Available online at www.sciencedirect.com
ScienceDirect
Polyhedron 27 (2008) 1–11
POLYHEDRON
www.elsevier.com/locate/poly

New insights on the Lewis acidity of diorganolead(IV) compounds: Diphenyllead(IV) complexes with N,O,S-chelating ligands

José S. Casas [a,*], Eduardo E. Castellano [b], Javier Ellena [b], María S. García-Tasende [a], Agustín Sánchez [a], José Sordo [a], Ángeles Touceda [a]

[a] *Departamento de Química Inorgánica, Facultade de Farmacia, Universidade de Santiago de Compostela, 15782 Santiago de Compostela, Galicia, Spain*
[b] *Instituto de Física de Sao Carlos, Universidade de Sao Paulo, Caixa Postal 369, CEP 13560, Sao Carlos, SP, Brazil*

Received 6 July 2007; accepted 7 August 2007
Available online 26 November 2007

Abstract

The reactions of $PbPh_2(OAc)_2$ with alkylglyoxylate thiosemicarbazones (HRGTSC, R = Et, Bu) afforded complexes of the type $[PbPh_2(GTSC)]\cdot H_2O$, $[PbPh_2(RGTSC)_2]$ and $[PbPh_2Cl(BuGTSC)]$. The structures of HRGTSC (R = Me, Et, Bu), $[PbPh_2(OAc)(RGTSC)]$(R = Me, Et, Bu), $[PbPh_2Cl(BuGTSC)]$ and $[PbPh_2(GTSC)]\cdot H_2O$ have been studied by X-ray diffraction. $[PbPh_2(OAc)(RGTSC)]$ and $[PbPh_2(GTSC)]\cdot H_2O$ have $[PbC_2NO_3S]$ kernels and the coordination sphere of the metal is pentagonal bipyramidal. $[PbPh_2Cl(BuGTSC)]$ has a $[PbC_2NOSCl]$ kernel and the coordination geometry around lead is pentagonal bipyramidal with one vacant site. Analysis of the bond distances in $[PbPh_2(GTSC)]\cdot H_2O$ suggests a significant affinity between diphenyllead(IV) and carboxylate donor groups, supporting a borderline acidic character for this organometallic cation. ^1H and ^{13}C NMR spectra in DMSO-d_6 suggest the partial dissociation of the acetate in $[PbPh_2(OAc)(RGTSC)]$ solutions and indicate some differences in the coordination mode of the two $RGTSC^-$ ligands in $[PbPh_2(RGTSC)_2]$ complexes.
© 2007 Elsevier Ltd. All rights reserved.

Keywords: Diphenyllead(IV) complexes; Thiosemicarbazone ligands; X-ray crystal structures; ^1H and ^{13}C NMR spectra

1. Introduction

Lead is a very toxic metal and occupies second place after arsenic in the priority list of hazardous substances published by the Agency for Toxic Substances and Disease Registry [1]. Since the ban on the use of tetraethyllead as an antiknock additive in gasoline in western countries, the main social concern has been focused on lead(II) compounds. However, organolead(IV) derivatives still represent a significant danger because they have not been prohibited everywhere and because they are more toxic than Pb(II) derivatives to mammals, a fact established a long time ago [2]. Moreover, there is no specific therapy for intoxication by this type of compound [3]. At present, chelation is the first option for the treatment of lead(II) poisoning but the chelating agents in clinical use do not seem to be effective against organolead(IV) intoxication [3]. In an effort to contribute to a solution for this problem, we are currently investigating the coordination chemistry of the $R_nPb^{(4-n)+}$ cations in a search for new chelate ligands that are able to fulfil the coordinative demand of these ions and are capable of playing an effective role in a detoxifying mechanism. For our studies we selected $PbPh_2^{2+}$ as a model organolead(IV) cation for two main reasons: it is fairly stable in solution and it is also less toxic than its aliphatic counterparts [2,4] helping to maintain a reasonable safety during the experimental work. On the other hand, it seems that the coordination behaviour of aromatic and non-aromatic organolead(IV) cations is analogous (e.g. [5]).

A search of the Cambridge Structural Database (CSD) [6] shows that complexes of the $PbPh_2^{2+}$ cation have

* Corresponding author.
E-mail address: qiscasas@usc.es (J.S. Casas).

0277-5387/$ - see front matter © 2007 Elsevier Ltd. All rights reserved.
doi:10.1016/j.poly.2007.08.027

coordination numbers from 4 to 8 and the choice of donor atoms is rather flexible. Thus, O, N, S or Cl donor atoms are common in $PbPh_2^{2+}$ coordination spheres and give rise to a large variety of kernels, a situation that also occurs in Pb(II) complexes [7].

In this work, we report the structural characterization of several complexes of diphenyllead(IV) with thiosemicarbazones derived from glyoxylic acid (see Scheme 1). According to our results, $PbPh_2^{2+}$ shows a significant affinity for deprotonated –SH and –C(O)OH donor groups, suggesting that this cation may have a borderline acidic character according to the HSAB principle of Pearson [8] – as does the Pb(II) cation [7].

2. Experimental

2.1. Materials and methods

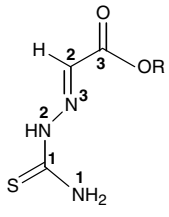
Di-*n*-butyl D-tartrate (Aldrich), diethyl L-tartrate (Aldrich), diphenyllead(IV) dichloride (Avocado), silver acetate (Fluka) and thiosemicarbazide (Merck) were used as received. Diphenyllead(IV) diacetate was prepared [*caution!* organolead(IV) compounds are very toxic; see Section 1] by reaction of diphenyllead(IV) dichloride and silver acetate in methanol. The AgCl was filtered off and the solution containing organolead(IV) acetate was used immediately in the preparation of the complexes.

Elemental analyses were performed with a FISONS 1108 analyser. Melting points were determined with a Büchi apparatus. The electrospray mass spectra of the complexes were measured on a Hewlett–Packard model LC-MSD 1100 instrument (positive ion mode, 98:2 MeOH/HCOOH as mobile phase, 20–100 V). The ^1H and ^{13}C NMR spectra of DMSO-d_6 solutions were recorded at room temperature using Bruker AMX 300 or AMX 500 spectrometers; chemical shifts in ppm were referred to TMS using the solvent signal.

2.2. Synthesis of the thiosemicarbazone ligands

Ethyl glyoxylate thiosemicarbazone (HEtGTSC) and *n*-butyl glyoxylate thiosemicarbazone (HBuGTSC) were both prepared in a similar way according to a previously described method [9]. The synthesis of HMeGTSC and the physical, analytical and spectroscopic properties for HBuGTSC and HMeGTSC will be reported elsewhere [10]. Physical, analytical and spectroscopic properties for HEtGTSC are as follows: mp 155 °C. *Anal.* Calc. for $C_5H_9N_3O_2S$: C, 34.3; H 5.1, N, 24.0; S, 18.3. Found: C, 34.3; H 5.2; N, 23.5; S, 17.8%. IR (cm^{-1}): 3340s, 3235s, 3168m ν(N–H), 1714s ν(C=O), 1601s ν(C=N), 834m, 651m ν(C=S). ^1H NMR (DMSO): 1.23 [t, 3H, C(5)H_3], 4.23 [q, 2H, C(4)H_2], 7.41 [s, 1H, C(2)H], 7.81 [s, 1H, N(1)H_2], 8.60 [s, 1H, N(1)H_2], 11.84 [s, 1H, N(2)H]. ^1H NMR ($CDCl_3$): 1.35 [t, 3H, C(5)H_3], 4.32 [q, 2H, C(4)H_2], 7.20 [s, 1H, C(2)H], 6.53 [s, 1H, N(1)H_2], 7.54 [s, 1H, N(1)H_2], 9.72 [s, 1H, N(2)H]. ^{13}C NMR (DMSO): 13.9 [C(5)H_3], 60.7 [C(4)H_2], 131.8 [C(2)], 162.6 [C(3)], 179.2 [C(1)].

Recrystallizations of HMeGTSC in methanol, HEtGTSC in ethanol and HBuGTSC in an ethanol:acetone mixture afforded crystals suitable for X-ray crystallography.

	R	Ligand
	-CH_2CH_3	**HEtGTSC**
	-$CH_2CH_2CH_2CH_3$	**HBuGTSC**
	-CH_3	**HMeGTSC**
	-H	**H_2GTSC**

Scheme 1. Thiosemicarbazone ligands used in this work.

2.3. Reactivity of $PbPh_2(OAc)_2$ towards thiosemicarbazone ligands

2.3.1. Reaction of HEtGTSC/$PbPh_2(OAc)_2$

A solution of freshly prepared $PbPh_2(OAc)_2$ in methanol (0.57 mmol in 20 ml of solvent) was slowly added to a solution of HEtGTSC (0.1 g, 0.57 mmol) in the same solvent (5 ml). This 1:1 molar ratio mixture was stirred for 6 h at room temperature, and the resulting solution was kept at a low temperature until yellow crystals, suitable for X-ray diffraction, were obtained. Mp 205 °C. *Anal.* Calc. for $C_{19}H_{21}N_3O_4SPb$ ([$PbPh_2$(OAc)(EtGTSC)]): C, 38.4; H 3.5; N, 7.1; S, 5.4. Found: C, 38.5; H 3.5; N, 7.0; S, 5.1%. MS (electrospray), *m/z* (%): 536 (61) [M−OAc]. ^1H NMR (DMSO) (the data for the major isomer are in italics): *1.00t*, 1.05t, 1.21t, 1.24t [3H, C(5)H_3]; 1.71s vb, 1.82sb [3H, CH_3COO], 4.21q, 4.15q, 4.13q, *4.08q* [2H, C(4)H_2], 7.34t, *7.39t* [t, 2H, H_p], *7.52t* [$^4J(^1H–^{207}Pb)$ = 73 Hz], 7.54t [4H, H_m]; 7.76d, *7.79d* [$^3J(^1H–^{207}Pb)$ = 186 Hz], 7.85d [d, 4H, H_o]; *7.54s*, 8.05s, 8.20s [1H, C(2)H]; 8.44s vb, 8.50 s vb [N(1)H_2]. ^{13}C NMR (DMSO): *13.8*, 13.9, 14.1 [C(5)H_3]; 23.2vb [CH_3(Ac)]; 60.2, 61.5, *61.9* [C(4)H_2]; 129.2, *129.8* [C_p]; 129.4, *129.9* [$^3J(^{13}C–^{207}Pb)$ = 186 Hz] [C_m]; 132.2, *132.7* [$^2J(^{13}C–^{207}Pb)$ = 119 Hz] [C_o]; *131.4*, 135.5, 136.3 [C(2)]; 163.7, *165.5*, 167.7, 169.0 [C(3)]; *165.2* [$^1J(^{13}C–^{207}Pb)$ = 1474 Hz], 166.0 [C_{ipso}]; 178.6vb [COO(OAc)]; 177.1, *179.6* [C(1)].

When this same reaction was carried out under heating and the solvent was partially removed, a mixture of pale yellow and yellow crystals, both suitable for X-ray diffraction, was obtained. *Pale yellow crystals*: Mp >250 °C. *Anal.* Calc. for $C_{18}H_{19}N_3O_4SPb$ ([$PbPh_2$(OAc)(MeGTSC)]): C, 37.2; H 3.3; N, 7.2; S, 5.5. Found: C, 37.1; H 3.3; N, 7.2; S, 5.4%. MS (electrospray), *m/z* (%): 522 (85) [M−OAc]. ^1H NMR (DMSO): 1.71sb, *1.82*sb [3H, CH_3COO^-];

*3.59*s, 3.64s, 3.69s, 3.75s [3H, C(4)H_3]; *7.39*s, 8.07s, 8.15s [1H, C(2)H], 7.39t, 7.44t [2H, H_p], 7.50t, 7.53t [t, 4H, H_m], *7.79*d, 7.85d [d, 4H, H_o], 8.50 [sb, 2H, N(1)H_2].

^{13}C NMR (DMSO): 23.5vb [CH_3(Ac)]; 51.5, 51.7, 52.2, *52.7* [C(4)H3]; 129.3, *130.0* [C_p]; 129.6, *130.1* [C_m]; 132.4, *132.8* [$^2J(^{13}C–^{207}Pb) = 118$ Hz, estimated] [C_o]; *131.6*, 136.0 [C(2)]; *168.2*, 169.0 [C(3)]; 165.4 [C_{ipso}]; 179.8 [C(1)]. *Yellow crystals*: Mp >250 °C. *Anal*. Calc. for $C_{15}H_{15}N_3O_3SPb$ ([$PbPh_2$(GTSC)] · H_2O): C, 34.4; H 2.9; N, 8.0; S, 6.1. Found: C, 33.8; H 2.9; N, 8.3; S, 6.1%. ^{1}H NMR (DMSO): 7.38 [t, 2H, H_p], 7.52 [t, 4H, H_m], 7.60 [s, 2H, N(1)H_2], 7.70 [s, 1H, C(2)H], 7.95 [d, 4H, H_o; $^3J(^1H–^{207}Pb) = 187.5$ Hz]. ^{13}C NMR (DMSO): 129.4 [C_p], 129.7 [C_m, $^3J(^{13}C–^{207}Pb) = 182$ Hz], 133.6 [C_o, $^2J(^{13}C–^{207}Pb) = \approx 120$ Hz], 140.8 [C(2)], 165.5 [C_{ipso}], 165.6 [C(3)], 178.3 [C(1)].

Table 1
Crystal and refinement data for ligands and complexes

	HEtGTSC	HBuGTSC	HMeGTSC	[$PbPh_2$(OAc)(MeGTSC)]
Molecular formula	$C_5H_9N_3O_2S$	$C_7H_{13}N_3O_2S$	$C_4H_7N_3O_2S$	$C_{18}H_{19}N_3O_4SPb$
Molecular weight	175.21	203.27	161.19	580.61
Temperature (K)	100(2)	120(2)	293(2)	120(2)
Wavelength (Å)	0.71073	0.71073	1.54180	0.71073
Crystal system	triclinic	triclinic	triclinic	monoclinic
Space group	$P\bar{1}$	$P\bar{1}$	$P\bar{1}$	C_2/c
a (Å)	8.4260(2)	10.0720(1)	5.8144(5)	22.4494(9)
b (Å)	9.7580(2)	10.3080(1)	7.7994(14)	10.4641(5)
c (Å)	10.9780(3)	11.0829(2)	8.8226(8)	19.7493(8)
α (°)	70.370(1)	73.542(1)	89.321(9)	
β (°)	76.927(1)	75.139(1)	75.689(5)	94.433(3)
γ (°)	80.921(1)	71.691(1)	70.871(11)	
V (Å^3)	824.83(3)	1029.77(2)	365.23(8)	4625.5(3)
Z	4	4	2	8
Absorption coefficient (mm^{-1})	0.349	0.289	3.538	7.409
F(000)	368	432	168	2224
Crystal size (mm)	0.23 × 0.11 × 0.08	0.25 × 0.20 × 0.07	0.64 × 0.24 × 0.04	0.08 × 0.04 × 0.04
θ Range for data collection (°)	2.00–25.00	1.95–25.00	5.19–72.89	1.03–25.01
Index ranges	−10, 10; −11, 11, −13, 11	0, 11; −11, 12; −12, 13	−6, 7, −9, 9, 0, 10	−26, 26; −12, 12; −23, 23
Reflections collected	5472	7018	1555	14631
Goodness-of-fit on F_2	1.164	1.195	1.053	1.052
R_1, wR_2 [$I > 2\sigma(I)$]	0.0328, 0.0967	0.0451, 0.1280	0.0829, 0.2238	0.0697, 0.1845
Largest difference peak and hole (e Å^{-3})	0.457 and −0.364	1.169 and −0.592	0.409 and −1.495	3.869 and −2.124
	[$PbPh_2$(OAc)(EtGTSC)]	[$PbPh_2$(OAc)(BuGTSC)]	[$PbPh_2Cl$(BuGTSC)]	[$PbPh_2$(GTSC)] · H_2O
Molecular formula	$C_{19}H_{21}N_3O_4SPb$	$C_{21}H_{25}N_3O_4SPb$	$C_{19}H_{22}ClN_3O_2PbS$	$C_{15}H_{15}N_3O_3SPb$
Molecular weight	594.64	622.69	599.10	524.55
Temperature (K)	293(2)	120(2)	120(2)	120(2)
Wavelength (Å)	0.71073	0.71073	0.71073	0.71073
Crystal system	triclinic	monoclinic	monoclinic	monoclinic
Space group	$P\bar{1}$	$P2_1/n$	$P2_1/n$	$C2/c$
a (Å)	8.5119(17)	14.0379(5)	9.6638(2)	24.5585(7)
b (Å)	9.4092(19)	10.5272(4)	15.8556(4)	9.7790(4)
c (Å)	15.0230(3)	15.7062(6)	14.1897(4)	17.9794(6)
α (°)	83.031(3)			
β (°)	87.134(3)	96.084(2)	102.388(2)	130.931(2)
γ (°)	63.961(3)			
V (Å^3)	1073.0(4)	2307.99(15)	2123.60(9)	3262.2(2)
Z	2	4	4	8
Absorption coefficient (mm^{-1})	7.987	7.431	8.187	10.489
F(000)	572	1208	1152	1984
Crystal size (mm)	0.26 × 0.15 × 0.13	0.14 × 0.12 × 0.04	0.19 × 0.17 × 0.09	0.22 × 0.07 × 0.05
θ Range for data collection (°)	1.37–26.51	3.25–25.00	3.21–25.00	2.20–27.47
Index ranges	−10, 10; −11, 11; −18, 18	−16, 16; −11, 12; −18, 18	−11, 11; −18, 16; −16, 16	−31, 31; −12, 12; −23, 23
Reflections collected	12357	13160	11403	13150
Goodness-of-fit on F_2	1.146	1.021	1.099	1.057
R_1, wR_2 [$I > 2\sigma(I)$]	0.0248, 0.0562	0.0453, 0.1140	0.0277, 0.0655	0.0469, 0.1114
Largest difference peak and hole (e Å^{-3})	1.063 and −1.181	1.497 and −2.389	1.951 and −1.469	2.094 and −2.754

The reaction with a 1:2 molar ratio also gave different results depending on the reaction temperature. At room temperature, and after partial removal of the solvent, a new yellow solid was obtained. Mp 208 °C. *Anal*. Calc. for $C_{22}H_{26}N_6O_4S_2Pb$ ([$PbPh_2(EtGTSC)_2$]): C, 37.2; H 3.7; N, 11.8; S, 9.0. Found: C, 36.1; H 3.7; N, 11.4; S, 8.8%. MS (electrospray), *m*/*z* (%): 536 (100) [M−EtGTSC]. ^{1}H NMR (DMSO): 1.06t, 1.24t [6H, C(5)H_3]; 4.12q, 4.20q [4H, C(4)H_2]; 7.32 [t, 2H, H_p]; 7.42s, 8.18s [2H, C(2)H]; 7.44 [t, 4H, H_m]; 7.74 [d, 4H, H_o, $^3J(^1H\text{-}^{207}Pb) = 200$ Hz]; 8.07sb, 8.22sb [s, 4H, N(1)H_2]. ^{13}C NMR (DMSO): 14.0, 14.1 [C(5)H_3], 60.3, 61.5 [C(4)H_2], 128.8 [C_p], 129.8 [C_m], 130.7 [C_o], 131.4 [C(2)], 166.0 [C(3)], 169.0 [C_{ipso}], 179.5 [C(1)]. An X-ray study of a yellow crystal of [$PbPh_2(EtGTSC)_2$]·H_2O, obtained after slow evaporation of the mother liquor, has been published previously [11].

The reaction under heating afforded the same compounds as obtained on using the 1:1 molar ratio.

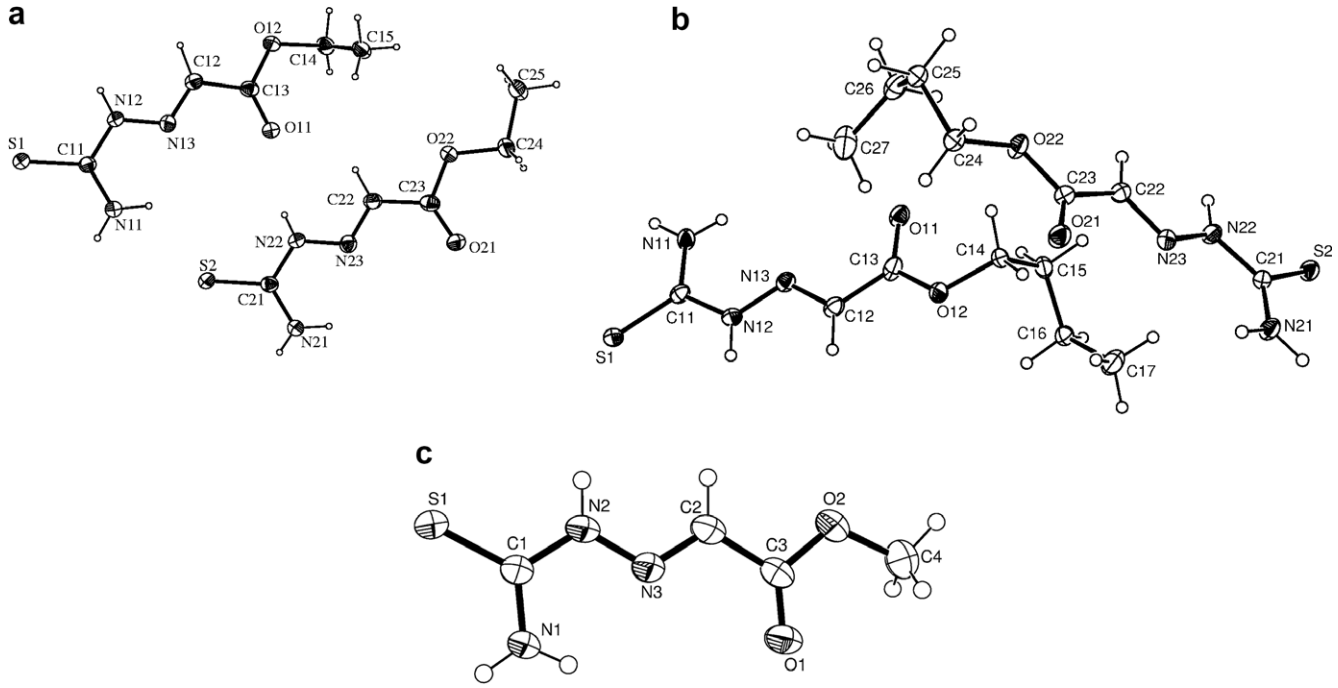


Fig. 1. Molecular structures of ligands HEtGTSC (a), HBuGTSC (b) and HMeGTSC (c).

Table 2
Selected bond distances (Å) and angles (°) for HEtGTSC, HBuGTSC and HMeGTSC

Molecule 1	HEtGTSC	HBuGTSC	HMeGTSC	Molecule 2	HEtGTSC	HBuGTSC
S(1)–C(11)	1.688(2)	1.687(2)	1.676(3)	S(2)–C(21)	1.685(2)	1.689(2)
O(11)–C(13)	1.214(3)	1.213(3)	1.202(4)	O(21)–C(23)	1.210(3)	1.211(3)
O(12)–C(13)	1.330(3)	1.364(11)	1.331(4)	O(22)–C(23)	1.340(3)	1.333(3)
O(12)–C(14)	1.470(3)	1.463(12)	1.452(4)	O(22)–C(24)	1.462(3)	1.45(2)
N(11)–C(11)	1.319(3)	1.316(3)	1.318(4)	N(21)–C(21)	1.321(3)	1.320(3)
N(12)–N(13)	1.359(3)	1.358(3)	1.352(4)	N(22)–N(23)	1.363(3)	1.360(3)
N(12)–C(11)	1.363(3)	1.364(3)	1.364(4)	N(22)–C(21)	1.359(3)	1.364(3)
N(13)–C(12)	1.281(3)	1.280(3)	1.274(4)	N(23)–C(22)	1.277(3)	1.283(3)
C(12)–C(13)	1.485(3)	1.475(4)	1.490(4)	C(22)–C(23)	1.487(3)	1.476(3)
C(13)–O(12)–C(14)	116.02(17)	121.3(8)	115.7(3)	C(23)–O(22)–C(24)	116.56(17)	118.0(8)
N(13)–N(12)–C(11)	117.87(19)	120.1(2)	117.8(3)	N(23)–N(22)–C(21)	119.2(2)	120.54(19)
C(12)–N(13)–N(12)	118.1(2)	116.5(2)	117.7(3)	C(22)–N(23)–N(22)	116.6(2)	115.16(19)
N(11)–C(11)–N(12)	117.3(2)	117.0(2)	116.6(3)	N(21)–C(21)–N(22)	116.3(2)	117.7(2)
N(11)–C(11)–S(1)	123.49(18)	124.39(19)	123.2(2)	N(21)–C(21)–S(2)	123.74(18)	124.67(18)
N(12)–C(11)–S(1)	119.24(16)	118.63(17)	120.2(2)	N(22)–C(21)–S(2)	119.96(17)	117.61(17)
N(13)–C(12)–C(13)	115.6(2)	117.7(2)	116.6(3)	N(23)–C(22)–C(23)	118.1(2)	118.9(2)
O(11)–C(13)–O(12)	124.9(2)	119.0(5)	124.6(3)	O(21)–C(23)–O(22)	124.9(2)	124.4(2)
O(11)–C(13)–C(12)	124.9(2)	126.3(2)	126.4(3)	O(21)–C(23)–C(22)	126.5(2)	126.9(2)
O(12)–C(13)–C(12)	110.19(19)	113.6(5)	109.1(3)	O(22)–C(23)–C(22)	108.59(19)	108.7(2)
O(12)–C(14)–C(15)	111.07(19)	112.2(6)		C(23)–O(22)–C(24)	116.56(17)	118.0(8)

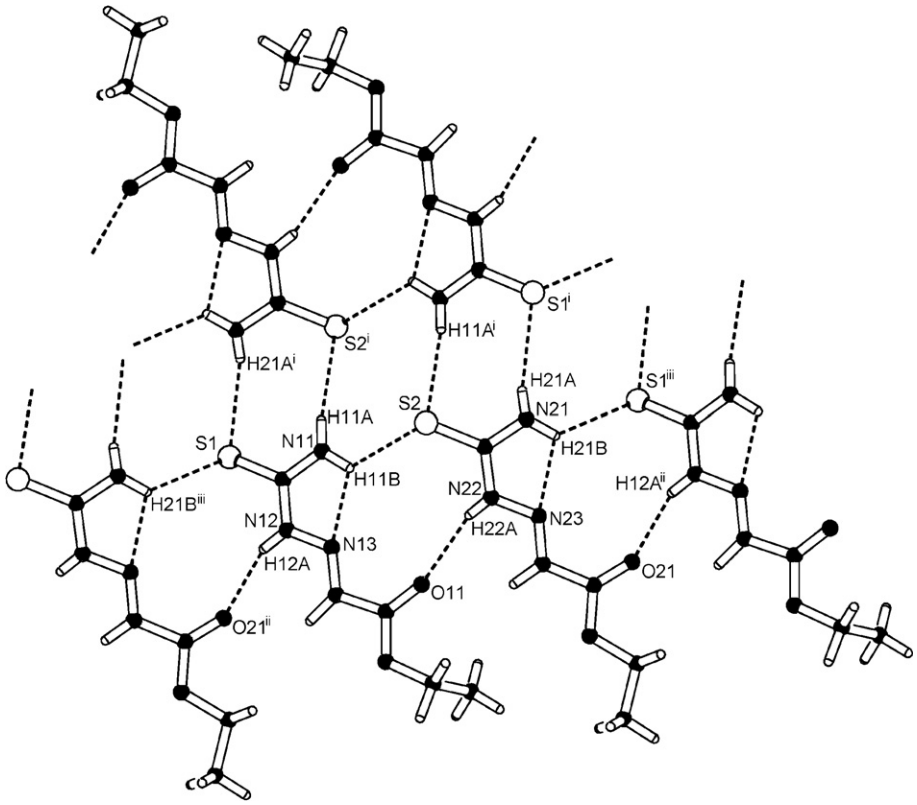


Fig. 2. Hydrogen bonds in HEtGTSC.

2.3.2. Reaction of HBuGTSC/PbPh$_2$(OAc)$_2$

A solution of HBuGTSC (0.1 g, 0.49 mmol) in methanol (5 ml) was slowly added to a solution of freshly prepared diphenyllead(IV) diacetate (0.49 mmol in 20 ml of methanol). This 1:1 molar ratio mixture was stirred for 6 h and the solvent was slowly evaporated until yellow crystals precipitated. Mp 180 °C. *Anal.* Calc. for $C_{21}H_{25}N_3O_4SPb$ ([PbPh$_2$(OAc)(BuGTSC)]): C, 40.2; H 4.0; N, 6.7; S, 5.1. Found: C, 40.2; H 4.0; N, 6.6; S, 5.0%. MS (electrospray), *m*/*z* (%): 564 (56) [M−OAc]. ^{1}H NMR (DMSO): *0.74t*, 0.87t, 0.90t [3H, C(7)H$_3$]; *1.06sext*, 1.40 m [2H, C(6)H$_2$]; *1.40m*, 1.58q [q, 2H, C(5)H$_2$]; *1.72sb*, 1.81sb [3H, CH_3COO^-]; *4.04t*, 4.10t, 4.17t [2H, C(4)H$_2$]; 7.37 [t, 2H, H$_p$]; 7.50 [t, 4H, H$_m$]; *7.77d*, 7.84d [d, 4H, H$_o$], *7.54s*, 8.04s, 8.13s [1H, C(2)H], 8.45s vb [N(1)H$_2$]. ^{13}C NMR (DMSO): 13.4 [C(7)H$_3$], 13.6 [C(7)H$_3$], 18.2 [C(6)H$_2$], 18.7 [C(6)H$_2$], 23.2 [C(8)H$_3$COO$^-$], 30.0 [C(5)H$_2$], 30.1 [C(5)H$_2$], 63.9 [C(4)H$_2$], 65.3 [C(4)H$_2$], 129.4 [C$_p$], 129.9 [C$_m$], 132.2 [C(2)], 132.6 [C$_o$], 165.2 [C(3)], 168.9 [C$_{ipso}$], 179.6 [C(1)]. Crystals suitable for the X-ray study were obtained from the mother liquor.

When the reaction was carried out under similar conditions, but using a 1:2 (M:L) molar ratio, the suspension was stirred for 6 h and kept at low temperature for 12 h. The resulting yellow solid was filtered off and dried under vacuum. Mp 171 °C. *Anal.* Calc. for $C_{26}H_{34}N_6O_4S_2Pb$ ([PbPh$_2$(BuGTSC)$_2$]): C, 40.7; H 4.4; N, 10.9; S, 8.3. Found: C, 39.6; H 4.4; N, 10.4; S, 8.0%. ^{1}H NMR (DMSO): 0.74t, 0.89t [3H, C(7)H$_3$]; 1.06sext, 1.36m [2H, C(6)H$_2$]; 1.36m, 1.61q [q, 2H, C(5)H$_2$]; 4.11t, 4.17t [2H, C(4)H$_2$]; 7.32 [t, 2H, H$_p$]; 7.43 [t, 4H, H$_m$]; 7.73d [d, 4H, H$_o$]; 7.42s, 8.13s [1H, C(2)H]; 8.08sb, 8.22sb [2H,

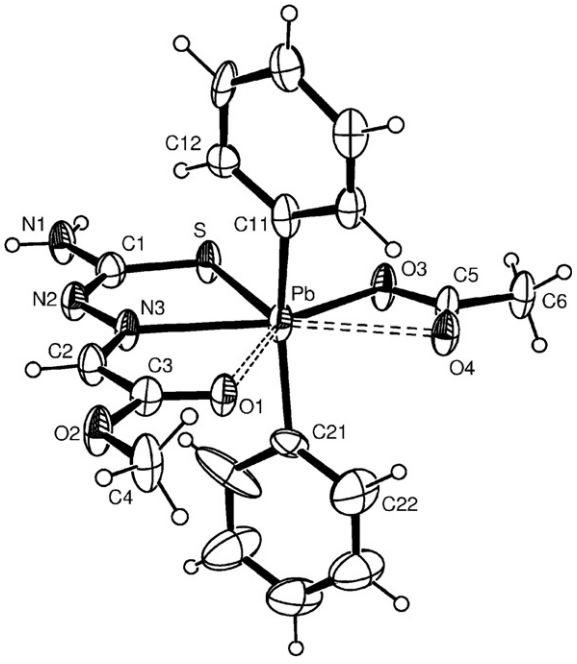


Fig. 3. Molecular structure of complex [PbPh$_2$(OAc)(MeGTSC)].

N(1)H_2]. ^{13}C NMR (DMSO): 13.4, 13.7 [C(7)H_3]; 18.2, 18.6 [C(6)H_2]; 30.2 [C(5)H_2]; 64.8, 64.0 [C(4)H_2]; 129.0 [C_p], 130.0 [C_m], 131.0, 131.6 [C_o], 135.3 [C(2)], 164.0, 166.2 [C(3)], 169.2 [C_{ipso}], 177.5, 179.6 [C(1)]. As a second fraction, a small amount of crystals suitable for an X-ray study were also obtained, showing the formation of a new complex [$PbPh_2Cl$(BuGTSC)]. When the reactions were carried out under reflux only unidentified products were obtained.

2.4. X-ray crystallography

Crystal data, experimental details and refinement results are listed in Table 1. Data were collected on Bruker Smart CCD 1000 or Enraf-Nonius CAD-4 diffractometers and were corrected for absorption by multi-scan [12] or SADABS [13]. The structures were solved using direct (ligands) or Patterson (complexes) methods, followed by conventional difference Fourier techniques. All of the H atoms were introduced in calculated positions except those in HEt-GTSC, which were all located in the Fourier difference map and refined isotropically, and the water protons in [$PbPh_2$(GTSC)]·H_2O (H1W and H2W), which were located and refined as a rigid model. The crystal of [$PbPh_2$(OAc)(MeGTSC)] shows disorder in regard to one of the phenyl rings (C21–C26), with two atomic sites observed for each of the atoms in this fragment. The site occupancy factors were determined as 0.65 and 0.35 and only the lengths of bonds and angles involving the atoms with the higher occupancy have been included in the Tables. The program used was SHELX-97 [14]. Molecular graphics were obtained with ORTEP [15] and PLATON [16].

Table 3
Selected bond distances (Å) and angles (°) for the complexes

	[$PbPh_2$(OAc)(MeGTSC)]	[$PbPh_2$(OAc)(EtGTSC)]	[$PbPh_2$(OAc)(BuGTSC)]	[$PbPh_2Cl$(BuGTSC)]	[$PbPh_2$(GTSC)]·H_2O
Pb–C(21)	2.083(13)	2.193(5)	2.171(6)	2.184(4)	2.178(10)
Pb–C(11)	2.197(15)	2.191(5)	2.172(7)	2.188(5)	2.200(10)
Pb–O(1)	2.803(10)	2.861(4)	2.808(5)	2.747(3)	2.580(8)
Pb–O(3)	2.330(8)	2.329(4)	2.316(5)		
Pb–N(3)	2.551(9)	2.613(4)	2.579(5)	2.554(4)	2.504(8)
Pb–S	2.609(3)	2.6036(14)	2.5987(17)	2.5399(11)	2.634(3)
Pb–O(4)	2.746(9)	2.637(4)	2.748(5)		
Pb–O(1)^i					2.645(7)
Pb–O(2)^i					2.708(6)
Pb–Cl				2.6976(9)	
S–C(1)	1.727(14)	1.730(6)	1.744(7)	1.735(4)	1.770(10)
O(1)–C(3)	1.213(15)	1.207(6)	1.214(7)		1.318(11)
O(2)–C(3)	1.357(15)	1.335(6)	1.352(7)		1.228(12)
O(3)–C(5)	1.290(15)				
O(3)–C(6)		1.276(6)			
O(4)–C(5)	1.237(16)				
O(4)–C(6)		1.244(7)			
O(3)–C(8)			1.274(8)		
O(4)–C(8)			1.248(8)		
N(1)–C(1)	1.346(17)	1.332(6)	1.350(8)		1.327(12)
N(2)–C(1)	1.345(18)	1.348(7)	1.322(9)		1.307(13)
N(2)–N(3)	1.364(14)	1.344(5)	1.366(7)		1.380(11)
N(3)–C(2)	1.305(16)	1.303(6)	1.298(9)		1.277(12)
C(2)–C(3)	1.431(18)	1.464(7)	1.456(9)		1.474(13)
C(5)–C(6)	1.510(18)				
C(6)–C(7)		1.508(8)			
C(8)–C(9)			1.516(10)		
C(11)–Pb–C(21)	153.4(6)	159.79(19)	149.9(3)	152.39(17)	157.7(4)
O(3)–Pb–S	77.6(2)	80.35(10)	78.09(12)		
N(3)–Pb–S	70.6(2)	70.52(10)	70.67(13)	71.55(8)	71.6(2)
O(3)–Pb–O(4)	50.5(3)	52.06(13)	50.69(16)		
N(3)–Pb–O(1)	62.4(3)	61.12(12)	62.17(15)	62.42(10)	64.2(2)
S–Pb–O(1)^i					71.44(16)
O(1)–Pb–O(4)	98.9(2)	96.09(12)	98.43(13)		
O(1)–Pb– Cl				145.93(7)	
Cl–Pb–S				80.17(3)	
O(1)–Pb–O(2)^i					102.7(2)
O(1)i–Pb–O(2)^i					50.3(2)

Symmetry operators: i = $-x+1/2$, $y+1/2$, $-z+1/2$.

3. Results and discussion

3.1. Synthesis

The reactions of the ligands HEtGTSC and HBuGTSC at room temperature with freshly prepared methanolic solutions of $PbPh_2(OAc)_2$ afforded complexes of the type $[PbPh_2(OAc)(RGTSC)]$ and $[PbPh_2(RGTSC)_2]$ (R = Et, Bu) when 1:1 and 1:2 M:L molar ratios were used, respectively. Furthermore, the reaction of HBuGTSC in the 1:2 molar ratio also afforded $[PbPh_2Cl(BuGTSC)]$ as a minor product, which probably results from the incomplete displacement of the Cl^- anions from $PbPh_2Cl_2$ during the $PbPh_2(OAc)_2$ synthesis (vide supra). All of the reactions with HBuGTSC, when heated under reflux, afforded unidentified products, while reactions with HEtGTSC rendered $[PbPh_2(OAc)(MeGTSC)]$ and $[PbPh_2(GTSC)]\cdot H_2O$, with the former produced through a transesterification process and the latter formed by hydrolysis of the initial ligand.

3.2. Crystal structures of the ligands

The molecular structures of the ligands HEtGTSC, HBuGTSC and HMeGTSC are shown in Fig. 1 together with the numbering scheme used. Selected bond distances and angles are shown in Table 2.

As can be seen from Fig. 1a and b, HEtGTSC and HBuGTSC both crystallize in a similar way with two slightly different molecules (molecules 1 and 2) in the asymmetric unit. The bond distances and bond angles in both molecules, as well as in HMeGTSC, are similar and within the values found for this class of compounds [17]. In all of these ligands the thiosemicarbazone chains adopt an *E*-configuration with respect to the C=N aldimine bonds and the C–S bonds are *trans* to the N–N bonds. As one would expect in this type of ligand, the E conformation is stabilized by the formation of intramolecular hydrogen bonds involving NH_2 groups and the aldimine nitrogen (see Table 4 and Fig. 2). Besides these hydrogen bonds, intermolecular $N(1)H_2\cdots S$ and $N(2)H\cdots O(1)$ hydrogen bonds link molecules to form a polymeric chain along the *z* (for HEtGTSC) or *x* (for HBuGTSC and HMeGTSC) axis. Furthermore, additional $N(1)H_2\cdots S$ intermolecular hydrogen bonds between two of these chains give rise to a double chain (see Fig. 2 for HEtGTSC).

3.3. Crystal structures of the complexes

The crystal structures of the three analogous compounds $[PbPh_2(OAc)(RGTSC)]$ (R = Me, Et, Bu) are similar and are represented in Fig. 3 and Figs. 1S and 2S. Selected bond distances and angles are given in Table 3. In all of these compounds – which have $[PbC_2NO_3S]$ kernels – the metal is bonded to the two carbon atoms from the phenyl groups, to the S, N(3) and O(1) atoms from a tridentate thiosemicarbazone ligand and to the two oxygen atoms, O(3) and O(4), from an anisobidentate acetate ($d_{Pb-O(3)} = 2.31$–2.32 Å; $d_{Pb-O(4)} = 2.64$–2.75 Å). These seven atoms adopt a very distorted pentagonal bipyramid around the metal, with the C(11) and C(21) atoms from the phenyl groups at the apexes and the S, N(3), O(1), O(3) and O(4) atoms in the equatorial plane, which also includes the Pb atom [Pb,S,N(3),O(1),O(3),O(4) plane; rms: 0.0326, 0.0493, 0.0304 for R = Me, Et and Bu, respectively]. The main distortion from the ideal bipyramid arises due to the narrow C–Pb–C angle [149.9(3)–159.79(19)°] and the short bite of the equatorial ligands.

The coordination of the three thiosemicarbazonates is roughly the same in the three complexes. The TSC^- ligands

Table 4
Intra- and intermolecular hydrogen bonds (Å, °) in ligands and complexes

D–H···A	d(D–H)	d(H···A)	d(D···A)	⟨(DHA)
HEtGTSC[a]				
N(11)–H(11A)···S(2)^{i}	0.85(3)	2.63(3)	3.467(2)	170(3)
N(11)–H(11B)···S(2)	0.93(3)	2.67(3)	3.289(2)	125(2)
N(11)–H(11B)···N(13)	0.93(3)	2.16(3)	2.604(3)	108(2)
N(12)–H(12A)···O(21)^{ii}	0.83(3)	2.16(3)	2.952(3)	159(3)
N(21)–H(21A)···S(1)^{i}	0.76(3)	2.62(3)	3.363(2)	165(3)
N(21)–H(21B)···S(1)^{iii}	0.90(3)	2.59(3)	3.241(2)	130(2)
N(21)–H(21B)···N(23)	0.90(3)	2.19(3)	2.608(3)	108(2)
N(22)–H(22A)···O(11)	0.74(3)	2.23(3)	2.949(3)	164(3)
HBuGTSC[b]				
N(11)–H(11A)···N(13)	0.88	2.29	2.643(3)	104.2
N(11)–H(11A)···S(2)^{i}	0.88	2.82	3.472(2)	132.3
N(11)–H(11B)···S(2)^{ii}	0.88	2.52	3.403(2)	177.3
N(12)–H(12A)···O(21)^{iii}	0.88	2.08	2.913(3)	158.6
N(21)–H(21A)···N(23)	0.88	2.32	2.670(3)	103.6
N(21)–H(21A)···S(1)^{iii}	0.88	2.69	3.401(2)	139.3
N(21)–H(21B)···S(1)^{iv}	0.88	2.55	3.433(2)	177.8
N(22)–H(22A)···O(11)^{i}	0.88	2.09	2.883(3)	150.4
HMeGTSC[c]				
N(1)–H(1A)···S(1)^{i}	0.86	2.55	3.190(3)	132.5
N(1)–H(1A)···N(3)	0.86	2.23	2.585(4)	105.0
N(1)–H(1B)···S(1)^{ii}	0.86	2.54	3.388(3)	168.4
N(2)–H(2)···O(1)^{iii}	0.86	2.10	2.942(3)	165.0
$[PbPh_2(OAc)(MeGTSC)]$[d]				
N(1)–H(1A)···O(4)^{i}	0.88	2.07	2.941(14)	170.6
$[PbPh_2(OAc)(EtGTSC)]$[e]				
N(1)–H(1A)···O(1)^{i}	0.86	2.33	3.091(6)	147.4
N(1)–H(1B)···O(4)^{i}	0.86	1.96	2.808(6)	166.4
$[PbPh_2(OAc)(BuGTSC)]$[f]				
N(1)–H(1A)···O(4)^{i}	0.88	2.06	2.925(7)	166.3
$[PbPh_2Cl(BuGTSC)]$[g]				
N(1)–H(1A)...N(2)^{i}	0.88	2.14	3.006(5)	169.0
N(1)–H(1B)...Cl^{ii}	0.88	2.49	3.293(4)	151.7
$[PbPh_2(GTSC)]\cdot H_2O$[h]				
N(1)–H(1B)···O(1W)	0.88	1.98	2.854(12)	169.8
O(1W)–H(2W)···O(2)^{ii}	0.85	2.02	2.792(10)	150.0

Symmetry transformations used to generate equivalent atoms: [a] i = $-x$, $-y$, $-z$; ii = x, y, $z+1$; iii = x, y, $z-1$; [b] i = $-x-1$, $-y+2$, $-z+2$; ii = $x+1$, $y-1$, $z-1$; iii = $-x$, $-y+2$, $-z+2$; iv = $x-1$, $y+1$, $z+1$; [c] i = $x+1$, y, z; ii = $-x$, $-y$, $-z+2$; iii = $x-1$, y, z; [d] i = x, $-y+1$, $z+1/2$; [e] i = $x-1$, y, z; [f] i = $x+1/2$, $-y+1/2$, $z+1/2$; [g] i = $-x+2$, $-y$, $-z+1$; ii = $-x+1$, $-y$, $-z+1$; [h] ii = $-x$, $1+y$, z.

form the strongest bond with the metal through the sulphur atom {d(Pb–S) ~ 2.60 Å; sum of the covalent radii Pb + S = 2.58 Å [18]} and also form a medium strength Pb–N(3) bond ($d_{Pb-N(3)}$ = 2.55–2.61 Å; sum of the covalent radii Pb + N = 2.24 Å [18]) and a Pb···O(1) secondary interaction {$d_{Pb-O(1)}$ = 2.80–2.82 Å; sum of the covalent radii Pb + O = 2.20 Å [18]}. It is worth noting that this close approach between lead and the carbonyl oxygen atom can be imposed simply by the stereochemistry of the ligand. The Pb–S bond distances are very similar in the three complexes. The Pb–N(3) and Pb–O(1) bond distances are also analogous in [$PbPh_2$(OAc)(MeTSC)] and [$PbPh_2$(OAc)(BuTSC)] but slightly longer in [$PbPh_2$(OAc)(EtTSC)]. This could be the reason why the acetate ligand is more strongly bound to the metal atom in the ethyl derivative.

The deprotonation and coordination of the HRGTSC ligands to the lead atom causes changes in its conformation, placing the C(1)–S bonds *cis* to the N(2)–N(3) bonds. Nevertheless, the *E*-conformation around C(2)–N(3), which has been observed in the free ligands, is retained in the complexes and allows the simultaneous coordination of the S, N(3) and O(1) atoms to the metal.

The strong Pb–S bond promotes a significant evolution of the ligands from the thione to the thiol form (the average value for the C–S bond distance is 1.685 Å in the ligands and this becomes 1.737 Å in the complexes).

In [$PbPh_2$(OAc)(MeTSC)] and [$PbPh_2$(OAc)(BuTSC)] an intermolecular hydrogen bond involving one hydrogen atom of the NH_2 group and the oxygen atom O(4) (see Table 4) associates the molecules in chains parallel to the *z*-axis in the methyl derivative (see Fig. 4) but bisecting the *xz*-plane in the butyl derivative. In [$PbPh_2$(OAc)(EtTSC)], in addition to the bond described above, there is another link between the same two molecules, in this case involving the second hydrogen atom of the NH_2 group and O(1). This gives rise to a polymeric chain (see Fig. 5) with more strongly associated molecules that extends along the *x*-axis.

The molecular structure of [$PbPh_2$Cl(BuGTSC)] is shown in Fig. 6 together with the numbering scheme used. Selected bond distances and angles are shown in Table 3.

In this complex the lead atom is coordinated to a monodeprotonated S,N(3),O(1)-donor thiosemicarbazone, to a chloro ligand and to two phenyl groups. The phenyl groups are in the axial positions and the S, N(3), O(1) and Cl atoms are in the equatorial plane of a distorted pentagonal bipyramid with a vacant position [Cl–Pb–O(1) = 145.93(7)°]. The C–Pb–C angle bends towards the unoccupied position of the polyhedron and it seems that there is no intermolecular interaction apart from the hydrogen bonds (the closest donor atom to lead, apart from those mentioned above, is an S atom located 4.9 Å away).

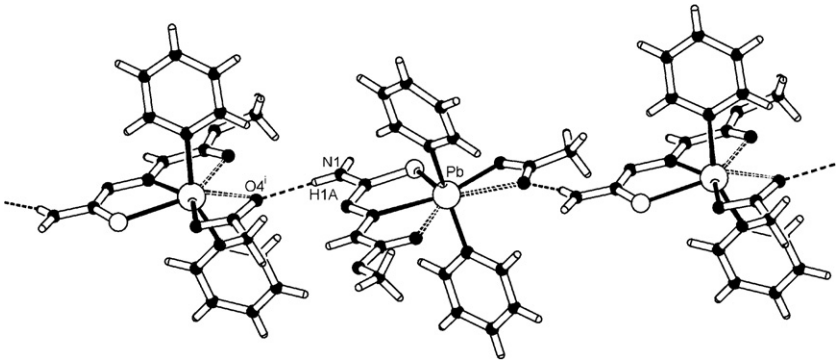


Fig. 4. Hydrogen bond in [$PbPh_2$(OAc)(MeGTSC)].

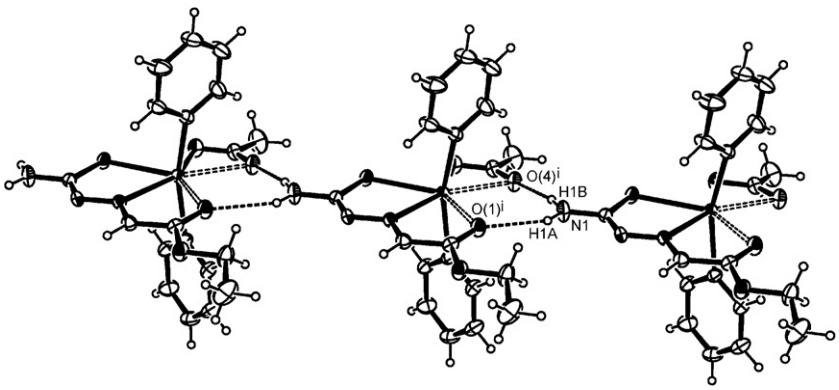


Fig. 5. Hydrogen bonds in [$PbPh_2$(OAc)(EtGTSC)].

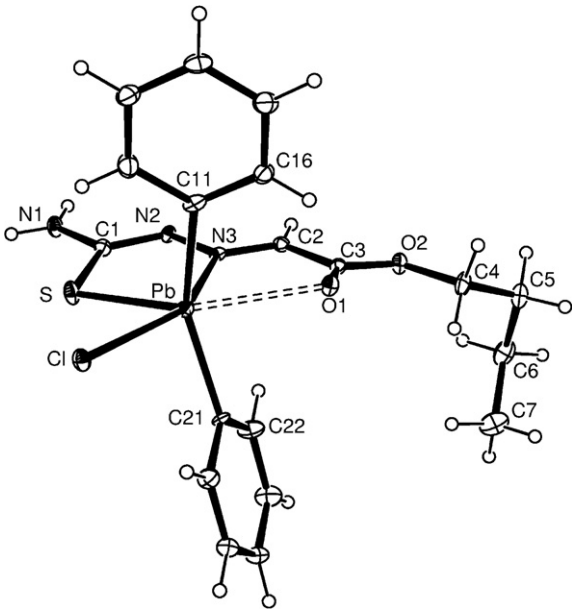


Fig. 6. Molecular structure of $[PbPh_2Cl(BuGTSC)]$.

The thiosemicarbazone ligand retains the *E*-conformation around the C=N bond (as in the free ligand) and the C–S bond length increases in accordance with the ligand evolution to the thiol form after deprotonation and coordination to the metal.

There are two intermolecular hydrogen bonds in the lattice and these involve the $N(1)H_2$ group and the Cl and N(2) atoms. These two weak interactions (see Table 4, Fig. 7) give rise to a polymeric chain parallel to the *x*-axis.

The asymmetric unit of $[PbPh_2(GTSC)] \cdot H_2O$ is represented in Fig. 8 and selected bond distances and angles are given in Table 3. In this compound, which also has a $[PbC_2NO_3S]$ kernel, the metal atom is bonded to the two C atoms from the phenyl groups, to the S, N(3) and O(1) atoms of a bideprotonated thiosemicarbazone and to the two oxygen atoms, $O(1)^i$ and $O(2)^i$, from the $-COO^-$ terminal group of a neighbouring molecule. These last two atoms occupy the sites of the acetate oxygen atoms in the $[PbPh_2(OAc)(RGTSC)]$ complexes described above. Thus, the ligand bridges two lead atoms and is tridentate with respect to one of them – through the S, N(3) and O(1) atoms – and bidentate with respect to the other (Pb^{ii}, ii = 0.5 − *x*, −0.5 + y, 0.5 − *z*) through the O(1) and O(2) atoms. Once again, the seven atoms in the coordination sphere adopt a very distorted pentagonal bipyramidal geometry around the metal, with the phenyl groups axial and the S, N(3), O(1), $O(1)^i$ and $O(2)^i$ atoms equatorial (rms = 0.0688 or 0.0732 if the Pb atom is also included). This arrangement gives rise to the polymeric chain parallel to the *y*-axis, as represented in Fig. 9.

In this complex the Pb–S bond can also be considered as a strong bond, although the bond distance is slightly longer than those in the $[PbPh_2(OAc)(RGTSC)]$ complexes. At the same time, the Pb–O(1) distance [and also the Pb–N(3) distance] diminishes. The reason for these changes is the higher donor capacity of the $-COO^-$ group in $[PbPh_2(GTSC)] \cdot H_2O$ with respect to the C=O group in $[PbPh_2(OAc)(RGTSC)]$. The consequent shortening of the Pb–O(1) bond displaces the carbamide group away from the metal. This stronger Pb–O bond supports the idea that diphenyllead(IV) has a good affinity for the carboxylate group and suggests a borderline Lewis acid character [8] for the diorganolead cations similar to that of Pb(II) [10].

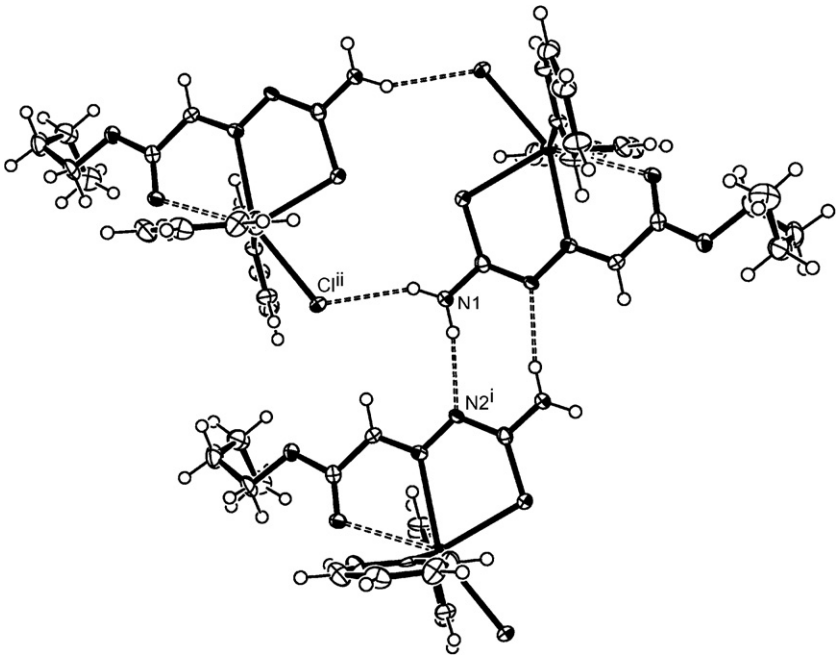


Fig. 7. Hydrogen bonds in $[PbPh_2Cl(BuGTSC)]$.

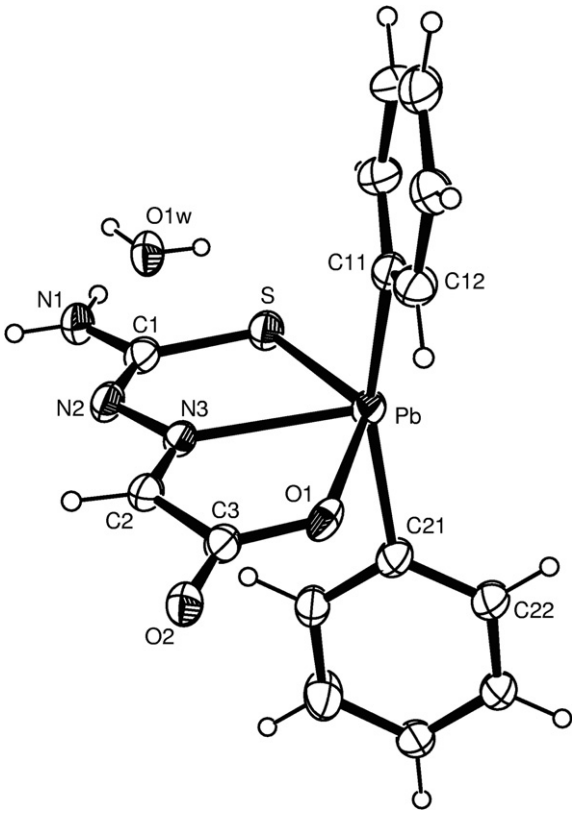


Fig. 8. Asymmetric unit in $[PbPh_2(GTSC)]\cdot H_2O$.

The water molecule in the lattice bridges, through hydrogen bonding, two molecules belonging to the polymeric chain described above (see Fig. 10 and Table 4).

3.4. Solution studies

The ^1H and ^{13}C NMR data from DMSO-d_6 solutions of the complexes are included in Section 2. Only the spectra of $[PbPh_2(GTSC)]\cdot H_2O$ allow a straightforward assignment, because this complex shows the expected signals for each hydrogen and carbon nucleus, suggesting the presence of only one species in solution. The spectra of the other complexes are more complicated and contain, e.g., two or more signals for the C(2)H, R and acetate groups and, in some cases, even for the organometallic fragment.

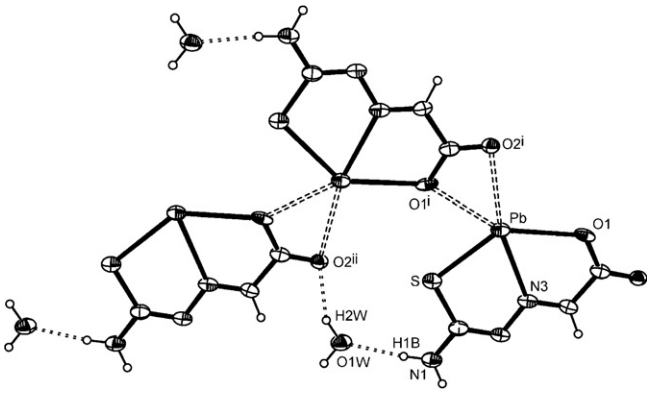


Fig. 10. Hydrogen bonds in $[PbPh_2(GTSC)]\cdot H_2O$.

In the heteroleptic derivatives, $[PbPh_2(OAc)(RTSC)]$, the complexity of the spectra may be due to the partial displacement of the acetate ligand from the coordination sphere of the metal in response to the donor competition of the solvent. This hypothesis is supported by the importance of the [M−OAc] species in the ESI spectra (methanolic solutions, see Section 2) and also by the presence of two signals associated with the methyl group of the acetate in the NMR spectra.

The complex spectral behaviour of the $[PbPh_2(RGTSC)_2]$ compounds (see Section 2) could be related to the versatile coordination mode of this type of thiosemicarbazone [11]. The presence of N^2,S- and N^3,S-coordinated $RGTSC^-$ ligands, as observed for the ethyl derivative in the solid state [11], should probably lead to perceptible spectral differences between the two non-equivalent thiosemicarbazonates.

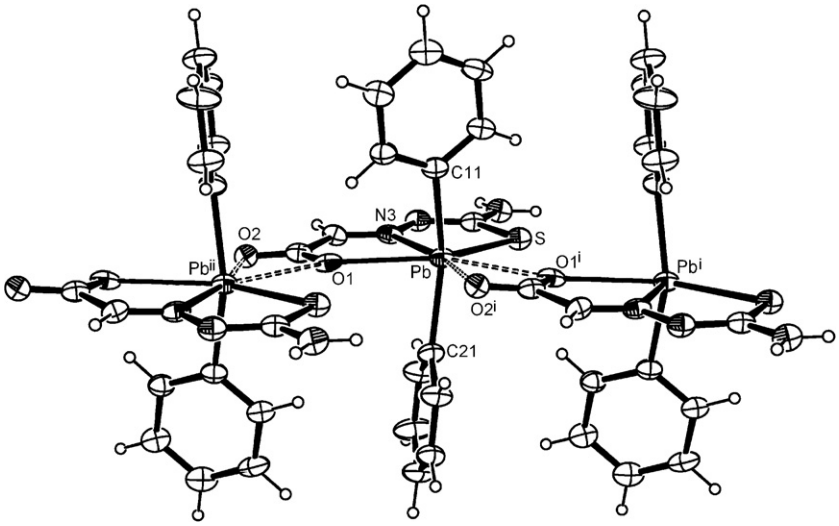


Fig. 9. Polymeric chain in $[PbPh_2(GTSC)]\cdot H_2O$.

Acknowledgement

Thanks are due to the Spanish Ministry of Science and Technology for financial support of this work under project CTQ2006-11805/BQU.

Appendix A. Supplementary material

CCDC 652794, 652795, 652796, 652797, 652798, 652799, 652800 and 652801 contain the supplementary crystallographic data for (HEtGTSC), (HBuGTSC), (HMeGTSC), ([$PbPh_2$(OAc)(MeGTSC)]), ([$PbPh_2$(OAc)(EtGTSC)]), ([$PbPh_2$(OAc)(BuGTSC)]), ([$PbPh_2$Cl(BuGTSC)]) and ([$PbPh_2$(GTSC)]). These data can be obtained free of charge from The Cambridge Crystallographic Data Centre via http://www.ccdc.cam.ac.uk/conts/retrieving.html or from Cambridge Crystallographic Data Centre, 12 Union Road, Cambridge, CB2 1EZ, UK fax: (+44) 1223-336-033; or e-mail: deposit@ccdc.cam.ac.uk. Supplementary data associated with this article: **Fig. 1S**, Molecular structure of [$PbPh_2$(OAc)(EtGTSC)]. **Fig. 2S**, Molecular structure of [$PbPh_2$(OAc)(BuGTSC)]. Supplementary data associated with this article can be found, in the online version, at doi:10.1016/j.poly.2007.08.027.

References

[1] http://www.atsdr.cdc.gov/cercla/supportdocs/text.pdf.
[2] J.S. Buck, D.M. Kumro, J. Phermacol. Exp. Ther. 38 (1930) 161.
[3] S.G. Schäfer, R.L.F. Dawes, B. Elsenhans, W. Forth, K. Schümann, in: H. Marquardt, S.G. Schäfer, R.O. McClellan, F. Welsch (Eds.), Toxicology, Academic Press, San Diego, 1999.
[4] H. Kleszczyńska, D. Bonarska, J. Sarapuk, S. Przestalski, J. Fluoresc. 14 (2004) 5.
[5] J.S. Casas, E.E. Castellano, J. Ellena, M.S. García-Tasende, F. Namor, A. Sánchez, J. Sordo, M.J. Vidarte, Eur. J. Inorg. Chem. 3742 (2007).
[6] F.H. Allen, Acta Crystallogr., Sect. B 58 (2002) 380.
[7] J.S. Casas, J. Sordo, M.J. Vidarte, in: J.S. Casas, J. Sordo (Eds.), Lead: Chemistry, Analytical Aspects, Environmental Impact and Health Effects, Elsevier, Amsterdam, 2006, p. 158.
[8] R.G. Pearson, Inorg. Chim. Acta 240 (1995) 93, and references cited therein.
[9] G. Werber, F. Maggio, Ann. Chim. 49 (1959) 2124.
[10] J.S. Casas, E.E. Castellano, J. Ellena, M.S. García-Tasende, A. Sánchez, J. Sordo, A. Touceda-Varela, unpublished work.
[11] J.S. Casas, E.E. Castellano, J. Ellena, M.S. García-Tasende, A. Sánchez, J. Sordo, A. Touceda-Varela, Inorg. Chem. Comm. 7 (2004) 1109.
[12] R.H. Blessing, Acta Crystallogr., Sect. A 51 (1995) 33.
[13] G.M. Sheldrick, SADABS, Program for Empirical Absorption Correction of Area Detector Data, University of Göttingen, Göttingen, Germany, 1997.
[14] G.M. Sheldrick, SHELX-97, An integrated system for solving and refining crystal structures from diffraction data, University of Göttingen, Göttingen, Germany, 1997.
[15] J.L. Farrugia, ORTEP III for Windows, J. Appl. Crystallogr. 30 (1997) 565.
[16] A.L. Spek, PLATON 99, A multipurpose crystallographic tool, University of Utrecht, Utrecht, The Netherlands, 1999.
[17] J.S. Casas, M.S. García-Tasende, J. Sordo, Coord. Chem. Rev. 209 (2000) 197.
[18] J. Emsley, The Elements, Oxford University Press, NY, 1998.

Available online at www.sciencedirect.com
ScienceDirect
Polyhedron 27 (2008) 12–24
POLYHEDRON
www.elsevier.com/locate/poly

Syntheses, characterization and crystal structures of mixed-ligand Cu(II), Ni(II) and Mn(II) complexes of *N*-(1-phenyl-3-methyl-4-propenylidene-5-pyrazolone)-salicylidene hydrazide containing ethanol or pyridine as a co-ligand

Guan-Cheng Xu, Li Zhang, Lang Liu, Guang-Fei Liu, Dian-Zeng Jia *

Institute of Applied Chemistry, Xinjiang University, Urumqi 830046, PR China

Received 25 June 2007; accepted 16 August 2007
Available online 22 October 2007

Abstract

Five new mixed-ligand complexes [CuL(EtOH)] (**1**), [NiL(EtOH)$_3$] (**2**), [$Mn_2L_2(\mu_2$-EtOH)$_2$(EtOH)$_2$] (**3**), [CuL(Py)] · MeOH (**4**) and [NiL(Py)$_3$] (**5**) (L^{2-} = *N*-(1-phenyl-3-methyl-4-propenylidene-5-pyrazolone)-salicylidene hydrazide anion, Py = pyridine) have been synthesized and characterized by elemental analyses, IR spectra, thermal analyses and single crystal X-ray diffraction. The crystallographic structural analyses of these complexes reveal that the ligand (H_2L) itself undergoes isomerization from the keto form to the enol form in the reaction, then loses two protons and acts as a double negatively charged tridentate chelating agent coordinated to the metal ion in the solution. The final results show that when a co-ligand was present in the synthetic reaction, other coordination sites around the metal ions Cu^{2+} and Ni^{2+} were completed either by the ethanol or pyridine molecules under the common solvent reaction or solvothermal syntheses conditions, respectively. In the case of the Mn^{2+} ion, it was still coordinated with the solvent molecules regardless of whether it was synthesized under the common solvent reaction or solvothermal syntheses with pyridine. The reason for this difference might be attributed to the fact that the coordination modes and bonding effect of the co-ligand with the metal ions are different, the final complexes tend to form the most stable compound.
© 2007 Elsevier Ltd. All rights reserved.

Keywords: Acyl pyrazolone derivatives; Crystal structures; Mixed-ligand complex; Copper(II); Nickel(II); Manganese(II)

1. Introduction

Pyrazolone-5 derivatives, especially 4-acyl pyrazolone, form an important class of organic compounds and represent a big scientific and applied interest in biological, analytical applications, catalysis, dye and extraction metallurgy, etc. [1–6]. Furthermore, 4-acyl pyrazolone derivatives have the potential to form different types of coordination compounds due to the several electron-rich donor centers [7–9] and tautomeric effect of the enol form and keto form [10–12]. Complexes containing these ligands are known for almost every transition and main group metal, often showing unusual structural and chemical properties [13,14]. Meanwhile, compounds containing hydrazide moieties and their complexes also possess biological activities, especially serving as potential inhibitors for many enzymes [15].

During the course of our research, we have synthesized a series of 4-acyl pyrazolone derivatives [16–18] and reported some transition metal complexes [19–21]. In order to further investigate the coordination abilities and complexation behaviors of pyrazolone-based ligands, we extended the study to the syntheses of new 4-acyl pyrazolone derivatives and their transition metal complexes. This paper presents the syntheses, characterization and crystal structures of the Cu(II), Ni(II) and Mn(II) mixed-ligand complexes of

* Corresponding author. Tel.: +86 991 8583083; fax: +86 991 8580032.
E-mail address: jdz@xju.edu.cn (D.-Z. Jia).

0277-5387/$ - see front matter © 2007 Elsevier Ltd. All rights reserved.
doi:10.1016/j.poly.2007.08.045

N-(1-phenyl-3-methyl-4-propenylidene-5-pyrazolone)-salicylidene hydrazide containing ethanol or pyridine as a co-ligand.

2. Experimental

2.1. Materials and general physical measurements

1-Phenyl-3-methyl-4-propionyl-5-pyrazolone and salicylic hydrazide were synthesized according to the Refs. [22,23]. Other chemicals and solvents were analytical grade and commercially available.

Elemental analyses of C, H and N were performed using a PE-240C analyzer. IR spectra were recorded on a BRUKER EQUINOX-55 spectrophotometer within the range 400–4000 cm^{-1}. The crystal structures were determined by a BRUKER SMART 1000 CCD detector and the SHELXTL-97 crystallographic software package. The simultaneous TG–DTA curves were obtained using a NETZSCH STA 449C model instrument, the experiments were carried out in dynamic air atmosphere with a flow rate of 30 cm^3 min^{-1}. Solvothermal syntheses experiments were performed in a Teflon-lined stainless steel autoclave with an inner volume of 40 mL.

2.2. Synthesis of the ligand H_2L

The ligand was synthesized by the same method described in the literature [26]. The yield was 72.6%. Molecular formula: $C_{20}H_{20}N_4O_3$. F.w.: 364.40. m.p.: 198–199 °C.

2.3. Syntheses of the complexes containing ethanol as a co-ligand

The synthesis procedure for [CuL(EtOH)] (**1**) was as follows: The ligand H_2L (1.5 mmol) was dissolved in 25 mL of hot anhydrous ethanol. To this solution was added dropwise an ethanolic solution of $Cu(CH_3COO)_2 \cdot H_2O$ (1.5 mmol) with constant stirring. The mixture was further refluxed for 3 h, then the green solution was filtered and the filtrate, as a clear solution, was slowly evaporated at room temperature and green block single crystals of **1** suitable for X-ray diffraction analysis were obtained.

The complexes [NiL(EtOH)$_3$] (**2**) and [$Mn_2L_2(\mu_2$-EtOH)$_2$(EtOH)$_2$] (**3**) were synthesized by the same procedure as for **1** with the corresponding metal acetate and ligand. Single crystals of **2** were obtained by slow evaporation of its ethanol solution. Single crystals of **3** were grown by slow evaporation of its ethanol and dichloromethane solution (volume rate 2:1) at room temperature.

2.4. Solvothermal syntheses of the complexes containing pyridine as a co-ligand

The synthesis procedure for [CuL(Py)] · MeOH (**4**) was as follows: The ligand H_2L (1 mmol) was dissolved by the addition of an aqueous solution of 1 M NaOH in 15 mL methanol. To this 8 mL of a methanolic solution of $Cu(CH_3COO)_2 \cdot H_2O$ (1 mmol) and 1.6 mL of a mixture of pyridine and acetonitrile with volume ratio of 1:1 were added in turn, then the mixture was stirred and loaded into a Teflon-lined stainless steel autoclave. The sealed autoclave was heated to 120 °C and kept isothermal for 48 h. After cooling to room temperature, brown crystals were collected by filtration and dried in air. Yield: 0.42 g (78.2% based on copper).

The complex [NiL(Py)$_3$] (**5**) was synthesized in a similar way, using $Ni(CH_3COO)_2 \cdot 4H_2O$ instead of $Cu(CH_3COO)_2 \cdot H_2O$. Yield: 0.55 g (83.5% based on nickel).

2.5. X-ray crystallography

The single crystal X-ray diffraction data collections for the complexes were performed on a BRUKER SMART 1000 CCD diffractometer, using graphite-monochromated MoKα radiation ($\lambda = 0.71073$ Å) at 293 K. Semi-empirical absorption corrections were applied using the SADABS program [24]. The structures were solved by direct methods and refined by full-matrix least squares on F^2 using the SHELXTL-97 program [25]. In complex **1**, the C21 and C22 atoms of the coordinated ethanol molecule are disordered into two positions, with site occupancy factors of 0.783 and 0.217. In complex **2**, the C1, C2, C3, C4, C5, C6 atoms of the phenyl group are disordered and have two positions with site occupation factors of 0.605 and 0.395. The C21 and C22, C23 and C24, C25 and C26 atoms of the three coordinated ethanol molecules are also disordered into two positions with site occupation factors of 0.292 and 0.708, 0.226 and 0.774, 0.568 and 0.432, respectively. All non-hydrogen atoms were refined anisotropically. The hydrogen atoms were generated geometrically and treated by a mixture of independent and constrained refinement. A summary of the crystal data, data collection parameters and convergence results are compiled in Table 1.

3. Results and discussion

3.1. Syntheses

Elemental analyses of the synthesized compounds are summarized in Table 2. The analytical data agree well with the proposed formula of the compounds. The synthetic mechanism of the principal ligand is shown in Scheme 1. The ligand can exist either in the enol form I or II or keto form III. However, the IR and X-ray crystallographic structural analyses of the ligand H_2L indicate that in the solid state it exists in keto form III. The molecular structure of the ligand [26] is depicted in Fig. 1.

The physical analyses results indicate that the complexes synthesized under the common solvent reaction have a 1:1 metal to ligand stoichiometry, in which the ligand H_2L converts to the enol form II, then loses two hydrogen atoms and functions as a doubly negatively charged tridentate chelating agent coordinated to the metal ion, while

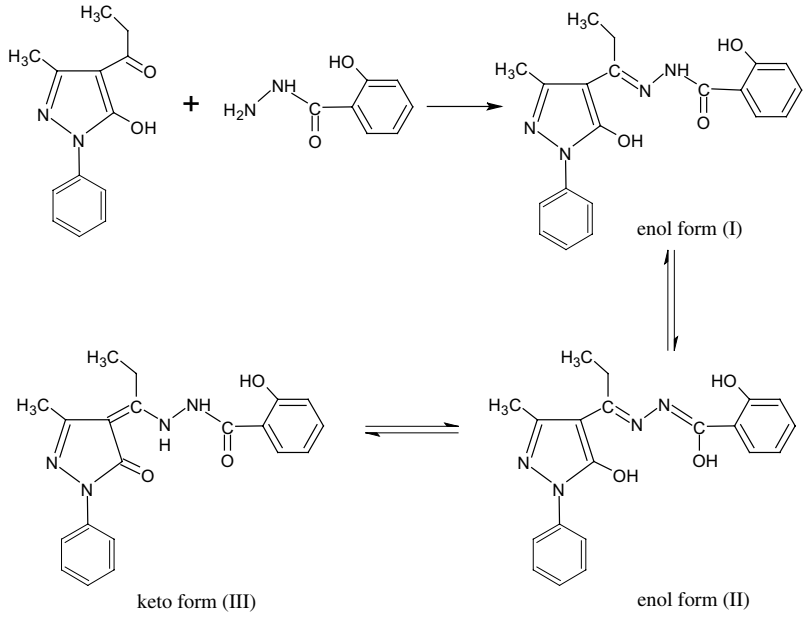
Table 1
Crystallographic data of the complexes

Complex	**1**	**2**	**3**	**4**	**5**
Empirical formula	$C_{22}H_{24}N_4O_4Cu$	$C_{26}H_{36}N_4O_6Ni$	$C_{48}H_{60}N_8O_{10}Mn_2$	$C_{26}H_{27}N_5O_4Cu$	$C_{35}H_{33}N_7O_3Ni$
Formula weight	471.99	559.30	1018.93	537.07	658.39
Crystal system	monoclinic	monoclinic	monoclinic	triclinic	triclinic
Space group	$P2(1)/n$	$P2(1)/n$	$P2(1)/n$	$P\bar{1}$	$P\bar{1}$
a (Å)	11.507(5)	9.335(5)	14.698(6)	7.5705(13	11.013(15)
b (Å)	12.296(5)	14.201(8)	9.410(4)	13.305(2)	11.087(16)
c (Å)	15.985(7)	21.832(12)	17.835(7)	13.753(2)	14.28(2)
α (°)	90	90	90	69.403(3)	109.47(2)
β (°)	108.050(6)	98.982(10)	99.279(6)	74.214(2)	97.35(2)
γ (°)	90	90	90	76.392(3)	99.99(2)
V (Å^3)	2150.4(15)	2859(3)	2434.5(16)	1232.7(4)	1586(4)
Z	4	4	4	2	2
D_{calc} (g cm^{-3})	1.458	1.300	1.390	1.447	1.379
Absorption coefficient (mm^{-1})	1.052	0.723	0.584	0.929	0.659
$F(000)$	980	1184	1068	558	688
Reflections collected	12266	14381	13572	6490	8186
Independent reflections (R_{int})	4427(0.0385)	5032(0.0942)	4941(0.0476)	4327(0.0217)	5509(0.0232)
Observed reflections	3028	2775	3501	3322	4224
Goodness-of-fit on F^2	1.027	1.001	1.087	1.040	1.071
Final R indices [$I > 2\ \sigma(I)$]	$R_1 = 0.0404$, $\omega R_2 = 0.0896$	$R_1 = 0.0638$ $\omega R_2 = 0.0998$	$R_1 = 0.0529$ $\omega R_2 = 0.0995$	$R_1 = 0.0384$ $\omega R_2 = 0.0884$	$R_1 = 0.0368$ $\omega R_2 = 0.0797$
R indices (all data)	$R_1 = 0.0769$ $\omega R_2 = 0.1031$	$R_1 = 0.1393$ $\omega R_2 = 0.1217$	$R_1 = 0.0880$ $\omega R_2 = 0.1111$	$R_1 = 0.0573$ $\omega R_2 = 0.0974$	$R_1 = 0.0582$ $\omega R_2 = 0.0926$
Largest difference peak and hole (e Å^{-3})	0.269 and −0.341	0.284 and −0.352	0.391 and −0.679	0.611 and −0.287	0.260 and −0.210

Table 2
Elemental analyses for the ligand and complexes

Compound	Formula weight	Color	Found (Calc.)%		
			C	H	N
H_2L	364.40	white	65.44(65.92)	5.81(5.53)	15.28(15.37)
1	471.99	green	55.96(55.98)	5.31(5.13)	11.80(11.87)
2	559.30	brown	55.15(55.84)	6.73(6.49)	9.86(10.02)
3	1018.93	maroon	56.83(56.58)	6.00(5.94)	10.88(11.00)
4	537.07	brown	58.32(58.15)	5.07(5.07)	13.21(13.04)
5	658.39	black red	63.94(63.85)	5.13(5.05)	14.78(14.89)

other coordination sites around the metal ion are completed by the ethanol molecules. When the same reactions were carried out in methanol solvent in the presence of pyridine by solvothermal syntheses, the pyridine molecules were coordinated to the metal ions in the prepared Cu(II) and Ni(II) complexes. However, when the Mn(II) complex was synthesized under the same conditions, the product $[Mn_2L_2(\mu_2\text{-MeOH})_2(MeOH)_2]$, which was confirmed by element analysis and TG analysis, was obtained. We guess its structure is similar to $[Mn_2L_2(\mu_2\text{-EtOH})_2(EtOH)_2]$ (**3**).



Scheme 1.

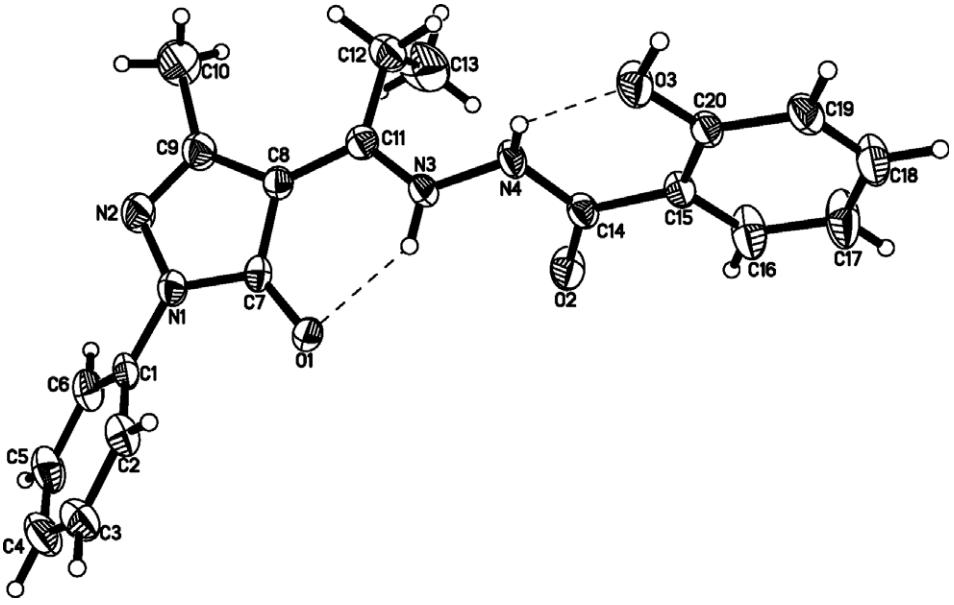


Fig. 1. Molecular structure and crystallographic numbering scheme for the ligand H_2L.

These complexes are stable in air and soluble in most common organic solvents and are readily soluble in DMF and DMSO.

3.2. Structural description

Selected bond lengths (Å) and bond angles (°) of the complexes are listed in Table 3. Hydrogen bonding interactions in the structures are listed in Table 4.

3.2.1. The structure of [CuL(EtOH)] (1)

A perspective view of **1** with the labelling scheme is given in Fig. 2. The Cu(II) ion is coordinated by an ONO tridentate ligand (pyrazolone oxygen atom O1, azomethine nitrogen N3 and enolate oxygen O2) and one oxygen atom (O4) from an ethanol molecule to form a $CuNO_3$ coordination environment with a square-planar geometry. The bond angles show that the complex is distorted from a regular square-planar structure, with O1–Cu1–O2 and O4–Cu1–N3 bond angles of 178.5(6) and 172.1(1)°, respectively, which are deviated from the ideal value of 180°. The deviation of the atom Cu1 from the plane defined by O1, N3, O2 and O4 (the mean deviation from the plane is 0.0278 Å) is 0.0430 Å, which indicates that the five atoms are almost coplanar.

The ligand H_2L itself undergoes isomerization from the keto form to the enol form (form II) in the reaction and acts as a tridentate chelating agent L^{2-}, coordinating to the Cu(II) ion in the solution. The fourth coordination site around the Cu(II) center is completed by the oxygen atom of an ethanol molecule.

Furthermore, it can be found that the hydrazone skeleton [C11=N3–N4=C14] and a certain degree of

Table 3
Selected bond lengths (Å) and angles (°) for the complexes

1			
Cu1–O1	1.880(2)	Cu1–O4	1.945(2)
Cu1–O2	1.902(2)	Cu1–N3	1.927(2)
O1–Cu1–O2	178.5(6)	N3–Cu1–O4	172.1(1)
O1–Cu1–N3	95.45(9)	O1–Cu1–O4	91.19(9)
2			
Ni1–O1	1.983(2)	Ni1–O4	2.104(2)
Ni1–O2	2.050(2)	Ni1–O5	2.062(2)
Ni1–N3	2.011(2)	Ni1–O6	2.111(2)
O1–Ni1–O2	172.6(6)	O4–Ni1–O6	177.6(6)
N3–Ni1–O5	173.5(6)	O1–Ni1–O6	92.3(4)
O1–Ni1–N3	91.5(5)	O2–Ni1–O5	92.6(6)
N3–Ni1–O2	81.1(1)	O1–Ni1–O5	94.9(9)
3			
Mn1–O1	1.923(2)	Mn1–N3	2.008(2)
Mn1–O2	1.947(2)	Mn1–O5A	2.202(2)
Mn1–O5	1.883(2)	Mn1–O4	2.283(2)
O5–Mn1–N3	173.5(5)	O1–Mn1–O2	167.0(1)
O5A–Mn1–O4	172.6(7)	O1–Mn1–O4	85.7(8)
O1–Mn1–N3	91.1(1)	O2–Mn1–N3	79.9(9)
O5–Mn1–O1	93.7(8)	O5–Mn1–O4	94.3(3)
O5–Mn1–O5A	79.2(2)	Mn1–O5–Mn1A	100.8(9)
4			
Cu1–O2	1.920(2)	Cu1–O3	1.897(2)
Cu1–N2	1.939(2)	Cu1–N5	1.996(2)
O3–Cu1–O2	177.1(1)	N2–Cu1–N5	175.1(2)
O3–Cu1–N2	94.6 (6)	O3–Cu1–N5	90.3(4)
5			
Ni1–O1	2.006(3)	Ni1–N5	2.132(3)
Ni1–O2	2.034(3)	Ni1–N6	2.082(3)
Ni1–N3	1.996(3)	Ni1–N7	2.148(3)
N3–Ni1–O1	93.4(1)	N6–Ni1–N5	87.6(1)
O1–Ni1–O2	173.8(9)	N3–Ni1–N6	173.6(6)
N5–Ni1–N7	175.4(5)	O1–Ni1–N5	90.4(1)
O1–Ni1–N7	88.4(1)	N3–Ni1–O1	93.4(1)

Table 4
Hydrogen bonding interactions for the complexes

1				
D–H···A	d(D–H) (Å)	d(H···A) (Å)	d(D···A) (Å)	<(DHA) (°)
O3–H30···N4	0.71(4)	1.95(4)	2.56(5)	144(5)
O4–H40···N2[a]	0.75(3)	2.00(4)	2.75(5)	175(4)
2				
O3–H3···N4	0.82	1.78	2.51(1)	146.8
O4–H4···N2[b]	0.85(5)	2.00(1)	2.85(5)	178.1(2)
O5–H5···O3[c]	0.85(3)	1.77(1)	2.60(0)	166.0(2)
O6–H6···O3[c]	0.84(5)	1.85(1)	2.65(5)	160(2)
3				
O3–H3···N4	0.85(1)	1.84(2)	2.59(9)	146(4)
O4–H4···N2[d]	0.85(1)	1.97(7)	2.82(1)	176(4)
4				
O1–H1···N1	0.98	1.63	2.55(5)	155.0
O4–H4A···N4[e]	0.82	2.13	2.89(8)	153.9
5				
O3–H3···N4	0.82	1.81	2.54(5)	147.2

Symmetry labels: (a) $x+1/2, -y+1/2, z+1/2$; (b) $-x, -y+2, -z$; (c) $-x+1/2, y-1/2, -z+1/2$; (d) $-x+3/2, y+1/2, -z+1/2$; (e) $-x+1, -y, -z+1$.

delocalized π-electrons of the pyrazolone ring appear in the complex, which results in coplanarity of plane I {N1N2C7C8C9}, plane II {O1C7C8C11N3Cu1} and plane III {N3N4C14O2Cu1}, of which the interplanar angles of plane I and III with II are 1.3° and 0.7°, respectively.

There are both intra- and intermolecular hydrogen bonds in the structure (Fig. 3). The amido N4 atom forms an intramolecular H-bond with HO3 of the phenolic hydroxyl group [O3···N4, 2.56(5) Å, 144(5)°], which links N4–C14–C15–C20–O3H30 to form a pseudo-six membered ring. Furthermore, the oxygen atom O4 of the coordinated ethanol molecule is intermolecularly hydrogen-bonded to the N2 atom of the pyrazolone ring of the adjacent unit, with an O4···N2 contact of 2.75(5) Å. Through the intermolecular hydrogen bonds, the complex units are linked into a supramolecule with a 1D chain structure.

3.2.2. The structure of $[NiL(EtOH)_3]$ (2)

The view of complex **2** as a monomeric unit is depicted in Fig. 4. The Ni(II) ion is in a distorted octahedral geometry, being hexa-coordinated by two oxygen atoms (O1, O2) and one nitrogen atom (N3) from the tridentate ligand and three oxygen atoms (O4, O5 and O6) from three ethanol molecules to form a NiNO5 coordination environment. The equatorial plane is made up of O1, O2, N3 and O5. The Ni1–O1, Ni1–O2, Ni1–O5 and Ni1–N3 bond lengths are 1.983(2), 2.050(2), 2.062(2) and 2.011(2) Å, respectively. While the axial positions of the distorted octahedral geometry are occupied by the O4 and O6 atoms of two other ethanol molecules, with two long Ni1–O distances of 2.104(2) and 2.111(2) Å. The average deviation of O1, O2, N3 and O5 with regard to the mean basal plane is 0.0076 Å. The Ni1 ion is displaced by −0.0137 Å from the equatorial plane. The ligand–metal–ligand bite angles differ from the ideal value of 90°, varying between 81.1(1)° [N3–Ni1–O2] and 94.9(9)° [O1–Ni1–O5]. The bond angles of O1–Ni1–O2, N3–Ni1–O5 and O4–Ni1–O6 are 172.6(6)°, 173.5(6)° and 177.6(6)°, respectively, which are slightly deviated from the theoretical value of 180°, these information indicate that the coordination sphere of Ni1 is best described as a slightly distorted octahedron. The longer Ni1–O(ethanol) bond lengths indicate that the oxygen atoms of the ethanol molecules coordinate less strongly than the donor atoms of the ligand.

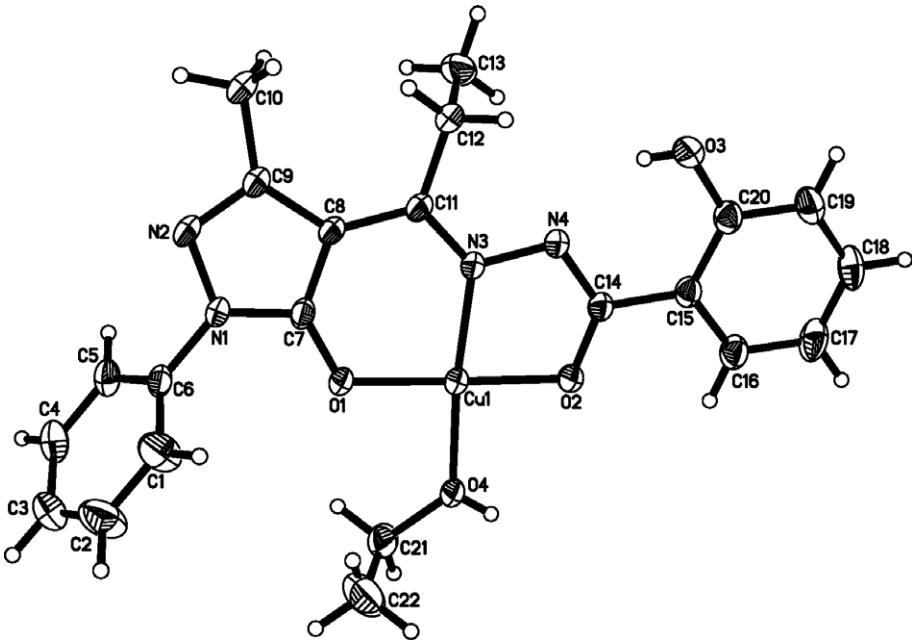


Fig. 2. A perspective view of **1** with the atom numbering scheme, thermal ellipsoids are at the 30% probability level.

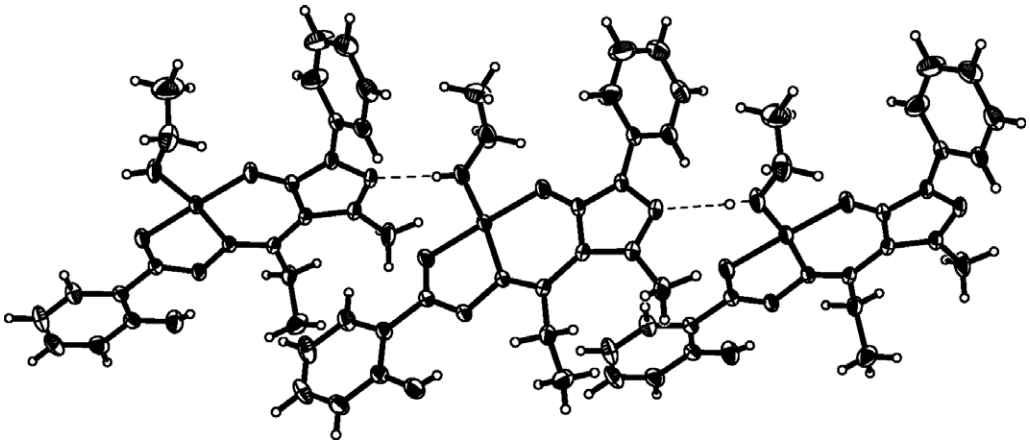


Fig. 3. The packing view of the unit cell for **1**.

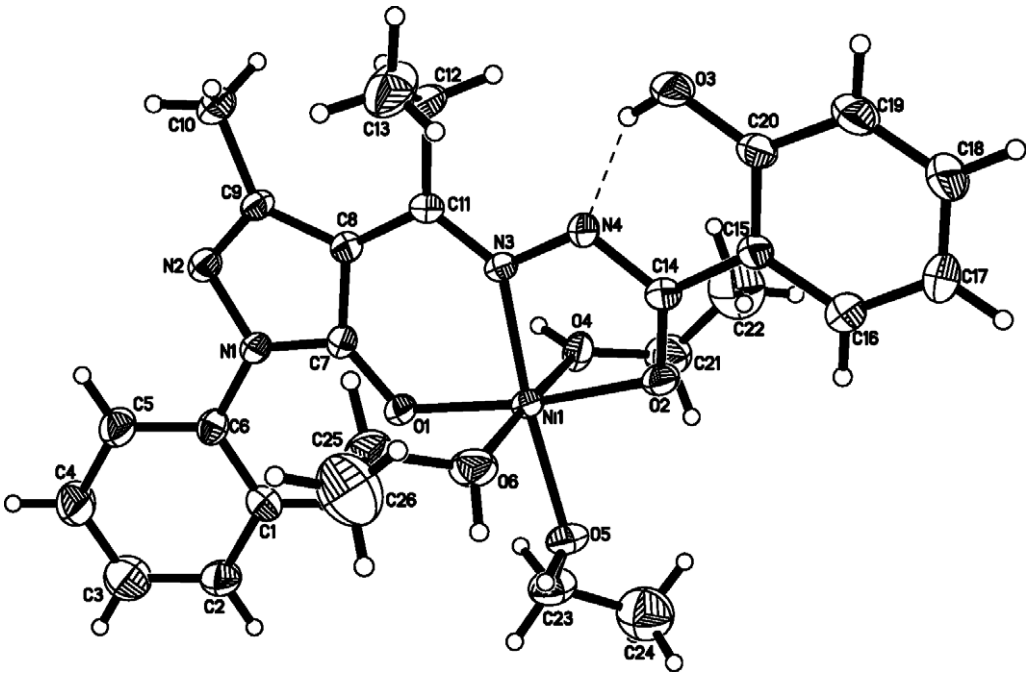


Fig. 4. The crystal structure of **2**, the thermal ellipsoids are drawn at the 30% probability level.

In the complex, the six-membered chelate ring {C7C8C11N3O1Ni1} and the five-membered chelate ring {N3N4C14O2Ni1} are coplanar with the pyrazolone ring. The dihedral angles are 2.7° and 4.0°, respectively. The plane defined by the {N4, C14, C15, C20, O3} atoms is also coplanar with the phenyl ring of {C15–C20}, the dihedral angle is 2.4°. These show that the ligand has favorable coplanarity.

Fig. 5 illustrates the packing diagram of **2**. The most interesting feature in the complex is that the intermolecular hydrogen bonds play an important role in the crystal packing and the stability of the complex. Adjacent units are cross-linked by two types of intermolecular hydrogen bonds (O–H···N and O–H···O), which stabilize the conformation. The oxygen atom (O4) of one ethanol molecule of a mononuclear unit is hydrogen bonded to a nitrogen atom (N2) of the pyrazolone ring of an adjacent complex unit (O4···N2 = 2.85(5) Å). The oxygen atoms (O5 and O6) of two other ethanol molecules are further hydrogen bonded to the hydroxyl oxygen atom (O3) of the third complex unit (O5···O3 = 2.60(0) Å, O6···O3 = 2.65(5) Å). Through the intermolecular hydrogen bonds, the units are linked into supramolecular 2D layers.

3.2.3. The structure of $[Mn_2L_2(\mu_2\text{-}EtOH)_2(EtOH)_2]$ (3)

The molecular structure of complex **3** is shown in Fig. 6. The crystal structure is built up of dinuclear centrosymmetric complex molecules, $[Mn_2L_2(\mu_2\text{-}EtOH)_2(EtOH)_2]$. Each Mn(II) is hexa-coordinated by one tridentate ligand, two bridging ethanol molecules and a coordinated ethanol

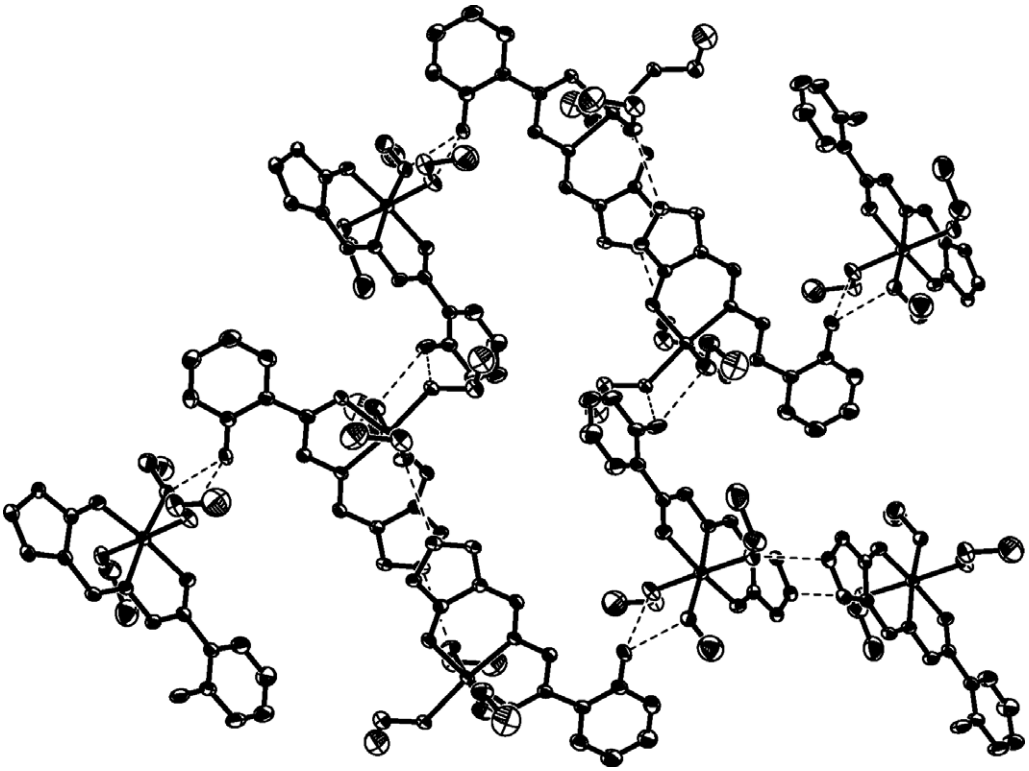


Fig. 5. The two-dimensional network structure of **2** formed by hydrogen-bonding interactions.

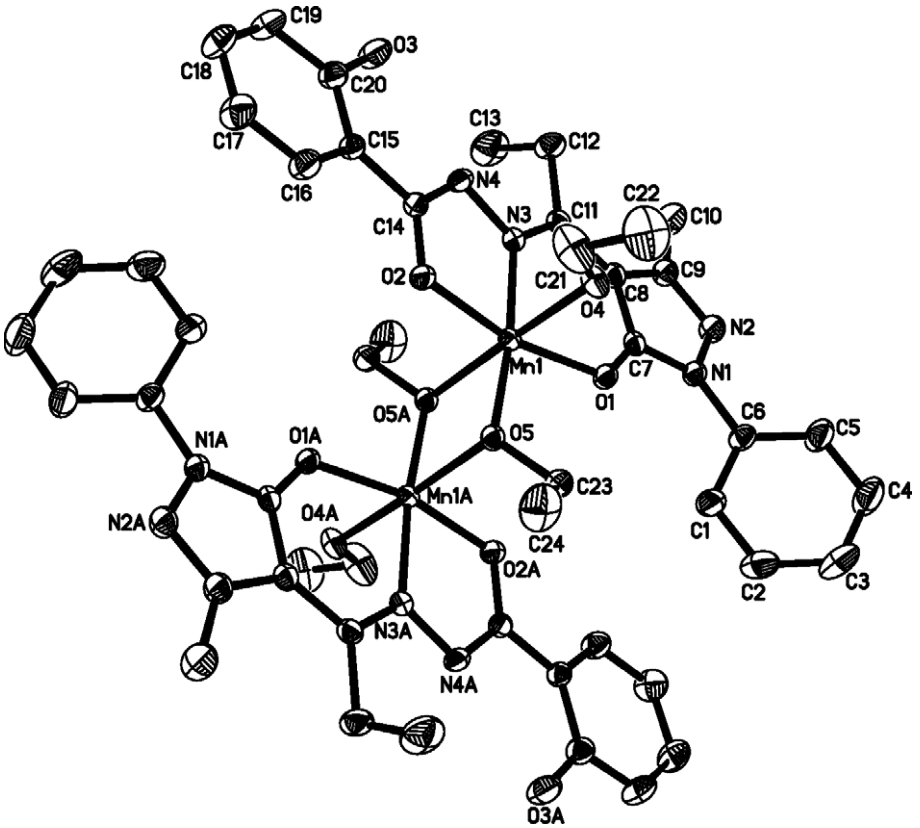


Fig. 6. Perspective view of **3** with 30% probability displacement ellipsoids.

molecule to form a MnNO5 coordination environment. The Mn1 ion has an octahedral geometry with the basal plane consisting of two oxygen atoms from the ligands (O1, O2), with Mn1–O distances of 1.923(2) and 1.947(2) Å, and two oxygen atoms of the ethanol molecules (O4, O5A), with Mn1–O distances of 2.283(2) and 2.202(2) Å. The axial positions are occupied by the azomethine nitrogen (N3) and ethoxo atom (O5). The average deviation of O1, O2, O4 and O5A with regard to the mean basal plane is 0.1367 Å. Mn1 is displaced by −0.0071 Å from the equatorial plane. The bond angles of O1–Mn1–O2, O4–Mn1–O5A and N3–Mn1–O5 are 167.0(1), 172.6(7) and 173.5(5)°, respectively. This indicates that the coordination sphere of the Mn1 ion is a slightly distorted octahedron.

In the binuclear unit, the two Mn(II) ions are connected by two oxygen atoms from two bridging ethanol molecules to define a centrosymmetric dimeric unit, in such a way a planar asymmetric bridge between the Mn ions is formed. Each bridging oxygen atom is more closely associated with a single Mn(II), with the bond lengths Mn1–O5 of 1.883(2) Å and Mn1–O5A of 2.202(2) Å (which are shorter than the bond length to the terminal oxygen, Mn1–O4 of 2.283(2) Å). The Mn1–O5–Mn1A bond angle of 100.8(9)°, and a Mn···Mn distance of 3.155 Å is observed in the complex. The formation of an oxygen bridged binuclear complex with high stability might be the reason for solvent molecule coordination regardless of whether the complex was synthesized under the common solvent reaction or by solvothermal synthesis with pyridine.

In the crystal structure, the complex molecules are interconnected through intermolecular O4–H4···N2 hydrogen bonds formed between O4 of the coordinated ethanol molecule and the N2 atom of the pyrazolone ring of a neighboring molecule (O4···N2 = 2.82(1) Å). Thus sheets of molecules parallel to the crystallographic *bc*-plane are formed (Fig. 7).

For the three complexes with ethanol as the co-ligand, the coordination number (CN) should be expected to be of the same order as for the ionic radii, i.e., Mn > Ni > Cu. However, the coordination number is Mn = Ni > Cu and the coordination geometry around Ni(II) and Mn(II) is a distorted octahedron while Cu(II) displays a square plane, which can be explained by the ionic radii of the cations and the well-known tetragonal Jahn-Teller distortion for Cu(II) [27]. The results also show that the interactions in the equatorial plane of Cu(II) were strengthened, as the in-plane Cu(II)–N and Cu(II)–O(ligand) distances are significantly shorter than those observed for the nickel(II) and manganese(II) complexes. On the other hand, it is found that the Mn(II) complex assumes a dimeric structure bridged by two ethanol molecules. It appears that Mn(II), with an ionic radius (0.84 Å) larger than the ionic radius of Ni(II) (0.69 Å), allows dimerization of the mononuclear units in **3** [28].

3.2.4. The structure of [CuL(Py)] · MeOH (4)

A perspective view of [CuL(Py)] · MeOH (**4**) with the labelling scheme is given in Fig. 8. The structure of **4** consists of an electroneutral Cu(II) mixed-ligand complex and one uncoordinated crystal methanol molecule. The Cu1 ion is tetra-coordinated with two oxygen atoms (O2, O3) and one nitrogen atom (N2) from the tridentate ligand and one nitrogen atom (N5) from a pyridine molecule to form a CuN2O2 coordination environment with a slightly distorted square-planar geometry. The derivations of the four donor atoms (O2, O3, N2 and N5) from their least-squares plane are 0.0027 Å, 0.0026 Å, −0.0022 Å and −0.0020 Å, respectively, and the Cu1 ion is displaced by −0.0012 Å out of the plane; all these figures show that the five atoms are almost coplanar. The bond angles show that the complex is distorted from a regular square-planar structure, with N2–Cu1–N5 and O2–Cu1–O3 bond angles of

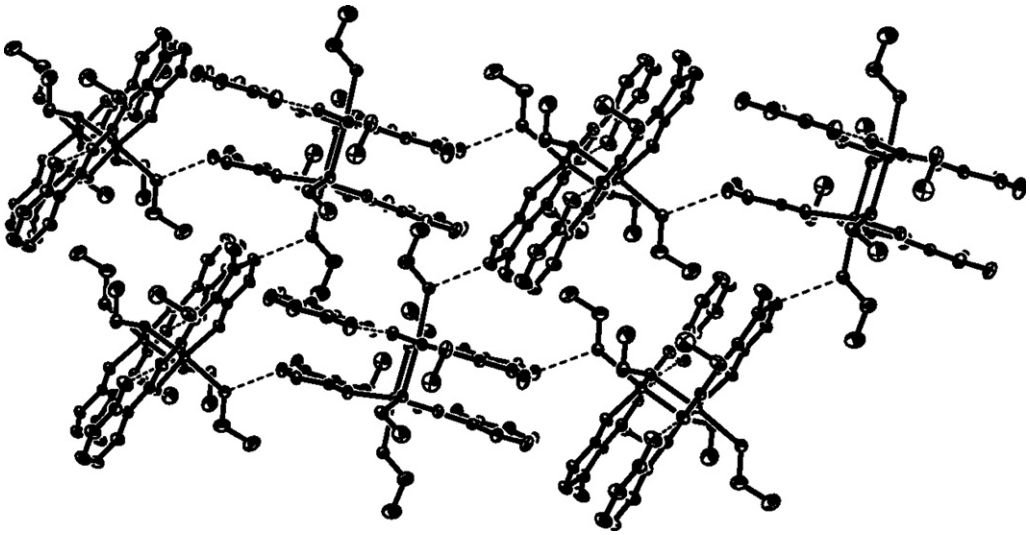


Fig. 7. 2-D network structure of **3** formed by hydrogen-bonding interactions.

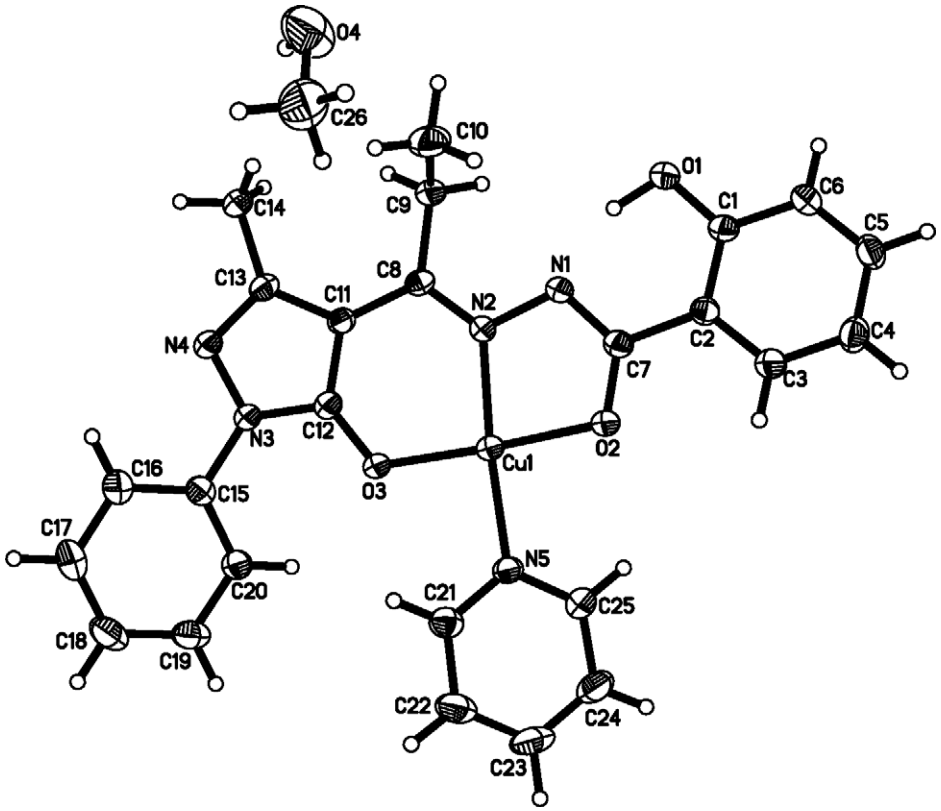


Fig. 8. The molecular structure of **4** with thermal ellipsoids shown at 30%.

175.1(2)° and 177.1(1)°, respectively, which are deviated from the ideal value of 180°.

In this complex, the ligand L^{2-} also adopts the enolic form II bonded to the Cu1 ion. The dihedral angle between the six-member chelating plane {O3C12C11C8N2Cu1} (mean derivation 0.0132 Å) and the pyrazolone ring (mean derivation 0.0027 Å) is 1.4°. The five-member chelating plane {O2C7N1N2Cu1} (mean derivation 0.0076 Å) is almost coplanar with the six-member chelating ring (dihedral angle 1.1°). It is concluded that there is considerable conjugation in the complex.

As shown in the packing diagram of **4** (Fig. 9), the O4 atom of the uncoordinated methanol molecule and the N4 atom of the pyrazolone ring provide the hydrogen bonding donor and acceptor, respectively. Atom O4 is hydrogen bonded to N4 at a N4···H(O4) distance of 2.13 Å, the

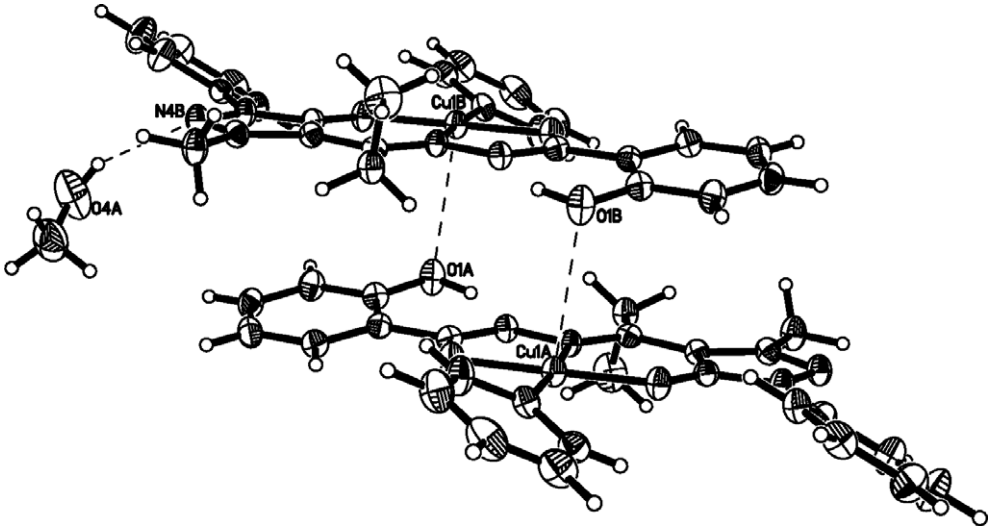


Fig. 9. Illustration of weak interactions between the phenolic oxygen atoms and central metal ions, broken lines indicate weak interactions and hydrogen bonds.

O4···N4 distance is 2.89(9) Å. The two complex units link to each other through a weak contact between the phenolic oxygen atoms and central metal ions (O1A···Cu1B, O1B···Cu1A) with a long distance (3.023 Å) to form a dimer. These O···Cu contacts suggest that there are π–π stacking interactions between the primary ligands.

3.2.5. The structure of [NiL(Py)$_3$] (5)

The molecular structure of **5**, together with the atom-numbering scheme is illustrated in Fig. 10. Selected bond lengths (Å) and bond angles (°) are listed in Table 3.

In the mixed-ligand complex **5**, the coordination geometry around the hexa-coordinated Ni(II) ion is described by a slight distorted octahedron, the Ni1 ion being coordinated by two oxygen atoms (O1 and O2) and one nitrogen atom (N3) of L^{2-} and three nitrogen atoms (N5, N6 and N7) from three pyridine molecules. The O1, O2, N3 and N6 atoms constitute the equatorial plane, while the axial positions are occupied by the N5 and N7 atoms. The average deviation of O1, O2, N3 and N6 with regard to the mean basal plane is 0.0051 Å. The Ni1 ion is displaced by 0.0099 Å from the equatorial plane. The bond angles of O1–Ni1–O2, N3–Ni1–N6 and N5–Ni1–N7 are 173.8(9)°, 173.6(6)° and 175.4(5)°, respectively, which are slightly deviated from the theoretical value of 180°. This indicates that the coordination geometry of the Ni1 ion is a slightly distorted octahedron. The average bond length of Ni1–N(pyridine) is 2.121 Å, in which the bond length Ni1–N6 (2.082(3) Å) is shorter than Ni1–N5 (2.132(3) Å) and Ni1–N7 (2.148(3) Å). The C7–O1 and C14–O2 bond distances are 1.279(3) and 1.274(3) Å, respectively, which are shorter than 1.43 Å for a C–O single bond and longer than 1.22 Å for a C=O double bond length. The C11–N3 (1.300(3) Å) and C14–N4 (1.322(3) Å) bond lengths are close to a C=N double bond (C=N, 1.28 Å), which confirms that the keto form III of the ligand isomerizes to the enol form II and then participates in bonding. Furthermore, after the coordination complex is formed, a hydrazone skeleton [C11=N3–N4=C14] appears with a certain degree of delocalization of the π-electrons of the pyrazolone ring and the hydrazone skeleton. This conjugation results in coplanarity of plane I {N1N2C7C8C9}, plane II {O1C7C8C11N3Ni1}, plane III {N3N4C14O2Ni1} and plane IV {C15–C20}, of which the interplanar angles of plane I and III with II are 8.7° and 5.8°, respectively; plane IV with II is 7.6°.

It is noteworthy that when the reactions of the ligand H_2L and the respective metal acetate were carried out in methanol solvent in the presence of pyridine, the pyridine molecule replaced methanol and coordinated to the metal ions Cu(II) and Ni(II) to complete the coordination requirement. However for Mn(II), the product [Mn_2L2-(μ_2-MeOH)$_2$(MeOH)$_2$], similar to [Mn_2L_2(μ_2-EtOH)$_2$-(EtOH)$_2$], was obtained. The preference for either pyridine or methanol is in fair agreement with Pearson's theory of hard and soft acids and bases, preferring bases of the same quality: the 'harder' Mn(II) binds intermediate base pyridine ligands much less compared to the 'intermediate' acid Ni(II), which prefers to bind with the 'harder' methanol molecule [29].

3.3. Comparison of the free ligand H_2L and these complexes

Useful information can be derived by comparing the structure of the ligand in free state and in the complexes. A comparison of the bond lengths of H_2L and the mixed-

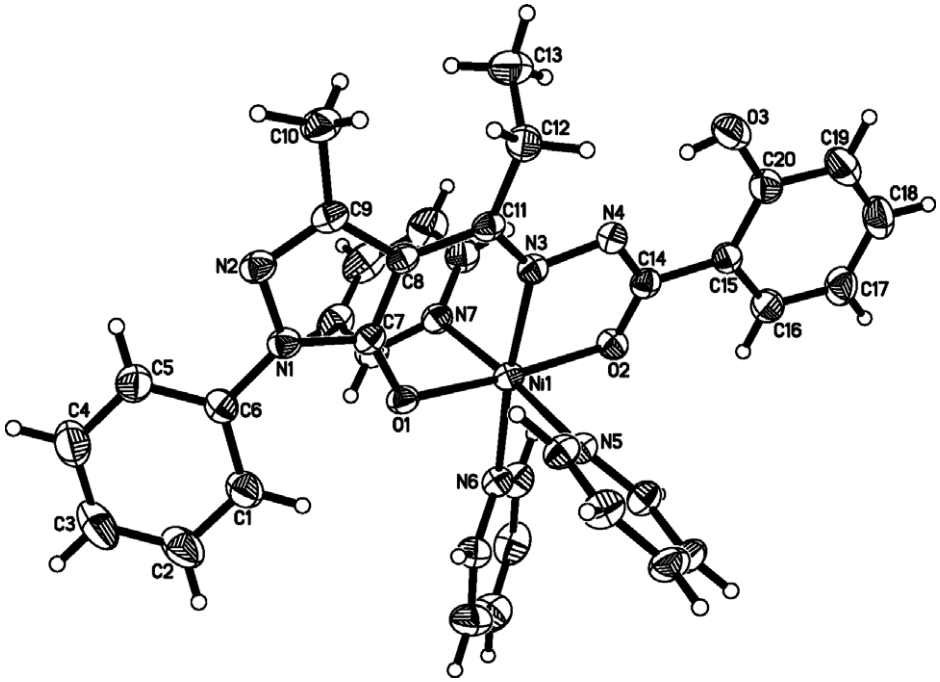


Fig. 10. The molecular structure of **5** with thermal ellipsoids shown at 30%.

ligand complexes are listed in Table 5. Some bond lengths are changed. As far as bond distances around the coordination atoms O1, O2 and N3 are concerned, the changes are the most obvious. In the free ligand, the bond distances of O1-C7 and O2–C14 are 1.266(3) and 1.218(3) Å, respectively, which is in good agreement with a C=O double bond. The bond length of C8–C11 is 1.400(4) Å, which is indicative of significant conjugate double bond character. While the C11–N3 bond distance is 1.311(4) Å, slightly shorter than a normal C–N bond distance. All of these demonstrate that the keto tautomer (form (III) in Scheme 1) is favored over the enol form (I) or (II) for the ligand. In the complexes, however, bonds O1–C7 and O2–C14 are lengthened, having values close to the value of a C–O single bond. While the bond lengths of N3–C11 and N4–C14 in the complexes are shorter than the corresponding C–N distance in the ligand. All these changes indicate that the ligand exists in the enol form II (in Scheme 1) in the reaction and acts as a tridentate ligand coordinated to the metal ion, with the other coordination sites around the metal ions being completed by the co-ligand.

In the free ligand, the pyrazolone ring (plane I) is coplanar with plane II defined by the C7, C8, C11, N3 and O1 atoms, the dihedral angle between them is only 0.8°. Plane III (N4, C14, C15, C20, O3) is also almost coplanar with plane IV (C15–C20), the dihedral angel between them is 8.9°. Moreover, the dihedral angle between plane II and plane III is 69.3°. These data indicate that the whole molecule is non-planar. However, in the structures of these complexes, the hydrazone skeleton [C11=N3–N4=C14] appears and there is a certain degree of delocalization of the π-electrons of the pyrazolone ring. This conjugation results in coplanarity of the pyrazolone ring, six-member chelating plane, five-member chelating plane and the plane defined by (C15–C20). Namely, the main body of the ligand is in a plane. These data reveal that the configuration of the ligand changed to planar in solution to facilitate the coordination of the enolic oxygen O2 to the metal ion.

3.4. IR spectra

The assignments of IR bands are observed to be in good agreement with the X-ray structural data. The main stretching frequencies of the IR spectra of the ligand H_2L and its mixed-ligand complexes are tabulated in Table 6.

Table 5
Comparison of bond lengths of H_2L and the complexes

Bond	H_2L	1	2	3	4	5
C7–O1	1.266(3)	1.290(3)	1.268(3)	1.295(3)	1.287(3)	1.279(3)
C14–O2	1.218(3)	1.290(3)	1.249(3)	1.303(3)	1.292(3)	1.274(3)
C20–O3	1.352(3)	1.352(4)	1.323(3)	1.361(4)	1.360(4)	1.346(4)
C11–N3	1.311(4)	1.311(3)	1.308(3)	1.314(3)	1.309(4)	1.300(3)
N3–N4	1.388(3)	1.397(3)	1.398(2)	1.408(3)	1.401(3)	1.400(3)
N4–C14	1.353(4)	1.313(3)	1.355(3)	1.312(4)	1.315(4)	1.322(3)
C7–C8	1.420(4)	1.408(4)	1.425(3)	1.412(4)	1.404(4)	1.406(4)
C8–C9	1.442(4)	1.421(4)	1.424(3)	1.423(4)	1.426(4)	1.431(4)
C8–C11	1.400(4)	1.421(4)	1.441(3)	1.426(4)	1.435(4)	1.447(4)

Table 6
IR band assignments for the ligand and the complexes

Compound	υ_{O-H}	υ_{N-H}	$\upsilon_{C=O}$	υ_{C-O^-}	$\upsilon_{C=N}$	$\upsilon_{C=N\ Py}$	υ_{C-OH}	υ_{M-O}	υ_{M-N}
H_2L	3249	3249	1663, 1614				1308		
1	3444			1453	1604		1305	512	472
2	3445			1450	1603		1304	517	459
3	3482			1454	1597		1304	514	461
4	3313			1453	1602	1576	1301	511	464
5	3176			1445	1599	1576	1305	506	457

The ligand spectrum shows a medium intensity band at around 3249 cm^{-1}, assigned to the hydrogen bond NH and OH stretching vibrations [30], the strong bands at 1663 and 1614 cm^{-1} are respectively allocated as υ(C=O) of the hydrazide and υ(C=O) of the pyrazolone-ring [4,31]. From the above analyses, it is concluded that the ligand exists in the keto form in the solid state. However, in the spectra of the complexes, the υ(C=O) bands are both absent. Meanwhile, a new band is observed at around 1450 cm^{-1} due to υ(C–O^-). The band at around 510 cm^{-1} is assigned to υ(M–O) [32]. From these observations, it is concluded that the ligand reacts in the enol form when coordinated to the metal ion in the solvent and the two enolic protons are replaced by M(II) in the complexes. The results are also confirmed by the crystal structure analyses above.

In the spectra of the complexes, the NH stretching vibration disappears and new bands at about 1600 and 1576 cm^{-1} appear, which are respectively allocated as υ(–C=N–N=C–) of the hydrazone and the coordinated pyridine nitrogen [30,33]. All of these demonstrate that the nitrogen atoms of the imino-group and the pyridine are coordinated to M(II). The new bands at 460 cm^{-1} for the complexes are assigned to υ(M–N), which further confirms the results [34].

In the ligand spectra, the strong band observed at 1308 cm^{-1} is assigned to the υ(C–OH) stretching vibration of the phenolic oxygen. This band shifts very feebly in the spectra of all the metal complexes, indicating the non-coordination of the phenolic oxygen to the central metal.

3.5. Thermal analyses

The thermal analyses results of these complexes are represented in Table 7. The results show that the complexes have very similar thermal behavior. In all cases the ethanol or pyridine moiety is removed first followed by the ligand moiety, leaving the respective metal oxide as the decomposition residue. The thermal decomposition behaviors of these complexes reflected the structural information as well. Only the thermal decomposition of complexes **3** and **5** are discussed here in detail.

3.5.1. Thermal analysis of $[Mn_2L_2(\mu_2\text{-}EtOH)_2(EtOH)_2]$ (3)

The simultaneous TG–DTG–DTA curves of complex $[Mn_2L_2(\mu_2\text{-}EtOH)_2(EtOH)_2]$ is shown in Fig. S1 and it

Table 7
Thermal analyses data for these mixed-ligand complexes

Complex	Stage	TG temperature range (°C)	DTG peak temperature (°C)	Removed group	TG mass loss%		Residue compound	Residue found (Calc.)%
					Found	Calculated		
1	I	115–165	140	EtOH	9.67	9.76	[CuL]	
	II	310–580	363	L	73.33	73.39	CuO	16.85 (16.85)
2	I	55–140	114	3EtOH	24.12	24.71	[NiL]	
	II	310–388	383	–Ph–OH	16.55	16.65	$[Ni(C_{14}H_{13}N_4O_2)]$	
	III	388–460	429	$C_{14}H_{13}N_4O$	44.90	44.93	NiO	13.84 (13.35)
3	I	105–175	155	2EtOH	10.13	9.04	$[Mn_2L_2(EtOH)_2]$	
	II	175–259	215, 236	2EtOH	8.11	9.04	$[Mn_2L_2]$	
	III	258–450	374	2L	66.36	67.99	Mn_2O_3	15.30 (15.49)
4	I	90–122	113	MeOH	5.42	5.96	[CuL(Py)]	
	II	152–244	207	Py	14.49	14.73	[CuL]	
	III	340–580	370	L	64.37	64.50	CuO	15.90 (14.81)
5	I	110–177	155	2Py	23.93	24.02	[NiL(Py)]	
	II	177–225	212	Py	11.95	12.01	[NiL]	
	III	368–485	403	L	52.30	52.20	NiO	11.75 (11.34)

indicates that the thermal decomposition takes place in three stages. In the first stage from 105 to 175 °C, two moles of ethanol molecules degrade, shown as one maximum in the DTG curve at 155 °C with a 10.13% mass loss (Calc.: 9.04%). The second stage starts at 175 °C and ends at 259 °C, the corresponding mass loss (8.11%) is due to the degradation of another two moles of ethanol molecules, which is in agreement with the calculated value (9.04%). The DTG curve shows two peaks at 215 and 236 °C for this stage. The third stage is related to the decomposition of the L^{2-} anion in the temperature range of 259–450 °C and shows a strong exothermic process with a DTA peak at 394 °C, the observed mass loss (66.36%) coincides with the theoretical value (67.99%). The decomposition completes at 450 °C and the final residue is qualitatively proved to be Mn_2O_3, with an observed mass of 15.30% as against the calculated value of 15.49%.

3.5.2. Thermal decomposition of [NiL(Py)$_3$] (5)

The simultaneous TG–DTG–DTA curves of the mixed-ligand complex [NiL(Py)$_3$] are shown in Fig. S2. The thermal decomposition of complex **5** is in three stages. The endothermic degradation of two moles of pyridine molecules takes place in the first stage between 110 and 177 °C with a mass loss of 23.93% (Calc.: 24.02%). The maximum rate of mass loss is indicated by the DTG peak at 155 °C. The residue at the first stage was found to be [NiL(Py)], and the second stage between 177 and 225 °C corresponds to decomposition of the remaining pyridine molecule, and one endotherm is observed in the DTA trace. The observed mass loss is 11.95% which is consistent with the theoretical value of 12.01%. With heating, the decomposition of the ligand followed. The third stage, which occurs in the temperature range 368–485 °C with a DTG peak at 403 °C, corresponds to the decomposition of the ligand, the observed mass loss (52.30%) is roughly coincident with the calculated value (52.20%). This step appears in the DTA curve as a broad exotherm with $T_{max} = 447$ °C and $\Delta H = 11$ kJ g^{-1}. The final residue, estimated as nickel oxide, has the observed mass 11.75% as against the calculated value of 11.34%.

4. Conclusion

A series of five new mixed-ligand complexes of the pyrazolone derivative ligand *N*-(1-phenyl-3-methyl-4-propenylidene-5-pyrazolone)-salicylidene hydrazide (H_2L) have been synthesized and characterized. X-ray crystallographic structural analyses of these complexes reveal that the ligand (H_2L) undergoes isomerization from the keto form to the enol form in the reaction and acts as a double negatively charged tridentate chelating agent coordinated to the metal ion in solution. Comparing with the reported results in this field, the strategy to design and utilize a pyrazolone derivative as a versatile ligand goes further. The final results also show that when a co-ligand was presented in the synthetic reaction, other coordination sites around the metal ions Cu^{2+} and Ni^{2+} were completed either by ethanol or pyridine molecules under the common solvent reaction or solvothermal syntheses conditions, respectively, this was not the case for the Mn^{2+} ion which was still coordinated with the solvent molecules. The different effects of the co-ligand on the structure of the compounds are also discussed.

Acknowledgements

This work was supported by the National Natural Science Foundation of China (No. 20366005 and 20462007), the Scientific Research Foundation in Xinjiang Educational Institutions (XJEDU2005S01) and Young Scholar Science Foundation of Xinjiang Educational Institutions (XJEDU2004E01).

Appendix A. Supplementary material

CCDC 297372, 297373, 297374, 259486 and 259485 contain the supplementary crystallographic data for **1**, **2**, **3**, **4** and **5**. These data can be obtained free of charge via http://www.ccdc.cam.ac.uk/conts/retrieving.html, or from the Cambridge Crystallographic Data Centre, 12 Union Road, Cambridge CB2 1EZ, UK; fax: (+44) 1223 336 033; or e-mail: deposit@ccdc.cam.ac.uk. Supplementary data associated with this article can be found, in the online version, at doi:10.1016/j.poly.2007.08.045.

References

[1] N. Raman, A. Kulandaisamy, A. Shunmugasundaram, K. Jeyasubramanian, Transit. Met. Chem. 26 (2001) 131.
[2] T. Yoshikuni, J. Mol. Catal. A: Chem. 148 (1999) 285.
[3] B.A. Uzoukwu, P.U. Adiukwu, S.S. Al-Juaid, P.B. Hitchcock, J.D. Smith, Inorg. Chim. Acta 250 (1996) 173.
[4] Z.Y. Yang, R.D. Yang, F.S. Li, K.B. Yu, Polyhedron 19 (2000) 2599.
[5] W.F. Yang, S.G. Yuan, Y.B. Xu, Y.H. Xiao, K.M. Fang, J. Radioanal. Nucl. Chem. 256 (2003) 149.
[6] P. Chiba, W. Holzer, M. Landau, G. Bechmann, K. Lorenz, B. Plagens, M. Hitzler, E. Richter, G. Ecker, J. Med. Chem. 41 (1998) 4001.
[7] A.K. El-Sawaf, D.X. West, Transit. Met. Chem. 23 (1998) 417.
[8] N. Kalarani, S. Sangeetha, P. Kamalakannan, D. Venkappayya, Russ. J. Coord. Chem. 29 (2003) 845.
[9] F. Marchetti, C. Rettinar, R. Pettinari, A. Cingolani, D. Leonesi, A. Lorenzotti, Polyhedron 18 (1999) 3041.
[10] O.N. Kataeva, A.T. Gubaidullin, I.A. Litvinov, O.A. Lodochnikova, L.R. Islamov, A.I. Movchan, G.A. Chmutova, J. Mol. Stuct. 610 (2002) 175.
[11] Y. Akama, A. Tong, Microchem. J. 53 (1996) 34.
[12] Y. Akama, A. Tong, N. Matsumoto, T. Ikeda, S. Tunaka, Vib. Spectrosc. 13 (1996) 113.
[13] A.L. Rheingold, W. King, Inorg. Chem. 28 (1998) 1715.
[14] C. Pettinari, F. Marchetti, C. Santini, R. Pettinari, A. Drozdov, S. Troyanov, G.A. attiston, R. Gerbasi, Inorg. Chim. Acta 315 (2001) 88.
[15] H. Adams, D.E. Fenton, G. Minardi, E. Mura, M. Angelo, Inorg. Chem. Commun. 3 (2000) 4.
[16] X.C. Tang, D.Z. Jia, K.B. Yu, X.G. Zhang, X. Xia, Z.Y. Zhou, J. Photochem. Photobiol. A: Chem. 134 (2000) 23.
[17] L. Liu, D.Z. Jia, Y.L. Ji, K.B. Yu, J. Photochem. Photobiol. A: Chem. 154 (2003) 117.
[18] B.H. Peng, G.F. Liu, L. Liu, D.Z. Jia, Tetrahedron 61 (2005) 5926.
[19] L. Zhang, L. Liu, D.Z. Jia, G.C. Xu, K.B. Yu, Inorg. Chem. Commun. 7 (2004) 1306.
[20] X. Hu, L. Zhang, L. Liu, G.F. Liu, D.Z. Jia, G.C. Xu, Inorg. Chim. Acta 359 (2006) 633.
[21] G.C. Xu, L. Liu, L. Zhang, G.F. Liu, D.Z. Jia, J.P. Lang, Struct. Chem. 16 (2005) 431.
[22] B.S. Jensen, Acta Chem. Scand. 13 (1959) 1668.
[23] R.Q. Huang, H.L. Wang, J. Zhou, Preparation of Organic Intermediates, Chemistry Industrial Press, China, 1997, p. 109.
[24] R.H. Blessing, Acta Crystallogr., Sect. A 51 (1995) 33.
[25] G.M. Sheldrick, SHELX SHELX-97: Programs for X-ray Crystallography, University of Gottingen, Gottingen, Germany, 1997.
[26] C. Hui, G.F. Liu, L. Liu, D.Z. Jia, Chinese J. Struct. Chem. 9 (2005) 117.
[27] C.E. Housecroft, A.G. Sharpe, Inorganic Chemistry, 1st ed., Ashford Colour Press Ltd., Gosport, 2001, p. 745.
[28] T. Shiga, T. Nakanishi, M. Ohba, H. Ōkawa, Polyhedron 24 (2005) 2732.
[29] C.E. Housecroft, A.G. Sharpe, Inorganic Chemistry, 1st ed., Ashford Colour Press Ltd., Gosport, 2001, p. 167.
[30] S.N. Rao, K.N. Munshi, N.N. Rao, M.M. Bhadbhade, E. Suresh, Polyhedron 18 (1999) 2491.
[31] M.F. Iskander, L. El-sayed, N.M.H. Salem, W. Haase, H.J. Linder, S. Foro, Polyhedron 23 (2004) 23.
[32] N.V. Thakkar, R.M. Patil, Synth. React. Inorg. Met. -Org. Chem. 30 (2000) 1159.
[33] H. Adams, D.E. Fenton, G. Minardi, E. Mura, A.M. Pistuddi, C. Solinas, Inorg. Chem. Commun. 3 (2000) 24.
[34] H. Temel, U. Cakir, B. Otludil, H.I. Ugras, Synth. React. Inorg. Met. Org. Chem. 31 (2001) 1323.

Available online at www.sciencedirect.com
ScienceDirect
Polyhedron 27 (2008) 25–34
POLYHEDRON
www.elsevier.com/locate/poly

Crystallographic and thermal investigations of organic ammonium tetrathiomolybdates

Bikshandarkoil R. Srinivasan [a,*], Sunder N. Dhuri [a], Ashish R. Naik [a], Christian Näther [b], Wolfgang Bensch [b]

[a] Department of Chemistry, Goa University PO, Goa 403 206, India
[b] Institut für Anorganische Chemie, Christian-Albrechts-Universität zu Kiel, Olshausenstraße 40, D-24098 Kiel, Germany

Received 26 June 2007; accepted 17 August 2007
Available online 27 September 2007

Dedicated to Prof. P.T. Manoharan on the occasion of his 72nd birthday

Abstract

The organic ammonium tetrathiomolybdates *N*-methylethylenediammonium tetrathiomolybdate (*N*-Me-enH$_2$)[MoS$_4$] (**1**), *N*-(3-aminopropyl)propane-1,3-diaminium tetrathiomolybdate (dipnH$_2$)[MoS$_4$] (**2**), 4-(2-ammonioethyl)piperazin-1-ium tetrathiomolybdate hemihydrate (2-pipH-1-EtNH$_3$)[MoS$_4$]$\cdot$ 1/2H$_2$O (**3**) and 2,2′-iminodiethanaminium tetrathiomolybdate (dienH$_2$)[MoS$_4$] (**4**), were synthesized by an aqueous reaction of ammonium tetrathiomolybdate with the organic amines *N*-methylethylenediamine (*N*-Me-en), bis(3-aminopropyl)amine (dipn), 2-piperazin-1-ylethanamine (2-pip-1-EtNH$_2$) and bis(2-aminoethyl)amine (dien), respectively. All compounds were characterized by elemental analysis, ^{1}H NMR, IR, Raman and UV–Vis spectra, and the crystal structures of compounds **1**–**3** were determined. The structures of **1**–**3** consist of diprotonated organic cations, which are linked to the tetrahedral $[MoS_4]^{2-}$ anions with the aid of several weak H-bonding interactions. The MoS$_4$ tetrahedron in all compounds is slightly distorted with one or more Mo–S bonds being elongated, which can be attributed to the H-bonding interactions. The difference Δ between the longest and the shortest Mo–S bond lengths for **1**–**3** are 0.0379, 0.0186 and 0.0302 Å, respectively. Unlike **1** and **2**, which are anhydrous, compound **3** is a hemihydrate. The water molecule in **3** occupies the pores between alternating layers of the cations and anions in the crystallographic *bc*-plane. Compound **3** exhibits four types of weak H-bonding interactions namely N–H$\cdots$S, N–H$\cdots$O, O–H$\cdots$S and C–H$\cdots$S. All four tetrathiomolybdates decompose endothermically forming amorphous disulfides containing C and N. A comparative structural description of 28 tetrathiomolybdates is presented.
© 2007 Elsevier Ltd. All rights reserved.

Keywords: *N*-Methylethylenediamine; Bis(3-aminopropyl)amine; 2-Piperazin-1-ylethanamine; Tetrathiomolybdate; Crystal structures

1. Introduction

The chemistry of tetrathiomolybdate is an area of current research interest in view of its usefulness as a precursor for the preparation of catalytically active metal sulfide materials [1]. A very important application is the routine use as a starting material in synthetic inorganic chemistry for the preparation of several Mo–S compounds [2,3]. In organic syntheses, tetrathiomolybdate has been used as a S-transfer reagent for the synthesis of several organo sulfur compounds [4]. The reactivity of tetrathiomolybdate has been investigated with several organic agents like alkyl halides [5], organic trisulfide [6] organic disulfide [7], thiophenol [8], 1,1-dithiolate disulfide [9], and more recently with organic amines [10–17]. Unlike the reactions of tetrathiomolybdate with other organic reagents like organic disulfides or thiophenol where the tetrathiomolybdate undergoes changes like for example the reduction of Mo(VI) to Mo(V), with organic amines the tetrahedral tetrathiomolybdate(VI) core is retained intact and the organic amines function as cations for charge balance [10–16]. From a structural point of view the acentric tetrahedral $[MoS_4]^{2-}$ unit can be used as a building block

* Corresponding author. Tel.: +91 832 6519316; fax: +91 832 2451184.
E-mail address: srini@unigoa.ac.in (B.R. Srinivasan).

0277-5387/$ - see front matter © 2007 Elsevier Ltd. All rights reserved.
doi:10.1016/j.poly.2007.08.023

to create non-centrosymmetric materials by an appropriate choice of counter cations, which can also be used as cationic handles to distort the MoS_4 tetrahedron by suitably altering the cation–anion interactions. In this context we are investigating the structural chemistry of group VI tetrathiometalates, and for tetrathiotungstates we have demonstrated that the reaction of $[WS_4]^{2-}$ with organic amines leads to the facile formation of organic ammonium tetrathiotungstates [15,18–24]. In many of these structurally characterized compounds, the WS_4 tetrahedron is slightly distorted with one or two of the W–S bonds elongated, which has been attributed to the S···H interactions between $[WS_4]^{2-}$ and the organic cation [21–25]. The importance of H-bonding interactions in the structural chemistry of tetrathiotungstates can also be evidenced by the fact that in some compounds the organic amines are only partially protonated. In view of this, it is of interest to investigate the reactions of tetrathiometalates with tri- or polyamines and alkyl substituted amines. In the present work, we have studied the reaction of $[MoS_4]^{2-}$ with the methyl substituted organic amine *N*-methylethylenediamine (*N*-Me-en) and three triamines bis(3-aminopropyl)amine (dipn), 2-piperazin-1-ylethanamine (2-pip-1-EtNH_2) and bis(2-aminoethyl)amine (dien). Herein we describe the synthesis, spectroscopic, and thermal characterization of the organic tetrathiomolybdates obtained by the above reaction. The structures of compounds **1**–**3** are reported here, while the structure of **4** has been reported by Pokrel et al. earlier [26]. Compounds **1**–**3** constitute new additions to the growing list of structurally characterized tetrathiomolybdates. The availability of structural information for several tetrathiomolybdates permits us to make a comparative study of the structural features, the details of which are described in this paper.

2. Experimental

2.1. Materials and physical measurements

The amines *N*-methylethylenediamine (*N*-Me-en), bis-(3-aminopropyl)amine (dipn), 2-piperazinyl-1-ethylamine (2-pip-1-EtNH_2), bis(2-aminoethyl)amine (dien), and the solvents were used as obtained from commercial sources with analytical purity. $(NH_4)_2[MoS_4]$ (ATM) was prepared by a literature method [27]. The details of the instrumentation used for the elemental analysis, IR, Raman and UV–Vis spectroscopy, thermal analysis were the same as described in our previous reports [11,12]. X-ray powder patterns were recorded in transmission geometry using a STOE STADI P diffractometer (Cu Kα = 1.54056 Å).

2.2. Preparation of compounds *1*–*4*

Freshly prepared ATM (260 mg, 1 mmol) was dissolved in 15 mL of distilled water containing 2 drops of 25% aqueous ammonia, and filtered. To the deep red coloured filtrate, *N*-Me-en (0.3 mL, 3.4 mmol) was added in drops at room temperature and the reaction mixture was left aside for crystallisation. After 1–2 days, red blocks of compound **1** slowly crystallized from the solution. The crystals were isolated by filtration, washed with a little ice-cold water (2 mL) followed by isopropanol (10 mL) and ether (10 mL) and dried under vacuum. Yield 75%. The use of dipn, 2-pip-1-EtNH_2 and dien instead of *N*-Me-en in above synthesis afforded the complexes **2**–**4** in 70% yield. All complexes are quite stable in air and dissolve in aqueous alkali solution, DMSO and DMF.

(*N*-Me-enH_2)[MoS_4] (**1**): *Anal*. Calc. for $C_3H_{12}N_2MoS_4$: C, 9.28; H, 3.12; N, 6.88; S, 33.04. Found: C, 9.34; H, 3.11; N, 6.88; S, 33.89%.

IR data: 3046, 2955, 2727, 1567, 1527, 1466, 1442, 1412, 1203, 1116, 1051, 1025, 935, 824, 766,496, 478 (ν_3), 460 (ν_3), 448 (ν_1), 433, 254, 166, 131, 99 cm^{-1}; Raman data: 475 (ν_3), 458 (ν_3), 449 (ν_1), 412, 202, 185, 170 cm^{-1}.

UV–Vis data (aqueous ammonia): 468, 317, 245 nm.

^{1}H NMR (DMSO-d_6): δ 2.59 (s, 3H), 3.12 (t, 2H, $J = 5$ Hz), 3.09 (t, 2H, $J = 5$ Hz) ppm.

(dipnH_2)[MoS_4] (**2**): *Anal*. Calc. for $C_6H_{19}N_2MoS_4$: C, 20.16; H, 5.37; N, 11.76; S, 35.88. Found: C, 20.15; H, 5.29; N, 11.57; S, 35.86%.

IR data: 3272, 3228, 2998, 1575, 1519, 1461, 1380, 1284, 1083, 989, 755, 477 (ν_3), 453 (ν_1), 219, 262, 194 cm^{-1}; Raman data: 475 (ν_3), 453 (ν_1), 189 (ν_4), 178 cm^{-1}.

UV–Vis data (aqueous ammonia): 468, 317, 241 nm.

^{1}H NMR (DMSO-d_6): δ 1.65 (p, 2H, $J = 7$ Hz), 2.57 (t, 2H, $J = 7$ Hz), 2.81 (t, 2H, $J = 7$ Hz) ppm.

(2-pipH-1-EtNH_3)[MoS_4] · 1/2H_2O (**3**): *Anal*. Calc. for $C_6H_{18}N_3MoS_4O_{0.5}$: C, 19.77; H, 4.98; N, 11.53; S, 35.19. Found: C, 19.62; H, 4.89; N, 11.39; S, 35.38%.

IR data: 3434, 3162, 3081, 2950, 1635, 1608, 1553, 1451, 1367, 1172, 1094, 1067, 993, 902, 509, 475 (ν_3), 451 (ν_1), 435, 363, 335, 279, 227, 202 (ν_4), 173, 139, 105, 88 cm^{-1}; Raman data: 477 (ν_3), 466 (ν_3), 451 (ν_1), 189, 179, 172, 110 cm^{-1}.

UV–Vis data (aqueous ammonia): 468, 317, 239 nm.

^{1}H NMR (DMSO-d_6): δ 2.57 (t, 4H, $J = 5$ Hz), 3.07 (t, 4H, $J = 5$ Hz), 2.89 (t, 2H, $J = 6$ Hz), 2.40 (t, 2H, $J = 6$ Hz) ppm.

(dienH_2)[MoS_4] (**4**): *Anal*. Calc. for $C_4H_{15}N_3MoS_4$: C, 14.58; H, 4.60; N, 12.76; S, 38.94. Found: C, 14.65; H, 4.56; N, 12.67; S, 38.87%.

IR data: 3257, 3054 (br), 1568, 1540, 1504, 1464, 1459, 1365, 1345, 1311, 1283, 1257, 1188, 1177, 1088, 1054, 1027, 987, 959, 932, 866, 838, 818, 797, 770, 676, 495, 464 (ν_3), 427, 320, 283, 204 (ν_4), 185 (ν_2), 171, 141, 125, 92 cm^{-1}; Raman data: 491, 479 (ν_3), 469 (ν_3), 451 (ν_1), 192 (ν_4), 182 cm^{-1}.

UV–Vis data (aqueous ammonia): 468, 317, 240 nm.

^{1}H NMR (DMSO-d_6): δ 2.82 (t, 2H, $J = 5.4$ Hz), 2.66 (t, 2H, $J = 5.54$ Hz) ppm.

2.3. Crystal structure determination

Single crystal X-ray work was performed using a AED-II 4-circle diffractometer from STOE & CIE (Mo Kα radiation; $\lambda = 0$ 71073 Å). The raw intensities were corrected

Table 1
Technical details of data acquisition and selected refinement results for **1**–**3**

Compound	**1**	**2**	**3**
Formula	$C_3H_{12}N_2S_4Mo$	$C_6H_{19}N_3S_4Mo$	$C_6H_{18}N_3S_4MoO_{0.5}$
Temperature (K)	293	293	293
Wavelength (pm)	71.073	71.073	71.073
Space group	$P2_12_12_1$	$Pca2_1$	$C2/c$
a (Å)	7.8805(11)	13.7377(13)	24.451(3)
b (Å)	11.8098(16)	7.4901(7)	7.1150(10)
c (Å)	11.9492(17)	13.4526(11)	17.864(2)
β (°)			115.030(10)
Volume (Å^3)	1112.1(3)	1384.2(2)	2815.9(6)
Z	4	4	8
μ [mm^{-1}]	1.874	1.522	1.501
$F(000)$	600	728	1480
Molecular weight (g/mol)	300.33	357.42	364.41
D_{calc} (g cm^{-3})	1.794	1.715	1.719
Crystal size (mm)	0.14 0.12 0.10	0.2 0.18 0.16	0.12 0.09 0.07
hkl Range	−11/1; −16/1; −16/1	−19/2; −10/1; −18/6	0/34; −1/10; −25/22
2θ Range (°)	4.84–60.08	5.44–60.04	3.68–60.06
Reflections collected	2227	4107	4833
Reflections unique	2141	2959	4095
Data ($F_o > 4\sigma(F_o)$)	1632	2385	3008
R_{int}	0.0367	0.0404	0.0223
Minimum/maximum transmission	0.7214/0.8381	0.7029/0.8501	0.7075/0.8530
$\Delta\rho$ (e Å^{-3})	−0.731/0.625	−0.568/0.574	−0.445/0.426
Parameters	93	129	134
R_1 [$F_o > 4\sigma(F_o)$]	0.0305	0.0295	0.0285
WR_2 for all unique data	0.0699	0.0700	0.0684
Flack x-parameter	−0.05(8)	−0.07(6)	
Goodness of fit	1.006	1.028	0985

for Lorentz, polarization effects and a numerical absorption correction was applied for all compounds. The structures of the compounds **1**–**3** were solved with direct methods using SHELXS-97 [28] and refinement was done against F^2 using SHELXL-97 [28]. All non-hydrogen atoms were refined using anisotropic displacement parameters. The hydrogen atoms were located in difference map but in most cases were positioned with idealized geometry (ammonium hydrogen atoms in **2** and **3** allowed to rotate but not to tip) and refined isotropically using a riding model. The H atom of the water in **3** was located in difference map, its bond lengths set to ideal values and afterwards it was refined using a riding model. The absolute structure for **1** and **2** was determined and is in agreement with selected setting. The technical details of data acquisition and some selected refinement results for **1**–**3** are summarised in Table 1.

3. Results and discussion

3.1. Synthesis

Compounds **1**–**4** were synthesized by a direct aqueous reaction of ATM with the corresponding organic amine. In this reaction the stronger organic bases displace the weaker ammonia from ATM and no change is observed with respect to the tetrathiomolybdate. This observation is in accordance with the known stability of $[MoS_4]^{2-}$ in alkaline medium [29,30]. The compounds analysed satisfactorily for the proposed formula containing $[MoS_4]^{2-}$ in association with the diprotonated cations of *N*-Me-en, dipn, 2-pip-1-EtNH_2 and dien in **1**–**4**, respectively. The presence of the organic amine and $[MoS_4]^{2-}$ could be inferred based on the NMR and UV–Vis spectral data, respectively. In earlier reports we have shown that the use of the cyclic diamine (±)*trans*-1,2-diaminocyclohexane (*trans*-1,2-cn) results in the formation of (*trans*-1,2-cnH)$_2$[MoS_4] containing the monoprotonated amine [14] while the use of the polyamine tris(2-aminoethylamine) (tren) leads to the formation of (trenH_2)[MoS_4]·H_2O [11]. The synthesis of compound **4** containing the diprotonated triamine dien has been reported earlier by an alternate method which involves passing of H_2S gas into an aqueous molybdate solution containing dien [26]. It is interesting to note that the central secondary amine functionality and one of the terminal N atoms of the triamine bis(3-aminopropyl)amine (dipn) are protonated in **2** unlike in the related triamine dien in **4** where the protonation of the terminal primary amine groups has been reported [26]. In **3** only two of the N atoms are protonated. It has been reported that MoO_3 dissolves in aqueous dien resulting in the formation of the hexacoordinated neutral complex [MoO_3(dien)] where dien functions as a neutral tridentate ligand [31,32]. The neutral compound is freely soluble in water and forms (dienH_2)[MoO_4] in solution [33]. While (dienH_2)[MoO_4] exists only in solution, the corresponding tetrathio analogue **4** can be crystallised as a stable solid indicating the difference in the chemistry of

oxo- and thiomolybdates. Our several efforts to prepare the neutral trithio complex [MoS_3(dien)] by the reaction of MoS_3 with dien were not successful as MoS_3 does not dissolve in aqueous dien unlike MoO_3. Furthermore, our attempts to obtain a 2:3 $[MoS_4]^{2-}$ complex of the fully protonated dipn and dien by changing the reaction stoichiometries were not successful. In all cases only the diprotonated ammonium compounds were obtained. As observed earlier [12] for other organic thiomolybdates, the aqueous reaction of **1**–**4** with $[Ni(en)_3]^{2+}$ resulted in a cation exchange leading to the quantitative formation of the known metal–organic tetrathiomolybdate $[Ni(en)_3][MoS_4]$ [34].

3.2. Crystal structure description of *1*–*3*

Compound **1** (*N*-Me-enH_2)[MoS_4] crystallises in the non-centrosymmetric orthorhombic space group $P2_12_12_1$ with all atoms located in general positions and its structure consists of tetrahedral $[MoS_4]^{2-}$ dianions and *N*-methylethylenediammonium cations (Fig. 1). Compound **1** is isostructural with the corresponding W analogue [22] in accordance with our earlier observation wherein a pair of $[MS_4]^{2-}$ (M = Mo, W) compounds linked to the same cation are isostructural. The MoS_4 tetrahedron is slightly distorted and the S–Mo–S bond angles range between 108.36(6)° and 110.65(5)° (average: 109.47°) (Table 2). The Mo–S distances vary from 2.1635(14) to 2.2014(12) Å with a mean Mo–S bond length of 2.1861 Å. An analysis of the crystal structure reveals that

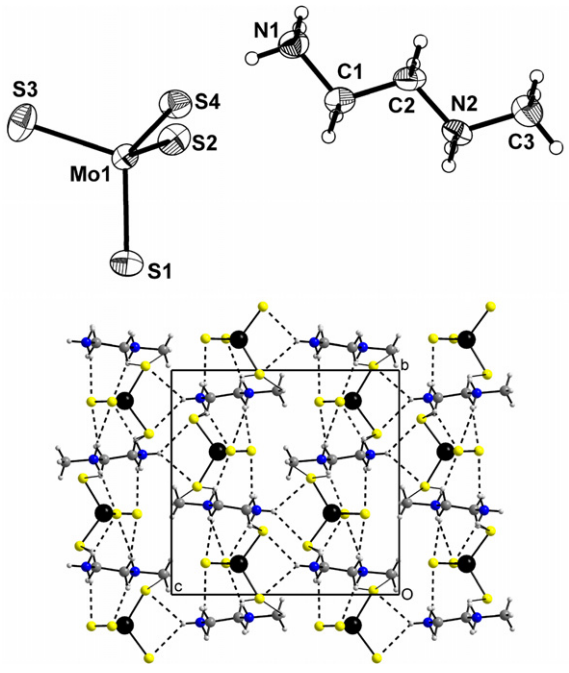


Fig. 1. The crystal structure of (*N*-Me-enH_2)[MoS_4] (**1**) showing the atom-labelling scheme. Displacement ellipsoids are drawn at 50% probability level except for the H atoms, which are shown as circles of arbitrary radius (top). A view of the packing diagram of **1** along *a*-axis (bottom). Hydrogen bonding is shown as dashed lines.

Table 2
Selected geometric parameters (Å, °) for compounds **1**–**3**

*(N-Me-enH$_2$)[MoS$_4$] (**1**)*			
Mo(1)–S(2)	2.1635(14)	Mo(1)–S(3)	2.1997(13)
Mo(1)–S(4)	2.1798(14)	Mo(1)–S(1)	2.2014(12)
S(2)–Mo(1)–S(4)	110.65(5)	S(2)–Mo(1)–S(1)	109.37(6)
S(2)–Mo(1)–S(3)	108.36(6)	S(4)–Mo(1)–S(1)	108.91(5)
S(4)–Mo(1)–S(3)	109.78(6)	S(3)–Mo(1)–S(1)	109.76(5)
*(dipnH$_2$)[MoS$_4$] (**2**)*			
Mo(1)–S(1)	2.1717(13)	Mo(1)–S(4)	2.1844(14)
Mo(1)–S(3)	2.1810(10)	Mo(1)–S(2)	2.1903(9)
S(1)–Mo(1)–S(3)	108.97(5)	S(1)–Mo(1)–S(2)	109.72(5)
S(1)–Mo(1)–S(4)	109.30(6)	S(3)–Mo(1)–S(2)	110.33(4)
S(3)–Mo(1)–S(4)	109.44(5)	S(4)–Mo(1)–S(2)	109.07(5)
*(2-pipH-1-EtNH$_3$)[MoS$_4$] · 1/2H$_2$O (**3**)*			
Mo(1)–S(4)	2.1703(7)	Mo(1)–S(2)	2.1884(7)
Mo(1)–S(3)	2.1750(7)	Mo(1)–S(1)	2.2005(8)
S(4)–Mo(1)–S(3)	109.43(3)	S(4)–Mo(1)–S(1)	108.51(3)
S(4)–Mo(1)–S(2)	110.34(3)	S(3)–Mo(1)–S(1)	110.29(3)
S(3)–Mo(1)–S(2)	108.82(3)	S(2)–Mo(1)–S(1)	109.45(3)

the each $[MoS_4]^{2-}$ anion is linked to four different cations with the aid of several weak N–H···S and C–H···S interactions (Table 3). A total of seven N–H···S interactions ranging from 2.362 to 2.868 Å and four C–H···S interactions between 2.825 and 2.953 Å are observed and all S···H contacts are shorter than the sum of their van der Waals radii [35]. The two longer Mo–S(3) and Mo–S(1) bonds at 2.2014(12) and 2. 1997(13) Å are involved in shorter N–H···S contacts accompanied by larger N–H–S angles while the other two shorter Mo–S bonds are involved in longer S···H contacts. Thus the strength and number of the S···H interactions can account for the observed distinct Mo–S bond distances. The three-dimensional H-bonded network is shown in Fig. 1. The difference Δ between the longest and shortest Mo–S bond lengths in **1** is 0.0379 Å and is quite larger than the Δ value of 0.0111 Å observed earlier (enH_2)[MoS_4] [10] (enH_2 is ethylenediammonium).

Compound **2** (dipnH_2)[MoS_4], crystallises in the non-centrosymmetric orthorhombic space group $Pca2_1$ with all atoms located in general positions. The structure consists of diprotonated $(dipnH_2)^{2+}$ cations and $[MoS_4]^{2-}$ anions (Fig. 2). The geometric parameters of the cation are in the normal range. Compound **2** is isostructural to its corresponding W analogue [23] and one of the primary N atoms and the central secondary N atoms are protonated. The MoS_4 tetrahedron is slightly distorted (S–Mo–S angles: 108.97 (5)–110.33 (4)°; average: 109.47°) with Mo–S bond distances ranging from 2.1717 (13) to 2.1903 (9) Å (average: 2.1818 Å) (Table 2). The observed Δ value of 0.0186 Å, is less than that for compound **1**. Cations and anions are involved in three varieties of H-bonding interactions, which include eight N–H···S, one N–H···N and four C–H···S bonds (Table 4). The resulting three-dimensional crystal-packing diagram is displayed in Fig. 2. $(dipnH_2)^{2+}$ and $[MoS_4]^{2-}$ are stacked in rods along

Table 3
Hydrogen-bonding geometry (Å, °) for (*N*-Me-enH$_2$)[MoS$_4$] (**1**)

D–H···A	*d*(D–H)	*d*(H···A)	*d*(D···A)	∠DHA	Symmetry code
N1–H1N1···S3	0.890	2.418	3.254	156.56	$-x+3/2, -y+1, z+1/2$
N1–H2N1···S4	0.890	2.663	3.368	136.84	
N1–H2N1···S2	0.890	2.746	3.411	132.57	
N1–H3N1···S1	0.890	2.442	3.280	157.13	$x+1/2, -y+1/2, -z+1$
N1–H3N1···S4	0.890	2.868	3.388	118.84	$x+1/2, -y+1/2, -z+1$
N2–H1N2···S3	0.900	2.362	3.190	152.89	$x-1/2, -y+1/2, -z+1$
N2–H2N2···S1	0.900	2.377	3.225	157.12	$-x+1/2, -y+1, z+1/2$
C1–H1A···S4	0.970	2.952	3.583	123.8	$x-1/2, -y+1/2, -z+1$
C2–H2A···S1	0.970	2.953	3.719	136.6	$x+1/2, -y+1/2, -z+1$
C2–H2B···S2	0.970	2.939	3.530	120.4	$-x+3/2, -y+1, z+1/2$
C3–H3A···S2	0.960	2.825	3.531	131.0	$-x+1/2, -y+1, z+1/2$

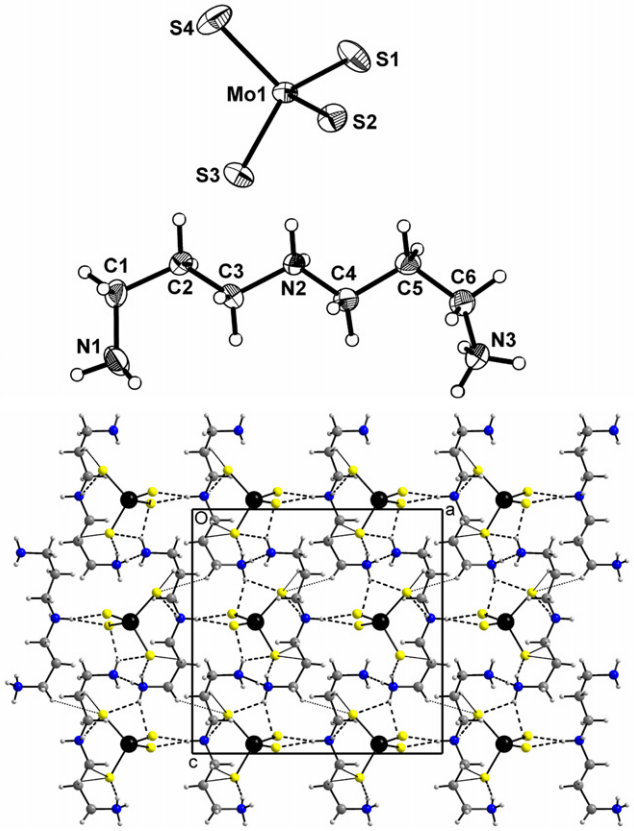


Fig. 2. The crystal structure of (dipnH$_2$)[MoS$_4$] (**2**) showing the atom-labelling scheme. Displacement ellipsoids are drawn at 50% probability level except for the H atoms, which are shown as circles of arbitrary radius (top). The three-dimensional extended network with view along *b*-axis (bottom). H-bonding is shown as dashed lines.

[0 0 1] to form a pseudo-hexagonal array. The cations and anions alternate along [1 0 0] and [0 1 0]. In the (0 1 0) plane a layer like arrangement is found with the anions being located in the pockets formed by three neighboring cations. A very short N3–H···N1 contact at 1.864 Å links the cations into a chain along the '*c*'-axis and each anion is surrounded by four cations and vice versa.

Compound **3** (2-pipH-1-EtNH$_3$)[MoS$_4$]·1/2H$_2$O (**3**), crystallises in the monoclinic space group *C*2/*c* and its structure consists of (2-pipH-1-EtNH$_3$)$^{2+}$, [MoS$_4$]$^{2-}$ located in general position and a crystal water with the oxygen located on a twofold axis (Fig. 3). The cyclic amine adopts the chair conformation with the ethylammonium group occupying equatorial position and the tertiary N remains unprotonated. The geometric parameters of the organic cation are in the normal range. Like for the other two compounds, the [MoS$_4$] tetrahedron is slightly distorted (S–Mo–S: 108.51 (3)–110.34 (3)°; Mo–S bond lengths: 2.1703 (7)–2.2005 (8) Å; average Mo–S distance: 2.1835 Å) (Table 2). The difference between the longest and shortest Mo–S distance Δ is 0.0302 Å and is comparatively larger than that for **2** but less than that observed in **1**. (2-pipH-1-EtNH$_3$)$^{2+}$, [MoS$_4$]$^{2-}$, and H$_2$O are linked via four varieties of H-bonding interactions consisting of five N–H···S, one N–H···O, one O–H···S and one C–H···S bonds (Table 5). It is interesting to note that the crystal water is H-bonded to two symmetry related [MoS$_4$]$^{2-}$ anions via O–H···S bonds while O11 forms H-acceptor bonds (N–H···O) with the organic cation leading to a tetrahedral coordination around the oxygen of water (Fig. 4). This unit linked via H$_2$O can be considered as a synthon to describe the extended supramolecular structure which consists of alternating layers of organic cations and anions with the water molecules occupying the pores between the alternating layers. The N–H···S and C–H···S interactions serve to link the layers of cations and anions (Fig. 4).

3.3. Spectral studies

Compounds **1**–**4** were characterised by using a combination of ^{1}H NMR, UV–Vis, infrared and Raman spectroscopic techniques. The observed chemical shifts (see Section 2) are in the normal range confirming the presence of the organic moieties in **1**–**4**. The electronic spectra of **1**–**4** recorded in dilute ammonia exhibit intense signals at around 468, 317 and 241 nm and the peak positions are identical within experimental error to ammonium tetrathiomolybdate [27]. These bands can be assigned to the charge transfer transitions of the [MoS$_4$]$^{2-}$ anion. The signals in the mid IR (up to 500 cm^{-1}) originate from the organic cations, while the vibrations of the [MoS$_4$]$^{2-}$ unit are observed at lower energies below 500 cm^{-1}. As expected the IR spectra of compounds **1**, **2** and **4** are

Table 4
Hydrogen-bonding geometry (Å, °) for $(dipnH_2)[MoS_4]$ (**2**)

D–H···A	*d*(D–H)	*d*(H···A)	*d*(D···A)	∠DHA	Symmetry code
N1–H2N1···S3	0.890	2.759	3.563	150.77	$-x+1, -y+2, z-1/2$
N1–H2N1···S1	0.890	2.768	3.345	123.78	$-x+1, -y+2, z-1/2$
N2–H1N2···S3	0.900	2.645	3.384	140.06	
N2–H1N2···S2	0.900	2.711	3.415	135.78	
N2–H2N2···S4	0.900	2.627	3.479	158.30	$x-1/2, -y+1, z$
N3–H1N3···N1	0.890	1.864	2.752	175.07	$-x+1/2, y, z+1/2$
N3–H2N3···S2	0.890	2.648	3.451	150.60	$-x+1, -y+1, z+1/2$
N3–H2N3···S4	0.890	2.890	3.510	128.08	$-x+1, -y+1, z+1/2$
N3–H3N3···S1	0.890	2.553	3.401	159.37	$x-1/2, -y+1, z$
C2–H2A···S4	0.970	2.837	3.675	145.16	$x-1/2, -y+1, z$
C4–H4B···S1	0.970	2.933	3.775	145.79	$x-1/2, -y+2, z$
C5–H5A···S1	0.970	2.808	3.638	144.03	$x-1/2, -y+1, z$
C6–H6A···S4	0.970	2.922	3.614	129.16	$-x+3/2, y, z+1/2$

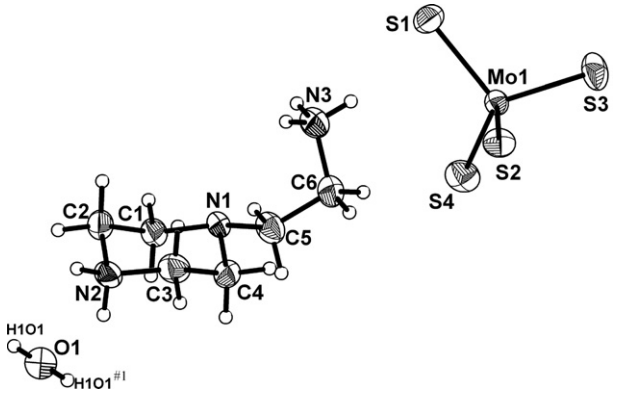


Fig. 3. Crystal structure of $(2\text{-pipH-1-EtNH}_3)[MoS_4]\cdot 1/2H_2O$ (**3**) showing the atom-labelling scheme. Displacement ellipsoids are drawn at 50% probability level except for the H atoms, which are shown as circles of arbitrary radius. Symmetry code: #1 $1-x, y, 1.5-z$.

identical with that of their W counterparts [22,23] with the signals due to the vibrations of $[MoS_4]^{2-}$ unit occurring at slightly higher energies. The strong band at 3434 cm^{-1}, which can be assigned to the O–H stretching vibration indicates the presence of water in the hemihydrate compound **3**. For all compounds the N–H region appears broad and shifted to lower wave numbers as compared to the free amines. This can be attributed to the change of amine group into the ammonium cation and the hydrogen bonding interactions between the organic cation and $[MoS_4]^{2-}$ anion. A broad signal due to the N–H vibration occurs at around 3046 cm^{-1} for **1** while for **2**–**4**, this vibration occurs at 2998, 3081 and 3054 cm^{-1}, respectively. However, the N–H region of **2** and **4** is quite different from that of **1**, as extra bands at 3272, 3228 cm^{-1} in **2** and 3257 cm^{-1} in **4**, are observed. These signals can be attributed to the N–H vibrations of the free amine part of the organic cations in **2**–**4**, indicating that the amines are partially protonated in **2**–**4**. Such signals have been earlier observed for the free amine functionality in $(trenH_2)[MoS_4]\cdot H_2O$ [11]. For the free tetrahedral $[MoS_4]^{2-}$ anion four characteristic bands $\nu_1(A_1)$, $\nu_2(E)$, $\nu_3(F_2)$, and $\nu_4(F_2)$ are expected [36,37]. All four bands are Raman active while only ν_3 and ν_4 are infrared active. When the T_d symmetry of MoS_4 is lowered to C_{2v} as in $[Ni(MoS_4)_2]^{2-}$ where $[MoS_4]^{2-}$ functions as a bidentate ligand, a splitting of the triply degenerate $\nu_3(F_2)$ vibration of the M–S bond occurs [36,37]. In $[Ni(MoS_4)_2]^{2-}$ the Mo–S bond to the bridging S atom is long (Mo–S–Ni) and the Mo–S bond to terminal S atom is short (2.151 Å). In our compounds the longer Mo–S bonds are always observed when strong S···H bonding interactions are present, and the Mo–S bond length distribution indicates a slight distortion of the tetrahedra. In **1** the asymmetric stretching vibration ν_3 appears as a split signal at 463 and 448 with a further shoulder at 433 cm^{-1}. The observed extra signals can be attributed to the distortion of MoS_4 tetrahedron and lowering of symmetry. All compounds exhibit a strong signal

Table 5
Hydrogen-bonding geometry (Å, °) for $(2\text{-pipH-1-EtNH}_3)[MoS_4]\cdot 1/2H_2O$ (**3**)

D–H···A	*d*(D–H)	*d*(H···A)	*d*(D···A)	∠DHA	Symmetry code
N2–H1N2···O1	0.900	2.349	3.064	136.29	
N2–H1N2···S2	0.900	2.706	3.445	140.07	$-x+3/2, y+1/2, -z+3/2$
N2–H2N2···S3	0.900	2.451	3.282	153.64	$x-1/2, y+1/2, z$
N3–H1N1···S2	0.890	2.529	3.320	148.39	$-x+3/2, -y+1/2, -z+1$
N3–H2N2···S1	0.890	2.558	3.415	161.85	
N3–H3N3···S1	0.890	2.714	3.378	132.31	$-x+3/2, -y+3/2, -z+1$
O1–H101···S4	0.820	2.670	3.443	157.88	$x-1/2, y-1/2, z$
C2–H2A···S3	0.970	2.856	3.773	158.05	$-x+3/2, -y+3/2, -z+1$
C5–H5A···S1	0.970	2.826	3.614	138.93	$-x+3/2, -y+1/2, -z+1$
C6–H6A···S4	0.970	2.975	3.598	123.15	

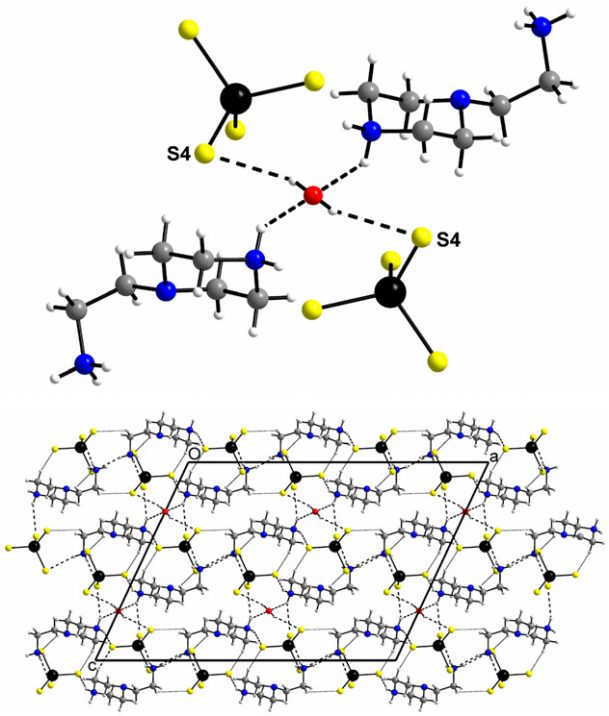


Fig. 4. Hydrogen bonding situation around the crystal water molecule in **3** showing the linking of two symmetry related cations and anions by the crystal water (top). A view of the extended H-bonded network in the crystallographic *ac*-plane, showing the formation of alternating layers (bottom). Hydrogen bonding is shown as dashed lines.

in their Raman spectrum at around 455 cm^{-1}, which can be assigned to the $\nu_1(A_1)$ vibration. The bands at around 200 and 190 cm^{-1} in the IR–Raman spectra of **1**–**4** can be assigned to the ν_4.

3.4. Comparative structural chemistry of tetrathiomolybdates

In addition to the tetrathiomolybdates **1**–**3** reported herein, several others have been structurally characterized [10–16,38–48]. The isolation of $[MoS_4]^{2-}$ anions with a variety of cations like ammonium, K^+, metal complex cations like $[Co_2(tren)_3]^{2+}$, $[Mn(dien)_2]^{2+}$, $[Ni(en)_3]^{2+}$, several organic ammonium cations like $(enH_2)^{2+}$, $(N\text{-Me-enH}_2)^{2+}$, $(dipnH_2)^{2+}$, $(1,3\text{-pnH}_2)^{2+}$, $(1,4\text{-bnH}_2)^{2+}$, $(trenH_2)^{2+}$, $(pipH_2)^{2+}$ (for the explanation of abbreviations see Table 6) tetralkylammonium cations, etc. indicates the flexibility of the MoS_4 tetrahedron to exist in different structural environments. The structural parameters of 28 tetrathiomolybdates are listed in Table 6 of which $(trenH_2)[MoS_4]\cdot H_2O$ and $(2\text{-pipH-1-EtNH}_3)[MoS_4]\cdot 1/2H_2O$ (**3**) are the only known structurally characterised hydrates and both exhibit more varieties of H-bonding interactions. A comparison reveals that the ammonium, K^+, Rb^+, Cs^+ and methylammonium tetrathiomolybdates are isostructural and crystallise in the centrosymmetric *Pnma* space group while three of the four known $[MoS_4]^{2-}$ compounds with metal complex cations crystallise in non-centrosymmetric space groups. The use of chiral amines like $[PhCH(CH_3)NH_2]$ results in tetrathiomolybdates crystallising in chiral space groups [15]. Interestingly the use of tetralkylammonium cations like $(NR_4)^+$ (R = methyl or butyl) results in non-centrosymmetric solids. It is to be noted that for the $(NEt_4)^+$ salt of $[MoS_4]^{2-}$ in addition to the reported triclinic $P\bar{1}$ form, a polymorphic $P2_12_12_1$ has been identified [41]. As observed recently for $[WS_4]^{2-}$ compounds, the $[MoS_4]^{2-}$ compounds derived from en, *N*-Me-en and dipn crystallise in non-centrosymmetric groups [22,23]. In all compounds the MoS_4 tetrahedron is slightly distorted (Table 6), which can be attributed to the cation–anion interactions. In an earlier report we had shown that the Δ value in tetrathiotungstates can be taken as a useful measure of the distortion of the WS_4 tetrahedron and a threshold value of 0.03 was estimated. A very high Δ value of 0.1541 Å was observed for $[Co(dien)]_2[MoS_4][MoOS_3]$ [42], where one of the S atoms is disordered and its position partially occupied by O resulting in a structure consisting of superimposed $[MoS_4]^{2-}$ and $[MoOS_3]^{2-}$ ions, being responsible for the unusually short Mo–S bond length. When the analysis is done keeping aside such compounds, it is observed that $(pipH_2)[MoS_4]$ [11] shows the longest Mo–S distance of 2.2114 Å as well as the maximum Δ value of 0.0431 Å, in analogy to the corresponding W compound. The average value of the Mo–S distance ranges from 2.1765 Å in $[Mn(dien)_2][MoS_4]$ [39] to 2.1921 Å in $[(n\text{-Bu})_4N]_2[MoS_4]$ [34]. In general the average Mo–S bond distance for all compounds scatters in a small range and the Δ value is around 0.02 Å. The Δ value for compound **1** is 0.0379 indicative of a distortion of the tetrahedron as evidenced by a comparison of the IR spectral bands in the Mo–S region (Fig. 5). In this analysis, a noticeable difference as compared to tetrathiotungstates is that more examples of non-centrosymmetric $[MoS_4]^{2-}$ compounds are observed.

3.5. Thermal investigations

It is well documented that ammonium tetrathiomolybdate undergoes a two-step decomposition to form MoS_2 [2,49] as shown below:

$$(NH_4)_2[MoS_4] \overset{\text{endo}}{\rightarrow} NH_3\uparrow + H_2S\uparrow + MoS_3 \overset{\text{exo}}{\rightarrow} MoS_2 + S\uparrow$$

In contrast, organic ammonium tetrathiomolybdates decompose endothermically in a single step in most cases [11,12] and the final amorphous residue always contains considerable amounts of C [50]. In a recent report we have shown that tetralkylammonium tetrathiomolybdates exhibit a complex thermal behaviour involving structural phase transitions as well as emissions of different organic fragments like disulfides and amines [50]. For the decomposition of **1**–**4** (argon atmosphere; heating rate of 4 K) no exothermic events were observed. Although the exact nature of the intermediates formed cannot be described in the absence of mass spectral data of the emitted fragments,

Table 6
Comparative structural parameters of tetrathiomolybdates

Compound	Space group	Mo–S long (Å)	Mo–S short (Å)	Difference Δ (Å)	Mo–S mean (Å)	Ref.
$(NH_4)_2[MoS_4]$	*Pnma*	2.186	2.171	0.015	2.178	[43]
$Rb_2[MoS_4]$	*Pnma*	2.1917	2.1782	0.0135	2.182	[38]
$Cs_2[MoS_4]$	*Pnma*	2.1935	2.1809	0.0126	2.1841	[45]
$K_2[MoS_4]$	*Pnma*	2.2000	2.1757	0.0243	2.1823	[46]
$(MeNH_3)_2[MoS_4]$	*Pnma*	2.1961	2.1762	0.0199	2.1841	[16]
$[Co(dien)_2]_2[MoS_4][MoOS_3]$*	$P2_1/n$	2.2041	2.050	0.1541	2.1568	[42]
$(tmenH_2)[MoS_4]$	$P2_1/n$	2.1983	2.1694	0.0289	2.1838	[12]
$(1,3\text{-}pnH_2)[MoS_4]$	$P2_1/c$	2.1882	2.1699	0.0183	2.1815	[12]
$(trenH_2)[MoS_4]\cdot H_2O$	$P2_1/c$	2.1951	2.1670	0.0281	2.1846	[11]
$(pipH_2)[MoS_4]$	$P2_1/c$	2.2114	2.1683	0.0431	2.1872	[11]
$(1,4\text{-}bnH_2)[MoS_4]$	$P\bar{1}$	2.1992	2.1749	0.0243	2.1814	[13]
$(trans\text{-}1,4\text{-}cnH_2)[MoS_4]$	$P\bar{1}$	2.1955	2.1774	0.0181	2.1865	[14]
$[(Et)_4N]_2[MoS_4]$τ	$P\bar{1}$	2.187	2.171	0.016	2.179	[44]
$(trans\text{-}1,2\text{-}cnH)_2[MoS_4]$	$C2/c$	2.1876	2.1751	0.0125	2.1814	[14]
$[(n\text{-}Pr)_4N]_2[MoS_4]$	$C2/c$	2.1928	2.1749	0.0179	2.1850	[11]
$(2\text{-}pipH\text{-}1\text{-}EtNH_3)[MoS_4]\cdot 1/2H_2O$ (**3**)	$C2/c$	2.2005	2.1703	0.0302	2.1835	this work
$[Co_2(tren)_3][MoS_4]$	*Fdd*2	2.1901	2.1631	0.0270	2.180	[39]
$[Ni(en)_3][MoS_4]$	$Pna2_1$	2.1865	2.1766	0.0099	2.1817	[34]
$[Mn(dien)_2][MoS_4]$	*I*-4	2.1765	2.1765	0.0	2.1765	[40]
$[(Me)_4N]_2[MoS_4]$#	$P2_12_12_1$	2.177	2.159	0.018	2.171	[41]
$[(n\text{-}Bu)_4N]_2[MoS_4]$	*Fdd*2	2.2047	2.1792	0.0255	2.1921	[41]
$(trienH_2)[MoS_4]$τ	$Pca2_1$	2.200	2.173	0.027	2.185	[47]
$(dabcoH)(NH_4)[MoS_4]$	$P2_13$	2.1854	2.1762	0.0092	2.1831	[48]
$(enH_2)[MoS_4]$	$P2_12_12_1$	2.1846	2.1735	0.0111	2.179	[10]
$R\text{-}[PhCH(CH_3)NH_3]_2[MoS_4]$	$P2_1$	2.2066	2.1644	0.0422	2.1840	[15]
$S\text{-}[PhCH(CH_3)NH_3]_2[MoS_4]$	$P2_1$	2.2056	2.1655	0.0401	2.1831	[15]
$(N\text{-}Me\text{-}enH_2)[MoS_4]$ (**1**)	$P2_12_12_1$	2.2014	2.1635	0.0379	2.1861	this work
$(dipnH_2)[MoS_4]$ (**2**)	$Pca2_1$	2.1903	2.1717	0.0186	2.1818	this work

Abbreviations used: $MeNH_2$ = methylamine; dien = bis(2-aminopropylamine); tmen = *N*,*N*,*N*′,*N*′-tetramethylethylenediamine; 1,3-pn = 1,3-propanediamine; tren = tris(2-aminoethyl)amine; pip = piperazine; 1,4-bn = butane-1,4-diamine; *trans*-1,4-cn = *trans*-1,4-diaminocyclohexane; Et = ethyl; *trans*-1,2-cn = *trans*-1,2-diaminocyclohexane; *n*-Pr = *n*-propyl; en = ethylenediamine; Me = methyl; *n*-Bu = *n*-butyl; trien = triethylenetetramine; dabco = 1,4-diazabicyclo-2,2,2-octane; $[PhCH(CH_3)NH_2]$ = α-methylbenzylamine. *One S atom is disordered. τTwo crystallographically independent $[MoS_4]^{2-}$ units; #three crystallographically independent $[MoS_4]^{2-}$ units. The cations are disordered; for compounds with more than one independent $[MoS_4]^{2-}$ units the parameters are listed for that unit which shows maximum Δ.

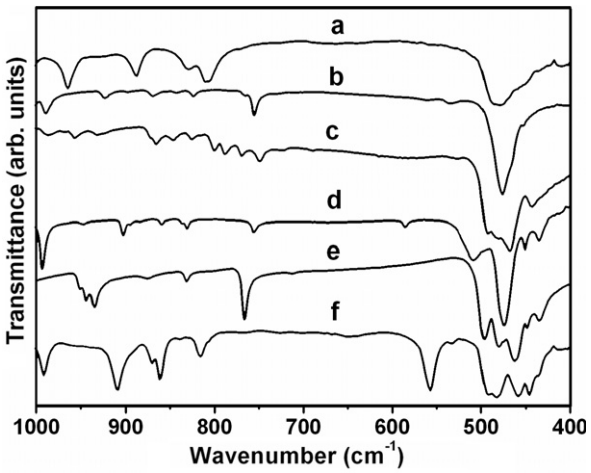


Fig. 5. IR spectra of (a) $(enH_2)[MoS_4]$, (b) $(dipnH_2)[MoS_4]$, (c) $(dienH_2)[MoS_4]$, (d) $(2\text{-}pipH\text{-}1\text{-}EtNH_3)[MoS_4]\cdot 1/2H_2O$, (e) $(N\text{-}Me\text{-}enH_2)[MoS_4]$, (f) $(pipH_2)[MoS_4]$ showing asymmetric stretching vibration (ν_3).

it is interesting to note that the thermal patterns exhibit a common trend. The decomposition temperatures and the composition of the final sulfide residues are collected in Table 7. The composition of the residues is in good agreement with that derived from EDX analysis. The X-ray powder patterns of the final C and N containing molybdenum sulfide residues of **1**–**4** showed only broad humps indicating their amorphous nature.

Compound **1** exhibits two endothermic events at 124 and 153 °C, assignable to the decomposition of the organic cation as well as tetrathiomolybdate. The total mass loss up to 600 °C is 37.6%. The elemental analysis of the final product showed the presence of C and N and can be formulated as $MoS_{2.3}C_{1.3}N_{0.4}$. For **2** the endothermic signal at 73 °C can be attributed to a phase transition and a similar behaviour was observed recently for tetralkylammonium thiomolybdates [50]. Compound **2** is thermally stable up to 116 °C and its decomposition is evidenced by the two endothermic events at 136 and 194 °C. The total mass loss up to 600 °C is 50.5% and is higher than expected for the loss of dipn and H_2S only (46.3%). The analysis of the residue is indicative of incomplete removal of organics.

In the TG–DTA curve of **3** (Fig. 6), the first mass loss around 100 °C, is accompanied by an endothermic peak at 107 °C. The mass loss of 2.68% and is in very good agreement for the loss of half mole of water (expected is 2.47%). The anhydrous compound thus formed starts

Table 7
Thermal characterization data for **1**–**4**

Complex	DTA temp (°C)	TG mass loss (%)	Elemental analysis of residue (%)	Final residue
(N-Me-enH_2)[MoS_4] (**1**)	124 endo 153 endo	37.60	C 8.15 H 0.25 N 3.19 S 37.97	$MoS_{2..3}C_{1.3}N_{0.4}$
(dipnH_2)[MoS_4] (**2**)	136 endo 183 endo	50.51	C 6.79 H 0.27 N 1.69 S 37.66	$MoS_{2.1}C_{1.01}N_{0.2}$
(2-pipH-1-EtNH_3)[MoS_4] · 1/2H_2O (**3**)	107 endo 160 endo	2.68 41.75	C 14.79 H 0.47 N 5.07 S 29.45	$MoS_{1.7}C_{2.4}N_{0.7}$
(dienH_2)[MoS_4] (**4**)	153 endo 187 endo	37.68	C 13.03 H 0.61 N 4.67 S 34.32	$MoS_{2.2}C_{2.2}N_{0.7}$

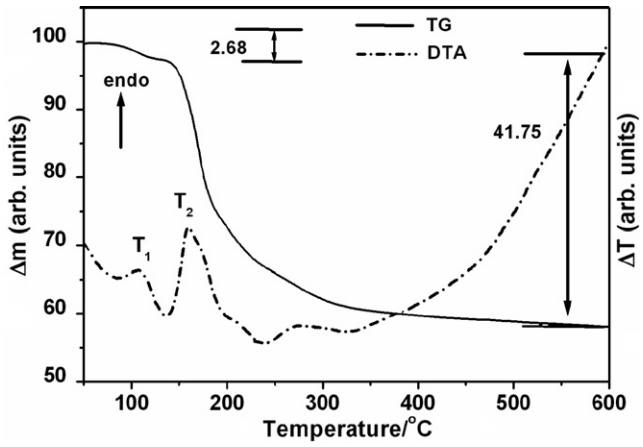


Fig. 6. TG and DTA curves for (2-pipH-1-EtNH_3)[MoS_4] · 1/2H_2O (**3**) (heating rate 4 K/min; Ar atmosphere; $T_1 = 107$ and $T_2 = 160$ °C are peak temperatures).

decomposing endothermically as evidenced by the signal at 160 °C and a sharp mass drop in the TG curve. A total mass loss of 44.43% up to 600 °C is quite less than expected for the removal of water, amine and H_2S (47.27%). Based on analytical data the residue can be formulated as $MoS_{1.7}C_{2.3}N_{0.7}$. The Mo:S ratio is 1:1.7 instead of 1:2 indicating the presence of some structural C. Compound **4**, which exhibits two endothermic events at 153 and 187 °C, is stable up to about 130 °C and decomposes with a total mass loss of 37.68% up to 500 °C, which is lower than expected for the emission of dien and H_2S (41.66%). The elemental analysis of the residue indicates $MoS_{2.2}C_{2.2}N_{0.7}$ as composition.

4. Conclusions

The organic ammonium tetrathiomolybdates **1**–**4** were synthesized by an aqueous reaction of $(NH_4)_2[MoS_4]$ with the corresponding organic amines. All the compounds were characterised by elemental analysis, spectroscopy methods, and the structures of **1**–**3** were determined. In compounds **2**–**4** the triamines are partially protonated forming dications. The characterization of such compounds demonstrates the ability of $[MoS_4]^{2-}$ to stabilise partially protonated organic ammonium cations. A comparative study of structural data of several tetrathiomolybdates highlights, that in most of the compounds the average Mo–S bond length scatters in a relatively narrow range, i.e. this structural parameter cannot be regarded as a good measure of the actual distortion of the anions. A more sensitive parameter is the difference Δ between the longest and shortest Mo–S bonds. Above a critical value for Δ the symmetry of the MoS_4 tetrahedron is reduced which is reflected by the appearance of extra signals in the Mo–S region of the infrared spectrum. The compounds **1**–**4** decompose endothermically and the resulting decomposition products are amorphous carbon contaminated metal sulfides with compositions $MoS_{2.3}C_{1.3}N_{0.4}$, $MoS_{2.1}C_{1.01}N_{0.2}$, Mo- $S_{1.7}C_{2.4}N_{0.7}$ and $MoS_{2.2}C_{2..2}N_{0.7}$, respectively.

Acknowledgements

B.R.S. thanks the Department of Science and Technology (DST), New Delhi, for financial support under Grant No. SR/S1/IC-41/2003. B.R.S. and W.B. thank the DST, New Delhi and Deutscher Akademischer Austauschdienst (DAAD) Bonn, for the sanction of a DST-DAAD (PPP) project.

Appendix A. Supplementary material

CCDC 651723, 651724, 651725 contain the supplementary crystallographic data for **1**, **2** and **3**. These data can be obtained free of charge via http://www.ccdc.cam.ac.uk/conts/retrieving.html, or from the Cambridge Crystallographic Data Centre, 12 Union Road, Cambridge

CB2 1EZ, UK; fax: (+44) 1223-336-033; or e-mail: deposit @ccdc.cam.ac.uk. Supplementary data associated with this article can be found, in the online version, at doi:10.1016/j.poly.2007.08.023.

References

[1] S.E. Skrabalak, K.E. Suslick, J. Am. Chem. Soc. 127 (2005) 9990.
[2] A. Müller, E. Diemann, R. Jostes, H. Bögge, Angew. Chem., Int. Ed. Engl. 20 (1981) 934.
[3] D. Coucouvanis, Adv. Inorg. Chem. 45 (1998) 1.
[4] K.R. Prabhu, N. Devan, S. Chandrasekaran, Synlett (2002) 1762.
[5] J.P. Lang, H. Nawaguchi, K. Tatsumi, J. Chem. Soc., Dalton Trans. (2002) 2573.
[6] E.D. Simhon, N.C. Baenziger, M. Kanatzidis, M.D. Coucouvanis, J. Am. Chem. Soc. 103 (1981) 1218.
[7] W.H. Pan, M.E. Leonowicz, E.I. Stiefel, Inorg. Chem. 22 (1983) 672.
[8] W.H. Pan, M.A. Harmer, T.R. Halbert, E.I. Stiefel, J. Am. Chem. Soc. 106 (1984) 459.
[9] C. McConnachie, E.I. Stiefel, Inorg. Chem. 38 (1999) 964.
[10] B.R. Srinivasan, B.K. Vernekar, K. Nagarajan, Indian J. Chem. 40A (2001) 563.
[11] B.R. Srinivasan, S.N. Dhuri, M. Poisot, C. Näther, W. Bensch, Z. Naturforsch. 59b (2004) 1083.
[12] B.R. Srinivasan, S.N. Dhuri, C. Näther, W. Bensch, Inorg. Chim. Acta 358 (2005) 279.
[13] B.R. Srinivasan, C. Näther, W. Bensch, Acta Crystallogr. E61 (2005) m2454.
[14] B.R. Srinivasan, C. Näther, W. Bensch, Acta Crystallogr. C62 (2006) m98.
[15] B.R. Srinivasan, A.R. Naik, C. Näther, W. Bensch, Z. Anorg. Allg. Chem. 633 (2007) 582.
[16] B.R. Srinivasan, A.R. Naik, C. Näther, W. Bensch, Acta Crystallogr. E62 (2006) m1635.
[17] B.R. Srinivasan, S.N. Dhuri, C. Näther, W. Bensch, Transition Met. Chem. 32 (2007) 64.
[18] B.R. Srinivasan, S.N. Dhuri, C. Näther, W. Bensch, Acta Crystallogr. E58 (2002) m622.
[19] B.R. Srinivasan, S.N. Dhuri, C. Näther, W. Bensch, Acta Crystallogr. C59 (2003) m124.
[20] B.R. Srinivasan, S.N. Dhuri, C. Näther, W. Bensch, Acta Crystallogr. E59 (2003) m681.
[21] B.R. Srinivasan, S.N. Dhuri, M. Poisot, C. Näther, W. Bensch, Z. Anorg. Allg. Chem. 631 (2005) 1087.
[22] B.R. Srinivasan, C. Näther, S.N. Dhuri, W. Bensch, Monats. Chem. 137 (2006) 397.
[23] B.R. Srinivasan, C. Näther, S.N. Dhuri, W. Bensch, Polyhedron 25 (2006) 3269.
[24] B.R. Srinivasan, A.R. Naik, C. Näther, W. Bensch, Acta Crystallogr. E62 (2006) m3491.
[25] U. Siemeling, F. Bretthauer, C. Bruhn, Z. Anorg. Allg. Chem. 632 (2006) 1027.
[26] S. Pokrel, K.S. Nagaraja, B. Varghese, J. Chem. Cryst. 35 (2003) 903.
[27] J.W. McDonald, G.D. Friesen, L.D. Rosenhein, W.E. Newton, Inorg. Chim. Acta 72 (1983) 205.
[28] G.M. Sheldrick, SHELXS-97 and SHELXL-97 Programs for Crystal Structure Solution and Refinement, University of Göttingen, Germany, 1997.
[29] B.R. Srinivasan, S.N. Dhuri, A.R. Naik, Tetrahedron Lett. 45 (2004) 2247.
[30] B.R. Srinivasan, J. Chem. Sci. 116 (2004) 251.
[31] W.E. Marzluff, Inorg. Chem. 3 (1964) 395.
[32] F.A. Cotton, R.C. Elder, Inorg. Chem. 3 (1964) 397.
[33] R.S. Taylor, P. Gans, P.F. Knowles, A.G. Sykes, J. Chem. Soc., Dalton 24 (1972).
[34] J. Ellermeier, C. Näther, W. Bensch, Acta Crystallogr. C55 (1999) 501.
[35] A. Bondi, J. Phys. Chem. 68 (1964) 441.
[36] K. Nakamoto, Infrared and Raman Spectra of Inorganic and Coordination Compounds, fifth ed., John Wiley, New York, 1997, p. 189.
[37] K.H. Schmidt, A. Müller, Coord. Chem. Rev. 14 (1974) 115.
[38] J. Ellermeier, C. Näther, W. Bensch, Acta Crystallogr. C55 (1999) 1748.
[39] J. Ellermeier, W. Bensch, Z. Naturforsch. 56b (2001) 611.
[40] J. Ellermeier, W. Bensch, Monatsh. Chem. 133 (2002) 945.
[41] M. Poisot, C. Näther, W. Bensch, Z. Naturforsch. 62b (2007) 209.
[42] M. Poisot, C. Näther, W. Bensch, Acta Crystallogr. E62 (2006) m1326.
[43] P.J. Lapasset, N. Chezeu, P. Belougne, Acta Crystallogr. B32 (1976) 3087.
[44] M.G. Kanatzidis, D. Coucouvanis, Acta Crystallogr. C39 (1983) 835.
[45] C.C. Raymond, P.K. Dorhout, S.M. Miller, Z. Kristallogr. 210 (1995) 775.
[46] M. Emirdag-Eanes, J.A. Ibers, Z. Kristallogr. New Cryst. Struct. 216 (2001) 484.
[47] S. Pokrel, K.S. Nagaraja, B. Varghese, J. Struct. Chem. 44 (2003) 689.
[48] S. Pokrel, K.S. Nagaraja, B. Varghese, J. Struct. Chem. 45 (2004) 900.
[49] T.P. Prasad, E. Diemann, A. Müller, J. Inorg. Nucl. Chem. 35 (1973) 1895.
[50] M. Poisot, W. Bensch, S. Fuentus, G. Alonso, Theromochim. Acta 444 (2006) 35.

Available online at www.sciencedirect.com
ScienceDirect
Polyhedron 27 (2008) 35–43
POLYHEDRON
www.elsevier.com/locate/poly

Spectral and structural studies of nickel(II) complexes of salicylaldehyde 3-azacyclothiosemicarbazones

Leji Latheef, Maliyeckal R. Prathapachandra Kurup *

Department of Applied Chemistry, Cochin University of Science and Technology, Kochi 682 022, Kerala, India

Received 12 June 2007; accepted 17 August 2007
Available online 24 October 2007

Abstract

Mononuclear nickel(II) complexes with two ONS donor thiosemicarbazone ligands {salicylaldehyde 3-hexamethyleneiminyl thiosemicarbazone [H_2L^1] and salicylaldehyde 3-tetramethyleneiminyl thiosemicarbazone [H_2L^2]} have been prepared and physico-chemically characterized. IR and electronic spectra of the complexes have been obtained. The thiosemicarbazones bind to the metal as dianionic ONS donor ligands in all the complexes except in $[Ni(HL^1)_2]$ (**1**). In compound **1**, the ligand is coordinated as a monoanionic (HL^-) one. The magnetic susceptibility measurements indicate that all the complexes are mononuclear and are diamagnetic. The complexes were given the formulae $[Ni(HL^1)_2]$ (**1**), $[NiL^1py]$ (**2**), $[NiL^1\alpha\text{-pic}]$ (**3**), $[NiL^1\gamma\text{-pic}]\cdot H_2O$ (**4**), $[NiL^2py]$ (**5**) and $[NiL^2\gamma\text{-pic}]$ (**6**). The structures of compounds **2** and **3** have been solved by single crystal X-ray crystallography and were found to be distorted square planar in geometry with coordination of azomethine nitrogen, thiolato sulfur, phenolato oxygen and pyridyl nitrogen atoms.
© 2007 Elsevier Ltd. All rights reserved.

Keywords: Thiosemicarbazone; Nickel(II) complex; Salicylaldehyde; Crystal structure

1. Introduction

The coordination chemistry of thiosemicarbazones with transition metals [1–4], which began with Jensen's work [5], has been more intensively investigated as compared to that of main group elements [6,7]. Thiosemicarbazones are an important group of multidentate ligands with potential binding sites available for a wide variety of metal ions [8–10]. These thiourea derivatives find substantial applications in different facets of contemporary scientific research. Thiosemicarbazones and their metal complexes are a broad class of biologically active compounds [4]. Due to this biological activity, there is considerable interest in metal complexes of heterocyclic thiosemicarbazones [4]. Nickel(II) complexes containing sulfur donors have received considerable attention due to the identification of a sulfur rich coordination environment in biological nickel centres, such as the active sites of certain ureases, methyl-*S*-coenzyme-M-methyl reductase and hydrogenases [11].

Spectral and, in some complexes, structural investigations of a series of nickel(II) complexes of ONS donor thiosemicarbazones [12–16] have been reported earlier. The thiosemicarbazone ligand usually coordinates with the metal through the imine nitrogen and sulfur atom. The ligands feature more than two covalent sites, the number of which depends on the aldehyde and on the tautomeric equilibrium of the thiosemicarbazone, although the most common way to coordinate is through the thiolate form [17]. We have reported Cu(II) [18] and Zn(II) [19] complexes of the present thiosemicarbazone ligands recently. Here, we report six mononuclear nickel (II) complexes of salicylaldehyde 3-hexamethyleneiminyl and 3-tetramethyleneiminyl thiosemicarbazones. These complexes were characterized by IR, electronic and magnetic data.

* Corresponding author. Tel.: +91 484 2575804; fax: +91 484 2577595.
E-mail address: mrp@cusat.ac.in (M.R. Prathapachandra Kurup).

0277-5387/$ - see front matter © 2007 Elsevier Ltd. All rights reserved.
doi:10.1016/j.poly.2007.08.048

2. Experimental

2.1. Materials

All the solvents used for the synthesis of the thiosemicarbazone ligands and their complexes were purified by distillation. Pyridine, α/β/γ-picoline, $Ni(OAc)_2 \cdot 4H_2O$ (Central drug house) were used as received. 4-Methyl-4-phenyl-3-thiosemicarbazide was prepared as reported previously [20].

2.2. Synthesis of the ligands

H_2L^1 was prepared using a reported procedure [21]. H_2L^2 was prepared as described by adapting the reported procedure [20,21]. A solution of 4-methyl-4-phenyl thiosemicarbazide (1 g, 5.52 mmol) in acetonitrile (5 ml) was treated with salicylaldehyde (0.60 ml, 5.52 mmol) and pyrrolidine (0.50 ml, 5.52 mmol) and refluxed for 20 min. The solution was allowed to cool and the fine colorless needles of the compound separated out. It was filtered off, washed with cold acetonitrile and dried *in vacuo* over P_4O_{10}. The compound was recrystallized from methanol. The structures of the two ligands are given in Scheme 1.

2.3. Synthesis of complexes

Complex **1** was prepared by refluxing an ethanolic solution of H_2L^1 with a methanolic solution of $Ni(OAc)_2 \cdot 4H_2O$ in a 2:1 molar ratio for 4 h. The brown colored complex that formed was filtered, washed with ethanol and then with ether and dried over P_4O_{10} *in vacuo*. The complexes **2**–**6** were prepared by refluxing an ethanolic solution of the corresponding ligands and heterocyclic bases with a methanolic solution of $Ni(OAc)_2 \cdot 4H_2O$ in a 1:1:1 molar ratio. The complexes that separated were filtered, washed with ethanol and finally with ether and dried over P_4O_{10} *in vacuo*. Crystals suitable for X-ray analysis for compounds **2** and **3** were obtained by slow evaporation of solutions of the compounds from an ethanol methanol mixture (1:1 v/v) over 10 days.

The colors and analytical data of the complexes, elemental analysis and magnetic susceptibilities are presented in Table 1.

2.4. Physical measurements

Elemental analyses were carried out using a Vario EL III CHN analyzer at SAIF, Kochi, India. Magnetic susceptibility measurements were carried out at IIT, Roorkee, India, at 298 K in the polycrystalline state on a PAR model 155 Vibrating sample magnetometer at 5 kOe field strength using $Hg[Co(SCN)_4]$ as a calibrant. The FT-IR spectra were recorded on a Thermo Nicolet AVATAR 370 DTGS FTIR spectrometer using KBr pellets in the range 400–4000 cm^{-1} at SAIF, Cochin University of Science and Technology, Kochi 22, India, and far IR spectra were recorded in the range 50–500 cm^{-1} on a Nicolet Magna 550 FT-IR spectrophotometer using polyethylene pellets at SAIF, IIT, Bombay, India. Electronic spectra were recorded on a UVD-3500 UV–VIS-Double beam Spectrophotometer from solutions in DMF. ^1H NMR spectra were recorded on a Bruker AMX 300 in $CDCl_3$ with TMS as an internal standard.

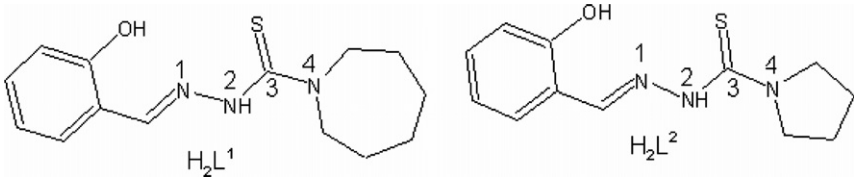
Table 1
Stoichiometries, colors and partial elemental analysis of complexes

Compound	*Anal.* Found (Calc.) (%)		
	C	H	N
$[Ni(HL^1)_2]$ (**1**)	55.9(55.30)	6.36(5.93)	14.04(13.74)
$[NiL^1py]$ (**2**)	55.20(55.23)	5.35(5.37)	13.55(13.56)
$[NiL^1\alpha\text{-pic}]$ (**3**)	56.21(56.23)	5.63(5.66)	13.11(13.12)
$[NiL^1\gamma\text{-pic}] \cdot H_2O$ (**4**)	54.11(53.90)	6.02(5.89)	12.59(12.58)
$[NiL^2py]$ (**5**)	53.12(53.02)	4.57(4.71)	14.42(14.55)
$[NiL^2\gamma\text{-pic}]$ (**6**)	54.02(54.16)	5.70(5.05)	14.16(14.04)

2.5. X-ray crystallography

Reddish brown crystals of compounds **2** and **3**, having approximate dimensions of $0.26 \times 0.21 \times 0.17$ and $0.35 \times 0.30 \times 0.20$ mm^3, respectively, were selected. The crystal data for compounds **2** and **3** were collected by CrysAlis CCD, Oxford Diffraction Ltd. with graphite-monochromated Mo Kα ($\lambda = 0.71073$ Å) radiation. In compound **2**, the atom C10 in the ring containing N3 is disordered as this carbon splits over two sets of positions. Restraints were applied to assist the geometry of the disordered atom. The ratio of major to minor disorder components for the C10 atom is 54:46. Compound **3** similarly has some disorder in the 7-membered ring. Even though refinement with restraints was applied to the 7-membered ring, the problems of the weak data could not be improved further. In spite of several attempts, we were unable to isolate single crystals of good quality.

In both of these compounds restraints were applied to assist the geometry of the disordered atoms. The trial structure was solved using SHELXS-97 [22] and refinement was



Scheme 1. The thiosemicarbazones H_2L^1 and H_2L^2.

Table 2
Crystal data for compounds **2** and **3**

	(**2**)	(**3**)
Empirical formula	$C_{19}H_{22}N_4NiOS$	$C_{20}H_{24}N_4NiOS$
Formula weight	826.35	427.20
Temperature (K)	150(2)	150(2)
Wavelength (Å)	0.71073	0.71073
Crystal system	orthorhombic	monoclinic
Space group	*Pbca*	$P2_1/a$
Unit cell dimensions		
a (Å)	13.7965(19)	10.567(3)
b (Å)	21.954(4)	10.933(3)
c (Å)	25.410(5)	17.439(6)
α (°)	90	90
β (°)	90	100.42(3)
γ (°)	90	90
Volume (Å^3)	7696(2)	1981.5(10)
Z	16	4
D_{calc} (g/cm^3)	1.426	1.432
Absorption coefficient (mm^{-1})	1.132	1.102
F(000)	3456	896
Crystal size (mm^3)	0.26 × 0.21 × 0.17	0.35 × 0.30 × 0.20
θ Range for data collection (°)	2.95–25	3.02–2
Index ranges	$-16 \leqslant h \leqslant 16$, $-26 \leqslant k \leqslant 25$, $-30 \leqslant l \leqslant 19$	$-12 \leqslant h \leqslant 12$, $-13 \leqslant k \leqslant 12$, $-20 \leqslant l \leqslant 20$
Reflections collected	37350	17298
Independent reflections (R_{int})	6769 (0.0865)	3476 (0.1093)
Refinement method	full-matrix on F^2	full-matrix on F^2
Data/restraints/parameters	6769/0/479	3476/52/232
Goodness-of-fit on F^2	0.761	0.787
Final *R* indices [$I > 2\sigma(I)$]	$R_1 = 0.0362$, $wR_2 = 0.0636$	$R_1 = 0.0600$, $wR_2 = 0.1418$
R indices (all data)	$R_1 = 0.1028$, $wR_2 = 0.0732$	$R_1 = 0.1798$, $wR_2 = 0.1691$

carried out by full-matrix least squares on F^2 (SHELXL) [22]. The molecular and crystal structures are illustrated by DIAMOND version 3.1d [23] and MERCURY [24]. All non-hydrogen atoms were refined anisotropically and hydrogen atoms were geometrically fixed at calculated positions. The crystallographic data and structure refinement parameters for the complexes are given in Table 2.

3. Results and discussion

The elemental analyses data are consistent with the general empirical formula $[M(HL)_2]$ for **1**, MLB for **2**, **3**, **4**, **5** and **6** where M is the nickel metal atom, L is the doubly deprotonated thiosemicarbazone ligand and B is the heterocyclic bases *viz.* py and α/β/γ pic. All the nickel complexes are reddish brown in color, which is common for complexes involving thiosemicarbazone coordination, resulting from the sulfur to metal charge transfer bands [25]. The complexes are insoluble in most common solvents. They are however soluble in DMF and DMSO.

The room temperature magnetic moments of the Ni(II) complexes suggest that they are all essentially diamagnetic. For the d^8 electronic configuration, diamagnetism generally implies that the metal ion has a square-planar configuration. The electronic spectra of the complexes in DMF solution are not well resolved owing to very intense charge transfer bands extending into the visible portion of the spectra.

3.1. Crystal structure of the compound [NiL^{1}py] and [NiL^{1}α-pic]

The molecular structures of [NiL^{1}py] (**2**) and [NiL^{1}α-pic] (**3**) along with the atom labelling schemes are shown in Figs. 1 and 2, and selected bond lengths and bond angles are summarized in Table 3. The ligand H_2L^1 gets doubly deprotonated to behave as an ONS tridentate ligand, coordinating *via* its phenolato oxygen, azomethine nitrogen and thiolate sulfur atom in the deprotonated form after thiol formation, giving a distorted square planar geometry around the nickel atom. The fourth coordination site is occupied by the nitrogen atom from the heterocyclic bases. The *E* configuration of the thiosemicarbazone chain about the C7–N1 bond is retained to facilitate the coordination of the thiolate sulfur to Ni in the two complexes. This reveals that no rotation has occurred about the azomethine bond for coordination. The coordination results in one 5-membered and one 6-membered chelate ring in the two complexes.

Compound **2** crystallizes with two monomers per asymmetric unit in the orthorhombic crystal system. The two molecules in the asymmetric unit are almost identical. So the discussion can be limited to one of the molecules. The Ni1 coordination is almost square planar with a maximum mean deviation of the coordinating atoms (phenolic oxygen O1, azomethine nitrogen N1, thiolate sulfur S1 and

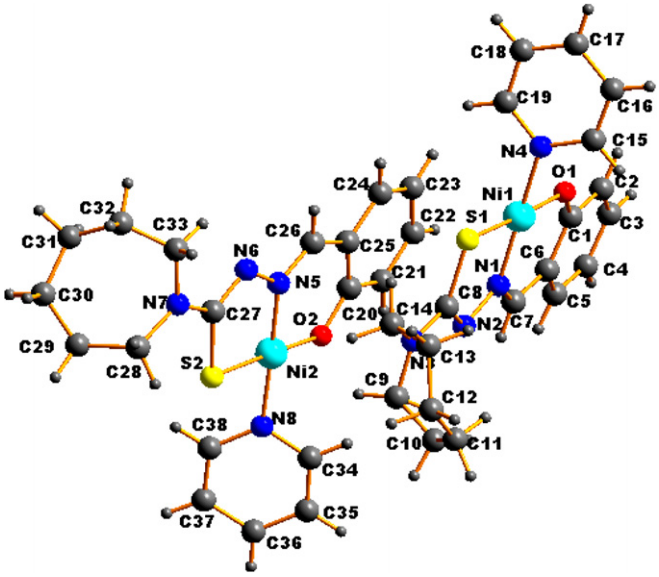


Fig. 1. Molecular structure of compound **2**.

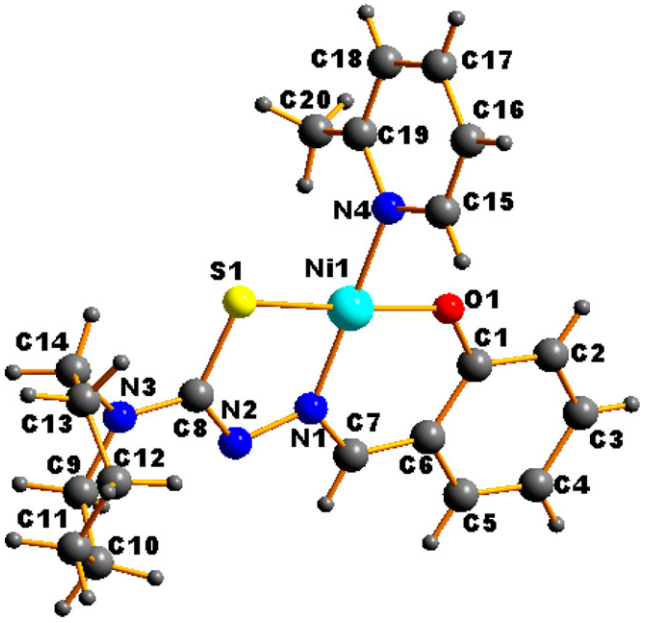


Fig. 2. Molecular structure of compound **3**.

pyridyl nitrogen N4) from their own plane of 0.0103 Å for N4. The thiosemicarbazonato moiety, C7–N1–N2–C8–S1–N3, also is almost planar and has a maximum mean plane deviation of 0.037(4) Å and an angle of 2.86(6)° to the plane of the four donor atoms, while the phenyl ring has an angle of 6.29(10)° to the donor plane of compound **2** indicating that the thiosemicarbazone moieties are close to coplanar with the nickel's coordination plane. Ring puckering analysis and least-square plane calculations show that the Cg(5) ring comprising of atoms N3, C9, C10, C11, C12, C13 and C14, and the Cg(10) ring comprising of atoms N7, C28, C29, C30, C31, C32 and C33 adopt a chair conformation [$Q_T = 0.696(6)$ Å (Cg(5)) and $Q_T = 0.650(6)$ Å (Cg(10))].

The bond angles O1–Ni1–N1 [96.16(12)°], O1–Ni1–N4 [85.35(11)°] and N1–Ni1–S1 [87.08(10)°] also reveal the distortion of the square plane comprising of Ni1, O1, S1, N1 and N4. The dihedral angle formed by the least square planes Cg(1) comprising of atoms Ni1, S1, N1, N2 and C8, and Cg(2) comprising of atoms Ni1, O1, N1, C1, C6 and C7 is 3.47(12)°. The C7–N1 bond distance of 1.305(4) Å lengthens compared to the corresponding C7–N1 bond distance (1.269(3) Å) in the ligand. The delocalization of electron density from the coordinating nitrogen onto the central metal atom gives rise to an elongated N1–N2 bond length (1.406(3) Å) compared to the uncomplexed thiosemicarbazone (1.356(3) Å). Also, the C7–N1–N2 bond angle decreases considerably compared to the ligand H_2L^1. The loss of the proton bound to N2 in H_2L^1 produces a negative charge which is delocalized on the N1–N2–C8 system. This is indicated by the lengthening of the bond C8–S1, 1.753(4) Å, compared to the value of 1.684(3) Å in the ligand. This thiolate formation is also supported by the decrease in bond length of N2–C8, 1.304(4) Å from the value of 1.362(3) Å found in the uncomplexed thiosemicarbazone. The bond angles O1–Ni1–N4 [85.35(11)°] and S1–Ni1–N1 [87.08(10)°] are also analogous, as expected on the basis of the similar square planar nature for all the complexes. Coordination of O1 results in O1–C1 decreasing by approximately 0.04–0.05 Å.

Compound **3** crystallizes with only one monomer per asymmetric unit in the monoclinic crystal system. The bond angles N1–Ni1–O1 [96.5(2)°], O1–Ni1–N4 [87.56(19)°] and N1–Ni1–S1 [86.77(19)°] reveal the distortion of the square planar geometry. The dihedral angle formed by the least square planes Cg(1) comprising of atoms Ni1, S1, N1, N2 and C8, and Cg(2) comprising of atoms Ni1, O1, N1, C1, C6 and C7 is 0.6(2)°. Similar to compound **2**, the

Table 3
Comparison of selected bond lengths (Å) and bond angles (°) for H_2L^1, **2** and **3**

	H_2L^{1a}	2	3
Bond lengths			
Ni1–O1		1.837(2)	1.859(4)
Ni1–N1		1.848(3)	1.847(5)
Ni1–N4		1.907(3)	1.906(4)
Ni1–S1		2.134(11)	2.151(2)
Ni2–O2		1.848(2)	
Ni2–N5		1.859(3)	
Ni2–N8		1.925(3)	
Ni2–S2		2.132(11)	
S1–C8	1.684(3)	1.753(4)	1.759(6)
S2–C27		1.752(4)	
N1–C7	1.269(3)	1.305(4)	1.320(7)
N1–N2	1.356(3)	1.406(3)	1.393(6)
N2–C8	1.362(3)	1.304(4)	1.302(7)
N3–C8		1.350(4)	1.362(7)
N4–C19		1.326(4)	1.388
N4–C15		1.327(4)	1.392
N5–C26		1.302(4)	
N5–N6		1.400(4)	
N6–C27		1.293(4)	
N7–C27		1.357(4)	
N8–C34		1.340(4)	
N8–C38		1.343(4)	
Bond angles			
O1–Ni1–N1		96.56(12)	96.5(2)
O1–Ni1–N4		85.35(11)	87.56(19)
N1–Ni1–N4		177.87(12)	174.4(2)
O1–Ni1–S1		176.35(8)	176.71(14)
N1–Ni1–S1		87.08(10)	86.77(19)
N4–Ni1–S1		91.01(8)	89.17(15)
O2–Ni2–N5		95.75(12)	
O2–Ni2–N8		86.96(11)	
N5–Ni2–N8		177.26(14)	
O2–Ni2–S2		176.83(8)	
N5–Ni2–S2		87.15(11)	
N8–Ni2–S2		90.16(9)	
C8–S1–Ni1		96.57(13)	95.8(3)
C27–S2–Ni2		96.11(16)	
C7–N1–N2	120.0(2)	113.3(3)	112.4(5)
N2–N1–Ni1		122.8(2)	123.8(4)
C26–N5–N6		113.6(3)	
C26–N5–Ni2		124.0(3)	
N6–N5–Ni2		122.4(2)	
C26–N5–N6		113.6(3)	

[a] Ref. [17].

C7–N1 bond length increases compared to the ligand. Thus on complexation, the azomethine C–N bond lengthens because of coordination of the azomethine nitrogen. Coordination lengthens the thiosemicarbazone moiety's C8–S1 bond length to 1.759(6) Å and shortens the N2–C8 bond length to 1.302(7) Å. The maximum deviation from the least square planes around the Ni(II) ion is 0.0626(5) Å for N1. The thiosemicarbazonato moiety, C7–N1–N2–C8–S1–N3, is almost planar with a maximum mean deviation of 0.028(6) for N2 and is at an angle of 1.46(9)° to the plane of the four donor atoms, while the dihedral angle formed by the phenyl ring is 1.95(2)° to the donor plane. The hexamethyleneiminyl ring adopts a chair conformation [$Q_T = 0.7269$ Å].

The dihedral angles formed by the least square planes Cg(1) and Cg(2) for the compounds support the distorted square planar conformation for these complexes, where greater distortion is observed for compound **2**. This small deviation from coplanarity would certainly not hinder the delocalization of electrons in the coordination sphere, and the stability of the complex is sustained.

The Ni–$N_{azomethine}$ bond lengths are shorter compared to the Ni–N_{base} bond lengths, indicating greater strength of the former bonds compared to the latter in the two complexes. The O1–Ni1–N1 bond angles are slightly greater compared to the similar Ni(II) ONS donor complexes [Ni(PTSC)(PPh_3)] 95.32(9)°, [Ni(PTSC)(PPh_3)].$CHCl_3$, 95.4(1)° [12] and [Ni($C_{18}H_{18}N_6O_2S_2$)](ClO_4)$_2 \cdot 2CH_4O$, 83.64(12)° [26], and the N1–Ni1–S1 bond angles are comparable. The N1–Ni1–S1 bond angles are greater compared to [Ni(Et-fbt)$_2$], 85.35(11)°, [Ni(fbt)$_2$], 84.90(10)° [27] and [Ni(NQTS)$_2$] · 2DMSO 81.47(16)° [28]. The C–$N_{azomethine}$ bond length is shorter compared to other C–N_{py} bond lengths in the complexes. This indicates that the bonding is dominated by the thiosemicarbazone moiety.

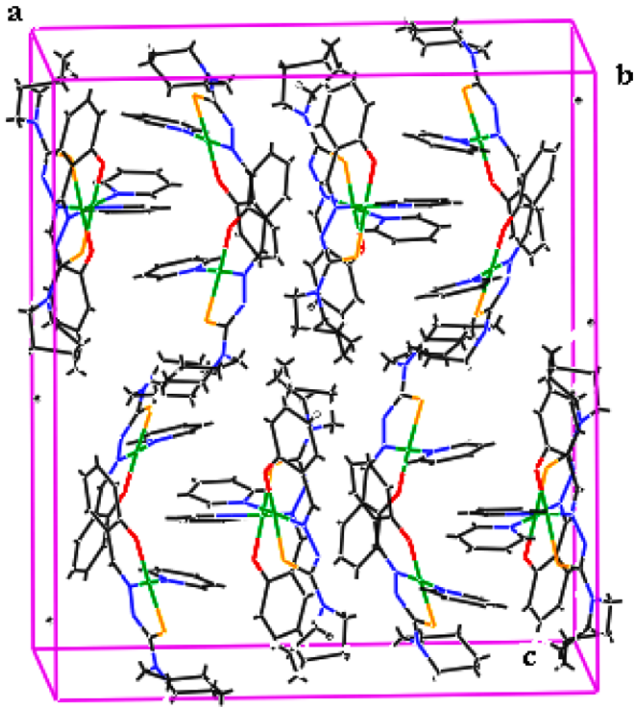


Fig. 3. Unit cell packing diagram of compound **2**.

In compound **2**, adjacent molecules are arranged in an offset manner within the unit cell when viewed along the *a* axis, as seen in Fig. 3, as a result of diverse π–π stacking, CH–π and hydrogen bonding interactions (Table 4).

The molecules of **3** are connected by various hydrogen bonding interactions and are arranged parallel along the *a* axis (Fig. 4). Though π–π interactions exist in the lattice of compound **3**, they are observed at distances greater than 4.0 Å, also there are no effective CH–π interactions (Table 5). adjacent molecules are arranged opposing directions within the unit cell.

3.2. Infrared spectra

The characteristic IR bands (50–4000 cm^{-1}) for the four free ligands differ from those of their complexes and pro-

Table 4
Interaction parameters of compound **2**

Cg(I)-Res 1···Cg (J)	Cg–Cg (Å)	α (°)	β (°)
π–π interactions			
Cg(1) [1] → Cg(9)[a]	3.747(2)	3.28	25.77
Cg(2) [1] → Cg(9)[a]	3.624(2)	6.74	24.05
Cg(3) [1] → Cg(8)[b]	3.856(2)	17.19	27.64
Cg(8) [1] → Cg(3)[b]	3.856(2)	17.19	12.31
Cg(9) [1] → Cg(1)[c]	3.747(2)	3.28	22.53
Cg(9) [1] → Cg(2)[c]	3.624(2)	6.74	24.30

Equivalent position code: a = 1/2 − *x*, 1/2 + *y*,*z*; b = 1/2 + *x*, *y*, 1/2 − *z*; c = 1/2 − *x*, −1/2 + *y*,*z*
α = Dihedral angle between planes I and J (°)
β = ∠Cg(I) → Cg(J) or Cg(I) → Me vector and normal to plane I (°)
Cg(1) = Ni1, S1, C8, N2, N1; Cg(2) = Ni1, O1, C1, C6, C7, N1; Cg(3) = N4, C15, C16, C17, C18, C19
Cg(8) = N8, C34, C35, C36, C37, C38; Cg(9) = C20, C21, C22, C23, C24, C25

XH(I)···Cg(J)	H···Cg (Å)	X–H···Cg (°)	X···Cg (Å)
CH–π interactions			
C(17)–H(17) [1] → Cg(6)[a]	2.69	144	3.4857
C(18)–H(18) [1] → Cg(1)[a]	2.69	139	3.4420
C(35)–H(35) [1] → Cg(9)[a]	2.67	153	3.5223
C(37)–H(37) [1] → Cg(4)[a]	2.90	141	3.6669

Equivalent position code: a = 1/2 + *x*,*y*, 1/2 − *z*
Cg(1) = Ni1, S1, C8, N2, N1; Cg(4) = C1, C2, C3,C4, C5, C6; Cg(6) = Ni2, S2, C27, N6, N5; Cg(9) = C20, C21, C22, C23, C24, C25

D–H···A	D···H (Å)	H···A (Å)	D···A (Å)	D–H···A (°)
H-bonding				
C15–H15···O2[a]	0.930	2.967(2)	3.539(5)	121.23(25)
C16–H16···O2[a]	0.930	2.827(2)	3.460(5)	126.33(26)
C3–H3···N7[b]	0.930	2.895(3)	3.589(5)	132.41(26)
C17–H17···N5[c]	0.930	2.755(3)	3.530(6)	141.42(29)
C18–H18···N1[c]	0.930	2.962(3)	3.445(5)	113.90(27)
C18–H18···N2[c]	0.930	2.859(3)	3.424(5)	120.36(28)
C36–H36···O1[c]	0.930	2.863(2)	3.723(5)	154.33(25)
C19–H19···N2[c]	0.930	2.699(3)	3.358(5)	128.52(24)

D, donor; A, acceptor. Equivalent position code: a = *x*, *y*, *z*; b = *x*, 1/2 − *y*, 1/2 + *z*; c = 1/2 + *x*, − *z* + 1/2 + 1.

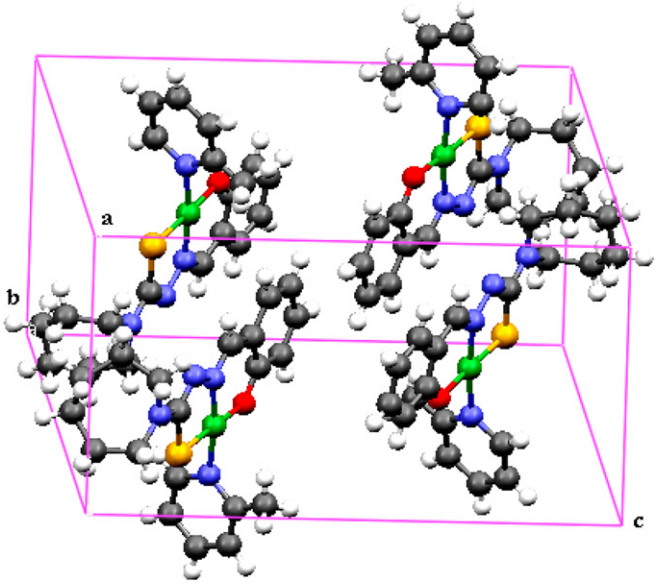


Fig. 4. Unit cell packing diagram of compound **3**.

Table 5
Interaction parameters of the compound **3**

D–H···A	D···H (Å)	H···A (Å)	D···A (Å)	D–H···A (°)
H-bonding				
C14–H14B···S1[a]	0.970	2.517(2)	3.021(8)	112.25(47)
C14–H14A···N2[b]	0.970	2.867(6)	3.540(11)	127.27(48)
C(17)–H17···N2[c]	0.930	2.858(5)	3.771(7)	167.25(27)
C18–H18···O1[d]	0.930	2.732(5)	3.596(9)	154.94(47)

D, donor, A, acceptor, Equivalent position code: a = x, y, z; b = $x-1/2, -y+1/2, +z$; c = $x, y-1, z$; d = $x-1/2, -y-1/2, +z$.

vide significant indications regarding the bonding sites of the ligands. IR spectral assignments of the ligands and the complexes are listed in Table 6. A medium band in the range 3070–3160 cm^{-1} in the free ligands, due to the $\nu(^2NH)$ vibration, disappears in the spectra of the complexes, providing strong evidence for ligand coordination around the Ni(II) ion in its deprotonated form.

The IR spectra of the ligands H_2L^1 and H_2L^2 exhibit intermolecular hydrogen bonded ν(OH) vibrations at 3315 and 3232 cm^{-1}, respectively, which disappear in the spectra of the complexes except for **1**. It is further corroborated with the decrease in stretching frequency by 60–80 cm^{-1} for ν(CO) as well as the appearance of a band in the 410–430 cm^{-1} region due to a ν(Ni–O) stretch in the spectra of the complexes [29]. It indicates coordination *via* the phenolic oxygen. In complex **1**, the phenolic group is not coordinated to the metal. The non-involvement of the phenolic group of the same thiosemicarbazone ligand in a zinc complex [19] has been proven by us. However, there is X-ray crystal structure evidence for the existence of the phenol rather than the phenolate form in a closely related salicylaldehyde thiosemicarbazone [30], with the ligand acting as an ONS donor.

On coordination of the azomethine nitrogen, $\nu(C{=}N_{azo})$ shifts to lower wavenumbers by 10–20 cm^{-1}, as the band shifts from 1613 cm^{-1} in the uncomplexed thiosemicarbazone spectrum to ~1596 cm^{-1} in the spectra of the complexes. Coordination of the azomethine nitrogen is confirmed by the presence of a new band in the range 450–490 cm^{-1}, assignable to ν(Ni–N) for these complexes [31]. The ν(N–N) band of the thiosemicarbazone is found in the 1030–1075 cm^{-1} range. The increase in the frequency of this band in the spectra of the complexes, due to the increase in the bond strength, again confirms coordination *via* the azomethine nitrogen [19].

The bands in the ranges 1320–1340 and 835–865 cm^{-1} due to thioamide {which is partly $\nu(C{=}S)$} stretching and bending vibrations, respectively, of the free ligands are shifted to lower values, indicating coordination of the thiolate sulfur to the Ni(II) ion. This negative shift of ν(CS) in the complexes has already been indicated by Campbell [1]. Coordination *via* the thiolato sulfur is confirmed with the presence of a new band in the range 320–350 cm^{-1}, assignable to ν(Ni–S) for these complexes [32]. In all the Ni(II) complexes, another strong band is found in the range 1530–1540 cm^{-1}, which may be due to the newly formed $\nu(C{=}^2N)$ bond formed as a result of enolization. The IR spectra of the complexes, except **1**, display bands characteristic of coordinated heterocyclic bases [33].

3.3. Electronic spectra

The electronic spectral assignments of the ligands and their complexes are given in Table 7. The thiosemicarbazones show a ring $\pi \rightarrow \pi^*$ band at ~36000 cm^{-1} and an

Table 6
IR spectroscopic assignments for the ligands and their nickel complexes

Compound	$\nu(C{=}N_{azo})$	$\nu(C{=}^2N)$	ν(N–N)	ν/δ[(C=S)/(C–S)]	ν(C–O)	ν(Ni–N)	ν(Ni–O)	ν(Ni–S)	Bands due to heterocyclic base
H_2L^1	1612		1037	1324, 861	1271				
$[Ni(HL^1)_2]$ (**1**)	1581	1530	1071	1267, 753	1270	466		350	
$[NiL^1py]$ (**2**)	1597	1536	1070	1288, 757	1207	463	430	345	1447, 691
$[NiL^1\alpha\text{-pic}]$ (**3**)	1601	1531	1063	1278, 752	1209	494	446	347	1448, 614
$[NiL^1\gamma\text{-pic}]\cdot H_2O$ (**4**)	1597	1537	1068	1270, 753	1208	460	420	332	1449, 714
H_2L^2	1622		1034	1338, 839	1288				
$[NiL^4py]$ (**5**)	1600	1538	1061	1290, 758	1210	490	422	334	1478, 693
$[NiL^4\gamma\text{-pic}]$ (**6**)	1600	1538	1055	1275, 757	1205	476	425	325	1480, 607

Table 7
Electronic spectral assignments of the ligands and their Ni(II) complexes

Compound	π–π*	n–π*	LMCT	d–d
H_2L^1	36110	29500		
$[Ni(HL^1)_2]$ (**1**)	35340	30210	26190	17240
$[NiL^1py]$ (**2**)	34840	30400	26450	16980
$[NiL^1\alpha\text{-pic}]$ (**3**)	35420	30920, 33000	23640, 26700	17060
$[NiL^1\gamma\text{-pic}]\cdot H_2O$ (**4**)	35580	30960, 33330	23980, 26740	17070
H_2L^2	36490	30210		
$[NiL^2py]$ (**5**)	36020	32680	23790, 26040	18480
$[NiL^2\gamma\text{-pic}]$ (**6**)	36230	30210, 33780	23980, 26380	18520

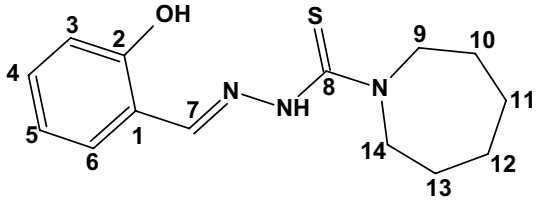


Fig. 5. The structure of the ligand H_2L^1 along with atom labelling scheme.

$n \rightarrow \pi^*$ band (involving transitions within the thiosemicarbazone moiety, mainly C(7)=N(1) and C(8)–S groups [16]) at ~30000 cm^{-1}. These bands are slightly shifted upon complexation. The shift of the $\pi \rightarrow \pi^*$ bands to a longer wavelength region in the complexes is the result of the C–S bond being weakened and the conjugation system being enhanced on complexation [34,35]. The $n \rightarrow \pi^*$ bands in the complexes show a blue shift due to donation of the lone pair of electrons to the metal and hence the coordination of the azomethine with a reduction of intensity.

In the case of complexes having ONS donor ligands, two ligand to metal charge transfer bands are found in the 25000–28000 and 23000–24500 cm^{-1} ranges. Their positions are dependent on the steric requirements of the N(4) substituents. That is, thiosemicarbazones with bulkier N(4)-substituents have these bands at somewhat higher energies. In most of the dianionic complexes, LMCT maxima of the phenolate complexes show line broadening with a tail running into the visible part of the spectrum. This may result from a phenolate to Ni(II) LMCT band being superimposed on the low energy side of the S → Ni(II) LMCT. Each complex has a broad d–d combination band that appears as a shoulder on the intraligand and charge-transfer bands. These nickel complexes show a trend of increasing size of the N(4)-substituent and lower energy of the d–d band maximum, presumably due to weakening of the coordinate bonding with increased bulkiness of the ligands. The absence of bands below 10000 cm^{-1} confirms the square planar nature of the complexes [36,37].

3.4. ^1H NMR spectra

The numbering scheme used in the ^1H NMR spectrum of the ligand H_2L^1 is given in Fig. 5 and the spectra of the complexes **1** and **4** are given in Figs. 6 and 7. The ^1H NMR spectrum of the ligand H_2L^1 has been discussed earlier [19]. ^1H NMR spectral assignments of the ligand and its Ni(II) complexes **1** and **4** are given in Table 8. The signals for ^2NH are absent from the spectra of these complexes, as expected, and the phenolic OH is absent in the spectrum of complex **4** because of its loss on complex formation, which is an evidence for the coordination of the ligand as a doubly deprotonated anion. The spectra of complexes **1** and **4** show a sharp singlet which integrates as one hydrogen at δ 7.44 and 7.83 ppm,

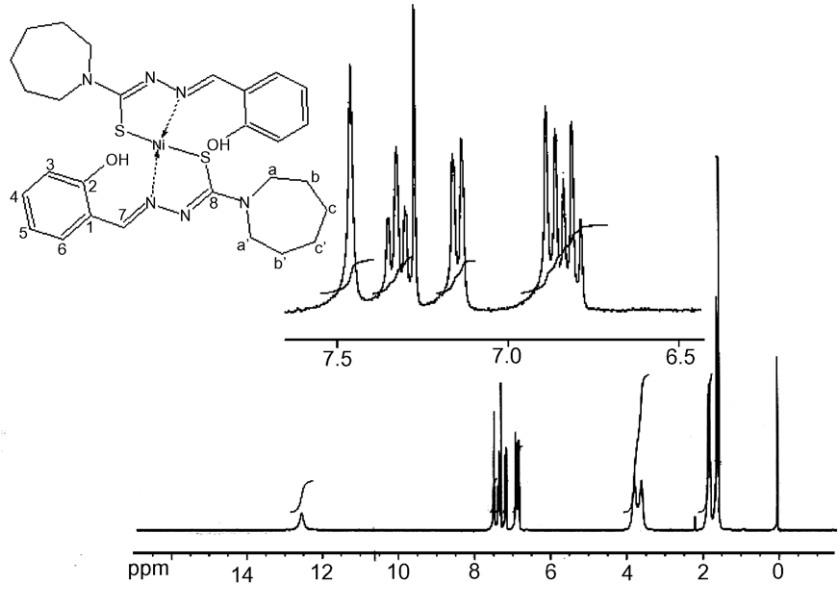


Fig. 6. ^1H NMR spectrum of compound **1**.

Table 8
^{1}H NMR ($CDCl_3$) assignments of the ligand H_2L^1 and its Ni(II) complexes (δ in ppm)

Compound	OH	Aromatic protons				^{8}CH=	^{a}CH$_2$	^{b}CH$_2$	^{c}CH$_2$
		H^6Ph	H^4Ph	H^3Ph	H^5Ph				
H_2L^1	11.3	7.09	6.97	6.80	6.67	7.99	3.63	1.66	1.42
$[Ni(HL^1)_2]$ (**1**)	12.51	7.45	7.31	7.13	6.82	7.45	3.67	1.79	1.56
$[NiL^1\gamma\text{-pic}]\cdot H_2O$ (**4**)		7.25	7.18	7.14	6.80	7.83	3.61	1.74	1.55

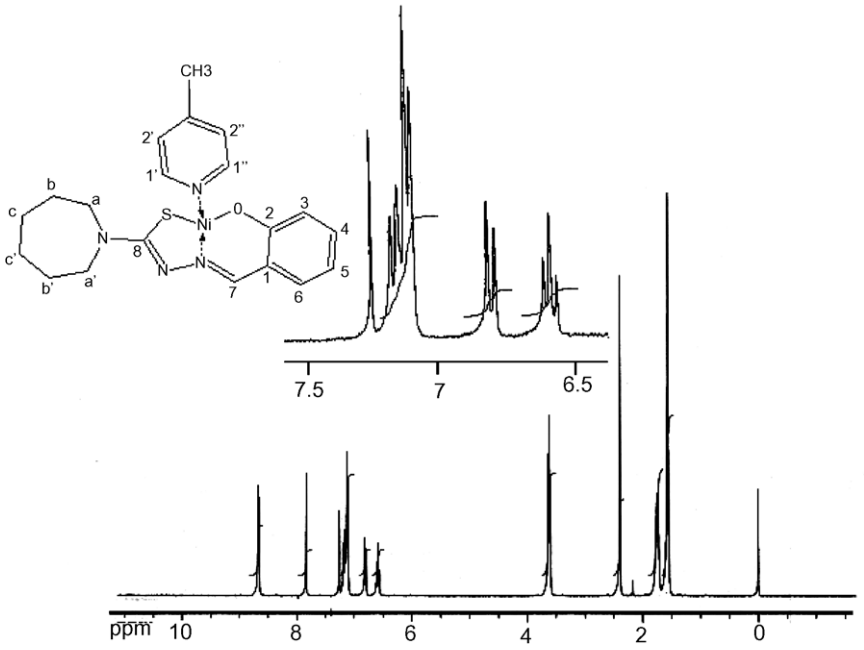


Fig. 7. ^{1}H NMR spectrum of compound **4**.

respectively, corresponding to ^{7}CH= present in the thiosemicarbazone moiety. Complex **1** shows a peak at δ 12.51 ppm due to the presence of the uncoordinated hydroxyl group. The more downfield shift of the OH protons compared to the uncomplexed thiosemicarbazone may be due to the overall loss of electron density and hydrogen bonding interactions. The ^{1}H NMR spectrum of **1** shows a multiplet which integrates as two hydrogens at δ *ca.* 6.82 ppm and is assigned to the protons attached to ^{3}C and ^{5}C of the phenyl ring. ^{4}CH and ^{6}CH protons of the phenyl ring appear at δ 7.13 and 7.31 ppm, respectively. In complex **4**, the protons of the aromatic ring ^{3}CH and ^{5}CH appear at δ 6.58 and 6.80 ppm. The spectrum also shows a multiplet which integrates as four hydrogens at δ *ca.* 7.15 ppm, corresponding to ^{4}CH, ^{6}CH and the base protons $H^{2'}$ and $H^{2''}$. The upfield shift of these base protons may be due to the presence of the electron releasing methyl group present in the pyridine ring. The heterocyclic base protons ($H^{1'}$ and $H^{1''}$) are present as a doublet, which integrates as two hydrogens at δ 8.66 ppm. The downfield shift of these protons may be the result of the withdrawal of electron density from the thiosemicarbazone moiety and the heterocyclic base, due to coordination with the metal atom [38]. Methyl protons appear as a singlet at δ 2.38 ppm (see Fig. 7).

Acknowledgements

L. Latheef thanks the Council of Scientific and Industrial Research, New Delhi, India, for financial support in the form of a fellowship. M.R.P. Kurup is thankful to the CSIR, New Delhi, India, for financial support. The authors also thank the National Single Crystal X-ray diffraction Facility, IIT, Bombay, for X-ray data collection.

Appendix A. Supplementary material

CCDC 603882 and 604196 contain the supplementary crystallographic data for **2** and **3**. The data can be obtained free of charge at www.ccdc.cam.ac.uk/conts/retrieving.html, or from the Cambridge Crystallographic Data Centre (CCDC), 12 Union Road, Cambridge, CB2, IEZ, UK fax: (+44)-1223-336-033; e-mail: deposit@ccdc.cam.ac.uk. Supplementary data associated with this article can be found, in the online version, at doi:10.1016/j.poly.2007.08.048.

References

[1] M.J.M. Campbell, Coord. Chem. Rev. 15 (1975) 279.
[2] S. Padhye, G.B. Kauffman, Coord. Chem. Rev. 63 (1985) 127.

[3] D.X. West, S.B. Padhye, P.B. Sonawane, Struct. Bond. (Berlin) 76 (1991) 4.
[4] D.X. West, A.E. Liberta, S.B. Padhye, R.C. Chikate, P.B. Sonawane, A.S. Kumbhar, R.G. Yerande, Coord. Chem. Rev. 123 (1993) 49.
[5] K.A. Jensen, E. Rancke-Madsen, Z. Anorg. Allergy Chem. 219 (1934) 243.
[6] C.E. Holloway, M. Melnik, J. Organomet. Chem. 495 (1995) 1.
[7] C.E. Holloway, M. Melnik, Main Group Met. Chem. 17 (1994) 799.
[8] J.S. Casas, M.S. Garcia-Tasende, J. Sordo, Coord. Chem. Rev. 209 (2000) 197.
[9] A. Sreekanth, S. Sivakumar, M.R.P. Kurup, J. Mol. Struct. 655 (2003) 47.
[10] R.P. John, A. Sreekanth, M.R.P. Kurup, A. Usman, I.A. Razak, H.K. Fun, Spectrochim. Acta 59A (2003) 1349.
[11] A.D. Naik, S.M. Annigeri, U.B. Gangadharmath, V.K. Revankar, V.B. Mahale, J. Mol. Struct. 616 (2002) 119.
[12] R. Prabhakaran, R. Karvenmbu, T. Hashimoto, K. Shimizu, K. Natarajan, Inorg. Chim. Acta 358 (2005) 2093.
[13] E. Labisbal, K.D. Haslow, A. Sousa-Pedrares, J. Valdes- Martinez, A.H. Ortega, D.X. West, Polyhedron 22 (2003) 2831.
[14] D.X. West, Y. Yang, T.L. Klein, K.I. Goldberg, A.E. Liberta, J. Valdes-Martinez, S.H. Ortega, Polyhedron 14 (1995) 3051.
[15] D.E. Barber, Z. Lu, T. Richardson, R.H. Crabtree, Inorg. Chem. 31 (1992) 4709.
[16] P. Bindu, M.R.P. Kurup, Indian J. Chem. 36A (1997) 1094.
[17] A.G. Quiroga, C.N. Ranninger, Coord. Chem. Rev. 248 (2004) 119.
[18] L. Latheef et al., Spectrochim. Acta (2007), doi:10.1016/j.saa.2007.07.015.
[19] L. Latheef et al., Polyhedron (2007), doi:10.1016/j.poly.2007.05.023.
[20] J.P. Scovill, Phosphorus Sulfur Silicon Relat. Elem. 60 (1991) 15.
[21] L. Latheef, E. Manoj, M.R.P. Kurup, Acta Crystallogr. C 62 (2006) 16.
[22] G.M. Sheldrick, SHELXL-97 and SHELXS-97 Program for the Solution of Crystal Structures, University of Göttingen, Germany, 1997.
[23] K. Brandenburg, DIAMOND version 3.1d, Crystal Impact GbR, Bonn, Germany, 2006.
[24] C.F. Macrac, P.R. Edgington, P. McCabe, E. Pidcock, G.P. Shields, R. Taylor, M. Towler, J. Van de Streek, J. Appl. Cryst. 39 (2006) 453.
[25] V. Suni, M.R.P. Kurup, M. Nethaji, Polyhedron 26 (2007) 3097.
[26] X.-H. Qiu, H.-Y. Wu, Acta Crystallogr. E 60 (2004) m 1151.
[27] M.B. Ferrari, S. Capacchi, F. Bisceglie, G. Pelosi, P. Tarasconi, Inorg. Chim. Acta 312 (2001) 81.
[28] Z. Afrasiabi, E. Sinn, W. Lin, Y. Ma, C. Campana, S. Padhye, J. Inorg. Biochem. 99 (2005) 1526.
[29] M. Mikuriya, H. Okawa, S. Kida, Bull. Chem. Soc. Jpn. 53 (1980) 3717.
[30] M. Zimmer, G. Schulte, X.-L. Luo, R.H. Crabtree, Angew. Chem., Int. Ed. Engl. 30 (1991) 193.
[31] P. Sousa, J.A. Garcia-Vasquez, J.R. Masaguer, Trans. Met. Chem. 9 (1984) 318.
[32] R. Roy, M. Chaudhury, S.K. Mondal, K. Nag, J. Chem. Soc., Dalton Trans. (1984) 1681.
[33] P.B. Sreeja, M.R.P. Kurup, Spectrochim. Acta 61A (2005) 331.
[34] V. Philip, V. Suni, M.R.P. Kurup, Polyhedron 25 (2006) 1931.
[35] I.-X. Li, H.A. Tang, Yi-Zhi Li, M. Wang, L.-F. Wang, C.-G. Xia, J. Inorg. Biochem. 78 (2000) 167.
[36] B.S. Garg, M.R.P. Kurup, S.K. Jain, Y.K. Bhoon, Trans. Met. Chem. 16 (1991) 111.
[37] H.B. Gray, C.J. Bauhausen, J. Am. Chem. Soc. 85 (1963) 260.
[38] D.X. West, Y. Yang, T.L. Klein, K.I. Goldberg, A.E. Liberta, J. Valdes-Martinez, R.A. Toscano, Polyhedron 14 (1995) 1681.

Available online at www.sciencedirect.com
ScienceDirect
Polyhedron 27 (2008) 44–52
POLYHEDRON
www.elsevier.com/locate/poly

Synthesis, structure and reactivity of *cis*-[PtL_2(1-alkenyl)$_2$] complexes

Akella Sivaramakrishna, Banothile C.E. Makhubela, Feng Zheng, Hong Su, Gregory S. Smith, John R. Moss *

Department of Chemistry, University of Cape Town, Rondebosch, 7701 Cape Town, South Africa

Received 10 May 2007; accepted 31 August 2007
Available online 23 October 2007

Abstract

The synthesis and characterization of several new bis(1-alkenyl)platinum(II) complexes have been carried out. The structure of *cis*-[Pt(dppp)($(CH_2)_6CH{=}CH_2)_2$] has been determined by X-ray crystallography. The stability and reactivity of the compounds, *cis*-[$PtL_2((CH_2)_nCH{=}CH_2)_2$] ($n = 3$ or 4 and L_2 = 1,3-bis(diphenylphosphino)propane (dppp), 1,2-bis(diphenylphosphino)ethane (dppe), L = PPh_3) is strongly dependent on the nature of ligand systems. It is found that the insertion of carbon monoxide into the metal–carbon bonds of the platinum alkenyl complexes is possible. Other reactions including transmetalation, intermolecular alkenyl migrations, oxidative addition of methyl iodide are described and the thermal decomposition of the bis(alkenyl) complexes are also reported.
© 2007 Elsevier Ltd. All rights reserved.

Keywords: Bis(alkenyl) complexes; Structure; Reactivity; Insertion reactions; Oxidative addition; Transmetalation

1. Introduction

Metal–alkenyl complexes are an important class of compounds. These compounds have been implicated as potential model compounds for intermediates in a number of catalytic cycles as well as other applications [1]. Metal–alkenyl complexes have been shown to act as precursors for the preparation of thin metal films, which can in turn be applied in the micro-electronics and catalysis industries [2]. Recently we have shown that bis(1-alkenyl)platinum complexes undergo a novel ring closing metathesis (RCM) reaction to give medium to large metallacycles [3–5]. Selective and quantitative isomerization of *cis*-[PtL_2(1-alkenyl)$_2$] to *cis*-[PtL_2(2-alkenyl)$_2$] complexes has also been observed [6]. In order to explore the reactivity pathways for these complexes, we have investigated some novel reactions of platinum alkenyl complexes. The present paper also explores the influence of the nature of phosphine ligands on the reactivity aspects of the title compounds.

* Corresponding author. Tel.: +27 21 650 2535; fax: +27 21 689 7499.
E-mail address: John.Moss@uct.ac.za (J.R. Moss).

0277-5387/$ - see front matter © 2007 Elsevier Ltd. All rights reserved.
doi:10.1016/j.poly.2007.08.036

2. Experimental

2.1. Materials and methods

All manipulations were carried out under a nitrogen atmosphere unless otherwise stated. Commercially available solvents were distilled from Na metal/benzophenone ketyl before use.

2.1.1. Nuclear magnetic resonance spectroscopy

^1H, ^{13}C and ^{31}P NMR spectra were recorded on a Bruker DMX-400 spectrometer and all ^1H chemical shifts are reported relative to the residual proton resonance in deuterated solvents (all at 298 K, C_6D_6).

2.1.2. Elemental analysis

Microanalyses were conducted with a Thermo Flash 1112 Series CHNS-O Elemental Analyzer instrument.

2.1.3. GC–MS analysis

GC analyses were carried out using a Varian 3900 gas chromatograph equipped with an FID and a 30 m × 0.32 mm CP-Wax 52 CB column (0.25 μm film

thickness). The carrier gas used was helium at 5.0 psi. The oven was programmed to hold at 32 °C for 4 min and then to ramp to 200 °C at 10 °C/min and then hold for 5 min. GC–MS analyses for peak identification were performed using an Agilent 5973 gas chromatograph equipped with MSD and a 60 m × 0.25 mm Rtx-1 column (0.5 μm film thickness). The carrier gas was helium at a flow rate of 0.9 ml/min. The oven was programmed to hold at 50 °C for 2 min and then ramp to 250 °C at 10 °C/min and then hold for 8 min.

2.1.4. Infrared spectroscopy

Infrared spectra were recorded on a Perkin–Elmer Spectrum One FT-IR Spectrometer.

2.1.5. Materials

All chemicals were obtained commercially and unless otherwise stated, were used as received without further purification. 1-Alkenyl Grignard reagents ($BrMgCH_2CH_2(CH_2)_nCH{=}CH_2$; $n = 1, 3, 4, 6$) [7], $Pt(COD)Cl_2$ [8], $Pt(dppe)Cl_2$, [9] $Pt(dppp)Cl_2$, [9] and $Pt(PPh_3)_2Cl_2$ [9] were prepared according to the literature procedures. Bis(1-octenyl)(dppp)platinum(II) (**1**), bis(1-hexenyl) *cis*- bis(triphenylphosphine)platinum(II) (**2**), bis(1-hexenyl)(dppp)platinum(II) (**3**), bis(1-pentenyl)*cis*-bis(triphenylphosphine)platinum(II) (**4**) and bis(1-pentenyl)(dppp)-platinum(II) (**5**) were prepared as reported earlier [4].

2.1.6. Crystallographic data for compound *1*

Single crystals of compound **1** were obtained by recrystallization and slow evaporation from Et_2O at room temperature. Intensity data for the compound **1** was collected at 113 K on a Nonius Kappa CCD diffractometer using graphite- monochromated Mo Kα radiation ($\lambda = 0.71073$ Å). $C_{43}H_{56}P_2Pt$, $M = 829.91$, triclinic, $P\bar{1}$, $a = 12.59740(10)$, $b = 12.98700(10)$, $c = 14.5363(2)$ Å, $\alpha = 110.3300(10)°$, $\beta = 90.6480(10)°$, $\gamma = 117.1230(10)°$, $V = 1943.33(3)$ Å^{-3}, $Z = 2$, $\mu = 3.720$ mm^{-1}, unique reflections = 55 624/7391 [R(int) = 0.0467], $R_1 = 0.0210$, $wR_2 = 0.0433$ [$I > 2\sigma(I)$].

2.2. Synthesis of the metal complexes

2.2.1. Preparation of bis(1-pentenyl)(dppe)platinum(II) (*6*)

$Pt(COD)Cl_2$ (506 mg, 1.352 mmol) in diethyl ether (20 ml) was cooled to −78 °C and of 1-pentenyl Grignard reagent (2.8 ml, 1.34 M, 3.75 mmol) was added. The solution was warmed to 0 °C and then stirred until the solution became clear. To this, solution dppe (539 mg, 1.353 mmol) was added and stirred for 30 h until a clear solution was formed. The excess Grignard reagent was removed by hydrolyzing the reaction mixture with saturated aqueous NH_4Cl (5 ml) at −78 °C. The aqueous layer was washed with dichloromethane (2 × 5 ml), dried with anhydrous magnesium sulfate and filtered. The solvent was removed under reduced pressure and the residue recrystallized from a CH_2Cl_2/hexane mixture (3 ml: 5 ml) at −10 °C for 48 h. The pale yellow crystalline solid was separated by decanting the mother liquor and dried under vacuum for 3 h. For compound **6**. Yield: 96%. M.p. 84–85 °C. *Anal*. Calc. for $C_{36}H_{42}P_2Pt$: C, 59.09; H, 5.79. Found: C, 58.98; H, 5.69%. IR (ν_{max}/cm^{-1}) in CH_2Cl_2: 1605(m), 1636(s); ^{1}H NMR (300 MHz, $CDCl_3$) δ: 7.36–7.91 (m, 20H, Ph); 5.55–5.72 (m, 2H, =CH); 4.68–4.82 (m, 4H, $=CH_2$); 1.96–2.22 (m, 4H, P-CH_2); 1.21–1.88 (m, 12H, –CH_2);^{13}C NMR (100 MHz, $CDCl_3$) δ: 141.01 (s, 2C);133.16–133.29 (m, 12C); 129.98 (s, 8C) 127.55–128.32 (m, 4C); 112.40 (s, 2C); 32.08–32.56 (m, 2C); 30.88 (s 2C); 29.03–29.79 (m, 2C); 22.57 (d, $J = 6.67$ Hz 2C) 21.60 (d, $J = 6.58$ Hz), $^{31}P\{^1H\}$ 45.76 (s) ($J_{Pt-P} = 1641$ Hz).

2.2.2. Carbonylation of compound 6

Compound **6** (262 mg, 0.358 mmol) was dissolved in toluene (25 ml) of. After bubbling CO through the contents of the flask for 5–6 min, the solution was stirred at room temperature under ambient pressure of carbon monoxide (balloon). After 72 h, the solvent was removed under the reduced pressure. The residue was filtered and recrystallized from a CH_2Cl_2/hexane mixture (2:1 v/v) to give compound **10a**. Yield: 62%. M.p. 118–126 °C. *Anal*. Calc. for $C_{38}H_{42}O_2P_2Pt$: C, 57.94; H, 5.37. Found: C, 58.16; H, 5.42%. IR (ν_{max}/cm^{-1}) in CH_2Cl_2: 1608(m), 1680(s). ^{1}H NMR (300 MHz, $CDCl_3$) δ: 7.24–7.91 (m, 20H, Ph); 5.54–5.69 (m, 2H, CH); 4.61–4.80 (m, 4H, $=CH_2$); 1.98–2.40 (m, 4H, P–CH_2); 1.16–1.86 (m, 12H, CH_2); ^{13}C NMR (100 MHz, $CDCl_3$) δ: 206.78 (s, 2C); 140.92 (s, 2C); 133.21–133.58 (m, 12C); 129 (s, 8C); 126.71–128.37 (m, 4C); 112.30 (s, 2C); 31.55 (m, 2C); 30.87 (s, 2C) 25.10 (d, $J = 8.66$ Hz); 24.14 (d, $J = 8.71$ Hz) $^{31}P\{^1H\}$ 46.00 (s) ($J_{Pt-P} = 2320$ Hz).

2.2.3. Carbonylation of compound *1*

A similar procedure was followed by taking compound **1** (61 mg, 0.073 mmol) in a round bottom flask containing toluene (15 ml). The reaction was carried out and worked-up as described above to give compound **10b** as colourless crystals. Yield: 86%. M.p. 104–105 °C. *Anal*. Calc. for $C_{45}H_{56}O_2P_2Pt$: C, 61.01; H, 6.37. Found: C, 61.16; H, 6.42%. IR (ν_{max}/cm^{-1}) in CH_2Cl_2: 1605(m), 1676(s). ^{1}H NMR (300 MHz, $CDCl_3$) δ: 7.21–7.97 (m. 20H, Ph); 5.40–5.70 (m, 2H, =CH); 4.63–4.73 (m, 4H $=CH_2$); 1.99–2.15 (m, 6H, P–CH_2); 1.23–1.92 (m, 24H, CH_2).

2.2.4. Reaction of $Pt(1\text{-pentenyl})_2(PPh_3)_2$ (*4*) with $[Cp^*IrCl_2]_2$

Compound **4** (232 mg, 0.271 mmol) and $[Cp^*IrCl_2]_2$ (0.104 mg, 0.135 mmol) were transferred into a Schlenk flask containing toluene (5 ml). The mixture was heated for 3 h at 85–90 °C. A colourless precipitate was formed during the reaction. The solvent was removed in vacuo. The mixture was treated with diethylether (5 ml). The insoluble crystalline solid was found to be a mixture of $[Pt(PPh_3)_2Cl_2]$ and $[IrCp^*(PPh_3)Cl_2]$. The products **13** and

14 from the solution were separated by using a *p*-TLC with CH_2Cl_2 as an eluent. The pale yellow band was extracted and compound **13** was obtained as a yellow oily substance (48 mg). The oil was treated with *n*-hexane (3 ml) and on cooling a yellow solid resulted which was shown to be compound **13**, bis(1-pentenyl)(tetramethylcyclopentadienyl)iridium(III)- (triphenylphosphine) Yield: 50%. M.p. 66–68 °C. *Anal.* Calc. for $C_{37}H_{46}IrP$: C, 62.24; H, 6.49. Found: C, 62.43; H, 6.59%. ^1H NMR (300 MHz, $CDCl_3$) δ: 6.99–8.10 (m, 15H, Ph); 5.63–5.94 (m, 2H, =CH); 4.88–5.13 (m, 4H, $=CH_2$); 4.19 (s, 1H, Cp^*–H); 0.76–2.12 (m, 12H, CH_2); $^{31}P\{^1H\}$ 25.88 (s).

2.2.5. Reaction of Pt(1-pentenyl)$_2$ (dppp) (5) with $[Cp^*IrCl_2]_2$

Compound **5** (202 mg, 0.272 mmol) and $[Cp^*IrCl_2]_2$ (0.105 mg, 0.136 mmol) were taken in to a Schlenk flask containing toluene (15 ml). The mixture was heated for 13 h at 85–90 °C. The colourless precipitate that formed during the reaction was found to be compound **11**, (η^3-dimethylallyl)[1,3-bis(diphenyl phosphino)propane]-platinum(II)chloride. Yield: 68%. M.p. 144–146 °C. *Anal.* Calc. for $C_{32}H_{35}P_2PtCl$: C, 53.97; H, 4.95. Found: C, 54.16; H, 4.88%. ^1H NMR (300 MHz, $CDCl_3$) δ: 7.23–7.78 (m, 20H, Ph); 3.30–3.87 (m, 3H, allylic-H); 2.17–2.67 (m, 4H, P–CH_2); 1.09–1.17 (m, 6H, CH_2); $^{31}P\{^1H\}$ −1.32 (s) (J_{Pt-P} = 3828 Hz). All the solvent was removed from the solution and the obtained pale yellow solid was recrystallized from 1:1 *n*-hexane-diethylether mixture to yield the compound **12**. Yield: 75%. M.p. 108–112 °C. *Anal.* Calc. for $C_{14}H_{22}IrCl$: C, 40.23; H, 5.31. Found: C, 40.46; H, 5.36%. ^1H NMR (300 MHz, $CDCl_3$) δ: 4.43 (s, 1H, Cp–H); 3.95 (m, 1H, CH); 2.95 (m, 1H, **CH**–CH_3); 2.20 (m, 2H, –CH_2), 1.81 (s, 12H, Cp–CH_3), 1.52–1.61 (m, 2H, CH_2); 0.92–1.06 (m, 3H, CH_3).

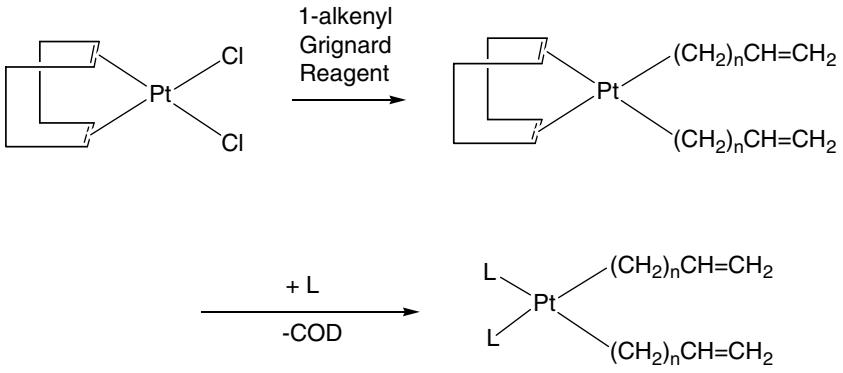
2.2.6. Reaction of Pt(1-pentenyl)$_2$ (dppp) (6) with MeI

Compound **6** (304 mg, 0.415 mmol) and 118 mg of MeI (0.832 mmol) were taken in to of CH_2Cl_2 (5 ml). After stirring at room temperature for 72 h, a pale yellow precipitate was formed. The precipitate was washed with diethylether (5 ml) and recrystallized from CH_2Cl_2–hexane mixture (1:1). The product was found to be compound **9b**. The product **9a** was isolated from the solution. After removing the solvent, the compound was recrystallized from a mixture of toluene (2 ml) and hexane (1 ml). The liquid product was found to be 5-iodo-1-pentene. For compound **9a**, (1-pentenyl)(methyl)[1,2-bis-(diphenylphosphino)ethane] platinum(II). Yield: 52%. M.p. 110–112 °C. *Anal.* Calc. for $C_{32}H_{36}P_2Pt$: C, 56.72; H, 5.35. Found: C, 56.66; H, 5.62%. ^1H NMR (300 MHz, $CDCl_3$) δ: 7.18–7.92 (m, 20H, Ph); 5.69–5.86 (m, 1H, =CH); 4.77–4.98 (m, 2H, $=CH_2$); 1.85–2.29 (m, 4H, P–CH_2); 1.15–1.67 (m, 6H, CH_2); $^{31}P\{^1H\}$ δ 45.96, 45.91 (d), 45.76, 45.70 (d) (1685 and 1635 Hz).

3. Results and discussion

3.1. Synthesis and characterization of compounds

The bis(alkenyl)–platinum complexes were prepared in high yields by reacting the appropriate Grignard reagents with $Pt(COD)Cl_2$. Several derivatives of these compounds were synthesized using various ligand systems, mainly, PPh_3, dppe and dppp (Scheme 1). All the data gathered for compounds (**1–6**) are consistent with the proposed formulations. The ^1H NMR spectra exhibit signals which are characteristic of species containing a vinylic functionality, while the ^{31}P NMR spectra showed sharp singlets with their respective platinum satellites. Single crystals of compound **1** were obtained by recrystallization from Et_2O at room temperature. Crystallographic data are listed



1, L_2 = dppp, n = 6;
2, L = PPh_3, n = 4;
3, L_2 = dppp, n = 4;
4, L = PPh_3, n = 3;
5, L_2 = dppp, n = 3;
6, L_2 = dppe, n = 3.

Scheme 1.

Table 1
Selected bond distances (Å) and angles (°) of compound **1**

Bond distances			
Pt(1)–C(61)	2.119 (3)	C(56)–C(55)	1.526 (4)
Pt(1)–C(51)	2.120 (3)	C(65)–C(66A)	1.5207 (7)
Pt(1)–P(1)	2.2766 (7)	C(57)–C(58)	1.292 (5)
Pt(1)–P(2)	2.2873 (7)	C(68A)–C(67A)	1.211 (7)
Bond angles			
C(61)–Pt(1)–C(51)	85.05 (10)	C(51)–Pt(1)–P(1)	89.86 (8)
C(61)–Pt(1)–P(2)	91.98 (7)	C(61)–Pt(1)–P(1)	174.78 (7)
P(1)–Pt(1)–P(2)	92.97 (2)	C(51)–Pt(1)–P(2)	173.58 (7)

in Section 2, and selected bond distances and angles are given in Table 1.

The molecular structure of compound **1** (Fig. 1) shows square-planar coordination geometry around the platinum. The Pt–C and Pt–P bonds of compound **1** are similar and comparable with the literature reports of similar compounds [10](2.119(3)–2.120(3) Å and 2.2766(7)–2.2873(7) Å, respectively), while the C=C distances range from 1.211(7) to 1.292(5) Å. The P–Pt–P, P–Pt–C and C–Pt–C bond angles in compound **1** are observed as 92.97(2), 89.86(8) to 91.98(7) and 85.05(10), respectively.

3.2. Reactivity of metal–alkenyl complexes

Generally, metal alkenyl complexes can show two distinct reaction pathways: (i) reaction at the M–C bond (ii) coordination of the pendant alkene. It is interesting to note that these special features impart novel chemistry to these compounds [1a].

The interaction of metal–alkenyls with electrophilic reagents such as acids and halogens gives the corresponding hydrocarbons or 1-haloalkenes resulting from the cleavage of metal–carbon bonds and the hydrogenation and hydroformylation reactions of some metal alkenyl compounds have been reported with the Lewis acid $TiCl_4$ [1b], we explored other novel reactions with various substrates. The group 10 metal-catalyzed cross-coupling reactions are very important in organic synthesis through oxidative addition, transmetallation, and reductive elimination steps [11]. Some of these reactions may have considerable potential in chemical synthesis, since they provide a method for the formation of new C–C bonds by reductive elimination or formation of C–X bonds. The effect of the length of the alkenyl chains, the influence of the solvent as well as the nature of ligand systems on the reactivity of the title compounds will be discussed.

3.3. Thermal decomposition and rearrangement reactions

Although thermal decomposition pathways of metal–alkenyl complexes may be similar to those of metallacycles or metal alkyl complexes, the products formed can differ considerably because of the pendant alkene functionality. The thermal stability of the metal–alkenyl complexes is dependent on the solvent system, thus halogenated solvents readily cleave the M–C bond to form metal halides irrespective of the ligand system. Bis(alkenyl) metal complexes can give various products on decomposition (Scheme 2).

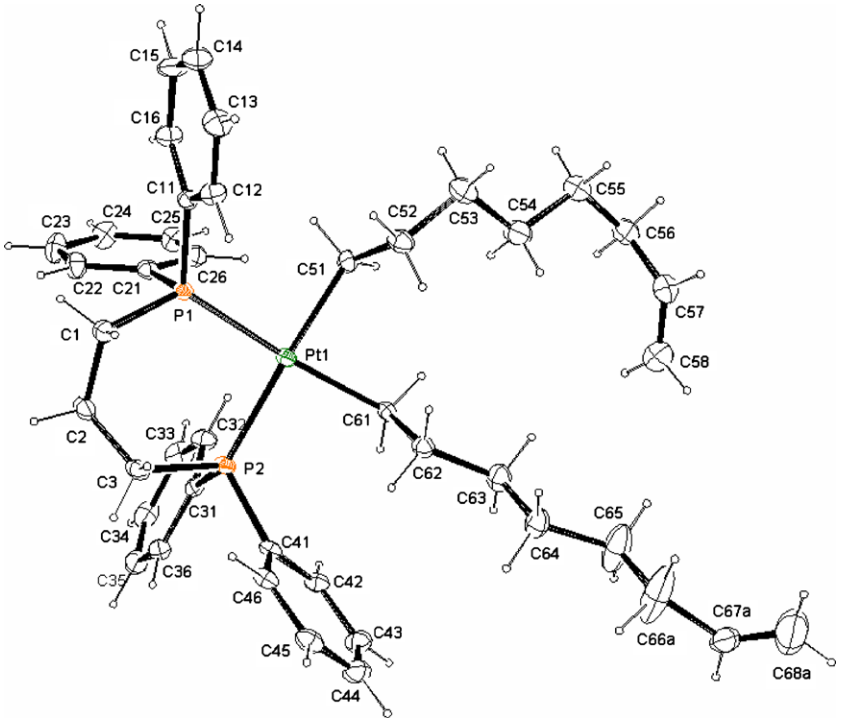
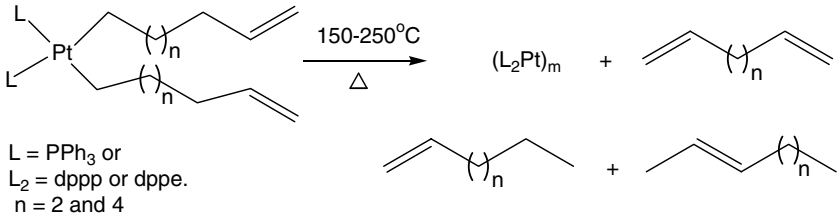


Fig. 1. Molecular structure and atom labeling scheme for compound **1**. Displacement ellipsoids are drawn at the 40% probability level and H atoms are shown as small spheres of arbitrary radii. Atom C67 was disordered over two positions: C67A with Site Occupancy 0.535 and C67B with Site Occupancy 0.465.



Scheme 2.

Our present experiments show that the organic products depend on the nature of the ligands, and this may relate to the stability and reactivity of the metal–alkenyl compounds in solution. Thus the triphenylphosphine complexes, $Pt(PPh_3)_2\{(CH_2)_nCH{=}CH_2\}_2$ were found to yield an intense red colour on decomposition which we believe to be due to $[(PPh_3)2Pt]_m$ clusters. In contrast, the $PtL_2[(CH_2)_3CH{=}CH_2]_2$ complexes (where $L_2 = $ dppp or dppe) were found to be quite stable up to 100 °C [6]. The diphosphine ligands have generally been found to increase the thermal stability of the complexes significantly. It is also believed that metal alkenyl species may be important intermediates in the decomposition of metallacycloalkanes through β-hydride elimination [12,13].

Several interesting trends were noted in the products isolated from the thermolysis reactions. First, all the decomposition reactions showed the presence of 2-alkene and cycloalkane as major components. Second, the organic product distributions are quite dependent on the time of heating as well as the medium of reaction whether in the solid state or in solution (Table 2). It can be seen that there is a significant decrease in the quantities of 1-alkene species with increasing the time of heating, with the exception of PPh_3 derivatives, which is in agreement with earlier reports [6]. Further thermal studies will be carried out to try and understand the mechanistic aspects for the formation of the organic products in these reactions.

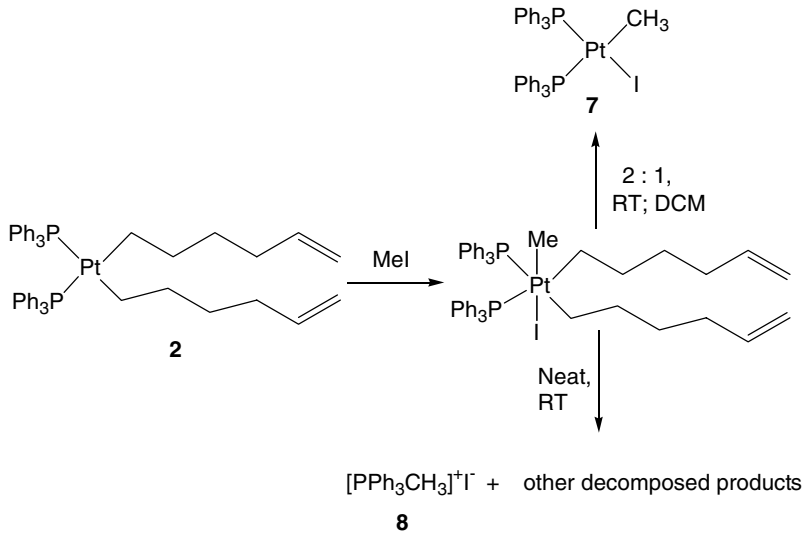
Table 2
Thermal decomposition of bis(1-hexenyl)(dppp)platinum(II) (**3**), at 175 °C

Medium	Observed products (%)*				
	n-Hexane	1-Hexene	2-Hexene (*cis*- + *trans*-isomers)	Cyclohexane	1,5-Hexadiene
Solid					
1 h	25	8	41	14	11
3 h	2	0	63	22	12
10 h	1	0	63	18	8
24 h	0	0	71	21	8
CH_2Cl_2	14	0	83	3	1

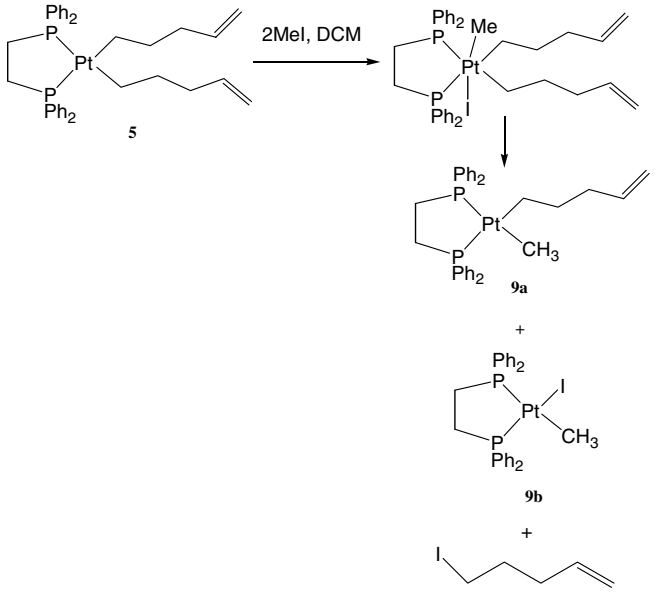
By GC–MS analysis.

3.4. Oxidative addition

The oxidative addition of organic molecules to unsaturated transition metal complexes is a fundamental process in organometallic chemistry and catalytic reactions [14]. It was found that the bis(alkenyl)platinum(II) complexes undergo oxidative addition reactions with methyl iodide to yield different products, depending on the experimental conditions (Schemes 3 and 4). It is presumed that the reaction proceeds via the formation of hexacoordinate platinum(IV) species by oxidative addition as reported earlier



Scheme 3.



Scheme 4.

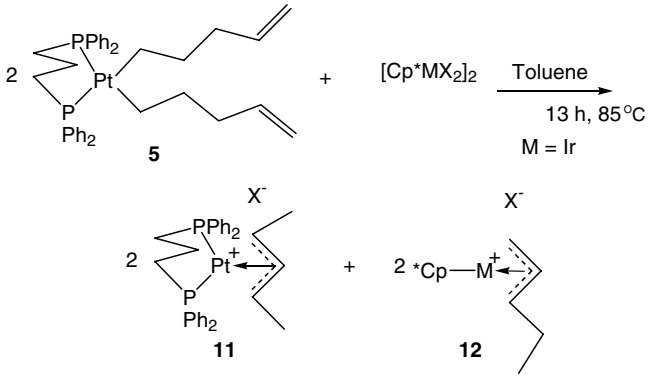
products. In contrast, the presence of excess MeI showed the quantitative formation of the known methylphosphonium iodide salt (**8**). The decomposed products could not be identified or isolated. The formation of the new compound **9a** (15%) and known compound **9b** (41%) [16] were evident when the ligand was dppe in the presence of 1:2 MeI (Scheme 4). The formation of 5-iodo-1-pentene (32%) was also confirmed. It is of interest to note that the addition of MeI allowed the formation of a new metal–carbon bond and breaking of already existing metal–carbon bond simultaneously, this is significant. The nature of ligand systems show a marked effect in oxidative addition reactions, which may be due to differences in steric, electronic and chelating effects in the ligands.

3.5. Carbonylation

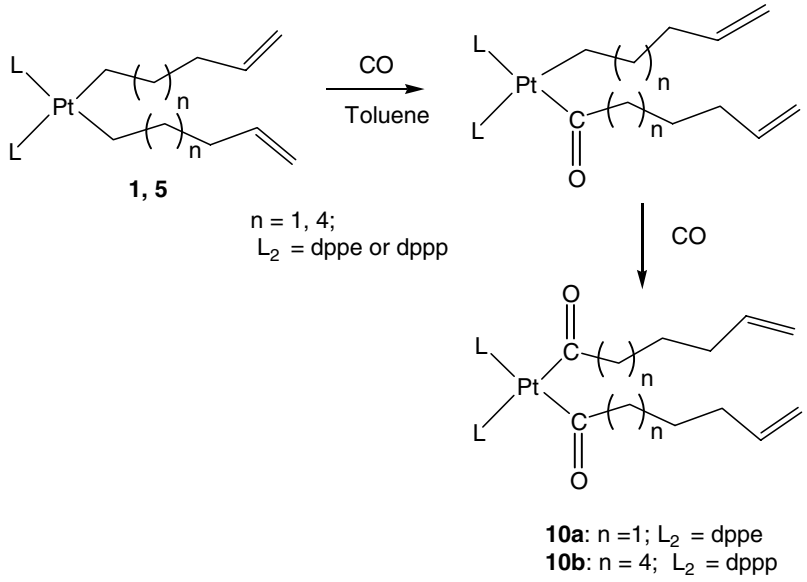
Carbon monoxide insertion into M-alkyl as well as M-acyl bonds to form M-acyl as well as α-ketoacyl complexes

[15]. The organic products were found to be 1-alkenes, 2-alkenes and α,ω-dienes. Attempts to isolate these intermediate hexacoordinate platinum(IV) species were unsuccessful.

Surprisingly, the oxidative addition of MeI to compound **2** afforded different products depending on the experimental conditions and ligand systems (Scheme 3). It is of interest to note that when MeI was allowed to react with **2** in 2:1 molar ratio, a 70% of known compound $Pt(PPh_3)_2MeI$ (**7**) [16] was isolated. The major organic products were found to be 1-hexene (56%), 2-hexene (23%), 1,5-hexadiene (5%) as well as other unidentified



Scheme 6.



Scheme 5.

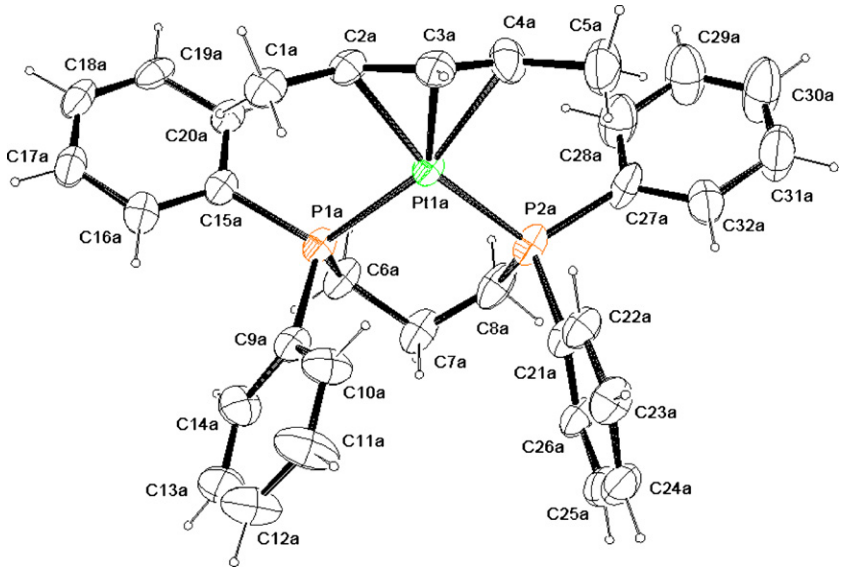


Fig. 2. Molecular structure and atom labeling scheme for the cationic part of the compound **11**, showing one of the two unique molecules (A and B) with the atom-numbering scheme; the suffix a denotes the crystallographically independent molecule A. Displacement ellipsoids are drawn at the 25% probability level and H atoms are shown as small spheres of arbitrary radii.

is well known in the literature [14,17]. It was found that the reaction of carbon monoxide with the bis(pentenyl)platinum(II) complex $L_2Pt[(CH_2)_3CH{=}CH_2]_2$ ($L_2 = dppe$) afforded the expected di(acyl) inserted products **10a** while the reactions with other bis(pentenyl) complexes gave unidentified products ($L_2 = COD$). The ^1H NMR spectra of the reaction mixture ($L = PPh_3$ and $L_2 = dppp$) showed very complex signals indicating the presence of the monoacyl intermediate, which was identified by the characteristic ^{31}P NMR spectrum. However, the reaction smoothly proceeds to the formation of compound **10a** over time. This was evidenced by the ^{13}C NMR which shows a signal in the region of δ 206.8 ppm for the carbonyl carbon as well as a signal at δ 31.5 ppm corresponding to the carbon α to the carbonyl carbon. The IR spectral analysis of the reaction mixture also indicated the presence of bands corresponding to the coordinated CO, which may be due to the replacement of PPh_3 with CO ligands, when $L = PPh_3$. A solution of compound **1** in toluene was subjected to carbonylation with carbon monoxide gas at room temperature. This resulted in the insertion of CO into the Pt–C σ bond to afford the di-acyl product as a colourless crystalline solid after 48 h (Scheme 5). Two strong IR bands at 1605 cm^{-1} (C=C) and 1676 cm^{-1} (C=O) were observed in the spectrum of compound **10b**.

3.6. Transmetalation reactions

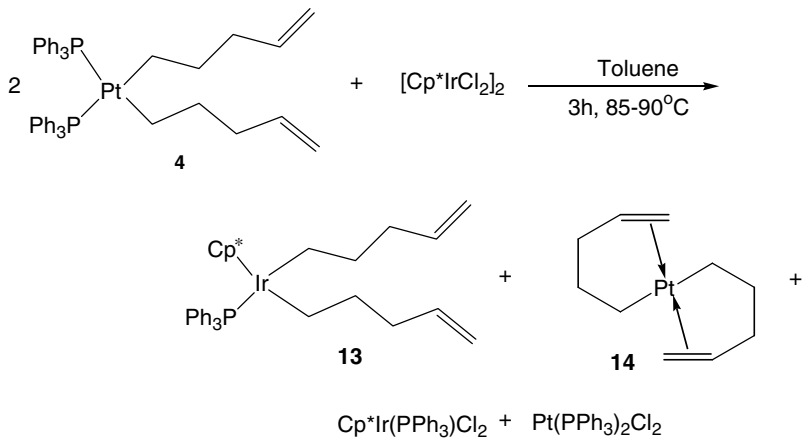
Transmetalation is a fundamental step in cross-coupling chemistry [11]. Various transmetalation reactions of group 10 metal halide complexes with organoboronic acid or organometallic reagents have received recent attention [18,19]. Clarke and Heydt have reported the importance of ligand steric effects on transmetalation reactions of some organometallic complexes [20].

The diphosphine ligand system allowed the quantitative formation of allylic metal complexes after reaction of compound **5** with the dimeric sandwich compounds of iridium (Scheme 6). Products **11** and **12** were isolated from diethylether solution and characterized by spectroscopically. Compound **11** was also characterized by X-ray analysis, but the structure was not fully refined.[1]

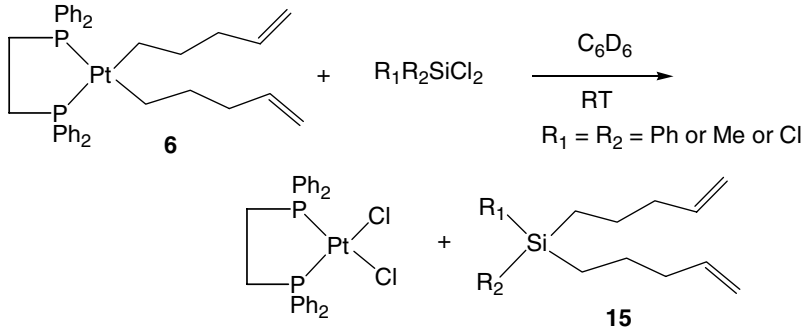
The Pt–P bonds of compound **11** are found to be 2.261(2) and 2.265(2) Å, while the Pt–C bond distances range from 2.156(10)–1.266(3) Å (Fig. 2). Strikingly, the distance between central allylic carbon (C_3) and metal is the shortest. The allylic carbon–carbon distances (C_2–C_3 and C_3–C_4), ranging from 1.349(18) to 1.427(16), showed the nature of double bond and the other C_1–C_2 and C_4–C_5 distances are found to be single bonds. The P–Pt–P, P_1–Pt–C_2 and C–Pt–C bond angles in compound **11** are observed as 94.69(11), 98.0(3) and 66.9(5), respectively.

In contrast, the PPh_3 ligand system shows a different trend in the reactivity by forming unexpected compounds **13** and **14** (Scheme 7). The compound can be easily assigned in the ^{31}P NMR, showing a signal at 26.4 ppm

[1] The cationic part of the structure was completely solved, but we failed to solve the counter anion because there were unidentified discrete solvent molecules in this structure. However, the positions for the atoms of cationic part of the compound 11 molecules were unambiguously placed and refined with reasonable anisotropic displacement parameters. The final *R* factor of 0.0591 is acceptable. We therefore report this structure here. The parameters for crystal data collection and structure refinements are in Table 1. The bond lengths, angles, torsion angles and other molecular parameters are in Table 2–6 (see supporting information for the tables and other details about the data collection).



Scheme 7.



Scheme 8.

without any satellites. $Pt(PPh_3)_2Cl_2$ and $Cp*Ir(PPh_3)Cl_2$ were also recovered from the reaction mixture as insoluble solids from a benzene solution. All these products were isolated and characterized. Data for compound **14** was in agreement with the literature [21].

3.7. Alkenyl group migration reactions

The reaction of platinum(II)-alkenyls with halosilanes yielded the corresponding alkenyl silane products (Scheme 8), with quantitative migration of the alkenyl chains from the platinum to the silicon center. In all the reactions, the products were isolated and identified. The characterization of compound **15** is in agreement with previously reported data [22].

4. Conclusions

Various reactions of bis(alkenyl) platinum complexes have been carried out and shown to yield interesting products. The chelating effect of diphosphine ligands is shown to affect the stability as well as the reactivity aspects of these title compounds significantly. It was also found that these compounds decomposed in the presence of halogenated solvents under light or heat. The length of alkenyl chains did not influence the reactivity of the alkenyl complexes. Studies are in progress which should yield information regarding further reactivity aspects and mechanisms of reactions of these platinum(II) alkenyls and other metal alkenyl compounds. Furthermore the scope of other insertion reactions in the presence of, oxygen, sulphur dioxide, carbon dioxide and elemental sulphur will be explored which may lead to produce some interesting organic products.

Acknowledgements

We thank Anglo Platinum Corporation Ltd., Johnson and Matthey, NRF and University of Cape Town for the financial support.

Appendix A. Supplementary material

CCDC 631341 contains the supplementary crystallographic data for **1**. These data can be obtained free of charge via http://www.ccdc.cam.ac.uk/conts/retrieving.html, or from the Cambridge Crystallographic Data Centre, 12 Union Road, Cambridge CB2 1EZ, UK; fax: (+44) 1223-336-033; or e-mail: deposit@ccdc.cam.ac.uk. Supplementary data associated with this article can be found, in the online version, at doi:10.1016/j.poly.2007.08.036.

References

[1] (a) A. Sivaramakrishna, H. Clayton, C. Kaschula, J.R. Moss, Coord. Chem. Rev. 251 (2007) 1294;
(b) L. Hermans, S.F. Mapolie, Polyhedron 16 (1997) 869.

[2] C.D. Tagge, R.D. Simpson, R.G. Bergman, M.J. Hosteler, G.S. Girolami, R.G. Nuzzo, J. Am. Chem. Soc. 118 (1996) 2634.

[3] K. Dralle, N.L. Jaffa, T. le Roex, J.R. Moss, S. Travis, N.D. Watermeyer, A. Sivaramakrishna, Chem. Commun. (2005) 3865.

[4] A. Sivaramakrishna, H. Su, J.R. Moss, Angew. Chem., Int. Ed. (Eng.) 46 (2007) 3541.

[5] A. Sivaramakrishna, H. Su, J.R. Moss, Dalton Trans., accepted for publication.

[6] (a) A. Sivaramakrishna, H. Su, J.R. Moss, Organometallics, in press;
(b) F. Zheng, A. Sivaramakrishna, J.R. Moss (2007) (unpublished results).

[7] J.X. McDermott, J.F. White, G.M. Whitesides, J. Am. Chem. Soc. 98 (1976) 6522.

[8] H.C. Clark, L.E. Manzer, J. Organomet. Chem. 59 (1973) 411.

[9] D.A. Slack, M.C. Baird, Inorg. Chim. Acta 24 (1977) 277.

[10] F.H. Allen, O. Kennard, D.G. Watson, R. Taylor, in: A.J.C. Wilson (Ed.), International Tables for Crystallography, vol. C, Kluwer Academic Publishers, Dordrecht, 1992.

[11] A.D. Meijere, F. Dieterich, Metal Catalyzed Cross-Coupling Reactions, Wiley, New York, 2004, and the references therein.

[12] (a) R.H. Grubbs, A. Miyashita, Fundamental Res. Homogeneous Catal. 3 (1979) 151;
(b) R.J. Puddephatt, Coord. Chem. Rev. 33 (1980) 149;
(c) R.J. Puddephatt, Comments Inorg. Chem. 2 (1982) 69;
(d) E. Lindner, Adv. Heterocyclic Chem. 39 (1986) 237.

[13] J. Cámpora, P. Palma, E. Carmona, Coord. Chem. Rev. 193–195 (1999) 207.

[14] J.P. Collman, L.S. Hegedus, J.R. Norton, R.G. Finke, Principles and Applications of Organo Transition Metal Chemistry, University Press, Mill Valley, CA, 1987.

[15] L.M. Rendina, R.J. Puddephatt, Chem. Rev. 97 (1997) 1735.

[16] (a) S. Otto, A. Roodt, J.G. Leipoldt, S. Afr. J. Chem. 48 (1995) 114;
(b) K.A. Hooton, J. Chem. Soc. [Sect.] A: Inorganic, Physical, Theoretical (1970) 1896.

[17] (a) J.B. Sheridan, S.H. Han, G.L. Geoffroy, J. Am. Chem. Soc. 109 (1987) 8097;
(b) F. Calderazzo, Angew. Chem., Int. Ed. Engl. 16 (1977) 299.

[18] T. Nishikata, Y. Yamamoto, N. Miyaura, Organometallics 23 (2004) 4317.

[19] K. Osakada, H. Onodera, Y. Nishihara, Organometallics 24 (2005) 190.

[20] M.L. Clarke, M. Heydt, Organometallics 24 (2005) 6475.

[21] C.D. Tagge, R.D. Simpson, R.G. Bergman, M.J. Hostetler, G.S. Girolami, R.G. Nuzzo, J. Am. Chem. Soc. 118 (1996) 2634.

[22] A.C. Church, J.H. Pawlow, K.B. Wagener, Macromolecules 35 (2002) 5746.

Available online at www.sciencedirect.com
ScienceDirect
Polyhedron 27 (2008) 53–58
POLYHEDRON
www.elsevier.com/locate/poly

Novel manganese (III) porphyrin containing peripheral "[RuCl(dppb)(X-bipy)]$^{+}$" cations [dppb = 1,4-bis(diphenylphosphino) butane and X = –CH_3, –OMe, –Cl]. X-ray structure of the *cis*-[RuCl(dppb)(bipy)(4-Mepy)]PF_6 complex

Lincoln Lucilio Romualdo [a], André Luis Bogado [a], Eliana M.A. Valle [a], Icaro S. Moreira [b], Javier Ellena [c], Eduardo E. Castellano [c], Márcio P. de Araujo [d,*], Alzir A. Batista [a,*]

[a] *Departamento de Química, Universidade Federal de São Carlos, C.P. 676, 13565-905 São Carlos, SP, Brazil*
[b] *Departamento de Química Orgânica e Inorgânica, Universidade Federal do Ceará, Fortaleza, CE, Brazil*
[c] *Instituto de Física de São Carlos, Universidade de São Paulo, São Carlos, SP, Brazil*
[d] *Departamento de Química, Universidade Federal do Paraná, C.P. 19081, CEP 81531-990, Curitiba, PR, Brazil*

Received 27 March 2007; accepted 20 August 2007
Available online 1 October 2007

Abstract

New tetraruthenated manganese (III) porphyrins were synthesized and characterized (^{31}P NMR, cyclic voltammetry, UV–Vis). This new system presents four units of cationic "[RuCl(dppb)(X-bipy)]$^{+}$". The electrochemical and catalytic properties of the central manganese (III) show dependence on the characteristics of the peripheral ruthenium complexes as evidenced by the $Mn^{(III)}/Mn^{(II)}$ reduction potential.

The catalytic oxidation reactions of olefins, cyclohexene and cyclohexane, were carried out in the presence of tetrapyridyl manganese (III) porphyrins containing cationic ruthenium complex and using iodosylbenzene as oxygen donor. The performance of these new tetraruthenated porphyrins systems were evaluated and compared with the manganese porphyrin.
© 2007 Elsevier Ltd. All rights reserved.

Keywords: Tetraruthenated porphyrins; Manganese porphyrins; Oxidation catalysis

1. Introduction

The metalloporphyrins are widely studied due to their participation in biological systems promoting, for example, oxygen transport, electron transferences and of note are the studies on mimetic catalytic oxidation reactions [1,2]. The primordial factor of these reactions is related to the formation of high valence Mn^{IV}=O and Mn^{V}=O species [3–6] via oxygen-donor agent, usually H_2O_2 and PhIO.

Usually, one way to introduce electronic and/or steric modifications on porphyrins is through *meso*-functionalization of the porphyrin rings leading to different properties [7–12].

Thus, tetrapyridyl substituted porphyrins are widely employed as building blocks for supramolecular systems construction [13–17]. The functionalization of the pyridyl group by linking ruthenium complexes can afford both electronic and steric changes on porphyrins making them very attractives and a fascinating way to manipulate the structure of such systems [13–17].

Some works on oxidation of organic substrates applying tetraruthenated manganese porphyrins can be found in the literature [16,18,19] and their activities are related to the electronic and steric effects of the peripheral ruthenium complexes.

* Corresponding author.
E-mail address: mparaujo@quimica.ufpr.br (M.P. de Araujo).

0277-5387/$ - see front matter © 2007 Elsevier Ltd. All rights reserved.
doi:10.1016/j.poly.2007.08.021

In this paper is presented the synthesis, characterization and catalytic evaluation of new supra-molecular manganese (III) porphyrins $\{Mn^{(III)}TPyP[RuCl(dppb)(X\text{-}bipy)]_4\}(PF_6)_5$, where dppb = 1,4-bis(diphenylphosphino)butane; X-bipy = 4,4′-substituted-2,2′-bipyridine; *X* = –Cl, –Me and –OMe). In addition, oxidation reactions were conducted using the porphyrin $[Mn^{(III)}TPyP]^+$ without any peripheral ruthenium complexes. X-ray structure of $[RuCl(dppb)(bipy)(4\text{-}Mepy)]PF_6$ is presented for understanding and visualization of how are the ruthenium peripherals in the manganese–porphyrin system.

2. Experimental

2.1. Materials and instrumentation

All manipulations were carried out under purified argon using standard Schlenk technique. Reagent grade solvents were appropriately distilled and dried before use. The $RuCl_3 \cdot 3H_2O$ was supplied by Johnson Matthey Ltd. or purchased from Aldrich. Methylenechloride (Baker) (DCM) HPLC grade was degassed prior to use. Cyclohexane (Aldrich) and cyclohexene (Aldrich) were distilled prior to use. The *cis*-$[RuCl_2(dppb)(X\text{-}bipy)]$ (X = –H, $–CH_3$, CH_3O–, –Cl) were synthesized as described in the literature [20,21]. The UV–Vis spectra were recorded on a Hewlett–Packard 8453A diode-array spectrophotometer. Cyclic voltammetry (CV) experiments were carried out at room temperature in CH_2Cl_2 using a BAS-100B/W Bioanalytical Systems Instruments; the working and auxiliary electrodes were stationary Pt foils, and the reference electrode was Ag/AgCl, 0.10 M $Bu_4N^+ClO_4^-$ (TBAP) (Fluka Purum), a medium in which ferrocene is oxidized at 0.43 V (Fc^+/Fc). Elemental analyses were performed in the Chemistry Department at Universidade Federal de São Carlos. The NMR data of the compounds were acquired using a Bruker DRX-400 spectrometers using D_2O/CH_2Cl_2 or $CDCl_3$ as deuterated solvent. Chemical shifts are reported with respect to the phosphorus signal of phosphoric acid (85%) for ^{31}P and residual solvent proton for ^1H. The *cis*- and *trans*- used in the text refer to the position of chlorides related to each other.

2.2. Iodosylbenzene (PhIO)

Iodosylbenzene was prepared from iodobenzene diacetate and NaOH [22,23], and its purity (>98%) was confirmed by the iodometric method. Samples were stored in freezer.

2.3. Oxidation reactions

The reactions were carried out in a 3 mL vial with screw cap containing a silicone teflon-coated septum. In a standard reaction, the solvent and cyclohexane were added to the vial containing the pre-catalyst and iodosylbenzene under argon atmosphere, and the flask was adapted in a dark chamber. The mixtures were magnetic stirred at room temperature (25 °C).

2.4. Product analysis

The oxidation products of the catalytic reactions were analyzed by gas-chromatography using hexadecane as internal standard. A Shimadzu 17A chromatograph with FID ($N_2 = 30$ mL min^{-1}: $H_2 = 40$ mL min^{-1}; compressed air = 500 mL min^{-1}) detector and Silica (25 m long and 0.5 mm inner diameter with 1 mm thick Silica as stationary phase) column were used. The yields of the reactions are referred to the amount of PhIO consumed in each reaction. The products of the reactions were analyzed by a comparison of their retention times with authentic samples. Control of all reactions was carried out under the same experimental conditions, but in the absence of pre-catalysts for all runs. The stability of the catalysts was checked by UV–Vis spectroscopy.

3. Synthesis

3.1. [RuCl(dppb)(bipy)(4-Mepy)]PF_6

To a methylenechloride (5.0 mL) solution of *cis*-$[RuCl_2(dppb)(bipy)]$ (100 mg; 0.132 mmols) the 4-methylpyridine ligand (12.3 mg; 0.132 mmols) and NH_4PF_6 (215 mg; 1.32 mmols) were added. The reaction was stirred at room temperature for 2 h. The solution was concentrated and addition of *n*-hexanes yielded a yellow solid, which was collected by filtration, washed well with deionized water and diethyl ether and dried under vacuum. Yield: 93%. Elemental *Anal.* Calc. for $C_{44}H_{43}ClN_3P_3F_6Ru \cdot CH_2Cl_2$: C, 51.86; H, 4.35; N, 4.03. Found: C, 51.78; H, 4.42; N, 4.20%. $^{31}P\{^1H\}$ NMR, r.t., δ 37.87 (s); 0 °C, 38.83 (d), 38.37 (d) ($^2J = 34.0$ Hz). The recrystallization of the complex from CH_2Cl_2/MeOH/ether gave yellow crystals suitable for X-ray analysis. The structure of the $[RuCl(dppb)(bipy)(4\text{-}Mepy)]PF_6$ complex can be used as a model for the structures of the porphyrin derivatives obtained in this work.

4. Porphyrins and porphyrins derivatives

4.1. Meso-tetra(4-pyridyl)porphynatemanganese(III) acetate, [$Mn^{(III)}$ TPyP](OAc) (MnP) where TPyP = meso-tetra(4-pyridyl)porphyrin

TPyP = meso-tetra(4-pyridyl)porphyrin, was done by adapting the method describe in the literature [24] refluxing the free-base (H_2TPyP, Aldrich, 97%) and manganese (II) acetate (Fluka) in glacial acetic acid during 4 h. The acid was removed in a rotary evaporator; the solid was dissolved in methylenechloride and filtered, the solvent was pumped out and manganese–porphyrin (MnP) was obtained.

A representative synthesis of {$Mn^{(III)}$-TPyP[RuCl(dppb)(X-bipy)]$_4$}$(PF_6)_5$ is as follow:

{$Mn^{(III)}$-TPyP[RuCl(dppb)(CH_3O-bipy)]$_4$}$(PF_6)_5$ (MeO–MnP). To a methylenechloride (5.0 mL) solution of [$Mn^{(III)}$TPyP](OAc) (3.0 mg; 4.2 μmols) a methylenechloride solution of *cis*-[$RuCl_2$(dppb)(CH_3O-bipy)] (14.0 mg; 17.4 μmol), and NH_4PF_6 (10.0 mg; 61.0 μmols) were added. The reaction was stirred at room temperature for 4 h. The solution was concentrated and addition of *n*-hexanes yielded a black solid, which was collected by filtration, washed well with deionized water and diethyl ether and dried under vacuum.

Yield: 93%. Elemental *Anal.* Calc. for $C_{200}H_{184}Cl_4F_{30}MnN_{16}O_8P_{13}Ru_4$: C, 53.22; H, 4.11; N, 4.97; Ru, 8.96; Mn, 1.22. Found: C, 53.35; H, 4.05; N, 4.62; Ru, 8.42; Mn, 1.08%.

{$Mn^{(III)}$-TPyP[RuCl(dppb)(CH_3-bipy)]$_4$}$(PF_6)_5$ (Me–MnP). Yield: 88%. Elemental *Anal.* Calc. for $C_{200}H_{184}Cl_4F_{30}MnN_{16}P_{13}Ru_4$: C, 54.78; H, 4.23; N 5.11; Ru, 9.22; Mn, 1.25. Found: C, 54.35; H, 4.05; N, 5.05; Ru, 9.42; Mn, 1.18%.

{$Mn^{(III)}$-TPyP[RuCl(dppb)(Cl-bipy)]$_4$}$(PF_6)_5$ (Cl–MnP). Yield: 87%. Elemental *Anal.* Calc. for $C_{192}H_{160}Cl_{12}F_{30}MnN_{16}P_{13}Ru_4$: C, 50.70; H, 3.55; N 4.93; Ru, 8.89; Mn, 1.21. Found:C, 50.61; H, 3.63; N, 4.66; Ru, 8.65; Mn, 1.07%.

4.2. X-ray diffraction data

Yellow single crystals of *cis*-[RuCl(dppb)(bipy)-(4-Mepy)]PF_6 suitable for X-ray structure analysis were obtained by recrystallization from dichloromethane solution. The X-ray data were performed on graphite monochromated Mo Kα ($\lambda = 0.71073$ Å) radiation on an Enraf-Nonius Kappa CCD diffractometer. Data were collected up to 50° in 2θ, with a redundancy of 4. The final unit cell parameters were based on all reflections. Data collections were done using the COLLECT program [25]; integration and scaling of the reflections were performed with the HKL Denzo–Scalepack system of programs [26]. Absorption corrections were carried out using the multi-scan method [27]. The structure was solved by direct methods with SHELXS-97 [28]. The model was refined by full-matrix least-squares on F^2 by means of SHELXL-97 [29]. All the hydrogen atoms were stereochemically positioned and refined with the riding model. All H atoms were located on stereochemical grounds. The data collections and experimental details for the complex are summarized in Table 1.

Table 1
Crystal data and structure refinement for the *cis*-[RuCl(dppb)(bipy)(4-Mepy)]PF_6 complex

Empirical formula	$[C_{44}H_{43}N_3P_2ClRu]PF_6 \cdot 0.4(CH_3OH) \cdot 1/2(H_2O)$
Formula weight	979.07
Temperature (K)	120(2)
Wavelength (Å)	0.71073
Crystal system	monoclinic
Space group	$P2_1/c$
Unit cell dimensions	
a (Å)	19.0149(5)
b (Å)	13.1118(4)
c (Å)	22.2038(7)
β (°)	124.158(2)
Volume (Å^3)	4580.9(2)
Z	4
D_{calc} (Mg/m^3)	1.420
Absorption coefficient (mm^{-1})	0.566
F(000)	2001
Crystal size (mm^3)	$0.15 \times 0.12 \times 0.04$
Θ Range for data collection (°)	2.02–25.00
Index ranges	$-22 \leqslant h \leqslant 22$, $-15 \leqslant k \leqslant 15$, $-26 \leqslant l \leqslant 24$
Reflections collected	25456
Independent reflections [R_{int}]	7842 [0.0599]
Completeness to theta = 25.00°	97.2%
Absorption correction	analytical
Maximum and minimum transmission	0.9791 and 0.9291
Refinement method	full-matrix least-squares on F^2
Data/restraints/parameters	7842/0/561
Goodness-of-fit on F^2	1.048
Final R indices [$I > 2\sigma(I)$]	$R_1 = 0.0584$, $wR_2 = 0.1495$
R indices (all data)	$R_1 = 0.0770$, $wR_2 = 0.1608$
Extinction coefficient	0.0014(3)
Largest differences in peak and hole (e Å^{-3})	1.486 and −0.863

5. Results and discussion

The ORTEP [30] molecular structure of the [RuCl(dppb)-(bipy)(4-Mepy)]PF_6 complex and selected bond length and angles are in Fig. 2.

The X-ray single crystal structure of the [RuCl(dppb)-(bipy)(4-Mepy)]PF_6 complex revealed that the Ru(II) ion is in a distorted octahedral geometry. The Ru–Cl, Ru–N, Ru–P distances found for the [RuCl(dppb)(bipy)-(4-Mepy)]PF_6 are in the expected range reported in the literature [31]. The Ru–N bond length is longer for those *trans* to P- atom than the one *trans* to chloride (see caption in Fig. 2). The stronger structural *trans* effect of the phosphines than the chloride can account for these differences in bond length [32,33].

The $^{31}P\{^1H\}$ NMR spectra of the precursors *cis*-[$RuCl_2$(dppb)(X-bipy)] show two doublets in the range 46 and 31 ppm ($^2J_{PP} \sim 36$ Hz) in CH_2Cl_2 (see Table 2) which is characteristic of a AX spin system. The formation of tetraruthenated porphyrins involves the dissociation of one chloride of the *cis*-[$RuCl_2$(dppb)(X-bipy)] complex and its coordination to the pyridyl groups leading to the formation of "[RuCl(dppb)(L)(X-bipy)]$^+$" unities (L = pyridyl group of the porphyrin ring). The substitution reaction is accompanied by a change in the spin system, the initial AX changes to an AB system. This change is indicative of the formation of such isomer where the pyridyl group is *trans* to P of the dppb ligand. The same behavior is observed in the reaction of *cis*-[$RuCl_2$(dppb)(X-bipy)] [34] with

Table 2
^{31}P NMR and electrochemical data

Compound	$^{31}P\{^{1}H\}$/ppm (mult.); ^{2}J (Hz)	Ru^{III}/Ru^{II}	Mn^{III}/Mn^{II}
cis-[$RuCl_2$(dppb)(CH_3O-bipy)][21]	46(d), 31(d); 36	570	
cis-[$RuCl_2$(dppb)(CH_3-bipy)][21]	42(d), 31(d); 36	600	
cis-[$RuCl_2$(dppb)(Cl-bipy)][21]	44(d), 31(d); 33	760	
[RuCl(dppb)(bipy)(4-Mepy)]PF_6	38.8(d), 38.4(d); 34[a]	1103	
$\{Mn^{(III)}$-TPyP[RuCl(dppb)(MeO-bipy)]$_4\}(PF_6)_5$	38(d), 36(d); 36	1021	113
$\{Mn^{(III)}$-TPyP[RuCl(dppb)(Me-bipy)]$_4\}(PF_6)_5$	39(d), 38(d); 36	1080	30
$\{Mn^{(III)}$-TPyP[RuCl(dppb)(Cl-bipy)]$_4\}(PF_6)_5$	40(d), 39(d); 36	1180	4

[a] $^{31}P\{^{1}H\}$ acquired at 0 °C.

N-donor ligands. As can be seen is Fig. 2, the 4-Mepy is in *trans* position with one P-atom of the diphosphine. In this way it is easy to attribute the formation of the tetraruthenated porphyrin and the isomer of the peripheral ruthenium complexes as proposed in Fig. 1.

It is worth of mention that the multiplicity of the phosphorus atoms of the dppb ligand is solvent and temperature dependent. This accidental degeneracy was observed before by James and by us [35,36]. For example, the complex $\{Mn^{(III)}$-TPyP[RuCl(dppb)(Me-bipy)]$_4\}(PF_6)_5$ in methylenechloride the ^{31}P NMR spectrum show a singlet, but in chloroform the AB quadruplet is resolved. The signals are broader than the analogues containing zinc metallated porphyrins due to the presence of a paramagnetic Mn(III) [36].

The cyclic voltammograms of the manganese complexes prepared consist of a pair of reversible peaks ($Ia/Ic \cong 1$), attributed to the one electron $Ru^{(III)}/Ru^{(II)}$ couple (Table 2) and another for $Mn^{(II)}/Mn^{(III)}$ couple. The higher potentials for Ru^{III}/Ru^{II} for the $\{Mn^{(III)}$-TPyP[RuCl(dppb)-(X-bipy)]$_4\}(PF_6)_5$ complex when compared with the starting ruthenium complexes, *cis*-[$RuCl_2$(dppb)(X-bipy)], can be explained by the dissociation of one donor (chloride), reducing the electron density on metal center and enormously increasing the potential.

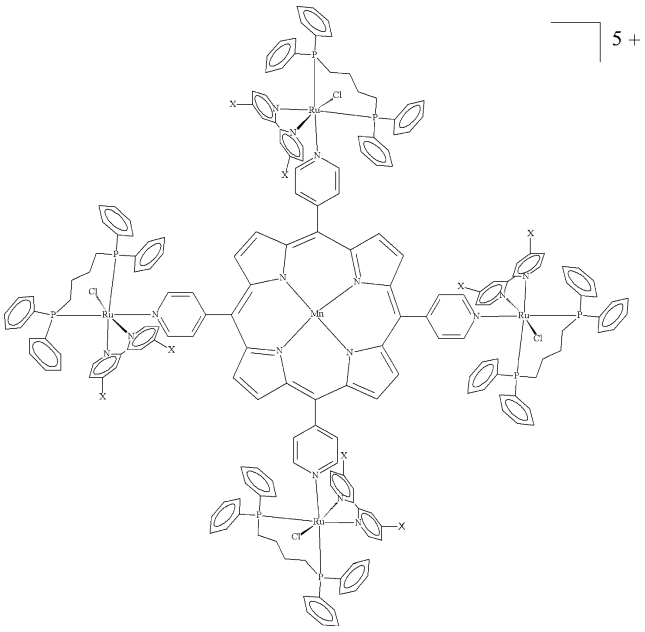


Fig. 1. Structure of $\{MnTPyP[RuCl(dppb)(X\text{-}bipy)]_4(PF_6)_5$, (X = –$CH_3$, –OMe, –Cl).

The manganese reduction potentials are higher for the tetraruthenated porphyrins than $Mn^{(III)}$-TPyP (−80 mV) which is in agreement with previously reported data [37]. The reduction potential variation for the peripheral ruthenium is inversely related to the manganese (see Table 2). This clearly shows that the electron density on $Mn^{(III)}$ can be tuned just changing the characteristics of the peripheral ruthenium complexes.

Typical bands in the UV/Vis spectra of $Mn^{(III)}$-TPyP porphyrin complex [38] are observed at 621, 584, 475 and 370 nm. The $\{Mn^{(III)}$-TPyP[RuCl(dppb)(X-bipy)]$_4\}(PF_6)_5$ complexes, besides the typical bands for the manganese porphyrin they show other arising from the ruthenium peripheral complex, such as $\pi \rightarrow \pi^*$ from the bipyridine ligand, in the UV region [21].

6. Catalytic activity

The catalytic mechanism involving manganese porphyrins is mentioned in the literature and is based on the formation of Mn^{IV}=O and Mn^{V}=O species [3–6,16]. One strategy to modulate the bulkiness environment or the electronic characteristics of the metalloporphyrin center is binding selected metal complexes in the peripheral nitrogens of the tetrapyridylporphyrin.

The oxidation of cyclohexane with PhIO in the presence of the $[Mn^{(III)}$-TPyP]OAc or of the supramolecular $\{Mn^{(III)}$-TPyP[RuCl(dppb)(X-bipy)]$_4\}(PF_6)_5$ species, at 25 °C, was found to yield cyclohexanol and cyclohexanone as major products. None of these products could be found in the absence of the porphyrins species, showing that they are, in fact, promoting the oxygen atom transfer to the substrate. The catalytic activity of $[Mn^{(III)}$-TPyP]OAc and $\{Mn^{(III)}$-TPyP[RuCl(dppb)(X-bipy)]$_4\}(PF_6)_5$ species for the epoxidation of cyclohexene by iodosylbenzene, in methylenechloride, was evaluated under identical experimental conditions [24].

The conversion of the oxidation reactions of cyclohexene and cyclohexane, based on iodosylbenzene, was up to 97%. For the epoxidation reactions the yields in epoxide were around 60% to MnP, 11% to MeO–MnP, 13% to Me–MnP and 10% Cl–MnP (reaction time = 1.5 h,

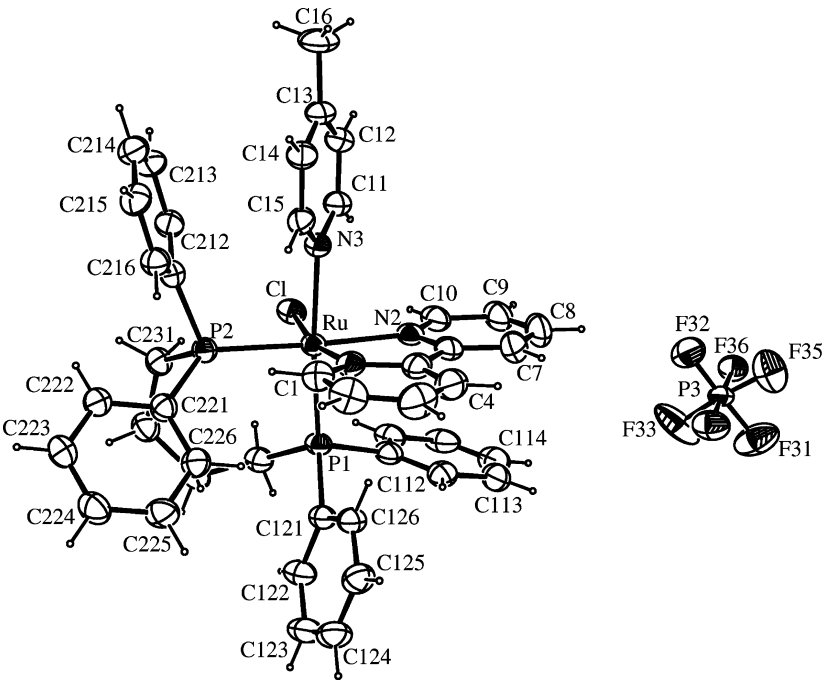


Fig. 2. X-ray structure of [RuCl(dppb)(bipy)(4-Mepy)]PF_6 (ORTEP plot with ellipsoids at the 50% probability). Bond lengths (Å): Ru–N(1) 2.096(4), Ru–N(2) 2.140(4), Ru–N(3) 2.203(4), Ru–P(1) 2.3571(12), Ru–P(2) 2.3645(13), Ru–Cl 2.4560(13). Bond angles (°): P(1)–Ru–P(2) 93.38(4), N(1)–Ru–Cl 168.25(12), N(2)–Ru–Cl 91.55(12), N(3)–Ru–Cl 87.47(11), P(1)–Ru–Cl 86.35(4), P(2)–Ru–Cl 87.94(4), N(1)–Ru–N(2) 77.74(17), N(1)–Ru–N(3) 86.60(15), N(2)–Ru–N(3) 83.93(14), N(1)–Ru–P(1) 98.29(11), N(2)–Ru–P(1) 89.74(10), N(3)–Ru–P(1) 171.03(11), N(1)–Ru–P(2) 102.48(12), N(2)–Ru–P(2) 176.80(10), N(3)–Ru–P(2) 92.89(11).

$[cat] = 4 \times 10^{-7}$ mol L^{-1}, cat:PhIO:cyclohexene molar ratio 1:30:2000) for both systems.

The [$Mn^{(III)}$-TPyP]OAc catalyst leds to the formation of cyclohexanol (14%) and cyclohexanone (6%) in a ratio C-ol:C-one of 2.3, but MeO–MnP, Me–MnP and Cl–MnP generated cyclohexanol (35%, 30% and 28%) and cyclohexanone (9%, 4% and 5%). However, the PhIO yields were 96%, 70%, 77% and 65% for MnP, MeO–MnP, Me–MnP and Cl–MnP, respectively. No detectable degradation of MnP catalyst (evaluated by the presence of the Soret band) was observed by UV–Vis spectroscopy. The high values on the total conversion based on the consumption of PhIO can be explained by the occurrence of parallel reactions in the systems as previously reported [4] especially reactions that involve allylic oxidations of the cyclohexene. Others species was formed during the reaction but it was not measured, but this justify the small yield for the epoxide formation Table 3.

Comparison of our system with the closest found in the literature [19] using the supramolecular {MnT4PyP[RuCl-(bipy)$_2$]$_4$}$^{5+}$, for the epoxidation reactions our system presents lower yield in epoxide, but for cyclohexane oxidation the ratio C-ol:C-one is higher, showing that our system has higher selectivity on cyclohexanol Table 4.

Very recently was shown that electron-rich manganese porphyrins decay faster than electron-deficient ones [39]. In this study this was not observed, probably because the electron density of the manganese centers are not too different when the highly reactive Mn^{V}=O site is formed in solution or because the peripheral groups prevent the degradation of the molecule under highly oxidizing conditions.

Table 3
Oxidation of cyclohexene by PhIO in CH_2Cl_2

Catalyst	Conversion[a] (%)	Epoxide (%)
MnP	97	60
MeO–MnP	97	11
Me–MnP	92	13
Cl–MnP	88	10

Conditions: Molar rather Cat/PhIO/cyclohexene 1:30:2000, DCM, 25 °C, time 1 h argon atmosphere.
[a] Yield based on iodosylbenzene.

Table 4
Oxidation of cyclohexane by PhIO in CH_2Cl_2

Catalyst	Conversion[a] (%)	Yield C-ol (%)	Yield C-ona (%)	Ratio C-ol:C-one
MnP	96	14	6	2.3
MeO–MnP	95	35	8	4.4
Me–MnP	96	30	4	7.5
Cl–MnP	97	28	5	5.6

Conditions: Molar rather Cat/PhIO/cyclohexane 1:30:2000, DCM, 25 °C, time 1 h argon atmosphere.
[a] Yield based on iodosylbenzene.

7. Conclusions

New tetraruthenated porphyrins were synthesized, characterized and their catalytic properties on oxidation of cyclohexanone and cyclohexane were evaluated. The properties of the porphyrins are practically not dependent on the characteristics of peripheral ruthenium complexes containing substituted bipyridines. The catalytic results obtained in this work allows to suggest that the yield and the selectivity of the products are modulated better by the presence or absence of steric effect than by the electronic effect induced by the peripheral ruthenium complexes on the central metal. The yield on epoxide is decreased comparing the non-tetraruthenated porphyrin with the tetraruthenated, but for cyclohexane the presence of peripheral ruthenium complexes increase the yield on cyclohexanol. The electron density of the manganese center does not affect significantly the yield and selectivity of the products of the catalytic reactions. Probably this difference on electron density of the metal center is not significant after the formation of the real catalytic Mn^{V}=O site, in solution.

Acknowledgements

We thank CNPq, CAPES, FINEP, PRONEX and FAPESP for financial support and Johnson Matthey plc for the loan of $RuCl_3$ (to M.P.A).

Appendix A. Supplementary material

CCDC 640693 contains the supplementary crystallographic data for *cis*-[RuCl(dppb)(bipy)(4-Mepy)]PF_6. These data can be obtained free of charge via http://www.ccdc.cam.ac.uk/conts/retrieving.html, or from the Cambridge Crystallographic Data Centre, 12 Union Road, Cambridge CB2 1EZ, UK; fax: (+44) 1223-336-033; or e-mail: deposit@ccdc.cam.ac.uk. Supplementary data associated with this article can be found, in the online version, at doi:10.1016/j.poly.2007.08.021.

References

[1] M.J. Gunter, P. Turner, Coordination Chemistry Reviews 108 (1991) 15.
[2] B. Meunier, Chemical Review 92 (1992) 1411.
[3] J.T. Groves, J.B. Lee, S.S. Marla, Journal of the American Chemical Society 119 (1997) 6269.
[4] J.T. Groves, M.K. Stern, Journal of the American Chemical Society 110 (1988) 8628.
[5] N. Jin, J.T. Groves, Journal of the American Chemical Society 121 (1999) 2923.
[6] A. Yamamoto, L.K. Phillips, M. Calvin, Inorganic Chemistry 7 (1968) 847.
[7] K. Kalyanasundaram, Inorganic Chemistry 23 (1984) 2453.
[8] I. Batinic-Haberle, I. Spasojevic, P. Hambright, L. Benov, A.L. Crumbliss, I. Fridovich, Inorganic Chemistry 38 (1999) 4011.
[9] P. Hambright, T. Gore, M. Burton, Inorganic Chemistry 15 (1976) 2314.
[10] P. Hambright, Inorganic Chemistry 16 (1977) 2987.
[11] P. Hambright, Journal of Inorganic and Nuclear Chemistry 39 (1977) 1102.
[12] A. Shamim, P. Hambright, Inorganic Chemistry 19 (1980) 564.
[13] L.R. Dinelli, Ph.D. Thesis UFSCAR (São Carlos), Brazil, 2003.
[14] H. Winnischofer, H.E. Toma, K. Araki, Journal of Nanoscience and Nanotechnology 6 (2006) 1701.
[15] T. Imamura, K. Fukushima, Coordination Chemistry Reviews 198 (2000) 133.
[16] G.S. Nunes, I. Mayer, H.E. Toma, K. Araki, Journal of Catalysis 236 (2005) 55.
[17] K. Araki, H.E. Toma, Quimica Nova 25 (2002) 962.
[18] K. Araki, H. Winnischofer, H.E.B. Viana, M.M. Toyama, F.M. Engelmann, I. Mayer, A.L.B. Formiga, H.E. Toma, Journal of Electroanalytical Chemistry 562 (2004) 145.
[19] I. Mayer, G.S. Nunes, H.E. Toma, K. Araki, European Journal of Inorganic Chemistry 2006 (2006) 850.
[20] S.L. Queiroz, A.A. Batista, G. Oliva, M. Gambardella, R.H.A. Santos, K.S. MacFarlane, S.J. Rettig, B.R. James, Inorganica Chimica Acta 267 (1998) 209.
[21] M.O. Santiago, C.L. Donicci, I.D. Moreira, R.M. Carlos, S.L. Queiroz, A.A. Batista, Polyhedron 22 (2003) 3205.
[22] H.J. Lucas, E.R. Kennedy, M. W Formo, Organic Synthesis Collective 3 (1955) 483.
[23] J.G. Sharefkin, H. Saltzmann, Organic Syntheses 43 (1963) 62.
[24] Y. Iamamoto, M.D. Assis, K.J. Ciuffi, C.M.C. Prado, B.Z. Prellwitz, M. Moraes, O.R. Nascimento, H.C. Sacco, Journal of Molecular Catalysis A – Chemical 116 (1997) 365.
[25] Enraf-Nonius (1997–2000). COLLECT. Nonius BV, Delft, The Netherlands.
[26] Z. Otinowski, W. Minor, HKL Denzo and Scalepack, in: C.W. CarterJr., R.M. Sweet (Eds.), Methods in Enzymology, vol. 276, Academic Press, New York, 1997, pp. 307–326.
[27] R.H. Blessing, Acta Crystallographica Section A 51 (1995) 33.
[28] G.M. Sheldrick, SHELXS-97, Program for Crystal Structure Resolution, University of Göttingen, Göttingen, Germany, 1997.
[29] G.M. Sheldrick, SHELXL-97, Program for Crystal Structures Analysis, University of Göttingen, Göttingen, Germany, 1997.
[30] L.J. Farrugia, ORTEP3 for Windows, Journal of Applied Crystallography (1997) 565.
[31] M.O. Santiago, A.A. Batista, M.P. de Araújo, C.L. Donnici, I.de S. Moreira, E.E. Castellano, J. Ellena, S. Dos Santos Jr., S.L. Queiroz, Transition Metal Chemistry 30 (2005) 170.
[32] D.A. Cavarzan, F.R. Caetano, L.L. Romualdo, F.B. do Nascimento, A.A. Batista, J. Ellena, A. Barison, M.P. de Araujo, Inorganic Chemistry Communications 9 (2006) 1247.
[33] B.J. Coe, S.J. Glenwright, Coordination Chemistry Reviews 203 (2000) 5.
[34] E.M.A. Valle, M.Sc. Dissertation, UFSCAR (São Carlos), Brazil, 2005.
[35] P.W. Cyr, B.O. Patrick, B.R. James, Chemical Communications (2001) 1570.
[36] L.L Romualdo, A.A. Batista, unpublished work.
[37] S. Dovidauskas, H.E. Toma, K. Araki, H.C. Sacco, Y. Iamamoto, Inorganica Chimica Acta 305 (2000) 206.
[38] L.J. Boucher, Journal of the American Chemical Society 90 (1968) 6640.
[39] W.J. Song, M.S. Seo, S.D. George, T. Ohta, R. Song, M.J. Kang, T. Tosha, T. Kitagawa, E.I. Solomon, W. Nam, Journal of the American Chemical Society 129 (2007) 1268.

Available online at www.sciencedirect.com
ScienceDirect
Polyhedron 27 (2008) 59–64
POLYHEDRON
www.elsevier.com/locate/poly

Synthesis, characterization, crystal structure and catalytic property of [Cu(SalAHE)$_2$] (SalAHE = salicylaldehydeimine-1-hydroxyethane) complex for the oxidation of 3,5-di-*tert*-butylcatechol

Ana C.D. Midões [a], Pedro E. Aranha [a], Mirian P. dos Santos [a], Érica Tozzo [b], Sandra Romera [a], Regina H. de A. Santos [b], Edward R. Dockal [a,*]

[a] *UFSCar, Universidade Federal de São Carlos, Rod. Washington Luiz (SP-310), Km235 São Carlos, SP, Brazil*
[b] *IQSC-USP – Av. Trabalhador Sãocarlense, 400, Centro, Caixa Postal 780, CEP13560-970 São Carlos, SP, Brazil*

Received 21 March 2007; accepted 20 August 2007
Available online 29 October 2007

Abstract

The crystal structure, spectroscopic properties and catalytic property of the copper(II) complex, prepared by the reaction between copper(II) diacetate with the bidentate Schiff base, SalAHE (SalAHE = salicylaldehydeimine-1-hydroxyethane), are reported. This complex is able to oxidize 3,5-di-*tert*-butylcatechol to the respective *o*-quinone. The oxidation reaction was studied in CH_3CN with molecular oxygen at 0, 5, 15 and 25 °C. The progress of the catalytic reaction was followed by gas chromatographic analyses (GC).
© 2007 Elsevier Ltd. All rights reserved.

Keywords: Copper complex; Schiff base; Catecholase activity; Crystal structure

1. Introduction

Copper has been known as an essential bioelement for some time but its biological role(s) has been recognized only in the last decades due to the rapid development of bioinorganic chemistry, a successful interaction between model complexes and protein biochemistry [1–8].

The environment around the metal center and its conformational flexibility are the key factors for a metalloprotein to carry out a specific physiological function, e.g. dioxygen binding, oxygen utilization, etc. In order to emulate the biological activity of metalloproteins, particularly their active sites, various model metal complexes containing Schiff base ligands have been synthesized and studied for their dioxygen uptake [9–15] and oxidative catalysis [16–20].

The oxidation of organic substrates with molecular oxygen under mild conditions is of great interest for industrial and synthetic processes both from an economical and environmental point of view. The synthesis and investigation of functional model complexes for metalloenzymes with catechol oxygenase or catechol oxidase activity is therefore of great promise for the development of new and efficient catalysts for oxidation reactions [21]. Two major enzymes play the key role in these reactions, catechol dioxygenases and catechol oxidases. Most functional mimics of catechol oxidase are mono- or dinuclear Cu(II) complexes [22–27].

As part of the ongoing investigations by our group for spectroscopic studies [28–31] and metal-salen catalyzed oxidations [32], we describe in this work the preparation, characterization, crystal structure and catalytic activity of [Cu(SalAHE)$_2$] for oxidation of catechol. The catalytic oxidation of 3,5-di-*tert*-butylcatechol by copper(II) complex in acetonitrile (CH_3CN) saturated with molecular oxygen was studied in a homogenous system.

* Corresponding author. Tel.: +55 16 3351 8095.
E-mail address: dockal@dq.ufscar.br (E.R. Dockal).

0277-5387/$ - see front matter © 2007 Elsevier Ltd. All rights reserved.
doi:10.1016/j.poly.2007.08.030

2. Experimental

2.1. Reagents

Ethanolamine, 99% (Riedel-de-Haën Inc.); salicylaldehyde, 98%; copper(II) acetate, 99% (Alfa Morton Thiokol Inc.); chloroform-*d* 99.8 at.% D, $CDCl_3$ (Aldrich Chemical Co.); acetonitrile, 99.9%; 3,5-di-*tert*-butylcatechol, 99%; 3,5-di-*tert*-1,2-benzoquinone, 98%. All other solvents and reagents were obtained commercially and were used without further purification.

2.2. Preparation of the copper(II) complex

The complex was prepared in a manner similar to that described [33]. Salicylaldehyde (3.0 mmol, 0.320 ml) and ethanolamine (3.0 mmol, 0.181 ml) were dissolved in 15 ml of methanol. The solution was stirred for 1 h at 60 °C, and then $Cu(CH_3COO)_2 \cdot H_2O$ (1.5 mmol, 0.2995 g) was added to the reaction mixture with continuous stirring for 4 h at 60 °C. The solution was then cooled to room temperature, filtered and the solid was purified with cold ethanol (5 ml at 5 °C) and dried over silica.

Green powder. Yield: 0.326 g, 55.6%. M.p. 178.2–178.7 °C (uncorrected). *Anal.* Calc. for $C_{18}H_{24}N_2O_6Cu$: C, 50.5; H, 5.65; N, 6.55. Found: C, 50.9; H, 5.75; N, 6.7%. Selected IR bands (KBr, cm^{-1}): 1636s, ν(C=N); 1396m, ν(C–N); 1327m, ν(Ph–O); 429w, ν(Cu–O). UV–Vis spectrum in CH_3CN [λ_{max} (nm), ε ($dm^3\,cm^{-1}\,mol^{-1}$)]: $268_{shoulder}$ (18650), 366 (7580), 631 (157).

2.3. Crystallography

Suitable single crystal of the [Cu(SalAHE)$_2$] complex was formed by slow evaporation of an ethanolic solution at room temperature. Diffraction data were acquired using a single crystal mounted on an Enraf-Nonius CAD4 diffractometer. Intensity data were obtained using Mo Kα radiation ($\lambda = 0.71073$ Å) monochromated with graphite using ω–2θ scan mode. The details of the X-ray data collection, structure solution and structure refinements were given in Table 1.

Unit-cell parameters were obtained by the least-squares fit of the setting angles of 25 reflections. Three standard reflections, checked every 2 h, showed no significant variations (±0.1%). The intensity data were corrected for Lorentz polarization and absorption effects on the basis of PSISCAN [34].

The structure was solved on the WinGX system with the localization of the position of the copper atom using the Patterson method with the program SIR97 [35]. The refinement was effected through SHELXL97 [36], with the simultaneous analysis of the geometric parameters of the structure made through system PLATON [37], incorporated the WinGX. Non-hydrogen atoms were refined anisotropically. The hydrogen atoms had been located geometrically, assuming thermal displacement as being equal the 1.3 times the Beq of the atom to which it is bonded.

Table 1
Crystal data and details of the structure determination for [Cu(SalAHE)$_2$]

Empirical formula	$CuC_{18}H_{20}N_2O_4$
Formula weight	391.91
Temperature (K)	293
Radiation (Å)	Mo Kα 0.71073
Crystal system	Monoclinic
Space group	*P*2 1/*c*
a (Å)	18.322(1)
b (Å)	4.804(3)
c (Å)	19.801(2)
β (°)	98.908(6)
V (Å^3)	1721(1)
Z	4
D_{calc} (g/cm^3)	1.512
μ (mm^{-1})	1.294
F(000)	812
Crystal size (mm)	$0.15 \times 0.18 \times 0.20$
θ Range (°)	2.5–30.0
Index ranges	$-25 \leqslant h \leqslant 25$; $-6 \leqslant k \leqslant 0$; $0 \leqslant l \leqslant 27$
Total reflections collected	5145
Independent reflections	5003 [$R_{int} = 0.026$]
Observed reflections $I \geqslant 2\sigma(I)$	2678
Number of parameters	229
R observations	0.0388
wR observations	0.1253
Goodness-of-fit	1.00
Maximum/minimum $\Delta\rho$ (e Å^3)	0.61/−0.57

The graphic representations of the molecules were done using the program ORTEP3 for Windows [38] with 50% probability displacement ellipsoids.

2.4. Physical measurements

Elemental microanalyses (C, H, N) were performed by the Microanalytical Laboratory of the Departamento de Química of the Universidade Federal de São Carlos, São Carlos, São Paulo with a Faison EA 1108 CHNS-O instrument. IR spectroscopy on KBr, dried and stored at 110 °C, pressed discs (1% by weight) with a Bomem Michelson 102 FT-IR instrument. Electronic spectra were recorded in the 190–1100 nm range using a Shimadzu MultSpec-1501 instrument. These spectra of the CH_3CN solutions were obtained at room temperature using matched 1.0 cm quartz cells.

2.5. Blank reactions without any catalyst

Reactions were run in a round-bottom flask at 25, 15, 5 and 0 °C by mixing 0.0222 g (1.0 mmol) of 3,5-di-*tert*-butylcatechol and 10.0 ml of CH_3CN as solvent, saturated with molecular oxygen, each reaction was monitored at 30 min for the first four hours and at 24 h by GC. The quantitative GC analysis of the catechol products was carried out using a SHIMADZU GC-2010 Chromatograph equipped with an FID detector and a J&W DB-5 capillary column (29 m × 0.25 mm × 0.25 μm). Hydrogen was used as carrier gas. The oxidation products yields were calcu-

lated from the chromatogram area, GC error for the determination was within ±3%. The products were characterized by ^{1}H NMR obtained using a Bruker ARX 200 MHz 4.7 T spectrometer with $CDCl_3$ as solvent and TMS with internal standard, and IR spectroscopy on KBr pressed discs (1% by weight) with a Bomem Michelson 102 FT-IR instrument.

2.6. Oxidation of 3,5-di-tert-butylcatechol with catalyst

The conditions of the oxidation reactions in the presence of the catalyst are the same as the blanks except that 0.0039 g, 0.01 mmol of the catalyst was added. The final substrate to catalyst ratio is 100:1.

3. Results and discussion

3.1. IR spectrum

The IR spectrum of the complex exhibits various bands in the 300–4000 cm^{-1} region. In the 3400–3100 cm^{-1} region, were observed two bands in 3329 and 3232 cm^{-1} attributed to O–H stretching. These O–H stretchings are due to the OH of the ligand and with water associated with the solid formed in the reaction since the KBr is stored at 110 °C until use. The microanalysis is consistent with the presence of two waters in the molecular formula. The characteristic C=N stretching frequencies are in the 1592–1640 cm^{-1} region as reported for similar ligands [28,39], the complex exhibits this band at 1636 cm^{-1}. The C–N stretching frequency has been reported in the 1350–1410 cm^{-1} region [41–43], for the complex the band is attributed in 1396 cm^{-1}. A band at 1327 cm^{-1} is attributed to ν(Ph–O) stretching, for similar ligands this band appears as a weak band within the 1290–1340 cm^{-1} range [40–45].

3.2. Molecular structure of [Cu(SalAHE)$_2$]

The structure of [Cu(SalAHE)$_2$] determined by X-ray crystallography consist of two independent half molecules in the asymmetric unit. The Cu atoms are located on the crystallographic inversion centers, giving rise (by $\bar{1}$ symmetry operation) to two independent molecules with different conformation as shown in Fig. 1, with label scheme of the atoms. As shown in Fig. 1, the central copper(II) atom is coordinated with two imine nitrogen atoms and two phenolate oxygen atoms of the two Schiff base ligands. The Schiff base SalAHE (salicylaldehydeimine-1-hydroxyethane) is a bidentate and monoanionic ligand, which results in a neutral copper complex. The X-ray crystallography symmetry imposes that the two ligands be oriented in a *trans* configuration, in which the hydroxyl groups are involved in hydrogen bonds. Contrary to the solid isolated from the reaction mixture that has two water molecules, the isolated crystal does not present either coordinated water or hydration water. In Table 2 selected bond lengths and angles for [Cu(SalAHE)$_2$] are presented. The angles O–Cu–N are 91.92(8)° and 88.08(8)° for the Cu1, and 91.33(9)° and 88.67(9)° for Cu_2. These bond angles are all close to 90°. The distorted square planar coordination is reinforced by the strictly planar arrangement around the Cu atoms. The bond length Cu–N is longer than that of Cu–O and is in agreement with others found in the literature [33,49]. The central copper atom and the ligands form two six-member rings which increase the stability of the complex. Table 3 shows the hydrogen interactions. The presence of hydrogen bonds O–H···O in the solid state makes a bidimensional supramolecular polymer, in the (1 0 0) crystallographic plane depicted in Fig. 2. The interactions C–H···O (Fig. 2) shows that the crystal packing is a very complex three-dimensional polymer, but the interactions are not negligible.

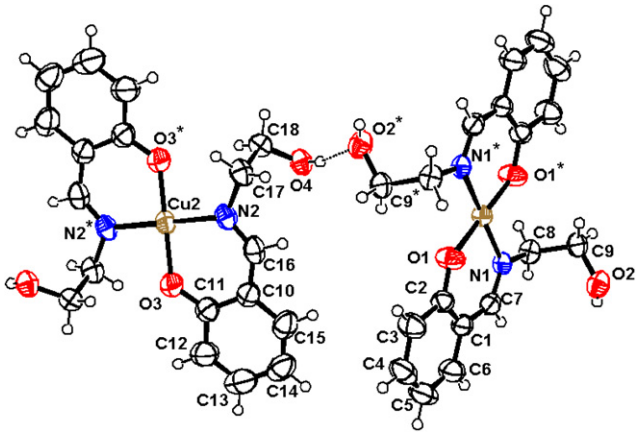


Fig. 1. An ORTEP drawing of [Cu(SalAHE)$_2$] and the atom numbering.

Table 2
Selected bonds and angles for the [Cu(SalAHE)$_2$]

Bonds lengths (Å)			
Cu(1)–O(1)	1.876(2)	Cu(2)–O(3)	1.885(2)
Cu(1)–N(1)	2.013(2)	Cu(2)–N(2)	1.999(2)
Bonds angles (°)			
O(1)–Cu(1)–N(1)	91.92(8)	O(3)–Cu(2)–N(2)	91.33(9)
O(1)–Cu(1)–O(1a)	180	O(3)–Cu(2)–O(3b)	180
O(1)–Cu(1)–N(1a)	88.08(8)	O(3)–Cu(2)–N(2b)	88.67(9)
N(1)–Cu(1)–N(1a)	180	N(2)–Cu(2)–N(2b)	180

3.3. Catalytic oxidation of 3,5-di-tert-butylcatechol

In general, 3,5-di-*tert*-butylcatechol is used as substrate to investigate the oxidation capability of copper complexes, due to its low redox potential, which makes it easy to oxidize to 3,5-di-*tert*butylquinone (DTBQ), and the presence of bulky, non-polar substituents, which prevent further oxidation reactions, such as ring opening reactions, and cyclization/tautomerization reactions [26].

Among the mononuclear copper(II) complexes, compounds possessing intermediate geometry between trigonal bipyramidal and square pyramidal [45] are considered to be

Table 3
Hydrogen bonds distances and angles for the [Cu(SalAHE)$_2$]

A	H	B	A–H (Å)	H···B (Å)	A···B (Å)	Angle (°)	Symmetry operation
O2	OH2	O4	0.82	2.00	2.742(3)	151	$3-x, -y, 2-z$
O4	OH4	O2	0.82	1.92	2.723(3)	165	$3-x, -1-y, 2-z$
C8	H8A	O1	0.97	2.37	2.763(3)	104	$3-x, -1-y, 2-z$
C9	H9B	O1	0.97	2.49	3.051(4)	116	$3-x, -1-y, 2-z$
C17	H17B	O3	0.97	2.33	2.755(4)	105	$2-x, -y, 2-z$
C18	H18A	O3	0.97	2.53	3.061(4)	115	$2-x, -y, 2-z$

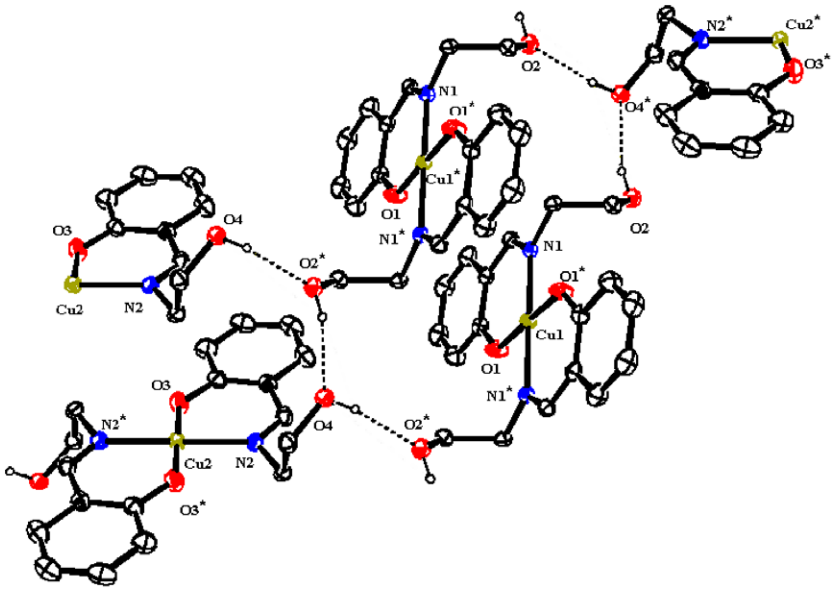


Fig. 2. Supramolecular bidimensional polymer of [Cu(SalAHE)$_2$].

potential models, due to its biological relevance in the geometrical rearrangement [46] during the tyrosinase substrate binding reaction. Kida and co-workers have studied a number of copper(II) complexes and have shown that dinuclear complexes catalyze the reaction while the mononuclear species are either not as efficient or inactive depending on the steric demands of the ligands [47]. Neves and co-workers studied the mononuclear and binuclear copper(II) complexes of the unsymmetrical, binucleating ligand, *N*,*N*,*N*-tris-(2-pyridylmethyl)-1,3-diaminopropan-2-ol, as models for the active site of catechol oxidase [48]. The mononuclear complex was inactive in this oxidation reaction while the binuclear complex is a potential model for the dinuclear copper site in catechol oxidase.

We have examined the catalytic activity of the mononuclear copper(II) complex, [Cu(SalAHE)$_2$], for oxidation of 3,5-di-*tert*-butylcatechol by molecular oxygen in oxygen saturated acetonitrile solutions. The initial rate for the catechol oxidation was determined by monitoring the appearance of the quinone peak in CG chromatogram. For reactions without catalyst at different temperatures the yields after 24 h were below 5%. The progress of the oxidation reactions of 3,5-di-*tert*-butylcatechol in presence of the copper(II) complex at four different temperatures, 0, 5, 15 and 25 °C, and without catalyst at 25 °C are shown in Fig. 3. The results of the catalytic oxidation of 3,5-di-*tert*-butylcatechol for the systems studied are given in Table 4.

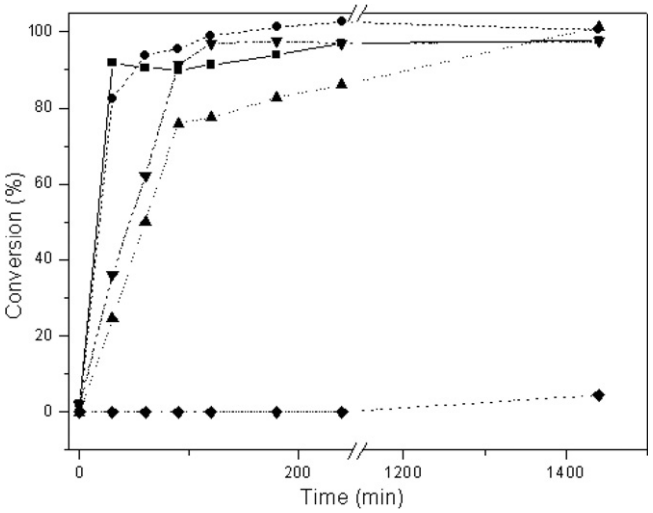


Fig. 3. Effect of temperature on the oxidation of 3,5-di-*tert*-butylcatechol; ■ 25 °C; ● 15 °C; ▼ 5 °C; ▲ 0 °C and ♦ for 25 °C without catalyst.

Table 4
3,5-Di-*tert*-butylcatechol conversion (mol%) at four different temperatures with $[Cu(SalAHE)_2]$ as catalyst and without the catalyst at 25 °C

Time (min)	25 °C	15 °C	5 °C	0 °C	25 °C (without catalyst)
30	92	82	36	24.5	0
60	91	94	62	50	0
90	90	96	91	76	0
120	91	99	97	77	0
180	94	100	98	83	0
240	97	100	97	86	0
1440	98	100	98	100	4.5

Table 5
Comparison of the kinetic parameters for different temperatures

Temperature (°C)	k_{cat} (s^{-1})	Yields (%)
0	0.76 ± 0.10	100
5	1.13 ± 0.19	98
15	3.35 ± 0.29	100
25	8.03 ± 0.43	98

The values of k_{cat}, determined considering a first order reaction for oxidation of catechol with the copper(II) complex as catalyst, at 0, 5, 15 and 25 °C are given in Table 5. The values of $\Delta H^{\neq}$ and $\Delta S^{\neq}$ for 25 °C, determined from temperature dependence studies, are 62.2 ± 4.1 kJ mol^{-1} and -10 ± 1 J K^{-1} mol^{-1}, respectively. The negative value of $\Delta S^{\neq}$ indicates the operation of an associative mode of activation.

The product of the catalytic oxidation of 3,5-di-*tert*-butylcatechol was characterized by IR and ^1H NMR. For the ^1H NMR spectra, a change for two of the hydrogen peaks on the aromatic ring was observed. For the substrate, 3,5-di-*tert*-butylcatechol, peaks appear at 6.78 and 6.91 ppm with $J = 2.1$ and for the reaction product, 3,5-di-*tert*-1,2-benzoquinone, these two peaks are shifted to 6.21 and 6.93 ppm respectively with $J = 2.2$. This is in accordance with a ^1H NMR spectra of commercial 3,5-di-*tert*-1,2-benzoquinone. In the IR spectra, the absence of bands at 3460 and 3260 cm^{-1} attributed to ν(O–H) present in substrate and the appearance of a band at 1680 cm^{-1} attributed to ν(C=O) of the product are the main changes observed.

4. Conclusions

A new Schiff base copper(II) complex $[Cu(SalAHE)_2]$ was synthesized and characterized. The crystal structure of this complex shows that the central part of the molecule strictly coplanar with the two ligands in the *trans* configuration. The crystal packing makes an infinite supramolecular polymer, using conventional and non-conventional H-bonds This mononuclear complex is able to oxidize 3,5-di-*tert*-butylcatechol to the respective *o*-quinone with molecular oxygen.

Acknowledgements

Financial support from the Conselho Nacional de Desenvolvimento Cientifico e Tecnológico, CNPq, and the Fundação de Amparo à Pesquisa do Estado de São Paulo, FAPESP, is gratefully acknowledged. We wish to thank FAPESP for providing an undergraduate scholarship to A.C.D.M. and the CNPq for graduate scholarships to P.E.A., M.P. dos S. and S.R.

Appendix A. Supplementary material

CCDC 612991 contains the supplementary crystallographic data for this paper. These data can be obtained free of charge via http://www.ccdc.cam.ac.uk/conts/retrieving.html, or from the Cambridge Crystallographic Data Centre, 12 Union Road, Cambridge CB2 1EZ, UK; fax: (+44) 1223-336-033; or e-mail: deposit@ccdc.cam.ac.uk. Supplementary data associated with this article can be found, in the online version, at doi:10.1016/j.poly.2007.08.030.

References

[1] K. Selmeczi, M. Réglier, M. Giorgi, G. Speier, Coord. Chemi. Rev. 245 (2003) 191.
[2] M.C. Linder, C. Goode, Biochemistry of Copper, Plenum Press, New York, 1991.
[3] W. Kaim, J. Rall, Angew. Chem., Int. Ed. Engl. 35 (1996) 43.
[4] N. Kitajima, Y. Moro-oka, Chem. Rev. 94 (1994) 737.
[5] K.D. Karlin, J.D. Hayes, Y. Gultneh, R.W. Cruse, J.W. McKown, J.P. Hutchinson, J. Zubieta, J. Am. Chem. Soc. 106 (1984) 2121.
[6] K.D. Karlin, Y. Gultneh, T. Nicholson, J. Zubieta, Inorg. Chem. 24 (1985) 3727.
[7] R.R. Jacobson, Z. Tyeklar, A. Farooq, K.D. Karlin, S. Liu, J. Zubieta, J. Am. Chem. Soc. 110 (1988) 3690.
[8] Z. Tyeklar, K.D. Karlin, Acc. Chem. Res. 22 (1988) 241.
[9] R. Klement, F. Stock, H. Elias, H. Paulus, P. Pelikán, M. Valko, M. Mazúr, Polyhedron 18 (1999) 3617.
[10] G. McLendon, A.E. Martell, Coord. Chem. Rev. 19 (1976) 1.
[11] E.C. Niederhoffer, J.A. Thommsons, A.E. Martell, Chem. Rev. 84 (1984) 137.
[12] T.D. Smith, J.R. Pilbrow, Coord. Chem. Rev. 39 (1981) 295.
[13] B.S. Tovrog, D.J. Kitko, R.S. Drago, J. Am. Chem. Soc. 98 (1976) 5144.
[14] A.E. Martell, D.T. Sawyer, Oxygen Complexes and Oxygen Activation by Transition Metals, Plenum Press, New York, 1988.
[15] D.H. Busch, N.W. Alcock, Chem. Rev. 94 (1994) 585.
[16] R.H. Holm, Chem. Rev. 87 (1987) 1401.
[17] K. Srinivasan, P. Michaud, J.K. Kochi, J. Am. Chem. Soc. 108 (1986) 2309.
[18] P.S. Dixit, K. Srinivasan, Inorg. Chem. 27 (1988) 4507.
[19] B. Rihter, S. SriHari, S. Hunter, J. Masnovi, J. Am. Chem. Soc. 115 (1993) 3918.
[20] S. SriHari, J. Masnovi, Inorg. Chem. 29 (1990) 3154.
[21] P. Gentschev, N. Möller, B. Krebs, Inorg. Chim. Acta 300–302 (2000) 442.
[22] M.G. Alvarez, G. Alzuet, J. Borras, S.G. Granda, J.M.M. Bernardo, J. Inorg. Biochem. 96 (2003) 443.
[23] K. Selmeczi, M. Reglier, M. Giorgi, G. Speier, Coord. Chem. Rev. 245 (2003) 191.
[24] C. Fernandes, A. Neves, A.J. Bortoluzzi, A.S. Mangrich, E. Rentschler, B. Szpoganiez, E. Schwingle, Inorg. Chim. Acta 320 (2001) 12.

[25] A. Majumder, S. Goswami, S.R. Batten, M.S. El Fallah, J. Ribas, S. Mitra, Inorg. Chim. Acta 359 (2006) 2375.
[26] M. Gullotti, L. Santagostini, R. Pagliarin, A. Granata, L. Casella, J. Mol. Catal. A: Chem. 235 (2005) 271.
[27] J. Gao, S. Zhong, J. Mol. Catal. A: Chem. 164 (2000) 1.
[28] J.R. Zamian, E.R. Dockal, Transition Met. Chem. 21 (1996) 370.
[29] P.E. Aranha, M.P. dos Santos, S. Romera, E.R. Dockal, Polyhedron 26 (2007) 1373.
[30] O. Signorini, E.R. Dockal, G. Castellano, G. Oliva, Polyhedron 15 (1995) 245.
[31] R.C. Felicio, E.T.G. Cavalheiro, E.R. Dockal, Polyhedron 20 (2001) 261.
[32] A.P. de A. Marques, E.R. Dockal, F.C. Skrobot, I.L.V. Rosa, Inorg. Chem. Commun. 10 (2007) 255.
[33] L.Z. Li, C. Zhao, T. Xu, H.W. Ji, Y.H. Yu, G.Q. Guo, H. Chao, J. Inorg. Biochem. 99 (2005) 1076.
[34] A.C.T. North, D.C. Phillips, F.S. Mathews, Acta Crystallogr., Sect. A 21 (1968) 351.
[35] A. Altomare, M.C. Burla, M. Camalli, G.L. Cascarano, C. Giacovazzo, A. Guagliardi, A.G.G. Moliterni, G. Polidori, R. Spagna, J. Appl. Cryst. 32 (1999) 115.
[36] G.M. Sheldrick, SHELX97 Programs for Crystal Structure Analysis (Release 97-2), Institüt für Anorganische Chemie der Universität, Tammanstrasse 4, D-3400 Göttingen, Germany, 1998.
[37] A.L. Spek, J. Appl. Cryst. 36 (2003) 7.
[38] L.J. Farrugia, J. Appl. Cryst. 30 (1997) 565.
[39] A. Vogt, S. Wolowiec, R.L. Prasas, A. Gupta, J. Skarzeviski, Polyhedron 17 (1998) 1231.
[40] F.A. Bottino, P. Finocchiaro, E. Libertini, J. Coord. Chem. 16 (1988) 341.
[41] P. Gluvchinsky, G.M. Mocler, E. Sinn, Spectrochim. Acta 33A (1977) 1073.
[42] X. Wang, X.M. Zang, H.X. Lin, Polyhedron 14 (1995) 293.
[43] K. Ueno, A.E. Martel, J. Phys. Chem. 60 (1956) 1270.
[44] J.A. Faniran, K.S. Patel, J.C. Bailar Jr., J. Inorg. Nucl. Chem. 36 (1974) 1547.
[45] G.C. Percy, J. Thornton, J. Inorg. Nucl. Chem. 35 (1973) 35, 2319.
[46] C.H. Kao, H.H. Wei, Y.H. Liu, G.H. Lee, Y. Wang, C.J. Lee, J. Inorg. Biochem. 84 (2001) 171.
[47] N. Oishi, Y. Nishida, K. Ida, S. Kida, Bull. Chem. Soc. Jpn. 53 (1980) 2847.
[48] C. Fernandes, A. Neves, A.J. Bortoluzzi, A.S. Mangrich, E. Rentschler, B. Szpoganicz, Erineu Schwingel, Inorg. Chim. Acta 320 (2001) 12.
[49] I. Castillo, J.M. Fernández-González, J.L. Gárate-Morales, J. Mol. Struct. 657 (2003) 25.

Available online at www.sciencedirect.com
ScienceDirect
Polyhedron 27 (2008) 65–70
POLYHEDRON
www.elsevier.com/locate/poly

Gold(I) phosphine-decorated 2,2′:6′,2″-terpyridine ligands

Edwin C. Constable *, Catherine E. Housecroft *, Markus Neuburger, Silvia Schaffner, Ellen J. Shardlow

Department of Chemistry, University of Basel, Spitalstrasse 51, 4056-Basel, Switzerland

Received 15 June 2007; accepted 20 August 2007
Available online 17 October 2007

Abstract

The synthesis and characterization of the ligands R_3PAu(**1**–H) (R = ^{n}Bu, Ph) and (**1**–H)Au(μ-dppe)Au(**1**–H) (**1** = HC≡CCH$_2$Otpy, tpy = 2,2′:6′,2″-terpyridine) are reported. The single crystal structures of $^n Bu_3PAu$(**1**–H) and (**1**–H)Au(μ-dppe)Au(**1**–H) have been determined, and weak hydrogen bonding rather than aurophilic interactions operate between the molecules in the solid state.
© 2007 Elsevier Ltd. All rights reserved.

Keywords: Gold(I); 2,2′:6′,2″-Terpyridine; Phosphine; Alkyne; Ligand

1. Introduction

The use of terminal C≡CH groups to produce organometallic complexes through M–C σ-bond formation is well documented, with platinum(II) and gold(I) derivatives being especially important [1–4]. Current interest is these derivatives arises from possible applications in advanced materials based upon their luminescent [5–9] and nonlinear optical [3,10–13] properties. We have recently reported a family of platinum(II)-centred ditopic 2,2′:6′,2″-terpyridine (tpy) ligands which are synthesized by coupling 4′-(2-propyn-1-oxy)-2,2′:6′,2″-terpyridine (HC≡CCH$_2$Otpy (**1**)) with *trans*-[PtI$_2$(PR$_3$)$_2$] (R = Et, ^{n}Bu, Ph) [14,15] or 4′-(4,7,10-trioxadec-1-yn-10-yl)-2,2′:6′,2″-terpyridine with *trans*-[PtI$_2$(PEt$_3$)$_2$] [16]. Metal binding by the tpy domains leads to the formation of [n + n] metallomacrocyclic products with n = 2, 3 or 4 for M = Fe(II). Mixtures of these products convert in solution to the thermodynamically favoured $[Fe_2L_2]^{4+}$ [15]. We have now turned our attention to gold(I) alkynyl derivatives [17], and report here a series of new ligands in which tpy domains are linked to C≡CAuPR$_3$ (R = ^{n}Bu, Ph) or C≡CAu(μ-dppe)AuC≡C units (dppe = bis(diphenylphosphino)ethane). Previous examples of gold(I) σ-acetylide-functionalized polypyridine ligands have been based upon 1,10-phenanthroline [18–21].

2. Experimental

2.1. General procedures

Infrared spectra were recorded on a Shimadzu FTIR-8400S spectrophotometer with samples as solids using a Golden Gate ATR accessory. ^{1}H, ^{13}C and ^{31}P NMR spectra were recorded on a Bruker Avance DRX 400 spectrometer; the numbering scheme adopted for the ligands are shown in the reaction schemes. Chemical shifts for ^{1}H and ^{13}C NMR spectra are referenced with respect to residual solvent peaks and TMS = δ 0 ppm; ^{31}P NMR signals are referenced with respect to 85% aqueous H_3PO_4. MALDI-TOF mass spectra were recorded using a PerSeptive Biosystems Voyager mass spectrometer with α-cyano-4-hydroxycinnamic acid matrix. Electronic absorption spectra were recorded on a Varian-Cary 5000 spectrophotometer.

Compound **1** [22] $^n Bu_3PAuCl$ [23] and ClAu(μ-dppe)AuCl [24–26] were prepared by literature methods. Ph_3PAuCl was purchased from ChemPur.

* Corresponding authors. Fax: +41 61 267 1018.
E-mail address: catherine.housecroft@unibas.ch (E.C. Constable).

0277-5387/$ - see front matter © 2007 Elsevier Ltd. All rights reserved.
doi:10.1016/j.poly.2007.08.034

2.2. Compound 2

Compound **1** (0.219 g, 0.763 mmol), $^{n}Bu_3PAuCl$ (0.330 g, 0.759 mmol) and CuI (14.7 mg, 77.2 μmol) were added to Et_3N (10 ml). The reaction mixture was stirred at room temperature for 4 h. Solvent was then removed and the product was separated by column chromatography (alumina, CH_2Cl_2–acetone 99:1). There was a single fraction, from which **2** was isolated as a white oil (0.233 g, 0.340 mmol, 44.8%). Crystals of **2** could be obtained by slow evaporation of the crude reaction mixture. Compound **2**: ^{1}H NMR (400 MHz, $CDCl_3$) δ (ppm) 8.65 (ddd, *J* 4.7, 1.8, 0.8 Hz, 2H, H^{A6}), 8.54 (dt, *J* 7.9, 0.9 Hz, 2H, H^{A3}), 8.04 (s, 2H, H^{B3}), 7.79 (dt, *J* 7.6, 2.0 Hz, 2H, H^{A4}), 7.26 (ddd, *J* 7.6, 5.1, 1.0 Hz, 2H, H^{A5}), 5.01 (s, 2H, OCH_2), 1.67 (m, 6H, PCH_2), 1.48 (m, 6H, PCH_2CH_2), 1.38 (sextet, *J* 7.6 Hz, 6H, CH_2CH_3), 0.87 (t, *J* 7.6 Hz, 9H, CH_3); $^{13}C\{^1H\}$ NMR (100 MHz, $CDCl_3$) δ (ppm) 166.4 (C^{B4}), 156.9 ($C^{B2/A2}$), 156.1 ($C^{B2/A2}$), 148.9 (C^{A6}), 136.5 (C^{A4}), 123.5 (C^{A5}), 121.2 (C^{A3}), 107.7 (C^{B3}), 96.6 ($C{\equiv}CAu$), 57.2 (OCH_2), 27.1 (s, CH_2CH_3), 25.4 (d, J_{PC} 33.0 Hz, PCH_2), 24.1 (d, J_{PC} 14.0 Hz, PCH_2CH_2), 13.5 (s, CH_3), signal for $C{\equiv}CAu$ not resolved; $^{31}P\{^1H\}$ NMR (162 MHz, $CDCl_3$) δ (ppm) 25.7. MALDI-MS *m*/*z* 686 $[M]^+$, 288 $[M-AuPBu_3]^+$. IR (ν, cm^{-1}) 2955 w, 2924 w, 2862 w, 2361 w, 2130 w, 1736 w, 1558 m, 1450 m, 1404 m, 1335 m, 1188 m, 1088 m, 1018 s, 879 w, 795 m, 741 m, 617 w, 563 w, 525 w. UV/Vis λ_{max}/nm 247, 277.

2.3. Compound 3

Compound **1** (0.0820 g, 0.285 mmol), Ph_3PAuCl (0.148 g, 0.299 mmol) and CuI (10.9 mg, 57.3 μmol) were added to Et_3N (12 ml) and CH_2Cl_2 (12 ml). The reaction mixture was stirred at room temperature for 2 h. The precipitate that formed was separated by filtration, and then solvent was then removed from the filtrate to give a yellow-green oil. Purification by column chromatography (alumina, CH_2Cl_2–acetone 99:1) gave one fraction yielding **3** as a white oil (0.145 g, 0.194 mmol, 68.1%). **2**: ^{1}H NMR (400 MHz, $CDCl_3$) δ (ppm) 8.67 (ddd, *J* 4.5, 2.0, 1.2 Hz, 2H, H^{A6}), 8.57 (dt, *J* 8.0, 1.2 Hz, 2H, H^{A3}), 8.09 (s, 2H, H^{B3}), 7.81 (dt, *J* 7.6, 1.6 Hz, 2H, H^{A4}), 7.47 (m, 9H, $H^{Ph3,4}$), 7.41 (m, 6H, H^{Ph2}), 7.28 (ddd, *J* 7.2, 4.8, 1.2 Hz, 2H, H^{A5}), 5.08 (s, 2H, OCH_2); $^{13}C\{^1H\}$ NMR (125 MHz, $CDCl_3$) δ (ppm) 166.5 (C^{B4}), 157.0 ($C^{B2/A2}$), 156.2 ($C^{B2/A2}$), 149.0 (C^{A6}), 136.6 (C^{A4}), 134.2 (d, J_{PC} 13.8 Hz, $C^{Ph2/3}$), 131.5 (s, C^{Ph4}), 129.9 (d, J_{PC} 140 Hz, $C{\equiv}CAu$), 129.5 (d, J_{PC} 55.0 Hz, C^{Ph1}), 129.1 (d, J_{PC} 11.3 Hz, $C^{Ph2/3}$), 123.6 (C^{A5}), 121.3(C^{A3}), 107.8 (C^{B3}), 96.8 (d, J_{PC} 26 Hz, $C{\equiv}CAu$), 57.2 (OCH_2); $^{31}P\{^1H\}$ NMR (162 MHz, $CDCl_3$) δ (ppm) 38.8. MALDI-MS *m*/*z* 748 $[M]^+$, 289 $[M-Ph_3PAu]^+$ (base peak). IR (ν, cm^{-1}) 3066 w, 2963 w, 2921 w, 2863 w, 2350 w, 2130 w, 1581 s, 1563 s, 1469 m, 1436 m, 1406 m, 1345 m, 1334 m, 1186 m, 1101 m, 1020 s, 795 m, 745 m, 692 s. UV/Vis λ_{max}/nm (2.39×10^{-5} mol dm^{-3}, CH_2Cl_2) 249 (ε/dm^3 mol^{-1} cm^{-1} 106,000), 278 (72,700).

2.4. Compound 4

Compound **1** (0.270 g, 0.941 mmol), ClAu(dppe)AuCl (0.405 g, 0.469 mmol) and CuI (9.4 mg, 49.4 μmol) were added to Et_3N (12 ml) and CH_2Cl_2 (12 ml). The reaction mixture was stirred at room temperature for 4 d. The crude product formed as a precipitate and was removed by filtration. It was purified by column chromatography (alumina, CH_2Cl_2–acetone 90:10). One fraction was eluted and from this, **4** was isolated as a white oil (0.253 g, 0.185 mmol, 39.4%). Crystalline 4 was obtained from a $CHCl_3$ solution left standing at room temperature. ^{1}H NMR (400 MHz, $CDCl_3$) δ (ppm) 8.63 (ddd, *J* 4.8, 1.8, 0.8 Hz, 4H, H^{A6}), 8.55 (dt, *J* 8.0, 0.8 Hz, 4H, H^{A3}), 8.06 (s, 4H, H^{B3}), 7.78 (dt, *J* 7.6, 1.8 Hz, 4H, H^{A4}), 7.56 (m, 8H, Ph), 7.7–7.3 (overlapping m, 12H, Ph), 7.25 (ddd, *J* 7.6, 4.8, 1.0 Hz, 4H, H^{A5}), 5.00 (s, 4H, OCH_2), 2.56 (br s, 4H, PCH_2); $^{13}C\{^1H\}$ NMR (100 MHz, $CDCl_3$) δ (ppm) 166.4 (C^{B4}), 157.0 ($C^{B2/A2}$), 156.1 ($C^{B2/A2}$), 149.0 (C^{A6}), 136.6 (C^{A4}), 134.9 (C^{Phipso}), 133.2 (t, J_{PC} 7 Hz, $C^{Ph2/3}$), 132.1 (C^{Ph4}), 129.5 (t, J_{PC} 5 Hz, $C^{Ph2/3}$), 123.7 (C^{A5}), 121.3 (C^{A3}), 107.7 (C^{B3}), 97.0 ($C{\equiv}CAu$), 57.1 (OCH_2), 23.7 (PCH_2), signal for $C{\equiv}CAu$ not resolved; $^{31}P\{^1H\}$ NMR (162 MHz, $CDCl_3$) δ (ppm) 36.5. MALDI-MS *m*/*z* 1388 $[M+Na]^+$. IR (ν, cm^{-1}) 3055 w, 2924 m, 2854 m, 1697 w, 1558 s, 1435 s, 1404 s, 1335 s, 1258 m, 1188 s, 1103 m, 1018 s, 879 s, 795 m, 725 s, 687 s. UV/Vis λ_{max}/nm (4.62×10^{-5} mol dm^{-3}, CH_2Cl_2) 233 (ε/dm^3 mol^{-1} cm^{-1} 55,500), 253 sh (37,900), 277 (30,400).

2.5. Crystal structure determinations: general

Data were collected on an Enraf Nonius Kappa CCD instrument; data reduction, solution and refinement used the programmes COLLECT [27], SIR92 [28], DENZO/SCALEPACK [29] and CRYSTALS [30].

2.6. Crystal data for 2

$C_{30}H_{39}AuN_3OP$, $M = 685.60$, triclinic, space group $P\bar{1}$, $a = 11.1882(2)$, $b = 11.3401(2)$, $c = 14.3037(2)$ Å, $\alpha = 92.6970(9)$, $\beta = 110.5440(7)$, $\gamma = 116.1495(8)°$, $U = 1480.86(5)$ $Å^3$, $Z = 2$, $D_{calc} = 1.537$ Mg m^{-3}, μ(Mo-Kα) = 5.047 mm^{-1}, $T = 173$ K, 8610 reflections collected. Refinement of 8555 reflections (325 parameters) with $I > 2.0\sigma I$) converged at final $R_1 = 0.0315$ (R_1 all data = 0.0498), $wR_2 = 0.0491$ (wR_2 all data = 0.0592), goodness-of-fit = 0.968.

2.7. Crystal data for 4 · 4CHCl3

$C_{66}H_{52}Au_2Cl_{12}N_6O_2P_2$, $M = 1842.49$, triclinic, space group $P\bar{1}$, $a = 8.7136(3)$, $b = 13.3106(4)$, $c = 15.9758(4)$ Å, $\alpha = 110.037(2)$, $\beta = 91.133(2)$, $\gamma = 95.801(2)°$, $U = 1728.92(9)$ $Å^3$, $Z = 1$, $D_{calc} = 1.770$ Mg m^{-3}, μ(Mo-Kα) = 4.797 mm^{-1}, $T = 173$ K, 7916 reflections collected. Refinement of 5094 reflections (442 parameters) with $I > 3.0\sigma$ *I*) converged at final $R_1 = 0.0325$ (R_1 all data = 0.0626),

$wR_2 = 0.0359$ (wR_2 all data = 0.0574), goodness-of-fit = 1.112.

3. Results and discussion

The reactions of alkyne **1** with $^{n}Bu_3PAuCl$ and Ph_3PAuCl were carried out using standard conditions [31] (Scheme 1). The yields of products **2** and **3** were affected by the choice of Et_3N or a mixture of Et_3N and CH_2Cl_2 as solvent. The MALDI mass spectra of **2** and **3** showed parent ions at m/z 686 and 748, respectively. Fragmentation by loss of the $AuPR_3$ unit was observed for both compounds. The $^{31}P\{^1H\}$ NMR spectrum of solutions of each of **2** and **3** exhibited one singlet (δ 25.7 ppm for **2**, δ 38.8 ppm for **3**). Both compounds were characterized by ^1H and ^{13}C NMR spectroscopies. In the ^1H NMR spectra, the signals assigned to the tpy protons of **2** and **3** were characteristic of a non-coordinated ligand, confirming that there had been no competition between alkyne and tpy domains for interaction with the gold(I) centre. The loss of the signal for the C≡CH proton in **1** was evidence for the formation of a C–Au bond. On going from **1** to **3**, the signals in the ^{13}C NMR spectrum assigned to the C≡C units shifted to higher frequency, from δ 77.6 and 76.3 ppm in **1** [22] to δ 129.9 and 96.8 ppm in **3**. Each of these signals was a doublet with coupling of the ^{31}P *trans* to the alkyne unit (J_{PC} 140 Hz, for C≡*C*Au and J_{PC} 26 Hz for *C*≡CAu). These chemical shifts and coupling constants are similar to data reported for other $RC{\equiv}CAuPR'_3$ species [32–36]. For compound **2**, the ^{13}C NMR signal for the *C*≡CAu carbon was observed at δ 96.6 ppm, but the resonance for the metal-bonded C atom could not be resolved. Single crystals of **2** suitable for X-ray crystallography were serendipitously grown by slow evaporation of the crude reaction mixture (CH_2Cl_2–Et_3N 1:1 solvent). Crystals of **2** (colourless plates) were separated from crystals of **1** (large blocks) by hand. The molecular structure of **2** is shown in Fig. 1 and selected bond parameters are listed in the caption. The tpy unit is in the *trans*,*trans*-conformation that is expected for a non-coordinated ligand. The terpy unit deviates slightly from planarity, with the angles between the least squares planes of the rings being 14.0(2)° (for rings containing N1 and N2) and 3.6(2)° (for rings containing N2 and N3). The fact that bond C8–O1 is shorter (1.367(4) Å) than O1–C16 (1.443(4) Å) is consistent with the O atom being sp^2 hybridized, and there being a degree of π-delocalization between the central pyridine ring and oxygen atom. The structural determination confirms the presence of a linear C–C≡C–Au–P unit. All other structural parameters are as expected. In the crystal lattice, molecules of **2** form dimeric motifs, supported by non-classical C–H···N hydrogen bonds (Fig. 2). Rows of dimers assemble along the *a*-axis, with weak C–H···π-alkyne interactions [37–42] operating between dimers (C15H151···C18 = 2.72 Å, C15H151···C17 = 3.00 Å). These rows are aligned so as to produce alternating domains of alkyl and tpy groups (Fig. 3). Interestingly, the weak C–H···N and C–H···π-alkyne interactions dictate the molecular packing, and there are no aurophilic [43,44] or π-stacking interactions.

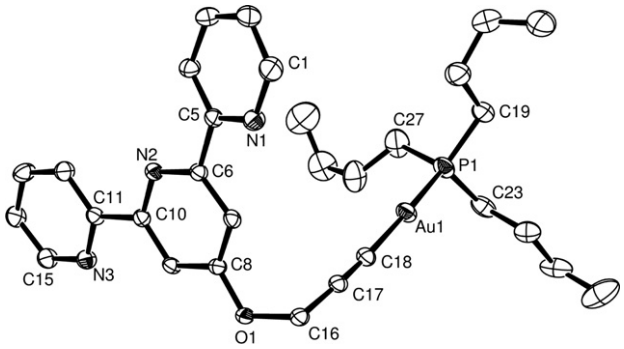
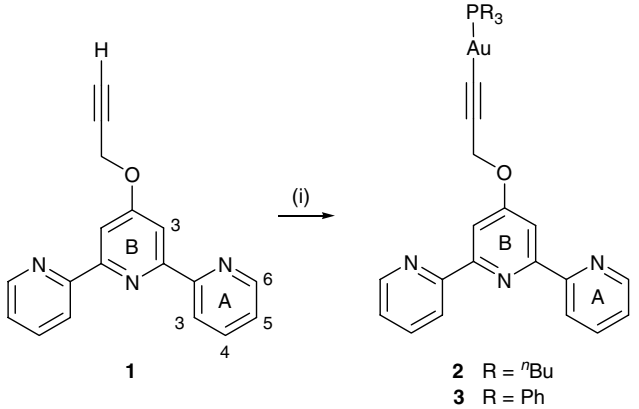


Fig. 1. The structure of **2** with displacement ellipsoids drawn at the 30% probability level; H atoms omitted for clarity. Selected bond lengths and angles: Au1–P1=2.279(1), Au1–C18 = 2.018(4), C17—C18 = 1.186(5), C16–C17 = 1.467(5), C16–O1 = 1.443(4), C8–O1 = 1.367(4), C5–C6 = 1.491(4), C10–C11 = 1.493(4) Å; P1–Au1–C18 = 175.1(1), Au1–C18–C17 = 175.3(3), C18–C17—C16 = 176.7(4), C17—C16–O1 = 111.5(3), C16–O1–C8 = 117.4(3)°.



Scheme 1. Reaction scheme for the formation of **2** and **3**: (i) R_3PAuCl, CuI in Et_3N (for **2**) or Et_3N/CH_2Cl_2 (for **3**). The ring labelling is used for NMR assignments.

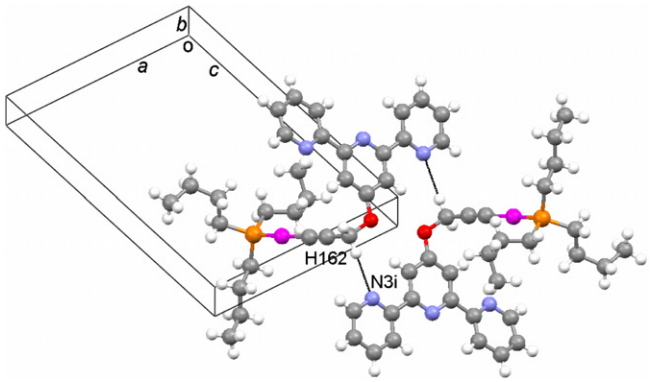


Fig. 2. Dimeric motif in the packing of **2**; symmetry code i = 2 − *x*, 2 − *y*, −*z*. C16H162···N3i=2.53, C16···N3i = 3.433(5) Å; C16–H162···N3i = 158.0°.

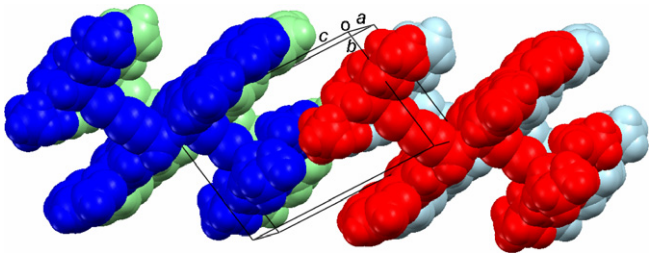
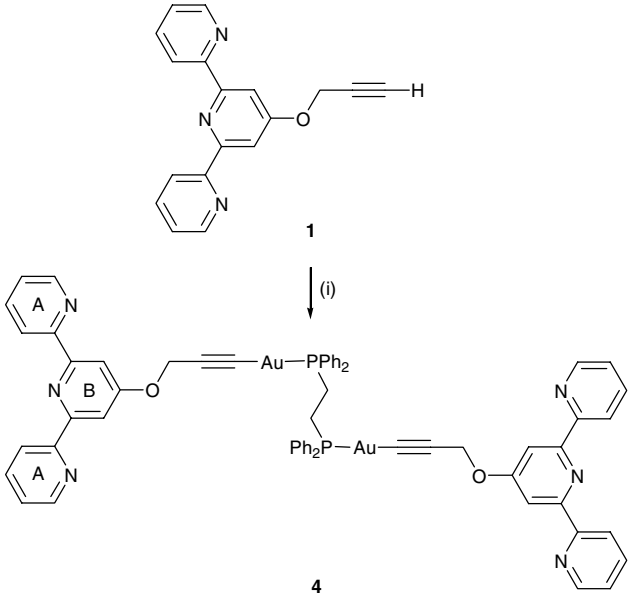


Fig. 3. Four dimers of **2** showing their assembly into rows along the *a*-axis, and the resulting domains of alkyl chains (centre of unit cell) and tpy groups.

Compounds **2** and **3** illustrate the success of the methodology of functionalizing a tpy metal-binding domain in the 4′-position with a gold(I) phosphine. However, in order to develop these systems further towards their use as building blocks in metallomacrocyclic or polymeric systems, it is necessary to incorporate a bridging bis(phosphine) ligand. For initial studies, we chose dppe. Ligand **1** reacts with ClAu(μ-dppe)AuCl in Et_3N/CH_2Cl_2 in the presence of CuI (Scheme 2) to yield **4** in moderate yield. In the MALDI mass spectrum, a peak at *m*/*z* 1388 was assigned to $[M + Na]^+$. The solution $^{31}P\{^1H\}$ NMR spectrum exhibited one signal (δ 36.5 ppm), consistent with the formation of a symmetrical product. The ^1H and $^{13}C\{^1H\}$ NMR spectra were also consistent with the presence of 2 equiv tpy units and a symmetrical dppe ligand. In **4**, the ^{13}C NMR signal for the $C{\equiv}CAu$ carbon was observed at δ 97.0 ppm, consistent with the chemical shifts observed for the analogous C centres in **2** and **3**. As in **2**, the signal for the gold-bonded C atom in **4** was not resolved.

Crystals of $\mathbf{4} \cdot 4CHCl_3$ suitable for an X-ray diffraction study were grown from a $CHCl_3$ solution. The structure of **4** is shown in Fig. 4. The molecule is centrosymmetric, with



Scheme 2. Reaction scheme for the formation of **4**: (i) ClAu(dppe)AuCl, CuI in Et_3N/CH_2Cl_2. The ring labelling is used for NMR assignments.

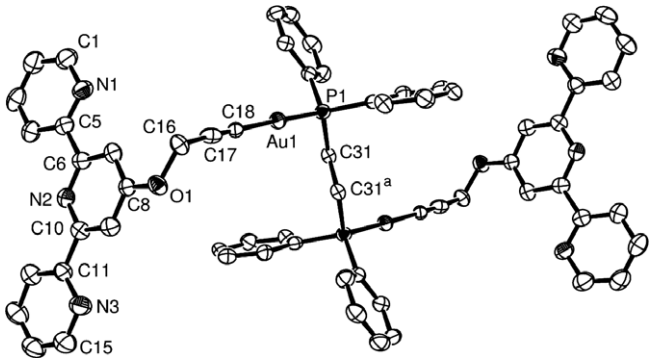


Fig. 4. The structure of **4** in $\mathbf{4} \cdot 4CHCl_3$ with displacement ellipsoids drawn at the 30% probability level; H atoms omitted for clarity. Selected bond lengths and angles: Au1–P1 = 2.275(1), Au1–C18 = 2.062(6), C17—C18 = 1.117(8), C16–C17 = 1.481(8), C16–O1 = 1.449(7), O1–C8 = 1.361(7) Å; P1–Au1–C18 = 178.8(2), Au1–C18–C17 = 177.6(5), C18–C17—C16 = 176.2(6), C17—C16–O1 = 112.3(5), C16–O1–C8 = 119.0(4)°.

the tpy groups adopting a *transoid* arrangement. As a result, there is no intramolecular Au···Au close contact. A search of the CSD [45] shows that in XAu(μ-dppe)AuX derivatives with relatively simple X substituents, a *transoid* arrangment of the Au(μ-dppe)Au unit is usually favoured [46–53], and the formation of an intramolecular Au···Au interaction appears not to drive the molecule towards adopting a *cisoid* arrangement. In several cases, intermolecular aurophilic interactions lead to the formation of polymeric chains [48,54,55]. The structure of ClAu(μ-dppe)AuCl is noteworthy. In both the unsolvated complex and ClAu(μ-dppe)AuCl · $0.4CH_2Cl_2$ [56,57], the Au(dppe)Au unit adopts a conformation between *cisoid* and *transoid*. Inspection of these structures using Mercury v. 1.4.2 [58] shows that in ClAu(μ-dppe)AuCl, intermolecular aurophilic interactions lead to the formation of cyclic dimers, while polymeric chains are present in ClAu(μ-dppe)AuCl · $0.4CH_2Cl_2$. In $\mathbf{4} \cdot 4CHCl_3$, one of the crystallographically independent solvate molecules is ordered, and the second is disordered over two sites (65:35%). The supramolecular interactions that dominate the packing of molecules of **4** are non-classical hydrogen bonds. The C–H···N and O···H–C interactions shown in Fig. 5a, along with those that are symmetry related to the latter, result in the assembly of hydrogen-bonded chains. Significantly, there are no intermolecular Au···Au or π-stacking interactions, and packing of the hydrogen-bonded chains (Fig. 5b) involves only very weak C–H···π-alkyne and C–H···π-aryl contacts along with hydrogen bonds between N2 and one $CHCl_3$ molecule (N2···H321C32 = 2.28 Å, N2···H321–C32 = 162°). Additional factors which may oppose the formation of Au···Au interactions are the steric demands of the substituents and the overall length of the molecule [59].

The isolation of compounds **2**–**4** illustrates the viability of attaching a gold(I) phosphine unit to an alkynyl-functionalized tpy to produce either a gold(I)-decorated monotopic ligand or a gold(I) phosphine bridged ditopic ligand. We now plan to undertake investigations of the coordination behaviour of these ligands.

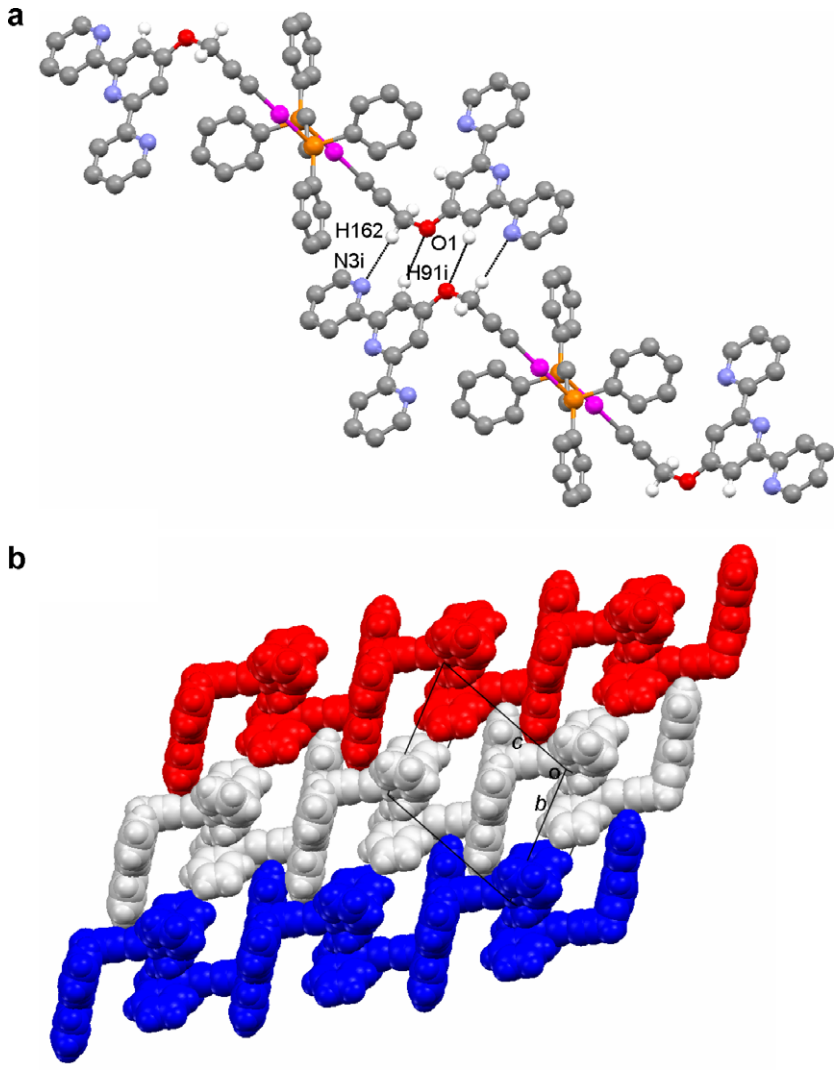


Fig. 5. (a) Non-classical hydrogen bonding interactions between molecules of **4**; symmetry code i = 1 − *x*, −1 − *y*, 1 − *z*. C16H162···N3i = 2.54, C16···N3i = 3.445(8) Å, C16–H162···N3i = 158°, O1···H91iC9i = 2.64, O1···C9i = 3.569(8) Å, O1···H91i–C9i = 162°. Hydrogen atoms other than those of the CH and CH_2 groups involved in hydrogen bonding are omitted for clarity. (b) Packing of hydrogen-bonded chains of **4**.

Acknowledgements

We thank the Swiss National Science Foundation and the University of Basel for financial support. Jonathon E. Beves is acknowledged for recording the 500 MHz NMR spectra.

Appendix A. Supplementary material

CCDC 648054 and 648054 contains the supplementary crystallographic data for **2** and **4**. These data can be obtained free of charge via www: http://www.ccdc.cam.ac.uk), or from the Cambridge Crystallographic Data Centre, 12 Union Road, Cambridge CB2 1EZ, UK; fax: (+44) 1223 336 033; or e-mail: deposit@ccdc.cam.ac.uk. Supplementary data associated with this article can be found, in the online version, at doi:10.1016/j.poly.2007.08.034.

References

[1] G.K. Anderson, in: E.W. Abel, F.G.A. Stone, G. Wilkinson (Eds.), Comprehensive Organometallic Chemistry II, Vol. 9, Pergamon, Oxford, 1995, Chapter 8.
[2] K. Osakada, in: R.H. Crabtree, D.M.P. Mingos (Eds.), Comprehensive Organometallic Chemistry III, Vol. 8, Elsevier, Oxford, 2007, Chapter 8.
[3] N.J. Long, C.K. Williams, Angew. Chem., Int. Ed. 42 (2003) 2586.
[4] H. Schmidbaur, A. Schier, in: R.H. Crabtree, D.M.P. Mingos (Eds.), Comprehensive Organometallic Chemistry III, Vol. 2, Elsevier, Oxford, 2007, Chapter 5.
[5] K.L. Cheung, S.K. Yip, V.W.W. Yam, J. Organomet. Chem. 689 (2004) 4451.
[6] V.W.W. Yam, J. Organomet. Chem. 689 (2004) 1393.
[7] V.W.W. Yam, W.Y. Lo, C.H. Lam, W.K.M. Fung, K.M.C. Wong, V.C.Y. Lau, N. Zhu, Coord. Chem. Rev. 245 (2003) 39.
[8] J. Fornies, J. Gomez, E. Lalinde, M.T. Moreno, Inorg. Chim. Acta 347 (2003) 145.
[9] V.W.W. Yam, K M-C. Wong, N. Zhu, Angew. Chem., Int. Ed. 42 (2003) 1400.

[10] M.P. Cifuentes, M.G. Humphrey, J. Organomet. Chem. 689 (2004) 3968, and references cited therein.
[11] R.H. Naulty, M.P. Cifuentes, M.G. Humphrey, S. Houbrechts, C. Boutton, A. Persoons, G.A. Heath, D.C.R. Hockless, B. Luther-Davies, M. Samoc, J. Chem. Soc., Dalton Trans. (1997) 4167.
[12] I.R. Whittall, M.G. Humphrey, M. Samoc, B. Luther-Davies, D.C.R. Hockless, J. Organomet. Chem. 544 (1997) 189.
[13] I.R. Whittall, M.G. Humphrey, S. Houbrechts, M. Joachim, A. Persoons, S. Schmid, D.C.R. Hockless, J. Organomet. Chem. 544 (1997) 277.
[14] E.C. Constable, C.E. Housecroft, M. Neuburger, S. Schaffner, E.J. Shardlow, Dalton Trans. (2005) 234.
[15] J.E. Beves, E.C. Constable, C.E. Housecroft, M. Neuburger, S. Schaffner, E.J. Shardlow, Dalton Trans. (2007) 1593.
[16] E.C. Constable, C.E. Housecroft, M. Neuburger, S. Schaffner, E.J. Shardlow, Inorg. Chim. Acta, in press. DOI:doi:10.1016/j.ica.2006.12.007.
[17] E.C. Constable, C.E. Housecroft, M. Neuburger, S. Schaffner, E.J. Shardlow, Dalton Trans. (2007) 2631.
[18] M. Shiotsuka, Y. Yamamoto, S. Okuno, M. Kitou, K. Nozaki, S. Onaka, Chem. Commun. (2002) 590.
[19] Y. Yamamoto, M. Shiotsuka, S. Okuno, S. Onaka, Chem. Lett. 33 (2004) 210.
[20] Y. Yamamoto, M. Shiotsuka, S. Onaka, J. Organomet. Chem. 689 (2004) 2905.
[21] I.E. Pomestchenko, D.E. Polyansky, F.N. Castellano, Inorg. Chem. 44 (2005) 3412.
[22] D. Armspach, E.C. Constable, C.E. Housecroft, M. Neuburger, M. Zehnder, J. Organomet. Chem. 550 (1997) 193.
[23] B.M. Sutton, F. McGusty, D.T. Waltz, M.J. DiMartino, J. Med. Chem. 11 (1972) 1095.
[24] S.J. Berners-Price, M.A. Mazid, P.J. Sadler, J. Chem. Soc., Dalton Trans. (1984) 969.
[25] F. Cariati, L. Naldini, G. Simonetta, L. Malatesta, Inorg. Chim. Acta 1 (1967) 315.
[26] C.A. McAuliffe, R.V. Parish, P.D. Randall, J. Chem. Soc., Dalton Trans. 11 (1979) 1730.
[27] COLLECT Software, Nonius BV 1997-2001.
[28] A. Altomare, G. Cascarano, G. Giacovazzo, A. Guagliardi, M.C. Burla, G. Polidori, M. Camalli, J. Appl. Crystallogr. 27 (1994) 435.
[29] Z. Otwinowski, W. Minor, in: C.W. CarterJr., R.M. Sweet (Eds.), Methods in Enzymology, Vol. 276, Academic Press, New York, 1997, p. 307.
[30] P.W. Betteridge, J.R. Carruthers, R.I. Cooper, K. Prout, D.J. Watkin, J. Appl. Crystallogr. 36 (2003) 1487.
[31] See for example: M.I. Bruce, E. Horn, J.G. Matisons, M.R. Snow, Aust. J. Chem. 37 (1984) 1163.
[32] See for example: H. Werner, H. Otto, T. Ngo-Khac, Ch. Burschka, J. Organmet. Chem. 262 (1984) 123.
[33] J. Vicente, M.-T. Chicote, M.-D. Abrisqueta, J. Chem. Soc., Dalton Trans. (1995) 497.
[34] J. Vicente, M.-T. Chicote, M.-D. Abrisqueta, P.G. Jones, Organometallics 16 (1997) 5628.
[35] O. Schuster, R.-Y. Liau, A. Schier, H. Schmidbaur, Inorg. Chim. Acta 358 (2005) 1429.
[36] N.C. Habermehl, D.J. Eisler, C.W. Kirby, N.L.-S. Yue, R.J. Puddephatt, Organometallics 25 (2006) 2921.
[37] G. Desiraju, Acc. Chem. Res. 35 (2002) 565.
[38] G. Desiraju, Chem. Commun. (2005) 2995.
[39] G. Desiraju, T. Steiner, The Weak Hydrogen Bond, Oxford University Press, Oxford, 1999.
[40] T. Steiner, Angew. Chem., Int. Ed. 41 (2002) 48.
[41] M. Nishio, CrystEngComm 6 (2004) 130.
[42] M. Nishio, M. Hirota, Y. Umezawa, The C–H$\cdots\pi$ Interaction: Evidence, Nature and Consequences, Wiley, Weinheim, 1998.
[43] P. Pyykkö, Angew. Chem., Int. Ed. 41 (2002) 3573.
[44] P. Pyykkö, Angew. Chem., Int. Ed. 43 (2004) 4412.
[45] F.H. Allen, Acta Crystallogr., Sect. B 58 (2002) 380.
[46] F. Bachechi, A. Burini, R. Galassi, B.R. Pietroni, M. Severini, J. Organomet. Chem. 575 (1999) 269.
[47] M. Mar Artigas, O. Crespo, M. Concepción Gimeno, P .G. Jones, A. Laguna, M. Dolores Villacampa, J. Organomet. Chem. 561 (1998) 1.
[48] S. Onaka, M. Yaguchi, R. Yamauchi, T. Ozeki, M. Ito, T. Sunahara, Y. Sugiura, M. Shiotsuka, K. Nunokawa, M. Horibe, K. Okazaki, A. Iida, H. Chiba, K. Inoue, H. Imai, K. Sako, J. Organomet. Chem. 690 (2005) 57.
[49] L.L. Marques, G.M. de Oliveira, E.S. Lang, R.A. Burrow, Z. Naturforsch. Teil B 60 (2005) 318.
[50] D.R. Smyth, B.R. Vincent, E.R.T. Tiekink, CrystEngComm 2 (2000) 115.
[51] W. Henderson, B.K. Nicholson, E.R.T. Tiekink, Inorg. Chim. Acta 359 (2006) 204.
[52] M. Bardaji, P.G. Jones, A. Laguna, A. Moracho, A.K. Fischer, J. Organomet. Chem. 648 (2002) 1.
[53] D.R. Smyth, E.R.T. Tiekink, Z. Kristallogr. 217 (2002) 361.
[54] U.E.I. Horvath, S. Cronje, J.M. McKenzie, L.J. Barbour, H.G. Raubenheimer, Z. Naturforsch. Teil B 59 (2004) 1605.
[55] B.C. Tzeng, A. Schier, H. Schmidbaur, Inorg. Chem. 38 (1999) 3978.
[56] D.S. Eggleston, D.F. Chodosh, G.R. Girard, D.T. Hill, Inorg. Chim. Acta 108 (1985) 221.
[57] P.A. Bates, J.M. Waters, Inorg. Chim. Acta 98 (1985) 125.
[58] I.J. Bruno, J.C. Cole, P.R. Edgington, M.K. Kessler, C.F. Macrae, P. McCabe, J. Pearson, R. Taylor, Acta Crystallogr., Sect. B 58 (2002) 389.
[59] P. Li, B. Ahrens, N. Feeder, P.R. Raithby, S.J. Teat, M.S. Khan, Dalton Trans. (2005) 874.

Available online at www.sciencedirect.com
ScienceDirect
Polyhedron 27 (2008) 71–79
POLYHEDRON
www.elsevier.com/locate/poly

Preparation, spectroscopic characterization and X-ray crystal and molecular structures of nickel(II), copper(II) and zinc(II) complexes of the Schiff base formed from isatin and *S*-methyldithiocarbazate (Hisa-sme)

M. Akbar Ali [a,*], Hjh Junaidah Hj Abu Bakar [b], A.H. Mirza [a], S.J. Smith [c], L.R. Gahan [c], Paul V. Bernhardt [c]

[a] *Department of Chemistry, Universiti Brunei Darussalam, BE 1410, Brunei Darussalam*
[b] *Department of Biology, Universiti Brunei Darussalam, BE 1410, Brunei Darussalam*
[c] *Department of Chemistry, The University of Queensland, Brisbane, Qld 4072, Australia*

Received 24 April 2007; accepted 21 August 2007
Available online 4 October 2007

Abstract

Complexes of general formula, $[M(isa\text{-}sme)_2]\cdot n(solvate)$ [$M = Ni^{2+}$, Cu^{2+}, Zn^{2+}, Cd^{2+}; isa-sme = monoanionic form of the Schiff base formed by condensation of isatin with *S*-methyldithiocarbazate; $n = 1$ or 1.5; solvate = MeCN, DMSO, MeOH or H_2O] have been synthesized and characterized by a variety of physicochemical techniques. An X-ray crystallographic structure determination of the $[Ni(isa\text{-}sme)_2]\cdot MeCN$ complex reveals a six-coordinate, distorted octahedral geometry. The two uninegatively charged, tridentate, Schiff base ligands are coordinated to the nickel(II) ion meridionally *via* the amide O-atoms, the azomethine N-atoms and the thiolate S-atoms. By contrast, the crystal structure of $[Zn(isa\text{-}sme)_2]\cdot MeOH$ shows a four-coordinate distorted tetrahedral geometry. The two dithiocarbazate ligands are coordinated as *N*,*S* bidentate chelates with the amide O-atom not coordinated. The structure of the copper(II) complex $[Cu(isa\text{-}sme)_2]\cdot DMSO$ is complicated and comprises two different complexes in the asymmetric unit, one four- and the other five-coordinate. The four-coordinate copper(II) has a distorted (flattened) tetrahedral geometry as seen in the Zn(II) analogue whereas the five-coordinate copper(II) has a distorted square-pyramidal geometry with one ligand coordinated to the copper(II) ion as a tridentate (*N*, *S*, *O*) ligand and the other coordinated as a bidentate *N*, *S* chelate. EPR spectroscopy indicates that in solution only one form is present, that being a distorted tetrahedral complex.
© 2007 Elsevier Ltd. All rights reserved.

Keywords: Isatin Schiff base of *S*-methyldithiocarbazate; Nickel(II), zinc(II), copper(II) and cadmium(II) complexes

1. Introduction

Metal complexes of thiosemicarbazones [1–5] and Schiff bases derived from *S*-alkyl/aryl esters of dithiocarbazic acid [6–10] have been the subjects of considerable study. The presence of hard N- and soft S-donor atoms in the backbones of these ligands enable them to react readily with both transition and main group metal ions yielding stable metal complexes some of which have been shown to exhibit interesting physico-chemical properties [11] and significant biological activities [12]. Istain (2,3-dihydroindole-2,3-dione) and its derivatives have also been shown to exhibit a wide range of biological activities [13–17]. Since thiosemicarbazones derived from heterocyclic aldehydes and ketones and Schiff bases derived from *S*-alkyl/aryl esters of dithiocarbazic acid often act as versatile chelating agents and exhibit promising bioactivities [12], it is likely that isatin thiosemicarbazones and their metal complexes might also exhibit

* Corresponding author. Tel.: +673 2 2463001x1341; fax: +673 2 461502.
E-mail address: akbar@fos.ubd.edu.bn (M. Akbar Ali).

0277-5387/$ - see front matter © 2007 Elsevier Ltd. All rights reserved.
doi:10.1016/j.poly.2007.08.022

useful biological activity. Consequently, in recent years, the coordination chemistry as well as biological potentials of some complexes of istain- and *N*-methyl isatin thiosemicarbazones have been studied [18–20]. However, so far there have been no reports on metal complexes of isatin Schiff bases of *S*-alkyl/aryl dithiocarbazates. As part of our general study of metal complexes of dithiocarbazic acid and its derivatives, we report here the preparation and characterization of metal complexes of the istain Schiff base of *S*-methyldithiocarbazate together with the X-ray crystal and molecular structures of the free ligand and its nickel(II), zinc(II) and copper(II) complexes.

A particularly novel feature of the coordination arises from the structural rigidity brought about by the fused heterocyclic ring system. Unlike other Schiff base derivatives of heterocyclic aldehydes or ketones, the ligand presented here are special in that the O=C–C=N chelating moiety is inflexible and the O–M–N coordinate bite angle cannot adapt to metal ions of different sizes in contrast to more flexible ligand systems. As we shall demonstrate, in some cases this prevents coordination by the O-donor to the metal yet this O-atom acts as a blocking group preventing coordination by other ligands in the site it has left vacant.

2. Experimental

2.1. Materials and instrumentation

Isatin was purchased from Aldrich Chemical Company. *S*-methyldithiocarbazate was prepared as described previously [21]. The electronic spectra were recorded with a Shimadzu UV-3100 spectrophotometer. The IR spectra were recorded as KBr discs with either a Perkin–Elmer 1600 FT IR or a Perkin–Elmer 2000 spectrometer. Conductance measurements were made by means of a CMD 400 conductivity meter. Magnetic susceptibilities were measured with a Sherwood Scientific magnetic susceptibility balance calibrated with $HgCo(NCS)_4$. Diamagnetic corrections were applied using Pascal's constants. NMR spectra were measured using Bruker AV300 (300 MHz), AV400 (400 MHz) and AV500 (500 MHz) instruments. Spectra were recorded in $CDCl_3$ or d^6-DMSO with chemical shifts reported in parts per million calibrated using the resonances for $CDCl_3$, ($\delta_H(CHCl_3) = 7.24$ ppm; $\delta_C(CDCl_3) = 77.0$ ppm) or d^6-DMSO ($\delta_H(DMSO) = 2.49$ ppm; $\delta_C(DMSO) = 39.5$ ppm). Abbreviations: s (singlet), d (doublet), t (triplet), and m (multiplet) are employed for reporting of spectral data. Where required water suppression sequences were applied. The electron paramagnetic resonance (EPR) spectrum was recorded at 77 K on a Bruker ER200D spectrometer at X-band frequency (9.307 GHz). The microwave power was 2 mW and the modulation amplitude was 10 G.

2.2. Preparation of the Schiff base

Isatin (1.50 g, 10 mmol) dissolved in boiling MeOH (100 cm^3) was mixed with a boiling solution of *S*-methyldithiocarbazate (1.22 g, 10 mmol) in the same solvent (50 cm^3). The resulting mixture was heated on a water bath for 10 min and then left to stand overnight. The yellow crystalline product which formed was separated by filtration, washed with MeOH and recrystallized from MeCN to obtain light yellow crystals (2.3 g; 88.0%); m.p. 228–230 °C. *Anal.* Calc. for $C_{10}H_9N_3OS_2$ requires: C, 47.79; H, 3.61; N, 16.72. Found: C, 47.69; H, 3.48; N, 16.51%. Selected IR data (KBr pellet, cm^{-1}): 3200 br (νNH); 1686 s (νCO); 1621 s (νCN); 1149 s (νN–N); 978m (νCSS). UV–Vis spectrum [λ_{max} DMF, nm, (ε, $mol^{-1}\,dm^3\,cm^{-1}$)]: 400 *sh*, 381(19100). ^{1}H NMR (d_6-DMSO): δ/ppm, 2.60 (s, 3H, SCH_3), 6.94 (d, 1H, Ph), 7.09 (t, 1H, Ph), 7.40(t, 1H, Ph), 7.53 (d, 1H, Ph); ^{13}C NMR (d_6-DMSO): δ/ppm 17.1 (S–CH_3); 111.4, 119.2, 121.1, 122.8, 132.4, 143.4 (isatin-Ph); 135.6 (C=N); 162.4 (C=O); 201.2 (C=S).

2.3. Preparation of complexes

2.3.1. General method of preparation of $[M(isasme_2)] \cdot xS$ (M=Ni^{2+},Cu^{2+}, Zn^{2+}, Cd^{2+}; S=CH_3CN, H_2O, CH_3OH; $(CH_3)_2SO$; x = 1, 1.5)

A solution of the appropriate hydrated metal nitrate salt (1.0 mmol) in hot MeOH (20 cm^3) was added to a boiling solution of the Schiff base (0.26 g; 0.002 mol) in MeCN (100 cm^3). The mixture was refluxed for 3–4 h and then left to stand overnight. The complexes that crystallized out of the reaction mixture were filtered off, washed with MeOH and dried over anhydrous silica gel in a desiccator (60–70%.). Crystals of $[Cu(isa\text{-}sme)_2] \cdot DMSO$ suitable for X-ray work were obtained by recrystallizing the copper complex from DMSO:MeOH (4:1).

2.3.2. $[Ni(isa\text{-}sme)_2] \cdot MeCN$ (**1**)

Anal. Calc. for $C_{22}H_{19}N_7NiO_2S_4$ requires: C, 44.01; H, 3.19; N, 16.33. Found: C, 43.65; H, 3.21; N, 16.15%. Selected IR data (KBr pellet, cm^{-1}): 3207 m (νNH); 1677 s (νCO); 1608 s (νCN); 1188 s (νN–N); 991 s, 1008 sh (νCSS). UV–Vis spectrum [λ_{max} (nm) DMF, (ε, mol^{-1} dm^3 cm^{-1})] 928 (1020), 484 (17989), 384 (25146). $\mu_B = 2.84$ B.M. Λ (DMF, $ohm^{-1}\,cm^2\,mol^{-1}$): 1.4.

2.3.3. $[Zn(isa\text{-}sme)_2] \cdot MeOH$ (**2**)

Anal. Calc. for $C_{21}H_{22}N_6O_5S_4Zn$ requires: C, 42.18, H, 3.37, N, 14.05. Found: C, 42.03; H, 3.66; N, 14.05%. ^{13}C NMR (d_6-DMSO): δ/ppm 16.1 (S–CH_3); 48.6 (CH_3 of MeOH); 111.9, 115.8, 123.4, 128.1, 134.3, 141.3, 144.3 (isatin-Ph); 166.1 (C=O); 198.0 (C=S). ^{1}H NMR (d_6-DMSO): δ/ppm 2.70 (s, 6H, SCH_3), 3.20 (s, CH_3 of MeOH); 7.04 (d, 2H, Ph), 7.20 (d, 2H), 7.48 (t, 2H, Ph), 8.09 (t, 2H, Ph). Selected IR data (KBr pellet, cm^{-1}): 3135 br, w (νNH); 1701 s (νCO); 1610 s (νCN); 1185 s (νN–N); 991 s, 1000 sh (νCSS). UV–Vis spectrum [λ_{max} DMF, nm, (ε, mol^{-1} $dm^3\,cm^{-1}$): 436 (28724), 381 (25224). Λ (DMF, $ohm^{-1}\,cm^2\,mol^{-1}$): 2.4.

2.3.4. [Cu(isa-sme)$_2$] · (CH$_3$)$_2$SO (3)

Anal. Calc. for $C_{22}H_{22}N_6O_5S_5Cu$ requires: C, 40.84; H, 3.55; N, 12.87. Found: C, 41.13; H, 3.45; N, 13.05%. Selected IR data (KBr pellet, cm^{-1}): 3423 br (νNH); 1717 s, 1676 s (νCO); 1615 s (νCN); 1189 s (νN–N); 996 s, 986 s (νCSS). UV–Vis spectrum [λ_{max} DMF, nm, (ε, mol^{-1} dm^3 cm^{-1})] 701 (356), 443 (19929), 364 (30055). $\mu_B = 2.10$. Λ (DMF, ohm^{-1} cm^2 mol^{-1}): 4.0.

2.3.5. [Cd(isa-sme)$_2$] · 1.5H$_2$O (4)

Anal. Calc. for $C_{20}H_{19}N_6O_{3.5}S_4Cd$ requires: C, 37.53; H, 2.99; N, 13.13. Found: C, 38.04; H, 3.40; N, 12.90%. ^{13}C NMR (d_6-DMSO): δ/ppm 15.9 (S–CH$_3$); 111.8, 116.1, 123.4, 127.7, 133.5, 140.6, 143.3 (isatin-Ph); 166.9 (C=O); 197.6 (C=S). ^{1}H NMR (d_6-DMSO): δ/ppm, 2.68 (s, 6H, SCH$_3$), 7.02 (d, 2H, Ph), 7.17 (t, 2H, Ph), 7.45 (t, 2H, Ph), 8.07 (d, 2H, Ph). Selected IR data (KBr pellet, cm^{-1}): 3205 m (νNH); 1705 s (νCO); 1610 s (νCN); 1185 s (νN–N); 987 s, 1007 w (νCSS). UV–Vis spectrum [λ_{max} DMF, nm, ε, mol^{-1} dm^3 cm^{-1}] 429 (33, 200), *ca.* 381 sh. Λ (DMF, ohm^{-1} cm^2 mol^{-1}): 19.3.

2.4. Crystallography

Cell constants were determined by a least-squares fit to the setting parameters of 25 independent reflections, measured on an Enraf-Nonius CAD 4 four-circle diffractometer using graphite monochromated Mo Kα radiation (0.71073 Å) and operating in the ω–2θ mode within the range $2 < 2\theta < 50°$. An empirical absorption correction (ψ scans) [22] and data reduction [23] were performed within the WINGX [24] suite of programs. The structures were solved by direct methods with SHELX86 [25] and refined by full-matrix least-squares analysis with SHELXL97 [26]. Non-hydrogen atoms were refined with anisotropic thermal parameters whereas H-atoms were included at estimated positions. Drawings of all molecules were produced with ORTEP3 [27]. A summary of the crystal data, structure solution and refinement parameters are given in Table 1. Selected bond lengths and angles are given in Table 2.

3. Results and discussion

3.1. Syntheses

Isatin is a highly conjugated compound with an intense orange colour but its condensation with *S*-methyldithiocarbazate produces a light yellow crystalline Schiff base compound. Like most thiosemicarbazones and Schiff bases derived from dithiocarbazic acid, it can exhibit thione-thiol tautomerism [28] (Fig. 1) since it has a thioamide functional group –NH–C(=S)SR.

The solid state IR spectrum of Hisa-sme does not reveal any νSH band at *ca.* 2700 cm^{-1} indicating that, in the solid state, it remains as the thione form (1a). Its ^{1}H NMR spectrum in $CDCl_3$ also does not exhibit any signal attributable to the SH proton indicating that in solution, it also remains predominantly as the thione form. However, upon depro-

Table 1
Crystal and refinement data

	1	2	3
Formula	$C_{22}H_{19}N_7NiO_2S_4$	$C_{21}H_{20}N_6O_3S_4Zn$	$C_{22}H_{22}N_6CuO_3S_5$
Formula weight	600.39	598.04	642.30
Temperature (K)	293(2)	293(2)	293(2)
Wavelength (Å)	0.71073	0.71073	0.71073
Crystal system	monoclinic	monoclinic	triclinic
Space group	$P2_1/c$	Cc	$P\bar{1}$
Unit cell dimensions			
a (Å)	10.1101(1)	10.448(2)	11.854(1)
b (Å)	13.359(2)	29.761(5)	13.726(2)
c (Å)	19.537(1)	8.714(2)	17.901(7)
α (°)			101.04(2)
β (°)	103.713(9)	110.08(2)	106.00(1)
γ (°)			91.60(1)
Volume, (Å^3)	2563.4(5)	2544.9(9)	2737.9(7)
Z	4	4	4
D_{calc} (g cm^{-3})	1.556	1.561	1.558
Absorption coefficient (mm^{-1})	1.118	1.329	1.216
F(000)	1232	1224	1316
Reflections collected	4691	2319	10118
Independent reflections	4429	2319	9608
R_{int}	0.0215	0.000	0.0498
Observed reflections [$I > 2\sigma(I)$]	2874	930	5775
Parameters	328	302	667
Goodness-of-fit on F^2	1.012	0.999	1.026
R_1 [$I > 2\sigma(I)$]	0.0371	0.0839	0.0550
wR_2 (all data)	0.0990	0.2476	0.1748

Table 2
Selected bond lengths (Å) and angles (°.)

	1	2	3 (four-coord.)[a]	3 (five-coord.)
M–N(2A)	2.008(3)	2.08(2)	2.037(4)	1.972(4)
M–N(2B)	1.995(3)	2.04(2)	1.999(4)	1.953(4)
M–S(1A)	2.385(1)	2.310(8)	2.215(2)	2.455(2)
M–S(2A)	2.382(1)	2.379(8)	2.241(2)	2.299(2)
M–O(1A)	2.228(3)			
M–O(1B)	2.294(3)			2.224(4)
C(1A)–S(1A)	1.715(4)	1.73(2)	1.713(6)	1.674(5)
C(1B)–S(1B)	1.707(4)	1.69(3)	1.711(7)	1.711(6)
C(1A)–N(1A)	1.329(4)	1.38(3)	1.300(7)	1.335(7)
C(1B)–N(1B)	1.315(4)	1.37(3)	1.314(7)	1.316(7)
N(1A)–N(2A)	1.329(4)	1.32(2)	1.378(6)	1.378(6)
N(1B)–N(2B)	1.315(4)	1.34(3)	1.380(6)	1.360(6)
C(3A)–N(2A)	1.297(4)	1.35(3)	1.299(7)	1.297(6)
C(3B)–N(2B)	1.288(4)	1.28(3)	1.287(7)	1.278(7)
C(4A)–O(1A)	1.240(4)	1.21(3)	1.218(7)	1.222(6)
C(4B)–O(1B)	1.227(4)	1.26(3)	1.214(7)	1.244(6)
N(1A)–M–N(1B)	172.6(1)	144.3(8)	110.1(2)	169.3(2)
S(1A)–M–S(1B)	98.23(4)	110.1(3)	98.60(7)	104.24(7)
N(2A)–M–S(1A)	81.01(9)	81.9(6)	85.38(13)	82.4(1)
O(1B)–M–S(1B)	158.08(7)			160.4(1)

[a] Replace atom labels A and B with C and D, respectively, i.e. N2C, N2D (instead of N2A and N2B).

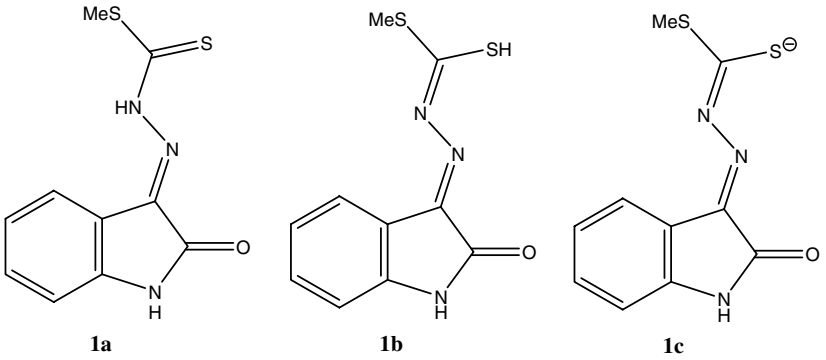


Fig. 1. The thione (**1a**) and thiol (**1b**) tautomeric forms of Hisa-sme and also the thiolate form of its monoanion (**1c**).

tonation, it is found in the thiolate form (1c) and is capable of coordination to divalent metal(II) ions to give compounds of the general formula, $[M(isa\text{-}sme)_2]\cdot n(solvate)$ ($M = Ni^{II}$, Cu^{II}, Zn^{II}, Cd^{II}; solvate = MeCN, DMSO, MeOH or H_2O; $n = 1, 1.5, 2.0$). Attempts to prepare mono-ligand complexes of the type $M(Hisa\text{-}sme)X_2$ or [M(isa-sme)X] ($M = Ni^{II}$, Zn^{II}, Cd^{II}; $X = Cl^-$, Br^-) were unsuccessful.

3.2. Crystallographic characterization

3.2.1. [Ni(isa-sme)$_2$] · MeCN (*1*)

The crystal structure of the nickel complex is shown in Fig. 2 and selected bond lengths and bond angles are given in Table 2. The structure reveals a six-coordinate nickel(II) ion in a distorted octahedral environment. An MeCN molecule (not shown here) is H-bonded to the amide N–H group of one ligand. The two isatin Schiff bases are coordinated to the nickel ion as uninegatively charged tridentate

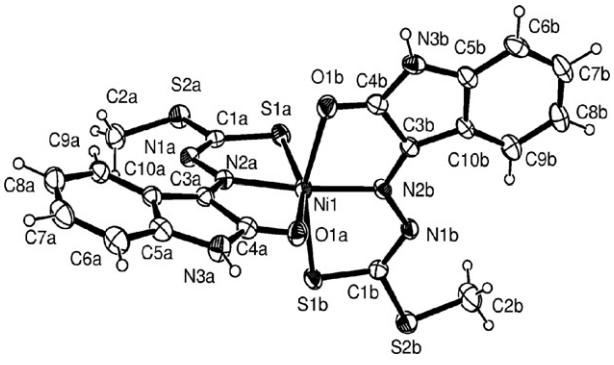


Fig. 2. The molecular structure of (**1**) Ni(isa-sme)$_2$ (30% probability ellipsoids). The MeCN molecule that co-crystallised is omitted for clarity.

chelating agents *via* the carbonyl oxygen atom, the azomethine nitrogen atom and the thiolate sulfur atom. Deprotonation of the ligand produces an iminothiolate ion with a

negative charge on the sulfur atom which is delocalized in the C–N–N–C chain of the dithiocarbazate moiety as indicated by the bond distances C(1A)–N(1A): 1.329(4) Å and C(1B)–N(1B): 1.315(4) Å; N(1A)–N(2A): 1.366(4) Å, N(1A)–N(2B): 1.372(4) Å; C(3A)–N(2A): 1.297(4) Å, C(3B)–N(2B): 1.288(4) Å which fall between the extrema anticipated for pure double or single bonds.

The Schiff bases are coordinated to the nickel(II) ion in meridional configurations with the azomethine N-atoms *trans* and the pairs of thiolate S- and carbonyl O-atoms *cis*. The angle between the two Ni···S···N···O planes defined by each ligand is 89°, i.e. the two ligands are essentially orthogonal. Similar meridional configurations have also been reported for related bis-ligand nickel(II) complexes of other *O*, *N*, *S* donor ligands [17,18,29]. The Ni–N bonds are the shortest and are similar to those of other six-coordinate high-spin nickel(II) complexes of related ligands [18–20]. The two Ni–S bond lengths are also similar to those of related bis-ligand nickel(II) complexes of isatin thiosemicarbazones [18–20]. The two Ni–O distances are different [2.228(3) Å, 2.294(3) Å] and also very long by comparison with the Ni–N distances. This is indicative of very weak coordination by these amide O-atoms. It is of note that similarly weak Ni–O coordinate bonds have been seen in an isatin-thiosemicarbazone complex $[Ni(isa\text{-}tsc)_2]\cdot EtOH$ [18]. This feature may be due to either an inherently poor nucleophilicity of the amide O-atom or it may be a consequence of rigidity in the chelate ring brought about by the bicyclic indole moiety which prevents any closer approach by the O-atom to the Ni ion. The C–S bond distances [1.715(4), 1.707(4) Å] in the complex are longer than that observed in related free Schiff base ligands derived from *S*-methyldithiocarbazate [28] confirming that the thiolate tautomer is present in the coordinated ligand (Fig. 1, structure 1c). For the purpose of comparison, Ni coordinate bond distances in closely related complexes are given in Table 3. The data indicate that bond distances in the most six-coordinate nickel(II) complexes of planar tridentate *O*, *N*, *S* ligands compare well, except that the Ni–S bond distances in the present nickel complex are longer than those in other such complexes, perhaps a reflection of the *mer* configuration and the resulting increased interaction between the sulfur donor atoms.

The stereochemistry of nickel(II) in the complex can be considered as a distorted octahedron. All coordinate angles within each five-membered chelate ring are around 80°, while the *trans* N(2B)–Ni(1)–N(2A) angle (172.6(1)) is somewhat distorted from linearity. A comparison of bond angles in the present nickel complex with those of related complexes of *O*, *N*, *S* chelates [18–20,28] indicates that none of the complexes of *O*, *N*, *S* donor ligands have regular octahedral geometries. The unequal field strengths provided by the three different donor atoms in this type of ligands are expected to cause substantial tetragonal distortion from octahedral symmetry which is what is actually observed in these complexes.

3.2.2. $[Zn(isa\text{-}sme)_2]\cdot MeOH$ (2)

The molecular structure of the zinc complex is shown in Fig. 3 and selected bond lengths and angles are included in Table 2. The structure shows that, in contrast with the bis-ligand nickel(II) complex which has a distorted octahedral

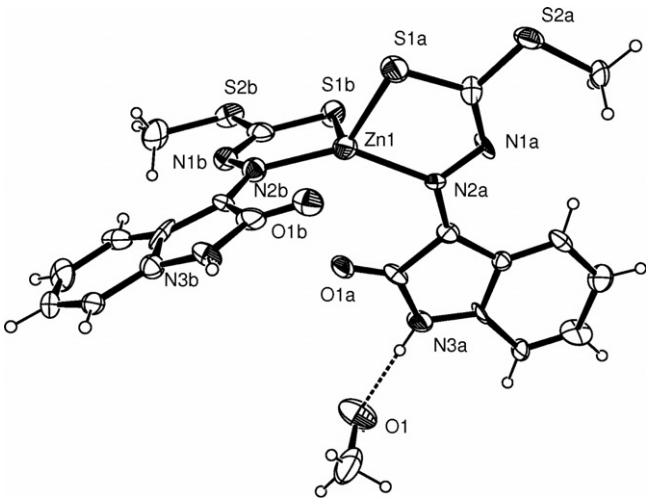


Fig. 3. View of (**2**) $[Zn(isa\text{-}sme)_2]\cdot MeOH$ structure (30% probability ellipsoids).

Table 3
Comparison of Ni-donor atom distances in bis-ligand six-coordinate nickel(II) complexes of ONS donor ligands

Compound[a]	Ni–S	Ni–$N_{azomethine}$	Ni–O	Ref.
$[Ni(isa\text{-}tsc)_2]\cdot C_2H_5OH$	2.368(2)	2.023(3)	2.226(3)	[17]
$[Ni(isa\text{-}tsc)_2]\cdot DMF$	2.378(3) 2.345(3)	2.027(6) 2.022(6)	2.177(5) 2.212(6)	[17]
$[Ni(Misa\text{-}tsc)_2]$	2.367(2)	2.005(6)	2.264(4)	[18]
$[Ni(mpsme)_2]$	2.3607(8) 2.3583(9)	2.014(2) 2.013(2)	2.218(2) 2.263(2)	[31]
$[Ni(isa\text{-}sme)_2]\cdot MeCN$	2.3847(11) 2.3818(11)	2.008(3) 1.995(3)	2.228(3) 2.294(3)	this work

[a] isa-tsc = monoanionic form of isatin thiosemicarbazone; misa-tsc = anionic form of 1-*N*-methyl isatin thiosemicarbazone; mpsme = anionic form of the methylpyruvate Schiff base of *S*-methyldithiocarbazate.

geometry, the zinc complex has a four-coordinate configuration in which the Schiff bases are coordinated to the zinc atom not as tridentate ONS ligands but as uninegatively charged NS bidentate chelating agents *via* the two azomethine nitrogen atoms and the two thiolate sulfur atoms. The methanol molecule is hydrogen bonded to the N3A atom of the isatin ring.

The angle between the two Zn···N···S planes is 80° thus the coordination geometry is best considered distorted tetrahedral. The coordinate angles are in the range 144.3(8)–81.3(7)°, the smallest being associated with the N2*n*-Zn–S1*n* chelate rings. The crystals for this structure determination were not of ideal quality and the precision is poorer than the other structures reported here. Nevertheless, the Zn–N [2.04(2) and 2.08(2) Å] and Zn–S [2.379(8) and 2.310(8) Å] bond distances are comparable with those of the analogous zinc(II) complex bis[*S*-methyl-b-*N*-(2-furylmethyl)methylenedithio-carbazato]zinc(II) of a bidentate *N*,*S* donor ligand, which also has a distorted tetrahedral geometry and the same ZnN_2S_2 coordination kernel [29]. As expected, the Zn–S and Zn–N bond lengths in the present zinc complex are shorter than similar bonds in octahedral zinc(II) complexes of tridentate *N*,*N*,*S* dithiocarbazate ligands [30]. The Zn···O distances are each in excess of 2.58 Å and thus are too long to be considered genuine coordinate bonds. Notwithstanding, it is very interesting that the amide O-atoms, due to their proximity to the Zn ion, effectively block coordination by any other monodentate ligands in these 'vacant' coordination sites.

3.2.3. [Cu(isa-sme)$_2$] · DMSO (3)

The crystal structure of the bis-ligand copper(II) complex is out of the ordinary in that it contains a four-coordinate copper(II) complex (Fig. 4a) and a five-coordinate copper(II) complex (Fig. 4b) within the asymmetric unit in addition to two DMSO molecules (one disordered). In the four-coordinate complex, the ligands are coordinated to the copper(II) ion *via* the thiolate S- and azomethine N-atoms. The Cu–S [2.215(3) and 2.242(2) Å] and Cu–N [2.037(4) and 1.998(4) Å] bond lengths are similar to those of the bis-chelated four coordinate copper(II) complex of related *p*-dimethylaminobenzaldehyde Schiff base of *S*-benzyldithiocarbazate [31]. The angle between the two Cu···N···S planes is 50° thus the CuN_2S_2 moiety is distorted to roughly half-way between a tetrahedral and a square planar geometry. The Cu···O distances are each in excess of 2.8 Å and are hence too remote to be included in the first coordination sphere.

In the five-coordinate copper(II) complex (Fig. 4b), one of the Schiff bases is coordinated to the copper(II) ion as a tridentate *O*,*N*,*S* chelate (as seen in the Ni(II) structure, Fig. 2) while the other ligand molecule is coordinated as a bidentate *N*,*S* chelate. The coordination geometry of the copper(II) ion in the five-coordinate unit can be considered as approximately square-pyramidal. The structural parameter τ is commonly used to describe 5-coordinate complexes distorted between an ideal square pyramid ($\tau = 0$) and a trigonal bipyramid ($\tau = 1$). The equation is $\tau = (\beta - \alpha)/60°$, with α and β being the two largest coordinate angles (160.4(1)° and 169.4(2)°, respectively in this case), to afford a value of 0.148 for this 5-coordinate complex.

The angle between the two Cu···N···S planes defined by the two coordinated ligands is 78° and clearly much closer to orthogonal than in the four-coordinate complex. The Cu–S bonds [2.455(2) and 2.379(8) Å] are very different and this disparity can be attributed to a Jahn–Teller distortion arising from the d^9 electronic configuration leading to elongation of the coordinate bonds along the Cu–S1A axis. This in part explains why O1A is not coordinated (CuÅ···O1A) > 2.62 Å as it lies along the same axis of elongation. The remaining equatorial coordinate bonds are shorter although once again an unusually elongated equatorial bond to the amide O-atom is seen (as with the Ni(II) analogue). The coordinate bonds compare well with other five-coordinate copper(II) complexes such as [Cu(NNS)(phen)]ClO_4 (where NNS = Schiff base formed from pyridine-2-*N*-oxide carbaldehyde Schiff base of

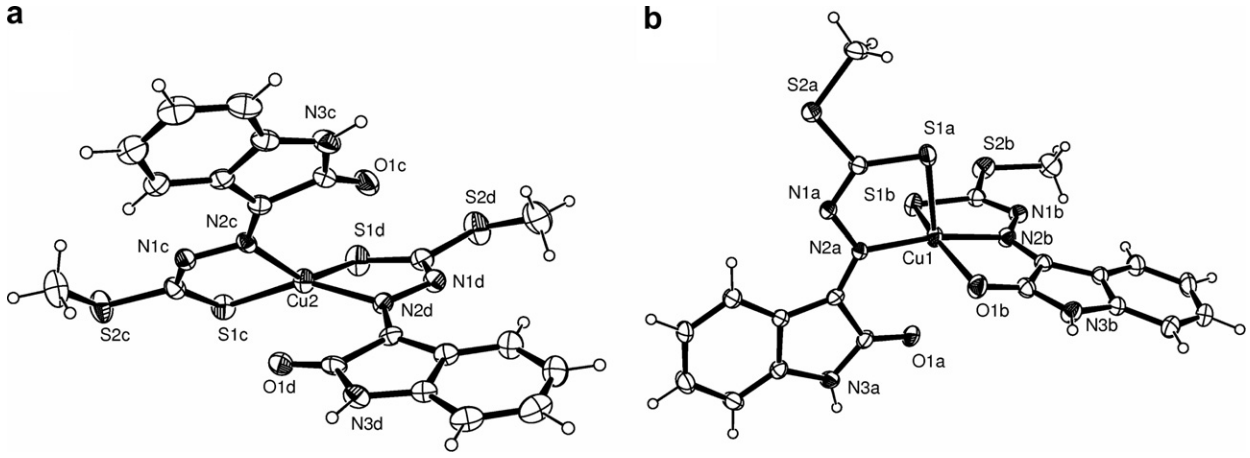


Fig. 4. The molecular structures of the complexes in (**3**): (a) four-coordinate Cu(isa-sme)$_2$ and (b) five-coordinate Cu(isa-sme)$_2$ found in the same asymmetric unit (30% probability ellipsoids). The DMSO molecules are omitted for clarity.

S-benzyldithiocarbazate) [32]. The bond distances in the dithiocarbazate chain are similar to those found in the nickel complex described above. In both copper(II) centres, the coordinate angles deviate significantly from the ideal values because of the restraint imposed by the five-membered chelate rings.

3.3. Physical and spectroscopic characterization of isa-sme complexes

The nickel(II), copper(II), zinc(II) and cadmium(II) complexes exhibit molar conductances of 1.4, 4.0, 2.4 and 19.3 $ohm^{-1}\,cm^2\,mol^{-1}$, respectively in DMF indicating that they behave essentially as non-electrolytes in this solvent. The non-electrolytic nature of the complexes also indicates that the ligands remain coordinated as monoanions in solution. The room-temperature magnetic moment of the nickel(II) complex (2.84 B.M.) indicates that it is high-spin and six-coordinate. The magnetic moment of the copper(II) complex (2.10 B.M.) is normal for a $3d^9$ metal ion in a magnetically dilute environment.

The IR spectrum of Hisa-sme exhibits a strong band at 1686 cm^{-1} assigned to the ν(C=O) of the carbonyl group. In the spectrum of the nickel(II) complex this band shifts to lower frequency in accordance with the observed coordination environment of the metal ion. The corresponding ν(C=O) band in the IR spectra of the zinc(II) and cadmium(II) complexes shifts to higher wave number suggesting that it is not coordinated. In contrast, for all three metal ions the IR spectrum exhibits a shift in the azomethine ν(C=N) band from the free ligand position (1621 cm^{-1}) to lower wave numbers indicates the involvement of this moiety in bonding in each case. The shift of the ν(N–N) band of the free ligand to higher wave numbers in the spectra of the complexes (from 1149 to *ca.*1185 cm^{-1}) supports the suggestion of the bonding of the azomethine nitrogen atom to the metal ions. The splitting of the νCSS band of the free ligand at 978 cm^{-1} in the spectra of the complexes is strong evidence that the ligand coordinates with the metal ions through one of the sulfur atoms [33].

The electronic spectrum of Ni(isa-sme)$_2$ (in DMF) displays bands at 928, 680 sh, 484 and 384 nm. Six-coordinate nickel(II) complexes are expected to exhibit three spin-allowed bands corresponding to the $^3A_{2g} \rightarrow {}^3T_{2g}$, $^3A_{2g} \rightarrow {}^3T_{1g}(F)$ and $^3A_{2g} \rightarrow {}^3T_{1g}(P)$ transitions. However, with sulfur-containing ligands the transition, $^3A_{2g} \rightarrow {}^3T_{1g}(P)$ is invariably obscured by $S \rightarrow M$ charge transfer bands and consequently, only two bands are generally observed. The bands at 928 and 680 nm are thus assigned to the $^3A_{2g} \rightarrow {}^3T_{2g}$ and $^3A_{2g} \rightarrow {}^3T_{1g}(F)$ transitions, respectively. For the six-coordinate nickel(II) complex of the methylpyruvate Schiff base of S-methyl dithiocarbazate, with the same $NiO_2N_2S_2$ chromophore, d–d bands at 915 and 550 nm were observed [28]. The intense band at 484 nm in the spectrum of [Ni(isa-sme)$_2$] is probably a combination of a d–d band corresponding to the transition $^3A_{2g} \rightarrow {}^3T_{1g}(P)$ and the $S \rightarrow Ni^{II}$ charge-transfer band. The electronic spectrum of the [Cu(isa-sme)$_2$]·DMSO exhibits a broad d–d band at 771 nm and $S \rightarrow Cu^{II}$ C.T. band at 443 nm. The presence of a S–Cu^{II} C.T. band is typical of copper(II) complexes of dithiocarbazate ligands [34–37]. The electronic spectra of the d^{10} zinc(II) and cadmium(II) complexes are similar to those of the free ligand although bathochromic shifts of the bands seen in the free ligand are apparent.

The X-ray structural data shows that the ligand is bound to nickel(II) ion *via* the carbonyl oxygen atom, the azomethine nitrogen atom and the thiolate sulfur atom. However, the non-electrolyte character and the differences in the IR spectra between the nickel(II) and the zinc(II) and cadmium(II) complexes suggest that the latter are coordinated to the isa-sme ligand through the azomethine nitrogen and thiolate sulfur atoms. No crystals of the Cd complex suitable for X-ray work were obtained so its structure remains unknown. A tetrahedral geometry of the kind seen in the Zn analogue is consistent with the very similar IR results of the Cd and Zn complexes, but in the absence of a crystal structure this is only a speculative assignment.

The identification of two distinctly different Cu(II) complexes in the crystal structure of [Cu(isa-sme)$_2$]·DMSO poses the question of its structure in solution. In other words does it exist as a distorted tetrahedral CuN_2S_2 complex or a tetragonally elongated (4 + 1) square pyramidal CuN_2OS_2 or perhaps as an equilibrium mixture of the two? The electronic spectrum of the complex does not discriminate between these possibilities. EPR spectroscopy is very sensitive to angular distortions at the Cu(II) centre; particularly those involving a distortion from planar to tetrahedral geometry [38]. A Cu(II) complex with tetragonally elongated (axial) symmetry will yield an EPR spectrum with two sets of resonances parallel with and perpendicular to the axis of symmetry (designated ∥ and ⊥). Hyperfine coupling with the Cu nucleus (^{63,65}Cu $I = 3/2$) generates two sets of four lines centred at $g_\parallel$ and $g_\perp$; the splitting of each set of four lines being equal to the hyperfine coupling constants $A_\parallel$ and $A_\perp$, respectively. As a general rule, distortion from planar towards tetrahedral geometry results in a decrease in $A_\parallel$ and increase in $g_\parallel$ as shown in a number of synthetic and biological examples involving Cu(II) [39,40]. The experimental X-band EPR spectrum of [Cu(isa-sme)$_2$]·DMSO is shown in Fig. 5. The spin Hamiltonian parameters were obtained by spectral simulation [42] (also shown in Fig. 5). The most relevant (and accurately determined) parameters are $A_\parallel$ (105 G) and $g_\parallel$ (2.185) while the remaining parameters $A_\perp$ (∼45 G) and $g_\perp$ (∼2.06) are less certain as these transitions (in particular the hyperfine splittings) are not resolved due to the linewidths of the transitions. Nevertheless, the $A_\parallel$ value is very small and in line with that of a dominantly tetrahedral CuN_2S_2 complex [39–41].

For comparison, the EPR spectra of a series of CuN_2S_2 complexes of a tetradentate ligand were reported [39], where the tetrahedral twist angle was varied by structural

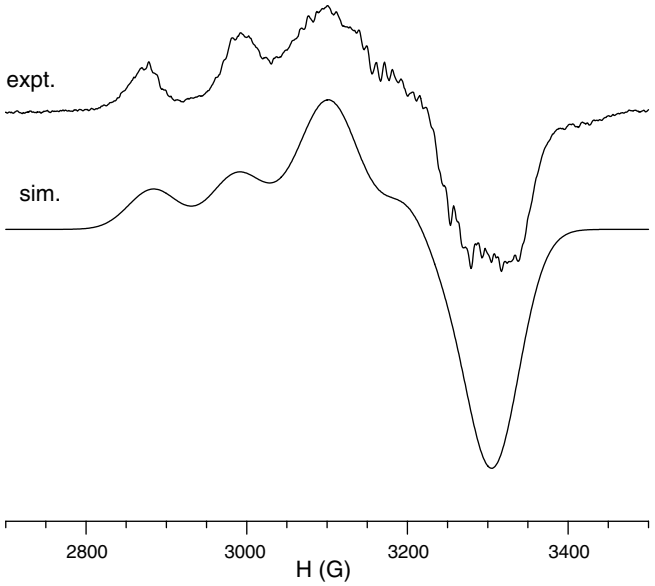


Fig. 5. Experimental and simulated X-band (9.307 GHz) EPR spectra of Cu(isa-sme)$_2$ in DMSO at 77 K (1 mM frozen solution). Simulation spin Hamiltonian parameters $g_{\|} = 2.185$, $A_{\|} = 105\ G$; $g_{\perp} = 2.06$ and $A_{\perp} = 45$ G. Linewidths 35 G, Lorentzian lineshapes.

changes to the chelate ring size. The Cu(II) complex exhibiting the greatest tetrahedral twist (57°) gave an EPR spectrum where $A_{\|}$ was 145 G, while a less twisted analogue (53°) gave an $A_{\|}$ value of 160 G. The even smaller $A_{\|}$ (105 G) seen in Cu(isa-sme)$_2$ is indicative of a tetrahedral twist angle greater that 57°. We contend that the solution structure of Cu(isa-sme)$_2$ approaches that of the Zn(II) analogue identified crystallographically where a twist angle of 80° was seen. Indeed this geometry can easily be derived from the 5-coordinate form of the complex seen in the crystal structure of [Cu(isa-sme)$_2$]·DMSO (twist angle 78°) by merely breaking the (already strained) Cu–O bond in the absence of any other conformational change. It is important to point out that the EPR spectrum of [Cu(isa-sme)$_2$]·DMSO is not consistent with a tetragonally elongated (4 + 1) Cu(II) complex (either square pyramidal or pseudo square planar) as both types of complexes invariably furnish EPR spectra where $A_{\|}$ is in the vicinity of 200 G [38–41]. In other words, we can conclude that the solid state structure of Cu(isa-sme)$_2$ is affected by packing forces and not representative of the structure of the complex in solution. The DMSO solvate molecules and the proximity of the 4- and 5-coordinate Cu(II) complexes in the structure results in distortions away from its ideal structure in solution.

4. Conclusions

The isatin Schiff base of *S*-methyldithiocarbazate behaves as a versatile chelating agent exhibiting variable denticity toward metal ions depending upon the requirements of the particular metal centre. Thus, it behaves as a uninegatively charged tridentate O,N,S chelate with nickel(II) forming a stable six-coordinate high-spin octahedral nickel(II) complex. However, with zinc(II) and cadmium(II) it behaves as an N,S bidentate chelating agent forming distorted tetrahedral complexes. With copper(II), in the solid state, it behaves both as a bidentate N,S ligand as well as a tridentate O,N,S donor chelate producing a novel structure comprising both 4- and 5-coordinate copper(II) complexes within the asymmetric unit. EPR spectroscopy of the Cu(II) complex reveals a homogeneous solution structure that is different to both of the crystallographically identified forms.

5. Supplementary material

CCDC 638441, 638442 and 638443 contain the supplementary crystallographic data for **1**, **2** and **3**. These data can be obtained free of charge via http://www.ccdc.cam.ac.uk/conts/retrieving.html, or from the Cambridge Crystallographic Data Centre, 12 Union Road, Cambridge CB2 1EZ, UK; fax: (+44) 1223-336-033; or e-mail: deposit@ccdc.cam.ac.uk.

Acknowledgements

M. Akbar Ali, Hjh Junaidah and A.H. Mirza gratefully acknowledge the financial support provided for this work by the Ministry of Development, Negara Brunei Darussalam by means of a Research Grant (No. HRD/UBD/BIO/001) and thank Awg Harrisman Ashady Bin Haji Ali for technical help. PVB acknowledges financial support of the Australian Research Council. Dr Tri. Le is warmly thanked for technical assistance with the EPR measurements.

References

[1] (a) D.X. West, S.B. Padhye, P.B. Sonawane, Struct. Bond (Berlin) 76 (1991) 1;
(b) D.X. West, A.E. Liberta, S.B. Padhye, R.C. Chikate, P.B. Sonawane, A.S. Kumbhar, R.G. Yerande, Coord. Chem. Rev. 123 (1993) 49;
(c) M.J.M. Campbell, Coord. Chem. Rev. 15 (1975) 279.
[2] I.G. Santos, A. Hagenbasch, U. Abram, J. Chem. Soc., Dalton Trans. (2004) 677.
[3] V. Philip, V. Suni, M.R.P. Kurup, M. Nethaji, Polyhedron 23 (2004) 1225.
[4] P.J. Blower, T.C. Castle, A.R. Cowley, J.R. Dilworth, P.S. Donnely, E. Labisbal, F.E. Sowrey, S.J. Teat, M.J. Went, J. Chem. Soc., Dalton Trans. (2003) 4416.
[5] N.C. Kasuga, K. Sekino, M. Ishikawa, A. Honda, M. Yokoyama, S. Nakano, N.C. Koumo, K. Nomiya, J. Inorg. Biochem. 96 (2003) 298.
[6] (a) M. Akbar Ali, A.H. Mirza, T.B.S.A. Ravoof, P.V. Bernhardt, Polyhedron 23 (2004) 2031;
(b) M. Akbar Ali, A.H. Mirza, T.B.S.A. Ravoof, P.V. Bernhardt, Polyhedron 23 (2004) 2037.
[7] (a) M. Akbar Ali, A.H. Mirza, C.W. Voo, A.L. Tan, P.V. Bernhardt, Polyhedron 22 (2003) 3433;
(b) M. Akbar Ali, A.H. Mirza, M. Nazimuddin, Raju Ahmed, L.R. Gahan, P.V. Bernhardt, Polyhedron 22 (2003) 1471;
(c) M. Akbar Ali, A.H. Mirza, See Tho Wai Keng, R.J. Butcher, Transition Met. Chem. 28 (2003) 241.

[8] (a) M. Akbar Ali, A.H. Mirza, R.J. Butcher, M.T.H. Tarafder, Tan Boon Keat, A. Manaf Ali, J. Inorg. Biochem. 92 (2002) 141;
(b) M. Akbar Ali, A.H. Mirza, M. Nazimuddin, H. Rahman, R.J. Butcher, Transition Met. Chem. 27 (2002) 268;
(c) M. Akbar Ali, A.H. Mirza, M. Nazimuddin, P.K. Dhar, R.J. Butcher, Transition Met. Chem. 27 (2002) 27;
(d) M. Akbar Ali, A.H. Mirza, R.J. Butcher, M.T.H. Tarafder, Manaf A. Ali, Inorg. Chim. Acta 320 (2001) 1.
[9] (a) K.A. Crouse, Kar-Benng Chew, M.T.H. Tarafder, A. Kasbollah, A.M. Ali, B.M. Yamin, H.-K. Fun, Polyhedron 23 (2004) 161;
(b) K.A. Crouse, Kar-Beng Chew, Bohari M. Yamin, Seik-Weng Ng, M.T.H. Tarafder, Acta Crystallogr., Sect. E 59 (2003) 148.
[10] (a) Yao-Cheng Shi, Hua-Mei Yang, Hai-Bin Song, Chao-Guo Yan, Xiao-Ya Hu, Polyhedron 23 (2004) 567;
(b) K.N. Zelenin, I.P. Bezhan, B.A. Ershov, A.K. Zelenin, Tetrahedron 50 (1994) 1147;
(c) W. Wang, F.L. Zeng, X. Wang, M.Y. Tan, Polyhedron 15 (1996) 1699.
[11] (a) Yu-peng Tian, Chun-ying Duan, Cun-yuan Zhao, Xiao-zeng You, T.C.W. Mak, Z.Y. Zhang, Inorg. Chem. 36 (1997) 1247;
(b) Z.H. Liu, C.Y. Duan, J. Hu, Inorg. Chem. 38 (1999) 1719;
(c) Z.H. Liu, S.R. Yang, C.Y. Duan, X.Z. You, Chem. Lett. Jpn. 10 (1999) 1063;
(d) Yu-Peng Tian, C.Y. Duan, Xiao-Zeng You, T.C.W. Mak, Q. Luo, Jian-Ying Hou, Transition Met. Chem. 23 (1998) 17;
(e) A. Abu-Raqabah, G. Davies, M.A. El-Sayed, A. El-Toukhy, S.N. Shaikh, J. Zubieta, Inorg. Chim. Acta 193 (1992) 43.
[12] (a) A.E. Liberta, D.X. West, BioMetals 5 (1992) 121;
(b) M.B. Ferrari, F. Bisceglie, G.G. Fava, G. Pelosi, P. Tarasconi, R. Albertini, S. Pinelli, J. Inorg. Biochem. 89 (2002) 36.
[13] R.W. Daisley, V.K. Shah, J. Pharm. Sci. 73 (1984) 407.
[14] S.N. Pandeya, D. Sriram, E. Declecq, C. Pannecouque, M. Mitvrouw, Indian J. Pharm. Sci. 60 (1999) 207.
[15] S.N. Pandeya, J.R. Dimmock, Pharmazie 48 (1993) 659.
[16] R. Boon, Antiviral Chem. Chemother. 8 (1997) 5.
[17] S.N. Pandeya, D. Siram, G. Nath, E. Declercq, Eur. J. Pharm. Sci. 9 (1999) 25.
[18] M.C. Rodriguez-Arguelles, A. Sanchez, M.B. Ferrari, G.G. Fava, C. Pelizzi, G. Pelosi, R. Albertini, P. Lunghi, S. Pinelli, J. Inorg. Biochem. 73 (1999) 7.
[19] M.B. Ferrari, C. Pelizzi, G. Pelosi, M.C. Rodrigues-Arguelles, Polyhedron 21 (2002) 2593.
[20] A. Bacchi, M. Cracelli, P. Pelagatti, G. Pelizzi, M.C. Rodriguez-Arguelles, D. Rogolino, C. Solinas, F. Zani, J. Inorg. Biochem. 99 (2005) 397.
[21] (a) G. Bahr, G. Schleitzer, Z. Anorg. Allg. Chem. 280 (1955) 176;
(b) M. Das, S.E. Livingstone, Inorg. Chim. Acta 19 (1976) 5.
[22] A.C.T. North, D.C. Phillips, F.S. Mathews, Acta Crystallogr., Sect. A 24 (1968) 351.
[23] K. Harms, S. Wocadlo, CAD4 Data Reduction, University of Marburg, Marburg, Germany, 1995.
[24] L. Farrugia, J. Appl. Cryst. 32 (1999) 837.
[25] G.M. Sheldrick, SHEXS86 – Program for Crystal Structure Solution, Institute für Anorganisch Chemie der Universität, Göttingen, Germany, 1986.
[26] G.M. Sheldrick, SHELXL97, Institüt für Anorganisch Chemie der Universität, Göttingen, Germany, 1998.
[27] L. Farrugia, J. Appl. Cryst. 30 (1997) 565.
[28] M. Akbar Ali, M. Nazimuddin, R. Saha, R.J. Butcher, J.C. Bryan, Polyhedron 17 (1998) 3955.
[29] M.T.H. Tarafder, Kar-Beng Chew, K.A. Crouse, A.M. Ali, B.M. Yamin, H.-K. Fun, Polyhedron 21 (2002) 2683.
[30] M.T.H. Tarafder, A. Kasbollah, K.A. Crouse, A.M. Ali, B.M. Amin, H.-K. Fun, Polyhedron 20 (2001) 2363.
[31] Yu-Peng Tian, Chun-Ying Duan, Xiao-Zeng You, T.C.W. Mak, Qing-Luo, Jian-Ying Zhou, Transition Met. Chem. 23 (1998) 17.
[32] S. Gou, X. You, Z. Xu, Z. Zhou, K. Yu, Polyhedron 10 (1991) 363.
[33] M. Akbar Ali, S.E. Livingstone, D.J. Phillips, Inorg. Chim. Acta 5 (1971) 119.
[34] M. Akbar Ali, A.H. Mirza, M.H.S.A. Hamid, P.V. Bernhardt, Polyhedron 24 (2005) 383.
[35] M. Akbar Ali, K.K. Dey, M. Nazimuddin, R.J. Butcher, J.P. Jasinski, J.M. Jasinski, Polyhedron 15 (1996) 3331.
[36] M.E. Hossain, M.N. Alam, J. Begum, M. Akbar Ali, M. Nazimuddin, F.E. Smith, R.C. Hynes, Inorg. Chim. Acta 249 (1996) 207.
[37] M. Akbar Ali, R.J. Butcher, J. Bryan, Inorg. Chim. Acta 287 (1999) 8.
[38] I. Bertini, G. Canti, R. Grassi, A. Scozzafava, Inorg. Chem. 19 (1980) 2198.
[39] R.D. Bereman, G.D. Shields, J. Bordner, J.R. Dorfman, Inorg. Chem. 20 (1981) 2165.
[40] J. Peisach, W.E. Blumberg, Arch. Biochem. Biophys. 165 (1974) 691.
[41] U. Sakaguchi, A.W. Addison, J. Chem. Soc., Dalton Trans. (1979) 600.
[42] R.A. Martinelli, G.R. Hanson, J.S. Thompson, B. Holmquist, J.R. Pilbrow, D.S. Auld, B.L. Vallee, Biochemistry 28 (1989) 2251.

Available online at www.sciencedirect.com
ScienceDirect
Polyhedron 27 (2008) 80–86
POLYHEDRON
www.elsevier.com/locate/poly

Synthesis and characterization of Ru^{II}/Au^{I}, Pd^{II}/Au^{I}, $Pd^{II}/2Au^{I}$, $Pt^{II}/2Au^{I}$ and $Cu^{I}/2Au^{I}$ heterometallic complexes of cyclodiphosphazane *cis*-{(*o*-$MeOC_6H_4O$)P(μ-N^{t}Bu)}$_2$

P. Chandrasekaran [a], Joel T. Mague [b], Maravanji S. Balakrishna [a,*]

[a] *Phosphorus Laboratory, Department of Chemistry, Indian Institute of Technology Bombay, Mumbai 400 076, India*
[b] *Department of Chemistry, Tulane University, New Orleans, Louisiana, LA 70118, USA*

Received 7 August 2007; accepted 22 August 2007
Available online 25 September 2007

Abstract

Mononuclear complexes of cyclodiphosphazane with an uncoordinated phosphorus centre [$RuCl_2$(η^6-cymene){L-κP}] (**1a**) (L = *cis*-{(*o*-$MeOC_6H_4O$)P(μ-N^{t}Bu)}$_2$) and [$PdCl_2$(PEt_3){L-κP}] (**1b**) react with 1 equiv. of [AuCl(SMe_2)] to afford Ru^{II}/Au^{I} and Pd^{II}/Au^{I} heterodinuclear complexes [$RuCl_2$(η^6-cymene){μ-L-κP,κP}AuCl] (**2**) and [$PdCl_2$(PEt_3){μ-L-κP,κP}AuCl] (**3**), respectively. Heterotrinuclear complexes [$PdCl_2${μ-L-κP,κP}$_2$($AuCl)_2$] (**4**), [$PtCl_2${μ-L-κP,κP}$_2$($AuCl)_2$] (**5**) and [CuI{μ-L-κP,κP}$_2$($AuCl)_2$] (**6**) containing $Pd^{II}/2Au^{I}$, $Pt^{II}/2Au^{I}$ and $Cu^{I}/2Au^{I}$ metal centers have been synthesized from the reactions of *trans*-[$PdCl_2${L-κP}$_2$] (**1c**), *cis*-[$PtCl_2${L-κP}$_2$] (**1d**) and [CuI{{L-κP}$_2$] (**1f**) respectively, with 2 equiv. of [AuCl(SMe_2)]. Molecular structures of complexes **2**, **3** and **4** were established by single crystal X-ray diffraction studies.
© 2007 Elsevier Ltd. All rights reserved.

Keywords: Cyclodiphosphazanes; Heterometallic complexes; Mono- and bidentate coordination; Crystal structures

1. Introduction

Over the past decade cyclodiphosphazanes have been extensively used for the syntheses of several phosphorus–nitrogen macrocycles and cages [1]. Stahl and Chivers utilized amide substituted cyclodiphosphazanes of the type *cis*-[(^{t}BuNH)P(E)(μ-N^{t}Bu)]$_2$ (E = lone pair, O, S, Se) to stabilize various main group and transition metals [2]. Earlier reports on the coordination chemistry of cyclodiphosphazanes were limited to group-6 and 10 metals [3]. Recently we investigated [4] the coordination behavior of the cyclodiphosphazane *cis*-[(*o*-$MeOC_6H_4O$)P(μ-N^{t}Bu)]$_2$ with various transition metal reagents and observed the *cis*-[(*o*-$MeOC_6H_4O$)P(μ-N^{t}Bu)]$_2$ ligand selectively forming mononuclear complexes with metal reagents such as [$RuCl_2$(η^6-cymene)]$_2$, [MCl(COD)]$_2$ (M = Rh, Ir), [$PdCl_2$-(PEt_3)]$_2$, [MCl_2(COD)] (M = Pd, Pt) and AgCN irrespective of the stoichiometry and the reaction conditions. In contrast, reactions with [$Rh(CO)_2Cl]_2$, [PdCl(η^3-C_3H_5)]$_2$, CuX (X = Cl, Br, I), AgOTf and AuCl(SMe_2) afforded complexes with ligand exhibiting both monodentate and bridged bidentate coordination modes. The bridging coordination mode of the cyclodiphosphazane leads to the formation of novel metallamacrocycles (Rh^{I}, Au^{I}) and one dimensional coordination polymers (Cu^{I} and Ag^{I}). The monodentate coordination of the cyclodiphosphazane leads to the complex having a free P^{III} site for further coordination. This interesting coordination behavior of *cis*-[(*o*-$MeOC_6H_4O$)P(μ-N^{t}Bu)]$_2$ can be utilized for the syntheses of numerous hetero-multinuclear complexes containing two or more different late transition metals. Heterometallic complexes containing two different early or late transition metals are difficult to synthesize due to the similar reactivity of late metals toward symmetrical ligands, whilst late-early heterometallic (LEHM) complexes can be conveniently prepared using amide or alkoxy functionalized phosphine ligands due to the preference of

* Corresponding author. Tel.: +91 22 2576 7181; fax: +91 22 2572 3480.
E-mail address: krishna@chem.iitb.ac.in (M.S. Balakrishna).

0277-5387/$ - see front matter © 2007 Elsevier Ltd. All rights reserved.
doi:10.1016/j.poly.2007.08.024

early metals for hard centers and late metals for soft metal centers [5]. Heterometallic complexes containing platinum metals which are far apart with out metal–metal interactions can be utilized as one pot catalysts to promote more than one type of catalytic reaction [6]. In this context, we report the syntheses of Ru^{II}/Au^{I}, Pd^{II}/Au^{I}, $Pd^{II}/2Au^{I}$, $Pt^{II}/2Au^{I}$ and $Cu^{I}/2Au^{I}$ heterometallic complexes anchored by the cyclodiphosphazane, *cis*-[(*o*-$MeOC_6H_4O$)-P(μ-N^{t}Bu)]$_2$ and also the molecular structures of Ru^{II}/Au^{I}, Pd^{II}/Au^{I}, $Pd^{II}/2Au^{I}$ heterometallic derivatives.

2. Experimental

All experimental manipulations were carried out under an atmosphere of dry nitrogen using Schlenk techniques. Solvents were dried and distilled prior to use by conventional methods [7]. The compounds [$RuCl_2$-(η^6-cymene){μ-L-κP}] (**1a**), [$PdCl_2(PEt_3)${μ-L-κP}] (**1b**), *trans*-[$PdCl_2${μ-L-κP}$_2$] (**1c**), *cis*-[$PtCl_2${μ-L-κP}$_2$] (**1d**) [4b], [CuI{μ-L-κP}$_2$] (**1e**) [4c] (**L** = *cis*-{(*o*-$MeOC_6H_4O$)P-(μ-N^{t}Bu)}$_2$) and [$AuCl(SMe_2)$] [8] were prepared according to the published procedures.

The ^{1}H and ^{31}P{^{1}H} NMR spectra were recorded using Varian Mercury Plus spectrometer operating at the appropriate frequencies using TMS and 85% H_3PO_4 as internal and external references, respectively. Microanalyses were performed on a Carlo Erba Model 1112 elemental analyzer. Mass spectrometry experiments were carried out using Waters Q-Tof micro-YA-105. Melting points were recorded in capillary tubes and are uncorrected.

2.1. Synthesis of [$RuCl_2$(η^6-cymene){μ-L-κP,κP}AuCl] (2)

A dichloromethane (7 mL) solution of [$AuCl(SMe_2)$] (20.2 mg, 0.069 mmol) was added dropwise to [$RuCl_2$-(η^6-cymene){μ-L-κP}] (**1a**) (52.3 mg, 0.069 mmol) in CH_2Cl_2 (5 mL) at room temperature with stirring. Stirring was continued for 6 h with minimum light exposure. The reaction mixture was concentrated to 5 mL under reduced pressure and to this was added 3 mL of hexane. Storage at −30 °C for one day afforded the product as dark orange crystals (52.5 mg, 77%). M.p.: 170–172 °C (dec). *Anal*. Calc. for $C_{32}H_{46}N_2P_2O_4Cl_3RuAu$: C, 38.85; H, 4.68; N, 2.83. Found: C, 38.59; H, 4.71; N, 3.05%. ^{1}H NMR (400 MHz; $CDCl_3$, 25 °C): δ_H = 7.26–6.90 (m, 8H, Ph), 5.47 (d, J_{HH} = 6 Hz, 2H, *MeC$_6$H$_4$^{i}Pr-p*), 5.34 (d, 2H, *MeC$_6$H$_4$^{i}Pr-p*), 3.85 (s, 3H, OMe), 3.86 (s, 3H, OMe), 2.92 (sep, 1H, CH), 2.16 (s, 3H, Me), 1.54 (s, 18H, ^{t}Bu), 1.28 (d, J_{HH} = 6.8 Hz, 6H, CMe_2) ppm. ^{31}P{^{1}H} NMR (161.9 MHz, $CDCl_3$, 25 °C): δ_P = 129.3 (s, 1P, PRu), 105.3 (s, 1P, PAu) ppm.

2.2. Synthesis of [$PdCl_2(PEt_3)${μ-L-κP,κP}AuCl] (3)

[$AuCl(SMe_2)$] (19.2 mg, 0.065 mmol) dissolved in 5 mL of dichloromethane was added to [$PdCl_2(PEt_3)${μ-L-κP}] (**1b**) (48.7 mg, 0.065 mmol) also in dichloromethane at room temperature. The resulting reaction mixture was stirred for 4 h, concentrated to 5 mL and diluted with 5 mL CH_3CN. Slow evaporation of CH_2Cl_2 from this solution at room temperature yielded the product as yellow crystals (58.6 mg, 92%). M.p.: 218–220 °C (dec). *Anal*. Calc. for $C_{28}H_{47}N_2O_4P_3PdAuCl_3$: C, 34.37; H, 4.84; N, 2.86. Found: C, 34.56; H, 4.98; N, 2.79%. ^{1}H NMR (400 MHz; $CDCl_3$, 25 °C): δ_H = 7.05–6.84 (m, 8H, Ph), 3.87 (s, 3H, OMe), 3.79 (s, 3 H, OMe), 2.27 (m, 2H, CH_2), 1.55 (s, 18H, ^{t}Bu), 1.26 (m, 3H, CH_3) ppm. ^{31}P{^{1}H} NMR (161.9 MHz, $CDCl_3$, 25 °C): δ_P = 108.9 (d, $^2J_{PP}$ = 39 Hz, 1P, AuP), 83.8 (dd, 1P, PdP), 30.2 (d, $^2J_{PP}$ = 16 Hz, 1P, $PdPEt_3$) ppm. MS(EI, *m*/*z*): 942.76 (M–Cl).

2.3. Synthesis of [$PdCl_2${μ-L-κP,κP}$_2$($AuCl)_2$] (4)

A dichloromethane solution (7 mL) of [$AuCl(SMe_2)$] (48.1 mg, 0.164 mmol) was added dropwise to a well-stirred dichloromethane solution (10 mL) of *trans*-[$PdCl_2$-{μ-L-κP}$_2$] (**1c**) (88.3 mg, 0.082 mmol) at room temperature. The yellow reaction mixture was stirred at room temperature for 4 h, concentrated to 10 mL under reduced pressure and diluted with 5 mL of CH_3CN. Storage at room temperature for 3 days afforded the product as yellow crystals (110 mg, 87%). M.p.: 206–208 °C (dec). *Anal.* Calc. for $C_{44}H_{64}N_4P_4O_8PdAu_2Cl_4$: C, 34.24; H, 4.18; N, 3.63. Found: C, 34.48; H, 4.27; N, 3.44%. ^{1}H NMR (400 MHz; $CDCl_3$, 25 °C): δ_H = 8.04–6.83 (m, 16 H, Ph), 3.88 (s, 6H, OMe), 3.86 (s, 6H, OMe), 1.63 (s, 36H, ^{t}Bu) ppm. ^{31}P{^{1}H} NMR (161.9 MHz, $CDCl_3$, 25 °C): δ_P = 105.0 (d, $^2J_{PP}$ = 40 Hz, 1P, PAu), 70.5 (d, 1P, PPd) ppm.

2.4. Synthesis of [$PtCl_2${μ-L-κP,κP}$_2$($AuCl)_2$] (5)

A dichloromethane solution (7 mL) of [$AuCl(SMe_2)$] (22.1 mg, 0.079 mmol) was added dropwise to a well-stirred dichloromethane solution (5 mL) of *cis*-[$PtCl_2${μ-L-κP}$_2$] (**1d**) (43.7 mg, 0.037 mmol) at room temperature. The reaction mixture was stirred for 4 h, concentrated to 5 mL and diluted with 3 mL of hexane. Storage at −30 °C for one day afforded a white crystalline product (41.1 mg, 68%). M.p.: 224–226 °C (dec). *Anal*. Calc. for $C_{44}H_{64}N_4O_8P_4Au_2PtCl_4$: C, 32.38; H, 3.95; N, 3.43. Found: C, 32.55; H, 4.12; N, 3.77%. ^{1}H NMR (400 MHz; $CDCl_3$, 25 °C): δ_H = 7.74–6.82 (m, 16 H, Ph), 3.87 (s, 6H, OMe), 3.83 (s, 6H, OMe), 1.45 (s, 36 H, ^{t}Bu) ppm. ^{31}P{^{1}H} NMR (161.9 MHz, $CDCl_3$, 25 °C): δ_P = 109.4 (d, $^3J_{PtP}$ = 81 Hz, 2P, AuP), 47.0 (d, $^1J_{PtP}$ = 5738 Hz, $^2J_{PP}$ = 36 Hz, 2P, PtP) ppm.

2.5. Synthesis of [CuI{μ-L-κP,κP}$_2$($AuCl)_2$] (6)

A solution of [$AuCl(SMe_2)$] (46.3 mg, 0.157 mmol) in 7 mL of CH_2Cl_2 was added dropwise to a well-stirred CH_2Cl_2 (5 mL) solution of [CuI{μ-L-κP}$_2$] (**1e**) (85.3 mg, 0.078 mmol) at room temperature. The colorless reaction

mixture was stirred for 4 h, concentrated to 5 mL under reduced pressure and diluted with 3 mL of hexane. Storage at −30 °C for one day afforded the product as a white crystalline solid (84.9 mg, 70%). M.p.: 194–196 °C (dec). *Anal.* Calc. for $C_{44}H_{64}N_4O_8P_4CuAu_2ICl_2$: C, 33.95; H, 4.14; N, 3.60. Found: C, 33.74; H, 4.06; N, 3.72%. ^{1}H NMR (400 MHz; $CDCl_3$, 25 °C): $\delta_H = 7.89–6.73$ (m, 16H, Ph), 3.85 (s, 6H, OMe), 3.77 (s, 6H, OMe), 1.52 (s, 36H, ^{t}Bu) ppm. $^{31}P\{^1H\}$ NMR (161.9 MHz, $CDCl_3$, 25 °C): $\delta_P = 120.9$ (br s, 2P, CuP), 105.9 (s, 2P, AuP) ppm.

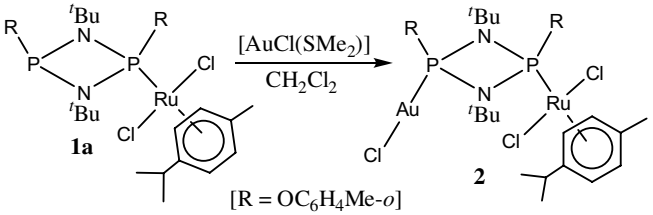
2.6. X-ray crystallography

Crystals of **2**, **3** and **4** were mounted in a CryoLoop with a drop of Paratone oil and placed in the cold nitrogen stream of the Kryoflex attachment of the Bruker APEX CCD diffractometer. Full spheres of intensity data were collected for each crystals as three sets of 400 scans in ω (0.5° per scan at $\phi = 0°$, 90° and 180°) and two sets of 800 scans in ϕ (0.45° per scan at $\omega = -30°$ and 210°). Intensity data were collected using the SMART software package [9] and these were reduced to F^2 values with the SAINT+ software [10] which also performed a global refinement of unit cell parameters using 9217 (for **2**), 9275 (for **3**) and 8300 (for **4**) reflections chosen from the full data set. Crystals of **2** and **3** proved to be twinned and the integration of the raw data was carried out with the two-component version of SAINT+ using the two-component orientation file prepared by CELL_NOW [11] and with the cell parameters of the second domain of the twin constrained to be identical to those of the first domain. Multiple measurements of equivalent reflections provided the basis for empirical absorption corrections as well as corrections for any crystal deterioration during the data collection (TWINABS [12] for **2** and **3** and SADABS [13] for **4**). The structures were solved by direct methods and refined by full-matrix least-squares procedures using the SHELXTL program package [14]. Hydrogen atoms were placed in calculated positions (C–H = 0.95 Å (aromatic rings) or 0.98 Å (methyl groups)) and included as riding contributions with isotropic displacement parameters 1.2 (aromatic rings) or 1.5 (methyl groups) times those of the attached non-hydrogen atoms.

3. Results and discussion

3.1. Synthesis of heterometallic complexes

Mononuclear Ru^{II} and Pd^{II} complexes $[RuCl_2(\eta^6\text{-cymene})\{\mu\text{-L-}\kappa P\}]$ (**1a**) and $[PdCl_2(PEt_3)\{\mu\text{-L-}\kappa P\}]$ (**1b**) containing one uncoordinated P^{III} site were prepared from the reaction of *cis*-$\{(o\text{-MeOC}_6H_4O)P(\mu\text{-N}^t\text{Bu})\}_2$ (**L**) with $[RuCl_2(\eta^6\text{-cymene})]_2$ and $[PdCl_2(PEt_3)]$, respectively [4b]. Interestingly, the cyclodiphosphazane *cis*-$\{(o\text{-MeOC}_6H_4O)P(\mu\text{-N}^t\text{Bu})\}_2$ afforded exclusively the mononuclear derivatives **1a** and **1b**, irrespective of the reaction conditions and stoichiometry. The Ru^{II}/Au^I heterobimetallic

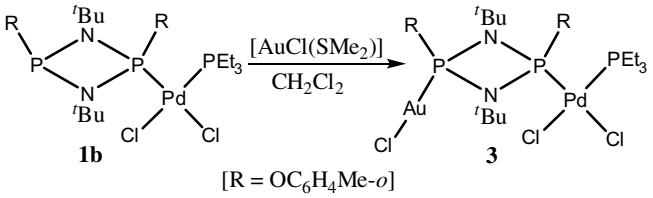


Scheme 1. Synthesis of Ru^{II}/Au^I complex.

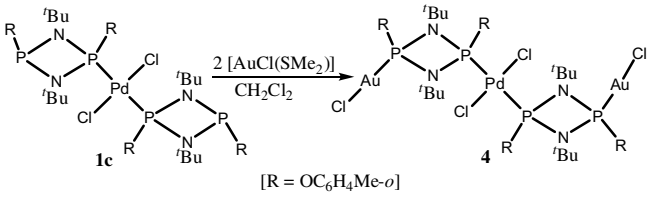
complex $[RuCl_2(\eta^6\text{-cymene})\{\mu\text{-L-}\kappa P,P\}AuCl]$ (**2**) was synthesized by treating **1a** with 1 equiv. of $[AuCl(SMe_2)]$ in dichloromethane as shown in Scheme 1. The ^{31}P NMR spectrum of **2** exhibits two single resonances at 129.3 and 105.3 ppm, respectively, for ruthenium and gold coordinated phosphorus centers of the cyclodiphosphazane. Surprisingly, no $^2J_{PP}$ coupling was observed although complex **1a** shows a $^2J_{PP}$ coupling of 8.7 Hz.

Addition of 1 equiv. of $[AuCl(SMe_2)]$ to a dichloromethane solution of $[PdCl_2(PEt_3)\{\mu\text{-L-}\kappa P\}]$ (**1b**) results in the formation of a Pd^{II}/Au^I heterobimetallic complex $[PdCl_2(PEt_3)\{\mu\text{-L-}\kappa P,\kappa P\}AuCl]$ (**3**) in quantitative yield (Scheme 2). The ^{31}P NMR spectrum of **3** exhibits three signals due to the presence of three P-centers. The phosphorus-31 resonance corresponding to the Au-coordinated centre appears as a doublet at 108.9 ppm, with a $^2J_{PP}$ coupling of 39 Hz, whereas the Pd-bound phosphorus of the cyclodiphosphazane appears as a doublet of doublets centered at 83.8 ppm due to the coupling with two different neighboring phosphorus centers. The signal corresponding to PEt_3 appears as a doublet at 30.2 ppm with a $^2J_{pp}$ coupling of 16 Hz.

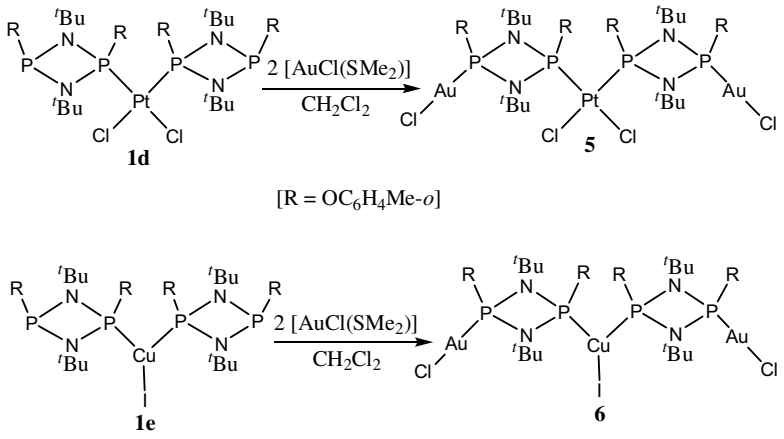
The reaction of 2 equiv. of *cis*-$\{(o\text{-MeOC}_6H_4O)P(\mu\text{-N}^t\text{Bu})\}_2$ with $[PdCl_2(NCPh)_2]$ or $[PdCl_2(SMe_2)_2]$ afforded *trans*-$[PdCl_2\{\mu\text{-L-}\kappa P\}_2]$ (**1c**) exclusively [4b]. The molecular structure of **1c** reveals the *trans* arrangement of two cyclodiphosphazanes with two uncoordinated P^{III} centers



Scheme 2. Synthesis of Pd^{II}/Au^I complex.



Scheme 3. Synthesis of $Pd^{II}/2Au^I$ complex.



Scheme 4. Synthesis of $Pt^{II}/2Au^{I}$ and $Cu^{I}/2Au^{I}$ complexes.

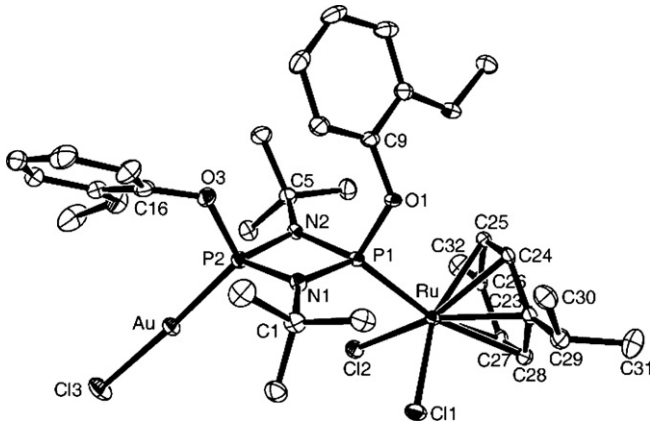


Fig. 1. ORTEP drawing of compound **2**. Thermal ellipsoids are drawn at the 50% probability level. All hydrogen atoms are omitted for clarity.

projecting in an anti-parallel manner so this compound can serve as an excellent metalloligand for designing hetero polynuclear complexes. The 1:2 reaction between *trans*-$[PdCl_2\{\mu\text{-L-}\kappa P\}_2]$ (**1c**) and $[AuCl(SMe_2)]$ in dichloromethane affords a $Pd^{II}/2Au^{I}$ hetero-trinuclear complex $[PdCl_2\{\mu\text{-L-}\kappa P,\kappa P\}_2(AuCl)_2]$ (**4**) as shown in Scheme 3. The ^{31}P NMR spectrum of **4** exhibits two doublets centered at 105 and 70.5 ppm, respectively, for Au and Pd coordinated centers with a $^{2}J_{PP}$ coupling of 40 Hz. Again, the $^{2}J_{PP}$ coupling is not observed in *trans*-$[PdCl_2\{\mu\text{-L-}\kappa P\}_2]$ (**1c**) which exhibited single resonances for coordinated and uncoordinated P-centers.

Heterotrinuclear complexes $[PtCl_2\{\mu\text{-L-}\kappa P,\kappa P\}_2(AuCl)_2]$ (**5**) and $[CuI\{\mu\text{-L-}\kappa P,\kappa P\}_2(AuCl)_2]$ (**6**) containing $Pt^{II}/2Au^{I}$ and $Cu^{I}/2Au^{I}$ metal centers were synthesized from

Table 1
Crystallographic information for **2**, **3** and **4**

	2	**3**	**4**
Formula	$C_{32}H_{46}AuCl_3N_2O_4P_2Ru$	$C_{28}H_{47}AuCl_3N_2O_4P_3Pd$	$C_{44}H_{64}Au_2Cl_4N_4O_8P_4Pd$
Formula weight	989.03	978.30	1543.03
Crystal system	monoclinic	monoclinic	monoclinic
Space group	$P2_1/c$	$P2_1/n$	$P2_1/c$
a (Å)	13.453(1)	10.973(1)	10.723(3)
b (Å)	13.589(1)	15.218(2)	19.685(1)
c (Å)	20.634(2)	21.589(3)	13.700(1)
α (°)	90	90	90
β (°)	97.982(1)	98.630(2)	107.307(1)
γ (°)	90	90	90
V (Å^3)	3735.7(6)	3564.3(8)	2760.8(3)
Z	4	4	2
ρ_{calc} (g cm^{-3})	1.759	1.823	1.856
μ (Mo Kα) (mm^{-1})	4.664	5.010	5.984
$F(000)$	1952	1928	1504
Crystal size (mm)	0.12 × 0.18 × 0.23	0.15 × 0.17 × 0.26	0.16 × 0.19 × 0.25
T (K)	100	100	100
2θ range (°)	2.1–28.4	2.2–28.3	2.2–28.3
Total number of reflections	23 530	23 926	48 400
Number of independent reflections [R_{int}]	9361 [0.074]	8888 [0.042]	6846 [0.032]
R_1[a]	0.0351	0.0341	0.0252
wR_2[b]	0.0776	0.0845	0.0681
Goodness-of-fit (F^2)	0.95	1.01	1.07

[a] $R = \sum\|F_o| - |F_c\|/\sum|F_o|$.
[b] $wR_2 = \{[\sum w(F_o^2 - F_c^2)/\sum w(F_o^2)^2]\}^{1/2}$; $w = 1/[\sigma^2(F_o^2) + (xP)^2]$ where $P = (F_o^2 + 2F_c^2)/3$.

the reaction of *cis*-[$PtCl_2$\{μ-L-κP\}$_2$] (**1d**) and [CuI\{μ-L-κP\}$_2$] (**1e**) with 2 equiv. of [$AuCl(SMe_2)$] in dichloromethane at room temperature (Scheme 4). The ^{31}P NMR spectrum of **5** exhibits a doublet centered at 109.4 ppm for the gold coordinated center with a $^2J_{PP}$ coupling of 36 Hz along with a $^3J_{PtP}$ coupling of 81 Hz. The platinum bound phosphorus center exhibits a doublet at 47.0 ppm along with very large $^1J_{PtP}$ coupling of 5738 Hz, which confirms the *cis* arrangement of the two cyclodiphosphazanes [15]. The ^{31}P NMR spectrum of complex **6** exhibits two singlets at 120.9 and 105.9 ppm, respectively, for copper and gold coordinated phosphorus centers of the cyclodiphosphazane.

3.2. Molecular structures of 2, 3 and 4

The molecular structure of complex **2** is shown in Fig. 1. Crystal data and details of the structure determination are presented in Table 1 while selected bond parameters are listed in Table 2. The X-ray quality crystals of **2** were obtained by slow diffusion of Et_2O into a dichloromethane solution of **2** at room temperature. In molecule **2**, the cyclodiphosphazane bridges {AuCl} and {$RuCl_2(\eta^6$-cymene)} fragments through P-coordination with the metals arranged in a *cis* orientation. The gold center is dicoordinated with a P2–Au–Cl3 angle of 176.51(2)°. The coordination geometry around the ruthenium center in **2** is the typical pseudo octahedral mode with a three-legged piano-stool arrangement commonly observed for half-sandwich phosphine complexes [16]. The Ru–P1 and Au–P2 bond distances are 2.348(1) and 2.205(1) Å, respectively, and agree well with reported values for similar complexes of the type [$Cp(PPh_3)$RuCl-{μ-$PPh_2(CH_2)_nPPh_2$}AuCl] [17].

Perspective views of the molecular structures of **3** and **4** are depicted in Figs. 2 and 3, respectively, with important bond parameters listed in Table 3. Single crystals of **3** and **4** suitable for X-ray diffraction studies were obtained by slow evaporation of dichloromethane from CH_3CN/CH_2Cl_2 solutions of the respective compounds at room temperature. In complexes **3** and **4** the cyclodiphosphazane ligand *cis*-{^{t}BuNP(OC_6H_4OMe-*o*)}$_2$ (L) bridges the gold and palladium centers to furnish Pd^{II}/Au^I, $Pd^{II}/2Au^I$ heterometallic complexes. The palladium atoms occupy the center of square planar ligand set with the corners occupied by two chlorides and two phosphorus atoms. As complex **4** has crystallographically-imposed centrosymmetry, the P1–Pd–P1^i and Cl1–Pd–Cl1^i bond angles in **4** are exactly linear and similar to the parent compound **1c** [4b]. The gold centers are linear in geometry with P–Au–Cl angles of 176.25(4)° and 179.27(3)°, respectively, for **3** and **4**. The Pd–P bond lengths in **3** and **4** are, respectively the same and slightly shorter than the corresponding bonds in the respective mononuclear complexes **1b** and **1c** [4b]. The exocyclic phenyl substituents on the phosphorus atoms are present in *exo,endo* orientations with respect to the planar P_2N_2 ring.

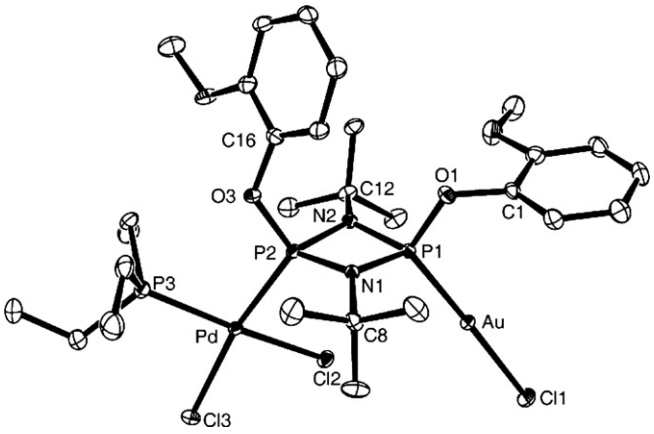


Fig. 2. ORTEP drawing of compound **3**. Thermal ellipsoids are drawn at the 50% probability level. All hydrogen atoms are omitted for clarity.

Table 2
Selected bond distances (Å) and bond angles (°) for **2**

Bond distances (Å)		Bond angles (°)	
Ru–P1	2.348(1)	P1–Ru–Cl1	96.51(2)
Ru–Cl1	2.406(1)	P1–Ru–Cl2	84.87(2)
Ru–Cl2	2.391(1)	C25–Ru–P1	94.34(7)
Ru–C23	2.236(3)	P2–Au–Cl3	176.51(2)
Ru–C24	2.207(3)	C24–Ru–P1	93.83(7)
Ru–C25	2.211(3)	C25–Ru–P1	94.34(7)
Ru–C26	2.249(3)	C28–Ru–P1	156.07(7)
Ru–C27	2.236(3)	C25–Ru–Cl2	116.06(7)
Ru–C28	2.221(3)	C28–Ru–Cl2	118.94(7)
Au–P2	2.205(1)	P1–N1–P2	96.77(11)
Au–Cl3	2.281(1)	P1–N2–P2	96.70(11)
P1–N1	1.706(2)	N1–P1–N2	81.96(11)
P1–N2	1.709(2)	N1–P2–N2	84.12(11)
P2–N1	1.672(2)	C1–N1–P1	134.85(18)
P2–N2	1.670(2)	C1–N1–P2	127.65(18)
P1–O1	1.616(2)	C9–O1–P1	128.52(15)
P2–O3	1.608(2)	C16–O3–P2	128.38(18)

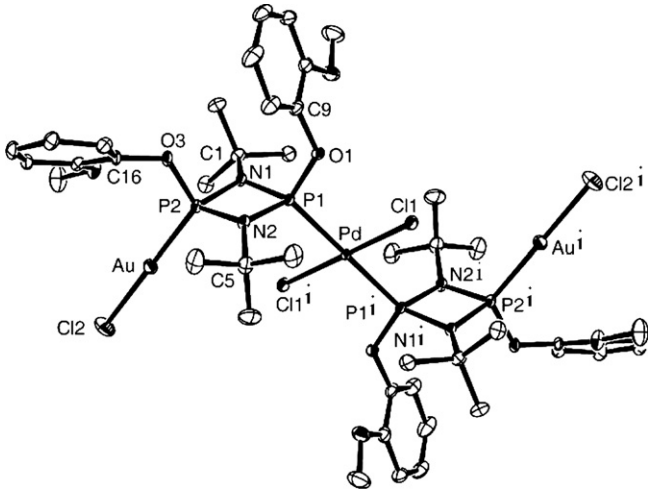


Fig. 3. ORTEP drawing of compound **4**. Thermal ellipsoids are drawn at the 50% probability level. All hydrogen atoms are omitted for clarity.

Table 3
Selected bond distances (Å) and bond angles (°) for **3** and **4**

Bond distances (Å)		Bond angles (°)	
Complex ***3***			
Au–P1	2.199(1)	P1–Au–Cl1	176.25(4)
Pd–P2	2.233(2)	P2–Pd–P3	96.88(4)
Pd–P3	2.281(2)	P2–Pd–Cl2	83.71(3)
Au–Cl1	2.277(1)	Cl2–Pd–Cl3	89.23(3)
Pd–Cl2	2.346(1)	P3–Pd–Cl3	91.21(3)
Pd–Cl3	2.334(2)	P1–N1–P2	95.31(16)
P1–N1	1.686(3)	P1–N2–P2	95.61(16)
P1–N2	1.687(4)	N1–P1–N2	83.81(16)
P2–N1	1.688(4)	N1–P2–N2	83.99(15)
P2–N2	1.679(3)	P1–O1–C1	121.7(2)
P1–O1	1.606(3)	P2–O3–C16	126.4(2)
P2–O3	1.603(3)	P1–N1–C8	129.4(2)
		P2–N1–C8	130.1(2)
Complex ***4***			
Pd–P1	2.287(1)	P1–Pd–Cl1	93.65(3)
Pd–Cl1	2.296(1)	P1–Pd–P1^{i}	180.00
Au–P2	2.208(1)	Cl1–Pd–Cl1^{i}	180.00
Au–Cl2	2.281(1)	Cl1–Pd–P1^{i}	86.35(3)
P1–N1	1.689(3)	P2–Au–Cl2	179.27(3)
P1–N2	1.684(3)	P2–N1–P1	95.74(13)
P2–N1	1.673(2)	P2–N2–P1	95.60(15)
P2–N2	1.682(3)	N2–P1–N1	83.83(12)
P1–O1	1.592(2)	N1–P2–N2	84.37(14)
P2–O3	1.607(2)	P1–N1–C1	133.3(2)
		P2–N1–C1	130.2(2)

4. Conclusions

Variable coordination modes exhibited by the cyclodiphosphazane *cis*-{(*o*-MeOC$_6$H$_4$O)P(μ-N^{t}Bu)}$_2$ with different transition metal precursors offer straightforward synthetic routes to make a variety of heterometallic complexes in excellent yield. We are investigating the catalytic reactions of these heterometallic complexes for various organic transformations.

Acknowledgements

We are grateful to the Department of Science and Technology (DST), New Delhi for funding through Grant SR/S1/IC-02/2007. P.C. thanks CSIR for Research Fellowship. J.T.M. thanks the Louisiana Board of Regents through Grant LEQSF(2002-03)-ENH-TR-67 for purchase of the Bruker APEX CCD diffractometer and the Chemistry Department of Tulane University for support of the X-ray laboratory.

Appendix A. Supplementary material

CCDC 652466, 652467 and 652468 contain the supplementary crystallographic data for **2**, **3** and **4**. These data can be obtained free of charge via http://www.ccdc.cam.ac.uk/conts/retrieving.html, or from the Cambridge Crystallographic Data Centre, 12 Union Road, Cambridge CB2 1EZ, UK; fax: (+44) 1223-336-033; or e-mail: deposit@ccdc.cam.ac.uk.

References

[1] (a) M.S. Balakrishna, D.J. Eisler, T. Chivers, Chem. Soc. Rev. 36 (2007) 650;
(b) F. Dodds, F. Garcia, R.A. Kowenicki, M. McPartlin, A. Steiner, D.S. Wright, Chem. Commun. (2005) 3733;
(c) F. Garcia, J.M. Goodman, R.A. Kowenicki, I. Kuzu, M. McPartlin, M.A. Silva, L. Riera, A.D. Woods, D.S. Wright, Chem. Eur. J. 10 (2004) 6066;
(d) S.S. Kumaravel, S.S. Krishnamurthy, T.S. Cameron, A. Linden, Inorg. Chem. 27 (1988) 4546;
(e) P. Kommana, K.C. Kumara Swamy, Inorg. Chem. 39 (2000) 4384;
(f) D. Dou, E.N. Duesler, R.T. Paine, Inorg. Chem. 38 (1999) 788;
(g) M. Vijjulatha, S. Kumaraswamy, K.C. Kumara Swamy, U. Engelhardt, Polyhedron 18 (1999) 2557;
(h) F. Garcia, J.M. Goodman, R.A. Kowenicki, M. McPartlin, L. Riera, M.A. Silva, A. Wirsing, D.S. Wright, Dalton Trans. (2005) 1764.
[2] (a) G.G. Briand, T. Chivers, M. Krahn, Coord. Chem. Rev. 233–234 (2002) 237;
(b) L. Stahl, Coord. Chem. Rev. 210 (2000) 203;
(c) I. Schranz, G.R. Lief, C.J. Carrow, D.C. Haagenson, L. Grocholl, L. Stahl, R.J. Staples, R. Boomishankar, A. Steiner, Dalton Trans. (2005) 3307;
(d) G.G. Briand, T. Chivers, M. Parvez, Angew. Chem. Int. Ed. 41 (2002) 3468;
(e) K.V. Axenov, V.V. Kotov, M. Klinga, M. Leskelä, T. Repo, Eur. J. Inorg. Chem. (2004) 695;
(f) G.R. Lief, D.F. Moser, L. Stahl, R.J. Staples, J. Organomet. Chem. 689 (2004) 1110.
[3] (a) M.S. Balakrishna, V.S. Reddy, S.S. Krishnamurthy, J.F. Nixon, J.C.T.R.B. St. Laurent, Coord. Chem. Rev. 129 (1994) l;
(b) M.S. Balakrishna, S.S. Krishnamurthy, J. Organomet. Chem. 424 (1992) 243;
(c) V.S. Reddy, S.S. Krishnamurthy, M. Nethaji, J. Organomet. Chem. 438 (1992) 99;
(d) V.S. Reddy, S.S. Krishnamurthy, M. Nethaji, J. Chem. Soc., Dalton Trans. (1994) 2661;
(e) V.S. Reddy, S.S. Krishnamurthy, M. Nethaji, J. Chem. Soc., Dalton Trans. (1995) 1933;
(f) T.K. Prakasha, S.S. Krishnamurthy, J. Organomet. Chem. 438 (1992) 241;
(g) J.C.T.R.B. St. Laurent, H.E. Hosseini, J. Sinclair, J.F. Nixon, Inorg. Chim. Acta 44 (1980) L17.
[4] (a) P. Chandrasekaran, J.T. Mague, M.S. Balakrishna, Organometallics 24 (2005) 3780;
(b) P. Chandrasekaran, J.T. Mague, M.S. Balakrishna, Inorg. Chem. 44 (2005) 7925;
(c) P. Chandrasekaran, J.T. Mague, M.S. Balakrishna, Inorg. Chem. 45 (2006) 6678;
(d) P. Chandrasekaran, J.T. Mague, M.S. Balakrishna, Inorg. Chem. 45 (2006) 5893;
(e) M.S. Balakrishna, P. Chandrasekaran, R. Venkateswaran, J. Organomet. Chem. 692 (2007) 2642;
(f) D. Suresh, J.T. Mague, M.S. Balakrishna, Tetrahedron Lett 28 (2007) 2283;
(g) P. Chandrasekaran, J.T. Mague, M.S. Balakrishna, Tetrahedron Lett. 28 (2007) 5227;
(h) M.S. Balakrishna, J.T. Mague, Organometallics 26 (2007) 4677.
[5] (a) N. Wheatley, P. Kalck, Chem. Rev. 99 (1999) 3379;
(b) A. Kless, C. Lefeber, A. Spannenberg, R. Kempe, W. Baumann, J. Holz, J.A. Boerner, Tetrahedron 52 (1996) 14599;
(c) B.E. Bosch, I. Brummer, K. Kunz, G. Erker, R. Frohlich, S. Kotila, Organometallics 19 (2000) 1255;
(d) H. Han, M. Elsmaili, S.A. Johnson, Inorg. Chem. 45 (2006) 7435;
(e) D.W. Stephan, Coord. Chem. Rev. 95 (1989) 41;
(f) A.H. Eisenberg, M.V. Ovchinnikov, C.A. Mirkin, J. Am. Chem. Soc. (125) (2003) 2836;

(g) M.F. Zuniga, G.B. Deacon, K. Ruhlandt-Senge, Chem.-Eur. J. 13 (2007) 1921;
(h) P. Braunstein, G. Clerc, X. Morise, R. Welter, G. Mantovani, Dalton Trans. (2003) 1601;
(i) S.E. Watkins, D.C. Craig, S.B. Colbran, J. Chem. Soc., Dalton Trans. (2002) 2423;
(j) D.A. Edwards, M.F. Mahon, T.J. Paget, Polyhedron 19 (2000) 757.

[6] (a) M.A.F. Hernandez-Gruel, J.J. Perez-Torrente, M.A. Ciriano, A.B. Rivas, F.J. Lahoz, I.T. Dobrinovitch, L.A. Oro, Organometallics 22 (2003) 1237;
(b) T. Hosokawa, M. Takano, S. Murahashi, H. Ozaki, Y. Kitagawa, K. Sakaguchi, Y. Katsube, J. Chem. Soc., Chem. Commun. (1994) 1433;
(c) J. Choudhury, S. Podder, S. Roy, J. Am. Chem. Soc. 127 (2005) 6162;
(d) D. Drommi, F. Nicolo, C.A. Arena, G. Bruno, F. Faraone, R. Gobetto, Inorg. Chim. Acta 221 (1994) 109;
(e) P.A. Robles-Dutenhefner, E.M. Moura, G.J. Gama, H.G.L. Siebald, E.V. Gusevskaya, J. Mol. Catal. A: Chem. 164 (2000) 39;
(f) E.K. Van Den Beuken, B.L. Feringa, Tetrahedron 54 (1998) 12985.

[7] W.L.F. Armarego, D.D. Perrin, Purification of Laboratory Chemicals, Fourth ed., Butterworth-Heinemann, Linacre House, Jordan Hill, Oxford, UK, 1996.

[8] M.-C. Brandys, M.C. Jennings, R.J. Puddephatt, J. Chem. Soc., Dalton Trans. (2000) 4601.

[9] Bruker-AXS, SMART, Version 5.625, Madison, WI, 2000.

[10] Bruker-AXS, SAINT+, Version 6.35A, Madison, WI, 2002.

[11] G.M. Sheldrick, CELL_NOW, University of Göttingen, Germany, 2005.

[12] (a) G.M. Sheldrick, TWINABS, University of Gottingen, Germany, 2002;
(b) G.M. Sheldrick, TWINABS, University of Gottingen, Germany, 2005.

[13] G.M. Sheldrick, SADABS, Version 2.05, University of Göttingen, Germany, 2002.

[14] (a) Bruker-AXS, SHELXTL, Version 6.10; Madison, WI, 2000;
(b) G.M. Sheldrick, SHELXS97 and SHELXL97, University of Göttingen, Germany, 1997.

[15] (a) C.J. Cobley, P.G. Pringle, Inorg. Chim. Acta 265 (1997) 107;
(b) M.S. Balakrishna, R. Panda, J.T. Mague, Inorg. Chem. 40 (2001) 5620.

[16] (a) R. Venkateswaran, J.T. Mague, M.S. Balakrishna, Inorg. Chem. 46 (2007) 808;
(b) S.I.M. Paris, F.R. Lemke, R. Sommer, P. Lönnecke, E.J. Hey-Hawkins, J. Organomet. Chem. 690 (2005) 1807;
(c) M.S. Balakrishna, D. Suresh, P.P. George, J.T. Mague, Polyhedron 25 (2006) 3215.

[17] (a) Y. Yang, K.A. Abboud, L. McElwee-White, Dalton Trans. (2003) 4288;
(b) D. Serra, K.A. Abboud, C.R. Hilliard, L. McElwee-White, Organometallics 26 (2007) 3085;
(c) G.A. Bowmaker, H. Schmidbaur, S. Kruger, N. Rosch, Inorg. Chem. 36 (1997) 1754.

Available online at www.sciencedirect.com
ScienceDirect
Polyhedron 27 (2008) 87–94
POLYHEDRON
www.elsevier.com/locate/poly

New *N*-heterocyclic carbene mercury(II) and silver(I) complexes

Qing-Xiang Liu [a,*], Li-Na Yin [a], Xiu-Mei Wu [a], Jin-Cheng Feng [a], Jian-Hua Guo [a], Hai-Bin Song [b]

[a] *Key Laboratory of Molecular Structure and Materials Performance, College of Chemistry and Life Science, Tianjin Normal University, Tianjin 300387, PR China*

[b] *State Key Laboratory of Element-Organic Chemistry, Nankai University, Tianjin 300071, PR China*

Received 9 May 2007; accepted 22 August 2007
Available online 22 October 2007

Abstract

The complexes [1-(9-anthracenylmethyl)-3-octylimy]$_2$Hg[HgCl$_4$] (**2a**) (imy = imidazol-2-ylidene) and [1-(9-anthracenylmethyl)-3-butylbimy]$_2$AgPF$_6$ (**2b**) (bimy = benzimidazol-2-ylidene) have been prepared and characterized. Crystal packing of complex **2a** revealed that 1D polymeric chains are formed by [1-(9-anthracenylmethyl)-3-octylimy]Hg and [HgCl$_4$]$^{2-}$ through weak Hg...Cl bonds. The packing diagram of **2b** showed that 1D supramolecular chains are formed by both benzimidazole ring head to tail π–π stacking interactions and anthracene ring face-to-face π–π stacking interactions.
© 2007 Published by Elsevier Ltd.

Keywords: Carbene complex; Mercury; Silver; π–π stacking interactions

1. Introduction

Since the discovery of free *N*-heterocyclic carbene [1], metal carbene complexes based on imidazol-2-ylidene (imy) have received considerable attention, and a variety of related transition-metal complexes have been synthesized through deprotonation of *N*,*N*′-disubstituted imidazolium salts [2]. In the complexes some reports on the imidazol-2-ylidene complexes of Hg(II) and Ag(I) have appeared [3]. A new discovery shows that Ag(I)–carbene complexes can be used as effective antimicrobial agents [4], and they are also good carbene transfer agents for the synthesis of Ni, Pd, Pt, Cu, Au, Rh, Ir and Ru carbene complexes, such a route affording a convenient method for the preparation of these metal carbene complexes [5]. *N*-heterocyclic carbene complexes have also been shown to be remarkably stable towards heat, air and moisture [6]. Also many organic reactions using metal–NHC complexes as catalysts have been investigated, such as Heck, Suzuki and Kumada couplings, and olefin metathesis [7]. We are interested in *N*-heterocyclic carbene complexes exhibiting fluorescence [8] owing to their potential application as fluorescent switches. We report here the synthesis, structure and fluorescent emission spectra of two new complexes [1-(9-anthracenylmethyl)-3-octylimy]$_2$Hg[HgCl$_4$] (**2a**) (imy = imidazol-2-ylidene) and [1-(9-anthracenylmethyl)-3-butylbimy]$_2$AgPF$_6$ (**2b**) (bimy = benzimidazol-2-ylidene).

2. Experimental

2.1. General procedures

1-(9-Anthracenylmethyl)-3-octylimidazolium chloride (**1a**) was obtained according to a reported procedure [8a]. All manipulations were performed using Schlenk techniques, and solvents were purified by standard procedures. All the reagents for the syntheses and analyses were of analytical grade and were used without further purification. Melting points were determined with a Boetius Block apparatus. ^{1}H and ^{13}C{^{1}H} NMR spectra were recorded on a

* Corresponding author. Tel.: +86 13820172297.
E-mail address: qxliu@eyou.com (Q.-X. Liu).

0277-5387/$ - see front matter © 2007 Published by Elsevier Ltd.
doi:10.1016/j.poly.2007.08.046

Varian Mercury Vx 300 spectrometer at 300 MHz and 75 MHz, respectively. Chemical shifts, δ, are reported in ppm relative to the internal standard TMS for both ^1H and ^{13}C NMR. J values are given in Hz. Elemental analyses were measured using a Perkin–Elmer 2400C Elemental Analyzer. The luminescent spectra were conducted on a Cary Eclipse Fluorescence spectrophotometer.

2.2. 1-(9-Anthracenylmethyl)-3-butylbenzimidazolium hexafluorophosphate (*1c*)

A THF solution of benzimidazole (10.170 g, 86 mmol) was added to a suspension of oil-free sodium hydride (3.977 g, 95 mmol) in THF (100 mL) and stirred for 1 h at 60 °C. Then a THF (50 mL) solution of butyl iodide (16.634 g, 90 mmol) was added dropwise to the above solution. The mixture was continued to be stirred for 24 h at 60 °C, and a yellow solution was obtained. The solvent was removed with a rotary evaporator and H_2O (100 mL) was added to the residue. Then the solution was extracted with CH_2Cl_2 (3×50 mL), and the extracting solution was dried with anhydrous $MgSO_4$. After removing CH_2Cl_2, yellow liquid 1-butylbenzimidazole was obtained. Yield: 14.500 g (96.7%).

1-(9Anthracenylmethyl)-3-butylbenzimidazolium chloride (**1b**) was prepared by the reaction of 1-butylbenzimidazole with 9-chloromethylanthracene according to the literature procedures [8d]. M.p.: 239–241 °C. *Anal.* Calc. for $C_{26}H_{25}ClN_2$: C, 77.89; H, 6.29; N, 6.99. Found: C, 77.80; H, 6.33; N, 6.76%. ^1H NMR (300 MHz, $CDCl_3$): 1.02 (t, $J = 5.4$, 3H, CH_3), 1.41–1.49 (m, 2H, CH_2), 2.01–2.06 (m, 2H, CH_2), 4.57 (t, $J = 5.4$, 2H, CH_2), 6.92 (d, $J = 6.3$, 1H, PhH), 6.99 (s, 2H, CH_2An), 7.12 (t, $J = 6.3$, 1H, PhH), 7.38 (t, $J = 6.3$, 1H, PhH), 7.54 (d, $J = 6.3$, 1H, PhH), 7.68 (t, $J = 8.4$, 2H, AnH) (An: anthracene), 7.72 (t, $J = 8.4$, 2H, AnH), 8.10 (d, $J = 8.4$, 2H, AnH), 8.56 (d, $J = 8.4$, 2H, AnH), 8.59 (s, 1H, AnH), 12.17 (s, 1H, 2-benzimiH) (benzimi: benzimidazole).

1-(9-Anthracenylmethyl)-3-butylbenzimidazolium hexafluorophosphate (**1c**) was formed by an ion-exchange reaction of **1b** with NH_4PF_6 according to the literature methods [8d]. ^1H NMR (300 MHz, $CDCl_3$): δ 0.96 (t, $J = 5.4$, 3H, CH_3), 1.28–1.36 (m, 2H, CH_2), 1.86–1.91 (m, 2H, CH_2), 4.40 (t, $J = 5.4$, 2H, CH_2), 6.59 (s, 2H, CH_2An), 7.34–7.42 (m, 2H, PhH), 7.52–7.57 (m, 3H, AnH and PhH) (An: anthracene), 7.62–7.70 (m, 3H, AnH and PhH), 8.10 (d, $J = 8.4$, 2H, AnH), 8.27 (d, $J = 8.4$, 2H, AnH), 8.64 (s, 1H, AnH), 8.97 (s, 1H, 2-benzimiH) (benzimi: benzimidazole).

2.3. [1-(9-Anthracenylmethyl)-3-octylimy]$_2$ Hg[HgCl$_4$] (*2a*)

A suspension of $KOBu^t$ (0.090 g, 0.8 mmol), precursor **1a** (0.200 g, 0.5 mmol) and anhydrous mercury(II) chloride (0.136 g, 0.5 mmol) in THF (20 mL) and acetonitrile (20 mL) was refluxed for 24 h. A brown solution was formed and the solvent was removed with a rotary evaporator. Water (30 mL) was added to the residue and the solution was extracted with CH_2Cl_2 (3×20 mL). The extracting solution was dried with anhydrate $MgSO_4$, then the solution was concentrated to 10 mL and hexane (2 mL) was added, as a result, a pale yellow powder was obtained. Yield: 0.178 g (56.5%), M.p.: 248–250 °C. *Anal.* Calc. for $C_{52}H_{60}Cl_4Hg_2N_4$: C, 48.64; H, 4.71; N, 4.36. Found: C, 48.35; H, 4.27; N 4.18%. ^1H NMR (300 MHz, DMSO-d_6): δ 0.82 (t, $J = 6.0$, 3H, CH_3), 1.20–1.28 (m, 10H, CH_2), 1.73–1.78 (m, 2H, CH_2), 4.23 (t, $J = 6.0$, 2H, CH_2), 6.51 (s, 2H, CH_2An) (An: anthracene), 6.81 (s, 1H, 4 or 5-imiH) (imi: imidazole), 7.47 (s, 1H, 4 or 5-imiH), 7.57–7.63 (m, 4H, AnH), 8.20 (d, $J = 8.0$, 2H, AnH), 8.37 (d, $J = 8.0$, 2H, AnH), 8.80 (s, 1H, AnH). ^{13}C NMR (75 MHz, DMSO-d_6): δ 14.5 (CH_3), 22.7 (CH_2), 26.4 (CH_2), 26.8 (CH_2), 29.2 (CH_2), 31.2 (CH_2), 31.8 (CH_2), 46.9 (CCH_2N), 51.2 ($AnCH_2N$), 122.1, 123.9, 124.3 and 126.2 (AnC or 4, 5-imiC), 128.3, 130.0, 130.6, 131.5 and 131.7 (AnC), 176.8 ($C_{carbene}$).

2.4. [1-(9-Anthracenylmethyl)-3-butylbimy]$_2$ AgPF$_6$ (*2b*)

To a solution of **1c** (0.200 g, 0.4 mmol) in dichloromethane (30 mL) was added silver oxide (0.050 g, 0.2 mmol), and the suspension solution was refluxed under nitrogen for 24 h. The resulting solution was filtered and concentrated to 5 mL, and Et_2O (5 mL) was added to precipitate a pale yellow powder. Isolation by filtration yielded **2b**. Yield: 0.106 g (55%), M.p.: 272–274 °C. *Anal.* Calc. for $C_{52}H_{48}AgF_6N_4P$: C, 63.61; H, 4.93; N, 5.71. Found: C, 63.44; H, 4.63; N, 5.81%. ^1H NMR (300 MHz, DMSO-d_6): δ 0.30 (t, $J = 5.4$, 3H, CH_3), 0.57–0.62 (m, 2H, CH_2), 1.13–1.18 (m, 2H, CH_2), 3.33 (t, $J = 5.4$, 2H, CH_2), 6.18 (s, 2H, CH_2), 7.24 (t, $J = 6.3$, 1H, PhH), 7.43 (t, $J = 8.4$, 2H, AnH), 7.52–7.58 (m, 2H, AnH), 7.80 (d, $J = 6.3$, 1H, PhH), 7.92 (d, $J = 8.4$, 2H, AnH) (An: anthracene), 8.02 (d, $J = 8.4$, 2H, AnH), 8.08 (d, $J = 6.3$, 1H, PhH), 8.61 (s, 1H, AnH). ^{13}C NMR (75 MHz, DMSO-d_6): δ 13.5 (CH_3), 19.5 (CH_2), 31.9 (CH_2), 44.0 (CH_2), 49.6 (NCH_2An), 112.6, 124.1, 125.0, 125.8, 126.8, 127.5, 127.9, 128.5, 129.8, 130.2, 131.0 131.6, 132.9, 134.8 (AnC or PhC), 186.5 ($C_{carbene}$).

2.5. X-ray crystallography

For compounds **1a**, **2a** and **2b**, selected single crystals were mounted on a Bruker SMART 1000 CCD diffractometer operating at 50 kV and 20 mA using Mo Kα radiation (0.71073 Å). Data collection and reduction were performed using SMART and SAINT software [9] with frames of 0.6° oscillation in the θ range $1.8 < \theta < 25°$. An empirical absorption correction was applied using the SADABS program [10]. The structures were solved by direct methods and all non-hydrogen atoms were subjected to anisotropic refinement by full-matrix least squares on F^2 using the SHELXTL package [11]. All hydrogen atoms were generated

Table 1
Selected bond lengths (Å) and angles (°) for **1a**, **2a** and **2b**

1a		**2a**		**2b**	
N(1)–C(1)	1.326(9)	Hg(1)–C(1)	2.074(6)	Ag(1)–C(27)	2.074(5)
N(1)–C(3)	1.340(1)	Hg(1)–C(27)	2.073(6)	Ag(1)–C(1)	2.077(6)
N(1)–C(4)	1.469(9)	Hg(2)–Cl(4)	2.463(1)	N(1)–C(8)	1.458(7)
N(2)–C(1)	1.302(9)	Hg(2)–Cl(2)	2.472(1)	N(2)–C(23)	1.463(6)
N(2)–C(2)	1.368(1)	Hg(2)–Cl(3)	2.478(1)	C(1)–Ag(1)–C(27)	177.2(2)
N(2)–C(19)	1.489(1)	Hg(2)–Cl(1)	2.498(1)	N(2)–C(1)–N(1)	105.6(5)
C(1)–N(1)–C(3)	107.8(7)	C(1)–Hg(1)–C(27)	174.8(2)	N(2)–C(1)–Ag(1)	125.0(4)
C(1)–N(1)–C(4)	125.7(7)	Cl(4)–Hg(2)–Cl(2)	105.2(7)	N(1)–C(1)–Ag(1)	129.1(4)
C(3)–N(1)–C(4)	126.4(8)	Cl(4)–Hg(2)–Cl(3)	130.2(7)	C(1)–N(1)–C(2)	110.6(5)
C(1)–N(2)–C(2)	108.2(7)	Cl(2)–Hg(2)–Cl(3)	101.2(6)	C(1)–N(1)–C(8)	127.2(5)
C(1)–N(2)–C(19)	125.9(8)	Cl(4)–Hg(2)–Cl(1)	101.6(6)	C(2)–N(1)–C(8)	122.2(5)
C(2)–N(2)–C(19)	125.9(8)	Cl(2)–Hg(2)–Cl(1)	121.4(7)	C(1)–N(2)–C(7)	112.0(5)
N(2)–C(1)–N(1)	109.2(8)	Cl(3)–Hg(2)–Cl(1)	99.0(7)	C(1)–N(2)–C(23)	123.3(5)
		N(2)–C(1)–N(1)	105.8(5)	C(7)–N(2)–C(23)	124.5(5)
		N(2)–C(1)–Hg(1)	126.2(4)		
		N(1)–C(1)–Hg(1)	127.9(5)		

Table 2
Crystal data and structure refinements for **1a**, **2a** and **2b**

	1a	**2a**	**2b**
Chemical formula	$C_{26}H_{32}ClN_2O_{0.5}$	$C_{52}H_{60}Cl_4Hg_2N_4$	$C_{52}H_{48}AgF_6N_4P$
f_w	415.99	1284.07	981.79
Crystal system	triclinic	monoclinic	triclinic
Space group	$P\bar{1}$	$P2(1)/n$	$P\bar{1}$
a (Å)	10.864(5)	9.3077(6)	13.057(4)
b (Å)	13.455(6)	35.453(2)	19.370(6)
c (Å)	17.512(8)	15.590(9)	19.439(6)
α (°)	76.396(9)	90	106.439(5)
β (°)	72.427(8)	100.459(1)	95.997(5)
γ (°)	79.068(9)	90	92.134(6)
V (Å^3)	2352.5(1)	5059.1(5)	4678.0(2)
Z	2	2	1
D_{calcd} (Mg/m^3)	1.175	1.686	1.395
Absorption coefficient (mm^{-1})	0.179	6.311	0.529
$F(000)$	892	2512	2018
Crystal size (mm)	$0.24 \times 0.22 \times 0.18$	$0.22 \times 0.20 \times 0.20$	$0.24 \times 0.22 \times 0.18$
θ_{min}, θ_{max} (°)	1.24, 25.00	1.76, 7.91	1.77, 25.93
T (K)	293(2)	293(2)	293(2)
Number of data collected	11723	34205	27167
Number of unique data	8182	11990	17663
Number of refined parameters	532	625	1263
Goodness-of-fit on F^2[a]	0.968	1.003	0.915
Final R indices[b] $[I > 2\sigma(I))]$			
R_1	0.1194	0.0427	0.0542
wR_2	0.2404	0.0918	0.1239
R indices (all data)			
R_1	0.3322	0.0982	0.1510
wR_2	0.3461	0.1080	0.1566

[a] Gof $= [\sum \omega(F_o^2 - F_c^2)^2/(n-p)]_{1/2}$, where n is the number of reflection and p is the number of parameters refined.
[b] $R_1 = \sum(||F_o| - |F_c||/\sum|F_o|$; $wR_2 = 1/[\sigma^2(F_o^2) + (0.0691P) + 1.4100P]$ where $P = (F_o^2 + 2F_c^2)/3$.

geometrically (C–H bond lengths fixed at 0.96 Å), assigned appropriated isotropic thermal parameters and included in structure factor calculations. Selected bond lengths (Å) and angles (°) and crystal data and structure refinement for **1a**, **2a** and **2b**, are presented in Tables 1 and 2.

3. Results and discussion

1-(9-Anthracenylmethyl)-3-butylbenzimidazolium chloride (**1b**) was prepared from benzimidazole by stepwise alkylation with butyl iodide followed by 9-chloromethylan-

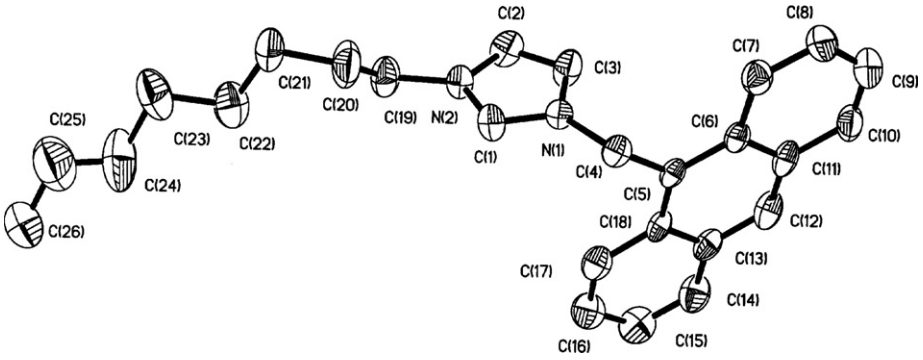
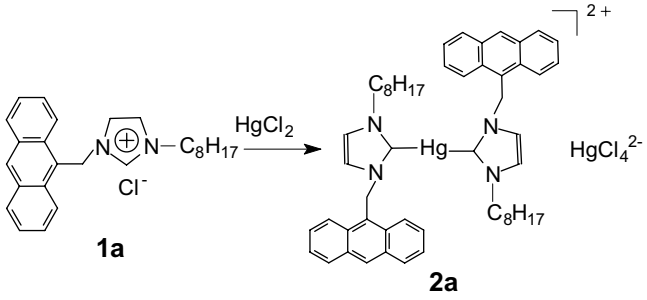


Fig. 1. Perspective view of **1a** and anisotropic displacement parameters depicting 30% probability. Hydrogen atoms have been omitted for clarity.

thracene in sequence. Compound **1b** was changed to 1-(9-anthracenylmethyl)-3-butylbenzimidazolium hexafluorophosphate (**1c**) by an anionic exchange reaction with NH_4PF_6. The compounds **1a** and **1c** are soluble in most polar organic solvents, such as CH_2Cl_2, CH_3OH and CH_3CN, and insoluble in diethyl ether and hydrocarbon solvents. In the ^1H NMR spectra of **1a** and **1c** the imidazolium proton signals (NCHN) appear at $\delta = 8.97$ and 11.45 ppm, which are consistent with the chemical shifts of known imidazolium salts [2]. Yellow crystals of **1a** were obtained by slowly evaporating its CH_2Cl_2 solution (Fig. 1). Although the poor quality of the crystal yielded a relatively high *R* value, nevertheless, the skeletal arrangement was correct. In the molecular structure of **1a** the dihedral angle between the imidazole ring and anthracene ring is 91.5°.

In CH_3CN and THF solution, compound**1a** was reacted with $HgCl_2$ in the presence of $KOBu^t$ to afford complex **2a** (Scheme 1). Complex **2a** is light-sensitive in solution, but

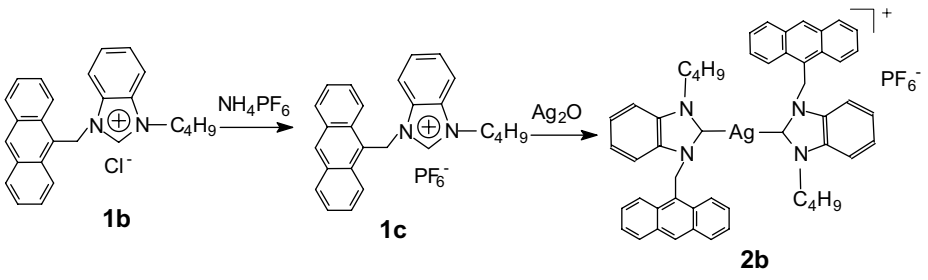


Scheme 1.

light-stable as a solid. In CH_2Cl_2 solution compound **1c** was reacted with Ag_2O to give complex **2b** (Scheme 2). Complexes **2a** and **2b** are soluble in DMSO, soluble partly in $CHCl_3$ and CH_3CN, and insoluble in diethyl ether and petroleum ether. Yellow crystals of **2a** and **2b** suitable for X-ray diffraction were obtained from slow diffusion of diethyl ether into their DMSO solutions, and they were characterized by elemental analysis and ^1H and ^{13}C NMR spectroscopy. In the ^1H NMR spectra of **2a** and **2b**, the disappearance of the resonances for the imidazolium (or benzimidazolium) protons (NCHN) shows the formation of the expected metal carbene complexes. In the ^{13}C NMR spectra the signals for the carbene carbon appears at 176.8 ppm for **2a** and 186.5 ppm for **2b**, which are characteristic for carbene metal complexes [3].

As depicted in Fig. 2a, the coordination geometry on the mercury atom in **2a** is essentially linear, with a C(1)–Hg(1A)–C(27) bond angle of 174.8(2)°. The C–Hg bond distance of 2.074(6) Å is slightly longer than those of known Hg–carbene complexes (2.02–2.06 Å) [3a,3b,3c,3d]. The internal ring angle (N–C–N) at the carbene center is 105.8(5)°, which is somewhat smaller than that of the precursor **1a** (109.2(8)°) but similar to those in some known mercury complexes. One of the imidazole rings forms dihedral angles of 14.6° and 86.4°, respectively, with another imidazole ring and adjacent anthracene ring. The dihedral angle between two anthracene rings is 14.7°. The two 9-anthracylmethyl groups and two octyl groups point to contrary directions due to steric demands.

A notable feature in the crystal packing of complex **2a** (Fig. 2b) is that one dimensional polymeric chains are formed by [1-(9-anthracenylmethyl)-3-octylimy]$_2$Hg and



Scheme 2.

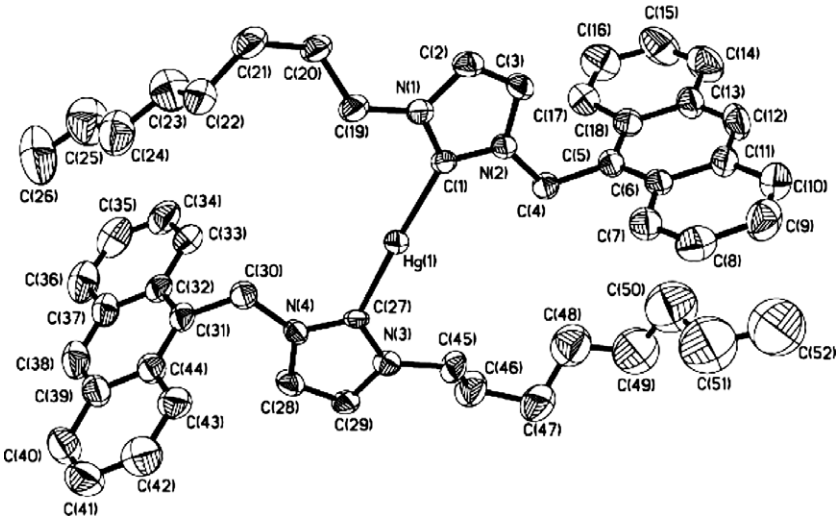


Fig. 2a. Perspective view of **2a** and anisotropic displacement parameters depicting 30% probability. Hydrogen atoms have been omitted for clarity.

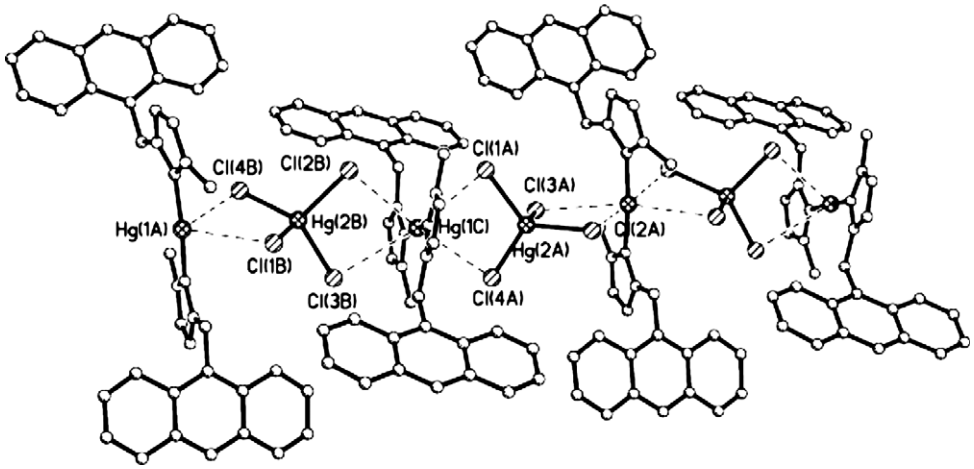


Fig. 2b. 1D polymeric chain by weak Hg...Cl bonds in **2a**. Seven carbon atoms of the octyl group have been omitted and only one carbon atom is reserved for clarity.

$[HgCl_4]^{2-}$ via weak Hg...Cl bonds (Hg...Cl bond separations being 3.1–3.4 Å, whereas regular Hg–Cl bond lengths are 2.4–2.5 Å). The Hg(1A)...Hg(2B) separation of 4.256 Å shows no metal–metal interactions. The atoms Hg(1A)...Cl(1B)–Hg(2B)–Cl(4B) (plane 1), Hg(2B)–Cl(2B)...Hg(1C)...Cl(3B) (plane 2) and Hg(1C)...Cl(1A)–Hg(2A)–Cl(4A) (plane 3) are coplanar. Plane 1 forms dihedral angles of 80.3° and 86.9° with the two adjacent imidazole rings. Plane 2 forms dihedral angles of 70.3° and 15.7°, respectively, with plane 1 and plane 3.

The X-ray structural analysis of **2b** shows that the central silver atom has a linear two-coordinate structure (Fig. 3a) with a C(1)–Ag(1)–C(27) bond angle of 177.2(2)°. The C–Ag bond distance of 2.077(6) Å is similar to those of some known NHC silver complexes [3e,3f,3g,3h,3i,3j,3k,3l]. In **2b** the two benzimidazole rings are almost perpendicular (the dihedral angle being 93.4°), and one of benzimidazole ring forms dihedral angles of 105.1° and 6°, respectively, with one anthracene rings

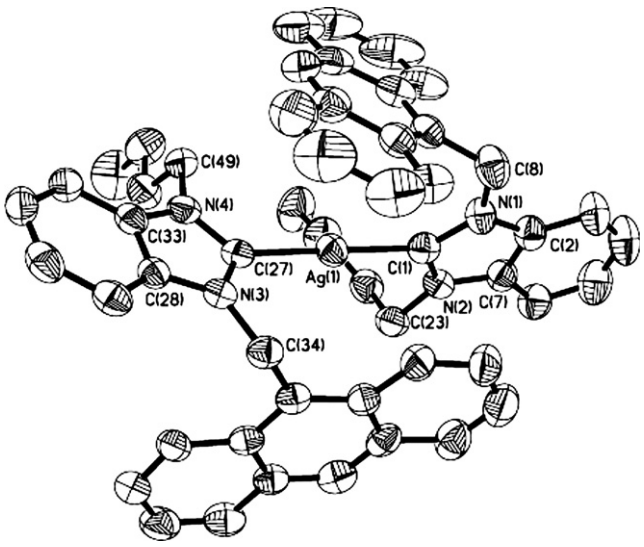


Fig. 3a. Perspective view of **2b** and anisotropic displacement parameters depicting 30% probability. Hydrogen atoms have been omitted for clarity.

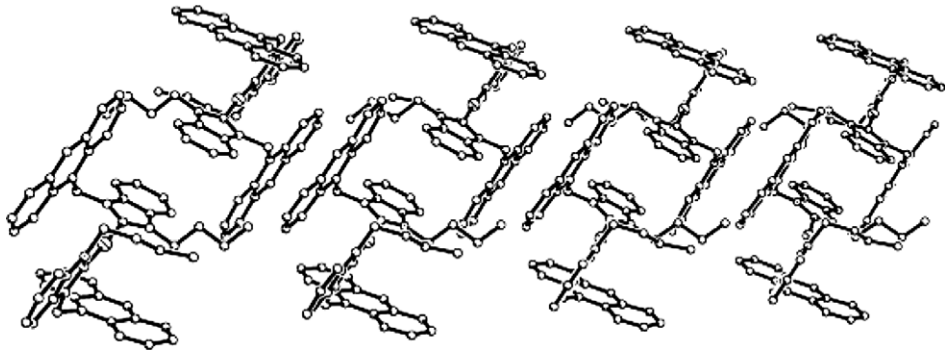


Fig. 3b. The 1D supramolecular chain by π–π stacking interactions from benzimidazole rings and anthracene rings in **2b**.

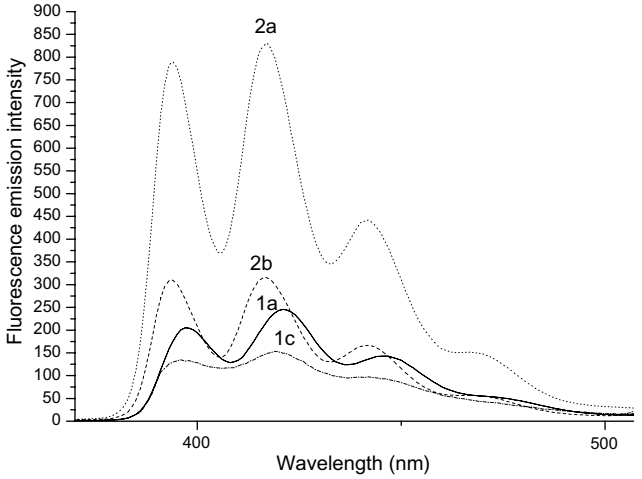


Fig. 4. Emission spectra of **1a** (—), **1c** (-·-·-), **2a** (· · ·) and **2b** (– – –) at 298 K upon excitation at 256 nm in CH_2Cl_2 (5.0×10^{-6} M).

from an identical ligand and another from a different ligand.

An interesting feature in the packing diagrams of **2b** is that both types of aromatic π–π stacking interactions are observed [12] (Fig. 3b). One type is the head to tail π–π stacking interactions from inter-molecular benzimidazole rings with an inter-planar separation of 3.541 Å (center-to-center separation: 3.890 Å), which form dimeric units. Another type is the face-to-face π–π interactions from inter-dimeric anthracene rings, which extends the dimeric units into 1D supramolecular chains. In the packing diagrams the distance of neighboring parallel anthracene rings is 3.261 Å, with a center-to-center separation of 4.960 Å. Thus aromatic π–π stacking interactions are mainly responsible for the formation of dimeric units and expanding the dimeric units to 1D supramolecular chains in **2b**.

The fluorescent emission spectra of **1a**, **1c**, **2a** and **2b** are shown in Fig. 4. In dichloromethane **2a** and **2b** showed an anthracene-type fluorescence emission in the region 370–510 nm, similar to but stronger than those of the corresponding precursors **1a** and **1c**. This can be attributed to the electron-withdrawing effect of mercury(II) or silver(I), which inhibits the photoinduced electron transfer (PET) process of the lone-pair electron of the nitrogen atom to the anthracene ring [13].

4. Conclusion

In summary, two new *N*-heterocyclic carbene Hg(II) and Ag(I) complexes have been synthesized and characterized. In complex **2a** 1D polymeric chains are formed by [1-(9-anthracenylmethyl)-3-octylimy]Hg and $[HgCl_4]^{2-}$ through weak Hg...Cl bonds. In complex **2b** 1D supramolecular chains are formed by both types of aromatic π–π stacking interactions. The fluorescent emission spectra of **2a** and **2b** are stronger than those of their corresponding precursors **1a** and **1c**. Further studies on new fluorescent organometallic compounds from precursor **1** and analogous ligands are underway.

Acknowledgement

We are grateful to the National Science Foundation of China (Project Grant No. 20672081) and Tianjin Natural Science Foundation (07JCYBJC00300).

Appendix A. Supplementary material

CCDC 631990, 631992 and 631991 contain the supplementary crystallographic data for **1a**, **2a** and **2b**. These data can be obtained free of charge via http://www.ccdc.cam.ac.uk/conts/retrieving.html, or from the Cambridge Crystallographic Data Centre, 12 Union Road, Cambridge CB2 1EZ, UK, fax: (+44) 1223-336-033, or e-mail: deposit@ccdc.cam.ac.uk. Supplementary data associated with this article can be found, in the online version, at doi:10.1016/j.poly.2007.08.046.

References

[1] A.J. Arduengo III, R.L. Harlow, M. Kline, J. Am. Chem. Soc. 113 (1991) 361.
[2] (a) D. Bourissou, O. Guerret, F.P. Gabbaï, G. Bertrand, Chem. Rev. 100 (2000) 39;
(b) P.L. Arnold, S. Pearson, Coord. Chem. Rev. 251 (2007) 596;
(c) D. Pugh, A.A. Danopoulos, Coord. Chem. Rev. 251 (2007) 610;

(d) M. Regitz, Angew. Chem., Int. Ed. Engl. 35 (1996) 725;
(e) W.A. Herrmann, C. Köcher, Angew. Chem., Int. Ed. 41 (2002) 1290;
(f) M. Alcarazo, S.J. Roseblade, A.R. Cowley, R. Fernandez, J.M. Brown, J.M. Lassaletta, J. Am. Chem. Soc. 127 (2005) 3290;
(g) L. Ackermann, A. Fürstner, T. Weskamp, F.J. Kohl, W.A. Herrmann, Tetrahedron Lett. 40 (1999) 4787;
(h) D.J. Nielsen, K.J. Cavell, B.W. Skelton, A.H. White, Organometallics 25 (2006) 4850;
(i) W.A. Herrmann, C. Köcher, Angew. Chem., Int. Ed. Engl. 96 (1997) 2162;
(j) J.C.C. Chen, I.J.B. Lin, J. Chem. Soc., Dalton Trans. (2000) 839;
(k) J. Huang, E.D. Stevens, S.P. Nolan, Organometallics 19 (2000) 1194;
(l) R.E. Douthwaite, M.L.H. Green, P.J. Silcock, P.T. Gomes, J. Chem. Soc., Dalton Trans. (2002) 1386;
(m) D.J. Nielsen, K.J. Cavell, B.W. Skelton, A.H. White, Inorg. Chim. Acta 327 (2002) 116;
(n) A.J. Arduengo III, F. Davidson, H.V.R. Dias, J.R. Goerlich, D. Khasnis, W.J. Marshall, T.K. Prakasha, J. Am. Chem. Soc. 119 (1997) 12742;
(o) F.M. Rivas, U. Riaz, A. Giessert, J.A. Smulik, S.T. Diver, Org. Lett. 3 (2001) 2673;
(p) D. Enders, K. Breuer, G. Raabe, J. Runsink, J.H. Teles, J.-P. Melder, K. Ebel, S. Brode, Angew. Chem., Int. Ed. Engl. 34 (1995) 284;
(q) F.E. Hahn, M.C. Jahnke, T. Pape, Organometallics 26 (2007) 150;
(r) N. Saino, D. Kogure, S. Okamoto, Org. Lett. 7 (2005) 3065;
(s) C. Fischer, S.W. Smith, D.A. Powell, G.C. Fu, J. Am. Chem. Soc. 128 (2006) 1472;
(t) J.C. Green, R.G. Scurr, P.L. Arnold, F.G.N. Cloke, Chem. Commun. (1997) 1963;
(u) L.J. Xu, W.P. Chen, J.F. Bickley, A. Steiner, J.L. Xiao, J. Organomet. Chem. 598 (2000) 409;
(v) A.A. Danopoulos, N. Tsoureas, S.A. Macgregor, C. Smith, Organometallics 26 (2007) 253.

[3] (a) X.J. Wan, F.B. Xu, Q.S. Li, H.B. Song, Z.Z. Zhang, Organometallics 24 (2005) 6066;
(b) U. Scheele, S. Dechert, F. Meyer, Inorg. Chim. Acta 359 (2006) 4891;
(c) J.C. Garrisen, R.S. Simons, J.M. Talley, C. Wesdemiotis, C.A. Tessier, W.J. Youngs, Organometallics 20 (2001) 1276;
(d) A. Caballero, E. Díez-Barra, F.A. Jalón, S. Merino, J. Tejeda, J. Organomet. Chem. 617–618 (2001) 395;
(e) A.M. Magill, D.S. Mcguinness, K.J. Cavell, G.J.P. Britovsek, V.C. Gibson, A.J.P. White, D.J. Williams, A.H. White, B.W. Skekton, J. Organomet. Chem. 617–618 (2001) 546;
(f) C.K. Lee, K.M. Lee, J.B.Ivan Lin, Organometallics 21 (2002) 10;
(g) Q.X. Liu, F.B. Xu, Q.S. Li, X.S. Zeng, X.B. Leng, Y.L. Chou, Z.Z. Zhang, Organometallics 22 (2003) 309;
(h) O. Guerret, S. Sole, H. Gornitzka, M.L. Teichert, G. Teingnier, G. Berte, J. Am. Chem. Soc. 119 (1997) 6668;
(i) R.Z. Ku, J.C. Huang, J.Y. Cho, F.M. Kiang, K.R. Reddy, Y.C. Chen, K.J. Lee, J.H. Lee, G.H. Lee, S.M. Peng, S.T. Liu, Organometallics 18 (1999) 2145;
(j) I.J.B. Lin, C.S. Vasam, Coord. Chem. Rev. 251 (2007) 642;
(k) K.M. Lee, J.C.C. Chen, I.J.B. Lin, J. Organomet. Chem. 617–618 (2001) 364;
(l) M.K. Samantaray, V. Katiyar, K. Pang, H. Nanavati, P. Ghosh, J. Organomet. Chem. 692 (2007) 1672.

[4] (a) A. Melaiye, Z. Sun, K. Hindi, A. Milsted, D. Ely, D.H. Reneker, C.A. Tessier, W.J. Youngs, J. Am. Chem. Soc. 127 (2005) 2285;
(b) A. Melaiye, R.S. Simons, A. Milsted, F. Pingitore, C. Wesdemiotis, C.A. Tessier, W.J. Youngs, J. Med. Chem. 47 (2004) 973;
(c) A.K. Nebioglu, M.J. Panzner, C.A. Tessier, C.L. Cannon, W.J. Youngs, Coord. Chem. Rev. 251 (2007) 884.

[5] (a) J.C. Garrison, W.J. Youngs, Chem. Rev. 105 (2005) 3978;
(b) H.M.F. Wang, I.J.B. Lin, Organometallics 17 (1998) 972;
(c) S. Liu, T. Hsieh, G. Lee, S. Peng, Organometallics 17 (1998) 993;
(d) W.A. Herrmann, S.K. Schneider, K. Öfele, M. Sakamoto, E. Herdtweck, J. Organomet. Chem. 689 (2004) 2441;
(e) D.J. Nielsen, K.J. Cavell, B.W. Skelton, A.H. White, Inorg. Chim. Acta 352 (2003) 143;
(f) H.M. Lee, J.Y. Zeng, C.H. Hu, M.T. Lee, Inorg. Chem. 43 (2004) 6822;
(g) H.M. Lee, P.L. Chiu, C.H. Hu, C.L. Lai, Y.C. Chou, J. Organomet. Chem. 690 (2005) 403;
(h) K.S. Coleman, H.T. Chamberlayne, S. Turberville, M.L.H. Green, A.R. Cowley, J. Chem Soc., Dalton Trans. (2003) 2917;
(i) P.L. Arnold, A.C. Scarisbrick, A.J. Blake, C. Wilson, Chem. Commun. (2002) 2340;
(j) J.J. Van Veldhuizen, J.E. Campbell, R.E. Giudici, A.H. Hoveyda, J. Am. Chem. Soc. 127 (2005) 6877;
(k) P.L. Arnold, M. Rodden, K.M. Davis, A.C. Scarisbrick, A.J. Blake, C. Wilson, Chem. Commun. (2004) 1612;
(l) S. Winston, N. Stylianides, A.A.D. Tulloch, J.A. Wright, A.A. Danopoulos, Polyhedron 23 (2004) 2813.

[6] (a) A.J. Arduengo III, R.H.V. Dias, R.L. Harlow, M. Kline, J. Am. Chem. Soc. 114 (1992) 5530;
(b) W.A. Herrmann, M. Elison, J. Fischer, C. Köcher, G.R.J. Artus, Chem. Eur. J. 2 (1996) 772;
(c) A.J. Arduengo III, J.R. Goerlich, W.J. Marshall, J. Am. Chem. Soc. 117 (1995) 11027;
(d) J.A. Loch, M. Albrecht, E. Peris, J. Mata, J.W. Faller, R.H. Crabtree, Organometallics 21 (2002) 700;
(e) V.M. Baker, D.H. Brown, V.J. Hesler, B.W. Skelton, A.H. White, Organometallics 26 (2007) 250;
(f) S. Caddick, F.G.N. Cloke, P.B. Hitchcock, J. Leonard, A.K.de K. Lewis, D. McKerrecher, L.R. Titcomb, Organometallics 22 (2003) 4318;
(g) A. Fürstner, G. Seidel, D. Kremzow, C.W. Lehmann, Organometallics 22 (2003) 907;
(h) H.V. Huynh, T.C. Neo, G.K. Tan, Organometallics 25 (2006) 1298;
(i) F. Hanasaka, K. Fujita, R. Yamaguchi, Organometallics 25 (2006) 4643;
(j) W.A. Herrmann, L.J. Goossen, M. Spiegler, Organometallics 17 (1998) 2162;
(k) L. Xu, W. Chen, J. Xiao, Organometallics 19 (2000) 1123;
(l) M. Hasan, I.V. Kozhevnikov, M.R.H. Siddiqui, C. Femoni, A. Steiner, N. Winterton, Inorg. Chem. 40 (2001) 795;
(m) S. Grundemann, M. Albrecht, A. Kovacevic, J.W. Faller, R.H. Crabtree, J. Chem. Soc., Dalton Trans. (2002) 2163;
(n) K.E. Krahulic, G.D. Enright, M. Parvez, R. Roesler, J. Am. Chem. Soc. 127 (2005) 4142.

[7] (a) J. Ruiz, G. Garcia, M.E.G. Mosquera, B.F. Perandones, M.P. Gonzalo, M. Vivanco, J. Am. Chem. Soc. 127 (2005) 8584;
(b) N. Hadei, E.A.B. Kantchev, C.J. Brien, M.G. Organ, Org. Lett. 7 (2005) 1991;
(c) J.J. Song, F. Gallou, J.T. Reeves, Z. Tan, N.K. Yee, C.H. Senanayake, J. Org. Chem. 71 (1991) 1273;
(d) D.S. McGuinness, K.J. Cavell, B.W. Skekton, A.H. White, Organometallics 18 (1999) 1596;
(e) J. Huang, S.P. Nolan, J. Am. Chem. Soc. 121 (1999) 9889;
(f) M.G. Gardiner, W.A. Herrmann, C.-P. Reisinger, J. Schwarz, M. Spiegler, J. Organomet. Chem. 572 (1999) 239;
(g) L.H. Gade, S.B. Laponnaz, Coord. Chem. Rev. 251 (2007) 718;
(h) W.J. Sommer, M. Weck, Coord. Chem. Rev. 251 (2007) 860;
(i) S.K. Schneider, C.F. Rentzsch, A. Krüger, H.G. Raubenheimer, W.A. Herrmann, J. Mol. Cat. A: Chem. 265 (2007) 50;
(j) M.A. Taige, A. Zeller, S. Ahrens, S. Goutal, E. Herdtweck, T. Strassner, J. Organomet. Chem. 692 (2007) 1519;
(k) J.J. Song, F. Gallou, J.T. Reeves, Z. Tan, N.K. Yee, C.H. Senanayake, J. Org. Chem. 71 (2006) 1273;

(l) E. Despagnet-Ayoub, R.H. Grubbs, Organometallics 24 (2005) 338.

[8] (a) Q.X. Liu, F.B. Xu, Q.S. Li, H.B. Song, Z.Z. Zhang, Organometallics 23 (2004) 610;
(b) Q.X. Liu, H.B. Song, F.B. Xu, Q.S. Li, X.S. Zeng, X.B. Leng, Z.Z. Zhang, Polyhedron 22 (2003) 1515;
(c) Q.X. Liu, F.B. Xu, Q.S. Li, H.B. Song, Z.Z. Zhang, J. Mol. Struct. 697 (2004) 131;
(d) Q.X. Liu, L.N. Yin, J.C. Feng, J.H. Guo, H.B. Song, Acta Crystallogr., Sect. E 62 (2006) o3604.

[9] SMART 5.0 and SAINT 4.0 for Windows NT, Area Detector Control and Integration Software, Bruker Analytical X-ray Systems, Inc., Madison, WI, USA, 1998.

[10] G.M. Sheldrick, SADABS, Program for Empirical Absorption Correction of Area Detector Data, Univ. of Göttingen, Germany, 1996.

[11] G.M. Sheldrick, SHELXTL 5.10 for Windows NT, Structure Determination Software, Brucker Analytical X-Ray Systems Inc., Madison, WI, USA, 1997.

[12] (a) C.K. Lee, J.C.C. Chen, K.M. Lee, C.W. Liu, I.J.B. Lin, Chem. Mater. 11 (2001) 1237;
(b) C.A. Hunter, J.K.M. Sanders, J. Am. Chem. Soc. 112 (1990) 5525;
(c) C.A. Janiak, J. Chem. Soc., Dalton Trans. (2000) 3885;
(d) A.N. Khlobystov, A.J. Blake, N.R. Champness, D.A. Lemenovskki, A.C. Majouga, N.V. Zyk, M. Schroder, Coord. Chem. Rev. 222 (2001) 155;
(e) A.J. Black, G. Baum, N.R. Champness, S.S.M. Chung, P.A. Cooke, D. Fenske, A.N. Khlobystov, D.A. Lemenovskki, W.S. Li, M. Schroder, J. Chem. Soc., Dalton Trans. (2000) 4285.

[13] B.P. de Silva, H.Q.N. Lgunaratne, T.L. Gunnlangsson, A.J.M. Unzley, C.P. McCoy, J.T. Rademacher, T.E. Rice, Chem. Rev. 97 (1997) 1515.

Available online at www.sciencedirect.com
ScienceDirect
Polyhedron 27 (2008) 95–104
POLYHEDRON
www.elsevier.com/locate/poly

Uranyl(VI) complexes of [*O*,*N*,*O*,*N*′]-type diaminobis(phenolate) ligands: Syntheses, structures and extraction studies

Harri Sopo [a,*], Ari Lehtonen [b], Reijo Sillanpää [a]

[a] *Department of Chemistry, University of Jyväskylä, P.O. Box 35, FIN-40351 Jyväskylä, Finland*
[b] *Department of Chemistry, University of Turku, Vatselantie, FIN-20014, Turku, Finland*

Received 13 July 2007; accepted 22 August 2007
Available online 26 October 2007

Abstract

The syntheses and crystal structures of four new uranyl complexes with [*O*,*N*,*O*,*N*′]-type ligands are described. The reaction between uranyl nitrate hexahydrate and the phenolic ligand [(*N*,*N*-bis(2-hydroxy-3,5-dimethylbenzyl)-*N*′,*N*′-dimethylethylenediamine)], H_2L1 in a 1:2 molar ratio (M to L), yields a uranyl complex with the formula $[UO_2(HL1)(NO_3)] \cdot CH_3CN$ (**1**). In the presence of a base (triethylamine, one mole per ligand mole) with the same molar ratio, the uranyl complex $[UO_2(HL1)_2]$ (**2**) is formed. The reaction between uranyl nitrate hexahydrate and the ligand [(*N*,*N*-bis(2-hydroxy-3,5-di-*t*-butylbenzyl)-*N*′,*N*′-dimethylethylenediamine)], H_2L2, yields a uranyl complex with the formula $[UO_2(HL2)(NO_3)] \cdot 2CH_3CN$ (**3**) and the ligand [*N*-(2-pyridylmethyl)-*N*,*N*-bis(2-hydroxy-3,5-dimethylbenzyl)amine], H_2L3, in the presence of a base yields a uranyl complex with the formula $[UO_2(HL3)_2] \cdot 2CH_3CN$ (**4**). The molecular structures of **1**–**4** were verified by X-ray crystallography. The complexes **1**–**4** are zwitter ions with a neutral net charge. Compounds **1** and **3** are rare neutral mononuclear $[UO_2(HLn)(NO_3)]$ complexes with the nitrate bonded in η^2-fashion to the uranyl ion. Furthermore, the ability of the ligands H_2L1–H_2L4 to extract the uranyl ion from water to dichloromethane, and the selectivity of extraction with ligands H_2L1, H_3L5 (*N*,*N*-bis(2-hydroxy-3,5-dimethylbenzyl)-3-amino-1-propanol), $H_2L6 \cdot HCl$ (*N*,*N*-bis(2-hydroxy-5-*tert*-butyl-3-methylbenzyl)-1-aminobutane · HCl) and $H_3L7 \cdot HCl$ (*N*,*N*-bis(2-hydroxy-5-*tert*-butyl-3-methylbenzyl)-6-amino-1-hexanol · HCl) under varied chemical conditions were studied. As a result, the most efficient and selective ligand for uranyl ion extraction proved to be $H_3L7 \cdot HCl$.
© 2007 Elsevier Ltd. All rights reserved.

Keywords: Uranyl complex; Uranyl ion extraction; Phenolate ligands; Crystal structures

1. Introduction

Ligands with a good selectivity towards particular metal ions in different chemical surroundings have found use in biological and environmental applications of coordination chemistry. For example, in a metal ion recognition ligand architecture is a key factor [1] which is clearly demonstrated, e.g. by Karmazin et al. [2]. Moreover, in industrially interesting applications of catalytically active coordination compounds, the three-dimensional geometry of the used complexes has a crucial role for the catalytic efficiency [3–5]. As an example, multidentate [*O*,*N*,*O*,*N*′]-type ligands and their metal complexes, among others, have been under intense research due to their versatility in chemistry. An indication of this is the number of crystal structure determinations of the complexes mentioned above [4,6–10] along with the number of reports presenting their use as catalysts in various chemical reactions [5,11–16]. Our group has earlier prepared uranyl complexes with [*O*,*N*,*O*,*O*′][17,18]- and [*O*,*N*,*O*][19]-type aminobis(phenolate) ligands in which the coordination of the aminobis(phenol) ligand to the UO_2^{2+} ion is associated with the protonation of the central nitrogen atom of the ligand backbone. This protonation evokes potentially tridentate, dianionic aminobis(phenol)s to react as bidentate, monoanionic ligands. To enlarge our studies concerning the chemistry of uranium(VI), we were interested in investigating the behavior of [*O*,*N*,*O*,*N*′]-type ligands with a UO_2^{2+}

* Corresponding author. Tel.: +358 14 260 2616; fax: +358 14 260 2501.
E-mail address: hasopo@jyu.fi (H. Sopo).

0277-5387/$ - see front matter © 2007 Elsevier Ltd. All rights reserved.
doi:10.1016/j.poly.2007.08.047

ion. This ligand type has two possible sites (two nitrogen donors) to accommodate the proton freed in the complexation process, a feature which may significantly affect the coordination mode of the ligand and consequently the properties of the formed complex, e.g. in catalysis or in extraction processes. Furthermore, the new uranyl ion complexes are of interest since the linear uranyl cation is present in the majority of naturally occurring uranium minerals and in nuclear waste reprocessing systems [20] and there thus exists a need to selectively extract the uranyl ion from other chemical species.

In our earlier studies concerning the complexation of the uranyl ion with various aminoalcoholbis(phenol)s (H_3L) [17,18], two structurally different type of uranyl complexes were isolated. In general, complexes of the type $[UO_2(H_2L)_2] \cdot S$ (one H^+ ion at the nitrogen atom) with solvent molecules (S), like acetonitrile, crystallized from the solutions, but in one case when $H_3L = N,N$-bis(2-hydroxy-3,5-dimethylbenzyl)-2-aminoethanol, also a dinuclear complex $[(UO_2)_2(H_2L)_2(NO_3)_2]$ was formed. If the ligands are aminoalkylbis(phenol)s (H_2L), only complexes with the formula $[UO_2(HL)_2] \cdot S$ (H^+ ion at the nitrogen) crystallized from the solutions [19]. When the monomeric complexes of type $[UO_2(HL)_2]$ were dissolved in coordinating solvents, such as DMSO or pyridine, they dissociate to produce $[UO_2(HL)(solvent)_n]^+$ complexes, but in chloroform the $[UO_2(HL)_2]$ species dissolve in the molecular form.

In this paper we report the complexation and extraction studies of the uranyl ion with selected diaminobis(phenol)s. The ligand family used is presented in Fig. 1.

The ligands H_3L5 (N,N-bis(2-hydroxy-3,5-dimethylbenzyl)-3-amino-1-propanol), $H_2L6 \cdot HCl$ (N,N-bis(2-hydroxy-5-*tert*-butyl-3-methylbenzyl)-1-aminobutane $\cdot$ HCl) and $H_3L7 \cdot HCl$ (N,N-bis(2-hydroxy-5-*tert*-butyl-3-methylbenzyl)-6-amino-1-hexanol $\cdot$ HCl), prepared in our earlier studies [17–19] and used in the uranyl extraction experiments in this paper, are presented in Fig. 2.

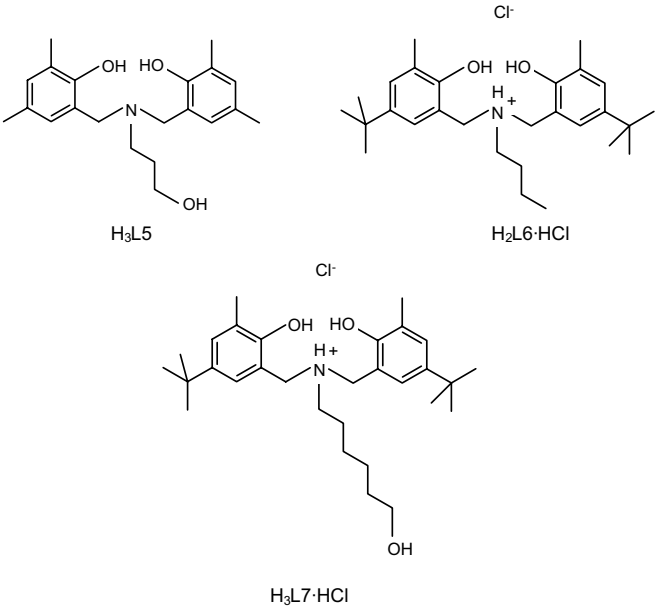


Fig. 2. Ligands H_3L5, $H_2L6 \cdot HCl$ and $H_3L7 \cdot HCl$ used in the uranyl extraction experiments.

2. Experimental

2.1. General information

The starting materials for all syntheses were purchased from Fluka, Merck or Riedel and were of reagent grade and used as received. Solvents were of HPLC grade and used as purchased. All syntheses and extraction experiments were performed under ambient laboratory atmosphere. The NMR spectra were recorded on a Bruker AVANCE DPX 250 FT-NMR spectrometer or Bruker AVANCE DRX 500 FT-NMR spectrometer. The ^1H and ^{13}C NMR spectra were recorded either in $CDCl_3$ or d_6-DMSO at 30 °C. The chemical shifts are reported in ppm and referenced internally using the residual protic solvent resonances relative to tetramethylsilane ($CDCl_3$ δ 7.26, ^1H NMR; δ 77.0, ^{13}C NMR; DMSO-d_6 δ 2.50, ^1H NMR; δ 39.50, ^{13}C NMR). IR spectra were recorded on a Perkin–Elmer System 2000 FT-IR spectrometer in KBr discs. Elemental analysis was performed using a VarioEl III elemental analyzer. Single crystal X-ray measurements were performed using an Enraf Nonius Kappa CCD area-detector diffractometer. The uranyl extraction samples were analyzed with inductively coupled plasma optical emission spectrometry (ICP-OES) at 385.958 nm using a Perkin–Elmer Optima 4300DV instrument. The pH values were measured with an ORION SA520 pH-meter.

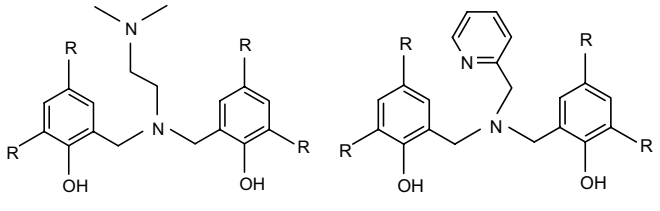


Fig. 1. Diaminobis(phenol) ligands used in this paper.

2.2. Ligand syntheses

The ligands H_2L3 and H_2L4 were prepared according to a known procedure [4]. H_2L1 and H_2L2 were prepared by a slightly modified method described below. The NMR spectra of the prepared ligands were in agreement with the literature [4,6,7,16].

2.2.1. H_2L1

To a solution of 2,4-dimethylphenol (3.00 g, 0.025 mol) in EtOH (15 ml) and water (3 ml), was added aqueous formaldehyde (37%, 3.26 g, 0.040 mol), N,N-dimethylethylenediamine (1.00 g, 0.011 mol) and triethylamine

($V = 0.500$ ml, 0.004 mol) for a catalyst. The resulting solution was kept in a water bath (50 °C) for 47 h. The colourless crystals formed were filtered, washed with cold MeOH (2×10 ml) and dried. Yield 3.41 g (87%). A single crystal X-ray analysis was done on one of these crystals and the results were in agreement with the literature [11,16].

2.2.2. H_2L2

Prepared as H_2L1, except the amount of water was 2 ml and that the time in the water bath (50 °C) was 140 h. Yield 3.22 g (56%) as colourless crystals.

2.3. $[UO_2(HL1)(NO_3)] \cdot CH_3CN$ (1)

Complex **1** was prepared by dissolving 0.053 g (0.15 mmol) of H_2L1 and 0.038 g (0.075 mmol) of $UO_2(NO_3)_2 \cdot 6H_2O$ in 10 ml of CH_3CN with 4 Å molecular sieves to remove water. The resulting red solution was kept in a freezer for three weeks leading to the formation of red crystals. After that the crystals were filtered off and dried. Yield 0.022 g (40%). The crystals are soluble in DMSO and acetone. ^{1}H NMR (DMSO-d_6, 250 MHz; Co for coordinated ligand and Un for uncoordinated ligand (20% of complex is dissociated, see NMR discussion)): 7.02, 6.99 (s, 4H, aryl, Co), 6.81, 6.74 (s, 1H, aryl, Un), 4.35 (m, 4H, N–CH_2-aryl, Co), 3.57 (s, 1H, N–CH_2-aryl, Un), 3.28 (m, 1H, N–CH_2CH_2–N, Un), 3.10, 2.87 (m, 4H, N–CH_2CH_2–N, Co), 2.59, 2.32 (s, 12H, aryl-CH_3, Co), 2.29, 2.14 (s, 3H, aryl-CH_3, Un), 2.14 (s, 6H, N–(CH_3)$_2$, Co) 2.08 (s, 1.5H, N–(CH_3)$_2$, Un), 2.07 (s, 4H, H_3CCN). ^{13}C NMR (DMSO-d_6, 63 MHz): 164.7–122.2 (aryl), 59.7 (N–CH_2–*C*(aryl)), 54.9, 51.5 (N–*C*H_2-aryl, N–(*C*H_2)$_2$–N), 46.1, 43.7 (N–(*C*H_3)$_2$), 19.9, 16.9, 16.0 (aryl-*C*H_3). IR (KBr, ν/cm^{-1}): 3428(m), 2913(m), 1610(w), 1472(s), 1382(s), 1263(s), 891(s), 858(m), 804(m), 790(m), 501(m). Elemental *Anal.* Calc. for $C_{24}H_{34}N_4O_7U$: C, 39.56; H, 4.70; N, 7.69. Found: C, 38.55; H, 4.30; N, 7.69%. Single crystal X-ray analysis was made for one of these crystals (Fig. 3).

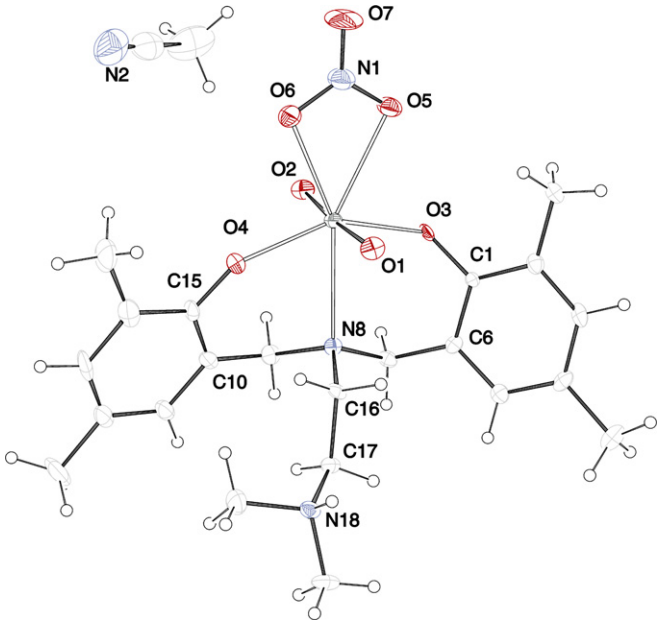


Fig. 3. Molecular structure of $[UO_2(HL1)(NO_3)] \cdot CH_3CN$ (**1**). Thermal ellipsoids have been drawn at the 30% probability level.

2.4. $[UO_2(HL1)_2]$ (2)

Complex **2** was prepared by dissolving 0.053 g (0.15 mmol) of H_2L1, 21.0 μl (0.15 mmol) of triethylamine and 0.038 g (0.075 mmol) of $UO_2(NO_3)_2 \cdot 6H_2O$ in 10 ml of CH_3CN. The resulting red solution was kept at room temperature for three days and in a freezer for one week, leading to the formation of orange crystals. The crystals were filtered off, washed twice with 10 ml of diethyl ether and dried. Yield 0.062 g (84%). The crystals are soluble in DMSO, $CHCl_3$ and slightly soluble in acetone. ^{1}H NMR (DMSO-d_6, 500 MHz; about 33% of complex is dissociated): 6.99, 6.94 (s, 4H, aryl, Co), 6.80, 6.72 (s, 2H, aryl, Un), 4.38 (m, 4H, N–CH_2-aryl, Co), 3.54 (s, 2H, N–CH_2-aryl, Un), 3.28 (m, 2H, N–CH_2CH_2–N, Un), 2.95, 2.48 (m, 4H, N–CH_2CH_2–N, Co), 2.60, 2.31 (s, 12H, aryl-CH_3, Co), 2.15, 2.14 (s, 6H, aryl-CH_3, Un), 2.07 (s, 3H, N–(CH_3)$_2$, Un), 1.81 (s, 6H, N–(CH_3)$_2$, Co). ^{13}C NMR (DMSO-d_6, 126 MHz): 164.7–122.2 (aryl), 59.7 (N–CH_2–*C*(aryl)), 55.3, 54.5, 50.8, 48.9, 47.0 (N–*C*H_2-aryl, N–(*C*H_2)$_2$–N), 45.4, 44.6 (N–(*C*H_3)$_2$), 20.0, 17.0, 16.0 (aryl-*C*H_3). IR (KBr, ν/cm^{-1}): 3435(w), 2906(m), 1610(w), 1472(s), 1310(m), 1270(s), 858(s), 811(s), 768(m), 497(m). Elemental *Anal.* Calc. for $C_{44}H_{62}N_4O_6U$: C, 53.87; H, 6.37; N, 5.71. Found: C, 54.05; H, 6.40; N, 5.91%. Single crystal X-ray analysis was made for one of these crystals (Fig. 4).

2.5. $[UO_2(HL2)(NO_3)] \cdot 2CH_3CN$ (3)

Complex **3** was prepared by dissolving 0.079 g (0.15 mmol) of H_2L2 and 0.038 g (0.075 mmol) of $UO_2(NO_3)_2 \cdot 6H_2O$ in 10 ml of CH_3CN which contained 4 Å molecular sieves to remove water. The resulting dark red solution was kept in a freezer for three weeks leading to the formation of red crystals. The crystals were filtered off and washed with 5 ml of cold diethylether. Yield 0.027 g (38%). The crystals are soluble in DMSO and acetone. ^{1}H NMR (DMSO-d_6, 500 MHz; about 33% of complex is dissociated): δ 7.35, 7.23 (d, 4H, aryl, Co), 7.10, 6.95 (d, 2H, aryl, Un), 4.92, 3.98 (m, 4H, N–CH_2-aryl, Co), 3.58 (s, 2H, N–CH_2-aryl, Un), 3.02, 2.76 (m, 4H, N–CH_2CH_2–N, Co), 2.62, 2.52 (m, 2H, N–CH_2CH_2–N, Un), 2.25 (s, 3H, N–(CH_3)$_2$, Un), 2.07 (s, H_3CCN), 1.92 (s, 6H, N–(CH_3)$_2$, Co), 1.67, 1.31 (s, 36H, aryl-*t*-butyl, Co), 1.33, 1.23 (s, 18H, aryl-*t*-butyl, Un). ^{13}C NMR (DMSO-d_6, 126 MHz): δ 165.4–122.2 (aryl), 61.3, 55.4, 54.6, 51.5, 48.4 (N–*C*H_2-aryl, N–(*C*H_2)$_2$–N), 44.1, 43.8 (N–(*C*H_3)$_2$), 34.7, 34.5, 33.7, 33.4 (aryl-*C*(CH$_3$)$_3$), 32.0, 31.4, 30.4, 29.4 (aryl-C(*C*H$_3$)$_3$)). IR (KBr, ν/cm^{-1}):

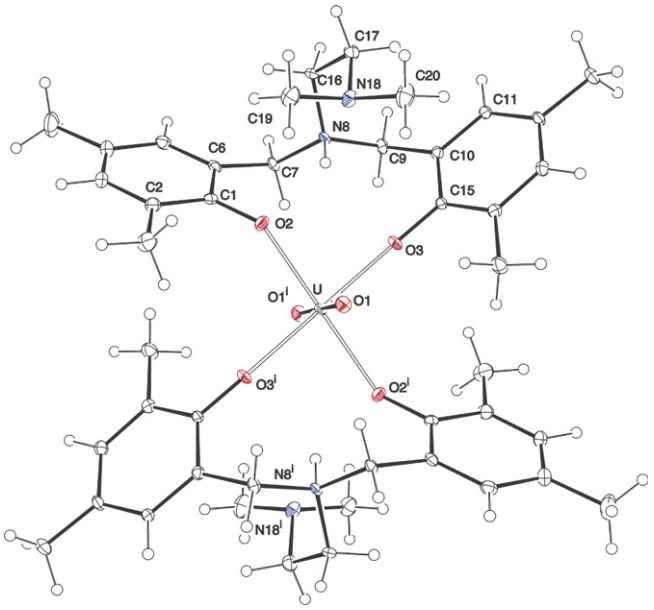


Fig. 4. Molecular structure of $[UO_2(HL1)_2]$ (**2**). Thermal ellipsoids have been drawn at the 30% probability level. Symmetry operation $i = -x, -y, -z$.

3587(m), 3500(m), 2949(s), 1603(m), 1472(s), 1382(s), 1306(s), 1274(s), 880(s), 851(m), 837(m), 797(s), 739(m), 529(m). Elemental *Anal.* Calc. for $C_{38}H_{61}N_5O_7U$: C, 48.66; H, 6.56; N, 7.47. Found: C, 48.01; H, 6.15; N, 6.99%. Single crystal X-ray analysis was made for one of these crystals (Fig. 5).

2.6. $[UO_2(HL3)_2] \cdot 2CH_3CN$ (*4*)

Complex **4** was prepared by dissolving 0.034 g (0.09 mmol) of H_2L3, 0.009 g (12.6 μl, 0.09 mmol) of triethylamine and 0.023 g (0.045 mmol) of $UO_2(NO_3)_2 \cdot 6H_2O$ in 10 ml of CH_3CN. The resulting red solution was kept in a freezer for three weeks leading to the formation of orange crystals. The crystals were filtered off and dried. Yield 0.023 g (46%). The crystals are soluble in DMSO, $CHCl_3$ and acetone. ^{1}H NMR (DMSO-d_6, 250 MHz; about 50% of complex is dissociated): 10.02 (s, 2H, aryl-O*H*, Un), 8.63 (m, 2H, pyridyl, Co (1H) and Un (1H)), 7.85 (m, 1H, pyridyl, Un), 7.56 (m, 1H, pyridyl, Co), 7.36 (m, 2H, pyridyl, Un), 7.26 (m, 1H, pyridyl, Co), 6.62 (m, 1H, pyridyl, Co), 6.95, 6.63 (s, 4H, aryl, Co), 6.80, 6.76 (s, 4H, aryl, Un), 4.52 (s, 4H, N–CH_2-aryl, Co), 4.33 (s, 2H, N–CH_2-pyridyl, Co), 3.80 (s, 2H, N–CH_2-pyridyl, Un), 3.66 (s, 4H, N–CH_2-aryl, Un), 2.62, 2.22 (s, 12H, aryl-CH_3, Co), 2.15, 2.08 (s, 12H, aryl-CH_3, Un), 2.07 (s, 6H, H_3CCN). ^{13}C NMR (DMSO-d_6, 63 MHz): δ 164.7– 121.5 (aryl, pyridyl), 59.3, 56.6, 55.3, 55.0 (N–*C*H_2-aryl, N–*C*H_2-pyridyl), 20.0, 17.1, 16.0 (aryl-*C*H_3). IR (KBr, ν/cm^{-1}): 3442(w), 2913(m), 1606(w), 1584(m), 1574(w), 1472(s), 1303(s), 1256(s), 862(s), 804(s), 743(m), 493(s). Elemental *Anal.* Calc. for $C_{52}H_{60}N_6O_6U$: C, 56.62; H, 5.48; N, 7.62. Found: C, 56.24; H, 5.21; N, 7.75%. Single crystal X-ray analysis was made for one of these crystals (Fig. 6).

2.7. X-ray crystallography

Crystals suitable for single crystal X-ray measurements were obtained directly from the reaction vessels. The crystal data for compounds **1**–**4** are summarized in Table 1 along with other experimental details. The crystallographic data were collected at 173 K on an Enraf Nonius Kappa CCD area-detector diffractometer using graphite monochromatized Mo Kα radiation ($\lambda = 0.71073$ Å). Data collection was performed using φ and ω scans and the data were processed using DENZO-SMN v0.93.0 [21]. SADABS [22a] absorption correction was applied for compounds **1**–**3** and SHELXA [22b] absorption correction for compound **4**. The structures were solved by direct methods using the

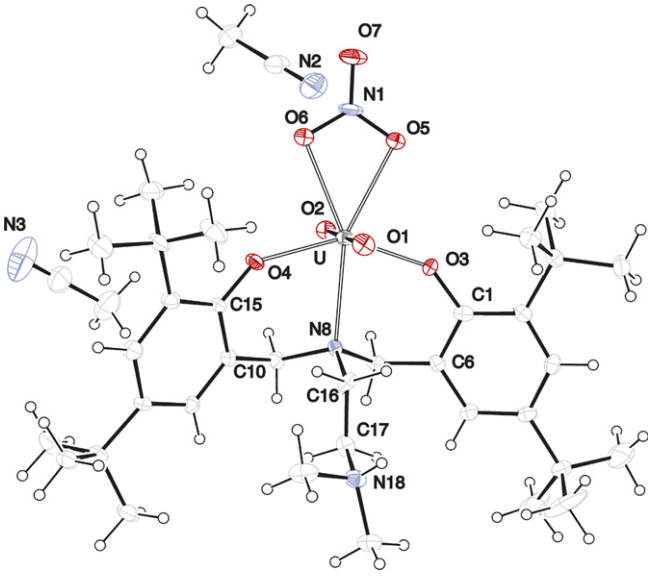


Fig. 5. Molecular structure of $[UO_2(HL2)(NO_3)] \cdot 2CH_3CN$ (**3**). Thermal ellipsoids have been drawn at the 30% probability level.

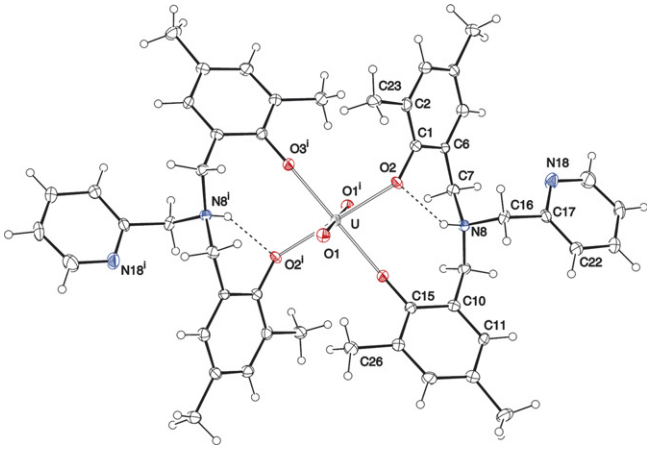


Fig. 6. Molecular structure of $[UO_2(HL3)_2] \cdot 2CH_3CN$ (**4**). Thermal ellipsoids have been drawn at the 30% probability level. Acetonitrile molecules are not shown. Symmetry operation $i = -x, -y, -z$.

Table 1
Summary of the crystallographic data for compounds **1**–**4** at 173(2) K

	1	**2**	**3**	**4**
Formula	$C_{24}H_{34}N_4O_7U$	$C_{44}H_{62}N_4O_6U$	$C_{38}H_{61}N_5O_7U$	$C_{52}H_{60}N_6O_6U$
M_r	728.58	981.01	937.95	1103.09
Crystal system	monoclinic	triclinic	monoclinic	triclinic
Space group (no.)	$P21/n$ (14)	$P\bar{1}(2)$	$P21/n$ (14)	$P\bar{1}(2)$
a (Å)	11.1926(3)	8.7429(3)	10.8839(5)	8.3987(3)
b (Å)	11.1027(5)	10.9914(3)	12.8823(4)	12.2755(4)
c (Å)	23.1515(10)	11.4877(5)	31.2601(14)	12.9163(4)
α (°)	90.0	102.602(2)	90.0	106.846(2)
β (°)	98.820(2)	91.642(2)	96.192(2)	94.387(2)
γ (°)	90.0	99.001(2)	90.0	110.086(2)
V (Å^3)	2842.97(19)	1061.81(7)	4357.4(3)	1173.81(7)
Z	4	1	4	1
D_{calc} (g cm^{-3})	1.702	1.534	1.430	1.560
μ(Mo Kα) (cm^{-1})	57.55	38.72	37.73	35.14
Observed reflections	5236	4630	6116	5658
R_{int}	0.0946	0.0371	0.0453	0.0866
Parameters	335	259	480	304
R_1^a	0.0822(0.0409)[b]	0.0300(0.0295)	0.0643(0.0430)	0.0620(0.0545)
wR_2^c	0.0812(0.0698)	0.0565(0.0562)	0.0962(0.0909)	0.1083(0.1031)
Peak, hole (e Å^{-3})	1.271, −1.518	0.625, −0.892	1.608, −1.907	1.487, −1.624

[a] $R_1 = \sum||F_o| - |F_c||/\sum|F_o|$.
[b] Values in parentheses for reflections with $I > 2.0\sigma(I)$.
[c] $wR_2 = \{\sum[w(F_o^2 - F_c^2)^2]/\sum[w(F_o^2)^2]\}^{1/2}$ and $w = 1/[\sigma^2(F_o^2) + (aP)^2 + bP)]$, where $P = (2F_c^2 + F_o^2)/3$.

SIR-97 program [23a] and full-matrix least-squares refinements on F^2 were performed using the SHELXL-97 program [23b]. Figures were drawn with ORTEP-3 for Windows [24]. For all compounds the heavy atoms were refined anisotropically. The CH hydrogen atoms were included at fixed distances using fixed displacement parameters from their host atoms while other H atoms were refined using fixed displacement parameters (1.2 times that of the host atom).

2.8. Uranyl extraction

Two-phase uranyl ion extraction studies from water to dichloromethane were performed at room temperature (21–22 °C) to determine the extraction ability of the ligands and the influence of several factors on the extraction process. The study consisted of three different tests:

1. The extraction ability for the uranyl ion of the ligands H_2L1–H_2L4 without stirring the extraction system (pH around 3).
2. The selectivity of the ligand toward several metal ions in an extraction process from water at pH 1.8 to dichloromethane. The ligands were H_2L1, H_3L5, $H_2L6 \cdot HCl$ and $H_3L7 \cdot HCl$ whereas the metal ions were $UO_2(aq)^{2+}$, $Fe(aq)^{3+}$, $Co(aq)^{2+}$, $Ni(aq)^{2+}$, $Cu(aq)^{2+}$ and $Zn(aq)^{2+}$.
3. This experiment was done as experiment 2, but now the metal ions were in an acetate buffer solution (225 mmol/L) at pH 4.2.

In the first experiment with the ligands H_2L1–H_2L4 the experimental setup was the following: into a test tube were placed 3 ml of CH_2Cl_2 with the ligand (0.210 mmol) and on top of this CH_2Cl_2 layer was placed 2 ml of a water solution of uranyl nitrate hexahydrate (0.0525 mmol) leading to a U:ligand ratio of 1:4. The samples for ICP ($V = 50$ μl, diluted to a 10 ml of H_2O) were taken from the water layer within a 120-h period of time. The samples were analyzed with ICP-OES at 385.958 nm using a Perkin–Elmer Optima 4300DV instrument in every experiment.

In the second experiment with the ligands H_2L1, H_3L5, $H_2L6 \cdot HCl$ and $H_3L7 \cdot HCl$ the experimental setup was as follows: into a test tube was placed 3 ml of CH_2Cl_2 with the ligand (0.320 mmol) and Et_3N (0.320 mmol, to neutralize HCl in $H_2L6 \cdot HCl$ and $H_3L7 \cdot HCl$) and on the top of this layer was placed 3 ml of water solution containing uranyl nitrate (0.078 mmol), iron(III) nitrate (0.078 mmol), copper(II) nitrate (0.078 mmol), nickel(II) nitrate (0.078 mmol), zinc(II) nitrate (0.078 mmol) and cobalt(II) nitrate (0.078 mmol) leading to a $UO_2(aq)^{2+}$:$Fe(aq)^{3+}$:$Co(aq)^{2+}$:$Ni(aq)^{2+}$:$Cu(aq)^{2+}$:$Zn(aq)^{2+}$:ligand ratio of 1:1:1:1:1:1:4 (the total ratio of the metal ions to the ligand being 6:4). One test tube containing no ligand and no base was also prepared. The solutions were stirred with a magnetic stirrer (900–1100 rpm) throughout the experiment. Before the samples were taken, the stirring was interrupted and the solutions were allowed to settle for 5 min. The samples for ICP (V = 50 μl, diluted to 10 ml) were taken from the water layer during a 44-h period of time.

The third experiment was done similarly to the second one with the exception that the pH of the water solution was adjusted to 4.2 with an acetate buffer.

3. Results and discussion

3.1. Complexation studies

In the reactions of the uranyl ion with the diaminobis(phenolato) ligands, two types of complexes are formed, i.e. $[UO_2(HLn)(NO_3)]$ ($n = 1, 2$) and $[UO_2(HLn)_2]$ ($n = 1,3$). For example, if the reaction between uranyl nitrate and H_2L1 is performed in a 1:2 metal to ligand ratio without any additional base and using acetonitrile as the solvent, a complex with the formula $[UO_2(HL1)(NO_3)]\cdot CH_3CN$ (**1**) can be isolated. When the reaction was carried out under similar conditions in the presence of a base (1:1 ratio of ligand to triethylamine), the reaction produced a complex with the formula $[UO_2(HL1)_2]$ (**2**). Apparently, in a higher stoichiometry, i.e. when the metal to ligand ratio in the reaction mixture is 1:2, one ligand molecule acts as a proton acceptor causing the formation of a 1:1 complex. The presence of an extra base (triethylamine) favours the formation of the 1:2 complexes. Both of the phenolic OH-groups are deprotonated during the complexation process, and principally either of the two nitrogen donors of the coordinated ligand could accept the proton to form a zwitter ion HLn^-. The site of the protonation defines the coordination mode of the ligand – the protonation of the bridging amino group makes the aminobis(phenol) coordinate as a bidentate $[O,O]$ donor, whereas the protonation of the side-arm nitrogen allows tridentate $[O,N,O]$ coordination. Certainly, in **1**, the proton is located on the side-arm amino group, whereas in **2** it is on the bridging nitrogen (see the structural part of the work). So, we can sum up that the ligand H_2L1 formed both 1:1 and 1:2 (metal–ligand ratio) complexes with the uranyl ion, while the ligand H_2L2 formed only a 1:1 complex (**3**) and the ligand H_2L3 formed solely a 1:2 complex (**4**) with the uranyl ion. The ligand H_2L2 did not form the 1:2 complex, apparently due to the steric reasons. Ligand H_2L4 formed a red solution with the uranyl ion, but no crystalline compound was formed under the applied conditions.

The slight discrepancy in the elemental analyses of compounds **1** and **3** originate from the fact that the crystals of **1** and **3** contain weakly bonded acetonitrile molecules, some of which are loosened during the sample preparation. On the other hand, if acetonitrile is removed in vacuum prior to analyses, the resulting solids can absorb atmospheric moisture. In both cases, the elemental analyses give slightly lower analytical results than the calculated ones.

3.2. NMR studies of the complexes in the solution

Complexes **1**–**4** were dissolved in deuterated DMSO and complex **2** also in deuterated chloroform and their behaviour in these solutions was studied by ^1H NMR. In DMSO the complexes **1**–**4** evoke two sets of peaks: one set for a coordinated ligand and the other set for an uncoordinated ligand. Dissociation of the uncoordinated ligand from the uranyl complex is possibly due to the protonation of the phenoxide moiety by possible proton sources, e.g. traces of water or the protonated side-arm aminogroup of the ligand. The degree of dissociation varies, e.g. for **2**, about 33% of the dissolved complex has been dissociated, whereas complex **4** seems to be predominantly in the dissociated form (the ratio of the coordinated ligand to the uncoordinated ligand being approximately 1:1).

The NMR for complex **2** in $CDCl_3$ revealed that compound **2** hydrolyses due to atmospheric moisture and traces of water in the solvent. This leads to the decomposition of the complex according to the following scheme (1–2):

$$[UO_2(HL1)_2](CDCl_3)_n + xH_2O \rightarrow [UO_2(HL1)(H_2O)_x]^+ + HL1^- + nCDCl_3 \quad (1)$$

$$[UO_2(HL1)(H_2O)_x]^+ + HL1^- \rightarrow [UO_2(HL1)(OH)(H_2O)_{x-1}] + H_2L1 \quad (2)$$

These reactions were followed with two different ^1H NMR samples: one sample was exposed to atmospheric moisture, while another sample was sealed under ambient conditions, so that the system contained only a small amount of water that was absorbed during the preparation of the sample. As a result, it was found that in the "open" tube the decomposition of the complex carried on until the experiment was interrupted after 216 h. In the sealed tube reaction the decomposition ended after about 72 h as all water molecules in the system were consumed in hydrolysis. After a follow-up of 144 h, the sealed sample tube was opened and exposed to air for 10 min. From the NMR spectra it could be clearly noticed that the solution immediately absorbed water from air and the complex decomposition started again, continuing until all the complex was decomposed. After 216 h the solution contained only the free ligand, whereas all the uranium was in the precipitate, which has the possible composition $[UO_2(HL1)(OH)(aq)]$. On the whole, the studied complexes seem to be remarkably less stable towards hydrolysis than their congeners without a basic side-arm donor.

3.3. Structural studies of the uranyl complexes

With the ligand H_2L1 used in the study, two types of complexes are formed, namely 1:1 complexes $[UO_2(HL1)(NO_3)]$ (Fig. 3) and 1:2 complexes $[UO_2(HL1)_2]$ (Fig. 4). Ligand H_2L2 formed only a $[UO_2(HL2)(NO_3)]$ complex (Fig. 5) and ligand H_2L3 formed a $[UO_2(HL3)_2]$ complex (Fig. 6) in the solid state. Crystals of the studied complexes were obtained from the reaction mixtures. Selected bond parameters for **1** and **3** are presented in Table 2 and for **2** and **4** in Table 3.

In complexes **1** and **3** the nitrate anion is coordinated in the bidentate mode and the ligand HL^- in a tridentate manner to the uranyl(VI) ion. This evokes a pentagonal bipyramidal geometry around the metal centre. These kinds of neutral mononitrate complexes of uranyl are very

Table 2
Selected bond lengths (Å) and angles (°) for **1** and **3**

	1	3
Bond lengths (Å)		
U–O1	1.766(5)	1.788(5)
U–O2	1.796(5)	1.789(5)
U–O3	2.258(4)	2.202(5)
U–O4	2.165(5)	2.195(5)
U–O5	2.551(5)	2.546(5)
U–O6	2.518(4)	2.526(6)
U–N8	2.662(5)	2.614(7)
N1–O5	1.262(8)	1.278(9)
N1–O6	1.270(8)	1.270(9)
N1–O7	1.196(7)	1.215(8)
C1–O3	1.371(7)	1.347(9)
C15–O4	1.328(8)	1.322(9)
Bond angles (°)		
O1–U–O2	174.8(2)	179.4(3)
O3–U–O4	146.13(15)	146.79(19)
O3–U–N8	76.07(16)	74.61(19)
O4–U–N8	71.18(16)	72.45(19)
O5–U–O6	50.21(16)	50.41(18)
O5–N1–O6	116.3(5)	115.9(8)
O5–N1–O7	122.1(7)	122.3(8)
O6–N1–O7	121.6(7)	121.7(8)
C1–O3–U	121.7(4)	142.9(5)
C15–O4–U	148.3(4)	146.4(5)
τ_1 vs. τ_2[a]	57.41(18)	52.89(23)

[a] Dihedral angle between the planes of the phenyl rings: C1, . . ., C6 and C10, . . ., C15.

Table 3
Selected bond lengths (Å) and angles (°) for **2** and **4**

	2	4
Bond lengths (Å)		
U–O1	1.794(2)	1.803(4)
U–O2	2.260(2)	2.296(3)
U–O3	2.251(2)	2.240(4)
C1–O2	1.343(4)	1.351(6)
C15–O3	1.332(4)	1.336(6)
Bond angles (°)		
O1–U–O2	90.37(9)	89.53(15)
O1–U–O3	90.06(9)	89.97(16)
O2–U–O3	84.52(8)	83.04(13)
O2–U–O3[a]	95.48(8)	96.96(13)
C1–O2–U	140.60(18)	131.6(3)
C15–O3–U	163.08(19)	159.6(4)
τ_1 vs. τ_2[b]	42.16(7)	48.06(16)

[a] Generated by inversion.
[b] Dihedral angle between the planes of the phenyl rings: C1, . . ., C6 and C10, . . ., C15.

rare. For example, $[UO_2(L)_x(NO_3)_2]$ complexes (L = neutral ligand with one to three donor atoms and x depending on the number of donor atoms in L) are quite common.[1] Only one example having the stoichiometry $[UO_2(L)(NO_3)]$ (L = monoanionic ligand) is reported [17], while four examples with a stoichiometry of $[UO_2(L)(L')(NO_3)]$ (L = a monoanionic ligand and L′ = a neutral ligand) are described [25]. However, all these five uranyl complexes are dinuclear ones, although one nitrate ion is coordinated to the uranyl ion in a η^2-fashion. The uranyl coordination in complexes **1** and **3** resembles that in the anionic uranyl complex with the bis[2-(2-hydroxyphenoxy)ethoxy]ethane dianion [26].

The ligand HL^- bonds to the uranyl ion in compounds **1** and **3** as a tridentate dianion via two phenoxo oxygens and the benzylic amine nitrogen, while the labile proton is located on the side-arm nitrogen N18. The η^2-coordinated nitrate oxygen atoms are at a distance of 2.518(4) and 2.551(5) Å from the U(VI) ion in **1** and at a distance of 2.526(6) and 2.546(5) Å in **3**. In the compound presented in Ref. [26] both η^2-coordinated nitrate oxygen atoms are at a distance of 2.521(7) Å from the uranyl ion. The U–N8 distances are also quite long, 2.662(5) Å for **1** and 2.614(7) Å for **3**. This causes the U–O(phenoxo) bonds in the $[UO_2(HLn)(NO_3)]$ complexes to be shorter than in the $[UO_2(HLn)_2]$ complexes. For example, the average of the alkoxo bonds in **1** and **3** is 2.205 Å and in **2** and **4** it is 2.262 Å. These bond distances are in agreement with the relevant bond lengths of the uranyl ion with alkoxide and phenoxide ligands [27].

The O=U=O groups are not exactly linear as the O=U=O angles are 174.8(2)° in **1** and 179.4(3)° in **3**. Non-linear O=U=O bonds are found generally in uranyl complexes with five non-symmetrically bonding equatorial ligands, two of them being nitrate oxygen atoms [17,25,26]. The presence of nitrate is not essential as the phenomenon is found in other uranyl complexes with oxygen donors [28]. The reason for the bending of the O=U=O bonds is presumably due to uneven π donation from the ligands to the UO_2^{2+} moiety, which results from the asymmetrical location of the donor atoms around the uranium caused by the pentacoordination [29].

It is interesting to note that the coordination sphere around the uranyl ion is less distorted in **3**, where the ligand has more bulky substituents than the ligand in **1**. In both structures, the packing of molecules is supported by intermolecular H-bonds (Table 4) and acetonitrile molecules, which fill the empty holes in both structures.

The $[UO_2(HLn)_2]$ type of complexes (**2** and **4**) show similar centrosymmetric structures as the earlier reported related complexes with aminoalcoholbis(phenolate) and aminoalkylbis(phenolate) ligands [17–19]. In the *xy*-plane (the linear O=U=O group is along the *z* axis) there are four phenoxo oxygens bonded to the uranyl ion. This results that the labile proton could be attached principally to two different nitrogen atoms (N8 and N18). In both ligands, the nitrogen N8 is protonated, which leads to the bidentate coordination mode of the ligand. The hydrogens at N8 form weak intramolecular H-bonds with O2 and O3 (Table 4).

[1] A search in the Cambridge Structure database (version 5.28, November 2006) gives about 120 entries with the $UO_2(NO_3)_2$ fragment.

Table 4
Hydrogen bond parameters (Å, °)

Compound	D–H···A	*d*(D–H)	*d*(H···A)	*d*(D···A)	∠(D–H···A)
1	N18–H18···O3[a]	0.79(7)	1.94(7)	2.713(7)	166(7)
2	N8–H8···O2	0.95(3)	2.12(3)	2.867(3)	135(3)
	N8–H8···O3	0.95(3)	2.32(3)	2.940(3)	123(3)
3	N18–H18···N2	0.78(10)	2.03(10)	2.813(12)	176(11)
4	N8–H8···O2	0.78(7)	2.06(7)	2.734(6)	144(7)
	N8–H8···O3	0.78(7)	2.46(7)	2.973(6)	125(6)

[a] Atom generated by symmetry transformation: $-x+1/2$, $y-1/2$, $-z+3/2$.

In Table 5 selected torsion angles in the coordinated ligands are presented. Clearly compounds **1** and **3** have similar torsion angles as do compounds **2** and **4**. The largest difference between **1** and **2** is in the torsion angle C16–N8–C9–C10, which has the values 43.0(7)° and 85.0(3)° for **1** and **2**, respectively. The intramolecular O···O distances in the aminobis(phenolato) ligands of **1** and **2** are 3.3033(3) and 4.214(7) Å, respectively. These changes in the torsion angles and intramolecular distances in the ligands in different uranyl complexes indicate the flexibility of these bisphenolate ligands in the complexation processes.

3.4. Uranyl ion extraction studies

The results of uranyl ion extraction studies with ligands H_2L1–H_2L4 (experiment 1) at room temperature are shown in Fig. 7. The ratio of the ligand to the uranyl ion was 4:1. The extraction was done without stirring at the pH of the 0.026 M uranyl nitrate in unbuffered water solution (pH around 3). The extraction curves show that the extraction abilities of these ligands under the applied conditions were not very good. Only about 28% of the uranyl ions are transferred into the dichloromethane phase, whereas in our previous studies with long chain aminoalcohol ligands they transferred more than 90% of the uranyl ions into the dichloromethane phase under similar conditions [18]. There are two possible reasons for the low extraction ability of the H_2L1–H_2L4 ligands. First, the ligands H_2L1–H_2L4 have very good solubility in dichloromethane and low solubility in water, so the low concentration of the ligand in the water phase leads to the slow extraction rate. Second, the low stability of the neutral $[UO_2(HLn)_2]$ complexes in moist CH_2Cl_2, as shown by the ^1H NMR studies, causes a quick transfer of the uranyl ions back to the water phase. Also, the presence of several uranyl(VI) ion complexes with water and nitrate in the water phase can affect the complexation kinetics and thus the extraction speed of the uranyl ion, as shown by Bühl et al. [30]. A reason for the deviation in the extraction curve of H_2L2 is that this di-*tert*-butyl substituted ligand formed a jelly-like gel in the water phase at the beginning of the extractions process which hindered the sample taking, leading to dilute samples.

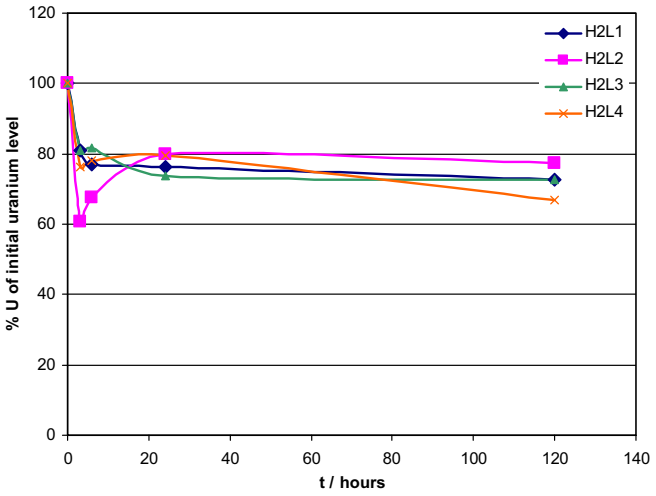


Fig. 7. Decrease of the uranyl ion concentration (%) in the water layer as a function of time during the extraction process with ligands H_2L1–H_2L4 (experiment 1).

In order to find out the selectivity of the several different aminobis(phenol) ligands, studied in this as well as in our earlier works, towards several metal ions, two tests were performed. The selectivity tests were performed with the metal ions in a water solution at two different pH values (1.8 and 4.2) using one ligand at a time as an extractor. During the extraction process the system was stirred in order to speed up the process. The first selectivity tests were done at pH 1.8, the value which was achieved after all the metal ions had been dissolved. The concentration of each metal ion ($UO_2(aq)^{2+}$, $Fe(aq)^{3+}$, $Co(aq)^{2+}$, $Ni(aq)^{2+}$, $Cu(aq)^{2+}$ and $Zn(aq)^{2+}$) in the water layer was 0.026 mol/l whereas the ligand concentration was 0.101 mol/l. Cations Co^{2+}, Ni^{2+} and Zn^{2+} were not extracted at all by any of the ligands H_2L1, H_3L5, $H_2L6 \cdot HCl$ and $H_3L7 \cdot HCl$ during the 44 h of extraction at pH 1.8.

Table 5
Selected torsion angles (°) for **1**–**4**

	1	**2**	**3**	**4**
C5–C6–C7–N8	111.1 (7)	127.7 (3)	120.6 (7)	135.2 (5)
C1–C6–C7–N8	−68.6 (8)	−57.4 (4)	−60.4 (9)	−48.6 (7)
N8–C9–C10–C11	−129.8 (7)	−119.3 (3)	−123.9 (8)	−117.6 (6)
N8–C9–C10–C15	53.0 (8)	62.7 (4)	59.3 (10)	67.7 (6)
C16–N8–C7–C6	−62.6 (7)	−61.0 (3)	−48.8 (8)	−60.4 (6)
C9–N8–C7–C6	173.5 (5)	171.6 (3)	−169.8 (6)	169.3 (4)
C16–N8–C9–C10	43.0 (7)	85.0 (3)	48.7 (8)	75.9 (6)
C7–N8–C9–C10	166.0 (5)	−149.4 (3)	169.8 (6)	−152.6 (5)

Ligands H_3L5 (extracted 38% of uranyl ions), $H_2L6 \cdot HCl$ (extracted 47% of uranyl ions) and $H_3L7 \cdot HCl$ (extracted 41% of uranyl ions) extracted quite selectively uranyl ions; only small amounts of iron(III) ions were also co-extracted and no copper(II) ions at all. Ligand H_2L1 instead preferred copper and iron over the uranyl ion. The concentrations of the metal salts in the control experiment were constant during the extraction follow-up.

In the third set of experiments, the extractions were done whilst stirring the solutions at pH 4.2 using an acetate buffer in a water phase. Again Co^{2+}, Ni^{2+} and Zn^{2+} ions were not extracted practically at all by any of the ligands H_2L1, H_3L5, $H_2L6 \cdot HCl$ and $H_3L7 \cdot HCl$ (only H_2L1 extracted 10% of Ni-ions). The uranyl ion was extracted quite well by ligands $H_2L6 \cdot HCl$ and $H_3L7 \cdot HCl$ (65%) with moderate amounts of Fe^{3+} ions (44% and 30%, respectively). H_2L1 extracted Fe^{3+} and Cu^{2+} ions practically quantitatively. H_3L5 extracted Fe^{3+} ions also quantitatively (97%) with 50% of uranyl ions. These results can be seen in Figs. 8–11. The concentrations of the metal ions in the water layer of the control sample were constant during the follow-up.

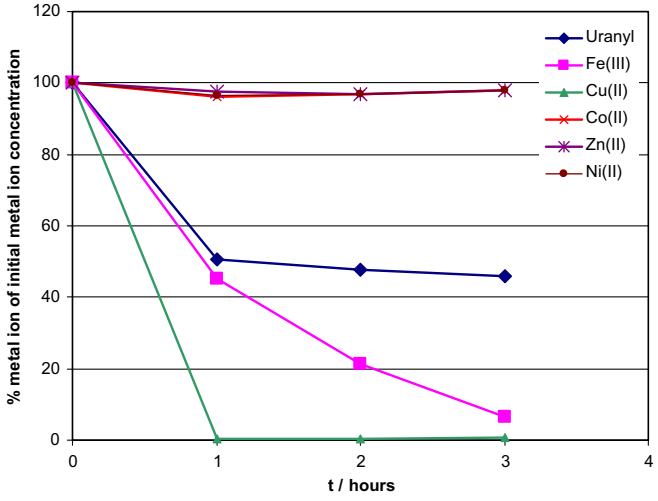


Fig. 8. Decrease of the metal ion concentrations (%) in the water layer as a function of time during the extraction process with H_2L1 at pH 4.2.

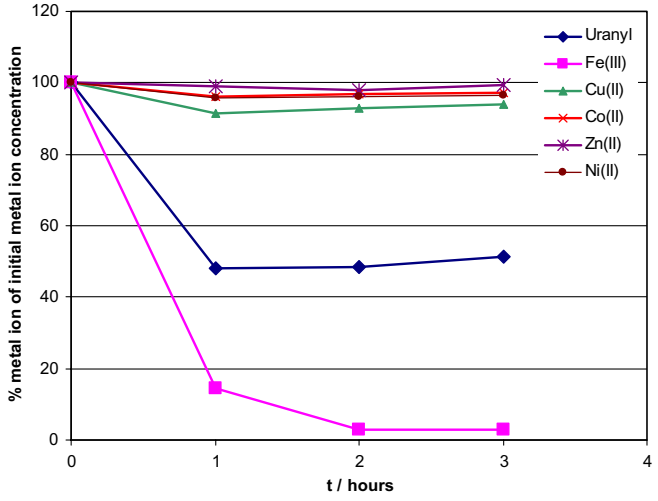


Fig. 9. Decrease of the metal ion concentrations (%) in the water layer as a function of time during the extraction process with H_3L5 at pH 4.2.

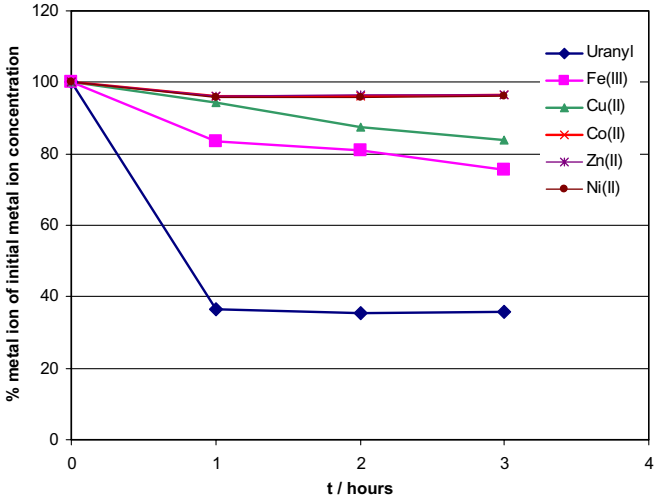


Fig. 10. Decrease of the metal ion concentrations (%) in the water layer as a function of time during the extraction process with $H_2L6 \cdot HCl$ at pH 4.2.

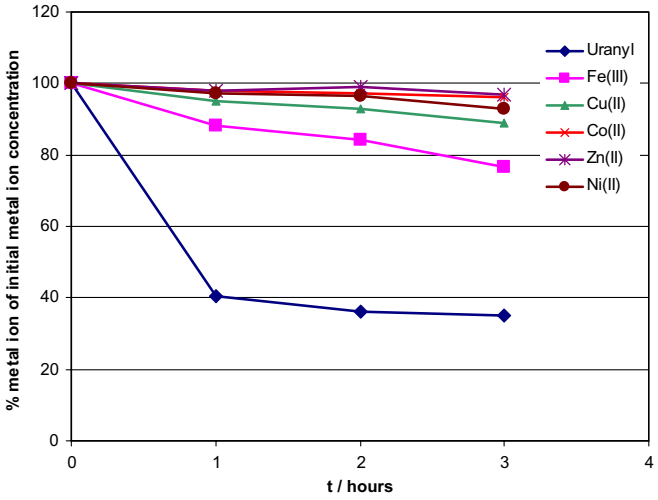


Fig. 11. Decrease of the metal ion concentrations (%) in the water layer as a function of time during the extraction process with $H_3L7 \cdot HCl$ at pH 4.2.

4. Conclusions

The diaminobisphenolates reported here can form two types of complexes with the uranyl ion: $[UO_2(HLn)(NO_3)] \cdot CH_3CN$ and $[UO_2(HLn)_2]$. Earlier studied amino-alcohol- and aminoalkylbis(phenolate)s are found to form only the latter type of complex. In these new $[UO_2(HLn)(NO_3)]$ complexes the organic ligand bonds tridentately and the nitrate ion bidentately to the uranyl ion. The possible reason for the formation of these new

uranyl complexes is the existence of two basic nitrogen atoms in the ligand, with which one can bond to the uranyl ion while the another acts as a proton acceptor.

The ^{1}H NMR studies show that the $[UO_2(HLn)_2]$ complexes reported are sensitive to water in organic solvents, as the complexes decompose slowly in chloroform. This can be one of the reasons why these diaminobis(phenol) ligands are weak uranyl ion extractors from water to dichloromethane, although the $[UO_2(HLn)_2]$ complexes are soluble in dichloromethane.

Even though the ligands H_2L1–H_2L4 did not show good uranyl ion extraction properties in the experiments made in this study, the ligand H_2L1 proved to be a good iron and copper extractor from water to dichloromethane. In the selectivity studies the ligands H_3L6 (*N*,*N*-bis(2-hydroxy-5-*tert*-butyl-3-methylbenzyl)-1-aminobutane · HCl) and H_3L7 · HCl (*N*,*N*-bis(2-hydroxy-5-*tert*-butyl-3-methylbenzyl)-6-amino-1-hexanol · HCl) showed good selectivity towards the uranyl ion in extraction experiments, thus possessing the potential ability to selectively extract uranyl under environmental and physiological conditions.

Acknowledgements

We are grateful to Prof. Matti Nurmia for correcting the language of this paper, to Dr. Ari Väisänen for performing the ICP measurements, to Elina Hautakangas for performing the elemental analysis and to Reijo Kauppinen for his assistance with NMR measurements.

Appendix A. Supplementary material

CCDC 652541, 652542, 652543 and 652544 contain the supplementary crystallographic data for **1**, **2**, **3** and **4**. These data can be obtained free of charge via http://www.ccdc.cam.ac.uk/conts/retrieving.html, or from the Cambridge Crystallographic Data Centre, 12 Union Road, Cambridge CB2 1EZ, UK; fax: (+44) 1223-336-033; or e-mail: deposit@ccdc.cam.ac.uk. Supplementary data associated with this article can be found, in the online version, at doi:10.1016/j.poly.2007.08.047.

References

[1] (a) D.H. Busch, Chem. Rev. 93 (1993) 847;
(b) R.D. Hancock, A.E. Martell, Chem. Rev. 89 (1989) 1875.
[2] L. Karmazin, M. Mazzanti, C. Gateau, C. Hill, J. Pécaut, Chem. Commun. (2002) 2892.
[3] (a) E.Y. Tshuva, S. Groysman, I. Goldberg, M. Kol, Z. Goldschmidt, Organometallics 21 (2002) 662;
(b) S. Groysman, S. Segal, M. Shamis, I. Goldberg, M. Kol, Z. Goldschmidt, E. Hayut-Salant, J. Chem. Soc., Dalton Trans. (2002) 3425.
[4] E.Y. Tshuva, I. Goldberg, M. Kol, Z. Goldschmidt, Organometallics 20 (2001) 3017.
[5] E.Y. Tshuva, I. Goldberg, M. Kol, J. Am. Chem. Soc. 122 (2000) 10706.
[6] (a) E.Y. Tshuva, I. Goldberg, M. Kol, Z. Goldschmidt, Inorg. Chem. 40 (2001) 4263;
(b) T. Andrea, E. Barnea, M. Botoshansky, M. Kapon, E. Genizi, Z. Goldschmidt, M.S. Eisen, J. Organomet. Chem. 692 (2007) 1074.
[7] T. Toupance, S.R. Dupperley, N.H. Rees, B.R. Tyrrell, P. Mountford, Organometallics 21 (2002) 1367.
[8] (a) A. Lehtonen, R. Sillanpää, Polyhedron 24 (2005) 257;
(b) A. Lehtonen, M. Wasberg, R. Sillanpää, Polyhedron 25 (2006) 767.
[9] F. Wolff, C. Lorber, R. Choukroun, B. Donnadieu, Inorg. Chem. 42 (2003) 7839.
[10] S. Groysman, I. Goldberg, M. Kol, Z. Goldschmidt, Organometallics 22 (2003) 3793.
[11] C. Lorber, F. Wolff, R. Choukroun, L. Vendier, Eur. J. Inorg. Chem. (2005) 2850.
[12] S. Gendler, S. Groysman, Z. Goldschmidt, M. Shuster, M. Kol, J. Polym. Sci. Part A: Polym. Chem. 44 (2006) 1136.
[13] A.J. Chmura, M.G. Davidson, M.D. Jones, M.D. Lunn, M.F. Mahon, J. Chem. Soc., Dalton Trans. (2006) 887.
[14] Y. Kim, J.G. Verkade, Organometallics 21 (2002) 2395.
[15] F.M. Kerton, A.C. Whitwood, C.E. Willans, J. Chem. Soc., Dalton Trans. (2004) 2237.
[16] M. Velusamy, M. Palaniandavar, R.S. Gopalan, G.U. Kulkarni, Inorg. Chem. 42 (2003) 8283.
[17] H. Sopo, J. Sviili, A. Valkonen, R. Sillanpää, Polyhedron 25 (2006) 1223.
[18] H. Sopo, A. Väisänen, R. Sillanpää, Polyhedron 26 (2007) 184.
[19] H. Sopo, K. Goljahanpoor, R. Sillanpää, Polyhedron 26 (2007) 3397.
[20] (a) M.J. Sarsfield, M. Helliwell, J. Raftery, Inorg. Chem. 43 (2004) 3170;
(b) K.A. Venkatesan, V. Sukumaran, M.P. Antony, P.R.V. Rao, J. Radioanal. Nucl. Chem. 260 (2004) 443;
(c) G. Schreckenbach, P.J. Hay, R.L. Martin, Inorg. Chem. 37 (1998) 4442;
(d) P.B. Duval, C.J. Burns, W.E. Buschmann, D.L. Clark, D.E. Morris, B.L. Scott, Inorg. Chem. 40 (2001) 5491;
(e) D.L. Clark, S.D. Conradson, R.J. Donahoe, D.W. Keogh, D.E. Morris, P.D. Palmer, R.D. Rogers, C.D. Tait, Inorg. Chem. 38 (1999) 1456;
(f) J.L. Sessler, D. Seidel, A.E. Vivian, V. Lynch, B.L. Scott, D.W. Keogh, Angew. Chem. Int. Ed. 40 (2001) 591.
[21] Z. Otwinowski, W. Minor, in: C.W. Carter, R.M. Sweet (Eds.), Methods in Enzymology: Part A, vol. 276, Academic Press, New York, 1997, pp. 307–326.
[22] (a) G.M. Sheldrick, SADABS, University of Göttingen, Germany, 2002.;
(b) G.M. Sheldrick, (anon) SHELX-97 (Release 97-2), A program for Crystal Structure Refinement, University of Göttingen, Germany, 1998.
[23] (a) A. Altomare, M. Cascarano, C. Giacovazzo, A. Guagliardi, M.C. Burla, G. Pilodori, M. Camalli, J. Appl. Crystallogr. 27 (1994) 435;
(b) G.M. Sheldrick, SHELXL-97, A Program for Crystal Structure Refinement, University of Göttingen, Germany, 1997.
[24] L.J. Farrugia, J. Appl. Crystallogr. 30 (1997) 565.
[25] (a) J.H. Burns, Inorg. Chem. 22 (1983) 1174;
(b) B. Kanellakopulos, E. Dornberger, R. Maier, B. Nuber, H.-G. Stammler, M. Ziegler, Z. Anorg. Allg. Chem. 619 (1993) 593;
(c) G.A. Doyle, D.M.L. Goodgame, A. Sinden, D.J. Williams, J. Chem. Soc., Chem. Commun. (1993) 1170;
(d) A.R. de Aquino, P.C. Isolani, J. Zukerman-Schpector, L.B. Zinner, C. Vicentini, J. Alloys Compd. 323 (2001) 18.
[26] P. Thuéry, M. Nierlich, B. Masci, Acta Cryst. C58 (2002) m84.
[27] (a) J. Harrowfield, Gazz. Chim. Ital. 127 (1997) 663;
(b) P. Thuéry, M. Nierlich, J. Harrowfield, J. Vicens (Eds.), Calixarenes 2001, Kluwer Academic Publishers, Dordrecht, 2001.
[28] (a) B. Masci, P. Thuéry, Acta Cryst. E61 (2005) m2278;
(b) P. Thuéry, H. Takemura, Acta Cryst. C59 (2003) m384.
[29] J.L. Sonnenberg, P.J. Hay, R.L. Martin, B.E. Bursten, Inorg. Chem. 44 (2005) 2255.
[30] M. Bühl, R. Diss, G. Wipff, Inorg. Chem. 46 (2007) 5196.

Available online at www.sciencedirect.com
ScienceDirect
Polyhedron 27 (2008) 105–112
POLYHEDRON
www.elsevier.com/locate/poly

A pyrazole-based orthogonal ferromagnetically coupled [2 × 2] homoleptic square Cu_4 grid: Magnetostructural correlations

Somnath Roy [a], Tarak Nath Mandal [a], Anil Kumar Barik [b], Samik Gupta [a], Ray J. Butcher [c], Mohamed Salah El Fallah [d,*], Javier Tercero [d], Susanta Kumar Kar [a,*]

[a] Department of Chemistry, University College of Science, 92, A.P.C. Road, Kolkata 700 009, India
[b] Department of Chemistry, St. Paul's C.M. College, 33/1, Raja Rammohan Roy Sarani, Kolkata 700 009, India
[c] Department of Chemistry, Howard University, 2400 Sixth Street, N.W., Washington, DC 200 59, USA
[d] Departament de Química Inorgànica, Facultat de Química, Universitat de Barcelona, Martí i Franquès 1-11, 08028 Barcelona, Spain

Received 4 July 2007; accepted 23 August 2007
Available online 23 October 2007

Abstract

The synthesis and structure of a pyrazole-based orthogonal ferromagnetically coupled tetracopper(II) 2 × 2 homoleptic grid complex $[Cu_4(PzOAPyz)_4(ClO_4)_2](ClO_4)_2 \cdot 6H_2O$ (**1**), formed by the reaction between the ditopic ligand PzOAPyz and $Cu(ClO_4)_2 \cdot 6H_2O$, are described. The ligand contains terminal pyrazole and pyrazine residues bound to a central flexible diazine subunit (N–N) as well as one potentially bridging alkoxo group. The two adjacent metal centers are linked by an alkoxo oxygen forming essentially a square $Cu_4(\mu\text{-}O_4)$ cluster. In the $Cu_4(\mu\text{-}O_4)$ core, out of the four copper centers, two copper centers are penta-coordinated and the remaining two are hexa-coordinated. In each case of hexa-coordination, the sixth position is occupied by one of the oxygen atoms of a coordinated perchlorate ion. Complex **1** has been characterized structurally and magnetically. Although the large Cu–O–Cu bridge angles (137–138°) and short Cu–Cu distances (3.964–3.970 Å) are suitable for the transmission of the expected antiferromagnetic coupling, the square-based $Cu_4(\mu\text{-}O_4)$ cluster exhibits an intramolecular ferromagnetic exchange ($J = 7.47\ cm^{-1}$) between the metal centers with an $S = 2$ magnetic ground state associated with the quasi orthogonal arrangement of the magnetic orbitals ($d_{x^2-y^2}$). The exchange pathway parameters have been evaluated from density functional calculations.
© 2007 Elsevier Ltd. All rights reserved.

Keywords: Tetranuclear copper 2 × 2 grid; Schiff base; X-ray structure; Magnetic property

1. Introduction

Self-assembly processes involving carefully designed multidentate ligands and metal ions with appropriate stereoelectronic preferences can lead to the efficient and specific formation of aesthetically looking sophisticated polynuclear grids [1,2]. Although at the beginning, many of these structures arose accidentally, recently worldwide systematic attempts are in line to determine the relationship between the number, type and spatial disposition of the binding sites of the ligand for a proper metal ion. This newly found relationship allows a considerable degree of control over the nature of the structure [3]. A significant amount of control can be exerted over the formation of relatively low nuclearity molecular clusters ($<M_6$) by the use of poly-functional and polytopic ligands with well defined and appropriately positioned coordination pockets. Hence, with the proper choice of paramagnetic metal ions to form complexes with these ligands, magnetic coupling can be fine-tuned in order to achieve the result of desired and interesting supramolecular magnetic properties. The major interest so far in these types of grid complexes has emerged from their remarkable and fantastic structures. The specific self-assembly processes leading to these grid-like complexes find immense application in information

* Corresponding authors. Tel.: +91 033 24322936; fax: +91 033 23519755.
E-mail addresses: salah.elfallah@qi.ub.es (M.S. El Fallah), skkar_cu@yahoo.co.in (S.K. Kar).

0277-5387/$ - see front matter © 2007 Elsevier Ltd. All rights reserved.
doi:10.1016/j.poly.2007.08.040

storage and processing technology [4–6]. However, there is also considerable scope for the study of magnetic interactions in these complexes where several metal ions are assembled in a well-defined spatial array linked by suitable bridging ligands to transmit the interaction. Physicochemical properties and magnetic exchange interactions have been extensively studied between the pairs of metal centers in tetranuclear complexes. Recently, the magnetic properties of high-nuclearity clusters have also created immense interest [2] for the development of new magnetic materials. Transition metal template cyclisations have successfully produced many tetranuclear Mn_4, Ni_4, Cu_4 and Zn_4 complexes, [7–13] in which the bridging arrays among the metal ions involve oxygen donor centers. Most of the so far reported alkoxo-bridged poly-nuclear grids [Mn(II), Co(II) and Ni(II)] show anti-ferromagnetic coupling [9–13], while a few Cu(II) grids [14–18] exhibit a ferromagnetic interaction. The origin of this ferromagnetic exchange emerges from the orthogonal orientation of the magnetic orbitals ($d_{x^2-y^2}$).

In continuation of our very recent report [15] of a square Cu_4-grid, in this paper we describe the syntheses, structural characterisation and magnetic properties of a tetranuclear copper(II) complex prepared from the simple multidentate chelating ligand PzOAPyz, containing pyrazine and pyrazole as heterocyclic rings. The assembly of this structure is driven by the stereoelectronic requirement of the copper(II) ion for an elongated tetragonal geometry. The resultant grid-like copper(II) complex contains arrays of four copper(II) ions linked by alkoxide bridges, which are known to be effective mediators of magnetic exchange interactions; accordingly, detailed magnetic susceptibility studies on this complex are described. A brief discussion of its DFT study has also been made.

2. Experimental

2.1. Materials

2-Cyanopyrazine was purchased from Aldrich Chemical Company. Other commercially available chemicals and solvents were used and purified by standard procedures [19].

2.2. Physical measurements

Elemental analyses (carbon, hydrogen and nitrogen) of the ligand PzOAPyz and the metal complex **1** were carried out with a Perkin-Elmer CHNS/O analyzer 2400 at the Indian Association for the Cultivation of Science, Kolkata. The electronic spectra of **1** in purified CH_3CN solution were recorded on a Hitachi model U-3501 spectrophotometer. IR spectra (KBr pellet, 4000–400 cm^{-1}) were recorded on a Perkin Elmer model 883 infrared spectrophotometer. The mass spectrum of the ligand was done at the Indian Institute for Chemical Biology, Kolkata with a JEOLJMS-AX 500 mass spectrometer. Room temperature magnetic susceptibility was measured with a PAR 155 vibrating sample magnetometer. Magnetic susceptibility measurements for the compound were carried out on polycrystalline samples at the Servei de Magnetoquímica of the Universitat de Barcelona, with a Quantum Design SQUID MPMS-XL susceptometer apparatus working in the range 2–300 K under magnetic field of approximately 500 G (2–30 K) and 1000 G (35–300 K). Diamagnetic corrections were estimated from Pascal Tables.

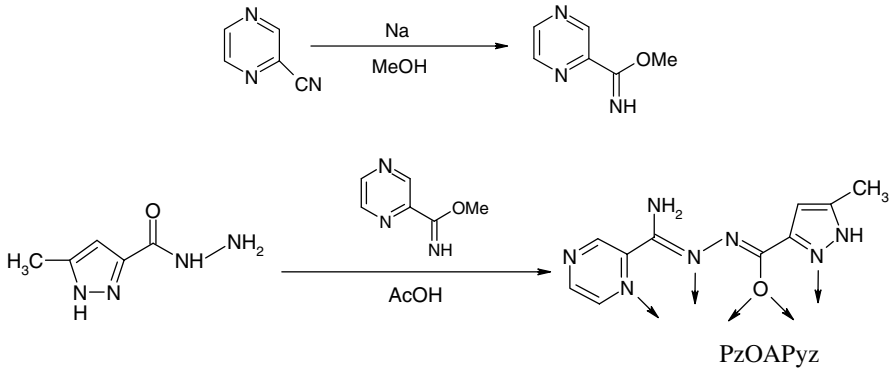
2.3. Synthesis and characterization of the ligand

2.3.1. Synthesis of 5-methylpyrazole-3-carbohydrazide

5-Methylpyrazole-3-carbohydrazide was prepared following an established method [20].

2.3.2. Synthesis of PzOAPyz

The methyl ester of iminopyrazine-2-carboxylic acid, isolated as a white precipitate, was prepared in situ (Scheme 1) by the direct reaction of 2-cyanopyrazine (1.75 g, 0.0166 mol) with sodium methoxide solution, preproduced by dissolving sodium metal (2.63 g, 0.114 mol) in dry methanol (10 mL) when required. 5-Methylpyrazole-3-carbohydrazide (3.5 g, 0.025 mol) in 15–20 mL dry methanol was added to the above precipitate with stirring. Within a few minutes, the white precipitate was found to be dissolved. The stirring was continued for an additional 1 h. Then the mixture was refluxed for 5 h and cooled to room temperature. Excess methanol was removed in a rotary



Scheme 1.

evaporator, leaving a red coloured oily sticky liquid. This was then mixed with water (30 mL) and neutralized with AcOH (pH ~5), which afforded a yellow shining powder. The solid was filtered off, washed thoroughly with methanol and dried in vacuo over fused $CaCl_2$. Yield (3.32 g, 60%). M.p. >250 °C. MS (*m*/*z*) 245 (M^+, 100%). IR/cm^{-1}: ν_{NH} 3350; $\nu_{CO/CN}$ 1659(s), 1548(s); $\nu_{N\text{-}Npz}$ 1065(s); ν_{py} 1020(s). *Anal.* Calc. for $C_{11}H_{12}N_6O$: C, 48.97; H, 4.49; N, 40.00. Found: C, 48.91; H, 4.51; N, 39.93%.

2.4. Preparation of the complex

2.4.1. $[Cu_4(PzOAPyz)_4(ClO_4)_2](ClO_4)_2 \cdot 6H_2O$ (1)

The ligand PzOAPyz (0.122 g, 0.5 mmol) was added to a hot solution of $Cu(ClO_4)_2 \cdot 6H_2O$ (0.185 g, 0.5 mmol) in H_2O–CH_3OH (30 mL) (60:40 v/v). The resulting suspension was stirred at 60 °C until complete dissolution of the ligand occurred. The resulting deep green solution was filtered to remove any undissolved ligand and left at room temperature. Dark green crystals suitable for X-ray diffraction were isolated from the filtrate after standing for several days (yield 0.108 g, 40%). IR/cm^{-1}: ν_{NH/H_2O} 3371, 3458; $\nu_{CO/CN}$ 1669(s), 1536(s); $\nu_{N\text{-}Npz}$ 1084(s); ν_{py} 1032(s). UV–Vis (λ_{max}): 316(sh), 400(sh), 730(br) nm. μ_{RT} 3.42 B.M. *Anal.* Calc. for $[Cu_4(PzOAPyz)_4(ClO_4)_2](ClO_4)_2 \cdot 6H_2O$ (**1**): C, 27.63; H, 2.99; N, 22.56. Found: C, 27.49; H, 3.12; N, 22.51%.

2.5. Crystallographic data collection and refinement of the structure

Selected crystal data for **1** are given in Table 1. Data collections for **1** were made using a Bruker SMART CCD area detector diffractometer equipped with a Mo Kα radiation ($\lambda = 0.71073$ Å) source in the ϕ and ω scan modes at 100(2) K. Cell parameters were determined and refined using SMART software [21]. Data reductions were carried out using the SAINT program [22]. The structure was solved by conventional direct methods and refined by full-matrix least square methods using F^2 data. SHELXS-97 and SHELXL-97 programs [23] were used for structure solution and refinement, respectively. H-atoms bonded to water oxygens had their coordinates refined. Refinement of F^2 was done against all reflections. The weighted *R*-factor *wR* and goodness-of-fit *S* are based on F^2, conventional *R*-factors *R* are based on *F*, with *F* set to zero for negative F^2. The threshold expression of $F^2 > 2\sigma(F^2)$ is used only for calculating *R*-factors (gt), etc. and is not relevant to the choice of reflections for refinement. *R*-factors based on F^2 are statistically about twice as large as those based on *F*, and *R*-factors based on all data will be even larger.

Table 1
Crystallographic data for **1**

Compound	**1**
Empirical formula	$C_{40}H_{52}Cl_4Cu_4N_{28}O_{26}$
Formula weight	1737.06
Temperature (K)	100(2)
Wavelength (Å)	0.71073
Crystal system	monoclinic
Space group	*P*2/*n*
Unit cell dimensions	
a (Å)	14.8346(19)
b (Å)	10.3371(13)
c (Å)	21.155(3)
β (°)	96.392(2)
Volume, Å^3	3223.9(7)
Z	2
D_{calc} (Mg/m^3)	1.789
Absorption coefficient (mm^{-1})	1.571
F(000)	1760
Crystal size (mm)	0.50 × 0.35 × 0.25
θ range for data collection (°)	1.60–30.61
Index ranges	$-21 \leqslant h \leqslant 21$, $-14 \leqslant k \leqslant 14$, $-30 \leqslant l \leqslant 29$
Reflections collected	37 159
Independent reflections [R_{int}]	9884 [0.0821]
Completeness to $\theta = 25.00°$	99.6%
Absorption correction	multiscan
Maximum and minimum transmission	1.000 and 0.617
Refinement method	full-matrix least-squares on F^2
Data/restraints/parameters	9884/37/534
Goodness-of-fit on F^2	1.037
Final *R* indices [$I > 2\sigma(I)$]	$R_1 = 0.0631$, $wR_2 = 0.1589$
R indices (all data)	$R_1 = 0.0889$, $wR_2 = 0.1780$
Largest difference in peak and hole (e Å^{-3})	1.969 and −1.871

3. Result and discussion

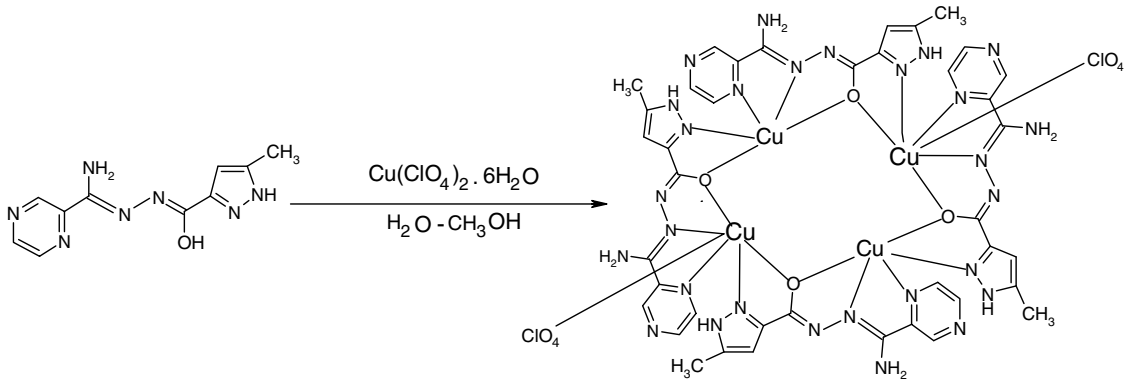
3.1. Syntheses

The ditopic ligand PzOAPyz (Scheme 1) on treatment with a water–methanol solution (60:40 v/v) of copper perchlorate hexahydrate in a 1:1 ratio yielded an interesting orthogonal ferromagnetically coupled tetracopper(II) 2 × 2 homoleptic square grid complex. In methanol, the complex readily precipitated out from the metal–ligand reaction mixture, hence a water–methanol (60:40 v/v) mixed solvent system was chosen as the reaction medium to prevent the precipitation. The formation and stability of this self-assembled square tetrameric complex may be visualized in the following way (Scheme 2).

Each of the four chelating ditopic ligands in the tetrameric $Cu_4(\mu\text{-}O_4)$ core coordinates to any two neighbouring Cu(II) centers, occupying three and two coordination sites respectively, using the alkoxide fragment as a bridger. The repetition of this process leads to the formation of the self-assembled square $Cu_4(\mu\text{-}O_4)$ unit, where the successive four ligand molecules are orthogonal in orientation.

3.2. Description of the crystal structure $[Cu_4(PzOAPyz)_4(ClO_4)_2](ClO_4)_2 \cdot 6H_2O$ (1)

The structure of the tetranuclear cluster cation complex is illustrated in Fig. 1. An ORTEP view of the asymmetric unit is shown in Fig. 2. Selected crystal data for **1** are summarized in Table 1. Important bond distances and angles



Scheme 2.

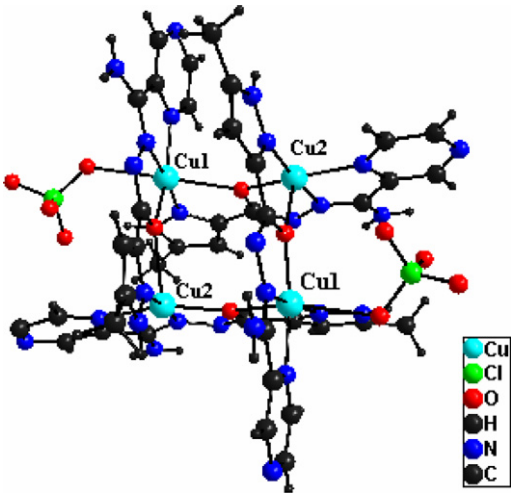


Fig. 1. Structural representation of the cationic complex **1**.

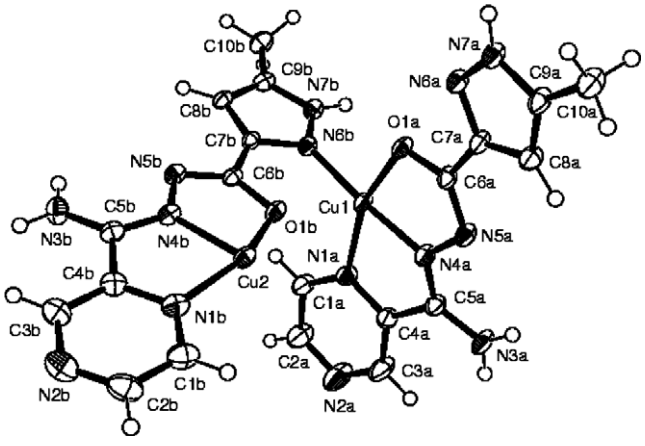


Fig. 2. Ortep diagram of the asymmetric unit and atom numbering scheme of the cationic complex **1**.

are listed in Table 2. A view of the tetranuclear core, depicting the immediate donor atoms only, is shown in Fig. 3. The cationic cluster fragment consists of a square arrangement of Cu(II) centers bridged just by alkoxide oxygen atoms. The two bridging oxygen atoms (O1A) are

Table 2
Selected bond distances (Å) and angles (°) in **1**

Cu(1)–N(1A)	2.052(3)	Cu(2)–N(6A)#1	1.966(3)
Cu(1)–N(4A)	1.906(3)	Cu(2)–N(1B)	2.048(3)
Cu(1)–N(6B)	1.967(3)	Cu(2)–N(4B)	1.908(3)
Cu(1)–O(1A)	1.965(2)	Cu(2)–O(1A)#1	2.279(2)
Cu(1)–O(1B)	2.285(2)	Cu(2)–O(1B)	1.970(2)
Cu(1)–O(13)	2.663(2)		
N(4A)–Cu(1)–O(1A)	79.92(11)	N(4B)–Cu(2)–N(6A)#1	175.20(12)
N(4A)–Cu(1)–N(6B)	174.19(12)	N(4B)–Cu(2)–O(1B)	79.22(11)
O(1A)–Cu(1)–N(6B)	99.43(10)	N(6A)#1–Cu(2)–O(1B)	101.35(11)
N(4A)–Cu(1)–N(1A)	79.79(12)	N(4B)–Cu(2)–N(1B)	79.82(12)
O(1A)–Cu(1)–N(1A)	159.70(11)	N(6A)#1–Cu(2)–N(1B)	98.62(12)
N(6B)–Cu(1)–N(1A)	100.81(12)	O(1B)–Cu(2)–N(1B)	156.24(11)
N(4A)–Cu(1)–O(1B)	110.46(11)	N(4B)–Cu(2)–O(1A)#1	108.91(10)
O(1A)–Cu(1)–O(1B)	92.06(9)	N(6A)#1–Cu(2)–O(1A)#1	75.72(10)
N(6B)–Cu(1)–O(1B)	75.30(10)	O(1B)–Cu(2)–O(1A)#1	100.72(9)
N(1A)–Cu(1)–O(1B)	94.55(10)	N(1B)–Cu(2)–O(1A)#1	96.56(10)
N(4A)–Cu(1)–O(13)	87.61(10)	Cu(1)–O(1A)–Cu(2)#1	138.10(12)
O(1A)–Cu(1)–O(13)	100.89(8)	Cu(2)–O(1B)–Cu(1)	137.69(12)
N(6B)–Cu(1)–O(13)	86.85(10)		
N(1A)–Cu(1)–O(13)	78.74(9)		
O(1B)–Cu(1)–O(13)	159.50(8)		

located below the Cu_4 plane and other two bridging oxygen atoms (O1B) are located above the plane in boat-like conformation. The two five coordinated and two six coordinated copper(II) centers of the Cu_4 (μ-O_4) core are arranged in a slightly distorted square (displacement of metals from the Cu_4 least square plane; two Cu(1) +0.122 Å, two Cu(2) −0.122 Å) and are bridged by four alkoxide oxygens (two O1A and two O1B) from the four deprotonated ligands, arranged in pairs above and below the Cu_4 pseudo plane in a boat-like conformation. The O–Cu–O angles fall in the range 92–100° and the Cu–Cu separations are close to 4 Å (Cu1–Cu2 3.97 Å, Cu2–Cu1 3.96 Å). The ligands allow an orientational distinction among its four moieties and are arranged in two groups of parallel pairs, with each ligand in a roughly eclipsed arrangement compared with its partner. The total coordination sites requirement of the four metals (22 bonds) is completed by four ligands, which fill 20 coordination sites and two ClO_4^- ions, binding to each of the diagonally related Cu1 centers. The square pyramidal Cu2 centers

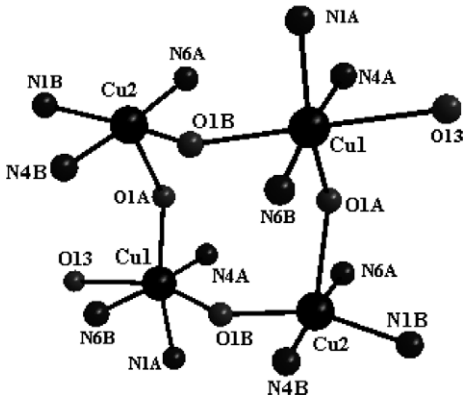


Fig. 3. Structural representation and atom numbering scheme of the tetranuclear core in **1**.

have a N_4O chromophore (all the donor centers are from ligand moieties), while the axially distorted octahedral Cu1 centers have a N_4O_2 chromophore (the additional sixth donor center is occupied by the perchlorate oxygen).

The copper–oxygen (alkoxide) bond distances are quite variable, but an interesting trend is observed based on the copper chromophore. The two Cu1 centres have long and short contacts to O1B and O1A, respectively (Cu1–O1B 2.285(2) Å, Cu1–O1A 1.965(2) Å). Similarly the other two Cu2 centres also have alternate long and short contacts to O1A and O1B respectively (Cu2–O1A 2.279(2) Å, Cu2–O1B 1.970(2) Å). This establishes an asymmetric, alternating long–short bridging arrangement within the Cu_4 square plane. The Cu–O–Cu angles fall in the range 137.69–138.10°. Both the separations and angle values are quite typical for these grid systems [14–16].

The most prominent feature of the structure involves the encapsulation of the two five-coordinate and two six-coordinate Cu(II) centers within the grid, an unusual feature in related non-homoleptic Cu_4 (2×2) square grid complexes [17,18]. Hexa-coordinated Cu(II) undergoes Jahn-Teller distortion and in this case each of two six-coordinate Cu(II) ions undergo a tetragonal elongation. The axis of elongation of the copper center includes two bridging oxygen connections (O1A and O1B), leading to a situation where the copper equatorial planes are tilted at 86.45° to the neighbouring penta-coordinated metal center. This orbital orthogonality situation leads to significant intramolecular ferromagnetic interaction. In the asymmetric unit, the two independent perchlorate groups are disordered, one about a twofold axis and the other about an inversion center. Systematic and regular solvent and perchlorate channels alternate in between the layer structures of the cluster molecules. This stabilizes the lattice structure through hydrogen bonding. In the tetrameric complex, there are also weak hydrogen bonds (Table 3) between H3AD and O3W and between H3W1 and O3W. This makes an infinite straight chain throughout the crystal.

The lattice structure involves a number of water molecules (here six) as is typical for grids in this class [14–18]. In this crystal structure, one of the water molecules (O1W) is present with unit-occupancy and there are also two half-occupancy water molecules (O2W, O3W) in the asymmetric unit.

Table 3
Hydrogen bonding parameters in **1** (Å) and (°)

D–H...A	*d*(D–H)	*d*(H...A)	*d*(D...A)	∠(DHA)
N(3A)–H(3AB)...O(3W)	0.88	2.11	2.980(6)	171.9
O(3W)–H(3W1)...O(11)#6	0.82	2.10	2.892(8)	160.3

Symmetry transformations used to generate equivalent atoms: #6 $-x+1$, $-y$, $-z+2$.

4. Magnetic behaviour

The variable temperature magnetic susceptibility data for the compound were recorded between 300 and 2 K. Plot of $\chi_m T$ versus T in Fig. 4 shows a ferromagnetic behavior. The $\chi_m T$ value is 1.568 $cm^3\ mol^{-1}$ K at 300 K, being close to that expected for four uncoupled $S = 1/2$ spins (with $g = 2.00$). $\chi_m T$ increases slightly when temperature is lowered and reached a maximum value of 2.885 $cm^3\ mol^{-1}$ K at 3 K. This maximum is consistent with that expected for ferromagnetically coupled copper(II) ions.

The structure of **1** consists of copper ions linked by the ligand (PzOAPyz), giving a tetranuclear compound. Taking into account the compound topology (slight distortion from square array, see crystallographic data), three coupling parameters J_1, J_2 and J_3 can be considered to interpret the magnetic interactions in the complex, using the Hamiltonian:

$$H = -J_1(S_1 \cdot S_2 + S_3 \cdot S_4) - J_2(S_1 \cdot S_4 + S_2 \cdot S_3) - J_3(S_1 \cdot S_3 + S_2 \cdot S_4)$$

Based on the structural data of the $Cu_4(\mu\text{-}O_4)$ core, we have considered that $J_1 = J_2 = J$ and $J_3 = 0$ (no cross-coupling connection). For this square disposition, the E_n value can

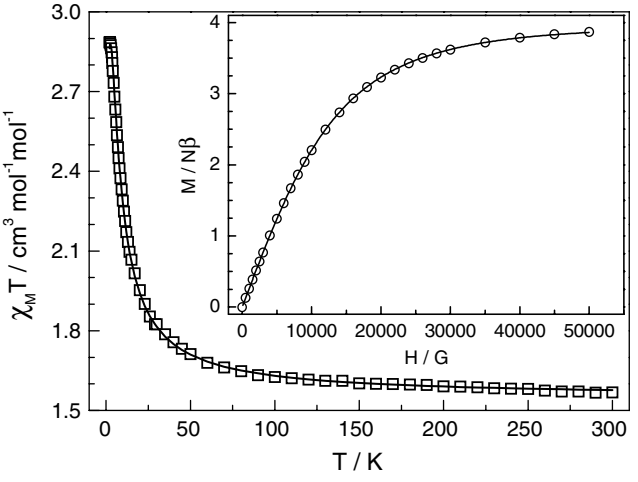


Fig. 4. Plots of $\chi_m T$ vs. T and M/Nβ vs. H at $T = 2$ K (inset) for **1**. Solid lines correspond to the best fit (see text).

be obtained by using the Kambe method [24] from the Hamiltonian:

$$H = -J_1(S_1 \cdot S_2 + S_2 \cdot S_3 + S_3 \cdot S_4 + S_1 \cdot S_4) \quad (1)$$

The analysis of the experimental susceptibility data have been performed by the use of the expression:

$$\chi_m T = Ng^2\beta^2 T(f(J,T)/3K) \quad (2)$$

Here

$$f(J,T) = \frac{6\exp(J/KT) + 12\exp(2J/KT) + 30\exp(3J/KT)}{1 + 3\exp(J/KT) + 7\exp(2J/KT) + 5\exp(3J/KT)} \quad (3)$$

The best fit parameters found are: $J = +7.47\ cm^{-1}$ and $g = 2.03$ with an error $R = 4.2 \times 10^{-5}$, where $R = \chi[(\chi_m T)_{obs} - (\chi_m T)_{calc}]^2/\chi(\chi_m T)_{obs}{}^2$. The field dependence of magnetization (0–5 T) measured at 2 K (Fig. 4, inset) suggests that the magnetization tends to 4.0 electrons, which is close to the expected value for the ferromagnetically coupled four Cu^{II} ions ($S = 1/2$ and $g = 2.03$).

4.1. Magneto-structural correlations

The value of the superexchange parameter $J = +7.47\ cm^{-1}$ for compound **1**, should be considered as normal, taking into account the structural and magnetic data reported in the literature [12,14,15,25]. In Table 4, we report significant structural data and the calculated J values for the published ferromagnetic [2 × 2] square Cu_4 complexes, along with those of complex **1**. These fit nicely into the list. It might be interesting to compare the ferromagnetic behavior of these complexes, which increases when the Cu–O distance decreases, as can be observed in Fig. 5. The variation observed can be rationalized-based on the Hay–Thibeault–Hoffmann model [26] where the global coupling constant is given by

$$J = 2K_{ab} - \frac{(\varepsilon_1 - \varepsilon_2)^2}{J_{aa} - J_{ab}} = J_F + J_{AF} \quad (4)$$

The poor overlap between the nearly orthogonal $d_{x^2-y^2}$ orbitals (Fig. 6) approaches to zero or reduces considerably the antiferromagnetic contributions (second term). In this situation, we would expect the first term, $2K_{ab}$, to dominate giving overall positive and large J values, which diminish with longer Cu–O distances as we can observe as a general trend (Fig. 5).

On the other hand, the DFT calculation carried out on the real structure of complex **1** confirms with accuracy the value of the magnetic interaction reported before, being $7.2\ cm^{-1}$. The computational methodology was reported recently in a similar case [15]. The analysis of the spin density distribution shows the predominance of a delocalization mechanism in the coordinated atoms to the copper ions (Fig. 6) [27]. The spin population on the copper atoms is around 0.63e−, and the missing spin density, relative to one unpaired electron, appears mainly to be delocalized over the bridging ligands (∼0.13e−). The topology of the SOMOs and the spin density map in this case indicates that adjacent copper(II) centres are quasi orthogonal, leading a ferromagnetic interaction.

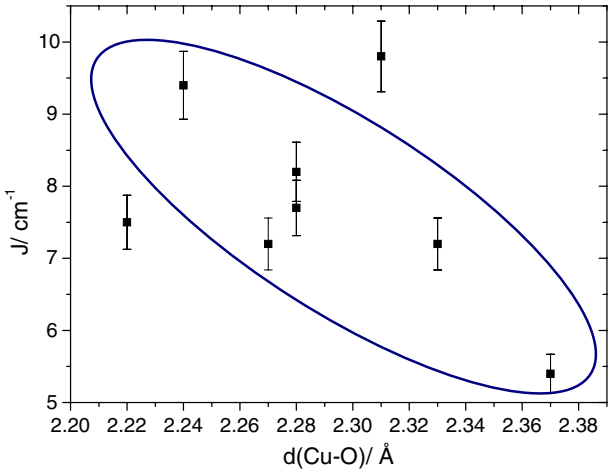


Fig. 5. Plot of the J values vs. longer d(Cu–O) distances (5% error bars were added) for the ferromagnetic [2 × 2] square Cu_4 complexes characterized to date (see Table 4).

Table 4
Significant average structural and magnetic data for ferromagnetic [2 × 2] square Cu_4 complexes

Compound[a]	d(Cu···O) (Å)	Cu–O–Cu (°)	d(Cu···Cu) (Å)	J_{exp} (cm^{-1})	Reference
$[Cu_4(POAP\text{-}H)_4(H_2O)_2](ClO_4)\cdot 4H_2O$				+7.3	[12]
$[Cu_4(POAPZ\text{-}H)_4(H_2O)](NO_3)_4\cdot 3H_2O$	2.31	140.6	4.04	+9.8	
$[Cu_4(6POAP\text{-}H)_4](ClO_4)_4$	2.24	139.3	3.97	+9.4	
$[Cu_4(PZOAP\text{-}H)_4](NO_3)_4\cdot 3H_2O$	2.28	140.6	4.05	+8.2	
$[Cu_4(MPOAP\text{-}H)_4](ClO_4)_4\cdot 8H_2O$	2.22	139.2	3.95	+7.5	[20]
$[Cu_4(IOAPM\text{–}H)_4](ClO_4)_4\cdot 3CH_3CN$	2.33	139.7	4.05	+7.2	
$[Cu_4(PzOAP)_4(NO_3)_2](NO_3)_2\cdot 4H_2O$	2.37	140.1	4.09	+5.4	[15]
$[Cu_4(pcoap\text{-}H)_2(pcaop\text{-}2H)_2](NO_3)_2\cdot 15H_2O$	2.27	139.7	4.02	+7.2	[14]
$[Cu_4(PzOAPyz)_4(ClO_4)_2](ClO_4)_2\cdot 6H_2O$	2.28	137.9	3.97	+7.7	this work

[a] *Abbreviations used:* POAP = N3-(2-pyridyl)-2-pyridinecarboxamidrazone; POAPZ = N3-(2-pyridyl)-2-pyrazinecarboxamidrazone, 6POAP = 6-hydroxy methyl-2-pyridine carboxylate; MPOAP = 6-methyl-2-picolinic acid; IOAPM = 4-methyl-5-imidazole carboxylic acid hydrazide; PzOAP = methyl-2-pyridine carboxylate; Pcoap = 6-methyloxycarbonyl-2-pyridinecarboxylic acid hydrazide; PzOAPyz = N3-(3-pyrazolyl)-2-pyrazinecarboxamidrazone.

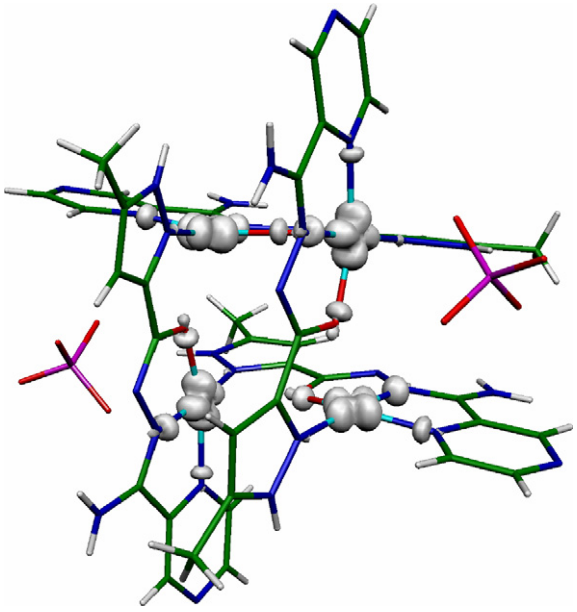


Fig. 6. Spin density distribution for **1**, corresponding to the $S = 2$ ground state, showing a nearly orthogonality between the adjacent copper(II) atoms. White regions indicate positive spin populations.

5. Concluding remarks

The mixed pyrazole-pyrazine-based ditopic ligand PzOAPyz forms a homoleptic 2×2 square grid-complex in the presence of the Cu(II) ion, in which the pyrazole rings remain protonated. The structural backbone of the ligand contains two diazine nitrogens linking two peripheral heterocyclic rings. The ligand is made by tracing the same synthetic route as before [15] in which a hydrazide was reacted with a methyl imino ester. This leads to the desired ligand with a pyrazole and a pyrazine fragment at the two ends. The alkoxide fragment (–OH group) in the ligand PzOAPyz plays an important role towards the self-assembly process, forming a grid by bridging two adjacent copper centers simultaneously. The –OH group is deprotonated during the course of the reaction and serves as a ferromagnetic mediator between the two adjacent paramagnetic copper ions. The $–NH_2$ groups are not involved in the coordination. The ligand donor set combination provides a template for binding the two adjacent metals which leads to the formation of the cluster by a self-assembly process. The four metal centers in the tetrameric complex are arranged in a distorted square shape with two pairs of roughly parallel ligands. The self-assembly mechanism is difficult to predict but one could rationalize an initial step of coordination of the ligand at three sites, one pyrazole or pyrazine nitrogen, one diazine nitrogen and the adjacent deprotonated –OH, in a meridional fashion.

In the present grid complex, the two copper centers are square pyramidal and other two are axially distorted octahedral. In the $Cu_4(\mu\text{-}O_4)$ core, alternative short and long contacts lead to an unsymmetrical orientation from a perfect square grid arrangement. However, in the $Cu_4(\mu\text{-}O_4)$ unit, the main backbone of the complex arises through a self-assembly process. This is controlled by employing the sense that a predetermined structural arrangement is logically based on the strategic positions of the donor groups within the ligand moiety. Variable temperature magnetic susceptibility studies show that the square copper cluster exhibits an intramolecular ferromagnetic spin exchange, associated with the orthogonal alkoxide bridging arrangement and the close proximity of the copper centers. The origin of this ferromagnetic coupling lies in the approximately orthogonal orientation of the magnetic orbitals $d_{x^2-y^2}$.

Acknowledgements

Financial support [01(1916)/04/EMR-II] from the Council of Scientific and Industrial Research (CSIR), New Delhi, India is gratefully acknowledged. M. S. El Fallah is grateful for the financial support given by the Spanish (CTQ2006-01759 and CTQ2005-08123-C02-02/BQU) and Catalan (2005SGR-00593 and 2005SGR-00036) governments. J. Tercero is grateful to the Centre de Computació de Catalunya (CESCA) with a grant provided by Fundació Catalana per a la Recerca (FCR) and the Universitat de Barcelona.

Appendix A. Supplementary material

CCDC 649860 contains the supplementary crystallographic data for **1**. These data can be obtained free of charge via http://www.ccdc.cam.ac.uk/conts/retrieving.html, or from the Cambridge Crystallographic Data Centre, 12 Union Road, Cambridge CB2 1EZ, UK; fax: (+44) 1223-336-033; or e-mail: deposit@ccdc.cam.ac.uk. Supplementary data associated with this article can be found, in the online version, at doi:10.1016/j.poly.2007.08.040.

References

[1] J.M. Lehn, Supramolecular Chemistry – Concepts and Perspective, VCH, Weinheim, 1995 (Chapter 9).
[2] L.K. Thompson, L. Zhao, Z. Xu, D.O. Miller, W.M. Reiff, Inorg.Chem. 42 (2003) 128, and references therein.
[3] T. Beissel, R.E. Powers, K.N. Raymond, Angew. Chem., Int. Ed.Engl. 35 (1996) 1084.
[4] O. Waldmann, R. Koch, S. Schromm, P. Müller, L. Zhao, L.K. Thompson, Chem. Phys. Lett. 332 (2000) 73.
[5] P.N.W. Baxter, J.M. Lehn, J. Fisher, M.T. Youinou, Angew. Chem., Int. Ed. Engl. 106 (1994) 2432.
[6] G.S. Hanan, D. Volkmer, U.S. Schubert, J.M. Lehn, G. Baum, D. Fenske, Angew. Chem., Int. Ed. Engl. 109 (1997) 1929.
[7] M.J. Grannas, B.F. Hoskins, R. Robson, J. Chem. Soc., Chem.Commun. (1990) 1644.
[8] M.J. Grannas, B.F. Hoskins, R. Robson, Inorg. Chem. 33 (1994) 1071.
[9] L.H. Uppadeine, J.P. Gisselbrecht, N. Kyritsakas, K. Ñattinen, K. Rissamen, J.M. Lehn, Chem. Eur. J. 11 (2005) 2549.
[10] L. Zhao, C.J. Matthews, L.K. Thompson, S.L. Heath, Chem. Commun. (2000) 265.
[11] D.M. Bassani, J.M. Lehn, K. Fromm, D. Fenske, Angew. Chem., Int. Ed. 37 (1998) 2364.

[12] C.J. Matthews, K. Avery, Z. Xu, L.K. Thompson, L. Zhao, D.O. Miller, K. Biradha, K. Poirier, M.J. Zaworotko, C. Wilson, A.E. Goeta, J.A.K. Howard, Inorg. Chem. 38 (1999) 5266.
[13] V. McKee, S.S. Tandon, J. Chem. Soc., Chem. Commun. (1988) 1334.
[14] (a) Z. Xu, L.K. Thompson, D.O. Miller, J. Chem. Soc., Dalton Trans. (2002) 2462;
(b) L.N. Dawe, T.S.M. Abedin, T.L. Kelly, L.K. Thompson, D.O. Miller, L. Zhao, C. Wilson, M.A. Leech, J.A.K. Howard, J. Mater. Chem. (2006) 2645.
[15] (a) S. Roy, T.N. Mandal, A.K. Barik, S. Pal, R.J. Butcher, M.S. El Fallah, J. Terceroe, S.K. Kar, J. Chem. Soc., Dalton Trans. (2007) 1229;
(b) K.D. Karlin, Z. Tyeklor (Eds.), Bioinorganic Chemistry of Copper, Chapman and Hall, New York, 1993;
(c) L.Q. Jun, A.E. True, Prog. Inorg. Chem. 38 (1990) 97.
[16] K.L.V. Mann, E. Psillakis, J.C. Jeffery, L.H. Rees, N.M. Harden, J.A. McCleverty, M.D. Ward, D. Gatteschi, F. Totti, F.E. Mabbs, E.J.L. McInnes, P.C. Riedi, G.M. Smith, J. Chem. Soc., Dalton Trans. (1999) 339.
[17] Z. Xu, L.K. Thompson, C.J. Matthews, D.O. Miller, A.E. Goeta, J.A.K. Howard, Inorg. Chem. 40 (2001) 2446.
[18] L.K. Thompson, C.J. Matthews, L. Zhao, Z. Xu, D.O. Miller, C. Wilson, M.A. Leech, J.A.K. Howard, S.L. Heath, A.G. Whittaker, R.E.P. Winpenny, J. Solid State Chem. 159 (2001) 308.
[19] D.D. Perrin, W.L.F. Armarigo, D.R. Perrin, Purification of Laboratory Chemicals, 2nd ed., Pergamon Press, Oxford, 1980.
[20] N. Saha, K.M. Dutta, J. Inorg. Nucl. Chem. 43 (1981) 1405.
[21] (a) Bruker, XPREP v2005/4, Bruker AXS Inc.: Madison, WI, USA, 2005;
(b) Bruker, SMART v5.631, Bruker AXS Inc.: Madison, WI, USA, 2001.
[22] Bruker, SAINT v7.34A., Bruker, AXS Inc., Madison, WI, USA, 2005.
[23] (a) Bruker, SHELXTL v6.12, Bruker AXS Inc.: Madison, WI, USA, 2005;
(b) G.M. Sheldrick, Acta Crystallogr., Sect. A 46 (1990) 467;
(c) G.M. Sheldrick, SHELXS 97, Program for the Automatic Solution of Crystal Structures, Universitate Gottingen, Gottingen, Germany, 1997.
[24] K. Kambe, J. Phys. Soc. Jpn. 5 (1950) 48.
[25] L.N. Dawe, T.S.M. Abedin, T.L. Kelly, L.K. Thompson, D.O. Miller, L. Zhao, C. Wilson, M.A. Leech, J.A.K. Howard, J. Mater. Chem. 16 (2006) 2645.
[26] P.J. Hay, J.C. Thibeault, R. Hoffmann, J. Am. Chem. Soc. 97 (1975) 4884.
[27] J. Cano, E. Ruiz, S. Alvarez, M. Verdaguer, Comm. Inorg. Chem. 20 (1998) 27.

Available online at www.sciencedirect.com
ScienceDirect
Polyhedron 27 (2008) 113–117
POLYHEDRON
www.elsevier.com/locate/poly

Synthesis, structure and spectral studies on mixed ligand copper(II) complexes of diimines and acetylacetonate

O.O.E. Onawumi [a,b], O.O.P. Faboya [b], O.A. Odunola [b], T.K. Prasad [a], M.V. Rajasekharan [a,*]

[a] School of Chemistry, University of Hyderabad, Hyderabad 500 046, AP, India
[b] Department of Pure and Applied Chemistry, Ladoke Akintota University of Technology, P.M.B 4000, Ogbomoso Oyo State, Nigeria

Received 16 May 2007; accepted 24 August 2007
Available online 22 October 2007

Abstract

Two new mixed ligand complexes of copper(II) with acetylacetonate (acac), 2,2′-bipyridine (bpy) and 1,10-phenanthroline (phen) belonging to the class of cytotoxic and antineoplastic compounds known as CASIOPEINAS® were synthesized and structurally characterized. Crystals of both complexes $[Cu(acac)(bpy)(H_2O)]NO_3 \cdot H_2O$ (**1**), [Cu(acac)(phen)Br] (**2**) contain square pyramidal Cu(II) complex species. In frozen solution both compounds give well resolved EPR spectra with very similar parameters.
© 2007 Elsevier Ltd. All rights reserved.

Keywords: Copper(II) complex; Mixed ligand chelate; EPR spectroscopy; UV–Vis spectroscopy; Casiopeinas®

1. Introduction

Mixed chelate complexes of Cu(II) having the general formulae $[Cu(NN)(OO)]^+$ and $[Cu(NN)(ON)]^+$ are reported to have potentially useful pharmacological properties [1–3]. In the above formulae, (NN) represents a diimine ligand, 2,2′-bipyridine (bpy) or 1,10-phenanthroline (phen) or their ring substituted derivatives, (OO) stands for acetyl acetonate and (ON) is an aminoacidate. The class of compounds [Cu(N–N)(O–O)]NO_3 has been registered under the trade name, CASIOPEINAS® [1,4]. As early as 1970, Fukuda and Sone reported the formation and absorption spectra of mixed ligand complexes of Cu(II) with acac and bpy/phen [5]. Subsequently, a number of mixed ligand complexes of copper (II) with acac and phen have been structurally characterized which include, $[Cu(acac)(phen)(OH_2)][hfac] \cdot H_2O$ (hfac = hexafluoroacetylacetonate) [6], [Cu(acac)(phen)NCS] [7], $[Cu(acac)(phen)H_2O]NO_3 \cdot 2H_2O$ [8], $[Cu(acac)(phen)NO_3] \cdot H_2O$ [9], $[Cu(acac)(2,9\text{-}Me_2phen)NO_3]$ [9], $[Cu(acac)(phen)ClO_4][Cu(acac)(phen)(CH_3CN)]ClO_4$ [10], $[Cu(acac)(phen)(H_2O)]ClO_4$ [11]. Azido bridged polynuclear complexes containing acac and phen/bpy have also been reported [12]. However, only the structure of one mononuclear mixed chelate of Cu(II) with bpy and acac, $[Cu(acac)(bpy)(H_2O)][Cu(acac)(bpy)N_3] \cdot 2ClO_4$ has been reported so far [13], although there were reports of $[Cu(acac)(4,4'\text{-}Me_2bpy)]^+$ [4,7]. Herein we report the synthesis, structure and spectral properties of $[Cu(acac)(bpy)(H_2O)]NO_3 \cdot H_2O$ (**1**), [Cu(acac)(phen)Br] (**2**).

2. Experimental

2.1. Materials and physical measurements

All the chemicals used were of the reagent grade and were used as received. IR spectra were recorded using KBr discs on a Jasco FT/IR 5300 spectrometer in the range 4000–400 cm^{-1}. Elemental analysis for C, H and N was performed on a Perkin–Elmer 240C elemental analyzer. Electronic spectral measurements were obtained using a Shimadzu UV-3101 PC spectrophotometer and the diffuse

* Corresponding author. Tel.: +91 40 2313 4857; fax: +91 40 2301 2460.
E-mail address: mvrsc@uohyd.ernet.in (M.V. Rajasekharan).

0277-5387/$ - see front matter © 2007 Elsevier Ltd. All rights reserved.
doi:10.1016/j.poly.2007.08.041

reflectance spectra with an ISR-3100 integrating sphere attachment. The EPR spectra of the frozen solution at 130 K in ethanol were collected on a JEOL JES – FA 200 spectrometer operating at X-band frequency. Spectra were simulated using a previously described computer program [14]. Powder diffractograms were measured using PW3710 model Philips Analytical X-ray diffractometer.

2.2. Synthesis

2.2.1. [Cu(acac)(bpy)(H_2O)]$NO_3 \cdot H_2O$ (1)

To a 25 mL of ethanolic solution of $Cu(NO_3)_2 \cdot 3H_2O$ (0.242 g, 1.00 mmol), acetylacetone (0.103 mL, 0.99 mmol) was added and stirred. To the resulting green solution solid 2,2′-bipyridine (0.156 g, 0.99 mmol) was added followed 2 mL aqueous solution of KOCN (0.081 g, 0.99 mmol). The resulting mixture was stirred for 30 min and a light blue precipitate was filtered off (0.045 g) and dark blue filtrate kept for evaporation at RT. In one week, dark blue crystals of **1** suitable for X-ray determination were formed. Yield: 0.281 g (0.674 mmol, 67%). *Anal.* Calc. for $C_{15}H_{19}CuN_3O_7$ (MW 416.87): C, 43.22; H, 4.59; N, 10.08. Found: C, 43.17; H, 4.73; N, 10.19%. IR (KBr disk, cm^{-1}) 3516, 3420, 1575, 1521, 1383, 1018, 1275, 821, 731.

2.2.2. [Cu(acac)(phen)Br] (2)

To a 20 mL ethanolic solution of acetylacetone (0.103 mL, 0.99 mmol) and 1,10-phenanthroline monohydrate (0.198 g, 1 mmol), solid $CuBr_2$ (0.223 g, 1.00 mmol) was added and stirred. The pH of the resulting brown solution was adjusted to 6–7 by adding dilute sodium hydroxide and stirring. The color of the solution changed to green, with the formation of green precipitate of **2** which was filtered and dried. Yield: 0.250 g (0.591 mmol, 59%). The filtrate was kept for evaporation at RT to get dark green crystals suitable for X-ray crystallography. Powder diffractograms revealed that both the crystals and the microcrystalline precipitate are identical. *Anal.* Calc. for $C_{17}H_{15}BrCuN_2O_2$ (MW 422.76): C, 48.30; H, 3.58; N, 6.63. Found: C, 47.88; H, 3.33; N, 6.36%. IR (KBr disk, cm^{-1}) 3414, 1585, 1518, 1429, 1381, 1273, 1018, 925, 855, 766, 722, 646.

2.3. X-ray crystallography

X-ray data were collected on a Bruker SMART APEX CCD X-ray diffractometer, using graphite-monochromated Mo Kα radiation ($\lambda = 0.71073$ Å) at 298 K. Data were reduced using SAINTPLUS [15] and a multi-scan absorption correction using SADABS [16] was performed. The structures were solved by direct method using SHELXS-97 and full-matrix least-square refinement was carried out using SHELXL-97 [17]. All ring hydrogen atoms were assigned on the basis of geometrical considerations and were allowed to ride upon the respective carbon atoms. Hydrogen atoms on the water molecules were located from the difference maps and geometrical constraints were applied. Drawings were made using ORTEP3 for windows [18] and Mercury [19].

3. Results and discussion

3.1. Synthesis

The adjustment of pH is essential for the formation of the mixed ligand complexes reported here. In the case of compound **1**, this was accomplished by the addition of KOCN while in the case of **2**, a dilute solution of NaOH could suffice. In the absence of KOCN, we could get only [Cu(bpy)(H_2O)$_3$(NO_3)]NO_3 [20]. The IR spectra of the initial precipitate formed as a minor product during the preparation shows peaks corresponding to NO_3^-, NCO^- and bpy ligands indicating a different compound than **1**. In fact, the role KOCN in the preparation of **1** was discovered while attempting to prepare a cyanate complex. It was found that compound **2** can be prepared also by the use of KOCN without adding any NaOH, but the yield of the product obtained was less and the side product formed was more. The side products are probably mixed ligand complexes containing coordinated cyanate, but they could not be obtained in a good crystalline form Table 1.

3.2. Structure of [Cu(acac)(bpy)(H_2O)]$NO_3 \cdot H_2O$ (1)

There are two molecules of [Cu(acac)(bpy)(H_2O)]-$NO_3 \cdot H_2O$ in the asymmetric unit, with slightly different geometric parameters (Fig. 1). The coordination around copper is distorted square pyramidal with acac and bpy

Table 1
Crystal data and structure refinement for **1** and **2**

	1	**2**
Formula	$C_{15}H_{19}CuN_3O_7$	$C_{17}H_{15}BrCuN_2O_2$
Formula weight	416.87	422.76
Crystal system	monoclinic	triclinic
a (Å)	14.160(5)	7.7005(10)
b (Å)	18.028(6)	9.1930(12)
c (Å)	15.241(5)	12.1728(16)
α (°)	90	84.575(2)
β (°)	111.719(5)	71.838(2)
γ (°)	90	86.398(2)
V (Å^3)	3615(2)	814.62(18)
Z	8	2
Space group	$P2_1/n$	$P\bar{1}$
Crystal size (mm)	$0.34 \times 0.16 \times 0.12$	$0.40 \times 0.26 \times 0.24$
μ (mm^{-1})	1.251	3.803
Reflections collected	36446	9362
Unique reflections, R_{int}, parameters	8461, 0.0405, 491	3757, 0.0171, 210
Observed reflections [$I > 2\sigma(I)$]	5195	3102
Completeness to $2\theta = 25.0$ (%)	99.1	99.6
Goodness-of-fit on F^2	1.003	1.037
$R(F_o^2)$[a] [$I > 2\sigma(I)$]	0.0642	0.0330
$R_w(F_o^2)$[b] [$I > 2\sigma(I)$]	0.1838	0.0938

[a] $R = \sum\|\|F_o\| - \|F_c\|\|/\sum|F_o|$.
[b] $R_w = [\sum w(F_o^2 - F_c^2)^2/\sum(wF_o^4)]^{1/2}$.

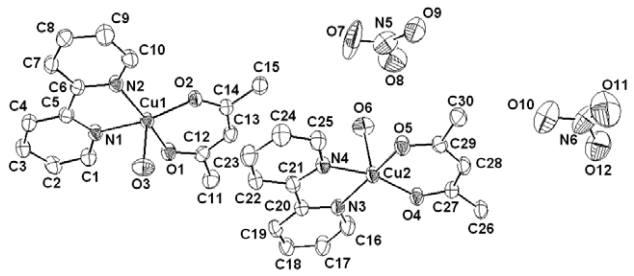


Fig. 1. ORTEP view of compound **1** showing atom labeling, thermal ellipsoids are drawn at the 50% probability ellipsoids and hydrogen atoms and solvent water molecules have been omitted for clarity.

in the equatorial plane and the water molecule at the axial position. The deviations (Å) of the Cu atoms from the mean equatorial coordination planes were 0.145(Cu1) and 0.182(Cu2). There exists in the lattice a 1-D H-bond network formed by the coordinated water molecule, solvent water molecules and the NO_3^- ion, with no H-bond contacts between these chains (Fig. 2). Selected bond lengths and angles are given in Table 2.

3.3. Structure of [Cu(acac)(phen)Br] (2)

The coordination around copper(II) is again a distorted square pyramidal with acac and phen in the equatorial plane and the Br^- ion coordinated at the axial position (Fig. 3). The mean plane deviation (Å) of the Cu from the equatorial plane was 0.282. Unlike in crystals of **1**, there is no H-bond network, as there are no solvent water molecules or anions in the lattice. The selected bond lengths and angles are given in Table 3.

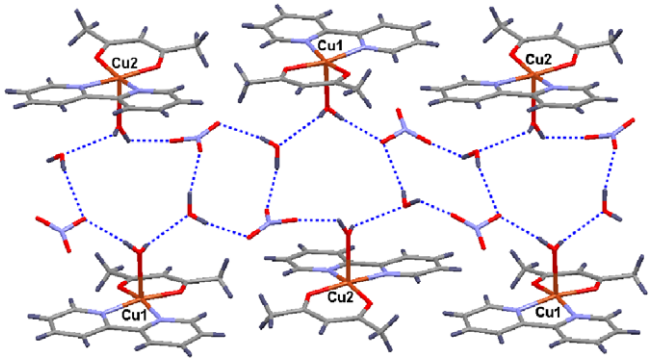


Fig. 2. 1D H-bonded network formed by the water molecules and nitrate ion existing in compound **1**.

3.4. Electronic and EPR spectra

Both solution (ethanol) and solid state (diffuse reflectance) spectra of compounds were measured. For compound **1** solid and solution spectra show similar trends with two broad peaks in the visible region at 11×10^3 cm^{-1}(sh) and 16.0×10^3 cm^{-1}. In square pyramidal Cu(II) complexes the plausible d-orbital energy level scheme (idealized symmetry group C_{4v}), is $d_{x^2-y^2} > d_{z^2} > d_{xy} > d_{xz}, d_{yz}$ so that the higher energy band can be assigned to $d_{xy} \rightarrow d_{x^2-y^2}$ and the lower energy band to $d_{z^2} \rightarrow d_{x^2-y^2}$. The other d–d bands are probably masked by intense $\pi \rightarrow \pi^*$ transitions with peaks at 32.0×10^3 cm^{-1} (shoulder), 33.5×10^3 cm^{-1}, and 40.8×10^3 cm^{-1} observed in both solution and solid. In the case of compound **2**, there were

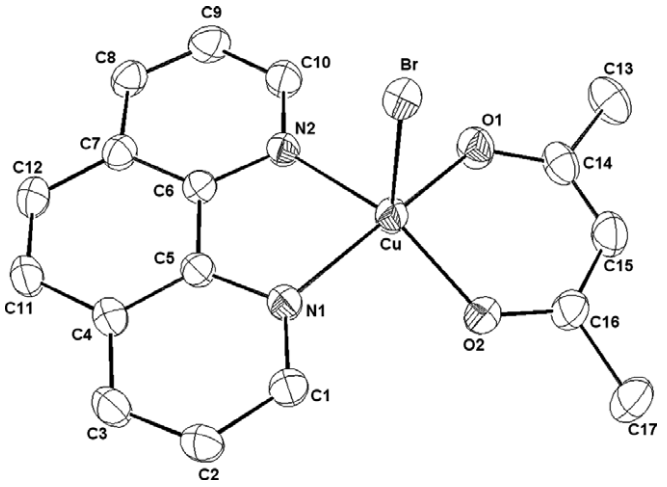


Fig. 3. ORTEP view of compound **2** showing atom labelling, thermal ellipsoids are drawn at the 50% probability ellipsoids and hydrogen atoms have been omitted for clarity.

Table 2
Selected bond lengths (Å) and angles (°) for **1**

Cu1–O1	1.911(3)	Cu1–O2	1.934(3)	Cu1–N1	2.011(4)
Cu1–N2	2.020(4)	Cu1–O3	2.282(5)	Cu2–O5	1.915(4)
Cu2–O4	1.919(4)	Cu2–N3	1.998(4)	Cu2–N4	2.008(5)
Cu2–O6	2.264(5)				
O1–Cu1–O2	94.37(15)	O1–Cu1–N1	90.64(17)	O2–Cu1–N1	168.48(18)
O1–Cu1–N2	169.33(18)	O2–Cu1–N2	93.11(16)	N1–Cu1–N2	80.67(17)
O1–Cu1–O3	94.97(18)	O2–Cu1–O3	98.11(19)	N1–Cu1–O3	91.77(19)
N2–Cu1–O3	91.49(18)	O5–Cu2–O4	93.86(16)	O5–Cu2–N3	169.6(2)
O4–Cu2–N3	92.27(16)	O5–Cu2–N4	91.01(18)	O4–Cu2–N4	164.95(19)
N3–Cu2–N4	81.01(18)	O5–Cu2–O6	96.64(19)	O4–Cu2–O6	99.01(19)
N3–Cu2–O6	90.7(2)	N4–Cu2–O6	94.5(2)		

Table 3
Selected bond lengths (Å) and angles (°) for **2**

Cu–O2	1.9226(18)	Cu–O1	1.9239(18)	Cu–N1	2.0165(19)
Cu–N2	2.036(2)	Cu–Br	2.6308(5)		
O2–Cu–O1	93.52(8)	O2–Cu–N1	89.17(8)	O1–Cu–N1	164.56(9)
O2–Cu–N2	160.14(9)	O1–Cu–N2	91.48(8)	N1–Cu–N2	81.16(8)
O2–Cu–Br	102.50(7)	O1–Cu–Br	97.46(7)	N1–Cu–Br	96.79(6)
N2–Cu–Br	95.87(6)				

significant differences between solution and solid-state band maxima. The two visible bands for the solid were observed at 9.9×10^3 cm^{-1}, 13.4×10^3 cm^{-1} and there were two broad UV bands at 28.5×10^3 cm^{-1} and 34.6×10^3 cm^{-1}. In solution the visible bands were greatly broadened and blue shifted to 10.4×10^3 cm^{-1} and 15.8×10^3 cm^{-1} while the UV bands remained narrow at 28.5×10^3 cm^{-1}, 33.8×10^3 cm^{-1} and 36.5×10^3 cm^{-1}. The low energy UV band which is most likely due to $Br^- \rightarrow Cu$ charge transfer has negligible intensity in solution. These observations lead to the following conclusion: in the case of compound **1**, the structure of the Cu(II) complex species is the same in both solid and solution while in the case of compound **2**, the bromide ligand is exchanged with the solvent or water present in the solvent.

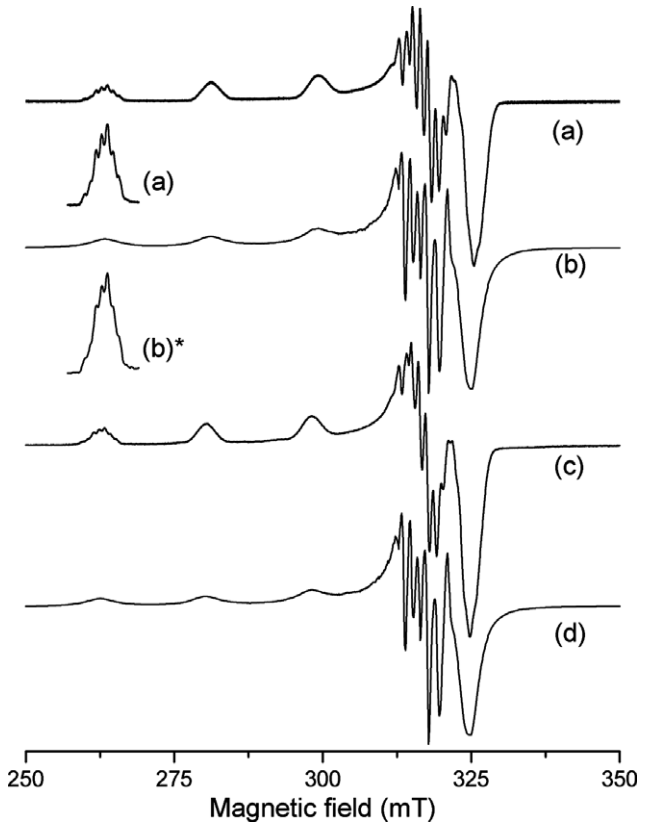


Fig. 4. Frozen solution EPR spectra, at X-band. Experimental: (a) compound **1**; (c) compound **2**. Simulated (with parameters given in the text): (b) compound **1**; (d) compound **2**. (b) * shows the simulated super-hyperfine splitting on the lowest field hyperfine component obtained as explained in the text.

The above conclusion is further supported by the observation of almost identical EPR spectra in frozen ethanol solutions for the two compounds (Fig. 4). The spectra correspond to an axial spin Hamiltonian with the following g and copper hyperfine coupling parameters (in units of 10^{-4} cm^{-1}) derived by computer simulation: $g_x = 2.048$, $g_y = 2.068$, $g_z = 2.250$ (compound **1**), 2.257 (compound **2**), $A_x = 20$, $A_y = 15$, $A_z = 187$. EPR spectra have been previously reported for some other members of the CASIOPEINAS® family [2] and the parameters are in agreement with a $d_{x^2-y^2}$ ground state and significant covalency. The most important feature, different from the previous reports, is the resolution of ^{14}N super-hyperfine (shf) splitting on the lowest field parallel component (Fig. 4). If the molecular structure found in the solid state is maintained in solution one should see a 5-line shf pattern corresponding to two equivalent N atoms in the equatorial plane. However the spectra clearly shows at least seven components on the lowest field parallel line. We considered three possible explanations. (i) Decomposition of the complex and formation of a species with three coordinated N atoms. This can be ruled out because it would have produced a mixture of different Cu(II) complex species and an overlapped EPR spectra. (ii) The shf pattern arises from unequal coupling to the two N atoms of the chelating ligand. The positions of the shf lines can be reproduced by assuming coupling constants of 8×10^{-4} cm^{-1} and 16×10^{-4} cm^{-1} for the two N atoms. This would mean that solvent perturbation and inherent plasticity of the Cu(II) coordination polyhedron leads to a distortion of the complex so as to make it an unsymmetrical chelate. However, this model fails to satisfactorily reproduce the intensity distribution within the multiplet. (iii) The additional lines arise from a resolution of ^{63}Cu/^{65}Cu hyperfine components on the lowest field line. In order to test this model we simulated the spectra for ^{65}Cu (using the hyperfine parameters give above) and ^{63}Cu with the coupling scaled down by a factor of 0.94 (the ratio of the nuclear g-factors) and added the two after weighting with the relative abundances (^{63}Cu:^{65}Cu = 0.69:0.31). This produces a satisfactory matching with the observed splittings (Fig. 4). ^{63,65}Cu resolution is often not seen in EPR from frozen solutions. In the present case, it results from narrow line widths combined with a high value for A_z.

4. Conclusions

Compound **1** is the simplest member of the CASIOPEINAS® family of compounds. Its synthesis in crystalline

form requires careful control of pH, this being accomplished in the present study by the use of potassium cyanate. Like other reported compounds in this series, both **1** and **2** contain five coordinate Cu(II) in distorted square pyramidal coordination in the solid state and presumably also in solution. Considering the electronic spectral data and the near identical EPR spectra of **1** and **2**, it would appear that in compound **2**, the coordinated bromide is displaced by the solvent, leading to similar structure for both compounds in solution.

Acknowledgements

We thank a referee for reminding us of the possible resolution of $^{63}Cu/^{65}Cu$ hyperfine splitting in EPR. O.O.O. thanks TWOWS (Third World Organization for Women in Science) for the award of fellowship and Ladoke Akintola University of Technology, Nigeria for study leave. A.S. Onawumi is highly appreciated for his support. The X-ray data were collected at the diffractometer facility at University of Hyderabad, established by the Department of Science and Technology, Government of India. Infrastructure support from UGC (UPE program) is also acknowledged. This work was supported by CSIR, India. T.K.P. thanks the CSIR for award of research fellowship.

Appendix A. Supplementary material

CCDC 639772 and 639773 contain the supplementary crystallographic data for this paper. These data can be obtained free of charge via http://www.ccdc.cam.ac.uk/conts/retrieving.html, or from the Cambridge Crystallographic Data Centre, 12 Union Road, Cambridge CB2 1EZ, UK; fax: (+44) 1223-336-033; or e-mail: deposit@ccdc.cam.ac.uk. Supplementary data associated with this article can be found, in the online version, at doi:10.1016/j.poly.2007.08.041.

References

[1] I. Gracia-Mora, L. Ruiz-Ramirez, C. Gomez-Ruiz, M. Tinoco-Mendez, A. Marquez-Quinones, L.R.-D. Lira, A. Marin-Hernandez, L. Macias-Rosales, M.E. Bravo-Gomez, Metal Based Drugs 8 (2001) 19.
[2] A. De Vizcaya-Ruiz, A. Rivero-Muller, L. Ruiz-Ramirez, G.E.N. Kass, L.R. Kelland, R.M. Orr, M. Dobrota, Toxicol. In Vitro 14 (2000) 1.
[3] L. Ruiz-Ramirez, I. Gracia-Mora, M.E. da le Rosa, H. Sumano, C. Gomez, F. Arenas, E. Gomez, E. Pimentel, M. Cruces, J. Inorg. Biochem. 51 (1993) 406.
[4] A. Tovar-Tovar, L. Ruiz-Ramirez, A. Campero, A. Romerosa, R. Moreno-Esparza, M.J. Rosales-Hoz, J. Inorg. Biochem. 98 (2004) 1045.
[5] Y. Fukuda, K. Sone, Bull. Chem. Soc. Jpn. 43 (1970) 556.
[6] N.A. Bailey, D.E. Fenton, M.V. Franklin, M. Hall, J. Chem. Soc., Dalton Trans. (1980) 984.
[7] A.M. Madalan, V.Ch. Kravtsov, D. Pajic, K. Zadro, Y.A. Simonov, N. Stanica, L. Ouahab, J. Lipkowski, M. Andruh, Inorg. Chim. Acta 357 (2004) 4151.
[8] S.I. Troyanov, A.N. Grigor'ev, A.A. Drozdov, L.I. Martynenko, Russ. J. Inorg. Chem. 37 (1992) 107.
[9] A. Paulovicova, U. El-Ayaan, Y. Fukuda, Inorg. Chim. Acta 321 (2001) 56.
[10] C.-C. Su, S.-P. Wu, C.-Y. Wu, T.-Y. Chang, Polyhedron 14 (1995) 267.
[11] A.M. Madalan, C. Ruiz-Perez, E. Melnic, V. Kravtsov, M. Andruh, Rev. Roum. Chim. 50 (2005) 11.
[12] A.M. Madalan, M. Noltemeyer, M. Neculai, H.W. Roesky, M. Schmidtmann, A. Muller, Y. Journaux, M. Andruh, Inorg. Chim. Acta 359 (2006) 459.
[13] A.M. Madalan, M. Andruh, L. Ouahab, S. Golhen, Rev. Roum. Chim. 46 (2001) 433.
[14] G. Swarnabala, M.V. Rajasekharan, Inorg. Chem. 28 (1989) 662.
[15] SAINTPLUS, Bruker AXS Inc., Madison, WI, USA, 2003.
[16] G.M. Sheldrick, SADABS, Program for Empirical Absorption Correction, University of Göttingen, Göttingen, Germany, 1996.
[17] G.M. Sheldrick, SHELX-97, Programs for Crystal Structure Analysis, University of Göttingen, Göttingen, Germany, 1997.
[18] L.J. Farrugia, J. Appl. Crystallogr. 30 (1997) 565.
[19] C.F. Macrae, P.R. Edgington, P. McCabe, E. Pidcock, G.P. Shields, R. Taylor, M. Towler, J. van de Streek, J. Appl. Crystallogr. 39 (2006) 453.
[20] H. Nakai, S. Ooi, H. Kuroya, Bull. Chem. Soc. Jpn. 50 (1977) 531.

Available online at www.sciencedirect.com
ScienceDirect
Polyhedron 27 (2008) 118–124
POLYHEDRON
www.elsevier.com/locate/poly

Complexes of Al(III) with D-gluconic acid

Andrea Lakatos [a], Tamás Kiss [a,b,*], Roberta Bertani [c,*], Alfonso Venzo [d], Valerio B. Di Marco [e]

[a] Bioinorganic Chemistry Research Group of the Hungarian Academy of Sciences, University of Szeged, P.O. Box 440, H-6701 Szeged, Hungary
[b] Department of Inorganic and Analytical Chemistry, University of Szeged, P.O. Box 440, H-6701 Szeged, Hungary
[c] Department of Chemical Processes and Engineering, Universita di Padova, Via Marzolo 9, 35131 Padova, Italy
[d] CNR Institute of Sciences and Molecular Technologies, Corso Stati Uniti 4, 35100 Padova, Italy
[e] Department of Chemical Sciences, University of Padova, Via Marzolo 1, 35131 Padova, Italy

Received 29 June 2007; accepted 29 August 2007
Available online 22 October 2007

Abstract

The complexation of Al(III) with D-gluconic acid was studied in solution by means of pH-potentiometry, ESI mass spectrometry and one- and two-dimensional NMR spectroscopy. Six complexes were found to form in solution from pH 2 to 10: $[AlL]^{2+}$, $[AlLH_{-1}]^{+}$, $[AlLH_{-2}]$, $[AlLH_{-3}]^{-}$, $[AlL_2H_{-1}]$ and $[AlL_2H_{-2}]^{-}$. NMR spectroscopy indicated very complicated chemical exchange processes between the free ligand and gluconic acid molecules bound in the metal complexes, with different coordination modes resulting in changes both of the chemical shift and of the line shape of the signals. A solid complex $[AlL_2H_{-1}] \cdot 2H_2O$ was isolated as a microcrystalline powder and characterized. The structures of the complexes are discussed on the basis of the spectroscopic results and MM force field calculations.
© 2007 Elsevier Ltd. All rights reserved.

Keywords: D-gluconic acid; Aluminium(III); Speciation; NMR; ESI-MS

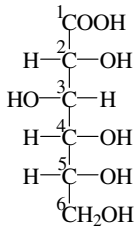
1. Introduction

Gluconic acid and its derivatives, especially sodium gluconate, have wide applications in food and pharmaceutical industry. This latter application is based on the outstanding properties of gluconic acid to chelate di- and trivalent metal ions. For example, calcium gluconate is used for treating calcium(II) deficiency, iron(III) gluconate is administered in iron therapy and zinc(II) gluconate is used as an ingredient for treating common cold and various diseases caused by zinc deficiency [1]. Due to its wide range of applications and good complexing ability, the study of metal gluconate complexes have received increasing attention in recent years [2–9] (see Scheme 1).

Al(III), as a typical hard metal ion, prefers coordination of oxygen donors, especially negatively charged ones, such as carboxylates, phosphates and alcoholates [10]. (Poly)hydroxy(poly)carboxylates including, citric acid [11], tartaric acid [12] and sugar carboxylates [2,13] are strong Al(III)-binders that are able to prevent hydrolysis of the metal ions under physiological conditions. Our previous study of C6 aldonic acids has revealed the versatile coordination possibilities of alcoholic OH/O^{-} groups which are in close proximity to negatively charged O-donors [13]. These sugar carboxylates act as polydentate ligands and form very stable complexes with Al(III). The solution state of Al(III)–gluconate was also studied in earlier works [14–16]. In these speciation studies only the occurrence of 1:1 complexes was considered. In recent investigations of the interactions between gluconate and trivalent metal ions (Fe(III) and lanthanides(III)) the

* Corresponding authors. Address: Bioinorganic Chemistry Research Group of the Hungarian Academy of Sciences, University of Szeged, P.O. Box 440, H-6701 Szeged, Hungary. Tel.: +36 62 544 337; fax: +36 62 420 505 (T. Kiss).
E-mail address: tkiss@chem.u-szeged.hu (T. Kiss).

0277-5387/$ - see front matter © 2007 Elsevier Ltd. All rights reserved.
doi:10.1016/j.poly.2007.08.035



Scheme 1.

formation of 1:2 complexes were also found by potentiometry and some spectroscopic methods [5–7]. Similar speciation model could be in principle assumed also for the trivalent Al(III) which questions the correctness of the results published so far in the literature [14–16].

The aim of the present work was to clarify the solution speciation and structure of the complexes formed in the Al(III)–gluconic acid system through the use of pH-potentiometry, ESI-MS and NMR spectroscopy. The results of these investigations could provide a basis for a better understanding of the transport and toxicity of Al(III) as Al(III)–gluconate solutions are often employed in the experimental toxicology and provide much higher bioavailability of Al(III) than Al(III)–citrate or Al(III)–maltolate [17].

2. Experimental

2.1. Reagents

D-gluconic acid sodium salt of the highest analytical purity (Aldrich product) was used without further purification. Stock solution of the ligand had a slightly basic pH to avoid lactonization of the ligand [5] and was prepared freshly every day. The exact concentrations of the ligand solutions were determined by potentiometric titration, using the Gran method [18]. The Al(III) stock solution was prepared from recrystallized $AlCl_3 \cdot 6H_2O$, and its metal ion concentration was determined gravimetrically through its oxinate. The stock solution contained 0.1 M HCl to prevent hydrolysis of the metal ion.

2.2. Potentiometric measurements

The stability constants of the proton and Al(III) complexes of the ligand were determined by pH-potentiometric titrations of 50 mL samples. To avoid lactonization of gluconic acid the solutions were acidified just before the beginning of the titration, and the pH was never lower than 2. The ligand concentration was 0.004 M and 0.002 M and the metal ion to ligand ratio was varied between 1:1 and 1:10. The titrations were performed with 0.2 M carbonate-free KOH solution of known concentration under purified argon atmosphere. The ionic strength of all solutions was adjusted to 0.2 M KCl and the samples were thermostatted at 25.0 ± 0.1 °C. Duplicate titrations were performed. The reproducibility of the titrations was within 0.005 pH unit. Titration points obtained when 5 min was not enough to attain pH equilibrium were omitted from the evaluation. The pH was measured with a Radiometer PHM 84 instrument with a CMAWL Russel combined glass electrode, which was calibrated for hydrogen ion concentration according to Irving et al. [19]. The concentration stability constants $\beta_{pqr} = [M_pL_qH_r]/[M]^p[L]^q[H]^r$ were calculated with the aid of the computer program PSEQUAD [20]. The stability constants used for the hydroxo species of Al(III) were taken from Ref. [21] and corrected to $I = 0.2$ M using the Davies equation: -5.49 for $[AlH_{-1}]^{2+}$, -13.54 for $[Al_3H_{-4}]^{5+}$, -108.62 for $[Al_{13}H_{-32}]^{7+}$ and -23.40 for $[AlH_{-4}]^{-}$.

2.3. Preparation of the complex $[Al(C_6H_{10}O_7)(C_6H_9O_7)] \cdot 2H_2O$ (1)

A mixture of 0.242 g (1 mmol) $AlCl_3 \cdot 6H_2O$ and 0.438 g (2 mmol) D-gluconic acid sodium salt was dissolved in 10 mL distilled water. The pH of the solution was adjusted to ~4 with KOH. Addition of absolute ethanol (~70 mL) yielded a microcrystalline powder, which was isolated by filtration and dried at 40 °C under vacuum for 12 h. The yield was 0.16 g (55.17%). FTIR(KBr): ν_{COO}: 1646 cm^{-1}. Elemental *Anal.* Calc. for the microcrystalline powder: C, 31.86; H, 5.53. Found: C, 30.05; H, 5.22%. An explanation of the big discrepancy in the analytical results might be the uncertainty of the structural water content of the complex. We found this in other cases too, when we had *X*-ray evidences for some unstoichiometric amount of bound water in the intersticia of the crystal [13].

2.4. NMR spectroscopy

^1H, ^{13}C NMR and two-dimensional spectra were recorded at 25 °C at 400.13 and 100.61 MHz, respectively, on a Bruker Avance DRX-400 spectrometer equipped with a VSP-400 reverse detector broad-band probe and a Bruker VST-100 temperature controller. Chemical shifts were referenced to the signal of DSS as an internal standard. The samples were prepared in D_2O and the pH was adjusted with concentrated NaOD and DCl, using the relationship $pD = pH + 0.4$. The concentrations of the solutions were 0.01–0.1 M in Al(III) and the metal ion:ligand ratio was 1:1 or 1:2.

Presaturation of the H_2O signal was performed, when necessary. Suitable integral values for the proton spectra were obtained with a pre-scan delay of 10 s. The proton resonances were assigned by means of standard chemical shift correlations and COSY, TOCSY and NOESY experiments. The ^{13}C resonances were assigned through 2D-heterocorrelated COSY experiments (HMQC with the *bird* sequence [22] and quadrature along F1, achieved with the TPPI method [23] for the H-bonded carbon atoms, and HMBC [24] for the quaternary ones).

2.5. ESI-MS measurements

The mass-spectrometric measurements were recorded on a LCQ Deca (Finnigan PAF) mass spectrometer equipped with an electrospray ion source. MS and multiple mass-spectrometric (MS^n) experiments were performed both in positive and in negative ion mode by direct infusion of an aqueous solution of the analyte at a flow rate of 5 μL/min. The instrumental conditions were as follows: source potential 4 kV, capillary temperature 270 °C, sheath gas (N_2) flow rate 40 arbitrary units. Collisional experiments on preselected ion species were performed by application of a supplementary rf voltage in the range 0–5 V with helium as a target gas.

2.6. Energy calculations

Energy calculations were performed using the MM2 force field algorithm [25] included in the computer programme CS Chem 3D Ultra 6.0 (CambridgeSoft.Com, Cambridge, USA, 2000). Atom types and parameters available in the software were used for the calculations. Energies were calculated for structures described in the NMR results section.

3. Results and discussion

3.1. Potentiometric titrations

The protonation constant of the ligand was found to be 3.36. If the differences in the experimental conditions (the ionic strength and the type of electrolyte used) are taken into account, this value is in fairly good agreement with those reported in the literature: 3.44 at 25 °C and 0.1 M KNO_3 [14], 3.50 at 25 °C and 0.1 M $NaClO_4$ [3].

The formation constants of the Al(III) complexes are listed in Table 1, together with some derived data.

The Al(III)–gluconic acid titration data were evaluated on the basis of the literature results. As mentioned above early potentiometric measurements were fitted considering only mononuclear complexes: Motekaitis and Martell [14] proposed the formation of species $[AlL]^{2+}$, $[AlLH_{-1}]^{+}$ and $[AlLH_{-3}]^{-}$ whereas Escandar et al. [16] assumed an even simpler complexation model involving the species $[AlLH_{-1}]^{+}$ and $[AlLH_{-3}]^{-}$. When these simple models were assumed in our calculations, rather poor fits were obtained between the experimental and the calculated titration curves. The speciation models obtained recently for other trivalent metal ions interacting with gluconic acid reveal the formation of bis complexes, besides mononuclear 1:1 complexes [5–7]. Other metal ions such as Cu(II) [2] and VO(IV) [8] were also proved to form 1:2 complexes with D-gluconic acid. When the formation of bis complexes was considered in our calculations the fitting parameter improved considerably as compared with the model including only mono complexes. The best fit between the experimental and the calculated titration curves was obtained with the species and stability constants listed in Table 1. The distribution of the complexes formed in the Al(III)–D-gluconic acid system as a function of pH is depicted in Fig. 1a.

Table 1
Stability constants for proton and Al(III) ion complexes [log β] of gluconic acid at 25 °C and $I = 0.2$ M (KCl)

Species	log β[a]
HL	3.36(2)
$[AlL]^{2+}$	2.38(3)
$[AlLH_{-1}]^{+}$	−1.49(6)
$[AlLH_{-2}]$	−5.95(15)
$[AlLH_{-3}]^{-}$	−11.94(3)
$[AlL_2H_{-1}]$	1.48(6)
$[AlL_2H_{-2}]^{-}$	−3.70(15)
Fitting [Δcm^3][b]	0.015
Number of points	360

[a] The uncertainty of the stability constants are given as 3SD values after the constants in parentheses.
[b] The average difference between the experimental and the calculated titration curves expressed in the volume of the titrant.

Complexation starts with the formation of the species $[AlL]^{2+}$ in the slightly acidic pH range. Stepwise deprotonations of this complex occur at higher pH with pK values of 3.87, 4.46 and 5.99 leading to the formation of species $[AlLH_{-1}]^{+}$, $[AlLH_{-2}]$ and $[AlLH_{-3}]^{-}$, respectively. The relatively low values of the first two constants (significantly lower than $pK_{Al(H_2O)_6} = 5.52$) suggest that the metal bound water molecules are not deprotonating. Thus, the species $[AlLH_{-1}]^{+}$ is most probably formed by the simultaneous coordination of the carboxylate group and the deprotonated alcoholic function in the α-position, and in the complex $[AlLH_{-2}]$ a (O^-, COO^-, O^-) tridentate coordination may be assumed. The species $[AlLH_{-3}]^{-}$ may be formed into two different ways: (i) by the deprotonation of another alcoholic group or (ii) by the deprotonation of one of the water molecules from the coordination sphere of the metal ion. The relatively high value of the deprotonation constant of $[AlLH_{-2}]$ indicates that process (ii) is more likely in this case. At ligand excess 1:2 species are also formed: $[AlL_2H_{-1}]$ and $[AlL_2H_{-2}]^{-}$. In these complexes again the parallel deprotonation and subsequent coordination of the alcoholic-OH functions or ionization of the Al(III) coordinated water molecules may be assumed in overlapping processes. Moreover, the ligand molecules can coordinate either in a bidentate or in a tridentate way involving one or two protonated OH groups of the polyalcoholic chain. Stability constant comparison with the formation constants of the corresponding Al(III) complexes of lactic acid [26,27] reveals that one of the ligand molecules coordinates in a tridentate way. Namely the basicity adjusted equilibrium constant $\log \beta_{AlL_2H_{-1}} - \log \beta_{HL}$ is 0.59 log unit higher for the Al(III)–gluconic acid complex than that for the corresponding Al(III)–lactic acid complex ($\log \beta_{AlL_2H_{-1}} - \log \beta_{HL} = 1.48–3.36 = -1.88$ for gluconic acid and −2.47 for lactic acid) suggesting the participation of an extra alcoholic-OH function in Al(III) binding in the

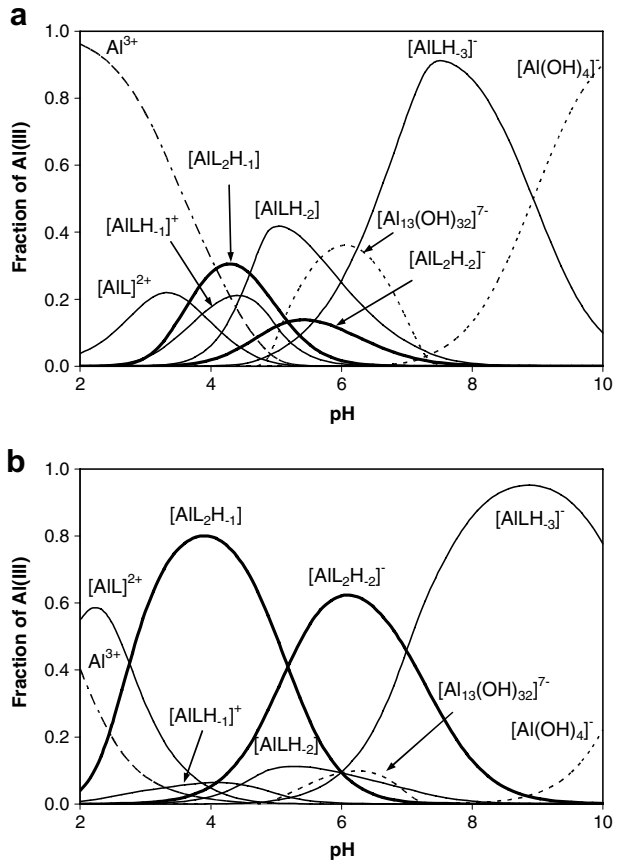


Fig. 1. Species distribution curves as a function of pH in the Al(III)–D-gluconic acid system at a metal ion to ligand ratio of 1:2 and at (a) $c_{Al(III)} = 0.002$ M; (b) $c_{Al(III)} = 0.1$ M. Solid lines indicate the 1:1, bold lines the 1:2 and dashed lines the binary hydroxo complexes.

case of the former ligand [26]. At pH 5 the complex $[AlL_2H_{-1}]$ starts to liberate a proton with a $pK = 5.18$. This, in accordance with other aliphatic hydroxycarboxylates [26,27] would rather be ascribed to the ionization of the water molecule in the coordination sphere of metal ion than to the deprotonation of a second alcoholic-OH group of the sugar carboxylate.

Further investigations were primarily focused on the characterizations of the bis complexes, since they are "new" species with respect to the literature data. Attempts have also been made to crystallize one of the two bis complexes which was partially successful as the neutral complex $[AlL_2H_{-1}]$ was obtained as a microcrystalline powder (**1**). Fig. 1b shows the species distribution calculated at concentrations used for preparation of the solid complex and used in the NMR spectroscopic measurements. In these conditions the bis complexes are the predominant species in the system in wide pH range (pH 3–7) except the acidic and the basic pH range.

3.2. ESI-MS measurements

ESI-MS measurements were carried out to prove the stoichiometry of the solid compound **1**. ESI-MS is often used to characterize metal–ligand complexes which seems to be not involved in solution equilibria. ESI-MS, however, is more and more widely used to study solutions at equilibrium (for example, to see the resulting species formed in solution upon dissolution of a solid complex) [28] and, despite of some limitations, it seems to be a suitable tool for the determination of the stoichiometry of species present in solution. The exact proton content of the complexes usually can not be determined by ESI-MS, because protonation reactions easily occur in the ESI chamber [28]. Our previous experiences show that in the case of Al(III)–ligand solution equilibria, ESI-MS gave a fairly good qualitative picture of the solution speciation as compared with the pH-potentiometric results [13,29,30].

ESI measurements were carried out both in positive and negative ion mode, in a solution containing 0.001 g of **1** dissolved in water/methanol 3:1 mixture. The spectra unambiguously proved the 1:2 metal to ligand stoichiometry in complex **1**. The main signals present in the spectra and their assignment are summarized in Table 2.

In negative ion mode two signals could be detected at m/z 195 and 415. The first peak is that of the free gluconic acid. The second is attributed to the complex ion $[AlL_2H_{-2}]^-$ originated from compound **1** ($[AlL_2H_{-1}]$), which loses a proton in the ESI source.

In positive ion mode the spectrum is richer in signals (Fig. 2) due to formation of Na^+ adducts. Adduct formation with alkali metal ions (especially sodium) in the ESI source is also a common feature of ESI-measurements. Thus **1** is detected as the protonated species $[AlL_2]^+$ (m/z 417) and two sodium adducts (m/z 439, 461). The latter signal is a result of the deprotonation of **1** and simultaneous addition of two sodium ions. The signal at m/z 221 corresponds to the mono complex $[AlLH_{-1}]^+$ which is a result of the partial dissociation of **1** upon dissolution. Mono complexes could not be detected in the negative ion mode. A reasonable explanation of this fact is that according to potentiometry at pH ~ 4.5 the two mono complexes are positively charged ($[AlLH_{-1}]^+$) and neutral ($[AlLH_{-2}]$). To be detectable in negative ion mode they should lose 2 and 1 protons, respectively. Their ion response factor is therefore smaller in negative ion mode than in positive.

Table 2
Main signals observed in the solution of the solid complex **1**

Detection mode	m/z	Relative abundance %	Stoichiometries
Negative ion	195	100	$[L]^-$
	415	55	$[AlL_2H_{-2}]^-$
Positive ion	219	14	$[LH \cdot Na]^+$
	221	20	$[AlLH_{-1}]^+$
	241	13	$[L \cdot 2Na]^+$
	417	30	$[AlL_2]^+$
	439	100	$[AlL_2H_{-1} \cdot Na]^+$
	459	32	$[2L \cdot 3Na]^+$
	461	60	$[AlL_2H_{-2} \cdot 2Na]^+$

[a]Expressed in the percentage of the intensity of the signal with maximum intensity (100%).

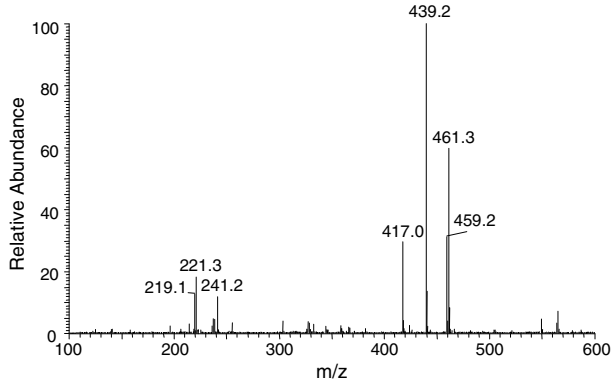


Fig. 2. ESI-MS spectrum of the solid compound **1** dissolved in water–methanol 3:1 mixture, recorded in positive ion mode.

Moreover, in-source deprotonation at acidic pH is less favoured than protonation. The free ligand is detected as sodium adducts at *m*/*z* 219, 241 and 459 corresponding to the species $[LH+Na]^+$, $[L+2Na]^+$ and $[2L+3Na]^+$ respectively. We should mention here, that gluconic acid has a high tendency to form adducts with Na^+: the ESI spectrum recorded in the solution containing only gluconic acid at pH ~ 4 shows the signals of a series of sodium adducts of the type $[nL+(n+1)Na]^+$, detected in the 100–2000 *m*/*z* range. MS^n experiments carried out on the ion at *m*/*z* 417 shows that the first two steps of fragmentation occur with the loss of two water molecules, whereas the third step is the simultaneous loss of two CO_2 molecules, most probably from the carboxylic group of the two ligands. This is another proof of the 1:2 metal–ligand stoichiometry of **1**.

4. NMR spectroscopy

The proton and carbon resonances of gluconic acid were assigned by two-dimensional H–H and C–H correlation measurements, and they are in agreement with the literature data. The chemical shift values of the ^1H and ^{13}C resonances obtained at p*D* 3.9 in a solution of 0.2 M gluconic acid are listed in Table 3.

The ^1H NMR spectrum recorded in the solution of **1** dissolved in D_2O (p*D* = 3.9) in a concentration of 0.1 M is depicted in Fig. 3b. A considerable downfield shift and selective broadening of the signals of H(2) and H(3) could be observed with respect to the free ligand (Fig. 3a). COSY and HMQC measurements show that also the peak corresponding to H(4) is shifted downfield; it appears under the signal of H(6a) at 3.816 ppm. The other resonances (those of H5, H(6a) and H(6b)) remain practically at the same positions as in the spectrum of gluconic acid alone. The ^{13}C spectrum recorded in the same sample presents a similar picture: the signals ascribed to C(1), C(2), C(3) and C(4) are shifted and broadened as compared with the signals of gluconic acid itself, whereas the signals corresponding to C(5) and C(6) are much less affected. This selective line broadening and chemical shift changes of some of the signals indicate that the affected protons and carbon atoms may be close to functional groups involved in the Al(III) coordination, namely the alcoholic/alcoholate groups of C2, C3 and C4 are assumed to participate in the metal chelation.

Table 3
Characteristic NMR parameters in D_2O at 25 °C for free gluconic acid and its complex $[AlL_2H_{-1}]$

	Chemical shifts in δ (ppm) at p*D* = 3.9					
	H2	H3	H4	H5	H6a	H6b
Free ligand	4.186	4.042	3.760	3.749	3.811	3.649
complex **1**	4.386	4.113	3.825	3.748	3.809	3.650
	C1	C2	C3	C4	C5	C6
Free ligand	180.85	76.50	73.70	75.15	73.98	65.43
complex **1**	very broad	78.96b	73.35b	75.84b	73.62	65.33

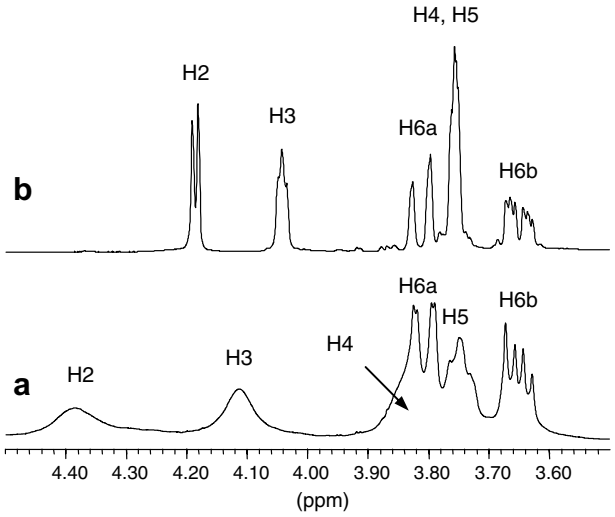


Fig. 3. ^1H NMR spectrum of (a) complex **1** dissolved in D_2O at autogenous p*D* = 4.2 and concentration of 0.1 M; (b) free gluconic acid at p*D* = 4.2.

Participation of the alcoholic-OH/alcoholate-O^- groups in the coordination is mostly determined by their steric arrangement within the molecule. MM force field calculations performed for AlL_2H_{-1} show that the more favoured structures are formed by the tridentate coordination of one ligand and a bidentate coordination of the other. The tridentate chelation of both ligands is less favoured, their steric energy level is about 20–30% higher and this increase is probably not counterbalanced by the bond energy of the additional Al-OH interaction. Among the species with tridentate-bidentate chelation, the (COO^-, C(2)–O^-, C(3)–OH) coordination of the tridentate ligand is the energetically less favoured structure. All the other possible binding namely e.g. (COO^-, C(2)–O^-, C(4)–OH) or (COO^-, C(3)–O^-, C(4)–OH) have fairly little energy differences and they can be considered equally probable. For the bidentate ligand, MM calculations can not distinguish among the three possible coordination modes, i.e. (COO^-, C(2)–

OH), (COO^-, C(3)–OH), (COO^-, C(4)–OH). Previous studies on Al(III)-(poly)hydroxycarboxylates show that the first is the main coordination mode in these systems [10,11,13]. Accordingly, we can assume that the tridentate (COO^-, C(2)–O^-, C(4)–OH) coordination of one of the ligand molecules and a bidentate (COO^-, C(2)–OH) coordination of the other one is the most favoured. This structure is depicted in Fig. 4 A similar structure, but with the tridentate (COO^-, C(2)–OH, C(4)–OH) coordination of the second ligand molecule was proposed for the ML_2H_{-1} complex of D-gluconic acid formed with praseodymium(III) ion [5].

The NMR spectra of complex **1** display one rather broad set of signals for the bound ligand (Fig. 3), but the phase sensitive NOESY spectrum indicates unambiguously the presence of exchange processes. These reactions may occur between the bis complex and the free gluconic acid molecules, (the presence of a small amount of the free ligand can be detected at this pH by pH-potentiometry, see Fig. 1b) and/or between the ligand molecules of the different coordination isomers of the bis complex. These processes are in the fast exchange regime on the NMR time-scale, and they explain the line broadening of the signals observed upon coordination of Al(III) to gluconic acid.

Fig. 5 depicts the pH dependence of the NMR signals at metal ion to ligand ratio of 1:2. In the more acidic pH range two sets of signals are detected in the ^{1}H NMR spectra. The assignment is straightforward if we compare the spectra recorded at 1:1 and 1:2 metal-to-ligand ratios at pD 2 (Fig. 5a and b) and take into account the pH-metric results. The signals, the intensities of which increase at 1:2 ratio, were ascribed to the bis complex $[AlL_2H_{-1}]$ and the other set of signals should belong to the mono complex $[AlL]^{2+}$. These two complexes are in slow ligand exchange between each other and in fast ligand exchange with the uncomplexed gluconic acid which has a significant concentration at pD 2. Thus, the observed chemical shifts of these two complexes are a weighted average of those corresponding to the complex and unbound ligand, and their position is dependent on the ratios between the complex and the free ligand. The upfield shift of these signals with increasing pH

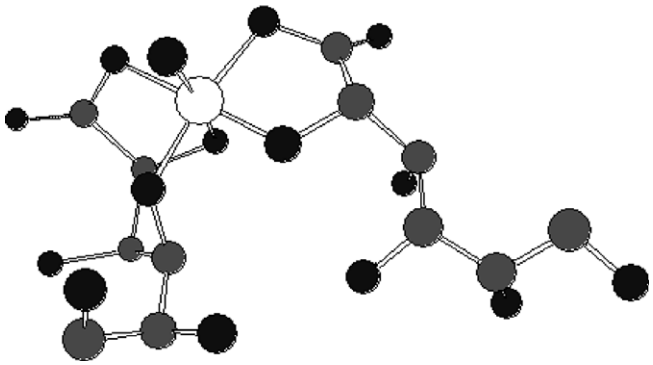


Fig. 4. Most probable structure of $[AlL_2H_{-1}]$.

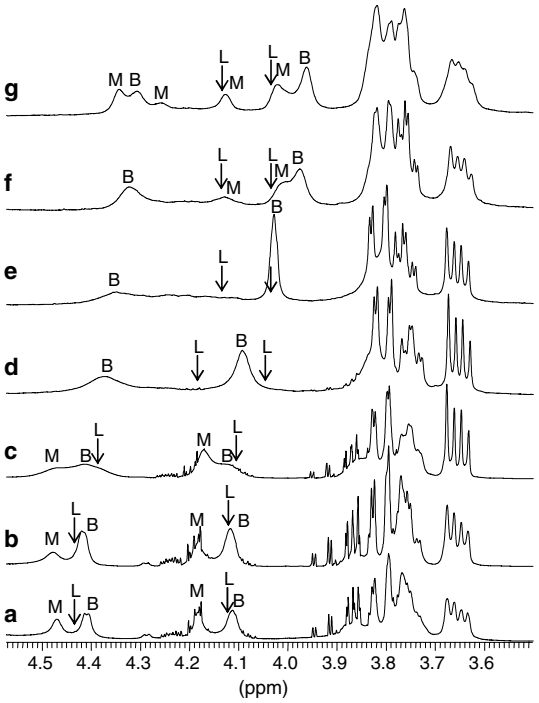


Fig. 5. ^{1}H NMR spectra obtained for the Al(III)–gluconic acid system at an Al(III) concentration of 0.1 M at ratios (a) 1:1 ratio, pD = 2.0; and 1:2 ratios at pD values of (b) pD =2.0, (c) pD = 2.6, (d) pD = 3.9, (e) pD = 5.4, (f) pD = 6.7, (g) pD = 7.6. The arrows indicates the chemical shifts of the H(2) and H(3) protons of gluconic acid taken from the spectra obtained in solution containing the ligand alone at the corresponding pD values. Notations: M = mononuclear complex, B = bis complex, L = free ligand.

is explained in one hand by the change in the complex/free ligand ratio, and in the other hand by the deprotonation of the complexes. The proton exchange reactions between the differently protonated complexes with the same metal to ligand ratios are fast in the NMR time-scale. Accordingly, until pH 4 $[AlL]^{2+}$ and $[AlL_2H_{-1}]^+$ are present in different ratios, whereas at pH > 4 the bis complex deprotonates to form $[AlL_2H_{-2}]^-$ and its signal shifts upfield.

Above pH 7 new signals (M) appear which could be ascribed to the complex $[AlLH_{-3}]^-$ found potentiometrically most probably present in the form of two coordination isomers, involving one or two deprotonated alcoholate functions in metal ion binding. MM calculations cannot distinguish between the two isomers, but in agreement with Escandar et al. [16] participation of two deprotonated alcoholate-O^- in Al(III) binding seems to be more probable.

5. Conclusions

The calculations from potentiometric experiments allowed us to conclude that besides the 1:1 species two bis complexes $[AlL_2H_{-1}]$ and $[AlL_2H_{-2}]^-$ are also formed in the Al(III)–gluconic acid system. These species have not been considered in earlier works. A basic question concerning the binding mode of the deprotonated mono and

bis complexes is whether the proton is liberated from a coordinated water molecule resulting in a mixed hydroxo species or from the ligand molecule through the formation of a gluconato complex with coordination of one or more alcoholate-O^- functions. The different methods: stability constant comparison, multinuclear NMR spectroscopy, ESI-MS and MM calculations provided enough information to suggest the most probable binding mode in these complexes. Accordingly, in the bis complexes a bidentate–tridentate coordination of the ligands is the most probable binding mode according to the MM calculations, the sixth position of Al(III) is occupied by a water molecule, which can deprotonate to form the mixed hydroxo species $[AlL_2H_{-2}]^-$. While, in the solid state this binding mode can be mostly assumed, in solution various binding isomers with the participation of alcoholic functions in C2, C3 and C4 carbon atoms may be formed, as indicated by NMR spectroscopy. Stability constant comparisons suggest that in the 1:1 complex the ligand also coordinates in a tridentate way, and depending on the stoichiometry of the species one or two alcoholic-OH groups are deprotonated due to a stepwise coordination to the metal ion. The ionization of one of the coordinated water molecules is an overlapping process, results finally in the formation of species $[AlLH_{-3}]^-$.

Acknowledgements

The authors thank to Nicola Bonato for his assistance in the experimental work. One of the authors (T.K.) is very thankful to Professors G. Bombi and B. Corain for the technical help and everyday useful discussions during his COST-PECO study in Padova. The work was mostly carried out in the frame of a bilateral collaboration agreement between the Academy Institutions of Italy and Hungary, CNR and HAS (Project Nos. 11/2004 and 11/2007). L.A. gratefully acknowledges financial support through the award of a János Bólyai research fellowship.

References

[1] S. Ramachandran, P. Fontanille, A. Pandey, C. Larroche, Food, Technol. Biotechnol. 44 (2006) 185, and references therein.
[2] B. Gyurcsik, L. Nagy, Coord. Chem. Rev. 203 (2000) 81, and references therein.
[3] T. Gajda, B. Gyurcsik, T. Jakusch, K. Burger, B. Henry, J.-J. Delpuech, Inorg. Chim. Acta 275–276 (1998) 130.
[4] A.A. Frutos, L.F. Sala, G.M. Escandar, M. Devillers, J.M. Salas Peregrin, M. Gonzalez Sierra, Polyhedron 18 (1999) 989.
[5] S. Giroux, P. Rubini, B. Henry, S. Aury, Polyhedron 19 (2000) 1567.
[6] S. Giroux, S. Aury, B. Henry, P. Rubini, Eur. J. Inorg. Chem. (2002) 1162.
[7] T. Bechtold, E. Burtscher, A. Turcanu, J. Chem. Soc., Dalton Trans. (2002) 2683.
[8] P.A.M. Williams, D.A. Barrio, S.B. Etcheverry, E.J. Baran, J. Inorg. Biochem. 98 (2004) 333.
[9] A. Szorcsik, L. Nagy, B. Gyurcsik, Gy. Vanko, R. Kramer, A. Vertes, T. Yamaguchi, K. Yoshida, J. Radioanal. Nucl. Chem. 260 (2004) 459.
[10] T. Kiss, E. Farkas, Perspect. Bioinorg. Chem. 3 (1996) 199, and references therein.
[11] A. Lakatos, I. Banyai, P. Decock, T. Kiss, Eur. J. Inorg. Chem. (2001) 461.
[12] E. Marklund, L.O. Öhman, J. Chem. Soc., Dalton Trans. (1990) 755.
[13] A. Lakatos, R. Bertani, T. Kiss, A. Venzo, M. Casarin, F. Benetollo, P. Ganis, D. Favretto, Chem. Eur. J. 10 (2004) 1281.
[14] R.J. Motekaitis, A.E. Martell, Inorg. Chem. 23 (1984) 18.
[15] A.A. Sheikh-Osman, R. Bertani, A. Tapparo, G.G. Bombi, B. Corain, J. Chem. Soc., Dalton Trans. (1993) 3229.
[16] G.M. Escandar, A.C. Olivieri, M. Gonzalez-Sierra, A.A. Frutos, L.F. Sala, J. Chem. Soc., Dalton Trans. (1995) 799.
[17] R.J. Ward, Y. Zhang, R.R. Crichton, J. Inorg. Biochem. 87 (2001) 9.
[18] G. Gran, Acta Chem. Scand. 4 (1950) 559.
[19] H.M. Irving, M.G. Miles, L.D. Pettit, Anal. Chim. Acta 38 (1967) 475.
[20] L. Zékány, I. Nagypál, G. Peintler, PSEQUAD for Chemical equilibria, Technical Software Distribution, Baltimore, 1991.
[21] L.O. Öhman, S. Sjöberg, Acta Chem. Scand. 36 (1982) 47.
[22] A. Bax, S. Subramian, J. Magn. Reson. 67 (1986) 565.
[23] (a) G. Otting, K. Wuthrich, J. Magn. Reson. 76 (1988) 569; (b) G. Drobny, A. Pines, S. Sinton, D.P. Weitekamp, D. Wemmer, Faraday Symp. Chem. Soc. 13 (1978) 49.
[24] A. Bax, M.F. Summers, J. Am. Chem. Soc. 108 (1986) 2093.
[25] N.L. Allinger, J. Am. Chem. Soc. 99 (1977) 8127.
[26] T. Kiss, I. Sovago, R.B. Martin, J. Pursiainen, J. Inorg. Biochem. 55 (1994) 53.
[27] P. Rubini, A. Lakatos, D. Champmartin, T. Kiss, Coord., Chem. Rev. 228 (2002) 137, and references therein.
[28] V.B. Di Marco, G.G. Bombi, Mass Spectrom. Rev. 25 (2006) 347.
[29] V.B. Di Marco, A. Károly-Lakatos, A. Venzo, R. Bertani, R. Seraglia, T. Kiss, Inorg. Chim. Acta 359 (2006) 4227.
[30] V. Di Marco, G.G. Bombi, M. Tubaro, P. Traldi, Rapid Commun. Mass Spectrom. 17 (2003) 2039.

Available online at www.sciencedirect.com
ScienceDirect
Polyhedron 27 (2008) 125–132
POLYHEDRON
www.elsevier.com/locate/poly

Synthesis, electrochemistry and *in situ* spectroelectrochemistry of a new Co(III) thio Schiff-base complex with *N*,*N*′-bis(2-aminothiophenol)-1,4-bis(carboxylidene phenoxy)butane

Ismail Yilmaz [a,*], Hamdi Temel [b], Hüseyin Alp [b]

[a] *Istanbul Technical University, Faculty of Arts and Sciences, Chemistry Department, 34469 Istanbul, Turkey*
[b] *Dicle University, Faculty of Education, Department of Chemistry, 21280 Diyarbakır, Turkey*

Received 2 March 2007; accepted 24 August 2007
Available online 22 October 2007

Abstract

A new cobalt Schiff-base complex, [Co(L)(OH)(H_2O)] (where L = [*N*,*N*′-bis(2-aminothiophenol)-1,4-bis(carboxylidene phenoxy)butane), was synthesized and its electrochemical and spectroelectochemical properties were investigated using cyclic voltammetry (CV), differential pulse voltammetry (DPV) and thin-layer spectro-electrochemistry in solutions of dimethyl sulfoxide (DMSO) and dichloromethane (CH_2Cl_2). The [Co(L)(OH)(H_2O)] complex displays two well-defined reversible reduction processes with the corresponding anodic waves. The half-wave potentials of the first and second reduction processes were displayed at $E_{1/2} = 0.08$ V and $E_{1/2} = -1.21$ V (scan rate: 0.100 Vs^{-1}) in DMSO, and $E_{1/2} = -0.124$ V and $E_{1/2} = -1.32$ V (scan rate: 0.100 Vs^{-1}) in CH_2Cl_2. The potentials of the reduction processes in DMSO are shifted toward negative potentials (0.220–0.112 V) compared to those in CH_2Cl_2. The electrochemical results are assigned to two one-electron reduction processes; $[Co(III)L] + {}^{-}e \rightarrow [Co(II)L]^{-}$ and $[Co(II)L]^{-} + {}^{-}e \rightarrow [Co(I)L]^{2-}$. The six-coordination of the complex remains unchanged during the reduction processes and the electron transfer processes were not followed by a chemical reaction upon scan reversal. It was also seen that [Co(L)(OH)(H_2O)] was reduced at a more positive potential than the corresponding salen analogs. The shift and reversibility are apparently related to the high degree of electron delocalization of the [Co(L)(OH)(H_2O)] complex, having a $N_2O_2S_2$ donor set and two additional benzene units. Additionally, *in situ* spectroelectrochemical measurements support Co(III)/Co(II) and Co(II)/Co(I) reversible reduction processes with the observation of the corresponding spectral changes with the applied potentials $E_{app} = -0.40$ and -1.60 V. Application of the spectroelectrochemical results allowed the determination of$E_{1/2}$ and n (the number of electrons) from the spectra of the fully oxidized and reduced species in one unified experiment as well. The results obtained by this method are in agreement with those by the CV and DPV methods.
© 2007 Elsevier Ltd. All rights reserved.

Keywords: Schiff-base; Thiosalen; Cobalt; Electrochemistry; Spectroelectrochemistry

1. Introduction

Transition metal Schiff-base complexes with tetradentate (N_2X_2) ligands (N is imine nitrogen; $X = O^{-}$ (salen), S^{-} (thiosalen), OR, SR, PR_2, etc.) have been extensively studied [1]. Some of these complexes have interesting applications, e.g., in catalytic oxidation reactions and electrochemical reduction processes [2], in metalloenzyme-mediated catalysis [3,1e] and asymmetric catalysis, as catalytically active materials to develop surface modified electrodes in many reactions [4], photochromism [5] and complexing towards certain toxic metals [6]. Among these metal complexes, cobalt Schiff-base complexes have especially attracted considerable interest due to their ability to bind reversibly O_2 and CO_2, their potential catalytic behavior for electrochemical reduction of organic halides, and their oxidative coupling catalytic reactions of phenols

* Corresponding author. Tel.: +90 212 285 6831; fax: +90 212 285 6386.
E-mail address: iyilmaz@itu.edu.tr (I. Yilmaz).

0277-5387/$ - see front matter © 2007 Elsevier Ltd. All rights reserved.
doi:10.1016/j.poly.2007.08.044

and oxidation of olefins [1b,1c,3a,7]. Recently, the discovery that cobalt(III) Schiff-base complexes are potent antiviral agents prompted researchers to initiate an investigation of Co(III) interactions with proteins and nucleic acids [8]. Co(III) Schiff-base complexes with two amines in axial positions have been used as antimicrobial agents as well [9]. On the other hand, electro-generated cobalt(I) salen complexes were described for the catalytic reduction of halogenated organic species [10]. Thiosalen derivatives are Schiff-base ligands where the sulfur atoms are substituted with oxygen atoms in salen ligands. The replacement of two phenoxide oxygen atoms in salen by two thiolate sulfur atoms should, in principle, lead to changes in the redox properties of the corresponding complexes. Since sulfur is a medium-strength soft base, whereas oxygen is a strong hard base, it is often expected that coordination by sulfur will stabilize metals in low oxidation states, i.e., lead to a decrease in the potential of the complex based on the metal [11]. There have been numerous transition metal complexes containing salen and thiosalen, with two sulfur and two nitrogen donor atoms (N_2S_2 donor set), [11b,12] but only a few examples of complexes containing a NSO donor set have been reported in the literature [13]. Recently, some complexes of bis(alkylthio)salen were studied in view of them acting as templates for Diels–Alder reactions and their potential surfactant character, and they were anticipated to have a wide range of interesting stereochemical, redox and physical properties [12d,14]. The study of transition metal thiolates is frequently complicated by air sensitivity and a tendency to form polymetallic complexes with bridging μ-SR groups. The air sensitivity of transition metal thiolates typically results in degradation of the enzymatic and catalytic sites due to disulfide formation, expulsion of metal ion and metal oxide formation [15]. Fine tuning of the electronic structure by the introduction of electron donating and withdrawing substituents in the equatorial or axial position of ligand is known to enhance the reactivity of Schiff-base complexes in particular applications.

In the present paper, we report the synthesis and characterization of a new thio Schiff- base ligand L (L = [*N*,*N*′-bis(2-aminothiophenol)-1,4-bis(carboxylidene phenoxy)butane]), involving an $N_2O_2S_2$ donor set, and its cobalt(III) complex. It is known that a combination of electrochemical and spectroelectrochemical methods provides a powerful tool to reveal the complementary nature of the molecular structure and to supply a better understanding of the electrochemical behavior of the electro-generated species in bulk solution [16–21]. Little attention has been given to transition metal Schiff-base complexes based on thiosalen, as compared to salen analogs. Moreover, no *in situ* spectroelectrochemical study on thiosalen or thiolate derivatives has been reported in the literature. The aim of this study is to present for the first time detailed information on the electro-spectroelectrochemical behavior of a new cobalt(III) thio Schiff-base complex bearing the $N_2O_2S_2$ donor set and two additional aromatic groups.

2. Experimental

2.1. Physical measurements

Conductivities of 10^{-3} M solutions of the complex were measured in DMF at 25 °C using a Conductivity Hand-Held Meter LF 330. The IR spectra of the complex were recorded with a Midac 1700 instrument in KBr pellets. ^{1}H NMR spectra were recorded on a BRUKER DPX-400 High Performance Digital FT-NMR spectrometer in DMSO-d_6. LC/MS-API-ES mass spectra were recorded using an AGILENT model 1100 MSD mass spectrophotometer. Magnetic moments were determined on a Sherwood Scientific magnetic moment balance (Model No: MK1) at room temperature (23 °C) using $Hg[Co(SCN)_4]$ as a calibrant: diamagnetic corrections were calculated from Pascal's constants [22]. The elemental analyses were conducted on a Carlo Erba instrument. UV–Vis spectra were recorded on an Agillent Model 8453 diode array spectrophotometer. Cyclic voltammograms (CV) were carried out using CV measurements with a Princeton Applied Research Model 2263 potentiostat controlled by an external PC. A three electrode system (BAS model solid cell stand) was used for CV measurements in DMSO and consisted of a 2 mm sized platinum disc electrode as the working electrode, a platinum wire counter electrode and an Ag/AgCl reference electrode. The reference electrode was separated from the bulk solution by a fritted-glass bridge filled with the solvent/supporting electrolyte mixture. The ferrocene/ferrocenium couple (Fc/Fc^+) was used as an internal standard but all potentials in the paper are referenced to the Ag/AgCl reference electrode. Solutions containing the complex were deoxygenated by a stream of high purity nitrogen for at least 5 min before running the experiment. The solution was protected from air by a blanket of nitrogen during the experiment. Controlled potential electrolysis (CPE) was performed with a Princeton Applied Research Model 2263 potentiostat/Galvanostat. A BAS model electrolysis cell with a fritted glass to separate the cathodic and anodic portions of the cell was used for bulk electrolysis. The sample and solvent were placed into the electrolysis cell under nitrogen. UV–Vis spectroelectrochemical experiments were performed with a home-built thin-layer cell that utilized a light transparent platinum gauze working electrode [23]. Potentials were applied and monitored with a Princeton Applied Research Model 2263 potentiostat. Time- and potential-resolved UV–Vis spectra were recorded on an Agillent Model 8453 diode array spectrophotometer.

2.2. Materials

All the chemicals and solvents were purchased from Merck and Fluka Chemical Co. 1,4-Bis(2-carboxyaldehyde phenoxy)butane was prepared as in the literature

[24]. Dimethyl sulfoxide (DMSO) was dried over a molecular sieve of 4 Å. Dichloromethane (CH_2Cl_2) was three times treated with H_2SO_4 and distilled over P_2O_5 and CaH_2 prior to use. Electrochemical grade tetrabutylammonium perchlorate (TBAP, Fluka Chemical Co.) was recrystallized from ethyl alcohol and dried in a vacuum oven at 40 °C for at least 1 week prior to use.

2.3. Synthesis of the ligand [N,N′-bis(2-aminothiophenol)-1,4-bis(carboxylidene phenoxy)butane]

A solution of 1,4-bis(2-carboxyaldehyde phenoxy)butane (10.0 mmol, 2.98 g) in 50 ml absolute ethanol was added dropwise over 2 h to a stirred solution of 2-aminothiophenol (20.0 mmol, 2.50 g) dissolved in 50 ml hot absolute ethanol. A solid mass separated out on cooling, which was kept in a refrigerator for better crystallization. It was then filtered and recrystallized from a mixture of absolute ethanol–DMF, m.p. 140–142 °C; yield: 4.11 g (80%). *Anal.* Calc. C, 70.3; H, 5.46; N, 5.47; S, 12.5. Found: C, 70.4; H, 5.67; N, 5.65; S, 12.6%. IR (KBr cm^{-1}): 3316 $\nu(N^+H)$, 3066 ν(Ar–C–H), 2953, 2916, 2870 ν(Aliph-C–H), 1599 ν(C=N), 1486, 1469, 1452 ν(Ar–C=C), 1280, 1241 ν(Ar–O), 1157, 1112, 1051 ν(R–O), 749, 740 ν(C–S). ^{1}H NMR (DMSO-d_6, δ ppm): 2.30 (CH_2–CH_2–O) (s), 4.45 (CH_2–O) (s), 7.10–8.00 (Arom-H) (m, $J = 8$ Hz), 8.40 (CH=N) (s). ^{13}C NMR (DMSO-d_6, δ ppm): C1: 26.7, C2: 68.7, C9: 163, Arom. C's: 111, 121, 121, 122, 123, 125, 126, 130, 132, 136, 152. UV–Vis (λ_{max}): $\lambda_1 = 229$ ($\varepsilon = 49100\ M^{-1}\ cm^{-1}$), $\lambda_2 = 282$ ($\varepsilon = 5880\ M^{-1}\ cm^{-1}$), $\lambda_3 = 322$ ($\varepsilon = 7720\ M^{-1}\ cm^{-1}$) (in ethanol). $\lambda_1 = 283$ ($\varepsilon = 10620\ M^{-1}\ cm^{-1}$), $\lambda_2 = 325$ ($\varepsilon = 14740\ M^{-1}\ cm^{-1}$) (in DMF). Mass spectra: 511.2 $[L-H]^+$ (M_A: 512 g/mol).

2.4. Synthesis of the Co(III) complex [Co(L)(OH)(H2O)]

To a stirred solution of 1,4-bis(2-carboxyaldehyde phenoxy)butane (0.447 g, 1.50 mmol) and $Co(CH_3COO)_2 \cdot 4H_2O$ (0.374 g, 1.50 mmol) in methanol (60 ml) was added dropwise 2-aminothiophenol (0.375 g, 3.00 mmol) in methanol (40 mL). After the addition was completed, the stirring was continued for 2 h. A blue colored precipitation was filtered off and washed with acetic acid and diethyl ether, respectively. The product was purified from a mixture of absolute ethanol–acetone, then dried in air. Yield: 0.702 g (80%). m.p. 188–189 °C. *Anal.* Calc. C, 59.6; H, 4.80; N, 4.64; S, 10.6. Found: C, 59.5; H, 4.95; N, 4.82; S, 10.4%. $\Lambda = 8.70\ \Omega^{-1}\ mol^{-1}\ cm^2$. $\mu_{eff} = 3.96$ B.M. IR (KBr, ν cm^{-1}): 3400 $\nu(H_2O)$, 3022 ν(Ar–CH), 2923, 2856 ν(Aliph-CH), 1542 ν(C=N), 1470, 1458, ν(Ar–C=C), 1283, 1247 ν(Ar–O), 1159, 1108, 1050 ν(R–O), 752, 739 ν(C–S), 520 ν(Co–O) 458 ν(Co–N). UV–Vis (λmax, nm) (DMSO): $\lambda_1 = 330$, $\lambda_2 = 579$, $\lambda_3 = 664$, $\lambda_3 = 809$. Mass spectra: m/z: 571.6 $[Co(L)–(H_2O)–(OH)]^+$ (M_A: 604 g/mol).

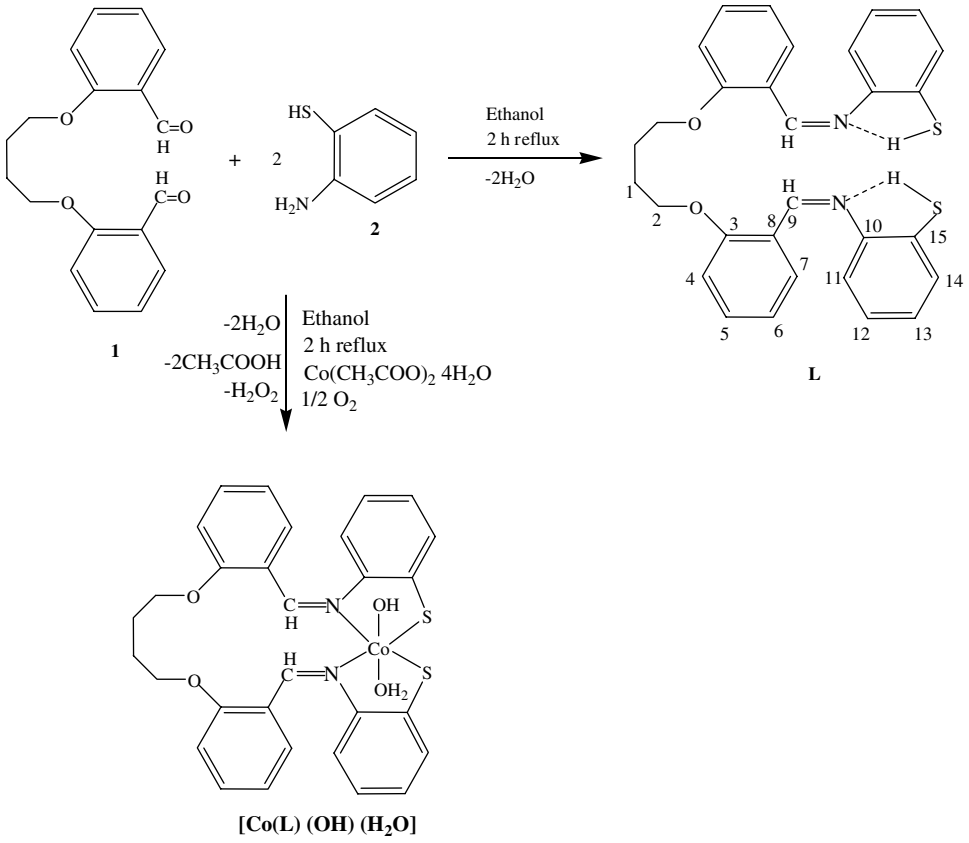
3. Results and discussion

3.1. Synthesis

The new thio Schiff-base [*N*,*N*′-bis(2-aminothiophenol)-1,4-bis(carboxylidene phenoxy)butane] (**L**) was synthesized by the condensation of 1,4-bis(2-carboxyaldehyde phenoxy)butane and 2-aminothiophenol in absolute ethanol. The preparation of the ligand (**L**) and its cobalt complex [Co(L)(OH)(H_2O)] is illustrated in Scheme 1. The stoichiometries of the ligand and its complex were confirmed by their elemental analyses. The molar conductance measured in DMF of a 10^{-3} M solution of the complex gave a value of 8.70 $ohm^{-1}\ cm^2\ mol^{-1}$, which indicated its non-electrolytic behavior [25–27]. The metal/ligand mole ratio was found to be 1:1, in accord with the elemental analysis (Scheme 1). The observed magnetic moment of the Co(III) complex is 3.96 B.M. This value suggests an octahedral stereochemistry of the complex. The proposed structure is presented in Scheme 1. The complex was fine powder hence we could not manage to prepare single crystals for X-ray crystallography.

The IR spectrum of the thio Schiff-base ligand exhibited a strong sharp band at 3316 cm^{-1}. This band was assigned to the stretching frequency of the N^+H group, due to the presence of the intramolecular hydrogen bond (N···SH) in the molecule (Scheme 1). This band disappeared in the IR spectrum of the cobalt complex, as previously reported in the literature [28]. It was seen from the solid state IR spectra of the ligand and its Co(III) complex that the C=N band of the complex shifted to a lower value compared with that of the ligand [25–27,29–31]. Conclusive evidence of the bonding was also shown by the observation that new bands in the spectra of the metal complex appeared at 458 and 520 cm^{-1}, assigned to (Co–O) and (Co–N) stretching vibrations, that were not observed in the spectrum of the ligand [25–27,29–31]. A broad and weak band around 3400 cm^{-1} is attributed to the OH vibration of water molecules in the complex [26]. A ^{1}H NMR spectrum of the Co(III) complex could not be obtained because of its paramagnetic nature. The data of the ^{1}NMR and ^{13}C NMR spectra of the ligand are given in experimental section. The mass spectra of the ligand and its cobalt complex showed peaks attributable to the molecular ions, m/z: 511.2 $[L-H]^+$ and 571.6 $[Co(L)–(H_2O)–(OH)]^+$, respectively.

The electronic spectrum of the ligand (**L**) in ethanol shows absorption bands at 229 ($\varepsilon = 49100\ M^{-1}\ cm^{-1}$), 282 ($\varepsilon = 5880\ M^{-1}\ cm^{-1}$) and 322 nm ($\varepsilon = 7720\ M^{-1}\ cm^{-1}$). The bands appearing at the low energy side are attributable to $\pi \rightarrow \pi^*$ transitions associated with the azomethine chromophores. The bands at higher energy arise from $\pi \rightarrow \pi^*$ transitions within the phenyl rings. The absorption bands of the complex are shifted to longer wave numbers compared to those of the ligand [32]. A moderately intensive band observed in the range of 325–345 nm is attributable to the $n \rightarrow \pi^*$ transitions of the complex. The most prominent feature in the visible region of the



Scheme 1. Synthesis of the ligand (**L**) and the cobalt complex, [Co(L)(OH)(H_2O)].

spectrum of the complex in DMSO solution is two main bands observed at 664 and 809 nm, which are attributed to thio S(σ) → Co(III) (dπ) and thio S(π) → Co(III) (dπ) ligand to metal charge transfer transitions (LMCT). The intense blue color of the complex is probably due to these LMCT transitions and is not sensitive to different solvent systems, indicating the inertness of the axial ligands coordinated to the central metal ion. The blue-green color is a prominent feature for thiosalen complexes.

3.2. Electrochemistry

The cyclic voltammograms (CVs) of the complex [Co(L)(OH)(H_2O)] in the potential range 1.10–1.50 V (versus Ag/AgCl) and for scan rates of 0.025–0.50 Vs^{-1} in DMSO and CH_2Cl_2 solutions containing 0.1 M TBAP supporting electrolyte are shown in Fig. 1, where the inset figures represent differential pulse voltammograms (DPV) under the same experimental conditions. As can be seen from Fig. 1a and b, [Co(L)(OH)(H_2O)] displays two well-defined reversible reduction processes with the corresponding anodic waves. The half-wave potentials for the reversible Co(III)/Co(II) and Co(II)/Co(I) redox couples were calculated as the average of the cathodic and anodic peak potentials of the processes. The half-wave potentials of the first and second reduction processes are displayed at $E_{1/2} = 0.08$ V and $E_{1/2} = -1.21$ V (scan rate: 0.100 Vs^{-1}) in DMSO, and $E_{1/2} = -0.124$ V and $E_{1/2} = -1.32$ V (scan rate: 0.100 Vs^{-1}) in CH_2Cl_2. The potentials of the reduction processes in DMSO are shifted toward negative potentials (0.220–0.112 V) compared to those in CH_2Cl_2 because of the different donor number effect under the same experimental conditions. The first reduction process has about a unit ratio of anodic to cathodic peak currents (i_{pa}/i_{pc}). The ratio observed for the second reduction process deviates from unity due to the residual current at low potential. These results are assigned to a simple one-electron processes: $[Co(III)L] + {}^{-}e \rightarrow [Co(II)L]^{-}$ and $[Co(II)L]^{-} + {}^{-}e \rightarrow [Co(I)L]^{2-}$. The value of the anodic to cathodic peak separation of the Co(III)/Co(II) and Co(II)/Co(I) couples are 68–117 mV (scan rate: 0.025–0.50 Vs^{-1}) and 70–110 mV (scan rate 0.025–0.50 Vs^{-1}) in DMSO, respectively. These values are a little larger than expected theoretically for a reversible one-electron process [33]. However, under our experimental conditions, the peak separation of the ferrocene/ferrocenium couple was observed to be 70–100 mV (scan rate: 0.025–0.50 Vs^{-1}), which can be used as a criterion for electrochemical reversibility. The peak separation increased only slightly with increasing scan rate, and this case was true for the ferrocene/ferrocenium couple under our experimental conditions. These reduction processes were diffusion controlled with the anodic current function ($I_{pa}/v^{1/2}$) independent of the scan rate (v) over the scan range 0.0250–0.500 Vs^{-1} [33]. Very similar electrochemical behavior was observed in CH_2Cl_2 under the same experimental conditions. Controlled potential electrolysis

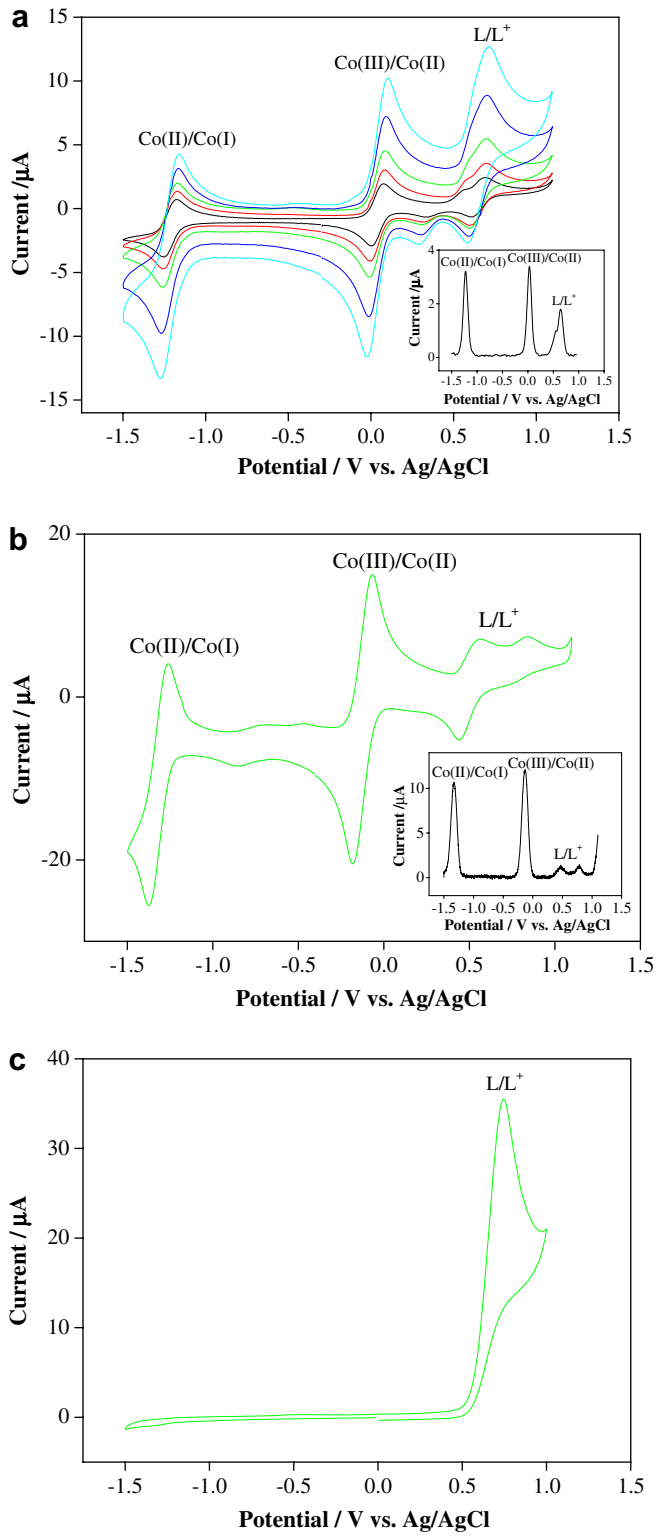


Fig. 1. Cyclic voltammograms (CV) of [Co(L)(OH)(H_2O)] in DMSO (a) and CH_2Cl_2 (b) solutions containing 0.1 M TBAP. Scan rates between 0.025 and 0.500 Vs^{-1} for (a) and 0.100 Vs^{-1} for (b) The inset figures in (a) and (b) represent differential pulse voltammograms (DPV). CV of ligand (**L**) in DMSO (scan rate 0.100 Vs^{-1}) (c).

revealed that a single electron was involved in each reduction step. The low peak separation observed for the Co(III)/Co(II) and Co(II)/Co(I) couples indicates that the six-coordination of the complex remains unchanged during the reduction processes and the electron transfer processes are not followed by a chemical reaction upon a reversal scan. On scanning through a second cycle, no change of the cathodic and anodic waves was observed for these electrode processes; the reductions occurred at the same potentials as observed in the first cycle. Multiple scans resulted in nearly superposable cyclic voltammograms, thereby showing the marked stability of the two reduction states of cobalt involved in the electrochemical study. It was reported in the literature that Co(III) salen complexes reduce to Co(II) species followed by a chemical reaction due to the loss of an axial ligand upon one electron being added to the d_{z^2} orbital. In this case, either the re-oxidation wave appeared at a higher potential or no corresponding anodic wave was observed upon reversal scan [34]. In our study, the reduction processes have reversible character, indicating that the axial ligands bound to the central atom are not released on the electrode surface in the timescale of the cyclic voltammetric measurement. It was also observed that [Co(L)(OH)(H_2O)] reduced at a more positive potential than the corresponding salen analogs. The shifts and reversibility are apparently related to the high degree of electron delocalization in the [Co(L)(OH)(H_2O)] complex, having a $N_2O_2S_2$ donor set and two additional benzene units. The high positive potential for the first reduction processes of some thiolate complexes was previously observed in the literature [12b]. The lower oxidation states, Co(I), are probably stabilized by the thio Schiff-base ligand system where the sulfur atom, having dπ orbitals, and imines groups (π^*) play an effective role with back donation [11]. It is known that increasing the number of aromatic rings or double bonds in the equatorial ligand facilitates reduction of Co(II) to Co(I) [11b]. The fact is clearly observed in our study. The electro-generated Co(I) species exhibiting reversible and stable character will likely facilitate a catalytic reduction of halogenated organic species as well as the Co(III)/Co(II) species [10]. The complex exhibited one oxidation wave at high scan rates (0.25–0.50 Vs^{-1}) and showed two peaks at low scan rates (0.25–0.50 Vs^{-1}). These two oxidation processes could be better differentiated by the CV (Fig. 1b) and DPV (Fig. 1b, the inset one) in CH_2Cl_2 solution. The ligand (**L**) exhibited one irreversible two electron-oxidation process without the corresponding cathodic wave (Fig. 1c). Its anodic peak potential (E_{pa}) was observed at 0.74 V. The anodic peak potentials of the complex appeared at almost same value in DMSO. So the oxidation processes of the complex are based on the ligand character. The splitting of the wave is probably due to the presence of two thiolate groups of the complex, oxidized at the different potentials.

3.3. UV–Vis spectra of the electro-oxidized and electro-reduced complexes

The spectroelectrochemical behavior of the [Co(L)-(OH)(H_2O)] complex was investigated using an *in situ*

spectroelectrochemical technique including chronoamperometry and UV–Vis spectroscopy in DMSO solution containing 0.2 M TBAP. The UV–Vis spectral changes for the reduced and oxidized species of the corresponding complex were obtained in a thin-layer cell the potentials were applied. The absorption spectra of the neutral complex and its electrochemically generated species are given in Fig. 2. The convenient applied potential values for the *in situ* spectroelectrochemical experiment were determined for each processes by taking CVs of the complexes in the thin-layer cell.

Fig. 2a shows the changes of the electronic spectrum of [Co(L)(OH)(H_2O)] during the first reduction process in the thin-layer cell. Well-defined isosbestic points were observed at 342, 442, 476 and 593 nm, confirming that the electrode reaction proceeded in a quantitative fashion and therefore with the absence of any coupled chemistry [16–21]. The main bands of the neutral complex observed at 664 and 809 nm can be attributed to the thio S(σ) → Co(III) (dπ) and thio S(π) → Co(III) (dπ) ligand to metal charge transfer transitions (LMCT). The intensity of these bands decreased and new bands formed at 571 and 389 nm, and a broad band at 315 nm in the timescale of the applied potential at $E_{app} = -0.4$ V (this process was completed within 300 s). A few new bands of low intensity were also observed between 300 and 600 nm. As a result of adding one electron to the Co(III) ion in the complex, one-electron reduction results in a Co(III) (d^6) → Co(II) (d^7) process, which makes the electron transition from the ligand to the metal harder. So the LMCT was observed at higher energy compared with that of the neutral complex, as expected. It is well known that spectroelectrochemistry provides the best knowledge on the redox process of complexes which is based on metal or ligand, reduction or oxidation [16–21]. The reduction process observed at the potential $E_{1/2} = 0.08$ V in DMSO and $E_{1/2} = -0.124$ V in CH_2Cl_2 was confirmed by this technique. As seen, the corresponding spectral changes were observed at low cathodic peak potential ($E_{app} = -0.4$ V) (Fig. 2a), but no spectral changes were observed with applied potentials at more positive values (E_{app}, 0.15–0.35 V) than the cathodic peak potential of the first reduction ($E_{pc} = 0.08$ V). It clearly indicates that this process is the first reduction of the complex based on the cobalt ion. The original spectrum of the complex was obtained upon re-oxidation during spectroelectrochemical measurement. It is concluded that the singly-reduced species remains stable and is not accompanied by a chemical reaction in the timescale of the spectroelectrochemical measurement. The fact that the axial ligand was not released from the metal during the first reduction process was verified by this way. The spectroelectrochemical results are also in agreement with the results of the cyclic voltammetric measurement. The controlled potential coulometric (CPC) study indicated that the number of electrons transferred for the forward and reverse electrochemical reaction of the complex was one for the reduction and re-oxidation processes based on the

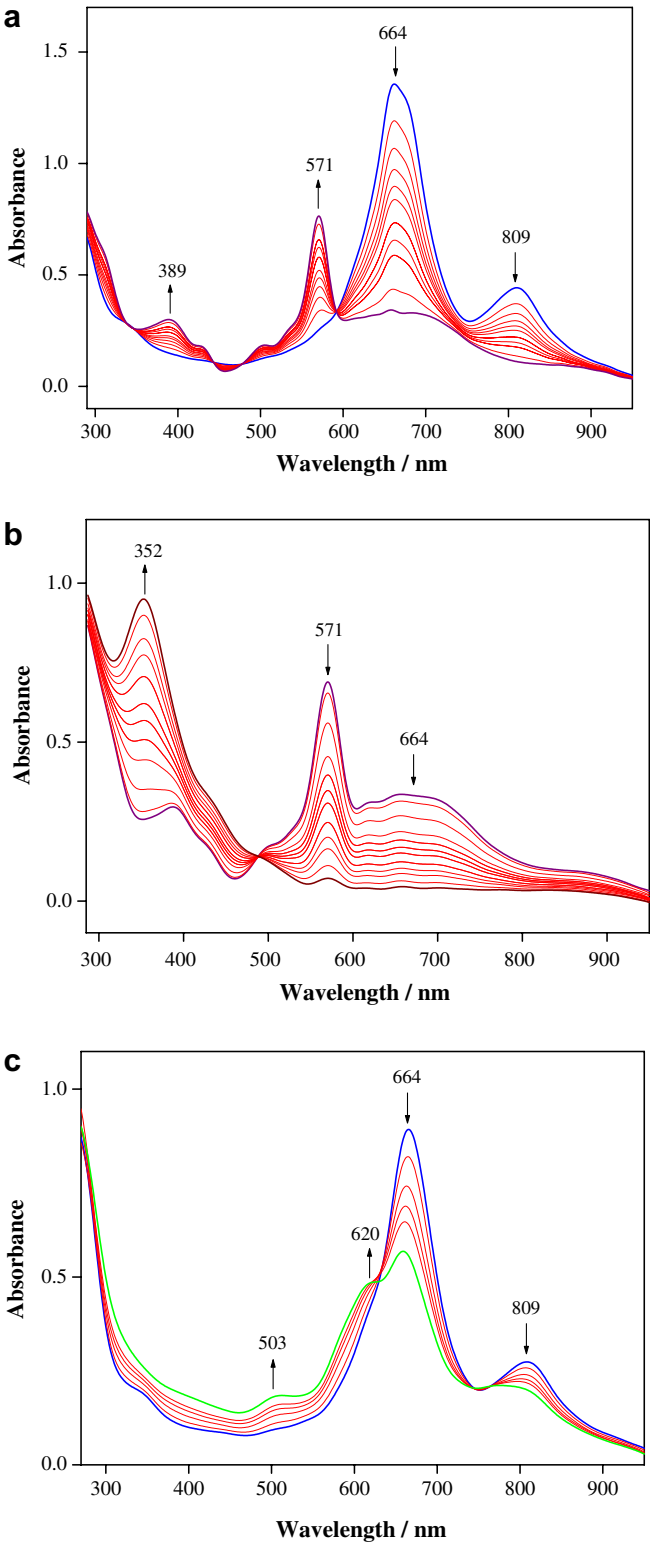


Fig. 2. Time-resolved UV–Vis spectral changes of [Co(L)(OH)(H_2O)] during the first reduction at $E_{app} = -0.4$ V (a), during the second reduction at $E_{app} = -1.60$ V (b), during the oxidation at $E_{app} = 1.0$ V (c), in DMSO solution containing 0.2 M TBAP.

Co(III)/Cu(II) couples. It was also seen by the *in situ* spectroelectrochemical measurement that the blue color of the complex changed to purple during the reduction process.

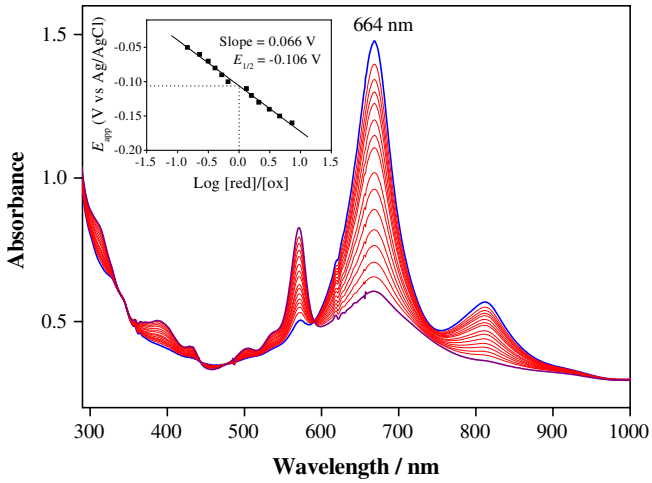


Fig. 3. Potential-resolved UV–Vis spectral changes of [Co(L)(OH)(H_2O)] during the first reduction (the potentials were applied in the range −0.05 to −0.20 V) in CH_2Cl_2 containing 0.2 M TBAP where the inset figure shows the plot of log([red]/[ox]) vs. applied potentials (E_{app}) for the Co(III)/Co(II) process.

It is known from the literature that some thiolate complexes with N_2S_2 or S_4 donor sets show absorptions in the visible region and have a blue-green color [12b,35].

The UV–Vis spectral changes upon the second reduction of [Co(L)(OH)(H_2O)] are shown in Fig. 2b. The isosbestic point is found at 487 nm, which clearly verifies the formation of the doubly-reduced species of the cobalt complex. As seen from Fig. 2b, the bands at 664 and 571 nm disappeared. Also, the band intensity corresponding to the 389 nm peak increases and its position shifts to lower energy (352 nm). This band is probably attributed to a metal to ligand charge transfer transition (MLCT) on the bases of the Co(II) (d^7) → Co(I) (d^8) process as a result of adding a second electron into the d orbital system. The original spectrum corresponding to the neutral complex was recovered upon re-reduction at the applied potential ($E_{app} = 0.25$ V).

The UV–Vis spectral changes upon oxidation of [Co(L)(OH)(H_2O)] are shown in Fig. 2c. The intensity of the main bands corresponding to the LMCT transition decrease and a shoulder develops at 620 nm. Isosbestic points are observed at 628 and 762 nm for the complex.

Application of the *in situ* spectroelectrochemical method allows determination of $E_{1/2}$, n (the number of electrons) with the spectra of fully oxidized and reduced species in one unified experiment. In this experiment, a series of potentials was applied to the optically transparent thin-layer cell in CH_2Cl_2, and individual spectra were measured after equilibrium was attained at each potential, as monitored by the current decay to a small, essentially zero value. Fig. 3 (potential-resolved spectra) shows such a result. The absorbance changes at a given wavelength (664 nm) can be related to the concentration ratio of the reduced to oxidized species by Eq. (1):

$$[R]/[O] = (A_2 - A_3)/(A_1 - A_2) \quad (1)$$

where A_2 is the absorbance of the mixture of oxidized and reduced forms, A_1 is the absorbance of the totally reduced form, and A_3 is the absorbance of the totally oxidized form. The Nernst Eq. (2)

$$E_{app} = E_{1/2} - (0.059)/n \log([R]/[O]) \quad (2)$$

indicates that a plot of E_{app} versus log[R]/[O] should be linear with a slope $59/n$ mV and an intercept of $E_{1/2}$, assuming Nernstian reversibility. For the $[Co(III)L] + {}^{-}e \rightarrow [Co(II)L]^{-}$ process, $E_{1/2} = -0.106$ V and $n = 0.90$ electron (slope = 66 mV, correlation coefficient = 0.997 for the plot) were found (Fig. 3, inset figure). These results are in agreement with those obtained from the cyclic voltammetric measurement and the bulk electrolysis.

4. Conclusion

A new cobalt Schiff-base complex, [Co(L)(OH)(H_2O)] (where L = [*N*,*N*′-bis(2-aminothiophenol)-1,4-bis(carboxylidene phenoxy)butane), was synthesized and its electrospectrochemical properties were investigated using CV, DPV and thin-layer spectroelectrochemical techniques in DMSO and CH_2Cl_2 solutions. This study presents for the first time detailed information on the electro-spectroelectrochemical behavior of the electro-generated species of a new thio Schiff-base cobalt (III) complex bearing the $N_2O_2S_2$ donor set and two additional aromatic groups. It is clear that this new blue cobalt(III) complex exhibits reversible and stable single- and double-reduced species in non-aqueous solution, based on the cobalt center, and has intense absorption bands in the visible region, and it will be a potential candidate molecule in electrocatalytic applications.

Acknowledgements

The support of the State Planning Organization (DPT, Project no. 90177) is gratefully acknowledged. This work has also been supported, in part, by the Turkish Academy of Sciences in the framework of the Young Scientist Award Program (TÜBA-GEBİP).

References

[1] (a) J. Vargas, J. Costamagna, R. Latorre, A. Alvardo, G. Mena, Coord. Chem. Rev. 119 (1992) 67;
(b) M.D. Hobday, T.D. Smith, Coord. Chem. Rev. 9 (1972) 311;
(c) S. Yamada, Coord. Chem. Rev. 192 (1999) 537;
(d) R.D. Jones, D.A. Summerville, F. Basolo, Chem. Rev. 79 (1979) 139;
(e) A. Christensen, H.S. Jensen, V. McKee, C.J. McKenzie, M. Munch, Inorg. Chem. 36 (1997) 6080.
[2] (a) L. Canali, D.C. Sherrington, Chem. Soc. Rev. 28 (1998) 85;
(b) E. Gallo, C. Floriani, H. Miyasaka, N. Matsumoto, Inorg. Chem. 35 (1996) 5964;
(c) W. Zhang, J.L. Loebach, S.R. Wilson, E.N. Jacobsen, J. Am. Chem. Soc. 112 (1990) 2801;
(d) D. Pletcher, H. Thompson, J. Electroanal. Chem. 464 (1999) 168.

[3] (a) E.C. Niederhoffer, J.H. Timmons, A.E. Martel, Chem. Rev. 84 (1984) 137;
(b) A. Vogler, H. Kunkely, Coord. Chem. Rev. 177 (1998) 81.
[4] (a) L. Mao, K. Yamamato, W. Zhou, L. Jin, Electroanalysis 12 (2000) 72;
(b) K. Chichak, U. Jacquembard, N.R. Branda, Eur. J. Inorg. Chem. 8 (2002) 357.
[5] J.D. Margerum, L.J. Miller, Photochromism, Interscience, Wiley, 1971, p. 569.
[6] W.J. Sawony, M. Riederer, Angew. Chem., Int. Ed. Engl. 16 (1977) 859.
[7] (a) D.H. Busch, N.W. Alcock, Chem. Rev. 94 (1994) 585;
(b) J. Losada, I. del Peso, L. Beyer, J. Hartung, V. Fernandez, M. Möbius, J. Electroanal. Chem. 398 (1995) 89;
(c) N.J. Henson, P.J. Hay, A. Redondo, Inorg. Chem. 38 (1999) 1618;
(d) C. Bianchini, R.W. Zoeliner, Adv. Inorg. Chem. 44 (1997) 263.
[8] A. Böttcher, T. Takeuchi, M.I. Simon, T.J. Meade, H.B. Gray, J. Inorg. Biochem. 59 (1995) 221.
[9] N. Raman, A. Kulandaisamy, C. Thangaraja, K. Jeyasubramanian, Trans. Met. Chem. 28 (2003) 29.
[10] (a) A.J. Fry, U.N. Sirisoma, J. Org. Chem. 58 (1993) 4919;
(b) D.L. Zhou, J. Gao, J.F. Rusling, J. Am. Chem. Soc. 117 (1995) 1127;
(c) D. Pletcher, H. Thompson, J. Electoanal. Chem. 464 (1999) 168.
[11] (a) M.H. Crisholm, E.R. Davidson, J.C. Hufmann, K.B. Quinian, J. Am. Chem. Soc. 123 (2001) 9652;
(b) K.P. Butin, A.A. Moiseeva, E.K. Beloglazkina, Y.B. Chudinov, A.A. Chizhevskii, A.V. Mironov, B.N. Trasevich, A.V. Lalov, N.V. Zyk, Russ. Chem. Bull. Int. Ed. 54 (2005) 173.
[12] (a) I. Bertini, L. Sacconi, G.P. Speroni, Inorg. Chem. 11 (1972) 1323;
(b) H.J. Krüger, R.H. Holm, Inorg. Chem. 26 (1987) 3647;
(c) A. Cristensen, H.S. Jensen, V. McKee, C.J. McKenzie, M. Munch, Inorg. Chem. 36 (1997) 6080;
(d) D.S. Bohle, A. Zafar, P.A. Goodson, D.A. Jaeger, Inorg. Chem. 39 (2000) 712;
(e) J.A. Ibers, R.H. Holm, Science 209 (1980) 223;
(f) M. Vaidyanathan, R. Balamurugan, U. Sivagnanam, M. Palaniandavar, J. Chem. Soc., Dalton Trans. (2001) 3498.
[13] (a) B. Turner, S. Swavey, Inorg. Chem. Commun. 10 (2007) 209;
(b) S. Sarkar, K. Dey, Spectrochim. Acta Part A 62 (2005) 383;
(c) A.A. Soliman, W. Linert, Thermochim. Acta 338 (1999) 67;
(d) D.C. Goodman, R.M. Buonomo, P.J. Farmer, J.H. Reibenspies, M.Y. Darensbourg, Inorg. Chem. 35 (1996) 4029.
[14] (a) L. Sacconi, F. Mani, A. Bencini, in: G. Wilkinson, R.D. Gillard, J.A. McCleverty (Eds.), Comprehensive Coordination Chemistry, 5, Pergamon, New York, 1987, Chapter 50;
(b) D.A. Nation, J.H. Reibenspies, M.R. Taylor, K.P. Wainwrigth, Inorg. Chim. Acta 258 (1997) 161;
(c) L.F. Lindoy, R.J. Smith, Inorg. Chem. 20 (1981) 1314.
[15] C.A. Grapperhaus, M.Y. Darensbourg, Acc. Chem. Res. 31 (1998) 451.
[16] I. Yilmaz, A.G. Gurek, V. Ahsen, Polyhedron 24 (2005) 791.
[17] I. Yilmaz, M. Kocak, Polyhedron 23 (2004) 1279.
[18] K.M. Kadish, T. Nakanishi, V. Ahsen, I. Yilmaz, J. Phys. Chem. B 105 (2001) 9817.
[19] I. Yilmaz, T. Nakanishi, A. Gürek, K.M. Kadish, J. Porhyrins Phthalocyanines 7 (2003) 227.
[20] T. Nakanishi, I. Yilmaz, N. Nakashima, K. M Kadish, J. Phys. Chem. B 107 (2003) 12789.
[21] (a) S. Arslan, I. Yilmaz, Inorg. Chem. Commun. 10 (2007) 385;
(b) I. Yilmaz, S. Arslan, S. Guney, I. Becerik, Electro Chim. Acta 52 (2007) 6611;
(c) S. Arslan, I. Yilmaz, Polyhedron 26 (2007) 2387;
(d) A. Kilic, E. Tas, B. Deveci, I. Yilmaz, Polyhedron 26 (2007) 4009.
[22] A. Earnshaw, Introduction to Magnetochemistry, Academic Press, London, 1968, p. 4.
[23] X.Q. Lin, K.M. Kadish, Anal. Chem. 57 (1985) 1498.
[24] (a) K.R. Adam, A.J. Leong, L.F. Lindoy, H.C. Lip, B.W. Skelton, A.H. White, J. Am. Chem. Soc. 105 (1983) 4645;
(b) L.F. Lindoy, L.G. Armstrong, Inorg. Chem. 14 (1975) 1322.
[25] H. Temel, J. Coord. Chem. 57 (2004) 723.
[26] H. Temel, S. İlhan, M. Sekerci, R. Ziyadanoğulları, Spectrosc. Lett. 35 (2002) 219.
[27] H. Temel, U. Çakır, V. Tolan, B. Otludil, H.I. Ugras, J. Coord. Chem. 57 (2004) 571.
[28] (a) M.M.H. Khalil, M.M. Aboaly, R.M. Ramadan, Spectrochim. Acta A 61 (2005) 157;
(b) M.M. Aboaly, M.M.H. Khalil, Spectrosc. Lett. 34 (2001) 495.
[29] H. Temel, U. Cakır, H.I. Ugras, M. Sekerci, J. Coord. Chem. 56 (2003) 943.
[30] (a) S. Ilhan, H. Temel, I. Yilmaz, M. Sekerci, Polyhedron 26 (2007) 2795;
(b) S. Ilhan, H. Temel, I. Yilmaz, M. Sekerci, J. Organomet. Chem. 692 (2007) 3855.
[31] H. Temel, B. Ziyadanoğulları, I. Aydın, F. Aydın, J. Coord. Chem. 58 (2005) 1177.
[32] L. Valencia, H. Adams, R. Bastida, D.E. Fenton, A. Macias, Inorg. Chim. Acta 45 (2001) 317.
[33] A.J. Bard, L.R. Faulkner (Eds.), Electrochemical Methods: Fundamentals and Applications, second ed., John Wiley & Sons, New York, 2001, pp. 228–234.
[34] (a) A.A. Khandar, B. Shaabani, F. Belaj, A. Bakhtiari, Polyhedron 25 (2006) 1893;
(b) A. Bötter, T. Takeuchi, K.I. Hardcastle, T.J. Meade, H.B. Gray, D. Cwikel, M. Kapon, Z. Dori, Inorg. Chem. 36 (1997) 2498.
[35] R. Fikar, S.A. Koch, M.M. Millar, Inorg. Chem. 24 (1985) 3311.

Available online at www.sciencedirect.com
ScienceDirect
Polyhedron 27 (2008) 133–138
POLYHEDRON
www.elsevier.com/locate/poly

Synthesis, characterization and DNA-binding of the mononuclear dioxouranium(VI) complex with ciprofloxacin

George Psomas *,[1], Alketa Tarushi [1], Eleni K. Efthimiadou

Institute of Physical Chemistry, NCSR "Demokritos", GR-15310 Aghia Paraskevi Attikis, Greece

Received 30 April 2007; accepted 24 August 2007
Available online 22 October 2007

Abstract

The mononuclear complex of the second-generation quinolone antibacterial agent ciprofloxacin with UO_2^{2+} has been prepared and characterized with physicochemical and spectroscopic techniques. In this complex, ciprofloxacin acts as a bidentate deprotonated ligand bound to the metal through the pyridone oxygen and one carboxylate oxygen. The central U(VI) atom is six-coordinate and a slightly distorted octahedral geometry is proposed. The lowest energy model structure of the complex has been determined with molecular modelling calculations. The biological activity of the complex has been evaluated by examining its ability to bind to calf-thymus DNA.
© 2007 Elsevier Ltd. All rights reserved.

Keywords: Ciprofloxacin; Quinolones; Uranyl(VI) complex; Molecular modelling; Interaction with calf-thymus DNA

1. Introduction

Ciprofloxacin, Hcf, (Fig. 1) is a typical second-generation quinolone (4-quinolone or quinolonecarboxylic acid) antibacterial agent used to treat diverse gram-negative infections [1]. Quinolones are a group of synthetic antibacterial agents [2], they can act as antibacterial drugs that effectively inhibit DNA replication and are commonly used as a treatment for many infections [3,4]. More specifically, ciprofloxacin can be used for the treatment of complicated and uncomplicated urinary tract infections and pyelonephritis, lower respiratory tract infections, skin and skin-structure infections, urethral and cervical gonococcal infections, bone and joint infections, infectious diarrhea, typhoid fever and acute sinusitis [1]. Because of its good penetration into bone, orally administered ciprofloxacin is a useful alternative to parenterally administered antibiotics for the treatment of osteomyelitis caused by susceptible organisms [5].

Ciprofloxacin can act as a bidentate ligand through the pyridone oxygen and one carboxylate oxygen. In the literature, the structures and the properties of diverse transition metal complexes of ciprofloxacin have been reported. More specifically, binary ciprofloxacin complexes with Cu(II) [2], $V(IV)O^{2+}$ [6], Cd(II), Co(II), Zn(II) [7,8], Mn(III) [8] and Mg(II) [9], as well as mixed-ligands ciprofloxacin complexes with Fe(III) [2], Cu(II) [10–12], Mn(II), Cd(II), Co(II), Zn(II), Ca(II), Ba(II), Sr(II) [8] and Ag(I) [13] have been structurally characterized.

The role of UO_2^{2+} as an element of biological interest is well known [14], while the biocoordination behavior of the uranyl cation is still relatively unexplored [15]. The uranyl(VI) ion has been used as a staining agent in electron microscopy [16], mainly due to its high affinity for the phosphates of the DNA backbone [17]. For UO_2^{2+}, three other quinolone complexes with pipemidato [18], *N*-propyl-norfloxacinato [19] and oxolinato ligands [20] have been studied.

We have initiated a study of the structure, spectroscopic and biological properties of diverse transition metal

* Corresponding author. Present address: Department of General and Inorganic Chemistry, Faculty of Chemistry, Aristotle University of Thessaloniki, P.O. Box 135, GR-54124 Thessaloniki, Greece. Tel.: +30 2310997790; fax: +30 2310997738.
E-mail address: gepsomas@chem.auth.gr (G. Psomas).
[1] Present address: Department of General and Inorganic Chemistry, Faculty of Chemistry, Aristotle University of Thessaloniki, GR-54124 Thessaloniki, Greece.

0277-5387/$ - see front matter © 2007 Elsevier Ltd. All rights reserved.
doi:10.1016/j.poly.2007.08.043

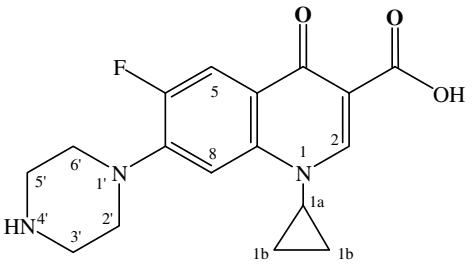


Fig. 1. Ciprofloxacin (Hcf = 1-cyclopropyl-6-fluoro-1,4-dihydro-4-oxo-7-(1-piperazinyl)-3-quinoline carboxylic acid) and H atom labelling.

complexes with various quinolone antibacterial drugs [18–27]. In this context, the interaction of UO_2^{2+} with deprotonated ciprofloxacin has been studied in an attempt to examine the mode of binding and possible synergetic effects. The resultant neutral mononuclear complex $UO_2(cf)_2$ has been characterized by elemental analysis and spectroscopic techniques. Molecular modelling techniques have been employed to assess the lowest energy model structure of the complex. The interaction of the complex with calf-thymus (CT) DNA has been studied with UV and circular dichroism (CD) spectroscopies.

2. Experimental

2.1. Materials

All the chemicals and solvents were reagent grade and were purchased from Aldrich Co., while ciprofloxacin was purchased from Sigma. Dimethylformamide (dmf) was distilled from calcium hydride (CaH_2) and CH_3OH from magnesium (Mg) and these solvents were stored over 3 Å molecular sieves. Diethyl ether and absolute ethanol were used without any further purification.

DNA stock solutions (5 mM) were prepared by dilution of CT-DNA with buffer (containing 150 mM NaCl and 15 mM trisodium citrate at pH 7.0), followed by exhaustive stirring at 4 °C for three days [28], and they were kept at 4 °C for no longer than a week. The nucleotide concentrations were determined by their absorption at 260 nm using $\varepsilon = 6600\ M^{-1}\ cm^{-1}$ (expressed as phosphate).

2.2. Synthesis of the complex $UO_2(cf)_2$ (1)

A methanolic solution (15 mL) of ciprofloxacin (0.4 mmol, 132 mg), deprotonated with KOH (0.4 mmol, 22 mg), was added to a methanolic solution (10 mL) of $UO_2(NO_3)_2 \cdot 6H_2O$ (0.2 mmol, 100 mg) and the reaction mixture was refluxed for 2 h. The solution was filtered and left for slow evaporation. After a few days a yellow-orange microcrystalline product was deposited, collected with filtration, washed with methanol and dried. Yield: 140 mg, 75 %. *Anal.* Calc. for $UO_2(cf)_2$ ($C_{34}H_{34}F_2N_6O_8U$) (MW = 930.71): C, 43.88; H, 3.68; N, 9.03. Found: C, 44.08; H, 3.80; N, 8.87%.

IR (KBr pellet, cm^{-1}): $\nu(C{=}O)_p$, 1635 (vs); $\nu(CO_2)_{asym}$, 1614 (vs); $\nu(CO_2)_{sym}$, 1385 (vs); $\nu(U{=}O)$, 935 (m). UV–Vis, λ (nm) (ε, $M^{-1}\ cm^{-1}$) as a nujol mull: 434 (sh), 347, 320, 294; in dmso: 433 (sh) (210), 370 (1350), 333 (1950), 292 (4700). ^1H NMR in dmso-d_6, δ (ppm): 1.20, (t, 4H, H1b); 1.45, (t, 1H, H1a); 3.40–3.55, (m, 4H, H2′ and H6′ or H3′ and H5′); 3.95, (m, 4H, H3′ and H5′ or H2′ and H6′); 7.45, (s, 1H, H8); 8.10, (s, 1H, H5); 8.85, (s, 1H, H2). The complex is soluble in dmso, dmf and partially soluble in water and is a non-electrolyte.

2.3. Instrumentation – physical measurements

Infrared (IR) spectra (400–4000 cm^{-1}) were recorded on a Nicolet Magna–IR 550 with samples prepared as KBr pellets. UV–Vis spectra (concentration range 2×10^{-5} – 10^{-3} M) were recorded on a Thermo Electron Corporation Helios α dual beam spectrophotometer. C, H and N elemental analysis was performed on a Perkin–Elmer 240B elemental analyzer. Electric conductance measurements were carried out with a WTW model LF 530 conductivity outfit and a type C cell, which had a cell constant of 0.996. NMR spectra were recorded with a Bruker Avance 500 MHz instrument and were processed by X-WIN NMR 2.6 (Bruker Analytik GmbH).

The interaction of complex **1** with CT DNA has been investigated with UV and CD spectroscopies. For the complex a DMSO stock solution (1 mM) was prepared, while for CT DNA the DNA aqueous stock solution, prepared as previously described, was used. In both techniques, the spectra of CT DNA in the presence of the complex have been recorded for a constant CT DNA concentration (3.125×10^{-4} M) in diverse complex:CT DNA mixing ratios (r) of the complex and CT DNA stock solutions. All the UV and CD spectra were recorded after incubation of the complex with CT DNA for 24 h at 37 °C.

The CD spectra were recorded on a Jasco J-700 spectropolarimeter using a 1.0 cm path quartz cell and the following acquisition parameters: $\lambda = 190$–400 nm, scan speed 50 nm min^{-1}, resolution step 0.2 nm, sensitivity 50 mdeg, response 1 s, bandwidth 1.0 nm, accumulations 10. In some cases, the spectra were averaged over an appropriate number of scans. The UV spectra were recorded in the region $\lambda = 200$–400 nm on a Thermo Electron Corporation Helios α dual beam spectrophotometer.

2.4. Molecular modelling

With the aim of presenting a molecular model for the complex that is unbiased by the starting structure, we have used Langevin dynamics with a simulated annealing protocol. Using this method, the mean total energy of an ensemble of structures guides the selection of the most favorable configuration for the complex. The starting structures were constructed using the program HyperChem and a MM+ force field that is based on Allinger's MM2 force field [29]. For the metal ion we have used a default parameter

set with $R^* = 2.20$ Å and $e^* = 0.02$ Kcal mol^{-1}, since the van der Waals interactions are not expected to play a major role in such bonded representations as in octahedral complexes. The metal–ligand bond lengths were corrected in the final model using harmonic restraints with equilibrium values that were extracted from crystallographic data of similar compounds [15,30,31] (Table S1). Non-bonded interactions were calculated in vacuo with no cutoff and the electrostatic energy term was treated using bond dipoles. Initial energy minimizations were carried out by a conjugate gradient method with rms gradient <0.01 as the convergence criterion.

Each model (Scheme S1) was subjected to 20 individual rounds of simulated annealing, setting different values to the seed for the assignment of the starting velocities. To integrate the Langevin equation [32] the step size was set to 1 fs and the collision frequency to 1 ps^{-1}. The annealing calculation comprised of three phases: (i) raising the temperature of the system from 10 to 1000 K over 2 ps, (ii) keeping the system at 1000 K for 3 ps and (iii) cooling the system down to 0 K over 15 ps. A tight coupling of the system with temperature (0.1 ps) was used for the heating and equilibration phases. During the cooling phase the bath relaxation time was gradually decreased from 5.0 ps (7000 steps), 2.0 ps (3000 steps), 1.0 ps (2000 steps), 0.5 ps (2000 steps) to 0.05 ps (1000 steps). At the final step all the structures had a rms gradient <0.01 and their total energy was recorded (Table S2). The model presented herein was selected from the lowest energy structures that were generated for each starting geometry. A final minimization of the energy was performed as above, but having applied the metal–ligand distance restraints.

3. Results and discussion

3.1. Spectroscopic study of the complex

The complex has been prepared in high yield (75%) via the addition of a methanolic solution of deprotonated ciprofloxacin to a methanolic solution of the UO_2^{2+} ion at a 2:1 metal–ligand ratio. The resultant complex **1** is soluble in dmso and dmf, is partially soluble in water and is a non-electrolyte.

In the IR spectrum of complex **1** the absorption at 1707 cm^{-1}, observed in the spectrum of Hcf and attributed to ν(C=O)$_{carb}$, has been replaced by two very strong characteristic bands at 1614 and 1385 cm^{-1}, assigned as ν(O–C–O) asymmetric and symmetric stretching vibrations, respectively. The difference $\Delta = \nu_{asym}(CO_2) - \nu_{sym}(CO_2)$, a useful characteristic for determining the coordination mode of carboxylato ligands, is 229 cm^{-1}, indicating the monodentate coordination mode of the carboxylato group [33]. The vibration ν(C=O)$_p$ is shifted from 1623 cm^{-1} to 1635 cm^{-1} upon bonding. The overall changes in the IR spectrum suggest that the ciprofloxacinato ligand is coordinated to central U(VI) atom via the pyridone oxygen and one carboxylato oxygen [2].

The UV–Vis spectra of the complex have been recorded as nujol mulls and in dmso solution. Practically, the spectra in solution are identical with those in nujol, with the exception of a few nm shifts in some cases. The UV–Vis spectra of the complex are practically identical with that of the ligand ciprofloxacin but slightly shifted, indicative of coordination through the pyridone oxygen and one carboxylate oxygen. Additionally, an absorption band at 433 nm ($\varepsilon = 210$ M^{-1} cm^{-1}) is present in the spectrum of **1** and can be assigned to a ligand-to-metal charge transfer transition for the quinolone ligand [18–27].

^{1}H NMR spectra of Hcf and UO_2 (cf)$_2$ have been recorded in dmso-d_6. The assignment of every signal has been achieved by comparing the ^{1}H NMR spectrum of the complex to that of the ligand and the spectra of other quinolone–metal complexes reported in the literature [18–20,34]. The results are shown in Table 1.

Comparison of the ^{1}H NMR spectrum of UO_2 (cf)$_2$ with that of Hcf shows a significant perturbation of the chemical shift (up to 0.6 ppm) of the aromatic protons H2 and H5, indicating that H2 and H5 are close to the coordination site of the ligand. The signals for the aromatic proton H8, the aliphatic protons H1a and H1b and the piperazine protons are practically unchanged since they lie far from the binding site of the ligand. The overall changes of the NMR spectrum of the complex are indicative of coordination of the ciprofloxacinato ligand to the central U(VI) atom via the pyridone oxygen and one carboxylate oxygen [18–20,34].

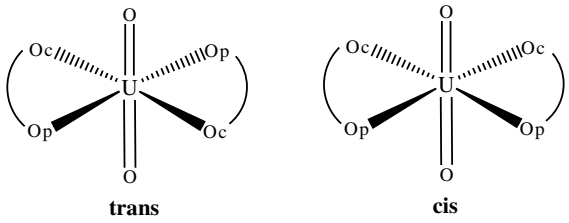
3.2. Proposed structure of the complex with molecular modelling

The complex was collected as a microcrystalline product. Diverse crystallization techniques were employed but no crystals of the complex suitable for determination of the structure with X-ray crystallography were obtained. In order to present a model for the complex, only the enantiomers having the two uranyl oxygen atoms in *trans* positions were constructed as starting models of UO_2(cf)$_2$ (Scheme 1). This is in accordance with the structure of all the uranyl(VI) complexes reported in the literature [15,30,31].

After the Langevin dynamics simulated annealing calculations, we obtained the total energy results of 20 different

Table 1
Chemical shifts (in ppm) in the ^{1}H NMR spectra of Hcf and UO_2(cf)$_2$ in dmso-d_6

	Hcf	UO_2(cf)$_2$
H2	8.60 (1H)	8.85 (1H)
H5	7.50 (1H)	8.10 (1H)
H8	7.42 (1H)	7.45 (1H)
H1a	1.47 (1H)	1.45 (1H)
H1b	1.21 (4H)	1.20 (4H)
H2′, H6′ or H3′, H5′	3.56 (4H)	3.40–3.55 (4H)
H3′, H5′ or H2′, H6′	3.85 (4H)	3.90 (4H)



Scheme 1. The two diastereoisomers of $UO_2(cf)_2$ employed in the simulated annealing calculations. Oc and Op are the carboxylate and the pyridone oxygen atoms, respectively, of the ciprofloxacinato ligands.

conformations for each starting model (Table S2). The average energy of the isomers is almost equal, as expected [35], and, since the energy difference is very low ($\sim$0.22 Kcal mol^{-1}), it is difficult to distinguish between *trans* or *cis* isomers. Nevertheless, the *cis*-isomers exhibit the lowest average energy and the lowest energy model structure found for the *cis*-isomers is presented in Fig. 2.

3.3. Interaction with DNA

DNA can provide three distinctive binding sites for quinolone metal complexes; namely, groove binding, binding to the phosphate group and intercalation [36]. This behavior is of great importance with regard to the relevant biological role of quinolone antibiotics in the body [37].

3.3.1. UV spectroscopy

The absorption spectra of the interaction of complex **1** with CT DNA have been recorded for a constant CT DNA concentration (3.125×10^{-4} M) with different r values. The UV spectra of the complex with CT DNA derived for diverse complex:CT DNA mixing ratios are shown in Fig. 3. The changes observed in the absorption spectra of the complex after mixing with CT DNA (either the increase of the intensity at $\lambda_{max} = 258$ nm or the shift of λ_{max} up to 265 nm) indicate that the interaction of complex **1** with CT DNA takes place by the direct formation of a new complex with double-helical CT DNA [38].

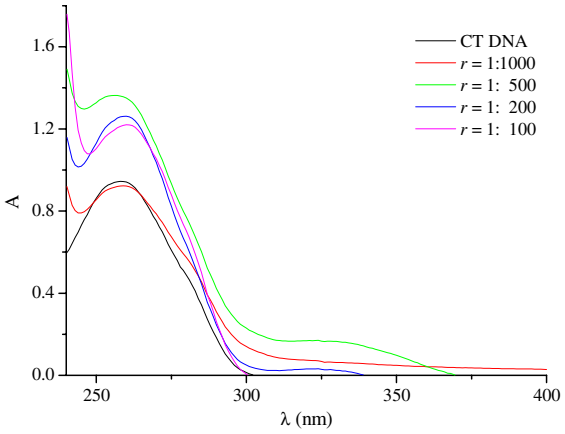


Fig. 3. Absorption spectra of complex **1** in the presence of CT DNA for diverse r values. The spectra were recorded at 25 °C after the complex had been incubated with CT DNA for 24 h at 37 °C.

3.3.2. CD spectroscopy

CD spectroscopy is useful in diagnosing changes in DNA morphology during drug–DNA interactions, as the positive band due to base stacking (273 nm) and the negative one due to right–handed helicity (246 nm) are quite sensitive to the mode of DNA interactions with small molecules [39,40]. The changes in the CD signals of DNA observed on interaction with drugs may often be assigned to the corresponding changes in the DNA structure [41]. Thus, simple groove binding and electrostatic interaction of small molecules show less or no perturbation on the base-stacking and helicity bands, while intercalation enhances the intensities of both the bands, stabilizing the right-handed B conformation of CT DNA, as observed for the classical intercalator methylene blue [42].

The CD spectra of the complex with double-stranded CT DNA for different r values can provide us with useful information concerning the complex–nucleotide interaction. The CD spectrum of free CT DNA is conservative and consists of a negative band at 246 nm and a positive one at 273 nm, characteristic of the B-form of DNA [43,44].

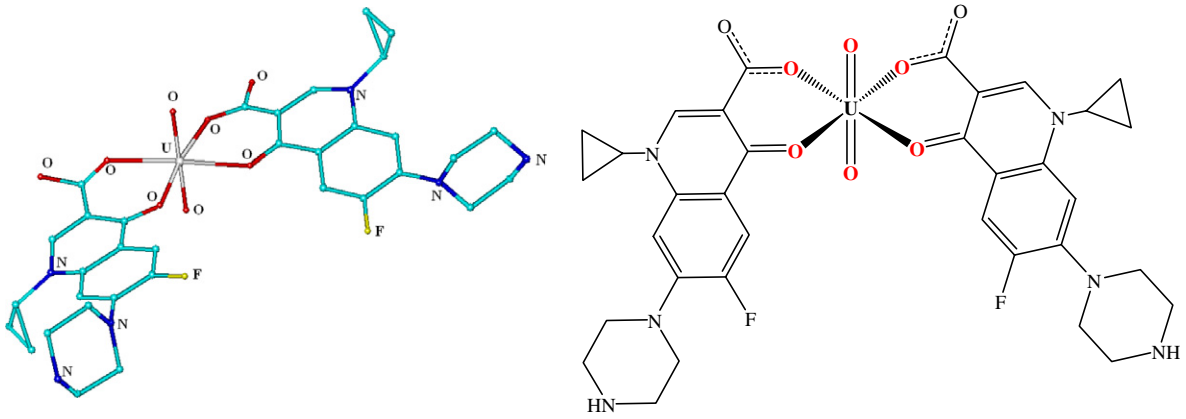


Fig. 2. Lowest energy model structure of $UO_2(cf)_2$.

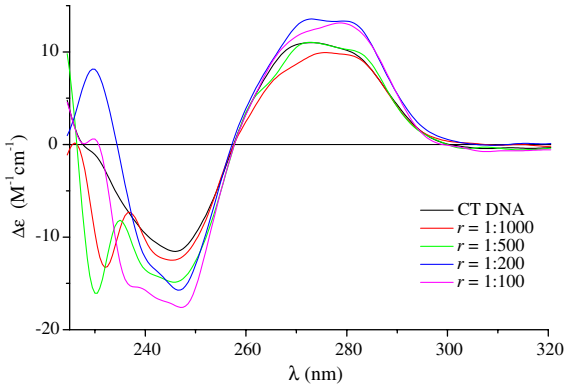


Fig. 4. CD spectra of CT DNA in 5 mM buffer (containing 150 mM NaCl and 15 mM trisodium citrate at pH 7.0) in the presence of complex **1** $UO_2(cf)_2$, with different *r* values. The spectra were recorded at 25 °C after the samples had been incubated with CT DNA for 24 h at 37 °C.

The CD spectra of CT DNA in the presence of complex **1** are shown in Fig. 4. For $r = 1{:}1000$, the spectrum consists of a strong negative band I at 245 nm and two discrete positive ones, band II at 273 nm and band III (observed as a shoulder) at 281 nm. When *r* increases up to 1:200, the position of the peaks remains unchanged, whilst a slight increase of both the intensities is observed. For a further increase of *r* (higher than 1:200), the two positive bands II and III cannot be distinguished, resulting in a unique broad band at $\lambda_{max} = 280$ nm and the intensity slightly increases. The λ_{max} value of 245 nm of the negative band I remains practically stable in all the spectra, while an increase of the intensity is observed with the increase of the *r* value.

The overall changes in the CD spectra indicate that the complex can be bound to CD DNA. The exact mode of binding cannot be safely concluded; nevertheless, the slight increase of the intensity of the negative band I and positive ones II–III shows that the intercalative mode between complex **1** and CT DNA is possible and it cannot be ruled out [36,38,45].

4. Conclusions

The synthesis and the characterization of a new ciprofloxacin mononuclear complex with UO_2^{2+} have been realized with physicochemical and spectroscopic methods. Ciprofloxacin is in the deprotonated mode and acts as a bidentate ligand bound to U(VI) through the pyridone oxygen and one carboxylate oxygen. The uranium(VI) atom is six-coordinate and the environment around it could be described as a distorted octahedron. With the use of molecular modelling, the lowest energy model structure of complex $UO_2(cf)_2$ has been determined, revealing the possible arrangement of the ligands around the metal. The study of the interaction of the complex with CT DNA has revealed that the complex can be bound to DNA, but the exact mode of binding cannot be safely concluded, although the intercalation is possible and cannot be ruled out.

Acknowledgement

We thank Dr. A. Papakyriakou, Institute of Physical Chemistry, NCSR "Demokritos", Greece, for the supply of the molecular modelling routine.

Appendix A. Supplementary material

Supplementary data associated with this article can be found, in the online version, at doi:10.1016/j.poly.2007.08.043.

References

[1] D.E. King, R. Malone, S.H. Lilley, Am. Fam. Physician 61 (2000) 2741.
[2] I. Turel, Coord. Chem. Rev. 232 (2002) 27, and references cited therein.
[3] D.C. Hooper, E. Rubinstein (Eds.), Quinolone Antimicrobial Agents, 3rd ed., ASM Press, Washington, DC, 2003.
[4] V.T. Andriole (Ed.), The Quinolones, 3rd ed., Academic Press, San Diego, 2000.
[5] P.S. Lietman, Drugs 49 (1995) 159.
[6] I. Turel, A. Golobic, A. Klavzar, B. Pihlar, P. Buglyo, E. Tolis, D. Rehder, K. Sepcic, J. Inorg. Biochem. 95 (2003) 199.
[7] M.P. Lopez-Gresa, R. Ortiz, L. Perello, J. Latorre, M. Liu-Gonzalez, S. Garcia-Granda, M. Perez-Priede, E. Canton, J. Inorg. Biochem. 92 (2002) 65.
[8] D.-R. Xiao, E.-B. Wang, H.-Y. An, Z.-M. Su, Y.-G. Li, L. Gao, C.-Y. Sun, L. Xu, Chem. Eur. J. 11 (2005) 6673.
[9] P. Drevensek, N. Poklar Ulrih, A. Majerle, I. Turel, J. Inorg. Biochem. 100 (2006) 1705.
[10] P. Drevensek, I. Leban, I. Turel, G. Giester, E. Tillmanns, Acta Crystallogr., Sect. C 59 (2003) m376.
[11] D.K. Saha, U. Sandbhor, K. Shirisha, S. Padhye, D. Deobagkar, C.E. Anson, A.K. Powell, Bioorg. Med. Chem. Lett. 14 (2004) 3027.
[12] N. Jimenez-Garrido, L. Perello, R. Ortiz, G. Alzuet, M. Gonzalez-Alvarez, E. Canton, M. Liu-Gonzalez, S. Garcia-Granda, M. Perez-Priede, J. Inorg. Biochem. 99 (2005) 677.
[13] Z.-F. Chen, L.-C. Yu, D.-C. Zhong, H. Liang, X.-H. Zhu, Z.-Y. Zhou, Inorg. Chem. Commun. 9 (2006) 839.
[14] J.D. Van Horn, H. Huang, Coord. Chem. Rev. 250 (2006) 765, and references cited therein.
[15] C.J. Burns, M.P. Neu, H. Boukhalfa, K.E. Gutowski, N.J. Bridges, R.D. Rogers, in: J.A. McCleverty, T.J. Meyer (Eds.), Comprehensive Coordination Chemistry II, Vol. 3, Elsevier, 2003, pp. 189–345, and references cited therein.
[16] P. Testillano, M. Sanchez-Pina, A. Olmedilla, M. Ollacarizqueta, C. Tandler, M. Risueno, J. Histochem. Cytochem. 39 (1991) 1427.
[17] P.E. Nielsen, C. Hiort, S.H. Sonnichsen, O. Buchardt, O. Dahl, B. Norden, J. Am. Chem. Soc. 114 (1992) 4967.
[18] E.K. Efthimiadou, Y. Sanakis, N. Katsaros, A. Karaliota, G. Psomas, Polyhedron 26 (2007) 1148.
[19] E.K. Efthimiadou, G. Psomas, Y. Sanakis, N. Katsaros, A. Karaliota, J. Inorg. Biochem. 101 (2007) 525.
[20] A. Tarushi, E.K. Efthimiadou, P. Christofis, G. Psomas, Inorg. Chim. Acta, in press (doi:10.1016/j.ica.2007.05.041).
[21] E.K. Efthimiadou, M. Katsarou, Y. Sanakis, C.P. Raptopoulou, A. Karaliota, N. Katsaros, G. Psomas, J. Inorg. Biochem. 100 (2006) 1378.
[22] E.K. Efthimiadou, Y. Sanakis, C.P. Raptopoulou, A. Karaliota, N. Katsaros, G. Psomas, Bioorg. Med. Chem. Lett. 16 (2006) 3864.
[23] G. Psomas, A. Tarushi, E.K. Efthimiadou, Y. Sanakis, C.P. Raptopoulou, N. Katsaros, J. Inorg. Biochem. 100 (2006) 1764.

[24] E.K. Efthimiadou, H. Thomadaki, Y. Sanakis, C.P. Raptopoulou, N. Katsaros, A. Scorilas, A. Karaliota, G. Psomas, J. Inorg. Biochem. 101 (2007) 64.
[25] E.K. Efthimiadou, N. Katsaros, A. Karaliota, G. Psomas, Bioorg. Med. Chem. Lett. 17 (2007) 1238.
[26] A. Tarushi, P. Christofis, G. Psomas, Polyhedron 26 (2007) 3963.
[27] E.K. Efthimiadou, N. Katsaros, A. Karaliota, G. Psomas, Inorg. Chim. Acta, in press (doi:10.1016/j.ica.2007.05.042).
[28] E. Tselepi–Kalouli, N. Katsaros, J. Inorg. Biochem. 37 (1989) 271.
[29] N.L. Allinger, J. Am. Chem. Soc. 99 (1977) 8127.
[30] P. Thuery, C. Villiers, J. Jaud, M. Ephritikhine, B. Masci, J. Am. Chem. Soc. 126 (2004) 6838, and references cited therein.
[31] A.D. Sutton, G.H. John, M.J. Sarsfield, J.C. Renshaw, I. May, L.R. Martin, A.J. Selvage, D. Collison, M. Helliwell, Inorg. Chem. 43 (2004) 5480, and references cited therein.
[32] M.P. Allen, D.J. Tildesley (Eds.), Computer Simulation of Liquids, Oxford University Press, 1989.
[33] K. Nakamoto, Infrared and Raman Spectra of Inorganic and Coordination Compounds, 4th ed., Wiley, New York, 1986.
[34] M. Sakai, A. Hara, S. Anjo, M. Nakamura, J. Pharm. Biomed. Anal. 18 (1999) 1057.
[35] P. Christofis, M. Katsarou, A. Papakyriakou, Y. Sanakis, N. Katsaros, G. Psomas, J. Inorg. Biochem. 99 (2005) 2197, and references cited therein.
[36] A. Rodger, B. Norden (Eds.), Circular Dichroism and Linear Dichroism, Oxford University Press, Oxford–New York–Tokyo, 1997.
[37] T.C. Jenkins, in: K.R. Fox (Ed.), Drug–DNA Interaction Protocols, Humana Press Inc., Totowa, NJ, 1997, pp. 195–218.
[38] G.S. Son, J-.A. Yeo, M.-S. Kim, S.K. Kim, A. Holmen, B. Akerman, B. Norden, J. Am. Chem. Soc. 120 (1998) 6451.
[39] P. Uma Maheswari, M. Palaniandavar, J. Inorg. Biochem. 98 (2004) 219.
[40] V.I. Ivanov, L.E. Minchenkova, A.K. Schyolkina, A.I. Poletayev, Biopolymers 12 (1973) 89.
[41] P. Lincoln, E. Tuite, B. Norden, J. Am. Chem. Soc. 119 (1997) 1454.
[42] B. Norden, F. Tjerneld, Biopolymers 21 (1982) 1713.
[43] O. Novakova, H. Chen, O. Vrana, A. Rodger, P.J. Sadler, V. Brabec, Biochemistry 42 (2003) 11544.
[44] W. Curtis-Johnson, in: K. Nakanishi, N. Berova, R.W. Woody (Eds.), CD of Nucleic Acids in Circular Dichroism, Principles and Applications, VHS, New York, 1994, pp. 523–540.
[45] G. Song, Y. He, Z. Cai, J. Fluoresc. 14 (2004) 705.

Available online at www.sciencedirect.com
ScienceDirect
Polyhedron 27 (2008) 139–150
POLYHEDRON
www.elsevier.com/locate/poly

N,*N*′-Bis(aryl)pyridine-2,6-dicarboxamide complexes of ruthenium: Synthesis, structure and redox properties

Moutusi Dasgupta [a], Sumon Nag [a], Gopal Das [b], Munirathinam Nethaji [c], Samaresh Bhattacharya [a,*]

[a] *Department of Chemistry, Inorganic Chemistry Section, Jadavpur University, Kolkata 700 032, India*
[b] *Department of Chemistry, Indian Institute of Technology, Guwahati 781 039, Assam, India*
[c] *Department of Inorganic and Physical Chemistry, Indian Institute of Science, Bangalore 560 012, India*

Received 16 July 2007; accepted 27 August 2007
Available online 23 October 2007

Abstract

Reaction of five *N*,*N*′-bis(aryl)pyridine-2,6-dicarboxamides (H_2L-R, where H_2 denotes the two acidic protons and R (R = OCH_3, CH_3, H, Cl and NO_2) the *para* substituent in the aryl fragment) with [Ru(trpy)Cl_3](trpy = 2,2′,2″-terpyridine) in refluxing ethanol in the presence of a base (NEt_3) affords a group of complexes of the type [Ru^{II}(trpy)(L-R)], each of which contains an amide ligand coordinated to the metal center as a dianionic tridentate N,N,N-donor along with a terpyridine ligand. Structure of the [Ru^{II}-(trpy)(L-Cl)] complex has been determined by X-ray crystallography. All the Ru(II) complexes are diamagnetic, and show characteristic ^{1}H NMR signals and intense MLCT transitions in the visible region. Cyclic voltammetry on the [Ru^{II}(trpy)(L-R)] complexes shows a Ru(II)–Ru(III) oxidation within 0.16–0.33 V versus SCE. An oxidation of the coordinated amide ligand is also observed within 0.94–1.33 V versus SCE and a reduction of coordinated terpyridine ligand within −1.10 to −1.15 V versus SCE. Constant potential coulometric oxidation of the [Ru^{II}(trpy)(L-R)] complexes produces the corresponding [Ru^{III}(trpy)(L-R)]$^+$ complexes, which have been isolated as the perchlorate salts. Structure of the [Ru^{III}(trpy)(L-CH_3)]ClO_4 complex has been determined by X-ray crystallography. All the Ru(III) complexes are one-electron paramagnetic, and show anisotropic ESR spectra at 77 K and intense LMCT transitions in the visible region. A weak ligand-field band has also been shown by all the [Ru^{III}(trpy)(L-R)]ClO_4 complexes near 1600 nm.
© 2007 Elsevier Ltd. All rights reserved.

Keywords: *N*,*N*′-Bis(aryl)pyridine-2,6-dicarboxamide ligands; Ruthenium complexes; Redox properties

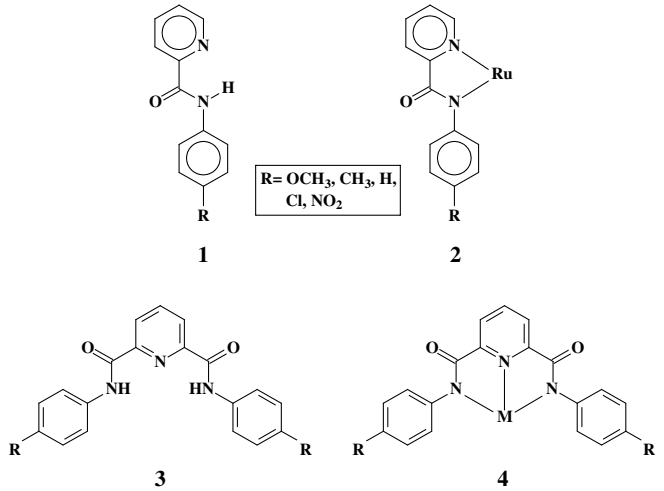
1. Introduction

The chemistry of ruthenium has been receiving considerable attention [1], primarily because of the fascinating redox, photophysical and photochemical properties exhibited by complexes of this metal. As properties are dependent mostly on the coordination environment around the metal center, complexation of ruthenium by ligands of selected types is of significant importance, and the present work has originated from our continued interest in this area in general [2], and our recent findings on the chemistry of some ruthenium amide complexes in particular [2j]. It may be relevant to mention here that chemistry of the amide ligands is of particular interest with reference to their role in biological processes [3]. For example, the amide linkage plays a key role in the formation and maintenance of protein architectures, which are crucial for their performance in biological systems [4]. Apart from their relevance in biological phenomena, coordination chemistry of the amide ligands is also interesting with regard to their variable binding modes. The amides usually display two modes of binding to metal ions, through the nitrogen (amidate mode) via dissociation of the N–H proton and through the oxygen (amide mode). While binding in the amidate mode is known to stabilize metal ions in their high oxidation states, that in the amide mode is reported to favor relatively lower oxidation states of a metal [5]. Interconversion between the amide and amidate modes

* Corresponding author. Tel.: +91 33 2414 6223; fax: +91 33 2414 6584.
E-mail address: samaresh_b@hotmail.com (S. Bhattacharya).

0277-5387/$ - see front matter © 2007 Elsevier Ltd. All rights reserved.
doi:10.1016/j.poly.2007.08.042

of binding has been efficiently utilized to manipulate redox properties of the metal center [6]. In a recent study on a group of tris-complexes of *N*-(aryl)picolinamides (**1**) [2j], where the amides are bound to ruthenium through the pyridine-nitrogen (N^p) and the amide-nitrogen (N^a) (as in **2**) creating a $N^p_3N^a_3$ coordination sphere, the trivalent state of ruthenium has been found to be highly stable as reflected in the Ru(III)–Ru(II) reduction potential (−0.38 V versus SCE, for the R = H complex). From the magnitude of this reduction potential it became evident that the bivalent state of ruthenium cannot be stabilized in the same $N^p_3N^a_3$ environment. In order to have stable ruthenium(II) complexes of such amides, a logical approach seems to be to reduce the number of hard amide nitrogens and increase that of soft pyridine nitrogens in the coordination sphere. Thus we have planned to create a $N^p_4N^a_2$ coordination sphere around ruthenium, and with this simple strategy a group of *N*,*N*′-bis(aryl)pyridine-2,6-dicarboxamides (**3**), derived from 2,2′-dipicolinic acid and five different *para*-substituted anilines, have been selected as the ligands and [Ru(trpy)Cl_3](trpy = 2,2′,2″-terpyridine) as the ruthenium starting material. The selected amides (**3**) are known to bind to metal ions usually as dianaionic tridentate N^a,N^p, N^a-donors (**4**) via loss of the two amide protons [7]. However, there are few instances where they also bind to metal ions as monoanaionic N^a,N^p,O-donors as well as neutral O,N^p,O-donors [8]. It may be mentioned here that though chemistry of amide complexes of many transition metals has been extensively studied [9], that of ruthenium appears to have received much less attention [2j,o,7a,10]. As the source of ruthenium the [Ru(trpy)Cl_3] complex has been selected because of its demonstrated ability to accommodate tridentate ligands via displacement of three chlorides and thus providing three pyridine nitrogens in the coordination sphere [11]. Reaction of the selected amides (**3**) with [Ru(trpy)Cl_3] has indeed been found to afford a family of complexes having the targeted $N^p_4N^a_2$ coordination sphere around ruthenium. An account of the chemistry of all these complexes is presented in this report, with special reference to their formation, characterization and, spectral and electrochemical properties.



2. Experimental

2.1. Materials

Commercial ruthenium trichloride was purchased from Arora Matthey, Kolkata, India. The *para*-substituted anilines, 2,2′,2″-terpyridine and 2,6-dipicolinic acid were obtained from Aldrich, India. All other chemicals and solvents were reagent grade commercial materials and were used as received. [Ru(trpy)Cl_3] was synthesized by following a reported procedure [12]. The *N*,*N*′-bis(aryl)pyridine-2,6-dicarboxamides (**3**, H_2L-R) were prepared by condensing 2,6-dipicolinic acid with *para*-substituted anilines [10a]. Purification of dichloromethane and acetonitrile, and preparation of tetrabutylammonium perchlorate (TBAP) for electrochemical work were performed as reported in the literature [13].

2.2. Synthesis

2.2.1. [Ru^{II}(trpy)(L-R)]

The [Ru^{II}(trpy)(L-R)] complexes were obtained by following a general procedure. Specific details are given below for a particular complex.

2.2.1.1. [Ru^{II}(trpy)(L-H)]. To a solution of the H_2L-H ligand (70 mg, 0.22 mmol) in ethanol (40 mL) was added triethylamine (70 mg, 0.70 mmol) followed by [Ru(trpy)Cl_3] (100 mg, 0.22 mmol), and the mixture was then refluxed for 24 h to yield a brown solution. The solvent was evaporated and the brown residue, thus obtained, was subjected to purification by thin layer chromatography on a silica plate. With 1:1 acetonitrile–toluene as the eluant, a brown band separated, which was extracted with acetonitrile. Evaporation of this acetonitrile extract gave [Ru^{II}(trpy)(L-H)] as a brown crystalline solid. Yield: 103 mg (70%).

2.2.1.2. [Ru^{II}(trpy)(L-OCH_3)]. Anal. Calc. for $C_{36}H_{28}N_6O_4Ru$: C, 60.93; H, 3.94; N, 11.84. Found: C, 60.83; H, 3.72; N, 11.95%. ^{1}H NMR in $CDCl_3$, δ ppm[1]: 3.57 (s, 6H, OCH_3); 5.55 (d, 4H, $J = 6.2$); 6.57 (d, 4H, $J = 6.2$); 7.32 (t, 2H, $J = 7.8$); 7.49–7.61 (4H)*; 7.78 (d, 2H, $J = 7.7$); 7.81 (d, 2H, $J = 7.7$); 8.15 (t, 2H, $J = 7.4$)*; 8.31 (2H)*.

2.2.1.3. [Ru^{II}(trpy)(L-CH_3)]. Anal. Calc. for $C_{36}H_{28}N_6O_2Ru$: C, 63.81; H, 4.13; N, 12.40. Found: C, 63.77; H, 4.04; N, 12.48%. ^{1}H NMR in $CDCl_3$, δ ppm[1]: 2.10 (s, 6H, CH_3); 5.35 (d, 4H, $J = 6.1$); 6.37 (d, 4H, $J = 6.2$); 7.34 (t, 2H, $J = 7.8$); 7.51–7.66 (4H)*; 7.77 (d, 2H,

[1] Chemical shifts are given in ppm and multiplicity of the signals along with the associated coupling constants (*J* in Hz) are given in parentheses. Overlapping signals are marked with an asterisk.

$J = 7.7$); 7.79 (d, 2H, $J = 7.7$); 8.11 (t, 2H, $J = 7.4$); 8.28 (2H)*.

2.2.1.4. [Ru^{II}(trpy)(L-H)]. Anal. Calc. for $C_{34}H_{24}N_6O_2Ru$: C, 62.86; H, 3.69; N, 12.94. Found: C, 62.45; H, 3.82; N, 13.01%. ^{1}H NMR in $CDCl_3$, δ ppm[1]: 5.33 (t, 2H, $J = 6.1$); 5.54 (t, 4H, $J = 6.1$); 6.45 (d, 4H, $J = 6.2$); 7.31 (t, 2H, $J = 7.8$); 7.43–7.62 (4H)*; 7.80 (d, 2H, $J = 7.7$); 7.82 (d, 2H, $J = 7.7$); 8.15 (d, 2H, $J = 7.7$); 8.32 (2H)*.

2.2.1.5. [Ru^{II}(trpy)(L-Cl)]. Anal. Calc. for $C_{34}H_{22}N_6O_2Cl_2Ru$: C, 56.82; H, 3.06; N, 11.69. Found: C, 56.95; H, 3.10; N 11.85%. ^{1}H NMR in $CDCl_3$, δ ppm[1]: 5.34 (d, 4H, $J = 6.1$); 6.48 (d, 4H, $J = 6.2$); 7.29 (t, 2H, $J = 7.8$); 7.43–7.62 (4H)*; 7.79 (d, 2H, $J = 7.7$); 7.86 (d, 2H, $J = 7.7$); 8.18 (d, 2H, $J = 7.4$); 8.26 (2H)*.

2.2.1.6. [Ru^{II}(trpy)(L-NO$_2$)]. Anal. Calc. for $C_{34}H_{22}N_8O_6Ru$: C, 55.20; H, 2.97; N, 15.15. Found: C, 55.30; H, 2.85; N, 15.25%. ^{1}H NMR in $CDCl_3$, δ ppm[1]: 5.36 (d, 4H, $J = 6.1$); 6.47 (d, 4H, $J = 6.2$); 7.33 (t, 2H, $J = 7.8$); 7.43–7.62 (4H)*; 7.75 (d, 2H, $J = 7.7$); 7.83 (d, 2H, $J = 7.7$); 8.13 (d, 2H, $J = 7.4$), 8.29 (2H)*.

2.2.2. [Ru^{III}(trpy)(L-R)]ClO$_4$

The [Ru^{III}(trpy)(L-R)]ClO$_4$ complexes were obtained by following a general procedure. Specific details are given below for a particular complex.

2.2.2.1. [Ru^{III}(trpy)(L-H)]ClO$_4$. A solution of [Ru^{II}(trpy)(L-H)] (22 mg, 0.03 mmol) in 50 mL of 1:9 dichloromethane–acetonitrile (0.1 M TBAP) was coulometrically oxidized at 0.4 V versus SCE. Color of the solution gradually changed from brown to green during the oxidation. After the electrolysis was complete ($Q_{observed} = 3.47$ C, $Q_{calculated} = 3.36$ C), the resulting acetonitrile solution was then layered over toluene. Green crystals of the [Ru^{III}(trpy)(L-H)]ClO$_4$ complex were obtained upon slow diffusion of toluene into the acetonitrile solution, which were collected manually. The yield was quantitative.

2.2.2.1.1. [Ru^{III}(trpy)(L-OCH$_3$)]ClO$_4$. Anal. Calc. for $C_{36}H_{28}N_6O_8ClRu$: C, 53.43; H, 3.46; N, 10.38. Found: C, 53.78; H, 3.34; N, 10.44%.

2.2.2.1.2. [Ru^{III}(trpy)(L-CH$_3$)]ClO$_4$. Anal. Calc. for $C_{36}H_{28}N_6O_6ClRu$: C, 55.63; H, 3.60; N, 10.81. Found: C, 55.92; H, 3.32; N, 10.94%.

2.2.2.1.3. [Ru^{III}(trpy)(L-H)]ClO$_4$. Anal. Calc. for $C_{34}H_{24}N_6O_6ClRu$: C, 54.50; H, 3.20; N, 11.22. Found: C, 54.62; H, 3.63; N, 11.10%.

2.2.2.1.4. [Ru^{III}(trpy)(L-Cl)]ClO$_4$. Anal. Calc. for $C_{34}H_{22}N_6O_6Cl_3Ru$: C, 49.90; H, 2.69; N, 10.27. Found: C, 49.75; H, 2.77; N, 10.45%.

2.2.2.1.5. [Ru^{III}(trpy)(L-NO$_2$)]ClO$_4$. Anal. Calc. for $C_{34}H_{22}N_8O_{10}ClRu$: C, 48.65; H, 2.62; N, 13.35. Found: C, 48.55; H, 2.80; N, 13.45%.

2.3. Physical measurements

Microanalyses (C, H, N) were performed using a Heraeus Carlo Erba 1108 elemental analyzer. IR spectra were obtained on a Perkin–Elmer 783 spectrometer with samples prepared as KBr pellets. Electronic spectra were recorded on a JASCO V-570 spectrophotometer. Magnetic susceptibilities were measured using a PAR 155 vibrating sample magnetometer fitted with a Walker Scientific L75FBAL magnet. NMR spectra were recorded in $CDCl_3$ solution with a Bruker AV 300 NMR spectrometer. ESR spectra were recorded with a JEOL JES-FA200 X-band spectrometer fitted with a quartz Dewar for measurements at 77 K (liquid dinitrogen). All ESR spectra were calibrated with an aid of DPPH ($g = 2.0037$). Electrochemical measurements were made using a CH Instruments model 600A electrochemical analyzer. A platinum disc working electrode, a platinum wire auxiliary electrode and an aqueous saturated calomel reference electrode (SCE) were used in the cyclic voltammetry experiments. A platinum-wire-gauge working electrode was used in the coulometric experiments. All electrochemical experiments were performed under a dinitrogen atmosphere. All electrochemical data were collected at 298 K and are uncorrected for junction potentials.

2.4. X-ray crystallography

Single crystals of [Ru^{II}(trpy)(L-Cl)] were obtained by slow evaporation of an acetonitrile solution of the complex. Single crystals of [Ru^{III}(trpy)(L-Me)]ClO$_4$ were obtained by slow diffusion of toluene into an acetonitrile solution of the complex. Data were collected on a Bruker SMART APEX CCD diffractometer using graphite monochromated and Mo Kα radiation ($\lambda = 0.71073$ Å). X-ray data reduction and, structure solution and refinement were done using SHELXS-97 and SHELXL-97 programs [14]. The structures were solved by the direct methods.

Crystal data for $C_{51}H_{33}N_9O_6Cl_3Ru_{1.5}$, $M = 1125.34$, $0.33 \times 0.34 \times 0.45$ mm^3, monoclinic, space group $C2/c$, $a = 32.244(7)$ Å, $b = 15.797(4)$ Å, $c = 19.331(4)$ Å, $\beta = 102.458(4)°$, $V = 9615(4)$ Å^3, $Z = 8$, $D_{calc} = 1.556$ Mg m^{-3}, $F(000) = 4536$, $\lambda = 0.71073$ Å, $T = 293$ K, $\mu = 0.702$ mm^{-1}, 49 734 reflections collected, 10 279 unique ($R_{int} = 0.036$). Final goodness-of-fit = 0.95, $R_1 = 0.0595$, $wR_2 = 0.2266$, R indices based on 8382 reflections with $I > 2\sigma(I)$ (refinement on F_2), 638 parameters.

Crystal data for $C_{36}H_{28}N_6O_6ClRu$, $M = 813.20$, $0.24 \times 0.28 \times 0.42$ mm^3, monoclinic, space group $P2_1/c$, $a = 14.0441(3)$ Å, $b = 21.9700(5)$ Å, $c = 12.5956(3)$ Å, $\beta = 115.2980(10)°$, $V = 3513.65(14)$ Å^3, $Z = 4$, $D_{calc} = 1.537$ mg m^{-3}, $F(000) = 1660$, $\lambda = 0.71073$ Å, $T = 273$ K, $\mu = 0.584$ mm^{-1}, 40 809 reflections collected, 8523 unique ($R_{int} = 0.032$). Final goodness-of-fit = 1.07, $R_1 = 0.0386$, $wR_2 = 0.1044$, R indices based on 8523 reflections with $I > 2\sigma(I)$ (refinement on F_2), 487 parameters.

3. Results and discussion

3.1. [Ru^{II}(trpy)(L-R)] complexes

3.1.1. Synthesis and crystal structure

As delineated in the introduction, the primary objective of the present study has been to synthesize a group of mixed-ligand complexes of ruthenium containing both 2,2′,2″-terpyridine and the *N*,*N*′-bis(aryl)pyridine-2,6-dicarboxamide (**3**). For this purpose five *N*,*N*′-bis(aryl)-pyridine-2,6-dicarboxamides with different substituents (R = OCH_3, CH_3, H, Cl and NO_2) at the *para* position of the two pendant phenyl rings have been used, in order to study their influence, if any, on the redox properties of the resulting ruthenium complexes. These amide ligands (**3**) are abbreviated in general as H_2L-R, where H_2 stands for the two dissociable protons and R for the substituents. Reactions of the selected amides (**3**) with [Ru(trpy)Cl_3] proceed smoothly in refluxing ethanol in the presence of triethylamine to afford the targeted mixed-ligand complexes of type [Ru^{II}(trpy)(L-R)] in decent yields. It may be noted here that during the synthetic reaction ruthenium has undergone a one-electron reduction, and triethylamine might have served as the reducing agent. Preliminary (microanalytical, spectroscopic, magnetic, etc.) characterizations on these complexes (vide infra) are found to be in well accordance with their compositions. In order to find out coordination mode of the *N*,*N*′-bis(aryl)pyridine-2,6-dicarboxamides in these complexes, structure of a representative member of this family, *viz*. [Ru^{II}(trpy)(L-Cl)], has been determined by X-ray crystallography. The structure is shown in Fig. 1 and selected bond parameters are listed in Table 1. The structure shows that the *N*,*N*′-bis(4′-chlorophenyl)pyridine-2,6-dicarboxamide is coordinated to ruthenium, via dissociation of two acidic protons, as a dianionic tridentate N,N,N-donor (**4**). A terpyridine is also coordinated to the metal center in the usual fashion. Ruthenium is therefore sitting in a N_6 coordination environment, which is distorted octahedral in nature, as reflected in all the bond parameters around ruthenium. The observed bond distances in the Ru(L-Cl) fragment are all quite normal [2j,n], and so are those in the Ru(trpy) fragment [11a]. In the crystal lattice of the [Ru^{II}(trpy)-(L-Cl)] complex, there are three molecules of water per two complex molecules. In order to find out the link between these water molecules and the complex molecule, packing pattern in the lattice has been scrutinized (Fig. 2), which shows that besides links with the water molecules, the complex molecules also have direct links between themselves. A closer inspection into the network reveals that three types of hydrogen-bonding interactions, *viz*. C–H–O, O–H–O, C–H–Cl and C–H–π, are active in the lattice. The amide oxygen is linked with one trpy C–H as well as O–H of water. A C–H fragment from the pyridine ring of the amide is hydrogen bonded to water molecule. The central C–H fragment from the pyridine ring of the amide is linked to the π-cloud over a terminal pyridine ring of trpy in a η^2-fashion. C–H fragments of the terpyridine and the pendent phenyl ring of the amide are found to be hydrogen bonded to the chlorine atom in the amide. One C–H fragment of the terpyridine is also hydrogen bonded to the π-cloud in the pendent phenyl ring of the amide. These hydrogen-bonding interactions appear to be responsible for holding the complex molecules together in the crystal lattice. It may be relevant to note here that such interactions are of significant importance in molecular recognition processes as well as in crystal engineering [15]. As all the [Ru^{II}(trpy)(L-R)] complexes have been synthesized similarly and they show similar properties (vide infra), the other four [Ru^{II}(trpy)(L-R)] (R ≠ Cl) complexes are assumed to have similar structure as the [Ru^{II}(trpy)-(L-Cl)] complex.

3.1.2. Spectral properties

^{1}H NMR spectra of these complexes show many signals, most of which are overlapping, and hence assignment of each signal to a specific proton has not been possible. However, two distinct doublets observed near 5.3 and 6.3 ppm in the complexes with R ≠ H, each integrating to four protons, are assignable to the hydrogens in the two pendent phenyl rings in the coordinated amide ligand. Signals for the methoxy and methyl groups in the [Ru^{II}(trpy)-(L-OCH_3)] and [Ru^{II}(trpy)(L-CH_3)] complexes are observed respectively at 3.57 and 2.10 ppm. The infrared and ^{1}H NMR spectral data of the [Ru^{II}(trpy)(L-R)] complexes are therefore consistent with their compositions.

Infrared spectra of each [Ru^{II}(trpy)(L-R)] complex shows many bands of different intensities in the 400–4000 cm^{-1} region. Assignment of each individual band to a specific vibration has not been attempted. However, comparison with spectrum of the respective uncoordinated ligand shows that the N–H stretch, observed near 3140 cm^{-1} in the uncoordinated ligands, is absent in the complexes. The amide C=O stretch, observed near 1680 cm^{-1} in the uncoordinated ligands, is also found to be shifted to around 1595 cm^{-1} in the complexes. Comparison with the spectrum of [Ru(trpy)Cl_3] shows the presence of some common bands (near 648, 670, 729, 781, 1240 and 1444 cm^{-1}) as well as some new bands (near 808, 1008, 1083, 1379 and 1595 cm^{-1}) in the spectra of the [Ru^{II}(trpy)-(L-R)] complexes indicating presence coordinated terpyridine and amide ligands [8a,2n,j]. The [Ru^{II}(trpy)-(L-R)] complexes are found to be diamagnetic, which is in accordance with the +2 oxidation state of ruthenium (low-spin d^6, $S = 0$) in these complexes.

The [Ru^{II}(trpy)(L-R)] complexes are soluble in acetone, acetonitrile, dichloromethane, chloroform, etc., producing deep brown solutions. Electronic spectra of the complexes have been recorded in dichloromethane solution. All the complexes show several intense absorptions in the visible and ultraviolet regions (Table 2). The absorptions in the ultraviolet region are attributable to transitions within the ligand orbitals and those in the visible region are probably due to charge-transfer transitions. To have a better

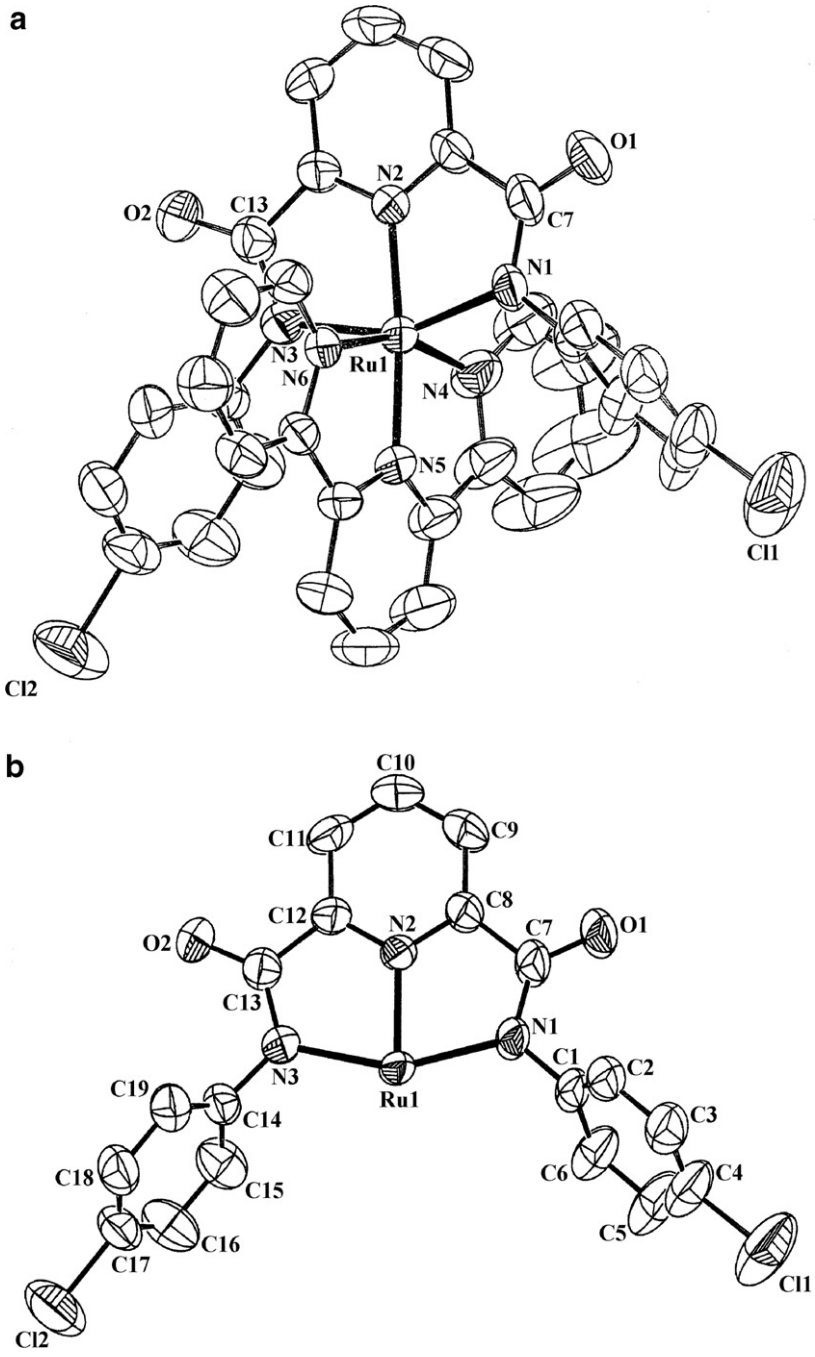


Fig. 1. (a) Structure of the [Ru^{II}(trpy)(L-Cl)] complex and (b) view of the Ru(L-Cl) fragment.

insight into the nature of the absorptions in the visible region, qualitative EHMO calculations have been performed [16] on the structurally characterized [Ru^{II}(trpy)-(L-Cl)] complex. Partial MO diagrams are shown in Fig. 3 and composition of selected molecular orbitals is presented in Table S1 (Supplementary material). The highest occupied molecular orbital (HOMO) and the next two filled orbitals (HOMO − 1 and HOMO − 2) have major (~60%) contribution from the ruthenium d_{xy}, d_{yz} and d_{zx} orbitals. These three occupied orbitals may therefore be regarded as the ruthenium t_2 orbitals. The lowest unoccupied molecular orbital (LUMO) has 70% contribution from the coordinated terpyridine and is dispersed over the entire ligand. Among the next few vacant orbitals (LUMO + 1, LUMO + 2, etc.), LUMO + 1 is primarily centered on the amide ligand and concentrated heavily on pyridine nitrogen, while LUMO + 2 is delocalized over both the amide ligand and terpyridine. The lowest energy absorption, displayed by the [Ru^{II}(trpy)(L-R)] complexes near 540 nm, may therefore be assigned to the charge-transfer transition taking place from the highest filled ruthenium t_2 orbital (HOMO) to the vacant orbital delocalized over the terpyridine (LUMO). The other intense absorptions in the visible region may be assigned to

Table 1
Selected bond distances (Å) and bond angels (°) for $[Ru^{II}(trpy)(L\text{-}Cl)]$ and $[Ru^{III}(trpy)(L\text{-}CH_3)]^+$

$[Ru^{II}(trpy)(L\text{-}Cl)]$			
Bond distance (Å)			
Ru1–N1	2.098(3)	Ru1–N4	2.047(4)
Ru1–N2	1.983(4)	Ru1–N5	1.946(4)
Ru1–N3	2.098(3)	Ru1–N6	2.053(4)
C7–O1	1.249(6)		
C13–O2	1.254(6)		
Bond angles (°)			
N1–Ru1–N2	77.22(14)	N4–Ru1–N5	78.64(16)
N2–Ru1–N3	77.81(14)	N5–Ru1–N6	79.43(15)
N1–Ru1–N3	155.01(15)	N4–Ru1–N6	158.01(16)
$[Ru^{III}(trpy)(L\text{-}CH_3)]^+$			
Bond distance (Å)			
Ru1–N1	1.981(2)	Ru1–N4	2.071(2)
Ru1–N2	2.023(2)	Ru1–N5	1.982(2)
Ru1–N3	2.042(2)	Ru1–N6	2.080(3)
C6–O1	1.224(3)		
C14–O2	1.235(3)		
Bond angles (°)			
N1–Ru1–N2	80.24(8)	N4–Ru1–N5	79.51(9)
N1–Ru1–N3	78.81(8)	N5–Ru1–N6	79.19(9)
N2–Ru1–N3	159.05(8)	N4–Ru1–N6	158.67(9)

charge-transfer transitions from the filled ruthenium t_2 orbitals to the higher energy vacant orbitals.

3.1.3. Electrochemical properties

Electrochemical properties of the $[Ru^{II}(trpy)(L\text{-}R)]$ complexes have been studied by cyclic voltammetry in 1:9 dichloromethane–acetonitrile solution (0.1 M TBAP).[2] Each complex shows two oxidative responses at potentials positive of the SCE reference electrode and a reductive response at negative potentials (Table 2). A representative voltammogram is shown in Fig. 4. The first oxidation, observed within 0.16–0.33 V, is reversible in nature, characterized by a peak-to-peak separation (ΔE_p) of ~70 mV, which remains unchanged upon changing the scan rate, and the anodic peak-current (i_{pa}) is almost equal to the cathodic peak-current (i_{pc}) as expected for a reversible electron-transfer process. In view of composition of the HOMO, this oxidation is assigned to Ru(II)–Ru(III) oxidation. It is interesting to note here that in the tris-complexes of *N*-(aryl)picolinamides (**1**) [2j], where ruthenium was nested in a $N_3^pN_3^a$ coordination sphere, the Ru(III)–Ru(II) couple appeared on the negative side of SCE (*e.g.* −0.38 V, for the R = H complex), whereas in these $[Ru^{II}(trpy)(L\text{-}R)]$ complexes, in which the coordination environment around the metal center has changed to $N_4^pN_2^a$, the same couple appears on the positive side of SCE (*e.g.* 0.20 V, for the R = H complex). Hence replacement of an amide nitrogen by a pyridine nitrogen in the coordination sphere of ruthenium has truly stabilized the bivalent state of the metal to a significant extent, which has been manifested in the positive shift of the Ru(II)–Ru(III) potential by about 580 mV.

The second oxidation, observed within 0.94–1.33 V, is quasi-reversible in nature, and is tentatively assigned to Ru(III)–Ru(IV) oxidation. Based on composition of the LUMO, the irreversible reduction observed around −1.1 V is assigned to reduction of the coordinated terpyridine ligand. Potential of Ru(II)–Ru(III) oxidation has been observed to be sensitive to nature of the substituent R in the *N*,*N*′-bis(aryl)pyridine-2,6-dicarboxamide. The potential ($E_{1/2}$) increases with increasing electron-withdrawing character of the substituent R. The plot of $E_{1/2}$ versus 2σ [σ = Hammett constant of R [17]; $OCH_3 = -0.27$, $CH_3 = -0.17$, $H = 0.00$, $Cl = 0.23$, $NO_2 = 0.78$] is linear for these complexes (Fig. S1, Supplementary material) with a slope (ρ) of 0.08 (ρ = reaction constant of this oxidation [18]). This linear correlation of the Ru(II)–Ru(III) oxidation potentials with the electronic nature of the substituents having a reasonable slope clearly shows that the substituent on the phenyl ring of the amide, which is six bonds away from the metal center, can still influence the metal-centered redox potential in a predictable manner. Similarly potential ($E_{1/2}$) of the Ru(III)–Ru(IV) oxidation also shows linear correlation with the electron-withdrawing nature (2σ) of substituent R with a slope (ρ) of 0.18 V (Fig. S1, Supplementary materials). The higher slope of the second plot indicates that the second oxidation probably involves an orbital having significant amide character. Potentials of the irreversible reductive responses do not show any systematic variation with the nature of the substituent.

3.2. $[Ru^{III}(trpy)(L\text{-}R)]^+$ complexes

3.2.1. Synthesis and crystal structure

Reversibility of the Ru(II)–Ru(III) oxidation in the $[Ru^{II}(trpy)(L\text{-}R)]$ complexes indicates that the one-electron oxidized species, *viz.* $[Ru^{III}(trpy)(L\text{-}R)]^+$, might be stable on a time scale much longer than the cyclic voltammetric time scale. To investigate this, each $[Ru^{II}(trpy)(L\text{-}R)]$ complex has been coulometrically oxidized at an appropriate potential[3] in acetonitrile solution (0.1 M TBAP). The oxidation has been smooth and quantitative, associated with a color change from brown to green, and the oxidized product has been isolated as $[Ru^{III}(trpy)(L\text{-}R)]ClO_4$ in the solid state. Preliminary characterization data on these complexes are found to be consistent with their compositions. To examine the difference in structural features, if any, associated with one-electron oxidation of the metal center, structure of a selected member of this new family, *viz.* $[Ru^{III}(trpy)(L\text{-}CH_3)]ClO_4$, has also been determined by X-ray crystallography. The structure (Fig. 5) shows that apart from small differences in the Ru–N lengths (Table 1),

[2] A little dichloromethane was necessary to take the complex into solution. Addition of large excess of acetonitrile was necessary to record the redox responses in proper shape.

[3] Coulometric oxidation has been carried out at a potential 200 mV higher than the E_{pa}.

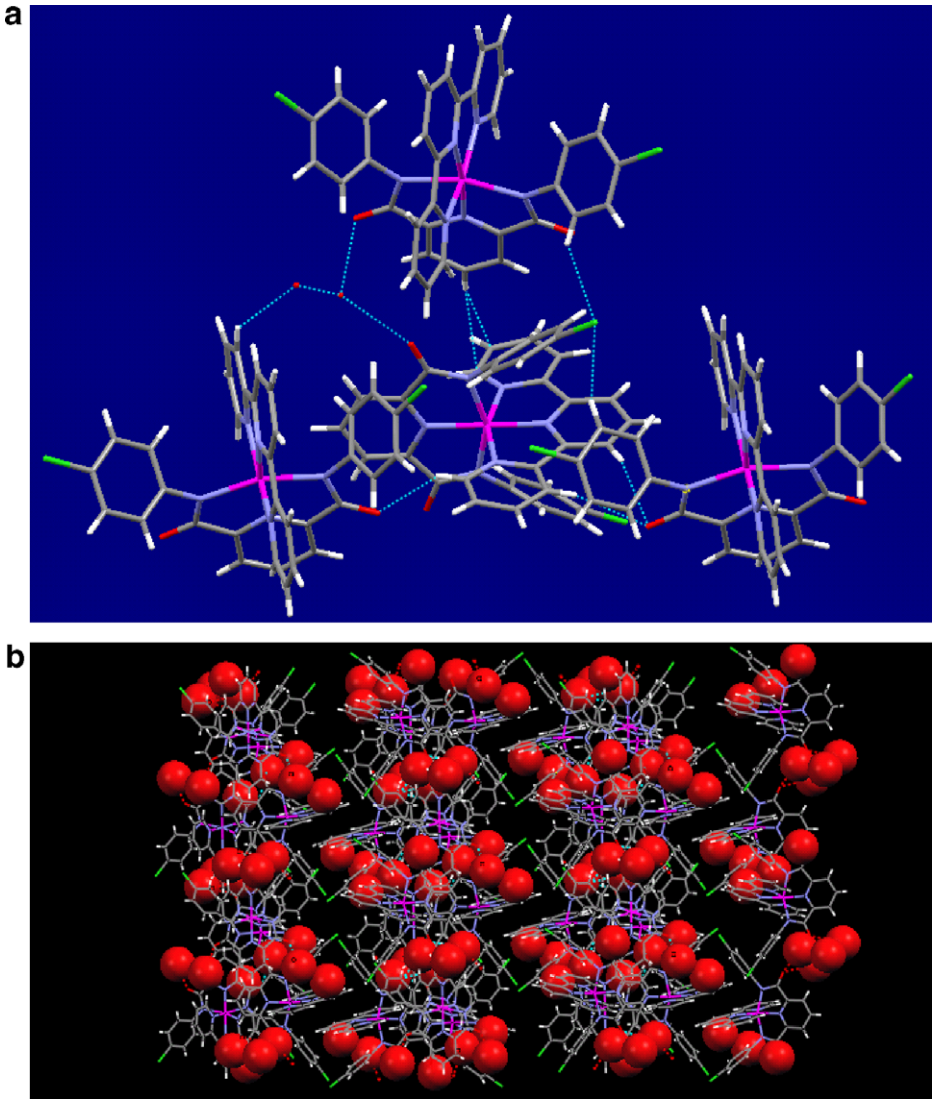


Fig. 2. Packing diagram of the [Ru^{II}(trpy)(L-Cl)] crystal.

Table 2
Electronic spectral and cyclic voltammetric data of [Ru^{II}(trpy)(L-R)]

Compound	Electronic spectral data[a] λ_{max}, nm (ε, M^{-1} cm^{-1})	Cyclic voltammetric data[b]
[Ru^{II}(trpy)(L-OCH_3)]	236 (20400), 277 (11000),[c] 314 (9500), 397 (5500), 435 (5000),[c] 541 (3400)	0.16[d] (70),[e] 0.94[d] (69),[e] −1.10[f]
[Ru^{II}(trpy)(L-CH_3)]	236 (19400), 278 (10600),[c] 315 (9400), 396 (4500), 432 (4300),[c] 540 (2700)	0.18[d] (74),[e] 0.99[d] (90),[e] −1.15[f]
[Ru^{II}(trpy)(L-H)]	235 (19900), 278 (11500),[c] 315 (9900), 395 (5100), 430 (5300),[c] 538 (3500)	0.20[d] (63),[e] 1.05[d] (96),[e] −1.11[f]
[Ru^{II}(trpy)(L-Cl)]	233 (19400), 278 (9900),[c] 314 (7400), 394 (3200), 432 (2300),[c] 540 (2200)	0.22[d] (76),[e] 1.15[d] (93),[e] −1.15[f]
[Ru^{II}(trpy)(L-NO_2)]	230 (19200), 277 (14500),[c] 316 (17800), 326 (17200), 431 (7100),[c] 541 (3500)	0.33[d] (66),[e] 1.33[d] (62),[e] −1.15[f]

[a] In dichloromethane solution.
[b] Solvent, 1:9 dichloromethane–acetonitrile; supporting electrolyte, TBAP; scan rate 50 mV s^{-1}.
[c] Shoulder.
[d] $E_{1/2} = 0.5(E_{pa} + E_{pc})$, where E_{pa} and E_{pc} are anodic and cathodic peak potentials respectively.
[e] $\Delta E_p = (E_{pa} - E_{pc})$.
[f] E_{pc} value.

the other features are qualitatively very similar to those of the [Ru^{II}(trpy)(L-R)] complex. The Ru–N distances in the Ru(L-R) fragment are shorter in the Ru(III) complex, probably due to enhanced electrostatic attraction of the dianionic amide ligand with the trivalent metal. The Ru–N lengths in the Ru(trpy) fragment are, however, slightly longer in the Ru(III) complexes, which is attributable to the lack of back-donation from the oxidized metal center that probably wins over the electrostatic effect. The packing pattern in the lattice (Fig. 6) shows that

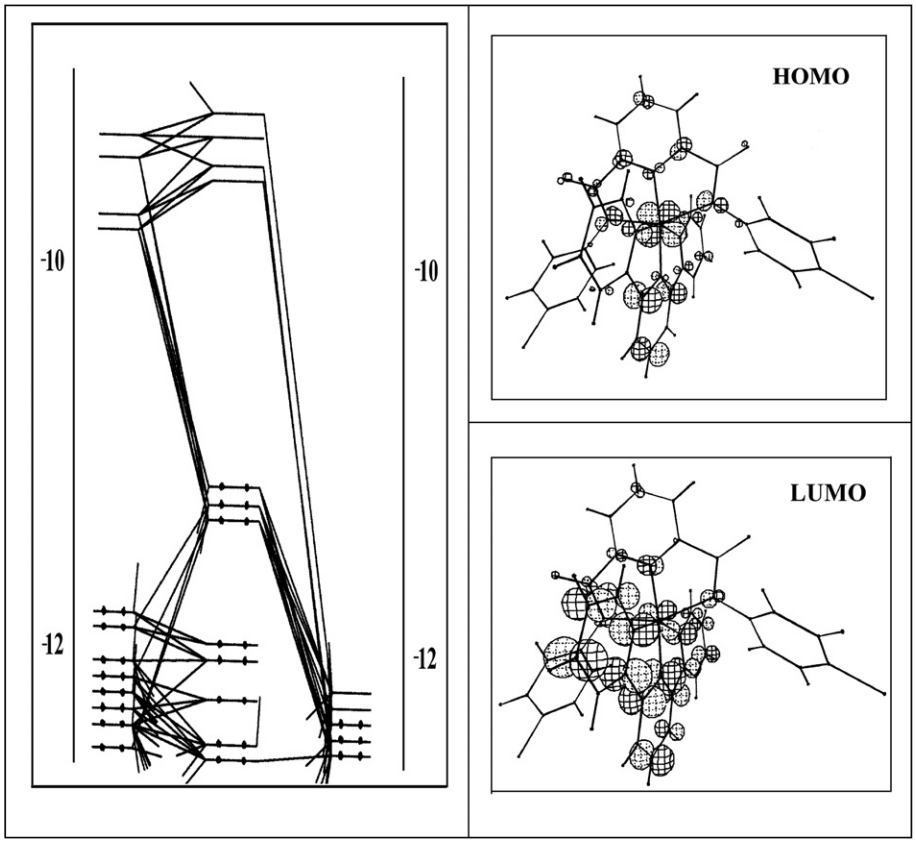


Fig. 3. Partial MO diagram of the $[Ru^{II}(trpy)(L\text{-}Cl)]$ complex.

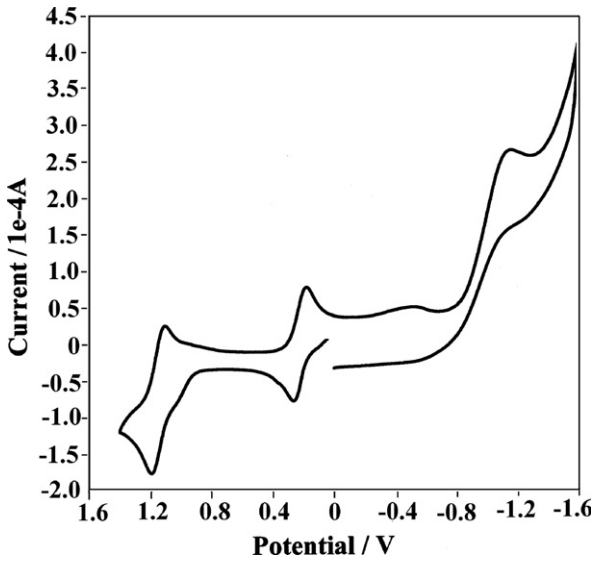


Fig. 4. Cyclic voltammogram of the $[Ru^{II}(trpy)(L\text{-}Cl)]$ complex in 1:9 dichloromethane–acetonitrile solution (0.1 M TBAP) at a scan rate of 50 mV s^{-1}.

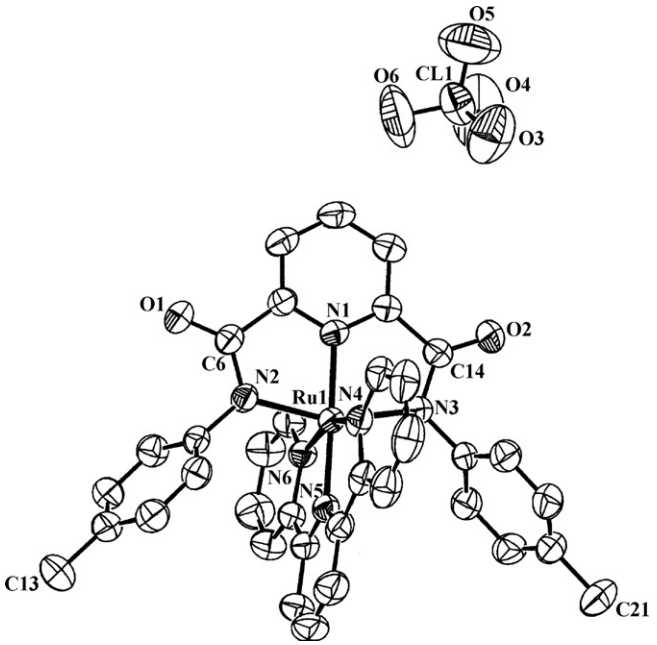


Fig. 5. Structure of the $[Ru^{III}(trpy)(L\text{-}CH_3)]ClO_4$ complex.

hydrogen-bonding interactions of three types, *viz.* C–H–O, O–H–O and C–H–π, are active. The perchlorate oxygens are hydrogen bonded to water and C–H fragment of the trpy ligand. The amide oxygen is also hydrogen bonded to water and C–H fragment of the trpy ligand. One C–H fragment of the trpy ligand is hydrogen bonded to the π-cloud over the tolyl ring of the amide ligand. Due to such hydrogen-bonded arrangements of the complex molecules, several nearly rectangular cavities have been created throughout the lattice. Based on the similarity in their syn-

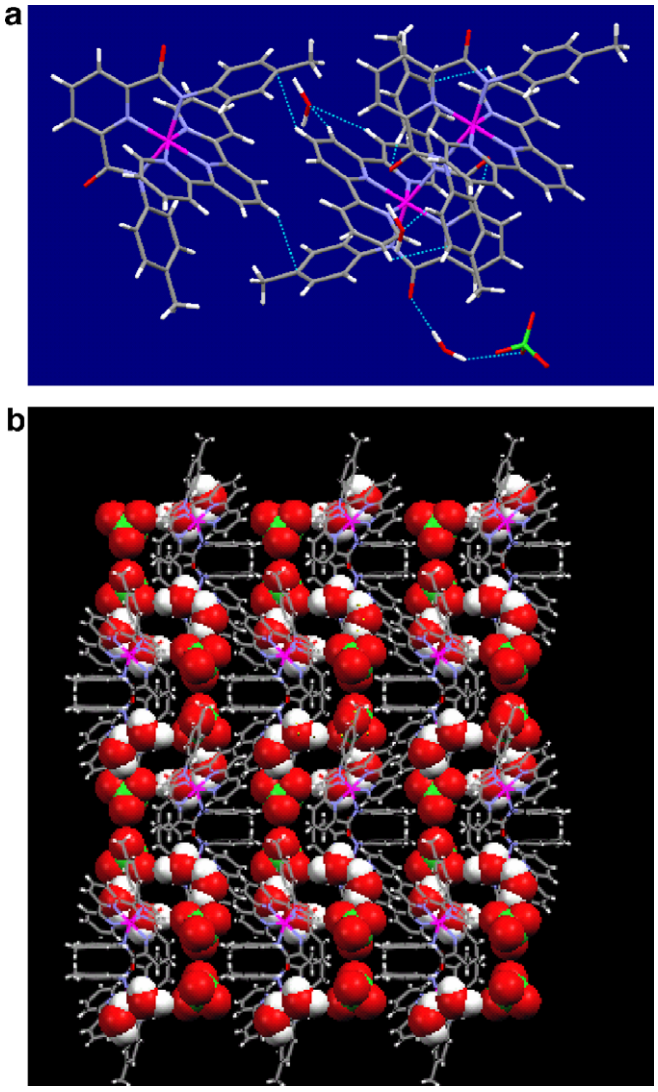


Fig. 6. Packing diagram of the $[Ru^{III}(trpy)(L\text{-}CH_3)]ClO_4$ crystal.

thesis and properties (*vide infra*), the other four $[Ru^{III}(trpy)(L\text{-}R)]ClO_4$ ($R \neq CH_3$) complexes are assumed to have similar structures as $[Ru^{III}(trpy)(L\text{-}CH_3)]ClO_4$.

3.2.2. Spectral properties

Apart from the appearance of two additional intense bands around 1100 and 620 cm^{-1} due to presence of the perchlorate anion and small shifts in the position of the other bands, infrared spectra of each $[Ru^{III}(trpy)(L\text{-}R)]ClO_4$ complex is qualitatively similar to that of the respective $[Ru^{II}(trpy)(L\text{-}R)]$ complex. Magnetic susceptibility measurements show that the $[Ru^{III}(trpy)(L\text{-}R)]ClO_4$ complexes are one-electron paramagnetic ($\mu_{eff} = 1.83$–$1.90\ \mu_B$), which corresponds to the +3 oxidation state of ruthenium (low-spin d^5, $S = 1/2$) in these complexes. ESR spectra of the $[Ru^{III}(trpy)(L\text{-}R)]ClO_4$ complexes have been recorded in 1:1 dichloromethane–toluene solution at 77 K. Each complex shows an axial ESR spectrum with two distinct signals ($g_\perp$ and $g_\parallel$; in the order of decreasing magnitude). A selected spectrum is shown in Fig. 7 and the spectral data for all complexes are given in Table 3. The anisotropy of the spectra reflects the asymmetry of the electronic environment around ruthenium in these $[Ru^{III}(trpy)(L\text{-}R)]ClO_4$ complexes. When an octahedral geometry suffers from an axial distortion (Δ), the t_2 level splits into a and e components (Fig. 7). Spin–orbit coupling causes minor additional changes in energy of all the three levels. Thus two closely spaced electronic transitions (transition energies ΔE_1 and ΔE_2; $\Delta E_1 < \Delta E_2$) are, in principle, probable within these three levels. All these energy parameters have been computed (Table 3) using the observed g values, the g-tensor theory of low-spin d^5 complexes [19], and a reported method [20]. The axial distortion is found to be around 6000 cm^{-1}.[4] The calculated values of ΔE_1 and ΔE_2 are also close to ~6000 cm^{-1} (~1670 nm), which indicate that two ligand-field transitions, which are close in energy, should take place in the near-infrared region, and indeed a broad band of weak intensity has been observed in the spectra of all the complexes near the predicted energy (*vide infra*). Closeness of the two expected transitions appears to have vitiated their resolution. The ESR spectral data thus show that these $[Ru^{III}(trpy)(L\text{-}R)]ClO_4$ complexes are significantly distorted from the ideal octahedral geometry, as was also indicated by the structure determination.

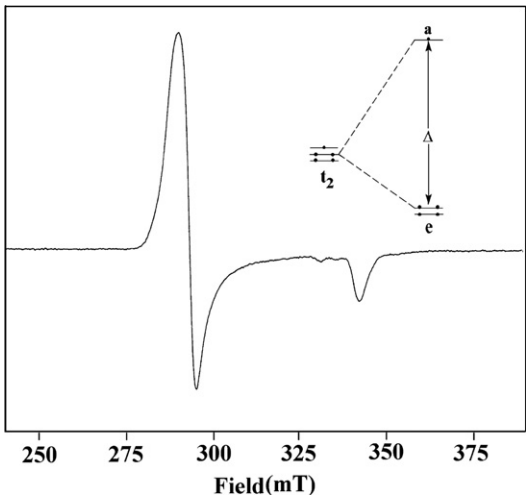


Fig. 7. ESR spectrum of the $[Ru^{III}(trpy)(L\text{-}Cl)]ClO_4$ complex in 1:1 dichloromethane–toluene solution at 77 K.

Electronic spectra of the green $[Ru^{III}(trpy)(L\text{-}R)]ClO_4$ complexes, recorded in acetonitrile solutions, show absorptions in the near-infrared, visible and ultraviolet regions (Table 4). The absorptions in the ultraviolet region are again believed to be due to transitions within the ligand orbitals. To understand the origin of the absorptions in the visible region, qualitative EHMO calculations have been performed on the structurally characterized $[Ru^{III}(trpy)(L\text{-}CH_3)]ClO_4$ complex. Composition of selected

[4] The spin–orbit coupling constant (λ) is taken to be 1000 cm^{-1} for complexed ruthenium(III) [20].

Table 3
ESR g-values[a] and derived parameters[b] of the $[Ru^{III}(trpy)(L\text{-}R)]ClO_4$ complexes

Compounds	$g_\perp$	$g_\parallel$	Δ, λ	ΔE_1, λ	ΔE_2, λ
$[Ru^{III}(trpy)(L\text{-}OCH_3)]ClO_4$	2.209	1.921	6.219	5.891	6.805
$[Ru^{III}(trpy)(L\text{-}CH_3)]ClO_4$	2.217	1.916	6.050	5.727	6.638
$[Ru^{III}(trpy)(L\text{-}H)]ClO_4$	2.222	1.914	5.988	5.667	6.577
$[Ru^{III}(trpy)(L\text{-}Cl)]ClO_4$	2.230	1.909	5.836	5.520	6.428
$[Ru^{III}(trpy)(L\text{-}NO_2)]ClO_4$	2.236	1.903	5.659	5.349	6.254

[a] In 1:1 dichloromethane–toluene solution at 77 K.
[b] Spin–orbit coupling constant (λ) for complexed Ru(III) is $\sim$1000 cm^{-1}.

Table 4
Electronic spectral data of $[Ru^{III}(trpy)(L\text{-}R)]ClO_4$

Compound	Electronic spectral data[a] λ_{max}, nm (ε, M^{-1} cm^{-1})
$[Ru^{III}(trpy)(L\text{-}OCH_3)]ClO_4$	232 (11200), 273 (5900),[b] 287 (5200),[b] 313 (5400), 338 (3500),[b] 424 (1400), 655 (850), 1553 (112)
$[Ru^{III}(trpy)(L\text{-}CH_3)]ClO_4$	231 (10100), 273 (4900),[b] 282 (4700),[b] 314 (4800), 332 (4000),[b] 420 (1300), 652 (1100), 1565 (136)
$[Ru^{III}(trpy)(L\text{-}H)]ClO_4$	226 (10000), 276 (6300),[b] 283 (6400),[b] 311 (5500), 338 (3400),[b] 421 (1900), 652 (1500), 1569 (130)
$[Ru^{III}(trpy)(L\text{-}Cl)]ClO_4$	231 (10900), 265 (5800),[b] 283 (5600),[b] 314 (5800), 337 (4300),[b] 425 (2000), 651 (1700), 1576 (143)
$[Ru^{III}(trpy)(L\text{-}NO_2)]ClO_4$	226 (11600), 271 (7800),[b] 283 (8700),[b] 319 (11200), 340 (8500),[b] 411 (2300), 646 (1100), 1581 (146)

[a] In dichloromethane.
[b] Shoulder.

molecular orbitals is given in Table S2 (Supplementary material) and partial MO diagram is shown in Fig. 8. In this complex, the HOMO (singly occupied), HOMO − 1 and HOMO − 2 are found to have large contributions (nearly 60%) from ruthenium d_{xy}, d_{yz} and d_{xz} orbitals, while the HOMO − 3 has predominant terpyridine character. The absorption near 650 nm may therefore be assigned to a ligand-to-metal charge-transfer transition from HOMO − 3 to HOMO (singly occupied). The weak absorption in the near-infrared region (near 1600 nm) has already been assigned to ligand-field transitions (*vide supra*).

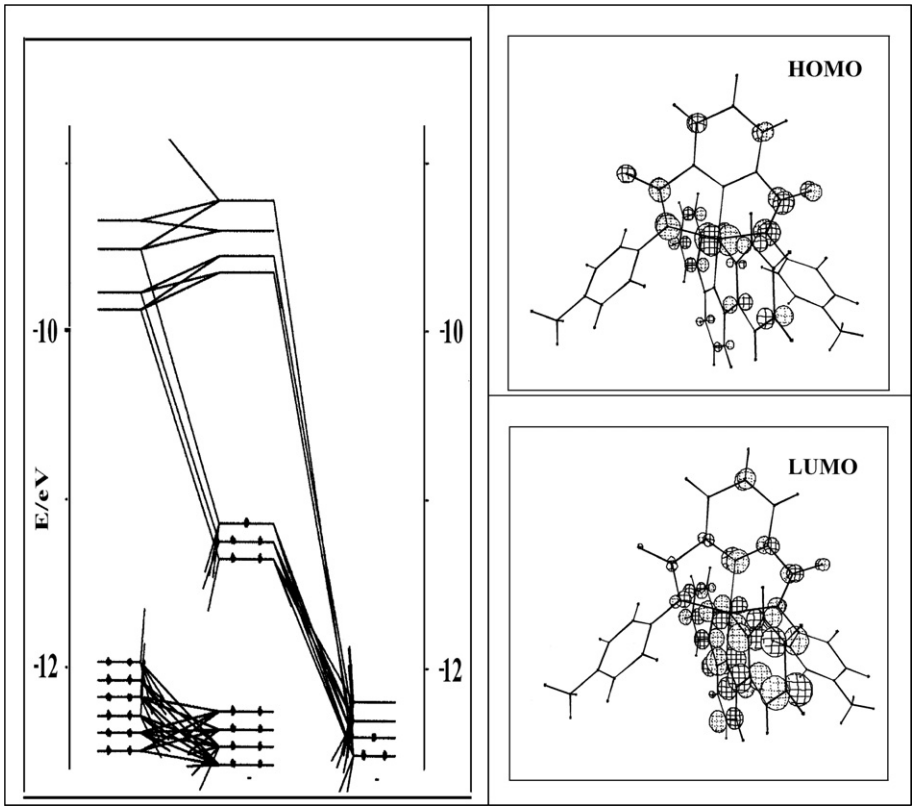


Fig. 8. Partial MO diagram of the $[Ru^{II}(trpy)(L\text{-}CH_3)]ClO_4$ complex.

3.2.3. Electrochemical properties

Cyclic voltammetric properties of the $[Ru^{III}(trpy)(L\text{-}R)]^{+}$ complexes are identical to those of their Ru(II) precursors, only the Ru(II)–Ru(III) couple appears as a reductive response. The green $[Ru^{III}(trpy)(L\text{-}R)]^{+}$ complexes could be quantitatively converted back, upon coulometric reduction at 0.0 V, to the respective brown $[Ru^{II}(trpy)(L\text{-}R)]$ complexes, identified by their characteristic electronic spectra. In terms of their Ru(II)–Ru(II) reduction potentials, these green $[Ru^{III}(trpy)(L\text{-}R)]^{+}$ complexes are very mild oxidants.

4. Conclusions

The present study shows that the *N*,*N*′-bis(aryl)pyridine-2,6-dicarboxamides (**3**) can efficiently bind to ruthenium(II) in the dianionic N,N,N-fashion (**4**) and in combination with 2,2′,2″-terpyridine can stabilize the metal in its +2 state. This study further demonstrates that binding by the amides (**3**) in the N,N,N-fashion (**4**) can also sufficiently stabilize the +3 oxidation state of ruthenium. The coordination environment provided by the *N*,*N*′-bis(aryl)pyridine-2,6-dicarboxamides and 2,2′,2″-terpyridine appears to be unique in supporting both the +2 and +3 states of ruthenium.

Acknowledgements

Financial assistance received from the University Grants Commission, New Delhi, [Grant No. F31-124/2005(SR)] is gratefully acknowledged. The authors thank Dr. Samar K. Das, School of Chemistry, University of Hyderabad, India, for his help with recording the ESR spectra. SN thanks the Council of Scientific and Industrial Research, New Delhi, for his fellowship [Grant No. 9/96(401)2003-EMR-I].

Appendix A. Supplementary material

CCDC 651197 and 651198 contain the supplementary crystallographic data for this paper. These data can be obtained free of charge via http://www.ccdc.cam.ac.uk/conts/retrieving.html, or from the Cambridge Crystallographic Data Centre, 12 Union Road, Cambridge CB2 1EZ, UK; fax: (+44) 1223-336-033; or e-mail: deposit@ccdc.cam.ac.uk. Supplementary data associated with this article can be found, in the online version, at doi:10.1016/j.poly.2007.08.042.

References

[1] (a) M. Turki, C. Daniel, Coord. Chem. Rev. 216–217 (2001) 31;
(b) V. Balzani, A. Juris, Coord. Chem. Rev. 211 (2001) 97;
(c) B.-Z. Shan, Q. Zhao, N. Goswami, D.M. Eichhom, D.P. Rillema, Coord. Chem. Rev. 211 (2001) 117;
(d) N.A.P. Kane-Maguire, J.F. Wheeler, Coord. Chem. Rev. 211 (2001) 145;
(e) L.-N. Ji, X.-H. Zou, J.-G. Liu, Coord. Chem. Rev. 216–217 (2001) 513;
(f) G. Simonneaux, P. Le Maux, Coord. Chem. Rev. 228 (2002) 43;
(g) H. Yersin, C. Kratzer, Coord. Chem. Rev. 229 (2002) 75;
(h) J.F. Endicott, H.B. Schlegel, M.J. Uddin, D.S. Seniveratne, Coord. Chem. Rev. 229 (2002) 95;
(i) S.I. Gorelsky, A.B.P. Lever, M. Ebadi, Coord. Chem. Rev. 230 (2002) 97;
(j) F. Hartl, M.P. Aarnts, H.A. Nieuwenhuis, J. van Slageren, Coord. Chem. Rev. 230 (2002) 106;
(k) C.-M. Che, J.-S. Huang, Coord. Chem. Rev. 231 (2002) 151;
(l) M.J. Clarke, Coord. Chem. Rev. 232 (2002) 69;
(m) E. Tfouni, M. Krieger, B.R. McGarvey, D.W. Franco, Coord. Chem. Rev. 236 (2003) 57;
(n) B. Serli, E. Zangrando, T. Gianferrara, L. Yellowless, E. Alessio, Coord. Chem. Rev. 245 (2003) 73;
(o) I. Ando, Coord. Chem. Rev. 248 (2004) 185;
(p) M.J. Clarke, Coord. Chem. Rev. 236 (2003) 209;
(q) M.A.S. Aquino, Coord. Chem. Rev. 248 (2004) 1025;
(r) R.F. Winter, S. Záli, Coord. Chem. Rev. 248 (2004) 1565;
(s) S. Rigaut, D. Touchard, P.H. Dixneuf, Coord. Chem. Rev. 248 (2004) 1585;
(t) M.K. Nazeeruddin, S.M. Zakeeruddin, J.-J. Lagref, P. Liska, P. Comte, C. Barolo, G. Viscardi, K. Schenk, M. Graetzel, Coord. Chem. Rev. 248 (2004) 1317;
(u) L. Spiccia, G.B. Deacon, C.M. Kepert, Coord. Chem. Rev. 248 (2004) 1329;
(v) Y. Saito, T. Azechi, T. Kitamura, Y. Hasegawa, Y. Wada, S. Yanagida, Coord. Chem. Rev. 248 (2004) 1469;
(w) Md.K. Nazeeruddin, C. Klein, P. Liska, M. Grätzel, Coord. Chem. Rev. 249 (2005) 1460.
[2] (a) F. Basuli, S.M. Peng, S. Bhattacharya, Inorg. Chem. 36 (1997) 5645;
(b) F. Basuli, M. Ruf, C.G. Pierpont, S. Bhattacharya, Inorg. Chem. 37 (1998) 6113;
(c) A.K. Das, A. Rueda, L.R. Falvello, S.M. Peng, S. Bhattacharya, Inorg. Chem. 38 (1999) 4365;
(d) A.K. Das, S.M. Peng, S. Bhattacharya, J. Chem. Soc., Dalton Trans. (2000) 181;
(e) F. Basuli, S.M. Peng, S. Bhattacharya, Inorg. Chem. 39 (2000) 1120;
(f) F. Basuli, S.M. Peng, S. Bhattacharya, Inorg. Chem. 40 (2001) 1126;
(g) I. Pal, F. Basuli, T.C.W. Mak, S. Bhattacharya, Angew. Chem., Int. Ed. 40 (2001) 2923;
(h) K. Majumder, R.J. Butcher, S. Bhattacharya, Inorg. Chem. 41 (2002) 4605;
(i) R. Acharyya, S.M. Peng, G.H. Lee, S. Bhattacharya, Inorg. Chem. 42 (2003) 7378;
(j) A. Das, S.M. Peng, G.H. Lee, S. Bhattacharya, New. J. Chem. 28 (2004) 712;
(k) S. Nag, P. Gupta, R.J. Butcher, S. Bhattacharya, Inorg. Chem. 43 (2004) 4814;
(l) P.K. Sinha, L.R. Falvello, S. Bhattacharya, Indian J. Chem. 43A (2004) 1846;
(m) P. Gupta, S. Dutta, F. Basuli, S.M. Peng, G.-H. Lee, S. Bhattacharya, Inorg. Chem. 45 (2006) 460;
(n) S. Halder, R. Acharyya, S.M. Peng, G.H. Lee, M.G.B. Drew, S. Bhattacharya, Inorg. Chem. 45 (2006) 9654;
(o) S. Nag, R.J. Butcher, S. Bhattacharya, Eur. J. Inorg. Chem. (2007) 1251.
[3] (a) P. Ford, D.E.P. Rudd, R.G. Gaunder, H. Taube, J. Am. Chem. Soc. 90 (1968) 1187;
(b) A.W. Zanella, P.C. Ford, Inorg. Chem. 14 (1975) 42;
(c) T. Matsubara, P.C. Ford, Inorg. Chem. 15 (1976) 1107;
(d) Y. Ilan, H. Taube, Inorg. Chem. 22 (1983) 1655;
(e) Y. Ilan, M. Kapon, Inorg. Chem. 25 (1986) 2350;
(f) H.Y. Huang, W.J. Chen, C.C. Yang, A. Yeh, Inorg. Chem. 30 (1991) 1862;

(g) M.H. Chou, C. Creutz, N. Sutin, Inorg. Chem. 31 (1992) 2318;
(h) M.H. Chou, B.S. Brunschwig, C. Creutz, N. Sutin, A. Yeh, R.C. Chang, C.-T. Lin, Inorg. Chem. 31 (1992) 5347;
(i) M.H. Chou, D.J. Szalda, C. Creutz, N. Sutin, Inorg. Chem. 33 (1994) 1674;
(j) S.M. Redmore, C.D.F. Rickard, S.J. Webb, L.J. Wright, Inorg. Chem. 36 (1997) 4743.

[4] B. Albert, D. Bray, J. Lewis, M. Raff, K. Roberts, J.D. Watson, Molecular Biology of the Cell, third ed., Garland Publishing, New York, 1994, Chapter 3.

[5] (a) H. Sigel, C.F. Naumann, B. Prijs, D.B. McCormick, M.C. Falk, Inorg. Chem. 16 (1977) 790;
(b) H. Sigel, Inorg. Chem. 14 (1975) 1535;
(c) M.F. El-Shazly, A. El-Dissowky, T. Salem, M. Osman, Inorg. Chim. Acta 40 (1980) 1;
(d) D.W. Margerum, Pure Appl. Chem. 23 (1983) 23;
(e) A.S. Borovik, T.M. Dewey, K.N. Raymond, Inorg. Chem. 32 (1993) 413;
(f) T.J. Collins, Acc. Chem. Res. 27 (1994) 279;
(g) M.J. Bartos, S.W. Gordon-Wylie, B.G. Fox, L.J. Wright, S.T. Weintraub, K.E. Kauffmann, E. Münck, K.L. Koskta, E.S. Uffelman, C.E.F. Rickard, K.R. Noon, T.J. Collins, Coord. Chem. Rev. 174 (1998) 361;
(h) A. White, X. Ding, J.C. vanderSpek, J.R. Murphy, D. Ringe, Nature 394 (1998) 502;
(i) E. Pohl, R.K. Holmes, W.G.J. Hol, J. Mol. Biol. 292 (1997) 653;
(j) B.M. Trost, C.B. Lee, J. Am. Chem. Soc. 123 (2001) 3671;
(k) M.D. Feese, B.P. Ingason, J. Goranson-Siekierke, R.K. Holmes, W.G.J. Hol, J. Biol. Chem. 276 (2001) 5959;
(l) T.J. Collins, Acc. Chem. Res. 35 (2002) 782;
(m) B.M. Trost, K. Dogra, I. Hachiya, T. Emura, D.L. Hughes, S. Krska, R.A. Reamer, M. Palucki, N. Yasuda, P.J. Reider, Angew. Chem., Int. Ed. 41 (2002) 1929;
(n) B.M. Trost, M. Crawley, J. Am. Chem. Soc. 124 (2002) 9328.

[6] T. Kojima, K. Hayashi, Y. Matsuda, Inorg. Chem. 43 (2004) 6793.

[7] (a) A.K. Singh, V. Balamurugan, R. Mukherjee, Inorg. Chem. 42 (2003) 6497;
(b) D.B. Dellamico, F. Calderazzo, F. Dicolo, G. Gugliemetti, L. Labella, F. Marchetti, Inorg. Chim. Acta 359 (2006) 127.

[8] Kalagouda B. Gudasi, Transition Met. Chem. 30 (2005) 569.

[9] (a) H. Sigel, R.B. Martin, Chem. Rev. 82 (1982) 385;
(b) H.E. Bryndza, W. Tam, Chem. Rev. 88 (1988) 1163;
(c) K. Severin, R. Bergs, W. Beck, Angew. Chem., Int. Ed. 37 (1998) 1634;
(d) J.R. Fulton, A.W. Holland, D.J. Fox, R.G. Bergman, Acc. Chem. Res. 35 (2002) 44.

[10] (a) S. Dutta, S. Pal, P.K. Bhattacharya, Polyhedron 18 (1999) 2157;
(b) S. Dutta, P.K. Bhattacharya, E. Horn, E.R.T. Tiekink, Polyhedron 20 (2001) 1815;
(c) S. Dutta, P.K. Bhattacharya, E.R.T. Tiekink, Polyhedron 20 (2001) 2027.

[11] (a) N.C. Pramanik, K. Pramanik, P. Ghosh, S. Bhattacharya, Polyhedron 17 (1998) 1525;
(b) P.K. Sinha, L.R. Falvello, S. Bhattacharya, Ind. J. Chem. 43 (2004) 1846;
(c) E. Lebon, I.M. Dixon, L. Vendier, A. Igau, P. Sutra, Inorg. Chim. Acta 360 (2007) 1235;
(d) M. Fabre, J. Jaud, M. Hliwa, J.P. Launay, J. Bonvoisin, Inorg. Chem. 45 (2006) 9332;
(e) H.S. Chow, E.C. Constable, C.E. Housecroft, M. Neuburger, S. Schaffner, Polyhedron 25 (2006) 1831.

[12] B.P. Sullivan, J.M. Calvert, T.J. Meyer, Inorg. Chem. 19 (1980) 1404.

[13] (a) D.T. Sawyer, J.L. Roberts Jr., Experimental Electrochemistry for Chemists, vol. 167, Wiley, New York, 1974, p. 167;
(b) M. Walter, L. Ramaley, Anal. Chem. 45 (1973) 165.

[14] G.M. Sheldrick, SHELXS-97 and SHELXL-97, Fortran Programs for Crystal Structure Solution and Refinement, University of Gottingen, Gottingen, Germany, 1997.

[15] (a) S.K. Burley, G.A. Petsko, Science 229 (1985) 23;
(b) H.C. Weiss, D. Blaser, R. Boese, B.M. Doughan, M.M. Haley, Chem. Commun. (1997) 1703;
(c) N.N.L. Madhavi, A.K. Katz, H.L. Carrell, A. Nangia, G.R. Desiraju, Chem. Commun. (1997) 1953;
(d) S.K. Burley, G.A. Petsko, Adv. Protein Chem. 39 (1988) 125;
(e) M. Nishio, M. Hirota, Y. Umezawa, The CH–π Interactions (Evidence, Nature and Consequences), Wiley-VCH, New York, 1998;
(f) Y. Umezawa, S. Tsuboyama, K. Honda, J. Uzawa, M. Nishio, Bull. Chem. Soc., Jpn. 71 (1998) 1207;
(g) G.R. Desiraju, T. Steiner, The Weak Hydrogen Bond (IUCr Monograph on Crystallography 9), Oxford Science Pub., 1999;
(h) M.J. Hannon, C.L. Painting, N.W. Alcock, Chem. Commun. (1999) 2023;
(i) B.J. Mcnelis, L.C. Nathan, C.J. Clark, J. Chem. Soc., Dalton Trans. (1999) 1831;
(j) K. Biradha, C. Seward, M.J. Zaworotko, Angew. Chem., Int. Ed. 38 (1999) 492;
(k) M.J. Calhorda, Chem. Commun. (2000) 801;
(l) C. Janiak, S. Temizdemir, S. Dechert, Inorg. Chem. Commun. 3 (2000) 271;
(m) C. Janiak, S. Temizdemir, S. Dechert, W. Deck, F. Girgsdies, J. Heinze, M.J. Kolm, T.G. Scarmann, O.M. Zipffel, Eur. J. Inorg. Chem. (2000) 1229.

[16] (a) C. Mealli, D.M. Proserpio, CACAO Version 4.0, Italy, 1994;
(b) C. Mealli, D.M. Proserpio, J. Chem. Educ. 67 (1990) 399.

[17] L.P. Hammett, Physical Organic Chemistry, second ed., McGraw Hill, New York, 1970.

[18] R.N. Mukherjee, O.A. Rajan, A. Chakravorty, Inorg. Chem. 21 (1982) 785.

[19] (a) J.S. Griffith, The Theory of Transition Metal Ions, Cambridge University Press, Cambridge, 1961, 364;
(b) B. Bleany, M.C.M. O'Brien, Proc. Phys. Soc. London, Sect. B 69 (1956) 1216.

[20] S. Bhattacharya, A. Chakravorty, Proc. Indian Acad. Sci. (Chem. Sci.) 95 (1985) 159.

Available online at www.sciencedirect.com
ScienceDirect
Polyhedron 27 (2008) 151–156
POLYHEDRON
www.elsevier.com/locate/poly

Synthesis, structure and characterization of $[Mg_7(\mu_3\text{-}OCH_2CH_2OMe)_6(\mu\text{-}OCH_2CH_2OMe)_6][Al(n\text{-}Bu)_4]_2$ – A cationic heptanuclear magnesium complex consisting of discrete cations and tetrabutylaluminate anions

Matthias Linnert [a], Clemens Bruhn [b], Harry Schmidt [a], Renate Herzog [a], Dirk Steinborn [a,*]

[a] Institut für Chemie, Martin-Luther-Universität Halle-Wittenberg, Kurt-Mothes-Straße 2, D-06120 Halle, Germany
[b] Fachbereich 18, Naturwissenschaften, Abt. Metallorganische Chemie, Universität Kassel, Heinrich-Plett-Straße 40, D-34132 Kassel, Germany

Received 1 August 2007; accepted 30 August 2007
Available online 25 October 2007

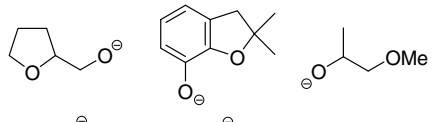
Abstract

Dibutylmagnesium (contaminated with $Al(n\text{-}Bu)_3$; n_{Mg}:n_{Al} ca. 1:0.2) was found to react with $MeOCH_2CH_2OH$ followed by the addition of PhSCH(Me)Ph in the presence of 0.2 equiv *n*-butyllithium yielding $[Mg_7(\mu_3\text{-}OCH_2CH_2OMe)_6(\mu\text{-}OCH_2CH_2OMe)_6][Al(n\text{-}Bu)_4]_2$ (**1**) as the principal product (yield 40–45% referred to $MeOCH_2CH_2OH$). The single-crystal X-ray diffraction analysis revealed that the centrosymmetric cationic heptamagnesium complex is built up from seven edge-shared MgO_6 octahedra. The $[Al(n\text{-}Bu)_4]^-$ anions adopt approximately a tetrahedral AlC_4 symmetry. ^1H, ^{13}C and ^{27}Al NMR spectroscopic measurements showed that in THF solution the structures both of the heptamagnesium complex and the tetrabutylaluminate anion are preserved and that there are no cation–anion interactions reducing the symmetry. The ^{27}Al resonance (151.6 ppm) was found to be very sharp ($w_{1/2} = 5$ Hz), the coupling constant $^1J(^{27}Al,^{13}C)$ amounts to 72.3 Hz.
© 2007 Elsevier Ltd. All rights reserved.

Keywords: Magnesium complexes; Oligonuclear complexes; Alkyl aluminates; ^{27}Al NMR spectroscopy; Crystal structures

1. Introduction

Metal alkoxides – among them magnesium alkoxides – have drawn increasing attention not only in chemical vapour decomposition processes but also as catalyst components for olefin polymerization or metathesis processes [1–4]. In this context, crystalline oligonuclear complexes – both monometallic and mixed-metal complexes – may have serious advantages due to their definite stoichiometry and structures. In the case of magnesium, bidentate alkoxo ligands of the types $RO\overset{\frown}{\ }O^-$ (**I**; $\overset{\frown}{\ } = C_2$ spacer) have been successfully used to build up oligonulcear magnesium complexes. Examples are the tetranuclear complexes ($[Mg_4(OCHMeCH_2OMe)_8]$ [5], $[Mg_4(THFFO)_6Cl_2]$ [6], $[Mg_4(DDBFO)_8]$ [7], $[Mg_4(OMe)_2(DDBFO)_6(MeOH)_5]$ [7]), the heptanuclear complex $[Mg_7(DDBFO)_{12}][FeCl_4]$ [8] and bimetallic complexes of the type $[Mg_4(THFFO)_6X_2]$ having terminal Ti and Si containing ligands X, respectively [7,9]. In all these complexes the ligands **II**–**IV** are bound with different coordination modes to the magnesium centres acting as bridging (μ_3,μ), chelating and/or as terminal ligands.



(THFFO$^{\ominus}$) (DDBFO$^{\ominus}$)

II **III** **IV**

* Corresponding author. Tel.: +49 345 5525620; fax: +49 345 5527028.
E-mail address: dirk.steinborn@chemie.uni-halle.de (D. Steinborn).

0277-5387/$ - see front matter © 2007 Elsevier Ltd. All rights reserved.
doi:10.1016/j.poly.2007.08.039

Here we report on a heptanuclear magnesium complex with the most simple bidentate alkoxo ligand of type **I**, namely with the 2-methoxyethoxo ligand ($MeOCH_2$-CH_2O^-). The complex $[Mg_7(OCH_2CH_2OMe)_{12}][Al(n\text{-}Bu)_4]_2$ (**1**) was obtained as the main product in a reaction that was directed to the metallation of a thioether using $MeOCH_2$-CH_2OMgBu/*n*-BuLi. As source of the aluminium a severe impurity of, likely, $Al(n\text{-}Bu)_3$, in the magnesiumdibutyl used has been identified.

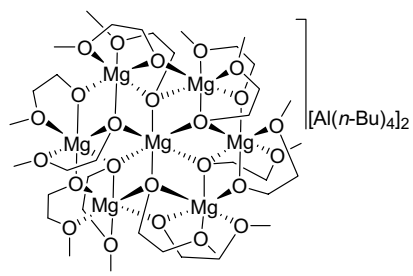
2. Results and discussion

2.1. Synthesis

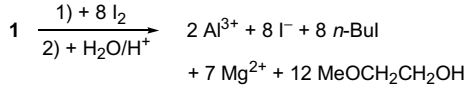
With the objective to metallate 1-(phenyl)ethyl phenyl sulfide (PhSCH(Me)Ph) with $MeOCH_2CH_2OMgBu$ yielding $MeOCH_2CH_2OMgC(Me)(Ph)SPh$, we let react in an one-pot reaction dibutylmagnesium with 2-methoxyethanol (1:1) followed by the addition of 1 equiv. PhSCH(Me)Ph and a substoichiometric amount (0.2 equiv.) of *n*-butyllithium. The synthesis resulted in the formation of a larger amount of well-shaped colourless crystals. Unexpectedly, single-crystal X-ray diffraction measurements revealed them to have the composition $[Mg_7(\mu_3\text{-}OCH_2CH_2OMe)_6(\mu\text{-}OCH_2CH_2OMe)_6][Al(n\text{-}Bu)_4]_2$ (**1**) consisting of a cationic heptamagnesium complex and tetra(*n*-butyl)aluminate anions (Scheme 1).

Analytical investigations of all starting materials made unambiguously clear that the source for the aluminium is the "dibutylmagnesium" solution in heptane that contained a considerable amount of aluminium (n_{Mg}:n_{Al} ca. 1:0.2) most likely as $Al(n\text{-}Bu)_3$. Although PhSCH(Me)Ph is not a constituent part of complex **1**, in the absence of the sulfide no formation of the complex was observed. All these findings prompted us to investigate the constitution of complex **1** carefully and independently from the X-ray crystallographic measurements.

Complex **1** is a colourless, air- and moisture-sensitive crystalline substance. It is the main product of the synthesis; the isolated yield of **1** is 40–45% referred to methoxyethanol. Furthermore, 40–45% and about 30% of the total amount of Al and Mg, respectively, were found in the complex **1**. In tetrahydrofuran complex **1** was found to react with iodine with cleavage of the Al–C bonds yielding AlI_3/I^- and butyliodide (Scheme 1). Iodometric titration (using an excess of I_2 and back titration of the surplus I_2 with $Na_2S_2O_3$) exhibited a very good agreement between the experimentally found consumption of I_2 (16.07 ± 0.36 mol I/mol **1**) and the calculated one (16.00 mol I/mol **1**). Furthermore, the constitution of complex **1** was unambiguously proven by the results of microanalysis as well as by ^1H, ^{13}C and ^{27}Al NMR investigations.



1



Scheme 1.

2.2. Structure

Crystals of compound **1** consist of tetra(*n*-butyl)aluminate anions and twofold-positively charged $[Mg_7(\mu_3\text{-}OCH_2CH_2OMe)_6(\mu\text{-}OCH_2CH_2OMe)_6]^{2+}$ cations that are shown in Fig. 1. Selected bond lengths and angles are given in Table 1. The filling of the unit cell in crystals of **1** is shown in Fig. 2. There are no specific cation–anion, cation–cation or anion–anion interactions; the shortest contacts between non-hydrogen atoms are 3.553(4) Å (C3···C19′), 3.851(4) Å (C2···C9′) and 3.962(5) Å (C30···C30′), respectively.

The $[Al(n\text{-}Bu)_4]^-$ anions adopt approximately a tetrahedral AlC_4 symmetry; all C–Al–C angles (108.9(1)–110.1(1)°) are very close to the tetrahedral one. The Al–C distances range from 2.006(3) to 2.024(3) Å (mean value: 2.014 Å). They are slightly longer than those in tetracoordinated organoaluminium compounds having the fragment "Al–R" (R = ethyl–butyl): median: 1.972 Å, lower/upper quartile: 1.955/1.991 Å, $n = 369$ (n – number of observations) [10].

The cation $[Mg_7(\mu_3\text{-}OCH_2CH_2OMe)_6(\mu\text{-}OCH_2CH_2OMe)_6]^{2+}$ exhibits crystallographically imposed inversion symmetry; overall, the symmetry is close to the point group S_6. The seven magnesium atoms build up a puckered hexagon with the magnesium atom Mg1 in the centre. Deviations of Mg2–Mg4 from the Mg_7 mean plane are between ±0.1586(8) and ±0.1595(7) Å. All Mg···Mg distances between neighboured magnesium atoms are between 3.1042(8) and 3.135(1) Å. Thus, the Mg···Mg separation is in a range that is expected for $[Mg^{II}O_6]$ coordination as found, for example, in the NaCl-type lattice of MgO (2.980 Å) [11]. Each three of the six Mg–μ_3-O bridging oxygen atoms lie above and below of the Mg_7 plane such that the central magnesium atom Mg1 adopts approximately an octahedral O_6 coordination (Mg1–O: 2.089(1)–2.099(2) Å; O–Mg1–O: 83.34(6)–96.66(6)°). Each of the six μ-O atoms bridges two peripheral magnesium atoms. Thus, each of them is coordinated by two μ-O and two μ_3-O bridging atoms as well as by two terminal ether oxygen atoms. Thus, all magnesium atoms are surrounded by six oxygen atoms and the Mg_7O_{24} unit is built up by seven MgO_6 octahedra linked by sharing edges (Fig. 1c). Comparison of the Mg–O bond lengths revealed the order Mg–μ-O (1.979(2)–2.019(2) Å) < Mg–μ_3-O (2.080(2)–2.122(2) Å) < $Mg\text{–}O_{terminal}$ (2.150(2)–2.205(2) Å).

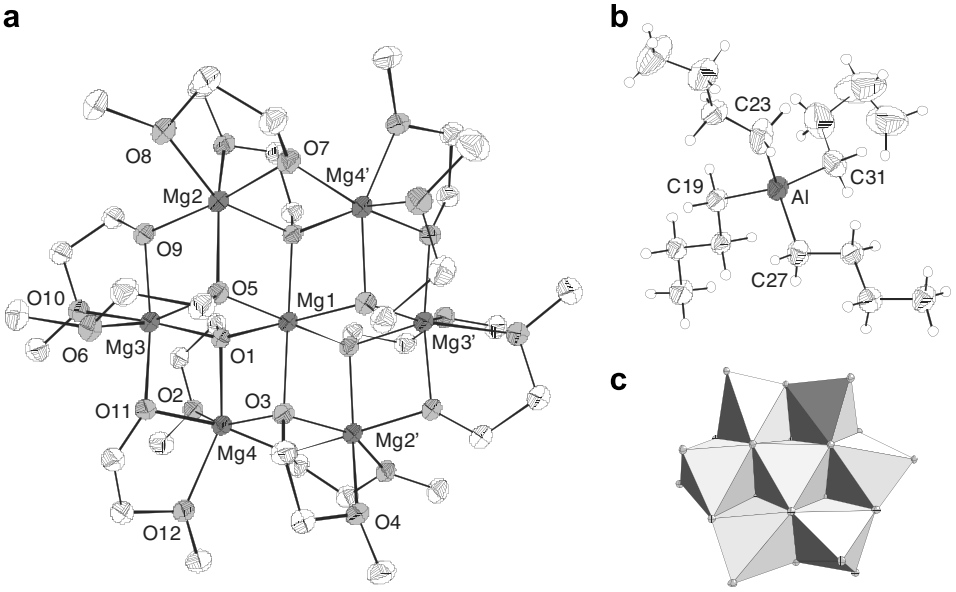


Fig. 1. Molecular structure of the cation (a) and anion (b) in crystals of $[Mg_7(\mu_3\text{-}OCH_2CH_2OMe)_6(\mu\text{-}OCH_2CH_2OMe)_6][Al(n\text{-}Bu)_4]_2$ (**1**) (displacement ellipsoids at 30 % probability; hydrogen atoms of the cation are omitted). (c) Structure of the Mg_7O_{24} unit in crystals of **1** shown as edge-shared MgO_6 octahedra.

Table 1
Selected interatomic distances (in Å) and angles (in deg) of **1**

Mg(μ-O)			
Mg2–O7	2.011(2)	Mg3–O11	1.985(2)
Mg2–O9	1.987(2)	Mg4–O7′	1.979(2)
Mg3–O9	2.011(2)	Mg4–O11	2.019(2)
Mg(μ$_3$-O)			
Mg1–O1	2.099(2)	Mg3–O1	2.107(2)
Mg1–O3	2.089(1)	Mg3–O5	2.080(2)
Mg1–O5	2.094(1)	Mg4–O1	2.093(2)
Mg2–O3′	2.096(2)	Mg4–O3	2.101(2)
Mg2–O5	2.122(2)		
Mg(O$_{terminal}$)			
Mg2–O4′	2.150(2)	Mg3–O10	2.160(2)
Mg2–O8	2.178(2)	Mg4–O2	2.176(2)
Mg3–O6	2.205(2)	Mg4–O12	2.168(2)
Mg···Mg			
Mg1···Mg4	3.1042(8)	Mg2···Mg3	3.128(1)
Mg1···Mg2	3.1349(8)	Mg2···Mg4′	3.132(1)
Mg1···Mg3	3.1194(7)	Mg3···Mg4	3.135(1)
Al–C			
Al–C19	2.016(3)	Al–C27	2.024(3)
Al–C23	2.010(4)	Al–C31	2.006(3)
O–Mg–O			
O7–Mg2–O9	166.61(8)	O9–Mg3–O11	168.65(8)
O5–Mg2–O4′	152.76(7)	O1–Mg4–O12	154.36(7)
O8–Mg2–O3′	153.90(8)	O2–Mg4–O3	153.47(7)
O1–Mg3–O6	153.64(7)	O11–Mg4–O7′	169.15(7)
O5–Mg3–O10	155.21(7)		
C–Al–C			
C19–Al–C23	109.6(1)	C23–Al–C27	109.9(2)
C19–Al–C27	110.1(1)	C23–Al–C31	109.4(2)
C19–Al–C31	108.9(1)	C27–Al–C31	109.0(1)

An analogous heptamagnesium complex with the bidentate alkoxo ligand $THFFO^{\ominus}$ (THFFOH: 2-tetrahydrofurfuryl alcohol) has been found in $[Mg_7(\mu_3\text{-}THFFO)_6(\mu\text{-}THFFO)_6][FeCl_4]\cdot 3CH_2Cl_2$ (**2**) prepared by the reaction of $Mg(THFFO)_2$ with $FeCl_2\cdot 1.5THF$ [8]. The cation in **2** has crystallographically imposed C_3 symmetry. It is worth noting that a tetranuclear magnesium complex, $[Mg_4(\mu_3\text{-}OCHMeCH_2OMe)_2(\mu\text{-}OCHMeCH_2OMe)_2(OCHMeCH_2OMe)_2]$, has been obtained with the 2-methoxypropoxo ligand that is structurally closely analogous to the ligand in the heptanuclear complex **1** [5]. In lithium and sodium tetraalkylaluminate complexes ($M[AlR_4]$, M = Li, Na; R = Me, Et, *n*-Pr) cation–anion contacts were found through Al–C–M bridges and/or agostic α-C–H···M interactions [12–14] and, likely, also in tetramethylaluminates of K, Rb and Cs [15,16]. On the other hand, tetraalkylaluminates were found to crystallize in discrete ions with bulky counter cations such as $[K(pmdta)_2][AlMe_4]$ [17], $[CoMe_2(bpy)_2][AlEt_4]$ [18] and $[Yb(\eta^5\text{-fluorenyl})(THF)_4][AlMe_4]$ [19]. In complex **1**, the bulkiness of the heptamagnesium complex cation having coordinatively saturated magnesium centres seems to be decisive to prevent cation–anion interactions. Recently, the solid-state structure of a complex was reported in which interstitial $[Mg(n\text{-}Bu)_4]^{2-}$ dianions within a polycationic network were found [20].

2.3. Spectroscopic investigation

^1H, ^{13}C and ^{27}Al NMR investigations confirm the constitution of complex **1**. All spectra show the expected signals; ^1H NMR signals exhibited the correct intensities. The assignment of the signals of the tetrabutylaluminate anion has been established by H,H and H,C COSY experiments. The signal of the α-C atom of the butyl group is split into six lines of equal intensity as expected for coupling with one ^{27}Al nucleus ($I = 5/2$, nat. abundance:

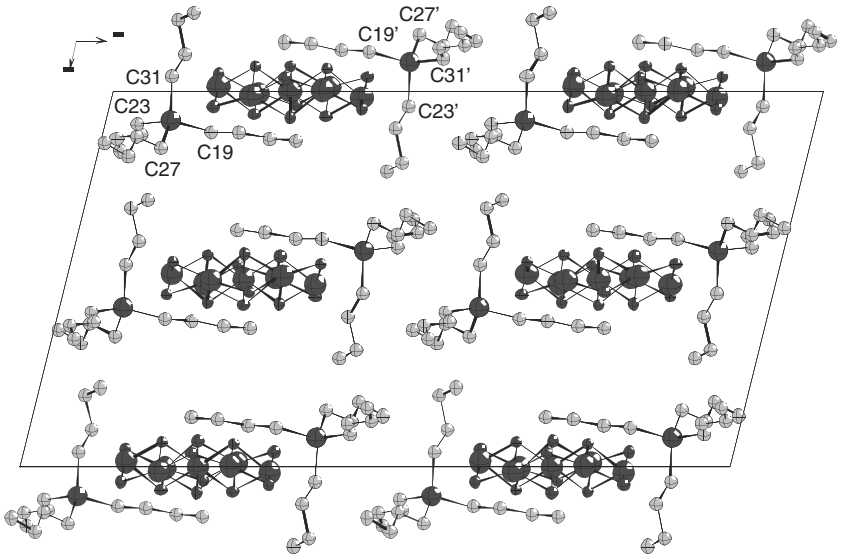


Fig. 2. View of the packing of cations (only the cluster core is shown) and anions in crystals of **1** along the monoclinic *b* axis.

100%), see Fig. 3. The coupling constant $^{1}J(^{27}Al,^{13}C)$ was found to be 72.3 Hz that is fully consistent with that in $[AlEt_4]^-$ (73.2 Hz) [21] and in $[AlMe_4]^-$ (71.2 Hz) [22]. Due to the very sharp resonance signals (see below), the Al–C coupling constant could also be obtained from the ^{13}C satellites in the ^{27}Al NMR spectrum.

The chemical shift (151.6 ppm) of the signal in the ^{27}Al NMR spectrum gives proof of tetracoordinated aluminium. Typical shift range of tetracoordinated aluminium is 125–180 ppm whereas in three- and fivecoordinated aluminium chemical shifts from 210 to 280 ppm and from 100 to 125 ppm, respectively, were found [23]. For quadrupole nuclei like ^{27}Al ($I = 5/2$) line broadening of NMR resonances is characteristic. Only in the case of highly symmetric ligand spheres, signals with normal line widths are observed [24]. Thus, the very sharp signal having a half line width of only 5 Hz indicates a much longer T_2 relaxation time. This suggests that the aluminium atom has local tetrahedral symmetry. The results of the NMR experiments show that in THF solution the structures both of the heptamagnesium complex and the tetrabutylaluminate anion are preserved and that there are no cation–anion interactions reducing the symmetry.

In conclusion, complex **1** is the first example of an oligonuclear main group metal complex with a tetraalkylaluminate counter anion that crystallizes in discrete ions and one of the few examples where the high symmetry of the tetraalkylaluminate anion is preserved even in THF solution exhibiting that the molecules exist, most likely, as solvent-separated ion pairs [25].

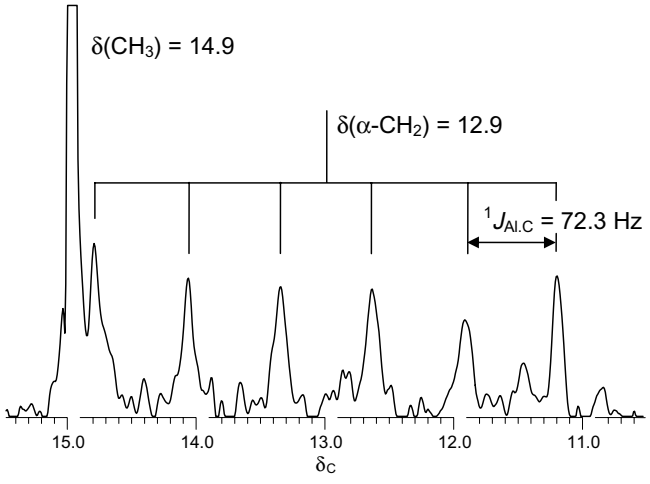


Fig. 3. 101 MHz ^{13}C NMR spectrum of **1** in THF-d_8 showing the resonance of the aluminium bound carbon atoms.

3. Experimental

3.1. General considerations

All reactions were performed under Ar atmospheres using standard Schlenk techniques. Toluene and THF were distilled from Na/benzophenone prior to use. Methoxyethanol was distilled under argon prior to use. NMR spectra were recorded on Varian VXR 400 and Unity 500 NMR spectrometers. Chemical shifts are relative to solvent signals (^1H, ^{13}C) as internal references and $Al(NO_3)_3$ (1 M in D_2O) as external reference (^{27}Al), respectively. PhSCH(Me)Ph was prepared according to [26] and *n*-BuLi (Aldrich) was used as supplied. $MgBu_2/Al(n\text{-}Bu)_3$ was purchased from Fluka (handled over Aldrich) supplied as dibutylmagnesium solution (1 M in heptane); the synthesis of **1** described below was reproducible with different bottles of the reagent. Hydrolysis of an aliquot followed by evaporation of all solvents in vacuo revealed a ratio of $n_{Mg}:n_{Al}$ ca. 1:0.2 (determined by X-ray fluorescence analysis using a RFA SRS 3000).

3.2. Synthesis of $[Mg_7(OCH_2CH_2OMe)_{12}][Al(n\text{-}Bu)_4]_2$ (1)

To $MgBu_2/Al(n\text{-}Bu)_3$ (8 mmol) in heptane/toluene (7/15 ml) methoxyethanol (8 mmol) was dropwise added. The reaction mixture was stirred for 20 min at room temperature. Then, PhSCH(Me)Ph (8 mmol) and after 10 min tetrahydrofuran (3 ml) were added by means of syringes. After about 1 h *n*-BuLi (1.6 mmol) in *n*-hexane (1 ml) was dropwise added with stirring. Standing (without stirring) for 12–24 h resulted in precipitation of well-shaped colourless crystals that were used for single-crystal X-ray diffraction measurements or were filtered off, washed with diethyl ether (5×2 ml) and dried in vacuo. Yield: 430–470 mg (40–45% referred to methoxyethanol).

$C_{68}H_{156}Al_2Mg_7O_{24}$ (1582.05) requires C 51.62; H 9.94. Found: C 51.01; H 9.82%. ^{1}H NMR (THF-d_8, 400 MHz): δ −0.43 (br, 2H, α-CH_2, butyl), 0.81 (t, 3H, CH_3, butyl), 1.20 ('tq', 2H, γ-CH_2, butyl), 1.35 (br, 2H, β-CH_2, butyl), 3.48 ('dd', 1H, CH_2), 3.54 ('dd', 1H, CH_2), 3.58 (s, 3H, OCH_3), 3.71 (s, 3H, OCH_3), 3.78 (m, 3H, CH_2), 3.88 ('dd', 1H, CH_2), 3.99 ('dt', 1H, CH_2), 4.19 ('dt', 1H, CH_2). H,H COSY spectrum revealed that signals at 3.48, 3.78 (1H), 3.88, 4.19 ppm and at 3.54, 3.78 (2H), 3.99 ppm belong to the same CH_2CH_2 moiety. ^{13}C NMR (THF-d_8, 101 MHz): δ 12.9 (sextet, $^1J(^{27}Al,^{13}C) = 72.3$ Hz, α-*C*H_2, butyl), 14.9 (s, *C*H_3, butyl), 31.0 (s (br), γ-*C*H_2, butyl), 32.5 (s, β-*C*H_2, butyl), 59.4/59.6 (s/s, $2 \times$ O*C*H_3), 61.9/62.8/75.5/76.6 (s/s/s/s, $4 \times$ *C*H_2). ^{27}Al NMR (THF-d_8, 130 MHz): δ 151.6 (s + d, $w_{1/2} = 5$ Hz, $^1J(^{27}Al,^{13}C) =$ 73 Hz). Two smaller signals (impurities) were found at 151.0 and 152.3 ppm.

3.3. Iodometric titration of 1

Under strictly anaerobic conditions, a Schlenk tube was filled with a standard solution of iodine in THF (25.0 ml; 0.025 M), additional THF (200–250 ml) and an ampoule containing 45–75 mg of **1**. Then, the ampoule was broken. After few minutes the Schlenk tube was opened, water (ca. 50 ml) was added and the excess of iodine was titrated with $Na_2S_2O_3$ (0.05 M) using starch as indicator.

3.4. X-ray crystal structure determination of 1

Intensity data of a suitable crystal ($0.54 \times 0.53 \times 0.31$ mm) were collected on a STOE IPDS2 diffractometer at 150(2) K with Mo–Kα radiation (0.71073 Å, graphite monochromator). A summary of the crystallographic data, the data collection parameters, and the refinement parameters is given in Table 2. Absorption correction was carried out numerically (T_{min}/T_{max} 0.90/0.95). The structure was solved by direct methods using SHELXS-97 and refined with full-matrix least-squares routines against F^2 using SHELXL-97 [27]. All non-H atoms were refined with anisotropic displacement parameters. The H atoms were added to the model in their calculated positions according to the riding model and refined isotropically.

Table 2
Crystallographic data for complex **1**

Empirical formula	$C_{68}H_{156}Al_2Mg_7O_{24}$
Fw	1582.06
Space group	*C*2/*c* (no. 15)
a (Å)	30.923(2)
b (Å)	17.908(1)
c (Å)	16.843(1)
β (°)	103.922(6)
V (Å^3)	9053(1)
Z	4
ρ_{calc} (g cm^{-3})	1.161
μ(Mo Kα) (mm^{-1})	0.145
F(000)	3464
Scan range (°)	1.36–25.00
Reflections collected	42 698
Reflections independent	7968 ($R_{int} = 0.0739$)
Data/restraints/parameters	7968/0/468
R_1/wR_2 ($I > 2\sigma(I)$)	0.0517/0.1467
R_1/wR_2 (all data)	0.0668/0.1548
Largest difference in peak and hole (e Å^{-3})	0.350 and −0.423

Acknowledgement

The authors thank Prof. H. Pöllmann (Institute of Mineralogy and Geochemistry of the University of Halle) for the determination of Mg/Al.

Appendix A. Supplementary material

CCDC-656051 contains the supplementary crystallographic data for **1**. These data can be obtained free of charge via http://www.ccdc.cam.ac.uk/conts/retrieving.html, or from the Cambridge Crystallographic Data Centre, 12 Union Road, Cambridge CB2 1EZ, UK; fax: (+44) 1223-336-033; or e-mail: deposit@ccdc.cam.ac.uk. Supplementary data associated with this article can be found, in the online version, at doi:10.1016/j.poly.2007.08.039.

References

[1] D.C. Bradley, Chem. Rev. 89 (1989) 1317.
[2] W.A. Herrmann, N.W. Huber, O. Runte, Angew. Chem. 107 (1995) 2371.
[3] T.P. Hanusa, in: J.A. McCleverty, T.J. Meyer (Eds.), Comprehensive Coordination Chemistry II, vol. 3, Elsevier/Pergamon, Amsterdam, 2004, p. 1.
[4] L. Resconi, J.C. Chadwick, L. Cavallo, in: D.M.P. Mingos, R.H. Crabtree (Eds.), Comprehensive Organometallic Chemistry III, vol. 4, Elsevier, Amsterdam, 2007, p. 1006.
[5] L. Albaric, N. Hovnanian, A. Julbe, C. Guizard, A. Alvarez-Larena, J.F. Piniella, Polyhedron 16 (1997) 587.
[6] P. Sobota, J. Utko, Z. Janas, S. Szafert, Chem. Commun. (1996) 1923.
[7] P. Sobota, J. Utko, K. Sztajnowska, J. Ejfler, L.B. Jerzykiewicz, Inorg. Chem. 39 (2000) 235.
[8] Z. Janas, L.B. Jerzykiewicz, P. Sobota, J. Utko, New J. Chem. (1999) 185.

[9] P. Sobota, J. Utko, J. Ejfler, L.B. Jerzykiewicz, Organometallics 19 (2000) 4929.
[10] Cambridge Structural Database (CSD): Cambridge Crystallographic Data Centre, University Chemical Laboratory, Cambridge, UK.
[11] V.G. Tsirelson, A.S. Avilov, Y.A. Abramov, E.L. Belokoneva, C.R. Kitaneh, D. Feil, Acta Crystallogr., Sect. B 54 (1998) 8.
[12] R.L. Gerteis, R.E. Dickerson, T.L. Brown, Inorg. Chem. 3 (1964) 872.
[13] J.H. Medley, F.R. Fronczek, N. Ahmad, M.C. Day, R.D. Rogers, C.R. Kerr, J.L. Atwood, J. Cryst. Spectr. Res. 15 (1985) 99.
[14] A.I. Sizov, T.M. Zvukova, B.M. Bulychev, V.K. Belsky, J. Organomet. Chem. 603 (2000) 167.
[15] R. Wolfrum, G. Sauermann, E. Weiss, J. Organomet. Chem. 18 (1969) 27.
[16] C. Schade, P.v. Ragué Schleyer, Adv. Organomet. Chem. 27 (1987) 169.
[17] F.J. Craig, A.R. Kennedy, R.E. Mulvey, M.D. Spicer, Chem. Commun. (1996) 1951.
[18] S. Komiya, T. Yamamoto, A. Yamamoto, Acta Crystallogr., Sect. B 35 (1979) 2702.
[19] H. Nakamura, Y. Nakayama, H. Yasuda, T. Maruo, N. Kanehisa, Y. Kai, Organometallics 19 (2000) 5392.
[20] P.C. Andrikopoulos, D.R. Armstrong, E. Hevia, A.R. Kennedy, R.E. Mulvey, C.T. O'Hara, Chem. Commun. (2005) 1131.
[21] H. Gizbar, Y. Vestfrid, O. Chusid, Y. Gofer, H.E. Gottlieb, V. Marks, D. Aurbach, Organometallics 23 (2004) 3826.
[22] O. Yamamoto, Chem. Lett. (1975) 511.
[23] M. Stender, U. Segerer, J. Sieler, E. Hey-Hawkins, Z. Anorg. Allg. Chem. 624 (1998) 85, and references cited therein.
[24] T.D.W. Claridge, High-resolution NMR Techniques in Organic Chemistry, Pergamon Press, Amsterdam, 1999, p. 41.
[25] Y. Marcus, G. Hefter, Chem. Rev. 106 (2006) 4585.
[26] A. Schöberl, A. Wagner, in: E. Müller (Ed.), Houben-Weyl, Methoden der Organischen Chemie, vol. IX, Thieme-Verlag, Stuttgart, 1955, p. 7, and 97.
[27] G.M. Sheldrick, SHELXL-97, Programs for Structure Determination, University of Göttingen, Göttingen, Germany, 1990;
G.M. Sheldrick, SHELXL-97, Programs for Structure Determination, University of Göttingen, Göttingen, Germany, 1997.

Available online at www.sciencedirect.com
ScienceDirect
Polyhedron 27 (2008) 157–166
POLYHEDRON
www.elsevier.com/locate/poly

Half-sandwich *para*-cymene ruthenium(II) naphthylazophenolato complexes: Synthesis, molecular structure, light emission, redox behavior and catalytic oxidation properties

K. Naresh Kumar [a], G. Venkatachalam [a], R. Ramesh [a,*], Y. Liu [b]

[a] *School of Chemistry, Bharathidasan University, Tiruchirappalli 620 024, India*
[b] *Institute of Inorganic Chemistry, University of Zürich, Winterthurerstrasse 190, CH-8057 Zürich, Switzerland*

Received 15 July 2007; accepted 31 August 2007
Available online 22 October 2007

Abstract

A series of conformationally rigid half-sandwich organoruthenium(II) complexes with the general formula [(η^6-*p*-cymene)RuCl(L)] (where L = mono anionic 2-(naphthylazo)phenolato ligands) have been synthesized from the reaction of [{(η^6-*p*-cymene)RuCl}$_2$-(μ-Cl)$_2$] with a set of 2-(naphthylazo)phenolato O,N-donor ligands. All the ruthenium complexes were fully characterized by FT-IR, ^{1}H NMR, and UV–Vis spectroscopy as well as elemental analysis. In dichloromethane solution all the metal complexes exhibits characteristic metal-to-ligand charge transfer bands (MLCT) and emission bands in the visible region. The molecular structure of one of the complexes [Ru(η^6-*p*-cymene)(Cl)(L2)] (**2**) was determined by X-ray crystallography. Electrochemical data of all the ruthenium complexes show a two metal centered voltammetric responses with respect to Ag/AgCl at scan rate 100 mV s^{-1}. Further, the complex (**2**) efficiently catalyzes the oxidation of a wide range of alcohols to their corresponding carbonyl compounds in the presence of *N*-methylmorpholine-*N*-oxide (NMO) up to 97%.
© 2007 Elsevier Ltd. All rights reserved.

Keywords: (η^6-*p*-Cymene)-ruthenium(II) complexes; Spectra; Crystal structure; Redox property; Oxidation of alcohols

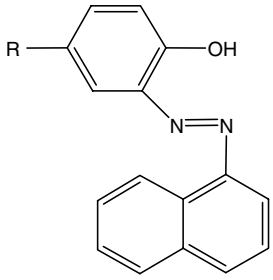
1. Introduction

For many decades arene ruthenium complexes are playing important role in organometallic chemistry [1]. There has been an increasing interest in the chemistry of half-sandwich organoruthenium(II) complexes due to numerous application in new catalytic systems for a variety of organic transformations [2,3]. Ruthenium(II)-arene complexes display a three-legged piano stool structure in which the metal center has a quasi-octahedral geometry were occupied by an arene ligands. This structural feature opens the possibility to introduce in the molecule two types of stereogenic centers: the metal and ligands. The O,N-donor type of ligands have been prepared to optimize the catalytic potential of their metal complexes [4]. It is well-known that the uses of nitrogen containing ligands lead to an increased catalytic activity [5]. Many methods for specific catalytic oxidation of various organic substrates such as alcohols, amines, amides and hydrocarbons have been studied extensively using low-valent metal complex catalysts [6,7]. It is to be noted that ruthenium compounds are intensively studied transition metal compounds and many methodologies have been developed with them [8–10]. Ru-based oxidation catalysis is a powerful and extremely versatile synthetic tool to afford selectively oxygenate products both in homogeneous and in heterogeneous conversions [11–14].

In early studies Oshima and co-workers reported that primary alcohols are selectively oxidized to aldehydes in the presence of secondary ones by using stoichiometric $Ru(PPh_3)_3Cl_2$ or a $Ru(PPh_3)_3Cl_2$ and TMSOOTMS system [15]. Ishii and co-workers successfully achieved aerobic

* Corresponding author. Fax: +91 431 2407045/20.
E-mail address: ramesh_bdu@yahoo.com (R. Ramesh).

0277-5387/$ - see front matter © 2007 Elsevier Ltd. All rights reserved.
doi:10.1016/j.poly.2007.08.037



(R = Cl : HL1 ; CH_3 : HL2 ; OCH_3 : HL3 ; OC_2H_5 : HL4 ; NO_2 : HL5)

Scheme 1. Structure of 2-(naphthylazo)phenolate ligands.

oxidation using $Ru(PPh_3)_3Cl_2$ as the catalyst in the presence of hydroquinone without diminishing chemoselectivity [16]. Though several ruthenium catalytic systems have been reported with a wide range of oxidants viz., *tert*-butyl hydroperoxide [17], chloramine-T [18], benzoquinone [19], hydrogen peroxide [20], molecular oxygen [21], iodosylbenzene [22] and $NaIO_4$ [23], *N*-methylmorpholine-*N*-oxide (NMO) as oxidant is less covered in the literature. To the best of our knowledge there are no reports available on catalytic oxidation of alcohols by (η^6-*p*-cyemene)ruthenium(II) 2-(naphthylazo)phenolato complexes incorporating N,O-donors in presence of NMO.

In this paper, we report the synthesis, characterization of (η^6-*p*-cyemene)Ru(II) complexes containing naphthylazophenolato ligands (Scheme 1). The molecular and electronic structure of the bivalent complexes are probed with the help of X-ray crystal structure in combination with spectral and emission studies. The redox properties of the complexes are monitored by cyclic voltammetry. Further, the catalytic activity of the (η^6-*p*-cyemene)Ru(II) complexes are investigated in the case of oxidation of primary and secondary alcohols in presence of NMO as oxidant.

2. Experimental

2.1. Materials and physical measurements

All the reagents used were chemically pure or analytical reagent grade. Solvents were purified and dried according to standard procedures. $RuCl_3 \cdot 3H_2O$ was purchased from Loba Chemie Pvt. Ltd., Bombay, India and was used without further purification. The alcohols and their corresponding ketones or aldehydes, which were used in the catalytic studies, were purchased from Merck and Aldrich. The analysis of carbon, hydrogen and nitrogen were performed in Carlo-Erba 1106-model 240 Perkin Elmer analyzer at Sophisticated Test and Instrumentation Centre (STIC), Cochin University, Kochi, India. FT-IR spectra were recorded in KBr Pellets with a JASCO 200 plus spectrophotometer. A CARY 300 Bio UV–Vis Varian spectrophotometer was used to record the electronic spectra. ^1H NMR spectra were recorded on a Bruker 400 MHz instrument using tetramethylsilane (TMS) as an internal reference. Emission intensity measurements were carried out by using a Jasco FP-6500 spectrofluorimeter with 5 nm exit slit. Electrochemical measurements were made using a Princeton EG and G-PARC model potentiostat using a glassy carbon working electrode, Pt wire as counter electrode and all the potentials were referenced to Ag/AgCl electrode. Melting points were recorded with a Boetius micro-heating table and are uncorrected. The catalytic yields were determined using HP 6890 series GC-FID with a DP-5 column of 30 m length, 0.32 mm diameter and 0.25 μm film thickness. The ruthenium(II) precursor complex $[\{(\eta^6\text{-}p\text{-cymene})RuCl\}_2(\mu\text{-}Cl)_2]$, was prepared according to literature method [24]. The 2-(naphthylazo)phenolate ligands were prepared by coupling diazotized α-naphthylamine with *p*-substituted phenols [25].

2.2. Synthesis of (η^6-*p*-cymene)Ru(II) 2-(naphthylazo)phenolate complexes

Synthesis of (η^6-*p*-cymene)Ru(II) 2-(naphthylazo)phenolate complexes were carried out under strictly anhydrous conditions. The (*p*-cymene)ruthenium(II)complex $[\{(\eta^6\text{-}p\text{-cymene})RuCl\}_2(\mu\text{-}Cl)_2]$ (0.163 mmol; 0.100 g) and 2-(naphthylazo)phenolate ligands (HL1-HL5) (0.163 mmol; 0.042-0.047 g) were taken in 1:1 molar ratio in methanol and kept stirring for 3 h. Then the solvent was removed through vaccum, the dark red mass was dissolved in chloroform (15 ml) and filtered through short path of silica gel column to remove insoluble materials. The red solution was then concentrated into 2 ml, addition of excess hexane dark-red product separated out, washed with diethylether and dried in vaccum (yield: 65–70%).

2.3. X-ray crystallography

Single crystals suitable for X-ray diffraction were grown from mixture of chloroform/acetonitrile solution at room temperature. The single crystals of suitable size was covered with Paratone oil, mounted on the top of a glass fiber, and transferred to a Stoe IPDS diffractometer using monochromated Mo Kα radiation ($\lambda = 0.71073$ Å). Data were collected at 183 K. Corrections were made for Lorentz and polarization effects as well as for absorption (numerical). Structures were solved with direct method using SHELXS-97 or SIR-97 [26–28] and were refined by full-matrix least-squares method [29] on F^2 with SHELXL-97. Non-hydrogen atoms were refined with anisotropy thermal parameters. All hydrogen atoms were geometrically fixed and allowed to refine using a riding model.

2.4. Procedure for catalytic oxidation

Catalytic oxidation of primary alcohols to corresponding aldehydes and secondary alcohols to ketones by (η^6-*p*-cymene)Ru(II) 2-(naphthylazo)phenolate complex was studied in the presence of NMO. A typical reaction using the complex [(η^6-*p*-cymene)RuCl(L2)] (**2**) as a catalyst

and primary or secondary alcohol as substrates at 1:100 molar ratio is described as follows. A solution of ruthenium complex (**2**) (0.01 mmol) in 20 ml CH_2Cl_2 was added to the solution of substrate (1 mmol) and NMO (3 mmol). The solution mixture was refluxed for 3 h and the solvent was then evaporated from the mother liquor under reduced pressure. The reaction mixture containing the complex **2** and the oxidized product was then extracted with pet. ether (60–80 °C) (20 ml). The complex **2** was precipitated as solid mass on addition of pet. ether and was recovered quantitatively for next catalytic cycle. Further, the oxidized product was separated out along with pet. ether and was analyzed by GC.

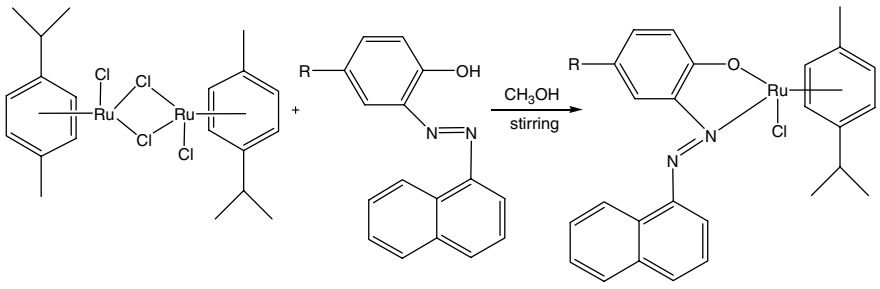
3. Results and discussion

3.1. Synthesis and characterization

The reaction of 2-(naphthylazo)phenolate ligands with chloro-bridged (η^6-*p*-cymene) ruthenium complex [{(η^6-*p*-cymene)RuCl}$_2$(μ-Cl)$_2$] in methanol at room temperature in 1:1 molar ratio resulted in the formation of conformationally rigid new monomeric ruthenium(II) complexes (Scheme 2). The complexes were found to be air stable and are soluble in polar solvents such as dichloromethane and acetone, but insoluble in non-polar solvents such as pentane and hexane. The diamagnetic nature of all the complexes is consistent with the +2 oxidation state and low spin character of the metal ions in these complexes. Elemental analyses (C, H and N) were consistent with the composition proposed for all complexes (Table 1).

Infrared spectra of all the ligands displayed strong bands around 1425–1438 and 1275–1284 cm^{-1} corresponding to $\nu_{-N=N-}$ and phenolic ν_{C-O} stretching, respectively. After complexation $\nu_{-N=N-}$ appears at 1360–1390 cm^{-1} and the red shifting is corroborated with N(azo) coordination. The coordination through phenolic oxygen is confirmed by the increase of C–O at higher frequencies in the region 1290–1325 cm^{-1} in all the complexes (Table 2). This is further supported by the disappearance of ν_{OH} band in the range 3440–3457 cm^{-1} in all the complexes. Further, all the complexes show strong bands corresponding to ν_{M-N} and ν_{M-O} in the region 440–464 and 510–545 cm^{-1}, respectively. The ν_{M-Cl} stretching frequency has been observed for all the complexes in the region 320 cm^{-1} [30–32].

The ^{1}H NMR spectra of the complexes have been recorded in $CDCl_3$ solution to probe the solution structure (Table 3) and the representative spectrum is shown in Fig. 1. All the complexes show multiplets at δ 6.8–8.6 ppm for the presence of naphthylazo phenol ligands. The methyl protons appear as singlet and isopropyl protons appear as two doublets of the *p*-cymene ligand in the range of δ 2.1–2.2 ppm and δ 0.8–0.9 ppm, respectively. The isopropyl CH protons appear as a septet in the range of δ 2.4–2.5 ppm and the *p*-cymene ring protons are observed in the ranges of δ 3.6–5.7 ppm as either four doublets (4H) or two doublets (2H) and one singlet (2H). Additional methyl signals are observed as singlet for complex **2** at δ 2.1 and methoxy signals are observed as singlet for complex **3** at δ 4.0 ppm. A triplet observed for methyl protons for complex **4** at δ 1.45 ppm and OCH_2 protons



(R = Cl : L1(**1**) ; CH_3 : L2(**2**) ; OCH_3 : L3(**3**) ; OC_2H_5 : L4(**4**) ; NO_2 : L5(**5**))

Scheme 2. Structure of (*p*-cymene)ruthenium(II) 2-(naphthylazo)phenolate complexes.

Table 1
Analytical data of (*p*-cymene)ruthenium(II) 2-(naphthylazo)phenolate complexes

S. no.	Complexes	Empirical formula	Found (calcd.) (%)		
			C	H	N
1	[Ru(η^6-*p*-cymene)(Cl)(L1)]	$C_{26}H_{24}N_2OCl_2Ru$	56.13(56.32)	4.52(4.73)	4.87(5.05)
2	[Ru(η^6-*p*-cymene)(Cl)(L2)]	$C_{27}H_{27}N_2OClRu$	60.58(60.72)	5.34(5.47)	5.13(5.24)
3	[Ru(η^6-*p*-cymene)(Cl)(L3)]	$C_{27}H_{27}$ N_2O_2ClRu	62.83(63.01)	5.47(5.68)	5.32(5.44)
4	[Ru(η^6-*p*-cymene)(Cl)(L4)]	$C_{28}H_{29}N_2O_2ClRu$	59.47(59.61)	5.36(5.54)	4.75(4.96)
5	[Ru(η^6-*p*-cymene)(Cl)(L5)]	$C_{26}H_{24}N_3O_3ClRu$	55.01(55.27)	4.27(4.64)	7.23(7.43)

Table 2
IR and UV–Vis[d] and fluorescence data[d,e] of (*p*-cymene)ruthenium(II) 2-(naphthylazo)phenolate complexes

Complexes	IR frequencies (cm^{-1})		λ_{max} (nm) (ε) ($dm^3\ mol^{-1}\ cm^{-1}$)	Fluorescence data λ_{max} (nm)	
	ν_{C-O}	$\nu_{N=N}$		Excitation	Emission
1	1290	1385	595(1295),[a] 418(3456),[a] 329[b](8214), 252[c](13474)	418	474
2	1310	1360	592(2072),[a] 412(3546),[a] 319[b](6975), 257[c](13428)	412	465
3	1295	1385	613(2248),[a] 414(3754),[a] 316[b](5648), 274[c](13428)	414	485
4	1325	1375	610(1986),[a] 410(3534),[a] 330[b](7150), 266[c](14548)	410	494
5	1320	1390	604(1986),[a] 417(2950),[a] 321[b](7156), 265[c](13418)	417	470

[a] Charge transfer transition.
[b] n–π*.
[c] π–π*.
[d] Solvent – dichloromethane.
[e] Excitation at the higher wavelength absorption peak.

Table 3
^{1}H NMR data of (*p*-cymene)ruthenium(II) 2-(naphthylazo)phenolate complexes

Complexes	^{1}H NMR data (ppm)
1	6.8–8.6 (ArH, m), 5.0, 5.6 (ring H, 2d), 5.3 (ring H, s), 3.6, 4.1 (ring H, 2d), 2.4 (CH, sp), 2.2 (Me, s), 1.06, 0.91 ($CHMe_2$, 2d)
2	6.8–8.5 (ArH, m), 5.1, 5.4 (ring H, 2d), 5.3 (ring H, s), 3.5, 4.3 (ring H, 2d), 2.5 (CH, sp), 2.3 (Me, s), 2.1 (Me, s), 1.06, 0.81 ($CHMe_2$, 2d)
3	6.8–8.5 (ArH, m), 5.07, 5.7 (ring H, 2d), 5.4 (ring H, s), 3.6, 4.1 (ring H, 2d), 4.0 (OMe, s), 2.4 (CH, sp), 2.2 (Me, s), 1.06, 0.91 ($CHMe_2$, 2d)
4	6.9–8.6 (ArH, m), 5.17, 5.5 (ring H, 2d), 5.3 (ring H, s), 3.6, 4.1 (ring H, 2d), 3.9 (OCH_2, q), 2.4 (CH, sp), 2.2 (Me, s), 1.45 (Me, t), 1.06, 0.91 ($CHMe_2$, 2d)
5	7.0–8.6 (ArH, m), 5.0, 5.7 (ring H, 2d), 5.4 (ring H, s), 3.6, 4.1 (ring H, 2d), 2.4 (CH, sp), 2.2 (Me, s), 1.06, 0.91 ($CHMe_2$, 2d)

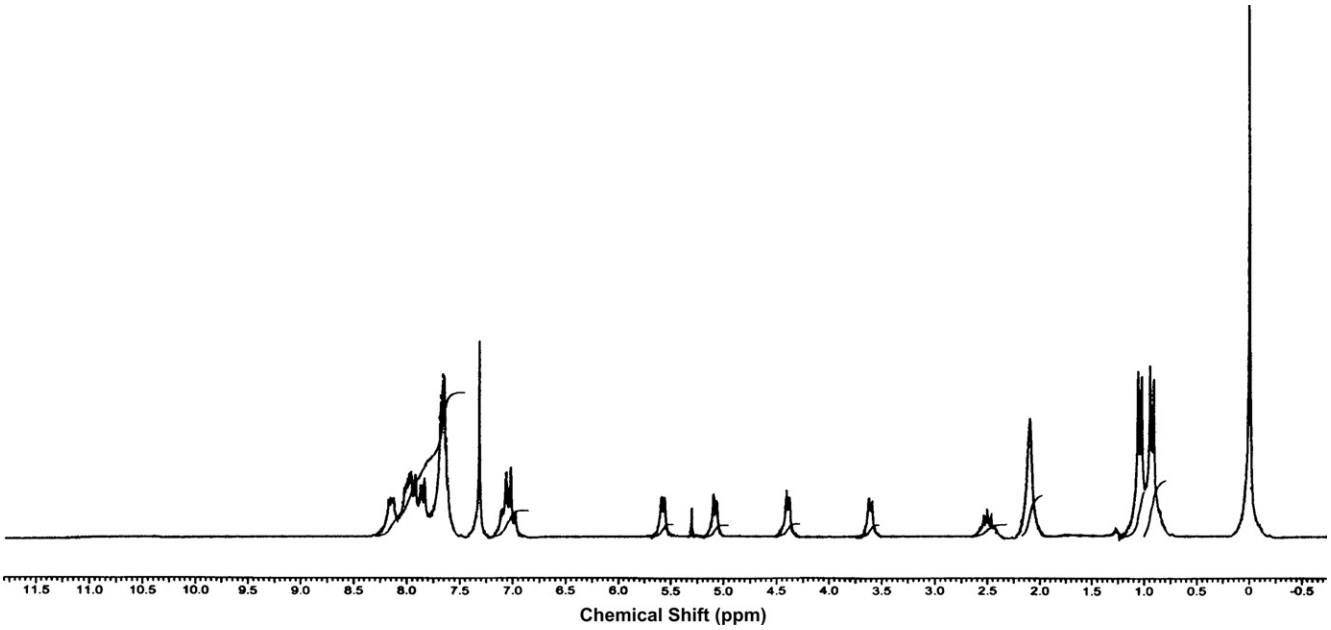


Fig. 1. ^{1}H NMR spectrum of [Ru(η^6-*p*-cymene)(Cl)(L1)] (**1**).

appeared as quartet in the region of 3.85 ppm. A sharp singlet appeared for OH protons of all the 2-(napthylazo) phenol ligands in the region δ 13.0 ppm was disappeared in all the complexes [33].

The electronic transition for all the complexes were recorded in dichloromethane solution and are listed in Table 2. All the (η^6-*p*-cymene) ruthenium(II) 2-(naphthylazo)phenolato complexes show three to four intense absorptions in the visible and ultraviolet region 613–252 nm. The intense absorption in the visible region at 613-592 nm and the absorption at 410–418 nm are probably due to metal-to-ligand charge transfer transitions. The charge transfer transitions taking place from the highest filled ruthenium t_2 orbital (highest occupied molecular orbital) to the vacant π^*(–N=N–) orbital of the 2-(naphthylazo)phenolato ligand (lowest unoccupied molecular orbital) or to the higher energy vacant orbitals of other fragment of ligands. It has been observed that many

charge-transfer transitions in such mixed-ligand complexes may result from the lower symmetry splitting of the metal level, the presence of different acceptor orbitals, and the mixing of singlet and triplet configurations in the excited state through spin–orbit coupling [34]. In addition, the other high intensity bands in the 330–252 nm regions were characterized by ligand-centered (LC) transitions taking place in the coordinated 2-(naphthylazo)phenolate ligands. The absorption in the ultraviolet region may be attributed to usual n–π^*, π–π^* transitions occurring within ligand orbitals. The pattern of the electronic spectra of all the complexes indicated the presence of an octahedral environment around ruthenium(II) ion, similar to that of other ruthenium(II) octahedral complexes [35].

The luminescent property of (η^6-*p*-cymene) ruthenium(II) complexes of ligand containing strong chromophoric groups often show in addition to intense MLCT transitions interesting luminescence properties [36,37], such properties have also been explored in the [(η^6-*p*-cymene)-RuCl(L)] complexes (Table 2). The luminescence studies were carried out in dichloromethane solution at ambient temperature (298 K). No emission was observed, when an excitation wavelength corresponding to the lowest energy absorption (~500 nm) was used. However, the excitation wavelength of ~400 nm was used, all the [(η^6-*p*-cymene)RuCl(L2)] complexes showed strong emission (Fig. 2) within 465–494 nm. This indicates that transition of a metal electron to metallated *p*-cymene ring (or) *p*-cresol ring leads to photochemical excited state, which is much more stable compared to excitation of metal electron to π^*(azo –N=N–) [38].

The structure of the compound (**2**) consist of neutral arene ring bonded to the ruthenium along with chloride and O,N-donors of 2-(napthylazo)phenolate ligands. The molecular structure of complex (**2**) with atom labeling scheme is shown in Fig. 3. The summary of single crystal X-ray structure refinement is shown in Table 4 and the selected bond parameters are presented in Table 5. The complexes crystallize in the *C*2/*c* space group. The *p*-cymene ligand is bonded to the ruthenium atom in η^6-fashion with ruthenium centroid of the ring being 1.710(4). The complexes adopt a typical three-legged piano stool conformation with N, O and Cl atoms as the legs. The 2-(naphthylazo)phenolate ligands bind the metal center at O and N forming the five membered chelate ring with bite angle 79.5(3) O(1)–Ru(1)–N(1) and bond lengths of Ru(1)–O(1) and Ru(1)–N(1) are 2.077(6) and 2.122(7), respectively. The Ru–Cl bond length is found to be 2.412(2). As all the complexes display similar spectral and electrochemical properties, the other four complexes are assumed to have similar structure to that of complex (**2**). The structural features correspond well with the reported Schiff base (*p*-cymene)ruthenium(II) complexes [39,40].

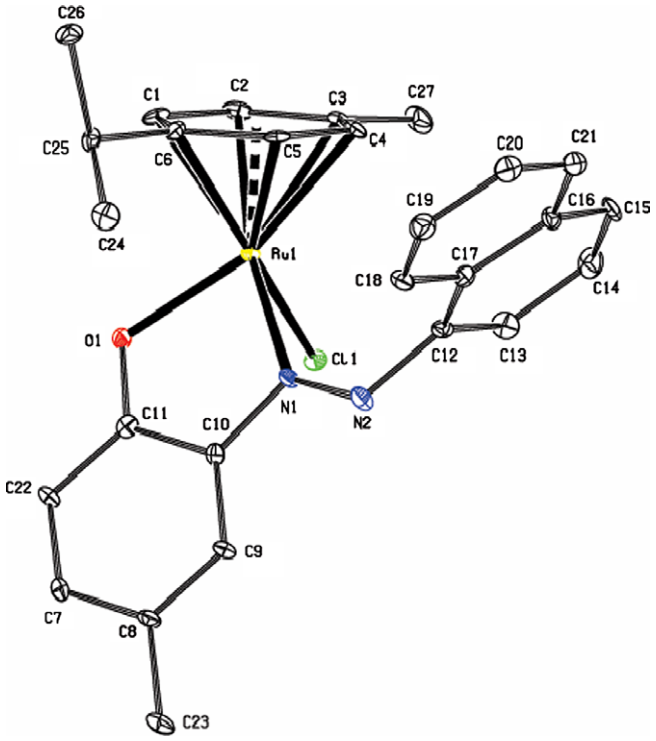


Fig. 3. Molecular structure of [Ru(η^6-*p*-cymene)(Cl)(L2)] (**2**), the hydrogen atoms were omitted for clarity.

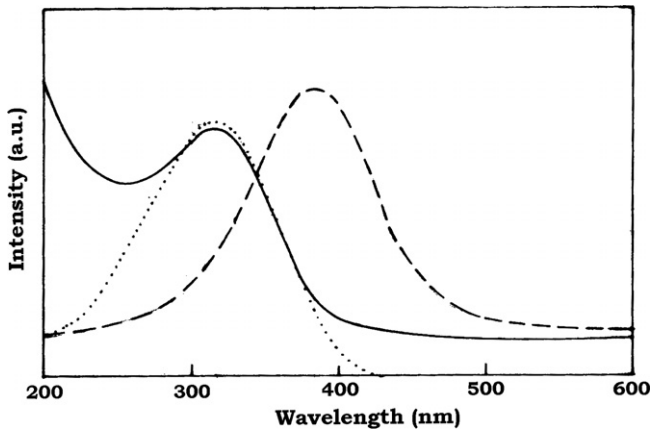


Fig. 2. Absroption (—), flurescence (- - -) and excitation (···) spectra of [Ru(η^6-*p*-cymene)(Cl)(L3)] (**3**).

The electrochemical property of all the complexes were studied by cyclic voltammetry. The electrochemical data are given in Table 6 and the representative voltammogram is shown in Fig. 4. Cyclic voltammogram of all the complexes were recorded in dichloromethane at glassy carbon working electrode and all the potentials are expressed with reference to Ag/AgCl. All the complexes (1×10^{-3}) show two metal centered voltammetric responses, a quasi-reversible oxidation (Ru^{III}/Ru^{II}) with $E_{1/2}$ values +0.89 to +1.07 V and an irreversible reduction with $E_{1/2}$ values −0.72 to −0.93 V with respect to the Ag/AgCl at scan rate 100 mV s^{-1}. The changes in oxidation and reduction potentials are probably due to the relative stabilization of the ruthenium(II) state over ruthenium(III) by a combination of σ and π effects exhibited by the ligand. The oxidation observed is quasi-reversible in nature, characterized by a

Table 4
Crystal data and structure refinement for complex [(η^6-*p*-cymene)-RuCl(L2)] (**2**)

Empirical formula	$C_{27}H_{27}ClN_2ORu$
Formula weight	532.03
Temperature (K)	183(2)
Wavelength (Å)	0.71073
Crystal system	monoclinic
Space group	*C*2/*c*
Unit cell dimensions	
a (Å)	29.527(6)
b (Å)	11.101(2)
c (Å)	16.781(3)
α (°)	90
β (°)	120.74(3)
γ (°)	90
Volume (Å^3)	4727.4(16)
Z	8
D_{calc} (Mg/m^3)	1.495
Absorption coefficient (mm^{-1})	0.798
F(000)	2176
Crystal size (mm)	0.15 × 0.12 × 0.10
θ Range for data collection (°)	1.60–23.00
Index ranges	$-32 \leqslant h \leqslant 26$, $-12 \leqslant k \leqslant 0$, $0 \leqslant l \leqslant 18$
Reflections collected	3287
Independent reflections	3287 [*R*(int) = 0.0000]
Completeness to theta = 23.00° (%)	99.8
Absorption correction	numerical
Maximum and minimum transmission	0.7192 and 0.5152
Refinement method	full-matrix least-squares on F^2
Data/restraints/parameters	3287/0/294
Goodness-of-fit on F^2	1.093
Final *R* indices [$I > 2\sigma(I)$]	$R_1 = 0.0571$, $wR_2 = 0.1568$
R indices (all data)	$R_1 = 0.0816$, $wR_2 = 0.1735$
Extinction coefficient	0.0006(2)
Largest difference peak and hole (e Å^{-3})	1.165 and −0.734

Table 5
Selected bond lengths (Å) and bond angles (°) of complex (**2**)

Bond lengths (Å)		Bond angles (°)	
Ru(1)–O(1)	2.077(6)	O(1)–Ru(1)–N(1)	79.5(3)
Ru(1)–N(1)	2.122(7)	O(1)–Ru(1)-Cl(1)	87.71(18)
Ru(1)–C(5)	2.192(8)	N(1)–Ru(1)-Cl(1)	83.5(2)
Ru(1)–C(6)	2.207(9)	C_g(1)–Ru(1)-Cl(1)	128.73(17)
Ru(1)–C(1)	2.232(9)	C_g(1)–Ru(1)–O(1)	125.6(2)
Ru(1)–C(2)	2.236(9)	C_g(1)–Ru(1)–N(1)	134.7(3)
Ru(1)–C(4)	2.245(9)		
Ru(1)–C(3)	2.267(9)		
Ru(1)–Cl(1)	2.412(2)		
O(1)–C(11)	1.304(11)		
C(10)–C(11)	1.432(13)		
N(1)–C(10)	1.414(12)		
N(2)–C(12)	1.426(12)		
Ru–C_g(1)	1.710(4)		

C_g = the centroid of the *p*-cymene ring.

rather large peak-to-peak separation (ΔE_p) of 110–220 mV and cathodic peak current (i_{pc}) is less than the anodic peak current (i_{pa}). The one electron nature of this oxidation has been verified by comparing its current height (i_{pa}) with that of the standard ferrocene–ferrocenium couple under identical experimental conditions [41]. The oxidation at more positive and less negative are believed to be corresponding metal oxidation and metal reduction, respectively.

Table 6
Cyclic voltammetric data of (*p*-cymene)ruthenium(II) 2-(naphthylazo)-phenolate complexes

Complexes	Ru^{III}/Ru^{II}				Ru^{II}/Ru^{I}
	E_{pa} (V)	E_{pc} (V)	$E_{1/2}$ (V)	ΔE_p (mV)	E_{pc} (V)
1	1.16	0.98	1.07	180	−0.82
2	1.17	0.96	1.06	210	−0.72
3	1.06	0.91	0.98	150	−0.75
4	0.96	0.82	0.89	140	−0.85
5	0.98	0.84	0.92	140	−0.93

Supporting electrolyte: NBu_4ClO_4 (0.005 M); complex: 0.001 M; solvent: CH_2Cl_2; $\Delta E_p = E_{pa} - E_{pc}$ where, E_{pa} and E_{pc} are anodic and cathodic potentials, respectively; $E_{1/2} = 0.5(E_{pa} + E_{pc})$; scan rate: 100 mV s^{-1}.

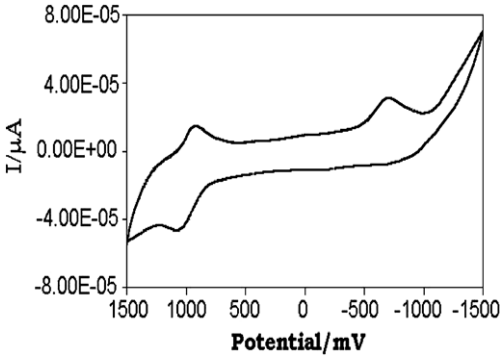


Fig. 4. Cyclic voltammogram of [Ru(η^6-*p*-cymene)(Cl)(L2)] (**2**).

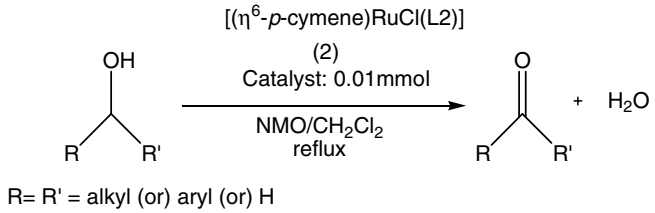
$$[(\eta^6\text{-}p\text{-cymene})Ru^{II}Cl(L)] \overset{\text{oxidation}}{\rightleftharpoons} [(\eta^6\text{-}p\text{-cymene})Ru^{III}Cl(L)] + e^-$$

$$[(\eta^6\text{-}p\text{-cymene})Ru^{II}Cl(L)] + e^- \overset{\text{reduction}}{\rightleftharpoons} [(\eta^6\text{-}p\text{-cymene})Ru^{II}Cl(L)]^-$$

From the electrochemical data, it is inferred that the present ligand system is ideally suitable for stabilizing the higher oxidation state of ruthenium ion and the electron transfer reactions take place without gross changes in the stereochemistry of the complexes [42,43].

3.2. Catalytic oxidation

The catalytic performance of complex [(η^6-*p*-cymene)-RuCl(L2)] (**2**) has been evaluated in a classical oxidation system developed for the oxidation of primary and secondary alcohols in CH_2Cl_2 in the presence of NMO (Scheme 3). Complex (**2**) oxidizes primary alcohols to the corresponding aldehydes and secondary alcohols to ketones with high conversion and the results are listed in Table 7 (entries 1–15). The crude reaction mixture were quantitatively analyzed by gas chromatography with authentic samples after 3 and 8 h (entries 6 and 7) of reaction with complex (**2**). The catalytic activity of the complex was



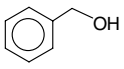
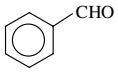
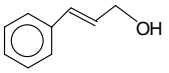
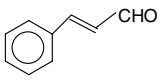
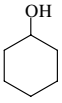
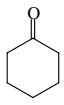
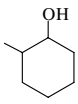
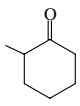
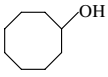
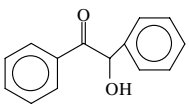
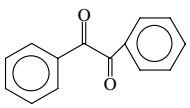
Scheme 3.

examined under a set of conditions (see Section 2 for reaction conditions) and a series of blank or control experiments suggest that none of ruthenium(II) 2-(naphthylazo)phenolate complexes and NMO alone causes these transformations under identical reaction conditions. This ascertained the necessity of ruthenium(II) complex to observe the ensuing catalytic organic transformations.

Results of the present investigation suggest that the complexes are able to react efficiently with NMO to yield high valent ruthenium-oxo species responsible for dehydrogenation of alcohols. This was further supported by spectral changes that occur by addition of NMO to a dichloromethane solution of the ruthenium(II) complexes. The appearance of peak at 390 nm is attributed to the formation of Ru^{IV}=O species, which is in conformity with other oxo ruthenium(II) complexes [44–46]. Further support in favor of the formation of such species was identified from the IR spectrum of the solid mass (obtained by evaporation of the resultant solution to dryness), which showed a band at 860 cm^{-1}, characteristic of Ru^{IV}=O species [45–47]. The *N*-methylmorpholine and water are the by products during the course of the reaction.

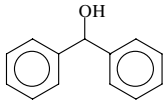
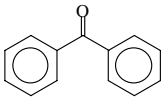
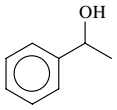
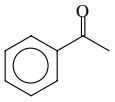
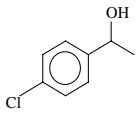
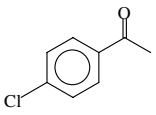
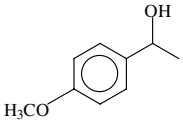
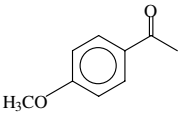
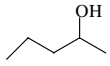
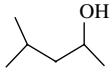
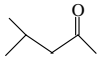
In the present study of oxidation, the catalytic oxidation of benzyl alcohol to benzaldehyde consequences 77%

Table 7
Catalytic oxidation of alcohols to corresponding aldehydes and ketones with complex (**2**) in the presence of NMO

Entry	Substrate	Product	Conversion[b] (%)	Turnover[c]
1			77	77
2			>94	94
3			>87	87
4			88	88
5			>91	91
6			>85[d]	85
7			>83[d]	83
8			56[a] 25[e] 33[f]	56 25 33

(*continued on next page*)

Table 7 (*continued*)

Entry	Substrate	Product	Conversion[b] (%)	Turnover[c]
9			90	90
10			>84	84
11			>94	94
12			92	92
13			97	97
14			>94	94
15			>95	95

Substrate (1 mmol); NMO (3 mmol); complex (0.01 mmol): solvent dichloromethane.

[a] Isolated yield, characterized by melting point, ^{1}H NMR and IR.

[b] Yield of product was determined using a HP 6890 series GC-FID with a DP-5 column of 30 m length, 0.32 mm diameter and 0.25 μm film thickness and by comparison with authentic samples.

[c] Moles of product per mole of catalyst.

[d] Reaction after 8 h.

[e] In presence of *t*-BuOOH.

[f] In presence of H_2O_2.

conversion. An important characteristic of ruthenium NMO system results in the selective oxidation at alcoholic group of unsaturated cinnamyl alcohol to cinnamaldehyde yielded >94% to tolerating other functional groups (double bond). The complex effectively catalyze the oxidation of allylic and benzylic alcohols with maximum selectivity to aldehydes with, importantly, no further oxidation to the corresponding carboxylic acids. Unsaturated aliphatic alcohols such as butan-2-ol, methylpropyl carbinol and isobutyl methyl carbinol are converted to corresponding ketones with high conversion >94%. In case of saturated aromatic secondary alcohols such as 1-phenyl ethanol, 4-chloro-1-phenyl ethanol and 4-methoxy-1-phenyl ethanol to undergo significant oxidation to give their corresponding ketones with high selectivity with 88%, 96% and 92%, respectively. The higher conversion in case of 4-chloro-1-phenyl ethanol and 4-methoxy-1-phenyl ethanol when compared to the 1-phenyl ethanol is due to the presence of substituents in the *para* position, which increase the reactivity by destabilizing the ruthenium-oxo intermediate making it a more reactive oxidant [48].

Further, the complex effectively catalyzes benzhydrol and benzoin to corresponding ketones. Particularly, in the case of benzoin the oxidation product was isolated and characterized by melting point, IR and ^{1}H NMR. In view of comparison, oxidation of benzoin was carried out in presence of *t*-BuOOH and H_2O_2 in addition to NMO. It was found that

the conversions are poor (Table 7) when compared to ruthenium/NMO catalytic system. Moreover, the complex efficiently catalyze the five, six, substituted six membered, seven and eight membered cyclic alcohols into corresponding ketones with high conversion >83%. It has been observed that the complex **2** has better catalytic efficiency in the case of oxidation of primary and secondary alcohols when compared to similar ruthenium complexes as catalysts in the presence of NMO/*t*-BuOOH reported earlier [44–49].

4. Conclusions

In conclusion, we have synthesized and characterized five mononuclear half-sandwich organoruthenium(II) naphthylazophenolato complexes. Complex **2** was structurally characterized by X-ray crystallography, which witnessed a typical three-legged piano stool conformation with N, O and Cl atoms as the legs. All the complexes exhibit characteristic metal-to-ligand charge transfer (MLCT) absorption and emission bands in the visible region. Further, the complex **2** efficiently catalyze the oxidation of variety of primary and secondary alcohol to the corresponding oxidized products in the presence of NMO.

Acknowledgements

We express sincere thanks to Dr. B. Spingler, Institute of Inorganic Chemistry, University of Zürich, Switzerland for crystallographic discussion. The author also thanks to Prof. P.R. Athappan, School of Chemistry, Madurai Kamaraj University, for cyclic voltammetry facility.

Appendix A. Supplementary material

CCDC 602827 contains the supplementary crystallographic data for **2**. These data can be obtained free of charge via http://www.ccdc.cam.ac.uk/conts/retrieving.html, or from the Cambridge Crystallographic Data Centre, 12 Union Road, Cambridge CB2 1EZ, UK; fax: (+44) 1223-336-033; or e-mail: deposit@ccdc.cam.ac.uk. Supplementary data associated with this article can be found, in the online version, at doi:10.1016/j.poly.2007.08.037.

References

[1] (a) M.H. Bennett, Coord. Chem. Rev. 166 (1997) 225;
(b) J.H. Rigby, M.A. Kondratenko, Top. Organomet. Chem. 7 (2004) 181.
[2] Y. Miyaki, T. Onishi, S. Ogoshi, H. Kurosawa, J. Organomet. Chem. 616 (2000) 135.
[3] (a) Y. Miyaki, T. Onishi, H. Kurosawo, Inorg. Chim. Acta 300 (2000) 369;
(b) D.P. Halbach, C.G. Hamaker, J. Organomet. Chem. 691 (2006) 3349;
(c) K. Severin, Corr. Org. Chem. 10 (2006) 217;
(d) L. Delande, A. Demonceau, A.F. Noels, Curr. Org. Chem. 210 (2006) 203.
[4] C.M. Thomas, R. Mafia, B. Thesrian, E. Rusanov, H. Stoeckkli-Evans, G. Suss-Fink, Chem. Eur. J. 8 (2002) 3343.
[5] F. Fache, E. Schulz, E.L. Tommasino, M. Lemaire, Chem. Rev. 100 (2000) 2159.
[6] (a) T. Punniyamurthy, S. Velusamy, J. Iqbal, Chem. Soc. Rev. 105 (2005) 2329;
(b) V.B. Sharma, L.S. Jain, B. Sain, J. Mol. Catal. A: Chem. 227 (2005) 47.
[7] S.I. Murahashi, Angew. Chem., Int. Ed. Engl. 34 (1995) 2443.
[8] R.A. Sheldon, J.K. Kochi, Metal-Catalyzed Oxidation of Organic Compounds, Academic Press, New York, 1991.
[9] A. Pijksmann, I.W.C.E. Arends, S. Shelton, J. Chem. Soc., Chem. Commun. (1999) 1591.
[10] G. Csjernyik, A.H. Ell, L. Fadini, B. Pugin, J.-E. Backvall, J. Org. Chem. 67 (2002) 657.
[11] I.W.C.E. Arends, T. Kodama, R.A. Sheldon, Oxidation using ruthenium catalyst, in: Topics in Organometallic Chemistry, Spinger, Berlin, 2004.
[12] M. Pagliaro, S. Campestrini, R. Ciriminna, Chem. Soc. Rev. 34 (2005) 837.
[13] D.G. Lee, E. Engh Vanden, in: W.S. Trahanovsky (Ed.), Oxidation in Organic Chemistry, Academic Press, New York, 1973.
[14] M.A. Bennett, T.W. Matheson, in: G. Wilkinson, F.G.A. Stone, E.W. Abel (Eds.), Comprehensive Organometallic Chemistry, vol. 4, Pergamon Press, Oxford, 1982, p. 931.
[15] S. Kanemote, S. Matsubara, K. Takai, K. Oshima, Tetrahedron Lett. 24 (1983) 2185.
[16] A. Hanyu, E. Takezwa, S. Sakaguchi, Y. Ishii, Tetrahedron. Lett. 39 (1998) 5557.
[17] D. Chatterjee, A. Mitra, S. Mukherjee, J. Mol. Catal. A: Chem. 165 (2001) 295.
[18] K.B. Sharpless, K. Akashi, K. Oshima, Tetrahedron Lett. 17 (1976) 2503, and references therein.
[19] J.E. Backvall, R.L. Chowdhury, U. Karlsson, J. Chem. Soc., Chem. Commun. (1991) 473.
[20] S. Campestrini, M. Carraro, U. Tonellato, M. Pagliaro, R. Ciriminna, Tetrahedron Lett. 45 (2004) 7283.
[21] C. Bilgrien, S. Davis, R.S. Drago, J. Am. Chem. Soc. 109 (1987) 3786.
[22] P. Muller, J. Godoy, Tetrahedron Lett. 22 (1981) 2361.
[23] W.S. Trahanosky, Oxidation of Organic Chemistry, Part B, Academic Press, 1973.
[24] M.A. Bennett, A.K. Smith, J. Chem. Soc., Dalton Trans. (1974) 233.
[25] A.I. Vogel, Text Book of Practical Organic Chemistry, 5th ed., Longman, London, 1989.
[26] CELL, 2.92, 1999 ed.; STOE & Cie, GmbH: Darmstadt, Germany, 1999.
[27] G.M. Sheldrick, SHELXS-97, Program fro Crystal Structure Solution, Göttingen, 1997.
[28] M.C. Altomare, M. Burla, G.L. Camalli, C. Cascarano, A. Giacovazzo, A.G. Guagliardi, G. Moliterni, G. Polidori, R. Spagna, J. Appl. Crystallogr. 32 (1999) 115.
[29] G.M. Sheldrick, SHELXL-97, Program for Crystal Structure Refinement, Göttingen, 1997.
[30] P. Byabartta, P.K. Santra, T.K. Misra, C. Sinha, C.H.L. Kennard, Polyhedron 20 (2001) 905.
[31] S. Goswami, R. Mukerjee, A. Chakravorty, Inorg. Chem. 22 (1983) 2825.
[32] K. Nakamoto, Infrared and Raman Spectra of Inorganic and Coordination Compounds, Wiley Interscience, New York, 1971.
[33] J.R. Dyer, Application of Absoption Spectroscopy of Organic Compounds, Prentice-Hall, New Jersey, 1978.
[34] A. Ceulemans, L.G. Vanquickenborne, J. Am. Chem. Soc. 103 (1981) 2238.
[35] A.B.P. Lever, Inorganic Electronic Spectroscopy, second ed., Elsiever, New York, 1984.
[36] J.V. Ortega, K. Khine, W.E. Vanderveer, J. Ziller, B. Hong, Inorg. Chem. 39 (2000) 6038.
[37] A.A. Harriman, R. Ziessel, M. Hissler, A. El-ghayoury, F. Wu, E.C. Riesgo, R.O. Thummel, Inorg. Chem. 39 (2000) 3590.

[38] P. Gupta, R.J. Butcher, S. Bhattacharya, Inorg. Chem. 42 (2003) 5405.
[39] (a) H. Brunner, R. Oeschwy, B. Nuber, Inorg. Chem. 34 (1995) 3349; (b) S. Mandal, A.R. Chakravarty, Inorg. Chem. 32 (1993) 3851.
[40] S. Roy, C. Sudha, A.R. Chakravarty, Ind. J. Chem. 37A (1998) 1045.
[41] S. Dutta, S. Peng, S. Bhattachrya, J. Chem. Soc., Dalton Trans. (2000) 4623.
[42] A.M. Bond, R. Colton, D.R. Mann, Inorg. Chem. 29 (1990) 4665.
[43] A. Basu, T.G. Kasan, N.Y. Sapre, Inorg. Chem. 27 (1998) 4639.
[44] (a) M.M.T. Khan, C. Sreelatha, S.A. Mirza, G. Ramachandriah, S.H.R. Abdi, Inorg. Chim. Acta 154 (1988) 102;
(b) A.S. Goldstein, R.S. Drago, J. Chem. Soc., Chem. Commun. (1991) 21.
[45] W.H. Leung, C.M. Chem, Inorg. Chem. 28 (1989) 4619.
[46] (a) M.S. El-Shahawi, A.F. Shoair, Spectrochim. Acta A 60 (2004) 121;
(b) R.S. Drago, Coord. Chem. Rev. 117 (1992) 185.
[47] D. Chatterjeea, A. Mitra, B.C. Roy, J. Mol. Catal. A 161 (2000) 17.
[48] N.S. Venkataramanan, G. Kuppuraj, S. Rajagopal, Coord. Chem. Rev. 249 (2005) 1249.
[49] Y. Tsuji, T. Ohta, T.T. Ido, H. Minbu, Y. Watanabe, J. Organomet. Chem. 270 (1984) 333.

Available online at www.sciencedirect.com
ScienceDirect
Polyhedron 27 (2008) 167–174
POLYHEDRON
www.elsevier.com/locate/poly

Self-cyclisation versus diynediol-promoted ring closure during the construction of coordinated crown-type macrocycles

Vladimir B. Golovko [a,b,*], Martin J. Mays [a], Gregory A. Solan [c,*]

[a] Department of Chemistry, Lensfield Road, Cambridge CB2 1EW, UK
[b] Department of Chemistry, Canterbury University, Private Bag 4800, Christchurch, New Zealand
[c] Department of Chemistry, University of Leicester, University Road, Leicester LE1 7RH, UK

Received 8 August 2007; accepted 31 August 2007
Available online 22 October 2007

Abstract

Treatment of $[Co_2(CO)_6(\mu\text{-}\eta^2\text{-}HOCH_2C{\equiv}CCH_2OH)]$ (**1a**) with a catalytic quantity of $HBF_4 \cdot OEt_2$ affords $[\{Co_2(CO)_6\}_2\{cyclo\text{-}\mu\text{-}\eta^2\text{:}\mu\text{-}\eta^2\text{-}OCH_2C{\equiv}CCH_2OCH_2C{\equiv}CCH_2\text{–}\}]$ (**2**) and $[\{Co_2(CO)_6\}_3\{cyclo\text{-}\mu\text{-}\eta^2\text{:}\mu\text{-}\eta^2\text{:}\mu\text{-}\eta^2\text{-}OCH_2C{\equiv}CCH_2OCH_2C{\equiv}CCH_2OCH_2C{\equiv}CCH_2\text{–}\}]$ (**3**), in which cyclodimerisation and cyclotrimerisation of **1a** has occurred, respectively. The molecular structures of **2** and **3** reveal non-bonding oxygen–oxygen separations within the macrocycles of 4.716 Å (**2**) and 3.968–5.045 Å (**3**). On the other hand, introduction of one equivalent of the cyclohexyl-substituted diyne-diol, (1-HO-*cyclo*-C_6H_{10})$C{\equiv}CC{\equiv}C$(1-HO-*cyclo*-C_6H_{10}), to the reaction furnishes the macrocyclic complexes $[\{Co_2(CO)_6\}_2\{cyclo\text{-}\mu\text{-}\eta^2\text{:}\mu\text{-}\eta^2\text{-}OCH_2C{\equiv}CCH_2OCH_2C{\equiv}CCH_2O(cyclo\text{-}C_6H_{10})C_2C_2(cyclo\text{-}C_6H_{10})\text{–}\}]$ (**4**) and $[\{Co_2(CO)_6\}_3\{cyclo\text{-}\mu\text{-}\eta^2\text{:}\mu\text{-}\eta^2\text{:}\mu\text{-}\eta^2\text{-}OCH_2C{\equiv}CCH_2OCH_2C{\equiv}CCH_2OCH_2C{\equiv}CCH_2O(cyclo\text{-}1\text{-}C_6H_{10})C_2C_2(cyclo\text{-}1\text{-}C_6H_{10})\text{–}\}]$ (**5**), in which the chain ends of the rigid 1,3-diyne unit are linked by either di- or tri-merised derivatives of **1a**. Also isolated in the reaction is the open-chain species $[\{Co_2(CO)_6\}_2(\mu\text{-}\eta^2\text{:}\mu\text{-}\eta^2\text{-}HOCH_2C{\equiv}CCH_2O(cyclo\text{-}1\text{-}C_6H_{10})C_2C_2(cyclo\text{-}1\text{-}C_6H_{10})\text{-}OCH_2C{\equiv}CCH_2OH)]$ (**6**). Inspection of the molecular structure of **4** reveals a 17-membered ring with the non-bonding oxygen–oxygen separations ranging from 4.958 to 7.257 Å.
© 2007 Elsevier Ltd. All rights reserved.

Keywords: Cobalt complexes; Alkyne; Self-cyclisation; 1,3-Diyne; Macrocycle; Nicholas reaction

1. Introduction

The amenability of the Nicholas reaction [1] to facilitate the assembly of cyclic structures has been the topic of a number of studies [2–4] in recent years due, in some measure, to the association the resulting materials have to natural products [2–4], molecular sensors [5] and nanoscience [6]. In particular, the acid-catalysed intermolecular reactions of butyne-1,4-diol-$Co_2(CO)_6$ (**1a**, Fig. 1) with suitable bifunctional nucleophiles [e.g., alkyldithiols, bis(mercaptoalkyl)sulfides/ethers] has allowed access to a diversity of unusual macrocycles containing a range of donor atoms [7,8]. As an extension to these studies our group [9] and others [4,10,11] have been attracted by the potential of the more extended bis(propargyl alcohol/ether)-$\{Co_2(CO)_6\}_2$ substrates (e.g., **1b**, Fig. 1) to act as building blocks for larger cyclic systems incorporating diyne units. During the course of our study we have found that self-cyclisation can be a competitive side reaction when **1b** is treated with a co-reactant that displays only modest nucleophilicity (e.g., alkyl diols) [9d]. Indeed, when **1b** is treated with catalytic quantities of acid alone, the cyclodimerised crown-type species 1,8-dioxacyclotetradeca-3,5,10,12-tetrayne-$\{Co_2(CO)_8\}_4$ (Fig. 1) can be isolated as the sole product [9d].

In this paper, we are concerned with examining whether **1a** has a similar propensity to undergo acid-catalysed self-cyclisation reactions. Martin et al. have disclosed the formation of 1,6-dioxa-cyclodeca-3,8-diyne-$Co_2(CO)_6$ from

* Corresponding authors. Tel.: +44 116 2522096 (G.A. Solan).
E-mail address: gas8@leicester.ac.uk (G.A. Solan).

0277-5387/$ - see front matter © 2007 Elsevier Ltd. All rights reserved.
doi:10.1016/j.poly.2007.08.038

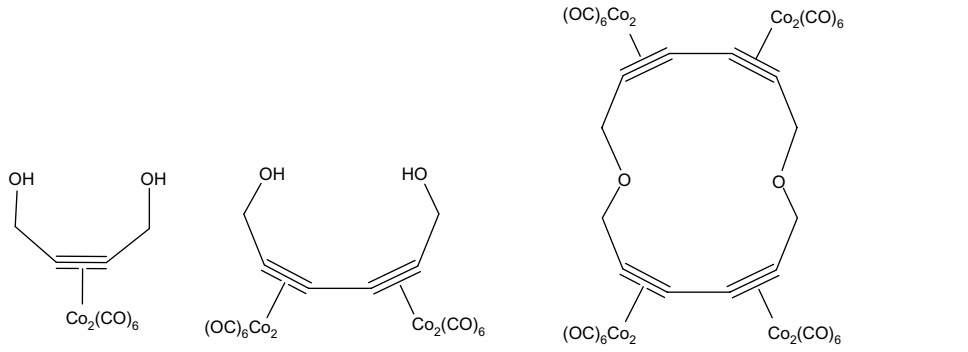
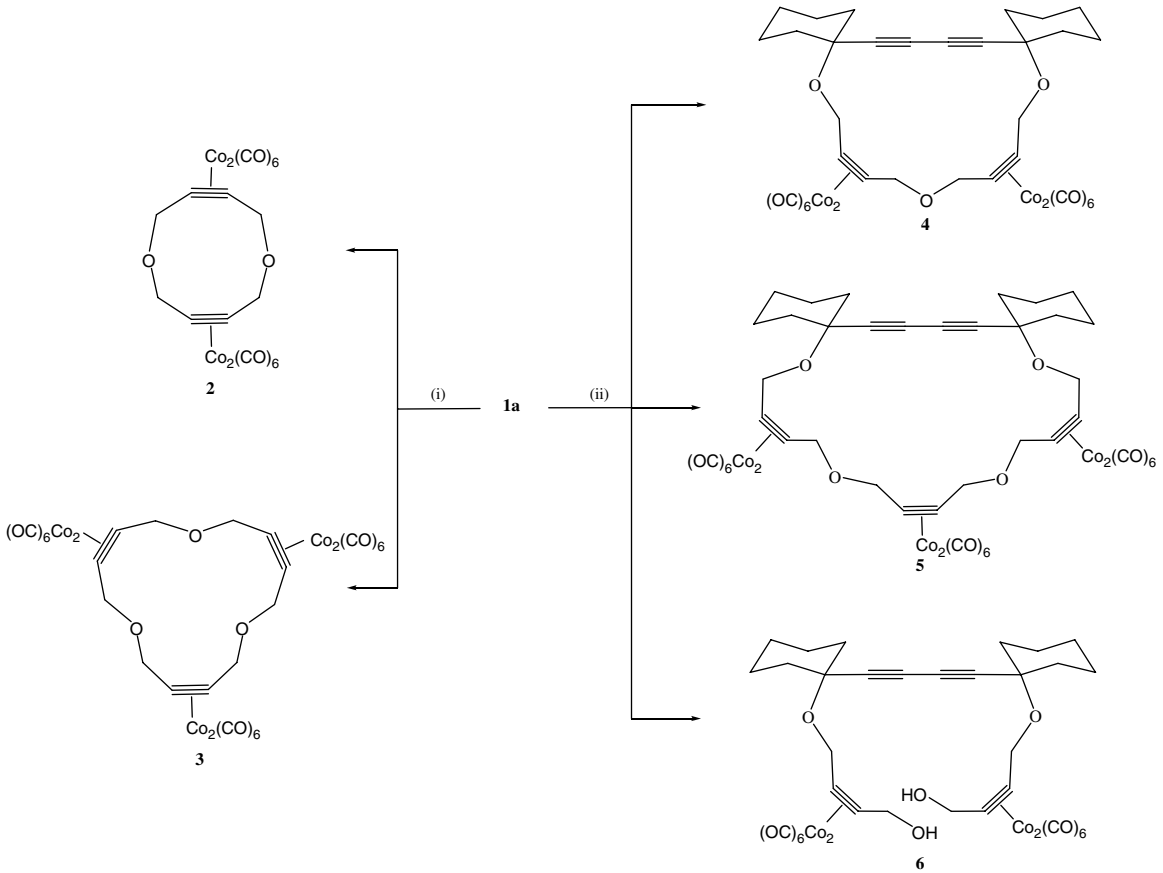


Fig. 1. Butyne-1,4-diol-$Co_2(CO)_6$ (**1a**), hexa-2,4-diyne-1,6-diol-$\{Co_2(CO)_6\}_2$ (**1b**) and 1,8-dioxacyclotetradeca-3,5,10,12-tetrayne-$\{Co_2(CO)_6\}_4$.

the reaction of **1a** with the non-coordinated butyne-1,4-diol [8] while, to the knowledge of the authors, no reports have appeared with regard to the reactivity of **1a** per se. In addition, we probe the potential of the free diyne diol (1-HO-*cyclo*-C_6H_{10})C≡CC≡C(1-HO-*cyclo*-C_6H_{10}) to undergo intermolecular cyclisation reactions with **1a** or its self-reacted derivatives [12]. This latter study is of added interest since alkyl-substituted 1,3-diyne diols of the type XC≡CC≡CX (X = C_5H_8OH [13], $C_6H_{10}OH$ [13], CMe_2OH [14]) when complexed with two $Co_2(CO)_6$ units have instead shown a preference to undergo dehydration reactions under Nicholas conditions.

2. Results and discussion

Treatment of [$Co_2(CO)_6$(μ-η^2-$HOCH_2$-C≡C-CH_2OH)] (**1a**) [15] in dichloromethane with a catalytic amount of $HBF_4 \cdot OEt_2$ at −78 °C afforded, following chromatographic work-up, the cyclic dimer [$\{Co_2(CO)_6\}_2$\{*cyclo*-μ-η^2:μ-η^2-OCH_2C≡CCH_2OCH_2C≡CCH_2–\}] (**2**) and the



Scheme 1. Reagents and conditions: (i) $HBF_4 \cdot OEt_2$ (catalyst), −78 °C, CH_2Cl_2; (ii) (1-HO-*cyclo*-C_6H_{10})CCCC(1-HO-*cyclo*-C_6H_{10}), $HBF_4 \cdot OEt_2$ (catalyst), −78 °C, CH_2Cl_2.

cyclic trimer [{$Co_2(CO)_6$}$_3${*cyclo*-μ-η^2:μ-η^2:μ-η^2-$OCH_2C{\equiv}CCH_2OCH_2C{\equiv}CCH_2OCH_2C{\equiv}CCH_2$–}] (**3**) in moderate yield (Scheme 1). Both complexes have been characterised by IR, ^{1}H and ^{13}C NMR spectroscopy, liquid secondary ion (LSI) mass spectrometry and gave satisfactory microanalyses (see Section 4). In addition, **2** and **3** have been the subject of single crystal X-ray diffraction studies.

The IR spectra of complexes **2** and **3** are characteristic of dicobalt hexacarbonyl-coordinated monoyne complexes [7,16], with three major CO stretching bands. The ^{1}H NMR spectra of **2** and **3** show singlet resonances for the propargyl CH_2 groups at ca. δ 4.90 consistent with symmetric structures which is further supported by the presence of only one type of alkynic carbon signal (at ca. δ 91.1) in their ^{13}C NMR spectra. The LSI mass spectra of both complexes show protonated molecular ion peaks (along with M^++Na peaks) corresponding to the proposed cyclic structures and also display fragmentation patterns that match with the loss of carbonyl groups from the molecular ions.

Crystals of **2** suitable for an X-ray diffraction study were grown from dichloromethane:hexane at 0 °C by slow vapour diffusion of additional hexane. The molecular structure of **2** is shown in Fig. 2; selected bond lengths and angles are collected in Table 1. The structure consists of a 10-membered 1,6-dioxa-cyclodeca-3,8-diyne ring in which each alkynic group is perpendicularly bound by dicobalt hexacarbonyl units. The Co_2C_2 cores adopt the expected tetrahedral arrangements with the Co–Co and C (alkyne)–C (alkyne) bond distances falling within the normal ranges [16,17]; the coordinated carbonyl ligands display the expected linear geometries. The C–C≡C *bend-back* angles [143.4(3)°, 143.9(3)°, 142.9(3)°, 143.2(3)°] are similar in magnitude and typical of those found in related macrocyclic complexes [7]. In comparison with the chair-like conformation found in the structure of the free 1,6-dioxa-cyclodeca-3,8-diyne ligand [18], **2** exhibits a more boat-like arrangement with the triple bonds no longer oriented in a parallel fashion and the oxygen–oxygen separation reduced [4.716 Å (**2**) versus 4.935 Å]. The separation between the complexed triple bonds in **2** is also slightly shorter than that found in its dithio analogue [{$Co_2(CO)_6$}$_2${*cyclo*-μ-η^2:μ-η^2-$SCH_2C{\equiv}CCH_2SCH_2C{\equiv}CCH_2$–}] [3.446 Å (**2**) versus 3.635 Å] [19]. An intermolecular interaction is apparent between a propargylic hydrogen atom in one molecule of **2** and an oxygen atom belonging to one of the bis-propargyl ether bridges in an adjacent molecule [H(20B)···O(14) 2.670 Å].

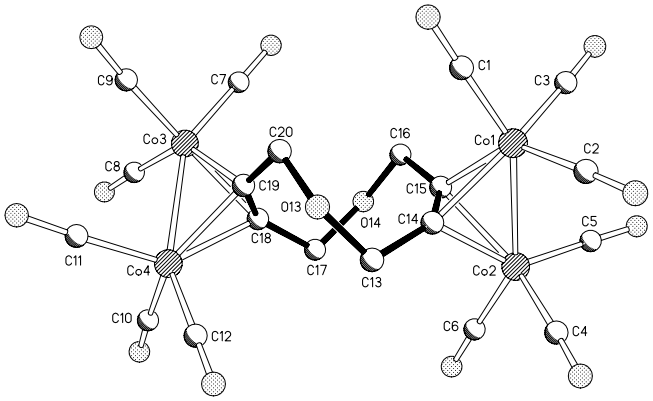


Fig. 2. Molecular structure of **2** with partial atom labeling scheme; all hydrogen atoms have been omitted for clarity.

Crystals of **3** suitable for an X-ray diffraction study were also grown from dichloromethane:hexane at 0 °C. The molecular structure of **3** is shown in Fig. 3; selected bond lengths and angles are listed in Table 2. The structure comprises a 15-membered 1,6,11-trioxa-cyclopentadeca-3,8,13-triyne ring in which each alkyne functionality is bound by a $Co_2(CO)_6$ unit. The expected tetrahedral arrangements are adopted by the Co_2C_2 cores and the Co–Co and C (alkyne)–C (alkyne) bond distances fall within the normal ranges [16,17]. The C–C≡C *bend-back* angles [141.8(2)°, 142.3(3)°, 142.4(3)°, 142.5(3)°, 147.7(3)°, 146.3(3)°] show some variation when compared with the values found in **2** indicating some uneven distribution of strain within the ring. The oxygen–oxygen separations within the macrocycle

Table 1
Selected bond distances (Å) and angles (°) for **2**

Bond lengths (Å)			
C(13)–C(14)	1.490(4)	C(20)–O(13)	1.429(3)
C(14)–C(15)	1.339(4)	O(13)–C(13)	1.422(3)
C(15)–C(16)	1.489(4)	Co(1)–Co(2)	2.4649(5)
C(16)–O(14)	1.423(3)	Co(3)–Co(4)	2.4631(5)
O(14)–C(17)	1.426(3)	Co–C (carbonyl)	1.786(3)–1.833(3)
C(17)–C(18)	1.487(4)	C–O (carbonyl)	1.125(3)–1.143(3)
C(18)–C(19)	1.338(4)	Co–C (alkyne)	1.974(3)–1.977(3)
C(19)–C(20)	1.484(4)		
Bond angles (°)			
C(13)–C(14)–C(15)	142.9(3)	C(17)–C(18)–C(19)	143.4(3)
C(14)–C(15)–C(16)	143.2(3)	C(18)–C(19)–C(20)	143.9(3)
C(15)–C(16)–O(14)	116.1(2)	C(19)–C(20)–O(13)	115.1(2)
C(16)–O(14)–C(17)	118.1(2)	C(20)–O(13)–C(13)	117.7(2)
O(14)–C(17)–C(18)	115.7(2)	O(13)–C(13)–C(14)	116.0(2)

also vary [O(19)···O(20) 5.045 Å, O(19)···O(21) 4.048 Å, O(20)···O(21) 3.968 Å] with the average value lower than that in **2**. Intermolecular short contacts are also a feature of the packing in **3** most noticeably between the oxygen atoms of the CO ligands in one molecule and the hydrogen atoms of the propargyl CH_2 groups in another [e.g., O(9)···H(19B) 2.540 Å, O(13)···H(27A) 2.696 Å, O(14)···H(23A) 2.837 Å, O(3)···H(26A) 2.794 Å].

The capacity of alkyl diols of the type HO-$(CH_2)_n$-OH ($n = 4$–6) to undergo ring closing reactions with the dppm-bridged derivative of **1a** has been previously been reported by Went et al. [7f]. We have been interested in exploring the use of less flexible alkyl diols (e.g., 1,3-diyne alkyl diols) in which ring closure of **1a** would be expected to proceed less efficiently. Thus, reaction of **1a** with the diynediol (1-HO-*cyclo*-C_6H_{10})C≡CC≡C(1-HO-*cyclo*-C_6H_{10}) in dichloromethane in the presence of a catalytic amount of $HBF_4 \cdot OEt_2$ gave, on work-up by TLC, [{$Co_2(CO)_6$}$_2${*cyclo*-μ-η^2:μ-η^2-$OCH_2C{\equiv}CCH_2OCH_2C{\equiv}CCH_2O$(*cyclo*-$C_6H_{10}$)$C_2C_2$(*cyclo*-$C_6H_{10}$)–}] (**4**), [{$Co_2(CO)_6$}$_3$-{*cyclo*-μ-η^2:μ-η^2:μ-η^2-$OCH_2C{\equiv}CCH_2OCH_2C{\equiv}CCH_2O$-$CH_2C{\equiv}CCH_2O$(*cyclo*-1-$C_6H_{10}$)$C_2C_2$(*cyclo*-1-$C_6H_{10}$)–}] (**5**) and [{$Co_2(CO)_6$}$_2$(μ-η^2:μ-η^2-$HOCH_2C{\equiv}CCH_2O$(*cyclo*-1-$C_6H_{10}$)$C_2C_2$(*cyclo*-1-$C_6H_{10}$)-$OCH_2C{\equiv}CCH_2OH$)] (**6**) (Scheme 1). Only low yields of **4**–**6** could be obtained which were further reduced by the need for repeated elution (with hexane) to allow satisfactory separation of the products. Nevertheless, the complexes have been characterised by a combination of IR, ^{1}H and ^{13}C NMR spectroscopy and LSI mass spectrometry (Table 1 and Section 4). In addition, **4** has been the subject of a single crystal X-ray diffraction study.

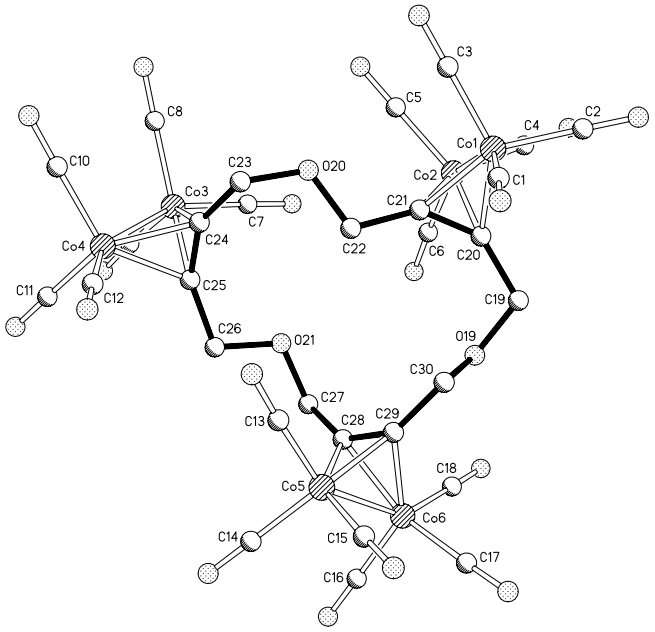


Fig. 3. Molecular structure of **3** with partial atom labeling scheme; all hydrogen atoms have been omitted for clarity.

Crystals of **4** were grown by prolonged standing at 0 °C of a hexane:dichloromethane solution containing the complex. The asymmetric unit of **4** contains two crystallographically independent molecules (A and B) differing in the orientations of the *cyclo*-hexyl groups with respect to the rigid diyne moiety. The molecular structure of one of the independent molecules of **4** is shown in Fig. 4a; selected bond lengths and angles are listed for both molecules in Table 3. The structure consists of a 17-membered 1,6,13-trioxa-cycloheptadeca-3,8,10,15-tetrayne ring in which two of the alkynic groups are η^2:η^2 bound by $Co_2(CO)_6$ units. Both cyclohexyl substituents adopt the "chair" conformation. As expected there is considerable variation in the magnitude of the C–C≡C *bend back* angles with those

Table 2
Selected bond distances (Å) and angles (°) for **3**

Bond lengths (Å)			
O(19)–C(19)	1.423(3)	C(27)–C(28)	1.483(4)
C(19)–C(20)	1.490(4)	C(28)–C(29)	1.341(4)
C(20)–C(21)	1.355(4)	C(29)–C(30)	1.473(4)
C(21)–C(22)	1.474(4)	C(30)–O(19)	1.425(3)
C(22)–O(20)	1.419(3)	Co(1)–Co(2)	2.4677(7)
O(20)–C(23)	1.424(3)	Co(3)–Co(4)	2.4615(5)
C(23)–C(24)	1.498(4)	Co(5)–Co(6)	2.4826(5)
C(24)–C(25)	1.330(4)	Co–C (carbonyl)	1.783(5)–1.830(4)
C(25)–C(26)	1.486(4)	C–O (carbonyl)	1.127(4)–1.145(5)
C(26)–O(21)	1.420(3)	Co–C (alkyne)	1.939(3)–1.970(3)
O(21)–C(27)	1.431(3)		
Bond angles (°)			
O(19)–C(19)–C(20)	112.1(2)	C(25)–C(26)–O(21)	109.0(2)
C(19)–C(20)–C(21)	142.4(3)	C(26)–O(21)–C(27)	113.4(2)
C(20)–C(21)–C(22)	142.5(3)	O(21)–C(27)–C(28)	113.8(2)
C(21)–C(22)–O(20)	109.0(2)	C(27)–C(28)–C(29)	141.8(3)
C(22)–O(20)–C(23)	112.4(2)	C(28)–C(29)–C(30)	142.3(3)
O(20)–C(23)–C(24)	113.6(2)	C(29)–C(30)–O(19)	108.5(2)
C(23)–C(24)–C(25)	147.7(3)	C(30)–O(19)–C(19)	112.7(2)
C(24)–C(25)–C(26)	146.3(3)		

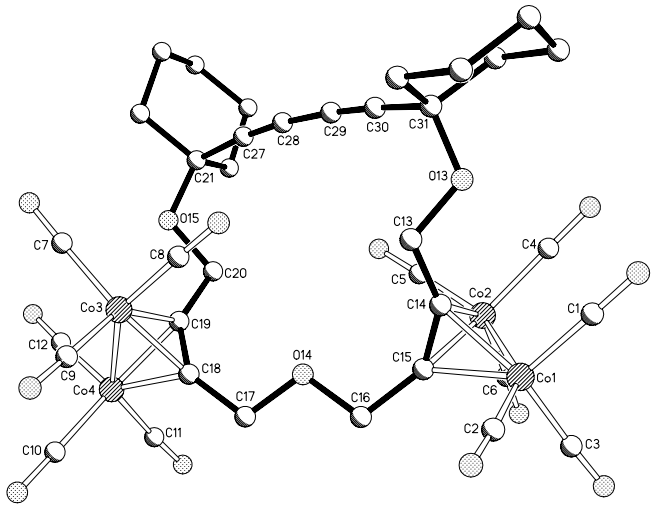


Fig. 4a. Molecular structure of **4** with partial atom labeling scheme; all hydrogen atoms have been omitted for clarity.

Table 3
Selected bond distances (Å) and angles (°) for **4**

	Molecule A	Molecule B
Bond lengths (Å)		
O(13)–C(13)	1.442(9)	1.428(9)
C(13)–C(14)	1.462(12)	1.473(11)
C(14)–C(15)	1.343(12)	1.344(11)
C(15)–C(16)	1.492(12)	1.494(11)
C(16)–O(14)	1.426(9)	1.425(9)
O(14)–C(17)	1.417(9)	1.414(9)
C(17)–C(18)	1.456(11)	1.507(11)
C(18)–C(19)	1.340(10)	1.348(11)
C(19)–C(20)	1.478(10)	1.457(12)
C(20)–O(15)	1.432(9)	1.440(9)
O(15)–C(21)	1.441(9)	1.433(9)
C(21)–C(27)	1.483(11)	1.467(11)
C(27)–C(28)	1.190(10)	1.210(1)
C(28)–C(29)	1.381(12)	1.383(11)
C(29)–C(30)	1.191(1)	1.173(10)
C(30)–C(31)	1.479(11)	1.503(11)
C(31)–O(13)	1.449(9)	1.444(9)
Co(1)–Co(2)	2.4684(16)	2.4730(16)
Co(3)–Co(4)	2.4760(16)	2.4749(17)
Co–C (carbonyl)	1.774(11)–1.828(11)	1.772(13)–1.843(10)
C–O (carbonyl)	1.121(13)–1154(10)	1.106(10)–1.147(10)
Co–C (alkyne)	1.949(7)–1.975(8)	1.952(7)–1.965(8)
Bond angles (°)		
O(13)–C(13)–C(14)	109.3(6)	108.5(6)
C(13)–C(14)–C(15)	144.4(8)	142.9(7)
C(14)–C(15)–C(16)	140.2(8)	140.7(7)
C(15)–C(16)–O(14)	108.4(6)	108.7(6)
C(16)–O(14)–C(17)	110.7(6)	110.0(6)
O(14)–C(17)–C(18)	110.7(7)	108.0(6)
C(17)–C(18)–C(19)	140.3(8)	140.5(8)
C(18)–C(19)–C(20)	143.7(7)	144.1(7)
C(19)–C(20)–O(15)	108.7(6)	108.3(6)
C(20)–O(15)–C(21)	116.3(5)	117.2(6)
O(15)–C(21)–C(27)	109.1(6)	110.0(6)
C(21)–C(27)–C(28)	173.7(8)	173.0(8)
C(27)–C(28)–C(29)	174.3(8)	176.0(8)
C(28)–C(29)–C(30)	176.0(8)	175.6(9)
C(29)–C(30)–C(31)	176.0(8)	174.0(8)
C(30)–C(31)–O(13)	109.1(6)	108.7(6)
C(31)–O(13)–C(13)	116.7(5)	116.7(5)

for the bound alkynes [144.4(8)°, 140.2(8)°, 140.3(8)°, 143.7(7)°] being significantly less than for the unbound ones [173.7(8)°, 176.0(8)°]. Nevertheless, the divergence from linearity in the 1,3-diyne unit suggests some strain within this section of the macrocycle. The bond parameters within the Co_2C_2 cores are unexceptional. The oxygen–oxygen separations [O(13)···O(14) 4.956 Å, O(13)···O(15) 7.257 Å, O(14)···O(15) 4.950 Å] indicate the cavity size of the macrocycle is larger than in both **2** and **3**.

Within the unit cell the four molecules assemble in such a way that the pseudo-linear diyne moieties within each molecule of **4** are oriented approximately parallel (Fig. 4b). Along the b axis the $-C{\equiv}CCH_2OCH_2C{\equiv}C-\{Co_2(CO)_6\}_2$ sections of the macrocycle line up facing each other as do the less polar neighbouring diyne sections. There are a number of intermolecular short contacts between the oxygen atoms of the CO ligands and the hydrogen atoms of both the propargyl CH_2 groups (shortest contact: 2.633 Å) and the cyclohexyl groups (shortest contact: 2.670 Å) in neighbouring molecules. In addition, disordered solvent molecules fill the voids between molecules of **4**.

As with **2** and **3**, the IR spectra of complexes **4**–**6** display the typical pattern of ν(CO) bands for alkyne-bridged $Co_2(CO)_6$ units [16]. In the case of **4** and **6**, broad weak bands attributable to the free alkyne units are also visible at ca. 2253 cm^{-1} [20]. In their ^1H NMR spectra, in addition to poorly resolved signals due to the C_6H_{10} groups, signals due to the propargyl CH_2 protons are seen as two singlets (at δ 4.84 and 4.75) for **4**, three singlets (at δ 4.82, 4.75 and 4.64) for **5** and two singlets (at δ 4.90 and 4.64) for **6**; consistent with a plane of symmetry that bisects the 1,3-diyne moieties. This is further supported in the ^{13}C NMR spectra which display either two (**4**: δ 72.2, 63.6), three (**5**: δ 72.2, 71.4, 63.7) or two (**6**: δ 72.1, 63.6) propargylic carbon signals. In the LSI mass spectra of **4** and **5** peaks corresponding to the protonated molecular ion (and M^++Na peaks) are visible along with fragmentation peaks corresponding to the loss of carbonyl groups.

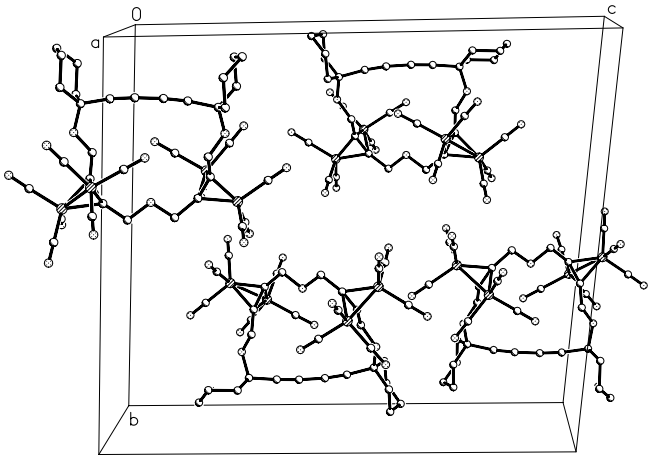


Fig. 4b. Packing in crystal of **4** with respect to the unit cell axis.

In our previous studies using the more extended **1b** as the substrate, we have shown that a 1,3-diyne-diol [viz. $HOR_2C{\equiv}CC{\equiv}CCR_2OH$ (R = H, Me)] can promote an acid-mediated intermolecular ring closure in **1b** leading to both monomeric and dimeric cyclic products [9d]. The reason for the absence of related oligomeric complexes during the reaction of **1a** with (1-HO-*cyclo*-C_6H_{10})$C{\equiv}CC{\equiv}$C(1-HO-*cyclo*-C_6H_{10}) is uncertain, but it would seem likely that the mis-match in size of **1a** with the diynediol employed prevents the facile formation of a monomeric cyclised product. To circumvent the latter pathway, it is possible that **1a** reacts with itself to form dimeric or trimeric cationic derivatives which are larger than the cation derived from **1a** itself and thus enable ring closure by the diynediol to take place (to give **4** or **5**). Alternatively, two molecules of **1a** react with both ends of the diynediol to give initially **6** (or its cationic derivative) which can then further react with itself to give **4** or with more **1a** to give **5**. Unfortunately, the limited quantities isolated of **6** have precluded a more thorough investigation.

3. Conclusions

The capacity of **1a** to undergo self-cyclisation reactions under acidic conditions to give crown-type macrocycles has been exploited with both dimeric (**2**) and trimeric species (**3**) being successfully isolated. In addition, the free cyclohexyl-substituted diyne-diol has been shown to undergo intermolecular cyclisation reactions, a reaction pathway not observed with the corresponding bis{$Co_2(CO)_6$}-coordinated derivative [13]. Furthermore, the products of the cyclisation (**5**, **6**) further illustrate the aptitude of **1a** to self-react in order to accommodate the rigid diyne unit into the macrocycle.

4. Experimental

4.1. General procedures and materials

Unless otherwise stated all experiments were carried out under an atmosphere of dry, oxygen-free argon, using standard Schlenk line techniques and solvents freshly distilled from appropriate drying agent [21]. NMR spectra were recorded in $CDCl_3$ using a Bruker DRX-500 or a AM-400 spectrometer with TMS as an external standard for ^1H and ^{13}C spectra. ^1H–^1H COSY and HMQC NMR experiments were employed to obtain ^1H–^1H and ^1H–^{13}C correlated spectra [22]. Infrared spectra were, unless otherwise stated, recorded in dichloromethane solution in 0.5 mm NaCl solution cells, using a Perkin–Elmer 1710 Fourier Transform Spectrometer. LSI (liquid secondary ion) mass spectra were recorded on a Micromass Autospec high resolution double focusing mass spectrometer at the EPSRC National Mass Spectrometry Service Centre at the University of Wales Swansea. Elemental analyses were performed at the Science Technical Support Unit, London Metropolitan University. Preparative TLC was carried out on 1 mm silica plates prepared at the University of Cambridge. All products are listed in order of decreasing R_f. Tetrafluoroboric acid (48 wt% in diethyl ether) was obtained from Aldrich Chemical Co. and 1,4-bis(1-hydroxycyclohexyl)-1,3-butadiyne from Alfa Aesar; both reagents were used without further purification. [$Co_2(CO)_6$(μ-η^2-$HOCH_2C{\equiv}CCH_2OH$)] (**1a**) was prepared by the literature method [15].

4.2. Reaction of *1a* in the presence of HBF_4

To a stirred solution of **1a** (0.372 g, 1.0 mmol) in dichloromethane (200 ml) at −78 °C was added three drops of 48% $HBF_4 \cdot OEt_2$ under a flow of argon. After stirring overnight at room temperature an excess of $NaHCO_3$ was added. Following filtration through a plug of $MgSO_4$, the solvent was removed on a rotary evaporator. The resulting residue was re-dissolved in the minimum amount of dichloromethane and applied to the base of preparative TLC plates. Repeated elution with hexane gave red-orange crystalline [{$Co_2(CO)_6$}$_3${*cyclo*-μ-η^2:μ-η^2:μ-η^2-$OCH_2C{\equiv}CCH_2OCH_2C{\equiv}CCH_2OCH_2C{\equiv}CCH_2$–}] (**3**) (0.032 g, 9%) and [{$Co_2(CO)_6$}$_2${*cyclo*-μ-η^2:μ-η^2-$OCH_2C{\equiv}CCH_2OCH_2C{\equiv}CCH_2$–}] (**2**) (0.110 g, 30%). Spectroscopic and analytical data for **2**: *Anal*. Calc. $C_{20}H_8O_{14}Co_4$: C, 33.91; H, 1.13. Found: C, 34.01; H, 1.25%. IR (*ν*(CO), cm^{-1}): 2091s, 2059vs, 2029vs; ^1H NMR ($CDCl_3$): *δ* 4.91 (s, 8H, CH_2); $^{13}C\{^1H\}$ NMR: *δ* 199.1 (CO), 90.9 (C≡C), 71.8 (CH_2); LSI mass spectrum: (MW for $C_{20}H_8O_{14}Co_4$: 708): MH^+: 709; M^+-nCO (*n* = 2–4): 653–597. Spectroscopic and analytical data for **3**: *Anal*. Calc. $C_{30}H_{12}O_{21}Co_6$: C, 33.91; H, 1.13. Found: C, 34.16; H, 1.27%. IR (*ν*(CO), cm^{-1}): 2093s, 2061vs, 2054sh, 2029vs; ^1H NMR ($CDCl_3$): *δ* 4.90 (s, 12H, CH_2); HMQC: *δ* 4.90 (72.0); $^{13}C\{^1H\}$ NMR: *δ* 199.2 (CO), 91.3 (C≡C), 72.0 (CH_2); LSI mass spectrum: (MW for $C_{30}H_{12}O_{21}Co_6$: 1062): MNa^+: 1086 (weak); MH^+: 1063 (weak); M^+-nCO (*n* = 2–5,7,10–13): 1006–923, 867, 783–699.

4.3. Reaction of *1a* with (1-HO-cyclo-C_6H_{10}-C≡C-)$_2$ in the presence of HBF_4

To a stirred suspension of (1-HO-*cyclo*-C_6H_{10})$C{\equiv}CC{\equiv}$C(1-HO-*cyclo*-C_6H_{10}) (0.246 g, 1.0 mmol) in dichloromethane (200 ml) was added **1a** (0.372 g, 1.0 mmol) in small portions under a flow of argon. Upon dissolution the mixture was cooled down to −78 °C and three drops of 48% $HBF_4 \cdot OEt_2$ introduced. The resulting deep red solution was allowed to warm to room temperature and stirred overnight. An excess of $NaHCO_3$ was added and the resulting mixture was filtered through a plug of $MgSO_4$. The solvent was removed on a rotary evaporator, the residue re-dissolved in the minimum amount of dichloromethane and applied to the base of preparative TLC plates. Repeated elution with hexane yielded red-orange crystalline [{$Co_2(CO)_6$}$_2${*cyclo*-μ-η^2:μ-η^2-$OCH_2C{\equiv}CCH_2OCH_2C{\equiv}CCH_2O$(*cyclo*-$C_6H_{10}$)$C_2C_2$(*cyclo*-$C_6H_{10}$)–}]

Table 4
Crystallographic and data processing parameters for **2**, **3** and **4**

Complex	**2**	**3**	**4**
Formula	$C_{20}H_8Co_4O_{14}$	$C_{30}H_{12}Co_6O_{21}$	$C_{36}H_{18}Co_4O_{15}.3/4CH_2Cl_2 \cdot 1/8C_6H_{14}$
Molecular weight	707.98	1061.98	1010.77
Crystal size (mm)	$0.14 \times 0.12 \times 0.12$	$0.18 \times 0.14 \times 0.09$	$0.23 \times 0.16 \times 0.05$
Temperature (K)	180(2)	180(2)	180(2)
Crystal system	orthorhombic	monoclinic	triclinic
Space group	*Pbca*	$P2_1/n$	$P\bar{1}$
Lattice parameters			
a (Å)	13.4260(4)	7.7575(2)	8.1123(3)
b (Å)	14.9180(3)	20.4962(5)	21.7497(12)
c (Å)	24.4940(9)	24.1957(6)	24.4716(14)
α (°)	90	90	94.731(2)
β (°)	90	95.730(2)	90.594(4)
γ (°)	90	90	95.305(3)
V (Å^3)	4905.9(3)	3827.88(17)	4283.9(4)
Z	8	4	4
D_{calc} (Mg m^{-3})	1.917	1.843	1.567
$F(000)$	2784	2088	2039
μ(Mo Kα) (mm^{-1})	2.728	2.622	1.680
Reflections collected	24498	25328	28513
Independent reflections	5589	8649	10720
R_{int}	0.0765	0.0763	0.0830
Parameters/restraints	343/0	514/0	1025/13
Final R indices [$I > 2\sigma(I)$]	$R_1 = 0.0383$, $wR_2 = 0.0690$	$R_1 = 0.0395$, $wR_2 = 0.0765$	$R_1 = 0.0645$, $wR_2 = 0.1663$
Final R indices (all data)	$R_1 = 0.0903$, $wR_2 = 0.1727$	$R_1 = 0.0738$, $wR_2 = 0.0884$	$R_1 = 0.1025$, $wR_2 = 0.1912$
Goodness-of-fit on F^2 (all data)	0.967	0.981	1.040

Data in common: graphite-monochromated Mo Kα radiation, $\lambda = 0.71073$ Å; $R_1 = \sum\|F_o| - |F_c\|/\sum|F_o|$, $wR_2 = [\sum w(F_o^2 - F_c^2)^2/\sum w(F_o^2)^2]^{1/2}$, $w^{-1} = [\sigma^2(F_o)^2 + (aP)^2]$, $P = [\max(F_o^2, 0) + 2(F_c^2)]/3$, where a is a constant adjusted by the program; goodness of fit $= [\sum(F_o^2 - F_c^2)2/(n-p)]^{1/2}$ where n is the number of reflections and p the number of parameters.

(**4**) (0.070 g, 15%), red-orange [{$Co_2(CO)_6$}$_3${*cyclo*-μ-η^2:μ-η^2:μ-η^2-$OCH_2C{\equiv}CCH_2OCH_2C{\equiv}CCH_2OCH_2C{\equiv}CCH_2O$(*cyclo*-1-$C_6H_{10}$)$C_2C_2$(*cyclo*-1-$C_6H_{10}$)–}] (**5**) (0.045 g, 10%) and red-orange crystalline [{$Co_2(CO)_6$}$_2$(μ-η^2:μ-η^2-$HOCH_2C{\equiv}CCH_2O$(*cyclo*-1-C_6H_{10})C_2C_2(*cyclo*-1-C_6H_{10})-$OCH_2C{\equiv}CCH_2OH$)] (**6**) (0.031 g, 6%). Spectroscopic and analytical data for **4**: IR (ν(C≡C), cm^{-1}) 2253 w, (ν(CO), cm^{-1}) 2092s, 2054vs, 2028vs; ^{1}H NMR ($CDCl_3$): δ 4.84 (s, 4H, CH_2O), 4.75 (s, 4H, CH_2O), 1.81–1.35 (groups of m, 20H, C_6H_{10}); $^{13}C\{^1H\}$ NMR: δ 199.5 (CO), 95.0, 89.8 ($Co_2(CO)_6$μ-η^2-*C*≡C), 82.6, 75.0 (C≡C), 72.2 (CH_2O), 69.9 (C, C_6H_{10}), 63.6 (CH_2O), 36.4, 25.2, 22.3 (CH_2, C_6H_{10}); LSI mass spectrum: (MW for $C_{36}H_{28}O_{15}Co_4$: 936.34): MNa^+: 960; MH^+: 938; ($M^+ - n$CO, $n = 5$–12): 797–599. Spectroscopic and analytical data for **5**: IR (ν(CO), cm^{-1}) 2093s, 2058vs, 2029vs; ^{1}H NMR ($CDCl_3$): δ 4.82 (s, 4H, CH_2O), 4.75 (s, 4H, CH_2O), 4.64 (s, 4H, CH_2O), 1.80–1.40 (groups of m, 20H, C_6H_{10}); $^{13}C\{^1H\}$ NMR: δ 199.4 (CO), 94.8, 91.6, 89.8 ($Co_2(CO)_6$μ-η^2-*C*≡C), 80.9, 74.4 (C≡C), 72.2, 71.4 (*C*H_2O), 69.9 (C, C_6H_{10}), 63.7 (*C*H_2O), 36.7, 25.2, 22.2 (CH_2, C_6H_{10}); LSI mass spectrum: (MW for $C_{46}H_{32}O_{22}Co_6$: 1290): MNa^+: 1312 (weak); MH^+: 1291 (weak); $M^+ - n$CO, ($n = 7$–18): 1095–786. Spectroscopic and analytical data for **6**: IR (ν(C≡C), cm^{-1}) 2254w, (ν(CO), cm^{-1}) 2092s, 2061s, 2052s, 2029vs.; ^{1}H NMR ($CDCl_3$): δ 4.90 (s, 4H, CH_2O), 4.64 (s, 4H, CH_2O), 1.90–1.40 (groups of m, 20H, C_6H_{10}); $^{13}C\{^1H\}$ NMR: δ 199.8, 199.2 (CO), 92.7, 91.3 ($Co_2(CO)_6$μ-η^2-*C*≡C), 80.8, 74.0 (C, C≡C), 72.1 (CH_2O), 69.6 (C, C_6H_{10}), 63.6 (CH_2O), 36.7, 25.2, 22.1 (CH_2, C_6H_{10}).

4.4. X-ray crystallography

Single crystal X-ray diffraction data for **2**, **3** and **4** were collected using a Nonius-Kappa CCD diffractometer, equipped with an Oxford Cryosystems cryostream and employing Mo Kα ($\lambda = 0.71073$ Å) irradiation from a sealed tube X-ray source. Cell refinement, data collection and data reduction were performed with the programs DENZO [23] and COLLECT [24] and multi-scan absorption corrections were applied to all intensity data with the program SORTAV [25]. All structures were solved and refined with the programs SHELXS-97 and SHELXL-97 [26], respectively. Hydrogen atoms were included in calculated positions (C–H = 0.96 Å) riding on the bonded atom with isotropic displacement parameters set to $1.5U_{eq}$(C) for methyl H atoms and $1.2U_{eq}$(C) for all other H atoms. Details of the data collection, refinement and crystal data are listed in Table 4.

Acknowledgements

We thank the Cambridge Overseas Trust for financial support to V.B.G. The help of the EPSRC mass spectrometry service, Swansea is gratefully acknowledged. Dr. John

E. Davies (Cambridge) is thanked for data collection and for the crystal structure determinations.

Appendix A. Supplementary material

CCDC 656639, 656638 and 656640 contain the supplementary crystallographic data for **2**, **3** and **4**. These data can be obtained free of charge via http://www.ccdc.cam.ac.uk/conts/retrieving.html, or from the Cambridge Crystallographic Data Centre, 12 Union Road, Cambridge CB2 1EZ, UK; fax: (+44) 1223-336-033; or e-mail: deposit @ccdc.cam.ac.uk. Supplementary data associated with this article can be found, in the online version, at doi:10.1016/j.poly.2007.08.038.

References

[1] For reviews see: (a) G.G. Melikyan, K.M. Nicholas, in: P.J. Stang, F. Diederich (Eds.), Modern Acetylene Chemistry, VCH, Weinheim, 1995, pp. 99–139 (Chapter 4);
(b) A.J.M. Caffyn, K.M. Nicholas, in: E.W. Abel, F.G.A. Stone, G. Wilkinson (Eds.), Comprehensive Organometallic Chemistry II, vol. 12, Pergamon Press, Oxford, 1995, pp. 685–702 (Chapter 7);
(c) M.E. Welker, Curr. Org. Chem. 5 (2001) 785;
(d) B.J. Teobald, Tetrahedron 58 (2002) 4133.

[2] See for example: (a) T. Baba, S. Takai, N. Svada, M. Isobe, Synlett (2004) 603;
(b) C. Yenjai, M. Isobe, Tetrahedron 54 (1998) 2509;
(c) S. Hosokawa, M. Isobe, Tetrahedron Lett. 39 (1998) 2609;
(d) S. Hosokawa, M. Isobe, Synlett (1996) 351;
(e) M. Isobe, S. Hosokawa, K. Kira, Chem. Lett. (1996) 473;
(f) R. Saeeng, M. Isobe, Tetrahedron Lett. 40 (1999) 1911.

[3] (a) A.B. Mohamed, J.R. Green, Chem. Commun. (2003) 2936;
(b) S.D.R. Christie, R.J. Davoile, M.R.J. Elsegood, R. Fryatt, R.C.F. Jones, G.J. Pritchard, Chem. Commun. (2004) 2474;
(c) D.D. Diaz, J.M. Betancourt, V.S. Martin, Synlett (2007) 343;
(d) T.F. Jamison, S. Shambayati, W.E. Crowe, S.L. Schreiber, J. Am. Chem. Soc. 119 (1997) 4353;
(e) T.F. Jamison, S. Shambayati, W.E. Crowe, S.L. Schreiber, J. Am. Chem. Soc. 116 (1994) 5505;
(f) T. Nakamura, T. Matsui, K. Tanino, I.J. Kuwajima, Org. Chem. 62 (1997) 3032.

[4] E. Alvaro, M.C. de la Torre, M.A. Sierra, Chem. Commun. (2006) 985.

[5] See for example: (a) R.M. Izatt, K. Pawlak, J.S. Bradshaw, R.L. Breuning, Chem. Rev. 91 (1991) 1721;
(b) L.F. Lindoy, Pure Appl. Chem. 69 (1997) 2179;
(c) F. Neve, M. Ghedini, M. Francescangeil, Liq. Cryst. 21 (1996) 625;
(d) A.J. Blake, A. Taylor, M. Schröder, J. Chem. Soc., Chem. Commun. (1993) 1097.

[6] P.I. Dosa, C. Erben, V.S. Iyer, K.P.C. Vollhardt, I.M. Wasser, J. Am. Chem. Soc. 121 (1999) 10430.

[7] (a) A. Gelling, G.F. Mohmand, J.C. Jeffery, M.J. Went, J. Chem. Soc., Dalton Trans. (1993) 1857;
(b) A. Gelling, J.C. Jeffery, D.C. Povey, M.J. Went, J. Chem. Soc., Chem. Commun. (1991) 349;
(c) F. Demirhan, A. Gelling, S. Irisli, J.C. Jeffery, S.N. Salek, O.S. Senturk, M.J. Went, J. Chem. Soc., Dalton Trans. (1993) 2765;
(d) F. Demirhan, S. Irisli, S.N. Salek, O.S. Senturk, M.J. Went, J.C. Jeffery, J. Organomet. Chem. C30 (1993) 453;
(e) M.J. Went, Adv. Organomet. Chem. 41 (1997) 69;
(f) S.C. Bennett, J.C. Jeffery, M.J. Went, J. Chem. Soc., Dalton Trans. (1994) 3171.

[8] D. Diaz, T. Martin, V.S. Martin, Org. Lett. 3 (2001) 3289.

[9] (a) L.J. Hope-Weeks, M.J. Mays, A.D. Woods, J. Chem. Soc., Dalton Trans. (2002) 1812;
(b) R.C.J. Atkinson, L.J. Hope-Weeks, M.J. Mays, G.A. Solan, J. Organomet. Chem. 692 (2007) 2076;
(c) V.B. Golovko, M.J. Mays, G.A. Solan, J. Organomet. Chem. 692 (2007) 4985;
(d) L.J. Hope-Weeks, M.J. Mays, G.A. Solan, Eur. J. Inorg. Chem. (2007) 3101.

[10] G.G. Melikyan, M.A. Khan, K.M. Nicholas, Organometallics 14 (1995) 2170.

[11] (a) R. Guo, J.R. Green, Chem. Commun. (1999) 2503;
(b) R. Gibe, J.R. Green, G. Davidson, Org. Lett. 5 (2003) 1003;
(c) R. Gibe, J.R. Green, Chem. Commun. (2002) 1550;
(d) R. Guo, J.R. Green, Synlett (2000) 746.

[12] S.C. Bennet, A. Gelling, M.J. Went, J. Organomet. Chem. 439 (1992) 189.

[13] V.B. Golovko, M.J. Mays, A.D. Woods, New J. Chem. 26 (2002) 1706.

[14] V.B. Golovko, L.J. Hope-Weeks, M.J. Mays, M. McPartlin, A.M. Sloan, A.D. Woods, New J. Chem. 28 (2004) 527.

[15] (a) H.W. Sternberg, H. Greenfield, R.A. Friedel, J. Wotiz, R. Markby, I. Wender, J. Am. Chem. Soc. 78 (1956) 120;
(b) M. Gruselle, B. Malezieux, J. Vaissermann, H. Amouri, Organometallics 17 (1998) 2337.

[16] R.S. Dickson, P.J. Fraser, Adv. Organomet. Chem. 12 (1974) 323, and references cited therein.

[17] See for example: (a) V. Calvo-Perez, A. Vega, P. Cortes, E. Spodine, Inorg. Chim. Acta 333 (2002) 15;
(b) H. Schottenberger, J. Lukassser, E. Reichel, A.G. Muller, G. Steiner, H. Kopacka, K. Wurst, K.H. Ongania, K. Kirchner, J. Organomet. Chem. 637 (2001) 558;
(c) D. Gregson, J.A.K. Howard, Acta Crystallogr., Sect.C 39 (1983) 1024;
(d) B. Happ, T. Bartik, C. Zucchi, M.C. Rossi, G. Varadi, G. Szalontai, I.T. Horvath, A. Chiesi-Villa, C. Guastini, Organometallics 14 (1995) 809;
(e) M. Zirngast, C. Marschner, J. Baumgartner, Organometallics 25 (2006) 4897.

[18] R. Gleiter, S. Rittinger, H. Irngartinger, Chem. Ber. 124 (1991) 365.

[19] B.J. Rausch, R. Gleiter, F. Rominger, J. Chem. Soc., Dalton Trans. (2002) 2219.

[20] See for example: M. Kamath, W.H. Kim, L. Li, J. Kumar, S. Tripathy, K.N. Babu, S.S. Talwar, Macromolecules 26 (1993) 5954.

[21] W.L.F. Armarego, D.D. Perrin, Purification of Laboratory Chemicals, 4th ed., Butterworths–Heinemann, London, 1996.

[22] (a) H. Friebolin, Basic One- and Two-Dimensional NMR experiments, Wiley–VCH, New York, 1998;
(b) S. Braun, H.O. Kalinowski, S. Berger, 100 and More Basic NMR Experiments, Wiley–VCH, New York, 1996.

[23] Z. Otwinowski, W. Minor, Methods Enzymol. 276 (1997) 307.

[24] R. Hooft, COLLECT, Nonius BV, Delft, The Netherlands, 1998.

[25] R.H. Blessing, Acta Crystallogr. 51 (1995) 33.

[26] G.M. Sheldrick, SHELXS-97 and SHELXL-97, University of Göttinghen, Göttinghen, Germany, 1997.

Available online at www.sciencedirect.com
ScienceDirect
Polyhedron 27 (2008) 175–180
POLYHEDRON
www.elsevier.com/locate/poly

Three- and four-coordinate copper(I) halide complexes of 2-(diphenylphosphano)benzaldehyde: Dimerization induced by thione-S ligation

M. Mamais [a], P.J. Cox [b], P. Aslanidis [a,*]

[a] Aristotle University of Thessaloniki, Faculty of Chemistry, Inorganic Chemistry Laboratory, P.O. Box 135, GR-541 24 Thessaloniki, Greece
[b] School of Pharmacy, The Robert Gordon University, Schoolhill, Aberdeen AB10 1FR, Scotland, UK

Received 14 June 2007; accepted 5 September 2007
Available online 1 November 2007

Abstract

Reactions of copper(I) halides with 2-(diphenylphosphano)benzaldehyde (PCHO) in 1:2 molar ratio afforded mononuclear complexes of the type $[CuX(PCHO)_2]$, whereas treatment of these compounds with equimolar amounts of pyridine-2-thione or pyrimidine-2-thione gave rise to the formation of mixed-ligand dimers of the formula $[CuX(PCHO)(thione)]_2$. The molecular structures of $[CuCl(PCHO)_2]$, $[CuBr(PCHO)_2]$ and $[CuCl(PCHO)(pymtH)]_2$ have been established by single-crystal X-ray diffraction. The two homoleptic complexes feature a trigonal copper(I) centre with the phosphane acting as a monodentate ligand via the P atom. In the structure of the dimeric mixed-ligand complex each of the two metal centres exhibit a distorted tetrahedral environment with the thione-S atoms acting in a doubly bridging mode.
© 2007 Elsevier Ltd. All rights reserved.

Keywords: Copper(I) halide complexes; 2-(Diphenylphosphano)benzaldehyde; Heterocyclic thiones; Structures

1. Introduction

There is much current interest in copper(I) coordination chemistry, mainly because of its participation in certain biochemical redox reactions [1]. Due to the favorable soft acid–soft base interaction, the chemistry of this closed-shell d^{10} metal ion is largely based upon coordination to ligands containing phosphorus and sulfur donor atoms. Thus, with tertiary phosphanes, copper(I) produces a vast number of complexes which feature an extraordinary stoichiometric and geometrical variety. Many of these complexes have been intensively employed in catalytic processes [2] and some of them were even found to exhibit antitumor activity [3]. As far as the sulfur containing ligands are concerned, heterocyclic thioamides represent a class of compounds that have attracted substantial interest over the last few decades, largely because of their relevance to biological systems [4,5].

Based on the rich chemistry so far found for each of the two aforementioned classes of ligands, we have been interested in examining univalent copper and silver mixed-ligand complexes bearing both neutral heterocyclic thiones and bulky triaryl phosphane ligands with respect to the factors that influence the structural characteristics of these compounds [6,7]. Since our findings showed the coordination number to be related to the steric requirements on the part of the phosphane ligand only [8], we recently focused on phosphanes that may introduce imposed steric effects around the metal centre. In the present work we report on the synthesis and characterization of some Cu^I complexes derived from 2-(diphenylphosphano)benzaldehyde (PCHO). Apart from its steric demands, the selection of PCHO as ligand is further based on its salient feature to bear, besides the "soft" phosphorus donor, a "hard" oxygen atom, thus being capable of behaving as a P,O-chelate [9].

* Corresponding author.
E-mail addresses: p.j.cox@rgu.ac.uk (P.J. Cox), aslanidi@chem.auth.gr (P. Aslanidis).

0277-5387/$ - see front matter © 2007 Elsevier Ltd. All rights reserved.
doi:10.1016/j.poly.2007.09.001

2. Experimental

2.1. Materials and instrumentation

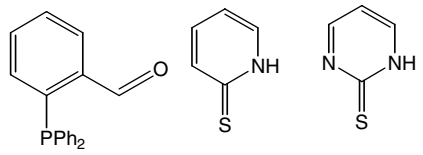
Commercially available copper(I) halides and 2-(diphenylphosphano)benzaldehyde (Aldrich) were used as received while the thiones (Merck) were re-crystallized from hot ethanol prior to their use (Scheme 1). All the solvents were purified by respective suitable methods and allowed to stand over molecular sieves. Infra-red spectra in the region of 4000–250 cm^{-1} were obtained in KBr discs with Perkin–Elmer FT-IR Spectrum 1 spectrophotometer, while a Perkin–Elmer-Hitachi 200 spectrophotometer was used to obtain the electronic absorption spectra. ^1H NMR spectra were recorded on a Brucker AM 300 spectrometer at 298 K with positive chemical shifts given downfield from internal TMS. Melting points were measured in open tubes with a STUART scientific instrument and are uncorrected.

2.2. Crystal structure determination

Single crystals suitable for crystal structure analysis were obtained by slow evaporation of acetonitrile/methanol solutions of the complexes at room temperature. X-ray diffraction data were collected on an Enraf-Nonius Kappa CCD area-detector diffractometer. The programs DENZO [10] and COLLECT [11] were used in data collection and cell refinement. Details of crystal and structure refinement are shown in Table 1. The structures were solved using program SIR97 [12] and refined with program SHELX-97 [13]. Molecular plots were obtained with program ORTEP-3 [14].

2.3. Synthesis of complexes **1–3**

A suspension of 0.25 mmol of copper(I) halide (24.75 mg for CuCl, 35.85.7 mg for CuBr, 47.6 mg for CuI) in 30 cm^3 of dry acetonitrile was stirred at 50 °C until a clear yellow solution was formed. To this, a solution of 145 mg (0.5 mmol) of 2-(diphenylphosphano)benzaldehyde in 25 cm^3 of dry acetonitrile was added and the mixture was stirred for 2 h at 50 °C. The resulting bright yellow solution was filtered off and left to evaporate at ambient. The microcrystalline solid, which was deposited upon standing for several days, was filtered off and dried *in vacuo*.



PCHO py2SH pymtH

Scheme 1. The phosphane and the heterocyclic thiones used as ligands with their abbreviations.

2.3.1. *[CuCl(PCHO)$_2$] (**1**)*

Orange crystals (21 mg, 12%), m.p. 232 °C; *Anal.* Calc. for $C_{38}H_{30}ClCuO_2P_2$: C, 67.16; H, 4.45. Found: C, 67.24; H, 4.58%. IR (cm^{-1}): 3054m, 2824w, 2761m, 1696vs, 1668vs, 1583m, 1561m, 1481s, 1392m, 1295m, 1200vs, 1096s, 864m, 764m, 748vs, 696vs, 527vs, 508vs, 462s. ^1H NMR ($CDCl_3$, δ ppm): 9.98 (s, 1H, –CHO), 7.83 (d, 1H, $J_{H-H} = 7.3$ Hz, H^3–PhCHO), 7.58 (t, 1H, $J_{H-H} = 7.3$ Hz, H^5–PhCHO), 7.49 (t, 1H, $J_{H-H} = 7.3$ Hz, H^4–PhCHO), 7.40 (m, 4H, Ph, $H^{2,6}$), 7.26 (m, 6H, Ph, $H^{2,6}$), 6.99 (d, $J_{H-H} = 7.3$ Hz, H^6-PhCHO).

2.3.2. *[CuBr(PCHO)$_2$] (**2**)*

Orange crystals (45 mg, 24%), m.p. 230 °C; *Anal.* Calc. for $C_{38}H_{30}BrCuO_2P_2$: C, 63.04; H, 4.18. Found: C, 62.98; H, 4.25%. IR (cm^{-1}): 3061m, 2839m, 2745m, 1697s, 1676vs, 1560s, 1479s, 1435vs, 1393m, 1294s, 1203vs, 1094s, 1091vs, 846vs, 760vs, 749vs, 703vs, 691vs, 676s, 529vs, 509vs, 462s. ^1H NMR ($CDCl_3$, δ ppm): 9.95 (s, 1H, –CHO), 7.84 (d, 1H, $J_{H-H} = 7.3$ Hz, H^3–PhCHO), 7.58 (t, 1H, $J_{H-H} = 7.3$ Hz, H^5–PhCHO), 7.50 (t, 1H, $J_{H-H} = 7.3$ Hz, H^4–PhCHO), 7.40 (m, 4H, Ph, $H^{2,6}$), 7.26 (m, 6H, Ph, $H^{2,6}$), 6.99 (d, $J_{H-H} = 7.3$ Hz, H^6-PhCHO).

2.3.3. *[CuI(PCHO)$_2$] (**3**)*

Yellow crystals (33 mg, 17%), m.p. 241 °C; *Anal.* Calc. for $C_{38}H_{30}ClCuO_2P_2$: C, 59.19; H, 3.92. Found: C, 60.09; H, 4.01%. IR (cm^{-1}): 3058m, 2839m, 2744m, 1697s, 1675vs, 1560m, 1479s, 1435vs, 1385m, 1294s, 1203vs, 1094m, 1091s, 847s, 759vs, 744s, 703s, 691vs, 677s, 529vs, 509vs, 462s. ^1H NMR ($CDCl_3$, δ ppm): 9.95 (s, 1H, –CHO), 7.88 (d, 1H, $J_{H-H} = 7.3$ Hz, H^3–PhCHO), 7.60 (t, 1H, $J_{H-H} = 7.3$ Hz, H^5–PhCHO), 7.52 (t, 1H, $J_{H-H} = 7.3$ Hz, H^4–PhCHO), 7.38 (m, 4H, Ph, $H^{2,6}$), 7.24 (m, 6H, Ph, $H^{2,6}$), 7.00 (d, $J_{H-H} = 7.3$ Hz, H^6-PhCHO).

2.4. Synthesis of complexes **4–6**

To a stirred solution of 0.25 mmol of copper(I) halide (24.75 mg for CuCl, 35.85.7 mg for CuBr) was suspended in 60 cm^3 of dry acetonitrile, solid 2-(diphenylphosphano)benzaldehyde (145 mg, 0.5 mmol) was suspended and the mixture was stirred for 2 h at 50 °C. The resulting clear solution was then treated with the appropriate thione (0.5 mmol) dissolved in a small amount (~20 cm^3) of methanol. The new reaction mixture was stirred for additional two hours at 50 °C and then was filtered off and left several days at ambient to provide a yellow microcrystalline product.

2.4.1. *[CuBr(PCHO)(py2SH)]$_2$ (**4**)*

Yellow crystals (32 mg, 23%), m.p. 179 °C; *Anal.* Calc. for $C_{48}H_{40}Br_2Cu_2N_2O_2P_2S_2$: C, 52.90; H, 3.70, N: 2.57. Found: C, 64.47; H, 4.81; N, 3.47%. IR (cm^{-1}): 3049m, 2965m, 2901m, 1691vs, 1606s, 1575vs, 1505s, 1436vs, 1366s, 1261s, 1200s, 1125vs, 1094s, 1080s, 996s, 822m, 747vs, 695vs, 521vs, 483s, 443m. ^1H NMR ($CDCl_3$, δ

Table 1
Crystal data and structure refinements for $[CuCl(PCHO)_2]$ (**1**), $[CuBr(PCHO)_2]$ (**2**) and $[CuCl(PCHO)(pymtH)]_2$ (**5**)

	1	**2**	**5**
Molecular formula	$C_{38}H_{30}ClCuO_2P_2$	$C_{38}H_{30}BrCuO_2P_2$	$C_{46.13}H_{38}Cl_2Cu_2N_4O_{2.13}P_2S_2$[a]
Formula weight	679.55	724.02	1006.63
Temperature (K)	120(2)	120(2)	120(2)
Wavelength (Å)	0.71073	0.71073	0.71073
Crystal system	monoclinic	monoclinic	monoclinic
Space group	$P2_1/n$	$C2/c$	$P2_1/n$
a (Å)	11.55790(10)	18.1960(6)	14.6594(3)
b (Å)	17.1727(3)	9.8615(3)	12.0067(3)
c (Å)	16.3545(3)	19.6831(8)	24.9499(6)
α (°)	90	90	90
β (°)	101.5490(10)	116.936(1)	91.9370(10)
γ (°)	90	90	90
Volume (Å^3)	3184.03(9)	3148.76(16)	4388.95(18)
Z	4	4	4
D_{calc} (Mg/m^3)	1.418	1.527	1.523
Absorption coefficient (mm^{-1})	0.904	2.099	1.303
$F(000)$	1400	1472	2056
Crystal size (mm)	$0.40 \times 0.25 \times 0.18$	$0.52 \times 0.24 \times 0.20$	$0.46 \times 0.36 \times 0.30$
θ Range for data collection (°)	3.09–27.49	2.42–27.61	3.18–27.49
Index ranges	$-14 \leqslant h \leqslant 14$, $-22 \leqslant k \leqslant 22$, $-21 \leqslant l \leqslant 21$	$-23 \leqslant h \leqslant 23$, $-12 \leqslant k \leqslant 12$, $-25 \leqslant l \leqslant 25$	$-19 \leqslant h \leqslant 19$, $-15 \leqslant k \leqslant 15$, $-32 \leqslant l \leqslant 24$
Reflections collected	36828	28527	47805
Independent reflections	7247 [$R_{int} = 0.0439$]	3639 [$R_{int} = 0.0488$]	10023 [$R_{int} = 0.0544$]
Completeness to θ	27.49°, 99.4%	27.61°, 99.5%	27.49°, 99.4%
Data/restraints/parameters	7247/0/397	3639/0/200	10023/0/550
Maximum and minimum transmission	0.8541 and 0.6368	0.6789 and 0.5233	0.6958 and 0.5495
Refinement method	full-matrix least square on F^2	full-matrix least square on F^2	full-matrix least square on F^2
Goodness-of-fit on F^2	1.031	1.044	1.018
Final R indices [$I > 2\sigma(I)$]	$R_1 = 0.0330$, $wR_2 = 0.0779$	$R_1 = 0.0261$, $wR_2 = 0.0638$	$R_1 = 0.0344$, $wR_2 = 0.0768$
R indices (all data)	$R_1 = 0.0526$, $wR_2 = 0.0845$	$R_1 = 0.0352$, $wR_2 = 0.0677$	$R_1 = 0.0529$, $wR_2 = 0.0829$
Final weighting scheme	calc $w = 1/[\sigma^2(F_o^2) + (0.0438P)^2 + 0.7341P]$ where $P = (F_o^2 + 2F_c^2)/3$	calc $w = 1/[\sigma^2(F_o^2) + (0.0358P)^2 + 2.9145P]$ where $P = (F_o^2 + 2F_c^2)/3$	calc $w = 1/[\sigma^2(F_o^2) + (0.0351P)^2 + 2.8449P]$ where $P = (F_o^2 + 2F_c^2)/3$
Largest difference in peak and hole (e Å^{-3})	0.406 and −0.522	0.305 and −0.520	0.454 and −0.419

[a] Decimal points for the number of C and O atoms due to a small impurity of doubly CHO-substituted phosphane.

ppm): 14.08 (br, 1H, NH), 10.35 (s, 1H, –CHO), 7.88 (d, 1H, $J_{H-H} = 7.3$ Hz, H^3–PhCHO), 7.60 (t, 1H, $J_{H-H} = 7.3$ Hz, H^5–PhCHO), 7.52 (t, 1H, $J_{H-H} = 7.3$ Hz, H^4–PhCHO), 7.36–7.28 (m, 10H, PPh), 7.00 (d, $J_{H-H} = 7.3$ Hz, H^6-PhCHO), 7.00 (t, 1H, H^3_{py2SH}), 6.89 (t, 1H, H^5_{py2SH}).

2.4.2. *[CuCl(PCHO)(pymtH)]$_2$ (**5**)*

Yellow crystals (25 mg, 20%), m.p. 196 °C; *Anal.* Calc. for $C_{46}H_{38}Cl_2Cu_2N_4O_2P_2S_2$: C, 55.09; H, 3.81, N: 5.59. Found: C, 54.98; H, 3.91; N, 5.66%. IR (cm^{-1}): 3054m, 2827m, 2632m, 1690vs, 1600s, 1572vs, 1479s, 1425s, 1326vs, 1196s, 1167vs, 1043s, 984s, 762s, 747s, 696vs, 528vs, 501s, 481s, 457s.

2.4.3. *[CuBr(PCHO)(pymtH)]$_2$ (**6**)*

Yellow crystals (29 mg, 21%), m.p. 191 °C; *Anal.* Calc. for $C_{46}H_{38}Br_2Cu_2N_4O_2P_2S_2$: C, 50.60; H, 3.51, N: 5.13. Found: C, 50.60; H, 3.48; N, 5.13%. IR (cm^{-1}): 3063m, 2925w, 2853w, 1677vs, 1603vs, 1584vs, 1568vs, 1474s, 1425s, 1321vs, 1210s, 1173vs, 989s, 973s, 751s, 743s, 698s, 530s, 504s, 462s.

3. Results and discussion

3.1. Synthesis

Treatment of 2-(diphenylphosphano)benzaldehyde and CuX (X = Cl, Br, I) resulted in the formation of orange-yellow colored crystalline compounds formulated as $[CuX(PCHO)_2]$ (compounds **1**–**3**), regardless of the molar ratio (1:1 or 2:1) applied. Aiming to obtain phosphane/thione mixed-ligand complexes, we further treated the solutions of these precursors, skipping their isolation, with a methanolic solution of 1 equiv. of a heterocyclic thione. Stirring of such a mixture at 50 °C gradually caused slight

darkening of the solution, from which, on slow evaporation, microcrystalline or powdery solids were deposited. These proved, however, to correspond to the desired pure compounds only in a few cases, although the described one-top two-step synthetic procedure applied has already produced a number of such copper(I) halide derivatives, virtually for any thione and copper(I) halide applied. In particular, pyridine-2-thione (py2SH) and pyrimidine-2-thione (pymtH) yielded small amounts of well-formed bright orange crystals, which could be satisfactory defined as compounds **4**–**6**, but inseparable mixtures of two or more products resulted in all the other cases. All prepared compounds are air stable diamagnetic solids, moderately soluble in acetonitrile, chloroform and acetone. Their solutions in common organic solvents are non-conducting.

3.2. Spectroscopy

The room temperature ^{1}H NMR spectra of the complexes under investigation, recorded in deuterated chloroform, are dominated by the presence of two separated multiplets in the regions $\delta = 7.40$ and $\delta = 7.25$ ppm attributed to the resonances of the non-substituted phenyl rings of the PCHO ligand. With respect to the complex multiplet assigned to the PPh_2 resonances of the un-coordinated phosphane, this splitting indicates coordination to the metal through the P atom which causes a typical upfield shift of the *ortho*-positioned protons by ca. 0.20 ppm. The resonances attributed to the formylated phenyl ring appear as well separated signals assignable to the discrete aromatic protons only for the thione-free compounds **1**–**3**, whereas for compounds **4**–**6** the extent of overlapping makes assignments of the splitting pattern for the individual phosphane and thione resonances very difficult.

The infrared spectra of compounds **1**–**6**, recorded in the range 4000–250 cm^{-1} display strong vibrational phosphane bands, which remain practically unshifted upon coordination. In addition, the spectra of the mixed-ligand complexes **4**–**6** contain the expected characteristic ''thioamide bands'', with shifts due to coordination indicative of an exclusive S-coordination mode. As expected, upon coordination no significant shift is noticed for the ν(C=O) vibration of the PCHO ligand.

3.3. X-ray structural investigations

The X-ray crystal structures of $[CuCl(PCHO)_2]$ (**1**), $[CuBr(PCHO)_2]$ (**2**) and $[CuCl(PCHO)(pymtH)]_2$ (**5**) (details of crystal and structure refinement are shown in Table 1) corroborate the spectroscopic results discussed above. Tables 2 and 3 list selected distances and angles of these complexes.

Compounds **1** and **2** crystallize in the monoclinic space group $P2_1/n$ and $C2/c$ respectively, both with four discrete formula units in the unit cell. Likewise, compound **5** crystallizes in the monoclinic space group $P2_1/n$ with four discrete formula units in the unit cell. It should be mentioned that there is a small impurity in the structure of **5**, indicated by the presence of a formyl substituent attached to C(25), apparently due to a small amount of doubly formylated phosphane. Hence a population parameter of 0.13 corresponds to C(47), O(3) and H(47), whereas the population parameter of H(25) is 0.87 (see also Table 1).

Table 2
Selected bond lengths (Å) and angles (°) for **1** and **2**

Compound **1**		Compound **2**	
Cu(1)–P(1)	2.2266(5)	Cu(1)–P(1)	2.2366(4)
Cu(1)–Cl(1)	2.2448(5)	Cu(1)–Br(1)	2.3364(4)
Cu(1)–P(2)	2.2486(5)	Cu(1)–P(1)[a]	2.2366(4)
P(1)–Cu(1)–P(2)	130.17(2)	P(1)–Cu(1)–P(1)[a]	123.53(2)
Cl(1)–Cu(1)–P(2)	108.350(18)	Br(1)–Cu(1)–P(1)	118.234(12)
P(1)–Cu(1)–Cl(1)	120.177(19)	P(1)[I]–Cu(1)–Br(1)	118.234(12)

[a] Symmetry transformations used to generate equivalent atoms: $-x+1$, y, $-z+1/2$.

Table 3
Selected bond lengths (Å) and angles (°) for **5**

Cu(1)–Cl(1)	2.3350(6)	Cu(2)–S(1)	2.3608(6)
Cu(1)–P(1)	2.2506(6)	Cu(2)–S(2)	2.4227(6)
Cu(1)–S(2)	2.3469(6)	S(1)–C(20)	1.722(2)
Cu(1)–S(1)	2.4025(6)	S(2)–C(43)	1.723(2)
Cu(2)–P(2)	2.2387(6)	Cu(1)···Cu(2)	2.9766(4)
Cu(2)–Cl(2)	2.3279(6)		
S(2)–Cu(1)–S(1)	103.23(2)	P(2)–Cu(2)–S(2)	113.46(2)
P(1)–Cu(1)–S(2)	112.33(2)	Cl(2)–Cu(2)–S(2)	99.89(2)
P(1)–Cu(1)–S(1)	123.13(2)	S(1)–Cu(2)–S(2)	102.23(2)
P(1)–Cu(1)–Cl(1)	105.12(2)	C(20)–S(1)–Cu(2)	113.18(7)
Cl(1)–Cu(1)–S(1)	100.19(2)	C(20)–S(1)–Cu(1)	99.62(7)
S(2)–Cu(1)–Cl(1)	112.32(2)	C(43)–S(2)–Cu(1)	110.94(7)
P(2)–Cu(2)–Cl(2)	118.93(2)	C(43)–S(2)–Cu(2)	110.08(7)
P(2)–Cu(2)–S(1)	111.39(2)	Cu(1)–S(2)–Cu(2)	77.211(18)
Cl(2)–Cu(1)–S(1)	109.20(2)	Cu(2)–S(1)–Cu(1)	77.344(18)
Hydrogen bridges			
N(2)–H(2)	0.8800	Cl(2)···N(2)	3.0650(18)
NH(2)–Cl(2)	2.2000	Cl(2)···H(2)–N(2)	168.8
N(4)–H(4)	0.8800	Cl(12)···N(4)	3.0419(18)
NH(4)–Cl(1)	2.1600	Cl(1)···H(4)–N(4)	179.5

By comparison to the vast number of known four-coordinate species, examples of three coordination among Cu^{I} complexes are far less common, mostly represented by cations of the type CuL_3^+. The more rarely reported neutral complexes of the formula CuL_2X are usually formed by bulky ligands such as triarylphosphanes or aromatic amines. A literature search of published data on Cu^{I} complexes of 2-(diphenylphosphano)benzaldehyde revealed that there were structures of six cationic species known [15,16], featuring tetrahedral or trigonal planar environment around Cu^{I}, thus the three structures presented here are the first examples of neutral Cu^{I} complexes bearing PCHO.

The crystal structures of compounds **1** and **2** (Figs. 1 and 2) are quite similar having in common trigonal coordination of the copper(I) centre. Nevertheless, considering the interligand bond angles involving the central metal atom in the two structures described here, there are some

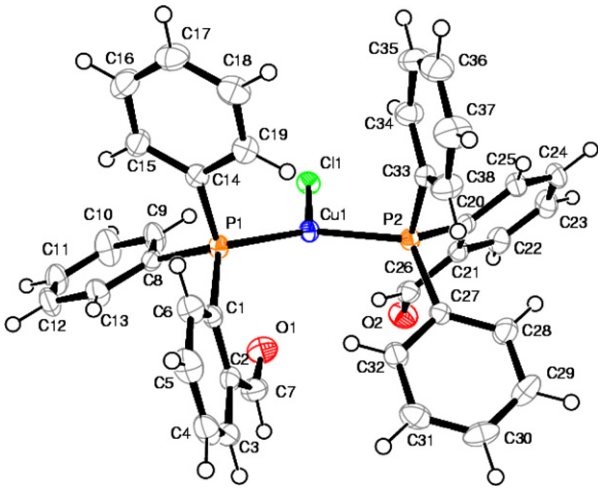


Fig. 1. A view of compound **1** with atom labels. Displacement ellipsoids are shown in the 50% probability level.

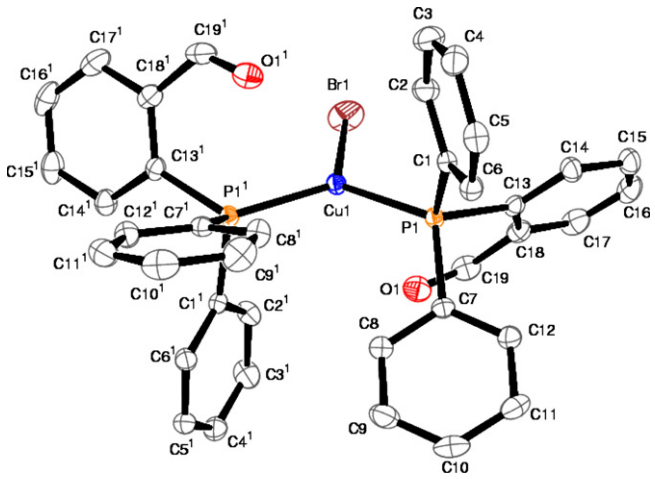


Fig. 2. A view of compound **2** with atom labels. Displacement ellipsoids are shown in the 50% probability level.

obvious differences. Thus, angular deviations from the ideal trigonal value in **1** are remarkable but not at all unexpected, at least regarding the appropriate opening up of the angle between the sterically demanding groups of the PHCO units. The sum of the three angles around Cu is 358.72°, and the Cu atom is displaced from the basal trigonal plane by 0.1465(3) Å. Another remarkable feature of **1** is the different orientation of the formyl groups of the two PCHO ligands, one of them having oriented its oxygen atom toward the copper atom to a distance of 2.804(2) Å, whereas the second one is twisted outwards. This short Cu(1)···O(1) contact is less than the sum of the van der Waal radii (1.40 (Cu) + 1.52 (O) = 2.92Å) and may be considered as a dipole–ion interaction [16,17]. The carbon–oxygen bond distance of the formyl group in the two individual PCHO units remains essential the same. Moreover, the formyl groups are both essentially coplanar with the C atoms of the attached phenyl rings.

Contrary to that, **2** exhibits a symmetric arrangement of the two PCHO units. Here the trigonal environment within

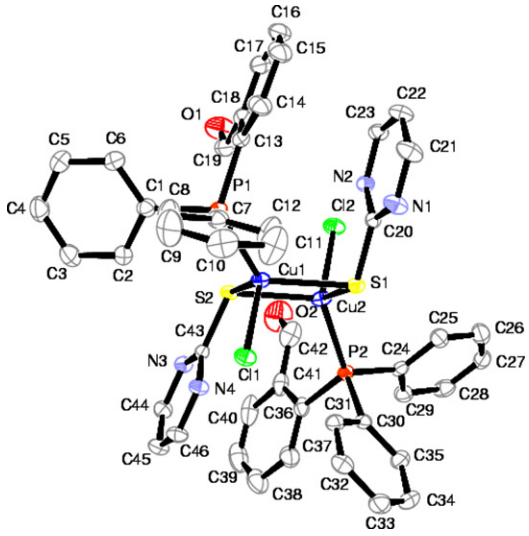


Fig. 3. A view of compound **5** with atom labels. Displacement ellipsoids are shown in the 50% probability level.

the exactly planar CuP_2Br core can be considered as essentially regular with the largest P–Cu–P angle deviating only by 3.5° from the ideal trigonal expectation of 120°. The Cu–P bond distances of 2.2266(5) and 2.2448(5) Å in **1** and 2.2366(4) Å in **2** are comparable to those found in PCHO ligated cationic Cu^{I} complexes such as $[Cu(PCHO)_2(CH_3CN)]BF_4$ or $[Cu(PCHO)_3]BF_4$ [15]. Moreover the PCHO units have both their formyl groups oriented toward the copper atom with a short Cu···O separation of 3.002(2) Å. As a further difference between the two structures, the co-planarity within the formyl groups and the C atoms of the attached phenyl rings in **2** is substantially distorted.

In the dimeric complex **5** each copper atom displays a distorted tetrahedral environment formed by one P atom from PCHO, one Br atom and two inequivalent bridging S atoms from the thione ligands. Within the essentially planar Cu_2S_2 central core respective bond lengths and angles around the two copper atoms differ slightly. This is in contrast to other related structures with simple monodentate arylphosphane ligands like triphenylphosphane or tri-tolylphosphanes, where doubly bridging S atoms were found to generate a Cu_2S_2 rhombus with the dimeric molecule generally having a crystallographic centre of symmetry. Nonetheless, this is another example of dicopper(I) halide complex comprising a neutral thione ligand coordinated in a μ_2-S bridging mode, which is in line with our assumption that primary control of the coordination behavior (terminal or bridging) of the thione and halide ligands can be achieved by the choice of the halide ligand, with the "soft" iodide being capable to serve as bridging ligand rather than the "hard" chloride which prefers, at least in the presence of a "soft" thione-S donor atom, the terminal coordination mode [18] (Fig. 3).

An interesting structural feature within molecule **5** is the almost parallel orientation of each of the six-membered pyrimidine rings relative to the formylated phenyl ring of the respective PCHO unit. The dihedral angle between the

C13–C18 and N1,N2,C20–C23 rings is 12.68(8)° and the dihedral angle between rings C36–C41 and N3,N4,C43–C46 is 16.12(5)°. The respective stacking distances between ring centroids are 3.743(1) and 3.728(1) Å, respectively, suggesting the presence of significant $\pi\cdots\pi$ interactions [19]. These may be considered to significantly contribute, together with the intramolecular hydrogen bonds (see Table 3), to the alignment of the molecule in the crystalline state.

4. Conclusion

The aim of this work was the study of the coordination capability of 2-(diphenylphosphano)benzaldehyde (PCHO) toward copper(I) halides. We have found that PCHO acts as a monodentate, coordinating to the metal exclusively via the "soft" phosphorus atom, whereas no bonding interaction could be proposed for the formyl group, despite the observed marked orientation of its oxygen atom towards the copper centre. Thus, the resulting complexes of composition $[CuX(PCHO)_2]$, are monomers with the copper atom in a fairly trigonal environment. These compounds prove to be good precursors for the preparation of other derivatives; in the course of the present study these are chosen for the synthesis of mixed-ligand dimeric complexes, which contain, besides the PCHO unit, a heterocyclic thioamide. The structure of the mixed-ligand complex presented here, comprising the neutral thione ligand coordinated in a μ_2-S bridging mode, confirms once more our assumption that primary control of the coordination behavior (terminal or bridging) of the thione and halide ligands in such dimers can be achieved by the choice of the halide.

Acknowledgement

We thank the EPSRC X-ray crystallography service at the University of Southampton for collecting the X-ray data.

Appendix A. Supplementary material

CCDC 612610, 612611 and 612609 contain the supplementary crystallographic data for **1**, **2** and **5**. These data can be obtained free of charge via http://www.ccdc.cam.ac.uk/conts/retrieving.html, or from the Cambridge Crystallographic Data Centre, 12 Union Road, Cambridge CB2 1EZ, UK; fax: (+44) 1223-336-033; or e-mail: deposit@ccdc.cam.ac.uk. Supplementary data associated with this article can be found, in the online version, at doi:10.1016/j.poly.2007.09.001.

References

[1] K.B. Karlin, J. Zubieta (Eds.), Copper Coordination Chemistry. Biochemical and Inorganic Perspectives, Adenine, New York, 1983.
[2] (a) R.J. Puddephatt, Chem. Soc. Rev. 12 (1983) 99;
(b) F.A. Cotton, K.R. Dunbar, M.G. Verbruggen, J. Am. Chem. Soc. 109 (1987) 5498;
(c) R.V. Kiress, R. Eisenberg, Inorg. Chem. 28 (1989) 3372.
[3] S.J. Bernes-Price, R.K. Johnson, C.K. Mirabelli, L.F. Faucette, F.L. McCabe, P.J. Sadler, Inorg. Chem. 26 (1987) 3383, and references therein.
[4] B. Krebs, G. Henkel, Angew. Chem., Int. Ed. Engl. 30 (1991) 769.
[5] (a) E.S. Raper, Coord. Chem. Rev. 61 (1985) 115;
(b) E.S. Raper, Coord. Chem. Rev. 129 (1994) 91;
(c) E.S. Raper, Coord. Chem. Rev. 153 (1996) 199;
(d) J.A. Garcia-Vazquez, J. Romero, A. Sousa, Coord. Chem. Rev. 193 (1999) 691;
(e) P.D. Akrivos, Coord. Chem. Rev. 213 (2001) 181.
[6] P. Aslanidis, S. Divanidis, P.J. Cox, P. Karagiannidis, Polyhedron 24 (2005) 853, and references therein.
[7] (a) P. Karagiannidis, P. Aslanidis, D.P. Kessissoglou, B. Krebs, M. Dartmann, Inorg. Chim. Acta 156 (1989) 47;
(b) S.K. Hadjikakou, P. Aslanidis, P. Karagiannidis, A. Hountas, A. Terzis, Inorg. Chim. Acta 184 (1991) 161;
(c) S.K. Hadjikakou, P. Aslanidis, P.D. Akrivos, P. Karagiannidis, B. Kojic-Prodic, M. Luic, Inorg. Chim. Acta 197 (1992) 31.
[8] (a) S.K. Hadjikakou, P. Aslanidis, P. Karagiannidis, D. Mentzafos, A. Terzis, Inorg. Chim. Acta 186 (1991) 199;
(b) S.K. Hadjikakou, P. Aslanidis, P. Karagiannidis, A. Aubry, S. Skoulika, Inorg. Chim. Acta 193 (1992) 129.
[9] (a) X. Chen, F.J. Femia, J.W. Babich, J. Zubieta, Inorg. Chim. Acta 351 (2001) 147;
(b) C.P. Lenges, M. Brookhart, P.S. White, Angew. Chem., Int. Ed. 38 (1999) 552;
(c) W.-Y. Yeh, C.-S. Lin, S.-M. Peng, G.-H. Lee, Organometallics 23 (2004) 917;
(d) T.B. Tauchfuss, J. Am. Chem. Soc. 101 (1979) 1045.
[10] Z. Otwinowski, W. Minor, in: C.W. CarterJr., R.M. Sweet (Eds.), Macromolecular Crystallography, Part A, Methods in Enzymology, Vol.276, Academic Press, 1997, p. 307.
[11] R. Hooft, COLLECT Data Collection Software, Nonius B.V., 1998.
[12] A. Altomare, M.C. Burla, M. Camalli, G.L. Cascarano, C. Giacovazzo, A. Guagliardi, A.G.G. Moliterni, G. Polidori, R. Spagna, J. Appl. Crystallogr. 32 (1999) 115.
[13] G.M. Sheldrick, SHELXL-97. Program for Crystal Structure Analysis (Release 97-2), University of Goettingen, Germany, 1997.
[14] L.J. Farrugia, J. Appl. Crystallogr. 30 (1997) 565.
[15] W.-Y. Yeh, Y.-C. Liu, S.-M. Peng, G.-H. Lee, Inorg. Chim. Acta 358 (2005) 1987.
[16] W.-Y. Yeh, G.-H. Lee, S.-M. Peng, Inorg. Chim. Acta 359 (2006) 659.
[17] J.N. Murrell, S.F.A. Kettle, J.M. Tedder, The Chemical Bond, second ed., Wiley, New York, 1985.
[18] S.K. Hadjikakou, C.D. Antoniadis, P. Aslanidis, P.J. Cox, A.C. Tsipis, Eur. J. Inorg. Chem. (2005) 1442, and references therein.
[19] X.-L. Zhao, Q.-M. Wang, T.C.W. Mak, Inorg. Chem. 42 (2003) 7872.

Available online at www.sciencedirect.com
ScienceDirect
Polyhedron 27 (2008) 181–186
POLYHEDRON
www.elsevier.com/locate/poly

Synthesis and spectral studies of the mesogenic Schiff-base, *N*,*N*′-di-(4′-pentyloxybenzoate) salicylidene-1,8-diamino-3,6-dioxaoctane and crystal structure of the Zn(II) complex

Angad Kumar Singh [a], Sanyucta Kumari [a], K. Ravi Kumar [b], B. Sridhar [b], T.R. Rao [a,*]

[a] *Department of Chemistry, Banaras Hindu University, Varanasi 221 005, India*
[b] *Indian Institute of Chemical Technology, Hyderabad, India*

Received 27 June 2007; accepted 5 September 2007
Available online 18 October 2007

Abstract

A novel Schiff-base, *N*,*N*′-di-(4′-pentyloxybenzoate)salicylidene-1,8-diamino-3,6-dioxaoctane (H_2L_4) with the mesogenic phase, *nematic droplets*, was prepared and its structure studied by elemental analyses and mass, NMR and IR spectra. The di-negative tetra-dentate bonding of the Schiff-base in the non-mesogenic complex, [ZnL_4], as implied on the basis of IR and NMR spectral data, was confirmed in the crystal structure of the monomeric tetrahedral Zn(II) complex. As per the crystal structure of the complex, the dinegative species of the ligand, L_4^{2-}, coordinates to the Zn(II) ion through two phenolate oxygens and two azomethine nitrogens, rendering the overall geometry around Zn(II) to distorted tetrahedron.
© 2007 Elsevier Ltd. All rights reserved.

Keywords: Mesogenic Schiff-base; Tetrahedral zinc(II) complex; Crystal structure; NMR spectra

1. Introduction

Liquid crystals with transition metal core groups are increasingly a topic of investigation since metals can impart useful shapes and properties which are not easily produced in totally organic liquid crystals [1]. A major distinction between metallomesogens and most organic mesogens is the greater tendency in the former type to exhibit intermolecular dative coordination in the solid state [1]. However, it should be noted that rigid tetrahedral molecules usually seem to prevent mesophase formation [2]. As a part of our investigation on systematic structural and spectroscopic studies of 3d metal complexes of a series of mesogenic organic Schiff-bases, we report here, synthesis and spectroscopic studies on the mesogenic Schiff-base, *N*,*N*′-di-(4′-pentyloxybenzoate)salicylidene-1,8-diamino-3,6-dioxaoctane (H_2L_4) and crystal structure of the corresponding Zn(II) complex. We have observed that despite the mesogenic behaviour of the [CuL_4] (unpublished work), the zinc homologue, [ZnL_4], does not exhibit liquid crystalline properties presumably due to the tetrahedral coordination of the latter [2].

2. Experimental

2.1. Materials

All reagents were purchased from the following and used as received: 4-hydroxy benzoic acid, 1-bromopentane, 2,4-dihydroxy benzaldehyde, *N*,*N*′-dicyclohexylcarbodiimide (DCC), *N*,*N*-dimethylaminopyridine (DMAP) and 1,8-diamino-3,6-dioxaoctane from Sigma–Aldrich, USA, and $Zn(OAc)_2 \cdot 2H_2O$ and KOH from Merck. The solvents received from commercial sources were used as such without further purification and were dried using standard methods [3] when required.

* Corresponding author. Tel.: +91 542 230726; fax: +91 542 2368127.
E-mail address: drtrrao@gmail.com (T.R. Rao).

0277-5387/$ - see front matter © 2007 Elsevier Ltd. All rights reserved.
doi:10.1016/j.poly.2007.09.002

2.2. Synthesis

The synthesis of *N*,*N*′-di-(4′-pentyloxybenzoate)-salicylidene-1,8-diamino-3,6-dioxaoctane (H_2L_4) (**3**), was achieved by proceeding through three major steps, viz., alkylation of 4-hydroxy benzoic acid with *n*-pentyl bromide, followed by esterification and Schiff-base formation; all the experimental details are given in Scheme 1.

2.2.1. Preparation of 4-pentyloxybenzoic acid (*1*)

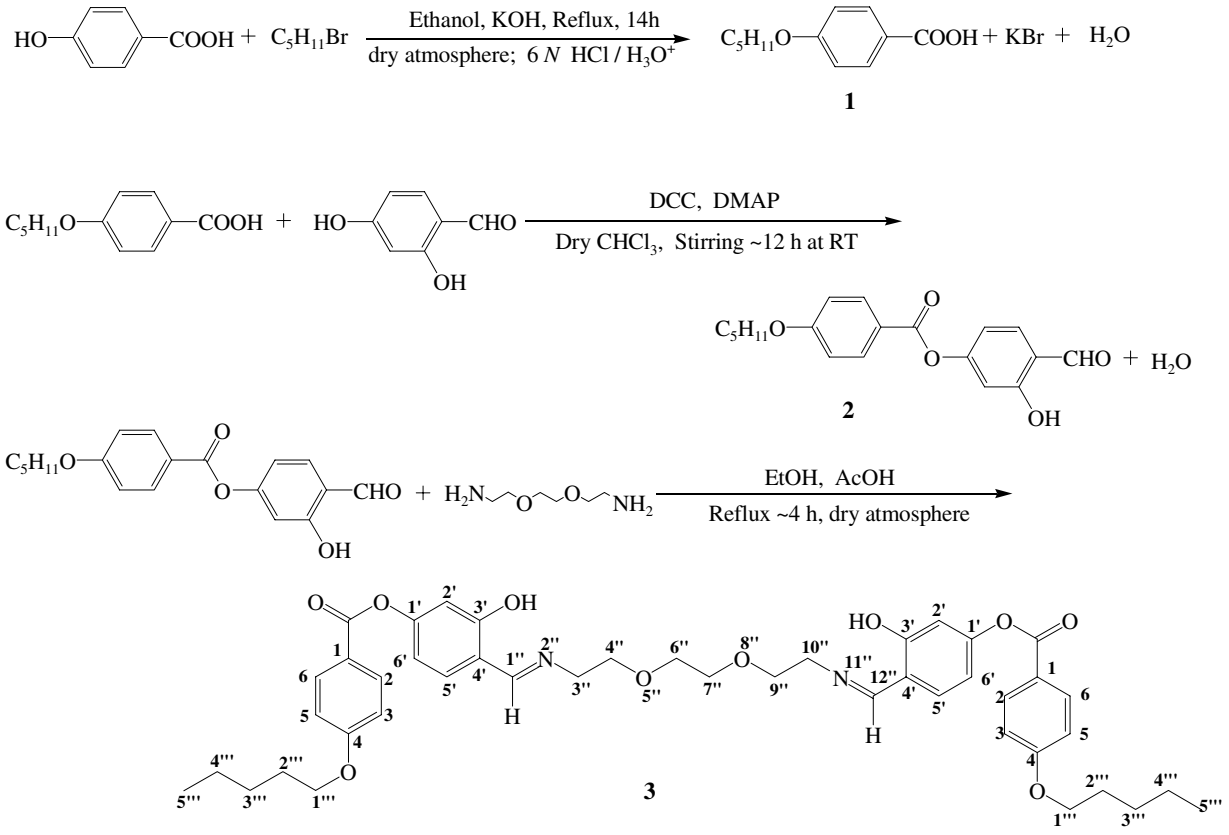
Solutions of 4-hydroxybenzoic acid (11.05 g, 80 mmol) in dry ethanol (150 mL) and of KOH (8.97 g, 160 mmol) in dry ethanol (50 mL) were magnetically stirred with simultaneous drop-wise addition of 1-bromopentane (10.00 mL, 80 mmol). The reaction mixture was refluxed for ~14 h under dry atmosphere and allowed to come to room temperature. The solid alkoxy potassium salt thus obtained was separated out by filtration under suction and treated with dilute HCl until the pH of the reaction mixture reached to ~2. The crude solid white product was filtered off, washed thoroughly with water and recrystallized successively from solutions of glacial acetic acid and toluene. Yield: 11.65 g (70%).

2.2.2. Preparation of 4-pentyloxy (4′-formyl-3′-hydroxy)-benzoate (*2*)

Solutions of 4-pentyloxy benzoic acid (10.40 g, 50 mmol in 50 mL), 2,4-dihydroxybenzaldehyde (6.90 g, 50 mmol in 50 mL), DCC (11.35 g, 55 mmol in 100 mL) in dry chloroform along with solid DMAP (0.3 g, 2.5 mmol as a catalyst) were magnetically stirred at room temperature for ~12 h. The byproduct (dicyclohexyl urea) was filtered off under suction and the solvent was removed on rotavapor. The crude product was recrystallized from hot solution of ethanol and purified by column chromatography over SiO_2 by eluting with a mixture of *n*-hexane and chloroform (v/v, 1:1); evaporation of this eluent yielded the ester, **2**, in the form of a white solid. Yield: 10.17 g (62%).

2.2.3. Synthesis of N,N′-di-(4′-pentyloxybenzoate)-salicylidene-1,8-diamino-3,6-dioxaoctane (*3*)

Absolute ethanolic solutions of 4-pentyloxy-(4′-formyl-3′-hydroxy)benzoate (6.56 g, 20 mmol, in 100 mL) and 1,8-diamino-3,6-dioxaoctane (1.50 mL, 10 mmol in 20 mL) were refluxed for ~4 h in presence of a few drops of acetic acid and the resultant solution was left over-night in the reaction flask at room temperature. The micro-crystalline yellow coloured product, **3**, was suction-filtered, thoroughly washed with ethanol, recrystallized from a solution of absolute ethanol/chloroform (v/v, 1/1) and dried at room temperature. Yield: 4.61 g (60%); m.p., 110 °C. ^{1}H NMR (300 MHz, $CDCl_3$, 25 °C, TMS): $\delta = 0.945$ (t, $^3J_{H-H} = 6.9$ Hz, 3H, CH_3), 1.847–1.390 (m, 6H, $H^{methylene}$), 3.614 (s, 2H, $H_{6''}$), 3.721 (s, 4H, $H^{3'',4''}$), 4.035 (t, $^3J_{H-H} = 6.6$ Hz, 2H, $H^{1'''}$), 6.720 (dd,



Scheme 1. Major reaction steps involved in the synthesis of *N*,*N*′-di-(4′-pentyloxy-benzoate)salicylidene-1,8- diamino-3,6-dioxaoctane (**3**) (H_2L_4).

$^3J_{H-H} = 6.3$ Hz, $^4J_{H-H} = 2.1$ Hz, 1H, $H^{6'}$), (d, $^4J_{H-H} = 1.8$ Hz, 1H, $H^{2'}$), 6.970 (d, $^3J_{H-H} = 8.7$ Hz, 1H, H^3), 7.277 (d, $^3J_{H-H} = 8.4$ Hz, 1H, $H^{5'}$), 8.126 (d, $^3J_{H-H} = 9.0$ Hz, 1H, H^2), 8.324 (s, 1H, N=CH), 13.813 (s, 1H, ϕ-OH) ppm. *FAB Mass*: the molecular ion (*m*/*e*, 769; 75% intensity) generates simultaneously four fragments, M_1–M_4, (*m*/*e*, fragment, % intensity): M_1: 398, $C_5H_{11}OC_6H_4COOC_6H_3(OH)CH{=}N(CH_2)_2OCH_2$-$CH_2^+$, 15; M_2: 370, $C_5H_{11}OC_6H_4COOC_6H_3(OH)CH{=}N(CH_2)_2O^+$, 11%; M_3: 340, $C_5H_{11}OC_6H_4COOC_6H_3(OH)$-$CH{=}NCH_2^+$, 12; M_4: 191, $C_5H_{11}OC_6H_4CO^+$, 100; $M_{4'}$ (generated from M_4): 121, $HOC_6H_4CO^+$, 97. IR (CCl_4, cm^{-1}): ν(O–H)$_{phenol}$ 3450b, ν(>C=O) 1742, ν(C=N) 1633, ν(C–O)$_{phenol}$ 1248, ν(C(O)O) 1149; (KBr, cm^{-1}): ν(O–H)$_{phenol}$ 3439b, ν(>C=O) 1722, ν(C=N) 1628, ν(C–O)$_{phenol}$ 1246, ν(C(O)O) 1145. *Anal.* Calc. for $C_{44}H_{52}N_2O_{10}$(768.0): C, 68.75; H, 6.77; N, 3.65. Found: C, 68.62; H, 6.50; N, 3.62%.

2.2.4. Synthesis of the zinc complex, [ZnL4]

Anhydrous solutions of *N*,*N*′-di-(4′-pentyloxybenzoate)salicylidene-1,8-diamino-3,6-dioxaoctane (**3**), (0.77 g, 1.0 mmol) in dichloromethane (30 mL) and of zinc acetate (0.22 g, 1.0 mmol) in ethanol (20 mL) were refluxed for ~6 h and the reaction mixture left over-night in the reaction flask after reducing the volume to ~10 mL. The crude solid complex, [ZnL_4], was filtered off under suction, washed repeatedly with cold ethanol, recrystallised from the solution of chloroform/ethanol and dried over fused $CaCl_2$ in a desiccator. Yield: 0.68 g (82%); m.p. 210 °C. ^{1}H NMR (300 MHz, $CDCl_3$, 25 °C, TMS): $\delta = 0.947$ (t, $^3J_{H-H} = 6.9$ Hz, 3H, CH_3), 1.850–1.392 (m, 6H, $H^{methylene}$), 4.040 (t, $^3J_{H-H} = 6.9$ Hz, 2H, $H^{1'''}$), 6.973 (d, $^3J_{H-H} = 8.1$ Hz, 1H, H^3), 7.185 (d, $^3J_{H-H} = 8.4$ Hz, 1H, $H^{5'}$), 8.133 (d, $^3J_{H-H} = 7.8$ Hz, 1H, H^2), 8.197 (s, 1H, N=CH) ppm. IR (KBr, cm^{-1}): ν(>C=O) 1730, ν(C=N) 1535, ν(C–O)$_{phenol}$ 1253, ν(C(O)O) 1151. *Anal.* Calc. for $C_{44}H_{50}N_2O_{10}Zn$ (832.23): C, 63.50; H, 6.06; N, 3.37; Zn, 7.86. Found: C, 63.27; H, 6.01; N, 3.22; Zn, 7.79%.

2.3. Physical measurements

Infrared spectra were recorded on a JASCO-5300 FT IR spectrophotometer and the ^{1}H and ^{13}C NMR spectra were recorded on a JEOL AL300 FT NMR spectrometer. Mass spectra were recorded on JEOL SX-102 (EI/CI/FAB) mass spectrometers. C, H, and N were micro-analyzed on Elementar Vario EL III Carlo Erba 1108 analyzer.

2.4. X-ray crystallographic data collection and refinement of the structure

X-ray data for the compound ZnL_4, [aq74m], was collected at room temperature using a Bruker Smart Apex CCD diffractometer with graphite monochromated Mo Kα radiation ($\lambda = 0.71073$ Å) with ω-scan method. Preliminary lattice parameters and orientation matrices were obtained from four sets of frames. Unit cell dimensions were determined from the setting angles of 7224 reflections in the range of $2.31° < \theta < 24.66°$. Integration and scaling of intensity data was accomplished using SAINT program [4]. The structure was solved by direct methods using SHELXS97 [5] and refinement was carried out by full-matrix least-squares technique using SHELXL97 [5]. Anisotropic displacement parameters were included for all non-hydrogen atoms. All other hydrogen atoms were positioned geometrically and treated as riding atoms, with C–H distances in the range of 0.93–0.96 Å and with U_{iso}(H) values of $1.5U_{eq}$(C) for methyl hydrogens and $1.2U_{eq}$(C) for other hydrogen atoms. The geometries of the atoms C17, C18 and C19 were restrained, where distances C17–C18=C18–C19 were set to the target value, 1.55 Å.

3. Results and discussion

3.1. Spectral investigation

The Schiff-base ligand (H_2L_4), **3**, is yellow-coloured while the Zn(II) complex, [ZnL_4] is colourless. Both

Table 1
Crystal data and structure refinement for aq74m, [ZnL_4]

Empirical formula	$C_{44}H_{50}N_2O_{10}Zn$
Formula weight	832.23
Cell axes	
a (Å)	8.7660 (6)
b (Å)	41.322(3)
c (Å)	11.5379(8)
Cell angles	
α (°)	90.000 (0)
β (°)	99.358 (1)
γ (°)	90.000 (0)
Cell volume *V* (Å)^3	4123.8 (5)
Crystal system	monoclinic
Crystal size	$0.22 \times 0.17 \times 0.09$ mm
Temperature (K)	294(2)
Wavelength (Å)	0.71073
Space group	$P2_1/n$
F(000)	1752
Density (Mg/m^3)	1.340
No. form Unit *Z*	4
Absorption coefficient (mm^{-1})	0.656
Reflections collected/unique	39 614/7261 [*R*(int) = 0.0251]
Completeness to $\theta = 25.00$	100.0%
Absorption correction	none
Refinement method	full-matrix least-squares on F^2
Data/restraints/parameters	7261/2/515
$H_{min,max}$	−10, 10
$K_{min,max}$	−49, 49
$L_{min,max}$	−13, 13
$\Theta_{min,max}$	0.99, 25.0
Goodness-of-fit on F^2	1.193
Final *R* indices	$[I > 2\sigma(I)]$ $R_1 = 0.0468$, $wR_2 = .1259$
R indices (all data)	$R_1 = 0.0540$, $wR_2 = 0.1338$
Largest diffraction peak and hole (e Å^{-3})	0.682 and −0.553

the parent ligand and the metal complex are soluble in chloroform, dichloromethane, DMF and DMSO but are insoluble in water, methanol, ethanol, and acetonitrile. The structures and purities of the Schiff-base ligand, **3**, and of the metal complex, [ZnL_4], were confirmed by IR and ^1H NMR spectroscopy and elemental analyses. The structure of the ligand was further confirmed by FAB Mass spectrum. The mass spectral features of H_2L_4 were characterized by the base peak ($m/e = 191$ corresponding to the fragment, $C_5H_{11}OC_6H_4CO^+$), the molecular ion peak with ~75% intensity ($m/e = 769$) and the major fragment peaks ($m/e = 398$, 370, 340, 121) due to $C_5H_{11}OC_6H_4COOC_6H_3(OH)CH{=}N(CH_2)_2OCH_2CH_2^+$, $C_5H_{11}OC_6H_4COOC_6H_3(OH)CH{=}N(CH_2)_2O^+$, $C_5H_{11}OC_6H_4COOC_6H_3(OH)CH{=}NCH_2^+$ and $HOC_6H_4CO^+$. A comparison of the ^1H and $^{13}C\{^1H\}$ NMR spectral data of the ligand with those of the Zn(II) complex shows the absence of the phenolic–OH signal (13.813 ppm in H_2L_4) and a significant shift (8.324–8.197 ppm) in the peak position of the –N=C*H* in the spectrum of the metal complex, which implies bonding through the phenolate anion and the azomethine nitrogen atom [6] of the ligand to the metal ion. Similar shifts observed in the $^{13}C\{^1H\}$ NMR spectra were of considerable magnitude in the case of the carbon atoms directly attached to the bonding atoms (phenolate–O and azomethine–N) while those observed for the carbons close to the bonding atoms were of lesser magnitude. Thus, the NMR spectral data imply tetradentate bonding of H_2L through the two >C=N groups and two phenolate oxygen atoms. In the IR spectrum of H_2L_4 the broad absorption centered on 3439 and 3450 cm^{-1}, in the solid and solution states, respectively, may be assigned to the O–H stretching vibration of the phenolic group [7]. The strong intensity band occurring at 1633 cm^{-1} may be assigned [8] to ν(C=N) absorption of the azomethine moiety. The strong bands occurring at 1722 cm^{-1} and 1145 cm^{-1} in the solution state of the parent ligand may be assigned [7] to ν(>C=O) and ν(C–O) stretching modes of aromatic ester. The characteristic response of ether in the infrared is associated with the stretching vibration of the C–O–C system. The bands appearing at 1246 and 1064 cm^{-1} may be assigned [7] to ν_{as}(C–O–C) and ν_s(C–O–C) stretching of aryl alkyl ether. Bonding of the parent ligand with the metal ions through phenolate oxygen and azomethine nitrogen was inferred [8] on the basis of (i) disappearance of the ν(O–H) (phenolic) band, and (ii) bathochromic shifts observed in the *ν*(>C=N) frequencies in the spectra of the metal complexes.

3.2. Crystal structure and molecular association

The crystal data and structure refinement details for [ZnL_4], [aq74m], are given in Table 1. The molecular structure and atomic labeling scheme of the complex, [ZnL_4], is as shown in Fig. 1.

As per the crystal structure of the complex, the ligand, H_2L_4, coordinates to the Zn(II) ion through two phenolate oxygens (O(1), O(5)) and two azomethine nitrogens (N(1), N(2)), rendering the overall

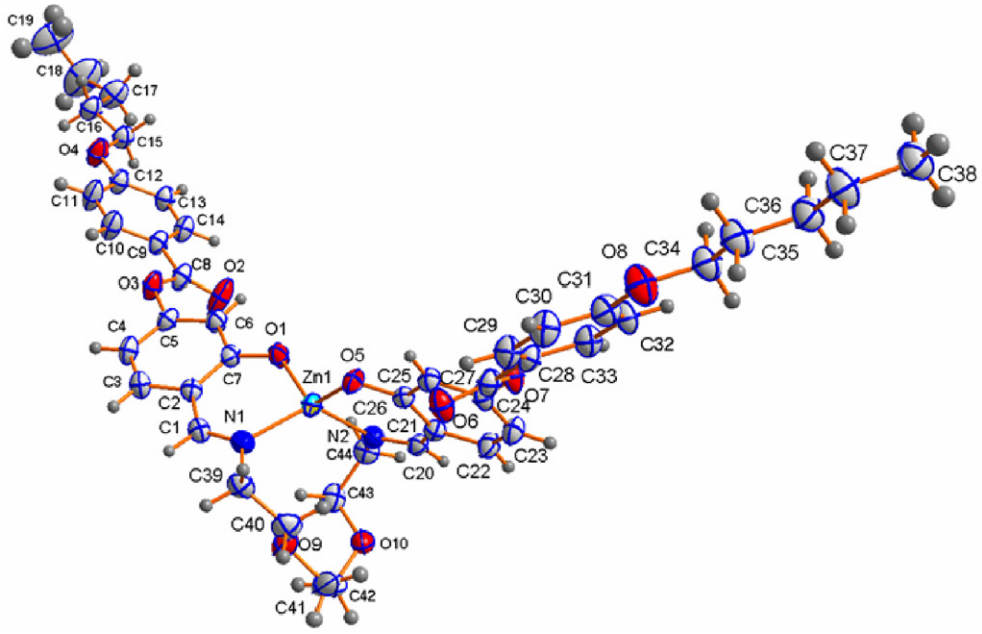


Fig. 1. Molecular structure and atomic labeling scheme of the Complex [ZnL_4].

Table 2
Bond lengths (Å) and angles (°) involved in the tetrahedral unit of the complex [ZnL_4]

N(1)–Zn(1)	2.003(2)	N(2)–Zn(1)	1.994(2)
O(1)–Zn(1)	1.9146(19)	O(5)–Zn(1)	1.9213(18)
O(1)–Zn(1)–O(5)	121.12(9)	O(1)–Zn(1)–N(2)	107.78(9)
O(5)–Zn(1)–N(2)	96.78(8)	O(1)–Zn(1)–N(1)	95.86(9)
O(5)–Zn(1)–N(1)	111.10(9)	N(2)–Zn(1)–N(1)	126.37(9)

Table 3
Hydrogen bonds geometry (Å, °) for the complex [ZnL_4]

D–H...A	*d*(D–H)	*d*(H...A)	*d*(D...A)	*d*(D...A)
C(30)–H(30)...O2^{i}	0.93	2.53	3.232(14)	132
C(39)–H(39B)...O10^{i}	0.97	2.47	3.350(4)	151

Symmetry code: (i) $1/2 + x$, $1/2 - y$, $1/2 + z$.

geometry around Zn(II) to distorted tetrahedron where the bond lengths and the bond angles are as shown in Table 2. The hydrogen bond geometry is tabulated in Table 3. The crystal structure is stabilized by intermolecular C–H···O interactions which exist between the atom C(30) of the benzoate ring and the carbonyl oxygen atom O(3). Similarly, the aliphatic atom C(39) forms an intermolecular C–H···O interaction with the ethereal oxygen atom O(10), thereby forming an infinite glide-related chain running along crystallographic *c*-axis. The packing diagram is depicted in Fig. 2. Considerable torsion has been observed between benzoate ring and salicylaldimine ring on either side of the metal atom.

4. Conclusion

The Schiff-base, *N*,*N*′-di-(4′-pentyloxybenzoate)salicylidene-1,8-diamino-3,6-dioxaoctane (H_2L_4) with the mesogenic phase, nematic droplets, coordinates to Zn(II) as a di-negative tetra-dentate species, to yield the non-mesogenic tetrahedral complex, [ZnL_4]. As per the crystal structure of the complex, the dinegative species of the ligand, L_4^{2-}, coordinates to the Zn(II) ion through two phenolate oxygens and two azomethine nitrogens, rendering the overall geometry around Zn(II) to distorted tetrahedron.

Acknowledgements

The authors wish to acknowledge the recording of FAB Mass spectra and elemental analyses at the Central Drug Research Institute, Lucknow. One of the authors, Prof. T.R. Rao, gratefully acknowledges the financial grant received from the Council of Scientific & Industrial Research, New Delhi [vide Grant No. 01(1834)/03/EMR-II dated 12-03-2003] and the University Grants Commission [vide Grant No. F.12-26/2003 (SR) dated 31 Mar 2003].

Appendix A. Supplementary material

CCDC 649423 contain the supplementary crystallographic data for this paper. These data can be obtained free of charge via http://www.ccdc.cam.ac.uk/conts/retrieving.html, or from the Cambridge Crystallographic Data Centre, 12 Union Road, Cambridge CB2 1EZ, UK; fax: (+44) 1223-336-033; or e-mail: deposit@ccdc.cam.ac.uk. Supplementary data associated with this article can be found, in the online version, at doi:10.1016/j.poly.2007.09.002.

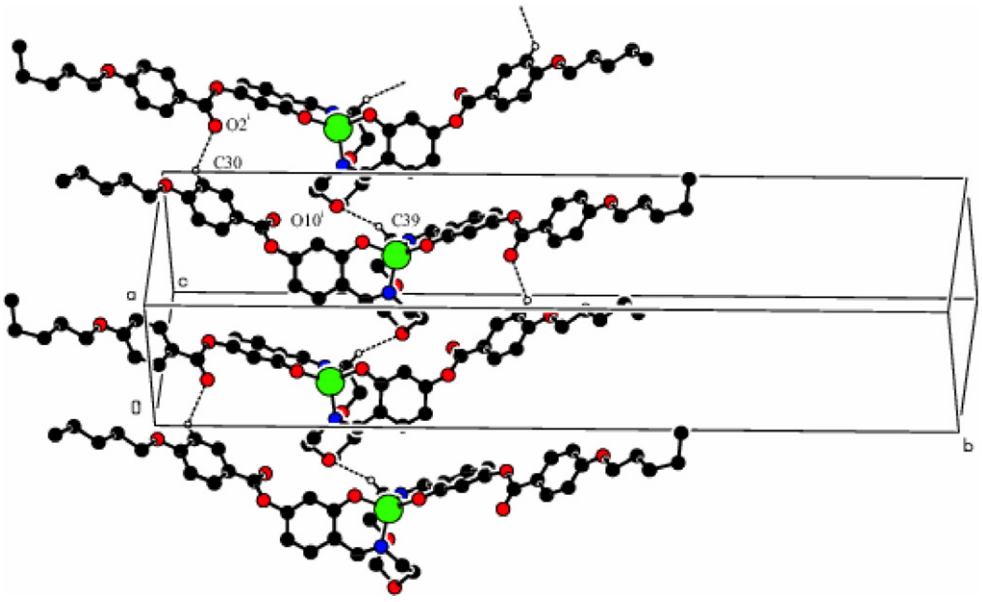


Fig. 2. Part of the crystal structure for [ZnL_4], viewed down *a*-axis. Dashed lines indicate C–H···O interaction. H atoms not involved in hydrogen bonding have been omitted for clarity.

References

[1] (a) A. Serrette, P.J. Carroll, T.M. Swager, J. Am. Chem. Soc. 114 (1992) 1887;
(b) A.M. Giroud-Godquin, P.M. Maitlis, Angew. Chem., Int. Ed. Engl. 30 (1991) 375.
[2] A. Pegenau, T. Hegmann, C. Tschierske, S. Diele, Chem. Eur. J. 5 (1999) 1643.
[3] A. Weisberger, F.S. Praskver, Organic Solvents, International Publishers Inc., New York, 1956, pp. 1263.
[4] SMART & SAINT, Software Reference Manuals. Versions 6.28a & 5.625, Bruker Analytical X-ray Systems Inc., Madison, WI, USA, 2001.
[5] G.M. Sheldrick, SHELXS97 and SHELXL97, Programs for Crystal Structure Solution and Refinement, University of Gottingen, Germany, 1997.
[6] K. Binnemans, K. Lodewyckx, R. van Deun, Y.G. Galyametdinov, D. Hinz, G. Meyer, Liquid Cryst. 28 (2001) 279.
[7] R.M. Silverstein, F.X. Webster, Spectroscopic Identification of Organic Compounds, 6th ed., John-Wiley & Sons. Inc., New York, 2002, pp. 82–98.
[8] A. Braibanti, F. Dallavalle, M.A. Pellinghelli, Inorg. Chem. 7 (1968) 1430.

Available online at www.sciencedirect.com
ScienceDirect
Polyhedron 27 (2008) 187–195
POLYHEDRON
www.elsevier.com/locate/poly

Synthesis, spectroscopic characterisation, crystal and molecular structure of [ReOBr(quin-2-c)$_2$] and [ReOCl(quin-2-c)$_2$] complexes: DFT and TD-DFT calculations for [ReOBr(quin-2-c)$_2$]

B. Machura [a,*], J. Kusz [b]

[a] Department of Crystallography, Institute of Chemistry, University of Silesia, 9th Szkolna Street, 40-006 Katowice, Poland
[b] Institute of Physics, University of Silesia, 4th Uniwersytecka Street, 40-006 Katowice, Poland

Received 1 May 2007; accepted 5 September 2007
Available online 23 October 2007

Abstract

Novel [ReOX(quin-2-c)$_2$] complexes (X = Cl, Br; quin-2-c = quinoline-2-carboxylate ion) have been prepared by treatment of [ReOX$_3$(AsPh$_3$)$_2$] with an excess of quinoline-2-carboxylic acid in acetonitrile. The complexes were characterised structurally and spectroscopically. The electronic structure of [ReOBr(quin-2-c)$_2$] has been calculated with the density functional theory (DFT) method, and additional information about binding has been obtained by NBO analysis. The UV–Vis spectrum of [ReOBr(quin-2-c)$_2$] has been discussed on the basis of TD-DFT calculations.
© 2007 Elsevier Ltd. All rights reserved.

Keywords: Rhenium oxo complexes; Quinoline-2-carboxylate ligand; X-ray and electronic structure; DFT calculations; NBO analysis

1. Introduction

There is considerable interest in the chemistry of inorganic compounds containing an oxygen atom that is multiply bonding to a transition metal in a high oxidation state. These compounds can transfer an oxygen atom to reductants such as phosphines, sulfides and alkenes. For many years they have been in the center of interest to those scientists engaged in basic research and to those trying to employ these complexes in catalytic processes. Oxygen atom transfer chemistry has been implicated in various reactions of industrial and biological importance, including olefin epoxidation and catalysis by cytochrome P-450 [1–3].

The chemistry of oxo rhenium complexes arouses particular interest among these compounds. Methyltrioxorhenium and its derivatives are among the most versatile oxidation catalysts known to date [4]. The oxorhenium(V) chelates [ReOCl$_2$(O–N)(PPh$_3$)] with pyridinecarboxylate ligands exhibit remarkable catalytic activity for the conversion of ethane, under relatively mild conditions, to a mixture of propionic and acetic acids in a single-pot process, with various advantages over the industrial ones [5]. The [CH$_3$ReO(pic)$_2$] complex is an active precursor in olefin oxidation and forms epoxides in a two-phase H_2O_2–H_2O/CH_2Cl_2 system [6].

Furthermore, favourable nuclear properties of ^{186}Re and ^{188}Re nuclides make the compounds with these radioisotopes useful for applications in radioimmunotherapy [7,8].

In this context, the design, synthesis and reactivity of novel rhenium oxocomplexes has become the aim of several laboratories, including ours.

Previously, we investigated the reactivity of oxorhenium(V) species – [ReO(OEt)X$_2$(PPh$_3$)$_2$], [ReOX$_3$(PPh$_3$)$_2$] and [ReOX$_3$(AsPh$_3$)(OAsPh$_3$)] (X = Cl or Br) – towards

* Corresponding author.
E-mail address: basia@ich.us.edu.pl (B. Machura).

0277-5387/$ - see front matter © 2007 Elsevier Ltd. All rights reserved.
doi:10.1016/j.poly.2007.09.010

pyrazole, 3,5-dimethylopyrazole, benzotriazole and pyrazine [9]. In this report, we focus on the examinations of the reactions of $[ReOX_3(AsPh_3)_2]$ with quinoline-2-carboxylic acid. Quinoline-2-carboxylic acid is the biological compound involved in the metabolism of tryptophan. It is a strong chelator providing a donor set similar to that responsible for binding the metal ion in PQQ (pyrroloquinilnequinone) cofactor of the quinoprotein family [10].

Here we present the synthesis, spectroscopic data and X-ray structures of $[ReOBr(quin\text{-}2\text{-}c)_2]$ and $[ReOCl(quin\text{-}2\text{-}c)_2]$. In addition, this paper includes density functional theory (DFT) and time-dependent DFT (TD-DFT) calculations for the bromide complex. Recently, the electronic structures of nitrido, oxo, carbonyl, nitrosyl and nitrile rhenium complexes, as well as their spectroscopic properties, bonding and reactivity have been theoretically studied at the HF, MP2, EHT and DFT levels of theory using various basis sets [11–20]. Gancheff and co-workers [13] have performed extended tests of the ability of the B3LYP method in LANL2DZ basis set for rhenium compounds in a geometry optimization and calculation of spectral properties. Although this is not a very extended basis set, its use with DFT has been shown to be sufficient for geometry optimization and calculation of spectral properties. The correctness of the B3LYP method with the LANL2DZ basis set for rhenium complexes has been also proven in this paper. The experimental geometry of $[ReOBr(quin\text{-}2\text{-}c)_2]$ is well reproduced and the calculated electronic spectrum is in good accordance with the experimental one.

2. Experimental

2.1. General procedure

All the reagents used in the synthesis were commercially available and were used without further purification. The $[ReOX_3(AsPh_3)_2]$ (X = Cl, Br) complexes were prepared according to the literature methods [21].

IR spectra were recorded on a Nicolet Magna 560 spectrophotometer in the spectral range 4000–400 cm^{-1} with the samples in the form of KBr pellets. Electronic spectra were measured on a spectrophotometer Lab Alliance UV–Vis 8500 in the range 1000–200 nm in acetonitrile solution. Elemental analyses (C H N) were performed on a Perkin–Elmer CHN-2400 analyzer.

2.2. Preparation of $[ReOBr(quin\text{-}2\text{-}c)_2]$

$[ReOBr_3(AsPh_3)_2]$ (0.5 g, 0.47 mmol) was added to quinoline-2-carboxylic acid (0.2 g, 1.15 mmol) in acetonitrile (50 ml) and the reaction mixture was refluxed for 6 h. The resulting solution was allowed to cool to room temperature and reduced in volume to ~10 ml. A brown crystalline precipitate of $[ReOBr(quin\text{-}2\text{-}c)_2]$ was filtered off and dried in the air. Yield: 85%. Single crystals of $[ReOBr(quin\text{-}2\text{-}c)_2]$ were obtained by recrystallization from acetonitrile.

Anal. Calc. for $C_{20}H_{12}BrN_2O_5Re$: C, 38.55; H, 1.90; N, 4.40. Found: C, 38.35; H, 1.93; N, 4.47%.

2.3. Preparation of $[ReOCl(quin\text{-}2\text{-}c)]$

A procedure similar to that for $[ReOBr(quin\text{-}2\text{-}c)_2]$ was used with $[ReOCl_3(AsPh_3)_2]$ (0.5 g, 0.54 mmol) and quinoline-2-carboxylic (0.2 g, 1.15 mmol). The crystalline precipitate of $[ReOCl(quin\text{-}2\text{-}c)_2]$ was collected in 90% yield.

Anal. Calc. for $C_{20}H_{12}ClN_2O_5Re$: C, 41.38; H, 2.11; N, 4.72. Found: C, 41.28; H, 2.08; N, 4.81%.

2.4. Crystal structure determination and refinement

The X-ray intensity data of $[ReOX(quin\text{-}2\text{-}c)_2]$ were collected on a KM-4-CCD automatic diffractometer equipped with a CCD detector and graphite-monochromated Mo Kα radiation ($\lambda = 0.71073$ Å) at a temperature of 295(2) K. Details concerning crystal data and refinement are given in Table 1. Lorentz, polarization and empirical absorption

Table 1
Crystal data and structure refinement for $[ReOX(quin\text{-}2\text{-}c)_2]$ complexes

Compound	$[ReOBr(quin\text{-}2\text{-}c)_2]$	$[ReOCl(quin\text{-}2\text{-}c)_2]$
Empirical formula	$C_{20}H_{12}BrN_2O_5Re$	$C_{20}H_{12}ClN_2O_5Re$
Formula weight	626.43	581.97
Temperature (K)	293(2)	293(2)
Wavelength (Å)	0.71073	0.71073
Crystal system	monoclinic	monoclinic
Space group	$P2_1/n$	$P2_1/n$
Unit cell dimensions		
a (Å)	10.0816(4)	10.1378(4)
b (Å)	14.3395(5)	14.2585(4)
c (Å)	13.0948(5)	12.9838(4)
β (°)	100.432(4)	100.942(3)
V (Å^3)	1861.76(12)	1842.69(11)
Z	4	4
D_{calc} (Mg/m^3)	2.235	2.098
Absorption coefficient (mm^{-1})	8.710	6.776
$F(000)$	1184	1112
Crystal size (mm)	$0.06 \times 0.22 \times 0.24$	$0.12 \times 0.16 \times 0.26$
θ Range for data collection (°)	2.75–25.00	3.17–25.00
Index ranges	$-11 \leqslant h \leqslant 11$, $-17 \leqslant k \leqslant 8$, $-15 \leqslant l \leqslant 15$	$-12 \leqslant h \leqslant 12$, $-16 \leqslant k \leqslant 16$, $-15 \leqslant l \leqslant 8$
Reflections collected	11 422	11 287
Independent reflections (R_{int})	3234 (0.0192)	3214 (0.0160)
Completeness to $2\theta = 50°$ (%)	99.9	99.3
Data/restraints/parameters	3234/0/262	3214/0/262
Goodness-of-fit on F^2	1.140	1.036
Final R indices [$I > 2\sigma(I)$]	$R_1 = 0.0259$, $wR_2 = 0.0818$	$R_1 = 0.0147$, $wR_2 = 0.0362$
R indices (all data)	$R_1 = 0.0314$, $wR_2 = 0.0835$	$R_1 = 0.0182$, $wR_2 = 0.0368$
Largest difference in peak and hole (e Å^{-3})	0.756 and −1.917	0.523 and −0.626

corrections using spherical harmonics implemented in SCALE3 ABSPACK scaling algorithm [22] were applied. The structures were solved by the Patterson method and subsequently completed by difference Fourier recycling. All the non-hydrogen atoms were refined anisotropically using the full-matrix, least-squares technique. The hydrogen atoms were treated as "riding" on their parent carbon atoms and assigned isotropic temperature factors equal to 1.2 times the value of the equivalent temperature factor of the parent atom. SHELXS-97 [23], SHELXL-97 [24] and SHELXTL [25] programs were used for all the calculations. Atomic scattering factors were those incorporated in the computer programs.

3. Computational details

The GAUSSIAN-03 program [26] was used in the calculations. The geometry optimization of [ReOBr(quin-2-c)$_2$] in a singlet state was carried out with the DFT method with the use of the B3LYP functional [27,28]. The electronic spectrum of [ReOBr(quin-2-c)$_2$] was calculated with the TD-DFT method [29], and the solvent effect was simulated using the polarizable continuum model with the integral equation formalism (IEF-PCM). The calculations were performed by using the ECP basis set on the rhenium atom, the standard 6-31+G** basis for bromine, oxygen and nitrogen, 6-31G* for carbon and 6-31G for hydrogen atoms [30,31]. The Xe core electrons of Re were replaced by an effective core potential and a DZ quality Hay and Wadt Los Alamos ECP basis set (LANL2DZ) [32] was used for the valence electrons. An additional d function with exponent $\alpha = 0.3811$ and f function with exponent $\alpha = 2.033$ on the rhenium atom were added [33].

Natural bond orbital (NBO) calculations were performed with the NBO code [34] included in GAUSSIAN-03.

4. Results and discussion

4.1. Preparation and infrared data

The [ReOX(quin-2-c)$_2$] complexes were prepared in good yields by ligand exchange reactions starting from [ReOX$_3$(AsPh$_3$)$_2$] complexes and quinoline-2-carboxylic acid in acetone:

$$[ReOX_3(AsPh_3)_2] + 2\text{quin-2-cH} \rightarrow [ReOX(\text{quin-2-c})_2] + 2HX + 2AsPh_3 \quad X = Cl, Br$$

They were isolated as brown microcrystalline solids, soluble in common organic solvents.

The selected frequencies observed in the IR spectra of the [ReOX(quin-2-c)$_2$] complexes are collected in Table 2. The IR spectra of the [ReOX(quin-2-c)$_2$] complexes show features comparable to those of mononuclear picolinato species [6]. In addition to strong bands assigned to $\nu_{sym}(CO_2)$ and $\nu_{as}(CO_2)$, there are sharp bands at $\approx$990 cm^{-1} assignable to the ν(Re=O) mode. The presence of the ν_s(Re=O) bands in the high end of the range observed for $\{ReO\}^{3+}$ core complexes suggests that the Re–carboxylate bond *trans* to the oxo ligand does not compete effectively for the d_{Re} orbitals, and the bond is relatively weak.

Table 2
Selected IR frequencies (cm^{-1}) of [ReOX(quin-2-c)$_2$] complexes

Complex	ν(Re=O)	ν_{as}(COO)	ν_s(COO)
[ReOBr(quin-2-c)$_2$]	987	1724, 1693	1317, 1304
[ReOCl(quin-2-c)$_2$]	988	1625, 1693	1318, 1305

4.2. Crystal structures

Both complexes are isostructural, they crystallise in the monoclinic space group $P2_1/n$ and their structures consist of discrete and well-separated monomers. Classical hydrogen bonds were not found in the [ReOX(quin-2-c)$_2$] structures, only some C—H···O weak inter- and intramolecular hydrogen bonds (Table 3) were detected [35,36].

The molecular structure of [ReOBr(quin-2-c)$_2$] is presented in Fig. 1, and the selected bond distances and angles of the [ReOX(quin-2-c)$_2$] complexes are collected in Tables 4 and 5, respectively.

The geometry of the [ReOX(quin-2-c)$_2$] compounds reveals typical features of quasi-octahedral oxorhenium(V) complexes with oxygenated bidentate ligands. For the complex [ReOBr(quin-2-c)$_2$], the rhenium atom is displaced 0.2852(18) Å from the equatorial plane formed by the two nitrogens, one oxygen and one bromide atom (plane A), and 0.0891(20) and 0.0192(17) Å from the axial planes formed, respectively, by the three oxygen and one nitrogen atom (plane B) and two oxygens, one bromide and one nitrogen atom (plane C). The least squares plane A is inclined at 89.14(9)° to plane B and 89.24(10)° to plane C. The planes B and C are inclined at 85.83(9)°. These values for the chloride analogue are, respectively, 0.2829(9), 0.0870(10) and 0.0137(8) Å, 89.38(5)°, 89.30(5)° and 85.25(5)°. Clear distortions of the pseudo-octahedral envi-

Table 3
Hydrogen bonds for [ReOX(quin-2-c)$_2$]

D	A	H···A (Å)	D···A (Å)	D–H···A (°)
[ReOBr(quin-2-c)$_2$]				
C(18)	O(1)	2.29	2.978(6)	130.0
C(7)	O(3)#1	2.41	3.191(8)	141.2
[ReOCl(quin-2-c)$_2$]				
C(18)	O(1)	2.29	2.981(3)	130.5
C(15)	O(4)#2	2.60	3.208(3)	123.8
C(7)	O(3)#2	2.41	3.191(4)	140.9

Symmetry codes: #1: $x - 1/2$, $-y + 1/2$, $z + 1/2$; #2: $x + 1/2$, $-y + 1/2$, $z - 1/2$.

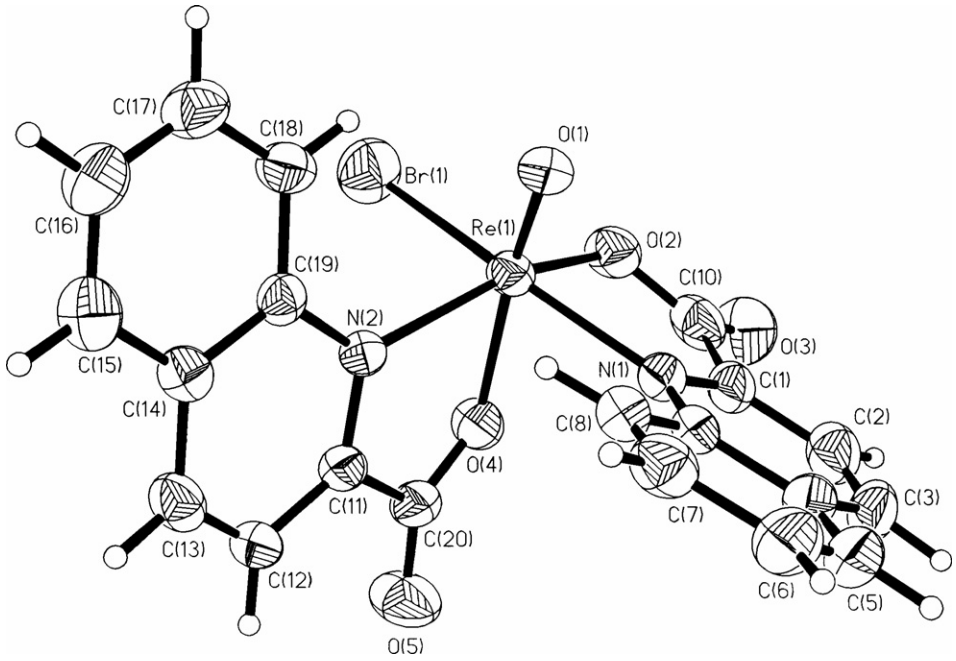


Fig. 1. The molecular structure of [ReOBr(quin-2-c)$_2$]. Displacement ellipsoids are drawn at 50% probability.

Table 4
Selected experimental and optimized bond lengths (Å), bond angles (°) and torsion angles (°) for [ReOBr(quin-2-c)$_2$]

	Experimental	Optimized
Bond lengths (Å)		
Re(1)–O(1)	1.668(4)	1.680
Re(1)–O(2)	1.982(4)	1.983
Re(1)–O(4)	2.039(3)	2.045
Re(1)–N(1)	2.159(4)	2.213
Re(1)–N(2)	2.169(4)	2.229
Re(1)–Br(1)	2.4509(7)	2.534
Bond angles (°)		
O(1)–Re(1)–O(2)	108.21(17)	106.82
O(1)–Re(1)–O(4)	161.18(17)	159.82
O(2)–Re(1)–O(4)	83.62(15)	86.21
O(1)–Re(1)–N(1)	88.65(17)	89.77
O(2)–Re(1)–N(1)	79.39(16)	78.66
O(4)–Re(1)–N(1)	79.00(15)	77.51
O(1)–Re(1)–N(2)	94.68(16)	93.80
O(2)–Re(1)–N(2)	157.11(16)	159.36
O(4)–Re(1)–N(2)	74.38(14)	74.29
N(1)–Re(1)–N(2)	102.07(15)	103.08
O(1)–Re(1)–Br(1)	100.80(12)	102.33
O(2)–Re(1)–Br(1)	87.24(12)	89.40
O(4)–Re(1)–Br(1)	94.22(11)	92.95
N(1)–Re(1)–Br(1)	165.55(12)	165.09
N(2)–Re(1)–Br(1)	88.15(10)	84.98
Torsion angles (°)		
N(1)–Re(1)–O(4)–C(20)	91.16(41)	99.52
O(2)–Re(1)–O(4)–C(20)	171.54(41)	178.73
O(2)–Re(1)–C(20)–C(11)	−175.14(28)	−172.26
N(2)–Re(1)–O(2)–C(10)	−80.55(56)	−88.24
Re(1)–N(1)–C(9)–C(5)	−177.03(51)	−171.25
Re(1)–N(2)–C(19)–C(15)	−177.26(50)	−179.18

ronment of the Re center in [ReOX(quin-2-c)$_2$] is induced by the multiple bonding ligand (terminal oxo ligand – O_t) and narrow bite angle of the chelating ligands.

Table 5
Experimental bond lengths (Å) and angles (°) for [ReOCl(quin-2-c)$_2$]

	Experimental
Bond lengths (Å)	
Re(1)–O(1)	1.6721(17)
Re(1)–O(2)	1.9781(18)
Re(1)–O(4)	2.0414(17)
Re(1)–N(1)	2.155(2)
Re(1)–N(2)	2.1706(19)
Re(1)–Cl(1)	2.3361(7)
Bond angles (°)	
O(1)–Re(1)–O(2)	107.93(8)
O(1)–Re(1)–O(4)	161.53(8)
O(4)–Re(1)–O(2)	83.63(7)
O(1)–Re(1)–N(1)	88.65(8)
O(2)–Re(1)–N(1)	79.38(8)
O(4)–Re(1)–N(1)	79.20(7)
O(1)–Re(1)–N(2)	94.67(8)
O(2)–Re(1)–N(2)	157.40(8)
O(4)–Re(1)–N(2)	74.66(7)
N(2)–Re(1)–N(1)	102.19(7)
O(1)–Re(1)–Cl(1)	101.01(7)
O(2)–Re(1)–Cl(1)	87.63(6)
O(4)–Re(1)–Cl(1)	93.66(5)
N(1)–Re(1)–Cl(1)	165.75(6)
N(2)–Re(1)–Cl(1)	87.57(5)

The Re–O_t bond lengths fall in the range 1.639–1.76 Å, which is typical of mononuclear complexes of rhenium(V) having $[ReO]^{3+}$ core, and indicates the presence of a triple Re≡O bond [37]. The interatomic distance between the rhenium atom and the oxygen atom of quin-2-c in the *trans* position to the terminal oxo ion is somewhat longer than the corresponding Re–O bond in the equatorial plane. This structural *trans* influ-

ence is common in mononuclear six-coordinate oxo Re(V) complexes with a monoanionic oxygen *trans* to the oxo group [38].

Table 6
Atomic charges from the natural population analysis (NPA) for [ReOBr(quin-2-c)$_2$]

Atom	Charge
Re(1)	1.432
O(1)	−0.480
O(2)	−0.671
O(4)	−0.714
N(1)	−0.472
N(2)	−0.473
Br(1)	−0.304

4.3. Geometry optimization, charge distribution, electronic structure and NBO analysis

The geometry of [ReOBr(quin-2-c)$_2$] was optimized in a singlet state by the DFT method with the B3LYP functional. The optimized geometric parameters of [ReOBr-(quin-2-c)$_2$] are gathered in Table 4. In general, the predicted bond lengths and angles are in agreement with the values based upon the X-ray crystal structure data, and the general trends observed in the experimental data are well reproduced in the calculations. The calculated least squares plane A is inclined at 89.22° to plane B and 88.77° to plane C. The planes B and C are inclined at 83.94°.

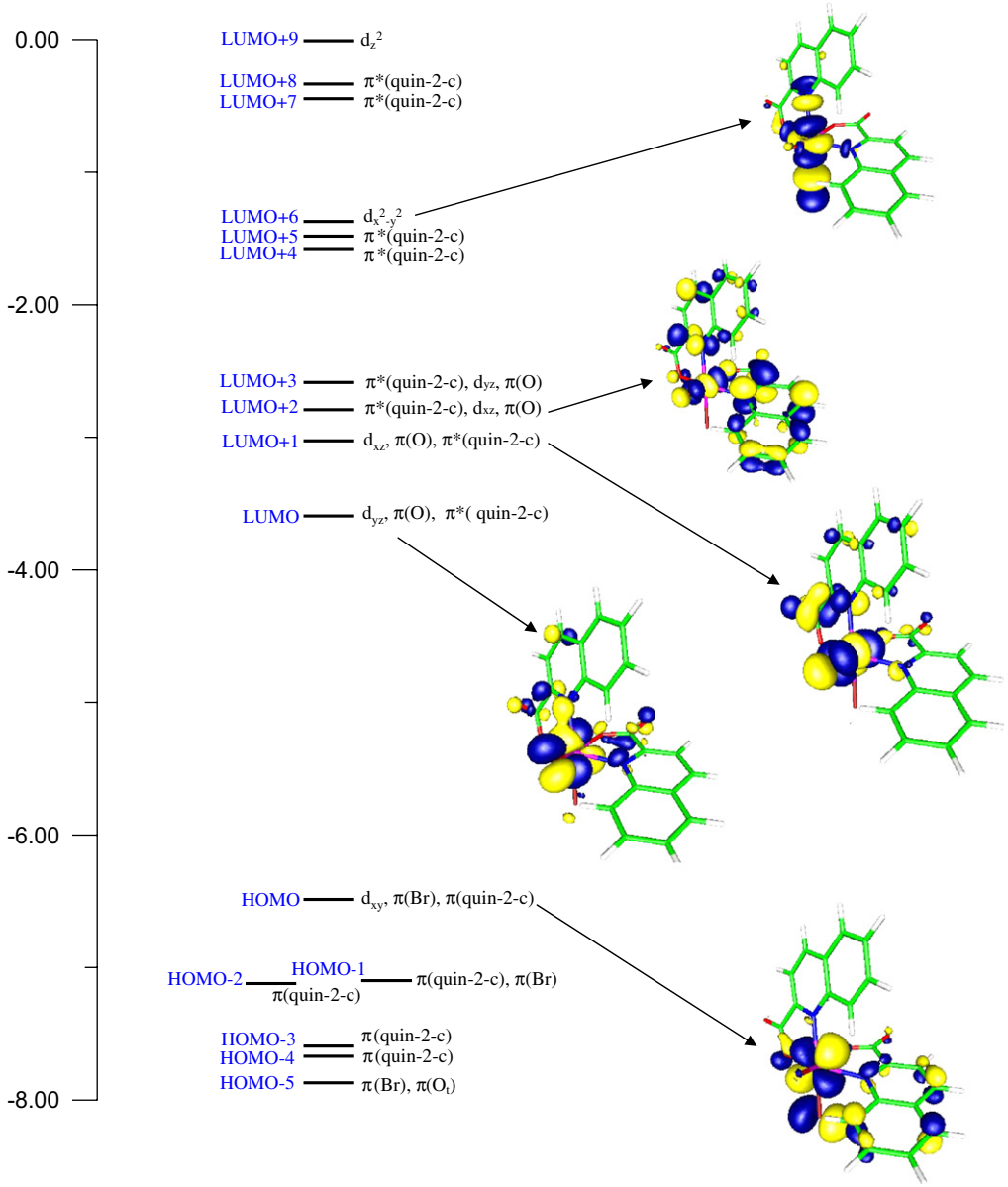


Fig. 2. The energy (eV), character and some contours of the occupied and unoccupied molecular orbitals of [ReOBr(quin-2-c)$_2$]. Positive values of the orbital contour are represented in blue (0.04 a.u.) and negative values in yellow (−0.04 a.u.). (For interpretation of the references to colour in this figure legend, the reader is referred to the web version of this article.)

Table 6 presents the atomic charges from the natural population analysis (NPA) for [ReOBr(quin-2-c)$_2$]. The calculated charge on the rhenium atom in [ReOBr(quin-2-c)$_2$] is considerable lower than the formal charge +5, corresponding to a d^2 configuration of the central ion. It results from significant charge donation from the ligands. The charges on the terminal oxo, bromide and oxygen atom of quin-2-c are significantly smaller than −2, −1 and −1, respectively. The terminal oxo ion is less negative in comparison with the oxygen atom of the quin-2-c ligand. It indicates higher electron density delocalization from the O_t ligand towards the central ion and corresponds to differences in the Re–$O_{carboxylate}$ and Re–$O_{terminal}$ bonds lengths.

The complex [ReOBr(quin-2-c)$_2$] has a closed-shell structure. Its molecular orbital diagram with several highest and lowest molecular orbital contours is presented in Fig. 2. The local symmetry of the rhenium center has been considered in the discussion: the *z*-axis goes along the O–Re–O linkage, and the *x*-axis through the N(2)–Re–O(2) bonds. The value of the energy separation between the highest occupied molecular orbital (HOMO) and the lowest unoccupied molecular orbital (LUMO) equals to 2.89 eV. This value is higher in comparison with the HOMO–LUMO gap (2.55 eV) calculated for the related [ReOBr(hqn)$_2$] complex (hqn = 8-hydroxyquinoline) [39]. The bigger absolute value of the gap energies means better stability of the title complex.

The highest occupied MO of [ReOBr(quin-2-c)$_2$] is of the d_{xy} type with some contributions from p_π bromide and quin-2-c orbitals. The remaining four d-type orbitals of rhenium are found among the unoccuppied MOs. It confirms the d^2 configuration of the rhenium atom. The LUMO and LUMO+1 can be ascribed as π-antibonding rhenium–oxygen molecular orbitals.

Table 7
The occupancy of the calculated natural bond orbitals (NBOs) between the rhenium and the oxo ligand for [ReOBr(quin-2-c)$_2$]

BD	Occupancy	Composition of NBO	BD*	Occupancy
Re–O_t	1.994	$0.552(d)_{Re} + 0.834(p)_O$	$0.834(d)_{Re} - 0.552(p)_O$	0.265
Re–O_t	1.984	$0.567(d)_{Re} + 0.824(p)_O$	$0.824(d)_{Re} - 0.567(p)_O$	0.273

BD denotes 2-center bond, * denotes antibonding NBO.

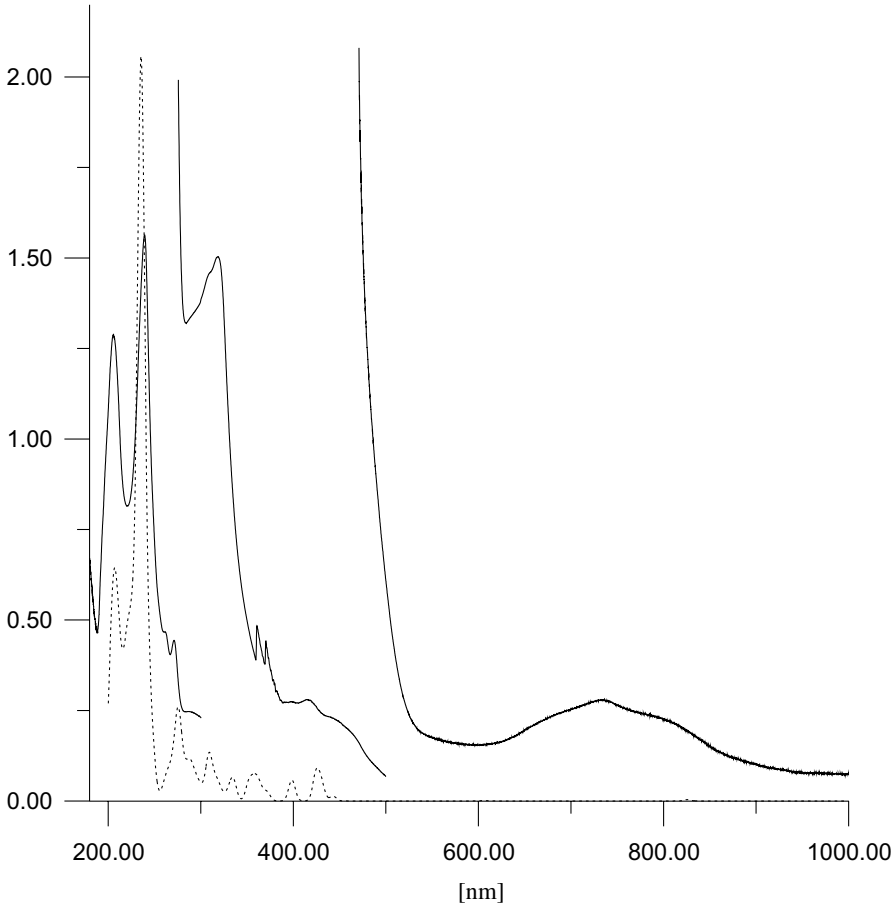


Fig. 3. The experimental (——) and calculated (------) electronic absorption spectra of [ReOBr(quin-2-c)$_2$].

Additional information about nature of the rhenium–terminal oxygen bonding has been obtained by NBO analysis. The occupancy and composition of the calculated Re–O_t natural bond orbitals (NBOs) are given in Table 7. Each natural bond orbital (NBO) σ_{AB} can be written in terms of two directed valence hybrids (NHOs) h_A and h_B on atoms A and B:

$$\sigma_{AB} = c_A h_A + c_B h_B$$

where c_A and c_B are polarization coefficients. Each valence bonding NBO must in turn be paired with a corresponding valence *anti*-bonding NBO:

$$\sigma^*_{AB} = c_B h_A - c_A h_B$$

to complete the span of the valence space. The Lewis-type (donor) NBOs are thereby complemented by the non-Lewis-type (acceptor) NBOs that are formally empty in

Table 8
The energy and molar absorption coefficients of experimental absorption bands and the electronic transitions calculated with the TD-DFT method for [ReOBr(quin-2-c)$_2$]

The most important orbital excitations	Character	λ (nm)	E (eV)	f	Experimental Λ (nm) (E (eV)) ε
H → L	d → d	825.7	1.50	*0.0018*	815.0 (1.52) 100
H → L + 1	d → d	606.3	2.04	*0.0006*	727.7 (1.70) 125
H − 1 → L	π(quin-2-c)/π(Br) → d	442.8	2.80	*0.0066*	435.4 (2.85) 2720
H − 2 → L	π(quin-2-c) → d	430.3	2.88	*0.0226*	
H → L + 2	d → π*(quin-2-c)	424.6	2.92	*0.0380*	417.9 (2.97) 3220
H → L + 3	d → π*(quin-2-c)	398.4	3.11	*0.0289*	
H − 3 → L	π(quin-2-c) → d	371.6	3.34	*0.0111*	370.3 (3.35) 5115
H − 2 → L + 1	π(quin-2-c) → d	361.4	3.43	*0.0104*	360.6 (3.44) 5600
H − 2 → L + 1	π(quin-2-c) → d	357.2	3.47	*0.0177*	
H − 4 → L	π(quin-2-c) → d				
H − 6 → L	π(Br)/π(quin-2-c) → d	351.9	3.52	*0.0239*	
H − 1 → L + 2	π(quin-2-c)/π(Br) → π*(quin-2-c)	335.3	3.70	*0.0246*	271.0 (4.59) 25650
H − 6 → L + 1	π(Br)/π(quin-2-c) → d	309.5	4.01	*0.0289*	
H − 4 → L + 1	π(quin-2-c) → d	308.7	4.03	*0.0333*	
H − 4 → L + 2	π(quin-2-c) → π*(quin-2-c)	287.4	4.31	*0.0379*	
H − 3 → L + 3	π(quin-2-c) → π*(quin-2-c)	282.0	4.40	*0.0207*	
H − 4 → L + 3	π(quin-2-c) → π*(quin-2-c)	276.6	4.48	*0.0301*	
H − 3 → L + 3	π(quin-2-c) → π*(quin-2-c)	275.0	4.51	*0.0706*	
H → L + 5	d → π*(quin-2-c)				
H − 2 → L + 6	π(quin-2-c) → π*(quin-2-c)	245.3	5.05	*0.0270*	239.1 (5.19) 90375
H − 1 → L + 4	π(quin-2-c)/π(Br) → π*(quin-2-c)	243.9	5.08	*0.0755*	
H − 14 → L	π(quin-2-c) → d	242.0	5.12	*0.0262*	
H − 10 → L + 1	π(quin-2-c)/π(O_t)/σ(Br) → d				
H − 14 → L	π(quin-2-c) → d	239.6	5.18	*0.0422*	
H − 2 → L + 5	π(quin-2-c) → π*(quin-2-c)	238.5	5.20	*0.1960*	
H → L + 9	d → d	237.5	5.22	*0.0226*	
H − 2 → L + 4	π(quin-2-c) → π*(quin-2-c)	235.4	5.27	*0.6979*	
H − 1 → L + 5	π(quin-2-c)/π(Br) → π*(quin-2-c)				
H − 12 → L + 1	π(quin-2-c)/π(O_t) → d	232.1	5.34	*0.1985*	
H − 9 → L + 3	π(quin-2-c)σ(Br) → π*(quin-2-c)				
H − 8 → L + 3	π(Br)/π(quin-2-c) → π*(quin-2-c)	231.0	5.36	*0.0318*	
H → L + 8	d → π*(quin-2-c)	225.8	5.49	*0.0471*	206.6 (6.00) 73950
H − 11 → L + 1	π(quin-2-c)/π(O_t) → d				
H − 12 → L + 2	π(quin-2-c)/π(O_t) → π*(quin-2-c)	225.7	5.49	*0.0612*	
H − 11 → L + 1	π(quin-2-c)/π(O_t) → d				
H − 3 → L + 4	π(quin-2-c) → π*(quin-2-c)	223.6	5.54	*0.0257*	
H − 4 → L + 5	π(quin-2-c) → π*(quin-2-c)	222.3	5.58	*0.0363*	
H − 11 → L + 2	π(quin-2-c)/π(O_t) → π*(quin-2-c)	219.6	5.65	*0.0416*	
H − 17 → L	π(quin-2-c)σ(Br) → d	219.2	5.66	*0.0376*	
H − 8 → L + 1	π(Br)/π(quin-2-c) → d	213.7	5.80	*0.0236*	
H − 6 → L + 5	π(Br)/π(quin-2-c) → π*(quin-2-c)	213.2	5.82	*0.0231*	
H − 15 → L + 2	π(quin-2-c) → π*(quin-2-c)	209.4	5.92	*0.0848*	
H − 15 → L + 2	π(quin-2-c) → π*(quin-2-c)	206.9	6.00	*0.0280*	
H − 11 → L + 3	π(quin-2-c)/π(O_t) → π*(quin-2-c)	206.5	6.00	*0.0626*	
H − 11 → L + 3	π(quin-2-c)/π(O_t) → π*(quin-2-c)	205.0	6.05	*0.0941*	
H − 13 → L + 3	π(quin-2-c)/π(O_t) → π*(quin-2-c)	201.8	6.14	*0.02101*	

ε, molar absorption coefficient (dm^3 mol^{-1} cm^{-1}); f, oscillator strength; H, highest occupied molecular orbital; L, lowest unoccupied molecular orbital.

an idealized Lewis picture. The interactions between 'filled' Lewis-type NBOs and 'empty' non-Lewis NBOs lead to loss of occupancy from the localized NBOs of the idealized Lewis structure into the empty non-Lewis orbitals, and they are referred to as 'delocalization' corrections to the zeroth-order natural Lewis structure [34].

The detected natural Re–O_t bond orbitals of [ReOBr(quin-2-c)$_2$] are π orbitals – the p_x and p_y oxygen orbitals and d_{xz} and d_{yz} rhenium orbitals are involved in their formation. Not detected, the $\sigma_{Re–Ot}$ bond has character of predominant Coulomb-type interactions between the central ion and ligands [40]. The terminal oxo ligand of [ReOBr(quin-2-c)$_2$] has two lone pair orbitals, and electron density from one of them is strongly delocalized into the non-Lewis rhenium orbital. Accordingly, NBO analysis confirms a triple bond between the rhenium and the terminal oxygen ligand.

4.4. Electronic spectra

The experimental and calculated electronic spectra of [ReOBr(quin-2-c)$_2$] are presented in Fig. 3. Each calculated transition is represented by a Gaussian function $y = c\,e^{-bx^2}$ with the height (c) equal to the oscillator strength and b equal to 0.04 nm^{-2}. The shape of the UV–Vis spectrum of [ReOCl(quin-2-c)$_2$] is the same as for the bromo analogue; the absorption bands of the chloro complex were recorded at 842.1, 731.7, 432.6, 370.4, 360.7 269.5, 241.2 and 208.7 nm.

The spin-allowed singlet–singlet electronic transitions calculated with the TD-DFT method for [ReOBr(quin-2-c)$_2$] are gathered in Table 8. For the high energy part of the spectrum, only transitions with oscillator strengths larger than 0.020 are listed in Table 8.

The TD-DFT/PCM calculations show that the two longest wavelength experimental bands of [ReOBr(quin-2-c)$_2$] at 815.0 and 743.7 nm originate in the HOMO → LUMO and HOMO → LUMO + 1 transitions, respectively. As d_{Re} orbitals take the main part in the HOMO, LUMO and LUMO + 1 orbitals, the HOMO → LUMO and HOMO → LUMO + 1 transitions may be attributed to transitions of d → d character. However, as it can be seen from Fig. 2, the HOMO, LUMO and LUMO + 1 orbitals are delocalized amongst the rhenium ion, bromide, oxo and quin-2-c ligands so a delocalized *MLLCT* (metal–ligand-to-ligand CT) description also can be used. In Table 8, the assignment of the calculated transitions to the experimental bands is based on consideration of main components of the molecular orbital.

The absorption bands with maxima at 435.4, 370.3 and 360.6 nm are assigned to the *Ligand–Metal Charge Transfer* transitions. The *Metal–Ligand Charge Transfer* transitions ($d \rightarrow \pi^*_{quin\text{-}2\text{-}c}$) make the largest contribution into the experimental band at 417.9 nm.

The experimental bands below 300 nm result mainly from *Ligand–Ligand Charge Transfer* and interligand (*IL*) transitions.

5. Supplementary material

CCDC 645437 and 645438 contain the supplementary crystallographic data for $C_{20}H_{12}BrN_2O_5Re$ and $C_{20}H_{12}ClN_2O_5Re$. These data can be obtained free of charge via http://www.ccdc.cam.ac.uk/conts/retrieving.html, or from the Cambridge Crystallographic Data Centre, 12 Union Road, Cambridge CB2 1EZ, UK; fax: (+44) 1223-336-033; or e-mail: deposit@ccdc.cam.ac.uk.

Acknowledgements

The GAUSSIAN-03 calculations were carried out in the Wrocław Centre for Networking and Supercomputing, WCSS, Wrocław, Poland.

References

[1] R.H. Holm, Chem. Rev. 87 (1987) 1401.
[2] C.C. Romão, F.E. Kühn, W.A. Hermann, Chem. Rev. 97 (1997) 3197.
[3] S.B. Seymore, S.N. Brown, Inorg. Chem. 39 (2000) 325.
[4] F.E. Kühn, A. Scherbaum, W.A. Herrmann, J. Organomet. Chem. 689 (2004) 4149.
[5] A.M. Kirillov, M. Haukka, M.V. Kirillova, A.J.L. Pombeiro, Adv. Synth. Catal. 347 (2005) 1435.
[6] A. Deloffre, S. Halut, L. Salles, J.-M. Brégeault, J.R. Gregorio, B. Denise, H. Rudler, J. Chem. Soc., Dalton Trans. (1999) 2897.
[7] W. Volkert, W.F. Goeckeler, G.J. Ehrhardt, A.R. Ketring, J. Nucl. Med. 32 (1991) 174.
[8] E.A. Deutsch, K. Libson, J.L. Vanderheyden, Technetium and Rhenium in Chemistry and Nuclear Medicine, Raven Press, New York, 1990.
[9] B. Machura, Coord. Chem. Rev. 249 (2005) 591.
[10] D. Dobrzyńska, T. Lis, L.B. Jerzykiewicz, Inorg. Chem. Commun. 8 (2005) 1090.
[11] A. Voigt, U. Abram, R. Böttcher, U. Richter, J. Reinhold, R. Kirmse, Chem. Phys. 253 (2000) 171.
[12] M. Lipowska, L. Hansen, R. Cini, X. Xu, H. Choi, A.T. Taylor, L.G. Marzilli, Inorg. Chim. Acta 339 (2002) 327.
[13] J. Gancheff, C. Kremer, E. Kremer, O.N. Ventura, J. Mol. Struct. (Theochem) 580 (2002) 107.
[14] M.L. Kuznestov, E.A. Klestova-Nadeeva, A.I. Dement'ev, J. Mol. Struct. (Theochem) 671 (2004) 229.
[15] N. Psaroudakis, K. Mertis, D.G. Liakos, E.D. Simandiras, Chem. Phys. Lett. 369 (2003) 490.
[16] X.-Y. Liu, S. Bouherour, H. Jacobsen, H.W. Schmalle, H. Berke, Inorg. Chim. Acta 330 (2002) 250.
[17] É. Bencze, J. Mink, I. Pápai, I.S. Butler, D. Lafleur, D.F.R. Gilson, J. Organomet. Chem. 616 (2000) 1.
[18] W.-Y. Wong, S.-H. Cheung, X. Huang, Z. Lin, J. Organomet. Chem. 655 (2002) 39.
[19] B. Machura, R. Kruszynski, M. Jaworska, Polyhedron 25 (2006) 1111.
[20] B. Machura, R. Kruszynski, Polyhedron 25 (2006) 1985.
[21] G. Rouschias, G. Wilkinson, J. Chem. Soc. A (1966) 465.
[22] CrysAlis RED, Oxford Diffraction Ltd., Version 1.171.29.2.
[23] G.M. Sheldrick, Acta Crystallogr., Sect. A 46 (1990) 467.
[24] G.M. Sheldrick, SHELXL-97: Program for the Refinement of Crystal Structures, University of Göttingen, Göttingen, Germany, 1997.
[25] G.M. Sheldrick, SHELXTL: Release 4.1 for Siemens Crystallographic Research Systems, 1990.
[26] M.J. Frisch, G.W. Trucks, H.B. Schlegel, G.E. Scuseria, M.A. Robb, J.R. Cheeseman, J.A. Montgomery Jr., T. Vreven, K.N. Kudin, J.C. Burant, J.M. Millam, S.S. Iyengar, J. Tomasi, V. Barone, B.

Mennucci, M. Cossi, G. Scalmani, N. Rega, G.A. Petersson, H. Nakatsuji, M. Hada, M. Ehara, K. Toyota, R. Fukuda, J. Hasegawa, M. Ishida, T. Nakajima, Y. Honda, O. Kitao, H. Nakai, M. Klene, X. Li, J.E. Knox, H.P. Hratchian, J.B. Cross, C. Adamo, J. Jaramillo, R. Gomperts, R.E. Stratmann, O. Yazyev, A.J. Austin, R. Cammi, C. Pomelli, J.W. Ochterski, P.Y. Ayala, K. Morokuma, G.A. Voth, P. Salvador, J.J. Dannenberg, V.G. Zakrzewski, S. Dapprich, A.D. Daniels, M.C. Strain, O. Farkas, D.K. Malick, A.D. Rabuck, K. Raghavachari, J.B. Foresman, J.V. Ortiz, Q. Cui, A.G. Baboul, S. Clifford, J. Cioslowski, B.B. Stefanov, G. Liu, A. Liashenko, P. Piskorz, I. Komaromi, R.L. Martin, D.J. Fox, T. Keith, M.A. Al-Laham, C.Y. Peng, A. Nanayakkara, M. Challacombe, P.M.W. Gill, B. Johnson, W. Chen, M.W. Wong, C. Gonzalez, J.A. Pople, GAUSSIAN-03, Revision B.03, Gaussian, Inc., Pittsburgh, PA, 2003.

[27] A.D. Becke, J. Chem. Phys. 98 (1993) 5648.

[28] C. Lee, W. Yang, R.G. Parr, Phys. Rev. B 37 (1988) 785.

[29] M.E. Casida, in: J.M. Seminario (Ed.), Recent Developments and Applications in Modern Density Functional Theory, Theoretical and Computational Chemistry, vol. 4, Elsevier, Amsterdam, 1996.

[30] P.C. Hariharan, J.A. Pople, Theor. Chim. Acta 28 (1973) 213.

[31] V.A. Rassolov, M.A. Ratner, J.A. Pople, P.C. Redfern, L.A. Curtiss, J. Comput. Chem. 22 (2001) 976.

[32] P.J. Hay, W.R. Wadt, J. Chem. Phys. 82 (1985) 299.

[33] K. Eichkorn, F. Weigend, O. Treutler, R. Ahlrichs, Theor. Chem. Acc. 97 (1997) 119.

[34] (a) E.D. Glendening, A.E. Reed, J.E. Carpenter, F. Weinhold, NBO (version 3.1);
(b) E. Reed, L.A. Curtiss, F. Weinhold, Chem. Rev. 88 (1988) 899.

[35] G.A. Jeffrey, W. Saenger, Hydrogen Bonding in Biological Structures, Springer, Berlin, 1994.

[36] G.R. Desiraju, T. Steiner, The Weak Hydrogen Bond in Structural Chemistry and Biology, Oxford University Press, Oxford, 1999.

[37] J.M. Mayer, Inorg. Chem. 27 (1988) 3899.

[38] F.H. Allen, Acta Crystallogr., Sect. B 58 (2002) 380.

[39] B. Machura, R. Kruszynski, Polyhedron 26 (2007) 2957.

[40] M.L. Kuznetsov, A.J.L. Pombeiro, J. Chem. Soc., Dalton Trans. (2003) 738.

Available online at www.sciencedirect.com
ScienceDirect
Polyhedron 27 (2008) 196–202
POLYHEDRON
www.elsevier.com/locate/poly

Synthesis and characterizations of *N*,*N*-bis(diphenylphosphino)ethylaniline derivatives and X-ray crystal structure of palladium (II), platinum (II) complexes

Feyyaz Durap [a,*], Nermin Biricik [a], Bahattin Gümgüm [a], Saim Özkar [b], Wee Han Ang [c], Zhaofu Fei [c], Rosario Scopelliti [c]

[a] *Department of Chemistry, University of Dicle, 21280 Diyarbakir, Turkey*
[b] *Department of Chemistry, METU, 06531 Ankara, Turkey*
[c] *Institut de Sciences et Ingénierie Chimiques, Ecole Polytechnique Fédérale de Lausanne, CH-1015 Lausanne, Switzerland*

Received 27 July 2007; accepted 5 September 2007
Available online 5 November 2007

Abstract

N,*N*-Bis(diphenylphosphino)ethylaniline compounds, $[Ph_2P]_2N\text{-}C_6H_4\text{-}C_2H_5$, with ethyl groups at the *ortho*- and *para*-positions have been synthesized. Oxidation of the aminophosphines with hydrogen peroxide, elemental sulfur and selenium gave the corresponding oxides, sulfides and selenides $[Ph_2P(E)]_2N\text{-}C_6H_4\text{-}C_2H_5$ (E = O, S, Se). Complexes $[MCl_2\{(Ph_2P)_2N\text{-}C_6H_4\text{-}(C_2H_5)\}]$ (M = Pd, Pt) and $[Cu\{(Ph_2P)_2N\text{-}C_6H_4\text{-}C_2H_5\}_2]PF_6$ were obtained by the reaction of *N*,*N*-bis(diphenylphosphino)ethylaniline with $[MCl_2(COD)]$ (M = Pd, Pt) and $[Cu(MeCN)_4]PF_6$. The new compounds were characterized by NMR, IR spectroscopy and microanalysis. In addition, representative solid-state structures of the palladium and platinum complexes were determined using single crystal X-ray diffraction analyses.
© 2007 Elsevier Ltd. All rights reserved.

Keywords: Aminophosphine; Synthesis; Oxidation; Complexation; X-ray structures

1. Introduction

The chemistry of aminophosphines containing direct P–N bonds is one of the most challenging areas in main group chemistry [1]. Among the numerous aminophosphines, bis(diphenylphosphino)alkylaniline derivatives are particularly interesting due to their relatively high stability and their ability to chelate transition metals such as palladium, platinum and copper [2,3]. Many aminophosphine ligands and their complexes have been investigated as co-catalysts in a number of catalytic processes [4,5]. Some aminophosphines and derivatives have also found application as anticancer drugs [6], herbicides and antimicrobial agents, as well as neuroactive agents [7,8]. The synthesis of bis(diphenylphosphino)alkylaniline is usually achieved in high yield via the aminolysis of aniline [9,10], which allows for the incorporation of additional functional groups such as O and N donors [11,12], or π-donors such as allyl groups [13]. The presence of the bulky groups attached to the phosphorus center renders the aminophosphine more stable against hydrolysis. The substituents at the aniline backbone can also play an important role in determining the outcome of the products [14]. In a recent study [15], we found that electron-donating groups often lead to the exclusive formation of aminophosphines [P(III)–N–P(III)], whereas electron-withdrawing groups, such as nitrile and trifluoromethyl at the *ortho*-position can lead to formation of iminobiphosphine [P(III)–P(V)=N] species.

* Corresponding author. Tel.: +90 4122488550; fax: +90 4122488300.
E-mail address: fdurap@dicle.edu.tr (F. Durap).

0277-5387/$ - see front matter © 2007 Elsevier Ltd. All rights reserved.
doi:10.1016/j.poly.2007.09.011

Herein, we describe the synthesis of new *N*,*N*-bis(diphenylphosphino)ethylaniline with an ethyl group at the *ortho*- and *para*-positions. In order to study their reactivities, we prepared their corresponding complexes with selected transition metals (Cu, Pd, Pt), and also the aminophosphine oxides, sulfides and selenides. The compounds were fully characterized using multi-nuclear NMR spectroscopic methods and the solid-state structures of two of the products were established by single crystal X-ray diffraction analyses.

2. Experimental

All reactions were performed under argon unless otherwise stated. Ph_2PCl and the ethyl anilines were purchased from Fluka and used directly. The starting materials $[MCl_2(COD)]$ (M = Pd, Pt, COD = 1,5-cyclooctadiene) [16,17] and $[Cu(MeCN)_4]PF_6$ [18] were prepared according to the literature procedures. Solvents were dried using the appropriate reagents and distilled prior to use. Infrared spectra were recorded as KBr pellets in the range 4000–400 cm^{-1} on a Mattson 1000 ATI UNICAM FT-IR spectrometer. ^1H NMR (400.1 MHz) spectra were recorded on a Bruker AC 400 spectrometer, and $^{31}P-\{^1H\}$ NMR spectra at 162 MHz with δ referenced to external 85% H_3PO_4. Microanalysis was carried out on a Fisons EA 1108 CHNS-O instrument.

2.1. General procedure for the synthesis of *N,N-bis(diphenylphosphino)ethylanilines*

2.1.1. *[(Ph$_2$P)$_2$N-C$_6$H$_4$-C$_2$H$_5$] (**1**, **2**)*

N,*N*-Bis(diphenylphosphino)ethylanilines were prepared by the aminolysis reaction of $H_2N-C_6H_4-C_2H_5$ (**1**: 2-C_2H_5; **2**: 4-C_2H_5) with two equivalents of Ph_2PCl according to the procedure given in the literature [19].

2.2. General procedure for the synthesis of the chalcogenides

2.2.1. *N,N-Bis(diphenyloxophosphino)ethylanilines [(Ph$_2$P(O))$_2$N-C$_6$H$_4$-C$_2$H$_5$] (**1a**, **2a**)*

A THF solution (10 mL) of *N*,*N*-bis(diphenylphosphino)ethylaniline (0.20 g, 0.420 mmol) and aqueous H_2O_2 (30% w/w, 0.083 mL) was stirred for 2 h at room temperature. The solution was evaporated to dryness under reduced pressure and the white solids **1a** and **2a** were obtained.

*N,N-Bis(diphenyloxophosphino)-2-ethylaniline (**1a**)*: Yield: 0.065 g, 25%, mp 180–181 °C. ^1H NMR ($CDCl_3$) δ (ppm): 6.85–7.89 (m, 24H, Ar H), 2.72–2.78 (q, 2H, CH_2, $^3J_{HH} = 7.4$ Hz), 0.90–0.94 (t, 3H, CH_3, $^3J_{HH} = 7.3$ Hz). $^{31}P-\{^1H\}$ NMR ($CDCl_3$) δ (ppm): 23.6 (s). Selected IR, ν (cm^{-1}): 901 (P–N–P), 1219 (PO). *Anal*. Calc. for $C_{32}H_{29}NP_2O_2$: C, 73.70; H, 5.56; N, 2.68. Found: C, 73.56; H, 5.47; N, 2.46%.

*N,N-Bis(diphenyloxophosphino)-4-ethylaniline (**2a**)*: Yield: 0.18 g, 70%, mp 215–217 °C. ^1H NMR ($CDCl_3$) δ (ppm): 6.74–7.88 (m, 24H, Ar H), 2.32–2.38 (q, 2H, CH_2, $^3J_{HH} = 7.8$ Hz), 0.96–1.00 (t, 3H, CH_3, $^3J_{HH} = 7.6$ Hz). $^{31}P-\{^1H\}$ NMR ($CDCl_3$) δ (ppm): 24.3 (s). Selected IR, ν (cm^{-1}): 909 (P–N–P), 1213 (PO). *Anal*. Calc. for $C_{32}H_{29}NP_2O_2$: C, 73.70; H, 5.56; N, 2.68. Found: C, 73.84; H, 5.36; N, 2.59%.

2.2.2. *N,N-Bis(diphenylthiophosphino)ethylanilines [(Ph$_2$P(S))$_2$N-C$_6$H$_4$-C$_2$H$_5$] (**1b**, **2b**)*

To solid *N*,*N*-bis(diphenylphosphino)ethylaniline (0.20 g, 0.420 mmol) and S_8 (0.027 g, 0.840 mmol) was added THF (20 mL) and this was refluxed for 6 h. The volume was concentrated in vacuum to ca. 1–2 mL and addition of *n*-hexane (20 mL) gave **1b** and **2b** as white solids which were collected by suction filtration.

*N,N-Bis(diphenylthiophosphino)-2-ethylaniline (**1b**)*: Yield: 0.117 g, 52%, mp 172–174 °C. ^1H NMR ($CDCl_3$) δ (ppm): 6.85–8.13 (m, 24H, Ar H), 2.43–2.48 (q, 2H, CH_2, $^3J_{HH} = 7.4$ Hz), 0.85–0.89 (t, 3H, CH_3, $^3J_{HH} = 7.5$ Hz). $^{31}P-\{^1H\}$ NMR ($CDCl_3$) δ (ppm): 68.3 (s). Selected IR, ν (cm^{-1}): 862 (P–N–P), 650 (P–S). *Anal*. Calc. for $C_{32}H_{29}NP_2S_2$: C, 69.44; H, 5.24; N, 2.53; S, 11.57. Found: C, 69.63; H, 5.18; N, 2.73; S, 11.62%.

*N,N-Bis(diphenylthiophosphino)-4-ethylaniline (**2b**)*: Yield: 0.132 g, 58%, mp 196–197 °C. ^1H NMR ($CDCl_3$) δ (ppm): 6.68–8.09 (m, 24H, Ar H), 2.32–2.34 (q, 2H, CH_2, $^3J_{HH} = 7.8$ Hz), 0.97–1.00 (t, 3H, CH_3, $^3J_{HH} = 7.6$ Hz). $^{31}P-\{^1H\}$ NMR ($CDCl_3$) δ (ppm): 68.8 (s). Selected IR, ν (cm^{-1}): 882 (P–N–P), 658 (P–S). *Anal*. Calc. for $C_{32}H_{29}NP_2S_2$: C, 69.44; H, 5.24; N, 2.53; S, 11.57. Found: C, 69.31; H, 5.30; N, 2.24; S, 11.41%.

2.2.3. *N,N-Bis(diphenylselenophosphino)ethylanilines [(Ph$_2$P(Se))$_2$N-C$_6$H$_4$-C$_2$H$_5$] (**1c**, **2c**)*

To solid *N*,*N*-bis(diphenylphosphino)ethylaniline (0.20 g, 0.420 mmol) and grey Se (0.064 g, 0.840 mmol) was added THF (20 mL) and this was refluxed for 6 h. The volume was concentrated in vacuum to ca. 1–2 mL and addition of *n*-hexane (20 mL) gave **1c** and **2c** which were collected by suction filtration.

*N,N-Bis(diphenylselenophosphino)-2-ethylaniline (**1c**)*: Yield: 0.155 g, 59%, mp 174–175 °C. ^1H NMR ($CDCl_3$) δ (ppm): 6.87–8.15 (m, 24H, Ar H), 2.38–2.44 (q, 2H, CH_2, $^3J_{HH} = 7.4$ Hz), 0.88–0.91 (t, 3H, CH_3, $^3J_{HH} = 7.4$ Hz). $^{31}P-\{^1H\}$ NMR ($CDCl_3$) δ (ppm): 67.5, $J_{(PSe)}$: 788 Hz. Selected IR, ν (cm^{-1}): 855 (P–N–P), 579 (P–Se). *Anal*. Calc. for $C_{32}H_{29}NP_2Se_2$: C, 59.35; H, 4.48; N, 2.16. Found: C, 59.34; H, 4.22; N, 2.03%.

*N,N-Bis(diphenylselenophosphino)-4-ethylaniline (**2c**)*: Yield: 0.176 g, 67%, mp 182–184 °C. ^1H NMR ($CDCl_3$) δ (ppm): 6.68–8.19 (m, 24H, Ar H), 2.32–2.35 (q, 2H, CH_2, $^3J_{HH} = 7.5$ Hz), 0.96–1.00 (t, 3H, CH_3, $^3J_{HH} = 7.5$ Hz). $^{31}P-\{^1H\}$ NMR ($CDCl_3$) δ (ppm): 69.6, $J_{(PSe)}$: 782 Hz. Selected IR, ν (cm^{-1}): 876 (P–N–P), 565 (P–Se). *Anal*. Calc. for $C_{32}H_{29}NP_2Se_2$: C, 59.35; H, 4.48; N, 2.16. Found: C, 59.48; H, 4.53; N, 2.07%.

2.3. General procedure for the synthesis of the complexes

2.3.1. Dichloro{*N,N*-bis(diphenylphosphino)ethylaniline}-palladium (II) (**1d, 2d**)

A solution of [$PdCl_2$(COD)] (0.049 g, 0.172 mmol) and *N,N*-bis(diphenylphosphino) ethylaniline (0.086 g, 0.175 mmol) in CH_2Cl_2 (10 mL) was stirred for 1.5 h. The volume was concentrated in vacuum to ca. 1–2 mL and addition of diethyl ether (20 mL) gave **1d** and **2d** as yellow solids which were collected by suction filtration and dried in vacuum.

*Dichloro{N,N-bis(diphenylphosphino)-2-ethylaniline}-palladium (II) (**1d**)*: Yield: 0.094 g, 85%, mp >300 °C. ^{1}H NMR ($CDCl_3$) δ (ppm): 6.57–7.94 (m, 24H, Ar H), 1.38–1.41 (q, 2H, CH_2, $^3J_{HH} = 7.4$ Hz), 0.91–0.95 (t, 3H, CH_3, $^3J_{HH} = 7.5$ Hz). ^{31}P–{^{1}H} NMR ($CDCl_3$) δ (ppm): 37.2 (s). Selected IR, ν (cm^{-1}): 900 (P–N–P). *Anal.* Calc. for $C_{32}H_{29}NP_2PdCl_2$: C, 60.86; H, 4.59; N, 2.22. Found: C, 60.77; H, 4.39; N, 2.05%.

*Dichloro{N,N-bis(diphenylphosphino)-4-ethylaniline}-palladium (II) (**2d**)*: Yield: 0.10 g, 97%, mp >300 °C. ^{1}H NMR ($CDCl_3$) δ (ppm): 6.43–7.92 (m, 24H, Ar H); 2.52–2.54 (q, 2H, CH_2, $^3J_{HH} = 7.5$ Hz), 1.15–1.18 (t, 3H, CH_3, $^3J_{HH} = 7.5$ Hz). ^{31}P–{^{1}H} NMR ($CDCl_3$) δ (ppm): 34.8 (s). Selected IR, ν (cm^{-1}): 913 (P–N–P). *Anal.* Calc. for $C_{32}H_{29}NP_2PdCl_2$: C, 60.86; H, 4.59; N, 2.22. Found: C, 60.66; H, 4.38; N, 2.33%. Slow diffusion of diethyl ether into a CH_2Cl_2 solution of **2d** over 48 h gave crystals suitable for X-ray diffraction.

2.3.2. Dichloro{*N,N*-bis(diphenylphosphino)ethylaniline}-platinum (II) (**1e, 2e**)

A solution of [$PtCl_2$(COD)] (0.034 g, 0.0860 mmol) and *N,N*-bis(diphenylphosphino)ethylaniline (0.0427 g, 0.0875 mmol) in CH_2Cl_2 (10 mL) was stirred for 1.5 h. The volume was concentrated in vacuum to ca. 1–2 mL and addition of diethyl ether (20 mL) gave **1e** and **2e** as white solids which were collected by suction filtration and dried in vacuum.

*Dichloro{N,N-bis(diphenylphosphino)-2-ethylaniline}-platinum (II) (**1e**)*: Yield: 0.056 g, 86%, mp 339–341 °C. ^{1}H NMR ($CDCl_3$) δ (ppm): 6.48–7.93 (m, 24H, Ar H), 1.21–1.25 (q, 2H, CH_2, $^3J_{HH} = 7.1$ Hz), 0.23–0.27 (t, 3H, CH_3, $^3J_{HH} = 7.2$ Hz). ^{31}P–{^{1}H} NMR ($CDCl_3$) δ (ppm): 22.3, $J_{(PtP)}$: 3348.6 Hz. Selected IR, ν (cm^{-1}): 900 (P–N–P). *Anal.* Calc. for $C_{32}H_{29}NP_2PtCl_2$: C, 50.86; H, 3.84; N, 1.85. Found: C, 50.84; H, 3.63; N, 1.67%. Slow diffusion of diethyl ether into a $CHCl_3$ solution of **1e** over 48 h gave crystals suitable for X-ray crystallography.

*Dichloro{N,N-bis(diphenylphosphino)-4-ethylaniline}-platinum (II) (**2e**)*: Yield: 0.057 g, 88%, mp 339–340 °C. ^{1}H NMR ($CDCl_3$) δ (ppm): 6.36–7.90 (m, 24H, Ar H), 2.51–2.56 (q, 2H, CH_2, $^3J_{HH} = 7.5$ Hz), 1.14–1.17 (t, 3H, CH_3, $^3J_{HH} = 7.5$ Hz). ^{31}P–{^{1}H} NMR ($CDCl_3$) δ (ppm): 20.6, $J_{(PtP)}$: 3324 Hz. Selected IR, ν (cm^{-1}): 906 (P–N–P). *Anal.* Calc. for $C_{32}H_{29}NP_2PtCl_2$: C, 50.86; H, 3.84; N, 1.85. Found: C, 50.71; H, 3.78; N, 1.76%.

2.3.3. Bis[*N,N*-bis(diphenylphosphino)ethylaniline]copper (I) hexafluorophosphates (**1f, 2f**)

To a solution of [$Cu(MeCN)_4$]PF_6 (0.071 g, 0.191 mmol) in CH_2Cl_2 (20 mL) was added *N,N*-bis(diphenylphosphino)ethylaniline (0.185 g, 0.380 mmol) and the resulting solution was stirred for 2 h. The volume was concentrated in vacuum to ca. 1–2 mL and addition of diethyl ether (20 mL) gave **1f** and **2f** as white solids which were collected by suction filtration and dried in vacuum.

*Bis[N,N-bis(diphenylphosphino)-2-ethylaniline]copper (I) hexafluorophosphate (**1f**)*: Yield: 0.183 g, 83%, mp 204–205 °C. ^{1}H NMR ($CDCl_3$) δ (ppm): 6.87–8.15 (m, 24H, Ar H), 1.21–1.27 (q, 2H, CH_2, $^3J_{HH} = 7.6$ Hz), 0.02–0.05 (t, 3H, CH_3, $^3J_{HH} = 7.5$ Hz). ^{31}P–{^{1}H} NMR ($CDCl_3$) δ (ppm): 87.7 (s), $\delta_{(PF6)}$: −144.3(m); $J_{(PF6)}$: 1418 Hz. Selected IR, ν (cm^{-1}): 843 (P–N–P). *Anal.* Calc. for $C_{64}H_{58}N_2P_5F_6Cu$: C, 64.73; H, 4.89; N, 2.36. Found: C, 64.69; H, 5.02; N, 2.21%.

*Bis[N,N-bis(diphenylphosphino)-4-ethylaniline]copper (I) hexafluorophosphate (**2f**)*: Yield: 0.20 g, 91%, mp 339–340 °C. ^{1}H NMR ($CDCl_3$) δ (ppm): 6.68–8.19 (m, 24H, Ar H), 2.45–2.51 (q, 2H, CH_2, $^3J_{HH} = 7.6$ Hz), 1.08–1.12 (t, 3H, CH_3, $^3J_{HH} = 7.6$ Hz). ^{31}P–{^{1}H} NMR ($CDCl_3$) δ (ppm): 88.2 (s), $\delta_{(PF_6)}$: −144.3(m); $J_{(PF_6)}$: 1424 Hz. Selected IR, ν (cm^{-1}): 848 (P–N–P). *Anal.* Calc. for $C_{64}H_{58}N_2P_5F_6Cu$: C, 64.73; H, 4.89; N, 2.36. Found: C, 64.79; H, 4.95; N, 2.41%.

2.3.4. Structure determination in the solid state

Data collection for **1e** and **2d** was performed on an Oxford-Kuma Xcalibur diffractor with a Sapphire CCD area detector at 140(2) K and data reduction was performed using CrysAlis RED [20]. The structures were solved by direct methods using SIR-92 [21], and refined by full-matrix least-squares refinement (against F^2) using SHELXTL [22,23], with all non-hydrogen atoms refined anisotropically. The hydrogen atoms were placed in their geometrically generated positions and treated as riding on their parent atoms with $U_{iso}(H) = 1.2U_{eq}(C)$, except for the terminal H-atoms on C8 where $U_{iso}(H) = 1.5U_{eq}(C)$. Empirical absorption corrections were applied using DELABS [24]. Relevant crystallographic data are compiled in Table 1 and graphical representations of the structures were made with DIAMOND [25].

3. Results and discussion

N,N-Bis(diphenylphosphino)ethylanilines, $(Ph_2P)_2N$-C_6H_4-C_2H_5 (**1**: 2-C_2H_5; **2**: 4-C_2H_5) were prepared from H_2-N-C_6H_4-C_2H_5 and Ph_2PCl by aminolysis in CH_2Cl_2 in accordance with our previous reports [19] (Scheme 1).

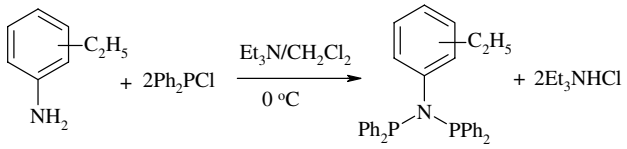
The reaction was monitored by ^{31}P–{^{1}H} NMR spectroscopy. In contrast to reactions of diphenylphosphorus chloride (Ph_2PCl) with anilines bearing electron-withdrawing groups [15], the reaction mixture of Ph_2PCl with 2-ethylaniline or 4-ethylaniline gave a single resonance at δ(P) 61.6 ppm for **1** and 68.5 ppm for **2**, and no formation of

Table 1
Crystallographic data for compounds **1e** · $CHCl_3$ and **2d** · CH_2Cl_2

Compound	**1e** · $CHCl_3$	**2d** · CH_2Cl_2
Chemical formula	$C_{32}H_{29}Cl_3NP_2Pt \cdot CHCl_3$	$C_{32}H_{29}Cl_3NP_2Pd \cdot CH_2Cl_2$
Formula weight	874.86	751.73
Crystal system	monoclinic	monoclinic
Space group	$P2_1/c$	$P2_1/n$
a (Å)	11.9722(6)	10.2901(10)
b (Å)	14.6887(4)	14.8786(15)
c (Å)	19.9617(10)	21.665(2)
α (°)	90	90
β (°)	106.536(5)	98.332(9)
γ (°)	90	90
Volume (Å^3)	3365.2(3)	3282.0(6)
Z	4	4
D_{calc} (g cm^{-3})	1.727	1.521
$F(000)$	1712	1520
μ (mm^{-1})	4.687	1.013
Temperature (K)	140(2)	140(2)
Wavelength (Å)	0.71073	0.71073
Measured reflections	19 557	19 146
Unique reflections	5737	5489
Unique reflections [$I > 2\sigma(I)$]	4218	1781
Number of data/ restraints/ parameters	5737/0/380	5489/192/371
R^a [$I > 2\sigma(I)$]	0.0264	0.0480
wR_2^a (all data)	0.0547	0.1051
Goodness-of-fit (GOF)[b]	0.891	0.677

[a] $R = \sum\|F_o\| - |F_c\|/\sum|F_o|$, $wR_2 = \{\sum[w(F_o^2 - F_c^2)^2]/\sum[w(F_o^2)^2]\}^{1/2}$.

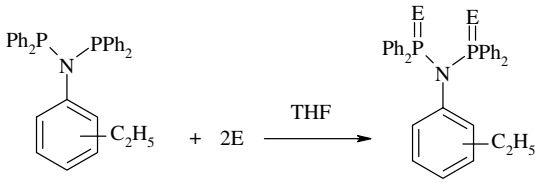
[b] GOF $= \{\sum[w(F_o^2 - F_c^2)^2]/(n-p)\}^{1/2}$ where n is the number of data and p is the number of parameters refined.



Scheme 1. Syntheses of *N*,*N*-bis(diphenylphosphino)ethylanilines by the aminolysis reaction of H_2N-C_6H_4-$C_2H_5$with Ph_2PCl (**1**: 2-C_2H_5; **2**: 4-C_2H_5).

iminobiphosphine species (Ph_2P–PPh_2=$NC_6H_4(C_2H_5)$) could be observed. The ^{31}P–{^1H} NMR signal of compound **1** is shifted upfield compared to that of **2**, although they both lie in the expected region of 60–70 ppm [26]. The compounds are air-stable solids but gradually undergo decomposition on exposure to moisture.

Oxidation of **1** and **2** with aqueous hydrogen peroxide, elemental sulfur and selenium gave the corresponding oxides **1a**, **2a**, sulfides **1b**, **2b** and selenides **1c**, **2c** (Scheme 2). The ^{31}P NMR spectrum of **1a** and **2a** displays one singlet at 23.6 ppm and 24.3 ppm, respectively, suggesting the two phosphorus atoms are chemically equivalent in both compounds. Similarly, singlet resonances were also found in the ^{31}P NMR spectra of **1b** and **2b** (68.3 ppm and



Scheme 2. Oxidation of $(Ph_2P)_2$N-C_6H_4-C_2H_5 with aqueous H_2O_2 (**1a**, **2a**), elemental sulfur (**1b**, **2b**) and powder selenium (**1c**, **2c**).

68.8 ppm) and **1c**, **2c** (67.5 ppm and 69.6 ppm). The composition of the oxidized derivatives **1a**, **2a**, **1b**, **2b**, **1c** and **2c** were further confirmed by using microanalysis and IR spectroscopy, and were found to be in good agreement with the theoretical values [12,13,15].

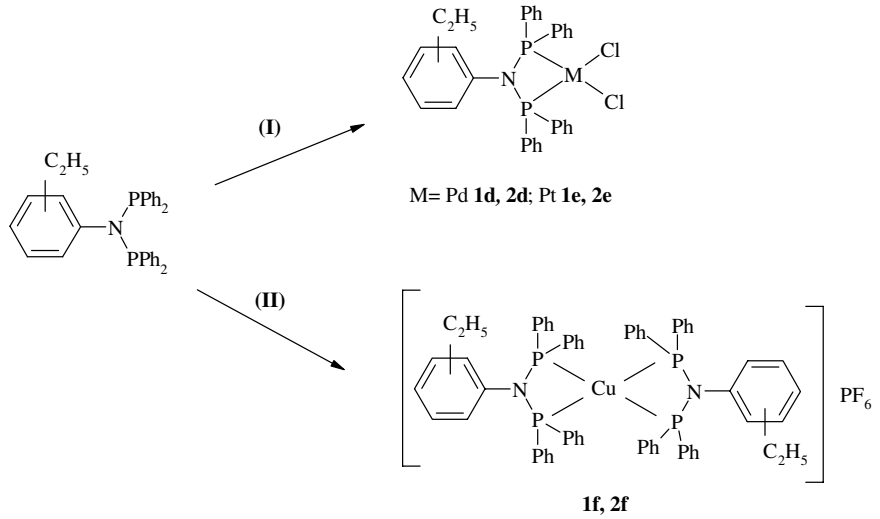
Reactions of compounds **1** and **2** with [M(COD)Cl_2] (M = Pd, Pt; COD = 1,5-cyclooctadiene) and [Cu(CH_3-$CN)_4$]PF_6 in CH_2C1_2 gave the corresponding complexes **1d**, **2d**, **1e**, **2e** [M{$(Ph_2P)_2$N-C_6H_4-C_2H_5}Cl_2] (M = Pd; Pt) and **1f**, **2f** [Cu{$(Ph_2P)_2$N-C_6H_4-C_2H_5}$_2$]PF_6 in good yields (Scheme 3).

The ^{31}P NMR chemical shifts of complexes **1d** and **2d** (37.2 ppm and 34.8 ppm) are within the range expected for structurally similar complexes where an electron-withdrawing group is attached to the aniline ring [27]. The chemical shifts of **1e**, **2e**, **1f** and **2f** in the ^{31}P NMR spectra are also within the expected range and they show minor solvent dependence [13]. In the ^1H NMR spectra, these complexes display overlapped multiplets in the region 6.70–8.10 ppm for the aromatic H-atoms, and a quartet at 2.50 ppm and a triplet at 1.15 ppm for the hydrogen atoms of the ethyl group.

Single crystals of **1e** and **2d** suitable for X-ray diffraction analyses were obtained by slow diffusion of diethyl ether into a solution of the complexes in chloroform and dichloromethane, respectively. They both crystallized as 1:1 solvent adducts and the crystallographic data of **1e** · $CHCl_3$ and **2d** · CH_2Cl_2 are listed in Table 1.

The molecular representation of complexes **1e** and **2d** are shown in Figs. 1 and 2, with key bond parameters given in the figure captions. In general, the key bond lengths and angles of complexes **1e** and **2d** in the solid state are very similar, with minimal structural differences due to the relocation of the ethyl groups. The P–N bond distances of 1.734(7) and 1.738(6) Å in complex **2d** are essentially the same, but they are longer than that of the platinum complex **1e** [1.715(4) and 1.719(4) Å], although they are within the expected value range on comparison to similar structures [27]. Both complexes form metallacycles, i.e. P–N–P–Pd and P–N–P–Pt, respectively, that are nearly planar with torsion angles P–N–P–Pd of 0.5(4)° in **2d** and P–N–P–Pt of 5.78(17)° in **1e**. Despite the difference of the two metal atoms, the P–Pd–P angle in **2d** [72.30(9)°] is not too different from that of the P–Pt–P angle in **1e** [72.80(4)°].

It is interesting to note that compounds **1e** and **2d** crystallised under similar conditions, both forming 1:1 adducts with solvent molecules, presumably driven by H-bonding interactions with the solvent molecules. In both instances,



Scheme 3. Reactions of aminophosphines **1** and **2** with $[M(COD)Cl_2]$ (M = Pd, Pt) and $[Cu(CH_3CN)_4]PF_6$ in CH_2C1_2.

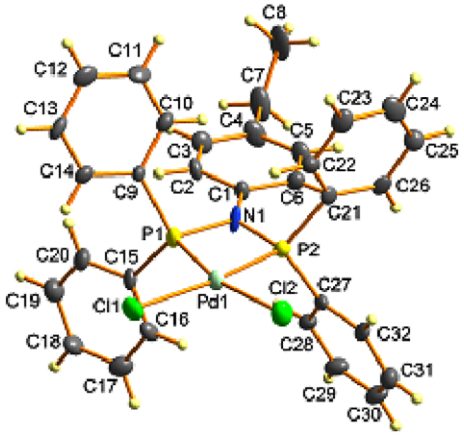


Fig. 1. Solid-state structure of compound **2d**; selected bond lengths (Å) and angles (°): Pd(1)–P(1), 2.212(3), Pd(1)–P(2), 2.215(3), Pd(1)–Cl(1), 2.373(2), Pd(1)–Cl(2), 2.379(3), N(1)–C(1), 1.419(11), N(1)–P(2), 1.734(7), N(1)–P(1), 1.738(6); P(1)–Pd(1)–P(2), 72.30(9), P(1)–Pd(1)–Cl(1), 95.18(9), P(2)–Pd(1)–Cl(1), 167.18(10), P(1)–Pd(1)–Cl(2), 165.81(9), P(2)–Pd(1)–Cl(2), 94.28(9), Cl(1)–Pd(1)–Cl(2), 98.41(9), C(1)–N(1)–P(2), 132.8(6), C(1)–N(1)–P(1), 129.5(6), P(2)–N(1)–P(1), 97.6(4).

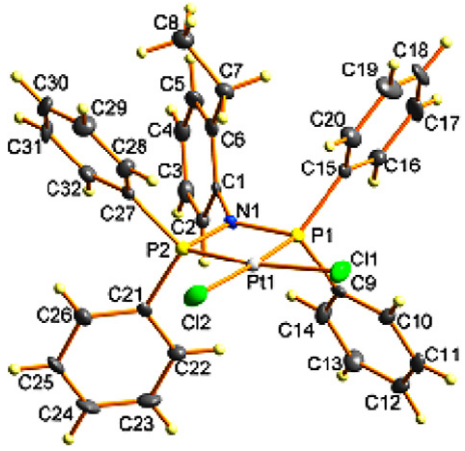


Fig. 2. Solid-state structure of compound **1e**; selected bond lengths (Å) and angles (°): Pt(1)–P(1), 2.2096(12), Pt(1)–P(2), 2.2151(12), Pt(1)–Cl(2), 2.3592(12), Pt(1)–Cl(1), 2.3633(12), N(1)–C(1), 1.449(5)N(1)–P(1), 1.715(4), N(1)–P(2), 1.719(4), P(1)–Pt(1)–P(2), 72.80(4), P(1)–Pt(1)–Cl(2), 171.69(5), P(2)–Pt(1)–Cl(2), 98.97(4), P(1)–Pt(1)–Cl(1), 97.54(5), P(2)–Pt(1)–P(1), 169.93(4), Cl(2)–Pt(1)–Cl(1), 90.74(4), C(1)–N(1)–P(1), 132.7(3), C(1)–N(1)–P(2), 126.9(3), P(1)–N(1)–P(2), 99.72(18).

the solvent molecule interacts via C–H bonds directly with the metal chloride bonds, the C–H···Cl(Pd) distance in **2d** and C–H···Cl(Pt) distance in **1e** being 2.589 and 2.471 Å, respectively. In addition, the chloride of the solvent molecules also interacts with the C–H bonds of the aromatic benzene ring, and the C–H···Cl values range from 2.80 to 2.90 Å (see Fig. 3).

4. Conclusion

In conclusion, we have prepared a series of aminophosphine compounds and their derivatives including oxides, sulfides, selenides, as well as transition-metal complexes containing Pd, Pt and Cu centers. Although the positions of the ethyl groups in the aniline substituent are different, they exhibit similar reactivities towards different oxidants due to the presence of the bulky diphenyl groups at the phosphorus atom. In addition, they also show similar coordination properties towards Pd, Pt and Cu. All these new compounds were characterized using NMR and IR spectroscopy, with two representative structures studied by single crystal X-ray diffraction analyses. Investigations of these compounds as potential catalysts are ongoing and will be reported separately.

5. Supplementary material

CCDC 643157 and 643158 contain the supplementary crystallographic data for this paper. These data can be

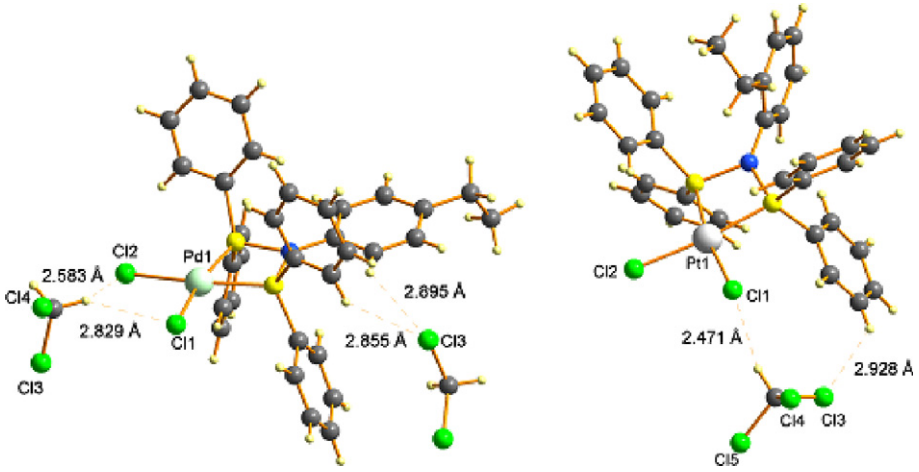


Fig. 3. Hydrogen bonding interactions in **2d** (left) and **1e** (right).

obtained free of charge via http://www.ccdc.cam.ac.uk/conts/retrieving.html, or from the Cambridge Crystallographic Data Centre, 12 Union Road, Cambridge CB2 1EZ, UK; fax: (+44) 1223-336-033; or e-mail: deposit@ccdc.cam.ac.uk.

Acknowledgments

We thank The Council of Dicle University (DUAPK-05-FF-19 and DUAPK-06-FF-41 projects) for financial support and Ecole Polytechnique Fédérale de Lausanne for X-ray structure analyses.

References

[1] (a) F.R. Hartley, The Chemistry of Organophosphorus Compounds, vol. 1, Wiley, Manchester, 1990;
(b) N.N. Greenwood, A. Earnshaw, Chemistry of the Elements, Pergamon Press, Oxford, 1984, p. 619.
[2] (a) M.S. Balakrishna, V. Sreenivasa Reddy, S.S. Krishnamurthy, J.F. Nixon, J.C.T.R. Burckett St. Laurent, Coord. Chem. Rev. 129 (1994) 1;
(b) F. Agbossou, J.F. Carpentier, F. Hapiot, Coord. Chem. Rev. 178–180 (1998) 1615;
(c) M.R.I. Zubiri, J.D. Woollins, Comment Inorg. Chem. 24 (5–6) (2003) 189;
(d) N. Biricik, F. Durap, B. Gümgüm, Z. Fei, R. Scopelliti, Transition Met. Chem. 32 (2007) 877.
[3] (a) T. Appleby, J.D. Woollins, Coord. Chem. Rev. 235 (2002) 121;
(b) Z. Fei, P.J. Dyson, Coord. Chem. Rev. 249 (2005) 2056.
[4] (a) I. Bachert, P. Braunstein, R. Hasselbring, New J. Chem. 20 (1996) 993;
(b) I. Bachert, P. Braunstein, M.K. McCart, F. Fabrizi de Biani, F. Lashi, P. Zanello, G. Kickelbick, U. Schubert, J. Organomet. Chem. 573 (1999) 47;
(c) I. Bachert, I. Bartussek, P. Braunstein, E. Guillon, J. Rose, G. Kickelbick, J. Organomet. Chem. 580 (1999) 257;
(d) B. Gümgüm, N. Biricik, F. Durap, İ. Ozdemir, N. Gurbuz, W.H. Ang, P.J. Dyson, Appl. Organomet. Chem. 21 (2007) 711.
[5] I.M.R. Zubiri, M.L. Clarke, D.F. Foster, D.J. Cole-Hamilton, A.M.Z. Slawin, J.D. Woollins, J. Chem. Soc., Dalton Trans. 969 (2001).
[6] J. Reedijk, J. Chem. Soc., Chem. Commun. 801 (1996).
[7] (a) D.J. Birdsall, J. Green, T.Q. Ly, J. Novosad, M. Necas, A.M.Z. Slawin, J.D. Woollins, Z. Zak, Eur. J. Inorg. Chem. 1445 (1999);
(b) P. Bhattacharyya, T.Q. Ly, A.M.Z. Slawin, J.D. Woollins, Polyhedron 20 (2001) 1803.
[8] P. Kafarski, P. Mastalerz, Beitr. Wriskstorfforch 21 (1984).
[9] (a) Z. Fei, R. Scopelliti, P.J. Dyson, Eur. J. Inorg. Chem. (2003) 3527;
(b) Z. Fei, R. Scopelliti, Paul J. Dyson, Eur. J. Inorg. Chem. (2004) 530;
(c) N. Biricik, Z. Fei, R. Scopelliti, P.J. Dyson, Eur. J. Inorg. Chem. (2004) 4232;
(d) I. Fernández, F. Breher, P.S. Pregosin, Z. Fei, P.J. Dyson, Inorg. Chem. 44 (2005) 7616.
[10] K.G. Gaw, M.B. Smith, A.M.Z. Slawin, New J. Chem. 24 (2000) 429.
[11] K.G. Gaw, M.B. Smith, J.W. Steed, J. Organomet. Chem. 664 (2002) 294.
[12] (a) Q. Zhang, S.M. Aucott, A.M.Z. Slawin, J.D. Woollins, Eur. J. Inorg. Chem. 7 (2002) 1635;
(b) M.L. Clarke, G.L. Holliday, A.M.Z. Slawin, J.D. Woollins, J. Chem. Soc., Dalton Trans. 6 (2002) 1093;
(c) A.M.Z. Slawin, M. Wainwright, J.D. Woollins, J. Chem. Soc., Dalton Trans. 4 (2002) 513;
(d) N. Biricik, Z. Fei, R. Scopelliti, P.J. Dyson, Helv. Chim. Acta 86 (2003) 3281;
(e) Z. Fei, D. Zhao, N. Biricik, R. Scopelliti, P.J. Dyson, Inorg. Chem. 44 (2004) 2228;
(f) A. Baysal, M. Aydemir, F. Durap, B. Gümgüm, S. Özkar, L.T. Yıldırım, Polyhedron 26 (2007) 3373.
[13] (a) A.M.Z. Slawin, H.L. Milton, J. Wheatley, J.D. Woollins, Polyhedron 23 (2004) 3125;
(b) A.M.Z. Slawin, J. Wheatley, J.D. Woollins, Phosphorus, Sulfur, Silicon Relat. Elem. 179 (4–5) (2004) 991;
(c) A.M.Z. Slawin, J. Wheatley, J.D. Woollins, Eur. J. Inorg. Chem. (2005) 713;
(d) B. Gümgüm, O. Akba, F. Durap, L.T. Yıldırım, D. Ülkü, S. Özkar, Polyhedron 25 (2006) 3133.
[14] Z. Fei, R. Scopelliti, P.J. Dyson, Inorg. Chem. 42 (2003) 2125.
[15] Z. Fei, R. Scopelliti, P.J. Dyson, J. Chem. Soc., Dalton Trans. (2003) 2772.
[16] D. Drew, J.R. Doyle, Inorg. Synth. 13 (1972) 47.
[17] J.X. McDermott, J.F. White, G.M. Whitesides, J. Am. Chem. Soc. 98 (1976) 6521.
[18] G.J. Kubas, Inorg. Synth. 19 (1979) 90.
[19] N. Biricik, F. Durap, C. Kayan, B. Gümgüm, Heteroatom Chem. 18 (6) (2007) 613.
[20] Oxford Diffraction Ltd., Abingdon, Oxfordshire, UK, 2002.
[21] A. Altomare, M.C. Burla, G. Camalli, G. Cascarano, C. Giacovazzo, A. Gualiardi, G. Polidori, J. Appl. Crystallogr. 27 (1994) 435.
[22] G.M. Sheldrick, University of Göttingen, Göttingen, Germany, 1997.
[23] G.M. Sheldrick, Bruker AXS, Inc., Madison, WI 53719, USA, 1997.

[24] DIAMOND 3.0a, Crystal Impact GbR, Bonn, Germany.
[25] N. Walker, D. Stuart DELABS, Acta Crystallogr., Sect. A 39 (1983) 158.
[26] Z. Fei, D. Zhao, N. Biricik, R. Scopelliti, P.J. Dyson, Inorg. Chem. 44 (2004) 2228.
[27] (a) H.L. Milton, M.V. Wheatley, A.M.Z. Slawin, J.D. Woollins, Inorg. Chem. Commun. 7 (10) (2004) 1106;
(b) Z. Fei, W.H. Ang, D. Zhao, R. Scopelliti, P.J. Dyson, Inorg. Chim. Acta 359 (2006) 2635.

Available online at www.sciencedirect.com
ScienceDirect
Polyhedron 27 (2008) 203–209
POLYHEDRON
www.elsevier.com/locate/poly

Synthesis, structure and thermal properties of polynuclear complexes with a new multidentate ligand, *N*,*N*′-bis(5-ethyl-1,3,4-thiadiazol-2-yl)-2,6-pyridinedicarboxamide

Xiao-Qing Shen [a], Hong-Chang Yao [b], Rui Yang [b], Zhong-Jun Li [b], Hong-Yun Zhang [b,*], Ben-Lai Wu [b], Hong-Wei Hou [b]

[a] *College of Material Science and Engineering, Zhengzhou University, Zhengzhou 450052, China*
[b] *Department of Chemistry, Zhengzhou University, Zhengzhou 450052, China*

Received 15 June 2007; accepted 5 September 2007
Available online 26 October 2007

Abstract

Based on *N*,*N*′-bis(5-ethyl-1,3,4-thiadiazol-2-yl)-2,6-pyridinedicarboxamide (H_2**L**) and inorganic Zn^{II} and Cd^{II} salts, three polynuclear complexes $[Zn_6(\mu_4\text{-}O)_2(L)_4]$ (**1**), $[Zn_3(\mu_3\text{-}O)_2(L)_2(H_2L)]$ (**2**) and $[Cd_5(\mu_3\text{-}O)_2(L)_3(H_2L)(CH_3OH)(DMF)]$ (**3**) have been prepared and their crystal structures have been determined by single-crystal X-ray analysis. The thermal behaviors of these complexes in nitrogen and the thermal decomposition kinetics of complex **2** in the temperature range 350–540 °C have been studied, and kinetic parameters were also obtained. Kinetic results show that the decomposition of complex **2** is double-step reaction: a 1st-order reaction (F1) is followed by an *n*th-order reaction (Fn).
© 2007 Published by Elsevier Ltd.

Keywords: Polynuclear complexes; Crystal structure; d^{10} Metals; Thermal properties

1. Introduction

Polynuclear complexes continue to attract a great deal of interest, not only because of their fascinating structural diversities, but also for their potential application in the fields of catalysis, functional materials and biological recognition [1], as models of active sites in metal enzymes [2–5], etc. So far, various preparation methods have been proposed to obtain such polynuclear complexes [6–9], of which, a successful strategy is to design a polytopic ligand for the coordination of metal centers [10–14]. Depending on these carefully designed ligands and the versatile coordination geometries of metal, a large number of polynuclear metal clusters with magnetic, optical or electronic properties have been synthesized. Diamides incorporating an –NH–CO–pyridine–CO–NH– core based on pyridine-2,6-dicarboxylic acid are versatile ligands and a number of novel architectures such as helicates, cages and metallamacrocycle have been prepared recently [15–20].

As part of our interest in preparing metalla-assemblies with ligands that contain 5-(ethyl-2-yl)-amide-1,3,4-thiadiazole, we have recently synthesized a new compound, *N*,*N*′-bis(5-ethyl-1,3,4-thiadiazol-2-yl)-2,6-pyridinedicarboxamide (H_2**L**). Obviously, this compound easily acts as a multidentate ligand to construct polynuclear complexes and its *pocket*-like nature can result in structurally complicated complexes. For example, it can take different bonding modes, such as **A**, **B** and **C** coordination fashions under different conditions (Fig. 1). In addition, the ligand still retains O and S donors for further hydrogen-bonding and/or metal–ligand interactions.

In this paper, we report the syntheses, structures and thermal behaviors of three polynuclear d^{10} metal complexes, namely, $[Zn_6(\mu\text{-}O)_2(L)_4]$ (**1**), $[Zn_3(\mu\text{-}O)_2(H_2L)(L)_2]$ (**2**) and

* Corresponding author. Tel.: +86 3717763675; fax: +86 3717761744.
E-mail address: wzhy917@zzu.edu.cn (H.-Y. Zhang).

0277-5387/$ - see front matter © 2007 Published by Elsevier Ltd.
doi:10.1016/j.poly.2007.09.015

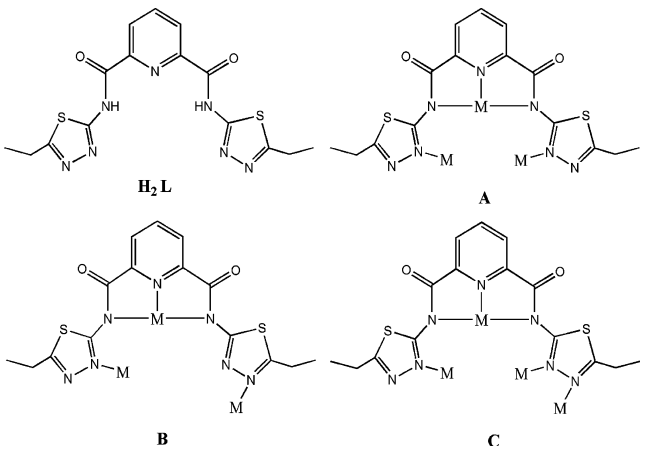


Fig. 1. Schematic diagrams of ligand H_2**L** and its potential coordination sites.

$[Cd_5(\mu_3\text{-}O)_2(H_2L)(L)_3(CH_3OH)\ (DMF)]$ (**3**). Based on the results of thermogravimetry (TG) analysis, the thermal decomposition mechanism of complex **2** in the temperature range 350–540 °C has been studied and kinetic parameters of the thermal decomposition reaction have been obtained by means of the non-linear regression method.

2. Experimental

The ligand precursor and metal salts were commercial samples and were used in the syntheses as received.

2.1. Ligand preparation (H_2**L**)

2,6-Pyridinedicarboxylic acid (1.67 g, 10 mmol) was dissolved in 10 ml of $SOCl_2$. The mixture was refluxed for 2 h until the white powder was dissolved completely. The residual $SOCl_2$ was then removed under reduced pressure. The resulting 2,6-pyridinedicarbonyl dichloride was dissolved and added dropwise to a 20 ml pyridine solution containing 5-ethyl-2-amino-1,3,4-thiadiazole (2.58 g, 20 mmol) whilst stirring. Two hours later, white precipitates were formed. The pure product was obtained by being filtered under reduced pressure, washed with water and recrystallized in absolute ethanol. Yields: 2.92 g (75%). M.P. 309–310 °C. *Anal*. Calc. for H_2**L** ($C_{15}H_{15}N_7O_2S_2$): C, 46.27; H, 3.86; N, 25.19. Found: C, 46.25; H, 3.79; N, 25.20%. ^{1}H NMR (DMSO): $\delta_H = 8.47$, 8.45 (m, 2H, CONH), 8.38-8.31(w, 3H, py), 3.09–3.05 (m, 4H, CH_2), 1.34 (s, 6H, CH_3) ppm. IR (KBr, cm^{-1}): 3295s, 3163s, 2937m, 1684s, 1534s, 1438m, 1298s, 1071m, 1001w, 888m, 704w, 650m.

2.2. Synthesis of $[Zn_6(\mu_4\text{-}O)_2(L)_4]$ (**1**)

An EtOH solution (10 ml) of $Zn(OAc)_2 \cdot 2H_2O$ (0.0587 g, 0.1 mmol) was added slowly to a DMF solution (10 ml) of H_2**L** (0.0389 g, 0.1 mmol) with continuous stirring. KSCN (0.0097 g, 0.1 mmol) in 10 ml of EtOH was then added to the above solution. The mixture was refluxed for 1 h and filtered. The filtrate was evaporated slowly at room temperature. After a week colorless crystals suitable for X-ray diffraction were obtained by being filtered, washed with cooled water and dried under vacuum. Yield: 36%. *Anal*. Calc. for **1** ($C_{60}H_{52}N_{28}O_{10}S_8Zn_6$): C, 36.51; H, 2.65; N, 19.87. Found: C, 36.54; H, 2.55; N, 19.88%. IR (KBr, cm^{-1}): 3448s, 3134s, 2975s, 2935w, 1660s, 1617s, 1593s, 1463s, 1442s, 1379s, 1308s, 1287m, 1073m, 956m, 845m, 696m.

2.3. Synthesis of $[Zn_3(\mu_3\text{-}O)_2(H_2L)(L)_2]$ (**2**)

$Zn(OAc)_2 \cdot 2H_2O$ (0.0587 g, 0.1 mmol) in 10 ml of methanol and KSCN (0.0097 g, 0.1 mmol) in 5 ml of water were added slowly to a 20 ml of ethanol solution containing H_2**L** (0.0389 g, 0.1 mmol) with continuous stirring for 1 h. The mixture was filtered and after a month light-yellow crystals were formed from the filtrate at room temperature. The crystals were collected, washed with water and dried under vacuum. Yield: 47%. *Anal*. Calc. for **2** $\cdot 4H_2O$ ($C_{45}H_{49}N_{21}O_{11}S_6Zn_3$): C, 37.36; H, 3.41; N, 20.31. Found: C, 73.31; H, 3.39; N, 20.24%. IR (KBr, cm^{-1}): 3422s, 3197s, 2971m, 1617m, 1593m, 1576s, 1456s, 1425s, 1387s, 1367s, 1306m, 1073w, 1045w, 963w, 903m, 762w, 675m.

2.4. Synthesis of $[Cd_5(\mu_3\text{-}O)_2(H_2L)(L)_3(CH_3OH)(DMF)]$ (**3**)

A solution of $Cd(NO_3)_2 \cdot 4H_2O$ (0.0308 g, 0.1 mmol) in EtOH (5 ml) and a solution of NaOOCH (0.007 g, 0.1 mmol) in EtOH (5 ml) were added to a solution of H_2**L** (0.0389 g, 0.1 mmol) in DMF (10 ml). The mixture was refluxed for 1 h and filtered. The filtrate was allowed to stand undisturbed at room temperature and colorless block crystals were obtained after six months. The crystals were washed with water and dried under vacuum. Yield: 20%. *Anal*. Calc. for **3** $\cdot H_2O$ ($C_{64}H_{67}N_{29}O_{13}S_6Cd_5$): C, 33.88; H, 2.98; N, 17.90%. Found: C, 33.82; H, 2.88, N, 17.85%. IR (KBr, cm^{-1}): 3411s, 2971m, 1660s, 1577s, 1490m, 1450s, 1420s, 1374s, 1354s, 1299w, 951m, 898m, 756m, 670m.

2.5. Physical measurements

Elemental analyses were performed on a Perkin–Elmer 240C analyzer and IR spectra were recorded on a Nicolet IR-470 spectrometer using KBr pellets in the range 4000–400 cm^{-1}. ^{1}H NMR spectra were obtained on a Bruke-DPX400 NMR spectrometer (300 MHz) at 25 °C in DMSO. The thermal decomposition experiments were carried out using a Netzsch TG 209 instrument under a nitrogen atmosphere. The heating rate for the thermal decomposition employed was 10 °C min^{-1}.

Data collection were made using graphite monochromated Mo Kα ($\lambda = 0.071073$ nm) radiation on a Rigaku Raxis-IV X-ray diffractometer at 291(2) K. The structures were solved by direct methods and refined on F^2 by

Table 1
Crystallographic data and refinement parameters for complex **1**–**3**

	1	**2** · $4H_2O$	**3** · H_2O
Empirical formula	$C_{60}H_{52}N_{28}O_{10}S_8Zn_6$	$C_{45}H_{49}N_{21}O_{11}S_6Zn_3$	$C_{64}H_{67}N_{29}O_{13}S_8Cd_5$
Formula weight	1974.00	2897.04	2268.95
Crystal system	Monoclinic	Monoclinic	Triclinic
Space group	$P2_1/n$	$C2/c$	$P\bar{1}$
a (Å)	15.025(3)	24.1903(18)	11.9828(16)
b (Å)	23.826(5)	16.8497(13)	17.987(2)
c (Å)	21.611(4)	16.8265(13)	21.914(3)
α (°)	90.0	90	100.022 (2)
β (°)	103.46(3)	115.5900(10)	99.054(2)
γ (°)	90.0	90	108.569 (2)
Volume (Å^3)	7524(3)	6185.7(8)	4293.0(10)
Z	4	4	2
D_{calc} (g cm^{-3})	1.743	1.555	1.755
μ (mm^{-1})	2.180	1.428	1.487
$F(000)$	3984	2960	2252
Total, unique data, R_{int}	18947, 11183, 0.0654	16200, 5647, 0.0784	39211, 20766, 0.0570
Observed data [$I > 2.0\sigma(I)$]	7734	2762	10836
R_1^a, wR_2^b	0.0758, 0.1693	0.0756, 0.2015	0.0564, 0.1209

[a] $R_1 = \sum\|F_o| - |F_c\|/\sum|F_o|$.
[b] $wR_2 = [\sum w(F_o^2 - F_c^2)^2/\sum w(F_o^2)^2]^{1/2}$.

Table 2
Selected bond distances (Å) and angles (°) for **1**

Bond distance			
Zn1–O9	1.963(5)	Zn3–N2	1.939(8)
Zn1–N3	2.234(7)	Zn3–N16	1.971(8)
Zn1–N4	2.019(7)	Zn4–O9	1.965(5)
Zn1–N5	2.220(7)	Zn4–O10	1.964(6)
Zn1–N9	2.004(7)	Zn4–N23	1.977(8)
Zn2–O9	1.955(5)	Zn5–O10	1.968(5)
Zn2–N6	2.024(7)	Zn5–N17	2.275(8)
Zn3–O9	1.962(6)	Zn6–O10	1.967(5)
Zn3–O10	1.968(5)	Zn6–N20	2.017(7)
Angle			
O9–Zn1–N4	140.1(3)	O9–Zn4–N23	111.8(3)
O9–Zn1–N9	106.7(3)	N13–Zn4–N23	112.3(4)
O9–Zn2–N6	108.8(3)	O10–Zn5–N19	98.3(2)
N6–Zn2–N12	102.6(2)	O10–Zn5–N27	104.5(2)
O9–Zn3–O10	92.7(2)	O10–Zn6–N20	104.9(3)
O9–Zn3–N2	114.6(3)	Zn1–O9–Zn2	107.6(3)
O9–Zn3–N16	111.9(3)	Zn3–O9–Zn4	87.3(2)
N2–Zn3–N16	113.5(4)	Zn3–O10–Zn4	87.2(2)
O9–Zn4–O10	92.8(2)	Zn5–O10–Zn6	106.4(2)

Table 3
Selected bond distances (Å) and angles (°) for **2**

Bond distance			
Zn1–O4	1.976(4)	Zn2–O4	1.865(7)
Zn1–N3	2.165(7)	Zn2–N11	2.043(8)
Zn1–N6#1	2.264(7)	Zn2–N2#1	2.440(6)
Zn1–N4	2.077(8)	Zn2–N10#1	2.199(5)
Zn1–N5	2.142(10)	Zn2–N10	2.199(5)
Zn1–N9	2.336(5)	Zn2–N2	2.440(6)
Angle			
O4–Zn1–N4	176.2(3)	O4–Zn2–N10#1	104.3(15)
N4–Zn1–N5	76.9(4)	O4–Zn2–N2	84.93(14)
N4–Zn1–N3	75.0(3)	N10#1–Zn2–N10	151.4(3)
N5–Zn1–N6#1	94.1(3)	N10#1–Zn2–N2	85.53(19)
O4–Zn1–N3	103.5(2)	N11–Zn2–N2	95.07(14)
N4–Zn1–N6#1	93.1(3)	O4–Zn2–N11	180.00(1)
N4–Zn1–N9	88.0(2)	Zn1–O4–Zn1#1	116.8(3)
O4–Zn1–N9	88.54(18)	Zn2–O4–Zn1#1	121.60(17)

Symmetry transformations used to generate equivalent atoms: #1 $-x, y, 1/2 - z$.

full-matrix least squares using SHELXTL [21]. Non-hydrogen atoms were located by direct phase determination and subjected to anisotropic refinement. All the hydrogen atoms were placed in calculated positions. Details of crystal structure determination of complexes **1**–**3** are listed in Table 1, and selected bond distances and angles are listed in Tables 2–4.

3. Results and discussion

3.1. Synthesis

The single crystals of **1** would not form unless in the presence of KSCN. Since KSCN did not participate in the formation of the structure of **1**, the role it played may be an improvement of the ionic strength (I) of the solution, which is the key factor in the self-assemble of the hexanuclear Zn complex. The same case appears in the process of the synthesis of complex **3**, but the strong electrolyte here is NaOOCH.

The synthetic method of crystal **2** is the same as that of crystal**1**, except the solvent. The different solvents result in the formation of hexanuclear and trinuclear Zn complexes, which indicate that the solvent used can affect the self-assembly process.

3.2. Crystal structure of $[Zn_6(\mu_4\text{-}O)_2(L)_4]$ (**1**)

Complex **1** crystallizes in the monoclinic space group $P2_{1/n}$. As shown in Fig. 2a, the complex motif contains a

Table 4
Selected bond distances (Å) and angles (°) for **3**

Bond distance			
Cd1–O9	2.558(6)	Cd2–N16	2.333(3)
Cd1–O12	2.189(2)	Cd3–O12	2.234(5)
Cd1–N9	2.290(3)	Cd3–N6	2.423(7)
Cd1–N5	2.316(3)	Cd3–N28	2.452(4)
Cd1–N3	2.340(3)	Cd4–O11	2.202(4)
Cd2–O9	2.424(3)	Cd4–N14	2.451(6)
Cd2–O10	2.276(7)	Cd4–N23	2.471(6)
Cd2–O11	2.216(4)	Cd5–O11	2.193(4)
Cd2–O12	2.292(2)	Cd5–N1	2.573(6)
Cd2–N2	2.456(3)	Cd5–N20	2.522(6)
Angle			
O9–Cd1–N9	176.42(9)	O11–Cd4–N18	175.55(10)
O12–Cd1–O9	76.03(9)	N1–Cd5–N20	173.83(10)
O12–Cd1–N9	102.20(10)	O11–Cd5–N25	176.10(9)
N2–Cd2–N16	174.13(12)	Cd5–O11–Cd4	105.97(10)
O11–Cd2–O9	164.12(9)	Cd5–O11–Cd2	121.16(9)
O12–Cd2–O9	77.16(9)	Cd4–O11–Cd2	114.67(10)
O12–Cd3–N12	113.19(10)	Cd1–O12–Cd3	101.27(10)
N6–Cd3–N28	162.12(9)	Cd1–O12–Cd2	102.57(9)
N14–Cd4–N23	168.58(10)	Cd3–O12–Cd2	147.58(10)

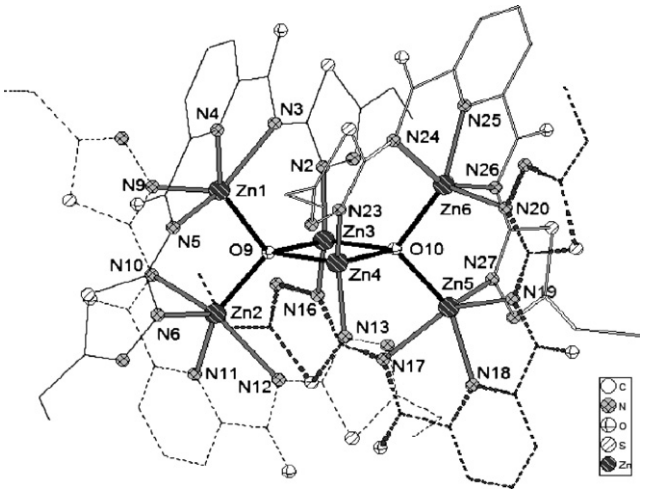


Fig. 2a. Molecular structure of complex **1**.

$[Zn_6(\mu_4\text{-}O)_2]$ core and can be considered as two tetrahedrons, in which μ_4-O (O9, O10) atoms occupy the centre of each tetrahedron (see Fig. 2b). The edge-shared (Zn3, Zn4) tetrahedrons constitute the core of complex **1**. On the other hand, the 6-atom Zn core can also be described as a contracted octahedron with Zn3 and Zn4 in the axial coordination sites of the minor axis. The Zn3···Zn4 distance of 2.711(19) Å indicates that there is a strong interaction between them. The outer coordination shell of the $[Zn_6(\mu_4\text{-}O)_2]$ core is occupied by four ligands.

Two types of Zn atoms can be distinguished (see Fig. 2a). In the first type (including Zn1, Zn2, Zn5 and Zn6), the distorted square pyramids of each Zn atom is completed by one μ_4-O, three nitrogen atoms of the –NH–CO–pyridine–CO–NH– core of one ligand and

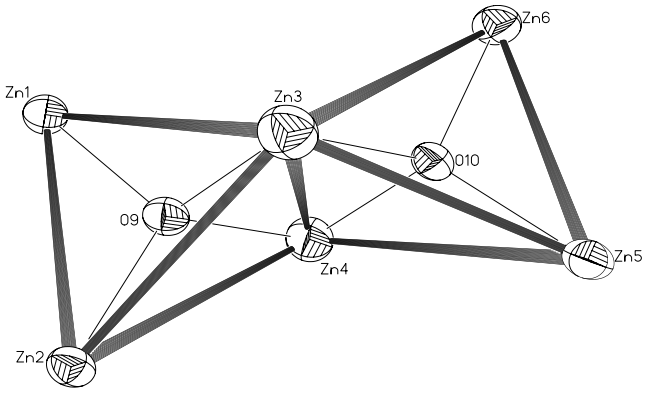


Fig. 2b. Edge-shared tetrahedron core of complex **1**.

another nitrogen atom from the thiadiazole of another ligand, forming a $ZnON_4$ coordination environment. The Zn–O bond lengths are almost the same (1.955(5)–1.968(5) Å), and the Zn–N bond distances fall in the range of 2.004(7)–2.275(8) Å. The large range of Zn–N bond distances suggests that these Zn–N bonds have different bond strength, and this may be caused by the difference in the steric hindrance of the rigid part (–NH–CO–pyridine–CO–NH–) of the ligand. A similar situation of M–N bonds can also be seen in those polynuclear complexes constructed from substituted pyridine ligands [15–17]. In the second type (Zn3 and Zn4), the tetrahedral sphere of each Zn is completed by two μ_4-O and two nitrogen atoms from the thiadiazole ring of two ligands, forming a ZnO_2N_2 coordination environment. The Zn–O bond distances (1.962(6)–1.968(5) Å) in this type are similar to the Zn–N bonds (1.939(8)–1.977(8) Å). In complex **1**, four $\mathbf{L}^{2-}$ chelate Zn atoms with the same coordination mode, namely the **A** type mode.

3.3. Crystal structure of $[Zn_3(\mu_3\text{-}O)_2(H_2L)(L)_2]$ (**2**)

Single-crystal structural analysis reveals that complex $\mathbf{2}\cdot 4H_2O$ crystallizes in the monoclinic space group $C2/c$ and in the structure there exists a twofold symmetric axis on which the Zn2, N11 and O4 atoms lie (Fig. 3). The lattice water molecules reside on three crystallographic sites with partial occupancies which are summed to "two". There are two crystallographically different Zn atoms in the structure. Each Zn atom has a distorted octahedral geometry with a μ_3-O atom and five nitrogen atoms. The Zn–O bond lengths in complex **2** are 1.865(7), 1.976(4) and 1.976(4) Å, and as is the case for complex **1**, a wide range for the Zn–N bond distances (2.043(8)–2.440(6) Å) are also caused by the steric hindrance of the ligand. Although the three ligands take the same coordination mode, **A** type, one of them is not deprotonated, as is deduced from charge balance and bond lengths. Thus, complex **2** has a cage-like structure with the conventional $[Zn_3(\mu_3\text{-}O)]$ core and two deprotonated $\mathbf{L}^{2-}$ ligands as well as one $H_2\mathbf{L}$.

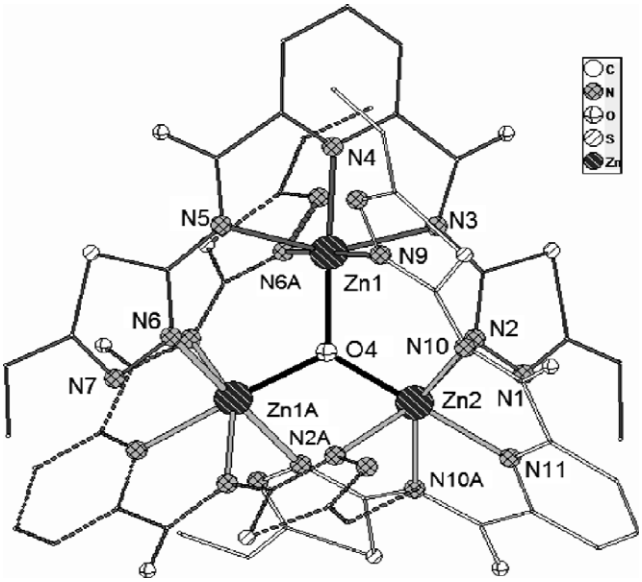


Fig. 3. Molecular structure of complex **2**.

A network of H-bonds is present in the structure. Six O atoms (O5A, O6A, O7A, O5B, O6B, O7B) of H_2O from two adjacent units connect each other to form a six-member ring through H-bonds, and O atoms in these rings further link all the neighboring acyl O atoms (O1, O2, O3) of the $[Zn_3(\mu_3\text{-}O)_2(H_2L)(L)_2]$ core to form a 3D structure.

3.4. Crystal structure of $[Cd_5(\mu_3\text{-}O)_2(H_2L)(L)_3(CH_3OH)(DMF)]$ (3)

Complex **3** · H_2O crystallizes in the triclinic space group $P\bar{1}$. The structure unit is shown in Fig. 4a. The core of **3** can be described as two trinuclear oxo-centered $[Cd_3(\mu_3\text{-}O)]$ units sharing one vertex (Cd2) through two ligands and two μ_3-oxygen atoms (Fig. 4b).

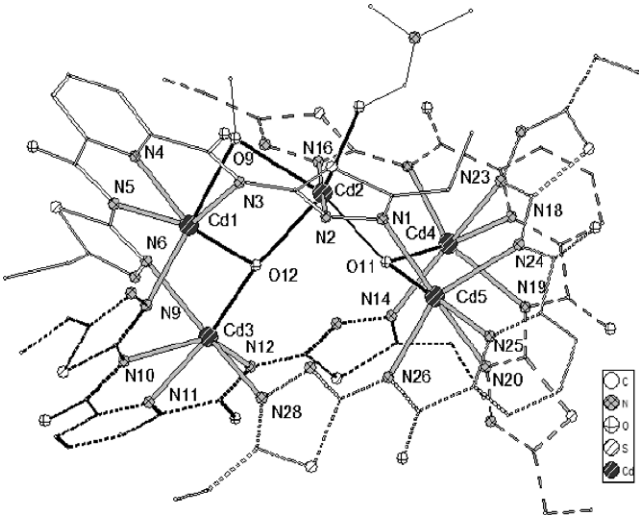


Fig. 4a. Molecular structure of complex **3**.

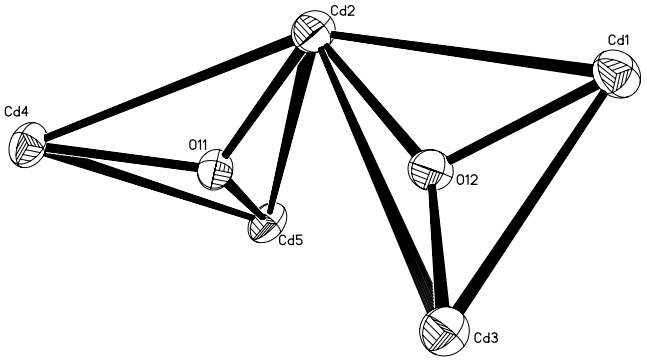


Fig. 4b. Vertex-shared core of complex **3**.

There are four different kinds of coordination modes for the Cd atoms. Cd1 is six-coordinated by three pyridinedicarboxamide nitrogen atoms (N3, N4, N5), one nitrogen atom of the 3-position of the thiadiazole ring (N9), one oxygen atom of methanol (O9) and a μ_3-O atom (O12). N3, N4, N5 and O12 constitute the equatorial plane, and N9 together with O9 occupy the axial positions. Cd2 also has an octahedral geometry but with a CdO_4N_2 coordinate environment, i.e. the two nitrogen atoms of the 3-position of the thiadiazole ring of two ligands (N2, N16) and four oxygen atoms, which come from solvent molecules (O9, O10) and μ_3-O (O11, O12). Cd3 has a CdN_5O coordination mode with one μ_3-O, three pyridinedicarboxamide nitrogen atoms and another two nitrogen atoms of the 3-position of the thiadiazole rings from different ligands. Cd4 and Cd5 have a similar coordination mode, except that one of the N atoms coordinating to Cd5 is a 4-position nitrogen of the thiadiazole ring. In complex **3**, the lengths of the Cd–N bonds are also in a wide range, 2.290(3)–2.573(6) Å, and are slightly longer than those of the Cd–O(μ_3-O) bonds (2.189(2)–2.292(2) Å) for the same reason mentioned above. Water molecules do not participate in hydrogen bonds and are only wrapped in the crystal.

The ligands in complex **3** have two distinguishable states, H_2**L** and deprotonated $\mathbf{L}^{2-}$. The H_2**L** ligand takes **B** type of coordination modes while the three deprotonated $\mathbf{L}^{2-}$ ligands employ **A**, **B** and **C** coordination fashions.

3.5. Thermal stabilities of the title complexes

Typical TG curves of the title complexes are shown in Fig. 5. The weight losses in the TG curves of complexes **2** and **3** appear at a temperature below 120 °C, and are related to the removal of lattice water in these crystals. Complexes **1** and **2** have the same decomposition temperature with onset at 411 °C, suggesting that they both have high thermal stabilities and may have similar decomposition pathways.

The mass losses that occurred in the temperature range 400–500 °C for complexes **1** and **2**, and 300–500 °C for complex **3** are mainly due to the breakage of coordinated bonds and the decomposition of the ligand, the values of which are 36%, 41% and 44% for complexes **1**, **2** and **3**,

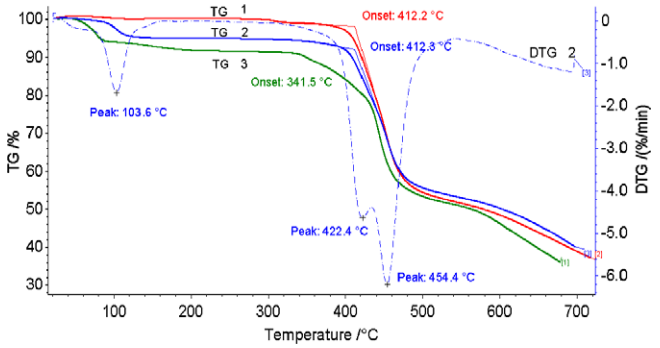


Fig. 5. TG–DTG curves of complexes **1**, **2** and **3**.

respectively. From Fig. 5 it can also be seen that the decomposition of complex **3** is different from that of complexes **1** and **2** because of the coordination of the solvent molecules in complex **3**.

The continuing weight losses in the TG curves of **1**, **2** and **3** above 540 °C are entirely caused by the gradual elimination of carbon deposition resulting from compound decomposition under the N_2 atmosphere [22].

In order to provide basic data for further investigation, kinetic studies of the thermal decomposition process of these complexes is needed, and we used complex **2** as an example to discuss the decomposition mode of the complexes within the temperature range 350–540 °C.

3.6. Non-isothermal kinetics of the complex $[Zn_3(\mu_3\text{-}O)(H_2L)(L)_2]$ (2)

A series of dynamic scans with different heating rates results in a set of data which exhibits the same degree of conversion (α) at different temperatures. TG curves of complex **2** in the temperature range 350–540 °C with heating rates of 5, 10, 20 and 30 °C min^{-1} were measured. The basic data (β, α, T) taken from the TG curves are used in the equations below:

Ozawa–Flynn–Wall equation [23],

$$\ln\beta = \ln\left(\frac{AE}{R}\right) - \ln g(\alpha) - 5.3305 - 1.052\cdot\frac{E}{RT} \quad (1)$$

where β is the heating rate, α degree of conversion, $g(\alpha)$ mechanism function, E activation energy, A pre-exponential factor and R gas constant.

From Eq. (1) it can be seen that the graphs $\ln\beta$ versus $1/T$ show straight lines with slopes $m = -1.052E/R$. The slopes of these straight lines are directly proportional to the reaction activation energy (E). The calculated results of the main decomposition process by using Eq. (1) are listed Table 5.

From Table 5 it can be seen that the activation energy is not a constant and two maximums appear at $\alpha = 0.5$ and 0.95 for the decomposition process, which indicates that the thermal decomposition of $[Zn_3(\mu_3\text{-}O)(H_2L)(L)_2]$ could be considered as a double-step reaction [24]. According to the OFW method, the activation energies and pre-exponential factors of thermal decomposition are approximately $E_1 = 416.9$ kJ mol^{-1}, $\lg(A_1/s^{-1}) = 28.09$ and $E_2 = 371.1$ kJ mol^{-1}, $\lg(A_2/s^{-1}) = 23.09$, respectively. These data would offer initial values for getting a reaction model by means of non-linear regression (NLR) and would be optimized finally.

Non-linear regression [25] allows a direct fit of the model to the experimental data without a transformation and there are no limitations with respect to the complexity of the model. For this reason, the NLR method can be employed for estimating the decomposition model of complex **2**. Selecting mechanism functions $f(\alpha)$ of different singular reaction types [26]; testing all double-step reaction types to which individual steps are linked for the first and second transition; Setting the initial values of the parameters of E and $\lg A$ according to the OFW method, calculated curves were obtained by means of NLR. During this procedure kinetic parameters of the initial values were optimized to get high fitting quality. Considering the fitting quality (characterized by the correlation coefficient and the relative precision), the mechanism of d:f, $A \overset{F_1}{\rightarrow} B \overset{F_n}{\rightarrow} C$, is the most suitable for the main decomposition of $[Zn_3(\mu_3\text{-}O)(H_2L)(L)_2]$. The calculated results are listed in Table 6 and the graphic presentation of the curve fitting is presented in Fig. 6, which shows that the non-linear regression curves fit the experimental data nicely.

Table 5
Parameters E (kJ mol^{-1}) and $\lg(A/s^{-1})$ for the main thermal decomposition of complex **2**

Partial mass loss (α)	E (kJ · mol^{-1})	$\lg(A/s^{-1})$
0.05	88.88 ± 4.87	7.06
0.10	141.47 ± 39.11	4.89
0.20	302.95 ± 77.44	20.29
0.30	307.75 ± 63.67	20.63
0.40	332.04 ± 53.31	22.16
0.50	416.89 ± 50.74	28.09
0.60	395.15 ± 26.26	26.34
0.70	360.75 ± 25.12	23.78
0.80	325.70 ± 27.32	21.09
0.90	326.39 ± 23.12	20.63
0.95	371.10 ± 48.05	23.09
0.98	353.57 ± 62.53	21.49

Table 6
Kinetic data and fitting quality on complex **2**

Corr. coeff.	Reg. par.	Step	Mode	E (kJ mol^{-1})	$\lg(A/s^{-1})$	Order
0.999456	0.00100	I	F_1	345.29049	24.22900	
		II	F_n	396.02971	26.69950	2.34924

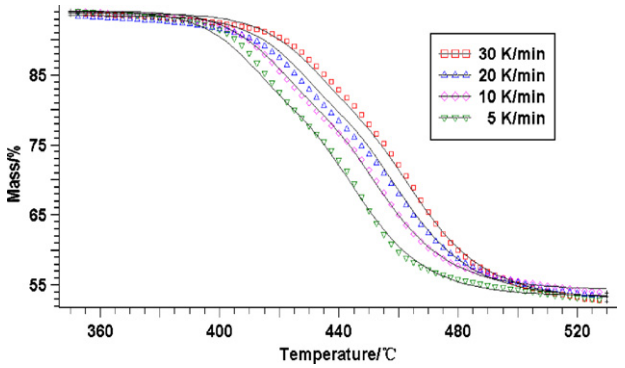


Fig. 6. Curve fitting of the second transition of **2**: ◇, △, ▽, □, experimental plots, — integral plots.

In short, the result of the kinetic analysis above shows the decomposition mode of the main process of $[Zn_3(\mu_3\text{-}O)(H_2L)(L)_2]$ is double-step, following the reaction, $A \xrightarrow{F_1} B \xrightarrow{F_n} C$, with $E_1 = 345.3$ kJ mol^{-1}, $\lg(A_1/s^{-1}) = 24.3$; $E_2 = 396.0$ kJ mol^{-1}, $\lg(A_2/s^{-1}) = 26.7$, $n = 2.35$.

4. Conclusion

Three polynuclear complexes have been prepared for the first time by using a new multidentate ligand, *N*,*N*′-bis-(5-ethyl-1,3,4-thiadiazol-2-yl)-2,6-pyridinedicarboxamide (H_2**L**). Structural studies reveal that μ-O plays an important role in the construction of all these complexes. The ligand in these complexes has two distinguishable states, H_2**L** and deprotonated $\mathbf{L}^{2-}$. Meanwhile, there are three coordination modes of the ligand shown as **A**, **B** and **C**, respectively, in these crystals.

Thermal analysis shows that complexes **1** and **2** possess high thermal stabilities and kinetics analysis of complex **2** shows that the mechanism of main decomposition process is a double-step reaction: a 1st-order reaction (F_1) with $E_1 = 345.3$ kJ mol^{-1} and $\lg(A_1/s^{-1}) = 24.23$ is followed by an *n*th-order reaction (F_n) with $E_2 = 396.0$ kJ mol^{-1}, $\lg(A_2/s^{-1}) = 26.7$ and $n = 2.35$.

Acknowledgement

We thank the Natural Science Foundation of China (20501017) for providing financial support.

Appendix A. Supplementary material

CCDC 287019, 299898 and 607432 contain the supplementary crystallographic data for **1**, **2** and **3**. These data can be obtained free of charge via http://www.ccdc.cam.ac.uk/conts/retrieving.html, or from the Cambridge Crystallographic Data Centre, 12 Union Road, Cambridge CB2 1EZ, UK; fax: (+44) 1223-336-033; or e-mail: deposit @ccdc.cam.ac.uk. Supplementary data associated with this article can be found, in the online version, at doi:10.1016/j.poly.2007.09.015.

References

[1] D. Gatteschi, R. Sessoli, Angew. Chem. Int. Ed. 42 (2003) 268.
[2] W.N. Lipscomb, N. Sträter, Chem. Rev. 96 (1996) 2375.
[3] D.E. Wilcox, Chem. Rev. 96 (1996) 2435.
[4] N. Sträter, W.N. Lipscomb, T. Klabunde, B. Krebs, Angew. Chem., Int. Ed. Engl. 35 (1996) 2024.
[5] H. Steinhagen, G. Helmchem, Angew. Chem., Int. Ed. Engl. 35 (1996) 2339.
[6] E.C. Sanudo, V.A. Grillo, M.J. Knapp, J.C. Bollinger, J.C. Huffman, D.N. Hendrickson, G. Christou, Inorg. Chem. 41 (2002) 2441.
[7] A. Bino, M. Ardon, D. Lee, B. Spingler, S.J. Lippard, J. Am. Chem. Soc. 124 (2002) 4578.
[8] S.T. Cheng, E. Doxiadi, R. Vilar, A.J.P. White, D.J. Williams, J. Chem. Soc., Dalton Trans. (2001) 2239.
[9] M. Soler, P. Artus, K. Folting, J.C. Huffman, D.N. Hendrickson, G. Christou, Inorg. Chem. 40 (2001) 4902.
[10] S. Wang, K. Folting, W.E. Streib, E.A. Schmitt, J.K. McCusker, D.N. Hendrickson, G. Christou, Angew. Chem., Int. Ed. Engl. 30 (1991) 305.
[11] J.K. McCusker, J.B. Vincent, E.A. Schmitt, M.L. Mino, K. Shin, D.K. Coggin, P.M. Hagen, J.C. Huffman, G. Christou, D.N. Hendrickson, J. Am. Chem. Soc. 113 (1991) 3012.
[12] S.C. Burdette, S.J. Lippard, Coord. Chem. Rev. 216–217 (2001) 333.
[13] E.Y. Tshuva, D. Lee, W. Bu, S.J. Lippard, J. Am. Chem. Soc. 124 (2002) 2416.
[14] Z. Huang, H.B. Song, M. Du, S.T. Chen, X.H. Bu, Inorg. Chem. 4 (2004) 931.
[15] Y. Wei, H. Hou, Y. Fan, Y. Zhu, Eur. J. Inorg. Chem. (2004) 3946.
[16] N.W. Alcock, G. Clarkson, P.B. Glover, G.A. Lawrance, P. Moore, M. Napitupulu, J. Chem. Soc., Dalton Trans. (2005) 518.
[17] H.A. Burkill, N. Robertson, R. Vilar, A.J.P. White, D.J. Williams, Inorg. Chem. 44 (2005) 3337.
[18] R. Pedrido, M.R. Bermejo, M.J. Romero, M. Vázquez, A.M. González-Noya, M. Maneiro, M.J. Rodriguez, M.I. Fernández, J. Chem. Soc., Dalton Trans. (2005) 572.
[19] H.A. Burkill, R. Vilar, A.J.P. White, D.J. Williams, J. Chem. Soc., Dalton Trans. (2002) 837.
[20] W.J. Vickaryous, E.R. Healey, O.B. Berryman, D.W. Johnson, Inorg. Chem. 44 (2005) 9247.
[21] G.M. Sheldrick, SHELXTL NT Version 5.1, Program for Solution and Refinement of Crystal Structures, University of Göttingen, Göttingen, Germany, 1997.
[22] X.Q. Shen, H.J. Zhong, H.Y. Zhang, H.Y. Mao, Q.A. Wu, Y. Zhu, Polyhedron 23 (2004) 876.
[23] T. Ozawa, Bull. Chem. Soc. Jpn 38 (1965) 1881.
[24] S. Vyazovkin, Int. J. Chem. Kinet. 28 (1996) 95.
[25] P.D.M. Benoit, R.G. Ferillo, A.H. Ganzow, Anal. Chim. Acta 124 (1985) 869.
[26] M.E. Brown, D. Dollimore, A.K. Galwey, Comprehensive Chemical Kinetics, Vol. 22, Reactions in the Solid State, Amsterdam, 1980.

Available online at www.sciencedirect.com
ScienceDirect
Polyhedron 27 (2008) 210–222
POLYHEDRON
www.elsevier.com/locate/poly

Thiocyanate complexes of the group 12 metals with pyridine-2-carboxamide: Synthesis and structural characterization

Marijana Đaković [a], Zora Popović [a,*], Gerald Giester [b], Maša Rajić-Linarić [c]

[a] Department of Chemistry, Laboratory of General and Inorganic Chemistry, Faculty of Science, University of Zagreb, Horvatovac 102a, HR-10000 Zagreb, Croatia
[b] Institute of Mineralogy and Crystallography, University of Vienna, Althan Strasse 14, A-1090 Vienna, Austria
[c] Laboratory for Thermal Analysis, Brodarski Institute-Marine Research and Special Technology, Av. V. Holjevca 20, HR-10000 Zagreb, Croatia

Received 1 June 2007; accepted 7 September 2007
Available online 26 October 2007

Abstract

Three complexes of picolinamide (pyridine-2-carboxamide, pia) and metal thiocyanates, $M(SCN)_2$, (M = Zn, Cd, Hg), namely two polymorphs of bis(picolinamide-*N,O*)-bis-(thiocyanato-*N*)zinc(II) (**1a** and **1b**), *catena*-[bis(μ-thiocyanato-*S,N*)-picolinamide-*N,O*-cadmium(II)] (**2**) and bis[(μ_2-thiocyanato-*S*-thiocyanato-*S*-picolinamide-*N,O*)mercury(II)] (**3**) have been prepared and characterized by spectroscopic, thermal and X-ray crystallographic methods. The IR and thermal data correlate with the structures of the complexes in the solid state. The vibration bands of diagnostic value are compared to the values of the free ligands.
© 2007 Elsevier Ltd. All rights reserved.

Keywords: Metal complexes of the group 12; Picolinamide; Thiocyanate; X-ray crystal structure; IR; NMR spectra; TGA/DTA analysis

1. Introduction

The carboxamide group, [–C(O)NH–], ubiquitous throughout Nature in the primary structure of proteins, is an important ligand construction unit for coordination chemists. The behavior of pyridine carboxamides towards biologically relevant d-block metals has been widely investigated while much lesser attention had been paid toward exclusively toxic metals such as cadmium and mercury. In our recent research we examined the behavior of pyridinemono- and dicarboxylic acids and their derivatives and established that they act as efficient competitive ligands toward halides for coordination sites of these metal centres coexisting as anionic *N,O*-bidentate [1–4], *N,O,O*-tridentate [5], *O*-monodentate [3] and *O,O*-bidentate ligands [6], as well as neutral molecules [2]. Our interest is currently engaged with exploring not only the coordination abilities of picolinamide with thiocyanate complexes of group 12 metals but also in getting some information possibly useful in understanding the role of the thiocyanate ion in biologically important processes recently discovered [7,8]. Here we report the synthesis of thiocyanate complexes of group 12 metals with picolinamide, their structural characterization by spectroscopic and diffraction methods as well as their thermal stability using TGA/DTA methods. The crystal and molecular structures of the two polymorphs $[Zn(NCS)_2(pia)_2]$ (**1a** and **1b**), and $[Cd(SCN)_2(pia)]_n$ (**2**) and $[Hg(SCN)_2(pia)]_2$ (**3**) were determined by single crystal X-ray diffraction.

2. Experimental

2.1. Materials and physical measurements

All reagents were supplied by Aldrich Chemical Co. and were used as received without further purification. The

* Corresponding author.
E-mail address: zpopovic@chem.pmf.hr (Z. Popović).

0277-5387/$ - see front matter © 2007 Elsevier Ltd. All rights reserved.
doi:10.1016/j.poly.2007.09.014

CHNS-microanalyses were performed by the Chemical Analytical Service of the Ruđer Bošković Institut, Zagreb.

Infrared spectra were obtained from KBr pellets within the range 4000–400 cm^{-1} with a Perkin–Elmer FTIR spectrometer 1600 Series.

The one-dimensional ^{1}H and ^{13}C NMR spectra were recorded with a Bruker AV 600 spectrometer, operating at 600.133 MHz and 150.971 MHz for the ^{1}H and ^{13}C nuclei, respectively. Samples were measured in DMSO-d_6 solution and chemical shifts (ppm) are referred to TMS.

The thermal measurements were performed using a simultaneous TGA–DTA analyzer (*TA Instruments*, SDT Model 2960). The TGA and DTA curves were obtained by placing samples of about 6 mg in mass, in small open platinum pans, with a heating rate of 10 °C/min and nitrogen (purity above 99.996%) pouring at a flow rate of 50 mL/min. All samples were heated from room temperature up to 700 °C. The SDT was calibrated with indium and silver.

2.2. Preparation of the complexes

2.2.1. Preparation of $[Zn(NCS)_2(pia)_2]$ (**1a** and **1b**)

A warm solution (50 mL) of picolinamide (0.24 g; 0.2 mmol) in water was slowly added to an aqueous solution (10 mL) of zinc nitrate hexahydrate (0.30 g; 0.1 mmol). Into the resulting solution was then added an aqueous solution (10 mL) of potassium thiocyanate (0.18 g; 0.2 mmol). After keeping the mother liquid for few days, white crystals suitable for further X-ray diffraction experiments were obtained. Total yield corresponds to 88% (0.37 g; 0.88 mmol) based on Zn. *Anal.* Calc. for $C_{14}H_{12}ZnN_6O_2S_2$ (**1**): C, 39.49; H, 2.84; N, 19.74; S, 15.06. Found: C, 39.61; H, 2.98; N, 19.95; S, 15.16%. Selected IR data (cm^{-1}, KBr pellets): 3330s, 3184s, 2096vs, 1688s, 1666vs, 1624m, 1612m, 1593s, 1585s, 1569s, 1423s, 1184w, 1160w, 1124w, 1109m-w, 1074w, 1056w, 1024m, 798w, 780w, 755m, 744m, 724m-w, 528w. From the reaction mixture, in which an excess of a picolinamide was present, **1a** together with a few crystals of another polymorph **1b** were obtained.

2.2.2. Preparation of $[Cd(SCN)_2(pia)]_n$ (**2**)

Compound **2** was prepared in an analogous way to **1**, only using cadmium nitrate tetrahydrate (0.31 g; 0.1 mmol) as the starting metal salt. Total yield corresponds to 77% (0.28 g; 0.77 mmol) based on Cd. *Anal.* Calc. for $C_8H_6CdN_4OS_2$ (**2**): C, 27.40; H, 1.72; N, 15.98; S, 18.29. Found: C, 27.48; H, 1.81; N, 16.03; S, 18.32%. Selected IR data (cm^{-1}, KBr pellets): 3408s, 3343m, 3284m, 3203s, 2119vs, 2094vs, 1669vs, 1610m-s, 1584s, 1571s, 1419s, 1181w, 1161w, 1117m, 1092w, 1054w, 1016s, 782w, 747s, 659s, 638m-w, 541m.

2.2.3. Preparation of $[Hg(SCN)_2(pia)]_2$ (**3**)

Into an aqueous solution (100 mL) of mercury(II) nitrate monohydrate (0.68 g; 2 mmol) with a few drops of diluted nitric acid (20% by weight), an aqueous solution (10 mL) of potassium thiocyanate (0.36 g; 4 mmol) was slowly added. After several hours colourless crystals of mercury(II) thiocyanate were obtained. The crystals were filtered off, washed with water and dried. Total yield 85% (0.54 g; 1.7 mmol). $Hg(SCN)_2$ was then dissolved in ethanol (0.32 g; 1 mmol in 100 mL) by gentle heating and the ethanol solution (30 mL) of picolinamide (0.24 g; 2 mmol) was added in it. The resulting mixture was refluxed for 1 h. The clear solution thus formed was allowed to stand for a few days to yield colourless crystals of compound **3** suitable for X-ray investigations. Total yield corresponds to 82% (0.36 g; 0.82 mmol) based on Hg. *Anal.* Calc. for $C_{16}H_{12}Hg_2N_8O_2S_4$ (**3**): C, 21.89; H, 1.38; N, 12.77; S, 14.61. Found: C, 21.95; H, 1.40; N, 12.82; S, 14.73%. Selected IR data (cm^{-1}, KBr pellets): 3409s, 3292s, 2130vs, 1691vs, 1616m-s, 1583s, 1568m, 1142w, 1095m, 1044w, 999m, 749s, 676m-w, 636m-w, 617m-s, 559m-s, 496m, 462m.

2.3. X-ray structural analysis

The general and crystal data, and summary of intensity data collection and structure refinement for compounds **1**–**3** are given in Table 1.

Data for structure **1a** were collected at 200 K on a Nonius KappaCCD diffractometer with a crystal-detector distance of 30 mm. The extraction and correction of the intensity data, absorption correction and the refinement of the unit cell parameters were performed with the program package DENZO-SMN [9].

Data for structures **1b**, **2** and **3** were collected at 293 K on an Oxford Diffraction Xcalibur four-circle kappa geometry single-crystal diffractometer with a Sapphire 3 CCD detector, by applying the CrysAlis software system [10]. The crystal-detector distance was 60 mm. Data reduction, including absorption correction, was done by the CrysAlis RED application of the CrysAlis software system [10].

The structures were solved by direct methods using the SHELXS97 program [11]. The coordinates and the anisotropic thermal parameters for all non-hydrogen atoms were refined by the least-squares methods based on F^2 using the SHELXL97 program [12]. The hydrogen atoms were generated geometrically using the riding model with the isotropic factor set at $1.2U_{eq}$ of the parent atom. Hydrogen atoms on the amide nitrogen atom, as well as on the oxygen atom of the H_2O molecule were located in the difference Fourier map at the final stage of the refinement and were refined freely. Graphical work has been performed by the program ORTEP-3 *for Windows* [13] and Mercury 1.4.1 [14]. The thermal ellipsoides are drawn at the 50% probability level.

3. Results and discussion

3.1. Preparation of the complexes

The zinc and cadmium thiocyanato complexes **1** (**1a** and **1b**) and **2** were prepared *in situ* from aqueous solutions. The mercury complex **3** could not be obtained in the same way due to very low solubility of mercuric thiocyanate in

Table 1
Crystal data and structure refinements for complexes **1**–**3**

Complex	**1a**	**1b**	**2**	**3**
Empirical formula	$C_{14}H_{12}ZnN_6O_2S_2$	$C_{14}H_{12}ZnN_6O_2S_2$	$C_8H_6CdN_4OS_2$	$C_{16}H_{12}Hg_2N_8O_2S_4$
Formula weight	425.83	425.83	350.72	877.80
Temperature (K)	200	296	296	296
Wavelength (Å)	0.71073	0.71073	0.71073	0.71073
Crystal system	monoclinic	monoclinic	triclinic	triclinic
Space group	$P2_1/c$	$C2/c$	$P\bar{1}$	$P\bar{1}$
a (Å)	6.754(2)	17.1396(5)	9.4097(6)	7.3949(7)
b (Å)	16.643(3)	8.2446(2)	10.4414(7)	7.4560(4)
c (Å)	17.384(4)	13.5627(4)	12.2651(4)	10.757(1)
α (°)	90	90	99.259(5)	100.124(8)
β (°)	110.18(3)	109.243(3)	90.292(4)	105.538(9)
γ (°)	90	90	93.124(5)	91.343(8)
Volume (Å^3)	1838.0(7)	1809.46(9)	1187.5(1)	560.97(9)
Z	4	4	4	1
ρ_{calc} (g/cm^3)	1.542	1.563	1.962	2.598
$F(000)$	864	864	680	404
Crystal size (mm)	$0.15 \times 0.20 \times 0.24$	$0.07 \times 0.28 \times 0.42$	$0.13 \times 0.31 \times 0.32$	$0.10 \times 0.22 \times 0.32$
Reflections collected	21 352	20 139	30 651	17 933
Unique reflections	5585	2637	6914	3264
Parameters	253	122	306	154
$R_{1,\text{all data}}$,	0.0434	0.0541	0.0296	0.0338
$R1$[a] $[I > 2\sigma(I)]$	0.0307	0.0312	0.0214	0.0280
$wR_{2,\text{all data}}$,	0.0788	0.0813	0.0534	0.0712
wR_2[b] $[I > 2\sigma(I)]$	0.0735	0.0703	0.0496	0.0677
g_1, g_2 in w[c]	0.0355, 0.6356	0.0389, 0.3787	0.0259, 0.3511	0.0345, 1.4834
S[d] on F^2	1.047	1.053	1.073	1.049
$\Delta\sigma_{min/max}$ (e Å^{-3})[e]	−0.410/0.399	−0.402/0.368	−0.549/0.692	−1.819/2.359
Extinction coefficient	0.0053(6)	none	0.0042(3)	0.027(1)

[a] $R = \sum\|F_o| - |F_c\|/\sum|F_o|$.
[b] $wR = [\sum(F_o^2 - F_c^2)^2/\sum w(F_o^2)^2]^{1/2}$.
[c] $w = 1/[\sigma^2(F_o^2) + [(g_1P)^2 + g_2P]]$ where $P = (F_o^2 + 2F_c^2)/3$.
[d] $S = \sum[w(F_o^2 - F_c^2)^2/(N_{obs} - N_{param})]^{1/2}$.
[e] The maximum electron density in the last difference Fourier map is near Hg.

water, while *in situ* reaction from an ethanol solution gave a mixture of products. Complex **3** was the only product from the reaction performed by refluxing the mixture of ethanolic solutions of mercuric thiocyanate and picolinamide. It was also established that in **1**–**3** the reaction products were not influenced by the molar ratio of the reactants (1:1 or 1:2 metal thiocyanate versus picolinamide). All complexes are soluble in solvents with pronounced coordination properties such as dimethyl sulfoxide (DMSO) and *N,N*-dimethyl formamide (DMF).

3.2. Structure descriptions

All crystals were grown by slow evaporation of the reaction mixture under ambient conditions in periods from two days to one week. Selected bond distances and bond angles relevant to the coordination of the central metal ions are given in Table 2, while the hydrogen bonds are presented in Table 1. The structures are shown in Figs. 1–4.

3.2.1. Crystal structure of $[Zn(NCS)_2(pia)_2]$ (**1a**) and (**1b**)

The compound **1** crystallizes in two polymorphic forms, **1a** and **1b**. The different packing in the unit cell is caused by the slight differences in their molecular structures.

The compound **1a** crystallizes in the space group $P2_1/c$. The crystal structure of bis(picolinamide-*N*,*O*)-bis(thiocyanato-*N*)zinc(II) consists of discrete octahedral complex molecules. An octahedral polyhedron is achieved through [4N + 2O] coordination of the zinc atom, where two nitrogen atoms originate from picolinamides and two from *cis*-positioned NCS-groups (Fig. 1a). The octahedron is almost regular with the two smallest angles being 75.06(5)° and 75.69(5)° for N3–Zn1–O1 and N5–Zn1–O2, respectively. All other angles around the zinc atom are in the range 87.44(5)–96.59(6)°, while all the opposite atoms in the coordination sphere form angles in the range 162.89(5)–171.51(5)°. The sums of four angles around the zinc atom closed by coordinating atoms lying in a plane are very close to 360° [359.06°, 359.44°, 361.35°], indicating the planarity of the planes containing the zinc(II) ion and thus also supporting the almost regular octahedral coordination of the central metal atom.

The Zn–N distances are in the range between 2.058(2) and 2.106(2) Å, with the Zn–NCS bonds [2.053(2) and 2.087(2) Å] being shorter than the Zn–N(pia) bonds [2.103(2) and 2.106(2) Å]. The Zn–O distances [2.258(1) Å and 2.218(1) Å] are somewhat longer than in other octahedral zinc complexes with picolinamide or its derivatives: 2.073(2) Å in $[Zn(picolinamide)_2(H_2O)_2I_2]$ [15] and

Table 2
Selected bond distances (Å) and angles (°) for complexes **1**–**3**

Complex **1a**			
In the coordination polyhedron			
Zn(1)–N(1)	2.058(2)	Zn(1)–O(1)	2.258(1)
Zn(1)–N(2)	2.087(2)	Zn(1)–O(2)	2.218(1)
Zn(1)–N(3)	2.106(2)		
Zn(1)–N(5)	2.103(2)		
N(1)–Zn(1)–N(2)	93.22(7)	N(1)–Zn(1)–O(2)	171.51(5)
N(1)–Zn(1)–N(5)	95.98(6)	N(2)–Zn(1)–O(2)	89.44(6)
N(2)–Zn(1)–N(5)	96.59(6)	N(5)–Zn(1)–O(2)	75.69(5)
N(1)–Zn(1)–N(3)	95.41(6)	N(3)–Zn(1)–O(2)	92.36(5)
N(2)–Zn(1)–N(3)	95.47(6)	N(1)–Zn(1)–O(1)	91.25(6)
N(5)–Zn(1)–N(3)	162.89(5)	N(2)–Zn(1)–O(1)	169.88(5)
O(2)–Zn(1)–O(1)	87.44(5)	N(5)–Zn(1)–O(1)	91.96(5)
		N(3)–Zn(1)–O(1)	75.06(5)
In the thiocyanate			
N(1)–C(1)	1.152(2)	C(1)–S(1)	1.629(2)
N(2)–C(2)	1.147(2)	C(2)–S(2a)	1.631(4)
		C(2)–S(2b)	1.623(6)
N(1)–C(1)–S(1)	178.2(2)		
N(2)–C(2)–S(2a)	172.0(4)		
N(2)–C(2)–S(2b)	167.0(5)		
Zn(1)–N(1)–C(1)	154.3(2)		
Zn(2)–N(2)–C(2)	147.9(2)		
Complex **1b**			
In the coordination polyhedron			
Zn(1)–N(1)	2.069(2)	Zn(1)–O(1)	2.197(2)
Zn(1)–N(1)[a]	2.069(2)	Zn(1)–O(1)[a]	2.197(2)
Zn(1)–N(2)	2.117(2)		
Zn(1)–N(2)[a]	2.117(2)		
N(1)–Zn(1)–N(2)	97.87(6)	N(1)–Zn(1)–O(1)	88.05(6)
N(1)–Zn(1)–N(2)[a]	95.82(6)	N(1)–Zn(1)–O(1)[a]	170.09(6)
N(1)–Zn(1)–N(1)[a]	97.45(7)	N(2)–Zn(1)–O(1)	75.19(5)
N(2)–Zn(1)–N(2)[a]	159.19(6)	N(2)–Zn(1)–O(1)[1]	89.73(5)
O(1)–Zn(1)–O(1)[a]	87.76(5)		
In the thiocyanate			
N(1)–C(1)	1.153(3)	C(1)–S(1)	1.628(2)
N(1)–C(1)–S(1)	178.5(2)		
Zn(1)–N(1)–C(1)	171.9(2)		
Complex **2**			
In the coordination polyhedron			
Cd(1)–N(1)	2.333(2)	Cd(1)–O(1)	2.369(1)
Cd(1)–N(2)	2.312(2)	Cd(1)–S(1)	2.6519(6)
Cd(1)–N(5)	2.333(2)	Cd(1)–S(2)	2.6328(6)
Cd(2)–N(3)	2.271(1)	Cd(2)–O(2)	2.373(1)
Cd(2)–N(4)	2.346(2)	Cd(2)–S(3)	2.7831(6)
Cd(2)–N(7)	2.352(2)	Cd(2)–S(4)	2.6154(6)
N(1)–Cd(1)–N(2)	176.65(7)	N(1)–Cd(1)–S(1)	96.10(5)
N(1)–Cd(1)–N(5)	91.17(7)	N(2)–Cd(1)–S(1)	86.65(6)
N(2)–Cd(1)–N(5)	90.30(7)	N(5)–Cd(1)–S(1)	98.41(4)
N(1)–Cd(1)–O(1)	95.29(6)	N(1)–Cd(1)–S(2)	84.63(5)
N(2)–Cd(1)–O(1)	82.40(7)	N(2)–Cd(1)–S(2)	92.93(5)
N(5)–Cd(1)–O(1)	69.77(5)	N(5)–Cd(1)–S(2)	159.02(5)
O(1)–Cd(1)–S(1)	163.74(4)		
S(1)–Cd(1)–S(2)	102.46(2)		
N(1)–Cd(2)–N(2)	176.65(7)	N(1)–Cd(2)–S(1)	96.10(5)
N(1)–Cd(2)–N(5)	91.17(7)	N(2)–Cd(2)–S(1)	86.65(6)
N(2)–Cd(2)–N(5)	90.30(7)	N(5)–Cd(2)–S(1)	98.41(4)
N(1)–Cd(2)–O(1)	95.29(6)	N(1)–Cd(2)–S(2)	84.63(5)
N(2)–Cd(2)–O(1)	82.40(7)	N(2)–Cd(2)–S(2)	92.93(5)
N(5)–Cd(2)–O(1)	69.77(5)	N(5)–Cd(2)–S(2)	159.02(5)
O(1)–Cd(2)–S(1)	163.74(4)		
S(1)–Cd(2)–S(2)	102.46(2)		
In the thiocyanate			
N(1)–C(1)	1.149(3)	C(1)–S(1)[b]	1.649(2)
N(2)–C(2)	1.148(3)	C(2)–S(2)[c]	1.641(2)
N(3)[d]–C(3)	1.148(3)	C(3)–S(3)	1.654(2)
N(4)–C(4)	1.150(3)	C(4)–S(4)[e]	1.650(2)
N(1)–C(1)–S(1)[b]	178.4(2)	N(3)–C(3)[d]–S(3)[d]	179.2(2)
N(2)–C(2)–S(2)[c]	177.3(2)	N(4)–C(4)–S(4)[e]	177.3(2)
Cd(1)–N(1)–C(1)	140.2(2)	Cd(2)–S(3)–C(3)	96.72(8)
Cd(1)–S(1)–C(1)[b]	96.60(7)	Cd(2)–N(3)–C(3)[e]	156.6(2)
Cd(1)–N(2)–C(2)	150.2(2)	Cd(2)–S(4)–C(4)[d]	97.55(7)
Cd(1)–S(2)–C(2)[c]	97.81(7)	Cd(2)–N(4)–C(4)	138.6(2)
Complex **3**			
In the coordination polyhedron			
Hg(1)–S(1)	2.612(1)	Hg(1)–O(1)	2.493(3)
Hg(1)–S(1)[f]	2.874(2)		
Hg(1)–S(2)	2.482(1)		
Hg(1)–N(3)	2.239(3)		
S(1)–Hg(1)–S(1)[f]	88.17(3)	N(3)–Hg(1)–S(1)	136.1(1)
S(1)–Hg(1)–S(2)	96.08(4)	N(3)–Hg(1)–S(2)	126.1(1)
S(2)–Hg(1)–S(1)[f]	99.58(4)	N(3)–Hg(1)–S(1)[f]	95.40(9)
O(1)–Hg(1)–S(1)	89.91(8)	N(3)–Hg(1)–O(1)	69.4(1)
O(1)–Hg(1)–S(1)[f]	155.17(9)		
O(1)–Hg(1)–S(2)	105.25(9)		
In the thiocyanate			
N(1)–C(1)	1.151(7)	C(1)–S(1)	1.679(5)
N(2)–C(2)	1.144(6)	C(2)–S(2)	1.668(5)
N(1)–C(1)–S(1)	176.7(4)		
N(2)–C(2)–S(2)	179.1(5)		
Hg(1)–N(1)–C(1)	106.0(2)	Hg(1)–N(2)–C(2)	96.5(2)
Hg(1)[f]–N(1)–C(1)	102.2(2)		

[a] $1-x, y, 1/2-z$.
[b] $-x+2, -y+1, -z$.
[c] $-x+1, -y+1, -z$.
[d] $-x+1, -y+2, -z+1$.
[e] $-x+2, -y+2, -z+1$.
[f] $-x+1, -y, 1-z$.

2.110(3) Å in [Zn(3-hydroxypicolinamide)$_2$(OH)$_2$] [16]. The set of bond lengths around zinc in **1a** indicates that the Zn–N bond involving the thiocyanate anion is stronger than that originating from picolinamide.

The NCS ligand, labelled as 1, (N(1)–C(1)–S(1)), shows a very small distortion from linearity (178.2(2)°), while the isothiocyanate ligand with a disordered sulfur atom deviates significantly [167.0(5)° and 172.0(4)°] and both NCS ligands bind to the metal in a non-linear mode with Zn–N–CS angles of 154.3(2)° and 147.9(2)°, which is generally usual for thiocyanates. The M–N–CS angle for zinc thiocyanate has been found to be in the range 132–180°, but is usually between 150° and 180° [17,18]. The pyridine rings are almost planar [torsion angles are 0.83(1)° and 1.27(1)°] while the chelate rings deviate from planarity [torsion angles 5.32(7)° and 8.36(7)°].

The crystal structure is predominantly determined by hydrogen bonding – there are N–H···O, N–H···S and

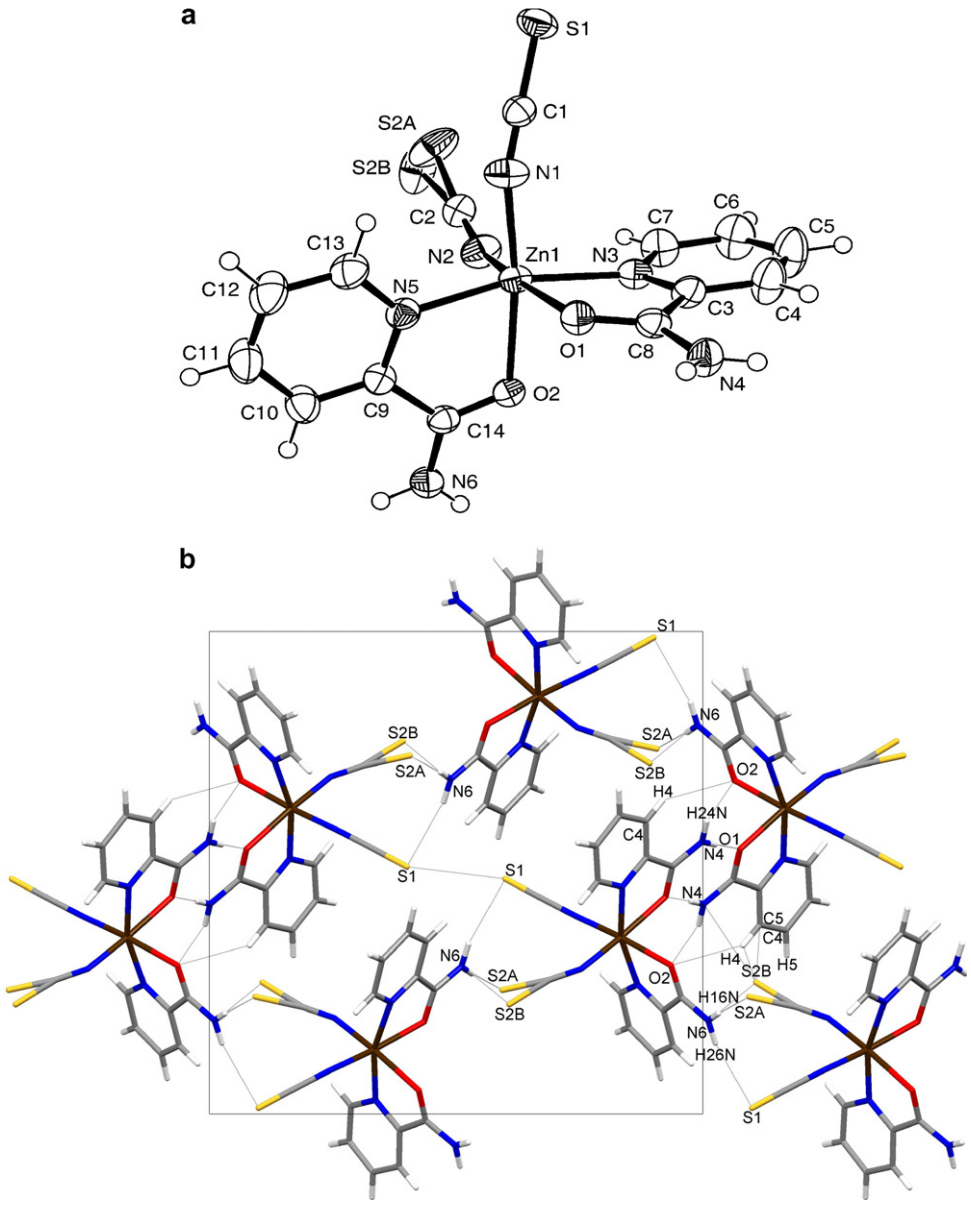


Fig. 1. (a) ORTEP3 drawing of the structural unit of complex **1a**; (b) perspective view along the *a*-axis; hydrogen bonds and contacts are drawn as dotted lines.

C–H···O types of hydrogen bonds. The geometric parameters of these bonds are given in Table 5. The amide nitrogen atoms from both picolinamide ligands, N(4) and N(6), are involved in two hydrogen bonds to two oxygen and two sulfur atoms, respectively (N(4)–H···O and N(6)–H···S). As a consequence of these two different hydrogen bondings the two carboxamide groups have different twist angles (13.0(1)° and 2.06(6)°). The amide nitrogen atom N(4) participates in a centrosymmetric head-to-head hydrogen bond of the R_2^2 (8) type with the amide oxygen atom O(1) from the neighbouring molecule (symmetry code: $-x$, $-y$, $1-z$). The same amide nitrogen atom N(4) also forms a hydrogen bond with the amide oxygen atom from the neighbouring molecule along the *a*-axis, O(2), which also acts as a bifurcated acceptor in the C(4)–H(4)···O(2) hydrogen bond. The amide nitrogen atom from the other picolinamide ligand, N(6), also participates in two hydrogen bonds, but of the N–H···S type. Thus each complex molecule bridges adjacent molecules forming chains along the *a*-axis. As shown in Fig. 1b, the molecules are further stabilized through short S···S contacts of the NCS ligands (3.392 Å).

The sulfur atom S(2), is found to be disordered. The same disorder is also observed in space groups of lower symmetries, $P2_1$ and *Pc*. It could, probably, be the consequence of the few short contacts resulting from the vicinity of neighbouring molecules: C(4)–H(4)···S(2b), C(4)···S(2b) and N(4)···S(2b), symmetry code: x, $1/2-y$, $-1/2+z$, and N(6)–H(16N)···S(2b), symmetry code: $1-x$, $1/2+y$, $1/2-z$, as designated in Fig. 1b.

In addition to hydrogen bonds there are also weak π···π interactions with a short distance between the centroids of

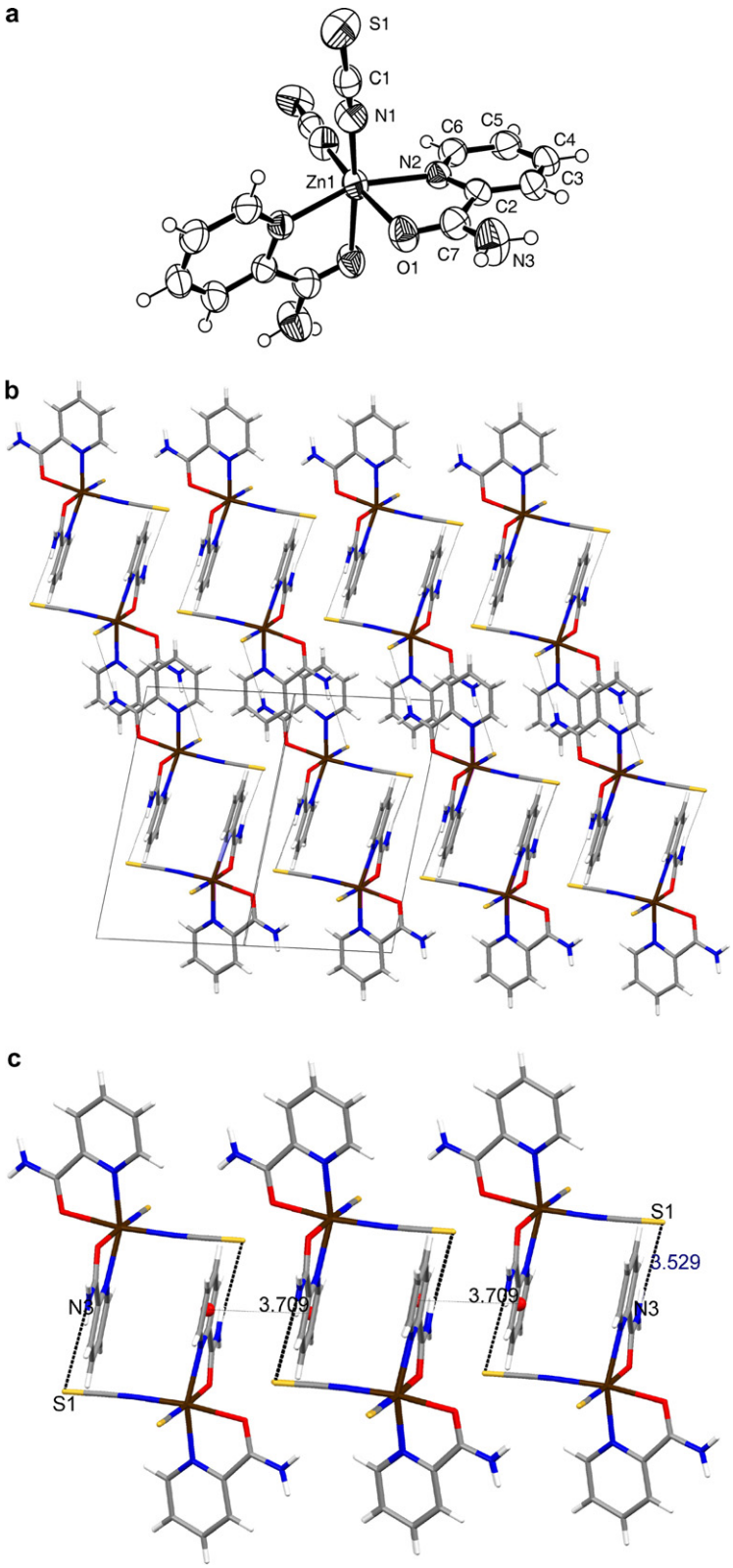


Fig. 2. (a) ORTEP3 drawing of the structural unit of complex **1b** with the atomic numbering scheme of asymmetric unit; (b) perspective view of the crystal packing of compound **1b** along the [101] direction; (c) π···π and N–H···S contacts are drawn as dotted lines.

the two aromatic rings N3,C3 → C7 and N5,C9 → C13, 4.434(2) Å (Table 5).

1b, the polymorph of **1a**, crystallizes in space group *C*2/*c* with a central metal ion in a special position. The octahedral coordination polyhedra of the zinc(II) ion was found in both polymorphs. Apart from deviations in the crystal packing of the two polymorphs, there are also some other discrepancies in the molecular geometry.

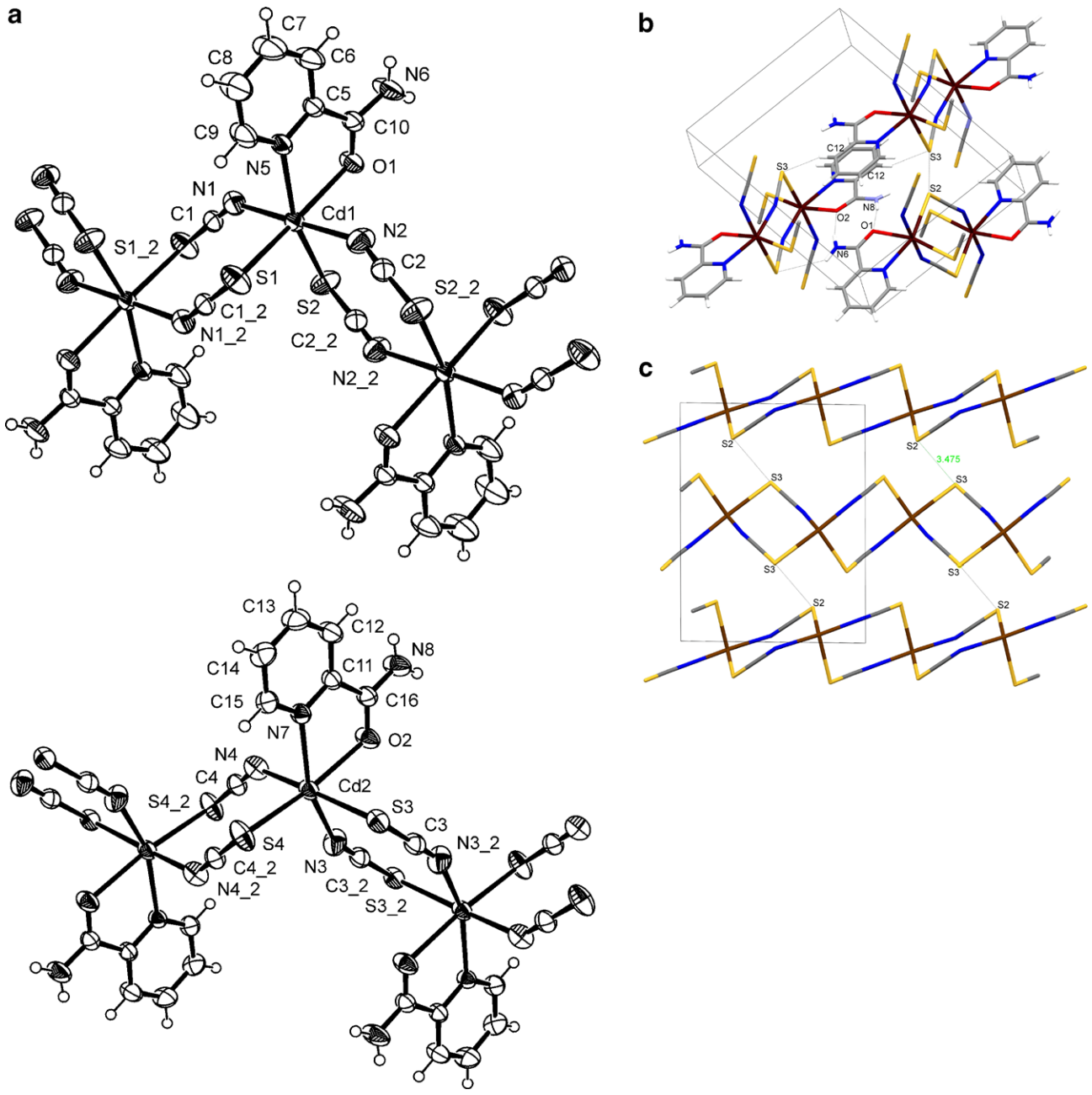


Fig. 3. (a) ORTEP3 drawing of the two crystallographically independent chains of complex **2** with the atomic numbering scheme of the asymmetric unit; (b) perspective view of intermolecular hydrogen bonds and S···S contacts between adjacent polymer chains; (c) a view of the $Cd(SCN)_2$ chains along the *b*-axis. The picolinamide ligands are omitted for clarity.

The bite angles of the chelate picolinamide ligands are retained in both polymorphs, while significant deviations in bond distances toward the zinc(II) ions are observed. The Zn–O(pia) bond length in polymorph **1b** is shorter than it is in polymorph **1a** [2.197(2) Å, **1b**; 2.258(1) Å and 2.218(1) Å, **1a**]. Further, the Zn–N(py) bond length is elongated to a somewhat smaller extend [2.117(2) Å, **1b**; 2.106(2) Å and 2.103(2) Å, **1a**]. But it is still the case, as in polymorph **1a**, that the thiocyanato ligand is bound to the central zinc(II) ion more tightly than the picolinamide ligand.

The isothiocyanato ligand is more tilted towards the carboxamide group in **1b** than in **1a**. Smaller N(NCS)–Zn–O [88.05(6)° **1a**; 89.44(6)° and 91.25(6)° **1b**] and larger N(NCS)–Zn–N(py) [97.89(6)° **1b**; 95.41(6)–96.59(6)° **1a**] angles in **1b** than in **1a** are established. The chelate ring also deviates more from planarity in polymorph **1b** than in **1a** (Table 3).

There are other differences in the crystal than in the molecular structures of both polymorphs. In crystal structure of **1b** hydrogen bonds are not pronounced. There is just one weak intermolecular interaction of the N–H···S

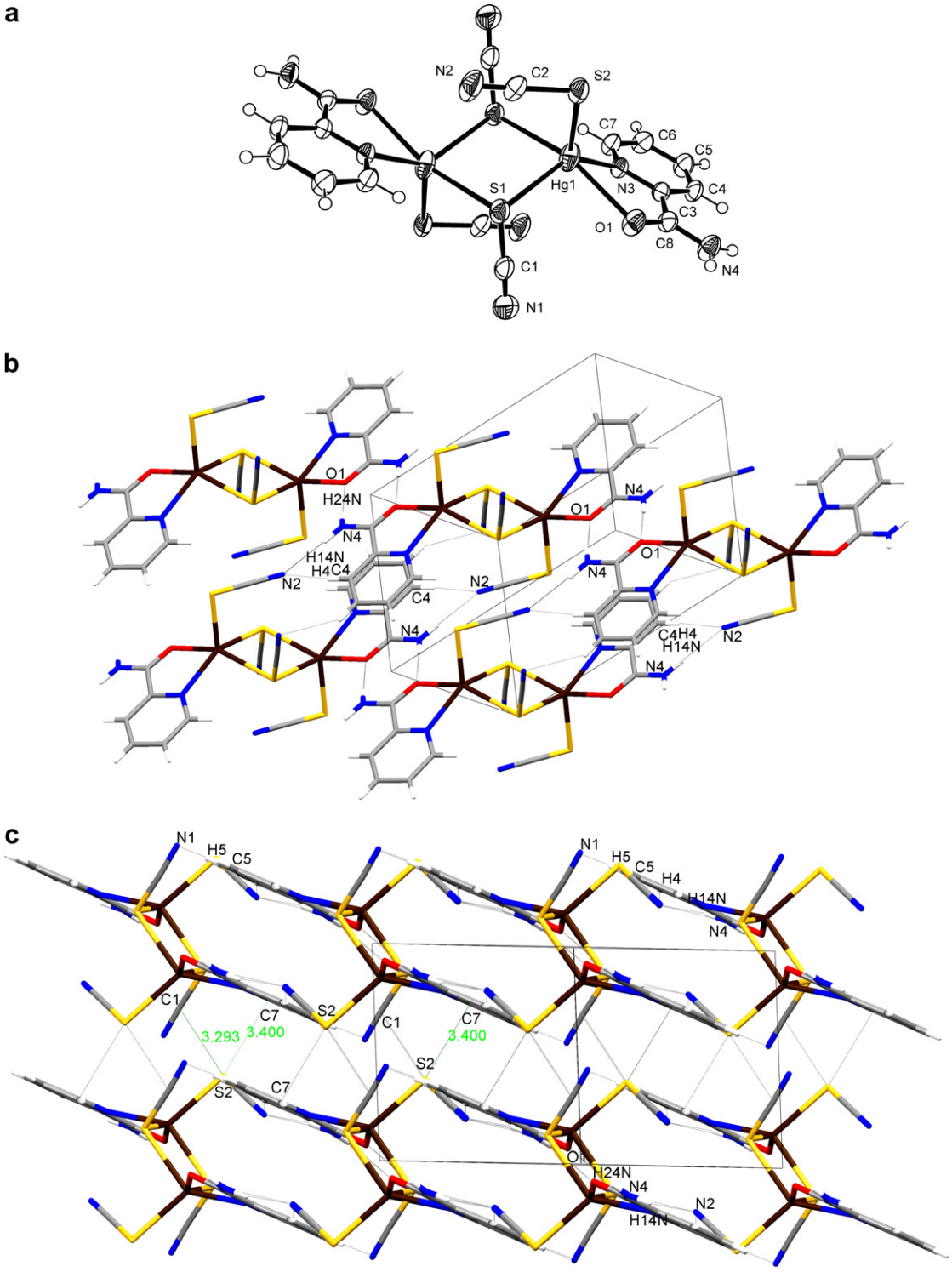


Fig. 4. (a) ORTEP3 drawing of the structural unit of complex **3**, [Hg $(SCN)_2$(pia)] with the atomic numbering scheme; (b) formation of the 2D architecture established by hydrogen bonds; the dotted lines represent hydrogen bonds; (c) the perspective view of the molecular packing of complex **3** showing the channels formed by the C···S interactions and hydrogen bonds.

type (3.529(2) Å) found between the nitrogen atom of the carboxamide group and the isothiocyanate sulfur atom. Two neighbouring molecules are held together by two interactions of this type forming stair like chains of complex molecules. Two adjacent molecules in this chains form 16-membered rings which leave the holes in crystal structure in the [1 0 1] direction. Two such formed neighbouring chains are held together by weak π–π interactions with *Cg*···*Cg* of distances 3.709(1) Å (Table 6). The differences in intermolecular interactions between these two poly-

Table 3
Selected torsion and dihedral angles (°)

	(**1a**)	(**1b**)	(**2**)	(**3**)
Py ring (I)	0.83(1)	0.7(1)	0.4(2)	1.2(3)
Py ring (II)	1.27(1)		0.7(1)	
Chelate ring (I)	5.32(7)	11.4(8)	5.52(8)	12.7(2)
Chelate ring (II)	8.36(7)		2.21(9)	
Py ring (I)–amido group (I)	13.0(1)	7.51(8)	3.5(1)	2.2(2)
Py ring (II)–amido group (II)	2.06(6)		2.3(1)	
Py (I)–Py (II)	85.47(9)			

morphs are also affirmed by different melting temperatures, 169.0(5) °C for **1a** and 167.1(5) °C for **1b**.

3.2.2. Crystal structure of $[Cd(SCN)_2(pia)]_n$ (**2**)

The molecular structure of *catena*-[bis(μ-thiocyanato-*S*,*N*)-picolinamide-*N*,*O*-cadmium(II)] comprises of two crystallographically independent chains along the *a*-axis (Fig. 3a). In both chains the cadmium atom shows a distorted octahedral environment with [3N + O + 2S] coordination. Two adjacent cadmium atoms are bridged by two inversely related μ-SCN^--*N,S* and the remaining coordination sites are occupied by the chelate picolinamide ligand, resulting in a structure comprising of eight-membered $(N–C–S–Cd)_2$ rings. These chains differ in the *cis*- and *trans*-orientation of the two bridging thiocyanato-*N* groups resulting in different chair conformations of the Cd–NCS skeleton, as illustrated in Fig. 3c. The intra-chain Cd···Cd distances from two crystallographically independent chains also differ: 5.743 Å and 5.847 Å for chains containing Cd(1) and Cd(2), respectively, the values are close to those already found for structures with two bridged thiocyanato ligands [19]. The Cd–N(NCS) (2.271(1)–2.346(2) Å) and Cd–S (2.6154(6)–2.7831(6) Å) distances are also very close to those ones reported for complexes containing eight-membered $[Cd_2(SCN)_2]$ rings [20,21]. The crystal structure is realized through various non-covalent interactions: (a) N–H···O (between two amido groups) head-to-head double hydrogen bonds of the $R_2^2(8)$ type (originated from the amide group of two picolinamide ligands coordinated on two symmetrically independent cadmium(II) atoms from adjacent chains, Cd(1) and Cd(2)), (b) N–H···S and (c) C–H···S interactions (Table 4), as well as (d) π–π stacking interactions (Table 6). The nitrogen atoms from each amide group are involved in N–H···O hydrogen bonds (N···O 2.948(3) Å and 2.983(3) Å) but the nitrogen atom from the amide group coordinated to Cd(1) also participates in a N–H···S interaction with a N···S distance of 3.456 Å, acting as a bifurcated donor. The weak intermolecular interaction C–H···S between two symmetrically related chains involves aromatic C(12)–H(12) and thiocyanate S(3) (Table 4). As shown in Fig. 3b, the layers are further packed into a three-dimensional framework also through weak S···S interactions of the NCS^- ligands (3.475(8) Å). The observed interaction is slightly shorter than in comparable cadmium complexes already reported [19]. In the present structure the pyridyl rings from each one-dimensional polymer chain π–π stack in an offset face to face arrangement with adjacent chains (3.817(1) Å) contributing to the stability of the crystal structure and resulting in the highest decomposition temperature of all three isolated complexes.

3.2.3. Crystal structure of $[Hg(SCN)_2(pia)]_2$ (**3**)

Bis[(μ$_2$-thiocyanato-*S*-thiocyanato-*S*-picolinamide-*N*,*O*)-mercury(II)] crystallizes in space group $P\bar{1}$ and the crystal lattice (molecular structure) consists of a neutral centrosymmetric dinuclear unit $[Hg_2(L)_2(SCN)_4]$, Fig. 4a. The coordination polyhedron around the mercury is best described as a distorted tetragonal pyramid. The metal ion is ligated by three sulfur atoms from thiocyanate, and an amide oxygen and an endocyclic nitrogen from the pic-

Table 4
Hydrogen bonds and contacts (Å and °) **1–3**

D–H···A	D–H	H···A	D···A	∠DHA	Symmetry code
Compound ***1a***					
N(4)–H(14N)···O(1)	0.90(3)	2.07(3)	2.962(2)	175(2)	$-x, -y, 1-z$
N(4)–H(24N)···O(2)	0.84(2)	2.53(3)	3.124(2)	161(2)	$1-x, -y, 1-z$
N(6)–H(16N)···S(2a)	0.82(3)	2.53(3)	3.347(6)	176(2)	$1-x, -1/2+y, 1/2-z$
N(6)–H(26N)···S(1)	0.88(2)	2.54(2)	3.356(2)	155.8(2)	$-x, -1/2+y, 1/2-z$
C(4)–H(4)···O(2)	0.95	2.53	3.300(2)	138	$1-x, -y, 1-z$
Compound ***1b***					
N(3)–H(13N)···S(1)	0.89(3)	2.65(3)	3.530(3)	167(3)	$1/2-x, 1/2-y, -z$
Compound ***2***					
N(8)–H(18N)···O(1)	0.84(3)	2.11(3)	2.948(3)	170(3)	
N(6)–H(16N)···O(2)	0.80(4)	2.20(4)	2.983(3)	166(4)	
N(6)–H(26N)···S(3)	0.83(3)	2.77(3)	3.456(2)	141(2)	$1-x, -y, 1-z$
C(12)–H(12)···S(3)	0.95	2.81	3.698(2)	160	$1-x, 1-y, 1-z$
Compound ***3***					
N(4)–H(14N)···N(2)	0.86(7)	2.10(7)	2.955(6)	169(7)	$x, y, -1+z$
N(4)–H(24N)···O(1)	0.75(6)	2.22(7)	2.957(6)	173(7)	$-x, -y, -z$
C(4)–H(4)···N(2)	0.95	2.53	3.437(6)	164	$x, y, -1+z$
C(5)–H(5)···N(1)	0.95	2.54	3.292(7)	138	$1-x, -y, -z$

Table 5
π···π interactions

π···π contacts	Cg···Cg (Å)	α (°)	β (°)	Cg···plane (Cg2)
Compound **1a**				
Cg(N3,C3 → C7)···Cg(N3, C3 → C7)[a]	5.823(2)	0.00	52.53	3.542
Cg(N3,C3 → C7)···Cg(N5, C9 → C13)[b]	4.434(2)	12.41	39.56	3.419
Compound **1b**				
Cg(N2,C2 → C6)···Cg(N2, C2 → C6)[c]	3.709(1)	0.00	23.06	3.413
Compound **2**				
Cg(N7, C11 → C15)···Cg(N7,C11 → C15)[d]	3.817(1)	0.00	25.99	3.431
Compound **3**				
Cg(N3, C3 → C7) ··· Cg(N3, C3 → C7)[e]	4.713(3)	0.02	42.80	3.458

[a] $1-x, -y, 1-z$.
[b] $1+x, 1/2-y, 1/2+z$.
[c] $1-x, 1-y, -z$.
[d] $-x, 1-y, 1-z$.
[e] $1-x, -y, -z$.

olinamide ligand. One thiocyanate ligand is terminal, while the other bridges two mercuric ions in an end-on fashion.

The distances in the thiocyanato ligands are 1.151(7) and 1.144(6) Å for N–C bonds, and 1.679(5) and 1.668(5) Å for C–S bonds, in the bridging and terminal ligand, respectively, as expected for *S*-coordination of thiocyanates [22]. The thiocyanates are coordinated in a linear fashion as can be seen from the N1–C1–S1 and N2–C2–S2 angles [176.7(4)° and 179.1(5)°], as evident, the bridging SCN-ligand deviates more from linearity than the terminal one.

The pyridyl and chelate rings deviate the most from planarity as compared with structures of **1** and **2** (Table 3) but the amide group, at the same time, closes the smallest torsion angle with the pyridyl ring.

Two dimers are connected together by a N–H···O hydrogen bond of the $R_2^2(8)$ type (Fig. 4b) forming infinite one-dimensional chains in the [101] direction (N(4)–H(24 N)···O(1), Table 4). The well known tendency of the mercury(II) ion towards soft basis, in this case the sulfur atom of the amibdentate thiocyanate ion, releases the thiocyanate nitrogen atom to participate in hydrogen bonding. So, both thiocyanate nitrogens, N(1) and N(2), from one chain of dimers participate in hydrogen bonds holding together two such adjacent chains. While N(1) participates in C–H···N bonding, N(2) acts as a bifurcated acceptor for C–H···N and N–H···N chelate hydrogen bonds. In such a way infinite two-dimensional sheets of channels, closed by two adjacent chains of dimers, are formed. These 2D sheets are probably held together by weak C···S contacts, C(1)···S(2) 3.293 Å and C(7)···S(2) 3.400 Å.

3.3. Spectroscopic properties

3.3.1. IR spectra

In general, C–N stretching frequencies, *ν*(CN), of thiocyanates are lower in *N*-bonded complexes (near or below 2050 cm^{-1}) than *S*-bonded complexes (near 2100 cm^{-1}). For bridging complexes (M–SCN–M) the CN stretching frequency is above 2100 cm^{-1} [23]. The stretching CN frequencies observed at 2096 cm^{-1} for **1a** and **1b**, at 2118 and 2094 cm^{-1} for **2** and at 2130 cm^{-1} for **3** clearly indicate a different coordination mode of the SCN-ligand. The thiocyanate is coordinated to zinc through the nitrogen atom, and to mercury through the sulfur atom, while cadmium is coordinated *via* both, *N*- and *S*- atoms. All above mentioned frequencies are significantly higher than the corresponding one found in the IR spectrum of KSCN (2048 cm^{-1} [24]). The SCN group is a good electron supplier and the electron transfer from SCN^- to Zn^{2+}, Cd^{2+} and Hg^{2+} ions cause the significant increase of the CN stretching frequency [25]. It is worth emphasising that in **1** the *ν*(CN) frequency is significantly higher (2096 cm^{-1}) than that in the reported zinc *N*-bonded thiocyanate complexes (2077 cm^{-1}, 2073 cm^{-1}) [26,27].

The position of the C–S stretching frequencies in the region 860–690 cm^{-1} is usually employed for differentiating *S*- from *N*-bonded terminal thiocyanates; *ν*(CS) bands that are observed in the range 860–780 cm^{-1} and 720–690 cm^{-1} indicate the *N*- and *S*-coordination mode of the SCN-ligand, respectively [28]. However, the *ν*(CS) modes in the IR spectra of compounds **1**–**3**, are overlapped by selected bands of the ligand in this region and make the assignment quite uncertain.

3.3.2. NMR spectra

The ^1H and ^{13}C NMR data of the parent picolinamide (pia) molecule together with the data of its zinc(II), cadmium(II) and mercury(II) thiocyanato complexes **1**, **2** and **3** are presented in Tables 6 and 7, respectively, while the Scheme 1 shows the labelling of the atoms. Complexation ^1H and ^{13}C NMR shifts are defined as the difference of proton and carbon shifts, respectively, in the complexes and the free ligand molecule. The ^1H NMR data of the free picolinamide in DMSO-d_6 are cited from the literature [29], and all other measurements are also performed in DMSO-d_6.

Table 6
^{1}H NMR chemical shifts (δ/ppm)[a], complexation shifts ($\Delta\delta$/ppm)[b,d] and H–H coupling constants (J_{HH}/Hz)[e] in the ligand molecule, picolinamide, and its complexes with zinc(II), cadmium(II) and mercury(II) thiocyanate, **1**, **2** and **3**

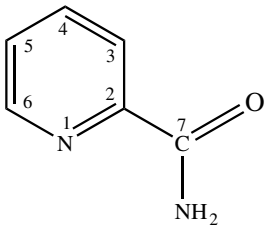
Compound		pia[c]	**1**	**2**	**3**
H-3	δ	8.43	8.24	8.14	8.13
	J_{HH}	8.1 (d)	7.64 (d)	7.77 (d)	7.59 (d)
	$\Delta\delta$		−0.19	−0.29	−0.30
H-4	δ	8.22	8.15	8.07	8.06
	J_{HH}	(m)	(m)	(m)	(m)
	$\Delta\delta$		−0.07	−0.15	−0.16
H-5	δ	7.81	7.75	7.68	7.68
	J_{HH}	(m)	(m)	(m)	(m)
	$\Delta\delta$		−0.06	−0.13	−0.14
H-6	δ	8.89	8.70	8.66	8.70
	J_{HH}	4.5 (d)	4.63 (d)	4.47 (d)	4.84 (d)
	$\Delta\delta$		−0.19	−0.23	−0.19
H-1(NH_2)	δ	8.1	8.09	7.94	7.86
	J_{HH}	broadened	broadened	broadened	broadened
	$\Delta\delta$		−0.01	−1.16	−0.24
H-2(NH_2)	δ	8.5	8.64	8.38	8.31
	J_{HH}	broadened	broadened	broadened	broadened
	$\Delta\delta$		0.14	−0.12	−0.19

[a] Refered to TMS in DMSO solutions.
[b] Complexation shift is defined as the ^{1}H chemical shift difference of corresponding nuclei in the complex and free picolinamide molecule.
[c] Taken from Ref. [29].
[d] Sign (+) denotes deshielding effect, while (−) denotes shielding effect.
[e] Digital resolution ±0.30 Hz: (s) singlet, (d) doublet, (m) multiplet.

Table 7
^{13}C NMR chemical shifts (δ/ppm)[a] and complexation shifts ($\Delta\delta$/ppm)[b,c] in the ligand molecule, picolinamide, and its complexes with zinc(II), cadmium(II) and mercury(II) thiocyanate, **1**, **2** and **3**

Compound		pia	**1**	**2**	**3**
C-2	δ	150.75	148.39	149.06	149.33
	$\Delta\delta$		−2.36	−1.69	−1.42
C-3	δ	122.35	122.49	122.32	122.38
	$\Delta\delta$		0.14	−0.03	0.03
C-4	δ	138.08	139.02	138.36	138.32
	$\Delta\delta$		0.94	0.28	0.24
C-5	δ	126.89	127.46	127.00	126.87
	$\Delta\delta$		0.57	0.11	−0.02
C-6	δ	148.90	147.87	148.55	148.80
	$\Delta\delta$		−1.03	−0.35	−0.1
C-7	δ	166.51	166.02	166.05	165.95
	$\Delta\delta$		−0.49	−0.46	−0.56
C(SCN)	δ		134.65	133.35	115.97

[a] Refered to TMS in DMSO solutions.
[b] Complexation shift is defined as the ^{13}C chemical shift difference of corresponding nuclei in complex and free picolinamide molecule.
[c] Sign (+) denotes deshielding effect, while (−) denotes shielding effect.



Scheme 1.

In the ^{1}H NMR spectra of all three complexes shielding of all protons is established. The only one exception found is the proton of the amido group of the zinc complex, which is deshielded. It is probably caused by different H-bonding in the Zn complex than in the free ligand. The greatest complexation shifts ($\Delta\delta$) are observed for the H-6 and H-3 protons, which are three or four bonds remote from the metal centers.

In the ^{13}C NMR spectra of all the complexes, in general, the greatest changes upon complexation were observed for the chemical shifts in the zinc complex (**1**), and the smallest changes were for the mercury complex (**3**). In all three complexes carbon atom C-2 is found to be the most shielded (−1.42 to −2.36 ppm). The carboxamido carbon atom is also greatly influenced by coordination to the metal centers and is the only C atom for which the greatest complexation shift is found for mercury in comparison with the other complexes. The C-4 carbon atom, which is *para* to the pyridine nitrogen atom, is found to be deshielded in all complexes due to delocalisation of π-electrons through the pyridine ring.

The formation of thiocyanate and isothiocyanate complexes can be easily detected by the characteristic ^{13}C signal for –SCN and –NCS groups that are usually found at ~111 and ~145 ppm, respectively [30]. In the ^{13}C spectra of the investigated thiocyanato complexes there are signals at 135, 133 and 116 ppm in the zinc, cadmium and mercury complexes respectively, indicating coordination of the thiocyanato ligands to the metal centers through *N*- in the cases of Zn (**1**) and Cd (**2**) and through *S*- in the case of Hg (**3**).

3.4. Thermal analysis

Thermal decomposition of the complex **1** is shown in Fig. 5. At normal temperature and pressure the crystals possess good stability and do not show any hygroscopic effect. The analysis of the TGA and DTA curves shows that the thermal decomposition of **1** starts around 160 °C. The first step is the decomposition of **1** to $Zn(SCN)_2$, corresponding to the endothermic DTA peaks at 172.9 °C. In the temperature range 270–700 °C two endothermic peaks (a main large one at 273 °C, and a second small around 350 °C) were observed.

The TGA curve of **2** (Fig. 6) shows a large weight loss in the range 200–350 °C followed by an endothermic DTA peak with a minimum at 251.6 °C, and subsequently continues with a weight loss in range up to 350 °C without any peak in the DTA curve. The decomposition process suggests that the loss of picolinamide and thiocyanate groups occurs almost simultaneously. The final product after 700 °C should mainly be CdS.

The thermal analysis of **3** reveals that the thermal decomposition of the complex involves three processes, two endothermal and one exothermal process (Fig. 7). The first step is the decomposition of **3** to $Hg(SCN)_2$ (minimum at 145.9 °C), and the second one is the decomposition of $Hg(SCN)_2$ due to elimination of CS_2, $(CN)_2$ and N_2 gases (maximum at 200.8 °C) The last one is the sublimation of HgS, corresponding to the endothermic peak in the temperature range 350–450 °C.

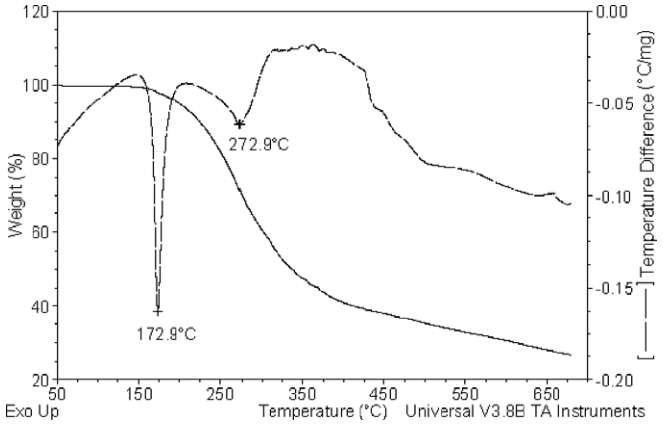


Fig. 5. TGA and DTA curve of **1**.

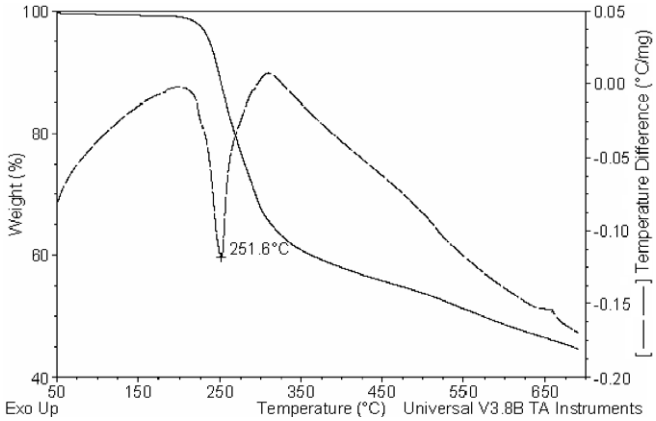


Fig. 6. TGA and DTA curve of **2**.

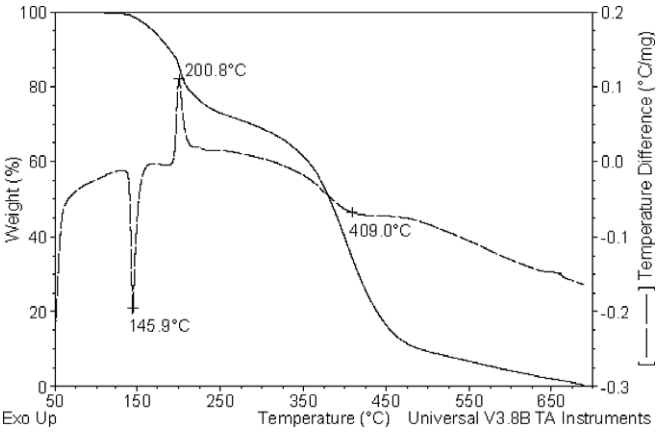


Fig. 7. TGA and DTA curve of **3**.

4. Conclusion

Three new heteroleptic complexes of the group 12 metals with picolinamide and thiocyanate have been synthesized. The zinc and cadmium complex have been readily prepared by the *in situ* reaction from water solution, while the mercury complex has been prepared by prior isolation of mercury(II) thiocyante. The isolated title compounds were investigated by X-ray analysis, spectroscopic and thermal methods.

Having the amide group in a *para* position to the endocyclic nitrogen atom, picolinamide acts as a chelating *N,O*-ligand towards all three metals of group 12, leaving the amido *N*-atom for participation in hydrogen bonding and contacts. The thiocyanate ion acts as *N*- for the zinc complex **1**, *S*-/μ-*S*- for the mercury complex **3** and a μ-*N,S*-donor ligand for the cadmium thiocyanato complex **2**. Compound **1** is comprised of monomeric units and compound **3** dimeric units, while compound **2** is comprised of polymeric units. The thiocyanate shows a great variety of bonding modes with the group 12 metals, as a terminal as well as a bridging ligand. As a terminal ligand it is bound to metal ion from almost linear in **1b** [∠M–N–

C = 171.9(2)°] to almost perpendicular bonding mode in **3** [∠M–S–C = 96.5(2)°]. It is also noticed that there is elongation of the C–S bond lengths for the *S*-coordination in **3** in comparison to the *N*-coordination of the terminal thiocyanate ligand in **1**, while as a bridging μ-*N,S*-ligand in **2** the C–S bond length is somewhere in between the values for **1** and **3**. Although Zn and Cd have the same coordination number and Hg a smaller one, the bite angle in the case of Cd and Hg is the same, and in the case of Zn it is somewhat larger.

Acknowledgement

This research was supported by the Ministry of Science, Education and Sport of the Republic of Croatia, Zagreb (Grants Nos. 119-1193079-1332 and 192-1252971-1982).

Appendix A. Supplementary material

CCDC 644422, 645305, 645306 and 646561 contain the supplementary crystallographic data for **1a**, **1b**, **2** and **3**. These data can be obtained free of charge via www.ccdc.cam.ac.uk/conts/retrieving.html [or from the Cambridge Crystallographic Data Centre (CCDC), 12 Union Road, Cambridge CB2 1EZ, UK; fax: +44(0)1223-336033; e-mail: deposit@ccdc.cam.ac.uk]. Supplementary data associated with this article can be found, in the online version, at doi:10.1016/j.poly.2007.09.014.

References

[1] Z. Popović, D. Matković-Čalogović, J. Popović, I. Vicković, M. Vinković, Polyhedron 26 (2007) 1045.
[2] Z. Popović, G. Pavlović, Ž. Soldin, Acta Crystallogr. C62 (2006) m272.
[3] Z. Popović, G. Pavlović, M. Vinković, D. Vikić-Topić, M. Rajić-Linarić, Polyhedron 25 (2006) 2353.
[4] J. Popović, D. Matković-Čalogović, G. Pavlović, Ž. Soldin, Z. Popović, Eleventh Slovenian–Croatian Crystallographic Meeting, 27–30 June, 2002, Bohinj, Slovenia, Book of Abstracts, pp. 35.
[5] D. Matković-Čalogović, J. Popović, Z. Popović, I. Picek, Ž. Soldin, Acta Crystallogr. C58 (2006) m39.
[6] Z. Popović, G. Pavlović, D. Matković-Čalogović, Ž. Soldin, Acta Crystallogr. C59 (2003) m165.
[7] M. Rosin, T. Kocher, A. Kramer, J, Clin. Peridontol. 28 (2001) 270.
[8] N. Goi, Y. Hirai, H. Harada, A. Ikari, T. Ono, Y. Terashima, N. Kinae, M. Hiramatsu, K. Nakamura, H. Tsuboi, K. Takagi, Brain, Behavior and Immunity 20 (2006) e17 (Abstract).
[9] Z. Otwinowski, W. Minor, in: C.W. Carter, R.M. Sweet (Eds.), Methods in Enzymology, Macromolecular Crystallography, part A, vol. 276, Academic Press, London, 1997, p. 307.
[10] Oxford Diffraction, 2004. Oxford Diffraction Ltd., Xcalibur CCD System, CrysAlis Software System, Version 171.26.
[11] Sheldrick, G.M. SHELXS97. Program for Solving of Crystal Structures, University of Göttingen, Germany, 1997.
[12] G.M. Sheldrick, SHELX97, Program for refinement of crystal structures, University of Göttingen, Germany, 1997.
[13] L.J. Farrugia, J. Appl. Crystallogr. 30 (1997) 565.
[14] I.J. Bruno, J.C. Cole, P.R. Edgington, M.K. Kessler, C.F. Macrae, P. McCabe, J. Pearson, R. Taylor, Acta Crystallogr. B58 (2002) 389.
[15] H. Paşaoğlu, S. Güven, Z. Heren, O. Büyükgüngör, J. Mol. Struct. 794 (2006) 270.
[16] K. Sakai, T. Imakubo, M. Ichikawa, Y. Taniguchi, J. Chem. Soc., Dalton Trans. (2006) 881.
[17] M.B.B. Drew, A.H.B. Othman, Acta Crystallogr. B31 (1975) 613.
[18] T. Ito, M. Kato, H. Ito, Bull. Chem. Soc. Jpn. 57 (1984) 2634.
[19] G. Yang, H.G. Zhu, B.H. Liang, X.M. Chen, J. Chem. Soc., Dalton Trans. (2001) 580.
[20] M. Taniguchi, Y. Sugita, A. Ouchi, Bull. Soc. Jpn. 59 (1986) 2299.
[21] M. Taniguchi, Y. Sugita, A. Ouchi, Bull. Soc. Jpn. 60 (1987) 1321.
[22] Z. Popović, D. Matković-Čalogović, J. Hasić, D. Vikić-Topić, Inorg. Chim. Acta 285 (1999) 208.
[23] R. Bala, R.P. Sarma, R. Sharma, B.M. Kariuki, Inorg. Chem. Commun. 9 (2006) 852.
[24] K. Nakamoto, Infrared and Raman Spectra of Inorganic and Coordination Compounds, Wiley, New York, 1986.
[25] X.Q. Wang, D. Xu, G.W. Lu, M.K. Lü, D.R. Yuan, G.H. Zhang, G.T. Lü, Y. Chen, Y.Q. Zhou, Chem. Phys. Lett. 360 (2002) 573.
[26] M.C. Suen, T.C. Keng, J.C. Wang, Polyhedron 21 (2002) 2705.
[27] F. Jin, J.F. Li, H.P. Zhou, J.Y. Wu, J.X. Yang, Y.P. Tian, M.H. Jiang, J. Mol. Struct. (2006), doi:10.1016/j.molstruct.2006.06.025.
[28] R. Kapoor, A. Kataria, A. Pathak, P. Venugopalan, G. Hundal, P. Kapoor, Polyhedron 24 (2005) 1221.
[29] W. Bruegel, Z. Elektrochem. Ber. Bunsenges. Phys. Chem. 66 (1962) 159.
[30] N. Iranpoor, H. Firouzabadi, H.R. Shaterian, Tetrahedron Lett. 43 (2002) 3439.

Available online at www.sciencedirect.com
ScienceDirect
Polyhedron 27 (2008) 223–231
POLYHEDRON
www.elsevier.com/locate/poly

Syntheses, IR spectra, thermal properties and crystal structures of novel cyano-bridged polymeric complexes of zinc^{II} and cadmium^{II} with tetracyanoplatinate^{II}

Ahmet Karadağ [a,*], İbrahim Önal [a], Ayşegül Şenocak [a], İbrahim Uçar [b], Ahmet Bulut [b], Orhan Büyükgüngör [b]

[a] *Chemistry Department, Gaziosmanpasa University, Tokat, Turkey*
[b] *Physics Department, Ondokuz Mayıs University, Samsun, Turkey*

Received 3 July 2007; accepted 7 September 2007
Available online 5 November 2007

Abstract

Two novel one-dimensional polymeric cyano-bridged platinum(II) complexes of *N*-(2-hydroxyethyl)-ethylenediamine (*hydeten*), $[M^{II}(hydeten)Pt(CN)_2(\mu\text{-}CN)_2]_n$ ($M^{II} = Zn^{II}$ (**1**) and Cd^{II} (**2**)), were synthesized and characterized by physico-chemical methods (elemental analysis, IR spectroscopy and thermoanalytical measurements) and X-ray diffraction. Thermal behaviours of **1** and **2** were followed using TG and DTA (DSC) techniques. The 1D chain structures of **1** and **2** were verified by X-ray diffraction studies. According to the positions of the bridging cyano groups, in complex **1** the polymeric chains are built up via the 2,2-CT type, while in complex **2** the polymeric chains are built up via the 2,2-TT type.
© 2007 Elsevier Ltd. All rights reserved.

Keywords: Tetracyanoplatinate(II); Zinc; Cadmium; *N*-(2-Hydroxyethyl)-ethylenediamine; Coordination polymers

1. Introduction

Cyano-bridged complexes, which have been of interest since the XVIIth century, have been shown to form polymeric structures by studies over the last few decades. These polymeric metal complexes are especially macromolecules formed by metal–metal or metal–ligand–metal bridge connections in one, two or three dimensions. These types of complexes have applications in the fields of chemistry, biology and material science and therefore they have been attracting increasing attention from scientists [1]. The applications are mainly focused on catalysts [2], non-linear optic, molecular magnets [3], molecular sieves and ion exchange materials [4].

Functional polymeric cyano complexes can be prepared with two or more dentate ligands. These types of materials are packed to form crystal structures due to bridging groups and intermolecular interactions. Cyano-bridged polymeric complexes structurally contain chains oriented in one dimension. These structures may be linear, zig-zag, stepwise, lateral and pipe shaped [5].

Cyano ligands are used to synthesize one, two- or three-dimensional structures in the branches of organometallic coordination and supramolecular structures because of their ability to behaving as σ-donors and π-acceptors at the same time, their negative charge and ambidentate character.

Hydeten (*N*-(2-hydroxyethyl)-ethylenediamine; alternatively named 2-(2-aminoethylamino)-ethanol {H_2NCH_2-$CH_2NHCH_2CH_2OH$}) is used in this study as a ligand which can coordinate to a metal ion through its three donor atoms. In our previous studies, we have observed two different coordination modes of the *hydeten* ligand. It

* Corresponding author. Tel.: +90 356 2521616; fax: +90 356 2521582.
E-mail address: akaradag@gop.edu.tr (A. Karadağ).

0277-5387/$ - see front matter © 2007 Elsevier Ltd. All rights reserved.
doi:10.1016/j.poly.2007.09.016

Table 1
Crystal data and structure refinement for complexes **1** and **2**

Formula	$C_{12}H_{24}N_8O_2PtZn$	$C_{12}H_{24}N_8O_2PtCd$
Formula weight	572.86	619.88
Temperature (K)	297(2)	297(2)
Wavelength (Mo Kα)	0.71073	0.71073
Crystal system	monoclinic	monoclinic
Space group	*C*2/*c*	*P*21/*c*
Unit cell dimensions		
a (Å)	9.9710(7)	7.7081(7)
b (Å)	11.3644(8)	13.6534(9)
c (Å)	17.8190(10)	10.1106(8)
β (°)	98.085(5)	109.153(6)
Volume (Å^3)	1999.10(2)	1005.16(14)
Z	4	2
D_{calc} (g cm^{-3})	1.9034(2)	2.0481(2)
μ (mm^{-1})	8.211	8.030
F(000)	1104	588
Crystal size (mm)	0.21 × 0.15 × 0.27	0.18 × 0.21 × 0.14
θ Range (°)	2.15, 28.19	2.18, 28.75
Index ranges	$-13 \leqslant h \leqslant 13$, $-14 \leqslant k \leqslant 14$, $-21 \leqslant l \leqslant 23$	$-10 \leqslant h \leqslant 10$, $-17 \leqslant k \leqslant 17$, $-13 \leqslant l \leqslant 13$
Reflections collected	13 702	14 506
Independent reflections [R_{int}]	2343 [0.060]	2370 [0.042]
Reflections observed (>2*σ*)	2200	1756
Absorption correction	integration	integration
Refinement method	full-matrix least-squares on F^2	Full-matrix least-squares on F^2
Data/restrains/parameters	2343/0/113	2370/0/113
Goodness-of-fit on F^2	1.100	1.046
Final *R* indices [$I > 2\sigma(I)$]	0.0718	0.0201
Largest difference in peak and hole (e Å^{-3})	0.72, −0.47	0.81, −0.37

was determined in these studies that it was either coordinated as a bidentate ligand to metal ion through its two *N*,*N*′ donor sites [6] or as a tridentate ligand through its *N*,*N*′,O donor sites [7].

Cyanocomplexes, such as tetracyanopalladate [8], and especially tetracyanonickelate complexes [9], have been systematically studied to evaluate their structural properties, but tetracyanoplatinate complexes have rarely appeared in the literature [10]. Apart from that, the importance of the Pt(II)–*hydeten* complex as a potential agent for cancer therapy [11] led us to synthesize two new cyano-bridged Pt(II)–*hydeten* complexes (**1** and **2**). This study reports the synthesis, spectroscopic, thermal and structural characterization of these two novel compounds by IR, TG/DTA (DSC) and X-ray diffraction techniques.

2. Experimental details

2.1. Materials and instrumentation

Zinc(II) chloride ($ZnCl_2$), cadmium(II) sulfate 8/3 hydrate ($CdSO_4 \cdot 8/3H_2O$), [*N*-(2-hydroxyethyl)-ethylenediamine ($C_4H_{12}N_2O$)], platinum(II) chloride ($PtCl_2$), and potassium cyanide (KCN) were purchased from commercial sources and used without further purification.

Microanalytical (C, N, H) data were performed by standard methods (TÜBITAK Ankara Test and Analysis Laboratory, Turkey). The IR spectra were recorded on a Jasco 430 FTIR spectrophotometer using KBr pellets in the 4000–200 cm^{-1} range. The TG, DTG and DTA curves were obtained using a PYRIS Diamond TG/DTA (DSC) apparatus in a dynamic nitrogen atmosphere (heating rate: 10 °C/min., platinum crucibles, mass ~10 mg and temperature range 35–1300 °C).

2.2. Syntheses

2.2.1. *[Zn(hydeten)$_2$Pt(CN)$_4$] (1)*

A solution of $PtCl_2$ (0.077 g, 0.29 mmol) in 1:1 ethanol:water (20 mL) was dropped with stirring onto solid KCN (4 mmol, 0.075 g). Afterwards, $ZnCl_2$ (1 mmol, 0.039 g) in ethanol (10 mL) was added slowly to the solution, resulting in a cloudy cream mixture. This was dissolved by effusion slowly into the bulk containing *hydeten* (2 mmol, 0.061 g) in 10 mL ethanol. The resultant light-yellow solution was filtered and left to crystallize at room temperature. White crystals of **1** suitable for X-ray measurements were formed by slow evaporation after a week. The yield was 153 mg, 92.26%. *Anal.* Calc. C, 25.16; H, 4.22; N, 19.56. Found: C, 25.31; H, 3.94; N, 19.60%.

Table 2
The important IR spectral data of the *hydeten*, $K_2[Pt(CN)_4]$, complex **1** and **2**

Group (1/*λ*, cm^{-1})	*hydeten*	$K_2[Pt(CN)_4]$	[Zn(*hydeten*)$_2$Pt(CN)$_4$]	[Cd(*hydeten*)$_2$Pt(CN)$_4$]
ν(O–H)–*ν*(N–H)	3355–3210			
ν(O–H)			3326	3365
ν(N–H)			3297	3325, 3301, 3271
ν(C–H)	2949, 2868		2960, 2941, 2914, 2881, 2845	2968, 2925, 2871, 2850
ν(C≡N)		2135	2156, 2142	2144, 2138
δ(N–H), *ν*(C–N) (–*HN*–*CH*$_2$–)	1616		1604	1608
δ(CH$_2$)	1469		1448	1436
ν(C–N) (*H*$_2$*N*–*CH*$_2$–)	1140		1109	1108
ν(C–O)	1067		1024	1039
ν(M–C)			501	499

2.2.2. [Cd(hydeten)$_2$Pt(CN)$_4$] (2)

Solid KCN (4 mmol, 0.087 g) was added to 20 mL $PtCl_2$ (0.089 g, 0.33 mmol) solution in a 1:1 ethanol:water mixture. $CdSO_4 \cdot 8/3H_2O$ (1 mmol, 0.086 g) was then added slowly to the solution and a cloudy cream mixture appeared. Then, the suspension was added slowly to *hydeten* (2 mmol, 0.069 g) with stirring. The resultant yellowish solution was left to crystallize at room temperature, and white crystals of **2**, suitable for X-ray analysis, formed by slow evaporation after about a week. The yield was 154 mg, 74.25%. *Anal*. Calc. C, 23.25; H, 3.90; N, 18.08. Found: C, 23.39; H, 3.10; N, 18.10%.

2.3. Crystal structure analysis

Suitable single crystals were mounted on a glass fiber and data collections were performed on a STOE IPDS(II) image plate detector system using Mo Kα radiation ($\lambda = 0.71019$ Å) at 298 K. Details of the crystal structures of **1** and **2** are given in Table 1. Data collection: Stoe X-AREA [12]. Cell refinement: Stoe X-AREA [12]. Data reduction: Stoe X-RED [12]. The structure was solved by direct-methods using SHELXS-97 [13] and anisotropic displacement parameters were applied to non-hydrogen atoms in a full-matrix least-squares refinement based on F^2 using SHELXL-97 [13]. All carbon hydrogens were positioned geometrically and refined with a riding model with U_{iso} 1.2 times that of the attached atoms, and remaining hydrogen atoms were found by Fourier difference. Molecular drawings were obtained using ORTEP-III [14].

3. Results and discussion

3.1. FTIR spectra

The significant absorption bands of *hydeten*, $K_2[Pt(CN)_4]$, complex **1** and complex **2** are given in Table 2. It is observed that ν(O–H) of **2** shifts to higher wavenumbers than ν(O–H) of **1**, it was observed in the Zn^{II}/Cd^{II}–Pd^{II} complexes [15]. The difference between the OH stretching vibrations of the complexes may be explained by the variations of the surroundings of the crystals. The ν(N–H) band of **1** splits into three, and two of those are shoulder peaks, while ν(N–H) of **2** splits into four, consistent with the Zn^{II}/Cd^{II}–Pd^{II} complexes [15]. The splitting of the NH stretching vibrations is probably due to coordination of the Zn^{II} and Cd^{II} ions with nitrogen atoms of the *hydeten* ligand. In addition, the splitting of the ν(C–H) bands of complexes **1** and **2** might be attributed to changing the moiety of the CH_2 groups in the complexes.

The ν(C≡N) vibrations are the most important absorption bands for complexes **1** and **2** since the ν(C≡N) vibrational peaks in the IR spectra are used to reveal the bridging formation in the polymeric complexes. For

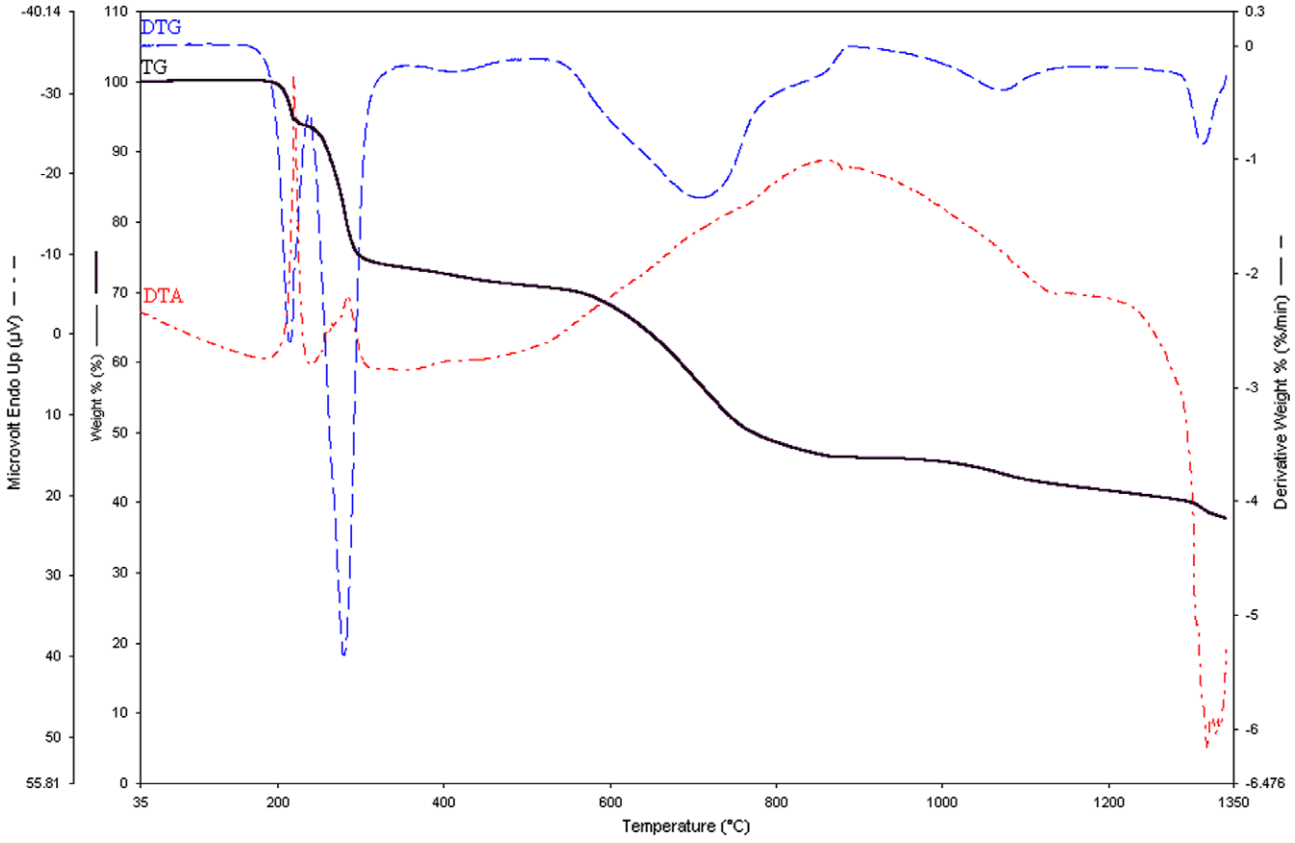


Fig. 1. Thermal curves of complex **1**.

complexes **1** and **2**, the $\nu(C{\equiv}N)$ vibrations are observed in the 2156–2138 cm^{-1} region. Taking into consideration the known structures of complexes **1** and **2**, the strong and sharp bands at 2142 and 2138 cm^{-1}, respectively, can be attributed to the stretching vibration of the terminal cyano groups, while those at 2156 and 2144 cm^{-1} arise from the bridging cyano groups. The bridging cyano frequencies in cyano-bridged complexes are generally observed at a higher frequency, due to the kinematic coupling which is a mechanical constraint upon the bridging-cyano confined to the second metal [16]. Besides, the N atoms at the *trans* position of the cyano groups of both **1** and **2** complexes are bonded to the second metal (Zn and Cd) to form a bridge, the D_{4h} local symmetry of the $[Pt(CN)_4]^{2-}$ ion changes slightly and reduces to D_{2h} symmetry.

In the low energy region of the spectra, Pt–C stretches and Pt–CN bending bands in the region 650–400 cm^{-1} were observed for complexes **1** and **2**. The bands observed at 501 and 432 cm^{-1} in the IR spectra of complex **1** might be attributed to the stretching vibrations of Pt–C and bending vibrations of Pt–CN, respectively. The same vibrational bands were observed at 499 and 411 cm^{-1} for complex **2**.

3.2. Thermal properties

The TG, DTG and DTA curves and data related to the thermal decomposition of complexes **1** and **2** are illustrated in Figs. 1, 2 and Table 3. The thermal decomposition of complex **1** follows a seven-step mechanism as seen in Fig. 1. The first four stages in the temperature range 185–648 °C correspond to the endothermic decomposition of the *hydeten* ligands (calc. 36.36%, found 35.93%). The decomposition of neutral *hydeten* ligands follows a multi-step process where the decomposition starts with the release of the CH_2CH_2OH groups of the *hydeten* ligands. Both weight losses and broadened DTG curve shows that the fourth and fifth decomposition steps are overlapped and on completion of *hydeten* decomposition (calc. 36.36%, found 35.93%), decomposition of the cyano groups starts at 650 °C. The decomposition of the anionic ligands are completed at the end of the fifth step, where $DTG_{max.}$ is 705 °C. Finally, there are Zn and Pt in the residual part (calc. 45.47%, found 46.11%). The boiling point of Zn is 907 °C and it is vaporized at the sixth and seventh steps of the decomposition mechanism. The vaporization of Zn is an exothermic process leaving only Pt in the medium above 1350 °C. Following scheme may be put forward for the thermal decomposition of complex **1**:

$$Zn(hydeten)_2Pt(CN)_4 \xrightarrow[2hydeten]{185\text{–}648\ ^\circ C} ZnPt(CN)_4 \xrightarrow[4CN]{648\text{–}954\ ^\circ C} Zn + Pt \xrightarrow[Zn]{954-(\cong 1350)^\circ C} Pt$$

The decomposition enthalpies (ΔH, J/g) of each stage were calculated by converting DTA signals to DSC data. The details are given in Table 3 which indicates that the

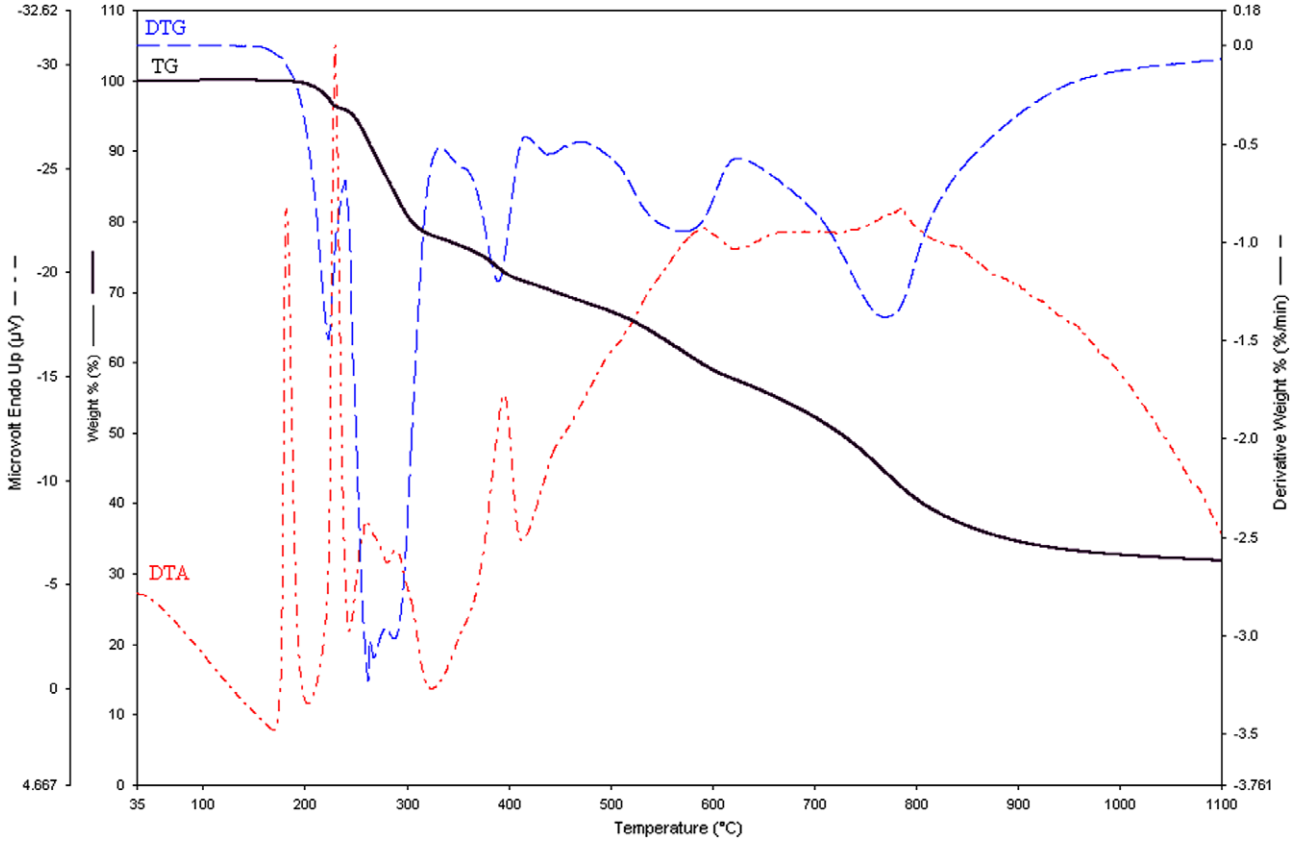


Fig. 2. Thermal curves of complex **2**.

Table 3
Thermoanalytical data for complexes **1** and **2**

Complex	Stage	Temperature range (°C)	DTG_{max} (°C)	ΔH (J/g)	Mass loss, Δm (%)	Total mass loss, Δm (%)		Residue (%)	
					Found	Found	Calc.	Found	Calc.
$[Zn(hydeten)_2Pt(CN)_4]$ $C_{12}H_{24}N_8O_2PtZn$									
	1	185–239	214	4948.17	6.60				
	2	239–352	281	3599.66	20.03				
	3	352–489	409	265.78	2.45				
	4	489–648	591		6.85	35.93	36.36	64.07 $[ZnPt(CN)_4]$	63.64
	5	648–954	708	23722.34	17.96	17.96	18.17	46.11 ZnPt	45.47
	6	954–1250	1070	−1589.23	5.29				
	7		1313	−6702.98				Pt	
$[Cd(hydeten)_2Pt(CN)_4]$ $C_{12}H_{24}N_8O_2PtCd$		182[a]		1268.46[a]					
	1	188–240	223	1459.67	4.25				
	2	240–265	262		5.19				
	3	265–280	267	374.37	4.32				
	4	280–335	289	169.63	8.75				
	5	335–418	390	1059.64	6.12				
	6	418–508	438	95.03	4.58	33.21	33..60	66.79 $[CdPt(CN)_4]$	66.40
	7	508–634	570	1290.52	9.92				
	8	634–725	675		6.93	16.85	16.79	49.94 CdPt	49.61
	9	725–1093		8551.60	18.02	18.02	18.13	31.92 Pt	31.48

[a] The solid–solid transition temperature and transformation enthalpy.

enthalpies of the first five decomposition stages are endothermic while those of the last two stages are exothermic.

It is revealed from the DTA analysis that complex **2** shows an endothermic transition at around 182 °C which is assigned to a solid–solid transition since there is no melting observed at this temperature. The same behaviour was also observed for the $[Cu(hydeten)_2Pd(CN)_4]$ complex [17]. The thermal decomposition of complex **2** is more complicated than that of complex **1**, as nine distinguishable stages, corresponding to separate releases of *hydeten* molecules and cyano groups decomposing were observed during its decomposition. The TG curve for complex **2** indicates that it is stable up to 188 °C, at which point slow decomposition begins. In the temperature range 188–508 °C, there are six processes and the total weight loss by 33.21% corresponds to the release of two *hydeten* ligands (calc. 33.60%) by an endothermic process. The cyano groups are liberated in two separated steps (7th and 8th steps in the 508–725 °C range), both connected with endothermic process. The 8th step is overlapped by the 9th process in the 725–1093 °C range, with a weight loss of 18.02%, corresponding to the vaporization of cadmium (calc. 18.13%), the boiling point of which is 765 °C. The final thermal decomposition product is metallic Pt (calc. 31.48%, found 31.91%). The most probable thermal decomposition scheme for complex **2** is:

$$Cd(hydeten)_2Pt(CN)_4 \xrightarrow[2hydeten]{188\text{–}508\ ^\circ C} CdPt(CN)_4 \xrightarrow[4CN]{508\text{–}725\ ^\circ C} Cd + Pt \xrightarrow[Cd]{725\text{–}1093\ ^\circ C} Pt$$

The enthalpy of some of the decomposition stages were given in total due to the consecutive stages. Thus, the decomposition enthalpy values were found to be 1459.67 J/g for the first stage, 374.37 J/g for the second and third stages, 169.63, 1059.64, 95.03, 1290.52 (J/g) for the fourth, fifth, seventh and eighth stages, respectively and 8551.60 J/g for the final two stages.

3.3. Structure of complexes *1* and *2*

Single crystal X-ray diffraction analysis revealed that both complexes $[Zn(hydeten)_2Pt(CN)_4]$ (**1**), {*catena-poly*[μ-cyano- 1:2κ^{2}C:N-dicyano-1 κ^{2}C-*trans*-bis[*N*-(2-hydroxyethyl)ethane-1,2-diamine-2κ^2*N,N′*] zinc(II) platinum(II)]-μ-cyano-1:2′κ^2 C:N]}, and $[Cd(hydeten)_2Pt(CN)_4]$ (**2**), {*catena-poly*[μ-cyano-1:2κ^{2}C:N-dicyano-1 κ^{2}C-*trans*-bis[*N*-(2-hydroxyethyl)ethane-1,2-diamine-2κ^{2}N, N′]cadmium(II)platinum(II)]-μ-cyano-1:2′κ^2 C:N]}, have a cyanide-bridged polymeric chain structure where Pt^{II} is coordinated by four cyanide ligands, and Zn^{II} and Cd^{II} ions are coordinated by two *hydeten* and two bridging cyanide ligands, as shown in Figs. 3 and 4. Both

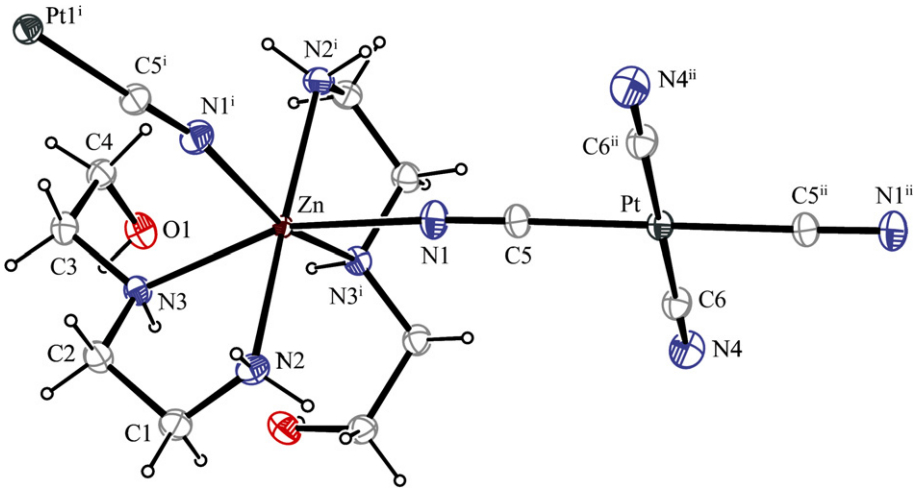


Fig. 3. An ORTEP plot of complex **1**.

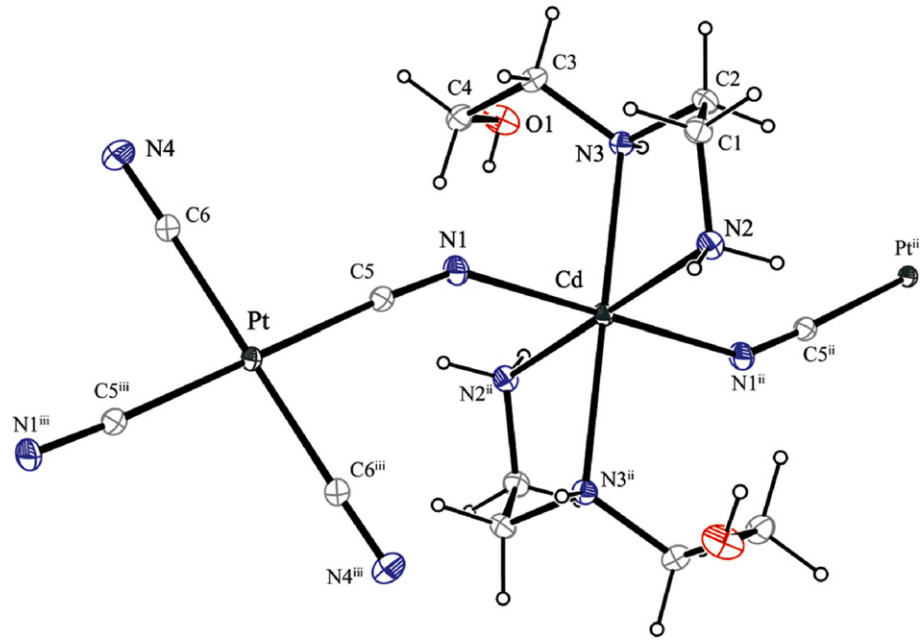


Fig. 4. An ORTEP plot of complex **2**.

complexes consist of a 1D polymeric chain –Zn(*hydeten*)$_2$–NC–Pt(CN)$_2$–CN–Zn(*hydeten*)$_2$ and –Cd(*hydeten*)$_2$–NC–Pt(CN)$_2$–CN–Cd(*hydeten*)$_2$ in which Zn^{II}–Pt^{II} and Cd^{II}–Pt^{II} atoms are linked by CN groups. The four cyanide-carbon coordinated Pt^{II} ion [two cyano groups are terminal in both complexes and the other two cyano groups (in the *cis* position for **1** and in the *trans* position for **2**) are bridged] has a square-planar geometry and the bond distances of Pt–C [1.963(13)–1.982(13) Å for **1** and 1.981(3)–1.987(3) Å for **2**] in the Pt(CN)$_4$ moiety are in accordance with the reported values for other tetracyanoplatinate complexes [18]. In complex **1**, the polymeric chains are built up via the 2,2-CT type in which one of the bridging cyano groups is in a *cis* position and the other cyano group is in a *trans* position, while in complex **2** the polymeric chains are built up via the 2,2-TT type in which both bridging cyano groups are in trans positions.

The coordination environment of the Zn^{II} and Cd^{II} ions can be described as distorted octahedral. In complex **1**, the basal plane is constructed by the coordination of three N atoms of the bidentate *hydeten* ligand and N1^{i} [symmetry code (i): $1 - x$, y, $0.5 - z$] atom of the cyanide group, whereas the N1 and N3 atoms occupy the axial positions. In complex **2**, four N atoms of two *hydeten* ligands form the basal plane, while the two cyanide N atoms are in the apical positions. The Zn–N and Cd–N distances reveal a small tetragonal distortion of the Zn–N4 and Cd–N4

planes, with the Zn–N and Cd–N bonds (Table 4) to the secondary amines [2.390(11) Å for **1** and 2.433(3) Å for **2**] being longer than the Zn–N and Cd–N bonds to the primary amines [2.359(13) Å for **1** and 2.284(3) Å for **2**]. This may be a consequence of the steric differences between the N atoms. These distances are found to be similar to those of our previously reported heteronuclear [Zn(*hydeten*)$_2$Pd(CN)$_4$], [Cd(*hydeten*)$_2$Pd(CN)$_4$] [15] and [Cd(*hydeten*)$_2$Ni(CN)$_4$] [6a] complexes.

All the N–Zn–N and N–Cd–N bond angles deviate significantly from the 90° and 180°, which is presumably the result of the steric constraints arising from the shape of the ligands. The angles subtended at the Zn(II) and Cd(II) atoms by the *hydeten* ligands are 73.8(4)° and 76.65(10)°, respectively, which are in agreement with previously reported values for other *hydeten* containing complexes [19,6b]. The C5≡N1–Zn and C5≡N1–Cd bond angles are 166.4(15)° and 147.1(3)°, respectively, which result in the formation of a one-dimensional zig-zag chain, while the Pt–C5≡N1 angle [178.7(15)° for **1** and 176.9(3)° for **2**] is essentially linear. The C5≡N1–Zn angle is comparable with that found in heteronuclear [Zn(*hydeten*)$_2$Pd(CN)$_4$], [Cd(*hydeten*)$_2$Pd(CN)$_4$] and [Cd(*hydeten*)$_2$Ni(CN)$_4$] complexes [C≡N–Zn: 168.70(2)° for [15], C≡N–Cd: 167.9(2)° for [15] and 167.3(1)° for [6a]. This deviation from linearity is greater than those observed in related structures [9c]. However, the C5≡N1–Cd angle is significantly smaller than the C5≡N1–Zn angle, indicating a degree of ionic character to the Cd–N bond. Similarly, in the [Cu(en)$_2$Pd(CN)$_4$] [8b] complex the C≡N–Cu angle [121.6(2)°; a bent bond value suggesting some degree of ionic character of the Cu–N bond] is found to be smaller than that of observed in the title compounds. The

Table 4
Selected bond lengths (Å) and bond angles (°) for complexes **1** and **2**

Complex **1**		Complex **2**	
Bond lengths (Å)			
C5–N1	1.16(2)	C5–N1	1.14(4)
C6–N4	1.16(2)	C6–N4	1.12(4)
C5–Pt	1.96(1)	C5–Pt	1.98(3)
C6–Pt	1.98(2)	C6–Pt	1.99(3)
N3–Zn	2.39(1)	N3–Cd	2.43(3)
N1–Zn	2.33(1)	N1–Cd	2.38(3)
N2–Zn	2.36(1)	N2–Cd	2.28(3)
Bond angles (°)			
C5–N1–Zn1	166.4(15)	C5–N1–Cd	147.1(3)
N3–Zn1–N2	73.8(4)	N3–Cd–N2	76.7(1)
N3–Zn1–N1	159.3(5)	N3–Cd–N1	90.7(1)
N2–Zn1–N1	86.6(6)	N2–Cd–N1	89.7(1)
N1–C5–Pt	178.7(15)	N1–C5–Pt	176.9(3)
N4–C6–Pt	177.4(17)	N4–C6–Pt	177.1(4)
C5–Pt–C6	90.5(6)	C5–Pt–C6	92.2(1)

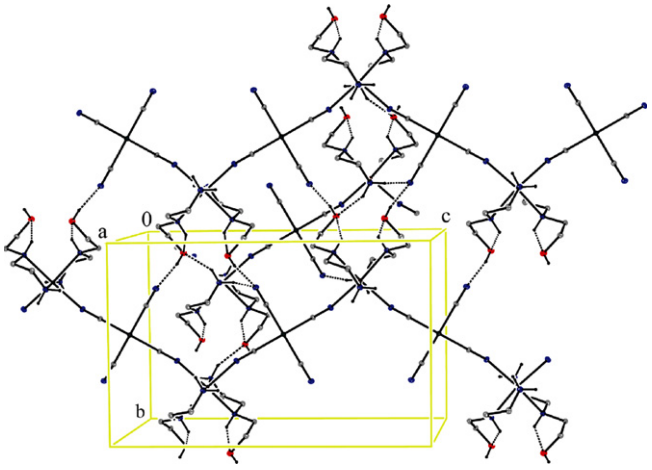


Fig. 5. Perspective view of the crystal structure with hydrogen bonds for complex **1**.

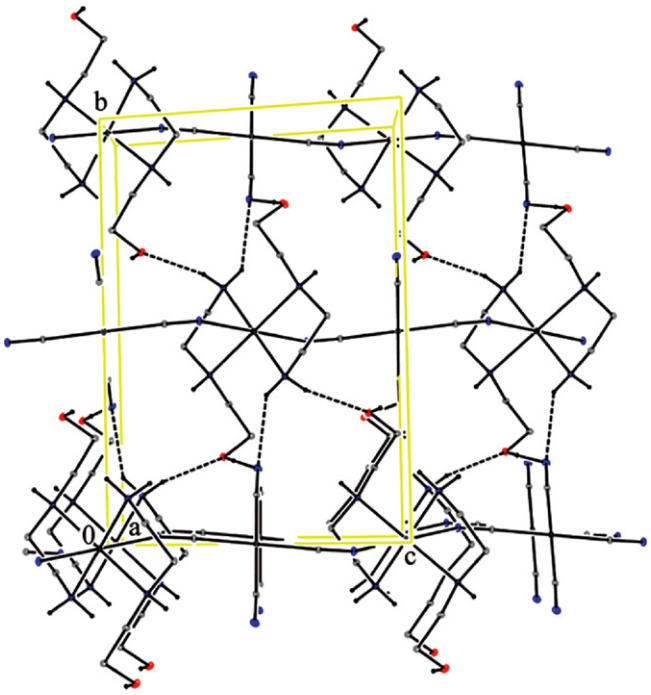


Fig. 6. Perspective view of crystal structure with hydrogen bonds for complex **2**.

Table 5
Hydrogen bonds (Å, °) for complexes **1** and **2**

D–H···A	*d*(D–H)	*d*(H···A)	*d*(D···A)	⟨(DHA)
Complex **1**				
N3–H3···O1	0.91	2.41	2.80(2)	106
N2–H2D···O1^{a}	0.90	2.24	3.06(2)	152
N2–H2C···N4^{b}	0.90	2.49	3.27(2)	145
O1–H1···N4^{c}	0.82	2.06	2.87(2)	169
Complex **2**				
N3–H3···O1	0.91	2.45	2.83(4)	105
N2–H2D···O1^{d}	0.90	2.21	3.01(4)	147
N2–H2C···N4^{e}	0.90	2.38	3.13(5)	141
O1–H1···N4^{f}	0.82	2.44	3.01(4)	127

Symmetry codes: (a) x, $-y+2$, $z-0.5$; (b) $-x+1.5$, $-y+1.5$; (c) $-z+1$, x, $-y+2$, $z-0.5$; (d) $-x+1$, $y-0.5$, $-z+1.5$; (e) $-x$, $y-0.5$, $-z+0.5$; (f) $-x+1$, $y+0.5$, $-z+1.5$.

Pt–C6≡N4 angles [177.4(17)° for **1** and 177.1(4)° for **2**] are found to be almost linear, as expected.

The crystal packing in both complexes shows interchain hydrogen bonding interactions between NH, NH_2 and OH groups. In both complexes, each polymeric chain is linked to a second chain via weak interchain N–H···N, N–H···O and O–H···N hydrogen bonding interactions (Figs. 5 and 6). These interactions are also effective in forming a layered structure, and the geometry of the interactions is illustrated in Table 5. The intramolecular $Zn\cdots Zn^{ii}$ and $Cd\cdots Cd^{iii}$ distances are 10.826(1) and 10.512(2) Å, respectively, whereas the shortest interchain $Zn\cdots Zn^{iv}$ and $Cd\cdots Cd^{v}$ distances are 7.559(1) and 7.708(1) Å, respectively [symmetry codes (ii) $1-x$, $1-y$, $1-z$, (iii) $-x$, $1-y$, $-z$, (iv) $x-0.5$, $y-0.5$, z, (v) $-x$, $1-y$, $1-z$].

4. Conclusion

Using $Zn(hydeten)_2^{2+}$ or $Cd(hydeten)_2^{2+}$ as bricks and the $[Pt(CN)_4]^{2-}$ anion as mortar, the novel binuclear one dimensional polymeric complexes **1** and **2** were prepared, and their structures were determined. The X-ray analysis revealed the formation of Zn^{II}–Pt^{II} and Cd^{II}–Pt^{II} polymers showing CT and TT chain structures, respectively. Also in our previous studies on Zn^{II}–Pd^{II} and Cd^{II}–Pd^{II} polymers the formation of TT and CT chains, respectively, was observed [15]. Pd^{II} and Pt^{II} polymers of Zn^{II} and Cd^{II} with the same ligand, *hydeten* resulted in a different orientation in the chain, which may be due to the difference in ionic diameters of Pd^{II} and Pt^{II}. The ionic diameter of Pt^{II} (94 pm) and Zn^{II} (88 pm) are similar and the Zn^{II}–Pt^{II} polymer forms a CT chain structure. A similarity is also observed in the ionic diameters of Pd^{II} (100 pm) and Cd^{II} (109 pm) which also formed a Cd^{II}–Pd^{II} polymer with *hydeten* with a CT chain structure. However, the differences between the ionic diameters of Cd^{II} and Pt^{II} and the ionic diameters of Zn^{II} and Pd^{II} are bigger than the differences between the ionic diameters of Zn^{II} and Pt^{II} and the ionic diameters of Cd^{II} and Pd^{II}, respectively. Probably for this reason, Cd^{II}–Pt^{II} and Zn^{II}–Pd^{II} polymers with *hydeten* formed a TT chain structure.

Acknowledgements

The authors wish to thank the Scientific and Technical Research Council of Turkey (TUBİTAK, Grant TBAG-104T205), and the Gaziosmanpasa University Research Foundation (Grant 2005-04), for financial support.

Appendix A. Supplementary material

CCDC 632067 and 632068 contain the supplementary crystallographic data for this paper. These data can be obtained free of charge via http://www.ccdc.cam.ac.uk/conts/retrieving.html, or from the Cambridge Crystallographic Data Centre, 12 Union Road, Cambridge CB2 1EZ, UK; fax: (+44) 1223-336-033; or e-mail: deposit@ccdc.cam.ac.uk. Supplementary data associated with this article can be found, in the online version, at doi:10.1016/j.poly.2007.09.016

References

[1] P.S. Mukherjeee, T.K. Maji, T. Mallah, E. Zangrando, L. Randaccio, N.R. Chaudhuri, Inorg. Chim. Acta 315 (2001) 249.
[2] (a) T. Funabiki, S. Yoshida, K. Tarama, J. Chem. Soc. Chem. Commun. (1978) 1059;
(b) R. Brahmi, C. Kappenstein, J. Černák, D. Duprez, A. Sadel, J. Chim. Phys. 96 (1999) 487;
(c) R. Brahmi, C. Kappenstein, J. Černák, D. Duprez, in: B. Delmon et al. (Eds.), Preparation of Catalysts, Elsevier, Amsterdam, 1998;
(d) E. Boellaard, A.M. van der Kraan, J.W. Geus, Scientific Basis for the Preparation of Heterogeneous Catalysts, vol. 3, Elsevier, Amsterdam, 1994.
[3] (a) R.K. Kumar, I. Goldberg, Angew. Chem., Int. Ed. Engl. 37 (1998) 3027;
(b) S.W. Keller, S. Lopez, J. Am. Chem. Soc. 121 (1999) 6306;
(c) W. Lin, O.P. Evans, R.G. Xiong, Z. Wang, J. Am. Chem. Soc. 120 (1998) 13272;
(d) R.H. Groeneman, L.R. MacGillvray, L. Atwood, Chem. Commun. (1998) 2735.
[4] M. Kämper, M. Wagner, A. Weiss, Angew. Chem. 91 (1979) 517.
[5] J. Černák, M. Orendáč, Ivan Potočňák, J. Chomič, A. Orendáčová, J. Skoršepa, A. Feher, Coord. Chem. Rev. 224 (2002) 51.
[6] (a) A. Karadağ, H. Paşaoğlu, G. Kaştaş, O. Büyükgüngör, Acta Crystallogr. Sect. C 60 (2004) m581;
(b) A. Karadağ, A. Bulut, O. Büyükgüngör, Acta Crystallogr. Sect. C 60 (2004) m402;
(c) A. Karadağ, H. Paşaoğlu, G. Kaştaş, O. Büyükgüngör, Z. Kristallogr. 220 (2005) 74.
[7] H. Paşaoğlu, A. Karadağ, F. Tezcan, O. Büyükgüngör, Acta Crystallogr. C61 (2005) m93.
[8] (a) M. Munakata, J.C. Zhong, I. Ino, T. Kuroda-Sowa, M. Maekawa, Y. Suenaga, N. Oiji, Inorg. Chim. Acta 317 (2001) 268;
(b) J. Černák, J. Skoršepa, K.A. Abboud, M.W. Meisel, M. Orendáč, A. Orendáčová, A. Feher, Inorg. Chim. Acta 326 (2001) 3;
(c) J. Kuchár, J. Černák, K.A. Abboud, Acta Crystallogr. Sect. C 60 (2004) m492.
[9] (a) J.A. Duimstra, C.L. Stern, T.J. Meade, Polyhedron 25 (2006) 2705;
(b) N.F. Curtisa, H. Puschmannb, Acta Crystallogr. Sect. C 60 (2004) m410;
(c) P.S. Mukherjee, T.K. Maji, T. Mallah, E. Zangrando, L. Randaccio, N.R. Chaudhuri, Inorg. Chim. Acta 315 (2001) 249;
(d) Z. Smékal, I. Císařová, J. Mroziński, Polyhedron 20 (2001) 3301;
(e) D. Ghoshal, A.K. Ghosh, T.K. Maji, J. Ribas, G. Mostafa, E. Zangrando, N.R. Chaudhuri, Inorg. Chim. Acta 359 (2006) 593;
(f) J.C. Byun, C.H. Han, K.J. Kim, Inorg. Chem. Commun. 9 (2006) 171.
[10] (a) M. Munakata, J.C. Zhong, I. Ino, T. Kuroda-Sowa, M. Maekawa, Y. Suenaga, N. Oiji, Inorg. Chim. Acta 317 (2001) 268;
(b) T. Akitsu, Y. Einaga, Inorg. Chim. Acta 360 (2007) 497.
[11] J.N. Jolley, A.I. Yanovsky, L.R. Kelland, K.B. Nolana, J. Inorg. Biochem. 83 (2001) 91.
[12] Stoe & Cie X-AREA (Version 1.18) and X-RED (Version 1.04), Stoe & Cie, Darmstadt, Germany, 2002.
[13] G.M. Sheldric, SHELXL97, University of Gottingen, Germany, 1997.
[14] M.N. Burnett, C.K. Johnson, ORTEP-III. Report ORNL-6895, Oak Ridge National Laboratory, Tenessee, USA, 1996.
[15] A. Karadağ, A. Bulut, A. Şenocak, İ. Uçar, O. Büyükgüngör, J. Coord. Chem. 60 (19) (2007) 2035.
[16] (a) S. Alvarez, C. Lopez, M.J. Bermejo, Transition Met. Chem. 9 (1984) 123;
(b) D.F. Shriver, J. Am. Chem. Soc. 85 (1963) 1405;

(c) D.A. Down, A. Haim, W.K. Wilmarth, J. Inorg. Nucl. Chem. 21 (1961) 33.
[17] A. Karadağ, Z. Kristallogr. 222 (2007) 39.
[18] (a) R.W. Gable, B.F. Hoskins, R. Robson, J. Chem. Soc., Chem. Commun. (1990) 762;
(b) C. Mühle, A. Karpov, J. Nuss, M. Jansen, Z. Naturforsch. 59b (2004) 567;
(c) L.R. Falvello, M. Thomás, Chem. Commun. (1999) 273.
[19] V.T. Yılmaz, A. Karadağ, C. Thone, J. Coord. Chem. 55 (6) (2002) 609.

Available online at www.sciencedirect.com
ScienceDirect
Polyhedron 27 (2008) 232–240
POLYHEDRON
www.elsevier.com/locate/poly

Syntheses and characterization of three novel W(Mo)/Cu/S cluster-based layered polymers with 1,3,4-thiadiazole-2,5-dithiolate (SSS): Intriguing coordination modes of SSS

Zhi-Hua Li, Ping Lin, Shao-Wu Du *

State Key Laboratory of Structural Chemistry, Fujian Institute of Research on the Structure of Matter, Chinese Academy of Sciences, Fujian, Fuzhou 350002, PR China
Graduate School of the Chinese Academy of Sciences, Beijing 100039, PR China

Received 1 June 2007; accepted 10 September 2007
Available online 22 October 2007

Abstract

Solvothermal reactions of H_2SSS (H_2SSS = 1,3,4-thiadiazole-2,5-dithiolate) with CuCN and $[WOS_3CuCN]^{2-}$ or $[W(Mo)S_4]^{2-}$ in organic solvents produced three novel 2D layered polymers, namely, $[Et_4N][WS_{3.5}O_{0.5}Cu_3(CN)_{0.5}(SSSH_{0.5})]$ (**1**), $[Et_4N][WS_4Cu_3(SSS)]$ (**2**) and $[Et_4N]_2[MoS_4Cu_4(CN)(SSSH_{0.5})_2]$ (**3**). X-ray diffraction analyses reveal that in **1** or **3**, the nest-shaped clusters $\{WS(O)S_3Cu_3\}$ or saddle-shaped clusters $\{MoS_4Cu_4\}$ are linked together by SSS ligands to form a double chain $[WS_{3.5}O_{0.5}Cu_3(SSSH_{0.5})]_n^{-1/2}$ or a zigzag chain $[MoS_4Cu_4(SSSH_{0.5})_2]_n^-$, respectively. The CN^- groups bridge the chains in **1** or **3** resulting in the formation of a 2D anionic network. Compound **2** is constructed from T-shaped $\{WS_4Cu_3\}$ subunits and SSS, also producing a 2D anionic sheet structure. The SSS ligand in **1** or **2** coordinates to five Cu atoms via its exocyclic sulfur and endocyclic nitrogen atoms in an unprecedented fashion, while in **3**, it acts as a rare tridentate ligand to connect three Cu atoms. Complexes **1**–**3** show optical transitions with band gaps ranging from 1.90 to 2.24 eV.
© 2007 Elsevier Ltd. All rights reserved.

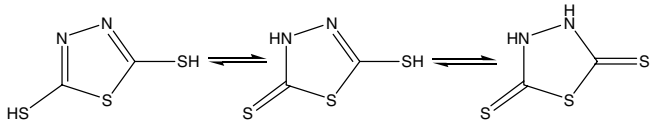
Keywords: 1,3,4-Thiadiazole-2,5-dithiolate; Heterobimetallic polymer; Coordination modes; Semiconductor; W(Mo)/Cu/S cluster

1. Introduction

N-heterocyclic thiones containing one or more thioamide groups are intriguing ligands in coordination chemistry since they can achieve versatile coordination modes by using exocyclic sulfur or endocyclic nitrogen atoms [1–11]. In the assembly reactions with metal ions, they usually show protoprotic tautomerism, acid–base equilibrium, and redox behavior based on a mercapto → disulfido conversion [2–8]. Among various N-heterocyclic thiones, 1,3,4-thiadiazole-2,5-dithiolate (H_2SSS, commonly known as "Bismuthiol I") is particularly interesting because its five available donor atoms in either protonated or deprotonated forms enable it to bind to one or more metal ions (Scheme 1) [5–9]. Compared to other N-heterocyclic thiones, only a few metal complexes containing SSS have been structurally determined due to the difficulties with insolubility and poor crystal habit [10d]. For example, several dinuclear transition metal (such as Au, Pt, etc.) complexes with SSS have been prepared and their structures, optical spectra and electrochemical properties have been studied [5–7]. A few main group metal thiol clusters with intriguing structures constructed from SSS, like the pentanuclear 35-membered tin macrocycle, have also been reported [7]. In addition, only two examples of coordination polymers constructed from SSS have been structurally characterized

* Corresponding author. Address: State Key Laboratory of Structural Chemistry, Fujian Institute of Research on the Structure of Matter, Chinese Academy of Sciences, Fujian, Fuzhou 350002, PR China. Tel./fax: +86 591 83709470.
E-mail address: swdu@fjirsm.ac.cn (S.-W. Du).

0277-5387/$ - see front matter © 2007 Elsevier Ltd. All rights reserved.
doi:10.1016/j.poly.2007.09.003



Scheme 1. Three tautomeric forms of H_2SSS.

[8c,11]. One is an infinite 1D polymer whose basic repeating unit is $[(Me)_2Sn(SSS)]$ [8c]. The other is the helical chain polymers $[Et_4N]_2[W(Mo)S_4Cu_2(SSS)]$ (**4**) reported previously by us [11]. In compound **4**, the SSS linked two $\{W(Mo)S_4Cu_2\}$ subunits by its exocyclic sulfur atoms leaving the nitrogen atoms uncoordinated [11]. As far as we are aware, no higher dimensional (2D or 3D) coordination polymers and supramolecular complexes containing SSS have been reported so far.

Recently, the rational design and construction of supramolecular structures based on metal clusters has attracted considerable attention due to the formation of fascinating structures and applications as functional materials [12–15]. The use of metal clusters instead of single metal ions as structural and functional building blocks may offer the possibility of rational design and allow for better control over the structural and physical properties of these extended solids [14]. So far, the construction of cluster-containing supramolecular compounds has mostly focused on using metal–oxygen clusters as a building block [12,14,15], there have only been a few reports on the employment of metal–sulfur clusters [16–19]. Typical examples are the supramolecular compounds based on Mo(W)/Cu/S clusters with rigid or flexible multi-dentate linkers like 4,4′-bipy or bix [bix = 1,4-bis(imidazole-1-ylmethyl)benzene] [17,19a]. We have recently employed bidentate thiolato ligands to assemble Mo(W)/Cu/S cluster-based supramolecular architectures. For example, the reactions of $[MOS_3]^{2-}$ (M = Mo, W) or $[WS_4]^{2-}$ with $CuS_2P(OR)_2$ (R = Et, Me) gave rise to 2D layered polymers $[Et_4N][MOS_3Cu_3\{S_2P(OMe)_2\}_2]$ or 1D polymers $[Et_4N][\{MS_4Cu_4\}\{S_2P(OEt)_2\}_3]$ [19b,19c]. As an extension of these studies, we have investigated the self-assembly reactions of $[WOS_3CuCN]^{2-}$ or $[W(Mo)S_4]^{2-}$ with CuCN in the presence of H_2SSS at elevated temperature and successfully isolated three novel 2D coordination polymers $[Et_4N][WS_{3.5}O_{0.5}Cu_3(CN)_{0.5}(SSSH_{0.5})]$ (**1**), $[Et_4N][WS_4Cu_3(SSS)]$ (**2**) and $[Et_4N]_2[MoS_4Cu_4(CN)(SSSH_{0.5})_2]$ (**3**). In contrast to **4**, the nitrogen atoms in SSS ligands in **1**–**3** are also involved in the coordination and the SSS ligands adopt novel coordination modes to connect W(Mo)/Cu/S cluster subunits leading to 2D cluster arrays.

2. Experimental

2.1. General remarks

H_2SSS and CuCN (AR) were purchased from Acrōs Organics and used as received without further purification. Compounds $[Et_4N]_2[WOS_3CuCN]$ and $[Et_4N]_2[W(Mo)S_4]$ were prepared according to literature procedures [20]. CH_3CN and acetone were purified by the standard method before use. Infrared spectra were recorded on a Nicolet Magna 750 FT-IR spectrophotometer (KBr pellets). Elemental analyses were carried out using a Perkin–Elmer 2400 II elemental analyzer. The diffuse-reflectance spectrum has been measured on a Lambda 900 spectrophotometer using $BaSO_4$ powder as 100% reflectance reference at room temperature.

It should be cautioned that all the manipulations should be carried out in a well-ventilated fumehood due to the production of toxic gases (HCN and/or H_2S) in the preparation of the title compounds.

2.2. Preparation of $[Et_4N][WS_{3.5}O_{0.5}Cu_3(CN)_{0.5}(SSSH_{0.5})]$ (1)

H_2SSS (12 mg, 0.08 mmol), CuCN (11 mg, 0.125 mmol), $[Et_4N]_2[WOS_3CuCN]$ (54 mg, 0.08 mmol) and 3.0 mL of CH_3CN were placed in a $15.0 \times 0.8 \times 0.8$ cm^3 glass tube. The tube was evacuated and sealed before it was heated at 160 °C for 24 h. After cooling to room temperature over 48 h, red crystals suitable for X-ray single-crystal diffraction were formed. Yield, 10% (based on CuCN). *Anal.* Calc. for **1**: C, 16.03; H, 2.63; N, 6.23. Found: C, 15.99; H, 2.89; N, 6.13%. IR (KBr pellet, cm^{-1}): ν(C≡N): 2144 (m); ν(C=N): 1456 (m); ν(W–O_t): 920 (m); ν(W–S_t): 500 (m); ν(W–μ_3-S): 432 (s).

2.3. Preparation of $[Et_4N][WS_4Cu_3(SSS)]$ (2)

Compound **2** was synthesized by a similar procedure as **1** with the exception that the reactants were H_2SSS (19 mg, 0.125 mmol), CuCN (22.5 mg, 0.25 mmol) and $[Et_4N]_2[WS_4]$ (71.6 mg, 0.125 mmol). After cooling to room temperature over 48 h, red crystals suitable for X-ray single-crystal diffraction were obtained. Yield, 26% (based on CuCN). *Anal.* Calc. for **2**: C, 15.37; H, 2.58; N, 5.38. Found: C, 15.34; H, 2.69; N, 5.40%. IR (KBr pellet, cm^{-1}): ν(C=N): 1455 (m); ν(W–μ_2-S): 470 (s); ν(W–μ_3-S): 432 (m).

2.4. Preparation of $[Et_4N]_2[MoS_4Cu_4(CN)(SSSH_{0.5})_2]$ (3)

The synthesis procedure was similar to that of **2**. A mixture of H_2SSS (12 mg, 0.08 mmol), CuCN (22.5 mg, 0.25 mmol), $[Et_4N]_2[MoS_4]$ (40 mg, 0.08 mmol) and 3 mL of acetone was heated at 120 °C for 48 h. After cooling to room temperature over 36 h, dark red crystals suitable for X-ray single-crystal diffraction were formed. Yield, 31% (based on CuCN). *Anal.* Calc. for **3**: C, 23.74; H, 3.89; N, 9.23. Found: C, 23.60; H, 4.26; N, 8.95%. IR (KBr pellet, cm^{-1}): ν(C≡N): 2137 (m); ν(C=N): 1453 (m); ν(Mo–μ_3-S): 443 (m).

2.5. X-ray crystallographic study

Suitable single crystals of the compounds were carefully selected and glued to thin glass fibers with epoxy resin.

Table 1
Crystallographic data for complexes **1**–**3**

	1	**2**	**3**
Empirical formula	$C_{10.5}H_{20.5}Cu_3N_{3.5}O_{0.5}S_{6.5}W$	$C_{10}H_{20}Cu_3N_3S_7W$	$C_{21}H_{41}Cu_4MoN_7S_{10}$
Formula weight	786.66	781.18	1062.31
Crystal system	monoclinic	monoclinic	monoclinic
Space group	$P2_1/c$	$P2_1/c$	$P2_1/n$
a (Å)	7.2683(4)	10.685(2)	15.804(1)
b (Å)	13.5858(7)	19.399(4)	12.9142(7)
c (Å)	22.375(1)	10.733(2)	19.774(1)
β (°)	94.260(3)	100.880(4)	105.317(3)
V (Å^3)	2203.3(2)	2184.7(8)	3892.5(4)
Z	4	4	4
ρ_{calc} (g cm^{-3})	2.371	2.375	1.813
μ (mm^{-1})	8.681	8.798	3.026
$F(000)$	1508	1496	2136
θ (°)	3.0177–27.4835	3.1484–27.4835	2.0675–27.4835
Reflections collected	16821	16763	29914
Independent reflections	5042	4988	8903
Parameters	258	217	388
R(int)	0.0355	0.0487	0.0604
R_1, wR_2 $[I > 2\sigma(I)]$[a,b]	0.0510, 0.1002	0.0329, 0.0784	0.0684, 0.1221
Goodness-of-fit on F^2	0.993	0.998	1.066

[a] $R_1 = \sum||F_o| - |F_c||/\sum|F_o|$.
[b] $wR_2 = [\sum w(F_o^2 - F_c^2)^2/\sum w(F_o^2)]^{0.5}$.

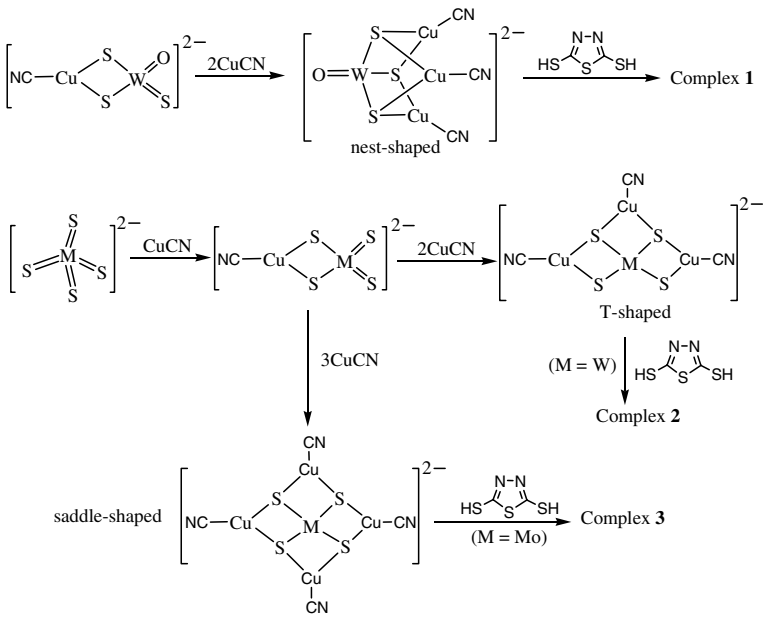
Intensity data were collected at room temperature on a Rigaku Mercury CCD area-detector diffractometer with a graphite monochromator utilizing Mo Kα radiation ($\lambda = 0.71073$ Å). The structures were solved by direct methods and refined on F^2 by full-matrix least-squares using the SHELXL-97 program package [21]. All non-hydrogen atoms were refined anisotropically. The hydrogen atoms in $[Et_4N]^+$ were treated as riding, with C–H 0.96 or 0.97 Å and U(H) values set as 1.2 or 1.5 times U_{eq}(C). In compounds **1** and **3**, the μ_2-bridging cyanides between two Cu atoms indicated disorder with respect to the C and N termini; this disorder was treated by adopting 50% C and N occupancies at those sites. In compound **1**, the unique C atom connected to N4 is disordered over two positions, and was refined as two atoms of 37% or 63% occupancy, viz. C3 and C31. The terminal O1 and S4 in compound **1** are disordered and was refined by adopting 50% O and S occupancies at the same site based on the best fit of the disorder. H2A in **1** and H2A, H4A in **3** were generated in calculated positions with half-occupancy for the balance of the charge and N–H distance being 0.86 Å. The crystallographic data for **1**–**3** are listed in Table 1.

3. Results and discussion

3.1. Synthetic considerations

As reported previously, the reactions of thiomolybdates or thiotungstates with CuCN in solution produced a number of heterometallic compounds with various structural types [20b,23]. The CN^- groups in these compounds can be partially or completely removed by other donor ligands, such as PhS^-, PPh_3 and bix to form either discrete complexes or polymeric compounds [19a,20b,24]. It was also observed that by acidifying a linear cluster anion $[NCCuS_2WS_2CuCN]^{2-}$ with acetic acid, some of the terminally bonded cyanides at Cu centers were easily removed resulting in the formation of a cyanide-bridged 2D layer framework [24d]. Since the H_2SSS ligand has five potential coordination sites, the replacement of CN^- groups at Cu atoms in W(Mo)/Cu/S clusters by SSS may lead to the assembly of new compounds with interesting structural motifs. In addition, the acidity of the H_2SSS ligand may facilitate this process. Thus, the reaction of CuCN, H_2SSS and $[Et_4N]_2[WOS_3CuCN]$ in CH_3CN at 160 °C for 24 h afforded red crystals of $[Et_4N][WS_{3.5}O_{0.5}Cu_3(CN)_{0.5}(SSSH_{0.5})]$ (**1**) in low yield. The formation of **1** may involve the addition of two CuCN moieties to the linear cluster $[Et_4N]_2[WOS_3CuCN]$ followed by the replacement of two cyanide groups by SSS ligands (Scheme 2). During the reaction a small amount of W=O groups were replaced by W=S, presumably due to the formation of H_2S gas under the solvothermal conditions and this has frequently been observed in the formation of other W(Mo)/Cu/S clusters [22].

Analogous reaction of CuCN with $[Et_4N]_2[WS_4]$ in the presence of H_2SSS produced $[Et_4N][WS_4Cu_3(SSS)]$ (**2**) as red crystals in moderate yield. As shown in Scheme 2, the initial step of the reaction may be the formation of a T-shaped cluster anion $[WS_4(CuCN)_3]^{2-}$, which by completely replacement of CN^- with SSS yields a 2D anionic layer of **2**. The composition of the anion seems to be independent upon the ratio of CuCN to $[Et_4N]_2[WS_4]$. Changing the ratio only decrease the yield of compound **2**. Similar procedures involving CuCN, H_2SSS and $[Et_4N]_2[MoS_4]$ failed to get any products. However, when the reaction



Scheme 2. The possible self-assembly pathways for the syntheses of **1**–**3**.

was carried out in acetone at 120 °C, dark-red crystals identified as $[Et_4N]_2[MoS_4Cu_4(CN)(SSSH_{0.5})_2]$ (**3**) were obtained. Apparently, the formation of **3** can be described as the displacement of three CN^- groups in the saddle-shaped cluster anion $[MoS_4(CuCN)_4]^{2-}$ with SSS leading to the formation of a 1D $[MoS_4Cu_4(SSSH_{0.5})_2]_n^-$ anionic chain. The remaining CN^- groups bridge these chain structures to generate a 2D layer.

3.2. Description of the crystal structure of $[Et_4N][WS_{3.5}O_{0.5}Cu_3(CN)_{0.5}(SSSH_{0.5})]$ 1

An X-ray crystal analysis reveals that the asymmetric unit of **1** contains a nest-shaped $\{WO(S)S_3Cu_3\}$ cluster anion, half of CN^- group, one SSS ligand and a $[Et_4N]^+$ cation. The selected bond lengths and angles for **1** are quoted in Table 2. The W atom lies in the center of the distorted tetrahedron $\{WO(S)S_3\}$, of which the terminal site is occupied by 1/2 S and 1/2 O with the length W–O(S) being 2.028(5) Å. All three copper centers in **1** adopt a distorted tetrahedral geometry but in different coordination environment: Cu1 coordinates to one nitrogen atom and one sulfur atom provided by SSS and two sulfur atoms from $\{WO(S)S_3\}$; Cu2 coordinates to two sulfur atoms from $\{WO(S)S_3\}$ and two sulfur atoms from different SSS; Cu3 coordinates to one C/N atom from CN^-, one S atom from SSS and two S atoms from $\{WO(S)S_3\}$. The interconnection of $\{WO(S)S_3Cu_3\}$ clusters by SSS linkers results in a double chain of $[WS_{3.5}O_{0.5}Cu_3(SSSH_{0.5})]_n^{-1/2}$ extended along the *a*-axis (Fig. 1a). Alternatively, the basic repeating unit of **1** can be described as a double incomplete cubane-like cluster where two incomplete cubane-like $\{WS_{3.5}O_{0.5}Cu_3(SSSH_{0.5})\}$ fragments are linked via a pair of SSS ligands in a fashion similar to those of $[Et_4N]_2[(OWS_3Cu_3)_2(\mu\text{-}SBu^t)_2]$ [25]. These double incomplete cubane-like clusters are connected via Cu1–S5 to form a unique chain. The adjacent double chains are further linked each other by bridging CN^- groups to form a 2D anionic layer that extends in the *ab*-plane (Fig. 1b). The $[Et_4N]^+$ cations are enchased between the adjacent layers.

In compound **1**, the SSS ligand acts as a k_5 (two-S/one-N) form to link five Cu atoms from three different $\{WO(S)S_3Cu_3\}$ subunits by S5, S7 and N3, of which S7 and N3 coordinate to two and one Cu atoms from the same $\{WO(S)S_3Cu_3\}$ subunit, respectively, while S5 connects two Cu atoms from two adjacent $\{WO(S)S_3Cu_3\}$ clusters (Fig. 1a). As can be seen from Scheme 3, which summarizes all the reported coordination modes of the SSS ligand, the SSS ligand in **1** presents an unprecedented coordination pattern (mode g). The bond lengths of Cu1–S5 and Cu2b–S5 [2.376(2) and 2.249(2) Å, respectively] are comparable to the Cu–S distances in the Cu(I) thiolates reported before [2c,2d,2e,2f,11]. The bond distances of Cu2a–S7 [2.617(3) Å] and Cu3a–S7 [2.589(3) Å] are slightly longer than the common Cu–S bond lengths, but are similar to those observed in the Cu(I) complexes containing N-heterocyclic thiones, such as 2.6572(13) Å in $[Cu(pymtH)I]_2$ (pymtH = pyrimidine-2-thione) and 2.5871(16) Å in $\{Cu_6I_6(2\text{-}SC_5H_4NH)_6\}_n \cdot 2n$MeCN [2c,2f]. The lengths of 1.724(8) and 1.710(8) Å for the S5–C1 and S7–C2 bonds, respectively, coincide with the fact that the SSS ligand in **1** is in the thiolate form rather than the thione form. The mean N=C distance in **1** (1.302(10)–1.304(10) Å) is only slightly longer than that of Au(I)–, Pt(II)– and Ru(II)–SSS complexes (1.292 Å) but close to that of Sn(II)–SSS complexes (1.305 Å). The lengthening of C=N may be due to the coordination of N to Cu atoms. The N2–N3 separation (1.391(9) Å) is normal and within the range for a

Table 2
Selected bond lengths (Å) and angles (°) for **1**–**3**

1							
W1–S1	2.246(2)	W1···Cu2	2.699(1)	Cu1–S3	2.312(2)	Cu3–S2	2.332(3)
W1–S2	2.251(2)	W1···Cu3	2.702(1)	Cu2–S1	2.314(2)	Cu3–S3	2.301(3)
W1–S3	2.251(2)	Cu1–S1	2.329(2)	Cu2–S2	2.287(3)	Cu3–N1/C11	1.906(8)
W1···Cu1	2.763(1)						
S1–W1–S2	107.27(8)	S2–W1–S4	107.8(2)	S1–Cu1–S5	104.71(9)	S2–Cu3–S3	104.17(9)
S1–W1–S3	107.95(8)	S3–W1–S4	111.1(2)	S3–Cu1–S5	109.68(9)	S2–Cu3–N1/C11	117.3(3)
S1–W1–S4	114.0(2)	S1–Cu1–S3	103.22(9)	S1–Cu2–S2	103.80(9)	S3–Cu3–N1/C11	125.1(3)
S2–W1–S3	108.56(9)						
2							
W1–S1	2.181(1)	W1···Cu2	2.6869(7)	Cu2–S2	2.310(1)	Cu3–S4	2.236(1)
W1–S2	2.251(1)	W1···Cu3	2.6465(7)	Cu2–S3	2.310(2)	S5–C1	1.736(4)
W1–S3	2.251(1)	Cu1–S1	2.309(2)	Cu2–S5	2.478(1)	S7–C2	1.730(4)
W1–S4	2.198(1)	Cu1–S2	2.301(1)	Cu3–S3	2.256(1)	N2–Cu2b	2.018(3)
W1···Cu1	2.6972(7)	Cu1–N1	2.208(3)				
S1–W1–S2	109.03(5)	S2–W1–S4	110.24(5)	S1–Cu1–N1	108.3(1)	S2–Cu2–S5	99.50(5)
S1–W1–S3	109.23(5)	S3–W1–S4	107.73(5)	S2–Cu1–N1	111.08(9)	S3–Cu2–S5	124.03(4)
S1–W1–S4	110.84(5)	S1–Cu1–S2	103.03(5)	S2–Cu2–S3	105.69(5)	S3–Cu3–S4	106.27(5)
S2–W1–S3	109.75(4)						
3							
Mo1–S1	2.224(2)	Mo1···Cu4	2.6931(9)	Cu2–S5	2.399(2)	S5–C1	1.710(6)
Mo1–S2	2.243(2)	Cu1–S1	2.331(2)	Cu3–S2	2.279(2)	S7–Cu4b	2.278(2)
Mo1–S3	2.221(2)	Cu1–S4	2.303(2)	Cu3–S3	2.310(2)	S10–Cu3a	2.277(2)
Mo1–S4	2.252(2)	Cu1–S8	2.445(2)	Cu3–N1	2.167(5)	S10–C4	1.708(7)
Mo1···Cu1	2.7032(9)	Cu1–C21/N21	1.927(6)	Cu4–S3	2.302(2)	N3–N4	1.393(7)
Mo1···Cu2	2.7053(9)	Cu2–S1	2.337(2)	Cu4–S4	2.263(2)	C3–N3	1.306(8)
Mo1···Cu3	2.7033(9)	Cu2–S2	2.290(2)	Cu4–N3	2.185(5)	C4–N4	1.307(8)
S1–Mo1–S2	109.09(6)	S1–Cu1–S4	103.60(6)	S8–Cu1–C21/N21	101.4(2)	S2–Cu3–N1	113.3(1)
S1–Mo1–S3	112.80(7)	S1–Cu1–S8	101.45(7)	S1–Cu2–S2	103.71(6)	S3–Cu3–N1	94.5(1)
S1–Mo1–S4	108.89(6)	S1–Cu1–C21/N21	121.6(2)	S1–Cu2–S5	101.26(7)	S3–Cu4–S4	105.21(6)
S2–Mo1–S3	108.36(6)	S4–Cu1–S8	113.43(6)	S2–Cu2–S5	116.04(6)	S3–Cu4–N3	96.6(2)
S2–Mo1–S4	109.30(6)	S4–Cu1–C21/N21	114.8(2)	S2–Cu3–S3	104.15(6)	S4–Cu4–N3	113.0(1)
S3–Mo1–S4	108.35(6)						

Symmetry transformations used to generate equivalent atoms: For **1**, a: $1-x, 1-y, 1-z$; b: $1+x, y, z$; For **2**, a: $x, 0.5-y, 0.5+z$; b: $x, 0.5-y, z-0.5$; c: $-x, y+0.5, 0.5-z$; For **3**, a: $1.5-x, 0.5+y, 0.5-z$; b: $1.5-x, y-0.5, 0.5-z$.

typical N–N single bond (1.40 Å) [26]. In SSS ligand, the uncoordinated azole-N atom is protonated, and the two adjacent SSS share one proton by forming a N2–H···N2 hydrogen bond (N–N distance is 2.59(1) Å).

3.3. Description of the crystal structure of $[Et_4N][WS_4Cu_3(SSS)]$ 2

As shown in Fig. 2a, the asymmetric anion of **2** contains one T-shaped cluster unit $\{WS_4Cu_3\}$ and one SSS ligand. The selected bond lengths and angles for **2** are listed in Table 2. The bond angles of Cu1–W1–Cu3, Cu1–W1–Cu2 and Cu2–W1–Cu3 are 169.15(2)°, 81.46(2)° and 87.81(2)°, respectively, indicating a slightly distorted T-shaped $\{WS_4Cu_3\}$ skeleton. The W–S and Cu–S separations are comparable to those in compound $[PPh_4][WS_4Cu_3(CN)_2]\cdot MeCN$ which also contains a T-shaped $\{WS_4Cu_3\}$ cluster core [23b]. There are two types of Cu atoms: (a) the tetrahedral Cu1 and Cu2 atoms coordinated to two S atoms of the $\{WS_4\}$ unit, one S atom from SSS and one N atom from another SSS and (b) the trigonal Cu3 atom coordinated to two S atoms of the $\{WS_4\}$ unit and one thio-S atom. The W···Cu3 [2.6465(7) Å] separation is slightly shorter than those of the other two [2.6972(7) and 2.6869(7) Å], suggesting that the interactions between the W and Cu are somewhat influenced by the coordination geometry of Cu [22]. As shown in Fig. 2b, the T-shaped cluster $\{WS_4Cu_3\}$ connects eight equivalent clusters through four SSS ligands to form a 2D anionic network that extends in the *bc*-plane. The $[Et_4N]^+$ cations are situated between the adjacent layers.

Similar to **1**, the SSS ligand in **2** also links five Cu atoms but in a slightly different way. The SSS ligand coordinates to Cu atoms from four different $\{WS_4Cu_3\}$ subunits through two nitrogen atoms and two sulfur atoms in an unprecedented k_5 (two-S/two-N) coordination mode (Scheme 3, mode h). Compared to **1**, where both the thio-S atoms function as μ_2-bridges, one of the thio-S atoms of SSS in **2** bridges two Cu atoms while the other coordinates to only one Cu atom. The other difference of the SSS coordination modes from **1** is that in **2**, both the azole-N atoms are bonded to Cu atoms. Although similar coordination mode of the SSS ligand has been proposed for the polymeric compound $[Au_2(SSS)_n]$, it has not been confirmed by X-ray crystallography [5c]. All the Cu–S bond lengths ranging from 2.185(1) to 2.478(1) Å are

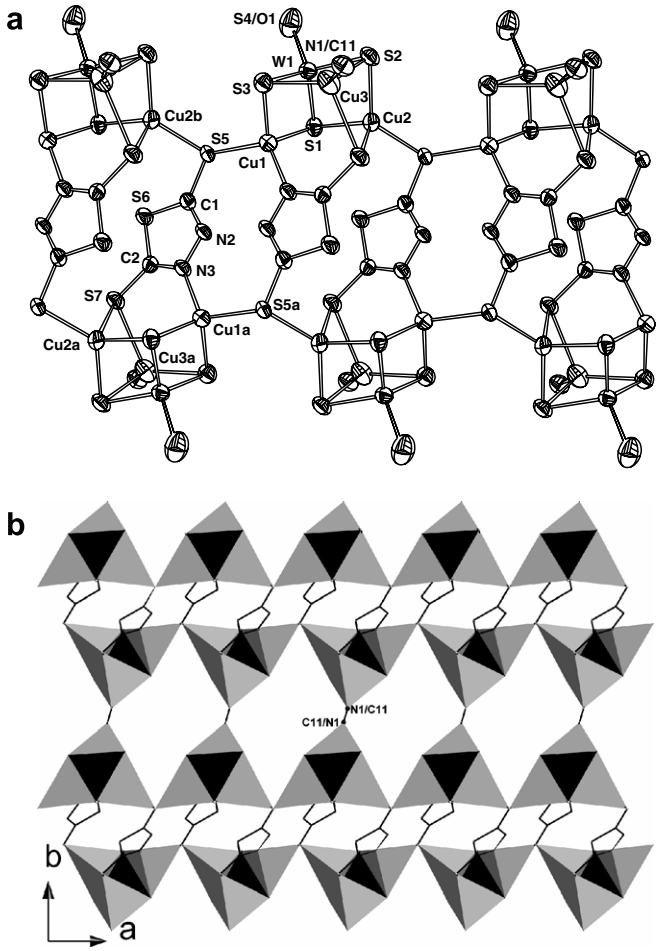
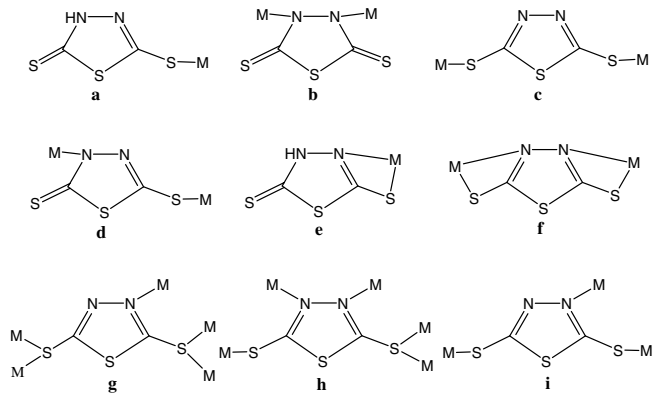


Fig. 1. (a) Part of the double chain linked by nest-shaped $WS(O)S_3Cu_3$ clusters and SSS in the anion of **1**, with partial atom numbering scheme (50% probability displacement ellipsoids, H atoms have been omitted for clarity). Symmetry transformations used to generate equivalent atoms – a: $1-x, 1-y, 1-z$; b: $1+x, y, z$. (b) Polyhedral and ball-stick view of part of the 2D anionic network within **1** ($WS(O)S_3$ as black and CuS_4 or $CuN(C)S_3$ as gray).



Scheme 3. The coordination modes of SSS.

normal compared to those for the Cu(I) thiolates reported [2c,2d,2e,2f,11]. Although both N-donors of the SSS unit are coordinated to Cu atoms, there is no significant length-

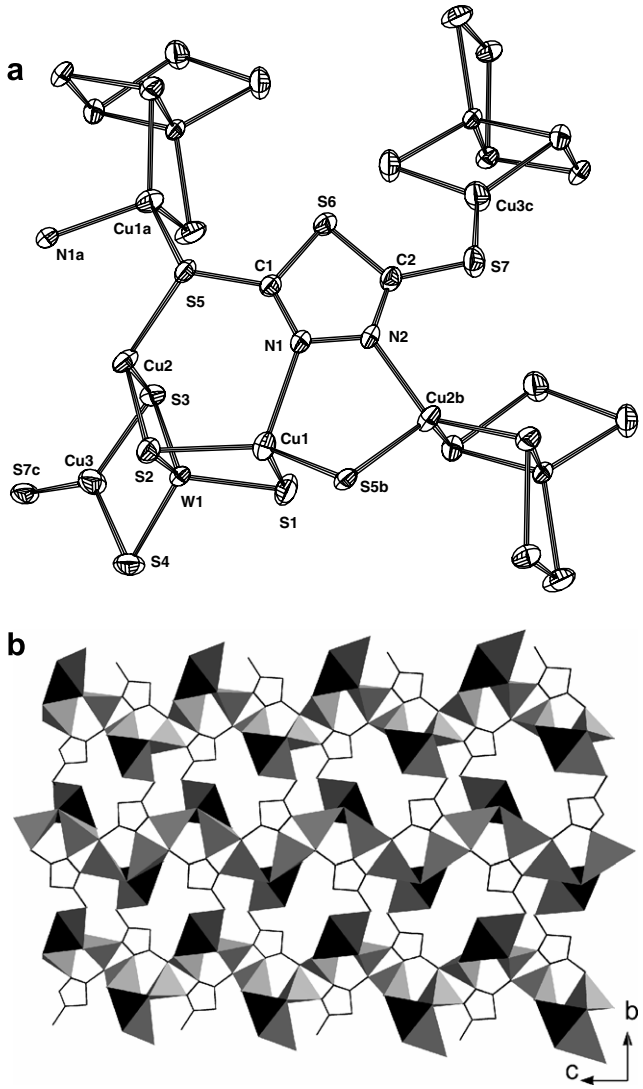


Fig. 2. (a) Fragment of the chain structure of $[WS_4Cu_3(C_2N_2S_3)]_n^{1-}$ anion in **2**, showing the coordination environment of the SSS ligand (50% probability displacement ellipsoids). Symmetry transformations used to generate equivalent atoms – a: $x, 0.5-y, 0.5+z$; b: $x, 0.5-y, z-0.5$; c: $-x, y+0.5, 0.5-z$; d: $-x, y-0.5, 0.5-z$. (b) Polyhedral and ball-stick view of part of the 2D anionic network within **2** (WS_4, black; $CuNS_3$/CuS_3, gray).

ening of the C=N distances (1.303(5) and 1.305(6) Å), as also observed in **1**. The N1–N2 distance (1.396(4) Å) is close to that of **1** and is considered to be a single bond.

3.4. Description of the crystal structure of $[Et_4N]_2[MoS_4Cu_4(CN)(SSSH_{0.5})_2]$ 3

Compound **3** crystallizes in the monoclinic space group $P2(1)/n$ and the asymmetric unit contains one saddle-shaped $\{MoS_4Cu_4\}$ core, one cyanide group, two SSS ligands and two $[Et_4N]^{2+}$ cations. The selected bond lengths and angles for **3** are given in Table 2. The anion $[MoS_4Cu_4(CN)(SSSH_{0.5})_2]^{2-}$ consists of a saddle-shaped $\{MoS_4Cu_4\}$ core, which closely resembles those in

$[MoS_4Cu_4L_4]^{2-}$ (L = Cl, CN, NCS, etc.) [16c,27]. The average Mo1–Cu, Mo1–μ_3-S, and Cu–μ_3-S bond lengths in the $\{MoS_4Cu_4\}$ core are similar to those in the related Mo/Cu/S clusters [27]. All four copper centers in **3** adopt a distorted tetrahedral coordination geometry. Cu1 or Cu2 coordinates to one C/N atom of the bridging cyanide, one thio-S atom and two S atoms provided by the $\{MoS_4\}$ moiety whereas Cu3 or Cu4 coordinates to one azole-N atom, one thio-S atom and two S atoms from the $\{MoS_4\}$ unit. Each $\{MoS_4Cu_4\}$ cluster is linked to two crystallographically equivalent clusters through four SSS ligands to form a zigzag chain of $[MoS_4Cu_4(SSSH_{0.5})_2]_n^-$ along the *b*-axis (Fig. 3a). The adjacent zigzag chains are further linked together by bridging CN^- groups to form a 2D anionic layer that extends in the *ab*-plane (Fig. 3b). The $[Et_4N]^+$ cations reside between two layers.

In compound **3**, the SSS moiety acts as a tridentate ligand in which two S atoms and one N atom links three Cu atoms of two $\{MoS_4Cu_4\}$ subunits (Scheme 3, mode i). This coordination mode is also rare for the SSS ligand and has been only reported most recently in a novel trinuclear Re(I) complex $[SSS(Re(CO)_5)_3](CF_3SO_3)$ [7]. The exocyclic S–C bond distances (range from 1.694(6) to 1.717(6) Å) are consistent with S–C single bonds as those observed in triphenyltin benzoxazole-2-thiolate (1.724 Å) [28]. The N1–N2 distance (1.381(6) Å) is slightly shorter than that of N3–N4 (1.393(7) Å), both of which are close to that of a single bond [26]. The C–N distances (range from 1.306(8) to 1.316(7) Å) are within the range of a C=N double bond and are comparable to those found in $[SSS(Re(CO)_5)_3](CF_3SO_3)$ (1.278(8)–1.317(8) Å) [7]. The bond parameters of the SSS ligand together with the IR spectral data further reveal that the coordinated SSS ligand in **3** takes thiolate form. The uncoordinated endocyclic nitrogen atom is protonated, and the adjacent two SSS ligands share one proton by a weak N–H···N hydrogen bond as observed in compound **1** (N–N distance is 2.62 Å).

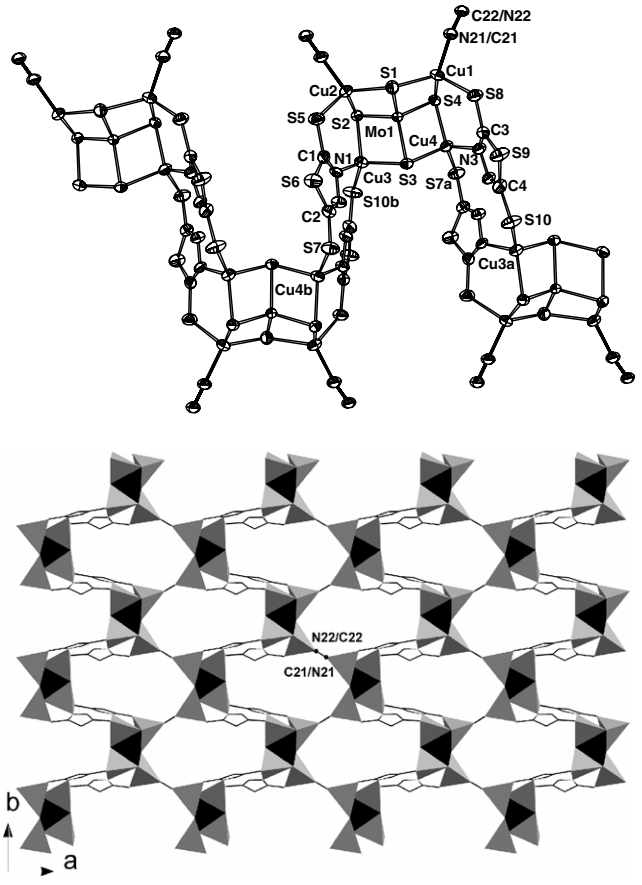


Fig. 3. (a) Part of the zigzig chain linked by saddle-shaped $\{MoS_4Cu_4\}$ clusters and SSS in the anion of **3**, with partial atom numbering scheme (50% probability displacement ellipsoids, H atoms have been omitted for clarity). Symmetry transformations used to generate equivalent atoms – a: $1.5 - x$, $0.5 + y$, $0.5 - z$; b: $1.5 - x$, $y - 0.5$, $0.5 - z$. (b) Polyhedral and ball-stick view of part of the 2D anionic network within **3** (MoS_4, black and $CuN(C)S_3$, gray).

3.5. IR and UV absorptional properties

In the infrared spectra of the title complexes, the bands ranging from 1453 to 1456 cm^{-1} are assigned to the C=N vibrations as those reported for complex Cu(SSSH) [6a]. The W(Mo)–S_t, W(Mo)–μ_2-S and W(Mo)–μ_3-S stretching vibrations are observed in the range of 520–400 cm^{-1}, which are comparable to those for the related W(Mo)/Cu/S complexes [11,19–25]. The observation of both ν(W–S_t) (500 cm^{-1}) and ν(W–O_t) (920 cm^{-1}) in compound **1** confirmed the partial replacement of W=O groups by W=S groups. The strong, sharp absorptions observed at 2144 and 2137 cm^{-1} in **1** and **3** are assigned to the vibrations of the bridging cyanides.

The optical absorption spectra of compounds **1**–**3** have been measured by diffuse-reflectance experiments. The UV–Vis absorption data were calculated from the reflectance data using the Kubelka–Munk function [29]: $\alpha/S = (1 - R)^2/2R$. Where R is the experimentally observed

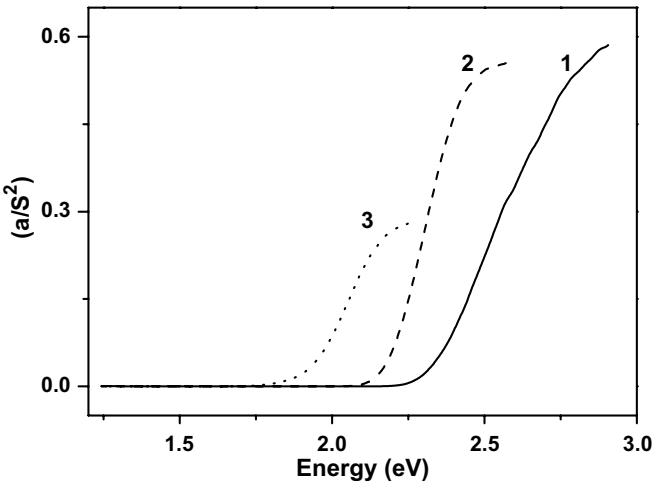


Fig. 4. Optical absorption spectra of compounds **1**–**3** at room temperature.

reflectance, α the coefficient and S the scattering coefficient. The spectra reveal the presence of the optical gaps, as shown in Fig. 4. The band gaps of **1**–**3** were assessed at ca. 2.24, 2.07 and 1.90 eV, respectively, determined as the intersection point by $(\alpha/S)^2 = 0$ in a $(\alpha/S)^2$ vs E plot [30]. These results show that compounds **1**–**3** may be classed as semiconductors.

4. Conclusion

In this paper, we demonstrated new approaches to the construction of three novel heterobimetallic complexes with layered structures. In these complexes, the nest-shaped $\{WS(O)S_3Cu_3\}$ core in **1**, the T-shaped $\{WS_4Cu_3\}$ core in **2** and the saddle-shaped $\{MoS_4Cu_4\}$ subunit in **3** serve as metal nodes whereas the SSS ligands function as multi-dentate linkers. The SSS ligand in **1** or **2** coordinates to five Cu atoms via its exocyclic sulfur and endocyclic nitrogen atoms in an unusual pattern, while in **3**, it acts as a rare tridentate ligand to connect three copper atoms. To the best of our knowledge, these complexes are the first examples of 2D metal-SSS coordination polymers determined by single crystal X-ray diffraction. The novel coordination fashions of SSS ligands observed in **1**–**3** imply that SSS is a very promising linker for the rational design and construction of cluster-based supramolecular compounds. In addition, the title complexes show optical transitions with band gaps varying from 1.90 to 2.24 eV, which indicates that they belong to semiconductors.

Acknowledgments

We thank the State Key Laboratory of Structural Chemistry, Fujian Institute of Research on the Structure of Matter, Chinese Academy of Sciences (CAS), National Basic Research Program of China (973 Program, 2007CB815306), the National Science Foundation of China (20333070 and 20673117) and Young Scientist's Foundation of Fujian Province (2006F3136) for financial support.

Appendix A. Supplementary material

CCDC 624217, 624218 and 624219 contain the supplementary crystallographic data for **1**, **2**, and **3**. These data can be obtained free of charge via http://www.ccdc.cam.ac.uk/conts/retrieving.html, or from the Cambridge Crystallographic Data Centre, 12 Union Road, Cambridge CB2 1EZ, UK; fax: (+44) 1223-336-033; or e-mail: deposit@ccdc.cam.ac.uk. Supplementary data associated with this article can be found, in the online version, at doi:10.1016/j.poly.2007.09.003.

References

[1] (a) E.S. Raper, Coord. Chem. Rev. 61 (1985) 115;
(b) E.S. Raper, Coord. Chem. Rev. 129 (1994) 91;
(c) E.S. Raper, Coord. Chem. Rev. 153 (1996) 199;
(d) E.S. Raper, Coord. Chem. Rev. 165 (1997) 475.
[2] (a) W.P. Su, M.C. Hong, J.B. Weng, R. Cao, S.F. Lu, Angew. Chem., Int. Ed. Engl. 39 (2000) 2911;
(b) W.P. Su, R. Cao, M.C. Hong, J.T. Chen, J.X. Lu, Chem. Commun. (1998) 1389;
(c) T.S. Lobana, Ri. Sharma, Re. Sharma, S. Mehra, A. Castineiras, P. Turner, Inorg. Chem. 44 (2005) 1914;
(d) J.K. Cheng, Y.G. Yao, J. Zhang, Z.J. Li, Z.W. Cai, X.Y. Zhang, Z.N. Chen, Y.B. Chen, Y. Kang, Y.Y. Qin, Y.H. Wen, J. Am. Chem. Soc. 126 (2004) 7796;
(e) J.K. Cheng, Y.B. Chen, L. Wu, J. Zhang, Y.H. Wen, Z.J. Li, Y.G. Yao, Inorg. Chem. 44 (2005) 3386;
(f) D. Li, W.J. Shi, L. Hou, Inorg. Chem. 44 (2005) 3907.
[3] (a) K. Umakoshi, T. Yamasaki, A. Fukuoka, H. Kawano, M. Ichikawa, M. Onishi, Inorg. Chem. 41 (2002) 4093;
(b) Y.J. Zhao, M.C. Hong, Y.C. Liang, R. Cao, W.J. Li, J.B. Weng, S.F. Lu, Chem. Commun. (2001) 1020;
(c) E. Block, G. Ofori-Okai, H. Kang, J. Wu, J. Zubieta, Inorg. Chem. 30 (1991) 4784;
(d) D.J. Rose, Y.D. Chang, Q. Chen, P.B. Kettler, J. Zubieta, Inorg. Chem. 34 (1995) 3973;
(e) E.S. Lang, G.M. Oliveira, G.A. Casagrande, E.M. Vázquez-López, Inorg. Chem. Commun. 6 (2003) 1297.
[4] (a) M. Berardini, J. Brennan, Inorg. Chem. 34 (1995) 6179;
(b) M. Berardini, J. Lee, D. Freedman, J. Lee, T.J. Emge, J.G. Brennan, Inorg. Chem. 36 (1997) 5772.
[5] (a) H. Tannai, K. Tsuge, Y. Sasaki, O. Hatozaki, N. Oyama, J. Chem. Soc., Dalton Trans. (2003) 2353;
(b) J.D.E.T. Wilton-Ely, A. Schier, N.W. Mitzel, H. Schmidbaur, Inorg. Chem. 40 (2001) 6266;
(c) J.D.E.T. Wilton-Ely, A. Schier, H. Schmidbaur, Organometallics 20 (2001) 1895;
(d) H. Tannai, K. Tsuge, Y. Sasaki, Inorg. Chem. 44 (2005) 5206;
(e) M.V. Castano, M.M. Plascencia, A. Macias, J.S. Casas, J. Sordo, E.E. Castellano, J. Chem. Soc., Dalton Trans. (1989) 1409.
[6] (a) S.A.A. Zaidi, D.K. Varshney, J. Inorg. Nucl. Chem. 37 (1975) 1804;
(b) S.A.A. Zaidi, A.S. Farooqi, D.K. Varshney, V. Islam, K.S. Siddiqi, J. Inorg. Nucl. Chem. 39 (1977) 581;
(c) P. Mura, B.G. Olby, S.D. Robinson, Inorg. Chim. Acta 97 (1985) 45;
(d) V.W. Lin Ng, S.L. Kuan, Z.Q. Weng, W.K. Leong, J.J. Vittal, L.L. Koh, G.K. Tan, L.Y. Goh, J. Organomet. Chem. 690 (2005) 2323.
[7] B.C. Tzeng, Y.L. Wu, G.H. Lee, S.M. Peng, New J. Chem. 31 (2007) 199.
[8] (a) C.L. Ma, J.H. Zhang, F. Li, R.F. Zhang, Eur. J. Inorg. Chem. (2004) 2775;
(b) C.L. Ma, F. Li, D.Q. Wang, H.D. Yin, J. Organomet. Chem. 667 (2003) 5;
(c) C.L. Ma, F. Li, Q. Jiang, R.F. Zhang, J. Organomet. Chem. 689 (2004) 96;
(d) K.M. Lo, S.W. Ng, Acta Cryst. E 60 (2004) m715.
[9] (a) W.J. Hunks, M.C. Jennings, R.J. Puddephatt, Inorg. Chem. 38 (1999) 5930;
(b) K. Henke, D.A. Atwood, Inorg. Chem. 37 (1998) 224;
(c) D.R. Corbin, L.C. Francesconi, D.N. Hendrickson, G.D. Stucky, Inorg. Chem. 18 (1979) 3069.
[10] (a) N. Oyama, T. Tatsuma, T. Sato, T. Sotomura, Nature 373 (1995) 598;
(b) R.J. Qu, C.M. Sun, C.N. Ji, C.H. Wang, G.Z. Zhao, D.S. Yu, Polym. Eng. Sci. (2005) 1515;
(c) R.J. Qu, C.M. Sun, C.N. Ji, C.H. Wang, Q. Xu, S.L. Lu, C.F. Li, G. Xu, G.X. Cheng, J. Appl. Polym. Sci. 101 (2006) 631;
(d) P. Ortega, L.R. Vera, M.E. Guzmán, Macromol. Chem. Phys. 198 (1997) 2949.
[11] Z.H. Li, S.W. Du, X.T. Wu, Polyhedron 24 (2005) 2988.

[12] (a) J.L.C. Rowsell, O.M. Yaghi, Angew. Chem., Int. Ed. Engl. 44 (2005) 4670;
(b) O.M. Yaghi, H.L. Li, C. Davis, D. Richardon, T.L. Groy, Acc. Chem. Res. 31 (1998) 474;
(c) N.L. Rosi, J. Eckert, M. Eddaoudi, D.T. Vodark, J. Kim, M. O'Keefe, O.M. Yaghi, Science 300 (2003) 1127;
(d) H.L. Li, M. Addaoudi, M. O'Keefe, O.M. Yaghi, Nature 402 (1999) 276;
(e) J.L.C. Rowsell, R. Andrew Millward, S.P. Sung, O.M. Yaghi, J. Am. Chem. Soc. 126 (2004) 5666.
[13] (a) F.A. Cotton, C. Lin, C.A. Murillo, Acc. Chem. Res. 34 (2001) 759;
(b) S. Jin, F.J. Disalvo, Chem. Mater. 14 (2002) 3448;
(c) B.B. Yan, C.S. Day, A. Lachgar, Chem. Commun. (2004) 2390.
[14] S.C. Xiang, X.T. Wu, J.J. Zhang, R.B. Fu, S.M. Hu, X.D. Zhang, J. Am. Chem. Soc. 127 (2005) 16352.
[15] (a) M.B. Zhang, J. Zhang, S.T. Zheng, G.Y. Yang, Angew. Chem., Int. Ed. Engl. 44 (2005) 1385;
(b) H.Y. An, E.B. Wang, D.R. Xiao, Y.G. Li, Z.M. Su, L. Xu, Angew. Chem., Int. Ed. Engl. 45 (2006) 904;
(c) C. Inman, J.M. Knaust, S.W. Keller, Chem. Commun. (2002) 156;
(d) J.S. Seo, D. Wang, H. Lee, S.I. Jun, J. Oh, Y.J. Jeon, K. Kim, Nature 404 (2000) 982.
[16] (a) C. Zhang, S. Takada, M. Kölzer, T. Matsumoto, K. Tatsumi, Angew. Chem., Int. Ed. Engl. 45 (2006) 3768;
(b) J.P. Lang, H. Kawaguchi, K. Tatsumi, Chem. Commun. (1999) 2315;
(c) J.M. Manoli, C. Potvin, F. Sécheresse, S. Marzak, Inorg. Chim. Acta 150 (1988) 257;
(d) C.P. Cui, S.M. Hu, J.J. Zhang, W.X. Du, X.T. Wu, Inorg. Chem. Commun. 8 (2005) 704.
[17] (a) Q.F. Zhang, Y.Y. Niu, W.H. Leung, Y.L. Song, I.D. Williams, X.Q. Xin, Chem. Commun. (2001) 1126;
(b) J.P. Lang, Q.F. Xu, R.X. Yuan, B.F. Abrahams, Angew. Chem., Int. Ed. Engl. 43 (2004) 4741;
(c) K. Liang, H.G. Zheng, Y.L. Song, M.F. Lappert, Y.H. Li, X.Q. Xin, Z.X. Huang, J.T. Chen, S.F. Lu, Angew. Chem., Int. Ed. Engl. 43 (2004) 5776;
(d) C.Y. Zhang, K. Liang, Q.Y. Chen, H.G. Zheng, X.Q. Xin, Chin. J. Inorg. Chem. 21 (2005) 783.
[18] (a) P. Lin, W. Clegg, R.W. Harrington, R.A. Henderson, A.J. Fletcher, J. Bell, K.M. Thomas, Inorg. Chem. 45 (2006) 4284;
(b) Y.V. Mironov, V.E. Fedorov, H. Bang, S.T. Kim, Eur. J. Inorg. Chem. (2006) 553;
(c) H.D. Selby, B.K. Roland, Z.P. Zheng, Acc. Chem. Res. 36 (2003) 933;
(d) N.F. Zheng, X.H. Bu, P.Y. Feng, J. Am. Chem. Soc. 124 (2002) 9688;
(e) J.L. Xie, X.H. Bu, N.F. Zheng, P.Y. Feng, Chem. Commun. (2005) 4916.
[19] (a) L. Song, J.R. Li, P. Lin, Z.H. Li, T. Li, S.W. Du, X.T. Wu, Inorg. Chem. 45 (2006) 10155;
(b) Z.H. Li, S.W. Du, X.T. Wu, Inorg. Chem. Commun. 9 (2006) 79;
(c) Z.H. Li, S.W. Du, X.T. Wu, Inorg. Chem. 43 (2004) 4776;
(d) J.R. Li, S.W. Du, X.T. Wu, J. Cluster Sci. 16 (2005) 489.
[20] (a) J.W. McDonald, G.D. Friessen, L.D. Rosenheim, W.E. Newton, Inorg. Chim. Acta 72 (1983) 205;
(b) S.F. Gheller, T.W. Hambley, J.R. Rodgers, R.T.C. Brownlee, M.J. O'connor, M.R. Snow, A.G. Wedd, Inorg. Chem. 23 (1984) 2519.
[21] (a) G.M. Sheldrick, SHELXS-97 Program for X-ray Crystal Structure Solution, University of Göttingen, Germany, 1997;
(b) G.M. Sheldrick, SHELXL-97 Program for X-ray Crystal Structure Refinement, University of Göttingen, Germany, 1997.
[22] J. Guo, T.L. Sheng, W.J. Zhang, X.T. Wu, P. Lin, Q.M. Wang, J.X. Lu, Inorg. Chem. 37 (1998) 3689.
[23] (a) A. Müller, M. Dartmann, C. Römer, W. Clegg, G.M. Sheldrick, Angew. Chem., Int. Ed. Engl. 20 (1981) 1060;
(b) H.W. Hou, H.G. Zheng, H.G. Ang, Y.T. Fan, M.K.M. Low, Y. Zhu, W.L. Wang, X.Q. Xin, W. Ji, W.T. Wong, J. Chem. Soc., Dalton Trans. (1999) 2953;
(c) J.P. Lang, C.M. Jiao, S.B. Qiao, W.H. Zhang, B.F. Abrahams, Inorg. Chem. 44 (2005) 3664;
(d) C. Zhang, Y.L. Song, Y. Xu, H. Fun, G.Y. Fang, Y.X. Wang, X.Q. Xin, J. Chem. Soc., Dalton Trans. (2000) 2823;
(e) S.B. Qiao, C.M. Jiao, Q.F. Xu, Y. Zhang, B.L. Li, J.P. Lang, Acta Cryst. C 59 (2003) m465.
[24] (a) S.W. Du, N.Y. Zhu, P.C. Chen, X.T. Wu, J.X. Lu, Polyhedron 11 (1992) 109;
(b) P. Lin, L. Smyth, A. Waldram, R.A. Henderson, J. Chem. Soc., Dalton Trans. (2005) 3173;
(c) J.P. Lang, Q.F. Xu, W. Ji, H.I. Elim, K. Tatsumi, Eur. J. Inorg. Chem. (2004) 86;
(d) Q.F. Xu, J.X. Chen, W.H. Zhang, Z.G. Ren, H.X. Li, Y. Zhang, J.P. Lang, Inorg. Chem. 45 (2006) 4055.
[25] Z.H. Li, S.W. Du, X.T. Wu, J. Chem. Soc., Dalton Trans. (2004) 2438.
[26] L. Pauling, The Nature of the Chemical Bond, third ed., Cornell University Press, Ithaca, New York, 1960, p. 224.
[27] (a) J.R. Nicholson, A.C. Flood, C.D. Garner, W. Clegg, Chem. Commun. (1983) 1179;
(b) J.P. Lang, K. Tatsumi, Inorg. Chem. 37 (1998) 6308;
(c) F. Sécheresse, S. Bernés, F. Robert, Y. Jeannin, J. Chem. Soc., Dalton Trans. (1991) 2875;
(d) N.R. Brooks, W. Clegg, M.H. Sadr, M. Esm-Hosseini, R. Yavari, Acta Cryst. E 60 (2004) m204.
[28] N.G. Fumanova, Y.T. Strchkov, E.M. Rokhlina, D.N. Kravtsov, J. Struct. Chem. Engl. Trans. 21 (1980) 766.
[29] (a) G. Kotüm, Reflectance Spectroscopy, Springer-Verlag, New York, 1969;
(b) W.W. Wendlandt, H.G. Hecht, Reflectance Spectroscopy, Interscience Publishers, New York, 1966.
[30] G. Cao, L.K. Rabenberg, C.M. Nunn, T.E. Mallouk, Chem. Mater. 3 (1991) 149.

Available online at www.sciencedirect.com
ScienceDirect
Polyhedron 27 (2008) 241–248
POLYHEDRON
www.elsevier.com/locate/poly

Reactivity of M(en)Cl_2 (M = Pd^{II}/Pt^{II}, en = 1,2-diaminoethane) with *N*,*N*′-bis(salicylidene)-*p*-phenylenediamine: Binding with hexafluorobenzene

Niraj Kumari, Rishikesh Prajapati, Lallan Mishra *

Department of Chemistry, Faculty of Science, Banaras Hindu University, Varanasi 221 005, India

Received 2 August 2007; accepted 10 September 2007
Available online 29 October 2007

Abstract

Schiff base *N*,*N*′-bis(salicylidene)-*p*-phenylenediamine (LH_2) complexed with Pt(en)Cl_2 and Pd(en)Cl_2 provided [Pt(en)L]$_2 \cdot 4PF_6$ (**1**) and Pd(Salen) (**2**) (Salen = *N*,*N*′-bis(salicylidene)-ethylenediamine), respectively, which were characterized by their elemental analysis, spectroscopic data and X-ray data. A solid complex obtained by the reaction of hexafluorobenzene (hfb) with the representative complex **1** has been isolated and characterized as **3** (**1** · hfb) using UV–Vis, NMR (^1H, ^{13}C and ^{19}F) data. A solid complex of hfb with a reported Zn-cyclophane **4** has also been prepared and characterized **5** (**4** · hfb) for comparison with complex **3**. The association of hfb with **1** and **4** has also been monitored using UV–Vis and luminescence data.
© 2007 Elsevier Ltd. All rights reserved.

Keywords: *N*,*N*′-Bis(salicylidene)-*p*-phenylenediamine; Pt^{II} based cyclophane; X-ray study; NMR spectra; Association constant

1. Introduction

Supramolecular chemistry involving self assembly, inclusion phenomena, molecular recognition and non-covalent interactions are at the forefront of modern chemistry. These phenomena are commonly accessed by various macrocycles and related assemblies. Diverse macrocycles such as crown ethers, cyclophanes, cyclodextrins, calixarenes, cryptands, spherands, clathrates, cryptophanes and molecular clefts as receptors are well known. The majority of these macrocycles are reasonably flexible organic molecules that preferentially interact with cationic guests [1–10]. Conformationally, more rigid macrocycles incorporating metal centres have emerged as interesting members of supramolecular assemblies [11]. Molecules containing larger cavities bearing several functional groups open the possibility of the encapsulation of various guest molecules. However, among intermolecular interactions, those involving organic fluorine have also been a field of current interest [12]. Several reports in the literature subscribe to the conclusion that organic fluorine hardly accepts hydrogen bonds and does not contribute to crystal packing [13,14]. We, therefore, thought to interact some fluorine containing moieties, especially a strong electron acceptor molecule like hexafluorobenzene, with newly synthesized metallocyclophanes and to evaluate their association behaviour. In this context, the tetradentate Schiff base *N*,*N*′-bis(salicylidene)-*p*-phenylenediamine was chosen for its condensation with well protected Pd^{II} and Pt^{II} metal centres. The association of hfb with a representative complex of Pt^{II}-based cyclophane **1** has been monitored using spectroscopic techniques. Its association behaviour has also been compared with the earlier reported Zn^{II} cyclophane [15].

2. Experimental

2.1. Materials and methods

$PdCl_2$ and K_2PtCl_4 purchased from Sigma–Aldrich were converted into Pd(en)Cl_2 and Pt(en)Cl_2 using the reported

* Corresponding author. Tel.: +91 542 2307321; fax: +91 542 2368174.
E-mail address: lmishrabhu@yahoo.co.in (L. Mishra).

0277-5387/$ - see front matter © 2007 Elsevier Ltd. All rights reserved.
doi:10.1016/j.poly.2007.09.017

procedures [16,17]. Elemental analysis and mass measurements were carried on a Carbo-Erba elemental analyzer 1108 and a JEOL SX-102 mass spectrometer, respectively. IR spectra were recorded as KBr pellets on a JASCO FT-IR 5300 spectrometer and ^{1}H NMR spectra were recorded on a JEOL AL 300 MHZ spectrometer using $CDCl_3$ and DMSO-d_6 as solvents and TMS as an internal reference. ^{19}F NMR spectra are recorded on a JEOL AL 300 MHz spectrometer using DMSO-d_6 as the solvent and trifluoroacetic acid as an external reference at 282.5 MHz. UV–Vis and luminescence measurements were made in the range 200–700 nm on a Shimadzu UV-1601 spectrometer and Perkin–Elmer LS-45 Luminescence spectrometer, respectively, and TGA-DTA measurements have been performed on a Perkin–Elmer Pyris diamond TG-DTA instrument at a heating rate of 20 °C/min in the temperature range 50–400 °C.

2.2. Preparation of *N,N′-bis(salicylidene)-p-phenylenediamine (LH$_2$)*

N,N′-Bis(salicylidene)-*p*-phenylenediamine (LH_2) was prepared and characterized using a reported procedure [18].

2.3. Preparation of *Pt^{II} complex 1*

A solution of Pt(en)Cl_2 (0.672 g, 2.0 mmol) in DMF (10 ml) was added to a solution of LH_2 (0.630 g, 2.0 mmol) in DMF followed by the addition of Et_3N (~5.0 mmol) while stirring. The resulting mixture was stirred whilst heating on a water bath for 5 h. The solid product obtained after the addition of an aqueous solution of NH_4PF_6 was filtered, washed with distilled water and methanol followed by diethyl ether and recrystallised with a DMSO/MeOH mixture and finally dried in vacuo as $[Pt(en)LH_2]_2 \cdot 4PF_6$ (**1**). However, crystals suitable for single crystal X-ray crystallography could not be obtained. Yield: 35%. m.p.: >230 °C (dec). Elemental *Anal.* Calc. for $C_{44}H_{48}N_8O_4P_4F_{24}Pt_2$: C, 30.66; H, 2.78; N, 6.50. Found: C, 30.78; H, 3.14; N, 6.72%. IR (KBr pellet, cm^{-1}): 1633 ($\nu_{HC=N}$), 1264 ($\nu_{O-H\ phenolic}$), 2924 ($\nu_{C-H\ phenyl}$), 846 (ν_{PF6}). ^{1}H NMR (DMSO-d_6, 300 MHz, ppm): δ 13.1 (s, 4H, OH), 9.0 (s, 4H, HC=N), 7.5 (m, 20H, aromatic), 7.0 (m, 8H, NH_2), 6.5 (m, 4H, aromatic), 3.6 (s, 4H, N–CH_2), 3.5 (s, 4H, N–CH_2). FAB-MS: *m/z*: 1722 $[M]^+$, 1577 $[M-PF_6]$, 1142 $[M-4PF_6]$. UV–Vis (DMSO, 10^{-4} M): $\lambda_{max/(nm)}$ (ε_{max} 10^4 M^{-1} cm^{-1}) 339 (1.69), 354 (1.68), 439 (0.43); Emission excited at λ 340 nm (DMSO, 10^{-4} M): $\lambda_{max\,(nm)}$ (intensity in a.u.) 493 (459). Conductivity: Λ_m (DMSO, 10^{-4} M) 360 Ω^{-1} cm^2 mol^{-1}.

2.4. Preparation of *Pd^{II} complex 2*

Pd^{II} complex **2** has also been prepared using a method similar to that adopted for complex **1** by the addition of a solution of Pd(en)Cl_2 (0.472 g, 2.0 mmol) in DMF (10 ml) to a solution of LH_2 (0.630 g, 2.0 mmol) in DMF containing Et_3N (~5.0 mmol) while stirring. The product, after heating on a sand bath for 4 h with stirring, was isolated after the addition of H_2O to the reaction mixture. It was then filtered and washed with distilled water and methanol followed by diethyl ether. The product was then recrystallized in dichloromethane and characterized. Yield: 40%. m.p.: >230 °C. Elemental *Anal.* Calc. for $C_{16}H_{14}N_2O_2Pd$: C, 51.56; H, 3.60; N, 8.56. Found: C, 50.56; H, 3.62; N, 8.03%. IR (KBr pellet, cm^{-1}): 1622 ($\nu_{HC=N}$), 2934 ($\nu_{C-H\ phenyl}$). ^{1}H NMR (DMSO-d_6, 300 MHz, ppm): δ 8.5 (s, 2H, HC=N), 7.4 (m, 8H, aromatic), 6.5–6.8 (m, 8H, aromatic), 4.0 (s, 4H, N–CH_2). FAB-MS: *m/z*: 372 $[M]^+$. UV–Vis (DMSO, 10^{-4} M): $\lambda_{max/(nm)}$ (ε_{max} 10^4 M^{-1} cm^{-1}) 403 (1.94). Emission: non-emissive. Conductivity: Λ_m (DMSO, 10^{-4} M) 11.4 Ω^{-1} cm^2 mol^{-1}.

This indicates that the Pd^{II} compound did not follow the same reaction pattern as is followed by the Pt^{II} compound. Instead it turned out to be a neutral Pd^{II}(Salen) [Salen = *N,N′*-bis(salicylidene)-ethylenediamine] complex.

2.5. Preparation of complex *3 (1 · hfb)*

The adduct of complex **1** with hexafluorobenzene was prepared by the dropwise addition of a methanolic solution of hfb to the solution of complex **1** in minimum amount of DMSO. The resulting solution was stirred for 4 h and cooled in a refrigerator for 24 h. After the addition of an aqueous solution of NH_4PF_6, the solid thus obtained was filtered and washed with methanol followed by diethyl ether. It was further purified by dissolving it in a minimum amount of DMSO followed by the addition of excess methanol. Finally, the crystallized solid was dried in vacuo and characterized as $[Pt(en)LH_2]_2 \cdot$ hfb **3**. Yield 30%; m.p.: >230 °C. Elemental *Anal.* Calc. for $C_{50}H_{48}N_8O_4P_4F_{30}Pt_2$: C, 31.44; H, 2.51; N, 5.87. Found: C, 31.78; H, 2.55; N, 5.63%. IR (KBr pellet, cm^{-1}): 1622 ($\nu_{CH=N}$), 1254 (ν_{OH}), 844 (ν_{PF6}). ^{1}H NMR (DMSO-d_6, 300 MHz, ppm): δ 13.04 (s, OH), 9.02 (s, HC=N), 7.6–7.4 (m, aromatic), 6.9 (m, aromatic + NH_2), 6.61 (m, aromatic), 3.6 (s, N–CH_2), 3.5 (s, 4H, N–CH_2), ^{19}F NMR (DMSO-d_6, 282.5 MHz, ppm): δ −71 (s; PF_6), 162.35 (s; Ar–F). FAB-MS: *m/z*: 1908 $[M]^+$, 1722 $[M-hfb]^+$, 1619 $[M-2PF_6+1]^+$, 1142 $[M-hfb-4PF_6]^+$, 1022 $[M-hfb-4PF_6-2en]^+$. UV/Vis (DMSO, 10^{-4} M): $\lambda_{max/nm}$ (ε_{max} 10^4 M^{-1} cm^{-1}) 343 (1.41), 358 (1.49), 258 (4.27). Emission excited at λ 340 nm (DMSO, 10^{-4} M): $\lambda_{max\,(nm)}$ (intensity in a.u.) = 503.39 (362). Conductivity: Λ_m (DMSO 10^{-4} M) 370 Ω^{-1} cm^2 mol^{-1}.

2.6. Preparation of *Zn^{II} complex 4*

The metallocyclophane $[Zn(bpy)L]_2$ (bpy = 2,2′-bipyridine) **4** was prepared and characterized using the reported procedure [15].

2.7. Preparation of complex 5 (4 · hfb)

The adduct of complex **4** with hfb was also prepared using a similar method as followed for **3** by the addition of a methanolic solution of excess hfb to the solution of complex **4** in minimum amount of DMSO. The resulting solution was stirred for 4 h then cooled in a refrigerator for 24 h. The solid thus obtained was filtered and washed with methanol followed by diethyl ether. It was further purified by dissolving in a minimum amount of DMSO followed by the addition of excess methanol. Finally, the crystallized solid was dried in vacuo and characterized as [**4** · hfb]. Yield: 36%. m.p.: >230 °C. Elemental *Anal*. Calc. (%) for $C_{66}H_{44}N_8O_4Zn_2F_6$: C, 63.1; H, 3.5; N, 8.9. Found: C, 63.4; H, 3.4; N, 8.6%. IR (KBr pellet, cm^{-1}): 1601 ($\nu_{CH=N}$), 1531 (ν_{phenyl}), 1149 (ν_{hfb}). ^1H NMR (DMSO-d_6, 300 MHz, ppm): δ 8.9 (s, 4H, HC=N), 6.4–6.7 (m, 12H, bpy), 7.3–7.5 (m, 12H, phenyl), 6.9–7.1 (s, 4H, phenyl). ^{19}F NMR (DMSO d_6, 282.5 MHz, ppm): δ 162.47 (s, 6F, Ar–F). FAB-MS: *m/z*: 1256 $[M]^+$, 1071 $[M-hfb+1]^+$, 1036 $[M-hfb-2OH]^+$, 1018 $[M-hfb-3OH+1]^+$. UV/Vis (DMSO, 10^{-4} M): $\lambda_{max/nm}$ (ε_{max} 10^4 M^{-1} cm^{-1}) 396 (1.59), 379 (2.40), 328 (1.41). Emission excited at λ 396 nm (DMSO, 10^{-4} M): $\lambda_{max\,(nm)}$ (intensity in a.u.) 532 (150). Conductivity: Λ_m (DMSO, 10^{-4} M) 5 Ω^{-1} cm^2 mol^{-1}.

3. Results and discussion

The complexes are soluble in DMF and DMSO, complex **1** and its adduct **3** show electrolytic behaviour (1:4) in DMSO (10^{-3} M), whereas complexes **2**,**4** and **5** are found to be non-electrolytic in nature [19].

In the infrared spectra, the peak observed at 1610 cm^{-1} (free ligand), assigned to ν(CH=N), shifted to 1633 cm^{-1} (complex **1**). This indicates that the HC=N groups had coordinated during complex formation. The peak observed at 1282 cm^{-1}, assigned to νOH, (free ligand) [18] remains constant in the spectrum of its complex and shows the presence of free OH groups. This observation is further supported by its ^1H NMR spectrum, which shows a peak at δ 13.1 ppm assigned to OH protons. Additionally, in the IR spectrum of adduct **3**, peaks due to νHC=N are observed at 1622 cm^{-1} as compared to 1633 cm^{-1} in complex **1**, showing that the HC=N groups are involved in the association with hexafluorobenzene.

Additionally, the peaks of the phenyl ring protons in the ^1H NMR spectrum of adduct **3** are broadened as compared to the peaks in the spectrum of complex **1**, in which they are sharp (Fig. 1). The broadening of aromatic protons could occur due to its restricted rotation on the NMR time-scale upon the inclusion of hexafluorobenzene in the cavity of complex **1**. This behaviour is consistent with an earlier report [20] on the inclusion complexes.

The UV/Vis spectra recorded in DMSO solution (10^{-4} M) showed that the single peak observed at λ_{max} 261 nm in the spectrum of free hfb is enhanced to twice the intensity in the spectrum of its adduct **3** at λ_{max} 260 nm. Additional peaks observed at λ_{max} 340, 356 and 378 nm in the spectrum of complex **1** are assigned to intra-ligand transitions, whereas the peak at λ_{max} 439 nm arises from a MLCT transition. In the adduct of **1** with hfb, most of the peaks, including that of the MLCT transition, are blue shifted. This indicates that hfb is bound with complex **1** internally.

The composition of complex **2**, assigned as Pd(Salen) on the basis of its elemental analysis and mass measurements, is further substantiated by its ^1H NMR spectrum which shows the presence of N–CH_2–CH_2-N and HC=N protons at $\delta = 4.0$ (s, 4H) and 8.5 (s, 2H) ppm, respectively. However, the disappearance of the signal of the phenolic OH proton of the free ligand shows that the deprotonated OH groups had coordinated with the Pd^{II} ion. To get additional support for its structure, it has been characterized by single crystal X-ray crystallography.

Suitable X-ray quality crystals of complex **2** were grown from a DMSO/MeOH solvent mixture at room temperature, and X-ray crystallographic data are recorded by mounting a single-crystal of sample **2** (0.26 × 0.18 ×

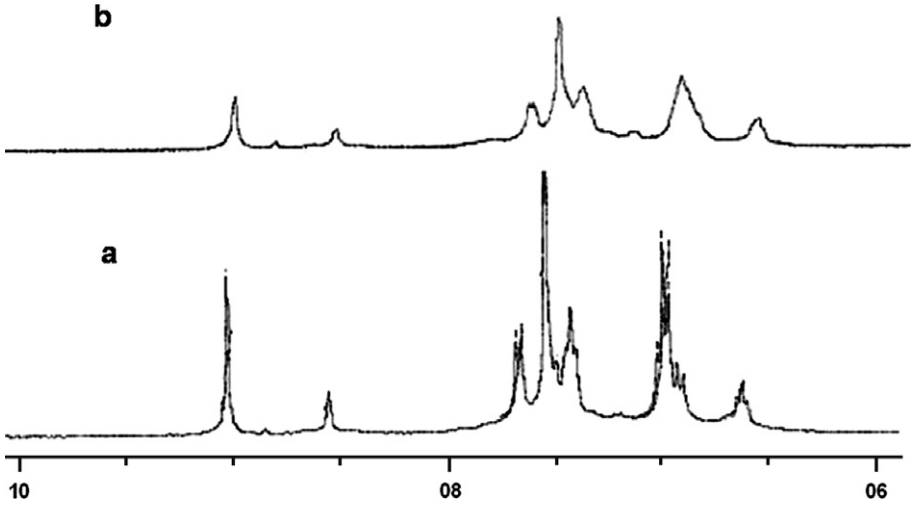


Fig. 1. Comparison of ^1H NMR spectra of complex **1** (a), and complex **3** (b) in the aromatic region.

Table 1
Crystal data and structure refinement for complex **2**

Empirical formula	$C_{16}H_{14}N_2O_2Pd$
Formula weight	372.69
Temperature (K)	293(2)
Wavelength (Å)	0.71073
Crystal system, space group	monoclinic, $P2_1/c$
Unit cell dimensions	
a (Å)	13.795(2)
b (Å)	7.252(10)
c (Å)	13.982(2
α (°)	90
β (°)	105.55(2)
γ (°)	90
Volume (Å^3)	1347.77(3)
Z, D_{calc} (Mg/m^3)	4, 1.837
Absorption coefficient (mm^{-1})	1.382
Reflections collected/unique [R_{int}]	21921/4494 [0.0268]
Data/restraints/parameters	4494/0/191
Goodness-of-fit on F^2	0.876
Final R indices [$I > 2\sigma(I)$]	$R_1 = 0.0312$, $wR_2 = 0.0909$
R indices (all data)	$R_1 = 0.0414$, $wR_2 = 0.1107$

Table 2
Selected bond lengths (Å) and bond angles (°) for complex **2**

Pd(1)–N(1)	1.952(2)
Pd(1)–N(2)	1.957(2)
Pd(1)–O(1)	1.9981(16)
Pd(1)–O(2)	2.0087(16)
O(1)–C(1)	1.311(3)
O(2)–C(16)	1.309(3)
N(1)–C(7)	1.286(3)
N(1)–C(8)	1.481(3)
N(2)–C(10)	1.285(3)
N(2)–C(9)	1.474(3)
N(1)–Pd(1)–N(2)	84.23(9)
N(1)–Pd(1)–O(1)	93.91(8)
N(2)–Pd(1)–O(1)	177.87(8)
N(1)–Pd(1)–O(2)	177.72(8)
N(2)–Pd(1)–O(2)	93.53(8)
O(1)–Pd(1)–O(2)	88.33(7)

0.16) mm^3 on a glass fiber. An Oxford diffraction XCALIBUR-S CCD area detector diffractometer equipped with an LN-2 low-temperature attachment was used for the cell determination and intensity data collection. Appropriate empirical absorption corrections using the programs multi-scan were applied. Monochromated Mo Kα radiation ($\lambda = 0.71073$ Å) was used for the measurements.

Important crystallographic data and the structure refinement details are listed in Table 1, selected bond lengths and bond angles are summarized in Table 2, and its ORTEP view is shown in Fig. 2. Crystallographic data shows that the Pd–N distance, observed to be about 1.95 Å, is shorter than the reported [20] value of 2.1 Å. The N–Pd–N bond angle of 84.2° is a bit smaller than that of a square (90°). Thus, the geometry around the Pd^{II} centre is a little deviated from the normal square planar. In other words, although, the molecule's shape is indeed that of a square, it is not planar. The deviation from planarity is about 3 Å. It is important to note that N1–C8–C9–N2 is largely deviated by 34.5°, which is quite logical as it contains a flexible alkyl chain. The deviation from planarity is also observed in the chelate ring but to a smaller extent (5 Å). It shows that this deviation is again caused by the flexible alkyl chain.

Thus, the formation of Pd(Salen) shows that upon the addition of Pd(en)Cl$_2$ to a solution of LH$_2$, the ligand rearranges itself into the formation of an imine linkage between ethylenediamine appended with Pd^{II} and salicylaldehyde (most likely formed due to hydrolysis of the imine groups followed by oxidation) as depicted in Scheme 1. The contribution of ethylenediamine in this type of condensation is further supported by the condensation of [Pd(bpy)Cl$_2$] with the Schiff base, which like the Pt^{II} complex, led to a (2 + 2) condensation instead of the formation of Pd(Salen).

As mentioned above, upon the complexation of Pt(en)Cl$_2$ with LH$_2$, a (2 + 2) condensation between the two components occurred and it resulted in the formation of a metallocyclophane, as reported earlier for the Zn(bpy) system [15].

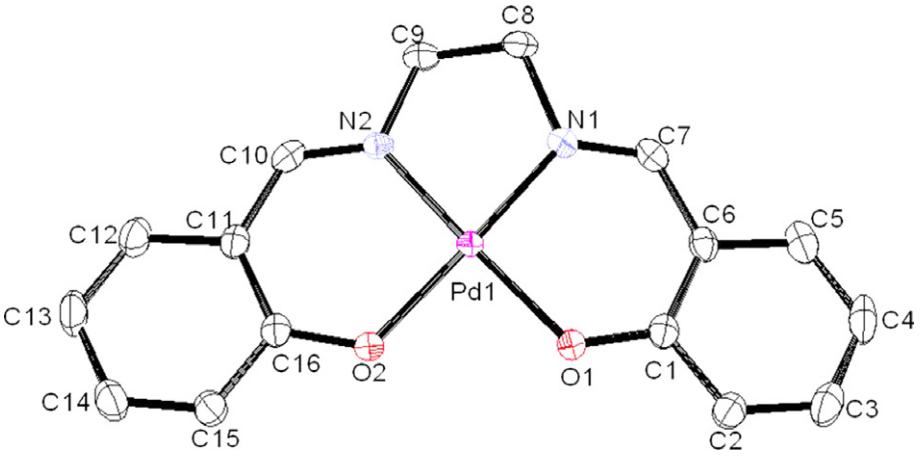
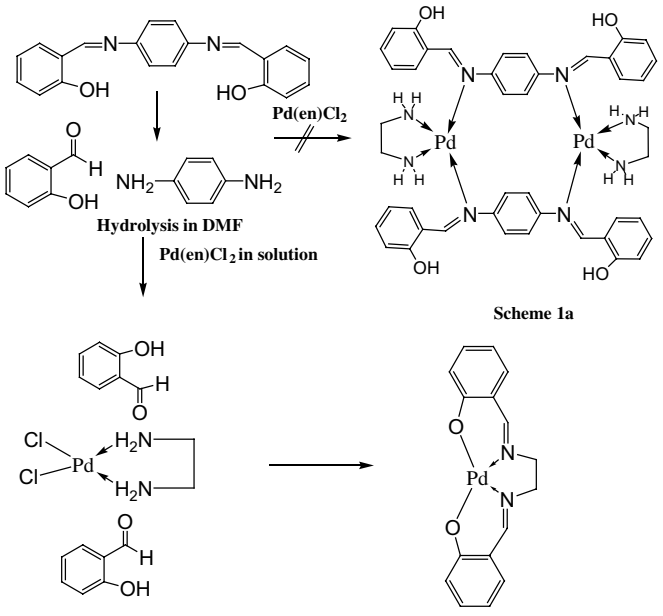


Fig. 2. ORTEP diagram of complex **2**. Thermal ellipsoids are at 50% probability.



Scheme 1.

Although the reason for this difference in reactivity of Pd^{II} and Pt^{II} with the Schiff base cannot be understood accurately, it may be considered in view of the stronger Pt–N=C bond as compared to the Pd–N=C bond [21]. Theoretical calculations also support that the relativistic bond stabilization is stronger for third-row transition metal complexes (Pt) than for second-row transition metal complexes (Pd) [22].

The crystal packing pattern of complex **2** in the solid state is shown in Fig. 4. The squares are stacked along the '*b*'-axis, resulting in long channel like cavities of ~25 Å diameter as shown by the centroid–centroid perpendicular distance ~3.3 Å and parallel distance of 8.2 Å. It is worth mentioning that π–π stacking between the phenyl rings produces a near contact between the two Pd centres, being separated by 3.206 Å, though the presence of a Pd–Pd bond between the metal centres has been ruled out in view of the literature report [23,24]. Furthermore, it is quite interesting to note that a cavity as desired from Scheme 1a could be looked upon from this stacking pattern. Thus, the stacking pattern of the complex as shown in Fig. 3 prompted us to make binding studies of phenol similar to that reported earlier with a Zn^{II} containing cyclophane. Since this structure is obtained by π–π stacking interactions, the association of phenol with this compound is considered to be weaker and in fact its binding constant [15] gave the value $K = 1.6 \times 10^4$, which is lower than that reported for the Zn^{II} analogue ($K = 7.5 \times 10^4$) [15].

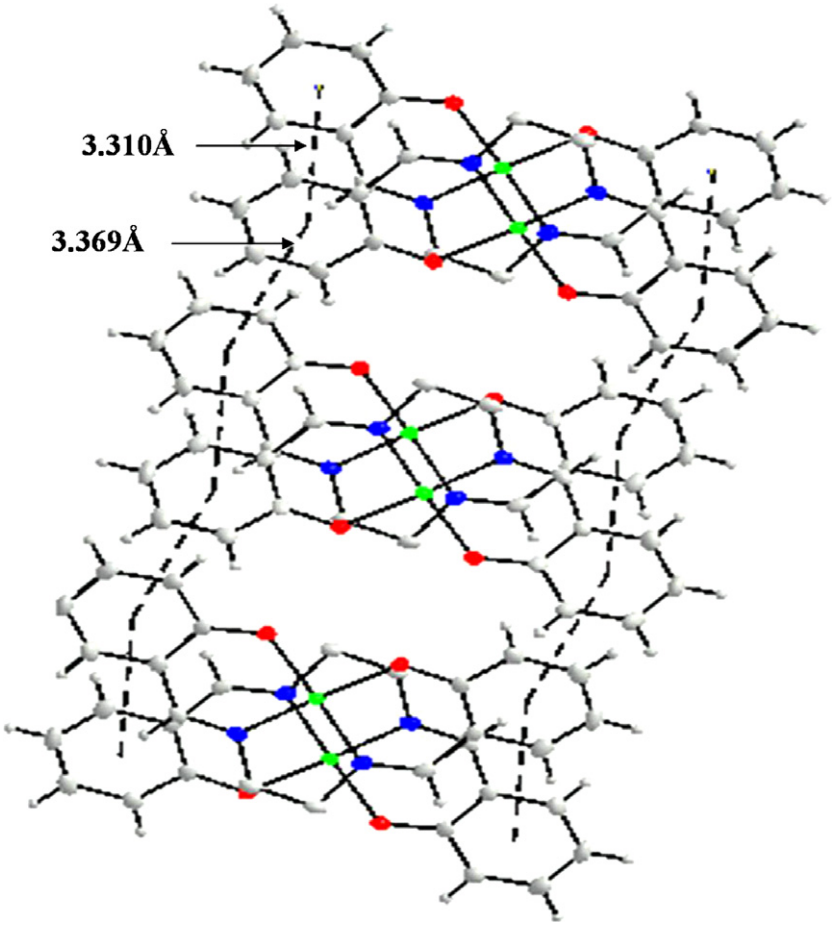


Fig. 3. Stacking pattern in complex **2**.

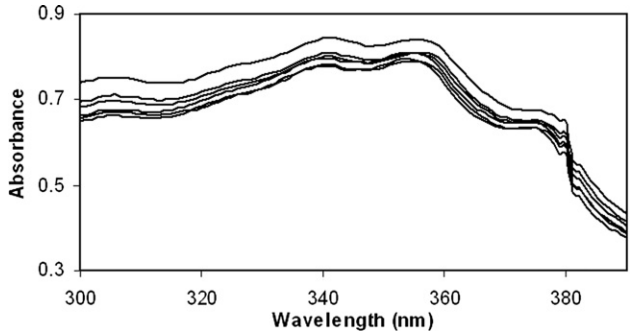


Fig. 4. UV/Vis absorption spectrum of **1** titrated against hexafluorobenzene.

Since the formation constant K_c is an important parameter that measures the extent of inclusion of a guest in a host complex, hexafluorobenzene being electron deficient in nature was considered as a novel guest. The selectivity of an electron acceptor molecule like hfb has been made in view of the possibility of the electron rich nature of the cavity of the macrocyclic frame due to the attachment of electron donor groups like 1,2-diaminoethanes to the metal centres as well as the presence of phenyl rings as electron sinks in the skeleton of the metallocyclophane. Thus, the binding of hexafluorobenzene with the representative complex **1** has been monitored by UV–Vis spectral data (Fig. 4). The variation of spectral pattern obtained by the addition of increasing concentrations of hexafluorobenzene (2×10^{-5}–1×10^{-4} M) to a fixed concentration of the complex (5×10^{-5} M) monitored at λ 340 nm is shown in Fig. 4. The formation constant as calculated using the Benesi-Hilde brand (BH) equation [15] is found to be 3.17×10^{4} M^{-1}.

To support the inclusion of hexafluorobenzene inside the cavity of the complex, the ^{19}F NMR spectrum of complex **3** was recorded. A ^{19}F signal observed at δ −162.35 ppm is found to be deshielded as compared to the signal observed at δ −161.54 for free hexafluorobenzene, as depicted in Fig. 5. It is worth mentioning that the observed difference in ^{19}F chemical shifts between the included hexafluorobenzene and the free hexafluorobenzene, being 0.8 ppm, is almost two orders higher than the digital resolution 0.01 ppm (acquisition time = 0.328 s). Thus, the observed difference in chemical shifts is definitely significant. It is further clear that upon heating, the ^{19}F signal shifts towards high field (tending towards the ^{19}F signal of free hfb). Additionally, upon heating, the number of ^{13}C peaks of the phenyl rings also get enhanced. This could happen only when hbf is included in the cavity since upon heating hfb would tend to come out of the cavity and get closer to the phenyl ring of ligand skeleton. A variable temperature ^{1}H NMR spectrum of adduct **3** was also recorded, and it shows extensive splitting of the phenyl protons in the temperature range 130–140 °C. For further support, ^{19}F VT NMR of adduct **3** was also recorded from room temperature 27.7 to 70 °C. The variable temperature ^{19}F NMR spectrum shows a substantial decrease in the change of chemical shift as compared to the position of the ^{19}F sig-

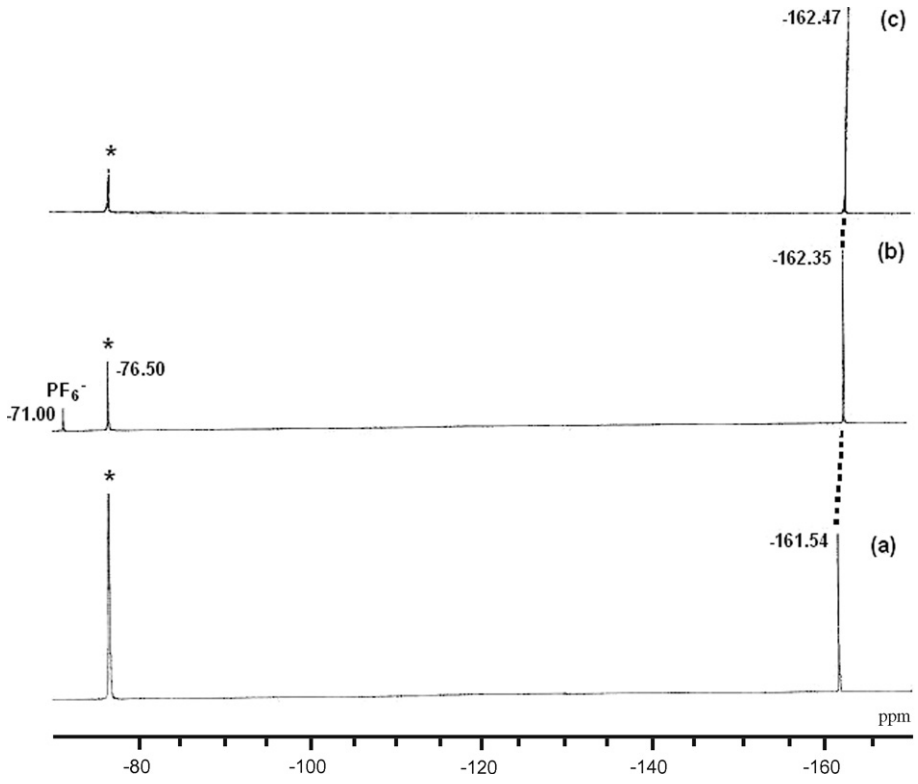


Fig. 5. Comparison of ^{19}F NMR spectra of free hexafluorobenzene (a); complex **3** (b) and complex **5** (c). The signal labelled with an asterisk represents trifluoroacetic acid (external reference).

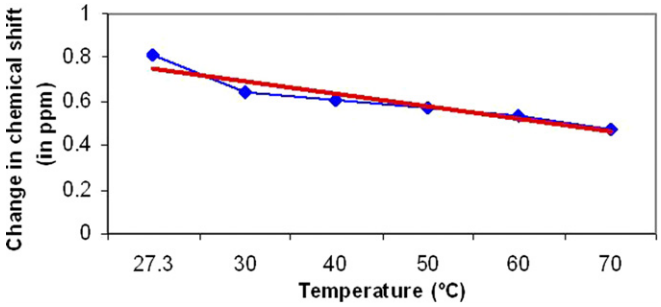


Fig. 6. Change in chemical shift in ^{19}F VT NMR spectra of complex **3** (blue), trendline (red). (For interpretation of the references to colour in this figure legend, the reader is referred to the web version of this article.)

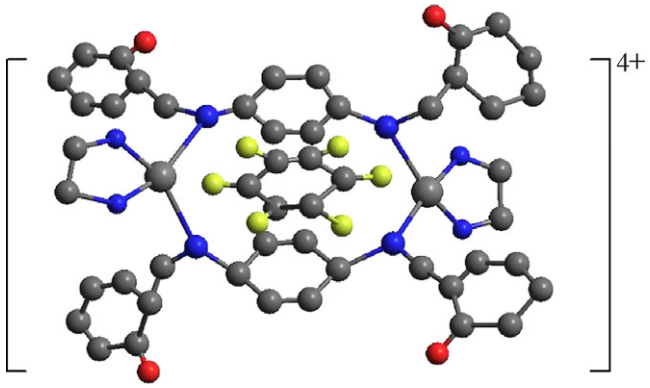


Fig. 7. Ball and stick model showing the fitting of one hfb molecule within the cavity of complex **1**. All H atoms have been omitted for clarity.

nal of free hfb with an increase in temperature, as depicted in Fig. 6.

Thus, the ^{1}H, ^{13}C and ^{19}F NMR spectral pattern of the adduct show that the guest is included in the cavity generated by the metallocyclophane **1**, consistent with the earlier report. Since suitable crystals could not be grown, a model of such host–guest binding was tried and is depicted in Fig. 7, which shows that hfb is accommodated by the cavity formed by metallocyclophane.

In order to compare the association of hfb with metallocyclophane **1**, hfb has also been allowed to interact with the earlier reported metallocyclophane **4** and the association constant thus evaluated was found to be 2.52×10^4 M^{-1}. An ^{19}F NMR spectrum of its adduct **5** along with the spectrum of free hfb is also shown in Fig. 5.

Thus, the results indicate that Pt^{II}–cyclophane derived from the Schiff base (LH_2) binds hexafluorobenzene more strongly compared to the earlier reported Zn^{II}–cyclophane.

To get evidence of guest mobility and framework stability, thermal gravimetric analysis of adduct **3** has been made and the corresponding thermogram is shown in Fig. 8. Crystalline sample **3** (2.128 mg) was heated at a constant rate of 20 °C min^{-1} in a N_2 atmosphere with 180 ml/min flow rate from 50 to 400 °C. Three weight-loss steps were observed: the first, corresponding to 9.39%, occurred between 50 and 130 °C, which could be attributed to the loss of the guest molecules (calculated 9.74%). This is further supported by its DTA thermogram which shows an endothermic peak for this temperature range, indicating that a phase transition occurs most likely due to the removal of hexafluorobenzene (guest) as reported for the metal organic frameworks [25]. The second weight loss of 30.39% between 200 and 240 °C is due to the removal of four counter PF_6^- anions (30.54%) in view of the decomposition temperature of complex **1**, i.e. >230 °C. The appearance of an exotherm at 230 °C in the DTA thermogram also strengthens this finding. The second weight loss in the TGA thermogram profile is followed by a third weight loss in the temperature range 250–400 °C. After 400 °C about 12% mass remains, which may be due to metal oxide.

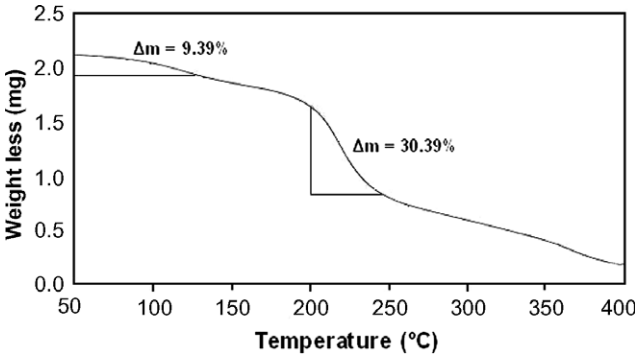


Fig. 8. TGA thermogram of complex **3**.

4. Conclusion

The present study shows the construction of a Pt^{II}-based metallocyclophane on the skeleton of a simple tetradentate Schiff base which provides an electron rich cavity. The space provided by the cavity is found to be suitable for comparatively stronger binding of an electron acceptor molecule like hexafluorobenzene. Additionally, the presently used Schiff base provides an alternate route to prepare the Pd(Salen) complex in the form of beautiful coloured crystals suitable for X-ray studies. This study also allows the difference in the reactivity of Pd^{II} and Pt^{II} complexes with a tetradentate Schiff base to be understood.

Acknowledgements

N.K. and R.P. thank UGC, New Delhi, India for financial assistance. The authors wish to thank CDRI, Lucknow, India for providing analytical data and IITB, Mumbai, India for X-ray data collection. We also wish to thank Dr. R.K. Mandal, Department of Metallurgical Engineering, BHU, India for recording TGA-DTA data.

Appendix A. Supplementary material

CCDC 647916 contains the supplementary crystallographic data for **2**. These data can be obtained free of

charge via http://www.ccdc.cam.ac.uk/conts/retrieving.html, or from the Cambridge Crystallographic Data Centre, 12 Union Road, Cambridge CB2 1EZ, UK; fax: (+44) 1223-336-033; or e-mail: deposit@ccdc.cam.ac.uk. Supplementary data associated with this article can be found, in the online version, at doi:10.1016/j.poly.2007.09.017.

References

[1] E.G. Samsel, K. Srinivasan, J.K. Kochi, J. Am. Chem. Soc. 107 (1985) 7606.
[2] K. Sriniwasan, P. Michaud, J.K. Kochi, J. Am. Chem. Soc. 108 (1986) 2309.
[3] J.D. Koola, J.K. Kochi, J. Org. Chem. 52 (1987) 4545.
[4] E.N. Jocobson, In: I. Ojima (Ed), Catalytic Asymmetric Synthesis, VCH, New York, 1993, p. 159.
[5] C.J. Chang, J.A. Labinger, H.B. Gray, Inorg. Chem. 36 (1997) 5927.
[6] D.A. Evas, D.M. Barnes, Tetrahedron Lett. 38 (1997) 57.
[7] R.E. Lowenthal, A. Abiko, S. Masamune, Tetrahedron Lett. 31 (1990) 6005.
[8] D.A. Evans, K.A. Woerpel, M.M. Hinman, U.M. Faul, J. Am. Chem. Soc. 113 (1991) 726.
[9] T. Fukauda, T. Katsuki, Tetrahedron 53 (1997) 7201.
[10] Y. Uozumi, H. Kyota, E. Kishi, K. Kitayama, T. Hayashi, Tetrahedron Asymmetry.
[11] F.C.J.M. van Veggel, W. Verboom, D.N. Reinhoudt, Chem. Rev. 94 (1994) 279, and references therein.
[12] A.R. Choudhary, R.G. Bhat, T.N. Guru Row, S. Chandrasekaran, Cryst. Growth Des. 7 (2007) 844.
[13] J.A.K. Howard, V.J. Hoy, D. O'Hagan, G.T. Smith, Tetrahedron 52 (1996) 12613.
[14] J.D. Dunitz, R. Taylor, Chem. Eur. J. 3 (1997) 89.
[15] L. Mishra, K. Bindu, S. Bhattachatya, Inorg. Chem. Commun. 7 (2004) 777.
[16] B.J. McCormick, E.N. Jaynes Jr., R.I. Laplan, Inorg. Syn. 13 (1972) 216.
[17] G.C. Johnson, Inorg. Syn. 8 (1966) 242.
[18] N. Hoshino, T. Inabe, T. Mitani, Y. Maruyama, Bull. Chem. Soc. Jpn. 61 (1988) 4207.
[19] W.J. Geary, Coord. Chem. Rev. 7 (1971) 81.
[20] M.A. Houghton, A. Bilky, M.M. Harding, P. Turner, T.W. Hambley, J. Chem. Soc., Dalton Trans. (1997) 2725.
[21] P.J. Stang, D.H. Cao, S. Saito, A.M. Arif, J. Am. Chem. Soc. 117 (1995) 6273.
[22] D.V. Deubel, J.K.-c. Lau, Chem. Commun. (2006) 2451.
[23] K. Mashima, M. Tanaka, K. Tani, Inorg. Chem. 35 (1996) 5244.
[24] J.H.K. Yip, J. Wu, K.-y. Yong, K.P. Ho, L.L. Koh, J.J. Vittal, Eur. J. Inorg. Chem. (2004) 1056.
[25] S. Kitagawa, R. Kitaura, S.-i. Noro, Angew. Chem., Int. Ed. 43 (2004) 2334.

Available online at www.sciencedirect.com
ScienceDirect
Polyhedron 27 (2008) 249–254
POLYHEDRON
www.elsevier.com/locate/poly

Synthesis, structure, spectroscopic, magnetic and electrochemical studies of a rare *syn–anti* acetate-bridged copper(II) complex

Hassan Hadadzadeh [a,*], S. Jamil A. Fatemi [b], Seyedeh Raziyeh Hosseinian [b], Hamid Reza Khavasi [c], Rainer Pöttgen [d]

[a] *Department of Chemistry, Isfahan University of Technology, Isfahan 84156-83111, Iran*
[b] *Department of Chemistry, Shahid Bahonar University, Kerman, Iran*
[c] *Department of Chemistry, Shahid Beheshti University, Evin, Tehran 19839-63113, Iran*
[d] *Institut für Anorganische und Analytische Chemie, Universität Münster, Corrensstrasse 30, D-48149 Münster, Germany*

Received 10 May 2007; accepted 10 September 2007
Available online 7 November 2007

Abstract

The structure, spectroscopy and electrochemical properties of a novel dinuclear copper(II) complex, $[\{Cu(phen)_2\}_2(\mu\text{-}CH_3COO)][PF_6]_3$ where phen = 1,10-phenanthroline, is reported. The crystal structure contains two independent Cu(II) ions, with different geometry around each copper center, which are bridged by an acetate anion. The acetate-bridged ligand shows a *syn–anti* coordination mode with a trigonal bipyramidal geometry for the Cu(1) center and a distorted square-based pyramidal geometry for the Cu(2) center. The angular structural index parameter τ for Cu(1) and Cu(2) is 0.9 and 0.33, respectively. The copper(II) atoms display a different geometry with a N_4O chromophore group and with Cu–O distances of 1.993(5)–1.996(5) Å and Cu–N distances which vary from 1.980(5) to 2.161(6) Å. The intra Cu...Cu separation is 4.9904(5) Å. The effective magnetic moment (μ_{eff}) of the complex was measured by the Evans method. The cyclic voltammogram of $[\{Cu(phen)_2\}_2(\mu\text{-}CH_3COO)][PF_6]_3$ shows two waves at positive potential which are assigned to the two Cu(II/I) reduction couples.
© 2007 Elsevier Ltd. All rights reserved.

Keywords: Crystal structure; Copper(II); Magnetic moment; Cyclic voltammetry; *syn–anti* coordination mode

1. Introduction

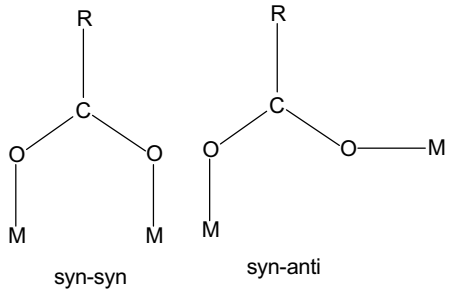
In recent decades, metal-carboxylate chemistry has received a great deal of attention in different fields ranging from metallobiochemistry to catalysis and materials science [1]. The main interest in the chemistry of metal-carboxylates arises from: (i) the versatility of the coordination modes of the simple carboxylate anions which leads to fascinating molecular architectures; (ii) the key role of the carboxylate as a ligand in biological systems involving mono- or polymetallic active sites; and (iii) the property of the carboxylate bridge to exhibit an exchange path mediating the interaction among spins that are localized on paramagnetic centers [2–7]. Carboxylate ligands exhibit several coordination modes to metal centers leading to a variety of polynuclear complexes ranging from discrete entities to multi-dimensional systems. One-dimensional copper(II) compounds containing carboxylate bridges are especially important in the area of molecule based magnets [8,9] and high-temperature oxide-superconductors [10].

Bridged dinuclear copper(II) carboxylato compounds with bidentate chelating ligands and a five coordination of the Cu(II) ion show an extensive range of compounds with a distortion between regular trigonal bipyramidal and regular square-based pyramidal. This feature can be useful for understanding the relationships between structural features and the value of the intramolecular magnetic exchange interaction in the dinuclear units [11].

With acetate as a bridging ligand, several interesting structures with special magnetic properties have been

* Corresponding author. Tel.: +98 311 3913240; fax: +98 311 3912350.
E-mail address: hadad@cc.iut.ac.ir (H. Hadadzadeh).

0277-5387/$ - see front matter © 2007 Elsevier Ltd. All rights reserved.
doi:10.1016/j.poly.2007.09.029



Scheme 1.

reported for a number of dinuclear Cu(II) compounds [12–16]. The acetate ligand can adopt two different bridging conformations; the *syn–syn* mode and the *syn–anti* mode (see Scheme 1). The *syn–anti* mode conformation is very rare and only a limited number of X-ray structures have been reported with this bridging mode [12,13,15,17–28].

In this investigation, we report the synthesis, crystal structure, spectroscopic characterization and magnetic and electrochemical behaviors of a novel copper(II) complex, $[\{Cu(phen)_2\}_2(\mu\text{-}CH_3COO)][PF_6]_3$, having the acetate ligand in a *syn–anti* bridging mode.

2. Experimental

2.1. Materials and physical measurements

All chemicals and solvents were reagent grade, obtained from either Merck or Aldrich and used without further purification. Elemental analysis was performed on a Perkin–Elmer 2400 CHNS/O elemental analyzer. IR spectra (4000–400 cm^{-1}) were measured on a FT-IR JASCO 460 spectrophotometer with KBr pellets. UV–Vis spectroscopy was performed on a JASCO 7850 spectrophotometer. The effective magnetic moment (μ_{eff}) of the complex was measured by the Evans method on a ^1H NMR Bruker DRX-500 MHz, Avance spectrometer at ambient temperature. Cyclic voltammograms were recorded using a Metrohm 694 apparatus. Three electrodes were utilized in this system, a platinum disk working electrode (RDE), a platinum wire auxiliary electrode and a Ag/AgCl reference electrode. The platinum disk working electrode was manually cleaned with 1-μm diamond polish prior to each scan. The supporting electrolyte, tetrabutylammonium hexafluorophosphate (TBAH), was twice recrystallized from 1:1 ethanol/water and vacuum-dried at 110 °C. Acetonitrile was dried over P_2O_5 and vacuum distilled. The solutions were deoxygenated by bubbling with argon (Ar) for 15 min. Ferrocene ($E^\circ = 0.665$ V) was used as an internal reference.

2.2. Synthesis of $[\{Cu(phen)_2\}_2(\mu\text{-}CH_3COO)][PF_6]_3$

A mixture of $Cu(CH_3COO)_2 \cdot H_2O$ (0.4 g, 2 mmol) and 1,10-phenanthroline (0.7 g, 4 mmol) was placed in 80 mL of EtOH and the solution was stirred and kept at 40 °C for 12 h. To the reaction mixture was then added excess NH_4PF_6 (1.5 g). The green precipitate, $[\{Cu(phen)_2\}_2(\mu\text{-}CH_3COO)][PF_6]_3$, which formed was collected by suction filtration, washed with ethanol and ether, and then air dried. The crude product was recrystallized by diffusion of diethyl ether into an acetonitrile solution of the complex. After 5 days, green crystals formed. Yield: 818 mg, 61%. *Anal*. Calc. for $C_{50}H_{35}Cu_2F_{18}N_8O_2P_3$: C, 44.75; H, 2.63; N, 8.35. Found: C, 45.11; H, 2.67; N, 8.46%.

2.3. X-ray crystallographic study of $[\{Cu(phen)_2\}_2(\mu\text{-}CH_3COO)][PF_6]_3$

A green single crystal of $[\{Cu(phen)_2\}_2(\mu\text{-}CH_3COO)][PF_6]_3$ with dimensions $0.40 \times 0.20 \times 0.12$ mm was chosen for the X-ray diffraction study. Diffraction measurements were carried out on a STOE IPDS II two-circle diffractometer using graphite-monochromated Mo Kα ($\lambda = 0.71073$ Å) radiation at 293(2) K. Unit cell parameters were determined by the least-squares procedures with the θ angle ranging from 1.67° to 26.86°. A numerical absorption correction was applied to the data with the help of the programs X-RED and X-SHAPE [29]. A total of 11 919 independent reflections were collected, giving 5752 observed reflections with $I > 2\sigma(I)$. The structure was solved by the direct method [30] and refined by full-matrix least-squares on F^2 using the X-STEP32 program package [31], giving a final $R_1 = 0.0878$, $wR_2 = 0.2224$ values. The R_1 value is slightly

Table 1
Crystallographic and data collection parameters for $[\{Cu(phen)_2\}_2(\mu\text{-}CH_3COO)][PF_6]_3$

Chemical formula	$C_{50}H_{35}Cu_2F_{18}N_8O_2P_3$
Formula weight	1341.85
Crystal size (mm)	$0.40 \times 0.20 \times 0.12$
Crystal system	monoclinic
Space group	$P2_1/c$ (no. 14)
Z	4
a (Å)	18.1272(14)
b (Å)	12.7180(7)
c (Å)	24.981(2)
β (°)	103.136(6)
Collection ranges	$-22 \leqslant h \leqslant 22$; $-16 \leqslant k \leqslant 16$; $-31 \leqslant l \leqslant 31$
Temperature (K)	293(2)
Volume (Å^3)	5608.6(7)
D_{calcd} (Mg m^{-3})	1.589
Radiation	Mo Kα ($\lambda = 0.71073$ Å)
Absorption coefficient (μ) (mm^{-1})	0.951
Absorption correction	numerical
$F(000)$	2688
θ range for data collection (°)	1.67–26.86
Observed reflections	42 454
Independent reflections	5752 ($R_{int} = 0.0732$)
Data/restraints/parameters	11 919/0/748
Goodness-of-fit on F^2	0.970
Final R indices [$I > 2\sigma(I)$]	$R_1 = 0.0878$, $wR_2 = 0.2224$
R indices (all data)	$R_1 = 0.1636$, $wR_2 = 0.2663$
Largest diffraction peak and hole (e Å^{-3})	1.169 and −0.395

Table 2
Selected bond lengths (Å) and bond angles (°) for $[\{Cu(phen)_2\}_2(\mu\text{-}CH_3COO)][PF_6]_3$

Bond lengths			
Cu(1)–N(4)	2.118(5)	Cu(2)–N(7)	1.997(6)
Cu(1)–N(2)	1.985(6)	Cu(2)–O(2)	1.996(5)
Cu(1)–O(1)	1.993(5)	Cu(2)–N(5)	1.993(6)
Cu(1)–N(1)	2.102(6)	Cu(2)–N(6)	2.161(6)
Cu(1)–N(3)	1.980(5)	Cu(2)–N(8)	2.059(7)
Bond angles			
N(4)–Cu(1)–N(2)	99.4(2)	N(7)–Cu(2)–O(2)	94.8(2)
N(4)–Cu(1)–O(1)	121.7(2)	N(7)–Cu(2)–N(5)	176.2(3)
N(2)–Cu(1)–O(1)	88.3(2)	O(2)–Cu(2)–N(5)	89.0(2)
N(4)–Cu(1)–N(1)	114.2(2)	N(7)–Cu(2)–N(6)	98.0(3)
N(2)–Cu(1)–N(1)	81.4(3)	O(2)–Cu(2)–N(6)	105.7(2)
O(1)–Cu(1)–N(1)	124.1(2)	N(5)–Cu(2)–N(6)	80.4(3)
N(4)–Cu(1)–N(3)	81.3(2)	N(7)–Cu(2)–N(8)	81.0(3)
N(2)–Cu(1)–N(3)	178.0(3)	O(2)–Cu(2)–N(8)	156.0(2)
O(1)–Cu(1)–N(3)	92.9(2)	N(5)–Cu(2)–N(8)	95.7(3)
N(1)–Cu(1)–N(3)	96.6(2)	N(6)–Cu(2)–N(8)	98.3(3)

high due to data collection at room temperature and is related to the high vibrational motion of the fluorine atoms of PF_6^- and also the carbon atoms in the Phen rings. These disorders are common especially with room temperature data collection when the structure contains PF_6^-, ClO_4^- and similar groups. We tried refining these atoms in two positions with reduced occupancy but while this model converged satisfactorily, there was no decrease in the *R* value and therefore we consider that our original refinement is the best that can be achieved and should be reported. The largest diffraction peak and hole on the final difference-Fourier map were 1.169 and -0.395 e Å^{-3}, respectively. The largest peak is not close to a heavy scatterer (the distance is more than 1 Å), so it is related to disordering of some atoms in the structure. Further details of the structural analyses are given in Table 1. Selected bond lengths and bond angles are listed in Table 2.

3. Results and discussion

The dinuclear Cu(II) complex was synthesized in good yield. $[\{Cu(phen)_2\}_2(\mu\text{-}CH_3COO)][PF_6]_3$ is air-stable and can be readily recrystallized. Elemental analysis of the complex was entirely consistent with its proposed stoichiometry. This complex was further characterized by IR, UV–Vis spectroscopies and cyclic voltammetry. Green crystals of $[\{Cu(phen)_2\}_2(\mu\text{-}CH_3COO)][PF_6]_3$ were grown by ether diffusion into an acetonitrile solution of the complex.

An ORTEP plot of $[\{Cu(phen)_2\}_2(\mu\text{-}CH_3COO)][PF_6]_3$ with the atomic labelling scheme is shown in Fig. 1, and selected bond lengths and bond angles are listed in Table 2. Both Cu(II) ions in the dinuclear unit are linked through a bridging acetate ligand with a *syn–anti* mode conformation. The molecular structures of five-coordinate copper(II) complexes show an extensive range from regular trigonal bipyramidal (RTBP) to regular square-based pyramidal (RSBP) [32,33]. The structure index parameter, $\tau = (\beta - \alpha/60)$, was evaluated by the two large angles ($\alpha < \beta$) in the five-coordinated geometry, where $\tau = 1.0$ for a RTBP geometry and $\tau = 0.0$ for a RSBP [34]. The coordination geometry of Cu(1) ($\tau = 0.9$) is best described as trigonal bipyramidal with the equatorial plane comprising of N(3), N(1), Cu(1) and O(1) (see Fig. 2). There is a small difference in the axial and equatorial Cu–N bond lengths. In the Cu(1) coordination site, the equatorial Cu–N bond lengths are considerably longer than the corresponding axial Cu–N bond lengths. The coordination geometry around Cu(2) is approximately square pyramidal with a N_4O donor set (see Fig. 2). This coordination geometry is slightly distorted from regular square-based pyramidal, as ascertained by the observed τ value of 0.33. One oxygen atom of the acetate bridge and three nitrogen atoms of the phen ligands constitute the basal plane of the square pyramid, and a nitrogen of phen occupies the apical position.

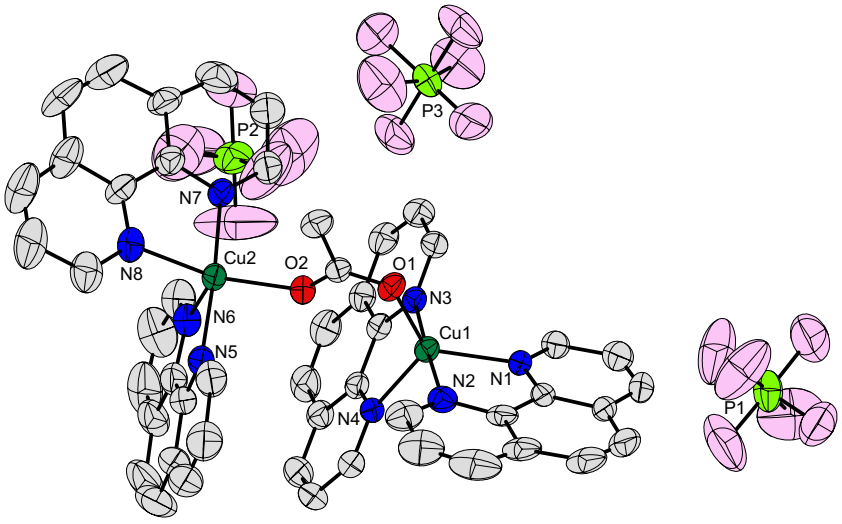


Fig. 1. ORTEP diagram of $[\{Cu(phen)_2\}_2(\mu\text{-}CH_3COO)][PF_6]_3$ showing 30% probability ellipsoids. Hydrogen atoms and some atoms numbering are deleted for clarity.

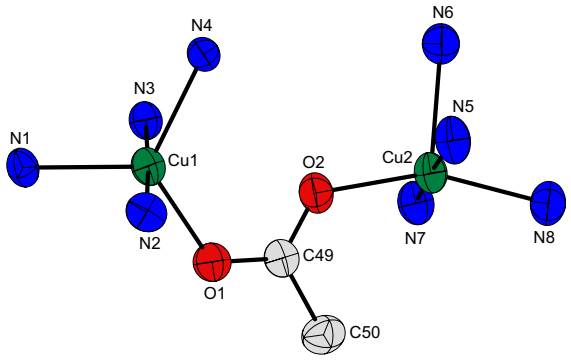


Fig. 2. The inner coordination sphere of the copper(II) ions bridged by acetate in $[\{Cu(phen)_2\}_2(\mu\text{-}CH_3COO)][PF_6]_3$.

The Cu(2) atom lies 0.223(3) Å above the basal plane. The Cu(II) centers are connected through a single *syn–anti* acetate bridge with a Cu...Cu separation of 4.9904(5) Å. In the crystal of this dinuclear complex, the distances between the copper(II) ions and the fluorine of PF_6^- are too great to suggest coordination. The lattice structure is further stabilized by a network of hydrogen bonds between the H atoms of the phen ligands and the F atoms of the PF_6^- anions, with C–H...F distances of 2.371(0.035)–3.931(0.001) Å. As is shown in Fig. 3, there are some weak π–π aromatic interactions between two of the four phenanthroline ligands, N(3)–N(4) and N(5)–N(6), and the angles between the phenanthroline planes are about 18° in the lattice.

The infrared spectrum of the complex exhibits the bands expected for the organic ligands and counter ions. Particularly, the asymmetric stretching vibration of the acetate anion, $\nu_{asym}(COO)$, is observed at 1613 cm^{-1}, while the band at 1449 cm^{-1} is assigned to the symmetric stretching vibration of the acetate anion ($\nu_{sym}(COO)$). The difference between $\nu_{asym}(COO)$ and $\nu_{sym}(COO)$ of about 164 cm^{-1} agrees with the bridging coordination mode for the acetate anion [12,15,35]. The strong absorption band at 841 cm^{-1} is assigned to ν(P–F) and demonstrates the existence of PF_6^- as a counter ion [35].

The electronic spectrum of the complex was taken in acetonitrile. The spectrum shows two absorption bands in the UV region and two absorption bands in the visible region. The absorption bands centered at 234 nm ($\log\varepsilon = 4.53$) and 313 nm ($\log\varepsilon = 4.18$) are assigned to ligand-centered ($\pi \rightarrow \pi^*$) transitions. The intense absorption band centered at 412 nm ($\log\varepsilon = 3.25$) is assigned to a LMCT transition. Due to the different coordination geometries around the Cu(II) centers, the ligand field transitions (LFT) overlap with each other and appear as a broad band around 700 nm ($\log\varepsilon = 1.22$) [36].

The effective magnetic moment (μ_{eff}) of $[\{Cu(phen)_2\}_2(\mu\text{-}CH_3COO)][PF_6]_3$ was measured to be 1.63 BM per Cu(II) ion by the Evans method [37]. The effective magnetic moment (μ_{eff}) is slightly below the theoretical value expected for a Cu(II) center with $S = 1/2$ and suggests antiferromagnetic exchange between the Cu(II) ions. As the Cu...Cu distance is fairly large (4.9904(5) Å), this antiferromagnetic interaction most likely occurs via the Cu–O–C–O–Cu pathway. This is consistent with a few other acetate-bridged complexes such as $\{[Cu(diethylenetriamine)(\mu\text{-}CH_3COO)]_n(ClO_4)_n\}$ and $\{[Cu\text{-}(dpa)(CH_3COO)](ClO_4)\cdot 0.5THF\}_n$, which also exhibit a weak antiferromagnetic interaction [38,39].

Cyclic voltammetry was performed on an acetonitrile solution of the complex with 0.1 M TBAH as a supporting electrolyte. The cyclic voltammograms of the

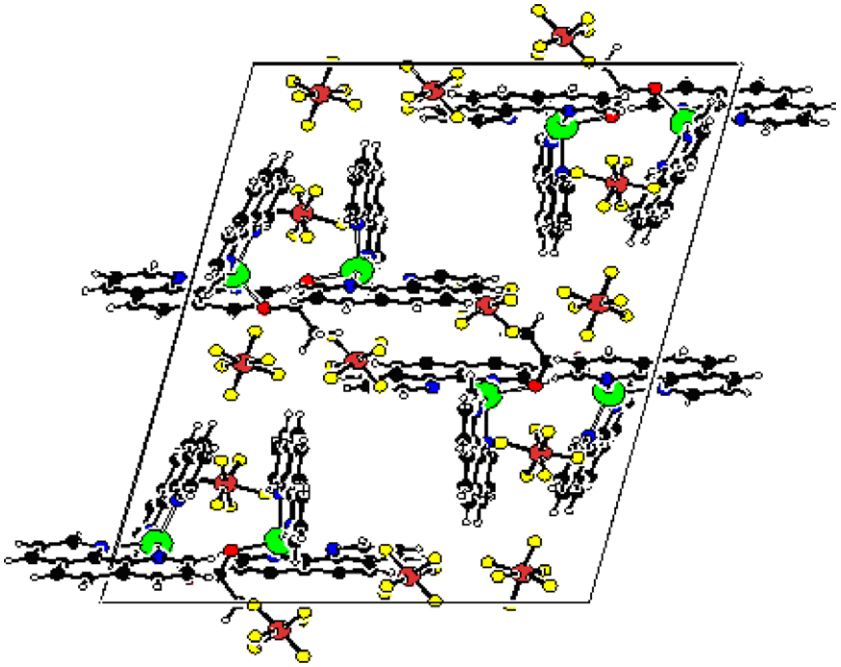


Fig. 3. Packing diagram of $[\{Cu(phen)_2\}_2(\mu\text{-}CH_3COO)][PF_6]_3$ viewed in the b-direction.

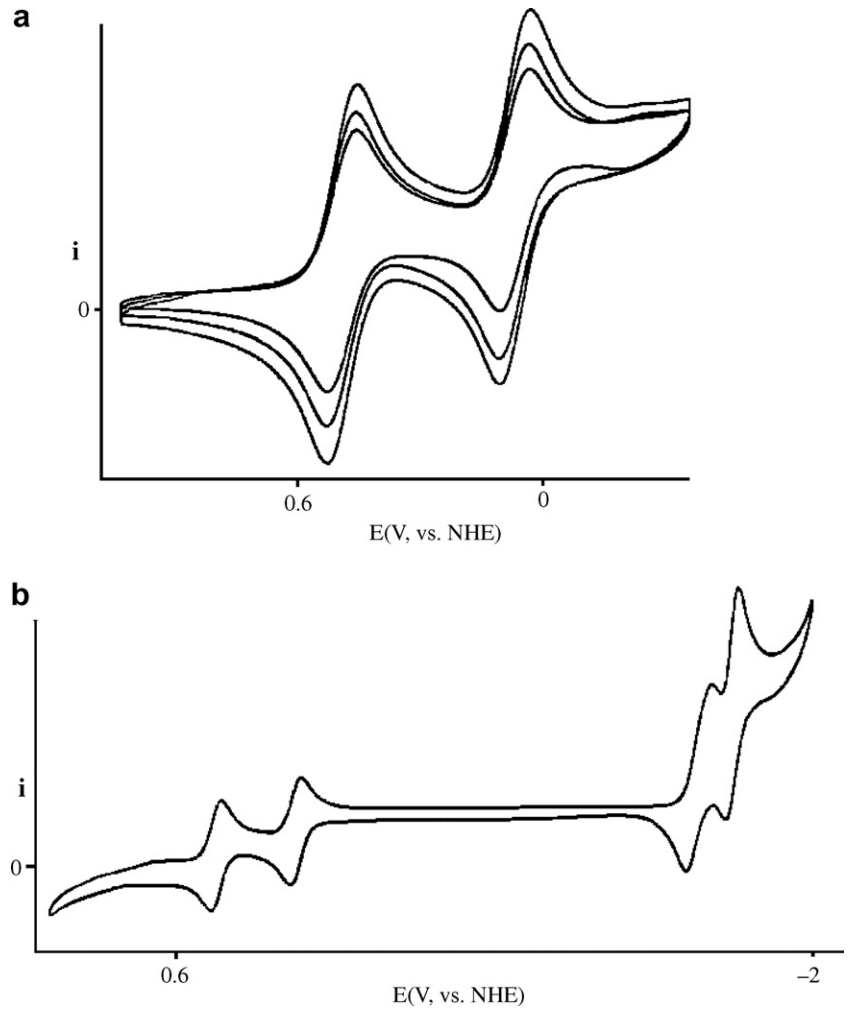


Fig. 4. Cyclic voltammograms of $[\{Cu(phen)_2\}_2(\mu\text{-}CH_3COO)][PF_6]_3$ in CH_3CN/0.1 M TBAH. (a) Scan rates of 100, 200 and 300 mV/s; (b) at a scan rate of 100 mV/s.

$[\{Cu(phen)_2\}_2(\mu\text{-}CH_3COO)][PF_6]_3$ complex are shown in Fig. 4. The copper redox couples in the dinuclear complex occur in approximately the same region as the Cu(II/I) of mononuclear Cu(II) complexes with phen ligands. However, these reduction couples are split into two one-electron waves at 0.544 and 0.135 V which correspond to Cu(II,II/II,I) and Cu(II,I/I,I), respectively, and is indicative of significant metal–metal coupling. These redox couples seem to be quasi-reversible with an average separation between the cathodic and anodic waves of 98 mV, which is independent of the scan rate between 100 and 400 mV/s.

The stability of a mixed-valance form can be quantified by the comproportionation equilibrium constant (K_c). The larger K_c is, the greater the electronic coupling. K_c is usually deduced from the difference in potential between metal center reduction couples, $\log K_c = 16.9(\Delta E)$. From the difference in Cu(II/I) couples of the dinuclear complexes (ΔE), the comproportionation constant (K_c) for the formation of the Cu(II/I) mixed-valence complex,

$$Cu(II) - Cu(II) + Cu(I) - Cu(I) \overset{K_c}{\rightleftharpoons} 2Cu(II) - Cu(I)$$

was determined to be 0.8×10^7. This value is on the borderline between Classes II and III behavior in the Robin and Day classification [40–45] and requires further study before an absolute assignment can be given. In particular, the difference in solid state coordination environments may significantly perturb the Cu(II/I) couples and hence make a contribution to the comproportionation equilibrium. Whether this difference exists in solution is at the present unknown. The two quasi-reversible reduction couples at negative potential are assigned to the sequential reductions of the phenanthroline ligands.

4. Conclusion

The combination of spectral, structural and electrochemical measurements we have described has illustrated the main features of the coordination, magnetic property and redox chemistry of a novel dinuclear Cu(II) complex, $[\{Cu(phen)_2\}_2(\mu\text{-}CH_3COO)][PF_6]_3$. The coordination geometry around the Cu(II) centers is different. The acetate-bridged ligand between two Cu(II) centers shows

a*syn–anti* coordination mode with a trigonal bipyramidal geometry for the Cu(1) center and a distorted square-based pyramidal geometry for the Cu(2) center. The effective magnetic moment is slightly less than the theoretical value expected for one non-coupled Cu(II) center. The magnitude of μ_{eff} suggests a weak antiferromagnetic interaction between the two paramagnetic Cu(II) centers. The comproportionation constant of this complex suggests strong coupling between the copper(II) ions, however the difference in coordination environment may also make a significant contribution.

5. Supplementary material

CCDC 629592 contains the supplementary crystallographic data for $[\{Cu(phen)_2\}_2(\mu\text{-}CH_3COO)][PF_6]_3$. These data can be obtained free of charge via http://www.ccdc.cam.ac.uk/conts/retrieving.html, or from the Cambridge Crystallographic Data Centre, 12 Union Road, Cambridge CB2 1EZ, UK; fax: (+44) 1223-336-033; or e-mail: deposit@ccdc.cam.ac.uk.

Acknowledgements

We are grateful to the Isfahan University of Technology (IUT) and Shahid Bahonar University for financial support. We are also very grateful to Professor R.J. Crutchley (Carleton University, Ottawa, Canada) for helpful discussions.

References

[1] A.C. Warden, M.T.W. Hearn, L. Spiccia, Inorg. Chem. 42 (2003) 868.
[2] M. Melnik, Coord. Chem. Rev. 42 (1982) 259.
[3] F.P.W. Agterberg, H.A.J. Provo Kluit, W.L. Driessen, H. Oevering, W. Buijs, M.T. Lakin, A.L. Spek, J. Reedijk, Inorg. Chem. 36 (1997) 4321.
[4] K.L. Oberhausen, J.F. Richardson, R.M. Buchanan, J.K. McCusker, D.N. Hendrikson, J.M. Latour, Inorg. Chem. 30 (1991) 1357.
[5] B. Graham, M.T. Hearn, P.C. Junk, F.E. Mabbs, B. Moubaraki, K.S. Murray, L. Spiccia, Inorg. Chem. 40 (2001) 1536.
[6] S. Chavan, D. Srinivas, P. Ratnasamy, Top. Catal. 11 (2000) 359.
[7] W. Wislecerus, W. Stoeber, Ber. Dtsch. Chem. Ges. 35 (1902) 539.
[8] D. Gatteschi, O. Kahn, J.S. Miller, F. Pallacio, Adv. Mater. 3 (1991) 161.
[9] C.N.R. Rao, S. Natarajan, R. Vaidhyanathan, Angew. Chem., Int. Ed. 43 (2004) 1466.
[10] H. Müller-Buschbaum, Angew. Chem., Int. Ed. 30 (1991) 723.
[11] C. Chailuecha, S. Youngme, C. Pakawatchai, N. Chaichit, G.A.V. Albaba, J. Reedijk, Inorg. Chem. Acta 359 (2006) 4168.
[12] B.H. Ye, L.N. ji, F. Xue, T.C.W. Mak, Polyhedron 17 (1998) 2687.
[13] D.K. Towle, S.K. Hoffmann, W.E. Hatfiled, P. Singh, P. Chaudhuri, Inorg. Chem. 27 (1998) 394.
[14] P. Gentschev, M. Lüken, N. Möller, A. Rompel, B. Zkrebs, Inorg. Chem. Commun. 4 (2001) 753.
[15] I.A. Koval, P. Games, O. Roubeau, W.L. Driessen, M. Lutz, A.L. Spek, J. Reedjik, Inorg. Chem. 42 (2003) 868.
[16] C.T. Zeyrek, A. Elmali, Y. Elerman, J. Mol. Struct. (Theochem.) 680 (2004) 159.
[17] L.G. Zhu, S. Kitagawa, Inorg. Chem. Commun. 5 (2002) 358.
[18] B. Chiari, O. Piovesana, T. Tarantelli, P.F. Zanazzi, Inorg. Chem. 32 (1999) 4834.
[19] C.A. Crawford, E.F. Day, W.E. Streib, J.C. Huffman, G. Christou, Polyhedron 13 (1994) 2933.
[20] S.P. Perelepes, E. Libby, W.E. Streib, K. Folting, G. Christou, Polyhedron 11 (1992) 923.
[21] S. Warzeska, R. Krämer, Chem. Ber. 128 (1995) 115.
[22] V. Tangoulis, C.P. Raptopoulou, A. Terzis, S. Paschalidou, S.P. Perlepes, E.G. Bakalbassis, Inorg. Chem. 36 (1997) 3996.
[23] J. Valo, M. Näsäkkälä, Acta Chem. Scan. 48 (1994) 20.
[24] M. Mikuriya, S. Kida, I. Murase, Bull. Chem. Soc. Jpn. 60 (1987) 1681.
[25] S. Youngme, T. Chotkhun, N. Chaichit, Acta Crystallogr., Sect. C 63 (2007) m59.
[26] P.A.N. Reddy, M. Nethaji, A.R. Chakravarty, Eur. J. Inorg. Chem. (2003) 2318.
[27] F.H. Allen, Acta Crystallogr., Sect. B 58 (2002) 380.
[28] I.J. Bruno, J.C. Cole, P.R. Edgington, M. Kessler, C.F. Macrae, P. McCabe, J. Pearson, R. Taylor, Acta Crystallogr., Sect. B 58 (2002) 389.
[29] (a) X-RED32 Version 1.28b, Program for Data Reduction and Absorption Correction, Stoe & Cie GmbH, Darmstadt, Germany, 2005.;
(b) X-SHAPE Version 2.05, Program for Crystal Optimization for Numerical, Stoe & Cie GmbH, Darmstadt, Germany, 2004.
[30] G.M. Sheldrick, SHELXS-97, Program for Crystal Structure Solution Refinement. University of Göttingen, Germany, 1997.
[31] X-STEP32, Version 1.07b, X-ray Structure Evaluation Package, Stoe & Cie GmbH, Darmstadt, Germany, 2000.
[32] M. Brophy, G. Murphy, C. O′Sullivan, B. Hathaway, B. Murphy, Polyhedron 18 (1999) 611.
[33] B. Murphy, B. Hathaway, Coord. Chem. Rev. 243 (2003) 237.
[34] A.W. Addison, T.N. Rao, j. Reedijk, J. VanRijn, G.C. Verschoor, J. Chem. Soc., Dalton Trans. (1984) 1349.
[35] K. Nakamato, Infrared and raman spectra of inorganic and coordination compounds Part II: application in coordination, 5th ed., Organometallic and Bioinorganic Chemistry, Wiley – Interscience, New York, 1997.
[36] A.B.P. Lever, Inorganic Electronic Spectroscopy, 2nd ed., Elsevier, Amsterdam, 1984.
[37] D.J. Mackey, S.V. Evans, J. Chem. Soc., Dalton. Trans. (1976) 2004.
[38] S. Youngme, P. Phuenghai, N. Chaichit, G.A. Van Albaba, S. Tanase, d J. Reedijik, Inorg. Chem. Acta 358 (2005) 3257.
[39] S. Tanase, G.A. Van Albaba, R. de Gelder, E. Bouwman, J. Reedijik, Polyhedron 24 (2005) 979.
[40] C. Creutz, M.H. Chou, Inorg. Chem. 26 (1987) 2995.
[41] M.B. Robin, P. Day, Adv. Inorg. Chem. Radiochem. 10 (1967) 247.
[42] R.J. Crutchley, Coord. Chem. Rev. 219–221 (2001) 125.
[43] P.J. Mosher, G.P.A. Yap, R.J. Crutchley, Inorg. Chem. 40 (2001) 1189.
[44] A.R. Rezvani, C.E.B. Evans, R.J. Crutchley, Inorg. Chem. 34 (1995) 4600.
[45] A.R. Rezvani, C. Bensimon, B. Cromp, C. Reber, J.E. Greedan, V.V. Kondrative, R.J. Crutchley, Inorg. Chem. 36 (1997) 3322.

Available online at www.sciencedirect.com
ScienceDirect
Polyhedron 27 (2008) 255–262
POLYHEDRON
www.elsevier.com/locate/poly

Synthesis, structure and metallation of spiro-$N_3P_3(O_2C_{12}H_8)(OC_5H_4N\text{-}2)_4$: A heptacoordinate Co(II) in the molecular structure of $N_3P_3(O_2C_{12}H_8)(OC_5H_4N\text{-}2)_4 \cdot Co(NO_3)_2$

Vadapalli Chandrasekhar *, Balasubramanian Murugesa Pandian, Ramachandran Azhakar

Department of Chemistry, Indian Institute of Technology, Kanpur, Kanpur 208 016, India

Received 25 July 2007; accepted 10 September 2007
Available online 14 November 2007

Abstract

Spiro-$N_3P_3(O_2C_{12}H_8)(OC_5H_4N\text{-}2)_4$ (**L**) is an efficient multi-site coordination ligand which binds with transition metal ions to afford the mononuclear complexes $[LCu(NO_3)_2]$, $[LCo(NO_3)_2]$ and $[LZnCl_2]$. In $[LCu(NO_3)_2]$ the copper atom is six-coordinate with the cyclophosphazene ligand coordinating to the metal ion through one skeletal ring nitrogen atom and two nitrogen atoms of geminal pyridyloxy substituents in a η^3-*gem*-N_3 mode. The two nitrate ligands provide monodentate as well as chelating coordination. In $[LCo(NO_3)_2]$ the coordination geometry around Co(II) is pentagonal bipyramidal with a 3N, 4O coordination environment. The cyclophosphazene ligand binds to the metal ion in a η^3-*non-gem*-N_3 mode. The two nitrate ligands function as chelating ligands and complete the coordination around cobalt. The coordination response of **L** in the complex $[LZnCl_2]$ is also η^3-*non-gem*-N_3. Two chloride ligands complete the coordination environment around zinc.
© 2007 Published by Elsevier Ltd.

Keywords: Cyclotriphosphazene; Hydroxypyridine; Metal complexes; Multi-site coordination ligand

1. Introduction

Cyclophosphazene-based ligand systems have been attracting a great deal of interest in recent times [1,2]. One of the important reasons for this is because it is possible to use the cyclophosphazene rings as supports for the design and assembly of a large variety of ligands each of which can provide unique steric and electronic environments for transition metal coordination. Such ligands possess multi-site coordination capabilities and are quite effective in binding transition and lanthanide metal ions [2–5]. Another reason of interest in the cyclophosphazene-based ligand systems is the close inter-relationship between cyclo- and polyphosphazenes which allows the cyclophosphazene chemistry to be readily translated to the polymeric analogues [1a]. Thus, we have recently shown the utility of pyrazolyl cyclophosphazenes and cyclophosphazene hydrazides in metallation reactions [6]. This chemistry could be readily adapted for the preparation of the corresponding polymers [7,8] some of which were used to generate recyclable polymeric catalysts for plasmid cleavage, phosphate ester hydrolysis as well as in the Heck reaction involving C–C bond formation [8]. In view of this success, we have been interested in extending this methodology to other types of ligands. Recently, we and others have shown that pyridyloxy cyclophosphazenes containing P–O bonds are quite effective in the preparation of mono-, di- and trinuclear metal complexes [9]. It is of interest to compare the coordination behavior of the hexakis(pyridyloxy)cyclophosphazenes with modified ligands where some sites on the cyclophosphazene are blocked by non-coordinating groups. Accordingly, herein we report the synthesis, structure and metallation studies of spiro-$N_3P_3(O_2C_{12}H_8)(OC_5H_4N\text{-}2)_4$ (**L**). The cobalt(II) complex formed from this ligand, $N_3P_3(O_2C_{12}H_8)(OC_5H_4N\text{-}2)_4 \cdot$

* Corresponding author. Fax: +91 512 2590007/2597436.
E-mail address: vc@iitk.ac.in (V. Chandrasekhar).

0277-5387/$ - see front matter © 2007 Published by Elsevier Ltd.
doi:10.1016/j.poly.2007.09.026

$Co(NO_3)_2$ shows a heptacoordinate Co(II) with a 3N, 4O coordination environment. This is the first example of stabilization of the rare hepta-coordination for Co(II) using cyclophosphazene ligands.

2. Experimental

2.1. Materials and instrumentation

Solvents and other general reagents used in this work were purified according to standard procedures. Hexachlorocyclotriphosphazene (Nippon Soda, Japan) was recrystallized from *n*-hexane before use. Anhydrous $ZnCl_2$ (Fluka, Switzerland), $Cu(NO_3)_2 \cdot 3H_2O$, $Co(NO_3)_2 \cdot 6H_2O$ (S.D. Fine Chemicals Mumbai, India) and 2-hydroxypyridine (Lancaster, UK) were used as obtained. Spiro-$N_3P_3(O_2C_{12}H_8)Cl_4$ (**1**) was prepared according to the procedure reported in the literature [10]. ^1H and $^{31}P\{^1H\}$ NMR spectra were recorded on a JEOL spectrometer operating at 400.0 and 161.7 MHz, respectively. Chemical shifts are reported with respect to internal tetramethylsilane (^1H) and external 85% H_3PO_4 (^{31}P). Mass spectra were recorded on a JEOL SX 102/DA 6000 mass spectrometer using xenon (6 kV, 10 mA) as the FAB gas. IR spectra were recorded as KBr pellets on a Bruker Vector 22 FT IR spectrophotometer operating from 400 to 4000 cm^{-1}. Electronic spectra were recorded on a Perkin–Elmer-Lambda 20 UV–Vis spectrometer and on a Shimadzu UV-160 spectrometer using chloroform as the solvent. EPR spectra were recorded on a Bruker EMX 1444 X-band EPR spectrometer (fitted with a quartz Dewar for measurements up to 120 K). The EPR spectra were calibrated with diphenylpicrylhydrazyl, DPPH ($g = 2.0037$). Magnetic susceptibility measurements were carried out by SQUID (Superconducting Quantum Interference Device) using a Quantum Design Magnetic property measurement system XL (USA) at 300 K and the results were corrected for the magnetization of the sample holder and capsule and the diamagnetic contributions to the samples, which were estimated from Pascal's constants [11]. Elemental analyses of the compounds were obtained on a Thermoquest CE instruments CHNS-O, EA/110 model.

2.2. Preparation of spiro-$N_3P_3(O_2C_{12}H_8)(O\text{-}C_5H_4N\text{-}2)_4$ (**L**)

A mixture of spiro-$N_3P_3(O_2C_{12}H_8)Cl_4$(**1**) (2.300 g, 5.00 mmol), 2-hydroxypyridine (2.300 g, 24.000 mmol) and anhydrous potassium carbonate (10.000 g, 72.500 mmol) was heated under reflux in acetone (150 mL) for 2 days. The volatiles were evaporated in vacuo and the residue was extracted twice with dichloromethane (2 × 40 mL). Evaporation of the solvent in vacuo gave spectroscopically and analytically pure compound **L** as a white solid. Yield: 2.8 g (79%). M.p.: 209 °C. ^1H NMR ($CDCl_3$, ppm): 6.73 (m, 2H, aromatic), 6.98–7.17 (m, 12H, aromatic), 7.38 (m, 2H, aromatic), 7.57 (m, 4H, aromatic), 8.17 (m, 4H, aromatic). $^{31}P\{^1H\}$ NMR ($CDCl_3$, ppm) 26.7 (t, $P(OC_{12}H_8)$), 7.8 (d, $P(O\text{-}C_5H_4N\text{-}2)_2$, ^2J(P–N–P) = 93.8 Hz). FAB-MS: 696 $[L]^+$. IR (KBr, cm^{-1}) 3429 (b), 3061 (m), 1590 (s), 1468 (s), 1431 (s), 1223 (m), 1094 (sh), 1000 (sh), 933 (m), 785 (s), 621 (s), 532 (m). *Anal.* Calc. for $C_{32}H_{24}N_7O_6P_3$: C, 55.26; H, 3.48; N, 14.10. Found: C, 55.06; H, 3.35; N, 13.85%.

2.3. Synthesis of metal complexes **2**–**4**

2.3.1. Spiro-$N_3P_3(O_2C_{12}H_8)(O\text{-}C_5H_4N\text{-}2)_4 \cdot Cu(NO_3)_2$ (**2**)

Hydrated copper nitrate, $Cu(NO_3) \cdot 3H_2O$ (0.070 g, 0.288 mmol), was added to a solution of **L** (0.200 g, 0.288 mmol) in dichloromethane (50 mL). The reaction mixture was stirred for 12 h at room temperature. Filtration, followed by removal of the solvent from the filtrate, gave **2**. Yield: 0.200 g (78.8%). M.p.:187–189 °C, FAB-MS: 821 $[L \cdot CuNO_3]^+$, 759 $[L \cdot Cu]^+$, 696 $[L]^+$. EPR: $g_\parallel = 2.35$, $A_\parallel = 146$ G, $g_\perp = 2.07$. Room temperature magnetic moment (after applying diamagnetic corrections), $\mu_B = 1.65$ BM. UV–Vis ($CHCl_3$): λ_{max} (ε_{max}) 768 nm (73 $M^{-1}\,cm^{-1}$). IR (KBr, cm^{-1}) 3427 (b), 3080 (m), 1599 (s), 1471 (s), 1434 (s), 1384 (s), 1290 (s), 1225 (sh), 1181 (s), 1097 (sh), 1001 (sh), 953 (s), 832 (s), 785 (s), 618 (s), 534 (s). *Anal.* Calc. for $C_{32}H_{24}N_9O_{12}P_3Cu$: C, 43.53; H, 2.74; N, 14.29. Found: C, 43.54; H, 2.75; N, 14.14%.

2.3.2. Spiro-$N_3P_3(O_2C_{12}H_8)(O\text{-}C_5H_4N\text{-}2)_4 \cdot Co(NO_3)_2$ (**3**)

Hydrated cobalt nitrate, $Co(NO_3) \cdot 6H_2O$ (0.084 g, 0.288 mmol), was added to a solution of **L** (0.200 g, 0.288 mmol) in dichloromethane (50 mL). The reaction mixture was stirred for 12 h at room temperature. Filtration, followed by removal of the solvent from the filtrate afforded **3**. Yield: 0.19 g (75.2%). M.p.: 178–179 °C, FAB-MS: 817 $[LCo(NO_3)]^+$, 755 $[LCo]^+$, 696 $[L]^+$. Room temperature magnetic moment (after applying diamagnetic corrections), $\mu_B = 4.02$ BM. UV–Vis ($CHCl_3$): $\lambda_{max(\epsilon max)}$ 506 nm (33 $M^{-1}\,cm^{-1}$). IR (KBr, cm^{-1}) 3404 (b), 3066 (m), 1647 (s), 1472 (s), 1434 (s), 1384 (s), 1291 (s), 1228 (sh), 1182 (s), 1095 (sh), 1043 (sh), 950 (s), 893 (s), 785 (s), 617 (s), 532 (s). *Anal.* Calc. for $C_{32}H_{24}N_9O_{12}P_3Co$: C, 43.75; H, 2.75; N, 14.35. Found: C, 43.54; H, 2.91; N, 13.94%.

2.3.3. Spiro-$N_3P_3(O_2C_{12}H_8)(O\text{-}C_5H_4N\text{-}2)_4 \cdot ZnCl_2$ (**4**)

Anhydrous zinc chloride (0.040 g, 0.288 mmol) was added to a solution of **L** (0.200 g, 0.288 mmol) in dichloromethane (50 mL) solution. The reaction mixture was stirred for 12 h at room temperature. Filtration, followed by removal of the solvent from the filtrate, yielded metal complex **4**. Yield: 0.18 g (73.2%). M.p.: 205–206 °C, ^1H NMR ($CDCl_3$, ppm): 6.74 (m, 2H, aromatic), 6.93 (m, 4H, aromatic), 7.08–7.25 (m, 8H, aromatic), 7.45 (m, 2H aromatic), 7.67 (m, 4H, aromatic), 8.41 (m, 4H, aromatic). $^{31}P\{^1H\}$ NMR ($CDCl_3$, ppm) 23.9 (t, $P(OC_{12}H_8)$), 7.6

(d, P(O-C_5H_4N-2)$_2$), ^2J(P–N–P) = 98.6 Hz. FAB-MS: 795 $[LZnCl]^+$, 696 $[L]^+$. IR (KBr, cm^{-1}) 3428 (b), 3065 (m), 1599 (s), 1471 (s), 1435 (s), 1299 (s), 1221 (m), 1164 (s), 1055 (sh), 941 (s), 894 (s), 789 (s), 759 (sh), 622 (s), 529 (s). *Anal*. Calc. for $C_{32}H_{24}N_7O_6P_3ZnCl_2$: C, 46.32; H, 2.91; N, 11.82. Found: C, 46.10; H, 2.89; N, 11.52%.

2.4. X-ray crystallography

A suitable crystal for **L** was obtained by slow evaporation of its dichloromethane solution. Suitable crystals for **2–4** were obtained by slow diffusion of *n*-hexane into their dichloromethane solutions. The crystal data for compounds **L** and **2–4** were collected on a Bruker SMART APEX CCD diffractometer. The program SMART (version 6.45) was used for integration of the intensity of reflections and scaling. The program SADABS was used for absorption correction. The crystal structures were solved and refined by full-matrix least-squares methods against F^2 by using the program SHELXTL (version 6.14) [12]. All non-hydrogen atoms were refined with anisotropic displacement parameters. Hydrogen positions were fixed at calculated positions and refined isotropically. Compounds **3** and **4** contained disordered solvent molecules that could not be modelled satisfactorily. These were removed by using the PLATON/SQUEEZE program [13]. The squeeze method found the electron count to be 169 and 21 e in a volume of 616.5 and 199.6 Å^3 in the solvent region in the unit cells of **3** and **4**, respectively. The calculated electron counts shows that 4 dichloromethane and 2 water molecules are present in the unit cells of **3** and **4**, respectively. The crystal data for **L** and **2–4** are given in Table 1.

3. Results and discussion

3.1. Synthetic and spectroscopic aspects

Spiro-$N_3P_3(O_2C_{12}H_8)Cl_4$ (**1**) has four reactive chlorine atoms which can be substituted quite readily. Utilizing this feature, we have synthesized spiro-$N_3P_3(O_2C_{12}H_8)$-(OC_5H_4N-2)$_4$ (**L**), by the reaction of **1** with 2-hydroxypyridine in the presence of anhydrous K_2CO_3 in refluxing acetone medium (Scheme 1). Ligand **L** showed a prominent parent ion peak at *m*/*e* 696 $[L]^+$ in its FAB-MS. $^{31}P\{^1H\}$ NMR of **L** is of the AB_2 type. A triplet centered at 26.7 ppm [*P*($OC_{12}H_8$)] and a doublet centered at 7.8 ppm [*P*(O-C_5H_4N-2)$_2$] were observed with a ^2J(P–N–P) value of 93.8 Hz. By comparison, in the parent tetrachloro derivative **1**, *P*($OC_{12}H_8$) resonates at 12.9 ppm while the signal for PCl_2 is seen at 24.8 ppm [^2J(P–N–P) = 71.2 Hz]. It is also of interest to note that the hexakis derivative, $N_3P_3(OC_5H_4N$-2)$_6$ shows a singlet in its $^{31}P\{^1H\}$ NMR spectrum at 6.4 ppm [14].

The reaction of **L** with hydrated copper and cobalt nitrates or anhydrous zinc chloride afforded 1:1 metal complexes (Scheme 2). The metal uptake does not increase upon varying the stoichiometry of the reactants. Further, in contrast to the hydrolytic sensitivity of other cyclophosphazene-based ligands, particularly pyrazolyl cyclophosphazenes, **L** is remarkably insensitive. It may also be noted that we have previously observed P–O bond scission in the reaction between N_3P_3(O-C_5H_4N-2)$_6$, $CuCl_2$ and $Co(NO_3)_2 \cdot 6H_2O$ [9d]. Such a P–O bond scission was also observed in the reaction of N_3P_3(O-C_5H_3-4-CH_3-N-2)$_6$ and $[Cu(MeCN)_4]PF_6$ [9c].

Metal complexes **2–4** were characterized by a variety of techniques. Although these complexes do not show the parent ion peaks in their FAB-MS, they do show prominent fragment ions: $[LCuNO_3]^+$, 821; $[LCu]^+$, *m*/*z* 759; $[LCo(NO_3)]^+$, *m*/*z* 817; $[LCo]^+$, *m*/*z* 755 and $[LZnCl]^+$, *m*/*z* 795.

Complexes **2** and **3** show a broad d–d band at 768 and 506 nm, respectively. The EPR spectrum of the copper complex **2** has been recorded in dichloromethane–toluene glass (120 K). It shows a resolved axial Cu(II) species with a four-line pattern in the parallel region ($g_\parallel = 2.35$; $A_\parallel = 146$ G; $g_\perp = 2.07$ for compound **2**). The *g* values obtained (greater than 2.0) as well as the observation that $g_\parallel > g_\perp$, indicates a $d_{x^2-y^2}$ ground state for the Cu(II) ion [15]. Room temperature magnetic studies of **2** and **3** support that the metal ions are in a divalent state. Thus, the room temperature magnetic moment value of complex **2** is 1.80 BM (*spin only* $\mu_B = 1.73$ BM) while the magnetic moment value of **3** is 4.02 BM (*spin only* $\mu_B = 3.87$ BM).

The $^{31}P\{^1H\}$ NMR spectra of complexes **2** and **3** were affected by the paramagnetic nature of the metal ions and were uninformative. The zinc complex **4**, on the other hand, shows a triplet at 23.9 ppm [which is slightly upfield shifted with respect to the free ligand (26.7 ppm)] and a doublet at 7.6 ppm (which is shifted by 0.2 ppm vis-a-vis the free ligand). The coupling constant ^2J(P–N–P) = 98.6 Hz in **4** is slightly higher than that observed in **L**. Infrared spectra of **2–4** reveal that ν(P=N) seen for the free ligand at 1223 cm^{-1} is altered upon complexation. New peaks at 1290 (s), 1225 (s) for **2**; 1291 (s), 1228 (s) for **3**; 1299 (s), 1221 (s) for **4** are seen, while the peak at 1223 $cm^{-1}$is split, indicating the involvement of the cyclophosphazene ring nitrogen atom in coordination to the metal ion. This feature is similar to that observed previously in the case of pyrazolyl cyclophosphazenes [6] as well as pyridyloxy cyclophosphazenes [9]. The involvement of the cyclophosphazene ring nitrogen coordination is confirmed by the X-ray crystal structure analysis of **2–4**.

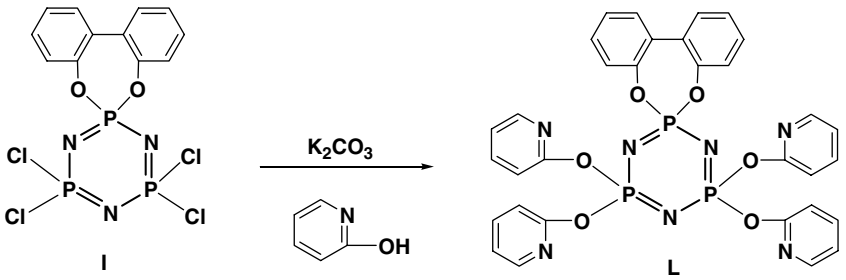
3.2. X-ray crystal structures of L and 2–4

The ligand **L** crystallized in the monoclinic cell system (*C*2/*c*). The molecular structure of **L** is shown in Fig. 1. One face of the molecule is non-coordinating because of the spirocyclic ring formation. The other side of the cyclophosphazene ring contains four pyridyloxy substituents as potential coordination sites. The cyclophosphazene ring is nearly planar. The P–N bond distances in **L** do not show large variations (Table 2).

Table 1
Crystal and structure refinement data for compounds **L** and **2**–**4**

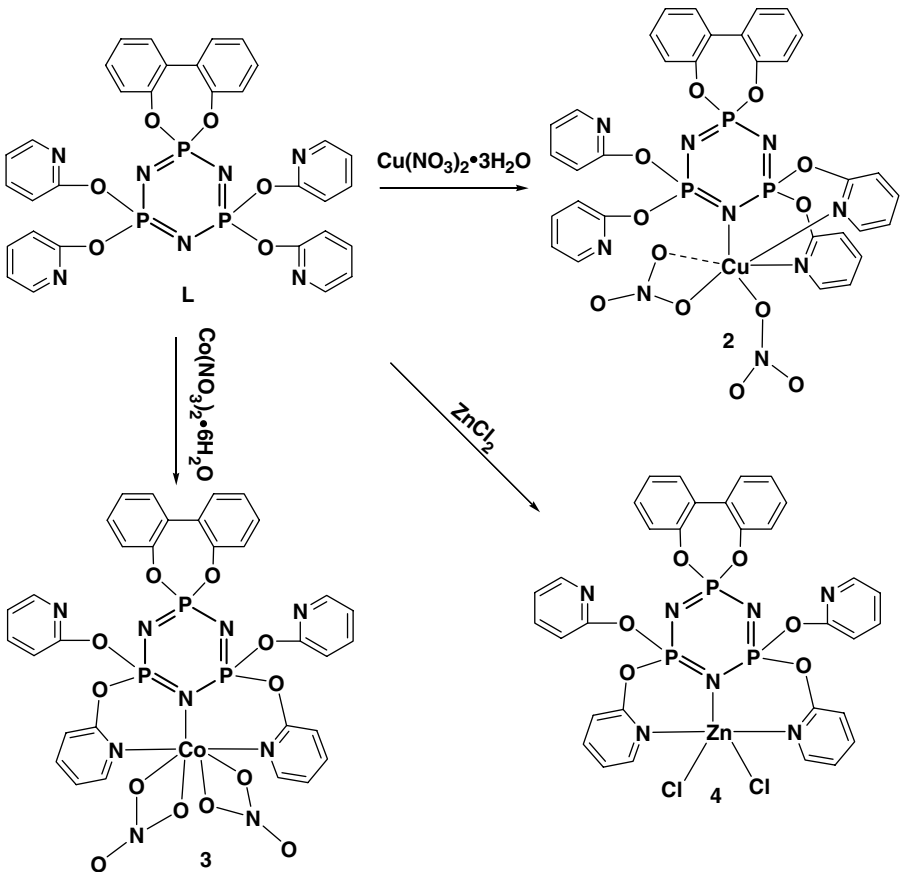
Parameters	L	2	3	4
Empirical formula	$C_{32}H_{24}N_7O_6P_3$	$C_{34}H_{28}N_9P_3O_{12}CuCl_4$	$C_{32}H_{24}N_9O_{12}P_3Co$	$C_{32}H_{24}N_7O_6P_3ZnCl_2$
Formula weight	695.49	1052.92	878.44	831.76
Temperature (K)	100(2)	273(2)	100(2)	100(2)
Wavelength (Å)	0.71073	0.71073	0.71073	0.71073
Crystal system	monoclinic	monoclinic	monoclinic	triclinic
Space group	$C2/c$	$P2_1/c$	$C2/c$	$P\bar{1}$
Unit cell dimensions				
a (Å)	20.2931(17)	15.863(11)	9.618(5)	9.3110(19)
b (Å)	10.5916(7)	16.891(12)	29.239(5)	13.924(3)
c (Å)	16.7110(13)	17.080(12)	14.776(5)	14.229(3)
α (°)	90	90	90	77.48(3)
β (°)	120.105(2)	98.338(13)	93.34(5)	87.79(3)
γ (°)	90	90	90	87.18(3)
V (Å^3)	3107.3(4)	4528(6)	4148(3)	1798.0(6)
Z	4	4	4	2
D_{calc} (Mg/m^3)	1.487	1.544	1.407	1.536
Absorption coefficient (mm^{-1})	0.250	0.892	0.597	1.019
F(000)	1432	2132	1788	844
Crystal size (mm)	0.2 × 0.1 × 0.2	0.2 × 0.1 × 0.1	0.1 × 0.2 × 0.1	0.1 × 0.1 × 0.1
θ Range for data collection (°)	2.25–28.29	2.03–28.28	1.96–28.34	2.19–28.27
Limiting indices	$-21 \leqslant h \leqslant 26$, $-13 \leqslant k \leqslant 14$, $-22 \leqslant l \leqslant 10$	$-20 \leqslant h \leqslant 20$, $-20 \leqslant k \leqslant 22$, $-22 \leqslant l \leqslant 14$	$-11 \leqslant h \leqslant 12$, $-38 \leqslant k \leqslant 38$, $-19 \leqslant l \leqslant 13$	$-11 \leqslant h \leqslant 12$, $-18 \leqslant k \leqslant 16$, $-15 \leqslant l \leqslant 18$
Reflections collected	10171	28420	13797	12061
Independent reflections (R_{int})	3807 (0.0233)	10987 (0.1072)	5115 (0.0305)	8540 (0.0176)
Data/restraints/parameters	3807/0/218	10987/0/568	5115/0/259	8540/0/460
Goodness-of-fit on F^2	1.057	0.975	0.954	1.045
Final R indices [$I > 2\sigma(I)$]	$R_1^a = 0.0350$, $wR_2^b = 0.0952$	$R_1 = 0.0611$, $wR_2 = 0.1565$	$R_1 = 0.0532$, $wR_2 = 0.1347$	$R_1 = 0.0405$, $wR_2 = 0.1036$
R indices (all data)	$R_1 = 0.0371$, $wR_2 = 0.0970$	$R_1 = 0.1480$, $wR_2 = 0.1877$	$R_1 = 0.0728$, $wR_2 = 0.1449$	$R_1 = 0.0481$, $wR_2 = 0.1074$
Largest difference in peak and hole (e Å^{-3})	0.545 and −0.330	0.834 and −0.646	0.407 and −0.294	0.569 and −0.362

[a] $R_1 = \sum\|(F_o| - |F_c\|)/\sum|F_o|$.
[b] $wR_2 = \{\sum[w(F_o^2 - F_c^2)^2]/\sum[w(F_o^2)^2]\}^{1/2}$.



Scheme 1. Synthesis of ligand **L**.

Compound **2** crystallized in the monoclinic cell system ($P2_1/c$). The molecular structure of **2** is shown in Fig. 2. The metric parameters of **2** are summarized in Table 2. The molecular structure of **2** reveals that the copper atom in **2** has a coordination number of six (3N, 3O) and is present in a distorted octahedral geometry (Fig. 2) with a facial coordination mode. The nitrogen coordination environment around copper can be described as η^3-*gem*-N_3 with two of the three coordinating nitrogen atoms being derived from the geminally substituted pyridyloxy groups. The third donor nitrogen atom is from the cyclophosphazene ring nitrogen atom which is located adjacent to the phosphorus atom bearing the coordinating pyridyloxy arms. The remaining coordination environment around copper is satisfied by the two nitrate ligands. One of the nitrate ligands is chelating while the other acts in a unidentate mode. The bond distance Cu–O8 [2.5867(7) Å] is considerably longer than the remaining Cu–O distances [average



Scheme 2. Synthesis of complexes **2**–**4** from ligand **L**.

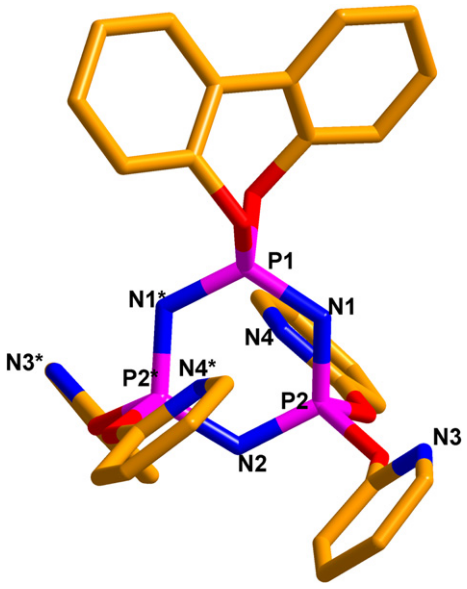


Fig. 1. Diamond view of **L**.

1.986(3) Å]. Among the Cu–N distances, while one, Cu–N6 [2.351(3) Å], is longer, the other two are slightly shorter [Cu–N7, 1.984(3) Å; Cu–N2, 2.057(3) Å]. It is interesting to compare the coordination behavior observed in the present instance with that seen in earlier instances involving $N_3P_3(O\text{-}C_5H_4N\text{-}2)_6$. In general, with the latter ligand coordination modes such as η^5-*gem*-N_5; η^3-*non-gem*-N_3 and η^2-*gem*-N_2 are seen. The η^3-*gem*-N_3 coordination mode observed in the present instance is quite rare. Previous examples of such coordination behavior are provided by the complexes $N_3P_3Ph_4(Me_2Pz)_2 \cdot M(CO)_3$ [M = Mo or W] [3b] and $[\{N_3P_3(MeNC_2H_4NMe)_2Pz_2\}Re(CO)_3]^+$ [5b].

Compound **3** crystallized in a monoclinic cell system (*C*2/*c* space group). The molecular structure of **3** is shown in Fig. 3a. It reveals that in **3** the cobalt atom has a coordination number of seven (3N, 4O) and is present in a pentagonal bipyramidal geometry (Fig. 3), with the two pyridyl groups axially disposed (N3 and N3*). The remaining ligands viz., two chelating nitrate anions and the linearly bound phosphazene nitrogen (N2, O4, O4*, O5 and O5*) occupy the equatorial positions. The nitrogen coordination environment around cobalt can be described as η^3-*non-gem*-N_3 with two of the three coordinating nitrogen atoms derived from the non-geminally substituted pyridyloxy groups; the third donor nitrogen atom is from the cyclophosphazene ring. Compound **3** represents the first example of the stabilization of a heptacoordinate Co(II) by any cyclophosphazene ligand. Among the Co–N distances, Co–N2 (involving the cyclophosphazene ring nitrogen atom) is shorter [2.053(3) Å] in comparison with the distances involving the pyridyloxy

Table 2
Important bond lengths (Å) and bond angles (°) for compounds **L** and **2**–**4**

Bond lengths (Å)		Bond angles (°)	
*Ligand **L***			
P1–N1	1.5826(10)	N1–P1–N1[a]	119.39(8)
P1–N1[a]	1.5827(10)	N1–P2–N2	117.75(6)
P2–N1	1.5805(11)	P2–N2–P1	119.48(7)
P2[a]–N1[a]	1.5805(11)	P2–N2–P2[a]	121.22(9)
P2–N2	1.5817(8)		
N2–P2[a]	1.5818(8)		
*Compound **2***			
P1–N1	1.579(3)	P2–N1–P1	124.07(19)
P1–N3	1.592(3)	P3–N2–P2	120.24(18)
P2–N1	1.561(3)	P3–N3–P1	122.00(18)
P2–N2	1.603(3)	N3–P3–N2	118.93(16)
P3–N2	1.625(3)	N1–P2–N2	116.50(15)
P3–N3	1.553(3)	N1–P1–N3	116.97(16)
Cu–N2	2.057(3)	O7–Cu–N7	157.56
Cu–N6	2.351(3)	O7–Cu–O10	85.99(11)
Cu–N7	1.984(3)	N7–Cu–O10	93.81(12)
Cu–O7	1.984(2)	O7–Cu–N2	92.98(11)
Cu–O10	1.989(3)	N7–Cu–N2	87.03(12)
Cu–O8	2.5867	O10–Cu–N2	178.92(10)
		O7–Cu–N6	89.88(11)
		N7–Cu–N6	112.43(12)
		O10–Cu–N6	95.67(12)
		N2–Cu–N6	84.63(10)
*Compound **3***			
P1–N1	1.578(2)	P2–N1–P1	121.17(12)
P2–N1	1.561(2)	P2–N2–P2[b]	120.47(2)
P2–N2	1.600(2)	P2–N2–Co	119.77(8)
Co–N2	2.053(3)	N1–P1–N1[b]	117.97(14)
Co–N3	2.236(3)	N1–P2–N2	117.34(11)
Co–O5	2.132(3)	N2–Co–O5	141.36(9)
Co–O4	2.393(3)	O5–Co–O5[b]	77.28(2)
		N2–Co–N3	90.24(6)
		O5–Co–N3	93.19(10)
		O5[b]–Co–N3	86.44(10)
		N3–Co–N3[b]	79.52(12)
		N2–Co–O4[b]	86.66(100)
		O5–Co–O4[b]	32.10(16)
		O5[b]–Co–O4[b]	54.66(11)
		N3–Co–O4[b]	98.39(10)
		N3[b]–Co–O4[b]	81.64(11)
*Compound **4***			
P1–N1	1.580(2)	N3–P1–N1	117.79(10)
P1–N3	1.577(2)	N1–P2–N2	118.10(10)
P2–N1	1.558(2)	N3–P3–N2	118.10(10)
P2–N2	1.609(2)	P2–N1–P1	121.85(11)
P3–N3	1.562(2)	P2–N2–P3	119.89(11)
P3–N2	1.608(2)	N2–Zn–Cl1	116.02(6)
Zn–N2	2.0685(18)	N2–Zn–Cl2	119.20(6)
Zn–Cl1	2.2495(8)	Cl1–Zn–Cl2	124.76(3)
Zn–Cl2	2.2504(8)	N2–Zn–N6	87.97(7)
Zn–N6	2.2856(2)	Cl1–Zn–N6	90.93(5)
Zn–N4	2.3029(2)	Cl2–Zn–N6	92.45(6)
		N2–Zn–N4	88.04(7)
		Cl1–Zn–N4	91.42(6)
		Cl2–Zn–N4	88.91(6)
		N6–Zn–N4	175.95(6)

[a] Symmetry transformations used to generate equivalent atoms: $1-x$, y, $-z+1/2$.
[b] Symmetry transformations used to generate equivalent atoms: $1-x+2$, y, $-z+1/2$.

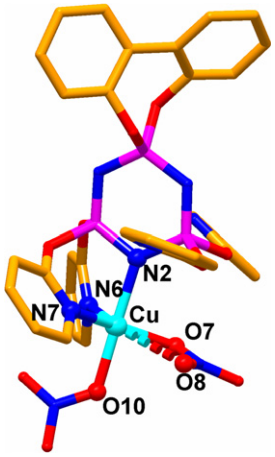


Fig. 2. Diamond picture of compound **2**. Hydrogen atoms have been omitted for clarity.

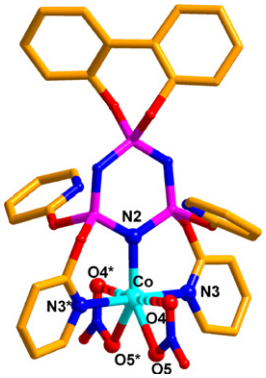


Fig. 3. Diamond picture of compound **3**. Hydrogen atoms have been omitted for clarity.

nitrogen atoms [2.235(3) Å]. The nitrate ligand is bound in an anisobidentate mode as shown by the presence of two types of Co–O distances [Co–O5, 2.132(3) Å; Co–O4, 2.393(3) Å]. The metric parameters for this compound are given in Table 2.

Compound **4** crystallized in a triclinic cell system ($P\bar{1}$). The molecular structure of **4** is shown in Fig. 4. Zinc has

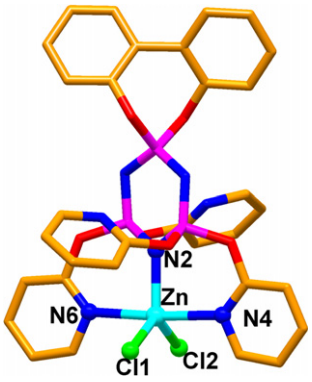


Fig. 4. Diamond picture of compound **4**. Hydrogen atoms have been omitted for clarity.

a coordination number of five (3N, 2Cl) and is present in a trigonal bipyramidal geometry (Fig. 4) with the two pyridyl groups being axially disposed (N4 and N6; N4–Zn2–N6: 175.95(6)°). Other ligands viz., the two chloride anions and the linearly bound phosphazene nitrogen atom are present in equatorial positions (N2, Cl1 and Cl2). The nitrogen coordination environment around zinc can be described as η^3-*non-gem*-N_3 with two of the three coordinating nitrogen atoms derived from the non-geminally substituted pyridyloxy groups; the third donor nitrogen atom is from the cyclophosphazene ring. This coordination mode leads to the generation of two six-membered rings (Zn-N6-C-O-P-N2 and Zn-N4-C-O-P-N2). The structural index τ which defines the extent of deviation from trigonal bipyramidal to square pyramidal geometry ($\tau = 1$ for a perfect trigonal bipyramidal; $\tau = 0$ for a perfect square based pyramid) [16] is 0.946 indicating only a small deviation from the regular trigonal bipyramidal geometry. The coordination response of **L** towards the zinc is similar to that found in dinuclear zinc complexes obtained from N_3P_3-(2-OC_5H_4N)$_6$ [9d] and N_3P_3(3,5-Me_2Pz)$_6$ [3d]. The Zn–N distances reveal that the distance involving the cyclophosphazene ring (Zn–N2; 2.0685(2) Å) is shorter than those involving the pyridyloxy nitrogen atoms (Zn–N4 2.303(3) Å and Zn–N6 2.2857(2) Å), consistent with the situation found in compounds **2** and **3** (Table 2).

3.3. Comparison of the structural features of the cyclophosphazene ring in *L* and *2–4*

The cyclophosphazene ring in ligand **L** is reasonably planar with two pairs of atoms (P2 and P2*) and (N1 and N1*) deviating slightly from the mean plane of the six-membered P_3N_3 ring. Interestingly, within each pair, the two atoms deviate from the mean plane in opposite directions (Table S1). The average P–N distance in **L** is 1.5816(11) Å. The average ring N–P–N angle is 118.57(8)° while the average P–N–P angle is slightly wider, 120.35(9)°. It must be mentioned here that in contrast to the situation found in metal complexes formed with pyrazolyl cyclophosphazenes, metallation does not cause any distortion in the cyclophosphazene ring skeleton in **2–4**. This feature is quite characteristic of pyridyloxy cyclophosphazenes and has been attributed to the flexibility of the coordinating pyridyloxy arms. It has been argued that the spacer oxygen atom acts as a hinge and provides rotational flexibility to the coordinating arm [9]. Because of this the ligand does not encounter any geometric constraint upon coordination to the metal ion. Whereas in **3** and **4** the metal is coplanar with the cyclophosphazene ring, in **2** the metal is deviated away by 0.19 Å. The P–N ring bond distances flanking the coordinating pyridyloxy arms are longer [average 1.614(3) Å for **2**, 1.601(2) Å for **3** and 1.608(2) Å for **4**], in comparison to the other P–N bond distances. This feature is similar to that observed in other cyclophosphazene metal complexes [9].

4. Conclusion

In conclusion, spiro-$N_3P_3(O_2C_{12}H_8)(OC_5H_4N\text{-}2)_4$ has been shown to be an efficient multi-site coordination ligand towards the transition metal ions Cu(II), Co(II) and Zn(II), affording mononuclear complexes [$LCu(NO_3)_2$], [$LCo(NO_3)_2$] and [$LZnCl_2$]. The η^3-*gem*-N_3 coordination mode in **2** is quite uncommon among pyridyloxy cylcophosphazenes, and in fact among other cyclophosphazene ligands also. In [$LCo(NO_3)_2$], Co(II) is heptacoordinate in a pentagonal bipyramidal geometry with a 3N, 4O coordination environment. This represents the first example where a heptacoordinate Co(II) is stabilized by a cyclophosphazene ligand. The coordination response of **L** in the complexes [$LCo(NO_3)_2$] and [$LZnCl_2$] is η^3-*non-gem*-N_3 and corresponds to a situation found with pyridyloxy cyclophosphazens [9], pyrazolyl cyclophosphazenes [2a,6a–c] as well as cyclophosphazene hydrazides [6d].

Acknowledgments

We thank the Department of Science and Technology, India and the Council of Scientific and Industrial Research, India for financial support. V.C. is a Lalith Kapoor Professor of Chemistry. V.C. is thankful for a J.C. Bose fellowship from the Department of Science and Technology. B.M.P. thanks the Council of Scientific and Industrial Research for a Senior Research Fellowship.

Appendix A. Supplementary material

CCDC 645826, 645827, 645828 and 645829 contain the supplementary crystallographic data for **L**, **2**, **3** and **4**. These data can be obtained free of charge via http://www.ccdc.cam.ac.uk/conts/retrieving.html, or from the Cambridge Crystallographic Data Centre, 12 Union Road, Cambridge CB2 1EZ, UK; fax: (+44) 1223-336-033; or e-mail: deposit@ccdc.cam.ac.uk. The supplementary material consists of Table S1. Supplementary data associated with this article can be found, in the online version, at doi:10.1016/j.poly.2007.09.026.

References

[1] (a) J.E. Mark, H.R. Allcock, R. West, Inorganic Polymers, Prentice-Hall, Englewood Cliffs, NJ, 1992;
(b) V. Chandrasekhar, V. Krishnan, Adv. Inorg. Chem. 53 (2002) 159;
(c) H.R. Allcock, Chemistry and Application of Polyphosphazenes, Wiley, Hoboken, NJ, 2003;
(d) M. Gleria, R. De Jaeger (Eds.), Applicative Aspects of Cyclophosphazenes, Nova Science Publishers, New York, 2004;
(e) V. Chandrasekhar, Inorganic and Organometallic polymers, Springer, Heidelberg, 2005.
[2] (a) V. Chandrasekhar, S. Nagendran, Chem. Soc. Rev. 30 (2001) 193;
(b) A. Steiner, S. Zacchini, P.I. Richards, Coord. Chem. Rev. 227 (2002) 193;

(c) V. Chandrasekhar, V. Krishnan, in: M. Gleria, R. De Jaeger (Eds.), Applicative Aspects of Cyclophosphazenes, Nova Science Publishers, New York, 2004 (Chapter 7);
(d) U. Diefenbach, in: M. Gleria, R. De Jaeger (Eds.), Applicative Aspects of Cyclophosphazenes, Nova Science Publishers, New York, 2004 (Chapter 8);
(e) V. Chandrasekhar, P. Thilagar, B. Murugesa Pandian, Coord. Chem. Rev. 251 (2007) 1045.

[3] (a) A. Chandrasekaran, S.S. Krishnamurthy, M. Nethaji, Inorg. Chem. 32 (1993) 6102;
(b) A. Chandrasekaran, S.S. Krishnamurthy, M. Nethaji, J. Chem. Soc., Dalton Trans. (1994) 63;
(c) A. Chandrasekharan, S.S. Krishnamurthy, M. Nethaji, Inorg. Chem. 33 (1994) 3085;
(d) D. Min, Y. Do, Chem. Lett. (1994) 1989.

[4] (a) G.T. Lawson, C. Jacob, A. Steiner, Eur. J. Inorg. Chem. (1999) 1881;
(b) P.I. Richards, A. Steiner, Inorg. Chem. 43 (2004) 2810.

[5] (a) B.H. Koo, Y. Byun, E. Hong, Y. Kim, Y. Do, Chem. Commun. (1998) 1227;
(b) M. Harmjanz, B.L. Scoot, C.J. Burns, Chem. Commun. (2002) 1386;
(c) M. Harmjanz, I.M. Piglosiewicz, B.L. Scott, C.J. Burns, Inorg. Chem. 43 (2004) 642;
(d) E.W. Ainscough, A.M. Brodie, A.B. Chaplin, J.M. O'Connor, C.A. Otter, J. Chem. Soc., Dalton Trans. (2006) 1264;
(e) E.W. Ainscough, A.M. Brodie, G.B. Jameson, C.A. Otter, Polyhedron 22 (2007) 460.

[6] (a) K.R.J. Thomas, V. Chandrasekhar, P. Pal, S.R. Scoot, R. Halford, A.W. Cordes, Inorg. Chem. 21 (1993) 673;
(b) K.R.J. Thomas, V. Chandrasekhar, S.R. Scoot, R. Halford, A.W. Cordes, J. Chem. Soc., Dalton Trans. (1993) 2589;
(c) K.R.J. Thomas, P. Tharmaraj, V. Chandrasekhar, C.D. Bryan, A.W. Cordes, Inorg. Chem. 33 (1994) 5382;
(d) V. Chandrasekhar, V. Krishnan, A. Steiner, J.F. Bickley, Inorg. Chem. 43 (2004) 166;
(e) V. Chandrasekhar, V. Krishnan, R. Azhakar, C. Madhavaiah, S. Verma, J. Chem. Sci. 43 (2005) 175.

[7] (a) V. Chandrasekhar, V. Krishnan, A. Athimoolam, G.T.S. Andavan, Can. J. Chem. 80 (2002) 1415;
(b) V. Chandrasekhar, V. Krishnan, P. Thilagar, C. R. Chim. 7 (2004) 915.

[8] (a) V. Chandrasekhar, A. Athimoolam, S.G. Srivatsan, P.S. Sundaram, S. Verma, A. Steiner, S. Zacchini, R.J. Butcher, Inorg. Chem. 41 (2002) 5172;
(b) V. Chandrasekhar, A. Athimoolam, Org. Lett. 4 (2002) 2113;
(c) V. Chandrasekhar, P. Deria, V. Krishnan, A. Athimoolam, S. Singh, C. Madhavaiah, S.G. Srivatsan, S. Verma, Bioorg. Med. Chem. Lett. 14 (2004) 1559;
(d) V. Chandrasekhar, A. Athimolam, V. Krishnan, R. Azhakar, C. Madhavaiah, S. Verma, Eur. J. Inorg. (2005) 1482.

[9] (a) E.W. Ainscough, A.M. Brodie, C.V. Depree, J. Chem. Soc., Dalton Trans. (1999) 4123;
(b) E.W. Ainscough, A.M. Brodie, B. Moubaraki, K.S. Murray, C.A. Otter, J. Chem. Soc., Dalton Trans. 20 (2005) 3337;
(c) E.W. Ainscough, A.M. Brodie, C.V. Depree, G.B. Jameson, C.A. Otter, Inorg. Chem. 44 (2005) 7325;
(d) V. Chandrasekhar, B. Murugesa Pandian, R. Azhakar, Inorg. Chem. 45 (2006) 3510;
(e) E.W. Ainscough, A.M. Brodie, C.V. Depree, G.B. Jameson, C.A. Otter, Polyhedron 25 (2006) 2341.

[10] G.A. Carriedo, L. Fernández-Catuxo, F.J.G. Alonso, P. Gómez-Elipe, P.A. González, Macromolecules 29 (1996) 5320.

[11] O. Khan, Molecular Magnetism, Wiley–VCH, New York, 1993.

[12] G.M. Sheldrick, SHELXTL, version 6.14, Bruker AXS Inc., Madison, WI, 2003.

[13] P. van der Sluis, A.L. Spek, Acta Crystallogr., Sect. A 46 (1990) 194.

[14] G.A. Carriedo, P.G. Elipe, F.J.G. Alonso, L. Fernández-Catuxo, M.R. Díaz, S.G. Granda, J. Organomet. Chem. 498 (1995) 207.

[15] M.C.B. De Oliveira, M. Scarpellini, A. Neves, H. Terenzi, A.J. Bortoluzzi, B. Szpoganics, A. Greatti, A.S. Mangrich, E.M. De Souza, P.M. Fernandez, M.R. Soares, Inorg. Chem. 44 (2005) 921.

[16] S. Tanase, I.A. Koval, E. Bouwman, R.D. Gelder, J. Reedijk, Inorg. Chem. 44 (2005) 7860.

Available online at www.sciencedirect.com
ScienceDirect
Polyhedron 27 (2008) 263–267
POLYHEDRON
www.elsevier.com/locate/poly

Hybrid inorganic–organic layered structures of $[AuCl_4]^-$ and protonated bipyridyl derivatives

Susan A. Bourne *, Lesego J. Moitsheki [1]

Department of Chemistry, University of Cape Town, Rondebosch 7701, South Africa

Received 13 August 2007; accepted 11 September 2007
Available online 22 October 2007

Abstract

Complexes of $[AuCl_4]^-$ with 4,4′-dipyridylethane, 4,4′-dipyridylethene and 4,4′-bipyridine-*N*,*N*′-dioxide have been prepared by a solvent layering method. All three complexes pack in distinct organic and inorganic layers: $[H_2\text{-dpa}][AuCl_4]Cl$ (**1**) and $[H_2\text{-dpe}][AuCl_4]Cl$ (**2**) are isostructural and consist of layers of $[AuCl_4]^-$ anions alternating with hydrogen-bonded dipyridyl···Cl···dipyridyl layers. In [H-bpdo][$AuCl_4$] (**3**), the organic layers consist instead of hydrogen-bonded bipyridyldioxide cations. This structure is the first report of a structure containing protonated 4,4′-bipyridine-1,1′-dioxide.
© 2007 Elsevier Ltd. All rights reserved.

Keywords: Gold(III)chloride complexes; Dipyridyl derivatives; Layered organic/inorganic structures

1. Introduction

Novel metal–organic compounds are of interest for their extensive structural diversity and potential functional properties [1–3]. A considerable amount of research has exploited bridging ligands such as 4,4′-bipyridine and its analogues, bound to different metals [4–8]. These complexes are usually held together by supramolecular interactions such as hydrogen bonding, van der Waals forces or π–π interactions, all of which play a role in the self-assembly process [9,10].

We have become interested in preparing self-assembled hybrid organic/inorganic materials as either coordination polymers or layered structures. In some cases the same components can be used to prepare metal–organic networks or inorganic–organic layered structures [11–13]. Among the latter, the hybrid perovskites [14] have attracted a great deal of interest because of their structural, magnetic, optical and electrical properties. These properties can be readily modified by replacement of the metal, halide or amine. The tendency of the hybrids to self-assemble from the solid or liquid phase arises from the range of interactions seen in these compounds, from van der Waals forces between organic components, hydrogen bonding within the organic layer or between organic and inorganic components to ionic and covalent bonds within the metal halide sheets [15,16]. This strategy has been extended to allow the preparation of a wide variety of ionic hydrogen-bonded materials, by combining perhalometallate anions with organic cations [17,18]. While [4,4′-H_2bipy] salts with MCl_4^{n-} are not uncommon, there are no reports of protonated dipyridylethane (4,4′-H_2dpa) or dipyridylethene (4,4′-H_2dpe) with $[MCl_4]^{n-}$ anions. Furthermore, a search of the CSD [19] showed that a protonated form of 4,4′-bipyridine-1,1′-dioxide $[H\text{-bpdo}]^+$ has never been reported in a crystal structure [20]. On the other hand, $[AuCl_4]^-$ has been found previously to be a poor acceptor of hydrogen bonds [21]. In this paper we report three structures of $[AuCl_4]^-$ with the protonated forms of 1,2-bis(4-pyridyl)ethane (H_2-dpa) (**1**), *trans*-1,2-bis(4-pyridyl)ethene (H_2-dpe) (**2**) and 4,4′-bipyridine-1,1′-dioxide (H-bpdo) (**3**).

* Corresponding author. Tel.: +27 21 6502563; fax: +27 21 6897499.
E-mail address: susan.bourne@uct.ac.za (S.A. Bourne).
[1] Present address: Institute of Applied Materials, University of Pretoria, Lynnwood Road, Pretoria 0002, South Africa.

0277-5387/$ - see front matter © 2007 Elsevier Ltd. All rights reserved.
doi:10.1016/j.poly.2007.09.007

2. Experimental

2.1. Materials and general methods

All the reagents for syntheses were commercially available and employed without further purification. Elemental analyses were performed on a Carlo Erba elemental analyzer Model 1106 and IR spectra on a Perkin–Elmer 983 IR spectrometer using KBr pellets.

2.2. Syntheses of complexes *1–3*

Single crystals of **1–3** suitable for X-ray analysis were obtained by the slow diffusion of layers containing 0.2 mmol of the respective dipyridyl compound (dissolved in 5 cm^3 methanol) and 3 cm^3 of $H[AuCl_4]$. Crystals suitable for X-ray diffraction were obtained after several weeks. Powder X-ray diffraction (Huber Guinier 670 Imaging Plate diffractometer with Cu Kα radiation, 1.542 Å) was used to confirm that the bulk sample crystallized matched that of the single crystal selected for structure elucidation in each case. Compounds **1–3** are thermally stable to temperatures above 200°C.

2.2.1. *[H_2-dpa][$AuCl_4$]Cl (**1**)*

IR (KBr pellet, cm^{-1}): 3192 ms, 3077 ms, 2029 w, 1953 w, 1633 s, 1591 s, 1503 vs, 1412 m, 1367 m, 1325 w, 1241 mw, 1184 m, 1088 w, 1017 w, 956 w, 817 s, 747 m, 527 m. Elemental *Anal.* Calc. for $C_{12}H_{14}AuCl_5N_2$: C, 25.72; H, 2.52; N, 5.00. Found: C, 25.83; H, 2.56; N, 4.83%.

2.2.2. *[H_2-dpe][$AuCl_4$]Cl (**2**)*

IR (KBr pellet, cm^{-1}): 3072 ms, 3056 ms, 2963 s, 2029 w, 1953 w, 1620 s, 1595 w, 1503 vs, 1367 w, 1345 m, 1283 m, 1237 m, 1190 s, 1088 m, 1016 w, 958 ms, 815 s, 731 m, 540 m. Elemental *Anal.* Calc. for $C_{12}H_{12}AuCl_5N_2$: C, 25.81; H, 2.17; N, 5.02. Found: C, 25.84; H, 2.16; N, 4.85%.

2.2.3. *[H-bpdo][$AuCl_4$] (**3**)*

IR (KBr pellet, cm^{-1}): 3102 s, 3050 m, 1931 w, 1624 ms, 1545 w, 1476 ms, 1455 w, 1426 m, 1313 w, 1280 ms, 1187 mw, 1036 m, 871 m, 841 s, 747 s, 698 s, 650 m, 578 m, 548 ms. Elemental *Anal.* Calc. for $C_{10}H_9AuCl_4N_2O_2$: C, 22.75; H, 1.72; N, 5.31. Found: C, 23.12; H, 1.52; N, 5.29%.

2.3. Crystal structure solution and refinement

Data for crystal and molecular structure determination were measured on a Nonius KappaCCD diffractometer using graphite-monochromated Mo Kα radiation (0.7107 Å) at 113 K. In each case, a series of frames were recorded with width ranging from 1° to 1.5° in ϕ or in ω (with $\kappa \neq 0$) to ensure completeness of the data collected to $\theta > 25°$. The unit cell was indexed from the first 20 frames and positional data were refined along with diffractometer constants to give the final cell parameters. Integration and scaling correction [22] resulted in unique data sets corrected for Lorentz-polarization effects and for the effects of crystal decay and absorption by a combination of averaging of equivalence reflections and an overall volume and scaling correction. The structures were solved using SHELXS-97 and refined using the full-matrix least-squares methods in SHELXL-97 [23] with the aid of the program XSEED [24].

Table 1
Summary of crystallographic data for compounds **1–3**

	1	**2**	**3**
Empirical formula	$(C_{12}H_{14}N_2)\cdot(AuCl_4)\cdot Cl$	$(C_{12}H_{12}N_2)\cdot(AuCl_4)\cdot Cl$	$(C_{10}H_9N_2O_2)\cdot(AuCl_4)$
M	560.47	558.45	527.96
Temperature (K)	113	113	113
Crystal system	triclinic	triclinic	orthorhombic
Space group	$P\bar{1}$	$P\bar{1}$	$Cmc2_1$
a (Å)	7.339(2)	7.280(2)	17.756(4)
b (Å)	7.503(2)	7.562(2)	21.268(4)
c (Å)	7.928(2)	7.796(2)	7.556(2)
α (°)	108.47(3)	106.82(3)	90
β (°)	90.31(3)	89.43(3)	90
γ (°)	96.27(3)	98.05(3)	90
V $(Å)^3$	411.2(2)	406.5(2)	2854(1)
Z	1	1	8
D_{calc} (g cm^{-3})	2.263	2.281	2.458
μ (mm^{-1})	9.746	9.858	11.056
R_1 $[I \geqslant 2\sigma I]$[a]	0.0179	0.0217	0.0216
wR_2 (all data)[b]	0.0368	0.0420	0.0396

[a] $R_1 = \sum(|F_o| - |F_c|)/|F_o|$.
[b] $wR_2 = \{\sum[w(F_o^2 - F_c^2)^2/\sum w(F_o^2)^2]\}^{1/2}$.

Crystal structure refinement data are given in Table 1. Non-hydrogen atoms were modelled anisotropically. Hydrogen atoms attached to pyridyl nitrogens (**1** and **2**) or pyridyl oxygen (**3**) were located in the difference electron density maps and refined independently, while other hydrogen atoms were assigned an isotropic thermal parameter 1.2 times that of their parent atom and refined using a 'riding' model. Compounds **1** and **2** are isostructural; to render this easier to see the unit cell of **2** is reported in the alternative, non-reduced setting. Images of crystal and molecular structures were rendered using the program POV-Ray [25].

Perspective diagrams, showing thermal ellipsoids and atom labels are shown in Fig. 1.

3. Results and discussion

Compounds **1** and **2** are isostructural, while in **3** the unit cell is significantly longer in two dimensions. The asymmetric unit in **1** (and **2)** consists of half a gold atom (on a centre of inversion at the origin), two coordinated chlorine atoms, one chloride ion and half a dipyridyl molecule (with the central C7–C7′ bond on the centre of inversion at (1/2, 1/2, 1)). The asymmetric unit of **3** consists of two half $[AuCl_4]^-$ units (Au1 and its associated chlorines lie on the mirror plane at Wyckoff position *a*, while Au2 lies on the mirror with its chlorines perpendicular to the mirror plane) and a complete $[H\text{-bpdo}]^+$ cation. In all three structures the immediate environment of the gold atom is square planar with chlorine atoms at distances 2.280(2)–

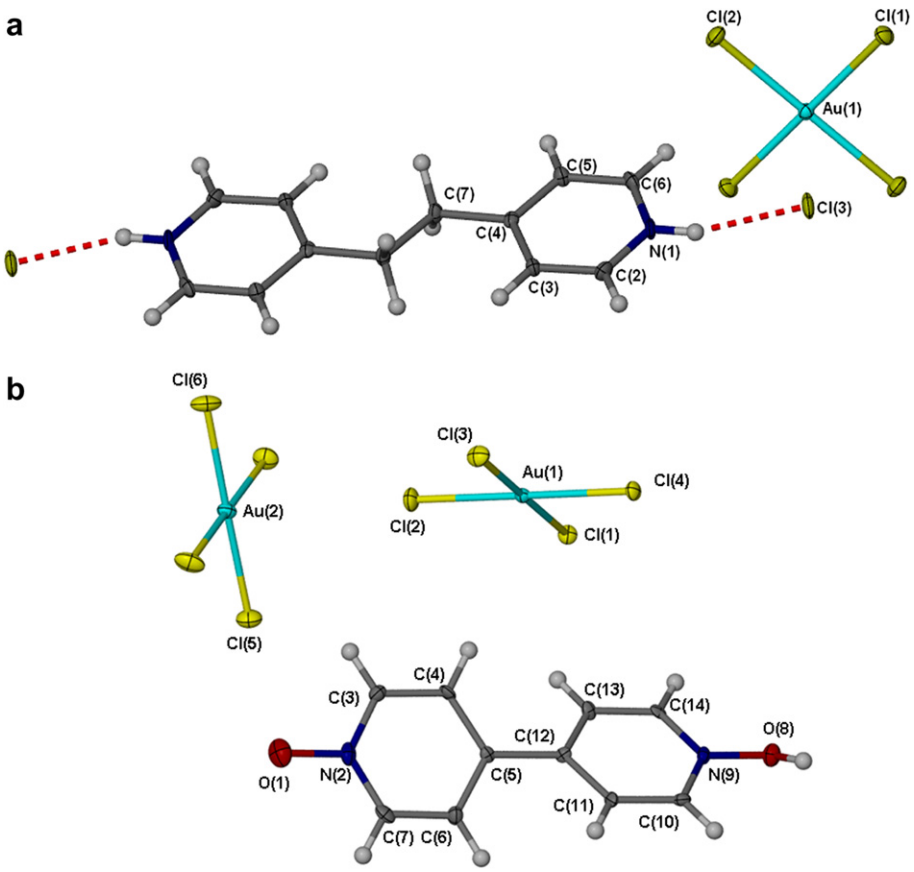


Fig. 1. Perspective diagrams of (a) **1** and (b) **3**, showing atomic displacement parameters (ellipsoids drawn at 50% probability) and atom labels.

2.291(2) Å and Cl–Au–Cl angles of 88.63(7)–90.90(6)°. In **1** and **2** there are also longer apical Au···Cl contacts with the chloride ion (3.670(1) Å in **1**; 3.640(1) Å in **2**), somewhat longer than the sum of van der Waals radii for Au and Cl (3.41 Å). This additional contact causes the Au^{III} centre to take on a distorted octahedral coordination environment and results in the formation of a polymeric $[AuCl_6]_n^{n-}$ anionic chain (Fig. 2). This is analogous to the polymeric chain formed in (*n*-butyl-3-methylimadazolium)$[AuCl_4]$ (Au···Cl 3.356 Å) and $[(H_7O_3)$(15-crown-5)$][AuCl_4]$[9] (Au···Cl 3.845 Å) [26]. Polymeric anionic chains with distorted square pyramidal gold ions and Au···Cl intermolecular interactions between 3.2 and 3.7 Å have also been reported [21,27]. There are no Au···Cl contacts in **3**, which lacks an uncoordinated chloride ion.

Fig. 2 also shows the N–H···Cl hydrogen bonds which link the $[H_2\text{-dpa}]^{2+}$ (**1**) or $[H_2\text{-dpe}]^{2+}$ (**2**) cations and the chloride ion. These are detailed in Table 2 and result in the formation of ribbons running along the crystallographic *b*-direction, with each layer of parallel $[AuCl_4]^-$ anions surrounded by ribbons of bipyridinium cations and Cl^- anions. All atoms in the pyridyl rings are within two standard deviations of the least-squares plane defined by the non-hydrogen atoms in the ring. The inversion symmetry forces coplanarity of the pyridyl rings in $[H_2\text{-dpa}]$ (**1**) and $[H_2\text{-dpe}]$ (**2**). Both $[H_2\text{-dpa}]$ and $[H_2\text{-dpe}]$ have been

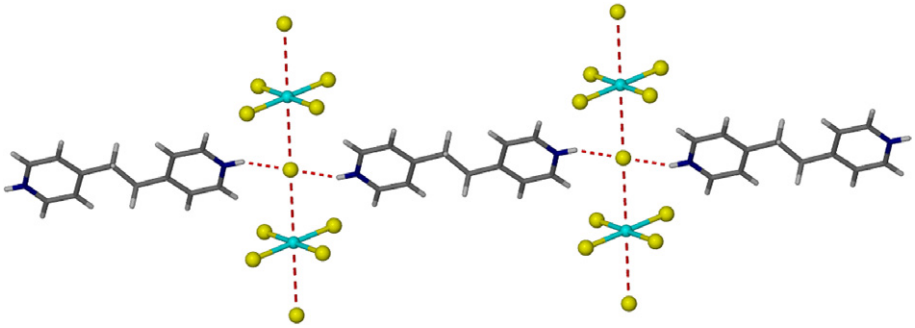


Fig. 2. Packing diagram of **1** showing the polymeric $AuCl_6$ chains and pyridinium–chloride hydrogen-bonded chains.

Table 2
Hydrogen bonds and intermolecular contacts

	D–H (Å)	D···A (Å)	D–H···A (°)	Symmetry operator
1				
N1–H1···Cl3	0.86(4)	3.022(3)	157(4)	x, y, z
2				
N1–H1···Cl3	0.91(5)	3.003(4)	165(4)	x, y, z
3				
O8–H8···O1	1.00(4)	2.433(5)	174(6)	$1/2 - x, y - 1/2, z$

crystallized with $[MnF_4(H_2O)_2]^{2-}$; the structures [28] (ERETEA and ERETIE) are isostructural and form extended hydrogen-bonded ribbons similar to those reported by Orpen *et al* for pyridyl cations with metal halides [29].

Fig. 3 shows layers of $[H\text{-bpdo}]^+$ cations surrounded by stacks of $[AuCl_4]^-$ anions which are arranged in an ···ABBA··· fashion (where A and B represent mutually perpendicular orientations). In **3**, the $[H\text{-bpdo}]^+$ cations are linked by short O–H···O hydrogen bonds (Table 2) into a chain running parallel to the crystallographic *b*-direction. The dihedral angle between least-squares planes through the linked pyridyl rings is 31.41°, a typical value for the bpdo molecule [20]. This twist between the rings causes a slight zigzag in the H-bonded chain (Fig. 3). The O···O distance in the [H-bpdo] diadduct is 2.433(5) Å, which is comparable to the 2.426(4) Å reported in the analogous 2,6-dimethylpyridine-*N*-oxide structure [30]. The oxygen atoms of the pyNO lie 2.974 Å from gold, completing a distorted octahedron around the gold atom, which is not the case in **3**. Nangia and co-workers recently studied short hydrogen bonds in pyrazine carboxylic acids by neutron diffraction [31]. Short O–H···O hydrogen bonds (O···O = 2.5–3.0 Å) are highly electrostatic in nature while very short hydrogen bonds (O···O = 2.2–2.5 Å) have an increasingly covalent character. Gilli and co-workers [32] report that very strong hydrogen bonds are of three main types: (i) negative charge-assisted H-bonds, O–H···O^-; (ii) positive charge-assisted H-bonds, O^+–H···O; (iii) resonance-assisted H-bonds, ···O=C–C=C–O–H··· **3** is of type (i), other examples of which include H-bonds between inorganic oxoacids and their conjugate bases and short, intramolecular H-bonds in dicarboxylic acids (O···O = 2.30–2.50 Å).

The CSD contains seven crystal structures of protonated pyridyl-*N*-oxide[2] but none containing protonated bpdo. A consideration of pK_a values may provide an explanation: the pK_a for pyridine-*N*-oxide (0.73 ± 0.15) is far lower than that of pyridine (5.23 ± 0.10). The pK_a for 4,4′-bipyridine is 3.27 ± 0.26, while that for 4,4′-bipyridine-1,1′-dioxide is not available in the literature. For comparison, pK_a values for 1,2-bis(4-pyridyl)ethane and *trans*-1,2-bis(4-pyridyl)ethene are 6.11 ± 0.20 and 5.50 ± 0.20. Compound **3** thus is the first report of a crystal structure containing $[H\text{-bpdo}]^+$. As expected, the N–O bonds are longer (1.348(5) and 1.351(5) Å) than the N–O bonds in free bpdo (1.301–1.343 Å, mean: 1.319(3) Å) and comparable to those in coordinated bpdo (1.291–1.365 Å, mean: 1.329(1) Å). The IR spectrum of **3** shows an intense and broad absorption within the 1600–400 cm^{-1} region, which appears instead of the usual OH stretching band in the

[2] CSD REFCODES: BALGUQ10, JIFREV, LOKFEW, LUPPUH, MIWYEW, PIKDES and QUSLUL.

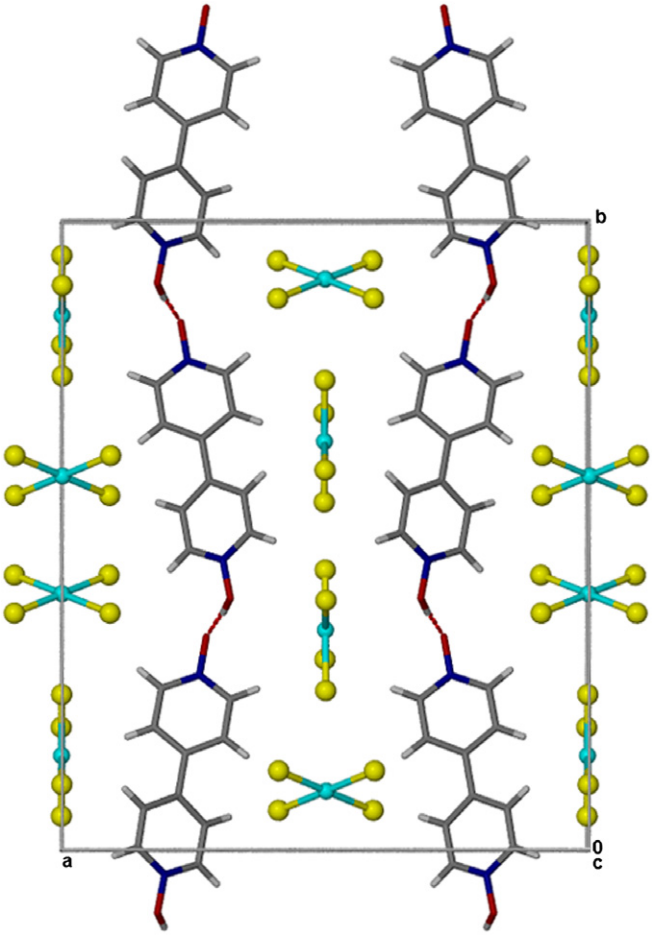


Fig. 3. Packing diagram of **3** showing the alternating stacks of $[AuCl_4]^-$ and $[H\text{-bpdo}]^+$ ions.

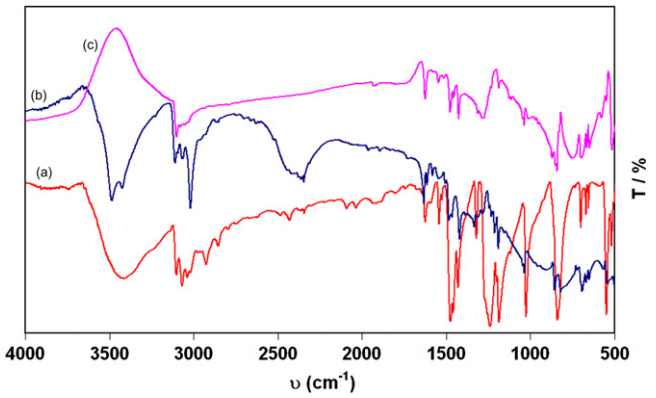


Fig. 4. Infrared spectrum of (a) bpdo, (b) bpdo protonated by addition of HCl, (c) compound **3**.

higher frequency region (Fig. 4). This absorption is characteristic of a short O–H···O bond [33] and was also observed for a protonated pyridine-*N*-oxide salt with sulfate [34].

4. Conclusion

The crystal structures of **1**–**3** contain distinct layers of $AuCl_4^-$ anions and protonated dipyridyl cations. The organic layers are stabilized by the formation of C–H···Cl (**1** and **2**) or O–H···O (**3**) hydrogen bonds. In **1** and **2**, Au···Cl contacts give rise to a polymeric $[AuCl_6]_n^{n-}$ anionic chain perpendicular to the hybrid layers. This paper is, to the best of our knowledge, the first report of a protonated bpdo structure, that of **3**.

Acknowledgements

We thank the South African National Research Foundation (FA2006030100003), the University of Cape Town Research Committee and the CSIR (L.J.M.) for financial support.

Appendix A. Supplementary material

CCDC 657040, 657041 and 657042 contain the supplementary crystallographic data for **1**, **2** and **3**. These data can be obtained free of charge via http://www.ccdc.cam.ac.uk/conts/retrieving.html, or from the Cambridge Crystallographic Data Centre, 12 Union Road, Cambridge CB2 1EZ, UK; fax: (+44) 1223-336-033; or e-mail: deposit @ccdc.cam.ac.uk. Supplementary data associated with this article can be found, in the online version, at doi:10.1016/j.poly.2007.09.007.

References

[1] T.M. Reineke, M. Eddaoudi, D. Moler, M. O' Keeffe, O.M. Yaghi, J. Am. Chem. Soc. 122 (2000) 4843.
[2] C.-B. Liu, S.-S. Tan, Z.-S. Wu, H.-L. Wen, Acta Crystallogr., Sect. E 62 (2006) m1496.
[3] N. Lah, I. Leban, Inorg. Chem. Commun. 9 (2006) 42.
[4] K. Biradha, M. Fujita, J. Chem. Soc., Dalton Trans. (2000) 3805.
[5] S.A. Bourne, J. Lu, B. Moulton, M.J. Zawarokto, Chem. Commun. (2001) 861.
[6] L.J. Moitsheki, S.A. Bourne, L.R. Nassimbeni, Acta Crystallogr., Sect. E 62 (2006) m542.
[7] S.J. Dalgarno, M.J. Hardie, J.L. Atwood, J.E. Warren, C.L. Raston, New J. Chem. 29 (2005) 649.
[8] D.-L. Long, A.J. Blake, N.R. Champness, M. Schröder, Chem. Eur. J. 8 (2002) 2026.
[9] G.R. Desiraju, Acc. Chem. Res. 35 (2002) 565.
[10] T. Steiner, Cryst. Rev. 6 (1996) 1.
[11] S.A. Bourne, Z. Mangombo, CrystEngComm 6 (2004) 437.
[12] S.A. Bourne, L.J. Moitsheki, CrystEngComm 7 (2005) 674.
[13] S.A. Bourne, L.J. Moitsheki, Polyhedron 26 (2007) 2719.
[14] D.B. Mitzi, J. Chem. Soc., Dalton Trans. (2001) 1.
[15] D.G. Billing, A. Lemmerer, CrystEngComm 9 (2007) 236.
[16] D.G. Billing, A. Lemmerer, CrystEngComm 8 (2006) 686.
[17] L. Brammer, J.K. Swearingen, E.A. Bruton, P. Sherwood, PNAS 99 (2002) 4956.
[18] C.J. Adams, P.C. Crawford, A.G. Orpen, T.J. Podesta, Dalton. Trans. (2006) 4078.
[19] F.H. Allen, Acta Crystallogr., Sect. B 58 (2002) 380.
[20] CSD Version 5.28, updated May 2007.
[21] M. Calleja, K. Johnson, W.J. Belcher, J.W. Steed, Inorg. Chem. 40 (2001) 4978.
[22] Z. Otwinowski, W. Minor, DENZO and SCALEPACK, in: M.G. Rossman, E. Arnold (Eds.), International Tables for Crystallography, vol. F, Kluwer, Dordrecht, 2000.
[23] G.M. Sheldrick, SHELXS97 and SHELXL97, Suite of Programs for Crystal Structure Determination and Refinement, University of Göttingen, 1997.
[24] L.J. Barbour, J. Supramol. Chem. 1 (2003) 189.
[25] Pov-Ray for Windows, Version 3.1e.watcom.win32, The Persistence of Vision Development Team, ©1991–1999.
[26] M. Hasan, I.V. Kozhevnikov, M.R.H. Siddiqui, A. Steiner, N. Winterton, Inorg. Chem. 38 (1999) 5637.
[27] (a) L.E. Pope, J.C.A. Boeyens, J. Cryst. Mol. Struct. 5 (1975) 47;
(b) M.R. Caira, L.R. Nassimbeni, A.L. Rodgers, Acta Crystallogr., Sect. B 31 (1975) 1112;
(c) A.A. Dvorkin, Yu.A. Simonov, T.I. Malinovskii, L.I. Budarin, E.V. Fesenko, Kristallografiya (Russ.) (Crystallogr. Rep.) 35 (1990) 342.
[28] P. Nunez, J.C. Ruiz-Morales, A.D. Lozano-Gorrin, P. Gili, V.D. Rodriguez, J. Gonzalez-Platas, T. Barriuso, F. Rodriguez, Dalton Trans. (2004) 273.
[29] (a) A. Angeloni, A.G. Orpen, Chem. Commun. (2001) 343;
(b) B. Dolling, A.L. Gillon, A.G. Orpen, J. Starbuck, X.-M. Wang, Chem. Commun. (2001) 567.
[30] M.S. Hussain, Polyhedron 15 (1996) 645.
[31] P. Vishweshwar, N.J. Babu, A. Nangia, S.A. Mason, H. Puschmann, R. Mondal, J.A.K. Howard, J. Phys. Chem. A 108 (2004) 9406.
[32] (a) V. Bertolasi, P. Gilli, V. Ferretti, G. Gilli, Chem. – Eur. J. 2 (1996) 925;
(b) P. Gilli, V. Bertolasi, L. Pretto, V. Ferretti, G. Gilli, J. Am. Chem. Soc. 126 (2004) 3845.
[33] S. Bratos, J. Lascombe, A. Novak, in: H. Ratajczak, W.J. Orville-Thomas (Eds.), Molecular Interactions, Vol. 1, Wiley, Chichester, 1980, p. 301.
[34] M. Szafran, E. Tykarska, Z. Dega-Szafran, J. Mol. Struct. 416 (1997) 81.

Available online at www.sciencedirect.com
ScienceDirect
Polyhedron 27 (2008) 268–274
POLYHEDRON
www.elsevier.com/locate/poly

Copper(II) complexes derived from substituted 2,2′-bis-(4-isopropyl-4-methyl-4,5-dihydro-1*H*-imidazol-5-one) ligands: Synthesis, structure and catalytic activity

Pavel Drabina [a,*], Petr Valenta [a], Petr Jansa [b], Aleš Růžička [c], Jiří Hanusek [a], Miloš Sedlák [a]

[a] *Department of Organic Chemistry, Faculty of Chemical Technology, University of Pardubice, Nám. Čs. legií 565, 53210 Pardubice, Czech Republic*
[b] *Institute of Organic Chemistry and Biochemistry, Academy of Science of the Czech Republic, Flemingovo Nám. 2, 16610 Prague 6, Czech Republic*
[c] *Department of General and Inorganic Chemistry, Faculty of Chemical Technology, University of Pardubice, Nám. Čs. legií 565, 53210 Pardubice, Czech Republic*

Received 19 July 2007; accepted 11 September 2007
Available online 31 October 2007

Abstract

New chiral *N*,*N*-bidentate 2,2′-bis-(4-isopropyl-4-methyl-4,5-dihydro-1*H*-imidazol-5-one) ligands have been prepared and characterised by their ^{1}H and ^{13}C NMR spectra and/or optical rotation. The ligands prepared were then tested for their ability to form complexes with copper(II) salts. It was found that the most stable complex is formed from the 2,2′-bis-(4-isopropyl-1,4-dimethyl-4,5-dihydro-1*H*-imidazol-5-one) ligand and copper(II) chloride. The structure of this complex was determined by means of quantum-chemical computations at the B3LYP or UB3LYP/6-31G(d,p) level. According to the computations, the geometry of the copper atom most resembles a tetrahedral arrangement, which was also confirmed by means of X-ray structural analysis. It was found that the structure of this copper(II) complex does not allow the copper atom to coordinate to additional ligands; therefore, it is catalytically inactive in the asymmetric *Henry* reaction.
© 2007 Elsevier Ltd. All rights reserved.

Keywords: Nitrogen bidentate ligands; 4,5-Dihydro-1*H*-imidazol-5-ones; Copper(II) complexes; B3LYP/6-31G(d,p); Asymmetric catalysis

1. Introduction

The importance of syntheses and tests of the properties of new nitrogen-containing heterocyclic compounds and their complex compounds with metals lies in the fact that they may be suitable catalysts in many chemical processes. If, in addition to that, the complex is formed by a heterocyclic system that involves a stereogenic centre, then the substance can be applied as a homogeneous or heterogeneous catalyst in many asymmetric syntheses [1]. Among such chiral nitrogen ligands are the derivatives of 4,5-dihydro-1*H*-imidazol-5-ones [2]. In our previous papers we dealt with the syntheses and catalytic properties of iron(III) [3], rhodium(III) [4] and copper(II) [5] complexes prepared from substituted 2-(4-alkyl-4-methyl-4,5-dihydro-1*H*-imidazol-5-on-2-yl)pyridines (Fig. 1A) [4] or 2,6-bis(4-alkyl-4-methyl-4,5-dihydro-1*H*-imidazol-5-on-2-yl)pyridines [3,4] (Fig. 1B). These chiral substituted 2-(4-alkyl-4-methyl-4,5-dihydro-1*H*-imidazol-5-on-2-yl)pyridines represented new types of *N*,*N*-bidentate and *N*,*N*-tridentate ligands, whose complexes were applied as enantioselective catalysts of the asymmetric *Henry* reaction [5] or as very effective catalysts of the deallylation reaction of substituted allyl malonates [4].

In the present paper we have dealt with the synthesis and characterisation of substituted 2,2′-bis-(4-isopropyl-4-methyl-4,5-dihydro-1*H*-imidazol-5-ones) (Scheme 1). The structure of these newly prepared chiral ligands is very similar to the well-known *N*,*N*-bidentate derivatives of oxazolines (“Boxes”) [6]. However, in comparison with the previous *N*,*N*-bidentate 2-(4,5-dihydro-1*H*-imidazol-

* Corresponding author. Tel.: +420 466 037 010; fax: +420 466 037 068.
E-mail address: pavel.drabina@upce.cz (P. Drabina).

0277-5387/$ - see front matter © 2007 Elsevier Ltd. All rights reserved.
doi:10.1016/j.poly.2007.09.018

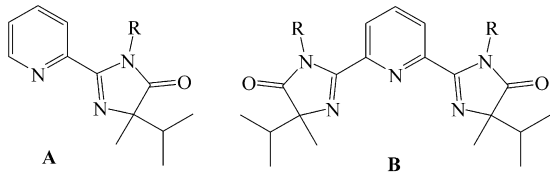


Fig. 1. Previous 4,5-dihydro-1 *H*-imidazol-5-one ligands.

5-on-2-yl)pyridine ligands (Fig. 1A), the present compounds contain two chiral centres and their structure is characterised by C_2-symmetry. Generally, complexes of ligands having this type of symmetry are very suitable for use as enantioselective catalysts, because they form a highly ordered chiral activated complex with the reactants, which results in formation of products of high optical purity. Hence, we decided to prepare copper(II) complexes of these ligands and to study their structure by means of both experimental and theoretical methods. The selected complexes were tested for enantiocatalytic properties in the asymmetric *Henry* reaction.

2. Results and discussion

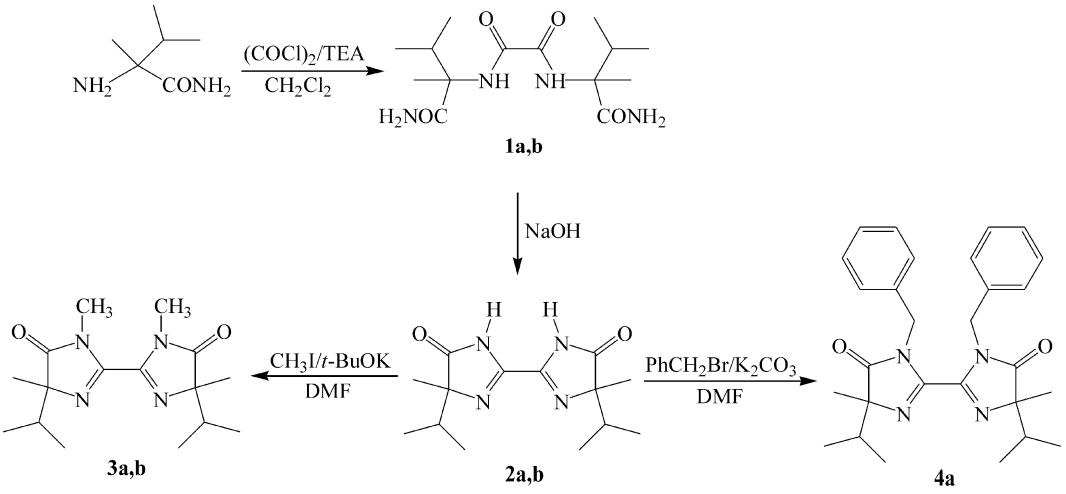
2.1. Syntheses and characterisation of the ligands and complexes

Substituted 2,2′-bis-(4-isopropyl-4-methyl-4,5-dihydro-1*H*-imidazol-5-ones) (**3a**,**b**; **4a**) were prepared by the sequence of reactions given in Scheme 1. First, we acylated the racemic or optically pure 2-amino-2,3-dimethylbutanamide [7] with oxalyl chloride in the presence of triethylamine. Acylaminobutanamide **1a**,**b** was obtained in a good yield of almost 90%. Subsequent base-catalysed ring closure of compounds **1a**,**b** gave racemic **2a** (93%) and (*S*,*S*)-2,2′-bis-(4-isopropyl-4-methyl-4,5-dihydro-1*H*-imidazol-5-one) (**2b**) (85%). The reaction time of the ring closure reaction was relatively long (2 days) to achieve the maximum conversion; however, it was not optimised, because the product formed is stable in basic medium. The alkylation of the nitrogen atom at the 1-position of the 1*H*-imidazol-5-one cycle in compound **2a**,**b** with methyl iodide or benzyl bromide in anhydrous dimethylformamide gave the final ligands **3**–**4** in the yields of 78–84%. 2,2′-Bis-(4-isopropyl-1,4-dimethyl-4,5-dihydro-1*H*-imidazol-5-one) (**3a**) was also prepared in the optically pure form of (*S*,*S*) **3b**. The base used in the alkylation with methyl iodide was *t*-BuOK, whilst in the reaction with benzyl bromide anhydrous K_2CO_3 was adopted [5]. The ligands synthesised were characterised by means of ^{1}H and ^{13}C NMR spectroscopy, elemental analysis, determination of melting point and their optical rotatory power.

Complexes **5a**,**b** were prepared by the reaction of copper(II) chloride dihydrate with the corresponding ligand in methanol in yields of 84% (**5a**) and 81% (**5b**). The complexes were characterised by elemental analyses, and the structure of complex (**5b**) was determined by X-ray structural analysis. Complexes **5a**,**b** were found to be readily soluble in organic solvents, particularly alcohols, chloroform and acetone; on the other hand, they are virtually insoluble in ether and alkanes. Isolation of the complex of 2,2′-bis-(1-benzyl-4-isopropyl-4-methyl-4,5-dihydro-1*H*-imidazol-5-one) (**4a**) with copper(II) chloride failed, probably due to its very low stability. The syntheses of the complexes of ligands **3a**, **3b** and **4** with copper(II) acetate failed too. Since ligand **4a** exhibits bad chelate-forming ability, i.e. it is not suitable for the study of enantiocatalytic activity, its optically pure form was not prepared.

2.2. Quantum-chemical computations of the structure and stability of the complexes

The complex-forming abilities of the ligands and the stabilities of the complexes were studied by means of quantum-chemical computations at the B3LYP or



Scheme 1. Synthesis of ligands (**3a**,**b** and **4a**).

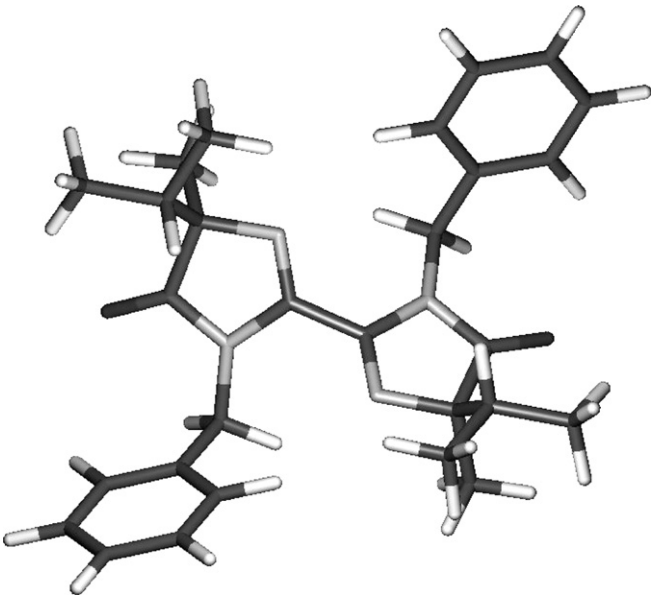


Fig. 2. Structure of ligand **4a** at the B3LYP/6-31G(d,p) level.

UB3LYP/6-31G(d,p) level; for details, see Section 4.5. It was found that compound **4a** assumes the most stable conformation, depicted in Fig. 2. Due to the presence of the bulky benzyl substituents, the 1*H*-imidazol-5-one cycles are deviated to such an extent that the molecule loses its property as an *N*,*N*-bidentate ligand. According to the potential energy surface (PES) scan there exists only one local minimum during rotation around the single bond connecting both cycles. Next there are four local energy minima during rotation of the benzyl or isopropyl groups, but none of these conformations are able to coordinate to a metal ion. The computation shows that the formation of a complex based on **4a** with $CuCl_2$ is energetically unfavourable by 21 kJ/mol. Such a complex should not be stable. This finding agrees with the experimental results.

Fig. 3 depicts the structure of the complex of ligand **3a** with $CuCl_2$. This representation shows that the substituents at the chiral centres disturb the usual planar geometry of the copper atom. The structure of this complex does not allow the copper atom to coordinate to a further two ligands. The absence of free coordination sites at the copper atom explains the lack of effectiveness of this complex in the enantioselective *Henry* reaction [5,9], because this reaction requires the presence of two free coordination sites at the transition metal atom [5]. These coordination properties of ligand **3a** also explain the lesser stability of the complex with $Cu(OAc)_2$. Stable complexes with acetates of transition metals are formed in those cases in which the anion of acetate behaves as an η^2-ligand [8]. In the complex of **3a** with $Cu(OAc)_2$ there are only two coordination sites per two acetate anions, hence the complex is less stable.

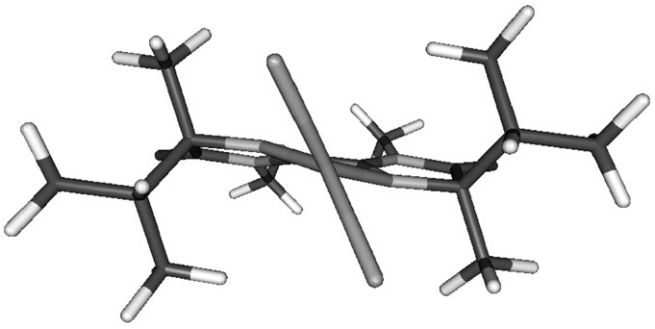


Fig. 3. Structure of complex **5a** at the UB3LYP/6-31G(d,p) level.

2.3. X-ray analysis of complex *5b*

The molecular structure of complex **5b** was determined by means of X-ray analysis (Fig. 4). The geometry of the copper atom most resembles a tetrahedral arrangement: Cl1–Cu1–Cl2 106.00(6)°, Cl1–Cu1–N1 103.69(13)°, Cl1–Cu1–N2 133.19(14)°, Cl2–Cu1–N1 131.79(14)°, Cl2–Cu1–N2 104.22(14)°, N1–Cu1–N2 80.78(18)°. However, the plane defined by atoms Cl1, Cl2 and Cu1 makes an angle of 65.2(4)° with the plane defined by atoms N1, N2 and Cu1. Hence, the chlorine atoms are considerably deviated from the ideal tetrahedral arrangement (90°). This deviation is probably caused by the large steric demands of the isopropyl groups of the ligand: there are van der Waals interactions between the hydrogen atoms of the carbons of the isopropyl group, C15 and C16, with chlorine atom Cl1 and/or an interaction among the hydrogen atoms at carbons C7 and C8 with the chlorine atom Cl2. The 1*H*-imidazol-5-one rings are not coplanar; their planes are mutually deviated by an angle of 12.11°. This anomaly probably follows from an interaction between the methyl groups at the 1-position of the 1*H*-imidazol-5-one ring (atoms C4 and C12). The experimental structure of complex **5b** agrees (Fig. 5) with the structure predicted by means of quantum-chemical methods. The two structures differ only in the position of the isopropyl group. The inter-atomic distances and bond angles in the 1*H*-imidazol-5-one rings are similar to those published earlier for the structures of copper(II) [5] and iron(III) [3] complexes of 1*H*-imidazol-5-one ligands.

2.4. Study of the enantioselectivity of ligand *3b*

The copper(II) complexes of ligand **3b** were studied as enantioselective catalysts of the asymmetric *Henry* reaction [5,9]. This choice of model reaction is rationalised by the fact that copper(II) complexes are amongst the most effective catalysts of the *Henry* reaction [9]. We found out that 5 mol% of ligand **3b** together with 5 mol% of copper(II) acetate catalyse the reaction of 4-nitrobenzaldehyde with nitromethane, the yield of the isolated 2-nitro-1-(4-nitrophenyl)ethanol being 75% after 22 days at room temperature, but the enantioselectivity was virtually zero ($\leqslant$3% ee). This result can be explained by the fact that the reaction is only catalysed by free copper(II) acetate, no

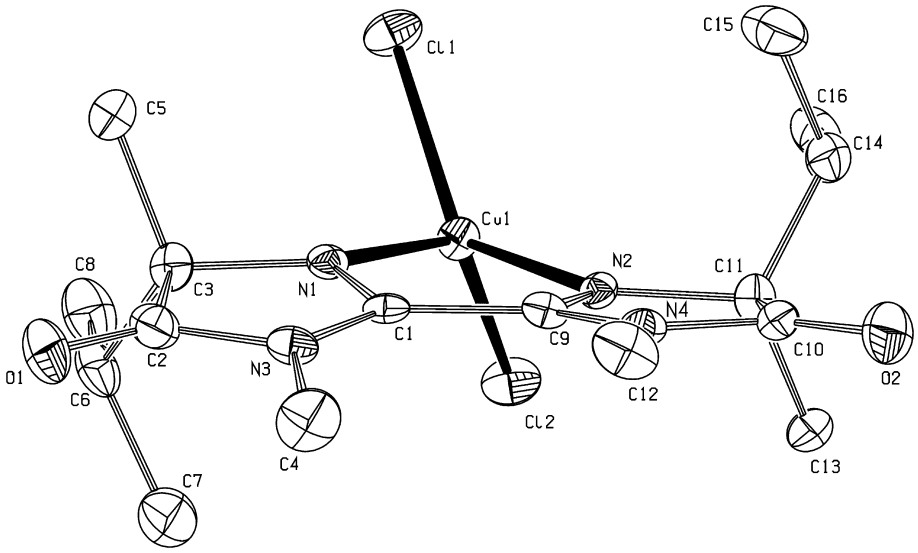


Fig. 4. Molecular structure of **5b**, ORTEP 40% probability level. Hydrogen atoms are omitted for clarity. Selected interatomic distances (Å) and angles (°): Cl1–Cu1 2.2153(14), Cl2–Cu1 2.2272(15), N1–Cu1 1.970(4), N2–Cu1 1.973(4), C1–N1 1.298(7), C9–N2 1.289(7), C1–C9 1.489(9), Cl1–N1 3.295(4), Cl1–N2 3.845(4), Cl2–N1 3.833(5), Cl2–N2 3.318(5), N1–N2 2.555(6), Cu1–C1 2.782(6), Cu1–C9 2.774(6); Cl1–Cu1–Cl2 106.00(6), Cl1–Cu1–N1 103.69(13), Cl1–Cu1–N2 133.19(14), Cl2–Cu1–N1 131.79(14), Cl2–Cu1–N2 104.22(14), N1–Cu1–N2 80.78(18), N1–C1–C9 113.4(5), N2–C9–C1 114.7(5), Cu1–N1–C1 115.2(4), Cu1–N2–C9 114.0(4), Cu1–N1–C3 135.1(4), Cu1–N2–C11 136.0(4).

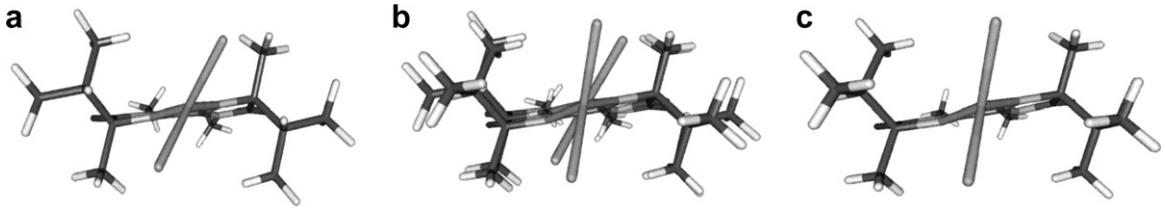


Fig. 5. (a) Structure of complex **5b** at the UB3LYP/6-31G(d,p) level, (b) overlay, and (c) X-ray analysis of complex **5b**.

complex being formed at all between copper(II) acetate and ligand **3b**. Although zero enantioselectivity was observed in both cases, it cannot be excluded that ligand **3b** may form catalytic systems with other metal ions, which may be effective in other asymmetric reactions.

3. Conclusion

While the *N*-methyl derivatives **3a** and **3b** form isolatable and air-stable complexes with copper(II) chloride, the *N*-benzyl derivative **4a** does not produce such complexes, since its structure lacks the properties of an *N*,*N*-bidentate ligand. Likewise, the isolation of complexes of ligands **3a** and **3b** with copper(II) acetate failed. These experimentally found complex-forming properties of the ligands were analysed by means of quantum-chemical methods. Using the B3LYP/6-31G(d,p) model we computed the structure of complex **5b**, in which the geometry of the copper atom most resembles a tetrahedral arrangement. Since the copper atom does not contain any further free coordination sites, it is not able to catalyse the *Henry* nitroaldol reaction. The structure of complex **5b** determined by the quantum-chemical computations was confirmed by X-ray structural analysis.

4. Experimental

4.1. NMR measurements

The ^{1}H and ^{13}C NMR spectra were recorded on a Bruker Avance spectrometer at 500.13 (^{1}H) and 125.76 MHz (^{13}C) in d_6-DMSO. The ^{1}H and ^{13}C chemical shifts were referenced to the central peaks of the solvent ($\delta = 2.55$ and 39.60, respectively).

4.2. Optical rotatory power determination

Optical rotation was measured on a Perkin–Elmer 341 Instrument, the concentration c is given in g/100 ml.

4.3. HPLC analyses

The optical purity of 2-nitro-1-(4-nitrophenyl)ethanol was determined by means of HPLC using a Chiralcel OD–

H column (85:15 hexane: propan-2-ol, 0.8 ml/min, 220 nm; (*R*)-isomer: $t_R = 21.0$ min, (*S*)-isomer: $t_R = 25.9$ min).

4.4. X-ray crystallography

The single crystals of **5b** were grown from ca. 10% methanol/ethyl acetate solution. The relevant crystallographic parameters and procedures are as follows: The data for a colourless crystal were collected at 150(1) K on a Nonius Kappa CCD diffractometer using Mo Kα radiation ($\lambda = 0.71073$ Å), a graphite monochromator, the structure was solved by direct methods (SIR92 [10]). All reflections were used in the structure refinement based on F^2 by the full-matrix least-squares technique (SHELXL97 [11]). Hydrogen atoms were mostly localised on a difference Fourier map; however, to ensure uniformity of the treatment of all crystals, all hydrogen atoms were recalculated into idealised positions (riding model) and assigned temperature factors $H_{iso}(H) = 1.2\ U_{eq}$ (pivot atom) or 1.5 U_{eq} for a methyl moiety (C–H = 0.96 Å for CH_3 and 0.98 Å for CH group hydrogen atoms). Absorption corrections were carried out using Gaussian integration from crystal shape (Coppens [12]). Empirical formula $C_{16}H_{26}Cl_2Cu_1N_4O_2$; Formula weight 440.85; Crystal system Orthorhombic; Space group $P2_12_12_1$; Unit cell dimensions *a*, *b*, *c* (Å) 6.8720(7), 13.8020(19), 20.447(4); Volume (Å^3) 1939.3(5); *Z* 4; Density (Mg/m^3) (calc.) 1.510; Absorption coefficient (mm^{-1}) 1.419; *F*(000) 916; Crystal size (mm) $0.27 \times 0.20 \times 0.06$; Theta range for data collection 1.0–27.5; *h* range $-8 \rightarrow 8$; *k* $-16 \rightarrow 17$; *l* $-26 \rightarrow 26$; Reflections collected 17153; T_{min}, T_{max} 0.806, 0.937; Independent/Observed reflections ($I > 2\delta(I)$) 4351/3344; R_{int} ($R_{int} = \sum|F_o^2 - F_{o,mean}^2|/\sum F_o^2$) 0.079; Absorption correction multi-scans (SORTAV) No. of parameters 226; *S* all data ($S = [\sum(w(F_o^2 - F_c^2)^2)/(N_{diffrs} - N_{params})]^{1/2}$) 1.156; R_1, wR_2 [$I > 2\delta(I)$] ($R(F) = \sum||F_o| - |F_c||/\sum|F_o|$, $wR(F^2) = [\sum(w(F_o^2 - F_c^2)^2)/(\sum w(F_o^2)^2)]^{1/2}$) 0.0525, 0.1165; R_1, wR_2 (all data) 0.0872, 0.1330; Flack parameter 0.00(2); $\Delta\rho_{max}$, $\Delta\rho_{min}$ (e/Å^3) 0.860, −0.772.

4.5. Computational method

Quantum-chemical computations were carried out with the GAUSSIAN03 program [13] employing the hybrid density functional B3LYP [14]. Full geometry optimisations were performed by using the 6-31G(d,p) basis set [15]. The nature of the stationary points was verified by analytical computations of harmonic vibration frequencies. Solvation effects were included using the polarizable continuum model (PCM) [16], (solvent: methanol as in Section 4.6.8). The starting structure for optimisation was obtained after energy minimisation using the software Chem3D Ultra 10.0. Full conformational analysis was performed using the potential energy surface (PES) scan method which is directly implemented in the Gaussian software. Scans for each bond where the free rotation is possible were evaluated for 12 conformations differing in dihedral angle (30° step). The $CuCl_2$ structure with four solvent molecules was used together with the PCM model.

4.6. Synthesis of the ligands and the copper(II) complexes

4.6.1. Preparation of (±)-N,N′-bis[1-(carbamoyl)-1,2-dimethylpropyl]ethanediamide (*1a*)

A solution of (±)-2-amino-2,3-dimethylbutanamide (2,6 g; 20 mmol) and triethylamine (2.8 ml; 20 mmol) in 20 ml dry CH_2Cl_2 was stirred at room temperature and a solution of oxalyl chloride (1.27 g; 10 mmol) in 15 ml CH_2Cl_2 was added drop by drop. The suspension obtained was stirred at room temperature for another 10 h, whereupon the mixture was evaporated, and the dry evaporation residue was thoroughly washed with water. Yield 2.76 g (88%) white crystalline solid melting at 196–198 °C. ^{1}H NMR (d_6-DMSO, δ ppm): 0.84 (d, $^3J = 6.8$ Hz, 6H, $1 \times i\text{Pr}CH_3$), 0.85 (d, $^3J = 6.8$ Hz, 6H, $1 \times i\text{Pr}CH_3$), 1.52 (s, 6H, CH_3), 2.19 (sp, $^3J = 6.8$ Hz, 2H, *i*Pr*CH*), 7.28 (bs, 2H, $1 \times CONH_2$), 7.41 (bs, 2H, $1 \times CONH_2$), 8.41 (bs, 2H, *CONH*). ^{13}C NMR (d_6-DMSO, δ ppm): 17.6, 17.7, 17.9, 34.6, 62.7, 158.8, 174.2. *Anal.* Calc. for $C_{14}H_{26}N_4O_4$: C, 53.47; H, 8.34; N, 17.82. Found: C, 53.31; H, 8.39; N, 17.63%.

4.6.2. Preparation of (S,S)-N,N′-bis[1-(carbamoyl)-1,2-dimethylpropyl]ethanediamide (*1b*)

Compound **1b** was prepared in the same way as compound **1a** in a yield of 89% and with a melting point of 266–267 °C; $[\alpha]_D^{25} = +38.0°$ ($c = 0.25$, CH_3OH). ^{1}H NMR (d_6-DMSO, δ ppm): 0.84 (d, $^3J = 6.8$ Hz, 6H, *i*PrCH_3), 0.86 (d, $^3J = 6.8$ Hz, 6H, *i*PrCH_3), 1.53 (s, 6H, CH_3), 2.20 (sp, $^3J = 6.8$ Hz, 2H, *i*Pr*CH*), 7.32 (bs, 2H, $1 \times CONH_2$), 7.40 (bs, 2H, $1 \times CONH_2$), 8.44 (bs, 2H, *CONH*). ^{13}C NMR (d_6-DMSO, δ ppm): 17.4, 17.5, 17.9, 34.6, 62.7, 158.9, 174.2. *Anal.* Calc. for $C_{14}H_{26}N_4O_4$: C, 53.47; H, 8.34; N, 17.82. Found: C, 53.64; H, 8.41; N, 17.60%.

4.6.3. Preparation of (±)-2,2′-bis-(4-isopropyl-4-methyl-4,5-dihydro-1H-imidazol-5-one) (*2a*)

A mixture of substance **1a** (2.51 g, 8 mmol) and 40 ml 1 M NaOH (40 mmol) was stirred at room temperature. After 2 days, the mixture was neutralised with concentrated HCl to pH ~7 and extracted with 4×30 ml CH_2Cl_2. The combined extracts were evaporated until dry to give 2.07 g (93%) product melting at 227–230 °C. ^{1}H NMR (d_6-DMSO, δ ppm): 0.77 (d, $^3J = 7.0$ Hz, 6H, *i*PrCH_3), 0.94 (d, $^3J = 7.0$ Hz, 6H, *i*PrCH_3), 1.23 (s, 6H, CH_3), 1.91 (sp, $^3J = 7.0$ Hz, 2H, *i*Pr*CH*), 11.50 (s, 2H, *NH*). ^{13}C NMR (d_6-DMSO, δ ppm): 16.4, 16.5, 20.6, 34.1, 74.9, 152.4, 185.9. *Anal.* Calc. for $C_{14}H_{22}N_4O_2$: C, 60.41; H, 7.97; N, 20.13. Found: C, 60.21; H, 8.19; N, 19.95%.

4.6.4. Preparation of (S,S)-2,2′-bis-(4-isopropyl-4-methyl-4,5-dihydro-1H-imidazol-5-one) (*2b*)

Compound **2b** was prepared in the same way as compound **2a** in a yield of 85% and with a melting point of

219–221 °C; $[\alpha]_D^{25} = -47.4°$ ($c = 0.50$, CH_3OH). ^1H NMR (d_6-DMSO, δ ppm): 0.77 (d, $^3J = 7.0$ Hz, 6H, *i*PrCH_3), 0.93 (d, $^3J = 7.0$ Hz, 6H, *i*PrCH_3), 1.23 (s, 6H, CH_3), 1.92 (sp, $^3J = 7.0$ Hz, 2H, *i*Pr*CH*), 11.59 (s, 2H, *NH*). ^{13}C NMR (d_6-DMSO, δ ppm): 16.4, 16.4, 20.5, 34.0, 74.7, 152.4, 185.9. *Anal.* Calc. for $C_{14}H_{22}N_4O_2$: C, 60.41; H, 7.97; N, 20.13. Found: C, 60.23; H, 7.85; N, 19.98%.

4.6.5. Preparation of (±)-2,2′-bis-(4-isopropyl-1,4-dimethyl-4,5-dihydro-1H-imidazol-5-one) (**3a**)

Compound **2a** (1.39 g, 5 mmol), kept under argon atmosphere, was treated with a solution of potassium *t*-butyl alcoholate (20 mmol, 2 equiv.) in *t*-butyl alcohol. The mixture was stirred at room temperature for 1 h, whereupon *t*-butyl alcohol was distilled off under reduced pressure. The evaporation residue was dissolved in 10 ml dry DMF, the reaction mixture was cooled to 0 °C, and methyl iodide (1.25 ml, 20 mmol) was added under an argon atmosphere. The suspension formed was stirred at room temperature overnight. Then the solvent was evaporated under reduced pressure, and the evaporation residue was purified by chromatography (silica gel; ethyl acetate) to give 1.21 g (79%) product melting at 60–62 °C. ^1H NMR (d_6-DMSO, δ ppm): 0.80 (d, $^3J = 6.8$ Hz, 6H, *i*PrCH_3), 1.00 (d, $^3J = 6.8$ Hz, 6H, *i*PrCH_3), 1.31 (s, 6H, CH_3), 2.00 (sp, $^3J = 6.8$ Hz, 2H, *i*Pr*CH*), 3.24 (s, 6H, NCH_3). ^{13}C NMR (d_6-DMSO, δ ppm): 16.7, 17.0, 20.5, 28.3, 34.1, 73.8, 152.4, 184.6. *Anal.* Calc. for $C_{16}H_{26}N_4O_2$: C, 62.72; H, 8.55; N, 18.29. Found: C, 62.86; H, 8.39; N, 18.18%.

4.6.6. Preparation of (S,S)-2,2′-bis-(4-isopropyl-1,4-dimethyl-4,5-dihydro-1H-imidazol-5-one) (**3b**)

Compound **3b** was prepared in the same way as compound **3a** in a yield of 84% and with a melting point of 63–65 °C; $[\alpha]_D^{25} = -51.3°$ ($c = 0.74$, CH_3OH). ^1H NMR (d_6-DMSO, δ ppm): 0.80 (d, $^3J = 6.8$ Hz, 6H, *i*PrCH_3), 1.01 (d, $^3J = 6.8$ Hz, 6H, *i*PrCH_3), 1.30 (s, 6H, CH_3), 2.01 (sp, $^3J = 6.8$ Hz, 2H, *i*Pr*CH*), 3.25 (s, 6H, NCH_3). ^{13}C NMR (d_6-DMSO, δ ppm): 16.7, 17.1, 20.5, 28.3, 34.2, 73.8, 152.3, 184.6. *Anal.* Calc. for $C_{16}H_{26}N_4O_2$: C, 62.72; H, 8.55; N, 18.29. Found: C, 62.68; H, 8.35; N, 18.17%.

4.6.7. Preparation of (±)-2,2′-bis-(1-benzyl-4-isopropyl-4-methyl-4,5-dihydro-1H-imidazol-5-one) (**4a**)

A mixture of compound **2a** (1.11 g, 4 mmol), anhydrous K_2CO_3 (1.66 g; 12 mmol), KI (50 mg) and benzyl bromide (2.05 g, 12 mmol) in 10 ml dry DMF was heated under an inert atmosphere at a temperature of 150 °C for a period of 2 days. After cooling, the mixture was filtered and the solid on the filter was washed with 3 × 10 ml DMF. The combined filtrates were evaporated under reduced pressure until dry. The residue was recrystallised from methanol with charcoal to give 1.43 g (78%) product melting at 107–117 °C. ^1H NMR (d_6-DMSO, δ ppm): 0.65 (d, $^3J = 6.9$ Hz, 6H, *i*PrCH_3), 0.95 (d, $^3J = 6.9$ Hz, 6H, *i*PrCH_3), 1.27 (s, 6H, CH_3), 2.03 (sp, $^3J = 6.9$ Hz, 2H, *i*Pr*CH*), 5.09–5.22 (m, 4H, BzCH_2), 6.95 (m, 4H, PhH_o), 7.19 (m, 6H, PhH_m,H_p). ^{13}C NMR (d_6-DMSO, δ ppm): 16.7, 17.0, 21.1, 34.6, 44.5, 74.6, 126.8, 127.2, 128.5, 136.9, 151.3, 185.0. *Anal.* Calc. for $C_{28}H_{34}N_4O_2$: C, 73.33; H, 7.47; N, 12.22. Found: C, 73.24; H, 7.67; N, 12.09%.

4.6.8. Synthesis of copper(II) complex **5a**

A solution of ligand **3a** (61.3 mg; 0.2 mmol) in 10 ml dry methanol was mixed with $CuCl_2 \cdot 2H_2O$ (34.1 mg; 0.2 mmol). The mixture was refluxed with exclusion of air moisture for 1 h. After cooling, the solvent was removed at reduced pressure, and the residue was suspended in 10 ml dry ether. The solid was collected by suction and washed with 20 ml ether. Yield 74 mg (84%) orange product. *Anal.* Calc. for $C_{16}H_{26}Cl_2CuN_4O_2$: C, 43.59; H, 5.94; N, 12.71. Found: C, 43.85; H, 6.16; N, 12.68%.

4.6.9. Synthesis of copper(II) complex **5b**

Compound **5b** was prepared in the same way as compound **5a** in a yield of 81%; $[\alpha]_D^{25} = -35.9°$ ($c = 0.51$, CH_3OH). *Anal.* Calc. for $C_{16}H_{26}Cl_2CuN_4O_2$: C, 43.59; H, 5.94; N, 12.71. Found: C, 43.77; H, 6.12; N, 12.59%.

4.6.10. Nitroaldol (Henry) reaction of 4-nitrobenzaldehyde with nitromethane

A typical procedure of the nitroaldol (*Henry*) reaction of 4-nitrobenzaldehyde with nitromethane is described in Ref. [5] (Method C and Method D).

Acknowledgements

The authors wish to acknowledge the financial support of the Ministry of Education, Youth and Sports (MSM 002 162 7501). The computational part of the study was supported by ME CR, Project No. LC 512 (special thanks to Petr Nachtigall for his help and discussion).

Appendix A. Supplementary material

CCDC 639679 contains the supplementary crystallographic data for this paper. These data can be obtained free of charge via http://www.ccdc.cam.ac.uk/conts/retrieving.html, or from the Cambridge Crystallographic Data Centre, 12 Union Road, Cambridge CB2 1EZ, UK; fax: (+44) 1223-336-033; or e-mail: deposit@ccdc.cam.ac.uk. Supplementary data associated with this article can be found, in the online version, at doi:10.1016/j.poly. 2007.09. 018.

References

[1] (a) I. Ojima (Ed.), Catalytic Asymmetric Synthesis, second ed., Wiley-VCH, New York, 2000;
(b) A. Pfaltz, J. Heterocyclic Chem. 36 (1999) 1437;
(c) J. Seyden-Penne, in: Chiral Auxiliaries and Ligands in Asymmetric Synthesis, Wiley-VCH, New York, 1995;
(d) J. Mulzer, H. Waldmann (Eds.), Organic Synthesis Highlights III, Wiley-VCH, Weinheim, 1998;

(e) E.N. Jacobsen, A. Pfaltz, H. Yamamoto (Eds.), Comprehensive Asymmetric Catalysis, Springer, Heildelberg, 1999.
[2] (a) M. Sedlák, A. Halama, P. Mitaš, J. Kaválek, V. Macháček, J. Heterocyclic Chem. 34 (1997) 1227;
(b) M. Sedlák, A. Halama, J. Kaválek, V. Macháček, V. Štěrba, Collect. Czech. Chem. Commun. 60 (1995) 150;
(c) M. Sedlák, A. Halama, J. Kaválek, V. Macháček, P. Mitaš, V. Štěrba, Collect. Czech. Chem. Commun. 61 (1996) 910;
(d) M. Sedlák, J. Kaválek, P. Mitaš, V. Macháček, Collect. Czech. Chem. Commun. 63 (1998) 406;
(e) M. Sedlák, J. Hanusek, R. Bína, J. Kaválek, V. Macháček, Collect. Czech. Chem. Commun. 64 (1999) 1629;
(f) M. Sedlák, P. Drabina, J. Hanusek, Heterocycl. Commun. 9 (2003) 129.
[3] M. Sedlák, P. Drabina, I. Císařová, A. Růžička, J. Hanusek, V. Macháček, Tetrahedron Lett. 45 (2004) 7723.
[4] M. Turský, D. Nečas, P. Drabina, M. Sedlák, M. Kotora, Organometallics 25 (2006) 901.
[5] M. Sedlák, P. Drabina, R. Keder, J. Hanusek, I. Císařová, A. Růžička, J. Organomet. Chem. 691 (2006) 2623.
[6] (a) G. Helmchen, A. Pfaltz, Acc. Chem. Res. 33 (2000) 336;
(b) J.S. Johnson, D.A. Evans, Acc. Chem. Res. 33 (2000) 325.
[7] (a) P.J. Weplo, Pestic. Sci. 29 (1990) 293;
(b) W.H. Gastrock, P.J. Wepplo, USP 4,683,324 (1987) (American Cyanamid Company), Chem. Abstr. 107 (1987) 198332.
[8] (a) B.J. Hathaway, G. Wilkinson, Copper, in: Comprehensive Coordination Chemistry, vol. 5. Pergamon Press, New York, 1987 (Chapter 53);
(b) B.J. Hathaway, D.E. Billing, Coord. Chem. Rev. 5 (1970) 143.
[9] (a) H. Sassai, T. Suzuki, S. Arai, T. Arai, M. Shibasaki, J. Am. Chem. Soc. 114 (1992) 4418;
(b) T. Arai, Y.M. A Yamada, N. Yamamoto, H. Sassai, M. Shibasaki, Chem. Eur. J. 2 (1996) 1368;
(c) B.M. Trost, V.S.C. Yeh, Org. Lett. 16 (2002) 2621;
(d) B.M. Trost, V.S.C. Yeh, Angew. Chem., Int. Ed. 41 (2002) 861;
(e) C. Christensen, K. Juhl, R.G. Hazell, K.A. Jørgensen, J. Org. Chem. 67 (2002) 4875;
(f) D.A. Evans, D. Seidel, M. Rueping, H.W. Lam, J.T. Shaw, C.W. Downey, J. Am. Chem. Soc. 125 (2003) 12692;
(g) C. Palomo, M. Oiarbide, A. Mielgo, Angew. Chem., Int. Ed. 43 (2004) 5442;
(h) H. Saisa, S. Watanabe, T. Suzuki, M. Shibasaki, F. Havas, N.A. Magomedov, D.J. Hart, Org. Synth. Coll. 10 (2004) 571;
(i) C. Palomo, M. Oiarbide, A. Laso, Angew. Chem., Int. Ed. 44 (2005) 3881;
(j) J. Boruwa, N. Gogoi, P.P. Saikia, N.C. Barua, Tetrahedron Asymmetry 17 (2006) 3315.
[10] A. Altomare, G. Cascarone, C. Giacovazzo, A. Guagliardi, M.C. Burla, G. Polidori, M. Camalli, J. Appl. Crystallogr. 27 (1994) 1045.
[11] G.M. Sheldrick, SHELXL-97, A Program for Crystal Structure Refinement, University of Göttingen, Germany, 1997.
[12] P. Coppens, in: F.R. Ahmed, S.R. Hall, C.P. Hber (Eds.), Crystallographic Computing, Copenhagen, Munksgaard, 1970, pp. 255–270.
[13] M.J. Frisch, G.W. Trucks, H.B. Schlegel, G.E. Scuseria,M.A. Robb, J.R. Cheeseman, J.A. Montgomery, Jr., T. Vreven, K.N. Kudin, J.C. Burant, J.M. Millam, S.S. Iyengar, J. Tomasi, V. Barone, B. Mennucci, M. Cossi, G. Scalmani, N. Rega, G.A. Petersson, H. Nakatsuji, M. Hada, M. Ehara, K. Toyota, R. Fukuda, J. Hasegawa, M. Ishida, T. Nakajima, Y. Honda, O. Kitao, H. Nakai, M. Klene, X. Li, J.E. Knox, H.P. Hratchian, J.B. Cross, V. Bakken, C. Adamo, J. Jaramillo, R. Gomperts, R.E. Stratmann, O. Yazyev, A.J. Austin, R. Cammi, C. Pomelli, J. Ochterski, P.Y. Ayala, K. Morokuma, G.A. Voth, P. Salvador, J.J. Dannenberg, V.G. Zakrzewski, S. Dapprich, A.D. Daniels, M.C. Strain, O. Farkas, D.K. Malick, A.D. Rabuck, K. Raghavachari, J.B. Foresman, J.V. Ortiz, Q. Cui, A.G. Baboul, S. Clifford, J. Cioslowski, B.B. Stefanov, G. Liu, A. Liashenko, P. Piskorz, I. Komaromi, R.L. Martin, D.J. Fox, T. Keith, M.A. Al-Laham, C.Y. Peng, A. Nanayakkara, M. Challacombe, P.M.W. Gill, B.G. Johnson, W. Chen, M.W. Wong, C. Gonzalez, J.A. Pople, GAUSSIAN03 (Revision B.4), Gaussian Inc., Pittsburgh, PA, 2003.
[14] (a) A.D. Becke, Phys. Rev. A 38 (1988) 3098;
(b) C. Lee, W. Yang, R.G. Parr, Phys. Rev. B 37 (1988) 785;
(c) A.D. Becke, J. Chem. Phys. 98 (1993) 5648.
[15] R. Ditchfield, W.L. Hehre, J.A. Pople, J. Chem. Phys. 54 (1971) 724.
[16] (a) S. Miertus, E. Scrocco, J. Tomasi, Chem. Phys. 55 (1981) 117;
(b) M. Cossi, G. Scalmani, N. Rega, V. Barone, J. Chem. Phys. 117 (2002) 43.

Available online at www.sciencedirect.com
ScienceDirect
Polyhedron 27 (2008) 275–282
POLYHEDRON
www.elsevier.com/locate/poly

Structural and spectral studies of nickel(II) complexes with *N*(4),*N*(4)-(butane-1,4-diyl) thiosemicarbazones

E. Manoj, M.R. Prathapachandra Kurup *

Department of Applied Chemistry, Cochin University of Science and Technology, Kochi 682 022, Kerala, India

Received 25 March 2007; accepted 11 September 2007
Available online 5 November 2007

Abstract

Nickel(II) complexes of quinoline-2-carbaldehyde *N*(4),*N*(4)-(butane-1,4-diyl) thiosemicarbazone (HL^1) and 2-benzoylpyridine *N*(4),*N*(4)-(butane-1,4-diyl) thiosemicarbazone (HL^2) have been synthesized and physico-chemically characterized by means of partial elemental analyses, molar conductance measurements, magnetic measurements, electronic and infrared spectral studies. Three complexes were given the formulae $[Ni(HL^1)_2]Cl_2$ (**1**), $[Ni(HL^2)L^2]ClO_4 \cdot 7H_2O$ (**2**) and $[NiL^2Cl] \cdot 0.5H_2O$ (**3**). The structure of compound **1** has been solved by single crystal X-ray crystallography and is found to be distorted octahedral. Compound **2**, when crystallized in DMSO solution, got deprotonated to form a new compound $[Ni(L^2)_2]$ (**2a**), with a distorted octahedral Ni(II) center. In compound **1**, HL^1 coordinates to the metal in the thione form, while in compounds **2a** and **3**, HL^2 coordinates in its deprotonated thiolate form.
© 2007 Elsevier Ltd. All rights reserved.

Keywords: Thiosemicarbazone; Ni(II) complex; Quinoline-2-carbaldehyde; 2-Benzoylpyridine; Crystal structure

1. Introduction

Heterocyclic thiosemicarbazones have aroused considerable interest in chemistry due to their remarkable coordination properties and in biology owing to a wide spectrum of potential biological activities [1–4]. The formation of complexes with transition metal ions has been proposed as a step in the biological activity of thiosemicarbazones and is related to its chelating ability with transition metal ions, bonding through nitrogen, nitrogen and sulfur atoms [4] or oxygen, nitrogen and sulfur atoms [5–7]. The activity of thiosemicarbazones depends very much on the parent aldehyde or ketone [8,9] and is affected also by the presence of *N*(4) substitution [10,11]. The real impetus towards developing the coordination chemistry of thiosemicarbazones has been provided by remarkable biological activities observed for these compounds, which has since been shown to be related to their metal complexing ability. Previously we have reported the synthesis, spectral and X-ray crystal studies of 2-benzoylpyridine-*N*(4),*N*(4)-(butane-1,4-diyl) thiosemicarbazone and its iron(III) [12], Cu(II) [13] and Mn(II) complexes [14]. Here we report the structural characterizations of one new thiosemicarbazone viz. quinoline-2-carbaldehyde *N*(4),*N*(4)-(butane-1,4-diyl) thiosemicarbazone (HL^1) and its Ni(II) complex along with two Ni(II) complexes of 2-benzoylpyridine-*N*(4),*N*(4)-(butane-1,4-diyl) thiosemicarbazone (HL^2).

2. Experimental

Quinoline-2-carbaldehyde (Aldrich), 2-benzoylpyridine (Aldrich) were used as received. 4-Methyl-4-phenyl-3-thiosemicarbazide was prepared as reported previously [15]. Nickel(II) chloride hexahydrate and nickel(II) perchlorate hexahydrate (Merck) were used as supplied and solvents were purified by standard procedures before use. *Caution*! Perchlorate complexes of metals with organic ligands are potentially explosive and should be handled with care.

* Corresponding author. Tel.: +91 484 2575804; fax: +91 484 2577595.
E-mail address: mrp@cusat.ac.in (M.R.P. Kurup).

0277-5387/$ - see front matter © 2007 Elsevier Ltd. All rights reserved.
doi:10.1016/j.poly.2007.09.023

2.1. Synthesis of the ligands

The thiosemicarbazone ligands (Scheme 1) were synthesized by adapting a reported procedure of Scovill [15].

HL^1: A solution of 1.000 g (5.52 mmol) of 4-methyl-4-phenyl-3-thiosemicarbazide in 10 ml of acetonitrile was refluxed with 0.392 g (5.52 mmol) of pyrrolidine and 0.894 g (5.52 mmol) of quinoline 2-carbaldehyde for 1.5 h. The solution was chilled (overnight) and the crystals that separated were collected and washed well with acetonitrile. The compound was recrystallized from ethanol and dried *in vacuo* over P_4O_{10}. Yield 46%. Elemental *Anal.* Calc.: C, 63.35; H, 5.67; N, 19.70; S, 11.28. Found: C, 63.15; H, 5.99; N, 19.66; S, 11.26%.

HL^2: The same procedure was followed for HL^2 also, except with the use of 1.021 g (5.52 mmol) of 2-benzoylpyridine instead of quinoline 2-carbaldehyde.

2.2. Synthesis of the complexes

The complexes were synthesized by a general method. To a hot solution of the respective ligand (0.5 mmol) {HL^1 for **1**, HL^2 for **2** and **3**} in 10 ml chloroform was added an equimolar amount of the nickel salt {nickel(II) chloride hexahydrate (0.120 g) for **1** and **3**, nickel(II) perchlorate hexahydrate (0.183 g) for **2**} dissolved in 20 ml hot methanol. The mixture was refluxed for an hour and allowed to stand at room temperature. The reddish brown compound that precipitated was filtered, washed with methanol and ether and dried *in vacuo* over P_4O_{10}.

$[Ni(HL^1)_2]Cl_2$ (**1**): Yield 53%. XRD quality single crystals of **1** were obtained by the slow evaporation of its methanol solution in air. Elemental *Anal.* Calc.: C, 51.60; H, 4.62; N, 16.05; S, 9.18. Found: C, 51.46; H, 5.01; N, 16.17; S, 9.09%.

$[Ni(HL^2)L^2]ClO_4 \cdot 7H_2O$ (**2**): Yield 78%. Elemental *Anal.* Calc.: C, 45.17; H, 5.46; N, 12.39; S, 7.09. Found: C, 44.65; H, 5.32; N, 12.28; S, 6.83%.

$[Ni(L^2)_2]$ (**2a**): The complex $[Ni(HL^2)L^2]ClO_4 \cdot 7H_2O$ (**2**) on crystallization in DMSO solution by slow evaporation in air yielded **2a** with deprotonation of HL^2 from **2**.

$[NiL^2Cl] \cdot 0.5H_2O$ (**3**): Yield 56%. Elemental *Anal.* Calc.: C, 49.49; H, 4.40; N, 13.58; S, 7.77. Found: C, 49.94; H, 4.15; N, 13.75; S, 7.72%.

2.3. Physical measurements

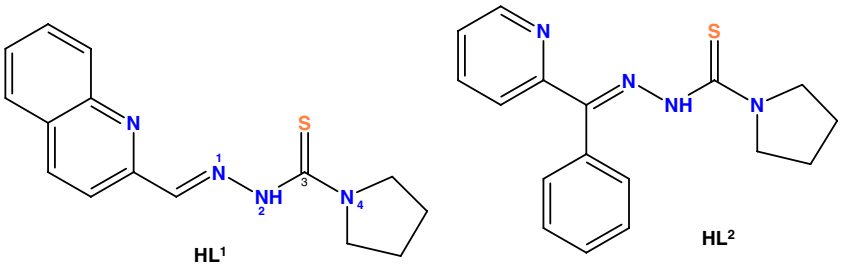
Elemental analyses were carried out using an Elementar Vario EL III CHNS analyzer at SAIF, Kochi, India. Infrared spectra were recorded on a Thermo Nicolet, AVATAR 370 DTGS model FT-IR spectrophotometer with KBr pellets and the ATR technique at SAIF, Kochi, India. The far IR spectra were recorded using polyethylene pellets in the 500–100 cm^{-1} region on a Nicolet Magna 550 FTIR instrument at the Regional Sophisticated Instrumentation Facility, Indian Institute of Technology, Bombay, India. Electronic spectra were recorded on a Cary 5000 version 1.09 UV–vis spectrophotometer from solutions in DMF. The magnetic susceptibility measurements were carried out at the Indian Institute of Technology, Roorkee, India at room temperature in the polycrystalline state on a PAR model 155 Vibrating Sample Magnetometer at 5 kOe field strength. The molar conductances of the complexes in DMF solutions (10^{-3} M) at room temperature were measured using a direct reading conductivity meter.

2.4. X-ray crystallography

The crystallographic data and structure refinement parameters for the compounds are given in Table 1. The data of single crystals of suitable dimensions of **1** and **2a** were collected using a CRYSALIS CCD, Oxford Diffraction Ltd. with graphite monochromated Mo Kα ($\lambda = 0.71073$ Å) radiation at a temperature of 150(2) K at the National Single Crystal X-ray Diffraction Facility, IIT, Bombay, India. Both crystals were found to be monoclinic. The trial structure was solved using SHELXS-97 [16] and refinement was carried out by full-matrix least squares on F^2 (SHELXL-97). One of the pyrrolidine groups is disordered over C(15) and C(16) in complex **2a**. All non-hydrogen atoms were refined anisotropically, while the hydrogen atoms were placed at calculated positions and allowed to ride on their parent atoms. The molecular graphics employed were ORTEP-III [17], PLATON [18] and MERCURY [19].

3. Results and discussion

Based on spectral and magnetic susceptibility studies, compounds **1** and **2** are found to be six coordinate around



Scheme 1. The thiosemicarbazones HL^1 and HL^2.

Table 1
Crystal data and structural refinement parameters of compounds $\mathbf{1}\cdot 2.5H_2O$ and $[Ni(L^2)_2]$ (**2a**)

Parameters	$[Ni(HL^1)_2]Cl_2\cdot 2.5H_2O$	$[Ni(L^2)_2]$
Empirical formula	$C_{30}H_{32}Cl_2N_8NiS_2O_{2.50}$	$C_{34}H_{34}N_8NiS_2$
Formula weight (M)	738.37	677.52
Colour, shape	Brown, plate	Brown, block
Temperature (T) K	150(2)	150(2)
Wavelength (Mo Kα) (Å)	0.71073	0.71073
Crystal system	monoclinic	monoclinic
Space group	$P21/n$	$P21/c$
Lattice constants		
a (Å)	9.3866(5)	10.684(2)
b (Å)	27.0204(10)	20.229(4)
c (Å)	13.8731(8)	14.7177(18)
α (°)	90.00	90.00
β (°)	108.385(6)	96.762(13)
γ (°)	90.00	90.00
Volume V (Å^3)	3339.0(3)	3158.8(9)
Z	4	4
D_{calc} (ρ) (Mg m^{-3})	1.469	1.425
Absorption coefficient, μ (mm^{-1})	0.910	0.785
F(000)	1528	1416
Crystal size (mm)	$0.35\times0.18\times0.13$	$0.21\times0.10\times0.10$
θ Range for data collection	3.02–25.00	2.9544–32.1616
Limiting indices	$-11\leqslant h\leqslant 11$, $-32\leqslant k\leqslant 32$, $-16\leqslant l\leqslant 15$	$-12\leqslant h\leqslant 12$, $-22\leqslant k\leqslant 24$, $-17\leqslant l\leqslant 17$
Reflections collected	30854	16787
Independent reflections (R_{int})	5857 (0.0694)	5521 (0.0685)
Refinement method	full-matrix least-squares on F^2	full-matrix least-squares on F^2
Data/restraints/parameters	5857/0/412	5521/21/425
Goodness-of-fit on F^2	1.087	1.089
Final R indices [$I>2\sigma(I)$]	$R_1=0.0693$, $wR_2=0.1942$	$R_1=0.0652$, $wR_2=0.1656$
R indices (all data)	$R_1=0.1087$, $wR_2=0.2218$	$R_1=0.1099$, $wR_2=0.2325$
Largest difference in peak and hole (e Å^{-3})	1.157 and −0.722	1.160 and −1.936

the Ni(II) centers, while compound **3** is four coordinate around the Ni(II) center. The stoichiometries of the complexes are in agreement with the partial elemental analyses and spectral studies. Infrared spectral evidences support the presence of coordination through the thione form of HL^1 in compound **1**, through the thiolate form of HL^2 in **3** and through the thione and thiolate forms of HL^2 in **2**. Molar conductivity measurements in 10^{-3} M DMF solution show non-electrolytic nature (8 ohm^{-1} cm^2 mol^{-1}) for **3**, a 1:1 electrolyte for **2** (89 ohm^{-1} cm^2 mol^{-1}) and a 2:1 electrolyte for **1** (138 ohm^{-1} cm^2 mol^{-1}). Like compound **2**, copper and cobalt complexes with both neutral and deprotonated forms of a thiosemicarbazone ligand in the same complexes with a perchlorate ion have been reported [20]. The room temperature effective magnetic moments μ_{eff} of the three compounds **1**, **2** and **3** are found to be 2.80, 2.66 and 0.89 μ_B, respectively; consistent with the octahedral geometry for complexes **1** and **2**. The anomalous magnetic moment of 0.89 μ_B shown by **3** is attributed to a four coordinated Ni(II) center. For a perfect square planar complex of Ni(II), diamagnetism is expected. The low magnetic moment may be due to deviation from a perfect square planar geometry or the presence of impurities. The structure of **1** has been confirmed by a single crystal X-ray study and it is found that a distorted octahedral geometry around the Ni(II) center is formed by two neutral HL^1 ligands. However the single crystal X-ray study of **2a** shows that the Ni(II) center is coordinated by two monodeprotonated ligands of HL^2 to form a distorted octahedral geometry around the Ni(II) center. The relevant bond lengths and bond angles of $[Ni(HL^1)_2]Cl_2\cdot 2.5H_2O$ ($\mathbf{1}\cdot 2.5H_2O$) and $[Ni(L^2)_2]$ (**2a**) are listed in Tables 2 and 3.

Table 2
Selected bond lengths (Å) and bond angles (°) of compound $\mathbf{1}\cdot 2.5H_2O$

Ni(1)–N(6)	2.006(5)	N(6)–Ni(1)–N(2)	168.86(19)
Ni(1)–N(2)	2.022(4)	N(6)–Ni(1)–N(5)	79.25(19)
Ni(1)–N(5)	2.139(5)	N(2)–Ni(1)–N(5)	105.29(18)
Ni(1)–N(1)	2.139(5)	N(6)–Ni(1)–N(1)	112.53(19)
Ni(1)–S(2)	2.3722(15)	N(2)–Ni(1)–N(1)	77.68(18)
Ni(1)–S(1)	2.4152(17)	N(5)–Ni(1)–N(1)	93.40(18)
S(1)–C(11)	1.704(6)	N(6)–Ni(1)–S(2)	81.86(14)
S(2)–C(26)	1.701(6)	N(2)–Ni(1)–S(2)	94.67(12)
N(2)–C(10)	1.274(7)	N(5)–Ni(1)–S(2)	159.64(14)
N(6)–C(25)	1.280(7)	N(1)–Ni(1)–S(2)	86.86(12)
N(2)–N(3)	1.358(6)	N(6)–Ni(1)–S(1)	88.34(14)
N(6)–N(7)	1.363(7)	N(2)–Ni(1)–S(1)	81.52(14)
N(3)–C(11)	1.364(7)	N(5)–Ni(1)–S(1)	90.29(13)
N(7)–C(26)	1.345(8)	N(1)–Ni(1)–S(1)	159.12(13)
N(4)–C(11)	1.307(7)	S(2)–Ni(1)–S(1)	96.71(6)
N(8)–C(26)	1.357(7)		

Table 3
Selected bond lengths (Å) and bond angles (°) of $[Ni(L^2)_2]$ (**2a**)

Ni(1)–N(6)	2.030(5)	N(6)–Ni(1)–N(2)	165.8(2)
Ni(1)–N(2)	2.035(5)	N(6)–Ni(1)–N(1)	92.40(19)
Ni(1)–N(1)	2.123(5)	N(2)–Ni(1)–N(1)	78.12 (19)
Ni(1)–N(5)	2.135(6)	N(6)–Ni(1)–N(5)	78.86(19)
Ni(1)–S(2)	2.4229(18)	N(2)–Ni(1)–N(5)	90.7(2)
Ni(1)–S(1)	2.4349(18)	N(1)–Ni(1)–N(5)	91.1(2)
S(1)–C(13)	1.729(6)	N(6)–Ni(1)–S(2)	79.96(14)
S(2)–C(30)	1.713(6)	N(2)–Ni(1)–S(2)	110.38(17)
C(6)–N(2)	1.301(8)	N(1)–Ni(1)–S(2)	90.76(15)
C(23)–N(6)	1.331(8)	N(5)–Ni(1)–S(2)	158.79(14)
N(2)–N(3)	1.353(7)	N(6)–Ni(1)–S(1)	109.03(14)
N(6)–N(7)	1.344(7)	N(2)–Ni(1)–S(1)	80.60(15)
N(3)–C(13)	1.334(8)	N(1)–Ni(1)–S(1)	158.54(14)
N(7)–C(30)	1.371(8)	N(5)–Ni(1)–S(1)	91.96(15)
		S(2)–Ni(1)–S(1)	94.03(6)

3.1. Crystal structures of $[Ni(HL^1)_2]Cl_2 \cdot 2.5H_2O$ ($\mathbf{1} \cdot 2.5H_2O$) and $[Ni(L^2)_2]$ (**2a**)

The molecular structures of $\mathbf{1} \cdot 2.5H_2O$ and **2a**, along with the atom numbering schemes, are depicted in Figs. 1 and 2. In compound $\mathbf{1} \cdot 2.5H_2O$, two molecules of the neutral ligand HL^1 are coordinated in the *meridional* fashion [21] using pairs of *cis* quinolyl nitrogen, *trans* azomethine nitrogen and *cis* thione sulfur atoms, while in compound **2a**, the Ni(II) ion is coordinated in a *meridional* fashion using pairs of *cis* pyridyl nitrogen, *trans* azomethine nitrogen and *cis* thiolate sulfur atoms [22–24] of two monoanionic ligands, resulting in two bicyclic chelate systems. The thione coordination as found in $\mathbf{1} \cdot 2.5H_2O$ is rare for thiosemicarbazones. In $\mathbf{1} \cdot 2.5H_2O$, the bicyclic chelate systems Ni(1), S(1), C(11), N(3), N(2), C(10), C(9), N(1) and Ni(1), S(2), C(26), N(7), N(6), C(25), C(24), N(5) are slightly deviated from planarity, as evidenced by the maximum deviation of 0.183(6) Å for C(9) and −0.121(5) Å for N(7), respectively, from their respective mean planes. However in **2a**, the bicyclic chelate system Ni(1), S(1), C(13), N(3), N(2), C(6), C(5), N(1) and Ni(1), S(2), C(30), N(7), N(6), C(23), C(22), N(5) are approximately planar with a maximum mean plane deviation of 0.100(5) Å for N(1) and −0.070(6) Å for C(23), respectively. The dihedral angle formed by the mean planes of the bicyclic chelate systems of each of the ligands is 83.50(10)° in $\mathbf{1} \cdot 2.5H_2O$, and 86.98(11)° in $[Ni(L^2)_2]$. In compound $\mathbf{1} \cdot 2.5H_2O$ the trans angles N(1)–Ni(1)–S(1), N(5)–Ni(1)–S(2) and N(2)–Ni(1)–N(6) are 159.12(13)°, 159.64(14)° and 168.86(19)°, respectively, while in compound **2a**, the angles N(1)–Ni(1)–S(1), N(5)–Ni(1)–S(2) and N(2)–Ni(1)–N(6) are 158.54(14)°, 158.79(14)° and 165.8(2)°, respectively. These factors suggest considerable distortion from an octahedral geometry around the Ni(II) centers in both complexes.

The bond lengths Ni–$N_{azomethine}$, Ni–N_{py} and Ni–S in **2a** increase in that order, as in similar compounds [21–25]. A similar increase is seen in the quinoline substi-

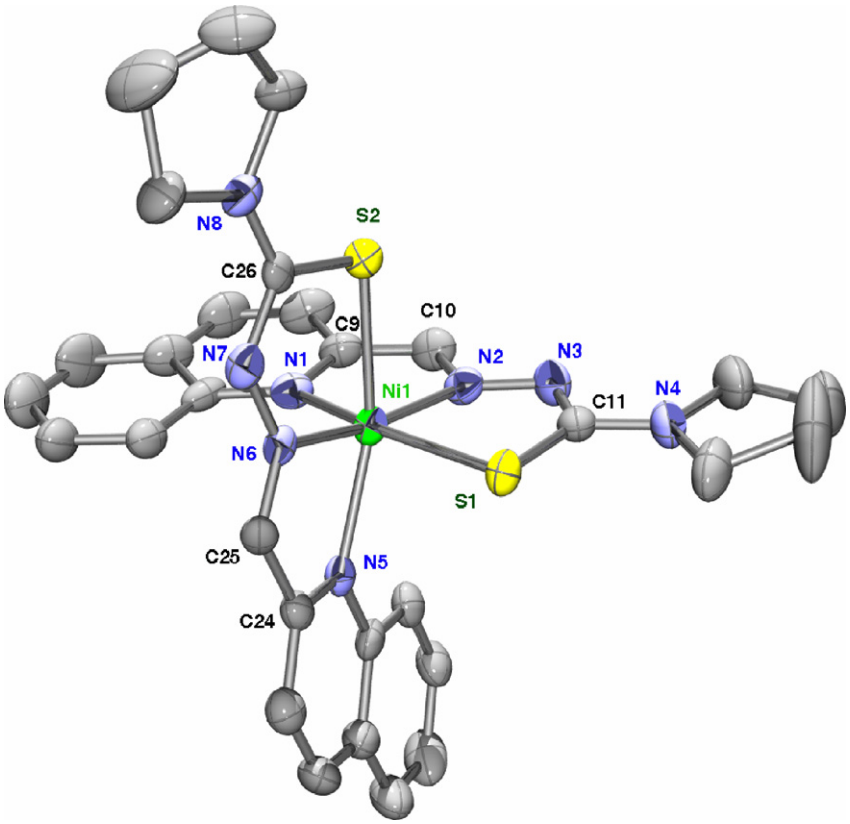


Fig. 1. ORTEP diagram of the cation of $[Ni(HL^1)_2]Cl_2 \cdot 2.5H_2O$ with 50% probability ellipsoids. Hydrogen atoms are omitted for clarity.

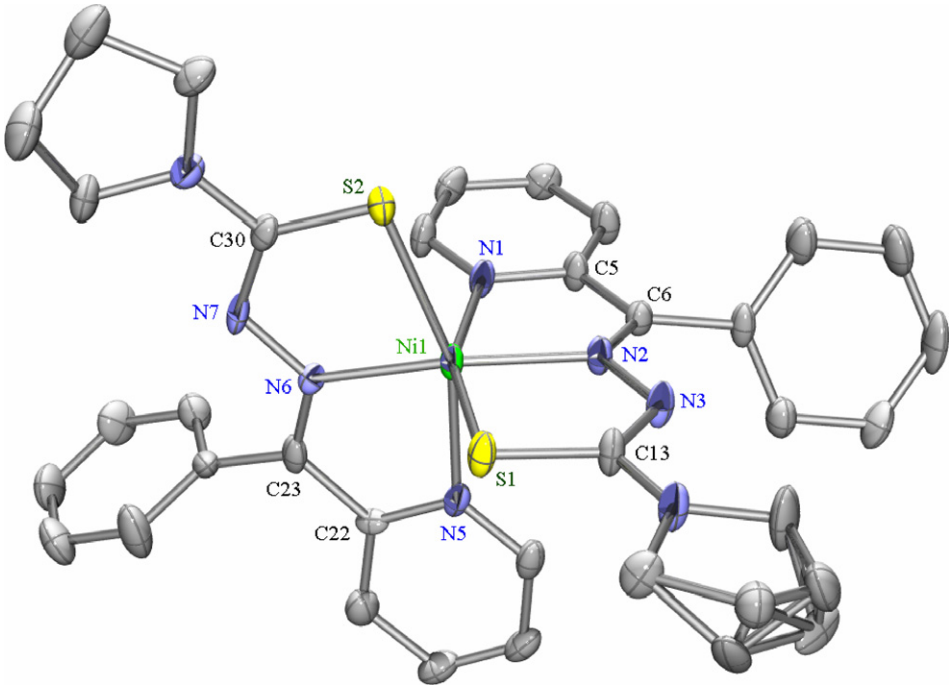


Fig. 2. ORTEP diagram for the compound $[Ni(L^2)_2]$ (**2a**) with 50% probability ellipsoids. Hydrogen atoms are omitted for clarity.

tuted compound $\mathbf{1}\cdot 2.5H_2O$. The Ni–N_{qu} bonds are of the same strength as both show lengths of 2.139(5) Å and are weaker compared to the Ni–N_{py} bonds in compound **2a**. The Ni–$N_{azomethine}$ bond lengths are less compared to Ni–$N_{py/qu}$ in complexes $\mathbf{1}\cdot 2.5H_2O$ and **2a**, indicating the higher strength of former bond than the latter. The Ni–S bond lengths in complex $\mathbf{1}\cdot 2.5H_2O$ are found to be less compared to that in **2a**, indicating stronger bonds in $\mathbf{1}\cdot 2.5H_2O$. However, the C–S bond lengths in compound **2a** are greater compared to the 1.681(3) Å seen in the free ligand HL^2 [12] and also compared to that in compound $\mathbf{1}\cdot 2.5H_2O$. Also the C–N bond lengths in **2a** {1.334(8) Å for N(3)–C(13) and 1.371(8) Å for C(30)–N(7)} are consistent with partial double bond character. These factors confirm the coordination through the thiolate form by deprotonation after enolization of the ligand HL^2 in compound **2a**. However in $\mathbf{1}\cdot 2.5H_2O$, the coordination occurs via the thione form of HL^1 as evidenced by the lesser C–S and greater C–$N_{azomethine}$ bond lengths. These bond lengths are comparable to that seen in thiosemicarbazones with delocalization of electron density [26].

In complex $\mathbf{1}\cdot 2.5H_2O$ the molecules are connected by various hydrogen bonding interactions including water molecules (Table 4) and are packed in the lattice (Fig. 3) in an ordered manner along the *c* axis by making use of C–H···π ring interactions. While in compound **2a**, the molecules are packed in the same manner along the *a* axis, as seen in Fig. 4, as a result of one intermolecular hydrogen bonding interaction and diverse C–H···π ring interactions (Table 5). However, no significant π···π interactions are found in the packing for both compounds.

Table 4
Interaction parameters of $[Ni(HL^1)_2]Cl_2\cdot 2.5H_2O$

C–H···π interactions			
X–H(I) Res(1)···Cg(J)	H···Cg (Å)	X···Cg (Å)	X–H···Cg (°)
C(2)–H(2) [1]···Cg(4)[a]	2.55	3.3546(67)	145
C(13)–H(13A) [1]···Cg(9)[b]	2.95	3.6529(91)	130

Cg(4) = Ni(1), N(5), C(24), C(25), N(6);
Cg(9) = C(1), C(2), C(3), C(4), C(5), C(6).

Hydrogen bonding interactions				
D–H···A	D–H (Å)	H···A (Å)	D···A (Å)	D–H···A (°)
N(3)–H(3)···O(w2)	0.86	1.88	2.702(8)	158
N(7)–H(7)···O(w1)[c]	0.86	2.51	2.911(9)	110
C(10)–H(10)···O(w2)	0.93	2.54	3.209(8)	129
C(17)–H(17)···N(2)	0.93	2.44	3.231(8)	143
C(23)–H(23)···Cl(1)	0.93	2.60	3.496(10)	163

D = donor, A = acceptor. Equivalent position codes: a = *x*, *y*, *z*; b = 1/2 + *x*, 1/2 − *y*, −1/2 + *z*; c = 1/2 + *x*, 1/2 − *y*, 1/2 + *z*.

3.2. IR and electronic spectral studies

The characteristic IR bands of the complexes differ from their free ligands HL^1 and HL^2, and provide significant indications regarding the coordination and bonding sites of the ligands. Relevant characteristic bands of all the compounds are listed in Table 6. The ligand HL^1 shows a broad peak at 3442 cm^{-1} which is attributed to a $\nu(^2N–H)$ vibration. In compound **1**, this peak is shifted slightly downwards but is indicative of the presence of $^2N–H$. However in compounds **2** and **3** due to the presence of lattice water broad bands are seen at frequencies 3415 and 3440 cm^{-1},

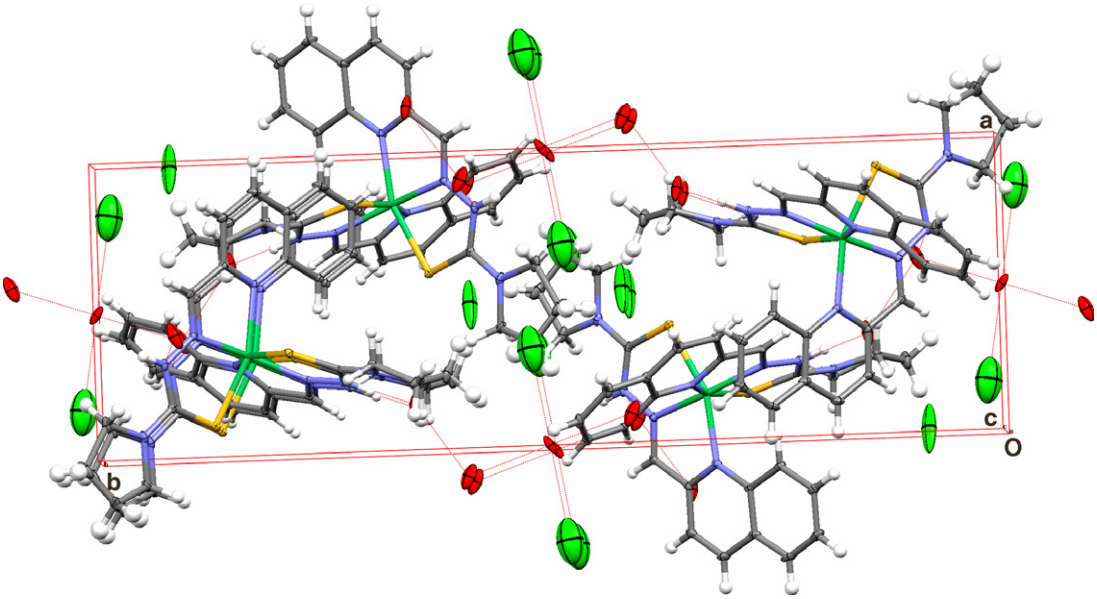


Fig. 3. A view of the unit cell of $[Ni(HL^1)_2]Cl_2 \cdot 2.5H_2O$ along the *c* axis showing the molecules packed along the *c* axis (left part) and connected through hydrogen bonding interactions involving chloride and water molecules.

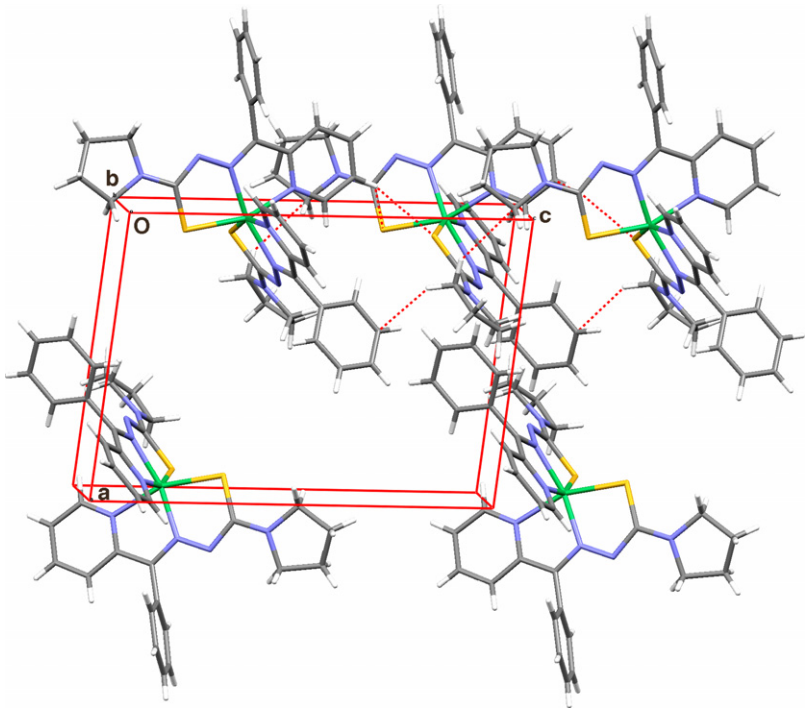


Fig. 4. Unit cell of the molecule $[Ni(L^2)_2]$ (**2a**) along the *b* axis showing molecules packed along the *c* axis (bottom part) and connected through intermolecular hydrogen bonding interactions with molecules of the nearby layer (top part).

respectively. No other bands in the nearby region may be due to the absence of N–H hydrogens. Also the strong peak at 1282, assigned as the ν(C=S) vibration for HL^1, shows only a marginal shift in compound **1**, supporting the coordination through the thione form. However for compound **2** two strong bands seen at 1337 and 1283 cm^{-1} are assigned to ν(C=S) and ν(C–S) frequencies, showing a shift from 1342 cm^{-1} assigned to the ν(C=S) band of HL^2 [12,13]. For compound **3** the strong band at 1296 cm^{-1} is assigned to a ν(C–S) band. Additionally, no band due to the SH group is observed between 2600 and 2500 cm^{-1} [27] in agreement with the deprotonated thiolate form of the ligand in these complexes. The bands seen at ~350 cm^{-1} for these complexes are assigned as νNi–S, which further supports their coordination. Bands ranging from 1600 to 1400 cm^{-1}, attributed to ν(C=C) and

Table 5
Interaction parameters of $[Ni(L^2)_2]$ (**2a**)

C–H···π interactions			
X–H(I) Res(1)···Cg(J)	H···Cg (Å)	X···Cg (Å)	X–H···Cg (°)
C(1)–H(1) [1]···Cg(15)[a]	2.73	3.160(6)	109
C(18)–H(18) [1]···Cg(14)[a]	2.69	3.113(7)	108
C(19)–H(19) [1]···Cg(15)[b]	2.55	3.310(6)	139

Cg(14) = Ni(1), S(1), C(13), N(3), N(2);
Cg(15) = Ni(1), S(2), C(30), N(7), N(6).

Hydrogen bonding interaction				
D–H···A	D–H (Å)	H···A (Å)	D···A (Å)	D–H···A (°)
C(27)–H(27)···S(2)[c]	0.93	2.79	3.510(8)	135

D = donor, A = acceptor. Equivalent position codes: a = x, y, z; b = x, $1/2 - y$, $1/2 + z$, c = $-1 + x$, y, z.

ν(C=N) vibration modes, in the spectra of the complexes suffer significant shifts and their mixing patterns are different from that in the spectra of the respective ligands. The azomethine ν(C=N) vibrations at 1580 and 1630 cm^{-1} in the free ligands HL^1 and HL^2, respectively, suffered negative shifts. These bands are seen at 1561 cm^{-1} in the spectrum of **1** and at 1553 and 1537 cm^{-1} in the spectra of compounds **2** and **3**, respectively. The new bands seen at frequencies 1590 and 1594 cm^{-1} for **2** and **3** are assigned to the newly formed $\nu(^2N{=}C)$ and this band is absent in the spectrum of **1**. The coordination through the azomethine nitrogen is further evidenced by the $\nu Ni–N_{azo}$ peaks ~440 cm^{-1} for these compounds. The shifts in the ν(N–N) frequencies also support coordination through the azomethine nitrogen in all the complexes. Coordination of the pyridine nitrogen atom is seen by the shifts in frequencies of the deformation mode bands that appear in the range 649–455 cm^{-1} in the spectrum of HL^2 [13]. This is further supported by $\nu Ni–N_{py/qu}$ bands seen at ~250 cm^{-1} for all these compounds.

The perchlorate complex **2** shows a broad band at 1090 cm^{-1} and strong band at 625 cm^{-1}, indicating the presence of ionic perchlorate [28]. The band at 1090 cm^{-1} is assignable to $\nu_3(ClO_4)$ and the unsplit band at 625 cm^{-1} assignable to $\nu_4(ClO_4)$. These indicate that the ClO_4 species is not coordinated (T_d symmetry). The other bands at 938 and 467 cm^{-1}, assignable to ν_1 and ν_2 vibrations of perchlorate, are very weak.

The electronic spectral data of the ligands and complexes in DMF solutions are summarized in Table 7. The intraligand electronic transitions of HL^1 suffered considerable shift on coordination, as evidenced by the absorptions obtained for **1**. The band with the highest molar absorptivity at 20750 cm^{-1} is assigned as a S→Ni LMCT transition. The ground state of Ni(II) in an octahedral coordination is $^3A_{2g}$ and expects three spin allowed transitions $^3T_{2g}(F) \leftarrow {}^3A_{2g}(F)(\nu_1)$, $^3T_{1g}(F) \leftarrow A_{2g}(F)(\nu_2)$ and $^3T_{1g}(P) \leftarrow {}^3A_{2g}(F)(\nu_3)$ in an increasing order of energy, with molar absorptivities generally below 20. However we could not locate any of these bands, probably due to masking by the high-intensity charge transfer bands. For compound **2** also the S→Ni charge transfer band at 22470 cm^{-1} masks the possible d–d bands in that region. For compound **3**, the CT band is obtained at 24150 cm^{-1}, assigned as an S→Ni LMCT. Another absorption obtained at 31250 cm^{-1} is assigned as an $n \rightarrow \pi^*$ transition. For a diamagnetic Ni(II) complex, as a consequence of eight electrons being paired in the four low-lying d orbitals with the upper orbital being $d_{x^2} - y^2$, the four lower orbitals are often so close in energy that individual transitions from them to the upper d level cannot be distinguished, resulting in a single absorption band. The shoulder band obtained at 19380 cm^{-1} (1870 $M^{-1}\,cm^{-1}$) for **3** may be attributed to a d–d band of this type. The d–d bands appearing as weak shoulders centered around the 20000 cm^{-1} region are typical of square planar monoligated Ni(II) complexes [29].

Table 6
IR spectral data of the ligands and complexes (cm^{-1})

Compounds	$\nu(C{=}^1N)$	$\nu(^2N{=}C)$	ν(N–N)	ν(C=S)/ν(C–S)	ν(C–H)	$\nu(Ni–N_{azo})$	ν(Ni–S)	$\nu(Ni–N_{py/qu})$
HL^1	1580		1102	1282	2970, 2870			
$[Ni(HL^1)_2]Cl_2$ (**1**)	1561		1110	1278	2969, 2870	459	352	240
HL^2	1630		1118	1342				
$[Ni(HL^2)L^2]ClO_4 \cdot 7H_2O$ (**2**)	1553	1590	1145	1337, 1283	2964, 2876	430	354	251
$[NiL^2Cl] \cdot 0.5H_2O$ (**3**)	1537	1594	1150	1296	2969, 2876	433	351	270

Table 7
Electronic spectral features of the ligands and complexes in DMF solutions

Compounds	Absorbance features λ_{max} cm^{-1} (ε $M^{-1}\,cm^{-1}$)
HL^1	34480 (139900), 31850 (150500), 30860 (155100), 29410 (165800), 28250 (161200)
$[Ni(HL^1)_2]Cl_2$ (**1**)	31250 (23640), 24510 (23230), 20750 (25280)
HL^2	36230 (8300), 29590 (9800), 23580 (2270)
$[Ni(HL^2)L^2]ClO_4 \cdot 7H_2O$ (**2**)	30030 (16550), 26530 (18080), 22470 (21200)
$[NiL^2Cl] \cdot 0.5H_2O$ (**3**)	31250 (7770), 24150 (12960), 19380 (1870)

Acknowledgements

E. Manoj thanks the University Grants Commission, New Delhi, India for financial support. M.R.P. Kurup is thankful to the CSIR, New Delhi, India for financial support.

Appendix A. Supplementary material

CCDC 626768 and 626767 contain the supplementary crystallographic data for $\mathbf{1} \cdot 2.5H_2O$ and **2a**. These data can be obtained free of charge via http://www.ccdc.cam.ac.uk/conts/retrieving.html, or from the Cambridge Crystallographic Data Centre, 12 Union Road, Cambridge CB2 1EZ, UK; fax: (+44) 1223-336-033; or e-mail: deposit @ccdc.cam.ac.uk. Supplementary data associated with this article can be found, in the online version, at doi:10.1016/j.poly.2007.09.023.

References

[1] P. Bindu, M.R.P. Kurup, T.R. Satyakeerthy, Polyhedron 18 (1999) 321.
[2] M. Joseph, V. Suni, M.R.P. Kurup, M. Nethaji, A. Kishore, S.G. Bhat, Polyhedron 23 (2004) 3069.
[3] D.S. Kalinowski, Y. Yu, P.C. Sharpe, M. Islam, Y.-T. Liao, D.B. Lovejoy, N. Kumar, P.V. Bernhardt, D.R. Richardson, J. Med. Chem. 50 (2007) 3716.
[4] D.L. Klayman, J.P. Scovill, J. Bruce, F. Bartosevich, J. Med. Chem. 27 (1984) 84.
[5] R.P. John, A. Sreekanth, V. Rajakannan, T.A. Ajith, M.R.P. Kurup, Polyhedron 23 (2004) 2549.
[6] S.K. Dutta, D.B. McConVille, W.J. Youngs, M. Chaudhuri, Inorg. Chem. 36 (1997) 2517.
[7] Z. Lu, C. White, A.L. Rheingold, R.H. Crabtree, Inorg. Chem. 32 (1993) 3991.
[8] S. Padhye, G.B. Kauffman, Coord. Chem. Rev. 63 (1985) 127.
[9] E. Lukevics, D. Jansone, K. Rubina, E. Abele, S. Germane, L. Leite, M. Shymaska, J. Popelis, Eur. J. Med. Chem. 30 (1995) 983.
[10] M. Joseph, M. Kuriakose, M.R.P. Kurup, E. Suresh, A. Kishore, S.G. Bhat, Polyhedron 25 (2006) 61.
[11] A.E. Liberta, D.X. West, Biometals 5 (1992) 121.
[12] A. Sreekanth, M.R.P. Kurup, Polyhedron 23 (2004) 969.
[13] A. Sreekanth, M.R.P. Kurup, Polyhedron 22 (2003) 3321.
[14] A. Sreekanth, M. Joseph, H.-K. Fun, M.R.P. Kurup, Polyhedron 25 (2006) 1408.
[15] J.P. Scovill, Phosphorous Sulfur Silicon 60 (1991) 15.
[16] G.M. Sheldrick, SHELXS97 and SHELXL97, Bruker AXS Inc., Madison, WI, USA, 1997.
[17] L.J. Farrugia, J. Appl. Crystallogr. 30 (1997) 565.
[18] A.L. Spek, J. Appl. Crystallogr. 36 (2003) 7.
[19] C.F. Macrae, P.R. Edgington, P. McCabe, E. Pidcock, G.P. Shields, R. Taylor, M. Towler, J. van de Streek, J. Appl. Crystallogr. 39 (2006) 453.
[20] P. Souza, A.I. Matesanz, V. Fernandez, J. Chem. Soc., Dalton Trans. (1996) 3011.
[21] I. Garcia, E. Bermejo, A.K. El Sawaf, A. Castineiras, D.X. West, Polyhedron 21 (2002) 729.
[22] K.A. Ketcham, I. Garcia, E. Bermejo, J.K. Swearingen, A.K. El Sawaf, E. Bermejo, A. Castineiras, D.X. West, Polyhedron 21 (2002) 859.
[23] N.C. Kasuga, K. Sekino, C. Koumo, N. Shimada, M. Ishikawa, K. Nomiya, J. Inorg. Biochem. 84 (2001) 55.
[24] V. Suni, M.R.P. Kurup, M. Nethaji, Polyhedron 26 (2007) 3097.
[25] A. Sreekanth, S. Sivakumar, M.R.P. Kurup, J. Mol. Struct. 655 (2003) 47.
[26] L. Latheef, E. Manoj, M.R.P. Kurup, Acta Crystallogr., Sect. C 61 (2006) o16.
[27] M.B. Ferrari, F. Bisceglie, G. Pelosi, M. Sassi, P. Tarasconi, M. Cornia, S. Capacchi, R. Albertini, S. Pinelli, J. Inorg. Biochem. 90 (2002) 113.
[28] B.S. Garg, M.R.P. Kurup, S.K. Jain, Y.K. Bhoon, Transition Met. Chem. 13 (1988) 309.
[29] M. Akbar Ali, S.M.G. Hossain, S.M.M.H. Majumder, M. Nazimuddin, M.T.H. Tazafder, Polyhedron 6 (1987) 1653.

Available online at www.sciencedirect.com
ScienceDirect
Polyhedron 27 (2008) 283–288
POLYHEDRON
www.elsevier.com/locate/poly

Two-dimensional lanthanide coordination polymers with bis(diphenylphosphino)hexane dioxide. The determination of the polymeric structure from twinned crystals

Zdenek Spichal [a], Vaclav Petricek [b], Jiri Pinkas [a], Marek Necas [a,*]

[a] Department of Chemistry, Masaryk University, Kotlarska 2, CZ-61137 Brno, Czech Republic
[b] Institute of Physics, Academy of Sciences of the Czech Republic, Na Slovance 2, CZ-18221 Praha, Czech Republic

Received 16 May 2007; accepted 12 September 2007
Available online 22 October 2007

Abstract

Lanthanide nitrates and bis(diphenylphosphino)hexane dioxide ($dpphO_2$) formed under solvothermal conditions a series of coordination polymers $[Ln(dpphO_2)_2(NO_3)_2](NO_3)$ (Ln = Pr (**1**), Nd (**2**), Sm (**3**), Dy (**4**), Lu (**5**)), featuring two-dimensional network structure of the (4,4) topology. The compounds $[Ln(dpphO_2)_2Cl_2]Cl$ (Ln = Pr (**6**), Nd (**7**), Gd (**8**)) were obtained from corresponding chlorides. Coordination polymer **7** formed regular single crystals of the orthorhombic $Pna2_1$ space group. The nitrate complexes crystallized in the orthorhombic $Aea2$ space group, however, the crystals were pseudo-merohedral twins simulating a tetragonal diffraction pattern. Unlike our previously characterized neutral polymers with bis(diphenylphosphino)ethane dioxide, all present coordination networks are cationic, with anions located between or within the two-dimensional layers.
© 2007 Elsevier Ltd. All rights reserved.

Keywords: Bis(diphenylphosphino)hexane dioxide; Lanthanides; Coordination polymers; X-ray crystallography; Twinning

1. Introduction

A current revolutionary increase in the number of synthesized and structurally characterized metal-organic coordination frameworks reflects the demand for new materials with predesigned functionalities [1]. The structures of polymeric networks and their properties are largely determined by a suitable combination of elemental building blocks, *e.g.* metal containing nodes and polyfunctional organic linkers. Their considerate choice together with synthetic strategy employed lead to different types of branching, topologies, and dimensionality [2]. Lanthanides are often utilized as nodes because of their propensity to high coordination numbers and inherent luminescent properties, which are essential for the formation of unusual network topologies and luminescent materials, respectively [3].

Our current investigations are focused on the reactivity of bis(diphenylphosphino)alkane dioxides $Ph_2P(O)–(CH_2)_n–P(O)Ph_2$ with lanthanide salts. In two recent articles we presented polymeric coordination compounds of 1,2-bis(diphenylphosphino)ethane dioxide and binuclear complexes of 1,4-bis(diphenylphosphino)butane dioxide with lanthanides. We also discussed factors affecting the structure of the products, *i.e.* the lanthanide atom size, the choice of the salt anion, and the ligand length [4]. To extend our knowledge of how the length of the ligand chain is related to the structure of the resulting complexes, we have performed a series of reactions of lanthanide salts with 1,6-bis(diphenylphosphino)hexane dioxide ($dpphO_2$).

The reactivity of $dpphO_2$ with metal cations is rather unexplored. A series of reports on spectroscopic and magnetic properties of Fe(II)/Fe(III) chelates with $dpphO_2$ was published in the 1980's [5]. According to the CSD, there are no crystallographically characterized molecular or polymeric $dpphO_2$ complexes [6]. However, aliphatic chain

* Corresponding author. Tel.: +420 549496060; fax: +420 549492443.
E-mail address: man@chemi.muni.cz (M. Necas).

0277-5387/$ - see front matter © 2007 Elsevier Ltd. All rights reserved.
doi:10.1016/j.poly.2007.09.004

based ligands of similar length were already used in the construction of metal-organic frameworks; for example 1,8-octanedioic (suberic) acid which possesses the same hexamethylene chain between the two carboxyl groups [7]. Dicarboxylic acids are only partially comparable with diphosphine dioxides as their terminal groups often feature in deprotonated anionic forms unlike the $Ph_2P(O)$ moieties. We can therefore expect that in case of diphosphine dioxides the displacement of other ligands from the coordination sphere of lanthanides might be less common and the resulting architectures different.

2. Results and discussion

The reaction mixture of $dpphO_2$ and praseodymium nitrate in methanol was heated in an autoclave at 140 °C for 24 h. After cooling and opening the autoclave, the product was obtained in the form of plate-shaped crystals which were markedly diagonally segmented into four overlapping triangular regions. The X-ray diffraction data of the entire segmented crystal showed a tetragonal Laue symmetry and the attempts to solve the structure by both direct and heavy atom methods were fruitless. Therefore one of the larger plates was carefully treated to cut out the fraction from within the overlapping wedges. This fragment gave diffraction data which strongly violated tetragonal symmetry and suggested rather the orthorhombic one. Using the latter dataset, we could solve the structure of $\{[Pr(dpphO_2)_2(NO_3)_2]^+(NO_3)^-\}_n$ (**1**). More details on the solution and subsequent refinement are given in Section 5. The solvothermal reactions of $dpphO_2$ with other lanthanide nitrates afforded similarly twinned crystals of **4** (Dy) and **5** (Lu). Using the information obtained during the solution and refinement of the structure of **1**, we carried out the refinement of **4** with comparable results. The Lu compound gave very poor data which were not suitable for the refinement. Nevertheless, the lattice parameters of **5** correspond to the lattice parameters of **1** and **4**.[1] On the basis of the lattice parameters and microanalytical data, we can conclude that the complexes of $dpphO_2$ with lanthanide nitrates are isostructural. Only the structure of **1** is described below, the general features are applicable to the Dy analogue **4** and most probably to other nitrate compounds.

The reactions of $dpphO_2$ with $PrCl_3$, $NdCl_3$, and $GdCl_3$ were also carried out in an autoclave, however, clear solutions were obtained in the Teflon liner after the autoclave was opened. The crystallization occurred spontaneously after the solutions were transferred to glass flasks. Single crystals suitable for X-ray diffraction were only available for $[Nd(dpphO_2)_2Cl_2]Cl$ (**7**).

A common feature of the coordination polymers containing the four atoms shorter $dppeO_2$ ligand and the present $dpphO_2$ compounds is the two-dimensional structure. Unlike the former, the latter are based on the 1:2 instead of 2:3 metal-to-ligand stoichiometry. The lanthanide coordination polyhedra of both nitrate and chloride complexes result from the addition of four Ph_2PO oxygens and the simultaneous displacement of either one nitrate or one chloride ligand from the original coordination sphere. Both polymeric networks are therefore of the (4,4) type and might be considered as derivatives of square grid architectures. As pointed out by Paine et al. the displacement of anions from the metal inner coordination sphere is quite uncommon with neutral donor ligands [8a]. However, it was observed that the diphosphine dioxide ligands may displace the inner-sphere nitrate ions from lanthanides under certain conditions [4a,8].

We first describe the structural features of compound **7** derived from $NdCl_3$, because it was crystallographically the simple case. Here the Nd center is octahedrally coordinated by four O and two *trans*-positioned Cl. The Nd–O–P bonds are almost linear and perpendicular to the adjacent hexamethylene chains, so that the structural motif closely resembles four-connected swastikas (Fig. 1). The Cl atoms displaced from the Nd(III) salt are located approximately in the centers of tetragonal building blocks. The polymeric layers are perpendicular to the crystallographic *b*-axis and the average interlayer separation, measured as a distance between the planes through the Nd atoms, is 9.35 Å.

The coordination polyhedron in $[Pr(dpphO_2)_2(NO_3)_2](NO_3)$ (**1**) contains two chelating (η^2) nitrate ligands in the *trans* geometry (Fig. 2). Because of the greater steric demand of nitrate anions in comparison to chlorides, the N–Pr–N arrangement is markedly less linear than Cl–Nd–Cl in **7** (167.4° versus 177.4°). The planes through

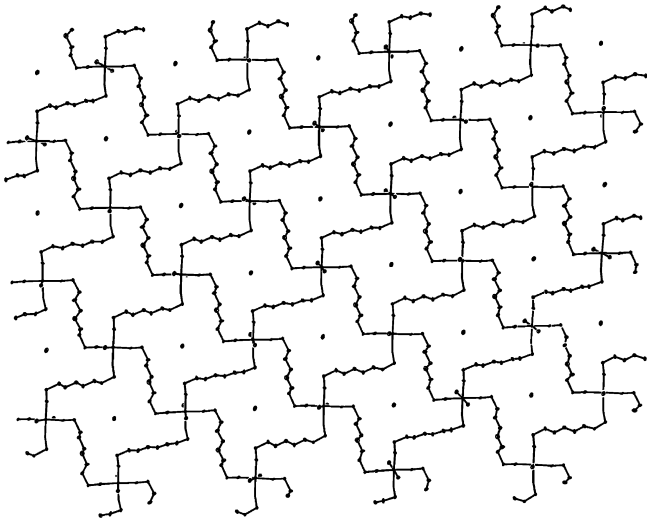


Fig. 1. Top view of 2D polymeric layer in $[Nd(dpphO_2)_2Cl_2]Cl$ (**7**). All hydrogen atoms and phenyl groups were omitted to emphasize the structural motif. Chloride anions are visible as isolated atoms throughout the network.

[1] Lattice parameters of **5**: $a = 25.855(2)$ Å, $b = 23.823(2)$ Å, $c = 23.744(2)$ Å, $V = 14625(2)$ Å^3.

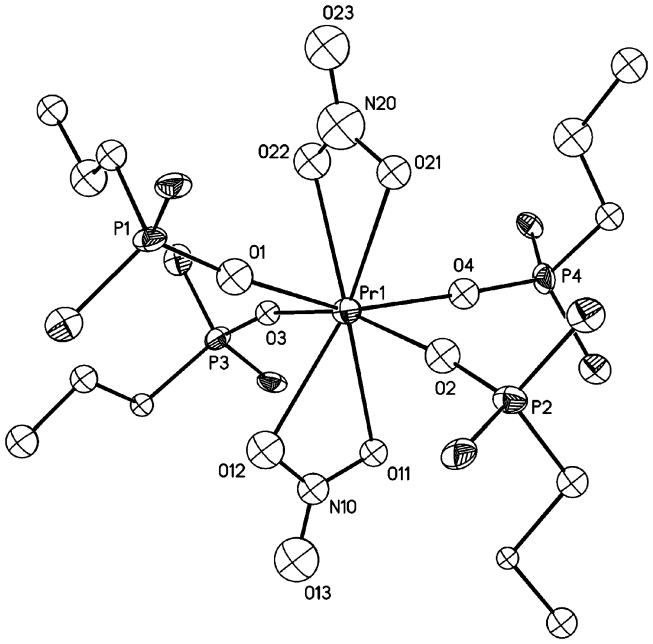


Fig. 2. Coordination polyhedron in $[Pr(dpphO_2)_2(NO_3)_2]NO_3$ (**1**). All hydrogen atoms were omitted and phenyl groups reduced to their *ipso* carbons for clarity. Thermal ellipsoids are drawn at the 50% probability level; the ellipsoids without octant shading represent atoms which were refined only isotropically.

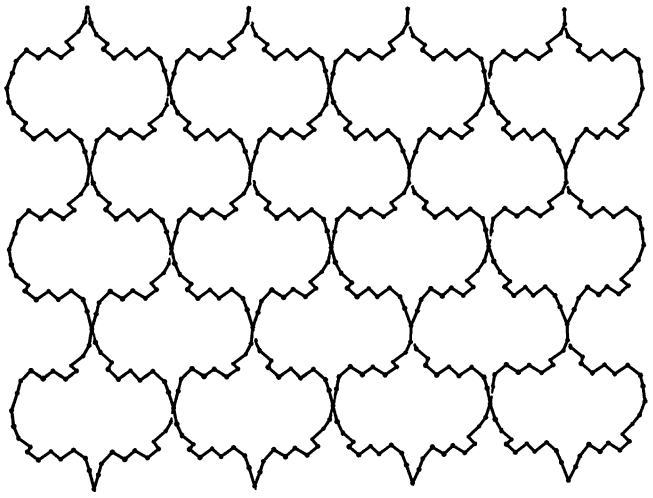


Fig. 3. Top view of 2D polymeric layer in $[Pr(dpphO_2)_2(NO_3)_2]NO_3$ (**1**). All hydrogen atoms, phenyl and nitrate groups were omitted to emphasize the structural motif.

the opposite nitrate ligands are almost perpendicular. Although we were not fully successful in definite positioning of the nitrate anions displaced from the $Ln(NO_3)_3$ centers to the second coordination sphere, we arrived at the general formula $[Ln(dpphO_2)_2(NO_3)_2](NO_3)$ for the nitrate compounds on the basis of electroneutrality, the presence of ionic nitrate bands in the IR spectra (below), and analogy with $[Nd(dpphO_2)_2Cl_2]Cl$ (**7**), in which the anion is also displaced from the coordination sphere. The layers are perpendicular to the crystallographic *a*-direction and the interlayer space is occupied by the nitrate anions and solvent molecules (methanol, water) (see Fig. 3). The distance between the 2D network layers, measured as a distance between the planes through the Pr atoms, is 12.85 Å.

The microanalytical results for C seemed to be systematically overestimated when compared to the calculated values whereas H analyses were lower for compounds **1** to **5**. This can be explained by the water of crystallization present in the crystals, which is visible as isolated maxima of varying density in residual Fourier maps. The experimental analytical values would require ca. 4–5 molecules of water per monomeric unit. The current model which includes two molecules of methanol and two and a half molecules of water per asymmetric part of the unit cell in **1** and **4** also fits the analyses quite well. Other data show that the crystalline products are chemically consistent (melting points on multiple randomly selected crystals, IR spectra). The IR spectra of all nitrate compounds show the presence of both chelating (1458–1506, 1300–1310, 1028–1029, and 817–818 cm^{-1}) and ionic nitrates (1384 cm^{-1}). Along with the chloride complexes, there are also very strong absorptions in the range of 1138–1150 cm^{-1} which is typical for the P=O stretch.

In spite of the 2D network structure of compounds **1**, **2**, **4**, and **5**, their solubility in water was sufficient to allow recording the ESI-MS spectra. All four compounds display the same kind of pattern with similar relative peak intensities. The parent peaks in all spectra belong to the binuclear $[Ln_2(dpphO_2)_2(NO_3)_5]^+$ fragments. The presence of two lanthanide atoms in these ions was clearly demonstrated by the correspondence of the measured and theoretical isotope patterns for the Nd complex **2**. The base peaks in the spectra are $[Ln(dpphO_2)_2(NO_3)_2]^+$ which are formed by the loss of a neutral $Ln(NO_3)_3$ moiety from the previous fragment as it was confirmed by the MS2 experiments. This sequence is completed by the expulsion of the $dpphO_2$ and the formation of $[Ln(dpphO_2)(NO_3)_2]^+$, the further fragmentation of which results in the HNO_2 loss. It is interesting to note that the polymeric $[Ln(dpphO_2)_2(NO_3)_2](NO_3)$ complexes with 1:2 metal-to-ligand stoichiometry provide the same fragmentation paths as the binuclear complexes $[Lu_2(dppeO_2)_3(NO_3)_6]$ [4a] and $[Ln_2(dppbO_2)_3(NO_3)_6]$ [4b] with 2:3 metal-to-ligand ratio.

3. Conclusion

We have described the structural determination of the coordination polymer from twinned crystals. From the chemical point of view, we have observed the formation of 2D cationic polymers by the interaction of the long-chain diphosphine dioxide ligand $dpphO_2$ with lanthanide cations (Pr, Nd, Sm, Gd, Dy, and Lu). Although the ligand possesses a rather flexible central part, the separation between the donor atoms is too large to allow the formation of chelates. Therefore, after obtaining the series of polymers with shorter ligands and molecular binuclear compounds with medium size ligands, we have prepared

the bis(diphenylphosphino)hexane dioxide complexes that again prefer the polymeric architecture. The present polymers do not afford porous structures, nevertheless, the preliminary experiments indicate promising luminescent properties.

4. Experimental

Commercially available 1,6-bis(diphenylphosphino)hexane was dissolved in tetrahydrofuran and oxidized by 30% aqueous solution of H_2O_2 to give $Ph_2P(O)$–$(CH_2)_6$–$P(O)Ph_2$ ($dpphO_2$). IR spectra (KBr pellets, 4000–400 cm^{-1}) were collected on an Equinox 55/S/NIR FTIR spectrometer. Microanalyses were performed using a Thermo Finnigan CHN Analyzer Flash EA 1112. Melting points were measured on a Boetius melting-point apparatus. The ion trap mass spectrometer Esquire 2000 (Bruker, Germany) with electrospray ionization was used for the ESI-MS analyses. Solid samples were dissolved in water and diluted in acetonitrile/water (1:1). The samples were injected directly into the electrospray ion source at a flow rate of 4 μl min^{-1}. The spectra were recorded both in positive and negative mode. The capillary voltage was 4500 V.

A mixture of $dpphO_2$ (250 mg, 0.514 mmol) and the hydrated lanthanide salt (0.257 mmol) in methanol (30 mL) was sealed in a 250-mL stainless-steel reactor Berghof HR-200 with a Teflon liner, heated for 24 h to 140 °C with a RHS-295 heater controlled by a BAR-945 unit, and then slowly cooled to room temperature. After additional 24 h the autoclave was opened. For nitrate complexes **1** to **5**, the crystals were already formed and could be collected. The chloride compounds yielded solutions which spontaneously crystallized after they were transferred to glass flasks (within 3 h). Alternatively, both nitrate and chloride compounds may be also prepared as powders by simple reactions of $dpphO_2$ with respective salts in methanol under laboratory conditions, as proven by consistent microanalytical data. However, these materials are amorphous to powder XRD and only the solvothermal reactions afforded the crystalline samples suitable for the X-ray diffraction.

$\{[Pr(dpphO_2)_2(NO_3)_2]^+(NO_3)^-\}_n$ (**1**). Yield: 315 mg (94.3%). Mp: 120–122 °C. *Anal.* Calc. C, 55.44; H, 4.96; N, 3.23. Found: C, 51.50; H, 5.24; N, 4.14%. IR: 514m, 543vs, 553w, 616vw, 669w, 695s, 720s, 744m, 789w, 818w, 855vw, 925vw, 997w, 1028m, 1072m, 1093s, 1121s, 1142vs, 1170s, 1183m, 1222vw, 1305s, 1384vs, 1437vs, 1458s, 1484s, 1591vw, 2333vw, 2359vw, 2863w, 2936w, 3055w, 3419m.

$\{[Nd(dpphO_2)_2(NO_3)_2]^+(NO_3)^-\}_n$ (**2**). Yield: 325 mg (97.0%). Mp: 121–124 °C. *Anal.* Calc. C, 55.29; H, 4.95; N, 3.22. Found: C, 50.40; H, 5.56; N, 2.68%. IR: 431vw, 511m, 543vs, 555w, 616vw, 669w, 694s, 722s, 744m, 790w, 818vw, 854vw, 892vw, 923vw, 942vw, 976vw, 997w, 1028m, 1072m, 1094s, 1122s, 1144vs, 1171s, 1222vw, 1305s, 1384vs, 1437vs, 1464s, 1486s,1591vw, 2359vw, 2863w, 2934w, 3055w, 3419w.

$\{[Sm(dpphO_2)_2(NO_3)_2]^+(NO_3)^-\}_n$ (**3**). Yield: 287 mg (85.4%). Mp: 122–125 °C. *Anal.* Calc. C, 55.04; H, 4.93; N, 3.21. Found: C, 52.84; H, 4.96; N, 2.78%. IR: 511m, 543vs, 553w, 616vw, 669w, 694s, 722s, 745m, 792w, 818w, 856vw, 892vw, 927vw, 943vw, 977vw, 997w, 1028m, 1072m, 1095s, 1122s, 1145vs, 1173m, 1222vw, 1307s, 1384vs, 1437vs, 1465s, 1485s, 1591vw, 2327vw, 2360vw, 2864w, 2934w, 3056w, 3393w.

$\{[Dy(dpphO_2)_2(NO_3)_2]^+(NO_3)^-\}_n$ (**4**). Yield: 316 mg (93.2%). Mp: 132–135 °C. *Anal.* Calc. C, 54.43; H, 4.88; N 3.18. Found: C, 49.81; H, 5.09; N, 2.57%. IR: 418vw, 511m, 543s, 553w, 618vw, 669w, 694s, 722m, 744m, 792w, 817vw, 855vw, 893vw, 923vw, 942vw, 980vw, 997w, 1028w, 1072m, 1096s, 1122s, 1147vs, 1179m, 1222vw, 1300m, 1384vs, 1437s, 1473m, 1487m, 1507m, 1591vw, 2361vw, 2864w, 2936w, 3054w, 3411w.

$\{[Lu(dpphO_2)_2(NO_3)_2]^+(NO_3)^-\}_n$ (**5**). Yield: 279 mg (81.3%). Mp: 138–141 °C. *Anal.* Calc. C, 54.02; H 4.84; N 3.15. Found: C, 49.60; H, 5.32; N, 2.52%. IR: 510m, 543vs, 553w, 616vw, 668w, 694s, 722s, 747m, 792w, 817vw, 828vw, 856vw, 925vw, 938vw, 997w, 1029m, 1072m, 1098s, 1122s, 1150vs, 1180m, 1223vw, 1301s, 1384vs, 1438s, 1477s, 1506m, 1591vw, 2342vw, 2360vw, 2865w, 2936w, 3056w, 3402w.

$\{[Pr(dpphO_2)_2Cl_2]^+Cl^-\}_n$ (**6**). Yield: 227 mg (72.5%). Mp: 270–272 °C. *Anal.* Calc. C, 59.05; H 5.29. Found: C, 57.80; H, 5.47%. IR: 431vw, 481vw, 513m, 544vs, 558w, 616vw, 699s, 716w, 725m, 730m, 745m, 757w, 793w, 854vw, 890vw, 939vw, 997w, 1026vw, 1075s, 1088vs, 1123vs, 1138vs, 1162w, 1184w, 1214vw, 1396vw, 1438vs, 1460vw, 1487vw, 1590vw, 2861w, 2897w, 2935w, 2990vw, 3017w, 3035w, 3052w.

$\{[Nd(dpphO_2)_2Cl_2]^+Cl^-\}_n$ (**7**). Yield: 213 mg (67.8%). Mp: 271–273 °C. *Anal.* Calc. C, 58.89; H, 5.24. Found: C, 57.32; H, 5.33%. IR: 431vw, 481vw, 513m, 545vs, 558w, 616vw, 699s, 726m, 746m, 793w, 856vw, 890vw, 924vw, 942vw, 997w, 1026vw, 1075m, 1089vs, 1122s, 1138vs, 1164w, 1185w, 1220vw, 1253vw, 1271vw, 1323vw, 1397vw, 1437s, 1460vw, 1487vw, 1589vw, 2862vw, 2900vw, 2932w, 2988vw, 3017vw, 3035w, 3051w, 3078vw, 3425vw.

$\{[Gd(dpphO_2)_2Cl_2]^+Cl^-\}_n$ (**8**). Yield: 249 mg (78.4%). Mp: 267–269 °C. *Anal.* Calc. C, 58.27; H, 5.22. Found: C, 57.38; H, 5.31%. IR: 430vw, 481vw, 514w, 545s, 559w, 616vw, 700m, 714w, 730w, 746w, 759w, 794w, 856vw, 890vw, 943vw, 997vw, 1026vw, 1076w, 1091s, 1122m, 1142vs, 1186vw, 1218vw, 1397vw, 1438m, 1461vw, 1488vw, 1589vw, 2865vw, 2898vw, 2932vw, 3018vw, 3036vw, 3050vw.

5. Crystallography

Diffraction data were collected on a KUMA KM-4 κ-axis diffractometer with Mo Kα radiation ($\lambda = 0.71073$ Å) equipped with a CCD detector. The temperature during data collection was 120(2) K. The intensity data were corrected for Lorentz and polarization effects; absorption cor-

rection was applied for all data. The structure of **7** was solved by direct methods and refined by standard methods using the SHELXTL software package [9]. The details of the data collection and structure refinement are summarized in Table 1 and the important bond lengths and angles are listed in Table 2.

The crystals of **1** were pseudo-merohedral twins simulating a tetragonal diffraction pattern and the attempts to solve the structure using the "tetragonal" data set were unsuccessful. Therefore the crystals were fragmented and the diffraction data recorded on one of the fragments were taken as a starting point for further investigation. The analysis of extinctions showed two most probable space groups *Aea*2 and *Aeam* related by the inversion center. A more detailed study showed that some relatively weak reflections violating the extinction conditions are generated by the twinning operation. This effect was much weaker for the small crystal but clearly apparent. This indicated that even the cut crystal is composed of twin domains. In the non-centrosymmetric space group *Aea*2, the direct methods on this data set gave a model, which was refined to a reasonable minimum using conventional techniques. The group-subgroup relationship between the idealized lattice symmetry 4/mmm and the orthorhombic Laue group led to the equivalent twinning matrices from which the fourfold axis, directed in the standard orthorhombic setting along the *a* axis, has been chosen. Introducing the twinning operation improved the fit significantly and ended with relatively small but significant volume fraction ~16.2(2)% for the minor domain. Unfortunately the small crystal had much worse statistics than the original one. This was the reason why the final refinement was made against the data collected from the original large crystal. The volume fraction of the second domain for the large crystal was about 49% which is in full accordance with the preliminary observations on the crystal morphology. In the final stages, the fact that the space group is non-centrosymmetric was taken into account and the additional twin domains were used that were related by the inversion center to already existing ones. The final refined values of the volume fractions of the four twin components (generated by operations 1, 4, −1 and −4) were 0.248(12), 0.373(13), 0.273(13) and 0.106(12) for **1**, and 0.286(13), 0.401(13), 0.286(13) and 0.027(12) for **4**.

The refinement was performed using JANA2000 crystallographic computing system [10]. We introduced the phenyl rings as rigid bodies whose average shapes were appropriately translated and rotated to address a rather unclear electron density in the vicinity of phosphorus atoms. The positioning of the ionic nitrate anions was only partially successful. One of the N–O vectors was found to coincide with the twofold axis so that only a half of the nitrate anion contributes to the asymmetric part of the unit cell. The other half of the anion has not been clearly identified in the electron density maps. The residual maxima are located between the polymeric layers rather than in the vicinity of the heavy atoms. However, the attempts to address the residual electron density peaks using the molecules of solvent (water or methanol) included in the model have not lead to meaningful results. The refinement of **1** converged to $R = 0.0476$, $Rw = 0.0541$.

The pseudo-merohedral twinning present in the crystal can generally lead to splitting of related diffraction spots. Due to the fact that the condition $b \approx c$ was closely fulfilled, no obvious splitting was detected. Nevertheless, the

Table 2
Selected average bond lengths (Å) and angles (°) for **1**, **4**, and **7** and the parent $dpphO_2$ ligand

	$dpphO_2$[b]	**1**	**4**	**7**
Ln–Cl				2.704
Ln–O (to N)		2.574	2.460	
Ln–O (to P)		2.377	2.270	2.336
P–O	1.488	1.498	1.496	1.505
P–C [a]	1.787	1.782	1.754	1.787
Ln–O–P		166.2	166.8	172.8
O–P–C [a]	114.7	112.1	111.1	110.9

[a] C is the carbon atom in the $(CH_2)_6$ central moiety.
[b] The values taken from CSD [6] Refcode WITHUC.

Table 1
Crystal data and structure refinement parameters

	1	**4**	**7**
Empirical formula	$C_{62}H_{77}PrN_3O_{17.5}P_4$	$C_{62}H_{77}DyN_3O_{17.5}P_4$	$C_{60}H_{66}Cl_3NdO_5P_4$
Formula weight	1409.1	1430.7	1241.60
Crystal system	orthorhombic	orthorhombic	orthorhombic
Space group	*Aea*2	*Aea*2	$Pna2_1$
a (Å)	25.8233(4)	25.7052(4)	25.0215(6)
b (Å)	23.7530(4)	23.6239(4)	18.6981(6)
c (Å)	23.6737(4)	23.4771(4)	12.9530(4)
Volume (Å^3)	14521.0(4)	14256.6(4)	6060.1(3)
Z	8	8	4
ρ (Mg/m^3)	1.289	1.333	1.361
μ (mm^{-1})	0.822	1.202	1.140
Reflection collected/unique	69 603/28 921	78 947/25 573	61 540/10 644
Data/parameters	15 614/274	12 793/274	10 644/668
Final *R* indices [$I > 2\sigma(I)$]	0.0476/0.0541	0.0479/0.0531	0.0402/0.0858
$\Delta\rho_{max}/\Delta\rho_{min}$ (e Å^{-3})	2.40/−1.41	2.15/−1.90	1.578/−0.512

integration has been preformed with a larger mask to avoid incomplete integration.

Acknowledgements

This work was supported by the Ministry of Education of the Czech Republic (MSM0021622410) and by the Grant Agency of the Czech Republic (202/06/0757). We thank Dr. Z. Zdrahal for recording ESI-MS spectra and Professor Z. Travnicek, Palacky University, Olomouc, for elemental analyses.

Appendix A. Supplementary material

CCDC 645713, 645714 and 645715 contain the supplementary crystallographic data for this paper. These data can be obtained free of charge via http://www.ccdc.cam.ac.uk/conts/retrieving.html, or from the Cambridge Crystallographic Data Centre, 12 Union Road, Cambridge CB2 1EZ, UK; fax: (+44) 1223-336-033; or e-mail: deposit @ccdc.cam.ac.uk. Supplementary data associated with this article can be found, in the online version, at doi:10.1016/j.poly.2007.09.004.

References

[1] (a) O.M. Yaghi, H. Li, C. Davis, D. Richardson, T.L. Groy, Acc. Chem. Res. 31 (1998) 474;
(b) N.W. Ockwig, O. Delgado-Friedrichs, M. O'Keeffe, O.M. Yaghi, Acc. Chem. Res. 38 (2005) 176;
(c) N.R. Champness, Dalton Trans. (2006) 877.
[2] (a) B. Moulton, M.J. Zaworotko, Chem. Rev. 101 (2001) 1629;
(b) C. Janiak, Dalton Trans. (2003) 2781;
(c) S. Kitagawa, R. Kitaura, S. Noro, Angew. Chem., Int. Ed. 43 (2004) 2334.
[3] (a) S.K. Ghosh, P.K. Bharadwaj, Inorg. Chem. 44 (2005) 3156;
(b) J.-C.G. Bünzli, C. Piguet, Chem. Soc. Rev. 34 (2005) 1048.
[4] (a) Z. Spichal, M. Necas, J. Pinkas, Inorg. Chem. 44 (2005) 2074;
(b) Z. Spichal, M. Necas, J. Pinkas, Z. Zdrahal, Polyhedron 25 (2006) 809.
[5] (a) T.S. Lobana, H.S. Cheema, S.S. Sandhu, Polyhedron 4 (1985) 717;
(b) T.S. Lobana, H.S. Cheema, S.S. Sandhu, J. Chem. Soc., Dalton Trans. (1983) 2039;
(c) T.S. Lobana, H.S. Cheema, S.S. Sandhu, J. Indian Chem. Soc. 59 (1982) 799;
(d) T.S. Lobana, H.S. Cheema, S.S. Sandhu, S.S. Spectrochim. Acta A42 (1986) 399;
(e) T.S. Lobana, S.S. Bhatti, Polyhedron 6 (1987) 1325.
[6] F.H. Allen, Acta Crystallogr., Sect. B 58 (2002) 380.
[7] Y.Q. Zheng, J. Sun, Y.F.J. Wang, Coord. Chem. 58 (2005) 1551.
[8] (a) B.M. Rapko, E.N. Duesler, P.H. Smith, R.T. Paine, R.R. Ryan, Inorg. Chem. 32 (1993) 2164;
(b) X. Gan, E.N. Duesler, R.T. Paine, P.H. Smith, Inorg. Chim. Acta 247 (1996) 29;
(c) E.M. Bond, E.N. Duesler, R.T. Paine, H. Nöth, Polyhedron 19 (2000) 2135;
(d) A.M.J. Lees, A.W.G. Platt, Inorg. Chem. 42 (2003) 4673.
[9] SHELXTL, Version 5.10, Bruker AXS Inc., Madison, WI, 1997.
[10] V. Petricek, M. Dusek, L. Palatinus, JANA2000, Crystallographic Computing System. 2000, Institute of Physics, Praha, Czech Republic.

Available online at www.sciencedirect.com
ScienceDirect
Polyhedron 27 (2008) 289–298
POLYHEDRON
www.elsevier.com/locate/poly

Deciphering the bonding mode of the trihalide ligands in a series of halogen carrier homo- and hetero-trihalide Cu(II) Schiff base complexes

Athanassios C. Tsipis [a,*], Paraskevas A. Karipidis [b]

[a] Laboratory of Inorganic and General Chemistry, Department of Chemistry, University of Ioannina, Ioannina 45110, Greece
[b] Laboratory of Applied Quantum Chemistry, Faculty of Chemistry, Aristotle University of Thessaloniki, 541 24, Thessaloniki, Greece

Received 2 May 2007; accepted 12 September 2007
Available online 18 October 2007

Abstract

Electronic structure calculation techniques (DFT) have been used to decipher the bonding of the trihalide ligands in a series of homo- and hetero-trihalide Cu(II) Schiff base complexes formulated as $[Cu(RdienR)(X)(XY_2)]$ (RdienR = Schiff base; R = furan, thiophene or pyrrol; X = Cl or Br; Y = Cl, Br or I). The association of the incoming Y_2 halogen molecule with one of the halide X ligands of the precursor $[Cu(RdienR)(X)_2]$ complexes alters their distorted trigonal bipyramidal stereochemistry which is transformed to a distorted square pyramidal geometry. The bonding mechanism between the halogen Y_2 molecule and the halide X ligand was thoroughly explored by means of various electronic parameters and charge decomposition analysis techniques. The bond dissociation energy of the Cu–XY_2 bond, $BDE_{Cu–XY_2}$, was estimated in the range of 61.9–68.4 kcal/mol, while the bond dissociation energy of the X–Y_2 bond, $BDE_{Cu–XY_2}$, was found in the range of 10.6–12.5 kcal/mol. It was found that the $X\cdots Y_2$ interactions correspond to weak hyperconjugative donor–acceptor interactions between a non-bonding n(X) molecular orbital (donor orbital) localized on the coordinated halide X ligand and an antibonding σ^*(Y–Y) molecular orbital (acceptor orbital) localized on the Y_2 halogen molecule. The n(X) $\rightarrow$ σ^*(Y–Y) donor–acceptor interactions are associated with a second-order perturbation stabilization energy, $\Delta E(2)$ of 34.5–52.5 kcal/mol. The loose association of the halogen molecules with the coordinated halide ligand renders the $[Cu(RdienR)(X)(XY_2)]$ complexes good halogen carrier molecules.
© 2007 Elsevier Ltd. All rights reserved.

Keywords: Trihalides; Schiff base; Copper(II) complexes; DFT; Bonding properties

1. Introduction

The structural features, the nature of the bonding and the relative stability of the "free" polyhalide anions $[X_mY_nZ_l]^-$ (X, Y, Z = F, Cl, Br or I; *m*, *n*, *l* integer numbers with $m + n + l =$ odd) has long been a subject of research and investigation both experimentally and theoretically [1–14]. Extensive theoretical studies have been devoted [15,16] to obtaining a detailed description of the electronic structure of the aforementioned anionic counterions of simple or complex cations and numerous crystal structures have been reported in the literature as well. From all possible combinations of the $[X_mY_nZ_l]^-$ anionic species, the most interesting and extensively studied are the trihalide anions $[XYZ]^-$ (X, Y, Z = Cl, Br or I). These species either homo- or hetero-nuclear adopt a linear or almost linear conformation, while for the homo-trihalide $[X_3]^-$ anions both symmetrical and unsymmetrical structures have been identified, depending on the type of the individual cations.

A decade ago Hoffmann et al. [15] have reported the results of a systematic, unified theoretical analysis concerning the bonding in the trihalides $[X_3]^-$, mixed trihalides $[XY_2]^-$ and hydrogen bihalides $[HY_2]^-$, based upon qualitative molecular orbital theory and DFT computational techniques. The authors showed that the nature of the

* Corresponding author. Tel.: +30 26510 98333; fax: +30 26510 44831.
E-mail address: attsipis@cc.uoi.gr (A.C. Tsipis).

0277-5387/$ - see front matter © 2007 Elsevier Ltd. All rights reserved.
doi:10.1016/j.poly.2007.09.005

bonding in all these species may be viewed as either electron-rich three-centre or as donor–acceptor bonding. The electron-rich three-centre bonding scheme resembles the "classical" view of the bonding in hypervalent molecules put forth by Pimentel [17] and Rundle [18] which invokes delocalized three-center σ bonding involving one bonding, one non-bonding and one antibonding molecular orbital. The alternative donor–acceptor view of the bonding corresponds to the interaction between closed-shell fragments, where X^- is the donor of a pair of electrons (occupied p_σ-orbital) and the Y_2 fragment acts as acceptor through its σ^* MO (σ^* LUMO). On the other hand, Kikuchi et al. [16] have studied the structure and dissociation of the heteronuclear $[XY_2]^-$ anions both in the gas phase and in solution using ab initio computational methods. They concluded that the $[X–Y–X]^-$ and $[Y–Y–X]^-$ isomers are energetically favoured over the $[Y–X–X]^-$ and $[Y–X–Y]^-$ ones, when Y is heavier than X. It was also suggested that the structures of $[Y–X–X]^-$ and $[Y–Y–X]^-$ anions in solution are quite different from those in the gas phase, being like an ion–dipole complex in aqueous solution.

Despite the vast number of theoretical and experimental works concerning the "free" $[XY_2]^-$ anions, the investigation of the structure and bonding of the homo- and hetero-trihalide anions occupying a coordination site in the coordination sphere of transition metal complexes is scarce. Very recently, we reported on the synthesis, structure elucidation, bioactivity and DNA-cleavage capability of a new series of Cu(II) trihalide complexes of the general formula $[Cu(RdienR)(X)(XY_2)]$, (R = furan, thiophene or pyrrole and X, Y = Cl, Br or I) (Scheme 1) [19]. Moreover, the crystal structure of the $[Cu(dpta)(Br)(BrI_2)]$ complex has recently also been reported [20].

In this paper, we explore the molecular and electronic structure of the $[Cu(RdienR)(X)(XY_2)]$ complexes and their $[Cu(RdienR)(X)_2]$ precursors with the help of DFT methods pursuing a twofold objective: (i) the understanding of the nature of the bonding between the $[XY_2]^-$ ligands and the Cu(II) central metal ion, and (ii) the unveiling of the effect, if any, of coordination on the bonding mechanism in the coordinated $[XY_2]^-$ ligands in comparison to that of the "free" $[XY_2]^-$ anions, using a variety of theoretical analysis techniques, which include charge decomposition analysis (CDA), natural bond orbital (NBO) population analysis, and percentage compositions of molecular orbitals.

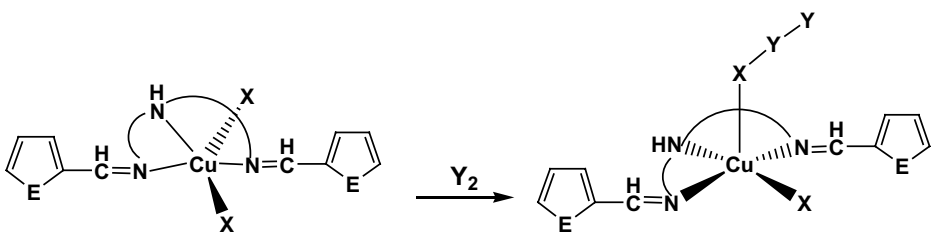
2. Computational details

The structural, electronic and energetic properties of all compounds under investigation were computed using the Becke's three parameter hybrid functional [21,22] combined with the Lee–Yang–Parr [23] correlation functional (B3LYP level of density functional theory) using an all-electron double-zeta (DZVP) basis set [24]. No constraints were imposed on the geometry. Full geometry optimization was performed for each structure using Schlegel's analytical gradient method [25], and the attainment of the energy minimum was verified by calculating the vibrational frequencies that result in an absence of imaginary eigenvalues. All the stationary points were identified for minima (number of imaginary frequencies NImag = 0). The computed electronic energy was corrected to constant pressure and 298 K, for zero point energy (ZPE) differences and for the contributions of the translational, rotational and vibrational partition functions. The natural bond orbital (NBO) population analysis was performed using Weinhold's methodology [26]. All calculations were performed using the GAUSSIAN 03 series of programs [27]. The charge decomposition analysis (CDA) and the extended charge decomposition analysis (ECDA) of Frenking and coworkers [28,29], were performed as implemented in the AOMIX program [30–32].

3. Results and discussion

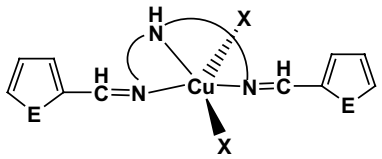
3.1. Equilibrium structures and electronic properties of the precursor [Cu(RdienR)(X)$_2$] (RdienR = Schiff base; X = Cl or Br) complexes

The equilibrium structures of the precursor $[Cu(RdienR)(X)_2]$ complexes (Scheme 2) computed at the B3LYP/DZVP level of theory correspond to a distorted trigonal bipyramidal geometry (TBP). The equilibrium geometry of the representative complex **1p** along with the coordinated atom numbering scheme is depicted schematically in Fig. 1. Selected geometrical, energetic and electronic parameters of **1p**–**6p** precursors are collected in Table 1.



E = O, S, NH, **X** = Cl, Br and **Y** = Br, I

Scheme 1.



E	X	Complex
O	Cl	**1p**
O	Br	**2p**
S	Cl	**3p**
S	Br	**4p**
NH	Cl	**5p**
NH	Br	**6p**

Scheme 2.

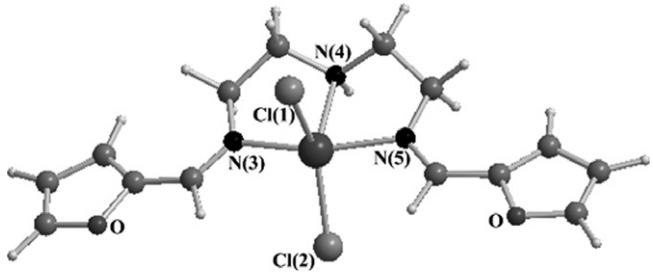


Fig. 1. The equilibrium structure of complex **1p** calculated at the B3LYP/DZVP level.

The two axial sites of the trigonal bipyramidal structure are occupied by the two N-donor atoms of the Schiff base ligand, while the equatorial sites are occupied by the third N-donor atom of the Schiff base and the two halide ligands. The X(1)–X(2)–N(4)–Cu dihedral angle is 180.0°. No significant structural differences are observed in the precursor Cu(II) complexes **1p**–**6p**. The only exception concerns the more acute ∠X(1)–Cu–X(2) bond angles in **5p** and **6p** complexes involving the pyrrole groups in the tridendate Schiff base ligand. It is interesting to be noticed that in all precursors the Cu–X(2) bond is slightly shorter than the Cu–X(1) bond. The different bond distances of the Cu–X(1) and Cu–X(2) bonds could be attributed to the participation of the X(2) halide ligand in hydrogen bond formation with the methylenic, CH_2, hydrogen atoms of the Schiff base ligand (the Cl(1)···H and Br(1)···H distances are found in the range of 2.822–2.906 and 3.052–3.205 Å, respectively) In general, the Cu–X bonds are predicted to be relatively strong with estimated bond dissociation energies, BDE_{Cu-X} in the range of 87.7–97.2 kcal/mol (Table 1).

Dissociation of the second halide X^- ligand from the cationic $[Cu(RdienR)(X)]^+$ species to yield the three-coordinated dicationic $[Cu(RdienR)]^{2+}$ species is much more difficult, the estimated bond dissociation energy was found in the range of 190–202 kcal/mol. This is due to the energy demand for the detachment of the negatively charged halide anion from the positively charged $[Cu(RdienR)(X)]^+$ species.

The calculated hardness, η, values given in Table 1 reflects the relative stability of the **1p**–**6p** precursors. The

Table 1
Selected geometrical (bond lengths in Å, bond angles in °), energetic and electronic parameters of the precursor **1p**–**6p** complexes calculated at the B3LYP/DZVP level

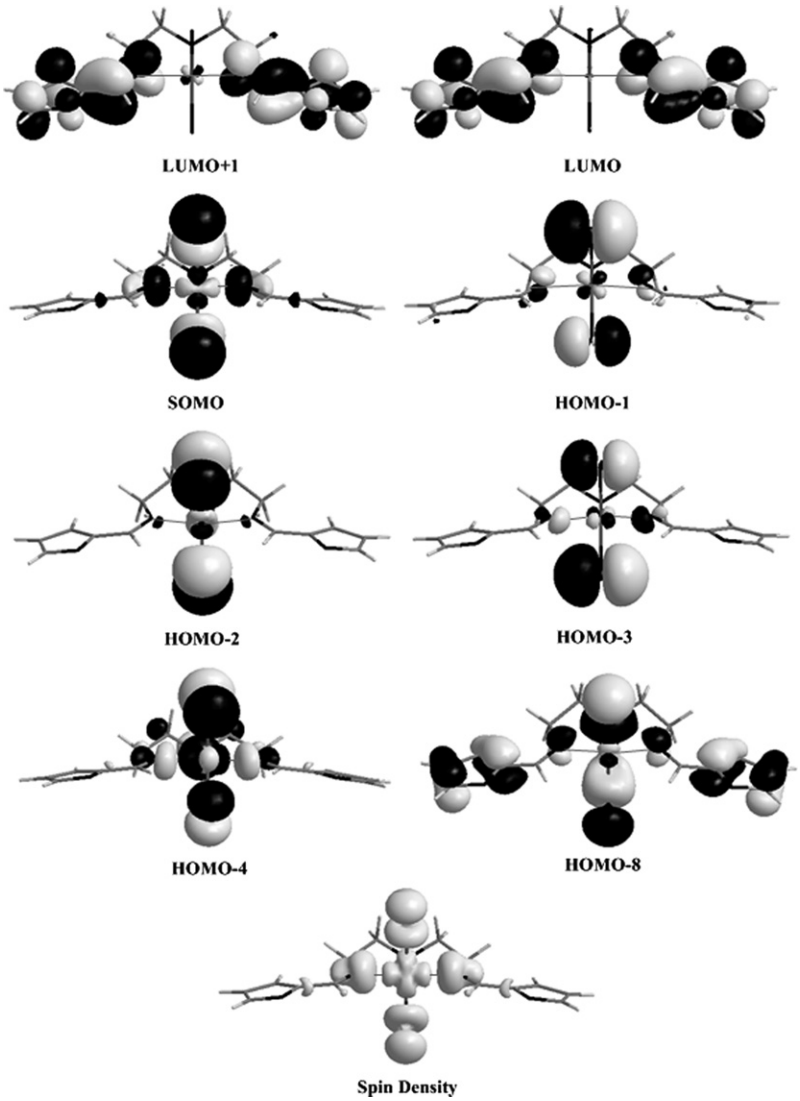
Parameter	1p	2p	3p	4p	5p	6p
$R_{Cu-X(1)}$	2.332	2.483	2.337	2.496	2.368	2.529
$R_{Cu-X(2)}$	2.305	2.473	2.306	2.467	2.341	2.497
$R_{Cu-N(4)}$	2.302	2.275	2.291	2.270	2.274	2.255
$R_{Cu-N(3)}$; $R_{Cu-N(5)}$	2.066[a]	2.064	2.067	2.058	2.050	2.049
∠N(3)–Cu–N(4)	80.0	80.6	80.1	80.9	79.9	80.4
∠N(3)–Cu–X(1)	92.6	91.8	92.4	92.0	93.8	101.3
∠N(4)–Cu–X(1)	98.6	104.9	99.2	104.4	97.3	93.0
∠X(1)–Cu–X(2)	145.2	148.3	142.0	145.4	131.7	132.5
ε_H (eV)[b]	−5.97	−5.78	−5.97	−5.78	−5.88	−5.66
ε_L (eV) [c]	−2.07	−2.11	−2.21	−2.25	−1.66	−1.71
η (eV)[d]	3.90	3.67	3.76	3.53	3.76	3.95
BDE_{Cu-X} (kcal/mol)	97.2	91.8	96.8	91.6	93.1	87.7
μ (D)[e]	6.8	6.5	6.5	6.3	4.2	3.9
Q^f_{Cu}	1.26	1.19	1.25	1.19	1.26	1.19
$Q_{X(1)}$	−0.83	−0.77	−0.84	−0.78	−0.85	−0.81
$Q_{X(2)}$	−0.73	−0.70	−0.73	−0.70	−0.74	−0.71
Spin density on Cu	0.53	0.53	0.54	0.49	0.49	0.49

[a] Average Cu–N bond length.
[b] ε_H is the highest occupied molecular orbital (HOMO) eigenvalue.
[c] ε_L is the lowest unoccupied molecular orbital (LUMO) eigenvalue.
[d] Hardness $\eta = \varepsilon_H - \varepsilon_L$.
[e] Dipole moment.
[f] Natural atomic charges.

computed dipole moments, μ, are of the same magnitude for **1p**–**4p** complexes (6.8–6.3 D), but are much lower (4.2 and 3.9 D) for **5p** and **6p** precursors. According to the natural bond orbital (NBO) population analysis the copper(II) central metal atom acquires a positive natural atomic charge of 1.2–1.3 |e|, thus accepting electron density from the ligands to both its 3d and 4s AOs. Noteworthy the X(1) halide ligand acquires higher negative natural atomic charge than the X(2) one illustrating that X(1) is more nucleophilic than X(2), thereby it would be expected to be the halide ligand which would interact with the incoming halogen molecule to afford the anionic trihalide ligand.

The pictures of the frontier molecular orbitals (FMOs) of the representative precursor **1p** are depicted in Scheme 3. Analogous are the relevant MOs of the rest of the precursor complexes **2p**–**6p**.

The degenerate lowest unoccupied molecular orbital (LUMO) and LUMO+1 are primarily localized on the furan rings (π^*-type MOs), while the singly occupied MO (SOMO) and the HOMO-1,2,3,4,8 are mainly composed from halide non-bonding np AOs. The SOMO is constructed from the out-of-phase combination of the $3d_{z^2}$ AO of Cu(II) with the p_σ AOs of the halide ligands. The nature of the occupied MOs strongly suggest that the halide ligands are the nucleophilic centers (donors) of the precursor [Cu(RdienR)$(X)_2$] complexes, thus accounting for their capability to associate with the electrophilic halogen Y_2 molecules (acceptors) converting the halide X^- to trihalide $[XY_2]^-$ ligands. Finally, the spin density on the Cu(II) central metal atom amounted to 0.54 and 0.49 |e| for the dichloro, **1p**–**3p**, and dibromo, **4p**–**6p**, derivatives, respectively comes primarily from the difference in 3d orbital occupation and highly altered by spin polarization of the s and p orbitals localized on the five coordinated donor atoms constituting the coordination sphere. Noteworthy is the higher polarization of the spin density for the dibromo **4p**–**6p** derivatives.



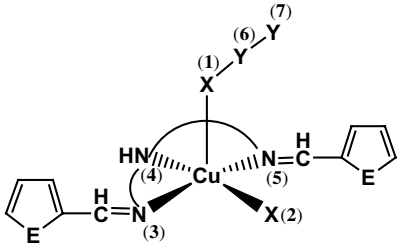
Scheme 3.

3.2. Equilibrium structures, bonding mechanism and electronic properties of the trihalide [Cu(RdienR)(X)(XY$_2$)] (RdienR = Schiff base; X = Cl or Br, Y = Cl, Br or I) complexes

The equilibrium structures of the [Cu(RdienR)(X)(XY$_2$)] complexes **1**–**12** (Scheme 4) computed at the B3LYP/DZVP level correspond to a distorted square pyramidal (SP) stereochemistry similar to that of a representative complex **1** depicted schematically in Fig. 2.

It can be seen that the trihalide ligand occupies the axial position of the square pyramidal structure, while the tridentate Schiff base and the halide ligands occupy the four sites in the basal square plane. In all cases, the two heterocyclic rings of the Schiff base are approximately coplanar with respect to the basal plane of the square pyramid. Noteworthy is the TBP → SP stereochemical change introduced by the balkier XY$_2$ ligand probably as a result of steric interactions. Selected geometrical parameters of the [Cu(RdienR)(X)(XY$_2$)] complexes are given in Table 2.

The trihalide [XY$_2$]$^-$ ligand adopting an almost linear configuration (∠X(1)–Y(6)–Y(7) bond angle found in the range of 176.4–178.0°) is coordinated with the copper(II) central atom in a bent fashion (the ∠Cu–X(1)–Y(6) bond angles range from 105.2° up to 114.6°). The latter depends on both the nature of the halide ligand which upon association with the incoming halogen molecule affords the trihalide [XY$_2$]$^-$ ligand and the nature of the R moiety of the Schiff base ligand, following the trend: pyrrol > furan > thiophene.



E	X	Y	Complex
O	Cl	Br	**1**
O	Cl	I	**2**
O	Br	Br	**3**
O	Br	I	**4**
S	Cl	Br	**5**
S	Cl	I	**6**
S	Br	Br	**7**
S	Br	I	**8**
NH	Cl	Br	**9**
NH	Cl	I	**10**
NH	Br	Br	**11**
NH	Br	I	**12**

Scheme 4.

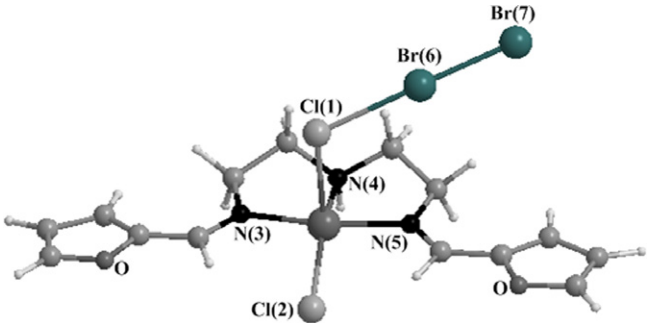


Fig. 2. The equilibrium structure of complex **1** calculated at the b3lyp/dgdzvp level along with the coordinated atom numbering scheme.

Selected energetic and electronic parameters of the [Cu(RdienR)(X)(XY$_2$)] complexes are compiled in Table 3.

Perusal of Table 3 reveals that the dissociation energy of the Cu–X(1) bond, BDE$_{Cu–X(1)}$ was predicted to be 61.9–68.4 kcal/mol. In contrast, the association of the Y$_2$ ligand with the halide ligand of the Cu(II) precursor complexes is characterized by weak interactions; the bond dissociation energy of the X(1)–Y(6) bond, BDE$_{X(1)–Y(6)}$ was predicted to be 10.6–12.5 kcal/mol at the B3LYP/DZVP level. The weak donor–acceptor interactions in the coordinated trihalide ligand is also reflected on the relatively long R$_{X(1)–Y(6)}$ bond distances (2.616–3.014 Å).

The X···Y interactions of the coordinated halide X$^-$ ligand with the halogen Y$_2$ molecules are much weaker than the X···Y interactions in the corresponding "free" [XY$_2$]$^-$ anionic species. Thus, the BDE$_{X–Y}$ values for the [Br$_3$]$^-$, [ClI$_2$]$^-$ and [BrI$_2$]$^-$ anions calculated by ADF methods [15] were 39.6, 37.0 and 36.6 kcal/mol, respectively. In the respective coordinated trihalide ligands the BDE$_{X–Y}$ values are 11.5, 10.9 and 10.8, respectively (Table 3). The stronger X···Y interactions in the "free" [XY$_2$]$^-$ anionic species is also reflected on the R$_{X–Y}$ and R$_{Y–Y}$ bond lengths, the former being shorter and the latter longer than the corresponding bond lengths in the coordinated [XY$_2$]$^-$ ligands (Table 2). It is interesting to be noticed that the Y–Y bond in the coordinated [XY$_2$]$^-$ ligands is elongated by 0.121–0.159 Å with respect to the Y–Y bond of the "free" halogen molecules.

According to the NBO analysis there is a charge transfer from the halide X(1) ligand to Y$_2$ molecule amounted to 0.17–0.26 |e|. The charge density is mainly transferred from the np AOs of the halide X(1) ligand to the np AOs of the terminal Y(7) halogen atom of the associated Y$_2$ molecule, which acquires a negative natural atomic charge of about −0.24 to −0.27 |e| (Table 3). In contrast, the natural atomic charge of the internal Y(6) halogen atom remains practically unaltered and was found to be close to zero. The stabilization energy $\Delta E(2)$ associated with the charge transfer (CT) interactions between the relevant donor–acceptor orbitals computed from the second-order perturbative estimates of the Fock matrix in the NBO analysis according to the equation:

$$\Delta E(2) = q_i F_{ij}^2/(\varepsilon_i - \varepsilon_j)$$

Table 2
Selected geometrical parameters (bond lengths in Å, bond angles in °) of the [Cu(RdienR)(X)(XY_2)] complexes computed at the B3LYP/DZVP level

Complex	$R_{Cu–X(1)}$	$R_{Cu–X(2)}$	$R_{X(1)–Y(6)}$	$R_{Y(6)–Y(7)}$	∠X(1)–Y(6)–Y(7)	∠Cu–X(1)–Y(6)	∠N(4)–Cu–X(2)
1	2.625	2.282	2.692	2.479	176.9	110.4	149.4
2	2.621	2.281	2.887	2.866	177.0	115.0	149.4
3	2.735	2.443	2.795	2.500	176.4	105.2	140.5
4	2.720	2.443	3.014	2.878	177.4	110.1	140.6
5	2.621	2.285	2.696	2.476	177.0	110.5	150.2
6	2.624	2.283	2.889	2.865	177.2	114.6	150.4
7	2.745	2.443	2.795	2.499	176.9	106.1	143.2
8	2.726	2.445	3.014	2.877	177.2	110.2	142.1
9	2.643	2.299	2.686	2.481	177.8	110.1	153.3
10	2.641	2.298	2.874	2.870	177.8	115.8	153.0
11	2.773	2.459	2.783	2.506	177.4	105.5	148.6
12	2.771	2.458	2.994	2.887	178.0	109.2	149.2
$[\mathbf{ClBr_2}]^-$			2.508 (2.453)[a]	2.627 (2.572)	179.9		
$[\mathbf{ClI_2}]^-$			2.677 (2.623)	3.017 (2.961)	180.0		
$[\mathbf{BrBr_2}]^-$			2.637 (2.640)[b]	2.647 (2.640)	178.9		
$[\mathbf{BrI_2}]^-$			2.823 (2.769)	3.028 (2.971)	179.3		

[a] Figures in parentheses are the bond lengths in the "free" trihalide anion taken from Ref. [16].
[b] Taken from Ref. [15].

Table 3
Selected electronic and energetic parameters of the [Cu(RdienR)(X)(XY_2)] complexes computed at the B3LYP/DZVP level

Complex	ε_{HOMO} (eV)	ε_{LUMO} (eV)	η (eV)	μ (D)	Q					$BDE_{Cu–X(1)}$ (kcal/mol)	$BDE_{X(1)–Y(6)}$ (kcal/mol)
					Cu	X(1)	X(2)	Y(6)	Y(7)		
1	−6.21	−2.58	3.64	12.2	1.26	−0.62	−0.71	−0.03	−0.25	68.4 (76.0)[a]	11.0 (−18.3)
2	−5.83	−2.60	3.26	12.7	1.26	−0.66	−0.71	0.01	−0.25	66.2 (−73.8)	10.9 (−17.1)
3	−6.19	−2.62	3.56	11.7	1.20	−0.53	−0.67	−0.07	−0.27	66.6 (−74.6)	11.5 (−18.8)
4	−5.86	−2.64	3.22	12.2	1.20	−0.59	−0.67	−0.03	−0.25	64.5 (−72.7)	10.8 (−16.2)
5	−6.20	−2.66	3.54	11.7	1.26	−0.62	−0.71	−0.03	−0.25	68.0 (−75.8)	11.0 (−18.0)
6	−5.81	−2.68	3.12	12.4	1.26	−0.67	−0.71	0.01	−0.24	65.8 (−73.6)	11.0 (−16.9)
7	−6.16	−2.72	3.44	11.2	1.20	−0.54	−0.67	−0.07	−0.27	66.2 (−73.7)	11.3 (−18.7)
8	−5.84	−2.72	3.12	11.8	1.20	−0.60	−0.67	−0.03	−0.25	64.1 (−72.3)	10.6 (−16.2)
9	−6.07	−2.25	3.82	10.7	1.26	−0.62	−0.72	−0.04	−0.26	65.7 (−72.9)	12.4 (−19.0)
10	−5.70	−2.31	3.39	11.5	1.26	−0.67	−0.72	0.01	−0.25	63.6 (−70.8)	12.5 (−18.0)
11	−6.00	−3.79	2.21	10.5	1.20	−0.54	−0.69	−0.08	−0.28		(−20.0)
12	−5.71	−2.39	3.32	11.4	1.21	−0.60	−0.68	−0.03	−0.26	61.9 (−68.8)	12.3 (−17.8)
$[\mathbf{ClBr_2}]^-$	−2.72	1.08	3.80	2.65			−0.51	−0.03	−0.46		40.0 (−49.2)
$[\mathbf{ClI_2}]^-$	−2.64	0.86	3.50	3.80			−0.57	0.04	−0.47		42.1 (−48.5)
$[\mathbf{BrBr_2}]^-$	−2.72	0.87	3.59	0.08			−0.46	−0.08	−0.46		36.7 (−46.3)
$[\mathbf{BrI_2}]^-$	−2.66	0.67	3.33	1.65			−0.52	−0.01	−0.47		38.2 (−44.9)

[a] Interaction energies (without BSSE corrections) between the respective fragments estimated by charge decomposition (CDA) analysis techniques.

accounts well for the elongation of the $R_{Y–Y}$ bond in the coordinated trihalide ligands. This equation evaluates the magnitude of the donor–acceptor interaction in terms of the spatial overlap of the NBO, using the off-diagonal Fock-matrix elements F_{ij} and the difference in energy between the NBOs, ε_i–ε_j, weighted by the occupancy of the donor NBO, q_i. The stabilization energies $\Delta E(2)$ introduced by the $n(X) \rightarrow \sigma^*(Y–Y)$ hyperconjugative (stereoelectronic) interactions in the [Cu(RdienR)(X)(XY_2)] complexes along with the occupation of the n(X) and σ^*(Y–Y) MOs are compiled in Table 4.

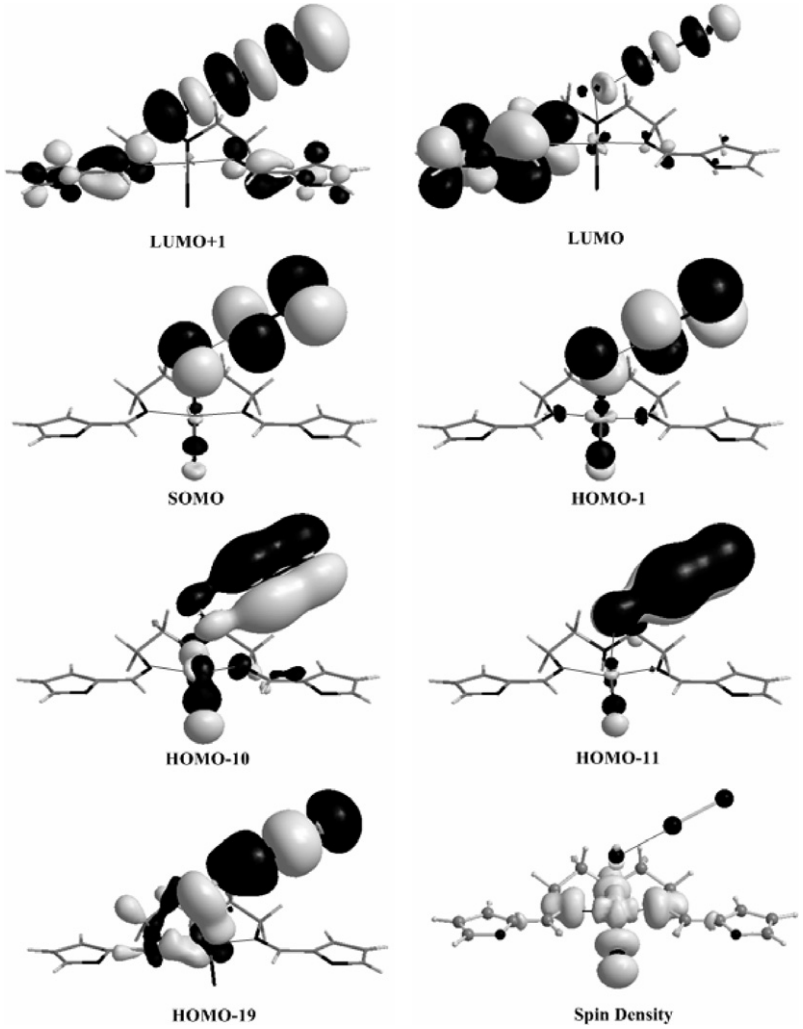
The most relevant MOs describing the Cl(1)···Br(6)–Br(7) interactions in **1** are depicted schematically in Scheme 5. Analogous are the pictures of the most relevant MOs of the rest complexes **2**–**12**.

The degenerate HOMO−10 and HOMO−11 are π-type MOs primarily localized on the incoming halogen molecules constructed from the np_π orbitals of the halogen

Table 4
Stabilization energies $\Delta E(2)$ (in kcal/mol) introduced by the n(X) → σ*(Y–Y) hyperconjugative interactions in the [Cu(RdienR)(X)(XY_2)] complexes along with the occupation of the n(X) ($P_{n(X)}$) and σ*(Y–Y) ($P_{\sigma^*(Y-Y)}$) MOs computed at the B3LYP/DZVP level

Complex	$\Delta E(2)$n(X) → σ*(Y–Y)	$P_{n(X)}$	$P_{\sigma^*(Y-Y)}$
1	42.6	1.702	0.281
2	34.8	1.748	0.232
3	49.9	1.647	0.336
4	37.3	1.710	0.267
5	41.8	1.706	0.277
6	34.5	1.750	0.231
7	49.7	1.649	0.334
8	37.3	1.711	0.266
9	44.2	1.697	0.287
10	36.3	1.742	0.239
11	52.5	1.636	0.345
12	40.7	1.696	0.281
$[ClBr_2]^-$	105.4	1.508	0.472
$[ClI_2]^-$	85.8	1.568	0.406
$[BrBr_2]^-$	111.4	1.463	0.518
$[BrI_2]^-$	91.0	1.523	0.452

atoms, while the degenerate SOMO and HOMO−1 are their antibonding π* counterparts. The HOMO−19 is a bonding σ-type MO with respect to the Cl(1)···Br(6)–Br(7) interaction constructed from the in-phase interaction of the np_σ orbitals of the halogen atoms (in other words it is a three orbital in-phase interaction localized on the Cl(1)–Br(6)–Br(7) nuclear framework), while the LUMO+1 is its antibonding counterpart. The HOMO−19 corresponds to the perturbative donor–acceptor interactions involving the n(X) donor orbitals localized on the coordinated halide ligand with the antibonding σ*(Y–Y) acceptor orbital localized on the Y–Y moiety. A qualitative orbital interaction diagram of the perturbative donor–acceptor interactions along with the 3D isosurface plot of the n(X) → σ*(Y–Y) hyperconjugative interactions in the representative complex **1** are given in Fig. 3. Finally, the LUMO is mainly localized on the furan ring of the Schiff base ligand in **1**. The spin density on the Cu(II) central metal atom amounted to 0.494 and 0.529 |e| comes primarily from the difference in 3d orbital occupation



Scheme 5.

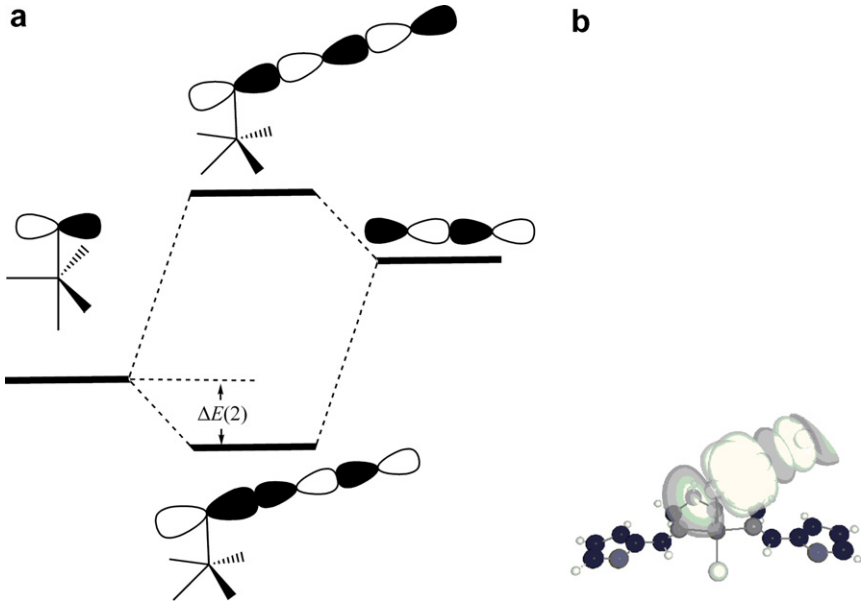


Fig. 3. (a) Perturbative donor–acceptor interactions involving a nonbonding n(X) donor orbital localized on the halide ligand with the antibonding σ*(Y–Y) acceptor orbital localized on the Y–Y moiety of the [Cu(RdienR)(X)(XY_2)] complexes (energy on an arbitrary scale). (b) 3D isosurface plot of the n(Cl) → σ*(Br–Br) hyperconjugative interactions in the representative complex **1**.

(0.522–0.556) and are highly altered by spin polarization of the s and p orbitals localized on the five coordination atoms constituting the coordination sphere.

The favourable n(X) → σ*(Y–Y) interactions primarily affect the $R_{Y–Y}$ bond length through electron delocalization. These hyperconjugative (stereoelectronic) interactions evolved in the course of the formation of the [Cu(RdienR)(X)(XY_2)] complexes upon reacting the precursor [Cu(RdienR)(X_2)] complexes with the Y_2 molecules lead to delocalization of negative charge due to the lone pair of electrons on the halide X^- ligand into the high-energy vacant antibonding σ*(Y–Y) orbital. This charge transfer is reflected on the occupation of the σ*(Y–Y) orbital, which amounts to 0.231–0.345 |e|. Therefore, the occupation of the n(X) orbital is lower than 2.000 (1.636–1.750 |e|). Noteworthy is the higher occupation of the σ*(Y–Y) orbital in the "free" $[XY_2]^-$ anions (0.406–0.518 |e|), while the occupation of the n(X) orbital is lower (1.463–1.568 |e|) than in the coordinated $[XY_2]^-$ ligand. Obviously, the lone pair (donor) → antibonding (acceptor) orbital interactions would have as a result the weakening of the Y–Y bond in the coordinated $[XY_2]^-$ ligand. It should be noticed that the occupation of the n(X) orbital follows the trend: n(Cl) → σ*(I–I) > n(Br) → σ*(I–I) > n(Cl) → σ*(Br–Br) > n(Br) → σ*(Br–Br). Noteworthy is the high contribution of the Y(6)–Y(7) fragment orbitals (FOs) to the bonding HOMO−10 and HOMO−11 and the antibonding SOMO that are involved in the X(1)···Y(6)–Y(7) interactions.

The results from CDA calculations on the complexes **1**–**12** are summarized in Table 5. In all cases the value of the rest term, Δ, in CDA is estimated to be essentially zero suggesting that compounds **1**–**12** could be considered as X(1) → Y(6)–Y(7) donor–acceptor complexes formed by donor–acceptor interactions between the X(1) halide ligand of the precursor complexes and the Y_2 molecule.

Table 5
Charge decomposition analysis of complexes **1**–**12** ($CT_{2→1}$ donation, $CT_{1→2}$ back-donation, $CT_{2→1} - CT_{1→2}$, net charge donation, and gross spin density on Cu, in |e|)[a]

Complex	$CT_{2→1}$	$CT_{1→2}$	$CT_{2→1} - CT_{1→2}$	Net charge donation	Gross spin density on Cu
1	0.203	0.035	0.168	0.138	0.529 (0.556)
2	0.211	0.035	0.176	0.122	0.529 (0.556)
3	0.212	0.049	0.163	0.157	0.494 (0.522)
4	0.212	0.041	0.171	0.133	0.493 (0.522)
5	0.200	0.033	0.167	0.137	0.528 (0.555)
6	0.210	0.033	0.177	0.122	0.528 (0.555)
7	0.212	0.047	0.165	0.158	0.494 (0.523)
8	0.212	0.040	0.172	0.133	0.494 (0.523)
9	0.205	0.028	0.177	0.143	0.528 (0.556)
10	0.217	0.027	0.190	0.128	0.528 (0.556)
11	0.217	0.043	0.174	0.164	
12	0.222	0.035	0.187	0.143	0.497 (0.527)
$[ClBr_2]^-$	0.294	−0.019	0.313	0.504	
$[ClI_2]^-$	0.332	−0.023	0.355	0.478	
$[BrBr_2]^-$	0.276	0.006	0.270	0.515	
$[BrI_2]^-$	0.309	−0.004	0.313	0.488	

[a] At the B3LYP/DZVP geometries.

Perusal of Table 5 shows that the X(1) → Y_2 donation is much larger than the X(1) ← Y_2 back-donation. As it is expected, the charge transferred from the halide ligand to the halogen molecule follows the trend: Cl → I_2 > Br → I_2 > Cl → Br_2 > Br → Br_2, in line with the trend followed by the occupation of the n(X) donor orbital of the complexes. The same holds true for the "free"

$[XY_2]^-$ anions (Table 5) where the charge transfer is much higher than in the corresponding coordinated anionic trihalide ligands. It is interesting to be noticed that the net charge donation between the fragments is not equal to the difference $CT_{2\rightarrow1} - CT_{1\rightarrow2}$, for the terms donation and back-donation in the CDA method do not include only charge transfer interactions but rather an overall reorganization of electronic density that includes both charge transfer between fragments and electronic polarization of fragments [30–32].

4. Conclusions

The equilibrium geometries and electronic properties of a series of [Cu(RdienR)(X)(XY_2)] (RdienR = Schiff base and X = Cl or Br, Y = Cl, Br or I) complexes and their precursors [Cu(RdienR)(X_2)] were calculated at the B3LYP/DZVP level. The [Cu(RdienR)(X)(XY_2)] complexes adopt a distorted square pyramidal geometry, while their precursors exhibit a trigonal bipyranidal stereochemistry.

According to the NBO population analysis, the association of the incoming halogen Y_2 molecule with a halide X(1) ligand of the precursor complexes correspond to donor–acceptor hyperconjugative interactions involving a nonbonding molecular orbital localized on the coordinated X(1) halide ligand, n(X), (donor orbital) and an antibonding molecular orbital localized on the Y_2 molecule, σ^*(Y–Y) (acceptor orbital). The n(X) $\rightarrow$ σ^*(Y–Y) donor–acceptor interactions are associated with a second-order perturbation stabilization energy, $\Delta E(2)$ of 34.5–52.5 kcal/mol. The n(X) $\rightarrow$ σ^*(Y–Y) interactions lead to delocalization of electron density from the n(X) to σ^*(Y–Y) orbitals resulting in the lowering of the occupation of the n(X) orbital (1.636–1.750 |e|) and the increase of the occupation of the σ^*(Y–Y) orbital (0.231–0.345 |e|). The occupation of the n(X) orbital follows the trend: n(Cl) $\rightarrow$ σ^*(I–I) > n(Br) $\rightarrow$ σ^*(I–I) > n(Cl) $\rightarrow$ σ^*(Br–Br) > n(Br) $\rightarrow$ σ^*(Br–Br). The dissociation energy of the Cu–X(1) bond, $BDE_{Cu-X(1)}$, was estimated in the range of 61.9–68.4 kcal/mol, while the bond dissociation energy of the X(1)–Y(6) bond, $BDE_{Cu-X(1)}$, was found in the range of 10.6–12.5 kcal/mol, thus reflecting the loose association of the Y_2 with the X(1) halide ligand. The loose association of the halogen molecules with the coordinated halide ligand renders the [Cu(RdienR)(X)(XY_2)] complexes good halogen carrier molecules.

The donor–acceptor n(X) $\rightarrow$ σ^*(Y–Y) bonding mechanism was also corroborated by CDA calculations. The estimated interaction energies between the precursor and the halogen molecules amounting −16.2 to −20.0 kcal/mol illustrate that these interactions are much weaker than the donor–acceptor interactions in the "free" $[XY_2]^-$ anions (the estimated interaction energies are found in the range of −44.9 to −49.2 kcal/mol). The charge transferred from the halide ligand to the halogen molecule in the [Cu(RdienR)(X)(XY_2)] complexes follows the trend: Cl $\rightarrow$ I_2 > Br $\rightarrow$ I_2 > Cl $\rightarrow$ Br_2 > Br $\rightarrow$ Br_2, in line with the trend followed by the occupation of the n(X) donor orbital of the complexes.

Acknowledgements

The financial support of this work by the Greek General Secretariat for Research and Technology and the European Commission within the frame of the PENED01 projects is thankfully acknowledged (Grant No. 01EΔ367).

References

[1] E. Dubler, L. Linowsky, Helv. Chim. Acta 58 (1975) 2604.
[2] A. Rabenau, H. Schulz, W. Stoeger, Naturwissenschaften 63 (1976) 245.
[3] M.F. Belicchi, G.G. Fava, C. Pelizzi, Acta Crystallogr. Sect. B 37 (1981) 924.
[4] E.M. Nour, L.H. Chen, J. Laane, J. Phys. Chem. 90 (1986) 2841.
[5] J.C. Bailar, H.J. Emeleus, R. Nyholm, A.F. Trotman-Dickenson, Comprehensive Inorganic Chemistry, vol. 2, Pergamon Press, Oxford, 1973.
[6] P. Deplano, J.R. Ferraro, M.L. Mercuri, E.F. Trogu, Coord. Chem. Rev. 188 (1999) 71.
[7] A. Tracz, J.K. Jeszka, J. Ulanski, T. Pakula, J.P. Rabe, Synth. Met. 94 (1998) 17.
[8] J. Ulanski, A. Tracz, J.K. Jeszka, E. Laukhina, T. Pakula, Synth. Met. 85 (1997) 1591.
[9] H. Mittag, P. Cikmacs, H. Fullbier, A. Lusis, G. Petrovskis, L. Schmidt, H. Stegemann, Soviet Electrochem. 25 (1989) 717.
[10] T. Okamoto, T. Utsunomiya, T. Uesugi, T. Kakinami, S. Kajigaeshi, Bull. Chem. Soc. Jpn. 62 (1989) 3748.
[11] T. Kakinami, H. Suenaga, T. Yamaguchi, T. Okamoto, S. Kajigaeshi, Bull. Chem. Soc. Jpn. 62 (1989) 3373.
[12] S.S. Mitra, K. Sreekumar, Eur. Polym. J. 34 (1998) 561.
[13] S.S. Mitra, K. Sreekumar, React. Funct. Polym. 32 (1997) 281.
[14] A. Butler, J.V. Walker, Chem. Rev. 93 (1993) 1937.
[15] G.A. Landrum, N. Goldberg, R. Hoffmann, J. Chem. Soc., Dalton Trans. (1997) 3605 (and references therein).
[16] Y. Ogawa, O. Takahashi, O. Kikuchi, J. Mol. Struct. (Theochem) 429 (1998) 187 (and references therein).
[17] G.C. Pimentel, J. Chem. Phys. 19 (1951) 446.
[18] R.J. Hach, R.E. Rundle, J. Am. Chem. Soc. 73 (1951) 4321.
[19] A.T. Chaviara, E.E. Kioseoglou, A.A. Pantazaki, A.C. Tsipis, P.A. Karipidis, D.A. Kyriakidis, C.A. Bolos, in preparation.
[20] A.T. Chaviara, A.C. Tsipis, P.J. Cox, C.A. Bolos, Eur. J. Inorg. Chem. (2005) 3491.
[21] A.D. Becke, J. Chem. Phys. 96 (1992) 215.
[22] A.D. Becke, J. Chem. Phys. 98 (1993) 5648.
[23] C. Lee, W. Yang, R.G. Parr, Phys. Rev. B B37 (1998) 785.
[24] N. Golbout, D.R. Salahub, J. Andzelm, E. Winner, Can. J. Chem. 70 (1992) 560.
[25] H.B. Schlegel, J. Comput. Chem. 3 (1982) 214.
[26] F. Weinhold, The Encyclopedia of Computational Chemistry, in: P.v.R. Schleyer (Ed.), John Wiley & Sons, Chichester, 1998, p. 1792.
[27] M.J. Frisch, G.W. Trucks, H.B. Schlegel, G.E. Scusseria, M.A. Robb, J.R. Cheeseman, V.G. Zakrzewski, J.A. Montgomery, T. Vreven, K.N. Kudin, J.C. Burant, J.M. Millan, S.S. Iyengar, J. Tomasi, V. Barone, B. Mennucci, M. Cossi, G. Scalmani, N. Rega, G.A. Petersson, H. Nakatsuji, M. Hada, M. Ehara, K. Toyota, F.R., J. Hasegawa, M. Ishida, T. Nakajima, Y. Honda, O. Kitao, H. Nakai, M. Klene, X. Li, J.E. Knox, H.P. Hratchian, J.B. Cross, C. Adamo, J. Jaramillo, R. Gomperts, R.E. Stratmann, O. Yazyev, A.J. Austin, R. Cammi, C. Pomelli, J.W. Ochterski, P.Y. Ayala, K. Morokuma, G.A. Voth, P. Salvador, J.J. Dannenberg, V.G. Zakrzewski, S. Dapprich, A.D. Daniels, M.C. Strain, O. Farkas, D.K. Malick, A.D. Rabuck, K. Raghavachari, J.B. Foresman, J.V. Ortiz, Q. Cui, A.G. Baboul, S.

Clifford, J. Cioslowski, B.B. Stefanov, G. Liu, A. Liashenko, P. Piskorz, I. Komaromi, R.L. Martin, D.J. Fox, T. Keith, M.A. Al-Laham, C.Y. Peng, A. Nanayakkara, M. Challacombe, P.M.W. Gill, B. Johnson, W. Chen, M.W. Wong, C. Gonzalez, J.A. Pople, GAUSSIAN 03, Revision B. 02, Gaussian, Inc., Pittsburgh, PA, 2003.
[28] S. Daprich, G. Frenking, J. Phys. Chem. 99 (1995) 9352.
[29] G. Frenking, N. Frohlich, Chem. Rev. 100 (2000) 717.
[30] S.I. Gorelsky, S. Ghosh, E.I. Solomon, J. Am. Chem. Soc. 128 (2006) 278.
[31] S.I. Gorelsky, AOMIX; Department of Chemistry, York University, Toronto, ON, 1997. <http://www.sg-chem.net>.
[32] S.I. Gorelsky, A.B.P. Lever, J. Organomet. Chem. 635 (2001) 187.

Available online at www.sciencedirect.com
ScienceDirect
Polyhedron 27 (2008) 299–303
POLYHEDRON
www.elsevier.com/locate/poly

Structure and magnetic properties of cyanide-bridged $Ni^{II}_9Mo^{V}_6$ cluster modified by bidentate capping ligands

Jung Hak Lim [a], Houng Sik Yoo [a], Jung Hee Yoon [a], Eui Kwan Koh [b], Hyoung Chan Kim [c], Chang Seop Hong [a,*]

[a] Department of Chemistry, Korea University, Seoul 136-713, Republic of Korea
[b] Nano-Bio System Research Team, Korea Basic Science Institute, Seoul 136-713, Republic of Korea
[c] Research and Development Division, Nuclear Fusion Research Center, Daejeon 305-333, Republic of Korea

Received 25 August 2007; accepted 13 September 2007
Available online 18 October 2007

Abstract

A cyanide-bridged Ni_9Mo_6 cluster (**1**) capped with chelating bidentate ligands was prepared by self-assembling $[Mo(CN)_8]^{3-}$, Ni^{2+}, and bipyridine in a stoichiometric ratio. Compound **1** crystallized in the triclinic system with space group $P\bar{1}$ shows a body-centered Ni cube capped with six Mo entities. The non-covalent π–π stackings present in **1** lead to the extension of the molecule to a 2D sheet. Magnetic data exhibit that intracluster ferromagnetic interactions in **1** are operative through the CN linkage coupled with zero-field splitting of the cluster with an $S = 12$ ground state.
© 2007 Elsevier Ltd. All rights reserved.

Keywords: Nickel; Molybdenum; Cluster compounds; Magnetic properties; Cyanides

1. Introduction

The chemical design of unique anisotropic materials such as single-molecule magnets (SMMs) and single-chain magnets (SCMs) is dependent on essential ingredients: paramagnetic metal ions as spin carriers and organic spacers as magnetic exchange couplers. The metal ions should be magnetically anisotropic to meet the requirements for SMMs and SCMs. As a useful ligand, cyanide merits to be considered because of its structural and magnetic predictabilities [1].

To achieve such anisotropic systems, blocked molecular precursors, $[M(CN)_pL_q]^{n-}$ (M = anisotropic metal ion, Fe^{III}, Mo^{III}, Re^{II}; L = polydentate ligand) were rationally chosen because the synthons are able to be propagated toward one direction and construct low-dimensional structures [2]. Incorporation of the precursors into their proper counterparts $[ML'_xL''_y]^{m+}$ (M = paramagnetic metal ion, L′ = capping ligand, L″ = labile group) formed discrete bimetallic clusters and one-dimensional (1D) coordination polymers, displaying superparamagnetic properties with slow relaxation of magnetization [2,3].

Among cyanide-bridged systems, some of the octacyanometallate-based clusters showed higher ground-state spins. For instance, the total spin in the ground state of bimetallic assemblies $[Mn\{Mn(MeOH)_3\}_8\{M'(CN)_8\}_6]\cdot x MeOH \cdot y H_2O$ (M′ = W, Mo) has been finally identified as an $S = 39/2$ state resulting from intracluster antiferromagnetic couplings between nine Mn^{II} ($S_{Mn} = 5/2$) and six M'^{V} ($S_{M'} = 1/2$) [4–6]. Subsequently, a family of $M_9M'_6$ clusters (M = Co, Ni; M′ = Mo, W) were characterized with $S = 21/2$ for M = Co and $S = 12$ for M = Ni, respectively [7,8]. In particular, the $Co_9M'_6$ complexes act as SMMs owing to the involvement of single-ion anisotropy of Co(II) [7]. On the other hand, it should be mentioned that all the prepared $M_9M'_6$ analogues to date are however subject to decomposition in air because of facile loss of labile terminal alcohol ligands. It is thus desirable to improve their chemical stability for physical measurements and practical uses.

* Corresponding author. Tel.: +82 2 3290 3138; fax: +82 2 3290 3121.
E-mail address: cshong@korea.ac.kr (C.S. Hong).

0277-5387/$ - see front matter © 2007 Elsevier Ltd. All rights reserved.
doi:10.1016/j.poly.2007.09.006

Recently, we demonstrated that the chemical modification of the Ni_9W_6 cluster led to the capped bimetallic molecule exhibiting SMM behavior [9]. To get more insights into structural and magnetic variations of related systems we attempted to examine a bimetallic Ni–Mo system in terms of structure and magnetism.

Herein we report the synthesis, structure, and magnetic properties of a new bimetallic cluster compound $[Ni\{Ni(bpy)(H_2O)\}_8\{Mo(CN)_8\}_6]\cdot 12H_2O$ (**1**) (bpy = 2,2′-bipyridine), which contains the chelating ligand bpy with aromatic pyridyl rings additionally capable of making intermolecular contacts. The ligand substitution on the periphery of the cluster, which gives rise to the symmetry lowering of the molecule and overall crystal system, makes the cluster stable when exposed to air. The intermolecular forces through the aromatic rings of the substituted ligands are established, which play a role in affecting the apparent magnetic nature.

2. Experimental

2.1. Materials

$(Bu_4N)_3[Mo(CN)_8]$ was prepared according to the literature procedure [10]. All the other chemicals and solvents in the synthesis were of reagent grade and used as received.

2.2. Preparation of $[Ni\{Ni(bpy)(H_2O)\}_8\{Mo(CN)_8\}_6]\cdot 12H_2O$ (1)

$(Bu_4N)_3[Mo(CN)_8]$ (0.10 mmol) in MeCN (8 mL) was slowly added on top of a mixed reaction solution of $Ni(ClO_4)_2\cdot 6H_2O$ (0.15 mmol) in H_2O (8 mL) and bpy (0.15 mmol) in MeCN (2 mL). In the dark, red crystals of $[Ni\{Ni(bpy)(H_2O)\}_8\{Mo(CN)_8\}_6]\cdot 38H_2O\cdot MeCN$ were formed after a few days, which are suitable for X-ray. The air-dried product $[Ni\{Ni(bpy)(H_2O)\}_8\{Mo(CN)_8\}_6]\cdot 12H_2O$ (**1**) was obtained in a yield of 8%. Elemental *Anal.* Calc. for $C_{128}H_{104}Mo_6N_{64}Ni_9O_{20}$ (**1**): C, 38.80; H, 2.65; N, 22.62. Found: C, 39.00; H, 2.35; N, 22.26%.

2.3. Physical measurements

Elemental analyses for C, H, and N were performed at the Elemental Analysis Service Center of Seoul Branch, Korea Basic Science Institute. Infrared spectra were obtained from KBr pellets with a Bomen MB-104 spectrometer. Magnetic susceptibilities for **1** were carried out using a Quantum Design MPMS-7 SQUID (dc) and PPMS (ac) susceptometers. Diamagnetic corrections of **1** were estimated from Pascal's tables.

2.4. X-ray structural analysis

X-ray data for **1** were collected on a Bruker SMART APEXII diffractometer equipped with graphite monochromated Mo Kα radiation ($\lambda = 0.71073$ Å). Preliminary orientation matrix and cell parameters were determined from three sets of ω scans at different starting angles. Data frames were obtained at scan intervals of 0.5° with an exposure time of 10 s per frame. The reflection data were corrected for Lorentz and polarization factors. Absorption corrections were carried out using SADABS [11]. The structure was solved by direct method and refined by full-matrix least-squares analysis using anisotropic thermal parameters for non-hydrogen atoms with the SHELXTL program [12]. All hydrogen atoms except for hydrogens bound to water molecules were calculated at idealized positions and refined with the riding models. Crystallographic data and the details of data collection are listed in Table 1.

Table 1
Crystal data and structure refinement for **1**

Formula	$C_{130}H_{159}Mo_6N_{65}Ni_9O_{46}$
Formula weight	4472.25
Crystal system	triclinic
Space group	$P\bar{1}$
a (Å)	18.4438(7)
b (Å)	20.5389(8)
c (Å)	29.4622(11)
α (°)	90.3680(10)
β (°)	102.8460(10)
γ (°)	116.5070(10)
V (Å^3)	9665.9(6)
Z	2
d_{calc} (g cm^{-3})	1.537
μ (mm^{-1})	1.314
$F(000)$	4532
θ Range (°)	0.71–28.38
Reflections collected	160741
Unique reflections	47538
Number of parameters	2303
R_1 [$I > 2\sigma(I)$]	0.0682
wR_2 [$I > 2\sigma(I)$]	0.1640

3. Results and discussion

3.1. Synthesis and characterization

A reaction of $(Bu_4N)_3[Mo(CN)_8]$:$Ni(ClO_4)_2\cdot 6H_2O$:bpy in a ratio of 2:3:3 in MeCN/H_2O mixed solvent produced red crystals of $[Ni\{Ni(bpy)(H_2O)\}_8\{Mo(CN)_8\}_6]\cdot 12H_2O$ (**1**) in 8% yield. No Cl–O stretching vibrations in the IR spectrum suggest the completion of the reaction. The peculiar CN bands occur at 2179w and 2152w cm^{-1}. The observation of the peaks at higher frequencies, compared with the $[Mo(CN)_8]^{3-}$ molecule (2139w and 2123w cm^{-1}), is definitely associated with the presence of bridging CN groups [13]. The shift stems from both the kinematic coupling, which takes place when a second mass is linked to the cyanide unit, and the fact that the N lone pair on CN is antibonding with respect to the C≡N bond [14].

3.2. Description of the structure

Compound **1** crystallizes in the triclinic system with space group $P\bar{1}$ as analyzed by X-ray crystallography. As

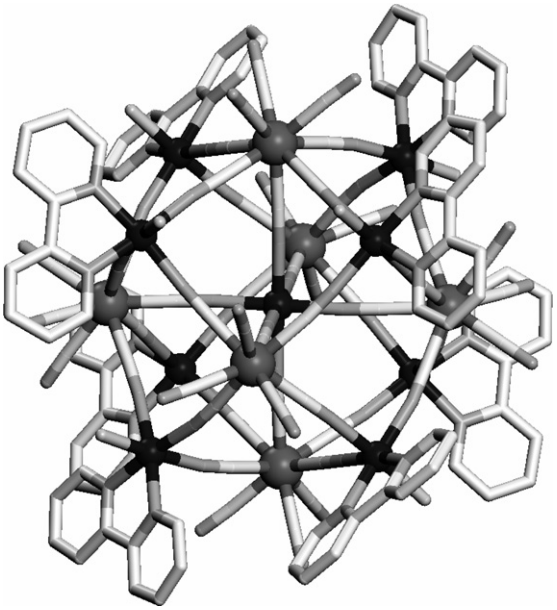


Fig. 1. Molecular view of **1**. Progressively darker shades of gray present C, O, N, Mo, and Ni, respectively.

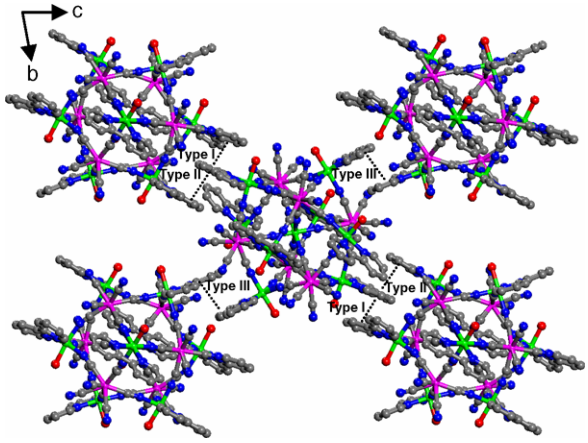


Fig. 2. Extended view of **1** showing three types of intermolecular π–π interactions, resulting in a 2D sheet structure.

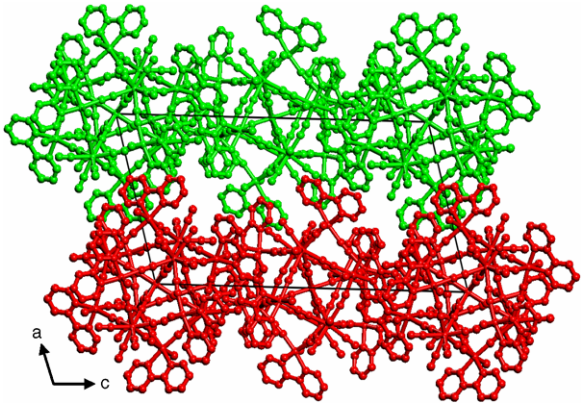


Fig. 3. Side view of **1** illustrating the extended layers.

shown in Fig. 1, the Mo center of $[Mo(CN)_8]^{3-}$ can be described as a distorted dodecahedron [5]. Five among the eight CN groups of octacyanomolybdate are subject to coordination to one central and four peripheral Ni atoms whereas the remaining ones are unbound. The intracluster distances between Ni and Mo atoms are in the range of 5.288–5.364 Å. The geometry of each terminal Ni atom is distorted octahedral, comprising three N atoms from bridging CN groups, two N atoms from bpy, and one O atom from a coordinated water molecule. The overall structure features a body-centered Ni cube capped with six Mo entities. It deserves to be noted that the cluster is air-stable, which is compared with other reported $M_9M'_6$ clusters that are readily decomposed upon exposure to air [4–8]. The stability of **1** evidently arises from the fact that the replacement of the alcohol molecules on the peripheral Ni atoms with the chelating bpy ligands and water molecules would prevent clusters from decomposing as a result of the loss of the labile solvent molecules.

The packing diagram of **1** (Fig. 2) depicts that each cluster has non-covalent π–π contacts where three types of π–π forces exist: the contact spacings are in the range of 3.366–3.774 Å for type I, 3.567–3.893 Å for type II, and 3.437–4.090 Å for type III. These non-covalent stackings generate an extended 2D sheet. In comparison, the bpy-capped Ni_9W_6 possesses only two types of π–π interactions (3.515–3.900 Å for type I and 3.398–3.907 Å for type II), constructing a 1D polymer [9]. Hence, clusters in **1** are more contacted than those in the Ni_9W_6 analogue. The shortest intermolecular metal–metal distance in **1** is 7.897 Å through the type I pathway, which is much longer by ~1 Å than the $M_9M'_6$ clusters [4–8]. Fig. 3 shows the side view of **1** in the ac plane, confirming the layered structure. Despite the longer intercluster distance, each cluster is not well isolated because of the pronounced intermolecular π–π stackings in **1** [15,16].

3.3. Magnetic properties

The cryomagnetic data were collected in the temperature range of 2–300 K (Fig. 4). The room-temperature $\chi_m T$ value is 15.49 cm^3 K mol^{-1}, which is somewhat larger than the spin-only case (11.25 cm^3 K mol^{-1}) expected for non-coupled nine Ni ($S_{Ni} = 1$) and six Mo ions ($S_{Mo} = 1/2$). Decreasing the temperature makes $\chi_m T$ increased to 117.24 cm^3 K mol^{-1}at 20 K and then abruptly reduced to 25.07 cm^3 K mol^{-1} at 2 K. The gradual rise in $\chi_m T$ on cooling indicates the operation of ferromagnetic interactions within the cluster and the drop at $T < 20$ K is relevant with the combined contributions from zero-field splitting, Zeeman effects under the applied field, and intercluster magnetic interactions. To roughly estimate the magnetic behavior among spin centers we fitted the high-temperature data ($T > 80$ K) with the Curie–Weiss equation, affording

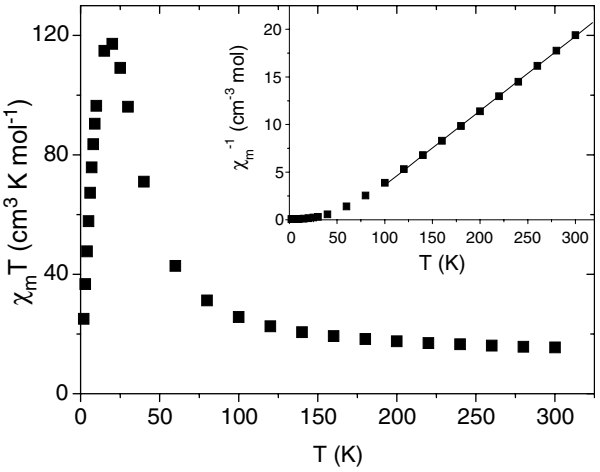


Fig. 4. Plot of $\chi_m T$ vs. T. The inset shows the inverse magnetic susceptibility data. The solid line denotes the result of the Curie–Weiss fit.

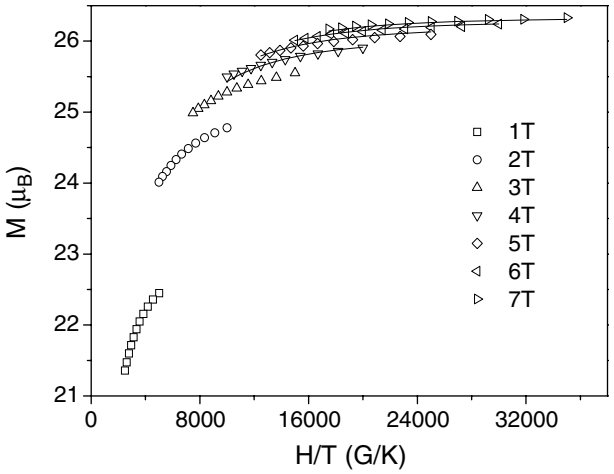


Fig. 6. Plot of reduced magnetization vs. H/T at several magnetic fields. The solid lines are fits to $S = 12$.

$\theta = 50.4$ K (inset of Fig. 4). The positive Weiss constant might indicate that ferromagnetic couplings are present between Ni(II) and Mo(V) spins through the CN bridges.

To inspect a ground state of the cluster the M(H) data were measured at 2 K (Fig. 5). The magnetization is rapidly saturated, reaching 26.27 μ_B at 7 T. The early saturation at low fields pertains to intracluster ferromagnetic interactions, which is affirmed by the theoretical curve (dotted line in Fig. 5) from the Brillouin function for magnetically isolated nine Ni(II) and six Mo(V) ions with $g = 2.2$. The ferromagnetic nature within the cluster can be interpreted on the basis of a simple orbital consideration. The magnetic 4d orbital of Mo matches in π-symmetry with the corresponding pπ orbital of C on the CN bridge whereas on the Ni side the e_g orbital is overlapped with the respective N pσ orbital on CN. As a consequence, the magnetic orbitals of the Mo and Ni centers are orthogonal to each other, eventually leading to the observed ferromagnetic behavior. The ground state of the cluster is confirmed to be an $S = 12$ as the experimental data are fairly reproduced by the Brillouin curve (solid line in Fig. 5) assuming $S = 12$.

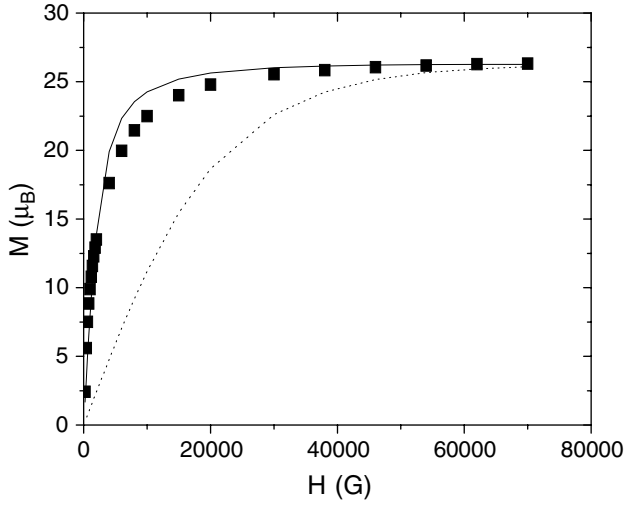


Fig. 5. Field dependence of the magnetization (M). The solid and dotted lines represent the theoretical curves calculated from the Brillouin function with $S = 12$ and non-interacting $9S_{Ni} + 6S_{Mo}$, respectively.

To examine the total spin ground state and the D parameter the reduced magnetization at low temperatures (2–4 K) and high magnetic fields (1–7 T) was investigated (Fig. 6). The isofield lines are not superimposable, clearly disclosing the onset of zero-field splitting. The fit of the data by using the ANISOFIT 2.0 program [17] is feasible only at $H = 4$–7 T, giving the values of $g = 2.2$, $D = -0.08$ cm^{-1}, and $E = 0.02$ cm^{-1}, where D and E denote the axial and rhombic zero-field splitting parameters, on the condition of an $S = 12$ and the absence of intermolecular magnetic interactions. This is because the low-field data are more significantly influenced by intercluster magnetic interactions and/or the population of low-lying excited states [18]. The surface modification of the solvated parent cluster by bpy causes the crystal system of **1** to change from monoclinic ($C2/c$) to triclinic ($P\bar{1}$), the lowest symmetry found in the $M_9M'_6$ family [4–8]. The lowering of the crystal symmetry may be associated with the observed magnetic anisotropy.

Fig. 7 illustrates out-of-phase ac susceptibility signals (χ''_m) at low temperatures and several oscillating frequencies. The observation of the frequency dependence supports that the magnetization is relaxed slowly, which is reminiscent of SMM properties. However, since no maxima in the $\chi''_m(T)$ plot are present, it is not possible to conclude the genuine magnetic nature and perform any quantitative analysis on spin dynamics. When compared with the bpy-capped Ni_9W_6 complex that exhibits peaks in $\chi''_m(T)$, the absence of the cusp temperatures in **1** probably concerns the weaker intracluster magnetic interactions and the more extended intermolecular contacts of **1**.

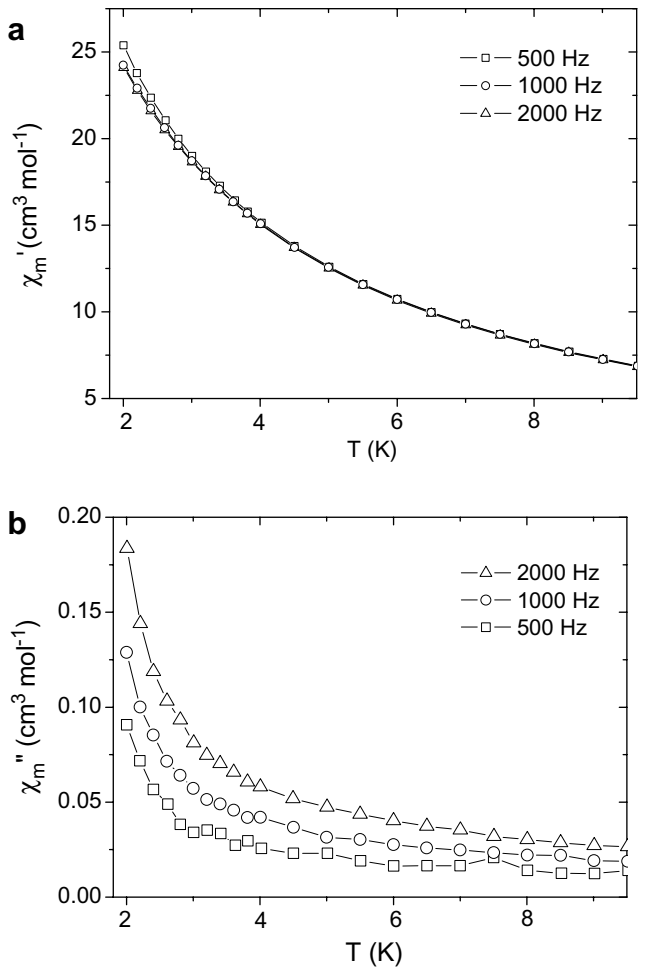


Fig. 7. Plots of (a) χ'_m and (b) χ''_m vs. T at an ac field of 5 G, zero dc field, and several frequencies.

4. Conclusion

In summary, we have prepared a cyanide-bridged Ni_9Mo_6 cluster (**1**) chelated with chelating bidentate ligands by self-assembling $[Mo(CN)_8]^{3-}$, Ni^{2+}, and bpy in a stoichiometric ratio. The 2D extended architecture is generated by the π–π interactions between pyridyl groups of bpy ligands. Magnetic data for **1** show that intracluster ferromagnetic interactions are mediated through the CN linkage and zero-field splitting of the cluster with an $S = 12$ ground state is present.

Acknowledgement

This work was supported by Korea Research Foundation Grant (MOEHRD) (KRF-2006-331-C00158) and KOSEF (R01-2007-000-10240-0) funded by Korean Government.

Appendix A. Supplementary material

CCDC 634635 contains the supplementary crystallographic data for **1**. These data can be obtained free of charge via http://www.ccdc.cam.ac.uk/conts/retrieving.html, or from the Cambridge Crystallographic Data Centre, 12 Union Road, Cambridge CB2 1EZ, UK, fax: (+44) 1223-336-033, or e-mail: deposit@ccdc.cam.ac.uk. Supplementary data associated with this article can be found, in the online version, at doi:10.1016/j.poly.2007.09.006.

References

[1] L.M.C. Beltran, J.R. Long, Acc. Chem. Res. 38 (2005) 325.
[2] (a) D. Li, S. Parkin, G. Wang, G.T. Yee, R. Clérac, W. Wernsdorfer, S.M. Holmes, J. Am. Chem. Soc. 128 (2006) 4214;
(b) J.J. Sokol, A.G. Hee, J.R. Long, J. Am. Chem. Soc. 124 (2002) 7656;
(c) E.J. Schelter, A.V. Prosvirin, K.R. Dunbar, J. Am. Chem. Soc. 126 (2004) 15004.
[3] L.M. Toma, R. Lescouëzec, J. Pasán, C. Ruiz-Pérez, J. Vaissermann, J. Cano, R. Carrasco, W. Wernsdorfer, F. Lloret, M. Julve, J. Am. Chem. Soc. 128 (2006) 4842.
[4] Z.J. Zhong, H. Seino, Y. Mizobe, M. Hidai, A. Fujishima, S.-I. Ohkoshi, K. Hashimoto, J. Am. Chem. Soc. 122 (2000) 2952.
[5] E. Ruiz, G. Rajaraman, S. Alvarez, B. Gillon, J. Stride, R. Clérac, J. Larionova, S. Decurtins, Angew. Chem., Int. Ed. 44 (2005) 2711.
[6] D.E. Freedman, M.V. Bennett, J.R. Long, Dalton Trans. (2006) 2829.
[7] Y. Song, P. Zhang, X.-M. Ren, X.-F. Shen, Y.-Z. Li, X.-Z. You, J. Am. Chem. Soc. 127 (2005) 3708.
[8] F. Bonadio, M. Gross, H. Stoeckli-Evans, S. Decurtins, Inorg. Chem. 41 (2002) 5891.
[9] J.H. Lim, J.H. Yoon, H.C. Kim, C.S. Hong, Angew. Chem., Int. Ed. 45 (2006) 7424.
[10] R.A. Pribush, R.D. Archer, Inorg. Chem. 13 (1974) 2556.
[11] G.M. Sheldrick, SADABS, A Program for Area Detector Absorption Corrections, University of Göttingen, Germany, 1994.
[12] G.M. Sheldrick, SHELXTL, version 5, Bruker AXS, Madison, WI, 1995.
[13] J.H. Lim, J.S. Kang, H.C. Kim, E.K. Koh, C.S. Hong, Inorg. Chem. 45 (2006) 7821.
[14] K.R. Dunbar, R.A. Heintz, Prog. Inorg. Chem. 45 (1997) 283.
[15] H. Miyasaka, M. Yamashita, Dalton Trans. (2007) 399.
[16] C. Boskovic, R. Bircher, P.L.W. Tregenna-Piggott, H.U. Güdel, C. Paulsen, W. Wernsdorfer, A.-L. Barra, E. Khatsko, A. Neels, H. Stoeckli-Evans, J. Am. Chem. Soc. 125 (2003) 14046.
[17] M.P. Shores, J.J. Sokol, J.R. Long, J. Am. Chem. Soc. 124 (2002) 2279.
[18] (a) W.-W. Ni, Z.-H. Ni, A.-L. Cui, X. Liang, H.-Z. Kou, Inorg. Chem. 46 (2007) 22;
(b) C. Boskovic, E.K. Brechin, W.E. Streib, K. Folting, J.C. Bollinger, D.N. Hendrickson, G. Christou, J. Am. Chem. Soc. 124 (2002) 3725.

Available online at www.sciencedirect.com
ScienceDirect
Polyhedron 27 (2008) 304–318
POLYHEDRON
www.elsevier.com/locate/poly

New ferromagnetic dinuclear triply-bridged copper(II) compounds containing carboxylato bridges: Synthesis, X-ray structure and magnetic properties

Sujittra Youngme [a,*], Jaturong Phatchimkun [a], Nanthawat Wannarit [a], Narongsak Chaichit [b], Siwaporn Meejoo [c], Gerard A. van Albada [d], Jan Reedijk [d]

[a] Department of Chemistry, Faculty of Science, Khon Kaen University, Khon Kaen 40002, Thailand
[b] Department of Physics, Faculty of Science and Technology, Thammasat University Rangsit, Pathumthani 12121, Thailand
[c] Department of Chemistry, Faculty of Science, Mahidol University, Bangkok 10400, Thailand
[d] Leiden Institute of Chemistry, Gorlaeus Laboratories, Leiden University, P.O. Box 9502, 2300 RA Leiden, The Netherlands

Received 14 July 2007; accepted 16 September 2007
Available online 23 October 2007

Abstract

The new triply-bridged dinuclear copper(II) complexes, $[Cu_2(\mu\text{-}O_2CH)(\mu\text{-}OH)_2(dpyam)_2](ClO_4)\cdot H_2O$ (**1**), $[Cu_2(\mu\text{-}O_2CCH_3)(\mu\text{-}OH)(\mu\text{-}OH_2)(dpyam)_2](S_2O_8)$ (**2**), $[Cu_2(\mu\text{-}O_2CCH_3)(\mu\text{-}OH)(\mu\text{-}OH_2)(bpy)_2](NO_3)_2$ (**3**), $[Cu_2(\mu\text{-}O_2CCH_3)(\mu\text{-}OH)(\mu\text{-}OH_2)(phen)_2](BF_4)_2\cdot 0.5H_2O$ (**4**), $[Cu_2(\mu\text{-}O_2CCH_2CH_3)(\mu\text{-}OH)(\mu\text{-}OH_2)(phen)_2](NO_3)_2$ (**5**) and $[Cu_2(\mu\text{-}O_2CCH_3)(\mu\text{-}OH)(\mu\text{-}Cl)(bpy)_2]Cl\cdot 8.5H_2O$ (**6**) (dpyam = di-2-pyridylamine, bpy = 2,2′-bipyridine, phen = 1,10-phenanthroline), have been synthesized and characterized crystallographically and also their spectroscopic and magnetic properties have been studied. A structural classification of this type of dimers, based on the data obtained from X-ray diffraction analysis in the present work and those reported in the literature has been performed. In these complexes, the local geometry around the copper centre is generally a distorted square pyramid and distorted trigonal bipyramid with different degrees of distortion. The global geometry of the dinuclear complexes can be described in terms of the relative arrangement of the two five-coordinate environments, giving rise to different classes (A–F) of complexes. The most logical explanations have been provided for each class describing different magnetic interactions. Practically, there is a clear correlation between structural data and *J* values of the class B complexes. Extended Hückel calculations were performed for the present complexes **1**–**6**, as well as for some other class B complexes, showing the different molecular orbitals involved in their corresponding frontier orbitals, together with their energy. The results are found to be useful for the proper interpretation and correlation of the magnetic data and the dinuclear structure of the present complexes.
© 2007 Elsevier Ltd. All rights reserved.

Keywords: Copper(II) complexes; Crystal structure; Triply-bridged; EPR; Magnetism

1. Introduction

Dinuclear copper(II) carboxylates with a pair of copper atoms held by carboxylato-O,O′ bridges are of interest toward understanding intramolecular magnetic exchange phenomena and for deriving magneto-structural correlations [1–12]. The magnetic interaction in the triply-bridged dinuclear copper(II) complexes can occur via bridging ligands in various pathways [2,7,13–15], which depends on the coordination geometry of copper(II) ion, the Cu···Cu separation, the bond angles at the bridging atoms, the dihedral angle between the planes containing the copper(II) ions and the copper-bridging ligand bond lengths. Structurally, the triply-bridged dinuclear copper(II) carboxylato compounds with didentate chelating ligands and a five coordination of the Cu(II) ion show an extensive

* Corresponding author. Fax: +66 043 202373.
E-mail address: sujittra@kku.ac.th (S. Youngme).

0277-5387/$ - see front matter © 2007 Elsevier Ltd. All rights reserved.
doi:10.1016/j.poly.2007.09.009

range of compounds with a distortion between regular trigonal bipyramidal and regular square-based pyramidal. This feature can be useful for understanding the relationships between structural features and the value of the intramolecular magnetic exchange interaction in the triply-bridged dinuclear unit.

Our previous reports [10–12] dealt with the distortion of the geometries ranging between regular trigonal bipyramidal and regular square-based pyramidal, and the structurally dependent magnetic properties displayed by the five-coordinate dinuclear copper(II) ions. The structures of complexes $[Cu_2(\mu\text{-}O_2CH)(\mu\text{-}OH)(\mu\text{-}Cl)(dpyam)_2](PF_6)$, $[Cu_2(\mu\text{-}O_2CH)_2(\mu\text{-}OH)(dpyam)_2](PF_6)$, $[Cu_2(\mu\text{-}O_2CH)(\mu\text{-}OH)(\mu\text{-}Cl)(dpyam)_2](ClO_4)\cdot 0.5H_2O$ [10,11] reveal a distorted trigonal bipyramidal stereochemistry, with a d_{z^2} ground state and thus the major lobe of the magnetic orbital will be axially directed towards a single bridging ligand: the hydroxido anion in these cases. This feature contributes to the observed ferromagnetic coupling between copper(II) magnetic centres. However, the structures of complexes $[Cu_2(\mu\text{-}O_2CCH_2CH_3)_2(\mu\text{-}OH)(dpyam)_2](ClO_4)$ [11], $[Cu_2(\mu\text{-}O_2CCH_2CH_3)(\mu\text{-}OH)(\mu\text{-}OH_2)(bpy)_2](ClO_4)_2$ [12] and $[Cu_2(\mu\text{-}O_2CCH_3)(\mu\text{-}OH)(\mu\text{-}OH_2)(phen)_2](ClO_4)_2$ [12], reveal a square-pyramidal stereochemistry with a $d_{x^2-y^2}$ ground state and the ferromagnetic coupling is still observed between copper(II) magnetic centres. On the contrary, the complex $[Cu_2(\mu\text{-}O_2CCH_3)_2(\mu\text{-}OCOCH_3)(dpyam)_2](BF_4)$ [12], which has a square-pyramidal stereochemistry with a $d_{x^2-y^2}$ ground state, reveals an antiferromagnetic interaction between the Cu(II) ions. For a better understanding of the magneto-structural correlation of the triply-bridged dinuclear copper(II) carboxylato complexes with different copper(II) environment and bridging configuration now an additional six new triply-bridged dinuclear copper(II) compounds are reported with different degrees of distortion, i.e. $[Cu_2(\mu\text{-}O_2CH)(\mu\text{-}OH)_2(dpyam)_2](ClO_4)\cdot H_2O$ (**1**), $[Cu_2(\mu\text{-}O_2CCH_3)(\mu\text{-}OH)(\mu\text{-}OH_2)(dpyam)_2](S_2O_8)$ (**2**), $[Cu_2(\mu\text{-}O_2CCH_3)(\mu\text{-}OH)(\mu\text{-}OH_2)(bpy)_2](NO_3)_2$ (**3**), $[Cu_2(\mu\text{-}O_2CCH_3)(\mu\text{-}OH)(\mu\text{-}OH_2)(phen)_2](BF_4)_2\cdot 0.5H_2O$ (**4**), $[Cu_2(\mu\text{-}O_2CCH_2CH_3)(\mu\text{-}OH)(\mu\text{-}OH_2)(phen)_2](NO_3)_2$ (**5**) and $[Cu_2(\mu\text{-}O_2CCH_3)(\mu\text{-}OH)(\mu\text{-}Cl)(bpy)_2]Cl\cdot 8.5H_2O$ (**6**). The compounds have been characterized by X-ray crystallography, IR, EPR and electronic spectra. The results of magnetic susceptibility measurements of compounds **1**–**6** from 5 to 250 K are investigated and discussed in relation with those of other relevant compounds. We have also undertaken a theoretical calculation using Extended Hückel methods on the different degree of structural distortion that influence their electronic and magnetic properties.

2. Experimental

2.1. Materials and measurements

1,10-Phenanthroline, 2,2′-bipyridyl and di-2-pyridylamine were purchased as commercial chemicals from Aldrich. All reagents are commercial grade materials and were used without further purification. Elemental analyses (C, H, N) were determined on a Perkin–Elmer PE 2400 CHNS/O Analyzer. IR spectra were recorded on Spectrum One FT-IR spectrophotometer as KBr disc in the 4000–450 cm^{-1} spectral range. Solid-state (diffuse reflectance) electronic spectra were measured as polycrystalline samples on a Perkin–Elmer Lambda2S spectrophotometer, over the range 8000–18 000 cm^{-1}. The X-band powder EPR spectra were recorded using a Bruker ESR-300 X-band instrument operating at room temperature with DPPH ($g = 2.0036$) as a reference. Magnetic susceptibility measurements (5–250 K) were carried out using a Quantum Design MPMS-5 5T SQUID magnetometer (measurements carried out at 0.1 T). Data were corrected for magnetisation of the sample holder and for diamagnetic contributions, which were estimated from the Pascal constants.

Molecular orbital calculations have been carried out with the CACAO (computer-aided composition of atomic orbitals) program [16], which is a program based on extended Hückel (EH) type of analysis, using the crystallographic coordinates. This approach was followed to obtain a better idea on how geometric distortion and the disposition of the magnetic orbitals of each Cu(II) ion influence their electronic and magnetic properties and to compare the magnitude of the ferromagnetic interaction of complexes within the same class. The present work has focused on class B complexes **2**–**6**, **8** and **9**, as well as class A complex **1**.

2.2. Synthesis

2.2.1. $[Cu_2(\mu\text{-}O_2CH)(\mu\text{-}OH)_2(dpyam)_2](ClO_4)\cdot H_2O$ (**1**)

A hot methanol solution (10 ml) of dpyam (0.171 g, 1.0 mmol) was added to a hot aqueous solution (20 ml) of $Cu(O_2CH)_2$ (0.154 g, 1.0 mmol). Then solid HCOONa (0.204 g, 3.0 mmol) was added, followed by solid $NaClO_4$ (0.195 g, 1.0 mmol). A green powder immediately formed, after which the mixture was warmed with adding methanol (10 ml) and water (10 ml), yielding a clear green solution. On slow evaporation at room temperature for two weeks product **1** was isolated as blue rod-shape crystals. They were filtered off, washed with the mother liquid and air-dried. Yield: ca. 30%. *Anal.* Calc. for $C_{21}H_{23}ClCu_2N_6O_9$: C, 37.87; H, 3.48; N, 12.62. Found: C, 37.59; H, 3.33; N, 12.53%.

2.2.2. $[Cu_2(\mu\text{-}O_2CCH_3)(\mu\text{-}OH)(\mu\text{-}OH_2)(dpyam)_2](S_2O_8)$ (**2**)

A hot methanol solution (10 ml) of dpyam (0.171 g, 1.0 mmol) was added to a hot methanol solution (20 ml) of $Cu(O_2CCH_3)_2\cdot H_2O$ (0.181 g, 1.0 mmol). Then a hot aqueous solution (10 ml) of $Na_2S_2O_8$ (0.119 g, 0.5 mmol) was added to the mixture, yielding a green solution. After two weeks, green-square crystals of compound **2** were obtained. The crystals were filtered off, washed with mother liquor and air-dried. Yield: ca. 60%. *Anal.* Calc.

for $C_{22}H_{24}Cu_2N_6O_{12}S_2$: C, 34.97; H, 3.20; N, 11.12. Found: C, 34.91; H, 3.09; N, 11.42%.

2.2.3. $[Cu_2(\mu\text{-}O_2CCH_3)(\mu\text{-}OH)(\mu\text{-}OH_2)(bpy)_2](NO_3)_2$ (3)

The warm methanol solution (20 ml) of bpy (0.156 g, 1.0 mmol) was added to a warm aqueous solution (5 ml) of $Cu(O_2CCH_3)_2 \cdot H_2O$ (0.181 g, 1.0 mmol). Then solid $NaNO_3$ (0.043 g, 0.5 mmol) was added to the mixture, yielding a clear blue solution. After one week, blue needle-shaped crystals of compound **3** were obtained. The crystals were filtered off, washed with mother liquor and air-dried. *Anal.* Calc. for $C_{22}H_{22}Cu_2N_6O_{10}$: C, 40.18; H, 3.37; N, 12.78. Found: C, 40.10; H, 3.31; N, 12.97%.

2.2.4. $[Cu_2(\mu\text{-}O_2CCH_3)(\mu\text{-}OH)(\mu\text{-}OH_2)(phen)_2](BF_4)_2 \cdot 0.5H_2O$ (4)

The warm methanol solution (20 ml) of phen (0.198 g, 1.0 mmol) was added to a warm aqueous solution (5 ml) of $Cu(O_2CCH_3)_2 \cdot H_2O$ (0.181 g, 1.0 mmol). Then solid $NaBF_4$ (0.055 g, 0.5 mmol) was added to the mixture, yielding a clear greenish-blue solution. After one week, violet-coloured crystals of compound **4** were obtained as needles. The crystals were filtered off, washed with mother liquor and air-dried. *Anal.* Calc. for $C_{26}H_{24}B_2Cu_2F_8N_4O_{4.5}$: C, 40.81; H, 3.16; N, 7.32. Found: C, 40.88; H, 2.91; N, 7.49%.

2.2.5. $[Cu_2(\mu\text{-}O_2CCH_2CH_3)(\mu\text{-}OH)(\mu\text{-}OH_2)(phen)_2](NO_3)_2$ (5)

The warm methanol solution (20 ml) of phen (0.198 g, 1.0 mmol) was added to a warm aqueous solution (5 ml) of $Cu(NO_3)_2 \cdot 3H_2O$ (0.241 g, 1.0 mmol). Then solid $NaO_2CCH_2CH_3$ (0.047 g, 0.5 mmol) was added to the mixture, yielding a blue solution. On slow evaporation, its color became greenish-blue. After one week, greenish-blue crystals of compound **5** were obtained. The crystals were filtered off, washed with mother liquor and air-dried. *Anal.* Calc. for $C_{27}H_{24}Cu_2N_6O_{10}$: C, 45.07; H, 3.36; N, 11.68. Found: C, 45.01; H, 3.25; N, 11.83%.

2.2.6. $[Cu_2(\mu\text{-}O_2CCH_3)(\mu\text{-}OH)(\mu\text{-}Cl)(bpy)_2]Cl \cdot 8.5H_2O$ (6)

The warm methanol solution (20 ml) of bpy (0.156 g, 1.0 mmol) was added to a warm aqueous solution (5 ml) of $Cu(O_2CCH_3)_2 \cdot H_2O$ (0.181 g, 1.0 mmol). Then solid NaCl (0.029 g, 0.5 mmol) was added to the mixture, yielding a clear blue solution. After one week, greenish-blue crystals of compound **6** were obtained. The crystals were filtered off, washed with mother liquor and air-dried. *Anal.* Calc. for $C_{22}H_{37}Cl_2Cu_2N_4O_{11.5}$: C, 35.72; H, 5.05; N, 7.57. Found: C, 35.55; H, 5.24; N, 7.61%.

2.3. Crystallography

The X-ray single-crystal data for all compounds were collected at 298 K on a 1 K Bruker SMART CCD area-detector diffractometer using graphite-monochromated Mo Kα radiation ($\lambda = 0.71073$ Å) at a detector distance of 4.5 cm and swing angle of −35°. A hemisphere of the reciprocal space was covered by combination of three sets of exposures; each set had a different ϕ angle (0, 88, 180°) and each exposure of 40 s covered 0.3° in ω. Data reduction and cell refinements were performed using the program SAINT [17] An empirical absorption correction by using the SADABS [18] program was applied, which resulted in transmission coefficients ranging from 0.683 to 1.000 for compound **1**, 0.862–1.000 for compound **2**, 0.679–1.000 for compound **3**, 0.744–1.000 for compound **4**, 0.764–1.000 for compound **5** and 0.581–1.000 for compound **6**.

The structures were solved by direct methods and refined by full-matrix least-squares method on $(F_{obs})^2$ with anisotropic thermal parameters for all non-hydrogen atoms using the SHELXTL-PC V 6.12 software package [19] All hydrogen atoms in **1, 2, 3** and **5** were located geometrically and refined isotropically while all hydrogen atoms in **4** and **6** were fixed and allowed to ride on attached atoms. A water molecule in **4** was located with an occupancy of 0.5. For the best results of the refinement of the structure of **6** the oxygen atoms of the overall 8.5 water molecules were refined without hydrogen atoms except a few of them. Two water molecules are disordered with site occupancy of 0.5 for both conformers and two water molecules are located with site occupancies 0.25. All non-H atoms in **6** were refined anisotropically except three oxygen atoms of water molecules. The ClO_4^- anion in **1**, $S_2O_8^{2-}$ in **2**, NO_3^- in **3** and **5**, and BF_4^- in **4** showed disorder; the occupancies of the disordered positions were initially refined and later fixed at 0.5. These disordered counterions have some unreasonable Cl/S/N···O distances with quite high U_{eq} values, which are usually found for the disordered groups. However, the average Cl/S/N···O distances are not significantly different from the normal ordered ones (ClO_4(**1**), 1.334–1.460 Å, $d_{av} = 1.408$ Å (1.414 Å); S_2O_8 (**2**), 1.344–1.671 Å, $d_{av} = 1.470$ Å (1.472 Å); NO_3 (**3**), 1.072–1.350 Å, $d_{av} = 1.222$ Å (1.239 Å); NO_3 (**5**), 1.069–1.350 Å, $d_{av} = 1.208$ Å (1.239 Å).

The molecular graphics were created by using the SHELXTL-PC [19] package. The crystal and refinement details for compounds **1**–**6** are listed in Table 1. Selected bond lengths and angles are given in Tables S4 and S5.

3. Results and discussion

3.1. Description of the crystal structures

3.1.1. Crystal structure of $[Cu_2(\mu\text{-}O_2CH)(\mu\text{-}OH)_2(dpyam)_2](ClO_4) \cdot H_2O$ (1)

The structure of **1** consists of a symmetric dinuclear $[Cu_2(\mu\text{-}O_2CH)(\mu\text{-}OH)_2(dpyam)_2]^+$ cation, with ClO_4^- counter anions. This unit is depicted in Fig. 1, together with the numbering scheme. Both copper(II) ions of the complex cation are linked through a double hydroxido

Table 1
Crystal and refinement data for complexes **1**–**6**

Complex	**1**	**2**	**3**	**4**	**5**	**6**
Empirical formula	$C_{21}H_{23}ClCu_2N_6O_9$	$C_{22}H_{24}Cu_2N_6O_{12}S_2$	$C_{22}H_{22}Cu_2N_6O_{10}$	$C_{26}H_{24}B_2Cu_2F_8N_4O_{4.5}$	$C_{27}H_{24}Cu_2N_6O_{10}$	$C_{22}H_{37}Cl_2Cu_2N_4O_{11.5}$
Formula weight	664.0	755.67	657.54	1526.35	719.62	730.40
T/K	293(2)	293(2)	293(2)	293(2)	293(2)	293(2)
Crystal system	monoclinic	monoclinic	triclinic	orthorhombic	monoclinic	triclinic
Space group	$C2/m$	$P2_1/m$	$P\bar{1}$	$P2_12_12_1$	$P2_1/n$	$P\bar{1}$
a (Å)	14.3312(5)	8.6702(2)	7.756	8.34520(10)	8.00060(10)	7.4607(2)
b (Å)	16.8446(7)	17.3735(4)	11.417	17.7730(2)	18.4031(2)	13.6636(3)
c (Å)	12.4728(5)	10.07380(10)	15.9420(2)	19.84770(10)	19.3110(3)	17.4330(4)
α (°)	90	90	74.8150(10)	90	90	83.2120(10)
β (°)	120.9700(10)	112.8730(10)	81.2370(10)	90	97.9530(10)	83.3470(10)
γ (°)	90	90	73.24	90	90	78.6260(10)
V (Å^3)	2581.72(17)	2470.85(5)	1299.939(16)	2943.80(5)	2815.92(6)	1722.17(7)
Z	4	2	2	2	4	2
D_{calc} (g cm^{-3})	1.708	1.795	1.680	1.722	1.697	1.409
μ (mm^{-1})	1.813	1.745	1.703	1.539	1.581	1.446
F(000)	1344	768	668	1528	1464	736
Crystal size (mm)	0.05 × 0.20 × 0.25	0.125 × 0.125× 0.125	0.325 × 0.225 × 0.075	0.425 × 0.175 × 0.150	0.300 × 0.225 × 0.050	0.500 × 0.250 × 0.200
Number of reflection collected	8117	7984	9432	18 402	20 148	9219
Number of unique reflections (R_{int})	3810 (0.0165)	2854 (0.0315)	7804 (0.0168)	3672 (0.0281)	8570 (0.0677)	6282 (0.0395)
Data/ restraints/ parameter	3810/0/219	2843/0/284	6895/0/503	6504/0/504	7983/0/556	6158/0/422
Goodness-of-fit	1.048	1.031	1.049	1.028	1.058	1.004
Final R indices [$I > 2\sigma(I)$]	$R_1 = 0.0525$, $wR_2 = 0.1455$	$R_1 = 0.0344$, $wR_2 = 0.0816$	$R_1 = 0.0380$, $wR_2 = 0.0902$	$R_1 = 0.0371$, $wR_2 = 0.0812$	$R_1 = 0.0670$, $wR_2 = 0.0943$	$R_1 = 0.0582$, $wR_2 = 0.1462$
R indices (all data)	$R_1 = 0.0708$, $wR_2 = 0.1594$	$R_1 = 0.0523$, $wR_2 = 0.0894$	$R_1 = 0.0518$, $wR_2 = 0.0988$	$R_1 = 0.0522$, $wR_2 = 0.0883$	$R_1 = 0.1540$, $wR_2 = 0.1162$	$R_1 = 0.0809$, $wR_2 = 0.1591$
Largest difference in peak and hole (e Å^3)	0.992 and −0.827	0.638 and −0.677	0.447 and −0.717	0.248 and −0.282	0.327 and −0.379	0.888 and −1.109

$R = \sum||F_o| - |F_c||/\sum|F_o|$, $R_w = [\sum w\{||F_o| - |F_c||\}^2/\sum w|F_o|^2]^{1/2}$.

and a formato bridge, leading to a Cu–Cu distance of 2.902(1) Å. The coordination environment around each copper(II) ion can be best described as tetrahedrally distorted square pyramidal CuN_2O_2O' chromophore with a τ value of 0.27, the structure index is defined as $\tau = (\beta - \alpha)/60$, where β and α are the largest coordination angles, $\tau = 0$ for square pyramidal (SP) and $\tau = 1$ for trigonal bipyramidal (TBP) geometry) [20]. The four shorter bonds in the basal plane involve two nitrogen atoms of the dpyam ligand (Cu–N 2.005(3) and 2.030(3) Å), two oxygen atoms of bridging hydroxido ligands (Cu–O 1.952(3) and 1.955 Å). An oxygen atom of the triatomic bridging formato ligand completes the five-coordination at Cu(1) atom (Cu–O(3) 2.345(3) Å), consistent with the typical square-pyramidal geometry. The four basal atoms are not coplanar, showing a significant tetrahedral distortion with a dihedral angle of 23.8° formed between CuO_2 and CuN_2 planes and the copper atom is displaced by 0.189 Å from the basal plane toward the O(3) atom. The dinuclear unit is nearly planar and the dihedral angle between the basal N_2O_2 planes is 165.6°. The bridging angles in the equatorial positions, Cu(1)–O(1)–Cu(1A) and Cu(1)–O(2)–Cu(1A) are 95.8(1)° and 96.0(1)°, respectively. This structural feature is comparable to the planar dihydroxido-copper(II) complexes to which their structures and magnetic properties are well characterized

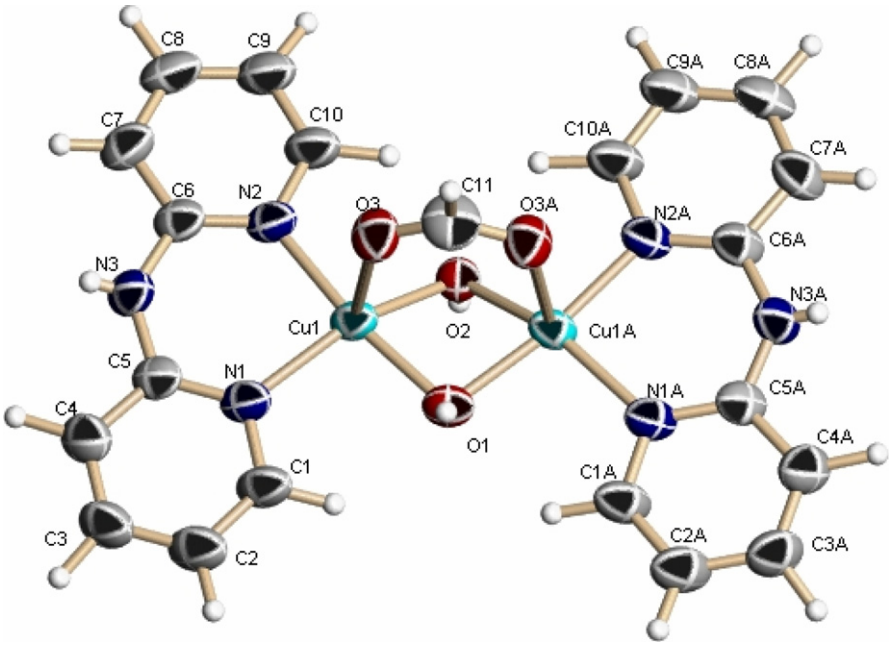


Fig. 1. ORTEP 50% probability plot of the cation in $[Cu_2(\mu\text{-}O_2CH)(\mu\text{-}OH)_2(dpyam)_2](ClO_4)\cdot H_2O$ (**1**), atoms with an "A" are generated by a mirror plane. The uncoordinating anion and water molecules are omitted for clarity.

experimentally and theoretically [21–28]. The dpyam ligands are essentially planar with small dihedral angles of 6.6° between the individual pyridine rings. The bite angles of the dpyam ligands (N–Cu–N, 91.9(1)°) are only slightly greater than 90°.

The lattice is further stabilized by a hydrogen bonding between the amine N and the oxygen atom of formato group with N···O contact of 2.796(1) Å; between the oxygen atom of bridging hydroxido group and the oxygen atom of lattice water molecules with O···O contacts of 2.865(1) Å; between the oxygen atom of bridging of both hydroxido groups O···O contacts of 2.855(1) Å along *a*- and *b*-axes, leading to a two dimensional supramolecular structure (see Fig. 2).

*3.1.2. Crystal structures of $[Cu_2(\mu\text{-}O_2CCH_3)(\mu\text{-}OH)(\mu\text{-}OH_2)(dpyam)_2](S_2O_8)$ (**2**), $[Cu_2(\mu\text{-}O_2CCH_3)(\mu\text{-}OH)(\mu\text{-}OH_2)(bpy)_2](NO_3)_2$ (**3**), $[Cu_2(\mu\text{-}O_2CCH_3)(\mu\text{-}OH)(\mu\text{-}OH_2)(phen)_2](BF_4)_2\cdot H_2O$ (**4**), $[Cu_2(\mu\text{-}O_2CCH_2CH_3)(\mu\text{-}OH)(\mu\text{-}OH_2)(phen)_2](NO_3)_2$ (**5**)*

The structure of compounds **2**–**5** are made up of a dinuclear $[Cu_2(\mu\text{-}O_2CCH_3/O_2CCH_2CH_3)(\mu\text{-}OH)(\mu\text{-}OH_2)(dpyam/bpy\text{ or }phen)_2]^+$ cation, an uncoordinated $S_2O_8^{2-}$, NO_3^-, BF_4^- and NO_3^- anion, respectively. This unit is depicted in Fig. 3 for complex **2** and Figs. S1–S3 for complexes **3**–**5**, together with the numbering scheme, with selected distances and angles listed in Tables S4 and S5. In complexes **2**–**5**, both Cu(II) ions in the dinuclear unit are linked through a hydroxido, an aqua and a didentate

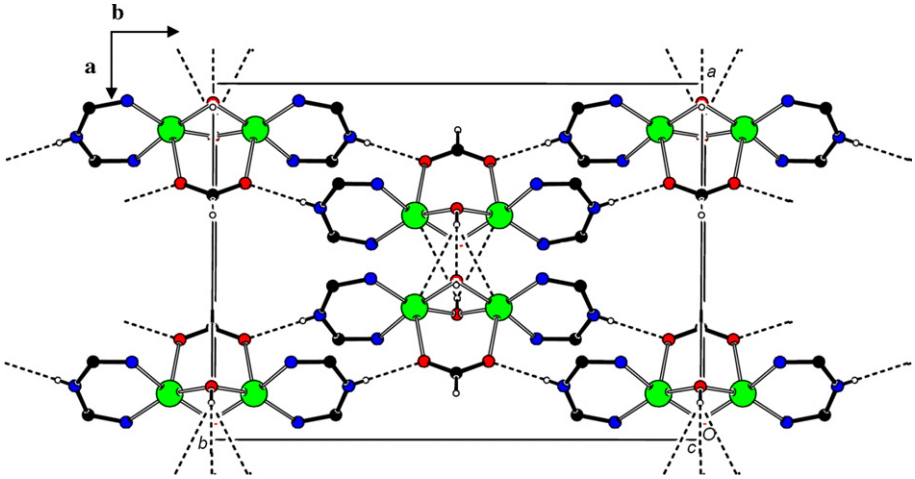


Fig. 2. H-bond system providing an two-dimensional array of complex **1**.

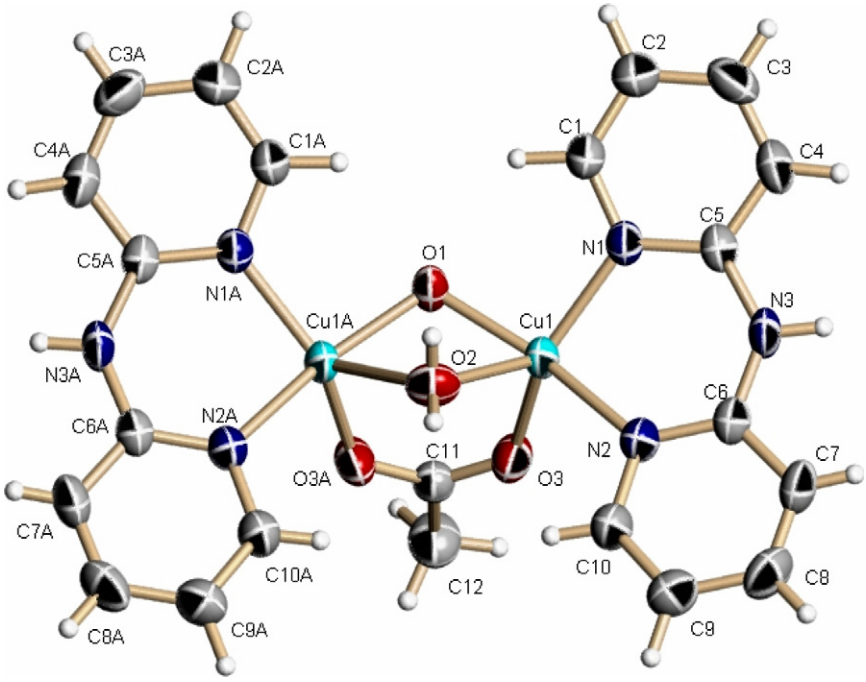


Fig. 3. ORTEP 50% probability plot of the cation in $[Cu_2(\mu\text{-}O_2CCH_3)(\mu\text{-}OH)(\mu\text{-}OH_2)(dpyam)_2](S_2O_8)$ (**2**), atoms with an "A" are generated by a mirror plane. The uncoordinating anion is omitted for clarity.

κ-O^1,O^2 bridging carboxylate ligand resulting in a five-coordinate species at each copper atom. The coordination environment around each Cu(II) ion can be best described as distorted square pyramidal, with a CuN_2O_2O' chromophore (see Fig. 3 and Figs. S1–S3) and the τ values of 0.43 for **2**, 0.21 and 0.19 for **3**, 0.21 and 0.16 for **4** and 0.08 and 0.19 for **5**. The carboxylate groups are in the didentate η^1:η^1:μ-bridging mode, locating in the equatorial positions. The fifth axial position is occupied by a bridging water molecule at a longer distance of 2.414(2) Å for **2**, 2.347(1) and 2.460(2) Å for **3**, 2.374(3) and 2.390(3) Å for **4** and, 2.344(4) and 2.368(4) Å for **5**. The copper atoms are displaced from the basal plane towards the apical O atom of aqua by 0.225(4) Å for **2**, 0.152(2) and 0.115(1) Å for **3**, 0.124(1) and 0.090(1) Å for **4** and 0.147(1) and 0.148(1) Å for **5**. The CuN_2O_2 chromophores are non-planar with dihedral angles of 40.4(1)° for **2**, 14.5(1) and 11.6(1)° for **3**, 17.0(1)° and 8.6(1)° for **4** and 14.6(1)° and 12.2(1)° for **5**, between the CuN_2 and CuO_2 planes. The dihedral angle between the basal planes is 164.4(1)° for **2**, 120.5(1)° for **3**, 114.6(3)° for **4** and 122.3(2)° for **5**.

For compound **2**, the lattice is stabilized by a hydrogen bonding between the amine N and the oxygen atom of S_2O_8 with N···O distance of 2.799–2.919 Å and between the oxygen atom of bridging hydroxido/aqueous groups and the oxygen atoms of S_2O_8 with O···O contacts of 2.659–3.364 Å parallel to *a*- and *b*-axes, leading to a two-dimensional supramolecular structure (see Fig. 4).

For compounds **3** and **5**, the lattice is stabilized by a hydrogen bonding between the oxygen atom of bridging hydroxido/aqueous groups and the oxygen atoms of NO_3^- with O···O contacts of 2.712–3.020 Å for **3** and 2.785–3.168 Å for **5**. That of compound **4** is stabilized by a hydrogen bonding between the oxygen atom of bridging hydroxido/aqueous groups and fluoride atoms of BF_4^- with O···F contacts of 2.744–3.390 Å.

3.1.3. Crystal structure of $[Cu_2(\mu\text{-}O_2CCH_3)(\mu\text{-}OH)(\mu\text{-}Cl)(bpy)_2]Cl \cdot 8.5H_2O$ (6)

The structure of compound **6** consists of a dinuclear $[Cu_2(\mu\text{-}OH)(\mu\text{-}O_2CCH_3)(\mu\text{-}Cl)(bpy)]^+$ cation, with Cl^- counter anions and 8.5 molecules of lattice water. This cation is depicted in Fig. 5, together with the numbering scheme, with selected distances and angles listed in Table S5. Each copper(II) ion has a distorted square pyramidal geometry of the CuN_2O_2Cl chromophore, with a τ value of 0.41 and 0.28 for Cu1 and Cu2, respectively. Two nitrogen atoms of the bpy ligand, two oxygen atoms of the bridging acetato and hydroxido ligands form the square bases. The axial site of each copper(II) atom is occupied by a chlorido ligand at distances of 2.632 and 2.657 Å. The *syn*,*syn*-coordinated acetato ligand bridges the two equatorial planes, giving a Cu–Cu distance of 3.040(1) Å. The CuN_2O_2 chromophore are non-planar with dihedral angles of 27.4(1)° and 18.9(1)° for **6**, between the CuN_2 and CuO_2 planes. The dihedral angle between the equatorial planes are 123.0(4)° for Cu1 and Cu2. The bridging angles (Cu(1)–O(1)–Cu(2) and Cu(1)–Cl(1)–Cu(2) are 103.3(1)° and 70.2(1)°, respectively.

The lattice is further stabilized by hydrogen bonding between the hydroxido O and the chloride anion with a short O···Cl contact of 2.910(1) Å.

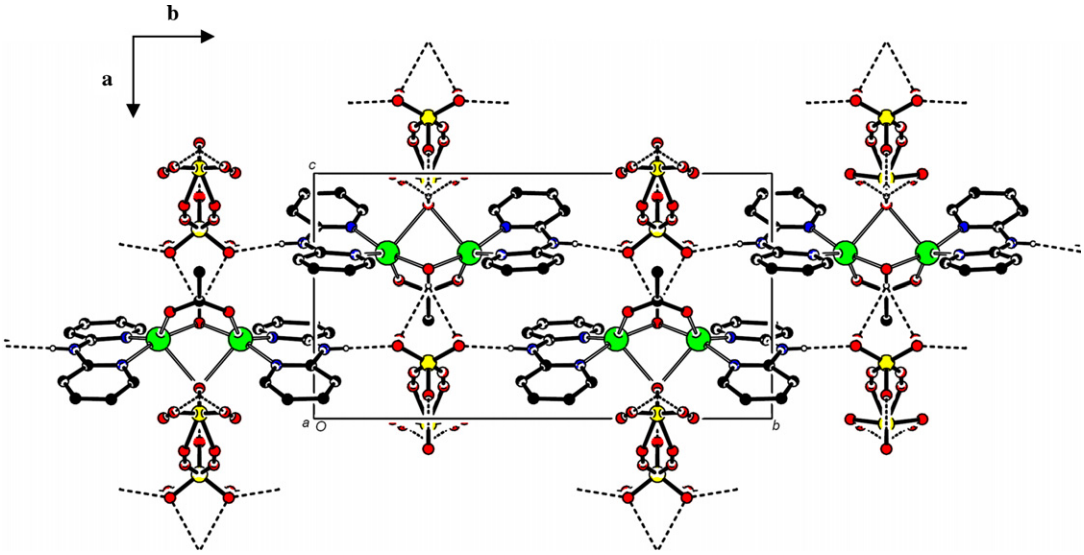


Fig. 4. H-bond system providing an two-dimensional array of complex **2**.

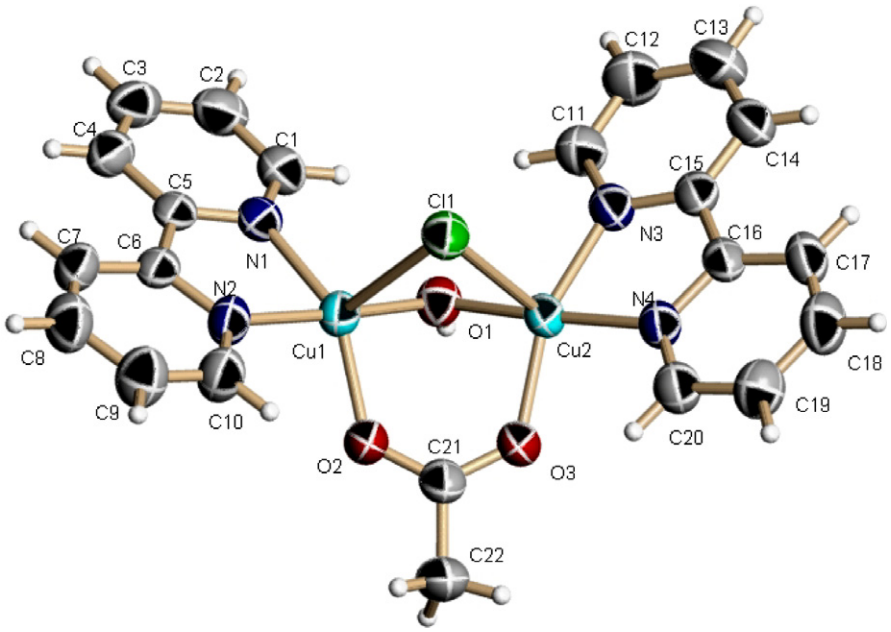


Fig. 5. ORTEP 50% probability plot of the cation in $[Cu_2(\mu\text{-}O_2CCH_3)(\mu\text{-}OH)(\mu\text{-}Cl)(bpy)_2]Cl \cdot 8.5H_2O$ (**6**). The uncoordinating anion and water molecules are omitted for clarity.

3.2. Structure comparison

The several structural and magnetic parameters of the compounds, together with those of a number of related dinuclear triply-bridged copper(II) compounds are listed in Table 2 and Fig. 6. The arrangement of the five-coordinate chromophores in the triply-bridged dinuclear copper(II) complexes containing a carboxylato bridge may be represented in six different classes (Scheme 1): (A) coplanar bases with a square pyramidal geometry for both Cu(II) environments and two dihydroxido bridges lying in the equatorial positions; (B) non-coplanar bases with a square pyramidal geometry for both Cu(II) ions, triatomic carboxylato and hydroxido bridges in the equatorial positions; (C) non-coplanar bases with a square pyramidal geometry for both Cu(II) ions and two triatomic carboxylato bridges lying in the equatorial positions; (D) non-coplanar bases with a square pyramidal geometry for both Cu(II) ions, one single-atom or triatomic bridge in an equatorial–equatorial configuration and two carboxylato (two triatomic or monoatomic/triatomic) bridges in an axial–equatorial configuration; (E) non-coplanar with a trigonal bipyramidal geometry for both Cu(II) ions and one hydroxido bridge in an axial–axial configuration; (F) non-coplanar bases with square pyramidal and trigonal bipyramidal geometries and two bridges, which occupy

Table 2
Structural and magnetic data for triply-bridged dinuclear copper(II) carboxylato compounds

Compound[a]	Coordination geometry[b]	τ	Angle between basal plane (°)	Tetrahedral twist (°)	Mode	Cu···Cu (Å)	Cu–X		J (cm^{-1})[c]	Cu–X–Cu (Å)	Reference
							Axial	Equatorial			
$[Cu_2(\mu\text{-}O_2CH)(\mu\text{-}OH)_2(dpyam)_2](ClO_4)\cdot H_2O$ (**1**)	Dist. Spy.	0.27	165.6	23.8	A	2.903	2.345	1.952–2.005	112.7	95.89 (OH) 96.09 (OH)	this work
$[Cu_2(\mu\text{-}O_2CCH_3)(\mu\text{-}OH)(\mu\text{-}OH_2)(dpyam)_2](S_2O_8)$ (**2**)	Dist. Spy.	0.43	164.4	40.4	B	3.124	2.414	1.911–2.023	n.d.	109.64 (OH) 80.66 (OH_2)	this work
$[Cu_2(\mu\text{-}O_2CCH_3)(\mu\text{-}OH)(\mu\text{-}OH_2)(bpy)_2](NO_3)_2$ (**3**)	Dist. Spy.	0.21, 0.19	120.5	14.5, 11.6	B	3.049	2.347, 2.460	1.938–2.017	n.d.	103.97 (OH) 78.70 (OH_2)	this work
$[Cu_2(\mu\text{-}O_2CCH_3)(\mu\text{-}OH)(\mu\text{-}OH_2)(phen)_2](BF_4)_2\cdot 0.5H_2O$ (**4**)	Dist. Spy.	0.21, 0.16	114.6	17.0, 8.6	B	3.002	2.374, 2.390	1.925–2.008	120.8	102.07 (OH) 78.12 (OH_2)	this work
$[Cu_2(\mu\text{-}O_2CCH_2CH_3)(\mu\text{-}OH)(\mu\text{-}OH_2)(phen)_2](NO_3)_2$ (**5**)	Dist. Spy.	0.08, 0.19	122.3	14.6, 12.2	B	3.026	2.344, 2.368	1.925–2.029	n.d.	103.58 (OH) 79.90 (OH_2)	this work
$[Cu_2(\mu\text{-}O_2CCH_3)(\mu\text{-}OH)(\mu\text{-}OH_2)(bpy)_2](ClO_4)_2$ (**7**)	Dist. Spy.	0.14, 0.25	118.1		B	3.035	2.379, 2.405	2.006–2.010	19.3	103.8 (OH) 78.7 (OH_2)	[1]
$[Cu_2(\mu\text{-}O_2CCH_3)(\mu\text{-}OH)(\mu\text{-}OH_2)(phen)_2](ClO_4)_2$ (**8**)	Dist. Spy.	0.02, 0.14	113.8	16.4, 8.2	B	2.989	2.360, 2.375	1.933–2.020	120.0	101.3 (OH) 78.3 (OH_2)	[12]
$[Cu_2(\mu\text{-}O_2CCH_2CH_3)(\mu\text{-}OH)(\mu\text{-}OH_2)(bpy)_2](ClO_4)_2$ (**9**)	Dist. Spy.	0.20, 0.16	120.1	15.0, 10.9	B	3.037	2.382, 2.415	1.920–2.005	148.9	104.5 (OH) 78.6 (OH_2)	[12]
$[Cu_2(\mu\text{-}O_2CCH_3)(\mu\text{-}OH)(\mu\text{-}Cl)(bpy)_2]Cl\cdot 8.5H_2O$ (**6**)	Dist. Spy.	0.41, 0.28	123.0	27.4, 18.9	B	3.040	2.632, 2.657	1.936–2.029	145.3	103.3 (OH)	this work
$[Cu_2(\mu\text{-}O_2CH)(\mu\text{-}OH)(\mu\text{-}Cl)(dpyam)_2](ClO_4)\cdot 0.5H_2O$ (**10**)	Dist. TBP.	0.67	90.0		E	3.036	1.916	1.975–2.158	79.1	104.8 (OH) 75.6 (Cl)	[10]
$[Cu_2(\mu\text{-}O_2CH)(\mu\text{-}OH)(\mu\text{-}Cl)(dpyam)_2](PF_6)$ (**11**)	Dist. TBP.	0.72	93.2		E	3.061	1.918	1.983–2.183	79.7	105.8 (OH) 77.3 (Cl)	[11]
$[Cu_2(\mu\text{-}O_2CH)(\mu\text{-}OH)(\mu\text{-}OMe)(dpyam)_2](ClO_4)$ (**12**)	Dist. TBP.	0.65			E	3.023	1.918	2.169–2.175	62.5	104.0 (OH) 88.3 (OMe)	[10]
$[Cu_2(\mu\text{-}O_2CH)(\mu\text{-}OH)(\mu\text{-}OCOH)(dpyam)_2](PF_6)$ (**13**)	Dist. TBP.	0.71	89.7		E	3.113	1.934	2.144–2.200	47.8	107.2 (OH) 93.1 (O_2CH)	[11]
$[Cu_2(\mu\text{-}O_2CCH_3)(\mu\text{-}OH)(\mu\text{-}OCOCH_3)(dpyam)_2](PF_6)\cdot H_2O$ (**14**)	Dist. Spy., Dist. TBP.	0.32, 0.51		25.32	F	2.988	2.313, 1.900	1.928–2.087 2.014–2.262	10.13	102.7 (OH) 86.8 ($OCOCH_3$)	[27]

$[Cu_2(\mu\text{-}O_2CC_2H_5)(\mu\text{-}OCOC_2H_5)(\mu\text{-}OH)(dpyam)_2](ClO_4)$ (**15**)	Dist. Spy.	0.22, 0.43		25.7, 34.4	D	3.006	2.236, 2.318	1.931–1.959	24.1	101.8 (OH) 86.4 ($O_2CCH_2CH_3$)	[11]
$[Cu_2(\mu\text{-}O_2CCH_3)_2(\mu\text{-}OCOCH_3)(dpyam)_2](BF_4)$ (**16**)	Dist. Spy.	0.07	120.1	32.1	C	3.402	2.144	1.967–2.002	−55.9	105.0 ($OCOCH_3$)	[12]
$[Cu_2(\mu\text{-}O_2CCH_3)_2(\mu\text{-}OCOCH_3)(bpy)_2](ClO_4)$ (**17**)	Dist. Spy.	0.14, 0.47			D	3.392	2.238, 1.930	1.939–1.977 1.974–2.169	3.6	109.8 ($OCOCH_3$)	[1]
$[Cu_2L(\mu\text{-}O_2CCH_3)_2](ClO_4)\cdot 3H_2O$ (**18**)	Dist. Spy.				D	3.263	2.169	1.942–2.046	−72	113.7 (OPh)	[32]

[a] *Abbreviations*: bpy = 2,2′-bipyridine; dpyam = di-2-pyridylamine; phen = 1,10′-phenanthroline; L = 2,6-bis(*N*-methylpiperazino)methyl-4-chlorophenol, n.d. = not determined.
[b] Dist. Spy. = distorted square pyramidal, Dist. TBP = distorted trigonal bipyramidal.
[c] J = singlet–triplet energy gap.

the axial–equatorial positions, the other one is in an equatorial–equatorial configuration. An example of each class is presented in Fig. 6.

3.3. Spectral characterization

The infrared spectra display a broad band at ~3500 cm^{-1}, which can be assigned to the bridging OH vibration of the hydroxido ligands and/or lattice water. The spectrum in complex **1** also exhibits a broad and intense band at 1570 cm^{-1}, corresponding to the $\nu_{as}(COO^-)$ vibration and a medium broad band at 1350 cm^{-1}, corresponding to the $\nu_s(COO^-)$ vibration, the difference Δ [$\Delta = \nu_{as}(COO^-) - \nu_s(COO^-)$; 220 cm^{-1}] is close to that of NaO_2CH (201 cm^{-1}) as expected for the triatomic bridging coordination mode of the formate anion within a dinuclear species [1,21]. Owing to the presence of two different coordination modes of carboxylate bridges in **2**–**6**, $\nu_{as}(COO^-)$ and $\nu_s(COO^-)$ bands are observed in their IR spectra (1556 and 1385 cm^{-1} bands for **2**, 1558 and 1384 cm^{-1} bands for **3**, 1559 and 1396 cm^{-1} bands for **4**, 1553 and 1395 cm^{-1} bands for **5** and 1549 and 1384 cm^{-1} for **6**). The IR spectra of compounds **1**–**5** show broad and intense bands of the ionic ClO_4^- anion (1089–1100 cm^{-1} for **1**), ionic $S_2O_8^{2-}$ (1232–1280 cm^{-1} for **2**), ionic NO_3^- anion (1365–1386 cm^{-1} for **3** and 1362–1384 cm^{-1} for **5**) and ionic BF_4^- anion (1084–1100 cm^{-1} for **4**) [29].

The electronic diffuse reflectance spectra of **1** and **2** show a single broad band centered at 14000 and 13300 cm^{-1}. This observed single broad peak is consistent with the tetrahedrally-distorted square pyramidal stereochemistry and assigned to be the $d_{z^2}, d_{xy}, d_{xz}, d_{yz} \rightarrow d_{x^2-y^2}$ transition [30].

The diffuse reflectance spectra of **3**–**6** display a broad band (16500, 16200, 16100 and 15600 cm^{-1} for **3**, **4**, **5** and **6**, respectively) and a lower energy shoulder (14200, 14100, 13600 and 13200 cm^{-1} for **3**, **4**, **5** and **6**, respectively), the relatively higher energy of this triply-bridged dinuclear species is unusual for the square-pyramidal geometry. However, they are consistent with those observed for the related dpyam, bpy and phen complexes [10–12] and the $d_{xy}, d_{yz} \rightarrow d_{x^2-y^2}$ and $d_{xz}, d_{z^2} \rightarrow d_{x^2-y^2}$ transitions are assigned for a broad band and a lower energy shoulder, respectively.

3.4. EPR and magnetic properties

The X-band EPR was measured on polycrystalline samples at RT and 77 K for all six compounds. All compounds (except compound **2**) showed at RT and at 77 K broad bands at the high field and at the low field side both at RT and 77 K, typical for triplet $S = 1$ signal with a large zero-field splitting. The occurrence of other peaks at high field indicates that the axial zero-field splitting parameter D is larger than the EPR quantum (ca. 0.3 cm^{-1}). No attempts were undertaken to determine the value of the zero-field splitting. Compound **1** shows,

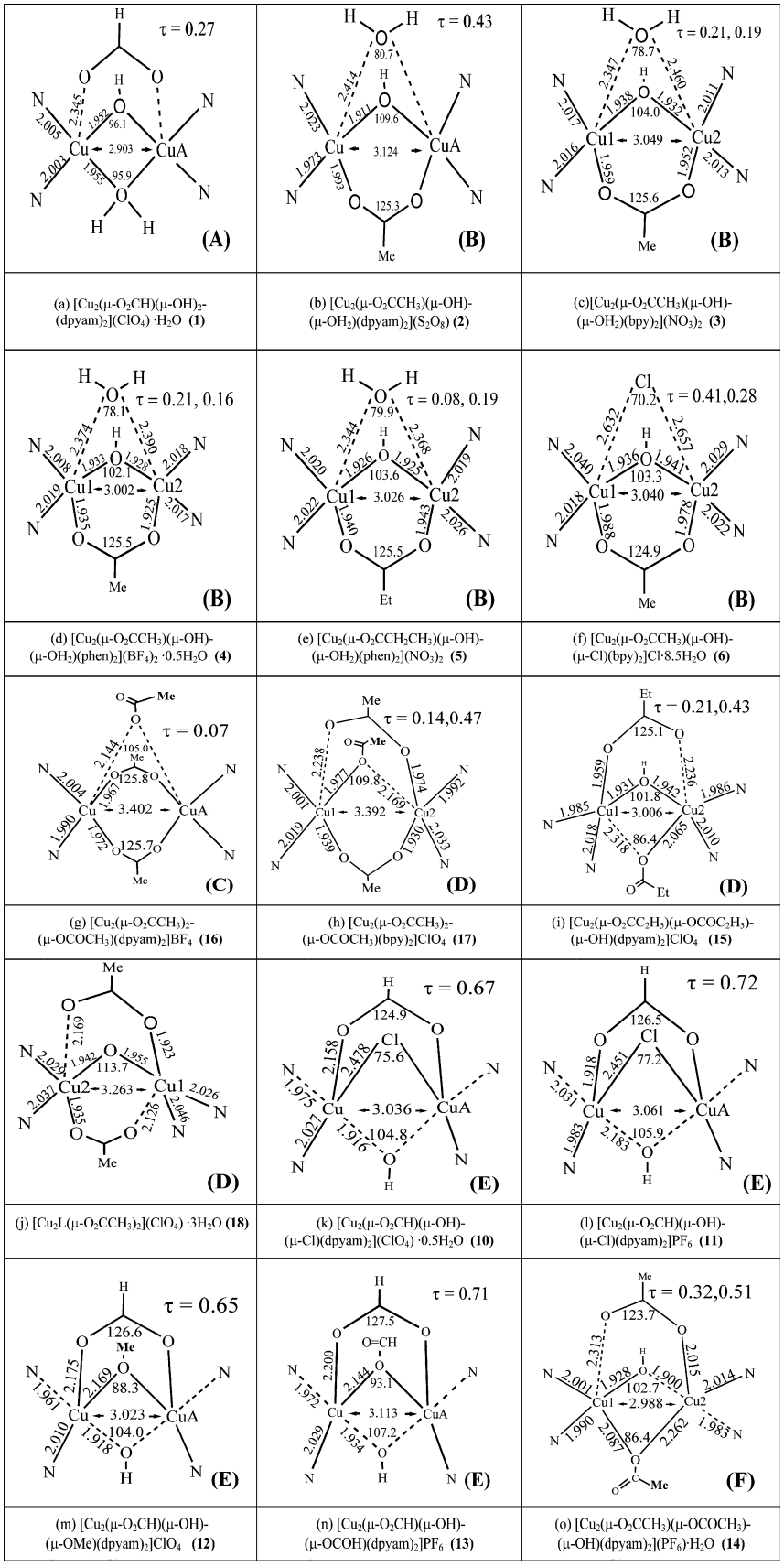
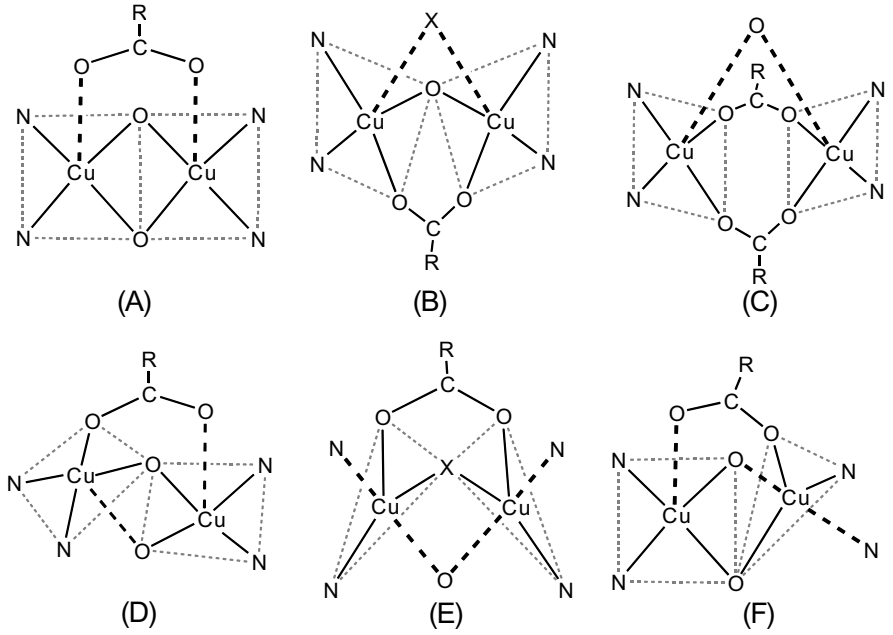


Fig. 6. Comparison of triply-bridged Cu(II) chromophores.



Scheme 1.

however, a somewhat more complicated $S = 1$ signal, which is stronger and more pronounced at 77 K (see Figs. S6 and S7), while compound **2** shows a peculiar, very broad signal at $g = 2.08$ and a small hump at $g = 24$ (see Fig. S8). All spectra also contain at around 320 mT a weak signal which arrises from a monomeric impurity, which is almost always present in dinuclear compounds. In compound **6** this signal is rather strong and sharp. Detailed analysis is not possible as the signals are too weak and too broad at 77 K, and as EPR at 4 K is not available. The same type of spectra was also observed for other triply-bridged compounds [10–12].

To investigate the magnetic behavior in more detail we undertook magnetic susceptibility measurements from 5 to 250 K for a selection of compounds, i.e. **1**, **4** and **6**. The susceptibility measurements from the other three compounds (**2**, **3** and **5**) did not give clear data, probably due to the fact that the structure gradually changes upon cooling and/or loosing solvent in the lattice. The magnetic properties are depicted in Figs. 7–9, for compounds **1**, **4** and **6**, respectively, in the form of μ_{eff} versus T plots for two Cu(II) ions. All three compounds show a similar behaviour. At 250 K the μ_{eff} is 2.75 μ_B per 2 Cu ions for compound **1** (2.64 μ_B, for **4** and 2.68 μ_B, for **4**) which agrees reasonable with the spin-only value calculated for two uncoupled spin $S = 1/2$ Cu(II) centres. Upon cooling μ_{eff} raises gradually to reach 2.87, 2.81 and 2.79 μ_B, at around 30 K, for compounds **1**, **4** and **6**, respectively. This behaviour is typical for a ferromagnetically coupled Cu(II) dinuclear compounds. Below that temperature, μ_{eff} then diminishes till a value around 2.47 μ_B for compound **1** (2.77 μ_B for **4** and 2.73 μ_B for **6**) at 5 K for the three compounds, which may originate from intermolecular antiferromagnetic interactions, and/or from zero-field splitting of the $S = 1$ state of the dinuclear species. The theoretical expression for the magnetic susceptibility for two interacting $S = 1/2$ centres, based on the general Hamiltonian [31] is: $H_{\text{ex}} = -JS_1S_2$, in which the exchange parameter J, is negative for antiferromagnetic and positive for ferromagnetic interaction. The magnetic data were fitted to the equation given in the literature for dinuclear copper compounds [31]: $\chi_m = (2Ng^2\beta^2)[kT - (2zJ'/(3 + \exp(-J/kT)))]^{-1}$ $[3 + \exp(-J/kT)]^{-1}(1 - p) + \chi_p p + \text{TIP}$, in which N, g, β, k and T have their usual meanings [31]. The parameter p denotes the fraction of paramagnetic impurity in the sample and zJ' the interaction between neighbouring dinuclear identities. A temperature independent paramagnetism (TIP) was also considered and fixed at 60×10^{-6} per copper ion. The fit was accomplished by minimisation of $R = \sum(\chi_m \cdot T_{\text{calc}} - \chi_m \cdot T_{\text{obs}})^2/(\chi_m \cdot T_{\text{obs}})^2$ by least-squares procedure.

The best fit was obtained for compound **1** with the following values: $J = 112.7\ \text{cm}^{-1}$, $g = 2.09$, $zJ' = -10.0\ \text{cm}^{-1}$, $p = 0.06$, with a final R of 2.0×10^{-3} (see solid line in Fig. 7). For compound **4** these values are $J = 120.8\ \text{cm}^{-1}$, $g = 1.98$, $zJ' = -0.21\ \text{cm}^{-1}$, $p = 0.0$, with a final R of $2.0 \cdot 10^{-3}$ (see solid line in Fig. 8). For compound **6** these values are $J = 145.3\ \text{cm}^{-1}$, $g = 1.98$, $zJ' = -0.8\ \text{cm}^{-1}$, $p = 0.06$, with a final R of 4.0×10^{-4} (see solid line in Fig. 9).

4. Magneto-structural correlation

For planar dihydroxido-bridged copper(II) dinuclear species, a linear correlation between the Cu–O–Cu bridging angle and the singlet–triplet energy gap (J) was first observed by Hodgson and co-workers [22,23]. An antiferromagnetic interaction is found when the Cu–O–Cu angle is larger than 97.5°, but when the Cu–O–Cu angle is smaller than 97.5°, a ferromagnetic interaction would be

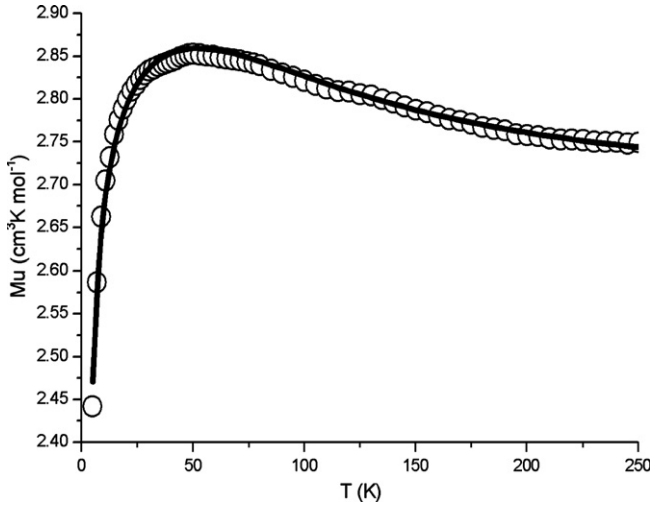


Fig. 7. A plot of the temperature dependence of μ_{eff} vs. T for compound **1**. The solid line represents the calculated curve (see text).

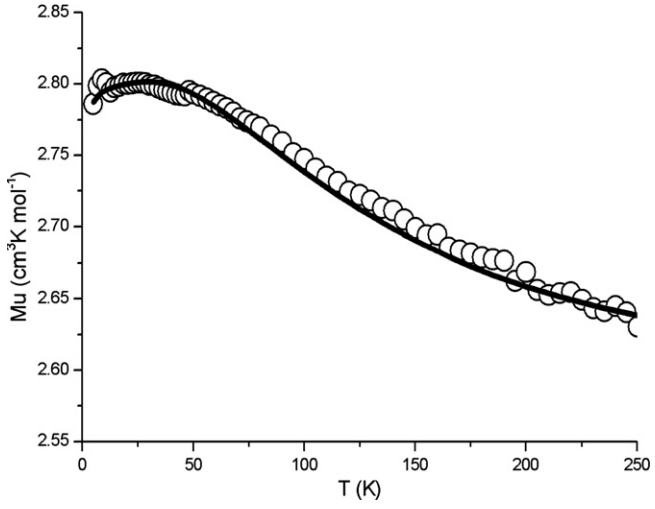


Fig. 8. A plot of the temperature dependence of μ_{eff} vs. T for compound **4**. The solid line represents the calculated curve (see text).

expected. Several theoretical approaches were applied to understand the behavior of the antiferromagnetic and ferromagnetic interaction of such dihydroxido-bridged copper(II) dinuclear species [22–27]. In this case, complex **1** can be analyzed using Hodgson and Hatfield's linear relationship to predict the magnetic properties in complex **1**.

Complex **1** exhibits a distorted square pyramidal geometry (class A), in which the unpaired electron is located in a $d_{x^2-y^2}$ type orbital. The $d_{x^2-y^2}$ magnetic orbital in **1** is directed toward the dihydroxido bridges, the Cu–O–Cu angles of 95.9° and 96.0°. For these bridging angles, a moderate ferromagnetic coupling ($J = 122.5\ cm^{-1}$) should be expected following Hodgson and Hatfield's linear relationship [22,23]. However, the tetrahedral distortion of the square bases may slightly reduce the magnitude of interaction. In fact, this feature can be predicted from the

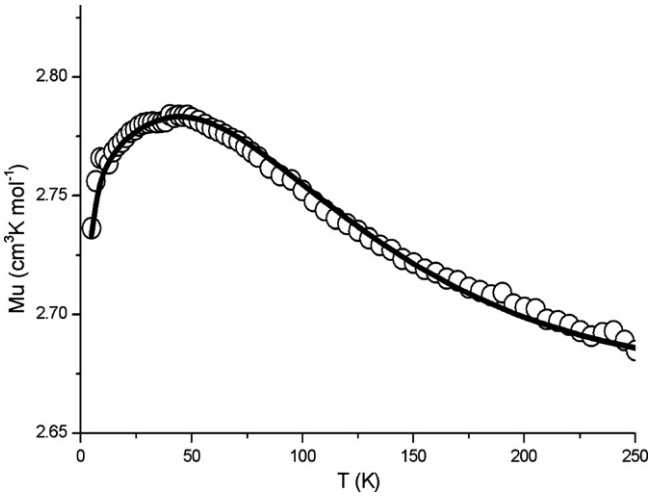


Fig. 9. A plot of the temperature dependence of μ_{eff} vs. T for compound **6**. The solid line represents the calculated curve (see text).

HOMO–LUMO energy gap using extended Hückel molecular orbital (EHMO) calculation (see Section 5).

Complexes **2**–**6** are classified in class B, Scheme 1 and Table 2, together with few relevant complexes with their previously reported J values, therefore the correlation between structure and magnetic exchange interaction can be performed for class B complexes with four data points (complexes **4**, **6**, **8**, **9**). These complexes offer the clear linear correlations in the plots of J versus Cu–OH–Cu (Fig. 10), J versus angle between basal planes (Fig. S9) and J versus Cu–Cu distance (Fig. S10). The J value increases upon increasing these structural parameters. Consequently, the J values of complexes **2**, **3** and **5** could be predicted to be 205.2, 146.1 and 142.0 cm^{-1}, respectively, following the J versus Cu–OH–Cu plot (see Fig. 10). However, a large number of the detailed structures and their magnetic properties are required for a clear correlation to be observed. An explanation for such a trend can be made in term of countercomplementary effect between the hydroxido bridge which generates ferromagnetic interaction due to the orbital orthogonality and one triatomic bridge in *syn–syn*. equatorial–equatorial configuration which usually contributes a weak antiferromagnetic interaction.

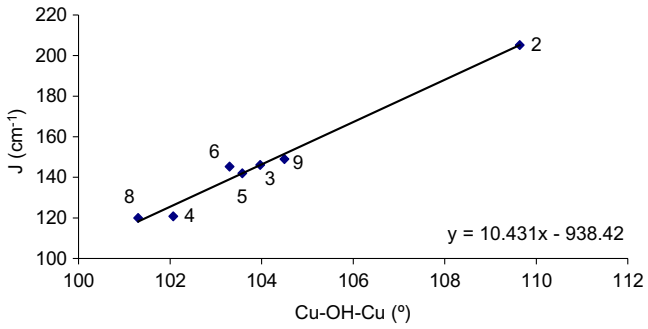


Fig. 10. Plot of J (cm^{-1}) vs. Cu–OH–Cu (°) for class B, the data points of complexes **2**, **3** and **5** are expected from this linear correlation.

Table 3
Energies and participation of atomic orbitals in HOMO and LUMO orbitals calculated for complexes **1**–**6**

Compound	**1**	**2**	**3**	**4**	**5**	**6**
Energy GAP between HOMO and LUMO orbitals (eV)	0.55	0.005	0.115	0.147	0.134	0.019
HOMO Cu d orbitals participation (%)	30	32	35	34	37	25
HOMO N p orbitals participation (%)	22	22	25	20	18	4
HOMO bridge O p orbitals participation (%)	8	3	2	2	5	12
LUMO Cu d orbitals participation (%)	4	32	34	36	34	28
LUMO N p orbitals participation (%)	20	21	18	15	14	5
LUMO bridge O p orbitals participation (%)	<1	<1	2	3	2	12

Class C complex **16** (see Table 2) revealed a moderate antiferromagnetic interaction with a J value of $-55\ cm^{-1}$, a similar trend found for the classical dinuclear paddle-wheel copper(II) species with four bridges, but with a different number of carboxylate bridges in complex **16**, leading to a smaller J value compared to those of the dinuclear paddle-wheel copper(II) species ($J = -142$ to $-300\ cm^{-1}$).

A possible magnetic exchange pathway for class-D complexes (see Fig. 6 and Table 2) is a single Cu–OH–Cu (101.8°) unit for complex **15** and a triatomic carboxylato bridge for complex**17** which links Cu(II) centres in an equatorial–equatorial configuration. This structure can occur with less electron density due to the nearly intermediate geometry ($\tau = 0.43$ for **15** and 0.47 for **17**) of one Cu(II) centre. Consequently, another possible pathway with less electron density is the triatomic carboxyato bridge for **15** and the monoatomic carboxylato Cu–O–Cu unit (109.8°) for **17**. Hence, a small J value ($24.5\ cm^{-1}$ for **15** and $3.6\ cm^{-1}$ for **17**) observed for both complexes may result from a countercomplementary effect between the monoatomic bridge with a small bridging angle which usually contributes the ferromagnetic interaction due to the orthogonality between the copper magnetic orbitals and the oxygen p-orbital, and the triatomic carboxylato bridge which usually contributes to an antiferromagnetic interaction. Another unique orientation of three bridges in the class-D complex was found in $[Cu_2L(\mu\text{-}O_2CCH_3)_2](ClO_4)\cdot 3H_2O$ (**18**) where LH = 2,6-bis(*N*-methypiperazino)methyl-4-chlorophenol (see Fig. 6 and Table 2) in which a possible pathway occurs via the Cu–O–Cu unit with an equatorial–equatorial configuration and a large bridging angle of 113.7°, leading to a negative J value of $-72\ cm^{-1}$ [32]. It is quite clear that the antiferromagnetic contribution increases upon increasing this bridging angle, thus allowing electron delocalization along the Cu–O–Cu unit. The remaining two triatomic carboxylato bridges which link Cu(II) centres in an axial–equatorial configuration provide a minor influence on the magnetic exchange interaction of the compound.

Class E complexes have a moderate ferromagnetic interaction. The superexchange mechanism for these complexes may be described in term of orbital orthogonality between the copper magnetic orbitals and oxygen p-orbital via Cu–OH–Cu unit allowing two unpaired electrons spins paralleled. As a result, it seems to be reliable to mention that the dominant ferromagnetic interaction increases with increasing in bridging angle Cu···Cu distance (compounds **10**–**12**, Table 2) till a certain maximum value, then decreases (compounds **10**–**13**, Table 2). However, no clear correlation has been observed for class E complexes reported in the literature. Hence, more detailed structures and magnetic properties are required to study the magneto-structural correlation in class E complexes.

A class F complex revealed a weak ferromagnetic nature. The τ values of 0.32 and 0.51 of Cu centres indicate magnetic orbital mainly to be $d_{x^2-y^2}$ and intermediate between $d_{x^2-y^2}$ and d_{z^2}, respectively. This situation usually results in a weak ferromagnetic interaction. Additionally, the presence of the $\eta^1{:}\eta^1{:}\mu$-carboxylate with axial–equatorial configuration may lead to countercomplementary effect giving rise to a small J value, Table 2.

5. Theoretical calculations

Extended Hückel molecular orbital (EHMO) calculations have been carried out on complexes **1**–**6, 8** and **9** (see Table 2) with the CACAO program [16], keeping the overall molecular structure unchanged to establish the mechanism of magnetic superexchange interaction through the triple bridges. The singlet–triplet energy gap could decrease with decrease in antiferromagnetic interaction. As the results, the calculated HOMO–LUMO energy gap are 0.55, 0.005, 0.115, 0.147, 0.134, 0.133, 0.162 and 0.111 eV for **1**–**6**, **8** and **9**, respectively. The results imply that a small difference in energy gap has a large influence on the magnetic interactions, the overall ferromagnetic interaction increases with decrease in energy gap as show in Fig. S11. This plot can confirm the predicted J value for class B complexes. The HOMO and LUMO of class B complexes (**2**–**6**, **8** and **9**) are close in energy while the energy gap of **1** is significantly larger. The complexes **1**–**6** are clarified drawing the two corresponding molecular orbitals (Figs. S12–S17). In both MOs the magnetic orbitals are mainly centered in the $d_{x^2-y^2}$ copper orbitals, in agreement with the geometry of the metal ions. The HOMO of **1** is delocalized on the atomic orbitals of both hydroxido bridging ligands, no overlapping through both hydroxido bridges is observed for the LUMO. The important contribution of each Cu(II) ion of 15% is found in the HOMO and a few contribution (2%) of each Cu(II) ion is found in LUMO orbitals. A possible reason of the large

HOMO–LUMO energy gap is the determining factor for the antiferromagnetic contribution to J (singlet–triplet energy difference) of compound **1**. This is in agreement with the large singlet–triplet energy difference observed for planar hydroxido-bridged copper(II) complexes [33].

The HOMO and LUMO of **2** are slightly different in energy and the overlap through the OH and carboxylate bridges is small, resulting ferromagnetic interaction. In complex **2**, the important contribution of each copper(II) ion of 16% is found in HOMO orbital (see Table 3).

The HOMO and LUMO of **3**–**6** are delocalized on the atomic orbital of hydroxido and O of carboxylate bridging and absent in the OH_2 (complexes **3**–**5**) or Cl (complex **6**) bridging which are in the axial position for each complex (see Table 3). In complexes **3**–**6**, the important contribution in HOMO of one of the copper(II) ions (21%, 23%, 21%, 18% in **3**–**6**, respectively) and smaller contribution to the other one (14%, 11%, 16%, 7% in **3**–**6**, respectively) are found. The HOMO and LUMO are slightly different in energy and the overlap through the OH and carboxylate bridges is small. This feature should result in a ferromagnetic interaction that can occur through this bridging ligand, as there is the orthogonality between the copper molecular orbital and the oxygen orbital of the OH bridge. A summary of the results obtained from EH analysis performed for **1**–**6** is shown in Table 3. However, DFT calculations have generally superseded EHMO, but if the results are not significantly different then EHMO is sufficient and faster. The theoretical investigation of magnetic properties are well studied for the dihydroxido-bridged [28], paddle-wheel carboxylato-bridged [34] and azido-bridged [35] dinuclear copper(II) complexes while that for the triply-bridged dinuclear copper(II) complexes has not been reported so far.

6. Conclusions

As a summary, a family of dinuclear triply-bridged copper(II) complexes bearing carboxylato bridges has been classified in terms of their relative arrangements of both local copper(II) chromophores, geometries and carboxylate bridging modes into different classes (A–F) and the efforts have been made to develop the magneto-structural correlation. The most logical explanation for their different magnetic behaviors have been provided in order to gain better understanding in the influence of various types of structures on the sign and magnitude of magnetic exchange interaction in this family of complexes. The results obtained from the EH calculations have proven to be useful for the proper interpretation and correlation of the magnetic and structural data. Linear correlations have been found for class B complexes and revealed that small geometric deviations may produce large energy gaps and therefore significant differences in the magnitude of the magnetic exchange interaction. So, more compounds with a careful inspection of structural parameters combined with their magnetic properties are demanded for both experimental and theoretical analyses which may lead to a very good magneto-structural correlation and using also the more accurate DFT calculations. A better understanding of factors that favor ferromagnetism in this family of complexes is expected to be useful for the design of novel ferromagnetic materials.

Acknowledgements

The authors gratefully acknowledge The Thailand Research Fund (Grant Nos. RTA 4880008 and BRG 4980007) and the Center for Innovation in Chemistry: Postgraduate Education and Research Program in Chemistry (PERCH-CIC), Thailand, for financial support. The work described in the present paper has been supported by the Leiden University Study group WFMO (Werkgroep Fundamenteel Materialen Onderzoek). Financial support and coordination by the FP6 Network of Excellence ''Magmanet'' (contract number 515767) is kindly acknowledged.

Appendix A. Supplementary material

CCDC 654135, 654136, 654137, 654138, 654139 and 654140 contain the supplementary crystallographic data for **1**, **2**, **3**, **4**, **5** and **6**. These data can be obtained free of charge via http://www.ccdc.cam.ac.uk/conts/retrieving.html, or from the Cambridge Crystallographic Data Centre, 12 Union Road, Cambridge CB2 1EZ, UK; fax: (+44) 1223-336-033; or e-mail: deposit@ccdc.cam.ac.uk. Supplementary data associated with this article can be found, in the online version, at doi:10.1016/j.poly.2007.09.009.

References

[1] G. Christou, S.P. Perlepes, E. Libby, K. Folting, J.C. Huffman, R.J. Webb, D.N. Hendrickson, Inorg. Chem. 29 (1990) 3657.
[2] S.P. Perlepes, J.C. Huffman, G. Christou, Polyhedron 10 (1991) 2301.
[3] S.P. Perlepes, J.C. Huffman, G. Christou, S. Paschalidou, Polyhedron 14 (1995) 1073.
[4] T. Tokii, M. Nagamatsu, H. Hamada, M. Nakashima, Chem. Lett. (1992) 1091.
[5] W. Huang, D. Hu, S. Gou, H. Qian, H.-K. Fun, S.S.S. Raj, Q. Meng, J. Mol. Struct. 649 (2003) 269.
[6] B. Graham, M.T.W. Hearn, P.C. Junk, C.M. Kepert, F.E. Mabbs, B. Moubaraki, K.S. Murray, L. Spiccia, Inorg. Chem. 40 (2001) 1536.
[7] T.M. Rajendiran, R. Kannappan, R. Venkatesan, P.S. Rao, M. Kandaswamy, Polyhedron 18 (1999) 3085.
[8] I. Chadjistamatis, A. Terzis, C.P. Raptopoulou, S.P. Perlepes, Inorg. Chem. Commun. 6 (2003) 1365.
[9] M. Lubben, R. Hage, A. Meetsma, K. Byma, B.L. Feringa, Inorg. Chem. 34 (1995) 2217.
[10] S. Youngme, C. Chailuecha, G.A. van Albada, C. Pakawatchai, N. Chaichit, J. Reedijk, Inorg. Chim. Acta 357 (2004) 2532.
[11] S. Youngme, C. Chailuecha, G.A. van Albada, C. Pakawatchai, N. Chaichit, J. Reedijk, Inorg. Chim. Acta 358 (2005) 1068.
[12] C. Chailuecha, S. Youngme, C. Pakawatchai, N. Chaichit, G.A. van Albada, J. Reedijk, Inorg. Chim. Acta 359 (2006) 4168.
[13] A. Yatani, M. Fujii, Y. Nakao, S. Kashino, M. Kinoshita, W. Mori, S. Suzuki, Inorg. Chim. Acta 316 (2001) 127.
[14] V. McKee, M. Zvagulis, C.A. Reed, Inorg. Chem. 24 (1985) 2914.

[15] H. Chowdhury, S.K. Rahaman, R. Ghosh, S.K. Sarkar, M. Corbella, B.K. Ghosh, Inorg. Chem. Commun. 9 (2006) 1276.
[16] C. Mealli, D.M. Proserpio, J. Chem. Educ. 67 (1990) 399.
[17] Siemens. SAINT, Version 4 Software Reference Manual, Siemens Analytical X-ray Systems, Inc., Madison, WI, USA, 1996.
[18] G.M. Sheldrick, SADABS: Program for Empirical Absorption correction of Area Detector Data, University of Göttingen, Göttingen, Germany, 1996.
[19] Bruker, XSHELL, Version 6.12 Reference Manual, Bruker AXS, Inc., Madison, WI, USA, 1999.
[20] A.W. Addison, T.N. Rao, J. Reedijk, J. van Rijn, G.C. Verschoor, J. Chem. Soc., Dalton Trans. (1984) 1349.
[21] M.S. Haddad, S.R. Wilson, D.J. Hodgson, D.N. Hendrickson, J. Am. Chem. Soc. 103 (1981) 384.
[22] V.H. Crawford, H.W. Richardson, J.R. Wasson, D.J. Hodgson, W.E. Hatfield, Inorg. Chem. 15 (1976) 2107.
[23] J.A. Barnes, D.J. Hodgson, W.E. Hatfield, Inorg. Chem. 11 (1972) 144.
[24] P.J. Hay, J.C. Thibeault, R. Hoffmann, J. Am. Chem. Soc. 97 (1975) 4884.
[25] A. Bencini, D. Gatteschi, Inorg. Chim. Acta 31 (1978) 11.
[26] L. Banci, A. Bencini, D. Gatteschi, J. Am. Chem. Soc. 105 (1983) 761.
[27] O. Kahn, M.F. Charlot, Inorg. Chem. 19 (1980) 1410.
[28] E. Ruiz, P. Alemany, S. Alvarez, J. Cano, Inorg. Chem. 36 (1997) 3683.
[29] K. Nakamoto, Infrared and Raman Spectra of Inorganic and Coordination Compounds: Part B, 5th ed., Wiley, New York, 1997.
[30] B.J. Hathaway, in: G. Wilkinson, R.D. Gill, J.A. McCleverty (Eds.), Comprehensive Coordination Chemistry, vol. 5, Pergamon Press, Oxford, 1987.
[31] O. Kahn, Molecular Magnetism, VCH, New York, 1993.
[32] K. Bertoncello, G.D. Fallon, J.H. Hodgkin, K.S. Murray, Inorg. Chem. 27 (1988) 4750.
[33] M.F. Charlot, O. Kahn, S. Jeannin, Y. Jeannin, Inorg. Chem. 19 (1980) 1410.
[34] M.E. Ali, S.N. Datta, J. Mol. Struct. (THEOCHEM) 775 (2006) 19.
[35] (a) E. Ruiz, J. Cano, S. Alvarez, P. Alemany, J. Am. Chem. Soc. 120 (1998) 11122;
(b) Y.S. Zhang, K.L. Yao, Z.L. Liu, J. Chem. Phys. 123 (2005) 124308.

Available online at www.sciencedirect.com
ScienceDirect
Polyhedron 27 (2008) 319–324
POLYHEDRON
www.elsevier.com/locate/poly

Synthesis of polylactide using a zinc complex containing (*S*)-*N*-ethyl-*N*-phenyl-2-pyrrolidinemethanamine

Jong Hwa Jeong [a,*], Young Hun An [a], Youn K. Kang [a], Quang Trung Nguyen [a], Hyosun Lee [a], Bruce M. Novak [b,*]

[a] *Department of Chemistry, Kyungpook National University, Taegu 702-701, Republic of Korea*
[b] *Department of Chemistry, North Carolina State University, Raleigh, NC 27695, United States*

Received 16 July 2007; accepted 13 September 2007
Available online 30 October 2007

Abstract

The reaction between $ZnCl_2$ and (*S*)-*N*-ethyl-*N*-phenyl-2-pyrrolidinemethanamine (***S*-EPP**) as a chiral ligand affords [$\mathbf{ZnCl_2}$(***S*-EPP**)], whose structure has been determined by X-ray crystallography. [$\mathbf{ZnEt_2}$(***S*-EPP**)] has demonstrated high activity toward the polymerization of *rac*-lactide with a maximum turnover frequency (TOF) of 121. Despite the intended stereocontrol by employing a chiral ligand, however, the observed heterotacticity was limited to under 0.6. The MWDs of the PLAs were found to be modulated by changing the solvent or controlling the concentration of the monomer in the solution. The glass transition temperature (T_g) was critically dependent on the MW within the narrow MWD regime, but the dependence became significantly shallow when the MWD was broadened.
© 2007 Elsevier Ltd. All rights reserved.

Keywords: (*S*)-*N*-ethyl-*N*-phenyl-2-pyrrolidinemethanamine; Chiral zinc complex; Polylactide; Stereocontrol of polylactide; X-ray structure

1. Introduction

Environmental pollution by the disposal of non-degradable plastics has emerged as a major concern worldwide. Poly(lactic acid) or polylactide (PLA), first synthesized half a century ago [1,2] has attracted great interest in recent years as a new environmentally friendly plastic material, not only because it degrades several orders of magnitude faster than petroleum-based polymers and thus can be composted locally into soil amendments but also it requires 30–50% less fossil fuel during the production step [3]. Also importantly, PLA's raw material is from annually renewable resources such as corn and sugar beats while many other polymers' are from continuously depleting petroleum sources. Despite these green benefits, the primary application of this material still remains in the medicinal purpose where the benefits of performance and the economical cost intersect. While its applications continue to expand to commodity purposes that include film, fiber and non-woven materials, the replacement of petroleum-based polymers, especially PET and flexible PVC, by PLA is expected to be accelerated as demands for preserving the environment are increasing.

The synthetic protocol of this material is mostly by the ring-opening polymerization of lactides [4]. This approach has been clearly advantageous in terms of a higher polymerization rate, a higher molecular weight, and a better conversion. A number of different kinds of metals have been used towards this purpose that include not only the relatively non-hazardous lithium [5,6], magnesium and zinc [7–10], aluminum [7,11–16], and iron [17,18], but also the highly toxic tin [4,9,19–22], lead and bismuth [23], and lanthanides [24–29]. Although many commercial PLAs with high molecular weight are currently produced by toxic transition metal catalysts, it is highly desirable for these catalyst residues to be completely absent in the final

* Corresponding authors. Tel.: +82 53 950 6343; fax: +82 53 950 6330 (J.H. Jeong).
E-mail address: jeongjh@knu.ac.kr (J.H. Jeong).

0277-5387/$ - see front matter © 2007 Elsevier Ltd. All rights reserved.
doi:10.1016/j.poly.2007.09.021

product for biomedical and food packaging applications. Since it is practically unviable to remove catalyst residues completely from the polymer, the use of environmentally friendly catalyst species must be a good approach.

The stereochemical control of PLA's microstructures has emerged as an important issue to establish the structure-property relationship of the PLA [3]. High P_r (the probability of a *R*,*R*-lactide unit to be enchained after a *S*,*S*-lactide unit or vice versa) values of over 0.90, for example, have been reported by Coates et al. [10] for the polymerization reaction of *meso*-lactide by employing the achiral catalyst [(BDI)Zn(O^{i}Pr)]$_2$ [(BDI) = 2-((2,6-dialkylphenyl)amido)-4-((2,6-diiso-propylphenyl)imino)-2-pentene]. However, only a limited body of work has been accumulated for the investigation of the microstructure related properties. More studies are thus necessary for a wider application of this material.

Within this view, we attempted to prepare PLA with a newly synthesized zinc catalyst containing (*S*)-*N*-ethyl-*N*-phenyl-2-pyrrolidinemethanamine (***S*-EPP**). The design motives of this catalyst species involve: (1) the use of non-toxic zinc as a central metal of the catalyst, (2) the incorporation of the chiral ***S*-EPP** ligand, which can be easily prepared from relatively inexpensive *L*-proline and possibly control the PLA's microstructure by stereospecific polymerization [30] (3) the easy synthesis of catalyst species by simple mixing of diethylzinc and the ***S*-EPP** ligand. Herein, we report the polymerization reaction of *rac*-lactide with the [**ZnEt$_2$**(***S*-EPP**)] complex. The X-ray crystal structure of the dichloro derivative of the catalyst species, [**ZnCl$_2$**(***S*-EPP**)], is also described.

2. Experimental

2.1. Materials

All manipulations were carried out under nitrogen prepurified by passage through an O_2 scrubbing tower (Schweizerhall R3-11 catalyst) and a drying tower (Linde 3Å molecular sieves) unless otherwise noted. Standard Schlenk techniques were employed to manipulate air sensitive materials. All solvents were purchased from Duksan Chemical Co. (reagent grade). Tetrahydrofuran (THF) and toluene were dried over Na/benzophenone ketyl, while CH_2Cl_2 was dried over CaH_2; these solvents were subsequently distilled from these reagents under nitrogen prior to use. The *rac*-Lactide was purchased from Aldrich and was sublimed prior to use. Zinc chloride and diethylzinc (1.1 M in toluene) were purchased from Aldrich. ***S*-EPP** was prepared as described in the literature [30].

2.2. Instrumentation

NMR spectra were recorded on a 400-MHz Bruker AD 400 FT NMR spectrometer. Chemical shifts for ^{1}H NMR spectra are relative to residual protons in the deuterated solvents ($CDCl_3$, $\delta = 7.24$). All coupling constants are reported in Hz. Gel permeation chromatography (GPC) analyses were carried out on a Waters Alliance GPCV2000, equipped with differential refractive index detectors. The GPC columns were eluted with tetrahydrofuran with a 1 ml/min rate at 25 °C and were calibrated with monodisperse polystyrene standards. Glass transition temperatures were measured on an Auto DSC 2910 system (TA instruments).

2.3. Synthesis of [*ZnCl$_2$*(***S*-EPP**)]

A 100 ml one-necked round-bottomed flask was charged with ***S*-EPP** (1.26 g, 6.19 mmol), $ZnCl_2$ (0.84 g, 6.16 mmol) and THF (20 ml). The mixture was stirred at room temperature for 3 days and then the solvent was removed under reduced pressure. The residual solids were dissolved in CH_2Cl_2 and filtered through a filter paper. The filtrate was evaporated in vacuo to afford white solids. Recrystallization of the crude product from the solvent pair of CH_2Cl_2/hexane gave white crystals (2.04 g, 97% yield). ^{1}H NMR (300 MHz, $CDCl_3$): δ 7.60 (d, 2H), 7.43 (t, 2H), 7.30 (t, 1H), 3.7–3.5 (m, 2H), 3.4–3.2(m, 3H), 2.06 (m, 1H), 1.83 (m, 1H), 1.59 (m, 1H), 0.97 (t, 3H).

2.4. Polymerization reaction with in situ generated [*ZnEt$_2$*(***S*-EPP**)]

To a 100 ml storage tube charged with $ZnEt_2$ (5.6 ml of 1.1 M solution in toluene, 6.2 mmol) and toluene (22 ml) was added ***S*-EPP** (1.26 g, 6.2 mmol in 5 ml toluene) at room temperature. After being stirred for 1 h, the resulting catalyst solution was used for the polymerization reaction. The general procedure for the polymerization reaction was as follows. A 100 ml Schlenk flask was charged with *rac*-Lactide (1.5 g, 10.4 mmol) and toluene (5 ml). The reaction was initiated by adding the catalyst solution (0.5 ml, 0.1 mmol) using a syringe. The reaction mixture was stirred at ambient temperature. This mixture was washed with water and all volatiles were removed under reduced pressure to obtain white crumbly solids (1.5 g, 99% based on *rac*-Lactide). ^{1}H NMR(400 MHz, $CDCl_3$): δ 5.19–5.04 (m, 1H), 1.52–1.47 (m, 3H).

2.5. X-ray crystallographic analysis

An X-ray quality single crystal of [**ZnCl$_2$**(***S*-EPP**)] was mounted in a thin-walled glass capillary on an Enraf-Noius CAD-4 diffractometer with Mo Kα radiation ($\lambda = 0.71073$ Å). Unit cell parameters were determined by least-squares analysis of 25 reflections ($10° < \theta < 13°$). Intensity data were collected with the θ range 1.88–24.97° in the $\omega/2\theta$ scan mode. Three standard reflections were monitored every 1 h during data collection. The data were corrected for Lorentz-polarization effects and decay. Empirical absorption corrections with ψ-scans were applied to the data. The structure was solved by using the Patterson method and refined by full-matrix least-

Table 1
Crystal data and structure refinement for [**ZnCl$_2$(*S*-EPP)**]

Empirical formula	$C_{13}H_{20}Cl_2N_2Zn$
Formula weight	340.58
Temperature (K)	293(2)
Wavelength (Å)	0.71073
Crystal system	monoclinic
Space group	$P2_1/c$
Unit cell dimensions	
a (Å)	9.8105(4)
b (Å)	11.1762(6)
c (Å)	14.400(1)
β (°)	92.940(4)
Volume (Å^3)	1576.7(1)
Z	4
D_{calc} (Mg/m^3)	1.435
Absorption coefficient (mm^{-1})	1.882
$F(000)$	704
Crystal size (mm)	$0.45 \times 0.45 \times 0.40$
θ Range for data collection (°)	2.31–25.47
Index ranges	$0 \leqslant h \leqslant 11$, $0 \leqslant k \leqslant 13$, $-17 \leqslant l \leqslant 17$
Reflections collected/unique [R_{int}]	3215/2926 [0.0102]
Reflections observed ($>2\sigma$)	2437
Data completeness	1.000
Refinement method	full-matrix least-squares on F^2
Data/restraints/parameters	2926/0/168
Goodness-of-fit on F^2	1.0651
Final R indices [$I > 2\sigma(I)$]	$R_1 = 0.024$, $wR_2 = 0.065$
R indices (all data)	$R_1 = 0.034$, $wR_2 = 0.067$
Largest difference in peak and hole (e Å^{-3})	0.321 and −0.237

squares techniques on F^2 using SHELXS-97 and SHELXL-97 program packages [31,32]. All hydrogen atoms were refined, positioned geometrically using the riding model with fixed isotropic thermal factors ($U = 0.08$ Å^2). The final cycle of the refinement converged with $R_1 = 0.034$ and $wR_2 = 0.067$. Crystal data, details of the data collection and refinement parameters are listed in Table 1.

3. Results and discussion

3.1. Synthesis and X-ray crystal structure of the [*ZnCl$_2$-(S-EPP)*] complex

[**ZnCl$_2$(*S*-EPP)**] was synthesized by a simple mixing of the ***S*-EPP** ligand and $ZnCl_2$ in THF solvent. The complexation reaction proceeded smoothly at room temperature and the product was easily purified by recrystallization. A single crystal suitable for X-ray crystallography was obtained by diffusional crystallization of [**ZnCl$_2$(*S*-EPP)**] in CH_2Cl_2 and hexane. The ORTEP drawing of the complex is shown in Fig. 1, with atomic labelling for non-hydrogen atoms. Selected bond distances and angles are listed in Table 2. The geometry of the complex is basically a tetrahedron comprising the zinc metal as a center linked with two N atoms of the ***S*-EPP** ligand in a bidentate coordination mode along with two chloro ligands. The Cl–Zn–Cl and N–Zn–N bond angles are 115.58(2)° and 86.66(7)°, respectively. These values are surprisingly similar with those found in dichloro(*N*,*N*,*N*′-trimethylethylenediamine)zinc(II) [33], which has a similar skeleton to [**ZnCl$_2$(*S*-EPP)**]. The average value of the N–Zn–N angle in TMEDA/zinc complexes (TMEDA = tetramethylethylenediamine) found in the Cambridge Structural Database (CSD) is 84.3 ± 2.7° [33]. The Zn–N bond distances are 2.036(2) Å for Zn–N(1) and 2.132(2) Å for Zn–N(2). The corresponding values for the dichloro(*N*,*N*,*N*′-trimethylethylenediamine)zinc(II) compound were 2.065(2) and 2.081(2) Å [33].

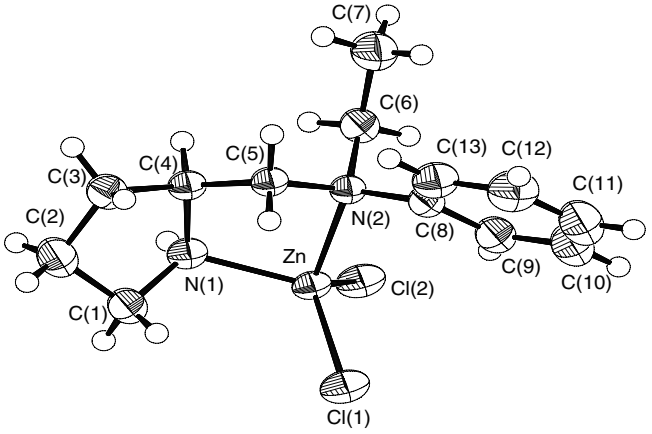


Fig. 1. An ORTEP drawing of [**ZnCl$_2$(*S*-EPP)**] with the numbering scheme.

Table 2
Selected bond lengths (Å) and angles (°) for [**ZnCl$_2$(*S*-EPP)**]

Zn–N(1)	2.036(2)	Zn–N(2)	2.132(2)
Zn–Cl(2)	2.2069(5)	Zn–Cl(1)	2.2191(5)
N(1)–C(1)	1.485(3)	N(1)–C(4)	1.497(2)
N(2)–C(8)	1.459(3)	N(2)–C(5)	1.494(2)
N(2)–C(6)	1.508(3)		
N(1)–Zn–N(2)	86.66(7)	N(1)–Zn–Cl(2)	117.13(5)
N(2)–Zn–Cl(2)	111.61(5)	N(1)–Zn–Cl(1)	112.09(5)
N(2)–Zn–Cl(1)	110.11(5)	Cl(2)–Zn–Cl(1)	115.58(2)
C(1)–N(1)–C(4)	105.7(2)	C(1)–N(1)–Zn	118.6(1)
C(4)–N(1)–Zn	108.6(1)	C(8)–N(2)–C(5)	112.9(2)
C(8)–N(2)–C(6)	110.2(2)	C(5)–N(2)–C(6)	112.9(2)
C(8)–N(2)–Zn	111.9(1)	C(5)–N(2)–Zn	99.4(1)
C(6)–N(2)–Zn	109.2(1)		

The synthesized [**ZnCl$_2$(*S*-EPP)**] has two stereogenic N atoms from the ligand (***S*-EPP**) possessing only one chiral center (Fig. 1). This is a diastereoselective reaction that gives rise to two chiral centers at the nitrogen atoms. Interestingly, the resolved structure was found to be enantiomerically pure, possessing two *S* configurations for both N(1) and N(2) atoms, respectively (*S*,*S*). The five-membered chelate ring made up of Zn–N(1)–C(4)–C(4)–N(2) atoms is thus in the λ-conformation. Being induced by the intrinsic chirality of the*S* configuration at the C(4) atom, the resulting *S* configuration at N(1) atom is not surprising. However, the *S* configuration at N(2) atom is not clear. Considering the

fact that this structural feature prevailed in the [(*S*)-2-(anilinomethyl)pyrrolidine-*N*,*N*′]chloro(η^6-*para*-cymene)ruthenium(II) chloride complex [34], one would expect that the *S* configuration at the N(2) atom might be thermodynamically favorable against the *R* configuration. Heat of formation data for two diastereomeric [**ZnCl$_2$**(***S*-EPP**)] complexes calculated by the PM3 method [35–37], however, were estimated to be −63.92 and −64.51 kcal/mol for the (*S*, *S*) and (*S*, *R*) configurations, respectively. The energy difference between these two enantiomers is only 0.59 kcal/mol, which is even smaller than the thermal energy at room temperature ($k_bT_{298} = 0.60$ kcal/mol). Since the difference in the entropic term for the two enantiomers is expected to be negligible, the observed crystal structure with only the (*S*, *S*) configuration is most likely due to packing effects.

3.2. Polymerization of rac-Lactide with in situ generated Zn catalyst

The polymerization reaction of *rac*-Lactide was carried out with in situ prepared Zn catalyst, [**ZnEt$_2$**(***S*-EPP**)]. The ***S*-EPP** ligand was mixed with diethylzinc in toluene at room temperature. Since an approximate pK_a value of pyrolidine is known to be ~44 in DMSO solvent [38], which is one of the highest among reported secondary amine compounds, and is expected to be further increased in a non-polar solvent, the chemical formula of the catalyst species is most likely [**ZnEt$_2$**(***S*-EPP**)]. This hypothesis can be supported by the work reported by Mimoun et al. in which two amine protons of (*S*,*S*)-*N*,*N*′-ethylenebis-(1-phenylethylamine) were not deprotonated after being reacted with dimethylzinc [39].

The polymerization reaction of *rac*-Lactide in three different solvents produced PLA in high conversion. The polymerization results are summarized in Table 3. In moderately polar CH_2Cl_2 and THF solvents, the polymerization reaction was completed within 1 h with a minimum 85% conversion. In non-polar toluene solvent, however, it took significantly more time to complete the reaction and the conversion varied from 43% to 99%. It should be noted that the relatively low conversions of entry 3 in THF and entries 7 and 8 in toluene (Table 3) were due to the unexpectedly early termination of the reaction by increased viscosity of the reaction mixture. Turnover frequency (TOF) calculated as moles of consumed lactide per moles of catalyst per hour ([Lactide]/[Cat]/h) was up to 121 (entry 2 in Table 3), indicating that the catalyst species is highly efficient for the formation of PLA.

Since it is commonly accepted that the polymerization reaction of lactide by an organometallic catalyst (or initiator) proceeds via a living polymerization mechanism [10,16], the number averaged molecular weight (M_n) of the polymer should be approximately $\sim C \times M \times R$, where *C* is the conversion, *M* is the molecular weight of the monomer, and *R* is the monomer/catalyst ratio. Observed M_n values of PLAs prepared in CH_2Cl_2 solvent were 13 700 and 26 000 for *R* values of 67 and 122, respectively. Although these values are a factor of ~1.5 larger than the theoretically calculated ones (8689 and 17 404) [10,16], it is important to note that both values are in good linear relationship. Slightly larger experimental M_n values relative to that of the theoretical counterparts are probably due to the reduction of the real catalyst amount by unexpected decomposition. Considering the fact that the conversion weighted theoretical M_n values are in good agreement with the experimental ones and the MWD of these polymers are near to 1, it is thus reasonable to affirm that the polymerization reactions of lactide by [**ZnEt$_2$**(***S*-EPP**)] in CH_2Cl_2 solvent are well controlled by a living polymerization mechanism.

The experimentally observed M_n values of PLAs are, however, not in a linear relationship with the theoretically calculated ones when the polymerization reaction was carried out in THF and toluene solvents. The ratio between experimentally observed M_n values and theoretically calculated ones varied 2.0–5.4 and 1.4–4.9 for the PLAs prepared in THF and toluene solvent, respectively. These large deviations even in the same solvent system cannot be merely explained by reduction of the catalyst amount

Table 3
Polymerization of *rac*-Lactide with in situ prepared [**ZnEt$_2$**(***S*-EPP**)]

Entry	Solvent	Concentration[a] (mM)	Time (h)	Conversion (%)	TOF	$M_n \times 10^3$	$M_w \times 10^3$	MWD	T_g (°C)
1[b]	CH_2Cl_2	3.47	1	90	60	13.7	18.5	1.35	41
2[c]		3.47	1	99	121	26.0	42.7	1.64	49
3[d]	THF	6.94	0.7	85	121	32.2	140.4	4.41	53
4[d]		3.47	0.8	93	116	48.1	75.2	1.56	50
5[d]		2.31	1	95	95	34.1	45.8	1.34	41
6[d]		1.73	1	99	99	41.8	56.3	1.34	49
7[d]	toluene	4.63	3	43	14	17.2	41.2	2.39	52
8[d]		3.47	4	76	19	40.6	99.3	2.45	55
9[d]		2.31	5	91	18	38.7	101.5	2.63	52
10[d]		1.73	7	99	14	46.5	111.5	2.40	53
11[d]		1.39	9	99	11	24.3	45.3	1.86	40

[a] Concentration of *rac*-Lactide.
[b] [Monomer]/[Cat] = 67.
[c] [Monomer]/[Cat] = 122.
[d] [Monomer]/[Cat] = 100.

due to the contamination. We thus emphasize that these results involve other factors as well. It should be noted that the MWDs of PLAs prepared in toluene were broader than those prepared in CH_2Cl_2 ($2.39 \leqslant MWD \leqslant 2.63$, entries 7–10 in Table 3). Even the MWD of PLA prepared from a high concentration solution of monomer in THF (6.94 mM) was exceptionally high (MWD = 4.41, entry 3 in Table 3). These results are most likely due to the fact that all the monomers were not in the solution phase, which causes inhomogeneity around the catalyst species during the polymerization process, and thus breaks the living polymerization condition.

The trend of the glass transition temperature (T_g) in relation to molecular weight and MWD deserve comments. In general, T_g of PLA is linearly dependent on the molecular weight until it reaches its maximum [18,40]. The T_g values of commercial PLA are in the range 55–70 °C for $100\,000 \leqslant M_w \leqslant 300\,000$. The tendency that T_g is dependent on molecular weight of PLA prevails in our results when the MWD is narrow (entries 1–6 in Table 3 except 3). However, to the PLAs synthesized in toluene solvent in which MWD is over 2 (entries 7–10 in Table 3), values of T_g were confined to within 52–55 °C over the $41\,200 \leqslant M_w \leqslant 112\,000$ range (Fig. 2). The relation between MWD and T_g has not been respected very much, probably due to the fact that most PLAs synthesized by the ring opening polymerization method in academic laboratories have MWD values near 1.0 [10,16]. Considering the effort devoted to lowering the T_g of PLA in order to reduce the brittleness of this polymer, the possibility to control T_g by a simple change of solvent and thus by modulating the MWD is worth further study.

Despite the intended stereocontrol of the PLA microstructure by employing a chiral catalyst, no pronouncing stereospecificity of PLA was observed. For instance, PLA

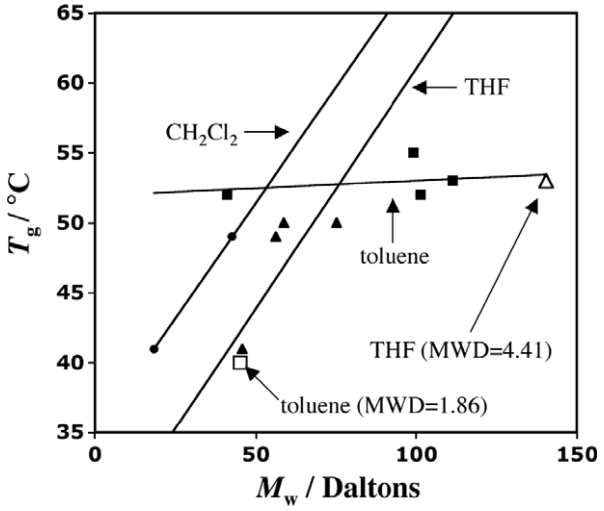


Fig. 2. The relation between T_g vs M_w of PLAs prepared in CH_2Cl_2 (circle), THF (triangle) and toluene (square) solvents. The open square and open triangle indicates entries 11 and 3 in Table 3, respectively.

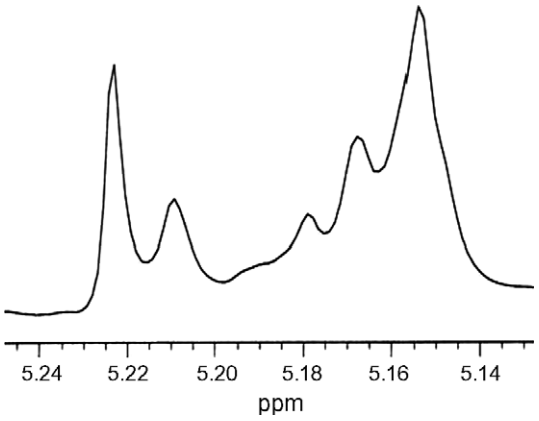


Fig. 3. Homonuclear decoupled ^1H NMR spectrum of PLA (for the preparation conditions, see entry 6 in Table 3).

synthesized in THF (entry 6 in Table 3) exhibit only 0.55 of heterotacticity (P_r), determined by homonuclear decoupled ^1H NMR spectra (Fig. 3) [41]. Given the very high heterotacticity ($P_r \geqslant 0.9$) of PLA polymerized with racemic [40] or achiral [10,42] catalysts, providing a chiral environment on the metal center by simply employing a chiral ligand might not be a clever approach for the stereochemical microstructure control of PLA.

4. Conclusion

The complex [**$ZnCl_2$(*S*-EPP)**] was synthesized for the first time and its structure was determined by X-ray crystallography. The diethyl derivative [**$ZnEt_2$(*S*-EPP)**], which is prepared in situ by the reaction of ***S*-EPP** ligand and $ZnEt_2$in toluene solvent, has demonstrated high activity on the polymerization of *rac*-Lactide, with a maximum TOF of 121. The polymerization reaction is controlled by the living polymerization mechanism due to the fact that the produced PLA has a narrow MWD near 1.0 and there is a linear dependence between the molecular weight and the catalyst/monomer ratio. However, the MWDs of PLAs were found to be modulated by changing the solvent or controlling the concentration of the monomer in the solution. T_g was critically dependent on the MW within the narrow MWD regime but the dependence became significantly shallow when the MWD was broadened. Despite the intended stereocontrol by employing a chiral ligand, the observed heterotacticity was limited to under 0.6.

Supplementary material

CCDC 654084 contain the supplementary crystallographic data for [**$ZnCl_2$(*S*-EPP)**]. These data can be obtained free of charge via http://www.ccdc.cam.ac.uk/conts/retrieving.html, or from the Cambridge Crystallographic Data Centre, 12 Union Road, Cambridge CB2 1EZ, UK; fax: (+44) 1223-336-033; or e-mail: deposit@ccdc.cam.ac.uk.

References

[1] E.M. Filachione, C.H. Fisher, US Patent, 1946, 2396994.
[2] T. Tsuruta, K. Matsuura, S. Inoue, Macromol. Chem. 75 (1964) 211.
[3] E. Chiellini, R. Solaro, Adv. Mater. 8 (1996) 305.
[4] W. Dittrich, R.C. Schulz, Angew. Macromol. Chem. 15 (1971) 109.
[5] H.R. Kricheldorf, C. Böttcher, Macromol. Chem. Phys. 194 (1993) 1665.
[6] B.T. Ko, C.C. Lin, J. Am. Chem. Soc. 123 (2001) 7973.
[7] H.R. Kricheldorf, M. Berl, N. Scharnagl, Macromolecules 21 (1988) 286.
[8] M. Bero, J. Kasperczyk, Z.J. Jedlinski, Macromol. Chem. Phys. 191 (1990) 2287.
[9] A.J. Nijenhuis, D.W. Grijpma, A.J. Pennings, Macromolecules 25 (1992) 6419.
[10] B.M. Chamberlain, M. Cheng, D.R. Moore, T.M. Ovitt, E.B. Lobkovsky, G.W. Coates, J. Am. Chem. Soc. 123 (2001) 3229.
[11] P. Dubois, C. Jacobs, R. Jerome, P. Teyssie, Macromolecules 24 (1991) 2266.
[12] N. Spassky, M. Wisniewski, C. Pluta, A. LeBorgne, Macromol. Chem. Phys. 197 (1996) 2627.
[13] T.M. Ovitt, G.W. Coates, J. Am. Chem. Soc. 121 (1999) 4072.
[14] C.P. Radano, G.L. Baker, M.R. Smith, J. Am. Chem. Soc. 122 (2000) 1552.
[15] N. Nomura, R. Ishii, M. Akakura, K. Aoi, J. Am. Chem. Soc. 124 (2002) 5938.
[16] P. Hormnirun, E.L. Marshall, V.C. Gibson, A.J.P. White, D.J. Williams, J. Am. Chem. Soc. 126 (2004) 2688.
[17] B.J. O'Keefe, S.M. Monnier, M.A. Hillmyer, W.B. Tolman, J. Am. Chem. Soc. 123 (2001) 339.
[18] X.Y. Wang, K.R. Liao, D.P. Quan, Q. Wu, Macromolecules 38 (2005) 4611.
[19] G. Schwach, J. Coudane, R. Engel, M. Vert, J. Polym. Sci., Part A: Polym. Chem. 35 (1997) 3431.
[20] K. Stridsberg, M. Ryner, A.C. Albertsson, Macromolecules 33 (2000) 2862.
[21] M. Moller, F. Nederberg, L.S. Lim, R. Kange, C.J. Hawker, J.L. Hedrick, Y.D. Gu, R. Shah, N.L. Abbott, J. Polym. Sci., Part A: Polym. Chem. 39 (2001) 3529.
[22] A. Finne, A.C. Albertsson, Biomacromolecules 3 (2002) 684.
[23] H.R. Kricheldorf, A. Serra, Polym. Bull. 14 (1985) 497.
[24] W.M. Stevels, M.J.K. Ankone, P.J. Dijkstra, J. Feijen, Macromolecules 29 (1996) 3332.
[25] V. Simic, N. Spassky, L.G. HubertPfalzgraf, Macromolecules 30 (1997) 7338.
[26] M.L. Yuan, C.D. Xiong, X.H. Li, X.M. Deng, J. Appl. Polym. Sci. 73 (1999) 2857.
[27] B.M. Chamberlain, Y.P. Sun, J.R. Hagadorn, E.W. Hemmesch, V.G. Young, R. Pink, M.A. Hillmyer, W.B. Tolman, Macromolecules 32 (1999) 2400.
[28] G.R. Giesbrecht, G.D. Whitener, J. Arnold, J. Chem. Soc., Dalton Trans. (2001) 923.
[29] M. Save, M. Schappacher, A. Soum, Macromol. Chem. Phys. 203 (2002) 889.
[30] M. Nakajima, I. Miyoshi, K. Kanayama, S. Hashimoto, M. Noji, K. Koga, J. Org. Chem. 64 (1999) 2264.
[31] G.M. Sheldrick, Program for the Solution of Crystal Structure, University of Göttingen, Göttinger, Germany, 1997.
[32] G.M. Sheldrick, Program for Crystal Structure Refinement, University of Göttingen, Göttinger, Germany, 1997.
[33] A. Johansson, M. Hakansson, Acta Crystallogr., Sect. E: Struct. Rep. Online 60 (2004) M955.
[34] M. Aitali, L. El Firdoussi, A. Karim, A.F. Barrero, M. Quiros, Acta Crystallogr., Sect. C: Cryst. Struct. Commun. 56 (2000) 1088.
[35] J.J.P. Stewart, J. Comput. Chem. 10 (1989) 209.
[36] J.J.P. Stewart, J. Comput. Chem. 10 (1989) 221.
[37] J.J.P. Stewart, J. Comput. Chem. 12 (1991) 320.
[38] F.G. Bordwell, G.E. Drucker, H.E. Fried, J. Org. Chem. 46 (1981) 632.
[39] H. Mimoun, J.Y. de Saint Laumer, L. Giannini, R. Scopelliti, C. Floriani, J. Am. Chem. Soc. 121 (1999) 6158.
[40] T.M. Ovitt, G.W. Coates, J. Am. Chem. Soc. 124 (2002) 1316.
[41] K.A.M. Thakur, R.T. Kean, E.S. Hall, J.J. Kolstad, T.A. Lindgren, M.A. Doscotch, J.I. Siepmann, E.J. Munson, Macromolecules 30 (1997) 2422.
[42] M. Cheng, A.B. Attygalle, E.B. Lobkovsky, G.W. Coates, J. Am. Chem. Soc. 121 (1999) 11583.

Available online at www.sciencedirect.com
ScienceDirect
Polyhedron 27 (2008) 325–334
POLYHEDRON
www.elsevier.com/locate/poly

New antimony-capped iron(II) and cobalt(III) clathrochelate precursors of the polytopic hybrid cage complexes: Synthesis, X-ray structures and electrochemistry

Yan Z. Voloshin [a,*], Oleg A. Varzatskii [c], Alexander S. Belov [a], Zoya A. Starikova [a], Alexander V. Dolganov [b], Tatiana V. Magdesieva [b]

[a] *Nesmeyanov Institute of Organoelement Compounds RAS, 119991 Moscow, Russia*
[b] *Lomonosov Moscow State University, 119992 Moscow, Russia*
[c] *Vernadskii Institute of General and Inorganic Chemistry NASU, 03680 Kiev, Ukraine*

Received 6 July 2007; accepted 16 September 2007
Available online 31 October 2007

Abstract

Direct template macrocyclization of the three dimethylglyoxime molecules on the iron(II) ion and the capping of nonmacrocyclic K_3CoDm_3 tris-dimethylglyoximate with triethylantimony(V) derivatives led to the formation of triethylantimony-capped iron(II) and cobalt(III) clathrochelates. The complexes obtained have been characterized using elemental analysis, MALDI-TOF mass, IR, UV–Vis, ^{57}Fe Mössbauer and ^{1}H and ^{13}C NMR spectroscopies, and X-ray crystallography. The influence of the nature of an encapsulated metal ion, the capping groups and the chelate fragments on a clathrochelate framework geometry is discussed. The cyclic voltammograms show oxidation and reduction waves assignable to $Fe^{2+/3+}$ and $Co^{2+/3+}$ couples of the encapsulated metal ion.
© 2007 Published by Elsevier Ltd.

Keywords: Clathrochelates; Macrocyclic compounds; Cobalt complexes; Iron complexes; Antimony compounds; X-ray crystallography; Electrochemistry

1. Introduction

Polytopic d-metals cage complexes with relatively spacially and electronically independent fragments that are linked by a system of σ- and π-bonds, have been proposed as promising entities for the design of molecular (photo)electronic devices and mechanical molecular machines [1,2].

The synthesis of such complexes by a direct template reaction is hindered or not possible in principle. The polytopic hybrid iron(II) α-oximehydrazonates and α-dioximates have been obtained by transmetallation reactions of the initially synthesized labile antimony-capped precursors [1–3] (Fig. 1). However, the presence of only one reactive macrobicyclic precursor of apically functionalized hybrid tris-dioximate clathrochelates, the triethylantimony-capped $FeNx_3(Sb(C_2H_5)_3)_2$ complex (where Nx^{2-} is cyclohexandione-1,2-dioxime (nioxime) dianion), limits the possibilities for obtaining such hybrid polytopic compounds. Moreover, the cobalt complexes of this type, which are most promising for the development of mentioned above devices and machines because of the formation of stable species with an encapsulated metal ion in different oxidation states (usually, the encapsulated cobalt(II) and cobalt(III) ions), have not been synthesized previously.

Therefore, we attempted to synthesize the di(triethylantimony)-capped iron(II) and cobalt(III) clathrochelates, which are derivatives of the available dimethylglyoxime, as potential precursors of polytopic iron(II) and cobalt(II,III) cage compounds. Using the X-ray crystallography data obtained, we also discuss the influence of the nature of an encapsulated metal ion, the capping groups and the chelate fragments on a clathrochelate framework geometry.

* Corresponding author.
E-mail address: voloshin@ineos.ac.ru (Y.Z. Voloshin).

0277-5387/$ - see front matter © 2007 Published by Elsevier Ltd.
doi:10.1016/j.poly.2007.09.008

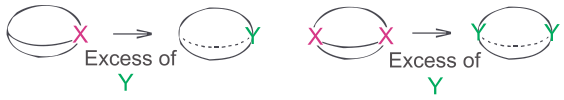


Fig. 1. Exchange of capping group(s) (transmetallation) reaction.

2. Experimental

2.1. General procedures

The reagents used, $FeCl_2 \cdot 4H_2O$, $CoCl_2 \cdot 6H_2O$, dimethylglyoxime (H_2Dm), sorbents, organic bases, and solvents were obtained commercially (Fluka). K_3CoDm_3 complex was prepared as described elsewhere [4]. The triethylantimony(V) dibromide was synthesized by known procedure [5]. The triethylantimony(V) carbonate was obtained from triethylantimony(V) dibromide with Na_2CO_3 in methanol.

The analytical, IR, UV–Vis, NMR, ^{57}Fe Mossbauer and electrochemicals data were obtained as described previously [2] (see Supplementary material for the experimental details, IR and NMR data).

2.2. Syntheses

2.2.1. $FeDm_3(Sb(C_2H_5)_3)_2$

$FeCl_2 \cdot 4H_2O$ (0.20 g, 1 mmol), dimethylglyoxime (0.38 g, 3.3 mmol) and $NaClO_4$ (1.5 g) were dissolved/suspended in methanol (15 ml) under argon. The reaction mixture was stirred at 50°C for 1.5 h and the solution of $(C_2H_5)_3SbCO_3$ (0.59 g, 2.2 mmol) in methanol (5 ml) was added. After stirring for 10 min, the reaction mixture was added dropwise to the stirring suspension of $CaCO_3$ (2 g) in 10% aqueous methanol (30 ml). The solution/suspension obtained was stirred for 30 min and then filtered. The precipitate was washed with methanol and dissolved in methylene dichloride. The methylene dichloride extract was filtered, evaporated to a small volume (~1.5 ml) and precipitated with hexane. The solid product was filtered, washed with hexane and dried *in vacuo*. Yield: 0.36 g (40%). *Anal.* Calc. for $C_{24}H_{48}N_6O_6FeSb_2$: C, 35.32; H, 5.94; N, 10.30; Fe, 6.84. Found: C, 35.20; H, 6.00; N, 10.31; Fe, 6.98%. MS (MALDI-TOF): *m/z* (*I*, %): 845(100) $[M + Et]^{+\cdot}$, 816(20) $[M]^{+\cdot}$, 729(70) $[M-3Et]^{+\cdot}$. UV–Vis (CH_2Cl_2): λ_{max}/nm ($\varepsilon \times 10^{-3}$, $mol^{-1}\,l\,cm^{-1}$) 270 (6.5), 300 (13), 330 (2.5), 355 (0.6), 389 (0.8), 424 (0.6), 450 (2.1), 476 (3.3), 536 (3.0).

2.2.2. $[CoDm_3(Sb(C_2H_5)_3)_2]Br$

Complex K_3CoDm_3 (1 g, 1.9 mmol) and $(C_2H_5)_3SbBr_2$ (1.55 g, 4.2 mmol) were dissolved in methanol (25 ml), the reaction mixture was stirred for 1 h and then rotary evaporated to dryness. The solid residue was washed with diethyl ether (20 ml) and filtered. The precipitate was washed with diethyl ether (30 ml, in 3 portions), and dissolved in methylene dichloride. The methylene dichloride solution was filtered and precipitated with hexane. The precipitate was washed with diethyl ether, reprecipitate from chloroform with hexane, washed with hexane and dried *in vacuo*. Yield: 0.90 g (50%). *Anal.* Calc. for $C_{24}H_{48}N_6O_6BrCoSb_2$: C, 32.06; H, 5.39; N, 9.35. Found: C, 32.22; H, 5.32; N, 9.41%. MS (MALDI-TOF): *m/z* 819 $[M-Br^-]^+$. UV–Vis (CH_2Cl_2): λ_{max}/nm ($\varepsilon \times 10^{-3}$, $mol^{-1}\,l\,cm^{-1}$) 256 (28), 278 (9.0), 299 (8.5), 337 (6.3), 382 (1.4), 408 (1.0).

2.3. X-ray crystallography

The details of crystal data collection and refinement parameters for $FeDm_3(Sb(C_2H_5)_3)_2$ and $[CoDm_3(Sb(C_2H_5)_3)_2]Br \cdot 2.5CHCl_3$ complexes are listed in Table 1. Single crystals of these complexes were grown from methylene dichloride – hexane and chloroform – heptane mixtures, respectively.

Data were collected with a Bruker SMART 1K CCD diffractometer using graphite monochromated Mo Kα radiation ($\lambda = 0.71073$ Å, ω-scans with a 0.3° step in ω and 10 s per frame exposure, $2\theta < 60°$) at 295 K $\{FeDm_3(Sb(C_2H_5)_3)_2\}$ and 120 K $\{[CoDm_3(Sb(C_2H_5)_3)_2]Br \cdot 2.5CHCl_3\}$. Reflections intensities were integrated using SAINT software [6] and corrected for absorption by semi-empirical method using SADABS program [7].

Due to the proximity of all angles to 90° in the $FeDm_3(Sb(C_2H_5)_3)_2$ unit cell, the choice of crystal system was done on the base of the detail analysis of the R_{int} values and systematic absences for all possible variants. All attempts to describe the crystal as a twin (monoclinic which emulate orthorhombic) gave no any change in the convergence factors as well as the standard deviations and residual Fourier electron density synthesis.

The structures were solved by the direct method and refined by full-matrix least squares method against F^2 of all data using SHELXTL-97 [8]. Non-hydrogen atoms were refined in anisotropic approximation (except for methyl groups in the $FeDm_3(Sb(C_2H_5)_3)_2$ molecules). Positions of hydrogen atoms were calculated and included in refinement in isotropic approximation by the riding model with $U_{iso}(H) = U_{eq}(C)$, where $n = 1.5$ for methyl groups and 1.2 for the other groups.

The terminal methyl groups in $FeDm_3(Sb(C_2H_5)_3)_2$ molecule are disordered at two positions with occupation 3:2 (C14 and C14′ atoms), 4:1 (C16 and C16′ atoms, C22 and C22′ atoms), 1:1 (C18 and C18′, C20 and C20′, C24 and C24′ atoms), and were included in refinement in isotropic approximation with constrained C–C bond lengths (1.50 Å). One of the chlorine atoms of one of the solvate chloroform molecules is disordered at two positions (Cl9 and Cl9′) with occupation 7:3.

3. Results and discussion

3.1. Synthesis

The synthesis of the labile in transmetallation reactions antimony-capped clathrochelates is a key step in the prep-

Table 1
Crystallographic data and experimental details for $FeDm_3(Sb(C_2H_5)_3)_2$ and $[CoDm_3(Sb(C_2H_5)_3)_2]Br \cdot 2.5CHCl_3$ complexes

	$FeDm_3(Sb(C_2H_5)_3)_2$	$[CoDm_3(Sb(C_2H_5)_3)_2]Br \times 2.5CHCl_3$
Empirical formula	$C_{24}H_{48}FeO_6N_6Sb_2$	$[C_{24}H_{48}CoO_6N_6Sb_2]^+ \times Br^- \ 2.5CHCl_3$
Formula weight	816.03	1197.44
Temperature (K)	295	120
Color, habit	dark-red, plate	yellow, plate
Crystal dimensions (mm)	$0.40 \times 0.30 \times 0.15$	$0.30 \times 0.25 \times 0.20$
a (Å)	27.443(3)	13.912(2)
b (Å)	14.475(2)	13.917(2)
c (Å)	8.577(1)	14.049(2)
α (°)	90.00	64.955(4)
β (°)	90.048(3)	75.246(3)
γ (°)	90.00	65.548(3)
V (Å^3)	3407.1(7)	2232.8(6)
Z	4	2
Crystal system	monoclinic	triclinic
Space group	$P2\bar{1}/c$	$P\bar{1}$
D_{cal} (g cm^{-3})	1.591	1.781
μ (mm^{-1})	0.2037	0.2954
Minimum/maximum transmission coefficient	0.453/0.665	0.472/0.802
θ_{max} (°)	0.74–26.00	1.62–27.50
Reflections collected	27966	16659
Independent reflections (R_{int})	6639 (R(int) = 0.0707)	9673 (R(int) = 0.0324)
Data/restraints/parameters	2985/0/346	6416/0/478
Weighting scheme	$1/\sigma_2(F_o^2) + (0.0012P)^2 + 0.3770P$, $P = 1/3(F_o^2 + 2F_c^2)$	$1/\sigma^2(F_o^2) + (0.0258P)^2 + 8.500P$, $P = 1/3(F_o^2 + 2F_c^2)$
R_1^a [$I > 2\sigma(I)$]	0.0617	0.0536
R_w^b	0.1748	0.1109
F(000)	1640	1182
Goodness-of-fit[c]	1.102	1.007
Maximum/minimum residual peak	1.017/−0.701	2.162/−0.687

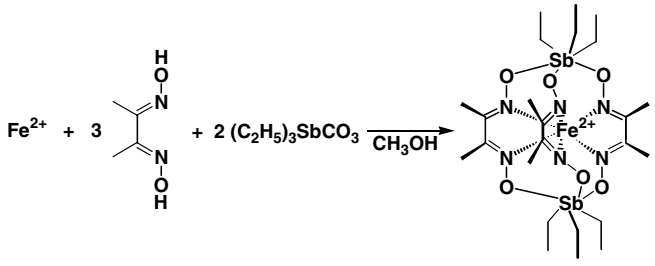
[a] $R_1 = (\sum \|\|F_o| - |F_c\|) / \sum |F_o|$.

[b] $R_w = \left[\sum (w(F_o^2 - F_c^2)^2) / \sum w(F_o^2)^2\right]^{1/2}$.

[c] $\mathrm{GOF} = \left[\sum (w(F_o^2 - F_c^2)^2) / (N_{obs} - N_{param})\right]^{1/2}$.

aration of macrobicycle-based hybrid compounds. While inert boron-, tin-, and germanium-capped clathrochelates can be synthesized in many cases using different pathways in high yields, the antimony-capped complexes are formed and isolated in the specific conditions only because of their lability. Therefore, the evaluation of such conditions is an important synthetic challenge.

The clathrochelate $FeDm_3(Sb(C_2H_5)_3)_2$ precursor was obtained by direct template macrocyclization of three dimethylglyoximate fragments with two molecules of a triethylantimony(V)-containing cross-linking agent as a Lewis acid



Scheme 1.

(Scheme 1) on the iron(II) ion matrix, analogous to the system for obtaining of the clathrochelate $FeNx_3(Sb(C_2H_5)_3)_2$ nioximate [9].

Despite the "one-pot" template synthetic procedure for the antimony-capped iron(II) clathrochelate, we failed to succeed with the same pathway for the synthesis of analogous cobalt(III) complex. Our attempts to use the nonmacrocyclic $Co(HDm)_3$ tris-dimethylglyoximate, initially synthesized by a known procedure [10], as a precursor led to a mixture of products, which was contaminated by paramagnetic Co^{2+} impurities. Further cross-linking of this mixture with triethylantimony(V) dibromide both in water and in methanol–water 1:1 medium in the presence of acetate buffer afforded mainly products that were insoluble in either chloroform or methylene dichloride. These products presumably had a polymeric structure, formed *via* cross-linking with Co^{2+} ions. As a result, either the yield of the target $[CoDm_3(Sb(C_2H_5)_3)_2]Br$ clathrochelate was low or the complex we obtained was contaminated by paramagnetic impurities. We also failed to obtain the target clathrochelate in water–methanol medium when we used the nonmacrocyclic tris-dimethylglyoximate $CoDm_3^{3-}$ anion as a precursor without isolating this initial complex from

the reaction mixture, because the clathrochelate product we obtained was also contaminated by paramagnetic impurities.

The nonmacrocyclic K_3CoDm_3 complex was isolated in the solid state as described in [4], and its reaction with $(C_2H_5)_3SbBr_2$ in methanol–water 1:1 mixture led to a light brown reaction mixture, which was extracted with chloroform. Most of the target product was found in this chloroform extract (the total yield was approximately 44%). In the same time, the initial K_3CoDm_3 complex was not extracted with chloroform from its aqueous solution. The reaction of nonmacrocyclic K_3CoDm_3 tris-dimethylglyoximate with $(C_2H_5)_3SbBr_2$ in methanol (Scheme 2) gave the target $[CoDm_3(Sb(C_2H_5)_3)_2]Br$ clathrochelate in 50% yield.

3.2. Structure and spectra

The parameters of ^{57}Fe Mössbauer spectrum of the $FeDm_3(Sb(C_2H_5)_3)_2$ clathrochelate (isomeric shift [IS] is equal to 0.33 mm/s; quadrupole splitting [QS] absolute value is equal to 0.24 mm/s) characterize it as low-spin complex of Fe^{2+} ion in the high field of the clathrochelate ligand. Because QSs for all antimony-capped clathrochelates have a negative sign [1–3], we suggested that QS for the $FeDm_3(Sb(C_2H_5)_3)_2$ complex also has a negative sign.

The solution ^1H and $^{13}C\{^1H\}$ NMR spectra of the diamagnetic iron(II) and cobalt(III) complexes we obtained confirmed the composition and C_3-symmetry of their molecules (in particular, the ratio of line integral intensities of the ethyl substituents in the apical capping triethylantimony fragment) and the methyl substituents in the α-dioximate chelate cycles in the ^1H NMR spectra as well as the number of signals of the carbon atoms of the clathrochelate framework, apical and ribbed substituents in the $^{13}C\{^1H\}$ NMR spectra.

The UV–Vis spectrum of the methylene dichloride solution of the $FeDm_3(Sb(C_2H_5)_3)_2$ complex in the visible region contains three bands with the same intensities ($\varepsilon \sim 2\text{–}3 \cdot 10^3$ mol^{-1} l;cm^{-1}), assigned to the metal – to – clathrochelate ligand $Fed \rightarrow L\pi^*$ charge transfer bands (CTBs). Such high-intensity CTBs mask the low-intensity d–d transitions bands of low-spin Fe^{2+} ion [11]. The same UV–Vis spectra were observed earlier for TAP tin-, antimony- and germanium-capped iron(II) clathrochelates [3,9,12–16].

The deconvoluted UV–Vis spectrum of the clathrochelate synthesized with an encapsulated low-spin cobalt(III) ion, which is isoelectronic (d^6) to iron(II) ion, contains in the visible and near UV regions two bands of d–d transitions $^1A_{1g} \rightarrow {}^1T_{1g}$ and $^1A_{1g} \rightarrow {}^1T_{2g}$ (Table 4). This allows one use equations from [17] to calculate both the ligand field Dq and the Racah B parameters for TAP cobalt complexes:

$$\nu_1 = E(^1A_{1g} \rightarrow {}^1T_{1g}) = 10Dq - C$$

$$\nu_2 = E(^1A_{1g} \rightarrow {}^1T_{2g}) = 10Dq - C + 16B$$

We calculated the Dq and B values with the estimation of $C = 4B$ as follows:

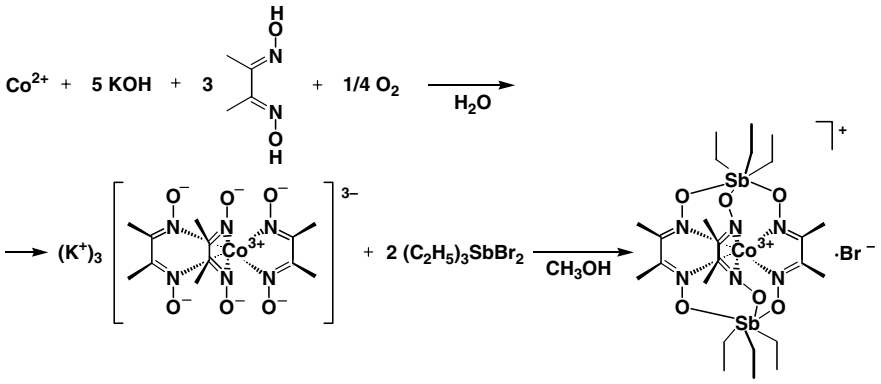
$$Dq = (3\nu_1 + \nu_2)/40$$

$$B = (\nu_2 - \nu_1)/16$$

The calculated values as well as the analogous data for the boron- and tin-capped clathrochelate tris-dioximate ligands [12] are listed in Table 5. As seen, all clathrochelate ligands of this type possess the same high ligand field strength, which results in high stability of the low-spin d^6 electronic configuration.

The X-ray crystallography data for the antimony-capped iron(II) and cobalt(III) clathrochelates we synthesized allow one to discuss the changes in the molecular structure of the given metal ion complexes in a series of the clathrochelate ligands with different boron-, tin- and antimony-capping fragments as well as to compare the geometry of the isoelectronic low-spin iron(II) and cobalt(III) complexes with a given clathrochelate ligand.

The intramolecular $FeDm_3(Sb(C_2H_5)_3)_2$ complex (Fig. 2) and the clathrochelate $[CoDm_3(Sb(C_2H_5)_3)_2]^+$ cation (Fig. 3) possess a geometry intermediate between that of a trigonal prism (TP, the distortion angle $\varphi = 0°$) and a trigonal antiprism (TAP, $\varphi = 60°$), which is characteristic of the hexadentate macrobicyclic ligands [12].



Scheme 2.

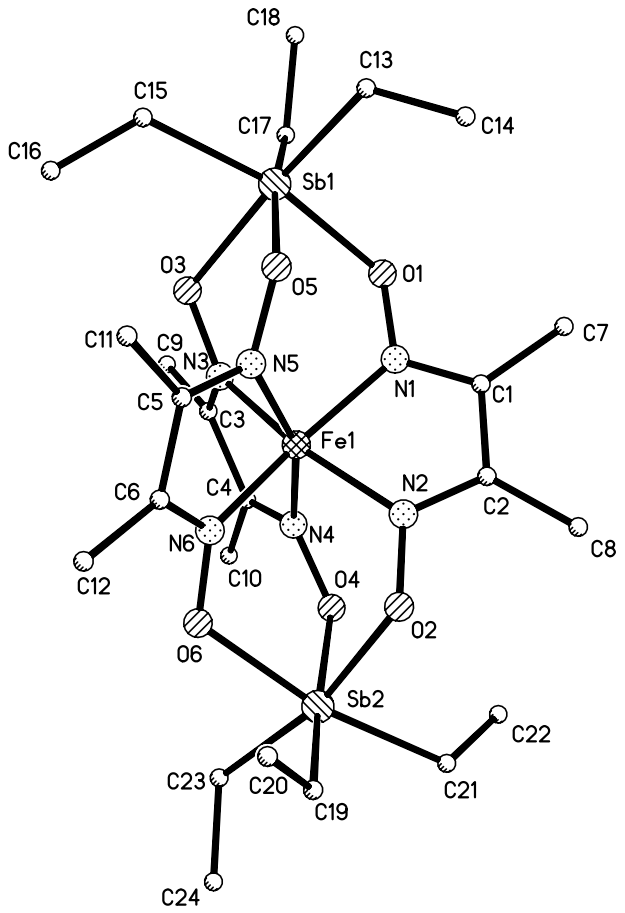


Fig. 2. Molecular structure of the $FeDm_3(Sb(C_2H_5)_3)_2$ clathrochelate (one of the two disordered methyl group is shown). Hydrogen atoms are omitted for clarity.

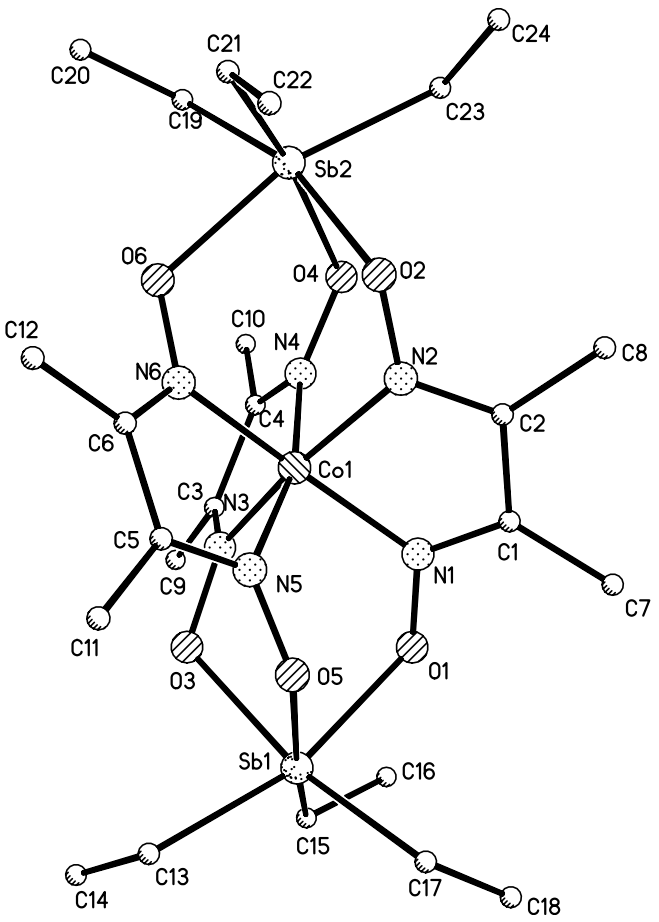


Fig. 3. Molecular structure of the clathrochelate $[CoDm_3(Sb(C_2H_5)_3)_2]^+$ cation. Hydrogen atoms are omitted for clarity.

A previously obtained [3] analogous nioximate $FeNx_3(Sb(C_2H_5)_3)_2$ clathrochelate has a similar molecular structure and geometric parameters close to those of the macrobicyclic framework (Table 2). The coordination N_6-polyhedra of the $FeDm_3(Sb(C_2H_5)_3)_2$ and $FeNx_3(Sb(C_2H_5)_3)_2$ complexes approach a TAP: their average distortion angles φ are close to 36°. The cyclic nature of the peripheral substituents in α-dioximate fragments of the $FeNx_3(Sb(C_2H_5)_3)_2$ molecule has a negligible effect on the orientation of these chelate rings to the symmetry C_3-pseudoaxis, which passes through the capping antimony atoms and the encapsulated iron(II) ion, but results in an increase in the height h of the coordination polyhedron from 2.24 Å for the $FeDm_3(Sb(C_2H_5)_3)_2$ molecule to 2.26 Å for the $FeNx_3(Sb(C_2H_5)_3)_2$ molecule.

The molecular structures of boron-capped iron(II) dimethylglyoximate $FeDm_3(BF)_2$ and nioximate $FeNx_3(Bn\text{-}C_4H_9)_2$ clathrochelates had previously been solved by X-ray crystallography [18]. Nevertheless, in the former clathrochelate molecule, the donor nitrogen atoms are disordered at various temperatures (298, 208 and 138 K), and this made it impossible to compare the data for this complex. The main geometric parameters for the $FeNx_3(Bn\text{-}C_4H_9)_2$ molecule are listed in Table 2, as well as the data for the fluoroboronic $FeBd_3(BF)_2$ [19,22] and $Fe(Cl_2Gm)_3(BF)_2$ [20] complexes with aromatic (phenyl) and halogenide (chloride) substituents, respectively, in the α-dioximate chelate fragments. For the former complex, the X-ray structures of two (chloroform and toluene) solvates have been described [19,22]. Because the molecular and crystal structure of the toluene solvate was solved with lower convergence factors [19], we discuss the X-ray data for this solvate.

We observe significant changes in the geometry of the clathrochelate framework as we move from the antimony-capped $FeDm_3(Sb(C_2H_5)_3)_2$ and $FeNx_3(Sb(C_2H_5)_3)_2$ complexes to their boron-containing $FeNx_3(Bn\text{-}C_4H_9)_2$, $FeBd_3(BF)_2$ and $Fe(Cl_2Gm)_3(BF)_2$ analogs. First, the distortion angle φ values for the encapsulated iron(II) ion coordination polyhedra decrease significantly (by 15–20°), whereas the Fe–N distances and bite angles α remain constant. As a result, the heights h increase by ~0.1 Å, the polyhedron geometry approaches that of a TP (average φ values are equal to 20°), and the deviation angles ω between the chelate rings and C_3-pseudoaxes decrease by approximately 10°. TAP distortion of the clathrochelate frameworks is determined by the nature of the apical capping atoms Q, rather than the alkyl, aryl, or halogenide

Table 2
The main geometrical parameters for clathrochelate iron(II) complexes

Complex	$FeDm_3(Sb(C_2H_5)_2)_3$	$FeNx_3(Sb(C_2H_5)_2)_3$ [3]	$FeNx_3(Bn\text{-}C_4H_9)_2$ [18]	$FeBd_3(BF)_2$ [19]	$Fe(Cl_2Gm)_3(BF)_2$ [20][h]	$[FeNx_3(SnCl_3)_2]^{2-}$ [21]	$[Fe(Cl_2Gm)_3(SnCl_3)_2]^{2-}$ [14]
Temperature	298	110	298	298	298	183	120
Fe–N(1,3,5) (Å)	1.911(7), 1.912(6), 1.919(6)	1.911, 1.914, 1.917	1.905, 1.913, 1.898	1.914, 1.914, 1.920	1.902, 1.915, 1.914	1.918, 1.928, 1.918	1.931, 1.899, 1.912
Fe–N(2,4,6) (Å)	1.920(7), 1.922(6), 1.932(7)	1.919, 1.906, 1.917	1.903, 1.907, 1.907	1.894, 1.931, 1.909		1.930, 1.915, 1.930	1.923, 1.902, 1.921
C=N(1,3,5) (Å)	1.307(9), 1.29(1), 1.298(9)	1.29, 1.315, 1.297	1.305, 1.299, 1.299	1.317, 1.317, 1.313	1.278, 1.284, 1.267	1.285, 1.310, 1.299	1.302, 1.296, 1.310
C=N(2,4,6) (Å)	1.308(9), 1.29(1), 1.307(9)	1.310, 1.32, 1.29	1.302, 1.305, 1.305	1.317, 1.314, 1.317		1.299, 1.305, 1.303	1.294, 1.320, 1.300
N–O (1,3,5) (Å)	1.368(8), 1.351(8), 1.378(8)	1.372, 1.365, 1.373	1.375, 1.370, 1.370	1.379, 1.368, 1.367	1.376, 1.365, 1.367	1.381, 1.376, 1.369	1.335, 1.341, 1.339
N–O (2,4,6) (Å)	1.366(8), 1.362(8), 1.362(8)	1.362, 1.373, 1.373	1.365, 1.371, 1.392	1.377, 1.367, 1.369		1.376, 1.378, 1.375	1.349, 1.360, 1.368
Q–O–N (°)	119.4–120.1	118.6–121.1	110.6–113.4	111.3 – 113.0	112.0–112.7	114.3–115.9	116.8–116.6
Q1–O(1,3,5) (Å)	2.134(6), 2.129(6), 2.125(6)	2.145, 2.131, 2.110	1.493, 1.490, 1.506	1.482, 1.507, 1.470	1.465, 1.464, 1.465	2.081, 2.113, 2.098	2.091, 2.128, 2.103
Q2–O(2,4,6) (Å)	2.128(6), 2.131(6), 2.134(6)	2.122, 2.141, 2.104	1.498, 1.506, 1.516	1.467, 1.476, 1.486		2.081, 2.104, 2.079	2.121, 2.099, 2.097
N=C–C=N (°)[a]	4.0, 6.0, 4.6	7.7, 5.4, 6.9	11.0, 6.5, 6.9	10.4, 8.0, 10.2	8.1, 8.1, 7.7	5.6, 5.0, 8.0	3.4, 3.2, 3.8
φ (°)[b]	36.3, 36.5, 36.4	35.5, 35.6, 36.1	20.1, 20.5, 20.2	23.5, 23.4, 23.7	17.3, 17.1, 17.1	37.8, 37.5, 37.3	40.9, 40.1, 40.2
α (°)[c]	39.6	39.8	39.1	39.0	39.0	39.5	40.5
h (Å)[d]	2.236	2.260	2.355	2.326	2.362	2.227	2.245
$\Delta Fe/N_3$ (Å)[e]	1.124(5), 1.118(5)	1.137, 1.124	1.177, 1.178	1.169, 1.157	1.181	1.107, 1.119	1.128, 1.117
N(1,3,5)//N(2,4,6) (°)[f]	0.70(3)	1.10	0.20	0.5	0.4	0.90	0.90
$\omega 1$, $\omega 2$, $\omega 3$ (°)[g]	23.6, 23.3, 23.8	22.5, 22.9, 22.9	12.6, 12.6, 13.2	14.9, 15.1, 14.7	10.5, 10.5, 11.2	24.8, 24.8, 24.5	25.5, 25.6, 25.4

[a] Mean deviation of the coordinated nitrogen atoms from the C–Fe–C plane.
[b] Distortion angle.
[c] Bite angle (half the chelate angle).
[d] Distance between the coordination polyhedron bases (the height of the distorted TP).
[e] Deviation of the iron(II) ion from N_6-coordination polyhedron trigonal bases.
[f] Dihedral angle between the N_6-coordination polyhedron trigonal bases.
[g] The angles between the chelate N...N and capping Q...Q axes.
[h] Iron(II) ion is in special position.

substituents in the chelate α-dioximate ribbed fragments. It should be noted that the distortion angle φ values for dianionic tin-capped $[FeNx_3(SnCl_3)_2]^{2-}$ [21] and $[Fe(Cl_2Gm)_3(SnCl_3)_2]^{2-}$ clathrochelates [14] are slightly higher (average 38–40°) then those for antimony-capped $FeDm_3(Sb(C_2H_5)_3)_2$ and $FeNx_3(Sb(C_2H_5)_3)_2$ complexes. In an attempt to explain the influence of the nature of capping atoms on the macrobicyclic ligand geometry, we compared both the bond lengths and angles in the coordination polyhedra of the encapsulated iron(II) ions for the $FeDm_3(Sb(C_2H_5)_3)_2$, $FeNx_3(Bn\text{-}C_4H_9)_3$, $FeBd_3(BF)_2$, and $Fe(Cl_2Gm)_3(BF)_2$ molecules, because their X-ray data were collected at similar temperatures and with approximately equal convergence factors. The average Fe–N distances in these molecules are the same, the C–N and N–O bond lengths are also practically constant. More significant differences are observed in the values of Sb–O–N and B–O–N bond angles (*av.* 119 and 112°, respectively). The distances between the encapsulated iron(II) ion and the N1.N3.N5 and N2.N4.N6 bases of a TP–TAP coordination polyhedron in the $FeNx_3(Bn\text{-}C_4H_9)_2$, $FeBd_3(BF)_2$ and $Fe(Cl_2Gm)_3(BF)_2$ molecules are significantly greater than those of the $FeDm_3(Sb(C_2H_5)_3)_2$ clathrochelate. The elongation of the Q–O bonds is caused by the small Shannon radius of the capping boron atom compared with that of the apical antimony atom. This results in a decrease in the average values of both the bond Q–O angles and the deviation angles ω between the chelate fragments and the Q...Q axis of the clathrochelate framework. As a result, the height h of the coordination polyhedron in boron-capped molecules increases. In the $FeDm_3(Sb(C_2H_5)_3)_2$ molecule, the average deviation angle ω between the Q...Q axis and the N...N axes in chelate fragments is equal to 23.5°, whereas in the $FeNx_3(Bn\text{-}C_4H_9)_2$, $FeBd_3(BF)_2$ and $Fe(Cl_2Gm)_3(BF)_2$ molecules, these angles are appreciably smaller (*av.* 13°).

We attribute major discrepancies in the geometry of the clathrochelate framework in the $[FeNx_3(SnCl_3)_2]^{2-}$ dianion and the $FeNx_3(Sb(C_2H_5)_3)_2$ intracomplex to slight differences in the Fe–N bond lengths and the mutual orientation of chelate cycles. The average Fe–N distance in the $[FeNx_3(SnCl_3)_2]^{2-}$ dianion is somewhat longer (1.923 Å) than that in the $FeNx_3(Sb(C_2H_5)_3)_2$ molecule (1.914 Å). In the former case, the bond angles at the oxygen atoms are reduced (*av.* 114.9°), whereas in the latter case, they are close to 120°, but the Sb–O and Sn–O distances are the same. In the tin-capped clathrochelate $[Fe(Cl_2Gm)_3(SnCl_3)_2]^{2-}$ anion, the Fe–N, Sn–O, C=N, and chelate C–C bond lengths, as well as the average Sn–O–N, O–N–C, and N=C–C bond angles in the clathrochelate framework, remain practically unchanged from those in its nioximate analog. However, the N–O distances in the $[Fe(Cl_2Gm)_3(SnCl_3)_2]^{2-}$ dianion are markedly lower than those in the $[FeNx_3(SnCl_3)_2]^{2-}$ anion (*av.* 1.349 and 1.376 Å, respectively).

The main geometric parameters of the clathrochelate $[CoDm_3(Sb(C_2H_5)_3)_2]^+$ cation and its macrobicyclic analogs with an encapsulated cobalt(III) ion are listed in Table 3. The coordination polyhedra of antimony- and tin-capped cobalt(III) clathrochelates approach a TAP: the distortion angles φ are in the range 40.5–46.4° and they are essentially higher than those of the analogous iron(II) complexes and those of the boron-capped $[CoDm_3(BF)_2]^+$ cation ($\varphi = 31.3°$). The TAP distortion of the cobalt(III) coordination polyhedra causes an increase in the deviation angle ω value, but the flatness of the chelate fragments remaines unaffected (the changes in the N=C–C=N torsion angles are negligible). The contraction along the Q...Q axis, which results in a decrease in the h values for the clathrochelate $[CoDm_3(Sb(C_2H_5)_3)_2]^+$, $[CoDm_3(SnBr_3)_2]^-$, and $[CoDm_3(SnCl_3)_2]^-$ ions, is larger than that of the $[CoNx_3(SnCl_3)_2]^-$ anion. The C=N and N–O bond length remain practically constant (within the experimental errors), whereas the Q–O distances and Q–O–N bond angles are characteristic of the corresponding capping atoms. The average Co–N distances in the clathrochelate $[CoDm_3(Sb(C_2H_5)_3)_2]^+$, $[CoNx_3(SnCl_3)_2]^-$, $[CoDm_3(SnBr_3)_2]^-$, $[CoDm_3(SnCl_3)_2]^-$, and $[CoDm_3(BF)_2]^+$ ions are close to those typical for low-spin tris-α-dioximate cobalt(III) complexes (1.89 Å) [26].

Thus, as seen in Tables 2 and 3, the C=N, N–O, and chelate C–C bond lengths and the N=C–C=N torsion angles remain practically unchanged in the different types of clathrochelate molecules. The Q–O–N bond angles are more sensitive to the nature of the clathrochelate framework. However, these angles are governed by a capping atom Q and, like the Q–O distances, are constant in the tris-dioximate clathrochelates with the same apical capping atoms.

The distortion angle φ, bite angle α, and height h values are the main characteristics of a TP–TAP coordination polyhedron (Table 4). These polyhedra for boron-capped clathrochelate molecules are contracted in the direction of the C_3-pseudoaxis compared with those for their tin- and antimony-capped analogs. This contraction correlates with the Shannon ionic radius values for the corresponding capping atoms Q (B^{3+} (0.25 Å), Sn^{4+} (0.83 Å) and Sb^{5+} (0.74 Å)): the B–O bond lengths are essentially shorter than the Sn–O and Sb–O lengths (*av.* 1.49, 2.10 and 2.13 Å, respectively). Because the N–O, C=N and chelate C–C bond lengths are equal for all α-dioximate clathrochelate molecules an, increase in the Q–O distances causes a decrease in the Q–O–N angles (112°, 115° and 119° for the boron-, tin-, and antimony-capped compounds, respectively) and the contraction of the coordination polyhedron (the height h decreases). In the case of TAP tin- and antimony-capped molecules, the deviation angle ω values are essentially higher than those of their TP boron-capped analogs.

The contraction (expansion) of the coordination N_6-polyhedron is also determined by the Shannon ionic radius of an encapsulated metal ion (the Shannon radii are equal to 0.75 and 0.68 Å for low-spin hexacoordinate Fe^{2+} and Co^{3+} ions, respectively). The average Fe^{2+}–N (~1.91 Å) and Co^{3+}–N (~1.89 Å) distances differ only slightly, but

Table 3
The main geometrical parameters for clathrochelate cobalt(III) complexes

Complex	$[CoDm_3(SbC_2H_5)_3]^+$	$[CoNx_3(SnCl_3)_2]^-$ [23]	$[CoDm_3(SnBr_3)_2]^-$ [23]	$[CoDm_3(SnCl_3)_2]^-$ [24][h]	$[CoDm_3(BF)_2]^+$ [25][h]
Temperature	120	153	153	298	298
Co–N(1,3,5) (Å)	1.901(4), 1.890(5), 1.908(4)	1.905, 1.904, 1.911	1.871, 1.892, 1.887	1.882, 1.916, 1.907	1.887, 1.907, 1.888
Co–N(2,4,6) (Å)	1.899(4), 1.904(4), 1.897(5)	1.933, 1.907, 1.919	1.850, 1.949, 1.914		
C=N(1,3,5) (Å)	1.305(7), 1.289(7), 1.302(7)	1.317, 1.289, 1.251	1.262, 1.300, 1.371	1.301, 1.264, 1.313	1.290, 1.285, 1.298
C=N(2,4,6) (Å)	1.299(7), 1.288(7), 1.277(7)	1.302, 1.285, 1.251	1.300, 1.176, 1.292		
N–O (1,3,5) (Å)	1.339(6), 1.343(6), 1.339(6)	1.366, 1.354, 1.385	1.382, 1.326, 1.308	1.375, 1.368, 1.372	1.361, 1.359, 1.361
N–O (2,4,6) (Å)	1.350(6), 1.345(6), 1.340(6)	1.301, 1.315, 1.357	1.321, 1.332, 1.352		
Q–O–N (°)	118.8(3)–119.8(3)	112.7–117.2	114.0–116.4	112.7–115.7	110.0–111.1
Q1–O(1,3,5) (Å)	2.155(4), 2.144(4), 2.202(4)	2.096, 2.092, 2.098	2.103, 2.160, 2.111	2.111, 2.099, 2.098	1.478, 1.488, 1.504
Q2–O(2,4,6) (Å)	2.144(4), 2.188(4), 2.155(4)	2.137, 2.133, 2.111	2.099, 2.141, 2.092		
N=C–C=N (°)[a]	9.7(7), 6.7(7), 7.9(7)	6.2, 7.6, 4.2	6.8, 5.9, 7.4	6.3, 6.3, 7.9	9.5, 9.5, 10.5
φ (°)[b]	42.3, 42.1, 42.2	41.1, 41.4, 40.5	46.4, 43.4, 45.4	42.3, 42.3, 43.7	31.5, 31.1, 31.1
α (°)[c]	40.6	40.5	41.0	40.2	40.0
h (Å)[d]	2.205	2.236	2.182	2.177	2.290
$\Delta Co/N_3$ (Å)[e]	1.103(3), 1.103(3)	1.092, 1.144	1.085, 1.097	1.089	1.145
N(1,3,5)/N(2,4,6) (°)[f]	0.9(3)	1.7	1.2	1.4	0
ω1, ω2, ω3 (°)[g]	26.0, 27.0, 27.5	25.8, 25.9, 26.1	29.9, 28.2, 27.4	27.8, 27.8, 27.1	19.6, 19.6, 19.4

[a] Mean deviation of the coordinated nitrogen atoms from the C–Co–C plane.
[b] Distortion angle.
[c] Bite angle (half the chelate angle).
[d] Distance between the coordination polyhedron bases (the height of the distorted TP).
[e] Deviation of the cobalt(III) ion from N_6-coordination polyhedron trigonal bases.
[f] Dihedral angle between the N_6-coordination polyhedron trigonal bases.
[g] The angles between the chelate N...N and capping Q...Q axes.
[h] Cobalt(III) ion is in special position.

Table 4
The main X-ray data (the average M–N distances and heights h [Å], angles φ, α and ω [°]) for clathrochelate iron(II) and cobalt(III) tris-dioximates

Complex	M–N	h	φ	α	ω
$FeDm_3(Sb(C_2H_5)_3)_2$	1.919	2.236	36.4	39.6	23.6
$FeNx_3(Sb(C_2H_5)_3)_2$ [3]	1.914	2.260	35.7	39.8	22.8
$[FeNx_3(SnCl_3)_2]^{2-}$ [21]	1.923	2.227	37.5	39.5	24.7
$[Fe(Cl_2Gm)_3(SnCl_3)_2]^{2-}$ [14]	1.911	2.245	40.4	40.5	25.5
$FeBd_3(BF)_2 \cdot 2C_6H_5CH_3$ [19]	1.914	2.326	23.5	39.0	14.9
$FeBd_3(BF)_2 \cdot 5CHCl_3$ [22]	1.91	2.29	29.3	39.3	18.6
$FeNx_3(Bn\text{-}C_4H_9)_2$ [18]	1.906	2.326	23.6	39.1	14.9
$Fe(Cl_2Gm)_3(BF)_2$ [20]	1.910	2.362	17.2	39.0	10.7
$[CoDm_3(Sb(C_2H_5)_3)_2]Br$	1.900	2.205	42.3	40.6	27.0
$[CoNx_3(SnCl_3)_2]^-$ [23]	1.913	2.236	41.0	40.6	25.9
$[CoDm_3(SnBr_3)_2]^-$ [23]	1.894	2.182	45.1	41.0	28.5
$[CoDm_3(SnCl_3)_2]^-$ [24]	1.902	2.177	42.8	40.2	27.6
$[CoDm_3(BF)_2]^+$ [25]	1.894	2.290	31.2	40.0	19.5

for the complexes with the same macrobicyclic ligand, the distortion angle φ value is significantly higher for the corresponding cobalt(III) clathrochelate than for its iron(II)-containing analog.

It should be noted that the height h is characteristic of a linear shift of the coordination polyhedron bases from each other, but does not indicate a change in the deviation angle ω. In contrast, the distortion angle φ is characteristic of the mutual angular distortion of these bases, but does not indicate a their linear shift. Both the height h and the distortion angle φ are independent parameters and change in the opposite directions, which allow one to describe the rotary-translational contraction (expansion) of the coordination polyhedron.

3.3. Electrochemistry

Electrochemical investigation of the new antimony-capped iron(II) and cobalt(III) clathrochelates was performed in two solvents with different polarity and donor numbers (methylene dichloride and acetonitrile). CVs obtained for both complexes are shown in Fig. 4. For the iron complex, the electrochemical response of the $Fe^{2+/3+}$ redox couple ($E_0 = 580$ mV) is diffusionally controlled (as follows from the linear relationship $I_p - \upsilon^{1/2}$, where υ is the scan rate) and quasi-reversible (the current ratio $I_c/I_a = 1$, and the peak separation ΔE_p is equal to 110 mV). Two additional peaks at 1460 and −2040 mV were assigned to the further oxidation and reduction of the clathrochelate framework followed by its destruction. The E_p values are listed in Table 6. The cobalt(III) clathrochelate differs from its iron(II)-containing analog by the presence of the outer-sphere Br^- counter-ion, which can be detected by two characteristic oxidation peaks at 1030 and 1280 mV (see Fig. 4) attributed to the consecutive oxidation of the Br^- and Br_3^- species [27].

Furthermore, the redox process assigned to the $Co^{3+/2+}$ redox couple ($E_0 = -810$ mV) is observed in the cathodic region of CV. As seen from the linear I_p–$\upsilon^{1/2}$ relationship, the reduction of the cobalt(III) clathrochelate is diffusionally controlled. The ratios of peak currents for direct (cathodic) and reverse (anodic) peaks I_a/I_c are equal to 1

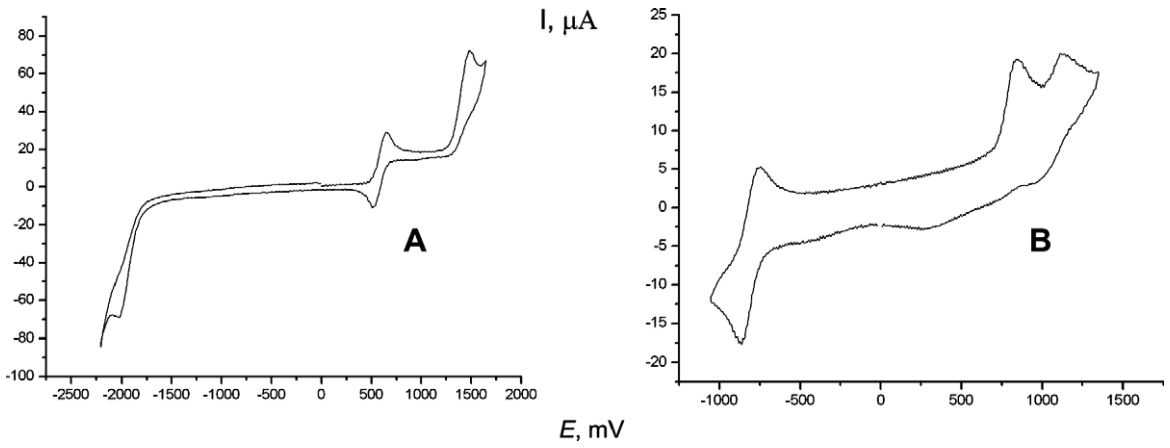


Fig. 4. Cyclic voltammograms for $FeDm_3(Sb(C_2H_5)_3)_2$ (A, in methylene dichloride) and $[CoDm_3(Sb(C_2H_5)_3)_2]Br$ (B, in acetonitrile) clathrochelates ($c = 0.7$ mM, Pt, 0.15 M $(Bu_4N)BF_4$, 100 mV/s, vs. Ag/AgCl/KCl).

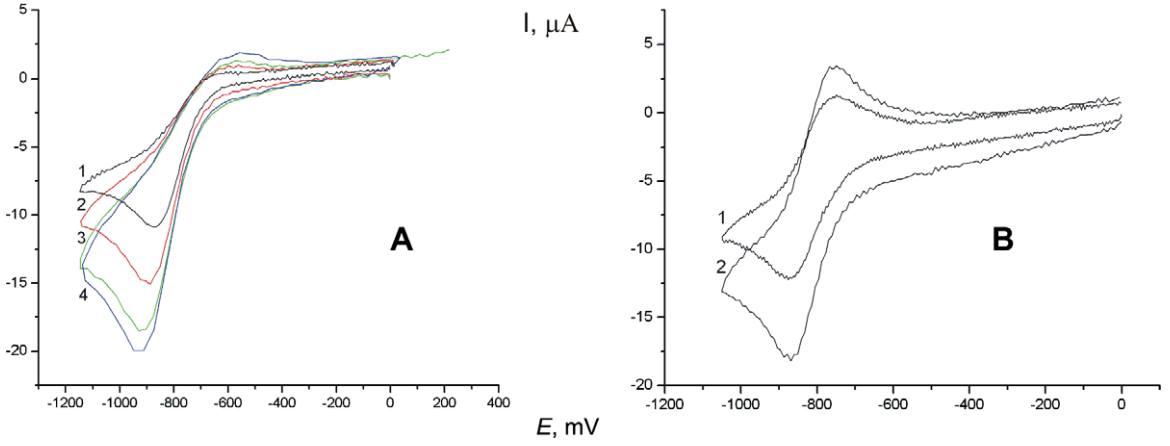


Fig. 5. Cyclic voltammograms for $[CoDm_3(Sb(C_2H_5)_3)_2]Br$ complex at the different potential scan rates in methylene dichloride (A, 100 (**1**), 200 (**2**), 300 (**3**) and 400 (**4**) mV/s) and in acetonitrile (B, 100 (**1**) and 200 (**2**) mV/s) solutions ($c = 0.7$ mM, Pt, 0.15 M $(Bu_4N)BF_4$, vs. Ag/AgCl/KCl).

at the potential scan rates of more than 50 mV/s (see Fig. 5). However, it should be noted that in acetonitrile solution the reduced cobalt(II) clathrochelate was more stable than this complex in methylene dichloride solution. The CVs of the $[CoDm_3(Sb(C_2H_5)_3)_2]Br$ clathrochelate, which were recorded in methylene dichloride at the scan rate lower than 200 mV/s, exhibited no reoxidation peaks. A small reoxidation peak appeared at the scan rate equal to 400 mV/s with $I_a/I_c = 0.45$. This allowed us to estimate the lifetime of the reduced $CoDm_3(Sb(C_2H_5)_3)_2$ macrobicycle in methylene dichloride solution in the time scale of the method. The $\tau_{1/2}$ value obtained falls within the interval

Table 5
The UV–Vis spectral and crystal field parameters (cm^{-1}) for cobalt(III) clathrochelates

Complex	$^1A_{1g} \rightarrow {}^1T_{2g}$ (ν_2)	$^1A_{1g} \rightarrow {}^1T_{1g}$ (ν_1)	Dq	B
$[CoDm_3(Sb(C_2H_5)_3)_2]Br$	26 200	24 500	2490	105
$[CoNx_3(BF)_2](BF_4)$ [12]	29 600	19 800	2240	600
$[CoDm_3(BF)_2](BF_4)$ [12]	30 200	19 800	2250	600
$[CoBd_3(BF)_2](BF_4)$ [12]	27 300	21 700	2300	420
$H[CoDm_3(SnCl_3)_2]$ [12]	26 300	21 800	2290	280
$H[CoNx_3(SnCl_3)_2]$ [12]	26 500	22 300	2330	245
$H[CoNx_3(SnBr_3)_2]$ [12]	25 200	20 900	2200	270

Table 6
Cyclic voltammetry data (mV, [a]) for iron(II) and cobalt(III) clathrochelates obtained

Complex	Solvent	Electrode material	Oxidation		Reduction	
			E_p^a	E_p	E_p	E_p^a
$FeDm_3$-$(Sb(C_2H_5)_3)_2$	CH_2Cl_2	Pt	640 1460	530	–2040	
		GC	640 1440	550	−2000	
$[CoDm_3(Sb$-$(C_2H_5)_3)_2]Br$	CH_2Cl_2	Pt	1030 1280		−910	−580
		GC	1050 1300		−880	−580
	CH_3CN	Pt	870 1150		−880	−730
		GC	910 1230		−870	−770

[a] 0.15 M $(Bu_4N)BF_4$, 200 mV/s, *vs.* Ag/AgCl/KCl.

of 2–3 s in methylene dichloride solution, whereas in acetonitrile solution the $\tau_{1/2}$ value is more than 5 s. However, the formal potential values for the Co^{3+}/Co^{2+} redox couple in methylene dichloride and acetonitrile are rather close ($E_0 = -750$ and -810 mV, respectively).

Changing of the working electrode material from platinum to glassy carbon did not influence the peak potential values observed for both complexes: as seen in Table 6, the potential values are almost identical.

Thus, the cyclic voltammetry data present information about the stability of the electrochemically generated forms of the cobalt clathrochelates in different solvents, and this allows one to choose the optimal preparative pathways and conditions for further synthesis and modifications of the polytopic cobalt(II) and cobalt(III) cage compounds.

Acknowledgements

The authors gratefully acknowledge support of the RFBR (Grants 05-03-33184, 05-03-33202, 05-03-32759, 06-03-32626 and 06-03-90903) and RAS (programme 7).

Appendix A. Supplementary material

CCDC 65013 and 65014 contain the supplementary crystallographic data for this paper. These data can be obtained free of charge via http://www.ccdc.cam.ac.uk/conts/retrieving.html, or from the Cambridge Crystallographic Data Centre, 12 Union Road, Cambridge CB2 1EZ, UK; fax: (+44) 1223-336-033; or e-mail: deposit@ccdc.cam.ac.uk. Supplementary data associated with this article (the experimental details for elemental analysis, IR, UV-vis, NMR, ^{57}Fe Mössbauer spectroscopies as well as IR and NMR data) can be found, in the online version, at doi:10.1016/j.poly.2007.09.008.

References

[1] Y.Z. Voloshin, O.A. Varzatskii, S.V. Korobko, V.Y. Chernii, S.V. Volkov, L.A. Tomachynski, V.I. Pehn'o, M.Y. Antipin, Z.A. Starikova, Inorg. Chem. 44 (2005) 822.
[2] Y.Z. Voloshin, I.A. Varzatskii, L.G. Tomilova, M.O. Breusova, T.V. Magdesieva, Y.N. Bubnov, R. Krämer, Polyhedron 26 (2007) 2733.
[3] Y.Z. Voloshin, O.A. Varzatskii, S.V. Korobko, M.Y. Antipin, I.I. Vorontsov, K.A. Lyssenko, D.I. Kochubey, S.G. Nikitenko, N.G. Strizhakova, Inorg. Chim. Acta 357 (2004) 3187.
[4] D.R. Boston, N.J. Rose, J. Amer. Chem. Soc. 95 (1973) 4163.
[5] K. Issleib, B. Hamann, Z. Anorg. Allg. Chem. 339 (1965) 289.
[6] SMART and SAINT, Release 5.0, Area detector control and integration software. Bruker AXS, Analytical X-ray Instruments, Madison, Wisconsin, USA, 1998.
[7] G.M. Sheldrick, SADABS: A Program for Exploiting the Redundancy of Area-detector X-ray Data, University of Gottingen, Gottingen, Germany, 1999.
[8] G.M.Sheldrick, SHELXTL-97, Version 5.10, Bruker AXS Inc., Madison, WI-53719, USA, 1997.
[9] Y.Z. Voloshin, O.A. Varzatskii, S.V. Korobko, Y.A. Maletin, Inorg. Chem. Commun. 1 (1998) 328.
[10] A. Nakahara, R. Tsuchida, J. Amer. Chem. Soc. 76 (1954) 3103.
[11] A.B.P. Lever, Inorganic Electronic Spectroscopy, Elsevier, Amsterdam, 1984.
[12] Y.Z. Voloshin, N.A. Kostromina, R. Krämer, Clathrochelates: Synthesis, Structure and Properties, Elsevier, Amsterdam, 2002.
[13] Y.Z. Voloshin, O.A. Varzatskii, N.G. Strizhakova, E.Y. Tkachenko, Inorg. Chim. Acta 299 (2000) 104.
[14] Y.Z. Voloshin, O.A. Varzatskii, A.V. Palchik, N.G. Strizhakova, I.I. Vorontsov, M.Y. Antipin, D.I. Kochubey, B.N. Novgorodov, New J. Chem. 27 (2003) 1148.
[15] Y.Z. Voloshin, N.A. Kostromina, A.Y. Nazarenko, E.V. Polshin, Inorg. Chim. Acta 185 (1991) 83.
[16] Y.Z. Voloshin, V.V. Trachevskii, E.V. Polshin, Polish J. Chem. 71 (1997) 428.
[17] K.B. Yatsimirskii, Y.D. Lampeka, Physicochemistry of Metal Complexes with Macrocyclic Ligands, Naukova Dumka, Kiev, 1985.
[18] S.A. Kubow, K.J. Takeuchi, J.J. Grzybowski, A.J. Jircitano, V.L. Goedken, Inorg. Chim. Acta 241 (1996) 21.
[19] R.F. See, M.R. Churchill, K.A. Lance, D.P. Mersman, K.R. Williams, Inorg. Chim. Acta 257 (1997) 285.
[20] Y.Z. Voloshin, O.A. Varzatskii, T.E. Kron, V.K. Belsky, V.E. Zavodnik, N.G. Strizhakova, A.V. Palchik, Inorg. Chem. 39 (2000) 1907.
[21] S.V. Lindeman, Y.T. Struchkov, Y.Z. Voloshin, J. Coord. Chem. 28 (1993) 319.
[22] S.V. Lindeman, Y.T. Struchkov, Y.Z. Voloshin, Inorg. Chim. Acta 184 (1991) 107.
[23] S.V. Lindeman, Y.T. Struchkov, Y.Z. Voloshin, J. Coord. Chem. 34 (1995) 203.
[24] Y.Z. Voloshin, V.K. Belsky, V.V. Trachevskii, Polyhedron 11 (1992) 1939.
[25] G.A. Zakrzewski, C.A. Ghilardi, E.C. Lingafelter, J. Am. Chem. Soc. 93 (1971) 4411.
[26] H.-B. Bürgi, J.D. Dunitz (Eds.), Structure Correlation, Vol.2, VCH, Weinheim – New York, 1994, p. 812.
[27] C.K. Mann, K.K. Barnes, Electrocheical Reaction in Nonaqueous systems, Marcel Dekker, New York, 1970, pp. 499.

Available online at www.sciencedirect.com
ScienceDirect
Polyhedron 27 (2008) 335–343
POLYHEDRON
www.elsevier.com/locate/poly

Synthesis, spectroscopic, electrochemical and structural characterization of Cu(II) complexes with asymmetric NN′OS coordination spheres

Eulália Pereira [a], Lígia R. Gomes [a,b,*], John N. Low [c], Baltazar de Castro [a]

[a] REQUIMTE/Faculdade de Ciências, Universidade do Porto, Rua do Campo Alegre, 687, P-4169-007 Porto, Portugal
[b] CIAGEB – Faculdade de Ciências da Saúde, Escola Superior de Saúde da UFP, Universidade Fernando Pessoa, Rua Carlos da Maia, 296, P-4200-150 Porto, Portugal
[c] Department of Chemistry, University of Aberdeen, Meston Walk, Aberdeen, AB24 3UE, Scotland, United Kingdom

Received 24 May 2007; accepted 16 September 2007
Available online 14 November 2007

Abstract

A set of four Cu(II) complexes, [Cu(cdnapen)], [Cu(cdnappd)], [Cu(cdMenappd)] and [Cu(cdMeMeOsalpd)], derived from Schiff base ligands with an asymmetric NN′OS coordination sphere have been synthesized. The molecular and the crystal structures have been determined by X-ray diffractometry. The structural results confirm that the complexes are tetra coordinated. The copper (II) ion coordinates to two nitrogen atoms from the imine moiety of the ligand, a sulfur atom from the methyl dithiocarboxylate moiety and a phenolic oxygen atom. The complexes show an unusual tetrahedral distortion to the square-planar geometry around the metal centre in spite of the pseudomacrocyclic skeleton of the ligand. The complexes were further characterized by cyclic voltammetry and electron paramagnetic resonance spectroscopy. The degree of tetrahedral distortion of the complexes appears to be dependent on the number of carbon atoms of the aliphatic bridge and the nature of the coordinating atoms.
© 2007 Elsevier Ltd. All rights reserved.

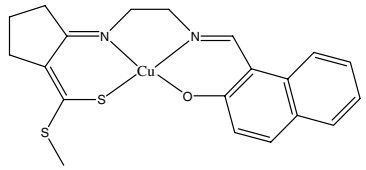
Keywords: Copper Schiff base complexes; X-ray crystal structures; EPR; Electrochemistry; Asymmetric Cu(II) complexes

1. Introduction

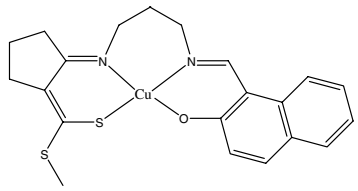
Cu(II)/Cu(I) chemistry has received renewed attention since the characterization and the structural elucidation of blue copper proteins [1–4], e.g. hemocyanin, tyrosinase, cytochrome *c* oxidase and laccase. These proteins have been reported to play an important role in electron transfer during biochemical metabolism. The metal centre responsible for the electron transfer has been identified as containing the redox pair Cu(II)/Cu(I) with quite positive reduction potentials. This feature has been attributed to the unusual coordination geometry around the metal centre. Blue copper proteins have an active copper centre with a N_2S_2 or a N_2OS_2 coordination sphere. Several attempts of preparing lower molecular weight compounds for modelling the redox behaviour of this active centre have been made [5–11]. The copper (II) moiety in biological proteins is asymmetric and, for the tetracoordinated active centre, the geometry around the Cu(II) ion seems to have a significant tetrahedral distortion from square planar geometry. We have prepared a series of Cu(II) complexes with a pseudomacrocyclic Schiff base ligand with a N_2OS asymmetric coordination sphere, as depicted in Scheme 1. The complexes have a sulfur donor atom that can act as a π acceptor, an oxygen donor atom as a π donor and the coordination around the copper ion allows for π electronic

* Corresponding author. Address: CIAGEB – Faculdade de Ciências da Saúde, Escola Superior de Saúde da UFP, Universidade Fernando Pessoa, Rua Carlos da Maia, 296, P-4200-150 Porto, Portugal. Tel.: +351 225 074 630; fax: +351 225 074 637.
E-mail address: lrgomes@ufp.pt (L.R. Gomes).

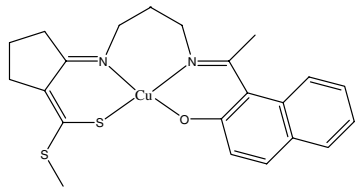
0277-5387/$ - see front matter © 2007 Elsevier Ltd. All rights reserved.
doi:10.1016/j.poly.2007.09.030



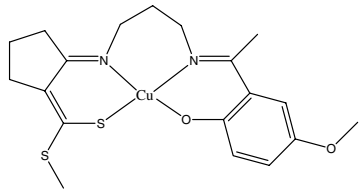
[Cu(cdnapen)]



[Cu(cdnappd)]



[Cu(cdMenappd)]



[Cu(cdMeMeOsalpd)]

Scheme 1.

delocalization. These complexes were characterized in the solid state by X-ray diffractometry in order to elucidate their molecular and crystal structures and to evaluate their degree of tetrahedral distortion to the square planar geometry. Also they have been characterized by EPR spectroscopy in solution at 298 K and at 77 K. Further, their electrochemical behaviour was studied by cyclic voltammetry. The structural and the electrochemical results are compared with those obtained for the corresponding symmetric N_2O_2 and N_2S_2 Cu(II) complexes.

2. Experimental

2.1. Reagents and solvents

All solvents and reagents used in the synthesis and characterization were of reagent grade and were used as received. Solvents used in the electrochemical studies (Merk *pro analysis*) were dried by standard methods. Tetra(*n*-butyl)ammonium perchlorate, TBAP, was prepared following published procedures [12]. *CAUTION*: perchlorates may be hazardous and may explode.

2.2. Synthesis of the ligands

Methyl 2-{*N*-(2-aminoethane)}-amino-1-cyclopentenedithiocarboxylate (Hcden) and methyl 2-{*N*-(2-aminopropane)}-amino-1-cyclopentenedithiocarboxylate (Hcdpd) were prepared by published methods [13,14]. The other ligands were prepared following the general published procedure [15,16].

2.3. Synthesis of the Cu(II) complexes

2.3.1. General procedure

A solution of copper (II) acetate monohydrate (0.1 mmol in 10 cm^3 of methanol) was added to 0.1 mmol of the appropriate ligand in chloroform/methanol (2:1) v/v solution. The mixture was stirred for about 20 min and allowed to react at room temperature for about 24 h. The resulting green or brown powder was recrystallized from acetonitrile/methanol (1:1) v/v. Single crystals for X-ray diffraction were obtained by slow evaporation of the acetonitrile/methanol (1:1) v/v solution.

Methyl 2-{[3-(2-hydroxynaphthyl)methyleneamino]ethylamino}(cyclopent-1-ene-1-dithiocarboxylato) copper (II), [Cu(cdnapen)]: Yield: 54%. *Anal*. Calc. for $C_{20}H_{20}N_2OS_2Cu$: C, 55.60; H, 4.66; N, 6.48; S, 14.84. Found: C, 55.65; H, 4.92; N, 6.45; S, 14.73%.

Methyl 2-{[3-(2-hydroxynaphthyl)methyleneamino]propylamino}(cyclopent-1-ene-1-dithiocarboxylato) copper (II), [Cu(cdnappd)]: Yield: 61%. *Anal*. Calc. for $C_{21}H_{22}N_2OS_2Cu$: C, 56.54; H, 4.97; N, 6.28; S, 14.37. Found: C, 56.59; H, 5.03; N, 6.30; S, 14.32%.

Methyl 2-{[3-(2-hydroxynaphthyl)-ethyl-1-ene-1-amino]ethylamino}(cyclopent-1-ene-1-dithiocarboxylato) copper (II), [Cu(cdMenappd)]: Yield: 14%. *Anal*. Calc. for $C_{22}H_{24}N_2OS_2Cu$: C, 57.43; H, 5.26; N, 6.09; S, 13.94. Found: C, 57.47; H, 5.29; N, 6.05; S, 13.57%.

Methyl 2-{[3-(2-hydroxy-5-methoxyphenyl)ethyl-1-ene-1-amino]ethylamino}(cyclopent-1-ene-1-dithiocarboxylato) copper (II), [Cu(cdMeMeOsalpd)]: Yield: 68%. *Anal*. Calc. for $C_{19}H_{24}N_2OS_2Cu$: C, 51.85; H, 5.50; N, 6.37; S, 14.57. Found: C, 51.90; H, 5.80; N, 6.38; S, 14.69%.

2.4. Instrumentation and electrochemical measurements

Elemental analysis (C, H and N) were performed at the Micro Analytical Laboratory, University of Manchester.

The electrochemical studies were performed with an EG&G PAR 362 instrument. Cyclic voltammetry was carried at room temperature under nitrogen atmosphere on a three-electrode system cell consisting of a microplatinum electrode, a platinum wire counter electrode and an Ag/AgCl (1 mol dm^{-3} NaCl) reference electrode. The cyclic voltammograms were recorded from $\sim 10^{-3}$ mol dm^{-3} solutions of the complexes in dmf, $(CH_3)SO$ and CH_3CN solutions. The potentials were corrected for the ferrocenium/ferrocene (Fc^+/Fc) couple. The potentials were scanned between 0.0 and −2.0 V at a scan rate of 50 mV s^{-1}. Vol-

tammograms were also obtained with scan rates from 20 to 500 mV s^{-1}, to check the reversibility of the redox process.

The EPR spectra were obtained with a Bruker ESP300E spectrometer (9 GHz) in a dual cavity, using diphenylpicrylhydrazyl ($g = 2.0037$) as an external standard; the magnetic field was calibrated with Mn^{2+} in MgO.

2.5. Structure determination

The data acquisition was made using a Stoe Stadi IV diffractometer for [Cu(cdnapen)] and [Cu(cdMeMeOsalpd)] and an image plate Stoe Ipds diffractometer for [Cu(cdnappd)] and [Cu(cdMenappd)], $\lambda = 0.71073$ nm. Intensities were corrected for Lorentz and polarization effects. Empirical absorption correction was performed for compounds [Cu(cdnapen)] and [Cu(cdMeMeOsalpd)] and numerical absorption correction was performed for [Cu(cdnappd)] and [Cu(cdMenappd)] using the package SADABS [17]. SHELX-97 [18] was used to make the structure solution and refinement. The structures were solved by direct methods and subsequent Fourier difference techniques. All non-hydrogen atoms were refined anisotropically by full-matrix least-squares on F^2. Hydrogen atoms were treated as riding atoms with C–H(aromatic) 0.93 Å, C–H(CH_2) 0.97 Å, C–H(CH_3) 0.96 Å, and given an isotropic displacement parameter equal to 1.2 (CH, CH_2) and 1.5 (CH_3) times the equivalent isotropic displacement parameter of the atom to which it is attached. Details for crystallographic data and refinement of the four complexes are shown in Table 1. Molecular and packing diagrams were generated by ORTEP-32 [19] and PLATON [20].

3. Results and discussion

3.1. Structures of the complexes

The X-ray structure determinations confirmed that the complexes show the expected molecular structure. For compounds [Cu(cdnapen)], [Cu(cdnappd)] and [Cu(cdMenappd)], the metal is bonded to the two imine nitrogen atoms, to the sulfur atom from the methyl dithiocarboxylate residue and to the naphtholic oxygen atom of the ligand, assuming a *cis* configuration. For the complex [Cu(cdMeMeOsalpd)], the ligand is a Schiff base that is formed with a fragment derived from the 5-methoxyketophenone and another one derived from the 2-aminocyclopentenedithiocarboxylate methyl ester. Complex [Cu(cdnapen)] has an ethylenic diimine chain while the remaining complexes have a propylenic one.

The structures of complexes are depicted in Figs. 1–5. The main bond lengths for the compounds studied as well as for the homologous compounds with a symmetric coordination sphere, are shown in Table 2. The bond lengths are within the expected range for copper (II) complexes with

Table 1
Crystallographic parameters for the data acquisition of the studied compounds

Compound	[Cu(cdnapen)]	[Cu(cdnappd)]	[Cu(cdMenappd)]	[Cu(cdMeMeOsalpd)]
Formula	$C_{20}H_{20}CuN_2OS_2$	$C_{21}H_{22}CuN_2OS_2$	$C_{22}H_{24}CuN_2OS_2$	$C_{19}H_{24}CuN_2O_4$
Molecular weight (mol dm^{-3})	432.05	442.07	460.09	440.07
Color	brown	green	green	brown
Crystal size (mm)	$0.4 \times 0.3 \times 0.3$	$0.4 \times 0.2 \times 0.1$	$0.3 \times 0.3 \times 0.2$	$0.4 \times 0.2 \times 0.1$
Space group	$P2_1/n$	$P2_1/c$	$P2_1/n$	$P2_1/c$
Crystal system	monoclinic	monoclinic	monoclinic	monoclinic
Temperature (K)	293(2)	203(2)	203(2)	293(2)
Unit cell dimensions				
a (Å)	14.976(7)	19.009(10)	16.104(4)	16.962(13)
b (Å)	14.583(7)	8.302(3)	7.207(4)	8.474(7)
c (Å)	16.829(8)	12.872(10)	17.462(4)	14.283(13)
β (°)	93.54(3)	94.05(6)	94.15(2)	110.72(7)
Volume ($Å^3$)	3668(3)	2026(2)	2021.4(13)	1920(3)
Z	8	4	4	4
μ (mm^{-1})	1.405	1.274	1.280	1.347
F(000)	1784	924	956	916
Minimum to maximum θ collected (°)	1.77–27.07	4.95–28.31	4.95–28.20	2.57–26.00
Index range	$0 \leqslant h \leqslant 16$, $0 \leqslant k \leqslant 18$, $-21 \leqslant l \leqslant 21$	$-22 \leqslant h \leqslant 23$, $-11 \leqslant k \leqslant 10$, $-16 \leqslant l \leqslant 17$	$-20 \leqslant h \leqslant 21$, $-9 \leqslant k \leqslant 9$, $-20 \leqslant l \leqslant 20$	$0 \leqslant h \leqslant 17$, $0 \leqslant k \leqslant 10$, $-20 \leqslant l \leqslant 19$
Absorption correction	empirical	multiscan	multiscan	empirical
Measured reflections (R_{int})	7676 (0.0331)	4747 (0.1633)	4711 (0.0728)	3776 (0,0472)
Data/parameters	7618/469	3735/245	4214/256	3771/238
Goodness-of-fit	1.037	1.056	1.083	1.031
R_1 and wR_2 ($I > 2\sigma I$)	$R_1 = 0.0479$, $wR_2 = 0.0991$	$R_1 = 0.0652$, $wR_2 = 0.1485$	$R_1 = 0.0490$, $wR_2 = 0.1095$	$R_1 = 0.0470$; $wR_2 = 0.1037$
R_1 and wR_2 (all data)	$R_1 = 0.1073$, $wR_2 = 0.1267$	$R_1 = 0.1277$, $wR_2 = 0.1790$	$R_1 = 0.0896$, $wR_2 = 0.1395$	$R_1 = 0.0991$; $wR_2 = 0.1158$
Extinction coefficient	0.013(3)	0.006(8)	0.014(2)	
Major difference (e $Å^{-3}$)	0.474 and −0.629	0.412 and 0.678	0.450 and −0.549	0.041 and −0.613

Table 2
Selected geometric parameters for the some copper (II) complexes with Schiff base ligands

Compound	Cu–N (Å)	Cu–S (Å)	Cu–O (Å)	S–C (Å)	O–C (Å)	Reference
[Cu(cden)]	1.966; 1.925	2.243; 2.258		1.728; 1.680		[26]
[Cu(napen)]	1.925		1.951			[28]
[Cu(cdnapen)]	1.930(4); 1.947(3); 1.940(4); 1.947(4)	2.2374(15); 2.2342(15)	1.921(3); 1.914(3)	1.725(4); 1.718(4)	1.305(5); 1.308(4)	this work
[Cu(salpd)]	1.938(11); 1.958(9)		1.857(10); 1.878(12)		1.293(17)	[31]
[Cu(cdpd)]	1.9498(30)	2.2225(11)		1.723(4)		[25]
[Cu(cdMeMeOsalpd)]	1.949(3); 1.993(3)	2.235(2)	1.888(3)	1.722(4)	1.307(4)	this work
[Cu(nappd)]	1.989(12); 1.971(13)		1.904(11); 1.917(12)			[30]
[Cu(cdnappd)]	1.921(5); 1.944(6)	2.227(3)	1.892(4)	1.697(7)	1.320(7)	this work
[Cu(cdMenappd)]	1.959(3); 2.002(3)	2.2295(11)	1.939(3)	1.713(4)	1.316(5)	this work

Schiff base ligands [21]. The analysis of the bond length within the metallocyclic part of the molecule is indicative of a strong delocalization of the π-electron density through the six member rings. For the cyclopentene fragment, the mean value for the S21–C221 bond length is 1.7150(7) Å, which is considerably lower than what is usually found for a single S–Csp^3 bond, 1.808(10) Å, and similar to the 1.712(17) Å attributed to the S–Csp^2 bond in thiophene, showing a high delocalization of the π-electron density in this part of the molecules [22]; in addition, the distances found between the C21/C41 and C22/C42 carbon atoms of the cyclopentene ring have a mean value within the range 1.439(5)–1.443(9) Å that is similar to the mean value for the Csp^2–Csp^2 bond in conjugated systems [22]. Finally, the similarity of the C21–N2 and C1–N1 bond length values is indicative that this fragment coordinates in a Schiff base mode. This electronic delocalization was reported for complexes containing this type of ligand with other metals [23,24] and for complexes of related ligands [25,26].

The cyclopropene ring defined by the atoms C*n*1–C*n*2–C*n*3–C*n*4–C*n*5 (where *n* is 2 or 4) is puckered in all cases except the compound [Cu(cdMenappd)]. This puckering can be quantified in terms of the pseudorotation parameters P and τ [27]. In all cases the reference bond is C*n*1–C*n*2. For [Cu(cdnapen)], the pucker values P and τ are $P = 296.8(19)°$, $\tau = 11.5(4)°$ corresponding to a twist on C24 and C25 for molecule **A**, and $P = 80.9(19)°$, $\tau = 10.4(4)°$ corresponding to an envelope on C44 for molecule **B**. For [Cu(cdnappd)] these values are $P = 98.6(12)°$, $\tau = 23.2(5)°$ corresponding to an envelope on C24 and for [Cu(cdMeMeOsalpd)] $P = 89.4(6)°$, $\tau = 29.8(3)°$ corresponding to an envelope on C24.

All the Cu(II) complexes show a square planar geometry but with different degrees of tetrahedral distortion. The degree of the distortion will be quantified by measuring the dihedral angle, θ, between planes formed by the N/Cu/O and N/Cu/S atoms of the two semi-coordination spheres.

3.1.1. [Cu(cdnapen)]

The ORTEP representation of the structure of this complex, including the atom numbering scheme is shown in Fig. 1. The crystal structure determination revealed the existence of two independent molecules in the asymmetric unit. These are assigned as molecule **A** (labelled as Cu1) and molecule **B** (labelled as Cu2). The two molecules have different tetrahedral distortions relative to the square-planar geometry. Molecule **A** presents a dihedral angle of 5.28(17)° and molecule **B** of 11.52(9)°. In both of them, the geometry around the coordination centre is more planar than that in the homologous N_2S_2 complex [Cu(cden)] that presents an dihedral angle of about 20° [21]. On the other hand, the analogous N_2O_2 [Cu(napen)] seems to be more planar with $\theta \approx 7°$ [28].

The minimum distance between the copper atoms is 3.879 Å which rules out the existence of an interaction between them. This observation contrasts with that described for the homologous symmetric N_2O_2 complex, [Cu(napen)], for which the crystallographic results pointed to the existence of an interaction between the copper ion (placed in an apical position) of the complex and the donor oxygen atom of the above one.

3.1.2. [Cu(cdnappd)]

The molecular diagram of this complex, together with the atom numbering scheme is depicted in Fig. 2. The molecular structure revealed that the geometry around the coordination centre is a square planar one with a tetrahedral distortion. The dihedral angle is 37.36(25)°, higher than that reported for [Cu(nappd)], 6.1° [30], the analogous symmetric N_2O_2 complex, but lower than that shown by the analogous N_2S_2 complex, [Cu(cdpd)], which has a value of ca. 50° [25]. The aliphatic chain is in the *twist* conformation.

In this compound C18 acts as a hydrogen bond donor to atom O12 in the molecule at $(x, 1.5 - y, 0.5 + z)$, so forming a C(6) chain [29] which runs parallel to the *c*-axis (Fig. 3). The C–H distance is 0.93 Å, the H···O distance is 2.48 Å and the C—O distance is 3.397(7) Å. The angle at H is 171°. The same O12 oxygen atom establishes a short contact with H1–C1 of the *c*-glide related complex, O12···H1–C1 (distance 2.64 Å).

3.1.3. [Cu(cdMenappd)]

The structure of [Cu(cdMenappd)] is depicted in Fig. 4. The propylenic aliphatic chain of the ligand assumes a

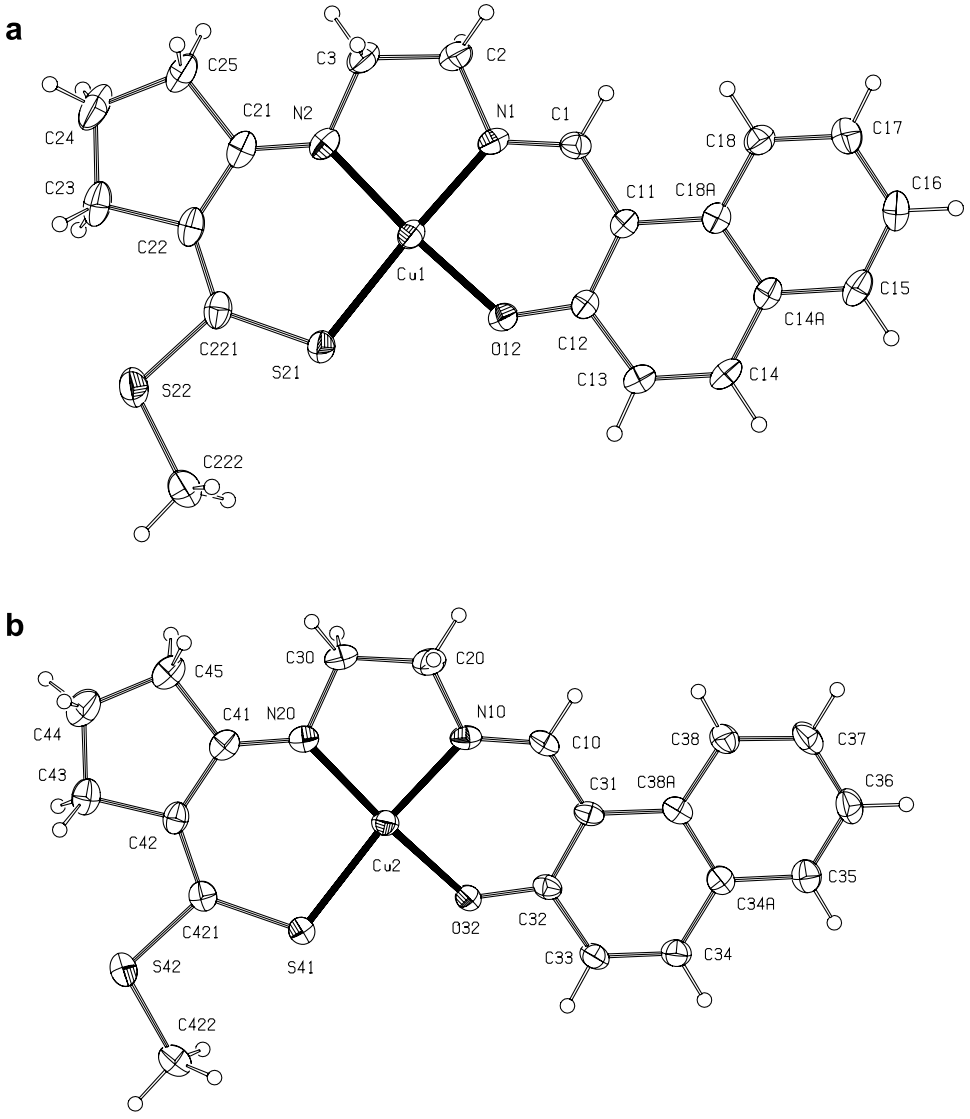


Fig. 1. A view of [Cu(cdnapen)] **A** (labelled with Cu1) and **B** (labelled with Cu2) with the adopted numbering scheme. Displacement ellipsoids are drawn at the 30% probability level.

"*boat*"-shape conformation in the complex. The coordination around the Cu(II) ion is square planar with a tetrahedral distortion. For this compound $\theta = 28.44(15)°$. This value is lower than that of 50° reported for [Cu(cdpd)] [25], and higher than the dihedral angle for the symmetric [Cu(nappd)], with a reported value of 6.1° [30].

3.1.4. [Cu(cdMeMeOsalpd)]

Fig. 5 shows the perspective view and the atomic numbering scheme for the [Cu(cdMeMeOsalpd)] complex. The trimethylenic chain of the ligand is *twisted* and the chelating rings assume an *umbrella* conformation relative to each other. The complex also presents some degree of tetrahedral distortion around the metal centre relative to the square-planar geometry. The dihedral angle between the N/Cu/S and N/Cu/O planes is 41.79(10)°. This complex is more tetrahedrally distorted than [Cu(salpd)] [31], for which the θ angle is ca. 21.0°, but the distortion value is similar to that for [Cu(Me_2salpd)], which is 43.8° [32]. Anyhow, the symmetric homologous N_2S_2 complex [Cu(cdpd)] [25] exhibits even higher distortion ($\theta = 50°$) showing that the presence of the sulfur atom also plays an important role in the geometrical distortion from the square planar shape in these complexes.

Our structural results point out some factors that can change the degree of tetrahedron distortion of these Cu(II) complexes, namely, (i) the number of ethylene groups in the ligand bridge and (ii) the type of donor atoms. Comparing the theta values for the [Cu(salen)]/[Cu(salpd)] (1.7° and 21°), [Cu(cden)]/[Cu(cdpd)] (20° and 50°) and [Cu(cdnapen)]/[Cu(cdnappd)] (5.5°/11.6° and 37.3°) set of pairs, it is clear that the three carbon atom chain induces a higher distortion than the two carbon atom chain. This has been reported for several other studies on Schiff base metal complexes that have even lower electronic preferences for square planar geometries.

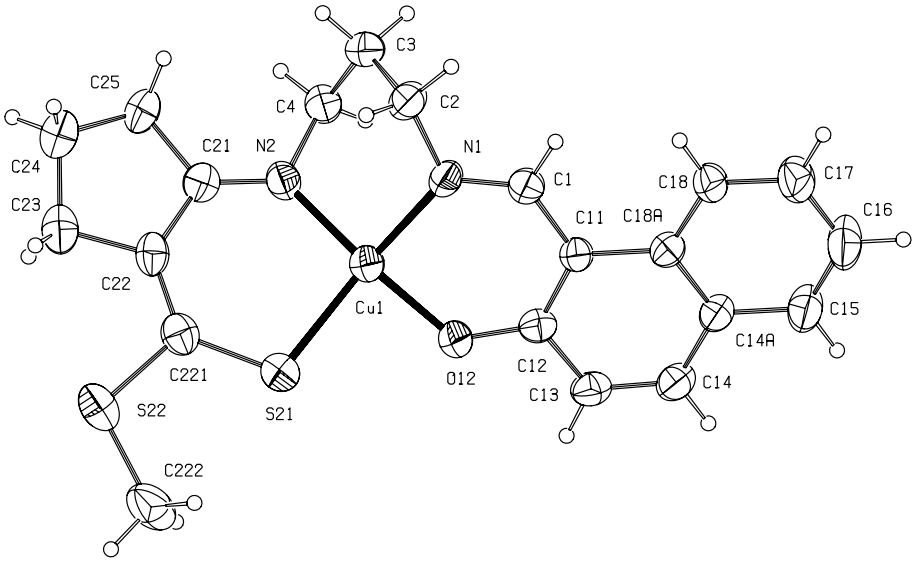


Fig. 2. A view of [Cu(cdnappd)] with the adopted numbering scheme. Displacement ellipsoids are drawn at the 30% probability level.

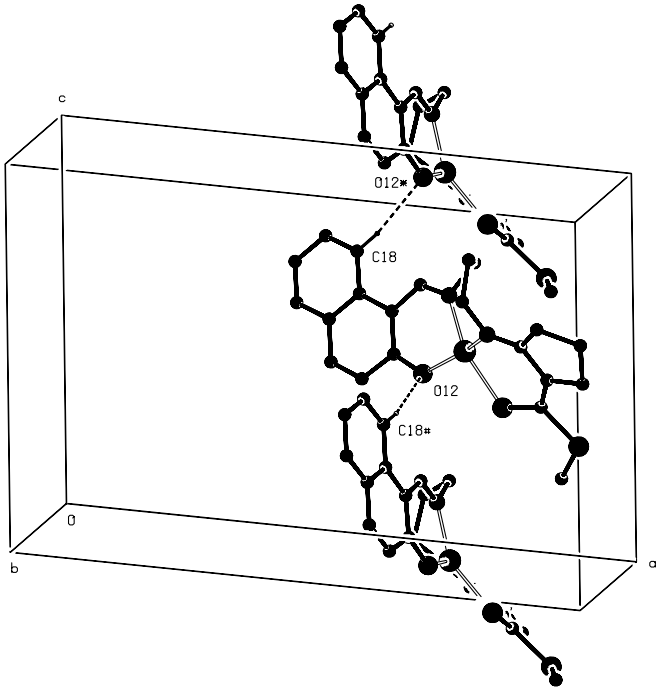


Fig. 3. Part of the structure of compound [Cu(cdnappd)] showing a C(6) chain running parallel to the *c*-axis. Hydrogen atoms not involved in the hydrogen bonding are omitted for clarity. The atom marked with an asterisk, (*), and hash, (#), are at symmetry positions (x, $1.5 - y$, $0.5 + z$) and (x, $1.5 - y$, $-0.5 + z$), respectively.

The complexes with an N_2O_2 coordination sphere are more planar than those with a N_2OS coordination sphere, that are, on the other hand, more planar than those with N_2S_2. A larger difference is observed for [Cu(nappd)]/[Cu(cdnappd)] and [Cu(cdpd)], which have 6.1°, 37° and 50° theta angles values, respectively. A sulfur donor, which gives a lower ligand field strength, shows a higher tendency than oxygen towards tetrahedral distortion.

3.2. Electron paramagnetic resonance spectroscopy

The EPR characterization of the complexes in dmf solution was made at room temperature and at 77 K. In Table 3, EPR parameters that were obtained after computational simulation of the experimental spectra are presented and in Fig. 6 a typical spectrum obtained for the complexes, together with the graphic computational simulation is shown.

The EPR parameters are in the range expected for tetra-coordinate copper (II) complexes with N_2S_2 and N_2O_2 coordination spheres and show the typical hyperfine splitting with the ^{63}Cu and ^{65}Cu nuclei. Super-hyperfine coupling with the two magnetically equivalent nitrogen nuclei (^{14}N, $I = 1$) is also observed either at room temperature or in frozen solution, in accordance with the similarity between the two nitrogen donor atoms revealed in the molecular structures of the complexes.

A comparison of the EPR parameters shows that the g and A values are very sensitive to the tetrahedral distortion of the complexes, as usually observed for tetra-coordinated copper (II), with a marked decrease of A values and an increase in g_1 with the tetrahedral distortion [33–36]. The dependence of the EPR parameters on the coordination sphere is not so important, and in fact the ERP parameters obtained for the N_2OS complexes are more similar to the N_2S_2 parent complexes than to the N_2O_2 copper (II) Schiff base complexes [37,38].

3.3. Electrochemistry

The results obtained in the electrochemical studies are summarized in Table 4. The symmetric N_2S_2 Cu(II) complexes were also studied under the same conditions for a direct comparison of the results. For all the complexes one anodic peak is observed in the potential range from

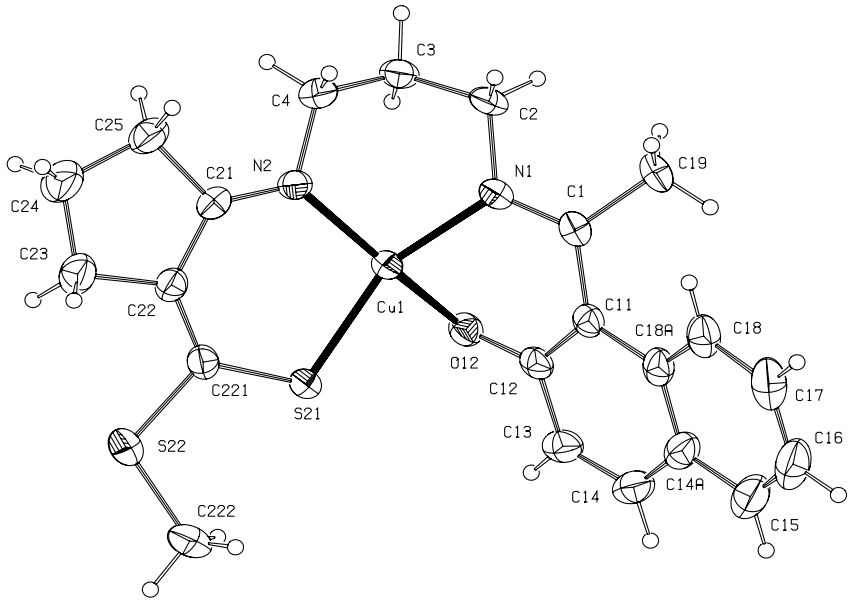


Fig. 4. A view of [Cu(cdMenappd)] with the adopted numbering scheme. Displacement ellipsoids are drawn at the 30% probability level.

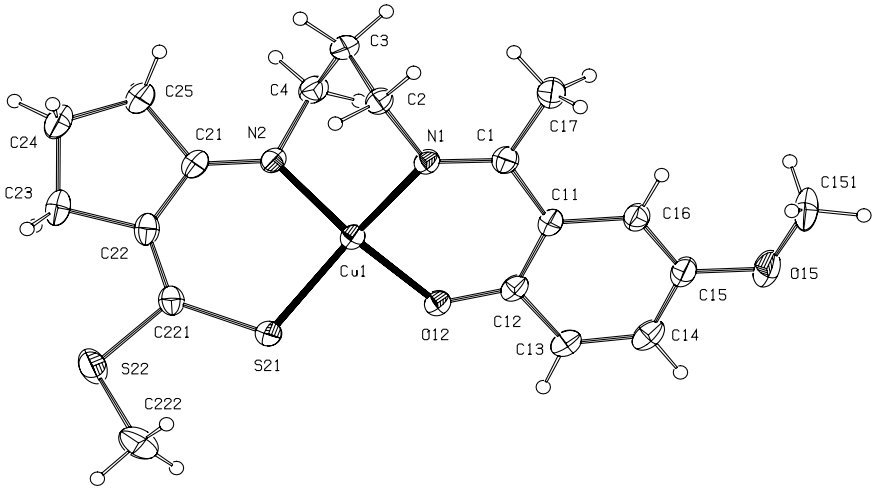


Fig. 5. A view of [Cu(cdMeMeOsalpd)] with the adopted numbering scheme. Displacement ellipsoids are drawn at the 30% probability level.

Table 3
EPR parameters for the studied complexes[a]

Complex	g_{iso}	A_{iso}	A_{iso}(N)	g_1	g_2	g_3	A_1	A_2	A_3	A_1(N)	A_2(N)	A_3(N)
[Cu(cdnapen)]	2.076	84.0	14.5	2.186	2.117	2.060	208.0	[b]	38.0	14.5	[b]	[b]
[Cu(cdnappd)]	2.084	77.0	12.0	2.188	2.049	2.012	186.0	20.0	[b]	[b]	9.0	[b]
[Cu(cdMenappd)]	2.084	77.0	12.0	2.168	2.053	2.036	189.0	37.6	[b]	[b]	12.7	[b]
[Cu(cdMeMeOsalpd)]	2.085	74.5	12.2	2.169	2.051	2.028	180.0	25.0	[b]	12.5	12.5	[b]

[a] Hyperfine coupling constants in 10^{-4} cm^{-1}.
[b] The spectral resolution did not allow the determination of this value.

+0.7 V to +0.9 V, but no evidence for a corresponding cathodic peak is observed, except for the compound [Cu(cdnapen)]. The voltammograms are not repeatable, and a dark material precipitates at the electrode. For the compound [Cu(cdnapen)], the i_{pc}/i_{pa} ratio increases with the scan rate, showing that the irreversible voltammetric behaviour is due to a slow chemical reaction after electron-transfer. In addition, in the negative potential scan, a cathodic peak is detected for all the complexes in the potential range from −0.8 V to −1.1 V. In this case, the corresponding anodic peaks are observed in the range from −0.6 V to −1.0 V, except for the compound

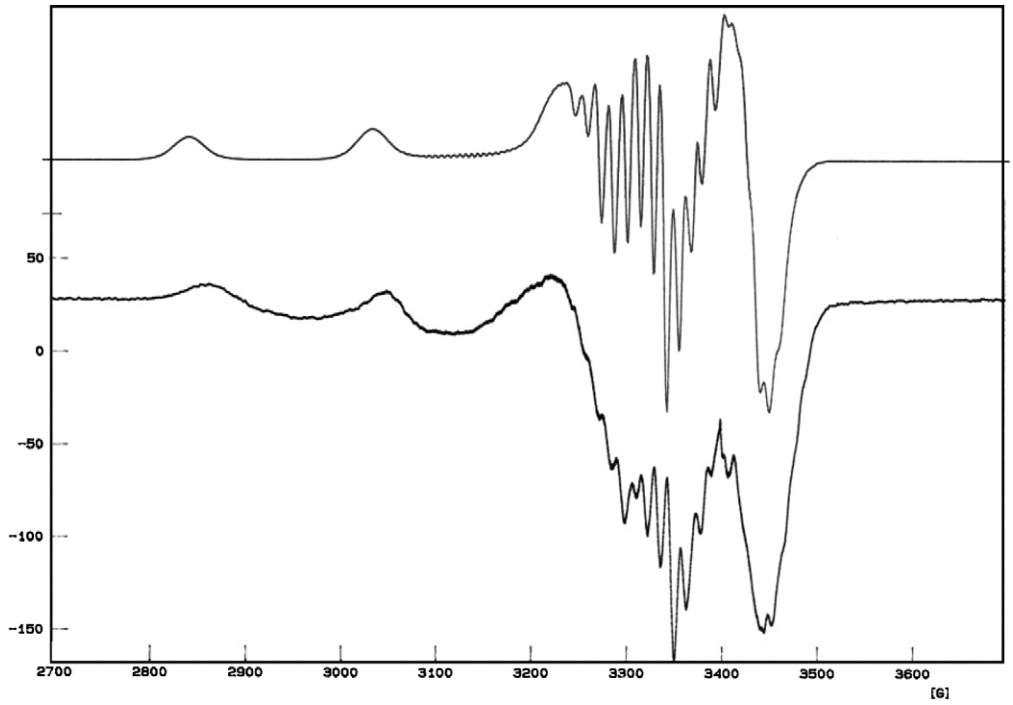


Fig. 6. EPR spectrum of [Cu(cdMenappd)] in DMF at 77 K (bottom) and simulation (top) using the software Symphonia WIN-EPR (Bruker).

Table 4
Voltammetric parameters obtained for the copper (II) complexes

Complex	E_{pa} (V)	E_{pc} (V)	ΔE (V)	i_{pa}/i_{pc}
[Cu(cdnapen)]	−0.978	−1.073	0.095	0.92[a]
[Cu(cdnappd)]	−0.780	−0.880	0.100	0.99[a]
[Cu(cdMenappd)]	−0.64	−0.80	0.16	[b]
[Cu(cdMeMeOsalpd)]	−0.770	−0.900	0.130	0.76[b]
[Cu(cden)]	−0.992	−1.070	0.078	0.93[a]
[Cu(cdpd)]	−0.80	−0.86	0.06	[b]

Potentials are reported in V relative to the Ag/AgCl (1 mol dm^{-3} NaCl) reference electrode and corrected for the Fc^+/Fc couple ($E_{1/2} = 0.485$ V). i_{pa} and i_{pc} values are base line corrected. Scan rate: 0.050 V s^{-1}.

[a] The i_{pa}/i_{pc} ratio decreases with the increase of scan rate.

[b] The i_{pa}/i_{pc} ratio increases with the increase in scan rate.

[Cu(cdMeMeOsalpd)], which shows totally irreversible behaviour. The variation of the CV parameters with scan rate shows that in all the other compounds the redox behaviour is not reversible. For compounds [Cu(cdnapen)], [Cu(cdnappd)] and [Cu(cden)], the i_{pc}/i_{pa} ratio decreases with the scan rate, typical of an irreversible electron transfer, whereas for compounds [Cu(cdMenappd)], [Cu(cdMeMeOsalpd)] and [Cu(cdpd)], the i_{pc}/i_{pa} ratio increases with the scan rate, showing that the reduced form undergoes a slow chemical reaction.

Due to the irreversible redox behaviour, it is not possible to correlate the redox potentials with the coordination spheres of the complexes, Nevertheless, the cathodic peak potential corresponding to the reduction of the copper (II) complexes seems to be lower for complexes with a dimethylene bridge than for those with propylene bridges. This trend is also observed for the reduction potentials for the Ni(II)/Ni(I) couple of the analogous Ni(II) complexes [15,16]. These observations have been attributed to the fact that the trimethylene bridge complexes are more tetrahedrally distorted and the distortion could favour the lower oxidation states for the metal complex. This is confirmed also for the compounds under study by the X-ray structural data. The reduction potentials obtained for the asymmetric complexes are similar to those obtained for homologous symmetric ones with the same number of ethylene residues in the bridge. This data is in agreement with the EPR results, and suggests that the change of a soft sulfur donor for a hardest oxygen donor does not significantly affect the properties of the complexes.

Acknowledgements

We thank the Institut fur Anorganische Chemie, Universitat Karlsruhe for allowing X-ray data collection. Lígia Gomes thanks financial support from the Fundação para a Ciência e Tecnologia (POCI/QUI/61873/2004).

Appendix A. Supplementary material

CCDC 640665, 640666, 640667 and 640668 contain the supplementary crystallographic data for [Cu(cdnapen)], [Cu(cdnappd)], [Cu(cdMenappd)] and [Cu(cdMeMeOsalpd)]. These data can be obtained free of charge via http://www.ccdc.cam.ac.uk/conts/retrieving.html, or from the Cambridge Crystallographic Data Centre, 12 Union Road, Cambridge CB2 1EZ, UK; fax: (+44) 1223-336-033; or e-mail: deposit@ccdc.cam.ac.uk. Supplementary data associated with this article can be found, in the online version, at doi:10.1016/j.poly.2007.09.030.

References

[1] A. Messerschmidt, Struct. Bond. 90 (1998) 37.
[2] E.I. Solomon, R.K. Szilagyi, S. DeBeer-George, L. Basumallick, Chem. Rev. 104 (2004) 419.
[3] Z. Zhu, L.M. Cunane, Z. Chen, R.C. Durley, F.S. Mathews, V.L. Davidson, Biochemistry 37 (1998) 17128.
[4] (a) A.G. Sykes, Adv. Inorg. Chem. 36 (1991) 377;
(b) A.G. Sykes, Struct. Bond. 73 (1990) 1.
[5] N. Daneshvar, A.A. Entezami, L.A. Khandar, L.A. Saghatforoush, Polyhedron 22 (2003) 1437.
[6] M.K. Taylor, D.E. Stevenson, L.E.A. Berlouis, A.R. Kennedy, J. Reglinski, J. Inorg. Biochem. 100 (2006) 250.
[7] N. Kitajima, K. Fujisawa, Y. Moro-oka, J. Am. Chem. Soc. 112 (1990) 3210.
[8] N. Kitajima, K. Fujisawa, Y. Moro-oka, J. Am. Chem. Soc. 114 (1992) 9232.
[9] P.L. Holland, W.B. Tolman, J. Am. Chem. Soc. 122 (2000) 6331.
[10] D.W. Randall, S.D. George, P.L. Holland, B. Hedman, K.O. Hodgson, W.B. Tolman, E.I. Solomon, J. Am. Chem. Soc. 122 (2000) 11632.
[11] W-Z. Lee, W.B. Tolman, Inorg. Chem. 41 (2002) 5656.
[12] S.T. Donald Jr., R.L. Julian, Experimental Electrochemistry for Chemistry, Wiley, New York, 1974.
[13] B. Bordás, P. Sohár, G. Matolcky, P. Berencsi, J. Org. Chem. 37 (1972) 1727.
[14] K. Nag, D.S. Jordar, Inorg. Chim. Acta 14 (1975) 133.
[15] E. Pereira, L. Gomes, B. Castro, J. Chem. Soc., Dalton Trans. (1998) 629.
[16] E. Pereira, L. Gomes, B. Castro, Inorg. Chim. Acta 271 (1998) 83.
[17] G.M. Sheldrick, SABABS: Bruker Nonious area detector scaling and absorption correction, 2003.
[18] (a) G.M. Sheldrick, Acta Crystallogr., Sect. A 46 (1990) 467;
(b) G.M. Sheldrick, SHELXS-97: Program for the Solution of Crystal Structure, University of Göttingen, Göttingen, Germany, 1997.
[19] L.J. Farrugia, J. Appl. Crystallogr. 30 (1997) 565.
[20] A.L. Spek, J. Appl. Crystallogr. 36 (2003) 3.
[21] (a) A.D. Garnovskii, A.L. Nivorozhkin, V.I. Minkin, Coord. Chem. Rev. 126 (1993) 1;
(b) S. Mandal, G. Das, R. Singh, K. Bhuradwaj, Coord. Chem. Rev. 160 (1997) 191.
[22] F.H. Allen, O. Kennard, D.G. Watson, G. Orpen, L. Brammer, R. Taylor, J. Chem. Soc., Perkin Trans. 2 (1987) S1.
[23] B. Castro, E. Pereira, L. Gomes, Acta Crystallogr., Sect. C 53 (1997) 572.
[24] E.M. Martin, R.D. Bereman, Inorg. Chim. Acta 188 (1991) 221.
[25] R.D. Beremenn, M.R. Churchill, G. Shields, Inorg. Chem. 18 (1979) 3117.
[26] R.D. Beremenn, J.R. Dorfmann, J. Bordener, D.P. Rillema, P. McCarthy, G.D. Shilds, J. Inorg. Biochem. 16 (1982) 47.
[27] S.T. Rao, E. Westhof, M. Sundaralingam, Acta Crystallogr., Sect. A 37 (1981) 421.
[28] Von C. Freiburg, W. Reicht, W. Melchers, B. Engelen, Acta Crystallogr., Sect. B 36 (1980) 1209.
[29] J. Bernstein, R.E. Davis, I. Shimoni, N-L. Chang, Agnew. Chem., Int. Ed. Engl. 34 (1995) 1555.
[30] F. Akhtar, M.G.B. Drew, Acta Crystallogr., Sect. B 38 (1982) 1149.
[31] M.G.B. Drew, Acta Crystallogr., Sect. C 41 (1985) 1755.
[32] K. Iide, J. Oonishi, A. Nakahara, J. Komiayma, Bull. Chem. Soc. Jpn. 43 (1970) 2347.
[33] B.J. Hathaway, D.E. Billing, Coord. Chem. Rev. 5 (1970) 143.
[34] K.D. Karlin, J. Zubieta (Eds.), Copper Coordination Chemistry: Biochemical and Inorganic Perspectives, Adenine Press, New York, 1983.
[35] H. Yokoi, A.W. Addison, Inorg. Chem. 16 (1977) 1341.
[36] I. Bertini, G. Canti, R. Grassi, A. Scozzatava, Inorg. Chem. 19 (1980) 2198.
[37] E.S. Marcus, R. Caballol, G. Trinquir, J.C. Barthelat, J. Chem. Soc., Dalton Trans. (1987) 1328.
[38] M.M. Bhadbhade, D. Srinivas, Inorg. Chem. 32 (1993) 6122.

Available online at www.sciencedirect.com
ScienceDirect
Polyhedron 27 (2008) 344–348
POLYHEDRON
www.elsevier.com/locate/poly

A new series of dinucleating macrocyclic ligands and their complexes of zinc(II)

Ze-Li Yuan [a], Qi-Long Zhang [a], Xue Liang [a], Bi-Xue Zhu [a,*], Leonard F. Lindoy [b,*], Gang Wei [c,*]

[a] Department of Chemistry, Guizhou University, Guizhou 550025, PR China
[b] Centre for Heavy Metal Research, School of Chemistry, The University of Sydney, NSW 2006, Australia
[c] CSIRO Materials Science and Engineering, P.O. Box 218, Lindfield, NSW 2070, Australia

Received 29 August 2007; accepted 18 September 2007
Available online 26 October 2007

Abstract

A new category of dinucleating macrocyclic Schiff base ligands with ring sizes from 34- to 52-membered have been synthesised employing metal template procedures involving the reaction of *o*-phenylenediamine with a series of α,ω-bis(3′-hydroxy-4′-formylphenyloxy)alkanes in the presence of calcium(II), barium(II) or manganese(II). The latter cations act as 'transient' templates for formation of the corresponding metal-free Schiff base macrocyclic ligands, H_4L^n (where *n* signifies the number of carbons in each linking bis-alkoxy chain); the macrocycles corresponding to $n = 4$, 6 and 8 were isolated and characterised while, for $n = 1$, in which single methylene groups acts as the bridges between salicyl moieties, the cyclic product was used directly for preparation of its dinuclear complex, $[Zn_2L^1]$, without prior isolation. Evidence for the templating role of barium in the preparation of H_4L^6 and H_4L^8 was obtained by isolation of the corresponding species of type $H_4L^n{\cdot}2Ba(ClO_4)_2$ ($n = 6$ or 8) as 'intermediates' before generation of the respective metal-free macrocycles. Reaction of zinc(II) acetate with the free macrocycles in methanol yielded complexes of type $[Zn_2L^n]$ in all cases. A related non-cyclic ligand, H_2L^0 and its corresponding mononuclear complex, $[ZnL^0]{\cdot}H_2O$, were also synthesised and its spectral properties compared with those of the macrocyclic derivatives. The elemental analyses, ^1H NMR, IR, UV–Vis and MS spectra of the respective zinc complexes in each case were in accord with the formation of the expected 2:2 condensation product. The results of DFT calculations to probe aspects of the electronic and structural natures of both H_2L^1 and H_4L^4 are briefly presented.
© 2007 Elsevier Ltd. All rights reserved.

Keywords: Zinc(II); Dinucleating macrocycles; Template synthesis; Schiff base

1. Introduction

Reflecting their usual relative ease of synthesis and excellent metal complexing properties, Schiff base complexes have been extensively investigated for more than a century and have been employed in areas that include analytical and bioinorganic chemistry, non-linear optics, fluorescence studies, catalysis and materials chemistry [1–12].

The metal coordination chemistry of dinucleating macrocyclic ligands remains an area of considerable research activity [13]. Apart from unusual properties (in particular, spectral, electrochemical and magnetic properties) [14,15] resulting from the proximity of the metal centres, there has long been an interest in such dinuclear species as model compounds for particular metallo-enzymes [16,17].

Beginning with the pioneering work of Robson [18], Schiff base linkages have been incorporated in many dinucleating macrocyclic derivatives [15,19] whose corresponding metal complexes exhibit a wide structure range. In many instances such complexes were prepared by metal template procedures and the ability of metal ions to promote the template synthesis of macrocyclic ligand species has been well documented for many years; in

* Corresponding authors. Tel.: +61 2 9351 4400; fax: +61 2 9351 3329.
E-mail address: lindoy@chem.usyd.edu.au (L.F. Lindoy).

0277-5387/$ - see front matter © 2007 Elsevier Ltd. All rights reserved.
doi:10.1016/j.poly.2007.09.012

particular, it is known to depend on a range of factors that relate to both the nature of the ligand precursors and the metal ion involved [20]. For example, metal ions with a 'symmetrical' electron shell such as Mn^{2+} (d^5), Zn^{2+} (d^{10}) or an alkaline earth cation have frequently been employed as templates. We now report the template synthesis of a series of new, potentially dinucleating macrocyclic Schiff base ligands of type H_4L^n ($n = 1$, 4, 6 and 8) along with the results of an investigation of their interaction with zinc(II). For comparison, the related open-chain complex of zinc(II) was also synthesised.

2. Experimental

2.1. General

Zinc acetate dihydrate, 1,4-dibromobutane, 1,6-dibromohexane, 1,8-dibromooctane, 4-hydroxy-salicylaldehyde were obtained commercially and 5,5′-methylene-bis-salicylaldehyde were synthesised using the reported procedure [21,22]. Solvents were purified according to literature methods [23]. The series of α,ω-bis(3′-hydroxy-4′-formylphenyloxy)alkanes (in which the alkyl bridge has four, six or eight carbons) were synthesised as reported elsewhere [24].

The ^{1}H NMR spectra were recorded on a JEOL ECX 500 MHz spectrometer. FT-IR spectra (KBr pellets) in the 400–4000 cm^{-1} range were recorded on a Bio-Rad FTIR spectrophotometer; selected assignments only are reported. Elemental analysis was performed on a Vario ELIII analyzer. ESI mass spectra were recorded on an Agilent 1100 Series ESI/MSD spectrometer. Density functional theory (DFT) calculations were carried out using GAUSSIAN03.

All new products were dried in a vacuum over silica gel.

2.2. Synthesis of $[ZnL^0]$ and H_2L^0

4-Dihydroxybenzaldehyde (1.106 g, 8.00 mmol) was added with stirring to *o*-phenylenediamine (0.432 g, 4.00 mmol) in methanol (25 mL) at room temperature. Zinc acetate dihydrate (0.698 g, 4.00 mmol) in methanol (20 mL) was added and the mixture was heated at reflux for 2 h. After allowing the solution to cool, the precipitate was collected by filtration, washed with water and dried; the yellow solid was crystallised from a THF/*n*-hexane mixture. Yield: 1.449 g (88%). MS (ESI) *m*/*z*: 412 (M^+). *Anal.* Calc. for $C_{20}H_{14}N_2O_4Zn$: C, 58.34; H, 3.43; N, 6.80. Found: C, 58.05; H, 3.38; N, 6.89%. NMR ^{1}H (DMSO-d_6) δ 9.79 (OH); 8.79 (s, CH=N); 6.03–6.04, 7.18–7.25, 7.75 (arom). FT-IR (KBr, cm^{-1}) 1612 ($\nu_{C=N}$); UV–Vis (DMSO, nm) λ_{max}: 258, 280, 315.

Repeat of the above synthesis in the absence of added zinc acetate, yielded a sample of metal-free H_2L^0. *Anal.* Calc. for $C_{20}H_{16}N_2O_4$: C, 68.96; H, 4.63; N, 8.04. Found: C, 68.56; H, 4.42; N, 6.91%. MS (ESI) *m*/*z*: 348 (M^+). NMR ^{1}H (DMSO-d_6) δ 13.41, 10.33 (OH); 8.73 (s, CH=N); 6.27–6.38, 7.29–7.43, 7.75 (arom). UV–Vis (DMSO, nm) λ_{max}: 265, 313, 390 and 425(sh).

2.3. Syntheses of the macrocyclic ligands and corresponding dinuclear zinc(II) complexes

2.3.1. Synthesis of $[Zn_2L^1]$ via H_4L^1

5,5′-Methylene-bis-salicylaldehyde (1.005 g, 4.00 mmol) in tetrahydrofuran (8 mL) was added slowly with stirring to *o*-phenylenediamine (0.425 g, 4.00 mmol) and $CaCl_2$ (0.45 g, 4.00 mmol) in methanol (25 mL) and the mixture was heated at reflux for 5 h. The solution was allowed to cool and the precipitate of H_4L^1 was collected by filtration and washed with methanol then water. Yield: 0.735 g (56%), m.p. 116–118 °C. MS (ESI) *m*/*z*: 656 (M^+). *Anal.* Calc. for $C_{42}H_{32}N_4O_4$: C, 76.81; H, 4.91; N, 8.43. Found: C, 77.02; H, 4.52; N, 8.52% FT-IR (KBr, cm^{-1}) 1618, 1610 ($\nu_{C=N}$). NMR ^{1}H (DMSO-d_6) δ 12.40 (OH); 8.79 (s, CH=N); 6.63–6.65, 7.10–7.52, 7.85 (arom); 3.75 (CH_2). UV–Vis (DMSO, nm) λ_{max}: 262, 301, 414.

Zinc acetate dihydrate (0.349 g, 2.00 mmol) in methanol (15 mL) was added to a solution of the above product (1.316 g, 2.00 mmol) in methanol (25 mL) at room temperature and the reaction solution was heated at reflux for 2 h. The solution was allowed to cool and the precipitate of $[Zn_2L^1]$ was collected by filtration and washed with methanol. Yield: 0.886 g (61%), m.p. 118–120 °C. MS (ESI) *m*/*z*: 783 (M^+). *Anal.* Calc. for $C_{42}H_{28}N_4O_4Zn_2{\cdot}H_2O$: C, 62.94; H, 3.77; N, 6.99. Found: C, 63.04; H, 3.52; N, 7.02%. FT-IR (KBr, cm^{-1}) 1618 ($\nu_{C=N}$), 621(ν_{Zn-O}), 511(ν_{Zn-N}). NMR ^{1}H (DMSO-d_6) δ 8.94 (s, CH=N); 6.63–6.65, 7.10–7.51 (arom); 3.68 (CH_2). UV–Vis (DMSO, nm) λ_{max}: 260, 274, 343.

2.3.2. Synthesis of H_4 L^n (where n = 4, 6 and 8)

2.3.2.1. H_4L^4. 1,4-Bis(3′-hydroxy-4′-formylphenyloxy)-butane (0.66 g, 2 mmol) in THF (8 mL) was added slowly, with stirring, to *o*-phenylenediamine (0.22 g, 2 mmol) and $MnCl_2{\cdot}4H_2O$ (0.396 g, 2 mmol) in methanol (25 mL). The mixture was heated at reflux for 5 h. After allowing the solution to cool, the yellow precipitate of H_4L^4 was collected by filtration and washed with hot methanol (3×5 mL). Yield: 0.322 g (40%), m.p. 145–147 °C. MS (ESI) *m*/*z*: 804 (M^+). *Anal.* Calc. for $C_{48}H_{44}N_4O_8$: C, 71.64; H, 5.47; N, 6.97. Found: C, 71.63; H, 5.51; N, 6.96%. FT-IR (KBr, cm^{-1}) 1640 ($\nu_{C=N}$). NMR ^{1}H (DMSO-d_6) δ 11.00 (OH); 9.99 (s, CH=N); 6.47–6.57, 7.59–7.62 (arom); 4.09 (OCH_2); 1.86 (CH_2). UV–Vis (DMSO, nm) λ_{max}: 253, 282, 320.

2.3.2.2. H_4L^6 via $H_4L^6{\cdot}2Ba(ClO_4)_2$. 1,6-Bis(3′-hydroxy-4′-formylphenyloxy)hexane 0.776 g (2 mmol) in THF (8 mL) was added slowly, with stirring, to *o*-phenylenediamine (0.22 g, 2 mmol) and $Ba(ClO_4)_2{\cdot}4H_2O$ (0.781 g, 2 mmol) in methanol (25 mL). The mixture was heated at reflux for 5 h and then allowed to cool. The yellow solid of $H_4L^6{\cdot}2Ba(ClO_4)_2$ was collected by filtration and washed with hot

methanol (3 × 5 mL). Yield: 1.103 g (72%), m.p. >300 °C. MS (ESI) *m/z*: 860 ($M^+-2Ba(ClO_4)_2$), 1333 ($M^+-2ClO_4^-$). *Anal.* Calc. for $C_{52}H_{52}N_4O_8{\cdot}2Ba(ClO_4)_2$: C, 40.73; H, 3.41; N, 3.65. Found: C, 41.01; H, 3.39; N, 3.61%.

Caution! Perchlorate salts are potentially explosive and need to be handled in small quantities with appropriate care and safeguards.

An aqueous solution of Na_2SO_4 (0.284 g, 2 mmol) was added slowly, with stirring, to a solution of $H_4L^6{\cdot}2Ba(ClO_4)_2$ (0.776 g, 2.00 mmol) in acetonitrile (50 mL). Stirring was continued for 1 h then the solution was filtered and the acetonitrile was removed under reduced pressure. The oily material that remained was extracted into $CHCl_3$ (3 × 10 mL) then the $CHCl_3$ was removed under reduced pressure to obtain H_4L^6 as an orange solid. Yield: 0.472 g (55%), m.p. 134–136 °C. MS (ESI) *m/z*: 860 (M^+). *Anal.* Calc. for $C_{52}H_{52}N_4O_8$: C, 72.56; H, 6.05; N, 6.51. Found: C, 72.54; H, 6.09; N, 6.68%. FT-IR (KBr, cm^{-1}) 1637, 1629 ($\nu_{C=N}$). NMR ^1H (DMSO-d_6) δ 11.00 (OH); 9.98 (s, CH=N); 6.43–6.53, 7.56–7.58 (arom); 4.00 (OCH_2); 1.70, 1.42 (CH_2). UV–Vis (DMSO, nm) λ_{max}: 253, 282, 319.

2.3.2.3. H_4L^8 via $H_4L^8{\cdot}2Ba(ClO_4)_2$. The synthetic procedure was similar to that employed for $H_4L^6{\cdot}2Ba(ClO_4)_2$ and H_4L^6 and used Ba^{2+} as a template. $H_4L^8{\cdot}2Ba(ClO_4)_2$ is an orange solid. Yield: 0.472 g (72%), m.p. > 300 °C. MS (ESI) *m/z*: 915 [$M^+-2Ba(ClO_4)_2$], 1389 ($M^+-2ClO_4^-$). *Anal.* Calc. for $C_{56}H_{60}N_4O_8{\cdot}2Ba(ClO_4)_2$: C, 42.31; H, 3.80; N, 3.52. Found: C, 41.96; H, 3.65; N, 3.28%. Yield: 0.472 g (52%), m.p. 125–127 °C. MS (ESI) *m/z*: 916 (M^+). *Anal.* Calc. for $C_{56}H_{60}N_4O_8$: C, 73.34; H, 6.59; N, 6.11. Found: C, 73.23; H, 6.59; N, 6.26%. FT-IR (KBr, cm^{-1}) 1639, 1627 ($\nu_{C=N}$). NMR ^1H (DMSO-d_6) δ 11.02 (OH); 9.98 (s, CH=N); 6.45–6.55, 7.58–7.60 (arom); 4.00 (OCH_2); 1.68–1.72, 1.21–1.39 (CH_2). UV–Vis (DMSO, nm) λ_{max}: 253, 282, 320.

2.3.3. Synthesis of $[Zn_2L^n]$ (n = 4, 6 and 8)

2.3.3.1. $[Zn_2L^4]2H_2O$. Zinc acetate dihydrate (0.111 g, 0.60 mmol) in methanol (10 mL) was added to H_4L^4 (0.201 g, 0.25 mmol) in methanol (20 mL). The solution was stirred for 5 h at room temperature and the precipitate of Zn_2L^4 that formed was filtered off and washed several times with methanol. Yield, 0.185 g (77%). MS (ESI) *m/z*: 931 (M^+). *Anal.* Calc. for $C_{48}H_{40}N_4O_8Zn_2{\cdot}2H_2O$: C, 59.81; H, 4.15; N, 5.82. Found: C, 59.58; H, 4.58; N, 5.79%. FT-IR (KBr, cm^{-1}) 1608 ($\nu_{C=N}$), 634 (ν_{Zn-O}), 420 (ν_{Zn-N}). NMR ^1H (DMSO-d_6) δ 9.97 (s, CH=N); 6.40–6.52, 7.24–7.42 (arom); 4.07 (OCH_2); 1.98, 1.55 (CH_2). UV–Vis (DMSO, nm) λ_{max}: 241, 282, 292, 322, 336, 363.

2.3.3.2. $[Zn_2L^6]$ and $[Zn_2L^8]$. The synthesis of these complexes, starting from the appropriate dialdehyde, was similar to that described above for $[Zn_2L^4]$.

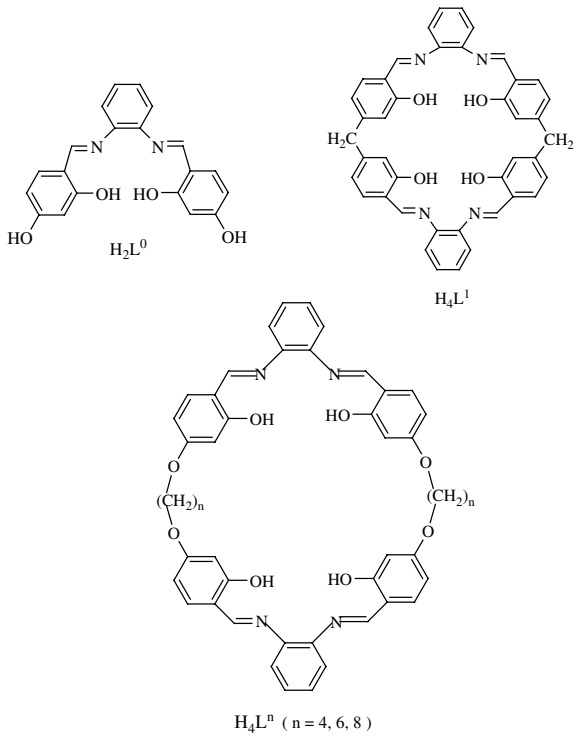
$[Zn_2L^6]$. Yield: 0.173 g (70%). MS (ESI) *m/z*: 987 (M^+). *Anal.* Calc. for $C_{52}H_{48}N_4O_8Zn_2$: C, 63.23; H, 4.90; N, 5.67. Found: C, 63.35; H, 4.88; N, 5.38%. FT-IR (KBr, cm^{-1}) 1608 ($\nu_{C=N}$), 655 (ν_{Zn-O}), 418 (ν_{Zn-N}). NMR ^1H (DMSO-d_6) δ 9.95 (s, CH=N); 6.40–6.52, 7.24–7.42 (arom); 4.03 (OCH_2); 1.45–1.73, 1.03–1.22 (CH_2). UV–Vis (DMSO, nm) λ_{max}: 241, 282, 292, 322, 335, 364.

$[Zn_2L^8]{\cdot}4H_2O$. Yield: 0.207 g (75%). MS (ESI) *m/z*:1043 (M^+). *Anal.* Calc. for $C_{56}H_{56}N_4O_8Zn_2{\cdot}2CH_3OH$: C, 60.27; H, 5.78; N, 5.02. Found: C, 60.23; H; 5.49; N, 5.21%. FT-IR (KBr, cm^{-1}) 1608 ($\nu_{C=N}$), 655 (ν_{Zn-O}), 419 (ν_{Zn-N}). NMR ^1H (DMSO-d_6) δ 9.95 (s, CH=N); 6.42–6.52, 7.56–7.58 (arom); 3.98 (OCH_2); 1.66–1.68, 1.32–1.37 (CH_2). UV–Vis (DMSO, nm) λ_{max}: 241, 282, 292, 322, 335, 363.

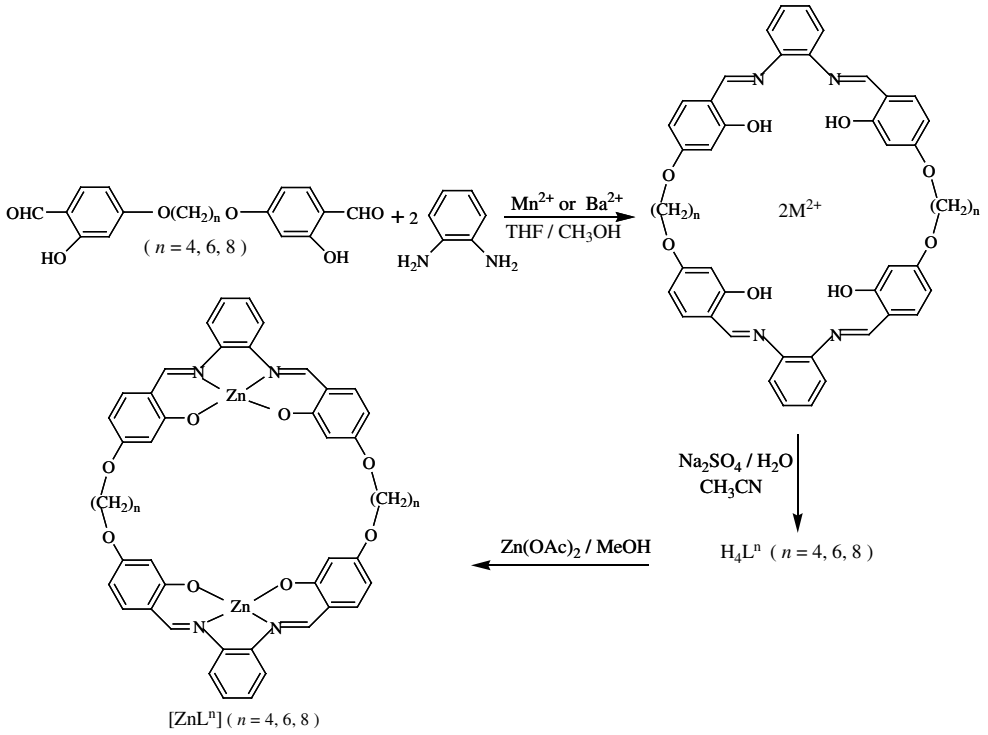
3. Results and discussion

The preparation of the new macrocyclic Schiff base ligands, H_4L^n ($n = 1$, 4, 6 and 8), in each case involved reaction of the corresponding dialdehyde and *o*-phenylenediamine in a 1:1 ratio in methanol in the presence of Ca^{2+}, Ba^{2+} or Mn^{2+} as 'transient' templates (Scheme 1). Indirect evidence for a templating role for Ba^{2+} in the preparation of H_4L^6 and H_4L^8 was given by the isolation of species of type $H_4L^n{\cdot}2Ba(ClO_4)_2$ ($n = 6$ and 8) as 'intermediates' before generation of the corresponding metal-free macrocycle. In the absence of a templating metal, the above Schiff base condensations produced oily solids which were assumed to be polymeric in nature.

Zinc(II) complexes of type $[Zn_2L^n]$ incorporating ligands of type H_4L^n, where $n = 1$, 4, 6 or 8, have also been synthesised by reaction of zinc acetate with the respective ligands in a 2.4:1 ratio in methanol (see Scheme 2 for the



Scheme 1. The ligands.



Scheme 2. Metal template synthesis of $[ZnL^n]$ ($n = 4$, 6, 8).

cases where $n = 4$, 6 or 8). For comparison, the related open-chain complex, $[ZnL^0]$, was also prepared by means of an *in situ* condensation between the required aldehyde derivative and *o*-phenylenediamine in a 2:1 ratio in methanol in the presence of zinc(II) acetate (see Scheme 2).

The FT-IR spectra of the free ligands and their corresponding complexes were determined. The O–H stretching frequencies of ligands are evident in the 3300–3800 cm^{-1} region but absent in the spectra of the corresponding complexes, again in keeping with the loss of the four hydroxy protons of each macrocycle on metal binding. The C=N stretching frequencies of the uncomplexed ligands and their zinc complexes fall in the range 1608–1640 cm^{-1} as reported for similar ligands and their complexes [25].

The ^1H NMR data (see Section 2) for the free ligands and their zinc complexes are in all cases consistent with the assigned structures. The peaks for the 'salicyl' OH protons in the free Schiff base ligands are present near 11–12 ppm and, as expected, are absent in the spectra of the corresponding zinc complexes confirming that loss of these protons occurs on uptake of zinc. Peaks with chemical shifts near 8.8–8.9 ppm are present for the HC=N protons in both H_2L^0 and H_4L^1 as well as for the corresponding zinc complexes, while they occur near 9.9 ppm For H_4L^4, H_4L^6 and H_4L^8 and their corresponding zinc complexes. The occurrence of this resonance in each of the above species as a 'clean' singlet is in keeping with the presence of intact (non hydrolyzed) imine groups in each case.

Attempts to obtain suitable crystals for X-ray structure determinations of the new ligands (or indeed, their zinc complexes) were unsuccessful. However, geometry optimizations were carried out using density functional theory (DFT) at the B3LYP/6-31 G* level employing Gaussing03 to probe the gas phase structures of H_4L^1 and H_4L^4. The minimum energy structure found for H_4L^1 has a rhomboidal-shaped cavity with the two phenyl rings derived from *o*-phenylenediamine inclined on the same side of the cavity to give the molecule a 'butterfly' shape when viewed laterally with respect to the cavity. In contrast, for H_4L^4 the dihedral angle between the *o*-phenylenediamine phenyl rings was calculated to be 89°, giving rise to a somewhat twisted, less symmetrical cavity. Gaussian03 was also employed to calculate the charge distributions for atoms in the HC=N double bonds of H_4L^1 and H_4L^4; the values obtained for the imine hydrogens are, respectively, 0.14*e* for ligand H_4L^1 and 0.11*e* for H_4L^4. Although the situation is not necessarily straight forward, these values correlate with the amount of shielding for each proton type obtained from the corresponding ^1H NMR chemical shifts (see Section 2); that is, the spectra indicated that the HC=N protons in H_4L^1 are more shielded than occurs for these protons in H_4L^4.

The electronic spectra of the two ligands in DMSO were recorded over 200–700 nm. Intense absorption bands for these conjugated aromatic systems were present at 262, 301and 414 nm for H_4L^1 and 253, 282 and 320 nm for H_4L^4. The calculated E(HOMO) for $H_4L^1$is −0.204 a.u. and −0.183 a.u. for H_4L^4. The E(LUMO) are −0.065 a.u. for H_4L^1 and −0.036 a.u. for H_4L^4. The ΔE(LUMO–HOMO) is thus 0.139 a.u. for H_4L^1 and 0.147 a.u. for H_4L^4. In general terms these results are in keeping with the electronic transitions in H_4L^4 occurring

at higher energies than in H_4L^1 and hence correlate with the observed blue shifts of the absorptions for H_4L^4 relative to those of H_4L^1.

4. Conclusions

In this report we describe the facile synthesis and characterisation of a series of new macrocyclic Schiff base ligands of varying ring size via a 'transient' metal template procedure. The ability of these derivatives to act as dinucleating ligands towards zinc has been demonstrated. The new macrocyclic ligands are now available for further studies. These include investigating the coordination behaviour of a range of other metal ions, use in synthesising new dinuclear complexes as models for selected metallo-enzymes and, in the case of complexes incorporating coordinately unsaturated metal centres, use as a 'platform' for the construction of extended molecular systems by reaction with appropriate bridging ligands such as 4,4′-bipyridine (or other suitable difunctional derivatives). Studies of these types are planned for the future in our laboratories.

Acknowledgements

The support of the Natural Science Foundation of China, the International Cooperation Foundation of the Guizhou Province of PR China, the "Chun-Hui" Fund of Chinese Ministry of Education and the Science and Technology Fund of Guizhou Province (Grant No. J-2005-2012) is gratefully acknowledged. B.-X. Zhu acknowledges Professor Z. Tao for helpful discussions and Professor Y.-B. Wang for assistance with the DFT calculations.

Appendix A. Supplementary material

Views of the DFT minimised structures of H_4L^1 and H_4L^4 as well as computed charge distributions for C and H in the HC=N functional groups of these two ligands are presented as supplementary data. Supplementary data associated with this article can be found, in the online version, at doi:10.1016/j.poly.2007.09.012.

References

[1] M.J. Sabater, M. Alvaro, H. Garcia, E. Palomares, J.C. Sherrington, Chem. Soc. Rev. 28 (1999) 85.
[2] S.R. Korupoju, N. Mangayarkarasi, S. Ameerunisha, E.J. Valente, P.S. Zacharias, J. Chem. Soc., Dalton Trans. (2000) 2845.
[3] S. Di Bella, Chem. Soc. Rev. 30 (2001) 355.
[4] P.G. Lacroix, Eur. J. Inorg. Chem. (2001) 339.
[5] S. Di Bella, I. Fragala, I. Ledoux, J. Zyss. Chem. Eur. J. 7 (2001) 3738.
[6] S. Di Bella, I. Fragala, New J. Chem. 26 (2002) 285.
[7] K.E. Splan, A.M. Massari, G.A. Morris, S.-S. Sun, E.R. Eina, S.T. Nguyen, J.T. Hupp, Eur. J. Inorg. Chem. (2003) 2348.
[8] J.T. Hupp, Eur. J. Inorg. Chem. (2003) 2348.
[9] C. Evans, D. Luneau, J. Chem. Soc., Dalton Trans. (2002) 83.
[10] P.G. Cozzi, L.S. Dolci, A. Garelli, M. Montalti, L. Prodi, N. Zaccheroni, New J. Chem. 27 (2003) 692.
[11] S.K. Dey, N. Mondal, M.S. El Fallah, R. Vicente, A. Escuer, X. Solans, M. Font-Bardia, T. Matsushita, V. Gramlich, S. Mitra, Inorg. Chem. 43 (2004) 2427.
[12] L. Lecren, W. Wernsdorfer, Y.-T. Li, A. Vindigni, H. Miyasaka, R. Clérac, J. Amer. Chem. Soc. 129 (2007) 5045.
[13] D.J. de Geest, A. Noble, B. Moubaraki, K.S. Murray, D.S. Larsen, S. Brooker, Dalton Trans. (2007) 467, and refs. therein.
[14] S. Brooker, T.C. Davidson, S.J. Hay, R.J. Kelly, D.K. Kennepohl, P.G. Plieger, B. Moubaraki, K.S. Murray, E. Bill, E. Bothe, Coord. Chem. Rev. 216–217 (2001) 3.
[15] U. Beckmann, S. Brooker, Coord. Chem. Rev. 245 (2003) 17.
[16] D.E. Fenton, H. Okawa, Perspect. Bioinorg. Chem. 2 (1993) 81.
[17] H. Okawa, H. Furutachi, D.E. Fenton, Coord. Chem. Rev. 174 (1998) 51.
[18] N.H. Pilkington, R. Robson, Aust. J. Chem. 23 (1970) 2255.
[19] See, for example: D. Black, R.L. Finn, L.F. Lindoy, A. Nezhadali, G. Rounaghi, P.A. Tasker, M. Schröder, Chem. Commun. (2002) 340.
[20] L.F. Lindoy, The Chemistry of Macrocyclic Ligand Complexes, Cambridge University Press, Cambridge, 1989.
[21] Z. Li, C. Jablonski, Chem. Commun. (1999) 1531.
[22] B.-X. Zhu, W.-J. Ruan, R.J. Yuan, Z.-A. Zhu, Chem. J. Chinese Univ. 26 (2005) 412.
[23] D.D. Perrin, L.F. Armarego, D.R. Perrin, Purification of Laboratory Chemicals, 2nd ed., Pergamon, Oxford, 1980.
[24] L. Cerrada, M. Pinol, L.J. Serrano, J. Polym. Sci. Part A: Poly Chem. 34 (1996) 2603.
[25] R.C. Felicio, E.T.G. Cavalheiro, E.R. Dockal, Polyhedron 20 (2001) 261.

Available online at www.sciencedirect.com
ScienceDirect
Polyhedron 27 (2008) 349–356
POLYHEDRON
www.elsevier.com/locate/poly

Mononuclear dioxomolybdenum(VI) complexes with the quinolones enrofloxacin and sparfloxacin: Synthesis, structure, antibacterial activity and interaction with DNA

Eleni K. Efthimiadou [a,b], Alexandra Karaliota [b], George Psomas [a,*]

[a] Institute of Physical Chemistry, NCSR "Demokritos", GR-15310 Aghia Paraskevi Attikis, Greece
[b] Department of Inorganic Chemistry, Faculty of Chemistry, National University of Athens, Panepistimioupoli Zographou, GR-15701 Athens, Greece

Received 24 June 2007; accepted 18 September 2007
Available online 30 October 2007

Abstract

The neutral mononuclear dioxomolybdenum(VI) complexes of the quinolone antibacterial agents enrofloxacin and sparfloxacin have been prepared and characterized with physicochemical and spectroscopic techniques. In these complexes, enrofloxacin and sparfloxacin act as bidentate deprotonated ligands bound to the metal through the pyridone oxygen and one carboxylate oxygen. The central molybdenum atoms are six-coordinate with slightly distorted octahedral geometry. The lowest energy model structure of each complex has been proposed with molecular modeling calculations. The antimicrobial activity of the complexes has been tested on three different microorganisms. The investigation of the interaction of the complexes with calf-thymus DNA has been performed with diverse spectroscopic techniques.
© 2007 Elsevier Ltd. All rights reserved.

Keywords: Quinolones; Enrofloxacin; Sparfloxacin; Dioxomolybdenum(VI) complexes; Interaction with calf-thymus DNA; MIC

1. Introduction

Quinolones is a term commonly used for the quinolonecarboxylic acids or 4-quinolones, a group of synthetic antibacterial agents containing a 4-oxo-1,4-dihydroquinoline skeleton [1–3]. Quinolones are extremely useful for the treatment of diverse infections [4–6]. The activity of quinolones as antibacterial drugs is due to the effective inhibition of DNA replication. The proposed mechanism of the interaction between quinolone and metal cations was chelation between the metal and the 4-oxo and adjacent carboxyl groups [7].

Enrofloxacin, Herx (Fig. 1a), is a typical second-generation quinolone antimicrobial drug with a broad spectrum of activity against a wide range of Gram-negative and Gram-positive bacteria, including those resistant to β-lactam antibiotics and sulfonamides [8,9]. Enrofloxacin is the first fluoroquinolone developed for veterinary application and is potentially available for the treatment of some urinary tract, respiratory tract and skin infectious diseases in pets and livestock [10–13]. It is also used for the treatment of uncomplicated and complicated urinary tract infections, pyelonephritis, sexually transmitted diseases, prostatitis, skin and tissue infections, urethral and cervical gonococcal infections [14–16]. Sparfloxacin, Hsf (Fig. 1b), is a third-generation quinolone antimicrobial drug mainly used for the treatment of acute exacerbations of chronic bronchitis and community-acquired pneumonia [17].

The role of molybdenum as an element of biological interest is well known [18–21]. Molybdenum can be found

* Corresponding author. Present address: Department of General and Inorganic Chemistry, Faculty of Chemistry, P.O. Box 135, Aristotle University of Thessaloniki, GR-54124 Thessaloniki, Greece. Tel.: +30 2310997790; fax: +30 2310997738.
E-mail address: gepsomas@chem.auth.gr (G. Psomas).

0277-5387/$ - see front matter © 2007 Elsevier Ltd. All rights reserved.
doi:10.1016/j.poly.2007.09.013

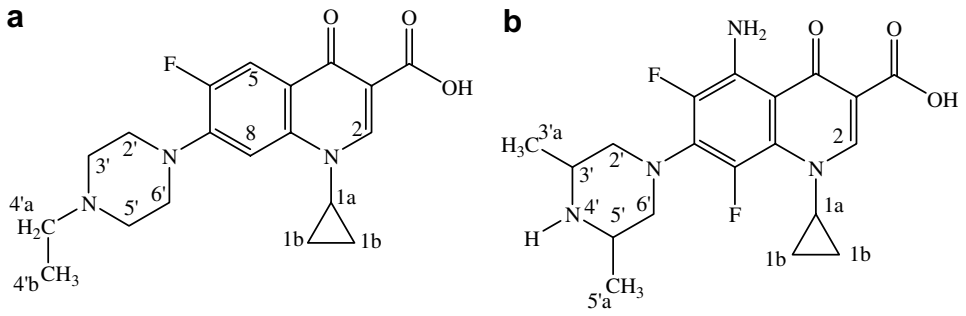


Fig. 1. (a) Enrofloxacin (Herx = 1-cyclopropyl-7-(4-ethyl-piperazin-1-yl)-6-fluoro-4-oxo-1,4-dihydro-quinoline-3-carboxylic acid) and (b) sparfloxacin (Hsf = 5-amino-1-cyclohexyl-7-(*cis*-3,5-dimethylpiperazino)-6,8-difluoro-1,4-dihydro-4-oxo-3-quinolinecarboxylic acid) and H atom labeling.

in the Mo nitrogenases [22] and in the molybdenum oxidases [23], enzymes that catalyze a number of biologically important oxotransfer reactions, such as the conversion of sulfite to sulfate, aldehyde to the corresponding carboxylic acid, or nitrate to nitrite [21]. For Mo, only two ciprofloxacin complexes as polyoxometalates have been characterized [24], while dioxomolybdenum(VI) binary complexes have been reported only with the first-generation quinolones pipemidic acid [25] and oxolinic acid [26] as well as with the second-generation quinolone *N*-propyl-norfloxacin [27].

We have initiated the study of the structure, spectroscopic and biological properties of diverse transition metal complexes with various quinolone antibacterial drugs [25–35]. Here, we present the interaction of MoO_2^{2+} with the second-generation quinolone enrofloxacin and third-generation quinolone sparfloxacin in an attempt to examine the mode of coordination and the biological properties of the resultant complexes. More specifically, the complexes have been synthesized and characterized with elemental analysis and diverse spectroscopic techniques (IR, UV–Vis and NMR spectroscopies). Molecular modeling techniques have been employed to assess the lowest energy model structure of the complexes. The biological activity of the complexes has been evaluated by determining the minimum inhibitory concentration (MIC) against three microorganisms. The interaction of the complexes with calf-thymus (CT) DNA has been investigated with UV and circular dichroism (CD) spectroscopy.

2. Experimental

2.1. Materials

Enrofloxacin, sparfloxacin and CT DNA were purchased from Sigma, NaCl was purchased from Merck, trisodium citrate was purchased from Riedel-de Haen, $MoO_2(acac)_2$, KOH and all the solvents were purchased from Aldrich Co. Agarose was purchased from BRL. Tryptone and yeast extract were purchased from Oxoid (Unipath, Hampshire, UK). All the chemicals for the synthesis of the compounds were reagent grade and were used as purchased.

DNA stock solutions (5 mM) were prepared by dilution of CT DNA to buffer (containing 150 mM NaCl and 15 mM trisodium citrate at pH 7.0) followed by exhaustive stirring at 4 °C for three days [36], and kept at 4 °C for no longer than a week. The nucleotide concentrations were determined by their absorption at 260 nm using $\varepsilon = 6600\ M^{-1}\ cm^{-1}$.

2.2. Synthesis of the complexes

2.2.1. $MoO_2(erx)_2$ (**1**)

A methanolic solution (10 mL) of enrofloxacin (0.6 mmol, 216 mg), deprotonated with KOH (0.6 mmol, 34 mg), was added to a methanolic solution (10 mL) of $MoO_2(acac)_2$ (0.3 mmol, 100 mg) and the reaction mixture was refluxed for 2.5 h. The solution was filtered and left for slow evaporation. After a few days a light yellow microcrystalline product was deposited, collected with filtration, washed with methanol and dried. Yield: 190 mg, 75%. *Anal.* Calc. for $MoO_2(erx)_2$ ($C_{38}H_{42}F_2N_6O_8Mo$) (MW = 844.72): C, 54.03; H, 5.01; N, 9.95. Found: C, 53.71; H, 4.85; N, 10.21%. The complex is soluble in DMSO and DMF and is a non-electrolyte.

2.2.2. $MoO_2(sf)_2$ (**2**)

In a similar way, complex **2** was prepared with the use of sparfloxacin (0.4 mmol, 235 mg). A light yellow microcrystalline product was collected. Yield: 135 mg, 75%. *Anal.* Calc. for $MoO_2(sf)_2$ ($C_{38}H_{42}F_4N_8O_8Mo$) (MW = 910.74): C, 50.12; H, 4.65; N, 12.30. Found: C, 50.41; H, 4.75; N, 12.20%. The complex is soluble in DMSO and DMF and is a non-electrolyte.

2.3. Instrumentation

IR spectra (400–4000 cm^{-1}) were recorded on a Nicolet Magna-IR 550 with samples prepared as KBr pellets. UV–Vis spectra were recorded as nujol mulls and in solution at concentrations in the range 10^{-5}–10^{-3} M on a Thermo Electron Corporation Helios α dual beam spectrophotometer. C, H and N elemental analysis were performed on a Perkin–Elmer 240B elemental analyzer. Electric conductance measurements were carried out with

a WTW model LF 530 conductivity outfit and a type C cell, which had a cell constant of 0.996. NMR spectra were recorded with a Bruker Avance 500 MHz instrument and were processed by X-WIN NMR 2.6 (Bruker Analytik GmbH).

The interaction of the complexes with CT DNA has been investigated with UV and CD spectroscopies. In both techniques, the spectra of CT DNA in the presence of each complex have been recorded for a constant CT DNA concentration (3.125×10^{-4} M) in diverse complex/CT DNA mixing ratios (r). All the UV and CD spectra were recorded after incubation of each complex with CT DNA for 24 h at 37 °C.

The CD spectra were recorded on a Jasco J-700 spectropolarimeter using a 1.0 cm path quartz cell and the following acquisition parameters: $\lambda = 190$–400 nm, scan speed 50 nm min^{-1}, resolution step 0.2 nm, sensitivity 50 mdeg, response 1 s, bandwidth 1.0 nm, accumulations 10. In some cases, the spectra were averaged over an appropriate number of scans.

2.4. Molecular modeling

With the aim to present a molecular model for each new complex that is unbiased by the starting structure, we have used Langevin dynamics with a simulated annealing protocol. Using this method, the mean total energy of an ensemble of structures guides the selection of the most favorable configuration for each complex. Starting structures were constructed using the program HYPERCHEM and the MM+ force field that is based on the Allinger's MM2 force field [37]. For molybdenum, we used a default parameter set with $R^* = 2.20$ Å and $e^* = 0.02$ kcal mol^{-1}, since the van der Waals interactions are not expected to play a major role in such bonded representations as in octahedral complexes. Metal–ligand bond lengths were corrected in the final models using harmonic restraints with equilibrium values that were extracted from crystallographic data of similar compounds [38–41] (Table S1). Non-bonded interactions were calculated in vacuo with no cutoff and the electrostatic energy term was treated using bond dipoles. Initial energy minimizations were carried out by a conjugate gradient method with RMS gradient <0.01 as convergence criterion.

Each model (Scheme S1) was subjected to 20 individual rounds of simulated annealing setting different value to the seed for the assignment of the starting velocities. To integrate the Langevin equation [42] the step size was set to 1 fs and the collision frequency to 1 ps^{-1}. The annealing calculation comprised three phases: (i) raising the temperature of the system from 10 to 1000 K over 2 ps, (ii) keeping the system at 1000 K for 3 ps and (iii) cooling the system down to 0 K over 15 ps. A tight coupling of the system with temperature (0.1 ps) was used for the heating and equilibration phases. During the cooling phase the bath relaxation time was gradually decreased from 5.0 ps (7000 steps), 2.0 ps (3000 steps), 1.0 ps (2000 steps), 0.5 ps (2000 steps) to 0.05 ps (1000 steps). At the final step all the resultant structures had RMS gradient <0.01 and their total energy was recorded (Tables S2 and S3). The models presented herein were selected among the lowest energy structures generated for each starting geometry. A final minimization of the energy was performed as above, but having applied the metal–ligand distance restraints.

2.5. Antibacterial activity – minimum inhibitory concentration

The antibacterial activity of the compounds (ligands and complexes) was studied against *Staphylococcus aureus* (*S. aureus*), *Escherichia coli* (*E. coli*) and *Pseudomonas aeruginosa* (*P. aeruginosa*). The microorganisms were maintained in the laboratory of "Chemical Biology" of NCSR "Demokritos". Screening was performed by determining the MIC. Two different media [Luria broth medium (=LB, containing 1% w/v tryptone, 0.5% w/v NaCl and 0.5% w/v yeast extract) and minimal medium salts broth (=MMS, containing 1.5% w/v glucose, 0.5% w/v NH_4Cl, 0.5% w/v K_2HPO_4, 0.1% w/v NaCl, 0.01% w/v $MgSO_4 \cdot 7H_2O$ and 0.1% w/v yeast extract)] were used. The compounds were dissolved in distilled water with twofold serial dilutions from 8 to 0.125 μg mL^{-1}. All the cultures were incubated at 37 °C. Control tests with no active ingredients were also performed.

MIC was determined using twofold serial dilutions in liquid media containing 0.125–8 μg mL^{-1} of the compound being tested. A preculture of bacteria was grown in LB overnight at the optimal temperature of each species. Two milliliters of MMS were inoculated with 20 mL of this preculture. This culture was used as a control to examine if the growth of the bacteria tested is normal. In a similar second culture, 20 μL of the bacteria as well as the tested compound at the desired concentration were added. A third sample containing 2 mL MMS supplemented with the same compound concentration was used as a second control to check the effect of the compound on MMS. All samples were measured in duplicate. We monitored bacterial growth by measuring the turbidity of the culture after 12 and 24 h. If a certain concentration of a compound inhibited bacterial growth, half the concentration of the compound was tested. This procedure was carried on to a concentration where bacteria grow normally. The lowest concentration that inhibited bacterial growth was determined as the MIC value. All the equipment and culture media were sterile.

3. Results and discussion

3.1. Synthesis and spectroscopic study of the complexes

The complexes have been prepared in high yield (75%) via the addition of methanolic solutions of the deprotonated quinolone to MoO_2^{2+} at a 2/1 ratio. Both complexes are soluble in DMSO and DMF and are non-electrolytes.

Table 1
Characteristic absorptions (in cm^{-1}) of the IR spectra of the complexes

	$\nu(C{=}O)_p$[a]	$\nu(CO_2)_{asym}$[a]	$\nu(CO_2)_{sym}$[a]	Δ[b]	ν(Mo=O)
Herx	1622	1733[c]			
$MoO_2(erx)_2$	1628	1606	1388	218	932, 904
$Cu(erx)_2(H_2O)$ [28]	1630	1611	1381	230	
Hsf	1641	1716[c]			
$MoO_2(sf)_2$	1634	1601	1392	209	931, 907
$Cu(sf)_2$ [29]	1635	1605	1385	220	

[a] p, pyridone; asym, asymmetric; sym, symmetric.
[b] $\Delta = \nu(CO_2)_{asym} - \nu(CO_2)_{sym}$.
[c] As ν(COOH).

In Table 1, the characteristic absorptions of the IR spectra of complexes **1** and **2** are listed. In the IR spectra of complexes **1** and **2**, the absorptions at 1733 cm^{-1} in the spectrum of Herx and at 1716 cm^{-1} for Hsf, respectively, attributed to the absorption of the $\nu(C{=}O)_c$ (c = carboxylato) have disappeared. Two very strong characteristic bands are present in the range of 1601–1606 cm^{-1} and at ~1390 cm^{-1} that could be assigned as ν(O–C–O) asymmetric and symmetric stretching vibrations, respectively, whereas $\nu(C{=}O)_p$ (p = pyridone) is slightly shifted from 1622 to 1629 cm^{-1} for **1** and from 1641 to 1634 cm^{-1} for **2** upon bonding. The difference $\Delta = \nu_{asym}(CO_2) - \nu_{sym}(CO_2)$ is a useful characteristic for determining the coordination mode of the ligands. The Δ values are 218 cm^{-1} for **1** and 209 cm^{-1} for **2**, indicating a monodentate coordination mode of the carboxylato group [43,44] of the ligands. These changes in the IR spectra suggest that enrofloxacinato and sparfloxacinato ligands are coordinated to molybdenum via the pyridone (O_p) and one carboxylato (O_c) oxygen atoms [1,25–35].

The existence and the number of the ν(Mo=O) absorptions is a useful diagnostic tool of the characterization of the complex. The existence of two ν(Mo=O) absorptions at ~930 cm^{-1} and ~905 cm^{-1} for both the complexes are indicative of a *cis* arrangement of the two dioxomolybdenum oxygen atoms around Mo [25–27].

The UV–Vis spectra of the complexes have been recorded as nujol mulls and in DMSO solution. Practically, the spectra in DMSO solution and those in nujol are alike, although in some cases they differ for a few nanometers, indicating that both complexes **1** and **2** retain their structure in solution. The UV–Vis spectral data for the complexes in DMSO solution are given in Table 2.

Table 2
Characteristic bands [λ_{max} in nm (ε in $M^{-1}\,cm^{-1}$)] in the UV–Vis spectra of the complexes in DMSO solution

	IL[a] bands			CT band[b]
Herx	280 (11200)	310(sh)[c] (6100)	335 (2800)	
$MoO_2(erx)_2$	287 (8200)	315 (4950)	340 (2910)	430(sh) (200)
Hsf	285 (6200)	320 (4100)	365 (2100)	
$MoO_2(sf)_2$	289 (5800)	322 (3950)	360 (2150)	432(sh) (210)

[a] IL, intraligand.
[b] CT, charge transfer.
[c] sh, shoulder.

The UV spectra of the complexes are practically identical with that of the quinolone ligands but slightly shifted, indicative of coordination through the O_p and one O_c. The complexes also exhibit an absorption band at ~430 nm ($\varepsilon \sim 200$–$210\ M^{-1}\,cm^{-1}$) which can be assigned to the ligand-to-metal charge-transfer transition for the quinolone ligand, as observed in a series of other quinolones binary complexes [25–35].

^{1}H NMR spectra of the ligands and the complexes have been recorded in DMSO-d_6. The assignment of every signal has been achieved by comparing the ^{1}H NMR spectra of the complexes to those of the ligands and to spectra reported in the literature [25–27,45]. The results are shown in Table 3.

Comparison of the ^{1}H NMR spectrum of complex **1** with that of Herx shows a significant perturbation of the chemical shift (up to 0.4 ppm) of the aromatic protons H2 and H5 indicating that H2 and H5 are close to the coordination site of the ligand. The signals for H8, the aliphatic H1a and H1b and the piperazine protons are practically unchanged since they lie far from the binding site of the ligand.

Quite similar results are derived from the comparison of the ^{1}H NMR spectrum of complex **2** with that of Hsf where a perturbation of the chemical shift (0.3 ppm) of the aromatic proton H2 is observed indicating adjacency to the coordination site of the ligand, while the rest protons (the aliphatic H1a and H1b, the piperazine H2′, H3′, H5′ and H6′ as well as the methyl protons H3′a and H5′a) lie far from the binding site of the ligand and their signals remain practically unchanged.

The overall changes in the NMR spectra of the complexes are indicative of coordination of the enrofloxacinato and sparfloxacinato ligands to molybdenum via the pyridone and one carboxylate oxygen atoms [25–27,45].

Table 3
Chemical shifts (ppm) in ^{1}H NMR spectra of Herx, $MoO_2(erx)_2$, Hsf and $MoO_2(sf)_2$ in DMSO-d_6

Atom	Herx	$MoO_2(erx)_2$
H1a[a]	1.49 (1H)	1.47 (1H)
H1b and H4′b	1.20 (7H)	1.20 (7H)
H2	8.85 (1H)	9.10 (1H)
H5	7.80 (1H)	8.20 (1H)
H8	7.40 (1H)	7.50 (1H)
H2′, H6′ or H3′, H5′	3.20–3.30 (4H), 3.65–3.70 (4H)	3.15–3.25 (4H), 3.75 (4H)
H4′a	3.35 (2H)	3.35 (2H)
	Hsf	$MoO_2(sf)_2$
H1a	1.47 (1H)	1.45 (1H)
H1b, H3′a, H5′a	1.20 (10H)	1.20 (10H)
H2	8.80 (1H)	9.10 (1H)
H2′, H6′ and H3′, H5′	3.20–3.40 (6H)	3.15–3.45 (6H)

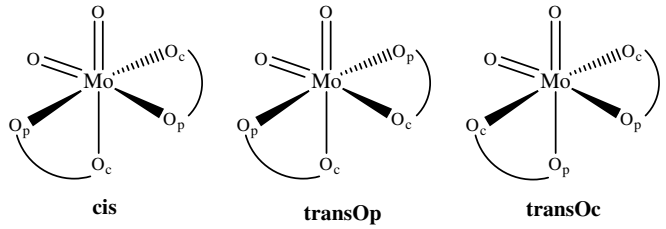
[a] Numbering of protons according to Fig. 1.

3.2. Molecular dynamics

Diverse crystallization techniques were employed in order to obtain a crystal suitable for the structure determination with X-ray crystallography. Nevertheless, the complexes were collected only as microcrystalline product. In order to present a model for each complex three pairs of enantiomers have been constructed as starting models for $MoO_2(erx)_2$ and $MoO_2(sf)_2$ (Scheme 1). After the Langevin dynamics simulated annealing calculations for each complex, we obtained the total energy results of 20 different conformations for each starting model, which guide us to select the lowest-energy isomers as the more favorable.

For $MoO_2(erx)_2$, the *transOc* isomers can be selected as the more favorable. Their average energy is almost equal, as expected [38], and is lower than the other four isomers by more than 3 kcal mol^{-1} (Table S2). We have applied a set of harmonic restraints at the metal–ligand bonds [39–41] during an additional minimization phase (Table S1). Based on these results, the lowest energy model structure of one *transOc*–$MoO_2(erx)_2$ enantiomer as the favorable configuration of the complex is illustrated in Fig. 2.

For $MoO_2(sf)_2$, the *transOc* isomers, with average energy lower than the other four isomers by more than 3 kcal mol^{-1} (Table S3), were also selected as the more favorable. The lowest energy model structure for $MoO_2(sf)_2$ has been found in the same way and is illustrated in Fig. S2. However, we can neither exclude the formation of any of the other isomers, nor unambiguously distinguish between the favorable enantiomers.



Scheme 1. The isomers of $MoO_2(erx)_2$ or $MoO_2(sf)_2$ that were employed in the simulated annealing calculations. O_c and O_p are the carboxylate and the pyridone oxygen atoms, respectively, of enrofloxacinato/sparfloxacinato ligands.

3.3. Antibacterial activity

The efficiencies of the ligands and the complexes have been tested against two Gram(−), *E. coli* and *P. aeruginosa*, and one Gram(+), *S. aureus*, microorganisms. The results are presented in Table 4.

It is evident (Table 4) that the ligands and the complexes have inhibitory action against all the microorganisms tested and the coordination of the quinolones enrofloxacin (MIC = 1–8 μg mL^{-1}) and sparfloxacin (MIC = 0.25–8 μg mL^{-1}) with MoO_2^{2+} results to a diverse biological activity (MIC for the complexes = 1–4 μg mL^{-1}). The antimicrobial activity of $MoO_2(acac)_2$ has also been investigated and it has been found that it does not exhibit antimicrobial activity, at the concentration range used to assay the activity of the complexes in this work. The MIC values found for the complexes are low and can be mainly attributed to the existence of the quinolone ligand in the molecule.

When the antimicrobial activity of metal complexes is investigated, the following principal factors [46–49] should be considered: (i) the chelate effect of the ligands; (ii) the nature of the N-donor ligands; (iii) the total charge of

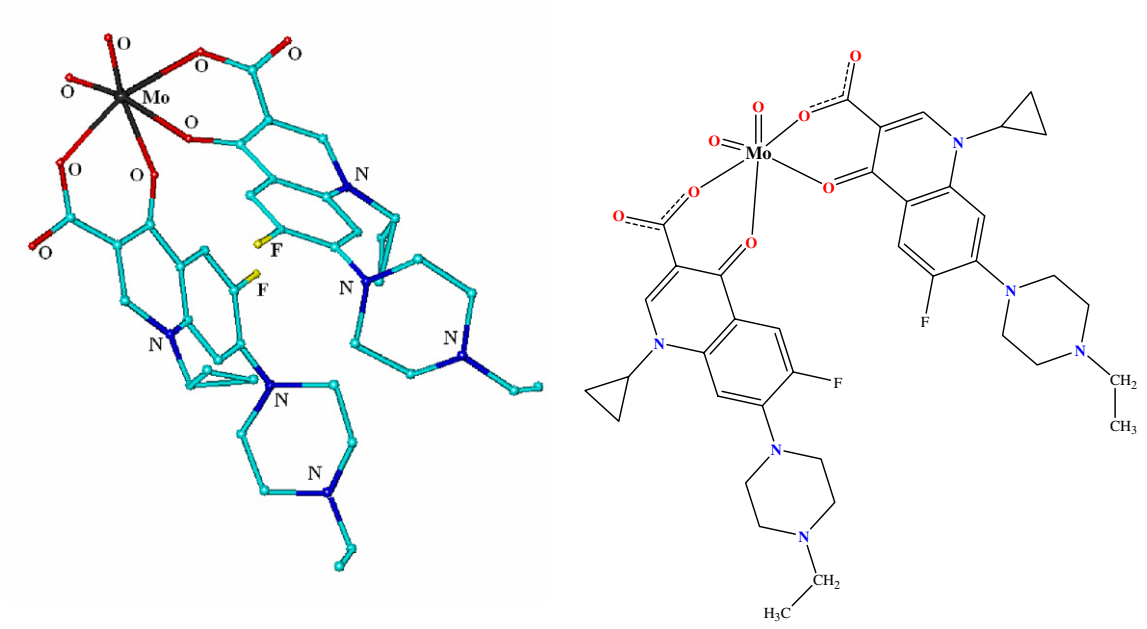


Fig. 2. Lowest energy model structure for $MoO_2(erx)_2$.

Table 4
MIC in μg mL^{-1}

	E. coli	*P. aeruginosa*	*S. aureus*
Herx	1 (2.78)[a]	1 (2.78)[a]	8 (22.22)[a]
$MoO_2(erx)_2$	1 (1.18)	1 (1.18)	4 (4.74)
$Cu(erx)_2(H_2O)$ [28]	0.125 (0.16)	0.125 (0.16)	4 (5.01)
$VO(erx)_2(H_2O)$ [32]	4 (4.99)	4 (4.99)	8 (9.98)
Hsf	8.0 (20.4)	0.25 (0.64)	0.5 (1.28)
$MoO_2(sf)_2$	4 (4.40)	1 (1.10)	2 (2.20)
$Cu(sf)_2$ [29]	2 (2.36)	0.25 (0.30)	1 (1.18)

[a] The values in parentheses represent the MIC in μM.

the complex; (iv) the existence and the nature of the ion neutralizing the ionic complex; and (v) the nuclearity of the metal center in the complex. For complexes **1** and **2**, only the first of these factors is present, i.e. the chelate effect of the ligand. This is probably one of the reasons for the diverse antibacterial activity shown by the complexes while the nature of the metal ion coordinated to the quinolone ligand may have a significant role to this diversity.

Complex **1** shows equal activity against the two Gram(−) microorganisms (MIC = 1 μg mL^{-1}) and is more active than Herx only against *S. aureus*. Comparing the activity of complex **1** to other enrofloxacinato complexes, $MoO_2(erx)_2$ is more active than $VO(erx)_2(H_2O)$ (MIC = 4–8 μg mL^{-1}) [32] against all the microorganisms tested and it is less active than $Cu(erx)_2(H_2O)$ against only the two Gram(−) microorganisms (MIC = 0.125 μg mL^{-1}) [28] while both complexes present equal inhibition (MIC = 4 μg mL^{-1}) against *S. aureus*.

On the other hand, complex **2** is more active than Hsf against *E. coli* (MIC = 4 μg mL^{-1}) and less active against *P. aeruginosa* (MIC = 1 μg mL^{-1}) and *S. aureus* (MIC = 2 μg mL^{-1}). Sparfloxacinato ligand shows a slightly better inhibition, against all the microorganisms tested, when it is coordinated to Cu(II) in $Cu(sf)_2$ (MIC = 0.25–2 μg mL^{-1}) [29].

3.4. Interaction of the complexes with DNA

DNA can provide three distinctive binding sites for quinolone metal complexes: namely, groove binding, binding to phosphate group and intercalation [50]. This behavior is of great importance with regard to the relevant biological role of quinolone antibiotics in the body [51].

3.4.1. UV spectroscopy

The absorption spectra of the interaction of complexes **1** and **2** with CT DNA have been recorded for a constant DNA concentration (3.125×10^{-4} M) in different complex: CT DNA mixing ratios (r) and are shown in Fig. 3. The changes observed (mainly the increase of the intensity at $\lambda_{max} = 258$ nm) in the UV spectra of the complexes after mixing with CT DNA indicate that complexes **1** and **2** can bind to CT DNA and the interaction of each complex, **1** and **2**, with CT DNA takes place by a direct formation of a new complex with double-helical CT DNA [52].

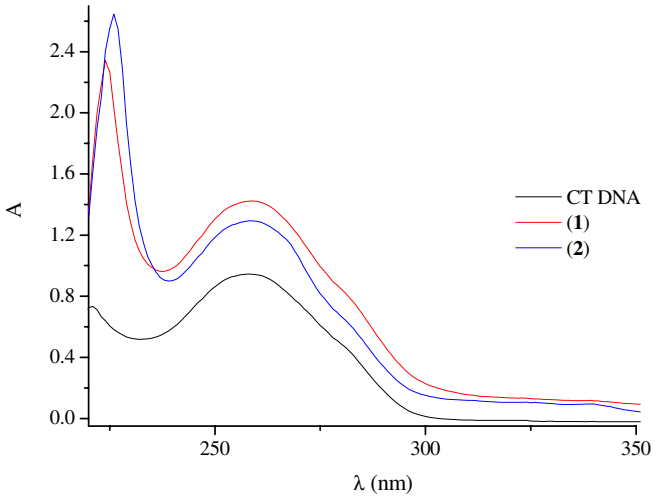


Fig. 3. UV spectra of CT DNA in the presence of complexes **1** and **2** for r = 1:200 (r = complex/CT DNA mixing ratio). The spectra were recorded at 25 °C after the complexes had been incubated with CT DNA for 24 h at 37 °C.

3.4.2. CD spectroscopy

CD spectroscopy is a useful tool to diagnose changes in DNA morphology during drug–DNA interactions, since the positive band due to base stacking (273 nm) and the negative one due to right-handed helicity (246 nm) are quite sensitive to the interaction mode of DNA with small molecules [53,54]. The changes in CD signals of DNA observed on interaction with drugs may often be assigned to the corresponding changes in DNA structure [55]. Thus, simple groove binding and electrostatic interaction of small molecules show less or no perturbation on the base-stacking and helicity bands, while intercalation enhances the intensities of both the bands stabilizing the right-handed B conformation of CT DNA as observed for the classical intercalator methylene blue [56].

The CD spectra of the complexes with double-stranded CT DNA for different r values can provide us with useful information concerning the complex–nucleotide interaction. The CD spectra of the interaction of the free ligands with CT DNA do not show any transitions because there is not any asymmetry or chirality in the molecules [25–35,52,57]. The CD spectrum of free CT DNA is conservative and consists of a negative band at 246 nm and a positive one at 273 nm, characteristic of the B-form of DNA [58].

The CD spectra of CT DNA in the presence of complex **1** are shown in Fig. 4. They consist of a strong negative band I at 246 nm and two discrete positive band II at 273 nm and band III (observed as a shoulder) at 280 nm. When complex **1** is incubated with CT DNA at diverse r values, the CD spectrum of CT DNA undergoes changes mainly in the positive bands showing that complex **1** is bound to CT DNA. For r values up to 1:400, each spectrum consists of one negative band I at 246 nm and two positive band II at 274 nm and band III at 280 nm. Upon increase of the r value, the λ_{max} of these three bands remain

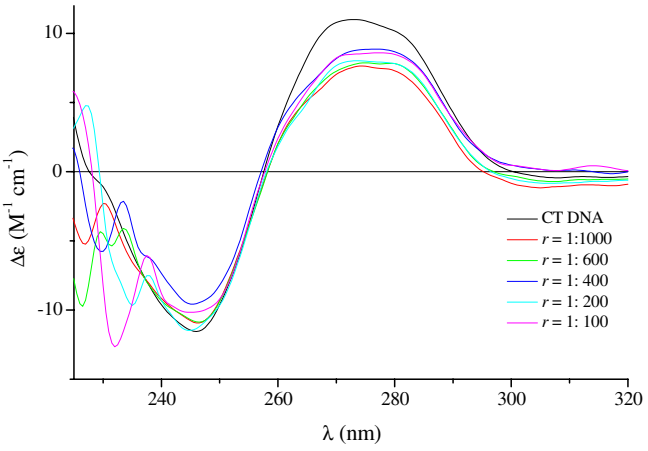


Fig. 4. CD spectra of CT DNA in 5 mM buffer (containing 150 mM NaCl and 15 mM trisodium citrate at pH 7.0) in the presence of complex $MoO_2(erx)_2$ (**1**) in different r values. The spectra were recorded at 25 °C after the samples had been incubated with CT DNA for 24 h at 37 °C.

practically unchanged and their intensities are marginally decreased. When r increases further (up to 1:100), the two positive bands II and III are consolidated and cannot be distinguished resulting to a unique broad band at $\lambda_{max} = 276$ nm while the intensity remains practically unchanged. On the other hand, the λ_{max} of the negative band I at 246 nm remains unchanged.

These changes indicate that **1** can be bound to CT DNA but we cannot safely suggest the exact mode of binding. Nevertheless, for high r values, the coexistence of bands II and III could be possibly concerned as a partial redshift of the CT DNA positive band (expected at 273 nm due to base stacking) to higher wavelengths being a hint for a probable B- to A-conformation DNA change due to $\pi \rightarrow \pi^*$ transitions [53,59], while for lower r values, where the dominating spectral feature is the lack of any perturbation on both bands I and II of CT DNA, the existence of simple groove binding or electrostatic interaction [56] could not be ruled out.

Quite similar behavior is observed in the CD spectra of CT DNA in the presence of complex **2**.

4. Conclusions

The synthesis and characterization of two neutral mononuclear MoO_2^{2+} complexes with the second and third-generation quinolone antibacterial drugs enrofloxacin and sparfloxacin, respectively, has been realized with physicochemical and spectroscopic methods. In both complexes, the quinolone ligands are bound to the metal via the pyridone and one carboxylate oxygen atoms. Each molybdenum(VI) atom is six-coordinate and the environment around could be described as distorted octahedron. With the use of molecular modeling calculations, we have proposed a low-energy model for the structures of both the complexes. The antimicrobial activity of the complexes has been tested on three different microorganisms. The complexes show a diverse biological activity in comparison to the free quinolone ligands and in some cases they provide better inhibition. The investigation of the interaction of the complexes with CT DNA has been performed with diverse spectroscopic techniques and has shown that the complexes can be bound to CT DNA.

Acknowledgements

The work was partially supported by E.L.K.E (70/4/6495) and the "Excellence in the Research Institutes" Program, Action 3.3.1 co-funded by the Greek Ministry of Development and E.U. We thank Dr. I. Eskioglou, Department of Medical Laboratories, Technological and Educational Institution of Larissa, Larissa, Greece for the supply of the microorganisms and Dr. A. Papakyriakou, Institute of Physical Chemistry, NCSR "Demokritos", Greece, for the supply of the molecular modeling routine.

Appendix A. Supplementary material

IR and UV–Vis spectral data and ^{1}H NMR chemical shifts for the ligands and the complexes. Scheme S1 for the diastereoisomers of $MoO_2(erx)_2$ and $MoO_2(sf)_2$ employed in the simulated annealing calculations. Table S1 for the metal–ligand distance restraints applied during the energy minimization phase in order to adjust the geometry of $MoO_2(erx)_2$ and $MoO_2(sf)_2$ models. Tables S2 and S3 for the energy statistics from the simulated annealing results of $MoO_2(erx)_2$ and $MoO_2(sf)_2$ diastereoisomers, respectively. Figs. S1 and S2 for the lowest energy model structures of the $MoO_2(erx)_2$ and $MoO_2(sf)_2$ enantiomers. Supplementary data associated with this article can be found, in the online version, at doi:10.1016/j.poly.2007.09.013.

References

[1] I. Turel, Coord. Chem. Rev. 232 (2002) 27.
[2] D.C. Hooper, E. Rubinstein (Eds.), Quinolone Antimicrobial Agents, 3rd ed., ASM Press, Washington, DC, 2003.
[3] V.T. Andriole (Ed.), The Quinolones, 3rd ed., Academic Press, San Diego, CA, 2000.
[4] D.T.W. Chu, P.B. Fernandes, in: B. Testa (Ed.), Advances in Drug Research, vol. 21, Academic Press, London, 1991, pp. 39–144.
[5] J.E.F. Reynolds (Ed.), Martindale: The Extra Pharmacopeia, 30th ed., The Pharmaceutical Press, London, 1993, pp. 145–147.
[6] H.C. Neu, Am. J. Med. 82 (1987) 395.
[7] R.E. Polk, Am. J. Med. 87 (1989) S76.
[8] M.J. e Souza, C.F. Bittencourt, L.M. Morsch, J. Pharm. Biomed. Anal. 28 (2002) 1197.
[9] M. Scheer, Vet. Med. Rev. 2 (1987) 90.
[10] P. Altreuther, Vet. Med. Rev. 2 (1987) 87.
[11] D.M. Boothe, Vet. Med. 89 (1994) 744.
[12] K. Tyczkowska, K.M. Heeden, D.P. Aucoin, A.l. Aronson, J. Chromatogr. B 493 (1989) 337.
[13] R. Bauditz, Vet. Med. Rev. 2 (1987) 122.
[14] J.-Y. Fan, D. Sun, H. Yu, S.M. Kerwin, L.H. Hurley, J. Med. Chem. 38 (1995) 408.

[15] S. Dessus-Babus, C.M. Bebear, A. Charron, C. Bebear, B. De Barbeyrac, Antimicrob. Agents Chemother. 42 (1998) 2474.
[16] S. Ameyama, Y. Shinmura, M. Takahata, Antimicrob. Agents Chemother. 47 (2003) 2327.
[17] D.E. King, R. Malone, S.H. Lilley, Am. Fam. Physician 61 (2000) 2741.
[18] E.I. Steifel, in: G. Wilkinson (Ed.), Comprehensive Coordination Chemistry, vol. 3, Pergamon Press, Oxford, 1989, pp. 1375–1420, and references cited therein.
[19] C.G. Young, in: J.A. McCleverty, T.J. Meyer (Eds.), Comprehensive Coordination Chemistry II, vol. 4, Elsevier, Amsterdam, 2003, pp. 415–527, and references cited therein.
[20] H. Arzoumanian, Coord. Chem. Rev. 178–180 (1998) 191, and references cited therein.
[21] J.M. Tunney, J. McMaster, C.D. Garner, in: J.A. McCleverty, T.J. Meyer (Eds.), Comprehensive Coordination Chemistry II, vol. 8, Elsevier, Amsterdam, 2003, pp. 459–477, and references cited therein.
[22] F. Barriere, Coord. Chem. Rev. 236 (2003) 71.
[23] J.T. Spence, Coord. Chem. Rev. 48 (1983) 59, and references cited therein.
[24] D.J. Wang, Z.D. Fang, D.Y. Han, Chem. Res. Chin. Univ. 21 (2005) 258.
[25] E.K. Efthimiadou, Y. Sanakis, N. Katsaros, A. Karaliota, G. Psomas, Polyhedron 26 (2007) 1148.
[26] A. Tarushi, E.K. Efthimiadou, P. Christofis, G. Psomas, Inorg. Chim. Acta 360 (2007) 3978.
[27] E.K. Efthimiadou, G. Psomas, Y. Sanakis, N. Katsaros, A. Karaliota, J. Inorg. Biochem. 101 (2007) 525.
[28] E.K. Efthimiadou, M. Katsarou, Y. Sanakis, C.P. Raptopoulou, A. Karaliota, N. Katsaros, G. Psomas, J. Inorg. Biochem. 100 (2006) 1378.
[29] E.K. Efthimiadou, Y. Sanakis, C.P. Raptopoulou, A. Karaliota, N. Katsaros, G. Psomas, Bioorg. Med. Chem. Lett. 16 (2006) 3864.
[30] G. Psomas, A. Tarushi, E.K. Efthimiadou, Y. Sanakis, C.P. Raptopoulou, N. Katsaros, J. Inorg. Biochem. 100 (2006) 1764.
[31] E.K. Efthimiadou, H. Thomadaki, Y. Sanakis, C.P. Raptopoulou, N. Katsaros, A. Scorilas, A. Karaliota, G. Psomas, J. Inorg. Biochem. 101 (2007) 64.
[32] E.K. Efthimiadou, N. Katsaros, A. Karaliota, G. Psomas, Bioorg. Med. Chem. Lett. 17 (2007) 1238.
[33] A. Tarushi, P. Christofis, G. Psomas, Polyhedron 26 (2007) 3963.
[34] E.K. Efthimiadou, N. Katsaros, A. Karaliota, G. Psomas, Inorg. Chim. Acta (2007), doi:10.1016/j.ica.2007.05.042.
[35] G. Psomas, A. Tarushi, E.K. Efthimiadou, Polyhedron (2007), doi:10.1016/j.poly.2007.08.043.
[36] E. Tselepi-Kalouli, N. Katsaros, J. Inorg. Biochem. 37 (1989) 271.
[37] N.L. Allinger, J. Am. Chem. Soc. 99 (1977) 8127.
[38] P. Christofis, M. Katsarou, A. Papakyriakou, Y. Sanakis, N. Katsaros, G. Psomas, J. Inorg. Biochem. 99 (2005) 2197, and references cited therein.
[39] E.J. Brown, A.C. Whitwood, P.H. Walton, A.-K. Duhme-Klair, Dalton Trans. (2004) 2458.
[40] Z.-H. Zhou, S.-Y. Hou, Z.-X. Cao, H.-L. Wan, S.-W. Ng, J. Inorg. Biochem. 98 (2004) 1037.
[41] A.-K. Duhme-Klair, G. Vollmer, C. Mars, R. Frohlich, Angew. Chem., Int. Ed. 39 (2000) 1626.
[42] M.P. Allen, D.J. Tildesley (Eds.), Computer Simulation of Liquids, Oxford University Press, Oxford, 1989.
[43] K. Nakamoto, Infrared and Raman Spectra of Inorganic and Coordination Compounds, 4th ed., Wiley, New York, 1986.
[44] G.B. Deacon, R.J. Phillips, Coord. Chem. Rev. 33 (1980) 227.
[45] M. Sakai, A. Hara, S. Anjo, M. Nakamura, J. Pharm. Biomed. Anal. 18 (1999) 1057.
[46] A.D. Russell, in: S.S. Block (Ed.), Disinfection, Sterilization and Preservation, 4th ed., Lea & Febinger, Philadelphia, PA, 1991, pp. 27–59.
[47] H.W. Rossmore, in: S.S. Block (Ed.), Disinfection, Sterilization and Preservation, 4th ed., Lea & Febinger, Philadelphia, PA, 1991, pp. 290–321.
[48] C. Dendrinou-Samara, G. Psomas, C.P. Raptopoulou, D.P. Kessissoglou, J. Inorg. Biochem. 83 (2001) 7.
[49] G. Psomas, C. Dendrinou-Samara, P. Philippakopoulos, V. Tangoulis, C.P. Raptopoulou, El. Samaras, D.P. Kessissoglou, Inorg. Chim. Acta 272 (1998) 24.
[50] A. Rodger, B. Norden (Eds.), Circular Dichroism and Linear Dichroism, Oxford University Press, Oxford, 1997.
[51] G. Song, Y. He, Z. Cai, J. Fluoresc. 14 (2004) 705.
[52] G.S. Son, J.-A. Yeo, M.-S. Kim, S.K. Kim, A. Holmen, B. Akerman, B. Norden, J. Am. Chem. Soc. 120 (1998) 6451.
[53] P. Uma Maheswari, M. Palaniandavar, J. Inorg. Biochem. 98 (2004) 219.
[54] V.I. Ivanov, L.E. Minchenkova, A.K. Schyolkina, A.I. Poletayev, Biopolymers 12 (1973) 89.
[55] P. Lincoln, E. Tuite, B. Norden, J. Am. Chem. Soc. 119 (1997) 1454.
[56] B. Norden, F. Tjerneld, Biopolymers 21 (1982) 1713.
[57] O. Novakova, H. Chen, O. Vrana, A. Rodger, P.J. Sadler, V. Brabec, Biochemistry 42 (2003) 11544.
[58] W. Curtis-Johnson, in: K. Nakanishi, N. Berova, R.W. Woody (Eds.), CD of Nucleic Acids in Circular Dichroism: Principles and Applications, VHS, New York, 1994, pp. 523–540.
[59] H. Robinson, A.H.J. Wang, Nucleic Acids Res. 24 (1996) 676.

Available online at www.sciencedirect.com
ScienceDirect
Polyhedron 27 (2008) 357–365
POLYHEDRON
www.elsevier.com/locate/poly

Anion dependent formation of linear trinuclear mixed valance cobalt(III/II/III) complexes and mononuclear cobalt(III) complexes of a pyrazole derived ligand – Synthesis, characterization and X-ray structures

Sachindranath Pal [a], Anil Kumar Barik [b], Samik Gupta [c], Somnath Roy [c], Tarak Nath Mandal [c], Arijit Hazra [c], Mohamed Salah El Fallah [d,*], Ray J. Butcher [e], Shie-Ming Peng [f], Gene-Hsiang. Lee [f], Susanta Kumar Kar [c,*]

[a] *Department of Chemistry, Sree Chaitanya College, Habra, North 24 Parganas, West Bengal, India*
[b] *Department of Chemistry, St. Paul's C.M. College, 33/1, Raja Rammohan Roy Sarani, Calcutta 700 009, India*
[c] *Department of Chemistry, University College of Science, 92 A.P.C. Road, Calcutta 700 009, India*
[d] *Departament de Química Inorgànica, Facultat de Química, Universitat de Barcelona, Martí i Franquès 1-11, 08028 Barcelona, Spain*
[e] *Department of Chemistry, Howard University, 2400 Sixth Street, N.W., Washington, DC 200 59, USA*
[f] *Department of Chemistry, National Taiwan University, Taipei 106, Taiwan, ROC*

Received 4 July 2007; accepted 20 September 2007

Abstract

Trinuclear mixed oxidation state Co(III/II/III) complexes with a different coordination geometry at each cobalt center of a pyrazole derived Schiff base and mononuclear cobalt (III) complexes of another pyrazole containing Schiff base having N-donor atoms have been prepared and structurally characterized. Reaction of 5-methyl-3-formylpyrazole (MPA) and 1,3-diamino-2-propanol (DAP) with $CoX_2 \cdot 6H_2O$ (X = Cl, Br) in a 2:1:1 ratio produces unusual trinuclear mixed-valent complexes $[Co_3(L_1)_2Cl_4]$ (**1**) and $[Co_3(L_1)_2Br_4]$ (**2**) [where $H_2L_1 = 1$, 3-bis(5-methyl-3-formylpyrazolylmethinimino)propane-2-ol], and the same reaction when carried out with $CoX_2 \cdot 6H_2O$ ($X = CH_3COO^-, ClO_4^-$ NO_3^-, BF_4^-) produces mononuclear $[Co(L_1)(H_2O)_2]X \cdot H_2O$, of which only $[Co(L_1)(H_2O)_2]CH_3COO \cdot H_2O$ (**3**) was isolated. In contrast, the reaction of 5-methyl-3-formylpyrazole (MPA) and 1,3-diamino-2-propanol (DAP) with $CoX_2 \cdot 6H_2O$ (where $X = ClO_4^- NO_3^-$, BF_4^-) in a 1:1:1 ratio produces mononuclear Schiff base complexes $[Co(L)_2]$ ClO_4 (**4**), $[Co(L)_2]$ NO_3 (**5**) and $[Co(L)_2]$ BF_4 (**6**) [where HL = 1-(5-methyl-3-formylpyrazolylmethinimino)-3-aminopropane-2-ol], whereas when X = Cl and Br a hygroscopic intractable material was isolated. Among the above species, **1** and **4** have been crystallographically characterized. In **1**, three cobalt atoms are arranged in a linear fashion and are bridged through pyrazolate rings. The terminal diamagnetic low spin cobalt(III) ions with a N_4Cl_2 chromophore are in a distorted octahedral environment. These two outer cobalt(III) complexes individually act as bidentate chelating ligands and encapsulate the central cobalt(II) ion, which adopts a distorted flattened, tetrahedral geometry with a N_4 chromophore. The interatomic separations are 3.794 Å (Co1···Co2) and 3.791 Å (Co2···Co3). In **4**, the cobalt(III) atom is also in a distorted octahedral geometry with a N_6 chromophore. Variable temperature (300–2 K) magnetic susceptibility measurements have been carried out for **1** and **2**. Zero field splitting of the tetrahedral cobalt(II) ion has been noticed. The EPR spectrum of **1** and **2** at low temperature is associated with a Kramer doublet $\pm 1/2$ arising from the $S = 3/2$ ground state. Some of the complexes are further characterized by UV–Vis, IR and electrochemical studies. The IR spectrum of **3** shows the typical vibration of ionic acetate at 1577 cm^{-1} (ν_{asym}) and 1397 cm^{-1} (ν_{sym}).
© 2007 Elsevier Ltd. All rights reserved.

Keywords: Trinuclear mixed oxidation state pyrazole bridged cobalt complexes; Schiff bases; X-ray structures; Magnetic properties; EPR spectra

* Corresponding authors. Tel.: +91 033 24322936; fax: +91 033 23519755.
E-mail addresses: Salah.elfallah@qi.ub.es (M.S. El Fallah), skkar_cu@yahoo.co.in (S.K. Kar).

0277-5387/$ - see front matter © 2007 Elsevier Ltd. All rights reserved.
doi:10.1016/j.poly.2007.09.037

1. Introduction

Multinuclear transition metal complexes have become a central theme of current research because of their potentially useful properties in the realm of relevant scientific and technological fields. They are involved in some notable catalytic processes [1]. Their important use for modelling the metal active sites of metalloproteins [2] and also their recent applications in the area of nanoscale materials [3] have drawn the focal point of attraction of modern chemists towards the synthesis and characterization of such metal complexes. Especially, there is currently a great deal of interest in the synthesis and characterization of polynuclear cobalt complexes due to their wide-ranging potential applications such as catalysts [4], electron transfer mediators in dye-sensitized solar cells [5], anti-viral agents [6] and molecular nano-magnets [7]. In particular, trinuclear cobalt complexes draw their speciality from their use as catalysts in epoxidation of olefins [8] and in the autoxidation of hydrocarbons [9]. One of the synthetic strategies to prepare polynuclear transition metal complexes is the use of simple metal ion complexes which have the appropriate functionality to act as ligands for another metal ion or ions. The speciality of these strategies is the use of a mononuclear transition metal complex as a bidentate chelate for a second metal ion. One attractive feature of this scheme is that the second metal ion will usually be in a different coordination pocket from the first one, potentially allowing the facile synthesis of homonuclear complexes in which the metals having different oxidation states are in different geometries.

Studies in metal ion mediated anion dependent formation of polynuclear Schiff base complexes has been one of the prime topics of our recent research [10]. In continuation of our earlier work, attempts have been made to prepare Co(II) complexes of the Schiff base ligand H_2L_1 [2:1 condensation product of MPA (5-methyl-3-formylpyrazole) and DAP (1,3-diamino-2-propanol)], employing the template methodology. Interestingly, when 2 equiv. of MPA and 1 equiv. of DAP are condensed in the presence of 1 equiv. of Co(II) chloride/bromide, the unusual mixed oxidation state pyrazolate bridged complexes $[Co_3(L_1)_2X_4]$, X = Cl, Br (**1** and **2**) are isolated. Under similar conditions $CoX_2 \cdot 6H_2O$ ($X = CH_3COO^-, ClO_4^-$, NO_3^-, BF_4^-) produces the mononuclear complexes $[Co(L_1)(H_2O)_2]X \cdot H_2O$, of which only the acetate complex (**3**) [$X = CH_3COO^-$] was isolated; the other products being intractable materials that could not be isolated. In contrast, the same reaction when carried out in MPA and DAP in a 2:2 equiv. ratio in the presence of 1 equiv. of $CoX_2 \cdot 6H_2O$ ($X = ClO_4^-$, NO_3^- and BF_4^-) ended in forming the desired mononuclear Schiff base complexes $[Co(L)_2]X$ ($X = ClO_4^-$, NO_3^- and BF_4^-) (**4**, **5** and **6**). An intractable green mass was obtained in the same reaction when Cl^-/Br^- were used as counterions. The structures of the ligands H_2L_1 and HL are given in Fig. 1.

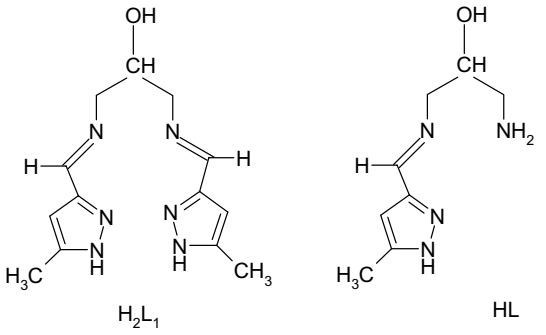


Fig. 1. Structure of the ligands.

All the observations are depicted in Scheme 1 for clarity.

2. Experimental

2.1. Materials

1,3-Diamino-2-propanol (DAP) was purchased from Aldrich, USA. 5-Methyl-3-formylpyrazole (MPA) was synthesized as described earlier [11]. Spectrograde solvents were used for physical measurements. All the other reagents and solvents were purchased from commercial sources and purified by standard procedures [12].

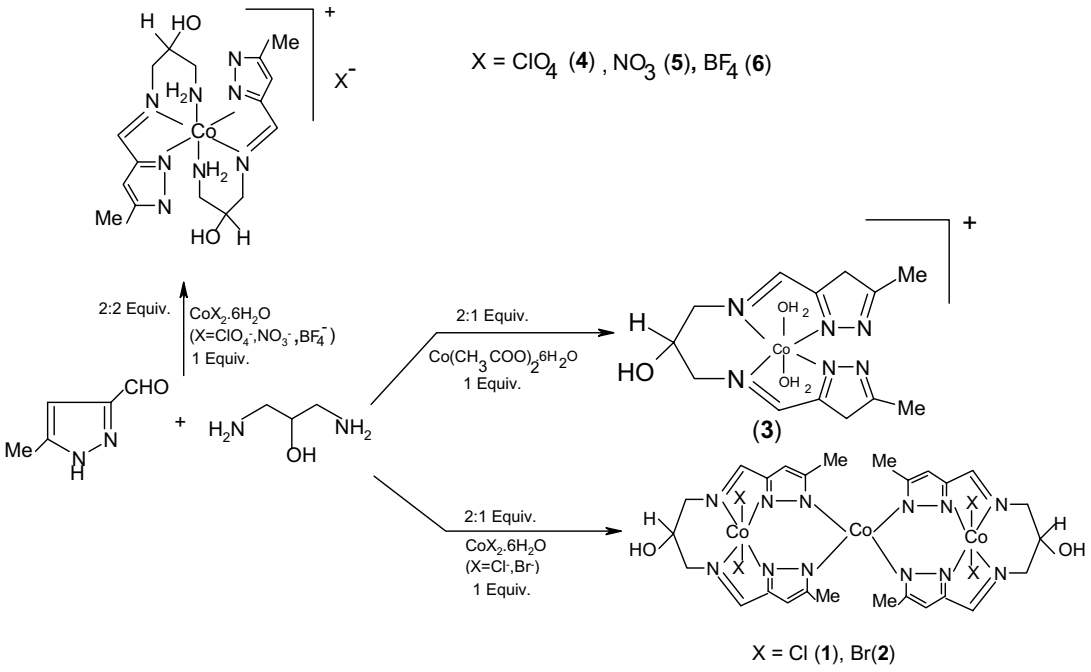
Synthesis: Warning! Perchlorate salts are potentially explosive and were handled only in small quantities with care.

2.2. Preparation of the Co(III/II) complexes $[Co_3(L_1)_2X_4]$ [X = Cl^- (1), Br^- (2)]

A mixture of MPA (0.22 g, 2 mmol) and DAP (0.09 g, 1 mmol) was refluxed for 4 h in 50 ml dry ethanol. The light red solution was filtered off, cooled to room temperature and the corresponding Co(II) salt (1 mmol) was added. Immediately a green precipitate was separated. The mixture was stirred for 2 h and filtered. The precipitate was washed with ethanol and dried over fused $CaCl_2$ in a desiccator. Yield 58% (**1**), 53% (**2**). X-ray quality crystals of **1** were grown by slow diffusion of *n*-hexane into a dichloromethane–ethanol (1:1 V/V mixture) solution of the compound.

Anal. Calc. for $C_{26}H_{32}Cl_4Co_3N_{12}O_2$ (**1**): C, 36.16; H, 3.70; N, 16.46. Found: C, 36.32; H, 3.73; N, 15.23%. IR (KBr; cm^{-1}): 3400, 3190, 2979 (ν_{OH}, ν_{NH}), 1605 ($\nu_{C=Niminyl}$), 1521 ($\nu_{C=NPz}$), 1035 (ν_{N-NPz}). Diffuse reflectance spectroscopy (DRS) (λ_{max}, nm): 1065, 644, 630, 590. UV–Vis (MeOH) (λ_{max}, nm) (ε, $1\,M^{-1}\,cm^{-1}$): 1075 (51), 587 (286), 565 (254), 542 (183). Molar conductivity (MeOH solution): $\Lambda_M = 16\,\Omega^{-1}\,cm^2\,mol^{-1}$. Magnetism (solid state, room temperature): $\mu_{eff} = 4.3$ B.M.

Anal. Calc. for $C_{26}H_{32}Br_4Co_3N_{12}O_2$ (**2**): C, 29.98; H, 3.07; N, 16.14. Found: C, 29.76; H, 3.19; N, 15.91%. IR



Scheme 1.

(KBr; cm^{-1}): 3401, 3210, 3100 (ν_{OH}, ν_{NH}), 1603 ($\nu_{C=Niminyl}$), 1523 ($\nu_{C=NPz}$), 1040 (ν_{N-NPz}). Diffuse reflectance spectroscopy (DRS) (λ_{max}, nm): 1073, 645, 629, 598. UV–Vis (DMF) (λ_{max}, nm) (ε, $1\,M^{-1}\,cm^{-1}$): 1060 (65), 648 (795), 625 (732), 595 (565). Molar conductivity (DMF solution): $\Lambda_M = 52\,\Omega^{-1}\,cm^2\,mol^{-1}$. Magnetism (solid state, room temperature): $\mu_{eff} = 4.2$ B.M.

2.3. Preparation of $[Co(L_1)(H_2O)_2]CH_3COO \cdot H_2O$ (3)

To a filtered solution of a mixture of MPA (0.22 g, 2 mmol) and DAP (0.09 g, 1 mmol) in 30 ml dry ethanol, prepared following the same procedure outlined above, the cobalt(II) salt $Co(II)X_2 \cdot xH_2O$ (1 mmol) was added ($X = ClO_4^-, BF_4^-, CH_3COO^-, NO_3^-$). The solution in each case was refluxed for 4 h to get a red solution. Only the complex with acetate as a counterion has been isolated, while in all other cases hygroscopic intractable materials were found. In spite of our several attempts, we were unsuccessful to isolate the X-ray quality crystals of **3**.

Anal. Calc. for $C_{15}H_{25}CoN_6O_6$ (**3**): C, 40.54; H, 5.68; N, 18.92%. Found: C, 40.51; H, 5.20; N, 18.45%. IR (KBr; cm^{-1}): 3600–2900 (v.b.) (ν_{OH}, ν_{H_2O}, ν_{NH}), 1610 ($\nu_{C=Niminyl}$), 1577 ($\nu_{C=NPz}$ and $\nu_{ionic\ acetate}$), 1397 ($\nu_{ionic\ acetate}$). Diffuse reflectance spectroscopy (DRS) (λ_{max}, nm): 462, 373. UV–Vis (MeOH) (λ_{max}, nm) (ε, $1\,M^{-1}\,cm^{-1}$): 505 (12). Molar conductivity (MeOH solution): $\Lambda_M = 82\,\Omega^{-1}\,cm^2\,mol^{-1}$. Magnetism (solid state, room temperature): $\mu_{eff} = 0$. TGA: Loss of lattice water (calc. 4.05%, found 4.12%) in the temperature range 75–85 °C and that of the coordinated water molecules (calc. 8.1%, found 7.98%) in the temperature range 170–195 °C.

2.4. Preparation of Co(III) complexes with HL: $[Co(L)_2]X$ [$X = ClO_4^-$ (4), NO_3^- (5), BF_4^- (6)]

A mixture of MPA (0.11 g, 1 mmol) and DAP (0.09 g, 1 mmol) was refluxed for 4–5 h in ethanol. To the light yellow filtrate, an ethanolic solution of the corresponding $CoX_2 \cdot 6H_2O$ ($X = ClO_4^-$, NO_3^-, BF_4^-) (1 mmol) was added and again refluxed for 4 h. The resulting deep red solution was left for slow evaporation at room temperature in a fused $CaCl_2$ desiccator. After 5 days red coloured crystalline compounds were isolated. Yield 60–65%. X-ray quality crystals of **4** were grown by the slow evaporation of a methanolic solution of the compound.

Anal. Calc. for $C_{16}H_{26}CoN_8ClO_6$ (**4**): C, 36.92; H, 5.03; N, 21.50. Found: C, 36.10; H, 4.98; N, 21.22%. IR (KBr: cm^{-1}): 3320 (br) (ν_{OH}, ν_{NH}), 1602 ($\nu_{C=N(iminyl)}$), 1563 (s, $\nu_{C=NPz}$), 1095 (s) (ν_{ClO4}) 1010 (ν_{N-NPz}). Diffuse reflectance spectroscopy (DRS) (λ_{max}, nm): 368, 453. UV–Vis (DMF), λ_{max}, nm (ε, $1\,M^{-1}\,cm^{-1}$): 449 (35). Molar conductivity (DMF solution): $\Lambda_M = 80\,\Omega^{-1}\,cm^2\,mol^{-1}$.

Anal. Calc. for $C_{16}H_{26}CoN_9O_5$ (**5**): C, 39.75; H, 5.38; N, 26.08. Found: C, 40.01; H, 5.21; N, 26.03%. IR (KBr: cm^{-1}): 3322 (br) (ν_{OH}, ν_{NH}), 1609 ($\nu_{C=N(iminyl)}$), 1563 (s, $\nu_{C=NPz}$), 1010 (ν_{N-NPz}). Diffuse reflectance spectroscopy (DRS) (λ_{max}, nm): 370, 453. UV–Vis (DMF) (λ_{max}, nm) (ε, $1\,M^{-1}\,cm^{-1}$): 448 (35). Molar conductivity (DMF solution): $\Lambda_M = 76\,\Omega^{-1}\,cm^2\,mol^{-1}$.

Anal. Calc. for $C_{16}H_{26}CoN_8O_2BF_4$ (**6**): C, 37.79; H, 5.11; N, 22.04. Found: C, 37.12; H, 5.02; N, 21.15%. IR (KBr: cm^{-1}): 3322 (br) (ν_{OH}, ν_{NH}), 1609 ($\nu_{C=N(iminyl)}$),

1563 (s, $\nu_{C=NPz}$), 1011 (ν_{N-NPz}). Diffuse reflectance spectroscopy (DRS) (λ_{max}, nm): 370, 453. UV–Vis (DMF) (λ_{max}, nm) (ε, $1\,M^{-1}\,cm^{-1}$): 445 (35). Molar conductivity (DMF solution): $\Lambda_M = 82\,\Omega^{-1}\,cm^2\,mol^{-1}$.

2.5. Physical methods

Infrared spectra were recorded on KBr disks (4000–400 cm^{-1}) with a Perkin–Elmer FTIR spectrophotometer. UV–Vis spectra were measured on a Hitachi U-3501 spectrophotometer. Room temperature magnetic moments were measured with a vibrating sample magnetometer. Variable temperature susceptibility measurements for **1** and **2** were carried out on polycrystalline samples at the Servei de Magnetoquimica of the Universitat de Barcelona with a Quantum Design SQUID MPMS-XL susceptometer apparatus working in the range 2–300 K under a magnetic field of approximately 200 G (2–30 K) and 5000 G (35–300 K). Diamagnetic corrections were estimated from Pascal Tables. The EPR spectra have been recorded on an X-band Bruker spectrometer (ESR 300E) working with an Oxford helium liquid cryostat for variable temperature measurements. The diffuse reflectance spectra of the reported complexes were recorded on a Hitachi U-3501 spectrophotometer. Electrical conductivity measurements were carried out in methanol solution using a Systronics model 304 digital conductivity meter. Elemental analyses were carried out at IACS, Calcutta with a Perkin–Elmer model 2400 CHN analyzer. Cyclic voltammetry was carried out using Sycopel model AEW2 1820F/S instrument. The measurements were performed at 300 K in DMF solutions containing 0.2 M TEAP and 10^{-3}–10^{-4} M cobalt complex **1** deoxygenated by bubbling with nitrogen. The working, counter and reference electrodes used were a platinum wire, a platinum coil and an SCE.

2.6. X-ray crystal structure analysis

Selected crystal data for **1** and **4** are given in Table 1. Data collections were made using a Bruker SMART CCD area detector (for **1**) and a Bruker P4 diffractometer (for **4**) equipped with a graphite monochromated Mo Kα radiation ($\lambda = 0.71073$ Å) source in the ω scan mode at 295(2) and 293(2) K, respectively. Cell parameter refinement and data reduction for **1** were carried out using the Bruker SAINT program [13]. For **4**, cell parameters were refined by Bruker XSCANS and the corresponding data reduction were done by Bruker SHELXTL software [14]. The structures were solved by conventional direct methods and refined by full-matrix least square methods using F^2 data. SHELXS-97 and SHELXL-97 programs [15] were used for structure solution and refinement, respectively. Positions of H-atoms were treated as riding on their parent atoms. For **4**, this was a room temperature structure containing perchlorate. As is usual for this group, it was disordered. However, an added complication was that this group was also near a symmetry element. This made it much harder to idealize this group during the refinement process. Because of symmetry one O atom was in two positions. The best model was obtained by constraining the Cl–O distance and the O–O separation.

Table 1
Crystallographic data and structure refinements for **1** and **4**

Complex	**1**	**4**
Empirical formula	$C_{26}H_{32}Cl_4Co_3N_{12}O_2$	$C_{16}H_{26}ClCoN_8O_6$
Formula weight	863.23	520.83
Temperature (K)	295(2)	293(2)
Wavelength (Å)	0.71073	0.71073
Crystal system	monoclinic	monoclinic
Space group	*C*2/*c*	*C*2/*c*
Unit cell dimensions		
a (Å)	35.5966(13)	10.5408(9)
b (Å)	8.1847(3)	12.0131(10)
c (Å)	32.8940(12)	17.8896(16)
β (°)	120.384(2)	95.378(5)
Volume	8267.3(10)	2255.3(3)
Z	8	4
D_{calc} (Mg/m^3)	1.387	1.534
Absorption coefficient (mm^{-1})	1.486	0.929
F(000)	3496	1080
Crystal size (mm)	$0.35 \times 0.10 \times 0.02$	$0.10 \times 0.70 \times 0.26$
θ Range for data collection (°)	1.33–25.00	2.29–27.49
Limiting indices	$-42 \leqslant h \leqslant 42$, $-9 \leqslant k \leqslant 9$, $-39 \leqslant 1 \leqslant 35$	$0 \leqslant h \leqslant 11$, $0 \leqslant k \leqslant 15$, $-23 \leqslant 1 \leqslant 23$
Reflections collected	27 333	2588
Independent reflections [R_{int}]	7285 [0.1215]	2452 [0.0194]
Completeness to $\theta = 27.50°$ (**1**), 25.00° (**4**)	99.9%	97.3%
Absorption correction	semi-empirical from equivalents	empirical
Maximum and minimum transmission	0.9709 and 0.6242	0.2864 and 0.2421
Refinement method	full-matrix least-squares on F^2	full-matrix least-squares on F^2
Data/restraints/parameters	7285/8/418	2452/7/165
Goodness-of-fit on F^2	1.050	1.059
Final *R* indices [$I > 2\sigma(I)$]	$R_1 = 0.0957$, $wR_2 = 0.2765$	$R_1 = 0.0589$, $wR_2 = 0.1635$
R indices (all data)	$R_1 = 0.1977$, $wR_2 = 0.3495$	$R_1 = 0.0758$, $wR_2 = 0.1808$
Largest differences in peak and hole (e $Å^{-3}$)	0.448 and −0.783	1.040 and −0.614

3. Results and discussion

The Schiff base ligand H_2L_1, acting as a binegative hexadentate ligand, forms linear trinuclear pyrazolate bridged mixed valent cobalt complexes $[Co_3(L_1)_2Cl_4]$ (**1**) and $[Co_3(L_1)_2Br_4]$ (**2**) in the presence of the Cl^- and Br^- anion, respectively. The same ligand forms mononuclear complexes $[Co(L_1)(H_2O)_2]X \cdot H_2O$ for other anions like CH_3COO^- (**3**), ClO_4^-, NO_3^- and BF_4^-, where it acts as a tetradentate binegative ligand. The other Schiff base HL, functioning as a uninegative tridentate ligand, forms mononuclear complexes $[Co(L)_2]ClO_4$ (**4**), $[Co(L)_2]NO_3$

(**5**) and $[Co(L)_2]BF_4$ (**6**). The crystal structures of **1** and **3** are depicted below.

3.1. Description of crystal structures

Fig. 2 shows a perspective view of compound **1** including the atom numbering scheme. The crystal data and selected bond lengths along with angles are presented in Tables 1 and 2, respectively. The crystal structure reveals the formation of a neutral, linear, trinuclear complex with mixed oxidation states of cobalt. The trinuclear cobalt complex locates at a general position in *C*2/*c*, there is no crystallographic symmetry in the complex. The hydroxyl group attached to C7 is disordered at the axial and equatorial positions with half occupancies. The other sites of the six-membered ring (Co3–N9–C19–C20–C21–N10) are seriously disordered on C20, C21 and O1 with half occupancies. Some restraints are applied in the refinement. The difference in bond lengths discriminate between the Co(II) and Co(III) ions. Each of the two terminal cobalt centers, Co1 and Co3, is clearly low spin octahedral cobalt(III) with short Co–N distances (av. 1.911 Å). Co1 has a six coordinate pseudo octahedral geometry in which N2, N3, N4 and N5 atoms of the deprotonated di-Schiff base $[L_1]^{2-}$ constitute the equatorial plane and two Cl [1 and 2] atoms define the axial directions of the *trans* isomer. The analysis of bond angle values Table 2 suggests a small deviation from the expected octahedral geometry. This is due to the restrictions imposed by the tetradentate ligand $[L_1]^{2-}$, the five- and six-membered chelate ring bite angles being 82° and 98°, respectively. The coordination environment around Co3 is very similar to that of Co1. Co3 is also in a pseudo octahedral environment in which the $[L_1]^{2-}$ ligand forms the equatorial plane [N(8), N(9), N(10), N(11)] and the two apical positions are occupied by two Cl-atoms [Cl3, Cl4]; here the five- and six-membered chelate ring bite angles are 82° and 97°, respectively.

Two of these mononuclear anionic $[trans\text{-}Co(L_1)Cl_2]^-$ complexes act as ligands to the central cobalt(II) center, [Co2] with the formation of four pyrazolate bridges. The metal ion sits in a slightly flattened tetrahedral geometry with an average Co2–N distance of 1.993 Å and an average chelate bite angle of 103°. The angle between the N1–Co2–N6 and N7–Co2–N12 chelate planes is 84°. This orthogonality in approach of the two ligands (obviously terminal octahedral complexes) is a consequence of the steric

Table 2
Selected bond distances (Å) and angles (°) involving **1** and **4**

1		**4**	
Bond distances (Å)			
Co1–N2	1.891(11)	Co–N(1)	1.902(3)
Co1–N3	1.943(12)	Co–N(1)#1	1.902(3)
Co1–N4	1.963(13)	Co–N(3)#1	1.945(3)
Co1–N5	1.875(10)	Co–N(3)	1.945(3)
Co2–N1	1.999(9)	Co–N(4)#1	1.972(3)
Co2–N6	1.979(11)	Co–N(4)	1.972(3)
Co2–N7	1.992(10)		
Co2–N12	2.002(10)		
Co3–Cl3	2.226(5)		
Co3–Cl4	2.249(5)		
Co3–N8	1.884(10)		
Co3–N9	1.925(16)		
Co3–N10	1.917(16)		
Co3–N11	1.889(10)		
Bond angles (°)			
N2–Co1–N3	81.8(5)	N(1)–Co–N(1)#1	92.70(18)
N2–Co1–N4	178.9(4)	N(1)–Co–N(3)#1	94.87(13)
N2–Co1–N5	98.7(5)	N(1)#1–Co–N(3)#1	82.00(13)
N3–Co1–N4	97.6(5)	N(1)–Co–N(3)	82.00(13)
N3–Co1–N5	179.4(5)	N(1)#1–Co–N(3)	94.87(13)
N4–Co1–N5	81.9(5)	N(3)#1–Co–N(3)	175.49(17)
N1–Co2–N6	102.7(4)	N(1)–Co–N(4)#1	87.92(14)
N1–Co2–N7	117.2(4)	N(1)#1–Co–N(4)#1	177.55(13)
N1–Co2–N12	107.3(4)	N(3)#1–Co–N(4)#1	95.59(13)
N6–Co2–N7	110.0(4)	N(3)–Co–N(4)#1	87.56(13)
N6–Co2–N12	117.0(4)	N(1)–Co–N(4)	177.55(13)
N7–Co2–N12	103.3(4)	N(1)#1–Co–N(4)	87.92(14)
N8–Co3–N9	82.8(6)	N(3)#1–Co–N(4)	87.57(13)
N8–Co3–N10	178.8(6)	N(3)–Co–N(4)	95.59(13)
N8–Co3–N11	99.3(5)	N(4)#1–Co–N(4)	91.60(2)
N9–Co3–N10	96.0(7)		
N9–Co3–N11	177.8(6)		
N10–Co3–N11	81.9(6)		

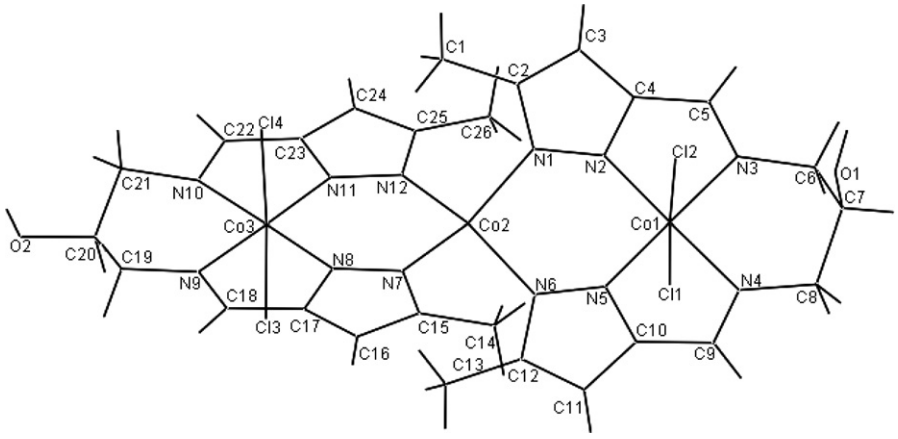


Fig. 2. Molecular structure of **1**.

hindrance of the interlacing methyl groups on the pyrazole rings. These methyl groups also effectively prevent the central Co(II) ion from adopting a higher coordination number.

The Co1···Co2 and Co2···Co3 interatomic distances are 3.794 Å and 3.791 Å, respectively. None of these distances is sufficiently short to imply any metal–metal bonding or allow intra-metal spin exchange through mutual interactions [16–18]. In the present complex, the Co(II)–N distances vary from 1.979(9) to 2.004(10) Å, and are typical for high spin Co(II)–N distances. The Co(III)–N distances are in the range 1.874(10)–1.963(11) Å, as expected for low spin Co(III) [16,19]. Thus the bond lengths about the terminal cobalt ions are significantly shorter than those about the central cobalt ion, indicating that the terminal ones are trivalent while the central one is divalent.

A perspective view of compound **4**, including the atom-numbering scheme, is shown in Fig. 3. The asymmetric unit consists of a $[Co(L)_2]^+$ cation and ClO_4^- anion. In the crystal structure the two potentially uninegative tridentate (NNN) donor ligand molecules form an octahedral geometry around the central cobalt atom. Each ligand molecule offers its respective deprotonated pyrazolyl nitrogen, azoimine nitrogen and terminal primary nitrogen atoms as the coordination sites, providing an N_6 chromophore. The equatorial plane of the octahedral geometry is defined by N1(deprotonated pyrazolide), N3(azoimine), N4(primary NH_2) and N3a(azoimine), and the two apical positions are coordinated by N1a (deprotonated pyrazolide) and N4a (primary NH_2). The coordination polyhedron of the said complex is best described as a distorted octahedron, which is reflected through the difference in N–Co–N bond angles. Quite obviously all the bond angles are deviated from the respective ideal bond angle values. The maximum deviation occurs for N1–Co–N3 [82.00(13)°], N3#1–Co–N3 [175.49(17)°], N3–Co–N4 [95.59(13)°]. The two Co–N pyrazolide bonds, being equal in length [1.902(3) Å], are still shorter than the two equal Co–N(azoimine) bonds [1.945(3) Å]. This difference in bond lengths is quite evident from the difference in the basic property between the deprotonated pyrazolide nitrogen (stronger base) and the neutral azoimine nitrogen (weaker base). The other two Co–N (terminal NH_2) bonds are also equal [1.972(3) Å] in themselves, but are longer than the other Co–N bonds. This is because of the difference in hybridization state (sp^2 for azoimine nitrogen and sp^3 for terminal NH_2). The two ligand molecules approach the central metal ion almost orthogonally, as suggested from the dihedral angle analysis (the dihedral angle being 88°). The ligands are coordinated to the central Co(III) ion in the meridional fashion (the pyrazolide and primary amine nitrogen atoms are cis to each other and the azoimine nitrogen atoms are *trans*). The origin of this meridional disposition arises from the maximum back bonding effect between the filled t_{2g} orbitals on the Co(III) ion and the vacant π^* M.O.s on the pyrazole ring. The perchlorate anion in this structure lies proximate to an inversion center. The crystal structure is stabilized through a network of both intramolecular and intermolecular H-bonding. The uncoordinated-OH of one ligand HL (in one asymmetric unit) forms a strong intermolecular H-bond with the pyrazolide N of another asymmetric unit [the O–N distance being 2.755(5) Å]. Likewise, the N4–O1 contact [3.011(5) Å] is also an indication of weak intramolecular H-bonding. The details of H-bond parameters are presented in Table 3. For clarity, the H-bonding interaction is shown in Fig. 4.

3.2. Diffuse reflectance and solution spectra

The spectral pattern in both DRS and in methanol solution of **1** (as a representative example) exhibits bands mainly characteristic of cobalt(II) in a tetrahedral geome-

Table 3
Hydrogen bonds for **4** (Å) and (°)

D–H···A	*d*(D–H)	*d*(H···A)	*d*(D···A)	∠(DHA)
O(1)–H(1A)···N(2)#1	0.82	1.94	2.760(4)	176.2
N(4)–H(4A)···O(1)#2	0.90	2.33	3.007(5)	132.3

Symmetry transformations used to generate equivalent atoms:
#1 $x-1/2, y-1/2, z$. #2 $-x+1, y, -z+1/2$.

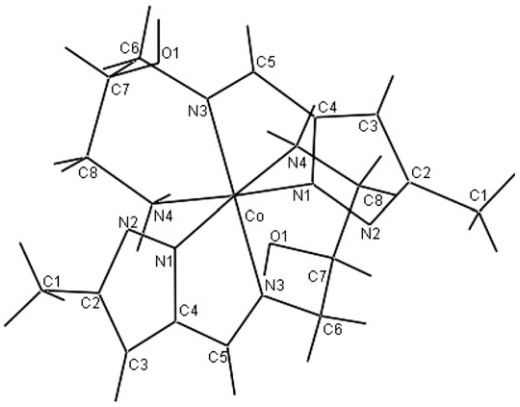


Fig. 3. Molecular structure of **4**.

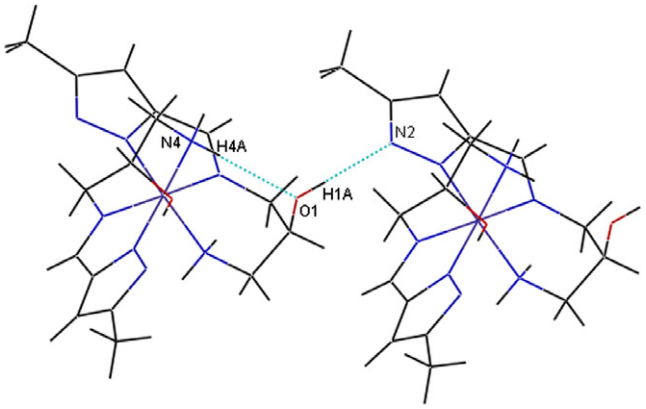


Fig. 4. H-bonding of **4**.

try. In the diffuse reflectance spectrum, in addition to the tetrahedral bands, (one spanning between 600–650 nm and the other between 1000–1100 nm) another spectral band is observed at *ca.* 400 nm, attributable to the low-spin octahedral Co(III) center. In solution, however, only Co(II) tetrahedral bands are obtained. Although three spin-allowed electronic transitions are expected to occur for tetrahedral Co(II), the visible spectrum is actually dominated by the highest energy transition, $^4A_2 \rightarrow {}^4T_1(P)$ with the $^4A_2 \rightarrow {}^4T_1(F)$ transition in the near IR region. The visible transition in tetrahedral complexes generally has complex envelopes because a number of transitions to doublet excited states occur in the same region, and these acquire some intensity by means of spin–orbit coupling. Thus from the above discussion it may be stated that, both in solid and in solution the weak absorption band at *ca.* 1065 nm and the strong one at *ca* 620 nm may be assigned as $^4A_2 \rightarrow {}^4T_1(F)$ (ν_2) and $^4A_2 \rightarrow {}^4T_1(P)$ (ν_3), respectively.

The diffuse reflectance spectrum of **3** exhibits two broad bands at 373 nm and 462 nm corresponding to two spin-allowed transitions ($^1A_{1g} \rightarrow {}^1T_{2g}$ and $^1A_{1g} \rightarrow {}^1T_{1g}$) for the low spin Co(III) octahedral species. The DMF solution of the complex does not display any band in the visible region. The d–d bands in the electronic spectrum of the present Co(III) complex is obscured by the intense CT bands [20].

The diffuse reflectance spectrum of **4** (as a representative example), exhibiting two bands at 368 nm ($^1A_{1g} \rightarrow {}^1T_{2g}$) and 453 nm ($^1A_{1g} \rightarrow {}^1T_{1g}$), indicates the low-spin octahedral geometry of the $[Co(L)_2]^+$ cation. The intense charge-transfer bands in the UV-region probably mask the other bands. The DMF solution of the complex displays a characteristic absorption in the UV–Vis region. The characteristic visible spectrum may be ascribed to transitions from $^1A_{1g}$ to $^1T_{1g}$ and $^1T_{2g}$ states, respectively. Here only one band at 449 nm ($^1A_{1g} \rightarrow {}^1T_{1g}$) is obtained. The second transition is obscured by either intense charge transfer bands or intraligand transitions [20].

3.3. Electrochemistry

The cyclic voltammetry experiment of **1** (Fig. 5) was performed in methanol solution within the potential range ±2 V versus Pt wire electrode at ambient temperature (300 K) using a three-electrode configuration. The complex exhibits no oxidation response. However, an irreversible reduction couple at −1.11 V is ascribed to a Co(III) → Co(II) reduction. The redox signal remains almost unaltered under different scan rates (0.02–1.0 vs^{-1}) in the temperature range 300–280 K.

3.4. Magnetic and EPR study of 1 and 2

The magnetic properties of compounds **1** and **2** are as expected, taking into account the linear trinuclear mixed valence cobalt(III/II/III) (Fig. 2) in which the surrounding Co(III) centres have an octahedral geometry with $S = 0$

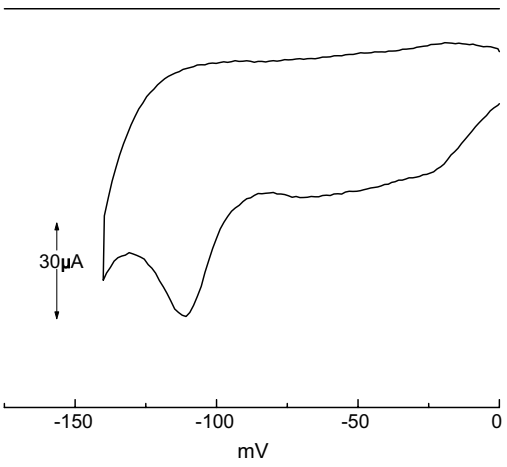


Fig. 5. Cyclic voltammogram of **1**.

and the central Co(II) centre has a distorted tetrahedral geometry possessing spin ($S = 3/2$) without spin–orbit splitting. Susceptibility measurements in the 300–2 K range shows a constant $\chi_M T$ value of 2.293 and 2.458 cm^3 K mol^{-1}, down to approximately 65 and 50 K, respectively, and below this temperature decrease to 1.373 and 1.476 cm^3 K mol^{-1} at 2 K for **1** and **2**, respectively (Fig. 6). Structural data of compound **1** indicate that it is a linear trinuclear cobalt complex with pyrazolate bridges and the main factor determining the decrease in the $\chi_M T$ value could be the Zero Field Splitting (ZFS) of the cobalt(II) ion in a distorted tetrahedral environment. To determine this parameter, we have fitted the experimental data to the following expression [21]:

$$\chi_M = \{[Ng^2\mu_\beta^2/KT][(1/4)(1 + 9e^{-2x})/(1 + e^{-2x})] + 2[1 + (3/4x)(1 - e^{-2x})/(1 + e^{-2x})]\}/3$$

where $x = D/KT$.

The best fit parameters obtained minimizing the function $R = (\sum \chi_M T_{calc} - \chi_M T_{obs})^2/(\sum \chi_M T_{obs})^2$ are $D = 16.1\ cm^{-1}$, $g = 2.21$ for **1** and $D = 12.3\ cm^{-1}$, $g = 2.28$ for

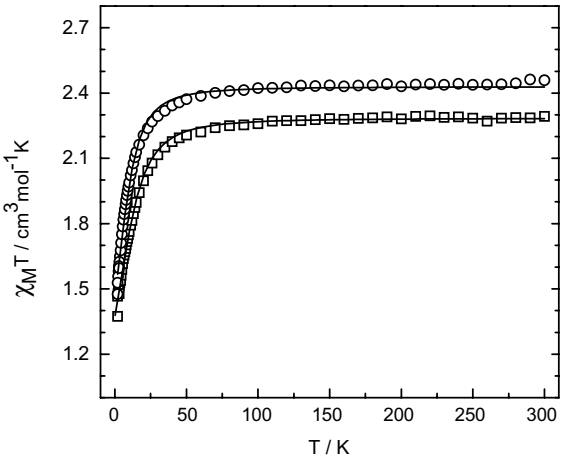


Fig. 6. Plot of $\chi_M T$ vs. T of a polycrystalline sample of **1** (□) and **2** (○). The solid line corresponds to the best fit.

2. In both cases the *R* factor value is found to be inferior to 10^{-5}. It should be pointed out that these D values seem to be too high because in the fits we do not take into account the intermolecular interactions (currently AF).

The field dependence of magnetization (0–5 T) measured at 2 K is shown in Fig. 7 in the form of M/Nβ per Co(III)–Co(II)–Co(III) unit versus H. The magnetization reaches a value of 1.91 and 2.25 electrons at 5 T for **1** and **2**, respectively. Comparison of the overall shape of the experimental plots with the Brillouin plot (solid plot) for one isolated ion with $S = 3/2$ system and $g = 2$ indicates slower magnetization, which is consistent with the presence of the ZFS effect.

The powder EPR spectra of **1** and **2** at 4 K are shown in Fig. 8. They exhibit a resonance with a maximum at approximately $g = 4.80$ and 5.13 and a broad band centred at $g = 2.16$ and 2.24 for **1** and **2**, respectively. No new transition is observed when the temperature is increased. These spectra are in good agreement with those expected for a $S_T = 3/2$ system: the spectrum at low temperature is associated with the Kramer doublet $\pm 1/2$ arising from the $S = 3/2$ ground state [22,23], which must present two signals approximately in the ratio $g_\perp = 2g_\parallel$.

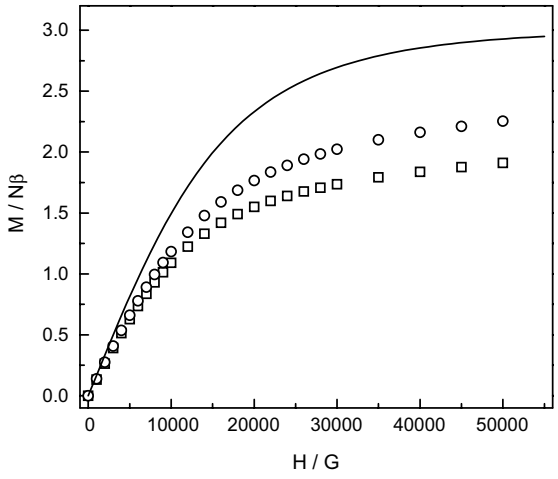


Fig. 7. Plot of reduced magnetization M/Nβ vs. applied field H at 2 K for **1** (□) and **2** (○). Solid line corresponds to the Brillouin function for an isolated $S = 3/2$ with $g = 2.0$.

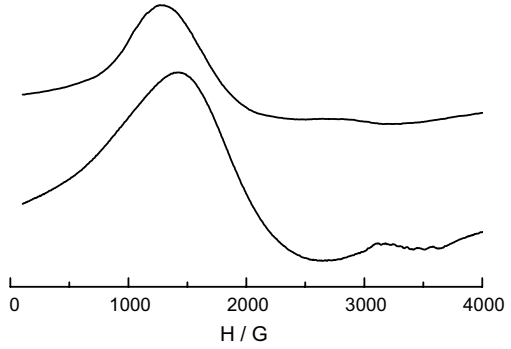


Fig. 8. Polycrystalline powder EPR spectra of **1** (bottom) and **2** (top) at 4 K.

4. Conclusion

The peculiarity of the coordinating behaviour of the same Schiff base (H_2L_1) towards Cu(II) and Ni(II) metal ions has already been reported in our earlier paper [10]. There we found that the composition of the metal complexes depends upon two factors – firstly the mole proportion of each of the aldehyde (MPA), the diamine (DAP) and the metal salt used and secondly the specification of the metal used. The compositions as well as internal cyclisation (in part) leading to the formation of a new ligand system are also related to the nature of the anion of the metal salt used [10]. This peculiarity was exclusively specific for the Cu(II) ion. Tracing the same synthetic route for the Co(II) ion, we find a different but unusual observation.

Using the aldehyde and amine (2:1 equiv.) and 1 equiv. of the Co(II) salts in the presence of Cl^- and Br^- ions, unusual linear trinuclear mixed valence Co(III/II/III) complexes of H_2L_1 are isolated, unlike the mononuclear Cu(II) complexes of H_2L_1 formed earlier in a similar reaction [10]. A mononuclear complex of Co(III) is formed when the CH_3COO^- salt is used. Whereas the mixed ligand system (HL_2 and partially cyclised HL_1), formed in situ by 1:1 condensation of MPA and DAP in the presence of Cu(II) nitrate, resulted in a tetra Cu(II) complex, and the same reaction when carried out with Ni(II) salts ClO_4^-, NO_3^-andBF_4^- formed intractable materials in our earlier work [10], whilst in the present study for Co(III) using the same counter ions the usual mononuclear bischelate complexes are isolated. When Cl^- and Br^- anions were used as counterions in this latest study, an intractable material was isolated.

Acknowledgements

Financial support [F. 30-65/2004(SR)] from the University Grants Commission, New Delhi, India, is gratefully acknowledged. Mohamed Salah El Fallah is grateful for the Grants sanctioned by the Ministerio de Ciencia y Tecnología (Programa Ramón y Cajal) and BQU2003/00539.

Appendix A. Supplementary material

CCDC 645553 and 645554 contain the supplementary crystallographic data for **1** and **4**. These data can be obtained free of charge via http://www.ccdc.cam.ac.uk/conts/retrieving.html, or from the Cambridge Crystallographic Data Centre, 12 Union Road, Cambridge CB2 1EZ, UK; fax: (+44) 1223-336-033; or e-mail: deposit @ccdc.cam.ac.uk. Supplementary data associated with this article can be found, in the online version, at doi:10.1016/j.poly.2007.09.037.

References

[1] (a) B. Meunier (Ed.), Biomimetic Oxidations Catalysed by Transition Metals, Imperial College Press, London, 2000;

(b) C. Christmas, J.B. Vincent, H.R. Chang, J.C. Huffman, G. Christau, D.N. Hendrickson, J. Am. Chem. Soc. 10 (1988) 823;
(c) A. Nishinaga, T. Yamada, H. Fujisawa, K. Ishizaki, H. Ihara, T. Matsuura, J. Mol. Catal. 48 (1988) 249;
(d) R.H. Holm, P. Kennepohl, E.I. Solomon, Chem. Rev. 96 (1996) 2239.
[2] S.J. Lippard, J.M. Berg, Principles of Bioinorganic Chemistry, University Science Books, Mill Valley, CA, 1994.
[3] (a) L. Chun, C.R. Kagan, J. Am. Chem. Soc. 125 (2003) 336;
(b) A. Bousseksou, G. Molnar, P. Demont, J. Menegotto, J. Mater. Chem. 13 (2003) 2069;
(c) J.S. Miller, Inorg. Chem. 39 (2000) 4392.
[4] J.-Y. Qi, H.-X. Ma, X.-J. Li, Z.-Y.M. Zhou, C.K. Choi, A.S.C. Chan, Q.-Y. Yang, Chem. Commun. (2003) 1294.
[5] H. Nusbaumer, J.-E. Moser, S.M. Zakeeruddin, M.K. Nazeeruddin, M. Grätzel, J. Phys. Chem. B 105 (2001) 10461.
[6] A. BÖttcher, T. Takeuchi, K.I. Hardcastle, T.J. Meade, H.B. Gray, D. Cwikel, M. Kapon, Z. Dori, Inorg. Chem. 36 (1997) 2498.
[7] M. Murrie, S.J. Teat, H. Stoeckli-Evans, H.U. Güdel, Angew. Chem., Int. Ed. 42 (2003) 4653.
[8] T. Szymanska-Buzar, J.J. Ziolkowski, J. Mol. Catal. 11 (1981) 371.
[9] D.E. Babushkin, E.P. Talsi, J. Mol. Catal. A 130 (1998) 131.
[10] S. Pal, A.K. Barik, S. Gupta, A. Hazra, S.K. Kar, S.M. Peng, G.H. Lee, R.J. Butcher, M.S.E. Fallah, J. Ribas, Inorg. Chem. 44 (2005) 3880.
[11] A.K. Barik, S. Paul, S.K. Kar, R.J. Butcher, J.C. Brayan, Polyhedron 18 (1999) 571.
[12] D.D. Perrin, W.L.F. Armargo, D.R. Perrin, Purification of Laboratory Chemicals, 2nd ed., Pergamon Prees, Oxford, 1980.
[13] Bruker, SAINT v7.34A, Bruker AXS Inc., Madison, WI, USA, 2005.
[14] Bruker, SHELXTL v6.12, Bruker AXS Inc., Madison, WI, USA, 2000.
[15] G.M. Sheldrick, SHELXL-97, Programs for Crystal Structure Solution and Refinement, University of Göttingen, Germany 1997.
[16] S. Chattopadhyay, G. Bocelli, A. Musatti, A. Ghosh, Inorg. Chem. Commun. 9 (2006) 1053.
[17] A. Gerli, K.S. Hagen, L.G. Marzilli, Inorg. Chem. 30 (1991) 4673.
[18] H. Kobayashi, K. Okhi, I. Tsujikawa, K. Osaki, N. Uryu, Bull. Chem. Soc. Jpn. 49 (1976) 1210.
[19] T.S. Billson, J.D. Crane, O.D. Fox, S.L. Heath, Inorg. Chem. Commun. 3 (2000) 718.
[20] A.K. Barik, S. Paul, R.J. Butcher, S.K. Kar, Polyhedron 19 (2000) 2651.
[21] O. Khan, Molecular Magnetism, VCH Publishers, New York, 1993, p. 21.
[22] J. Ribas (Ed.), Quimica de Coordination, S.A. Omega, Bercelona, 2000, p. 525.
[23] R. Vicente Escuer, J. Ribas, Polyhedron 11 (1992) 857.

Available online at www.sciencedirect.com
ScienceDirect
Polyhedron 27 (2008) 366–374
POLYHEDRON
www.elsevier.com/locate/poly

Reactivity of oxorhenium(V) complexes towards 8-hydroxyquinoline-2-carboxylic acid: X-ray structure of $[ReOCl_2(hquin\text{-}2\text{-}COOH)(AsPh_3)] \cdot MeCN$ and $[ReOCl_2(hquin\text{-}2\text{-}COOH)(PPh_3)] \cdot MeCN$ complexes. DFT and TDDFT calculations for $[ReOCl_2(hquin\text{-}2\text{-}COOH)(AsPh_3)]$

B. Machura [a,*], J. Kusz [b]

[a] Department of Crystallography, Institute of Chemistry, University of Silesia, 9th Szkolna Street, 40-006 Katowice, Poland
[b] Institute of Physics, University of Silesia, 4th Uniwersytecka Street, 40-006 Katowice, Poland

Received 5 September 2007; accepted 25 September 2007
Available online 5 November 2007

Abstract

The reactions of $[ReOX_3(EPh_3)_2]$ with 8-hydroxyquinoline-2-carboxylic acid (Hhquin-2-COOH) have been examined and $[ReOX_2(hquin\text{-}2\text{-}COOH)(EPh_3)] \cdot MeCN$ (X = Cl, Br; E = As, P) complexes have been obtained. All the complexes were characterised by IR, UV–Vis spectroscopy and elemental analysis. The crystal and molecular structures have been determined for $[ReOCl_2(hquin\text{-}2\text{-}COOH)(AsPh_3)] \cdot MeCN$ and $[ReOCl_2(hquin\text{-}2\text{-}COOH)(PPh_3)] \cdot MeCN$. The electronic structure of $[ReOCl_2(hquin\text{-}2\text{-}COOH)(AsPh_3)]$ has been calculated with the density functional theory (DFT) method, and TDDFT calculations have been employed to produce a hundred of singlet excited-states starting from the ground-state geometry optimized in the gas phase.
© 2007 Elsevier Ltd. All rights reserved.

Keywords: Rhenium oxo complexes; 8-Hydroxyquinoline-2-carboxylic acid; X-ray and electronic structure; DFT calculations; NBO analysis

1. Introduction

For many years inorganic compounds containing an oxygen atom multiply bonding to a transition metal have been in the centre of interest to those scientists engaged in basic research and to those trying to employ these complexes in catalytic processes. Oxygen atom transfer chemistry has been implicated in various reactions of industrial and biological importance, including olefin epoxidation and catalysis by cytochrome P-450 [1–3].

The chemistry of oxo rhenium complexes arouses particular interest among these compounds. Methyltrioxorhenium and its derivatives are among the most versatile oxidation catalysts known to date [4]. The oxorhenium(V) chelates $[ReOCl_2(O\text{–}N)(PPh_3)]$ with pyridinecarboxylate ligands exhibit a remarkable catalytic activity for the conversion of ethane, under relatively mild conditions, to a mixture of propionic and acetic acids in a single-pot process with various advantages over the industrial ones [5].

Furthermore, the favourable nuclear properties of ^{186}Re and ^{188}Re nuclides make the compounds with these radioisotopes useful for applications in radioimmunotheraphy [6,7]. Consequently, the inorganic chemistry studies with the naturally occurring non-radioactive rhenium isotopes are very attractive in order to clearly establish the molecular structure of ^{99m}Tc- and $^{186/188}Re$-based radiopharmaceuticals.

In this context, the design, synthesis and reactivity of novel rhenium oxocomplexes has become the aim of several laboratories, including ours.

* Corresponding author.
E-mail address: basia@ich.us.edu.pl (B. Machura).

0277-5387/$ - see front matter © 2007 Elsevier Ltd. All rights reserved.
doi:10.1016/j.poly.2007.09.019

Previously, we investigated the reactivity of oxorhenium(V) species – $[ReOX_3(PPh_3)_2]$ and $[ReOX_3(AsPh_3)_2]$ (X = Cl or Br) – towards 8-hydroxyquinoline (Hhqn) and quinoline-2-carboxylic acid (quin-2-c) [8,9]. In this report we focus on the examinations of the reactions of $[ReOX_3(AsPh_3)_2]$ and $[ReOX_3(PPh_3)_2]$ with 8-hydroxyquinoline-2-carboxylic acid (hquin-2-COOH). This compound contains both hydroxy and carboxylate fragments, and can be considered as a bidentate or tridentate chelating agent. Similar to 8-hydroxyquinoline and quinoline-2-carboxylic acid, 8-hydroxyquinoline-2-carboxylic acid is a biological compound. It is one of the tryptophan metabolites formed through the kynurenine metabolic pathway [10].

Here we present synthesis and spectroscopic data for $[ReOCl_2(hquin\text{-}2\text{-}COOH)(AsPh_3)]\cdot MeCN$ (**1** · MeCN), $[ReOBr_2(hquin\text{-}2\text{-}COOH)(AsPh_3)]\cdot MeCN$ (**2** · MeCN), $[ReOCl_2(hquin\text{-}2\text{-}COOH)(PPh_3)]\cdot MeCN$ (**3** · MeCN) and $[ReOBr_2(hquin\text{-}2\text{-}COOH)(PPh_3)]\cdot MeCN$ (**4** · MeCN) complexes. X-ray studies have been performed for **1** · MeCN and **3** · MeCN, and electronic structure of **1** has been calculated with the density functional theory (DFT). TDDFT calculations have been employed to produce a hundred of singlet excited-states starting from the ground-state geometry optimized in the gas phase, and the UV–Vis spectrum of the complex has been discussed on this basis.

Currently density functional theory (DFT) is commonly used to examine the electronic structure of transition metal complexes. It meets with the requirements of being accurate, easy to use and fast enough to allow the study of relatively large molecules of transition metal complexes [11]. Recent calculations with TDDFT method for open- and closed-shell of 5d-metal complexes (including rhenium complexes) have also supported the TDDFT method to be applicable for such systems giving good assignment of experimental spectra [12,13].

Some theoretical investigations have been carried out on rhenium compounds. The electronic structures of nitrido, oxo, carbonyl, nitrosyl and nitrile rhenium complexes, as well as their spectroscopic properties, bonding and reactivity have been theoretically studied at the HF, MP2, EHT and DFT levels of theory using various basis sets [14–22]. Gancheff et al. [16] have performed extended tests of the ability of the B3LYP method in LANL2DZ basis set for rhenium compounds in a geometry optimization and calculation of spectral properties. Although this is not a very extended basis set, its use with DFT has shown to be sufficient for the geometry optimization and calculation of spectral properties. It gives good agreement with the experimental data and its use is justified in the case of large molecules.

2. Experimental

2.1. General procedure

The reagents used to the synthesis were commercially available and were used without further purification. The $[ReOX_3(AsPh_3)_2]$ and $[ReOX_3(PPh_3)_2]$ complexes were prepared according to the literature methods [23].

IR spectra were recorded on a Nicolet Magna 560 spectrophotometer in the spectral range 4000–400 cm^{-1} with the samples in the form of KBr pellets. Electronic spectra were measured on a spectrophotometer Lab Alliance UV–Vis 8500 in the range 1000–180 nm in acetonitrile solution. Elemental analyses (C H N) were performed on a Perkin–Elmer CHN-2400 analyzer.

2.2. Preparation of $[ReOCl_2(hquin\text{-}2\text{-}COOH)(AsPh_3)]\cdot MeCN$ (**1** · MeCN)

A mixture of $[ReOCl_3(AsPh_3)_2]$ (0.50 g, 0.54 mmol), 8-hydroxyquinoline-2-carboxylic acid (0.12 g, 0.63 mmol) and acetone (50 ml) was stirred at room temperature for 3 h. Half of the solvent was removed and diethyl ether (50 ml) was added to precipitate the product as a brown solid, which was filtered off and dried. Yield 80%. Crystals suitable for X-ray investigation were obtained by recrystallization from acetonitrile.

Anal. Calc. for $C_{30}H_{24}Cl_2N_2O_4AsRe$: C, 44.56; H, 2.99; N, 3.46. Found: C, 44.70; H, 3.06; N, 3.55%.

2.3. Preparation of $[ReOBr_2(hquin\text{-}2\text{-}COOH)(AsPh_3)]\cdot MeCN$ (**2** · MeCN)

A procedure similar to that for $[ReOCl_2(hquin\text{-}2\text{-}COOH)(AsPh_3)]\cdot MeCN$ was used with $[ReOBr_3(AsPh_3)_2]$ (0.50 g, 0.47 mmol) and 8-hydroxyquinoline-2-carboxylic acid (0.11 g, 0.58 mmol). Crystalline precipitate of $[ReOBr_2(hquin\text{-}2\text{-}COOH)(AsPh_3)]\cdot MeCN$ was collected in 85% yield.

Anal. Calc. for $C_{30}H_{24}Br_2N_2O_4AsRe$: C, 40.15; H, 2.70; N, 3.12. Found: C, 40.29; H, 2.72; N, 3.20%.

2.4. Preparation of $[ReOCl_2(hquin\text{-}2\text{-}COOH)(PPh_3)]\cdot MeCN$ (**3** · MeCN)

A procedure similar to that for $[ReOCl_2(hquin\text{-}2\text{-}COOH)(AsPh_3)]\cdot MeCN$ was used with $[ReOCl_3(PPh_3)_2]$ (0.50 g, 0.60 mmol) and 8-hydroxyquinoline-2-carboxylic acid (0.13 g, 0.69 mmol). Crystalline precipitate of $[ReOCl_2(hquin\text{-}2\text{-}COOH)(PPh_3)]\cdot MeCN$ was collected in 80% yield.

Anal. Calc. for $C_{30}H_{24}Cl_2N_2O_4PRe$: C, 47.13; H, 3.16; N, 3.66. Found: C, 47.35; H, 3.12; N, 3.78%.

2.5. Preparation of $[ReOBr_2(hquin\text{-}2\text{-}COOH)(PPh_3)]\cdot MeCN$ (**4** · MeCN)

A procedure similar to that for $[ReOCl_2(hquin\text{-}2\text{-}COOH)(AsPh_3)]\cdot MeCN$ was used with $[ReOBr_3(PPh_3)_2]$ (0.50 g, 0.52 mmol) and 8-hydroxyquinoline-2-carboxylic acid (0.12 g, 0.63 mmol). Crystalline precipitate of $[ReOBr_2(hquin\text{-}2\text{-}COOH)(PPh_3)]\cdot MeCN$ was collected in 85% yield.

Anal. Calc. for $C_{30}H_{24}Br_2N_2O_4PRe$: C, 42.22; H, 2.83; N, 3.28. Found: C, 42.37; H, 2.73; N, 3.35%.

2.6. Crystal structures determination and refinement

The X-ray intensity data of **1** · MeCN and **3** · MeCN were collected on a KM-4-CCD automatic diffractometer equipped with CCD detector and graphite monochromated Mo Kα radiation ($\lambda = 0.71073$ Å) at room temperature. Details concerning crystal data and refinement are given in Table 1. Lorentz, polarization and absorption correction [24] were applied. The structures were solved by the Patterson method and subsequently completed by the difference Fourier recycling. All the non-hydrogen atoms were refined anisotropically using full-matrix, least-squares technique. The hydrogen atoms were treated as ''riding'' on their adjacent atoms and assigned isotropic temperature factors equal 1.2 times the value of equivalent temperature factor of the aromatic parent atoms and equal 1.5 times the value of equivalent temperature factor of the methyl parent carbon atom and oxygen atom (OH). SHELXS97 [25], SHELXL97 [26] and SHELXTL [27] programs were used for all the calculations. Atomic scattering factors were those incorporated in the computer programs.

Table 1
Crystal data and structure refinement for **1** · MeCN and **3** · MeCN complexes

	1 · MeCN	**3** · MeCN
Empirical formula	$C_{30}H_{24}AsCl_2N_2O_4Re$	$C_{30}H_{24}PCl_2N_2O_4Re$
Formula weight	808.53	764.58
Temperature (K)	293(2)	293(2)
Wavelength (Å)	0.71073	0.71073
Crystal system	monoclinic	monoclinic
Space group	$P2_1/c$	$P2_1/c$
Unit cell dimensions		
a (Å)	14.8430(7)	14.7672(7)
b (Å)	10.0433(4)	10.0811(4)
c (Å)	20.4824(9)	20.2228(8)
β (°)	104.297(5)	104.323(4)
Volume (Å^3)	2958.8(2)	2917.0(2)
Z	4	4
D_{calc} (Mg/m^3)	1.815	1.741
Absorption coefficient (mm^{-1})	5.435	4.442
F(000)	1568	1496
Crystal size (mm)	$0.04 \times 0.04 \times 0.32$	$0.02 \times 0.07 \times 0.14$
θ Range for data collection (°)	2.81–25.00	2.80–25.00
Index ranges	$-17 \leqslant h \leqslant 17$, $-10 \leqslant k \leqslant 11$, $-23 \leqslant l \leqslant 24$	$-17 \leqslant h \leqslant 17$, $-11 \leqslant k \leqslant 6$, $-24 \leqslant l \leqslant 24$
Reflections collected	17530	17928
Independent reflections (R_{int})	5172 (0.0214)	5055 (0.0213)
Completeness to $2\theta = 50°$ (%)	99.3	98.7
Data/restraints/parameters	5172/0/363	5055/0/363
Goodness-of-fit on F^2	1.013	0.934
Final R indices [$I > 2\sigma(I)$]	$R_1 = 0.0189$ $wR_2 = 0.0423$	$R_1 = 0.0190$ $wR_2 = 0.0423$
R indices (all data)	$R_1 = 0.0374$ $wR_2 = 0.0445$	$R_1 = 0.0331$ $wR_2 = 0.0446$
Largest difference in peak and hole (e Å^{-3})	0.815 and −0.591	0.690 and −0.829

3. Computational details

The gas phase geometry of **1** was optimized in the singlet ground-state with the DFT method using the hybrid B3LYP [28,29] functional of GAUSSIAN-03 [30]. The LANL2DZ with additional d function with exponent $\alpha = 0.3811$ and f function with exponent $\alpha = 2.033$ basis set [31,32] was chosen for the rhenium atom and the standard 6-31G basis set for all the other atoms. For chloride, oxygen, phosphorous and nitrogen atoms, diffuse and polarization functions were added [33,34]. TDDFT calculations were employed to produce a hundred singlet excited-states starting from the ground-state geometry optimized in the gas phase. The solvent (acetonitrile) effect was simulated using the polarizable continuum model (PCM) [35].

Natural bond orbital (NBO) calculations were performed with the NBO code [36,37] included in GAUSSIAN03.

4. Results and discussion

4.1. Preparation and infrared data

The $[ReOX_2(hquin\text{-}2\text{-}COOH)(EPh_3)]$ (X = Cl, Br; E = As, P) complexes were prepared in good yields by ligand exchange reactions starting from $[ReOX_3(EPh_3)_2]$ complexes and 8-hydroxyquinoline-2-carboxylic acid in acetone:

$$ReOX_3(EPh_3)_2] + \text{hquin-2-COOH} \rightarrow [ReOX_2(\text{hquin-2-COOH})(EPh_3)] + HX + EPh_3,$$
$$X = Cl, Br;\ E = As, P$$

They were isolated as brown microcrystalline solids, soluble in common organic solvents.

The selected frequencies observed in the IR spectra of $[ReOX_2(hquin\text{-}2\text{-}COOH)(EPh_3)]$ complexes are collected in Table 2. The non-coordinated carboxylic acid group of the *hquin-2-COOH* ligand is characterized by the ν_{O-H} absorption situated in the range 3050–3060 cm^{-1} and $\nu_{C=O}$ absorption observed at ≈1720 cm^{-1} [38,39].

The strong ν(Re=O) stretching bands of $[ReOX_2(hquin\text{-}2\text{-}COOH)(EPh_3)]$ compounds are in the higher end of the

Table 2
Selected IR frequencies (cm^{-1}) values of $[ReOX_2(hquin\text{-}2\text{-}COOH)(EPh_3)]$ complexes

Complex	ν_{OH} (COOH)	$\nu_{C=O}$(COOH)	ν(Re=O)
1	3064	1719	972
2	3052	1715	971
3	3060	1719	972
4	3060	1720	972

range observed for $\{ReO\}^{3+}$ core complexes. Similar to the reported previously $[ReOX_2(hqn)(EPh_3)]$ and $[ReOX_2$-(quin-2-c)$(EPh_3)]$ complexes, the Re–hydroxy bond *trans* to the oxo ligand does not compete effectively for the d_{Re} orbitals. Moreover, the narrow range in which the ν(Re=O) bands appear is very similar to those observed for Re(V)-oxo complexes with 8-quinolinolato or quinoline-2-carboxylate ligands [8,9].

4.2. Crystal structures

Both complexes crystallise as acetonitrile solvates in the monoclinic space group $P2_1/c$. The hydroxyl oxygen O(4) atoms of **1** · MeCN and **3** · MeCN are involved in an intermolecular O(4)—H(4A)···O(3) $(1-x, 1-y, -z)$ hydrogen bond, resulting in formation of carboxylic dimer synthons (Fig. 3 and Table 3). The other intra- and intermolecular contacts presented in Table 3 can be considered as weak hydrogen bonds [40,41]. Table 4 presents short analysis of π···π stacking interactions detected between the rings of the *hquin-2-COOH* ligand and one of the triphenyl phosphine rings, and between the ring of the *hquin-2-COOH* ligand and a symmetry related partner $(1-x, -y, -z)$ [42].

Table 3
Hydrogen bonds for **1** · MeCN, and **3** · MeCN complexes

D	A	H···A	D···A	D–H···A
1 · MeCN				
C(6)	O(2)	2.46	3.211(4)	137.6
O(4)	O(3)#1	1.86	2.645(3)	159.7
C(20)	N(99)#2	2.58	3.488(6)	165.0
3 · MeCN				
C(14)	O(2)	2.36	3.101(4)	136.4
C(2)	Cl(1)	2.80	3.632(3)	149.6
O(4)	O(3)#1	1.85	2.654(3)	164.8

#1: $-x+1, -y+1, -z$; #2: $-x+1, y-1/2, -z+1/2$.

Table 4
Analysis of short contacts between the *hquin-2-COOH* rings and triphenyl arsine (or phospine) ring (distances in Å and angles in degree)

R(I)	R(J)	Cg···Cg	α	β	d_p
1 · MeCN					
Cg(1)	Cg(3)	3.7415	21.87	10.45	3.254
Cg(2)	Cg(3)	4.0798	22.96	25.82	3.827
Cg(1)	Cg(1)#1	3.7896	0.00	27.69	3.356
3 · MeCN					
Cg(1)	Cg(4)	3.6545	21.12	12.39	3.220
Cg(2)	Cg(4)	3.9544	22.25	25.91	3.758
Cg(1)	Cg(1)#1	3.7561	0.03	3.7561	3.333

R1, R2, R3, R4 indicates the centroids of aromatic rings containing N(1), C(24), C(13), C(7) atoms respectively, α is a dihedral angle between planes I and J, β is an angle between Cg(I)–Cg(J) vector and normal to plane I and d_p is a perpendicular distance of Cg(I) on ring J plane.
#1: $1-x+1, -y, -z$.

The molecular structures of **1** · MeCN and **3** · MeCN are presented in Figs. 1 and 2, and the selected bond distances and angles are collected in Tables 5 and 6, respectively.

The geometry of $[ReOX_2(hquin\text{-}2\text{-}COOH)(EPh_3)]$ compounds reveals typical features of quasi-octahedral oxorhenium(V)complexes with oxygenated bidentate ligands. The deformation of the octahedron is caused by the presence of

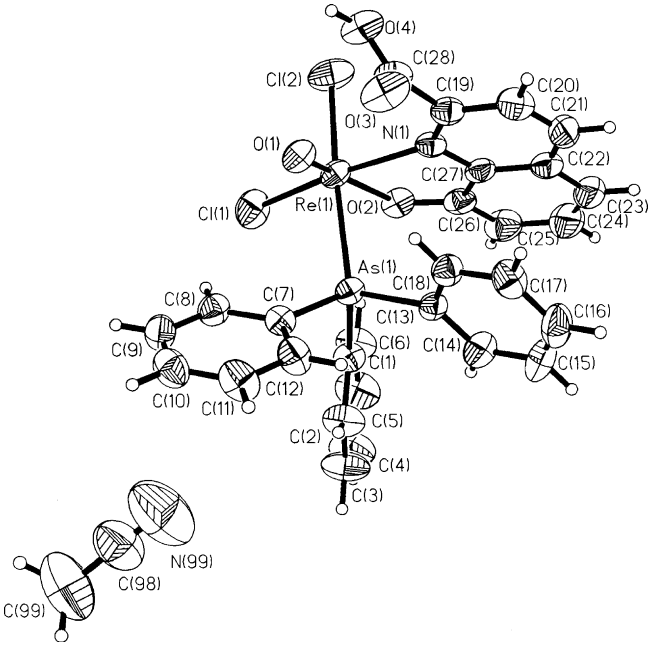


Fig. 1. The molecular structure of **1** · MeCN. Displacement ellipsoids are drawn at 50% probability.

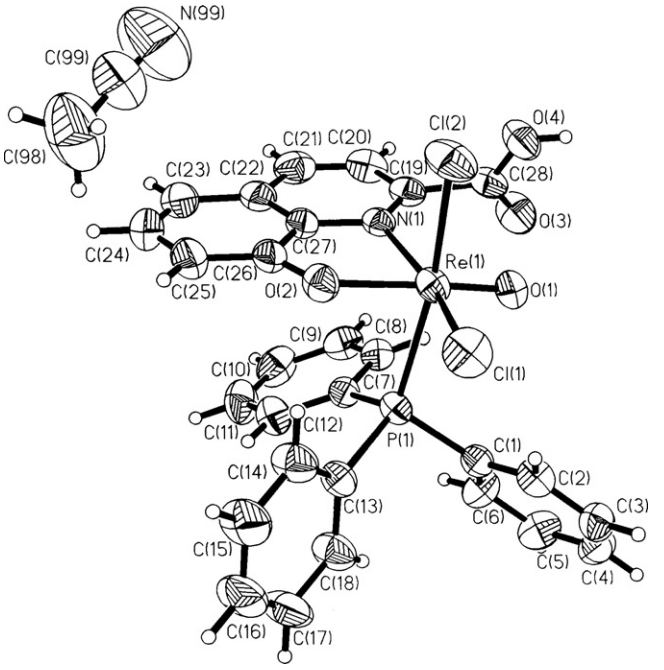


Fig. 2. The molecular structure of **3** · MeCN. Displacement ellipsoids are drawn at 50% probability.

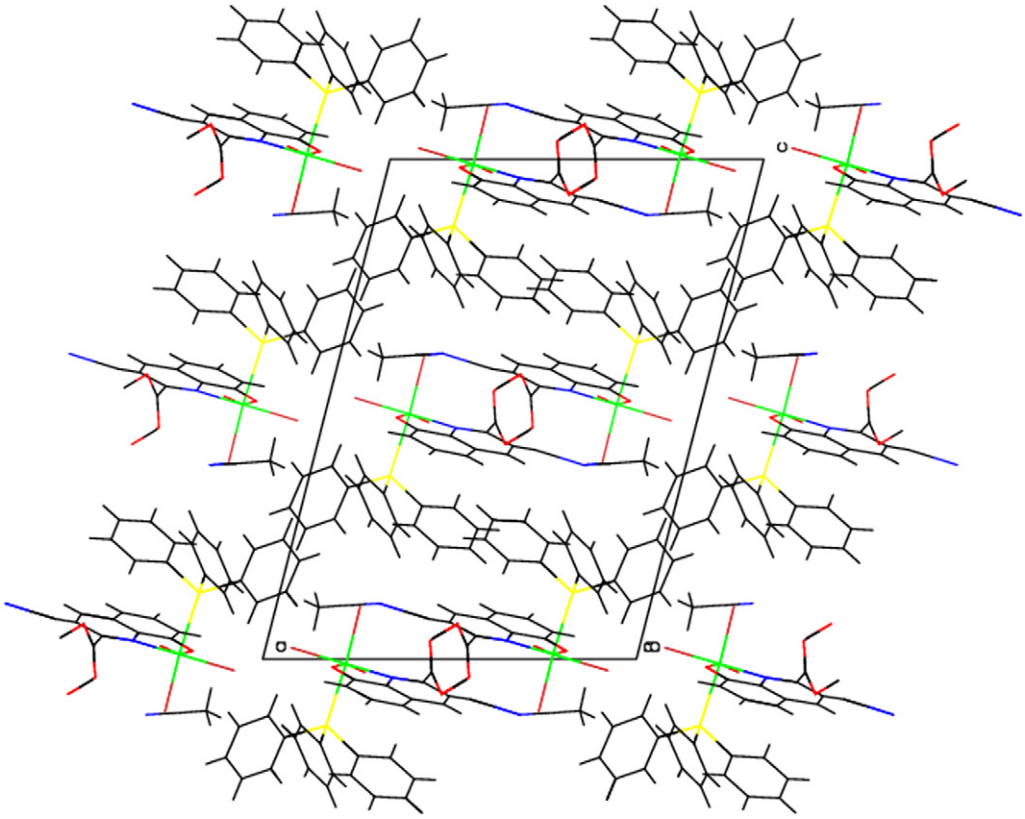


Fig. 3. Packing diagram of **1** · MeCN showing the shortest intermolecular interactions.

Table 5
The experimental and optimized bond lengths (Å) and angles (°) for **1**

Bond lengths	Experimental	Optimized	Bond angles	Experimental	Optimized
Re(1)–O(1)	1.6771(19)	1.680	O(1)–Re(1)–O(2)	161.21(9)	159.60
Re(1)–O(2)	1.9798(19)	2.023	O(1)–Re(1)–N(1)	89.18(9)	88.48
Re(1)–N(1)	2.177(2)	2.212	O(2)–Re(1)–N(1)	76.02(9)	75.27
Re(1)–Cl(1)	2.3389(9)	2.398	O(1)–Re(1)–Cl(1)	104.26(8)	104.36
Re(1)–Cl(2)	2.3659(8)	2.425	O(2)–Re(1)–Cl(1)	90.66(7)	92.52
Re(1)–As(1)	2.5707(3)	2.625	N(1)–Re(1)–Cl(1)	166.54(6)	167.05
			O(1)–Re(1)–Cl(2)	101.64(7)	102.67
			O(2)–Re(1)–Cl(2)	89.66(6)	88.77
			N(1)–Re(1)–Cl(2)	88.51(6)	86.41
			Cl(1)–Re(1)–Cl(2)	89.48(3)	89.06
			O(1)–Re(1)–As(1)	86.84(7)	87.44
			O(2)–Re(1)–As(1)	82.06(5)	81.82
			N(1)–Re(1)–As(1)	91.31(6)	94.80
			Cl(1)–Re(1)–As(1)	88.73(2)	87.57
			Cl(2)–Re(1)–As(1)	171.51(2)	169.85

multiple bonding ligand in the coordination sphere and narrow bite angle of the chelating ligand. The high concentration of electronic density along the Re—O_t (O_t – terminal oxo ligand) axis strongly influences the positions of the adjacent halogen atoms, which are pushed away. In each complex, the rhenium atom is coordinated by a terminal oxygen atom, two halide ions in *cis* arrangement, the phosphorus or arsine atom from EPh_3 molecule, and the bidentate N,O donors of the *hquin-2-COOH* ligand. The oxygen atom of *hquin-2-COOH* ligand lies in *trans* position to the terminal oxo ion.

The Re–O_t bond lengths of [$ReOX_2$(hquin-2-COOH)-(EPh_3)] complexes fall in the range 1.639–1.76 Å, typical of mononuclear complexes of rhenium(V) having $[ReO]^{3+}$ core, and indicate the presence of a triple bond Re≡O [43]. The interatomic distances between the rhenium atom and the oxygen atom of *hquin-2-COOH* ligand are somewhat shorter than an ideal single Re–O bond length (ca. 2.04 Å) [44], indicating small delocalization in the O(2)–Re(1)–O(1) moiety. The similar trend is observed for many Re(V)–oxo complexes with an monoanionic oxygen *trans* to the oxo group [45].

Table 6
The experimental bond lengths (Å) and angles (°) for **3**

Bond lengths	Experimental	Bond angles	Experimental
Re(1)–O(1)	1.6767(18)	O(1)–Re(1)–O(2)	161.32(9)
Re(1)–O(2)	1.9812(18)	O(1)–Re(1)–N(1)	89.19(9)
Re(1)–N(1)	2.181(2)	O(2)–Re(1)–N(1)	75.74(8)
Re(1)–Cl(1)	2.3372(9)	O(1)–Re(1)–Cl(1)	104.59(7)
Re(1)–Cl(2)	2.3831(8)	O(2)–Re(1)–Cl(1)	90.96(7)
Re(1)–P(1)	2.4815(7)	N(1)–Re(1)–Cl(1)	166.16(6)
		O(1)–Re(1)–Cl(2)	101.69(7)
		O(2)–Re(1)–Cl(2)	88.77(6)
		N(1)–Re(1)–Cl(2)	87.30(6)
		Cl(1)–Re(1)–Cl(2)	88.63(3)
		O(1)–Re(1)–P(1)	87.15(7)
		O(2)–Re(1)–P(1)	82.60(6)
		N(1)–Re(1)–P(1)	92.47(6)
		Cl(1)–Re(1)–P(1)	89.54(3)
		Cl(2)–Re(1)–P(1)	171.15(3)

The Re1–X(2) distances *trans* to the phosphorus or arsine atom of EPh_3 molecule are slightly longer than the Re1–X(1) bonds *trans* to the nitrogen atom of the *hquin-2-COOH* ligand. It is a consequence of *structural trans* effect of the EPh_3 ligands.

Table 7
Atomic charges from the natural population analysis (NPA) for **1**

Atom	Charge
Re(1)	1.023
O(1)	−0.454
O(2)	−0.684
N(1)	−0.454
Cl(1)	−0.364
Cl(2)	−0.405
As(1)	1.396

4.3. Geometry optimisation, charge distribution, electronic structure and NBO analysis

The geometry of **1** was optimised in a singlet state by the DFT method with the B3LYP functional. The optimized geometric parameters of **1** are gathered in Table 5. In general, the predicted bond lengths and angles are in

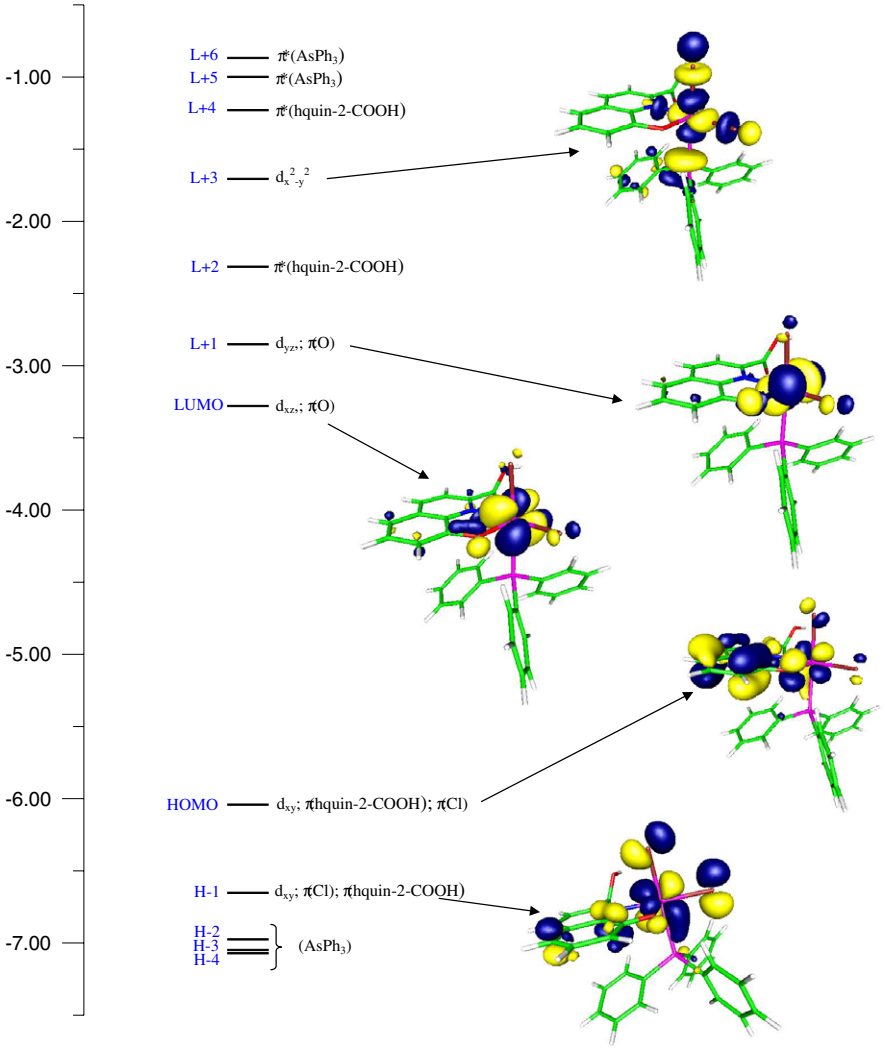


Fig. 4. The energy (eV), character and some contours of the unoccupied molecular orbitals of **1**. Positive values of the orbital contour are represented in blue (0.04 a.u.) and negative values – in yellow (−0.04 a.u.). (For interpretation of the references in colour in this figure legend, the reader is referred to the web version of this article.)

Table 8
The occupancy of the calculated natural bond orbitals (NBOs) between the rhenium and the oxo ligand for **1**

BD	Occupancy	BD	BD*	Occupancy
Re–O_t	1.993	$0.570(d)_{Re} + 0.822(p)_O$	$0.822(d)_{Re} - 0.570(p)_O$	0.310
Re–O_t	1.984	$0.568(d)_{Re} + 0.823(p)_O$	$0.823(d)_{Re} - 0.568(p)_O$	0.256

BD denotes 2-center bond, * denotes antibond NBO.

agreement with the values based upon the X-ray crystal structure data, and the general trends observed in the experimental data (discussed above) are well reproduced in the calculations.

Table 7 presents the atomic charges from the Natural Population Analysis (NPA) for **1**. The calculated charge on the rhenium atom in **1** is considerable lower than the formal charge +5, corresponding d^2 configuration of the central ion. It results from charge donation from the oxo ligands, halide ions and arsine molecule. ligands. The As atom is positively charged, and the charges on the terminal oxo, halide and oxygen atom of *hquin-2-COOH* are significantly smaller than −2, −1 and −1, respectively. The terminal oxo ions are less negative in comparison with the oxygen atoms of *hquin-2-COOH* ligand. It confirms the higher electron density delocalization from the terminal ligand towards the rhenium center and corresponds to differences in the Re–O(1) and Re–O(2) bond lengths.

The $[ReOX_2(hquin\text{-}2\text{-}COOH)(EPh_3)]$ complexes are closed-shell structures. The energies and characters of several highest occupied and lowest unoccupied molecular orbitals of **1** are presented in Fig. 4. The local symmetry of the rhenium center has been considered in the discussion: *z*-axis goes along the O–Re–O linkage, and *x*-axis – through the As–Re–Cl bonds. The HOMO–LUMO gap equals to 2.76 eV. Two highest occupied MOs are delocalized among d_{xy} rhenium orbital, chloride and *hquin-2-COOH* orbitals. The LUMO and LUMO + 1 are predominately localized on the rhenium atom (d_{xz} and d_{yz} orbitals) with some contribution of p_π oxygen orbitals. They can be ascribed as π-antibonding rhenium–oxygen molecular orbitals. The LUMO + 3 is of $d_{x^2-y^2}$ character, and d_{z^2} rhenium orbital contributes to the LUMO + 12.

Since the rhenium atom has d^2 electronic configuration, the empty $5d_{xz}$ and $5d_{yz}$ orbitals are available to overlap with $2p_x$ and $2p_y$ orbitals of the terminal oxygen to form an effective triple bond.

The nature of rhenium–terminal oxygen interaction in **1** has been studied by NBO analysis. Each natural bond orbital (NBO) σ_{AB} is written in terms of two directed valence hybrids (HHOs) h_A and h_B on atoms A and B:

$$\sigma_{AB} = c_A h_A + c_B h_B$$

where c_A and c_B are polarization coefficients. Each valence bonding NBO must in turn be paired with a corresponding valence *anti*-bonding NBO:

$$\sigma^*_{AB} = c_B h_A - c_A h_B$$

to complete the span of the valence space. The Lewis-type (donor) NBOs are thereby complemented by the non-Lewis-type (acceptor) NBOs that are formally empty in an idealized Lewis picture. The interactions between 'filled' Lewis-type NBOs and 'empty' non-Lewis NBOs lead to loss of occupancy from the localized NBOs of the idealized Lewis structure into the empty non-Lewis orbitals, and they are referred to as 'delocalization' corrections to the zeroth-order natural Lewis structure [36,37].

The results of NBO analysis for complex **1** are shown in Table 8. Two detected natural Re–O_t bond orbitals are of π character – they arise from overlap of the two occupied oxygen p_π orbitals with the empty d_{xz} and d_{yz} metal orbitals. Not detected σ_{Re-Ot} bond has character of predominant Coulomb-type interactions between the central ion

Table 9
Band position (nm) and molar absorption coefficient ($dm^3\ mol^{-1}\ cm^{-1}$) (in brackets) of $[ReOX_2(hquin\text{-}2\text{-}COOH)(EPh_3)]$ complexes

1	2	3	4
693.4 (310)	695.6 (280)	686.0 (270)	688.0 (270)
386.9 (5850)	405.6 (5790)	411.2 (5925)	409.8 (5740)
254.1 (59160)	250.4 (49780)	256.3 (50815)	256.3 (41000)
208.1 (117800)	210.2 (122670)	209.1 (121260)	369.9 (127590)

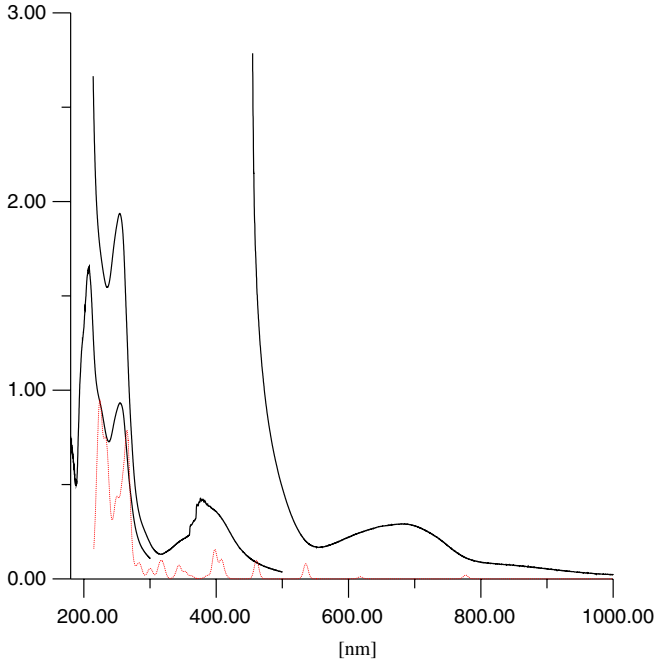


Fig. 5. The experimental (black solid line) and calculated (red dotted line) electronic absorption spectra of **1**. (For interpretation of the references in colour in this figure legend, the reader is referred to the web version of this article.)

and terminal oxo ligand [46]. The O_t ligand has two lone pair orbitals, and electron density from one of them is strongly delocalized into non-Lewis rhenium orbital. Accordingly, the rhenium–oxygen interaction in the investigated complexes can be described as a triple bond.

4.4. Electronic spectra

The electronic spectra of $[ReOX_2$(hquin-2-COOH)-$(EPh_3)]$ complexes are very similar in terms of the position, intensity and shape of the bands in the whole region 1000–180 nm. The positions and molar absorption coefficients of electronic bands for $[ReOX_2$(hquin-2-COOH)$(EPh_3)]$ complexes are given in Table 9.

The experimental and calculated electronic spectra of **1** are presented in Fig. 5. Each calculated transition is represented by a gaussian function $y = ce^{-b(x-x_0)^2}$ with the height (c) equal to the oscillator strength and b equal to 0.04 nm^{-2}. Table 10 presents the calculated singlet–singlet electronic transitions of **1** and their assignments to the experimental bands. For the high energy part of the spectrum, only transitions with oscillator strengths larger than 0.020 are listed in Table 10.

The assignment of the calculated transitions to the experimental bands is based on the criterion of the energy and oscillator strength of the calculated transitions. In the description of the electronic transitions the HOMO orbital is described as d_{Re} orbital, whereas the participation of d_{Re} in the H-1 orbital is omitted.

The longest wavelength experimental band at 693.4 nm is attributed to the transitions of d → d character. The broad and asymmetrical absorption band with maximum at 386.9 nm results mainly from *Ligand–Metal Charge Transfer* (π(Cl)/π(hquin-2-COOH) → d). However the contribution of the *Metal–Ligand Charge Transfer* excitations (d → π*(hquin-2-COOH)) into this band is also confirmed by the calculations. The *Ligand–Metal Charge Transfer* transitions occurring from the triphenylarsine orbitals to the *d* rhenium orbitals make the largest contribution into the experimental band at 254.1 nm. The absorption band at 208.1 nm is assigned to *Ligand–Ligand Charge Transfer* and interligand (IL) transitions.

Table 10
The energy and molar absorption coefficients of experimental absorption bands and the electronic transitions calculated with the TDDFT method for **1**

The most important orbital excitations	Character	λ [nm]	E [eV]	f	Experimental Λ [nm] (E [eV]) ε
H → L	d → d	777.1	1.60	0.0066	693.4 (1.79) 350
H → L + 1	d → d	618.0	2.01	0.0037	
H-1 → L + 1	π(Cl)/π(hquin-2-COOH) → d	460.8	2.69	0.0327	386.9 (3.20) 5850
H-1 → L + 3	π(Cl)/π(hquin-2-COOH) → d	407.9	3.04	0.0329	
H → L + 3	d → d				
H → L + 2	d → π*(hquin-2-COOH)	397.8	3.12	0.0513	
H-1 → L + 2	π(Cl)/π(hquin-2-COOH) → π*(hquin-2-COOH)	343.6	3.61	0.0226	
H-1 → L + 3	π(Cl)/π(hquin-2-COOH) → d	320.1	3.87	0.0189	
H → L + 3	d → d				
H-10 → L	π(Cl)/n(As) → d	315.4	3.93	0.0174	
H-2 → L + 3	$\pi(AsPh_3)$ → d	266.2	4.66	0.1064	254.1 (4.88) 59160
H-2 → L + 3	$\pi(AsPh_3)$ → d	265.5	4.67	0.1097	
H-3 → L + 3	$\pi(AsPh_3)$ → d	260.8	4.75	0.0517	
H-1 → L + 4	π(Cl)/π(hquin-2-COOH) → π*(hquin-2-COOH)	257.8	4.81	0.0412	
H-5 → L + 3	$\pi(AsPh_3)$ → d	257.1	4.82	0.0251	
H-12 → L + 1	π(Cl)/π(hquin-2-COOH) → d	256.8	4.83	0.0273	
H → L + 8	d → π*$(AsPh_3)$	251.1	4.94	0.0272	
H → L + 8	d → π*$(AsPh_3)$	250.1	4.96	0.0248	
H → L + 9	d → π*(hquin-2-COOH)				
H-14 → L + 1	π(Cl)/π(hquin-2-COOH)/π(O) → d	249.1	4.98	0.0292	
H-17 → L	π(O) → d	245.9	5.04	0.0232	
H-1 → L + 5	π(Cl)/π(hquin-2-COOH) → π*$(AsPh_3)$				
H-2 → L + 4	$\pi(AsPh_3)$ → π*(hquin-2-COOH)	236.4	5.24	0.0262	208.1 (5.96) 117800
H-9 → L + 3	π(Cl)/n(As) → d	235.6	5.26	0.0235	
H-3 → L + 4	$\pi(AsPh_3)$ → π*(hquin-2-COOH)	234.0	5.30	0.0550	
H-18 → L	π(hquin-2-COOH)/π(O) → d	232.4	5.34	0.0270	
H-2 → L + 5	$\pi(AsPh_3)$ → π*$(AsPh_3)$	231.4	5.36	0.0595	
H-6 → L + 4	$\pi(AsPh_3)$ → π*(hquin-2-COOH)	225.3	5.50	0.0402	
H-2 → L + 6	$\pi(AsPh_3)$ → π*$(AsPh_3)$	225.1	5.51	0.0737	
H-12 → L + 2	π(Cl)/π(hquin-2-COOH) → π*(hquin-2-COOH)				
H-10 → L + 3	π(Cl)/n(As) → d	224.6	5.52	0.0231	
H-5 → L + 5	$\pi(AsPh_3)$ → π*$(AsPh_3)$	224.2	5.53	0.0356	
H-1 → L + 8	π(Cl)/π(hquin-2-COOH) → π*$(AsPh_3)$	223.2	5.55	0.0262	
H-6 → L + 5	$\pi(AsPh_3)$ → π*$(AsPh_3)$	221.7	5.59	0.0603	
H-3 → L + 6	$\pi(AsPh_3)$ → π*$(AsPh_3)$	219.8	5.64	0.0222	

ε – molar absorption coefficient [dm^3 mol^{-1} cm^{-1}]; f – oscillator strength; H – highest occupied molecular orbital; L – lowest unoccupied molecular orbital.

5. Supplementary material

CCDC 659331 and 659332 contain the supplementary crystallographic data for $C_{30}H_{24}AsCl_2N_2O_4Re$ and $C_{30}H_{24}PCl_2N_2O_4Re$. These data can be obtained free of charge via http://www.ccdc.cam.ac.uk/conts/retrieving.html, or from the Cambridge Crystallographic Data Centre, 12 Union Road, Cambridge CB2 1EZ, UK; fax: (+44) 1223-336-033; or e-mail: deposit@ccdc.cam.ac.uk.

Acknowledgement

The GAUSSIAN03 calculations were carried out in the Wrocław Centre for Networking and Supercomputing, WCSS, Wrocław, Poland.

References

[1] R.H. Holm, Chem. Rev. 87 (1987) 1401.
[2] C.C. Romão, F.E. Kühn, W.A. Hermann, Chem. Rev. 97 (1997) 3197.
[3] S.B. Seymore, S.N. Brown, Inorg. Chem. 39 (2000) 325.
[4] F.E. Kühn, A. Scherbaum, W.A. Herrmann, J. Organomet. Chem. 689 (2004) 4149.
[5] A.M. Kirillov, M. Haukka, M.V. Kirillova, A.J.L. Pombeiro, Adv. Synth. Catal. 347 (2005) 1435.
[6] W. Volkert, W.F. Goeckeler, G.J. Ehrhardt, A.R. Ketring, J. Nucl. Med. 32 (1991) 174.
[7] E.A. Deutsch, K. Libson, J.L. Vanderheyden, Technetium and Rhenium in Chemistry and Nuclear Medicine, Raven Press, New York, 1990.
[8] B. Machura, S. Michalik, R. Kruszynski, J. Kusz, Polyhedron 26 (2007) 2837.
[9] B. Machura, R. Kruszynski, Polyhedron 26 (2007) 3686.
[10] V.W. Rodwell, Harper's Review of Biochemistry, in: D.W. Martin Jr., P.A. Mayes, V.W. Rodwell (Eds.), 19th ed., Maruzen Asia Ltd., Singapore, 1983, p. 292.
[11] H. Chermette, Coord. Chem. Rev. 178–180 (1998) 699.
[12] M.C. Aragoni, M. Arca, T. Cassano, C. Denotti, F.A. Devillanova, F. Isaia, V. Lippolis, D. Natali, L. Niti, M. Sampietro, R. Tommasi, G. Verani, Inorg. Chem. Commun. 5 (2002) 869.
[13] P. Romaniello, F. Lelj, Chem. Phys. Lett. 372 (2003) 51.
[14] A. Voigt, U. Abram, R. Böttcher, U. Richter, J. Reinhold, R. Kirmse, Chem. Phys. 253 (2000) 171.
[15] M. Lipowska, L. Hansen, R. Cini, X. Xu, H. Choi, A.T. Taylor, L.G. Marzilli, Inorg. Chim. Acta 339 (2002) 327.
[16] J. Gancheff, C. Kremer, E. Kremer, O.N. Ventura, J. Mol. Struct. (Theochem) 580 (2002) 107.
[17] M.L. Kuznestov, E.A. Klestova-Nadeeva, A.I. Dement'ev, J. Mol. Struct. (Theochem) 671 (2004) 229.
[18] N. Psaroudakis, K. Mertis, D.G. Liakos, E.D. Simandiras, Chem. Phys. Lett. 369 (2003) 490.
[19] X.-Y. Liu, S. Bouherour, H. Jacobsen, H.W. Schmalle, H. Berke, Inorg. Chim. Acta 330 (2002) 250.
[20] É. Bencze, J. Mink, I. Pápai, I.S. Butler, D. Lafleur, D.F.R. Gilson, J. Organomet. Chem. 616 (2000) 1.
[21] W.-Y. Wong, S.-H. Cheung, X. Huang, Z. Lin, J. Organomet. Chem. 655 (2002) 39.
[22] B. Machura, R. Kruszynski, Polyhedron 25 (2006) 1985.
[23] G. Rouschias, G. Wilkinson, J. Chem. Soc. A (1966) 465.
[24] STOE & Cie, X-RED. Version 1.18, STOE & Cie GmbH, Darmstadt, Germany, 1999.
[25] G.M. Sheldrick, Acta Cryst. A 46 (1990) 467.
[26] G.M. Sheldrick, SHELXL97. Program for the Refinement of Crystal Structures, Springer, Germany, 1997.
[27] G.M. Sheldrick, SHELXTL: release 4.1 for Siemens Crystallographic Research Systems, 1990.
[28] A.D. Becke, J. Chem. Phys. 98 (1993) 5648.
[29] C. Lee, W. Yang, R.G. Parr, Phys. Rev. B 37 (1988) 785.
[30] M.J. Frisch, G.W. Trucks, H.B. Schlegel, G.E. Scuseria, M.A. Robb, J.R. Cheeseman, J.A. Montgomery Jr., T. Vreven, K.N. Kudin, J.C. Burant, J.M. Millam, S.S. Iyengar, J. Tomasi, V. Barone, B. Mennucci, M. Cossi, G. Scalmani, N. Rega, G.A. Petersson, H. Nakatsuji, M. Hada, M. Ehara, K. Toyota, R. Fukuda, J. Hasegawa, M. Ishida, T. Nakajima, Y. Honda, O. Kitao, H. Nakai, M. Klene, X. Li, J.E. Knox, H.P. Hratchian, J.B. Cross, C. Adamo, J. Jaramillo, R. Gomperts, R.E. Stratmann, O. Yazyev, A.J. Austin, R. Cammi, C. Pomelli, J.W. Ochterski, P.Y. Ayala, K. Morokuma, G.A. Voth, P. Salvador, J.J. Dannenberg, V.G. Zakrzewski, S. Dapprich, A.D. Daniels, M.C. Strain, O. Farkas, D.K. Malick, A.D. Rabuck, K. Raghavachari, J.B. Foresman, J.V. Ortiz, Q. Cui, A.G. Baboul, S. Clifford, J. Cioslowski, B.B. Stefanov, G. Liu, A. Liashenko, P. Piskorz, I. Komaromi, R.L. Martin, D.J. Fox, T. Keith, M.A. Al-Laham, C.Y. Peng, A. Nanayakkara, M. Challacombe, P.M.W. Gill, B. Johnson, W. Chen, M.W. Wong, C. Gonzalez, J.A. Pople, GAUSSIAN 03, Revision B.03, Gaussian, Inc., Pittsburgh PA, 2003.
[31] P.J. Hay, W.R. Wadt, J. Chem. Phys. 82 (1985) 299.
[32] K. Eichkorn, F. Weigend, O. Treutler, R. Ahlrichs, Theor. Chem. Acc. 97 (1997) 119.
[33] P.C. Hariharan, J.A. Pople, Theor. Chim. Acta 28 (1973) 213.
[34] V.A. Rassolov, M.A. Ratner, J.A. Pople, P.C. Redfern, L.A. Curtiss, J. Comp. Chem. 22 (2001) 976.
[35] M.E. Casida, in: J.M. Seminario (Ed.), Recent Developments and Applications in Modern Density Functional Theory, Theoretical and Computational Chemistry, vol. 4, Elsevier, Amsterdam, 1996.
[36] E.D. Glendening, A.E. Reed, J.E. Carpenter, F. Weinhold, NBO (version 3.1).
[37] A.E. Reed, L.A. Curtiss, F. Weinhold, Chem. Rev. 88 (1988) 899.
[38] K. Nakamoto, Infrared and Raman Spectra of Inorganic and Coordination Compounds, fourth ed., Wiley Interscience, New York, 1986.
[39] L. Wei, J. Babich, J. Zubieta, Inorg. Chim. Acta 358 (2005) 2413.
[40] G.R. Desiraju, T. Steiner, The Weak Hydrogen Bond in Structural Chemistry and Biology, Oxford University Press, 1999.
[41] G.A. Jeffrey, W. Saenger, Hydrogen Bonding in Biological Structures, Springer-Verlag, 1994.
[42] C.A. Hunter, J.K.M. Sanders, J. Am. Chem. Soc. 112 (1990) 5525.
[43] J.M. Mayer, Inorg. Chem. 27 (1988) 3899.
[44] S.R. Fletcher, A.C. Skapski, J. Chem. Soc., Dalton (1972) 1073.
[45] E. Shuter, H.R. Hoveyda, V. Karunaratne, S.J. Retting, C. Orvig, Inorg. Chem. 35 (1996) 368.
[46] M.L. Kuznetsov, A.J.L. Pombeiro, J. Chem. Soc., Dalton Trans. (2003) 738.

Available online at www.sciencedirect.com
ScienceDirect
Polyhedron 27 (2008) 375–382
POLYHEDRON
www.elsevier.com/locate/poly

Synthesis of a new *N*,*N*′-ethane-1,2-bis(4-methoxyphenyl)carbothioamide ligand and its Cu(I) and Ag(I) complexes

Nand K. Singh [a,*], Mamata Singh [a], Pratibha Tripathi [a], Ajay K. Srivastava [a], Ray J. Butcher [b]

[a] *Department of Chemistry, Banaras Hindu University, Varanasi 221 005, India*
[b] *Department of Chemistry, Howard University, 525 College Street NW, Washington, DC 20059, USA*

Received 26 June 2007; accepted 23 September 2007
Available online 3 December 2007

Abstract

$[Cu(H_2L)(PPh_3)_2]NO_3 \cdot 0.5H_2O$ (**2**) and $[Ag(H_2L)(PPh_3)_2]NO_3 \cdot 0.5H_2O$ (**3**) complexes of a new flexible thioamide ligand; *N*,*N*′-ethane-1,2-bis(4-methoxyphenyl)carbothioamide H_2L (**1**) have been synthesized using PPh_3 as a coligand. The synthesized compounds have been characterized with the help of elemental analyses, IR, ^1H, ^{13}C and ^{31}P NMR spectroscopy. The ligand and its Cu(I) complex have been studied by single crystal X-ray crystallography. The ligand acts as a neutral S-donor and forms a nine-membered chelate ring in $[Cu(H_2L)(PPh_3)_2]NO_3 \cdot 0.5H_2O$. The molecular packing is stabilized by an anionic cavity formed by intermolecular hydrogen bonding between the basal plane of the complex molecule and the nitrate ions. The square shaped columnar channel has dimensions of 5.489(25) [N(11)–H(11A)···O(13)···H(21A)N(21)] × 3.693(7) [N(11)–C(11)–C(21)–N(21)] Å.
© 2007 Elsevier Ltd. All rights reserved.

Keywords: Thioamide ligand; β-Sheet hydrogen bonding; Cu(I) and Ag(I) complexes; Nine-membered chelate ring

1. Introduction

The role of copper(I) is evident in several biologically important reactions [1–3], such as a dioxygen carrier and models for several enzymes [4]. Following our interest in the coordination properties of ligands containing the –NH–C(=S)– group, and their potential biological activity, which is probably related to their chelating ability towards vital metal ions, we have recently reported copper(II) and manganese(III) complexes of *N*′-[(2-hydroxyphenyl)carbothioyl]pyridine-2-carbohydrazide: a novel therapeutic agent for cancer [5]. The use of such Cu(II) systems is bound to involve the reduction of Cu(II) to Cu(I) in the cell (especially in the presence of S), thus the stability of the Cu(I) species is crucial to biological activity. However, the low solubility of copper (I and II) complexes has restricted us studying the structures from single crystal X-ray crystallography. The presence of tertiary phosphines are known to play an important role in enhancing the solubility of Cu(I) compounds of heterocyclic thioamide ligands [6].

From the above viewpoints and with the aim of elucidating the coordination geometry of ligands containing the –NH–C(=S)– moiety, *N*,*N*′-ethane-1,2-bis(4-methoxyphenyl)carbothioamide and its Cu(I) and Ag(I) complexes with PPh_3 as a coligand, viz. $[Cu(H_2L)(PPh_3)_2]NO_3 \cdot 0.5H_2O$ and $[Ag(H_2L)(PPh_3)_2]NO_3 \cdot 0.5H_2O$, have been prepared and characterized. The ligand and the Cu(I) complex have been characterized by X-ray crystallography.

* Corresponding author. Tel.: +91 542 2318529; fax: +91 542 2368127.
E-mail address: nksingh@bhu.ac.in (N.K. Singh).

0277-5387/$ - see front matter © 2007 Elsevier Ltd. All rights reserved.
doi:10.1016/j.poly.2007.09.035

2. Experimental

2.1. Materials and methods

Commercial reagents were used without further purification and all experiments were carried out in the open atmosphere. 4-Methoxybenzaldehyde (Sigma Aldrich) and ethylenediamine (Loba Chemie) were used as such. All the solvents were purchased from Merck Chemicals, India and used after purification. Ammonium polysulfide [7] and the sodium salt of (4-methoxyphenyl)carbothioylthioacetic acid [8] were prepared by the reported methods. The orange yellow colored (4-methoxyphenyl)carbothioylthioacetic acid was recrystallized from MeOH in the presence of charcoal. M.p. 127 °C (lit. [8] 122–125 °C). [$M(PPh_3)_2NO_3$], [M = Cu(I) and Ag(I)] were prepared according to literature procedures [9].

2.2. Preparation of the ligand

N,*N*′-Ethane-1,2-bis(4-methoxyphenyl)carbothioamide-(H_2L) (**1**) was prepared by reacting an aqueous NaOH (1 N, 10 mL) solution of (4-methoxyphenyl)carbothioylthioacetic acid (10 mmol) with ethylenediamine (en) (6 mmol). The mixture was kept at room temperature for 2 h and then acidified with dilute AcOH (20% v/v), whereupon a white precipitate formed. It was suction filtered, washed with water, dried under reduced pressure and recrystallized from a MeOH–$CHCl_3$ mixture (50:50 v/v).

2.2.1. Compound (*1*)

White single crystals of (**1**) suitable for X-ray analyses were obtained by slow evaporation of its methanol–chloroform (50:50 v/v) solution over a period of 4 days. Yield 60%; m.p. 108 °C; *Anal.* Calc. for $C_{18}H_{20}N_2O_2S_2$ (360.48): C, 59.97; H, 5.59; N, 7.77; S, 17.79; Found: C, 59.97; H, 5.54; N, 7.78; S, 17.79%. IR (ν cm^{-1}, KBr): ν(NH) 3308 m, [β(NH) + ν(CN)] (thioamide I) 1417 s, [ν(NH)+β(CN)] (thioamide II) 1377 s, [ν(C–N) + ν(C–S)] (thioamide III) 1008 s, ν(C=S) (thioamide IV) 835 m. ^{1}H NMR (DMSO-d_6, δ ppm): 9.36 (m, 2H, –NH), 2.9 (m, 4H, –CH_2–), 3.58 (s, 6H, –OCH_3), 6.89,7.99 (multiplets, 8H, benzene ring). ^{13}C NMR (DMSO-d_6, δ ppm): 202.03 (>C=S), 49.02 (>CH_2), 56.85 (–OCH_3), 134.2 (C3A, C3B), 130.5 (C4A, C4B, C8A, C8B), 113.5 (C5A, C5B, C7A, C7B), 164.11 (C6A, C6B). The structure was further confirmed by XRD (Fig. 1).

2.3. Preparation of complexes (*2*) and (*3*)

An equimolar amount (1 mmol) of a methanolic solution of the metal precursor complexes [$Cu(PPh_3)_2NO_3$], (M = Cu(I) and Ag(I)) were refluxed with a $CHCl_3$solution of H_2L for 2 h. The soluble complexes were filtered off to remove any co-precipitated impurity. The pale yellow, air stable complexes [$M(H_2L)(PPh_3)_2]NO_3 \cdot 0.5H_2O$ (M = Cu(I) and Ag(I)) were obtained by adding hexane to the solution. Pale yellow single crystals of (**2**) suitable for X-ray analyses, were obtained by slow evaporation of its methanol–chloroform (50:50 v/v) solution over a period of 10 days. Yield 53%; m.p. 185 °C; *Anal.* Calc. for $C_{54}H_{51}CuN_3O_{5.5}P_2S_2$ (1019.58): C, 63.61; H, 5.04; N, 4.12; S, 6.29. Found: C, 63.60; H, 5.04; N, 4.16; S, 6.32%. IR (ν cm^{-1}, KBr): ν(NH) 3209 m, [β(NH) + ν(CN)] (thioamide I) 1433 s, [ν(NH) + β(CN)] (thioamide II) 1385 s, ν(C–N) + ν(C–S) (thioamide III) 1028 s, ν(C=S) (thioamide IV) 742 m, ν(P–C_{ph}) 1093 s, (NO_3^-) 1307, 1091, 839. ^{1}H NMR (DMSO-d_6, δ ppm): 10.35 (m, 2H, –NH), 4.05 (m, 4H, –CH_2–), 3.81 (s, 6H, –OCH_3), 6.97, 7.81 (multiplets, 8H, benzene ring) 7.38, 7.78 (multiplets, 30H, phenyl ring). ^{13}C NMR (DMSO-d_6, δ ppm): 194.58 (>C=S), 43.54 (>CH_2), 55.50 (–OCH_3), 132.46 (C13, C23), 132.09 (C14, C18, C24, C28), 113.35 (C15, C17, C25, C27), 162.05 (C16, C26), 133.34 ($C1_{ph}$), 133.15 ($C2_{ph}$, $C6_{ph}$), 128.86 ($C3_{ph}$, $C5_{ph}$), 128.75 ($C4_{ph}$). ^{31}P NMR (DMSO-d_6, δ ppm): −1.63.

2.3.1. Compound (*3*)

Yield 74%; m.p. 147 °C; *Anal.* Calc. for $C_{54}H_{51}AgN_3O_{5.5}P_2S_2$ (1063.90): C, 60.99; H, 4.83; N, 3.95; S, 6.03; Found: C, 60.52; H, 4.80; N, 3.95; S, 6.07%. IR (ν cm^{-1}, KBr): ν(NH) 3302 m, [β(NH) + ν(CN)] (thioamide I) 1435 s, [ν(NH) + β(CN)] (thioamide II) 1383 s, ν(C–N) + ν(C–S) (thioamide III) 1026 s, ν(C=S) (thioamide IV) 744 m, ν (P–C_{ph}) 1072 s, (NO_3^-) 1305, 1091, 839. ^{1}H NMR (DMSO-d_6, δ ppm): 10.19 (m, 2H, –NH), 4.04 (m, 4H, –CH_2–), 3.80 (s, 6H, –OCH_3), 6.95, 7.83 (multiplets, 8H, benzene ring) 7.44, 7.82 (multiplets, 30H, phenyl ring). ^{13}C NMR (DMSO-d_6, δ ppm): 196.58 (>C=S), 44.34 (>CH_2), 55.44 (–OCH_3), 130.15 (C13, C23), 129.30 (C14,

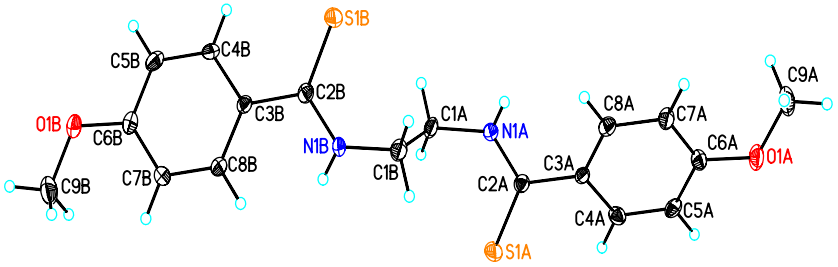


Fig. 1. ORTEP plot of H_2L showing atomic numbering scheme with ellipsoids of 30% probability.

C18, C24, C28), 113.14, (C15, C17, C25, C27), 161.64 (C16, C26), 133.33 ($C1_{ph}$), 133.11 ($C2_{ph}$, $C6_{ph}$), 128.96 ($C3_{ph}$, $C5_{ph}$), 128.85 ($C6_{ph}$). ^{31}P NMR (DMSO-d_6, δ ppm): 6.23.

2.4. Physical measurements

Carbon, hydrogen, nitrogen and sulfur contents were estimated on a Carlo Erba 1108 model microanalyser. Electronic spectra of **1**, **2** and **3** were recorded on a CARY 100 Varian EL01055314 UV–Vis spectrophotometer in MeOH–$CHCl_3$ (50:50 v/v). IR spectra were recorded in the 4000–400 cm^{-1} region as KBr pellets on a JASCO FT-IR-5300 spectrophotometer. ^1H and ^{13}C NMR spectra were recorded in DMSO-d_6 on a JEOL AL300 FT NMR spectrometer using TMS as an internal reference. ^{31}P NMR spectra were recorded in DMSO-d_6 using PCl_3 as an external reference.

3. Crystal structure determination

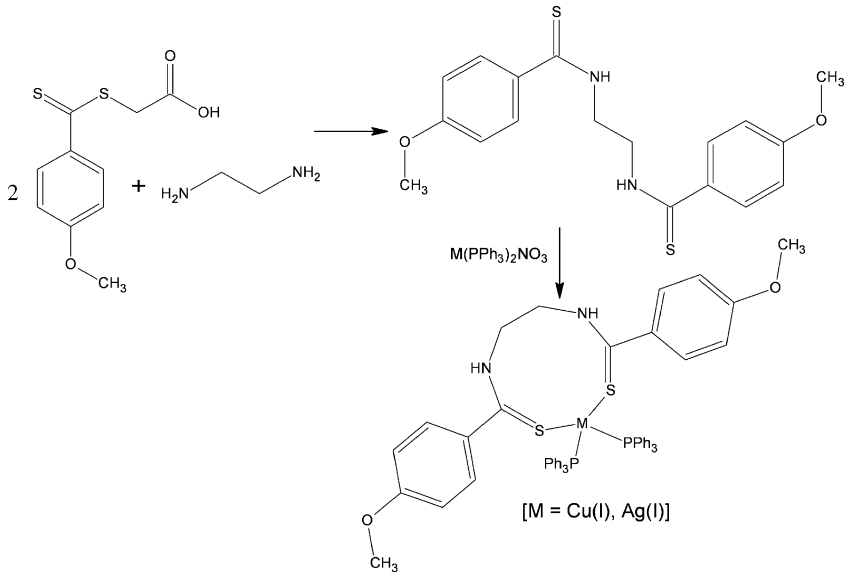
Data for the structure were obtained at 298 K(2) on a Bruker three-circle diffractometer equipped with a SMART 6000 CCD diffractometer using a graphite monochromated Mo Kα ($\lambda = 0.71073$ Å) radiation source. Intensity measurements were performed on a rapidly cooled crystal. The structure was solved by direct methods (SHELX-97) and refined against all data by full-matrix least-squares on F^2 using anisotropic displacement parameters for all non-hydrogen atoms. All hydrogen atoms were included in the refinement at geometrically ideal positions and refined with a riding model [10,11]. The MERCURY and DIAMOND package was used for molecular graphics [12,13]. Crystal structure diagrams were generated by use of the ORTEP-3 for Windows program [14].

4. Results and discussion

The ligand (4-methoxyphenyl-C(S)–NH–CH_2)$_2$ reacts with $[M(PPh_3)_2NO_3]$ in a MeOH–$CHCl_3$ mixture to give $[M(H_2L)(PPh_3)]NO_3 \cdot 0.5H_2O$, [M = Cu(I) and Ag(I)]. The complexes are stable towards air and moisture for several days. The soft Lewis bases H_2L (S-donor) and Ph_3P (P-donor) have stabilized the Cu(I) state, which is otherwise susceptible to oxidation by air. Scheme 1 shows the formation of Cu(I) and Ag(I) complexes with H_2L as a ligand and Ph_3P as a coligand. All the compounds are soluble in methanol–chloroform mixture and other polar solvents such as DMF and DMSO.

4.1. IR spectra

The ligand H_2L contains the –NH–C(=S)– group which may adopt either the thione –NH–C(=S)– or thiol –N=C(–SH)– form. However, the ligand adopts the thione form in the free state and in the complexes. This is evident by the absence of the ν(SH) band in the region ca. 2500 cm^{-1} and by the presence of ν(NH) at 3308 cm^{-1}. Since H_2L contains the thioamide group, –NH–C(=S)–, it gives rise to four characteristic bands, namely thioamide I, II, III and IV at 1417, 1377, 1008 and 835 cm^{-1} which have contributions from [β(NH) + ν(CN)], [β(CN) + ν(NH)], [ν(C–N) + ν(C–S)] and ν(C=S) modes of vibrations, respectively. The IR spectra of the complexes show the presence of the ν(N–H) band in the region 3200–3305 cm^{-1}, suggesting that H_2L is coordinated to M(I) in the neutral form. A negative shift in the ν(N–H) band is probably due to the hydrogen bonding in the complexes. The thioamide I and II bands shift slightly towards the higher frequency region, indicating the involvement of the C=S group in coordination. This is also supported



Scheme 1. Preparation of the ligand and the complexes.

by the negative shift of the ν(C=S) band. All these observations clearly indicate the involvement of the C=S group in coordination. Bonding through the sulfur atom is favored because copper(I), being a soft acid, should prefer to interact with a soft base such as sulfur. Further, the characteristic ν(P–C_{ph}) bands at 1050-1100 cm^{-1} show an increase in frequency and intensity, indicating P-metal coordination. The uncoordinated nature of the anion is inferred from its peaks in the region 1500–700 cm^{-1} where the characteristic absorption bands (1307, 1091 and 839) of the free nitrate ion appear [15].

4.2. Electronic spectra

The electronic spectrum of the complexes in a MeOH–$CHCl_3$ mixture exhibits two strong broad absorptions with maxima at 245 and 333 nm. Considering the fact that the spectrum of the free phosphine reveals a band at 245 nm, which usually remains unshifted upon coordination to Cu(I) [16], the rather strong first band corresponds to intraligand phosphine excitation. The second one can be considered as a thione originating intraligand band which exhibits a small red shift (11 nm) relative to that observed in the spectrum of the free ligand, and suggests that it contains some MLCT character.

4.3. ^1H and ^{13}C NMR spectra

The ^1H NMR spectrum of H_2L shows peaks due to –NH, –CH_2–, –OCH_3 and multiplets in the aromatic region. The ^{13}C NMR spectrum exhibits peaks due to C=S, >CH_2, –OCH_3 and benzene rings, as expected for the structure shown in Fig. 1.

The ^1H NMR spectra of the complexes in DMSO-d_6 reveal the presence of NH (thioamide) protons in the range of ca. 10.19–10.35 ppm which are downfield compared to the free ligand, indicating that the ligand coordinates to the metal ions as a neutral ligand, probably through the sulfur atoms only [17,18].

The ^{13}C NMR spectra of the complexes display signals associated with H_2L and PPh_3. The position and integrated intensities of various resonances supported well the presence of H_2L and the formulation of the complexes. The thione carbon in the complexes resonates in the range 194.58–196.58 ppm, which are upfield compared to the free ligand [19], suggesting involvement of the thione sulfur in bonding.

The ^{31}P NMR spectra of complexes (**2**) and (**3**) in DMSO-d_6 show a single resonance at $\delta_p = -1.63$ and 6.23 ppm, respectively, indicating that all the phosphorus atoms are chemically equivalent, which is also in accordance with the mononuclear nature of the complexes. As expected, only one sharp ^{31}P NMR signal for triphenylphospine is observed in the complexes with a downfield shift as compared to −4.50 ppm for free triphenylphosphine [20]. The downfield shift in the peak indicates coordination of PPh_3 with the metal ion.

4.4. Crystal structure of H_2L

The crystallographic data and structural refinement details are given in Table 1. The main bond distances and bond angles of the free ligand and the Cu(I) complex are given in Table 2. The relatively non-rigid functional group (*N*,*N* substituted-1,2-diaminoethane moiety) can attain a *cis* or *trans* configuration with two *p*-methoxyphenyl rings positioned on opposite sides. However, it has been observed that the HN–CH_2–CH_2–NH group acquires a staggered configuration (the torsion angle being −179.0(4)°), which is also energetically favored. This also favors the *anti* orientation of the symmetrical halves (if bisected along the C1A–C1B axes) of the molecule to minimize the steric hindrance by the bulkier groups placed on C(2). The structure is in turn stabilized by intermolecular

Table 1
Crystallographic data for the ligand (**1**) and the Cu(I) complex (**2**)

	H_2L (1)	$[Cu(H_2L)(PPh_3)]NO_3 \cdot 0.5H_2O$
Empirical formula	$C_{18}H_{20}N_2O_2S_2$	$C_{54}H_{51}CuN_3O_{5.50}P_2S_2$
Formula weight	360.48	1019.58
Temperature (K)	298(2)	298(2)
λ (Å)	0.71073	0.71073
Crystal system	triclinic	triclinic
Space group	$P\bar{1}$	$P\bar{1}$
a (Å)	5.8879(16)	10.399(3)
b (Å)	12.247(3)	12.933(3)
c (Å)	12.885(4)	20.330(4)
α (°)	71.730(5)	88.887(6)
β (°)	80.209(5)	85.594(7)
γ (°)	79.632(5)	69.275(6)
V (Å^3)	861.4(4)	2549.6(11)
Z	2	2
ρ_{calc} (Mg/m^3)	1.390	1.328
μ (mm^{-1})	0.322	0.624
F(000)	380	1062
Crystal size (mm)	0.39 × 0.11 × 0.04	0.39 × 0.26 × 0.10
θ Range for data collection (°)	1.68–24.49	1.68–26.40
Index ranges	$-6 \leqslant h \leqslant 6$, $-14 \leqslant k \leqslant 14$, $-15 \leqslant l \leqslant 15$	$-12 \leqslant h \leqslant 12$, $-16 \leqslant k \leqslant 16$, $0 \leqslant l \leqslant 25$
Number of reflections collected	6715	10859
Number of independent reflections (R_{int})	2804 (0.0771)	10868 (0.0000)
Number of data/restraints/parameters	2804/0/227	10868/3/620
Goodness-of-fit on F^2	0.963	0.871
R_1, $wR_2^{a,b}$ [$(I > 2\sigma(I))$]	0.0634, 0.1185	0.0640, 0.1445
R_1, $wR_2^{a,b}$ (all data)	0.1532, 0.1516	0.1221, 0.1655
Largest difference in peak and hole (e Å^{-3})	0.331 and −0.253	1.004 and −0.999

[a] $R_1 = \Sigma\|F_o| - |F_c\|/\Sigma|F_o|$.
[b] $R_2 = [\Sigma w(|F_o^2| - |F_c^2|)^2/\Sigma w|F_o^2|^2]^{1/2}$.

Table 2
Selected bond lengths (Å) and angles (°)

	H_2L	$[Cu(H_2L)(PPh_3)_2]NO_3 \cdot 0.5H_2O$
Bonds		
S(1A)–C(2A), S(1B)–C(2B)	1.666(5), 1.663(5)	
N(1A)–C(2A), N(1B)–C(2B)	1.317(6), 1.331(6)	
N(1A)–C(1A), N(1B)–C(1B)	1.463(5), 1.440(6)	
C(1A)–C(1B)	1.504(6)	
Cu–P(1), Cu–P(2)		2.3216(10), 2.3292(11)
Cu–S(1), Cu–S(2)		2.3910(11), 2.4212(11)
S(1)–C(12), S(2)–C(22)		1.697(3), 1.700(3)
N(11)–C(12), N(21)–C(22)		1.325(4), 1.327(4)
N(11)–C(11), N(21)–C(21)		1.440(4), 1.445(4)
C(11)–C(21)		1.509(5)
Angles		
C(2A)–N(1A)–C(1A)	126.6(4)	
C(2B)–N(1B)–C(1B)	126.9(4)	
N(1A)–C(1A)–C(1B)	111.4(4)	
N(1B)–C(1B)–C(1A)	111.7(4)	
N(1A)–C(2A)–S(1A)	120.5(4)	
N(1B)–C(2B)–S(1B)	119.8(4)	
N(11)–C(12)–S(1)		122.3(2)
N(21)–C(22)–S(2)		123.2(2)
P(2)–Cu–P(1)		122.19(3)
S(1)–Cu–S(2)		132.56(4)
P(2)–Cu–S(1)		103.26(3)
P(1)–Cu–S(2)		96.47(4)
P(1)–Cu–S(1)		104.44(3)
P(2)–Cu–S(2)		100.46(3)
C(12)–S(1)–Cu		122.34(11)
C(22)–S(2)–Cu		124.87(11)
Torsion angles		
C(2A)–N(1A)–C(1A)–C(1B)	87.1(6)	
C(2B)–N(1B)–C(1B)–C(1A)	−83.7(7)	
C(1A)–N(1A)–C(2A)–C(3A)	178.6(4)	
C(1B)–N(1B)–C(2B)–C(3B)	−172.6(5)	
C(1A)–N(1A)–C(2A)–S(1A)	−0.6(7)	
C(1B)–N(1B)–C(2B)–S(1B)	5.5(8)	
N(1A)–C(1A)–C(1B)–N(1B)	−179.0(4)	
C(11)–N(11)–C(12)–S(1)		−7.2(5)
C(21)–N(21)–C(22)–S(2)		0.5(5)
N(11)–C(12)–C(13)–C(14)		−20.2(5)
N(21)–C(22)–C(23)–C(28)		147.8(3)
N(11)–C(11)–C(21)–N(21)	−175.7(3)	

NH···SH-bonding, responsible for producing a β-sheet pattern [21]. The C–S bond distance of 1.666(5) Å in H_2L agrees well with that in related compounds, being intermediate between 1.82 for a C–S single bond and 1.56 Å for a C=S double bond [22]. The corresponding C(2A)–N(1A) and C(2B)–N(1B) bond distances [1.317(6) and 1.331(6) Å] are indicative of some double bond character. The methoxy groups are almost coplanar (torsion angle −11.0(7)° and −9.5(7)° with respect to A and B moieties, respectively) (Fig. 1), however the *p*-methoxyphenyl rings are observed to be twisted with a dihedral angle of 60.98° between the best defined planes of $(C(=S)NHCH_2)_2$ and $(CH_3O–C_6H_4)$.

The intermolecular N–H···S hydrogen bonds, involving the imino-N and thione-S atoms, form an infinite chain along the *b* axis [23,24] (as shown in Fig. 2). The two

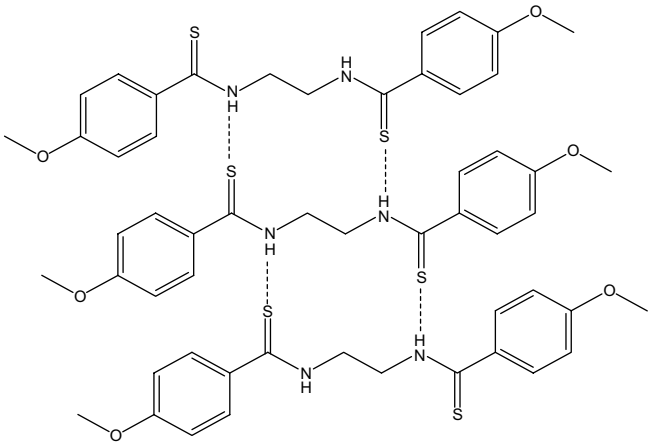


Fig. 2. β-Sheet hydrogen bond pattern of H_2L.

Table 3
Hydrogen bonds for H_2L (Å and °)

D–H···A	*d*(D–H)	*d*(H···A)	*d*(D···A)	∠(DHA)
N(1A)–H(1A)···S(1A)#1	0.72(4)	2.68(4)	3.299(5)	145(4)
N(1B)–H(1B)···S(1B)#2	0.78(4)	2.66(5)	3.305(5)	142(4)

Symmetry transformations used to generate equivalent atoms: #1 $x-1, y, z$; #2 $x+1, y, z$.

N···S distances of 3.299(5) and 3.305(5) Å (Table 3) are close to the mean N···S distance reported for NH···S hydrogen bonds by Srinivasan and Chacko [25]. The sheet further grows in the *a* direction by O1A···H9BA–C9B hydrogen bonding.

4.5. Crystal structure of complex (*2*)

Fig. 3 shows a Mercury view of the Cu(I) complex with the atomic numbering scheme. Reaction of $[Cu(PPh_3)_2NO_3]$ with H_2L in boiling methanol–chloroform gave the complex $[Cu(H_2L)(PPh_3)_2]NO_3 \cdot 0.5H_2O$ which consists of a mononuclear metal cation $[Cu(H_2L)(PPh_3)_2]^+$, (NO_3^-) anion and an isolated water between two molecules (Fig. 4). The metal centre is bonded to the ligand through the sulfur atom in an isobidentate fashion forming a nine-membered chelate ring. The geometry around the CuS_2P_2 core is approximately tetrahedral [26]. Geometrical distortion from ideal angles can be explained by the need to accommodate the bulky triphenylphosphine groups and the nine-membered chelate ring. The Cu–S bond lengths are 2.3910(11) and 2.4212(11) Å, consistent with values found for tetrahedrally coordinated Cu(I) with S-donor atoms [27]. The P–Cu–P angle [122.19(3)°] is in good agreement with the value reported for other bis(triphenylphosphine)copper(I) compounds, such as 125.0(2)° for $[Cu(PyZSH)(PPh_3)_2Br]$ [28], 121.71(3)° for $[Cu(PPh_3)_2(bzintH_2)Cl]$ [29] and 123.8(2)° for $[Cu(PPh_3)_2(C_2H_4N_2S_2)Br]$ [30]. The Cu–P bond distances 2.3216(10) and 2.3292(11) Å are slightly longer than the sum of the covalent radii (2.27 Å) and the values reported for other copper(I)–phos-

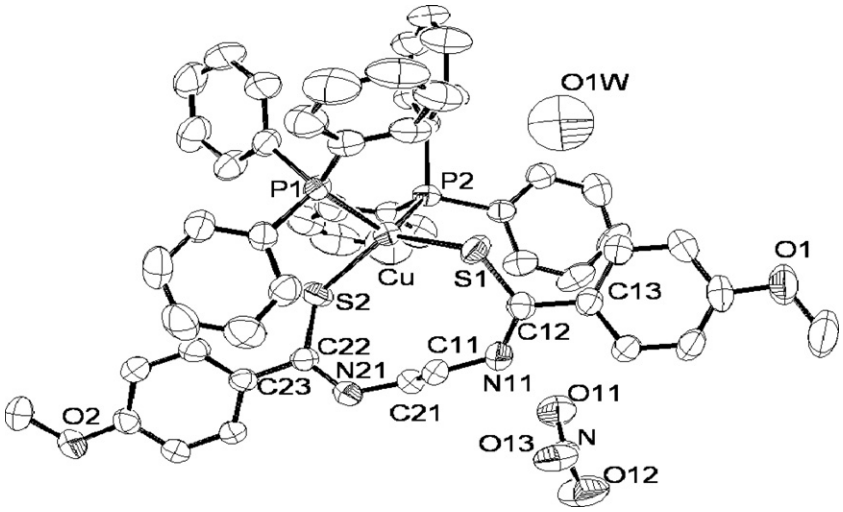


Fig. 3. ORTEP plot of $[Cu(H_2L)(PPh_3)_2]NO_3 \cdot 0.5H_2O$ showing atomic numbering scheme with ellipsoids of 30% probability. Hydrogen atoms are omitted for clarity.

phine complexes, ranging between 2.15 and 2.30 Å [31]. On the other hand, the S(1)–Cu–S(2) angle [132.56(4)°] is larger than that observed in $[Cu(PPh_3)(quintH)]$ [32] [114.24(7)°], indicating repulsion between the thiones caused by their negative charges. The C–S bond distances, 1.697(3) and 1.700(3) Å, are closer than that observed (1.66–1.72 Å) for $[CuX(4\text{-}H_2tsc)Ph_3P]$ (X = Br, I) [27].

Nine-membered chelate rings are very rare mainly because of their destabilization caused by non-bonding interactions within the nine-membered rings due to unfavorable torsion angles imposed by the ring size. It has been observed that –NH–C(=S)– containing ligands prefer to bridge metals to give polynuclear products [33] rather than forming a mononuclear chelate with an 8–11 membered ring [34]. The flexibility within the $(–C(=S)–NH–CH_2–)_2$ backbone, the presence of suitably positioned sterically demanding substituents, and heteroatoms (–NH– or –S–) stabilize the large ring. Additionally, the presence of two *p*-methoxyphenyl rings on the backbone probably contributes to the stability of the nine-membered chelate ring.

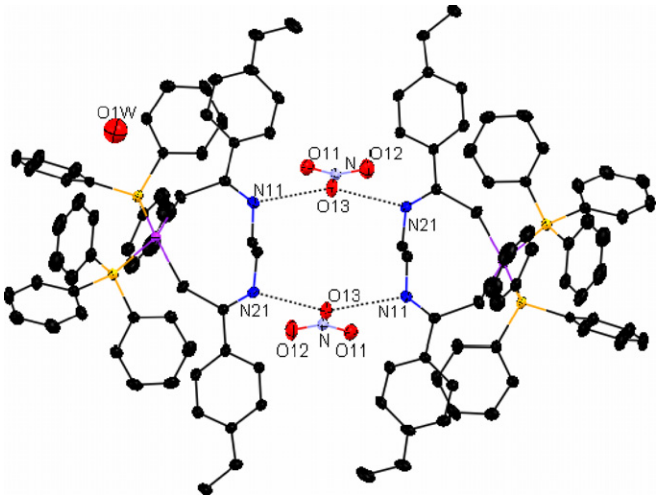


Fig. 4. Rectangular anionic column in the structure of $[Cu(H_2L)(PPh_3)]NO_3 \cdot 0.5H_2O$.

4.6. Molecular packing of the complex

The molecular packing is dominated by hydrogen bonding offered by the (NO_3^-) ion and the basal plane of the CuS_2 chelate ring. The anion, which exhibits no disorder even at room temperature, is held in the *x*,*y*,*z* plane by intermolecular hydrogen bonds (Table 4). Another symmetry related (NO_3^-) ion lies parallel but in an inverted manner along the *a* axis. The specific arrangement of two nitrate ions and two complex cations results in the formation of a rectangular shaped anionic channel (Fig. 4). The intermolecular N11–H11A···O13#1 hydrogen bond is one component of a bifurcated interaction based on O13(*x*,*y*,*z*); while the second one is O13···H21A–N21#2 of the symmetry related complex molecule (−*x*, 1 − *y*, 1 − *z*). The other amide hydrogen atom of H_2L#1 is involved in a similar N21–H21A···O13#2 (−*x*, 1 − *y*, 1 − *z*) interaction and O13#2 further with H11A–N11#2. Thus four intermolecular contacts effectively link two molecules of the complex into a 2-dimensional structure resulting in an unstrained chair-like close cavity. The rectangular shaped cavity has dimensions

Table 4
Hydrogen bonds for $[Cu(H_2L)(PPh_3)_2]NO_3 \cdot 0.5H_2O$ (Å and °)

D–H···A	*d*(D–H)	*d*(H···A)	*d*(D···A)	∠(DHA)
O(1W)–H(1W2)···S(1)	1.07(14) 2.8(5)	3.6(4)	132(18)	
N(11)–H(11)···O(13)	0.93	2.49	3.2(6)	132
N(21)–H(21)···O(13)	0.93	2.03	2.9(6)	150

Symmetry transformations used to generate equivalent atoms.

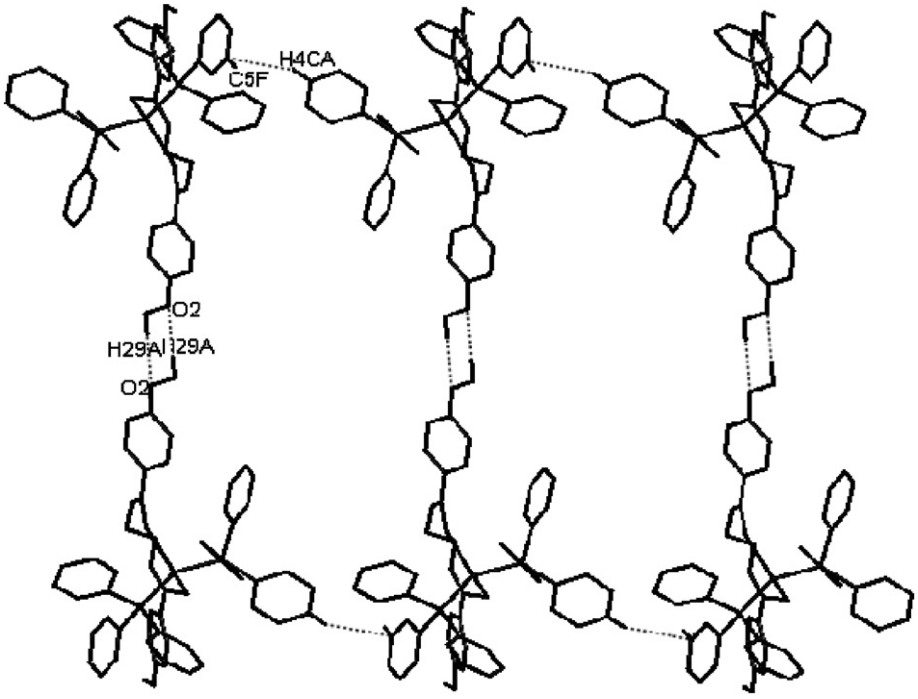


Fig. 5. Molecular packing of complex (**2**) showing C–H···π interactions (NO_3 and hydrogens atoms for more clarity, expect H4CA, H5FA, H29A).

of 5.489(25) [N11–H11A···O13···H21AN21] × 3.693(7) [N11–C11–C21–N21] Å, as shown in Fig. 4.

The water molecule in the complex forms intermolecular hydrogen bonding with the sulfur atom present in the CuS_2 chelate ring. The intermolecular H1W2···S2 hydrogen bond is 2.686 Å and H1W1···S1 is 2.797 Å, which interlink two complex molecules together and thus stabilize the whole structure. The edge-to-face C–H···π interaction formed between C5F···H4CA is found to be 2.895 Å, and this propagates the chain along the a axis. This tendency appears to have facilitated the position and orientation of the molecules, forming a cavity. The methoxy protons and oxygen of two different molecules are involved in forming intermolecular hydrogen bonding, with dimensions of 2.656[O2···H29A] × 1.984 [O2–C29] Å. The C–H···π interactions together with intermolecular hydrogen bonding [O2···H29A] leads to a supramolecular continuum (Fig. 5).

5. Conclusion

New mononuclear tetrahedral Cu(I) and Ag(I) complexes obtained from a flexible thioamide ligand contain a nine-membered chelate ring structure with the MS_2P_2 core. Complex **2** involves face to edge weak interactions in its molecular packing.

Acknowledgement

This work was supported by CSIR Grant No. 01/(1835)/03/EMR-II.

Appendix A. Supplementary material

CCDC 645978 and 645979 contain the supplementary crystallographic data for **1** and **2**. These data can be obtained free of charge via http://www.ccdc.cam.ac.uk/conts/retrieving.html, or from the Cambridge Crystallographic Data Centre, 12 Union Road, Cambridge CB2 1EZ, UK; fax: (+44) 1223-336-033; or e-mail: deposit@ccdc.cam.ac.uk. Supplementary data associated with this article can be found, in the online version, at doi:10.1016/j.poly.2007.09.035.

References

[1] M.G. Patch, H. Choi, R.D. Bau, V. McKee, C.A. Reed, Inorg. Chem. 29 (1990) 110.
[2] S. Banerji, R.E. Byrne, S.E. Livingstone, Transition Met. Chem. 7 (1982) 5.
[3] V. McKee, M. Xzvagulus, J.V. Dagdigan, M.G. Patch, C.A. Reed, J. Am. Chem. Soc. 106 (1984) 4765.
[4] R. Lantie, Copper Proteins and Copper Enzymes, vol. 1–3, CRC Press, Boca Raton, FL, 1984.
[5] A. Shrivastava, N.K. Singh, P. Tripathi, T. George, J.R. Dimmock, R.K. Sharma, Biochimie 88 (2006) 1209.
[6] T.S. Lobana, A. Castineiras, Polyhedron 21 (2002) 1603.
[7] R.W. Bost, J. Am. Chem. Soc. 73 (1951) 25.
[8] K.A. Jensen, C. Pedersen, Acta Chem. Scand. 15 (1961) 1087.
[9] F.A. Cotton, D.M.L. Goodgame, J. Chem. Soc. Part IV (1960) 5267.
[10] G.M. Sheldrick, Acta Crystallogr., Sect. A 46 (1990) 467.
[11] G.M. Sheldrick, SHELXL-97, Program for Crystal Structure Refinement, University of Göttingen, Göttingen, Germany, 1997.
[12] I.J. Bruno, J.C. Cole, P.R. Edgington, M. Kessler, C.F. Macrae, P. McCabe, J. Pearson, R. Taylor, Acta Crystallogr., Sect. B 58 (2002) 389.

[13] K. Brandenburg, H. Putz, DIAMOND. Version 3.0, University of Bonn, Germany, 2004.
[14] L.J.J. Farrugia, Appl. Crystallogr. 30 (1997) 565.
[15] K. Nakamoto, Infrared and Raman Spectra of Inorganic and Coordination Compounds, fourth ed., Wiley Interscience, New York, 1986.
[16] (a) A.A.D. Paggio, D.R. McMillin, Inorg. Chem. 22 (1983) 691;
(b) S.W. Orchard, C. Kutal, Inorg. Chem. 21 (1982) 538;
(c) C. Kutal, Coord. Chem. Rev. 99 (1990) 213.
[17] P.P. Singh, R. Rivest, Can. J. Chem. 46 (1968) 2361.
[18] B. Singh, M.M. Rukhaivar, R.J. Sinha, J. Inorg. Nucl. Chem. 39 (1977) 29.
[19] N.K. Singh, S.B. Singh, Synth. React. Inorg. Met.-Org. Chem. 32 (1) (2002) 25.
[20] T.S. Lobana, S. Paul, A. Castineiras, Polyhedron 16 (1997) 4023.
[21] M. Sarkar, K. Biradha, Chem. Commun. (2005) 2229.
[22] L.E. Sutton, Tables of Interatomic Distances and Configuration in Molecules and Ions, Special Publication No. 18. The Chemical Society, London, 1965.
[23] C.-Y. Zhao, C.-Y.A. Duan, Y.-P. Tian, X.-Z. You, T.C.W. Mak, Acta Crystallogr., Sect. C 53 (1997) 1151.
[24] R. Mattes, H. Weber, J. Chem. Soc., Dalton Trans. (1980) 423.
[25] R. Srinivasan, K.K. Chacko, Conformation of Biopolymers, vol. 2, Academic Press, New York, 1967.
[26] R. Singh, S.K. Dikshit, Polyhedron 11/16 (1992) 2099.
[27] (a) H.-G. Zheng, D.-X. Zeng, X.-Q. Xina, W.-T. Wong, Polyhedron 16/20 (1997) 3499;
(b) P. Karagiannidis, P. Aslanidis, S.P. Mentzafos, A. Hountas, A. Terzis, Polyhedron 9 (1990) 981.
[28] P. Karagiannidis, P. Aslanidis, B. Krebs, M. Dartmann, D.P. Kessissodlou, D.P.K. Krebs, Inorg. Chim. Acta 156 (1) (1989) 47.
[29] S. Skoulika, P. Karagianidis, A. Aubry, P. Aslanidis, S. Papastefanou, Inorg. Chim. Acta 183 (1) (1999) 207.
[30] N.T. Akinchan, R. Akinchan, P.M. Drozdewski, Y.H. Yang, T.L. Klein, D.X. West, Synth. React. Inorg. Met.-Org. Chem. 26 (1996) 735.
[31] T.S. Lobana, A. Sánchez, J.S. Casas, A. Castiñeiras, J. Sordo, M.S. García-Tasende, E.M. Vázquez-López, J. Chem. Soc., Dalton Trans. (1997) 4289.
[32] P. Cecchi, B. Bovio, G.G. Lobbia, C. Pettinari, D. Leonesi, Polyhedron 14/17–18 (1995) 2441.
[33] L.J. Ashfield, A.R. Cowley, J.R. Dilworth, P.S. Donnelly, Inorg. Chem. 43 (2004) 4121.
[34] (a) P.A. Cooke, S.D. Peresa, B.L. Shaw, M. Thornton-Pett, J.D. Vessey, J. Chem. Soc., Dalton Trans. (1997) 435;
(b) N.A. Al-Salem, H.D. Empsall, R. Markham, B.L. Shaw, B. Weeks, J. Chem. Soc., Dalton Trans. (1979) 1972;
(c) A. Constable, W.S. McDonald, B.L. Shaw, J. Chem. Soc., Dalton Trans. (1979) 496.

Available online at www.sciencedirect.com
ScienceDirect
Polyhedron 27 (2008) 383–392
POLYHEDRON
www.elsevier.com/locate/poly

Antiferromagnetic spin-coupling between Mn^{II} and amminium radical cation ligands: Models for coordination polymer magnets

Richard J. Bushby *, Colin Kilner, Norman Taylor, Rhidian A. Williams

Self-Organising Molecular Systems (SOMS) Centre and School of Chemistry, University of Leeds, Leeds LS2 9JT, United Kingdom

Received 15 August 2007; accepted 27 September 2007
Available online 5 November 2007

Abstract

One- and two-electron oxidation of the manganese(II) complex $[L_2Mn(hfac)_2]$ (L = 4″,4‴-di-*tert*-butyl-2′,2″,2‴trimethoxy-{4-(4′-diphenylaminophenyl)pyridine}) were studied by ultra violet/visible/near infra red spectroscopy, cyclic voltammetry and magnetometry. A one-electron oxidation converts the triarylamine ligand to its radical cation and gives a complex in which the antiferromagnetic coupling between the spin on the ligand and that on the metal J/k_b is −1.5 K. In a dilute frozen matrix and at low temperature this behaves as an $S = 2$ system. A two-electron oxidation gives $[L_2Mn(hfac)_2]^{2\bullet+}$ which at low enough temperatures behaves as an $S = 3/2$ system but the spin-coupling between the metal and the ligand is weaker ($J/k_b = -0.3$ K). The weakness of these spin-couplings mean that Mn^{II}/amminium radical cation complexes are not promising systems on which to base coordination polymer magnets. The equivalent copper(II) complex $[L_2Cu(hfac)_2]$ was also investigated but this decomposes when an attempt is made to oxidise the ligand to its amminium radical cation.
© 2007 Elsevier Ltd. All rights reserved.

Keywords: Manganese(II); Copper(II); Molecular magnet; Crystal structures

1. Introduction

One of the most successful strategies for producing molecular magnets is that originally pioneered by Gatteschi and co-workers [1,2] which relies on the creation of coordination polymers in which spin-bearing ligands and spin-bearing transition metal centres alternate with each other. At low enough temperatures, such systems can show bulk magnetic properties regardless of whether the coupling between metal and ligand is ferromagnetic or antiferromagnetic [2]. Systems of this type include a vanadium/TCNE complex which has a Curie temperature which is above room temperature but in most such systems there is weak or very weak spin-coupling between the ligand and the metal and, as a result, Curie temperatures are also low [3]. Most other examples exploit nitroxide [4] or nitronyl nitroxide [2,5] as the spin-bearing ligand although several others have been investigated [6,7]. This paper explores the possibility of using amminium radical cation ligands. We have used the monopyridyl functionalised triarylamine ligand **3** to make the model 'monomers' **4** and **5** (Scheme 1) and then tried to oxidise the ligands to the amminium radical cation level. The sign of the spin coupling between the ligand radical cation and the metal ion centre in the resulting $\mathbf{4}^{n\bullet+}$ and $\mathbf{5}^{n\bullet+}$ complexes is expected to depend on whether the spin orbitals overlap or are orthogonal [7]. In the Mn^{II} complexes, the non-zero overlap between spin orbitals should result in an antiferromagnetic interaction but, in the case of the copper complex the spin orbitals are orthogonal and the interaction should be ferromagnetic [8].

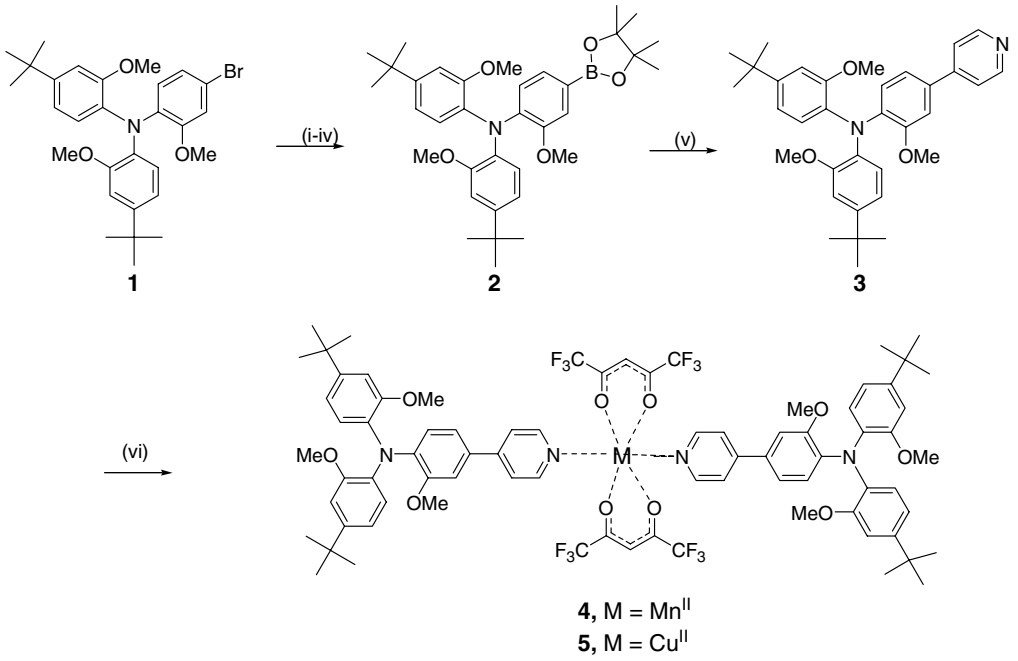
2. Results

2.1. Synthesis and X-ray crystal structures

As shown in Scheme 1, the ligand **3** was prepared by a Suzuki coupling reaction between the monoboronic acid

* Corresponding author. Tel.: +44 113 3436509; fax: +44 113 3436452.
E-mail address: r.j.bushby@leeds.ac.uk (R.J. Bushby).

0277-5387/$ - see front matter © 2007 Elsevier Ltd. All rights reserved.
doi:10.1016/j.poly.2007.09.020



Scheme 1. Synthesis of the complexes: Reagents: (i) *n*-BuLi/THF/−78 °C; (ii) $B(O^iPr)_3$/THF/−78 °C; (iii) H^+/H_2O/−78 °C; (iv) pinacol/4 Å molecular sieve/Δ, 46% (overall); (v) 4-bromopyridine hydrochloride/$Pd(PPh_3)_4$/$Ba(OH)_2$/DME/Ar atmosphere/Δ; and (vi) $[Cu(hfac)_2]$ or $[Mn(hfac)_2]$/heptane/ether/DCM.

2 (from the bromocompound **1** [9]) and 4-bromopyridine. The required 2:1 complexes **4** and **5** were obtained by mixing solutions of the ligand with $[Mn(hfac)_2]$ or $[Cu(hfac)_2]$. Recrystalisation of the complexes **4** and **5** from THF/hexane gave orange and green crystals, respectively. Single crystal X-ray structures were obtained for all three compounds **3**–**5**, the derived molecular structures are shown in Fig. 1 and crystal structure refinement data are given in Section 4 and Table 1. As expected, ligand **3** shows a propeller-like twist of the aryl residues around an almost planar central nitrogen. Like other triarylamines, the dihedral angles range between 53° and 74°. The torsional angle between the pyridine and benzene rings of 36° is also similar to that in related compounds [10]. As expected, the geometry of the ligand is only slightly changed on forming the complexes **4** and **5** and complexation occurs through the pyridyl rather than arylamine nitrogen. The Mn complex **4** has dihedral angles between 56° and 68° with a torsional angle of 29° and in the Cu complex **5** the dihedral angles range between 56° and 69° with a torsional angle of 31°.

2.2. Cyclic voltammetry

A cyclic voltammogram for the ligand **3** is shown in Fig. 2 [11]. There is a clean one-electron redox process at 0.71 V (versus silver/silver chloride) with a width at half height of about 0.1 V. Both forward and reverse scans match in amplitude and there are no additional peaks of the type associated with benzidine formation, even after many cycles [10]. This indicates that a fast reversible electrochemical process is occurring and that the amminium radical cation $\mathbf{3}^{\bullet+}$ is chemically stable on the CV timescale. Both of the complexes **4** and **5** show oxidation potentials and peak widths that are essentially the same as those of the uncomplexed ligand **3**.[1] This is the first indication that oxidation is occurring at the ligand rather than at the metal centre: something that is confirmed by the spectroscopy and magnetometry studies described below. This is not surprising since oxidation of manganese(II) to manganese(III) in similar complexes is known to require much higher potentials [12]. If each of the ligands in turn is being oxidised to the radical cation level and the complex remains intact (for example, **4**, $[Ar_3NMn^{II}Ar_3N] \rightarrow \mathbf{4}^{\bullet+}$, $[Ar_3N^{\bullet+}\text{-}Mn^{II}Ar_3N] \rightarrow \mathbf{4}^{2,\bullet+}$, $[Ar_3N^{\bullet+}Mn^{II}Ar_3N^{\bullet+}]$) one could argue that there should be shifts in ligand oxidation potentials arising from coulombic repulsion between the charge on the ligand and that on the metal ion (as in $\mathbf{4}^{\bullet+}$) and between the charges on the two ligands (as in $\mathbf{4}^{2,\bullet+}$). However, the charged centres are well separated from each other and in dichloromethane these systems are strongly ion-paired so that the charge–charge repulsion is screened out by the counter-ion. Based on data reported by McGill and coworkers [13] for related ion-paired dication diradical species in dichloromethane and given the separation between the charged centres (which is known from crystal structure data) the shifts in the oxidation potentials due to such coulombic repulsions would be <25 mV. Such small differences would be difficult to observe and so the similarity of the CV data for complexed and uncomplexed ligands does not indicate whether or not the complexes remain intact.

[1] See supplementary material.

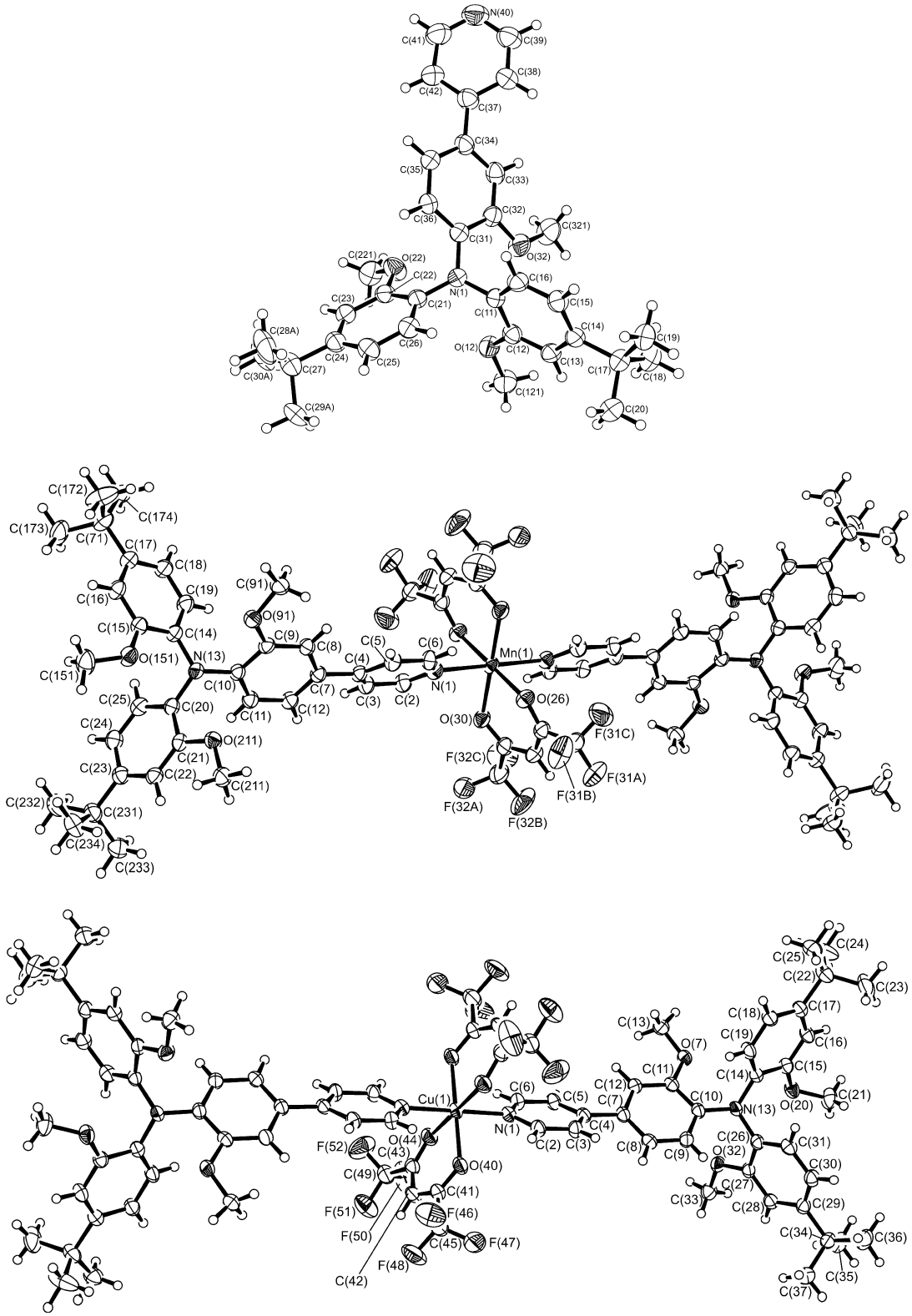


Fig. 1. X-ray derived structures of the ligand **3** (top), manganese complex **4** (middle) and copper complex **5** (bottom). For the complexes the Mn and Cu are on inversion centres. Ellipsoid probabilities are 50%.

2.3. Ultra violet/visible/near infra red spectroscopic studies

These studies were carried out using thianthrenium tetrafluoroborate ($THBF_4$) as the oxidant [14]. This has the advantage of being dichloromethane soluble so that it can be used in a quantitative titration. The results of these titrations are shown in Fig. 3 and the numerical data are summarised in Section 4. The electronic absorption

Table 1
Crystallographic data for compounds **3**–**5**

Compound	**3**	**4**	**5**
Formula	$C_{34}H_{40}N_2O_3$	$C_{94}H_{114}F_{12}MnN_4O_{14}$	$C_{94}H_{114}CuF_{12}N_4O_{14}$
Formula weight	524.68	1806.83	1815.43
Crystal system	monoclinic	triclinic	triclinic
Space group	$C2/c$	$P\bar{1}$	$P\bar{1}$
a (Å)	17.2432(3)	11.9670(2)	11.8763(2)
b (Å)	17.0393(3)	13.9279(3)	13.9797(3)
c (Å)	20.5000(4)	15.5052(4)	15.4469(3)
α (°)	90	83.1310(10)	81.8890(10)
β (°)	97.005(2)	74.3390(10)	73.0810(10)
γ (°)	90	66.5150(10)	66.5500(9)
V (Å^3)	5978.2(2)	2282.05(9)	2250.02(8)
Z	8	1	1
ρ_{calc} (g cm^{-3})	1.166	1.315	1.340
μ (mm^{-1})	0.074	0.233	0.333
T (K)	150(2)	150(2)	150(2)
Measured reflections	46881	43394	43337
Independent reflections	5838	8913	8847
R_{int}	0.0963	0.0643	0.0719
R_1 (F)[a] [$I > 2\sigma(I)$]	0.0642	0.0536	0.0591
wR_2 (F^2)[b] (all data)	0.1787	0.1440	0.1672
$\Delta\rho_{min,max}$ (e Å^{-3})	−0.230, 0.406	−0.490, 0.566	−0.628, 1.082

[a] $R_1 = \sum[||F_o| - |F_c||]/\sum|F_o|$.
[b] $wR_2 = [\sum w(F_o^2 - F_c^2)/\sum wF_o^4]^{1/2}$.

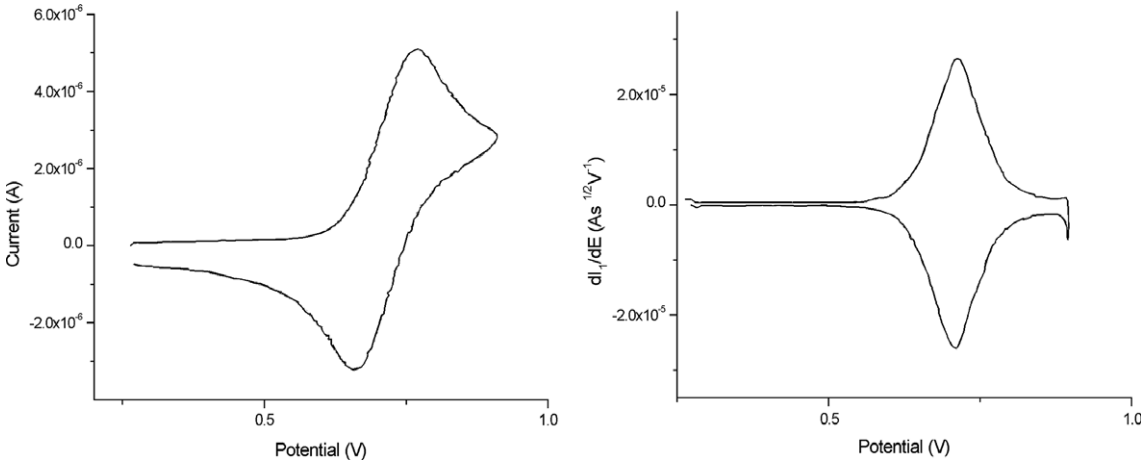


Fig. 2. (Left) Cyclic voltammogram for 10^{-3} M solutions of ligand **3** in DCM with 0.1 M tetrabutylammonium hexafluorophosphate as the supporting electrolyte. Potential relative to Ag/AgCl. (Right) Corresponding deconvoluted dI_i/dE plot. Sweep rate 500 mV s^{-1}.

spectrum (250–1250 nm) for the neutral amine **3** in dichloromethane shows one main absorption band at 354 nm. When it is oxidised with one molar equivalent of $THBF_4$ the spectrum is replaced by that of the radical cation $\mathbf{3}^{\bullet+}$ showing bands at 467, 620 and 920 nm. Because of the lowered symmetry the D_0–D_1 transition is split [10,15]. There are sharp isosbestic points at 297 and 377 nm, indicating a clean oxidation. Relative to the uncomplexed ligand $\mathbf{3}^{\bullet+}$, the spectrum of the complex $\mathbf{4}^{\bullet+}$ (Fig. 3, bottom) is slightly shifted with the main absorption band at 370 nm. On adding another equivalent of $THBF_4$, both of the ligands are oxidised to the radical cation level. The resulting diradical dication $\mathbf{4}^{2,+}$ shows three bands at 469, 619 and 925 nm. These changes parallel those for the uncomplexed ligand **3** but all of the bands are all slightly shifted. This confirms that the complex does not dissociate upon oxidation. There is a clean isosbestic point for the first one-electron oxidation step although this is less clear for the second (Fig. 3, insets). Whereas the results for the oxidation of the ligand **3** and of the manganese complex **4** are straightforward and easy to interpret the results obtained for the copper complex **5** are not. As expected the electronic absorption spectrum for the neutral complex **5** in dichloromethane shows one main absorption band at 369 nm but on oxidation, using either $THBF_4$ or $NOBF_4$ as the oxidant, a complex series of

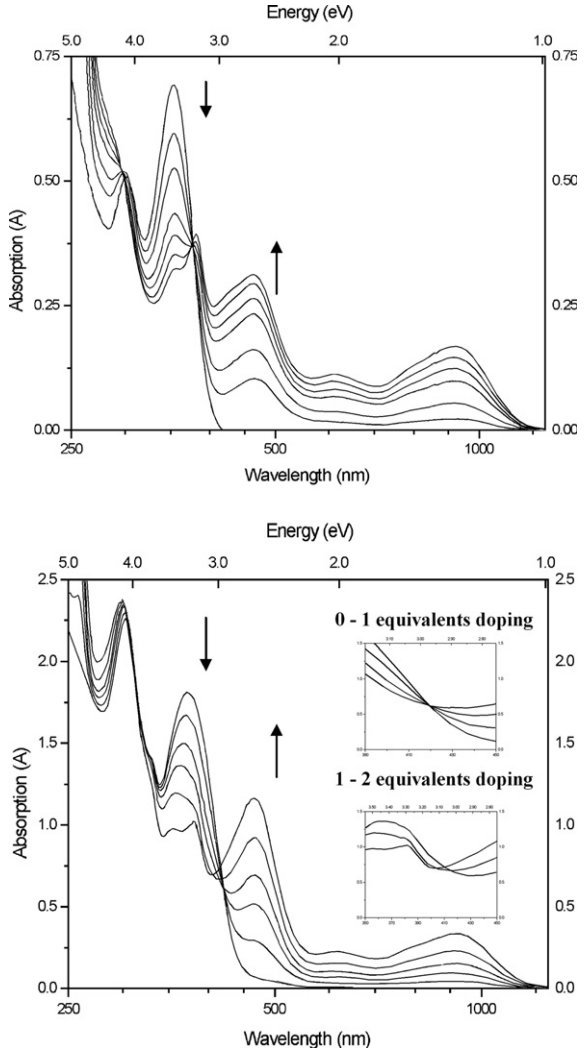


Fig. 3. (Top) Ultra violet/visible/near infra red spectra for the oxidation for monopyridyl ligand **3** to the radical cation species $\mathbf{3}^{+}$. (Bottom) UV spectra for the oxidation for Mn complex **4** to the diradical dication species $\mathbf{4}^{2+}$. Oxidation performed in dichloromethane using $THBF_4$ at room temperature.

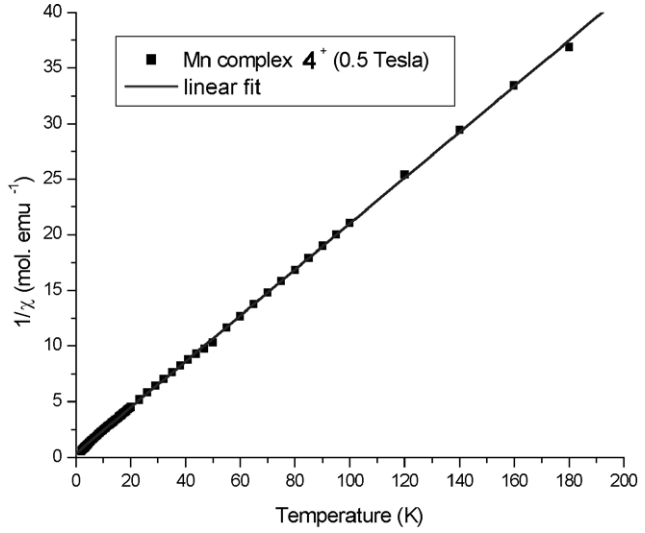
changes occurs which is quite different to those normally associated with amminium radical cation formation. It appears that even though the amminium ion/copper complexes are stable on the short time-scale of the cyclic voltammetry experiments they are not stable on the longer time-scale of these spectroscopic studies.

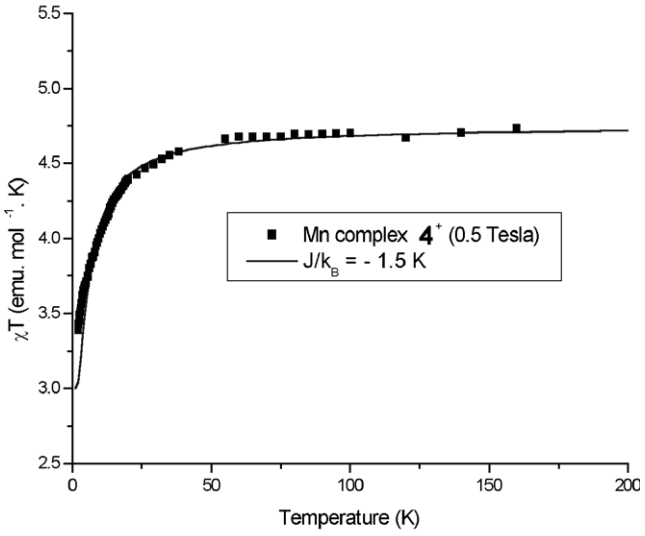
2.4. Magnetometry

Magnetometry studies were carried out using dilute frozen solutions which were prepared by the mixture of syringe and vacuum line techniques described previously [9]. This method minimises exposure to air during sample preparation and transfer, and requires less material than using dry powered samples. It also has the advantage that intermolecular spin interactions, which can complicate the interpretation of the data, can be ignored. The disadvantage is that, at higher temperatures, the signal becomes weak relative to the diamagnetic correction and the errors can be larger. Magnetic measurements were made on the neutral complex **4**, the monoradical monocation $\mathbf{4}^{\cdot+}$ and diradical dication complex $\mathbf{4}^{2,+}$. For the neutral Mn complex **4**, since we have a dilute frozen matrix, the individual manganese(II) $S = 5/2$ centres are expected to behave independently. It was found that the Curie law was obeyed and χT was 4.35 emu K mol^{-1} which is about the value expected for a dilute paramagnet of $S = 5/2$. This is confirmed by plots of the normalized magnetisation versus the ratio of magnetic field and temperature (M/M_{sat} versus H/T) which is consistent with a Brillouin function of $S = 5/2$ at both 2 and 5 K.[1] Magnetic data for the mono and diradical complexes were obtained by selectively oxidising the sample with one or two equivalents of $THBF_4$, respectively. For the monoradical monocation $\mathbf{4}^{\cdot+}$ the Curie law is obeyed. Hence, the plot ($1/\chi$ versus T) at low field (0.5 T) is linear as shown in Fig. 4 (top) and intercepts around 0 K. The product of susceptibility and temperature versus temperature (χT versus T) gradually increases from 2 K and flattens out around 50 K giving a high temperature χT value of 4.71 emu K mol^{-1} (Fig. 4, middle). This is close to the value expected for a system with isolated $S = 1/2$ and $S = 5/2$ spins. However, at low enough temperatures the spins are antiferromagnetically coupled and the system behaves as if comprised of isolated $S = (5/2 - 1/2) = 2$ spin centres. This is confirmed by plots of the normalized magnetisation versus the ratio of magnetic field and temperature (M/M_{sat} versus H/T) which fit reasonably closely to a Brillouin function of $S = 2$ (Fig. 4, bottom). The strength of the spin coupling (J_{ab}) was determined by fitting the χT versus T curve using the Bleaney–Bowers equation [16] for a system with an antiferromagnetic interaction between $S = 5/2$ and $S = 1/2$ spins [17].

$$\chi T = Ng^2\mu_B^2 T/k_B T \cdot [28 + 10\exp(-6J/k_B T)]/[7 + 5 \times \exp(-6J/K_B T)] + N_\alpha$$

The experimental data best fits a weak intramolecular antiferromagnetic coupling of $J/k_B = -1.5$ K. For the dication $\mathbf{4}^{2,+}$, the Curie law is obeyed, the plot ($1/\chi$ versus T) at low field (0.5 T) is linear as shown in Fig. 5 (top) and intercepts around 0 K. The product of susceptibility and temperature versus temperature (χT versus T) gradually increases from 2 K and flattens out around 30 K giving a high temperature χT value of 5.06 emu K mol^{-1} (Fig. 5, middle). This value is close to that expected for a system with isolated $S = 5/2$ and a pair of isolated $S = 1/2$ spins. If, at low enough temperatures the spins are antiferromagnetically coupled we should get magnetically isolated $S = (5/2 - 1/2 - 1/2) = 3/2$ spin centres. This is confirmed by plots of the normalized magnetisation versus the ratio of magnetic field and temperature (M/M_{sat} versus H/T) which fit reasonably closely to a Brillouin function of $S = 3/2$ at 2 and 5 K (Fig. 5, bottom). The strength of the intramolecular coupling (J_{ab}) was determined by fitting the χT versus T





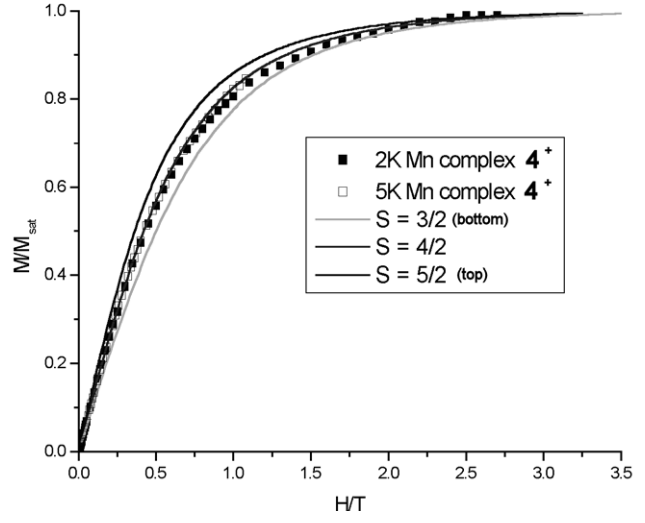
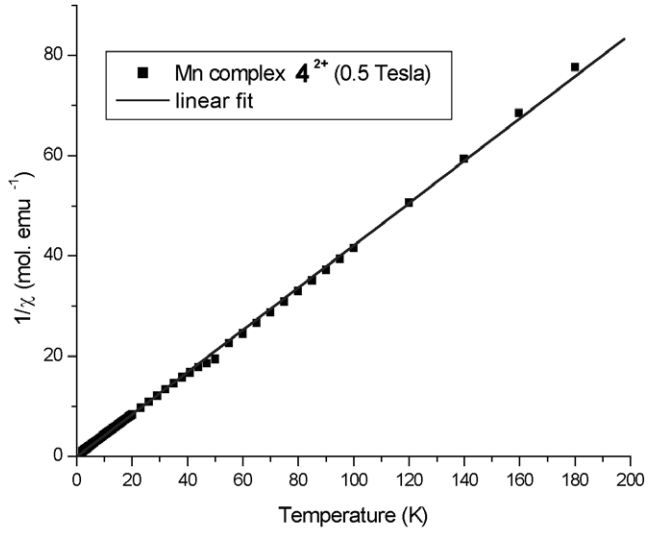
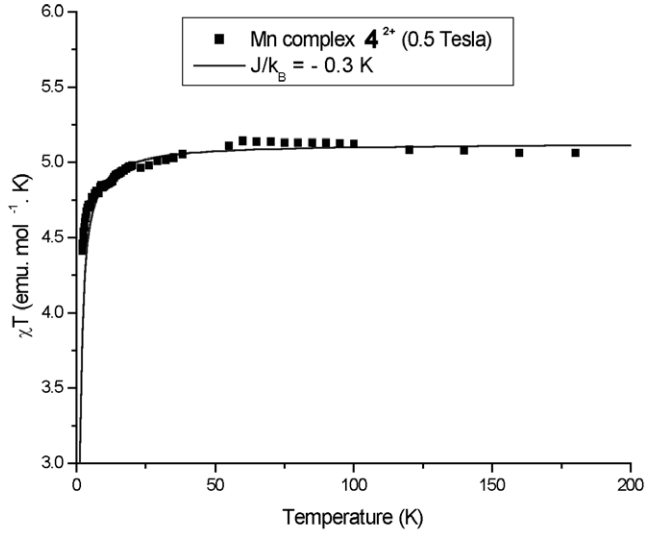


Fig. 4. (Top) 'Curie' law plot of the reciprocal of magnetic susceptibility (χ) vs. temperature for a frozen dilute solution of the radical cation $\mathbf{4}^{\bullet+}$. (Middle) Plot of product of susceptibility and temperature (χT vs. T) fitted to the Bleaney–Bowers equation. (Bottom) Plot of normalized magnetisation vs. ratio of field and temperature (Brillouin plot).





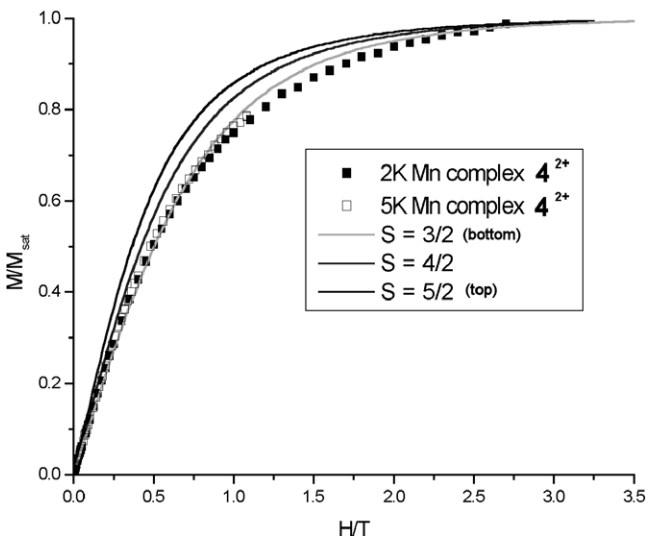


Fig. 5. (Top) 'Curie' law plot of the reciprocal of magnetic susceptibility (χ) vs. temperature for a frozen dilute solution of the diradical dication $\mathbf{4}^{2\bullet+}$. (Middle) Plot of product of susceptibility and temperature (χT vs. T) fitted to the Bleaney–Bowers equation. (Bottom) Plot of normalized magnetisation vs. ratio of field and temperature (Brillouin plot).

curve using the Bleaney–Bowers equation for a symmetrical ($S = 1/2$)–($S = 5/2$)–($S = 1/2$) system with antiferromagnetic coupling between the $S = 5/2$ and $S = 1/2$ centres and zero coupling between the two $S = 1/2$ centres [18].

$$\chi = \left\{Ng^2\mu_B^2 T/4k_B T\right\} \cdot \{[84\exp(5J/k_B T) + 35\exp(-2J/k_B T) + 10\exp(-7J/k_B T) + 35]/[4\exp(5J/k_B T) + 3\exp(-2J/k_B T) + 2\exp(-7J/k_B T) + 3]\} + N_\alpha$$

The experimental data best fits weak intramolecular antiferromagnetic coupling with a value of $J/k_B = -0.3$ K (Fig. 5, middle).

For a dilute frozen solution of the neutral Cu^{II} complex **5** the Curie law is obeyed and the plot intercepts around 0 K indicating that there is negligible intermolecular interactions. χT is 0.39 emu K mol^{-1}; a value which is consistent with $\chi T = 0.37$ emu K mol^{-1} calculated for a dilute paramagnet of $S = 1/2$, indicating that the unpaired d electron of copper(II) is magnetically isolated. Plots of the normalized magnetisation versus the ratio of magnetic field and temperature (M/M_{sat} versus H/T) which is consistent with a Brillouin function of $S = 1/2$ at 2 and 5 K.[1]

3. Discussion

It is very difficult to design a high-spin polymer that is purely organic [19,20] because both the range of ferromagnetic coupling units [21] and the number of stable free radicals is very limited. On the other hand, coordination polymers allow us to exploit the d orbitals of stable metal complexes and because we can use two metals with different moments or a metal and ligand with different moments it is not even necessary to engineer ferromagnetic coupling. This is a much easier strategy. One way to view the relationship between the purely organic high-spin polymers and the coordination polymers is illustrated in Fig. 6. As can be seen, in terms of the spin-coupling pathways, either a transition metal centre or an organic ferromagnetic coupling unit (metaphenylene, 3,4′-disubstituted biphenyl or 4,4″-disubstituted metaterphenyl, etc.) [21] can have the same function. It mediates an overall ferromagnetic coupling between radical, radical ion or carbene centres. Hence, the copper(I) in **6** [22] has the same function of feromagnetically coupling perchlorotrityl centres as the tertrachlorometaphenylene in **7** [24], the manganese(II) in **8** [25] has the same function of coupling carbene centres as the metaphenylene in **9** [23] and the manganese(II) in **10**[2] has the same function of coupling triarylamminium radical cation centres as the 4,4″-disubstituted metaterphenyl in **11** [9,13,26]. However, in all systems, whether purely organic or organometallic, the strength of the interaction is critical [9,10,20] Unfortunately, couplings are often weak and so low Curie temperatures result. In our work aimed at purely organic systems

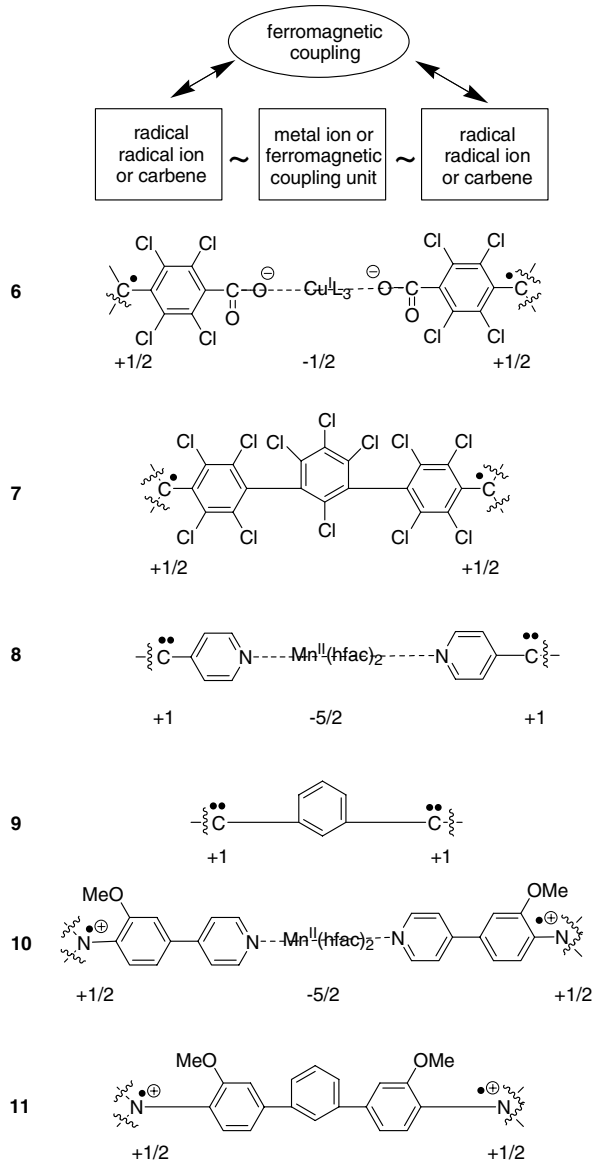


Fig. 6. Schematic of the parallels between spin-coupling pathways in high-spin organic polymers and those in coordination polymer magnets (see text).

we used amminium ion spin-bearing centres ferromagnetically coupled 1,3 through benzene, 3,4′-through biphenyl or (mostly) 4,4″-through metaterphenyl [9,10,13,26] In the present work, we have explored the coupling of similar amminium ion spin-bearing centres through Mn^{II}. These were generated by one- and two-electron oxidation of a neutral triarlyamine/Mn^{II} complex **4**. The complex remained stable when the ligands were oxidised to the amminium ion level but the antiferromagnetic spin-coupling between amminium ion and Mn^{II} centres proved to be weak in the monoradical monocation $\mathbf{4}^{\bullet+}$ and weaker still in the diradical dication $\mathbf{4}^{2,+}$. This seems to indicate a decrease in the overlap of the spin orbitals when the second electron is removed. A possible explanation is in terms of a space charge effect: that increased

[2] This work.

coulombic repulsion in the diradical dication leads to a small extension of the Mn–pyridyl bonds and a decrease in the d–π overlap. If space charge is indeed the cause it is clear that using radical ion spin-bearing centres is a less good strategy than using neutral radicals in designing coordination polymer magnets.

4. Experimental

4.1. General details

The general procedures adopted in the synthetic work were the same as those described in previous papers [9,10].

4.2. Synthesis

4.2.1. 4″,4‴-Ditertbutyl-2′,2″,2‴trimethoxy-{4-(4′-diphenylaminophenyl)pyridine} (3)

4-Bromopyridine hydrochloride (580 mg, 3.0 mmol) was added to a mixture of ethylene glycol 1,2-dimethyl ether (40 ml) and water (2 ml). Argon was bubbled through the mixture for 0.5 h. Tetrakis-triphenylphosphine palladium (0) (32 mg, 28 μmol) was added under a stream of argon. The boronic ester **2** (1.3 g, 2.5 mmol) [9] was dissolved in DME (10 ml) and degassed under a stream of argon for 0.5 h. The boronic ester solution was cannulated into the reaction vessel, barium hydroxide (1.54 g, 10 mmol) was finally added and the reaction mixture was refluxed for 48 h. The reaction was left to cool and the organic phase was extracted with dichloromethane (3 × 20 ml) washed with water (2 × 50 ml) and dried over anhydrous magnesium sulfate. Purification by flash chromatography gave *the amine* **3** as small light red crystals (1.1 g, 84%). *Anal.* Calc. for $C_{34}H_{40}N_2O_3$: C, 77.82; H, 7.68; N, 5.33. Found: C, 77.50; H, 7.90; N, 5.20%. MS (EI+) *m*/*z*: 524.1 (M^+, 100%).m.p. 167.3 °C. ^{1}H NMR (C_6D_6, 300 MHz) δ_H: 8.60 (2H, dd, *J* 7.2 and 1.55), 7.01 (2H, d, *J* 8.1), 7.0 (1H, m), 6.89 (2H, m), 6.86 (2H, d, *J* 2.14), 6.76 (2H, dd, *J* 8.2 and 2.2), 3.28 (12H, s, OMe), 3.17 (6H, s, OMe), 1.15 (36H, s, Bu). ^{13}C NMR (300 MHz, C_6D_6) δ_C: 154.2, 154.0, 153.8, 151.1, 147.9, 145.2, 140.5, 136.2, 126.1, 125.0, 121.3, 120.4, 118.6, 112.8, 111.8, 56.3, 56.2, 34.9, 32.0.

4.2.2. Manganese complex (4)

A solution of [Mn(hfac)$_2 \cdot 3H_2O$] (45 mg, 0.068 mmol) was prepared in *n*-heptane (15 ml) by the addition of the minimum amount of dry diethyl ether (ca. 1 ml). To this solution was added a solution of ligand **3** (100 mg, 0.190 mmol) in dichloromethane (5 ml) under nitrogen. The resulting solution was left under a flow of nitrogen for 12 h. The resulting orange precipitate was collected. The complex **4** was obtained as orange crystals (ca. 90 mg crude) and recrystalised from THF/hexane. *Anal.* Calc. for $C_{78}H_{82}N_4O_{10}F_{12}Mn$: C, 61.70; H, 5.44; N, 3.69. Found: C, 61.50; H, 5.35; N, 3.90%.

4.2.3. Copper complex (5)

In the same manner, the complex **5** was obtained as green crystals by recrystalisation from THF/hexane. *Anal.* Calc. for $C_{78}H_{82}N_4O_{10}F_{12}Cu$: C, 61.35; H, 5.41; N, 3.67. Found: C, 61.20; H, 5.55; N, 3.40%.

4.3. X-ray crystallography

Crystallographic data for **3**, **4** and **5** were collected at 150 K using a Nonius Kappa CCD diffractometer (with graphite-monochromated Mo Kα radiation; $\lambda = 0.71073$ Å) fitted with an Oxford Cryosystems nitrogen-cooled low-temperature device. Data processing for all structures was carried out using DENZO [27] while an absorption correction was applied using SORTAV [28]. The structures were all solved by direct methods and refined on F^2 using full-matrix least-squares methods with SHELXL-97 [29]. Hydrogen atoms were placed geometrically and treated with a riding model. Data are summarised in Table 1. In 4″,4‴-di-*tert*-butyl-2′,2″,2‴ trimethoxy-{4-(4′-diphenylaminophenyl)pyridine} (**3**), the *tert*-butyl group centred on C27 is disordered and was modelled over two positions with relative occupancies of 0.71:0.29. The Mn atom in the complex **4** lies on a centre of inversion and so the asymmetric unit contains half the complex molecule together with two disordered molecules of THF. Each THF molecule was modeled over two positions with relative occupancies of 0.73:0.27 in one case and 0.72:0.28 for the other. The Cu atom in the complex **5** lies on a centre of inversion and so the asymmetric unit contains half the complex molecule together with two molecules of THF, one of which is disordered. The disordered molecule was modeled over two positions with equal occupancies.

4.4. Cyclic voltammetry

These studies were carried out using a conventional three electrode system coupled to an EG&G Model 362 scanning potentiostat and the system was controlled by a PC unit running the 'Condecon 320' cyclic voltammetry software. The working electrode was a small platinum disc, ca. 2 mm diameter; the counter electrode was a platinum coiled wire and the reference electrode, a silver wire immersed in a saturated lithium chloride–dichloromethane mixture containing the supporting electrolyte tetrabutylammonium hexafluoroborate (0.1 M). Prior to use, solvents were thoroughly dried and degassed and the concentrations for the amines were approximately 1 mg cm^{-3}. The ferrocene/ferrocenium couple (fast electron transfer) was used as a standard and its oxidation potential was checked before and after each experiment for the solvent used. For the voltammograms shown in Fig. 2 the potential was swept in the anodic direction (upper trace) and the lower trace represents the reverse sweep in the cathodic direction.

4.5. Ultra violet/visible/near infra red spectroscopic studies

UV/Vis spectra in the range of 200–650 nm were recorded using a Perkin–Elmer Lambda 3000 UV/Vis/IR Spectrophotometer with a resolution of 0.1 nm in dichloromethane. Experiments were carried out using a pair of quartz cells with the corresponding solvent as reference. The path length of the cells was 10 mm. In a typical experiment, a dilute solution of the model diamine (1.6×10^{-5} mol l^{-1}) in dichloromethane was titrated against a known concentration of $THBF_4$ (1 mol l^{-1}), also in dichloromethane [14]. Ligand **3**, λ_{max} 354 nm, 3.50 eV ($\log_{10}\varepsilon$, 4.08); radical cation $\mathbf{3}^{\bullet+}$, λ_{max} 467 nm, 2.66 eV ($\log_{10}\varepsilon$, 4.01); 620, 2.02 (3.56); 920(s), 1.34 (3.75); isosbestic points $\mathbf{3}/\mathbf{3}^{\bullet+}$, 297 nm; 377. Complex **4**, λ_{max} 370 nm, 3.31 eV ($\log_{10}\varepsilon$, 4.78); diradical dication $\mathbf{4}^{\bullet+}$, λ_{max} 354 nm, 3.50 eV ($\log_{10}\varepsilon$, 4.46); 469, 2.66 (4.58); 619, 2.00 (3.87); 925, 1.34 (4.01); isosbestic point $\mathbf{4}/\mathbf{4}^{2,+}$, 419 nm. Complex **5**, λ_{max} 369 nm, 3.40 eV ($\log_{10}\varepsilon$, 4.56).

4.6. Magnetometry

Magnetic measurements were carried out using a SQUID magnetometer (MPMS, Quantum Design) at the University of Sheffield. Samples were prepared as a dilute frozen matrix using the same apparatus and combination of vacuum line and syringe techniques as previously described in detail in Ref. [9].

Acknowledgements

We thank EPSRC for funding this work and Dr. H. Blythe (Physics, University of Sheffield) for assistance with the SQUID magnetometry.

Appendix A. Supplementary material

CCDC 634674, 186580 and 636674 contain the supplementary crystallographic data for ligand **3**, Mn complex **4** and Cu complex **5**. These data can be obtained free of charge via http://www.ccdc.cam.ac.uk/conts/retrieving.html, or from the Cambridge Crystallographic Data Centre, 12 Union Road, Cambridge CB2 1EZ, UK; fax: (+44) 1223-336-033; or e-mail: deposit@ccdc.cam.ac.uk. Supplementary data associated with this article can be found, in the online version, at doi:10.1016/j.poly.2007.09.020.

References

[1] (a) A. Caneschi, D. Gatteschi, P. Rey, R. Sessoli, Inorg. Chem. 27 (1988) 1756;
(b) A. Caneschi, D. Gatteschi, J.P. Renard, P. Rey, R. Sessoli, Inorg. Chem. 28 (1989) 1976, 2940 and 3314.
[2] A. Caneschi, D. Gatteschi, R. Sessoli, P. Rey, Acc. Chem. Res. 22 (1982) 392.
[3] J.M. Manriquez, G.T. Yee, R.S. McLean, A.J. Epstein, J.S. Miller, Science 252 (1991) 1415.
[4] (a) K. Inoue, H. Iwamura, J. Chem. Soc., Chem. Commun. (1994) 2273;
(b) K. Inoue, T. Hayamizu, H. Iwamura, D. Hashizume, Y. Ohashi, J. Am. Chem. Soc. 118 (1996) 1803.
[5] (a) K. Fegy, D. Luneau, E. Belorizky, M. Novac, J.L. Tholence, C. Paulsen, T. Ohm, P. Rey, Inorg. Chem. 37 (1998) 4524;
(b) K. Fegy, D. Luneau, C. Paulsen, T. Ohm, P. Rey, Angew. Chem., Int. Ed. 37 (1998) 1270;
(c) A. Caneschi, D. Gatteschi, N. Lalioti, C. Sangregorio, R. Sessoli, G. Venturi, A. Vindigni, A. Rettori, M.G. Pini, M.A. Novak, Angew. Chem., Int. Ed. 40 (2001) 1760;
(d) M. Minguet, D. Luneau, C. Paulson, E. Lhotel, A. Gorski, J. Waluk, D.B. Amabilino, J. Veciana, Polyhedron 22 (2003) 2349.
[6] (a) N. Koga, Y. Ishimaru, H. Iwamura, Angew. Chem., Int. Ed. 35 (1996) 755;
(b) Y. Sano, M. Tanaka, N. Koga, K. Matsuda, H. Iwamura, P. Rabu, M. Drillon, J. Am. Chem. Soc. 119 (1997) 8246;
(c) S. Karasawa, H. Kumada, N. Koga, H. Iwamura, J. Am. Chem. Soc. 123 (2001) 9685.
[7] Y. Takano, Y. Kitagawa, T. Onishi, Y. Yoshioka, K. Yamaguchi, N. Koga, H. Iwamura, J. Am. Chem. Soc. 124 (2002) 450.
[8] W.T. Borden, E.R. Davidson, J. Am. Chem. Soc. 99 (1977) 4587.
[9] R.J. Bushby, N. Taylor, R.A. Williams, J. Mater. Chem. 17 (2007) 955.
[10] R.J. Bushby, C. Kilner, N. Taylor, M.E. Vale, Tetrahedron 63 (2007) 11458.
[11] (a) K.B. Oldham, J. Spanier, J. Electroanal. Chem. 26 (1970) 331;
(b) K.B. Oldham, Anal. Chem. 44 (1972) 196;
(c) M. Grenness, K.B. Oldham, Anal. Chem. 44 (1972) 1121.
[12] J. Britten, N.G.R. Hearns, K.E. Preuss, J.F. Richardson, S. Bin-Salamon, Inorg. Chem. 46 (2007) 3934.
[13] R.J. Bushby, D.R. McGill, K.M. Ng, N. Taylor, J. Chem. Soc., Perkin Trans. 2 (1997) 1405.
[14] B. Boduszek, H.J. Shine, J. Org. Chem. 53 (1988) 5142.
[15] S. Amthor, B. Noller, C. Lambert, Chem. Phys. 316 (2005) 141.
[16] B. Bleaney, K.D. Bowers, Proc. Roy. Soc. Lond. Ser. A 214 (1952) 451.
[17] H. Kumada, A. Sakane, N. Koga, H. Iwamura, J. Chem. Soc., Dalton Trans. (2000) 911.
[18] M.H. Dickman, L.C. Porter, R.J. Doedens, Inorg. Chem. 86 (1986) 2595.
[19] (a) K. Itoh, in: D. Gatteschi, O. Kahn, J.S. Miller, F. Palacio (Eds.), Magnetic Molecular Materials, Kluwer, Dordrecht, 1991;
(b) M.M. Murray, P. Kaszynski, D.A. Kaisaki, W.H. Chang, D.A. Dougherty, J. Am. Chem. Soc. 116 (1994) 8152;
(c) R.J. Bushby, D.R. McGill, K.M. Ng, in: O. Kahn (Ed.), Magnetism a Supermolecular Function, Kluwer, Dordrecht, 1996;
(d) P.M. Lathi, in: P.M. Lathi (Ed.), Magnetic Properties of Organic Materials, Marcel Dekker, New York, 1999;
(e) A. Rajca, J. Wongsriratanakul, S. Rajca, Science 294 (2001) 1503;
(f) N.A. Zaidi, S.R. Giblin, I. Terry, A.P. Monkman, Polymer 45 (2004) 5683.
[20] (a) A.H. Oka, T. Tamura, Y. Miura, Y. Teki, J. Mater. Chem. 11 (2001) 1364;
(b) A. Rajca, Chem. Rev. 94 (1994) 871.
[21] D.A. Dougherty, Acc. Chem. Res. 24 (1991) 88.
[22] D. Maspoch, D. Ruiz-Molina, K. Wurst, J. Vidal-Gancedo, J. Veciana, Dalton Trans. (2004) 1073.
[23] (a) K. Itoh, in: D. Gatteschi, O. Kahn, J.S. Miller, F. Palacio (Eds.), Magnetic Molecular Materials, Kluwer, Dordrecht, 1991;
(b) K. Matsuda, N. Nakamura, K. Takahashi, K. Inoue, N. Koga, H. Iwamura, ACS Sym. Ser. 644 (1996) 142.

[24] J. Veciana, C. Rovira, M.I. Crespo, O. Armet, V.M. Domingo, F. Palacio, J. Am. Chem. Soc. 113 (1991) 2552.
[25] S. Karasawa, H. Kumada, N. Koga, H. Iwamura, J. Am. Chem. Soc. 123 (2001) 9685.
[26] (a) R.J. Bushby, D. Gooding, M. Thornton-Pett, M.E. Vale, Mol. Cryst. Liq. Cryst. 334 (1999) 167;
(b) R.J. Bushby, D. Gooding, M.E. Vale, Philos. Trans. Roy. Soc. A 357 (1999) 2939;
(c) R.J. Bushby, in: J.S. Miller, M. Drillon (Eds.), Magnetism: Molecules to Materials II, Molecule-Based Materials, Wiley, New York, 2001.
[27] Z. Otwinowski, W. Minor, Methods Enzymol. 276 (1997) 307.
[28] R.H. Blessing, Acta Crystallogr., Sect. A 51 (1995) 33.
[29] G.M. Sheldrick, SHELXL-97: Program for the Refinement of Crystal Structures, University of Göttingen, Göttingen, Germany, 1997.

Available online at www.sciencedirect.com
ScienceDirect
Polyhedron 27 (2008) 393–405
POLYHEDRON
www.elsevier.com/locate/poly

Crystal structure and optical properties of novel $(N(C_2H_5)_4)[Nd(hfa)_4(H_2O)]$ tetrakis complex

Agnieszka Mech

Institute of Low Temperature and Structure Research, Polish Academy of Sciences, ul. Okólna 2, 54-422 Wrocław, Poland

Received 2 September 2007; accepted 27 September 2007
Available online 13 November 2007

Abstract

Crystal and molecular structure of the novel tetrakis hexafluoroacetyloacetonate neodymium(III) single crystal, $(N(C_2H_5)_4)[Nd(hfa)_4(H_2O)]$ (*hfa* – hexafluoroacetylacetone), obtained by us, has been determined by X-ray diffractometry. The complex was characterized using IR spectroscopy and thermogravimetric analysis. An absorption spectrum of the single crystal was recorded and parameterized in terms of Judd–Ofelt intensity parameters Ω_λ. The experimental values of Ω_λ have been compared with those calculated based on the crystallographic data and taking into account the forced electric dipole and dynamic coupling mechanisms. Our study reveals a strong effect of hydrogen bonds, formed between the ligand's ketone oxygens and the water molecule from the neighboring complex anion, on the polarisation of the chemical environment of Nd^{3+} ions as well as a high value of Ω_2 intensity parameter. The molecular structure of the complex can be satisfactorily predicted by the SMLC/AM1 (sparkle model for the calculation of lanthanide complexes within Austin model 1) method.
© 2007 Elsevier Ltd. All rights reserved.

Keywords: Neodymium tetrakis complex; β-Diketone; Crystal structure; Judd–Ofelt analysis; Infrared and UV–Vis spectra

1. Introduction

The lanthanides are known to form stable complexes with different groups of the organic ligands like calixarenes, ligands containing heterobiaryl groups or macrocyclic ligands [1]. Especially, worth attention are the lanthanide complexes with β-diketones [2], which in the last three decades have been intensively studied due to their potential applications in design of chelate lasers [3], efficient organic light emitting diodes (OLEDs) [4] and polymer light emitting diodes (PLEDs) [5], as NMR shift reagents [6], in analytical applications and as a modern antibody catalysts in biochemistry [7], to name just a few examples.

The most of hitherto studied rare-earth β-diketonate complexes belong to the group of tris complexes of the type M(β-diketone)$_3$L or M(β-diketone)$_3$L$_2$. Here, the two unoccupied coordination positions are usually filled up by additional neutral organic ligands L, which can serve as an antenna providing efficient pathway for excitation of lanthanide ion. Moreover, the L ligands prevent water or other solvent molecules, which possess a high energy vibrations and thus might quench efficiently the lanthanide complexes emission, from entering into the first coordination sphere. An alternative possibility is the complex of the type $(C^+)[ML_4^-]$, where all metal coordination positions are filled up by ligand donor atoms and the charge neutrality is provided by a C^+ counter cation, not coordinated to the lanthanide. An additional advantage of this type of complexes is that they exhibit usually a higher thermal stability compared to their tris-type counterparts. This property is of primary importance for applications as polymer light emitting diodes (PLEDs) and polymeric optical waveguides and amplifiers. Survey of the literature reveals, however, only a few reports on the lanthanide complexes of the general formula $(C^+)[Ln(\beta\text{-diketone})_4^-]$ [8–10]. Moreover, the search of the Cambridge Crystallographic Data Base results in only 20 crystal structures determined for

E-mail address: A.Mech@int.pan.wroc.pl

0277-5387/$ - see front matter © 2007 Elsevier Ltd. All rights reserved.
doi:10.1016/j.poly.2007.09.031

lanthanide tertakis complexes in general, and only one for neodymium tetrakis complex. Therefore, in view of potential applications of tetrakis(β-diketonates) type of complexes and scarcity of relevant data in the literature, studies of physico-chemical properties of these group of compounds are timely.

In this paper the synthesis of a new $(N(C_2H_5)_4)[Nd(hfa)_4(H_2O)](N(C_2H_5)_4)$ (*hfa* = hexafluoroacetyloacetone) compound, belonging to the tetrakis(β-diketonates) type of complexes, and its characterisation, are presented. The crystal structure at 100 K was determined by a single crystal X-ray measurements. The molecular structure of the complex was also calculated using the SMLC/AM1 (sparkle model for the calculation of lanthanide complexes within Austin model 1) method [11]. The thermal stability of the compound was studied using the TGA measurements. The detailed assignment of vibrational bands observed in the IR spectra was made, whereas the room and low-temperature absorption spectra of the single crystal were recorded to obtain the insight into the optical properties of the material. The observed transition intensities have been theoretically interpreted in terms of the Judd–Ofelt Ω_λ intensity parameters.

2. Experimental

2.1. Materials and sample preparation

The starting materials were $NdCl_3 \cdot 6H_2O$ (99.99%, Aldrich), 1,1,1,5,5,5-hexafluoro-2,4-pentanedione (*hfa*, hexafluoroacetylacetone) (99%, Aldrich) and $N(C_2H_5)_4Cl$ monohydrate (99.8%, Merck). The $(N(C_2H_5)_4)[Nd(hfa)_4(H_2O)]$ was prepared by deprotonating 22 mmols of the hexafluoroacetylacetone ligand with NaOH in absolute ethanol, followed by addition of 10 mmoles of ethanolic solution of $N(C_2H_5)_4Cl$, and subsequent dropwise addition of 5 mmoles of the $NdCl_3 \cdot 6H_2O$ also dissolved in absolute ethanol. The sodium chloride, which precipitates immediately after the first drop of the counter ion is added to the solution, was filtered off. The obtained solution was concentrated by heating until the crystallization started. Afterwards, the small amount of absolute ethanol was added to dissolve the solid and the so obtained clear solution was then left at room temperature overnight. The formed light-violet single crystals of a good optical quality were separated by filtering and dried in air at room temperature. *Anal.* Calc. for $NdC_{28}H_{26}NO_9F_{24}$ (M_r = 1124.74): C, 30.08; N, 1.27; H, 2.37. Found: C, 30.0; N, 1.25; H, 2.3%.

2.2. Crystallography

A crystal suitable for X-ray analysis was cut from a larger one and mounted on a Kuma KM4 diffractometer with κ geometry and a graphite monochromator. The data were collected at 100 K and the unit cell parameters were refined from angular settings of 25 005 reflections with 2θ between 18° and 27°. The obtained data were corrected for Lorentz and polarisations factors as well as for extinction.

The position of the neodymium ion was found from the Patterson map; those of other atoms were found subsequently from the difference Fourier syntheses. The C-bonded hydrogen atoms were located from geometry, with the C–H distances constrained to 0.96 Å, and the position of the hydrogen atom in the water molecule was found from the difference Fourier syntheses. The structure was refined with a full-matrix least-squares method with all non-hydrogen atoms anisotropic and hydrogen atoms isotropic with common temperatures factors. Four (F(19), F(20), F(21) and F(24)) of the 24 F atoms reflect high anisotropic temperature factors, therefore in the crystal

Table 1
Crystal data, data collection and structure refinement details of $(N(C_2H_5)_4)[Nd(hfa)_4(H_2O)]$

Crystal data	
Formula weight	1120.74
Crystal system	monoclinic
Space group	$P2_1/n$
a (Å)	15.9257(7)
b (Å)	12.5939(5)
c (Å)	20.3604(8)
α (°)	90.00
β (°)	105.701(4)
γ (°)	90.00
Volume (Å^3)	3931.2(3)
D_{calc} (Mg m^{-3})	1.894
Z	4
Absorption coefficient (mm^{-1})	1.484
Crystal size (mm)	0.1 × 0.1 × 0.05
Crystal form	needle
Crystal color	light violet
Data collection	
Diffractometer	Kuma KM4 automatic diffractometer
Monochromator	graphite
Radiation type	Mo Kα
Temperature (K)	100(2)
θ Range (°)	3.04–28.55
Index range	$-21 \leqslant h \leqslant 16$, $-16 \leqslant k \leqslant 16$, $-25 \leqslant l \leqslant 26$
Absorption correction	analytical from crystal shape
T_{min}/T_{max}	0.212/0.572
Number of measured reflections	25 005
Number of independent reflections	9223
Number of observed reflections	6725
R_{int}	0.0438
$\Delta\rho_{min}/\Delta\rho_{max}$ (e Å^{-3})	−0.920/1.525
Refinement	
Refinement on	F^2
Data/restraints/parameters	9223/11/568
$R(F_o > 4\sigma(F_o))$	0.0527
R (all data)	0.0900
wR^2	0.0875
Goodness-of-fit	1.172
Weighting parameters a	0.0338
Weighting parameters b	0
$w=1/[(\sigma^2/(F_o)^2) + (aP)^2 + bP]$	$P = (\max(F_o^2,0) + 2F_c^2)/3$

structure refinement the disordered model was applied. Thus, in the refinement they were split over two sites with an assumed 50/50 occupancy.

The crystal structure calculations were performed with SHELXS-97 [12] and SHELXL-97 [13] programs. Other details of the data collection and the structure refinement are given in Table 1. Figs. 1–3 presenting the crystal structure of the title compound were drawn using with the DIAMOND 2.1d program [14].

2.3. Measurements

Electronic absorption spectra were recorded on a Cary 50 UV–Vis–NIR spectrophotometer in the 2500–28 000 cm^{-1} range. For the low temperature measurements the crystal was mounted in a helium Oxford Instruments optical cryostat and cooled to ~4.2 K. The FIR and IR spectra in the 60–600 cm^{-1} and 600–4000 cm^{-1} spectral range, respectively, were obtained in the room temperature with a BRUKER 113v FTIR spectrophotometer. The KBr disc and Nujol mull suspension techniques were applied. The DSC measurements were performed with a PERKIN–ELMER DSC-7 instrument equipped with a CCA-7 low-temperature accessory. The sample of the mass of ca. 18.2 mg was sealed in the aluminium pan. The measurements were carried out in the temperature range between 100 and 420 K.

3. Results and discussion

3.1. Crystal structure

The $(N(C_2H_5)_4)[Nd(hfa)_4(H_2O)]$ crystallizes in the $P2_1/n$ space group of the monoclinic system. The determined parameters describing the geometry of the first coordination sphere of the Nd^{3+} ion are presented in Table 2.

The structure of the $(N(C_2H_5)_4)[Nd(hfa)_4(H_2O)]$ consists of the $[Nd(hfa)_4^-]$ complex anion and the $N(C_2H_5)_4^+$ cation, presented in Fig. 1, which arranged alternately are forming chains in the [0 1 0] direction. These chains, shown in Fig. 2, determine the molecular packing of the crystal. The packing diagram of the ions in the unit cell is presented in Fig. 3.

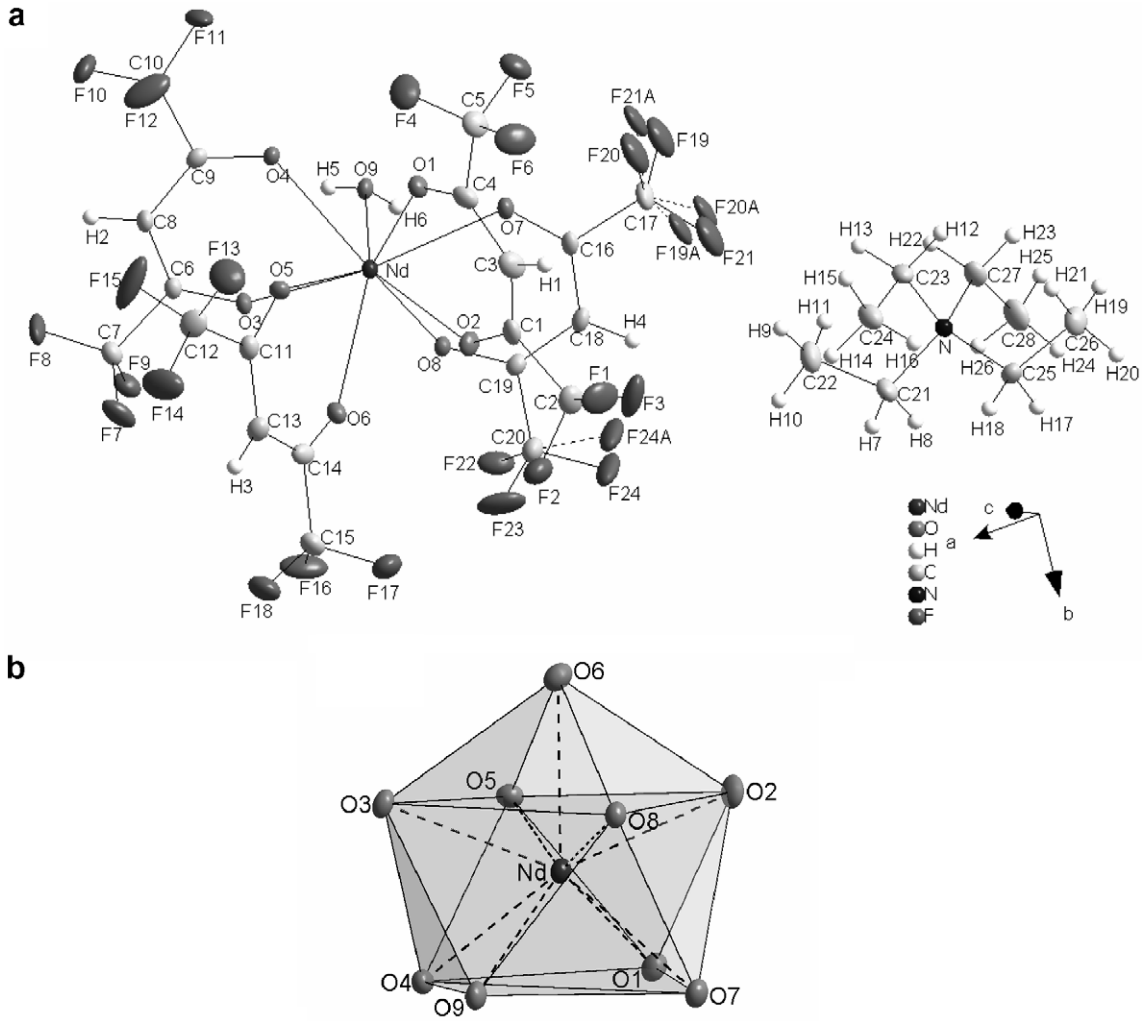


Fig. 1. (a) The molecular structure of the $(N(C_2H_5)_4)[Nd(hfa)_4(H_2O)]$. Displacement ellipsoids are shown at 30% probability. The hydrogen atoms are shown as a small circle of arbitrary radii. (b) The coordination geometry of the Nd^{3+} ion in the distorted capped square antiprism.

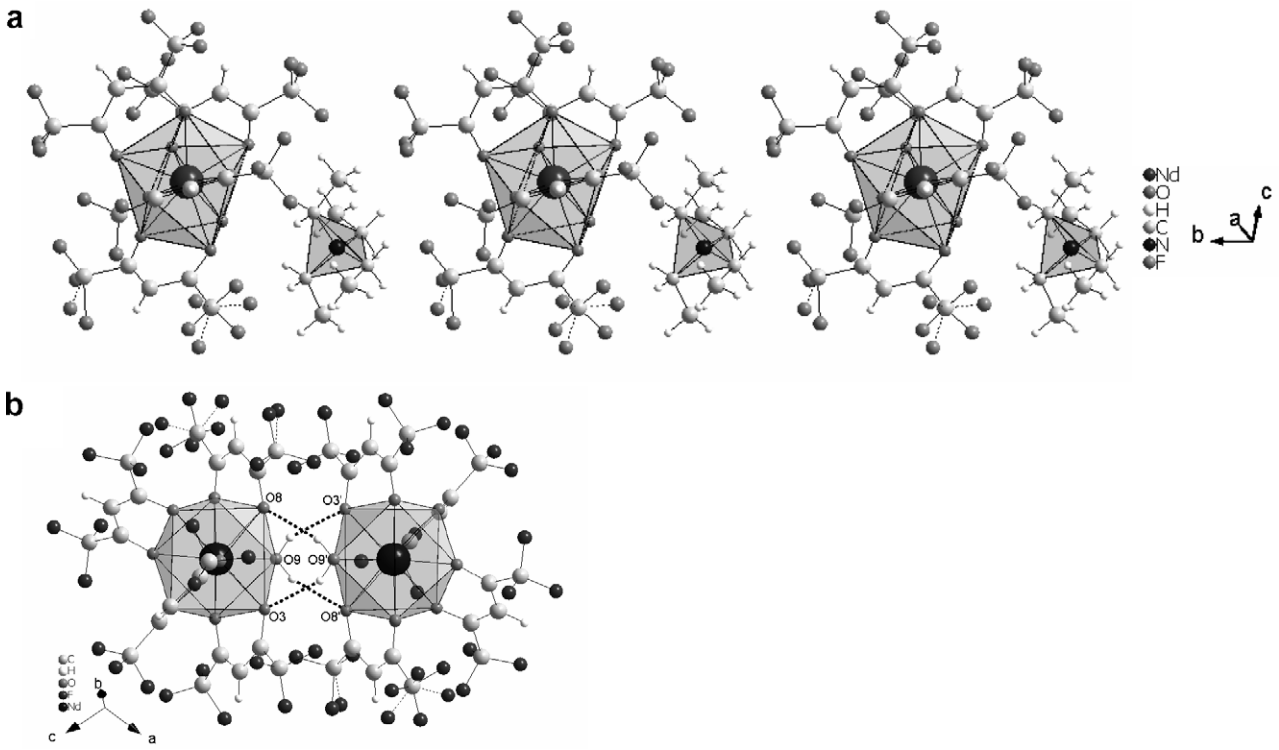


Fig. 2. (a) The fragment of the $(N(C_2H_5)_4)^+[Nd(hfa)_4(H_2O)]^-$ chain viewed along [1 0 1] direction. (b) The view of the pseudo-dimer with the dashed lines showing strong O–H···O hydrogen bonds; symmetry code is: (′) $-x+1, -y+1, -z$. All atoms are shown as a circle of arbitrary radii.

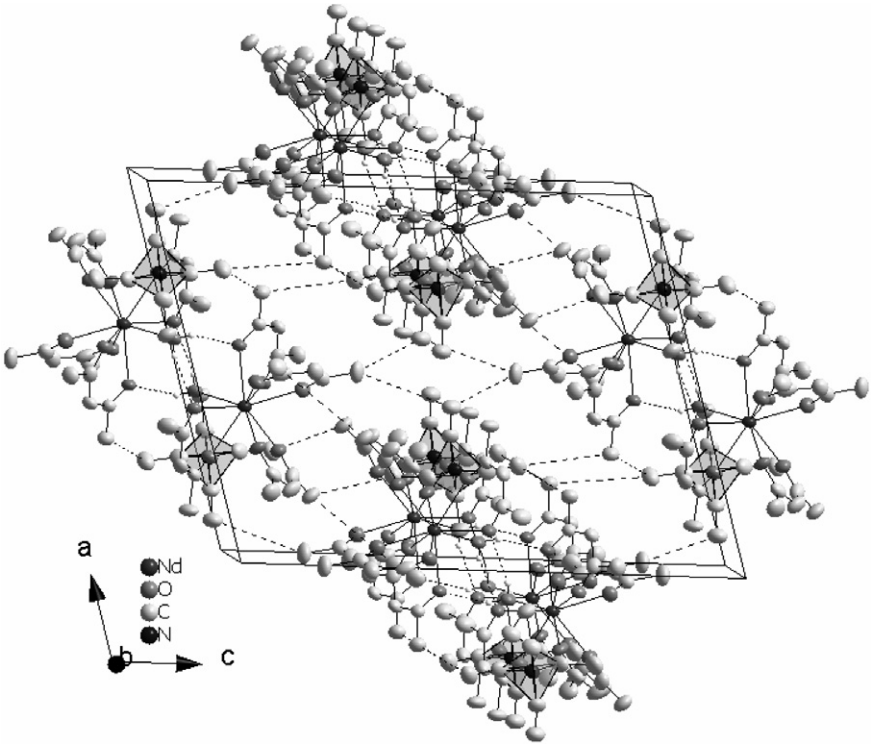


Fig. 3. The crystal packing diagram of the $(N(C_2H_5)_4)[Nd(hfa)_4(H_2O)]$. The fluorine and hydrogen atoms are omitted for clarity. The hydrogen bonds are shown as the dashed lines (D···A).

The each neodymium ion is coordinated by nine oxygen atoms. Eight of them originate from the four hexafluoroacetyloacetonate chelating ligands and one from the water molecule. The Nd–O distances range from 2.437(3) to 2.572(4) Å (Table 2) and are shorter by ca. 0.05–0.15 Å then those reported for the neodymium eight-coordinated

Table 2
Principal interatomic distances (Å), bond angles (°) and torsion angles (°) in the $(N(C_2H_5)_4)[Nd(hfa)_4(H_2O)]$ crystal

Distance (Å)		Distance (Å)		Distance (Å)	
Nd–O1	2.454(3) (2.524/2.531)	O5–C11	1.249(5)	C11–C12	1.525(6)
Nd–O2	2.438(3) (2.545/2.536)	O6–C14	1.245(5)	C13–C14	1.411(6)
Nd–O3	2.472(3) (2.530/2.536)	O7–C16	1.245(5)	C14–C15	1.527(7)
Nd–O4	2.503(3) (2.528/2.533)	O8–C19	1.266(5)	C16–C18	1.393(6)
Nd–O5	2.434(3) (2.540/2.531)	C1–C3	1.382(7)	C16–C17	1.517(6)
Nd–O6	2.478(3) (2.543/2.539)	C1–C2	1.530(7)	C18–C19	1.383(6)
Nd–O7	2.533(3) (2.539/2.531)	C3–C4	1.397(7)	C19–C20	1.538(6)
Nd–O8	2.465(3) (2.546/2.540)	C4–C5	1.522(6)	C15–F18	1.313(5)
Nd–O9	2.567(3) (2.539/2.536)	C6–C8	1.377(6)	C15–F16	1.331(5)
O1–C4	1.262(5)	C6–C7	1.534(6)	C15–F17	1.348(5)
O2–C1	1.259(5)	C8–C9	1.415(6)	C21–N	1.513(5)
O3–C6	1.265(5)	C9–C10	1.533(6)	C23–N	1.513(5)
O4–C9	1.247(5)	C11–C13	1.392(6)	C25–N	1.510(5)
Angle (°)		Angle (°)		Torsion angle (°)	
O2–Nd–O1	70.27(10) (70.6/63.2)	O2–C1–C3	126.9(5)	O1–Nd–O2–C1	0.4(4) (5.6/2.9)
O3–Nd–O4	69.37(9) (62.1/61.7)	O1–C4–C3	127.7(4)	O3–Nd–O4–C9	33.7(3) (26.5/22.6)
O5–Nd–O6	69.40(9) (62.1/62.2)	C13–C11–C12	117.4(4)	O6–Nd–O5–C11	5.7(4) (5.5/0.6)
O1–Nd–O8	131.42(9) (140.9/133.3)	C11–C13–C14	119.4(4)	O8–Nd–O7–C16	−38.4(3) (−31.5/−24.8)
O2–Nd–O6	66.81(10) (70.6/76.1)	C6–C8–C9	121.6(4)	O3–C6–C8–C9	−0.6(7)
O3–Nd–O9	72.05(10) (71.9/66.8)	N–C21–C22	115.0(4)	C6–C8–C9–O4	−6.8(7)
C6–O3–Nd	127.8(3) (140.4/141.6)	N–C25–C26	114.6(4)	C17–C16–C18–C19	−174.6(4)
C19–O8–Nd	127.1(3) (139.0/141.0)	C23–N–C21	111.6(3)	C26–C25–N–C23	−57.8(5)
C14–O6–Nd	134.8(3) (144.1/144.3)	C25–N–C27	110.7(3)	C24–C23–N–C25	−56.8(5)
C9–O4–Nd	129.6(3) (141.6/143.1)	F2–C2–F1	106.7(4)	C22–C21–N–C27	−63.6(5)

In parentheses the values calculated by means of SMLC/AM1 method are given for Nd(1)/Nd(2) – see text for details.

$Nd(tta)_4Pyr$ (tta = thenoyltrifluoroacetylacetonate) β-diketone complex [15]. The O–Nd–O angles observed in the chelate ring range from 68.16° to 70.28° and are somewhat lower as compared to those found in the neodymium tris(β-diketonates) type of complexes [16]. The average length of the C–O bond equals to 1.262 Å and is much shorter then in other lanthanide tris [17,18] and neodymium tetrakis β-diketonates [19], which might reflect the lower π electron delocalization of the C=O double bond in the $(N(C_2H_5)_4)$-$Nd(hfa)_4(H_2O)]$ complex. Furthermore, the C1–C3 distances (1.382(7) Å) between two carbon atoms in the chelating ring are much shorter then the $C(1)–C(2)F_3$ distances (1.570(7) Å), which suggests the enhancement of the double character of the C=C bond inside the ring. In fact, the C1–C3 bond length is very close to the value of 1.34 Å expected for the C=C double bond [20]. This conclusion is further confirmed by results of the IR spectra analysis, presented in Section 3.2.

The Nd atoms are located at C_1 symmetry sites, which have an approximate 2-fold axis. The geometry around the Nd atom may be seen as a distorted capped square antiprism (CSA). A view of the coordination polyhedra is presented in Fig. 1b. The non-capped base is spanned by the O(1), O(4), O(7) and O(9) atoms, whereas the O(2), O(3), O(5) and O(8) atoms form the capped one, and the O(6) atom is the cap.

Unlike other Ln^{3+} (Ln = Sm–Yb) ions, which form anhydrous complexes of the $(N(C_2H_5)_4)[Ln(hfa)_4]$ type, the tetrakis complex of the Nd^{3+} ion with *hfa* ligand contains one-coordinated water molecule, and thus is not isostructural with its heavier lanthanide analogues [19]. The presence of the water molecule coordinated to the Nd^{3+} cation influences the conformations of the ligands chelate rings, and for those two that are the nearest neighbors of the water molecule, the deviation from the planarity with the mean value of 1.757(4) Å is observed.

The characteristic feature of the $(N(C_2H_5)_4)[Nd(hfa)_4]$ structure is the existence of strong hydrogen bonds between the O(3) and O(8) oxygen atoms, originating from the β-diketonate chelating ring, and the water molecule of the neighboring complex anion, with the lengths equal to 2.084(5) and 2.092(5) Å, respectively. They link the neodymium nine-coordinated polyhedra into pseudo-dimers, with the Nd–Nd distance equal to 6.694 Å. The weaker hydrogen bonds, with the lengths ranging from 2.470(6) to 2.570(6) Å, are observed between the fluorine atoms of the anion and the CH_3 group belonging to the $N(C_2H_5)_4^+$ counter cation. These bonds link the neighboring chains into a three dimensional network. The details of the proposed hydrogen-bond geometry are given in Table 3.

3.2. IR spectra

The IR absorption spectra of the $(N(C_2H_5)_4)[Nd(hfa)_4(H_2O)]$ measured in the 60–4000 cm^{-1} range are shown in Fig. 4. The proposed assignment of the observed fundamental bands is given in Table 4. Only one broad

Table 3
Geometry of proposed hydrogen bonds

D–H–A	*d*(D–H)	*d*(H–A)	*d*(D–A)	Angle DHA	Symmetry
O9–H5···O8	0.860	2.09(3)	2.942(3)	169(2)	O8 [$-x+1, -y+1, -z$]
O9–H6···O3	0.860	2.09(3)	2.885(3)	154(6)	O3 [$-x+1, -y+1, -z$]
C22–H10···F3	0.960	2.77(4)	3.457(7)	129(5)	
C22–H11···F5	0.960	2.82(3)	3.783(4)	132(7)	F5 [$-x, -y+1, -z$]
C27–H22···F5	0.970	2.70(4)	3.429(4)	175(7)	F5 [$-x, -y+1, -z$]
C21–H8···F13	0.970	2.79(4)	3.548(4)	135(4)	F13 [$1/2+x$, 1 1/2 + y, 1/2 + z]
C28–H25···F4	0.960	2.68(4)	3.409(4)	133(7)	F4 [$-x, -y+1, -z$]
C23–H13···F19	0.970	2.64(3)	3.552(4)	155(5)	F19 [$-x, -y+1, -z$]
C24–H15···F7	0.960	2.87(3)	3.773(4)	157(4)	F7 [$x, y+1, z$]
C22–H9···F21A	0.960	2.73(4)	3.324(7)	121(8)	F21A [$-x, -y+1, -z$]
C26–H20···F17	0.960	2.70(4)	3.149(3)	109(7)	F19 [$-x, -y+2, -z$]
C26–H20···F23	0.960	2.79(3)	3.336(7)	117(5)	F23 [$-x, -y+2, -z$]
C28–H26···F13	0.960	2.61(4)	3.553(4)	167(7)	F13 [$1/2+x$, 1 1/2 + y, 1/2 + z]
C24–H14···F15	0.960	2.61(4)	3.532(6)	161(7)	F15 [1 1/2 $-x$, 1/2 + y, 1 1/2 $-z$]
C24–H15···F10	0.960	2.67(4)	3.378(4)	131(7)	F10 [1 1/2 $-x$, 1/2 + y, 1 1/2 $-z$]
C24–H16···F16	0.960	2.72(5)	3.463(4)	135(9)	F16 [$x+1, y, z$]
C26–H21···F16	0.960	2.64(4)	3.415(4)	138(7)	F16 [$x+1, y, z$]
C26–H19···F22	0.960	2.61(4)	3.134(7)	115(8)	F22 [$x+1, y, z$]
C26–H19···F11	0.960	2.66(4)	3.515(7)	149(8)	F11 [$-x, -y+1, -z$]
C25–H17···F2	0.970	2.61(4)	3.467(7)	147(6)	F2 [$-x, -y+2, -z$]
C21–H8···F2	0.970	2.80(4)	3.590(6)	140(10)	F2 [$-x, -y+2, -z$]
C28–H24···F11	0.960	2.67(4)	3.143(4)	111(8)	F11 [$-x, -y+1, -z$]

band is observed at 3460 cm^{-1} in the spectral region between 1700 and 4000 cm^{-1}. It is associated with the O–H vibrations of the water molecule.

Although, in the 2000–4000 cm^{-1} spectral range both the asymmetric and symmetric CH_2 and CH_3 stretching modes are expected, we did not observe any bands, except for some very low intensity features. Similarly, all other bands ascribable to the vibrational modes of the tetraethylammonium molecule are very week, see e.g. σ(C–C–N) in Fig. 4a, and only a few among the numerous expected bands could have been localized in the spectrum. This unusual phenomenon is observed also for other $(N(C_2H_5)_4)[Ln(hfa)_4(H_2O)]$ type complexes and is related to the centrosymmetricity of the crystal [19].

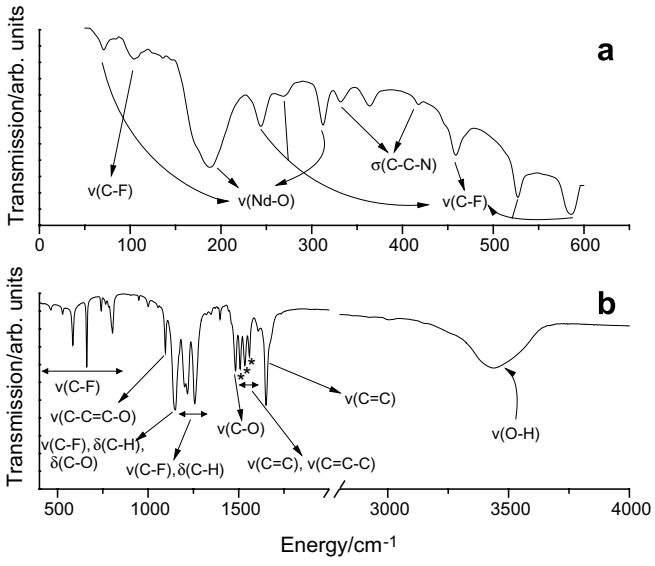


Fig. 4. (a) FIR and (b) NIR spectrum of the $(N(C_2H_5)_4)[Nd(hfa)_4(H_2O)]$ compound at room temperature.

The single band observed at 1650 cm^{-1}, that is within the region of C=O and C=C vibrations, should be assigned to the C=C stretching mode. Similarly, in the IR spectra of the $(N(C_2H_5)_4)[Ln(hfa)_4]$ [19] or $Cr(hfa)_3$ [21] complexes, unlike in the spectra of free hexafluoroacetylacetone or trifluoroacetylacetone ligands, only one single band has been observed at 1651 cm^{-1}. The absence of any feature attributable to the C=O stretching mode, otherwise observed as the intense band at about 1700 cm^{-1} and being characteristic for the keto form, confirms the coordination of both β-diketone's oxygen atoms to the Nd^{3+} ion [22].

In the 1470–1580 cm^{-1} region the group of relatively intense bands is observed. The band centered at 1482 cm^{-1} should be assigned to the C–O stretching vibration. However, over the years there has been extensive dispute in the literature [22] on the assignment of three remaining bands of this group, marked with asterisks in Fig. 4, usually observed in the IR spectra of metal ions β-diketonate complexes. These bands, which are not characteristic for the β-diketone itself, were proposed [21] to be due to delocalisation of the π-electron in the chelate ring forming in the complex. Our assignment of these bands, given in Table 4, is in agreement with that presented in Refs. [22,23]. Comparison of the IR spectra of metal complexes with different type of β-diketonates indicates that the intensity of these bands increases with increasing distance between ketonate oxygen atoms [24]. Since in the $(N(C_2H_5)_4)[Nd(hfa)_4(H_2O)]$ compound the O···O distance is rather

Table 4
Fundamental band assignment of $(N(C_2H_5)_4)[Nd(hfa)_4(H_2O)]$

Frequency (cm^{-1})	Proposed assignments[a]
3437, vs	ν(O–H)[b]
1670, vs	ν(C═C)[b]
1609, w	δ(O–H)[b]
1560, s	ν(C–C═C)[b]
1535, s	ν(C═C)[b], [ν(C–C–C)[b]]
1515, s	ν(C═C–C)[b]
1482, s	ν(C–O)[b], [σ(H–C–H/CH_2 + CH_3) [c]]
1460, w	δ(C–H)[b], ν(C–O)[b], σ(H–C–H/CH_3)[c]
1443, vw	[σ(H–C–H/CH_2 + CH_3) [c]]
1398, m	[ω(H–C–H/CH_3)[c]]
1348, vw	ω(H–C–H/CH_2 + CH_3)[c]
1260, vs	ν(C–F)[b], δ(C–H)[b]
1219, vs	ν(C–F)[b],δ(C–H)[b]
1198	δ(C–H)[b], ν(C–O)[b], ν(C–F)[b]
1146, w	ν(C–F)[b], δ(C–H)[a], δ(C–O)[b]
1099, vs	δ(C–F)[b], ν_s(C–C═C–O)[b], ν(C–N)[c]
1003, w	ν(C–O)[a], ν(C–C)[b], [c], ν(C–N)[c]
1003, w	ν(C–O)[a], ν(C–C)[b,c], ν(C–N)[c]
951, w	ν(C═C–C)[b], ν(C–O)[b]
801, m	δ(C–H) [b], ν(C–C)[b], ν(N–C)[c]
781, w	ν(C–F)[b], ν(C–N)[c]
765, w	ν(C–F)[b], ν(C–H)[b]
743, w	ν(C–F)[b]
663, s	ν(C–F)[b]
589, m	δ(C–F)[b]
529, w	combination band involving ν(Nd–O)[b], ν(C–F)[b]
459, w	combination band involving ν(Nd–O)[b]
417, w	σ(C–C–N)[c]
365, vw	τ(C–C–N)[c]
332, vw	τ(C–C–N)[c], ν(C–F)[b]
312, w	ν(C–F)[b], γ(C–CF_3)[b]
270, w	ν(C–F)[b]
244, m	ν(C–F)[b], ν(Nd–O)
190, bm	ν(C–F)[b], (ν(Nd–O)−171 cm^{-1}), [ring deformation]
105, w	ν(Nd–O)
70, w	γ(C–F)[b]

[a] s – strong, vs – very strong, m – medium, w – weak, vw – very weak, b – broad, ν – stretching, δ – in-plane bending, γ – out-of-plane bending, τ – twisting mode, ω – wagging mode, σ – scissoring mode; the assignments which are not unambiguous are given in the square brackets.
[b] $[Nd(hfa)_4 \cdot H_2O]^-$.
[c] $[N(C_2H_5)_4]^+$.

long (~2.82 Å), one observes in the IR spectrum three quite intense peaks at 1510 cm^{-1}, 1545 cm^{-1}, and 1570 cm^{-1}. This reveals the relatively high delocalisation of the π-electron and the enhancement of the double character of the C═C bond.

In the 400–1300 cm^{-1} spectral range the abundance of week bands, most of them corresponding to the C–F and C–N vibrations, is observed. The band at 1142 cm^{-1} is attributed to the CH in-plane bending mode, whereas the very strong band at 1187 cm^{-1} is assigned to the out-of-plane asymmetric CF_3 stretching mode. The strong band at 1099 cm^{-1} is due to the ν_s(C–C═C–O) coupled to the ν(C–F) mode.

Most of the bands at energy lower than 600 cm^{-1} can be assigned to the ν(C–F) as well as the δ(C–C–N) vibrations occurring within the counter ion. The expected intensive bands due to the metal–oxygen stretching modes are very weak in the recorded spectrum, which results from the presence of CF_3 groups. This phenomenon has been already reported by Nakamoto [24] and confirmed by Liang et al. [22] for lanthanide β-diketonates. It was ascribed to the strong positive inductive effect of the CF_3 groups strengthening the C═C bonds and weakening the metal–oxygen bonds.

3.3. Differential scanning calorimetry

In Fig. 5 two DSC curves measured for the $(N(C_2H_5)_4)[Nd(hfa)_4(H_2O)]$ are shown. They have been obtained when the sample was first heated to 460 K and then cooled to 170 K, under the same experimental conditions.

The DSC measurement does not reveal any low-temperature phase transition. However, two first-order phase transitions are found at above room temperature, as is indicated by the single peak at 297 K and the composed peak at ca. 405 K observed on DCS curve on heating.

The first up-temperature DSC scan, Fig. 5a, exhibits only one broad endothermic peak at approximately 361 K, corresponding to the loss of the water molecule. The down-temperature DSC curve (Fig. 5b) reveals the structural phase transition occurring at 297 K. This first-order type transition turns out to be characteristic for the anhydrous $(N(C_2H_5)_4)[Ln(hfa)_4]$ type compounds [19]. Hence, its occurrence implies that the anhydrous $(N(C_2H_5)_4)[Nd(hfa)_4]$ complex, which is formed after loosing of water molecule at 360 K, is isostructural with its lanthanide analogous. The compound melts at 408 K and just below this temperature another anomaly is observed on the

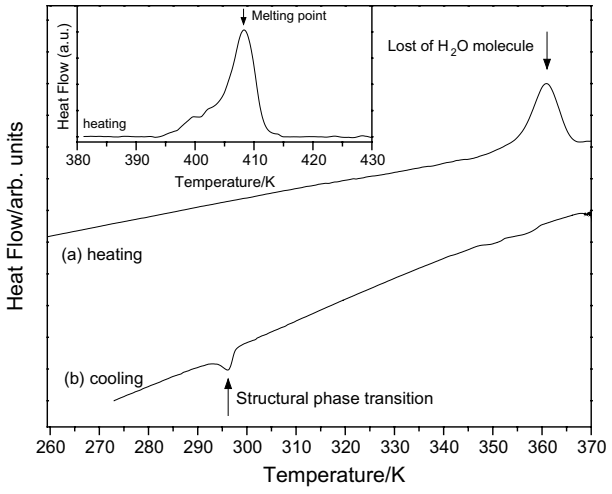


Fig. 5. Differential Scanning Calorimetry up-temperature (a) and down-temperature (b) curves recorded for $(N(C_2H_5)_4)[Nd(hfa)_4(H_2O)]$ in the 170–420 K temperature range. The inset shows the anomalies observed on the heating curve at temperatures close to the melting point.

heating DSC curve (inset in Fig. 5). This feature may be also associated with the structural phase transition and it has been observed, similarly as that at 361 K, in all other hitherto studied anhydrous $(N(C_2H_5)_4)[Ln(hfa)_4]$ complexes [19]. The thermal data determined by the DSC measurements are summarised in Table 5.

3.4. Absorption spectra

In Fig. 6 the survey absorption spectrum recorded at 298 K in the 3500–30 000 cm^{-1} range, is shown. The observed lines result from the intraconfigurational $4f^3 \rightarrow 4f^3$ transitions from the Stark components of the ground $^4I_{9/2}$ multiplet to the crystal-field levels of the excited $^{2S+1}L_J$ multiplets of the Nd^{3+} ion. The SLJ labels of terminal levels are indicated in Fig. 6. The lines occurring in the 3800–4600 cm^{-1} spectral range may result from Nd^{3+} $^4I_{9/2} \rightarrow {}^4I_{13/2}$ transitions expected in this region, or may be due to overtones and combinations of vibrational bands.

In 4.2 K spectrum (inset (b) in Fig. 6) the $^4I_{9/2} \rightarrow {}^2P_{1/2}$ transition is observed as a single, sharp peak at 23312 cm^{-1}, with a FWHM of 6 cm^{-1}. This is indicative of a single site occupancy of Nd^{3+} ions, in accordance with the crystal structure data. Due to the low symmetry of the Nd^{3+} ion environment the absorption spectrum is dominated by electronic origins and vibronic lines are not observed.

Since, there is one water molecule in the first Nd^{3+} coordination sphere, the emission from the excited states is very efficiently quenched by the multiphonon relaxation process with participation of OH vibrations. Thus the five crystal-field components resulting from the splitting of the $^4I_{9/2}$ ground multiplet could not be experimentally determined from emission spectra. However, from analysis of the hot bands observed at 298 K in the region of the $^4I_{9/2} \rightarrow {}^4F_{3/2}$ and $^4I_{9/2} \rightarrow {}^2P_{1/2}$ absorption transitions, the three crystal-field components of the $^4I_{9/2}$ ground multiplet could be assigned at 204, 355 and 426 cm^{-1}.This relatively large splitting of the ground multiplet indicates rather strong CF effect in the studied compound.

The edge of broad and very intense bands, attributed to the ligand absorption transitions, is observed above 28 000 cm^{-1}. These bands totally obscure the f–f transitions occurring in this range of the spectrum.

Table 5
Thermal data (onset, peak temperature and energy) obtained by Differential Scanning Calorimetry for the $(N(C_2H_5)_4)[Nd(hfa)_4(H_2O)]$

Onset (K)	Peak from–to (K)	Energy (J g^{-1})
297	291–298	0.93
355	346–367	17.47
403	391–414	55.70

3.5. f–f transition intensities

The experimental intensities of the induced electric dipole transitions are analyzed in terms of the Judd–Ofelt theory [25,26], whereas the theoretical calculations of 4f–4f intensities are performed using the procedure proposed by de Sá et al. [27] The experimental dipole strengths of transitions from the ground $^4I_{9/2}$ multiplet to the excited states have been determined from the unpolarized room

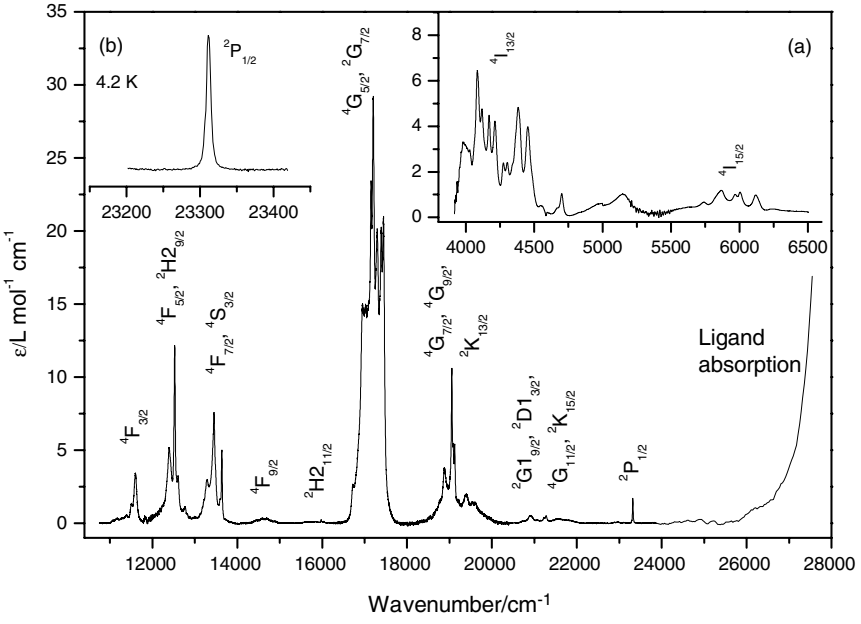


Fig. 6. UV–Vis electronic absorption spectrum recorded at 298 K for $(N(C_2H_5)_4)[Nd(hfa)_4(H_2O)]$ monocrystal. The inset (a) shows the absorption transitions in the IR spectral region. All transitions start from the $^4I_{9/2}$ ground state of Nd^{3+} and the terminal multiplets are labeled in the figure. The inset (b) shows the $^4I_{9/2} \rightarrow {}^2P_{1/2}$ transition recorded at 4.2 K.

temperature absorption spectrum measured for the random orientation of the crystal. The observed absorption bands were integrated and the dipole strengths (D) expressed in the squared Debye units (D^2) ($D = 3.3356 \times 10^{-30}$ Cm) were determined from the equation

$$D = \frac{9.188 \cdot 10^{-3}}{C \cdot d} \int \frac{A(\bar{\nu})}{\bar{\nu}} d\bar{\nu}, \quad (1)$$

where C is the molar concentration (mol l^{-1}) of the neodymium ions in the crystal, d – the optical path length (cm), A – the absorbance ($A = -\log(I/I_0)$) and $\bar{\nu}$ – the wavenumber (cm^{-1}). All transitions observed in the analyzed region of the spectrum are the induced electric dipole transitions. The assignment of absorption transitions observed in 10 000–25 000 cm^{-1} region and their experimental dipole strengths are listed in Table 6.

According to the Judd–Ofelt theory, the intensity of the lines resulting from the electric dipole transitions, is described in terms of three phenomenological intensity parameters Ω_λ, which are related to D in Eq. (1) as

$$D = \frac{10^{36}}{2J+1} \chi_{ed} e^2 \sum_{\lambda=2,4,6} \Omega_\lambda |\langle \mathrm{SLJ}|U^{(\lambda)}|S'L'J'\rangle|^2 \quad (2)$$

where the correction factor for bulk refractivity χ_{ed} is defined as $\chi_{ed} = \frac{(n^2+2)^2}{9n}$ and, for the assumed value of an average index of refraction $n = 1.5$, typical for rare-earth β-diketonate complexes [27], $\chi_{ed} = 1.34$. The factor 10 [36] converts the esu cm units into squared Debye (D^2) units, e is the elementary charge (4.803×10^{-10} esu), $(2J+1 = 10)$ is the degeneracy of the ground state, and $|\langle \mathrm{SLJ}|U^{(\lambda)}\ |S'L'J'\rangle^2|$ are the squared reduced matrix elements. We have applied the reduced matrix elements calculated on the basis of free-ion parameters obtained from the crystal-field analysis of the investigated complex [28]. In the case of overlapping transitions, the sum of the appropriate reduced matrix elements of the component multiplets was taken as the reduced matrix element.

The Ω_λ parameters have been determined by a least-squares adjustment of $\sum_{i=1-n}(D_{\mathrm{exp}}(i) - D_{calc}(i))^2$, where $D_{\mathrm{exp}}(i)$ and $D_{\mathrm{calc}}(i)$ are the experimental and calculated dipole strengths of the ith transition. The fitting yields $\Omega_2 = (15.3 \pm 1.1) \times 10^{-20}$ cm^2, $\Omega_4 = (7.3 \pm 1.5) \times 10^{-20}$ cm^2 and $\Omega_4 = (3.9 \pm 1.3) \times 10^{-20}$ cm^2 with the r.m.s. deviation of 79×10^{-6} D^2. The calculated dipole strengths are given in Table 6.

Similarly as for tris β-diketonates complexes [27], the high value of Ω_2 parameter resulted from our calculations for $(N(C_2H_5)_4)[Nd(hfa)_4(H_2O)]$. The dominance of the Ω_2 intensity parameter may be related to the hypersensitive nature of the $^4I_{92} \rightarrow (^4G_{5/2} + {}^2G_{7/2})$ transition, suggesting also the important contribution of the dynamic coupling mechanism to the transition intensities [29,30].

To gain the deeper insight into the mechanism governing the f–f intensities, we have calculated the intensity parameters Ω_λ using the theoretical expression [27]

$$\Omega_\lambda = (2\lambda+1) \sum_{t,\mathrm{p}} \frac{|B_{\lambda \mathrm{tp}}|^2}{(2t+1)}, \quad (3)$$

where the $B_{\lambda \mathrm{tp}}$ intensity parameters are given by

$$B_{\lambda \mathrm{tp}} = \frac{2}{\Delta E} \langle r^{t+1} \rangle \theta(t,\lambda) \gamma_{\mathrm{p}}^t - \left[\frac{(\lambda+1)(2\lambda+3)}{(2\lambda+1)}\right]^{1/2} \times \langle r^\lambda \rangle (1-\sigma_\lambda) \langle f \| C^{(\lambda)} \| f \rangle \Gamma_{\mathrm{p}}^t \delta_{\mathrm{t},\lambda+1}. \quad (4)$$

In Eq. (4) ΔE is the energy difference between the barycenters of the excited $4f^{N-1}$ 5d and ground $4f^N$ configuration, $\theta(t,\lambda)$ – a numerical factor, σ_λ is a screening factor, $C^{(\lambda)}$ – a Racah tensor operator of rank λ and $\delta_{\mathrm{t},\lambda+1}$ – the Kronecker delta function [27]. The quantities γ_{p}^t and Γ_{p}^t account for the dependence of transition intensities on geometry and chemical environment of the lanthanide ion; Γ_{p}^t is given by

$$\Gamma_{\mathrm{p}}^t = \left(\frac{4\pi}{2t+1}\right)^{1/2} \sum_j \frac{\alpha_j}{R_j^{t+1}} Y_{\mathrm{p}}^{t^*}(\theta_j, \varphi_j), \quad (5)$$

where α_j is the isotropic polarizability of the jth ligand atom at distance R_j and Y_{p}^t are the spherical harmonics of rank t [27]. According to the simple overlap model (SOM) [31] the parameters γ_{p}^t can be expressed as

$$\gamma_{\mathrm{p}}^t = \left(\frac{4\pi}{2t+1}\right)^{1/2} e^2 \sum_j \rho_j (2\beta_j)^{t+1} \frac{g_j}{R_j^{t+1}} Y_{\mathrm{p}}^{t^*}(\theta_j, \varphi_j), \quad (6)$$

where ρ_j is the magnitude of the total overlap between the 4f wave functions and the ligand ones, $\beta_j = 1/(1 \pm \rho_j)$ and

Table 6
Measured (D_{exp}) and calculated (D_{calc}) dipole strengths for absorption transitions of $(N(C_2H_5)_4)[Nd(hfa)_4(H_2O)]$

Transition $^4I_{9/2} \rightarrow {}^{2S'+1}L'_{J'}$	Wavenumber (cm^{-1})	$D_{\mathrm{exp}}/\times 10^6$ (D^2)	$D^{\mathrm{a}}_{\mathrm{calc}}/\times 10^6$ D^2	$D_{\mathrm{exp}} - D_{\mathrm{exp}}/\times 10^6$ D^2	$D_{\mathrm{exp}}/D_{\mathrm{calc}}$
$^4F_{3/2}$	11 380	526	586	−60	0.90
$^4F_{5/2} + {}^2H2_{9/2}$	12 520	1167	1220	−53	0.96
$^4F_{7/2} + {}^4S_{3/2}$	13 430	919	902	17	1.02
$^4F_{9/2}$	14 682	78	75	3	1.04
$^2H2_{11/2}$	15 834	28	19	9	1.45
$^4G_{5/2} + {}^2G_{7/2}$	17 170	6040	6050	−10	0.99
$^4G_{7/2} + {}^4G_{9/2} + {}^2K_{13/2}$	19 210	1122	959	163	1.17
$^2G1_{9/2} + {}^2D1_{3/2} + {}^4G_{11/2} + {}^2K_{15/2}$	21 340	136	153	−17	0.88
$^2P_{1/2}$	23 320	31	93	−62	0.33

[a] Judd–Ofelt parameters used for obtaining of D_{calc} values are: $\Omega_2 = (15.3 \pm 1.1) \times 10^{-20}$ cm^2, $\Omega_4 = (7.3 \pm 1.5) \times 10^{-20}$ cm^2 and $\Omega_4 = (3.9 \pm 1.3) \times 10^{-20}$ cm^2. The r.m.s. value is 79×10^{-6} D^2.

g_j are the charge factors. It may be assumed that overlap ρ_j vary with the distance as $\rho_j = 0.05(R_0/R_j)^{3.5}$, where R_0 is the smallest among the R_j's. Further details pertinent to this model may be found in Ref. [27] and references cited therein.

For the Eu^{3+} ion the values of the screening factors in Eq. (4) were assumed as $\sigma_2 = 0.6$, $\sigma_4 = 0.139$, and $\sigma_6 = 0.1$ [30]. A somewhat larger value of σ_2 is expected for Nd^{3+}. The σ_2 screening factors computed by the Sternheimer method equal to 0.686 and 0.714 for Eu^{3+} and Nd^{3+}, respectively [32]. Thus, in our calculations we use $\sigma_2 = 0.62$ for Nd^{3+} ion. The numerical values of $\langle r^k \rangle$ radial integrals were taken from Ref. [33] and for ΔE we assumed the value of 55 000 cm^{-1} [34].

The charge factors g_j for coordination compounds usually differ significantly from the nominal valence of the ligating atoms. As is discussed in Ref. [36], g_j should be rather interpreted as a measure of the "capacity" of an atomic species to donate charge to the formation of a bond in a molecule and may be identified with an ionic specific valence (ISV). Therefore, in our calculations the g_j were treated as adjustable parameters to be optimized until the best agreement between the calculated and experimental Ω_λ intensity parameters is obtained. The polarizabilities α_j, which depend not only on the type of atoms, but also on the chemical group in which it is present, as well as on its geometry and the next nearest neighbors, were also treated as variable parameters in fitting the experimental Ω_λ intensity parameters. Each Ω_λ depends, however, on both g_j and α_j. Note that the even rank crystal-field parameters of the SOM model, which describe the Stark splitting of the SLJ manifolds, are given by $B^k_q = \langle r^k \rangle \gamma^k_q$ (where γ^k_q are defined by Eq. (6)) and thus depend parametrically on g_j only, assuming that the relation $\rho_j = 0.05(R_0/R_j)^{3.5}$ holds for the overlap [27].

The CF parameters B^k_q can be related to quadratic rotational invariants $s_k{}^2$ (Ref. [35]):

$$s_k^2 = (1/(2k+1)) \sum_{q=-k}^{q=k} |B_q^k|^2 \tag{7}$$

and thus, in turn, to the quadratic moments of the multiplets, $(\sigma_2(\mathrm{SLJ}))^2$,

$$(\sigma_2(\mathrm{LSJ}))^2 = (1/(2J+1) \sum_{k=2,4,6} s_k^2 \langle \mathrm{LSJ} \| C^{(k)} \| \mathrm{LSJ} \rangle^2, \tag{8}$$

where $\langle \mathrm{SLJ} \| C^{(k)} \| \mathrm{SLJ} \rangle$ is a reduced matrix element. Finally, the quadratic moment, $(\sigma_2(\mathrm{SLJ}))^2$, is defined as [35]

$$(\sigma_2(\mathrm{SLJ}))^2 = (1/(2J+1) \sum_i [E_i(\mathrm{SLJ}) - E^0(\mathrm{SLJ})]^2 \tag{9}$$

where E^0 is the mean energy of the SLJ multiplet.

The splitting of the $^4F_{3/2}$ multiplet is usually easily available experimentally In the case of Nd^{3+} ion. For the studied compound the two Stark components of $^4F_{3/2}$ are observed at 11 500 and 11 597 cm^{-1}. From these, the $(\sigma_2(\mathrm{SLJ}))^2$ moment is obtained as 1176 cm^{-1}. For the $^4F_{3/2}$ multiplet only the $\langle {}^4F_{3/2} \| C^{(2)} \| {}^4F_{3/2} \rangle$ matrix element has non-zero value (0.1144 – calculated for the free-ion parameters resulted from CF analysis [28]. Substituting of $(\sigma_2(\mathrm{SLJ}))^2$ and the matrix element value into Eq. (8) yields $s_2 = 202.8$ cm^{-1}. Hence, the charge factors g_i can be optimized by minimizing the difference between thus determined experimental s_2 value and those calculated from Eqs. (7) and (6).

In our calculations for $(N(C_2H_5)_4)[Nd(hfa)_4(H_2O)]$ we use the axis system centered at Nd^{3+} ions with the z-axis along the Nd–O(9) direction (O(9) is the water molecule oxygen) and the y-axis coinciding with the Nd–O(1) bond. The spherical coordinates of ligating atoms forming the first coordination sphere in this axis system are listed in Table 7.

The charge factors g_j and polarizabilities α_j were optimized by least-square fittings of the calculated and experimental Ω_λ intensity parameters as well as the Stark splittings of the $^4F_{3/2}$ multiplet. Initially, we assume g_1 (α_1) for each β-diketonate oxygen and g_2 (α_2) for water molecule oxygen. However, this assumption yields reasonable agreement for Ω_6 and $^4F_{3/2}$ splitting only, whereas Ω_2/Ω_4 ratio was significantly lower than the experimental ratio. To obtain a good agreement with the experiment for all Ω_λ parameters and the $^4F_{3/2}$ splitting, and particularly to reproduce the high value of Ω_2, it was necessary to distinguish the two oxygen atoms, O(3) and O(8). Thus we allow the polarizablilities for these atoms to take on values different from those for remaining β-diketonate's oxygens. To avoid, however, the pitfall of overparameterisation (the number of parameters exceeding the number of observables), we arbitrary fix the polarizability of water molecule oxygen at the value of 4.0, typical for Eu^{3+} tris complexes [36]. Thus, in the final procedure a total of four parameters were varied and determined simultaneously. The results are listed in Table 8. In Table 9 the experimental and calculated Ω_λ intensity parameters as well as the s_2 rotational invariants are listed.

The agreement between calculated and experimental Ω_λ and s_2 parameters so excellent, should not be overvalued, since four adjustable parameters were fitted to four experimental quantities. More meaningful is to comment shortly on the g_j and α_1 values. The g_j determine almost exclusively

Table 7
Spherical coordinates of the bonding β-diketone's oxygens (O1–08) and water molecule oxygen (O9) in coordination system centered at Nd^{3+} ion, with z and y axis coincide with Nd–O(9) and Nd–O(1) bonds, respectively

Ligand	R (Å)	θ (°)	φ (°)
O1	2.453	111.32	90.00
O2	2.437	137.52	173.67
O3	2.469	72.01	−48.02
O4	2.501	68.68	26.40
O5	2.438	135.64	3.99
O6	2.479	125.73	−92.42
O8	2.471	72.40	−141.77
O9	2.570	0.00	0.00

Table 8
Optimized values of charge factors (g) and polarizabilities (α) obtained for $(N(C_2H_5)_4)[Nd(hfa)_4(H_2O)]$

Ligand	G	α (Å^3)
O1, O2, O4 − O7	0.78	4.25
O3, O8	0.78	2.32
O9	0.52	4.0

The O1–O8 oxygen atoms are from β-diketone's ligands, whereas the O9 atom is from the coordinated water molecule.

Table 9
Experimental and theoretical Ω_λ ($\times 10^{-20}$ cm^2) and s_2 (in cm^{-1})

	Experimental	Theoretical
Ω_2	15.3	15.4
Ω_4	7.3	7.3
Ω_6	3.9	3.8
s_2	202.8	201.7

the values of Ω_6 and s_2. The obtained charge factors of 0.78 for β-diketonate oxygen atoms are very close to values of 0.88 and 0.87 determined for $Eu(tta)_3 \cdot 2H_2O$ and $Eu(btfa)_3 \cdot 2H_2O$ [36]. The charge factor of 0.52 for oxygen from the water molecule is lower as compared to 1.48 and 1.24 determined experimentally [36], but not far from the values of 0.61 and 0.71 calculated theoretically, for the europium tris complexes [36]. Thus the charge factors g_1 and g_2 seems to be determined reliably.

Also the resulting values of polarizabilities fall in the physically acceptable range and do not deviate from those reported earlier for europium tris β-diketonate complexes [36]. An intriguing question is, however, the reason for the lower values obtained for the polarizabilities for O(3) and O(8) atoms, as compared to the remaining β-diketonate's oxygens. We are aware that the absolute values of polarizabilities may be not well determined, since they strongly depends also, e.g. on σ_λ screening factors, however, even in a such case, the trend emerging from calculations is unambiguous and in spite of many efforts we have not been able to obtain satisfactory results, without allowing the lower α_j values for those two atoms. The answer to this question may result from inspection of the molecular structure of the complex described in previous sections. Both the O(3) and O(8) atoms participate in formation of the H–O–H···O–Nd hydrogen bonds with water molecule coordinated to the adjacent Nd atom. This interaction may change the electron density on O(3) and O(8) atoms and, thus also their polarizabilities. Thus the β-diketonate's oxygens not bounded by hydrogen bonds have softer character as compared to O(3) and O(8). Probably, also the charge factors for those two oxygen atoms may be lower as well, however, the attempt to include this effect would lead to the number of adjustable parameters larger than that of the experimental quantities.

In Eq. (4) the first term corresponds to the forced electric dipole mechanism and the second one to the dynamic coupling mechanism. Comparison of intensity parameters $B_{\lambda tp}$ calculated for both mechanisms separately indicates, that contribution from the latter strongly dominates. Moreover, if one assumes the same polarizabilities for all β-diketonate's oxygens the contribution from the dynamic coupling mechanism decreases and the calculated Ω_2 value would be significantly lower as compared to the experimental one. It seems therefore, that the formation of hydrogen bonds is a factor responsible for the polarisation of chemical environment of Nd^{3+} ions, thus increasing the contribution from the dynamic coupling mechanism and leading to the high value of Ω_2 intensity parameter.

3.6. Structure optimization

The knowledge of the ground state geometry of the complex is required for theoretical predictions, e.g. of its electronic spectrum. For some complexes the experimental structural data are not available, for instance due to the difficulties in obtaining of X-ray quality crystals. Then the molecular structure may be predicted using theoretical methods. Moreover, it has been shown [37] than even if experimental structure is known, the use of calculated molecular structure instead of experimental one as the input geometry for the spectral calculation results in a better agreement between calculated and measured spectrum. The ground state geometry of the large lanthanide complexes can be successfully optimized using a SMLC/AM1 model (sparkle model for the calculation of lanthanide complexes within Austin model 1) [27]. However, most of the existing calculations have been performed for europium complexes. The $(N(C_2H_5)_4)[Nd(hfa)_4(H_2O)]$ complex seems to be an interesting subject for such modelling. Since the X-ray structure of this compound is available, it is possible to compare the calculated results with the experimental ones. Moreover, the presence of the coordinated water molecule affects the molecular structure of the complex. Particularly, the hydrogen bonds link two adjacent complex anions into pseudo-dimers (Fig. 2b) with a relatively short Nd–Nd distances of 5.913 Å. Thus, it is interesting to examine to what extent the molecular structure of the complex is correctly reflected by model calculations.

In the present work we use SMLC/AM1 for Nd(III) implemented within the MOPAC 6.00 program [11]. The geometry of the complex determined by X-ray diffraction was used as the input data in our calculations performed for the single $[Nd(hfa)_4(H_2O)]^-$ complex anion as well as for the $[Nd_2(hfa)_8(H_2O)_2]^{2-}$ pseudo-dimer. The results indicate that inclusion or omission of the counter ion has no noticeable influence on the geometry of the anion and in both cases the Nd–O distances are predicted with similar accuracy. However, in the calculations for the single $[Nd(hfa)_4(H_2O)]^-$ anion the bending of the chelate rings is not accurately reproduced. The obtained torsion angle between O8–Nd–O7–C16 atoms of about −15° is significantly lower than that determined by the X-ray diffraction

(−38.4°). Even worse correspondence is observed for the second ring, which was calculated to be almost flat, with the torsion angle between O3–Nd–O4–C9 atoms of about 5°, whereas the experimental value is 33.7°. Thus, though some steric effect of the water molecule is observed, our modelling suggests that this effect is not the most important one. Far better correspondence between calculated and experimental geometry is found in the calculations carried out for the pseudo-dimer. Some of the calculated Nd–O distances as well as angles and torsion angles between atoms are included in Table 2 (values in brackets). However, whereas in the real structure the both anions forming the pseudo-dimer are symmetrically equivalent, in the calculations slightly different surroundings are obtained for two Nd atoms, which therefore are denoted in Table 2 as Nd(1) and Nd(2). The Nd–O distances are predicted with a good accuracy, with an average deviation of 18 calculated values from experimental ones of 0.056 Å, and the largest difference between calculated and experimental distance equal to 0.107 Å. The agreement between the bond angles is not so good, although still acceptable. The calculated O3–Nd–O4–C9 and O8–Nd–O7–C16 torsion angles are somewhat lower compared to those determined experimentally. This probably results from the larger Nd–Nd distance (6.694 Å) resulted from calculations as compared to that of 5.913 Å found from X-ray determined structure, which decreases the steric effect. Nevertheless, the model calculations prove unambiguously that the steric hindrance between the two anions forming the pseudo-dimer, linked by hydrogen bonds, is responsible for the bending of chelate rings of the water adjoining ligands.

4. Summary

In this paper, the synthesis of a novel $(N(C_2H_5)_4)$-$[Nd(hfa)_4(H_2O)]$ (hfa = hexafluoroacetylacetonate) compound, belonging to the tetrakis (β-diketonates) type of complexes is presented. This complex crystallizes in the $P2_1/n$ space group of the monoclinic system. The neodymium ion is coordinated by nine oxygen atoms forming a distorted capped square antiprism. It is worth to notice that, to the best of our knowledge, this is only the second crystal structure reported hitherto for a tetrakis β-diketonate complex containing neodymium ions.

In contrast to other Ln^{3+}(Ln = Sm–Yb) ions, which form tetrakis(hexafluoroacetylacetone) anhydrous complexes of the $(N(C_2H_5)_4)[Ln(hfa)_4]$ type, the complex of Nd^{3+} with hfa contains one-coordinated water molecule and hence is not isostructural with its heavier lanthanide analogues. Further studies aimed at verification whether this feature is typical for all light lanthanides are currently under progress. The DSC analysis shows the loss of the water molecule at 361 K. After that the compound exhibits the first-order phase transitions at 297 K and ~403 K, typical for anhydrous $(N(C_2H_5)_4)[Ln(hfa)_4]$ type compounds.

Unexpectedly, the usually intense bands corresponding to the vibrational modes of the tetraethylammonium molecule, are very week or unobserved in the IR spectrum of the studied complex, which can be ascribed to the centrosymmetricity of the crystal. Moreover, the analysis of the IR spectra proves the coordination of both β-diketones oxygen atoms to the Nd^{3+} ion and indicates the relatively high delocalisation of the π-electron in the chelate ring forming in the metal–β-diketonate complex.

Analysis of the experimental absorption spectrum enables determination of the Ω_λ intensity parameters as: $\Omega_2 = (15.3 \pm 1.1) \times 10^{-20}$ cm^2, $\Omega_4 = (7.3 \pm 1.5) \times 10^{-20}$ cm^2 and $\Omega_6 = (3.9 \pm 1.3) \times 10^{-20}$ cm^2. The theoretical calculations indicate, that the important factor responsible for the high value of the Ω_2 parameter is formation of the hydrogen bonds by two of β-diketonate's oxygens, which leads to the polarisation of the chemical environment of Nd^{3+} ion and increases the contribution from the dynamic coupling mechanism to the $B_{\lambda tp}$ intensity parameters. The ground state geometry of the studied complex can be reasonably well predicted by means of the SMLC/AM1 method. The calculations reveal, that the bending of the chelate rings of two ligands adjoining the water molecule is caused by the steric effect arising in the pseudo-dimer, formed by two complex anions linked by the hydrogen bonds. This also leads to the shortening of the Nd–Nd distance to 5.913 Å, as compared to about 9.2–9.9 Å observed for analogous anhydrous tetrakis complexes [19].

Supplementary material

CCDC 631505 contains the supplementary crystallographic data for $(N(C_2H_5)_4)[Nd(hfa)_4(H_2O)]$. These data can be obtained free of charge via http://www.ccdc.cam.ac.uk/conts/retrieving.html, or from the Cambridge Crystallographic Data Centre, 12 Union Road, Cambridge CB2 1EZ, UK; fax: +44 1223 336 033; or e-mail: deposit@ccdc.cam.ac.uk.

Acknowledgements

This work was partially supported by the Polish Ministry of Science and Higher Education (Project No. 1 T09A 146 30) and the European Union – European Social Fund. Polish Foundation for Science Scholarship and the Max Born Scholarship are also gratefully acknowledged.

References

[1] J.C.G. Bünzli, P. Froidevaux, J.M. Harrowfild, Inorg. Chem. 32 (1993) 3306.
[2] W.W. Horrocks De Jr., P. Bolender, W.D. Smith, R.M. Supkowski, J. Am. Chem. Soc. 119 (1997) 5972.
[3] A. Lempicki, H. Samelson, Phys. Lett. 4 (1963) 133.
[4] C.W. Tang, S. A Vanslyka, Appl. Phys. Lett. 51 (1987) 2902.
[5] J.H. Burroughes, D.D.C. Bradley, A.B. Holmes, Nature 347 (1990) 539.
[6] T.J. Wenzel, in: T.C. Morrill (Ed.), Lanthanide Shift Reagents in Stereochemical Analysis, VCH Publishers, Weinheim, 1986, pp. 151–173 (Chapter 5).

[7] I.A. Hemmila, Application of Fluorescence in Immunoassays, Wiley, New York, 1991.
[8] L.M. Sweeting, A.L. Rheingold, J. Am. Chem. Soc. 109 (1987) 2652.
[9] M.J. Bennett, F.A. Cotton, P. Legzdins, J. Lippard, Inorg. Chem. 7 (1968) 1770.
[10] K. Binnemans, in: K.A. GschneidnerJr., J.-C.G. Bünzli, V. Pecharsky (Eds.), Handbook on the Physics and Chemistry of Rare Earths, vol. 35, Elsevier, Amsterdam, 2005, pp. 107–272 (Chapter 225).
[11] C.C. Bastos, R.O. Freire, G.B. Rocha, A.M. Simas, J. Photochem. Photobiol. A 177 (2006) 225.
[12] G.M. Sheldrick, SHEXSL-97, Program for the Solution of the Crystal Structures, University of Göttingen, Germany, 1997.
[13] G.M. Sheldrick, SHEXL-97, Program for the Refinement of the Crystal Structures, University of Göttingen, Germany, 1997.
[14] K. Brandenburg. DIAMOND, Version 2.1d. Crystal Impact GbR Created, November 16, 2000, Serial No. 9-48100.
[15] J.G. Leipoldt, L.D.C. Bok, S.S. Basson, A.E. Laubscher, J.S. Vollenhoven, J. Inorg. Nucl. Chem. 39 (1977) 301.
[16] X.F. Chen, S. Liu, Ch. Duan, Y. Xu, X. You, J.M. Min, N. Min, Polyhedron 17 (1998) 1883.
[17] J.G. Leipoldt, L.D.C. Bok, A.E. Laubscher, S.S. Basson, J. Inorg. Nucl. Chem. 37 (1975) 2477.
[18] J.G. Leipoldt, L.D.C. Bok, S.S. Basson, A.E. Laubscher, J. Inorg. Nucl. Chem. 38 (1976) 1477.
[19] A. Mech, A. Pietraszko, K. Gofryk, W. Ryba-Romanowski, unpublished work.
[20] T.L. Brown, H.E. LeMay Jr., Chemistry: The Central Science, second ed., Prentice-Hall, New Jersey, 1981, p. 191.
[21] S.F. Tayyari, T.H. Zeegers- Huyskens, J.L. Wood, Spectrochim. Acta A 35 (1979) 1289.
[22] C.Y. Liang, E.J. Schimitschek, J.A. Trias, J. Inorg. Nucl. Chem. 32 (1970) 811.
[23] S. Pinchas, B.L. Silver, I. Laulicht, J. Chem. Phys. 46 (1967) 1506.
[24] K. Nakamoto, Infrared Spectra of Inorganic and Coordination Compounds, Wiley, New York, 1964.
[25] B.R. Judd, Phys. Rev. 27 (1962) 750.
[26] G.S. Ofelt, J. Chem. Phys. 37 (1962) 511.
[27] G.F. de Sá, O.L. Malta, C. de Melo Donegá, A.M. Simas, R.L. Longo, P.A. Santa-Cruz, E.F. da Silva Jr., Coord. Chem. Rev. 196 (2000) 165.
[28] A. Mech, Z. Gajek. M. Karbowiak, C. Rudowicz, unpublished work.
[29] R.D. Peacock, Struct. Bond. 22 (1975) 83.
[30] O.L. Malta, M.A. Couto dos Santos, L.C. Thompson, N.K. Ito, J. Lumin. 69 (1996) 77.
[31] O.L. Malta, Chem. Phys. Lett. 87 (1982) 27.
[32] R.P. Gupta, S.K. Sen, Phys. Rev. A 7 (1973) 850.
[33] J.P. Desclaux, A.J. Freeman, J. Magn. Magn. Mater. 8 (1978) 119.
[34] L. van Pieterson, M.F. Reid, R.T. Wegh, S. Soverna, A. Meijerink, Phys. Rev. B 65 (2002) 045113.
[35] Y.Y. Yeung, Invariants and Moments, in: D.J. Newman, B. Ng (Eds.), Crystal Field Handbook, Cambridge University Press, 2000, pp. 160–175.
[36] O.L. Malta, H.J. Batista, L.D. Carlos, Chem. Phys. 282 (2002) 21.
[37] H.J. Batista, A.V.M. de Andrade, R.L. Longo, A.M. Simas, G.F. de Sá, L.C. Thompson, J. Lumin. 72–74 (1997) 159.

Available online at www.sciencedirect.com
ScienceDirect
Polyhedron 27 (2008) 406–410
POLYHEDRON
www.elsevier.com/locate/poly

Imidazole-based bifunctional chelates for the "*fac*-$[Re(CO)_3]^+$" core

Zenixole R. Tshentu [a,*], Thomas I.A. Gerber [b], Ryan Walmsley [a], Peter Mayer [c]

[a] *Department of Chemistry, Rhodes University, P.O. Box 94, Grahamstown 6140, South Africa*
[b] *Department of Chemistry, Nelson Mandela Metropolitan University, P.O. Box 77000, Port Elizabeth 6031, South Africa*
[c] *Department of Chemistry, Ludwig-Maximilians University, D-81377 München, Germany*

Received 14 September 2007; accepted 27 September 2007
Available online 5 November 2007

Abstract

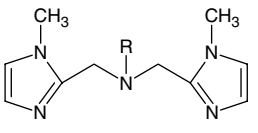
Three monocationic rhenium(I) complexes of the type $[Re(CO)_3(L)]Br$, containing the bis-imidazole tridentate ligands bis-(2-(1-methylimidazolyl)methyl)amine (L^1), bis-(2-(1-methylimidazolyl)methyl)aminoethanol (L^2) and bis-(2-(benzimidazolyl)ethyl)sulfide (L^3), were prepared and characterized by ^1H NMR and IR spectroscopy. The complex salt $[Re(CO)_3(L^2)]Br$ (**2**) was also characterized by X-ray crystallography. The structure consists of discrete monocationic monomers with a *fac*-$[Re(CO)_3]^+$ coordination unit, and the remaining three sites are occupied by one amine and two imidazolyl nitrogen donor atoms.
© 2007 Elsevier Ltd. All rights reserved.

Keywords: *fac*-$[Re(CO)_3]^+$; Tridentate; Imidazole; Crystal structure

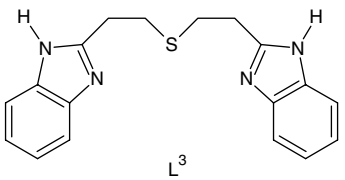
1. Introduction

The widespread interest in the development of rhenium radiopharmaceuticals is a direct result of the ideal nuclear properties of the $^{186/188}Re$ isotopes (strong β-emission energies of 1070 keV and 2120 keV, and long half-lives of 90 h and 17 h, respectively) which are suitable for targeted radiotherapy of cancers [1–3]. Recently, the interest in the chemistry of the *fac*-$[M(CO)_3]^+$ (M = Tc and Re) complexes has accelerated research in this field due to the easy availability of the $[M(OH_2)_3(CO)_3]^+$ precursor, which can be obtained directly from MO_4^- in aqueous solution [4,5]. Its convenient synthesis and quantitative preparation is in line with the principles of radiopharmaceutical synthesis, which are based on "instant kit" formulation and clean radio-labelling procedures from accessible radioisotopes of these metals [6,7]. The substitutional lability of the coordinated water molecules allows for the preparation of a range of *fac*-$[Re(CO)_3]^+$ complexes which are both thermodynamically and kinetically stable. However, this robust core only possesses three coordination sites to exploit with functional groups, and most work has been done with tridentate ligands to further enhance the kinetic inertness of the low-spin d^6 system [8,9]. The real challenge still rests in the adaptation of biomolecules to act as carrier groups in order to achieve the cellular specificity and localization of the complexes *in vivo*.

We have synthesized the tridentate imidazole-containing ligands bis-(2-(1-methylimidazolyl)methyl)amine (L^1), bis-(2-(1-methylimidazolyl)methyl)aminoethanol (L^2) and bis-(2-(benzimidazolyl)ethyl)sulfide (L^3) to study their coordination behaviour with rhenium(I), by using $[Re(OH_2)_3(CO)_3]Br$ or $(NEt_4)_2[ReBr_3(CO)_3]$ as precursor compounds. The two imidazole rings can be viewed as primitive models for multi-histidine coordination in biological systems [10].



$R^1 = H$ (L^1); $R^2 = CH_2CH_2OH$ (L^2)



L^3

* Corresponding author. Tel.: +27 46 603 8846; fax: +27 46 622 5109.
E-mail address: z.tshentu@ru.ac.za (Z.R. Tshentu).

0277-5387/$ - see front matter © 2007 Elsevier Ltd. All rights reserved.
doi:10.1016/j.poly.2007.09.022

2. Experimental

2.1. Reagents and instrumentation

$Re(CO)_5Br$, 1-methylimidazole, *o*-phenylenediamine, 3,3′-thiodipropionic acid, 2-aminoethanol, deuterated chloroform, and deuterated dimethylsulfoxide were purchased from Sigma–Aldrich and used as received. The reagents 1-methyl-2-aminomethylimidazole dihydrochloride [11], 1-methyl-2-imidazolecarboxaldehyde [11], 2-chloromethyl-1-methylimidazole hydrochloride [12], $[Re(OH_2)_3(CO)_3]Br$ [13] and $(NEt_4)_2[ReBr_3(CO)_3]$[14] were synthesized using published procedures. The ligands L^1, L^2 and L^3 were prepared from methods in the literature [11,15,16]. Solvents were purified and dried before use.

IR spectra were recorded in KBr pellets on a Perkin–Elmer spectrum 200 FTIR spectrophotometer. ^1H HMR spectra were recorded by using either a Bruker EMX-400 MHz or a Bruker AMX-300MHz NMR spectrometer. All chemical shifts are relative to TMS. Reversed phase HPLC separations were performed at a flow rate of 1 ml/min on a Phenomenex Luna 10m C18 column, gradient on an Agilent HP1100 LC-MSD (consisting of a quaternary pump, a degasser, a DAD detector, an 1100 MSD and a ChemStation for data acquisition and processing). Conductivity measurements (in units $cm^2\,\Omega^{-1}\,mol^{-1}$) were carried out with 10^{-3} M solutions in DMF at 293 K on a Phillips PW9509 digital conductometer. Elemental analyses were carried out by the Department of Chemistry at the University of Cape Town.

2.2. Synthesis

2.2.1. $[Re(CO)_3(L^1)]Br$ (1)

Under a nitrogen blanket, a mixture of $(NEt_4)_2[ReBr_3(CO)_3]$ (100 mg, 171 μmol) and L^1 (56 mg, 179 μmol) was dissolved in 10 ml of methanol. The solution was heated to reflux for an hour, and then 2 ml of water was added. The solution was allowed to cool to room temperature, and was left to stand for 3 days, after which a white precipitate was collected. It was washed with cold methanol and dried in an oven at 50 °C. Yield = 88%. *Anal.* Calc. for **1**: C, 28.11; H, 2.72; N, 12.61. Found: C, 28.23; H, 2.77; N, 12.55%. ^1H NMR (300 MHz): 3.61 (6H, s, $2\times CH_3$); 4.48 (4H, s, $2\times CH_2$); 7.06 and 7.23 (4H, 2xd, Ar-*H*) ppm. IR (cm^{-1}): *ν*(N–H) 2965; *ν*(C≡O) 1885, 2005, 2024; *ν*(C=N) 1621; *ν*(C=N–C=C) 1458. Conductivity (10^{-3} M) = 75.6.

2.2.2. $[Re(CO)_3(L^2)]Br$ (2)

The synthetic procedure was similar to that for **1** above, except that 1 ml of water was added, and the solution was allowed to stand at 5 °C to deposit crystals that were suitable for X-ray analysis. Yield = 92%. *Anal.* Calc. for **2**: C, 30.05; H, 3.19; N, 11.69. Found: C, 29.98; H, 3.21; N, 11.75%. ^1H NMR (D_2O, 300 MHz): 3.47 (6H, s, H(12), H(15)); 3.82 (2H, t, H(13)); 3.98 (2H, t, H(14)); 4.52 (4H, s, H(7), H(8)); 6.86 (2H, d, Ar–H(5), H10); 7.00 (2H, d, H(4), H(11)) (see Fig. 3 for labelling). IR (cm^{-1}): *ν*(C≡O) 1895, 1930, 2025; *ν*(C=N) 1624; *ν*(CH_2–O) 1263. Conductivity (10^{-3} M) = 79.2.

2.2.3. $[Re(CO)_3(L^3)]Br$ (3)

This procedure was the same as for **1**, except that the product crystallised out at room temperature in methanol, without addition of water. Yield = 78%. Anal. Calc. for **3**: C, 37.50; H, 2.70; N, 8.33; S, 4.77. Found: C, 37.44; H, 2.76; N, 8.49; S, 4.83%. ^1H NMR (400 MHz): 3.21 (4H, t, H(6)); 3.41 (4H, t, H(5)); 7.23 (2H, t, H(2)); 7.29 (2H, d, H(1)); 7.37 (2H, t, H(3)); 7.64 (2H, d, H(4)); 13.64 (2H, s, NH) ppm (see Fig. 2 for labelling). IR (cm^{-1}): *ν*(N–H) 3385; *ν*(C=N) 1618, *ν*(C≡O) 1909, 2004, 2027; *ν*(C=N–C=C) 1460. Conductivity (10^{-3} M) = 69.7.

2.3. X-ray crystallography

A single crystal of $[Re(CO)_3(L^2)]Br$ (**2**) was used for data collection on a Nonius Kappa CCD diffractometer with graphite-monochromated Mo Kα radiation ($\lambda = 0.71073$ Å). Details of the crystal data and refinement are given in Table 1, with selected bond lengths and angles in Table 2. Unit cell and space group determinations were carried out in the usual manner [17]. The structure was solved by direct methods and refined by full-matrix least-squares procedures using SHELXL-97 [18]. Non-hydrogen atoms were refined anisotropically, and the hydrogen atoms were

Table 1
Crystal data and structure refinement data for **2**

Property	$[Re(CO)_3(L^2)]Br$ (**2**)
Chemical formula	$C_{15}H_{19}N_5O_4BrRe$
Formula weight	599.45
Temperature (K)	200(2)
Crystal system	monoclinic
Space group	$P2_1/c$
Unit cell dimensions	
a (Å)	14.4065(4)
b (Å)	9.5493(3)
c (Å)	13.8649(2)
β (°)	91.874(1)
Crystal size (mm)	$0.04\times0.06\times0.19$
Volume ($Å^3$)	1906.40(8)
Z	4
D_{calc} (Mg/m^3)	2.089
Absorption coefficient (mm^{-1})	8.500
θ Range for data collection (°)	3.2–27.5
Index ranges	$-18\leqslant h\leqslant 16$, $-12\leqslant k\leqslant 12$, $-17\leqslant l\leqslant 17$
Reflections measured	33043
Number of independent reflections [*R*]	4364 [0.031]
Number of observed reflections [$I>2\sigma(I)$]	3954
Data/restraints/parameters	4364/0/241
Goodness-of-fit on F^2	1.14
Final *R* indices [$I>2\sigma(I)$]	$R = 0.0226$, $wR_2 = 0.0506$
Largest difference peak and hole ($e/Å^3$)	1.14, −0.94

Table 2
Selected bond lengths (Å) and bond angles (°) for **2**

Re–C(1)	1.922(3)	N(2)–C(5)	1.381(4)
Re–C(2)	1.913(3)	N(2)–C(6)	1.346(4)
Re–C(3)	1.909(4)	N(4)–C(9)	1.319(4)
Re–N(1)	2.154(3)	N(4)–C(11)	1.381(4)
Re–N(3)	2.302(3)	N(5)–C(9)	1.337(4)
Re–N(4)	2.154(3)	N(5)–C(10)	1.375(5)
N(1)–C(6)	1.312(4)	C(4)–C(5)	1.351(4)
N(1)–C(4)	1.381(4)	C(10)–C(11)	1.350(5)
C(1)–O(1)	1.149(4)	C(2)–O(2)	1.153(4)
N(1)–Re–N(3)	77.07(9)	N(1)–C(6)–C(7)	123.8(3)
N(3)–Re–N(4)	76.8(1)	N(4)–C(9)–C(8)	121.9(3)
N(1)–Re–N(4)	82.5(1)	Re–N(3)–C(7)	108.9(1)
C(1)–Re–C(3)	90.1(1)	Re–N(3)–C(8)	109.0(2)
N(1)–Re–C(1)	174.8(1)	Re–N(3)–C(13)	110.9(1)
N(3)–Re–C(2)	174.3(1)	Re–C(1)–O(1)	178.3(3)
N(4)–Re–C(3)	169.4(1)	Re–C(2)–O(2)	178.1(3)
N(3)–C(13)–C(14)	115.4(2)	Re–C(3)–O(3)	177.0(3)

geometrically constrained. An ORTEP view of **2** along with the atom numbering scheme is given in Fig. 3.

3. Results and discussion

3.1. Synthesis

Complexes **1**–**3** were prepared from methanolic solutions of $(NEt_4)_2[ReBr_3(CO)_3]$ and the ligands L^{1-3} in slight excess to obtain white solids as products in good yields. Small amounts of water were added for **1** and **2** to prevent the co-precipitation of NEt_4Br with the complexes. $(NEt_4)_2[ReBr_3(CO)_3]$ was rather used as starting material instead of the ideal and accessible $[Re(OH_2)_3(CO)_3]Br$, mainly to isolate and characterize the complexes at a macroscopic level. Attempts to isolate pure crystalline solids using $[Re(OH_2)_3(CO)_3]Br$ proved difficult due to the oily nature of the products that resulted under the same experimental conditions employed as above (reflux in methanol, followed by slow evaporation or cold crystallization).

However, the interaction of $[Re(OH_2)_3(CO)_3]Br$ and L^2 was studied in solution state by HPLC analyses with methanol as the mobile phase, but the chromatographic conditions were not optimised and the results are semi-quantitative. The formation of the complex (monitored using a UV detector at 254 nm) was verified by co-injection of the complex isolated at a microscopic level (RT = 2.6 min) with the reaction products. The starting materials, $[Re(OH_2)_3(CO)_3]Br$ and L^2 both showed the same retention time of 2.8 min. Interestingly, on mixing equimolar (4 μmol) amounts of these materials together in methanol in a vial and incubating at 50 °C for 15 min resulted in the formation of more than 60% of the desired complex (Fig. 1a). An almost quantitative formation was obtained on incubating the mixture at 60 °C for 1 h (Fig. 1b). This is an indication of the ease of substitution of the labile water molecules and the relevance of this ligand moiety of L^2 for coordination to $[M(OH_2)_3(CO)_3]Br$ ($M = {}^{99m}Tc$, ^{186}Re and ^{188}Re) in radiopharmaceutical preparations.

The conductivity measurements of **1**–**3** in DMF suggest 1:1 electrolytes. Conductivity readings between 65 and 90 $\Omega^{-1}\,mol^{-1}\,cm^2$ are consistent with 1:1 electrolytes in DMF [19]. Complexes **1** and **2** show a greater solubility in water than **3**, and all three complexes are soluble in polar organic solvents such as methanol, DMF, and DMSO.

3.2. Spectral characterization

In the infrared spectra of **1**–**3** three strong ν(CO) stretching bands appear in the region of 1880–2030 cm^{-1}, indicating the presence of the *fac*-$[Re(CO)_3]^+$ core [20]. Coordination of the imidazolyl nitrogens is indicated by the shifts of ν(C=N) from 1645 cm^{-1} in the free ligand (L^1) to 1620 cm^{-1} in **1**, and from 1655 to 1624 cm^{-1}, and from 1621 to 1618 cm^{-1} in **2** and **3**, respectively. This coordination-induced frequency change is typical for ring systems of this type [21,22].

In the ^1H NMR spectra of **1** and **2** the imidazole ring protons appear as two doublets, and are shifted markedly downfield relative to the free ligands (from 6.78 and 6.89 ppm to 7.06 and 7.23 ppm, respectively in **1**; and 6.76 and 6.91 ppm to 6.86 and 7.00 ppm in **2**). These signals also signify the symmetrical coordination of the imidazolyl groups to the *fac*-$[Re(CO)_3]^+$ core. The NH proton signal was absent in the spectrum of **1**, however, the coordination of the aliphatic amine nitrogen in **2** was confirmed by the significant shifts in H(13) and H(14) signals which appear as triplets at 2.89 and 3.68 ppm in the free ligand, and at 3.82 and 3.98 ppm in the complex. The signals of the methylene protons (H(7) and H(8) for **2**, see Fig. 3 for labelling) confirm the coordination of the amine nitrogen in both **1** and **2**, and appear as singlets at 3.82 and 3.81 ppm in the free ligands and at 4.48 and 4.52 ppm, respectively, in **1** and **2**. The ^1H NMR spectrum of **3** also confirms the tridentate coordination of L^3. The triplet signals of the methylene protons (H(6), see Fig. 2 for labelling) show a downfield shift from 3.04 ppm in the free ligand to 3.21 ppm, indicating the coordination of the sulfur atom; and the shift of the NH signal from 12.31 ppm in L^3 to 13.64 ppm in **3** is indicative of the coordination of the benzimidazole groups. The H(2) and H(3) proton signals appear as clearly resolved triplets at 7.23 and 7.37 ppm in the complex, but appeared as a multiplet in the free ligand (see Fig. 2); and this is also indicative of the coordination of the benzimidazolyl group.

3.3. Crystal structure

The crystallization of **2** in methanol/water gave crystals that were suitable for X-ray crystallography. The rhenium(I) ion lies in a distorted octahedral environment, with the amine and two imidazolyl nitrogen donors of L^2 in a facial arrangement, imposed by the *fac*-$[Re(CO)_3]^+$ core (Fig. 3). Ligand L^2 therefore acts as a neutral tridentate

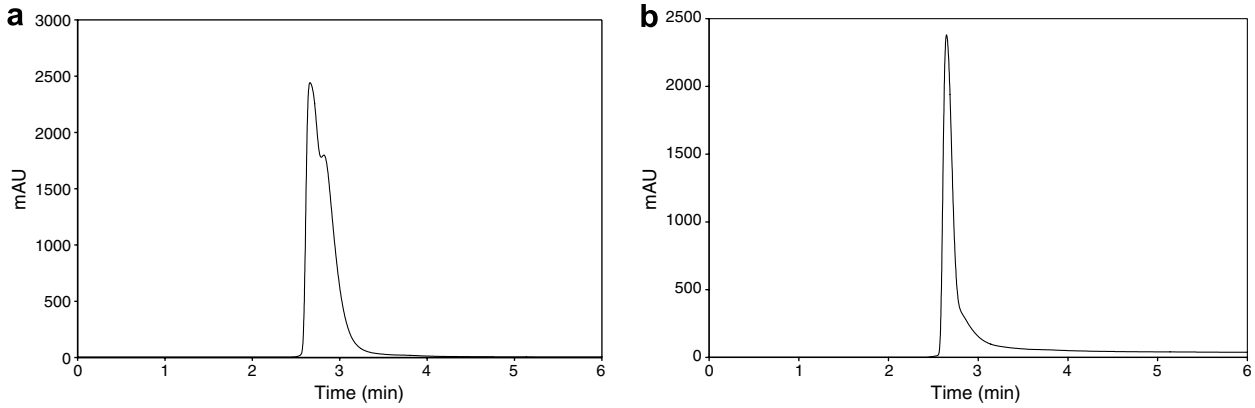


Fig. 1. The HPLC chromatograms of $[Re(OH_2)_3(CO)_3]Br + L^2$ after (a) 15 min at 50 °C (RT = 2.6 min for **2** and 2.8 for the unreacted $[Re(OH_2)_3(CO)_3]Br$ and L^2), and (b) after 1 h at 60 °C (RT = 2.6 min).

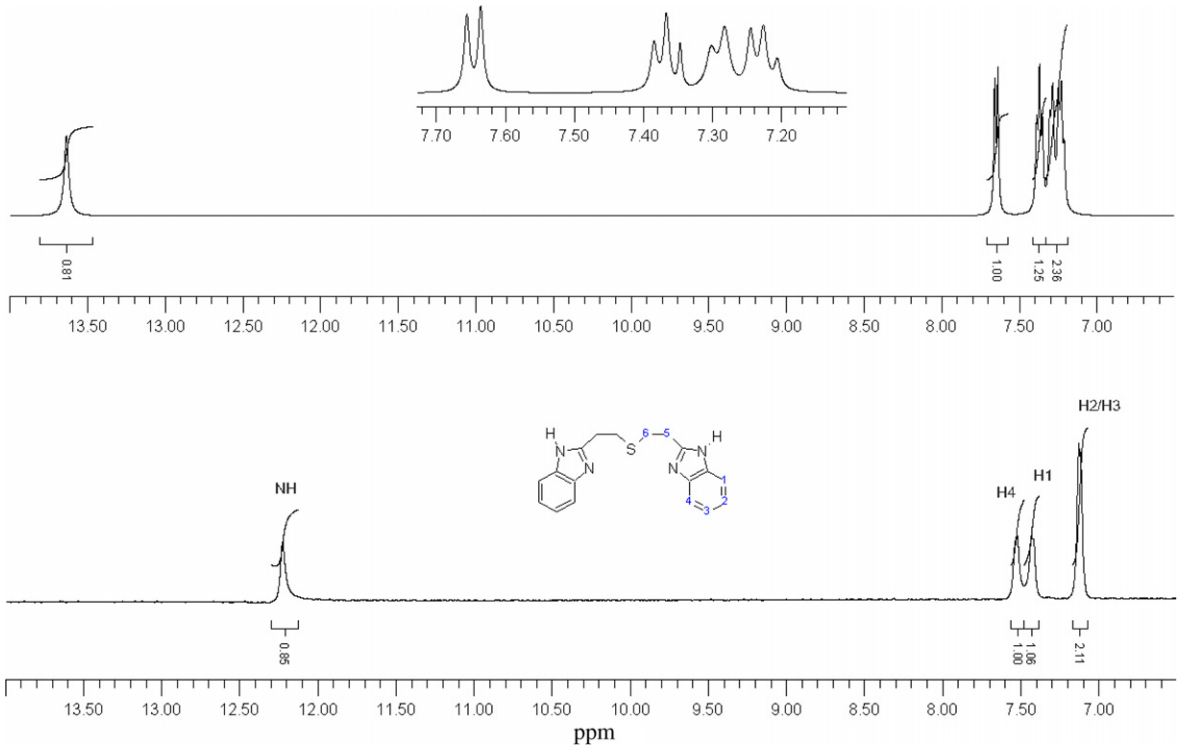


Fig. 2. The ^1H NMR overlay spectra of L^3 (bottom) and $[Re(CO)_3(L^3)]Br$ (**3**) (top).

chelate, with the alcohol pendant arm not interacting with the metal center. This terminal alcohol group presents possibilities to derivatize the ligand with, for example, carbohydrates, which have been shown to be selective in targeting tumour cells [23]. The closest contact of the discrete bromide counterion is with a hydrogen atom on C(7) (2.728 Å), and it is also involved in weak hydrogen-bonds with O(4)H, C(7)H and C(12)H.

The Re–C(carbonyl) bond distances (1.909–1.922(3) Å) are similar to those in related complexes [24–26]. The Re–N(3) distance of 2.302(3)Å is significantly longer than that of Re–N(1) and Re–N(4) (both at 2.154(3) Å), signifying the π-acidity of the imidazolyl ring systems compared to the σ basicity of the sp^3 hybridized amine nitrogen N(3). The two bite angles of the ligand L^2, N(1)–Re–N(3) (77.07(9)°) and N(3)–Re–N(4) (76.8(1)°), contribute significantly to the distortions in the molecule, resulting in the non-linear *trans* angles N(1)–Re–C(1) (174.8(1)°), N(3)–Re–C(2) (174.3(1)°) and N(4)–Re–C(3) (169.4(1)°). The bond angles around N(3) result in an approximately tetrahedral environment, with all the angles close to 109°.

The imidazole rings remain planar, as can be expected from an aromatic system, with torsion angles C(6)–N(1)–C(4)–C(5) = −0.6(4)° and C(9)–N(5)–C(10)–C(11) = 0.1(4)°, for example. The C(4)–C(5) and C(10)–C(11) bonds are double at 1.351(4) Å and 1.350(5) Å, respec-

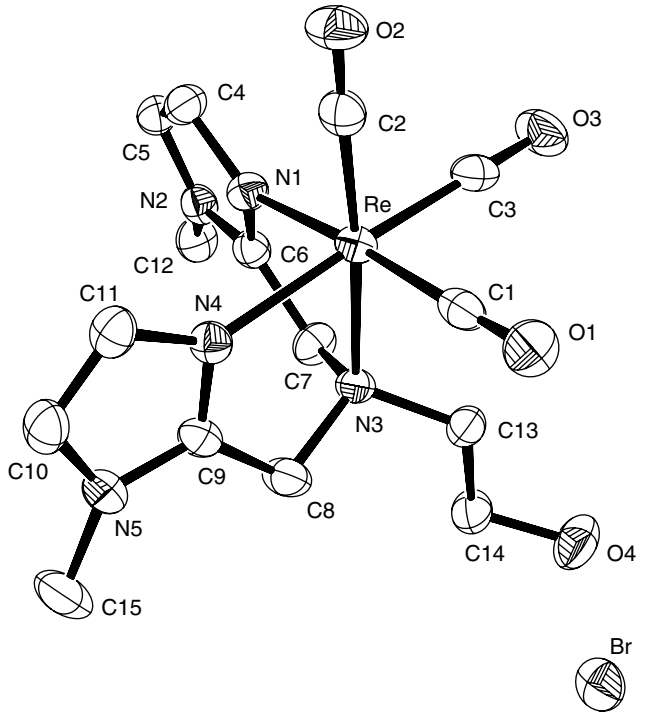


Fig. 3. An ORTEP view of $[Re(CO)_3(L^2)]Br$ (**2**), showing the atom labelling scheme and 50% probability ellipsoids.

tively, with the N(1)–C(4), N(2)–C(5), N(4)–C(11) and N(5)–C(10) all single bonds at an average of 1.380(5) Å. There are delocalized double bonds over the N(1)–C(6)–N(2) and N(4)–C(9)–N(5) parts of the imidazole rings, with the bonds N(1)–C(6) = 1.312(4), N(2)–C(6) = 1.346(4), N(4)–C(9) = 1.319(4) and N(5)–C(9) = 1.337(4) Å. The bond angles N(1)–C(6)–C(7) (123.8(3)°) and N(4)–C(9)–C(8) (121.9(3)°) illustrate the sp^2 hybridization of the imidazole carbon atoms C(6) and C(9).

There is nothing unusual about the backbone of the L^2 chelate. However, the angle N(3)–C(13)–C(14) = 115.4(2)° is bigger than expected for a sp^3 hybridized carbon. Significantly, the torsion angle N(3)–C(13)–C(14)–O(4) equals −175.6(3)°, with a strong hydrogen-bond (2.36(6) Å) between O(4)H and the bromide counterion.

In a previous study $(Et_4N)[Re(CO)_3Br_3]$ was reacted with tridentate N,N,N,-donor derivatives of benzimidazole, quinoline and tryptophan (N_3) to also give complex salts of the type *fac*-$[Re(CO)_3(N_3)]Br$ [27].

4. Supplementary material

CCDC 658077 contains the supplementary crystallographic data for **2**. These data can be obtained free of charge via http://www.ccdc.cam.ac.uk/conts/retrieving.html, or from the Cambridge Crystallographic Data Centre, 12 Union Road, Cambridge CB2 1EZ, UK, fax: (+44) 1223-336-033, or e-mail: deposit@ccdc.cam.ac.uk.

Acknowledgements

The authors are grateful for financial assistance from the Rhodes University JRC Fund and the Nelson Mandela Metropolitan University's Research Development Fund. Special thanks to Prof. J.G.H. du Preez from Nelson Mandela Metropolitan University for supplying $Re(CO)_5Br$ to us and Prof. M.T. Davies-Coleman from Rhodes University for his assistance with HPLC studies.

References

[1] J.R. Dilworth, S.J. Parrott, Chem. Soc. Rev. 27 (1998) 43.
[2] R. Alberto, R. Schibli, R. Waibel, U. Abram, A.P. Schubiger, Coord. Chem. Rev. 190–192 (1999) 901.
[3] N. Lazarova, J. Babich, J. Valliant, P. Schaffer, S. James, J. Zubieta, Inorg. Chem. 44 (2005) 6763.
[4] R. Alberto, R. Schibli, A. Egli, A.P. Schubiger, J. Am. Chem. Soc. 120 (1998) 7987.
[5] R. Schibli, R. Schwarzbach, R. Alberto, K. Ortner, H. Schmalle, C. Dumas, A. Egli, P.A. Schubiger, Bioconjugate Chem. 13 (2002) 750.
[6] R. Schibli, P.A. Schubiger, Eur. J. Nucl. Med. 29 (2002) 1529.
[7] G.J. Ehrhardt, A.R. Ketring, A.R. Ayers, Appl. Radiat. Isot. 49 (1998) 295.
[8] H.J. Pietzsch, A. Gupta, M. Reiggys, A. Drews, S. Seifert, R. Syhre, H. Spies, R. Alberto, U. Abram, P.A. Schubiger, Bioconjugate Chem. 11 (2000) 414.
[9] R. Schibli, R. La Bella, R. Alberto, E. Garcia-Garayoa, K. Ortner, U. Abram, P.A. Schubiger, Bioconjugate Chem. 11 (2000) 345.
[10] S. Abuskhuna, J. Briody, M. McCann, M. Devereux, K. Kavanagh, J.B. Fontecha, V. McKee, Polyhedron 23 (2004) 1249.
[11] K.J. Oberhausen, J.F. Richardson, R.M. Buchanan, Polyhedron 8 (1989) 659.
[12] M.M. Mtotywa, Ph.D. Thesis, University of Port Elizabeth, South Africa, 2002.
[13] N. Lazarova, S. James, J. Babich, J. Zubieta, Inorg. Chem. Comm. 7 (2004) 1023.
[14] R. Alberto, A. Egli, U. Abram, K. Hegetschweiler, V. Gramlich, A.P. Schubiger, J. Chem. Soc., Dalton Trans. (1994) 2815.
[15] T.I.A. Gerber, P. Mayer, Z.R. Tshentu, J. Coord. Chem. 60 (2007) 237.
[16] J.V. Dagdigian, C.A. Reed, Inorg. Chem. 18 (1979) 2623.
[17] G.M. Sheldrick, Acta Crystallogr., Sect. A 46 (1990) 467.
[18] G.M. Sheldrick, SHELXL-97, Programs for Structure Solution and Refinement, University of Göttingen, Germany, 1997.
[19] W.J. Geary, Coord. Chem. Rev. 7 (1971) 81.
[20] M. Allali, S. Cousinié, M. Gressier, C. Tessier, A.L. Beauchamp, Y. Coulais, M. Dartiguenave, E. Benoist, Inorg. Chim. Acta 359 (2006) 2128.
[21] T.J. Lane, I. Nakagawa, J.L. Walker, A.J. Kandathil, Inorg. Chem. 1 (1962) 267.
[22] J. Reedijk, J. Inorg. Nucl. Chem. 33 (1971) 179.
[23] P. Klüfers, O. Krotz, M. Oßberger, Eur. J. Inorg. Chem. (2002) 1919, and references therein.
[24] T. Storr, Y. Sugai, C.A. Barta, Y. Mikata, M.J. Adam, S. Yano, C. Orvig, Inorg. Chem. 44 (2005) 2698.
[25] S.R. Banerjee, M.K. Levadala, N. Lazarova, L. Wei, J.F. Valliant, K.P. Stephenson, J.W. Babich, K.P. Maresca, J. Zubieta, Inorg. Chem. 41 (2002) 6417.
[26] L. Wei, J.W. Babich, J. Zubieta, Inorg. Chim. Acta 358 (2005) 3691.
[27] L. Wei, J.W. Babich, W. Ouellette, J. Zubieta, Inorg. Chem. 45 (2006) 3057.

Available online at www.sciencedirect.com
ScienceDirect
Polyhedron 27 (2008) 411–419
POLYHEDRON
www.elsevier.com/locate/poly

Novel octahedral nickel(II) dithiocarbamates with bi- or tetradentate *N*-donor ligands: X-ray structures of $[Ni(Bzppzdtc)(phen)_2]ClO_4 \cdot CHCl_3$ and $[Ni(Bz_2dtc)_2(cyclam)]$

Zdeněk Trávníček [a,*], Richard Pastorek [a], Václav Slovák [b]

[a] *Department of Inorganic Chemistry, Faculty of Science, Palacký University, Křížkovského 10, CZ-771 47 Olomouc, Czech Republic*
[b] *Department of Chemistry, Faculty of Science, University of Ostrava, 30. dubna 22, CZ-701 03 Ostrava, Czech Republic*

Received 12 July 2007; accepted 28 September 2007
Available online 5 November 2007

Abstract

A series of novel octahedral nickel(II) dithiocarbamate complexes involving bidentate nitrogen-donor ligands (phen = 1,10-phenanthroline, bpy = 2,2′-bipyridine) or a tetradentate ligand (cyclam = 1,4,8,11-tetraazacycloteradecane) of the composition $[Ni(BzMetdtc)(phen)_2]ClO_4$ (**1**), $[Ni(Pe_2dtc)(phen)_2]ClO_4$ (**2**), $[Ni(Bzppzdtc)(phen)_2]ClO_4 \cdot CHCl_3$ (**3**), $[Ni(Bzppzdtc)(phen)_2](SCN)$ (**4**), $[Ni(BzMetdtc)(bpy)_2]ClO_4 \cdot 2H_2O$ (**5**), $[Ni(Pe_2dtc)(cyclam)]ClO_4$ (**6**), $[Ni(BzMetdtc)_2(cyclam)]$ (**7**), $[Ni(Bz_2dtc)_2(cyclam)]$ (**8**) and $[Ni(Bz_2dtc)_2(phen)]$ (**9**) (BzMetdtc = *N*,*N*-benzyl-methyldithiocarbamate(1-) anion, Pe_2dtc = *N*,*N*-dipentyldithiocarbamate(1-) anion, Bz_2dtc = *N*,*N*-dibenzyldithiocarbamate(1-) anion, Bzppzdtc = 4-benzylpiperazinedithiocarbamate(1-) anion), have been synthesized. Spectroscopic (electronic and infrared), magnetic moment and molar conductivity data, and thermal behaviour of the complexes are discussed. Single crystal X-ray analysis of **3** and **8** confirmed a distorted octahedral arrangement in the vicinity of the nickel atom with a N_4S_2 donor set. They represent the first X-ray structures of such type complexes. The catalytic influence of complexes **2**, **3**, **6**, and **7** on graphite oxidation was studied and discussed.
© 2007 Elsevier Ltd. All rights reserved.

Keywords: Nickel(II); Dithiocarbamates; X-ray structures; Graphite oxidation

1. Introduction

Generally, it is well known that square-planar dithiocarbamates (dtc) of nickel(II) of the type $[Ni(dtc)_2]$ react very unreadily with nitrogen-donor ligands. To date, only a few data regarding this topic have been found in the literature. For instance, Coucouvanis and Fackler [1] studied reactions of the mentioned Ni(II)-dithiocarbamates with monodentate N-donor ligands and synthesized paramagnetic octahedral complexes $[Ni(H_2dtc)_2(\gamma\text{-pic})_2]$, $[Ni(H_2dtc)_2(py)_2]$ and $[Ni(HRdtc)_2(\gamma\text{-pic})_2]$ (R = chlorophenyl; γ-pic = γ-picoline, py = pyridine). Moreover, the authors also found that $[Ni(Et_2dtc)_2]$ (Et = ethyl) forms adducts with pyridine and γ-picoline at liquid nitrogen temperature. The same conclusion was also confirmed by Dingle [2]. On the contrary, Ramalingam and co-workers [3] were unsuccessful in the preparation of pyridine and ethylenediamine (en) adducts of $[Ni(Et_2dtc)_2]$, $[Ni(HEadtc)_2]$ and $[Ni(Ea_2dtc)_2]$ (H_2Eadtc = ethanoldithiocarbamic acid). They had only found that in the case of attempts to prepare the discussed adducts with ethylenediamine, the reactions led to the formation of $[Ni(en)_3]^{2+}[(dtc)_2]^{2-}$ and/or $[Ni(en)_3]S_2O_3$, respectively.

Formerly, as a continuation in our systematic study of dithiocarbamate transition metal complexes, especially of nickel, we have prepared and characterized a binuclear complex $\{[Ni(Ea_2dtc)_2]_2(\mu\text{-en})\}$ in which two nickel(II) ions

* Corresponding author. Tel.: +420 58 5634350; fax: +420 58 5634352.
E-mail address: zdenek.travnicek@upol.cz (Z. Trávníček).

0277-5387/$ - see front matter © 2007 Elsevier Ltd. All rights reserved.
doi:10.1016/j.poly.2007.09.024

are connected via an ethylenediamine bridge [4]. We have also synthesized octahedral [Ni(Bz^{i}Prdtc)$_2$(cyclam)] and [Ni(Bz^{i}Prdtc)(cyclam)]X complexes, where cyclam = 1,4,8,11-tetraazacyclodecane, Bz^{i}Prdtc = *N*,*N*-benzylisopropyldithiocarbamate, (X = ClO_4, BPh_4) [5]. Moreover, the [Ni(Bz^{i}Prdtc)(cyclam)]$BPh_4 \cdot CHCl_3$ complex has been structurally characterized by single crystal X-ray analysis. In search for X-ray structures deposited within the Cambridge Structural Database [6] involving any transition metal in combination with a dithiocarbamate moiety and any N-donor ligand, and bearing a N_4S_2 donor set, ten molecular structures complying with the above-mentioned requirement have been found, i.e. four mononuclear Ru(II) complexes [7–9], three dinuclear Mo(V) complexes [10–12], two mononuclear Co(III) [13,14] complexes, and one mononuclear Ni(II) complex [15].

In this paper, we report the synthesis and characterization of novel octahedral Ni(II)-dithiocarbamate complexes **1**–**9** along with the single crystal X-ray structures of **3** and **8**. Moreover, the methods of thermal analysis have been used for the study of influence of selected complexes on graphite oxidation. This possible practical utilization of Ni(II)-dithiocarbamates have been also described and discussed recently in case of similar complexes [16,17].

2. Experimental

2.1. Materials

Dipentylamine (97%), 1-benzylpiperazine (98%), 1,4,8,11-tetraazacyclodecane (cyclam), nitromethane and K[PF_6] were supplied by FLUKA Co. 1,10-Phenanthroline (phen), 2,2′-bipyridine (bpy), $LiClO_4 \cdot 3H_2O$ and dibenzylamine (97%) were acquired from SIGMA ALDRICH Co. and *N*-benzylamine (97%) from LANCASTER Co. The remaining reagents were obtained from LACHEMA Co., all of p.a. purity.

2.2. Syntheses

2.2.1. [Ni(BzMetdtc)$_2$]

The complex was prepared by a slightly modified procedure described previously [18]. *N*-Benzylmethylamine (64 mL, 50 mmol) was added drop-wise into a solution of CS_2 (3 mL, 50 mmol) in ethanol (96%, 25 mL) with stirring. The reaction mixture was left to stand at room temperature for a short time period. Then, a warm solution of $NiCl_2 \cdot 6H_2O$ (5.9 g, 25 mmol) in distilled water (50 mL) was added. After the solution addition, the light green precipitate of [Ni(BzMetdtc)$_2$] appeared. It was filtered off, washed with warm water (until negative reaction on Cl^- ions) and dried at 40 °C under an infrared lamp. Yield: 72%. *Anal.* Calc. for $C_{18}H_{20}N_2NiS_4$: C, 47.9; H, 4.5; N, 6.2; Ni, 13.0; S, 28.4. Found: C, 48.0; H, 4.4; N, 5.9; Ni, 12.8; S, 28.7%.

2.2.2. [Ni(BzMetdtc)(phen)$_2$]ClO_4 (**1**) and [Ni(BzMetdtc)(bpy)$_2$]$ClO_4 \cdot 2H_2O$ (**5**)

To a suspension of finely powdered [Ni(BzMetdtc)$_2$] (0.23 g, 0.5 mmol) in an ethanol/chloroform mixture (30/30 mL), $NiCl_2 \cdot 6H_2O$ (0.11 g, 0.5 mmol), $LiClO_4 \cdot 3H_2O$ (0.16 g, 1 mmol) and bpy (0.31 g, 2 mmol) or phen (0.39 g, 2 mmol) were added in this sequence. The reaction mixture was stirred under reflux for 20 h and then filtered. The solid formed after 5 days. It was filtered off, washed with ethanol and diethyl ether, and recrystallized from a chloroform solution with activated carbon. The substance which formed, was filtered off, washed with diethyl ether and dried under an infrared lamp at 40 °C. Yields: 56% (**1**) and 73% (**5**). *Anal.* Calc. for $C_{33}H_{26}N_5NiS_2ClO_4$ (**1**): C, 55.4; H, 3.7; N, 9.8; Ni, 8.2; S, 9.0; Cl, 5.0. Found: C, 54.9; H, 3.4; N, 9.5; Ni, 8.3; S, 8.8; Cl, 4.8%. *Anal.* Calc. for $C_{29}H_{30}N_5NiS_2ClO_6$ (**5**): C, 49.6; H, 4.3; N, 10.0; Ni, 8.3; S, 9.1; Cl, 5.0. Found: C, 49.8; H, 4.2; N, 10.2; Ni, 8.2; S, 8.9; Cl, 4.7%.

2.2.3. [Ni(Pe$_2$dtc)(phen)$_2$]ClO_4 (**2**)

Phen (0.40 g, 2 mmol) and $LiClO_4 \cdot 3H_2O$ (0.16 g, 1 mmol) were added in this sequence to a suspension of finely powdered [Ni(Pe$_2$dtc)$_2$] [8] (0.52 g, 1 mmol) in methanol (15 mL). The reaction mixture was stirred under reflux until the colour of the solution turned to red (2 h). Then, the solution was filtered with activated carbon and the filtrate was left to stand at room temperature. After several hours, crystals formed in the mother liquor from which single crystals suitable for X-ray analysis were selected. The remaining portion of the crystalline product was filtered off, washed with methanol and diethyl ether and dried under an infrared lamp at 40 °C. Yield: 81%. *Anal.* Calc. for $C_{35}H_{38}N_5NiS_2ClO_4$ (**2**): C, 56.0; H, 5.1; N, 9.3; Ni, 7.8; S, 8.5; Cl, 4.7. Found: C, 56.1; H, 5.0; N, 9.3; Ni, 8.0; S, 8.3; Cl, 4.8%.

2.2.4. [Ni(Bzppzdtc)$_2$]

The complex was prepared by a slightly modified procedure described previously [18]. 1-Benzylpiperazine (8.7 mL, 50 mmol) was added drop-wise to a solution of CS_2 (3 mL, 50 mmol) in ethanol (96%, 25 mL) with stirring. A white precipitate, which formed during the above reaction, was dissolved by adding a solution of NaOH (1.9 g, 50 mmol) in water (10 mL). The resulting solution was filtered and a warm solution of $NiCl_2 \cdot 6H_2O$ (5.9 g, 25 mmol) in water (50 mL) was added with stirring to the filtrate. Subsequent steps are identical to those described for the preparation of [Ni(BzMetdtc)$_2$] (see Section 2.2.1). Yield: 81%. *Anal.* Calc. for $C_{24}H_{30}N_4NiS_4$: C, 51.3; H, 5.4; N, 10.0; Ni, 10.5; S, 22.8. Found: C, 51.0; H, 5.1; N, 9.8; Ni, 10.6; S, 22.5%.

2.2.5. [Ni(Bzppzdtc)(phen)$_2$]$ClO_4 \cdot CHCl_3$ (**3**)

A mixture of finely powdered [Ni(Bzppzdtc)$_2$] (0.39 g, 2 mmol), phen (0.39 g, 2 mmol), $NiCl_2 \cdot 6H_2O$ (0.11 g, 0.5 mmol) and $LiClO_4 \cdot 3H_2O$ (0.16 g, 1 mmol) were suspended in an ethanol/chloroform mixture (15/15 mL).

The reaction mixture was stirred under reflux until all components dissolved and the colour of the solution turned to dark red (*ca.* 4 h). Then, the solution was filtered with activated carbon and the filtrate was left to stand at room temperature for 7 days. During this period, a green substance appeared and it was separated by filtration and discarded. Subsequently, brown crystals suitable for X-ray analysis formed in the mother liquor after several days. They were filtered off, washed with hexane and dried under an infrared lamp at 40 °C. Yield: 56%. *Anal.* Calc. for $C_{37}H_{32}N_6NiS_2Cl_4O_4$ (**3**): C, 50.0; H, 3.6; N, 9.4; Ni, 6.6; S, 7.2; Cl, 15.9. Found: C, 50.4; H, 3.3; N, 9.5; Ni, 6.3; S, 7.0; Cl, 15.6%.

2.2.6. *[Ni(Bzppzdtc)(phen)$_2$](SCN) (**4**)*

Finely powdered [Ni(Bzppzdtc)$_2$] (0.28 g, 0.5 mmol) together with phen (0.39 g, 2 mmol) and $Ni(SCN)_2 \cdot 2H_2O$ (0.11 g, 0.5 mmol) were suspended in an ethanol/chloroform mixture (15/15 mL) and stirred under reflux for 4 h. After filtration of the reaction mixture with activated carbon, a light brown precipitate formed in the mother liquor in the course of a few days. The product was filtered off, washed with hexane and dried under an infrared lamp at 40 °C. Yield: 57%. *Anal.* Calc. for $C_{37}H_{31}N_7NiS_3$ (**4**): C, 61.0; H, 4.3; N, 13.5; Ni, 8.1; S, 13.2. Found: C, 60.4; H, 4.2; N, 13.2; Ni, 7.9; S, 13.5%.

2.2.7. *[Ni(Pe$_2$dtc)(cyclam)]ClO$_4$ (**6**)*

A suspension of finely powdered [Ni(Pe$_2$dtc)$_2$] (0.52 g, 1 mmol) in chloroform (5 mL) was mixed while stirring with 1,4,8,11-tetraazacyclodecane (0.2 g, 1 mmol) in 96% ethanol (5 mL) and $LiClO_4 \cdot 3H_2O$ (0.16 g, 1 mmol) in 96% ethanol (3 mL). The reaction mixture was stirred under reflux for 10 h. The resulting violet solution was filtered with activated carbon and left to stand at room temperature. After one week, a viscous product was obtained which was extracted with diethyl ether. After three days, the viscous product was formed again from which a powdered substance was isolated by means of diethyl ether. It was filtered off and dried under an infrared lamp at 40 °C. Yield: 46%. *Anal.* Calc. for $C_{21}H_{46}N_5NiS_2ClO_4$ (**6**): C, 42.7; H, 7.8; N, 11.8; Ni, 9.9; S, 10.8; Cl, 6.0. Found: C, 42.5; H, 7.5; N, 11.6; Ni, 9.8; S, 10.5; Cl, 5.5%.

2.2.8. *[Ni(BzMetdtc)$_2$(cyclam)] (**7**) and [Ni(Bz$_2$dtc)$_2$(cyclam)] (**8**)*

These compounds were obtained by the reaction of finely powdered [Ni(Bz$_2$dtc)$_2$] (0.6 g, 1 mmol) or [Ni(BzMetdtc)$_2$] (0.45 g, 1 mmol) in chloroform (5 mL) with 1,4,8,11-tetraazacyclodecane (cyclam) (0.2 g, 1 mmol) in 96% ethanol (10 mL). The mixture was stirred under reflux for 10 h and the resulting violet solution was filtered. During a few days, violet crystals, or a violet powder substance appeared. The product was recrystallized from chloroform by addition of methanol or hexane. The violet powder substance and violet crystals were isolated in the case of (**7**), and (**8**), respectively, which were washed with methanol or hexane and dried under an infrared lamp at 40 °C. Yields: 62% (**7**) and 58% (**8**). *Anal.* Calc. for $C_{28}H_{44}N_4NiS_4$ (**7**): C, 51.6; H, 6.8; N, 12.9; Ni, 9.0; S, 19.7. Found: C, 51.1; H, 7.2; N, 12.8; Ni, 8.9; S, 19.5%. *Anal.* Calc. for $C_{40}H_{52}N_6NiS_4$ (**8**): C, 59.8; H, 6.5; N, 10.4; Ni, 7.3; S, 16.0. Found: C, 59.3; H, 6.9; N, 10.5; Ni, 7.8; S, 15.7%.

2.2.9. *[Ni(Bz$_2$dtc)$_2$(phen)] (**9**)*

Phen (0.20 g, 1 mmol) and $LiClO_4 \cdot 3H_2O$ (0.16 g, 1 mmol) were added to a suspension of finely powdered [Ni(Bz$_2$dtc)$_2$] (0.60 g, 1 mmol) in methanol (15 mL) with stirring and the mixture was refluxed for 30 min. Then, a yellow substance formed. It was filtered off, washed with methanol, and dried under an infrared lamp at 40 °C. Yield: 85%. *Anal.* Calc. for $C_{42}H_{36}N_4NiS_4$ (**9**): C, 64.4; H, 4.6; N, 7.1; Ni, 7.5; S, 16.4. Found: C, 64.1; H, 4.2; N, 7.4; Ni, 7.3; S, 16.1%.

2.3. Physical measurements

The nickel content was determined by chelatometric titration using murexide as an indicator [19]. Chlorine content was determined by the Schöniger method [20]. CHNS analyses were performed on an EA 1108 analyzer (Fisons Instruments) instrument with satisfactory results for all the prepared complexes. Room temperature magnetic susceptibilities were measured by Faraday method on a laboratory designed instrument equipped with a Sartorius 4434 MP-8 microbalance, using Co[Hg(NCS)$_4$] as a calibrant. The correction for diamagnetism was performed using Pascal constants. Conductivities were measured with an LF 330/SET conductivity meter (WTW GmbH) at 25 °C. Diffuse-reflectance (45 000–9090 cm^{-1}) and DMFA solution (30 000–9090 cm^{-1}) electronic spectra were carried out on a Perkin–Elmer Lambda35 UV/Vis spectrometer. Nujol technique. IR spectra (4000–450 cm^{-1}) were recorded on a Perkin–Elmer Spectrum One FT-IR spectrometer using the KBr technique. TG/DTA analyses were performed on an Exstar TG/DTA 6200 (Seiko Instruments, Inc.) with the heating rate of 2.5 °C min^{-1}, sample weight of 7–11 mg, and temperature range of 20–1050 °C.

The study the catalytic influence of the complexes **2**, **3**, **6**, and **7** on graphite was performed on a Netzsch STA 449C device with an α-Al_2O_3 crucible without a standard, heating rate of 10 °C min^{-1}, a sample weight of 4.4–5.1 mg, and in a dynamic atmosphere (air, 100 cm^3 min^{-1}). Samples for the study were prepared by the mixing of graphite (0.6 g, diameter of particles less than 0.1 mm, ash residue max. 0.2%, mass drying loss max. 0.2%) with an acetone solution (2 mL) of the appropriate complex (**2**, **3**, **6** and **7**; [Ni] = 2.5 mM). All samples were homogenized by means of stirring and drying at room temperature for 24 h. Each experimental result is represented as an arithmetic mean of three independent experiments. The kinetic parameters were calculated by a direct non-linear regression method [21].

Table 1
Crystal data and structure refinement for $[Ni(Bzppzdtc)(phen)_2]ClO_4 \cdot CHCl_3$ (**3**) and $[Ni(Bz_2dtc)_2(cyclam)]$ (**8**)

	3	**8**
Empirical formula	$C_{37}H_{32}Cl_4N_6NiO_4S_2$	$C_{40}H_{46}N_6NiS_4$
Formula weight	889.32	797.78
Temperature (K)	105(2)	105(2)
Wavelength (Å)	0.71073	0.71073
Crystal system, space group	$P2_1/c$	$P2_1/c$
a (Å)	12.799(3)	9.2729(3)
b (Å)	16.864(3)	19.7667(5)
c (Å)	17.691(5)	10.8490(4)
α (°)	90	90
β (°)	92.18(2)	97.151(3)
γ (°)	90	90
Volume (Å^3)	3815.7(17)	1973.09(117)
Z, calculated density (g cm^{-3})	4, 1.548	2, 1.343
Absorption coefficient (mm^{-1})	0.948	0.740
$F(000)$	1824	840
Crystal size	$0.40 \times 0.35 \times 0.30$ mm	$0.40 \times 0.40 \times 0.30$ mm
θ range for data collection (°)	2.68–25.00	2.80–25.00
Index ranges	$-15 \leqslant h \leqslant 15$, $-20 \leqslant k \leqslant 20$, $-15 \leqslant l \leqslant 21$	$-11 \leqslant h \leqslant 10$, $-23 \leqslant k \leqslant 13$, $-12 \leqslant l \leqslant 12$
Reflections collected/unique	33494/6713 ($R_{int} = 0.0282$)	10042/3462 ($R_{int} = 0.0201$)
Refinement method on F^2	full-matrix least-squares	full-matrix least-squares
Goodness-of-fit on F^2	0.983	1.020
Final R indices [$I > 2\sigma(I)$]	$R_1 = 0.0424$, $wR_2 = 0.1197$	$R_1 = 0.0594$, $wR_2 = 0.1265$
R indices (all data)	$R_1 = 0.0562$, $wR_2 = 0.1289$	$R_1 = 0.0762$, $wR_2 = 0.1329$
Largest difference in peak and hole (e Å^{-3})	0.727 and −0.979	0.820 and −0.552

2.4. X-ray structures

X-ray data collections for **3** and **8** were performed on an Oxford Diffraction Xcalibur™2 equipped with a Sapphire2 CCD detector using Mo Kα radiation at 105 K. The CRYSALIS program package (version 1.171.32.5, Oxford Diffraction) was used for data collection and reduction. The molecular structure of **3** was solved by direct methods [SHELXS-97] [22] and all non-hydrogen atoms were refined anisotropically on F^2 using full-matrix least-squares procedure [SHELXL-97] [23] with weight: $w = 1/[\sigma^2(F_o)^2 + (0.08P)^2 + 5.00P]$, where $P = ({F_o}^2 + 2{F_c}^2)/3$. All H-atoms of **3** were found in differential maps of electron density and their parameters were refined using the riding model with the C–H distance of 0.95, 0.99, and 1.00 Å, respectively, and with $U_{iso}(H) = 1.2U_{eq}(C)$. Additional calculations were performed using the DIAMOND program [24]. The molecular structure of **8** was solved by direct methods [SHELXS-97] and all non-hydrogen atoms were refined anisotropically on F^2 using full-matrix least-squares procedure [SHELXL-97] with weight: $w = 1/[\sigma^2(F_o)^2 + (0.03P)^2 + 5.00P]$. The structure of **8** consists of a centrosymmetric $Ni_{1/2}(Bz_2dtc)(cyclam)_{1/2}$ moiety which is connected with its second part by means of an inversion centre [symmetry code: [a] $-x, -y+1, -z+1$] lying in the middle of Ni1···Ni1a distance. The separation of Ni1···Ni1a is 2.3962(16) Å. The N2–N4 and C20 atoms of the moiety belonging to cyclam are disordered over two positions with the occupancy of 36% (for N2 and N4), 64% (for N3), 32% (for C20) and 33% (for C20b), and 14% (for N2a and N4a), 36% (for N3a), 15% (for C20a) and 20% (for C20c). Owing to the high degree of disorder, a relatively high number of restrains (≈91) have been applied during the structural refinement of **8**, and moreover, a few H-atoms were not included into the refinement. H-atoms were positioned theoretically and refined using the riding model with the C–H distances of 0.95 and 0.99 Å, and N–H distance of 0.93 Å. Crystal data and structure refinements for both the structures are given in Table 1.

3. Results and discussion

3.1. General characterization

Colours, magnetic moment, molar conductivity and spectral data of all the prepared complexes **1**–**9** are summarized in Table 2. All complexes are paramagnetic with values of effective magnetic moments ranging from 3.02 to 3.41 μ_{eff}/μ_B. These values indicate the presence of two unpaired electrons and show on octahedral geometry in the vicinity of the nickel atom [25]. The octahedral geometry can also be supported by the d–d transition bands revealed both in electronic diffuse-reflectance and DMFA solution spectra at 10280–11720, 16180–19960 and 21929–26230 cm^{-1} (see Table 3). They may be assigned to the $^3A_{2g} \rightarrow {}^3T_{2g}$ (ν_1), $^3A_{2g} \rightarrow {}^3T_{1g}$ (F) (ν_2), and $^3A_{2g} \rightarrow {}^3T_{1g}(P)$ (ν_3) transitions, respectively [26]. The maxima above 30000 cm^{-1} are probably caused by charge-transfer transitions. An ionic nature of complexes **1**–**6** may be supported by their molar conductivity data. It has been found that the complexes behave as 1:1 electrolytes in acetone or DMFA solution [27]. Their molar conductivity values are

Table 2
Colour, molar conductivity, magnetic moment, spectral and thermal data for the complexes

	Colour	λ_M (S cm^2 mol^{-1})	μ_{eff}/μ_B	IR (cm^{-1})			TA[a] (°C)
				ν (C—S)	ν (C—N)		
1	yellow	148.6[b]	3.04	994m	1515w	$\nu_3(ClO_4^-)$: 1089vs; $\nu_4(ClO_4^-)$: 623s	[c]
2	dark red	146.2[b]	3.21	992m	1515s	$\nu_3(ClO_4^-)$: 1096vs; $\nu_4(ClO_4^-)$: 623vs	[c]
3	dark brown	132.8[b]	3.16	996m	1514m	$\nu_3(ClO_4^-)$: 1095vs; $\nu_4(ClO_4^-)$: 622s	[c]
4	light brown	147.2[d]	3.41	996s	1515vs	ν_{as}(C≡N): 2083vs	193
5	yellow	135.5[b]	3.02	992m	1514m	$\nu_3(ClO_4^-)$: 1084m; $\nu_4(ClO_4^-)$: 626m	[c]
6	light violet	111.1[b]	3.07	995m	1493s	$\nu_3(ClO_4^-)$: 1087vs; $\nu_4(ClO_4^-)$: 624vs	[c]
7	light violet	3.4[b]	3.07	996m	1522m		134
8	violet	25.2[d]	3.12	983vs	1493s		163
9	grey	10.0[d]	3.20	999vs	1513m		190

(**1**) [Ni(BzMetdtc)(phen)$_2$]ClO_4; (**2**) [Ni(Pe$_2$dtc)(phen)$_2$]ClO_4; (**3**) [Ni(Bzppzdtc)(phen)$_2$]$ClO_4 \cdot CHCl_3$; (**4**) [Ni(Bzppzdtc)(phen)$_2$](SCN); (**5**) [Ni(BzMetdtc)(bpy)$_2$]$ClO_4 \cdot 2H_2O$; (**6**) [Ni(Pe$_2$dtc)(cyclam)]ClO_4; (**7**) [Ni(BzMetdtc)$_2$(cyclam)]; (**8**) [Ni(Bz$_2$dtc)$_2$(cyclam)]; (**9**) [Ni(Bz$_2$dtc)$_2$(phen)].
[a] The beginning of thermal decomposition.
[b] Measured in acetone.
[c] Did not studied owing to the explosiveness.
[d] Measured in DMFA solution.

Table 3
UV/Vis spectral data for the complexes

	Diffuse-reflectance	UV/Vis[a] Solution[b]	ε (dm^3 cm^{-1} mol^{-1})
1	11 720	10 834	14
	26 230	11 363	27
	31 100	17 391	87
		25 125	675
2	11 810	10 294	14
	19 620	11 194	28
		19 792	17
		25 252	512
3	11 540	10 718	17
	19 810	11 376	24
		19 960	131
		25 316	532
4	10 680	10 256	8
	17 790	11 641	10
		16 181	31
		20 040	96
5	11 690	10 638	12
	167·80	16 393	36
	24 050	20 000	96
	30 030	24 398	156
6	11 240	10 752	47
	17 790	11 350	55
	31 480	17 921	73
		23 201	75
7	10 530	10 791	35
	16 180	11 287	44
	22 440	18 116	67
	30 100	22 676	77
8	11 320	10 799	16
	18 110	11 363	17
		18 018	28
		24 937	72
9	10 280	10 706	15
	16 280	11 389	24
	20 390	20 040	80
		21 929	86

[a] Absorption maxima in cm^{-1}.
[b] Measured in DMFA solutions [$c_M = 10^{-3}$ mol dm^{-3} for **1**–**7**; $c_M = 10^{-2}$ mol dm^{-3} for **8**–**9**].

in the interval of 111.1–148.6 S cm^2 mol^{-1}. On the other hand, the values obtained for complexes **7**–**9** clearly show on the fact that they are non-electrolytes (see Table 2). Characteristic IR bands and their assignment are given in Table 2.

3.2. IR spectral studies

For all complexes **1**–**9**, the bands belonging to ν(C···S) and ν(C···N) vibrations were observed at 983–999 cm^{-1}, and 1493–1542 cm^{-1}, respectively [28,29]. These values clearly characterize the dithiocarbamate moiety. Owing to the fact that intensive bands pertaining to ν(C···S) are not splitted into two components, we can conclude that dithiocarbamate anion is coordinated to nickel in a bidentate fashion. The presence of ClO_4^- in complexes **1**–**3**, **5** and **6**, as well as its ionic nature, can be supported by bands at 1084–1096 cm^{-1} (ν_3) and 622–626 cm^{-1}(ν_4) [30]. The peak recorded at 2083 cm^{-1} in the spectrum of **4** may be assigned to an asymmetric stretching vibration of an ionic bonded NCS^- anion [31]. The conclusions following from the interpretation of IR spectral data of [Ni(BzMetdtc)$_2$(cyclam)] (**7**) and [Ni(Bz$_2$dtc)$_2$(cyclam)] (**8**) are not unambiguous and at this point, and unfortunately, we cannot make decision if the bidentate manner of coordination of dithiocarbamate would be possible in the case of the discussed complexes. Generally, we may assume the tetradentate coordination of cyclam and the bidentate coordination of each of two dithiocarbamate ligands, and thus, to accept the non-ionic nature of the complexes as determined by conductivity measurements. It would point out that the coordination number for nickel would be eight, and evidently, this is not possible in the case of the ligand's combination used. However, the manner of ligand coordinations in **7** and **8** has been resolved by means of single crystal X-ray analysis and will be explained and discussed in greater details in the Section 3.3.

3.3. X-ray structures of $[Ni(Bzppzdtc)(phen)_2]ClO_4 \cdot CHCl_3$ (3) and $[Ni(Bz_2dtc)_2(cyclam)]$ (8)

The molecular structure of complex **3** and **8** is depicted in Figs. 1 and 2, respectively. Selected bond lengths and angles are given in Table 4. The molecular structure of $[Ni(Bzppzdtc)(phen)_2]ClO_4 \cdot CHCl_3$ (**3**) consists of the $[Ni(Bzppzdtc)(phen)_2]^+$ cation, perchlorate anion, and $CHCl_3$ as a solvent molecule. The nickel(II) ion is six-coordinated by four nitrogen atoms from two phen ligands and two sulphur atoms from 4-benzylpiperazinedithiocarbamate anion in a distorted octahedral geometry. The $[Ni(Bzppzdtc)(phen)_2]^+$ cation contains three different rings, i.e. the phen ligand containing N1 and N2 atoms (ring 1), phen ligand containing N3 and N4 atoms (ring 2) and a part of dithiocarbamate moiety together with the nickel atom involving a NiS_2C moiety (ring 3). All three rings are nearly planar with maximal deviation being 0.099(5) Å for C(8), 0.054(4) Å for C(20) and 0.074(4) Å for C(25) in rings 1–3, respectively [24]. The dihedral angle between rings 1 and 2, 1 and 3, and 2 and 3 are equal to 81.88(4)°, 88.65(4)°, and 86.02(4)°, respectively. The delocalization of π-electron density over the S_2CN moiety, as typical for a bidentate coordination of any dithiocarbamate anion to a transition metal, may be evident from the C–N and C–S bond length values (see Table 4). For comparison, mean values for C–N, C=S and C–S bonds, as found in Cambridge Structural Database (CSD Version 5.28), are 1.331 Å (valid for S_2CNR_2 moiety), 1.661 Å (valid for S_2CNR_2 moiety), and 1.753 Å (valid for R–S–R), respectively [6]. On the other hand, the C–S bond lengths in **3** and **8** are comparable to those as determined for bidentate coordinated dithiocarbamate moieties in case of Ni-complexes (the mean value in delocalized C–S bonds is 1.713 Å) [6]. The ionic nature of ClO_4^- in **3** can be seen from the Ni···Cl separation which is 6.5912(13) Å.

The structure of **8** consists of a centrosymmetric $Ni_{1/2}(Bz_2dtc)(cyclam)_{1/2}$ moiety which is connected with its second part by means of inversion centre [symmetry code: [a] $-x, -y+1, -z+1$]. Thus, the Ni1 atom and some atoms of cyclam adopt non-unit occupancy factors. The crystallographically independent part of the complex molecule is connected with its second centrosymmetric part through partially disordered cyclam ligand. The separation of Ni1···Ni1a is 2.3962(16) Å. The presence of the above-mentioned symmetry operation together with the disorder causes that each of the two parts of the nickel atom is six coordinated by four N atoms from cyclam and two S atoms from a bidentate coordinated dithiocarbamate ligand. Moreover, it also explains why may be coordinated the dithiocarbamate ligand to nickel via two S atoms. It also clearly supports conclusions following from IR data. Similarly as in **3**, a significant delocalization of π-electron density over the S_2CN moiety in **8**, as typical for a bidentate coordination of any dithiocarbamate anion to a transition metal, may be evident from the C–N and C–S bond length values (see Table 4).

In conclusion of this section, it is necessary to emphasize that the discussed structures represent the first examples of structurally characterized octahedral Ni-dithiocarbamate complexes bearing a combination of the ligands used.

3.4. TG and DTA studies

Thermal stability studies were performed for complexes **4**, **7**, **8** and **9**. The remaining compounds, i.e. those containing perchlorate anions, were not studied for safety reasons.

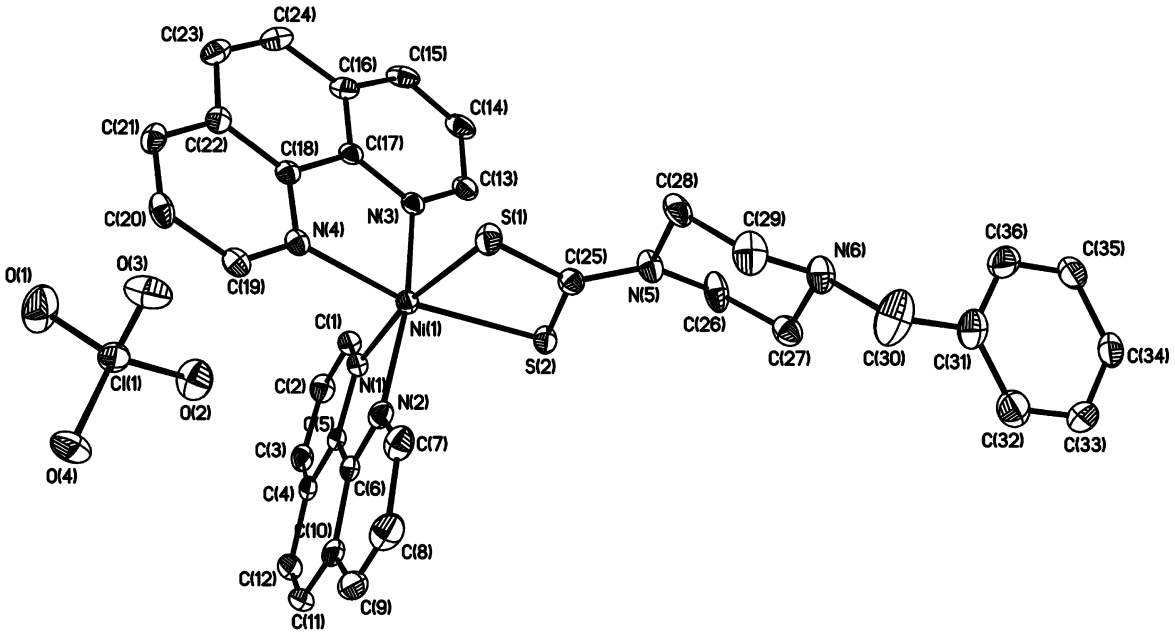


Fig. 1. The molecular structure of $[Ni(Bzppzdtc)(phen)_2]ClO_4 \cdot CHCl_3$ (**3**) with the atom labelling scheme. Thermal ellipsoids are drawn at the 40% probability level. H-atoms and $CHCl_3$ molecule have been omitted for clarity.

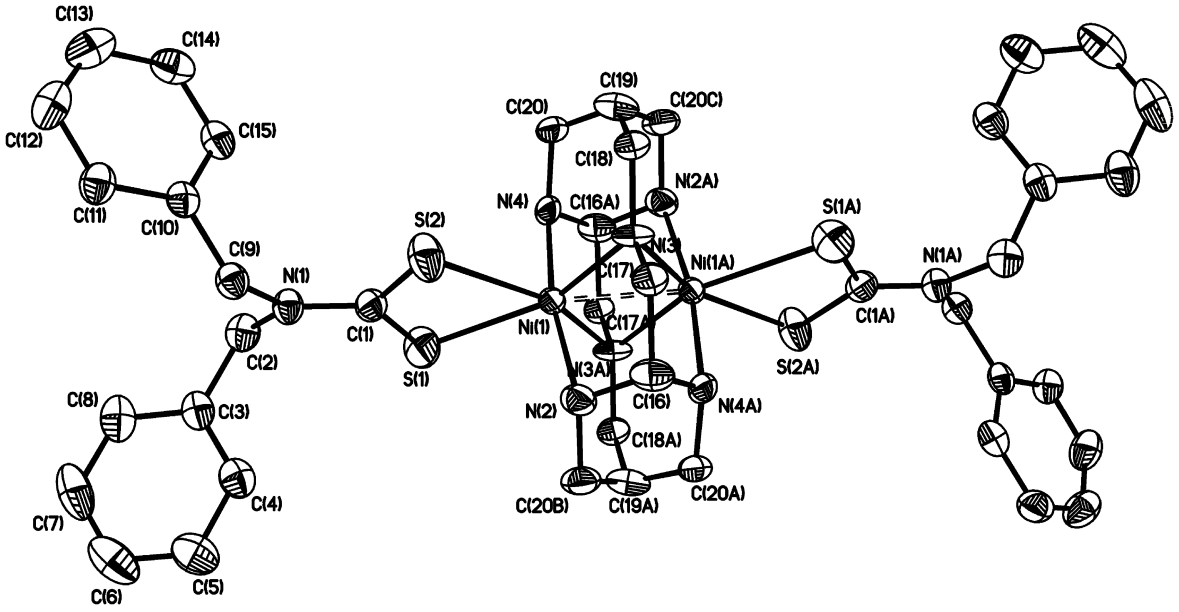


Fig. 2. The molecular structure of $[Ni(Bz_2dtc)_2(cyclam)]$ (**8**) with the atom labelling scheme, showing partially disordered cyclam ligand. Thermal ellipsoids are drawn at the 40% probability level. H-atoms and some of disordered cyclam atoms have been omitted for clarity.

Table 4
Selected bond lengths (Å) and angles (°) for $[Ni(Bzppzdtc)(phen)_2]ClO_4 \cdot CHCl_3$ (**3**) and $[Ni(Bz_2dtc)_2(cyclam)]$ (**8**)

3				**8**			
Ni(1)–N(1)	2.096(3)	N(1)–Ni(1)–N(2)	79.29(12)	Ni(1)–N(2)	2.133(9)	N(3)–Ni(1)–N(4)	89.3(5)
Ni(1)–N(2)	2.099(3)	N(3)–Ni(1)–N(4)	79.53(12)	Ni(1)–N(2a)	2.17(3)	N(3)–Ni(1)–N(2)	84.2(5)
Ni(1)–N(3)	2.072(3)	S(1)–Ni(1)–S(2)	73.85(3)	Ni(1)–N(3)	2.022(12)	N(4)–Ni(1)–N(2)	170.5(3)
Ni(1)–N(4)	2.099(3)	N(3)–Ni(1)–N(2)	168.69(10)	Ni(1)–N(3a)	1.99(2)	S(2)–Ni(1)–S(1)	69.22(4)
Ni(1)–S(1)	2.4020(11)	N(1)–Ni(1)–S(1)	170.75(7)	Ni(1)–N(4)	2.085(9)	S(2)–C(1)–S(1)	119.0(2)
Ni(1)–S(2)	2.4438(9)	N(4)–Ni(1)–S(2)	165.63(7)	Ni(1)–N(4a)	2.13(2)	C(1)–S(1)–Ni(1)	85.66(13)
S(1)–C(25)	1.719(3)	C(25)–S(1)–Ni(1)	85.53(11)	Ni(1)–S(1)	2.5958(15)	C(1)–S(2)–Ni(1)	86.08(13)
S(2)–C(25)	1.713(4)	C(25)–S(2)–Ni(1)	84.34(11)	Ni(1)–S(2)	2.5898(13)		
N(5)–C(25)	1.334(5)	S(1)–C(25)–S(2)	116.08(18)	S(1)–C(1)	1.715(4)		
				S(2)–C(1)	1.703(4)		
				N(1)–C(1)	1.344(4)		

Generally, we can note that the studied complexes are not comparatively thermally stable. They start to decompose within a relatively broad temperature interval of 134–193 °C. In the case of complexes **4**, **7** and **8**, the decays proceed without formation of thermally stable intermediates in several steps and are not finished even at 1050 °C. The decompositions are accompanied by several *exo*-effects on DTA curves in the case of the discussed complexes. The dominant *exo*-effects were observed at *ca.* 480 °C and it may be probably connected with the decomposition of the organic part of the complex. As for the thermal decay of **9**, the situation is a little bit different. That is why we will discuss it in greater detail. The complex **9** starts to decompose at 190 °C and the beginning of the decay is accompanied by significant decrease in the sample weight (*ca.* 56%). At the first stage of the decomposition, three small *endo*-effects can be seen on the DTA curve with the minimum at 236, 267, and 350 °C, respectively (see Fig. 3). The *endo*-effect with the maximum at 236 °C may be related to melting of the sample which was determined using melting point apparatus to be 234 °C. Next thermal decay proceeds in two waves and is finished at 705 °C. A sharp *exo*-effect with the maximum at 476 °C is clearly seen on the DTA curve, and is probably connected with the burning of the organic part of the molecule. Then, a plateau exists on the TG curve between 706 and 1050 °C. It has been found that the end-product of the thermal degradation is NiO (Δm found/calcd., 89.2/91.7%). The product was identified using the Bede ZDS program package [32] and PDF-2 database [33] as NiO (PDF-2 card number: 47–1049).

3.5. The catalytic study

For representative complexes **2**, **3**, **6** and **7**, their influence on graphite oxidation was studied. In quest to evaluate obtained results objectively, we also measured the oxidation of pure graphite (gr) and considered an impact of pure acetone (sample 0), as a solvent used for the preparation of the

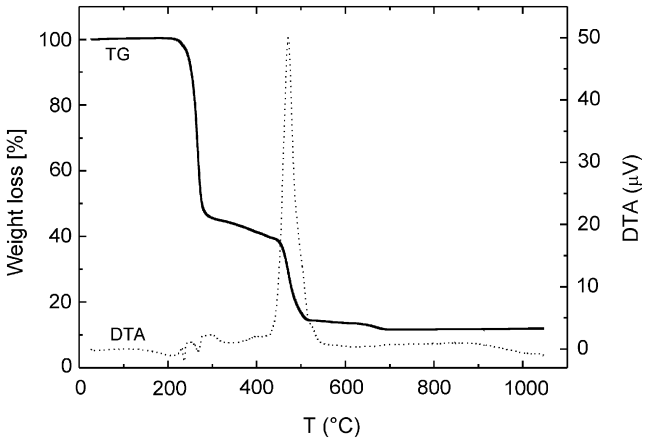


Fig. 3. TG and DTA curves for [Ni(Bz_2dtc)$_2$(phen)] (**9**).

samples containing the complexes, on the course of the oxidation. A comparison of the oxidation courses of the abovementioned samples is depicted in the form of their DTG curves in Fig. 4. Characteristic temperatures and kinetic parameters obtained from TG curves are summarized in Tables 5 and 6, respectively. It has been found that acetone application has no significant impact on the graphite oxidation. However, its presence causes only small decrease in temperature of the oxidation (*ca.* 10 °C) together with the decreasing of the activation energy of the process. The presence of the complexes even in applied trace amount (Ni content is about 100 mol ppm) has significant impact on the course of the graphite oxidation, however, this effect is practically independent on the quality of the admixture used, i.e. on the complexes themselves. In the presence of the complexes, the oxidation of graphite starts about 60 °C lower as compared to the sample containing graphite and acetone but the temperature relating to the termination of graphite oxidation is not influenced much. It follows that the width of the temperature interval in which the graphite oxidation with the samples proceeds is about 50 °C greater as compared to pure graphite. It can be seen from shapes of DTG curves that the presence of complexes causes bifurcating of the formerly simple DTG peak, thus graphite enriched by the complexes is oxidized in two steps in comparison of pure graphite.

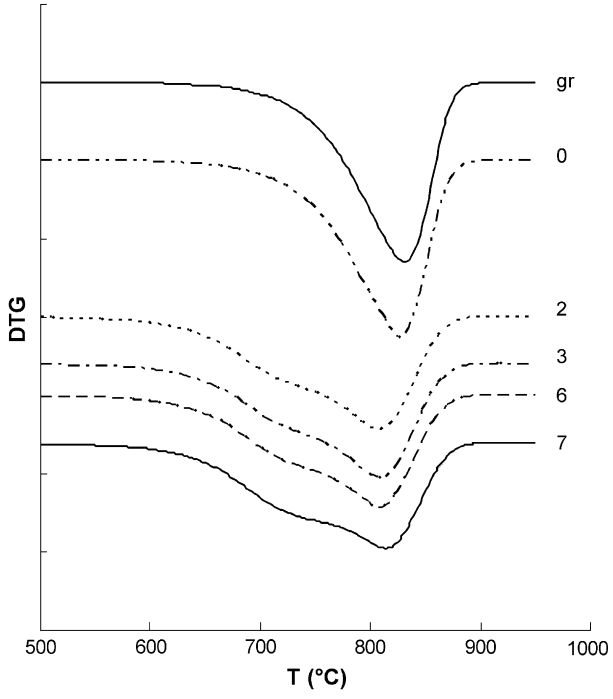


Fig. 4. DTG curves of graphite samples containing complexes **2**, **3**, **6** and, their comparison with DTG curves for pure graphite (gr) and pure acetone (0).

Table 5
Characteristic temperatures (°C) of graphite, acetone and their mixtures with complexes

Sample	T_p	T_m	T_k	$T_k - T_p$
Pure graphite (gr)	775	834	862	87
Pure acetone (0)	763	822	854	91
2	704	806	848	144
3	706	804	846	140
6	705	807	848	143
7	702	807	849	147

T_p – the beginning of oxidation; T_m – oxidation rate maximum; T_k – the end of oxidation.

Table 6
Kinetic parameters of oxidation of graphite, acetone and their mixtures with complexes

Sample	Step	n	A (s^{-1})	E (kJ mol^{-1})	w (%)
Pure graphite (gr)		0.7	9.50×10^8	241	
Pure acetone (0)		0.7	1.47×10^8	222	
2	I	1.0	5.36×10^5	160	53.66
	II	1.3	1.17×10^{17}	400	46.34
3	I	0.9	1.24×10^5	150	58.30
	II	1.1	1.35×10^{14}	341	41.70
6	I	1.0	6.00×10^5	162	60.91
	II	1.4	3.92×10^{20}	474	39.09
7	I	1.0	2.43×10^5	155	63.13
	II	1.2	3.23×10^{17}	412	36.87

n – reaction order; A – frequency factor, E – activation energy, w – mass of sample oxidized.

The calculated values of activation energies (E) and frequency factors (A) show that two observed oxidative steps of the enriched graphite differ significantly. A bigger portion of graphite is oxidized in the first step with activation energy values of 150–160 kJ mol^{-1} and frequency factors in the order of 10^5–10^6 s^{-1}. Significantly higher values of both parameters were determined for the second step. The reaction order was determined to be slightly higher for both steps ($n = 1.0$–1.4; see Table 6) as compared to free graphite ($n = 0.7$). It shows the fact that the kinetics of pure graphite is determined by its contracting volume ($n = 2/3$ corresponds to phase boundary controlled reaction, i.e. mechanism R3), however, the kinetics of oxidation of

graphite enriched by the complexes can be described better by the model of the first-order reaction.

Acknowledgements

The financial support of this work by The Ministry of Education, Youth and Sports of the Czech Republic (a grant no. MSM6198959218) is gratefully acknowledged. Authors also wish to thank to Mrs. Regina Mencelová for help with the preparation of some complexes, Dr. Zdeněk Šindelář for magnetic susceptibility measurements and Mr. Pavel Štarha for performing of TG/DTA measurements.

Appendix A. Supplementary material

CCDC 625271 and 652556 contain the supplementary crystallographic data for complexes **3** and **8**, respectively. These data can obtained free of charge via http://www.ccdc.cam.ac.uk/conts/retrieving.html, or from the Cambridge Crystallographic Data Centre, 12 Union Road, Cambridge CB2 1EZ, UK; fax: (+44) 1223-336-033; or e-mail: deposit@ccdc.cam.ac.uk. Supplementary data associated with this article can be found, in the online version, at doi:10.1016/j.poly.2007.09.024.

References

[1] D. Coucouvanis, J.P. Fackler Jr., Inorg. Chem. 6 (1967) 2047.
[2] R. Dingle, Inorg. Chem. 10 (1971) 1141.
[3] K. Ramalingam, G. Aravamudan, V. Ventachalam, Bull. Chem. Soc. Jpn. 66 (1993) 1554.
[4] R. Pastorek, F. Březina, Z. Šindelář, M. Klečková, Acta Univ. Palacki. Olom. 97 (1990) 19.
[5] R. Pastorek, J. Kameníček, M. Pavlíček, J. Husárek, Z. Šindelář, Z. Žák, Acta Univ. Palacki. Olom. 40 (2001) 57.
[6] F.H. Allen, Acta Crystallogr. Sect. B – Struct. Sci. 58 (2002) 380.
[7] Ng. Szeman, J.W. Ziller, P.J. Farmer, Inorg. Chem. 43 (2004) 8301.
[8] V. Shklover, T. Haibach, B. Bolliger, M. Hochstrasser, M. Erbudak, H.U. Nissen, S.M. Zakeeruddin, M.K. Nazeeruddin, M. Gratzel, J. Solid State Chem. 132 (1997) 60.
[9] S.M. Zakeeruddin, Md.K. Nazeeruddin, R. Humphy-Baker, M. Gratzel, V. Shklover, Inorg. Chem. 37 (1998) 5251.
[10] G.D. Forster, G. Hogarth, J. Chem. Soc., Dalton Trans. (1993) 2539.
[11] T.A. Coffey, G.D. Forster, G. Hogarth, J. Chem. Soc., Dalton Trans. (1995) 2337.
[12] G. Hogarth, I. Richards, Dalton Trans. (2005) 760.
[13] M. Kita, K. Yamanari, Y. Shimura, Bull. Chem. Soc. Jpn. 62 (1989) 23.
[14] S.P. Sovilj, K.B. Babic-Samardzija, Hemijska Industrija (Chem. Ind.) 54 (2000) 534.
[15] R. Vicente, A. Escuer, J. Ribas, A. Dei, X. Solans, T. Calvet, Polyhedron 9 (1990) 1729.
[16] R. Pastorek, J. Kameníček, B. Cvek, V. Slovák, M. Pavlíček, J. Coord. Chem. 59 (2006) 911.
[17] R. Pastorek, J. Kameníček, H. Vrbová, V. Slovák, M. Pavlíček, J. Coord. Chem. 59 (2006) 437.
[18] R. Pastorek, J. Kameníček, B. Cvek, M. Pavlíček, Z. Šindelář, Z. Žák, J. Coord. Chem. 56 (2003) 1123.
[19] R. Přibil, Komplexometrické titrace, SNTL, Praha, 1955, p. 22.
[20] M. Jureček, Organická analýza II, ČSAV, Praha, 1957, p. 140.
[21] V. Slovák, Thermochim. Acta 372 (2001) 175.
[22] G.M. Sheldrick, Acta Crystallogr. A 46 (1990) 467.
[23] G.M. Sheldrick, SHELXL-97, Program for crystal structure refinement, University of Göttingen, Göttingen, Germany, 1997.
[24] K. Brandenburg, H. Putz, DIAMOND (Version 3.1e), Crystal and molecular structure visualization, Crystal Impact GbR, Postfach 1251, Bonn, Germany, 2007.
[25] S.G. Vulfson, Molecular Magnetochemistry, Gordon and Breach Science Publishers, The Netherlands, 1998, p. 354.
[26] A.B.P. Lever, Inorganic Electronic Spectroscopy, second ed., Elsevier, Amsterdam, 1984, p. 534.
[27] W.J. Geary, Coord. Chem. Rev. 7 (1971) 81.
[28] C.A. Tsipis, D.P. Kessissoglou, G.A. Katsoulos, Chim. Chron., New Series 14 (1985) 195.
[29] I.E. Černikova, I.A. Chartonik, D.S. Umrejko, A.B. Kavrikov, V.I. Afanov, Koord. Chim. 15 (1989) 1695.
[30] R.P. Scholer, E.A. Merbach, Inorg. Chim. Acta 15 (1975) 15.
[31] K. Nakamoto, Infrared and Raman Spectra of Inorganic and Coordination Compounds: Part B: Applications in Coordination, Organometallic, and Bioinorganic Chemistry, fifth ed., Wiley, New York, 1997, p. 116.
[32] Bede ZDS Search/Match for Windows, Ver. 4.53, Bede Scientific Instruments Ltd., Durham, United Kingdom, 2000.
[33] PDF-2 Database Sts 1-47, (1997). ICDD, 12 Campus Boulevard, Newtown Square, Pennsylvania 19073-3273, USA.

Available online at www.sciencedirect.com
ScienceDirect
Polyhedron 27 (2008) 420–428
POLYHEDRON
www.elsevier.com/locate/poly

Syntheses, characterizations and crystal structures of monomeric or macrocyclic compounds of di- or triorganotin (IV) moieties with 4,4′-thiodibenzenethiol

Chun-Lin Ma [a,b,*], Zhi-Fo Guo [a], Ru-Fen Zhang [a]

[a] *Department of Chemistry, Liaocheng University, Liaocheng 252059, PR China*
[b] *Taishan University, Taian 271021, PR China*

Received 17 September 2007; accepted 28 September 2007
Available online 19 November 2007

Abstract

Six organotin compounds with 4,4′-thiodibenzenethiol (LH_2) of the type $R_nSnL_{4-n}SnR_n$ ($n = 3$: R = Me **1**, Ph **2**, $PhCH_2$ **3**, $n = 2$: R = Me **4**, Ph **5**, $PhCH_2$ **6**) have been synthesized. All compounds were characterized by elemental analysis, IR and NMR (^1H, ^{13}C, and ^{119}Sn) spectra. The structures of compounds **1**, **2**, **4**, **5** and **6** were also determined by X-ray diffraction analysis, which revealed that compounds **1** and **2** were monomeric structures, compounds **4**, **5** and **6** were centrosymmetric dinuclear macrocyclic structures, and all the tin(IV) atoms are four-coordinated. Furthermore, supramolecular structures were also found in compounds **1**, **2**, **4**, **5** and **6**, which exhibit one-dimensional chains, two-dimensional networks or three-dimensional structures through intermolecular C–H···S weak hydrogen bonds (WHBs), non-bonded Sn···S interactions or C–H···π interactions.
© 2007 Elsevier Ltd. All rights reserved.

Keywords: S ligand; Macrocyclic compounds; Crystal structure; Tin

1. Introduction

Recently, developments in coordination chemistry have produced numerous macrocyclic compounds through the appropriate coordination geometry of organometallic compounds and certain organic ligands [1]. Furthermore, noncovalent weak molecular forces (such as hydrogen bonds, van der Waals forces, non-bonded contacts and C–H···π interactions), capable of connecting these metallic subunits into looser and more intriguing supramolecular infrastructures, have been widely investigated in structural biology, structural chemistry and the pharmaceutical sciences [2]. Among them organotin compounds are attracting more and more attention mainly due to their intriguing, and often complicated, architectures and topologies [3], and also for their potential industrial applications and biological activities [4]. More recently, flexible multidentate ligands have been employed in order to gain access to topologies not available from logical combinations of rigid building blocks. de Sousa, for example, has reported a series of diorganotin compounds based on the flexible 2,6-diacetylpyridine ligand [5], Silva et al. have reported some five- and six-membered chelate organotin mercaptide compounds [6], and in particular Baul and co-workers have reported a cyclic dinuclear organotin compound [7]. In our previous work, we have reported several novel organotin mercaptide compounds which were obtained from flexible multidentate ligands, such as pentacoordinated compounds with 2,5-dithiobiurea [8], tetranuclear or dinuclear monomers or three-dimensional polymers with *meso*-2,3-dimercaptosuccinic acid [9]. To continue our research on organotin(IV) complexes in this field, we choose another interesting ligand: 4,4′-thiodibenzenethiol.

* Corresponding author. Address: Department of Chemistry, Liaocheng University, Liaocheng 252059, PR China. Tel.: +86 635 8230660; fax: +86 538 6715521.
E-mail address: macl@lcu.edu.cn (C.-L. Ma).

0277-5387/$ - see front matter © 2007 Elsevier Ltd. All rights reserved.
doi:10.1016/j.poly.2007.09.033

This ligand was chosen for the following reasons: first, it has two thiol groups so it should form strong covalent bonds with an organotin moiety; second, the conformational flexibility of this ligand will allow for the formation of various and interesting molecular and supramolecular structures; third, 4,4′-thiodibenzenethiol can bond to more than one organotin moiety in one discrete molecule, which will increase the opportunities for supramolecular assembly from these compounds through intermolecular weak interactions. Here, we report the syntheses and characterizations of six organotin compounds constructed from 4,4′-thiodibenzenethiol (LH_2). With a 1:2:2 molar ratio of LH_2:R_3SnCl:EtONa three dinuclear monomeric compounds (**1**–**3**) of the type $R_3SnLSnR_3$ [R = Me **1**, Ph **2**, $PhCH_2$ **3**] were obtained, and with a 1:1:2 molar ratio of LH_2:R_2SnCl_2:EtONa three dinuclear macrocyclic compounds (**4**–**6**) of the type $(R_2SnL)_2$ [R = Me **4**, Ph **5**, $PhCH_2$ **6**] were obtained.

2. Experimental

2.1. Materials and measurements

Trimethyltin chloride, triphenyltin chloride, dimethyltin dichloride, diphenyltin dichloride and 4,4′-thiodibenzenethiol are commercially available, and they were used without further purification. Dibenzyltin dichloride and tribenzyltin chloride were prepared by a standard method reported in the literature [10]. The melting points were obtained with a Kofler micro-melting point apparatus and were uncorrected. Infrared-spectra were recorded on a Nicolet-6700 spectrophotometer using KBr discs and sodium chloride optics. ^1H, ^{13}C and ^{119}Sn NMR spectra were recorded on a Varian Mercury Plus 400 spectrometer operating at 400, 100.6 and 149.2 MHz, respectively. The spectra were acquired at 298 K; ^{13}C spectra are broadband proton decoupled. The chemical shifts are reported in ppm with respect to the references and are stated relative to external tetramethylsilane (TMS) for ^1H and ^{13}C NMR, and neat tetramethyltin for ^{119}Sn NMR. Elemental analyses were performed with a PE-2400II apparatus.

2.2. X-ray crystallography

Crystals were mounted in Lindemann capillaries under nitrogen. All X-ray crystallographic data were collected on a Bruker SMART CCD 1000 diffractometer with graphite monochromated Mo Kα radiation (λ = 0.71073 Å) at 298(2) K. A semi-empirical absorption correction was applied to the data. The structures were solved by direct methods using SHELXS-97 and refined against F^2 by full-matrix least squares using SHELXL-97. Hydrogen atoms were placed in calculated positions. Crystal data and experimental details of the structure determinations are listed in Table 1.

2.3. Syntheses of the complexes *1*–*6*

2.3.1. *$[(CH_3)_3SnSC_6H_4]_2S$ (1)*

The reaction was carried out under a nitrogen atmosphere. 4,4′-Thiodibenzenethiol (0.250 g, 1 mmol) and sodium ethoxide (0.136 g, 2 mmol) were added to benzene (20 ml) in a Schlenk flask and stirred for 5 min. Trimethyltin chloride (0.399 g, 2 mmol) was added to the reaction mixture, which was then stirred for 12 h at 40 °C. After filtration the solvent was gradually removed by evaporation under vacuum until a solid product was obtained. The solid was recrystallized from ether-petroleum and colorless crystals were formed. Yield: 86%. M.p. 97–99 °C. *Anal.* Calc.

Table 1
Crystal, data collection and structure refinement parameters for compounds **1, 2, 4, 5** and **6**

Compound	**1**	**2**	**4**	**5**	**6**
Empirical formula	$C_{18}H_{26}S_3Sn_2$	$C_{48}H_{38}S_3Sn_2$	$C_{28}H_{28}S_6Sn_2$	$C_{48}H_{36}S_6Sn_2$	$C_{52}H_{44}S_6Sn_2$
M	575.95	948.34	794.24	1042.51	1098.61
Crystal system	Monoclinic	Triclinic	Monoclinic	Triclinic	Monoclinic
Space group	$P2(1)/c$	$P1$	$P2(1)/n$	$P\bar{1}$	$P2(1)/n$
a (Å)	22.923(7)	9.829(4)	6.378(2)	9.051(3)	14.762(4)
b (Å)	7.341(2)	9.853(4)	14.684(5)	10.305(4)	11.832(3)
c (Å)	14.155(4)	12.685(5)	16.205(6)	13.480(5)	15.370(4)
α (°)	90	87.932(5)	90	68.961(4)	90
β (°)	97.828(5)	76.041(5)	92.584(6)	71.938(4)	117.664(3)
γ (°)	90	63.765(4)	90	82.460(5)	90
V (Å^3)	2359.7(13)	1065.9(8)	1516.0(9)	1115.4(7)	2377.6(11)
Z	4	1	2	1	2
μ (mm^{-1})	2.380	1.350	2.078	1.433	1.349
Reflections collected	11 522	5450	7224	5756	12 080
Independent reflections	4075	4426	2667	3836	4198
R_{int}	0.0881	0.0213	0.0562	0.0361	0.0544
$R_1[I > 2\sigma(I)]/R_1$	0.0672	0.0584	0.0423	0.0552	0.0443
(all data)	0.1679	0.0701	0.0679	0.0933	0.0915
$wR_1[I > 2\sigma(I)]/wR_1$	0.1554	0.1459	0.0945	0.0812	0.0900
(all data)	0.2117	0.1556	0.1090	0.0906	0.1144

for $[(CH_3)_3SnSC_6H_4]_2S$: C, 37.53; H, 4.55. Found: C, 37.26; H, 4.30%. IR (KBr, cm^{-1}): ν(Sn–C), 557; ν(Sn–S), 312. ^1H NMR ($CDCl_3$, ppm): δ 0.34 (s, 9H, $^2J_{SnH} = 27.2$ Hz), 7.06 (d, 2H), 7.23 (d, 2H). ^{13}C NMR ($CDCl_3$, ppm): δ 29.6 ($^1J(^{119}Sn–^{13}C) = 390.4$ Hz), 131, 131.6, 133.3, 134, 135, 135.2. ^{119}Sn NMR ($CDCl_3$, ppm): 100.4.

2.3.2. $[Ph_3\ SnSC_6H_4]_2S$ (2)

Compound **2** was prepared in the same way as that for compound **1**. Yield: 92%. M.p. 153–155 °C. *Anal.* Calc. for $[Ph_3SnSC_6H_4]_2S$: C, 60.79; H, 4.04. Found: C, 60.50; H, 3.90%. IR (KBr, cm^{-1}): ν(Sn–C), 546; ν(Sn–S), 309. ^1H NMR ($CDCl_3$, ppm): δ 6.8 (d, 2H), 7.2 (d, 2H), 7.2–7.7 (m, 15H). ^{13}C NMR ($CDCl_3$, ppm): δ 124.9 ($^1J(^{119}Sn–^{13}C) = 402.8$ Hz), 128.7–129.2, 129.9–130.9, 131.67, 133.7, 135.4–135.7, 136.2–137.0, 137.3, 137.4. ^{119}Sn NMR ($CDCl_3$, ppm): −60.5.

2.3.3. $[(PhCH_2)_3\ SnSC_6H_4]_2S$ (3)

Compound **3** was prepared in the same way as that for compound **1**. Yield: 80%. M.p. 100–102 °C. *Anal.* Calc. for $[(PhCH_2)_3SnSC_6H_4]_2S$: C, 62.81; H, 4.88. Found: C, 62.96; H, 4.74%. IR (KBr, cm^{-1}): ν(Sn–C), 551; ν(Sn–S), 322. ^1H NMR ($CDCl_3$, ppm): δ 2.4 (s, 6H), 6.7–7.4 (m, 19H). ^{13}C NMR ($CDCl_3$, ppm): δ 22.7 ($^1J(^{119}Sn–^{13}C) = 440.3$ Hz), 124.7, 124.8, 127.9–128.1, 128.7–129.1, 130.9–131.5, 132.4, 134, 135.8–135.9, 139.4. ^{119}Sn NMR ($CDCl_3$, ppm): 37.7.

2.3.4. $[(CH_3)_2Sn(SC_6H_4)_2S]_2$ (4)

The reaction was carried out under a nitrogen atmosphere. 4,4′-Thiodibenzenethiol (0.250 g, 1 mmol) and sodium ethoxide (0.136 g, 2 mmol) were added to benzene (20 ml) in a Schlenk flask and stirred for 5 min. Dimethyltin dichloride (0.219 g, 1 mmol) was added to the reaction mixture, which was then stirred for 12 h at 40 °C. After filtration, the solvent was gradually removed by evaporation under vacuum until a solid product was obtained. The solid was recrystallized from ether–petroleum and colorless crystals were formed. Yield: 89%. M.p. 199–201 °C. *Anal.* Calc. for $[(CH_3)_2Sn(SC_6H_4)_2S]_2$: C, 42.34; H, 3.55. Found: C, 42.10; H, 3.32%. IR (KBr, cm^{-1}): ν(Sn–C), 575; ν(Sn–S), 319. ^1H NMR ($CDCl_3$, ppm): δ 0.6 (s, 6H), 7.1 (d, 2H), 7.3 (d, 4H), 7.4 (d, 2H). ^{13}C NMR ($CDCl_3$, ppm): δ 30.0 ($^1J(^{119}Sn–^{13}C) = 502.2$ Hz), 128.2, 128.6, 130.5, 132.4, 132.5. ^{119}Sn NMR ($CDCl_3$, ppm): 86.4.

2.3.5. $[(Ph)_2Sn(SC_6H_4)_2S]_2$ (5)

Compound **5** was prepared in the same way as that for compound **4**. Yield: 81%. M.p. 160–162 °C. *Anal.* Calc. for $[(Ph)_2Sn(SC_6H_4)_2S]_2$: C, 55.30; H, 3.48. Found: C, 55.05; H, 3.20%. IR (KBr, cm^{-1}): ν(Sn–C), 558; ν(Sn–S), 305. ^1H NMR ($CDCl_3$, ppm): δ 6.8–7.5 (m, 18H). ^{13}C NMR ($CDCl_3$, ppm): δ 128.8 ($^1J(^{119}Sn–^{13}C) = 503.3$ Hz), 129.1, 129.4, 130.2, 131.1, 131.8, 133.8, 135.8, 136.0, 136.7, 136.9, 137.5. ^{119}Sn NMR ($CDCl_3$, ppm): −61.2.

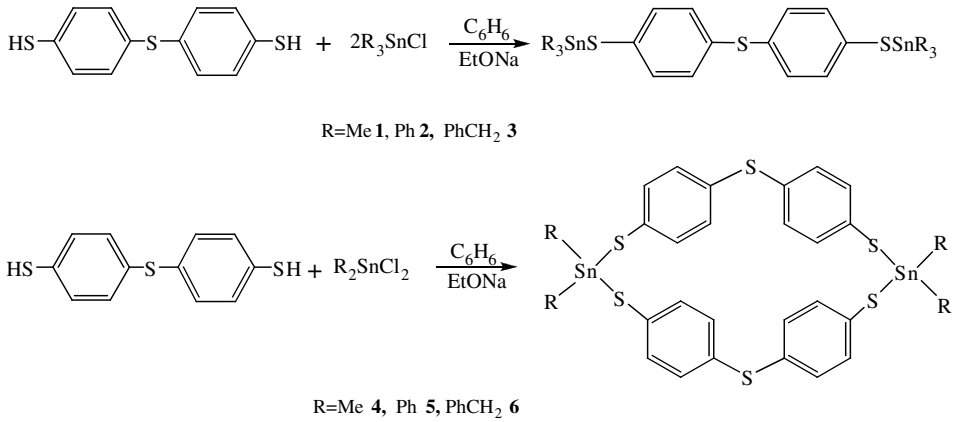
2.3.6. $[(PhCH_2)_2Sn(SC_6H_4)_2S]_2$ (6)

Compound **6** was prepared in the same way as that for compound **4**. Yield: 79%. M.p. 143–145 °C. *Anal.* Calc. for $[(PhCH_2)_2Sn(SC_6H_4)_2S]_2$: C, 56.84; H, 4.04. Found: C, 56.62; H, 3.81%. IR (KBr, cm^{-1}): ν(Sn–C), 530; ν(Sn–S), 320. ^1H NMR ($CDCl_3$, ppm): δ 2.5 (s, 4H), 6.7–7.4 (m, 18H). ^{13}C NMR ($CDCl_3$, ppm): δ 26.0 ($^1J(^{119}Sn–^{13}C) = 443.8$ Hz), 27.9, 125.4, 128.0–128.4, 128.8–128.9, 130.7–131.4, 134.9, 135.8, 136.4, 136.5, 137.2. ^{119}Sn NMR ($CDCl_3$, ppm): 23.0.

3. Results and discussion

3.1. Syntheses

The reactions of triorganotin(IV) chloride with 4,4′-thiodibenzenethiol in a 2:1 stoichiometry and diorganotin(IV) dichloride with 4,4′-thiodibenzenethiol in a 1:1 stoichiometry, depending on the nature of the starting acceptor and reaction conditions, afforded air-stable compounds. The syntheses procedures are shown in Scheme 1.



Scheme 1.

3.2. IR spectra

The IR spectra show that the strong absorption at 2560 cm^{-1} in the free ligand due to the –SH group is absent in the spectra of all the compounds **1–6**, and at the same time a new absorption appears in the region 305–322 cm^{-1}. All these values are located within the range for Sn–S vibrations observed in common organotin thiolate derivatives (300–400 cm^{-1}) [11], consequently, they can be assigned to ν(Sn–S).

3.3. NMR spectra

The ^{1}H NMR data show that the signal of the –SH proton in the spectrum of the ligand is absent in all of the compounds, indicating the removal of the –SH proton and the formation of Sn–S bonds. The $^{2}J_{SnH}$ values of compounds **1** and **4** are 27.2 Hz and 83.2 Hz, which are similar to those previously reported for four-coordinated tetrahedral tin(IV) adducts [12]. The ^{13}C NMR spectra of all the compounds show a significant downfield shift of all carbon resonances, compared with the free ligand.

The ^{119}Sn NMR data show that compounds **1–6** have only one signal (100.4, −60.5, 37.7, 86.4, −61.2 and 23 ppm, respectively), they are all well in accordance with values that have been reported in the literature which lie in the range from +200 to −60 ppm [13].

3.4. X-ray crystallographic studies

3.4.1. Crystal structures of *1* and *2*

The molecular structures of compounds **1** and **2** are illustrated in Figs. 1 and 3, respectively. Selected bond lengths (Å) and angles (°) are listed in Table 2.

X-ray crystal structure analysis reveals that compounds **1** and **2** are monomeric with one ligand bonding to two tin atoms through Sn–S bonds. Each of the tin atoms is four-coordinated. Distortion from strict tetrahedral coordination is partly because of the bonding variance. The four primary bonds to Sn are three methyl groups and one sulfur atom for **1** and three phenyl groups and one sulfur atom for **2**. The Sn–C bond lengths are consistent with those reported in other triorganotin derivatives [14]. The

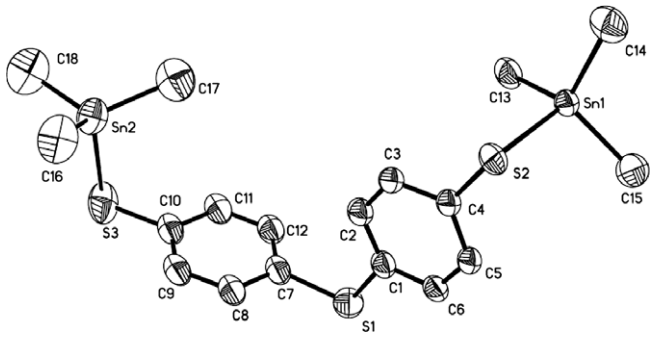


Fig. 1. Molecular structure of compound **1**; ellipsoids at 30% probability; hydrogen atoms have been removed for clarity.

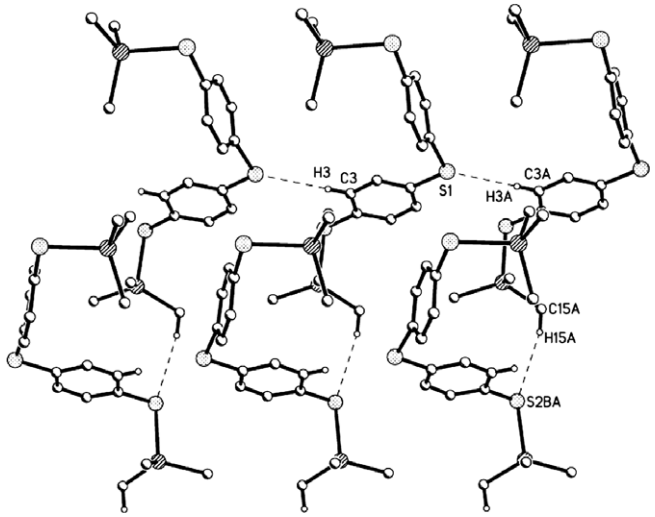


Fig. 2. Two-dimensional network of compound **1** connected through C–H···S WHBs, unattached hydrogen atoms have been removed for clarity.

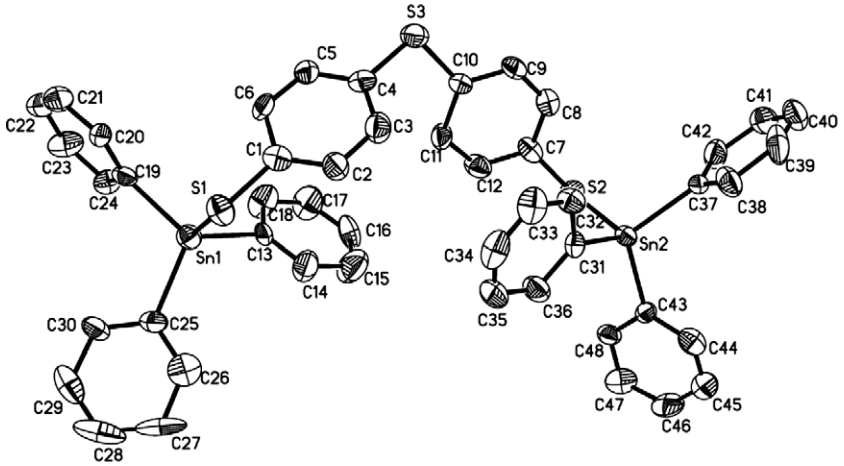


Fig. 3. Molecular structure of compound **2**; hydrogen atoms have been removed for clarity.

Table 2
Selected bond lengths (Å) and bond angles (°) for compounds **1** and **2**

[(CH$_3$)$_3$SnSC$_6$H$_4$]$_2$S (**1**)			
Sn(1)–C(14)	2.10(15)	Sn(2)–C(16)	2.07(19)
Sn(1)–C(15)	2.11(15)	Sn(2)–C(17)	2.08(2)
Sn(1)–C(13)	2.12(13)	Sn(2)–C(18)	2.11(2)
Sn(1)–S(2)	2.44(4)	Sn(2)–S(3)	2.43(6)
C(14)–Sn(1)–C(15)	114.7(6)	C(16)–Sn(2)–C(17)	109.8(8)
C(14)–Sn(1)–C(13)	113.1(6)	C(16)–Sn(2)–C(18)	108.4(8)
C(15)–Sn(1)–C(13)	112.3(6)	C(17)–Sn(2)–C(18)	119.2(9)
C(14)–Sn(1)–S(2)	103.5(4)	C(16)–Sn(2)–S(3)	107.5(6)
C(15)–Sn(1)–S(2)	106.3(4)	C(17)–Sn(2)–S(3)	107.4(6)
C(13)–Sn(1)–S(2)	105.8(4)	C(18)–Sn(2)–S(3)	103.8(6)
[Ph$_3$SnSC$_6$H$_4$]$_2$S (**2**)			
Sn(1)–C(25)	2.12(15)	Sn(2)–C(31)	2.10(17)
Sn(1)–C(13)	2.15(16)	Sn(2)–C(43)	2.13(12)
Sn(1)–C(19)	2.17(14)	Sn(2)–C(37)	2.15(13)
Sn(1)–S(1)	2.43(4)	Sn(2)–S(2)	2.42(3)
C(25)–Sn(1)–C(13)	111.4(6)	C(31)–Sn(2)–C(43)	112.6(6)
C(25)–Sn(1)–C(19)	110.4(6)	C(31)–Sn(2)–C(37)	112.8(6)
C(13)–Sn(1)–C(19)	112.9(6)	C(43)–Sn(2)–C(37)	112.5(5)
C(25)–Sn(1)–S(1)	107.6(4)	C(31)–Sn(2)–S(2)	106.8(4)
C(13)–Sn(1)–S(1)	105.7(5)	C(43)–Sn(2)–S(2)	104.5(3)
C(19)–Sn(1)–S(1)	108.5(4)	C(37)–Sn(2)–S(2)	107.0(4)

Sn–S bonds lengths [the Sn–S bond lengths are between 2.43(6) and 2.44(4) Å] are slightly less than the sum of the covalent radii of Sn and S (2.44 Å) [15].

Compounds **1** and **2** exhibit interesting intermolecular interactions as shown in Figs. 2, 4 and 5: the molecules of **1** are connected through C(15)–H(15)···S(2) (C···S, 3.85 Å; H···S, 2.94 Å; C–H···S, 158.5°) and C(3)–H(3)···S(1) WHBs (C···S, 3.91 Å; H···S, 2.99 Å; C–H···S, 175.9°) into a two-dimensional network in the *bc* plane. In compound **2**, there are two loose two-dimensional networks through different WHBs in different directions: one that consists of discrete molecules connected through C(24)–H(24)···S(3) (C···S, 3.70 Å; H···S, 2.98 Å; C–H···S, 135.1°) and C(28)–H(28)···S(2) (C···S, 3.80 Å; H···S, 2.99Å; C–H···S, 146.3°) WHBs (Fig. 4) in the *bc* plane, and another that is connected through C(30)–H(30)···π (37–42) [H···π (centroid), 3.51 Å; C–H···π (centroid), 122.0°] and C(46)–H(46)···π (37–42) [H···π (centroid), 3.38 Å; C–H···π (centroid), 138.1°] interactions (Fig. 5) along the [1 1 $\bar{1}$] and [$\bar{1}$ 1 0] directions.

The values for the C–H···S WHB are longer than an intramolecular C–H···S WHB in (r-2, c-4)-3-benzyl-2,4,5,5-tetraphenyl-1,3-thiazolidine (C···S, 3.04 Å; H···S, 2.55 Å and C–H···S, 110°) [16], but they are closely in agreement with values that have been reported in the literature [15,17], whilst the parameters for the C–H···π interactions in the compound are in agreement with those that have been reported in the literature [17,18].

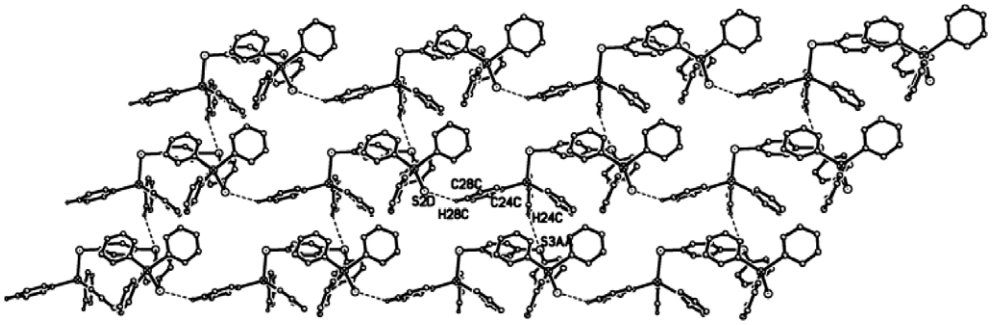


Fig. 4. Two-dimensional network of compound **2** by C–H···S WHBs along the *bc* plane, unattached hydrogen atoms have been removed for clarity.

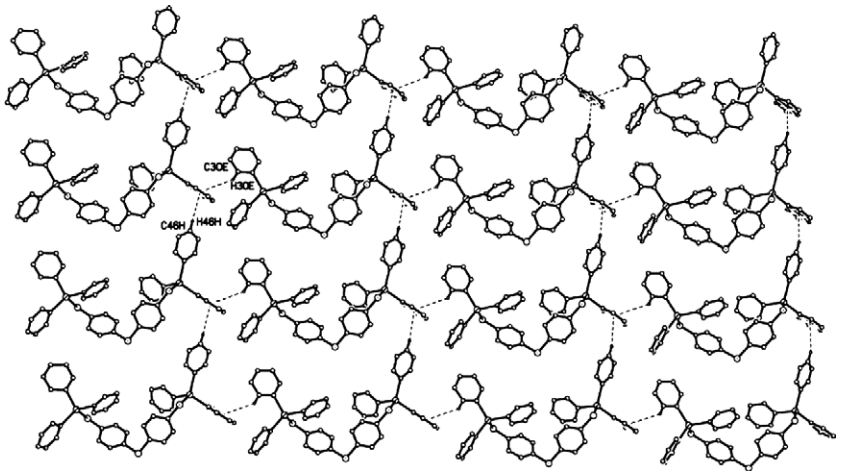


Fig. 5. Two-dimensional network of compound **2** connected through C–H···π interactions along the [1 1 $\bar{1}$] and [$\bar{1}$ 1 0] directions, unattached hydrogen atoms have been removed for clarity.

*3.4.2. Crystal structure of **4**, **5** and **6***

Perspective view of the molecular structures of compounds **4**, **5** and **6** are illustrated in Figs. 6, 8 and 10, respectively. Selected bond lengths (Å) and angles (°) are listed in Table 3.

Compounds **4**, **5** and **6** all proved to be centrosymmetric dinuclear macrocyclic compounds with 4,4′-thiodibenzenethiol bridging the adjacent tin atoms with a twenty-four member $Sn_2S_6C_{16}$ ring, and the ring can be valued by the transcyclic distances (Sn(1)–Sn(1)# = 12.51 Å and C(2)–

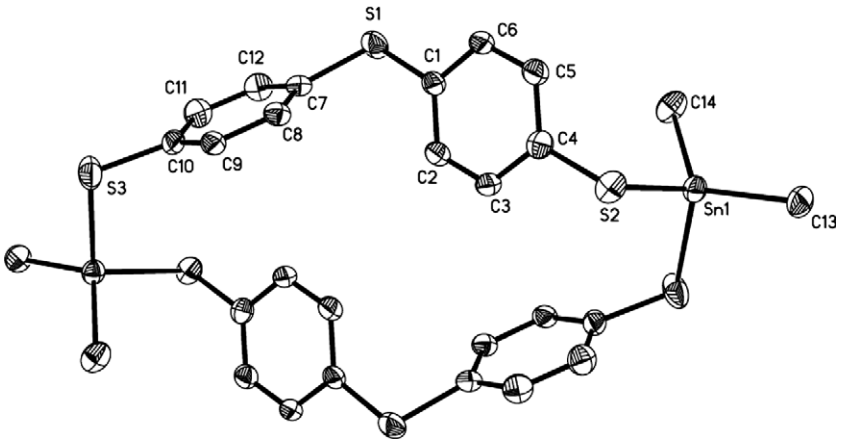


Fig. 6. Molecular structure of compound **4**; ellipsoids at 30% probability; hydrogen atoms have been removed for clarity.

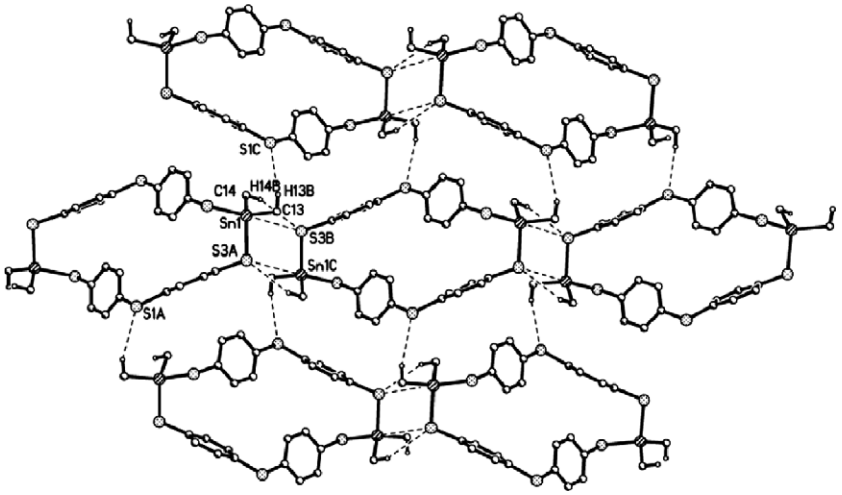


Fig. 7. Two-dimensional network of compound **4** connected through C–H···S WHBs and non-bonded Sn···S contacts, unattached hydrogen atoms have been removed for clarity.

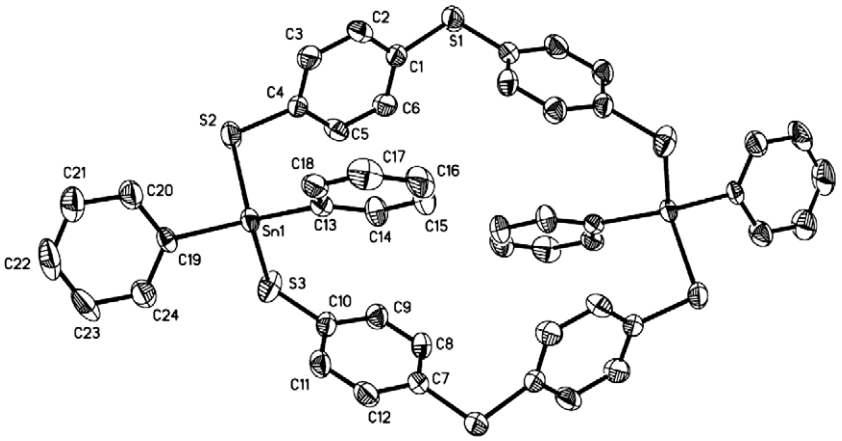


Fig. 8. Molecular structure of compound **5**; ellipsoids at 30% probability; hydrogen atoms have been removed for clarity.

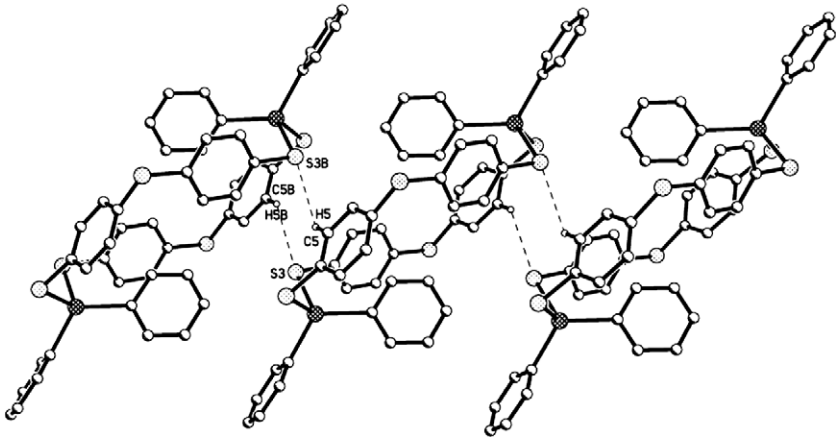


Fig. 9. One-dimensional chain of compound **5**, unattached hydrogen atoms have been removed for clarity.

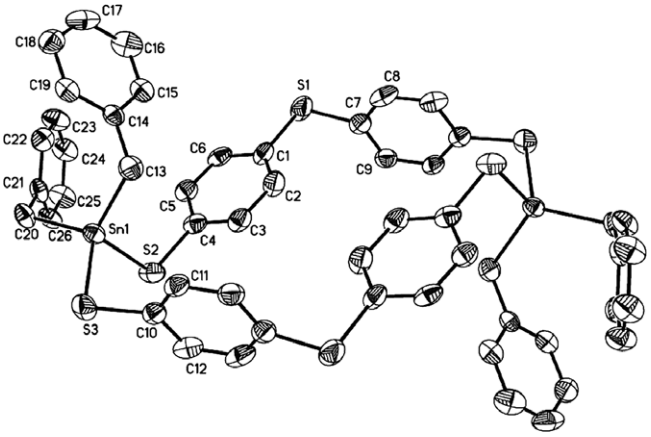


Fig. 10. Molecular structure of compound **6**; ellipsoids at 30% probability; hydrogen atoms have been removed for clarity.

Table 3
Selected bond lengths (Å) and bond angles (°) for compounds **4**, **5** and **6**

*[(CH$_3$)$_2$Sn(SC$_6$H$_4$)$_2$S]$_2$ (**4**)*			
Sn(1)–C(14)	2.12 (7)	Sn(1)–S(2)	2.42 (17)
Sn(1)–C(13)	2.12 (6)	Sn(1)–S(3)#1	2.45(2)
C(14)–Sn(1)–C(13)	120.8(3)	C(14)–Sn(1)–S(3)#1	107.6(2)
C(14)–Sn(1)–S(2)	107.8(18)	C(13)–Sn(1)–S(3)#1	104.0(19)
C(13)–Sn(1)–S(2)	107.5(19)	S(2)–Sn(1)–S(3)#1	108.7(6)
*[(Ph)$_2$Sn(SC$_6$H$_4$)$_2$S]$_2$ (**5**)*			
Sn(1)–C(13)	2.12(6)	Sn(1)–S(3)	2.42(19)
Sn(1)–C(19)	2.13(5)	Sn(1)–S(2)	2.42(18)
C(13)–Sn(1)–C(19)	120.9(2)	C(13)–Sn(1)–S(2)	107.8 (15)
C(13)–Sn(1)–S(3)	112.2(17)	C(19)–Sn(1)–S(2)	101.1(16)
C(19)–Sn(1)–S(3)	107.5(19)	S(3)–Sn(1)–S(2)	105.7(7)
*[(PhCH$_2$)$_2$Sn(SC$_6$H$_4$)$_2$S]$_2$ (**6**)*			
Sn(1)–C(20)	2.15(6)	Sn(1)–S(2)	2.41(18)
Sn(1)–C(13)	2.15(6)	Sn(1)–S(3)	2.43(19)
C(20)–Sn(1)–C(13)	115.7(2)	C(20)–Sn(1)–S(3)	114.4(16)
C(20)–Sn(1)–S(2)	108.0(17)	C(13)–Sn(1)–S(3)	106.7(19)
C(13)–Sn(1)–S(2)	111.5(19)	S(2)–Sn(1)–S(3)	99.4(7)

C(2)# = 3.89 Å for **4**; Sn(1)–Sn(1)# = 10.42 Å and C(8)–C(8)# = 6.75 Å for **5**; Sn(1)–Sn(1)# = 11.42 Å and C(2)–C(2)# = 4.44 Å for **6**). The units are [(CH$_3$)$_2$SnL], [(Ph)$_2$SnL] and [(PhCH$_2$)$_2$SnL], respectively, in which the primary bonds of the ligand to tin occur through the two sulfur atoms. To the best of our knowledge, dinuclear macrocyclic compounds in common organotin derivatives of thionate have so far only rarely been reported [19].

Each of the tin atoms in compounds **4**, **5** and **6** has a distorted tetrahedral coordination. The four primary bonds to Sn are two Sn–C and two Sn–S bonds. The Sn–C bond lengths are consistent with those found in compounds **1** and **2**. The Sn–S bond lengths are 2.42(17) Å [Sn(1)–S(2)], 2.45(2) Å [Sn(1)–S(3)#1] (#1 = $-x+2, -y+1, -z+1$) for **4**; 2.42(19) Å [Sn(1)–S(3)], 2.42(18) Å [Sn(1)–S(2)] for **5** and 2.41(18) Å [Sn(1)–S(2)], 2.43(19) Å [Sn(1)–S(3)] for **6**, similar to those found in compounds **1** and **2**. Distortion from a strict tetrahedral coordination is partly because of the bonding variance. The deviation from an ideal tetrahedron is manifested by the bond angles (see Table 3), all of which deviate from the idea value of 109.5°.

Analyses of the supramolecular infrastructure of the compounds **4**, **5** and **6** reveal that weak intermolecular non-bonded Sn···S contacts, C–H...S and C–H···π WHBs play important roles in the supramolecular arrangements. The C–H···π interactions can also be viewed as an edge-to face π–π interaction [18d].

The supramolecular structure of compound **4** is a two-dimensional network in the *bc* plane, as shown in Fig. 7, in which the discrete molecules are connected through intermolecular C–H···S (C···S, 3.62–3.75 Å; H···S, 2.87–2.96 Å; C–H···S, 135.0–140.6°) WHBs. This loose structure is further stabilized by non-bonded Sn(1)···S(3) interactions. The Sn(1)···S(3) distance (3.700 Å) is shorter than that in compounds (PhCH$_2$)$_2$Sn(SC$_5$H$_5$N$_2$)$_2$ and (PhCH$_2$)$_2$SnCl(SC$_5$H$_5$N$_2$) [20], and also shorter than the sum of the Van der waals radii of Sn and S (4.0 Å) [21].

In compound **5**, an intermolecular C(5)–H(5)···S(3) (C···S, 3.65Å; H···S, 2.97 Å; C–H···S, 130.3°) WHB connects the discrete molecules into a linear chain, as shown in Fig. 9.

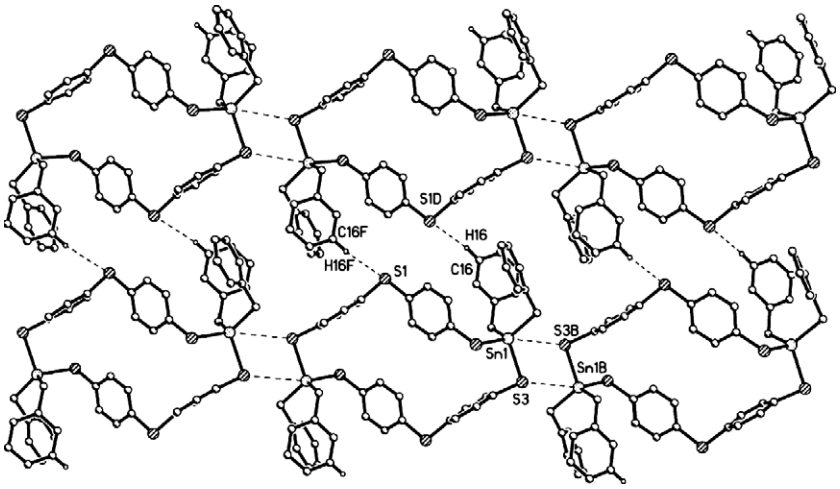


Fig. 11. Two-dimensional network of compound **6** connected through C–H···S WHBs and non-bonded Sn···S contacts, unattached hydrogen atoms have been removed for clarity.

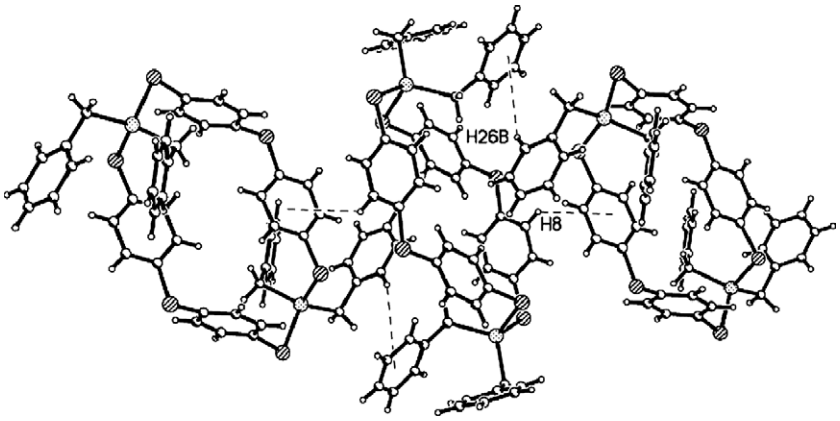


Fig. 12. One dimensional chain of compound **6** connected through C–H···π interactions along the [1 1 1] direction.

In compound **6**, the two-dimensional network in the *ac* plane (as shown in Fig. 11) is connected by C–H···S WHBs (C···S, 3.81Å; H···S, 2.95 Å; C–H···S, 153.6°) and non-bonded Sn···S interactions, and the linear chain along the [1 1 1] direction is connected by C–H···π [H···π (centroid), 3.36–3.51 Å; C–H···π (centroid), 131.5–136.3°] interactions at the same time (as shown in Fig. 12), forming a three-dimensional structure.

4. Conclusion

4,4′-Thiobisbenzenethiol has been shown to be able to form monomeric compounds with triorganotin moieties, and also to form dinuclear macrocyclic compounds with diorganotin moieties due to the flexibility of the ligand and the nature of the starting acceptor. The supramolecular structures described in this paper demonstrate that weak intermolecular interactions have enormous potential for assembling discrete molecular systems into one-dimensional chains, two-dimensional networks or three-dimensional structures, in which the subunits are organometallic compounds.

The current study also provides aids in the fundamental understanding of molecular recognition, and insight into the interpretation of supramolecular aggregation in crystal engineering.

5. Supplementary material

CCDC 636269, 636268, 636266, 636267, 636265 contains the supplementary crystallographic data for **1**, **2**, **4**, **5** and **6**. These data can be obtained free of charge via http://www.ccdc.cam.ac.uk/conts/retrieving.html, or from the Cambridge Crystallographic Data Centre, 12 Union Road, Cambridge CB2 1EZ, UK; fax: (+44) 1223-336-033; or e-mail: deposit@ccdc.cam.ac.uk.

Acknowledgement

We thank the National Natural Science Foundation of China (20271025) for financial support.

References

[1] (a) M. Eshel, A. Bino, Inorg. Chim. Acta 320 (2001) 127;
(b) E. Kiss, K. Petrohan, D. Sanna, E. Garribba, G. Micera, T. Kiss, Polyhedron 19 (2000) 55;
(c) D. Dakternieks, A. Duthie, B. Zobel, Organometallics 21 (2002) 647;
(d) M. Verdenelli, S. Parola, L.G. Hubert-Pfalzgraf, S. Lecocq, Polyhedron 19 (2000) 2069;
(e) T.P. Lockhart, Organometallics 7 (1988) 1438;
(f) Ok-Sang Tung, Y.S. Sohn, J.A. Ibers, Inorg. Chem. 25 (1986) 2273.

[2] (a) For recent reviews see: T. Steiner, W. Saenger, J. Am. Chem. Soc. 114 (1992) 10146;
(b) K.N. Houk, S. Menzer, S.P. Newton, F.M. Raymo, J.F. Stoddart, D.J. Williams, J. Am. Chem. Soc. 121 (1999) 1479;
(c) G.R. Desiraju, Acc. Chem. Res. 29 (1996) 441;
(d) M. Iwaoka, S. Tomoda, J. Am. Chem. Soc. 116 (1994) 4463;
(e) R. Boese, M.T. Kirchner, W.E. Billups, L.R. Norman, Angew. Chem. 115 (2003) 1921. Angew. Chem., Int. Ed., 42 (2003) 1961;
(f) G.R. Desiraju, Acc. Chem. Res. 29 (1996) 441;
(g) T. Steiner, Crystallogr. Rev. 6 (1996) 1;
(h) T. Steiner, Chem. Commun. (1997) 727;
(i) M.C.T. Fyfe, J.F. Stoddart, Coord. Chem. Rev. 183 (1999) 139.

[3] (a) M. Hill, M.F. Mahon, K.C. Molloy, J. Chem. Soc., Dalton Trans. (1996) 1857;
(b) S. Bhandari, C.G. Frost, E. Hague, M.F. Mahon, K.C. Molloy, J. Chem. Soc., Dalton Trans. (2000) 663;
(c) V. Berceanc, C. Crainic, I. Haiduc, M.F. Mahon, K.C. Molloy, M.M. Venter, P.J. Wilson, J. Chem. Soc., Dalton Trans. (2002) 1036;
(d) R. García-zarracino, J. Ramos-Quiñones, H. Hopfl, Inorg. Chem. 42 (2003) 3835.

[4] S.K. Duboy, U. Roy, Appl. Organomet. Chem. 17 (2003) 3.

[5] G.F. de Sousa, V.M. Deflon, M.T. do P. Gambardella, R.H.P. Francisco, J.D. Ardisson, E. Niquet, Inorg. Chem. 45 (2006) 4518.

[6] A.P.G. de Sousa, R.M. Silva, A. Cesar, J.L. Wardell, J.C. Huffman, A. Abras, J. Organomet. Chem. 605 (2000) 82.

[7] T.S.B. Baul, K.S. Singh, A. Lyčka, M. Holčapek, A. Linden, J. Organomet. Chem. 690 (2005) 1581.

[8] R.F. Zhang, J.F. Sun, C.L. Ma, Heteroatom Chem. 17 (2006) 93.

[9] C.L. Ma, Q.F. Zhang, Eur. J. Inorg. Chem. (2006) 3244.

[10] K. Sisido, Y. Takeda, Z. Kinugawa, J. Am. Chem. Soc. 83 (1961) 538.

[11] J.R. May, W.R. Mc Whinnie, R.C. Poller, Spectrochim. Acta 27A (1971) 969.

[12] T.P. Lockhart, W.F. Manders, Inorg. Chem. 25 (1986) 892.

[13] J. Holecek, M. Nadvornik, K. Handlir, A. Lycka, J. Organomet. Chem. 315 (1986) 299.

[14] C.L. Ma, J.F. Sun, Y. Shi, R.F. Zhang, J. Organomet. Chem. 690 (2005) 1560.

[15] L. Pauling, The Nature of the Chemical Bond, 3rd ed., Cornell University Press, Ithaca, 1960, pp. 64.

[16] M. Domagala, S.J. Grabowskia, K. Urbaniakb, G. Mloston, J. Mol. Struct. 690 (2004) 69.

[17] C.L. Ma, Q.F. Zhang, R.F. Zhang, D.Q. Wang, Chem. Eur. J. 12 (2006) 420.

[18] (a) P.K.C. Paul, Cryst. Eng. 5 (2002) 3;
(b) J.G. Planas, C. Masalles, R. Sillanpää, R. Kivekäs, F. Teixidor, C. Viñas, Cryst. Eng. 8 (2005) 75;
(c) H.W. Roesky, M. Andruh, Coord. Chem. Rev. 236 (2003) 91;
(d) M. Nishio, CrystEngComm. 6 (2004) 130.

[19] (a) K. Jurkschat, W. Uhlig, C. Mugge, A. Tzschach, B. Schmidt, M. Drager, Z. Anorg. Allg. Chem. 556 (1988) 161;
(b) H. Preut, K. Gratz, F. Huber, Acta. Crystallogr., Sect. C 40 (1984) 941;
(c) Ok-Sang Jung, Youn Soo Sohn, J.A. Ibers, Inorg. Chem. 25 (1986) 2273;
(d) F.E. Hahn, A. Dittler-Klingemann, T. Lugger, Z. Naturforsch., Teil. B 58 (2003) 1030.

[20] C.L. Ma, J.H. Zhang, G.R. Tian, R.F. Zhang, J. Organomet. Chem. 690 (2005) 519.

[21] J.S. Casas, A. Castineiras, E.G. Martinez, A.S. González, A. Sánchez, J. Sordo, Polyhedron 16 (1997) 795.

Available online at www.sciencedirect.com
ScienceDirect
Polyhedron 27 (2008) 429–439
POLYHEDRON
www.elsevier.com/locate/poly

Synthesis, structure, dehydration transformations and ion exchange characteristics of iron-silicate with various Si and Fe contents as mixed oxides

I.M. Ali *, E.S. Zakaria, M.M. Ibrahim, I.M. El-Naggar

Hot Labs. Center, Atomic Energy Authority, P.C. 13759 Cairo, Egypt

Received 31 May 2007; accepted 30 September 2007
Available online 11 December 2007

Abstract

The synthesis of a new series of impregnated metal oxides with different Fe/Si ratios (0.5, 1 and 2) was obtained by the direct precipitation method. Physico-chemical properties and molecular formula of the obtained products were identified with different analytical techniques, such as chemical stability, XRD, IR, elemental and thermal analyses. Thermal kinetic parameters, such as order (n) and activation energy (E_a), of the solid-state phase transformations of the first dehydration process have been studied for the obtained materials from DTA thermograms. The ion exchange applications and the sorption properties of the materials with some radioactive nuclides have been studied, depending on the Fe/Si molar ratios. These investigations indicated that the ion exchange capacities as well as the selectivities of different materials towards the studied nuclides show the order $Co^{2+} > Cs^{+} > Na^{+}$ at a certain pH.
© 2007 Elsevier Ltd. All rights reserved.

Keywords: Iron silicate; Kinetic studies; Solid-state dehydration; Ion exchange; Radioactive waste

1. Introduction

Ion exchange technologies are widely used for water and waste treatment, in hydrometallurgy, biochemistry, medicine, environmental protection, etc. Among various components, oxides and hydrous oxides (including oxyhydroxides and hydroxides) of Fe, Al and Si are important sorbents because of their abundance in the natural geologic environment and their high sorption capacity [1–3]. The sorption characteristics of the materials, however, are not easy to describe unambiguously, because they are controlled by a number of complicated physical and chemical interfacial properties. Tochiyama et al. reported [4] that amorphous-$Fe_2O_3 \cdot 3.5H_2O$ was obtained when NH_4OH was used as a precipitating agent while α-$FeOOH \cdot 0.6H_2O$ was obtained when NaOH was used for precipitation. Also, the same authors studied the sorption of Np(V) on various iron oxides and hydrous iron oxides [5]. Qualitative evidence for the chemical interaction of silicic acid with iron(III) in dilute aqueous solution has been reported earlier [6], but neither information regarding the nature of the interaction nor that of the chemical species formed is available. In 1965 Weber and Stumm [7] reported UV absorption data used to study the equilibrium relationships for complex formation between Fe(III) (in dilute acidic aqueous solutions of $HClO_4$) and orthosilicic acid. The data indicated that Fe^{3+} forms relatively stable $FeSiO(OH)_2^{2+}$ complexes with $Si(OH)_4$ according to the equation:

$$Fe^{3+} + Si(OH)_4 === FeSiO(OH)_2^{2+} + H^{+} \quad (1)$$

Recently, a method for preparing iron(III)-based binary oxide adsorbents in a granulated form for arsenic removal was studied [8]. The addition of silica enhanced the granulated adsorbent strength but reduced the arsenic adsorption capacity. Several iron(III) oxides, such as amorphous hydrous ferric oxide (FeOOH), poorly crystalline hydrous ferric oxide (ferrihydrite) and goethite (α-FeOOH), are

* Corresponding author. Tel.: +20 105787044.
E-mail address: ismail_m_ali@yahoo.com (I.M. Ali).

0277-5387/$ - see front matter © 2007 Elsevier Ltd. All rights reserved.
doi:10.1016/j.poly.2007.09.034

promising adsorptive materials for removing both As(V) and As(III) from aqueous solutions [9–13]. However, most iron(III) oxides are available only as fine powders or are generated in situ as gels or suspensions in aqueous solution. These forms of iron(III) oxides retain their strong affinities for As(V) and As(III), but are limited to reactor configurations incorporating large sedimentation and filtration units, which cause difficulty in solid/liquid separation [14]. Thus, they are not suitable for column adsorption in water and waste water treatment. Furthermore, iron(III) oxide alone is not suitable as a filter medium due to its low hydraulic conductivity [15].

In principle, silica sol can be produced by reacting a sodium silicate solution with hydrochloric acid. Initially, silica acid ($Si(OH)_4$) is released,

$$Na_2SiO_3 + H_2O + 2HCl ==== = (Si(OH)_4) + 2NaCl \quad (2)$$

Also, amorphous-FeOOH can be prepared by mixing iron(III) salt and caustic solution in terms of the following reaction:

$$Fe^{3+} + 3OH^- ======= Fe_2O_3 + H_2O \quad (3)$$

Condensing free silicic acid with the elimination of water then forms polymeric silicic acid and further leads to gelling, i.e. formation of hydro gel [16]. When $Si(OH)_4$ contacts with FeOOH, polymerization of silicic acid on FeOOH likely occurs to form silicato-iron(III) surface complexes between Si and Fe [17–19], possibly by the following scheme.

Fe-O-Si(OH)$_3$ Fe-O(OH)$_2$-Si(OH)$_3$ (OH)Si-Fe-(OH)O-O-O(OH)-Fe-Si(OH)

(a) (b) (c)

Schematic bonding between $Si(OH)_4$ and FeOOH (a) bonding with $Si(OH)_4$ monomer, (b) polymerization, and (c) siloxane linkage between $Si(OH)_4$ monomers [17].

It is known that iron(III) salt solution is strongly acidic. If iron(III) salt solution, for example, $FeCl_3$, is mixed with a mixture of Na_2SiO_3 and NaOH, the above reactions (2) and (3) should occur simultaneously. This means that FeOOH and $Si(OH)_4$ form instantly in situ. Under such circumstance, FeOOH sol and SiO_2 sol are believed to have a better contact and Fe–Si complexes are most likely to form. The complexation between Fe and Si likely enhances the binding of FeOOH microns and hence increases the physical strength of the adsorbents produced. Since the crystallization of iron oxides, for instance the transformation of ferrihydrite to goethite, is strongly retarded by the presence of silicate species [20–23], the FeOOH formed through co-precipitation with silicate should be in an amorphous (or poorly crystalline) form. However, the quantity of the silica sol to be added in the adsorbent should be determined as the balance of two factors: strength of the adsorbent (resistance to disintegration) and adsorption capacity for any designated species.

Based on the above data, the aim of this study was directed to synthesize a new extensive series of impregnated metal oxides with Fe/Si ratios equal to 0.5, 1 and 2 by using ammonium hydroxide as a precipitating agent, so that a direct comparison of the structure, solid-state dehydration and ion exchange properties between the different metal oxides could be done. A correlation between the metal ratios, the water contents and the structures and/or the ion exchange properties towards some radionuclides was investigated.

2. Experimental

2.1. Reagents and analytical procedures

All reagents were of analytical grade (Aldrich, Merk) and were used without further purification. The radioactive ^{22}Na, ^{134}Cs, ^{60}Co and ^{144}Ce tracers for the ion exchange studies were obtained from Amersham International.

2.2. Synthesis

An extensive series of iron(III) silicates were synthesized by dropwise addition of equimolar solutions (0.5 M) of iron trichloride and sodium silicate. Different volumes of Fe/Si ratios equal to 1.0, 0.5 and 2.0 were used to obtain the FeSi-I, FeSi-II and FeSi-III series, respectively, as given in Table 1. In the formation reactions, 1 M of ammonia solution was added to the reaction mixtures until the pH of the supernatant solutions was about 5. After overnight standing, the resultant mixtures of each reaction containing the precipitate was divided into two equal portions; one of the portions was filtered directly and the other portion was treated with 0.1 M HNO_3 for 24 h to produce the H^+-form of the iron silicate products. The precipitates were washed several times with bidistilled water, filtered by using a centrifuge (about 10^4 rpm), and dried at 50 °C. The glassy brown solid products were cracked with bidistilled water in order to remove fine adherent particles, then redried at 50 °C. The products were ground, sieved and finally air dried at room temperature and stored in a dark bottle. Details of the precipitations are summarized in Table 1.

2.3. Characterization of iron(III) silicates

The physico-chemical properties of the prepared silicates (FeSi-I, FeSi-II and FeSi-III) were identified with different analytical techniques, such as XRD, FTIR, Thermal analysis (DTA/TG), elemental analysis and chemical stability.

Powder X-ray diffraction patterns were carried out using Shimadzu X-ray diffractometer, Model XD 490 Shimadzu, Kyoto (Japan) with a nickel filter and Cu Kα radiation tube.

FTIR spectra were measured with BOMEM FTIR spectrometer, model MB 147 (Canada) using the KBr disc technique in the range 400–4000 cm^{-1}.

Table 1
Details of precipitation, chemical formula and some physical properties of the obtained iron silicates

Exchanger	Reactant molar ratios Fe:Si	Fe/Si ratio	Chemical formula	M.Wt.	XRD	Color
FeSi-I	1:1	1.0	$(Fe_2O_3)_{1.14}.SiO_2 \cdot 3.8H_2O$	264.45	amorphous	D.B*
FeSi-II	1:2	0.5	$(Fe_2O_3)_{0.55}.SiO_2 \cdot 1.3H_2O$	172.22	amorphous	D.B*
FeSi-III	2:1	2.0	$(Fe_2O_3)_{1.83}.SiO_2 \cdot 6.0H_2O$	460.90	amorphous	D.B*

D.B* = dark brown.

Thermal stability, water content and solid-state dehydration changes of the obtained products were carried out using a Shimadzu DT-60H thermal analyzer, Shimadzu, Kyoto, Japan by heating the samples up to 1000 °C.

The chemical composition of the iron silicates was obtained by X-ray fluorescence (XRF) of solid samples with a Philips XRF detector, Holland. Iron(III) oxide (Aldrich) and silica (Merk) were thoroughly ground together to obtain solid reference samples for calibration. The error in the Fe:Si calibration curve was ±0.1. The chemical data of the products and some physical properties are given in Table 1.

The number of water molecules (n) per mole of the material can be calculated from the Alberti equation [24]:

$$18n = x(M + 18n)/100$$

where x is the percent of water content and $M + 18n$ is the molecular weight of the materials.

The chemical stability of the iron silicates was determined in water, nitric and hydrochloric acids by mixing of 0.05 g of the exchanger with 10 ml of 0.1–3 M acid. The mixtures were equilibrated in a thermostated shaker water bath for one week at room temperature. The slurry was filtered of and the solid was determined gravimetrically while the Si and iron in the filtrate were detected by using an ICP Shemadzu Model 1200 product, from Shemadzu-Kyoto (Japan).

2.4. Ion exchange study

2.4.1. Capacity measurements

The capacities of the iron(III) silicate samples for Na^+, Cs^+ and Co^{2+} ions were determined by batch experiment techniques. 0.05 g of the solid materials were equilibrated with 2.5 ml (V/m ratio 50 $cm^3\ g^{-1}$) of the nitrate solutions of sodium, cesium and cobalt ions. Equilibration was done in a thermostated shaker water bath at 25 ± 1 °C until equilibrium was attained. The procedures were repeated until no further adsorption of cations occurred. The capacity (meq/g) was calculated from the formula:

$$\text{Capacity} = C_0 \times Z \times \frac{\%\ \text{uptake}}{100} \times \frac{V}{m} \times (\text{meq/g}) \qquad (4)$$

where C_0 is the initial concentration of solution (g/l), V is the solution volume (ml), M is the weight of the exchanger (g) and Z is the charge of the metal ion adsorbed.

2.4.2. Distribution coefficient (k_d) measurements

The affinity of the product materials for the ions of interest was expressed in terms of distribution coefficient (K_d, ml/g) values. A batch technique was followed to determine the distribution coefficient values of iron(III) silicates as a function of pH. The pH values of the solutions were adjusted using nitric acid solutions, where 0.05 g of the exchanger was added to 2.5 ml of 10^{-3} M of the metal nitrate solutions (Na^+, Cs^+, Co^{2+} and Ce^{3+}) labelled with ^{22}Na, ^{134}Cs, ^{60}Co and ^{144}Ce, respectively. The batch equilibrations were settled overnight (sufficient to attain equilibrium) at a V/m ratio of 50 cm^3/g in a thermostated shaker waterbath. The mixtures were centrifuged and the pH of the solution after equilibration was determined. The values of distribution coefficient (k_d) were calculated using the relation:

$$K_d = \frac{A_0 - A_f}{A_f} \times \frac{V}{m}\,\text{ml/g} \qquad (5)$$

where A_0 is the initial counting rate of the considered element in solution, A_f is the final counting rate of the considered element in solution at equilibrium, V is the volume of the solution (ml) and m is the mass of the exchanger (g).

All the experiments were conducted in triplicate and average values were used in the data analysis, and the results agreed to ±3%.

3. Results and discussion

3.1. Preparation and characterization of iron(III) silicates

Initial forms of iron(III) silicates as cation exchange materials were prepared by adding equimolar solutions of iron trichloride and sodium silicate of different volumes to obtain different Fe/Si molar ratios of 1.0, 0.5 and 2.0 of FeSi-I, FeSi-II and FeSi-III, respectively, as given in Table 1. All the samples of the iron silicates were hard granules in nature and suitable to use in a packed column. All of the three products of iron silicates still exhibit their original brown color after rough washing with distilled water and drying at 50 °C. Gradual changes in color from brown to reddish brown then dark brown were observed when the prepared materials were heated from 50 to 400 °C and finally up to 850 °C. Physico-chemical properties of these silicate samples were identified by using different techniques as given in Table 1.

3.1.1. Chemical stability

Chemical stability (solubility) of synthetic inorganic ion exchangers plays an important role in their analytical applications. Exchangers which have a high solubility in water as well as in acid media may not be useful for separation investigations. It is therefore advisable to have a guide of the solubility of an ion exchanger. In this concern, the chemical stability of the prepared iron silicate samples was investigated in water, nitric and hydrochloric acids at different concentrations (0.1–3.0 M). The results of the chemical stability of the prepared materials (FeSi-I, FeSi-II and FeSi-III) under different conditions are presented in Table 2. From the data in Table 2, it was found that all the prepared materials are stable in water and in the acids up to 1 M, while they partially dissolved in the 2–3 M range of acid concentrations. As far as the chemical stability of the prepared samples with respect to the composition of the materials is concerned (Table 2). Unexpected results of chemical stability of the iron silicates were obtained at higher acid concentrations (>1 M), where the samples are partially dissolved with the formation of two phases. The first is a white residual phase obtained at the bottom of the glass tube, while the filtrate phase is a brownish color solution that can be precipitated with alkali, forming dark brown hydrous iron(III) oxide. The white precipitate represents the silica content of the materials.

Furthermore, the chemical stability experiments indicated that the iron silicate samples follow the stability order:

$$\text{FeSi-II}(\text{Si/Fe} = 2.0) > \text{FeSi-I}(\text{Si/Fe} = 1) > \text{FeSi-III}(\text{Si/Fe} = 0.5)$$

Similar behaviors have been observed and reported [17–22]. From the analysis of the chemical stability measurement results, it can be concluded that the materials behave as mixed oxides of Fe_2O_3 and SiO_2 and the solubility of Fe_2O_3 is the fact which determines the stability of the mixed products. In another way, the results confirm that the obtained silicato-iron(III) is not one phase but a homogenous mixture with a better contact of Fe(III) and silica, and Fe–Si complexes are most likely to form. Also, the presence of Si indicates that the stabilization of the materials is probably related to its incorporation into the structure of the hydrous iron oxide as previously suggested [25]. Thus, the results of chemical stability measurements as well as the elemental analysis of the obtained silicates confirmed the chemical formula given in Table 1.

3.1.2. IR spectra

The IR spectra of the iron silicates preheated at different temperatures (50, 200, 400, 600 and 850 °C) were studied (Fig. 1 shows the IR spectra of FeSi-II as an example). The spectral analysis of different samples are nearly the same, just with slightly differences in details, and this may be due to the difference in the preparation conditions (Fe/Si ratios) and/or surface structural differences among the Fe–Si oxides. In all the spectra, three main absorption bands at ~3400, ~1600 and ~600 cm^{-1} were detected. The first band at ~3400 cm^{-1} is due to strong inter- and intra-molecular stretching vibrations of hydrogen bonds [26]. The second observed band at ~1600 cm^{-1} is related to the water in the crystal lattice of the iron silicate samples. Finally, the smallest third band, which is observed at ~600 cm^{-1}, may be ascribed to the metal oxygen bond [26]. In addition, semi-quantitative IR spectra of all the materials reveal that the characteristic bands of vibrational water (~3400 and ~1600 cm^{-1}) are still present up to 600 °C, while these bands suffer from a slight decrease in intensity on increasing the heating temperatures. This decrease may be assigned to molecular water dehydration on increasing the drying temperature [27]. In contrast, the peaks at 600 cm^{-1} become more intense on increasing the drying temperatures up to 850 °C, which supports the relative dehydration of mixed hydrous oxides of Fe–Si to the more stable oxide forms.

3.1.3. X-ray diffraction patterns

The powder X-ray diffraction patterns of the prepared materials preheated at 50, 200, 400, 600 and 850 °C indicated that all the samples (FeSi-I, FeSi-II and FeSi-III) are mostly amorphous materials under all the conditions studied, and there is no change in the structures on increasing the drying temperature up to 850 °C. From the aforementioned data, we can suggest that the basic structures of the prepared materials remain unchanged even on changing the metal ratios or even by heating these materials up to 850 °C. According to the literature [4], heat treatment of the laboratory prepared hydrous iron oxides revealed that the hydrous oxides retained their original amorphous structures below 200 °C and gradually changed

Table 2
Chemical stability of the different iron(III) silicates (g/l) at 25 ± 1 °C

Exchanger	Solubility, mg/L							
	H_2O	HNO_3 (M)				HCl (M)			
		0.1	0.5	2.0	3.0	0.1	0.5	2.0	3.0
FeSi-I	B.D	0.02	0.04	0.05	P.D	0.04	0.06	0.07	P.D
FeSi-II	B.D	0.02	0.02	0.04	0.09	0.03	0.05	0.06	P.D
FeSi-III	B.D	0.03	0.04	0.60	P.D	0.05	0.06	0.09	P.D

B.D: Below detection, P.D: partially dissolved.

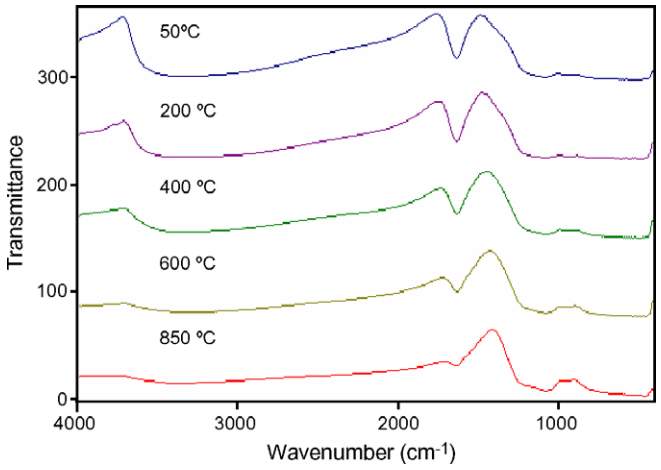


Fig. 1. Infrared spectra of FeSi-II at different drying temperatures.

into the α-Fe_2O_3 structure above 300 °C [4]. In this work, all the obtained materials retained their original amorphous structures after heating up to 850 °C. This unexpected result may be because either the hydrous oxides suffer from reversible phase transformation phenomena or the transformation of amorphous-Fe_2O_3 to metastable α-Fe_2O_3 is strongly retarded by the presence of silicate species. These probabilities can be confirmed by different tools of analyses, such as IR spectra and DTA/TG, as will be discussed later.

3.1.4. Thermal analysis

Fig. 2a–c shows the DTA/TGA of the different synthesized iron silicates, FeSi-I, FeSi-II and FeSi-III, respectively. Fig. 2a shows two endothermic peaks with maxima at $T_{m1} \approx 86$ °C resulting from a 12% mass loss and at $T_{m2} \approx 178$ °C resulting from an 8% mass loss from FeSi-I. The first peak is possibly assigned to dehydration of free absorbed water and the second one is possibly due to the loss of coordinated water molecules. The mass loss is continuous up to 500 °C, indicating a total loss of ≈22%, equivalent to 3.8 mol of water (Table 3).

Fig. 2b represents the DTA/TG thermogram of (FeSi-II) which indicates that there is only one endothermic peak at $T_{max} = 86.5$ °C, resulting from an 11.36% mass loss. This mass loss may be assigned to dehydration of surface absorbed water. The mass loss is continuous up to ~500 °C, giving a total mass loss of ≈14.75%, equivalent to 1.34 mol of water (Table 3). Finally, Fig. 2c shows the DTA/TG thermogram of FeSi-III which displays an endothermic peak at $T_{max} = 95$ °C, resulting from a 23.3% mass loss, equivalent to 6.0 mol of water. It is worth noting that, as shown in Tables 1 and 3, the water content of different silicate samples increased on increasing the iron species, in the order:

$$\text{FeSi-II}(\text{Fe/Si} = 0.5, \text{H}_2\text{O} = 14.7\%) > \text{FeSi-I}(\text{Fe/Si} = 1.0, \text{H}_2\text{O} = 22\%) > \text{FeSi-III}(\text{Fe/Si} = 2.0, \text{H}_2\text{O} = 23.3\%)$$

On the other hand, another alternative measurement of the DTA/TG of the iron silicate samples preheated at ≈150 °C then equilibrated with moist air were made and the results are shown in Fig. 3a–c. Fig. 3a of FeSi-I preheated at 150 °C also reveals two endothermic peaks, but they are shifted to higher temperatures (being at 93 and 215 °C, respectively) with a total mass loss of ≈15%. This result may confirm that the amorphous iron oxide changes to a new temporarily high thermally stable phase (α-Fe_2O_3 of lower water content instead of amorphous-Fe_2O_3) in parallel with restoring its water content to be nearly equal that of the original FeSi-I (22%). At the same time, Fig. 3a supports the IR spectra of the heated sample (Fig. 1), where the bands corresponding to water molecules are still present.

Based on the literature data [28,29], the structural water molecules may play an important rule as exchange sites. Also, from the view point of separation chemistry, especially in the field of fission products and removal of hazards elements, the last results of high chemical and thermal stability caused by increasing the silica content (besides the moisture reversibility nature) may reinforce our efforts on studying the application of impregnated Fe–Si oxides in new forms as promising exchange materials.

3.1.4.1. Kinetic studies of silicato-iron solid-state transformations processes. As indicated, the XRD patterns of heated Fe-silicates still show completely clear amorphous nature at higher temperatures (850 °C) in a parallel with their water restoring properties. This may be proven by the reversible endothermic peaks (DTA peaks) of the phase transformation processes of these materials, as observed from their DTA thermograms (Figs. 3a–c). The kinetics of the solid-state transformation processes of FeSi-I, FeSi-II and FeSi-III samples can be calculated from DTA thermograms by the T_{max} peak of the dehydration processes. Thus, the order of reactions (n) of the first dehydration processes of compounds FeSi-I, FeSi-II and FeSi-III, corresponding to T_{max} values of 89, 86.5 and 95.4 °C, respectively (Figs. 2a–c), may be calculated using the Kissingar empirical relation [30,31]:

$$n = 1.26S^{1/2} \quad \text{and} \quad S = a/b \tag{6}$$

where n is the reaction order, S is the peak shape factor and a and b are the length in cm on the base line of the dehydration peak (Fig. 2b). Additionally, it can be considered that the dehydration transformation process is one of the solid-state reactions, namely the solid-state reaction of a single reactant, according to the equation:

$$A_{(s)} \rightarrow \overline{A}_{(s)} + \text{H}_2\text{O}_{(g)} \tag{7}$$

Thus, for the materials studied, the FeSi-I dehydration can be represented by the equation:

$$(\text{Fe}_2\text{O}_3)_{1.14} \cdot \text{SiO}_2 \cdot 3.8\text{H}_2\text{O}_{(s)} \overset{89\ ^\circ\text{C}}{\rightarrow} (\text{Fe}_2\text{O}_3)_{1.14} \cdot \text{SiO}_2 \cdot 2.6\text{H}_2\text{O}_{(s)} + 1.2\text{H}_2\text{O}_{(g)} \tag{8}$$

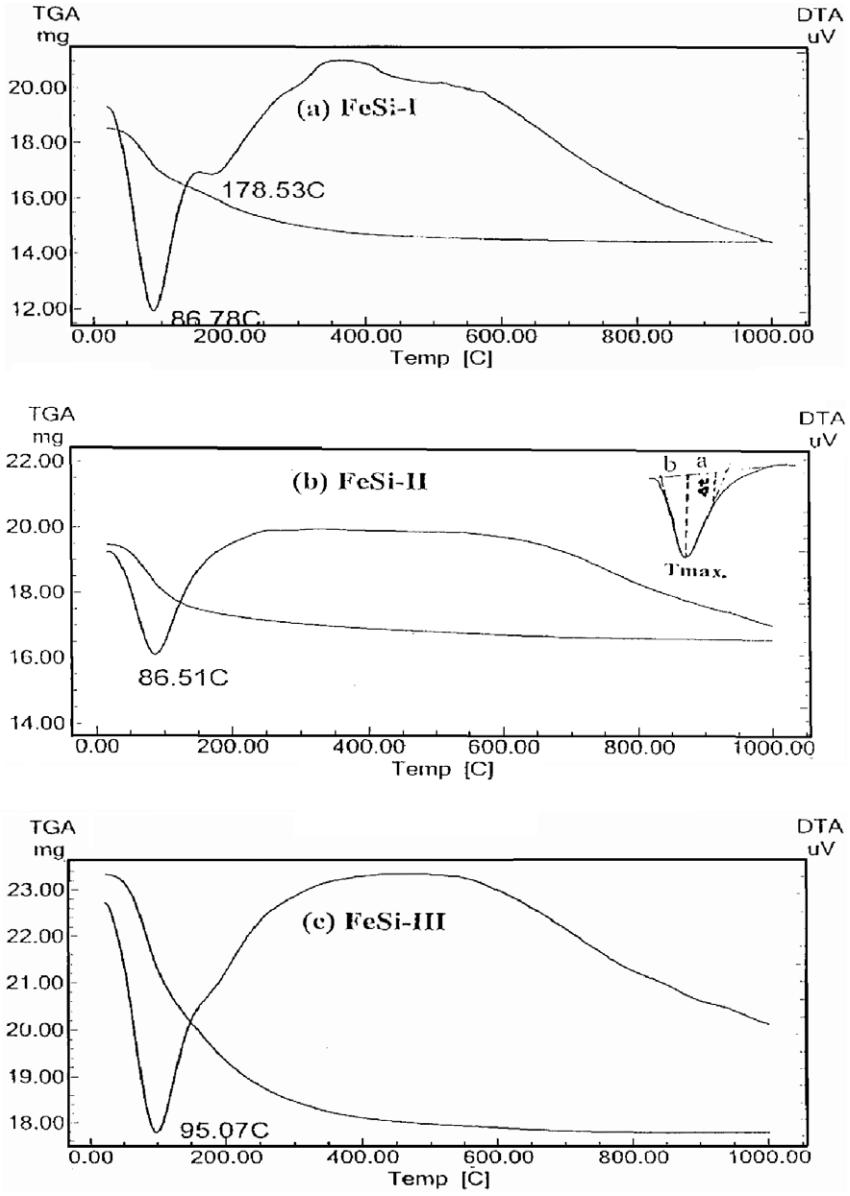


Fig. 2. DTA–TG thermograms of iron silicate with different Fe/Si ratios (a) 1, (b) 0.5 and (b) 2.

Table 3
Water contents of iron silicates in their initial forms and their different loaded forms

Exchanger	% water content		
	FeSi-I	FeSi-II	FeSi-III
Initial form	21.95	14.75	23.40
Cs^{+}-loaded	21.47	21.09	25.35
Na^{+}-loaded	17.96	17.93	23.20
Co^{2+}-loaded	22.40	22.03	24.865
Ce^{3+}-loaded	21.30	22.38	24.579

This type of reaction is assumed to be controlled by nucleation, diffusion and phase boundary advancement or by partial liquefaction, depending on the values of n. So, the order of the dehydration processes are calculated by employing the above equation and, given in Table 4, the values are found to be close to unity. From these results we can conclude that the dehydration processes of the different silicate samples are solid-state reactions that follow first order kinetics and the rate-determining step is the nucleation process [32,33]. Also, the activation energy (E_a) of the transformation dehydration process of all the prepared samples (FeSi-I, FeSi-II and FeSi-III) to form the semi-anhydrous products can be calculated using the Piloyan et al. equation [33]:

$$\ln \Delta t = C - \frac{E_a}{RT} \tag{9}$$

where Δt is the deviation from the base line (its value being taken directly from the DTA curve in length units of cm or mm, as shown in Fig. 2b), C is a constant, E_a is the energy of activation, R is the universal gas constant and T is the

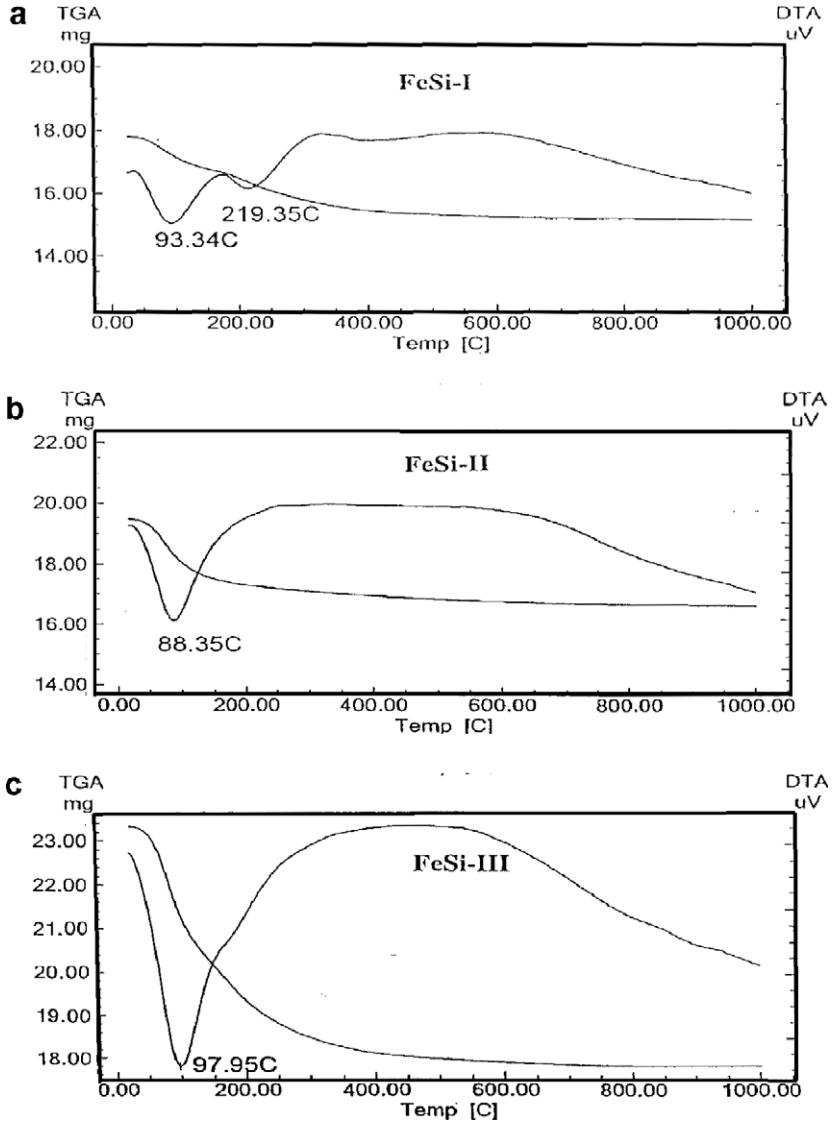


Fig. 3. DTA–TG thermograms of iron silicates preheated at 150 °C.

Table 4
The activation energy and order of dehydration reactions of the iron silicates in different forms

Compound	n	E_a (kJ/mol)	T_{max} (°C)	% loss
FeSi-I	1.18 1st	2.23	86.8	12.00
FeSi-II	1.37 1st	1.58	86.5	11.36
FeSi-III	1.47 1st	1.88	95.1	19.20

absolute temperature. The plot of $\ln\Delta t$ versus $1000/T$ gave a straight line, represented in Fig. 4 for all compounds, with a slope of $-E_a/R$. From these lines, the calculated values of E_a were found and these are given in Table 4. Table 4 shows low values of E_a for all the dehydration processes indicating the ease of water evaporation in the dehydration reactions. Also, the E_a values of the different silicates decrease in the order:

FeSi-I(2.23) > FeSi-III(1.88) > FeSi-II(1.58)

This indicates that FeSi-II has the lowest energy consumption for removal of water molecules.

3.2. Ion exchange and distribution studies

The potential use of the prepared iron silicates in removal and separation of some radioactive nuclides, including cesium, sodium, cobalt and cerium ions, were studied in order to assess and evaluate the prepared materials for the application as adsorbents.

Initially, the ion exchange capacity (IEC) of Na^+, Cs^+ and Co^{2+} ions on various iron silicates (FeSi-I, FeSi-II and FeSi-III) in both initial (treated with water), protonated (pretreated with 0.1 M HNO_3) forms and those dried at different temperatures (50, 200, 400 and 850 °C) are given in Table 5. The data in Table 5 shows clearly that all the iron silicates in the H^+-form (acidic form) have extremely low ion affinity compared to their initial forms.

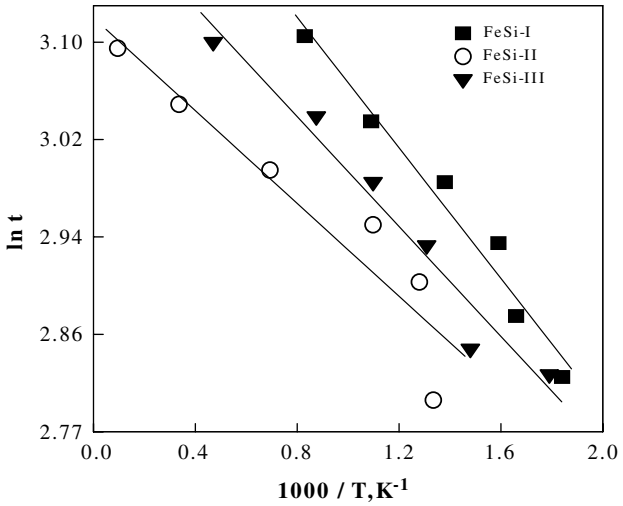


Fig. 4. Plot of $\ln \Delta t$ vs. $1000/T$ (K^{-1}) for iron silicates of different Fe/Si molar ratios.

The low sorption affinity of the H^+-forms of the different prepared iron silicates is expected, as many studies have reported the same behavior [34]. We can say that the lower values of the IEC of acid pretreated iron silicates may indicate a disturbance in the elemental structure (Fe/Si ratios). This disturbance may be due to either the dissolving of iron oxide [5] or the high affinity of the solid towards H^+ compared to the Na^+ ions (Na^+ ions are initially present in the silicate matrix by in situ precipitation from sodium silicate). These positive results of sorption experiments direct our attention towards the initial forms of the obtained silicates. This is very important from an economic point of view.

Generally, it is found that: (i) The ion exchange capacity of the prepared materials towards the studied cations (Na^+, Cs^+ and Co^{2+} ions) increases in the order:

FeSi-II > FeSi-I > FeSi-III

This trend may be due to the increase of acidities of materials on increasing the silicon content (high electronegativity) which may lead to an increase of electrostatic interaction of the counter ions with the exchange sites [35]. (ii) The ion exchange capacities of all the studied cations are slightly decreased by increasing the drying temperatures from 50 to 200 °C, this is then followed by a fast decrease with continuous heating up to 850 °C. *Firstly*, the slightly decrease in the ion exchange capacity for samples heated up to 200 °C, which is not accompanied by crystalline changes, may be discussed from the view point of DTA/TG and IR analyses for samples preheated at 200 °C. The IR peaks at 3400 and 1600 cm^{-1} of OH^- groups are still present after drying up to 200 °C, as shown in Fig. 1.

Table 5
Ion exchange capacities (meq/g) and percentage water content of the iron silicates at different drying temperatures

Exchanger	Drying temperature	% Water content	Ion exchange capacity (meq/g)		
			Na^+	Cs^+	Co^{2+}
FeSi-I	50	22.0	0.42 (0.04)[a]	0.45 (0.06)[a]	0.62 (0.06)[a]
	150	10.1	0.38 (0.04)[a]	0.40 (0.06)[a]	0.55 (0.06)[a]
	200	6.9	0.25 (0.05)[a]	0.32 (0.05)[a]	0.37 (0.06)[a]
	400	6.4	0.08 (0.04)[a]	0.13 (0.05)[a]	0.10 (0.07)[a]
	850	5.0	0.03	0.06	0.05
FeSi-II	50	14.7	0.44 (0.06)[a]	0.49 (0.07)[a]	0.72 (0.06)[a]
	150	4.6	0.40 (0.06)[a]	0.45 (0.07)[a]	0.65 (0.06)[a]
	200	3.5	0.29 (0.52)[a]	0.36 (0.07)[a]	0.38 (0.05)[a]
	400	1.6	0.15 (0.04)[a]	0.21 (0.06)[a]	0.20 (0.04)[a]
	850	0.1	0.07	0.12	0.15
FeSi-III	50	22.7	0.22 (0.02)[a]	0.30 (0.02)[a]	0.39 (0.03)[a]
	150	9.3	0.20 (0.02)[a]	0.25 (0.02)[a]	0.30 (0.03)[a]
	200	5.9	0.14 (0.02)[a]	0.19 (0.02)[a]	0.24 (0.03)[a]
	400	0.7	0.04 (0.02)[a]	0.50 (0.03)[a]	0.10 (0.04)[a]
	850	0.3	0.02	0.03	0.02

[a] For samples pretreated with 0.1 M HNO_3.

Furthermore, the reversibility of the first endothermic peaks of the DTA/TG for all the silicate samples (Figs. 2 and 3) shows that the iron silicate samples still reveal a high percentage water content. This result can be considered as being based on a reversible phase transformation nature of the iron silicates. Hence, silicate samples heated at 200 °C retain their original structures, where water molecules are restored to near equality of the original forms. The results support the idea of construction of new active sites by pre-heated iron silicates when equilibrated with moist air. A similar trend was observed in the case of goethite (α-FeO-OH) [5]. *Secondly*, the fast decrease of the ion exchange capacity of the iron silicates at higher temperatures (400 to 850 °C) may be related to the condensation of the surface OH^- groups which may act as the sites of exchange [36,37]. This result is also noticed from the IR spectra (Fig. 1) where the peaks due to water molecules become low in intensity on increasing the drying temperatures, which may suggest a decrease of active sites. (iii) The ion exchange capacity of the prepared iron silicates (FeSi-I, FeSi-II and FeSi-III) for the studied cations takes the order,

$$Co^{2+} > Cs^{+} > Na^{+}.$$

This order of ion exchange capacity (Table 5) agrees with the fundamental theory of hydrous ionic radii of these cations [38]. It must be notice that although the water molecules play an important role as exchange sites in the obtained materials, the sorption affinity trend of the iron silicates does not depend on the percentage of water molecules only. Other factors may have an affect, such as channel loading, diffusion of ions, pH, pore size, porosity, surface area and ordinal structuring of these materials.

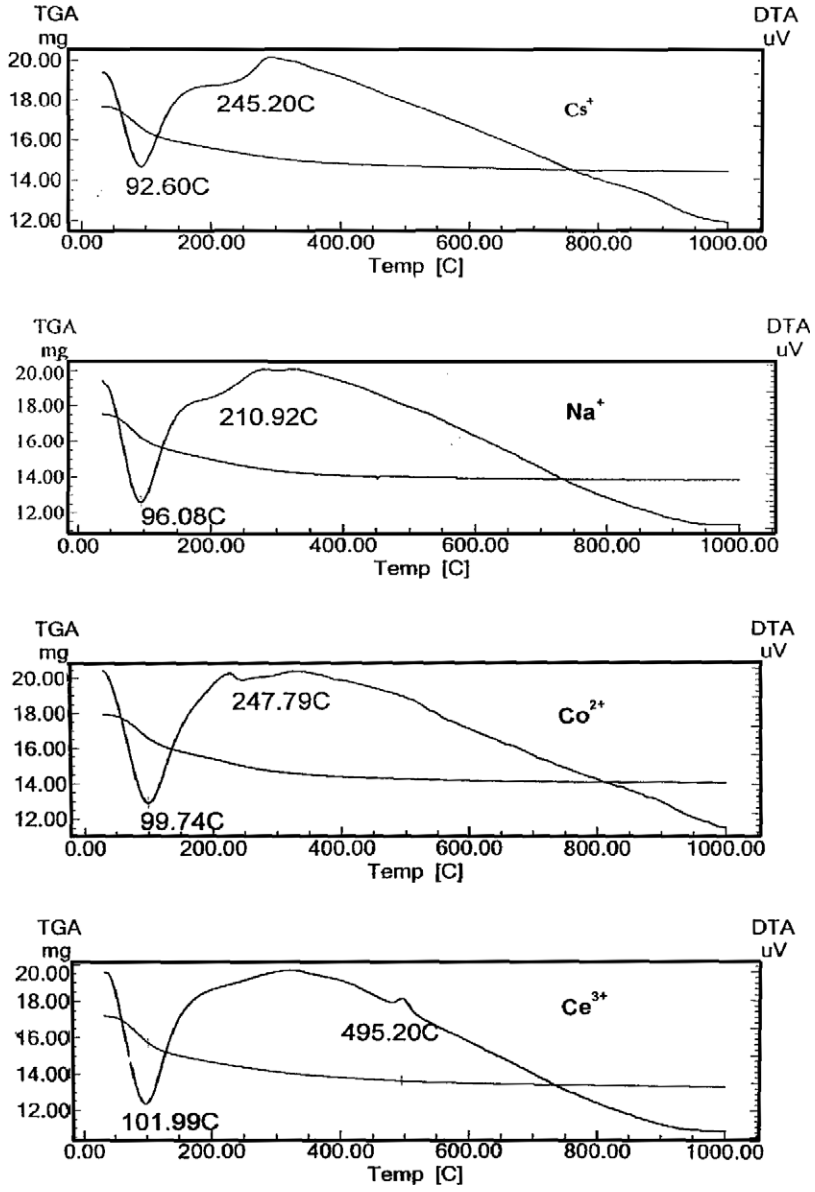


Fig. 5. DTA–TG thermograms of FeSi-II loaded with Cs^+, Na^+, Co^{2+} and Ce^{3+} ions.

Additional studies on the thermal behavior of iron silicates in different cation forms (-Na^+, -Cs^+, -Co^{2+} and -Ce^{3+}) have been carried out. Based on a comparison of the percentage water content for all the iron silicate samples (initial and their perspective cationic form) obtained from TG analysis and given in Table 3, it is clear that each of the Na^+, Cs^+, Co^{2+} and Ce^{3+} ions were adsorbed in their coordinated form in the case of FeSi-II, while this behavior is in contrast to that which occurs for FeSi-I and FeSi-III samples. The same result was confirmed from the DTA thermograms of Na–FeSi-II, Cs–FeSi-II, Co–FeSi-II and Ce–FeSi-II, as shown in Fig. 5. Fig. 5 indicates that a new second endothermic peak at ≈211, 245, 248 and 495 °C for Na–FeSi-II, Cs–FeSi-II, Co–FeSi-II and Ce–FeSi-II, respectively, was obtained. This peak may correspond to the dehydration of coordination water of different adsorbed cations. Thus the different FeSi-II cation forms can be arranged in the following order, according to the percentage water content:

$$\text{FeSi-II}(14.75\%) < \text{Na–FeSi-II}(17.93\%) < \text{Cs–FeSi-II}(21.1\%) < \text{Co–FeSi-II}(22.03\%) < \text{Ce–FeSi-II}(22.3\%)$$

On the other hand, the preliminary investigation indicates that the time for equilibration for the exchange of Cs^+, Na^+, Co^{2+} and Ce^{3+} ions with the initial form of the iron silicates were within 24 h (sufficient to attain the equilibrium). In this concern, to investigate the selectivity of the prepared materials for the studied metal ions, distribution coefficients (K_d) were determined in different pH values using different concentrations of HNO_3 of each of Cs^+, Na^+, Co^{2+} and Ce^{3+} labelled with ^{134}Cs, ^{22}Na, ^{60}Co and ^{142}Ce, respectively. Fig. 6a–c shows the results of variations of $\log K_d$ versus pH of solutions for the studied cations and it can be found that the distribution coefficients for all the metal ions increased on increasing the pH of

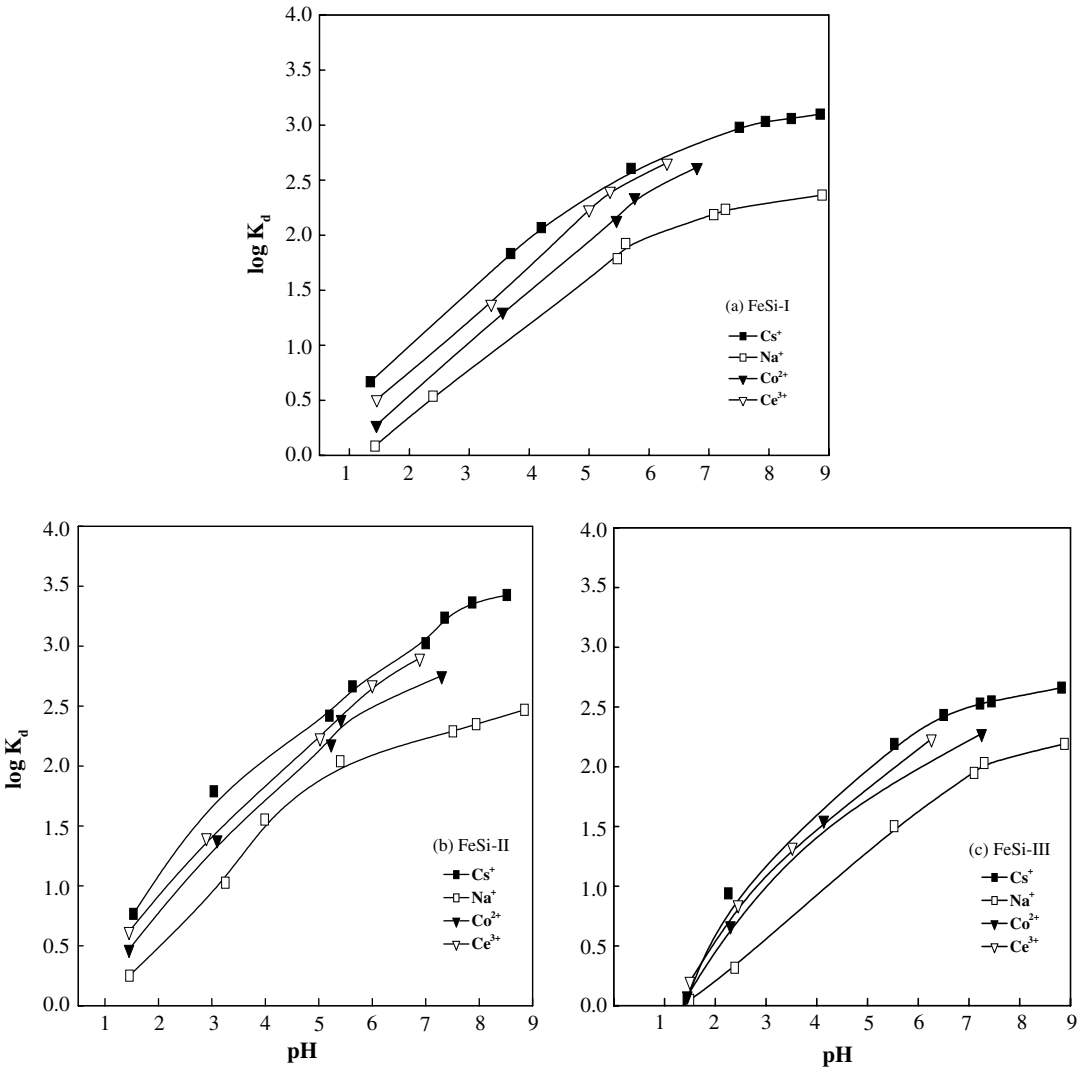


Fig. 6. Distribution coefficients of Cs^+, Na^+, Co^{2+} and Ce^{3+} ions as a function of pH on FeSi-I, FeSi-II and FeSi-III (dried at 50 °C) at 25 ± 1 °C.

the solutions. This trend is an obvious phenomenon and was observed by others [28,37–40]. Also, from the plots of $\log K_d$ at infinitesimal exchange versus pH of solutions of different cations (Fig. 6a–c) of the prepared materials (FeSi-I, FeSi-II and FeSi-III), a linear relationship with a slope smaller than the valences of the studied cations were obtained, indicating that the ion exchange reaction deviated from the ideal process. The non-ideality may due to a different mechanism such as physical adsorption, chemical reaction or other effects, that takes place besides the ion exchange process.

4. Conclusions

Composites of Fe–Si oxides were obtained from iron oxide impregnation with silica in different Fe/Si molar ratios. A chemical stability investigation indicated that the silicato-iron products were mixed oxides and the iron oxide is partially soluble in high acidic media, while the solubility decreased with increasing silica content. Kinetics of dehydration transformation indicated a 1st order process for different silicate ratios. Application of the materials as ion exchangers showed a high affinity for ions of different charges on increasing the solution pH as well as with the silica content increasing.

References

[1] U. Schwertmann, R.M. Taylor, Iron oxides, in: Minerals in soil environments, Soil Science Society of America, Inc., 1989, p. 379.
[2] P.H. Hsu, Minerals in soil environments, Soil Science Society of America, Inc., 1989, p. 331.
[3] D.G. Kinniburgh, M.L. Jackson, Ann Arbor Sci. (1981) 91.
[4] O. Tochiyama, S. Endo, Y. Inoue, Radiochem. Acta 68 (1995) 105.
[5] O. Tochiyama, H. Yamazaki, T. Mikami, Radiochem. Acta 73 (1996) 191.
[6] F. Hazel, R.U. Schock Jr., M. Grodon, J. Am. Chem. Soc. 71 (1949) 2256.
[7] W.J. Weber, W. Stumm, J. Inorg. Nucl. Chem. 27 (1965) 237.
[8] Le Zeng, Water Res. 37 (2003) 4351.
[9] M.L. Pierce, C.B. Moore, Water Res. 16 (1982) 1247.
[10] T.H. Hsia, S.L. Lo, C.F. Lin, Colloid. Surf. A 5 (1994) 1.
[11] J.A. Wilkie, J.G. Hering, Colloid. Surf. A 107 (1996) 97.
[12] K.P. Raven, A. Jain, R.H. Loeppert, Environ. Sci. Technol. 32 (1998) 344.
[13] X. Sun, H.E. Doner, Soil Sci. 163 (4) (1998) 278.
[14] S.L. Lo, T.-Y. Chen, Chemosphere 35 (5) (1997) 919.
[15] T.L. Theis, R. Iyer, S.K. Ellis, JAWWA 84 (1992) 101.
[16] R.P.W. Scott, Silica gel and bonded phases: their production, properties, and use in LC, J. Wiley, New York, 1993, 261.
[17] P.J. Swedlund, J.G. Webster, Water Res. 33 (16) (1999) 3413.
[18] A.J. Herbillon, J.Tran Vinh An, J. Soil Sci. 20 (2) (1969) 223.
[19] J.E. Schenk Jr, W.J. Weber, J. Am. Water Works Assoc. 2 (1968) 199.
[20] U. Schwertmann, R.M. Cornell, Iron oxides in the laboratory: preparation and characterization, VCH Publishers, New York, 1990.
[21] R.M. Cornell, R. Giovanoli, P.W. Schindler, Clays Clay Miner. 35 (1) (1987) 21.
[22] R.M. Cornell, R. Giovanoli, J. Chem. Soc., Chem. Commun. 6 (1987) 413.
[23] P. Anderson, M.M. Benjamin, Environ. Sci. Technol. 19 (1985) 1048.
[24] G. Albert, E. Toracca, A. Conte, J. Nucl. Chem. 28 (1996) 607.
[25] G. Aguila, S. Guerrero, F. Gracia, P. Araya, Appl. Catal. A: Gen. 305 (2006) 219.
[26] N. Nakamoto, Infrared and Raman spectra of Inorganic and Coordination Compounds, John Willey & Sons, NY, 1998.
[27] I.M. El-Naggar, M.A. El- Absy, H.F. Aly, Colloid. Surf. 66 (1992) 281.
[28] I.M. Ali, J. Radioanal. Nucl. Chem. 260 (1) (2004) 149.
[29] I.M. El-Naggar, M.M. Abdel-Hamid, S.A. Shady, H.F. Aly, Radioactive Waste Manage. Environ. Radiat., ASME (1995).
[30] H.E. Kissinger, Anal. Chem. 29 (1957) 1702.
[31] T. Rich, Polym. Lett. 4 (1966) 423.
[32] N. Akhmetov, General and Inorganic Chem, Mir Publishers, Moscow, 1983.
[33] W.E. Brouern, D. Dollinore, A.K. Golwey, Radiation in Solid State, Elsevier Scientific Publishers, NY, 1980.
[34] A.I. Bortun, L.N. Bortun, A. Clearfield, Solvent Extr. Ion Exc. 15 (2) (1997) 305.
[35] R. Koivula, R. Harjula, J. Lehto, Micropor. Mesopor. Mater. 55 (2002) 231.
[36] I.M. El-Naggar, E.S. Zakaria, S.A. Shady, H.F. Aly, in: Sixth Int. Conf. on Nuclear Science and Appl. Cairo, 1996.
[37] I.M. El-Naggar, M.M. Abdel- Hamid, H.F. Aly, Solvent Extr. Ion Exc. 12 (3) (1994) 651.
[38] I.M. El-Naggar, M.M. Abdel- Hamid, M.A. El- Absy, H.F. Aly, in: Second Arab Conf. on Peaceful uses of Atomic Energy, Cairo, 1994.
[39] E.S. Zakaria, I.M. Ali, I.M. El-Naggar, Colloid. Surf. 210 (2002) 33.
[40] E.S. Zakaria, I.M. Ali, H.F. Aly, J. Radianal. Nucl. Chem. 260 (2) (2004) 389.

Available online at www.sciencedirect.com
ScienceDirect
Polyhedron 27 (2008) 440–446
POLYHEDRON
www.elsevier.com/locate/poly

Synthesis, spectral characterization of the zinc(II) mixed-ligand complexes of *N*(4)-allyl thiosemicarbazones and *N*,*N*,*N*′,*N*′-tetramethylethylenediamine, and crystal structure of the novel [ZnL_2(*tmen*)] compound

Tülay Bal-Demirci

Department of Chemistry, Istanbul University, 34320 Avcilar, Istanbul, Turkey

Received 27 June 2007; accepted 1 October 2007
Available online 5 November 2007

I dedicate this paper to B. Ulkuseven, *the mentor of my research career*, on the occasion of his 50th birthday.

Abstract

Mixed-ligand zinc complexes with *N*,*N*,*N*′,*N*′-tetramethylethylenediamine (*tmen*) and R-salicylaldehyde N(4)-allyl thiosemicarbazones (R: 3-OCH_3 (L_1), 5-Br(L_2)), [$ZnL_{1,2}$(*tmen*)], were synthesized and the complexes were characterized by elemental analysis, atomic absorption spectrometer, magnetic susceptibility, molar conductivity, electrospray ionization (ESI) and atmospheric pressure chemical ionization (APCI) mass spectra and IR, UV–Vis, ^{1}H NMR and ^{15}N spectroscopies. Crystal of [ZnL_2(*tmen*)] have a slightly distorted square pyramid involving O, N, S atoms of thiosemicarbazone and one N atom of *tmen* in basal plane and the other N atom of *tmen* in apex of the pyramid. The non-coordinated allyl group is disordered.
© 2007 Elsevier Ltd. All rights reserved.

Keywords: Thiosemicarbazone; Salicylaldehyde; *N*,*N*,*N*′,*N*′-Tetramethylethylenediamine (*tmen*); Zinc complex; Crystal structure

1. Introduction

Thiosemicarbazones and their transition metal complexes are of considerable interest because of biological activities as antiviral [1,2], antifungal [3], antibacterial [4,5], antitumor [6,7], anticancerogenic [8–10] and insulin mimetic properties [11]. The thiosemicarbazones have also been used for analysis of metal as analytical reagent [12–14], for device applications relative to telecommunications, optical storage and optical information processing [15,16]. Biological activities of the metal complexes of thiosemicarbazones have been found in some instances to have enhanced depending on metal ion [17] and the parent aldehyde or ketone [5]. There are reports that the presence of alkyl groups at the terminal N(4) position can considerably increase their activity [18]. Moreover, most transition metal complexes of thiosemicarbazones have more activities than free ligands as regards biological activities [19,20].

In recent years a considerable amount of work has been done in the biological activities and synthesis of zinc(II) with thiosemicarbazone [21–27]. Perez et al. found that cytotoxic activity of zinc and cadmium complexes of *p*-isopropylbenzaldehyde thiosemicarbazone are resemble antitumor drug cisplatin, even they are much more active than cisplatin in cells resistant to cisplatin [28,29]. Zinc is an essential constituent of the enzymes catalysing hydrolyses and complexes of zinc(II) are catalysts for the cleavage of RNA target [30–34]. Thiosemicarbazones are effective inhibitors of ribonucleotide reductase (RR), and of key regulatory enzymes as well [35,36]. It had been reported that zinc complexes of thiosemicarbazones are antioxidant [37] and have an effect in vitro on cell proliferation and differentiation [38–40]. Therefore, the aim of this

E-mail address: tulaybal@istanbul.edu.tr

0277-5387/$ - see front matter © 2007 Elsevier Ltd. All rights reserved.
doi:10.1016/j.poly.2007.10.001

work was to synthesis mixed-ligand Zn(II) complexes with N(4)-allyl thiosemicarbazone and *N,N,N′,N′*-tetramethylethylenediamine (*tmen*) and to define the X-ray structure of the complex.

No reaction of *tmen* with thiosemicarbazone in the presence metal ion, so far as I know, gave mixed-ligand complex because dimeric complex was obtained [41,42]. In the present paper, I report the synthesis, spectroscopic data and crystal structure of Zinc(II) complex of [Zn(tsc)(*tmen*)]. The compound is the first mixed-ligand complex of zinc(II)–thiosemicarbazone with a *tmen* ligand.

2. Experimental

2.1. General procedures

All chemicals were of reagent grade and used as commercially purchased without further purification. The elemental analyses were determined on a Thermo Finnigan Flash EA 1112 Series Elemantar Analyser and Varian Spectra-220/FS Atomic Absorption spectrometer. I.r. spectra of the compounds were recorded on KBr pellets with a Mattson 1000 FT-infrared spectrometer. UV/Vis Spectra were obtained from ATI-Unicam UV/Visible Spectrometer UV2 Series. The ^{1}H, and ^{15}N Nuclear Magnetic Resonance spectra were recorded on Bruker AVANCE- 500 model spectrometer. Magnetic measurements were carried out at room temperature by the Gouy technique with an MK I model device obtained from Sherwood Scientific. The molar conductivities of the compounds were measured in 10^{-3} M DMSO solution at 25 ± 1 °C using a digital WPA CMD 750 conductivity meter. The ESI-MS and APCI-MS analyses were carried out in positive ion modes using a Thermo Finnigan LCQ Advantage MAX LC/MS/MS. Hypersil Betabasic-8 (5 μm, 100 mm × 4.6 mm) column was used at a flowrate of 0.3 ml/min at 25 °C. The mobile phase consisted of MeOH. ESI-MS/APCI-MS inlet conditions in the positive ion mode: heated capillary temp., 200/200 °C; sheath gas flow rate, 70/70 U; capillary voltage, 32/46 V and tube lens offset, 30/55 V.

2.2. Synthesis of ligands and complexes

2.2.1. Ligands

The 5-bromo- and 3-methoxysalicylaldehyde N(4)-allyl thiosemicarbazone were prepared according to the literature [10]. The colours, m.p., yields, Rf (CH_2Cl_2), Elemental Analysis, I.r., UV–Vis and ^{1}H NMR data of $\mathbf{L}_{1-2}$ were given as follows:

$\mathbf{L}_1$: cream; 229–230 °C; %94; 0.2065; *Anal*. Calc. for $C_{12}H_{15}N_3O_2S$ (265 g): C, 54.34; H, 5.66; N,15.85; S, 12.07. Found: C, 54.32; H, 5.61; N, 15.91; S, 11.96%. FT-IR (KBr, cm^{-1}): *ν*(NH) 3451, 3307, *ν*(OH) 3550–3250, *δ*(NH) 1646, 1615, *ν*(C=N) 1584, *ν*(C=CH_2) 3092, 3007, *ν*(–OCH_3) 2846, *ν*(–CS–NH) 1538, *ν*(–C=S) 1215. UV–Vis spectrum in $CHCl_3$ [λ_{max} (nm), *ε* ($dm^3\,cm^{-1}\,mol^{-1}$)]: 217 (7340), 240 (5890), 320 (11 600), 346 (shoulder). ^{1}H NMR (DMSO-d_6, 25 °C, ppm): 11.19 (s, 1H, OH), 9.13 (s, 1H, NH), 8.34 (t, 1H, N*H*-allyl), 8.16 (s, 1H, CH=N), 7.27 (d, *J*: 7.91, 1H, *d*), 6.74 (d, *J*: 7.82, 1H, *b*), 6.57 (t, *J*: 7.97, 1H, *c*), 5.65 (m, 1H, –CH=), 4.89 (m, 2H, =CH_2), 3.96 (d, *J*: 5.12, 2H, N–CH_2–), 3.56 (s, 1H, –OCH_3).

$\mathbf{L}_2$: light yellow; 179–180 °C; %69; 0.1848; *Anal*. Calc. for $C_{11}H_{12}N_3OSBr$ (314 g): C, 42.04; H, 3.82; N, 13.37; S, 10.19. Found: C, 42.09; H, 3.79; N, 13.46; S, 10.25%. FT-IR (KBr, cm^{-1}): *ν*(NH) 3407, 3153, *ν*(OH) 3600–3300, *δ*(NH) 1646, 1623, *ν*(C=N) 1607, *ν*(C=CH_2) 3092, 3000, *ν*(–CS–NH) 1538, *ν*(–C=S) 1230. UV–Vis spectrum in $CHCl_3$ [λ_{max} (nm), *ε* ($dm^3\,cm^{-1}\,mol^{-1}$)]: 218 (8450), 248 (10 450), 315 (14 040), 346 (15 000). ^{1}H NMR (DMSO-d_6, 25 °C, ppm): 11.21 (s, 1H, OH), 10.30 (s, 1H, NH), 8.51 (t, 1H, N*H*-allyl), 8.07 (s, 1H, CH=N), 7.89 (d, *J*: 2.24, 1H, *d*), 7.11 (dd, *J*: 2.49, *J*: 8.71, 1H, *b*), 6.60 (d, *J*: 8.72, 1H, *a*), 5.65 (m, 1H, –CH=), 4.89 (d, *J*: 1.52, *J*: 17.88, 1H, =CH_{2a}), 4.86 (dd, *J*: 1.28, *J*: 10.69, 1H, =CH_{2b}), 3.96 (d, *J*: 5.03, 2H, N–CH_2–).

2.2.2. Complexes

[**ZnL**$_1$(***tmen***)]: 3-Methoxysalicylaldehyde *N*(4)-allyl thiosemicarbazone (0.5 g, 1 mmol) in 20 ml EtOH was added to the solution of *N,N,N′,N′*-tetramethylethylenediamine (0.219 g, 0.28 ml, 1 mmol) in 20 ml of dry EtOH at 20 °C. The reaction mixture was poured with continuous stirring to 20 ml of an ethanol solution containing of $Zn(CH_3COO)_2 \cdot 2H_2O$ (0.41, 1 mmol). The resulting solution was stirred for 5 h at room temperature in nitrogen atmosphere. The solvent was removed on a rotary evaporator under reduced pressure. The residue was dissolved in ethanol (10 ml) and mixed with ether (10 ml). The mixture was kept for 48 h at 0 °C. The yellow coloured crystals were separated, filtered and dried in vacuo.

[ZnL_2(*tmen*)] complex was obtained by using 5-bromosalicylaldehyde *N*(4)-allyl thiosemicarbazone as to above procedure. The colours, m.p., yields, Rf (CH_2Cl_2), elemental analysis, molar conductivity, I.r., UV–Vis, ^{1}H NMR, ^{15}N NMR and mass (ESI, APCI) spectra, data of [ZnL_1(*tmen*)] and [ZnL_2(*tmen*)] were given as follows:

[ZnL$_1$(***tmen***)]: yellow; 192–193 °C; %62; 0.2212; *Anal*. Calc. for $C_{18}H_{29}N_5O_2SZn$ (444,37 g): C, 48.61; H, 6.53; N,15.75; S, 7.20; Zn, 14.71. Found: C, 48.57; H, 6.38; N, 15.69; S, 7.80; Zn, 14.66%; *Λ* (in 10^{-3} M DMSO, $\omega^{-1}\,cm^2\,mol^{-1}$): 9.2. FT-IR (KBr, cm^{-1}): *ν*(NH) 3385, *δ*(NH) 1643, *ν*(C=N) 1575, *ν*(C=CH_2) 3060, 2996, *ν*(–CH_3, –CH_2–) 2968, 2916, 2889, 2848, 2804, *ν*(N–CH_3) 1333, *ν*(–C–S) 1162. UV–Vis spectrum in $CHCl_3$ [λ_{max} (nm), *ε* ($dm^3\,cm^{-1}\,mol^{-1}$)]: 243 (980), 319 (10 950), 369 (6650), 581 (150), 658 (70). ^{1}H NMR (DMSO-d_6, 25 °C, ppm): 8.33 (s, 1H, CH=N), 6.64 (d, *J*: 7.91, 1H, *d*), 6.69 (s, 1H, N*H*-allyl), 6.68 (d, *J*: 7.41, 1H, *b*), 6.54 (t, *J*: 7.94, 1H, *c*), 5.87 (m, 1H, –CH=), 5.07 (d, *J*: 18.7, 1H, =CH_{2a}; dd, *J*: 10.2, 1H, =CH_{2b}), 3.86 (s, 2H, allyl, N–CH_2–), 3.56 (s, 3H, –OCH_3), 2.53 (s, 4H, *tmen*, –$(CH_2)_2$–), 2.23 (s, 12H, *tmen*, 2(–N–$(CH_3)_2$)); ^{15}N NMR: 318.56, 200.00, 199.97, 196.99, 195.12; *m/z* (+*c* ESI-MS, %relative abundance):

444 (100.00), 443 (18.35), 445 (26.62), 773 (20.46), 890 (18.53), 1218 (14.16), 1332 (18.42), 1430 (18.09), 1546 (6.05), 1662 (4.41); *m/z* (+*c* APCI-MS, %relative abundance): 444 (100.00), 328 (15.15), 443 (18.05), 445 (27.02), 774 (9.56), 890 (11.03), 1218 (10.71), 1332 (9.16), 1431 (6.54), 1546 (4.41), 1662 (4.20).

[**ZnL$_2$(tmen)**]: yellow; 175–176 °C; %79; 0.1956; *Anal.* Calc. for $C_{17}H_{26}N_5OSBrZn$ (493.28 g): C, 41.36; H, 5.27; N,14.19; S, 6.49; Zn, 13.25. Found: C, 41.57; H, 5.32; N, 14.32; S, 6.50; Zn, 13.29%; Λ (in 10^{-3} M DMSO, $\Omega^{-1}\,cm^2\,mol^{-1}$): 8.4. FT-IR (KBr, cm^{-1}): ν(NH)3349, δ(NH) 1643, ν(C=N) 1592, ν(C=CH$_2$) 3060, 2998, ν(–CH$_3$, –CH$_2$–) 2968, 2914, 2887, 2848, 2806, ν(N–CH$_3$) 1331, ν(–C–S) 1173. UV–Vis spectrum in $CHCl_3$ [λ_{max} (nm), ε ($dm^3\,cm^{-1}\,mol^{-1}$)]: 247 (11 350), 315 (7880), 371 (6570), 587 (180), 654 (100). ^{1}H NMR (DMSO-d_6, 25 °C, ppm): 8.24 (s, 1H, CH=N), 7.26 (dd, *J*: 2.59, *J*: 8.81, 1H, *d*), 7.07 (dd, *J*: 2.59, *J*: 8.8, 1H, *b*), 6.84 (s, 1H, N*H*-allyl), 6.54 (d, *J*: 8.8, 1H, *a*), 5.87 (m, 1H, –CH=), 5.11 (dd, *J*: 1.62, *J*: 17.14, 1H, =CH$_{2a}$), 5.00 (dd, *J*: 1.41, *J*: 10.2, 1H, =CH$_{2b}$), 3.87 (t, *J*: 5.35, 2H, allyl, N–CH$_2$–), 2.53 (s, 4H, *tmen*, –(CH$_2$)$_2$–), 2.24 (s, 12H, *tmen*, 2(–N–(CH$_3$)$_2$)). ^{15}N NMR: 316.76, 202.97, 199.97, 199.02, 195.06; *m/z* (+*c* ESI-MS, %relative abundance): 493 (100.00), 196 (6.82), 377 (8.22), 491 (59.53), 492 (17.36), 494 (29.00), 495 (62.83), 674 (25.52), 872 (14.28), 988 (17.17), 1247 (13.02), 1363 (21.16), 1626 (4.01), 1742 (2.03); *m/z* (+*c* APCI-MS, %relative abundance): 493 (100.00), 494 (30.43), 495 (64.91), 491 (66.68), 378 (49.47), 756 (11.72), 872 (7.17), 986 (24.23), 1247 (9.58), 1366 (7.02), 1626 (5.42), 1743 (4.48).

3. Results and discussion

3-Methoxy/5-bromosalicylaldehyde N(4)-allyl thiosemicarbazidato *N*,*N*,*N*′,*N*′-tetramethylethylenediamine zinc(II) complexes, [ZnL$_1$(*tmen*)] and [ZnL$_2$(*tmen*)], were obtained from reaction of *N*,*N*,*N*′,*N*′-tetramethylethylenediamine and thiosemicarbazone ligands in presence of $Zn(CH_3COO)_2\cdot 2H_2O$ in 1:1:1 molar in nitrogen atmosphere. The tridentate thiosemicarbazone ligands (L$_1$, L$_2$) coordinate to zinc(II) atom through the phenolic oxygen, imine nitrogen and thiolato sulphur atom, bidentate *tmen* ligand coordinates to zinc(II) atom through nitrogen atoms. The elemental analyses of complexes suggest the general formula as [ZnL$_1$(*tmen*)] and [ZnL$_2$(*tmen*)] according to Scheme 1.

Ligands melt at 229–230 °C (L$_1$) and 179–180 °C (L$_2$). [ZnL$_1$(*tmen*)] and [ZnL$_2$(*tmen*)] have melting points at 192–193 °C and 175–176 °C, respectively. The complexes compounds insoluble in H_2O, but soluble in alcohol, halocarbone solvents and polar organic solvents such as DMSO and MeCN. The μ_{eff} values of zinc chelates showed that they are diamagnetic. The molar conductance values are in the range 9.2–8.4 $\Omega^{-1}\,cm^2\,mol^{-1}$, indicating non-electrolytic behavior.

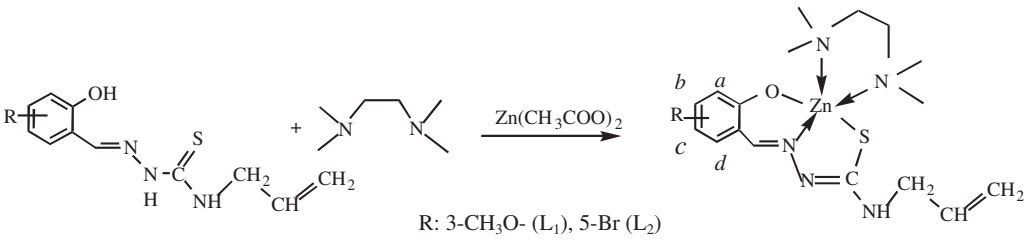
3.1. Structural characterization

3.1.1. X-ray structural determination of [ZnL$_2$(tmen)] structure

Suitable single crystal of complex [ZnL$_2$(*tmen*)] was obtained by crystallization from ethanol by ether diffusion. A yellow block crystal of $C_{17}H_{26}N_5OBrZnS$ having approximate dimensions of $0.40\times0.30\times0.20$ mm was mounted on a glass fiber. All measurements were made on a Rigaku RAXIS RAPID imaging plate area detector with graphite monochromated Mo Kα radiation. The structure was solved by direct methods (SHELXS-97) [43]. The non-hydrogen atoms were refined anisotropically. Unique F^2 data (3693) were used in the final cycle of the full-matrix least-squares refinement of 254 variables. Additional information to the structure determinations are given in Table 1. Selected bond distances, angles and torsion angles are listed in Table 2.

H atoms were positioned geometrically and treated using a riding model, fixing the bond lengths. In the molecule, (C10–C11) group shows positional disorder and the refined site-occupancy factors of the disordered parts, *viz*. C10A–C11A and C10B–C11B, are 64(1)% and 36(1)%, respectively. The disordered atoms were refined using the following restraints of SHELXL97: SIMU, DELU and SADI [44].

Compound [ZnL$_2$(*tmen*)] crystallizes in the triclinic space group, *P*21/*n*.The complex is described as a square pyramid with a phenolic oxygen atom [Zn(1)–O(1): 1.949(3) Å], an imin nitrogen atom [Zn(1)–N(1): 2.138(4) Å], a thiolato sulphur atom [Zn(1)–S(1): 2.3467(14) Å] and an nitrogen atom of *tmen* ligand [Zn(1)–N(4): 2.235(4) Å] at the corners of pyramidal base and the other nitrogen atom of *tmen* ligand [Zn(1)–N(5): 2.144(4) Å] at the top of pyramid (Fig. 1). The



Scheme 1. General synthesis of [ZnL$_1$(*tmen*)] and [ZnL$_2$(*tmen*)] complexes.

Table 1
Crystal and refinement data for [**ZnL**$_2$(***tmen***)]

Empirical formula	$C_{17}H_{26}N_5OBrZnS$
Formula weight	493.77
Temperature (K)	293
Wavelength (Å)	0.71073
Crystal system	monoclinic
Space group	$P2_1/n$
Unit cell	
a (Å)	12.1394(3)
b (Å)	8.3179(2)
c (Å)	21.3189(6)
β (°)	95.625(2)
V (Å^3)	2142.30(10)
Z	4
D_{calc} (g/cm^3)	1.531
μ (Mo Kα) (cm^{-1})	31.25
F_{000}	1008.00
h,k,l Range	$-14 \leqslant h \leqslant 14$, $-9 \leqslant k \leqslant 9$, $-25 \leqslant l \leqslant 25$
Reflections collected	37478
Unique reflections	3693
R_{int}	0.0402
Observed reflections	3627
R [$I > 2\sigma(I)$]	0.0554
Rw [$I > 2\sigma(I)$]	0.1314
Goodness-of-fit on indicator	1.113

angle [N(4)$_{tmen}$–Zn(1)–N(5)$_{tmen}$] between the apical and basal nitrogen atoms of the pyramid is 83.91°. The Zn–N(4)$_{tmen}$ and Zn–N(5)$_{tmen}$ distances are somewhat longer than those of other zinc(II) complexes containing *tmen*; [Zn–N(1)$_{tmen}$: 2.132(1) Å, Zn–N(2)$_{tmen}$: 2.079(1) Å] [45], [Zn–N(1)$_{tmen}$: 2.192(1) Å, Zn–N(2)$_{tmen}$: 2.150(1) Å] [46].

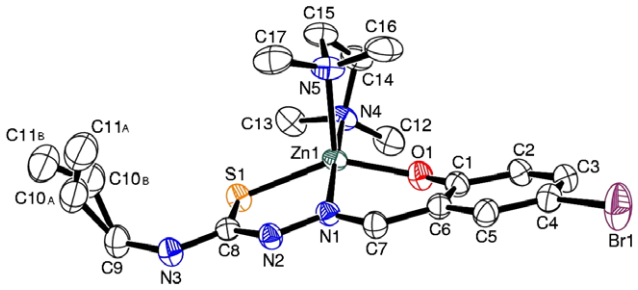


Fig. 1. A view of [ZnL$_2$(*tmen*)], showing 30% probability displacement ellipsoids and the atom-numbering scheme. The H atoms have been omitted for clarity.

Terdentate thiosemicarbazone ligand shows a Z configuration about N(2)–C(8) [torsion angle N(1)–N(2)–C(8)–N(3)] and N(1)–C(7) [torsion angle N(2)–N(1)–C(7)–C(6)] bonds, whereas an E configuration about N(2)–C(8) [torsion angle N(1)–N(2)–C(8)–S(1)] and Zn(1)–N(4) [torsion angle S(1)–Zn(1)–N(4)–C(13)] bonds is shown.

There is intermolecular hydrogen bonding in [**ZnL**$_2$-(***tmen***)]. C(9)–H(9B) interacts with a non-bonding pair of electrons on a coordinated thiolato sulphur Table 3. Configuration at the stereogenic centers, C(9) and C(10) of allyl moiety showed static disorder due to large thermal vibrations. Torsion angle N(3)–C(9)–C(10A)–C(11A) is 21.7(18) in conformation A, while torsion angle N(3)–C(9)–C(10B)–C(11B) is −105(2) in conformation B. The bond lengths and angles for allyl moiety in both conformations A and B are listed in Table 2.

In the molecular structure of [**ZnL**$_2$(***tmen***)], two intramolecular interactions are observed. One of these is between

Table 2
Bond lengths and selected bond and torsion angles for [**ZnL**$_2$(**tmen**)]

Bond lengths (Å)		Coordinate bond angles		Torsion angle	
Br(1)–C(4)	1.896(5)	O(1)–Zn(1)–N(1)	87.85(14)	N(4)–Zn(1)–S(1)–C(8)	−176.0(19)
Zn(1)–O(1)	1.949(3)	O(1)–Zn(1)–N(5)	103.99(18)	S(1)–Zn(1)–N(1)–C(7)	170.8(4)
Zn(1)–N(1)	2.138(4)	N(1)–Zn(1)–N(5)	102.55(16)	N(5)–Zn(1)–N(1)–N(2)	93.0(3)
Zn(1)–N(5)	2.144(4)	O(1)–Zn(1)–N(4)	90.31(16)	S(1)–Zn(1)–N(1)–N(2)	−13.7(3)
Zn(1)–N(4)	2.235(4)	N(1)–Zn(1)–N(4)	173.53(16)	Zn(1)–N(1)–N(2)–C(8)	10.9(5)
Zn(1)–S(1)	2.3467(14)	N(5)–Zn(1)–N(4)	83.91(17)	Zn(1)–N(1)–C(7)–C(6)	−5.7(7)
S(1)–C(8)	1.742(5)	O(1)–Zn(1)–S(1)	147.48(12)	Zn(1)–N(1)–N(2)–C(8)	10.9(5)
O(1)–C(1)	1.299(6)	N(1)–Zn(1)–S(1)	80.77(10)	S(1)–Zn(1)–N(4)–C(13)	5.2(4)
N(1)–C(7)	1.295(6)	N(5)–Zn(1)–S(1)	108.19(15)	N(2)–N(1)–C(7)–C(6)	−178.6(4)
N(1)–N(2)	1.380(5)	N(4)–Zn(1)–S(1)	97.60(12)	N(1)–N(2)–C(8)–N(3)	178.9(4)
N(2)–C(8)	1.324(6)	C(8)–S(1)–Zn(1)	96.54(16)	N(1)–N(2)–C(8)–S(1)	1.5(6)
N(3)–C(8)	1.347(6)	C(1)–O(1)–Zn(1)	127.4(3)	N(3)–C(9)–C(10A)–C(11A)	21.7(18)
N(3)–C(9)	1.428(7)	C(7)–N(1)–Zn(1)	123.5(3)	N(3)–C(9)–C(10B)–C(11B)	−105(2)
N(4)–C(13)	1.466(7)	N(2)–N(1)–Zn(1)	120.7(3)	N(3)–C(9)–C(10A)–C(11A)	21.7(18)
N(4)–C(14)	1.473(7)	C(13)–N(4)–Zn(1)	112.7(3)	N(4)–C(14)–C(15)–N(5)	59.5(7)
N(4)–C(12)	1.482(7)	C(14)–N(4)–Zn(1)	101.3(3)	N(5)–Zn(1)–S(1)–C(8)	−89.9(2)
N(5)–C(16)	1.465(8)	C(12)–N(4)–Zn(1)	114.2(3)	N(5)–Zn(1)–O(1)–C(1)	71.7(4)
N(5)–C(17)	1.473(8)	C(16)–N(5)–Zn(1)	110.3(4)	N(5)–Zn(1)–N(1)–C(7)	−82.5(4)
N(5)–C(15)	1.478(7)	C(17)–N(5)–Zn(1)	110.3(4)	N(5)–Zn(1)–N(1)–N(2)	93.0(3)
C(9)–C(10A)	1.452(10)	C(15)–N(5)–Zn(1)	105.0(3)	N(5)–Zn(1)–N(4)–C(13)	−102.4(4)
C(9)–C(10B)	1.459(11)			O(1)–C(1)–C(6)–C(7)	3.7(8)
C(10A)–C(11A)	1.183(12)			C(9)–N(3)–C(8)–S(1)	−12.4(7)
C(10B)–C(11B)	1.183(13)			C(9)–N(3)–C(8)–N(2)	170.0(5)
C(14)–C(15)	1.469(8)			C(10A)–C(9)–C(10B)–C(11B)	−7(2)

Table 3
Hydrogen bond parameters (Å and °) in [**ZnL$_2$(tmen)**]

D–H···A	*d*(D–H)	*d*(H···A)	*d*(D···A)	∠(DHA)
C(12)–H(12B)···O(1)	0.96	2.49	3.029(7)	115.2
C (9)–H(9B)···S(1)	0.97	2.51	3.039(6)	114.1
N (3)–H(3N)···N(2)[a]	0.86	2.28	3.134(5)	171.8

[a] Symmetry code: $-x+1, -y+2, -z$.

the methyl H atom belonging to the *tmen* and the O atom. The second is between the methylene H atom belonging to the allyl group and the S atom. Each of these interactions leads to the formation of five-membered ring with graph-set descriptor *S*(5) [47]. Examination of the structure with *PLATON* [48] reveals that the molecules of compound [ZnL$_2$(tmen)] are linked into centrosymmetric R_2^2 (8) – dimers (Fig. 2) by paired N–H···N hydrogen bonds [49–51]. Thioamide nitrogen atom N(3) in the molecule at (x, y, z) acts as hydrogen-bond donor to imin N(2) atom in the molecule at ($1-x$, $2-y$, $-z$), so forming a centrosymmetric R_2^2 (8) ring centred at (1/2, 1, 0). The detailed geometry of the intra- and intermolecular interactions is given in Table 3.

3.1.2. IR spectroscopy

IR spectral data of the thiosemicarbazone ligands show *v*(–NH–) stretchings of –NH–C(S)–NH– moiety at 3451 (L_1), 3407 (L_2) and at 3307 (L_1), 3153 (L_2). The absence of any band *v*(–SH–) in the 2700–2500 cm^{-1} region of the IR spectrum of ligands signify thione tautomer of free ligand in the solid state. The broad stretching band *v*(–OH–) in the range 3600–3250 cm^{-1} and the band at 3307 cm^{-1} (L_1) or 3153 cm^{-1} (L_2) corresponding to *v*(–N^{2}H–) disappear in the spectra of the complexes due to the deprotonation in the presence of Zn(II) and *tmen* ligand, and coordinates to zinc(II) ion via thiolate sulphur atom and phenolic oxygen. The *v*(–N^{4}H–) band and *v*(C=N) band of thiosemicarbazone ligands shift to lower wave numbers in the spectra of complexes. The bands assigned to *v*(CH$_3$–N), *v*(C–N–C), *v*(–CH$_2$–) and *v*(–CH$_3$) of *tmen* ligand are shown in the 1331–1306 cm^{-1}, 1175–1173 cm^{-1}, 2998–2860 cm^{-1} region, respectively.

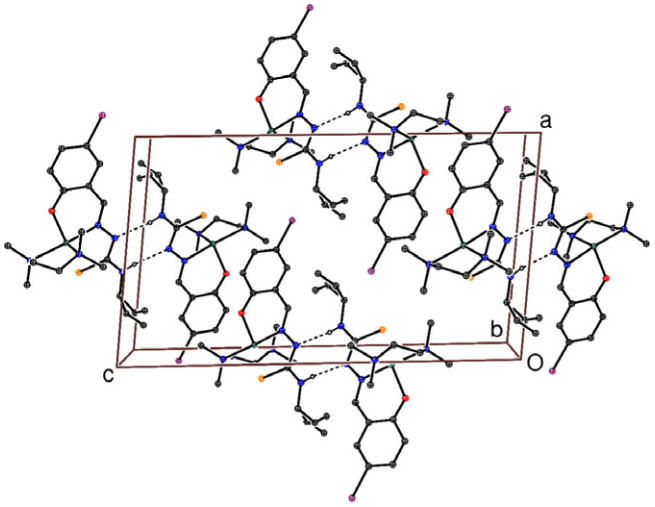


Fig. 2. Part of the crystal structure of [ZnL$_2$(*tmen*)], showing the formation of centrosymmetric R_2^2 (8) dimers. Hydrogen bonds are shown as dashed lines. For the sake of clarity, H atoms not involved in the motif shown have been omitted.

3.1.3. UV–Vis spectra

The UV–Vis spectra of the ligands in chloroform show four bands at *ca.* 217 nm which corresponds to $\pi \rightarrow \pi^*$ transition of phenol, at *ca.* 245 nm which corresponds to $\pi \rightarrow \pi^*$ transition of aromatic ring and at *ca.* 317 nm which corresponds to $n \rightarrow \pi^*$ transition of azomethine group and at *ca.* 346 nm with a shoulder which corresponds to $\pi \rightarrow \pi^*$ transition of thioamide. In the spectra of the complexes, the band of *tmen* ligand overlaps with the intense phenyl at *ca.* 245 nm. The band of at *ca.* 370 nm is attributable to the thioamide $n \rightarrow \pi^*$ transition on the complexation of the thiolato sulphur due to tautomer form.The higher energy bands can be assigned to d–d transitions at *ca.* 584 and 656 nm.

3.1.4. NMR spectra

^{1}H NMR spectra of the thiosemicarbazone ligands show a sharp singlet at 11.19 ppm (L_1) and 11.21 ppm (L_2) due to the OH group. These bands are not found in the spectra of the complexes, which is consistent with deprotonation of these ligands upon metal complexation. Moreover, in the ^{1}H NMR spectrum of the complexes, the absence of signals assigned N^{2}H of the free ligands at 9.13 ppm (L_1) and 10.30 ppm (L_2) confirms that N^2 deprotonates and thiosemicarbazon coordinate to zinc atom via thiolate sulphur atom. The complexation by azomethine nitrogen affects the chemical shift of the C=N protons about 0.2 ppm. The signals of *tmen* as a second ligand are observed in the range 3.87–2.53 ppm.

^{15}N NMR spectra of the complexes show five signal at *app.* 317 ppm, 201 ppm, 199 ppm, 198 ppm.

3.1.5. Mass spectra

Molecular ions are present at *m*/*z* 493 (100% relative abundance) in the both spectra of [ZnL$_2$(*tmen*)]. The peaks at *m*/*z* 495, 494, 492 and 491 correspond to (MH_2^+), (MH^+), (M^+-H), (M^+-2H), respectively. In the APCI-MS spectrum of [ZnL$_2$(*tmen*)], low mass ions below *m*/*z* 493 are present at 377 and 281, respectively, corresponding to *tmen* ligand molecule and Br–C$_6$H$_3$–(O)–CH=N–N– fragment. The spectrum shows seven prominent ions at *m*/*z* 756, 872, 986, 1247, 1366, 1626, 1743, respectively, corresponding to {2[ZnL$_2$(*tmen*)] + 2H$^+$ − 2*tmen*}, {2[ZnL$_2$(*tmen*)] + 2H$^+$ − 1*tmen*}, {2[ZnL$_2$(*tmen*)]}, {3[ZnL$_2$-(*tmen*)] − 2*tmen*}, {3[ZnL$_2$(*tmen*)] + 3H$^+$ − 1*tmen*}, {4[ZnL$_2$-(*tmen*)] + 2H$^+$ − 3*tmen*}, {4[ZnL$_2$(*tmen*)] + 3H$^+$ − 2*tmen*}. In the ESI-MS spectrum of [ZnL$_2$(*tmen*)], low mass ions below *m*/*z* 493 are present at 377 and 196, respectively, *tmen* ligand molecule and Br–C$_6$H$_3$–(O)–CH=N–N–CS–NH–C$_2$H$_2$– fragment. The spectrum shows seven prominent ions

at m/z 674, 872, 988, 1247, 1363, 1626, 1742, respectively, corresponding to {[ZnL_2 (*tmen*)] + Zn(*tmen*)}, {2[ZnL_2-(*tmen*)] + $2H^+$ − 1*tmen*}, {2[ZnL_2(*tmen*)] + $2H^+$}, {3[ZnL_2-(*tmen*)] − 2*tmen*}, {3[ZnL_2(*tmen*)] − 1*tmen*}, {4[ZnL_2(*tmen*)] + $2H^+$ − 3*tmen*}, {4[ZnL_2(*tmen*)] + $2H^+$ − 2*tmen*}. In comparison with the ESI-MS, APCI-MS shows a similar pattern of peaks above molecular ion peak, m/z 493. The higher mass ions are condensation products of lower mass ions. The polymer peaks in the spectrum must be formed by the association of the initially formed molecular ion with the neutral *tmen* molecule.

Molecular ions are present at m/z 444 (100% relative abundance) in the both spectra of [ZnL_1(*tmen*)]. In the APCI-MS spectrum of [ZnL_1(*tmen*)], the peaks at m/z 328, 443, 444, 445, 774, 890, 1218, 1332, 1431, 1546, 1662 corresponds to (M^+−*tmen*), (M^+−H), (M^+), (MH^+), {2[ZnL_1 (*tmen*)] + $2H^+$ − 1*tmen*}, {2[ZnL_1 (*tmen*)] + $2H^+$}, {3[ZnL_1(*tmen*)] + $2H^+$ − 1*tmen*}, {3[ZnL_1(*tmen*)]}, {4[ZnL_1(*tmen*)] + + $3H^+$ − 3*tmen*}, {4[ZnL_1(*tmen*)] + $2H^+$ − 2*tmen*}, {4[ZnL_1(*tmen*)] + $2H^+$ − 1*tmen*}, respectively. In the ESI-MS spectrum of [ZnL_1(*tmen*)], the peaks at m/z 328, 443, 444, 445, 773, 890, 1218, 1332, 1430, 1546, 1662 corresponds to (M^+ -*tmen*), (M^+−H), (M^+), (MH^+), {2[ZnL_1(*tmen*)] + $1H^+$ − 1*tmen*}, {2[ZnL_2(*tmen*)] + $2H^+$}, {3[ZnL_2(*tmen*)] + $2H^+$ − 1*tmen*}, {3[ZnL_2(*tmen*)]}, {4[ZnL_2-(*tmen*)] + $2H^+$ − 3*tmen*}, {4[ZnL_2(*tmen*)] + $2H^+$ − 2*tmen*}, {4[ZnL_2(*tmen*)] + $2H^+$ − 1*tmen*}, respectively.

4. Conclusion

I have presented the synthesis and characterisation of two novel zinc complexes containing chelating ligands. The mixed ligand complexes of type [ZnL(*tmen*)] are obtained with bidendate chelating *tmen* and dianionic thiosemicarbazone ligands. Up to this study, I know that the reaction of *tmen* with thiosemicarbazone in the presence metal ion gave dimeric complex containing no *tmen* molecule [18,19]. In this study, the presence of coordinated *tmen* molecule was confirmed by X-ray structure analysis, elemental analysis, atomic absorption spectrometer, magnetic susceptibility, molar conductivity, electrospray ionization (ESI) and atmospheric pressure chemical ionization (APCI) mass spectra and IR, UV–Vis, ^{1}H NMR and ^{15}N spectroscopies.

Acknowledgement

This work was supported by the Research Fund of Istanbul University. Project Number, 233/29042004.

Appendix A. Supplementary material

CCDC 643822 contains the supplementary crystallographic data for this paper. These data can be obtained free of charge via http://www.ccdc.cam.ac.uk/conts/retrieving.html, or from the Cambridge Crystallographic Data Centre, 12 Union Road, Cambridge CB2 1EZ, UK; fax: (+44) 1223-336-033; or e-mail: deposit@ccdc.cam.ac.uk.. Supplementary data associated with this article can be found, in the online version, at doi:10.1016/j.poly.2007.10.001.

References

[1] C.Q. Debra, A.K. Kathy, R.K. Earl, Antivir. Res. 71 (1) (2006) 24.
[2] Y. Teitz, D. Ronen, A. Vansover, T. Stematsky, J.L. Riggs, Antivir. Res. 24 (4) (1994) 305.
[3] M.C. Rodríguez-Argüelles, E.C. López-Silva, J. Sanmartín, P. Pelagatti, F. Zani, J. Inorg. Biochem. 99 (2005) 2231.
[4] M.C. Rodríguez-Argüelles, E.C. López-Silva, J. Sanmartín, A. Bacchi, C. Pelizzi, F. Zani, Inorg. Chim. Acta 357 (2004) 2543.
[5] A. Cukurovali, I. Yilmaz, S. Gur, C. Kazaz, Eur. J. Med. Chem. 41 (2) (2006) 201.
[6] A. Murugkar, B. Unnikrishnan, S. Padhye, R. Bhonde, S. Teat, E. Triantafillou, E. Sinn, Metal-Based Drugs 6 (3) (1999) 177.
[7] Y. Teitz, N. Barko, M. Abramoff, D. Ronen, Chemotherapy 40 (1994) 195.
[8] W.X. Hu, W. Zhou, C. Xia, X. Wen, Bioorg. Med. Chem. Lett. 16 (2006) 2213.
[9] Z. Afrasiabi, E. Sinn, S. Padhye, S. Dutta, S. Padhye, C. Newton, C.E. Anson, A.K. Powell, J. Inorg. Biochem. 95 (2003) 306.
[10] T. Bal, B. Atasever, Z. Solakoğlu, S. Erdem-Kuruca, B. Ülküseven, Eur. J. Med. Chem. 42 (2007) 161.
[11] M. Campana, C. Laborie, G. Barbier, R. Assan, R. Milcent, Eur. J. Med. Chem. 26 (1991) 273.
[12] K. Uesugi, L.J. Sik, H. Nishioka, T. Kumagai, T. Nagahiro, Microchem. J. 50 (1) (1994) 88.
[13] R.B. Singh, B.S. Garg, R.P. Singh, Talanta 25 (1978) 619.
[14] M.Y. Khuhawar, G.M. Arain, Talanta 68 (2006) 535.
[15] Y. Tian, C. Duan, C. Zhao, X. You, Inorg. Chem. 36 (1997) 1247.
[16] P. Ren, T. Liu, J. Qin, C. Chen, Spectrochim. Acta A 59 (2003) 1095.
[17] Ah. Altun, M. Kumru, A. Dimoglo, J. Mol. Struct. 535 (2001) 235.
[18] A.E. Liberta, D.X. West, BioMetals 5 (2) (1992) 121.
[19] L.A. Saryan, E. Ankel, C. Krishnamurti, D.H. Petering, H. Elford, J. Med. Chem. 22 (10) (1979) 1218.
[20] W. Rodhe, P. Mikelens, J. Jackson, J. Blackman, J. Whitcher, W. Levinson, Antimicrob. Agents Ch. 10 (2) (1976) 234.
[21] G. Atassi, P. Dumont, J.C.E. Harteel, Eur. J. Cancer 15 (4) (1979) 451.
[22] N.M. Samus, A.P. Gulya, V.I. Tsapkov, Yu.M. Chumakov, T. Roshu, Russ. J. Gen. Chem. 76 (7) (2006) 1100.
[23] A. Castiñeiras, D.X. West, J. Mol. Struct. 604 (2002) 113.
[24] E. Bermejo, A. Castiñeiras, I. García-Santos, D.X. West, Z. Anorg. Allergy Chem. 631 (2005) 2011.
[25] E. Labisbal, A. Sousa-Pedrares, A. Castiñeiras, J.K. Swearingen, D.X. West, Polyhedron 21 (2002) 1553.
[26] A.I. Matesanza, I. Cuadradoa, C. Pastorb, P. Souzaa, Z. Anorg. Allergy Chem. 631 (2005) 780.
[27] Z.M. Xue, Y.P. Tian, D. Wang, M.H. Jiang, Dalton Trans. (2003) 1373.
[28] J.M. Perez, A.I. Matesanz, A. Martinambite, P. Navarro, C. Alonso, P. Souza, J. Inorg. Biochem. 75 (1999) 255.
[29] Z. Iakovidou, E. Mioglou, D. Mourelatos, A. Kotsis, M.A. Demertzis, A. Papagoergiou, P.N. Yadav, D. Kovala-Demertzi, Anti-cancer Drug. 12 (2001) 65.
[30] Clifford S. Rossiter, Ryan A. Mathews, Janet R. Morrow, J. Inorg. Biochem. 101 (2007) 925.
[31] J.R. Morrow, O. Iranzo, Curr. Opin. Chem. Biol. 8 (2004) 192.
[32] T. Nittymaeki, H. Lonnberg, Org. Biomol. Chem. 4 (2006) 15.
[33] Y. Jin, J.A. Cowan, J. Am. Chem. Soc. 128 (2006) 410.
[34] K. Michaelis, M. Kalesse, Angew. Chem., Int. Ed. 38 (1999) 2243.

[35] R.W. Sidwell, J.H. Huffman, T.W. Schafer, C. Shipman, Chemotherapy 36 (1990) 58.
[36] S.R. Turk, C. Shipman Jr., J.C. Drach, Biochem. Pharmacol. 35 (9) (1986) 1539.
[37] M. Karatepe, F. Karatas, Cell Biochem. Funct. 24 (2006) 547.
[38] M.C. Rodriguez-Arguelles, M. Belicchi Ferrari, G. Gasparri Fava, C. Pelizzi, P.A. Tarasconi, R. Albertini, P.P. Dall'Aglio, P. Lunghi, S. Pinelli, J. Inorg. Biochem. 58 (1995) 157.
[39] D.T. Minkel, C. Chan-Stier, D.H. Petering, Mol. Pharmacol. 12 (1976) 1036.
[40] D. Kovala-Demertzi, P.N. Yadav, J. Wiecek, S. Skoulika, T. Varadinova, M.A. Demertzis, J. Inorg. Biochem. 100 (2006) 1558.
[41] H.S. Seleem, A.A. Emara, M. Shebl, J. Coord. Chem. 58 (2005) 1003.
[42] H.S. Seleem, B.A. El-Shetary, S.M.E. Khalil, M. Mostafa, M. Shebl, J. Coord. Chem. 58 (2005) 479.
[43] G.M. Sheldrick, SHELXS-97, Program for Crystal Structure Solution, University of Göttingen, Germany, 1997.
[44] G.M. Sheldrick, SHELXL-97, Program for Crystal Structure Refinement, University of Göttingen, Germany, 1997.
[45] V.I. Ovcharenko, S.V. Fokin, G.V. Romanenko, I.V. Korobkov, P. Rey, Russ. Chem. Bull. 48 (1999) 1519.
[46] F. Marchetti, C. Pettinari, R. Pettinari, D. Arriva, S. Troyanov, A. Drozdov, Inorg. Chim. Acta 307 (2000) 97.
[47] J. Bernstein, R.E. Davis, L. Shimoni, N.-L. Chang, Angew. Chem., Int. Ed. Engl. 34 (1995) 1555.
[48] A.L. Spek, J. Appl. Cryst. 36 (2003) 7.
[49] K. Brandenburg, DIAMOND. Release 3.1d. Crystal Impact GbR, Bonn, Germany, 2006.
[50] L.J. Farrugia, J. Appl. Cryst. 30 (1997) 565.
[51] L.J. Farrugia, J. Appl. Cryst. 32 (1999) 837.

Available online at www.sciencedirect.com
ScienceDirect
Polyhedron 27 (2008) 447–452
POLYHEDRON
www.elsevier.com/locate/poly

Synthesis and characterization of a bis-μ,η^1-carboxylate-bridged dinuclear manganese(II) complex containing a tetradentate tripodal ligand, *N*-(benzimidazol-2-ylmethyl)iminodiacetic acid

Dohyun Moon [a], Junghyun Kim [a], Minhak Oh [a], Byoung Jin Suh [b], Myoung Soo Lah [a,*]

[a] *Department of Chemistry and Applied Chemistry, Hanyang University, Ansan, Kyunggi-do 426-791, Republic of Korea*
[b] *Department of Physics, Catholic University of Korea, Puchon, Kyunggi-do 420-473, Republic of Korea*

Received 11 July 2007; accepted 30 September 2007
Available online 7 November 2007

Abstract

The dinuclear Mn(II) complex, $[Mn_2(Hbida)_2(H_2O)_2]$, was prepared using a tetradentate tripodal ligand, *N*-(benzimidazol-2-ylmethyl)iminodiacetic acid (H_3bida) which has two carboxylate and one benzimidazole groups. The manganese ions are doubly bridged using μ,η^1-bridging monodentate carboxylate oxygen atoms. The Mn–Mn bond distance of 3.446 Å in the complex is comparable to that observed in the active site of the native *manganese arginase* enzyme (3.30 Å). The geometry of the complex with four carboxylates in two different types of binding modes, non-bridging monodentate and μ,η^1-type bridging monodentate, mimics the active site structure of *manganese arginase*. The magnetic properties of the complex show a coupling constant of $J = -0.471(1)$ cm^{-1}, which is consistent with weakly coupled antiferromagnetic Mn^{II} ($S = 5/2$) centers. The cyclic voltammograms of the Mn(II) complex in DMF show irreversible oxidation occurring around 570 mV (versus Ag/AgCl).
© 2007 Elsevier Ltd. All rights reserved.

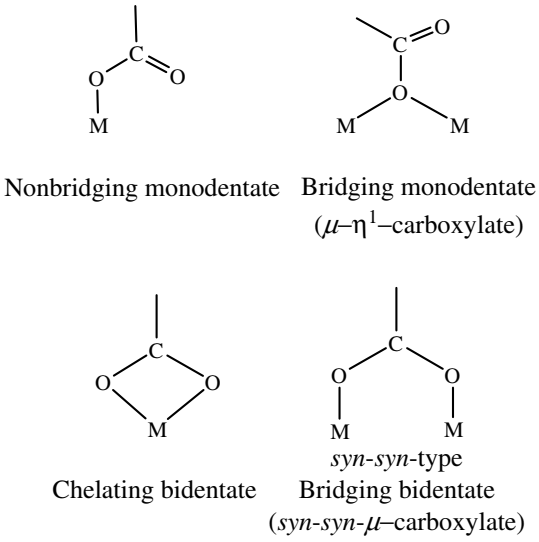
Keywords: Dinuclear manganese complex; Carboxylate bridge; Tetradentate tripodal ligand; Arginase

1. Introduction

Many of the studies on the synthesis and characterization of multinuclear manganese complexes have been directed towards the development of synthetic models [1–3] for diverse manganese enzymes, such as manganese arginase [4], manganese catalase [5] and the oxygen-evolving complex (OEC) of photosystem II [6]. These synthetic complexes have been prepared using multidentate ligands having various donor groups, among which a carboxylate donor group is important because of its role in forming the active site of metalloenzymes [7]. Various binding modes of carboxylates have been observed at the active sites of manganese metalloenzymes [4–7b,7d] (Scheme 1). The active site of manganese arginase that catalyzes the hydrolysis of L-arginine to L-ornithine and urea contains a dinuclear manganese center associated with four carboxylate groups, with all of which are in different binding modes [4f]. The manganese(II) ions in the arginase are bridged by a *syn–syn*-μ-carboxylate group, a μ,η^1-carboxylate group, and a water molecule, which leads to a Mn–Mn bond distance of 3.3 Å [4f]. Each manganese coordination sphere is completed by a histidine and either a monodentate carboxylate or a chelating bidentate carboxylate group, giving either a penta-coordinate square pyramidal or a hexa-coordinate distorted octahedral manganese center, respectively. The bridging water molecule is involved in a hydrogen bond interaction with the monodentate carboxylate oxygen atom and is supposed to participate in the hydrolysis of L-arginine through a metal-activated hydroxide mechanism [4d]. Even though numerous model complexes for either the manganese catalase [2] or the OEC [3] have been proposed and characterized,

* Corresponding author. Tel.: +82 31 400 5496; fax: +82 31 436 8100.
E-mail address: mslah@hanyang.ac.kr (M.S. Lah).

0277-5387/$ - see front matter © 2007 Elsevier Ltd. All rights reserved.
doi:10.1016/j.poly.2007.09.028



Scheme 1. The carboxylate binding modes observed in various manganese metalloproteins.

only a few manganese model complexes for the arginase have been reported so far [1].

Here we report on the preparation and characterization of a dinuclear manganese(II) complex, which has two important structural features of the active site of the manganese arginase: the bridging μ,η^1-carboxylate group and intramolecular hydrogen bonding between the ligated water molecule and a non-bridging monodentate carboxylate. The complex was prepared using a manganese(II) acetate tetrahydrate and a tripodal tetradentate ligand, *N*-(benzimidazol-2-ylmethyl)iminodiacetic acid (H_3bida) that contains two carboxylate and one benzimidazole groups.

2. Experimental

2.1. Materials

The following commercially available chemicals were purchased and used without further purification: Mn(II) acetate tetrahydrate from Yakuri; methanol from Junsei; and pyridine from Aldrich Chemicals. *N*-(benzimidazol-2-ylmethyl)iminodiacetic acid (H_3bida) was prepared according to a literature procedure [8].

2.2. Physical measurements

Elemental analysis was performed at the Organic Chemistry Research Center in Sogang University (Korea) using a TE Flash EA 1112 series elemental analyzer. Infrared spectra were recorded using KBr pellets in the range 4000–400 cm^{-1} employing a Varian FTS 1000 FT-IR spectrometer.

2.3. Synthesis

$[Mn_2(Hbida)_2(H_2O)_2]$ (**1**) 0.132 g (0.502 mmol) of H_3bida was dissolved in 10 mL of methanol and 10 mL of pyridine. Then 0.123 g (0.502 mmol) of Mn(II) acetate tetrahydrate was added to the solution. The solution was stirred until the solution became clear, and then it was allowed to stand for a period of 7 days. Pale yellow crystals were separated from the solution, washed with methanol and water, and vacuum dried. (0.088 g, 53% yield). *Anal.* Calc. for $[Mn_2(Hbida)_2(H_2O)_2]$ ($Mn_2C_{24}H_{26}N_6O_{10}$) ($fw = 668.38$): C, 43.13; H, 3.92; N, 12.57. Found: C, 43.10; H, 3.99; N, 12.61%. IR (cm^{-1}): 3391.7(br), 3208.4(br), 3115.6(w), 3063.3(w), 2922.2(w), 1638.5(w), 1626.3(m), 1612.2(s), 1592.0(m), 1490.4(m), 1467.2(w), 1453.7(s), 1435.8(w), 1402.7(s), 1367.0(s), 1328.4(s), 1316.4(w), 1277.2(s), 1264.1(m), 1129.4(s), 1116.7(m), 1039.3(s), 1003.6(s), 977.0(s), 932.5(s), 911.0(m), 899.1(s), 844.7(w), 768.8(m), 754.1(s), 622.1(m), 428.9(m).

2.4. Electrochemistry

Electrochemical measurements were performed using a BAS CV-50W under an argon atmosphere in a conventional three-electrode cell consisting of an Ag/AgCl (3 M KCl) reference electrode, Pt wire counter electrode, and a glassy carbon working electrode. The glassy carbon electrode was freshly polished using alumina before each scan. The cyclic voltammogram of complex **1** was recorded using a DMF solution of the complex ($\sim$1 mmol/dm^3) with 0.1 mol/dm^3 of tetrabutylammonium tetrafluoroborate ($[CH_3(CH_2)_3]_4NBF_4$) as the supporting electrolyte.

2.5. Magnetic measurements

Magnetization measurements were carried out on powdered sample using a SQUID magnetometer (Quantum Design MPMS-7XL). Field-cooled magnetization data were collected in an applied magnetic field of $H = 500$ Oe in the temperature range $2\ K < T < 300\ K$. All the data shown were corrected for the diamagnetic background.

2.6. X-ray crystallography

A crystal was coated with paratone oil to prevent loss of crystallinity on exposure to air. The data collection was performed at -100 °C using Mo Kα radiation ($\lambda = 0.71073$ Å) employing a Bruker SMART CCD equipped with a graphite crystal, incident-beam monochromator. The SMART and SAINT software packages [9] were used for data collection and integration, respectively. The collected data were corrected for absorbance using SADABS [10] based upon Laue symmetry using equivalent reflections. Structures were solved by direct methods, and refined using full-matrix least-squares calculations employing the SHELXTL-PLUS software package [11]. All non-hydrogen atoms were refined anisotropically. Hydrogen atoms, except those attached to the lattice solvents, were found by difference Fourier peaks, and refined isotropically. Two pyridine sites were found as lattice solvents: one was located at a general position and the other was on a crys-

Table 1
Crystal structure and refinement data for $[Mn_2(Hbida)_2(H_2O)_2]\cdot 3py$ (**1**)

Empirical formula	$Mn_2C_{39}H_{41}N_9O_{10}$
Formula weight (g/mol)	905.69
Temperature (K)	173(2)
Crystal system, space group	monoclinic, $P2_1/c$
Unit cell dimensions	
a (Å)	14.001(4)
b (Å)	14.797(4)
c (Å)	9.974(3)
β (°)	107.674(5)
Volume (Å^3)	1968.9(10)
Z, D_{calc} (mg/m^3)	2, 1.528
Absorption coefficient (mm^{-1})	0.713
Reflections collected/unique [R_{int}]	11679/4651 [0.0748]
Final R indices [$I > 2\sigma(I)$]	$R_1 = 0.0685$, $wR_2 = 0.1490$
R indices (all data)	$R_1 = 0.1500$, $wR_2 = 0.1818$
Maximum/minimum residual density (e Å^{-3})	0.533/−0.526

tallographic inversion center. The position of the largest electron density in the pyridine site of the general position was assigned as pyridyl nitrogen because there were no other indications, such as the involvement of a hydrogen bonding interaction, for any atoms around the site. All the atoms of the other pyridine site with the inversion symmetry were treated using the PART instruction to refine each position as 5/6 carbon and 1/6 nitrogen atom site, because the pyridyl nitrogen had to be disordered and it was not possible to distinguish it from other carbon atoms. Hydrogen atoms of the pyridine molecule on the inversion center were not included in the final least-squares refinement. Crystal and intensity data are given in Table 1.

3. Results and discussion

3.1. Preparation and characterization

$[Mn_2(Hbida)_2(H_2O)_2]$ (**1**) was prepared using manganese(II) acetate tetrahydrate as a metal source and $Hbida^{2-}$ as a dianionic tripodal tetradentate ligand in the presence of pyridine as base (Scheme 2). Two different sets of carboxylate peaks in the IR spectrum of complex **1** suggest the presence of two different binding modes of the carboxylate groups. The bands occurring at 1612 cm^{-1} and 1403 cm^{-1} were assigned to an asymmetric and symmetric stretching vibrational mode of the bridging monodentate carboxylate group, respectively, and the bands occurring at 1592 cm^{-1} and 1454 cm^{-1} were assigned to an asymmetric and symmetric stretching vibrational mode of the non-bridging monodentate carboxylate group [12]. The $\Delta(\mu_{as} - \mu_s)$ splittings of 209 and 138 cm^{-1} for the carboxylate groups are similar to those of manganese complexes that have both a bridging monodentate carboxylate group and a non-bridging monodentate carboxylate group [13a,13c,14]. The two different carboxylate binding modes in complex **1** were identified from the single crystal structural analysis of the compound.

3.2. Molecular structure

An ORTEP drawing [15] of $[Mn_2(Hbida)_2(H_2O)_2]\cdot 3py$ (**1**) is shown in Fig. 1. Each hexa-coordinate manganese(II) center in the dinuclear complex with an inversion symmetry has an N_2O_4 donor environment, where the nitrogen (N1) atom is from the benzimidazolyl group and the other nitrogen (N3) atom is from the tertiary amine nitrogen of the ligand, one oxygen (O5) atom is from a water molecule,

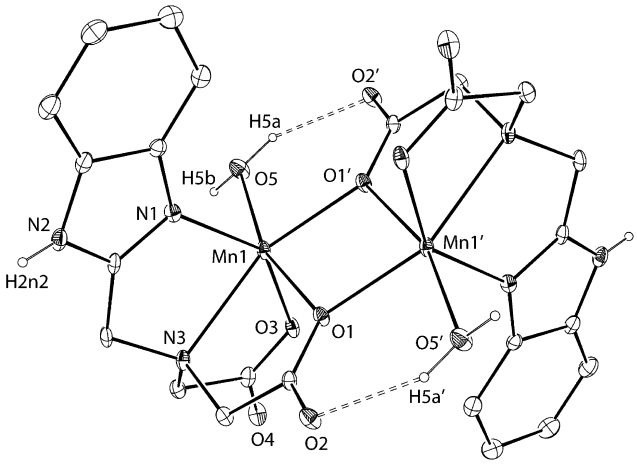
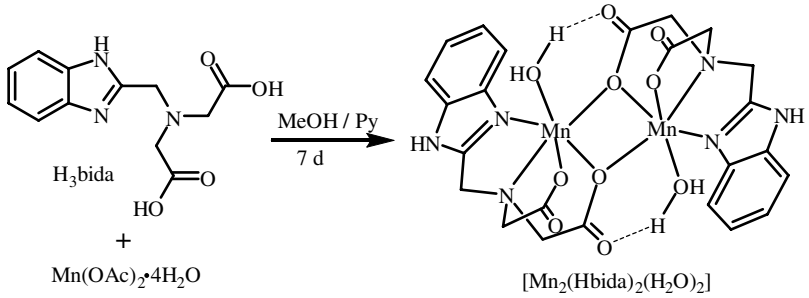


Fig. 1. An ORTEP drawing of $[Mn_2(Hbida)_2(H_2O)_2]\cdot 3py$ (**1**) at 30% probability thermal ellipsoids. Only the hydrogen atoms involved hydrogen bonding are shown, and the lattice solvent molecules have been omitted for clarity.



Scheme 2. Reaction scheme for $[Mn_2(Hbida)_2(H_2O)_2]$ (**1**).

and the remaining three oxygen atoms (O1, O1′, and O3) are from the carboxylate groups. The distorted octahedral coordination geometry of the manganese center is not unusual for a high-spin six-coordinate Mn(II) ion [16] (Table 2). The Mn–O bond distances (2.140(4)–2.184(3) Å) are in the range of the usual Mn^{II}–O bond distances. The distance between the manganese and the nitrogen atoms of the tertiary amine, 2.399(4) Å, is long for a Mn^{II}–N bond distance. This type of weak coordination has also been reported in the other Mn^{II} complexes having similar tertiary nitrogen atoms [13,17]. The two carboxylate groups in $Hbida^{2-}$ are in different binding modes: one in the non-bridging monodentate binding mode and the other in the bridging monodentate, μ,η^1-binding mode. This bridging mode leads to a dinuclear metal complex with a bis-μ,η^1-bridging Mn_2O_2 core. The Mn–Mn distance in this dinuclear complex (3.446(8) Å) is shorter than that of any known bis-μ,η^1-bridging dinuclear manganese model complex (3.489–4.091 Å range) [13,17,18], and nearly equal to that of the manganese arginase core (3.3 Å) [4f]. The sixth coordination site of the manganese(II) center is occupied by a water molecule, which is involved in intramolecular hydrogen bonding as the water molecule in the active site of the arginase. While the water molecule in the active site of the arginase enzyme bridges the two manganese(II) ions and participates in intramolecular hydrogen bonding with a non-coordinating oxygen atom of a monodentate terminal carboxylate, in complex **1**, the non-bridging terminal water molecule participates in intramolecular hydrogen bonding with a non-coordinating oxygen atom of a μ,η^1-bridging monodentate carboxylate. In addition to this intramolecular hydrogen bonding, the coordinate water molecule simultaneously participates in intermolecular hydrogen bonding with the carboxylate oxygen atom of the neighboring dinuclear complex (Table 3). A similar simultaneous intra- and intermolecular hydrogen bonding pattern has already been reported in a hepta-coordinated bis-μ,η^1-bridging dinuclear manganese complex prepared using a tripodal tetradentate ligand with two imidazole and one carboxylate groups [17a]. It is reported that the reaction of H_3bida with other transition metal ions such as V(IV), Ni(II), Co(II), and Zn(II) ions has led to only mononuclear six-coordinate complexes, where none of the carboxylates of the ligand are involved in any bridging modes [19]. While the reaction with Cu(II) ion in the presence of an additional chelating bidentate ligand has also led to a mononuclear complex [19b], but in the absence of the additional chelating bidentate ligand one-dimension coordination polymer has been obtained, where one carboxylate group is involved in a *syn–anti*-type bridging mode [19c]. Even though numerous carboxylate-bridged manganese complexes have been reported, most of these are of the *syn-syn*-type carboxylate-bridged complexes [20], and only a few μ,η^1-bridged manganese complexes have been reported in the literature [13,17]. All known μ,η^1-bridged manganese complexes have only one type of carboxylate group [13b,17]. μ,η^1-Bridged manganese complexes with more than one type of carboxylate group are: $[Mn^{II}_2(2,6\text{-dimethoxybenzoate})_4(Me_2Phen)_2(H_2O)_2]\cdot 2EtOH$ [13a] and $Mn^{II}_2(2,6\text{-dimethoxybenzoate})_4(bpy)_2(H_2O)_2$ [13c]. These complexes contain four carboxylate groups of two different types, where one is a non-bridging monodentate carboxylate group and the other is a μ,η^1-bridging monodentate group. Complex **1** is another example of a bis-μ,η^1-bridging dinuclear manganese complex with two different types of carboxylate groups prepared using a tripodal tetradentate ligand with two carboxylates and an benzimidazole group that provides a N_2O_2 coordination environment.

Table 2
Selected bond distances (Å) and angles (°) for **1**

Mn(1)–O(1)	2.184(3)	Mn(1)–O(1)[a]	2.161(3)
Mn(1)–O(3)	2.149(3)	Mn(1)–O(5)	2.140(4)
Mn(1)–N(1)	2.210(4)	Mn(1)–N(3)	2.399(4)
Mn(1)–Mn(1)[a]	3.446(8)		
O(1)–Mn(1)–O(1)[a]	75.0(1)	O(1)–Mn(1)–O(3)	94.3(1)
O(1)–Mn(1)–O(5)	162.5(2)	O(1)–Mn(1)–N(1)	88.5(1)
O(1)–Mn(1)–N(3)	75.7(1)	O(3)–Mn(1)–O(1)[a]	109.2(1)
O(5)–Mn(1)–O(1)[a]	87.4(2)	O(1)[a]–Mn(1)–N(1)	104.4(1)
O(1)[a]–Mn(1)–N(3)	150.8(1)	O(3)–Mn(1)–O(5)	90.9(2)
O(3)–Mn(1)–N(1)	145.8(1)	O(3)–Mn(1)–N(3)	73.3(1)
O(5)–Mn(1)–N(1)	96.5(2)	O(5)–Mn(1)–N(3)	121.8(2)
N(1)–Mn(1)–N(3)	74.5(1)	Mn(1)–O(1)–Mn(1)[a]	105.0(1)

Symmetry transformations used to generate equivalent atoms: [a] $-x+1$, $-y+1$, $-z+2$.

Table 3
Hydrogen bonds for **1** (Å and °)

D–H···A	d(D–H)	d(H···A)	d(D···A)	∠(DHA)
O(5)–H(5a)···O(2)[a]	0.89(8)	1.97(8)	2.768(6)	148(6)
O(5)–H(5b)···O(4)[b]	0.83(7)	1.84(7)	2.661(6)	166(7)
N(2)–H(2n2)···O(3)[c]	0.78(7)	2.30(7)	3.027(6)	155(8)
N(2)–H(2n2)···O(4)[c]	0.78(7)	2.30(7)	2.976(6)	145(8)

Symmetry transformations used to generate equivalent atoms: [a] $-x+1$, $-y+1$, $-z+2$, [b] $-x+1$, $-y+1$, $-z+1$, [c] $-x+1$, $y-1/2$, $-z+3/2$.

3.3. Magnetic properties

The magnetic susceptibility of complex **1** was measured in the temperature range 2–300 K. The effective magnetic moment (μ_{eff}) decreases slightly with decreasing temperature from 8.16 μ_B at 300 K to 7.88 μ_B at 30 K. Below 30 K, μ_{eff} decreases rapidly, and reaches a value of 4.57 μ_B at 2 K (Fig. 2). This behavior is typical of a weakly coupled antiferromagnetic system. We analyzed the χ_{mol} data by fitting it to the Eq. (1) derived from the isotopic Heisenberg exchange Hamiltonian $H = -2JS_1 \cdot S_2$ (where $S_1 = S_2 = 5/2$ for Mn^{II} high-spin d^5 ion systems) [21]. N is the Avogadro's number, μ_B is Bohr magneton, g is the Landé g-value, J is the exchange integral, and k is the Boltzmann's constant. A good fit curve was obtained for $J = -0.471(1)\ cm^{-1}$ and $g = 1.940$. This weakly antiferromagnetically coupled value of J for complex **1** is similar

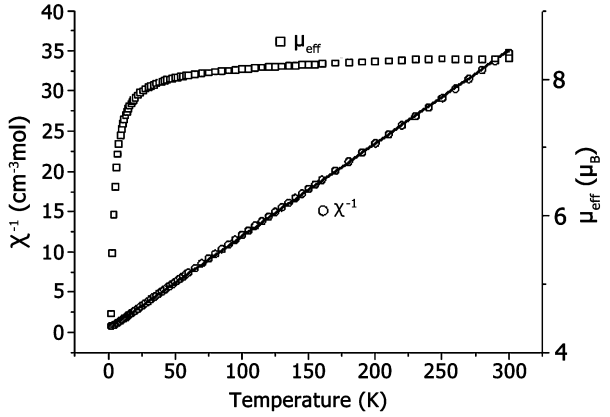


Fig. 2. The effective magnetic moment, μ_{eff}, of **1** and the Curie–Weiss plot ($1/\chi_{mol}$ vs. T).

to that of the other bis-μ,η^1-carboxylate bridged manganese complexes [13b,14a,17]

$$\chi_{mol} = \frac{2Ng^2\mu_B^2}{kT} \times \left[\frac{e^{J/kT} + 5e^{3J/kT} + 14e^{6J/kT} + 30e^{10J/kT} + 55e^{15J/kT}}{1 + 3e^{J/kT} + 5e^{3J/kT} + 7e^{6J/kT} + 9e^{10J/kT} + 11e^{15J/kT}}\right] \quad (1)$$

3.4. Electrochemical properties

The cyclic voltammogram of complex **1** in a DMF solution showed an irreversible oxidation wave around 570 mV (versus Ag/AgCl) as shown in Fig. 3. This irreversible redox feature of complex **1** is also similar to those in the other manganese(II) complexes with bis-μ,η^1-bridged carboxylate groups [13b,17b].

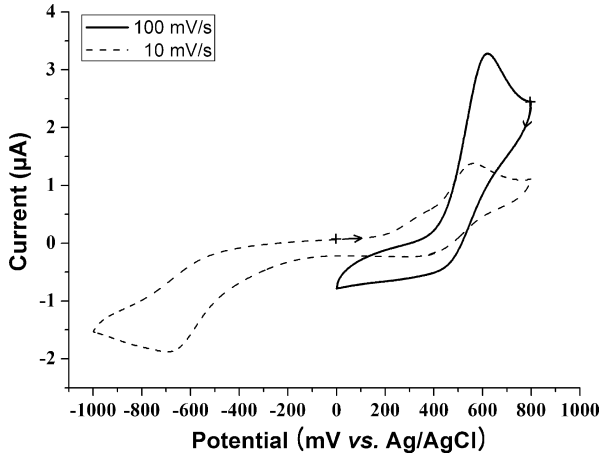


Fig. 3. Cyclovoltammogram of $[Mn_2(Hbida)_2(H_2O)_2]$ (**1**) in DMF with 0.1 mol/dm^3 of $[CH_3(CH_2)_3]_4NBF_4$ as supporting electrolyte. The scan presented with dashed lines was performed from 0 mV with initial anodic sweep at 10 mV/s scan rate, followed by cathodic sweep till −1000 mV, and then reversed back to 0 mV. The scan presented with solid line was performed from 800 mV with initial cathodic sweep at 100 mV/s scan rate, and then reversed at 0 mV.

4. Conclusions

We have characterized a hexa-coordinate dinuclear manganese(II) complex prepared using a tripodal tetradentate ligand, *N*-(benzimidazol-2-ylmethyl)iminodiacetic acid, having one benzimidazole and two carboxylate podal units. The coordination environment of complex **1** resembles that of the first coordination sphere of the native manganese *arginase*. Complex **1** mimics important structural features of the *manganese arginase* active site, such as the Mn–Mn distance, the hydrogen bonding pattern, the presence of four carboxylate groups with the same μ,η^1-bridging monodentate and non-bridging monodentate carboxylate groups. The Mn–Mn distance of 3.446 Å in complex **1** is closer to the value observed in the native *manganese arginase* core (Mn–Mn distance, 3.3 Å) than in any other dinuclear manganese complexes with the same μ,η^1-bridging monodentate carboxylate group. A similar intramolecular hydrogen bonding structure was also observed between the coordinated water molecule and the oxygen atom of the carboxylate group that is not involved in the coordination, as in the active site of the arginase. The magnetic properties and the redox behavior of complex **1** are similar to those reported in other bis-μ,η^1-bridging manganese(II) complexes [13,17].

Supplementary materials

CCDC 642507 contains the supplementary crystallographic data for **1**. These data can be obtained free of charge via http://www.ccdc.cam.ac.uk/conts/retrieving.html, or from the Cambridge Crystallographic Data Centre, 12 Union Road, Cambridge CB2 1EZ, UK; fax: (+44) 1223-336-033; or e-mail: deposit@ccdc.cam.ac.uk.

Acknowledgements

Authors wish to acknowledge the financial support of KOSEF (R01-2005-000-10490-0), ITEP (M1–0213–03–0004), and CBMH (R11-2003-019-02001-0).

References

[1] (a) C. He, S.J. Lippard, J. Am. Chem. Soc. 120 (1998) 105;
(b) B.-H. Ye, T. Mak, I.D. Williams, X.-Y. Li, Chem. Commun. (1997) 1813.
[2] (a) A.J. Wu, J.E. Penner-Hahn, V.L. Pecoraro, Chem. Rev. 104 (2004) 903;
(b) M.U. Triller, W.-Y. Hsieh, V.L. Pecoraro, A. Rompel, B. Krebs, Inorg. Chem. 41 (2002) 5544;
(c) J. Gao, S.H. Zhong, J. Mol. Catal. A: Chem. 186 (2002) 25;
(d) J.-J. Zhang, Q.-H. Luo, C.-Y. Duan, Z.-L. Wang, Y.-H. Mei, J. Inorg. Biochem. 86 (2001) 573;
(e) T.C. Brunold, D.R. Gamelin, T.L. Stemmler, S.K. Mandal, W.H. Armstrong, J.E. Penner-Hahn, E.I. Solomon, J. Am. Chem. Soc. 120 (1998) 8724.
[3] (a) A.K. Poulsen, A. Rompel, C.J. McKenzie, Angew. Chem., Int. Ed. 44 (2005) 6916;
(b) S. Mukhopadhyay, S.K. Mandal, S. Bhaduri, W.H. Armstrong, Chem. Rev. 104 (2004) 3981.

[4] (a) D.W. Christianson, Acc. Chem. Res. 38 (2005) 191;
(b) L.D. Costanzo, G. Sabio, A. Mora, P.C. Rodriguez, A.C. Ochoa, F. Centeno, D.W. Christianson, Proc. Natl. Acad. Sci. USA 102 (2005) 13058;
(c) E. Cama, D.M. Colleluori, F.A. Emig, H. Shin, S.W. Kim, N.N. Kim, A.M. Traish, D.E. Ash, D.W. Christianson, Biochemistry 42 (2003) 8445;
(d) J.D. Cox, E. Cama, D.M. Colleluori, S. Pethe, J.-L. Boucher, D. Mansuy, D.E. Ash, D.W. Christianson, Biochemistry 40 (2001) 2689;
(e) J.D. Cox, N.N. Kim, A.M. Traish, D.W. Christianson, Nature 6 (1999) 1043;
(f) Z.F. Kanyo, L.R. Scolnick, D.E. Ash, D.W. Christianson, Nature 383 (1996) 554.

[5] (a) V.V. Barynin, M.M. Whittaker, S.V. Antonyuk, V.S. Lamzin, P.M. Harrison, P.J. Artymiuk, J.W. Whittaker, Structure 9 (2001) 725;
(b) S.V. Antonyuk, V.R. Melik-Adamyan, A.N. Popov, V.S. Lamzin, P.D. Hempstead, P.M. Harrison, P.J. Artymyuk, V.V. Barynin, Cryst. Rep. 45 (2000) 105.

[6] (a) B. Loll, J. Kern, W. Saenger, A. Zouni, J. Biesiadka, Nature 438 (2005) 1040;
(b) K.N. Ferreira, T.M. Iverson, K. Maghlaoui, J. Barber, S. Iwata, Science 303 (2004) 1831;
(c) N. Kamiya, J.-R. Shen, Proc. Natl. Acad. Sci. USA 100 (2003) 98;
(d) A. Zouni, H.-T. Witt, J. Kern, P. Fromme, N. Krauß, W. Saenger, P. Orth, Nature 409 (2001) 739.

[7] (a) T. Dudev, C. Lim, Acc. Chem. Res. 40 (2007) 85;
(b) N. Mitić, S.J. Smith, A. Neves, L.W. Guddat, L.R. Gahan, G. Schenk, Chem. Rev. 106 (2006) 3338;
(c) E.Y. Tshuva, S.J. Lippard, Chem. Rev. 104 (2004) 987;
(d) G.C. Dismukes, Chem. Rev. 96 (1996) 2909.

[8] (a) L.A. Cescon, A.R. Day, Org. Chem. 27 (1962) 581;
(b) J.G. Wilson, F.C. Hunt, Aust. J. Chem. 36 (1983) 2317.

[9] SMART and SAINT, Area Detector Software Package and SAX Area detector Integration Program; Bruker Analytical X-ray: Madison, WI, 1997.

[10] SADABS, Area Detector Absorption Correction Program; Bruker Analytical X-ray: Madison, WI, 1997.

[11] G.M. Sheldrick, SHELXTL-PLUS, Crystal Structure Analysis Package, Bruker Analytical X-ray, Madison, WI, 1997.

[12] G.B. Deacon, R.J. Phillips, Coord. Chem. Rev. 33 (1980) 227.

[13] (a) E. Garribba, G. Micera, M. Zema, Inorg. Chim. Acta 357 (2004) 2038;
(b) C. Baffert, M.-N. Collomb, A. Deronzier, S. Kjærgaard-Knudsen, J.-M. Latour, K.H. Lund, C.J. McKenzie, M. Mortensen, L.P. Nielsen, N. Thorup, Dalton Trans. (2003) 1765;
(c) T. Glowiak, H. Kozlowski, L.S. Erre, G. Micera, Inorg. Chim. Acta 236 (1995) 149.

[14] (a) S. Durot, C. Policar, G. Pelosi, F. Bisceglie, T. Mallah, J.-P. Mahy, Inorg. Chem. 42 (2003) 8072;
(b) M.J. Baldwin, J.W. Kampf, M.L. Kirk, V.L. Pecoraro, Inorg. Chem. 34 (1995) 5252;
(c) M.-B. Zhang, Y.-M. Chen, S.-T. Zheng, G.-Y. Yang, Eur. J. Inorg. Chem. (2006) 1423;
(d) C. Policar, F. Lambert, M. Cesario, I. Morgenstern-Badarau, Eur. J. Inorg. Chem. (1999) 2201.

[15] ORTEP-3 for Windows L.J. Farrugia, J. Appl. Crystallogr. 30 (1997) 565.

[16] B. Trzaskowski, A. Les, L. Adamowicz, Int. J. Mol. Sci. 4 (2003) 503.

[17] (a) C. Policar, S. Durot, F. Lambert, M. Cesario, F. Ramiandrasoa, I. Morgenstern-Badarau, Eur. J. Inorg. Chem. (2001) 1807;
(b) H. Iikura, T. Nagata, Inorg. Chem. 37 (1998) 4702.

[18] M.J. Plater, M.R.S.J. Foreman, R.A. Howie, J.M.S. Skakle, E. Coronado, C.J. Gómez-García, T. Gelbrich, M.B. Hursthouse, Inorg. Chim. Acta 319 (2001) 159.

[19] (a) D.C. Crans, A.D. Keramidas, S.S. Amin, O.P. Anderson, S.M. Miller, J. Chem. Soc., Dalton Trans. (1997) 2799;
(b) S. Bandyopadhyay, G.N. Mukherjee, M.G.B. Drew, Inorg. Chim. Acta 358 (2005) 3786;
(c) S. Bandyopadhyay, A. Das, G.N. Mukherjee, A. Cantoni, G. Bocelli, S. Chaudhuri, J. Ribas, Inorg. Chim. Acta 357 (2004) 3563.

[20] (a) Y. Gultneh, Y.T. Tesema, T.B. Yisgedu, R.J. Butcher, G. Wang, G.T. Yee, Inorg. Chem. 45 (2006) 3023;
(b) M.A.M. Abu-Youssef, A. Escuer, V. Langer, Eur. J. Inorg. Chem. (2006) 3177;
(c) V.B. Romakh, B. Therrien, L. Karmazin-Brelot, G. Labat, H. Stoeckli-Evans, G.B. Shul'pin, G. Süss-Fink, Inorg. Chim. Acta 359 (2006) 1619;
(d) A. Magnuson, P. Liebisch, J. Högblom, M.F. Anderlund, R. Lomoth, W. Meyer-Klaucke, M. Haumann, H. Dau, J. Inorg. Biochem. 100 (2006) 1234;
(e) M. Murugesu, W. Wernsdorfer, K.A. Abboud, G. Christou, Angew. Chem., Int. Ed. 44 (2005) 892;
(f) A. Grirrane, A. Pastor, A. Galindo, D. del Río, A. Oralandini, C. Mealli, A. Ienco, A. Caneschi, J.F. Sanz, Angew. Chem., Int. Ed. 44 (2005) 3429;
(g) J. Vicario, R. Eelkema, W.R. Browne, A. Meetsma, R.M.L. Crois, B.L. Feringa, Chem. Commun. (2005) 3936;
(h) P. Christian, G. Rajaraman, A. Harrison, M. Helliwell, J.J.W. McDouall, J. Raftery, R.E.P. Winpenny, Dalton Trans. (2004) 2550.

[21] R.L. Carlin, Magnetochemistry, Springer-Verlag, Berlin, Heidelberg, New York, 1986.

Available online at www.sciencedirect.com
ScienceDirect
Polyhedron 27 (2008) 453–464
POLYHEDRON
www.elsevier.com/locate/poly

In vitro and *in vivo* studies of *N*,*N*′-bis[2(2-pyridyl)-methyl]pyridine-2,6-dicarboxamide–copper(II) and rheumatoid arthritis

Sebusi Odisitse, Graham E. Jackson *

Department of Chemistry, University of Cape Town, Private Bag Rondebosch, 7701 Cape Town, South Africa

Received 6 June 2007; accepted 28 September 2007
Available online 19 November 2007

Abstract

The thermodynamic equilibria of copper(II), zinc(II) and calcium(II) with *N*,*N*′-bis[2(2-pyridyl)-methyl]pyridine-2,6-dicarboxamide (L1) have been studied at 25 °C and an ionic strength of 0.15 mol dm^{-3}. Spectroscopic studies suggest metal ion complexation promotes deprotonation and coordination of the amide nitrogens resulting in overall tetragonal coordination of Cu^{2+}. Blood–plasma modelling predicts that Cu(II) competes effectively against Zn(II) and Ca(II) for L1 *in vivo*. Octanol–water partition coefficient studies show that Cu(II)–L1 complexes are reasonably lipophilic. However, the $CuL1H_{-2}$ species which predominates at the physiological pH of 7.4 has poor superoxide dismutase activity. Bio-distribution experiments showed activity accumulation and retention in the body of about 50% of the injected dose for the [^{64}Cu]Cu(II)–L1 complex after 24 h.
© 2007 Elsevier Ltd. All rights reserved.

Keywords: Thermodynamic; Potentiometry; Spectroscopic; Speciation; Complexation; Bio-distribution

1. Introduction

Rheumatoid arthritis (RA) is a chronic, debilitating disease for which there is no cure [1,2]. It is characterized by joint pain and swelling, joint destruction and pannus formation [2,3]. RA remains a medical challenge because it affects about 1% of the general population [4] and so far the exact cause of the disease is still unknown. However, the symptoms and progression of the disease can be treated using immunosuppressive and anti-inflammatory drugs [3,5]. Cu^{2+} has been observed to be effective in the treatment of RA [6]. Elevation of low molecular mass (lmm) Cu(II) complex species concentration in the plasma and synovial fluids of RA patients is well documented [6–8]. This suggests that Cu^{2+} may be a natural defence against inflammation and so an increase in lmm copper from either endogenous or exogenous sources may be beneficial.

With this hypothesis in mind, we have embarked on a programme of ligand design [9–11] with the aim of increasing lmm copper concentration *in vivo*. Recently, we have shown that 3,5-diaminodiamido-4-oxahexacyclododecane (cageL) (Fig. 1), forms stable, lipophilic, Cu(II) complexes capable of surviving *in vivo* as demonstrated by speciation calculations using a blood–plasma model and animal bio-distribution experiments [12]. In order to further improve the lipophilicity, the *N*,*N*′-bis[2(2-pyridyl)-methyl]pyridine-2,6-dicarboxamide (L1) shown in Fig. 1 was synthesised. This ligand has pyridyl groups which are found in most of the non-steroidal anti-inflammatory drugs (NSAIDs) and Cu(II)–NSAIDs complexes are reported to be more effective than their parent compounds [13]. The aromatic ring would also be able to increase the rigidity to the ligand system due to the aromatic ring system. Pre-organisation of the ligand structure for coordination as

* Corresponding author. Tel.: +27 21 650 2531; fax: +27 21 689 7499.
E-mail address: Graham.Jackson@uct.ac.za (G.E. Jackson).

0277-5387/$ - see front matter © 2007 Elsevier Ltd. All rights reserved.
doi:10.1016/j.poly.2007.09.032

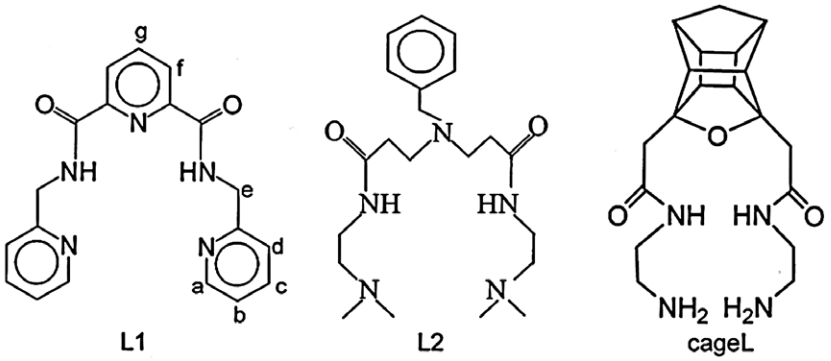


Fig. 1. Schematic structures of ligands discussed.

well as the aromatic groups on the ligand should increase both complex stability and lipophilicity.

The coordination chemistry of L1 with Cu^{2+} was explored by potentiometry, molecular mechanics (MM) calculation and, nuclear magnetic resonance (NMR), infrared (IR) and UV–Vis spectroscopy. Bio-modelling experiments include blood–plasma model simulations, octanol–water partition coefficients and superoxide dismutase (SOD) mimetic activity studies of the copper complexes. The *in vivo* verification of the modelling results was carried out by performing bio-distribution and dermal absorption studies on mice using radioactive ^{64}Cu(II) as a tracer. As Zn^{2+} and Ca^{2+} are potential *in vivo* competitors of Cu(II), their speciation with L1 has also been measured.

2. Experimental

2.1. Synthesis of N,N′-bis[2(2-pyridyl)-methyl]pyridine-2,6-dicarboxamide (L1)

N,*N*′-bis[2(2-pyridyl)-methyl]pyridine-2,6-dicarboxamide was synthesised following the method of Marlin et al. [14] and Hirao et al. [15]. Under nitrogen atmosphere 2,6-pyridinedicarbonyl dichloride (5 g, 0.0245 mol) in 100 cm^3 chloroform was added dropwise to a stirred solution of 2(2-aminomethyl)-pyridine (7.95 g, 0.0735 mol) in 150 cm^3 chloroform at 0 °C. The mixture was stirred for 1 h and then heated to reflux at 60 °C for 2 h. The solvent and excess 2(2-aminomethyl)-pyridine were removed under reduced pressure using a rotary evaporator. Recrystallisation from acetone gave a white solid that was dried under vacuum. The structure of the compound was confirmed by NMR spectroscopy, melting point and elemental micro analysis (CHN).

Yield: 5.1 g (60%), m.p. 150–154 °C (lit. 151–153 °C) [14] ^1H NMR(400 MHz) δ_H ($CDCl_3$) 4.81 (d, 4H, NCH_2), 7.23 (m, 2H, Py–H), 7.39 (m, 2H, Py–H), 7.68 (m, 2H, Py–H), 8.01 (t, 1H, Py–H), 8.34 (d, 2H, Py–H), 8.47 (dd, 2H, Py–H), 9.18 (t, 2H, C(O)NH), ^{13}C NMR(100.6 MHz) δ_C ($CDCl_3$) 44.43 ($NHCH_2$), 122.49, 122.66, 124.78, 137.27, 138.73, 148.75 (Py–C), 148.71, 157.08 (Py–C_{tert}), 163.74 (C(O)NH). Elemental *Anal*. Calc. for $C_{19}H_{17}N_5O_2$) C, 64.00; H, 4.90; N, 19.70. Found: C, 63.30; H, 4.89; N, 19.26%.

2.2. Potentiometric measurements

All solutions for potentiometry were prepared in glass distilled water which had been boiled to remove dissolved carbon dioxide. Recrystallized NaCl was used as background electrolyte at an ionic strength of 0.15 mol dm^{-3} (Cl^-). Other reagents, copper(II) chloride dihydrate, zinc(II) chloride, calcium chloride dihydrate, HCl, NaOH and EDTA (Merck) were commercially available and of analytical grade. These were used without purification. The 0.1 mol dm^{-3} solutions of NaOH and HCl were prepared from Merck Titrisol ampoules and standardized by titrating with potassium hydrogen phthalate (KHP) and sodium tetra borate decahydrate (Borax), respectively. The NaOH solutions were further standardized against the standard HCl solution. Acid–base titration was also used to check carbonate contamination of the sodium hydroxide titrant solution using the Gran method [16]. Otherwise these standardised solutions were used within a short period of time after preparation and were discarded whenever there were signs of carbonate contamination.

The potentiometric titrations were performed under an inert atmosphere of purified nitrogen, at 25 °C, using Radiometer PHM 84 research pH meter and Metrohm Dosimat 665 piston burette, which were linked and controlled by a computer. The pH meter was equipped with a Metrohm 6.0222.100 glass electrode, its slope determined from a buffer line and the response intercept, E^0, determined *in situ*. Titrations were performed in the pH range 2–11 in the concentration range 3×10^{-4}–1×10^{-3} mol dm^{-3} at metal ion to ligand ratios ranging from 1: 1 to 1: 3. Precipitation was observed in the titrations at metal to ligand ratio 1: 1 and at a pH > 8. The data were analysed using the ESTA suite of computer programs [17] which gave only models given in Table 1 for Cu(II), Zn(II) and Ca(II) systems. Various speciation models were tried based on the experimental Z_M-bar and Q_M-bar curves. The water ionization constant was determined to be 13.73 log units. The protonation constants of the ligand and the overall formation

Table 1
Formation constants ($\log \beta_{pqr}$) for Cu(II), Zn(II) and Ca(II) complexes of L1, $\beta_{pqr} = [M_pL_qH_r]/[M]^p[L]^q[H]^r$, $I = 0.15$ mol dm^{-3} (NaCl), $T = 25$ °C

Metal	pqr	log β_{pqr} (σ_{pqr})	R^H	R^H_{lim}
H^+	011	4.62 (0.01)	0.01	0.01
	012	8.13 (0.01)		
	013	10.11 (0.05)		
Cu(II)	111	8.42 (0.03)	0.01	0.01
	110	4.34 (0.03)		
	11−1	0.58 (0.02)		
	11−2	−4.68 (0.03)		
Zn(II)	111	6.90 (0.03)	0.01	0.01
	110	2.76 (0.04)		
	11−1	−3.90 (0.03)		
	11−2	−10.98 (0.01)		
Ca(II)	111	6.61 (0.04)	0.01	0.01
	110	2.46 (0.01)		

σ_{pqr} denotes standard deviation in log β_{pqr}, R^H and R^H_{lim} are the Hamiltonian R-factor and its limit. The general formula of a complex is $M_pL_qH_r$.

constants of the Cu(II), Zn(II) and Ca(II) systems were computed using general expressions given as

$$pM + qL + rH \rightleftharpoons M_pL_qH_r \quad (1)$$

$$\beta_{pqr} = [M_pL_qH_r]/[M]^p[L]^q[H]^r \quad (2)$$

where p, q and r are stoichiometric coefficients of the components in the complex.

2.3. Spectroscopic and molecular mechanics measurements

UV–Vis spectra were recorded at 25 °C on a Cary 100 Conc spectrophotometer. Aqueous solutions containing 1:2 ratio of Cu(II):L1 were investigated in the pH range 2–11 and wavelength region 340–800 nm. Small amounts of 0.1 mol dm^{-3} NaOH or HCl were used to adjust the pH during the titration. NMR samples were prepared in D_2O at ligand concentration of 0.015 mol dm^{-3} and a Cu(II) concentration of 0.007 mol dm^{-3}. ^{1}H NMR spectra were recorded on a Varian Unity Plus 400 MHz instrument. The pH values were corrected for the deuterium isotope effect using Eq. (3) [18].

$$pH = 0.929pH^* + 0.41 \quad (3)$$

where pH* is a direct reading in D_2O solution of the H_2O-calibrated pH meter.

IR spectra were recorded at 25 °C on a Perkin Elmer Spectra One FT-IR spectrometer (Overhead–ATR ZnSe top plate). Solutions of ligand concentration of 0.1 mol dm^{-3} and a Cu(II) concentration of 0.09 mol dm^{-3} were prepared in D_2O and scanned in the pH range 1–12 and wavenumber region 1400–1700 cm^{-1}. The pH of the solutions was adjusted using NaOD or DCl for both NMR and IR studies.

Molecular mechanics calculations were performed using the Discover 3 module of the Accelrys life sciences molecular modelling software, InsightII [19]. For the free ligand, the cvff force field was used while for the metal complex the esff force field was used.

2.4. Bio-modelling measurements

Blood–plasma modelling was performed using a blood–plasma equilibrium database consisting of 10 metal ions and more than 5000 ligands [20]. To this database, the protonation and Cu(II), Zn(II) and Ca(II) formation constants determined in this study were added. The database was used together with typical constituent concentrations of blood–plasma [20] to calculate the speciation of the system and the plasma mobilizing index (pmi) of the ligand. This was achieved using the evaluation of constituent concentration in large equilibrium systems (ECCLES) program [21]. Pmi is a measure of the ability of a ligand to move metal ion from a protein bound form to a low molecular weight form. It is defined by:

$$\text{pmi} = \frac{(\text{total concentration of low-molecular-weight metal complex species in the presence of drug})}{(\text{total concentration of low-molecular-weight metal complex species in normal plasma})}$$

The superoxide dismutase (SOD) mimetic activity of the Cu(II)–L1 system was measured using the nitro blue tetrazolium (NBT) assay at a physiological pH of 7.4 [22–24]. Standard solutions of (i) 0.0004 M xanthine, (ii) 0.0001 M EDTA, (iii) 0.0001 g/cm^3 of catalase, (iv) 0.018 U/cm^3 xanthine oxidase and (v) 0.001 mol dm^{-3} solutions of Cu(II)–L1 complex in 0.05 M phosphate buffer were prepared. In a 4 cm^3 cuvette, 0.6 cm^3 xanthine, 0.2 cm^3 EDTA, 0.2 cm^3 NBT, 0.1 cm^3 catalase and 2.9 cm^3 of phosphate buffer were added and this constituted a blank solution. In a control experiment, in addition to these compounds, 0.4 cm^3 xanthine oxidase and 2.5 cm^3 instead of 2.9 cm^3 phosphate buffer solution were added while in the test solutions, varying volumes of the Cu(II)–L1 complex solutions were added prior to the addition of xanthine oxidase. The concentrations of Cu(II)–L1 SOD mimics ranged from 2.5×10^{-6} mol dm^{-3} to 4.5×10^{-4} mol dm^{-3}. The absorbance readings at 560 nm were obtained at 30 s intervals for a total period of 10 min for the control and experimental SOD solutions. For each set of readings corresponding to a control and a particular concentration of the complex, the absorbance was plotted against time and the slopes of the resulting plots were computed. The %inhibition of the reduction of NBT to formazan was calculated and IC_{50}

values similarly determined from plots of %inhibition versus concentration of the Cu(II)–L1 complex.

Partition coefficients were measured at 25 °C and an ionic strength of 0.15 mol dm^{-3} (Cl^-) using ^{64}Cu and the shake flask method [10,25]. Briefly, into 15 20 cm^3 glass vials, 5 cm^3 portions of Cu(II) (0.001 mol dm^{-3})–L1 (0.002 mol dm^{-3}) solutions were pipetted. The first vial was left at pH 3.0 while the rest of the vials were adjusted in 0.5 pH increments apart using 0.1 mol dm^{-3} of NaOH. These solutions were then spiked with $^{64}CuCl_2$ solution of activity 5 mCi. To each vial containing the spiked metal–ligand solution, 5 cm^3 portions of water saturated 1-octanol were added. These were then stoppered and shaken for 10 min, swirled to collect droplets from the sides of the vials and set aside to allow the two phases to separate at a constant temperature of 25 °C. 1 cm^3 of each phase was pipetted into radioactive counting vials using a microlitre pipette and activity of each phase counted for 5 min in a Minaxi Auto gamma counter (5000 Series-Packard) using a window set at 340–540 eV.

2.5. Bio-distribution and dermal absorption studies

^{64}Cu was prepared by neutron irradiation of 1.7–2.5 mg copper(II) oxide (99.9999%, Aldrich Chem. Co., WI, USA) for 24 h at a thermal neutron flux of 1.0×10^{14} neutrons cm^{-2} s^{-1} in a Safari-1 Research Reactor. The targets were dissolved in 1.0 ml, 1.0 M HCl and diluted to 3.0 ml with 1.0 M HCl. Typical specific activities of 98% radioactively pure ^{64}Cu of ~600 MBq mg^{-1} target material were obtained.

^{64}Cu-labelled Cu(II)–L1 complexes were prepared by spiking 20 cm^3 of Cu^{2+} (0.001 mol dm^{-3})–L (0.003 mol dm^{-3}) solutions with 10–14 mCi $^{64}CuCl_2$(aq). Bio-distribution studies were carried out by injecting 6–8 weeks old Balb/c mice with 0.2 cm^3 of 5 μCi [^{64}Cu]Cu(II)–L1 solutions or $^{64}CuCl_2$(aq) as a control. The mice were kept individually in polycarbonate cages and allowed water and food *ad libitum*. At 6 and 24 h post-injection time points, groups of mice (three at a time) were anaesthetized by carbon dioxide inhalation and aliquots of blood taken from the heart. Various samples were removed, rinsed with NaCl (0.9%), dried and then weighed. The radioactivity in these samples as well as the collected urine were counted using a Minaxi Auto-gamma 5000 Series counter with the window set at 340–540 keV. Dermal absorption experiments were performed by applying 0.2 cm^3 of 5 μCi solutions to an enclosed portion of skin on the anterior dorsal side of the test animals. The application site was prepared 15 h prior to dosing by clipping an area of approximately 2×2 cm on the dorsal side of the test animals. The animals were anaesthetized with a saline solution of ketamine/xylazine following clipping and a small tubing ring (1.2 cm diameter and 0.5 cm height) was fixed to their backs using cyanoacrylate adhesive. At 24 h post-dosing, groups of mice (four at a time) were anaesthetized by carbon dioxide inhalation and the same procedure followed as above. The percentages of radio-activity dose per organ and/or per gram (g) tissue were computed from the mean organ weights after correction for radio-activity decay.

The bio-distribution and dermal absorption studies on mice were approved by the Research Animals Ethics Committee of the University of Cape Town (permission number 005/039). The authority to possess and use radioactive nuclide ^{64}Cu was granted by the university's radiation protection and health safety committee in conjunction with Department of Health (authority number 33/01/0327).

Caution: ^{64}Cu decays by positrons emissions, which annihilate to produce tissue penetrating high energy γ-radiation. Therefore, it is advisable to use low activity of ^{64}Cu and perform all experiments behind lead bricks inside a fume cupboard.

3. Results and discussion

3.1. Potentiometry

The three measurable acid dissociation (protonation) constants corresponding to the pyridyl nitrogens of L1 are given in Table 1. Deprotonation of the amide nitrogens was not observed because they are too basic ($pK_a \geqslant 15$) [11,26,27] for the measurable pH range 2–11 of our glass electrode system. The $pK_{a1} = 1.98$ is assigned to the protonation of the central pyridyl nitrogen whereas $pK_{a2} = 3.51$ and $pK_{a3} = 4.62$ are for the protonation of the terminal pyridyl nitrogens. The low value of the first protonation constant (pK_{a1}) is due to the electronic repulsion effect and the base weakening effect of the adjacent amide groups [28]. The pK_a values of pyridine and 2-methylpyridine are reported as 5.34 and 6.14, respectively [29], whereas the introduction of a carbonyl group in 2-methylpyridine resulted in a pK_a value of 2.66 [30]. Therefore, it would be expected that the protonation constant corresponding to the central pyridyl nitrogen in L1 should decrease further when two amide groups are present. The difference of 1.11 log units between pK_{a2} and pK_{a3} indicates electronic repulsion on addition of a proton to a charged species or rather to an already doubly protonated molecule. On statistical grounds a difference of only 0.6 is expected for equivalent protonation sites.

The complex formation (Z_M-bar) and the deprotonation (Q_M-bar) functions [10,25] derived from the experimental data have been used to visualize the experimental data and to decide on the speciation model. The Z_M-bar function measures the number of ligands bound per metal ion while Q_M-bar indicates the number of protons released upon metal ion complexation. The two functions are derived from the free and total concentrations of the participating components as well as the measured protonation constants. The classical complex formation function should level at a Z_M-bar value of 1 for mononuclear ML species formation. This was not observed to be the case for the Cu^{2+}, Zn^{2+} and Ca^{2+}-L1 systems. Fig. 2a shows the

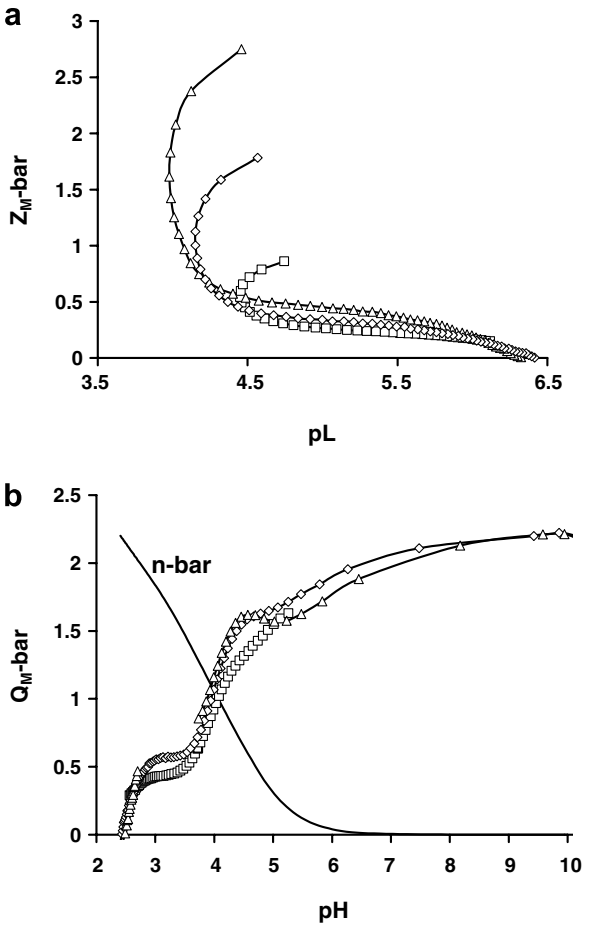


Fig. 2. Experimental and theoretical (solid line) (a) formation function and (b) deprotonation function curves for Cu(II)–L1 system at 25 °C and an ionic strength 0.15 M (Cl^{-1}). M:L ratios 1:1 (□), 1:2 (◇) and 1:3 (Δ) are displayed. The theoretical line was calculated using the model given in Table 1.

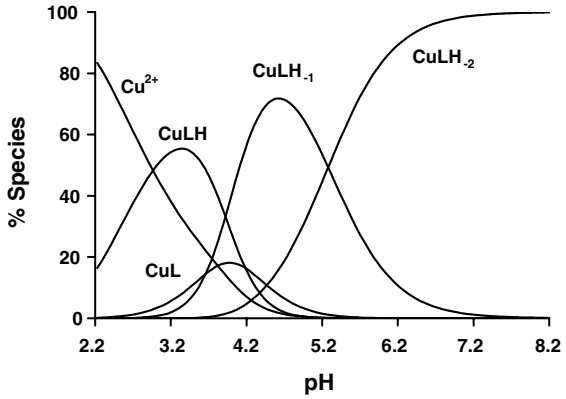


Fig. 3. Calculated speciation distribution graphs for a Cu(II)–L1 solution ([M] = 0.00051 mol dm^{-3}, [L] = 0.00101 mol dm^{-3}) as a function of pH.

Z_M-bar function plotted against pL (−log[L]). The Z_M-bars level off at 0.5 indicating that ML is not the predominant species in solution. The splitting of the curves for different metal to ligand ratios is due to the presence of polynuclear or protonated species. In fact the protonated CuLH is a majority species in solution as shown by the speciation graphs in Fig. 3. The fanning back of the curves is indicative of hydroxo and/or mixed hydroxo species formation.

The Q_M-bar function (Fig. 2b) rises vertically at pH 2.5 indicating that complexation occurs at the beginning of the titrations. In fact the speciation graphs in Fig. 3 show that CuLH is already formed (18% formation) at the start of the titration. The Q_M-bar curves rise from 0 to a maximum value of about 2.3 (n-bar > 2) indicating that approximately three protons have been released as a result of complexation. The n-bar function measures the average number of protons that would be bound to the ligand in the absence of the metal ion. Since a complete deprotonation (n-bar = 0) of L1 occurs at pH 6.2, the metal assisted deprotonation of the amide is likely to occur at an early stage thus forming $CuLH_{-1}$ and/or $CuLH_{-2}$. The analysis of these curves using the ESTA suite of programs [17,31], yielded the results given in Table 1. Despite the split of the curves at different metal to ligand ratios, the reproducibility of repeat titrations, low standard deviations and the Hamilton R-factors as well as an excellent agreement between the theoretical and experimental complex formation and deprotonation functions lend confidence to the results. The Zn(II) system showed similar complexation behaviour while for the Ca(II) system, no amide deprotonation was detected.

The formation constants (log β'_{pqr}s) for the MLH, ML, MLH_{-1} and MLH_{-2} complexes of the Cu(II)–L1 are given in Table 1. These values are lower than the corresponding values for the Cu(II)–cageL and Cu(II)–L2 systems [12,32]. The decrease in stability is due to the incorporation of the less basic or rather acidic pyridyl groups in L1. Zn(II) and Ca(II) were also found to form reasonably stable complexes with L1 but their stability is much lower than that of Cu(II). The order of stability Cu(II) > Zn(II) > Ca(II) is as expected [33]. Although Ca(II) and Zn(II) are weaker chelators than Cu(II), the *in vivo* concentration of these two essential metal ions is far higher than that of Cu(II) and so they could potentially compete for the ligand. The speciation distribution curves given in Fig. 3 show that $CuLH_{-2}$ is the predominant species at a physiological pH of 7.4.

From potentiometric data alone it is not possible to deduce the structure of the different complexes formed in solution. Therefore, spectroscopic measurements and molecular mechanics (MM) calculations were carried out in order to support or verify the potentiometric results.

3.2. Nuclear magnetic resonance studies

Nuclear magnetic resonance has been used to determine the sequence of protonation of L1 and also to gain some insights into the sites of metal coordination. Fig. 4 shows plots of chemical shifts as a function of pH where (a), (b), (c), (d), (e), (f) and (g) refer to the chemical shifts of the protons attached to carbons labelled (a)–(f) in Fig. 1. The

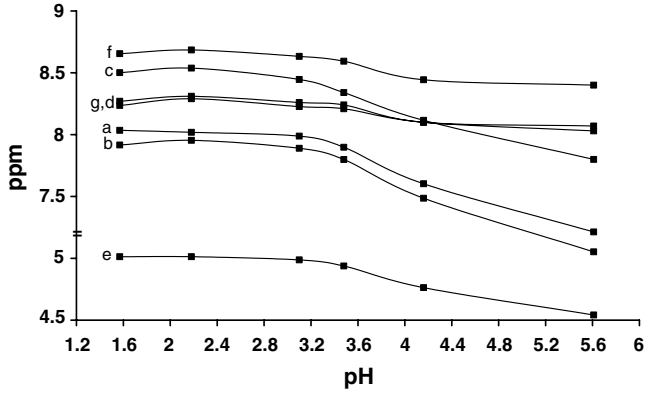


Fig. 4. Change in proton chemical shift (ppm) as a function of pH for L1 system. The protons are labelled according to Fig. 1.

assignment of these resonances is based on their chemical shifts and coupling patterns. Since the molecule is symmetrical and the protons undergo rapid chemical exchange, only a single set of resonances is seen for each species. A single inflection is seen in Fig. 4 with protons (a), (b) and (c) being most affected. These protons must be closest to the protonation site and hence confirm that it is the terminal pyridines that are being protonated. The inflection point in the chemical shift curves can be used to estimate a single pK_a value of 4.3 for these two protonation sites. This value is in good agreement with the potentiometric results. The chemical shift changes in the pH range 1.2–3.0 are too small to reliably estimate the pK_a of the central pyridine.

Fig. 5 shows the effect of Cu(II) on the spectrum of L1. Cu(II) is paramagnetic which can affect both the chemical

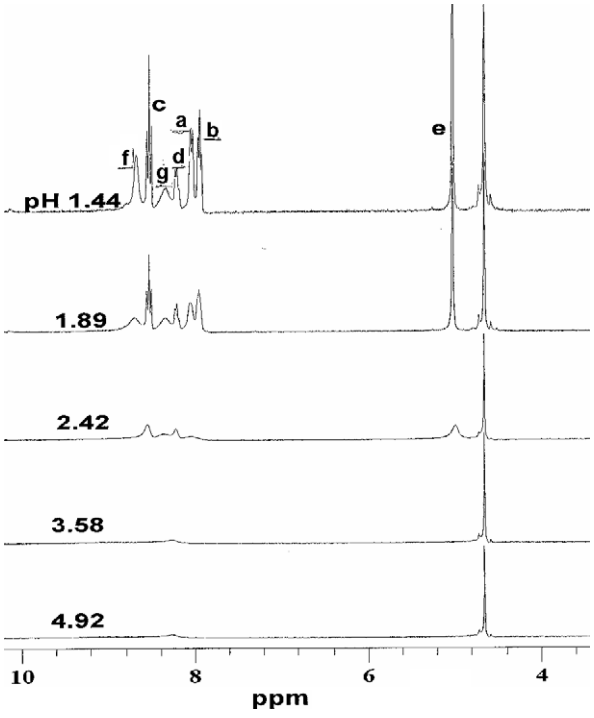


Fig. 5. Proton NMR spectra for the complexation of Cu(II) with L1 ([M] = 0.0075 mol dm^{-3}, [L] = 0.015 mol dm^{-3}) as a function of pH. The protons are labelled according to Fig. 1.

shift and relaxation time of the protons [34]. This manifests in a broadening and shifting of the NMR signals. Unless there is pseudo-contact shift, the broadening effect is usually more apparent. This is attenuated by $1/r^6$, where r is the internuclear distance between the Cu(II) and the observed proton. Cu(II) exchange for non-macrocyclic ligands is normally very rapid and so only average spectra will be seen. The spectrum shows that there is complexation at pH 1.44, with the (f) and (g) protons being preferentially broadened suggesting that the central pyridine is coordinated to the Cu(II). The fact that the other protons are not substantially broadened indicates that the terminal pyridines are not coordinated at this low pH. Between pH 1.89 and 2.44, the protons of the terminal pyridines and the methylene protons also broaden, indicating coordination of the terminal pyridine/s to the Cu(II). At this pH, the MLH species predominates (Fig. 3). These results support the structure postulated for MLH in Fig. 7. Further, the NMR results suggest that another species, presumably MLH_2 is formed at low pH. This species would not have been detected in our potentiometric study whose lower limit was pH 2.0.

3.3. Infrared studies

We have used infrared spectroscopy to establish the involvement of the amide oxygen or nitrogen in the course of the complexation process [19,35]. The infrared spectral data of the asymmetric amide carbonyl stretching vibration for L1 system are given in Table 2. Protonated L1 has an amide carbonyl band frequency of 1656 cm^{-1} and this band shifts slightly to lower frequency at higher pH. At pH 3.0, upon complexation by Cu(II), besides the 1656 cm^{-1} band, two new absorption bands at 1568 and 1591 cm^{-1} appear. The 1656 cm^{-1} band indicates that there is uncoordinated carbonyl amide present in the complex. Steenland et al. have assigned the 1591 cm^{-1} band to a carbonyl group with strong coordination through the oxygen. The 1568 cm^{-1} band was assigned to an amide carbonyl with coordination through the amide nitrogen. At pH 3.0, the MLH species predominates and the observed IR bands accord with the structure proposed in Fig. 7. Above pH 3 the ML and MLH_{-1} species begin to appear and a new band at 1578 cm^{-1} appears. This band can be assigned to a second amide nitrogen coordination [35]. At pH 5.4 no MLH is present and the 1656 cm^{-1} band disap-

Table 2
Infrared spectral data of the asymmetric amide carbonyl stretching vibration in the Cu(II) complexes of L1 in D_2O solution at 25 °C as a function of pH

Metal–ligand	pH	Wave number (cm^{-1})			
H–L1	1.21	1656			
Cu(II)–L1	2.58	1656	1591	1568	
	2.97	1656	1591	1565	
	3.34	1656	1594	1578	1565
	5.40		1594	1578	1565

pears. In Fig. 7, two possible structures are proposed for the MLH_{-1} species. The IR data support structure 7a because both amide are coordinated. The results would also suggest that for the ML species, the second amide carbonyl is also coordinated.

3.4. UV–Vis spectrophotometry

Distinct changes were observed in the colour of a solution of Cu(II) and L1 as the pH of the solution was increased. This was a result of the changing speciation of the solution, different species with different absorption spectra predominating at different pH values. Fig. 6 shows the absorption spectra for the Cu(II)–L1 system as a function of pH. At pH 2.39, an absorption maximum of 660 nm is seen indicating that there is already complexation at the start of titration. This was also observed in the potentiometric (Fig. 3) and NMR (Fig. 5) studies. As the pH increases, the band increases in intensity and shifts to shorter wavelength. Above pH 5.81 a slight red shift is observed. The spectra were deconvoluted using the UV-SPEC program [36] to yield spectra for the individual species. This deconvolution was based on the metal ion speciation calculated from the potentiometric model given in Table 1 and incorporated into an expanded Beer–Lambert Law which was then solved for the molar absorptivity of the different species at each wavelength. The smoothness of these spectra lends confidence to the potentiometric model. A single broad absorption band was obtained which envelopes the expected three spin allowed $^2A_{1g} \leftarrow {}^2B_{1g}$, $^2B_{2g} \leftarrow {}^2B_{1g}$ and $^2E_g \leftarrow {}^2B_{1g}$ transitions of a tetragonally distorted Cu(II) complex [37,38].

Analysis of the data yielded wavelength absorption maxima (λ_{max}) and molar extinction coefficients (ε) listed in Table 3 for the MLH, ML, MLH_{-1} and MLH_{-2} complexes. The electronic spectra are useful because the coordination sphere of the metal ion influences the energy of the transition. Therefore, λ_{max} affords a measure of the solution structure of the complex. Billo [39] and subsequently Sigel and Martin [40] have proposed a simple empirical method for estimating the electronic energy of a proposed configuration. In addition to contributions by donors

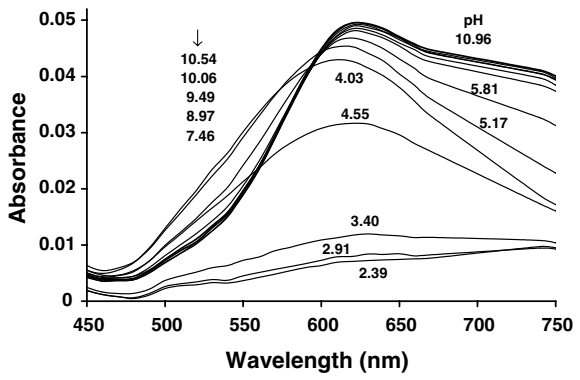


Fig. 6. Electronic absorption spectra of Cu(II)–L1 solution as a function of pH ([M] = 0.00051 mol dm^{-3}, [L] = 0.00101 mol dm^{-3}) at 25 °C.

Table 3
Wavelength absorption maxima (λ_{max}) corresponding to molar extinction coefficients (ε) of the various Cu(II)–L1, Cu(II)-L2 and Cu(II)-cageL complex species in solution

Ligand	λ_{max} (nm) ε (mol^{-1} dm^{-3} cm^{-1})			MLH_{-1}	MLH_{-2}
	Cu^{2+}	MLH	ML		
L1	760(22)	660(24)	610(15)	600(92)	620(95)
L2	780(20)	600(40)	580(115)	580(120)	540(110)
CageL	790(20)	720(40)	660(115)	590(120)	

reported by these authors, we deduced contribution due to the pyridine nitrogen ($\nu_{py-N} = 4.22 \times 10^3$ cm^{-1}) from the study by Osz et al. [41]. The MLH species has a $\lambda_{max}(\varepsilon)$ of 660 nm (24 mol^{-1} dm^{-3} cm^{-1}) which is close to a calculated λ_{max} of 668 nm, calculated for when the metal ion is coordinated to oxygen and two pyridine nitrogens. The blue shift in λ_{max} in forming MLH from hydrated Cu(II) reflects the increased ligand field splitting of L1 as opposed to H_2O. Similarly, the λ_{max} (ε) value, 610 nm (15 mol^{-1} dm^{-3} cm^{-1}) for the ML species is close to the 613 nm, calculated for the structure proposed in Fig. 7. However, the λ_{max} of 600 nm (92 mol^{-1} dm^{-3} cm^{-1}) observed for the MLH_{-1} species is significantly different from the values calculated for the structures MLH_{-1} (a) (551 nm) and MLH_{-1} (b) (571 nm) in Fig. 7. Notwithstanding this, we believe that the MLH_{-1} (a) structure in Fig. 7 is the correct structure and the red shift in the spectrum is due to the considerable distortion of the metal coordination sphere. This distortion is supported by the extinction coefficient of the complex. Marlin et al. obtained a band with λ_{max} at 613 nm ($\varepsilon = 220$ mol^{-1} dm^{-3} cm^{-1}) for this system in methanol [42].

The MLH_{-2} species shows a red shift of 20 nm which suggests axial coordination of a fifth nitrogen donor as in the structure Fig. 7 MLH_{-2} (b). A red shift of 50 nm was also observed for the formation of $[Cu(NH_3)_5(H_2O)]^{2+}$ complex from $[Cu(NH_3)_4(H_2O)_2]^{2+}$ [37]. The absorption maxima for the Cu(II)–L1 system is somewhat red shifted as compared to those of Cu(II)–cageL and Cu(II)–L2 given in Table 3 [12,32]. The coordination geometry of the MLH_{-2} species in this system is likely to be overall tetragonal with only weak axial coordination of the fifth nitrogen. A strong axial interaction by nitrogen donor in MLH_{-2} would certainly shift its d–d absorption band to lower wave numbers relative to MLH_{-1} resulting from weakening of the in-plane ligand field by a synergic effect [26,38].

The structures proposed for the MLH_{-2} complex from potentiometric, NMR, IR and UV–Vis studies are supported by crystal structures of L1 and related ligands with Cu(II), Ni(II) and Zn(II) [42,43]. Using a tridentate ligand *N*,*N*′-dimethylpyridine-2,6-dicarboxamide, Marlin et al. [44] found that Cu(II) promoted deprotonation of the amide nitrogens. Using L1, it was found that again coordination was through the central pyridine, the two deprotonated amide nitrogens and one of the terminal pyridines [42,43].

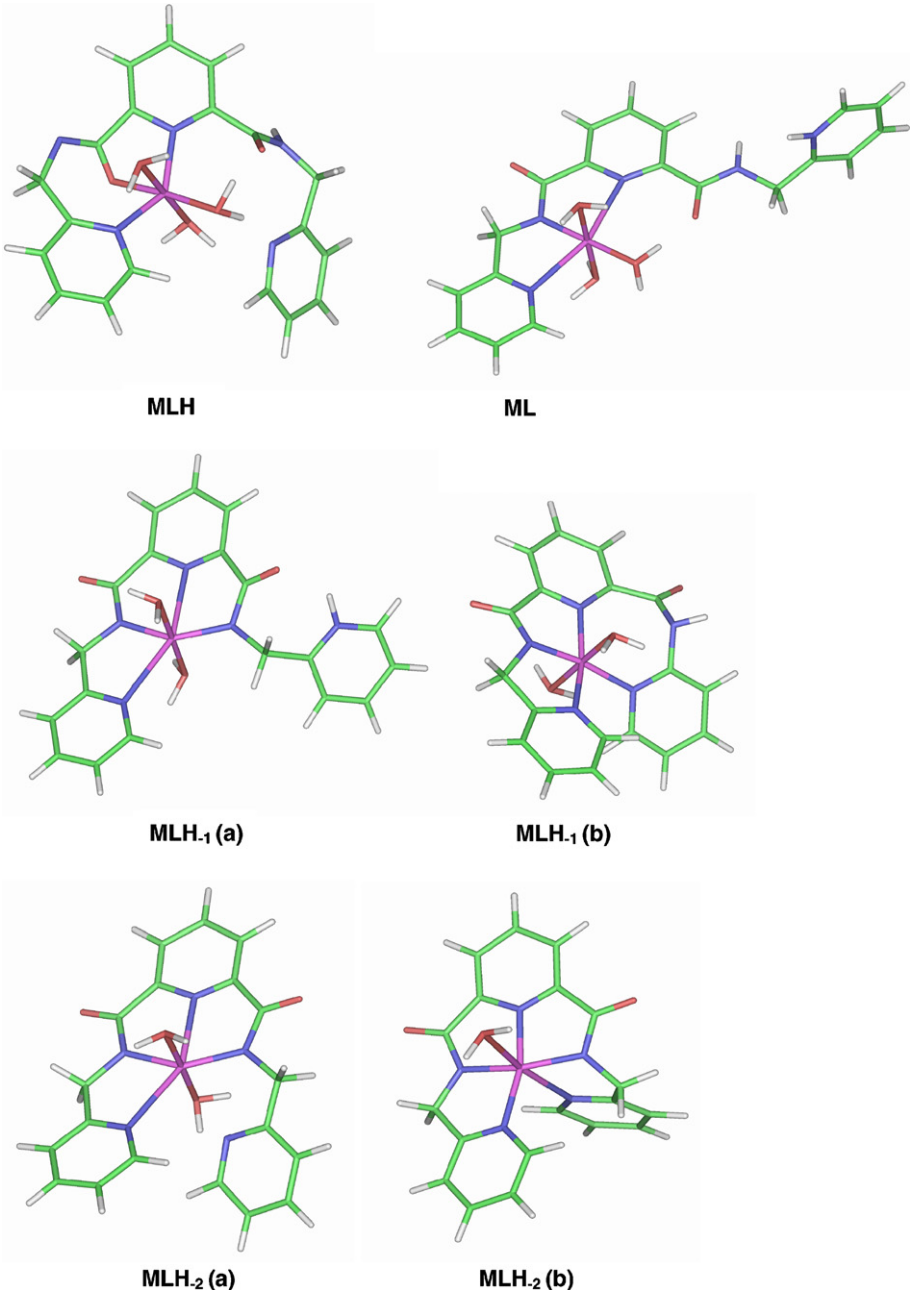


Fig. 7. Energy minimised structures for the Cu(II)–L1 species.

3.5. Molecular mechanics calculations

Molecular mechanics (MM) is a very popular tool for describing the structures and relative energies of many classes of molecules [45,46]. Its wide use is primarily due to its computational simplicity and efficiency whereas quantum mechanical modelling is far more computationally intensive and until recently, has been used only rarely for metal complexes. In this study, we have used MM to calculate the internal energy (strain energy) of different possible ligand conformations found in the different metal complexes. This strain energy would be one of the energy contributions to the overall stability of the complex. The chelate effect, as an entropic contribution, and the ligand field stabilisation energy of the metal ion, are two other important energy contributions, but are not taken into account in these calculations.

Fig. 7 shows the energy minimised structures for the different, mostly likely, formed isomers of Cu(II)–L1. In the structure proposed for MLH (Fig. 7), the central nitrogen, one terminal pyridyl group, and a carbonyl oxygen are coordinated to the metal ion whereas in ML, an amide nitrogen donor atom is coordinated instead of the carbonyl oxygen. The MLH species has a larger strain energy than ML. This may be due to the rigidity of the pyridine moiety that contributes more to the strain energy when the car-

bonyl oxygen donor atom is coordinated to the metal ion. Two different coordination modes are presented for the MLH_{-1} and MLH_{-2} species. For the MLH_{-1} species, the isomer MLH_{-1}(a), has a larger strain energy than MLH_{-1}(b) whereas MLH_{-2}(b) is more strained than MLH_{-2}(a). The strain energy corresponding to chelate ring formation is in the order $5,5,5,5 > 5,5,5 > 5,5 > 5,8,5 > 5,5,8$, where the numbers refer to the size of the chelate rings.

It is worth noting that molecular mechanics has been used as a simple computational tool for providing more evidence in support of the potentiometric and spectroscopic studies. In all calculations, no account was taken of electronic contribution, Jahn-Teller distorsion of Cu(II), entropy or solvent effects.

3.6. Blood–plasma simulation

In the design of copper based anti-inflammatory agents, blood–plasma modelling has been used to estimate the ability of L1 to mobilize Cu(II) *in vivo* [21]. This was done by calculating the plasma mobilizing index (pmi) of the ligand using a thermodynamic model of blood–plasma. The pmi of a ligand for a metal ion is defined as the percentage increase in the total concentration of low molecular mass (lmm) complexes of the metal ion caused by the ligand. This takes into account competition between the ligand and all the endogenous metal ions and l.m.m ligands present in blood–plasma. In calculating the pmi curves use has been made of the ECCLES model [47,48] of blood–plasma to which constants determined in this study have been added.

Fig. 8a gives the pmi curves for L1 and related ligands. In comparison, L1 is three to four orders of magnitude better at mobilizing Cu(II) *in vivo* than cageL. The improved mobilizing ability of L1 compared to cageL is related to the stable complexes it forms with Cu(II). However, it is poorer than 3,6,9,12-tetra-azatetradecanedioic acid (TTDA) [47] by about six orders of magnitude. Inspection of Fig. 8b shows that L1 is selective to Cu(II) *in vivo* relative to Zn(II) and Ca(II). In fact, the remarkably high mobilizing ability of this ligand is related to this selectivity. At a total ligand concentration of 3.1×10^{-3} mol dm^{-3} for L1, the pmi's for Zn(II) and Ca(II) pmi's are very low (<0.01). In addition, the predominant copper complex present at physiological pH is the neutral $CuLH_{-2}$ species.

3.7. Superoxide dismutase activity studies

Along with hydrogen peroxide and the hydroxyl radical, superoxide has been implicated in oxidative damage phenomena related to aging, inflammation and post-ischemic injury via reperfusion [49,50]. The beneficial role of copper in minimizing inflammation has been attributed to its redox activity, particularly that of copper in such enzymes as superoxide dismutase (SOD) [22,50]. The important requirements for SOD-like activity are a medium donor

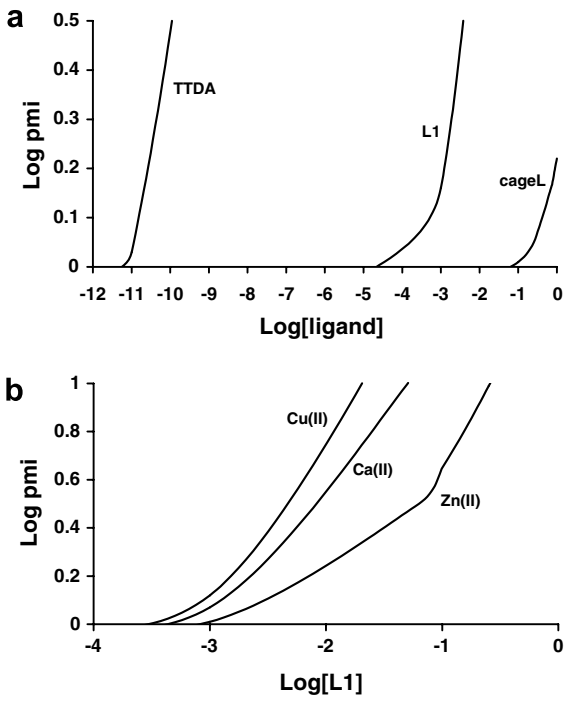


Fig. 8. Plasma mobilizing index for (a) Cu(II) with L1, cageL and TTDA, and (b) L1 with Cu(II), Zn(II) and Ca(II).

power and flexibility of the ligand, in order to facilitate the reduction and the accommodation of Cu(I), which is known to prefer tetrahedral or linear environments [51]. Of importance in this study is copper–zinc SOD which provides a cellular defence against the oxidative stress by catalyzing superoxide dispropotionation into less toxic dioxygen and hydrogen peroxide. The coordination geometry of the native SOD enzyme is distorted square-pyramidal for the Cu(II) and distorted tetrahedral for Zn(II).

Copper(II) complexes, including those of low molecular mass ligands and polypeptides, have been reported to exhibit SOD-mimic activity and thus are viewed as alternative human therapeutics to remove pro-inflammatory superoxide anion radical *in vivo* [22,52,53]. Although this is not an essential feature of or ligand design, we investigated the SOD activity of the [Cu(II)–$L1H_{-2}$] complex using the NBT assay [22–24]. EDTA was added to mimic the coordinating environment found *in vivo* because the Cu(II)EDTA complex has no SOD activity. An IC_{50} value of 275 μmol dm^{-3} for the [Cu(II)–$L1H_{-2}$] species was determined. This value is far higher than that of native CuZn-SOD (0.011 μmol dm^{-3}) [54]. The low activity of [Cu(II)–$L1H_{-2}$], relative to the native enzyme, may be due to the lack of suitable binding sites for the superoxide anion radical to coordinate to the metal ion.

3.8. Octan-1-ol–water partition coefficient studies

When administered orally and intravenously, copper(II) complexes do increase available copper. However, it is difficult to move this coordinated metal ion through a series

of body compartments without protein binding [21]. Transport across the skin and bio-membranes in general, is a process of limited diffusion governed by the drug's chemical and physical properties such as lipophilicity and protein binding [55,56]. We have determined the octanol–water partition coefficients of our copper complexes in order to ascertain if they can be applied as topical agents in the alleviation of the inflammatory process in RA.

Fig. 9 shows the partition coefficients ($\log P_{oct/aq}$) as a function of pH for the CuII)–L1 system. From this, it is possible to estimate the $\log P_{oct/aq}$'s of the individual species. The MLH species that is formed at the start of the titration (pH 2.2) has a $\log P_{oct/aq}$ value of −2.21. The low $\log P_{oct/aq}$ value is a result of high concentration of hydrated Cu(II) complex. The ML species coexists with MLH and MLH_{-1} and so it is difficult to measure its partition coefficient. However, the MLH_{-1} species predominates at pH 4.8 which corresponds to a $\log P_{oct/aq}$ value of −0.98. At a physiological pH of 7.4, MLH_{-2} is the predominant species and has a $\log P_{oct/aq}$ value of −0.58. Although these complexes are relatively hydrophilic, they are more lipophilic than previously studied copper complexes [12,32]. Pehourcq et al. [25] have reported positive $\log P_{oct/aq}$ values in the range 0.618–4.128 of some anti-inflammatory drugs. However, several workers have reported negative values in the range −1.60 to −3.02 for ^{64}Cu-labeled complexes [57–59].

For percutaneous absorption the drug should not be too lipophilic or it will be trapped in the epidermis. With our system, 19% of the Cu(II)–L1 complex was extracted into the organic phase of the octanol–water mixture at pH 7. We ascribe this to the presence of the bulky aromatic groups which suggests the importance of such groups in percutaneous drug administration.

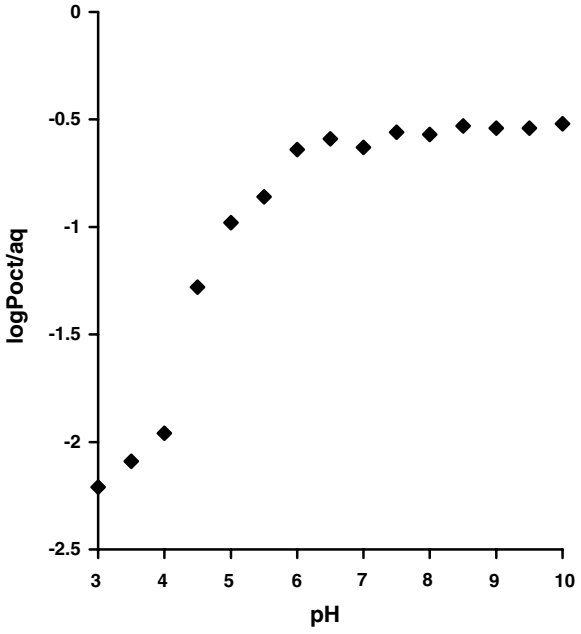


Fig. 9. Octanol–water partition coefficients of Cu(II)–L1 as a function of pH.

3.9. Bio-distribution and dermal absorption studies

Since the *in vitro* and bio-modelling showed encouraging results, we performed *in vivo* bio-distribution experiments. The bio-distribution was measured as a function of time in mice using ^{64}Cu(II) as a tracer or radiolabel. Table 4 shows the bio-distribution of ^{64}Cu(II) labelled Cu(II)–L1 and $CuCl_2$ at 6 and 24 h post-injection. The results show an initial rapid clearance from blood circulation and rapid uptake by the liver for both systems. The observed uptake of more than 60% of the administered dose by the liver is expected because copper storage and metabolism occur in this organ.

[^{64}Cu(II)]$CuCl_2$ used as a control, was rapidly excreted *via* hepatobiliary and renal routes. The Cu(II)–L1 complex has a much longer biological half-life than the copper complexes recently studied by Jackson et al. [9,32]. The activity retention over 24 h in the body of >50% dose for the [^{64}Cu]Cu(II)–L1 system is more or less the same as that of [^{64}Cu]Cu(II)-cageL [12]. This compares with only 20% of the [^{64}Cu]$CuCl_2$ control. Of interest is the fact that the carcass activity is higher after 24 h than 6 h. This is because after the rapid clearance from the blood by the liver, it is slowly released and redistributed into other tissues. For the control, most of the copper is excreted in the urine while for L1, there is a substantial amount in the intestines and retained in the liver.

Since the preferred route of administration is as a cream via the skin, bio-distribution studies were also performed using dermal absorption. The results in Table 5 show that a significant amount of activity is absorbed within 24 h.

Table 4
% Dose per organ and per gram tissue (in brackets) for bio-distribution in Bulb/c mice of [^{64}Cu]Cu(II)–L1 complexes following intravenous injection via the tail vein (mean ± std.dev., $n = 3$) after 6 and 24 h post-injection

Organ	[^{64}Cu]Cu(II)–L1		[^{64}Cu]$CuCl_2$	
	6 h	24 h	6 h	24 h
Blood	1.2 ± 0.3	2.1 ± 0.2	0.8 ± 0.2	0.9 ± 0.2
	(1.0 ± 0.4)	(1.6 ± 0.3)	(0.6 ± 0.2)	(0.7 ± 0.2)
Carcass	7 ± 2	12.0 ± 0.3	8 ± 2	11 ± 2
	(0.6 ± 0.1)	(1.1 ± 0.2)	(0.6 ± 0.2)	(1.0 ± 0.2)
Head	1.6 ± 0.1	3.4 ± 0.1	1.94 ± 0.04	8 ± 3
	(0.6 ± 0.1)	(1.1 ± 0.1)	(0.59 ± 0.02)	(3 ± 1)
Heart	0.21 ± 0.02	0.46 ± 0.05	0.19 ± 0.02	0.2 ± 0.1
	(1.8 ± 0.2)	(4 ± 1)	(1.6 ± 0.2)	(1.7 ± 0.4)
Intestines	12 ± 1	30 ± 4	22 ± 3	12 ± 7
	(4.2 ± 0.7)	(9 ± 2)	(8 ± 1)	(4 ± 2)
Kidney	2.2 ± 0.9	2.3 ± 0.3	1.0 ± 0.2	1.0 ± 0.4
	(6.3 ± 0.2)	(6.2 ± 0.4)	(3.1 ± 0.4)	(3 ± 1)
Liver	64 ± 3	36 ± 9	64 ± 5	11 ± 7
	(59 ± 4)	(30 ± 10)	(56.2 ± 0.5)	(11.3 ± 0.6)
Lung	0.6 ± 0.1	1.00 ± 0.03	0.53 ± 0.08	0.4 ± 0.2
	(4.0 ± 0.6)	(6.2 ± 0.5)	(1.9 ± 0.3)	(2.3 ± 0.3)
Muscle	0.06 ± 0.03	0.12 ±0.03	0.06 ± 0.04	0.04 ± 0.03
	0.4 ± 0.2)	(0.8 ±0.2)	(0.4 ± 0.1)	(0.3 ± 0.1)
Spleen	0.14 ± 0.03	0.3 ± 0.1	0.23 ± 0.04	0.12 ± 0.02
	(2.0 ± 0.5)	(3 ± 1)	(1.7 ± 0.1)	(1.3 ± 0.1)
Urine	11 ± 2	13 ± 4	2 ± 1	55 ± 9

Table 5
% Dose per organ and per gram tissue for the bio-distribution in Bulb/c mice of [^{64}Cu]Cu(II)–L1 complexes (mean ± std.dev., $n = 3$) after 24 h of dermal absorption

Organ	[^{64}Cu]Cu(II)–L1		[^{64}Cu]$CuCl_2$	
	Per organ	Per gram	Per organ	Per gram
Blood	0.34 ± 0.02	0.3 ± 0.1	2.25 ± 0.08	1.5 ± 0.2
Carcass	10 ± 6	0.9 ± 0.6	14 ± 10	0.9 ± 0.6
Head	18 ± 9	7 ± 3	3.3 ± 0.7	1.0 ± 0.2
Heart	0.07 ± 0.01	0.6 ± 0.1	0.37 ± 0.07	2.1 ± 0.4
Intestines	16 ± 6	6 ± 2	21 ± 3	6.3 ± 0.7
Kidney	0.30 ± 0.03	0.9 ± 0.1	1.74 ± 0.3	3.6 ± 0.6
Liver	2.1 ± 0.4	2.0 ± 0.2	18 ± 3	14 ± 3
Lung	0.10 ± 0.03	0.63 ± 0.06	0.7 ± 0.1	3.0 ± 0.5
Muscle	0.02 ± 0.01	0.10 ±0.03	0.13 ± 0.03	0.6 ± 0.3
Spleen	0.03 ± 0.01	0.3 ± 0.1	0.19 ± 0.02	2.1 ± 0.4
Urine	53 ± 12		38 ± 13	

Of note in these results is that the same bio-distribution as intravenous injection is not obtained. This is because of the different route of administration. Less activity is excreted in the urine and more activity is retained in the body. For the control, substantial hepatobiliary and urinary excretion is seen. This is the normal route of excretion of Cu(II). It was observed that up to 37% of the dose applied to the enclosed skin was absorbed over a period of 24 h. The activity accumulation and retention over 24 h in the body is encouraging and merits evaluation of this copper chelating agent for possible use in chemotherapy.

No attempt was made to isolate the excreted copper so it is not possible to say whether the complex remained intact or not. However, because different bio-distribution results were obtained for $CuCl_2$ and Cu(II)–L1 we conclude that the speciation of the metal ion is different in the two systems *in vivo*.

4. Conclusion

The ligand L1 is quite selective towards Cu(II) over Zn(II) and Ca(II) due to the ease with which Cu(II) deprotonates the amide nitrogen groups. The rigidity of the pyridyl moiety and pyridyl nitrogen that acts as an anchor enhanced the ionization of the amide protons in the presence of the metal ion. The geometries of the different species in solution were successfully determined by potentiometric, NMR, IR, UV–Vis and MM calculation studies. The $CuL1H_{-2}$ species predominates at the physiological pH of 7.4 and is reasonably lipophilic according to octanol–water partition coefficient measurements. However, the complex has limited SOD activity. Animal studies showed that L1 changed the bio-distribution of the copper upon both intravenous and dermal absorption.

Previous studies have shown that simple copper salts have anti-inflammatory activity, although the mechanism is unknown. The purpose of this study, then, was to design ligands that would increase the level of endogenous copper through dermal absorption and retention of copper in the body. This would increase the amount of bio-available copper. This objective has been achieved and the results warrant the testing of this system in animal models of arthritis. The lack of SOD activity is not important as simple copper salts do not have SOD activity either.

Acknowledgements

The authors thank the National Research Foundation (NRF), Canon Collins Trust and Council of the University of Cape Town for financial support. We are also grateful to Dr. J.R. Zeevaart and D. Jansen (South African Nuclear Energy Cooperation (Ltd.) for supplying us with $^{64}CuCl_2$ and, J. Boniaszczuk (Nuclear Medicine Dept), J. Visser (Animal Unit), Dr. J.N. Zvimba and C. Jackson for technical assistance with animal experiments.

References

[1] G.E. Jackson, B.S. Nakani, J. Chem. Soc., Dalton Trans. (1996) 1373.
[2] C.M. Weyand, Rheumatology 39 (Suppl. 1) (2000) 3.
[3] A. Aeschlinmann, B.R. Simmen, B.A. Michel, in: H. Baumgartner, J. Dvorak, D. Grob, U. Munzinger, B.R. Simmen (Eds.), Rheumatoid Arthritis, Thieme Medical Publishers, Inc., New York, 1995.
[4] M. Fischbach, Rheumatoid Arthritis, Churchill Livingstone, New York, 1991.
[5] R.F. Wilkens, S.L. Dahl, Therapeutic Controversies in the Rheumatic Disease, Grune and Stratton, Inc., Orlando, 1987.
[6] J.R.J. Sorenson, in: H. Sigel (Ed.), Metal Ions in Biological Systems, Inorganic Drugs in Deficiency and Disease, vol. 14, Marcel Dekker, Inc., 1982, p. 77.
[7] P.M. May, D.R. Williams, in: H. Sigel (Ed.), Metal Ions in Biological Systems, Inorganic Drugs in Deficiency and Disease, vol. 12, Marcel Dekker, Inc., 1981, p. 283.
[8] J.R.J. Sorenson, Prog. Med. Chem. 19 (1976) 135.
[9] G.E. Jackson, L. Mkhonta-Gama, A. Voyé, M. Kelly, J. Inorg. Biochem. 9 (2000) 147.
[10] T.E. Nomkoko, G.E. Jackson, B.S. Nakani, W.K.A. Louw, J.R. Zeevaart, J. Chem. Soc., Dalton Trans. (2004) 741.
[11] E.T. Nomkoko, G.E. Jackson, B.S. Nakani, J. Chem. Soc., Dalton Trans. (2004) 1432.
[12] S. Odisitse, G.E. Jackson, T. Govender, H.G. Kruger, A. Singh, J. Chem. Soc., Dalton Trans. (2007) 1140.
[13] J.E. Weder, T.C. Dillion, W.T. Hambley, J.B. Kennedy, A.P. Lay, J.R. Biffin, L.H. Regtop, M.N. Davies, Coord. Chem. Rev. 232 (2002) 95.
[14] D.S. Marlin, M.M. Olmstead, P.K. Mascharack, Inorg. Chem. 38 (1999) 3258.
[15] T. Hirao, T. Moriuchi, T. Ishikawa, K. Nishimura, S. Mikami, Y. Ohshiro, I. Ikeda, J. Mol. Cat. A 113 (1996) 117.
[16] J.C. Rossotti, H. Rossotti, J. Chem. Education. 42 (1965) 375.
[17] K. Murray, P.M. May, ESTA (Equilibrium Simulation for Titration Analysis) manual, Version 3, UWIST, Cardiff, Wales, 1989.
[18] A. Krezel, W. Bal, J. Inorg. Biochem. 98 (2004) 161.
[19] InsightII. System Guide, Issued by Accelrys, Cambridge, UK, July 2005.
[20] P.M. May, P.W. Linder, D.R. Williams, J. Chem. Soc., Dalton Trans. (1977) 588.
[21] G.E. Jackson, P.M. May, D.R. Williams, J. Inorg. Nucl. Chem. 40 (1978) 1227.
[22] M. Gonzalez-Alvarez, G. Alzuet, J. Borras, L.A. del Castillo, J.M. Montego-Bernado, S. Garcia-Granda, J. Biol. Inorg. Chem. 8 (2003) 112.
[23] C. Auclair, E. Voisin, in: R.A. Greenwald (Ed.), CRC Handbook of Methods for Oxygen Radical research, CRC Press, Boca Raton, FL, 1985.

[24] I. Fridovich, in: R.A. Greenwald (Ed.), CRC Handbook of Methods for Oxygen Radical research, CRC Press, Boca Raton, Fl, 1985.
[25] F. Pehourcq, M. Matoga, C. Jarry, B. Bannwarth, J. Liq. Chromatogr. Relat. Technol. 24 (2001) 2177.
[26] C. Jubert, A. Mohamadou, C. Gerard, S. Brandes, A. Tabard, J.P. Barbier, J. Chem. Soc., Dalton Trans. (2002) 2660.
[27] D. Chen, Y. Sun, A.E. Martell, M.J. Welch, Inorg. Chim. Acta 235 (2002) 119.
[28] M.W.A. Steenland, I. Dierck, G.G. Herman, B. Devreese, W. Lippens, J. van Beeumen, A.M. Goeminne, J. Chem. Soc., Dalton Trans. (1997) 3637.
[29] L.E. Kapinos, H. Sigel, Inorg. Chim. Acta 37 (2002) 131.
[30] E.A. Martell, R.M. Smith, R.J. Motekaitis, NIST Critical Stability Constants of the Metal Complexes Database, Texas A &M, University College Station, 1993.
[31] P.M. May, K. Murray, D.R. Williams, Talanta 35 (1985) 825.
[32] T.E. Nomkoko, G.E. Jackson, B.S. Nakani, R. Hunter, J. Chem. Soc., Dalton Trans. (2006) 4029.
[33] D.R. Williams, The Metals of Life, van Nonstrand Reinhold Company, London, 1971.
[34] P.S. Pregosin (Ed.), Transition Metal Nuclear Magnetic Resonance, Studies in Inorganic Chemistry, Elsevier Science Publisher B.V., Amsterdam, 1991.
[35] M.W.A. Steenland, P. Westbroek, I. Dierck, G.G. Herman, W. Lippens, E. Temmerman, A.M. Goeminne, Polyhedron. 18 (1999) 3417.
[36] G.E. Jackson, UV-SPEC, Private Communication, University of Cape Town, South Africa, 2003.
[37] H.H. Jaffé, M. Orchin, Theory and Application of Ultraviolet Spectroscopy, John Wiley & Sons, New York, 1962.
[38] A.B.P. Lever, Inorganic Electronic Spectroscopy, Elsevier, New York, 1984.
[39] E.J. Billo, Inorg. Nucl. Chem. Lett. 10 (1974) 613.
[40] H. Sigel, R.B. Martin, Chem. Rev. 82 (1982) 385.
[41] K. Osz, K. Varnagy, I. Sovago, L. Lennert, H. Suli-Vargha, D. Sanna, G. Micera, New J. Chem. 25 (2001) 700.
[42] D.S. Marlin, M.M. Olmstead, P.K. Mascharack, Inorg. Chim. Acta 323 (2001) 1.
[43] N.W. Alcock, G. Clarkson, P.B. Glover, G.A. Lawrance, P. Moore, M. Napitupulu, J. Chem. Soc., Dalton Trans. (2005) 518.
[44] D.S. Marlin, M.M. Olmstead, P.K. Mascharack, Inorg. Chem. 40 (2001) 7003.
[45] P. Comba, T.W. Hambley, Molecular Modelling of Inorganic Compounds, Wiley–VCH, Weinheim, 2001.
[46] A.M.T. Bygott, A.M. Sargeson, Inorg. Chem. 37 (1998) 4795.
[47] G.E. Jackson, M.J. Kelly, J. Chem. Soc., Dalton Trans. (1989) 2429.
[48] G.E. Jackson, M.J. Kelly, J. Chem. Soc., Dalton Trans. (1990) 1889.
[49] I. Fridovich, J. Biol. Chem. 264 (1989) 7761.
[50] V. Pelmenschikov, P.E.M. Siegbahn, Inorg. Chem. 44 (2005) 3311.
[51] G. Tabbi, W.L. Driessen, J. Reedijk, R.P. Bonomo, N. Veldman, A.L. Spek, Inorg. Chem. 36 (1997) 1168.
[52] R.N. Patel, K.B. Pandega, J. Inorg. Biochem. 72 (1998) 109.
[53] N.A. Roberts, P.A. Robinson, Br. J. Rheumatol. 24 (1985) 128.
[54] H.-L. Zhu, L.-M. Zheng, D.-G. Fu, X.-Y. Huang, M.-F. Wu, W.-X. Tang, J. Inorg. Biochem. 70 (1998) 211.
[55] S.K. Poole, C.F. Poole, J. Chromatogr. B. 797 (2003) 3.
[56] G. Klopman, H. Zhu, Mini-Rev. Med. Chem. 5 (2005) 127.
[57] X. Sun, M. Wuest, Z. Kovacs, A.D. Sherry, R. Motekaitis, Z. Wang, A.E. Martell, M.J. Welch, C.J. Anderson, J. Biol. Inorg. Chem. 8 (2003) 217.
[58] X. Sun, M. Wuest, G.R. Weisman, E.H. Wong, D.P. Reed, C.A. Boswell, R.J. Motekaitis, A.E. Martell, M.J. Welch, C.J. Anderson, J. Med. Chem. 45 (2002) 469.
[59] A.B. Packard, J.F. Kronauge, P.J. Day, S.T. Treves, Nucl. Med. Bio. 25 (1998) 531.

Available online at www.sciencedirect.com
ScienceDirect
Polyhedron 27 (2008) 465–472
POLYHEDRON
www.elsevier.com/locate/poly

Synthesis, spectroscopic and structural investigation of $Zn(NCS)_2(nicotinamide)_2$ and $[Hg(SCN)_2(nicotinamide)]_n$

Marijana Đaković [a], Zora Popović [a,*], Gerald Giester [b], Maša Rajić-Linarić [c]

[a] *Laboratory of General and Inorganic Chemistry, Department of Chemistry, Faculty of Science, University of Zagreb, Horvatovac 102a, HR-10000 Zagreb, Croatia*
[b] *Institute of Mineralogy and Crystallography, University of Vienna, Althan Strasse 14, A-1090 Vienna, Austria*
[c] *Laboratory for Thermal Analysis, Brodarski Institute, Marine Research and Special Technology, Av. V. Holjevca 20, HR-10000 Zagreb, Croatia*

Received 10 September 2007; accepted 30 September 2007
Available online 11 December 2007

Abstract

Zinc(II) and mercury(II) thiocyanate complexes with nicotinamide, bis(nicotinamide-*N*)-bis(thiocyanato-*N*)zinc(II) (**1**) and *catena*-[nicotinamide-*N*-(μ-thiocyanato-*S*,*N*)(thiocyanato-*S*)mercury(II)] (**2**), have been prepared and characterized by spectroscopic, thermal and X-ray crystallographic methods. The vibrational bands of diagnostic value are compared to the values of the free ligand and the data are in good correlation with the X-ray results. Centrosymmetrical hydrogen bonded dimers are found, $R_2^2(10)$ in **1** and $R_2^2(8)$ in **2**.
© 2007 Elsevier Ltd. All rights reserved.

Keywords: Zinc and mercury(II) thiocyanate complexes; Nicotinamide; X-ray crystal structure; IR, NMR spectra; TGA/DTA analysis

1. Introduction

Nicotinamide (pyridine-3-carboxamide, niacinamide, commonly known as vitamin B_3) shows important biological activity *e.g.* in the form of a coenzyme called NAD, nicotinamide adenine dinucleotide, it participates in many amino acid and carbohydrate metabolic reactions; it is also a vital compound in the drug industry. Metal complexes of biologically important ligands are sometimes more effective than the free ligand. Due to the relatively high abundance of zinc in living organisms and its participation in a large number of enzymatic reactions, the zinc complexes of nicotinamide are of great interest – especially those of the heteroleptic type [1]. In this context, we have chosen a thiocyanate ion, a well known ambidentate ligand, which is able to form different molecular architectures through its versatile ligation modes [2]. Beside this, it is interesting that thiocyanates have been found in human biofluids, saliva and cerebrospinal fluid, and recently it was established that psychological stress induces them in oral cavities [3–5]. In addition, the nicotinamide molecule can form a variety of molecular associations via hydrogen bonding, and the present work stems from our interest in finding out the predominant factors to form complexes with desired structural properties so as to create functional ones [6]. In this paper we report the preparation, IR and NMR characterization and structure analysis of $Zn(NCS)_2(nicotinamide)_2$ and $[Hg(SCN)_2(nicotinamide)]_n$. The thermal behaviour of the complexes has also been investigated by TG and DTA techniques. The structural features are compared with a congeneric cadmium(II) nicotinamide complex as well as with analogous zinc complexes, $ZnX_2(nicotinamide)_2$ (X = Cl, Br, I).

2. Experimental

2.1. Materials and physical measurements

All reagents were supplied by Aldrich Chemical Co. and were used as received without further purification. The CHNS microanalyses were measured by the Chemical Analytical Service of the Ruđer Bošković Institute, Zagreb.

* Corresponding author. Tel.: +385 1 4606 354.
E-mail address: zpopovic@chem.pmf.hr (Z. Popović).

0277-5387/$ - see front matter © 2007 Elsevier Ltd. All rights reserved.
doi:10.1016/j.poly.2007.09.036

Infrared spectra were obtained from KBr pellets within the range 4000–400 cm^{-1} with a Perkin–Elmer FTIR spectrometer 1600 Series.

The one-dimensional ^1H and ^{13}C NMR spectra were recorded with a Bruker AV 600 spectrometer, operating at 600.133 MHz and 150.971 MHz for the ^1H and ^{13}C nuclei, respectively. Samples were measured in DMSO-d_6 solution and chemical shifts (ppm) are referred to TMS.

The thermal measurements were performed using a simultaneous TGA–DTA analyser (*TA Instruments*, SDT Model 2960). The TGA and DTA curves were obtained by placing the samples of about 6 mg in mass in small open platinum pans, with a heating rate of 10 °C/min and a nitrogen (purity above 99.996%) flow rate of 50 mL/min. All samples were heated from room temperature up to 700 °C. The SDT was calibrated with indium and silver.

2.2. Preparation of the complexes

2.2.1. Preparation of *[Zn(NCS)$_2$(nia)$_2$]* (**1**)

A warm aqueous solution of nicotinamide (nia) (0.24 g, 0.2 mmol in 50 mL of H_2O) was added to an aqueous solution of zinc nitrate hexahydrate (0.30 g, 0.1 mmol in 10 mL of H_2O). Into the resulting solution was then added an aqueous solution of potassium thiocyanate (0.18 g, 0.2 mmol in 10 mL of H_2O). After keeping the mother liquid for few days, white crystals suitable for X-ray diffraction study were obtained. Total yield corresponds to 85% (0.36 g, 0.87 mmol) based on Zn. *Anal.* Calc. for $C_{14}H_{12}ZnN_6O_2S_2$ (**1**): C, 39.49; H, 2.84; N, 19.74; S, 15.06. Found: C, 39.64; H, 2.94; N, 20.03; S, 15.26%. IR data (cm^{-1}, KBr pellets): 3340s, 3283m-s, 3176m, 3053w, 2358vw, 2343vw, 2094vs, 2044m, 1665vs, 1608s, 1593m, 1482w, 1445w, 1428m-s, 1399m-s, 1338w-m, 1239w, 1202m, 1151w, 1129w, 1113w, 1060m, 1032vw, 961vw, 944w, 855w, 832w-m, 796w, 763w, 704m, 668w-m, 657m, 638m, 589m, 540m.

2.2.2. Preparation of *[Hg(SCN)$_2$(nia)]$_2$* (**2**)

In an aqueous solution of mercury(II) nitrate monohydrate (0.68 g, 0.2 mmol in 100 mL of H_2O) containing a few drops of nitric acid (20% by weight), an aqueous solution of potassium thiocyanate (0.36 g, 4 mmol in 10 mL of H_2O) was added. In a few hours a white crystalline product of mercury(II) thiocyanate was obtained. The crystals were filtered off, washed with water and dried. Total yield of 85% (0.54 g, 1.7 mmol).

Afterwards $Hg(SCN)_2$ was dissolved in ethanol (0.32 g, 1 mmol in 100 mL) by gentle heating and into this still warm solution an ethanol solution of nicotinamide (2 mmol in 30 mL) was added. The mixture was refluxed for 1 h. The clear solution was kept for a few days until white crystals of **2** suitable for X-ray diffraction study were obtained. Total yield corresponds to 77% (0.34 g, 0.77 mmol) based on Hg. *Anal.* Calc. for $C_8H_6HgN_4OS_2$ (**2**): C, 21.89; H, 1.38; N, 12.77; S, 14.61. Found: C, 22.03; H, 1.52; N, 12.89; S, 14.83%. IR data (cm^{-1}, KBr pellets): 3852w, 3452s, 3356s, 2112vs, 1671vs, 1601s, 1572m, 1476w, 1422m, 1394m-s, 1200w-m, 1135w, 1045w, 1028w-m, 829w, 785w, 747w-m, 704m, 641m, 513m.

2.3. X-ray structural analysis

The general and crystal data, and summary of intensity data collection and structure refinement for compounds **1** and **2** are given in Table 1.

Data for structure **1** were collected at 200 K on a Nonius KappaCCD diffractometer with a crystal-detector distance of 30 mm. The extraction and correction of the intensity data, absorption correction and the refinement of the unit cell parameters were performed with the program package DENZO-SMN [7].

Data for structure **2** were collected 293 K on an Oxford Diffraction Xcalibur four-circle kappa geometry single-crystal diffractometer with a Sapphire 3 CCD detector, by applying the CRYSALIS software system [8]. The crystal-detector distance was 60 mm. Data reduction, including absorption correction, was done by the CRYSALIS RED application of the CRYSALIS software system [8].

The structures were solved by direct methods implemented in the SHELXS-97 program [9]. The coordinates and the anisotropic thermal parameters for all non-

Table 1
Crystal data and structure refinement for complexes **1** and **2**

Complex	**1**	**2**
Empirical formula	$C_{14}H_{12}ZnN_6O_2S_2$	$C_8H_6HgN_4OS_2$
Formula weight	425.83	438.90
Temperature (K)	200	296
Wavelength (Å)	0.71073	0.71073
Crystal system	monoclinic	monoclinic
Space group	$C2/c$	$P2_1/c$
a (Å)	18.254(2)	15.1425(7)
b (Å)	4.786(1)	5.8701(3)
c (Å)	21.363(3)	13.5242(7)
β (°)	109.65(1)	96.122(4)
Volume (Å^3)	1757.7(5)	1195.3(1)
Z	4	4
ρ_{calc} (g/cm^3)	1.609	2.439
$F(000)$	864	808
Crystal size (mm)	0.20 × 0.22 × 0.25	0.14 × 0.45 × 0.55
Reflections collected	4825	32416
Unique reflections	2557	3487
Parameters	123	154
$R_{1,\text{all data}}$, R_1^a [$I > 2\sigma(I)$]	0.0275; 0.0238	0.0366; 0.0345
$wR_{2,\text{all data}}$, wR_2^b [$I > 2\sigma(I)$]	0.0650; 0.0632	0.0652; 0.0430
g_1, g_2 in w^c	0.033, 1.0224	0.0204, 2.3946
S^d on F^2	1.061	1.176
$\Delta\sigma_{min/max}$ (e Å^{-3})^e	−0.363/0.463	−1.157/1.025
Extinction coefficient	0.0016(4)	0.0010(2)

[a] $R = \sum ||F_o| - |F_c|| / \sum |F_o|$.

[b] $wR = \left[\sum (F_o^2 - F_c^2)^2 / \sum w(F_o^2)^2\right]^{1/2}$.

[c] $w = 1/\left[\sigma^2(F_o^2) + (g_1P)^2 + g_2P\right]$ where $P = (F_o^2 + 2F_c^2)/3$.

[d] $S = \sum \left[w(F_o^2 - F_c^2)^2 / (N_{obs} - N_{param})\right]^{1/2}$.

[e] The maximum electron density in the last difference Fourier map for **2** is near Hg.

hydrogen atoms were refined by the least-squares method based on F^2 using the SHELXL-97 program [10]. The hydrogen atoms were generated geometrically using the riding model with the isotropic factor set at 1.2 U_{eq} of the parent atom. Hydrogen atoms on carboxamide nitrogen atoms were located in the difference Fourier map at the final stage of the refinement and were refined freely. Graphical work has been performed by the program ORTEP-3 *for Windows* [11] and Mercury 1.4.1 [12]. Thermal ellipsoids are drawn at the 50% probability level.

3. Results and discussion

3.1. Preparation of the complexes

The zinc thiocyanato complex was prepared *in situ* from aqueous solutions by reacting of all the components at room temperature. The mercury complex could not be obtained in the analogous way due to the very low solubility of mercuric thiocyanate in water. By addition of an ethanol solution under *in situ* conditions a mixture of products was obtained instead. But by refluxing the mixture of ethanol solutions of mercuric thiocyanate and nicotinamide, one can prepare the pure titled mercury compound.

3.2. Structure descriptions

All crystals were grown by slow evaporation of the reaction mixture under ambient conditions in a period of two days to one week. Selected bond distances, bond angles and hydrogen bonds are presented in Table 2. The structures are shown in Figs. 1 and 2.

3.2.1. Crystal structure of $Zn(NCS)_2(nia)_2$ (1)

In the molecular structure of bis(nicotinamide-*N*)-bis(thiocyanato-*N*)zinc(II), the zinc atom is located on a center of symmetry and is four coordinated by *N*-atoms from two nicotinamide and two isothiocyanate ligands, as shown in Fig. 1a. The coordination sphere around the central ion is distorted tetrahedral. The angles that deviate the most from regularity are N2–Zn1–N2[1] and N1–Zn1–N1[1] (symmetry code: (1) $-x$, y, $-z+3/2$), closed by two nia and two NCS^- ligands, 112.42(6)° and 123.82(8)°, respectively. Comparing the aforementioned angles in the title compound with the corresponding ones in the analogous tetrahedral zinc(II) halide complex [$ZnX_2(nia)_2$, X = Cl, Br, I] [13–15], compound **1** shows the greatest deviation from an ideal tetrahedral geometry (see Table 3). The largest deviation from ideal tetrahedral angles in all three reported structures occurs for the angles between the same ligands, ∠(X–Zn–X) and ∠(N–Zn–N)py, and this deviation is inversely proportional to the size of the coordinating atom; a small digression in the structure of the bromine complex was observed, Table 3. The Zn–N1/N1[1] (symmetry code: (1) $-x$, y, $-z+3/2$) bond distance (1.928(1) Å) is in the range for reported Zn–N(NCS) bonds in tetrahedral zinc(II) thiocyanate complexes with *m*-substituted pyridine ligands [16–18]. All other bond lengths and angles follow the usual values [19]. The NCS^- groups are almost linear with a N–C–S angle of 177.9(1)° and are coordinated to the zinc ion in a linear fashion with a Zn–N–C angle of 178.8(1)°. The pyridine rings are essentially planar (with a maximum deviation from the mean plane of 0.020(1)Å for the N atom) and the carboxamide group has a dihedral angle of 39.37(7)° with the pyridine plane, Table 4.

Table 2
Selected bond distances (Å) and angles (°) for complexes **1** and **2**

Complex ***1***			
Zn(1)–N(1)	1.928(2)	N(1)–C(1)	1.160(2)
Zn(1)–N(2)	2.033(1)	C(1)–S(1)	1.613(1)
		C(7)–O(1)	1.232(2)
N(1)–Zn(1)–N(1)[1]	123.82(8)	N(1)[1]–Zn(1)–N(2)[1]	104.96(5)
N(2)–Zn(1)–N(1)[1]	105.40(5)	N(1)–Zn(1)–N(2)[1]	105.40(5)
N(1)–Zn(1)–N(2)	104.96(5)	N(2)–Zn(1)–N(2)[1]	112.42(6)
Zn(1)–N(1)–C(1)	178.8(1)		
N(1)–C(1)–S(1)	177.9(1)		
Complex ***2***			
Hg(1)–S(1)	2.459(1)	N(1)–C(1)[2]	1.143(5)
Hg(1)–S(2)	2.419(1)	N(2)–C(2)	1.141(7)
Hg(1)–N(1)	2.387(4)	C(1)–S(1)	1.659(4)
Hg(1)–N(3)	2.333(3)	C(2)–S(2)	1.658(5)
		C(8)–O(1)	1.223(5)
N(1)–Hg(1)–N(3)	91.0(2)	N(3)–Hg(1)–S(1)	104.4(1)
S(1)–Hg(1)–S(2)	128.74(4)	N(3)–Hg(1)–S(2)	116.5(1)
N(1)–Hg(1)–S(1)	106.3(1)	Hg(1)–S(1)–C(1)	94.3(2)
N(1)–Hg(1)–S(2)	102.7(1)	Hg(1)–S(2)–C(2)	98.2(2)

[1] $-x$, y, $-z+3/2$.
[2] x, $y+1$, z.

Fig. 2b shows the crystal packing of **1**, viewed down the *b* axis. In the crystal structure three types of hydrogen bonds, N–H···O, N–H···S and C–H···O, are established. The geometrical parameters are given in Table 5. The centrosymmetric head-to-head hydrogen bond of $R_2^2(8)$ type, usually found in amide structures, is not established in the crystal structure of complex **1**. The carboxamide oxygen atom O(1) participates in a centrosymmetric hydrogen bond of the $R_2^2(10)$ type [20], Scheme 1, with the C4 atom from a pyridine ring of the adjacent molecule [C–H···O, 3.397(2) Å; symmetry code: $1-x$, $2-y$, $-z$]. The oxygen atom is a bifurcated acceptor and it simultaneously accepts an amide hydrogen atom of the neighbouring molecule down the *b* axis [N–H···O, 2.895(2) Å; symmetry code: x, $-1+y$, z] thus forming C(4) hydrogen bond chains in the [0 1 0] direction. The short S···S contacts, very often present in thiocyanate structures [21,22], were not found in the crystal structure of **1**. The sulfur atom from the thiocyanate ligand participates in a N–H···S hydrogen bond with the amide nitrogen [N–H···S, 3.526(2) Å; symmetry code: $1/2-x$, $1/2-y$, $-z$]. Very short Zn···Cg contacts (3.886 Å) between the zinc atom and the pyridine ring of a neighbouring complex molecule located in the direction of the *b* axis are found. Similar short contacts between the metal ion and the aromatic ring have been observed in the crystal structures of aromatic amino acids complexes [23].

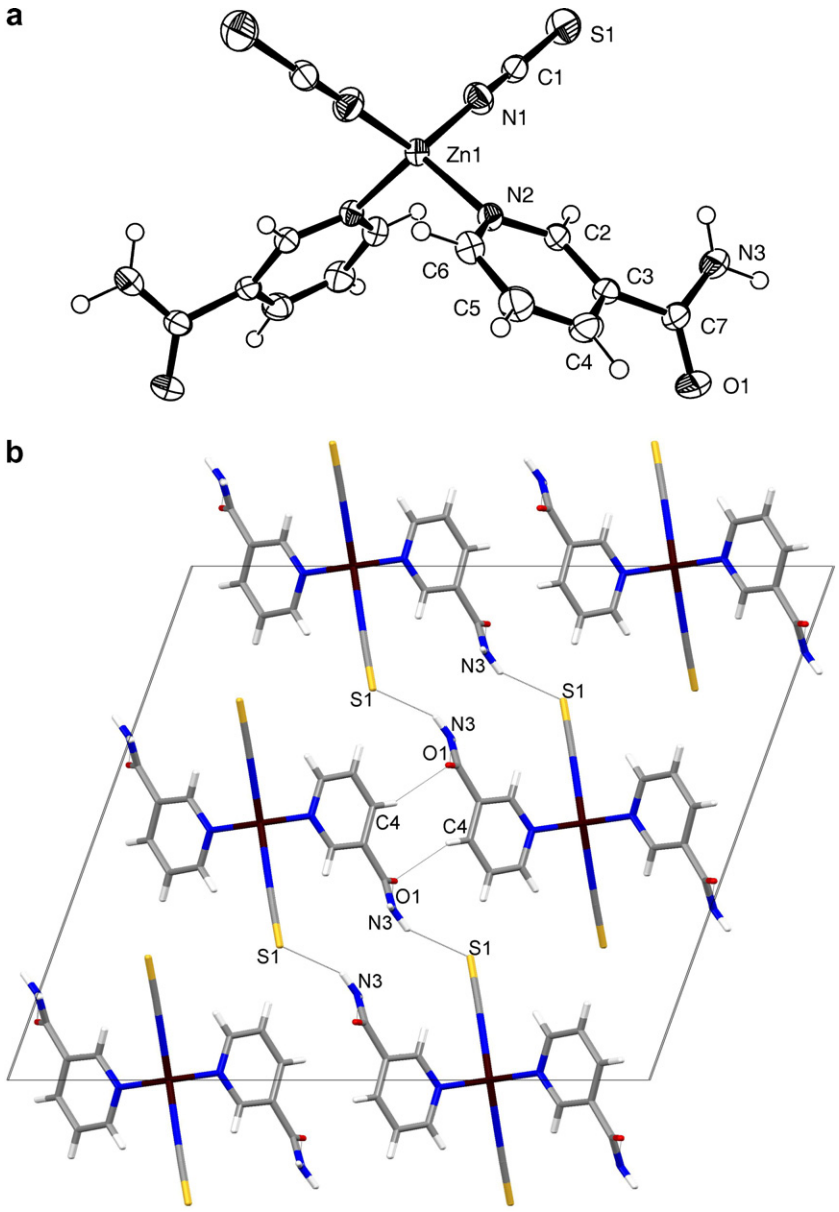


Fig. 1. (a) The ORTEP-3 drawing of the structural unit of complex **1** with the atomic numbering scheme; (b) crystal packing of complex **1** viewed down the *b* axis; hydrogen bonds are represented by dotted lines.

3.2.2. Crystal structure of $[Hg(SCN)_2(nia)]_n$ (**2**)

The X-ray structure analysis of **2** revealed the formation of a single-stranded chain structure, as is displayed in Fig. 2a. Each mercury(II) atom is four coordinated by two bridging μ-SCN-*S*,*N*, one terminal thiocyanate and one nicotinamide ligand in a quite distorted tetrahedral S_2N_2 geometry (the bond angles around the mercury atom are in the range 91.0(2)° to 128.74(4)°, Table 2). The Hg–N as well as the Hg–S bond distances are in the range of those distances found in other Hg^{II} thiocyanate complexes of substituted pyridine-*N* ligands [24–28]. As is expected, both bridging bond distances of coordinated thiocyanate ligands, Hg–N1 [2.387(4) Å] and Hg–S1 [2.459(1) Å] are somewhat longer than those ones of terminal ligands [Hg–N3 2.333(3) Å and Hg–S2 2.419(1) Å]. In **2**, the pyridine ring is less deformed in comparison with **1**, Table 4, and the dihedral angle closed by the pyridine ring and the carboxamide group is also much smaller in **2** than in **1**. Both thiocyanate ligands, bridging and terminal, are coordinated to mercury in a non-linear fashion [∠Hg1–S1–C1 94.3(2)°; ∠Hg1–S2–C2 98.2(2)°], especially the terminal one; its coordination geometry is probably caused by formation of hydrogen bonds. The terminal thiocyanate nitrogen atom is a very common H-bond acceptor and usually participates in more than one hydrogen bonding interaction [22]. In **2** it is a trifurcated acceptor. It participates in two *intra*molecular N–H···N and C–H···N hydrogen bonds of S(10) and S(7) type, respectively, and one *inter*molecular C–H···N hydrogen bond, forming C(7) chains.

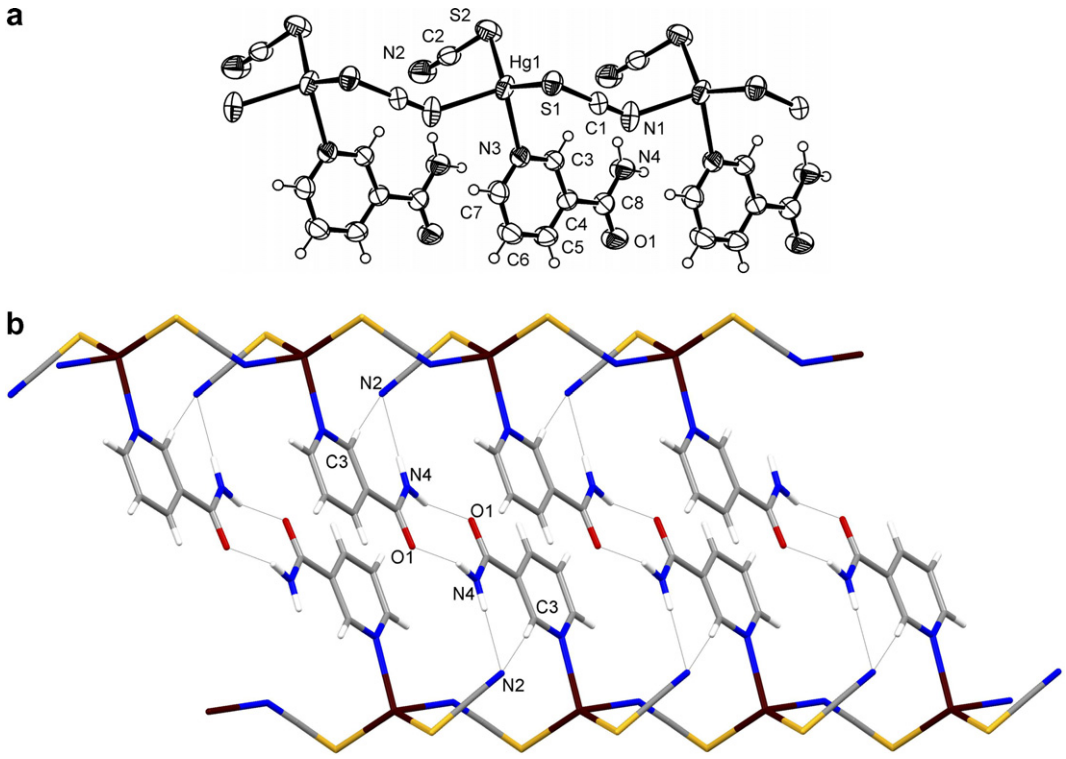


Fig. 2. (a) The ORTEP-3 drawing with the atom-labelling scheme of the structural unit of complex **2**; (b) packing diagram of **2** showing the formation of double-chains by head-to-head double hydrogen bonds of the $R_2^2(8)$ type; hydrogen bonds are represented by dotted lines.

Table 3
Comparison of angles closed by the same ligands in the coordination sphere of complex **1** and analogous halide complexes with nicotinamide [13–15]

	∠(X–Zn–X) (°)	∠(N–Zn–N)py (°)	Zn–N(py) (Å)	CSDB
$Zn(NCS)_2(nia)_2$	123.82(6)	112.42(4)	2.033(1)	
$ZnCl_2(nia)_2$	121.81(5)	101.8(1)	2.058(3)	WUKZAD [13]
			2.057(4)	
$ZnBr_2(nia)_2$	118.9*	96.1*	2.065(3)	BANDUQ [14]
$ZnI_2(nia)_2$	114.72(5)	98.8(1)	2.059(2)	WEMROW [15]

* Deviations are not given by the authors.

Table 4
Selected torsion and dihedral angles (°)

	(**1**)	(**2**)
Py ring (I)	2.16(8)	0.5(3)
Py ring (I) – amido group (I)	39.37(7)	3.0(3)

The details of the hydrogen bonding geometry of **2** are shown in Fig. 2b and geometric parameters are included in Table 4. As shown in Fig. 2b, the polymeric chains are further linked through centrosymmetrical amide–amide hydrogen bonds of the $R_2^2(8)$ type [N···O 2.922(6) Å; symmetry code: $1-x, -y, 1-z$] and in such a way double-chains are formed. These double-chains are packed into a 3D network by the above mentioned C–H···N H–bond in the *c* axis direction. Short C···S contacts [C···S 3.455 Å] are also observed in the structure of **2** between two parallel thiocyanate chains. *Intra* chain pyridine rings, although coplanar, are apart from each other, and no π–π stacking interactions are found.

3.3. Spectroscopic properties

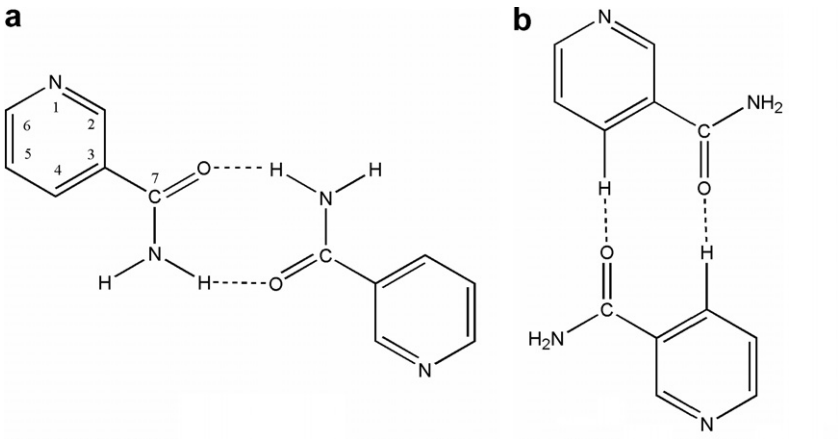
3.3.1. IR spectra

There are two possibilities for nicotinamide to coordinate to a central metal atom, either through the endocyclic nitrogen or the carboxamide oxygen atom. In its Zn and Hg complexes it usually behaves as a monodentate ligand through the pyridine ring nitrogen atom. The coordination mode of the nia ligand could easily be deduced from IR spectra by comparing the IR spectra of the free ligand and the complex molecule. The absorption bands of the carbonyl group (1697, 1679 cm^{-1}) are shifted to lower values if the amide oxygen atom is involved in coordination. In the case of coordination through the pyridine ring nitrogen atom, a significant negative shift of the carbonyl absorption bands takes place [15].

The IR bands of complexes **1** and **2** were assigned by comparing with the free ligand data. In both complexes a shift to lower wavenumbers of *ν*(CO) is observed (1665 cm^{-1} in **1**; 1671 cm^{-1} in **2**). It could be concluded that nia-*O* coordination occurred. Concerning the facts (a) that the CO stretching of picolinamide (pia) in

Table 5
Hydrogen bonds (Å and °) for compounds **1** and **2**

D–H···A	D–H	H···A	D···A	∠DHA	Symmetry code
Compound ***1***					
N(3)–H(23N)···O(1)	0.84(2)	2.08(2)	2.895(2)	163(2)	$x, -1+y, z$
N(3)–H(13N)···S(1)	0.85(2)	2.76(2)	3.526(2)	151(2)	$1/2-x, 1/2-y, -z$
C(4)–H(4)···O(1)	0.95	2.52	3.397(2)	153	$1-x, 2-y, -z$
Compound ***2***					
N(4)–H(14N)···O(1)	0.89(6)	2.03(6)	2.922(6)	175(6)	$1-x, -y, 1-z$
N(4)–H(24N)···N(2)	0.88(7)	2.20(6)	3.064(8)	170(7)	$x, -1+y, z$
C(3)–H(3)···N(2)	0.93	2.44	3.317(8)	135	$x, 5/2-y, -1/2-z$
C(7)–H(7)···N(2)	0.93	2.59	3.370(7)	176	$-1/2+x, 1/2-y, z$



Scheme 1. The bridging modes of nicotinamide established in complexes (a) **1** and (b) **2** with the labelling mode used in the discussion of the NMR data.

acetonitrile solution occurs at 1690 cm^{-1} while it is observed at around 1660 cm^{-1} in solid pia and its complexes [15] where such a negative shift is attributed to hydrogen bonding in the solids, and (b) that halide Zn complexes with nia, as well as Hg complexes with py ligands, are *N*-coordinated, it can be concluded that it could also be the case here, which is confirmed by the X-ray results. Moreover, a greater shift to lower frequencies observed in **1** compared to **2** could be explained by the fact that the carbonyl oxygen atom in **1** participates in two H-bonds as a bifurcated acceptor and significant elongation of C=O bond occurs in comparison to **2** where the carboxamide *O*-atom participates in one H-bond [C–O: 1.232(2) Å in **1**, 1.223(5) Å in **2**].

The *ν*(NH) absorption bands of the amide group in nia appear at 3368 and 3161 cm^{-1}. In both complexes some positive shifts of NH bands occur, and in **1** they are split, while in **2** they are broadened. These shifts to higher frequencies are obviously the consequence of hydrogen bonding in the crystalline state of the complexes. The broadening in **2** could be attributed to three hydrogen bonds in which the amide N-atom is involved as a trifurcated acceptor.

Concerning the C–N stretching frequencies of thiocyanates in general, *ν*(CN) are lower in *N*-bonded complexes (near or below 2050 cm^{-1}) than *S*-bonded complexes (near 2100 cm^{-1}). For bridging complexes (M–SCN–M) the CN stretching frequency is above 2100 cm^{-1} [29]. The stretching CN frequencies of compounds **1** and **2** were observed at 2094 and 2112 cm^{-1}, from which it could be clearly seen that the thiocyanate is coordinated to zinc through the nitrogen atom and to mercury through the sulfur atom. No separate bands were observed for bridging and terminal thiocyanate groups in the mercury complex **2**.

The position of the C–S stretching frequencies in the region 860–690 cm^{-1} is usually employed for differentiating *S*- from *N*-bonded terminal thiocyanates; *ν*(CS) in the range 860–780 cm^{-1} and 720–690 cm^{-1} for *N*- and *S*-coordinated, respectively [30]. However, the *ν*(CS) modes are, for both compounds **1** and **2**, overlapped by pyridine ligand stretching and deformation bands, making the assignment of the C–S stretches quite uncertain.

3.3.2. NMR spectra

The ^{1}H and ^{13}C data for **1** and **2**, together with the literature values of the parent nicotinamide molecule, are presented in Tables 6 and 7, respectively. Scheme 1 shows the labelling of the atoms. The ^{1}H and ^{13}C NMR data of free nia are cited from the literature [31], while the other measurements are performed in DMSO-d_6 solutions. The complexation ^{1}H and ^{13}C NMR shifts are defined as the difference of the proton and carbon shifts, respectively, in the complexes and the free ligand molecule.

Table 6
^{1}H NMR chemical shifts (δ ppm^{-1})[a], complexation shifts ($\Delta\delta$ ppm^{-1})[b,d] and H–H coupling constants (J_{HH}/Hz)[e] in the ligand molecule, nicotinamide, and their complexes with zinc(II) and mercury(II) thiocyanate, **1** and **2**

Compound		nia[c]	**1**	**2**
H-2	δ	9.08	9.04	9.06
	J_{HH}	(s)	(s)	(s)
	$\Delta\delta$		−0.04	−0.02
H-4	δ	8.25	8.24	8.29
	J_{HH}	7.9 (d)	7.94 (d)	7.96 (d)
	$\Delta\delta$		−0.01	0.04
H-5	δ	7.53	7.53	7.59
	J_{HH}	7.9 (d)	7.89 (d)	7.92 (d)
	$\Delta\delta$	4.9 (d)	4.88 (d)	4.96 (d)
			0.00	0.06
H-6	δ	8.74	8.76	8.73
	J_{HH}	4.9 (d)	4.81 (d)	4.76 (d)
	$\Delta\delta$		0.02	−0.01
H-1(NH_2)	δ	7.67	7.62	7.66
	J_{HH}	broadened	broadened	broadened
	$\Delta\delta$		−0.05	−0.01
H-2(NH_2)	δ	8.22	8.18	8.21
	J_{HH}	broadened	broadened	broadened
	$\Delta\delta$		−0.04	−0.01

[a] Referred to TMS in DMSO solutions.
[b] Complexation shifts are defined as the difference of proton chemical shifts between the complex and parent molecule.
[c] Taken from Ref. [31].
[d] Sign (+) denotes deshielding effect, while (−) denotes shielding effect.
[e] Digital resolution ±0.30 Hz: (s) singlet, (d) doublet.

Table 7
^{13}C NMR chemical shifts (δ ppm^{-1})[a] and complexation shifts ($\Delta\delta$ ppm^{-1})[b,d] in the ligand molecule, nicotinamide, and their complexes with zinc(II) and mercury(II) thiocyanate, **1** and **2**

Compound		nia[c]	**1**	**2**
C-2	δ	151.78	151.84	151.85
	$\Delta\delta$		0.06	0.07
C-3	δ	129.70	129.79	130.05
	$\Delta\delta$		0.09	0.35
C-4	δ	135.07	135.39	135.91
	$\Delta\delta$		0.32	0.84
C-5	δ	123.29	123.54	123.82
	$\Delta\delta$		0.25	0.53
C-6	δ	148.65	148.71	148.93
	$\Delta\delta$		0.06	0.28
C-7	δ	166.49	166.43	166.19
	$\Delta\delta$		−0.06	−0.30
C(SCN)	δ		135.05	116.07
	$\Delta\delta$			

[a] Referred to TMS in DMSO solutions.
[b] Complexation shift is defined as the difference of carbon chemical shifts in the complex and the parent molecule.
[c] Taken from Ref. [31].
[d] Sign (+) denotes deshielding effect, while (−) denotes shielding effect.

The ^{1}H spectra of both complexes display six signals, four belonging to aromatic protons and two to carboxamide ones. The signals of the amido group protons as well as the aromatic H–2 proton are found to be shielded in both complexes **1** and **2**.

In the ^{13}C spectra of both complexes **1** and **2**, all the aromatic carbon atoms are shifted 0.06–0.84 ppm downfield relatively to the corresponding ones in the parent ligand molecule. On the basis of the ^{13}C spectra it could be concluded that the aromaticity of the pyridine ring is preserved upon complexation, which can be supported by the short ring C–C distances obtained from the X-ray analysis. The greatest change of ^{13}C chemical shift upon complexation was found at C-4 which is *para* to the nitrogen and *ortho* to the amide group. The complexation shifts of the aromatic carbon atoms are found to be more pronounced by on average 2–3 times more in the mercury complex **2** than in the zinc complex **1**, except for carbon C-2 where the differences in complexation shift are negligible. The carboxamide carbons in **1** and **2** are found to be shielded and the shielding is more pronounced in **2**. In the crystal structure of **1**, the carboxamide oxygen atom participates in two H-bonds as a bifurcated acceptor. This elongates the carbonyl bond and withdraws electron density towards the O-atom more than just one hydrogen bond in which the carboxamide oxygen atom of **2** participates, so the shielding complexation effect is smaller in **1** than in **2**. The hydrogen bonds of the carboxamide groups found in the crystal structure probably also exist in solution.

The formation of thiocyanate and isothiocyanate complexes can be easily detected by the characteristic ^{13}C signal for the -SCN and -NCS groups that are usually found at ~111 and ~145 ppm, respectively [32]. In the ^{13}C spectra of the investigated thiocyanate complexes there are signals at 135 and 116 in the zinc and mercury complex, respectively, indicating the coordination of the thiocyanate ligands to the metal centers through (SCN)-*N* in **1** and through the (SCN)-*S* atom in **2**.

3.4. Thermal analysis

The analysis of the TGA and DTA curves showed that the thermal decomposition of **1** consists of three steps. The first one is the decomposition of **1** to $Zn(SCN)_2$, which corresponds to an endothermic DTA peak at 232.5(5) °C. In the temperature range 250–400 °C two endothermic peaks (a main large one at 283.6(5) °C and a second small one at 351.7(5) °C) were observed. This can be attributed to the thermal decomposition of $Zn(SCN)_2$, and the final residue is ZnS (about 23%).

The thermal analysis of **2** reveals that the thermal decomposition of the investigated complex involves three major processes; two endothermal and an exothermal one. The first endothermal peak corresponds to the melting process of **2** (minimum at 127.8(5) °C). The second one (exothermal at 218.8(5) °C) is followed and overlapped by a small endothermal peak, presenting degradation of the ligands. The incurred $Hg(SCN)_2$ continues the decomposition followed

by sublimation of HgS, corresponding to the endothermic peak with a maximum at 431.2(5) °C.

4. Conclusion

Zinc(II) and mercury(II) thiocyanato complexes with nicotinamide have been synthesized, the zinc complex by the *in situ* reaction in aqueous solution, while the mercury complex by using the previously isolated mercury(II) thiocyanate complex as the mercury starting reagent. The isolated complexes were investigated by X-ray structural analysis, spectroscopic and thermal methods.

The nicotinamide, with the carboxamide group in the *m*-position to the pyridine nitrogen atom acts as a monodentate-*N* ligand for the zinc(II) and mercury(II) ions, coordinating to the metal ions through the pyridine nitrogen atom and leaving both carboxamide moieties available for participation in hydrogen bond formation. The centrosymmetrical amide–amide hydrogen bonds of the $R_2^2(8)$ type, usually found in the structures of amides, are also established in the mercury(II) complex **2**, but in the zinc(II) complex **1**, the presence of a centrosymmetrical head-to-head hydrogen bond of the $R_2^2(10)$ type was found, comprising the aromatic carbon and carboxamide nitrogen atom, Scheme 1. The thiocyanate ion acts as a *N*-donor ligand for zinc, **1**, and a *S*-/μ-*S*,*N*-donor ligand for the mercury complex, **2**. In the thiocyanate complexes of the group 12 metals, the thiocyanate ligand shows its versatile coordination modes, from almost linear in **1** to almost perpendicular in **2**, and with the M-(SCN) angle intermediate in its congeneric cadmium complex [21]. Moreover, in **1** monomeric zinc–thiocyanate units are formed, in **2** there are one-dimensional mercury–thiocyanate chains, while in the cadmium complexes [21] two-dimensional cadmium–thiocyanate sheets are found.

Acknowledgements

This research was supported by the Ministry of Science, Education and Sport of the Republic of Croatia, Zagreb (Grants Nos. 119-1193079-1332 and 192-1252971-1982).

Appendix A. Supplementary material

CCDC 655345 and 655344 contain the supplementary crystallographic data for **1** and **2**. These data can be obtained free of charge via http://www.ccdc.cam.ac.uk/conts/retrieving.html, or from the Cambridge Crystallographic Data Centre, 12 Union Road, Cambridge CB2 1EZ, UK; fax: (+44) 1223-336-033; or e-mail: deposit@ccdc.cam.ac.uk. Supplementary data associated with this article can be found, in the online version, at doi:10.1016/j.poly.2007.09.036.

References

[1] P. Krogsgaard-Larsen, T. Liljefors, U. Madsen, Textbook of Drug Design and Discovery, third ed., Taylor & Francis, London, 2002, p. 365.
[2] H. Zhang, X. Wang, K. Zhang, B.K. Teo, Coord. Chem. Rev. 183 (1999) 157.
[3] P.B. Paul, M.L. Smith, J. Anal. Toxicol. (2006) 511.
[4] N. Goi, Y. Hirai, H. Harada, A. Ikari, T. Ono, Y. Terashima, N. Kinae, M. Hiramatsu, K. Nakamura, H. Tsuboi, K. Takagi, Abstr., Brain, Behav. Immun. 20 (2006) e17.
[5] M. Rosin, T. Kocher, A. Kramer, J. Clin. Periodontol. 28 (2001) 270.
[6] E. Akalin, S. Akyuz, Vib. Spectrosc. 42 (2006) 333.
[7] Z. Otwinowski, W. Minor, in: C.W. Carter, R.M. Sweet (Eds.), Methods in Enzymology, Macromolecular Crystallography, Part A, vol. 276, Academic Press, London, 1997, p. 307.
[8] Oxford Diffraction. Oxford Diffraction Ltd., Xcalibur CCD System, CRYSALIS Software System, Version 171.26, 2004.
[9] G.M. Sheldrick, SHELXS-97, Program for the Automatic Solution of Crystal Structures, University of Göttingen, Germany, 1997.
[10] G.M. Sheldrick, SHELXL-97, Program for the Refinement of Crystal Structures, University of Göttingen, Germany, 1997.
[11] L.J. Farrugia, J. Appl. Crystallogr. 30 (1997) 565.
[12] I.J. Bruno, J.C. Cole, P.R. Edgington, M.K. Kessler, C.F. Macrae, P. McCabe, J. Pearson, R. Taylor, Acta Crystallogr. B 58 (2002) 389.
[13] S. Ide, A. Ataç, Ş. Yurdakul, J. Mol. Struct. 605 (2002) 103.
[14] E. Şahin, S. Ide, A. Ataç, Ş. Yurdakul, J. Mol. Struct. 616 (2002) 253.
[15] H. Paşaoglu, S. Güven, Z. Heren, O. Büyükgüngör, J. Mol. Struct. 794 (2006) 270.
[16] W.-L. Pan, X.-L. Niu, W. Tang, C.-W. Hu, Acta Crystallogr. E 63 (2007) m304.
[17] S. Chantrapromma, H.-K. Fun, X.-J. Feng, J.-X. Yang, J.-Y. Wu, Y.-P. Tian, Acta Crystallogr. E 61 (2005) m733.
[18] F. Bigoli, A. Braibanti, M.A. Pellinghelli, A. Tiripicchio, Acta Crystallogr. B 29 (1973) 2708.
[19] F.H. Allen, O. Kennard, D.G. Brammer, L. Orpen, R. Taylor, J. Chem. Soc., Perkin Trans. 2 (1987) S1.
[20] J. Bernstein, R.E. Davis, L. Shimoni, N.-L. Chang, Angew. Chem., Int. Ed. Engl. 34 (1995) 1555.
[21] G. Yang, H.G. Zhu, B.H. Liang, X.M. Chen, J. Chem. Soc., Dalton Trans. (2001) 580.
[22] M. Đaković, Z. Popović, G. Giester, M. Rajić-Linarić, Polyhedron, in press, doi:10.1016/j.poly.2007.09.014.
[23] K. Aoki, H. Yamazaki, J. Chem. Soc., Dalton Trans. (1987) 2017.
[24] H.-P. Zhou, Y.-P. Tian, J.-Y. Wu, J.-Z. Zhang, D.-M. Li, Y.-M. Zhu, Z.-J. Hu, X.-T. Tao, M.-H. Jiang, Y. Xie, Eur. J. Inorg. Chem. (2005) 4976.
[25] A. Morsali, A. Ramazani, A.R. Mahjuob, A.A. Soudi, Z. Anorg. Allg. Chem. 629 (2003) 2058.
[26] A. Morsali, L.-G. Zhu, Helv. Chim. Acta 89 (2006) 81.
[27] A.R. Mahjoub, A. Morsali, R.E. Nejad, Z. Naturforsch. 59b (2004) 1109.
[28] A. Morsali, A.R. Mahjoub, A. Ramazani, J. Coord. Chem. 57 (1994) 347.
[29] R. Bala, R.P. Sarma, R. Sarma, B.M. Kariuki, Inorg. Chem. Commun. 9 (2006) 852.
[30] R. Kapoor, A. Kataria, A. Pathak, P. Venugopalan, G. Hundal, P. Kapoor, Polyhedron 24 (2005) 1221.
[31] SDBSWeb: http://www.aist.go.jp/RIODB/SDBS/ (National Institute of Advanced Industrial Science and Technology, 18.01.2007).
[32] N. Iranpoor, H. Firouzabadi, H.R. Shaterian, Tetrahedron Lett. 43 (2002) 3439.

Available online at www.sciencedirect.com
ScienceDirect
Polyhedron 27 (2008) 473
POLYHEDRON
www.elsevier.com/locate/poly

Corrigendum

Corrigendum to "Three novel trinuclear zinc(II)/nickel(II) complexes with pentadentate ligands *N*-nitrobenzoylsalicylhydrazidate" [Polyhedron 26 (2007) 4793–4798]

Shen Lin [a,b,*], Ming-Xing Yang [a,b], Shi-Xiong Liu [c]

[a] *College of Chemistry and Material Science, Fujian Normal University, Fuzhou 350007, PR China*
[b] *State Key Laboratory of Structural Chemistry, Fujian Institute of Research on the Structure of Matter, Chinese Academy of Sciences, Fuzhou 350002, China*
[c] *Central Laboratory, Fuzhou University, Fuzhou 350002, PR China*

Available online 26 November 2007

In the "Acknowledgements" section on page 4798 the current text is incomplete. The number of financial support program for the National Natural Science Foundation of China should be added. Therefore, the acknowledgment text should read:

This work was supported financially by the Natural Science Foundation of Fujian Province, China (No. E0510012) and the National Natural Science Foundation of China (No. 20771024).

DOI of original article: 10.1016/j.poly.2007.01.028.
* Corresponding author. Address: College of Chemistry and Material Science, Fujian Normal University, Fuzhou 350007, PR China. Tel.: +86 591 22868169; fax: +86 591 83465393.
E-mail address: shenlin@fjnu.edu.cn (S. Lin).

0277-5387/$ - see front matter © 2007 Elsevier Ltd. All rights reserved.
doi:10.1016/j.poly.2007.10.014

Available online at www.sciencedirect.com
ScienceDirect
Polyhedron 27 (2008) 475–484
POLYHEDRON
www.elsevier.com/locate/poly

Synthesis and spectroscopic characterization of piperidine/chloranil and piperidine/7,7′,8,8′-tetracyanoquinodimethane charge transfer complexes: X-ray crystal structure of a 7,7-dicyano-8,8-di-piperidinoquinodimethane adduct

Moamen S. Refat [a,*], Lamia A. El-Zayat [a], Okan Zafer Yeşilel [b]

[a] *Chemistry Department, Faculty of Education, Port Said, Suez Canal University, Egypt*
[b] *Department of Chemistry, Faculty of Arts and Sciences, Eskişehir Osmangazi University, 26480 Eskişehir, Turkey*

Received 5 June 2007; accepted 13 September 2007
Available online 5 November 2007

Abstract

Charge transfer reactions of piperidine with *p*-chloranil (CHL) and 7,7′,8,8′-tetracyanoquinodimethane (TCNQ) in chloroform have produced stable complexes with the general formula [$(Pip)_2$(acceptor)] with a 1:2 acceptor:donor molar ratio. Elemental analysis (CHN), electronic spectra, photometric titration, mid infrared spectra, ^{1}H NMR spectra and thermogravimetric analysis (TGA/DTG) were used to predict the position of the charge transfer interaction between the donating and accepting sites. The crystal structure of the Pip/TCNQ system was determined by single crystal X-ray diffraction.
© 2007 Elsevier Ltd. All rights reserved.

Keywords: Piperidine; TCNQ; X-ray crystal structure; Thermogravimetric analysis

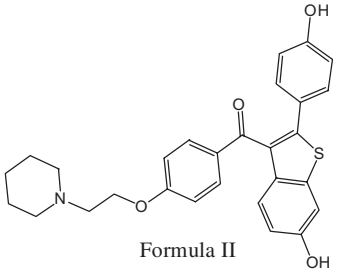
1. Introduction

Piperidine (Formula I) is an organic compound with the molecular formula $C_5H_{11}N$. It is a cyclic amine with a six-member ring. The piperidine skeleton is present in numerous natural alkaloids such as piperine, the main active chemical agent in black pepper and relatives, pharmaceutical drugs such as raloxifene (Formula II) and minoxidil (Formula III).

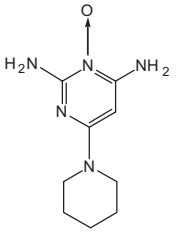
The major industrial application of piperidine is for the production of dipiperidinyl dithium tetrasulfide, which is used as a rubber vulcanization accelerator.



Formula I



Formula II



Formula III

* Corresponding author.
E-mail address: msrefat@yahoo.com (M.S. Refat).

0277-5387/$ - see front matter © 2007 Elsevier Ltd. All rights reserved.
doi:10.1016/j.poly.2007.09.025

Its charge transfer (CT) interaction has been widely reported recently. Charge transfer complexes are known to take part in many chemical reactions like addition, substitution and condensation [1,2]. These complexes have had great attention for non-linear optical materials and electrical conductivity [3–6]. The electron donor–acceptor (EDA) interaction is also important in the field of drug-receptor binding mechanisms [7], in solar energy storage [8] and in surface chemistry [9] as well as in many biological fields [10]. On the other hand, the EDA reactions of certain π-acceptors have successfully utilized in pharmaceutical analysis [11]. For these wide applications extensive studies on CT complexes of π-acceptors have been performed [12].

A literature survey [13–16] reveals that little attention has been paid to thermodynamic and electronic spectral characteristics, and it does not contain any information on the structural behavior of the CT interactions of this compound (Pip) with σ- and π-acceptors.

Charge transfer complexes of organic species are intensively studied because of their special type of interaction, which is accompanied by the transfer of an electron from the donor to the acceptor [17,18]. Also, protonation of the donor by acidic acceptors is generally the route for the formation of ion pair adducts [19–21].

Charge transfer (CT) complexes formed between piperidine (Pip) as the donor with *p*-chloranil (CHL) and 7,7′,8,8′-tetracyanoquinodi methane (TCNQ) as π-acceptors have been studied spectrophotometrically. The synthesis and characterization of piperidine CT complexes of *p*-chloranil, [(Pip)$_2$(CHL)] (**1**) and 7,7′,8,8′-tetracyanoquinodimethane, [(Pip)$_2$(TCNQ)] (**2**) are described. These complexes are readily prepared from the reaction of Pip with CHL and TCNQ using $CHCl_3$ as the solvent. IR,^{1}H NMR, mass spectra, UV–Vis techniques and elemental analyses (CHN), characterize the two piperidine charge-transfer complexes. Benesi-Hildebrand and its modification methods were applied for the determination of the association constant (K) and molar extinction coefficient (ε).

2. Experimental

Pure piperidine, *p*-chloranil (CHL) and 7,7,8,8-tetracyanoquinodimethane (TCNQ) were obtained from (Merck) and were used without further purification.

2.1. Materials and measurements

The electronic absorption spectra were recorded in the region 800–200 nm using a UV–Vis spectrophotometer, model Jenway 6405, with a quartz cell of 1.0 cm path length. The mid infrared spectra of the reactants and the resulted CT-complexes were measured from KBr discs using a Gensis II FT IR spectrophotometer. ^{1}H NMR spectra were obtained on a Varian spectrophotometer Gemini 200 MHz using TMS as an internal reference and d_6-DMSO as the solvent.

Thermogravimetric (TG) and differential (DTG) analyses were carried out in the temperature range 25–600 °C in nitrogen atmosphere using a Shimadzu TGA 50 H thermal analyzer. The experimental conditions were: aluminium crucible with a definite mg of sample, nitrogen atmosphere (nitrogen flow 30 ml/min) and heating rate of 15 °C/min. The elemental analyses were performed by the microanalysis unit at Cairo University, Egypt using a Perkin Elmer CHN 2400. The data of the elemental analyses (CHN) of the reaction products, the CT-complexes, were matched with the molar ratio results from the photometric titrations.

The two solid CT-complexes formed in the reaction of Pip with CHL and TCNQ were isolated by the addition of 1.0 mmol of Pip (10 ml) to a 1.0 mmol solution of CHL and TCNQ (20 ml) in chloroform followed by stirring for about 30 min. Dark brown and yellow precipitates were formed in the case of Pip/CHL and Pip/TCNQ, respectively, and these were filtered off, washed several times with $CHCl_3$ and dried in vacuo. The products were identified as: [(Pip)$_2$(CHL)] (**1**) ($C_{16}H_{22}N_2O_2Cl_4$; $M_w = 416$, m.p. 155 °C). *Anal.* Calc.: C, 46.20; H, 5.29; N, 6.73. Found: C, 46.12; H, 4.85; N, 6.69%; and 7,7-dicyano-8,8-di-piperidinoquinodimethane adduct (**2**) ($C_{20}H_{24}N_4$; $M_w = 320$, m.p. 187 °C). *Anal.* Calc.: C, 75.00; H, 7.50; N, 17.50. Found: C, 74.78; H, 7.46; N, 17.29%.

2.2. Crystallographic analysis

Data collection was performed on a Bruker SMART CCDC area detector diffractometer using Mo Kα radiation (α = 0.71073 Å). The structure was solved by direct-methods using SIR97 [22] and anisotropic displacement parameters were applied to non-hydrogen atoms in a full-matrix least-squares refinement based on F^2 using SHELXL-97 [23]. Molecular drawings were obtained using ORTEP-III [24].

Crystallographic data for [(Pip)$_2$(TCNQ)]: crystal dimensions $0.38 \times 0.29 \times 0.23$ mm; $F_w = 320.43$ g mol^{-1}, triclinic, space group $P\bar{1}$, $a = 8.7775(6)$, $b = 13.5503(9)$, $c = 16.2521(11)$ Å, $\alpha = 95.596(1)°$, $\beta = 101.804(1)°$, $\gamma = 104.797(1)°$; $V = 1806.3(2)$ Å^3, $Z = 4$, $D_c = 1.178$ Mg m^{-3}, $R_{int} = 0.050$ and $wR = 0.224$ for 7765 independent reflections; $S = 1.265$.

3. Results and discussion

3.1. Electronic absorption spectra of the Pip/CHL and Pip/TCNQ systems

In the case of the Pip/CHL system, once beginning the addition of CHL to a solution of Pip in chloroform, the color of the solution changes in four steps until it is constant: light blue → yellow → gray → olive green. On the other hand, in the case of the Pip/TCNQ system, upon addition of TCNQ to the donor (Pip) dissolved in chloroform, a dark green precipitate was formed immediately. The electronic absorption spectra of the reaction mixtures

containing CHL and TCNQ with piperidine as donor in $CHCl_3$ were recorded. Fig. 1A and B shows the spectra in the 800–200 nm region of the reactants piperidine (Pip), *p*-chloranil (CHL) and 7,7′,8,8′-tetracyanoquinodimethane (TCNQ) and the final products, with a concentration of each in the order of 1.0×10^{-4} M in $CHCl_3$. The electronic absorption spectra of the resultant Pip charge transfer complexes, shown in Fig. 1A and B, revealed new strong absorption bands assigned to the CT interaction. These bands are not present in the spectra of the free reactants (Pip, CHL and TCNQ) and were at 248, 330, 449 and 575 nm for Pip/CHL and at 324 nm for Pip/TCNQ. In the photometric titration measurements [25], the concentration of CHL and TCNQ was kept fixed at 1.00×10^{-4} M, while the concentration of Pip was varied over the range 0.25×10^{-4}–4.00×10^{-4} M. Furthermore, photometric titrations measurements between (Pip) and the defined acceptors CHL and TCNQ in $CHCl_3$ based on the characteristic absorption bands which refer to the CT complexes, Fig. 2A and B, proved that the molar ratio of the resultant complexes is 2:1 Pip:acceptor. A comparison of the absorption spectra of the free piperidine donor and the π-acceptor reveals that the two new CT complexes synthesized were characterized by definite maximum absorption bands at the wavelengths 330 and 575 nm, and 324 nm for the Pip/CHL and Pip/TCNQ systems, respectively. The formation of 1:2 complexes was supported by both elemental analysis and thermal measurements.

It was necessary to calculate the values of the equilibrium constant, the extinction coefficient, ε, and the oscillator strength, *f*, of the Pip complexes, $[(Pip)_2(CHL)]$ and $[(Pip)_2(TCNQ)]$ in chloroform solvent. The known equation for 1:2 complexes [26] was used in the calculations

$$\frac{C_A^{0^2} C_D^0}{A} = \frac{1}{K\varepsilon} + \frac{1}{\varepsilon} \cdot C_A^0 (4C_D^0 + C_A^0) \quad (1)$$

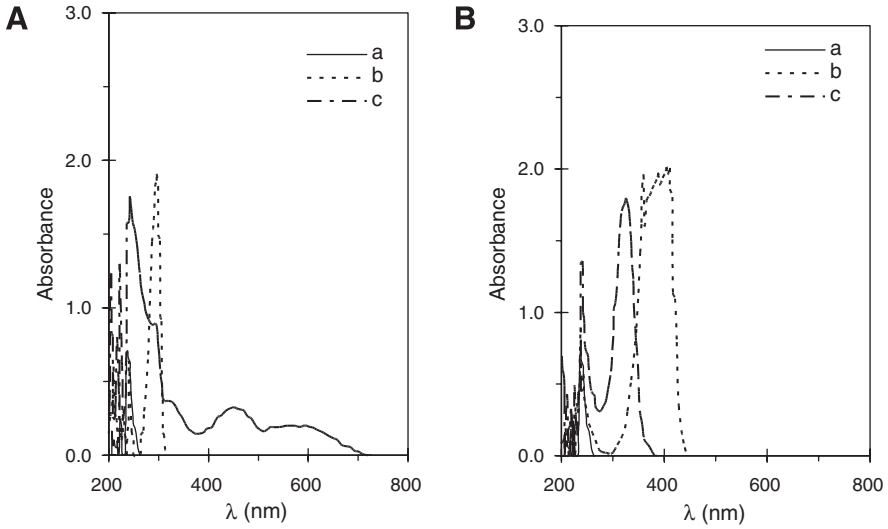


Fig. 1. Electronic absorption spectra of (A) Pip–CHL and (B) Pip–TCNQ reactions in $CHCl_3$. (a) Donor (1.0×10^{-4} M), (b) acceptor (1.0×10^{-4} M) and (c) CT-complex.

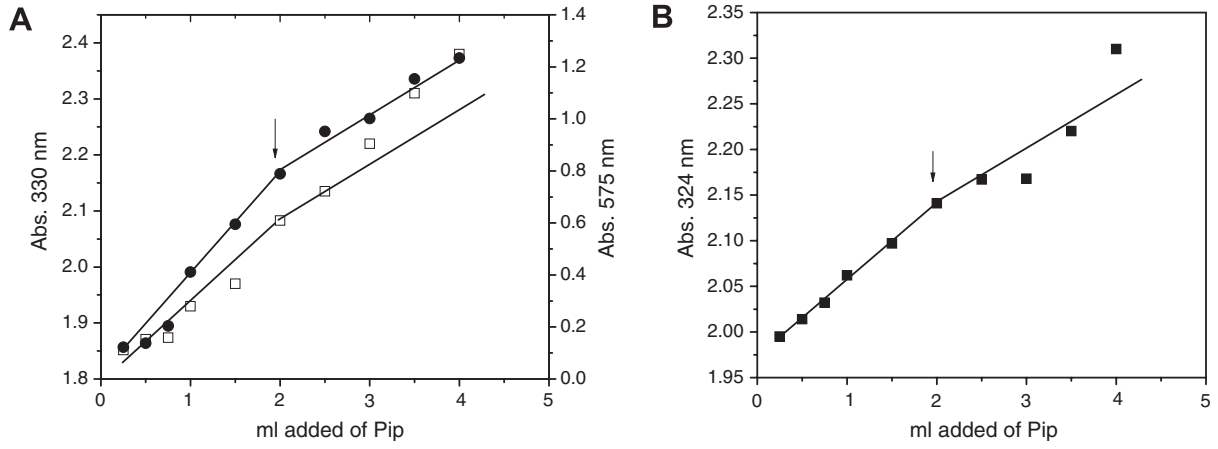


Fig. 2. Photometric titration curves for (A) the Pip–CHL system in $CHCl_3$ at 330 and 575 nm, and (B) the Pip–TCNQ system in $CHCl_3$ at 324 nm.

where C_A^{02} and are the initial concentration of the π-acceptor and donor (Pip), respectively, and A is the absorbance of the detected CT-band. By plotting $(C_A^{02} \cdot C_D^0)/A$ values versus $C_A^0(4C_D^0 + C_A^0)$, straight lines were obtained with a slope of $1/\varepsilon$ and an intercept of $1/K\varepsilon$, as shown in Fig. 3A and B for the reaction mixtures in $CHCl_3$. The values of both K and ε associated with these complexes, [(Pip)$_2$(CHL)] and [(Pip)$_2$(TCNQ)], are given in Table 1. The oscillator strength (f), which is a dimensionless quantity used to express the transition probability of the CT band [27], and the transition dipole moment (μ) of the CT-complexes [28], Table 1, have been calculated from Eqs. (2) and (3), respectively [29]. The high values of both the formation constant (K) and extinction coefficient (ε) of the resultant CT complexes caused high stabilities of the formed CT complexes to be expected as a result of the expected high donation of the Pip nucleus.

The dissociation energy (W) of the Pip/CHL CT-complex system can be calculated by applying Eq. (4), and this value is 4.13 eV. The ionization potential (I_p) of the free donor of the highest filled molecular orbital on the donor was determined from the CT energies of the CT band of its complexes with CHL and TCNQ using Eqs. (5)–(7) [30–32]:

$$f = (4.319 \times 10^{-9})\,\varepsilon_{max} \cdot \nu_{1/2} \quad (2)$$

$$\mu = 0.0958[\varepsilon_{max}\nu_{1/2}/\nu_{max}]1/2 \quad (3)$$

$$E_{CT} = I_p - E_A - W \quad (4)$$

$$I_p\ (\text{eV}) = 5.00 + 1.53 \times 10^{-4}\nu\text{CHL}\ (\text{cm}^{-1}) \quad (5)$$

$$I_p\ (\text{eV}) = a + b(h\nu_{max}) \quad (6)$$

where $h\nu_{max}$ is the lowest n–π^* transition energy in electron volts; a and b are 5.11 and 0.701 [32], respectively.

$$E_{CT} = 1243.667/\lambda_{CT}\ (\text{nm}) \quad (7)$$

where λ_{CT} is the wavelength of the complexation band.

3.2. Infrared spectra of the [(Pip)$_2$(CHL)] and [(Pip)$_2$(TCNQ)] solid complexes

The band assignments of the infrared spectra of the reactants CHL, TCNQ and the reaction products [(Pip)$_2$(CHL)] and [(Pip)$_2$(TCNQ)] are presented in Table 2.

The resultant charge transfer complexes produced from the interaction of Pip with CHL and TCNQ contain the characteristic bands of the Pip donor and acceptors (CHL and TCNQ) with an observed shift in the frequencies (Table 2), as well as some change in the band intensities. This could be assigned to the expected symmetry and electronic structure changes upon the formation of the CT-complexes. The infrared interpretation for the CT-complexes was dealt with as follows;

(i) In the case of the [(Pip)$_2$(CHL)] CT-complex: the vibration frequency of the ν(N–H) group for Pip, observed at 3393 cm^{-1}, is shifted to 3424 cm^{-1} in the IR spectrum of the Pip/CHL complex; this new band has a strong broad intensity for the (2Pip–H_2CHL) charge transfer complex. The assignment of this band is, interestingly, due to the ν(O–H) stretching vibration of the hydrogen of donor against the oxygen of the two carbonyl groups of the acceptor. The group of bands at 2948, 2840, 2808 and 2737 cm^{-1}

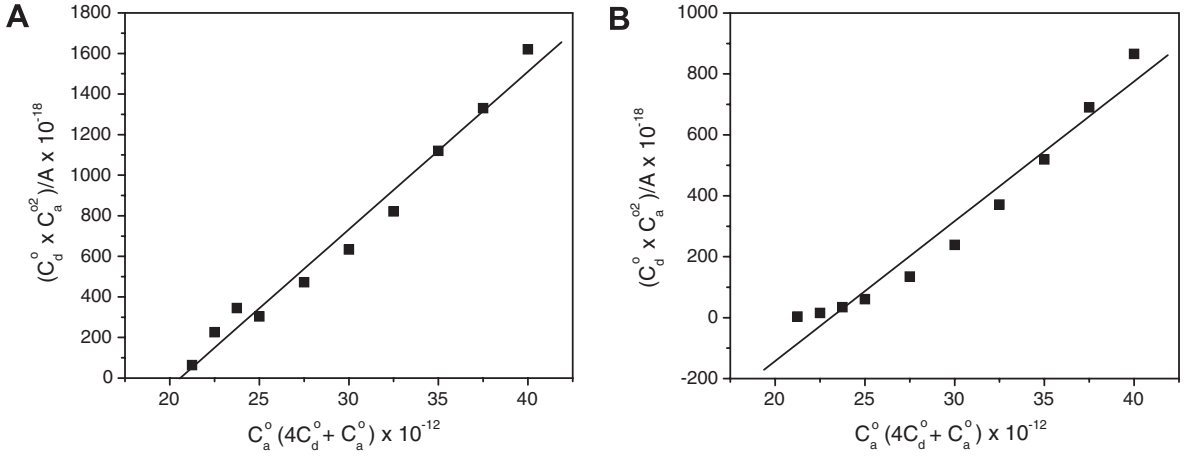


Fig. 3. The plot of $C_A^0(4C_D^0 + C_A^0)$ against $C_D^0 \cdot C_A^{02}/A$, for the (A) [(Pip)$_2$(CHL)] and (B) [(Pip)$_2$(TCNQ)] CT-complexes at 575 and 324 nm, respectively.

Table 1
Spectrophotometric results of the CT-complexes of (A) [(Pip)$_2$(CHL)] and (B) [(Pip)$_2$(TCNQ)] CT-complexes

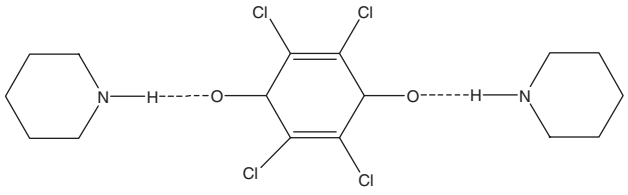
Solvent	λ_{max} (nm)	E_{CT} (eV)	K (l mol^{-1})	ε_{max} (l mol^{-1} cm^{-1})	f	μ	I_p
A	575	2.16	4.86×10^{10}	1.29×10^4	4.46	23.30	7.66
B	324	3.84	4.33×10^{10}	2.18×10^4	22.60	39.40	7.80
Average							7.73

Table 2
Infrared frequencies[a] (cm^{-1}) and tentative assignments for CHL, TCNQ, [$(Pip)_2$(CHL)] and 7,7-dicyano-8,8-di-piperidinoquinodimethane compounds

CHL	TCNQ	[$(Pip)_2$(acceptor)] CT-complexes		Assignments[b]
		CHL	TCNQ	
3354 ms	3405 br	3424 s, br	3443 w, br 3394 w	$\nu_{(O-H)}$; H_2O of KBr
	3137 mw	3184 vw	3023 ms	$\nu_{s(C-H)} + \nu_{as(C-H)}$
	3050 s	2948 vs	2931 s	
	2969 mw	2840 s	2896 ms	
	2851 mw	2808 s	2858 ms	
		2737 s		
		2629 s		hydrogen bonding
		2519 s		
		2421 s		
	2220 s		2120 vs 2132 vs	$\nu_{(C\equiv N)}$; TCNQ
1685 vs		1648 s		$\nu_{(C=O)}$
1567 vs 1487 w	1540 vs	1554 vs 1457 s 1440 s	1595 vs 1568 vs 1471 vs 1443 s	$\nu_{(C=C)}$ + C–H deformation
1316 w	1352 ms	1398 ms	1366 mw	$\nu_{(C-C)} + \nu_{(C-N)}$
1257 s	1285 vw	1359 ms	1305 vs	CH, in-plane bend
1232 s	1205 vw	1280 mw	1266 s	
1210 vw	1117 ms	1237 s	1174 s	
1110 vs	1044 vw	1194 s	1014 s	
		1155 ms		
		1110 ms		
		1079 mw		
		1028 s		
903 s	997 vw	978 ms	952 mw	δ_{rock}; NH
750 s	962 vw	946 ms	908 ms	CH-deformation
709 s		911 w		$\nu_{(C-Cl)}$; CHL
	860 vs	878 w	830 vs	skeletal vibration
	808 vw	850 w		CH bend
		724 ms		
471 mw	473 vs	556 ms	512 ms	CH out of plane bend
		530 w	470 mw	skeletal vibration
		438 ms	448 ms	CNC def.
			424 ms	

[a] s = strong, w = weak, m = medium, sh = shoulder, v = very, br = broad.
[b] ν, stretching; δ, bending.

in this complex were assigned to ν_s(C–H) + ν_{as}(C–H) vibrations, with the same positional wavenumbers as compared with free Pip. The spectrum of the [$(Pip)_2$(CHL)] CT-complex includes a few medium strong absorption bands located at 2629, 2519 and 2421 cm^{-1}, which could be assigned to hydrogen bonding [33]. The stretching vibration of the ν(C=O) absorption band in the case of free CHL appears at 1685 cm^{-1}, but under complexation this band was shifted to a lower value (1648 cm^{-1}). Doubtless, the IR spectra strongly supported that the CT-interaction in the case of the Pip/CHL complex take place through a n–π^* transition (Scheme 1). Evidently, in the spectrum of the [$(Pip)_2$(CHL)] complex, the vibrations group of δ(N–H), ν(C–N) and CNC deformation clearly show changes compared with those of free Pip, Table 2. The bands associated with the ν(C–Cl) vibration that appeared at 903, 750 and 709 cm^{-1} in free CHL were shifted to lower wavenumbers, with decreasing intensities of the characteristic peaks. This result is due to the increase in electron density around the CHL moiety, and therefore the charge transfer interaction and deprotonation of the donor upon complexation. This observation proves that the complexation of (Pip) with CHL takes place via the –NH group, with the formation of hydrogen bonding as shown in Scheme 1.



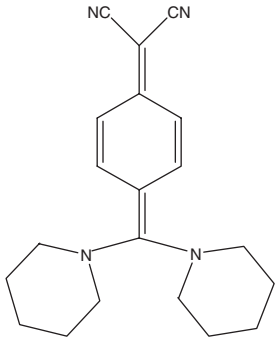
Scheme 1. The structure of the [$(Pip)_2$(CHL)] CT-complex.

(ii) In the case of the [$(Pip)_2$(TCNQ)] CT-complex: the IR spectrum of the solid reaction product 7,7-dicyano-8,8-di-piperidinoquinodimethane contains characteristic bands for both Pip (donor) and TCNQ (acceptor). The CN stretching of TCNQ show a drastic shift to a lower wavenumber. The distinguish stretching vibration, ν(C≡N), of free TCNQ is observed at 2220 cm^{-1} as single peak, but in the case of the Pip/TCNQ complex, after complexation two peaks at 2120 and 2132 cm^{-1} values were

detected, having very strong band intensities. This shift is indicative of higher charge density on the cyano groups of the TCNQ charge transfer complex. On the other hand, the –NH stretching bands of Pip were shifted to higher frequencies in the spectrum of the Pip/TCNQ complex. This is reasonably based on the increasing polarity of the NH band during complexation. The interaction of TCNQ and piperidine causes the formation of a stable adduct which is assigned the structure 7,7-dicyano-8,8-di-piperidinoquinodimethane (Scheme 2) on the basis of spectroscopic investigation and elemental analysis.

3.3. ^1H NMR spectrum of 7,7-dicyano-8,8-di-piperidinoquinodimethane adduct

The ^1H NMR spectrum of the 7,7-dicyano-8,8-di-piperidinoquinodimethane adduct in d_6-DMSO displayed distinct signals with the appropriate multiplets, Fig. 4. The singlet accounting for six protons centered at δ 1.673 ppm (6H; $3 \times CH_2$) is assigned to the protons of three methyl groups of piperidine, and the other singlet peak at δ 2.523 ppm should be due to the hydrogen protons of the two methyl groups attached with the nitrogen atom of the Pip donor (4H; $N(CH_2)_2$). The strong singlet peak at δ 3.365 ppm was ^1H (HDO), which is seen in protic solvents due to exchange with the solvent deuteriums. The aromatic region corresponds to four protons in the TCNQ ring (4H; aromatic TCNQ ring) – doublets centered at δ 6.863, 6.906, 7.294 and 7.336 ppm for the TCNQ ring. Comparison between the free reactants and the new stable adduct reveals that the signal of –NH (2.24 ppm) of the free donor disappeared, this indicates that two of the CN groups of TCNQ participate with two hydrogen atoms of two Pip donors (elimination reaction, −2HCN), Scheme 2.



Scheme 2. The structure of the 7,7-dicyano-8,8-di-piperidinoquinodimethane adduct.

3.4. Crystal structure of the 7,7-dicyano-8,8-di-piperidinoquinodimethane adduct

The asymmetric unit of the 7,7-dicyano-8,8-di-piperidinoquinodimethane adduct is composed of two crystallographic independent $[(pip)_2TCNQ]_2$ units, as shown in Fig. 5. The piperidine rings of each of the two independent molecules exhibit a chair conformation, while the TCNQ fragment is nearly planar (Fig. 5), with deviations from the mean planes of 0.025 Å for the CN groups (molecule A), and 0.0015 Å for the CN groups (molecule B). The dihedral angles between the mean planes of the piperidine rings is 75.8(3)° in molecule A and 76.4(3)° in molecule B and between the piperidine and TCNQ fragments 45.4(2)° and 48.4(2)° in molecule A and 43.4(2)° and 53.0(2)° in molecule B (see Fig. 6).

3.5. Thermal investigations of the $[(Pip)_2(TCNQ)]$ and 7,7-dicyano-8,8-di-piperidinoquinodimethane adducts

Thermal analysis (TGA and DTG) play an important role to study the physicochemical behaviors and the stability of the CT complexes. Thermal data of the complexes are given in Table 3.

The thermal analysis curve of the Pip/CHL CT complex, of the general formula $[(Pip)_2(CHL)]$, is shown in Fig. 7. It gives a pattern of four maximum stages of decomposition supported by DTG data (Table 3). The first step in the decomposition is from 25 to 175 °C, with a maximum peak at (158 °C) and corresponds to the decomposition of one HCl molecule from a CHL molecule, with an estimated mass loss of 8.35% (calc. mass loss 8.77%), while the subsequent second step is from 175 °C to 242 °C at $DTG_{max} = 214$ °C and is accompanied by the loss of

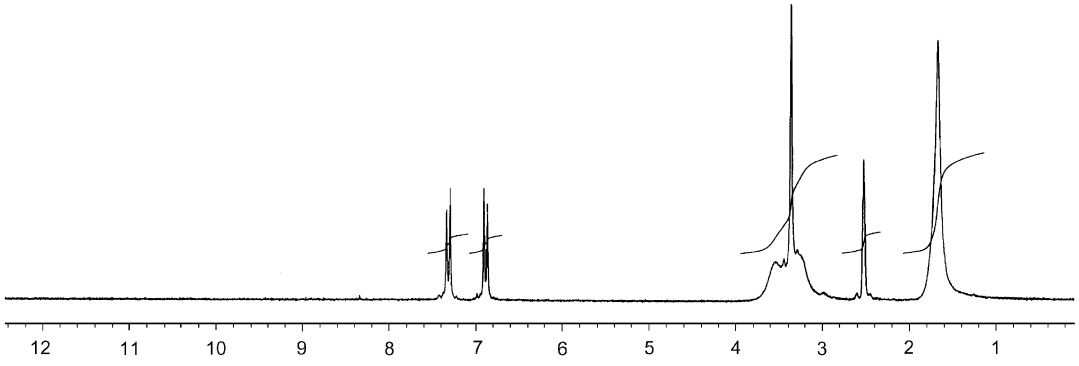


Fig. 4. ^1H NMR spectra of the 7,7-dicyano-8,8-di-piperidinoquinodimethane adduct.

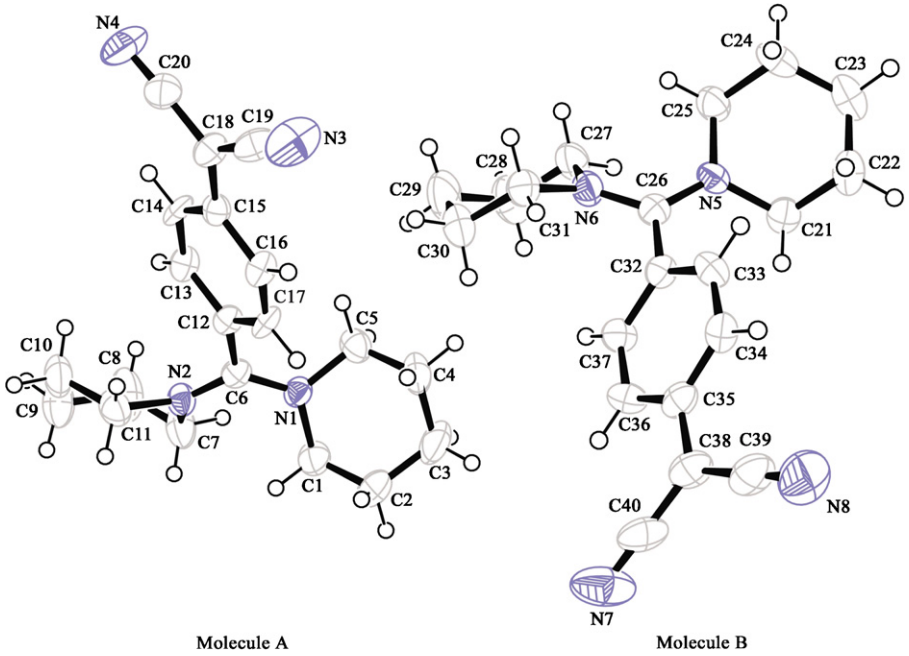


Fig. 5. ORTEP III view of the 7,7-dicyano-8,8-di-piperidinoquinodimethane adduct with the atom numbering scheme (50% probability ellipsoids).

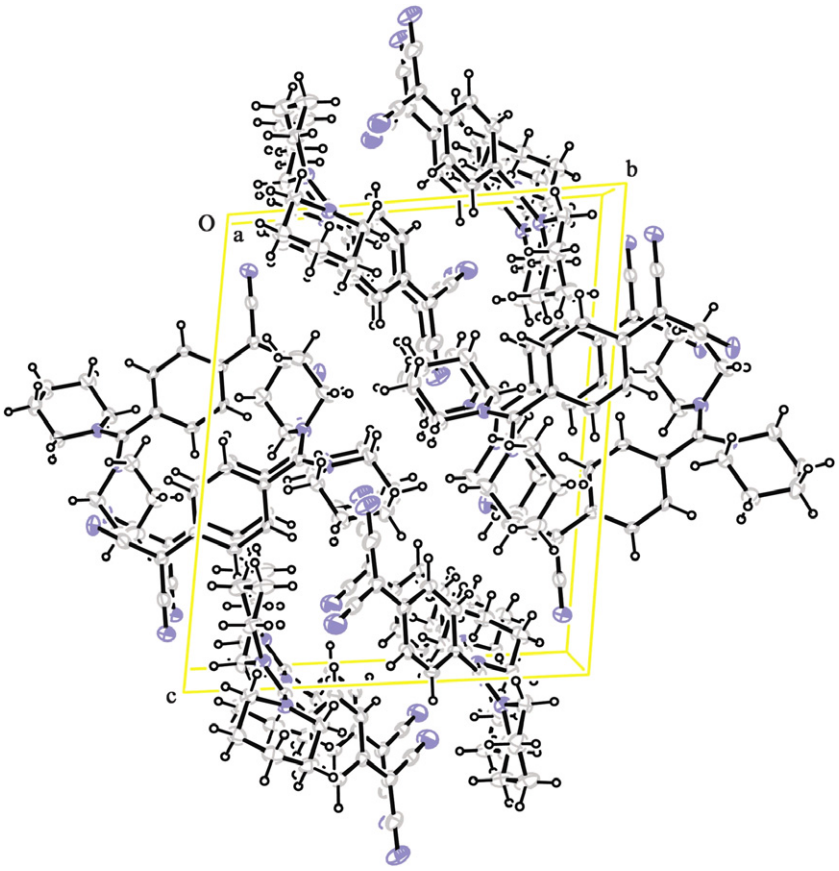


Fig. 6. Crystal packing of the 7,7-dicyano-8,8-di-piperidinoquinodimethane adduct.

2HCl molecules with a weight loss 16.70% (calc. 17.50%). The third and fourth stages are in the range 242–600 °C, with maximum peaks at 283 and 581 °C, respectively, and involve the loss of $HCl + C_6H_{18}N_2O_2$, leaving ten carbon atoms as a residue resulting from the process of decomposition under nitrogen. The remains of 10 carbon atoms

Table 3
Thermo analytical results for the (A) $[(Pip)_2(CHL)]$ and (B) 7,7-dicyano-8,8-di-piperidinoquinodimethane compounds

Samples	Stage	TGA range (°C)	DTG_{max} (°C)	Weight loss (%)		Evolved moiety
				Found	Calc.	
A	I	25–175	158	8.35	8.77	HCl
	175–242	214	16.70	17.50	2HCl	
	242–600	283, 581	46.70	44.90	$HCl + C_6H_{18}N_2O_2$	
	residue					10C
B	I	30–600	376	58.10	58.80	$C_9H_{24}N_4$
	residue					11C

confirm that the interaction between donor:acceptor occurs in a 2:1 molar ratio, in agreement with that obtained from the elemental analysis, this fact proves that the Pip/CHL complex contain two piperidine moieties. The overall weight loss amounts to 71.76% (calc. 71.20%).

Interestingly, Fig. 8, the thermogravimetric curve (TGA) of the new adduct, 7,7-dicyano-8,8-di-piperidinoquinodimethane, formed from the elimination reaction between two molecules of Pip and the powerful acceptor TCNQ has only one maximum peak at 376 °C, this result proves that the formed compound is a new organic compound that has only one sharp melting point. The thermograms of the Pip/TCNQ adduct shows one decomposition step within the temperature range 30–600 °C which corresponds to the loss of the $C_9H_{24}N_4$ organic moiety with a mass loss of 58.10% (calc. 58.80%).

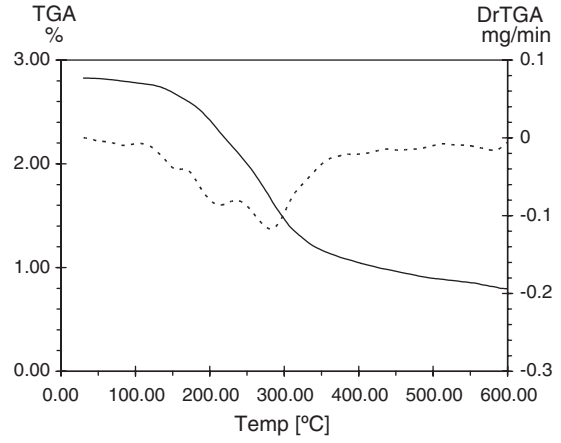


Fig. 7. TGA/DTG thermal diagram of the $[(Pip)_2(CHL)]$ CT complex.

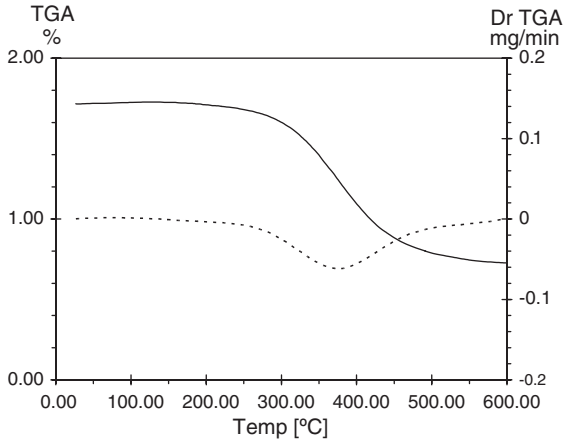


Fig. 8. TGA/DTG thermal diagram of the 7,7-dicyano-8,8-di-piperidinoquinodimethane adduct.

3.6. Kinetic studies of the $[(Pip)_2(TCNQ)]$ and 7,7-dicyano-8,8-di-piperidinoquinodimethane adducts

In recent years there has been increasing interest in determining the rate dependent parameters of solid-state non-isothermal decomposition reactions by analysis of TG curves. Several equations [34–41] have been proposed as a means of analyzing a TG curve and obtaining values for kinetic parameters. Many authors [34–38] have discussed the advantages of this method over the conventional isothermal method. The rate of a decomposition process can be described as the product of two separate functions of temperature and conversion [35], using

$$d\alpha/dt = k(T)f(\alpha) \tag{8}$$

where α is the fraction decomposed at time t, $k(T)$ is the temperature dependent function and $f(\alpha)$ is the conversion function dependent on the mechanism of decomposition. It has been established that the temperature dependent function $k(T)$ is of the Arrhenius type and can be considered as the rate constant k.

$$k = Ae^{-E*/RT} \tag{9}$$

where, R is the gas constant in (J mol^{-1} K^{-1}). Substituting Eq. (9) into Eq. (8), we get,

$$d\alpha/dT = (A/\phi e^{-E*/RT})f(\alpha) \tag{10}$$

where ϕ is the linear heating rate dT/dt. On integration and approximation, this equation can be obtained in the following form

$$\ln g(\alpha) = -E^*/RT + \ln[AR/\phi E^*] \tag{11}$$

where $g(\alpha)$ is a function of α, dependent on the mechanism of the reaction. The integral on the right-hand side is known as the temperature integral and has no closed solution. So, several techniques have been used for the evaluation of the temperature integral. Most commonly used methods for this purpose are the differential method of

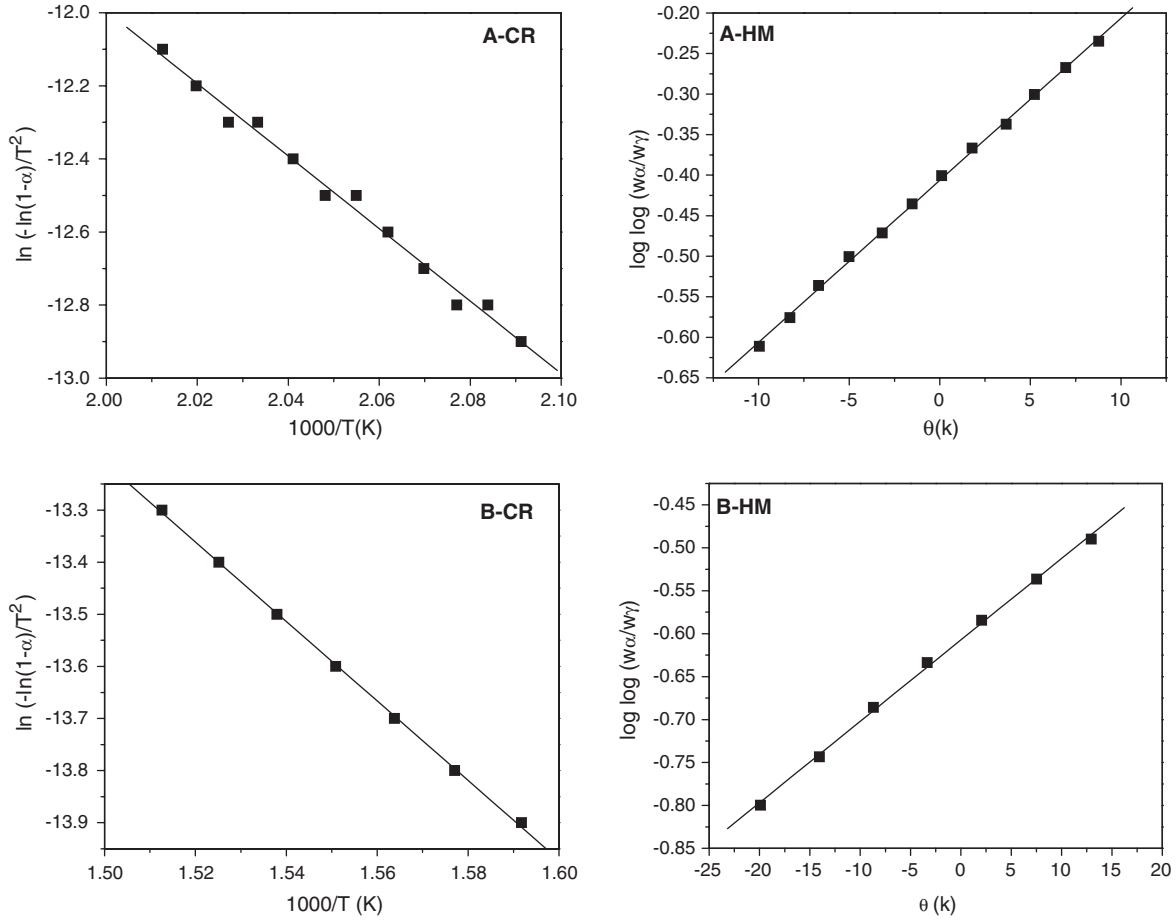


Fig. 9. Kinetic diagrams of the Coats–Redfern (CR) and Horowitz–Metzger (HM) equations for (a) the [(Pip)$_2$(CHL)] and (b) the 7,7-dicyano-8,8-dipiperidinoquinodimethane compounds.

Table 4
Kinetic data of the (A) [(Pip)$_2$(CHL)] and (B) 7,7-dicyano-8,8-dipiperidinoquinodimethane compounds for the essential stage

Compounds	Parameters[a]	From Coats–Redfern equation	From Horowitz–Metzger equation
A	E	8.25×10^{4}	9.12×10^{4}
	A	6.36×10^{6}	6.62×10^{7}
	ΔS	-1.19×10^{2}	-9.93×10^{1}
	ΔH	7.84×10^{4}	8.72×10^{4}
	ΔG	1.36×10^{5}	1.36×10^{5}
	r	0.9948	0.9995
B	E	6.34×10^{4}	7.63×10^{4}
	A	1.12×10^{4}	7.63×10^{3}
	ΔS	-1.74×10^{2}	-1.77×10^{2}
	ΔH	5.80×10^{4}	7.09×10^{4}
	ΔG	1.71×10^{5}	1.86×10^{5}
		0.9997	0.9993

[a] Units of parameters: E in kJ mol^{-1}, A in s^{-1}, ΔS in J mol^{-1} k^{-1}, ΔH and ΔG in kJ mol^{-1}.

Freeman and Carroll [34], the integral method of Coat and Redfern [36] and the approximation method of Horowitz and Metzger [39].

In the present investigation the general thermal behaviors of the two Pip CT complexes in terms of stability ranges, peak temperatures and values of kinetic parameters, are shown in Fig. 9 and Table 4. The kinetic parameters have been evaluated using the following methods and the results obtained by these methods are compared with one another. The following two methods are discussed briefly.

3.6.1. Coats–Redfern equation

The Coats–Redfern Eq. (12), which is a typical integral method, can be represented as

$$\int_0^{\alpha}\frac{d\alpha}{(1-\alpha)^n}=\frac{A}{\varphi}\int_{T_1}^{T_2}\exp\left(\frac{-E^*}{RT}\right)dt \tag{12}$$

For convenience of integration, the lower limit T_1 is usually taken as zero. This equation on integration gives

$$\ln[-\ln(1-\alpha)/T^2]=-E^*/RT+\ln[AR/\varphi E^*] \tag{13}$$

A plot of the left-hand side (LHS) against $1/T$ was drawn. E^* is the energy of activation in kJ mol^{-1} and is calculated from the slope, and A in (s^{-1}) is obtained from the intercept value. The entropy of activation ΔS^* in (J K^{-1} mol^{-1}) was calculated using

$$\Delta S^*=R\ln(Ah/k_BT_s) \tag{14}$$

where k_B is the Boltzmann constant, h is Plank's constant and T_s is the DTG peak temperature [42].

3.6.2. Horowitz–Metzger equation

The Horowitz–Metzger equation is illustrative of the approximation methods. These authors derived the relation:

$$\log[\{1-(1-\alpha)^{1-n}\}/(1-n)] = E^*\theta/2.303RT_s^2 \quad \text{for} \quad n \neq 1 \tag{15}$$

when $n = 1$, the LHS of Eq. (14) would be $\log[-\log(1-\alpha)]$. For a first-order kinetic process the Horowitz–Metzger Eq. (16) may be written in the form:

$$\log[\log(w_\alpha/w_\gamma)] = E^*\theta/2.303RT_s^2 - \log 2.303 \tag{16}$$

where $\theta = T - T_s$, $w_\gamma = w_\alpha - w$, $w_\alpha =$ mass loss at completion of the reaction; $w =$ mass loss up to time t. A plot of $\log[\log(w_\alpha/w_\gamma)]$ versus θ was drawn and found to be linear from the slope, from which E^* was calculated. The pre-exponential factor, A, was calculated from:

$$E^*/RT_s^2 = A/[\varphi \exp(-E^*/RT_s)] \tag{17}$$

The enthalpy activation, ΔH^*, and Gibbs free energy, ΔG^*, were calculated from:

$$\Delta H^* = E^* - RT \tag{18}$$

$$\text{and}\Delta G^* = \Delta H^* - T\Delta S^* \tag{19}$$

The kinetic parameters E^*, ΔH^*, ΔS^* and ΔG^* calculated with the Coats–Redfern and Horowitz–Metzger equations are tabulated in Table 4. Taking the main decomposition steps as a criterion, the values of the activation entropies, $-\Delta S^*$ in these two compounds indicate that the activated complexes have a more ordered structure than the reactants, this deduced the formation of the Pip CT complexes.

4. Supplementary material

CCDC 648793 contains the supplementary crystallographic data for [$(Pip)_2$(TCNQ)]. These data can be obtained free of charge via http://www.ccdc.cam.ac.uk/conts/retrieving.html, or from the Cambridge Crystallographic Data Centre, 12 Union Road, Cambridge CB2 1EZ, UK; fax: (+44) 1223-336-033; or e-mail:deposit@ccdc.cam.ac.uk.

References

[1] F.P. Fla, J. Palou, R. Valero, C.D. Hall, P. Speers, JCS Perkin Trans. 2 (1991) 1925.
[2] T. Roy, K. Dutta, M.K. Nayek, A.K. Mukherjee, M. Banerjee, B.K. Seal, JCS Perkin Trans. 2 (2000) 531.
[3] F. Yakuphanoglu, M. Arslan, Opt. Mater. 27 (2004) 29.
[4] F. Yakuphanoglu, M. Arslan, Solid State Commun. 132 (2004) 229.
[5] F. Yakuphanoglu, M. Arslan, M. Kucukislamoglu, M. Zengin, Sol. Energy 79 (2005) 96.
[6] B. Chakraborty, A.S. Mukherjee, B.K. Seal, Spectrochim. Acta Part A 57 (2001) 223.
[7] A. Korolkovas, Essentials of Medical Chem, 2nd ed., Wiley, New York, 1998 (Chapter 3).
[8] K. Takahasi, K. Horino, T. Komura, K. Murata, Bull. Chem. Soc. Jpn. 66 (1993) 733.
[9] S.M. Andrade, S.M.B. Costa, R. Pansu, J. Colloid Interf. Sci. 226 (2000) 260.
[10] A.M. Slifkin, Charge-Transfer Interaction of Biomolecules, Academic Press, New York, 1971.
[11] F.M. Abou Attia, Farmaco 55 (2000) 659.
[12] K. Basavaiah, Farmaco 59 (2004) 315.
[13] T. Fukunaga, H. Ishida, Acta Crystallogr., Sect. E 59 (11) (2003) 1793.
[14] N.I. Abdel Sayed, K. El Badry, H.M. Abdel Mohsen, J. Chin. Chem. Soc. 50 (2) (2003) 193.
[15] N.G. Kandile, T.M.A. Latif, J. Chem. Soc. Pak. 10 (3) (1988) 333.
[16] U. Muralikrishna, Y.V.S.K. Seshasayi, M. Krishnamurthy, National Acad. Sci. Lett. (India) 6 (11) (1983) 383.
[17] S.K. Das, G. Krishnamoorthy, S.K. Dofra, Can. J. Chem. 78 (2000) 191.
[18] G. Jones, J.A.C. Jimenez, Tetrahedron Lett. 40 (1999) 8551.
[19] G. Smith, R.C. Bott, A.D. Rae, A.C. Willis, Aust. J. Chem. 53 (2000) 531.
[20] G. Smith, D.E. Lynch, R.C. Bott, Aust. J. Chem. 51 (1998) 159.
[21] G. Smith, D.E. Lynch, K.A. Byriel, C.H.L. Kennard, J. Chem. Crystallogr. 27 (1997) 307.
[22] A. Altomare, M.C. Burla, M. Camalli, G.L. Cascarano, C. Giacovazzo, A. Guagliardi, A.G.G. Moliterni, G. Polidori, R. Spagna, J. Appl. Cryst. 32 (1999) 115.
[23] G.M. Sheldrick, SHELXL-97, University of Göttingen, Germany, 1997.
[24] M.N. Burnett, C.K. Johnson, ORTEPIII. Report ORNL-6895. OAK Ridge National Laboratory, TN, USA, 1996.
[25] D.A. Skoog, Principle of Instrumental Analysis, 3rd ed., Saunders College Publishing, New York, USA, 1985 (Chapter 7).
[26] A. El-Kourashy, Spectrochim. Acta 37A (1981) 399.
[27] A.B.P. Lever, Inorganic Electronic Spectroscopy, 2nd ed., Elsevier, Amsterdam, 1985, p. 161.
[28] H. Tsubomura, R.P. Lang, J. Am. Chem. Soc. 86 (1964) 3930.
[29] R. Rathone, S.V. Lindeman, J.K. Kochi, J. Am. Chem. Soc. 119 (1997) 9393.
[30] G.G. Aloisi, S. Pignataro, J. Chem. Soc., Faraday Trans. 69 (1973) 534.
[31] R. Foster, Organic Charge Transfer Complexes, Academic Press, London, 1969;
M. Kinoshita, Bull. Chem. Soc. Jpn. 1609 (1962).
[32] D.C. Wheat, Hand Book of Chemistry and Physics, 50th ed., 1969–1970.
[33] L.J. Bellamy, The Infrared Spectra of Complex Molecules, Chapman & Hall, London, 1975.
[34] E.S. Freeman, B. Carroll, J. Phys. Chem. 62 (1958) 394.
[35] J. Sestak, V. Satava, W.W. Wendlandt, Thermochim. Acta 7 (1973) 333.
[36] A.W. Coats, J.P. Redfern, Nature 201 (1964) 68.
[37] T. Ozawa, Bull. Chem. Sot. Jpn. 38 (1965) 1881.
[38] W.W. Wendlandt, Thermal Methods of Analysis, Wiley, New York, 1974.
[39] H.W. Horowitz, G. Metzger, Anal. Chem. 35 (1963) 1464.
[40] J.H. Flynn, L.A. Wall, Polym. Lett. 4 (1966) 323.
[41] P. Kofstad, Nature 179 (1957) 1362.
[42] J.H.F. Flynn, L.A. Wall, J. Res. Natl. Bur. Stand. 70A (1996) 487.

Available online at www.sciencedirect.com
ScienceDirect
Polyhedron 27 (2008) 485–492
POLYHEDRON
www.elsevier.com/locate/poly

Selenated Schiff bases of 2-hydroxyacetophenone and their palladium(II) and platinum(II) complexes: Syntheses, crystal structures and applications in the Heck reaction

Arun Kumar, Monika Agarwal, Ajai K. Singh *

Department of Chemistry, Indian Institute of Technology, New Delhi 110 016, India

Received 20 August 2007; accepted 13 September 2007
Available online 14 November 2007

Abstract

Selenated Schiff bases 2-HO-$C_6H_4C(CH_3)$=$N(CH_2)_n$SePh ($n = 2$, $\mathbf{L}^1$; $n = 3$, $\mathbf{L}^2$) and their complexes with Pd(II) and Pt(II), viz [Pd($\mathbf{L}^1$–H)Cl] (**1**), [Pt($\mathbf{L}^1$–H)Cl] (**2**), [Pd($\mathbf{L}^2$–H)Cl] (**3**) and [Pt$\mathbf{L}^2Cl_2$] (**4**), have been synthesized and characterized with proton, carbon-13 and ^{77}Se{^{1}H} NMR spectra. In the ^{77}Se{^{1}H} NMR spectrum of **2** the signal at δ 387.4 ppm appears as a triplet due to $^1J(^{195}Pt–Se)$ coupling (2043 Hz). The single-crystal structures of $\mathbf{L}^1$, $\mathbf{L}^2$, **1** and **2** were solved. The C–Se–C bond angles in $\mathbf{L}^1$ and $\mathbf{L}^2$ have been found to be around 99°. The geometry around Pd and Pt is square planar. The Pd–Se and Pt–Se bond distances are 2.3669(11) and 2.3543(16) Å, respectively. Complexes **1** and **2** are the first examples of crystal structures of Pd and Pt complexes of a (Se, N, O^-) ligand. Complex **1** has been explored as a homogeneous catalyst for a Heck type C–C coupling reaction between methyl acrylate and *p*-iodonitrobenzene (yield ~80%; reaction time 14 h).
© 2007 Elsevier Ltd. All rights reserved.

Keywords: Selenated Schiff base; Selenium ligand; Palladium; Platinum; Complex synthesis; Single-crystal structure; X-ray diffraction; Heck reaction; Catalysis

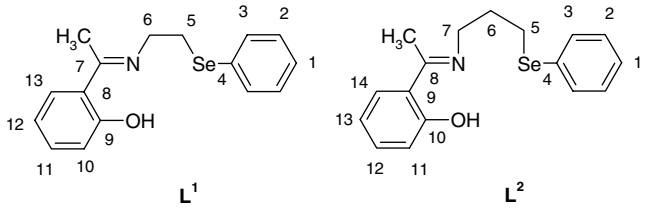
1. Introduction

Schiff bases constitute an important class of ligands, which have very rich and extensive chemistry, reviewed recently by Vigato and Tamburini [1]. Metal complexes of Schiff bases have found diverse applications in addition to interesting structural chemistry. Ruthenium complexes containing bidentate Schiff bases have been used [2] in catalyzing Kharasch addition, enol-ester synthesis, alkyne dimerization, olefin metathesis and atom transfer radical polymerization. Metal complexes of chiral binaphthyl Schiff bases have been used for stereoselective organic transformations [3]. Oxovanadium(III–V) complexes of tetradentate Schiff bases have the potential for multi-electron redox catalysis [4]. Metal complexes containing Schiff-base ligands have also been found to show mesomorphic behaviour [5]. Among Schiff bases, 'Salen' and related derivatives have been found to be very interesting. Their complexes with transition metals are suitable catalysts for epoxidation reactions [6–10] and a variety of other reactions like dehydrogenation plus intramolecular Diels-Alder cycloaddition [11], enantioselective conjugate addition [12] and ring opening polymerization [13]. However, selenated Schiff bases of mono ketones or aldehydes have not been studied in detail so far and recently we have reported such tellurated derivatives [14,15]. The presence of Se as a donor site in Schiff bases may modify significantly their known catalytic roles. Therefore, such systems are worth exploring. A wide range of selenated Schiff-base ligands may be designed by the reaction of a selenated amine with different aldehydes or ketones. To use this strategy we have made

* Corresponding author. Tel.: +91 011 26591379; fax: +91 011 26862037.
E-mail addresses: aksingh@chemistry.iitd.ac.in, ajai57@hotmail.com (A.K. Singh).

0277-5387/$ - see front matter © 2007 Elsevier Ltd. All rights reserved.
doi:10.1016/j.poly.2007.09.027

$NH_2CH_2CH_2SePh$ and $NH_2CH_2CH_2CH_2SePh$ [3], which have been used for designing selenated Schiff bases. Thus $\mathbf{L}^1$ and $\mathbf{L}^2$ and their complexes with Pd(II) and Pd(II), in which a metal–selenium bond is formed, have been synthesized. Selenium being a very "soft" donor in nature does not coordinate with 3-d transition metal ions in their common oxidation states. The ligands $\mathbf{L}^1$ and $\mathbf{L}^2$ and their complexes were characterized by NMR spectroscopy (including $^{77}Se\{^1H\}$) and X-ray diffraction studies, when single crystals were obtained. The results of these investigations are reported in this paper. The catalytic activity of the selenide–Pd(II) complexes not only rivals but may outperform that of the corresponding phosphorus and sulfur analogues [16,17]. Practical advantages of the selenium-based catalysts for the Heck reaction have been reported as their straightforward synthesis and high activity in the absence of any additives as well as the enhanced stability of the selenide ligands toward air oxidation [17]. Therefore, **1** was thought to be a good candidate for exploring for the Heck reaction. Preliminary results of these explorations are also reported in this paper.



2. Experimental

The C and H analyses were carried out with a Perkin–Elmer 2400 Series II C, H, N analyzer. The ^1H, $^{13}C\{^1H\}$ and $^{77}Se\{^1H\}$ NMR spectra were recorded on a Bruker Spectrospin DPX-300 NMR spectrometer at 300.13, 75.47 and 57.24 MHz, respectively. IR spectra in the range 4000–250 cm^{-1} were recorded on a Nicolet Protége 460 FT-IR spectrometer as KBr pellets. The melting points determined in open capillary are reported as such. The conductivity measurements were carried out in CH_3CN (concentration ca 1 mM) using an ORION conductivity meter model 162.

Single-crystal diffraction studies were carried out with a Bruker AXS SMART Apex CCD diffractometer using Mo Kα (0.71073 Å) radiation at 298(2) K. The software SADABS was used for absorption correction (if needed) and SHELXTL for space group, structure determination and refinements [18a,18b]. All non-hydrogen atoms were refined anisotropically. Hydrogen atoms were included in idealized positions with isotropic thermal parameters set at 1.2 times that of the carbon atom to which they are attached. The least-squares refinement cycles on F^2 were performed until the model converged.

2-(Phenylseleno)ethylamine [19] and 3-(phenylseleno)-propylamine [19] were prepared by the reported methods [$^{77}Se\{^1H\}$ NMR (vs Me_2Se, 25 °C) δ, ppm: 256.6 and 257.5, respectively].

2.1. Synthesis of L^1

2-(Phenylseleno)ethylamine (1.00 g, 5.0 mmol) was stirred in dry ethanol (20 mL) at room temperature for 0.5 h. *o*-Hydroxyacetophenone (0.68 g, 5.0 mmol), dissolved in dry ethanol (20 mL), was mixed dropwise with stirring. The mixture was stirred further at room temperature for 2 h. The solvent was evaporated on a rotary evaporator which resulted in a yellow precipitate. The precipitate on recrystallization from chloroform–hexane (1:1) gave yellow coloured single-crystals of $\mathbf{L}^1$. Yield 1.43 g (~90%); m.p. 84–85 °C. $\Lambda_M = 0.88\ cm^2\ mol^{-1}\ \Omega^{-1}$. *Anal.* Calc. for $C_{16}H_{17}NOSe$: C, 60.33; H, 5.34; N, 4.39. Found: C, 60.46; H, 5.28; N, 4.46%. NMR (^1H, $CDCl_3$, 25 °C, vs $SiMe_4$) δ, ppm: 2.25 (s, 3H, CH_3), 3.22 (t, $J = 6.9$ Hz, 2H, $SeCH_2$), 3.81 (t, $J = 6.9$ Hz, 2H, H_6), 6.78 (t, $J = 7.2$ Hz, 1H, H_{12}), 6.94 (d, $J = 8.4$ Hz, 1H, H_{13}), 7.25–7.30, (m, 4H, H_2, H_1 and H_{11}), 7.49 (d, $J = 8.4$ Hz, 1H, H_{10}), 7.52–7.55 (m, 2H, H_3), 15.93 (bs, 1H, OH) ($^{13}C\{^1H\}$, $CDCl_3$, 25 °C vs $SiMe_4$) δ, ppm: 14.6 (CH_3), 27.8 ($SeCH_2$), 49.4 (C_6), 117.2 (C_{10}), 118.5 (C_{12}), 119.3 (C_8), 127.2 (C_1), 128.0 (C_{13}), 129.1 (C_2), 129.2 (C_4), 132.4 (C_{11}), 133.0 (C_3), 163.2 (C_9), 171.8 (C_7) ($^{77}Se\{^1H\}$, $CDCl_3$, 25 °C vs Me_2Se) δ, ppm: 282.3. IR (KBr, cm^{-1}): 3484, 1607, 470, 734.

2.2. Synthesis of L^2

3-(Phenylseleno)propylamine (1.07 g, 5.0 mmol) was stirred in dry ethanol (20 mL) at room temperature for 0.5 h. *o*-Hydroxyacetophenone (0.68 g, 5.0 mmol), also dissolved in dry ethanol (20 mL), was added to it dropwise with stirring. The mixture was stirred further at room temperature for 2 h. On evaporating the solvent on a rotary evaporator a yellow precipitate of $\mathbf{L}^2$ was obtained, which on recrystallization from a chloroform–hexane mixture (1:1) afforded yellow single-crystals of $\mathbf{L}^2$. Yield 1.49 g (~90%); m.p. 82–83 °C. *Anal.* Calc. for $C_{17}H_{19}NOSe$: C, 61.40; H, 5.71; N, 4.21. Found: C, 61.45; H, 5.73; N, 4.28%. NMR (^1H $CDCl_3$, 25 °C, vs $SiMe_4$) δ, ppm: 2.15 (quintet, $J = 6.6$ Hz, 2H, H_6), 2.29 (s, 3H, CH_3), 3.06 (t, $J = 6.9$ Hz, 2H, $SeCH_2$), 3.66 (t, $J = 6.6$ Hz, 2H, H_7), 6.77 (t, $J = 7.5$ Hz, 1H, H_{13}), 6.92 (d, $J = 8.1$ Hz, 1H, H_{14}), 7.23–7.31 (m, 4H, H_2, H_1 and H_{12}), 7.48–7.50 (m, 2H, H_{11} and H_3), 16.40 (bs, 1H, OH) ($^{13}C\{^1H\}$ $CDCl_3$, 25 °C, vs $SiMe_4$) δ, ppm: 14.3 (CH_3), 25.2 ($SeCH_2$), 30.46 (C6), 48.4 (C_7), 116.9 (C_{11}), 118.7 (C_{13}), 119.1 (C_9), 126.8 (C_1), 127.9 (C_{14}), 129.0 (C_2), 129.7 (C_4), 132.4 (C_{12}), 132.5 (C_3), 164.0 (C_{10}), 172.0 (C_8) (^{77}Se $\{^1H\}$, $CDCl_3$, 25 °C, vs Me_2Se) δ, ppm: 286.6. IR (KBr, cm^{-1}): 1612, 461, 734.

2.3. Synthesis of [PdCl(L^1–H)] (1)

An aqueous solution (5 mL) of $Na_2[PdCl_4]$ (0.294 g, 1 mmol) was mixed with a solution of $\mathbf{L}^1$ (0.3182 g,

1 mmol) prepared in acetone (10 mL) with vigorous stirring. An orange precipitate of **1**, obtained instantaneously, was filtered and dried. It was recrystallized from chloroform–hexane (2:1) mixture. Single-crystals of **1** were obtained from the same solvent system (a few drops of MeOH were added additionally). Yield ca. 0.3626 g (~79%); m.p. 159 °C. $\Lambda_M = 7.0\ cm^2\ mol^{-1}\ \Omega^{-1}$. *Anal.* Calc. for $C_{16}H_{16}ClNOPdSe$ (powder form): C, 41.83; H, 3.49; N, 3.05. Found: C, 41.68; H, 3.41; N, 3.10%. NMR (^1H, $CDCl_3$, 25 °C, vs $SiMe_4$) δ, ppm: 2.22 (s, 3H, CH_3), 2.69–2.72 (m, 1H, H_5), 3.56–3.71 (m, 2H, $H_5 + H_6$), 4.48–4.53 (m, 1H, H_6), 6.62 (t, $J = 7.8$ Hz, 1H, H_{12}), 7.12 (d, $J = 8.7$ Hz, 1H, H_{13}), 7.23–7.38 (m, 2H, H_{11} and H_{10}), 7.41–7.43 (m, 3H, H_2 and H_1), 8.16–8.19 (m, 2H, H_3) ($^{13}C\{^1H\}$, $CDCl_3$, 25 °C, vs $SiMe_4$) δ, ppm: 19.7 (CH_3), 32.4 ($SeCH_2$), 60.7 (=NCH_2), 115.4 (C_{10}), 121.6 (C_{12}), 123.4 (C_4), 125.7 (C_8), 129.9 (C_2), 130.1 (C_{11}), 131.1 (C_1), 133.4 (C_{13}), 133.6 (C_3), 164.2 (C_9), 168.1 (C_7). ($^{77}Se\{^1H\}$ $CDCl_3$, 25 °C vs Me_2Se) δ, ppm: 440.4. IR (KBr, cm^{-1}): 1572, 463, 747.

2.4. Synthesis [PtCl(**L**^{1}–H)] (**2**)

$K_2[PtCl_4]$ (0.415 g, 1 mmol) was dissolved in water (5 mL). A solution of $\mathbf{L}^1$ (0.3182 g, 1 mmol) prepared in acetone (10 mL) was added to it with vigorous stirring. An orange precipitate of **2** was obtained, which was filtered and dried. The orange solid was recrystallized from chloroform–hexane (2:1). Single-crystals of **2** were obtained from the same solvent system. Yield ca. 0.3626 g (~79%); m.p. 162 °C $\Lambda_M = 5.0\ cm^2\ mol^{-1}\ \Omega^{-1}$. *Anal.* Calc. for $C_{16}H_{16}ClNOPtSe$: C, 35.10; H, 2.92; N 2.56. Found: C, 35.50; H, 2.96; N, 2.51%. NMR (^1H, $CDCl_3$, 25 °C, vs $SiMe_4$) δ, ppm: 2.14 (s, 3H, CH_3), 2.55 (t of d, $J = 2.7$ Hz, $J = 12.3$ Hz, 1H, H_5), 3.38 (d of t, $J = 4.2$ Hz, $J = 12$ Hz, 1H, H_5), 3.56 (d of t, $J = 3.9$ Hz, 12.3 Hz, 1H, H_6) 4.37 (t of d, $J = 2.4$ Hz, $J = 13.5$ Hz, 1H, H_6), 6.66 (t, $J = 7.2$ Hz, 1H, H_{12}), 7.20 (d, $J = 8.4$ Hz, 1H, H_{13}), 7.34 (t, $J = 8.4$ Hz, 1H, H_{11}), 7.39–7.42 (m, 3H, H_2, H_1), 7.47 (d, $J = 8.4$ Hz, H_{10}), 8.10–8.13 (m, 2H, H_3) ($^{13}C\{^1H\}$, $CDCl_3$, 25 °C, vs $SiMe_4$) δ, ppm: 20.6 (CH_3), 34.2 ($SeCH_2$), 61.9 (=NCH_2), 116.4 (C_{10}), 122.0 (C_{12}), 123.1 (C_4), 124.7 (C_8), 129.5 (C_2), 130.2 (C_{11}), 130.5 (C_1), 132.9 (C_{13}), 133.1 (C_3), 162.5 (C_9), 163.7 (C_7) ($^{77}Se\{^1H\}$, 25 °C, vs Me_2Se) δ, ppm: 387.36. IR (KBr, cm^{-1}): 1572, 465, 747.

2.5. Synthesis of [PdCl(**L**^{2}–H)] (**3**)

$Na_2[PdCl_4]$ (0.294 g, 1 mmol) dissolved in water (5 mL) and a solution of $\mathbf{L}^2$ (0.332 g, 1 mmol) prepared in acetone (10 mL) were stirred together vigorously. An orange precipitate of **3** was immediately obtained, which was filtered and dried. It was recrystallized from a chloroform–hexane (60:40) mixture. Yield ~0.42 g (~90%); m.p. 170 °C. $\Lambda_M = 6.0\ cm^2\ mol^{-1}\ \Omega^{-1}$ *Anal.* Calc. for $C_{17}H_{18}NOSePdCl$: C, 43.12; H, 3.80; N, 2.95. Found: C, 42.82; H, 3.99; N, 3.15%. NMR (^1H, $CDCl_3$, 25 °C, vs $SiMe_4$) δ, ppm: 2.02–2.07 (m, 2H, H_6), 2.34 (s, 3H, CH_3), 2.88 (d of t, $J = 4.2$ Hz, 1H, H_5), 3.10 (d of t, $J = 4.2$ Hz, $J = 11.1$ Hz, 1H, H_5), 3.65–3.69 (m, 2H, H_7), 6.65 (t, $J = 7.8$ Hz, 1H, H_{13}), 7.10 (d, $J = 8.7$ Hz, 1H, H_{14}), 7.22 (t, $J = 7.5$ Hz, 1H, H_{12}), 7.33–7.44 (m, 4H, H_{11}, H_2, H_1), 8.05–8.07 (m, 2H, H_3) ($^{13}C\{^1H\}$ $CDCl_3$, 25 °C, vs $SiMe_4$) δ, ppm: 19.6 (CH_3), 26.3 ($SeCH_2$), 29.7 (C6), 53.4 (NCH_2), 116.0 (C_{11}), 121.8 (C_{13}), 126.6 (C_9), 129.7 (C_4), 129.8 (C_2), 129.8 (C_{12}), 130.3 (C_1), 133.3 (C_3), 134.1 (C_{14}), 164.6 (C_{10}), 169.1 (C_8) ($^{77}Se\{^1H\}$, 25 °C, vs Me_2Se) δ, ppm: 293.6. IR (KBr, cm^{-1}): 1592, 468, 748.

2.6. Synthesis [PtCl(**L**^{2})] (**4**)

$K_2[PtCl_4]$ (0.415 g, 1 mmol) was dissolved in water (5 mL). A solution of $\mathbf{L}^2$ (0.332 g, 1 mmol) in acetone (10 mL) was added with vigorous stirring. An orange coloured precipitate of **4** was immediately obtained, which was filtered and dried. It was recrystallized from a chloroform–hexane (60:40) mixture. Yield ~0.415 g (~50%); m.p. 147 °C. $\Lambda_M = 6.8\ cm^2\ mol^{-1}\ \Omega^{-1}$. *Anal.* Calc. for $C_{17}H_{19}NOSePtCl_2$: C, 34.11; H, 3.18; N, 2.34. Found: C, 33.67; H, 3.58; N, 2.43%. NMR (^1H, CDCl3, 25 °C, vs $SiMe_4$) δ, ppm: 2.21–2.41 (m, 5H, $H_6 + CH_3$), 3.10 (t of d, $J = 3.6$ Hz, $J = 8.1$ Hz, 1H, H_5), 3.54–3.58(m, 1H, H_5), 3.65–3.66 (m, 2H, NCH_2), 6.78 (t, $J = 7.2$ Hz, 1H, H_{13}), 6.91 (d, $J = 8.4$ Hz, 1H, H_{14}), 7.28 (t, $J = 8.1$ Hz, 1H, H_{12}), 7.34–7.42 (m, 3H, H_2, H_1), 7.49 (d, $J = 7.8$ Hz, H_{11}), 7.86–7.89 (m, 2H, H_3), 16.28 (bs, 1H, OH); ($^{13}C\{^1H\}$ $CDCl_3$, 25 °C, vs $SiMe_4$) δ, ppm: 14.6 (CH_3), 28.2 ($SeCH_2$), 31.6 (C_6) 48.7 (NCH_2), 117.3 (C_{11}), 118.5 (C_{13}), 119.3 (C_9), 128.1 (C_{14}), 129.6 (C_2), 130.2 (C_1), 132.5 (C_{12}), 132.9 (C_4), 133.0 (C_3), 163.4 (C_{10}), 172.5 (C_8); ($^{77}Se\{^1H\}$, 25 °C, vs Me_2Se) δ, ppm: 337.4, 338.5. IR (KBr, cm^{-1}): 3395, 1582, 465, 739, 685.

2.7. Procedure for the homogeneous catalytic Heck reaction with **1**

A mixture of methyl acrylate (0.172 g, 2 mmol), *p*-iodonitrobenzene (0.62 g, 2.5 mmol), Et_3N (0.54 g, 3.0 mmol), *p*-xylene (2.0 mL) and **1** (22.95 mg) was stirred for 14 h at 140 °C and cooled thereafter to room temperature. It was treated with chloroform (40 mL) and filtered. The filtrate was evaporated on a rotary-evaporator to obtain the product.

It was purified through a silica gel column using hexane:ethylacetate mixture (9:1); yield 0. 33 g (~80%); NMR (^1H, $CDCl_3$, 25 °C, vs TMS) δ, ppm: 3.84 (s, 3H, OCH_3), 6.58 (d, $J = 15.9$ Hz, 1H, =CH–COOMe), 7.69 (d, 2H, $J = 9$ Hz, ArH, *o* to NO_2), 7.74 (d, $J = 15.9$ Hz, 1H, =CH–Ar), 8.27 (d, 2H, $J = 9$ Hz, Ar H, *m* to NO_2).

3. Results and discussion

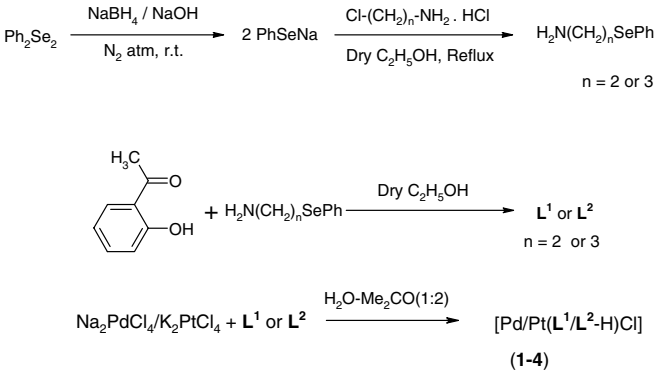
The ligands $\mathbf{L}^1$ and $\mathbf{L}^2$ and their complexes have been synthesized by the reactions given in Scheme 1. The ligands are stable and can be stored under ambient conditions up to 6 months. They have good solubility in $CHCl_3$, CH_2Cl_2, CH_3CN, MeOH, EtOH and acetone. In hexane both ligands are sparingly soluble. Both ligands are non-electrolytes. Complexes **1**–**4** are stable under ambient conditions and are soluble in $CHCl_3$, CH_2Cl_2, CH_3CN, EtOH, MeOH and acetone, but insoluble in hexane. All of them are non-ionic in nature. In the IR spectra of complexes **1**–**4** the $\rangle C{=}N-$ stretching frequency has been observed to be red shifted by 20–35 cm^{-1} with respect to those of $\mathbf{L}^1$ and $\mathbf{L}^2$, indicating the involvement of its nitrogen in coordination. Elemental analyses of **1** and **2** were carried out using their non-crystalline samples.

3.1. NMR spectra

The ^1H NMR spectra of both $\mathbf{L}^1$ and $\mathbf{L}^2$ have been found characteristic. On complexation of $\mathbf{L}^1$ with Pd(II) the $-CH_2$ groups in the $-Se-CH_2-CH_2-N$ system show a group of three signals, two correspond to a single proton and one to two protons (one from each $NCH_2 + SeCH_2$). Their assignments are based on the HMQC NMR spectrum of **1**. However in the case of complex **2**, the $-Se-CH_2-CH_2-N$ system shows a group of four signals, each one corresponding to one proton. These assignments are also in agreement with the HMQC NMR spectrum of **1**. On complexation of $\mathbf{L}^1$ with Pd(II)/Pt(II) one signal for the H_6 protons is deshielded by ~0.60–0.70 ppm and the other one is shielded by ~0.14–0.25 ppm. Similarly, of the two signals of H_5, one shows shielding of 0.52–0.67 ppm and the other deshielding of 0.16–0.38 ppm. The CH_3 signal shifts to upfield marginally (up to 0.1 ppm) on complexation. The H_{13} signal shows deshielding of the order of 0.18–0.26 ppm on the formation of **1** and **2**. The deshielding of the H_3 signal was found to be between 0.58 and 0.64 ppm on complexation. In complex **3** the signal of H_6 was observed as a multiplet (upfield ~0.1 ppm). The NCH_2 signal was also found to be a multiplet and deshielded by an amount <0.02 ppm. The pattern of the $-SeCH_2$ signals were found to be similar to those of **1**, but deshielded by up to 0.2 ppm only. The lower deshielding appears to be the effect of one six membered ring formed in the case of **3**. In the proton spectrum of **4**, the OH signal was observed but shielded insignificantly (~0.1 ppm). The signals of H_6 and CH_3 were found to be overlapping but not much shifted with respect to those of the free ligand $\mathbf{L}^2$. The signal of H_7 was found as a multiplet, but unshifted with respect to that of free $\mathbf{L}^2$. The protons of the $SeCH_2$ group give a multiplet deshielded by 0.5 ppm with respect to those of free $\mathbf{L}^2$ and a triplet of doublets at a position similar to that of $\mathbf{L}^2$.

The $^{13}C\{^1H\}$ NMR spectra of both $\mathbf{L}^1$ and $\mathbf{L}^2$ are also characteristic. On formation of **1** and **2** signals of carbon atoms C_2, C_3, C_9, C_{10} and C_{11} exhibit deshielding of up to 12.5 ppm. The signal of C_6 shows maximum deshielding (11.3–12.5 ppm) on complexation. The deshielding of the C_1, C_5, C_8 and C_{13} signals is of the order of 3–6 ppm. The signals of C_4, C_7 and C_{11} have been observed to be shielded by 2–8 ppm with respect to those signals of free $\mathbf{L}^1$. On formation of **3** signals of carbon atoms C_1, C_7, C_9, C_{13}, C_{14} and CH_3 exhibit deshielding between 3.0 and 7.5 ppm. Of them, the signal of C_9 shows maximum deshielding (7.5 ppm) on complexation. The deshielding of signals C_2, C_3, C_5 and C_{10} is of the order of 0.8 –1.0 ppm. The signals of C_4, C_6, C_8, C_{11} and C_{12} have been observed to be shielded (by up to 2.8 ppm) with respect to those of free $\mathbf{L}^2$. On complexation of $\mathbf{L}^2$ with Pt(II), the signals of most of the carbon atoms are shifted marginally (0.1–0.6 ppm), except those of C_1, C_4 and C_5 which are deshielded by 3.3, 3.2 and 3.0 ppm, respectively. These observations suggest that in **1**–**3** the ligands $\mathbf{L}^1$ and $\mathbf{L}^2$ coordinate in a tridentate mono-anionic mode. The bonding of $\mathbf{L}^2$ with Pt(II) appears to be through N and Se only.

In the $^{77}Se\{^1H\}$ NMR spectra, ligands $\mathbf{L}^1$ and $\mathbf{L}^2$ exhibit singlets at 282.3 and 286.6 ppm, respectively, which are deshielded (~25–29 ppm) with respect to those of the precursor selenated amines. On complexation of $\mathbf{L}^1$ with Pd(II) and Pt(II), the signals in the $^{77}Se\{^1H\}$ NMR spectra were found to be shifted downfield by 158 and 105 ppm respectively. In the case of **2**, the signal at 387.4 appears as a triplet because of $^1J(^{195}Pt–Se)$ coupling (2043 Hz). On formation of **3** and **4**, the deshielding of the signals in the ^{77}Se NMR spectra was found only to be 6.9 and 51.3 ppm. This is probably due to formation of one six membered ring in these cases (see Table 1).



Scheme 1.

3.2. Crystal structures

The crystal structures of $\mathbf{L}^1$, $\mathbf{L}^2$, **1** and **2** were solved. The structures of **1** and **2** are isomorphous. The molecular structure of $\mathbf{L}^1$ is shown in Fig. 1 and its selected bond lengths and angles are given in Table 2. The C–Se bond lengths of 1.916(4) and 1.953(4) Å are consistent with the earlier reports (1.939 Å) [20]. The Se–C(Ar) bond distance is somewhat shorter than the Se–C(alkyl) distance, as

Table 1
Crystal data and structural refinements for $\mathbf{L}^1$, $\mathbf{L}^2$, **1** and **2**

Compound	$\mathbf{L}^1$	$\mathbf{L}^2$	**1**	**2**
Empirical formula	$C_{16}H_{17}NOSe$	$C_{17}H_{19}NOSe$	$C_{17}H_{17}Cl_4NOPdSe$	$C_{17}H_{17}Cl_4NOPtSe$
Formula weight	318.27	332.29	578.50	667.16
Crystal size (mm)	$0.363 \times 0.217 \times 0.156$	$0.480 \times 0.190 \times 0.160$	$0.463 \times 0.215 \times 0.167$	$0.363 \times 0.217 \times 0.156$
Crystal system	monoclinic	monoclinic	monoclinic	monoclinic
Space group	$P2(1)/n$	$P2(1)/c$	$P2(1)/c$	$P2(1)/c$
Unit cell dimensions				
a (Å)	6.8629(16)	16.474(3)	14.854(2)	14.814(3)
b (Å)	29.966(7)	6.7098(11)	17.861(3)	17.863(3)
c (Å)	7.3948(18)	14.689(2)	15.917(2)	15.998(3)
β (°)	107.114(0)	108.084(2)	102.150(3)	101.672(4)
Volume (Å^3)	1453.4(60)	1543.5(40)	4128.3(10)	4145.9(13)
Z	4	4	8	8
D_{calc} (Mg m^{-3})	1.454	1.430	1.862	2.138
Absorption coefficient (mm^{-1})	2.575	2.428	3.186	9.046
$F(000)$	648	680	2256	2512
θ Range (°)	1.36–25.50	1.30–25.00	1.40–25.50	1.40–25.50
Index ranges	$-8 \leqslant h \leqslant 8$, $-36 \leqslant k \leqslant 36$, $-8 \leqslant l \leqslant 8$	$-19 \leqslant h \leqslant 19$, $-7 \leqslant k \leqslant 7$, $-17 \leqslant l \leqslant 17$	$-17 \leqslant h \leqslant 17$, $-21 \leqslant k \leqslant 21$, $-19 \leqslant l \leqslant 19$	$-17 \leqslant h \leqslant 17$, $-21 \leqslant k \leqslant 21$, $-19 \leqslant l \leqslant 19$
Reflections collected	14406	13862	40756	40899
Independent reflections (R_{int})	2701(0.1000)	2706 (0.367)	7669(0.0765)	7698(0.0946)
Maximum/minimum transmission	0.671/0.515	0.678/0.529	0.580/0.442	0.246/0.104
Data/restraints/parameters	2701/1/174	2706/0/186	7668/0/457	7690/0/453
Final R indices [$I > 2\sigma(I)$]	$R_1 = 0.0490$, $wR_2 = 0.1259$	$R_1 = 0.0412$, $wR_2 = 0.1183$	$R_1 = 0.0712$, $wR_2 = 0.1357$	$R_1 = 0.0801$, $wR_2 = 0.1407$
R indices (all data)	$R_1 = 0.0626$, $wR_2 = 0.1411$	$R_1 = 0.0490$, $wR_2 = 0.1260$	$R_1 = 0.0960$, $wR_2 = 0.1490$	$R_1 = 0.1028$, $wR_2 = 0.1521$
Largest difference peak/hole (e Å^{-3})	0.761/−0.458	0.749/−0.687	0.824/−0.606	1.235/−2.728

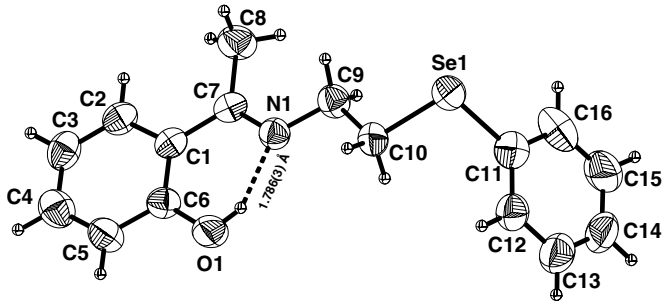


Fig. 1. ORTEP diagram of $\mathbf{L}^1$ with 50% probability ellipsoids.

Table 2
Selected bond lengths (Å) and angles (°) of $\mathbf{L}^1$

Bond length		Bond angle	
Se(1)–C(11)	1.916(4)	C(11)–Se(1)–C(10)	99.1(2)
Se(1)–C(10)	1.953(4)	C(7)–N(1)–C(9)	121.3(3)
N(1)–C(7)	1.284(4)	N(1)–C(7)–C(8)	122.4(3)
N(1)–C(9)	1.455(4)	N(1)–C(9)–C(10)	109.5(3)
C(9)–C(10)	1.518(5)	N(1)–C(7)–C(1)	117.6(3)
O(1)–C(6)	1.343(4)	C(12)–C(11)–Se(1)	120.9(3)
H(1)···N(1)	1.786(3)	C(16)–C(11)–Se(1)	120.2(3)

expected. Similarly the C–Se–C bond angle of 99.1(2)° was found as expected. Intramolecular hydrogen bonding, O–H···N, exists in the structure of $\mathbf{L}^1$. A perspective view of the structure of $\mathbf{L}^2$ is shown in Fig. 2. It also has intramolecular hydrogen bonding, O–H···N. The Se–C bond

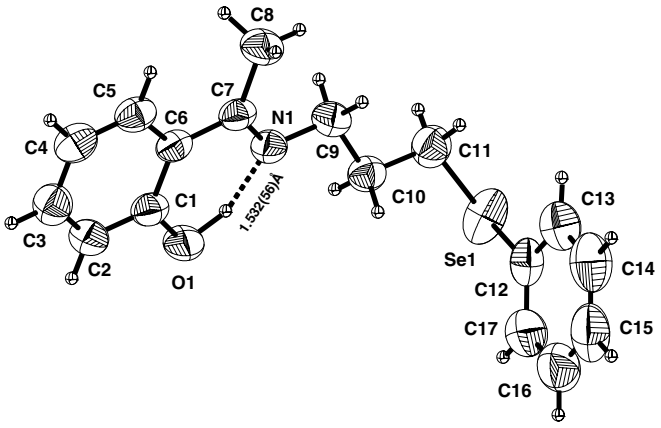


Fig. 2. ORTEP diagram of $\mathbf{L}^2$ with 50% probability ellipsoids.

distances, 1.914(3) and 1.956(3) Å and the C–Se–C bond angle are consistent with those of $\mathbf{L}^1$ and earlier reports [20]. In this case it is also found that the Se–C(Ar) bond distance is shorter than the Se–C(alkyl) bond distance (see Table 3).

The molecular structure of **1** is shown in Fig. 3 and its selected bond distances and angles are given in Table 4. In the asymmetric unit there are two chemically similar but crystallographically independent molecules and two molecules of chloroform solvent. The **1** is the first example of a crystal structure of a Pd complex of a (Se, N, O^-) ligand. The geometry around Pd is square planar. The Pd–Se

Table 3
Selected bond lengths (Å) and angles (°) of $\mathbf{L}^2$

Bond length		Bond angle	
Se(1)–C(12)	1.914(3)	C(12)–Se(1)–C(11)	99.5(1)
Se(1)–C(11)	1.956(3)	C(7)–N(1)–C(9)	122.0(2)
N(1)–C(7)	1.284(4)	N(1)–C(7)–C(6)	117.6(2)
N(1)–C(9)	1.458(4)	N(1)–C(7)–C(8)	123.0(3)
C(9)–C(10)	1.513(4)	N(1)–C(9)–C(10)	110.7(2)
O(1)–C(1)	1.330(3)	C(17)–C(12)–Se(1)	119.1(3)
H(1)···N(1)	1.53(6)	C(13)–C(12)–Se(1)	121.8(3)

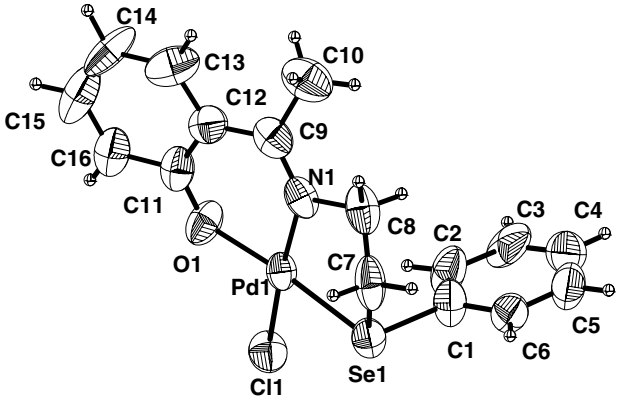


Fig. 3. ORTEP diagram of **1** with 50% probability ellipsoids.

Table 4
Selected bond lengths (Å) and angles (°) of **1** and **2**

(**1**)		(**2**)	
Bond lengths (Å)			
Pd(1)–Se(1)	2.3669(11)	Pt(1)–Se(1)	2.3543(16)
Pd(1)–Cl(1)	2.305(2)	Pt(1)–Cl(1)	2.306(4)
Pd(1)–N(1)	2.003(7)	Pt(1)–N(1)	1.988(12)
Pd(1)–O(1)	1.977(6)	Pt(1)–O(1)	1.976(10)
Se(1)–C(1)	1.929(8)	O(1)–C(6)	1.314(15)
Se(1)–C(7)	1.947(9)	N(1)–C(7)	1.316(18)
N(1)–C(8)	1.493(10)	N(1)–C(9)	1.512(18)
N(1)–C(9)	1.309(11)	Se(1)–C(10)	1.95 (2)
O(1)–C(11)	1.312(10)	Se(1)–C(11)	1.938(14)
Bond angles (°)			
O(1)–Pd(1)–N(1)	93.0(3)	O(1)–Pt(1)–N(1)	93.1(5)
O(1)–Pd(1)–Cl(1)	88.3(2)	O(1)–Pt(1)–Cl(1)	86.7(3)
N(1)–Pd(1)–Cl(1)	173.4(2)	N(1)–Pt(1)–Cl(1)	174.5(3)
O(1)–Pd(1)–Se(1)	176.0(2)	O(1)–Pt(1)–Se(1)	175.4(3)
N(1)–Pd(1)–Se(1)	90.5(2)	N(1)–Pt(1)–Se(1)	90.9(4)
Cl(1)–Pd(1)–Se(1)	88.40(7)	Cl(1)–Pt(1)–Se(1)	89.6(1)
C(1)–Se(1)–C(7)	98.8(4)	C(11)–Se(1)–C(10)	98.8(7)
C(1)–Se(1)–Pd(1)	104.3(2)	C(11)–Se(1)–Pt(1)	107.0(5)
C(7)–Se(1)–Pd(1)	91.5(3)	C(10)–Se(1)–Pt(1)	91.7(5)
C(9)–N(1)–Pd(1)	125.3(6)	C(7)–N(1)–Pt(1)	127.2(5)
C(8)–N(1)–Pd(1)	114.4(6)	C(9)–N(1)–Pt(1)	114.7(5)
C(9)–N(1)–C(8)	119.3(7)	C(7)–N(1)–C(9)	117.7(1)
C(11)–O(1)–Pd(1)	123.8(5)	C(6)–O(1)–Pt(1)	123.2(9)
O(1)–C(11)–C(12)	125.8(8)	O(1)–C(6)–C(5)	115.7(1)
O(1)–C(11)–C(16)	115.9(8)	O(1)–C(6)–C(1)	126.5(1)

bond length, 2.3669(11) Å, is shorter than those reported for $[Pd(PEt_3)_2(SePh)(PO(OPh)_2)]$ (2.518(9) Å) [21] and $[Pd(Me_2PCH_2CH_2PMe_2)(Me)(SeC_6H_4\text{-}4\text{-}Cl)]$ (2.4483(8) Å) [22]. The shorter Pd–Se bond in **1** may be attributed to the tridentate nature of ligand $\mathbf{L}^1$, which makes two chelate rings and forces Se to bind with Pd(II) somewhat strongly in comparison to those complexes in which the selenium ligand is a monodentate one. The Pd–N, Pd–O and Pd–Cl bond distances, 2.003(7), 1.977(6) and 2.305(2) Å, respectively, are consistent with earlier reports [Pd–N = 2.01(1) Å, Pd–O = 2.03(1) Å and Pd–Cl = 2.290 (4) Å] on a Pd(II) complex of a tridentate ligand of the (Te, N, O^-) type [14]. In Fig. 4 the molecular structure of **2** is shown. In Table 4 selected bond lengths and angles are given. In the unit cell of the crystal of **2** also there are two almost similar molecules. One molecule of chloroform per molecule of **2** is also present in the lattice. The structure of **2** is also the first example of a crystal structure of a Pt-complex of a (Se, N, O^-) ligand. The geometry around Pt is nearly square planar. The Pt–Se bond length, 2.3543(16) Å, is consistent with the earlier reported value in the case of $[CH_3SeCH_2CH_2CH(COOMe)NH_2 \cdot PtCl_2]$ (2.3697(8) Å) [23], but is shorter than those reported for *cis*-$[Pt(SePh)_2(PPh_3)_2]$ (2.4970(9), 2.4604(10) Å) [24] and *trans*-$[Pt(SePh)_2$(2,9-dimethyl-1,10-phenanthroline)(MeOOCCH=CHCOOMe)] (2.5197, 2.5142 Å) [25]. The shorter Pt–Se bond in **2** may again be attributed to the tridentate nature of the ligand $\mathbf{L}^1$, as in the case of the Pd(II) complex mentioned above. The absence of the *trans* influence may also contribute, particularly in comparison with *trans*-$[Pt(SePh)_2$(2,9-dimethyl-1,10-phenanthroline)(MeOOCCH=CHCOOMe)]. The Pt–N and Pt–Cl bond distances, 1.988(12) and 2.306(4) Å, respectively, are consistent with the earlier reports [23], 2.043(5) and 2.294(2), 2.322(2) Å, respectively. The Pt–O bond length of 1.976(10) Å is comparable with earlier reports (2.034 Å) [26]. On comparing Pd/Pt–N, Pd/Pt–O, Pd/Pt–Cl and Pd/Pt–Se bond lengths with the sum of their covalent radii 2.03/2.05, 2.01/2.03, 2.27/2.29 and 2.44/2.46 Å. respectively, it appears that the observed bond distances are shorter than this sum, except in the case of Pd/Pt–Cl where the observed values are marginally higher. This indicates that coordination of $\mathbf{L}^1$ is quite strong with Pd as well as with Pt.

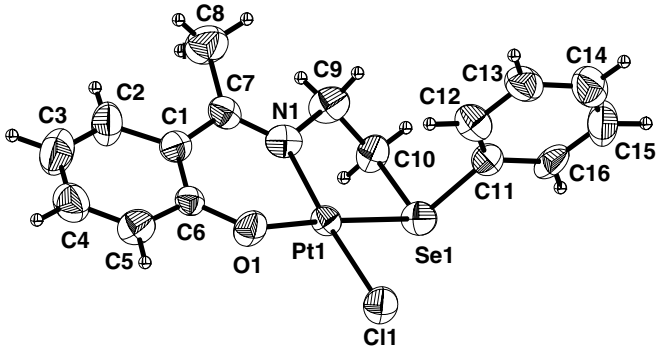


Fig. 4. ORTEP diagram of **2** with 50% probability ellipsoids.

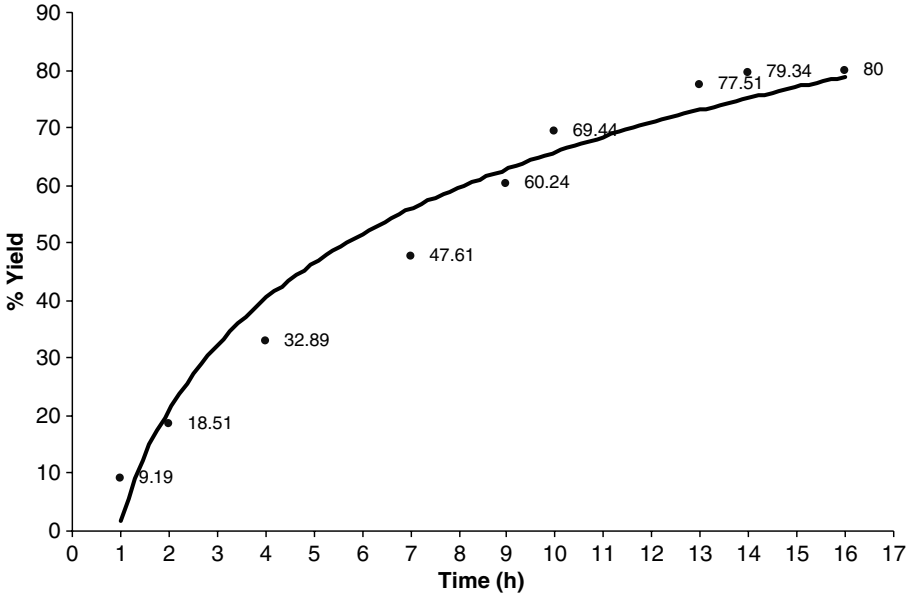
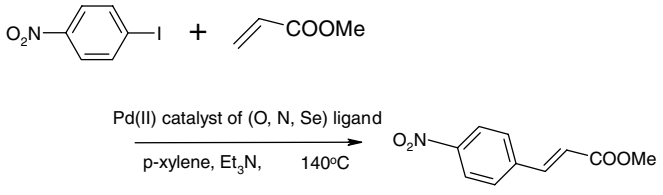


Fig. 5. Kinetic profile of the Heck reaction.

3.3. Application as a homogeneous catalyst for the Heck reaction

1 was found to be suitable to catalyze the Heck coupling reaction, as shown below with ~80% yield.



Using **1**, the time for completion of the reaction is only 14 h, less than that of a recently reported palladium(II) complex of a bidenate Se-ligand (20–90 h at a similar reaction temperature) [17]. The kinetic profile of the above reaction followed by proton NMR is shown in Fig. 5. The temperature cannot be much increased beyond 140 °C as the yield decreases. However at a lower temperature, around 100 °C, the yield goes down to 40–45%. The reaction was carried out in the presence of Na_2CO_3 at 140 °C and the yield was found to be only 20–25%. The trialkylamines (alkyl group = Me, Et, *n*-Bu or *t*-Bu) give the maximum yield.

4. Conclusion

Selenated Schiff bases 2-OH-$C_6H_4C(CH_3)$=$N(CH_2)_n$SePh ($n = 2$, $\mathbf{L^1}$; $n = 3$, $\mathbf{L^2}$) have been designed as such species are scantly known and explored for complexation with Pd(II)/Pt(II). Proton, carbon-13 and selenium-77 NMR spectra of the complexes support the coordination of $\mathbf{L^1}$ and $\mathbf{L^2}$ through Se. In the case of **2**, satellites due to coupling with ^{195}Pt were observed (^1J (^{195}Pt–Se) = 2043 Hz). **1** and **2** are the first examples of crystal structures of Pd and Pt complexes of a (Se, N, O^-) ligand. **1**is explored for the homogeneous catalysis of the Heck reaction between methyl acrylate and *p*-iodonitrobenzene. The yield is ~80% and the reaction time is only 14 h.

Acknowledgements

The authors thank the Department of Science and Technology (India) for Research Project No. SR/S1/IC-23/06. A.K. thanks the Council of Scientific and Industrial Research (India) for the award of a Junior/Senior Research Fellowship. Authors also thank Department of Science and Technology (India) for partial financial assistance given to establish single crystal X-ray diffraction facility under its FIST programme.

Appendix A. Supplementary material

CCDC 651260, 651261, 651259 and 655400 contain the supplementary crystallographic data for $\mathbf{L^1}$, $\mathbf{L^2}$, **1** and **2**. These data can be obtained free of charge via http://www.ccdc.cam.ac.uk/conts/retrieving.html, or from the Cambridge Crystallographic Data Centre, 12 Union Road, Cambridge CB2 1EZ, UK, fax: (+44) 1223-336-033, or e-mail: deposit@ccdc.cam.ac.uk. Supplementary data associated with this article can be found, in the online version, at doi:10.1016/j.poly.2007.09.027.

References

[1] P.A. Vigato, S. Tamburini, Coord. Chem. Rev. 248 (2004) 1717.
[2] R. Drozdzak, B. Allaert, N. Ledoux, I. Dragutan, V. Dragutan, F. Verpoort, Coord. Chem. Rev. 249 (2005) 3055.

[3] C.-M. Che, J.-S. Huang, Coord. Chem. Rev. 242 (2003) 97.
[4] E. Tsuchida, K. Oyaizu, Coord. Chem. Rev. 237 (2003) 213.
[5] R. Ziessel, Coord. Chem. Rev. 216–217 (2001) 195.
[6] E.M. McGarrigle, D.G. Gilheany, Chem. Rev. 105 (2005) 1563.
[7] D. Wang, M. Wang, X. Wang, Y. Chen, A. Gao, L. Sun, J. Catal. 237 (2006) 248.
[8] R. Ferreira, H. Garcia, B. de Castro, C. Freire, Eur. J. Inorg. Chem. (2005) 4272.
[9] A. Martinez, C. Hemmert, C. Loup, G. Barre, B. Meunier, J. Org. Chem. 71 (2006) 1449.
[10] H. Zhang, S. Xiang, C. Li, Chem. Commun. (2005) 1209.
[11] C.P. Chow, K.J. Shea, J. Am. Chem. Soc. 127 (2005) 3678.
[12] M.S. Taylor, D.N. Zalatan, A.M. Lerchner, E.N. Jacobsen, J. Am. Chem. Soc. 127 (2005) 1313.
[13] D.J. Darensbourg, P. Ganguly, D. Billodeaux, Macromolecules 39 (2006) 2722.
[14] R. Kumar P., A.K. Singh, P. Sharma, J.E. Drake, M.B. Hursthouse, M.E. Light, Inorg. Chem. Commun. 7 (2004) 502.
[15] R. Kumar P., A.K. Singh, R.J. Butcher, P. Sharma, R.A. Toscano, Eur. J. Inorg. Chem. (2004) 1107.
[16] J. Kjellgren, J. Audin, O.A. Wallner, I.V. Saltaova, K.J. Szabo, Chem. Eur. J. 11 (2005) 5260.
[17] Q. Yao, E.P. Kinney, C. Zheng, Org. Lett. 6 (2004) 2997.
[18] (a) G.M. Sheldrick, Acta Crystallogr., Sect. A 46 (1990) 467;
(b) G.M. Sheldrick, SHELXL-NT Version 6.12, University of Gottingen, Germany, 2000.
[19] A. Khanna, A. Bala, B.L. Khandelwal, J. Organomet. Chem. 494 (1995) 199.
[20] B. Umezawa, O. Hoshino, S. Sawaki, H. Sashida, K. Mori, Y. Hamada, K. Kotera, Y. Iitaka, Tetrahedron 40 (1984) 1783.
[21] L.-B. Han, N. Choi, M. Tanaka, J. Am. Chem. Soc. 118 (1996) 7000.
[22] A.J. Canty, M.C. Denney, J. Patel, H. Sun, B.W. Skelton, A.H. White, J. Organomet. Chem. 689 (2004) 672.
[23] M. Carland, B.F. Abrahams, T. Rede, J. Stephenson, V. Murray, W.A. Denny, W.D. McFadyen, Inorg. Chim. Acta 359 (2006) 3252.
[24] V.P. Ananikov, I.P. Beletskaya, G.G. Aleksandrov, I.L. Eremenko, Organometallics 22 (2003) 1414.
[25] V.G. Albano, M. Monari, I. Orabona, A. Panunzi, F. Ruffo, J. Am. Chem. Soc. 123 (2001) 4352.
[26] K. Sakai, S. Takahashi, Acta Crystrallogr., Sect. E 59 (2003) m532.

Available online at www.sciencedirect.com
ScienceDirect
Polyhedron 27 (2008) 493–501
POLYHEDRON
www.elsevier.com/locate/poly

The effect of steric hindrance on the Fe(II) complexes of triazine-containing ligands

Elaine A. Medlycott [a], Garry S. Hanan [a,*], Tareque S.M. Abedin [b,1], Laurence K. Thompson [b,1]

[a] *Département de Chimie, Université de Montréal, Montréal, Québec, Canada H3T 1J4*
[b] *Department of Chemistry, Memorial University, St. John's, Newfoundland, Canada A1B 3X7*

Received 12 June 2007; accepted 3 October 2007
Available online 7 November 2007

Abstract

Fe(II) complexes based on ligands containing a 1,3,5-triazine core have been synthesised and characterised and their electrochemical, spectroscopic and magnetic properties have also been investigated. The incorporation of various substituted metal-binding heterocycles into the 2,4-positions of the triazine allows the properties of the complexes to be modified considerably. Whereas the magnetic moments of the pyridyl (**1b**: 2.4 B.M.) and pyrazyl (**1c**: 4.2 B.M.) substituents lead to spin transitions, the 6-picolyl (**1d**: 5.4 B.M.) substituent is a pure Curie paramagnet at 300 K. Interestingly, the Fe(II) complex of bromo-phenyl-2,2′:6″,2‴-terpyridine (**1a**) displays significant anion effects in the solid state, with the ClO_4 salt exhibiting major diamagnetic contributions (2.1 B.M. at 300 K) and the PF_6 salt has more significant paramagnetic contributions (3.5 B.M. at 300 K). The Fe–N bond distances observed in the 6-picolyl complex $[Fe(\mathbf{1d})_2](ClO_4)_2$ for both the central rings 2.084 (5) Å and the distal rings 2.254 (4) and 2.369 (4) Å are significantly longer than those of the pyridyl complex $[Fe(\mathbf{1b})_2](ClO_4)_2$ (centre: 1.869 (4) Å; distal: 1.992 (4) Å; distal: 2.005 (4) Å) due to steric strain, thus generating high-spin $[Fe(\mathbf{1d})_2](ClO_4)_2$.
© 2007 Elsevier Ltd. All rights reserved.

Keywords: Tridentate N ligands; Transition metal complexes; Halogen–halogen interactions; Structure elucidation; Ligand design

1. Introduction

The ability to control and fine-tune the magnetic and electronic properties of transition metal complexes is fundamental to the development of efficient molecular electronic devices based on metal ions [1]. Transition metal ions have therefore been included in a wide variety of supramolecular materials [2,3]. Complexes with the potential to undergo a change in spin state are particularly good targets for development of molecular switches as the optical, magnetic and geometric properties may change significantly following a change in spin state [4]. In this regard, complexes with d^6 to d^7 electronic configurations are of great interest as they are able to undergo spin transitions between their low-spin and high-spin states and, consequently, Fe(II) and Co(II) coordination complexes have been intensely studied [5].

In general, Fe(II) complexes incorporating polypyridine ligands are low spin and diamagnetic at room temperature which allows temperature-induced changes in spin state to be monitored by NMR spectroscopy [6]. The spin state of the complexes may also be manipulated by incorporating electron-donating or -accepting groups onto the ligand framework and through the introduction of steric bulk, steric strain or mechanical strain within the ligand [7–10]. These modifications allow both low- and high-spin complexes to be obtained, as well as complexes in which the Fe(II) cations are able to access both states. Another approach to alter the properties of the complexes involves

* Corresponding author. Fax: +1 514 343 2468.
E-mail addresses: garry.hanan@umontreal.ca (G.S. Hanan), lthomp@mun.ca (L.K. Thompson).
[1] Fax: +1 709 737 3702.

0277-5387/$ - see front matter © 2007 Elsevier Ltd. All rights reserved.
doi:10.1016/j.poly.2007.10.002

substitution of the pyridyl rings within the tpy-motif with different heterocycles as substitution of distal pyridyl rings in the tpy core is relatively facile [11–19]. There are, however, fewer examples of Fe(II) complexes of tridentate ligands in which the central ring has been substituted [20,21]. One example of such a ligand is 2,4,6-tris(2′-pyridyl)-1,3,5-triazine (tpt), which is readily synthesised and commercially available [22]. The $Fe(tpt)_2^{2+}$ complex is diamagnetic and stable at room temperature [23–26], although due to the nature of the tridentate ligand, further functionalisation is difficult.

We have previously shown that a pendant phenyl ring in triazine ligands of the type 2,4-di(2′-pyridyl)-6-(phenyl)-1,3,5-triazine can be readily functionalised, thus enabling fine tuning of the electronic and redox properties in Ru(II) and Co(II) complexes [27–30]. For example, if a bromophenyl-functionalised triazine ligand is employed, the arrangement of the cations in the solid state is dictated by non-covalent, halogen–halogen interactions (Fig. 1) [28,30]. As such, the weak ligand field strength and facile functionalisation of these ligands make them a perfect platform to investigate the electrochemical, magnetic and spectroscopic properties in their Fe(II) complexes.

Herein, we report the synthesis, electronic and magnetic properties of a series of triazine-based Fe(II) complexes. Whilst functionalisation of the pendant phenyl ring has proved effective in the fine tuning of the electronic properties, functionalisation or substitution of the pyridyl rings provides coarse changes in the electronic, redox and magnetic properties of the assembled complexes.

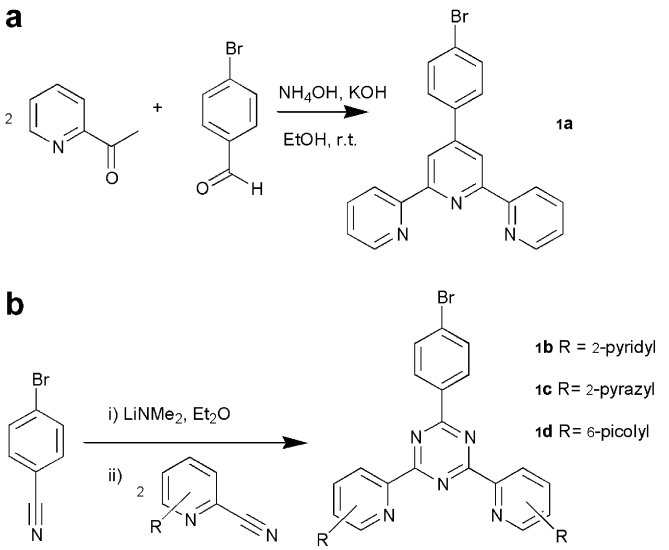
2. Results and discussion

2.1. Synthesis

In order to develop novel properties in a series of Fe(II) complexes, we required a flexible synthetic strategy to obtain various ligands. Triazine appeared to be the best choice for incorporation into the ligand design as it has a weaker ligand field strength than pyridine, thereby favouring the formation of high-spin complexes. Thus, in a similar fashion to the one-step synthesis of tpy (Scheme 1a) [32], we examined a triazine ring-forming reaction to afford variably substituted ligands (Scheme 1b) [27–29,33].

The synthetic procedure reported for triazine ligands, Fig. 1b, is general for a range of R groups substituted on the phenyl ring. As seen in Fig. 2, we were interested in retaining the bromo-phenyl pendant ring and in examining the versatility of this reaction by methyl substitution on the distal pyridyl rings (Fig. 2, **1c**) or replacing the pyridyl rings with an alternative heterocycle (pyrazine, Fig. 2, **1d**). For the synthesis of **1c** and **1d**, bromobenzonitrile was added to a stirred solution of $LiNMe_2$ in anhydrous diethyl ether. The amidinate intermediate that forms reacts with 2 equiv. of 2-cyanopyrazine or 2-cyano-6-methylpyridine and cyclisation affords ligands **1c** and **1d**, respectively, on work-up.

Fe(II) complexes of ligands **1a** and **1b** could be synthesised as both the PF_6^- and ClO_4^- salts, however, complexes of ligands **1c** and **1d** were only isolated as perchlorate salts due to the instability of the complexes to counter-ion exchange. Complexes $[Fe(\mathbf{1a})_2](PF_6)_2$ and $[Fe(\mathbf{1b})_2](PF_6)_2$



Scheme 1. Synthesis of ligands with variable R groups: (a) one-step terpyridine synthesis and (b) triazine ring-forming reaction.

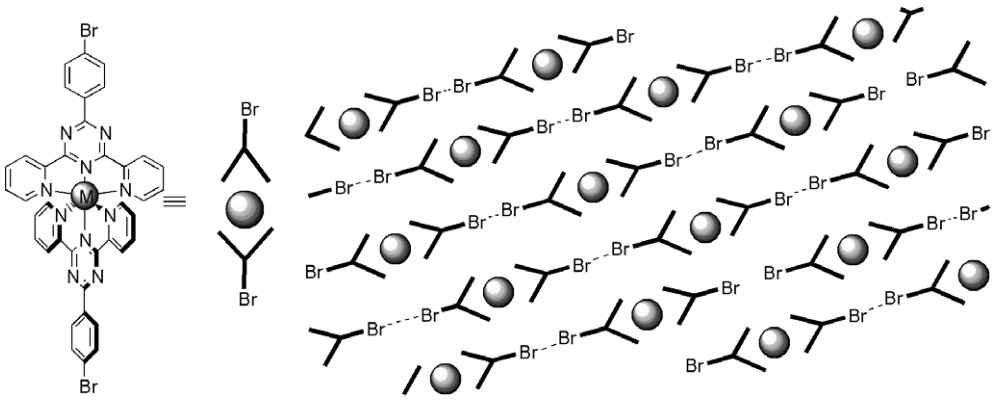


Fig. 1. Halogen–halogen interactions in Ru(II), Fe(II), Co(II) and Cu(II) complexes of bromine-functionalised triazine ligands [31].

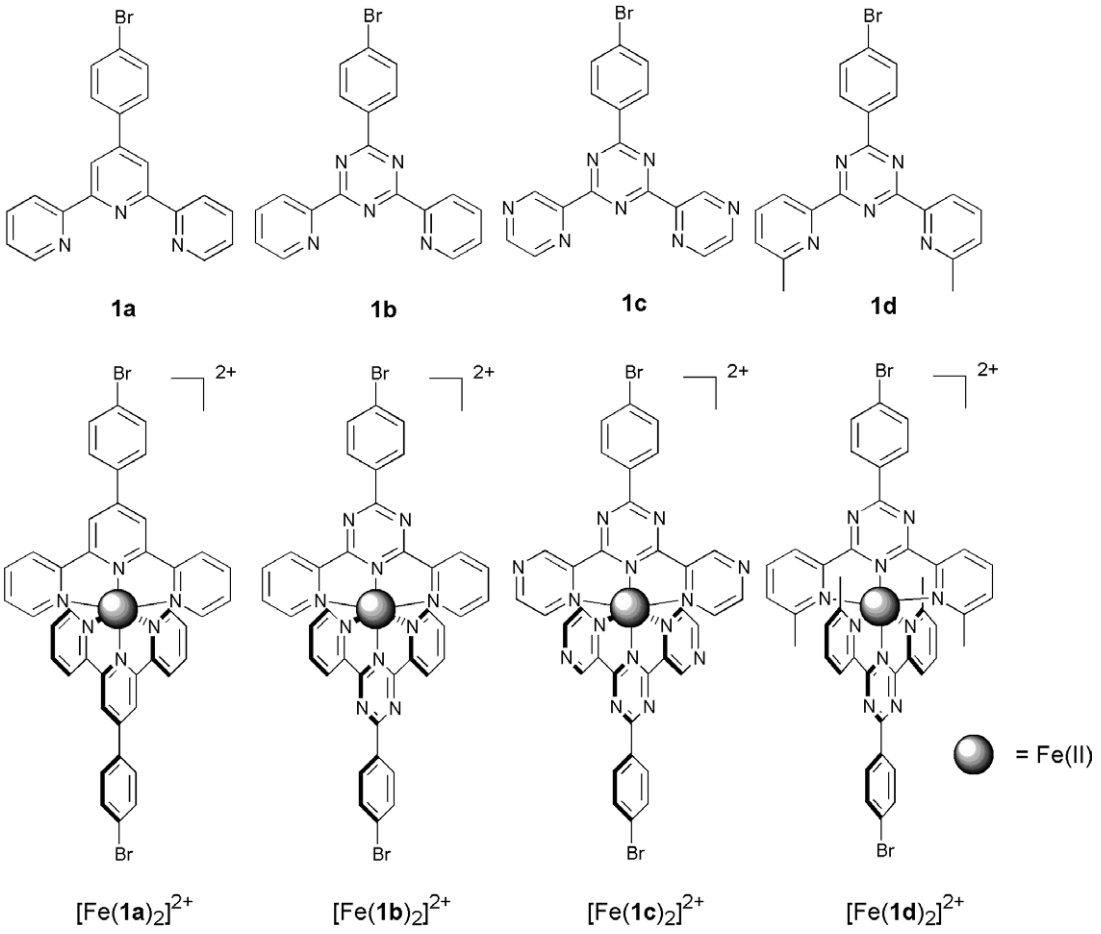


Fig. 2. The brominated terpyridine and triazine ligands and their Fe(II) complexes used in this study.

were synthesised by adapting a reported procedure [31]. Complexes of the type $Fe(L)_2(ClO_4)_2$ were synthesised by addition of $Fe(ClO_4)_2 \ldots 6H_2O$ in acetonitrile to a stirred solution of the ligand in acetonitrile. After 20 min of heating, the solvent was removed under reduced pressure and the mixture was taken up in a small amount of acetonitrile and precipitated in Et_2O. The purple or red product was isolated by filtration and dried.

The ligands and complexes were characterised by ^1H NMR and their chemical shifts are shown in Table 1. The variable temperature spectra of complex $[Fe(\mathbf{1b})_2](PF_6)_2$ are shown in Fig. 3.

Complexes $[Fe(\mathbf{1a})_2]^{2+}$, $[Fe(\mathbf{1b})_2]^{2+}$ and $[Fe(\mathbf{1c})_2]^{2+}$ showed signals in the 7–11 ppm range at room temperature indicating the presence of low-spin complexes. However, less resolution was observed for the ^1H signals closest to the coordinating N-atom in $[Fe(\mathbf{1b})_2]^{2+}$ and $[Fe(\mathbf{1c})_2]^{2+}$ as their PF_6^- and ClO_4^- salts. Increasing the temperature resulted in the loss of signal structure of the next closest signals, H_3 and H_5, followed by H_4, furthest from the coordinating site (Fig. 3). The phenyl protons maintained their doublet character without any broadening as they are furthest from the metal centre.

The shift to low field of H_6 is unexpected as compared to structurally similar paramagnetic complexes based on the $Fe(tpt)_2^{2+}$ motif in which a high-field shift is observed into the negative ppm range [9]. In addition, other complexes showing spin-crossover properties had ^1H NMR spectra

Table 1
^1H NMR signals obtained in CD_3CN at room temperature for **1c**, **1d** and the Fe(II) complexes of **1a-d** as their perchlorate salts

Cpd	3, 3″	4, 4″	5, 5″	6, 6″	3′, 5′	3‴, 5‴	2‴, 6‴	Me
1c	9.98		8.94	8.87		7.77	8.69	
1d	8.63	7.85	7.41			7.71	8.67	2.80
$[Fe(\mathbf{1a})_2]^{2+}$	8.63	7.93	7.11	7.20	9.19	8.02	8.26	
$[Fe(\mathbf{1b})_2]^{2+}$	9.16	8.10	7.37	7.76		8.10	9.11	
$[Fe(\mathbf{1c})_2]^{2+}$	10.26		8.71	8.32		8.12	9.11	
$[Fe(\mathbf{1d})_2]^{2+}$	52.5/53.8	13.08	52.5/53.8			7.66	3.33	−1.56

Chemical shifts are shown in ppm.

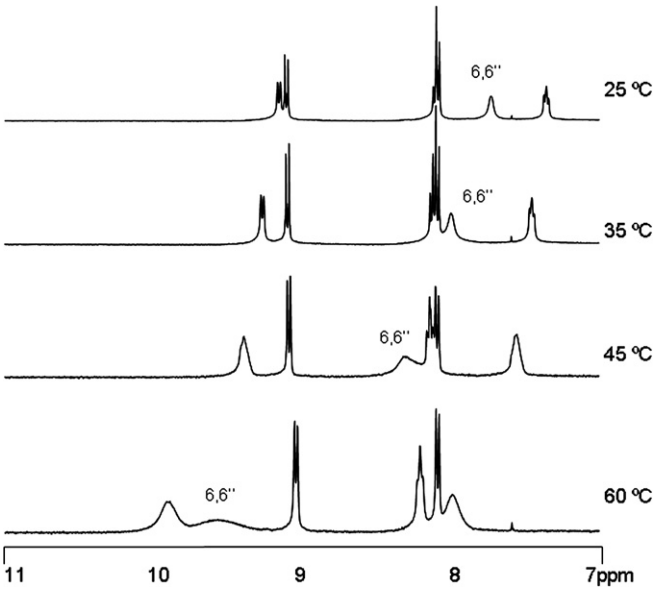


Fig. 3. Variable temperature ^{1}H NMR spectra $[Fe(\mathbf{1b})_2]^{2+}$ as its PF_6^- salt in CD_3CN at 400 MHz.

with paramagnetic signals corresponding to the high-spin complex and diamagnetic sub-spectrum as a result of slow exchange of the two states. However, no clear sub-spectrum or paramagnetic spectrum was observed for $[Fe(\mathbf{1b})_2](PF_6)_2$ indicating that the exchange of spin states is occurring faster than the NMR time scale. The room temperature spectrum is more characteristic of a low spin complex despite the broadening observed, suggesting that the diamagnetic contribution is greater in the equilibrium between spin states. $[Fe(\mathbf{1d})_2](ClO_4)_2$ displays paramagnetic shifts in its ^{1}H NMR spectra regardless of temperature and solvent. The signals were assigned by comparison to the previously published paramagnetic spectra of Fe (II) tpy-type complexes [9].

2.2. X-ray crystallography

Purple crystals of $[Fe(\mathbf{1b})_2](ClO_4)_2$ (Fig. 4) and $[Fe(\mathbf{1d})_2](ClO_4)_2$ (Fig. 5) were obtained by slow diffusion of isopropyl ether into acetonitrile solutions of the complexes. Efforts to obtain crystals of $[Fe(\mathbf{1c})_2](ClO_4)_2$ were unsuccessful, however, addition of excess NH_4PF_6 to the acetonitrile solution followed by filtration and crystallisation by slow diffusion yielded purple crystals as the mixed salt (Fig. 5). Attempts to crystallise $[Fe(\mathbf{1a})_2](ClO_4)_2$ were also unsuccessful, but acceptable crystals were obtained as the PF_6^- salt (Fig. 4). A summary of the crystal and structure refinement data for the complexes is gathered in Table 2 and bond length and angle data is in Table 3.

Both complexes $[Fe(\mathbf{1a})_2](PF_6)_2$ and $[Fe(\mathbf{1b})_2](ClO_4)_2$ crystallised in the triclinic space group $P\bar{1}$ with one complete molecule, two counter-ions and two or three acetonitrile solvent molecules in the asymmetric unit (Fig. 4). Complexes $[Fe(\mathbf{1c})_2](ClO_4)(PF_6)$ and $[Fe(\mathbf{1d})_2](ClO_4)_2$ crystallised in the monoclinic space group $C2/c$ (Fig. 5).

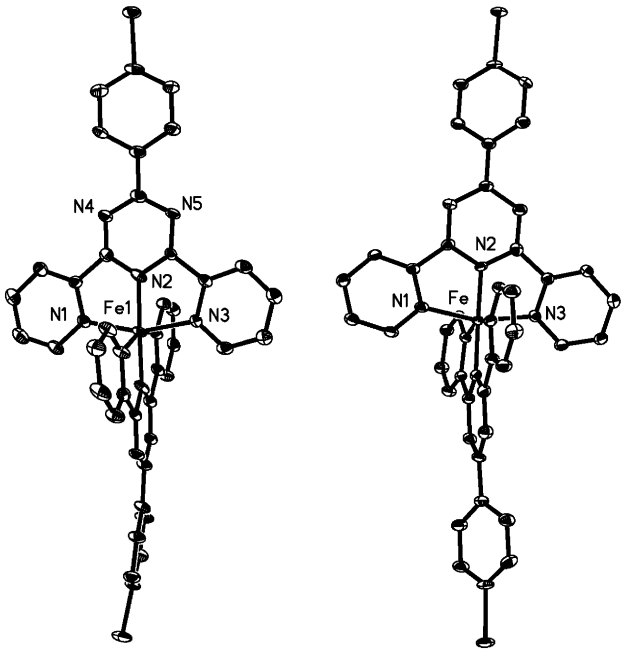


Fig. 4. X-ray crystal structures of complexes $[Fe(\mathbf{1a})_2](PF_6)_2$ and $[Fe(\mathbf{1b})_2](ClO_4)_2$ as ORTEP representations. Thermal ellipsoids are set at 50%. The anions and solvent molecules of crystallisation have been omitted for clarity.

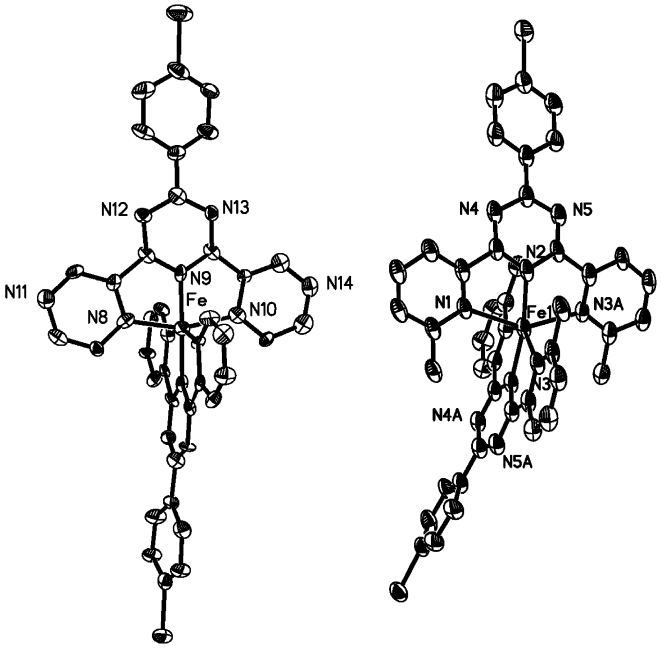


Fig. 5. X-ray crystal structures of complexes $[Fe(\mathbf{1c})_2](ClO_4)(PF_6)$ and $[Fe(\mathbf{1d})_2](ClO_4)_2$ as ORTEP representations. Thermal ellipsoids are set at 50%. The anions and solvent molecules of crystallisation have been omitted for clarity.

The Fe–N (centre) bond distances in all the complexes are shorter than the Fe–N (distal) bond distances (Table 3). The Fe–N bond distances of $[Fe(\mathbf{1a})_2](PF_6)_2$ were unexceptional for Fe(tpy)-type complexes and those for complex $[Fe(\mathbf{1b})_2](ClO_4)_2$ were similar to those found in the

Table 2
Summary of crystal data and structure refinement for Fe(II) complexes of **1a–d**

Compound	$[Fe(\mathbf{1a})_2](PF_6)_2$	$[Fe(\mathbf{1b})_2](ClO_4)_2$	$[Fe(\mathbf{1c})_2](ClO_4)(PF_6)$	$[Fe(\mathbf{1d})_2](ClO_4)_2$
Formula	$C_{46}H_{34}Br_2F_{12}FeN_8P_2$	$C_{44}H_{33}Br_2Cl_2Fe\ N_{13}O_8$	$C_{42}H_{32}Br_2ClF_6FeN_{18}O_4P$	$C_{46}H_{38}Br_2Cl_2FeN_{12}O_8$
Crystal system	triclinic	triclinic	monoclinic	monoclinic
T (K)	100(2)	100(2)	100(2)	150(2)
λ (Å)	1.54178	1.54178	1.54178	1.54178
Space group	$P\bar{1}$	$P\bar{1}$	$C2/c$	$C2/c$
a (Å)	10.1585 (2)	10.7253 (9)	27.0294 (15)	19.4190 (4)
b (Å)	11.4649 (2)	15.1165 (11)	9.2400 (5)	10.2896 (2)
c (Å)	22.6626 (3)	15.5248 (10)	39.652 (2)	24.4899 (5)
α (°)	93.4240 (10)	74.638 (5)		
β (°)	100.5180 (10)	73.791 (5)	106.461 (3)	98.8900 (10)
γ (°)	113.1240 (10)	89.096 (5)		
V (Å^3)	2361.24 (7)	2326.0 (3)	9497.3 (9)	4834.63 (17)
Z	2	2	8	4
D (Mg m^{-3})	1.694	1.654	1.747	1.612
μ (mm^{-1})	6.003	6.254	6.135	6.019
Maximum 2θ (°)	73.02	73.34	55.13	58.20
Number of reflections collected	29279	27650	38944	20606
Number of independent reflections	9061	8842	5939	3342
Data/restraints/parameters	9061/0/642	8842/0/634	5939/0/641	3342/69/387
R	0.0515	0.0711	0.0779	0.0603
wR_2	0.1366	0.2312	0.2373	0.1700
Goodness-of-fit on F^2	1.035	1.023	1.011	0.951

Table 3
Selected bond distances and angles for the Fe(II) complexes of **1a–d**

	$[Fe(\mathbf{1a})_2](PF_6)_2$	$[Fe(\mathbf{1b})_2](ClO_4)_2$	$[Fe(\mathbf{1c})_2](ClO_4)(PF_6)$	$[Fe(\mathbf{1d})_2](ClO_4)_2$
Bond distances (Å)				
Fe–N (centre)	1.876 (3)	1.869 (4)	1.879 (9)	2.084 (5)
Fe–N	1.970 (4)	1.986 (4)	1.983 (8)	2.254 (4)
Fe–N	1.972 (3)	2.005 (4)	1.987 (8)	2.369 (4)
Fe–N (centre)	1.877 (3)	1.870 (4)	1.876 (9)	
Fe–N	1.974 (3)	1.996 (4)	1.982 (9)	
Fe–N	1.974 (3)	2.006 (4)	1.993 (9)	
Selected angles (°)				
Trz–phenyl twist	30.6 (2)/28.30 (2)	14.3 (3)/10.6 (3)	7.9 (3)/11.7 (4)	11.9 (3)
Trz–pyridyl twist	9.8 (2)/2.8 (3)	2.4 (4)/8.7 (3)	3.7 (3)/3.2 (3)	10.2 (3)/3.6 (1)
N(trz)–Fe–N(trz) (ϕ)	178.8 (1)	175.9 (2)	178.0 (4)	169.1 (2)
N(py)–Fe–(Npy) bite angle	162.1 (1)/162.2 (1)	159.6 (2)/159.1 (2)	159.9(4)/159.5 (4)	146.7 (2)

previously reported structure reported as the PF_6^- salt [31]. The Fe–N bond distances in $[Fe(\mathbf{1c})_2](ClO_4)(PF_6)$ were lengthened to the central triazine ring as compared to $[Fe(\mathbf{1b})_2](ClO_4)_2$, but shorter to the peripheral pyrazine rings when compared to the pyridyl rings of $[Fe(\mathbf{1b})_2](ClO_4)_2$.

A significant elongation of Fe–N bond distances is observed in complex $[Fe(\mathbf{1d})_2](ClO_4)_2$ for both the central rings and the distal rings due to a combination of steric strain imposed by the methyl substituents and the consequential occupation of anti-bonding metal-based orbitals in the high-spin complex (Table 3). The bond elongations are consistent with the formation of a high-spin complex [9]. Smaller bite angles (72–73°) are reported for the high-spin complex due to the elongation of the Fe-N bonds consistent with observations made from high-spin tpy-based complexes [9].

Intermolecular Br–Br interactions are observed in all of the complexes in the extended lattice similar to those reported for Co(II) complexes of related ligands [29,31]. Intermolecular Br–Br distances of 3.46, 3.42 and 3.55 Å are observed for $[Fe(\mathbf{1a})_2](PF_6)_2$, $[Fe(\mathbf{1b})_2](ClO_4)_2$ and $[Fe(\mathbf{1d})_2](ClO_4)_2$, respectively, which are all shorter than the sum of the van der Waals radii for Br giving rise to 1-dimensional tapes running throughout the lattice. In complex $[Fe(\mathbf{1c})_2](ClO_4)(PF_6)$, the Br–Br contacts have lengthened to 4.26 Å.

2.3. Electrochemistry and electronic spectroscopy

The redox potentials for the Fe(II) complexes as their ClO_4^- salts are shown in Table 4. The Fe(III)/(II) couples dominate the anodic region and ligand-based reductions dominate the cathodic region of the cyclic voltammograms.

Table 4
Electrochemical data in CH_3CN solutions at 293 K[a]

	$E_{1/2}$ (ox)	$E_{1/2}$ (red)			
$[Fe(\mathbf{1a})_2]^{2+}$	1.11 (75)	−1.20 (68)	−1.32 (57)		
$[Fe(\mathbf{1b})_2]^{2+}$	1.38 (106)	−0.69 (66)	−0.84 (67)	−1.52 (82)	−1.82 (irr)
$[Fe(\mathbf{1c})_2]^{2+}$	1.89 (irr)	−0.42 (69)	−0.51 (69)	−1.13 (82)	−1.40 (55)
$[Fe(\mathbf{1d})_2]^{2+}$	1.62 (irr)	−0.51 (54)	−0.78 (76)	−1.62 (irr)	−1.80 (irr)
$[Fe(tpy)_2]^{2+}$[c]	1.10 (70)	−1.13 (70)	−1.27 (60)	−1.94 (70)	

[a] Potentials are in volts vs SCE for acetonitrile solutions, 0.1 M in TBAP, recorded at 25 ± 1 °C at a sweep rate of 200 mV/s. Unless otherwise stated couples are reversible.
[b] Irreversible; potential is given for the cathodic wave. (ΔE_p in parentheses (mV)).
[c] From Ref. [26].

The Fe(III)/(II) couples of the triazine-based complexes are irreversible as their ClO_4^- salts, although the same couple of $[Fe(\mathbf{1b})_2](PF_6)_2$ is reversible, presumably due to the improved solubility of the PF_6^- salts in acetonitrile solution [31]. The metal-based oxidation of $[Fe(\mathbf{1a})_2](ClO_4)_2$ is observed at +1.11 V, which is in agreement with the parent complex $[Fe(tpy)_2]^{2+}$ (+1.10 V) indicating that bromo-phenyl substitution of the tpy core has a minimal effect on the metal-based orbitals. The same Fe(III)/(II) couple in the triazine-based complexes occurs at a significantly more positive potential (1.38–1.89 V) due the electron-deficient nature of the triazine ligands as compared to the tpy ligand.

Similarly, the triazine-based complexes are easier to reduce than the terpyridine complexes. In complex $[Fe(\mathbf{1a})_2](ClO_4)_2$, a one-electron reduction of one terpyridine is observed followed by a second one-electron reduction of the second terpyridine ligand with a peak separation of 120 mV between the reductions. The separation between the reductions of the first and second triazine-based ligand in $[Fe(\mathbf{1b})_2](ClO_4)_2$ is 150 mV, which indicates greater sensitivity of the triazine ligands to reductive processes. An additional triazine-based reduction is observed on both ligands to give a total of four reductions for the complexes of triazine ligands.

The Fe(II) centres of complexes $[Fe(\mathbf{1c})_2](ClO_4)_2$ and $[Fe(\mathbf{1d})_2](ClO_4)_2$ are more difficult to oxidise and the ligands easier to reduce than triazine complex $[Fe(\mathbf{1b})_2](ClO_4)_2$ (Fig. 6). The pyrazine rings are more electron deficient than the pyridyl rings in $[Fe(\mathbf{1b})_2](ClO_4)_2$, thereby withdrawing more electron-density away from the metal centre. The positive shift, despite the introduction of electron-donating methyl groups in $[Fe(\mathbf{1d})_2](ClO_4)_2$, is a consequence of the high spin-state and weaker ligand field imposed by the elongation of the Fe–N bond distances.

The absorption data for the complexes are gathered in Table 5 and the absorption spectra of $[Fe(\mathbf{1a})_2](ClO_4)_2$, $[Fe(\mathbf{1b})_2](ClO_4)_2$ and $[Fe(\mathbf{1d})_2](ClO_4)_2$ are shown in Fig. 7. The UV regions of the electronic spectra for all of the Fe(II) complexes are dominated by ligand-centred $\pi \rightarrow \pi^*$ and $n \rightarrow \pi^*$ transitions. The visible regions are dominated by MLCT bands, albeit they are much less intense in the high-spin complex $[Fe(\mathbf{1d})_2](ClO_4)_2$ compared to the remaining complexes. The change in intensity may be a result of poor overlap between the ligand and metal orbitals due to the elongated bond distances. The ^{1}MLCT absorption band in complex $[Fe(\mathbf{1a})_2](ClO_4)_2$ is relatively sharp (569 nm) with a high energy shoulder. The transition

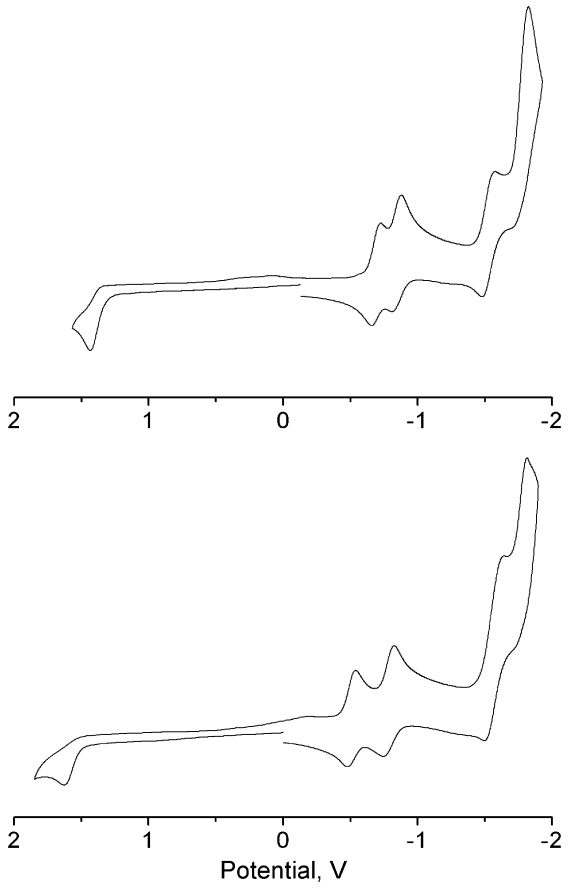


Fig. 6. Cyclic voltammograms of (above) $[Fe(\mathbf{1b})_2](ClO_4)_2$ and $[Fe(\mathbf{1d})_2](ClO_4)_2$ (below) in CH_3CN at room temperature.

Table 5
Spectroscopic data in CH_3CN solutions at 293 K

	Absorption, λ_{max}, nm (ε, $M^{-1}\,cm^{-1} \times 10^{-3}$)
$[Fe(\mathbf{1a})_2]^{2+}$	286 (67.3), 319 (42.7), 359 (7.2, sh), 568 (19.3)
$[Fe(\mathbf{1b})_2]^{2+}$	288 (67.1), 316 (40.3, sh), 548 (10.5), 597 (13.8)
$[Fe(\mathbf{1c})_2]^{2+}$	285 (71.3), 326 (43.4, sh), 533 (11.5), 576 (15.4)
$[Fe(\mathbf{1d})_2]^{2+}$	290 (52.9), 328 (26.9, sh), 400 (1.2, sh), 507 (0.4)

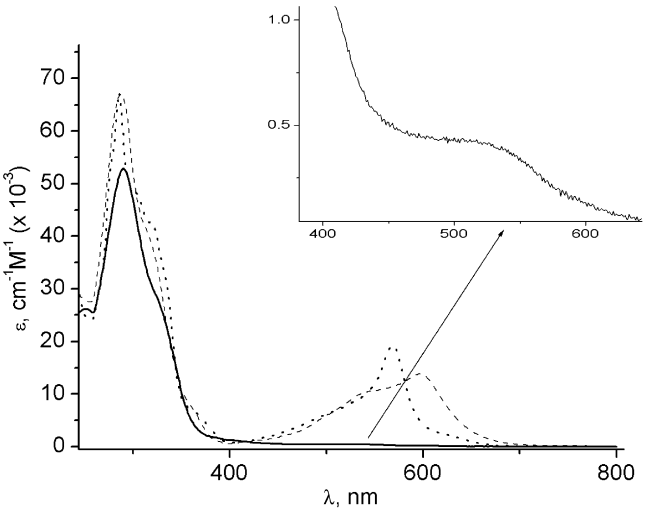


Fig. 7. Electronic spectra in acetonitrile for complexes $[Fe(\mathbf{1a})_2](ClO_4)_2$ (dotted-line), $[Fe(\mathbf{1b})_2](ClO_4)_2$ (dashed-line) and $[Fe(\mathbf{1d})_2](ClO_4)_2$ (solid line). $[Fe(\mathbf{1d})_2](ClO_4)_2$ is expanded in the visible region in the inset.

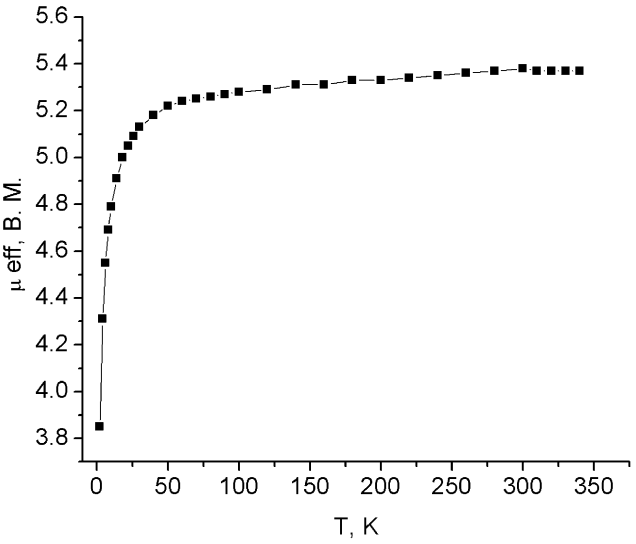


Fig. 8. Plot of the variable temperature magnetic moment of $[Fe(\mathbf{1d})_2](ClO_4)_2$.

is red-shifted compared to the parent complex $[Fe(tpy)_2]^{2+}$ (552 nm) as the bromo-phenyl substituent lowers the energy of the ligand-based LUMO [35]. The triazine complex, $[Fe(\mathbf{1b})_2](ClO_4)_2$, has two resolved MLCT bands at 542 and 597 nm, which may be a consequence of transitions to a triazine-based LUMO and a second, low-lying, triazine-based LUMO + 1 in the ligand. Thus, the two transitions may be considered as MLCT transitions to the ligand-based LUMO and LUMO + 1.

2.4. Magnetic measurements

The magnetism of the complexes was studied in solution at room temperature using the modified Evan's method and in the solid state using a SQUID magnetometer from 2 to 300 K. In solution, it was confirmed that $[Fe(\mathbf{1a})_2]^{2+}$ with both PF_6^- and ClO_4^- cations are diamagnetic at room temperature, consistent with the diamagnetic solution behaviour previously reported for an Fe(II) complex of a tolyl-tpy ligand [7]. The parent complex, $[Fe(tpy)_2]^{2+}$, is considered low spin at room temperature regardless of its counter-anion [34]. In contrast, $[Fe(\mathbf{1a})_2](PF_6)_2$ has significant paramagnetic contributions to the magnetic moment (3.5 B.M.) at 300 K in the solid state, whereas the perchlorate salt remains largely diamagnetic [7]. The magnetic moment of complex $[Fe(\mathbf{1b})_2]^{2+}$ as both the PF_6^- and ClO_4^- salts differ marginally between 2 and 300 K, with the PF_6^- salt having slightly greater paramagnetic contribution (2.5 B.M.) and a more gradual increase in the magnetic moment up to room temperature. Complex $[Fe(\mathbf{1c})_2](ClO_4)_2$ shows behaviour similar to complex $[Fe(\mathbf{1b})_2](ClO_4)_2$ with a magnetic moment of 4.2 B.M. at 300 K, more characteristic of a high-spin complex.

A plot of $1/\chi$ versus temperature for complex $[Fe(\mathbf{1d})_2](ClO_4)_2$ indicates a zero value for the Weiss constant, thereby suggesting that complex $[Fe(\mathbf{1d})_2](ClO_4)_2$ is a pure Curie paramagnet. The magnetic moment measured between 20 and 300 K corresponds to a high-spin Fe(II) complex ($S = 2$), with 5.4 B.M. measured at 340 K (Fig. 8). Below 20 K there is a reduction in the magnetic moment, down to 3.9 B.M. at 4 K, associated with zero-field splitting of the spin quintet state.

3. Conclusions

In solution, $[Fe(\mathbf{1a})_2]^{2+}$ is low spin, with no evidence of a paramagnetic contribution, whereas solid state measurements indicate significant high-spin contributions as the PF_6^- salt but not as the ClO_4^- salt. The solution and solid state magnetic data for complexes $[Fe(\mathbf{1b})_2](ClO_4)_2$ and $[Fe(\mathbf{1c})_2](ClO_4)_2$, on the other hand, indicate a small paramagnetic contribution to a largely diamagnetic ground state, due to the weaker ligand field strength of the triazine-containing ligands. Modification of complex $[Fe(\mathbf{1b})_2](ClO_4)_2$ with methyl substituents in the 6-position of the pyridyl rings induces sufficient steric strain to force a high-spin configuration over the temperature range 20–300 K. As too much steric strain leads to paramagnetic complexes, removing some of the steric strain may lead to spin-crossover complexes. We are currently undertaking further investigations of phenyl-tpy type ligands and the effects of substitution at other positions on the ligands on the magnetic and electrochemical properties of Fe(II) complexes of tridentate ligands.

4. Experimental

4.1. Materials and instrumentation

Nuclear magnetic resonance (NMR) spectra were recorded in CD_3CN at room temperature (r.t.) on a Bruker AV400 spectrometer at 400 MHz for ^1H NMR and at

100 MHz for ^{13}C NMR. Chemical shifts are reported in part per million (ppm) relative to residual solvent protons (1.93 ppm for acetonitrile-d_3) and the carbon resonance of the solvent. Absorption spectra were measured in deaerated acetonitrile at r.t. with a Cary 500i UV–Vis–NIR Spectrophotometer.

Electrochemical measurements were carried out in argon-purged acetonitrile at room temperature with a BAS CV50W potentiostat interfaced to a PC. The working electrode was a Pt electrode. The counter electrode was a Pt wire, and the pseudo-reference electrode was a silver wire. The reference was set using an internal 1 mM ferrocene/ferrocinium sample at 395 mV versus SCE in acetonitrile and 432 mV in DMF. The concentration of the compounds was 1 mM. Tetrabutylammonium hexafluorophosphate (TBAP) was used as supporting electrolyte and its concentration was 0.10 M. Cyclic voltammograms were obtained at scan rates of 50, 100, 200, and 500 mV/s. For irreversible oxidation processes, the cathodic peak was used as E, and the anodic peak was used for irreversible reduction processes. The criteria for reversibility were the separation of 60 mV between cathodic and anodic peaks, the close to unity ratio of the intensities of the cathodic and anodic currents, and the constancy of the peak potential on changing scan rate. The number of exchanged electrons was measured with OSWV, and by taking advantage of the presence of ferrocene used as the internal reference.

Variable temperature magnetic data were obtained with a Quantum Design MPMS5S Squid magnetometer operating in DC mode. Samples were prepared in gelatine capsules or aluminium cups, and measured data were corrected for sample holder response, and underlying sample diamagnetism using Pascal corrections.

Experimental uncertainties are as follows: absorption maxima, ±2 nm; molar absorption coefficient, 10%; redox potentials, ±10 mV.

X-ray crystallographic data for all complexes were collected from a single crystal sample, which as obtained by slow diffusion of isopropyl ether into acetonitrile solutions of the complexes, were mounted on loop fibers. Data were collected using a Bruker Platform diffractometer, equipped with a Bruker SMART 2K Charged-Coupled Device (CCD) Area Detector using the program SMART and normal focus sealed tube source graphite monochromated Cu Kα radiation.

Empirical adsorption corrections were applied using the SADABS program.

The structures were solved by direct method and refined using full-matrix least squares on F^2 using the SHELXTL suite of programs [36]. The H atoms were generated geometrically and were included in the refinement in the riding model approximation.

4.2. Synthetic procedures

Complexes **1a**, **1b** and $Fe(L)_2(PF_6)_2$ were synthesised as previously described [29,31,32].

4.2.1. *1c*

^{n}BuLi (1.6 M in hexanes, 11.0 mL, 0.018 mol) was added dropwise to a stirring solution of $HNMe_2$ (2 M in THF, 8.8 mL, 0.018 mmol) in anhydrous Et_2O (150 mL) under an inert atmosphere. The mixture was stirred until a white suspension formed (20 min) and *p*-bromo-benzonitrile (3.00 g, 0.016 mol) was added to the mixture as a solid. The mixture was stirred for 1 h, followed by addition of 2-cyanopyrazine (3.47 g, 0.033 mol). The reaction was stirred under N_2 for 4 h and in air for a further 30 min. The solid was collected by filtration, recrystallised from ethanol:water 1:2, washed with diethyl ether and dried to afford **1c** as a white powder (1.00 g, 16% yield).

^1H NMR (400 MHz, $CDCl_3$): 9.98, d, 2H, ($J = 1$ Hz), $H_{3,3''}$; 8.94 (t, $J = 2$ Hz, 2H) $H_{5,5''}$; 8.87 (d, $J = 2$ Hz, 2H) $H_{6,6''}$; 8.69 (d, $J = 9$ Hz, 2H) $H_{2''',6'''}$; 7.77 (d, $J = 9$ Hz, 2H) $H_{3''',5'''}$. ^{13}C {^1H} NMR (100 MHz, $CDCl_3$): 128.65, 130.56, 131.97, 133.21, 144.65, 145.87, 147.01, 148.02, 170.37, 172.12. High Res ESMS *m/z* calc. for $C_{17}H_{11}N_7Br$: $[M + H]^+$ 392.02594. Found: 392.02582.

4.2.2. *1d*

^{n}BuLi (1.6 M in hexanes, 1.45 mL, 2.32 mmol) was added dropwise to a stirring solution of $HNMe_2$ (2 M in THF, 1.16 mL, 2.32 mmol) in anhydrous Et_2O (30 mL) under an inert atmosphere. The mixture was stirred until a white suspension formed (20 min) and *p*-bromo-benzonitrile (0.38 g, 2.11 mmol) was added to the mixture as a solid. The mixture was stirred for 1 h, followed by addition of 2-cyano-6-methylpyridine (0.50 g, 4.23 mmol). The reaction was stirred under N_2 overnight and in air for a further 30 min. The solid was collected by filtration, recrystallised from ethanol:water 1:2, washed with diethyl ether and dried to afford **1d** as a white powder (333 mg, 38% yield).

^1H NMR ($CDCl_3$, 400 MHz): 8.67 (d, $J = 9$ Hz, 2H) $H_{2''',6'''}$; 8.63 (d, $J = 8$ Hz, 2H) $H_{3,3''}$; 7.85 (t, $J = 8$ Hz, 2H) $H_{4,4''}$; 7.71 (d, $J = 9$ Hz, 2H) $H_{3''',5'''}$; 7.41 (d, $J = 7$ Hz, 2H) $H_{5,5''}$; 2.80 (s, 6H) $H_{6,6''}$. ^{13}C {^1H} NMR ($CDCl_3$, 100 MHz): 23.90, 121.84, 126.37, 127.71, 130.29, 131.63, 133.95, 137.09, 151.96, 159.14, 171.11, 171.17. *Anal*. Calc. for $C_{21}H_{16}BrN_5$: C, 60.30; H, 3.86; N, 16.74. Found C, 59.87; H, 3.88; N, 16.52%.

4.3. The Fe(II) complexes

$[Fe(\mathbf{1a})_2](ClO_4)_2$: **1a** (198 mg, 0.51 mmol) was dissolved in acetonitrile (30 mL) and heated gently. In a separate flask, the $Fe(ClO_4)_2.6\,H_2O$ (65 mg, 0.26 mmol) was heated in acetonitrile (5 mL) and was then added on stirring to the ligand solution. An intense purple colour was immediately observed and stirring and heating were continued for a further 10 min. The solution was filtered, cooled and the solvent removed. The solid was dissolved in a minimum amount of acetonitrile and added to diethyl ether (200 mL). The solid was collected and dried to afford $[Fe(\mathbf{1a})_2](ClO_4)_2$ as a purple powder (150 mg, 57% yield).

ESMS: $[M]^{2+}$416.4. *Anal.* Calc. for $C_{42}H_{28}N_6Br_2Fe_1(ClO_4)_2 \cdot H_2O$: C, 48.08; H, 2.88; N, 8.01. Found: C, 47.94; H, 2.37; N, 7.89%.

$[Fe(\mathbf{1b})_2](ClO_4)_2$: The same method of preparation was used as $[Fe(\mathbf{1a})_2](ClO_4)_2$, starting with $Fe(ClO_4)_2.6H_2O$ (65 mg, 0.26 mmol) and **1b** (199 mg, 0.51 mmol). $[Fe(\mathbf{1b})_2](ClO_4)_2$ was isolated as a purple powder (115 mg, 44% yield).

ESMS: $[M]^{2+}$418.3. *Anal.* Calc. for: $C_{38}H_{24}N_{10}Br_2Fe_1 \cdot (ClO_4)_2$: C, 44.09; H, 2.34; N, 13.53. Found: C, 43.77; H, 1.86; N, 13.41%.

$[Fe(\mathbf{1c})_2](ClO_4)_2$: The same method of preparation was used as $[Fe(\mathbf{1a})_2](ClO_4)_2$, starting with $Fe(ClO_4)_2.6H_2O$ (65 mg, 0.26 mmol) and **1c** (200 mg, 0.51 mmol). $[Fe(\mathbf{1c})_2](ClO_4)_2$ was isolated as a purple powder (162 mg, 56% yield).

High Res ESMS *m/z* calc. for $C_{34}H_{20}N_{14}Br_2Fe$: $[M]^{2+}$ 419.9845; found: 419.9846. *Anal.* Calc. for $C_{34}H_{20}N_{14}Br_2Fe_1(ClO_4)_2 \cdot 0.5(H_2O)$: C, 38.96; H, 2.02; N, 18.71. Found: C, 39.30; H, 1.94; N, 18.87%.

$[Fe(\mathbf{1d})_2](ClO_4)_2$: The same method of preparation was used as $[Fe(\mathbf{1d})_2](ClO_4)_2$, starting with $Fe(ClO_4)_2.6H_2O$ (30 mg, 0.12 mmol) and **1d** (100 mg, 0.24 mmol). $[Fe(\mathbf{1d})_2](ClO_4)_2$ was isolated as a red solid (80 mg, 61% yield).

High Res ESMS *m/z* calc. for $C_{34}H_{20}N_{14}Br_2Fe$: $[M]^{2+}$ 445.0263; found: 445.0270. *Anal.* Calc. for $C_{42}H_{32}N_{10}Br_2Fe_1(ClO_4)_2 \cdot H_2O$: C, 45.47; H, 3.09; N, 12.63. Found: C, 45.72; H, 2.64; N, 12.81%.

Acknowledgements

G.S.H. and L.K.T. thank the Natural Sciences and Engineering Research Council of Canada and GSH thanks the Centre for Self-Assembled Chemical Structures and the Université de Montréal for financial support. EAM thanks the Commonwealth Scholarship Programme for a doctoral scholarship and Francine Belanger for assistance with the X-ray crystallography.

Appendix A. Supplementary material

CCDC 619603, 619604, 619605 and 619606 contain the supplementary crystallographic data for complexes $[Fe(\mathbf{1a})_2](PF_6)_2$, $[Fe(\mathbf{1b})_2](ClO_4)_2$, $[Fe(\mathbf{1c})_2](ClO_4)(PF_6)$ and $[Fe(\mathbf{1d})_2](ClO_4)_2$. These data can be obtained free of charge via http://www.ccdc.cam.ac.uk/conts/retrieving.html, or from the Cambridge Crystallographic Data Centre, 12 Union Road, Cambridge CB2 1EZ, UK; fax: (+44) 1223-336-033; or e-mail: deposit@ccdc.cam.ac.uk. Supplementary data associated with this article can be found, in the online version, at doi:10.1016/j.poly.2007.10.002.

References

[1] S.J. Loeb, Chem. Soc. Rev. 36 (2007) 226.
[2] S. Bonnet, J.-P. Collin, M. Koizumi, P. Mobian, J.-P. Sauvage, Adv. Mat. 18 (2006) 1239.
[3] U. Mueller, M. Schubert, F. Teich, H. Puetter, K. Schierle-Arndt, J. Pastre, J. Mat. Chem. 16 (2006) 626.
[4] P. Gütlich, Y. Garcia, H.A. Goodwin, Chem. Soc. Rev. 29 (2000) 419.
[5] P. Gütlich, P.J. Koningsbruggen, F. Renz, Struct. Bond. 107 (2004) 27.
[6] H.A. Goodwin, Top. Curr. Chem. 233 (2004) 59.
[7] J. Chambers, B. Eaves, D. Parker, R. Claxton, P.S. Ray, S.J. Slattery, Inorg. Chim. Acta 359 (2006) 2400.
[8] D.J. Hathcock, K. Stone, J. Madden, S.J. Slattery, Inorg. Chim. Acta 282 (1998) 131.
[9] E.C. Constable, G. Baum, E. Bill, R. Dyson, R. Van Eldik, D. Fenske, S. Kaderli, D. Morris, A. Neubrand, M. Neuburger, D.R. Smith, K. Wieghardt, M. Zehnder, A.D. Zuberbuhler, Chem. Eur. J. 5 (1999) 498.
[10] Y. Bodenthin, U. Pietsch, H. Moehwald, D.G. Kurth, J. Am. Chem. Soc. 127 (2005) 3110.
[11] C.A. Kilner, M.A. Halcrow, Polyhedron 25 (2006) 235.
[12] P. Manikandan, K. Padmakumar, K.R. Justin Thomas, B. Varghese, H. Onodera, P.T. Manoharan, Inorg. Chem. 40 (2001) 6930.
[13] F.A. Al-mutlaq, P.G. Potvin, A.I. Philippopoulos, P. Falaras, Eur. J. Inorg. Chem. (2007) 2121.
[14] D.L. Reger, J.R. Gardinier, M.D. Smith, A.M. Shahin, G.J. Long, L. Rebbouh, F. Grandjean, Inorg. Chem. 44 (2005) 1852.
[15] R. Liegghio, P.G. Potvin, A.B.P. Lever, Inorg. Chem. 40 (2001) 5485.
[16] C. Enachescu, J. Linares, F. Varret, K. Boukheddaden, E. Codjovi, S.G. Salunke, R. Mukherjee, Inorg. Chem. 43 (2004) 4880.
[17] T. Ayers, R. Turk, C. Lane, J. Goins, D.L. Jameson, S.J. Slattery, Inorg. Chim. Acta 357 (2004) 202.
[18] M.A. Halcrow, Coord. Chem. Rev. 249 (2005) 2880, and references therein.
[19] U. Ziener, E. Breuning, J.-M. Lehn, E. Wegelius, K. Rissanen, G. Baum, D. Fenske, G. Vaughan, Chem. Eur. J. 6 (2000) 4132.
[20] V.A. Money, J. Elhaik, I.R. Evans, M.A. Halcrow, J.A.K. Howard, Dalton Trans. (2004) 65.
[21] J. Elhaik, V.A. Money, S.A. Barrett, C.A. Kilner, I.R. Evans, M.A. Halcrow, Dalton Trans. (2003) 2053.
[22] F.H. Case, E. Koft, J. Am. Chem. Soc. 81 (1959) 905.
[23] G.K. Pagenkopf, D.W. Margerum, Inorg. Chem. 7 (1968) 2514.
[24] D. Sedney, M. Kahjehnassiri, W.M. Reiff, Inorg. Chem. 20 (1981) 20.
[25] F.H. Fraser, P. Epstein, D.J. Macero, Inorg. Chem. 11 (1972) 2031.
[26] C. Arana, S. Yan, M. Keshavarz-K, K.T. Potts, H.D. Abruña, Inorg. Chem. 31 (1992) 3680.
[27] M.I.J. Polson, N.J. Taylor, G.S. Hanan, Chem. Commun. (2002) 1356.
[28] M.I.J. Polson, E.A. Medlycott, G.S. Hanan, L. Mikelsons, N.J. Taylor, M. Watanabe, Y. Tanaka, F. Loiseau, R. Passalacqua, S. Campagna, Chem. Eur. J. 10 (2004) 3640.
[29] E.A. Medlycott, I. Theobald, G.S. Hanan, Eur. J. Inorg. Chem. (2005) 1223.
[30] E.A. Medlycott, G.S. Hanan, Inorg. Chem. Commun. 10 (2007) 229.
[31] E.A. Medlycott, K.A. Udachin, G.S. Hanan, Dalton Trans. (2007) 430.
[32] (a) J. Wang, G.S. Hanan, Synlett (2005) 1251;
(b) S. Vaduvescu, P.G. Potvin, Eur. J. Inorg. Chem. (2004) 1763;
(c) L. Masciello, P.G. Potvin, Can. J. Chem. 81 (2003) 209;
(d) S. Vaduvescu, P.G. Potvin, Inorg. Chem. 41 (2002) 4081.
[33] E.A. Medlycott, G.S. Hanan, F. Loiseau, S. Campagna, Chem. Eur. J. 13 (2007) 2837.
[34] E.C. Constable, M.D. Ward, Inorg. Chim. Acta 141 (1988) 201.
[35] J.M. Rao, D. Macero, M. Hughes, Inorg. Chim. Acta 41 (1980) 221.
[36] G.M. Sheldrick, SHELXTL, 2001 and 1997, Bruker Analytical X-Ray Systems, Madison, WI.

Available online at www.sciencedirect.com
ScienceDirect
Polyhedron 27 (2008) 502–512
POLYHEDRON
www.elsevier.com/locate/poly

Crystal structures, theoretical calculations, spectroscopic and electrochemical properties of Cr(III) complexes with dipicolinic acid and 1,10-phenantroline

Ana C. González-Baró [a], Reinaldo Pis-Diez [a], Oscar E. Piro [b], Beatriz S. Parajón-Costa [a,*]

[a] *Centro de Química Inorgánica (CEQUINOR, CONICET/UNLP), Facultad de Ciencias Exactas, Universidad Nacional de La Plata, C.C. 962, 1900 La Plata, Argentina*
[b] *Departamento de Física, Facultad de Ciencias Exactas, Universidad Nacional de La Plata and IFLP (CONICET), C.C. 67, 1900 La Plata, Argentina*

Received 28 June 2007; accepted 3 October 2007
Available online 19 November 2007

Abstract

The crystal structures of compounds $Na[Cr(dipic)_2]\cdot 2H_2O$ (**1**) and $[Cr(dipic)(phen)Cl]\cdot 1/2H_2O$ (**2**), dipic = dipicolinate, phen = 1,10-phenantroline, were determined. In both complexes, Cr(III) is in a distorted octahedral environment. In complex (**1**), the metal is coordinated to two nearly perpendicular dipic anions acting as tridentate ligands through one oxygen of each carboxylate group and the pyridinic nitrogen atom. In complex (**2**), Cr(III) ion is similarly coordinated to a dipic anion, defining a ligand equatorial plane. The phen molecule bridges the remaining equatorial coordination site and one of the axial positions through its N-atoms. The other axial position is occupied by a chloride ion.

The optimized geometries of both compounds and their corresponding harmonic vibrational frequencies were calculated using methods of density functional theory. The infrared, Raman and electronic spectra of the complexes were recorded. Assignments of the most characteristic bands are reported and discussed. Their electrochemical properties were also investigated. Both compounds exhibit similar redox behavior; they undergo two main reduction processes involving the metal center and the dipicolinato ligand. No Cr(III) oxidation processes were found.
© 2007 Elsevier Ltd. All rights reserved.

Keywords: Chromium-complexes; X-ray structure; Spectroscopy; Density functional calculations; Redox properties

1. Introduction

Numerous studies have been developed with the aim of determining the chromium function at molecular level but its biological role is still controversial and not well understood. Some compounds of Cr(VI) are well-established carcinogens [1,2]. Chromium enters mammalian cells in the hexavalent form and it is reduced by intracellular materials to Cr(III), which binds to DNA via guanine N-7 atoms and phosphate groups [3]. The long-term toxicity effects observed in workers exposed to occupational Cr(VI) was proposed to be attributed to reoxidation of accumulated Cr(III), previously reduced within the cell [1].

In contrast, Cr(III) is considered an essential trace element for humans, enhancing the activity of insulin in glucose and fat metabolism and it is recognized as a dietary supplement [4–6]. However, some divergence is found actually with respect to this role [2,7–10]. Studies carried out with the popular dietary supplement $Cr(pic)_3$ (pic = picolinate) show that this compound produces oxidative stress and DNA damage [11–14]. Recently, it was also suggested that the antidiabetic activities of Cr(III)-containing nutritional supplements could involve the formation of

* Corresponding author. Tel./fax: +54 221 4259485.
E-mail address: beatrizp@quimica.unlp.edu.ar (B.S. Parajón-Costa).

0277-5387/$ - see front matter © 2007 Elsevier Ltd. All rights reserved.
doi:10.1016/j.poly.2007.10.005

genotoxic Cr(V/VI) species, by intra or extra cellular oxidation, which acts similarly to well-known insulin-mimetic V(V) compounds [15].

Mechanistic studies of biologically relevant redox reactions of chromium complexes in different oxidation states have been recently reviewed [16]. The involvement of Cr(III) in intracellular redox reactions, that generate species capable to produce DNA damage and mutation in bacterial and mammalian cells, has been postulated and some mechanisms were proposed [17–19]. Cr(III) compounds containing aromatic imines as ligands have shown mutagenic effects in bacterial assays. Electrochemical studies reveal that, for these compounds, the Cr(III)/Cr(II) redox couple is reversible and exhibits reduction potential within the range of cellular reductant agents. Thus, it was suggested that the mutagenic compounds could be reduced intracelullary and generate DNA damaging hydroxyl radicals via Fenton-like reactions. In contrast, non-mutagenic Cr(III) complexes show irreversible behavior and more negative Cr(III)/Cr(II) reduction potential [19].

As part of our studies on metal complexes of biological interest, containing dipicolinic acid and related ligands [20–22] and in an attempt to contribute to a better understanding of the physicochemical properties of Cr(III) complexes containing organic ligands, $Na[Cr(dipic)_2]\cdot 2H_2O$ (**1**) and $[Cr(dipic)(phen)Cl]\cdot 1/2H_2O$ (**2**) were investigated. Dipicolinic acid (H_2dipic, 2,6-pyridinedicarboxylic acid) is a relevant N–O chelating agent, present in many natural compounds, that shows various biological functions and potential pharmacological activity. Even though 1,10-phenantroline has no significant biological role, complexes of this ligand with Cr(III) have been extensively studied as models of metal centers coordinated by aromatic bases [17–19].

In the present paper, the optimized geometries, calculated by means of the density functional theory were compared with crystallographic data and the experimental vibrational modes were assigned with the help of calculated frequencies. The electrochemical study of both complexes was performed in dimethysulfoxide (DMSO) solutions. The results were complemented with electronic spectroscopy and the assignment of experimental bands was accomplished with the aid of calculated electronic transitions obtained through the time dependent density functional theory.

2. Experimental

2.1. Reagents

$CrCl_3\cdot 6H_2O$, dipicolinic acid and 1,10-phenantroline (analytical grade, Sigma) were used without further purification. High purity DMSO (Aldrich) was used for the electrochemical measurements. Tetrabutylammonium hexafluorophosphate ($TBAPF_6$), employed as supporting electrolyte, was purchased from Fluka (electrochemical grade).

2.2. Synthesis of complexes

2.2.1. $Na[Cr(dipic)_2]\cdot 2H_2O$ (1)

Dipicolinic acid (H_2dipic, 0.12 g, 0.72 mmol) was dissolved in ethanol (25 ml) and drop wise added, under continuous stirring, to an ethanolic solution (25 ml) of $CrCl_3\cdot 6H_2O$ (0.14 g, 0.53 mmol). After 60 min stirring, at room temperature, 0.1 M NaOH was drop wise added to the resulting dark green solution until a color change, first to blue and finally to violet, was observed. The reaction mixture was stirred during 60 min more and then left to stand at room temperature. After two weeks, purple crystals suitable for X-ray structural analysis were obtained. The yield was 57%. *Anal.* Calc. for $C_{14}H_{10}CrN_2O_{10}Na$: C, 38.1; H, 2.3; N, 6.3. Found: C, 37.8; H, 2.5; N, 6.1%.

2.2.2. $[Cr(dipic)(phen)Cl]\cdot 1/2H_2O$ (2)

Even though the complex was prepared following the reported procedure [23], crystals suitable for X-ray structural analysis were obtained in the present case. To an ethanolic solution (50 ml) of $CrCl_3\cdot 6H_2O$ (0.27 g, 1.0 mmol) was added drop-by-drop an ethanolic solution (50 ml) of dipicolinic acid (0.17 g, 1.0 mmol). The mixture was stirred at room temperature for 60 min, when it turned deep green colored. Afterwards, an ethanolic solution (50 ml) of phenantroline (0.20 g, 1.1 mmol) was dropwise added and the stirring was continued for 60 min, at room temperature, until a violet solution was obtained. The system was kept at room temperature and after two weeks it showed the precipitation of purple single crystals. The yield was 42%. *Anal.* Calc. for $C_{19}H_{12}CrN_3O_{4.5}Cl$: C, 51.6; H, 2.7; N, 9.5. Found: C, 51.2; H, 2.5; N, 9.7%.

2.3. Physicochemical characterization

Elemental analysis (C, H, N) was performed using a Carlo Erba EA 1108 analyzer. FTIR spectra (4000–200 cm^{-1}) were measured using the KBr pellet technique with a Bruker 113v instrument. Raman spectra were obtained with a Bruker IFS 66 FTIR spectrophotometer, using the FRA 106 Raman accessory and the 1064 nm line of a Nd:YAG solid state laser for excitation. The electronic absorption spectra of the complexes and the ligands were measured on freshly prepared DMSO solutions in the 200–800 nm spectral range. They were recorded with a Hewlett–Packard 8452-A diode array spectrometer, using 10 mm quartz cells. Cyclic voltammetry was carried out with a computer controlled Princeton Applied Research (PAR) Potentiostat/Galvanostat model 263A. A standard three-electrode cell was used with a glassy carbon electrode as the working electrode, a platinum wire as the counter electrode and an Ag/(10^{-3} M) $AgNO_3$ in CH_3CN as the reference electrode. This electrode was calibrated against the $[Fe(C_5H_5)_2]/[Fe(C_5H_5)_2]^+$ redox couple, for which a potential of +0.4 V vs NHE was assumed [24,25]. All potentials reported here are referred to NHE in volts. Measurements were performed in oxygen purged 10^{-3} M DMSO solutions

with 0.1 M $TBAPF_6$ as supporting electrolyte. During the measurements, a continuous nitrogen stream was passed over the solutions.

2.4. Theoretical calculations

The GAUSSIAN 03 package [26] was used both for geometry optimizations and vibrational frequencies calculations. Becke's three parameters hybrid density functional [27] with the gradient-corrected correlation functional due to Lee et al. [28], a combination that gives rise to the well-known B3LYP method, was employed. The 6-31G(d,p) basis set was utilized for all atoms.

The ADF package [29–31] was used to calculate the electronic spectra of both complexes. The gradient-corrected exchange-correlation functional due to Perdew et al. [32] was used for the self-consistent field calculations, whereas the adiabatic local density approximation [33] was utilized for the time dependent density functional kernel. The atomic orbitals of all atoms were represented by a basis set of Slater functions having triple-zeta quality in the valence space and including two sets of polarization functions. The frozen core approximation up to the 1s orbital for C, N, and O, and up to the 2p orbital for Cr was used.

2.5. X-ray diffraction data and crystal structure determination

Diffraction data were collected on an Enraf-Nonius CAD4 diffractometer with EXPRESS [34] and reduced with XCAD4 [35]. The data were corrected numerically for absorption with PLATON [36]. The structures were solved by direct and Fourier methods with SHELXS [37] and its non-H atom refined by full-matrix least-squares with SHELXL [38]. The hydrogen atoms of the organic molecules in both substances were positioned stereo-chemically and refined with the riding model. The H-atoms of one crystallization water molecule of $Na[Cr(dipic)_2]\cdot 2H_2O$ were found in a difference Fourier map and refined isotropically with Ow-H and H···H distances restrained to target values of 0.86(1) and 1.36(1) Å, respectively. The H-atoms of the other water molecule could not be positioned reliably and therefore they were not included in the refinement. The crystallization water molecule of the $[Cr(dipic)(phen)Cl]\cdot 1/2H_2O$ complex showed positional disorder around a crystal inversion center. It was modeled in term of two sites for the oxygen atom and refined isotropically with occupation factor of 1/2 for each site.

3. Results and discussion

3.1. Theoretical calculations

The geometry of both complexes were optimized in the gas phase using tools from the density functional theory [39–41]. Calculations were carried out without specifying any symmetry for the complexes. A quartet electronic state corresponding to a high-spin electronic configuration for the Cr(III) ion was considered for both compounds, thus unrestricted Kohn–Sham calculations were accomplished throughout. No countercations were taken into account in the calculations for complex (**1**).

A vibrational analysis was performed for the optimized geometries to verify whether they are local minima or saddle points on the potential energy surface of the molecules. No scale factor was used to correct the calculated frequencies.

The electronic excitations of both complexes were calculated using the time dependent density functional theory [42,43].

3.2. Structural results

Crystal data and refinement results for compounds (**1**) and (**2**) are summarized in Table 1. Experimental and calculated bond distances and angles around Cr(III) ion are presented in Tables 2 and 3. Figures 1 and 2 show the ORTEP [44] drawings of the molecules.

$Na[Cr(dipic)_2\cdot 2H_2O$: Cr(III) ion is in a distorted octahedral environment, coordinated to two dipic anions acting as tridentate ligands through its carboxylic oxygen atoms [Cr–O distances in the range from 1.985(5) to 1.998(4) Å] and the nitrogen atoms [d(Cr–N1) = 1.972(5) and d(Cr–N2) = 1.980(5) Å]. The dipic ligands are nearly planar [rms deviation of atoms from the corresponding least-squares planes less than of 0.07 Å] and perpendicular to each other [dihedral angle of 81.73(5)°]. The metal ion lies close onto the intersection of the coordination planes (along the N1···N2 direction).

Table 1
Crystal data, structure solution methods and refinement results for $Na[Cr(dipic)_2]\cdot 2H_2O$ (**1**) and $[Cr(dipic)(phen)Cl]\cdot 1/2H_2O$ (**2**)

Compound	**1**	**2**
Chemical formula	$C_{14}H_{10}CrN_2NaO_{10}$	$C_{19}H_{12}CrClN_3O_{4.5}$
Formula weight	441.23	441.44
Temperature (K)	296(2)	296(2)
Crystal system	monoclinic	triclinic
Space group	*Cc* (no. 9)	$P\bar{1}$ (No. 2)
a (Å)	15.000(4)	8.636(2)
b (Å)	12.255(3)	9.754(2)
c (Å)	8.690(1)	12.402(2)
α (°)		68.34(2)
β (°)	92.96(2)	89.08(1)
γ (°)		79.65(2)
Volume (Å^3)	1595.3(6)	953.7(3)
Z	4	2
D_{calc} (Mg/m^3)	1.837	1.538
Crystal size	$0.24\times0.16\times0.02$	$0.2\times012\times0.06$
μ (mm^{-1})	6.793	6.531
Radiation (Å)	Cu Kα, $\lambda = 1.54184$	Cu Kα, $\lambda = 1.54184$
$R_1(F_o)$[a] $[I > 2\sigma(I)]$	0.0486	0.0573
$wR_2(F_o^2)$[b]	0.0544	0.0756

[a] $R_1 = \sum\|F_o| - |F_c\|/\sum|F_o|$.
[b] $wR_2 = [\sum w(|F_o|^2 - |F_c|^2)^2/\sum w(|F_o|_2)^2]^{1/2}$.

Table 2
Experimental and calculated bond distances (Å) and angles (°) around chromium for complex (**1**)

	Experimental	Calculated
Bond distances (Å)		
Cr–N1	1.972(5)	1.992
Cr–N2	1.980(5)	1.992
Cr–O11	1.996(5)	2.000
Cr–O13	1.998(4)	2.000
Cr–O21	1.986(5)	2.000
Cr–O23	1.985(5)	2.000
Bond angles (°)		
N1–Cr–N2	172.9(2)	180.0
N1–Cr–O11	79.0(2)	78.6
N1–Cr–O13	78.4(2)	78.6
N1–Cr–O21	107.7(2)	101.4
N1–Cr–O23	94.9(2)	101.4
N2–Cr–O11	98.0(2)	101.4
N2–Cr–O13	104.8(2)	101.4
N2–Cr–O21	78.6(2)	78.6
N2–Cr–O23	78.8(2)	78.6
O11–Cr–O13	157.2(2)	157.3
O11–Cr–O21	89.4(2)	92.2
O11–Cr–O23	94.2(2)	92.2
O13–Cr–O21	94.8(2)	92.2
O13–Cr–O23	90.4(2)	92.2
O21–Cr–O23	157.4(2)	157.3

Table 3
Experimental and calculated bond distances (Å) and angles (°) around chromium for complex (**2**)

	Experimental	Calculated
Bond distances (Å)		
Cr–N1	1.969(4)	1.975
Cr–N21	2.075(4)	2.126
Cr–N22	2.081(3)	2.153
Cr–O11	1.999(3)	1.978
Cr–O13	1.975(3)	1.978
Cr–Cl	2.290(1)	2.294
Bond angles (°)		
N1–Cr–O11	78.5(1)	79.2
N1–Cr–O13	79.4(1)	79.2
N1–Cr–N21	177.2(1)	173.8
N1–Cr–N22	97.8(1)	96.2
O11–Cr–N21	101.3(1)	100.3
O11–Cr–N22	88.4(1)	87.3
O13–Cr–N21	100.5(1)	100.3
O13–Cr–N22	89.7(1)	87.3
O13–Cr–O11	157.4(1)	157.0
N21–Cr–N22	79.4(1)	77.6
N1–Cr–Cl	90.8(1)	93.1
N21–Cr–Cl	92.0(1)	93.1
N22–Cr–Cl	171.2(1)	170.7
O11–Cr–Cl	91.8(1)	94.5
O13–Cr–Cl	93.4(1)	94.5

The sodium ion is in a compact sixfold coordination with four carboxylic oxygen atoms of neighboring dipic groups [Na···O distances in the range from 2.406(6) to 2.651(6) Å] and the two water molecules [d(Na···O1w) = 2.329(6) Å and d(Na···O2w) = 2.412(5) Å].

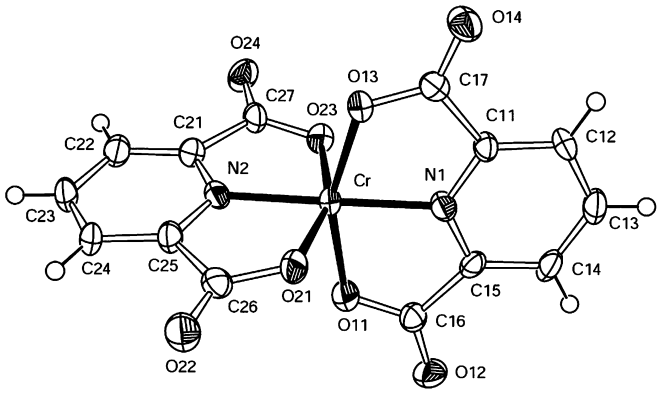


Fig. 1. Molecular plot of the $[Cr(dipic)_2]^-$ anion showing the labeling of the non-H atoms and their displacement ellipsoids at the 50% probability level. Chromium-ligand bonds are indicated by full lines.

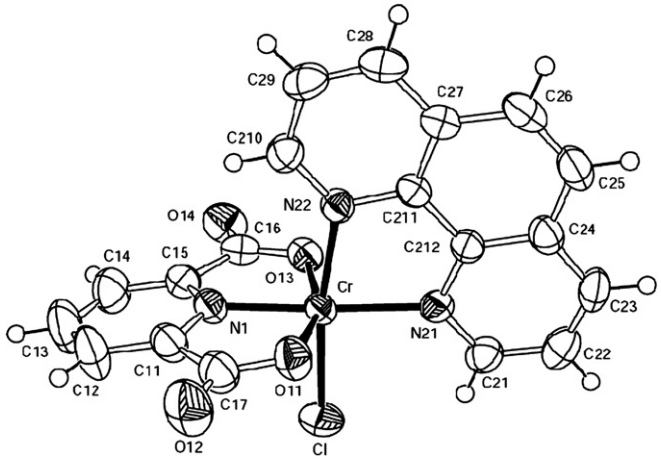


Fig. 2. Molecular diagram showing the [Cr(dipic)(phen)Cl] complex.

As the geometry optimization within the density functional framework was accomplished in the gas phase, that is without any perturbation as the ones arising from crystal packing effects, the two dipic ligands are located symmetrically around the metal ion, as can be seen from Table 2. This fact is in clear contrast with the experimental N1–Cr–N2 bond angle, which amounts to ca. 173°. Moreover, experimental N–Cr–O bond angles, in which N belongs to one of the dipic ligands and O belongs to the other dipic ligand, deviate from the gas phase value of 101.4°. It can also be observed in Table 2 that experimental N2–Cr–O11 and N2–Cr–O13 bond angles differ by about 3° with respect to the gas phase value, whereas N1–Cr–O21 and N1–Cr–O23 bond angles differ by about 6°. These findings seem to indicate that countercations interact differently with the two dipic ligands.

[*Cr(dipic)(phen)Cl*] · *1/2H*$_2$*O*: Cr(III) ion is in a sixfold environment, coordinated to one dipic ion defining a ligand equatorial plane [Cr–O distances of 1.975(3) and 1.999(3) Å and d(Cr–N) = 1.969(4) Å] and to a phen molecule acting as a bidentate ligand that bridges the fourth equatorial coordination site and one axial position through

its nitrogen atoms [Cr–N distances of 2.075(4) and 2.081(3) Å, respectively]. The other axial position is occupied by a chlorine ion [d(Cr–Cl) = 2.290(1) Å]. The dipic and phen molecules are nearly planar [rms deviation of atoms from the corresponding least-squares planes less than of 0.045 Å for both ligands] and close to mutual perpendicularity [angled at 86.60(7)° from each other]. As for the sodium salt, the Cr(III) ion nearly lies on the intersection of the coordination planes (along the N1···N21 direction).

The agreement between theoretical and experimental data is better than for complex (**1**) as can be seen in Table 3. The most relevant differences are observed when the N1–Cr–N21, N1–Cr–N22 and N21–Cr–N22 bond angles are compared. The ideal, gas phase values are 173.8° and 96.2°, respectively, whereas the experimental ones are 177.2° and 97.8°, respectively. These facts suggest that the phen ligand becomes stabilized in the solid state in a rather strained conformation. This can also be confirmed by comparing the experimental and gas phase values of the N21–Cr–N22 bond angle, which amount to 79.4° and 77.6°, respectively, thus differing by about 1.8°.

3.3. Vibrational spectra

Data of some of the most characteristic IR and Raman bands of the compounds are presented in Table 4 along with those of the H_2dipic and phen ligands. Main differences between the spectra of the ligands and the complexes were found below 700 cm^{-1}.

The O–H stretching modes of the crystallization water molecules give rise to two bands of medium intensity at 3475–3200 cm^{-1} in the IR spectrum of (**1**). For compound (**2**), this mode is superimposed with the ν(CH) mode of phen and appears as one broad and weak IR band centered at 3400 cm^{-1}.

In the compounds spectra, all the bands involving O–H motions of the carboxylate group are absent, namely the O–H stretching of the COOH groups, the C–OH in-plane bending and out-of-plane O–H deformation modes, hence showing deprotonation of the –COOH group and coordination to the metal [45], as disclosed by the X-ray structure. The characteristic IR carboxylate bands of the free acid, ν(C=O) and ν(C–O), are transformed into the asymmetric, ν_{as}(COO), and symmetric, ν_s(COO), stretching vibrations of the carboxylate group and as expected they are shifted after complex formation. The frequency difference between these bands is consistent with unidentate coordination of the carboxylate moiety to the metal [46]. Moreover, the δ(COO) mode, which appears in the spectra of the ligand as a strong band at 701 cm^{-1}, is shifted to higher frequency upon complexes formation. This behavior is similar to that observed in some complexes containing the dipic ligand [21, and references therein]. From the calculations, the splitting observed in the ν_{as}(COO) bands is attributed to the presence of in-phase and out-of-phase motions due to vibrational coupling between both terminal groups. Nevertheless, both calculated frequencies for complex (**1**) have almost coincident values (1771 cm^{-1}). In the symmetric mode, coupling with the C–COO stretching is also predicted. The calculated spectra also allow assigning differentially the vibrations for each free ligand, which are usually coupled with other modes. As expected, they undergo changes in intensity and position upon complexation [46,47].

The changes observed in the spectra of the complexes in the 700–200 cm^{-1} region are attributed to the coordination of the ligands to the metal. A new band of medium intensity at 683 cm^{-1} can be assigned to the out-of-plane ring deformation of the dipic, coupled with out-of-plane deformation of the Cr–N–C–C–O rings (Cr–L rings in Table 4).

Furthermore, a band at ca. 450 cm^{-1} with two shoulders, at higher and lower frequencies respectively, is present in both complexes. Calculations allow the assignment of these shoulders to ν(Cr–N) and to ν(Cr–O) stretchings. Some bands in this low-frequency region can be attributed to out-of-plane Cr–L rings deformations. The very weak bands at 395 cm^{-1} and at 226 cm^{-1} can be assigned to the Cr–Cl stretching and to the out-of-plane deformation of Cr–L ring, coupled with a Cr–Cl stretching in complex (**2**), respectively.

3.4. Electrochemical results

Cyclic voltammograms (CV) of the compounds were performed, in the potential range where they are electroactive, at incremental scan rates (v) from 0.05 V/s to 2.5 V/s. They were compared with those obtained with $CrCl_3$ and H_2dipic under similar experimental conditions. Data of the reduction and oxidation peaks at $v = 0.25$ V/s are summarized in Table 5.

The phen ligand was not active within the investigated potential range. The CV of H_2dipic display two overlapping irreversible reduction peaks at −1.36 V and −1.56 V which do not show associated oxidation processes in the reverse scan, even at the highest scan rate. Moreover, at more positive potentials one small couple is observed. The anomalous behavior of this couple and its dependence with electrode pretreatment suggest adsorption on the electrode surface.

Figure 3, curve A, shows the voltammetric behavior of the $Na[Cr(dipic)_2]\cdot 2H_2O$ compound, at $v = 0.25$ V/s. Two redox couples labeled I/I′ and II/II′, are observed.

The reduction current associated with peak II was measured from decaying baseline of peak I. The results indicates that the current ratio I/II is close to one at all scan rates investigated, suggesting that in both reduction the same number of electrons is involved.

On the other hand, although the separations of anodic (E_{pa}) and cathodic (E_{pc}) peak potentials of each process is larger than the value expected for a reversible charge transfer, the separation between the peak and half peak potential ($E_{pc} - E_{p/2}$) is 58 mV. This fact seems to point

Table 4
Assignment of the some characteristics IR and Raman bands of dipicolinic acid (H_2dipic), 1,10-phenantroline (phen), $Na[Cr(dipic)_2]\cdot 2H_2O$ (**1**) and $[Cr(dipic)(phen)Cl]\cdot 1/2H_2O$ (**2**) compounds

H_2dipic		Complex (**1**)		Calculated	Assignment	Phen		Complex (**2**)		Calculated	Assignment
IR	Ra	IR	Ra			IR	Ra	IR	Ra		
2800[a] s,b	2600[a] vw				ν(OH)						
1705[a] vs,b	1644 m,b				ν(C=O)						
		1672 s	1687 m	1771	$\nu_{as}(COO^-)$ip			1666 s	1693 w	1797	$\nu_{as}(COO^-)$ip
		1631 sh	1657 vw	1771	$\nu_{as}(COO^-)$op			1633 sh	1630 vw	1787	$\nu_{as}(COO^-)$op
1576 s	1576 m	1598 m	1600 m	1649	ν(ring)			1595 m	1604 w	1648	ν(ring)dipic
						1503 m	1507 w	1497 vw		1484	ν(ring)phen
1417 m					δ(OH)						
1332 s	1325 w				ν(C–O)						
1301 s	1296 w										
		1333 s	1345 s	1337	$\nu_s(COO^-) + \nu$(C–COO^-)			1319 s	1314 m	1324	$\nu_s(COO^-) + \nu$(C–COO^-)
927 m,b					γ(OH)						
		920 m		918	ν(C–COO^-) + δ(OCO)			916 w		917	ν(C–COO^-) + δ(OCO)
890 sh					ν(C–COOH)						
701 s	762 s	750 m		753	δ(OCO) + δ(ring)			748 m		753	δ(OCO) + δ(ring)dipic
649 s	647 w	698 sh	687 w	706	δ(ring)			697 vw		704	δ(ring)dipic
		683 m		676	γ(ring) + γ(Cr-Lring)			682 m		674	γ(ring) + γ(Cr-Lring)dipic
						623 m		619 vw			δ(ring)phen
		466 sh		448	ν(Cr–N)			463 sh		437	ν(Cr–N)dipic
419 vw		451 m	443 sh	463	γ(ring)dipic			453 m	450 sh	459	γ(ring)dipic
		438 sh	418 m	437	ν(Cr–O)			435 sh	429 m	443	ν(Cr–O)
						412 w	410 m,w	410 w		429	γ(ring)phen
								395 vw		377	ν(Cr–Cl) + γ(CH)dipic
		356 m	357 vw	357	γ(Cr-Lring)			358 m		368	γ (Cr-Lring)dipic
								226 vw		245	ν(Cr–Cl) + γ(Cr-Lring)

vs: very strong; s: strong; m: medium; w: weak; vw: very weak, sh: shoulder, b: broad; δ: in-plane deformation, γ: out-of-plane deformation, ip: in-phase, op: out-of-phase, ρ: torsion.
Band positions are in cm^{-1}.
[a] Centered.

Table 5
Cathodic (E_{pc}) and anodic (E_{pa}) peak potentials of chromium compounds and dipicolinic acid, at $v = 0.25$ V/s

Compound	E_{pc} (V)					E_{pa} (V)		
				I	II		I′	II′
H_2dipic				−1.36/−1.56				
$CrCl_3 \cdot 6H_2O$			−1.28			−0.64		
$CrCl_3 \cdot 6H_2O + H_2$dipic			−1.26 (sh)	−1.32	−1.75	−0.75	−1.12	−1.53
$Na[Cr(dipic)_2] \cdot 2H_2O$				−1.30	−1.73		−1.18	−1.60
$[Cr(dipic)(phen)Cl] \cdot 1/2H_2O$	−0.74	−0.99		−1.30	−1.75	−0.81	−1.18	−1.57

sh = shoulder.

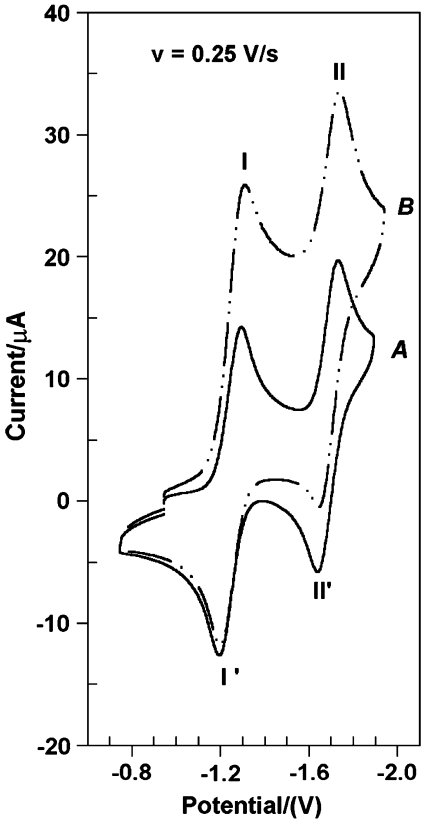


Fig. 3. Cyclic voltammograms of $Na[Cr(dipic)_2] \cdot 2H_2O$ in DMSO solution at $v = 0.25$ V/s (A) and after addition of dipicolinic acid (B).

to a reversible one electron transfer for these processes (a reversible diffusion-controlled process should have $(E_p - E_{p/2})$ values of 56.5/n mV) [48–50]. In addition, the peak current of both reductions increases with the square root of the scan rate ($v^{1/2}$), approaching a single straight-line plot, in accordance with diffusion control, and the ratio of anodic to cathodic peak currents (i_{pa}/i_{pc}) is near unity. These observations are indicative that the products of these reductions are stable during the time of the measurements.

To determine the origin of couples I and II, a complementary set of experiments was performed:

(a) 1 mM solution of $CrCl_3 \cdot 6H_2O$ was first measured in the absence of the ligand (see Table 5). Subsequently, H_2dipic was added to this solution. For ligand to metal concentration ratio L/M = 2 a new species is formed. Two main processes, at similar potential to that found for the complex, and a cathodic shoulder at *ca.* −1.26 V were observed. This last contribution corresponds to the reduction of a fraction of "free" Cr(III), since it appears at similar potential to that found when a solution of $CrCl_3$ in the absence of ligand was measured.

(b) Cyclic voltammograms of 1 mM complex solution were recorded at selected scan rates, and afterwards, an equimolar amount of H_2dipic was added. In Figure 1, curve B, a representative voltammogram at 0.25 V/s, is presented. After ligand addition, the cathodic current of peak I increases while the one related to peak II, measured from decaying baseline of peak I, remains unchanged. In this case, and for all scan rates investigated, the ratio I/II was close to 1.85, in contraposition with the value of 1, found when a solution of the complex alone was measured. The cyclic voltammogram of the free ligand in solution exhibited also one reduction peak at similar potential to that observed for peak I (−1.36 V), which remains irreversible at all scan rates investigated. In a similar way, after addition of the ligand, the oxidation current *I′*, associated with peak I, remains almost unchanged.

Therefore, based upon the discussed results, it can be assumed that the first peak corresponds to a ligand-centered reduction. The coordination with the metal changes the kinetic of this process from an irreversible to a reversible charge transfer [49]

$$\text{Peak I} \quad [Cr^{III}(dipic)_2]^- + e^- \rightleftharpoons [Cr^{III}(dipic)_2]^{2-}$$
$$E_{1/2} = -1.24\ \text{V} \qquad \text{(a)}$$

In addition, process II can be attributed to the reduction and subsequent oxidation of the metal center:

$$\text{Peak II} \quad [Cr^{III}(dipic)_2]^{2-} + e^- \rightleftharpoons [Cr^{II}(dipic)_2]^{3-}$$
$$E_{1/2} = -1.68\ \text{V} \qquad \text{(b)}$$

Figure 4 shows that a compound (**2**) holds a qualitatively similar cyclic voltammetric behavior. In fact, the electrochemical results indicate that $[Cr(dipic)(phen)Cl] \cdot 1/2H_2O$ dissociates in solution generating $[Cr(dipic)_2]^-$, as principal product. The two main couples, which appear at similar potential and display analogous behavior to that observed for complex (**1**), can be also described by means of Eqs. (a) and (b).

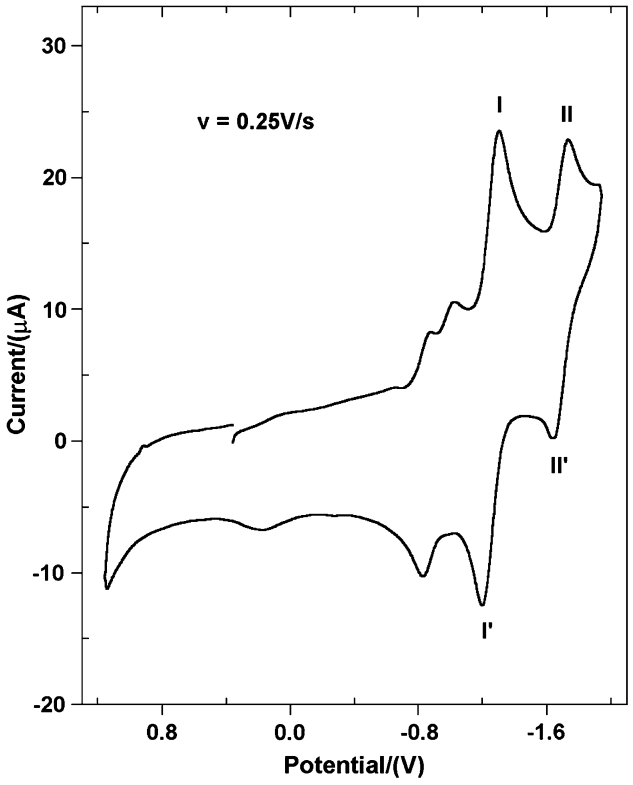


Fig. 4. Cyclic voltammograms of $[Cr(dipic)(phen)Cl]\cdot 1/2H_2O$ in DMSO solution at $v = 0.25$ V/s.

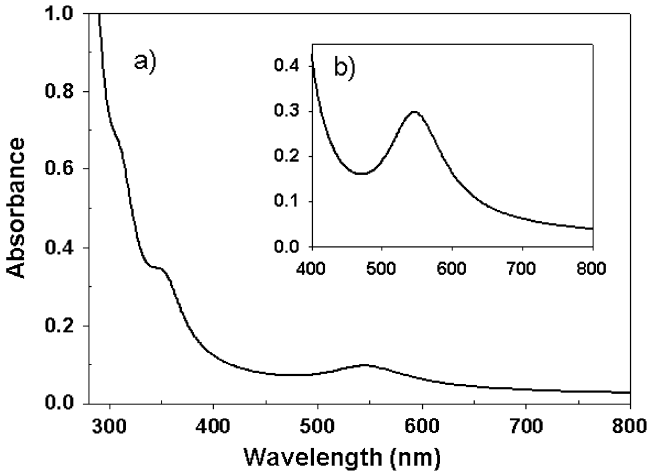


Fig. 5. Electronic spectra of $Na[Cr(dipic)_2]\cdot 2H_2O$ in DMSO solution. (a) 2×10^{-4} M; (b) 1×10^{-3} M, in a restricted wavelength range.

In addition, the small cathodic peaks and their anodic counterpart, that are absent in complex (**1**), can be attributed to new species in solution that contain phen, chloro and probably solvent molecules in their coordination spheres. The characteristic couple $2Cl^-/Cl_2$, which appears at 1.18 V in the $CrCl_3$ solution, is absent in this case, thus denoting that the chloride ligand remains attached to the metal.

3.5. Electronic spectra

The electronic spectra of complex (**1**) in DMSO solution is shown in Figure 5. The positions of the absorption maxima are listed in Table 6, together with the calculated transitions, which are selected according their respective oscillator strengths. The composition of the molecular orbitals, shown in Table 7, is determined in terms of atomic gross populations obtained through a Mulliken population analysis. Atomic percent contributions to molecular orbitals are summed up for each ligand in complex (**1**).

The experimental spectrum of complex (**2**) differs appreciably from the calculated one and, furthermore, it is very similar to the experimental spectrum corresponding to complex (**1**). These facts seem to suggest that complex (**2**) undergoes some reaction in solution in accordance with the electrochemical studies, which predict the same final species in solution for both complexes. Then, the assignments for both experimental spectra are discussed in terms of the calculated transitions for complex (**1**). Theoretical electronic transitions, the corresponding assignments, and the molecular orbital composition of non-dissociated complex (**2**) are available as Supplementary material.

Both ligands show strong absorptions at short wavelengths and up to ca. 300 nm. In addition, the phen spectrum presents a band of lower intensity around 320 nm.

Calculated transitions at ca. 432 nm in complex (**1**), attributed to d–d transitions, are not seen in the experimental spectrum. It can be assumed to be hidden by the more intense charge-transfer bands.

According to the analysis of the orbitals involved in the transitions, the broad band with maximum at 548 nm for complex (**1**) can be assigned to Cr → dipic charge-transfer transitions, mainly involving ligand rings. The strong absorption at the short wavelength end of the spectrum presents two shoulders, located at 353 nm and 312 nm. The first one can be considered as a combination of intraligand and dipic → Cr charge-transfer transitions, involving the oxygen atoms of the ligands. The shoulder at higher energy can be mainly attributed to dipic → Cr charge-transfer transitions, from the oxygen atoms.

Two high-intensity transitions at 656 nm and 604 nm are calculated for complex (**2**). They involve molecular orbitals having large contributions from dipic and phen ligands. Since those absorption bands are not observed in the experimental spectrum, it could be suggested that none species in solution contains simultaneously both ligands. Moreover, the experimental spectrum of complex (**2**) exhibits a small shoulder at 422 nm, which is not observed for complex (**1**) and that can be assigned to a Cr → phen charge-transfer transition, according to the theoretical results.

The above results support the proposal that complex (**2**) undergoes decomposition in DMSO solution, giving rise to new minor species containing phen, but no dipic, in the

Table 6
Experimental and calculated electronic transitions for complex (**1**)

Exp	Calc.	Oscillator strength	Assignment[a]
548	547	0.082091	HOMO → LUMO + 3 (24.13%) HOMO − 1 → LUMO (20.07%) HOMO → LUMO (18.76%) (β)
[b]	432	0.003037	HOMO − 1 → LUMO + 4 (61.98%)
	431	0.001341	HOMO − 2 → LUMO + 4 (49.74%)
353	342	0.007860	HOMO − 7 → LUMO (35.52%) (β) HOMO − 3 → LUMO + 4 (12.43%) HOMO − 4 → LUMO + 4 (11.07%)
	359	0.007048	HOMO − 4 → LUMO + 2 (34.16%) (β) HOMO − 7 → LUMO (32.49%)
312	293	0.009415	HOMO − 5 → LUMO + 5 (47.88%)
	315	0.008956	HOMO − 3 → LUMO + 5 (23.00%) HOMO − 11 → LUMO + 1 (22.27%) (β)
	311	0.008323	HOMO − 4 → LUMO + 5 (47.33%)
	315	0.007468	HOMO − 5 → LUMO + 4 (33.48%) HOMO − 11 → LUMO + 1 (14.90%) (β)
	309	0.005796	HOMO − 6 → LUMO + 4 (31.32%) HOMO − 9 → LUMO + 3 (13.46%)

Wavelengths are in nm, oscillator strengths in atomic units. Only the dominant one-electron transitions are taken into account for the assignment. The percent contribution of each one-electron transition is given in parenthesis.

[a] The one-electron transitions involve alpha molecular orbitals only, except for those cases in which it is explicitly stated that beta molecular orbitals are implied.

[b] d–d transitions are not observed in the experimental spectrum of complex (**1**). See text.

Table 7
Mulliken gross molecular orbital populations in terms of atoms for complex (**1**)

	% Cr	% L1	% L2
α-*OM*			
HOMO − 9	2.72	36.59	51.90
HOMO − 7	0.00	50.28	45.76
HOMO − 6	2.88	6.57	78.66
HOMO − 5	1.46	77.21	7.65
HOMO − 4	0.00	0.00	89.31
HOMO − 3	0.00	87.88	0.00
HOMO − 2	58.05	21.67	9.32
HOMO − 1	58.39	7.33	19.70
HOMO	68.50	11.07	9.66
LUMO	4.31	19.83	64.47
LUMO + 1	4.40	66.31	17.66
LUMO + 2	0.00	9.57	74.56
LUMO + 3	2.52	77.66	5.57
LUMO + 4	67.47	9.89	6.76
LUMO + 5	65.02	9.58	11.36
β-*OM*			
HOMO−11	7.44	26.69	46.48
HOMO−7	4.03	70.11	7.96
HOMO−4	0.00	51.32	45.57
HOMO	0.00	89.14	0.00
LUMO	19.63	19.74	46.16
LUMO + 1	16.61	48.47	18.22
LUMO + 2	5.32	3.75	73.21

Contributions from atoms in dipicolinic ligands are summed up to overall ligand contributions named L1 and L2.

coordination sphere. These species could be responsible for the slight differences observed in the spectrum of this solution with respect to that of complex (**1**).

4. Conclusions

The IR and Raman properties of the compounds $Na[Cr(dipic)_2]\cdot 2H_2O$ and $[Cr(dipic)(phen)Cl]\cdot 1/2H_2O$, dipic = dipicolinate, phen = 1,10-phenantroline, are in good agreement with the results of X-ray crystallography. Unidentate coordination of the carboxylate moiety to the metal, determined from the difference between $\nu(COO)_{as}$ and $\nu(COO)_s$, is in accordance with the structural and theoretical results. Important changes, that can be attributed to metal coordination, were observed in the IR spectra of the compounds when compared with the ligands, in the 700–200 cm^{-1} region. Out-of-plane deformations involving the five member ring (Cr–N–C–C–O) formed upon coordination of chromium with the dipic ligand, as well as the ν(Cr–N) and ν(Cr–O) vibrations modes, were clearly identified in the low-frequency region of the spectra with the help of harmonic vibrational frequencies, calculated in this work.

Both compounds are stable in air in the crystalline state. Electrochemical and electronic spectroscopy measurements show that the complex $[Cr(dipic)(phen)Cl]\cdot 1/2H_2O$ undergoes decomposition in DMSO solution generating $[Cr(dipic)_2]^-$ as major product.

It was also established by cyclic voltammetry that the Cr(III) center is not oxidized to Cr(VI) or Cr(V) genotoxic species within the potential range investigated. The complexes experienced two main redox processes, corresponding to the ligand and to the metal center reduction, respectively. The Cr(III)/Cr(II) redox couple does not lie within the range of biological reductants. It was found at

more negative potential that than reported for chromium mutagenic compounds.

Acknowledgments

This work has been supported by CONICET and the National University of La Plata, Argentina. The X-ray diffraction data were collected at LANADI (CONICET), Argentina. A.C.G.B., R.P.D, O.E.P, and B.S.P.C. are Research Fellows of CONICET.

Appendix A. Supplementary material

CCDC 628817 and 628818 contain the supplementary crystallographic data for **1** and **2**. These data can be obtained free of charge via http://www.ccdc.cam.ac.uk/conts/retrieving.html, or from the Cambridge Crystallographic Data Centre, 12 Union Road, Cambridge CB2 1EZ, UK; fax: (+44) 1223-336-033; or e-mail: deposit @ccdc.cam.ac.uk. Supplementary data associated with this article can be found, in the online version, at doi:10.1016/j.poly.2007.10.005. Complete data of IR and Raman frequencies and assignments, theoretical electronic transitions, the corresponding assignments and molecular orbital composition of non-dissociated complex (**2**), atomic fractional coordinates and equivalent isotropic displacement parameters, full intra-molecular bond distances and angles, atomic anisotropic displacement parameters, and hydrogen atoms positions are available from the authors on request.

References

[1] R. Codd, C.T. Dillon, A. Levina, P.A. Lay, Coord. Chem. Rev. 216–217 (2001) 537.
[2] D. Bagchi, S.J. Stohs, B.W. Downs, M. Bagchi, H.G. Preuss, Toxicology 180 (2002) 5.
[3] H. Arakawa, R. Ahmad, M. Naoui, H.A. Tajmir-Riahi, J. Biol. Chem. 275 (2000) 10150.
[4] J.B. Vincent, Acc. Chem. Res. 33 (2000) 503.
[5] C.M. Davis, J.B. Vincent, J. Biol. Inorg. Chem. 2 (1997) 675.
[6] H. Wang, A. Kruszewski, D. Brautigan, Biochemistry 44 (2005) 8167.
[7] J.B. Vincent, Polyhedron 20 (2001) 1.
[8] D.D.D. Hepburn, J.B. Vincent, J. Inorg. Biochem. 94 (2003) 86.
[9] V. Juturu, J.R. Komorowski, Toxicology 186 (2003) 171.
[10] D. Bagchi, S.J. Stohs, B.W. Downs, M. Bagchi, H.G. Preuss, Toxicology 186 (2003) 175.
[11] J.K. Speetjens, R.A. Collins, J.B. Vincent, S.A. Woski, Chem. Res. Toxicol. 12 (1999) 483.
[12] D.M. Stearns, S.M. Silveira, K.K. Wolf, A.M. Luke, Mutat. Res. 513 (2002) 135.
[13] D.D.D. Hepburn, M. Burney, S.A. Woski, J.B. Vincent, Polyhedron 22 (2003) 455.
[14] V.H. Coryell, D.M. Stearns, Mutat. Res. 610 (2006) 114.
[15] I. Mulyani, A. Levina, P.A. Lay, Angew. Chem., Int. Ed. 43 (2004) 4504.
[16] A. Levina, P.A. Lay, Coord. Chem. Rev. 249 (2005) 281.
[17] C.L. Weeks, A. Levina, C.T. Dillon, P. Turner, R.R. Fenton, P.A. Lay, Inorg. Chem. 43 (2004) 7844.
[18] C.T. Dillon, P.A. Lay, A.M. Bonin, M. Choleva, G.J.F. Legge, Chem. Res. Toxicol. 13 (2000) 742.
[19] K.D. Sudgen, R. Deer, S.J. Rogers, Biochemistry 31 (1992) 11626.
[20] A.C. González -Baró, E.E. Castellano, O.E. Piro, B.S. Parajón-Costa, Polyhedron 24 (2005) 49.
[21] B.S. Parajón-Costa, O.E. Piro, R. Pis-Diez, E.E. Castellano, A.C. González-Baró, Polyhedron 25 (2006) 2920.
[22] B.S. Parajón-Costa, C.C. Wagner, E.J. Baran, Z. Anorg. Allg. Chem. 629 (2003) 1085.
[23] P.B. Samnani, P.K. Battacharya, P.A. Ganeshpure, V.J. Kosky, S. Satish, J. Mol. Catal. A: Chem. 110 (1996) 89.
[24] H.M. Koepp, H. Went, H.Z. Strehlow, Z. Elektrochem. 64 (1960) 483.
[25] R.R. Gagné, C.A. Koval, G.C. Lisensky, Inorg. Chem. 19 (1980) 2854.
[26] M.J. Frisch, G.W. Trucks, H.B. Schlegel, G.E. Scuseria, M.A. Robb, J.R. Cheeseman, J.A. Montgomery Jr., T. Vreven, K.N. Kudin, J.C. Burant, J.M. Millam, S.S. Iyengar, J. Tomasi, V. Barone, B. Mennucci, M. Cossi, G. Scalmani, N. Rega, G.A. Petersson, H. Nakatsuji, M. Hada, M. Ehara, K. Toyota, R. Fukuda, J. Hasegawa, M. Ishida, T. Nakajima, Y. Honda, O. Kitao, H. Nakai, M. Klene, X. Li, J.E. Knox, H.P. Hratchian, J.B. Cross, V. Bakken, C. Adamo, J. Jaramillo, R. Gomperts, R.E. Stratmann, O. Yazyev, A.J. Austin, R. Cammi, C. Pomelli, J.W. Ochterski, P.Y. Ayala, K. Morokuma, G.A. Voth, P. Salvador, J.J. Dannenberg, V.G. Zakrzewski, S. Dapprich, A.D. Daniels, M.C. Strain, O. Farkas, D.K. Malick, A.D. Rabuck, K. Raghavachari, J.B. Foresman, J.V. Ortiz, Q. Cui, A.G. Baboul, S. Clifford, J. Cioslowski, B.B. Stefanov, G. Liu, A. Liashenko, P. Piskorz, I. Komaromi, R.L. Martin, D.J. Fox, T. Keith, M.A. Al-Laham, C.Y. Peng, A. Nanayakkara, M. Challacombe, P.M.W. Gill, B. Johnson, W. Chen, M.W. Wong, C. Gonzalez, J.A. Pople, Gaussian 03, Revision D.01, Gaussian, Inc., Wallingford CT, 2004.
[27] A.D. Becke, J. Chem. Phys. 98 (1993) 5648.
[28] C. Lee, W. Yang, R.G. Parr, Phys. Rev. B 37 (1988) 785.
[29] G. te Velde, F.M. Bickelhaupt, S.J.A. van Gisbergen, C. Fonseca Guerra, E.J. Baerends, J.G. Snijders, T. Ziegler, J. Comput. Chem. 22 (2001) 931.
[30] C. Fonseca Guerra, J.G. Snijders, G. te Velde, E.J. Baerends, Theor. Chem. Acc. 99 (1998) 391.
[31] SCM, Theoretical Chemistry, Vrije Universiteit, Amsterdam, The Netherlands, http://www.scm.com, ADF2006.01.
[32] J.P. Perdew, K. Burke, M. Ernzerhof, Phys. Rev. Lett. 77 (1996) 3865.
[33] E.K.U. Gross, W. Kohn, Phys. Rev. Lett. 55 (1985) 2850.
[34] CAD4 Express Software, Enraf-Nonius, Delft, The Netherlands, 1994.
[35] K. Harms, S. Wocadlo, XCAD4-CAD4 Data Reduction, University of Marburg, Marburg, Germany, 1995.
[36] PLATON, A Multipurpose Crystallographic Tool, Utrecht University, Utrecht, The Netherlands, AL Spek, 1998.
[37] G.M. Sheldrick, SHELXS-97. Program for Crystal Structure Resolution, University of Göttingen, Göttingen, Germany, 1997.
[38] G.M. Sheldrick, SHELXL-97. Program for Crystal Structures Analysis, University of Göttingen, Göttingen, Germany, 1997.
[39] W. Kohn, L.J. Sham, Phys. Rev. 140 (1965) A1133.
[40] P. Hohenberg, W. Kohn, Phys. Rev. 136 (1964) B864.
[41] R.G. Parr, W. Yang, Density Functional Theory of Atoms and Molecules, Oxford University Press, 1989.
[42] S.J. A van Gisbergen, J.G. Snijders, E.J. Baerends, Comput. Phys. Commun. 118 (1999) 119.
[43] F. Wang, T. Ziegler, Mol. Phys. 102 (2004) 2585.
[44] C.K. Johnson, ORTEP-II.A Fortran Thermal-Ellipsoid Plot Program. Report ORNL-5318, Oak Ridge National Laboratory, Tennessee, USA, 1976.
[45] D. Lin-Vien, N.B. Colthup, W.G. Fately, J.G. Grasselli, Infrared and Raman Characteristic Frequencies of Organic Molecules, Academic Press, Boston, 1991.
[46] K. Nakamoto, Infrared and Raman Spectra of Inorganic and Coordination Compounds, fifth ed., J. Wiley, New York, 1997.
[47] S.K. Sengupta, S.K. Shani, R.N. Kapoor, J. Indian Chem. Soc. LX (1983) 821.

[48] R.S. Nicholson, I. Shain, Anal. Chem. 36 (1964) 706.
[49] A.J. Bard, L.R. Faulkner, Electrochemical Methods: Fundamentals and Applications, second ed., J. Wiley & Sons, New York, 2001.
[50] E.R. Brown, R.F. Large, Electrochemical Methods, in: A. Weisberger, B.W. Rositer (Eds.), Physical Methods of Chemistry, Part IIA, Interscience, New York, 1971, Chapter 6.

Available online at www.sciencedirect.com
ScienceDirect
Polyhedron 27 (2008) 513–516
POLYHEDRON
www.elsevier.com/locate/poly

Synthesis of ethyl zinc fluoroalkoxide complexes and the crystal structure of $[EtZn(py)\{\mu\text{-}OCH(CF_3)_2\}]_2$

Seigi Suh, Liliana A. Mîinea, Saba Javed, David M. Hoffman *

Department of Chemistry, University of Houston, Houston, TX 77204-5003, USA

Received 13 July 2007; accepted 3 October 2007
Available online 28 November 2007

Abstract

Fluorinated alkoxide complexes of zinc were synthesized for possible use as precursors to fluorine-doped ZnO films. Diethyl zinc reacted with fluorinated alcohols to form $[EtZn(OR_f)]_n$ ($R_f = CH(CF_3)_2$, CMe_2CF_3, $CMe(CF_3)_2$) compounds. The $[EtZn(OR_f)]_n$ compounds reacted with excess pyridine to yield the pyridine adducts $[EtZn(py)(\mu\text{-}OR_f)]_2$. The X-ray structure of $[EtZn(py)\{\mu\text{-}OCH(CF_3)_2\}]_2$ showed that it has virtual C_i symmetry.
© 2007 Elsevier Ltd. All rights reserved.

Keywords: Zinc; Alkyl; Alkoxide; Fluoroalkoxide; ZnO films

1. Introduction

Jones, O'Beiwn, and co-workers reported using methyl zinc isopropoxide, $[MeZn(\mu_3\text{-}O\text{-}i\text{-}Pr)]_4$, and methyl zinc *tert*-butoxide, $[MeZn(\mu_3\text{-}O\text{-}t\text{-}Bu)]_4$, as single-source metal–organic chemical vapor deposition (MOCVD) precursors to undoped ZnO films with high resistivities (300–900 Ω cm) [1]. In this paper, we describe the synthesis of ethyl zinc fluoroalkoxide complexes that are related to the ZnO precursors employed by Jones, O'Brien, and co-workers. Our motivation for incorporating fluorine in the alkoxide ligands was the possibility that the complexes could be used as MOCVD precursors to conductive fluorine-doped zinc oxide films where the fluorine originates via a "self-doping" process [2,3].

2. Experimental

All manipulations were carried out in a nitrogen-filled glove box or by using standard Schlenk techniques. Diethyl zinc was obtained from Akzo Chemicals Inc. and used as received. The alcohols were purchased from Aldrich and DCR Inc. and were degassed before being used. Standard distillation procedures were used to purify and dry the solvents, which were stored in the glove box over 4-Å molecular sieves after they were collected. Oneida Research Services, Whitesboro, NY, and Midwest Microlab, LLC, Indianapolis, IN, performed the elemental analyses.

2.1. Synthesis of $[EtZn\{OCH(CF_3)_2\}]_n$

$(CF_3)_2CHOH$ (3.23 g, 19.2 mmol) was added slowly to a cold (−78 °C) solution of Et_2Zn (2.50 g, 20.2 mmol) in hexanes (20 ml) over a period of 20 min. A white precipitate formed during the addition. The reaction mixture was warmed slowly to room temperature. During the warming process, the precipitate dissolved. After stirring the reaction mixture for 3 h at room temperature, the volatile components were removed in vacuo to give a colorless liquid, which was distilled in vacuo (b.p. 48 °C, 0.05 mmHg). Some decomposition occurred during distillation (yield 2.6 g, 49%;). *Anal.* Calc. for $C_5H_6OF_6Zn$: C, 22.97; H, 2.31. Found: C, 22.76; H, 2.25%.

^1H NMR (C_6D_6): δ 3.84 (septet, 1, $^3J_{HF} = 6.0$ Hz, $OCH(CF_3)_3$), 1.26 (t, 3, $J_{HH} = 8.1$ Hz, CH_2CH_3), 0.56

* Corresponding author. Tel.: +1 713 743 3255.
E-mail address: hoffman@uh.edu (D.M. Hoffman).

0277-5387/$ - see front matter © 2007 Elsevier Ltd. All rights reserved.
doi:10.1016/j.poly.2007.10.010

(q, 2, $J_{HH} = 8.1$ Hz, CH_2CH_3). $^{13}C\{^1H\}$ NMR (C_6D_6): 122.5 (q, 2, $J_{CF} = 285$ Hz, $OCH(CF_3)_2$), 72.6 (septet, 1, $^2J_{CF} = 32$ Hz, $OCH(CF_3)_2$), 11.3 (s, 1, CH_2CH_3), −0.1 (s, 1, CH_2CH_3). IR (Nujol, CsI, cm^{-1}): 1375 m, 1289 s, 1231 s, 1196 s, 1138 s, 1101 s, 984 s, 912 w, 895 m, 860.3 m, 745 m, 689 m, 637 w, 544 w, 525 m, 457 w.

2.2. Synthesis of $[EtZn(py)\{\mu\text{-}OCH(CF_3)_2\}]_2$

Excess pyridine (2.0 g, 25 mmol) was added dropwise to a solution of $[EtZn\{OCH(CF_3)_2\}]_n$ (0.50 g, 1.9 mmol) in ether (10 ml) at room temperature. After stirring the mixture for 15 min, the volatile components were removed in vacuo, leaving a white solid. The solid was dissolved in a minimum amount of toluene. The solution was cooled (−35 °C), which resulted in the formation of large colorless blocks. The mother liquor was decanted and the crystals were dried in vacuo, producing a white solid (yield 0.61 g, 94%). The product could be sublimed in vacuo (80–86 °C, 0.05 mmHg). *Anal.* Calc. for $C_{20}H_{22}N_2O_2F_{12}Zn_2$: C, 35.27; H, 3.26; N 4.11. Found: C, 35.04; H, 3.19; N, 4.38%.

^1H NMR (C_6D_6): δ 8.46 (m, 4, *o*-py), 6.88 (m, 2, *p*-py), 6.64 (m, 4, *m*-py), 4.30 (septet, 2, $^3J_{HF} = 6.6$ Hz, $OCH(CF_3)_2$) 1.76 (t, 6, $J_{HH} = 8.1$ Hz, CH_2CH_3), 0.85 (q, 4, $J_{HH} = 8.1$ Hz, CH_2CH_3). $^{13}C\{^1H\}$ NMR (C_6D_6): 148.7 (4, *o*-py), 139.0 (2, *p*-py), 124.6 (4, *m*-py), 123.7 (q, 4, $J_{CF} = 287$ Hz, $OCH(CF_3)_2$), 73.5 (septet, 2, $^2J_{CF} = 31$ Hz, $OCH(CF_3)_2$), 13.5 (s, 2, CH_2CH_3), −3.3 (s, 2, CH_2CH_3). IR (Nujol, KBr, cm^{-1}): 1607 s, 1287 s, 1260 s, 1209 s, 1152 s, 1098 s, 1070 m, 1042 m, 1013 m, 986 w, 957 w, 887 m, 854.5 s, 756 m, 701 s, 685 s, 633 w.

2.3. Synthesis of $[EtZn(OCMe_2CF_3)]_n$

A solution of $(CF_3)Me_2COH$ (1.0 g, 7.7 mmol) in ether (10 mL) was added slowly to a cold (−78 °C) solution of Et_2Zn (1.0 g, 8.1 mmol) in ether (15 ml). The colorless reaction mixture was warmed slowly to room temperature whereupon it was left to stir overnight. The volatile components were removed in vacuo to yield a white solid. The solid was extracted with ether (10 ml), the extract was filtered, and the filtrate was concentrated in vacuo to ca. 4 mL. The clear filtrate was cooled slowly to −35 °C whereupon colorless crystals formed. The mother liquor was decanted and the crystals were dried in vacuo to give a white solid (yield 1.6 g, 89%). *Anal.* Calc. for $C_6H_{11}OF_3Zn$: C, 32.58; H, 5.00. Found: C, 32.26; H, 5.07%.

^1H NMR (C_6D_6): δ 1.38 (t, 3, $J_{HH} = 8.1$ Hz, CH_2CH_3), 1.26 (s, 6, $OCCF_3(CH_3)_2$), 0.59 (q, 2, $J_{HH} = 8.1$ Hz, CH_2CH_3). $^{13}C\{^1H\}$ NMR (C_6D_6): 127.0 (q, 1, $J_{CF} = 286$ Hz, $OCCF_3(CH_3)_2$), 75.5 (q, 1, $^2J_{CF} = 28$ Hz, $OCCF_3(CH_3)_2$), 24.9 (s, 2, $OCCF_3(CH_3)_2$), 12.3 (s, 1, CH_2CH_3), 6.1 (s, 1, CH_2CH_3). IR (Nujol, KBr, cm^{-1}): 1395 m, 1321 m, 1224 m, 1161 s, 1125 s, 999 w, 968 s, 939 w, 868 s, 756 m, 619 m, 592 w.

2.4. Synthesis of $[EtZn(py)(\mu\text{-}OCMe_2CF_3)]_2$

Excess pyridine (0.320 g, 4.06 mmol) was added dropwise to a solution of $[EtZn(OCMe_2CF_3)]_n$ (0.300 g, 1.35 mmol) in ether (10 ml) at room temperature. After stirring the solution overnight, the volatile components were removed in vacuo, leaving a white solid. The solid was dissolved in ether, and the solution was cooled (−35 °C). This produced colorless blocks, which were isolated by decanting the mother liquor and drying in vacuo (yield 0.37 g, 91%). The compound could be sublimed in vacuo (80–82 °C, 0.05 mmHg). *Anal.* Calc. for $C_{22}H_{32}N_2O_2F_6Zn_2$: C, 43.95; H, 5.37; N, 4.66. Found: C, 43.96; H, 5.42; N, 4.57%.

^1H NMR (C_6D_6): δ 8.61 (m, 4, *o*-py), 6.90 (m, 2, *p*-py), 6.63 (m, 4, *m*-py), 1.86 (t, 6, $J_{HH} = 8.1$ Hz, CH_2CH_3), 1.24 (s, 12, $OCCF_3(CH_3)_2$), 0.83 (q, 4, $J_{HH} = 8.1$ Hz, CH_2CH_3). $^{13}C\{^1H\}$ NMR (C_6D_6): 149.1 (4, *o*-py), 138.2 (2, *p*-py), 128.5 (q, 2, $J_{CF} = 288$ Hz, $OC(CF_3)(CH_3)_2$), 124.3 (4, *m*-py), 72.8 (q, 2, $^2J_{CF} = 27$ Hz, $OCCF_3(CH_3)_2$), 26.2 (s, 4, $OCCF_3(CH_3)_2$), 14.0 (s, 2, CH_2CH_3), −0.3 (s, 2, CH_2CH_3). IR (Nujol, KBr, cm^{-1}): 1603 s, 1447 s, 1383 s, 1319 s, 1217 s, 1120 s, 1071 m, 1037 m, 997 s, 949 w, 876 s, 754 s, 700 s, 629 w, 603 w.

2.5. Synthesis of $[EtZn\{OCMe(CF_3)_2\}]_n$

A solution of $(CF_3)_2MeCOH$ (6.60 g, 36.4 mmol) in hexanes (10 ml) was added dropwise to a cold (−78 °C) solution of Et_2Zn (5.00 g, 40.5 mmol) in hexanes (30 ml) over a period of 30 min. The reaction mixture was warmed slowly to room temperature, whereupon it was left to stir for an additional 30 min. The volatile components were removed in vacuo to yield a colorless liquid. The liquid was pure product as judged by an ^1H NMR spectrum. The compound could be distilled under vacuum (b.p. 48–49 °C at 0.05 mm Hg; yield, 8.93 g, 80%). *Anal.* Calc. for $C_6H_8OF_6Zn$: C, 26.16; H, 2.93. Found: C, 26.09; H, 2.89%.

^1H NMR (C_6D_6): δ 1.28 (t, 3, $J_{HH} = 8.1$ Hz, CH_2CH_3), 1.17 (s, 3, $OCCH_3(CF_3)_2$), 0.56 (q, 2, $J_{HH} = 8.1$ Hz, CH_2CH_3). $^{13}C\{^1H\}$ NMR (C_6D_6): 124.8 (q, 2, $J_{CF} = 287$ Hz, $OCCH_3(CF_3)_2$), 76.4 (septet, 1, $^2J_{CF} = 29$ Hz, $OCCH_3(CF_3)_2$), 19.1 (s, 1, $OCCH_3(CF_3)_2$), 10.9 (s, 1, CH_2CH_3), 2.0 (s, 1, CH_2CH_3). IR (Nujol, KBr, cm^{-1}): 1310 s, 1265 w, 1215 s, 1161 s, 1127 m, 1082 s, 997 w, 961 s, 870 m, 762 m, 704 s, 652 m, 629 m.

2.6. Synthesis of $[EtZn(py)\{\mu\text{-}OCMe(CF_3)_2\}]_2$

Excess pyridine (0.260 g, 3.27 mmol) was added dropwise to a solution of $[EtZn\{OCMe(CF_3)_2\}]_n$ (0.300 g, 1.09 mmol) in ether (10 ml) at room temperature. After stirring the solution for 15 h, the volatile components were removed in vacuo, leaving a white solid. The solid was dissolved in ether, and the solution was cooled in the freezer (−35 °C). Colorless crystals formed, which were isolated by decanting the mother liquor and drying in

vacuo (yield 0.34 g, 88%). The compound could be sublimed in vacuo (85–90 °C, 0.05 mmHg). *Anal.* Calc. for $C_{22}H_{26}N_2O_2F_{12}Zn_2$: C, 37.26; H, 3.69; N, 3.95. Found: C, 37.29; H, 3.71; N, 3.94%.

^{1}H NMR (C_6D_6): δ 8.54 (m, 4, *o*-py), 6.86 (m, 2, *p*-py), 6.61 (m, 4, *m*-py), 1.84 (t, 6, $J_{HH} = 8.1$ Hz, CH_2CH_3), 1.35 (s, 6, $OCCH_3(CF_3)_2$), 0.89 (q, 4, $J_{HH} = 8.1$ Hz, CH_2CH_3). ^{13}C{^{1}H}NMR (C_6D_6): 149.0 (4, *o*-py), 138.7 (2, *p*-py), 124.4 (4, *m*-py), 125.2 (q, 4, $J_{CF} = 291$ Hz, $OCCH_3(CF_3)_2$), 77.2 (septet, 2, $^2J_{CF} = 28$ Hz, $OCCH_3(CF_3)_2$), 19.8 (s, 2, $OCCH_3(CF_3)_2$), 13.5 (s, 2, CH_2CH_3), −0.5 (s, 2, CH_2CH_3). IR (Nujol, KBr, cm^{-1}): 1607 s, 1460 s, 1304 s, 1215 s, 1165 s, 1117 m, 1074 s, 1040 m, 1013 w, 961 m, 862 w, 756 m, 700 s, 611 w.

2.7. Crystal structure determination of [EtZn(py)-{μ-OCH(CF$_3$)$_2$}]$_2$

The crystals for this study (colorless square columns) were grown from a concentrated toluene solution at −35 °C. All measurements were made with a Siemens SMART platform diffractometer equipped with a CCD area detector. The programs used in the X-ray crystallographic analysis were as follows: Data collection, APEX2 v1.0–27 software (Bruker-Nonius, 2005); cell refinement and data reduction, SAINT v7.12A software (Bruker-Nonius, 2004); and structure solution and refinement, SHELXL v5.10.

Crystal data: $C_{20}H_{22}N_2O_2F_{12}Zn_2$, monoclinic, space group $P2_1/n$, $a = 10.2183(4)$, $b = 17.3567(7)$, $c = 15.0818(6)$ Å, $\beta = 94.494(1)°$, $T = 223(1)$ K, $V = 2666.62(18)$ Å^3, $Z = 4$, $D_{calc} = 1.697$ g/cm^3, $F(000) = 1360$, μ(Mo Kα) = 1.903 mm^{-1}, crystal size: 0.45 × 0.25 × 0.20 mm. There were 12095 reflections measured of which 4132 reflections were unique ($R_{int} = 0.0278$). Final R indices for 2905 reflections with $I > 4\sigma(I)$ were $R_1 = 0.0299$ and $wR_2 = 0.0772$ and for all data $R_1 = 0.0400$ and $wR_2 = 0.0832$.

The ethyl and alkoxide ligands are significantly disordered. The disordered ligands were treated during refinement by using distance constraints. Ideal rigid body models were used for each of the CF_3 groups. Occupancy factors for each disordered group were estimated based on comparison of isotropic displacement parameters.

3. Results and discussion

The fluorinated alcohols $HOCH(CF_3)_2$, $HOCMe_2CF_3$, and $HOCMe(CF_3)_2$ reacted with slightly more than one equivalent of diethyl zinc at room temperature in hexanes to yield hydrocarbon-soluble $[EtZn(OR_f)]_n$ compounds (Eq. (1)). A slight excess of diethyl zinc was required to maximize reaction yields. The $R_f = CH(CF_3)_2$ and $CMe(CF_3)_2$ derivatives were volatile distillable liquids, albeit the hexafluoroisopropoxide complex partially decomposed on distillation. The decomposition product from the distillation of $[EtZn\{OCH(CF_3)_2\}]_n$ was a white solid that was not soluble in benzene but was soluble in acetonitrile. An ^{1}H NMR spectrum of the solid in CD_3CN revealed resonances consistent with one type each of Et and $CH(CF_3)_2$ groups in an approximately 1:3 ratio, respectively. Based on these data, the solid is probably an alkoxide-rich oligomer. The $R_f = CMe_2CF_3$ derivative was a solid that decomposed upon attempted sublimation. An ^{1}H NMR spectrum of the benzene-soluble residue from the attempted sublimation was uninformative.

Attempts to characterize $[EtZn(OCMe_2CF_3)]_n$ by X-ray crystallographic analysis failed because a suitable crystal could not be grown. The structures of all three derivatives are presumably tetrameric cubes analogous to the structurally characterized alkoxide complexes $[MeZn(\mu_3\text{-}OR)]_4$, where R = Me or *t*-Bu. Proton and C-13 NMR spectra had resonances consistent with the presence of only one type of alkoxide ligand. This is in agreement with a cube structure as well as other possible structures.

$$Et_2Zn + R_fOH \xrightarrow{-78\ ^\circ C} [EtZn(OR_f)]_n + EtH$$
$$R_f = CH(CF_3)_2, CMe_2CF_3, CMe(CF_3)_2 \quad (1)$$

In an effort to prepare a derivative of the $[EtZn(OR_f)]_n$ complexes for X-ray characterization, they were reacted with excess pyridine at room temperature to yield hydrocarbon-soluble pyridine adducts, $[EtZn(py)(\mu\text{-}OR_f)]_2$ (Eq. (2)). These results are consistent with the earliest reactivity studies of $[RZn(\mu_3\text{-}OR')]_4$ compounds by Coates and Ridley [4], who found that alkoxide tetramers did not react with pyridine, whereas the phenoxide tetramer $[MeZn(\mu_3\text{-}OPh)]_4$ reacted readily with pyridine to form the dimer $[MeZn(py)(\mu\text{-}OPh)]_2$. Coates and Ridley explained this

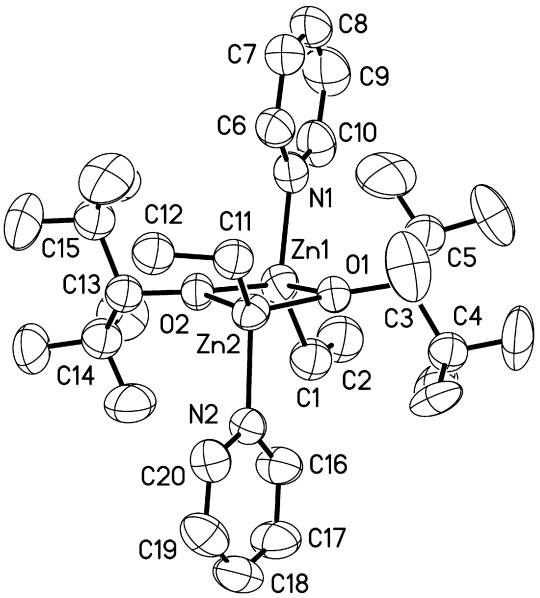


Fig. 1. Plot of the $[EtZn(py)\{\mu\text{-}OCH(CF_3)_2\}]_2$ molecule with hydrogens omitted (40% equiprobability envelopes). Only one orientation of each disordered group is shown. Selected bond lengths (Å) and angles (°): Zn(1)–O(2) 2.019(2); Zn(1)–O(1) 2.061(2); Zn(2)–O(1) 2.014(2); Zn(2)–O(2) 2.036(2); Zn(1)–N(1) 2.093(3); Zn(2)–N(2) 2.111(3); Zn(1)···Zn(2) 3.138(1); O(2)–Zn(1)–O(1) 78.38(8); O(1)–Zn(2)–O(2) 79.04(8); O(2)–Zn(1)–N(1) 101.14(9); O(2)–Zn(2)–N(2) 98.76(9); O(1)–Zn(1)–N(1) 96.03(9); O(1)–Zn(2)–N(2) 99.73(9).

difference in reactivity by pointing out that the phenoxide was a weaker donor than the alkoxides, and therefore the pyridine donor could break the phenoxide cube apart but could not disrupt the alkoxide cubes. In the present instance, the trifluoromethyl substituents make the alkoxide ligands weaker donors than their non-fluorinated counterparts, and thus the tetramers react with pyridine to form the dimeric pyridine adducts.

$$[EtZn(OR_f)]_n + \text{excess pyridine} \rightarrow [EtZn(py)(\mu\text{-}OR_f)]_2$$
$$R_f = CH(CF_3)_2, CMe_2CF_3, CMe(CF_3)_2 \quad (2)$$

An X-ray crystallographic analysis of $[EtZn(py)\{\mu\text{-}OCH(CF_3)_2\}]_2$ revealed a dimer structure in which the pyridine ligands are in an anti configuration (Fig. 1). The ethyl ligands were severely disordered, precluding any discussion of distances or angles with respect to $Zn–C_1$ or $Zn–C_{11}$. The Zn–O distances, 2.014(2)–2.061(2) Å, are within the range of distances found for $[(Me_3SiCH_2)Zn(\mu\text{-}O\text{-}2,6\text{-}i\text{-}Pr_2C_6H_3)]_2$ (1.934(10)–1.975(11) Å), $[(Me_3SiCH_2)Zn(\mu\text{-}O\text{-}2,4,6\text{-}t\text{-}Bu_3C_6H_2)]_2$ (1.948(6)–2.021(4) Å), $[(Me_3SiCH_2)Zn(\mu\text{-}O\text{-}1\text{-adamantyl})]_4$ (2.048(2)–2.121(3) Å), $\{Zn[(\mu\text{-}O\text{-}2,6\text{-}i\text{-}Pr_2C_6H_3)_2Zn(CH_2SiMe_3)]_2\}$ (1.933(3)–1.985(2) Å) [5], $[EtZn(\mu\text{-}O\text{-}2,6\text{-}t\text{-}Bu_2C_6H_3)]_2$ (1.970 (1)–1.990(1) Å) [6], $[MeZn(\mu_3\text{-}O\text{-}t\text{-}Bu)]_4$ (2.06(2) Å) [7], and $[MeZn(\mu_3\text{-}OMe)]_4$ (2.039(14)–2.114(15) Å) [8], while the Zn–N distances (2.093(3) and 2.111(3) Å) are comparable to those in $ZnX_2(py)_2$ (X = C l, 2.046(5) and 2.052(6) Å) and (X = I, 2.05(1) and 2.06(1) Å) [9,10].

The ^1H NMR spectrum of $[EtZn(py)(\mu\text{-}OCMe_2CF_3)]_2$ in toluene-d_8 revealed a quartet and triplet arising from the methylene and methyl groups of the ethyl ligand, respectively, and two closely spaced singlet resonances for the alkoxide methyl protons. These data are consistent with the solid-state structure of $[EtZn(py)\{\mu\text{-}OCH(CF_3)_2\}]_2$. In benzene-$d_6$ the alkoxide methyl resonances are accidentally degenerate.

4. Conclusion

The fluorinated alkoxide complexes $[EtZn(OR_f)]_n$ (R_f = $CH(CF_3)_2$, CMe_2CF_3, $CMe(CF_3)_2$) were synthesized for possible use as CVD precursors to fluorine-doped ZnO films. The compound $[EtZn\{OCMe(CF_3)_2\}]_n$, a volatile liquid that distills without decomposition at low temperature (b.p. 48–49 °C, 0.05 mm Hg), is the most promising precursor candidate because of its physical properties. Pyridine adducts (py/Zn = 1) of the new complexes were prepared, and the X-ray structure of $[EtZn(py)\{OCH(CF_3)_2\}]_2$ was determined.

Acknowledgements

We thank the Robert A. Welch Foundation for financial support and Dr. James Korp for his technical assistance with the X-ray crystallographic analysis.

Appendix A. Supplementary material

CCDC 653327 contains the supplementary crystallographic data for $[EtZn(py)\{\mu\text{-}OCH(CF_3)_2\}]_2$. These data can be obtained free of charge via http://www.ccdc.cam.ac.uk/conts/retrieving.html, or from the Cambridge Crystallographic Data Centre, 12 Union Road, Cambridge, CB2 1EZ, UK; fax: (+44) 1223-336-033; or e-mail: deposit @ccdc.cam.ac.uk. Supplementary data associated with this article can be found, in the online version, at doi:10.1016/j.poly.2007.10.010.

References

[1] J. Auld, D.J. Houlton, A.C. Jones, S.A. Rushworth, M.A. Malik, P. O'Brien, G.W. Critchlow, J. Mater. Chem. 4 (1994) 1249.
[2] R.G. Gordon, Mat. Res. Soc. Symp. Proc. 426 (1996) 419.
[3] J. Hu, R.G. Gordon, Solar Cells 30 (1991) 437.
[4] G.E. Coates, D. Ridley, J. Chem. Soc. (1965) 1870.
[5] M.M. Olmstead, P.P. Power, S.C. Shoner, J. Am. Chem. Soc. 113 (1991) 3379.
[6] M. Parvez, G.L. BergStresser, H.G. Richey Jr., Acta Crystallogr. C48 (1992) 641.
[7] W.A. Herrmann, S. Bogdanovic', J. Behm, M. Denk, J. Organomet. Chem. 430 (1992) C33.
[8] H.M.M. Shearer, C.B. Spencer, Acta Crystallogr. B36 (1980) 2046.
[9] W.L. Steffen, G.J. Palenik, Acta Crystallogr. B32 (1976) 298.
[10] J.F. Le Querler, M.M. Borel, A. Leclaire, Acta Crystallogr. B33 (1977) 2299.

Available online at www.sciencedirect.com
ScienceDirect
Polyhedron 27 (2008) 517–522
POLYHEDRON
www.elsevier.com/locate/poly

The chemistry of vanadate chelate esters of monoionized aromatic diols and methoxyphenolate

Samir Das *

Indian Association for the Cultivation of Science, Department of Inorganic Chemistry, Jadavpur, Kolkata 700 032, India

Received 12 June 2007; accepted 3 October 2007
Available online 14 November 2007

Abstract

Two ONO donor tridentate Schiff base ligands, two aromatic 1,2-diols and a monomethyl ether derivative of aromatic 1,2-diol are used in this work. The ONO donor ligands are deprotonated forms of *N*-(1-hydroxyphenyl)salicylaldimine (H_2L^1) and *N*-(1-hydroxyphenyl)napthaldimine(H_2L^2) (general abbreviation H_2L). The concerned diols are catechol (H_2cat), its 3, 5-Bu^t_2 derivative (H_2dbcat) and the monomethyl ether derivative of aromatic 1,2-diol is 2-methoxyphenol (HMecat), commonly known as guaiacol. The syntheses of hexa-/penta-coordinated vanadate esters of monoionized aromatic 1,2-diols and 2-methoxyphenolate, with diionized *N*-salicylidene/*N*-napthalidine-α-aminophenol as coligands are described and the reactivities of the compounds are reported. The concerned vanadate esters are [VO(L)(Hcat)], [VO(L)(Hdbcat)] and [VO(L)(Mecat)], where Hcat, Hdbcat and Mecat are monoionised forms of H_2cat, H_2dbcat and HMecat, respectively. The complexes are electroactive in MeCN solution. Molecular oxygen reacts smoothly with the oxovanadium(V) complexes quantitatively, furnishing the corresponding *o*-quinone. In the presence of the aromatic diol or guaiacol the reaction becomes catalytic. The X-ray structure of [VO(L^2)(Mecat)] has also been reported.
© 2007 Elsevier Ltd. All rights reserved.

Keywords: Oxovanadium(V); Catecholase reaction; Catalytic cycle; Aromatic 1,2-diols, 2-methoxyphenol

1. Introduction

The past few years have seen a rapid development in the chemistry and biochemistry of vanadium(V). It has been documented for a long time that the vanadium, like phosphorous, forms ester mainly in the pentavalent state [1–3]. The functional motif characterizing such species is oxovanadium alkoxides [4,5]. The rich chemistry of vanadate ester is however emerging only in recent years. A sizeable number of compounds representing diverse forms of structure and reactivity are available [6]. Oxovanadium alkoxides have been documented to act as selective redox reagent [7,8], as mimics in studies of phosphorylation [9] and insulin action [10,11]. Vanadium is also found in the haloperoxides of some marine algae and in nitrogen-fixing enzymes in some bacteria [12]. Extensive reviews of these biochemical functions of vanadium have recently been published [13]. The topic that has generated a considerable amount of interest is the chemistry of reaction between vanadate and 1,2-diol functionalities [6]. Herein the synthesis, characterization and reactivity of a family of vanadate esters of monoionised aromatic 1,2-diols and 2-methoxyphenolate, with diionized *N*-salicylidene/*N*-napthalidine-α-aminophenol as coligands, are reported.

The complexes are stable in solid state but undergo spontaneous oxidation in solution in the presence of oxygen affording quinone and an oxovanadium(V) product. In presence of excess free aromatic 1,2-diol or 2-methoxyphenol the oxidation process becomes catalytic [14]. Some aspects of the rate and nature of the reaction have been scrutinized. The spectral and electrochemical features of the complexes along with a X-ray structure of a 2-methoxyphenate complex are reported.

* Present address. Department of Chemistry, Washington State University, Pullman, WA 99164-4630, United States. Tel.: +1 509 335 5334; fax: +1 509 335 8867.
E-mail address: sdas@wsu.edu

0277-5387/$ - see front matter © 2007 Elsevier Ltd. All rights reserved.
doi:10.1016/j.poly.2007.10.004

2. Experimental

Commercially available $VOSO_4 \cdot 5H_2O$, salicylaldehyde, 2-hydroxynapthaldehyde, aminophenol, guaiacol, catechol, substituted catechol and dimethyl sulfate were used as received. $[VO(acac)_2]$ [15], $[V_2O_3(ONO)_2]$ [16] and tetraethylammonium perchlorate (TEAP) [17] were prepared as reported. All the other chemicals and solvents were of AR grade and used as obtained.

2.1. Physical methods

UV–Vis spectra were recorded on a Shimadzu UVPC 1601 PC spectrometer fitted with thermostated cell compartments. IR spectra were measured with Nicolet Magna IR 750 series II spectrometer. Proton NMR spectral measurements were carried out with a Brucker FT 300 MHz spectrometer. The atom-numbering scheme used for ^{1}H NMR is the same as that used in crystallography. Spin–spin structures are abbreviated as follows: s, singlet, d, doublet, t, triplet. The electrochemical measurements were performed on a PAR 370-A electrochemical system [18], using a Pt working electrode with reference to saturated calomel electrode (SCE). Perkin–Elmer 2400 is used for elemental analysis.

2.2. Rate measurements

The representative case of the reaction of $[VO(L^1)(Hdbcat)]$ in O_2-saturated Me_2CO (298 K) will be described. The initial O_2 concentration in O_2-saturated Me_2CO, determined by using an O_2 sensitive electrode, was found to be 9.0×10^{-4} M. The concentration of the complex was varied in the range $(4–10) \times 10^{-5}$ M. The spectrum of a solution of $[VO(L^1)(Hdbcat)]$ in O_2-saturated Me_2CO (298 K) was followed spectrophotometrically (quartz cell path length, 1 cm) by measuring the absorbance (A_t) at 610 nm as function time, t. The absorbance A_∞ at the end of 19 h of reaction was also measured. The values of k_{obs} were obtained from the slope of the linear plot of $-\ln(A_t - A_\infty)$ versus t.

2.3. Synthesis of the ligands

Two tridentate Schiff base ligands H_2L^1 and H_2L^2 (general abbreviation H_2L) have been employed in the present work. The ligands were prepared by the same general method.

2.4. Preparation of H_2L^2 ligand

To a MeOH (50 cm^3) solution of 2-hydroxynapthaldehyde (740 mg, 4.6 mmol), 2-aminophenol (500 mg, 4.6 mmol) was added while stirring at room temperature. After 2 h, a canary yellow precipitate appeared which was filtered, washed with cold MeOH, dried over P_4O_{10} for 48 h. Yield: 78%. *Anal.* Calc. for $C_{17}H_{13}NO_2$: C, 77.55; H, 4.98; N, 5.32. Found: C, 77.44; H, 5.09; N, 5.23%. IR (KBr): ν(OH) 3410; ν(C=N) 1598 cm^{-1}. ^{1}H NMR [($CDCl_3$), δ, (J/Hz)]: 9.40 (s, 1H, H(7)), 8.30 (d, 1H, H(2), $J = 8.02$), 7.42 (d, 1H, H(3), $J = 7.80$), 6.97 (d, 1H, H(9), $J = 8.00$), 7.12 (t, 1H, H(10), $J = 8.10$), 6.88 (t, 1H, H(11), $J = 7.90$), 7.89 (d, 1H, H(12), $J = 8.19$), 7.32 (d, 1H, H(14), $J = 7.90$), 7.10 (t, 1H, H(15), $J = 8.04$), 7.16 (t, 1H, H(16), $J = 8.01$), 7.09 (d, 1H, H(17), $J = 8.02$), 9.75 (br, 2H, H(OH)).

2.5. Preparation of H_2L^1 ligand

Salicyaldehyde (1 g, 8.0 mmol) and aminophenol (800 mg, 8.0 mmol) were employed. Yield: 83%. *Anal.* Calc. for $C_{13}H_{11}NO_2$: C, 73.22; H, 5.19; N, 6.56. Found: C, 73.27; H, 5.29; N, 6.47%. IR (KBr): ν(OH) 3405; ν(C=N) 1590 cm^{-1}. ^{1}H NMR [($CDCl_3$), δ, (J/Hz)]: 8.92 (s, 1H, H(7)), 7.28 (d, 1H, H(2), $J = 7.81$), 7.34 (t, 1H, H(3), $J = 7.79$), 7.11 (t, 1H, H(4), $J = 7.09$), 7.41 (d, 1H, H(5), $J = 7.80$), 6.94 (d, 1H, H(9), $J = 7.79$), 7.11 (t, 1H, H(10), $J = 8.00$), 6.81 (t, 1H, H(11), $J = 8.06$), 7.00 (d, 1H, H(12), $J = 8.10$), 9.73 (s, 2H, H(OH)).

2.6. Synthesis of the complexes

[VO(L)(Hcat)] and [VO(L)(Hdbcat)], type (**1**) complexes reported in this work were prepared by the same general method. Details are given for the case of $[VO(L^1)(Hcat)]$.

2.7. Preparation of $[VO(L^1)(Hcat)]$

To a stirred Me_2CO (30 cm^3) solution of $[V_2O_3(L^1)_2]$ (50 mg, 0.09 mmol), H_2cat (29 mg, 0.27 mmol) was added under N_2 atmosphere. After 0.5 h the reaction mixture was concentrated 10 cm^3 and the greenish solution then kept in cold. The precipitate thus obtained was filtered off, washed with hexane and dried in vacuum. Yield: 70%. *Anal.* Calc. for $C_{19}H_{14}NO_5V$: C, 58.92; H, 3.64; N, 3.62. Found: C, 58.81; H, 3.69; N, 3.51%. ^{1}H NMR [$(CD_3)_2CO$, δ, (J/Hz)]: 9.94 (s, 1H, H(7)), 8.11 (d, 1H, H(2), $J = 8.31$), 7.99 (t, 1H, H(3), $J = 8.7$), 7.01 (t, 1H, H(4), $J = 7.90$), 7.01 (d, 1H, H(5), $J = 8.40$), 7.54 (d, 1H, H(9), $J = 7.70$), 7.61 (t, 1H, H(10), $J = 8.00$), 7.81 (t, 1H, H(11) $J = 8.00$), 7.80 (d, 1H, H(12), $J = 8.1$), 6.92 (d, 1H, H(19), $J = 8.30$), 6.82 (t, 1H, H(20), $J = 7.00$), 6.94 (t, 1H, H(21), $J = 8.43$), 6.92 (d, 1H, H(22), $J = 8.10$), 10.03 (br, 1H, H(OH)). VO^{3+}–VO^{2+} couple (CH_2Cl_2–CH_3CN (1:1)): $E_{1/2}$, −1.32 V (100 mV) and E_p, 1.34 V.

2.8. Preparation of $[VO(L^1)(Hdbcat)]$

$[V_2O_3(L^1)_2]$ (50 mg, 0.09 mmol) and H_2dbcat (49 mg, 0.27 mmol) were employed. Yield: 75%. *Anal.* Calc. for $C_{27}H_{30}NO_5V$: C, 64.93; H, 6.05; N, 2.80. Found: C, 64.87; H, 6.01; N, 2.71%. ^{1}H NMR [$(CD_3)_2CO$, δ, (J/Hz)]: 9.93 (s, 1H, H(7)), 8.01 (d, 1H, H(2), $J = 8.3$), 8.03 (t, 1H, H(3), $J = 8.8$), 7.00 (t, 1H, H(4), $J = 8.0$), 7.02 (d, 1H, H(5), $J = 9.1$), 7.51 (d, 1H, H(9), $J = 7.9$), 7.64 (t, 1H, H(10), $J = 8.1$), 7.95 (t, 1H, H(11), $J = 8.0$), 7.80 (d,

1H, H(12), $J = 8.1$), 6.80 (s, 1H, H(19)), 1.56 (s, 3H, C(20)(Me_3)) 6.90 (s, 1H, H(21)), 1.25 (s, 3H, C(22) (Me_3)), 10.09 (br, 1H, H(OH)). VO^{3+}–VO^{2+} couple (CH_2Cl_2–CH_3CN (1:1)): $E_{1/2}$, −1.35 V (100 mV) and E_p, 1.36 V.

2.9. Preparation of [VO(L^2)(Hcat)]

[$V_2O_3(L^2)_2$] (50 mg, 0.07 mmol) and H_2cat (23 mg, 0.21 mmol) were employed. Yield: 71%. *Anal.* Calc. for $C_{23}H_{16}NO_5V$: C, 63.23; H, 3.74; N, 3.22. Found: C, 63.16; H, 3.79; N, 3.31%. ^{1}H NMR [$(CD_3)_2CO$, δ, (J/Hz)]: 9.90 (s, 1H, H(7)), 8.10 (d, 1H, H(2), $J = 8.04$), 8.03 (d, 1H, H(3), $J = 8.80$), 7.00 (d, 1H, H(9), $J = 8.01$), 7.99 (t, 1H, H(10), $J = 9.10$), 7.88 (t, 1H, H(11), $J = 7.90$), 7.89 (d, 1H, H(12), $J = 8.19$), 7.05 (d, 1H, H(14), $J = 7.90$), 7.20 (t, 1H, H(15), $J = 8.14$), 7.06 (t, 1H, H(16), $J = 8.14$), 7.05 (d, 1H, H(17), $J = 8.24$), 6.96 (d, 1H, H(19), $J = 8.2$), 6.84 (t, 1H, H(20), $J = 6.86$), 6.96 (t, 1H, H(21), $J = 8.24$), 6.92 (d, 1H, H(22). $J = 7.92$), 10.02 (br, 1H, H(OH)). VO^{3+}–VO^{2+} couple (CH_2Cl_2–CH_3CN (1:1)): $E_{1/2}$, −1.32 V (100 mV) and E_p, 1.34 V.

2.10. [VO(L)(Mecat)], type (**2**)

Two complexes were prepared by the same general procedure based on the reaction of [$V_2O_3L_2$] with HMecat in Me_2CO at room temperature. Details are given for the case of [VO(L^2)(Mecat)].

2.11. Preparation of [VO(L^2)(Mecat)]

To a stirred Me_2CO (30 cm^3) solution of [$V_2O_3(L^2)_2$] (50 mg, 0.07 mmol) was added HMecat (130 mg, 1.10 mmol) at ambient condition. After 1 h the reaction mixture was concentrated 10 cm^3 and the dark solution then kept in slow evaporation. After two days a dark crystalline compound was obtained. The complex was recrystallized from dichloromethane–methanol mixture in presence of excess guaiacol. Yield: 67%. *Anal.* Calc. for $C_{25}H_{20}NO_5VCl_2$: C, 55.99; H, 3.76; N, 2.61. Found: C, 55.90; H, 3.66; N, 2.53%. ^{1}H NMR [$CDCl_3$, δ, (J/Hz)]: 9.97 (s, 1H, H(7)), 8.29 (d, 1H, H(2), $J = 8.4$), 8.02 (d, 1H, H(3), $J = 9.09$), 7.58 (d, 1H, H(9), $J = 8.01$), 7.69 (t, 1H, H(10), $J = 8.00$), 7.98 (t, 1H, H(11), $J = 7.98$), 7.85 (d, 1H, H(12), $J = 8.10$), 7.25 (d, 1H, H(14), $J = 7.70$), 7.00 (t, 1H, H(15), $J = 8.04$), 7.00 (t, 1H, H(16), $J = 8.04$), 7.05 (d, 1H, H(17), $J = 8.00$), 6.96 (d, 1H, H(19), $J = 8.2$), 6.84 (t, 1H, H(20), $J = 6.86$), 6.96 (t, 1H, H(21), $J = 8.20$), 6.92 (d, 1H, H(22). $J = 6.92$), 3.32 (s, 3H, C(24)). VO^{3+}–VO^{2+} couple (CH_2Cl_2–CH_3CN (1:1)): $E_{1/2}$, −1.28 V (100 mV) and E_p,1.33 V.

2.12. Preparation of [VO(L^1)(Mecat)]

[$V_2O_3(L^1)_2$] (50 mg, 0.09 mmol) and HMecat (150 mg, 1.20 mmol) were employed. Yield: 71%. *Anal.* Calc. for $C_{20}H_{16}NO_5V$: C, 59.86; H, 4.02; N, 3.49. Found: C, 59.76; H, 3.89; N, 3.59%. ^{1}H NMR [$CDCl_3$, δ, (J/Hz)]: 9.15 (s, 1H, H(7)), 7.65 (d, 1H, H(2), $J = 6.00$), 7.59 (t, 8.7, 1H, H(3), $J = 7.2$), 7.19 (t, 1H, H(4), $J = 8.10$), 7.03 (d, 1H, H(5), $J = 5.40$), 7.04 (d, 1H, H(9), $J = 6.0$), 7.94 (t, 1H, H(10), $J = 9.00$), 7.01 (t, 1H, H(11) $J = 8.40$), 7.51 (d, 1H, H(12), $J = 8.1$), 6.82 (d, 1H, H(19), $J = 8.1$), 6.85 (t, 1H, H(20), $J = 6.15$), 6.82 (t, 1H, H(21) $J = 6.23$), 6.82 (d, 1H, H(22), $J = 8.10$), 3.36 (s, 3H, C(24)). VO^{3+}–VO^{2+} couple (CH_2Cl_2–CH_3CN (1:1)): $E_{1/2}$, −1.30 V (100 mV) and E_p, 1.35 V.

Table 1
X-ray crystallographic data for [VO(L^2)(Mecat)] · CH_2Cl_2

Empirical formula	$C_{25}H_{20}Cl_2NO_5V$
F_w	536.26
Crystal system, space group	triclinic, $P\bar{1}$
a (Å)	9.749(10)
b (Å)	11.085(11)
c (Å)	11.889(7)
α (°)	74.90(6)
β (°)	78.94(6)
γ (°)	67.31(7)
V (Å^3)	1138(2)
Z	2
T (K)	293
d_{calc} (mg/m^3)	1.565
μ (mm^{-1})	0.709
R_1^a (wR_2^b)	0.0540 (0.1379)
Goodness-of-fit on F^2	1.038

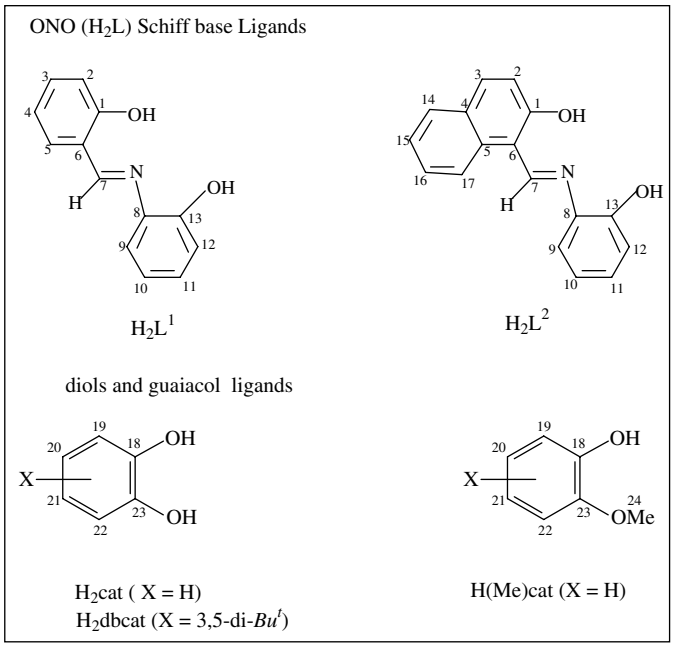
[a] $R_1 = \sum||F_o| - |F_c||/\sum|F_o|$.
[b] $wR2 = [\sum[w(F_o^2 - F_c^2)_2]/\sum[w(F_o^2)^2]]^{1/2}$.

2.13. Crystal structure determination

Single crystals of [VO(L^2)(Mecat)] ($0.40 \times 0.35 \times 0.35$) were grown by slow evaporation of a solution in dichloromethane–methanol, in presence of excess HMecat. The cell parameters were determined by least squares fit of 30 machine centred reflections ($14° \leqslant 2\theta \leqslant 28°$). Data were collected by ω-scan method in the range $2\theta = 3$–50° on a Siemens R3m/V diffractometer with graphite-monochromated Mo Kα radiation ($\lambda = 0.71073$ Å). Two check reflections measured after every 198 reflections showed on significant intensity reduction. Data were collected for Lorentz-polarization effects. An empirical absorption correction was done on the both sets of data on the basis of azimuthal scans [19]. All calculations for the data reductions, structure solution and refinement were done with the programs of SHELXTL Version 5.03 [20]. The structure of [VO(L^2)(Mecat)] was solved by direct methods and was refined by full-matrix least-squares anisotropic. All the H atoms were directly located in difference Fourier maps. Significant crystal data are listed in Table 1.

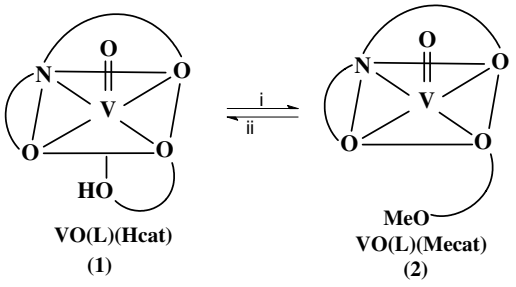
3. Results and discussion

The structures of the tridentate Schiff base ligands, aromatic diols and 2-methoxyphenol used in the present work are given in Box 1.



Box 1.

The potentially dissociable H atoms belong to the phenol groups. To ensure that only mononuclear configuration is attained we used the strategy of blocking three oxovanadium coordination positions leaving just two/one (assuming hexa-/pentacoordination) position for possible chelation by phenol/phenoxidic or phenoxidic functions [6].



Scheme 1. (i) Me_2SO_4 in alkaline MeOH/H_2O, stir. (ii) O_2 saturated Me_2CO/H_2O, stir.

The reaction of $[V_2O_3L_2]$ with excess aromatic diol (H_2cat/H_2dbcat) or guaiacol in Me_2CO under N_2 conditions afforded a dark colored solution. The complexes precipitated in cold. Monoionised aromatic diol chelation is rare in transition metal chemistry. A notable example, relevant to catechol dioxygens activity [21], occurs in iron chemistry [22]. The type **1** complexes undergo methylation in presence of dimethyl sulfate in alkaline aqueous methanol solution leading to the formation of type **2** complexes. Type **2** complexes readily form type **1** complexes in oxygen saturated aqueous acetone solution. The interconversion is shown in Scheme 1.

The complexes display strong V=O stretch in the region 986–991 cm^{-1} and type (**1**) species display OH stretching and very broad ^1H NMR spectrum. In UV–Vis spectra the complexes display moderately strong absorption band near 560–610 nm in visible region. The absorption and IR spectral data are set out in Table 2. All the reported complexes are electroactive in MeCN solution. The complexes display a quasi-reversible reductive one-electron response of V^V/V^{VI} at negative potentials and a irreversible oxidative response of catecholate/semiquinonate at positive potentials.

3.1. Structure

The X-ray structure of $[VO(L^2)(Mecat)]$ has been determined. Molecular view is shown in Fig. 1 and selected bond parameters are listed in Table 3. The VO^{3+} moiety is coordinated to the phenoxidic O4 atom of guaiacol and O2, N1 and O3 atoms of the meridionally tridentate Schiff base ligand, the N1 atom lying *trans* to O4.

The V=O [1.567(3) Å] and V–O(phenoxiodic) 1.806(3) Å are similar to these in polyol [23] and hexacoordinated mono-/diionised catechol complexes [14]. In monoionised catechol complexes the V–O (phenolic) distance is lengthened by the V=O trans influence so as to lie within 2.34 ± 0.05 Å [14]. A remarkable feature of $[VO(L^2)(Mecat)]$ is the usually long V–O(phenolic) contact 2.502(3) Å signifying the virtual absence of bonding. In effect $[VO(L^2)(Mecat)]$ is a square pyramidal complex.

Since the V=O length in $[VO(L^2)(Mecat)]$ is normal, the state of the V–O(phenolic) contact cannot be ascribed to

Table 2
UV–Vis and IR spectral data for the complexes

Complexes	UV–Vis data[a]	IR data[c] (cm^{-1})		
	λ_{max} (nm) (ε[b] (M^{-1} cm^{-1}))	$\nu_{V=O}$	$\nu_{C=N}$	ν_{OH}
$[VO(L^1)(Hcat)]$	572 (5200), 436 (7740), 384 (9270), 332 (10200)	986	1603	3060
$[VO(L^1)(Hdbcat)]$	611 (8150), 449 (8750), 382 (9580), 328 (10350)	991	1605	2959
$[VO(L^2)(Hcat)]$	562 (3200), 452 (3750), 385 (4290), 334 (4700)	984	1603	2926
$[VO(L^1)(Mecat)]$	578 (2720), 464 (8050), 444 (8420), 331 (9800)	991	1595	
$[VO(L^2)(Mecat)]$	572 (3500), 483 (5530), 393 (4750), 341 (6250)	988	1595	

[a] Solvent is CH_2Cl_2.
[b] Extinction coefficient.
[c] In KBr disk.

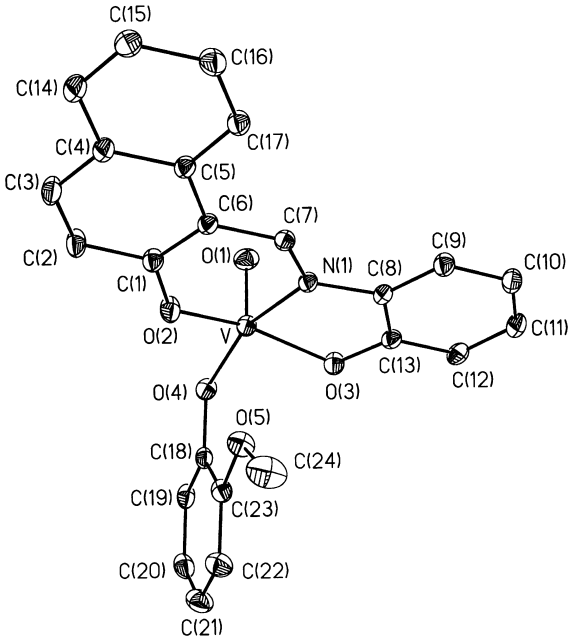


Fig. 1. Molecular view and atom labeling scheme for [VO(L^2)(Mecat)]. All non hydrogen atoms are represented by 30% thermal probability ellipsoids. Hydrogen atoms and solvent molecule have been omitted for clarity.

any augmented trans influence. The V–O2, V–N1 and V–O3 distance within the Schiff base fragment are similar to these observed elsewhere [24]. The atoms O2, O3, O4 and N1 constitute an excellent plane (mean deviation ca. 0.04 Å) from which the metal atom displacement is larger than that observed in monoionised diols [6].

3.2. Reaction with oxygen

The complexes are stable only in solid state. Their dark solutions which are otherwise stable, get progressively bleached in presence of oxygen. The products isolated from the yellowish brown solutions are dimeric $[V_2O_3L_2]$ [14] and the corresponding *o*-quinone (Q) of the used diols and guaiacol. The reaction has been quantitated in the case of [VO(L^1)(Hdbcat)] complex, Eq. (1). The progress of the reaction is scrutinized by both electronic and ^{1}H NMR spectra. Time evolution electronic spectra are characterized by a isosbestic point, and is shown in Fig. 2. In time evolution ^{1}H NMR spectra, the *tertiary*-butyl signals in oxygen saturated acetone-d_6 at δ 1.56 and 1.25 decay with time due to decrease of concentration of coordinated monoionized ditertiarybutylcatechol and those at δ 1.27 and 1.26 grow with time due to increase in concentration of free ditertiarybutylquinone.

$$[VO(L^1)(Hdbcat)] + 1/2\ O_2 \rightarrow 1/2[V_2O_3(L^1)_2] + Q + 1/2H_2O \quad (1)$$

Under pseudo-first-order conditions (saturated), the rates are proportional to the concentration of the VO^{3+} complex and the observed rate constant is k_{obs}. The value of k_{obs} increases with increasing electron withdrawing properties of ONO donor ligands ($H_2L^2 > H_2L^1$) and electron donating properties of momoionized diols ($Hdbcat^- > Hcat^-$). Rate data are listed in Table 4.

Upon adding free H_2dbcat to the solution during the reaction or after its completion the ester is regenerated to the original level and the reaction of Eq. (1) can start over again. A catalytic cycle for the oxidation of H_2dbcat into corresponding quinone (Q) by oxygen is clearly realized by combining two reactions (Eqs. (2) and (3)). It is a rare catecholase reaction in which the active intermediate, [VO(L^1)(Hdbcat)] and the catalyst, $[V_2O_3L_2]$, are vanadium complexes (Fig. 3) [14].

$$[V_2O_3(L)_2] + 2H_2dbcat \rightarrow 2[VO(L)(Hdbcat)] + H_2O \quad (2)$$

$$2H_2dbcat + O_2 \rightarrow 2Q + 2H_2O \quad (3)$$

Table 3
Selected bond lengths (Å) and angles (°) for [VO(L^2)(Mecat)]

Bond lengths			
V–O1	1.567(3)	V–N1	2.088(3)
V–O2	1.837(3)	N1–C8	1.405(4)
V–O3	1.855(3)	N1–C7	1.291(4)
V–O4	1.806(3)	C1–O2	1.304(4)
C23–O5	1.354(4)	C13–O3	1.325(4)
C18–O4	1.338(4)	C24–O5	1.388(5)
Bond angles			
O1–V–O4	103.05(14)	O1–V–O2	102.6(2)
O4–V–O2	98.23(13)	O1–V–O3	102.8(2)
O4–V–O3	91.33(12)	O2–V–O3	150.04(13)
O2–V–N1	82.87(12)	O4–V–N1	159.11(11)
O1–V–N1	97.01(14)	O3–V–N1	78.46(11)

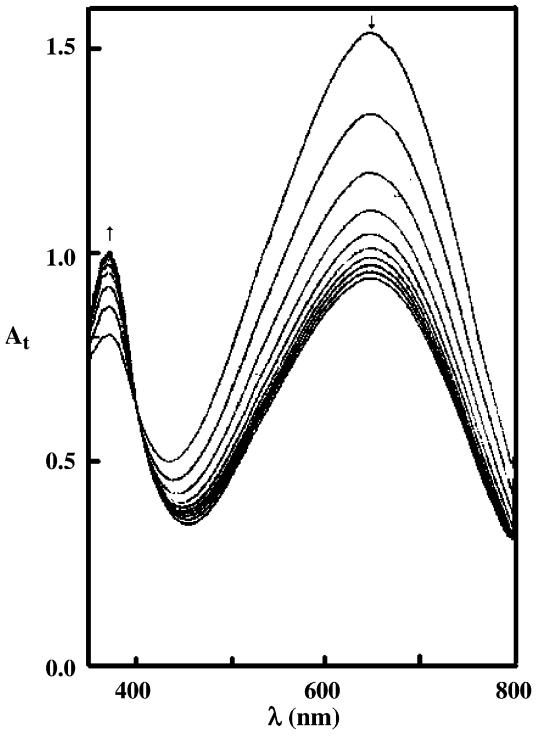


Fig. 2. Time evolution spectra of [VO(L^1)(Hdbcat)] in oxygen saturated acetone solution at 298 K, A_t absorbance.

Table 4
Rate constants for the quinone formation in oxygen saturated acetone solution at 298 K[a]

Compound	[Compound] ($M \times 10^5$)	$10^3 \times k_{obs}$ (s^{-1})	$10^3 \times k_{obs}$(average) (s^{-1})
[VO(L^1)(Hcat)]	9.44	1.98 (0.03)	2.06 (0.05)
	8.01	2.13 (0.07)	
	9.32	2.07 (0.05)	
[VO(L^1)(Hdbcat)]	5.10	7.12 (0.04)	7.40 (0.03)
	4.30	7.73 (0.03)	
	4.03	7.34 (0.02)	
[VO(L^2)(Hcat)]	6.01	3.05 (0.08)	3.20 (0.06)
	6.70	3.14 (0.03)	
	4.37	3.41 (0.06)	
[VO(L^1)(Mecat)]	5.32	0.53 (0.02)	0.58 (0.02)
	4.51	0.57 (0.03)	
	7.88	0.64 (0.02)	
[VO(L^2)(Mecat)]	5.80	0.71 (0.06)	0.74 (0.07)
	5.96	0.79 (0.05)	
	7.41	0.72 (0.09)	

[a] Least-squares deviations are given in parentheses.

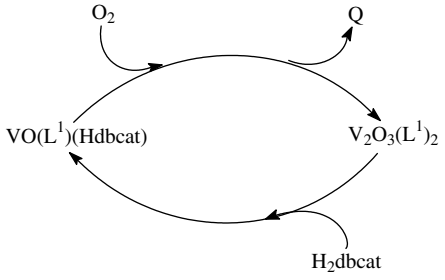


Fig. 3. Catalytic cycle based on catecholase reaction of [VO(L^1)(Hdbcat)] in oxygen saturated acetone solution.

4. Conclusion

The important aspects of this paper can now be summarized. The oxovanadium(V) complexes synthesized by chelation with catechols and guaiacol have been characterized. The complexes are oxidized spontaneously and quantitatively by O_2 in solution furnishing the corresponding quinone (Q) and $[V_2O_3L_2]$, which is reconverted to the original active complex upon addition of diol or guaiacol. These reactions provided a method for catalytic oxidation (catecholage reaction) of aromatic 1,2-diols and guaiacol to corresponding quinone.

5. Supplementary material

CCDC 288154 contains the supplementary crystallographic data for $[VO(L^2)(Mecat)] \cdot CH_2Cl_2$. These data can be obtained free of charge via http://www.ccdc.cam.ac.uk/conts/retrieving.html, or from the Cambridge Crystallographic Data Centre, 12 Union Road, Cambridge CB2 1EZ, UK; fax: (+44) 1223-336-033; or e-mail: deposit@ccdc.cam.ac.uk.

Acknowledgements

The author is grateful to Prof. Animesh Chakravorty and Dr. Bharat Baurah for technical advice and useful suggestions. This work is financially supported by the Department of Science and Technology and Council of Scientific and Industrial Research, India.

References

[1] W. Prandtl, L.Z. Hess, Z. Anorg. Chem. 82 (1913) 103.
[2] A.J. Blair, D.A. Pantony, G.J. Minkoff, J. Inorg. Nucl. Chem. 5 (1958) 316.
[3] F. Carton, C.N. Caughlan, J. Phys. Chem. 64 (1960) 1756.
[4] C.N. Caughlan, H.M. Smith, K. Watenpaugh, Inorg. Chem. 5 (1966) 2131.
[5] W.R. Scheidt, Inorg. Chem. 12 (1973) 1758.
[6] B. Baurah, S. Das, A. Chakravorty, Coord. Chem. Rev. 237 (2003) 135.
[7] T. Hirao, M. Nori, Y. Ohshiro, J. Org. Chem. 55 (1990) 358.
[8] T. Hirao, T. Fujii, T. Tanaka, Y. Ohshiro, J. Chem. Soc., Perkin Trans. 1 (1994) 3.
[9] D.C. Crans, C.M. Simone, J.S. Blanchard, J. Am. Chem. Soc. 144 (1992) 4926, and the references theirin.
[10] B.I. Posner, R. Faure, J.W. Burgess, A.P. Bevan, D. Lachance, G. Zhang Sun, I.G. Fantus, J.B. Ng, D.A. Hall, B. Soo Lum, A. Shaver, J. Biol. Chem. 269 (1994) 4596.
[11] P.J. Stankiewicz, A.S. Tracey, D.C. Crans, H. Sigel, A. Sigel (Eds.), Metal Ions in Biological system, Marcel Dekker Inc., New York, 1995, p. 287.
[12] J.M. Arber, E. de Boer, C.D. Garner, S.S. Hasnain, R. Wever, Biochemistry 28 (1989) 7968.
[13] X. Zhang, A.S. Tracey, Acta Chem. Scand. 46 (1992) 1170.
[14] B. Baruah, S. Das, A. Chakravorty, Inorg. Chem. 41 (2002) 4502.
[15] R.A. Rowe, M.M. Jones, Inorg. Synth. 5 (1957) 133.
[16] L.T. Theriot, G.O. Carlisle, J. Hu, J. Inorg. Nucl. Chem. 31 (1969) 2841.
[17] D.T. Sawyer, J.L. Roberts Jr., Experimental for Chemists, Wiley, New York, 1974, p. 212.
[18] G.K. Lahiri, S. Bhattacharya, B.K. Ghosh, A. Chakravorty, Inorg. Chem. 26 (1987) 4324.
[19] A.C.T. North, D.C. Philips, F.S. Mathews, Acta Crystallogr., Sect. A 24 (1968) 351.
[20] G.M. Sheldrick, SHELXTL, Version 5.03, Siemens Analytical Instruments Inc., Madison, WI, 1994.
[21] H.-J. Kruger, in: B. Meunier (Ed.), Biomimetic Oxidation by Transition Metal Complexes, Imperial College Press, London, UK, 2000, p. 363.
[22] L. Shu, Y.-M. Chiou, A.M. Orville, M.A. Miller, J.D. Lipscomb, L. Que Jr., Biochemistry 34 (1995) 6649.
[23] S. Mondal, S.P. Rath, K.K. Rajak, A. Chakravorty, Inorg. Chem. 37 (1998) 1713.
[24] S.P. Rath, K.K. Rajak, S. Mondal, A. Chakravorty, J. Chem. Soc., Dalton Trans. (1998) 2097.

Available online at www.sciencedirect.com
ScienceDirect
Polyhedron 27 (2008) 523–529
POLYHEDRON
www.elsevier.com/locate/poly

Single-crystal electronic spectra of some quadrate chromium(III) complexes

Chamindra S. Williams *,[1], Nelse C. Miller, John A. Collins

Department of Chemistry, Florida Atlantic University, 777 Glades Road, Boca Raton, FL 33431, United States

Received 12 July 2007; accepted 3 October 2007
Available online 14 November 2007

Abstract

Polarised electronic spectra of *trans*-$[Cr(tmd)_2F_2](ClO_4)$, *trans*-$[Cr(en)_2(dma)_2](ClO_4)_3$, *trans*-$[Cr(en)_2(dmf)Cl](ClO_4)_2$ and *trans*-$[Cr(en)_2(dmf)Br](ClO_4)_2$ have been measured at 77 K (tmd = trimethylenediamine; dma = *N*,*N*-dimethylacetamide; dmf = *N*,*N*-dimethylformamide; en = ethylenediamine, pn = propylenediamine). The observed quartet bands have been given definitive quadrate assignments based on polarisation characteristics. The four-component quadrate quartet bands have been uncovered and assigned also in the unpolarised crystal spectrum of *trans*-$[Cr(en)_2(dmf)_2](ClO_4)_3$ at 77 K and the solution spectrum of *trans*-$[Cr(en)(pn)F_2]^+$. The band maxima derived by gaussian analysis in these spectra have been fitted with the theoretical energy equations of d^3 configuration in quadrate ligand fields including full configuration interaction. The ligand field parameters *Dq*, *Dt*, and *Ds* and the election correlation parameter, *B*, extracted by such a fitting, have been compared with those obtained for other similar systems earlier. The significance of the ligand field symmetry parameters and the translated angular overlap model parameters is discussed.
© 2007 Elsevier Ltd. All rights reserved.

Keywords: Single-crystal electronic spectra; Chromium(III) complexes

1. Introduction

Most of the spectra of quadrate chromium(III) complexes that have been studied and interpreted were obtained either in solution or by diffuse reflectance [1–5]. Spectra of polarised single-crystals of quadrate chromium(III) complexes studied so far are still limited [6–11]. This study extends the list of polarised single-crystal spectra, as well as the list of unpolarised and solution spectra by providing an analysis of the polarised single-crystal spectra of *trans*-$[Cr(tmd)_2F_2]ClO_4$, *trans*-$[Cr(en)_2(dma)_2](ClO_4)_3$, *trans*-$[Cr(en)_2(dmf)Cl](ClO_4)_2$ and *trans*-$[Cr(en)_2(dmf)Br](ClO_4)_2$, unpolarised crystal spectrum of *trans*-$[Cr(en)_2(dmf)_2](ClO_4)_3$, and solution spectrum of *trans*-$[Cr(en)(pn)F_2]^+$.

2. Experimental

The complexes have been prepared as described in the literature [12–15]. Single-crystals of the complexes were grown by one of the following methods: (i) slow evaporation of a saturated solution (*trans*-$[Cr(en)_2(dma)_2](ClO_4)_3$, *trans*-$[Cr(en)_2(dmf)Br](ClO_4)_2$), (ii) slow evaporation of a saturated solution in 3:1 ethanol–water (*trans*-$[Cr(en)_2(dmf)Cl](ClO_4)_2$, *trans*-$[Cr(en)_2(dmf)_2](ClO_4)_3$), and (iii) a 3 mL volume of ice-cold 2 M perchloric acid was saturated with the complex to which acetone was added and the mixture was cooled in a refrigerator for 24 h, yielding single-crystals at the interface of the two layers (*trans*-$[Cr(tmd)_2F_2]ClO_4$). Single-crystals of *trans*-$[Cr(en)_2(dmf)Cl](ClO_4)_2$, *trans*-$[Cr(en)_2(dmf)Br](ClO_4)_2$ and *trans*-$[Cr(en)_2(dmf)_2](ClO_4)_3$ showed pink to green, deep-blue to green and orange to pink dichroism, respectively.

All compounds were analysed for Cr^{3+} content [16] by boiling with alkaline hydrogen peroxide and then measuring absorbance of the resulting CrO_4^{2-} at 372 nm; analysis

* Corresponding author.
E-mail address: cwilli74@fau.edu (C.S. Williams).
[1] Taken in part from the Ph.D. dissertation (2005) of Chamindra S. Williams.

0277-5387/$ - see front matter © 2007 Elsevier Ltd. All rights reserved.
doi:10.1016/j.poly.2007.10.003

Table 1
Observed band maxima

	Parallel (cm^{-1})	Perpendicular (cm^{-1})
trans-$[Cr(tmd)_2F_2]ClO_4$	29882	29829
	24806	24848
	21587	21578
	18776	18663
trans-$[Cr(en)_2(dma)_2](ClO_4)_3$	29356	29355
	26608	26400
	21362	21859
	19518	19243
trans-$[Cr(en)_2(dmf)Cl](ClO_4)_2$	27509	27600
	25546	25751
	22536	22547
	18181	18293
trans-$[Cr(en)_2(dmf)Br](ClO_4)_2$	27143	27172
	24708	24766
	22229	22247
	17846	18119
trans-$[Cr(en)_2(dmf)_2](ClO_4)_3$	28900	
	26950	
	23052	
	19600	
trans-$[Cr(pn)(en)F_2]^+$	28630	
	25035	
	20997	
	18366	

gave 98.6–99.9% of the calculated value for chromium content.

Spectral measurements were carried out as described in detail in the literature [6,9,17].

3. Results and discussion

3.1. Spectral data and band assignment

For all the systems studied, bands in each of the spectra were resolved into gaussian components.[2] Values of band maxima for complexes studied are listed in Table 1. The earlier studies [6] of the *dmf* systems only made tentative assignments for the second cubic band components $^4A_{2g}$ and ^4E_g of $^4T_{1g}$ based on shifts of the band maxima in different polarisations. For these systems, the experimental data were reproduced and gaussian analysis was carried out to obtain accurate band maxima for a definitive band assignment.

For complexes with d^3 configuration with octahedral geometry, three spin-allowed bands should be observed as follows: $^4A_2^C \rightarrow {}^4T_2^C$, $^4A_2^C \rightarrow {}^4T_1^C$ and $^4A_2^C \rightarrow {}^4T_1^C$, where $^4A_2$ represents the ground state and $^4T_2$ and $^4T_1$ represent the quartet excited states to which transitions are allowed. The third high-energy transition is usually not seen as it is buried in charge-transfer bands. The lower two transitions are expected to spilt into two components each as the symmetry of the complex is lowered when the axial ligands are different from those on the equatorial plane (D_{4h} to C_{4v}). In the lower symmetry, the ground state is $^4B_1$ and gives rise to the following transitions: $^4B_1^Q \rightarrow {}^4B_2^Q(^4T_2)$, $^4B_1^Q \rightarrow {}^4E^Q(^4T_2)$, $^4B_1^Q \rightarrow {}^4A_2^Q(^4T_1)$ and $^4B_1^Q \rightarrow {}^4E^Q(^4T_1)$.

In the case of D_{4h} complexes, vibronic selection rules predict [7–9] that the ^4E components are both 'z' ($\|$) and 'xy' ($\perp$) polarised whereas the $^4A_2$ and $^4B_2$ components are 'xy' polarised but not 'z' polarised. In the case of strictly C_{4v} complexes, however, the $^4A_2$ component becomes allowed in the 'z' polarisation by vibronic mechanism, although it is orbitally forbidden which means the $^4A_2$ may appear in 'z' polarisation, although with weak intensity. In addition, it is predicted [2,18] that among the two components of the lowest energy cubic band, $^4T_2$, the $^4B_2$ component will be at higher energy than the ^4E component for complexes with negative parameter Dt. This prediction has been verified in all the systems studied by polarised measurements [6–9]. These observations were used in making definitive assignments of the bands in the spectra of the systems studied. Spectra are those of energy (given in kiloKayser, $1\ kK = 1000\ cm^{-1}$) versus optical density (crystals) or extinction coefficient (solution).

3.1.1. *trans*-$[Cr(tmd)_2F_2]ClO_4$

Owing to the well-resolved spectra in each of the polarisations, band assignment for this complex was relatively straight-forward (Fig. 1). Bands in the perpendicular polar-

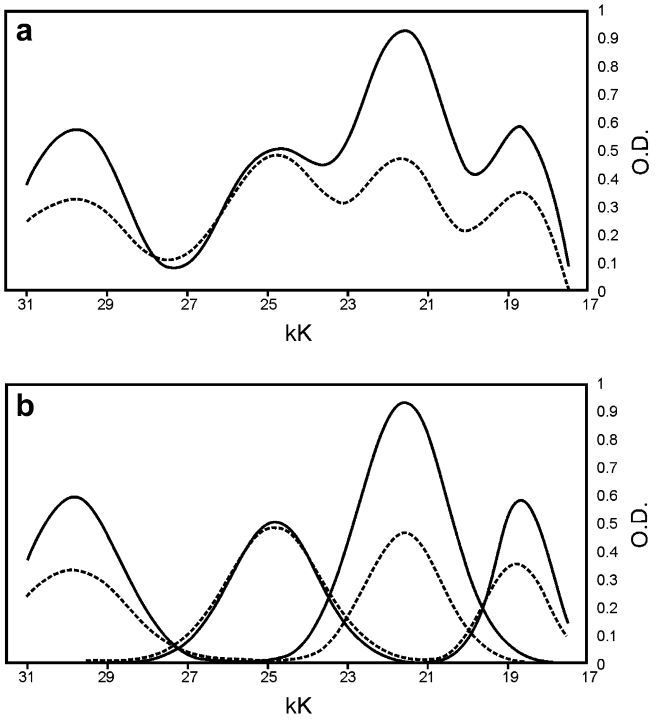


Fig. 1. (a) Polarised single-crystal spectrum of *trans*-$[Cr(tmd)_2F_2]ClO_4$ at 77 K and (b) gaussian fit. In both graphs, the solid line represents perpendicular polarisation and dashed line that of parallel polarisation.

[2] The generosity of Prof. P.A. Snyder for the use of software for this purpose is acknowledged.

isation are seen to occur at 18 663 cm^{-1}, 21 578 cm^{-1}, 24 848 cm^{-1} and 29 829 cm^{-1}. Those in the parallel polarisation are seen to occur at 18 776 cm^{-1}, 21 587 cm^{-1}, 24 806 cm^{-1} and 29 882 cm^{-1}. In all cases, band maxima (when comparing the two polarisations) are separated by no more than 100 cm^{-1}, with the lowest separation being 9 cm^{-1}. The lowest energy band in each case (18 663 cm^{-1} and 18 776 cm^{-1}) is assigned to $^4B_1^Q \rightarrow {}^4E^Q(^4T_2)$. The assignment of the second lowest energy band (at 21 578 cm^{-1} and 21 587 cm^{-1}) is made to $^4B_1^Q \rightarrow {}^4B_2^Q$ since its intensity is considerably lower in the parallel polarisation. Looking at the intensities of the next two bands, the marked reduction of the intensity in the highest energy band (at 29 829 cm^{-1} and 29 882 cm^{-1}) allows assignment to $^4B_1^Q \rightarrow {}^4A_2^Q$, which leaves the penultimate band (at 24 806 cm^{-1} and 24 848 cm^{-1}) in both polarisations assigned to $^4B_1^Q \rightarrow {}^4E^Q(^4T_1)$.

3.1.2. *trans*-[Cr(en)$_2$(dma)$_2$](ClO$_4$)$_3$

Single-crystal polarised spectra of the above complex were obtained in the parallel and perpendicular orientations (Fig. 2). Bands in the parallel polarisation are seen to occur at 19 518 cm^{-1}, 21 362 cm^{-1}, 26 608 cm^{-1} and 29 356 cm^{-1}. Those in the perpendicular polarisation are seen to occur at 19 243 cm^{-1}, 21 859 cm^{-1}, 26 400 cm^{-1} and 29 355 cm^{-1}. In looking at the spectra, in both polarisations it appears that the lowest energy band appears as a shoulder. Since the intensity of this band is not reduced significantly, it is assigned to $^4B_1^Q \rightarrow {}^4E^Q(^4T_2)$. The second lowest energy band is then assigned as $^4B_1^Q \rightarrow {}^4B_2^Q$. The last two assignments were somewhat difficult, as the reduction of intensity on one band in one polarisation was accompanied by an increase in intensity of the second band in the next polarisation. With greater weight given to the disappearance of one of the bands in the parallel polarisation, the assignment of $^4B_1^Q \rightarrow {}^4E^Q(^4T_1)$ is given to those bands at 26 608 cm^{-1} and 26 400 cm^{-1} in the two polarisations. The significant reduction in intensity of the band at 29 356 cm^{-1} in the parallel polarisation requires this and the one at 29 355 cm^{-1} in the perpendicular polarisation to be assigned to $^4B_1^Q \rightarrow {}^4A_2^Q$.

3.1.3. *trans*-[Cr(en)$_2$(dmf)Cl](ClO$_4$)$_2$

Bands in the spectrum of this complex in the perpendicular polarisation are seen to occur at 18 293 cm^{-1}, 22 547 cm^{-1}, 25 751 cm^{-1} and 27 600 cm^{-1} (Fig. 3). Those in the parallel polarisation are seen to occur at 18 181 cm^{-1}, 22 536 cm^{-1}, 25 546 cm^{-1} and 27 509 cm^{-1}. Looking at the relative intensities of the peaks, it is evident that the lowest energy band, in both cases, can be assigned to the transition $^4B_1^Q \rightarrow {}^4E^Q(^4T_2)$. The justification for this assignment is the almost-unchanged intensity of the band in both polarisations. The assignment of the second band, done so simultaneously, is made as $^4B_1^Q \rightarrow {}^4B_2^Q$. Here too, justification is made based on the consideration of intensity, in this case, a pronounced reduction in intensity, as expected for this band in the parallel polarisation. Again, using the criterion of intensity, the third transition

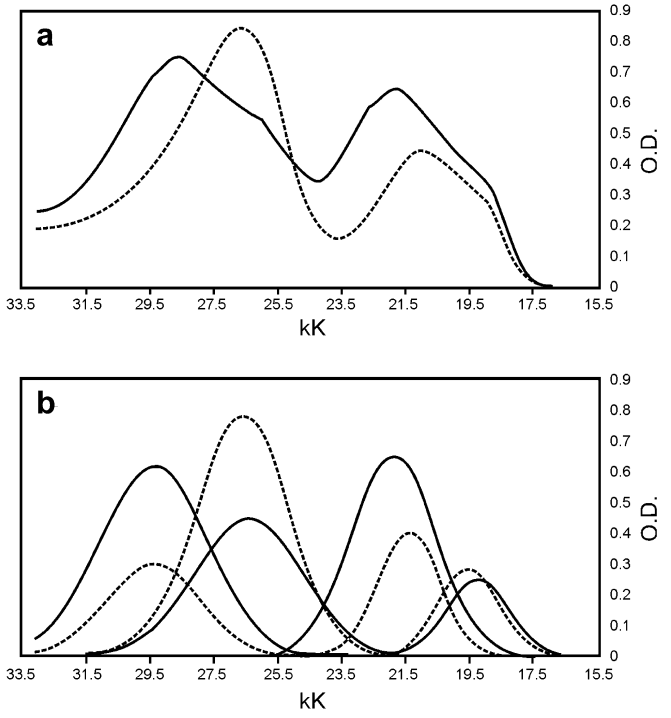


Fig. 2. (a) Polarised single-crystal spectrum of *trans*-[Cr(en)$_2$(dma)$_2$](ClO$_4$)$_3$ at 77 K and (b) gaussian fit. In both graphs, the solid line represents perpendicular polarisation and dashed line that of parallel polarisation.

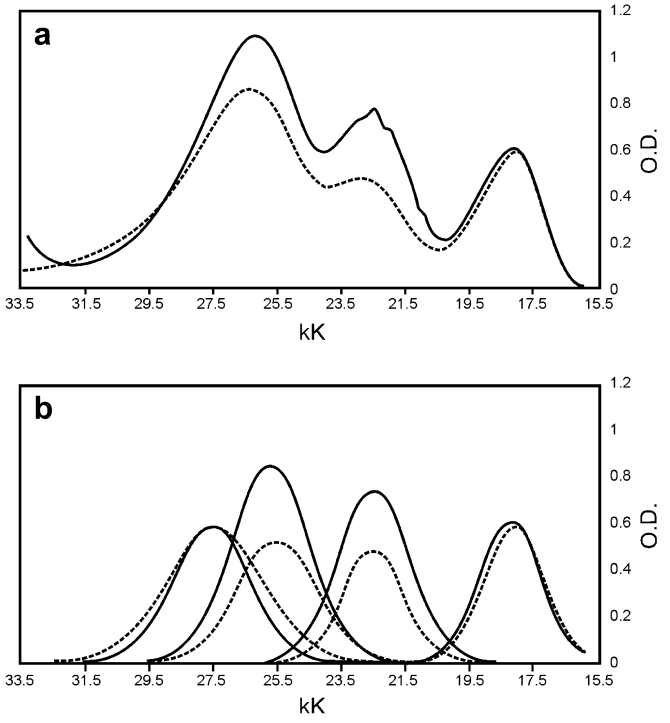


Fig. 3. (a) Polarised single-crystal spectrum of *trans*-[Cr(en)$_2$(dmf)Cl](ClO$_4$)$_2$ at 77 K and (b) gaussian fit. In both graphs, the solid line represents perpendicular polarisation and dashed line that of parallel polarisation.

$^4B_1^Q \rightarrow {}^4A_2^Q$ is characterised by bands at 25 546 cm^{-1} (parallel) and 25 751 cm^{-1} (perpendicular). Bands at 27 509 cm^{-1} and 27 600 cm^{-1} are assigned to the $^4B_1^Q \rightarrow {}^4E^Q(^4T_1)$ transition. A prominent feature of the analysis presented here, different from that given in earlier work, is the increased splitting of the second spin-allowed transition. A spin-forbidden band at 21 950 cm^{-1} is tentatively assigned to $^4B_1^Q \rightarrow {}^2B_2(^2T_{2g})$ transition.

3.1.4. *trans*-[Cr(en)$_2$(dmf)Br](ClO$_4$)$_2$

As was the case with *trans*-[Cr(en)$_2$(dmf)Cl](ClO$_4$)$_2$, an analysis of the spectra with gaussian fitting is made (Fig. 4). Bands in the perpendicular polarisation are seen to occur at 18 119 cm^{-1}, 22 247 cm^{-1}, 24 766 cm^{-1} and 27 172 cm^{-1}. Those in the parallel polarisation are seen to occur at 17 846 cm^{-1}, 22 229 cm^{-1}, 24 708 cm^{-1} and 27 143 cm^{-1}. Again, as was the case with *trans*-[Cr(en)$_2$(dmf)Cl](ClO$_4$)$_2$, by looking at the relative intensities of the peaks, the lowest energy band, in both cases, can be assigned to the transition $^4B_1^Q \rightarrow {}^4E^Q(^4T_2)$. As before, the justification for this assignment is the almost-unchanged intensity of the band in both polarisations while observing that the band at higher energy is lowered, as expected. The assignment of the second band is $^4B_1^Q \rightarrow {}^4B_2^Q$. The band at 24 766 cm^{-1} is assigned to the $^4B_1^Q \rightarrow {}^4A_2^Q$ transition since it is lowered in intensity in the parallel polarisation and the band at 27 369 cm^{-1} which has the same intensity in both polarisations is assigned to the $^4B_1^Q \rightarrow {}^4E^Q(^4T_1)$. A spin-forbidden band at 21 186 cm^{-1} is tentatively assigned to $^4B_1^Q \rightarrow {}^2B_2$, $^2E(^2T_{2g})$ transitions.

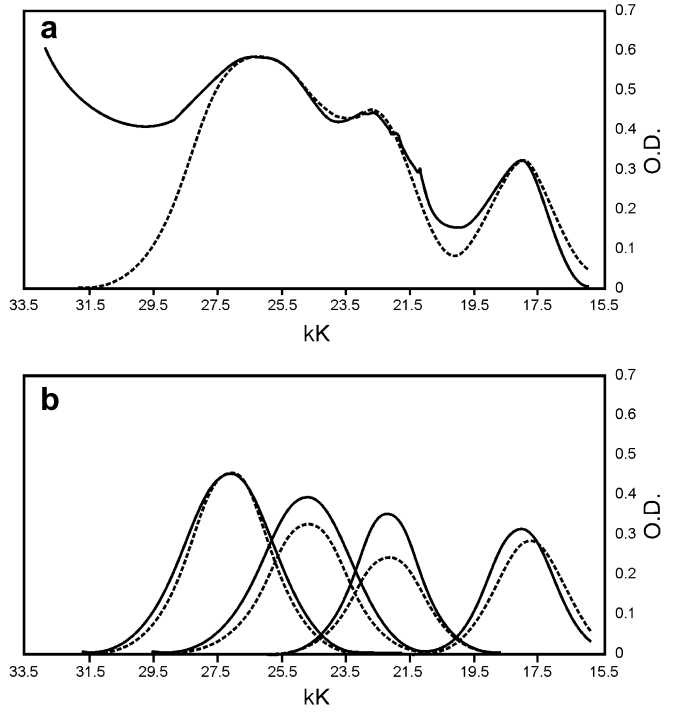


Fig. 4. (a) Polarised single-crystal spectrum of *trans*-[Cr(en)$_2$(dmf)Br](ClO$_4$)$_2$ at 77 K and (b) gaussian fit. In both graphs, the solid line represents perpendicular polarisation and dashed line that of parallel polarisation.

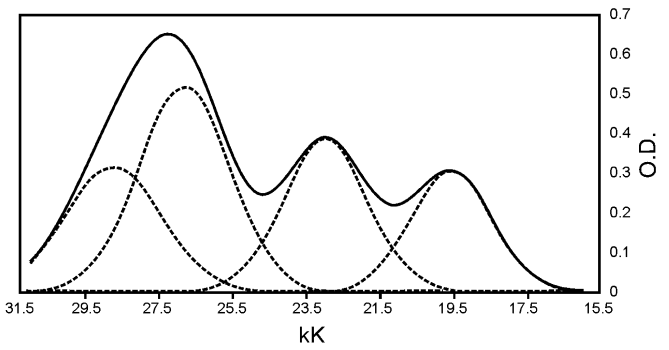


Fig. 5. Unpolarised single-crystal spectrum of *trans*-[Cr(en)$_2$(dmf)$_2$](ClO$_4$)$_3$ at 77 K and gaussian fit. The solid line represents the experimental spectrum and the dashed line represents the gaussian fit.

3.1.5. *trans*-[Cr(en)$_2$(dmf)$_2$](ClO$_4$)$_3$

Attempts to obtain polarised spectra of this complex were unsuccessful. Consequently, an analysis of the unpolarised crystal spectra with gaussian fitting is performed (Fig. 5). Bands are seen to occur at 19 600 cm^{-1}, 23 052 cm^{-1}, 26 950 cm^{-1} and 28 900 cm^{-1}. These bands can be assigned on the basis of a comparison with the corresponding *bis(dma)* and *di-aqua* systems which were studied [8] by the analysis of polarised spectra.[3] In addition to a spin-forbidden band at 22 270 cm^{-1}, two other spin-forbidden bands were uncovered for this system [6] at very high energy, i.e. 32 447 cm^{-1} and 32 658 cm^{-1}. These spin-forbidden bands have been thoroughly interpreted earlier [19].

3.1.6. *trans*-[Cr(en)(pn)F$_2$]$^+$

Even though repeated attempts to grow single-crystals were unsuccessful, this is perhaps one of the very few systems that exhibits all four components clearly in the solution spectrum, hence it has been included in this study (Fig. 6). The four obvious band positions gave a correspondingly similar gaussian fit which resulted in the following band assignments: The lowest energy band is assigned to $^4B_1^Q \rightarrow {}^4E^Q(^4T_2)$ and the next band to $^4B_1^Q \rightarrow {}^4B_2^Q$. Considering the other ligands in the complex, the other two bands are assigned as follows: the band at 25 035 cm^{-1} is assigned to $^4B_1^Q \rightarrow {}^4E^Q(^4T_1)$ and that at 28 630 cm^{-1} is assigned to $^4B_1^Q \rightarrow {}^4A_2^Q$. These assignments are similar to those in the well-known [7] complex *trans*-[Cr(en)$_2$F$_2$]ClO$_4$. These and all other assignments can be found in Table 2.

3.2. Fitting and analysis of parameters

Once the band assignments have been established, ligand field parameters *Dq*, *Dt*, *Ds* and *B* are determined according to the following: The parameter *Dq* is obtained from the band position of $^4B_2$, as this level has an energy of 10*Dq*. The difference in energy between $^4B_2$ and ^4E (i.e. splitting in the first cubic band) is $-\frac{35}{4}Dt$. The difference in energy between the $^4A_2$ and ^4E (i.e. the splitting

[3] This work.

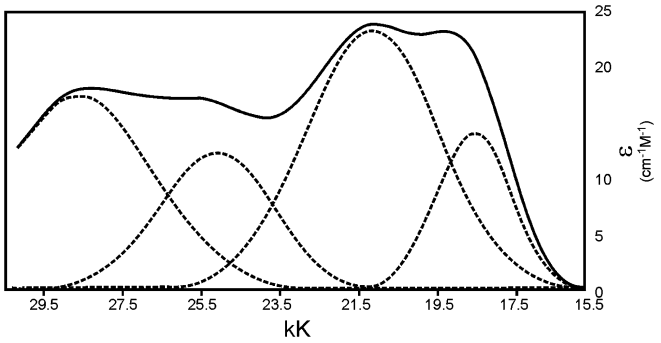


Fig. 6. Solution spectrum of *trans*-$[Cr(en)(pn)F_2]^+$ at 298 K and gaussian fit. The solid line represents the experimental spectrum and the dashed line represents the gaussian fit.

in the second cubic band) is $6Ds - \frac{5}{4}Dt$ and can be rearranged for Ds. The last parameter B, is obtained as $12B$, by taking the difference of the averages of the components of the two cubic bands, $^4T^C_{2g}$ and $^4T^C_{1g}$. These *initial* parameters are then varied until all observed bands in the spectra are fitted *exactly*. The manner in which this was achieved was to assume a linear effect of each of the parameters on the individual energy level and then solve a system of linear equations repeatedly until an exact fitting was obtained. The summary of these calculations are shown below in Table 3 along with the angular overlap model (AOM) parameters (to be discussed) calculated using equations given below.

A discussion of the parameters follows. The parameter Dt, is given by

$$Dt = -\frac{4}{7}(Dq_E - Dq_A),$$

where Dq_E and Dq_A are the Dqs of the equatorial ligands and axial ligands, respectively, of the octahedral complexes. Since *en* is of greater ligand-field strength than any of the ligands used in the axial position here, a negative value of Dt is expected and this is what is seen in the values tabulated (Table 3).

It should be noted that the value of Dq of the quadrate complex is predicted [2,17] to be very similar to the value of Dq_E. Considering the parameter Dq in the complex $Cr(en)_3$, the value reported [18] is 2185 cm^{-1}. Inspection of the values of Dq for all complexes shows a range of 2136–2305 cm^{-1}, indicating that the Dq value of the hexa-coordinated complex is approximately the same as the Dq value of the substituted complex with the ligand

Table 2
Band assignments for all complexes studied

Complex/polarisation		Band positions (cm^{-1})			
		$^4B_{1g} \rightarrow {}^4E_g$	$\rightarrow {}^4B_{2g}$	$\rightarrow {}^4E_g$	$\rightarrow {}^4A_{2g}$
trans-$[Cr(tmd)_2F_2]ClO_4$	⊥	18663	21578	24848	29829
	∥	18776	21587	24806	29882
trans-$[Cr(en)_2(dma)_2](ClO_4)_3$	⊥	19243	21859	26400	29355
	∥	19518	21362	26608	29356
trans-$[Cr(en)_2(dmf)Cl](ClO_4)_2$	⊥	18293	22547	27600	25751
	∥	18181	22536	27509	25546
trans-$[Cr(en)_2(dmf)Br](ClO_4)_2$	⊥	18119	22247	27172	24766
	∥	17846	22229	27143	24708
trans-$[Cr(en)_2(dmf)_2](ClO_4)_3$		19600	23052	26950	28900
trans-$[Cr(en)(pn)F_2]^+$		18366	20997	25035	28630

Table 3
Calculated parameters

		Ligand field symmetry parameters (cm^{-1})				AOM parameters (cm^{-1})			
		Dq	Ds	Dt	B	$e'_\sigma(xy)$	$e'_\pi(xy)$	$e'_\sigma(z)$	$e'_\pi(z)$
trans-$[Cr(tmd)_2F_2]ClO_4$	⊥	2158	943	−317	653	7190	0	8290	2200
	∥	2159	956	−302	638	7200	0	8350	2190
trans-$[Cr(en)_2(dma)_2](ClO_4)_3$	⊥	2186	530	−298	710	7290	0	7600	1540
	∥	2136	506	−208	721	7120	0	7610	1280
trans-$[Cr(en)_2(dmf)Cl](ClO_4)_2$	⊥	2255	−363	−455	664	7516	0	5653	593
	∥	2256	−382	−464	656	7512	0	5588	588
trans-$[Cr(en)_2(dmf)Br](ClO_4)_2$	⊥	2225	−451	−435	611	7420	0	5430	410
	∥	2223	−458	−462	627	7410	0	5340	470
trans− $[Cr(en)_2(dmf)_2]\,(ClO_4)_3$		2305	301	−393	651	7680	0	7300	1430
trans-$[Cr(en)(pn)F_2]^+$		2100	667	−296	682	7000	0	7590	1740

Table 4
Calculated and observed values of Dq of axial ligand

Complex	Calculated Dq_A (cm^{-1})	Observed Dq_A (cm^{-1})
trans-$[Cr(tmd)_2F_2]ClO_4$	1617	1490 [1]
trans-$[Cr(en)_2(dma)_2](ClO_4)_3$	1718	1517 [20]
trans-$[Cr(en)_2(dmf)Cl](ClO_4)_2$	1440	1444[a]
trans-$[Cr(en)_2(dmf)Br](ClO_4)_2$	1439	1408[a]
trans-$[Cr(en)_2(dmf)_2](ClO_4)_3$	1617	1517[b]
trans-$[Cr(en)(pn)F_2]^+$	1582	1490 [1]

[a] See Section 3.2 on averaging of parameters.
[b] Bonding similarities between *en*-Cr, *pn*-Cr and *dmf*-Cr, *dma*-Cr, allow interchange of Dq values.

occupying the equatorial positions. With the extracted values of Dq and Dt, it is possible, by rearranging the above formula and setting $Dq = Dq_E$, to calculate a value for Dq_A which can be compared to reported values of Dq for the hexa-coordinated complex having the axial ligand in all six coordination sites. This comparison is shown in Table 4.

Since the bonding between the metal and the ligands *dmf* and *dma* is expected to be very similar, the reported value of Dq for *dma* is used for the similar complex with *dmf* in Table 4. For the complexes *trans*-$[Cr(en)_2(dmf)Cl]^{2+}$ and *trans*-$[Cr(en)_2(dmf)Br]^{2+}$, since the axial positions are occupied by two different ligands, the observed Dq_A reported in Table 4 is the average of the values of Dq of the two axial ligands. The additional parameter values of Dq needed for this purpose are of $[CrCl_6]^{3-}$ (1370 cm^{-1}) and $[CrBr_6]^{3-}$ (1300 cm^{-1}).

In the case of $CrBr_6^{3-}$, a value of 1300 cm^{-1} was used after consideration of the Dq values of the other hexa-halo complexes. Inspection of the calculated and observed values of Dq for the axial ligands shows that although a good correlation is observed in the case of dmf(Cl), dmf(Br) complexes, in all the others a deviation of 100 cm^{-1} is observed (except in the case of the *dma* complex, in which the deviation is 200 cm^{-1}). Any large deviation implies that the bonding of the ligands in an octahedral complex does not remain the same when they are the axial ligands in a quadrate complex.

In order to analyse these parameters further, those of the angular overlap model (AOM) are used. This model has been widely used in the analysis of the spectra of transition-metal complexes [21]. The relationships of interest are listed here:

$$e_\sigma(E) = \frac{10}{3}Dq$$

$$e_\sigma(A) = \frac{10}{3}Dq + 2Ds + \frac{5}{2}Dt$$

$$e_\pi(A) = \frac{3}{2}Ds - \frac{5}{2}Dt$$

$$e_\pi(E) = 0.$$

These calculated AOM parameters are also presented in Table 3. Since these parameters are expected to be characteristic of the ligands, the AOM parameters obtained for similar systems in a previous study [7–9] are listed in Table 5. This table also includes, for comparison, parameters obtained for the $[Cr(pn)_2(dmf)_2]^{3+}$ and $[Cr(tmd)_2F_2]^+$ systems in a diffuse-reflectance spectral study [3]. These parameters are very similar to those extracted in the present study.

Table 5
Reported AOM parameters for complexes of Cr^{3+}

Complex	AOM parameters (cm^{-1})			
	$e'_\sigma(E)$	$e'_\pi(E)$	$e'_\sigma(A)$	$e'_\pi(A)$
trans-$[Cr(en)_2F_2]^+$	7267	0	8061	1930
trans-$[Cr(en)_2Cl_2]^+$	7540	0	5755	1103
trans-$[Cr(en)_2Br_2]^+$	7500	0	5155	766
trans-$[Cr(en)_2BrCl]^+$	7540	0	5363	826
trans-$[Cr(en)_2(H_2O)_2]^{3+}$	7787	0	7418	1630
trans-$[Cr(pn)_2(dmf)_2]^{3+}$	7833	0	7380	1402
trans-$[Cr(tmd)_2F_2]^+$	7457	0	8394	1933

4. Conclusions

In this study, the polarised electronic spectra of a number of *trans*-disubstituted bis(ethylenediamine) chromium(III) complexes have been measured at 77 K. The ligand field parameters Dq, Dt, and Ds and the election correlation parameter, B, extracted with the use of theoretical energy equations of d^3 configuration, have been compared with those obtained for similar systems. A favourable comparison of the parameters extracted in this study as well as the relationship to the AOM parameters has been shown. This study contributes to the data available for the growing comparison to results obtained through an analysis using density functional theory [22–25].

Acknowledgements

The authors thank Prof. J.R. Perumareddi for helpful discussion and guidance.

References

[1] C.K. Jorgensen, Absorption Spectra and Chemical Bonding in Complexes, Addison-Wesley, Reading, MA, 1962.
[2] J.R. Perumareddi, Coord. Chem. Rev. 4 (1969) 73.
[3] T.J. Barton, R.C. Slade, J. Chem. Soc., Dalton Trans. (1975) 650.
[4] J. Glerup, O. Monsted, C.E. Schaffer, Inorg. Chem. 15 (1976) 1399.
[5] B. Schatschneider, J.R. Perumareddi, Inorg. Chim. Acta 358 (2005) 4571.
[6] N.C. Miller, M.S. Thesis, Florida Atlantic University, 1974.
[7] L. Dubicki, M.A. Hitchman, P. Day, Inorg. Chem. 9 (1970) 188.
[8] L. Dubicki, P. Day, Inorg. Chem. 10 (1971) 2043.
[9] R.L. Klein, N.C. Miller, J.R. Perumareddi, Inorg. Chim. Acta 7 (1973) 685.
[10] T. Schönherr, I. Mutsuyoshi, A. Urushiyama, Bull. Chem. Soc. Jpn. 68 (1995) 2271.
[11] T. Schönherr, I. Mutsuyoshi, A. Urushiyama, Bull. Chem. Soc. Jpn. 68 (1995) 594.
[12] J. Glerup, C.E. Schaffer, et al., Acta Chem. Scand. 23 (1970) 247.
[13] W.W. Fee, J.N. Harrowfield, W.G. Jackson, J. Chem. Soc. A 16 (1970) 2612.
[14] I.R. Lantzke, D.W. Watts, Aust. J. Chem. 20 (1967) 35.

[15] J.W. Vaughn, J. Marzowski, Inorg. Chem. 12 (1973) 2346.
[16] W.W. Fee, C.S. Garner, J.N. Harrowfield, Inorg. Chem. 6 (1967) 87.
[17] M.M. Seifollahi, J.R. Perumareddi, Polyhedron 8 (1989) 2283.
[18] J.R. Perumareddi, J. Phys. Chem. 71 (1967) 3155.
[19] C.S. Williams, N.C. Miller, J.R. Perumareddi, Inorg. Chim. Acta 360 (2007) 2842.
[20] R.S. Drago, D.W. Meek, M.D. Joesten, L. LaRoche, Inorg. Chem. 2 (1963) 125.
[21] B.N. Figgis, M.A. Hitchman, Ligand Field Theory and Its Applications, Wiley–VCH, New York, 2000.
[22] C. Anthon, J. Bendix, C.E. Schaffer, Inorg. Chem. 42 (2003) 4088.
[23] J. Telser, J. Braz. Chem. Soc. 17 (2006) 1501.
[24] M. Atanasov, C.A. Daul, C. Rauzy, Chem. Phys. Lett. 367 (2003) 737.
[25] J.A. McCleverty, T.J. Meyer (Eds.), Comprehensive Coordination Chemistry II, vol. 2, Elsevier, Oxford, 2004.

Available online at www.sciencedirect.com
ScienceDirect
Polyhedron 27 (2008) 530–536
POLYHEDRON
www.elsevier.com/locate/poly

A general route for the synthesis of hydrido-carboxylate complexes of the type $MH(CO)(\kappa^3\text{-}OCOR)(PPh_3)_2$ [M = Ru, Os; R = CH_3, CH_2Cl, C_6H_5, $CH(CH_3)_2$] and their use as precatalysts for hydrogenation and hydroformylation reactions

Merlín Rosales [a,*], Beatriz Alvarado [a], Federico Arrieta [b], Carlos De La Cruz [c], Ángel González [a], Karely Molina [a], Otto Soto [a], Yslamar Salazar [a]

[a] La Universidad del Zulia (L.U.Z.), Facultad Experimental de Ciencias, Departamento de Química, Laboratorio de Química Inorgánica, Maracaibo, Venezuela
[b] Laboratorio de Química Inorgánica Teorica, Maracaibo, Venezuela
[c] Laboratorio de Espectroscopía Molecular y Atómica, Maracaibo, Venezuela

Received 28 April 2007; accepted 4 October 2007
Available online 26 November 2007

Abstract

The synthesis and solid-state IR, ^1H and $^{31}P\{^1H\}$ NMR spectroscopic characterization of complexes of the type $MH(CO)(\kappa^3\text{-}OCOR)(PPh_3)_2$ [M = Ru, Os; R = CH_3, CH_2Cl, C_6H_5 and $CH(CH_3)_2$] are reported in this paper. These compounds were obtained by reaction of the respective cationic complex $[MH(CO)(NCMe)_2(PPh_3)_2]BF_4$ with the sodium salt of the corresponding carboxylic acid in a 1:1 v/v dichloromethane/methanol solution at room temperature. The spectroscopic data of these complexes and some DFT calculations reveal an octahedral geometry with a bidentated carboxylate, two equivalent triphenylphosphines in a mutually *trans* positions, a linear hydride and a linear carbonyl both in the *cis*-positions of the coordination sphere. The catalytic results indicate that these complexes are efficient and regioselective precatalysts for the quinoline hydrogenation and for the hydroformylation of 1-hexene, under mild reaction conditions (130 °C and 4 atm H_2 and 120 °C and 15 atm H_2/CO, respectively). For benzothiophene hydrogenation, the osmium complexes showed low activities whereas the analogous ruthenium complexes were catalytically inactive under somewhat more drastic reaction conditions to those of the quinoline hydrogenation (140 °C and 10 atm H_2).
© 2007 Elsevier Ltd. All rights reserved.

Keywords: Ruthenium; Osmium; Carboxylate; Quinoline; Benzothiophene; Hydrogenation; 1-Hexene; Hydroformylation

1. Introduction

The chemistry of ruthenium and osmium complexes containing hydrido, carbonyl and trivalent phosphorus co-ligands has attracted continuous attention because of the wide variety of structures and reactivities exhibited by these compounds [1,2]. Perhaps the Vaska and Diluzio's complex $RuHCl(CO)(PPh_3)_3$ [3] is the most thoroughly studied compound of this series [2]. Interaction of this compound, or alternatively of $RuH_2(CO)(PPh_3)_3$, with carboxylic acids produces $RuCl(\kappa^3\text{-}OCOR)(CO)(PPh_3)_2$ and $RuH(\kappa^3\text{-}OCOR)(CO)(PPh_3)_2$, where R = CH_3 [4,5], C_2H_5, C_6H_5 [4], $C(CH_3)_3$, C_6H_{11}, CH_2Cl, CF_2Cl, CF_3 [5]. Examples of analogous osmium-complexes are rather scarce in the literature [6] and, to our knowledge, complexes of the type $OsH(\kappa^3\text{-}OCOR)(CO)(PPh_3)_2$ have not been synthesized.

* Corresponding author. Fax: +58 261 7598125.
E-mail address: merlin2002@cantv.net (M. Rosales).

0277-5387/$ - see front matter © 2007 Elsevier Ltd. All rights reserved.
doi:10.1016/j.poly.2007.10.007

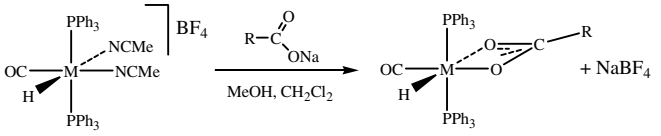
Furthermore, interest in hydrido-carboxylate complexes of transition-metals have been further enhanced by their catalytic activity in a number of industrially important chemical reactions [7].

In the present paper, we reported the synthesis and spectroscopic characterization of a group of complexes with general formulae $MH(\kappa^3\text{-}OCOR)(CO)(PPh_3)_2$ [M = Ru and Os; R = CH_3, CH_2Cl, C_6H_5 and $CH(CH_3)_2$]; these were tested as precatalysts for the homogeneous hydrogenation of polynuclear heteroaromatic nitrogen and sulfur compounds (quinoline and benzothiophene) and for the olefin hydroformylation (1-hexene).

2. Results and discussion

2.1. Synthesis and characterization of complexes $MH(CO)(\kappa^3\text{-}OCOR)(PPh_3)_2$

The complexes $MH(CO)(\kappa^3\text{-}OCOR)(PPh_3)_2$ (**III**–**X**) were synthesized in high yields (>70%) by reaction of the respective cationic complex $[MH(NCMe)_2(CO)(PPh_3)_2]BF_4$ (Ru = **I** and Os = **II**) with the sodium salt of the corresponding carboxylic acid in a 1:1 v/v dichloromethane/methanol solution, at room temperature (see Eq. (1)).



M = Ru; R = CH_3 (**III**), CH_2Cl (**IV**), $CH(CH_3)_2$ (**V**) and C_6H_5 (**VI**)
M = Os; R = CH_3 (**VII**), CH_2Cl (**VIII**), $CH(CH_3)_2$ (**IX**) and C_6H_5 (**X**)

(1)

The products **III**–**X** were white unstable solids that had to be manipulated and stored strictly under N_2 atmosphere. Three of the hydrido-carboxylate ruthenium complexes (R = CH_3, CH_2Cl and C_6H_5) were reported early by Dobson and Robinson [4] by the reaction of $RuH_2(CO)(PPh_3)_3$ with the corresponding carboxylic acid and by Sánchez-Delgado et al. [5] by slight modifications of the Robinson's method. However, this method is not of general use for Ru complexes, in the sense that the reaction time, the amount of the carboxylic acid added and the solvent used depend of the carboxylate ligand. On the other hand, the synthetic route that we are reporting in this article is of general application and allowed us to prepare the osmium analogues which, to our knowledge, were unknown to the date. No satisfactory analytical data could be obtained for these complexes, which darken after a few hours even under inert atmosphere at room temperature. Structural characterization of these complexes had to be based on their FT-IR and NMR spectroscopic properties and by comparison of those with the spectra from well-known complexes.

The FT-IR spectra of all complexes **III**–**X** showed medium-to-weak absorptions between 2150 and 2000 cm^{-1}, and very strong and broad bands between 1900 and 1950 cm^{-1}. Comparison with the reported data for $RuH(CO)(\kappa^3\text{-}OCOCMe_3)(PPh_3)_2$[1] and $OsHCl(CO)(PPh_3)_3$ [8][2] allowed us to assign the main bands in these wavenumber regions to the ν(MH) and ν(CO) vibrations of terminal MH and linear MCO groups, respectively [9]. The C–O distance is estimated to be 1.15 ± 0.02 Å for the carbonyls of these complexes [9b]. The wide wavenumber range found for the ν(MH) vibration relative to the ν(CO)-range shows the high sensitivity of the metal–hydrogen bond to changes in electron density around the central metal atom [9b]. This is affected by the type of metal in question [i.e. ν(RuH) = 2010–2070 cm^{-1} whereas ν(OsH) = 2090–2133 cm^{-1}] and by charge donation or withdrawal of the other co-ligands [e.g. ν(RuH) = 2019 or 2036 cm^{-1} for $RuH(CO)(\kappa^3\text{-}OCOCH_3)(PPh_3)_2$ or $RuH(CO)(\kappa^3\text{-}OCOCH_2Cl)(PPh_3)_2$, respectively].

The infrared spectra of the new complexes (with the exception of the Os-complex **VII**) also show the two expected, symmetry-allowed, infrared-active absorptions of the carboxylate group at 1560–1521 [ν_{asym}(OCO)] and 1457–1425 [ν_{sym}(OCO)] cm^{-1}. These values indicate bidentated coordination between the two equivalent oxygen atoms of the OCOR groups and the Ru or Os atom. Indeed when the carboxyl group is monodentated, one of the C–O bonds should have enhanced double bond character and therefore give rise to a high frequency band in the 1590–1650 cm^{-1}-region which is not observed in our spectra [10].

High field ^1H NMR spectra showed triplets between −16.3 and −16.9 ppm with coupling constants close to 20 Hz for the ruthenium complexes, whereas for the corresponding osmium ones the triplets appear between −19.3 and −20.0 ppm ($^2J_{HP}$ close to 16 Hz). These values are consistent with a hydride ligand coupled to two equivalent triphenylphosphines in mutually *trans* positions [5]. This is further supported by the spectra from the $^{31}P\{^1H\}$NMR experiments which show singlets between 41.8 and 46.4 ppm and between 23.3 and 25.2 ppm for the Ru and Os compounds, respectively.

Our results and interpretations are summarized in Table 1. It clearly indicates an octahedral geometry with four monodentated ligands (hydride, carbonyl and two PPh_3) and one bidentated carboxylate group coordinated to the central Ru or Os atom.

A more detailed analysis of the infrared spectra in the 2100–1850 cm^{-1} region (Fig. 1) indicates the presence of two isomers for the above octahedral complexes in solid state, as may be observed by the presence of two hydride bands. For complexes with the general formula $RuH(CO)(\kappa^3\text{-}OCOR)(PPh_3)_2$, four geometrical isomers could be drawn, which are shown in Fig. 2; for convenience we refer to these below as the *trans*-PPh_3/*trans*-PPh_3 (**A**), *trans*-CO/*trans*-PPh_3 (**B**), *trans*-H/*trans*-PPh_3 (**C**) and *trans*-H/*trans*-CO (**D**) isomers.

[1] For $RuH(CO)(OCO(CH_3)_3)(PPh_3)_2$; IR: ν(Ru–H) = 2000 cm^{-1} and ν(CO) = 1925 cm^{-1}.

[2] For $OsHCl(CO)(PPh_3)_3$. IR: ν(Os–H) = 2097 and ν(CO) = 1912 cm^{-1}.

Table 1
Selected FT-IRS, ^{1}H and $^{31}P\{^{1}H\}$ NMR data for $[MH(\eta^3\text{-}OCOR)(CO)(PPh_3)_2]$ {M = Ru and R = CH_3 (**V**), CH_2Cl (**VI**), $CH(CH_3)$ (**VII**), Ph (**VIII**); M = Os and R = CH_3 (**IX**), CH_2Cl (**X**) $CH(CH_3)_2$ (**XI**) and Ph (**XII**)}

Complex	FT-IRS				^{1}H NMR[a]			$^{31}P\{^{1}H\}$ NMR[b]
	Wavenumbers (cm^{-1}) and relative intensities[c]				Chemical shifts (ppm) and coupling constants (Hz)[d]			
	ν(MH)	ν(CO)	ν_{asym}(OCO)	ν_{sym}(OCO)	$\delta(RCO_2)$	δ(MH)	J(PH)	$\delta(PPh_3)$
III	2019 (m)	1929 (vs)	1531 (s)	1457 (s)	1.7 (s)	−16.7 (t)	20	46.4 (s)
IV	2036 (m)	1933 (vs)	1560 (s, br)	1432 (s, br)	2.4 (s)	−16.9 (t)	20	42.8 (s)
V	2070 (sh)	1909 (vs)	1523 (s)	1425 (s)	1.2 (sept) 0.1 (d, J = 7.1)	−16.3 (t)	21	41.8 (s)
VI	2010 (m)	1925 (vs)	1521 (s)	1425 (s)	7.6 (m)	−16.4 (t)	20	46.0 (s)
VII	2110 (br)	1928 (s)	Obscured by other bands		1.7 (s)	−19.6 (t)	16	24.7 (s)
VIII[e]	2133 (m)	1925 (vs)	1550 (s, br)	1432 (s)	2.0 (s)	−20.0 (t)	16	25.2 (s)
IX	2090 (sh)	1909 (vs)	1556 (s)	1433 (s, br)	1.1 (sept) 0.1 (d, J = 6.3)	−19.3 (t)	17	23.3 (s)
X	2105 (m)	1915 (vs)	1551 (s)	1431 (s)	7.1 (m)	−19.5 (t)	16	24.2 (s)

[a] Negative values are upfield from the signal of external $SiMe_4$.
[b] Positive values are downfield from the signal of external 85% H_3PO_4.
[c] FT-IRS abbreviations: ν = bond-stretching, vs = very strong, s = strong, m = medium, w = weak, vw = very weak, br = broad and sh = shoulder.
[d] NMR abbreviations: s = singlet, d = doublet, t = triplet, sept = septuplet, m = multiplet.
[e] The infrared spectrum also shows bands at 3480 (s, br), 2200 (vw, br), 2050 (vw, br), 1910 (s, br), 1610 (vs), 1490 (m), 1410 (s), 1380 (s), 1325 (m) and 1100 (vs) cm^{-1}. These can be assigned to vibrational modes of water, N≡C M–H, C=O, P–Ph_3 and BF_4^-. They indicate a mixture of small amounts of $[OsH(NCMe)_2(CO)(PPh_3)_2]BF_4$ and $OsH(OCOCH_2Cl)(CO)(PPh_3)_2$ (**VIII**) which probably adsorbed water during the pressing-disc procedure.

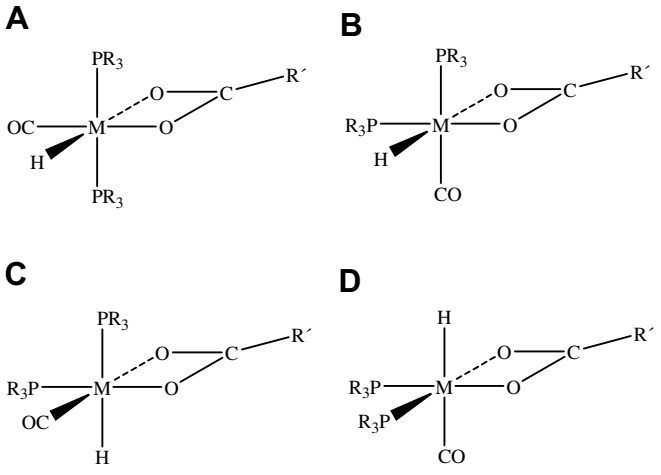


Fig. 1. Possible isomers for complexes $MH(CO)(\kappa^3\text{-}OCOR)(PPh_3)_2$ (M = Ru, Os).

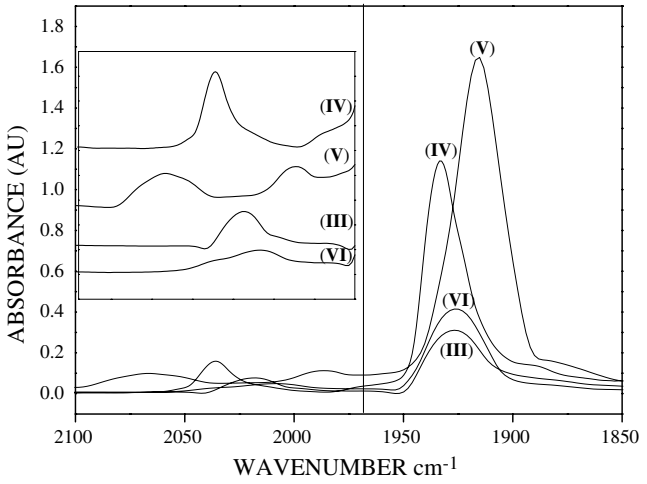


Fig. 2. FTIR for complexes $RuH(CO)(\kappa^3\text{-}OCOR)(PPh_3)_2$ in the 2100–1850 cm^{-1} region.

In other to determine the stability of these isomers, theoretical DFT-calculations were performer for these four isomers with the $FeH(CO)(OOCH)(PH_3)_2$ models using the STO/6-31+G(d,p) extended basis; in Table 2 are listed the calculated energies of these four isomers. As may be observed the isomer **A**, which present the two phosphine ligands in a mutually *trans* position was the more stable isomer, having an energy 20.1, 12.0 and 24.4 kJ mol^{-1} lesser than those of **B**, **C** and **D**, respectively. Isomers **B** and **D** were the least stable of the four isomers. The order of stability was **A** < **C** < **B** < **D**. In view of these results, we proposed that, in solid state, isomer **A** was the major isomer whereas **C** was the minor one. Halide complexes of the type $MX(CO)(\kappa^3\text{-}OCOR)(PPh_3)_2$ have been found to have similar structure to that of **A** (M = Ru, X = Cl) or **C** (M = Os, X = Br) isomers.

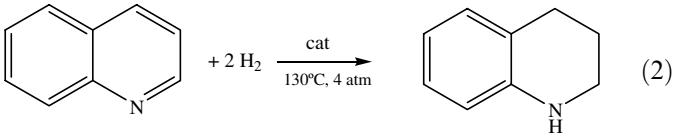
Table 2
Optimized total energies (hartrees) of the isomers of the model compound $Fe(H)(CO)(OOCH)(PH_3)_2$

Isomer	Energy
A	−2253.089846
B	−2253.082210
C	−2253.085265
D	−2253.080594

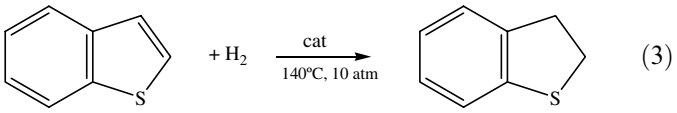
Although small amounts of the isomer **C** of complexes **III**–**X** can be presented (less than 10%) in the solid state, the spectroscopic data in solution are in agreement with a stereochemistry in which the two triphenylphosphine are in a mutually *trans* position, the carboxylate ligand is bonded in a bidentated fashion and the hydride and the carbonyl ligand occupy the *cis* positions of the coordination sphere (isomer **A**).

2.2. Catalytic activities of complexes MH(CO)(κ^3-OCOR)(PPh_3)$_2$

The new Rh and Os complexes MH(CO)(κ^3-OCOR)(PPh_3)$_2$ were tested as catalytic homogeneous precursors for the regioselective hydrogenation of quinoline (Q) to 1,2,3,4-tetrahydroquinoline (THQ) and of benzothiophene (BT) to 2,3-dihydrobenzothiophene (DHBT) under mild temperatures and low hydrogen pressures; see Eqs. (2) and (3).



(2)



(3)

The hydrogenation of the heterocyclic ring of polynuclear heteroaromatic nitrogen and sulfur compounds is an area of considerable interest in connection with the industrially important hydrodenitrogenation (HDN) and hydrodesulfurization (HDS) reactions, respectively [11]. Although some Rh- and Ir-complexes have been used for the hydrogenation of the heterocyclic ring of Q and related compounds, the only ruthenium and osmium precatalysts used in this reaction were $RuHCl(PPh_3)_3$ [12], $[MH(CO)(NCMe)_2(PPh_3)_2]^+$ (M = Ru or Os) [13] and $RuCl_2(NCMe)_4$/tris(pyrazolyl)borate [14]. Recently, Borowski et al. [15] reported the regioselective hydrogenation of the non-heterocyclic rings of Q, by using $[RuH_2(\eta^2\text{-}H_2)_2(PCy_3)_2]$ (Cy = cyclohexyl) as the precatalyst. For the BT hydrogenation, the complexes $[Ru(NCMe)_3(triphos)]^{+2}$ [16] and $[RuH_2(\eta^2\text{-}H_2)_2(PCy_3)_2]$ [17] were the only precursors that showed very high activities for this reaction.

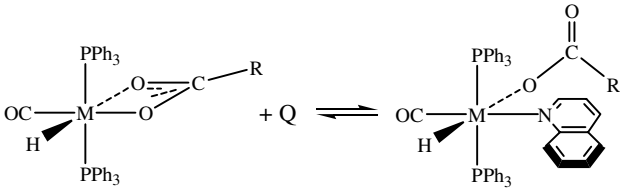
The hydrogenation of Q to THQ was achieved by all of the ruthenium and osmium hydrido-carboxylate complexes with high catalytic activities; the results are collected in Table 3 together with the pK_a values of the R groups of the carboxylate ligand of the Ru and Os complexes. As may be observed, the ruthenium complexes were twice more active than the corresponding osmium ones. It is clear that the hydrogenation activities of these compounds (except for the hydrido-isobutyrate cases where steric effects seem to be important) are affected by the electron-releasing character of the carboxylate substituents. Thus, for example, a plot of $\log r_i$ versus pK_a of the acid from which the carboxylate ligand is derived shows an excellent correlation [$\log r_i(\mathrm{Ru}) = -6.48 + 0.09\mathrm{p}K_a$, $r^2 = 0.99$], as may be observed in Fig. 3; for the osmium complexes, a similar tend was observed [$\log r_i(\mathrm{Os}) = -7.17 + 0.17\mathrm{p}K_a$, $r^2 = 0.99$]. Sánchez-Delgado et al. [7] found the contrary effect for the propionaldehyde hydrogenation, which was explained through a mechanism involving equilibrium between species containing the carboxylate ligand coordinated in a bi- and monodentated mode. In our case, we propose that the equilibrium between these two species (Eq. (4)) is very fast and, therefore, is not the rate-determining step of the catalytic reaction. Preliminary kinetic studies indicate that the hydrogenation rate is independent of the amount of quinoline present in the reaction mixture; these results are consistent with the opening of the carboxylate ligand and the coordination of Q molecule being a very fast step.

Table 3
Quinoline hydrogenation catalyzed by MH(CO)(κ^3-OCOR)(PPh_3)$_2$

R	pK_a[a]	$10^7 r_i$ (ms^{-1})	
		Ru	Os
CH_2Cl	2.86	6.13 ± 0.12	2.05 ± 0.06
C_5H_6	4.20	6.94 ± 0.15	3.51 ± 0.08
CH_3	4.76	9.24 ± 0.09	4.23 ± 0.08
$CH(CH_3)_2$	4.86	8.00 ± 0.05	2.65 ± 0.05

Conditions: $[cat] = 1.0 \times 10^{-3}$ M, $[Q] = 0.17$ M, $p(H_2) = 4$ atm, $T = 130$ °C, solvent = xylene, r_i (initial rate) are expressed in means ± SEM; $P = 0.05$.

[a] pK_a of the acid from which the carboxylate ligand is derived. Yield: 70–80% for Ru complexes and 40–50% for Os ones.



(4)

On the other hand, the hydrogenation of BT to DHBT was observed only with the osmium hydrido-carboxylate complexes (Table 4), the activities being very low (less than 10% conversion); the analogous ruthenium complexes were catalytically inactive for this reaction. Because of the close and very small activities of these osmium systems, no conclusions may be extracted on the relation between activity and the donor character of the carboxylate substituent.

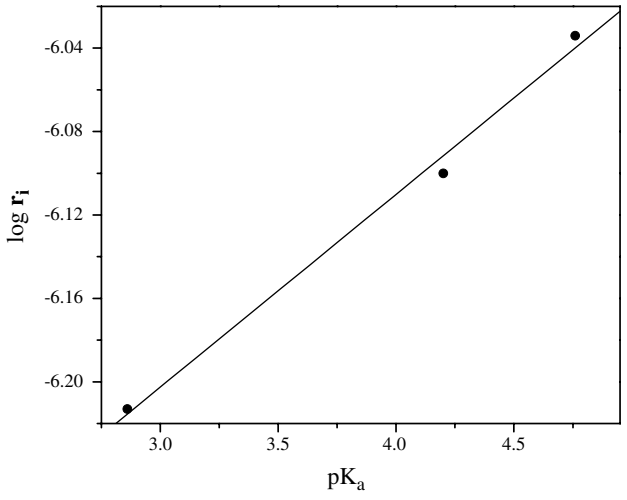
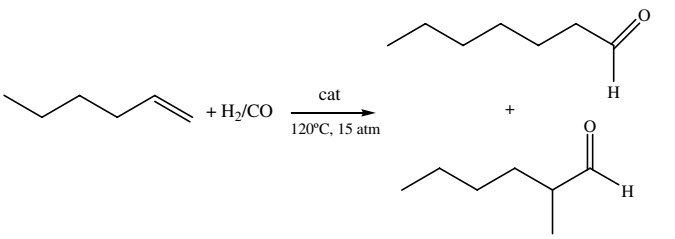


Fig. 3. Hydrogenation of quinoline catalyzed by RuH(CO)(κ^3-OCOR)(PPh_3)$_2$ showing the relation between initial rate (r_i) and the nature of the carboxylate ligand. Conditions as in Table 3.

In order to find new and lesser expensive precatalysts than the rhodium ones for the alkene hydroformylation, in the present work we used the hydrido-carboxylate complexes $MH(CO)(\kappa^3\text{-}OCOR)(PPh_3)_2$ as catalyst precursors for this reaction. This reaction is a well-known synthetic tool for a wide range of organic molecules of commercial value and it is also one of the largest scale applications of homogeneous catalysis in industry. The major capacity is based on the processes using phosphine-modified cobalt [18] and rhodium carbonyl systems [19] but some ruthenium precatalysts have been used for this reaction, such as $RuH_2(CO)_2(PPh_3)_2$ [20], $[RuH(CO)(NCMe)_2(PPh_3)_2]BF_4$ [21], $[Ru(CO)_2(\eta^5\text{-}Cp)]_2$ [22] and $RuH_2(CO)_2(TPPMS)_2$ [23].

The ruthenium and osmium hydrido-carboxylate complexes were efficient and regioselective precatalysts for the hydroformylation of 1-hexene towards heptanal and 2-methyl-hexanal (Eq. (5)), under mild reaction conditions (120 °C and 15 atm H_2/CO) in toluene as the solvent; the results in turnover frequency (TF) are showed in Table 5.



(5)

The ruthenium complexes were more active than the corresponding osmium ones and similar to the Q hydrogenation described before, the complexes with carboxylates presenting donor groups were more active than those containing electron-withdrawing substituents. Again, this effect may be explained through a mechanism which did not involve the opening of the carboxylate ligand as the rate-determining step. For the ruthenium complexes, a plot of log TF versus pK_a of the acid from which the carboxylate ligand is derived shows a very good correlation, $\log TF(Ru) = 0.61 + 0.32pK_a$, $r^2 = 0.96$ (Fig. 4); a similar graph may be constructed for the osmium analogues [$\log TF(Ru) = 0.41 + 0.20pK_a$, $r^2 = 0.92$]. Finally, the regioselectivity find for ruthenium complexes, measured as the linear to branch ratio (l/b), is ranging between 2.5 and 3.5, which is somewhat higher that those found for other ruthenium complexes; the l/b ratio for the osmium analogues varied from 0.8 to 1.6.

Table 4
Benzothiophene hydrogenation catalyzed by $OsH(CO)(\kappa^3\text{-}OCOR)(PPh_3)_2$

R	Conversion (%)
CH_2Cl	8.9
C_5H_6	6.2
CH_3	8.7
$CH(CH_3)_2$	9.1

Conditions: [cat] = 1.0×10^{-3} M, [BT] = 0.1 M, $p(H_2)$ = 15 atm, T = 140 °C, t = 8 h, solvent = xylene.

Table 5
Hydroformylation of hex-1-ene catalyzed by $MH(CO)(\kappa^3\text{-}OCOR)(PPh_3)_2$ (M = Ru, Os)

R	pK_a[a]	TF (l/b)	
		Ru	Os
CH_2Cl	2.86	38 (2.8)	10 (1.6)
C_5H_6	4.20	80 (3.5)	15 (0.8)
CH_3	4.76	155 (2.5)	22 (1.2)
$CH(CH_3)_2$	4.86	180 (3.0)	27 (0.9)

Conditions: [cat] = 3.3×10^{-3} M, [1-hexene] = 1 M, $p(H_2)$ = 15 atm, T = 120 °C, solvent = toluene, TF = mole of product per mole of catalyst per hour, l/b = linear to isoaldehyde ratio.
[a] pK_a of the acid from which the carboxylate ligand is derived.

The results found both for the Q and BT hydrogenation reactions as for the 1-hexene hydroformylation are promising for two reasons. First, although the Ru precatalysts synthesized in this work are close to one magnitude order less active than Rh ones, ruthenium is a metal less expensive than rhodium and, on the other hand, it is possible through the variation of the electronic properties of the carboxylate and phosphine ligands to increase the catalytic activities of our systems. Finally, it is convenient to mention that Fe complexes have shown to have less catalytic activity for both reactions. For example, $Fe(CO)_5$ is inactive for quinoline hydrogenation and $Fe(CO)_4(PBu_3)$ presented low activity (1% in 5 h) for hydrogenation of 5,6-benzoquinoline under drastic water-gas shift reaction conditions [27], whereas the activities of the Fe systems for olefin hydroformylation are four magnitude order lower than those of the ruthenium ones [18c].

More detailed kinetic and coordination chemistry studies of these catalytic reactions (hydrogenation of Q and BT and olefin hydroformylation) are in progress, aimed at better understanding these systems and at improving even more both the activity as the selectivity properties of the hydroformylation reaction.

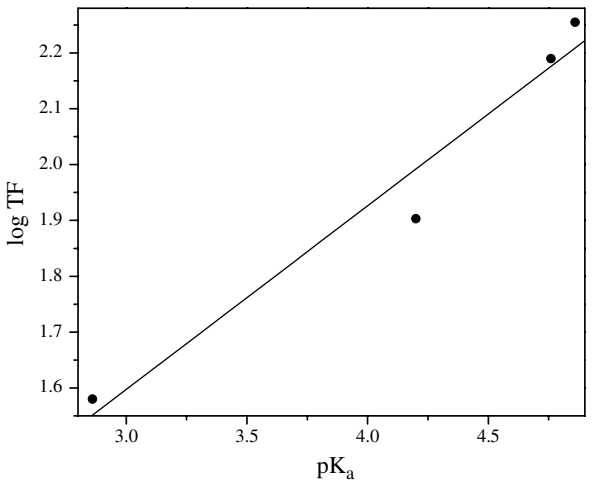


Fig. 4. Hydroformylation of 1-hexene catalyzed by $RuH(CO)(\kappa^3\text{-}OCOR)(PPh_3)_2$ showing the relation between turnover frequency (TF) and the nature of the carboxylate ligand. Conditions as in Table 5.

3. Experimental

3.1. General considerations

All manipulations were performed under argon using standard Schlenck techniques. Solvents, $MCl_3 \cdot 3H_2O$ (M = Ru, Os) for the home-made preparation of $[MH(NCMe)_2(CO)(PPh_3)_2]BF_4$, M = Ru (**I**) [21] and Os (**II**) [13c], quinoline, benzothiophene and 1-hexene were obtained as high purity compounds from Aldrich. Prior to use solvents, quinoline and 1-hexene were distilled over appropriate standard agents under nitrogen. Research grade H_2 and CO gases were obtained from Praxair Venezuela. Before use, these gases were dried by passing them through a column containing $CaSO_4$.

3.2. Analytical procedures

FT-IR spectra of dried discs (i.e. solid samples + KBr) were obtained using a 13-mm-die, 13-mm disk holder, a Caver hydraulic press (>12 ton), a vacuum pump and a Shimadzu FTIR-8300 interferometer. High resolution ^1H and $^{31}P\{^1H\}$ NMR spectra of the samples dissolved in $CDCl_3$were obtained at 300 MHz and 121 MHz, respectively, in a Bruker AC-300 instrument at room temperature; ^1H- and ^{31}P-chemical shifts are expressed in part per million down-field and up-field from $SiMe_4$ and H_3PO_4, respectively.

Gas chromatographic analyses were performed in a 3300 Series VARIAN instrument fitted with a flame ionization detector (FID) and a 2 m 20% SP-2100 on a 0.1% carbowax 100/120 Supelcoport column, using N_2 as carrier gas and naphthalene (for the Q and BT hydrogenation) and *n*-heptane (for hydroformylation of 1-hexene) as internal standards. The results were quantified with a VARIAN 4400 microcomputer.

3.3. Synthesis of complexes

$RuH(\kappa^3\text{-}OCOR)(CO)(PPh_3)_2$ [R = CH_3 (**III**), CH_2Cl (**IV**), $CH(CH_3)_2$ (**V**), and Ph (**VI**)] were prepared by the following method. To a solution of $[RuH(NCMe)_2(CO)(PPh_3)_2]BF_4$ (**I**) (0.5 mmol) in a 1:1 v/v mixture of $CHCl_2$ and MeOH (25 mL) was added the corresponding carboxylic Na salt (1.5 mmol). The mixture was stirred vigorously at room temperature for 3–4 h, giving a pale yellow solution which was evaporated under vacuum to about, one-third of its initial volume, obtaining a white precipitate. This solid was washed with methanol and diethylether, and then dried in vacuum. It affords white solids (yields: 70–80%).

The corresponding $OsH(\kappa^3\text{-}OCOR)(CO)(PPh_3)_2$ complexes [where R = CH_3 (**VII**), $CH(CH_3)_2$ (**IX**), Ph (**X**)] were synthesized by a similar method but with a reaction time of approximately 7 h. All products were white solids (yields: 70–80%). However, reaction of $[OsH(NCMe)_2(CO)(PPh_3)_2]BF_4$ (**II**) with $Na[OCOCH_2Cl]$ afforded a amourphous, white solid which darken after few minutes even in inert atmosphere. The infrared spectrum of this solid as KBr pellet revealed a solid mixture of small amounts of compound **II** and $OsH(OCOCH_2Cl)(CO)(PPh_3)_2$ (**VIII**) (see footnote e of Table 1). So increasing amounts of the Na salt and a longer period of reaction time (8 h) were needed to obtain white microcrystals of complex **VIII**. ^1H- and proton-decoupled ^{31}P NMR spectra indicated that only compound **VIII** was present in the $CDCl_3$ solutions.

3.4. Computational details

The optimized energy calculations of complexes $MH(\kappa^3\text{-}OCOR)(CO)(PPh_3)_2$ were carried out using Fe as metal, R = H and the simplified PH_3 analogues in order to have a better calculation level. These were performed with the GAUSSIAN-98 computational package by using the B3LYP [24] hybrid method of density functional density theory (DFT); the optimizations were carried out with the 6-31+G(d,p) basis sets [25].

3.5. Details of the catalytic runs

The apparatus and the reaction procedure for the catalytic runs of hydrogenation [13] and hydroformylation reactions [26] have been described in details elsewhere. Briefly, a solution of the precatalyst, substrate, internal standard and solvent were placed in a high pressure reactor which was flushed three times with argon. When this system reached thermal equilibrium, H_2 (or an H_2/CO mixture) was admitted into the reactor at the desired pressure. The reactions were followed by both measuring the gas pressure-drop as a function of time and by gas chromatography. Each reaction was repeated at least twice in order to ensure reproducibility of the results. All straight lines were fitted by conventional linear regression programs to $r^2 > 0.98$.

Acknowledgements

This work was supported from Consejo de Desarrollo Científico y Humanístico through Project (CONDES-0174-02) and for the acquisition of a gas chromatograph. We thank Dr. José Ortega for his valuable help to record the NMR spectra.

References

[1] (a) C.A. McAuliffe (Ed.), Transition Metal Complexes of Phosphorus, Arsenic and Antimony Ligands, MacMillan, London, 1973, pp. 72–86;
(b) C.A. McAuliffe, W. Levanson (Eds.), Phosphine, Arsine and Stibine Complexes of the Transition Elements, Elsevier, Amsterdam, 1979, pp. 112–126.
[2] R.A. Sánchez-Delgado, M. Rosales, Trends Inorg. Chem. 3 (1993) 479.
[3] L. Vaska, J.W. Diluzio, J. Am. Chem. Soc. 83 (1961) 1262.
[4] (a) A. Dobson, S.D. Robinson, Platinum Met. Rev. 20 (1976) 36;
(b) A. Dobson, S.D. Robinson, Inorg. Chem. 16 (1977) 321.

[5] R.A. Sánchez-Delgado, U. Thewalt, N. Valencia, A. Andriollo, R.-L. Márquez-Silva, J. Puga, H. Schöllhorn, H.-P. Klein, B. Fontal, Inorg. Chem. 25 (1986) 1097.
[6] (a) J.E. Amstrong, W.R. Robinson, R.A. Walton, J. Chem. Soc., Chem. Commun. (1981) 1120;
(b) J.E. Amstrong, W.R. Robinson, R.A. Walton, Inorg. Chem. 22 (1983) 1301;
(c) D.C. Moore, A.S. Alves, G. Wilkinson, J. Chem. Soc., Chem. Commun. (1981) 1164;
(d) D.A. Tocher, M.D. Walkinshaw, J. Organomet. Chem. 232 (1982) C51;
(e) T. Behing, G. Wilkinson, T.A. Stephenson, D.A. Tocher, M.D. Walkinshaw, J. Chem. Soc., Dalton Trans. (1983) 2109;
(f) A.R. Chakravarty, F.A. Cotton, D.A. Tocher, J. Chem. Soc., Chem. Commun. (1984) 501;
(g) F.A. Cotton, A.R. Chakravarty, D.A. Tocher, T.A. Stephenson, Inorg. Chim. Acta 87 (1984) 115;
(h) S.M. Tetrick, V.T. Coombe, G.A. Heath, T.A. Stephenson, R.A. Walton, Inorg. Chem. 23 (1984) 4567;
(i) A.R. Chakravarty, F.A. Cotton, D.A. Tocher, Inorg. Chem. 23 (1984) 4697;
(j) A. Dobson, S.D. Robinson, M.F. Uttley, J. Chem. Soc., Dalton Trans. (1975) 370;
(k) D. Robinson, M.F. Uttley, J. Chem. Soc., Dalton Trans. (1973) 1912.
[7] R.A. Sánchez-Delgado, N. Valencia, R.-L. Márquez-Silva, A. Andriollo, M. Medina, Inorg. Chem. 25 (1986) 1106.
[8] L. Vaska, J. Am. Chem. Soc. 88 (1966) 4100.
[9] (a) C. De La Cruz, Norman Sheppard, J. Mol. Struct. 22 (1990) 141;
(b) C. De La Cruz, Act. Cient. Venezolana 43 (1992) 269;
(c) S.L. Morrison, J.J. Turner, J. Mol. Struct. 317 (1994) 39.
[10] K. Nakamoto, Infrared Spectra of Inorganic and Coordination Compounds, 4th ed., Wiley–Interscience, New York, 1986.
[11] (a) H. Topsoe, B.S. Clausen, F.E. Massoth, Hydrotreating Catalysis, Springer, Berlin, 1996;
(b) R.A. Sánchez-Delgado, in: B.R. James, P.W.N.M. van Leeuwen (Eds.), Organometallic Modeling of the Hydrodesulfurization and Hydrodenitrogenation Reactions, Kluwer Academic Publishers, Dordrecht, 2000.
[12] (a) R.H. Fish, J.L. Tan, A.D. Thormodsen, J. Org. Chem. 49 (1984) 4500;
(b) R.A. Sánchez-Delgado, E. González, Polyhedron 8 (1989) 1431.
[13] (a) M. Rosales, Y. Alvarado, M. Boves, R. Rubio, R. Sánchez-Delgado, H. Soscún, Transition Met. Chem. 20 (1995) 246;
(b) M. Rosales, J. Navarro, L. Sánchez, A. González, Y. Alvarado, R. Rubio, C. De La Cruz, T. Rajmankina, Transition Met. Chem. 21 (1996) 11;
(c) M. Rosales, A. González, J. Navarro, H. Soscún, J. Zárraga, Inorg. Chim. Acta 257 (1997) 131;
(d) M. Rosales, F. Arrieta, J. Castillo, A. González, J. Navarro, R. Vallejo, Stud. Surf. Sci. Catal. 130D (2000) 3357;
(e) M. Rosales, J. Castillo, A. González, L. González, K. Molina, J. Navarro, I. Pacheco, Transition Met. Chem. 29 (2004) 221.
[14] Y. Alvarado, M. Busolo, F. López-Linares, J. Mol. Catal. 142 (1999) 163.
[15] A.F. Borowski, S. Sabo-Etienne, B. Donnadieu, B. Chaudret, Organometallics 22 (2003) 1630.
[16] C. Bianchini, A. Meli, S. Moneti, W. Oberhauser, F. Vizza, V. Herrera, A. Fuentes, R.A. Sánchez-Delgado, J. Am. Chem. Soc. 121 (1999) 7071.
[17] A.F. Borowski, S. Sabo-Etienne, B. Donnadieu, B. Chaudret, Organometallics 22 (2003) 4803.
[18] (a) J.P. Collman, L.S. Hegedus, J.R. Norton, R.G. Finke, Principles and Applications of Organotransition Metal Chemistry, University Science Book, Mill Valley, 1988, pp. 564–567;
(b) B. Cornils, W. A Herrmann (Eds.), Applied Homogeneous Catalysis with Organometallic Compounds, VCH, Weinhein, 1996, pp. 571–618;
(c) S. Bhaduri, D. Mukesh, Homogeneous Catalysis. Mechanisms and Industrial Applications, Wiley, New York, 2000, pp. 55–89.
[19] P. Van Leeuwen, C. Claver (Eds.), Rhodium Catalyzed Hydroformylation, Kluwer Academic Publishers, Dordrecht, 2000.
[20] R.A. Sánchez-Delgado, J.S. Bradley, G. Wilkinson, J. Chem. Soc., Dalton Trans. (1976) 309.
[21] R.A. Sánchez-Delgado, M. Rosales, A. Andriollo, Inorg. Chem. 30 (1991) 1170.
[22] E. Cesarotti, A. Fusi, R. Lugo, G.M. Zanderighi, J. Mol. Catal. 4 (1978) 205.
[23] P.J. Baricelli, E. Lujano, M. Modroño, A.C. Marrero, Y.M. García, A. Fuentes, R.A. Sánchez-Delgado, J. Organomet. Chem. 689 (2004) 3782.
[24] (a) A.D. Becke, J. Chem. Phys. 98 (1993) 5648;
(b) C. Lee, W. Yang, R.G. Parr, Phys. Rev. B 37 (1988) 785;
(c) B. Miehlich, A. Savin, H. Stoll, H. Preuss, Chem. Phys. Lett. 157 (1989) 200.
[25] (a) J.B. Collins, P.V.R. Schleyer, J.S. Binkley, J.A. Pople, J. Chem. Phys. 64 (1967) 5142;
(b) K.D. Dobbs, W.J. Hehre, J. Comput. Chem. 8 (1987) 880;
(c) M.S. Gordon, Chem. Phys. Lett. 76 (1980) 163;
(d) K. Raghavachari, G.W. Trucks, J. Chem. Phys. 91 (1989) 1062.
[26] M. Rosales, A. González, Y. Guerrero, I. Pacheco, R.A. Sánchez-Delgado, J. Mol. Catal. A 270 (2007) 141.
[27] R.H. Fish, Ann. N. Y. Acad. Sci. 415 (1983) 292.

Available online at www.sciencedirect.com
ScienceDirect
Polyhedron 27 (2008) 537–546
POLYHEDRON
www.elsevier.com/locate/poly

Crystal structures and physico-chemical properties of Zn(II) and Co(II) tetraaqua(3-nitro-4-hydroxybenzoato) complexes: Their anticonvulsant activities as well as related (5-nitrosalicylato)–metal complexes

Jean d'Angelo [a,*], Georges Morgant [a,*], Nour Eddine Ghermani [b,c], Didier Desmaële [a], Bernard Fraisse [c], François Bonhomme [b], Emma Dichi [d], Mehrez Sghaier [d], Yanling Li [e], Yves Journaux [e], John R.J. Sorenson [f,*]

[a] Laboratoire BioCIS, UMR CNRS 8076, IFR 141, Faculté de Pharmacie, Université Paris-Sud, 5 rue J.-B. Clément, 92296 Châtenay-Malabry, France
[b] Laboratoire PPB, UMR CNRS 8612, IFR 141, Faculté de Pharmacie, Université Paris-Sud, 5 rue J.-B. Clément, 92296 Châtenay-Malabry, France
[c] Laboratoire SPMS, UMR CNRS 8580, Ecole Centrale Paris, Grande Voie des Vignes, 92295 Châtenay-Malabry, France
[d] Laboratoire CPMB, Faculté de Pharmacie, Université Paris-Sud, 5 rue J.-B. Clément, 92296 Châtenay-Malabry, France
[e] Laboratoire CIMM, UMR CNRS 7071, Université Pierre et Marie Curie Paris 6, 4 Place Jussieu, 75005 Paris, France
[f] Division of Medicinal Chemistry, Department of Pharmaceutical Sciences, University of Arkansas, Medical Sciences Campus, Slot 522, 4301 West Markham Street, Little Rock, AR 72205, USA

Received 4 September 2007; accepted 4 October 2007
Available online 14 November 2007

Abstract

Purposes of these studies were to synthesize Zn(II) and Co(II) complexes of 3-nitro-4-hydroxybenzoic acid, determine their structures through X-ray crystallography, and obtain their anticonvulsant activities. Thermogravimetric, differential scanning calorimetry, impedance of aqueous solutions and magnetic properties analyses were also determined. Anticonvulsant and related activities of these complexes as well as Zn(II), Co(II), Ni(II) and Mg(II) (5-nitrosalicylato) complexes were determined by the National Institutes of Health, Antiepileptic Development Program. Results of these analyses are presented to document unique bonding features and physical properties of these compounds and their anticonvulsant activities. It is concluded that these compounds have chemical and physical properties that can be used to account for their anticonvulsant activities.
© 2007 Elsevier Ltd. All rights reserved.

Keywords: Crystal structures; 3-Nitro-4-hydroxybenzoic acid ligand; Zn(II) and Co(II) complexes; Anticonvulsant activity

1. Introduction

Besides their relevance to solid state structure and supramolecular design [1–3], (salicylato)–metal complexes have attracted considerable attention, because of their promising anti-inflammatory and anticonvulsant activities [4–10]. As part of a systematic program devoted to the study of structure–activity relationships of (salicylato)–metal complexes, we recently reported the preparation and crystal structures of (5-nitrosalicylato) complexes of Mg(II), Zn(II), Co(II) and Ni(II). The building units of these complexes self-assemble via π–π stacking and extensive intermolecular hydrogen bonding, resulting in a 3D supramolecular architecture [5]. Although the 5-nitrosalicylate ligand, 5-nsa, has a very versatile coordination behavior, an exciting feature in this series is the possibility of modifying the original structure by moving groups attached to the aromatic nucleus. By shifting the hydroxyl group from C-2 to the C-4 position of the 5-nsa ligand, a

* Corresponding authors. Tel.: +33 146835699; fax: +33 146835752 (J. d'Angelo); tel.: +33 146835463 (G. Morgant); tel.: +1 501 686 6494; fax: +1 501 526 6510 (J.R.J. Sorenson).
E-mail addresses: jean.dangelo@u-psud.fr (J. d'Angelo), georges.morgant@u-psud.fr (G. Morgant), sorensonjohnrj@uams.edu (J.R.J. Sorenson).

0277-5387/$ - see front matter © 2007 Elsevier Ltd. All rights reserved.
doi:10.1016/j.poly.2007.10.006

suitable set of ligands for intermolecular anchoring through hydrogen bonding was thus obtained for our intended evaluations.

Herein we report the crystal structures of (3-nitro-4-hydroxybenzoato) complexes of Zn(II) and Co(II). A key aspect of these structures is that the individual units self-assemble via extensive hydrogen bonding, leading to an original 3D continuum. Although, in the strict sense, the present complexes are not salicylate derivatives but 4-OH regioisomers, their anticonvulsant properties were determined to examine the effect of this structural change on the structural and physical properties of these complexes in relation to their pharmacological effects. For the sake of comparison, the anticonvulsant activities of related transition metalloelement 5-nsa complexes were also determined [5]. Interestingly, promising pharmacological responses were obtained for these complexes as anticonvulsants. Critical to the knowledge of the mode of action of present anticonvulsant metal complexes was the identification of the actual pharmacologically active entity that crosses the blood–brain barrier. Toward this end, this report presents: (1) the conducting properties of the metal complexes in dilute aqueous solution and (2) water/1-octanol extraction experiments which revealed an unexpected equilibrium between these complexes and the corresponding free ligands.

2. Experimental

2.1. Materials

High purity 3-nitro-4-hydroxybenzoic acid, zinc sulfate heptahydrate and cobalt sulfate heptahydrate were purchased from Acros (USA) and used without further purification.

2.2. Physical measurements

Elemental analyses (C, H and N) were performed with a Perkin–Elmer 2400 analyzer. Infrared spectra were recorded with a Bruker Vector 22 spectrometer. Thermogravimetric analyses (TGA) were performed with a TA Instruments TGA Q500 apparatus. Calibrations were performed at different temperatures using Curie magnetic transitions for the recommended materials: alumel (163 °C) and nickel (354 °C). Mass calibrations were performed using a standard mass of 100 mg. The furnace was calibrated between 100 and 900 °C to verify thermocouple performance. All experiments were performed under dry nitrogen, with a flow rate of 6×10^{-2} l min^{-1}. Analysis of compounds following nitrogen purging was conducted using a heating rate of 20 °C min^{-1} in order to determine percent mass loss with optimal precision. Differential Scanning Calorimetry (DSC) experiments were performed with a TA Instruments Universal V4.2E apparatus under nitrogen. Samples were introduced in aluminum pans and covered with holed caps in view to avoid uncontrolled variation of pressure. Calibration of temperature was performed with 5 N quality indium at 156.6 °C and tin at 231.9 °C and a heating rate of 10 °C min^{-1}. Impedance measurements of aqueous solutions were performed using a VoltaLab 80 (Radiometer Analytical) with a 2-pole cell with two platinum plates. The signal amplitude was 100 mV. A continuous potential of 0 mV was imposed. Solutions, preserved under nitrogen, were placed in a double walled glass cell ensuring thermal stabilization. Measurements were obtained at 20 °C. Magnetic measurements in the 2–300 K temperature range were carried out with a MPMS5 SQUID susceptometer (Quantum Design Inc.).

2.3. Synthesis of complexes

2.3.1. $C_{14}H_{16}N_2O_{14}Zn$ (**1**)

Sodium 3-nitro-4-hydroxybenzoate was prepared by neutralizing 3-nitro-4-hydroxybenzoic acid (0.915 g, 5 mmol) with 5 ml of 1 M NaOH in deionized water. To this solution was added $ZnSO_4 \cdot 7H_2O$ (0.720 g, 2.5 mmol) in 3 ml of water. After a few days **1** was filtered, crystallized from water, and dried over anhydrous magnesium sulfate. Yield: 0.939 g (75%). *Anal.* Calc. for $C_{14}H_{16}N_2O_{14}Zn$ (**1**): C, 33.52; H, 3.21; N, 5.58. Found: C, 33.43; H, 3.18; N, 5.56%. IR (neat, cm^{-1}): 3254 (s), 1621 (s), 1587 (s), 1526 (s), 1420 (s), 1379 (s), 1323 (s), 1264 (s), 1178 (s), 1153 (s), 1118 (s), 1074 (s), 942 (m), 916 (m), 858 (m), 825 (m), 789 (s), 764 (s), 684 (s), 638 (s).

2.3.2. $C_{14}H_{16}N_2O_{14}Co$ (**2**)

Sodium 3-nitro-4-hydroxybenzoate was prepared by neutralizing 3-nitro-4-hydroxybenzoic acid (0.915 g, 5 mmol) with 5 ml of 1 M NaOH in deionized water. To this solution was added $CoSO_4 \cdot 7H_2O$ (0.702 g, 2.5 mmol) in 3 ml of water. After a few days **2** was filtered, crystallized from water, and dried over anhydrous magnesium sulfate. Yield: 0.943 g (76%). *Anal.* Calc. for $C_{14}H_{16}N_2O_{14}Co$ (**2**): C, 33.95; H, 3.25; N, 5.66. Found: C, 34.05; H, 3.18; N, 5.64%. IR (neat, cm^{-1}): 3259 (m), 1621 (s), 1586 (s), 1545 (s), 1524 (s), 1418 (s), 1381 (s), 1323 (s), 1264 (s), 1179 (s), 1153 (s), 1117 (s), 1073 (m), 938 (m), 915 (m), 859 (m), 825 (m), 807 (s), 789 (s), 763 (s), 685 (s), 638 (s).

2.4. X-ray diffraction measurements

Diffraction data were collected with a Bruker-SMART three axis diffractometer equipped with a SMART 1000 CCD area detector using graphite monochromated Mo Kα X-radiation (wavelength $\lambda = 0.71073$ Å) at 100.0(1) K. The low temperature was reached by an evaporated liquid nitrogen stream over the crystal, provided by the Oxford Cryosystem device. Data collection and processing were performed using Bruker SMART programs [11] and empirical absorption correction was applied using SADABS computer program [11]. The structure was solved by direct methods using SIR97 [12], and refined by full-matrix least-

Table 1
Crystal data and structure refinement parameters for $C_{14}H_{16}N_2O_{14}M$ (**1**, M = Zn and for **2**, M = Co)

Compound	1	2
Empirical formula	$C_{14}H_{16}N_2O_{14}Zn$	$C_{14}H_{16}N_2O_{14}Co$
Molecular weight	501.67	495.22
Color	yellowish	pink
Crystal system	triclinic	triclinic
Space group	$P\bar{1}$	$P\bar{1}$
a (Å)	6.209(5)	6.197(5)
b (Å)	10.071(5)	5.047(5)
c (Å)	14.729(5)	14.671(5)
α (°)	83.579(5)	83.992(5)
β (°)	79.084(5)	99.698(5)
γ (°)	89.427(5)	89.944(5)
V (Å^3)	898.6(9)	449.5(6)
Z	2	1
D_{calc} (g cm^{-3})	1.854	1.829
Absorption coefficient (mm^{-1})	1.452	1.040
$F(000)$	512	253
Crystal size (mm)	$0.17 \times 0.22 \times 0.27$	$0.18 \times 0.22 \times 0.25$
θ Ranges (°)	1.42–29.78	2.83–29.54
$h/k/l$	−8, 8/−13, 13/0, 19	−6, 6/−8, 7/0, 19
T (K)	100	100
Number of reflections collected	6383	3064
Number of reflections used $\geqslant 3\sigma(I)$	4266	1834
Parameters	281	142
R [F^2]	0.0243	0.0346
wR [F^2]	0.0581	0.0821
Goodness-of-fit on F^2	0.9011	0.8934
Residual density (e Å^{-3})	−0.64; 0.64	−0.51; 0.58
Refine ls shift/su.max	0.0019	0.0003

squares based on F^2 using CRYSTALS software [13]. The molecule was drawn using the CAMERON program [14]. All non-hydrogen atoms were anisotropically refined. Hydrogen atoms were located in difference Fourier maps. H atoms were refined isotropically with $U_{iso} = 1.20U_{eq}$ where U_{eq} is the equivalent isotropic atomic displacement parameter of the attached atom. Crystal parameters, data collection and the refinement details of compounds **1** and **2** are reported in Table 1.

2.5. Determination of anticonvulsant activities and Rotorod toxicity

Anticonvulsant activities and Rotorod toxicity of $C_{14}H_{16}N_2O_{14}Zn$ (**1**) and $C_{14}H_{16}N_2O_{14}Co$ (**2**), as well as previously reported related complexes **3**–**6** [5], were determined by the National Institute of Health-National Institute of Neurological Disorders and Stroke-Antiepileptic Drug Development program for the detection and evaluation of compounds as anticonvulsant agents (USA). *Maximal electroshock seizure* were elicited with a 60 cycle alternating current of 50 mA, five to seven times that necessary to elicit minimal electroshock seizures, delivered for 0.2 s via corneal electrodes. *Psychomotor seizures test*: the delivery of a less intense electric stimulation, which produces less intense brain inflammation, via corneal electrodes of 6 Hz, 44 mA or lower, for 3 s is used to produce psychomotor seizures, following instillation of a drop of 0.9% saline prior to this application of electric current. Abolition of the visual stereotypic behavior characterized as minimal clonic automatistic behaviors. *Subcutaneous* (*sc*) *pentylenetetrazol* (*Metrazol*) *seizure threshold test*: a dose of pentylenetetrazol, a potent CNS stimulant (Central Nervous System), which produces seizures in greater than 97% of treated mice, 85 mg/kg of body mass, was administered sc as a 0.5% solution in saline at the posterior neck midline. Animals were observed for 30 min. Failure to observe even a threshold seizure, a single episode of clonic spasms of at least 5 s duration, is defined as anticonvulsant activity. *Rotating rod test*: mice or rats are placed on a 1 inch diameter knurled plastic rod rotating at six revolutions per min. Normal mice and rats can remain on a rod rotating at this speed indefinitely. Neurologic toxicity, either CNS stimulation or depression, is evidenced by a failure of the mouse or rat to remain on the rotating rod for 1 min.

3. Results and discussion

3.1. Description of the $C_{14}H_{16}N_2O_{14}Zn$ (**1**) and $C_{14}H_{16}N_2O_{14}Co$ (**2**) structures based upon X-ray crystallography

Complexes **1** and **2** can be represented by the general formula $(C_7H_4NO_5)_2M(H_2O)_4$, where $M = Zn^{II}$ or Co^{II}. The canonical drawings of these complexes are represented in Fig. 1 and the CAMERON molecular structures in Figs. 2 and 3, with the atom numbering system used in Table 2 which lists the most relevant bond distances and angles.

The formula units of complexes **1** and **2** can be represented by $(C_7H_4NO_5)_2M(H_2O)_4$ where M = Zn or Co. For complex **2**, the asymmetric unit consists of the half of formula unit. In both complexes, the coordination octahedron around the metal atom involves one carboxylato O-atom from each 3-nitro-4-hydroxybenzoate ligand (acting as a monodentate linker) and the O-atoms of the four water molecules harnessed to the metal atom. In $(C_7H_4NO_5)_2Zn(H_2O)_4$ (**1**), the octahedron is slightly distorted. The *cis* angles around the Zn center vary between 85.97(7)° and 92.95(7)° while the *trans* angles vary from 175.70(5)° to 178.68(5)°. The Zn–O(26) and Zn–O(36) distances, 2.074(2) and 2.052(2) Å, respectively, are notably shorter than those for Zn–O(10), Zn–O(11), Zn–O(12), and Zn–O(13); 2.186(2), 2.114(2), 2.092(2), and 2.118(2) Å, respectively.

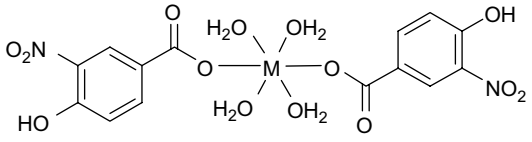


Fig. 1. Canonical representation of $(C_7H_4NO_5)_2M(H_2O)_4$ (**1**, M = Zn; **2**, M = Co).

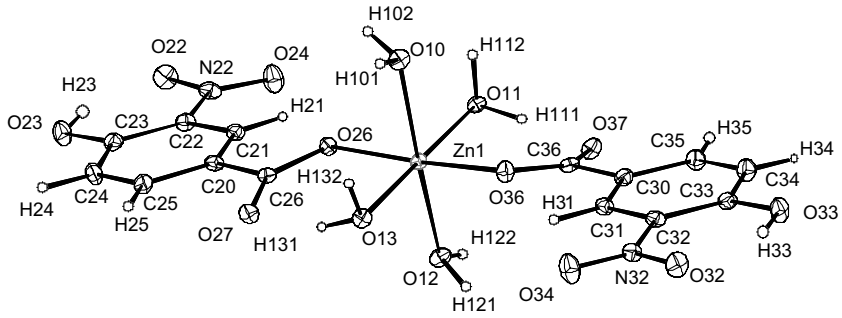


Fig. 2. Labeled CAMERON diagram of $(C_7H_4NO_5)_2Zn(H_2O)_4$ (**1**). Ellipsoids are drawn at a 50% probability level.

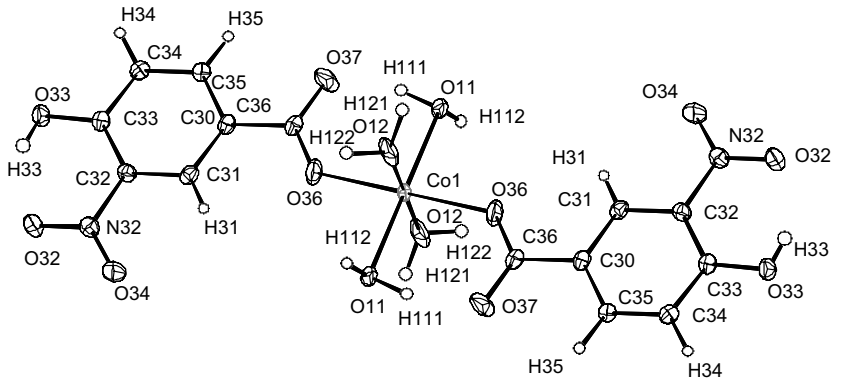


Fig. 3. Labeled CAMERON diagram of $(C_7H_4NO_5)_2Co(H_2O)_4$ (**2**). Ellipsoids are drawn at a 50% probability level.

In contrast, the structure of $(C_7H_4NO_5)_2Co(H_2O)_4$ (**2**) consists of centrosymmetric monomers with the metal atom occupying the inversion center at 0, 1/2, 1/2 of the triclinic unit cell. This symmetry is revealed by two identical metal–carboxylato O-atom lengths of 2.070(2) Å and two pairs of metal–O (water) distances of 2.100(2) and 2.070(2) Å. On the other hand, the *cis* angles around the Co center consist of six centrosymmetrically-related pairs, while identical values were observed for the three *trans* angles, 180.00(8)°. Since complexes **1** and **2** exhibit very close structural features, only details of the packing in **1** were arbitrarily chosen for presentation and discussion in the present paper. The presence of four water molecules around the metal center led to a very extensive and complicated H-bonding network. A list of the most probable atoms involved in H-bonds with their related angles is given in Tables 3 and 4. Fig. 4 shows the H-bonding in **1** around the Zn center. The crystal cohesion is thus ensured by fourteen hydrogen bonds per formula unit.

The individual zero-dimensional units (0D) of **1** are linked together through intermolecular hydrogen bonding implying their *ortho*-nitrophenol groups ends, $O(23)^{iv}$–$H(23)^{iv}\cdots O(32)$ and $O(33)$–$H(33)\cdots O(22)^{iv}$ forming infinite 1D chains (Figs. 5 and 6). The intrachain separation of the Zn centers is 18.82 Å (18.85 Å for Co–Co in complex **2**). It is noteworthy that the *ortho*-nitrophenol groups are also implied in intramolecular hydrogen bonding, $O(23)^{iv}$–$H(23)^{iv}\cdots O(22)^{iv}$ and $O(33)$–$H(33)\cdots O(32)$, which clearly reinforces the cohesion of these chains.

Table 2
Selected bond distances (Å) and bond angles (°) for $(C_7H_4NO_5)_2Zn(H_2O)_4$ (**1**) and $(C_7H_4NO_5)_2Co(H_2O)_4$ (**2**)

1		**2**	
Bond lengths		*Bond lengths*	
Zn–O(10)	2.186(2)	Co–O(11)	2.127(2)
Zn–O(11)	2.114(2)	Co–O(12)	2.100(2)
Zn–O(12)	2.092(2)	Co–O(36)	2.070(2)
Zn–O(13)	2.118(2)		
Zn–O(26)	2.074(2)		
Zn–O(36)	2.059(2)		
Bond angles		*Bond angles*	
O(10)–Zn–O(12)	177.58(6)	$O(11)^{vi}$–Co–O(11)	180.00(8)
O(11)–Zn–O(13)	178.68(5)	$O(12)^{vi}$–Co–O(12)	180.00(8)
O(26)–Zn–O(36)	175.70(5)	$O(36)^{vi}$–Co–O(36)	180.00(8)
O(10)–Zn–O(11)	86.57(6)	$O(11)^{vi}$–Co–$O(36)^{vi}$	93.26(8)
O(10)–Zn–O(13)	92.61(6)	O(11)–Co–O(36)	93.26(8)
O(10)–Zn–O(26)	89.03(6)	$O(11)^{vi}$–Co–$O(12)^{vi}$	88.40(9)
O(10)–Zn–O(36)	86.98(6)	O(11)–Co–O(12)	88.40(9)
O(12)–Zn–O(11)	91.03(7)	$O(12)^{vi}$–Co–O(11)	91.60(9)
O(12)–Zn–O(13)	89.78(6)	$O(11)^{vi}$–Co–O(12)	91.60(9)
O(12)–Zn–O(26)	91.21(6)	$O(36)^{vi}$–Co–O(12)	89.68(9)
O(12)–Zn–O(36)	92.84(6)	$O(12)^{vi}$–Co–O(36)	89.68(9)
O(11)–Zn–O(26)	88.42(7)	$O(11)^{vi}$–Co–O(36)	86.74(8)
O(11)–Zn–O(36)	92.95(7)	$O(36)^{vi}$–Co–O(11)	86.74(8)
O(13)–Zn–O(26)	92.60(7)	$O(12)^{vi}$–Co–$O(36)^{vi}$	90.32(9)
O(13)–Zn–O(36)	85.97(7)	O(12)–Co–O(36)	90.32(9)

Symmetry code: ^{vi} $-x, -y+1, -z+1$.

The parallel chains are further engaged in hydrogen bonding implying H(102), H(112) and H(121) with interchain separations of 4.904 Å and 5.200 Å (5.047 Å for com-

Table 3
H-bond donor/acceptor scheme (Å, °) for $(C_7H_4NO_5)_2Zn(H_2O)_4$ (**1**)

D–H···A	*d*(D–H)	*D*(H···A)	∠(DHA)
O(23)–H(23)···O(22)	0.795(2)	1.865(2)	153.13(9)
O(33)–H(33)···O(32)	0.815(2)	1.902(2)	143.30(9)
O(11)–H(111)···O(37)	0.940(2)	1.714(2)	161.11(9)
O(13)–H(131)···O(27)	0.940(2)	1.720(2)	160.63(8)
O(10)–H(101)···O(37)^{i}	0.934(2)	1.939(2)	147.17(9)
O(13)–H(132)···O(37)^{i}	0.940(2)	1.769(2)	164.39(9)
O(12)–H(122)···O(27)^{ii}	0.932(2)	1.912(2)	166.64(9)
O(11)–H(112)···O(26)^{iii}	0.939(2)	1.779(2)	166.97(8)
O(10)–H(102)···O(11)^{iii}	0.936(2)	1.938(2)	154.65(8)
O(33)–H(33)···O(22)^{iv}	0.814(2)	2.345(2)	139.78(9)
O(23)^{iv}–H(23)^{iv}···O(32)	0.794(2)	2.401(2)	130.98(9)
O(23)–H(23)···O(32)^{v}	0.794(2)	2.401(2)	130.98(9)
O(33)^{v}–H(33)^{v}···O(22)	0.814(2)	2.345(2)	139.78(9)
O(12)–H(121)···O(13)^{vi}	0.927(2)	1.888(2)	174.50(8)

Symmetry codes: ^{i} $x+1, y, z$; ^{ii} $x-1, y+z$; ^{iii} $-x, -y, -z+1$; ^{iv} $x-1, y+1, z+1$; ^{v} $x+1, y-1, z-1$; ^{vi} $-x, -y+1, -z+1$.

Table 4
H-bond donor/acceptor scheme (Å, °) for $(C_7H_4NO_5)_2Co(H_2O)_4$ (**2**)

D–H···A	*d*(D–H)	*D*(H···A)	∠(DHA)
O(11)–H(111)···O(37)	0.954(4)	1.673(2)	163.01(8)
O(11)–H(112)···O(36)^{i}	0.951(7)	2.162(3)	158.83(6)
O(12)–H(122)···O(11)^{ii}	0.944(7)	1.860(3)	170.02(9)
O(12)–H(121)···O(37)^{iii}	0.947(5)	1.834(3)	161.37(9)
O(33)–H(33)···O(32)	0.810(5)	1.898(3)	144.75(6)
O(33)–H(33)···O(32)^{iv}	0.810(5)	2.346(2)	138.38(5)
O(33)^{iv}–H(33)^{iv}···O(32)	0.810(5)	2.346(2)	138.38(5)

Symmetry codes: ^{i} $x+1, y, z$; ^{ii} $x, y-1, z$; ^{iii} $-x+1, -y+1, -z+1$; ^{iv} $-x-2, -y+2, -z+2$.

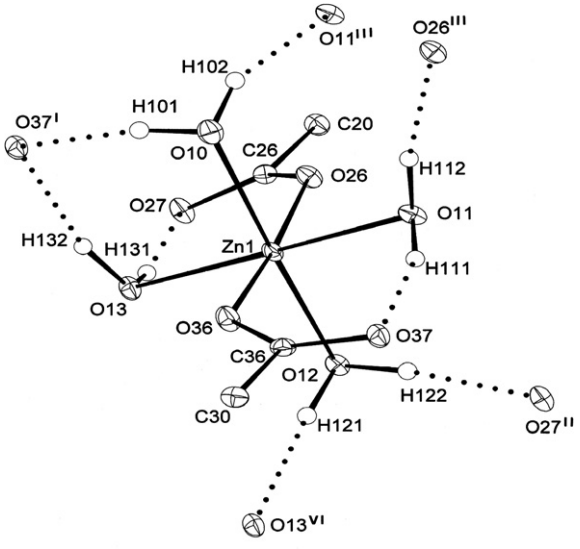


Fig. 4. Labeled diagram of $(C_7H_4NO_5)_2Zn(H_2O)_4$ (**1**) focusing on the hydrogen bonding system around the Zn atom (dashed lines).

plex **2**) resulting in 2D sheets (Fig. 7). These, in turn, self-assemble via hydrogen bonds implying H(122) and H(132) with an interplanar separation of 6.209 Å (7.996 Å for complex **2**) yielding a 3D supramolecular architecture (Fig. 8).

One of the most salient features of this architecture is the compact 3D arrangement of the metal atoms. In complex **1**, the Zn atoms are close to each other, with distances of 4.904, 5.200 and 6.209 Å (Fig. 9a). A centrosymmetric metal arrangement pattern was observed for complex **2** with Co – Co distances of 5.047 and 6.197 Å (Fig. 9b).

3.2. Thermal analysis: TGA and DSC measurements

TGA analysis of **1** revealed a mass loss of 14.8% on heating from 50 to 180 °C, corresponding to a loss of four crystalline water molecules (Calc. 14.4%). TGA analysis of **2** revealed a mass loss of 15.1% on heating from 80 to 180 °C, corresponding to a loss of four crystalline water molecules (Calc. 14.5%). On heating **2** from 80 to 550 °C, an overall mass loss of 85.5% was observed. The non-volatile residue, 14.5% of the starting material, corresponds to one molecule of CoO (Calc. 15.1%). The DSC study of **1** revealed, as the main event, a narrow endotherm centered at 141 °C corresponding to loss of water and a narrow exotherm centered at 342 °C. A similar thermal pattern was observed for complex **2**, with an endotherm centered at 130 °C and exotherm centered at 349 °C.

3.3. Electrochemical impedance measurements

The electrochemical impedance $Z(\omega)$ of the studied sample between the two plates of the conductivity cell is a complex number which can be represented, in polar coordinates by its module $|Z|$ and its phase, in Cartesian representations by its real part Z' and its imaginary part Z'' with $Z(\omega) = Z' + i\,Z''$. At the time of frequency scanning, the experimental points were distributed on a curve having the form of an arc of a circle. The obtained curve is called a Nyquist diagram ($-Z''$ versus Z'). Z'_1 to high frequency, HF, and Z'_2 to low frequency, LF, are the impedance when 'Z' crosses the OZ axis (real axis). The Nyquist curves for 1×10^{-4} M solutions of complexes **1** and **2** (a concentration close to the doses administered in the anticonvulsant and toxicity assays, see Section 3.6) are shown in Fig. 10. The existence of a half circle is typical of the presence of a simple charge transfer. Table 5 gives the electrochemical conductances $(1/Z')$ of complexes **1** and **2** at concentrations of 1×10^{-4} M and 5×10^{-4} M in deionized water. At LF, conductances $(1/Z'_2)$ of solutions of complexes **1** and **2** at identical concentrations are very similar (compare entries 1 and 5 in one hand, and 3 and 7 in the other hand). These values are notably higher than the conductance of deionized water employed in the present experiments (entry 9), that is to say, approximately 25 times for a concentration of 1×10^{-4} M and 130 times for a concentration of 5×10^{-4} M. Note that at LF, the cell capacitance is assumed to be so small that it may be neglected. However, at HF, conductances $(1/Z'_1)$ for solutions of both complexes are of the same order of magnitude, irrespective of

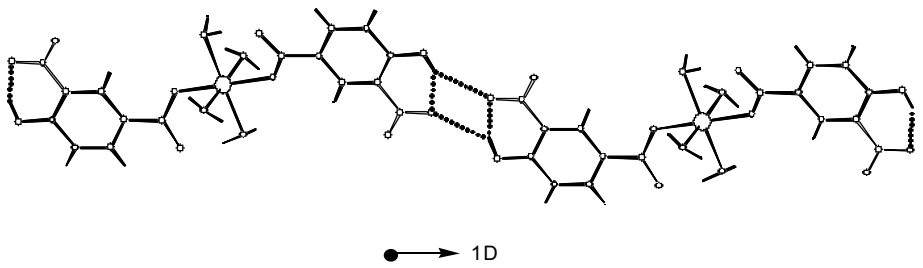


Fig. 5. Part of $[(C_7H_4NO_5)_2Zn(H_2O)_4]_n$ (**1**)$_n$ showing the 1D chain structure with intrachain hydrogen bonds (dashed lines). Zn centers are symbolized by large circles.

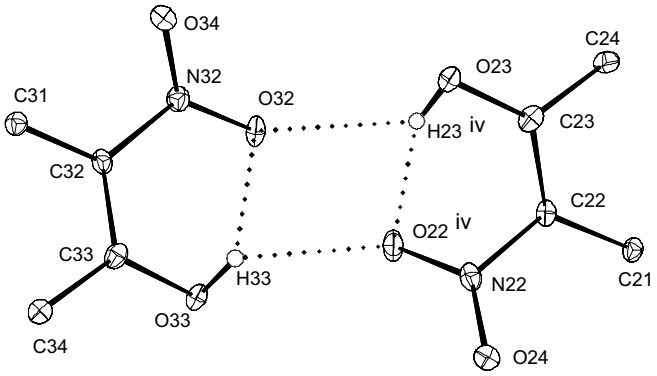


Fig. 6. Labeled diagram of $(C_7H_4NO_5)_2Zn(H_2O)_4$ (**1**) focusing on the hydrogen bonding system around the *ortho*-nitrophenol groups (dashed lines).

concentrations of these complexes (entries 2, 4, 6 and 8), and close to that of deionized water (entry 10). Clearly, at HF, the cell capacitance now markedly competes with the cell resistance, leading to fatal errors in conductance measurements. LF measurements indicate that the conductances of the 1×10^{-4} M and 5×10^{-4} M complex solutions do not differ greatly from those of KCl solutions at these concentrations (entries 11 and 12). Complexes **1** and **2** are therefore strong electrolytes.

3.4. Magnetic measurements

The magnetic properties of Co-complex **2** are shown in Fig. 11. At room temperature, $\chi_M T$ is equal to 3.02 cm^3 K mol^{-1}, value expected for an isolated Co(II) ion. Upon cooling, the $\chi_M T$ values steadily decrease up to 7 K. Below this temperature, the decrease of $\chi_M T$ is steeper to reach a value of 1.62 cm^3 K mol^{-1} at 2 K. In fact, in the 300–30 K temperature range, the experimental curve can be fitted using the theoretical behavior of a distorted octahedral isolated cobalt ion [15]. The best fit of the data by full-matrix diagonalization of the appropriate spin Hamiltonian is obtained with the following parameter $\lambda = -117$, $D = 605$ and $\kappa = 1$ where λ, D and κ stand for spin–orbit constant, axial distortion and orbital reduction factor, respectively. As shown in the inset of Fig. 11, below 30 K the experimental data deviate from the theoretical curve. First, between 30 and 3 K the experimental data are above the theoretical curve indicating that ferromagnetic interaction between Co ions is operative within the

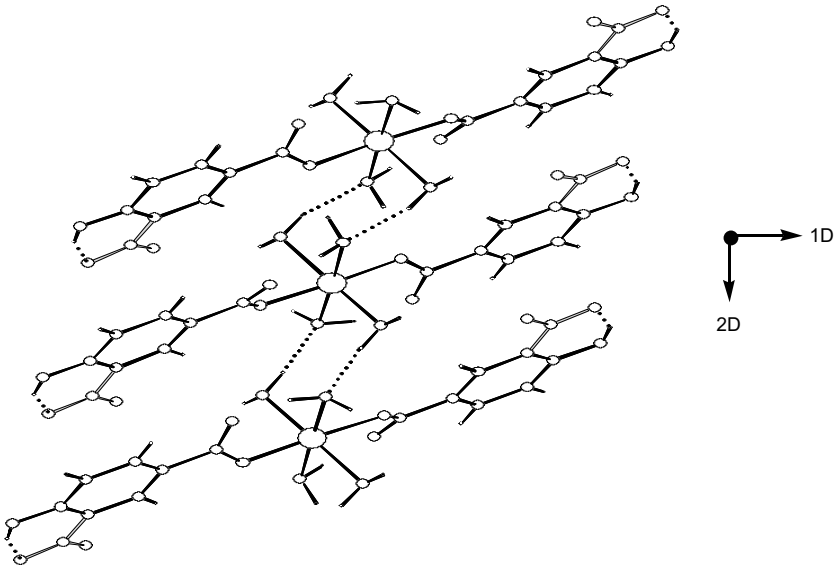


Fig. 7. Packing of $(C_7H_4NO_5)_2Zn(H_2O)_4$ (**1**) showing the H-bonded 2D continuum as dashed lines. Zn centers are symbolized by large circles.

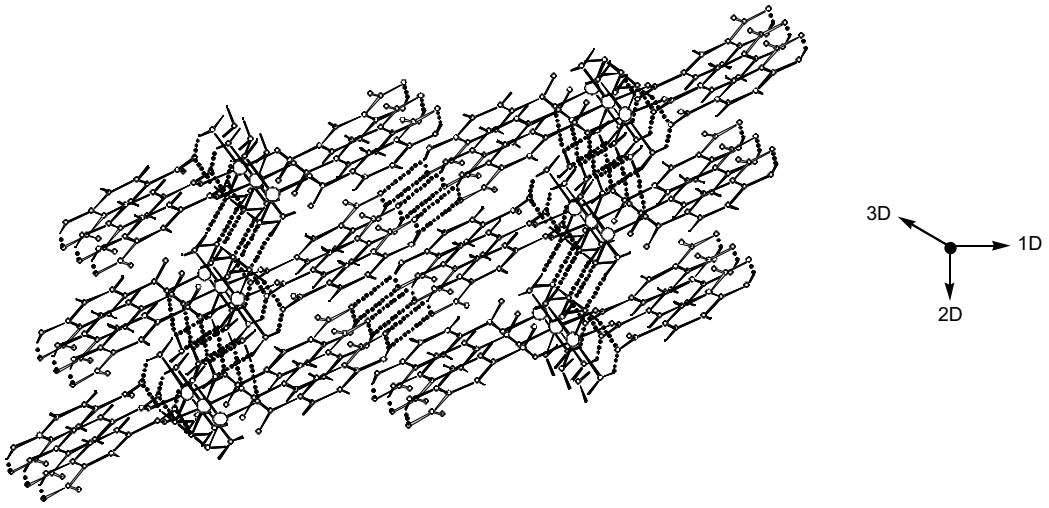


Fig. 8. Packing of $(C_7H_4NO_5)_2Zn(H_2O)_4$ (**1**) showing the H-bonded 3D continuum as dashed lines. Zn centers are symbolized by large circles.

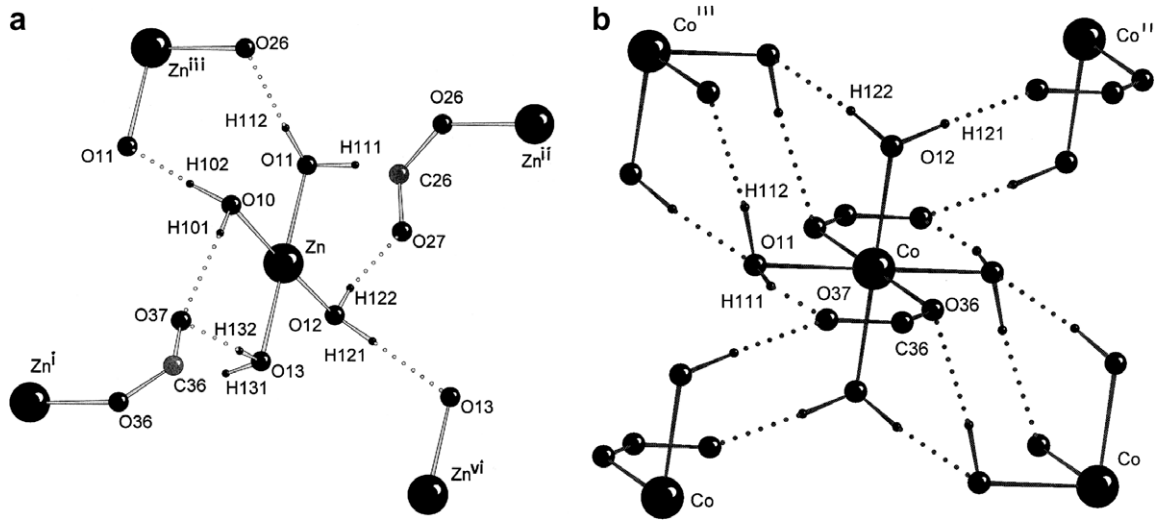


Fig. 9. Packing of $(C_7H_4NO_5)_2Zn(H_2O)_4$ (**1**) (a) and $(C_7H_4NO_5)_2Co(H_2O)_4$ (**2**) (b) concentrating on the 3D arrangement of the metal atoms. Hydrogen bonds are symbolized by dashed lines. Metal–metal distances for Zn–Zn^{iii}: 4.904 Å, Zn–Zn^{vi}, 5.200 Å and Zn–Zn^{i} = Zn–Zn^{ii}, 6.209 Å. Symmetry codes: i: $x+1$, y, z; ii: $x-1$, $y+z$; iii: $-x$, $-y$, $-z+1$; vi: $-x$, $-y+1$, $-z+1$. Metal–metal distances for Co–Co^{iii}: 5.047 Å and Co–Co^{ii}, 6.197 Å. Symmetry codes: iii: $-x+1$, $-y+1$, $-z+1$; ii: x, $y-1$, z.

crystal. Secondly, at very low temperature (3–2 K) the experimental values becomes lower than the theoretical curve showing that a weak antiferromagnetic interaction is also present in **2**. These results are in agreement with the two first levels of hydrogen bonds network in Co-complex **2** (Fig. 9b). On this basis, one can conclude that, magnetically, the cobalt ions are ferromagnetically coupled through the hydrogen bonds network of water molecules (Co^{iii}–O_{11}–O_{10}–Co, Co–Co = 5.047 Å) forming 1D ferromagnetic chains which are antiferromagnetically coupled by the hydrogen bonds developed through the *ortho*-nitrophenol groups of 3-nitro-4-hydroxybenzoate ligand.

3.5. Water/1-octanol extraction experiments

Only the details of the extraction experiment involving Zn-complex **1** are given below. Similar results were obtained with Co-complex **2**. Complex **1** (306 mg, 6.1×10^{-4} mol) was dissolved in deionized water (15 ml).

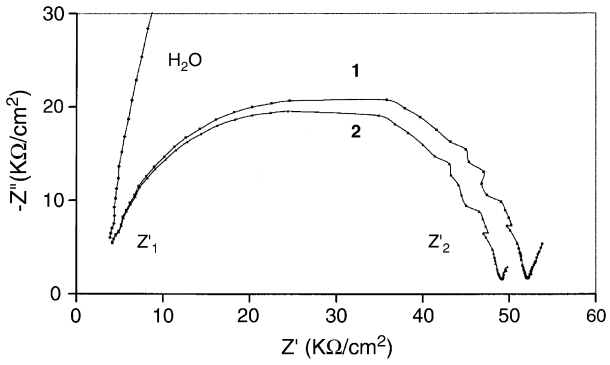


Fig. 10. Nyquist diagrams of complexes **1** and **2** at concentration of 1×10^{-4} M.

Table 5
Electrochemical conductance for complexes **1** and **2** at 20 °C[a]

Entry	Compound	Concentration (M)	Frequency (kHz)	$1/Z'$ (Ω^{-1} cm^{-1})
1	**1**	1×10^{-4}	3	2.02×10^{-5}
2	**1**	1×10^{-4}	>100	3.57×10^{-4}
3	**1**	5×10^{-4}	18	9.90×10^{-5}
4	**1**	5×10^{-4}	>100	4.54×10^{-4}
5	**2**	1×10^{-4}	3	2.16×10^{-5}
6	**2**	1×10^{-4}	>100	3.33×10^{-4}
7	**2**	5×10^{-4}	28	1.18×10^{-4}
8	**2**	5×10^{-4}	>100	3.57×10^{-4}
9	Deionized water		0.01	8.35×10^{-7}
10	Deionized water		18	2.22×10^{-4}
11	KCl	1×10^{-4}	1.4	1.47×10^{-5}
12	KCl	5×10^{-4}	0.12	7.98×10^{-5}

[a] Cell constant = 0.973.

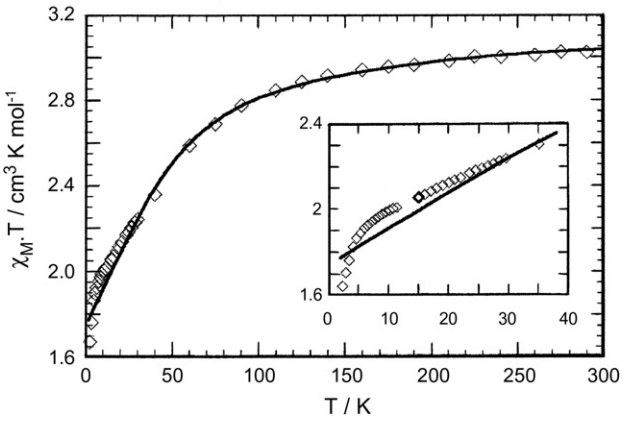


Fig. 11. $\chi_M T$ vs. T plot of Co-complex **2**, experimental (◇) and calculated (——). The inset shows the deviation of the experimental $\chi_M T$ values from the Co monomer behavior.

This solution was extracted with 1-octanol (15 ml) at room temperature. The extraction was repeated four times and the 1-octanol extracts combined. After removal of 1-octanol by vacuum distillation at 1 Torr, 3-nitro-4-hydroxybenzoic acid (111 mg, 6.1×10^{-4} mol), compound **C** in Fig. 12, was obtained as a pale yellow solid, which was unambiguously identified by comparison with an authentic sample using R_f values in thin layer chromatography and IR, UV, and ^{1}H NMR spectra. During this experiment, the color of the aqueous phase changed from pale yellow to bright orange. Evaporation of this solution at room temperature under vacuo gave a microcrystalline orange solid which was successively washed with THF and diethyl ether. Elemental analysis of this solid (Found: C, 30.71; H, 2.41; N, 5.05; Zn, 22.99%) is consistent with the molecular formula $C_7H_3NO_5Zn(H_2O)_2$ (Calc: C, 29.79; H, 2.48; N, 4.96; Zn, 23.14%) corresponding to a salt of type **D** (Fig. 12) in which the ligand **C** and Zn atom components are in the ratio of 1 to 1 (while starting complex **1** comprises two ligands **C** per Zn atom). Two water molecules are linked to each Zn atom of this salt, in order to satisfy the tetrahedral coordination of the metal. The IR spectrum of this salt, (neat, cm^{-1}): 3226 (m, ν O–H), 1596 (s, ν_{as} COO$^-$), 1518 (s), 1391 (s, ν_s COO$^-$), 1324 (s), 1248 (s), 1192 (m), 1153 (s), 1073 (m), 927 (m), 831 (m), 783 (s), 763 (s), 709 (s), 643 (s), is in agreement with the proposed molecular structure. The above outcome can be interpreted on the basis of the putative two-step equilibrium of complexes **1** and **2** in aqueous medium depicted in Fig. 12. The first step of this process involves the dissociation of the complexes into cation **A** and anion **B** [16] (note that similar discrete ionic entities were found in the crystal structures of 5(nsa)-metal complexes **3** and **4**, regioisomers of **1** and **2**, respectively, see Fig. 13). These, in turn, may interconvert through proton transfer into ligand **C** and salt **D** (in which each metal atom is coordinated to two ligand molecules acting as bidendate linkers through their carboxylato and phenoxo groups). Because of its marked lipophilicity (calculated $\log P = 1.78$) [17], ligand **C** is extractable with 1-octanol (an operation that drives the equilibrium towards **C** and **D** partners), while hydrophilic salt **D** remains in the aqueous phase.

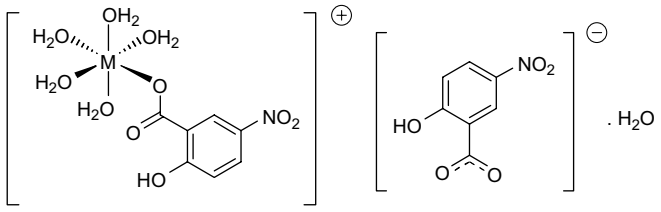


Fig. 13. Crystal structure-based canonical representation of $[M(H_2O)_5(5\text{-nsa})]^+(5\text{-nsa})^- \cdot H_2O$ (**3**, M = Zn; **4**, M = Co; **5**, M = Ni; **6**, M = Mg) [5].

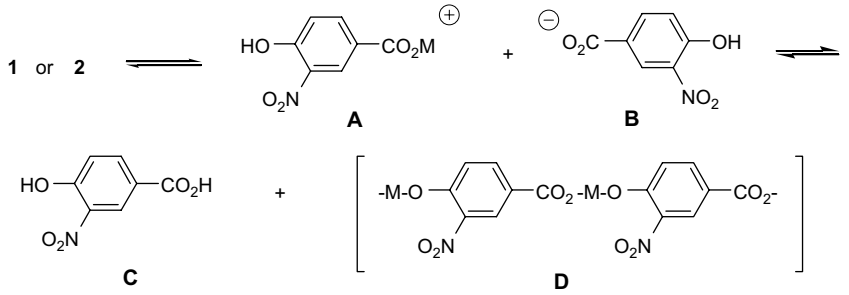


Fig. 12. Putative equilibrium of complexes **1** and **2** in aqueous solution (M = Zn or Co). The water molecules coordinated to the metal atoms have been omitted for clarity.

Table 6
Comparative anticonvulsant activities and Rotorod toxicity for complexes **1** to **6** (μmol/kg of body mass)

Compound [Reference]	MES[a]	Minimal clonic seizure[b]	scMET[c]	Rotorod toxicity[d]
1 [this work]	I at 600 ip^m at 0.5 h	A at 198 ip^m at 0.25 h	A at 198 ip^m at 0.25 h	A at 700 ip^m at 1 h
2 [this work]	I at 610 ip^m at 0.5 h	A at 200 ip^m at 1 h	A at 200 ip^m at 0.5 h	A at 610 at 0.5 h
3 [5]	I at 560 ip^m at 0.5 h	A at 185 at 0.25 h	A at 185 ip^m at 1 h	A at 185 ip^m at 0.25 h
4 [5]	A at 93 o^r at 0.25 h	A at 185 ip^m at 2 h	I at 560 ip^m at 4 h	A at 185 ip^m at 0.5 h
5 [5]	I at 570 ip^m at 4 h	A at 57 ip^m at 1 h	I at 570 ip^m at 4 h	A at 57 ip^m at 0.5 h
6 [5]	I at 600 ip^m at 4 h	A at 199 ip^m at 0.5 h	I at 600 ip^m at 4 h	I at 600 ip^m at 4 h

[a] MES = maximal electroshock seizure test.
[b] Psychomotor seizure or minimal clonic seizures are usually produced with the delivery of 6 Hz (32 mA) or slightly higher current designed to detect compounds that are missed with the MES tests which employs a larger current of 50 mA. It is a much less intense stimulation of the CNS than the MES test.
[c] scMET = subcutaneous Metrazol seizure threshold test, and Rotorod toxicity test.
[d] Rotorod toxicity, an inability to grasp the rotating rod, may be due to CNS depression due to sedative and/or hypnotic activities, or a state of eminent death, due to medullary paralysis at high doses, a common unwanted side effect caused by high doses of all anticonvulsant drugs. A = Activity at indicated dose and time of challenge. I = Inactive, ip = intraperitoneal, o = oral, m = mice, r = rats.

3.6. Anticonvulsant activities

Anticonvulsant activities for compounds **1** and **2**, as well as related (5-nitrosalicylato)–metal complexes [5] (compounds **3**–**6**, Fig. 13), are presented in Table 6.

Only **4** was found to have activity against MES-induced seizures. This modest activity was observed at a relatively low and non-toxic dose given orally to rats. Compounds **1**–**6** had activity in protecting against the less intense minimal clonic seizure with an apparent activity order being $\mathbf{5} > \mathbf{2} \cong \mathbf{1} > \mathbf{3} \cong \mathbf{6}$ and **4**, based upon these preliminary results. Only compounds **1**, **2**and **3** afforded some protection against the MET-induced seizure and the relative order of effectiveness was $\mathbf{1} > \mathbf{2} > \mathbf{3}$.

4. Conclusion

We have shown that the individual subunits of the (3-nitro-4-hydroxybenzoato) complexes of Zn(II) (**1**) and Co(II) (**2**) self-assemble via extensive hydrogen bonding involving water molecules leading to a 3D supramolecular architecture. The electrochemical impedance measurements show that these complexes are strong electrolytes in dilute aqueous solution. On the other hand, magnetic measurement of Co-complex indicates that the Co ions are ferromagnetically coupled thought the hydrogen bonds network of water molecules forming 1D ferromagnetic chains.

The anticonvulsant activities of complexes **1** and **2** as well as related Zn(II), Co(II), Ni(II) and Mg(II) (5-nitrosalicylato) complexes (**3**, **4**, **5** and **6**, respectively) where also determined. The pharmacological responses obtained for these complexes are consistent with those obtained for many related metal complexes [4–10].

The transport of therapeutics across the blood–brain barrier (BBB) is critical for the treatment of disorders of the central nervous system. There is a good correlation between BBB penetration *in vivo* and lipid solubility of a drug, the latter being conventionally expressed as its partition coefficient (*P*), calculated as the ratio of solubilities in 1-octanol and water [18]. Because of their marked hydrophilicity, revealed by their notable water solubility (Section 2.3) and the important conductance of their aqueous solutions (Section 3.3), metal salts **1** and **2** can have direct access to the systemic circulation *via* blood plasma. Lipophilic ligand **C**, which is in equilibrium with complexes **1** and **2** in aqueous medium (Section 3.5), can then penetrate the BBB by diffusion (passive translocation *via* a lipophilic pathway). On this basis, we may hypothesize that the active form of these anticonvulsant metal complexes might be free ligand **C**, the metal salts playing the role of hydrosoluble vectors that release the drug at BBB level. This hypothesis is in full agreement with a previous investigation of (salicylato)–copper complex equilibrium under physiological conditions, which ruled out any implication of the copper complex in the anti-inflammatory activity, since the salicylate anion cannot significantly mobilize plasma copper into tissue–diffusible complexes. Even though the salicylate ligand can effectively promote the gastrointestinal absorption of copper, the reciprocal effect of the metal upon the drug seems to be negligible, except for high metal-to-drug ratios [19–21].

Acknowledgements

Financial support of Université Paris XI, CNRS and Ecole Centrale Paris is gratefully acknowledged. The authors thank Mrs. S. Mairesse-Lebrun for performing elemental analyses. We are also thank Mr. James Stables for his assistance in obtaining data pertain to the anticonvulsant and Rotorod toxicities of our compounds *via* the DHHS, NIH, NINDS ADD program (USA).

Appendix A. Supplementary material

CCDC 647852 and 647853 contain the supplementary crystallographic data for **1** and **2**. These data can be obtained free of charge via http://www.ccdc.cam.ac.uk/conts/retrieving.html, or from the Cambridge Crystallographic Data Centre, 12 Union Road, Cambridge CB2

1EZ, UK; fax: (+44) 1223-336-033; or e-mail: deposit@ccdc.cam.ac.uk. Supplementary data associated with this article can be found, in the online version, at doi:10.1016/j.poly.2007.10.006.

References

[1] F.D. Rochon, G. Massarweh, Inorg. Chim. Acta 304 (2000) 190.
[2] S.H. Rahaman, D. Bose, H. Chowdhury, G. Mostafa, H.-K. Fun, B.K. Ghosh, Polyhedron 24 (2005) 1837.
[3] N.E. Ghermani, G. Morgant, J. d'Angelo, D. Desmaële, B. Fraisse, F. Bonhomme, E. Dichi, M. Sghaier, Polyhedron 26 (2007) 2880.
[4] J.R. J Sorenson, Free Radic. Biol. Med. 13 (1992) 593.
[5] G. Morgant, N. Bouhmaida, L. Balde, N.E. Ghermani, J. d'Angelo, Polyhedron 25 (2006) 2229.
[6] J.R.J. Sorenson, J. Med. Chem. 19 (1976) 135.
[7] J.R.J. Sorenson, Prog. Med. Chem. 15 (1978) 211.
[8] B. Viossat, J.-C. Daran, G. Savouret, G. Morgant, F.T. Greenaway, N.-H. Dung, V.A. Pham-Tran, J.R.J. Sorenson, J. Inorg. Biochem. 96 (2003) 375.
[9] P. Lemoine, B. Viossat, N.H. Dung, A. Tomas, G. Morgant, F.T. Greenaway, J.R.J. Sorenson, J. Inorg. Biochem. 98 (2004) 1734.
[10] B. Viossat, F.T. Greenaway, G. Morgant, J.-C. Daran, N.-H. Dung, J.R.J. Sorenson, J. Inorg. Biochem. 99 (2005) 355.
[11] ASTRO (5.00), SAINT (5.007) and SADABS (5.007). Data Collection and Processing Software for the SMART System (5.054). Siemens (BRUKER-AXS) Analytical X-ray Instruments Inc., Madison, WI, 1998.
[12] A. Altomare, M.C. Burla, M. Camalli, G.L. Cascarano, G. Giacovazzo, A. Guagliardi, A. Grazia, G. Moliterni, G. Polidori, R. Spagna, J. Appl. Crystallogr. 32 (1999) 115.
[13] D.J. Watkin, C.K Prout, J.R. Carruthers, P.W. Betteridge, R.I. Prout, CRYSTALS Issue 11. Chemical Crystallography Laboratory, University of Oxford, UK, 2001.
[14] D.J. Watkin, C.K. Prout, L.J. Pearce, CAMERON, Chemical Crystallography Laboratory, University of Oxford, UK, 1996.
[15] O. Kahn, Molecular Magnetism, VCH, New York, 1993.
[16] L.H.J. Lajunen, R. Portanova, J. Piispanen, M. Tolazzi, Pure Appl. Chem. 69 (1997) 329.
[17] N. Bodor, P. Buchwald, J. Phys. Chem. B 101 (1997) 3404.
[18] N.J. Abbott, I.A. Romero, Mol. Med. Today (1996) 106.
[19] V. Brumas, B. Brumas, G. Berthon, J. Inorg. Biochem. 57 (1995) 191.
[20] H. Miche, V. Brumas, G. Berthon, J. Inorg. Biochem. 68 (1997) 27.
[21] B. Halova-Lajoie, V. Brumas, M.M.L. Fiallo, G. Berthon, J. Inorg. Biochem. 100 (2006) 362.

Available online at www.sciencedirect.com
ScienceDirect
Polyhedron 27 (2008) 547–551
POLYHEDRON
www.elsevier.com/locate/poly

2-Pyridinoformamide-derived thiosemicarbazones and their iron(III) complexes: Potential antineoplastic activity

Angelica E. Graminha [a], Felipe S. Vilhena [b], Alzir A. Batista [a], Sonia R.W. Louro [c], Roberta L. Ziolli [b], Letícia R. Teixeira [b,*], Heloisa Beraldo [d]

[a] *Departamento de Química, Universidade Federal de São Carlos, 1365-905 São Carlos, Brazil*
[b] *Departamento de Química, Pontifícia Universidade Católica do Rio de Janeiro, 22453-900 Rio de Janeiro, Brazil*
[c] *Departamento de Física, Pontifícia Universidade Católica do Rio de Janeiro, 22453-900 Rio de Janeiro, Brazil*
[d] *Departamento de Química, Universidade Federal de Minas Gerais, 31270-901 Belo Horizonte, Brazil*

Received 12 July 2007; accepted 6 October 2007
Available online 19 November 2007

Abstract

The iron(III) complexes $[Fe(2Am4DH)_2]Cl$ (**1**), $[Fe(2Am4Me)_2]Cl$ (**2**) and $[Fe(2Am4Et)_2]Cl$ (**3**) with 2-pyridineformamide thiosemicarbazone (H2Am4DH) and its *N*(4)-methyl (H2Am4Me) and *N*(4)-ethyl (H2Am4Et) derivatives were obtained and characterized by means microanalyses, infrared and EPR spectra. The electrochemical behavior of the complexes was investigated. The thiosemicarbazones and complexes (**1**) and (**2**) presented toxicity against *Artemia salina* at low concentrations. Since this bioassay has a good correlation with cytotoxic activity in human solid tumors, the studied compounds present potential pharmacological applications.
© 2007 Elsevier Ltd. All rights reserved.

Keywords: 2-Pyridineformamide thiosemicarbazones; Iron complexes; Cytoxicity; *Artemia salina*

1. Introduction

Thiosemicarbazones and their metal complexes present a wide range of bioactivities [1,2]. The pharmacological profile of a variety of α(N)-heterocyclic thiosemicarbazones derived from pyridine has been extensively investigated, as well as the role of metal coordination in the mechanism of action of these compounds [1,3,4].

It has been shown that the antitumoral action of α(N)-heterocyclic thiosemicarbazones occurs through the inhibition of ribonucleotide diphosphate reductase (RDR), a key enzyme involved in the conversion of ribonucleotides into deoxyribonucleotides during DNA syntheses [5–7]. The active form of the drugs are their iron(II) complexes [8,9]. In the proposed mechanism of action oxidation of the iron(II) complex occurs with release of one electron, which inactivates a tyrosyl free radical present in the structure of the enzyme. Our group suggested that reduction of the iron(III) to the iron(II) complex by cellular thiols could be part of this pathway [10–13]. Hence the preparation of new iron complexes with thiosemicarbazones constitutes an interesting strategy in designing antitumoral drug candidates.

Although the literature reports some structural and spectral studies on 2-pyridineformamide-derived thiosemicarbazones [14–18], to our knowledge their pharmacological applications have not so far been investigated. Our group recently started the study of the possible pharmacological applications of this class of compounds.

In the present work, iron(III) complexes with 2-pyridineformamide thiosemicarbazone (H2Am4DH) and its *N*(4)-methyl (H2Am4Me) and *N*(4)-ethyl (H2Am4Et) derivatives (Fig. 1) were obtained. The toxicity of the

* Corresponding author.
E-mail address: lregina@qui.puc-rio.br (L.R. Teixeira).

0277-5387/$ - see front matter © 2007 Elsevier Ltd. All rights reserved.
doi:10.1016/j.poly.2007.10.008

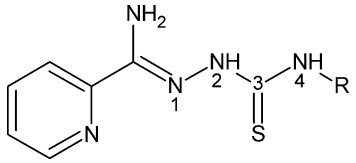


Fig. 1. General structure of 2-pyridineformamide-derived thiosemicarbazones: R = H (H2Am4DH); R = CH_3 (H2Am4Me); R = CH_2CH_3 (H2Am4Et).

thiosemicarbazones and their metal complexes against *Artemia salina* was assayed as a prescreening of antitumoral action.

2. Experimental

2.1. Apparatus

Partial elemental analyses were performed on a Perkin Elmer CHN 2400 analyzer. Infrared spectra were recorded on a Perkin Elmer FT-IR Spectrum GX spectrometer using KBr pellets; an YSI model 31 conductivity bridge was employed for molar conductivity measurements. Magnetic susceptibility measurements were carried out on a Johnson Matthey MSB/AUTO balance. Electron paramagnetic resonance (EPR) spectra of samples in the solid state and in frozen methanol solution were obtained in quartz tubes of 3 mm of internal diameter at liquid N_2 temperature (77 K) on a Bruker ESP300E equipment with modulation frequency of 100 kHz and modulation amplitude of 1.1 mT. Spectral simulations were performed using EasySpin [19].

The electrochemical experiments were carried out at room temperature in aqueous solution containing 0.1 mol L^{-1} KCl, using an electrochemical analyzer from Bioanalytical Systems Inc. (BAS), model 100BW. The working and auxiliary electrodes were stationary Pt foils, and the reference electrode was Ag/AgCl a medium in which ferrocene is oxidized at 0.48 V (Fc^+/Fc).

2.2. Synthesis of the iron(III) complexes with 2-pyridinoformamide thiosemicarbazone (H2Am4DH) and its N(4)-methyl (H2Am4Me) and N(4)-ethyl (H2Am4Et) derivatives

The thiosemicarbazones were obtained as reported in the literature [14]. The iron(III) complexes were obtained by mixing the desired thiosemicarbazone with $FeCl_3 \cdot 6H_2O$ in acetone at room temperature in 1:2 metal-to-ligand molar ratio. The solids which precipitate were filtered off and washed with diethyl ether.

2.2.1. Bis(2-pyridineformamidethiosemicarbazonato)-iron(III) chloride [Fe(2Am4DH)$_2$]Cl (1)

Brown solid. *Anal.* Calc. for $FeC_{14}H_{16}N_{10}S_2Cl$: C, 35.05; H, 3.36; N, 29.19. Found: C, 35.15; H, 3.29; N, 29.28%; FW: 479.77 g mol^{-1}. IR (KBr, cm^{-1}): ν(C=N)+ ν(C=S) 1509, ν(C=S) 786, ρ(py) 656, ν(Fe–N) 459, ν(Fe–S) 376, ν(Fe–N_{py}) 333. Molar conductivity (1×10^{-3} mol L^{-1} H_2O): 89.8 μS cm^{-1}. Effective magnetic moment = 1.62 (BM). Yield: 82%. Melting point 220–221 °C.

2.2.2. Bis(N(4)-methyl-2-pyridineformamidethiosemicarbazonato)iron(III) chloride [Fe(2Am4Me)$_2$]Cl (2)

Green solid. *Anal.* Calc. for $FeC_{16}H_{20}N_{10}S_2Cl$: C, 37.84; H, 3.97; N, 27.58. Found: C, 37.61; H, 3.94; N, 27.33%; FW: 507.83 g mol^{-1}. IR (KBr, cm^{-1}): ν(C=N)+ ν(C=S) 1551, ν(C=S) 774, ρ(py) 661, ν(Fe–N) 459, ν(Fe–S) 397, ν(Fe–N_{py}) 354. Molar conductivity (1×10^{-3} mol L^{-1} H_2O): 87.9 μS cm^{-1}. Effective magnetic moment = 1.66 (BM). Yield: 70%. Melting point 217–218 °C.

2.2.3. Bis(N(4)-ethyl-2-pyridineformamidethiosemicarbazonato)iron(III) chloride [Fe(2Am4Et)$_2$]Cl (3)

Green solid. *Anal.* Calc. for $FeC_{18}H_{24}N_{10}S_2Cl$: C, 40.34; H, 4.51; N, 26.14. Found: C, 40.48; H, 4.46; N, 26.25%; FW: 535.88 g mol^{-1}. IR (KBr, cm^{-1}): ν(C=N)+ ν(C=S) 1575, ν(C=S) 789, ρ(py) 612, ν(Fe–N) 457, ν(Fe–S) 389, ν(Fe–N_{py}) 349. Molar conductivity (1×10^{-3} mol L^{-1} H_2O): 83.2 μS cm^{-1}. Effective magnetic moment = 1.59 (BM). Yield: 73%. Melting point 205–206 °C.

2.3. Assay of toxicity against Artemia salina

The *Artemia salina* (brine shrimp) lethality test was employed as an antitumor prescreen. Lethality towards brine shrimp was assayed using procedures related in the literature [20,21]. Lethal dose (LD_{50}) is the amount of a substance which causes the death of 50% of a group of test animals. Determination of LD_{50} is an indication of the short-term poisoning potential (acute toxicity) of a compound.

Artemia salina encysted eggs (10 mg) were incubated in 100 mL of seawater under artificial light at 28 °C, pH 7–8. After incubation for 24 h, nauplii were collected with a Pasteur pipette and kept for an additional 24 h under the same conditions to reach the metanauplii stage. The samples to be assayed were dissolved in 1% DMSO (dimethylsulfoxide) and diluted in five different concentrations in seawater. About 10 nauplii were added to each set of tubes containing the samples. Controls containing 1% DMSO in seawater were included in each experiment. Forty-eight hours later, the number of survivors was counted, recorded and the lethal dose 50% (LD_{50} value) and 95% confidence intervals were calculated by Probit analysis [22]. The repeatability of the method was evaluated using at least three replicates of concentration of each sample.

3. Results and discussion

Microanalyses suggest the formation of [Fe(2Am4DH)$_2$]-Cl (**1**), [Fe(2Am4Me)$_2$]Cl (**2**) and [Fe(2Am4Et)$_2$]Cl (**3**) in which the thiosemicarbazones coordinate as anionic ligands. The molar conductivity data reveal that the complexes

are 1:1 electrolytes, in accordance with the proposed formulations.

The values of magnetic moments in the 1.59–1.66 BM range are close to the calculated value of 1.73 BM, characteristic of the presence of one unpaired electron as in low spin iron(III) complexes.

3.1. Infrared spectra

The ν(C=C)+ ν(C=N) composed mode observed in the 1593–1611 cm^{-1} range in the spectra of the thiosemicarbazones shifts to 1551–1575 cm^{-1} in the spectra of the complexes, indicating coordination of the azomethine nitrogen N_2 [14,23].

The ν(C=S) absorption at 850–856 cm^{-1} in the spectra of the uncomplexed thiosemicarbzones is observed at 774–789 cm^{-1} in those of the complexes, in accordance with coordination through a thiolate sulfur. The 61–66 cm^{-1} shift observed upon complexation is compatible with coordination of an anionic thiosemicarbazone in all cases [24–27]. The pyridine in-plane deformation mode at 601–617 cm^{-1} in the spectra of the free bases shifts to 612–661 cm^{-1} in those of the complexes, suggesting coordination of the heteroaromatic nitrogen [14,23]. In addition, new absorptions at 457–459 cm^{-1} and 333–354 cm^{-1} have been attributed to ν(Fe–N) and ν(Fe–N_{py}), respectively, and bands in the 376–397 cm^{-1} range have been assigned to ν(Fe–S) [14,23,28,29].

The infrared data for the complexes indicate coordination of the thiosemicarbazones through the N_{py}–N–S chelating system.

3.2. EPR spectra

The EPR spectra of the frozen methanol solutions in liquid nitrogen (77 K) (Fig. 2a) are very similar and show three different g values (orthorhombic g tensor) characteristic of low-spin Fe^{III} with rhombic distortion. The similarity between the EPR spectra indicates that the iron coordination spheres in the three complexes are similar. The small deviation of the anisotropic g values from 2.0 suggests that the unpaired electron is in the d_{xy} orbital, indicating a $d^2_{xz}d^2_{yz}d^1_{xy}$ ground state configuration for the complexes [23,28,29].

The polycrystalline samples of the three compounds, on the other hand, present different EPR spectra (Fig. 2b). The spectrum of [Fe(2Am4DH)$_2$]Cl (**1**) is mainly isotropic ($g_{iso} = 2.119$), with very small shoulders at $g_1 = 1.990$ and $g_3 = 2.220$. The spectrum of [Fe(2Am4Me)$_2$]Cl (**2**) is anisotropic, with three different g values, and that of [Fe(2AMEt)$_2$]Cl (**3**) has almost axial symmetry.

Spectral simulations were performed for a simple orthorhombic system, a single low-spin Fe^{III} ($S = 1/2$) with given g_1, g_2, and g_3 values (principal values of the g tensor), Lorentzian or Gaussian line-shapes, and magnetic field strain, to account for orientation dependent line-widths. The g values and line-width parameters are presented in Table 1. The simulated spectra are presented in Fig. 2 as dotted lines superimposed to the experimental spectra.

Table 1 shows that the three complexes dissolved in methanol (77 K) have basically the same EPR parameters. The spectral shapes were simulated using a Gaussian uniform broadening ($\Delta B_{FWHM} = 1.5$ mT), and B_{strain}

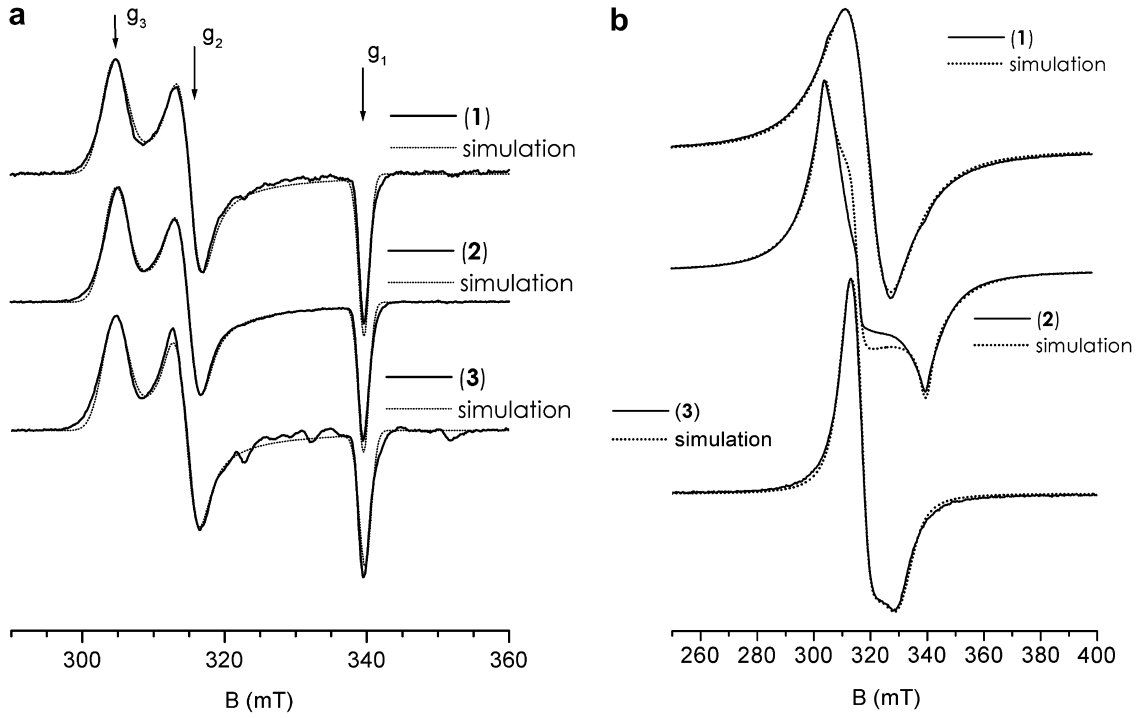


Fig. 2. EPR spectra of complexes **1**–**3** (a) in methanol and (b) in the polycrystalline state at 77 K.

Table 1
EPR spectral parameters for complexes **1**–**3** (77 K), obtained by spectral simulations using the software EasySpin (FWHM: full width at half height)

	ΔB_{FWHM} (mT) Gauss	B_{strain} (mT)	g_1	g_2	g_3	g_{av}
Complex in MeOH						
$[Fe(2Am4DH)_2]Cl$ (**1**)	1.5	0.0, 3.1, 4.1	1.991	2.147	2.221	2.120
$[Fe(2Am4Me)_2]Cl$ (**2**)	1.5	0.0, 3.1, 3.9	1.991	2.147	2.219	2.119
$[Fe(2Am4Et)_2]Cl$ (**3**)	1.7	0.0, 2.9, 4.0	1.990	2.149	2.220	2.119
Polycrystalline complex						
$[Fe(2Am4DH)_2]Cl$ (**1**)	16.0		2.119	2.119	2.119	2.119
$[Fe(2Am4Me)_2]Cl$ (**2**)	13.0	10; 0.0; 0.0	1.991	2.145	2.226	2.120
(2 components)	3.2	0.0; 1.5; 2.0				
$[Fe(2Am4Et)_2]Cl$ (**3**)	4.8	6.5; 0.0; 4.2	2.047	2.132	2.161	2.110

broadening components of about 3 and 4 mT for g_2 and g_3, respectively.

Contrary to the frozen methanol solutions, the spectral shapes of the polycrystalline samples were simulated using a Lorentzian line-shape, which is characteristic of homogeneous broadening. The polycrystalline spectrum of **1** was simulated with an isotropic $g = 2.119$, and $\Delta B_{FWHM} = 16$ mT. Complex **2** on the other hand, presented an anisotropic polycrystalline spectrum ($g_1 \neq g_2 \neq g_3$), with narrow peaks but wide wings. It was not possible to fit this spectrum using a single component, but it was almost completely simulated using two components with equal g values but different line-widths (see Table 1), suggesting the presence of two different populations of iron(III) ions. Polycrystalline **3** has almost axial symmetry ($g_1 \neq g_2 \approx g3$), and the g values differ from those in methanol. It is interesting to note that the average g values for the crystalline complexes **1** and **2**, and for the methanol solutions of the three complexes are the same.

The line-widths of the polycrystalline samples are much larger than in methanol (Table 1), and decrease in the following order: **1** > **2** > **3**. Large line-widths are usually due to spin–spin interactions in concentrated samples. In fact, the distances between the iron atoms are much smaller in the crystals than in the frozen methanol solutions. Among the polycrystalline samples, the distances between the iron atoms are expected to be greater for complexes with thiosemicarbazones containing the bulkier substituents. Indeed, it is observed that the line-width for **3** is the smallest one (Table 1).

3.3. Electrochemical studies

The cyclic voltammograms of complexes **1**–**3** (see Fig. 3) show one quasi-reversible process in the −0.17 to −0.19 V range, attributed to the Fe^{II}/Fe^{III} oxidation, followed by the corresponding reduction at −0.24 to −0.27 V. A second quasi-reversible process is observed at 0.55–0.66 V, attributed to the Fe^{III}/Fe^{IV} oxidation followed by the corresponding reduction at 0.47–0.54 V. The remaining wave in the −0.70 to −0.79 V range was attributed to a reduction process of the thiosemicarbazone (Table 2). The resemblance of electrochemical behaviors of the three complexes suggests that their structures in solution are also very similar.

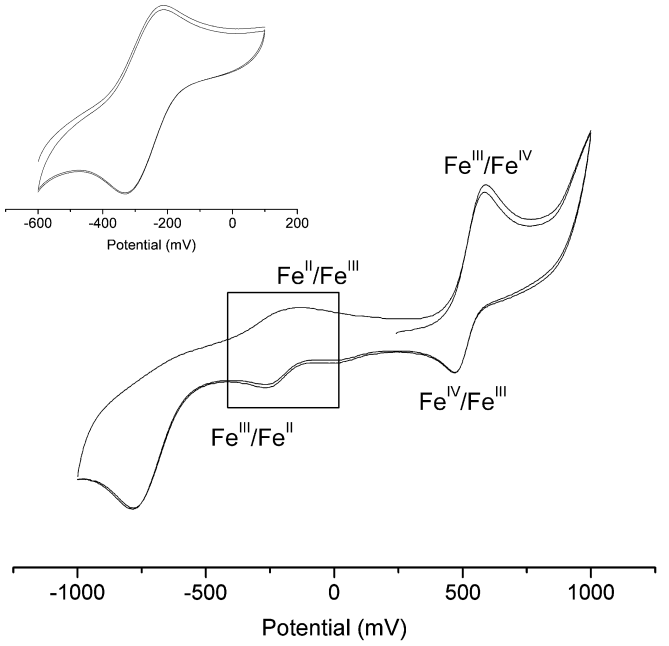


Fig. 3. Cyclic voltammogramm of $[Fe(2Am4Et)_2]Cl$ (**3**) (0.100 V s^{-1}, H_2O, 0.1 mol L^{-1} KCl).

Table 2
Cyclic voltammetry data for complexes **1**–**3** (0.100 V s^{-1}, H_2O, 0.1 mol L^{-1} KCl)

	Fe^{II}/Fe^{III}V	Fe^{III}/Fe^{II}V	Fe^{III}/Fe^{IV}V	Fe^{IV}/Fe^{III}V
$[Fe(2Am4DH)_2]Cl$ (**1**)	−0.17	−0.24	0.66	0.54
$[Fe(2Am4Me)_2]Cl$ (**2**)	−0.19	−0.27	0.55	0.48
$[Fe(2Am4Et)_2]Cl$ (**3**)	−0.17	−0.27	0.58	0.47

3.4. Toxicity against Artemia salina

LD_{50} average values for the thiosemicarbazones and their iron(III) complexes are reported in Table 3. We

Table 3
LD_{50} values for 2-pyridineformamide-derived thiosemicarbazones and their iron(III) complexes against *Artemia salina*

Compound	LD_{50}^{a}, μmol L^{-1} ± SD
H2Am4DH	35.24 ± 7.11
[Fe(2Am4DH)$_2$]Cl (**1**)	30.14 ± 1.93
H2Am4Me	26.09 ± 3.96
[Fe(2Am4Me)$_2$]Cl (**2**)	14.12 ± 0.98
H2Am4Et	31.89 ± 3.38
[Fe(2Am4Et)$_2$]Cl (**3**)	> 90

[a] LD_{50}, lethal dose which causes the death of 50% of a group of test animals; SD, standard deviation.

obtained $LD_{50} = 6.88$ mg L^{-1} (35.24 μM); 5.46 mg L^{-1} (26.09 μM) and 7.12 mg L^{-1} (31.89 μM) for H2Am4DH, H2Am4Me and H2Am4Et, respectively. For complexes **1** and **2** we found $LD_{50} = 14.46$ mg L^{-1} (30.14 μM) and 7.17 mg L^{-1} (14.12 μM), respectively. Complex **3** did not show activity up to the concentration of 48 mg L^{-1} (90 μM). The tested compounds were found to be more active than lapachol ($LD_{50} = 68$ μg $mL^{-1} = 281$ μM), which is known as reference compound [30].

Upon complexation with formation of complexes **1** and **2** the values of LD_{50} decrease, indicating higher toxicity. Complex **2** proved to be the most promising ($LD_{50} =$ 14.12 μM). In addition, the complexes are water-soluble, which strongly helps in vivo toxicity assays.

4. Conclusions

The toxicity against *Artemia salina* bioassay has a good correlation with cytotoxic activity in some human tumors [30]. The low values of LD_{50} obtained for the studied compounds in this assay indicate that they could present antineoplastic properties. Moreover, the determined values of Fe^{III}/Fe^{II} redox potentials for **1**–**3** fall in the range of cellular reductants [31]. Therefore, if the complexes present antitumoral activity, their biochemical pathway could involve Fe^{III}/Fe^{II} reduction by cellular thiols, as suggested previously by us for iron complexes of other thiosemicarbazones [10–13].

References

[1] H. Beraldo, D. Gambino, Mini-rev. Med. Chem. 4 (2004) 31.
[2] D.X. West, A. Liberta, S.B. Padhye, R.C. Chikate, P.B. Sonawane, A.S. Kumbhar, R.G. Yerande, Coord. Chem. Rev. 123 (1993) 49.
[3] A.E. Liberta, D.X. West, Biometals 5 (1992) 121.
[4] D.X. West, S. Padhye, P.B. Sonawane, Struct. Bond. 76 (1991) 127.
[5] D.R. Richardson, Crit. Rev. Oncol./Hematol. 42 (2002) 267.
[6] L. Thelander, A. Graslund, J. Biol. Chem. 286 (1983) 4063.
[7] L. Thelander, A. Graslund, M. Thelander, Biochem. Biophys. Res. Commun. 110 (1983) 859.
[8] R.A. Finch, M.C. Liu, A.H. Cory, J.G. Cory, A.C. Sartorelli, Adv. Enz. Reg. 39 (1999) 3.
[9] R.A. Finch, M.C. Liu, S.P. Grill, W.C. Rose, R. Loomis, K. Vasquez, Y. Cheng, A.C. Sartorelli, Adv. Biochem. Pharmacol. 59 (2000) 983.
[10] R.H.U. Borges, E. Paniago, H. Beraldo, J. Inorg. Biochem. 65 (1997) 267.
[11] H. Beraldo, E. Fantini, R.H.U. Borges, M.A. Rocha, L. Tosi, A. Abras, Inorg. Chim. Acta 172 (1990) 113.
[12] H. Beraldo, L. Tosi, J. Roy. Netherlands Chem. Soc. 106 (1987) 390.
[13] R.H. Borges, A. Abras, H. Beraldo, J. Bras. Chem. Soc. 8 (1997) 1.
[14] D.X. West, J.K. Swearing, J. Valdés-Martínez, S. Hernández-Ortega, A.K. El-Sawaf, F. van Merus, A. Castiñeiras, I. Garcia, E. Bermejo, Polyhedron 18 (1999) 2919.
[15] A. Castiñeiras, I. Garcia, E. Bermejo, D.X. West, Zeit. Naturforsch. B: Chem. Sci. 55 (2000) 511.
[16] E. Bermejo, A. Castiñeiras, I. Garcia-Santos, D.X. West, Zeit. Anorgan. Allg. Chem. 631 (2005) 2011.
[17] E. Bermejo, A. Castiñeiras, L.M. Fostiak, I. Garcia-Santos, J.K. Swearingen, D.X. West, Polyhedron 23 (2004) 2303.
[18] I. Garcia, E. Bermejo, A.K. El Sawaf, A. Castiñeiras, D.X. West, Polyhedron 21 (2002) 729.
[19] S. Stoll, A. Schweiger, J. Magn. Reson. 178 (2006) 42.
[20] B.N. Meyer, N.R. Ferrigni, J.E. Putnam, L.B. Jacobsen, D.E. Nichols, J.L. McLaughlin, J. Med. Plant Res. 45 (1982) 31.
[21] I.A. Nascimento, M.M.S. Araújo, Ecotoxicol. Environ. Restor. 2 (1999) 41.
[22] D.J. Finney, Probit Analysis, Cambridge University Press, Cambridge, 1971.
[23] M. Joseph, A. Sreekanth, V. Suni, M.R. Prathapachandra Kurup, Spectrochim. Acta Part A 64 (2006) 637.
[24] A.S. Dobek, D.L. Klayman, J.P. Scovill, E.T. Dickson Jr., J. Chemother. 32 (1986) 25.
[25] A.P. Rebolledo, M. Vieites, D. Gambino, O.E. Piro, E.E. Castellano, C.L. Zani, E.M. Souza-Fagundes, L.R. Teixeira, A.A. Batista, H. Beraldo, J. Inorg. Biochem. 99 (2005) 698.
[26] A.P. Rebolledo, G.M. De Lima, L.N. Gambi, N.L. Speziali, D.F. Maia, C.B. Pinheiro, J.D. Ardisson, M.E. Corte's, H. Beraldo, Appl. Organometal. Chem. 17 (2003) 945.
[27] R.F.F. Costa, A.P. Rebolledo, T. Matencio, H.D.R. Calado, J.D. Ardisson, M.E. Cortès, B.L. Rodrigues, H. Beraldo, J. Coord. Chem. 58 (2005) 1307.
[28] A. Sreekanth, M.R. Prathapachandra Kurup, Polyhedron 23 (2004) 969.
[29] A. Sreekanth, Hoong-Kun Fun, M.R. Prathapachandra Kurup, J. Mol. Struct. 737 (2005) 61.
[30] L.P. Santos Pimenta, G.B. Pinto, J.A. Takahashi, L.G.F. Silva, M.A.D. Boaventura, Phytomedicine 10 (2003) 209.
[31] D.C. Ware, B.D. Palmer, W.R. Wilson, W.A. Denny, J. Med. Chem. 36 (1993) 1839.

Available online at www.sciencedirect.com
ScienceDirect
Polyhedron 27 (2008) 552–558
POLYHEDRON
www.elsevier.com/locate/poly

Synthesis, crystal structure, electrochemical and magnetic properties of $(NBu_4)[ReCl_5(L)]$ with L = pyrimidine and pyridazine

Livia Arizaga [a], Ricardo González [a], Raúl Chiozzone [a,*], Carlos Kremer [a], María Fernanda Cerdá [b], Donatella Armentano [c], Giovanni De Munno [c], Francesc Lloret [d], Juan Faus [d]

[a] Cátedra de Química Inorgánica, Facultad de Química, Universidad de la República, Avda. Gral. Flores 2124, CC 1157 Montevideo, Uruguay
[b] Laboratorio de Biomateriales, Facultad de Ciencias, Universidad de la República, Iguá 4225, Montevideo, Uruguay
[c] Dipartimento di Chimica, Università della Calabria, via P. Bucci 14/c, 87036 Rende, Cosenza, Italy
[d] Departamento de Química Inorgánica/Instituto de Ciencia Molecular, Facultad de Química, Universidad de Valencia, Dr. Moliner 50, 46100 Burjassot, Valencia, Spain

Received 5 June 2007; accepted 6 October 2007
Available online 19 November 2007

Abstract

Two novel rhenium(IV) compounds, namely $(NBu_4)[ReCl_5(pym)]$ (**1**) and $(NBu_4)[ReCl_5(pyd)]$ (**2**) (pym = pyrimidine, pyd = pyridazine and NBu_4 = *n*-tetrabutylammonium cation), have been obtained by reaction of $[ReCl_6]^{2-}$ and the diazine in dmf, and their crystal structures determined by single-crystal X-ray diffraction. The structures of **1** and **2** consist of $[ReCl_5(pym)]^-$ or $[ReCl_5(pyd)]^-$ anions and NBu_4^+ cations held together by electrostatic forces and van der Waals interactions. Stacking interactions are present only in **1**. The coordination sphere of the Re^{IV} ion is defined by five chloride anions and one nitrogen atom of a monodentate diazine, resulting in a distorted octahedral environment. Voltammetric profiles in CH_3CN show a one-electron reduction step at ca. −0.5 V vs. NHE for both complexes. Magnetic measurements reveal weak antiferromagnetic interactions among the metal centers in the crystal lattices of **1** and **2**, superimposed to the well-known zero-field splitting of Re(IV) compounds.
© 2007 Elsevier Ltd. All rights reserved.

Keywords: Rhenium(IV) complexes; Pyrimidine and piridazine; X-ray structure; Cyclic voltammetry; Magnetic properties

1. Introduction

In recent years it has been reported the synthesis of several new coordination compounds of Re^{IV} by ligand substitution onto $[ReX_6]^{2-}$ (X = Cl, Br) [1–6]. Some of these mononuclear complexes can in turn act as ligands towards other transition metal ions, leading to structurally diverse heterometallic compounds with interesting magnetic properties [1a–3,7].

Two aspects related to the use of $[ReX_6]^{2-}$ precursors in synthetic work have required some attention. First, Re(IV) complexes are inert to substitution, and then the full exchange of the halide ligands is commonly hindered. For example, the reaction of $[ReX_6]^{2-}$ with the bidentate O-donor ligands oxalato (ox) or malonato (mal) in refluxing 2-propanol or hot dmf leads to $[ReX_4(O^{\frown}O)]^{2-}$ ($O^{\frown}O$ = ox, mal) and $[ReX_2(O^{\frown}O)_2]^{2-}$ ($O^{\frown}O$ = ox), but never $[Re(O^{\frown}O)_3]^{2-}$ [1,2]. A similar situation is observed with the bidentate N-donor ligand 2,2′-bipyrimidine (bpym), where only the neutral species $[ReX_4(N^{\frown}N)]$ have been isolated [5]. The complete substitution of chloride ligands has been only reported for the synthesis of $[Re(CN)_7]^{3-}$ in dmf with a huge excess of $(NBu_4)CN$ [6] and of $[Re(NCS)_6]^{2-}$ in molten KNCS [8].

Second, the compounds $[ReX_4(N^{\frown}N)]$ can be easily reduced to $[ReX_4(N^{\frown}N)]^-$ in CH_3CN or dmf, but the analogous reduction of $[ReX_4(O^{\frown}O)]^{2-}$ was not evidenced.

* Corresponding author. Fax: +5982 9241906.
E-mail address: rchiozzo@fq.edu.uy (R. Chiozzone).

0277-5387/$ - see front matter © 2007 Elsevier Ltd. All rights reserved.
doi:10.1016/j.poly.2007.10.009



pym pyd

Scheme 1.

This fact agrees with a higher affinity of Re^{III} respect to Re^{IV} for bpym, as indicated by the Re–N bond distances in this family of compounds, and reflects the π-accepting ability of the ligand.

In this work, we explore the possibilities of synthesizing new Re(IV) complexes with the ligands pyrimidine (pym) and pyridazine (pyd), which are structurally related to bpym (Scheme 1). These diazines were studied by several authors as potentially bent-bridging ligands and, in many compounds where bridging was observed, their magnetic properties have also been investigated [9,10].

Here, we report the synthesis and crystal structure of the two novel complexes, $(NBu_4)[ReCl_5(pym)]$ (**1**) and $(NBu_4)[ReCl_5(pyd)]$ (**2**). Also, we present the results of our investigations into their electrochemical behaviour and their magnetic properties.

2. Experimental

2.1. General procedure

All reagents were used as received from commercial sources. Potassium hexachlororhenate was prepared from $KReO_4$ following the literature procedure [11]. Solvents were dried by standard methods when necessary. *N*,*N*-dimethylformamide (dmf) was stored with Linde type 4 Å molecular sieves before use.

Infrared spectra were recorded with a Bomen MB 102 FTIR spectrophotometer as KBr pellets in the 4000–200 cm^{-1} region. UV–Vis spectra were recorded with a Shimadzu UV-1603 spectrophotometer in CH_3CN.

The voltammetric profile of the systems were evaluated in CH_3CN with tetraethylammonium perchlorate 0.04 M as supporting electrolyte. The analysed solutions were 1 mM in the Re^{IV} complexes and 1 mM in the ligands. Voltammetric measurements were carried out in a one compartment conic cell, using a polycrystalline (pc) Au disc (3 mm diameter) as working electrode, a Pt sheet as counter electrode and an $Ag/AgNO_3$ 0.1 M in the supporting electrolyte ($E = 0.60$ V vs. NHE) as the reference. Two different electrochemical routines were applied: (a) cyclic voltammetry run at scan rates v varying between $0.005\ V\ s^{-1} \leqslant v \leqslant 0.10\ V\ s^{-1}$ from a cathodic switching potential $E_c = -0.85$ V to an anodic switching potential $E_a = +1.20$ V, and (b) repetitive triangular potential scans at $v = 0.05\ V\ s^{-1}$ with either constant E_c and gradual changes of E_a or constant E_a and gradual changes of E_c.

The magnetic measurements on polycrystalline samples were carried out with a Quantum Design SQUID magnetometer in the temperature range 1.9–300 K and under an applied magnetic field of 1 T ($T > 25$ K) and 250 G ($T < 25$ K) to avoid any problem of magnetic saturation. The device was calibrated with $(NH_4)_2Mn(SO_4)_2 \cdot 6H_2O$. Diamagnetic corrections of the constituent atoms were estimated from Pascal's constants.

2.2. Preparation of $(NBu_4)[ReCl_5(pym)]$ (1)

K_2ReCl_6 (72 mg, 0.15 mmol) and pym (120 mg, 1.5 mmol) were stirred in dmf (1 mL) for 5 h at 125 °C. After cooling the solution was filtered and evaporated at 60 °C until complete elimination of the solvent. The residue was extracted with 10 mL of CH_3CN/MeOH (1:1, v/v) and $(NBu_4)Cl$ (50 mg, 0.18 mmol) was added. Any undissolved material was removed by filtration if necessary. The filtrate was allowed to evaporate slowly, producing bright green crystals of **1** in 80% yield after 3 days. X-ray quality crystals were obtained directly from the mother liquors. Selected IR data [KBr, ν_{max}/cm^{-1}] 3088w, 1647w, 1594s, 1555m, 1407s, 1230m, 1174m, 817m, 699s, 641m, 367w, 349m, 312 vs. UV–Vis [CH_3CN, λ_{max}/nm ($\varepsilon/dm^3\ mol^{-1}\ cm^{-1}$)] 249 (6600), 285 (13 000), 639 (6), 666sh, 680 (7), 719sh, 737 (12). *Anal.* Calc. for $C_{20}H_{40}Cl_5N_3Re$: C, 35.0; H, 5.9; N, 6.1. Found: C, 34.6; H, 6.0; N, 5.9%.

2.3. Preparation of $(NBu_4)[ReCl_5(pyd)]$ (2)

Compound **2** was prepared in 40% yield by a similar procedure, replacing pyd for pym and stirring in dmf for 3 h. Selected IR data [KBr, ν_{max}/cm^{-1}] 3069w, 1641m, 1579w, 1567m, 1419s, 1289w, 964m, 778s, 679w, 641w, 425w, 385w, 344m, 312 vs. UV–Vis [CH_3CN, λ_{max}/nm ($\varepsilon/dm^3\ mol^{-1}\ cm^{-1}$)] 256 (7500), 284 (16 000), 636 (6), 669sh, 683 (7), 719sh, 740 (10). *Anal.* Calc. for $C_{20}H_{40}Cl_5N_3Re$: C, 35.0; H, 5.9; N, 6.1. Found: C, 34.6; H, 5.7; N, 6.0%.

2.4. Crystal structures determination and refinement

Suitable crystals were mounted on a Bruker-Nonius X8-APEXII CCD area detector system and used for data collection. Diffraction data were collected at room temperature, by using graphite-monochromated Mo Kα radiation ($\lambda = 0.71073$ Å). Unfortunately crystals of **2** are too small and not of good quality, diffracting very poorly at higher theta value than 21°. Furthermore, any of our attempt to grow more suitable crystals to perform a better structure determination than the reported one failed. Consequently, the data of **2** were collected with a shorter crystal-to-detector distance (40 mm) and an higher exposure time (30 s) respect to **1** (50 mm and 5 s, respectively). A total of 6317 (**1**) and 5063 (**2**) frames of data were collected using a narrow-frame method with scan widths of 0.3° in ω and ϕ (**1**–**2**). These data were processed through the SAINT [12] reduction and SADABS [13] absorption software to yield a total of 44 083 (**1**) and 33 891 (**2**) reflections. The unit cell

parameters were based upon least-squares refinement of 9588 (**1**) and 7176 (**2**) reflections. Information concerning crystallographic data collection and structure refinements is summarized in Table 1. The structures were solved by standard Patterson methods through the SHELXTL structure determination package [14] and subsequently completed by Fourier recycling. In the structure of compound **2** nitrogen atom N(2) shows large displacements in one direction suggesting that it is affected by thermal disorder. Also carbon atoms of the pyd ring in **2** result very disordered. Consequently, the better model has been found refining them isotropically and with restrains. Both structures show large thermal motion on chains of *n*-tetrabutylammonium as often found in other complexes containing this cation. The refinement was done with terminal carbon atoms of the butyl side chains C13–C16 and C17–C20 treated with restrains on C–C bond distances and C–C–C angles. All non-hydrogen atoms were refined anisotropically except carbon atoms of pyd ligand and C16, C17, C18, C19 and C20 atoms of cation in **2**. The hydrogen atoms were set in calculated positions and refined as riding atoms with a common fixed isotropically thermal parameter. Full-matrix least-squares refinements on F^2, carried out by minimizing the function $\Sigma w(|F_o| - |F_c|)^2$, reached convergence with values of the discrepancy indices given in Table 1. The final geometrical calculations were carried out with the PARST program [15]. The graphical manipulations were performed using the XP utility of the SHELXTL structure determination package. The main interatomic bond distances and angles are listed in Table 2 (**1**–**2**).

Table 1
Crystal data and structure refinement for $(NBu_4)[ReCl_5(pym)]$ (**1**) and $(NBu_4)[ReCl_5(pyd)]$ (**2**)[a]

Compound	**1**	**2**
Formula	$C_{20}H_{40}Cl_5N_3Re$	$C_{20}H_{40}Cl_5N_3Re$
Formula weight	686.00	686.00
Crystal system	triclinic	monoclinic
Space group	$P(\bar{1})$	$P2_1/n$
Z	2	4
a (Å)	8.863(1)	10.853(1)
b (Å)	10.546(1)	19.204(1)
c (Å)	10.402(2)	13.933(1)
α (°)	96.302(2)	90.0
β (°)	92.249(2)	104.280(2)
γ (°)	110.694(2)	90.0
V (Å^3)	1420.5(2)	2814.2(3)
D_c (g cm^{-3})	1.604	1.619
$F(000)$	682	1364
μ (mm^{-1})	4.759	4.805
Reflection collected/observed	44083/9842	33891/3114
Goodness-of-fit on F^2	1.064	1.208
R_1 $[I > 2\sigma(I)]$[b]	0.0185	0.0434
wR_2[c,d]	0.0425	0.1087
Largest difference in peak and hole (e Å^{-3})	0.622 and −0.794	1.535 and −0.852

[a] Details in common: $T = 293(2)$ K.
[b] $R_1 = \Sigma||F_o| - |F_c||/\Sigma|F_o|$.
[c] $wR_2 = \{\Sigma[w(F_o^2 - F_c^2)^2]/[(w(F_o^2))^2]\}^{1/2}$.
[d] $w = 1/[\sigma^2(F_o^2) + (aP)^2 + bP]$ *with* $P = [F_o^2 + 2F_c^2]/3$, $a = 0.0184$ (**1**) and 0.0303 (**2**), $b = 0.4528$ (**1**) and 24.3462 (**2**).

Table 2
Selected bond distances (Å) and angles (°) for compounds **1**–**2**[a]

	1 (L = pym)	**2** (L = pyd)
Re(1)–N(1)	2.170(2)	2.123(6)
Re(1)–Cl(1)	2.3420(5)	2.338(3)
Re(1)–Cl(2)	2.3434(6)	2.341(3)
Re(1)–Cl(3)	2.3131(6)	2.319(3)
Re(1)–Cl(4)	2.3455(5)	2.341(3)
Re(1)–Cl(5)	2.3436(5)	2.335(3)
N(1)–Re(1)–Cl(1)	87.85(4)	87.4(2)
N(1)–Re(1)–Cl(2)	87.16(5)	88.0(2)
N(1)–Re(1)–Cl(3)	179.29(4)	178.2(2)
N(1)–Re(1)–Cl(4)	87.02(4)	88.5(2)
N(1)–Re(1)–Cl(5)	87.27(4)	88.9(2)
Cl(1)–Re(1)–Cl(2)	90.23(2)	91.0(1)
Cl(1)–Re(1)–Cl(3)	92.44(2)	91.2(1)
Cl(1)–Re(1)–Cl(4)	174.83(2)	175.6(1)
Cl(1)–Re(1)–Cl(5)	90.35(2)	89.7(1)
Cl(2)–Re(1)–Cl(3)	93.49(3)	90.9(1)
Cl(2)–Re(1)–Cl(4)	88.94(2)	90.4(1)
Cl(2)–Re(1)–Cl(5)	174.37(2)	176.8(1)
Cl(3)–Re(1)–Cl(4)	92.70(2)	92.9(1)
Cl(3)–Re(1)–Cl(5)	92.07(3)	92.2(1)
Cl(4)–Re(1)–Cl(5)	89.98(2)	88.7(1)

[a] Estimated standard deviations in the last significant digits are given in parentheses.

3. Results and discussion

3.1. Description of the structures

Compounds **1** and **2** consist of discrete $[ReCl_5(L)]^-$ [where L = pym (**1**) or pyd (**2**)] anions and $[(n\text{-}C_4H_9)_4N]^+$ cations held together by means of electrostatic and van der Waals interactions. Stacking interactions between aromatic rings are observed only in **1**. A perspective drawing of the structures showing the atom numbering is depicted in Fig. 1, while selected bond lengths and angles are listed in Table 2. Each $[ReCl_5(L)]^-$ unit contains a Re(IV) atom in a distorted octahedral geometry, being bonded to a monodentate pym/pyd molecule and five chloride anions. The Re–N and the average Re–Cl bond distances [2.170(2) and 2.338(1) Å in **1** and 2.123(6) and 2.335(3) Å in **2**] are in agreement with those found in the literature [5,16–18]. The Re–Cl bond lengths in *trans* position to the nitrogen donors are slightly shorter than those in *cis* position. The N(1), Cl(2), Cl(3), and Cl(5) set of atoms constitute the best equatorial plane around Re, the largest deviation from planarity being 0.006(1) and 0.023(3) Å at N(1) in **1** and **2**, respectively. The Re atom is 0.0110(4) Å out of this plane in **1** and practically placed in plane in **2**. The pyrimidine/pyridazine ring is planar and the C–C and C–N bond lengths are as expected. The dihedral angle between the pyrimidine/pyridazine mean plane and the equatorial one are 45.5(1)° and 38.5(4)° in **1** and **2**, respectively.

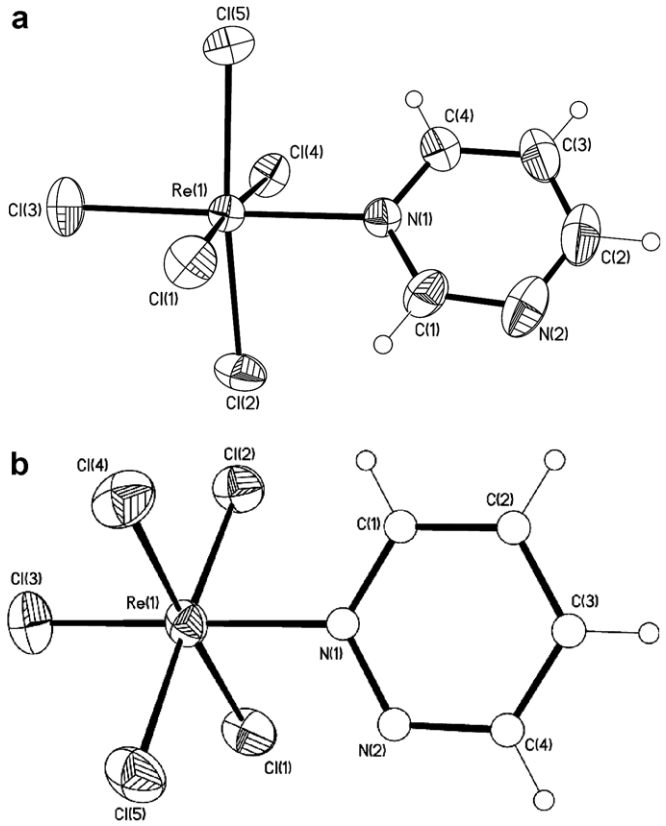


Fig. 1. Perspective drawing of the anionic $[ReCl_5(pym)]^-$ unit in **1** (a) and the $[ReCl_5(pyd)]^-$ unit in **2** (b) showing the atom numbering scheme. Thermal ellipsoids are drawn at 30% of probability level.

In compound **1**, the $[ReCl_5(pym)]^-$ anions show short Cl···Cl distances between them of 4.361(1) Å [Cl(5)···Cl(2a); (a) $= x+1, y, z$] that define chains developing along x axes, with a related Re(1)···Re(1a) distance of 8.863(1) Å. Adjacent chains of anions are packed through π–π interactions which take place between pyrimidine rings with an interplanar distance of 3.63 Å and an efficiency of overlap of about 60% (Fig. 2). The Re···Re distance between these stacked units is 8.517(1) Å [Re(1)···Re(1b); (b) $= -x+1, -y+1, -z+1$], the shortest observed in the structure. The resulting compound could be viewed as pairs of chains intercalating $[(n\text{-}C_4H_9)_4N]^+$ cations.

In compound **2**, even if there are aromatic groups no π–π interactions are present and anions are packed through weak forces. Also in **2** there are short Cl···Cl distances between $[ReCl_5(pyd)]^-$ units of 4.627(1) Å [Cl(1)···Cl(5a); (a) $= -x+1, -y, -z+1$] that lead to *pseudo*-dimers, as shown in Fig. 3, lying on layers intercalated by $[(n\text{-}C_4H_9)_4N]^+$ cations. The value of Re(1)···Re(1a) distance within dimers is 7.206(1) Å and corresponds to the shortest Re···Re distance observed in compound **2**. The pseudo-dimers anions have four nearest complex ions, with rhenium–rhenium distances of 9.020(1) Å.

The distances and angles of each tetrahedral $[(n\text{-}C_4H_9)_4N]^+$ cations in **1** and **2** are as expected. The scatter in the N–C and C–C distances and in the N–C–C and C–C–C angles doubtless arises from the considerable thermal motion, which is quite a common feature observed in most of the crystals containing this organic cation.

3.2. Electrochemical studies

The voltammetric profiles for compounds **1** and **2** in CH_3CN solution are shown in Fig. 4. Both complexes exhibit an electron transfer controlled process for the Re^{IV}/Re^{III} redox couple at practically the same potential peak values. For the pyridazine complex, this couple is located at −0.48 V vs. NHE, showing a slow electron transfer electrochemical reaction with an asymmetry parameter higher than 0.5. The intensity current peak ratio (i_{pc}/i_{pa}) is smaller

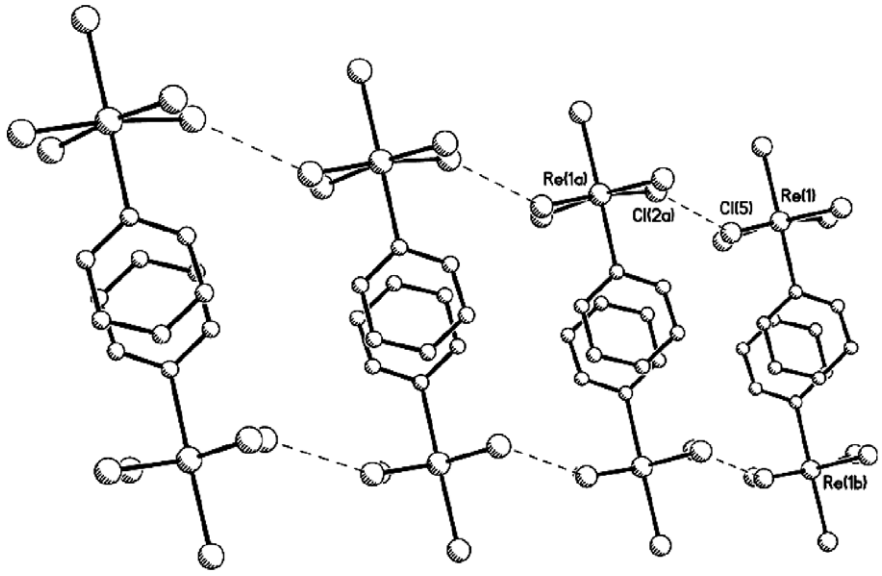


Fig. 2. Perspective view of the short Cl···Cl contacts (dotted lines) between anions and the stacking interactions between adjacent chains in **1**.

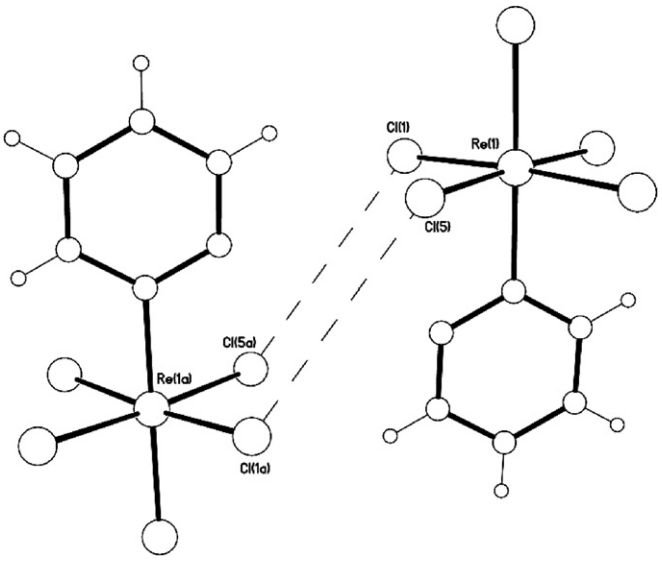


Fig. 3. View of the short Cl···Cl contacts (dotted lines) between anions in **2**.

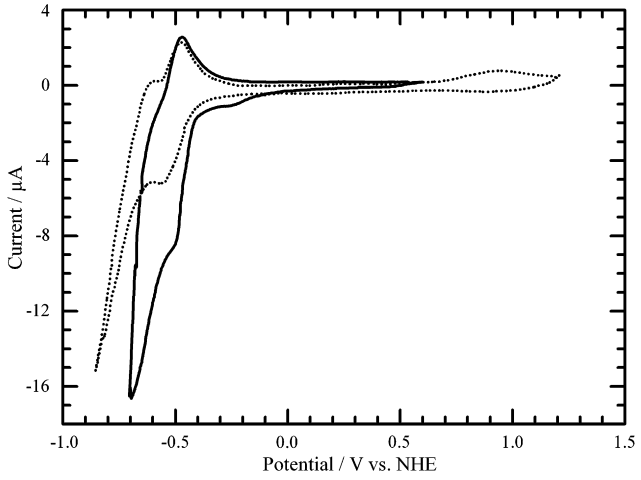


Fig. 4. Voltammetric profile of Au-pc in 1 mM $[ReCl_5(pym)]^-$ (solid line) and $[ReCl_5(pyd)]^-$ (dotted line) in 0.04 M tetraethylammonium perchlorate in acetonitrile at $v = 0.050$ V s^{-1}.

than 1, the potential peak value difference ($E_{pa} - E_{pc}$) is higher than 0.06 V, and the anodic potential peak E_{pa} shifts with ln v (slope = 0.010 V decade^{-1}) with an important overlapping with the contributions coming from the ligand-supporting electrolyte-solvent system. Moreover, the electron transfer is so slow that for $v < 0.010$ V s^{-1} the cathodic contribution is not detected. In addition, the electroactive species diffuses onto the electrode, as assessed by the linear relationship between i_{pa} and $v^{1/2}$.

For the pyrimidine complex, the Re^{IV}/Re^{III} couple is located at –0.50 V vs. NHE, with $\Delta E_p = 0.10$ V. The potential peak values for the anodic and cathodic contributions are the same for all v. The process is electron transfer controlled and involves the diffusion of the electroactive species. In addition, due to the overlapping with the contributions from the ligand-supporting electrolyte-solvent system, it is not possible to quantify the intensity of the related cathodic contribution.

Cyclic voltammetry in the same experimental conditions shows that the compound $(NBu_4)_2[ReCl_6]$ is not reduced to Re^{III} within the applied potentials range. Also, it is worthwhile to recall that for $[ReCl_4(bpym)]$ in CH_3CN, a reversible Re^{IV}/Re^{III} couple was located at more positive potential peak values ($E'^{\circ} = +0.19$ V vs. NHE) [5].

3.3. Magnetic properties

The magnetic properties of both complexes under the form of $\chi_m T$ vs. T plot (χ_m being the molar magnetic susceptibility) are shown in Fig. 5. At room temperature, the values of $\chi_m T$ are 1.51 and 1.55 cm^3 mol^{-1} K for **1** and **2**, respectively, as expected for non-interacting Re^{IV} ions ($S = 3/2$) with $g \approx 1.8$. Upon cooling, the curves remain practically constant down to until $T = 100$ K and then decrease at lower temperatures to reach values of 0.48 (**1**) and 0.72 cm^3 mol^{-1} K (**2**) at 1.9 K. No maximum of susceptibility is observed for **1** or **2** in the temperature range studied.

This behaviour could be attributed to zero-field splitting, that has been previously shown to be very important for Re^{IV} in pseudo-octahedral environments. However, the $\chi_m T$ values at 1.9 K are smaller than the expected for a magnetically diluted mononuclear Re^{IV} complexes (ca. 0.9 cm^3 mol^{-1} K) which would support the occurrence of noticeable antiferromagnetic interaction between the spin carriers.

Thus, we have analysed the magnetic data through the theoretical expressions for the magnetic susceptibility according to Eq. (1b) derived from the Hamiltonian in Eq. (1a) [19]:

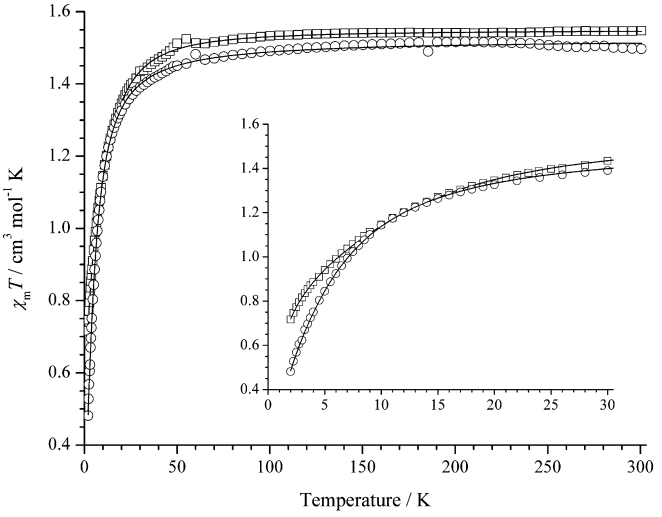


Fig. 5. Thermal dependence of $\chi_m T$ for **1** (circles) and **2** (squares). The solid lines are the calculated curves (see text).

$$\mathbf{H} = D[\mathbf{S}_z^2 - S(S+1)/3] + g_{//}\mu_B H_z \mathbf{S}_z + g_\perp \mu_B (H_x \mathbf{S}_x + H_y \mathbf{S}_y) \quad (1a)$$

$$\chi_{//} = \frac{N\mu_B^2 g_{//}^2}{4k(T-\theta)} \frac{1 + 9\exp(-2D/kT)}{1 + \exp(-2D/kT)}$$
$$\chi_\perp = \frac{N\mu_B^2 g_\perp^2}{k(T-\theta)} \frac{1 + (3kT/4D)[1 - \exp(-2D/kT)]}{1 + \exp(-2D/kT)} \quad (1b)$$
$$\chi_m = \frac{\chi_{//} + 2\chi_\perp}{3}$$

where $2D$ is the energy gap between $\pm 3/2$ and $\pm 1/2$ Kramers doublets, and a θ term has been added to account for magnetic coupling among the mononuclear units.

If θ is set to zero, the calculated curves do not match very well the experimental data, specially in the low temperature range. But when θ is included, and assuming $g_{//} = g_\perp = g$ in order to avoid overparametrization, an excellent agreement between experimental and calculated data is achieved. The best least-squares fit parameters are then $|2D| = 12.4(4)\ \mathrm{cm}^{-1}$, $g = 1.803(1)$, $\theta = -2.33(5)$ K and $R = 2.26 \times 10^{-5}$ for **1** and $|2D| = 28.2(2)\ \mathrm{cm}^{-1}$, $g = 1.818(1)$, $\theta = -0.75(1)$ K and $R = 0.82 \times 10^{-5}$ for **2** (R is the agreement factor defined as $\Sigma_i[(\chi_m T)_{obs}(i) - (\chi_m T)_{calc}(i)]^2 / \Sigma_i[(\chi_m T)_{obs}(i)]^2$).

4. Conclusions

The reaction of $[ReCl_6]^{2-}$ with an excess of pym or pyd in hot dmf leads to the monosubstituted anions $[ReCl_5(pym)]^-$ and $[ReCl_5(pyd)]^-$, respectively, which can be isolated as tetrabutylammonium salts. No further chloride substitution was observed in our studies.

Voltammetric profiles in CH_3CN show that both complexes can be electrochemically reduced, the quasi reversible Re^{IV}/Re^{III} couples being located at -0.50 V (**1**) and -0.48 V (**2**). These results suggest that so long as N-donor π-acceptor ligands contribute to stabilizing Re^{III} with respect to Re^{IV}, the higher the number of Re^{IV}–N bonds, the more oxidant the complex is.

Finally, compounds **1** and **2** have very similar magnetic behaviours. The thermal variation of the product $\chi_m T$ can be mainly attributed to the large zero-field splitting of Re^{IV}. In addition, the separations between the anions in the lattices make possible some weak antiferromagnetic interactions. The magnitude of these interactions given by the θ values can be roughly related to the Cl···Cl intermolecular distances in the crystal.

Acknowledgements

The authors thank the finantial support from the Comisión Sectorial de Investigación Científica (Project 290) and the Programa de Desarrollo de Ciencias Básicas (Uruguay), the EU (Project QueMolNa MRTN-CT-2003-504880), the Ministerio Español de Educación y Ciencia (Project CTQU2004-03633) and the Italian Ministero dell'Istruzione, dell'Università e della Ricerca.

Appendix A. Supplementary material

CCDC 642871 and 642872 contains the supplementary crystallographic data for **1** and **2**. These data can be obtained free of charge via http://www.ccdc.cam.ac.uk/conts/retrieving.html, or from the Cambridge Crystallographic Data Centre, 12 Union Road, Cambridge CB2 1EZ, UK; fax: (+44) 1223-336-033; or e-mail: deposit@ccdc.cam.ac.uk. Supplementary data associated with this article can be found, in the online version, at doi:10.1016/j.poly.2007.10.009.

References

[1] (a) R. Chiozzone, R. González, C. Kremer, G. De Munno, J. Cano, F. Lloret, M. Julve, J. Faus, Inorg. Chem. 38 (1999) 4745;
(b) A. Tomkiewicz, T.J. Bartczak, R. Kruszynski, J. Mrozinski, J. Mol. Struct. 595 (2001) 225;
(c) R. Chiozzone, A. Cuevas, R. González, C. Kremer, D. Armentano, G. De Munno, J. Faus, Inorg. Chim. Acta 359 (2006) 2194.
[2] A. Cuevas, R. Chiozzone, C. Kremer, L. Suescun, A. Mombrú, D. Armentano, G. De Munno, F. Lloret, J. Cano, J. Faus, Inorg. Chem. 43 (2004) 7823.
[3] A. Cuevas, C. Kremer, M. Hummert, H. Schumann, F. Lloret, M. Julve, J. Faus, Dalton Trans. (2007) 342.
[4] J. Martínez-Lillo, D. Armentano, G. De Munno, F. Lloret, M. Julve, J. Faus, Inorg. Chim. Acta 359 (2006) 3291.
[5] R. Chiozzone, R. González, C. Kremer, M.F. Cerdá, D. Armentano, G. De Munno, J. Martínez-Lillo, J. Faus, Dalton Trans. (2007) 653.
[6] M.V. Bennett, J.R. Long, J. Am. Chem. Soc. 125 (2003) 2394.
[7] (a) R. Chiozzone, R. González, C. Kremer, G. De Munno, D. Armentano, J. Cano, F. Lloret, M. Julve, J. Faus, Inorg. Chem. 40 (2001) 4242;
(b) R. Chiozzone, R. Gonzalez, C. Kremer, G. De Munno, D. Armentano, F. Lloret, M. Julve, J. Faus, Inorg. Chem. 42 (2003) 1064;
(c) J. Martínez-Lillo, D. Armentano, G. De Munno, W. Wernsdorfer, M. Julve, F. Lloret, J. Faus, J. Am. Chem. Soc. 128 (2006) 14218.
[8] R.A. Bailey, S.L. Kozak, Inorg. Chem. 6 (1967) 419.
[9] (a) Z.N. Chen, J. Qiu, W.X. Tang, K.B. Yu, Inorg. Chim. Acta 224 (1994) 171;
(b) T. Ishida, T. Nogami, Recent Res. Dev. Pure Appl. Chem. (1997) 1;
(c) F. Lloret, M. Julve, J. Cano, G. De Munno, Mol. Cryst. Liq. Cryst. 334 (1999) 569;
(d) T. Ishida, S. Mitsubori, T. Nogami, N. Takeda, M. Ishikawa, H. Iwamura, Inorg. Chem. 40 (2001) 7059;
(e) Y. Doi, T. Ishida, T. Nogami, Bull. Chem. Soc. Japan 75 (2002) 2455;
(f) V. Niel, A. Galet, A.B. Gaspar, M.C. Muñoz, J.A. Real, Chem. Commun. (2003) 1248;
(g) F.S. Delgado, J. Sanchiz, C. Ruiz-Pérez, F. Lloret, M. Julve, Cryst. Eng. Commun. 5 (2003) 280;
(h) J.L. Manson, J. Gu, J.A. Schlueter, H.-H. Wang, Inorg. Chem. 42 (2003) 3950;
(i) J.L. Manson, T. Lancaster, L.C. Chapon, S.J. Blundell, J.A. Schlueter, M.L. Brooks, F.L. Pratt, C.L. Nygren, J.S. Qualls, Inorg. Chem. 44 (2005) 989.
[10] (a) T. Otieno, S.J. Rettig, R.C. Thompson, J. Trotter, Inorg. Chem. 34 (1995) 1718;
(b) J. Cano, G. De Munno, F. Lloret, M. Julve, Inorg. Chem. 39 (2000) 1611;
(c) A. Escuer, R. Vicente, F.A. Mautner, M.A.S. Goher, M.A.M. Abu-Youssef, Chem. Commun. (2002) 64.
[11] C.L. Rulfs, R.J. Meyer, J. Am. Chem. Soc. 77 (1955) 4505.
[12] SAINT - Version 6.45 Copyright (c) Bruker Analytical X-ray Systems, Madison 2003.

[13] G.M. Sheldrick, SADABS Program for Absorption Correction, Version 2.10, Analytical X-ray Systems, Madison 2003.
[14] SHELXTL, Bruker Analytical X-ray Instruments, Madison 1998.
[15] M. Nardelli, Comput. Chem. 7 (1983) 95.
[16] (a) W.A. Herrmann, W.R. Thiel, E. Herdtweck, Chem. Ber. 123 (1990) 271;
(b) B. Machura, J.O. Dzięgielewski, R. Kruszynski, T.J. Bartczak, J. Kusz, Polyhedron 22 (2003) 2573.
[17] C. Pearson, A.L. Beauchamp, Inorg. Chem. 37 (1998) 1242.
[18] J. Mroziński, A. Kochel, T. Lis, J. Mol. Struct. 610 (2002) 53.
[19] (a) R.L. Carlin, Magnetochemistry, Springer, Berlin, 1986;
(b) O. Kahn, Molecular Magnetism, VCH, New York, 1993.

Available online at www.sciencedirect.com
ScienceDirect
Polyhedron 27 (2008) 559–573
POLYHEDRON
www.elsevier.com/locate/poly

Syntheses, crystal structures and magnetic properties of mono- and polynuclear [bis(2-arylcarbonyl)amidate]copper(II) complexes

Danielle Cangussu de Castro Gomes [a,b], Luminita Marilena Toma [b], Humberto O. Stumpf [a], Harry Adams [c], Jim A. Thomas [c], Francesc Lloret [b], Miguel Julve [b,*]

[a] *Departamento de Química, ICEX, Universidade Federal de Minas, Gerais, Av. Antônio Carlos 6627, Belo Horizonte-MG, 31270-901, Brazil*
[b] *Departament de Química Inorgànical Instituto de Ciencia, Molecular, Universitat de València, Polígono La Coma s/n, 46980 Paterna (València), Spain*
[c] *Department of Chemistry, Daiton Building, University of Sheffield, Brook Hill, Sheffield S3 7HF, United Kingdom*

Received 24 July 2007; accepted 7 October 2007
Available online 28 November 2007

Abstract

Five copper(II) complexes of formulas [Cu(bpcam)(CN)(H_2O)] (**1**), [Cu(bpcam)(N_3)(H_2O)]$_2$ (**2**), [Cu(bpcam)(NCS)(H_2O)] (**3**), [Cu(bpcam)(dca)(H_2O)]$_2$ (**4**) and [Cu(bpca)(tcm)]$_n$ (**5**) [bpcam = bis(2-pyrimidylcarbonyl)amidate, bpca = bis(2-pyridylcarbonyl)amidate, dca = dicyanamide and tcm = tricyanomethanide] have been prepared and their structures determined by single crystal X-ray diffraction. Compounds **1** and **3** are mononuclear species where each copper atom is five coordinated with a tridentate bpcam and a terminally bound cyanide (**1**)/thiocyanate (**3**) ligands creating a basal plane with a water molecule in the axial position of a distorted square pyramid. Compound **2** is made of neutral di-μ-1,1-azidobis[(aqua)(bpcam)copper(II)] dinuclear and aqua(azido)(bpcam)copper(II) mononuclear units. The copper–copper separation in the dinuclear entity is 3.730(5) Å. The structure of **4** consists of neutral di-μ-1,3-dcabis[(aqua)(bpcam)copper(II)] units, the intramolecular copper–copper distance being 5.701(3) Å. Compound **5** is a uniform copper(II) chain where the [Cu(bpca)]$^+$ units are connected through single μ-1,5-tcm bridges which link one equatorial position of a copper atom with the apical position of the adjacent copper. The intrachain copper–copper separation in **5** is 7.688(3) Å. Magnetic susceptibility measurements of **2**, **4** and **5** in the temperature range 1.9–295 K show the occurrence of weak antiferromagnetic interactions between the copper(II) ions, $J = -1.7$ (**2**), -0.53 (**4**) and -0.64 cm^{-1} (**5**) [the Hamiltonians used being defined as $\hat{H} = -J\hat{S}_1 \cdot \hat{S}_2$ (**2** and **4**) and $\hat{H} = -J\sum_i \hat{S}_i \cdot \hat{S}_{i+1}$ (**5**)].
© 2007 Elsevier Ltd. All rights reserved.

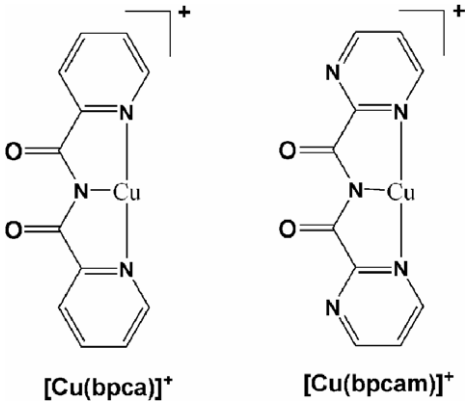
Keywords: Copper(II); Magnetism; Crystallography; Bridging ligands; Coordination chemistry

1. Introduction

Copper(II)-assisted hydrolysis of the substituted triazines 2,4,6-tris(2-pyridyl)-1,3,5-triazine (tpyt) and 2,4,6-tris(2-pyrimidyl)-1,3,5-triazine (tpymt) in mild conditions affords the highly stable [Cu(bpca)]$^+$ and [Cu(bpcam)]$^+$ species (see Scheme 1) where bpca and bpcam are the bis(2-pyridylcarbonyl)amidate and bis(2-pyrimidylcarbonyl)amidate anions, respectively. They were isolated and structurally characterized as the mononuclear complexes of formula [Cu(bpcam)(H_2O)$_n$]X · $p$$H_2O$ [$n = 2$ and $p = 3$ (X = ClO_4^-) and $n = 3$ and $p = 2$ (X = NO_3^-)] [1,2] and [Cu(bpca)(H_2O)$_2$]NO_3 · 2H_2O [3], where the tridentate bpcam and bpca groups and either two or three coordinated water molecules achieve the five- or six-coordination around the copper atoms. The facile replacement of these water molecules by potentially bridging ligands has allowed the preparation of homo- [2,4–8] and heterometallic [9,10]

* Corresponding author.
E-mail address: miguel.julve@uv.es (M. Julve).

0277-5387/$ - see front matter © 2007 Elsevier Ltd. All rights reserved.
doi:10.1016/j.poly.2007.10.017



Scheme 1.

polynuclear species exhibiting interesting magnetic properties. For instance, intramolecular ferromagnetic interactions were observed between the copper(II) ions through oxalate [5a,d,e] and 1,2-dithiosquarate (1,2-dtsq) [7] bridges and also between copper(II) and low-spin iron(III) ions across the cyanide bridge [10].

Additionally, the tridentate bpca ligand can also adopt a bidentate coordination through its two carbonyl-carbon atoms as illustrated for the first time by the copper(II) chain $[Cu(bpca)]ClO_4$ [11]. This result together with the fact that the bpca ligand is able to form mononuclear complexes $[M(bpca)_2]^{0/+}$ with di- [M = Mn^{II}, Fe^{II}, Ni^{II}, Cu^{II}, Zn^{II} and Rh^{II}] [12–16] and trivalent [M = Fe^{III} and Rh^{III}] [13,16,17] transition metal ions have allowed the preparation of variable-dimensionality magnetic compounds: homo- and heterotrimetallic complexes [14,18,19], single-chain magnets [20] and honeycomb layered materials [18b,21].

In the context of our previous magneto-structural studies with the bis(2-arylcarbonyl)amidatecopper(II) complexes as precursors of polynuclear species, we have now prepared five new compounds of formulas $[Cu(bpcam)(CN)(H_2O)]$ (**1**), $[Cu(bpcam)(N_3)(H_2O)]_2$ (**2**), $[Cu(bpcam)(NCS)(H_2O)]$ (**3**), $[Cu(bpcam)(dca)(H_2O)]_2$ (**4**) and $[Cu(bpca)(tcm)]_n$ (**5**), (dca = dicyanamide and tcm = tricyanomethanide). The syntheses and X-ray structures of **1**–**5** together with the investigation of the variable-temperature magnetic behaviour of **2**, **4** and **5** are included herein.

2. Experimental

2.1. Materials

The potassium salts of cyanide, thiocyanate and tricyanomethanide and the sodium salts of azide and dicyanamide were purchased from commercial sources and used as received. $[Cu(bpcam)(H_2O)_3]NO_3 \cdot 2H_2O$ and $[Cu(bpca)(H_2O)_2]NO_3 \cdot 2H_2O$ were prepared by the copper(II)-assisted hydrolysis of the tpymt and tptz ligands, respectively, as previously reported [1,3]. Elemental analysis (C, H, N) was conducted by the Microanalytical Service of the Universidad Autónoma de Madrid.

2.2. Synthesis

2.2.1. $[Cu(bpcam)(CN)(H_2O)]$ (1)

Single crystals of **1** as blue blocks were grown by slow diffusion in an H-shaped tube of aqueous solutions of $[Cu(bpcam)(H_2O)_3]NO_3 \cdot 2H_2O$ (0.094 g, 0.2 mmol) in one arm and KCN (0.013 g, 0.2 mmol) at the other one. The yield is practically quantitative after one month on standing in a hood at room temperature. *Anal.* Calc. for $C_{11}H_8CuN_6O_3$ (**1**): C, 39.36; H, 2.38; N, 25.03. Found: C, 39.19; H, 3.30; N, 29.91%.

2.2.2. $[Cu(bpcam)(N_3)(H_2O)]_2$ (2)

This compound is obtained as a polycrystalline blue solid by the reaction of aqueous solutions containing stoichiometric amounts of $[Cu(bpcam)(H_2O)_3]NO_3 \cdot 2H_2O$ and sodium azide. The yield is quantitative. X-ray quality crystals of **2** as blue blocks were grown by slow diffusion in an H-shaped tube of aqueous solutions of $[Cu(bpcam)(H_2O)_3]NO_3 \cdot 2H_2O$ (0.094 g, 0.2 mmol) in one arm and NaN_3 (0.013 g, 0.2 mmol) at the other arm. The yield is practically quantitative after one month. *Anal.* Calc. for $C_{10}H_8CuN_8O_3$ (**2**): C, 34.15; H, 2.28; N, 31.85. Found: C, 34.08; H, 2.23; N, 31.60%.

2.2.3. $[Cu(bpcam)(NCS)(H_2O)]$ (3)

X-ray quality crystals of **3** as blue plates were grown by slow diffusion in water as done for **1** and **2**, the starting chemicals being $[Cu(bpcam)(H_2O)_3]NO_3 \cdot 2H_2O$ (0.094 g, 0.2 mmol) and KSCN (0.019 g, 0.2 mmol). The yield is practically quantitative after three weeks. *Anal.* Calc. for $C_{11}H_8CuN_6O_3S$ (**3**): C, 35.93; H, 2.18; N, 22.84. Found: C, 35.81; H, 2.11; N, 22.73%.

2.2.4. $[Cu(bpcam)(dca)(H_2O)]_2$ (4)

Single crystals of **4** as blue blocks were grown by slow diffusion of aqueous solutions of $[Cu(bpcam)(H_2O)_3]NO_3 \cdot 2H_2O$ (0.094 g, 0.2 mmol) and Nadca (0.018 g, 0.2 mmol). The yield is practically quantitative after one month. *Anal.* Calc. for $C_{12}H_8CuN_8O_3$ (**4**): C, 38.36; H, 2.13; N, 29.81. Found: C, 38.25; H, 2.08; N, 29.72%.

2.2.5. $[Cu(bpca)(tcm)]_n$ (5)

The reaction of $[Cu(bpcam)]^+$ with tcm^- in water afforded crystals of [Cu(bpam)(tcm)] (**6**) which poorly diffract. Then, the corresponding system with bpca instead of bpcam was investigated and X-ray quality cystals of **5** as blue plates were grown by slow diffusion of aqueous solutions of $[Cu(bpca)(H_2O)_2]NO_3 \cdot 2H_2O$ (0.085 g, 0.200 mmol) and Ktcm (0.026 g, 0.100 mmol). The yield is practically quantitative after six weeks. *Anal.* Calc. for $C_{16}H_8CuN_6O_2$ (**5**): C, 50.61; H, 2.11; N, 22.12. Found: C, 50.53; H, 2.04; N, 22.05%.

2.3. Physical techniques

Infrared spectra of **1**–**5** were recorded with a Bruker IF S55 spectrophotometer as KBr pellets in the 4000–400 cm^{-1} region. The magnetic susceptibility measurements on polycrystalline samples of **2**, **4** and **5** were performed in the temperature range 1.9–295 K with a Quantum Design SQUID susceptometer, using an applied magnetic field of 1000 G. Diamagnetic corrections of the constituent atoms of **2**, **4** and **5** per mol of copper atoms were estimated from Pascal's constants [22] as -150×10^{-6} (**2**), -160×10^{-6} (**4**) and -168×10^{-6} cm^3 mol^{-1} (**5**). A value of 60×10^{-6} cm^3 mol^{-1} was used for the temperature-independent paramagnetism of the copper(II) ion.

2.4. X-ray data collection and structure refinement

Diffraction data for complexes **1**–**5** were collected with a Bruker Smart CCD area detector diffractometer equipped with Oxford Cryosystems low temperature system. Crystal parameters and refinement results are listed in Table 1. The reflections of **1**–**5** were measured from an hemisphere of data collected of frames each covering 0.3° in ω. They were corrected for Lorentz and polarisation effects and for absorption by semiempirical methods based on symmetry-equivalent and repeated reflections [minimum and maximum transmission coefficients 0.5724 and 0.8135 (**1**), 0.5342 and 0.7875 (**2**), 0.5131 and 0.8273 (**3**), 0.5116 and 0.5720 (**4**) and 0.5137 and 0.9411 (**5**)]. All five structures were solved by direct methods and refined by full-matrix least-squares methods on F^2. All non-hydrogen atoms were refined anisotropically. The hydrogen atoms were placed geometrically and refined with a riding model and with U_{iso} constrained to be 1.2 times U_{eq} of the carrier atom. The refinements for all reflections converged at final R/R_w values which are listed in Table 1. The values of the minimum and maximum final electron density peaks are −0.805 and 0.985 (**1**), −0.611 and 0.836 (**2**), −0.459 and 0.546 (**3**), −0.377 and 0.303 (**4**) and −0.923 and 0.909 e $Å^{-3}$ (**5**). A weighting scheme $w = 1/[\sigma(F_o)^2 + (mP)^2 + nP]$, where $P = (F_o + 2F_c^2)/3$ with $m = 0.0603$ (**1**), 0.0452 (**2**), 0.0486 (**3**), 0.0387 (**4**) and 0.0568 (**5**) and $n = 0.0000$ (**1**), 0.4605 (**2**), 0.0272 (**3**), 0.2182 (**4**) and 0.7295 (**5**), was used in the latter stages of refinement. Complex scattering factors were taken from the program package SHELXTL [23] as implemented on the Viglen Pentium computer. Selected bond lengths and angles are listed in Table 2 (**1**), Table 3 (**2**), Table 4 (**3**), Table 5 (**4**) and Table 6 (**5**).

3. Results and discussion

3.1. Synthesis and infrared spectra of 1–5

The tridentate coordination of the bpcam ligand to the copper(II) ion through the imido and two pyrimidine nitrogen atoms affords a very robust $[Cu(bpcam)]^+$ scaffold which has been used as a building block in the design of both homo- (**1**–**10**) and heterometallic (**11**) complexes (see

Table 1
Summary of crystal data and structure refinement for $[Cu(bpcam)(CN)(H_2O)]$ (**1**), $[Cu(bpcam)(N_3)(H_2O)]_2$ (**2**), $[Cu(bpcam)(NCS)(H_2O)]$ (**3**), $[Cu(bpcam)(dca)(H_2O)]_2$ (**4**), and $[Cu(bpca)(tcnm)(H_2O)]_n$ (**5**)[a]

Compound	**1**	**2**	**3**	**4**	**5**
Formula	$C_{11}H_8N_6O_3$	$C_{10}H_8CuN_8O_3$	$C_{11}H_8CuN_6O_3S$	$C_{12}H_8CuN_8O_3$	$C_{16}H_8CuN_6O_2$
Formula weight	335.77	351.78	367.83	375.80	379.82
Crystal system	triclinic	triclinic	triclinic	triclinic	monoclinic
Space group	$P(\bar{1})$	$P(\bar{1})$	$P(\bar{1})$	$P(\bar{1})$	$P2_1/c$
a (Å)	6.8545(11)	7.2122(13)	7.2453(15)	7.1779(6)	10.440(4)
b (Å)	11.749(2)	9.9625(18)	10.047(2)	10.0853(9)	18.517(7)
c (Å)	24.320(4)	18.469(3)	10.405(2)	10.9618(10)	7.688(3)
α (°)	80.111(3)	91.490(3)	109.550(3)	115.8010(10)	90
β (°)	88.587(3)	97.148(3)	103.913(3)	97.8520(10)	103.50(7)
γ (°)	73.418(3)	109.298(3)	96.683(3)	97.4050(10)	90
U ($Å^3$)	1848.5(5)	1239.5(4)	676.6(2)	691.77(11)	1444.9(10)
Z	6	4	2	2	4
D_c (Mg m^{-3})	1.810	1.885	1.806	1.804	1.746
μ(Mo Kα) (mm^{-1})	1.794	1.792	1.791	1.612	1.537
Maximum θ (°)	1.70–27.55	2.17–27.54	2.18–27.55	2.11–27.53	2.01–27.63
Reflections collected	21 286	13 978	5818	7733	15 705
Independent reflections	8276	5554	2574	3068	3287
R_{int}	0.0474	0.0563	0.0334	0.0215	0.0726
Reflect. [$I > 2\sigma(I)$]	6340	5253	5440	5440	6082
Data/restraints/parameters	8276/0/574	5554/0/397	2996/0/201	3068/0/217	3287/0/226
Goodness-of-fit on F^2	1.053	1.039	1.051	1.067	1.033
R [$I > 2\sigma(I)$]	0.0424	0.0381	0.0338	0.0245	0.0364
R_w [$I > 2\sigma(I)$]	0.01039	0.0916	0.0861	0.0659	0.0917
R (all data)	0.0673	0.0590	0.0411	0.0268	0.0637
R_w (all data)	0.1148	0.1007	0.0897	0.0670	0.1064

[a] Details in common: $T = 150(2)$ K and $\lambda = 0.71073$ Å.

Table 2
Selected bond lengths (Å) and angles (°) for [Cu(bpcam)(CN)(H_2O)] (**1**)

Copper coordination sphere					
Cu(1)–N(3B)	1.950(3)	Cu(1A)–N(3A)	1.956(3)	Cu(1B)–N(3)	1.948(3)
Cu(1)–C(11B)	1.963(4)	Cu(1A)–C(11A)	1.968(4)	Cu(1B)–C(11)	1.955(4)
Cu(1)–N(4B)	2.036(3)	Cu(1A)–N(4A)	2.014(3)	Cu(1B)–N(4)	2.023(3)
Cu(1)–N(1B)	2.036(3)	Cu(1A)–N(1A)	2.022(3)	Cu(1B)–N(1)	2.026(3)
Cu(1)–O(1WB)	2.250(2)	Cu(1A)–O(1WA)	2.259(3)	Cu(1B)–O(1W)	2.264(2)
N(3B)–Cu(1)–C(11B)	165.86(14)	N(3A)–Cu(1A)–C(11A)	170.89(14)	N(3)–Cu(1B)–C(11)	165.94(14)
N(3B)–Cu(1)–N(4B)	80.78(11)	N(3A)–Cu(1A)–N(4A)	80.81(11)	N(3)–Cu(1B)–N(4)	80.97(11)
C(11B)–Cu(1)–N(4B)	80.70(9)	C(11A)–Cu(1A)–N(4A)	98.89(13)	C(11)–Cu(1B)–N(4)	98.45(13)
N(3B)–Cu(1)–N(1B)	80.51(11)	N(3A)–Cu(1A)–N(1A)	80.65(11)	N(3)–Cu(1B)–N(1)	81.18(11)
C(11B)–Cu(1)–N(1B)	98.54(13)	C(11A)–Cu(1A)–N(1A)	98.00(13)	C(11)–Cu(1B)–N(1)	97.38(13)
N(4B)–Cu(1)–N(1B)	160.41(11)	N(4A)–Cu(1A)–N(1A)	159.38(12)	N(4)–Cu(1B)–N(1)	161.13(11)
N(3B)–Cu(1)–O(1WB)	95.23(10)	N(3A)–Cu(1A)–O(1WA)	92.41(10)	N(3)–Cu(1B)–O(1W)	95.94(10)
C(11B)–Cu(1)–O(1WB)	98.89(13)	C(11A)–Cu(1A)–O(1WA)	96.69(13)	C(11)–Cu(1B)–O(1W)	92.12(12)
N(4B)–Cu(1)–O(1WB)	97.19(10)	N(4A)–Cu(1A)–O(1WA)	94.11(10)	N(4)–Cu(1B)–O(1W)	92.83(10)
N(1B)–Cu(1)–O(1WB)	90.26(10)	N(1A)–Cu(1A)–O(1WA)	95.60(10)	N(1)–Cu(1B)–O(1W)	95.04(10)
Cyanide ligand					
N(6B)–C(11B)	1.140(4)	N(6A)–C(11A)	1.136(5)	N(6)–C(11)	1.139(4)
N(6B)–C(11B)–Cu(1)	179.1(4)	N(6A)–C(11A)–Cu(1A)	178.1(4)	N(6)–C(11)–Cu(1B)	177.9(3)

D–H···A	D–H (Å)	H···A (Å)	D···A (Å)
Hydrogen bonds[a,b]			
O(1W)–H(1W)···O(1)#1	0.85	2.21	2.847(3)
O(1W)–H(1W)···O(2)#1	0.85	2.29	3.048(3)
O(1W)–H(2W)···N(6)#2	0.85	2.06	2.823(4)
O(1WB)–H(1WB)···O(2A)#3	0.86	2.26	2.933(3)
O(1WB)–H(1WB)···O(1A)#3	0.86	2.28	3.022(3)
O(1WA)–H(1WA)···O(2B)#4	0.85	2.15	2.865(3)
O(1WA)–H(1WA)···O(1B)#4	0.85	2.31	3.015(3)
O(1WB)–H(2WB)···N(6A)	0.85	2.08	2.885(4)
O(1WA)–H(2WA)···N(6B)	0.85	2.01	2.849(4)

[a] D = donor and A = acceptor.
[b] Symmetry operations used to generate equivalent atoms: #1 = $-x+2$, $-y+1$, $-z$;#2 = $-x+2$, $-y$, $-z$; #3 = x, $y-1$, z; #4 = x, $y+1$, z.

Scheme 2) where the bpcam group acts as a terminal ligand. Its possible coordination modes as a bridge (either through the two carbonyl-carbon atoms and/or through each carbonyl-carbon atom and the adjacent free pyrimidine nitrogen) remain unknown in contrast to the situation for the related bpca ligand where the bridging mode as tridentate/bidentate (through the three nitrogen atoms at one side and through the two carbonyl-carbon atoms at the other side) has been established [11,18–21].

Mono- (**1**–**3** and **9**) and polynuclear (**2**, **4**, **6**–**8**, **10** and **11**) compounds are obtained depending on the coordination properties of the anion used to neutralize the positive charge of the $[Cu(bpcam)]^+$ unit and on the solubility of the neutral species resulting from the charge balance. The synthesis of **9** and **10**, both compounds being obtained as products from the same reaction, deserves a brief comment [2]. The latter is a dinuclear copper(II) complex with a μ-1,2-sulfate as a bridge whereas the former is an ionic salt with a monodentate sulfate in the anionic fragment. So, **9** can be viewed as the precursor of **10**: the removal of a coordinated water molecule from the $[Cu(bpcam)(H_2O)_2]^+$ cation followed by the subsequent coordination of the terminally bound sulfate from the $[Cu(bpcam)(H_2O)(SO_4)]^-$ anion would afford compound **10**. In the present work, the insolubility of the neutral compounds **1** and **3** in water [with cyanide (**1**) and thiocyanate (**3**) acting as terminal ligands] precludes any polymerization. Curiously, the neutral [Cu(bpcam)(N_3)(H_2O)] (mononuclear) and [Cu(bpcam)(N_3)(H_2O)]$_2$ (dinuclear) species coexist in **2** with monodentate azide and di-μ-1,1-azide groups, respectively. Double μ-1,3-dca bridges occur in **4** leading to the neutral [Cu(bpcam)(dca)(H_2O)]$_2$ dinuclear complex. Finally, although the structure of [Cu(bpcam)(tcm)] (**6**) could not be solved, the determination of the crystal structure of the related bpca-containing complex (**5**) strongly supports the occurrence of a copper(II) chain with single μ-1,5-tcm bridges. The variation in the nuclearity of species **1**–**6** constitutes a suitable example to illustrate the difficulties associated with the structural predictions concerning neutral products when using ligands that can adopt both terminal and bridging coordination modes.

The infrared spectra of **1**–**6** all display a strong intensity peak at 1730–1720 (**1**–**4** and **6**) and 1715 (**5**) cm^{-1}; this indicates the presence of coordinated bpcam and bpca ligands [ν_{as}(CO)], respectively [1,2,11]. The high-frequency region of the ir spectra of **1**–**4** is dominated by strong and broad absorptions in the range 3500–3380 cm^{-1} [ν(OH) stretching vibration] which is due to the presence of coordinated

Table 3
Selected bond lengths (Å) and angles (°) for $[Cu(bpcam)(N_3)(H_2O)]_2$ (**2**)

Copper coordination sphere			
Cu(1A)–N(6A)	1.944(2)	Cu(1B)–N(2B)	1.947(2)
Cu(1A)–N(2A)	1.954(2)	Cu(1B)–N(6B)	1.954(2)
Cu(1A)–N(3A)	2.027(2)	Cu(1B)–N(1B)	2.026(2)
Cu(1A)–N(1A)	2.031(2)	Cu(1B)–N(3B)	2.040(2)
Cu(1A)–O(3A)	2.232(2)	Cu(1B)–N(6B)#1	2.896(5)
Cu(1B)–O(3B)	2.312(2)		
N(6A)–Cu(1A)–N(2A)	163.86(12)	N(2B)–Cu(1B)–N(6B)	166.15(11)
N(6A)–Cu(1A)–N(3A)	91.38(10)	N(2B)–Cu(1B)–N(1B)	81.21(9)
N(2A)–Cu(1A)–N(3A)	80.70(9)	N(6B)–Cu(1B)–N(1B)	104.68(10)
N(6A)–Cu(1A)–N(1A)	130.90(10)	N(2B)–Cu(1B)–N(3B)	80.77(9)
N(2A)–Cu(1A)–N(1A)	81.30(9)	N(6B)–Cu(1B)–N(3B)	92.52(10)
N(3A)–Cu(1A)–N(1A)	160.17(10)	N(1B)–Cu(1B)–N(3B)	161.89(9)
N(6A)–Cu(1A)–O(3A)	96.72(9)	N(2B)–Cu(1B)–O(3B)	95.01(8)
N(2A)–Cu(1A)–O(3A)	98.06(9)	N(6B)–Cu(1B)–O(3B)	97.52(10)
N(3A)–Cu(1A)–O(3A)	95.88(8)	N(1B)–Cu(1B)–O(3B)	89.71(8)
N(1A)–Cu(1A)–O(3A)	94.80(8)	N(3B)–Cu(1B)–O(3B)	93.70(8)
N6(B)#1–Cu(B)–N1(B)	89.1(4)		
N6(B)#1–Cu(B)–N2(B)	86.2(8)		
N6(B)#1–Cu(B)–N3(B)	87.8(5)		
N6(B)#1–Cu(B)–N6(B)	81.3(4)		
N6(B)#1–Cu(B)–O3(B)	178.1(2)		
Azide ligand			
N(6A)–N(7A)	1.199(3)	N(6B)–N(7B)	1.191(3)
N(7A)–N(8A)	1.154(3)	N(7B)–N(8B)	1.160(3)
N(8A)–N(7A)–N(6A)	176.2(3)	N(8B)–N(7B)–N(6B)	175.6(3)
N(7A)–N(6A)–Cu(1A)	130.2(2)	N(7B)–N(6B)–Cu(1B)	134.1(2)
Cu(1B)–N(6B)–Cu(1B)#1	98.6(6)		

D–H···A	D–H (Å)	H···A (Å)	D···A (Å)
Hydrogen bonds[a,b]			
O(3A)–H(3AA)···O(1A)#1	0.85	2.15	2.754(3)
O(3A)–H(3AA)···O(2A)#1	0.85	2.27	3.049(3)
O(3A)–H(3AB)···O(2A)#5	0.85	2.05	2.875(3)
O(3A)–H(3AB)···N(5A)#5	0.85	2.61	3.105(3)
O(3B)–H(3BA)···O(1B)#6	0.85	1.93	2.767(3)
O(3B)–H(3BB)···O(2B)#2	0.85	2.27	2.875(3)
O(3B)–H(3BB)···O(1B)#2	0.85	2.41	3.180(3)

[a] D = donor and A = acceptor.
[b] Symmetry operations used to generate equivalent atoms: #1 $1-x$, $-2-y$, $-z$; #2 $-x$, $1-y$, $-z$; #3 $x-1$, $2-y$, $1-z$; #4 $-x$, $1-y$, $1-z$; #5 $-1+x$, y, z; #6 $1+x$, y, z.

water molecules that are involved in hydrogen bonds. The C–N stretching frequency of 2150 cm^{-1}, which is observed in the ir spectrum of **1** as a weak absorption, agrees with the presence of a terminally bound cyanide. For the sake of comparison, this absorption appears 2136 and 2111 cm^{-1} in the ir spectra of the five-coordinated mononuclear copper(II) complexes $[Cu(phen)_2)(CN)]NO_3 \cdot H_2O$ [24] and $[Cu(tpa)(CN)]ClO_4 \cdot 3\ H_2O$ [25] [phen = 1,10-phenanthroline and tpa = tris(2-pyridylmethyl)amine] where the cyanide group acts as a terminal ligand. A strong peak at 2055 cm^{-1} in the ir spectrum of **2** corresponds to the ν_{as} stretching of the azide ligand. The shift to higher wavenumbers of this vibration when compared to the free azide (2133 cm^{-1} for sodium azide) indicates that it is coordinated to the copper atom [26]. The ν_s stretching of the azide (vibration which is ir active for the terminal or end-on bridging mode) that is predicted to occur near 1300 cm^{-1} could not be observed because this region is obscured for several absorptions of the bpcam or bpca ligands. The pattern of the vibrational modes of the thiocyanate ligand of **3** [2090s (ν_{CN}), 810m (ν_{CS}) and 495m cm^{-1} (δ_{NCS})] is indicative of thiocyanato-N coordination [27], as confirmed by the crystal structure. The ir spectrum of **4** shows three stretch frequencies in the 2300–2170 cm^{-1} region [sharp and strong peaks at 2295s ($\nu_{as} + \nu_s(C{\equiv}N)$), 2237 ($\nu_{as}(C{\equiv}N)$) and 2177 cm^{-1} ($\nu_s(C{\equiv}N)$)] which are close to those of the dca anion in its sodium salt (2286, 2232 and 2179 cm^{-1}, respectively). As the monodentate coordination of dca has been found to exert a minor influence on the values of the stretching vibrations of free dca [28], a monodentate coordination of dca in **4** can be inferred. This is consistent with the X-ray structure of **4** where dca is found

Table 4
Selected bond lengths (Å) and angles (°) for [Cu(bpcam)(NCS)(H_2O)] (**3**)

Copper coordination sphere			
Cu(1)–N(6)	1.926(2)	Cu(1)–N(1)	2.028(2)
Cu(1)–N(3)	1.9362(19)	Cu(1)–O(3)	2.2429(16)
Cu(1)–N(5)	2.0190(19)		
N(6)–Cu(1)–N(3)	167.43(8)	N(6)–Cu(1)–N(5)	98.44(9)
N(3)–Cu(1)–N(5)	81.03(8)	N(6)–Cu(1)–N(1)	97.21(9)
N(3)–Cu(1)–N(1)	81.39(8)	N(5)–Cu(1)–N(1)	161.09(8)
N(6)–Cu(1)–O(3)	95.18(8)	N(3)–Cu(1)–O(3)	97.39(7)
N(5)–Cu(1)–O(3)	92.39(7)	N(1)–Cu(1)–O(3)	96.70(7)
Thiocyanate ligand			
N(6)–C(11)	1.163(3)	S(2)–C(11)	1.624(2)
C(11)–N(6)–Cu(1)	169.6(2)	N(6)–C(11)–S(2)	179.3(2)
D–H···A	D–H (Å)	H···A (Å)	D···A (Å)
Hydrogen bonds[a,b]			
O(3)–H(32)···O(2)#1	0.85	1.95	2.765(2)
O(3)–H(31)···O(1)#2	0.85	2.11	2.789(2)
O(3)–H(31)···O(2)#2	0.85	2.38	3.117(2)

[a] D = donor and A = acceptor.
[b] Symmetry operations used to generate equivalent atoms: #1 $x-1$, y, z; #2 $-x+2$, $-y$, $-z+1$.

Table 5
Selected bond lengths (Å) and angles (°) for [Cu(bpcam)(dca)(H_2O)]$_2$ (**4**)

Copper coordination sphere			
Cu(1)–N(2)	1.9412(13)	Cu(1)–N(3)	2.0445(14)
Cu(1)–N(4)	1.9473(15)	Cu(1)–O(3)	2.2655(12)
Cu(1)–N(1)	2.0236(14)	Cu(1)–N(5)#3	2.817(2)
N(2)–Cu(1)–N(4)	170.16(6)	N(1)–Cu(1)–N(3)	161.37(6)
N(2)–Cu(1)–N(1)	81.09 (6)	N(2)–Cu(1)–O(3)	96.87(5)
N(4)–Cu(1)–N(1)	99.62(6)	N(4)–Cu(1)–O(3)	92.95(5)
N(2)–Cu(1)–N(3)	81.12(5)	N(1)–Cu(1)–O(3)	90.61(5)
N(4)–Cu(1)–N(3)	96.98(6)	N(3)–Cu(1)–O(3)	96.96(5)
N(5)#3-Cu(1)–N(1)	89.6(8)	N(5)#3-Cu(1)–N(2)	87.5(9)
N(5)#3-Cu(1)–N(3)	84.0(9)	N(5)#3-Cu(1)–N(4)	82.6(1)
N(5)#3-Cu(1)–O(3)	175.5(3)		
Dicyanamide ligand			
N(4)–C(11)	1.156(2)	N(5)–C(12)	1.321(3)
N(5)–C(11)	1.292(2)	N(6)–C(12)	1.149(2)
C(11)–N(4)–Cu(1)	165.22(15)	N(4)–C(11)–N(5)	172.57(19)
C(11)–N(5)–C(12)	122.76(16)	N(6)–C(12)–N(5)	173.11(18)
C(11)–N(5)–Cu(1)#3	110.9(0)		
D–H···A	D–H (Å)	H···A (Å)	D···A (Å)
Hydrogen bonds[a,b]			
O(3)–H(3A)···O(1)#1	0.84	1.92	2.7527(16)
O(3)–H(3AA)···O(2)#2	0.84	2.09	2.7751(16)
O(3)–H(3AA)···O(1)#2	0.84	2.42	3.1462(16)

[a] D = donor and A = acceptor.
[b] Symmetry operations used to generate equivalent atoms: #1 = $x-1$, y, z; #2 = $-x+2$, $-y$, $-z+1$; #3 = $1-x$, 2, $-y$, $2-z$.

to coordinate to the copper atom through one of its cyano nitrogen atoms. Finally, the presence of three strong intensity peaks at 2180, 2198 and 2251 cm^{-1} in the ir spectrum of **5** (2186, 2204 and 2256 cm^{-1} for **6**), which are asigned to ν_{CN} stretches of the tcm group [to be compared with the strong absorption at 2178 cm^{-1} for the free tricyanomethanide in its potassium salt), suggests the coordination of this ligand to the copper atom. This is confirmed by the structure of **5** where the tcm adopts the μ-1,5-bridging mode. The quasi identical ir pattern of tcm in **5** and **6** strongly supports the same coordination mode of this ligand in both species.

Table 6
Selected bond lengths (Å) and angles (°) for $[Cu(bpcam)(tcm)]_n$ (**5**)[a]

Copper coordination sphere			
Cu(1)–N(1)	2.006(2)	Cu(1)–N(5)#1	1.974(2)
Cu(1)–N(2)	1.946(2)	Cu(1)–N(4)	2.210(2)
Cu(1)–N(3)	1.996(2)		
N(1)–Cu(1)–N(2)	82.35(10)	N(2)–Cu(1)–N(5)#1	158.64(9)
N(1)–Cu(1)–N(3)	163.67(10)	N(2)–Cu(1)–N(4)	100.79(9)
N(1)–Cu(1)–N(5)#1	97.08(10)	N(3)–Cu(1)–N(5)#1	95.37(10)
N(1)–Cu(1)–N(4)	95.49(10)	N(3)–Cu(1)–N(4)	92.57(10)
N(2)–Cu(1)–N(3)	82.21(10)	N(4)–Cu(1)–N(5)#1	100.52(9)
Tcm ligand			
N(4)–C(13)	1.150(4)	N(5)–C(15)	1.148(3)
C(13)–C(14)	1.410(4)	C(14)–C(16)	1.419(4)
C(14)–C(15)	1.404(4)	N(6)–C(16)	1.150(3)
C(13)–N(4)–Cu(1)	160.2(2)	C(15)–C(14)–C(16)	120.1(2)
N(4)–C(13)–N(14)	176.4(3)	N(6)–C(16)–C(14)	178.3(3)
C(13)–C(14)–C(15)	120.5(3)	N(5)C(15)–C(14)	178.2(3)
C(13)–C(14)–C(16)	119.5(2)	C(15)#1–N(5)#1–Cu(1)	168.9(2)

[a] Symmetry operation used to generate equivalent atoms: #1 = x, y, $z+1$.

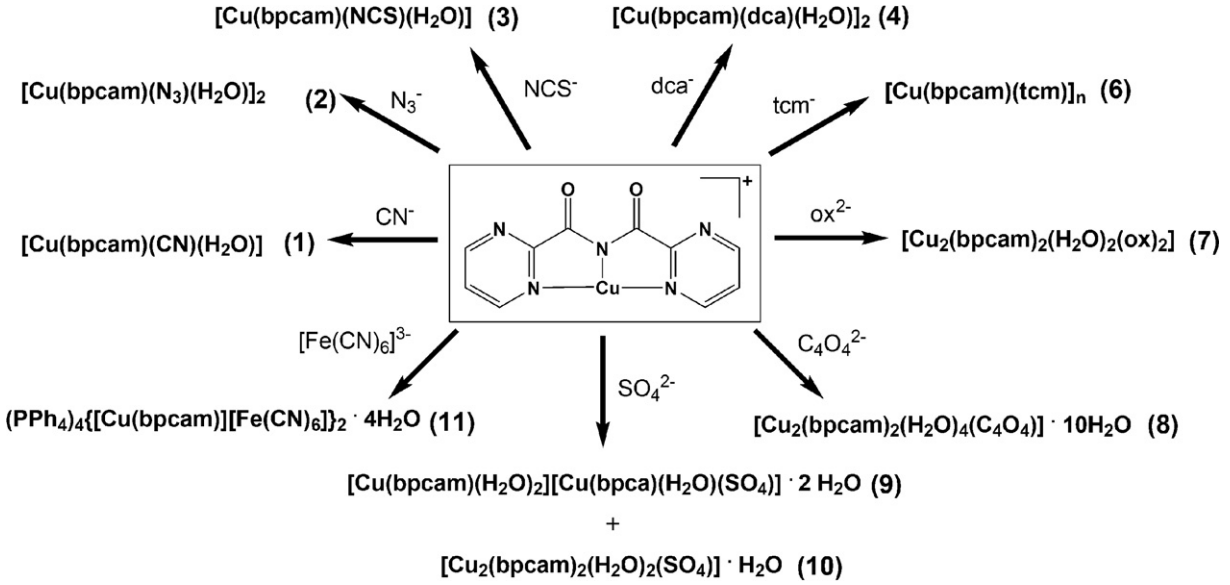
3.2. Description of the structures

3.2.1. [Cu(bpcam)(CN)(H$_2$O)] (1)

The structure of **1** is made up of three neutral and crystallographically independent [Cu(bpcam)(CN)(H_2O)] units (**I**–**III** in Fig. 1) which are interlinked through hydrogen bonds involving the water molecule, the cyanide-nitrogen atom and the two carbonyl-carbon atoms of the bpcam ligand (see end of Table 2). This leads to two types of chains of the copper(II) units through hydrogen bonds: one with regular alternating of **I** and **II** units and the other having only **III** as the repeating unit (Fig. 2).

The three crystallographically independent copper atoms [Cu(1) (**I**), Cu(1A) (**II**) and Cu(1B) (**III**)] exhibit a distorted square pyramidal surrounding, the values of the trigonality parameter τ being 0.01 (**I**), 0.20 (**II**) and 0.08 (**III**) ($\tau = 0$ and 1 for ideal square pyramid and trigonal bipyramid, respectively) [30]. The basal plane is formed by three nitrogen atoms from the tridentate bpcam ligand [Cu–N bonds varying in the range 1.948(3)–2.036(3) Å] and the cyanide-carbon atom [Cu–N = 1.955(4)–1.968(4) Å] whereas the apical position is filled by a water molecule [Cu–O_w = 2.250(2)–2.264(2) Å]. The values of the Cu–N distances agree with those observed in other bpcam-containing copper(II) complexes [1,2,5e,10]. The values of the bond length for the copper to cyanide carbon in **I**–**III** compare well with those observed in other five-coordinated cyano-containing copper(II) complexes: 1.94(1), 1.970(5) and 1.98(1) Å for $[Cu(phen)_2](CN)]NO_3 \cdot H_2O$ [24], $[Cu(phen)_2(CN)]tcm \cdot 2H_2O$ [29] and $[Cu(tpa)(CN)]ClO_4 \cdot 3H_2O$ [25], respectively. The angles in the basal plane are distorted from the ideal square-planar value mainly due to the constrained geometry of the tridentate bpcam ligand. So, the angles subtended at the copper atoms of **I**–**III** by the bpcam ligand vary in the range 80.51(11)–81.18(11)° evidencing the small bite size of the corresponding five-membered chelate rings. The copper atom is shifted by 0.1233 (**I**), 0.1877 (**II**), and 0.1269 Å (**III**) from the mean basal plane toward the axial water molecule. This significant out-of-plane displacement of the copper atom is accompanied by large deviations from the ideal value of 180° in the angles at the copper atom of the trans ligands [values varying in the range 159.38(12)–165.94(14)°].

The bond lengths and angles involving the cyanide ligand are all normal the C–N bond distance and C–N–Cu bond angle varying in the range 1.136(5)–1.140(4) Å and 177.9(3)–179.1(4)°, respectively]. The pyrimidyl rings of the bpcam ligand in **I**–**III** are essentially planar and the dihedral angles *between* these rings within each bpcam moiety are 6.8 [at Cu(1)], 8.7 [at Cu(1A)] and 8.4°



Scheme 2.

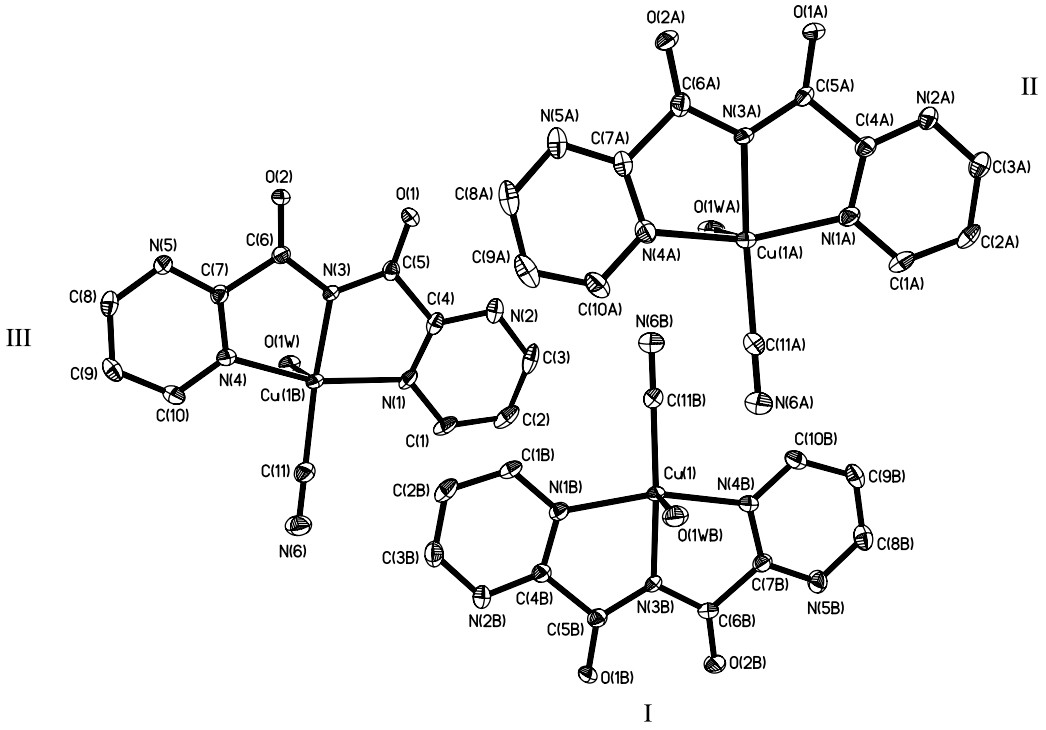


Fig. 1. A perspective view of the three crystallographically independent copper(II) units **I**–**III** in **1** with the atom numbering. Thermal ellipsoids are drawn at the 50% probability level and the hydrogen atoms are omitted by simplicity.

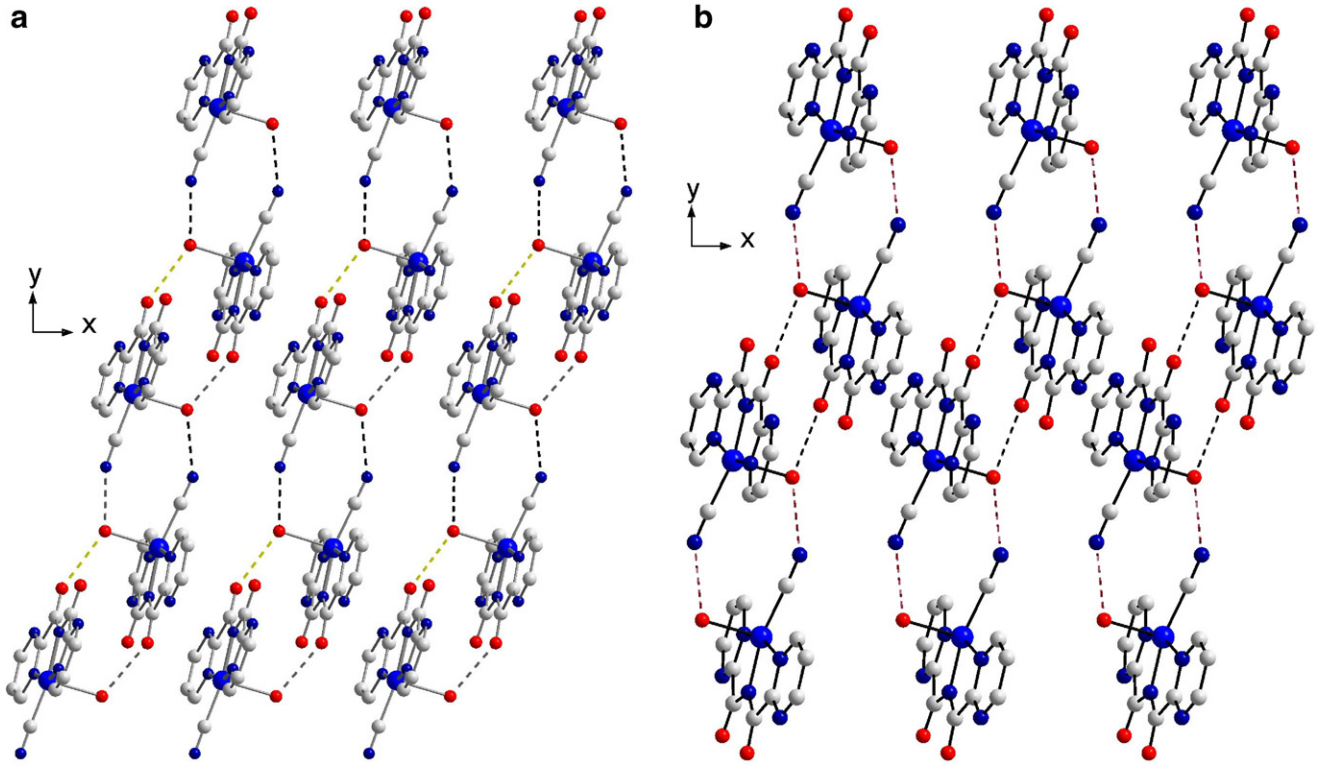


Fig. 2. Views on the *xy* plane showing the hydrogen bonds linking the **I** and **II** (dashed yellow line) and **III** (dashed pink lines) mononuclear units of **1**.

[at Cu(1B)]. Bond lengths and angles of the bpcam group in **I**–**III** agree with those reported for this ligand in previous structurally characterized bpcam-containing copper(II) complexes [1,2,5e,10].

The values of the intermolecular copper–copper separation are all greater than 6.0 Å [6.275 and 6.098 Å for Cu(1)···Cu(1A)#5 and Cu(1B)···Cu(1B)#5, respectively; #5 = 1 − *x*, 1 − *y*, 1 − *z*].

3.2.2. $[Cu(bpcam)(N_3)(H_2O)]_2$ (2)

The structure of **2** consists of two crystallographically independent neutral units of formula $[Cu(bpcam)(N_3)(H_2O)]$ which are noted as A and B (Fig. 3). The azide group in the A unit acts as a terminal monodentate ligand whereas it adopts the asymmetric end-on bridging mode in the B unit leading to mono- and dinuclear copper(II) units, respectively (Fig. 4). Both entities are stacked along the *y* axis through hydrogen bonds involving the carbonyl-oxygen atoms from the bpcam ligand and the coordinated water molecule (see Fig. 4 and the end of Table 3). The value of the copper–copper separation through the

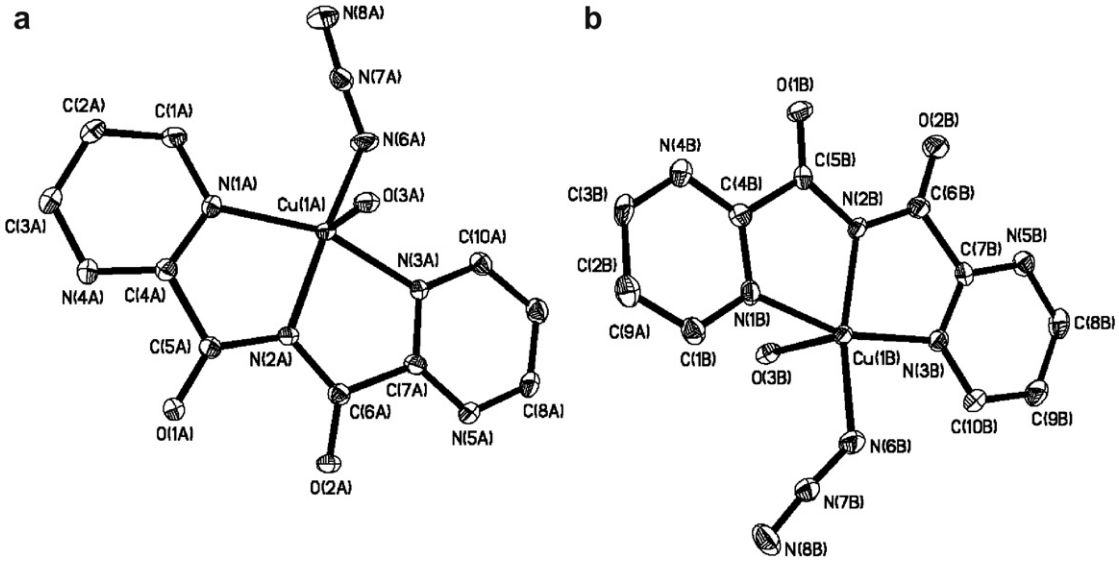


Fig. 3. A perspective view of the crystallographically independent units of **2** with the atom numbering. Thermal ellipsoids are drawn at the 50% probability level and the hydrogen atoms are omitted for simplicity.

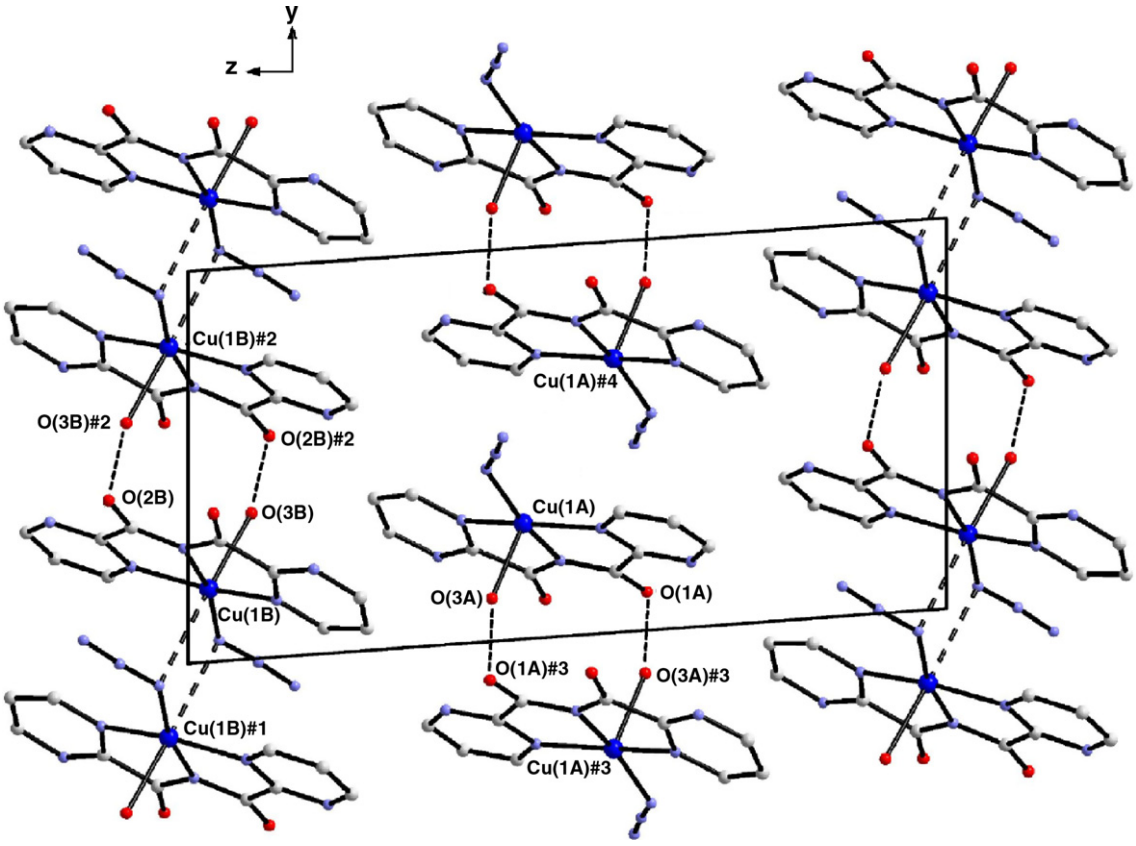


Fig. 4. A projection down the *a* axis of the unit cell contents of **2** showing the relative arrangement of the A (orange) and B (green) units. The double μ-1,1-azido bridge (B) and part of the hydrogen bonds between the coordinated water and carbonyl-carbon atoms (A and B) are shown as broken lines.

di-μ-1,1-azido bridge is 3.730(5) Å [Cu(1B)···Cu(1B)#1; #1 = 1 − x, 2 − y, −z] [to be compared to 4.600(8) Å for Cu(1A)···Cu(1A)#4; #4 = −x, 1 − y, 1 − z]. These values are much shorter than those of the metal–metal separation through the hydrogen bonds, 6.614(16) [Cu(1A)···Cu(1A)#3; #3 = 1 − x, 2 − y, 1 − z] and 6.928(15) Å [Cu(1B)···Cu(1B)#2; #2 = −x, 2 − y, −z].

The copper environment of the A and B units differs. While the A unit can be described as square pyramidal with the basal plane defined by the bpcam and azide nitrogen donors, the B unit is described as distorted octahedral: the equatorial plane being formed by four nitrogen atoms, three from bpcam [N(1B), N(2B) and N(3B)] and one from an azide group [N(6B)], whereas the axial positions are filled by a water molecule [O(3B)] and a nitrogen atom of a symmetry-related azido group [N(6B)#1]. The values of the Cu–N(bpcam) bond lengths vary in the ranges 1.944(5)–2.031(3) [at Cu(1A)] and 1.946(4)–2.040(3) Å [at Cu(1B)] agreeing with those observed in **1** and in other bpcam-containing copper(II) complexes [1,2,5e,10]. As in **1**, the small bite size of the two five-membered chelate rings subtended by the tridentate bpcam at the copper atom causes the deviations from the ideal value of 90° [81.30(9)° and 80.70(9)° for N(1A)–Cu(1A)–N(2A) and N(2A)–Cu(1A)–N(3A); 81.21(9)° and 80.77(9)° for N(1B)–Cu(1B)–N(2B) and N(3B)–Cu(1B)–N(2B)]. As might be expected, in the case of the pseudo-octahedral Cu(B) unit, the equatorial Cu–N(azide) bond distance [1.954(2) Å] is shorter than that of the axial one [2.896(5) Å for Cu(1B)–N(6B))#1]. The copper atom is shifted from the mean basal plane toward the axial water molecule by 0.1735 [Cu(1A)] and 0.0391 Å [Cu(1B)].

The pyrimidyl rings of the bpcam ligand at the two copper atoms are essentially planar and the dihedral angles between these rings within each bpcam moiety are 10.24° [at Cu(1A)] and 8.17° [at Cu(1B)]. The azido groups are quasi linear and two different nitrogen–nitrogen bond distances occur within them. As expected, the longer bond involves the end that is equatorially bound to the copper atom. The value of the angle at the equatorially bound azide nitrogen [130.2(2) and for N(7A)–N(6A)–Cu(1A) and 134.1(2)° for N(7B)–N(6B)–Cu(1B), respectively] is greater than the ideal 120° predicted for a sp^2 hybridization.

3.2.3. [Cu(bpcam)(NCS)(H$_2$O)] (3)

The crystal structure of **3** consists of discrete, neutral units of formula [Cu(bpcam)(NCS)(H$_2$O)] (Fig. 5) which are linked by hydrogen bonds involving the coordinated water molecule and two carbonyl-oxygen atoms from two bpcam ligands (see Fig. 6 and end of Table 4). This compound is isostructural with the complex [Cu(bpca)(NCS)(H$_2$O)] [31] where the bpca ligand substitutes for bpcam.

The coordination sphere of the copper atom in **3** is best described as a distorted square pyramid, the value of the trigonality parameter τ being 0.11. The basal plane is formed by three nitrogen atoms from the tridentate bpcam ligand [N(1), N(3) and N(5)] and the nitrogen atom from the monodentate thiocyanate group [N(6)] whereas the apical position is occupied by a water molecule [O(3)]. The values of Cu–N(bpcam) bond distances ranging from 1.9362(19) to 2.028(2) Å are close to those reported for the previous structures. The Cu(1)–N(6) bond length is 1.926(2) Å, a value which is practically identical to those observed in the structures of the mononuclear complexes [Cu(bpca)(NCS)(H$_2$O)] [31] and [Cu(paphy)(NCS)(SCN)] (paphy = pyridine-2-aldehyde-2′-pyridylhydrazone) [32]. The axial Cu–O$_w$ bond [2.2429(16) Å] is somewhat longer than the basal ones. The coordinated nitrogen atoms are nearly coplanar with deviations from the mean plane of 0.280 Å and the copper atom is displaced from this mean plane by 0.1837 Å toward the apical position. The angles subtended by the bpcam ligand at the copper atom are 81.03(8)° [N(3)–Cu(1)–N(5)] and 81.39(8)° [N(3)–Cu(1)–N(1)].

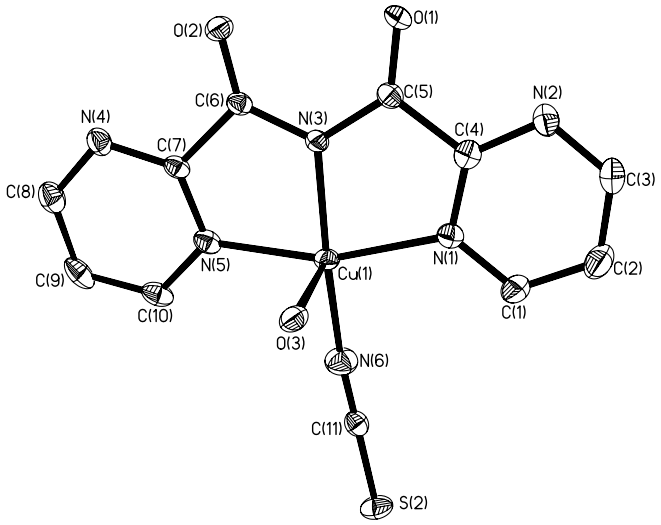


Fig. 5. A perspective view of the structure of **3** with the atom numbering. Thermal ellipsoids are drawn at the 50% probability level and the hydrogen atoms are omitted for simplicity.

The bpcam ligand is nearly planar within 0.0382 Å, although it is subject of a significant angular strain as evidenced by the values of the angles at the carbonyl-carbon atoms [110.74(19)° and 110.35(19)° for N(3)C(5)C(4) and N(3)C(6)C(7), respectively]. The thiocyanate ligand is linear but its coordination to the copper atom *via* the nitrogen atom is achieved in a significant bending mode [169.6(2)° for Cu(1)–N(6)–C(11)]. The values of the intraligand N–C and C–S bond distances have their typical values. The value of the shortest intermolecular copper–copper separation is 5.058(11) Å [Cu(1)···Cu(1)#3; #3 = 1 − x, −y, −z].

3.2.4. [Cu(bpcam)(dca)(H$_2$O)]$_2$ (4)

The structural building block of **4** is the neutral [Cu(bpcam)(dca)(H$_2$O)] complex in which the three bpcam-nitrogen atoms and a nitrile-dca nitrogen bind to copper in equatorial positions, and a water molecule occupies an

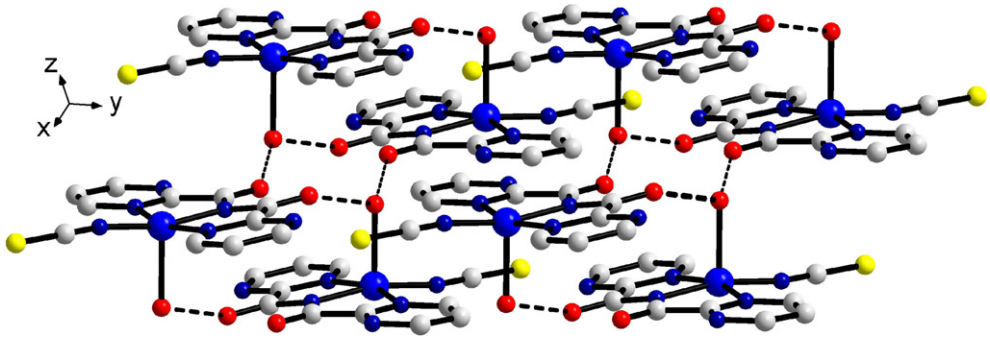


Fig. 6. A view of the packing in **3** showing the hydrogen bonding pattern as broken lines.

apical position. Considering only these interactions, the copper environment may be described as distorted square pyramidal [Cu(1)–N = 1.9412(13) Å–2.0445(14) Å and Cu(1)–O(3) = 2.2655(12) Å] with $\tau = 0.15$. The amide dca nitrogen atom of a centrosymmetrically related unit is semi-coordinated to copper [Cu(1)–N(5)#3 = 2.817(2) Å; #3 = $1-x$, $2-y$, $2-z$], resulting in a dinuclear entity (Fig. 7). These units are interlinked through hydrogen bonds involving the water molecule and the carbonyl-carbon atoms of the bpcam ligand (see Fig. 8 and the end of Table 5). This compound is isostructural with [Cu(bpca)(dca)$(H_2O)]_2$ [8] where the bpca ligand occurs instead of bpcam.

The atoms defining the equatorial plane of copper are approximately coplanar (maximum atomic deviation being 0.0205 Å) and the copper atom is displaced by 0.1448 Å from this plane toward the apical oxygen. The atoms of the dca bridge are also coplanar (maximum atomic deviation 0.0086 Å) and this plane forms an angle of 37.2° with the equatorial plane of the copper atom to which the dca is coordinated. The bpcam group acts as a tridentate ligand through its three nitrogen atoms, the copper to amido-nitrogen bond being significantly shorter than the two copper to pyrimidine–nitrogen ones, as observed in the structures described above. The pyrimidyl rings of bpcam are planar and the dihedral angle between these rings is 6.0°. The values of the nitrile [1.156(2) and 1.149(2) Å] and amide [1.292(2) and 1.321(3) Å] carbon–nitrogen distances in the dca group are consistent with the triple and single carbon–nitrogen bond character.

The copper–copper separation within the dinuclear unit is 5.701(3) Å [Cu(1)···Cu(1)#3], a value which is very close to the distance of 5.732(2) Å in the related bpca-containing complex. The shortest interdimer metal–metal separation in **4** is 6.755 Å [Cu(1)···Cu(1)#4; #4 = $-x$, $2-y$, $1-z$].

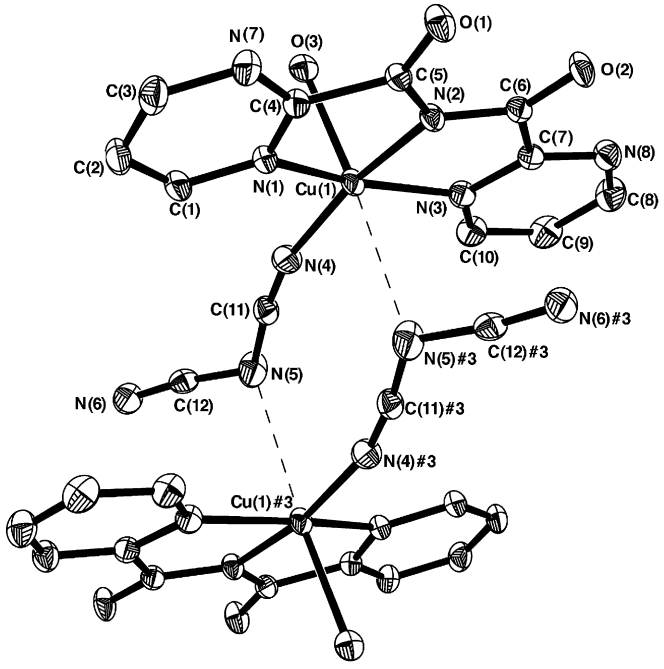


Fig. 7. A perspective view of the dinuclear unit in **4** [Cu(bpcam)(dca)$(H_2O)]_2$. Thermal ellipsoids are drawn at the 50% probability level and the hydrogen atoms are omitted for simplicity.

3.2.5. *[Cu(bpca)(tcm)]$_n$* (**5**)

A chain structure is present in this compound with the tcm group serving as a μ-1,5-bridging ligand between the [Cu(bpca)] units (Fig. 9). The chains extend along the *c* axis in a zigzag fashion and they are stacked in a zipper arrangement (Fig. 10) in the *ac* plane.

The copper atom is five-coordinated in a somewhat distorted square pyramidal surrounding, the value of the trigonality parameter being $\tau = 0.08$. The equatorial positions are defined by the three bpca-nitrogen atoms [N(1), N(2) and N(3)] and a nitrile-nitrogen [N(5)#1; #1 = x, y, $z+1$] from a tcm group whereas the apical position is occupied also by a nitrile-nitrogen [N(4)] from another tcm ligand. The four atoms in the equatorial positions around the copper atom are practically coplanar with the metal atom being displaced by 0.1065 Å from this plane toward the apical nitrile-nitrogen. The values of the dihedral angle between the equatorial plane and the mean planes of the bpca and tcm ligands are 4.0° and 11.4°, respectively. The bpca group acts as a tridentate ligand through its three nitrogen atoms, the copper to amido-nitrogen bond being significantly shorter than the two copper to pyridine–nitrogen ones, as observed in other bpca-containing copper(II) complexes [3–5a,5d–13,31]. Bond lengths and angles within the bpca ligand are in agreement

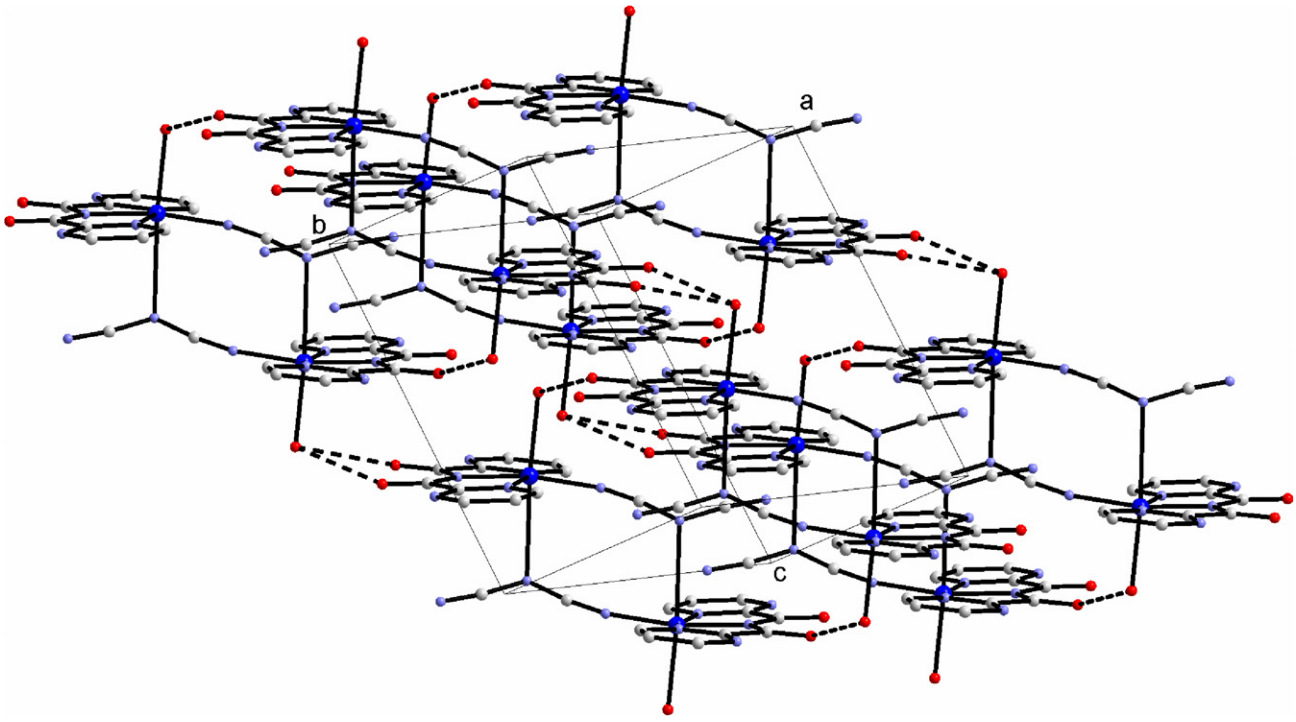


Fig. 8. A view of the packing in **4** showing the hydrogen bonds (broken lines) which link the double dca-bridged dicopper(II) units.

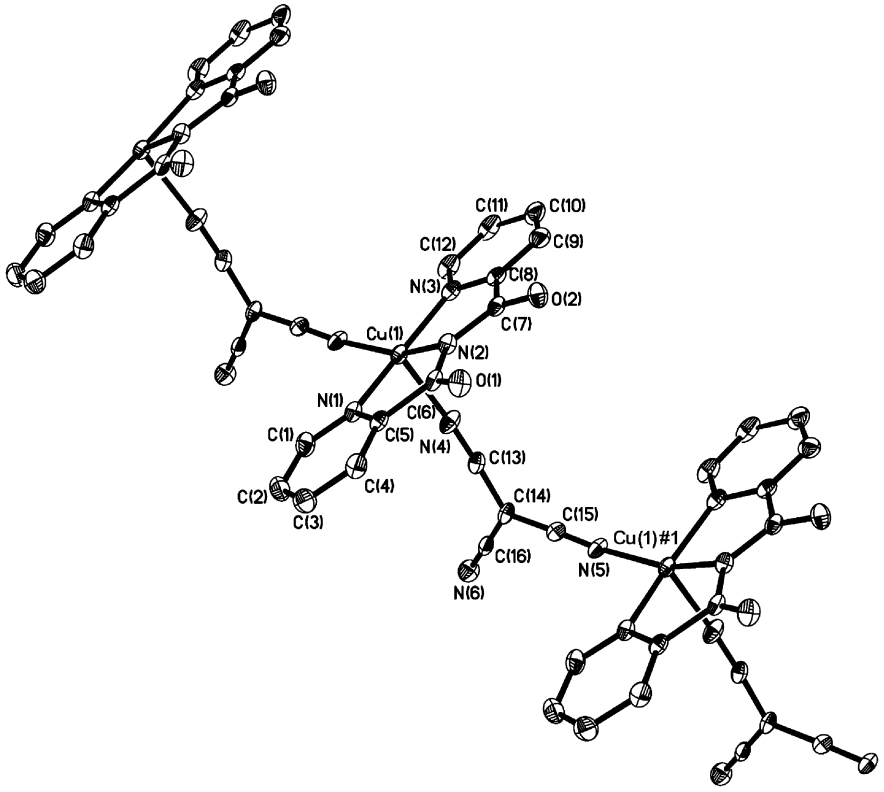


Fig. 9. Section of the $[Cu(bpca)(tcm)]_n$ chain (**5**) showing the atom numbering. Thermal ellipsoids are drawn at the 30% probability level and the hydrogen atoms are omitted for clarity.

with those reported previously [3–5a,d–13,31]. The pyridyl rings of the bpca are planar and the dihedral angle between them is 3.9°.

The values of the C–N and C–C bond lengths and the CCC bond angles of the tcm ligand in **5** remain in rather narrow ranges, 1.148(3)–1.150(4), 1.404(4)–1.419(4) Å and

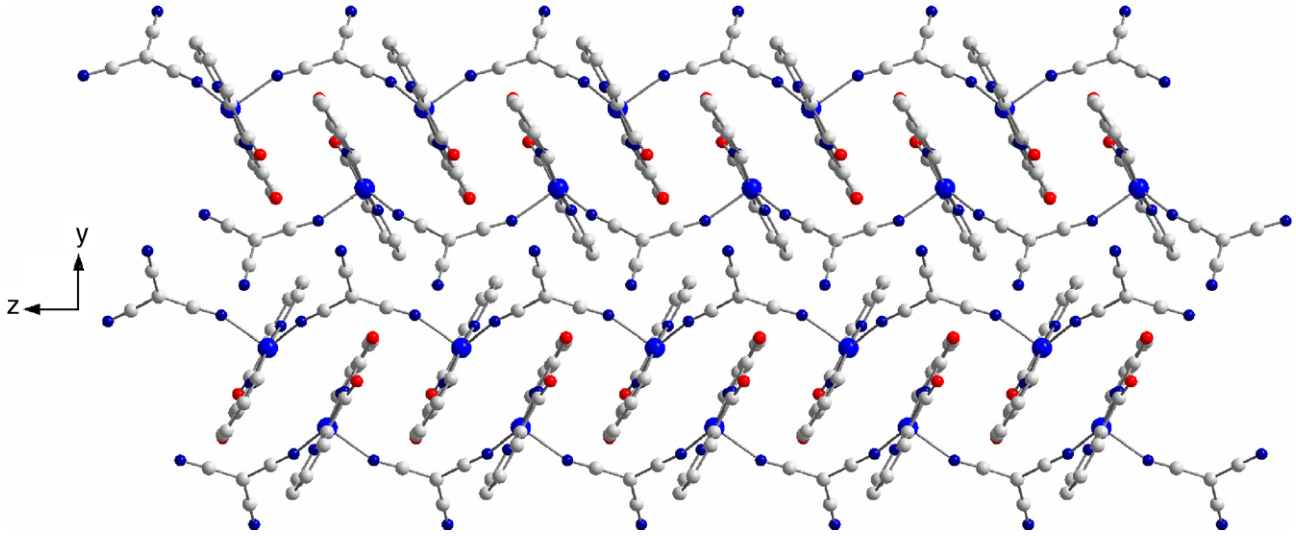


Fig. 10. A view of the stacking of the chains of **5** in the *bc* plane.

119.5(2)–120.5(3)°, respectively. This is in agreement with almost ideal sp^2 hybridisation of the central carbon atom. The asymmetric μ-1,5-bridging mode of the tcm ligand which occurs in **5** was also observed in other compounds [33,34] but as far as we know, **5** is the first structurally characterized example of uniform copper(II) chain with a single μ-1,5 tcm bridge. It is worthy to note that the analogous copper(II) complex with dca of formula $[Cu(bpca)(dca)(H_2O)]_2$ is a dinuclear compound with double μ-1,3-dca bridges [8]. The intrachain copper–copper distances in **5** is 7.688(3) Å [Cu(1)···Cu(1)#1], a value which is much longer than the the shortest interchain metal–metal separation [4.291(9) Å for Cu(1)···Cu(1)#3; #3 = 2 − *x*, −*y*, 1 − *z*].

3.3. Magnetic properties of 2, 4 and 5

The magnetic properties of the complexes **2**, **4** and **5** under the form of $\chi_M T$ versus T plot [χ_M is the magnetic susceptibility per copper(II) ion] are shown in Fig. 11. A Curie law behaviour of a magnetically isolated copper(II) ion, the values of $\chi_M T$ remaining practically constant from room temperature [values at 295 K varying in the range 0.44–0.41 $cm^3\,mol^{-1}$ K] until $T \leqslant 20$ K, and then they decrease to ca. 0.28 (**2**), 0.38 (**4**) and 0.32 $cm^3\,mol^{-1}$ K (**5**) at 1.9 K. No maximum is observed in the corresponding magnetic susceptibility versus T plots. The smooth decrease of $\chi_M T$ in the low temperature range for **2**, **4** and **5** is indicative of the occurrence of a weak antiferromagnetic interactions.

Having in mind the dinuclear structure of **4**, its magnetic data were analyzed through a simple Bleaney-Bowers expression for two interacting spin doublets [Eq. (1)] which is derived from the isotropic Hamiltonian in Eq. (2)

$$\chi_M = (2N\beta^2 g^2/kT)[3 + \exp(-J/kT)]^{-1} \quad (1)$$

$$\hat{H} = -J\hat{S}_A \cdot \hat{S}_B \quad (2)$$

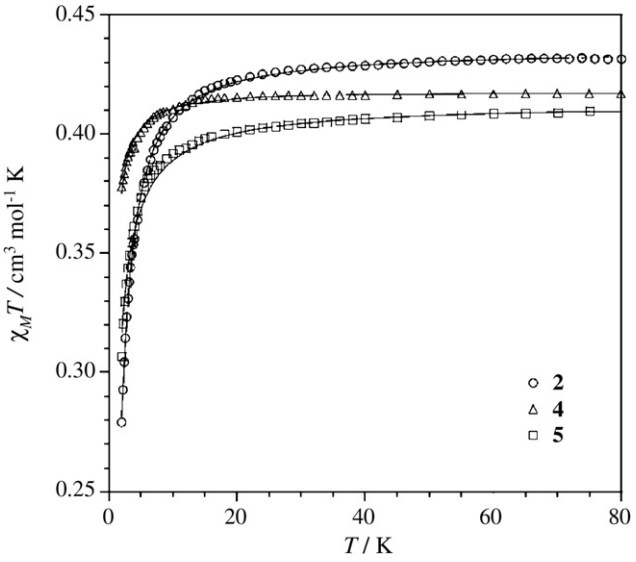


Fig. 11. Thermal dependence of $\chi_M T$ for **2**, **4** and **5** at $T \leqslant 80$ K. The solid lines are the best-fit curves (see text).

where N, g and β have their usual meanings and J is the spin coupling parameter. The best-fit parameters are $J = -0.53$ cm^{-1}, $g = 2.11$ and $R = 5.0 \times 10^{-6}$ (R is the agreement factor defined as $\sum_i[(\chi_M)_{obs(i)} - (\chi_M)_{calc(i)}]^2 / \sum_i[(\chi_M)_{obs(i)}]^2$). In the case of **2**, because of the coexistence of the di-μ-1,1-azido-bridged dicopper(II) unit [Cu(1B)···Cu(1B))#6] and the monuclear copper(II) entity [Cu(1A)], its magnetic data were analyzed through Eq. (3) (per four copper atoms)

$$\chi_M = (2N\beta^2 g^2/kT)[3 + \exp(-J/kT)]^{-1} + N\beta^2 g^2/2kT \quad (3)$$

where the first term is the Bleaney-Bowers expression for a copper(II) dimer and second term is the Curie law for two magnetically isolated copper(II) ions. The same average Landé factor (g) is assumed for the dinuclear and mononuclear copper(II) units. The best-fit parameters for **2** through Eq. (3) (per one copper atom) are $J = -3.3$ cm^{-1}, $g = 2.15$

and $R = 4.5 \times 10^{-6}$. The calculated curves in **2** and **4** match the experimental data very well. Given that **5** is a uniformly spaced chain of copper(II) ions, its magnetic data were analyzed through the theoretical expression proposed by Hall [35] for a uniform chain of local spins S = 1/2 [Eq. (4)] which is derived from the isotropic Hamiltonian in Eq. (5)

$$\chi_M = (N\beta^2 g^2/kT)[0.25 + 0.14995x + 0.30094x^2) / (1 + 1.9862x + 0.68854x^2 + 6.0626x^3) \quad (4)$$

$$\hat{H} = -J \sum_i \hat{S}_i \cdot \hat{S}_{i+1} \quad (5)$$

where $x = |J|/kT$ and J is the exchange coupling constant describing the magnetic interaction between two nearest-neighbour spin doublets. This expression, which derives from the numerical results from Bonner and Fisher [36], has been widely used to treat the magnetic data of uniform copper(II) chains. Least-squares fit of the magnetic data of **5** through Eq. (3) leads to the following parameters: $J = -0.64$ cm^{-1}, $g = 2.10$ and $R = 6.7 \times 10^{-5}$.

The magnetic interactions in **2**, **4** and **5** are all weak and antiferromagnetic. This can be understood by looking at the respective orientation of the magnetic orbitals involved, that is, the molecular orbitals which define the unpaired electron on each copper(II) ion. The unpaired electron on each copper atom in this family of complexes is essentially located in the equatorial plane and it is roughly defined by a $d_{x^2-y^2}$ type orbital [the x and y axes being roughly defined by the Cu–N(imido) (**2**, **4** and **5**) and Cu–N(pyrimidine/pyridine) (**2** and **4**/**5**) bonds, respectively]. Given that the spin density in the apical position is very weak, the overlap between the parallel magnetic orbitals of the adjacent copper(II) ions is very small. Under these conditions, the exchange coupling is expected to be very weak or zero [37]. In all three compounds, the out-of-plane exchange pathway is involved through double end-on azido (**2**)/μ-1,3-dca (**4**) and single μ-1,5-tcm (**5**) bridges. At this respect, a literature survey shows that weak ferro- [38,39] and antiferromagnetic [40,41] interactions occur in asymmetric double end-on azido-bridged copper(II) complexes, their nature and magnitude being dependent on several structural parameters such as the angle at the end-on azide nitrogen, the value of τ, the axial azido-nitrogen to copper bond length and the intramolecular copper–copper separation (see Table 7). The antiferromagnetic coupling in **4** is also very weak ($J = -0.53$ cm^{-1}). This feature together with the lack of magnetic coupling in the related dinuclear complex [Cu(bpca)(dca)(H$_2$O)]$_2$ [8] (isostructural to **4**) demonstrate that the asymmetric μ-1-3-dca bridge between copper(II) ions is a very poor exchange mediator. Finally, the value of the antiferromagnetic coupling in **5** ($J = -0.64$ cm^{-1}) is very close to that reported for the ladder-like compound of formula [Cu(tn)(tcm)$_2$]$_n$ (tn = 1,3-diaminopropane) ($J = -0.7$ cm^{-1}) [34] where the rods and the rungs are asymmetric single- and double μ-1,5 tcm bridges, respectively. The magnetic behaviour of this last compound was modelled through a uniform copper(II) chain model, the single tcm bridge that connects one equatorial position of one copper atom to an axial one of the adjacent copper atom being considered the only operative exchange pathway. These magneto-structural investigations show the low efficiency of the tcm bridge as exchange mediator.

4. Conclusions

The combined use of cyanide (**1**), azide (**2**), thiocyanate (**3**), dicyanamide (**4**) and tricyanomethanide (**5**) as ligands toward the stable building block bis(2-arylcarbonyl)amidatecopper(II) [aryl = pyrimidyl (**1**–**4**) and pyridyl (**5**)] afforded the neutral mononuclear species [Cu(bpcam)(CN)(H$_2$O)] (**1**) and [Cu(bpcam)(NCS)(H$_2$O)] (**3**), the mononuclear (**2**)/dinuclear (**2** and **4**) complexes [Cu(bpcam)(N$_3$)(H$_2$O)]$_2$ (**2**) and [Cu(bpcam)(dca)(H$_2$O)]$_2$ (**4**) and the chain compound [Cu(bpca)(tcm)]$_n$ (**5**). The monodentate coordination of cyanide (**1**) and thiocyanate (**3**) to copper(II) produces neutral mononuclear species which are insoluble in water and this insolubility precludes their polymerization. However, in the case of the azide and dicyanamide coligands, dinuclear compounds result because of

Table 7
Magneto-structural data for asymmetric end-on azido-bridged copper(II) complexes

Compound[a]	J (cm^{-1})	θ[b] (°)	τ	R[c] (Å)	d[d] (Å)	Ref.
[Cu$_2$L$_2$(N$_3$)$_2$]	+24	86.9	0.18	2.55	3.17	[38]
[Cu(bipy)(N$_3$)$_2$]$_n$[e]	+4.6	96.2	0.01	2.60	3.43	[39]
[Cu(terpy)(H$_2$O)(N$_3$)]$_2$(PF$_6$)$_2$	−2.9	95.7	0.06	2.85	3.60	[40]
[Cu(bipy)(N$_3$)$_2$]$_n$[e]	−2.7	96.8	0.06	2.68	3.51	[39]
[Cu(dpp)(N$_3$)$_2$]$_n$	−2.3	96.9	0.12	2.74	3.57	[41]
2[f]	−3.3	98.6	0.09	2.89	3.73	This work

[a] Abbreviations used: L = 7-amino-4-methyl-5-aza-3-hepten-2-onato; bipy = 2,2′-bipyridine; terpy = 2,2′:6′,2″-terpyridine; dpp = 2,3-bis(2-pyridyl)-pyrazine.
[b] Value of the Cu···N$_{(azide)}$···Cu bridging angle.
[c] Axial azide–nitrogen to copper bond distance.
[d] Copper–copper separation across the double end-on azido bridge.
[e] The two compounds with the same formula are uniform and alternating chain compounds, respectively.
[f] These values refer to the Cu(1B)···Cu(1B)#6 dinuclear unit.

the μ-1,1-azido (**2**) and the μ-1,3-dca (**4**) adopted bridging modes. Surprisingly, the mononuclear [Cu(bpcam)(N_3)-(H_2O)] unit containing a terminally bound azide ligand is also present in **2**. Finally, the tcm group in **5** adopts the μ-1,5-bridging mode linking an equatorial position at one copper atom with the apical one at the adjacent metal atom leading to a uniform chain of copper(II) ions. Weak intradimer (**2** and **4**)/intrachain (**5**) antiferromagnetic interactions between the copper(II) ions are observed through the out-of-plane exchange pathway across the double μ-1,1-azido (**2**) and μ-1,5-dca (**4**) bridges and the single μ-1,5-tcm (**5**) group.

Acknowledgements

Thanks are due to the Spanish Ministry of Science and Education (Project BQU2004-03633) and the Royal Society (J.A.T.). One of us acknowledges the Ministério da Educação do Brasil for a CAPES predoctoral grant (D.C.).

Appendix A. Supplementary material

CCDC 641184, 641185, 641186, 641187 and 641188 contain the supplementary crystallographic data for **1**, **2**, **3**, **4** and **5**. These data can be obtained free of charge via http://www.ccdc.cam.ac.uk/conts/retrieving.html, or from the Cambridge Crystallographic Data Centre, 12 Union Road, Cambridge CB2 1EZ, UK; fax: (+44) 1223-336-033; or e-mail: deposit@ccdc.cam.ac.uk.

References

[1] (a) E.I. Lerner, S.J. Lippard, J. Am. Chem. Soc. 98 (1976) 5397;
(b) E.I. Lerner, S.J. Lippard, Inorg. Chem. 16 (1977) 1546.
[2] D. Cangussu, H.O. Stumpf, F. Lloret, M. Julve, V. González, H. Adams, J.A. Thomas, Inorg. Chim. Acta 358 (2005) 1113.
[3] I. Castro, J. Faus, M. Julve, J.M. Amigó, J. Sletten, T. Debaerdemaeker, J. Chem. Soc., Dalton Trans. (1990) 891.
[4] J.V. Folgado, E. Coronado, D. Beltrán-Porter, R. Burriel, A. Fuertes, C. Miravitlles, J. Chem. Soc., Dalton Trans. (1988) 3041.
[5] (a) I. Castro, J. Faus, M. Julve, M. Mollar, A. Monge, E. Gutiérrez-Puebla, Inorg. Chim. Acta 161 (1989) 97;
(b) I. Castro, J. Faus, M. Julve, Y. Journaux, J. Sletten, J. Chem. Soc., Dalton Trans. (1991) 2533;
(c) I. Castro, J. Sletten, J. Faus, M. Julve, Y. Journaux, F. Lloret, S. Alvarez, Inorg. Chem. 31 (1992) 1889;
(d) M.L. Calatayud, I. Castro, J. Sletten, F. Lloret, M. Julve, Inorg. Chim. Acta 300–302 (2000) 846;
(e) D. Cangussu, H.O. Stumpf, H. Adams, J.A. Tomas, F. Lloret, M. Julve, Inorg. Chim. Acta 358 (2005) 2292.
[6] J. Sletten, M. Julve, F. Lloret, I. Castro, G. Seitz, K. Mann, Inorg. Chim. Acta 250 (1996) 219.
[7] I. Castro, M.L. Calatayud, J. Sletten, F. Lloret, J. Cano, M. Julve, G. Seitz, K. Mann, Inorg. Chem. 38 (1999) 4680.
[8] B. Vangdal, J. Carranza, F. Lloret, M. Julve, J. Sletten, J. Chem. Soc., Dalton Trans. (2002) 566.
[9] R. Lescouëzec, G. Marinescu, J. Vaissermann, F. Lloret, J. Faus, M. Andruh, M. Julve, Inorg. Chim. Acta 350 (2003) 131.
[10] L.M. Toma, R. Lescouëzec, D. Cangussu, R. Llusar, J. Mata, S. Spey, J.A. Thomas, F. Lloret, M. Julve, Inorg. Chem. Commun. 8 (2005) 382.
[11] A. Cantarero, J.M. Amigó, J. Faus, M. Julve, T. Debaerdemaeker, J. Chem. Soc., Dalton Trans. (1988) 2033.
[12] D. Marcos, J.V. Folgado, D. Beltrán-Porter, M.T. Do Prado-Gambardella, S.H. Pulcinelli, R.H. De Almeida-Santos, Polyhedron 9 (1990) 2699.
[13] S. Wocadlo, W. Massa, J.V. Folgado, Inorg. Chim. Acta 207 (1993) 199.
[14] A. Kamiyama, T. Noguchi, T. Kajiwara, T. Ito, Inorg. Chem. 41 (2002) 507.
[15] D. Marcos, R. Martínez-Máñez, J.V. Folgado, A. Beltrán-Porter, D. Beltrán-Porter, A. Fuertes, Inorg. Chim. Acta 159 (1989) 11.
[16] P. Paul, B. Tyagi, A.K. Bilakhiya, M.M. Bhadbhade, E. Suresh, J. Chem. Soc., Dalton Trans. (1999) 2009.
[17] (a) P. Paul, B. Tyagi, M.M. Bhadbhade, E. Suresh, J. Chem. Soc., Dalton Trans. (1997) 2273;
(b) P. Paul, B. Tyagi, A.K. Bilakhiya, M.M. Bhadbhade, E. Suresh, G. Ramachandraiah, Inorg. Chem. 37 (1998) 5733.
[18] (a) T. Kajiwara, R. Sensui, T. Noguchi, A. Kamiyama, T. Ito, Inorg. Chim. Acta 337 (2002) 299;
(b) A. Kamiyama, T. Noguchi, T. Kajiwara, T. Ito, CrystEngComm 5 (2003) 231.
[19] F. Pointillart, K. Bernot, R. Sessoli, D. Gatteschi, Chem. Eur. J. 13 (2007) 1602.
[20] T. Kajiwara, M. Nakano, Y. Kaneko, S. Takaishi, T. Ito, M. Yamashita, A. Igashira-Kamiyama, H. Nojiri, Y. Ono, N. Kojima, J. Am. Chem. Soc. 127 (2005) 10150.
[21] A. Kamiyama, T. Noguchi, T. Kajiwara, T. Ito, Angew. Chem. Int. Ed. 39 (2000) 3130.
[22] A. Earnshaw, Introduction to Magnetochemistry, Academic Press, London and New York, 1968.
[23] G.M. Sheldrick, SHELXTL/PC, An Integrated System for Solving and Refining Crystal Structures from Diffraction Data, Revisión 5.1, Bruker AXSINC., Madison, WI, USA, 1998.
[24] O.P. Anderson, Inorg. Chem. 14 (1975) 730.
[25] R.J. Parker, L. Spiccia, B. Moubaraki, K.S. Murray, B.W. Skelton, A.H. White, Inorg. Chim. Acta 300–302 (2000) 922.
[26] K. Nakamoto (Ed.), Infrared and Raman Spectra of Inorganic and Coordination Compounds, 4th ed., Wiley, New York, 1986.
[27] R.A. Bailey, S.L. Kozak, T.W. Michelson, W.N. Mills, Coord. Chem. Rev. 6 (1971) 407.
[28] A.M. Golub, H. Köhler, V.V. Skopenko, Chemistry of Pseudohalogenides, Elsevier, Amsterdam, 1986.
[29] I. Potocnák, M. Dunaj-Jurco, D. Miklos, L. Jäger, Acta Crystallogr. C52 (1996) 48.
[30] A.W. Addison, T.N. Rao, J. Reedijk, J. Van Rijn, G.C. Verschoor, J. Chem. Soc., Dalton Trans. (1984) 1349.
[31] G. Madariaga, F.J. Zúñiga, T. Rojo, J.V. Folgado, Acta Crystallogr. C47 (1991) 1632.
[32] J.L. Mesa, T. Rojo, M.I. Arriortua, G. Villeneuve, J.V. Folgado, A. Beltrán-Porter, D. Beltrán-Porter, J. Chem. Soc., Dalton Trans. (1989) 52.
[33] S.R. Batten, K.S. Murray, Coord. Chem. Rev. 246 (2003) 103, and references therein.
[34] F. Thétiot, S. Triki, J. Sala Pala, S. Golhen, Inorg. Chim. Acta 350 (2003) 314.
[35] J.W. Hall, Ph.D. Dissertation, University of North Carolina, Chapell Hill, NC, 1977.
[36] J.C. Bonner, M.E. Fisher, Phys. Rev. A 135 (1964) 640.
[37] O. Kahn, Molecular Magnetism, VCH, Weinheim, Germany, 1993.
[38] J.P. Costes, F. Dahan, J. Ruiz, J.P. Laurent, Inorg. Chim. Acta 239 (1995) 53.
[39] G. De Munno, M.G. Lombardi, M. Julve, F. Lloret, J. Faus, Inorg. Chim. Acta 282 (1998) 82.
[40] R. Cortés, M.K. Urtiaga, L. Lezama, J.I.R. Larramendi, M.I. Arriortua, T. Rojo, J. Chem. Soc., Dalton Trans. (1993) 3685.
[41] H. Grove, M. Julve, F. Lloret, P.E. Kruger, K.W. Törnroos, J. Sletten, Inorg. Chim. Acta 325 (2001) 115.

Available online at www.sciencedirect.com
ScienceDirect
Polyhedron 27 (2008) 574–582
POLYHEDRON
www.elsevier.com/locate/poly

One-dimensional and two-dimensional coordination polymers constructed from copper(II) nodes and polycarboxylato spacers: Synthesis, crystal structures and magnetic properties

Cristian D. Ene [a], Floriana Tuna [b], Oscar Fabelo [c], Catalina Ruiz-Pérez [c], Augustin M. Madalan [a], Herbert W. Roesky [d], Marius Andruh [a,*]

[a] *Inorganic Chemistry Laboratory, Faculty of Chemistry, University of Bucharest, Str. Dumbrava Rosie 23, 020464 Bucharest, Romania*
[b] *School of Chemistry, University of Manchester, Oxford Road, Manchester M13 9PL, UK*
[c] *Laboratorio de Rayos X y Materiales Moleculares, Departamento de Fisica Fundamental II, Facultad de Física, Universidad de La Laguna, Tenerife, Spain*
[d] *Institut für Anorganische Chemie der Universität, Tammannstr. 4, D-37077 Göttingen, Germany*

Received 4 September 2007; accepted 9 October 2007
Available online 19 November 2007

Abstract

Four new coordination polymers were obtained by employing polycarboxylato spacers and cationic copper(II) complexes as nodes: $^{\infty}_{2}[Cu_3(trim)_2(NH_3)_6(H_2O)_3]$ (**1**); $^{\infty}_{1}[Cu(tmen)(dhtp)]$ (**2**), $^{\infty}_{1}[Cu(tmen)(hitp)(H_2O)]$ (**3**), $^{\infty}_{1}[Cu(tmen)(nitp)]$ (**4**). (H_3trim = trimesic acid, H_2dhtp = 2,5-dihydroxy-terephthalic acid; H_2hitp = 5-hydroxy-isophthalic acid, H_2nitp = 5-nitro-isophthalic acid; tmen = *N*,*N*,*N*′,*N*′-tetramethyl-ethylenediamine). The crystal structures of the four compounds have been solved. Compound **1** consists of 2D coordination polymers with heart-shaped meshes, while compounds **2**–**4** contain infinite zigzag chains. The role of the hydrogen bond interactions in sustaining the supramolecular solid-state architectures in compounds **1** and **3** is discussed. The cryomagnetic investigation of compounds **1**, **2**, and **4** reveals antiferromagnetic interactions between the copper ions.
© 2007 Elsevier Ltd. All rights reserved.

Keywords: Copper complexes; Coordination polymers; Polycarboxylato ligands; Crystal structures; Magnetic properties

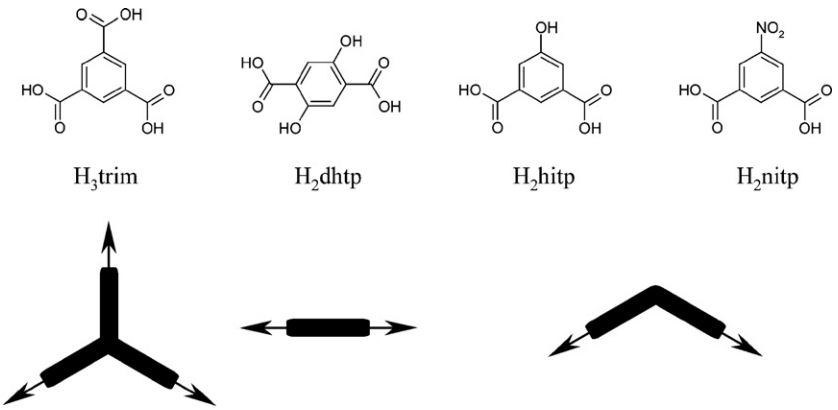
1. Introduction

Polycarboxylates are extremely popular as ligands in designing coordination polymers with various dimensionalities and network topologies [1]. The increasing interest in metal–organic frameworks arises not only from their intrinsic beauty, but also from their potential applications in gas storage, catalysis or ion exchange processes [2]. The main factors which influence the rich structural variety of the coordination polymers constructed from polycarboxylato ligands are: (i) the number of the carboxylato groups attached to the organic ligand; (ii) the spatial orientation of the carboxylato groups; (iii) the various coordination modes exhibited by each COO^- group; (iv) the presence of the coligands in the coordination sphere of the metal ions.

Both flexible aliphatic and rigid aromatic carboxylates are extensively used as linkers. From the last category we mention here the trimesic acid, H_3trim, which was found to generate both high-nuclearity clusters [3], and 1D, 2D, and 3D coordination polymers [4]. Most of these polymers are constructed from copper(II) ions. Let us recall some of them, which are relevant to this paper. A one-dimensional coordination polymer, $[Cu(Htma)(H_2O)_3]$ results from a neutral solution containing cupric ions and trimesic

* Corresponding author.
E-mail address: marius.andruh@dnt.ro (M. Andruh).

0277-5387/$ - see front matter © 2007 Elsevier Ltd. All rights reserved.
doi:10.1016/j.poly.2007.10.011



Scheme 1.

acid [4]. In the presence of sodium hydroxide, it results a bimetallic coordination polymer, $[NaCu(trim)(H_2O)_4]\cdot 2H_2O$, with a double-sheet architecture [5]. The reaction between copper(II) nitrate and trimesic acid, under hydrothermal conditions, affords a spectacular nanoporous material, $[Cu_3(trim)_2(H_2O)_3]$ [6]. The porosity, catalytic [7], and the magnetic properties [8] of this material were intensively investigated. The network topology of the coordination polymers constructed from trimesate linkers is strongly influenced by ancillary ligands attached to the copper(II) ions. For example, 2D coordination polymers, $[Cu_3(tmen)_3(trim)_2(H_2O)_2]\cdot 6.5H_2O$ and $[Cu_3(Ph_2SNH)_6(trim)_2]$, were obtained by employing *N*,*N*,*N*′,*N*′-tetramethylethane-1,2-diamine (tmen) [9] or *S*,*S*′-diphenylsulfimide (Ph_2SNH)[10] as coligands.

In this paper we report on four coordination polymers constructed from aromatic polycarboxylato spacers and assembling copper(II) complex cations. The following acids were employed: 1,3,5-benzenetricarboxylic acid (trimesic acid, H_3trim), 2,5-dihydroxy-terephthalic acid (H_2dhtp); 5-hydroxy-isophthalic acid, (H_2hitp), 5-nitro-isophthalic (H_2nitp) – Scheme 1.

2. Experimental

2.1. Materials

All the chemicals were purchased from commercial sources and used without any further purification. The [Cu(acac)(tmen)](ClO$_4$) complex has been previously reported [10]. The tetrafluoroborate derivative, [Cu(acac)(tmen)](BF$_4$), was prepared by an alternative method, as follows: two solutions, one containing acetylacetone (200.2 mg, 2 mmol) and triethylamine (202 mg, 2 mmol) in 10 mL ethanol, and the other one containing *N*,*N*,*N*′,*N*′-tetramethyl-ethylenediamine (232.4 mg, 2 mmol) in 10 mL ethanol, were added rapidly into 20 mL ethanolic solution of $Cu(BF_4)_2\cdot xH_2O$ (474.3 mg, 2 mmol). The slow evaporation of the resulted mixture gives dark blue crystals.

2.2. Syntheses

2.2.1. $^{\infty}_{2}[Cu_3(trim)_2(NH_3)_6(H_2O)_3]$ (**1**)

An ethanolic solution (15 mL) of trimesic acid (84 mg, 0.4 mmol) and triethylamine (121.4 mg, 1.2 mmol) was mixed with a solution of $Cu(CF_3SO_3)_2$ (217 mg, 0.6 mmol) in 10 mL water and stirred for about 30 min. An aqueous ammonia solution was added to the resulted mixture under stirring until the light blue precipitate dissolved. The resulted blue solution was allowed to slowly evaporate at room temperature and the reaction vessel was sealed when the first crystals appeared. Blue single crystals suitable for X-ray diffraction were collected after 1 week. Selected IR data (KBr, cm^{-1}): 3330, 3188, 2925, 1615, 1552, 1438, 1362, 1255, 759, 723.

2.2.2. $^{\infty}_{1}[Cu(tmen)(dhtp)]$ (**2**)

A solution of 2,5-dihydroxy-terephthalic acid (118.9 mg, 0.6 mmol) and triethylamine (121.4 mg, 1.2 mmol) in 10 mL methanol was slowly added to a methanol solution (10 mL) of [Cu(acac)(tmen)](BF$_4$) (219.4 mg, 0.6 mmol). The resulted mixture was filtered and the slow evaporation of the filtrate gave after several days a microcrystalline blue complex. Single crystals suitable for X-ray diffraction were obtained by recrystallisation from methanol. The crystals were collected by filtration and washed with small amounts of water and methanol. Selected IR data (KBr, cm^{-1}): 2985, 2922, 1587, 1479, 1439, 1420, 1383, 1359, 1240, 1020, 870, 815, 792.

2.2.3. $^{\infty}_{1}[Cu(tmen)(hitp)(H_2O)]$ (**3**)

A water/methanol (1:1, v/v) solution (10 mL) of 5-hydroxy-isophthalic acid (36.4 mg, 0.2 mmol) and triethylamine (40.4 mg, 0.4 mmol) was slowly added to a methanol solution (10 mL) of [Cu(acac)(tmen)](BF$_4$) (73.1 mg, 0.2 mmol). After 2 weeks, a microcrystalline blue compound separated from the resulted mixture on evaporation at room temperature. Blue single crystals of X-ray diffraction quality were obtained by recrystallisation from

methanol. Selected IR data (KBr, cm^{-1}): 3071, 2981, 1578, 1471, 1411, 1349, 1298, 1277, 1216, 1022, 919, 783, 714.

2.2.4. $^{\infty}_{1}$[Cu(tmen)(nitp)] (4)

An aqueous solution (10 mL) of 5-nitro-isophthalic acid (63.3 mg, 0.3 mmol) and triethylamine (60.7 mg, 0.6 mmol) was mixed with a solution of *N*,*N*,*N*′,*N*′-tetramethyl-ethylenediamine (34.8 mg, 0.3 mmol) in 5 mL water. The resulted mixture was slowly added to a solution of $Cu(CF_3SO_3)_2$ (108.5 mg, 0.3 mmol) in 10 mL water and allowed to evaporate at room temperature. Small blue crystals suitable for X-ray diffraction were separated after several days. Selected IR data (KBr, cm^{-1}): 2894, 1617, 1586, 1565, 1532, 1460, 1346, 1288, 1020, 808, 733.

2.3. Physical measurements

The IR spectra were recorded as KBr pellets with a Bio-Rad FTS 135 spectrophotometer in the 4000–400 cm^{-1} range. Magnetic data were obtained with a Quantum Design MPMS XL SQUID magnetometer. Magnetic susceptibility measurements were performed in the 1.8–300 K temperature range at 1000 G applied magnetic field. Diamagnetic corrections were applied by using Pascal's constants [11]. Isothermal magnetization measurements as a function of the external magnetic field were performed up to 7 T at 2 K and 4 K.

2.4. X-ray crystallography

X-ray diffraction data on single crystals of **1** and **2**–**4** were collected on a Huber four circle cradle equipped with a BRUKER SMART CCD detector and a Nonius Kappa CCD diffractometer respectively, using graphite-monochromated Mo Kα radiation ($\lambda = 0.71073$ Å). Crystal data and details of the refinement for compounds **1**–**4** are listed in Table 1. All calculations for data reduction, structure solution, and refinement were done by standard procedures (WINGX) [12].

The structures of **1**–**4** were solved by direct methods using the SHELXS97[b] computational program. All non-hydrogen atoms were refined anisotropically by full-matrix least-squares technique on F^2 through the SHELXL97 program [13]. The hydrogen atoms for all compounds were located from difference Fourier maps and refined with isotropic temperature factors. The final geometrical calculations and the graphical manipulations were carried out with PARST97 [14] and DIAMOND [15] programs, respectively.

3. Results and discussion

3.1. Description of the structures

Four new coordination polymers were obtained: $^{\infty}_{2}[Cu_3(trim)_2(NH_3)_6(H_2O)_3]$ (**1**); $^{\infty}_{1}$[Cu(tmen)(dhtp)] (**2**), $^{\infty}_{1}[Cu(tmen)(hitp)(H_2O)]$ (**3**), $^{\infty}_{1}$[Cu(tmen)(nitp)] (**4**), and their crystal structures were solved. Selected bond lengths and angles for the four compounds are listed in Table 2.

The first compound was obtained by reacting copper triflate with trimesic acid in the presence of ammonia. Its structure consists of 2D layers built up by two crystallographically independent copper(II) ions (Fig. 1). The Cu1 ions, located on a C_2-axis, are heptacoordinated by two ammonia, one aqua and two unsymmetrically chelating carboxylato groups from two $trim^{3-}$ ligands (one of the carboxylato oxygens is semicoordinated, Cu1–O4 = 2.825(2) Å). The Cu2 ions show a strongly distorted octahedral

Table 1
Crystallographic data and structure refinement parameters for compounds **1**–**4**

Compound	**1**	**2**	**3**	**4**
Chemical formula	$C_{18}H_{30}Cu_3N_6O_{15}$	$C_{14}H_{20}CuN_2O_6$	$C_{14}H_{22}CuN_2O_6$	$C_{14}H_{19}CuN_3O_6$
M (g mol^{-1})	761.10	375.86	377.87	388.86
Temperature (K)	103(2)	293(2)	293(2)	293(2)
Wavelength (Å)	0.71073	0.71073	0.71073	0.71073
Crystal system	monoclinic	orthorhombic	orthorhombic	monoclinic
Space group	*C*2/*c*	*Pbca*	*Pbca*	$P2_1/n$
a (Å)	13.9591(8)	16.2826(18)	14.3045(13)	12.266(2)
b (Å)	17.2160(8)	14.9850(12)	14.4687(16)	10.5200(12)
c (Å)	12.5358(7)	13.4020(17)	16.3079(9)	13.811(3)
α (°)	90	90	90	90
β (°)	115.0840(10)	90	90	111.030(16)
γ (°)	90	90	90	90
V (Å^3)	2728.5(3)	3270.0(6)	3375.2(5)	1663.4(5)
Z	4	8	4	4
D_{calc} (g cm^{-3})	1.853	1.527	1.487	1.545
μ (mm^{-1})	2.400	1.367	1.325	1.346
F (000)	1548	1560	1576	800
Goodness-of-fit on F^2	1.019	1.046	1.072	1.045
Final R_1, wR_2 [$I > 2(I)$]	0.0285; 0.0750	0.0519; 0.1030	0.0393; 0.0760	0.0676; 0.0917
R_1, wR_2 (all data)	0.0301; 0.0762	0.1145; 0.1269	0.0707; 0.0871	0.1500; 0.1109
Largest difference peak and hole (e Å^{-3})	0.630; −0.348	0.562; −0.491	0.413; −0.346	0.469; −0.413

Table 2
Selected bond distances (Å) and angles (°) for compounds **1**–**4**

Compound ***1***					
Cu1–N1	2.0182(18)	N1–Cu1–O3	92.37(8)	N2–Cu2–O1	87.51(7)
Cu1–O3	2.0064(15)	N1–Cu1–O3^{ii}	87.26(8)	N2–Cu2–O6^{i}	92.73(7)
Cu1–O4	2.825(2)	N1–Cu1–O4	82.30(7)	N2–Cu2–O11	82.09(7)
Cu1–O10	2.214(3)	N1–Cu1–O4^{ii}	87.99(7)	N3–Cu2–O1	90.71(7)
Cu2–N2	1.9821(18)	N1–Cu1–O10	96.07(6)	N3–Cu2–O5^{i}	86.77(7)
Cu2–N3	1.9690(18)	N1–Cu1–N1^{ii}	167.86(13)	N3–Cu2–O6^{i}	89.07(7)
Cu2–O1	2.0066(15)	O3–Cu1–O3^{ii}	176.47(9)	N3–Cu2–N2	178.19(8)
Cu2–O5^{i}	2.666(2)	O3–Cu1–O4	51.61(5)	O1–Cu2–O5^{i}	111.15(6)
Cu2–O6	1.9989(15)	O3–Cu1–O10	91.77(4)	O1–Cu2–O6^{i}	165.78(6)
Cu2–O11	2.512(2)	O4–Cu1–O4^{ii}	73.97(4)	O1–Cu2–O11	106.38(6)
				O5^{i}–Cu2–O6^{i}	54.64(6)
				O5^{i}–Cu2–O11	142.09(6)
				O6^{i}–Cu2–O11	87.72(6)
Compound ***2***					
Cu1–N1	2.023(4)	N1–Cu1–N2	85.96(16)	O2–Cu1–N2	93.85(14)
Cu1–N2	2.012(4)	N1–Cu1–O2	162.95(18)	O2–Cu1–O5	91.11(13)
Cu1–O1	2.473(4)	N2–Cu1–O5	162.55(16)	O5–Cu1–N1	94.12(16)
Cu1–O2	1.993(3)	O1–Cu1–O2	57.97(13)	O5–Cu1–O6	56.54(16)
Cu1–O5	1.961(3)	O1–Cu1–O6	138.55(14)		
Cu1–O6	2.562(3)				
Compound ***3***					
Cu1–N1	2.015(2)	N1–Cu1–N2	86.58(10)	O2–Cu1–O5	109.44(8)
Cu1–N2	2.067(2)	N1–Cu1–O16	176.95(10)	O2–Cu1–O16	90.50(9)
Cu1–O2	2.2241(17)	N2–Cu1–O16	90.58(10)	O5–Cu1–N1	89.22(8)
Cu1–O5	1.9719(18)	O2–Cu1–N1	90.99(8)	O5–Cu1–N2	152.77(9)
Cu1–O16	1.974(2)	O2–Cu1–N2	97.53(8)	O5–Cu1–O16	92.79(9)
Compound ***4***					
Cu1–N2	2.022(4)	N2–Cu1–N3	86.80(16)	O1–Cu1–O2	58.25(17)
Cu1–N3	2.033(4)	N2–Cu1–O1	95.20(14)	O1–Cu1–O4^{vi}	89.97(14)
Cu1–O1	2.000(3)	N2–Cu1–O4^{vi}	164.12(14)	O2–Cu1–O3^{vi}	95.65(15)
Cu1–O2	2.464(5)	N3–Cu1–O1	158.74(14)	O3^{vi}–Cu1–O4^{vi}	53.10(13)
Cu1–O3^{vi}	2.758(4)	N3–Cu1–O4^{vi}	93.80(15)		
Cu1–O4^{vi}	1.939(3)				

Symmetry code: (i) $0.5 - x$, $-0.5 + y$, $1.5 - z$; (ii) $-x$, y, $2.5 - z$; (iii) $x - 0.5$, $-y + 0.5$, $z - 0.5$.

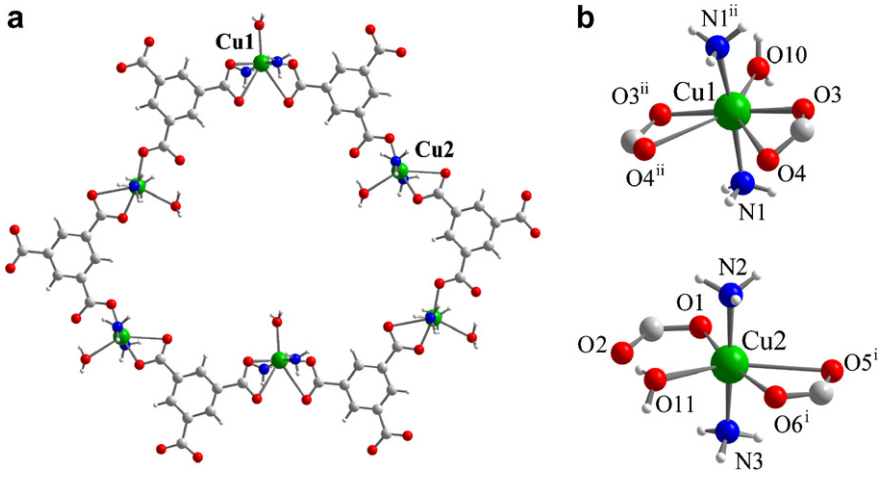


Fig. 1. Coordination environments of the copper ions in crystal **1**.

geometry, being coordinated by one chelating carboxylato group, one oxygen from a monodentate carboxylato arising from another trimesate ion, one aqua and two ammonia ligands. Two out of the *trans* Cu–O oxygen bonds [Cu2–O11 = 2.516(2) and Cu2–O5^{i} = 2.666(2) Å ($^{i} = 0.5 - x$, $-0.5 + y$, $1.5 - z$)] are much longer than the other four bonds [Cu2–O1 = 2.0066(15); Cu2–O6^{i} = 1.9989(15); Cu2–N2 = 1.9821(18); Cu2–N3 = 1.9690(18) Å].

The construction of the coordination polymer in **1** can be described as follows: the $trim^{3-}$ ligands connect with two of the carboxylato groups the Cu2 ions, resulting in zigzag chains. These chains are further interconnected by the Cu1 ions, which are coordinated to the third carboxylato group arising from trimesate ions belonging to two different chains. The coordination fashion of the trimesate ion is chelating bis-bidentate and unidentate. Two-dimensional layers with heart-shaped mashes, which are parallel to the *bc* crystallographic plane, are thus formed. The distance between the copper ions within a mesh are: Cu1···Cu2 = 10.159; Cu2···Cu2′ = 8.726; Cu1′···Cu2′ = 9.285 Å (Fig. 2a). Intralayer hydrogen bonds are established between the aqua ligand coordinated to Cu2 and an oxygen atom from the unidentate carboxylato group (O11–H11···O2 = 1.937 Å – Fig. 3a). It is interesting to recall that within the $3M^{2+}$: $2trim^{3-}$ stoichiometry, the following network topologies have been observed so far (M^{2+} = various transition metal ions): (1) honeycomb layers with the trimesate ion located on a threefold axis with all the metal centres crystallographically equivalent [16–18]; (2) herringbone (parquet flooring) [16]; (3) brick wall network [16]; (4) layers with heart-shaped mashes [19]; (5) double stranded chain [19]; (6) single zigzag chains with both connecting and terminal metal ions [3b,20]; (7) T-shaped bilayer [21].

The view along the *b* crystallographic axis reveals a stair-like conformation of the layers (Fig. 2b). The layers stack in the crystal as follows: ABAB··· The adjacent A and B layers (Fig. 3a) interact through hydrogen bonds established between the aqua ligands coordinated to the Cu1 and Cu2 ions from one layer and the carboxylato oxygen atoms that are semicoordinated to Cu2 and Cu1 from the other layer: (Cu1)O10···$O5^{iii}$(Cu2) = 2.669 Å ($^{iii} = -x$, $2 - y$, $2 - z$); (Cu2)O11···$O4^{iv}$(Cu1) = 2.792 Å ($^{iv} = -x$, $1 - y$, $2 - z$). Hydrogen bonds are also established between the first and the third layer (Fig. 3b), and involve the ammonia ligands: (Cu1)N1···$O11^{v}$(Cu2) = 3.039 Å ($^{v} = -0.5 + x$, $0.5 + y$, z), with O11 from the aqua ligand; (Cu2)N2···$O3^{vi}$(Cu1) = 3.044 Å ($^{vi} = 0.5 + x$, $-0.5 + y$, z); (Cu2)N3···$O2^{vii}$(Cu2) = 2.936 Å ($^{vii} = -x$, y, $1.5 - z$); O2 and O3 arise from carboxylato groups.

During the preparation of this manuscript, Long et al. published the synthesis and crystal structure of another copper complex that contains the same ligands: aqua, ammonia and trimesate. This compound, obtained via hydrothermal synthesis, has a different composition, $[Cu_3(trim)_2(NH_3)_4(H_2O)_3]\cdot 3H_2O$, and a different crystal structure, namely a threefold parallel interpenetration of 2D layers [22].

Compound **2** was obtained by reacting [Cu(tmen)(acac)][BF_4] with 2,5-dihydroxy-terephthalic acid (acac = acetylacetonato). The investigation of its crystal structure reveals the formation of infinite zigzag chains constructed from {Cu(tmen)} nodes and $dhtp^{2-}$ spacers (Fig. 4). The copper ions are hexacoordinated with a distorted octahedral geometry: two nitrogen atoms from the tmen ligand [Cu1–N1 = 2.023(4); Cu1–N2 = 2.012(4) Å], and four oxygens from two chelating carboxylato groups arising from two spacer molecules [Cu1–O1 = 2.473(4); Cu1–O2 = 1.993(3); Cu1–O5 = 1.961(3); Cu1–O6 = 2.562(3) Å]. The hydroxo groups are not involved in the coordination, but form strong intramolecular hydrogen bonds with one oxygen from each carboxylato groups (O1···O3 = 2.579 Å, O4···O6 = 2.581 Å). Each $CuN_2O_2O'_2$ chromophore is chiral, being related through an inversion centre to the neighbouring copper chromophore, so the chains are not chiral.

The third compound, $^{\infty}_{1}$[Cu(tmen)(hitp)(H_2O)] (**3**), consists also of infinite zigzag chains with {Cu(tmen)} nodes connected through 5-hydroxy-isophthalato linkers (Fig. 5). The copper ions are pentacoordinated with a strongly distorted square-pyramidal geometry. The basal plane is formed by two nitrogen atoms from the tmen molecule [Cu1–N1 = 2.015(2); Cu1–N2 = 2.067(2) Å], one aqua ligand [Cu1–O16 = 1.974(2) Å], and one carboxylato oxygen [Cu1–O5 = 1.9719(18) Å]; the apical position is occupied by one carboxylato oxygen from another spacer [Cu1–O2 = 2.2241(17) Å]. A measure of trigonal distortion

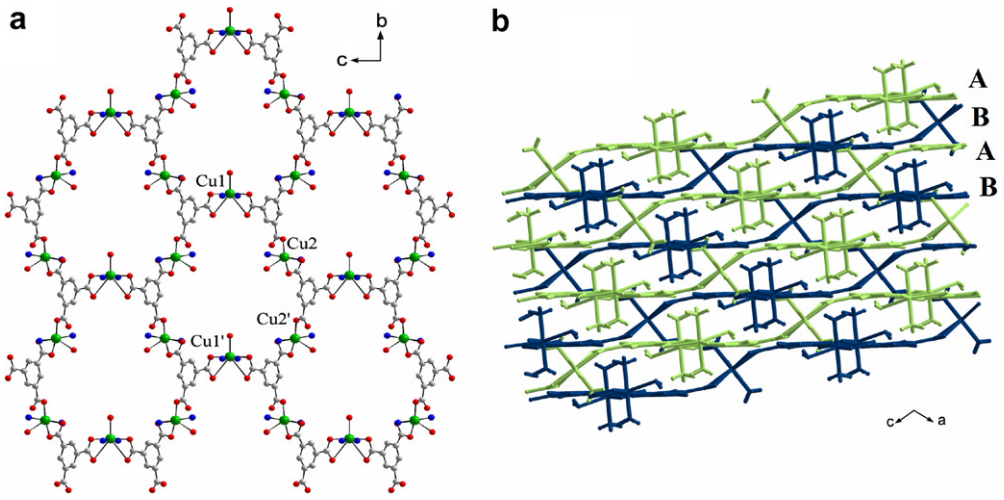


Fig. 2. (a) View along crystallographic *a*-axis of the 2D coordination polymer in **1**; (b) view of the layers along the *b*-axis.

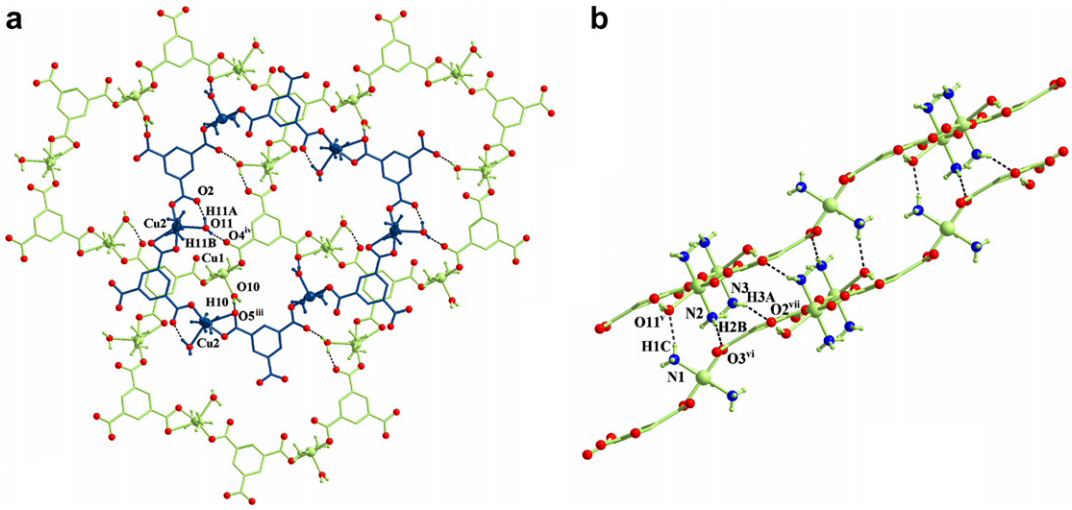


Fig. 3. (a) Packing diagram showing the hydrogen bond interactions established between the A and B layers for the sake of clarity, the semicoordinate Cu1–O4 and Cu1–O4^{ii} have been omitted (b) packing diagram showing the hydrogen bond interactions established between the A layers (see text) dotted.

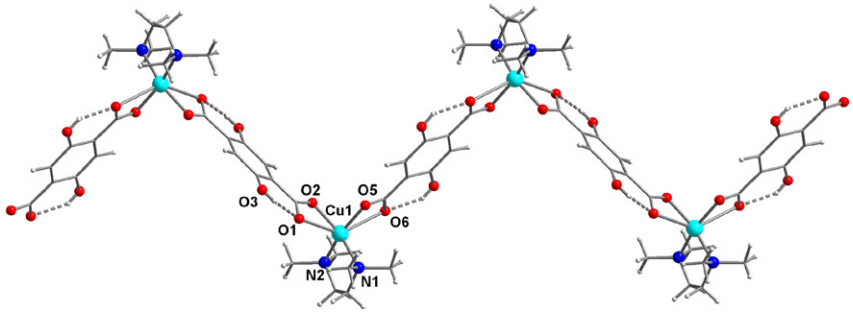


Fig. 4. Perspective view of a zigzag chain in crystal **2**, along with the atom numbering scheme.

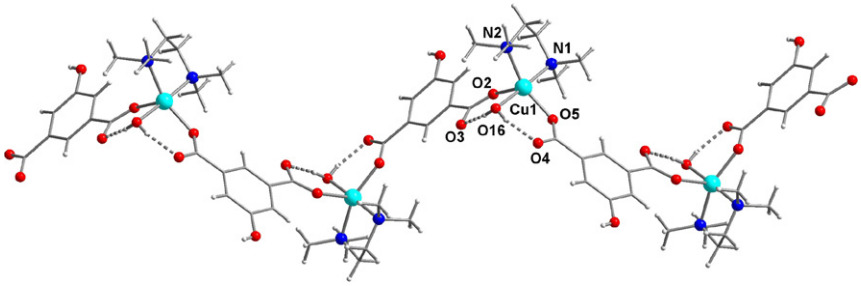


Fig. 5. Perspective view of a zigzag chain in crystal **3**, along with the atom numbering scheme.

for a square-pyramidal geometry can be described using the parameter τ, defined as $[(\theta-\varphi)/60]\times 100$, where θ and φ are the angles between the donor atoms and the Cu(II) ion forming the diagonals of the basal plane in a square-pyramidal geometry [23]. The value of τ for the coordination polyhedron of the Cu(II) ion is $\tau = 40.3$. Strong intrachain hydrogen bond interactions are established between the aqua ligand and the uncoordinated oxygens from two carboxylato groups: O16···O3 = 2.632(2); O16···O4^{i} = 2.573(2) Å ($^{i} = 0.5 - x, -y, 0.5 + z$).

The chains are interconnected through hydrogen bonds involving the OH group, from one chain, and one carboxylato oxygen from another one [O1···O3^{v} = 2.652 Å; ($^{v} = -0.5 + x, y, 0.5 - y$)], resulting in layers paralleling the crystallographic *ac* plane (Fig. 6). The shortest intrachain Cu···Cu distance is 9.919(2) Å.

The relative position of the OH group with respect to the carboxylate influences the coordination and the hydrogen bond abilities of such ligands: the *ortho* OH group favours the chelating behaviour of the hydroxy-carboxylic

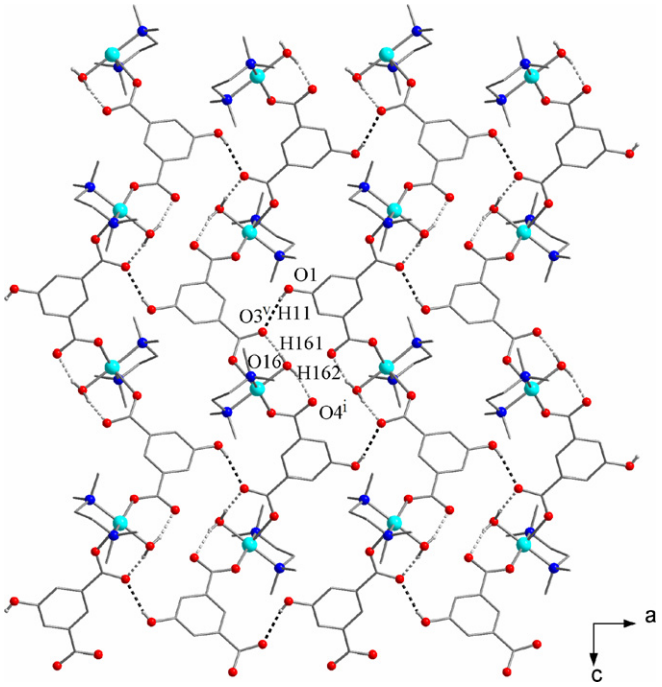


Fig. 6. Packing diagram for crystal **3** showing the hydrogen bonds connecting the chains.

acid or the formation of intramolecular hydrogen bonds (as in the case of compound **2**). The *meta* OH is too far away to coordinate together with the carboxylato group to the same metal ion, but it can be involved in intermolecular hydrogen bonds, as observed with compound **3**. The geometrical parameters associated to the hydrogen bonds in crystals **1**–**3** are listed in Table 3.

Compound **4**, $^{\infty}_{1}$[Cu(tmen)(nitp)], has been constructed by employing the 5-nitro-isophthalate as a spacer. Its structure consists of the zigzag chains similar to those found in crystal **3** (Fig. 7). The copper ions are hexacoordinated by one tmen molecule and two chelating carboxylato groups, with a strongly distorted octahedral geometry. The equatorial plane is described by the nitrogen atoms [Cu1–N2 = 2.022(4); Cu1–N3 = 2.033(4) Å], and by two carboxylato oxygen atoms arising from two spacers [Cu1–O1 = 2.000(3); Cu1-O4^{vi} = 1.939(3) Å with (vi) = $x - 0.5$, $-y + 0.5$, $z - 0.5$]; the apical positions are occupied by the other carboxylato oxygens [Cu1–O2 = 2.464(5); Cu1–O3^{vi} = 2.758(4) Å]. The distance between the neighbouring copper ions within a chain is 9.562(5) Å. Unlike compound **3**, the chains are not connected through hydrogen bonds, since the hydroxo group in the isophthalic acid is replaced by the nitro one.

Table 3
Geometrical parameters of strong hydrogen bonds in complexes **1**–**3**

D–H···A	H···A(Å)	D···A(Å)	D–H···A(°)
Compound ***1***			
O11–H11A···O2	1.937	2.733	164.1
O10–H10···O5^{iii}	1.859	2.669	170.0
O11–H11B···O4^{iv}	1.998	2.792	166.9
N1–H1C···O11^{v}	2.241	3.039	167.8
N2–H2B···O3^{vi}	2.171	3.044	160.7
N3–H3A···O2^{vii}	2.085	2.936	155.2
Compound ***2***			
O3–H3···O1	1.836	2.579	157.9
O4-H4···O6	1.878	2.581	149.3
Compound ***3***			
O16–H161···O3	1.824	2.632	170.1
O16–H162···O4^{i}	1.856	2.573	163.2
O1–H11···O3^{v}	2.022	2.652	168.7

Symmetry codes for complex **1**: (iii) $-x$, $2 - y$, $2 - z$; (iv) $-x$, $1 - y$, $2 - z$; (v) $-0.5 + x$, $0.5 + y$, z; (vi) $0.5 + x$, $-0.5 + y$, z; (vii) $-x$, y, $1.5 - z$.
Symmetry codes for complex **3**: (i) $0.5 - x$, $-y$, $0.5 + z$; (v) $-0.5 + x$, y, $0.5 - y$.

3.2. Magnetic properties

Compounds **1**, **2**, and **4** have been magnetically characterized by following the temperature dependence of the magnetic susceptibility as well as the field dependence of the magnetization at 2 and 4 K. Let us start with compound **1**. The $\chi_M T$ versus T curve is shown in Fig. 8 (χ_M is the magnetic susceptibility per Cu_3 unit). At room temperature, the value of the $\chi_M T$ product (1.20 cm^3 mol^{-1} K) corresponds to the one expected for three uncoupled copper ions. By decreasing the temperature, $\chi_M T$ remains constant down to 200 K, when it starts to decrease slowly, then more and more, reaching 0.46 cm^3 mol^{-1} K at 2 K. This behaviour indicates an antiferromagnetic interaction between the copper ions within the 2D layers. Antiferromagnetic interactions between the layers, mediated by the hydrogen bonds, may also occur.

The $\chi_M T$ versus T curves for compounds **2** and **4** (Figs. 9 and 10) suggest that the intrachain exchange interactions between the copper ions are very weak (we assume that the absence of the interchain hydrogen bonds prevents the intermolecular exchange interactions). For such chains of equally spaced copper(II) ions, the temperature dependence of the magnetic susceptibility is described by the Bonner and Fisher's equation [24]:

$$\chi_M = \frac{Ng^2\beta^2}{kT}\frac{A}{B}$$
$$A = 0.25 + 0.074975x + 0.075235x^2$$
$$B = 1.0 + 0.9931x + 0.172135x^2 + 0.757825x^3$$
$$\text{with } x = |J|/kT$$

The best fit to the data, by including the temperature independent paramagnetism (TIP), leads to the following values: $J = -0.12$ cm^{-1}, $g = 2.05$, TIP $= 2.0 \times 10^{-5}$ cm^3 mol^{-1} (compound **2**); $J = -0.53$ cm^{-1}, $g = 2.15$, TIP $= 4.1 \times 10^{-5}$ cm^3 mol^{-1} (compound **4**). For compounds **2** and **4** the magnetization saturates by increasing the magnetic field, and reaches the expected value ($\sim 1\ N\beta$ mol^{-1}) at 2 K (see insets to Figs. 9 and 10). In the case of compound **1**, the magnetization does not reach saturation even at 2 K (inset to Fig. 8), indicating stronger Cu(II)–Cu(II)

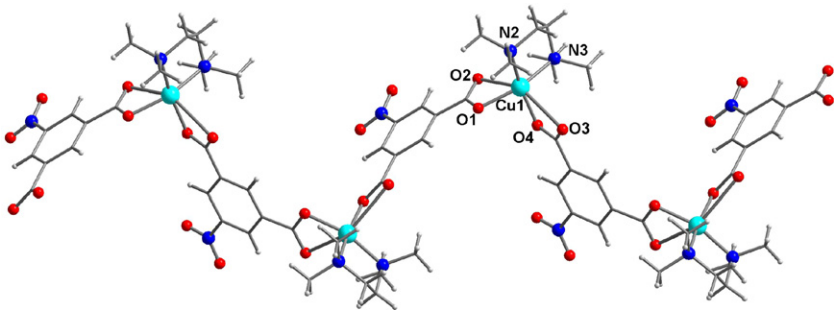


Fig. 7. Perspective view of a chain in crystal **4**, along with the atom numbering scheme.

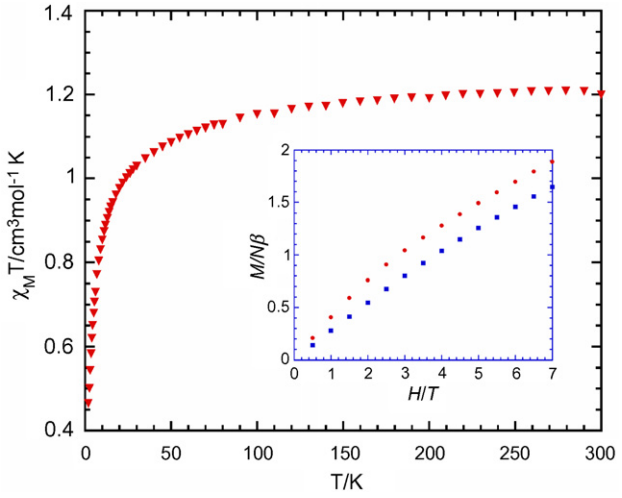


Fig. 8. $\chi_M T$ vs. T curve for compound **1** Inset: the field dependence of the magnetization at $T = 2$ K (circles) and 4 K (squares).

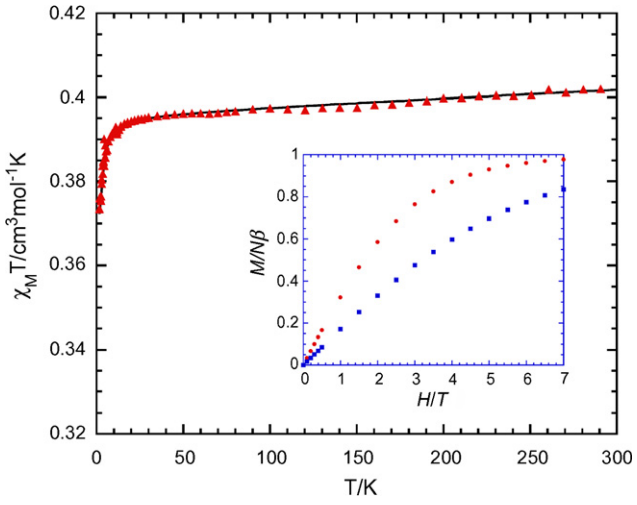


Fig. 9. $\chi_M T$ vs. T curve for compound **2** (the solid line represents the best fit curve). Inset: the field dependence of the magnetization $T = 2$ K (circles) and 4 K (squares).

antiferromagnetic interactions than those found in **2** and **4**. The magnitude of the exchange interactions in **1** can not be estimated, lacking the appropriate $\chi_M(T)$ equation for its complicated topology of the spin carriers.

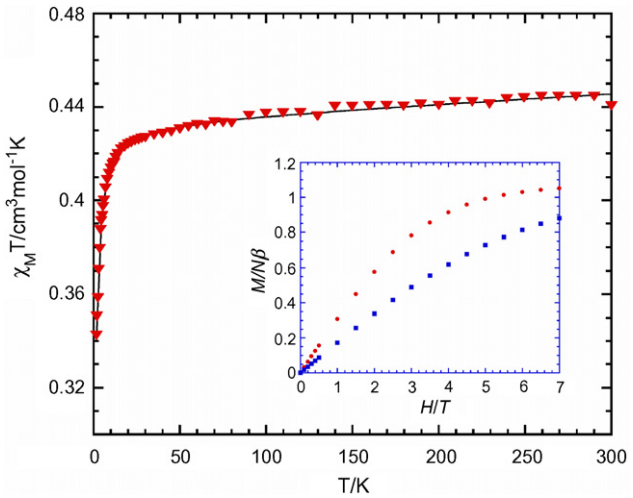


Fig. 10. $\chi_M T$ vs. T curve for compound **4** (the solid line represents the best fit curve). Inset: the field dependence of the magnetization $T = 2$ K (circles) and 4 K (squares).

4. Conclusions

In conclusion, we have illustrated with new examples the richness of the chemistry generated by polycarboxylato ligands acting as bridges. The ancillary ligands attached to the copper ions influence the topology of the metallic centers as well. The case of the trimesato complexes is quite interesting: as mentioned in the Introduction and illustrated by compound **1**, coordination polymers with various dimensionalities and solid-state architectures can be obtained by changing the ancillary ligands.

The values of the exchange parameters were found to be very low, as expected for polycarboxylato bridges, which impose long distance between the paramagnetic centres [3c,9,25,26].

5. Supplementary material

CCDC 658431, 658432, 658433 and 658434 contain the supplementary crystallographic data for compounds **1**, **2**, **3** and **4**. These data can be obtained free of charge via http://www.ccdc.cam.ac.uk/conts/retrieving.html, or from the Cambridge Crystallographic Data Centre, 12 Union Road,

Cambridge CB2 1EZ, UK; fax: (+44) 1223-336-033; or e-mail: deposit@ccdc.cam.ac.uk.

Acknowledgement

Financial support from the Alexander von Humboldt Foundation is gratefully acknowledged.

References

[1] (a) S. Kitagawa, R. Kitaura, S. Noro, Angew. Chem., Int. Ed. 43 (2004) 2334;
(b) C.N.R. Rao, S. Natarajan, R. Vaidhyanathan, Angew. Chem., Int. Ed. 43 (2004) 1466.
[2] (a) See, for example M. Eddaoudi, H.L. Li, O.M. Yaghi, J. Am. Chem. Soc. 122 (2000) 1391;
(b) M. Eddaoudi, D.B. Moler, H.L. Li, B.L. Chen, T.M. Reinecke, M. O'Keeffe, O.M. Yaghi, Acc. Chem. Res. 34 (2001) 319;
(c) O.M. Yaghi, H.L. Li, C. Davis, D. Richardson, T.L. Groy, Acc. Chem. Res. 31 (1998) 474;
(d) J.L.C. Rowell, O.M. Yaghi, Micropor. Mesopor. Mater. 73 (2004) 3;
(e) J.S. Seo, D. Whang, H. Lee, S.I. Jun, J. Oh, Y.J. Jeon, K. Kim, Nature 404 (2000) 982;
(f) B. Gomez-Lor, M. Gutiérez-Puebla, M.A. Monge, C. Ruiz-Valero, N. Snejko, Inorg. Chem. 41 (2000) 2429;
(g) E.V. Anokhina, M. Vouga-Zanda, X. Wang, A.J. Jacobson, J. Am. Chem. Soc. 127 (2005) 15000.
[3] (a) H. Oshio, H. Ichida, J. Phys. Chem. 99 (1995) 3294;
(b) W. Zhang, S. Bruda, C.P. Landee, J.L. Parent, M.M. Turnbull, Inorg. Chim. Acta 342 (2003) 193;
(c) M. Pascu, F. Lloret, N. Avarvari, M. Julve, M. Andruh, Inorg. Chem. 43 (2004) 5189.
[4] R. Pech, J. Pickard, Acta Crystallogr. C44 (1988) 992.
[5] S.S.Y. Chui, A. Siu, I.D. Williams, Acta Crystallogr. C55 (1999) 194.
[6] S.S.Y. Chui, S.M.F. Lo, J.P.H. Charmant, A. Guy Orpen, I.D. Williams, Science 283 (1999) 1148.
[7] (a) W. Böhlmann, A. Pöppl, M. Sabo, S. Kaskel, J. Phys. Chem. B 110 (2006) 20177;
(b) A. Vishnyakov, P.I. Ravikovith, A.V. Neimark, M. Bullow, Q.M. Wang, Nano Lett. 3 (2003) 713;
(c) S. De Rosa, G. Giordano, T. Granato, A. Katovic, A. Siciliano, F. Tripicchio, J. Agric. Food Chem. 53 (2005) 8306;
(d) K. Schlichte, T. Kratzke, S. Kaskel, Micropor. Mesopor. Mater. 73 (2004) 81.
[8] X.X. Zhang, S.S.Y. Chui, I.D. Williams, J. Appl. Phys. 87 (2000) 6007.
[9] S. Konar, P.S. Mukherjee, E. Zangrando, M.G.B. Drew, C. Diaz, J. Ribas, N.R. Chaudhuri, Inorg. Chim. Acta 358 (2005) 29.
[10] C.-C. Su, S.P. Wu, C.-Y. Wu, T.-Y. Chang, Polyhedron 14 (1995) 267.
[11] A. Earnshaw, Introduction to Magnetochemistry, Academic Press, London and New York, 1968.
[12] L.J. Farrugia (WINGX), J. Appl. Crystallogr. 32 (1999) 837.
[13] G.M. Sheldrick, SHELX97, Programs for Crystal Structure Analysis (Release 97-2), Institüt für Anorganische Chemie der Universität, Tammanstrasse 4, D-37077 Göttingen, Germany, 1998.
[14] M. Nardelli, J. Appl. Crystallogr. 28 (1995) 659.
[15] DIAMOND 2.1d, Crystal Impact GbR, CRYSTAL IMPACT, K. Brandenburg & H. Putz GbR, Postfach 1251, D-53002 Bonn, Germany, 2000.
[16] K.E. Holmes, P.F. Kelly, M.R.J. Elsegood, Dalton Trans. (2004) 3488.
[17] B. Liu, L. Xu, Inorg. Chem. Commun. 9 (2006) 364.
[18] J.W. Ko, K.S. Min, M.P. Suh, Inorg. Chem. 41 (2002) 2151.
[19] M.J. Plater, M.R. St. J. Foreman, E. Coronado, C.J. Gómez-García, A.M.Z. Slawin, J. Chem. Soc., Dalton Trans. (1999) 4209.
[20] O.M. Yaghi, H. Li, T.L. Groy, J. Am. Chem. Soc. 118 (1996) 9096.
[21] J.-C. Dai, X.-T. Wu, Z.-Y. Fu, C.-P. Cui, S.-M. Hu, W.-X. Du, L.-M. Wu, H.-H. Zhang, R.-Q. Sun, Inorg. Chem. 41 (2002) 1391.
[22] W.-X. Chen, S.-T. Wu, L.-S. Long, R.-B. Huang, L.-S. Zheng, Cryst. Growth Des. 7 (2007) 1171.
[23] A.W. Addison, T.N. Rao, J. Reedijk, J. van Rijn, G.C. Verschor, J. Chem. Soc., Dalton Trans. (1984) 1349.
[24] O. Kahn, Molecular Magnetism, VCH, New York, 1973, pp. 251–252.
[25] K.-S. Bürger, P. Chaudhuri, K. Wieghardt, B. Nuber, Chem.-Eur. J. 1 (1995) 583.
[26] (a) See, for example S.S. Massoud, F.A. Mautner, R. Vicente, H.N. Sweeney, Inorg. Chim. Acta 359 (2006) 1489;
(b) A. Das, G. Pilet, D. Luneau, M.S. El Fallah, J. Ribas, S. Mitra, Inorg. Chim. Acta 359 (2005) 4581;
(c) T.K. Maji, M. Ohba, S. Kitagawa, Inorg. Chem. 44 (2005) 9225;
(d) B. O Patrick, C.L. Stevens, A. Storr, R.C. Thompson, Polyhedron 24 (2005) 2242.

Available online at www.sciencedirect.com
ScienceDirect
Polyhedron 27 (2008) 583–592
POLYHEDRON
www.elsevier.com/locate/poly

Syntheses and characterizations of four metal coordination polymers constructed by the pyridine-3,5-dicarboxylate ligand

Ya-Hui Zhao, Zhong-Min Su *, Yao-Mei Fu, Kui-Zhan Shao, Peng Li, Yong Wang, Xiang-Rong Hao, Dong-Xia Zhu, Si-Dong Liu

Institute of Functional Material Chemistry, Faculty of Chemistry, Northeast Normal University, Changchun, Jilin 130024, PR China

Received 9 June 2007; accepted 8 October 2007
Available online 21 December 2007

Abstract

A series of metal-organic frameworks, namely $[Ni(PDB)(H_2O)]_n$ (**1**), $[Pb(PDB)(H_2O)]\cdot(H_2O)$ (**2**), $[Co_2(PDB)_2(bpy)_2(H_2O)_4]\cdot 4H_2O$ (**3**) and $[Co_2(PDB)_2(phen)_2]_n$ (**4**) (H_2PDB = pyridine-3,5-dicarboxylic acid, bpy = 2,2′-bipyridine, phen = 1,10-phenanthroline), have been synthesized based on pyridine-3,5-dicarboxylate acid and two neutral chelate ligands, with different metal ions such as Ni^{II}, Co^{II} and Pb^{II}, under hydrothermal conditions. The framework structures of these polymeric complexes have been determined by the X-ray single crystal diffraction technique. In the four complexes, the pyridine-3,5-dicarboxylate acid ligand exhibits diverse coordination modes, which play an important role in the construction of metal-organic frameworks. The thermal analyses of these four complexes have been measured and discussed. In addition, complex **2** shows strong phosphorescent emission at room temperature and the magnetic measurement of the polymer of **4** reveals a typical antiferromagnetic exchange.
© 2007 Elsevier Ltd. All rights reserved.

Keywords: Coordination polymer; Pyridine-3,5-dicarboxylate acid; Crystal structure; Phosphorescence; Magnetic property

1. Introduction

The construction of metal-organic framework (MOF) structures is receiving increasing attention because of the potential applications of novel functional materials such as magnetism, gas storage, molecular sieves, size- and shape-selective catalysis and electric conductivity [1,2]. However, rational design and synthesis of MOFs with unique structures and functions is still hard work. Therefore, the rational exploitation of the knowledge of the coordination geometry of a metal and ligand structure continues to be an important synthetic strategy widely used in the construction of metal-organic framework structures [3]. Organic aromatic polycarboxylate ligands as an important family of multidentate O-donors have been employed in the preparation of such metal-organic compounds [4]. Pyridyl dicarboxylic acids containing N- and O-donors are also particularly attractive as excellent building blocks with charge and multi-connecting ability [5]. In particular, pyridine-2,4-dicarboxylate acid, pyridine-3,4-dicarboxylate acid, pyridine-2,5-dicarboxylate acid and pyridine-2,6-dicarboxylate acid have been widely used by Kitagawa, Wang, Cao, Zhu and their co-workers in the construction of high-dimensional structures with large pores or undulated layers [5–8]. In contrast, pyridine-3,5-dicarboxylic acid [9], as a member of the multicarboxylate ligands containing N-donors, is rarely used. In this context, the majority of this research focuses on the synthesis, structural elements and properties of complexes constructed from different divalent metal ions and pyridine-3,5-dicarboxylic acid as well as two chelate bpy-liked ligands, and the utility of these versatile ligands in the fabrication of functional organic–inorganic hybrid materials is contemplated. In this paper, four new coordination complexes, namely,

* Corresponding author. Tel.: +86 431 85099108; fax: +86 431 85684009.
E-mail address: zmsu@nenu.edu.cn (Z.-M. Su).

0277-5387/$ - see front matter © 2007 Elsevier Ltd. All rights reserved.
doi:10.1016/j.poly.2007.10.020

[Ni(PDB)(H_2O)] (**1**), [Pb(PDB)(H_2O)]·(H_2O) (**2**), [Co_2(PDB)$_2$(bpy)$_2$(H_2O)$_4$]·4H_2O (**3**) and [Co_2(PDB)$_2$(phen)$_2$] (**4**) (H_2PDB = pyridine-3,5-dicarboxylic acid, bpy = 2,2′-bipyridine, phen = 1,10-phenanthroline), were prepared and investigated to determine the influence of metal ions and chelate ligands on the formation of such metal-organic frameworks. In addition, the photoluminescent property of complex **2** and the magnetic property of complex **4** were measured and discussed.

2. Experimental

2.1. Materials and analyses

All chemicals were commercially purchased and used without further purification. Elemental analyses (C, H and N) were performed on a Perkin–Elmer 2400CHN Elemental Analyzer. FT-IR spectra were recorded in the range 400–4000 cm^{-1} on an Alpha Centaurt FT/IR spectrophotometer as KBr pellets. The emission/excitation spectra were recorded on a Varian Cary Eclipse spectrometer. TG analyses were performed on a Perkin–Elmer TGA7 instrument in flowing N_2 with a heating rate of 10 °C min^{-1}. Variable-temperature magnetic susceptibility data were obtained on a SQUID magnetometer (Quantum Design, MPMS-5) in the temperature range 5–300 K with an applied field of 1000 Oe.

2.2. Syntheses of the complexes

2.2.1. [Ni(PDB)(H_2O)] (*1*)

A mixture of $NiCl_2 \cdot 6H_2O$ (0.072 g, 0.3 mmol), pyridine 3,5-dicarboxylate acid (0.05 g, 0.3 mmol), NaOH (0.024 g, 0.6 mmol) and H_2O (10 ml) was heated at 150 °C for 3 days in a 25 ml Teflon-lined stainless steel vessel under autogenous pressure. After the reaction mixture was slowly cooled down to room temperature, green block crystals were produced in a yield of 60%. Elem. *Anal.* Calc. for complex $C_7H_5NiNO_5$ (**1**) (241.83): C, 34.77; H, 2.07; N, 5.79. Found: C, 34.80; H, 2.11; N, 5.71%. IR (cm^{-1}, KBr): 3398 (br), 1607 (s), 1560 (s), 1432 (m), 1377 (s), 1302 (m), 1124 (m), 1035 (w), 936 (w), 835 (m), 775 (m), 697 (m), 564 (sm), 437 (m).

2.2.2. [Pb(PDB)(H_2O)]·(H_2O) (*2*)

An identical procedure to **1** was followed to prepare **2** except $NiCl_2 \cdot 6\,H_2O$ was replaced by $Pb(NO_3)_2$ (0.099 g, 0.3 mmol), yield 65%. Elem. *Anal.* Calc. for complex $C_7H_7PbNO_6$ (**2**) (408.33): C, 20.59; H, 1.71; N, 3.43. Found: C, 20.50; H, 1.75; N, 3.40%. IR (cm^{-1}, KBr): 3396 (br), 3080 (m), 1603 (s), 1557 (s), 1361 (vs), 1261 (m), 1147 (ms), 1208 (w), 958 (w), 911 (w), 821 (m), 767 (m), 725 (s), 681 (m), 669 (w), 573 (w), 515 (w), 430 (w).

2.2.3. [Co_2(PDB)$_2$(bpy)$_2$(H_2O)$_4$]·4H_2O (*3*)

A mixture of $Co(OAc)_2 \cdot 4H_2O$ (0.075 g, 0.3 mmol), pyridine 3,5-dicarboxylate acid (0.05 g, 0.3 mmol), 2,2′-bipyridine (0.031 g, 0.02 mmol), NaOH (0.024 g, 0.6 mmol) and H_2O (10 ml) was heated at 150 °C for 3 days in a 25 ml Teflon-lined stainless steel vessel under autogenous pressure. After the reaction mixture was slowly cooled down to room temperature, pink block crystals were produced in a yield of 70%. Elem. *Anal.* Calc. for complex $C_{34}H_{38}Co_2N_6O_{16}$ (**3**) (904.56): C, 45.15; H, 4.20; N, 9.29. Found: C, 45.10; H, 4.27; N, 9.31%. IR (cm^{-1}, KBr): 3420 (br), 1608 (vs), 1566 (s), 1489 (w), 1478 (w), 1438 (m), 1397 (m), 1375 (s), 1282 (w), 1151 (w), 1125 (w), 932 (w), 771 (s), 736 (mm), 695 (m), 529 (m), 439 (m).

2.2.4. [Co_2(PDB)$_2$(phen)$_2$] (*4*)

An identical procedure to **3** was followed to prepare **4** except 2,2′-bipyridine was replaced by 1,10-phenanthroline (0.031 g, 0.02 mmol), yield 50%. Elem. *Anal.* Calc. for complex $C_{38}H_{22}Co_2N_6O_8$ (**4**) (808.48): C, 56.45; H, 2.72; N, 10.39. Found: C, 56.38; H, 2.81; N, 10.32%. IR (cm^{-1}, KBr): 3420 (br), 3056 (m), 2359 (w), 1663 (s), 1610 (s), 1576 (s), 1516 (m), 1496 (w), 1442 (m), 1404 (s), 1354 (s), 1311 (s), 1284 (s), 1226 (w), 1144 (w), 1125 (m), 1104 (w), 1047 (w), 1031 (w), 936 (w), 918 (w), 866 (w), 846 (s), 818 (w), 771 (s), 725 (s), 715 (m), 696 (m), 641(w), 610(w), 564 (w), 438 (w).

2.3. X-ray crystallography analysis

Crystal data, data collection and refinement details for **1**–**4** are given in Table 1. X-ray diffraction measurements were performed using a Bruker APXII CCD diffractometer with graphite monochromated Mo Kα ($\lambda = 0.71073$ Å) radiation. An empirical absorption correction was applied using the SADABS computer program [10]. The coordinates of the heavy atoms were determined by direct methods with the SHELXS program [11]. The coordinates and anisotropic thermal displacement parameters for all non-hydrogen atoms were refined by the least squares methods based on F^2 using the SHELXL97 program [12]. The H atoms attached to C atoms were positioned geometrically, with U_{iso} values derived from U_{eq} values of the corresponding C atom. The hydrogen atoms from water molecules were directly located from successive Fourier differences syntheses and were included in the calculation with estimated isotropic displacement parameters without refinement, with O–H distances restrained (DFIX) to 0.85(2) Å, in order to ensure a chemically reasonable geometry for these molecules.

3. Results and discussion

3.1. Description of the structures

Crystallographic and structural refinement data for the compounds are given in Table 1. Selected bond distances and angles for **1**, **2**, **3** and **4** are shown in Tables 2–5, respectively.

Table 1
Crystal data and structure refinement for **1**–**4**

	1	**2**	**3**	**4**
Empirical formula	$C_7H_5NiNO_5$	$C_7H_7PbNO_6$	$C_{34}H_{38}Co_2N_6O_{16}$	$C_{38}H_{22}Co_2N_6O_8$
Formula weight	241.83	408.33	904.56	808.48
T(K)	293(2)	293(2)	293(2)	293(2)
λ(Å)	0.71069	0.71069	0.71069	0.71069
Crystal system	monoclinic	monoclinic	triclinic	monoclinic
Space group	$P2_1/c$	$P2_1/n$	$P\bar{1}$	$P2_1/c$
a (Å)	7.751(5)	10.3826(6)	9.542(5)	9.677(5)
b (Å)	15.049(5)	6.8387(4)	12.351(5)	31.194(5)
c (Å)	6.435(5)	12.7710(8)	16.654(5)	11.181(5)
α (°)	90	90	84.766(5)	90
β (°)	108.440(5)	92.277(1)	73.737(5)	108.069(5)
γ (°)	90	90	86.728(5)	90
V (Å^3)	712.1(8)	906.07(9)	1875.3(14)	3029(2)
Z	4	4	2	4
D_{calc} (g cm^{-3})	2.256	2.993	1.602	1.674
μ (mm^{-1})	2.716	18.630	0.968	1.103
F(000)	488	744	932	1640
Reflections collected	4335	5039	11 709	19 926
Independent reflections [R_{int}]	1654	2132	8435	7628
Data/restraints/parameters	1654/0/135	2132/0/152	8435/24/587	7628/0/487
Goodness-of-fit on F^2	1.039	1.004	0.985	0.940
R_1^a	0.0290	0.0222	0.0366	0.0393
wR_2^b	0.0752	0.0492	0.1148	0.1064

[a] $R_1 = \sum||F_0| - |F_c||/\sum|F_0|$.
[b] $wR_2 = \sum[w(F_0^2 - F_c^2)^2]/\sum[w(F_0^2)^2]^{1/2}$.

Table 2
Selected bond lengths (Å) and angles (°) for compound **1**

Ni(1)–O(4)	2.005(2)	Ni(1)–N(2)	2.064(2)
Ni(1)–O(3)	2.094(3)	Ni(1)–O(1)	2.115(2)
Ni(1)–O(5)	2.120(3)	Ni(1)–O(2)	2.143(2)
O(4)–Ni(1)–N(2)	109.67(8)	O(4)–Ni(1)–O(3)	87.39(9)
N(2)–Ni(1)–O(3)	89.0(1)	O(4)–Ni(1)–O(1)	92.35(7)
N(2)–Ni(1)–O(1)	157.85(8)	O(3)–Ni(1)–O(1)	89.7(1)
O(4)–Ni(1)–O(5)	92.37(7)	N(2)–Ni(1)–O(5)	91.35(8)
O(3)–Ni(1)–O(5)	179.64(9)	O(1)–Ni(1)–O(5)	90.07(8)
O(4)–Ni(1)–O(2)	153.80(7)	N(2)–Ni(1)–O(2)	96.17(8)
O(3)–Ni(1)–O(2)	88.88(8)	O(1)–Ni(1)–O(2)	61.70(7)
O(5)–Ni(1)–O(2)	91.22(7)		

Table 3
Selected bond lengths (Å) and angles (°) for compound **2**

Pb(1)–O(1W)	2.392(4)	Pb(1)–O(2)	2.463(3)
Pb(1)–O(5)	2.492(3)	Pb(1)–O(1)	2.685(3)
Pb(1)–N(1)	2.824(3)		
O(1W)–Pb(1)–O(2)	77.9(1)	O(1W)–Pb(1)–O(5)	74.8(1)
O(2)–Pb(1)–O(5)	83.1(1)	O(1W)–Pb(1)–O(1)	74.4(1)
O(2)–Pb(1)–O(1)	50.7(1)	O(5)–Pb(1)–O(1)	128.5(1)

Table 4
Selected bond lengths (Å) and angles (°) for compound **3**

Co(1)–O(1)	2.039(2)	Co(2)–O(8)	2.069(2)
Co(1)–O(2W)	2.075(3)	Co(2)–O(3W)	2.079(3)
Co(1)–O(1W)	2.136(3)	Co(2)–O(4W)	2.093(3)
Co(1)–N(1)	2.102(3)	Co(2)–N(4)	2.123(3)
Co(1)–N(2)	2.128(3)	Co(2)–N(3)	2.147(3)
Co(1)–N(6)	2.186(3)	Co(2)–N(5)[a]	2.196(3)
O(1)–Co(1)–(1W)	90.5(1)	O(3W)–Co(2)–N(3)	94.5(1)
N(1)–Co(1)–O(1W)	176.5(1)	O(8)–Co(2)–N(4)	93.6(1)
O(1)–Co(1)–N(1)	93.0(1)	N(4)–Co(2)–N(3)	77.0(1)
O(1)–Co(1)–N(2)	169.8(1)	O(8)–Co(2)–O(3W)	94.8(1)
N(1)–Co(1)–N(2)	76.9(1)	O(3W)–Co(2)–N(4)	171.6(1)
N(2)–Co(1)–O(1W)	99.6(1)	O(8)–Co(2)–N(3)	169.3(1)
O(2W)–Co(1)–N(6)	172.9(1)	O(4W)–Co(2)–N(5)[a]	175.0(1)

Symmetry transformations used to generate equivalent atoms: (a) x, $y+1$, z.

3.1.1. [Ni(PDB)(H$_2$O)] (**1**)

Single crystal X-ray diffraction analysis shows that the asymmetric unit of compound **1** contains one Ni^{II} ion, one PDB ligand and one coordinated water molecule. As shown in Fig. 1, each Ni^{II} ion adopts distorted octahedral coordination geometry supplied by one N atom and five O atoms. Three carboxylate oxygen atoms (O1, O2, O4) and the nitrogen atom (N2) (Ni1–N2 2.064(2) Å) comprise the equatorial plane, and the other carboxyl oxygen atom (O5C) and the oxygen atom (O3) from a coordinated water molecule occupy the axial positions (O3–Ni–O5C = 179.64(2)°), the Ni–O (2.005(2)–2.143(2) Å) and Ni–N (2.064(2) Å) bond distances are similar to those found in related Ni(II) complexes [13] (see Figs. 2a and 2b).

The coordination modes of PDB in this work are summarized in Scheme 1. As can be seen in Scheme 1c, one carboxylate bridges two metal atoms in a carboxylate *O,O′* mode, and the other links to the third Ni atom in bidentate–chelate mode. The pyridyl N atom bonds to the fourth Ni center, and thus, each pydc ligand acts as a tetra-connector. Interestingly, one carboxylate group is roughly coplanar with the adjacent pyridine ring and the other is

Table 5
Selected bond lengths (Å) and angles (°) for compound **4**

Co(1)–O(1)	2.076(2)	Co(2)–O(3)	2.226(2)
Co(1)–O(3)[a]	2.089(2)	Co(2)–O(5)	1.985(2)
Co(1)–O(7)[b]	2.107(2)	Co(2)–O(8)[d]	2.079(2)
Co(1)–N(5)	2.141(3)	Co(2)–O(1)[e]	2.082(2)
Co(1)–N(1)[c]	2.163(3)	Co(2)–N(2)	2.137(3)
Co(1)–N(6)	2.166(3)	Co(2)–N(3)	2.102(3)
N(5)–Co(1)–N(6)	77.0(1)	N(3)–Co(2)–N(2)	78.0(1)
O(7)[b]–Co(1)–N(6)	165.6(1)	O(8)[d]–Co(2)–N(2)	89.7(1)
O(3)[a]–Co(1)–O(7)[b]	84.23(8)	O(8)[d]–Co(2)–O(1)[e]	88.08(9)
O(3)[a]–Co(1)–N(5)	171.38(9)	O(1)[e]–Co(2)–N(2)	176.77(9)
O(3)[a]–Co(1)–N(6)	109.6(1)	O(8)[d]–Co(2)–N(3)	163.3(1)
O(7)[b]–Co(1)–N(5)	88.87(9)	O(1)[e]–Co(2)–N(3)	103.7(1)
O(1)–Co(1)–N(1)[c]	174.75(9)	O(5)–Co(2)–O(3)	165.60(9)

Symmetry transformations used to generate equivalent atoms: (a) $x+1$, y, z; (b) $x+1$, $-y+1/2$, $z-1/2$; (c) $x+1$, y, $z-1$; (d) x, $-y+1/2$, $z-1/2$; (e) $x-1$, y, z.

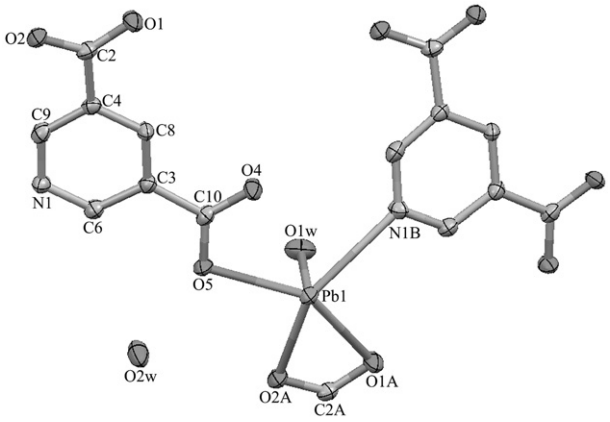


Fig. 3. ORTEP diagram showing the coordination environment of the Pb atom in **2**. Symmetry code A: $x+1$, y, z.

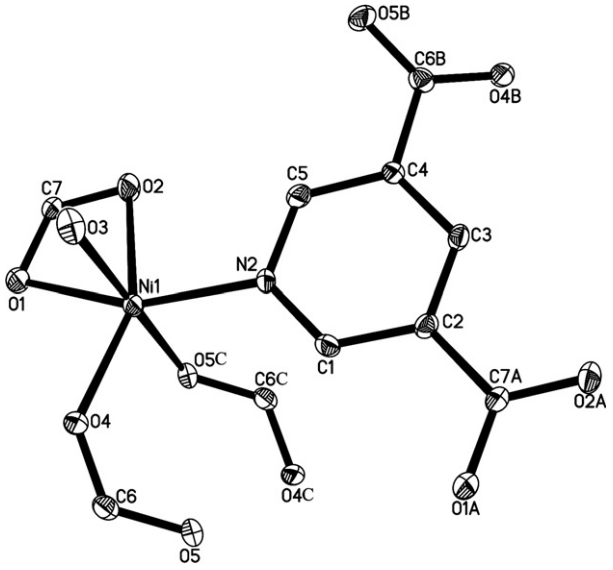


Fig. 1. ORTEP diagram showing the coordination environment for the Ni atoms in **1**. Symmetry code A: $x-1$, y, z; B: x, $-y+1/2$, $z+1/2$; C: $-x$, $-y+1$, $-z$.

deviated from the plane with a dihedral angle of 21.55°, nipping two Ni atoms located in adjacent single layers. Such a regular crossing-plane coordination fashion is still rare in the system of multi-carboxylates, and it plays an important role in the construction of the 3D metal-organic framework (see Fig. 4b). Moreover, the hydrogen bondings between the water molecule and carboxylic O atoms (O3···O1i = 2.708(3) Å, i: $1-x$, $1-y$, $1-z$; O3···O5ii = 3.143(4) Å, ii: x, y, $1+z$) further stabilize the framework.

3.1.2. *[Pb(PDB)(H$_2$O)]·(H$_2$O) (**2**)*

The structural analysis of complex **2** reveals that it is a 2D layer structure containing (6,3) topology. The Pb atom is in a square-pyramidal coordinated geometry with four O atoms and one N atom from three separated PDB ligands and one aqua ligand (Fig. 3). Three oxygen atoms (Pb1–O2 = 2.463(3) Å, Pb1–O5 = 2.492(3) Å, Pb1–O1 = 2.685(3) Å) from two carboxylic groups of the PDB ligands and one pyridyl N atom (Pb1–N1 = 2.824(3) Å) are ligated to the Pb^{II} ion in the quasi-plane, with another oxygen atom belonging to a water molecule (Pb1–O1W =

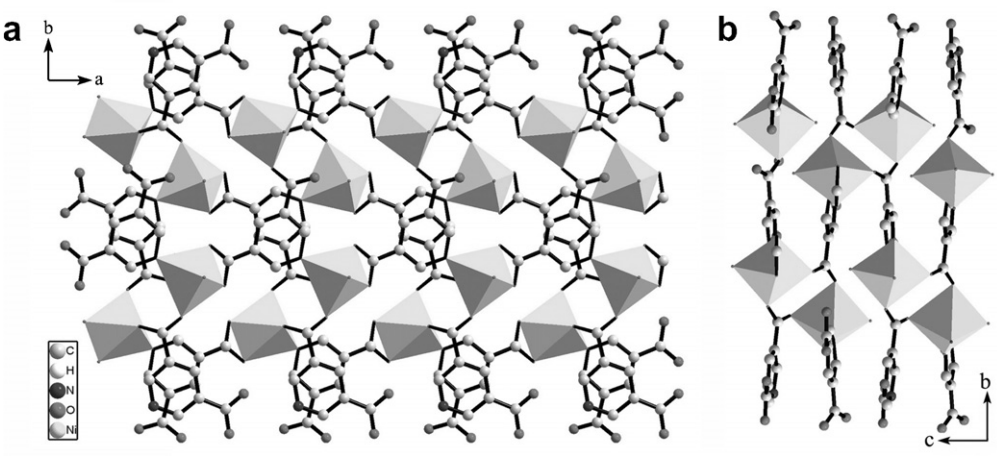
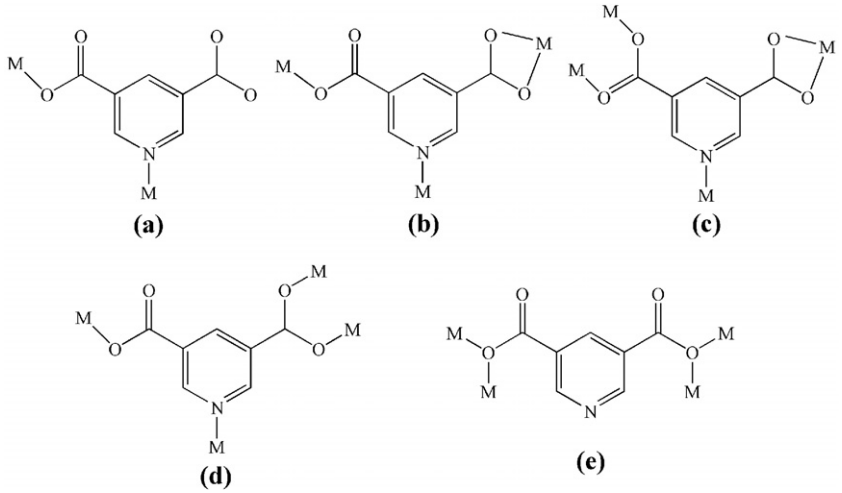


Fig. 2. Views of the 2D layer structure of **1** viewed down along the (a) *c*-axis; (b) *a*-axis.



Scheme 1. Coordination modes of the PDB ligand in compounds **1**–**4**.

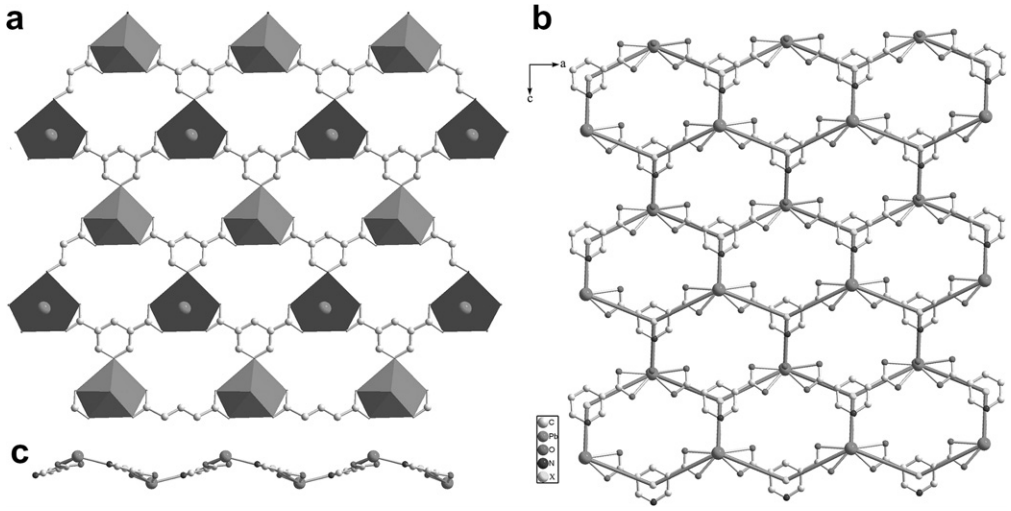


Fig. 4. (a) 2D layer structure of **2** viewed along the *b*-axis; (b) undulated along the *c*-axis; (c) projection of **2** showing the (6, 3) net based on the Pb atoms and PDB ligands.

2.392(4) Å) located in the axial position, as displayed in Fig. 4a. Longer distances are observed between Pb and O4 (2.781(4) Å); some long Pb–O weak bonds have also been reported in other lead complexes [14].

Different from that of complex **1**, each PDB ligand acts as a tri-connector linking three Pb atoms in complex **2** (Scheme 1b), one of carboxylate groups connects with one Pb atom through a mono-dentate O atom, the other bonds with the second Pb atom; the pyridyl N atom binds to the third Pb atom, consequently resulting in the formation of a 2D layer. In compound **2**, two carboxylate groups and the pyridine ring of the ligand are both distorted. The twist angles between the two $-CO_2$ planes and the pyridyl ring plane of PDB are 9.39° (O4, O5) and 14.51° (O1, O2), so the 2D layer is developed in an undulated layer pattern parallel to the *ab*-plane. By treating the Pb atom as a single node and connecting the nodes according to the connectivity defined by the geometrical centers of the benzene rings of the BTC ligands, a distorted 2D (6, 3) network sustained by 3-connected nodes is then yielded, as illustrated in Fig. 4c. The multipoint hydrogen-bonding interactions among free water molecules, coordinated water molecules and carboxylic O atoms extend the 2D layer into a 3D supramolecular net.

3.1.3. $[Co_2(PDB)_2(bpy)_2(H_2O)_4]\cdot 4H_2O$ (**3**)

When the chelate neutral ligand 2,2′-bpy is introduced, and simultaneously replacing the divalent lead salt with a divalent cobalt salt, complex **3** is obtained. Single-crystal X-ray diffraction analysis reveals that complex **3** crystallizes in a triclinic space group $P\bar{1}$ and there are two crystallographically independent cobalt atoms, two PDB, two bpy, four aqua ligands and four free water molecules in the asymmetric unit. The Co atom, in a distorted octahedral geometry (Fig. 5), is bounded by two N atoms from one bpy molecule, two O atoms from coordinated water

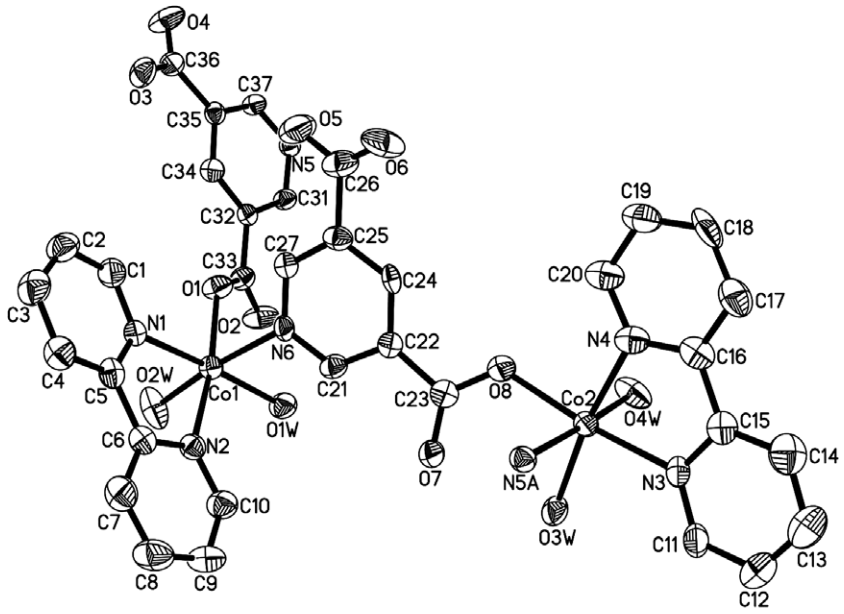


Fig. 5. ORTEP diagram showing the coordination environment of two Co atoms in **3**. Symmetry code A: x, $y+1$, z.

molecules (Co–O(water) 2.075(3)–2.136(3) Å), one pyridyl N atom and one carboxylic O atom from two PDB ligands.

Each PDB ligand acts as a bridge to connect with between Co^{II} centers through one carboxyl O atom and the pyridyl N atom (Scheme 1a), and thus a one-dimensional zig-zag chain is generated, as shown in Fig. 6. Two types of supramolecular interactions, $\pi\cdots\pi$ stacking interactions between bpys of adjacent layer (3.375 Å) and multipoint hydrogen-bonding interactions between lattice water molecules, and coordinated water molecules, as well as uncoordinated carboxylate O atoms, contribute to the formation of the three-dimensional supramolecular architecture.

3.1.4. $[Co_2(PDB)_2(phen)_2]$ (**4**)

When another chelate ligand, phen, is used, we obtained complex **4** under similar reaction conditions. The asymmetry unit of complex **4** contains two Co ions, two phen ligands and two PDB ligands. As shown in Fig. 7, the two crystallographically unique cobalt atoms exhibit two different coordination geometries. The Co1 site shows a distorted-octahedral geometry, being chelated by two N atoms from one phen ligand. The remaining four coordination sites are occupied by one N atom and three oxygen atoms from three pydc ligands. The Co1–O bond lengths are in the range 2.076(2)–2.107(2) Å and the Co1–N bond lengths are 2.141(3) and 2.166(3) Å. The Co2 ion is also six-coordinated in a more distorted octahedral symmetry with a N2O4 donor set. The equatorial plane is occupied by two N-donors from a phen molecule and two O-donors from carboxylate groups of two PDB ligands, and the axial positions are completed by two oxygen atoms from another two PDB ligands. The Co2–O bond lengths are in the range 1.985(2)–2.226(2) Å and Co2–N bond lengths are 2.102(3) and 2.137(3) Å.

In complex **4**, PDB ligands adopt two coordination modes different from those in complexes **1**–**3**: one acts as

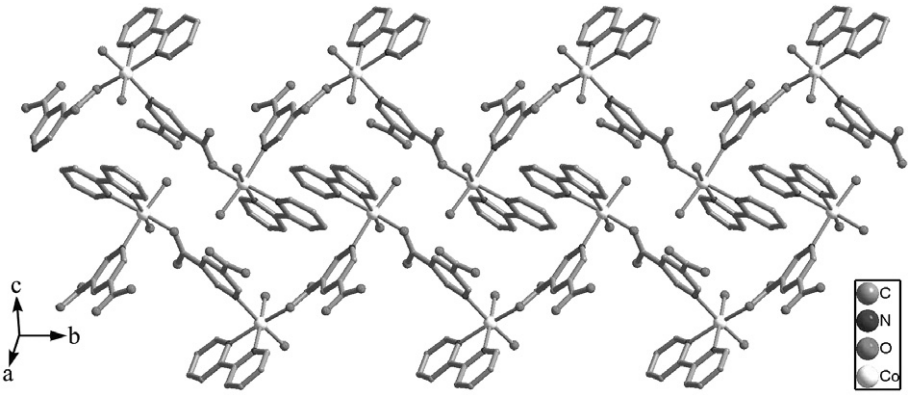


Fig. 6. View of the 1D zigzag chain highlighting the π–π interactions between pyridine rings in adjacent chains in **3**.

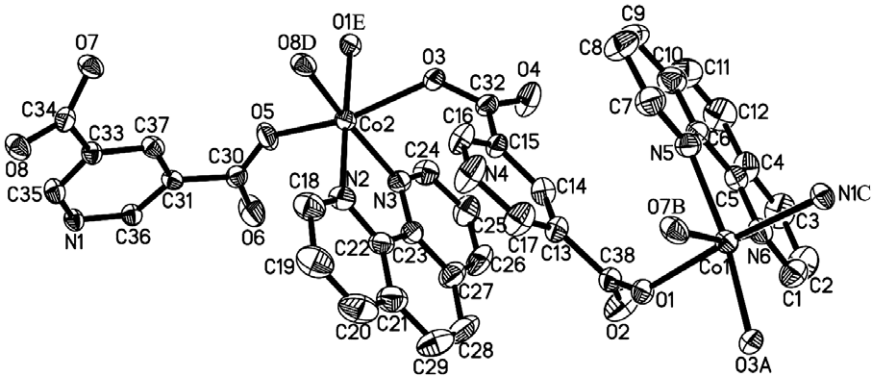


Fig. 7. ORTEP diagram showing the coordination environment for the two Co atoms in **4**. Symmetry code A: $x+1$, y, z; B: $x+1$, $-y+1/2$, $z-1/2$; C: $x+1$, y, $z-1$; D: x, $-y+1/2$, $z-1/2$; E: $x-1$, y, z.

a tetra-connector to link four Co atoms through two monodentate carboxylic O atoms from two carboxylic groups in the μ-O mode, containing an uncoordinated pyridyl N atom; the other, also being a tetra-connector, bonds with four Co atoms through one pyridyl N atom, one monodentate carboxylic O atom from one carboxylate group and two bis-monodentate carboxylic O atom from the other carboxylate group, as depicted in Scheme 1d–e.

A pair of μ-O atoms link to two adjacent Co atoms, generating a $[Co_2O_2]$ unit with a Co1···Co2 separation of 3.202 Å, in which the distances are in the normal range compared with those reported (3.076–3.393 Å) in the literature [15]. As shown in Fig. 8, firstly, one kind of PDB ligand bridges to two $[Co_2O_2]$ units to form a 2D net. Interestingly, when viewed along the *b*-axis, the two-dimensional layer contains rectangular windows with a dimensions of ca. 9.129×10.557 Å^2 that are occupied by phen ligands. Secondly, the other kind of PDB ligand connects with three $[Co_2O_2]$ units in two layers, consequently resulting in the formation of a bilayer structure (see Fig. 9).

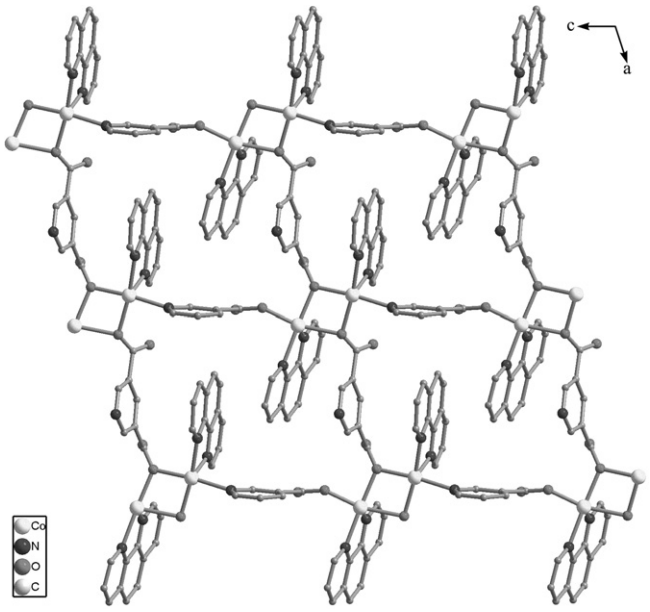


Fig. 8. View of the 2D net showing the rectangular window in **4**.

3.2. Properties

3.2.1. Luminescent properties

Luminescent compounds are of great current interest because of their various applications in chemical sensors, photochemistry and electroluminescent (EL) displays [16]. Recently, the luminescent properties of complexes containing Pb^{II} have been reported [17]. In this work, we investigated the photoluminescent property of compound **2** in the solid-state at room temperature. The free pyridine-3,5-dicarboxylic acid ligand only shows a fluorescent emission band at $\lambda_{max} = 378$ nm under 320 nm excitation (see Fig. 1S), whereas, the complex exhibits an emission peak located at about 475 nm (upon excitation at 330 nm), and undergoes a red shift by 97 nm compared to the acid ligand, as shown in Fig. 10. Hence, the emissions of compound **2** in this work might be assigned to be derived from a ligand to metal charge transition (LMCT). The low-energy emissions associated with large Stokes shifts for complex **2** have been commonly observed for other s^2-metal complexes [18]. The heavy-atom effect of lead(II) increases the spin–orbit coupling and facilitates intersystem crossing, so the phosphorescence is fast enough to successfully compete with radiationless deactivations [18d]. The observation indicates that complex **2** may be an excellent candidate for potential photoactive materials.

3.2.2. Magnetic properties

The magnetic property of polymer **4** has been investigated over the temperature range 5–300 K at 1000 Oe. The temperature dependence of the molar magnetic susceptibility is illustrated in Fig. 11. The $\chi_m T$ value of **4** remains almost constant from 300 to 115 K (5.659 cm^3 K mol^{-1}), and then decreases on further cooling, reaching a value of 0.793 cm^3 K mol^{-1} at 5 K. This behavior indicates a dominant weak antiferromagnetic interaction between the Co^{II} ions in the structure. In **4**, the Co···Co distance

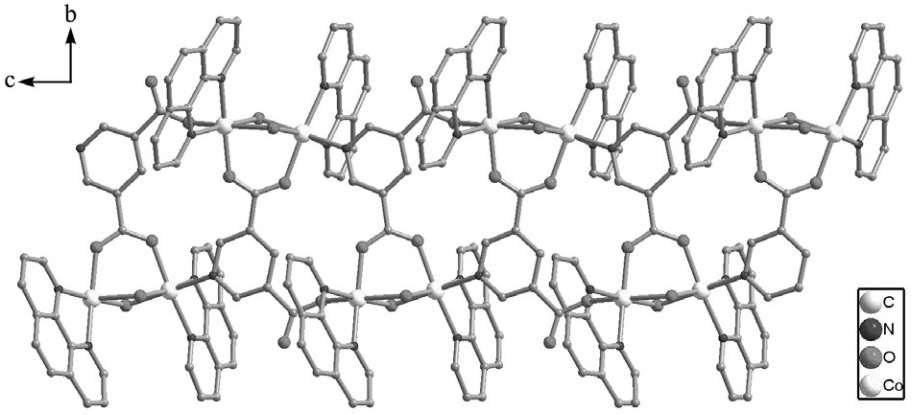


Fig. 9. View of the bilayer structure in **4**.

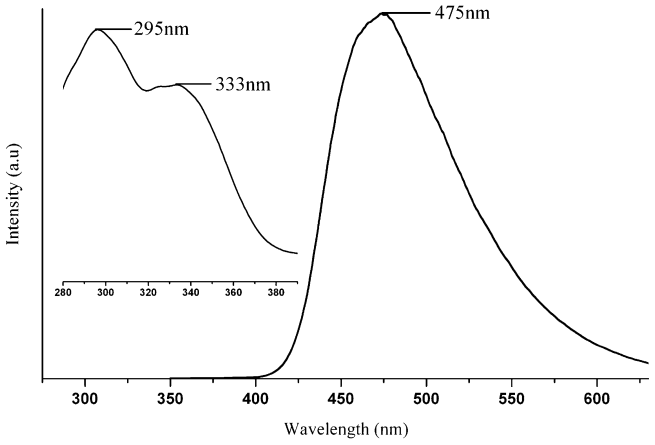


Fig. 10. Absorption (left) and phosphorescence (right) spectra of complex **2** in the solid state.

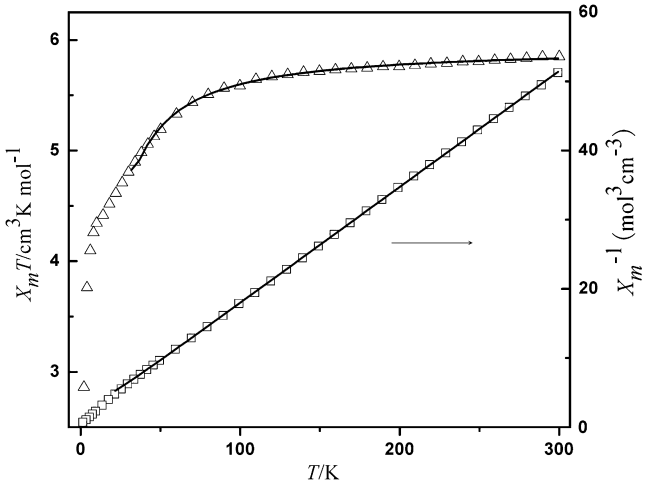


Fig. 11. Thermal variations of $\chi_M T$ and $\chi_M{}^{-1}$ for complex **4**.

through two μ_2-O atoms is 3.202 Å. Even small changes in these parameters could lead to changes in the Co···Co interaction. For polymer **4**, Co–O bridge distances ranging from 2.076(2) to 2.226(2) Å are slightly longer than those in the literature [19], but the lengths of the pathways are about 4.6 Å, which is a very short transmittance distance, helpful for magnetic coupling. The variation of $\chi_M{}^{-1}$ is well described by the Curie–Weiss law in the experimental temperature range 5–300 K with $C = 5.86\ \mathrm{cm^3\ K\ mol^{-1}}$ and $\theta = -3.69$ K.

The experiment data of complex **4** was fitted using the theoretical expression of the magnetic susceptibility, (Eq. (1)) which was deduced from the Heisenberg spin Hamiltonian $H = -JS_1 \cdot S_2$, where J is the intradimer interaction parameter between the Co(II) ions [20].

$$\chi_{\mathrm{dim}} = \frac{2Ng^2\beta^2}{kT} \times \frac{e^{5x} + 5e^{3x} + 14}{7 + e^{6x} + 3e^{5x} + 5e^{3x}} \tag{1}$$

where $x = -J/kT$. Taking into consideration the possibility of an interdimer interaction in the crystal lattice, the following correction of the molecular field is made:

$$\chi_{\mathrm{M}} = \frac{\chi_{\mathrm{dim}}}{1 - \chi_{\mathrm{dim}}(zJ'/N^2\beta^2)} \tag{2}$$

The best fitting of the experimental magnetic data by Eq. (2) gives the following parameters: $g = 2.52$, $J = -4.67\ \mathrm{cm^{-1}}$, $zJ' = 0.878\ \mathrm{cm^{-1}}$ and $R = 9.98 \times 10^{-4}$, where $R = \sum[(\chi_m T)_{\mathrm{obs}} - (\chi_m T)_{\mathrm{calcd}}]^2/\sum[(\chi_m T)_{\mathrm{obs}}]^2$. The results suggest that the interlayer interactions are weak compared with the intralayer interaction. The negative J value suggests the occurrence of an obvious antiferromagnetic Co(II)–Co(II) interactions in **4**, being in good agreement with the $\chi_m T$ versus T curve behavior in the temperature range 300–5 K. It is difficult to estimate the exchange interaction accurately within the Co(II) complexes because of the effect of spin–orbit coupling.

3.2.3. Thermal properties

Thermal gravimetric analyses (TGA) were carried out to examine the thermal stabilities of **1**–**4**. The results show that complexes **1**–**4** are very stable in air at ambient temperature, which make them potential candidates for practical applications. The samples were heated up in air at 1 atm pressure with a heating rate of 10 °C min^{-1}. The TGA curve shows that **1** is stable up to 127 °C. A weight loss of 7.6% occurred in the temperature range 127–226 °C, pre-

sumably due to the removal of a coordinated water molecule per formula unit (calcd. 7.4%). Another weight loss of 60.9% occurred in the temperature range 297–465 °C, corresponding to the removal of two PDB ligands per formula unit (calcd. 61.7%), no weight losses were observed up to 800 °C indicating the complete deposition of the complex with the formation of NiO as the final product. The TGA curve of **2** shows that the first weight loss of 4.2% between 46 and 90 °C corresponds to the loss of the lattice water molecules (calcd. 4.4%). A total weight loss of 41.2% occurred in the temperature range 215–513 °C, mainly corresponding to the removal of the one coordinated water molecule and one PDB ligand per formula unit (calcd. 40.9%), no weight losses were observed up to 800 °C indicating the complete deposition of the complex with the formation of PbO as the final product. The TGA curve of **3** shows that the first weight loss of 16.01% between 40 and 172 °C corresponds to the loss of the lattice water molecules and coordinated water molecules (calcd. 15.92%), and then it is stable up to 280 °C. The framework collapsed in the temperature range 280-800 °C before the final formation of a metal oxide. The TGA curve shows that **4** is stable up to 350 °C. The framework collapsed in the temperature range 350–800 °C, suggesting that the organic ligands decompose slowly over a wide temperature range. The results indicate that a 3D porous framework constrained by the N–H···N self-complementary hydrogen bonds is more stable than 2D sheets.

4. Conclusion

In summary, we have synthesized four novel metal-organic frameworks based on pyridine-3,5-dicarboxylic acid and two chelate ligands by hydrothermal reactions. The successful syntheses of the four compounds indicate that it is promising to build up unusual architectures via combining transition metals or main group elements and pyridine–carboxylate ligands, thus opening up a new field in the preparation of metal coordination polymers with potential magnetic and luminescent properties.

5. Supplementary material

CCDC 625481, 625482, 625483 and 625484 contain the supplementary crystallographic data for **1**, **2**, **3** and **4**. These data can be obtained free of charge via http://www.ccdc.cam.ac.uk/conts/retrieving.html, or from the Cambridge Crystallographic Data Centre, 12 Union Road, Cambridge CB2 1EZ, UK; fax: (+44) 1223-336-033; or e-mail: deposit@ccdc.cam.ac.uk.

Acknowledgement

The authors acknowledge financial support from the National Natural Science Foundation of China (Project Nos. 20373009 and 20573016).

References

[1] (a) S. Kitagawa, R. Kitaura, S. Noro, Angew. Chem., Int. Ed. 43 (2004) 2334;
(b) O.M. Yaghi, M. O'Keeffe, N.W. Ockwing, H.K. Chae, M. Eddaoudi, J. Kim, Nature 423 (2003) 705;
(c) C. Janiak, J. Chem. Soc., Dalton Trans. (2003) 2781;
(d) M.E. Davis, Nature 417 (2002) 813;
(e) O.R. Evans, W. Lin, Acc. Chem. Res. 35 (2002) 511;
(f) M. Eddaoudi, D.B. Moler, H. Li, B. Chen, T. Reineke, M. O'Keeffe, O.M. Yaghi, Acc. Chem. Res. 34 (2001) 319;
(g) D. Maspoch, D.R. Molinaa, J. Veciana, Chem. Soc. Rev. 36 (2007) 770.

[2] (a) S.L. Zheng, M.L. Tong, X.M. Chen, Coord. Chem. Rev. 246 (2003) 185;
(b) S.R. Batten, K.S. Murray, Coord. Chem. Rev. 246 (2003) 103;
(c) L. Carlucci, G. Ciani, D.M. Proserpio, Coord. Chem. Rev. 246 (2003) 247;
(d) A.J. Blake, N.R. Champness, P. Hubberstey, W.S. Li, M.A. Withersby, M. Schröder, Coord. Chem. Rev. 183 (1999) 117;
(e) N.R. Champness, J. Chem. Soc., Dalton Trans. (2006) 877;
(f) A.Y. Robin, K.M. Fromm, Coord. Chem. Rev. 250 (2006) 2127;
(g) C. Kepert, Chem. Commun. (2006) 695.

[3] (a) D.Q. Chu, J.Q. Xu, L.M. Duan, T.G. Wang, A.Q. Tang, L. Ye, Eur. J. Inorg. Chem. (2001) 1135;
(b) M. Du, X.J. Jiang, X.J. Zhao, Inorg. Chem. 46 (2007) 3984;
(c) S.J. Dalgarno, P.K. Thallapally, L.J. Barbour, J.L. Atwood, Chem. Soc. Rev. 36 (2007) 236.

[4] (a) S.P. Watton, P. Fuhrmann, L.E. Pence, A. Caneschi, A. Cornia, G.L. Abbati, S.J. Lippard, Angew. Chem., Int. Ed. Engl. 36 (1997) 2774;
(b) M.R. Brügstein, M.T. Gamer, P.W. Roesky, J. Am. Chem. Soc. 126 (2004) 5213.

[5] (a) Y.C. Liang, R. Cao, W.P. Su, M.C. Hong, W.J. Zhang, Angew. Chem., Int. Ed. 39 (2000) 3304;
(b) M.L. Tong, S. Kitagawa, H.Ch. Chang, M. Ohba, Chem. Commun. (2004) 418;
(c) Y.L. Wei, H.W. Hou, L.K. Li, Y.T. Fan, Y. Zhu, Cryst. Growth Des. 5 (2005) 1405;
(d) X.L. Wang, C. Qin, E.B. Wang, Y.G. Li, N. Hao, C.W. Hu, L. Xu, Inorg. Chem. 43 (2004) 1850.

[6] (a) S.K. Ghosh, P.K. Bharadeaj, Inorg. Chem. 42 (2003) 8250;
(b) S.K. Ghosh, P.K. Bharadeaj, Inorg. Chem. 43 (2004) 2293;
(c) S.K. Ghosh, J. Ribas, P.K. Bharadeaj, CrystEngComm 6 (2004) 250;
(d) B. Zhao, P. Cheng, Y. Dai, C. Cheng, D.Z. Liao, S.P. Yan, Z.H. Jiang, G.L. Wang, Angew. Chem., Int. Ed. 42 (2003) 934.

[7] (a) M.L. Tong, J. Wang, S. Hu, S.R. Batten, Inorg. Chem. Commun. 8 (2004) 48;
(b) X.L. Wang, C. Qin, E.B. Wang, Y.G. Li, C.W. Hu, L. Xu, Chem. Commun. (2004) 378;
(c) C. Qin, X.L. Wang, E.B. Wang, L. Xu, J. Mol. Struct. 738 (2005) 91;
(d) J.F. Eubank, R.D. Walsh, P. Poddar, H. Srikanth, R.W. Larsen, M. Eddaoudi, Cryst. Growth Des. 5 (2006) 1453.

[8] (a) D. Min, S.S. Yoon, D.Y. Jung, C.Y. Lee, Y. Kim, W.S. Han, S.W. Lee, Inorg. Chim. Acta 324 (2001) 293;
(b) R. García-Zarracino, H. Höpfl, Angew. Chem., Int. Ed. 43 (2004) 1507;
(c) S.M. Humphrey, P.T. Wood, J. Am. Chem. Soc. 126 (2004) 13236;
(d) Y.L. Liu, V.C. Kravtsov, D.A. Beauchamp, J.F. Eubank, M. Eddaoudi, J. Am. Chem. Soc. 127 (2005) 7266;
(e) Y.L. Wei, H.W. Hou, L.K. Li, Y.T. Fan, Y. Zhou, Cryst. Growth Des. 15 (2005) 1405;
(f) C. Qin, X.L. Wang, E.B. Wang, Z.M. Su, Inorg. Chem. 44 (2005) 7122.

[9] (a) Y.L. Lu, J.Y. Wu, M.C. Chan, S.M. Huang, C.S. Lin, T.W. Chiu, Y.H. Liu, Y.S. Wen, C.H. Ueng, T.M. Chin, C.H. Hung, K.L. Lu, Inorg. Chem. 45 (2006) 2430;

(b) C.L. Ma, J.K. Li, R.F. Zhang, J. Coord. Chem. 59 (2006) 1891;
(c) D. Min, S.W. Lee, Inorg. Chem. Commun. 5 (2002) 978;
(d) D.W. Min, S.S. Yoon, J.H. Lee, M. Suh, S.W. Lee, Inorg. Chem. Commun. (2001) 297;
(e) H.T. Xu, N.W. Zheng, H.H. Xu, Y.G. Wu, R.Y. Yang, E.Y. Ye, X.L. Jin, J. Mol. Struct. 610 (2002) 47.

[10] ASTRO (5.00), SAINT (5.007), SADABS (5.007), Data Collection and Processing Software for the SMART System (5.054). Siemens (BRUKER-AXS) Analytical X-ray Instruments Inc., Madison, WI, 1998.

[11] G.M. Sheldrick, SHELXS-97, A Program for Automatic Solution of Crystal Structure, University of Göttingen: Göttingen, Germany, 1997.

[12] G.M. Sheldrick, SHELXL-97, A Programs for Crystal Structure Refinement, University of Göttingen: Göttingen, Germany, 1997.

[13] (a) Q. Yue, J. Yang, G.H. Li, G.D. Li, W. Xu, J.S. Chen, S.N. Wang, Inorg. Chem. 44 (2005) 5241;
(b) Z. He, C. He, E.Q. Gao, Z.M. Wang, X.F. Yang, C.S. Liao, C.H. Yan, Inorg. Chem. 42 (2003) 2206;
(c) T. Sanada, T. Suzuki, S. Kaizaki, J. Chem. Soc., Dalton Trans. (1998) 959.

[14] J.G. Mao, Z. Wang, A. Clearfield, Inorg. Chem. 41 (2002) 6106.

[15] (a) P.M. Forster, A.R. Burbank, C. Livage, G. Ferey, A.K. Cheetham, Chem. Commun. (2004) 368;
(b) H. Kumagai, Y. Oka, S. Kawata, M. Ohba, K. Inoue, M. Kurmoo, H. Okawa, Polyhedron 22 (2003) 1917;
(c) X.J. Li, X.Y. Wang, S. Gao, R. Cao, Inorg. Chem. 45 (2006) 1508;
(d) P.M. Forster, A.R. Burbank, M.C. O'Sullivan, N. Guillou, C. Livage, G. Ferey, Solid State Sci. 7 (2005) 1549;
(e) Y.Z. Zheng, M.L. Tong, W.X. Zhang, X.M. Chen, Chem. Commun. (2006) 165;
(f) K.S. Gavrilenko, S.V. Punin, O. Cador, S. Golhen, L. Ouahab, V.V. Pavlishchuk, J. Am. Chem. Soc. 127 (2005) 12246.

[16] (a) Q. Wu, M. Esteghamatian, N.X. Hu, Z.D. Popovic, G. Enright, Y. Tao, M. D'Iorio, S. Wang, Chem. Mater. 12 (2000) 79;
(b) J.E. McGarrah, Y.J. Kim, M. Hissler, R. Eisenberg, Inorg. Chem. 40 (2001) 4510;
(c) G. De Santis, L. Fabbrizzi, M. Licchelli, A. Poggi, A. Taglietti, Angew. Chem., Int. Ed. Engl. 35 (1996) 202.

[17] (a) A. Vogler, H. Nikol, Pure Appl. Chem. 64 (1992) 1311;
(b) A. Strasser, A. Vogler, J. Photochem. Photobiol. A165 (2004) 115;
(c) A. Strasser, A. Vogler, Inorg. Chem. Commun. (2004) 528;
(d) S.K. Dutta, M.W. Perkovic, Inorg. Chem. 41 (2002) 6938;
(e) Y.H. Zhao, H.B. Xu, K.Z. Shao, Y. Xing, Z.M. Su, J.F. Ma, Cryst. Growth Des. 7 (2007) 513;
(f) Y.H. Zhao, Z.M. Su, Y. Wang, Y.M. Fu, S.D. Liu, P. Li, Inorg. Chem. Commun. 10 (2007) 410.

[18] (a) P.C. Ford, A. Vogler, Acc. Chem. Res. 26 (1993) 220;
(b) A. Vogler, A. Paukner, H. Kunkely, Coord. Chem. Rev. 33 (1980) 227;
(c) H. Nikol, A. Becht, A. Vogler, Inorg. Chem. 31 (1992) 3277;
(d) Q.Y. Liu, L. Xu, Eur. J. Inorg. Chem. (2006) 1620.

[19] (a) P.M. Forster, A.R. Burbank, C.LivageG. Féreyb, A.K. Cheetham, Chem. Commun. (2004) 368;
(b) H. Kumagai, Y. Oka, S. Kawata, M. Ohba, K. Inoue, M. Kurmoo, H. Ōkawa, Polyhedron 22 (2003) 1917.

[20] (a) J.M. Rueff, N. Masciocchi, P. Rabu, A. Sironi, A. Skoulios, Chem. Eur. J. 8 (2001) 1813;
(b) J.M. Rueff, N. Masciocchi, P. Rabu, A. Sironi, A. Skoulios, Eur. J. Inorg. Chem. (2002) 2843;
(c) S.M. Ostrovsky, K. Falk, J. Pelikan, D.A. Brown, Z. Tomkowics, W. Haase, Inorg. Chem. 45 (2006) 688;
(d) S.Q. Bai, E.Q. Gao, Z. He, C.J. Fang, C.H. Yan, New J. Chem. (2005) 935.

Available online at www.sciencedirect.com
ScienceDirect
Polyhedron 27 (2008) 593–601
POLYHEDRON
www.elsevier.com/locate/poly

Syntheses, characterization and X-ray crystal structures of Co(III) and Mn(II) complexes of pyrimidine derived Schiff base ligands

Somnath Roy [a], Tarak Nath Mandal [a], Anil Kumar Barik [b], Samik Gupta [a], Ray J. Butcher [c], Munirathinam Nethaji [d], Susanta Kumar Kar [a,*]

[a] Department of Chemistry, University College of Science, 92, A.P.C. Road, Kolkata 700 009, India
[b] Department of Chemistry, St. Paul's C.M. College, 33/1, Raja Rammohan Roy Sarani, Kolkata 700 009, India
[c] Department of Chemistry, Howard University, 2400 Sixth Street, N.W., Washington, DC 200 59, USA
[d] Department of Inorganic and Physical Chemistry, Indian Institute of Science, Bangalore 560 012, India

Received 21 August 2007; accepted 15 October 2007
Available online 26 November 2007

Abstract

Two pyrimidine based NNS tridentate Schiff base ligands *S*-methyl-3-((2-*S*-methyl-6-methyl-4-pyrimidyl)methyl)dithiocarbazate [HL_1] and *S*-benzyl-3-((2-*S*-methyl-6-methyl-4-pyrimidyl)methyl)dithiocarbazate [HL_2] have been synthesised by 1:1 condensation of 2-*S*-methylmercapto-6-methylpyrimidine-4-carbaldehyde and *S*-methyl/*S*-benzyl dithiocarbazate. One Co(III) and one Mn(II) complex of HL_1 and one Mn(II) complex of HL_2 have been prepared and characterized by elemental analyses, molar conductivities, magnetic susceptibilities and spectroscopic studies. All the bis-chelate complexes have a distorted octahedral arrangement with an N_4S_2 chromophore around the central metal ion. Each ligand molecule binds the metal ion using pyrimidyl nitrogen, azomethine nitrogen and the thiolato sulfur atoms. In the free ligand moieties, the pyrimidine nitrogen atoms, azomethine nitrogen atoms and thione sulfur atoms are in EEE orientation to each other. During chelation, all the donor sites of the ligands are reoriented to ZEZ configuration in order to facilitate the chelation process. In all the complexes, the respective ligand molecule functions as the monoanionic tridentate one. All complexes were analyzed by single crystal X-ray diffraction and significant differences concerning the distortion from octahedral geometry of the coordination environment were observed.
© 2007 Elsevier Ltd. All rights reserved.

Keywords: Cobalt(III) and manganese(II) complexes; Pyrimidine derived dithiocarbazate ligands; X-ray structures; Spectroscopy

1. Introduction

Thiosemicarbazones of *S*-alkyl dithiocarbazate are one of the most important classes of NNS donor ligands, which have considerable pharmacological interest due to their significant antibacterial, antimalarial, antileprotic and anticancer activities [1–14]. Moreover, metal complexes of pyrimidine derived thiosemicarbazones have been extensively studied in recent years because of presence of the pyrimidine ring which is an integral part of the active sites of several enzymes [15–22]. Most of the metal complexes of thiosemicarbazones particularly with copper, cobalt, platinum and palladium show marked and diverse biological activity [23–28]. However, manganese is also an essential trace element, forming the active sites of a number of metalloproteins [29]. In these metalloproteins, manganese does exist in any of the five oxidation states or in mixed valence states. The most important role of manganese is in the oxidation of water in green plant photosynthesis where its presence in photosystem II is essential [30,31]. Manganese complexes exhibit interest due to their catalytic anti-oxidant activity, in blocking oxidant trace in vitro [32]. Synthesis, characterization, structure and reactivity studies of pyrimidine derived NNS donor ligands lead to valuable

* Corresponding author. Tel.: +91 033 24322936; fax: +91 033 23519755.
E-mail address: skkar_cu@yahoo.co.in (S.K. Kar).

0277-5387/$ - see front matter © 2007 Elsevier Ltd. All rights reserved.
doi:10.1016/j.poly.2007.10.012

information toward understanding the functions of different enzymes at the molecular level [15]. Attention has been given towards the chemistry of Co(III) and Mn(II) complexes with pyrimidine derived thiosemicarbazones primarily because of their coordination mode, novel electrochemical and electronic properties as well as their biological importance [33–37]. Although there has been considerable interest in transition metal complexes derived from pyridine and pyrazole containing heterocyclic thiosemicarbazones but a scanty attention has been centered towards the coordinating properties of pyrimidine derived thiosemicarbazones. In continuation of our previous work [38], here we report the synthesis and structural characterization of Co(III) and Mn(II) complexes of *S*-methyl-3-((2-*S*-methyl-6-methyl-4-pyrimidyl)methyl)dithiocarbazate [HL_1] and Mn(II) complex of *S*-benzyl-3-((2-*S*-methyl-6-methyl-4-pyrimidyl)methyl)dithiocarbazate [HL_2]. The crystal and molecular structures, room temperature magnetic properties, electrochemical properties and electronic spectra of $[Co(L_1)_2]ClO_4 \cdot H_2O$, $[Mn(L_1)_2]$ and $[Mn(L_2)_2]$ complexes have been investigated.

2. Experimental

2.1. Materials

Ethyldiethoxyacetate were purchased from Aldrich Chemical Company, USA and were used as received. All other solvents and reagents were obtained from commercial sources and purified by standard procedures [39]. *S*-methy/*S*-benzyl dithiocarbazate and 2-*S*-methylmercapto-6-methylpyrimidine-4-carbaldehyde were synthesized following the reported methods [40,41].

Caution! Since perchlorate compounds in presence of organic ligands are explosive, only a small amount of the material should be prepared and it should be handled with care.

2.2. Physical measurement

Elemental analyses [carbon, hydrogen, nitrogen and sulfur] of **1** and **2** complexes were determined with a Perkin–Elmer CHNS/O analyzer 2400 at the Indian Association for the Cultivation of Science, Kolkata. The molar conductance values of the complexes were measured in purified methanolic solution with a Systronic model 304 digital conductivity meter. The electronic spectra of the complexes in purified acetonitrile solution were recorded on a Hitachi model U-3501 spectrophotometer. IR spectra [KBr pellet, 4000–400 cm^{-1}] were recorded on a Perkin–Elmer model 883 infrared spectrophotometer. Room temperature magnetic susceptibilities were measured with a PAR 155 vibrating sample magnetometer. Cyclic voltammetry was carried out using Sycopel model AEW2 1820 F/S instrument. The measurements were performed at 300 K in acetonitrile solution containing 0.2 (M) TEAP as the supporting electrolyte and 10^{-3}–10^{-4} (M) of the Co(III) and Mn(II) complexes, deoxygenated by bubbling with nitrogen. The working, counter and reference electrodes used were a platinum wire, a platinum coil and an SCE.

2.3. Preparation of the ligands

S-methyl-3-((2-*S*-methyl-6-methyl-4-pyrimidyl)methyl)dithiocarbazate [HL_1] and *S*-benzyl-3-((2-*S*-methyl-6-methyl-4-pyrimidyl)methyl)dithiocarbazate [HL_2] were synthesized following the method as reported earlier [38]. The two ligands HL_1 and HL_2 were synthesized in a similar way by refluxing a methanolic solution (10 cm^3) of 2-*S*-methylmercapto-6-methylpyrimidine-4-carbaldehyde (0.168 g, 1 mmol) with *S*-methyl dithiocarbazate (0.122 g, 1 mmol) and *S*-benzyl dithiocarbazate (0.198 g, 1 mmol), respectively, also taken in methanol (10 cm^3). Reflux was continued for ca. 2 h at water bath temperature during which a solid microcrystalline compound separated. It was filtered off, washed several times with cold methanol and dried in vacuo over fused $CaCl_2$. Single crystals of HL_1 and HL_2, suitable for X-ray diffraction were obtained by slow evaporation of the respective methanolic solution of the ligand.

HL_1: pale yellow; yield, 0.217 g (80%); m.p. (°C) 186, *m*/*z* 272 (M+, 100%). *Anal*. Calc. for $C_9H_{12}N_4S_3$: C, 39.70; H, 4.41; N, 20.58; S, 35.29. Found: C, 39.83; H, 4.72; N, 20.52; S, 35.23%.

HL_2: yellow; yield, 0.278 g (80%); m.p. (°C) 175, *m*/*z* 348 (M+, 100%). *Anal*. Calc. for $C_{15}H_{16}N_4S_3$: C, 51.72; H, 4.59; N, 16.09; S, 27.05. Found: C, 51.84; H, 4.89; N, 16.01; S, 27.51%.

2.4. Preparation of the complexes

In continuation of our previous work which described the preparation and structural studies of Ni(II) complex of HL_1 and Co(III) and Fe(III) complexes of HL_2, here three complexation reactions of these ligands (HL_1 and HL_2) have been investigated with Co(III) and Mn(II) of HL_1 and Mn(II) of HL_2. All the complexes [**1**–**3**] were obtained from suitable reaction mixtures of the respective ligand and the corresponding hydrated metal salts, taken in 2:1 molar proportion in suitable solvent. The oxidation to Co(III) occurs during preparation of the complex. Although the mechanism of this oxidation is not proven we can safely assume that the starting cobalt(II) salt presumably undergoes aerial oxidation in presence of the ligand in methanolic solution.

2.4.1. $[Co(L_1)_2]ClO_4 \cdot H_2O$ (**1**)

A methanolic solution (5 cm^3) of $Co(ClO_4)_2 \cdot 6H_2O$ (0.0915 g, 0.25 mmol) was added dropwise to a solution of HL_1 (0.136 g, 0.5 mmol) in the same solvent (15 cm^3) with constant stirring. The resulting pink coloured solution was further stirred for ca. 15 min and then refluxed at water bath temperature for ca. 2 h. The solution was cooled to room temperature and filtered. The filtrate was kept for slow evaporation. After two days, X-ray quality crystals

of **1** were isolated. Yield, 0.45 g (70%). *Anal.* Calc. for $C_{18}H_{22.5}ClCoN_8O_{4.25}S_6$ (**1**): C, 30.61; H, 3.19; N, 15.87; S, 27.21. Found: C, 30.69; H, 3.25; N, 15.85; S, 27.20%. IR: ν (cm^{-1}) 2925(ν_{NH}); 1596($\nu_{C=Npym}$); 1510($\nu_{CH=N}$); 1267($\nu_{C=S}$); 1079(ν_{N-N}); 741($\nu_{C=S}$); UV–Vis, λ_{max}: 343, 413, 711 nm. DRS, λ_{max}: 436, 517, 703 nm. λ_M (MeOH, Ω^{-1} cm^2 mol^{-1}): 93. μ_{eff} (at 298 K): 0.00 B.M.

2.4.2. [Mn(L_1)$_2$] (2)

HL_1 (0.136 g, 0.5 mmol) was dissolved in chloroform (20 cm^3). Solid $Mn(ClO_4)_2 \cdot 6H_2O$ (0.362 g, 1 mmol) was added to the above solution with constant stirring using a magnetic stirrer and few drops of methanol was added to dissolve $Mn(ClO_4)_2 \cdot 6H_2O$. To it two drops of triethyl amine were added. The resulting red coloured solution was stirred for an additional 2 h. The solution was filtered and the filtrate was kept for slow evaporation. After two days, a red coloured sticky mass was obtained. This was dried over fused $CaCl_2$ and dissolved in purified CH_3CN. It was filtered and the filtrate was kept for slow evaporation. After three days, single crystals, suitable for X-ray diffraction were separated. Yield, 0.16 g (60%). *Anal.* Calc. for $C_{18}H_{22}MnN_8S_6$ (**2**): C, 36.12; H, 3.68; N, 18.74; S, 32.12. Found: C, 36.20; H, 3.72; N, 18.72; S, 32.15%. IR: ν (cm^{-1}) 2920(ν_{NH}); 1582($\nu_{C=Npym}$); 1508($\nu_{CH=N}$); 1268($\nu_{C=S}$); 1074(ν_{N-N}); 749($\nu_{C=S}$). UV–Vis, λ_{max}: 425 nm. λ_M (MeOH, Ω^{-1} cm^2 mol^{-1}): 20. μ_{eff} (at 298 K): 5.82 B.M.

2.4.3. [Mn(L_2)$_2$] (3)

Complex **3** was prepared using the same procedure and reaction stoichiometry as for **2**. The colour of the resulting reaction mixture was red. Yield, 0.16 g (60%). *Anal.* Calc. for $C_{30}H_{30}MnN_8S_6$ (**3**): C, 48.00; H, 4.00; N, 14.93; S, 25.60. Found: C, 48.15; H, 4.12; N, 14.91; S, 25.57%. IR: ν (cm^{-1}) 2929(ν_{NH}); 1575($\nu_{C=Npym}$); 1512($\nu_{CH=N}$); 1334, 1267($\nu_{C=S}$); 1072(ν_{N-N}); 745($\nu_{C=S}$). UV–Vis, λ_{max}: 352, 428 nm. λ_M (MeOH, Ω^{-1} cm^2 mol^{-1}): 25. μ_{eff} (at 298 K): 5.85 B.M.

2.5. Single crystal X-ray crystallography

Relevant crystallographic data are summarized in Table 1. The intensity data for the ligand HL_1 and the complexes **1**, **2** and **3** were collected on a Bruker SMART CCD diffractometer, using graphite monochromated Mo Kα radiation [$\lambda = 0.71073$ Å] in the ω and φ scan mode and ω scan mode at 100(2) K, 296(2) K, 293(2) K and 273(2) K for HL_1, **1**, **2** and **3**, respectively. Accurate unit cell parameters and orientation matrices for data collection were obtained from least-squares refinement using the programs SMART and SAINT [42] and the data were corrected for absorption using SADABS [42]. All structures were solved using SHELXTL and the SHELX-97 packages of programmes [42] i.e. SHELXS-97 for the solution of the structure and refined by full-matrix least-squares technique based on F^2 [SHELXL-97]. Positions of H-atoms were treated as riding on their parent atoms.

3. Results and discussion

3.1. Syntheses

These newly formed three complexes (**1**–**3**) were characterized by elemental analyses, solution electrical conductivity, magnetic susceptibility, IR, UV–Vis spectra and electrochemical property. The results are consistent with the proposed mononuclear formulation. The complexes were found to be fairly soluble in most of the common organic solvents. Molar conductivity value of **1** is in accord with 1:1 electrolyte behavior but the molar conductivity values of **2** and **3** show non-electrolytic behavior in nature. The complex **1** is diamagnetic in nature. The effective magnetic moment values (5.82 B.M. for **2** and 5.85 B.M. for **3**) suggest the high spin nature of the paramagnetic complexes with five unpaired electrons.

3.2. Description of crystal structures

Structural representation of the ligand HL_1 and that of the complexes **1**, **2** and **3** with atom numbering schemes are shown in Figs. 1–4, respectively. Selected metrical parameters are listed in Table 2. The unit cell of both HL_1 and **1** comprises of two molecules and those of both **2** and **3** comprise of eight molecules. A packing diagram of **2** and **3** are shown in Figs. 5 and 6, respectively.

3.2.1. Structural description of HL_1

The structure of HL_1 (Fig. 1) shows that the neutral tridentate ligand has a EEE configuration based on the C(6)–C(7), N(2)–C(7) and N(4)–C(8) bonds for the donor centers nitrogen, nitrogen and sulfur, respectively. But, on coordination to the metal ion, the ligand undergoes structural reorientation about the C(6)–C(7), N(2)–C(7) and N(4)–C(8) changes from EEE to ZEZ configuration. This suggests that a possible rotation about the azomethine double bond on coordination to the metal ion and this ZEZ configuration is necessary for its participation as a tridentate NNS chelate ligand. From the analysis of the bond lengths (Table 2) of HL_1, we may conclude that the ligand exists in thione form in its solid state but in presence of metal ions, the ligand behaves as a monoanionic tridentate one in its thiol tautomer with concomitant deprotonation of the thiol hydrogen. The tridentate ligand is nearly planar which is evident from the analysis of torsion angles of HL_1 (Table 3).

3.2.2. Structural description of 1

The complex **1** contains $[Co(L_1)_2]^+$ cation and a ClO_4^- anion. The single crystal X-ray diffraction studies show a distorted octahedral geometry for the compound. A list of selected bond parameters and angles of **1** is presented in Table 2. The Co(III) center is coordinated in an N_4S_2 meridional manner by two monodeprotonated ligand moieties using pairs of *cis*-pyrimidyl-N, *trans*-azomethine-N and *cis*-thiolate-S atoms and form four five membered

Table 1
Experimental data for crystallographic analysis

Compound	HL_1	**1**	**2**	**3**
Empirical formula	$C_9H_{12}N_4S_3$	$C_{18}H_{22.5}ClCoN_8O_{4.25}S_6$	$C_{18}H_{22}MnN_8S_6$	$C_{30}H_{30}MnN_8S_6$
Formula weight	272.44	705.68	597.74	374.96
Temperature (K)	100(2)	296(2)	293(2)	273(2)
Wavelength (Å)	0.71073	0.71073	0.71073	0.71073
Crystal system	triclinic	triclinic	monoclinic	monoclinic
Space group	$P\bar{1}$	$P\bar{1}$	C_2/c	C_2/c
Unit cell dimensions				
a (Å)	7.2222(4)	8.9950(18)	16.261(5)	22.449(10)
b (Å)	9.3683(6)	12.560(2)	12.510(4)	14.372(6)
c (Å)	10.3845(6)	13.426(3)	26.392(12)	12.328(5)
α (°)	68.4650(10)	78.834(3)		
β (°)	72.4370(10)	88.597(3)	99.132(7)	111.395(7)
γ (°)	89.5870(10)	75.617(3)		
Volume (Å^3)	618.84(6)	1441.0(5)	5301(3)	3703(3)
z	2	1	8	8
D_{calc} (Mg m^{-3})	1.462	1.627	1.498	1.345
Absorption coefficient (mm^{-1})	0.577	1.165	0.994	0.727
$F(000)$	284	721	2456	1548
Crystal size (mm)	$0.30 \times 0.55 \times 0.65$	$0.03 \times 0.21 \times 0.28$	$0.29 \times 0.32 \times 0.34$	$0.29 \times 0.32 \times 0.35$
θ Range (°) for data collection	2.35–30.53	2.52–29.25	2.50–27.00	1.7–27.5
Index ranges	$-10 \leqslant h \leqslant 10$, $-13 \leqslant k \leqslant 13$, $-14 \leqslant l \leqslant 14$	$-12 \leqslant h \leqslant 11$, $-17 \leqslant k \leqslant 17$, $-18 \leqslant l \leqslant 18$	$-20 \leqslant h \leqslant 21$, $-15 \leqslant k \leqslant 10$, $-32 \leqslant l \leqslant 33$	$-25 \leqslant h \leqslant 28$, $-18 \leqslant k \leqslant 19$, $-16 \leqslant l \leqslant 16$
Goodness-of-fit on F^2	1.083	0.983	0.986	0.835
Completeness to $\theta = 25.00°$ (%)	99.9	98.4	100	100
Independent reflections [R_{int}]	3744 [0.0130]	8037 [0.0676]	5811 [0.1526]	4309 [0.138]
Absorption correction	multi-scan	multi-scan	empirical	empirical
Maximum and minimum transmission	none	0.7362 and 0.9659	0.7273 and 0.7620	0.7829 and 0.8174
Refinement method	full-matrix least-squares on F^2	full-matrix least-squares on F^2	full-matrix least-squares on F^2	full-matrix least-squares on F^2
Data/restraints/parameters	3744/0/148	8037/3/358	5811/0/304	4309/0/206
Reflections collected	7479	16175	10916	15295
Final R indices [$I > 2\sigma(I)$]	$R_1 = 0.0301$, $wR_2 = 0.0820$	$R_1 = 0.0567$, $wR_2 = 0.1429$	$R_1 = 0.0859$, $wR_2 = 0.1843$	$R_1 = 0.0827$, $wR_2 = 0.2099$
R Indices (all data)	$R_1 = 0.0314$, $wR_2 = 0.0833$	$R_1 = 0.0971$, $wR_2 = 0.1609$	$R_1 = 0.1728$, $wR_2 = 0.2245$	$R_1 = 0.2040$, $wR_2 = 0.2955$
Largest difference in peak and hole (e Å^{-3})	0.508 and −0.222	1.235 and −0.995	0.779 and −1.097	0.75 and −0.81

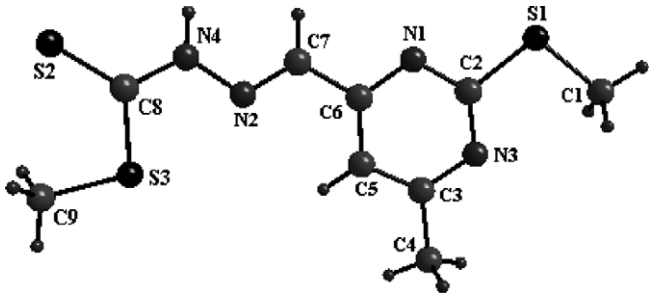


Fig. 1. Structural representation and atom numbering scheme of HL_1.

chelate rings. The meridional configurations of the NNS tridentate thiosemicarbaone ligands around the metal ion have been found in other bis-ligated metal chelates [43,44]. Consequently, the two pyrimidyl nitrogen atoms [N(1A) and N(1B)] and two thiolato sulfur atoms [S(1A) and S(1B)] are positioned in a square plane. In **1**, the atoms defining the equatorial plane lie −0.257, 0.256, −0.236 and 0.236 Å, respectively, are out of the least squares plane through them. The axial positions are occupied by the two remaining azomethine nitrogen atoms [N(2A) and N(2B)] which is evident from the N(2A)–M–N(2B) angle [169.60°]. From the bond angles Table 2, it is observed that the coordination geometry is quite far from a perfect octahedron due to the steric interactions and asymmetric nature of the ligand molecules. The maximum distortions from the ideal octahedral geometry occur for N(1A)–Co–N(2A) [81.43°] and N(1B)–Co–N(2B) [81.36°] angles in Co(III) complex [38]. The dihedral angle formed by the mean planes of the bicyclic chelate systems of each of the ligands is 88.78°. The C(8)–S(1) [A and B] bond distances appear to be longer than those reported for free thiosemicarbazone such as 1.678(2) Å in 4-formylpyridinethio-

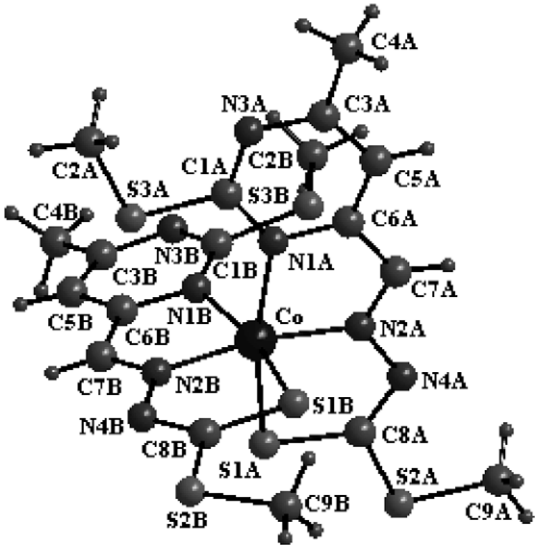


Fig. 2. Structural representation and atom numbering scheme of cationic complex **1**.

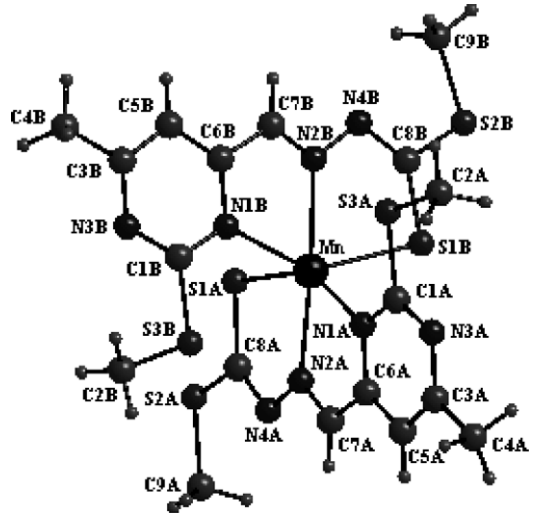


Fig. 3. Structural representation and atom numbering scheme of **2**.

semicarbazone [45] and 1.684(4) Å in 2-keto-3-ethoxybutyraldehyde-bis(thiosemicarbazone) [46].

3.2.3. Structural descriptions of *2* and *3*

Structural representations of $[Mn(L_n)_2]$ (where $n = 1$ and 2) with atom numbering schemes are shown in Figs. 3 and 4, respectively. The anionic ligands HL_1 and HL_2 act as tridentate ones which coordinate to manganese(II) through the pyrimidyl nitrogen N(1), azomethine nitrogen N(2) and thiolato sulfur S(1) atoms with ZEZ configuration based on the C(6)–C(7), N(2)–C(7) and N(4)–C(8) bonds for the NNS donor set. Like **1**, the manganese atoms (in **2** and **3**) are also coordinated in a distorted octahedral arrangement in a *trans*-N(2)-*cis*-N(1)-*cis*-S(1) fashion. Of these sulfur involving rings are somewhat planar and slightly puckered, while the other two are almost planar. In complexes **2** and **3**, the atoms defining the equatorial plane [N(1) and S(1)] (A and B) lie −0.796, 0.787, −0.623 and 0.664 Å in **2** and −0.776, 0.776, −0.616 and 0.616 Å in **3** are out of the least squares plane through them. The two thiolato sulfur atoms are observed to be deviated farthest from the central Mn(II) atoms, at

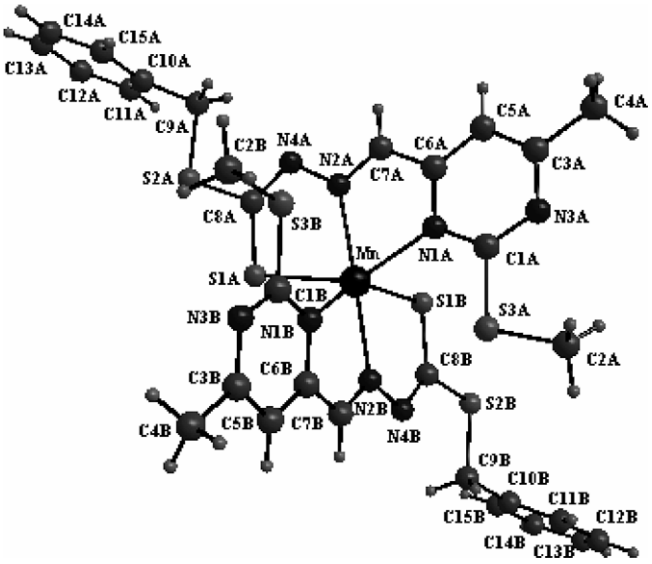


Fig. 4. Structural representation and atom numbering scheme of **3**.

Table 2
Selected bond distances (Å) and angles (°) involving HL_1, **1**, **2** and **3** (here M stands for the corresponding metal ion)

HL_1			**1**	**2**	**3**
Bond distances (Å)					
S2–C8	1.6595(12)	M–S1A	2.2195(12)	2.519(3)	2.555(2)
N2–C7	1.2792(16)	M–S1B	2.2196(11)	2.546(2)	2.555(2)
C6–C7	1.4666(16)	M–N1A	2.021(3)	2.307(5)	2.332(5)
N4–C8	1.3478(16)	M–N1B	2.033(3)	2.382(5)	2.332(5)
		M–N2A	1.896(3)	2.234(5)	2.233(5)
		M–N2B	1.899(3)	2.250(5)	2.233(5)
		S1A–C8A	1.737(4)	1.727(8)	1.717(6)
		S1B–C8B	1.709(4)	1.694(8)	1.717(6)
		N2A–C7A	1.284(5)	1.289(9)	1.279(9)
		N2B–C7B	1.288(5)	1.258(9)	1.279(9)
		N4A–C8A	1.295(5)	1.303(8)	1.314(8)
		N4B–C8B	1.315(5)	1.321(9)	1.314(8)

	1	**2**	**3**
Bond angles (°)			
S1A–M–S1B	90.99(4)	100.59(8)	104.90(8)
S1A–M–N1A	166.54(8)	146.72(14)	145.92(12)
S1A–M–N1B	89.88(8)	94.42(13)	89.81(12)
S1A–M–N2A	85.21(9)	75.44(14)	74.91(13)
S1A–M–N2B	87.58(9)	93.69(14)	101.49(13)
S1B–M–N1A	89.91(8)	92.95(14)	89.81(12)
S1B–M–N1B	166.72(8)	143.33(13)	145.92(12)
S1B–M–N2A	87.20(8)	103.07(14)	101.49(13)
S1B–M–N2B	85.44(8)	75.05(14)	74.91(13)
N1A–M–N1B	92.32(11)	92.43(18)	94.82(16)
N1A–M–N2A	81.43(11)	71.92(18)	72.07(16)
N1A–M–N2B	105.88(11)	119.25(18)	112.07(17)
N1B–M–N2A	106.08(11)	113.07(18)	112.07(17)
N1B–M–N2B	81.36(11)	70.72(18)	72.07(16)
N2A–M–N2B	169.60(11)	168.56(19)	174.25(17)

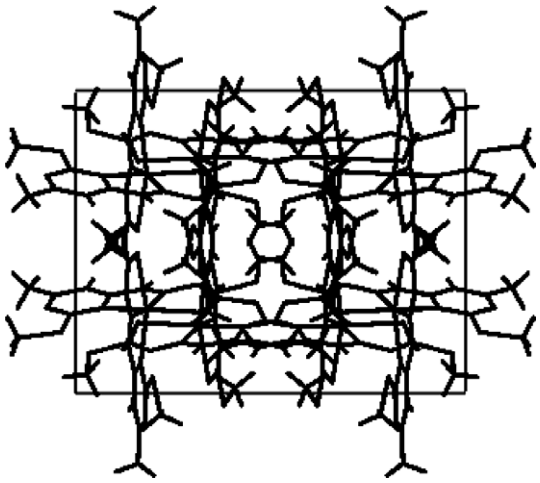


Fig. 5. Packing diagram of **2** along *c* axis.

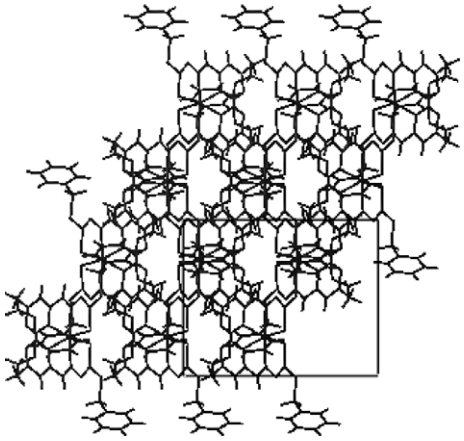


Fig. 6. Packing diagram of **3** along *c* axis.

distances of 2.519(3) Å [Mn–S(1A)] and 2.546(2) Å [Mn–S(1B)] for **2** and 2.555(2) Å [Mn–S(1)] (A and B) for **3**, while the Mn–N(1) and Mn–N(2) bonds are observed at an average distances of 2.33 Å and 2.23 Å, respectively. The Mn–$N_{azomethine}$, Mn–N_{pym} and Mn–S bond lengths are comparable well with the previously reported manganese(II) complexes [47,48]. These comparatively larger bond lengths are indicative of weak bonding of the ligand to the metal. The coordination process lengthens the C(8A)–S(1A) bond by 0.068 Å, C(8B)–S(1B) by 0.035 Å for **2** and C(8)–S(1) (A and B) bond by 0.061 Å for **3**. The decrease in bond length of N(4A)–C(8A), N(4B)–C(8B) by 0.045 and 0.027 Å for **2** and N(4)–C(8), N(4)–C(8) (A and B) by 0.036 Å for **3**, respectively, on coordination confirms the deprotonation after enolization [49]. The S–Mn–S angles are much greater than 90° [100.59(8)° for **2** and 104.90(8)° for **3**]; it is closer to the tetrahedral value and demonstrates that the two ligands exert significant steric effects on each other. The –S–CH_2–Ph in **3** exerting greater steric congestion over –S–CH_3 in **2**, registers higher S–Mn–S angle in **3**. The negative charge of the monoanionic ligands is delocalised over the main backbone of the respective ligand and the increased S–C bond distances are consistent with the single bond character, while the imine C–N distances and both thioamide C–N distances (**2** and **3**) indicate considerable double bond character. In both the cases, the tridentate ligands are nearly planar. The displacement from coplanarity is indicated by the dihedral angle between the pyrimidyl ring and the plane defined by the five membered chelate rings Mn–S–C–N–N, 0.94° and 2.34° for **2** and 7.87° for **3**. The pyrimidine ring thus makes an extended coplanar system with the two chelate rings. This extended coplanar ring system of the two ligands (HL_1 and HL_2) face each other orthogonally. This is supported from the analysis of their dihedral angles [88.52° for **2** and 81.66° for **3**].

4. Characterization of the complex species

All the three complexes gave satisfactory C, H, N and S analyses. Spectral properties of these complexes are described below in details.

4.1. IR spectra of the complexes

A comparative study of the IR spectral data of the reported complexes with those of the uncomplexed ligand gives supportive information regarding bonding sites of the ligand molecules. The Schiff base contains a proton adjacent to the thiocarbonyl group and consequently can exhibit thione–thiol tautomerism. The IR spectra of the ligands, however, display no band at ca. 2600 cm^{-1} corresponding to ν_{S-H} [50] indicating that the ligands remain as a thione tautomer. The ligand (HL_1) when dissolved in methanol in presence of Co(II) salts, quickly converts to the corresponding 'thiol' form with the concomitant formation of cobalt(III) complexes of the deprotonated mercaptide form of the ligand.

Some characteristic and recognizable spectral changes have been noticed in the IR spectra of the complexes as compared to that of the free ligands and the data can be

Table 3
Selected torsion angles (°) involving HL_1, **1**, **2** and **3** torsion angles (°)

HL_1			**1**	**2**	**3**
N1–C6–C7–N3	−175.62(10)	N1A–C6A–C7A–N2A	0.8(5)	4.1(9)	1.0(9)
N3–N4–C8–S2	175.95(8)	N2A–N4A–C8A–S1A	−0.1(5)	0.3(9)	−5.0(8)
		N1B–C6B–C7B–N2B	−2.3(5)	8.1(10)	1.0(9)
		N2B–N4B–C8B–S1B	−0.3(4)	−4.0(10)	−5.0(8)

successfully utilized for an additional support of the bonding mode. The corresponding spectral data of the two ligands are described in our earlier report [38]. A red shift of $\nu_{(C=N)}$ from 1511 cm^{-1} (in HL_1) and 1523 cm^{-1} (in HL_2) to 1510 cm^{-1} (in **1**), 1508 cm^{-1} (in **2**), 1512 cm^{-1} (in **3**) is consistent with coordination of azomethine nitrogen [51]. The presence of a band at ca. 550 $cm^{-1}$is also assignable to (ν_{M-N}) [38] (here M stands for the corresponding metal ion). A blue shift of $\nu_{(C=Npym)}$ from 1570 cm^{-1} in the uncomplexed ligand toward ca. 1584 cm^{-1} in all the complexes is also consistent with coordination of pyrimidine nitrogen [51]. For all the complexes, the thioamide band at ca. 775 cm^{-1} in the free ligand owing to $\nu_{(C=S)}$ undergoes a red-shift by ca. 30 cm^{-1}, pointing to the sulfur atom of thiol as a possible coordination site [51]. The low frequency band appearing in the region at ca. 315–320 cm^{-1}, 340–360 cm^{-1} and 490–515 cm^{-1} in all the three complexes are assigned as $\nu_{M-N(pym)}$, ν_{M-S} and $\nu_{M-N(azomethine)}$, respectively [52].

4.2. UV–Vis and DRS of the complexes

The DRS of **1** exhibits a broad band at ca. 436 nm with two distinct shoulders at low energy side (at ca. 517 nm and ca. 703 nm). The broad band is due to the S → Co(III) charge transfer transition as is also evident from the solution spectral study. The other two bands may be assigned as $^1A_{1g} \rightarrow {}^1T_{1g}$ and $^1A_{1g} \rightarrow {}^3T_{2g}$ transitions, respectively, [53]. In methanolic solution, it displays S → Co(III) charge transfer transition (LMCT) at 413 nm with one d–d band at 711 nm. The intense band at ca. 343 nm is due to the intraligand CT band.

The UV–Vis spectral data of HL_1 and HL_2 have already been reported in our previous communication. The complex **2** in CH_3CN displays the absorption band at 425 nm, which is assigned as the intraligand CT band ($n \rightarrow \pi^*$ transition of imine portion of the TSC moiety) [54]. The intense band of the complex **3** in CH_3CN are exhibited at 428 and 352 nm which are due to $n \rightarrow \pi^*$ transition of imine portion of the TSC moiety and $\pi \rightarrow \pi^*$ transition of the aromatic ring, respectively [55]. The absorption of the organic ligand tailing into the visible region obscure the very weak d–d absorption bands of the manganese(II) complexes [55].

5. Electrochemistry

Figs. 7 and 8 show the cyclic voltametric profile of the complexes **2** and **3**, respectively. Cyclic voltametric tests on the complexes reveal the presence of an irreversible, anodic process ($E_p = +0.79$ V for **2** and +0.82 V for **3**) and quasi-reversible reduction ($E_{1/2} = -1.06$ V for **2** and −1.04 V for **3**), which regenerates in the reverse scan of the oxidation of the original complexes. On this basis, the oxidation may be attributed to the Mn(II)/Mn(III) couple, where the Mn(III) complex after its formation, being quite unstable in the original geometry, evolves to an unidentified differently coordinated species (fragmentation can not be ruled out), which, however upon reduction regenerates the Mn(II) complex. Similar type of observation was recorded by Godbole et al. [56] in their $[Mn(mesalim)_2Cl]$ complex (Hmesalim is methyl salicylimidate) where manganese being in originally in +III stable oxidation state is electrochemically oxidized to unstable Mn(IV) species. From the comparison of $E_{1/2}$ values of Mn(III)/Mn(II) couple for **2** and **3**, we may state that $E_{1/2}$ for **3** being comparatively of higher value and hence HL_2 stabilizes Mn(II) more than HL_1.

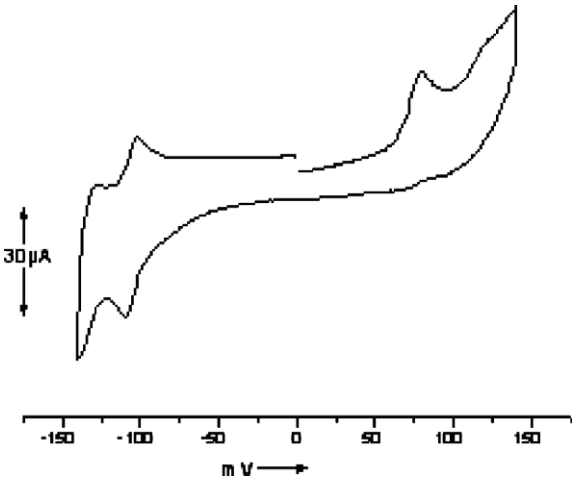


Fig. 7. Cyclic voltammogram of **2**. Scan rate 50 mV/s.

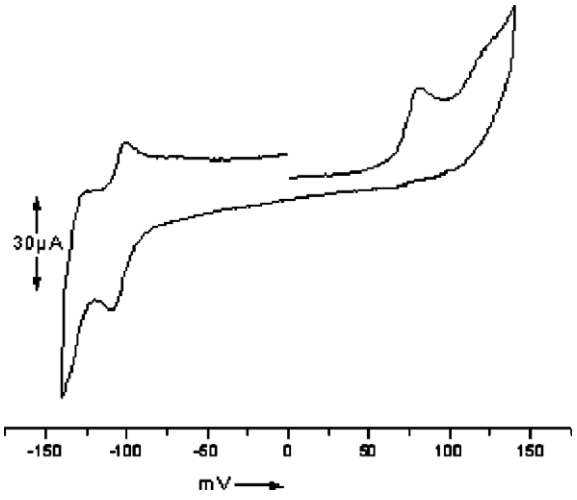


Fig. 8. Cyclic voltammogram of **3**. Scan rate 50 mV/s.

6. Concluding remarks

We have prepared Co(III) and Mn(II) complexes of HL_1 and a Mn(II) complex of HL_2 where HL_1 and HL_2 are pyrimidine derived similar Schiff base ligands. In all the complexes, the ligands HL_1 and HL_2 behave as the monoanionic NNS tridentate one through deprotonation of one proton from their corresponding thiol tautomer. Each of them forms bis-chelate with the metal ions having distorted

octahedral geometry. The deprotonation accompanied with tautomerization produces a delocalised ring system with overall intermediate interatomic bond distances on the ligand network. Cyclic voltametric studies show an irreversible anodic process and a quasi-reversible reduction.

Acknowledgement

Financial support [01(1916)/04/EMR-II] from Council of Scientific and Industrial Research (CSIR), New Delhi, India, is gratefully acknowledged.

Appendix A. Supplementary material

CCDC 657938, 657939, 657940 and 657941 contain the supplementary crystallographic data for HL_1, **1**, **2** and **3**. These data can be obtained free of charge via http://www.ccdc.cam.ac.uk/conts/retrieving.html, or from the Cambridge Crystallographic Data Centre, 12 Union Road, Cambridge CB2 1EZ, UK; fax: (+44) 1223-336-033; or e-mail: deposit@ccdc.cam.ac.uk. Supplementary data associated with this article can be found, in the online version, at doi:10.1016/j.poly.2007.10.012.

References

[1] E.S. Roper, Coord. Chem. Rev. 61 (1985) 115.
[2] J.S. Casas, E.E. Castellans, M.D. Louce, J. Ellena, A. Sanchez, J. Sordo, C. Taboada, J. Inorg. Biochem. 11 (2006) 1858.
[3] M.J. Campbell, Coord. Chem. Rev. 15 (1975) 297.
[4] D.X. West, S.B. Padhye, P.B. Sonawane, Struct. Bond (Berlin) 76 (1991) 4.
[5] Y.P. Tian, C.Y. Duan, Z.L. Lu, X.Z. You, H.K. Fun, S. Kandasamy, Polyhedron 15 (1996) 2263.
[6] S.K. Jain, B.S. Garg, Y.K. Boon, J.P. Scovill, D.L. Klayman, Spectrochim. Acta 24 (1985) 407.
[7] S.B. Padhye, G.B. Kanffman, Coord. Chem. Rev. 63 (1985) 127.
[8] D.X. West, A.E. Liberta, S.B. Padhye, R.C. Chilate, P.B. Sonawane, A.S. Kumbhar, R.G. Yerande, Coord. Chem. Rev. 123 (1993) 49.
[9] T.S. Lobana, P.K. Bhatia, J. Sci. Ind. Res. 48 (1989) 394.
[10] M.C. Rodriguez-Arguelles, S.J. Pinelli, J. Inorg. Biochem. 58 (1995) 157.
[11] J.S. Casas, M.S. Garcia-Tasende, C. Maichel-Mossmer, M.C. Rodriguez-Arguelles, A. Sanchez, J. Sordo, A. Vazquez-Lopez, S. Pinelli, P. Lunghi, R. Albertini, J. Inorg. Biochem. 62 (1996) 41.
[12] M.B. Ferrari, G.G. Fava, G. Tarasconi, R. Albertini, S. Pinelli, R. Starcich, J. Inorg. Biochem. 53 (1994) 13.
[13] T. Lobana, Proc. Indian Acad. Sci. (Chem. Sci.) 112 (2000) 323.
[14] U. Koch, B. Attenni, S. Malancona, S. Colarusso, I. Conte, M.D. Filippo, S. Harper, B. Pacini, C. Giomini, S. Thomas, I. Incitti, L. Tomei, R.D. Francesco, S. Altamura, V.G. Matassa, F. Narjes, J. Med. Chem. 49 (2006) 1693.
[15] A. Mullar, B. Krebs (Eds.), Sulfur its Significance for Chemistry, for the Geo- and Cosmosphere and Technology, Studies in Inorganic Chemistry, vol. 5, Elsevier Science Publishers, Amsterdam, 1984.
[16] S.D. Conradsson, B.K. Burgess, W.W. Newton, K.O. Hodgson, J.W. Mcdonald, J.F. Robinson, S.F. Gheller, L.E. Mortenson, M.W.W. Adams, P.K. Mascharak, W.A. Armstrong, R.H. Holm, J. Am. Chem. Soc. 107 (1985) 7935.
[17] E.C. Constable, Coord. Chem. Rev. 93 (1989) 205.
[18] T. Yamamoto, Z. Zhou, T. Kanbara, M. Shimura, K. Kizu, T. Maruyama, Y. Nakamura, T. Fukuda, B. Lee, N. Ooba, S. Tomaru, T. Kurihara, T. Kaino, K. Kubota, S. Sasaki, J. Am. Chem. Soc. 118 (1996) 10389.
[19] F. Lloret, G. De Munno, M. Julve, J. Cano, R. Ruiz, A. Caneschi, Angew. Chem., Int. Ed. 37 (1998) 135.
[20] R. Cortes, M.K. Urtiaga, L. Lezama, J.L. Pizarro, M.I. Arriortua, T. Rojo, Inorg. Chem. 36 (1997) 5016.
[21] S.W. Keller, Angew. Chem., Int. Ed. 36 (1997) 247.
[22] B. Neuman, T. Hegmann, R. Wolf, C. Tschierske, Chem. Commun. (1998) 105.
[23] D. Kovala-Demertzi, M.A. Demertzis, J.R. Miller, C. Padadopoulou, C. Dodorou, G. Filousis, J. Inorg. Biochem. 86 (2001) 555.
[24] A.G. Quiroga, J.M. Pérez, L. Solera, J.R. Masaguer, A. Luque, P. Román, A. Edwards, C. Alonso, C.N. Ranninger, J. Med. Chem. 41 (1998) 1399.
[25] D.H. Petering, Bioinorg. Chem. 1 (1972) 255.
[26] D. Kovala-Demertzi, A. Domopoulou, M.A. Demertzis, G. Valle, A. Papageorgiou, J. Inorg. Biochem. 68 (1997) 147.
[27] D. Kovala-Demertzi, P.N. Yadav, M.A. Demertzis, M. Coluccia, J. Inorg. Biochem. 78 (2000) 347.
[28] D.T. Minkel, D.H. Petering, Cancer Res. 38 (1978) 117.
[29] D.F. Xiang, C.Y. Duan, X.S. Tan, Q.W. Hang, W.X. Tang, J. Chem. Soc., Dalton Trans. (1998) 1201.
[30] P.E. Siegbahn, R.H. Crabtree, J. Am. Chem. Soc. 121 (1999) 117.
[31] K. Wieghardt, Angew. Chem., Int. Ed. 28 (1989) 1153.
[32] B.J. Day, Drug Discov. Today 13 (9) (2004) 557.
[33] Jh. Cory, A.E. Fleischeher, Cancer Res. 39 (1979) 4600.
[34] A.C. Sartorelli, K.C. Agarwal, A.S. Tsiftsoglou, E.C. Moore, Adv. Enzyme Regul. 15 (1977) 117.
[35] W.G. Rice, C.A. Schaeffer, L. Graham, D. Clanton, R.W. Buckheit Jr., D. Zaharevitz, M.F. Summers, A. Wallqvist, D.G. Covell, J. Med. Chem. 39 (1996) 3606.
[36] M. Otsuka, M. Fujita, Y. Sugiura, J. Med. Chem. 37 (1994) 4267.
[37] T. Hitoshi, N. Tamao, A. Hideykki, F. Manabu, M. Takayuki, Polyhedron 16 (1997) 3787.
[38] S. Roy, T.N. Mandal, A.K. Barik, S. Pal, S. Gupta, A. Hazra, R.J. Butcher, A.D. Hunter, M. Zeller, S.K. Kar, Polyhedron 26 (2007) 2603.
[39] D.D. Perrin, W.L.F. Armarigo, D.R. Perrin, Purification of Laboratory Chemicals, 2nd ed., Pergamon Press, Oxford, 1980.
[40] (a) M.A. Ali, S.E. Livingstone, D.J. Phillips, Inorg. Chim. Acta 7 (1973) 179;
(b) R. Bose, M.A. Ali, J. Inorg. Nucl. Chem. 39 (1977) 265.
[41] H. Bredereck, R. Sell, F. Effenberger, Chem. Ber. 97 (1964) 3406.
[42] (a) Bruker, XPREP v2005/4, Bruker AXS Inc., Madison, WI, USA, 2005;
(b) Bruker, SMART v5.631, Bruker AXS Inc., Madison, WI, USA, 2001;
(c) Bruker, SAINT v7.34A, Bruker AXS Inc., Madison, WI, USA, 2005;
(d) Bruker, SHELXTL v6.12, Bruker AXS Inc., Madison, WI, USA, 2000;
(e) Bruker, SADABS v2004/1, Bruker AXS Inc., Madison, WI, USA, 2004;
(f) G.M. Sheldrick, Acta Crystallogr., Sect. A 46 (1990) 467.
[43] A.K. Barik, S. Paul, S.K. Kar, R.J. Butcher, J.C. Bryan, Polyhedron 18 (1999) 571.
[44] M.A. Ali, S.M.M. Majumder, R.J. Butcher, J.P. Jasinski, J.M. Jasinski, Polyhedron 16 (1997) 2749.
[45] E.J. Gabe, M.R. Taylor, J.P. Pickworth Glusker, J. Minkin, A.L. Patterson, Acta Crystallogr., Sect. B 25 (1969) 1620.
[46] N.F. Curtis, in: G.A. Melson (Ed.), Coordination Chemistry of Macrocyclic (24 of c) Compounds, Plenum, New York, 1979.
[47] A. Usman, I.A. Razak, S. Chantrapromma, H.-K. Fun, A. Sreekanth, S. Sivakumar, M.R.P. Kurup, Acta Crystallogr., Sect. C 58 (2002) m461.
[48] M. Hoogenraad, K. Ramkisoensing, H. Kooijman, A.L. Spek, E. Bouwman, J.G. Haasnoot, J. Reedijk, Inorg. Chim. Acta 279 (1998) 217.

[49] A. Sreekanth, M. Joseph, H.-K. Fun, M.R.P. Kurup, Polyhedron 25 (2006) 1408.
[50] M.M. Mostafa, A. Hammid, A.M. Shallaby, A.A. El-Asmy, Transition Met. Chem. 6 (1981) 303.
[51] S.K. Chattopadhyay, D. Chattopadhyay, T. Banerjee, R. Kuroda, S. Ghosh, Polyhedron 6 (1997) 1925.
[52] D.X. West, J.S. Ives, G.A. Bain, A.E. Liberta, J. Valdes-Martinez, K.H. Ebert, S. Hernandez-Ortega, Polyhedron 16 (1997) 1895.
[53] A. Castineiras, D.X. West, H. Gebremedhin, T.J. Romack, Inorg. Chim. Acta 216 (1994) 229.
[54] D. Kovala-Demertzi, A. Domopoulou, G. Valle, M.A. Demertzis, A. Papageorgiou, J. Inorg. Biochem. 6 (1997) 147.
[55] D. Kovala-Demertzi, S.K. Hadjikakou, M.A. Demertzis, Y. Deligiannakis, J. Inorg. Biochem. 69 (1998) 223.
[56] M.D. Godbole, E. Grigiotti, P. Zanello, A.M. Mills, A.L. Spek, E. Bouwman, Inorg. Chim. Acta 358 (2005) 233.

Available online at www.sciencedirect.com
ScienceDirect
Polyhedron 27 (2008) 602–608
POLYHEDRON
www.elsevier.com/locate/poly

Crystal structure and spectral characterization of hexanuclear oxo titanium(IV) clusters: $[Ti_6O_6(OSi(CH_3)_3)_6(OOCR)_6]$ ($R = Bu^t$, CH_2Bu^t, $C(CH_3)_2Et$)

P. Piszczek *, M. Richert, A. Wojtczak

Faculty of Chemistry, Nicolaus Copernicus University, 87-100 Toruń, ul. Gagarina 7, Poland

Received 31 May 2007; accepted 15 October 2007
Available online 3 December 2007

Abstract

Hexanuclear oxo titanium(IV) siloxo carboxylate complexes with the general formula $[Ti_6O_6(OSi(CH_3)_3)_6(OOCR)_6]$ ($R = Bu^t$ (**1**), CH_2Bu^t (**2**), $C(CH_3)_2Et$ (**3**)) were synthesized in quantitative yield, by the reaction of $Ti(OSiMe_3)_4$ with the appropriate organic acid. Crystal structure determination revealed that molecules of **1**–**3** are composed of $[Ti_6\text{-}(\mu_3\text{-}O)_6]$ cores stabilized by six *syn–syn* carboxylato bridges and six terminal siloxide ligands. Each metal atom is surrounded by six oxo atoms, capping the triangular faces of the distorted octahedron. Spectral characterization (IR, NMR) of **1**–**3** revealed a significant non-equivalence of the carboxylate group interactions, resulting from the asymmetry of the Ti-μ-OOC bonds of the *syn–syn* bridges. The thermal stability of the studied compounds was determined from TGA/DTA analysis.
© 2007 Elsevier Ltd. All rights reserved.

Keywords: Titanium(IV) siloxides; Titanium(IV) carboxylato derivatives; Crystal structure; NMR; IR; TGA

1. Introduction

Multinuclear oxo titanium(IV) carboxylato alkoxide complexes are used as precursors mainly in sol–gel methods for manufacturing titanium oxide ceramics, TiO_2 nanoparticle layers and organic–inorganic hybrid polymers [1,2]. We have recently shown that the thermal properties of selected complexes also enable their application as CVD precursors for the preparation of thin titanium dioxide layers [3,4]. Especially interesting are hexanuclear oxo titanium(IV) alkoxide carboxylates, synthesized in the reaction of titanium(IV) alkoxides with carboxylic acids. X-ray diffraction studies revealed that molecules of these compounds consist of clusters formed by titanium(IV) oxo cores stabilized by carboxylate bridges and terminal alkoxide ligands [5–9]. The type and the thermal properties of Ti(IV) oxo-clusters depend on the $Ti(OR)_4/R'COOH$ stoichiometry, the type of carboxylate ligands and alkoxide groups [5,6]. The sensitivity of titanium carboxylato alkoxides to moisture was significantly lower than the parent alkoxides. However, during longer storage in air (2–4 months) their partial decomposition was observed. Therefore, in order to moderate the reactivity of these complexes, the titanium(IV) alkoxides have been replaced by titanium(IV) siloxides.

The most popular among the Ti(IV) siloxide derivatives is $Ti(OSiPh_3)_4$ [10,11], used in the epoxidation of alkenes. The reaction of $[(Cp)Ti(CHPh)_2]$ or $[Cp_2TiCl]$ with Ph_3SiOH leads to the formation of complexes of the general formula $[(Cp)(Ph_3SiO)Ti(CHPh)_2]$ [12] and $[Cp_2TiCl(OSiPh_3)]$ [13]. The crystal structure of these compounds consists of a regular tetrahedron of $Ti(OSiPh_3)_4$ surrounded by cyclopentadienyl ligands. Polyhedral titansiloxanes containing Si–O–Ti bonds were used as model systems for titanium doped zeolites [14]. The Ti(IV) complexes mentioned above were synthesized from a $Ti(OR)/R'Si(OH)_3$ mixture.

* Corresponding author. Fax: +48 056 654 24 77.
E-mail address: piszczek@chem.uni.torun.pl (P. Piszczek).

0277-5387/$ - see front matter © 2007 Elsevier Ltd. All rights reserved.
doi:10.1016/j.poly.2007.10.018

They form a multinuclear ring system, composed of 2–8 titanium atoms. The silicon atoms were four-coordinated, whilst the titanium atoms show coordination numbers from four to six [15–17]. Moreover, cubic titanosiloxanes were obtained in the reaction of titanium(IV) alkoxides with suitable silanotriols in the molar ratio 1:7 or 4:4 [18,19]. The titanium(IV) silanol derivatives of the general formula $[Ti(OSiOBu^t)_4]$ [20] and $[(Bu^tO)_3Si–O–Ti(OBu^t)_3]$ [21] have also been used as precursors in CVD methods. However, there are no data concerning the structure and thermal properties of Ti(IV) complexes formed during the reaction of $Ti(OSi(R)_3)_4$ and organic acids. Therefore, the aim of the reported research was to synthesise and structurally characterise multinuclear Ti(IV) oxo sioloxo carboxylate derivatives formed in the reaction between $Ti(OSi(CH_3)_3)_4$ and branched organic acids (RCOOH; $R = Bu^t$, CH_2Bu^t, $C(CH_3)_2Et$). The structures of the novel group of complexes have been studied by single crystal X-ray diffraction, IR and NMR spectroscopy. The thermal properties of the obtained compounds have been determined using thermogravimetric analysis.

2. Results and discussion

2.1. Synthesis

Hexanuclear oxo Ti(IV) siloxo carboxylate derivatives were synthesized under the conditions described in earlier reports concerning $[Ti_6O_6(OPr^i)_6(OOCBu^t)_6]$ [5–7] (molar ratio titanium siloxide/organic acid = 1:1, Ar atmosphere, room temperature). Yellowish crystals suitable for single crystal X-ray studies or fine-crystalline powders were grown by slow solvent evaporation (glovebox, RT) over one week. The results of the elemental analysis of the powders confirms the formation of complexes of the general formula $[Ti_6O_6(OSi(CH_3)_3)_6(OOCR)_6]$ ($R = Bu^t$ (**1**), CH_2Bu^t (**2**), $C(CH_3)_2Et$ (**3**)). The obtained compounds showed stability against moisture higher than that of the corresponding hexanuclear oxo Ti(IV) isopropoxo carboxylate derivatives [7].

2.2. Description of the structures

Analysis of X-ray data, collected at 293 K, shows that **1** and **3** crystallize in the triclinic space group $P\bar{1}$ (no. 2) and **2** in the monoclinic group $C2/c$ (no. 15). Table 1 lists the main X-ray data collection parameters for the synthesized complexes. The X-ray diffraction studies showed the presence of toluene in the crystal lattice of **1**. That is the main reason for the observed differences in the crystal packing between this complex and **2**. The poor quality of crystals obtained for **3** made their crystallographic studies impossible. Selected bond distances and angles of the studied complexes are presented in Table 2.

The structures of the investigated compounds consist of hexanuclear titanium oxo cores ($[Ti_6$-$(\mu_3$-$O)_6]$) surrounded by carboxylate bridges and siloxide ligands (Fig. 1). Six equivalent titanium atoms are arranged in the corners of an octahedron. The average Ti···Ti distances in the $[Ti_6$-$(\mu_3$-$O)_6]$ cores of **1** and **2** vary from 3.141(9) to 4.699(25) Å (Table 2) and are longer than the analogous distances in the structure of $[Ti_6O_6(OPr^i)_6(OOCBu^t)_6]$ (3.098 Å [6,7]). The center of the hexameric cluster is empty, with the internal diameter of the $[Ti$-$(\mu_3$-$O)]_3$ ring being 3.69–3.71 Å. Each titanium atom is surrounded by three oxygen atoms of μ_3-O bridges, two μ-O of a carboxylate bridge, and the oxygen atom of the terminal siloxide ligand capping the triangular faces in a distorted octahedron (μ_3-O–Ti–OSi angles 177.6(1)–178.9(2)° for (**1**) and 177.3(1)–178.0(1)° for (**2**); μ_3-O–Ti–OOC1 – 157.4(1)–160.1(2)° for (**1**) and 158.2(1)–158.8(1)° for (**2**); μ_3-O–Ti–OOC2 – 160.1(1)–162.8(1)° for (**1**) and 160.7(1)–161.1(1)° for (**2**)).

The titanium-oxide bond lengths of the μ_3-O bridges change in the range 1.863(2)–2.220(16) Å. The Ti–O distances of the respective bonds within the $[Ti–(\mu_3$-$O)]_3$ rings (1.863(2)–1.903(6) Å) are significantly shorter than those between planes of $[Ti–(\mu_3$-$O)]_3$ rings (2.200(19)–2.220(16) Å). Simultaneously, the lengths of these bonds are similar to the analogous titanium–(μ_3-O) distances in the $[Ti_6–(\mu_3$-$O)_6]$ cores of $[Ti_6O_6(OPr^i)_6(OOCR)_6]$ (R = H [5] and Bu^t [7]). Values of Ti–(μ_3-O)–Ti angles in the plane of the $[Ti–(\mu_3$-$O)]_3$ rings and between them are 134.9(1)–136.5(1)° and 99.6(1)–100.8(2)°, respectively. The hexanuclear titanium oxide core is stabilized by six asymmetric, carboxylate *syn–syn* bridges (μ-OOCR), with the length of the shorter bonds being 2.032(7)–2.068(6) Å and the longer ones 2.049(4)–2.073(8) Å (Table 2). The length of the Ti–OSi bonds change from 1.771(14) to 1.794(15) Å in the cluster of **1** and 1.776(8)–1.782(10) Å in **2** (Table 2), which is typical for Ti–OSi bonds of titanium(IV) siloxides (1.78–1.80 Å) [22,23].

3. NMR spectroscopy

The structures of **1–3** have also been characterized by multinuclear NMR spectroscopy in the solid phase and in solution ($[D_8]$ toluene). Results of our studies are listed in Table 3. The coordination effects were studied mainly as a result of the chemical shift of resonance signals descended from carbon atoms of the carboxylate ligands. However, changes in the electronic density of carbon atoms in hydrocarbon aliphatic chains remote from the coordination core can also influence the shift of the resonance peaks. The crystallographic similarity of **1** and **3** explains the analogical shifts and the splitting of COO carbon signals in ^{13}C NMR spectra, as well as the shift of the silicon peak in the ^{29}Si NMR spectra (Tables 1 and 3). Three resonance signals at $\delta = 183.95$, 184.15, 184.31 ppm and $\delta = 183.74$, 184.05, 184.24 ppm, attributed to the carbon atoms of the COO group, were found in the ^{13}C NMR spectra of **1** and **3** (crystallizing in the triclinic system), respectively. In the spectrum of **2**, which crystallizes in the monoclinic system, two peaks for the carboxylate

Table 1
Crystallographic data and data collection details

	1	2	3
Formula sum	$Ti_6Si_6O_{24}C_{55}H_{108}$	$Ti_6Si_6O_{24}C_{54}H_{120}$	$Ti_6Si_6O_{24}C_{54}H_{120}$
Formula weight	1609.35	1609.44	1609.50
Temperature (K)	293 (2)	293 (2)	293 (2)
Wavelength (Å)	0.71073	0.71073	0.71073
Crystal system	triclinic	monoclinic	triclinic
Space group	$P\bar{1}$ (no.2)	$C2/c$ (no.15)	$P\bar{1}$ (no.2)
Unit cell dimensions			
a (Å)	13.896(1)	27.386(2)	13.562(3)
b (Å)	15.113(1)	19.314(1)	14.317(1)
c (Å)	23.554(2)	19.344(1)	14.369(1)
α (°)	83.51(7)	90	67.00(1)
β (°)	79.85(7)	99.12(1)	68.36(1)
γ (°)	63.37(1)	90	68.85(1)
Volume (Å^3)	4349.4(6)	10102.3(10)	2309.3(6)
Z	2	4	
D (calc) (Mg/m^3)	1.229	1.058	
Absorption coefficient (mm^{-1})	0.667	0.574	
F(000)	1692	3408	
Crystal size (mm)	$0.37 \times 0.36 \times 0.31$	$0.44 \times 0.41 \times 0.16$	
θ Range for data collection (°)	2.27–31.46	2.36–31.35	
Index ranges	$-20 \leqslant h \leqslant 20$, $-22 \leqslant k \leqslant 21$, $-22 \leqslant l \leqslant 34$	$-38 \leqslant h \leqslant 34$, $-27 \leqslant k \leqslant 27$, $-26 \leqslant l \leqslant 28$	
Reflections collected	43387	49609	
Independent reflections	25,575 [$R_{int} = 0.1325$]	15,490 [$R_{int} = 0.1180$]	
Transmission Maximum/Minimum	0.8200/0.7905	0.9212/0.7947	
Refinement method	full-matrix LS on F^2	full-matrix LS on F^2	
Data/restraints/parameters	25575/0/825	15490/0/424	
Goodness-of-fit on F^2	0.932	1.022	
Final R indices [$I > 2\sigma(I)$]	$R_1 = 0.0825$, $wR_2 = 0.2065$	$R_1 = 0.0960$, $wR_2 = 0.2749$	
R indices (all data)	$R_1 = 0.1788$, $wR_2 = 0.2612$	$R_1 = 0.1536$, $wR_2 = 0.3216$	
Largest diffraction peak and hole (e Å^{-3})	0.714 and −0.598	1.507 and −0.768	

[a] $R_1 = \sum\|F_0| - |F_c\|/\sum|F_0|$.
[b] $wR_2 = [\sum w(F_0^2 - F_c^2)^2/\sum(w|F_0|^2)^2]^{1/2}$.

carbon, at $\delta = 178.42$ and 178.70 ppm have been detected. Comparison of these data with chemical shifts of carboxylate carbons in the spectra of the corresponding acids ($\delta = 186.12$ ppm (**1**), 179.85 ppm (**2**)) suggests a significant influence of the type of the carboxylate ligand on the shift of the resonance signals of the COO group. The crystal data reported in this paper show that carboxylate ligands form non-equivalent interactions with titanium ions of [Ti$_6$–(μ_3-O)$_6$] cores (Table 2). It suggests that the asymmetry of the COO bridges causes the splitting of the resonance signals of the carboxylate atoms, observed in the ^{13}C NMR spectra of **1**–**3**.

^{29}Si NMR studies of **1**–**3** revealed the presence of single resonance signals, attributed to coordinated OSi(CH$_3$)$_3$ groups in the spectra of **1** and **2**, and a double signal in the spectrum of **3** (Table 3). The chemical shift of the silicon peaks in the spectra of **1**–**3** have been compared to the spectrum of Ti(OSi(CH$_3$)$_3$)$_4$ ($\delta = 13.24$ ppm). In the spectrum of **1**, a shift of the silicon signal by about 0.28 ppm toward higher values of the magnetic field was found. The corresponding signal was shifted towards lower field by 1.27 ppm in the spectrum of **2**. Analysis of ^{29}Si and ^{13}C NMR spectra of **3** showed a significant splitting of the silicon ($\delta = 13.58$ and 14.43 ppm) and carbon ($\delta = 1.67$, 1.95, 2.18 ppm) resonance signals of the OSi(CH$_3$)$_3$ groups (Table 3). That suggests the presence of significant differences in the strength of the Ti–OSi(CH$_3$)$_3$ interactions in [Ti$_6$O$_6$(OSi(CH$_3$)$_3$)$_6$ (OOC(CH$_3$)$_2$Et)$_6$] clusters in comparison to **1** and **2**.

NMR spectra of [D$_8$] toluene solutions were recorded in order to determine the structural changes caused by ligand dissociation or interactions of the complex molecules with solvent. In the ^{1}H and ^{13}C NMR spectra of **1**–**3** C$_7$D$_8$ solutions, signals assigned to OOCR resonance signals and signals due to the methyl moiety of the OSiMe$_3$ ligand were found. A comparison of ^{13}C NMR spectra of the solid complexes with their solutions revealed single peaks attributed to the carbon of the carboxylate groups. This indicates that symmetrical multinuclear Ti(IV) carboxylato siloxo clusters are also present in solution.

4. Analysis of IR spectra

Differences in the strength of the metal-ligand interactions in the crystalline structures of **1**–**3** have been determined using IR spectroscopy. The frequency of the

Table 2
Selected bond lengths (Å) for $[Ti_6O_6(OSi(CH_3)_3)_6(OOCR)_6]$ (R = Bu^t(**1**), CH_2Bu^t (**2**))

Distances (Å)	**1**		**2**	
Ti–(μ_3-O)	O19–Ti3	2.200(19)	O1–Ti1	2.202(12)
	O19–Ti4	1.894(10)	O1–Ti2	1.898(5)
	O19–Ti6	1.875(4)	O1–Ti3^i	1.866(6)
	O21–Ti2	2.211(19)	O2–Ti2	2.201(10)
	O21–Ti1	1.888(4)	O2–Ti1	1.862(2)
	O21–Ti5	1.868(10)	O2–Ti3	1.903(0)
	O22–Ti6	2.216(18)	O3–Ti3	2.205(12)
	O22–Ti3	1.884(7)	O3–Ti1^i	1.903(6)
	O22–Ti5	1.897(6)	O3–Ti2	1.863(2)
	O23–Ti1	2.212(18)		
	O23–Ti2	1.890(7)		
	O23–Ti4	1.874(6)		
	O24–Ti5	2.215(16)		
	O24–Ti2	1.874(11)		
	O24–Ti6	1.896(7)		
	O25–Ti4	2.220(16)		
	O25–Ti1	1.872(7)		
	O25–Ti3	1.893(11)		
Ti–$OSiMe_3$	O6–Ti6	1.771(14)	O11–Ti3	1.782(10)
	O11–Ti4	1.782(13)	O21–Ti2	1.776(8)
	O14–Ti5	1.782(12)	O11–Ti1	1.782(10)
	O16–Ti1	1.782(13)		
	O18–Ti3	1.794(15)		
	O17–Ti2	1.781(15)		
Ti–(μ-OOCR)	O2–Ti5	2.064(4)	O12–Ti1	2.055(0)
	O10–Ti2	2.038(8)	O13–Ti3^i	2.040(0)
	O7–Ti6	2.062(8)	O22–Ti2	2.057(2)
	O13–Ti5	2.053(4)	O23–Ti1	2.043(6)
	O1–Ti1	2.032(7)	O32–Ti2	2.043(4)
	O12–Ti4	2.049(4)	O33–Ti3	2.062(8)
	O9–Ti3	2.073(8)		
	O8–Ti4	2.068(6)		
	O4–Ti2	2.066(11)		
	O15–Ti1	2.061(7)		
	O3–Ti3	2.047(11)		
	O5–Ti6	2.050(7)		
Ti···Ti	Ti1···Ti4	3.141(9)	Ti1···Ti3^i	3.147(12)
	Ti1···Ti2	3.165(25)	Ti1···Ti2	3.146(3)
	Ti1···Ti5	3.467(8)	Ti1···Ti2^i	3.481(8)
	Ti1···Ti3	3.496(17)	Ti1···Ti3	3.483(0)
	Ti1···Ti6	4.699(25)	Ti1···Ti1^i	4.696(8)

Symmetry codes:
1 – (i) $1-x, 1-y, 1-z$.
2 – (i) $0.5-x, 0.5-y, -z$.

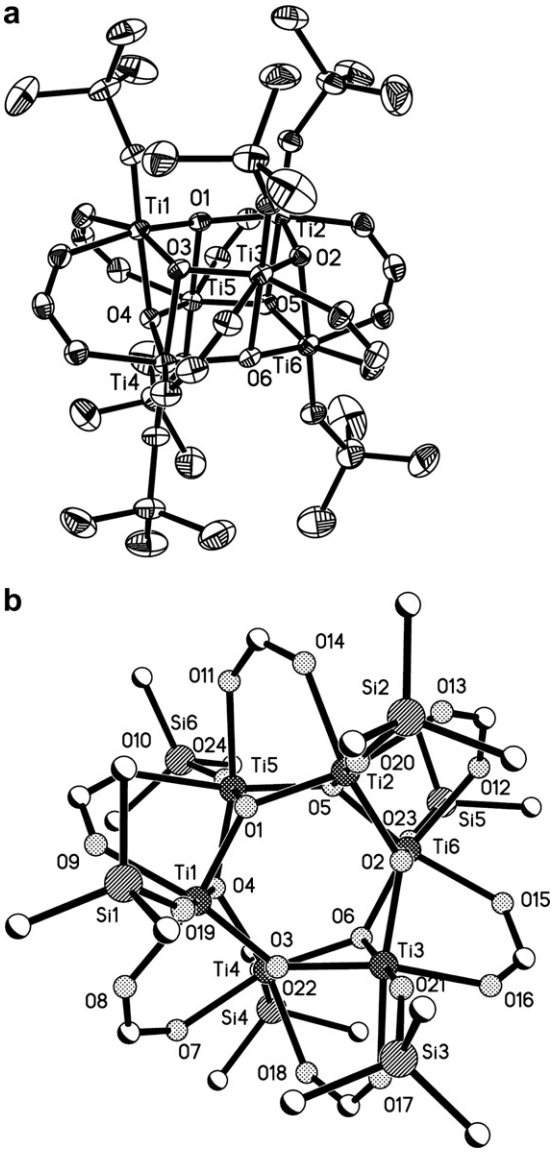


Fig. 1. The structure of $[Ti_6O_6(OSi(CH_3)_3)_6(OOCBu^t)_6]$ (**1**); (a) thermal ellipsoid plot and (b) ball and stick plot of the cluster, hydrocarbon groups are not shown for clarity.

fundamental vibrations of Ti–L functional groups (L = OOCR, $OSi(CH_3)_3$, μ_3-O), detected in spectra registered at room temperature (RT), are listed in Table 4.

4.1. Carboxylate bridge vibrations

Bands attributed to symmetric and asymmetric stretching vibrations of the coordinated carboxylate groups were observed between 1528 and 1594 cm^{-1} (ν_{as}(COO)), and 1380–1434 cm^{-1} (ν_s(COO)) (Table 4). Values of the Δ parameter (calculated as the difference between ν_{as}(COO) and ν_s(COO)), being 153–156 and 115–121 cm^{-1}, correspond to a bidentate coordination of the carboxylate groups participating in *syn–syn* bridges stabilizing the $[Ti_6(\mu_3\text{-}O)_6]$ cores. Differences in the mutual orientation of the carboxylate groups linking the $[Ti_3(\mu_3\text{-}O)_3]$ rings and the asymmetry of the carboxylate ligands are factors which cause the splitting of the COO stretching bands.

Analysis of data presented in Table 4 also reveals significant shifts of ν_{as}(COO) and ν_s(COO) bands towards lower wavenumbers in the sequence **2** > **1** > **3**. This effect can be explained by the influence of the type of alkyl group on the strength of the Ti–OOC interactions. According to the crystallographic data, the average metal-oxide distances of the carboxylate groups change from 2.043, 2.058 Å for **2** to 2.049, 2.060 Å for **1**. Two medium intensity bands between 470 and 472 cm^{-1}, and 421–444 cm^{-1} have been attributed to the stretching Ti–(μ-OOC) and bending (COO) modes. The mild splitting of these bands

Table 3
The solid state and solution (toluene-*d*) NMR studies of $[Ti_6O_6(OSi(CH_3)_3)_6(OOCR)_6]$ (R = Bu^t (**1**), Bu^{t}CH$_2$ (**2**), C(CH$_3$)$_2$Et (**3**))

NMR	δ (ppm) $[Ti_6O_6(Osi(CH_3)_3)_6(OOCBu^t)_6]$ (**1**)					
	$CH_3(Bu^t)$		$C(Bu^t)$	C(COO)	$CH_3((CH_3)_3Si)$	$Si((CH_3)_3Si)$
^{13}C-s.st.	26.98		39.27	183.95 184.15 184.31	2.09	
^{29}Si-s.st.						12.96
$^{13}C–C_7D_8$	27.80		39.50	184.88	2.18	
$^{1}H–C_7D_8$	1.19				0.45	
	δ (ppm) $[Ti_6O_6(OSi(CH_3)_3)_6(OOCCH_2Bu^t)_6]$ (**2**)					
	$CH_3(Bu^t)$	CH_2	$C(Bu^t)$	C(COO)	$CH_3((CH_3)_3Si)$	$Si((CH_3)_3Si)$
^{13}C-s.st.	30.25	50.13	31.33	178.42 178.70	2.09	
^{29}Si-s.st.						14.51
$^{13}C–C_7D_8$	30.12 30.29	50.01	31.57	179.17	1.99 2.13	
$^{1}H–C_7D_8$	1.05(s)	1.28(s)			0.46	
	δ(ppm) $[Ti_6O_6(OSi(CH_3)_3)_6(OOCC(CH_3)_2Et)_6]$ (**3**)					
	CH_3(Et)	CH_2(Et)	$CH_3C(CH_3)_2$	$C(C(CH_3)_2)$	C(COO)	$CH_3((CH_3)_3Si)$	$Si((CH_3)_3Si)$
^{13}C-c.st	9.06 9.69 10.27	32.52 34.62	25.03 25.77 27.23	43.68 43.35	183.74 184.05 184.24	1.67 1.95 2.18	
^{29}Si-s.st.							13.58 14.43
$^{13}C–C_7D_8$	10.22	34.48	25.39	43.51	184.39	2.30	
$^{1}H–C_7D_8$	0.96 (t) $J_{H–H}$ 7.5 Hz	1.61 (q) $J_{H–H}$ 4.4 Hz	1.23 1.25 (s)			0.51	

Table 4
Wavenumbers (cm^{-1}) for the fundamental vibrations of $[Ti_6O_6(OSi(CH_3)_3)_6(OOCR)_6]$ (R = Bu^t (**1**), Bu^{t}CH$_2$ (**2**), C(CH$_3$)$_2$Et (**3**))

	1	**2**	**3**
ν_{as}(COO)	1587 (s)	1594 (s)	1584 (s)
ν_{as}(COO)	1530 (m)	1539 (m)	1528 (s)
$\delta_{as}(CH_3)/(CH_2)$	1485 (m)	1478 (m)	1479 (m)
$\delta_{as}(CH_3)/(CH_2)$	1458 (w)	1463 (s)	1465 (w)
ν_s(COO)	1434 (s)	1441 (m)	1428 (m)
ν_s(COO)	1415 (m)	1418 (s)	1412 (w)
$\delta_{as}(CH_3)/(CH_2)$	1382 (w)	1398 (w)	1380 (w)
$\delta_{as}(CH_3)/(CH_2)$	1363 (w)	1371 (m)	1362 (w)
$\delta_{as}(CH_3)/(CH_2)$			1329 (w)
		1303 (w)	1293 (m)
ν(CSi)	1246 (s)	1247 (m)	1253 (w)
ν(C–C)	1230 (s)	1233 (w)	1246 (m)
ν(O–Si)	921 (s)	923 (s)	918 (s)
ν(C–Si)	842 (s)	843 (s)	843 (s)
ν(Ti–O–Ti)	753 (m)	754 (m)	754 (m)
ν(Ti–O–Ti)	710 (s)	704 (s)	710 (s)
	647 (w)	639 (s)	646 (w)
			634 (w)
ν_{as}(Ti–OSi)	607 (s)	566 (m)	599 (s)
δ_{as}(SiOC)	527 (s)	525 (m)	531 (m)
ν_{as}(Ti–OOC)	470 (m)	471 (m)	472 (m)
δ_{as}(COO)	444 (m)	421 (m)	436 (w)

is caused by the differences in the symmetry of the carboxylic groups interaction in the $[Ti_6O_6(OSiMe_3)_6(OOCR)_6]$ clusters.

4.2. Fundamental frequencies of –OSiMe$_3$ terminal ligands

The bands at 919–923 cm^{-1} and 525–647 cm^{-1} were assigned to vibrations of the trimethylsiloxide ligands. According to previous reports [24], the first band can be assigned to Si–O stretching vibrations of siloxide groups (ν(SiO)), whereas the second one to Ti–OSi modes (ν(Ti–O)). In comparison to $[Ti(OSi(CH_3)_3)_4]$, the frequencies of Si–O (ν(SiO), 918 cm^{-1}) and Ti–OSi (ν(Ti–O), 517 cm^{-1}) vibrations are shifted towards higher wavenumbers by 1–5 cm^{-1} and 8–14 cm^{-1}, respectively (Table 4). That can be explained by stronger Ti–OSi interactions in hexanuclear clusters in comparison with $[Ti(OSi(CH_3)_3)_4]$. Slight differences in the frequencies corresponding to the modes mentioned above indicate the formation of equivalent Ti–OSi interactions in the $[Ti_6O_6(OSi(CH_3)_3)_6(OOCR)_6]$ clusters, independent of the type of carboxylate ligands. The obtained spectral results are consistent with the structural analysis presented in this paper.

4.3. Fundamental frequencies of Ti–O–Ti vibrations of $[Ti_6–(\mu_3\text{-}O)_6]$ clusters

Two bands, which were detected in the spectra of **1**–**3** at 704–710 and ~754 cm^{-1}, can be attributed to vibrations of Ti–O–Ti non-linear bridges of the $[Ti_6–(\mu_3\text{-}O)_6]$ cores. In contrast to the complexes discussed in this paper, in the

spectra of $[Ti_6O_6(OPr^i)_6(OOCR)_6]$ ($R = Bu^t$, CH_2Bu^t, $C(CH_3)_2$- Et) [4,7], single ν_{as}(Ti–O–Ti) bands between 720 and 750 cm^{-1} were detected. Analysis of the crystallographic data suggest that the symmetry of the $[Ti_6–(\mu_3\text{-}O)_6]$ core is the main difference between the $[Ti_6O_6(OSi(CH_3)_3)_6$-$(OOCR)_6]$ and $[Ti_6O_6(OPr^i)_6(OOCR)_6]$ clusters. Differences in the length of the Ti–O bonds in the $[Ti_3–(\mu_3\text{-}O)_3]$ ring and mutual "twisting" of these rings causes the splitting of ν_{as}(Ti–O–Ti) bands, detected in the IR spectra of the compounds reported here.

5. Thermal stability

The thermal properties of the synthesized complexes were studied using thermogravimetric methods (TGA/DTA) over the temperature range 25–600 °C. According to these data, the thermal decomposition of **1** proceeds in five endothermic steps (maxima at 47, 107, 269, 366 and 402 °C). The mass of the decomposition residue (31.9%) was consistent with titanium dioxide, and this was confirmed by XRD measurements. The biggest weight loss (39%), between 134 and 291 °C, suggests the formation of fragments containing titanium oxide species, which are detached at these temperatures. In the case of **2** and **3**, the maxima of the endothermic steps were detected at 125, 247, 346, 411 °C and 181, 276, 398 °C, respectively. The mass of the decomposition residue, 29.3% and 29.1%, indicates that TiO_2 is also the main decomposition product in these cases. The biggest weight losses for **2** and **3** were detected in range 182–286 °C (41.2%) and 208–318 °C (47.4%), respectively. The lowest temperature of conversion with the biggest weight loss was found for compound **1**, which can be assigned to the higher volatility of this compound in comparison with **2** and **3**.

6. Conclusions

Titanium trimethylsiloxide ($Ti(OSiMe_3)_4$) modified by branched organic acids ($HOOCR'$; $R' = Bu^t$, CH_2Bu^t, $C(CH_3)_2Et$) in the molar ratio 1:1 resulted in novel titanium oxo siloxo carboxylate complexes of the general formula $[Ti_6O_6(OSi(CH_3)_3)_6(OOCR')_6]$ ($R' = Bu^t$ (**1**), CH_2Bu^t(**2**), $C(CH_3)_2Et$ (**3**)). The structure of **1** was solved in the triclinic space group $P\bar{1}$ (no. 2) and the structure of **2** in the monoclinic group $C2/c$ (no. 15). The space group determined for **3** was triclinic $P1$ (no. 2). In comparison with known hexanuclear titanium oxo alkoxo carboxylate clusters, the titanium atoms form a similar type of cluster in the crystal lattice of **1**–**3**. Spectral analysis (IR, ^{13}C NMR) of **1**–**3** powders proved that the obtained complexes form a similar type of structure of the general formula $[Ti_6O_6(OSi(CH_3)_3)_6(OOCR')_6]$. Although significant differences in the length of the bonds and angles inside the cluster of **1** have not been found, the results of spectroscopic studies revealed the clear influence of the carboxylate ligand type on the strength of the Ti–OOC interactions with $[Ti_6(\mu_3\text{-}O_6)]$ clusters. The following factors affect the non-equivalence of the carboxylate bridge interactions in complexes **1**–**3**: (a) asymmetry of the carboxylate group interactions, (b) the type of hydrocarbon group of the organic acid, and (c) different orientation of the COO groups in the cluster. Thermogravimetric analysis of the synthesized compounds suggests that the volatile properties of **1** are better than those of **2** and **3**.

7. Experimental

The studied compounds were synthesized under an argon atmosphere using standard Schlenk line and glovebox techniques. $Ti(OSi(CH_3)_3)_4$ and the acids $R'COOH$ ($R' = Bu^t$, CH_2Bu^t, $C(CH_3)_2Et$, Aldrich) were used as received. The synthesized compounds were characterized using IR and NMR spectroscopy. IR spectra were registered on a Perkin–Elmer Spectrum 2000 spectrometer within the range 400–4000 cm^1 with a medium slit width and a peak resolution of 4.0 cm^{-1}. The crystals were studied as a powder dispersed in a KBr pellet (400–4000 cm^{-1}) and as a Nujol suspension between CsI plates (160–700 cm^{-1}). Solution ^1H and ^{13}C NMR spectra (toluene-d_8) were recorded using a 5 mm solution probe on a Varian Gemini 200. Solid state ^{13}C NMR spectra were registered on Bruker AMX 300. Thermogravimetric analysis (TGA) was carried out using SDT 2960 TA Instruments, in nitrogen atmosphere from 25 to 600 °C at a ramp rate of 3° min^{-1}.

7.1. Preparation of $Ti_6O_6(OSi(CH_3)_3)_6(OOCR)_6$

$Ti(OSi(Me)_3)_4$ (1.00 g, 2.47 mmol) was added to a solution of organic acid (0.25 g, 2.47 mmol of Bu^tCOOH, 0.28 g of Bu^tCH_2COOH or 0.28 g of $Et(CH_3)_2CCOOH$) in toluene (3.00 cm^3), and stirred for 12 h. Crystals were grown by slow evaporation of the reaction mixture under an argon atmosphere (glovebox). Yellowish crystals were obtained after 2–3 days. Crystalline powders of the obtained complexes were dried in a vacuum before further analysis.

7.2. $Ti_6O_6(OSi(CH_3)_3)_6(O_2CBu^t)_6$ (**1**)

Crystalline yield: 0.39 g (61.3%). The % Ti was gravimetrically determined as TiO_2, according to the Meth-Cohn et al. method [25] *Anal.* Calc. for $C_{48}H_{96}O_{24}Ti_6Si_6$: C, 37.80; H, 7.09; Ti, 18.86. Found: C, 37.30; H, 7.21; Ti, 18.50%.

7.3. $Ti_6O_6(OSi(CH_3)_3)_6(O_2\ CCH_2Bu^t)_6$ (**2**)

Yield: 0.25 g (42.42%). *Anal.* Calc. for $C_{54}H_{120}O_{24}$-Ti_6Si_6: C, 40.28; H, 7.46; Ti, 17.86. Found: C, 40.78; H, 7.60; Ti, 17.61%.

7.4. $Ti_6O_6(OSi(CH_3)_3)_6(O_2\ C(CH_3)_2Et)_6$ (**3**)

Yield: 0.28 g (45.45%). *Anal.* Calc. for $C_{54}H_{120}O_{24}$-Ti_6Si_6: C, 40.23; H, 7.46; Ti, 17.86. Found: C, 40.51; H, 7.68; Ti, 17.55%.

7.5. X-ray data collection and structure determination

The yellowish single crystals of all the compounds were crystallized by slow evaporation from toluene solution. The X-ray data were collected with an Oxford Sapphire CCD diffractometer using Mo Kα radiation ($\lambda = 0.71073$ Å), at 293(2) K, by the $\omega - 2\theta$ method. A shape-based absorption correction was applied for **1**–**3** (RED171 package of programs, Oxford Diffraction, 2000 [26,27]) with maximum and minimum transmissions of 0.8200/0.7905, 0.9138/0.7863 and 0.97047/0.88027 for **1**–**3**, respectively. The structures were solved by direct methods and refined with the full-matrix least-squares method on F^2 using the SHELX-97 program package [28]. No extinction correction was applied. The data collection and refinement processes are summarized in Table 1. Selected bond lengths and angles of **1** and **2** are presented in Table 2.

8. Supplementary material

CCDC 648858 and 648859 contain the supplementary crystallographic data for this paper. These data can be obtained free of charge via http://www.ccdc.cam.ac.uk/conts/retrieving.html, or from the Cambridge Crystallographic Data Centre, 12 Union Road, Cambridge CB2 1EZ, UK; fax: (+44) 1223-336-033; or e-mail: deposit@ccdc.cam.ac.uk.

Acknowledgements

The authors wish to acknowledge the Ministry of Scientific Research and Information Technology for financial support, Grant no. N204 11631/2635.

References

[1] (a) N. Yamada, I. Yoshinaga, S. Katayama, J. Sol–Gel Sci. Tech. 17 (2000) 123;
(b) U. Schubert, J. Sol–Gel Sci. Tech. 26 (2004) 47;
(c) K. Hoon, P. Nimai Chand, Y. Ahn, B. Seok, S. Il, Phys. Stat. Solidi (A), Appl. Res. 203 (2006) 962.
[2] U. Schubert, Chem. Mater. 13 (2001) 3487.
[3] P. Piszczek, M. Richert, A. Grodzicki, E. Talik, J. Heimann, Chem. Vap. Deposition 11 (2005) 399.
[4] P. Piszczek, Polyhedron 26 (2007) 93.
[5] R. Papiernik, L.G. Hubert-Pfalzgraf, J. Vaissermann, M.C. Henriques Baptista Goncalves, J. Chem. Soc., Dalton Trans. (1998) 2285.
[6] T.J. Boyle, T.M. Alam, C.J. Tafoya, B.L. Scott, Inorg. Chem. 37 (1998) 5588.
[7] P. Piszczek, A. Grodzicki, M. Richert, A. Wojtczak, Inorg. Chim. Acta 357 (2004) 2769.
[8] T.J. Boyle, T.M. Alam, E.R. Mechenbier, B.L. Scott, J.W. Ziller, Inorg. Chem. 36 (1997) 3293.
[9] N. Steunou, F. Robert, K. Boubekeur, F. Ribot, C. Sanchez, Inorg. Chim. Acta 279 (1998) 144.
[10] D.C. Bradley, I.M. Thomas, J. Chem. Soc. (1959) 3404.
[11] B.F.G. Johnson, M.C. Klunduk, C.M. Martin, G. Sankar, S.J. Teate, J.M. Thomas, J. Organomet. Chem. 596 (2000) 221.
[12] R. Duchateau, U. Cremer, R.J. Harmsen, S.J. Mohamud, H.C.L. Abbenhuis, R.A. van Santen, A. Meetsma, B.K.-H. Thiele, M.F.H. van Tol, M. Krannenburg, Organometallics 18 (1999) 5447.
[13] D. Wolff von Guedenberg, H.-C. Kang, W. Massa, K. Dehnicke, C. Maichte-Mossmer, J. Strahle, Z. Anorg. Allg. Chem. 620 (1994) 1719.
[14] J.M. Thomas, G. Sankar, Acc. Chem. Res. 34 (2001) 571.
[15] H.M. Lindemann, M. Schneider, B. Neumann, H.-G. Stammler, A. Stammler, P. Jutzi, Organometallics 21 (2002) 3009.
[16] J.-O. Nolte, M. Schneider, B. Neumann, H.-G. Stammler, P. Jutzi, Organometallics 22 (2003) 3010.
[17] M. Crocker, R.H.M. Herold, A.G. Orpen, M.T.A. Overgaag, J. Chem. Soc., Dalton Trans. (1999) 3791.
[18] F.J. Feher, T.A. Budzichowski, Polyhedron 14 (1996) 3239.
[19] A. Voight, R. Murugavel, V. Chanrasekhar, N. Winkhofer, H.W. Roesky, H.-G. Schmid, I. Usón, Organometallics 33 (1996) 1352.
[20] M.P. Coles, C.G. Lugmair, K.W. Terry, T.D. Tilley, Chem. Mater. 12 (2000) 122.
[21] Ch.K. Narula, A. Varshney, U. Riaz, Chem. Vap. Deposition 2 (1996) 13.
[22] B. Marciniec, H. Maciejewski, Coord. Chem. Rev. 223 (2001) 301.
[23] B.F.G. Johnson, M.C. Klunduk, C.M. Martin, G. Sankar, S.J. Teate, J.M. Thomas, J. Organ. Chem. 596 (2000) 221.
[24] C.G. Barraclough, D.C. Bradley, J. Lewis, I.M. Thomas, J. Chem. Soc. (1961) 2601.
[25] O. Meth-Cohn, D. Thorpe, H.J. Twitchett, J. Chem. Soc. (C) (1970) 132.
[26] CRYSALIS CCD171 and RED 171 package of programs, Oxford Diffraction (2000).
[27] G.M. Sheldrick, T.M. Schneider, Method Enzymol. 277B (1997) 319.
[28] G.H. Sheldrick, SHELX 97 and SHELXL 97, University of Götingen, Germany, 1997.

Available online at www.sciencedirect.com
ScienceDirect
Polyhedron 27 (2008) 609–616
POLYHEDRON
www.elsevier.com/locate/poly

Oxidation of S(IV) by the dodecatungstocobaltate(III) ion over an extended pH range using acetic acid–acetate buffer: Different kinetics, oxidation product and mechanism ☆

Manu Mehrotra, Vimal Soni, Raj N. Mehrotra *

Department of Chemistry, JNV University, Jodhpur 342 005, India

Received 19 June 2007; accepted 15 October 2007
Available online 26 November 2007

Abstract

The reinvestigation of the title reaction over the extended pH range, $3.25 \leqslant pH \leqslant 6.3$, has shown that the reaction is first-order in $[Co(III)W]^{5-}$, [SIV] and $[M^+]$ where M^+ is the alkali metal ion, with SO_4^{2-} as the exclusive product. The alkali metal ions form ion-pairs with SO_3^{2-} and $[Co(III)W]^{5-}$ (abbreviation for 12-tungstocobaltate(III)) ions and also act as a bridge between the ion-pairs in the formation of the activated complex, the decomposition of which is rate limiting. A mechanism based on the above fact explains the kinetics results. Because of the nature of the rate dependence on M^+ and H^+, the application of the extended Marcus theory involving work terms could not be applied, but the application in its simple form does support that the reaction is outer-sphere.
© 2007 Elsevier Ltd. All rights reserved.

Keywords: 12-Tungstocobatate(III); Sulfite: S(IV), kinetics, mechanism, oxidation and redox reaction

1. Introduction

The mechanism of oxidation of S(IV) or SO_2(aq), catalysed by transition metals, relevant to atmospheric processes has been reviewed [1]. The oxidation product could be SO_4^{2-}, $S_2O_6^{2-}$ or a mixture of the two ions [2]. The kinetics with two-electron oxidants such as hypochlorite [3], hypobromite [4], tetrachloroaurate(III) [5], tetrachloroaurate(III), *trans*-dicyanodichloroaurate(III) and *trans*-dicyanodibromoaurate(III) ions [6], tetrahydroxyargentate(III) [7], hexaaquothalium(III) [8], aquopentaammineplatinum(IV) [9], hexachloroplatinum(IV) [10], *trans*-tetracyanohydroxobromoplatinum(IV) [11] and tetracyanodichloroplatinum(IV) [12], and extensively by one-electron oxidants [13] including the studies with tetraamine(phenanthroline)Ru(III) [14], tris-(2,2-bipyridyl)Os(III) [15], Co(III)dipicolinate [16], tris(acetylacetonato)Mn(III) [17] were studied in acidic solutions whereas those by $Mn(cdta)^-$ ions [18,19] were studied in acetic acid–acetate buffer.

The recent studies include metal ion catalysed oxidations by non-metal oxidants such as dioxygen and the $S_2O_8^{2-}$ ion. CdS and Mn(II) [20], and diaminesilver(I) [21] catalysts are used in the dioxygen oxidation; Ag(I) [22] and Cu(II)–tetramine [23] catalysts are used in the $S_2O_8^{2-}$ ion oxidation in acetate and ammonia buffered solutions, respectively.

The oxidation by the one-electron oxidant dodecatungstocobaltate(III) [24], $[CoW_{12}O_{40}]^{5-}$, here after referred to as $Co(III)W^{5-}$, was studied in the pH range $1.5 \leqslant pH \leqslant 3.5$. The ratio of $Co(III)W^{5-}$ and S(IV) decided the exclusive formation of $S_2O_6^{2-}$, or its formation in combination with SO_4^{2-} from the reaction mixtures having an excess of $Co(III)W^{5-}$ or SO_2(aq) in a slight excess. There were mixed first and second orders pathways in S(IV), observed in the oxidation by Cr(VI) [25], $[Fe(phen)_3]^{3+}$ [26] (phen = 1,10-phenanthroline) and $Mn(cdta)^-$ ions [18]. The formation of dithionate is considered to indicate an inner-sphere process whereas the sulfate ion is the exclusive product in the outer-sphere process [15]. An inner-sphere mechanism

☆ This work was supported by the UGC Grant F.12-59/1997.
* Corresponding author. Tel.: +91 291 2721478.
E-mail address: mehrotra_rn@yahoo.co.in (R.N. Mehrotra).

0277-5387/$ - see front matter © 2007 Elsevier Ltd. All rights reserved.
doi:10.1016/j.poly.2007.10.013

with $Co(III)W^{5-}$, which is substitution inert, is most unlikely. The use of the Marcus theory [27–29], which has given good correlations for metal complexes oxidising S(IV) by an outer-sphere mechanism [14], is desirable to decide upon the nature of the mechanism.

The reinvestigated reaction over the extended pH range, $3.25 \leqslant pH \leqslant 6.32$, has given altogether different results with a stoichiometry ratio $Co(III)W^{5-}$:S(IV) = 2:1 under the conditions of excess and deficient concentrations of $Co(III)W^{5-}$ over [S(IV)]. SO_4^{2-} is the exclusive oxidation product under any concentration conditions because dithionate was not detected, and there were no parallel first- and second-order paths in S(IV). The application of the Marcus theory [27–29] to the present reaction supports an outer-sphere nature of the mechanism which is consistent with the absence of dithionate as the product of the reaction [15].

2. Experimental

2.1. Material

The solutions of potassium salts of 12-tungstocobaltate(III), $[CoW_{12}O_{40}]^{5-}$ and 12-tungstocobaltate(II), $[CoW_{12}O_{40}]^{6-}$ were prepared, characterised and standardised by the method described in the literature [30,31] ($CoW_{12}O_{40}^{5-}$: $\varepsilon_{390} = 1215 \pm 5$, pH 4.63; ε_{390} [32] = 1207, ε_{390} [33] = 1225 $dm^3\ mol^{-1}\ cm^{-1}$; $CoW_12O_{40}^{6-}$: $\varepsilon_{625} = 214$; ε_{624} [34] = $212 \pm 4\ dm^3\ mol^{-1}\ cm^{-1}$, pH 4.63).

The solutions of sodium sulfite (Fluka, puriss), found stable over a period of a few hours, were freshly prepared in twice distilled water purged with nitrogen for sufficient time and used within 2 h. The solutions were standardised as described earlier [18].

The sodium acetate–acetic acid buffer solutions of different pH were prepared by mixing a 0.2 mol dm^{-3} solution of sodium acetate (Merck, GR) and acetic acid (Qualigen, GR) in volumes as described elsewhere [35]. The pH of the buffer solutions was checked with a Systronics 335 digital pH meter with a glass electrode.

The stock solution of lithium perchlorate, used to adjust the ionic strength, was prepared by neutralising a calculated amount of lithium hydroxide(Sigma, LR) by a calculated volume of the standard perchloric acid (Merck, GR) solution. The solution was standardised gravimetrically [36].

All other chemicals were of highest purity and were used as received. The twice distilled water was used in the preparation of all the solutions. The nitrogen purged reactant solutions were mixed to initiate the reaction.

The spectral studies were made on a HP 8452A UV–Vis spectrometer with a 2 nm band width and an integration time of 1 s.

2.2. Rate measurement

A union Giken RA-401 stopped flow spectrophotometer with a dead time of 0.5 ms for a 2 mm flow-cell was used to study the kinetics of the reaction under pseudo first-order conditions ($[S(IV)] \geqslant 10[Co(III)W^{5-}]$) at constant ionic strength (1.0 mol dm^{-3}, $LiClO_4$) in acetate–acetic acid buffered solutions. The reactant solutions, previously purged with nitrogen to remove the dissolved oxygen, were thermostated in the storage cylinders which along with the reaction cell were maintained at the desired temperature (±0.1 °C) by circulating water from a Haake-D8G refrigerated circulatory water-bath.

The rate in general was measured in terms of disappearance of $[Co(III)W]^{5-}$ at 390 nm, though some identical runs were repeated with the appearance of $[Co(II)W]^{6-}$ at 625 nm with almost the same results. At least 8–10 runs were studied for any given condition. The spectrophotometer is interfaced with a SORD microcomputer for collecting and analysing the data involving averaging the volt time curves of replicate runs, displaying the plots of log absorbance against time, which were linear over the entire range of the reaction studied, and reporting the averaged k_{obs} values. The averaged k_{obs} value was within ±3–5% of the value from the individual runs. The linear log absorbance-time plots are against a simultaneous second-order dependence in $[SO_2(aq)]$ [24].

Finally all the statistical calculations are based on the use of the EXCEL program which is also used to draw the plots given in the paper.

2.3. Stoichiometry

The stoichiometry of the reaction was estimated under two conditions at pH 4.63 and 25 °C. In one set of experiments $[Co(III)W^{5-}]$ was in excess over $[SO_2(aq)]$. After sufficient time the $[Co(III)W^{5-}]$, left unreacted, was generally estimated spectrometrically at 390 nm though in a few cases $[Co(II)W^{6-}]$ was also estimated at 625 nm. In the other set of experiment $[SO_2(aq)]$ was in excess over the $Co(III)W^{5-}$ ion. The unreacted sulfite was estimated titrimetrically using iodine solution. The results from the two sets of experiments, Table 1, indicate that $\Delta[Co(III)W]^{5-}/\Delta[SO_2(aq)] = 1.95 \pm 0.04$, which is the basis of the stoichiometric Eq. (1).

$$2Co(III)W^{5-} + SO_2(aq) + 2H_2O \rightarrow 2Co(II)W^{6-} + SO_4^{2-} + 4H^+ \quad (1)$$

The present stoichiometry result is, therefore, in disagreement with the results of the previous study [24], which reported a 1:1 ($[Co(III)W]^{5-}$:[S(IV)]) stoichiometry from the reaction mixtures having excess of $SO_2(aq)$.

2.4. Oxidation product

The spent reaction mixtures prepared under both the conditions were heated and nitrogen gas was bubbled through the solution over a period of time to remove $SO_2(aq)$. The treatment of these solutions with an excess of $BaClO_4$ solution resulted in the formation of an insoluble white precipitate which was filtered for gravimetric

Table 1
The estimation of stoichiometry ratio at pH 4.63 and 25 °C

S.no.	$10^3[Co(III)W^{5-}]_o$	$10^3[S(IV)]_o$	$10^3[Co(II)W^{6-}]_o$	$\frac{\Delta[Co(II)W^{6-}]}{\Delta[S(IV)]}$
1	1.50	0.272	0.528[a]	1.94
2	1.86	0.272	0.516[b]	1.90
3	2.02	0.296	0.606[a]	2.05
4	2.02	0.404	0.782[b]	1.93
5	3.60	1.23	2.42[a]	1.97
6	6.00	1.72	3.31[a]	1.92
			$10^3[S(IV)]$ used	
7	4.90	5.62	2.52	1.94
8	6.55	10.1	3.32	1.97
9	8.20	12.5	4.25	1.93

Mean $\frac{\Delta[Co(II)W^{6-}]}{\Delta[S(IV)]} = 1.95 \pm 0.04$.
[a] Based on the estimation of $[Co(II)W^{6-}]$ at 625 nm.
[b] Based on the estimation of $[Co(III)W^{5-}]$ at 390 nm.

estimation. The estimated amount of SO_4^{2-} ion was in fair agreement with the amount expected from Eq. (1).

In a separate experiment the spent reaction mixtures after degasification with nitrogen gas were treated with a dilute strongly acidified dichromate solution in the manner described in the previous study [24]. The back estimated concentration of dichromate at 348 nm was almost the same as that of the added dichromate indicating that $S_2O_6^{2-}$ was not present, if any formed, in the spent reaction mixtures.

These results are also contradictory to the previous study because $S_2O_6^{2-}$ was not detected as the oxidation product, which is exclusively the SO_4^{2-} ion whatever the conditions of $[Co(III)W^{5-}]$, present in excess or in a deficient amount.

The reason for the totally different results with respect to both the stoichiometry and the oxidation product could be the use of more dilute solutions of $Co(III)W^{5-}$ and $SO_2(aq)$ than used in the previous study [24]. The possible bearing of the concentration of the $SO_2(aq)$ solution on the reaction product will be discussed later along with a general discussion.

2.5. Test for free radical

The buffered solutions of $Co(III)W^{5-}$ and $SO_2(aq)$, in separate glass stoppered flasks, were degassed with nitrogen before 2 ml of acrylonitrile was added to each of the flasks. The two solutions, that remained clear even after 5–7 min of adding the monomer, were mixed and swirled, and left for sometime. A cloudiness appeared which changed to a thick white precipitate of polyacrylonitrile, indicating the formation of free radicals. Convincing esr evidence for the formation of a free sulfur radical in the solution has been known for a long time [37,38].

2.6. Distribution of the species of $SO_2(aq)$ different pH

The very soluble SO_2 in aqueous solution has the following speciation [39].

$$SO_2 + nH_2O \rightleftharpoons SO_2 \cdot nH_2O \quad \text{or} \quad SO_2(aq) \tag{2}$$

$$SO_2(aq) \overset{K}{\rightleftharpoons} H_2SO_3 \tag{3}$$

$$SO_2(aq) \overset{K_{a1}}{\rightleftharpoons} HSO_3^- + H^+ \tag{4}$$

$$HSO_3^- \overset{K_{a2}}{\rightleftharpoons} SO_3^{2-} + H^+ \tag{5}$$

The equilibrium constant $K \lll\lll 1$ so much so that H_2SO_3 is either not present or is present in an infinitesimal quantity in the aqueous solution [39]. The fraction distribution of the species $SO_2(aq)$, HSO_3^- and SO_3^{2-}, based on the equilibria (4) and (5), was calculated using the equilibrium constants $K_{a1} = 4.30 \times 10^{-2}$ and $K_{a2} = 4.57 \times 10^{-7}$ mol dm^{-3}, respectively, at 25 °C [40]. The equilibrium (6), $K_d = 8.8 \times 10^{-2}$ dm^3 mol^{-1} at 25 °C [41], was neglected because a second-order dependence in $[S(IV)]_o$, the analytical concentration, was not shown by the reaction and $S_2O_6^{2-}$ was not detected as the reaction product.

Table 2
The calculated fractions (=concentration of the species/$[S(IV)]_o$) of the species $SO_2(aq)$, HSO_3^- and SO_3^{2-} at different pH for $[S(IV)]_o = 0.01$ mol dm^{-3}

pH	$SO_2(aq)$	HSO_3^-	SO_3^{2-}
1	7×10^{-1}	3×10^{-1}	1.37×10^{-6}
1.5	4.2×10^{-1}	5.8×10^{-1}	8.3×10^{-6}
2	1.88×10^{-1}	8.1×10^{-1}	3.69×10^{-5}
2.5	6.8×10^{-2}	9.3×10^{-1}	1.34×10^{-4}
3	2.3×10^{-2}	9.8×10^{-1}	4.44×10^{-4}
3.25	1.3×10^{-2}	9.9×10^{-1}	8×10^{-4}
3.5	7×10^{-3}	9.9×10^{-1}	1.43×10^{-3}
3.88	3×10^{-3}	9.9×10^{-1}	3.42×10^{-3}
4.15	1.6×10^{-3}	9.9×10^{-1}	6.4×10^{-3}
4.45	8×10^{-4}	9.84×10^{-1}	1.3×10^{-2}
4.63	5×10^{-4}	9.8×10^{-1}	1.9×10^{-2}
4.9	2.8×10^{-4}	9.6×10^{-1}	3.5×10^{-2}
5.65	4×10^{-5}	8.3×10^{-1}	1.7×10^{-1}
6	2×10^{-5}	6.86×10^{-1}	3.1×10^{-1}
6.32	6×10^{-6}	5.1×10^{-1}	4.9×10^{-1}

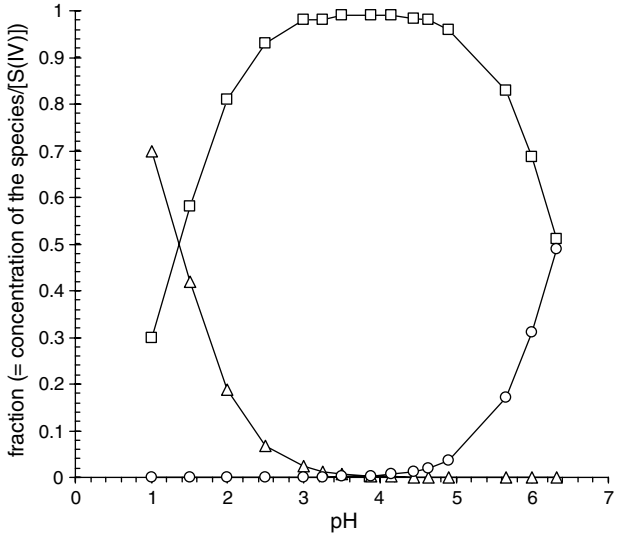


Fig. 1. The distribution of $SO_2(aq)$ (△), HSO_3^- (□) and SO_3^{2-} (○) species as a fraction (=concentration of the species/$[SO_2(aq)]_o$) at different pH at 25 °C for the initial $[SO_2(aq)]_o = 0.1$ mol dm^{-3}.

$$2HSO_3^- \overset{K_d}{\rightleftharpoons} S_2O_5^{2-} + H_2O \quad (6)$$

The fraction distribution (fraction = concentration of the species/[S(IV)]) of SO_2(aq), HSO_3^- and SO_3^{2-} species over different pH values is numerically given in Table 2 and graphically shown in Fig. 1. The SO_2(aq) fraction decreases with increasing pH, becoming negligible around pH 3.6 and beyond. The HSO_3^- fraction increases with pH and attains a plateau around pH 3.1–4.5 and thereafter it decreases and around pH 6.2 its concentration is equal to that of the fraction SO_3^{2-} which is negligible at pH $\leqslant$ 3.1 and thereafter increases continuously until its concentration equals that of HSO_3^-. Hence, the reactive species in the pH range 3.2–6.3 are possibly HSO_3^- and SO_3^{2-} ions since SO_2(aq) is negligible in this range.

3. Results

The $k_{obs} = 0.0663 \pm 0.0018\ s^{-1}$ was obtained when [Co(III)W^{5-}] was varied in the range $(0.25–4.0) \times 10^{-4}$ mol dm^{-3} at constant ionic strength (1 mol dm^{-3}), pH 4.15 and [SO_2(aq)] = 0.025 mol dm^{-3} at 40 °C. The result is, therefore, consistent with Eq. (7).

$$\frac{-d[Co(III)W^{5-}]}{dt} = k_{obs}[Co(III)W^{5-}]_o \quad (7)$$

A proportionate increase in k_{obs}, over a twenty-fivefold variation in [S(IV)] at five temperatures, Table 3, resulted in linear plots of k_{obs} against $[S(IV)]_o$, passing through the origin at all temperatures, Fig. 2, indicating the applicability of Eq. (8).

$$k_{obs} = k[S(IV)]_o \quad (8)$$

Eq. (8) is significant in the sense that it does not have an additional second-order term in $[S(IV)]_o$ [24], despite the fact that relatively high concentrations of S(IV) and higher pH were used.

The results over the pH range 3.25–6.32, Table 4, indicate that k_{obs} increased with the increase in the pH of the reaction. The plots of k_2^{-1} ($k_2 = k_{obs}/[S(IV)]_o$) against [H^+] (10^{-pH}) are linear with the intercept as shown in Fig. 3 for all temperatures.

Table 3
The dependence of k_{obs} on [S^{IV}] at different temperatures 10^4[Co(III)$W]^{5-} = 2.0$; $\mu = 1.0$ mol dm^{-3} and pH 4.15

[S^{IV}] (mol dm^{-3})	k_{obs} (s^{-1})				
	30 °C	36 °C	40 °C	45 °C	50 °C
0.01	0.0148	0.0224	0.0242	0.0291	0.0386
0.015	0.0225	0.0321	0.0361	0.0454	0.0578
0.025	0.0352	0.0519	0.0665	0.0741	0.111
0.035	0.0519	0.0769	0.0848	0.113	0.126
0.050	0.0738	0.102	0.111	0.146	0.202
0.075	0.117	0.156	0.181	0.218	0.276
0.100	0.138	0.206	0.232	0.311	0.388
0.125	0.183	0.266	0.314	0.361	0.449
0.250	0.366	0.527	0.592	0.749	0.943

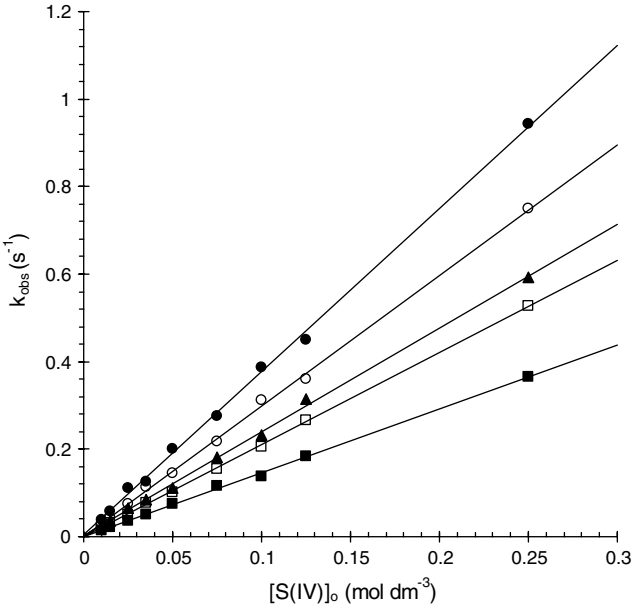


Fig. 2. The plots of k_{obs} against $[S(IV)]_o$ that pass through the origin at 30° (■), 35 °C (□), 40 °C (▲), 45 °C (○) and 50 °C (●).

The data in Table 5 is from an earlier study [24]. It has been analysed for the effect of ionic strength on k_{obs} in terms of Eq. (9), proposed by Davies [42].

$$\log k_{obs} = \log k_o + z_a z_b \left(\frac{\sqrt{\mu}}{1+\sqrt{\mu}} - 0.05\mu \right) \quad (9)$$

where z_a and z_b are the charges on the reacting species. The plot of log k_{obs} against $\left(\frac{\sqrt{\mu}}{1+\sqrt{\mu}} - 0.05\mu\right)$ is shown in Fig. 4. The slope of the plots corresponding to the variation of the ionic strength using salts of Li^+ (4.35), Na^+ (4.13) and K^+ (3.91) are averaged to 4.13 ± 0.22, and are therefore independent of the nature of the salt used. The significance of the average slope value $\cong 4$ in the context of the proposed mechanism is discussed later.

4. Mechanism and discussion

A different mechanism in the extended range of pH is indicated because the order with respect to S(IV) is strictly one against a simultaneous first and second-order dependence in the earlier study [24]. The inverse dependence on [H^+] is indicative of a deprotonation equilibrium prior to the rate limiting step where the deprotonated species, a stronger reducing agent than the protonated one, behaves as the sole reactive entity or is in combination with the protonated one. This equilibrium is likely to involve S(IV) species in aqueous solution because Co(III)W^{5-} species are not affected by H^+ ions [43].

The distribution pattern of the S(IV) species, Fig. 1, indicated that HSO_3^- and SO_3^{2-} are the major species in the pH range 3.25 $\leqslant$ pH $\leqslant$ 6.32 and are singularly or collectively treated as reactive entities in all the reactions [2–26]. A mechanism based on these species was initially

Table 4
The dependence of k ($=k_{obs}/[S^{IV}]$) at different pH and temperatures $10^4[Co(III)W^{5-}] = 2.0$; $[S^{IV}] = 0.10$ and $[\mu] = 1.0$ mol dm^{-3}

pH	k_{obs} (s^{-1})						
	$10^5[H^+]$	20 °C	25 °C	30 °C	35 °C	40 °C	45 °C
3.25	56.2	0.139	0.191	0.251	0.352	0.446	0.562
3.50	31.6	0.237	0.317	0.446	0.617	0.800	1.09
3.88	13.2	0.498	0.694	1.02	1.29	1.90	2.50
4.15	7.08	0.746	1.14	1.38	2.06	2.32	3.11
4.45	3.55	1.21	1.74	2.86	3.61	5.32	8.55
4.63	2.34	2.57	3.27	4.46	6.62	8.10	10.9
4.90	1.26	2.78	4.40	6.62	14.5	19.5	26.9
5.65	0.224	4.42	6.99	11.97	48.8	103.1	158.7
6.0	0.100	4.93	8.62	12.56	66.7	127.1	219.3
6.32	.0479	5.24	9.43	13.91	128.2	205.3	287.3

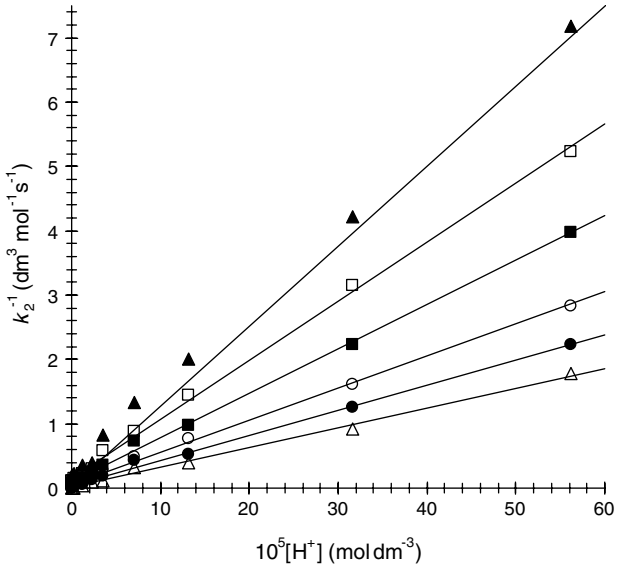


Fig. 3. The plots of k_2^{-1} ($k_2 = k_{obs}/[S(IV)]_o$) against $[H^+]$ ($=10^{-pH}$) with intercepts at 20 °C (▲), 25 °C (□), 30° (■), 35° (○), 40 °C (●) and 45 °C (△).

considered and rejected[1] because the deduced rate equation suggested a different correlation between k_{obs} and $[H^+]$ and a slope value between 5 and 8 for the plot in Fig. 4 (the observed value is 4).

The anionic species are likely to form an ion-pair with the cationic species of the alkali metal ion used to adjust the ionic strength. The following mechanism is based on this consideration and is treated as the most probable mechanism of the reaction.

[1] Only basic steps of the reaction are considered in the following mechanism.

$$HSO_3^- + Co(III)\ W^{5-} \xrightarrow{k_1} HSO_3^{\cdot} + Co(II)W^{6-}$$

$$SO_3^{2-} + Co(III)W^{5-} \xrightarrow{k_1} SO_3^{-\cdot} + Co(II)W^{6-}$$

$$= \frac{-d[Co(III)W^{5-}]_o}{dt} = \frac{(k_1[H^+] + k_2K_{a2})[S(IV)]_o}{K_{a2} + [H^+]}$$

$$SO_2(aq) \overset{K_{a1}}{\rightleftharpoons} HSO_3^- + H^+ \quad (4)$$

$$HSO_3^- \overset{K_{a2}}{\rightleftharpoons} SO_3^{2-} + H^+ \quad (5)$$

$$HSO_3^- + M^+ \overset{K_1}{\rightleftharpoons} MSO_3^- + H^+ \quad (10)$$

$$SO_3^{2-} + M^+ \overset{K_2}{\rightleftharpoons} MSO_3^- \quad (11)$$

$$[Co(III)W]^{5-} + M^+ \overset{K_5}{\rightleftharpoons} [Co(III)W\cdots M]^{4-} \quad (12)$$

$$[Co(III)W\cdots M]^{4-} + M^+ + MSO_3^- \overset{K_M}{\rightleftharpoons} MCo(III)W^{4-}\cdots M^+\cdots{}^-O_3SM \quad (13)$$

$$MCo(III)W^{4-}\cdots M^+\cdots{}^-O_3SM \xrightarrow{k} [Co(II)W\cdots M]^{5-} + MSO_3^{\cdot} + M^+ \quad (14)$$

$$[Co(III)W\cdots M]^{4-} + MSO_3^{\cdot} + H_2O \xrightarrow{fast} [Co(II)W\cdots M]^{5-} + MSO_4^- + 2H^+ \quad (15)$$

The $SO_3^{-\cdot}$ (which is the same as $MSO_3^{\cdot}$) radical had been proposed as an intermediate in the mechanism of transition-metal ion catalysed oxidation [44] of SO_2(aq). Since Eq. (14) is rate limiting, the rate is expressed by Eq. (16)

$$\text{rate} = k[MCo(III)W^{4-}\cdots M^+\cdots{}^-O_3SM] \quad (16)$$

$$= kK_MK_5K_2K_{a2}[Co(III)W^{5-}][HSO_3^-][M^+]^3/[H^+] \quad (17)$$

The derivation of Eq. (19) is based on the correlation expressed in Eq. (18).

$$[Co(III)W^{5-}]_o = [Co(III)W^{5-}] + [MCo(III)W^{4-}] \quad (18)$$

therefore,

$$[Co(III)W^{5-}] = \frac{[Co(III)W^{5-}]_o}{1 + K_5[M^+]} \quad (19)$$

Similarly, Eq. (21), derived with the assumption that $[H^+] + K_1\{M^+\} \gg K_{a2}K_2\{M^+\}$, is based on the mass balance of the S(IV) species given in Eq. (20), neglecting SO_3^{2-} because of its negligible concentration compared to the concentration of the MSO_3^- ion.

$$[S(IV)]_o = [HSO_3^-] + [MSO_3^-] + [MSO_3^-] \quad (20)$$

Table 5
The deduced values of k_{obs} (s^{-1}) from the plot between k_{obs} and $[M^+]$ in Ref. [19] $10^4[Co(III)W]^{5-} = 2.0$, $[S^{IV}] = 0.01$ mol dm^{-3}, pH 3.50 at 25 °C

$[M^+]$ (mol dm^{-3})	μ[a] (mol dm^{-3})	$10^4 k_{obs}$ (Li^+)	$10^4 k_{obs}$ (Na^+)	$10^4 k_{obs}$ (K^+)
0.09	0.103	1.72	5.16	13.8
0.27	0.283	5.16	12.0	31.0
0.48	0.493	6.88	17.2	43.0
0.68	0.693	10.4	26.7	65.4
0.98	0.993	15.5	42.1	99.8

[a] The ionic strength is calculated considering the concentrations of the alkali metal salts and S^{IV}. Since $[CH_3COO^-]$ used in the buffer solution is not reported, its contribution is not included and that of $[Co(III)W]^{5-}$ is neglected.

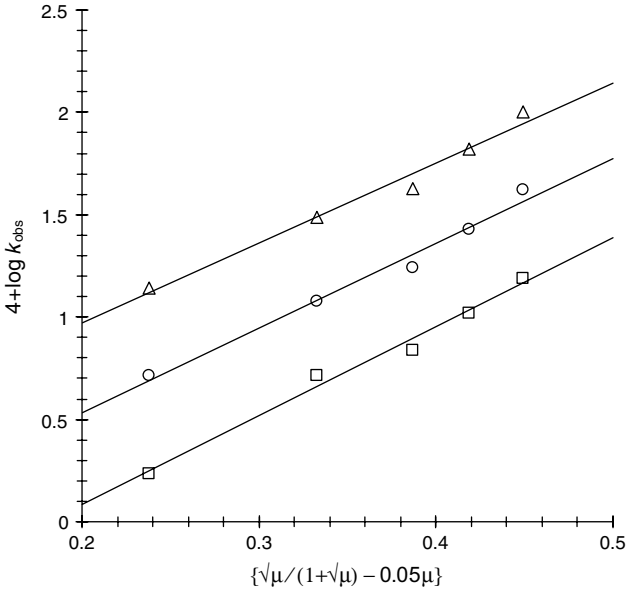


Fig. 4. The plots of log k_{obs} against $\{\sqrt{\mu}/(1+\sqrt{\mu}) - 0.05\mu\}$ where the ionic strength is varied with the salts of Li^+ (□, slope = 4.3), Na^+ (○, slope = 4.1) and K^+ (△, slope 3.9). The data is taken from Ref. [24].

therefore,

$$[HSO_3^-] = \frac{[S(IV)]_o[H^+]}{[H^+] + K_1[M^+]} \quad (21)$$

Eq. (17) is expressed by Eq. (22) on the proper substitution of the values of $[Co(III)W^{5-}]$ and $[MSO_3^-]$ given in Eqs. (19) and (21).

$$k_{obs} = \frac{-d[Co(III)W^{5-}]_o}{dt[Co(III)W^{5-}]_o} = \frac{kK_MK_5K_2K_{a2}[S(IV)]_o[M^+]^3}{[H^+] + K_5[M^+][H^+] + K_1[M^+] + K_5K_1[M^+]^2}. \quad (22)$$

Eq. (22) is simplified to Eq. (23) with the assumption that $K_5[M^+][H^+] + K_5K_1[M^+]^2 \gg [H^+] + K_1[M^+]$

$$k_2 = \frac{k_{obs}}{[S(IV)]_o} = \frac{kK_MK_2K_{a2}[M^+]^2}{[H^+] + K_1[M^+]} \quad (23)$$

$$\frac{1}{k_2} = \frac{[H^+]}{kK_MK_2K_{a2}[M^+]^2} + \frac{K_1}{kK_MK_2K_{a2}[M^+]} \quad (24)$$

Eq. (23) is consistent with the linear plots of k_{obs} against $[S(IV)]_o$, Fig. 2, that pass through the origin. Eq. (24), the inverted form of Eq. (23), is consistent with the linear plots of k_2^{-1} against $[H^+]$ with intercepts (Fig. 3). The values of the intercept and slope from the figure are in Table 5. In view of the excellent agreement between the observed results and the deduced rate Eq. (22), the above mechanism is acceptably very probable.

Eq. (23) could also be expressed as Eq. (25) under the rational assumption that $K_1[M^+] \gg [H^+]$. Eq. (25) is consistent with the linear plot of k_{obs} against $[M^+]$ that pass through the origin [24].

$$k_{obs} = \frac{kK_MK_2K_{a2}}{K_1}[S(IV)]_o[M^+] \quad (25)$$

The alkali metal ions M^+ (=Li^+, Na^+, K^+) either enhance or inhibit the rate of reactions [31,45–47]. Rate enhancement has been reported in several $[Co(III)W]^{5-}$ oxidations [24,48,49]. The data in Table 6 is from the linear plot between k_{obs} and $[M^+]$, shown in the earlier study [24], and an attempt has been made to analyse it in ways discussed below.

The M^+ ions may facilitate the approach of the anionic species. However, retardation rather than acceleration in the rate is expected with increasing size of Li^+ to Cs^+ ion [50]. The presence of M^+ ions could also affect the oxidation–reduction potential which is related to the rate of electron-transfer. The increase in the oxidation–reduction potential for the $Fe(CN)_6^{3-}$–$Fe(CN)_6^{4-}$ system from Li^+ to Cs^+ is in the same direction as the increase in the rate [51].

The possibility of ion pair formation ($[KFe(CN)_6]^{2-}$ and $[KFe(CN)_6]^{3-}$) is well known [52,53]. The formation of an

Table 6
The intercept and slope values of the plots in Fig. 3 at different temperatures

Temperature (°C)	20	25	30	35	40	45
Slope (S) $(kK_MK_2K_a[M^+]^2)^{-1}$	12460	9170	6910	5010	3935	3090
Intercept (I) $(K_1/kK_MK_2K_a[M^+])^{-1}$	0.255	0.157	0.0896	0.0470	0.0285	0.0106
$I/S = K_1[M^+]$	2.05	1.71	1.30	0.94	0.72	0.34

ion pair between M^+ and $[Co(III)W]^{5-}$ is supported by the increase in the optical density of the $[Co(III)W]^{5-}$ solution with increasing $[M^+]$, similar to that reported with $[Co(II)W]^{6-}$ [54]. It is, therefore, assumed that a similar ion pair, MSO_3^-, is formed between the M^+ and SO_3^{2-} ions. Therefore, the likely reactive species are MSO_3^- and $[MCo(III)W]^{4-}$ ions, which are consistent with the slope value 4.13 ± 0.22 obtained in the plot in Fig. 4.

Yet another possibility is the formation of a bridge between two anions [47,50,55,56]. In the bridge model a large sized alkali metal ion associated with a high value of polarisability [57] is likely to be more effective as a bridge between two anions. The greater polarisability of the larger cations [58] and the polarisability of the organic ligand acting as a bridge in the electron-transfer between metal ions are reported [59]. This view is strengthened by the linear plot of $k_{obs}/[M^+]$ against $\propto_{M+}$, as shown in Fig. 5. A similar plot is reported in the oxidation of $Co(III)W^{6-}$ with MnO_4^- [54] and the oxidation of $[Mo(CN)_8]^{4-}$ by $[Mn(cdta)]^-$(cdta = 1,2-diaminocyclohexanetetra-acetic acid) [60].

In view of the above discussion the formation of a bridge by the M^+ ions is very likely. Two types of bridges are possible. In one case the bridge may be $Co(III)W^{5-}\cdots M^+\cdots{}^-O_3SM$, in which one of the M^+ ions, which is part of the ion-pairs, acts as a bridge. The other bridge could be $MCo(III)W^{4-}\cdots M^+\cdots{}^-O_3SM$, in which the ion-pairs are bridged by an additional M^+ ion. The later one seems more likely in view of the linear plot of k_{obs} against $[M^+]$ that passes through the origin. This is consistent with MSO_3^- as the reactive entity.

The earlier study reported that scanning of the reaction mixture (pH not mentioned) gave an isosbestic point at 510 nm, indicating the absence of a complex [24], which is consistent with the substitution inert nature of $[Co(III)W]^{5-}$ and suggestive of an outer-sphere nature of the reaction. The outer-sphere nature of the reaction could have been supported with the application of the Marcus theory [27–29] which in its usual form involving work terms is inapplicable because of the high ionic strength ($\mu = 1$ mol dm^{-3}) adjusted with the alkali metal salt and the M^+ ion which accelerates the rate. As a measure of approximation the theory, under the present experimental conditions when the work terms cancel, the driving force is not too large and the term f approximates to zero, and in its simplest form is given by Eq. (26).

$$k_{12} = (k_{11}k_{22}K_{12})^{0.5} \tag{26}$$

The calculated value of k_{12}, using $E^\circ_{22} = 1.01$ [61], k_{22} (obtained by extrapolation at $\mu = 1$ mol dm^{-3}) = 1.15 dm^3 mol^{-1} s^{-1} [62], $E^\circ_{11} = 0.72$ V and $k_{11} = 4$ dm^3 mol^{-1} s^{-1} [14] at 25 °C where the subscripts 22 and 11 stand for $[Co(III)W]^{5-/6-}$ and SO_3^{2-}/HSO_3^- couples, is 4.75 dm^3 mol^{-1} s^{-1}, which is in fair agreement with the value 3.17 at pH 3.5 at 25 °C (Table 4) from where the fraction of SO_3^{2-} starts increasing with the pH. If the agreement is not too close then it is also not wide enough to conclude against the outer-sphere mechanism.

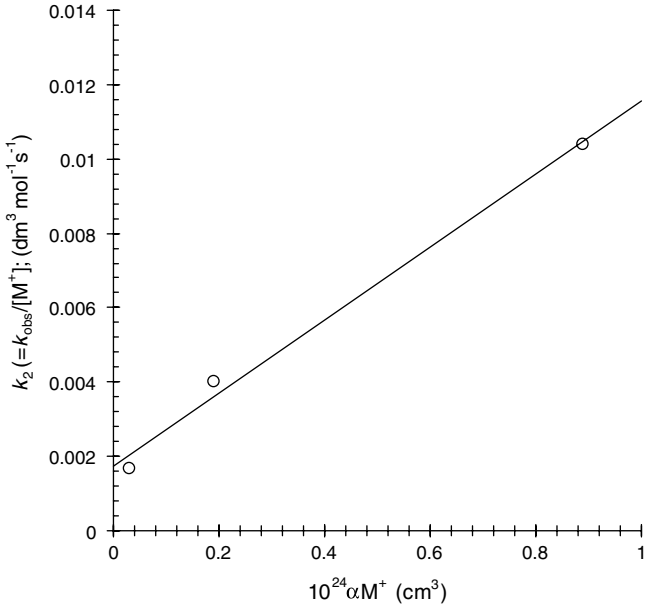


Fig. 5. The plot of k_2 (=k_{obs}/[akali metal ion, M^+]) against α_{M^+}, the polarisability of M^+.

5. Conclusion

In conclusion, the reaction studied at the extended pH range $3.25 \leqslant pH \leqslant 6.3$ has different kinetics results from the previous study [24] carried out at pH $\leqslant 3.5$. In the studied pH range the reaction is first-order in $[Co(III)W]^{5-}$, [SIV] and $[M^+]$ where M^+ is the alkali metal ion, with the SO_4^{2-} ion as the exclusive product. The M^+ ions form ion-pairs with $[Co(III)W]^{5-}$ and the species of [SIV] and also act as a bridge in the formation of the activated complex. The outer-sphere nature of the reaction is supported by the application of the Marcus theory [27–29] in its simple form because the extended theory is inapplicable to rate having dependence on H^+ and M^+ ions.

Acknowledgements

The financial grants from UGC (F.12-59/1997) and (F.12-147/2001) are acknowledged with thanks. Thanks are also due to the Department of Science and Technology (DST) for sanctioning grant (2/17/83/ STP-III) for the purchase of the stopped flow instrument.

References

[1] C. Brandt, R. Van Eldik, Chem. Rev. 95 (1995) 119.
[2] W.D. M Yost, H. Russell Jr., Systematic Inorganic Chemistry, Prentice-Hall, New York, 1944, p. 858.
[3] K.D. Fogelman, D.M. Walker, D.W. Margerum, Inorg. Chem. 28 (1989) 986.
[4] R.C. Tray, D.W. Margerum, Inorg. Chem. 30 (1991) 3538.
[5] K.K. Sengupta, S. Das, S. Sengupta, Transition Met. Chem. 13 (1988) 261.

[6] J. Berglund, L.I. Elding, Inorg. Chem. 34 (1995) 513.
[7] L.J. Kirschenbaum, I. Kouadio, E. Mentasti, Polyhedron 8 (1989) 1299.
[8] J. Berglund, P. Werndrup, L.I. Elding, J. Chem. Soc., Dalton Trans. (1994) 1435.
[9] K.C. Koshy, G.M. Harris, Inorg. Chem. 22 (1983) 2947.
[10] K.K. Sengupta, S. Das, S. Sengupta, Transition Met. Chem. 12 (1987) 417.
[11] W.K. Wilmarth, Y. -T. Fanchiang, J.E. Byrd, Coord. Chem. Rev. 51 (1983) 141.
[12] J. Berglund, R. Voigt, S. Fronaeus, L.I. Elding, Inorg. Chem. 33 (1994) 3346.
[13] See references 1–21 cited in the above Ref. [10].
[14] R. Sarala, M.A. Islam, S.B. Rabin, D.M. Stanbury, Inorg. Chem. 29 (1990) 1133.
[15] R. Sarala, D.M. Stanbury, Inorg. Chem. 29 (1990) 3456.
[16] M. Ali, S.K. Saha, P. Banerjee, Bull. Chem. Soc. (Jpn.) 64 (1991) 2497.
[17] S. Mukhopadhyay, R. Banerjee, J. Chem. Soc., Dalton Trans. (1993) 993.
[18] V.M. Bobba, G. Giraudi, E. Mentasti, Transition Met. Chem. 13 (1988) 256.
[19] U. Chandrawat, A. Prakash, R.N. Mehrotra, Can. J. Chem. 73 (1995) 1531.
[20] M.V. Sreedharan, R. Singh, M. Sharma, K.S. Gupta, Indian J. Chem. A 39 (2000) 507.
[21] K.S. Gupta, Pinky Bhargava, Manoj, V. Sreedharan, Transition Met. Chem. 26 (2001) 71.
[22] K.S. Gupta, Pinky Bhargava, Manoj, V. Sreedharan, Indian J. Chem. A 38 (1999) 692.
[23] K.S. Gupta, Pinky Bhargava, Manoj, V. Sreedharan, Transition Met. Chem. 25 (2000) 274.
[24] M. Ali, S.K. Saha, P. Banerjee, J. Chem. Soc., Dalton Trans. (1990) 187.
[25] G.P. Haight Jr., E. Perchonoex, F. Emmengger, G. Gordon, J. Am. Chem. Soc. 87 (1965) 3835.
[26] D.W. Carlyle, J. Am. Chem. Soc. 94 (1972) 4525.
[27] R.A. Marcus, J. Phys. Chem. 67 (1963) 853.
[28] R.A. Marcus, J. Phys. Chem. 72 (1968) 891.
[29] R.A. Marcus, Annu. Rev. Phys. Chem. 15 (1964) 155.
[30] L.C.W. Baker, T.P. McCutcheon, J. Am. Chem. Soc. 78 (1956) 4503.
[31] P.G. Rasmussen, C.H. Brubaker, Inorg. Chem. 3 (1964) 977.
[32] A.W. Chester, J. Org. Chem. 35 (1970) 1797.
[33] E. Baciocchi, M. Crescenzi, E. Fasella, M. Mattioli, J. Org. Chem. 57 (1992) 4684.
[34] A.L. Nolan, R.C. Burns, G.A. Lawrance, J. Chem. Soc., Dalton Trans. (1998) 3041.
[35] M. Mehrotra, R.N. Mehrotra, J. Chem. Soc., Dalton Trans. (2003) 3606.
[36] Ms. Rekha, A. Prakash, Raj N. Mehrotra, Can. J. Chem. 71 (1993) 2164.
[37] R.O.C. Norman, P.M. Storey, J. Chem. Soc., B (1971) 119.
[38] B.D. Fockhart, K.J. Ivin, R.C. Pink, B.D. Sharma, J. Chem. Soc., Chem. Commun. (1971) 339.
[39] F.A. Cotton, G. Wilkinson, Advanced Inorganic Chemistry, third ed., Wiley, Eastern, New Delhi, 1986, p. 447.
[40] R.M. Smith, A.E. Martell, Critical Stability Constants, vol. 6, Plenum, New York, 1989, p. 16 and 450.
[41] R.E. Connick, T.M. Tam, E. von Deuster, Inorg. Chem. 21 (1982) 103.
[42] C.W. Davies, Ion Association, Butterwoths, London, 1962, p. 39.
[43] R.N. Mehrotra, S. Dholia (nee Gatiyala), K. Sharma, A. Prakash, Indian J. Chem. A 37 (1998) 973.
[44] H.L.J. Bäckström, Z. Phys. Chem. B 25 (1934) 122.
[45] R.J. Campion, C.F. Deck, P.J. King, A.C. Wahl, Inorg. Chem. 6 (1967) 672.
[46] G. Grtzner, K. Danksagmüler, V. Gutmann, J. Electroanal. Chem. 72 (1976) 177.
[47] M. Sphorer, G. Ron, A. Lowenstein, G. Navon, Inorg. Chem. 4 (1965) 4358.
[48] S. Dholiya, A. Prakash, R.N. Mehrotra, J. Chem. Soc., Dalton Trans. (1992) 819.
[49] (a) S.K. Saha, M.C. Ghosh, P. Banerjee, J. Chem. Soc., Dalton Trans. (1986) 1301;
(b) M. Gupta, S.K. Saha, P. Banerjee, J. Chem. Soc., Perkin Trans. 2 (1988) 1781;
(c) S.K. Saha, P. Bhattacharya, M. Ali, P. Banerjee, Bull. Chem. Soc. Jpn. 62 (1989) 3320;
(d) S.K. Saha, M.C. Ghosh, P. Banerjee, Inorg. Chim. Acta 126 (1987) 29;
(e) S.K. Saha, M.C. Ghosh, P. Banerjee, Int. J. Chem. Kinet. 20 (1988) 699.
[50] H. Taube, Advan. Inorg. Chem. Radiochem. 1 (1959) 1.
[51] I.M. Kolthoff, W.J. Tomsicek, J. Phys. Chem. 39 (1935) 945.
[52] Y. Abdul Majid, K.E. Howlett, J. Chem. Soc. A (1968) 679.
[53] R.W. Chlebek, M.W. Lister, Can. J. Chem. 49 (1971) 2943.
[54] R. Shah, M. Mehrotra, A. Prakash, R.N. Mehrotra, Indian J. Chem. A 40 (2001) 819.
[55] M. Sphorer, G. Ron, A. Lowenstein, G. Navon, Inorg. Chem. 4 (1965) 361.
[56] J.F. Kirby, L.C.W. Baker, J. Am. Chem. Soc. 117 (1995) 10010.
[57] C.N.R. Rao, A Handbook of Chemistry and Physics, Affiliated East–West Press, New Delhi, 1967, p. 234.
[58] J.A.A. Ketelaar, Chemical Constitution, Elsevier, 1958, p. 91.
[59] J.K. Halpern, L.E. Orgel, Faraday Discuss. Soc. 29 (1960) 32.
[60] R.N. Mehrotra, U. Chandrawat, A. Prakash, Indian J. Chem. A 36 (1997) 857.
[61] L. Eberson, J. Am. Chem. Soc. 105 (1983) 3192.
[62] P. Rasmussen, C.H. Brubaker Jr., Inorg. Chem. 3 (1964) 977.

Available online at www.sciencedirect.com
ScienceDirect
Polyhedron 27 (2008) 617–622
POLYHEDRON
www.elsevier.com/locate/poly

A unique chain of trinuclear Cu(II) units containing both neutral and anionic *N*-(pyrimidin-2-yl) acetamide (Haapm, resp. aapm) as a ligand and dicyanamide (dca): Synthesis, characterization, X-ray structure and magnetism of $[Cu_3(\mu\text{-aapm})_2\text{-}(\mu\text{-dca})_2(Haapm)_2](CF_3SO_3)_2$

Gerard A. van Albada [a], Isja Dominicus [a], Marta Viciano-Chumillas [a], Ilpo Mutikainen [b], Urho Turpeinen [b], Jan Reedijk [a,*]

[a] *Leiden Institute of Chemistry, Gorlaeus Laboratories, Leiden University, P.O. Box 9502, 2300 RA Leiden, The Netherlands*
[b] *Laboratory of Inorganic Chemistry, Department of Chemistry, P.O. Box 55 (A.I.Virtasen aukio 1), 00014 University of Helsinki, Finland*

Received 4 September 2007; accepted 16 October 2007
Available online 26 November 2007

Abstract

The synthesis, crystal structure, as well as the electronic and magnetic properties, of a new trinuclear-based Cu(II) compound $[Cu_3(\mu\text{-aapm})_2(\mu\text{-dca})_2(Haapm)_2](CF_3SO_3)_2$, containing the ligands *N*-(pyridin-2yl)acetamide (Haapm) and dicyanamide (dca) is reported.

The central Cu1 atom has a distorted elongated octahedral coordination with the basal plane comprised of two nitrogens from two different tetrachelating dehydronated aapm ligands and two nitrogen atoms of two dca anions (Cu–N distances 2.016(2) and 1.988(3) Å). The apical positions are occupied by two nitrogen atoms of the two different tetrachelating aapm ligands (Cu–N distance 2.539(3) Å), with a trans angle of 180°. Also the N–Cu–N angle is extremely small (58.25(9)°), due to the four-membered chelate ring. The outer Cu2 ions have also a distorted octahedral geometry with the basal plane formed of two nitrogens and two oxygen atoms from a tetrachelating dehydronated aapm ligand (which is bridging between Cu1 and Cu2) and from a Haapm ligand (Cu–N/O distances vary from 1.95.4(2) and 2.022(2) Å), with basal angles of 177.29(9)° and 171.12(8)°. The apical positions are occupied by an oxygen atom of a triflate anion (Cu–O distance 2.534(3) Å) and a nitrogen atom of a neighbouring dca anion (Cu–N distance 2.314(3) Å), with an angle of 171.92(8)°. The Cu–Cu distance within the trinuclear unit is 5.23 Å. The dca anions are connected in an end-to-end fashion to a neighbouring Cu(II) ion (Cu–Cu distance 8.54 Å), forming in this way a chain of trinuclear units bridged by two dca anions.

The EPR as a powdered solid revealed a weak $S = 1$ triplet spectrum at RT. The magnetic susceptibility measurements, measured from 5 to 200 K, revealed a weak ferromagnetic interaction between the Cu(II) ions.
© 2007 Elsevier Ltd. All rights reserved.

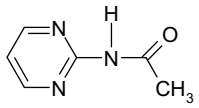
Keywords: Crystal structure; Copper; Dicyanamide; Trinuclear; Chain compound

1. Introduction

The coordination properties of acid amide ligands are known for several decades, and in all cases coordination of neutral acid amides takes part via the lone pair of the amide oxygen atom. The lone pair at the N atom is conjugated with the amide and therefore not available for metal–ion binding. Only when the N atom is ionized it can bind to metal ions. Pyridine-substituted acetamides were investigated some decades ago for the first time [1–3], Nonoyama et al. [4] synthesized several transition-metal compounds

* Corresponding author. Tel.: +31 71 527 4459.
E-mail address: reedijk@chem.leidenuniv.nl (J. Reedijk).

0277-5387/$ - see front matter © 2007 Elsevier Ltd. All rights reserved.
doi:10.1016/j.poly.2007.10.015



Scheme 1. *N*-(pyrimidin-2-yl)acetamide (Haapm).

with the ligand *N*-(pyridin-2yl)acetamide (abbreviated as Haap). Also a number of X-ray crystal structures with Haap and aap were published in later years [5].

The ligand Haap might have biological interest, and as a free ligand it was tested as an inducer for some types of Leukemia cells [6]. Very recently the pairwise arrangement of a donor and acceptor H bond group was realized and the molecule was used as a highly effective co-crystallizing agent for carboxylate acids [7].

More recently we investigated Cu(II) compounds with this ligand in more detail and also synthesized the new ligand *N*-(pyrimidin-2-yl)acetamide (abbreviated as Haapm) (see Scheme 1) and synthesized Cu(II) compounds with different anions [8].

On the other hand compounds of transition-metals and the ligand dicyanamide (abbreviated as dca = $N(CN)_2$) have gained much attention the last decade because of their interesting coordination, physical and magnetic properties [9–16], also due to the fact that the dca anion itself is a most interesting bridging ligand with three potential donor sites. As a result the co-ligand can vary from monodentate to even pentadentate [9–23]. The first generation of magnetically interesting compounds of the type Metal$(dca)_2$ compounds were, however, quite limited in structural types. Introducing co-ligands various new and exciting structures in the field of crystal engineering showing one-, two- and three-dimensional compounds have been obtained [9–23].

In this study the synthesis, X-ray crystal structure, characterization and magnetic behavior of a new linear trinuclear Cu(II) compound with the formula [Cu_3-(μ-aapm)$_2$(μ-dca)$_2$(Haapm)$_2$] $(CF_3SO_3)_2$ has been investigated. Linear trinuclear Cu(II) compounds have gained much interest in the field of magnetism [24].

However, linear trinuclear Cu(II) compounds, of which the trinuclear units forming a chain bridged via dca ligands are quite rare, *i.e.* to the best of our knowledge only one such compound, although not completely linear, has been reported [25].

2. Experimental

2.1. General

C, H, N determinations were performed on a Perkin–Elmer 2400 Series II analyzer. Ligand-field spectra were obtained on a Perkin–Elmer Lambda900 spectrophotometer using the diffuse reflectance technique, with MgO as a reference. X-band powder EPR spectra were obtained on a Jeol RE2x electron spin resonance spectrometer using DPPH ($g = 2.0036$) as a standard. FTIR spectra were obtained on a Perkin–Elmer Paragon 1000 FTIR spectrophotometer equipped with a Golden Gate ATR device, using the reflectance technique (4000–300 cm^{-1}, resp. 4 cm^{-1}).

Magnetic susceptibility measurement (5–200 K) were carried out (at 0.1 T) using a Quantum Design MPMS-5S SQUID magnetometer. Data were corrected for the magnetization of the sample holder and for diamagnetic contributions, which were estimated from standard Pascal constants.

2.2. Synthesis of the coordination compound

The ligand dipm was prepared by the method reported in the literature [8]. All other chemicals were used as received without further purification.

Synthesis of the compound: 1.2 mmol of Cu(II) triflate and 2.4 mmol of the ligand were each dissolved in 20 ml ethanol. The ligand salt solution was then added slowly to the Cu(II) solution. Then 1.2 mmol of sodium dicyanamide dissolved in about 2 ml of water was added slowly, while stirring, to the solution. The solution was filtered to remove any non-dissolved material. After one week a blue crystalline product separated. This product was isolated by filtration and dried in air. Yield 65%. *Anal.* Calc. for $C_{30}H_{26}Cu_3F_6N_{18}O_{10}S_2$: C, 31.2; H, 2.2; N, 22.4; S, 5.4. Found: C, 30.9; H, 2.2; N, 22.4; S, 5.4%.

Table 1
Crystallographic data for the title compound

Formula	$C_{30}H_{26}Cu_3F_6N_{18}O_{10}S_2$
Molecular weight	1167.43
Crystal system	triclinic
T (K)	173(2)
Space group	$P\bar{1}$
a (Å)	8.981(2)
b (Å)	9,002(2)
c (Å)	16.208(3)
α (°)	105.73(3)
β (°)	90.62(3)
γ (°)	119.38(3)
V (Å^3)	1082.8(4)
Z	1
D_{calc} (g cm^{-3})	1.790
$F(000)$	585
μ (mm^{-1})	1.658
Crystal size (mm)	$0.12 \times 0.10 \times 0.08$
Colour, shape	blue, plate
θ_{min}, θ_{max} °	2.64–27.50
Total reflections	16472
Total unique reflections (R_{int})	4950 (0.0446)
Number of refined parameters	315
R^a, wR_2^b, S^c	0.0351, 0.0829, 1.008
Minimum and maximum residual density (e/Å^3)	−0.566; 0.588

[a] $R_1 = \sum||F_o| - |F_c||/\sum|F_o|$.
[b] $wR_2 = [\sum[w(F_o^2 - F_c^2)^2]/\sum[w(F_o^2)^2]]^{1/2}$.
[c] Goodness-of-fit $S = [\sum w(F_o^2 - F_c^2)^2/(n-p)]^{1/2}$, where n is the number of reflections and p the number of parameters.

2.3. Crystal structure determination and refinement

A suitable crystal for the title compound was selected from the mother liquid and mounted to a glass fibre using the oil-drop method [26] data were collected on a Nonius KappaCCD diffractometer (graphite-monochromated Mo Kα radiation). The structures were solved by direct methods. The programs COLLECT [27], SHELXS-97 [28], SHELXL-97 [29] were used for data reduction, structure solution and structure refinement, respectively. Refinement of F^2 was done against all reflections. All non-hydrogen atoms were refined anisotropically. The water H atoms were picked from a difference map and refined isotropically. All other H atoms were introduced in calculated positions and refined with fixed geometry with respect to their carrier atoms. Crystallographic data of the compound is summarized in Table 1.

3. Results and discussion

3.1. Description of the crystal structure

A thermal ellipsoid plot, together with the numbering scheme is shown in Fig. 1, with selected bond lengths and bond angles given in Table 2. The unit structure consist of a three Cu atoms, two Haapm ligands, two dehydronated aapm ligands, two triflate anions and two dca anions. A centre of symmetry is located at the Cu1 atom.

The central Cu1 atom has a distorted elongated octahedral coordination with the basal plane comprised of two nitrogens from two different tetrachelating dehydronated aapm ligands and two nitrogen atoms of two dca anions (Cu–N distances 2.016(2) and 1.988(3) Å), with basal angles of 180°. The apical positions are occupied by two nitrogen atoms of the two different tetrachelating aapm ligands (Cu–N distance 2.539(3) Å), with a trans angle of 180°. Another interesting feature is that one N–Cu–N angle is extremely small (N15–Cu1–N17 = 58.25(9)°), as a result of the four-membered chelate ring. The outer Cu2 ions have also a distorted octahedral geometry with the basal plane formed of two nitrogens and two oxygen atoms from a tetrachelating dehydronated aapm ligand (which is bridging between Cu1 and Cu2) and from a Haapm ligand (Cu–N/O distances vary from 1.95.4(2) and 2.022(2) Å), with basal angles of 177.29(9)° and 171.12(8)°. The apical positions are occupied by an oxygen atom of a triflate anion (Cu–O distance 2.534(3) Å) and a nitrogen atom of a neighboring dca anion (Cu–N distance 2.314(3) Å), with an angle of 171.92(8)°.

Table 2
Selected bond lengths (Å) and angles (°) for the compound $[Cu_3(\mu\text{-aapm})_2(\mu\text{-dca})_2(Haapm)_2](CF_3SO_3)_2$

Cu1–N1	1.988(3)	Cu1–N17	2.015(2)
Cu1–N15	2.539(3)		
Cu2–O19	1.954(2)	Cu2–O29	1.977(2)
Cu2–N11	2.009(2)	Cu2–N21	2.022(2)
Cu2–N5b	2.314(3)	Cu2–O11	2.534(3)
N1–Cu1–N17a	89.29(10)	N1–Cu1–N17	90.72(10)
N1a–Cu1–N17	89.28(10)	N15–Cu1–N17	58.25(9)
O19–Cu2–O29	171.12(8)	O19–Cu2–N11	89.21(9)
O29–Cu2–N11	91.49(9)	O19–Cu2–N21	90.38(9)
O29–Cu2–N21	88.50(9)	N11–Cu2–N21	177.29(9)
O19–Cu2–N5b	87.90(9)	O29–Cu2–N5b	100.91(9)
N11–Cu2–N5b	92.28(10)	N21–Cu2–N5b	90.38(9)
O11–Cu2–N5b	171.92(8)		

a = − x, −y, −z; b = − x + 1, −y, −z

	D–H	H···A	D···A	D–H···A
Hydrogen bond parameters				
N27–H27A···O13 [1 − x, 2 − y, −1 − z]	0.88	2.04	2.847(4)	151

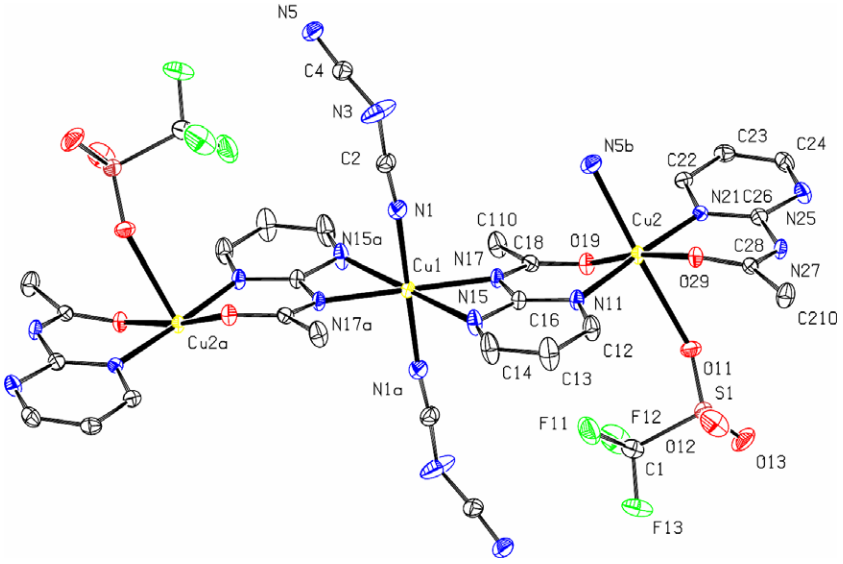


Fig. 1. Atomic displacement plot (50% probability level) of the molecular structure of $[Cu_3(\mu\text{-aapm})_2(\mu\text{-dca})_2(Haapm)_2](CF_3SO_3)_2$. H atoms have been omitted for clarity.

The Cu–Cu distance within the trinuclear unit is 5.23 Å. The dca anions are connected in an end-to-end fashion to a neighboring Cu(II) ion (Cu–Cu distance 8.54 Å), forming in this way a chain of trinuclear units bridged by two dca anions (Fig. 2). The lattice structure is stabilized by stacking between the pyrimidine rings of different units (Shortest Ring–Ring distances of 3.509 Å) and by a strong hydrogen-bonding between the amide N–H of the Haapm ligand and an oxygen atom of a triflate anion (N27···O13 2.847(4) Å), forming in this way a 3D array (see Fig. 3).

3.2. Spectroscopy and EPR

The ligand-field transition measured as a solid with the diffuse reflectance technique is observed as a very broad band with a maximum at about $14.4 \times 10^3\ cm^{-1}$, with a shoulder at around $10.0 \times 10^3\ cm^{-1}$. These are normal ligand-field transitions for (distorted) octahedral geometries [30].

In the IR a clear broad vibration band is observed at 3265 cm^{-1}, which is assigned to the NH of the Haapm molecule. Furthermore strong absorptions are observed in the 2370–2150 cm^{-1} region corresponding to the combination modes of vibration of the dca anion. These bands are characteristic of the $\nu_{s(C-N)} + \nu_{as(C-N)}$ and $\nu_{(C\equiv N)}$ vibrations [9,31]. The bands are observed as strong sharp vibrations at 2306, 2251 and 2183 cm^{-1}. The $\nu_{as(S=O)}$ bands in the compound are observed at 1276, 1249 cm^{-1} and the $\nu_{as(S=O)}$ bands at 1222 and 1032 cm^{-1}. All these bands are in agreement with the literature for monodentate and/or H-bonded triflate absorptions [32,33].

The amide bands of the Haapm ligand are observed at 1646, 1613, 1577 and 1532 cm^{-1}. In the mononuclear compound $Cu(Haapm)_2(CF_3SO_3)_2$ these bands are observed at 1641, 1604 and 1527 cm^{-1} [8], concluding that the extra band in the trinuclear compound originates from the two different Haapm/aapm ligands present in the compound.

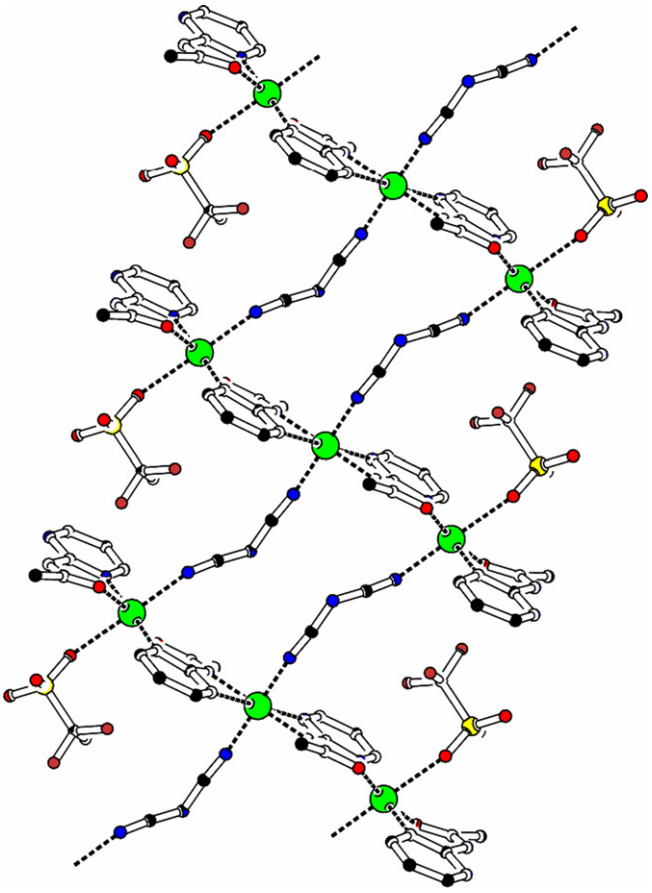


Fig. 3. Packing diagram of the title compound showing the links via the dca anions.

The EPR spectra of the title compound was recorded as a polycrystalline powder at RT and 77 K. At RT a strong isotropic band was observed with $g = 2.11$ and furthermore weak to very weak triplet bands are observed at 160, 230, 265 and 410 mT, indicating a weak zero-field splitting. At 77 K also the isotropic signal was observed at $g = 2.11$, while now only a very weak half-field signal was observed

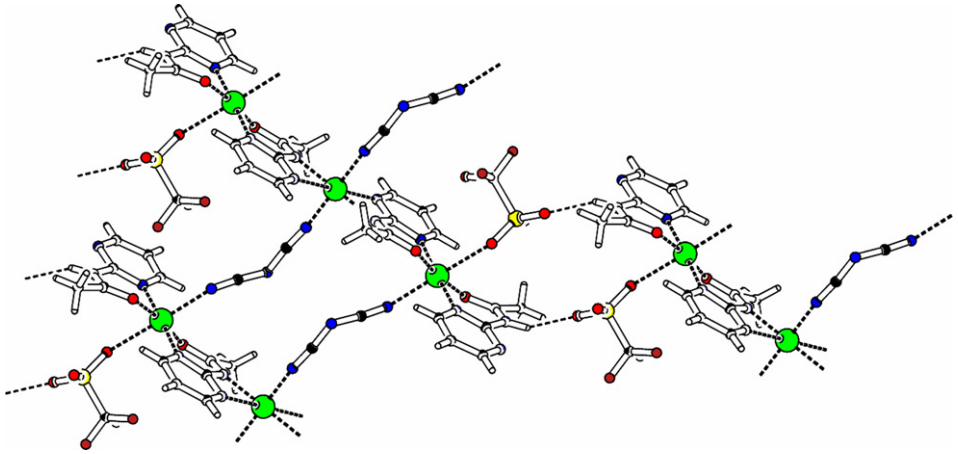


Fig. 2. Illustration of the H-bonding interactions between the triflate anion and the Haapm ligand.

at 160 mT. This signal is consistent with the trinuclear nature of the compound and the magnetic susceptibility measurements (*vide infra*).

3.3. Magnetic susceptibility

The temperature-dependent magnetic susceptibility of the title compound, measured as a powdered sample from 5 to 200 K, is depicted in Fig. 4 in the form $\chi_M T$ *versus* T and χ_M *versus* T. At 200 K, the $\chi_M T$ product is equal to 1.33 $cm^3\,mol^{-1}$ K, *i.e.* a value that is close to the expected value for three non-interacting copper(II) ions with $S = 1/2$($\chi_M T = 1.125\ cm^3\,mol^{-1}$ K). By lowering the temperature, the $\chi_M T$ value remains almost constant until 100 K where after it increases, reaching a value of 1.95 $cm^3\,mol^{-1}$ K at 5 K. This type of behavior arises from dominant ferromagnetic interactions between the three linear copper(II) within the trinuclear unit. The experimental data were fitted with the equation derived from the Hamiltonian $\widehat{H} = J(\widehat{S}_1\widehat{S}_2 + \widehat{S}_2\widehat{S}_3) + J'\widehat{S}_1\widehat{S}_3$ given as follows [24]:

$$\chi_M = \frac{N\beta^2 g^2}{4kT}\cdot\frac{1+\exp((J_1-J_2)/kT)+10\exp(3J_1/2kT)}{1+\exp((J_1-J_2)/kT)+2\exp(3J_1/2kT)} + \mathrm{TIP}$$

where J_1 is the interaction between neighboring copper(II) ions and J_2 represents the exchange parameter between the terminal copper(II) ions. A TIP value of $60\times10^{-6}\ cm^3\,mol^{-1}$ per each copper(II) was considered. The g value is the average of the three Cu(II) ions calculated from the fit of the magnetization *versus* field plot (Fig. 5). The best-fit parameters were found to be $g = 2.13$, $J_1 = 7.84\ cm^{-1}$ and $J_2 = 2.45\ cm^{-1}$, which are obtained from a fit of the experimental data from 5 to 200 K, with $R = 8\times10^{-5}$. Intermolecular interactions (zJ') between the chains formed by trinuclear copper units bridged by dca^- ligand also have been considered [34]. The best fitting parameters were found in this case: $J_1 = 8.98\ cm^{-1}$, $J_2 = 3.36\ cm^{-1}$, $zJ' = -0.019\ cm^{-1}$ and $g = 2.10$, with $R = 2\times10^{-5}$.

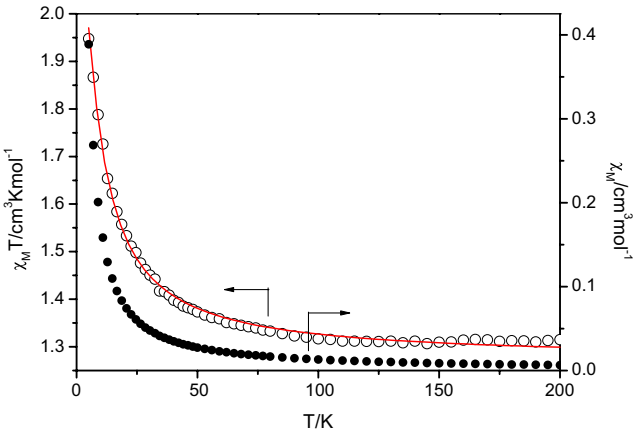


Fig. 4. Plot of $\chi_M T$ *vs* T (○) and χ_M *vs* T (●) for in the range of 5–200 K at 0.1 T applied field. The solid line represents the fit with $J_1 = 7.84\ cm^{-1}$ and $J_2 = 2.45\ cm^{-1}$ (see text).

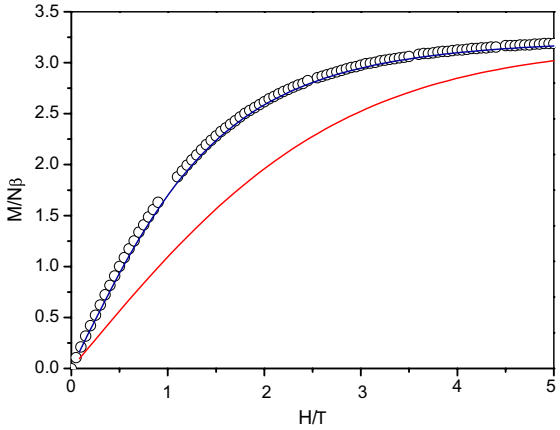


Fig. 5. The field dependence of the magnetization measured at 2 K (the red and the blue solid line represent the theoretical curve calculated with the Brillouin function for three copper(II) ions non-interacting and ferromagnetically coupled, respectively). (For interpretation of the references to color in this figure legend, the reader is referred to the web version of this article.)

The effective exchange pathway is through the Haapm ligand, while the dca^- bridge can be considered with negligible contribution as this group acts only by linking an equatorial site of one copper(II) ion with an axial position of a copper(II) ion belonging to an adjacent trinuclear unit (Cu···Cu = 8.54 Å) [35,36]. Each copper(II) ion within the trinuclear unit is octahedrally coordinated with $d_{x^2-y^2}$ being the magnetic orbital. As the bridging ligands are coordinated in the xy plane, the non-coplanarity of the coordination plane corresponding to the terminal copper(II) ion and central copper(II) ion could be a possible origin of the observed ferromagnetic interaction. The dihedral angle between the two coordination planes amounts to 19.09°, which is likely to have an effect on the orientation of the magnetic orbitals. More detailed analyses would be required to relate this distortion to the observed ferromagnetism. This is beyond the scope of the present study.

4. Conclusion

In this study a unique linear trinuclear CU compound in which the Cu ions are connected via end-to-end dca molecules forming a 1D chain has been synthesized and fully characterized. Also the magnetic susceptibility has been studied in detail.

In the literature only one trinuclear Cu(II) compound, although not completely linear, has been reported with end-to-end dca molecules bridging trinuclear units and forming a 1D chain, *i.e.* the compound {[Cu_3(dca)$_2$(nicotinato)$_4$(H_2O)$_8$](H_2O)$_2$} [25]. The Cu–Cu distances in this compound are 7.176(4) Å (Cu–Cu in trinuclear species) and 7.235(2) (Cu–Cu via dca bridge), compared to 5.23 and 8.54 Å in the title compound. The magnetic susceptibility revealed a weak ferromagnetic interaction contributed from the Cu–Cu interactions from the trinuclear

units, while the interaction via the dca anions are negligible, similar to the observation for the nicotinato compound [25].

5. Supplementary material

CCDC-653725 contains the supplementary crystallographic data for the title compound. These data can be obtained free of charge via http://www.ccdc.cam.ac.uk/conts/retrieving.html, or from the Cambridge Crystallographic Data Centre, 12 Union Road, Cambridge CB2 1EZ, UK; fax: (+44) 1223-336-033; or e-mail: deposit@ccdc.cam.ac.uk.

Acknowledgements

The work described in the present paper has been supported by the Leiden University Study group WFMO (Werkgroep Fundamenteel Materialen Onderzoek). Support of the NRSC Catalysis (Research School Combination of HRSMC and NIOK) is kindly acknowledged. Financial support and coordination by the FP6 Network of Excellence ''Magmanet''(contract number 515767) is kindly acknowledged. Dr. Stefania Tanase-Grecea is kindly acknowledged for useful discussions.

References

[1] M. Mikami, I. Nakagawa, T. Shimanouchi, Spectrochim. Acta 25A (1969) 365.
[2] M. Sekizaki, K. Yamasaki, Inorg. Chim. Acta 4 (1970) 296, and references cited therein.
[3] M. Sekizaki, Acta Crystallogr. B29 (1973) 327, and references cited therein.
[4] M. Nonoyama, S. Tomita, K. Yamasaki, Inorg. Chim. Acta 12 (1975) 33, and references cited therein.
[5] V. Sheller-Krattiger, K.H. Scheller, E. Sinn, R.B. Martin, Inorg. Chim. Acta 60 (1982) 45.
[6] C. Li, L.S. Rittmann, A.S. Tsiftsoglou, K.K. Bhargava, A.S. Sartorelli, J. Med. Chem. 21 (1978) 874.
[7] C.B. Aakeröy, I. Hussain, J. Desper, Crystal Growth Des. 6 (2006) 474.
[8] G.A. van Albada, I. Dominicus, I. Mutikainen, U. Turpeinen, J. Reedijk, Polyhedron 26 (2007) 3731.
[9] J. Kohout, L. Jäger, M. Hvastijová, J. Kožíšek, J. Coord. Chem. 51 (2000) 169, and references cited therein.
[10] J.S. Miller, J.L. Manson, Acc. Chem. Res. 34 (2001) 563.
[11] S.R. Batten, K.S. Murray, Coord. Chem. Rev. 246 (2003) 103, and references cited therein.
[12] W.-Z. Shen, X.-Y. Chen, P. Cheng, D.-Z. Liao, S.-P. Yan, Z.-H. Jiang, Z. Anorg. Allg. Chem. 629 (2003) 2591.
[13] D. Ghoshal, H. Bialas, A. Escuer, M. Font-Bardía, T.K. Maji, J. Ribas, X. Solans, R. Vicente, E. Zangrando, N.R. Chaudhuri, Eur. J. Inorg. Chem. (2003) 3929.
[14] A. Majunder, G. Pilet, M.T.G. Rodriguez, S. Mitra, Polyhedron 25 (2006) 2550.
[15] R. Boča, M. Boča, M. Gembický, L. Jäger, C. Wagner, H. Fuess, Polyhedron 23 (2004) 2337.
[16] S.R. Batten, J. Bjernemose, P. Jensen, B.A. Leita, K.S. Murray, B. Moubaraki, J.P. Smitl, H. Toftlund, J. Chem. Soc., Dalton Trans. (2004) 3370.
[17] A.M. Kutasi, A.R. Harris, S.R. Batten, B. Moubaraki, K.S. Murray, Cryst. Growth Des. 4 (2004) 605.
[18] Y.-J. Shi, X.-T. Chen, Y.-Z. Li, Z. Xue, X.-Z. You, New J. Chem. 26 (2002) 1711.
[19] D. Ghoshal, G. Mostafa, T.K. Maji, E. Zangrando, T.-H. Lu, K. Ribas, N.R. Chaudhuri, New J. Chem. 28 (2004) 1204, and references cited therein.
[20] Q. Shi, M.-L. Hu, H.-P. Xiao, X.-H. Li, Inorg. Chem. Commun. 8 (2005) 1169.
[21] G.A. van Albada, M.E. Quiroz-Castro, I. Mutikainen, U. Turpeinen, J. Reedijk, Inorg. Chim. Acta 298 (2000) 221.
[22] G.A. van Albada, W.J.J. Smeets, A.L. Spek, J. Reedijk, J. Chem. Cryst. 30 (2000) 11.
[23] A. Mohamadou, G.A. van Albada, H. Kooijman, B. Wieczorek, A.L. Spek, J. Reedijk, New J. Chem. 27 (2003) 983.
[24] O. Kahn, Molecular Magnetism, VCH Publ., NY, 1993.
[25] A.M. Madalan, C. Paraschiv, J.-P. Sutter, M. Schmidtmann, A. Müller, M. Andruh, Cryst. Growth Des. 5 (2005) 707.
[26] T. Kottke, D. Stalke, J. Appl. Crystallogr. 26 (1993) 615.
[27] Nonius, COLLECT, Nonius BV, Delft, The Netherlands, 2002.
[28] G.M. Sheldrick, SHELXS-97, Program for Crystal Structure Determination, University of Göttingen, Germany, 1997.
[29] G.M. Sheldrick, SHELXL-97, Program for the Refinement of Crystal Structures, University of Göttingen, Germany, 1997.
[30] B.J. Hathaway, in: G. Wilkinson, R.D. Gill, J.A. McCleverty (Eds.), Comprehensive Coordination Chemistry, vol. 5, Pergamon Press, Oxford, 1987 (Chapter 53).
[31] J. Carranza, J. Sletten, F. Lloret, M. Julve, Inorg. Chim. Acta 357 (2004) 3304, and references cited therein.
[32] G.A. van Albada, W.J.J. Smeets, A.L. Spek, J. Reedijk, Inorg. Chim. Acta 260 (1997) 260, 151 and references cited therein.
[33] G.A. van Albada, W.J.J. Smeets, A.L. Spek, J. Reedijk, J. Chem. Cryst. 28 (1998) 427.
[34] Y. Song, C. Massera, M. Quesada, A.M. Manotti Lanfredi, I. Mutikainen, U. Turpeinen, J. Reedijk, Inorg. Chim. Acta 358 (2005) 1171.
[35] B. Vangdal, J. Carranza, F. Lloret, M. Julve, J. Sletten, J. Chem. Soc., Dalton Trans. (2002) 566.
[36] M. Du, X.-J. Zhao, S.R. Batten, J. Ribas, Cryst. Growth Des. 5 (2005) 901.

Available online at www.sciencedirect.com
ScienceDirect
Polyhedron 27 (2008) 623–632
POLYHEDRON
www.elsevier.com/locate/poly

Study of protonation and Zn(II), Cd(II), Cu(II) and Mn(II) complexation with a glutamic acid *N*-pyrimidine derivative: Crystal structure of a neutral Cd(II) complex of the bianionic ligand

P. Arranz-Mascarós [a], M.D. Gutiérrez-Valero [a], R. López-Garzón [a,*], M.D. López-León [a], M.L. Godino-Salido [a], A. Santiago-Medina [a], H. Stoeckli-Evans [b]

[a] *Department of Inorganic and Organic Chemistry, University of Jaén, 23071 Jaén, Spain*
[b] *Institute of Chemistry, University of Neuchâtel, CH-2007 Neuchâtel, Switzerland*

Received 4 July 2007; received in revised form 17 October 2007; accepted 18 October 2007
Available online 20 December 2007

Abstract

The compound *N*-(4-amino-1-methyl-5-nitroso-6-oxo-1,6-dihydropyrimidin-2-yl)-(s)-glutamic acid (H_3L) was synthesised and structurally characterised by analytical methods and ^1H, ^{13}C and ^{15}N NMR spectroscopy. This compound (H_3L) shows the same topology as other model receptors previously used to develop chemical functionalization at the surface of an active carbon when they adsorb on it. Protonation of H_3L and its coordination ability towards Cd^{2+}, Zn^{2+}, Cu^{2+} and Mn^{2+} ions in water solution was also studied by potentiometric methods, UV–Vis and ^1H, ^{13}C NMR spectroscopies. The obtained results allow us to fit the operative conditions for the use of the activated carbon–H_3L adsorbent for the retaining of the above-mentioned metal ions in aqueous solutions. The molecular structure of $\{[Cd(HL)H_2O]\cdot 3H_2O\}_n$ was solved by single-crystal X-ray diffraction methods.
© 2007 Elsevier Ltd. All rights reserved.

Keywords: Cadmium; Zinc; Manganese and copper complexes; Adsorption; Ligand design; Crystal structures

1. Introduction

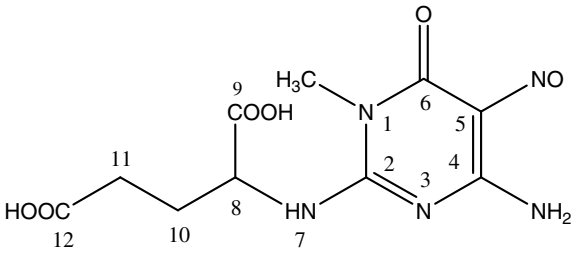
Environmental contamination from a wide variety of sources has become an increasingly serious problem in recent years. Activated carbons have been extensively used for the purification or recovery of pollutant metals in waste waters [1–3]. In recent works [4,5], we have described a new method to add chemical functionality to the surface of an active carbon based on adsorbing the above-mentioned model compounds on it. That adsorption, which takes place when pyrimidine residues interact with carbon arene centres, favours adsorbed compounds acting as metal–ion receptors. This method provides specific chemical functionalization of the carbon surface provided by the substituent existing at the C2 position of the pyrimidine.

Previous results point out that in the case of analogous molecular compounds derived from single amino acids L-alanine, L-valine, L-methionine, L-serine and L-glycylglycine, the adsorption capacity of adsorbents AC-molecular receptors to different metal ions was improved in relation to AC. It was also proved that this fact is due to the metal-binding capacity of the carboxyl function existing at the C2 substituent [6].

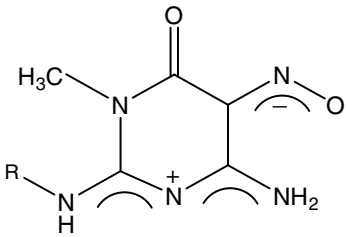
The model compound *N*-2-(4-amino-1,6-dihydro-1-methyl-5-nitroso-6-oxo-pyrimidin,2-yl) L-glutamic acid, H_3L (Scheme 1), shows the metal binding bicarboxylate COO^-–CHR–CH_2–CH_2–COO^- at the C2 position of the pyrimidine moiety. Thus, it is expected that the metal binding ability of the amino acid residue would improve the

* Corresponding author. Tel.: +34 953212186; fax: +34 953211876.
E-mail address: rlopez@ujaen.es (R. López-Garzón).

0277-5387/$ - see front matter © 2007 Elsevier Ltd. All rights reserved.
doi:10.1016/j.poly.2007.10.028



Scheme 1.



Scheme 2. Structure with charge delocalization

single monocarboxyl function existing at the single amino acid derivatives previously studied. In this work, we present the synthetic procedure for the H_3L compound and its structural characterization by thermal analysis, NMR and UV–Vis spectroscopy. The coordinating behaviour of H_3L to Zn(II), Cd(II), Cu(II) and Mn(II) metal ions has been recognized by studying the reactivity of the different H_3L/metal systems. The aim of this recognition was establishing the experimental conditions at which the bi-carboxyl function of the adsorbed ligand on an activated carbon is operative to metal ions, and also providing the thermodynamic properties of such a function for the above-mentioned metal ions. Reactivity studies were carried out using potentiometric, ^{13}C NMR and UV–Vis methods. The structure of the $\{[Cd(HL)H_2O]\cdot 3H_2O\}_n$ complex, which was solved by X-ray single crystal methods [7], is also reported.

2. Results and discussion

2.1. Synthesis and characterization of the molecular receptor

H_3L was prepared by a synthetic procedure [8] consisting of condensation of L-glutamic acid and 4-amino-1,6-dihydro-1-methyl-5-nitroso-6-oxo-pyrimidine [8,9]; this reaction takes place by the nucleophilic attack of the α-NH_2 amino group of L-glutamic acid on the C2 atom of the pyrimidine [8,9]. The structure of H_3L was determined by ^1H–^1H, ^1H–^{13}C and ^1H–^{15}N bi-dimensional spectra (see Section 4). Assignments are in accordance with the structural data of the H_3L unit, which were obtained by single X-ray diffraction methods [8].

The pyrimidine moiety shows alike structural and electronic features to a series of analogous compounds obtained by condensation of the above-mentioned pyrimidine derivatives with a series of single amino acids [10]. These data show extensive π-electron delocalization at the cyclic moiety which also involves the C2NH_2, C6O, C5NO and C4NH_2 exocyclic substituents. The somewhat long bond length values in the NH–C2–N3–C4–NH_2 fragment and the short bond distances in the C5NO grouping point out the location of a positive charge at the former fragment, and a negative charge at the latter; for example, the bipolar character of the aromatic moiety. These features have already been observed in the case of analogous amino acid derivatives [10] (Scheme 2).

2.2. Ligand protonation

The Brönsted acid–base behaviour of H_3L in aqueous solution was studied as a previous step on the study of the reactivity of the H_3L/metal ion systems in aqueous solutions. The protonation pattern of the ligand was also determined by following the dependence of the ^{13}C NMR signals of a H_3L solution on pH.

The protonation equilibrium of the ligand in solution (0.1 mol dm^{-3}KCl, 25 °C) within a 2.5–10.5 pH range was determined by a potentiometric method (see Section 4) and results are reported in Table 1.

Distribution plots of the protonated species of the ligand were obtained from the data of Table 1 and are shown in Fig. 1. The tri-anion L^{3-}, which exists at high pH values, binds four protons in the pH range investigated (2.0–10.5).

Table 1
Protonation constants ($\log K$) of the ligand H_3L (0.1 mol dm^{-3} KCl, 298.1 K)

Reaction	$\log K$[a]
	H_3L
$L^{3-} + H^+ = [HL]^{2-}$	12.11 (2)
$[HL]^{2-} + H^+ = [H_2L]^-$	4.43 (3)
$[H_2L]^- + H^+ = [H_3L]$	3.00 (1)
$[H_3L] + H^+ = [H_4L]^+$	1.90 (2)

[a] Values in parentheses are standard deviations in the last significant number.

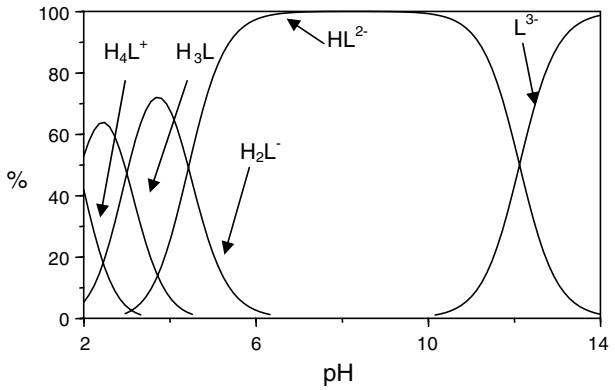


Fig. 1. Distribution species diagram as a function of pH for the ligand H_3L (10^{-3} mol dm^{-3}) in aqueous solution (0.1 mol dm^{-3} KCl) at 298.1 K.

The $\log K_{HL}$ value corresponding to the protonation of the tri-anion, $L^{3-} + H^+ = HL^{2-}$ (12.12), indicates that the corresponding binding site is strongly basic. The two protonation processes corresponding to the neutralization of the resulting bi-anion markedly overlap (see Fig. 1), and their matching constants are found within the expected range for the protonation of the two carboxylate residues existing at the *F* function of the ligand [11] ($\log K_{H_2L} = 4.43$, $\log K_{H_3L} = 3.00$). Bearing in mind the presence of a long spacer between terminal carboxylate groups, their basicities should be analogous; therefore the differences between both $\log K$ values can be attributed to statistical effects [12]. Finally, a protonation step corresponding to the $H_3L + H^+ = H_4L^+$ equilibrium (with $\log K_{H4L} = 1.9$) points out the very weak basic character of the corresponding proton binding site.

The addition of two protons to the HL^{2-} species, which takes place under the pH range 3–7 (see Fig. 1), does not produce any change in the UV–Vis spectrum of the ligand. On the other hand, as shown in Fig. 2, an increasing shielding of the ^{13}C NMR signal corresponding to the CH_2 groups at positions 8, 10 and 11 and of the two C atoms of the carboxyl groups (C(9) and C(12)) is observed in the above pH range as the pH decreases, indicating the protonation of the two COO^- anions.

The onset of H_3L protonation, which takes place at pH 3.5 (Fig. 1), is accompanied by changes in the UV and visible spectra of the compound (Fig. 3). Among these changes, the vanishing of a band at 524 nm stands out, which is assigned to a forbidden $n_N \rightarrow \pi^*$ transition of the C5NO chromophore (see Fig. 3), indicating that the protonation site is the nitrogen atom of the above mentioned group [13,14].

Deprotonation of HL^{2-}, which onsets at pH ca. 10.32, is accompanied by UV and visible spectral changes (see Figs. 1 and 3). Moreover this process is accompanied by significant shifts of the C(2) signal in the ^{13}C NMR spectra of H_3L, suggesting that the group involved in this protonation

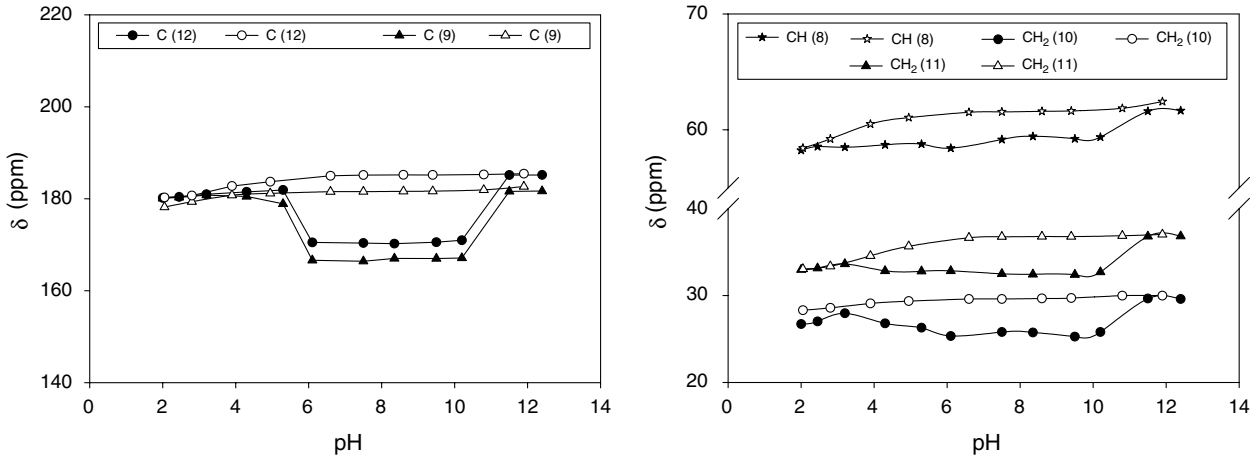


Fig. 2. ^{13}C NMR chemical shifts of C(8), C(10), C(11) and C(12) carbon atoms vs. pH of an H_3L D_2O solution (white points) and an H_3L/Cd^{2+} (1/1 molar ratio) D_2O solution (black points).

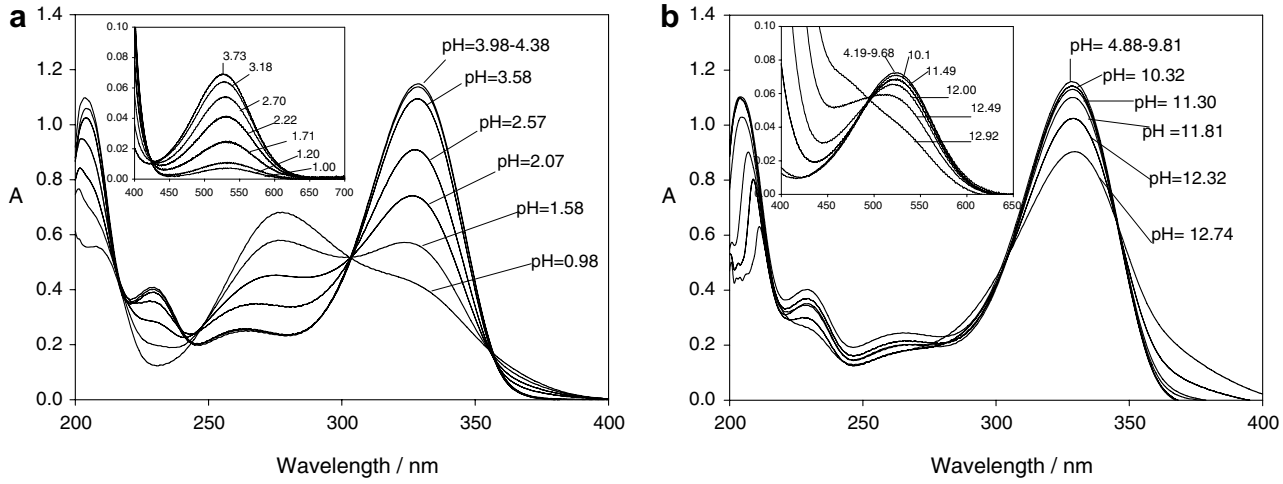


Fig. 3. pH-Dependence of the absorption spectra of H_3L in the UV ($[H_3L] = 5 \times 10^{-5}$ mol dm^{-3}, 0.1 mol dm^{-3} KCl), and visible ($[H_3L] = 10^{-3}$ mol dm^{-3}, 0.1 mol dm^{-3} KCl) regions, (a) in acidic media and (b) in basic media.

step is C2HN, which is conjugated with the pyrimidine moiety.

2.3. Complex formation in aqueous solution

As it has been previously said [4–6], the main adsorption mechanism of ligands analogous to H_3L and also of the H_3L ligand [15] on the activated carbon involves a plane-to-plane interaction between the pyrimidine moiety of the former and the arene centres of the graphite planes of the AC. This kind of interaction blocks the basic functions of the pyrimidine moiety, limiting the reactivity of the ligand (AC–H_3L) anchored with metal–ions to that of the amino acid residue of H_3L. Therefore, the main objectives of the studies of ligand–metal ion complex formation in solution are to obtain the data necessary to fit pH conditions at which the bi-carboxyl function of the anchored H_3L are operative for metal–ion binding, and also determine its coordinating ability to these ions, (i.e., to characterize its coordination patterns and stabilities) which would state the metal adsorption capacities of the AC–H_3L adsorbent.

The complex formation equilibria and the corresponding constants in aqueous solutions for the studied H_3L/metal ion systems were obtained from the potentiometric-titration data of the corresponding ligand/metal ion mixtures ([H_3L]/[metal ion] = 1/1), which were processed with the HYPERQUAD software [16]. The best fit of the experimental data for each of the studied systems corresponds to those summarized in Table 2. The corresponding species distribution plots appear in Fig. 4.

Data displayed in Table 2 and Fig. 4 highlight that the highest reactivities and the most stable complexes are displayed in ligand/Cu^{2+} and ligand/Cd^{2+} systems, whereas the lowest are shown in the ligand/Mn^{2+} system.

In all the studied systems, mononuclear complexes showing 1/1 ligand/metal–ion stoichiometries are formed, even though the ligand can be found in the following forms: neutral (H_3L), monoanionic (H_2L^-), bianionic (HL^{2-}) and trianionic (L^{3-}). Additionally, a mononuclear complex with a 2/1 ligand to metal–ion stoichiometry is formed in the case of the ligand/Cd^{2+} system. Moreover, binuclear complexes (e.g., with 1/2 ligand/metal–ion stoichiometries) which contain the ligand partially deprotonated, as the bi and/or

Table 2
Equilibrium constants (0.1 mol dm^{-3} KCl, 298.1 K) for Cu(II), Zn(II), Cd(II) and Mn(II) complexes with H_3L in aqueous solution

Reaction	log *K*			
	Cu(II)	Zn(II)	Cd(II)	Mn(II)
$M^{2+} + L^{3-} \rightleftarrows [M(L)]^-$	10.71			
$M^{2+} + HL^{2-} \rightleftarrows [M(HL)]$	4.18	2.41	3.95	
$M^{2+} + H_2L^- \rightleftarrows [M(H_2L)]^+$	3.98	2.70		2.31
$M^{2+} + H_3L \rightleftarrows [M(H_3L)]^{2+}$	3.75		3.76	
$2M^{2+} + H_2L^- \rightleftarrows [M_2(H_2L)]^{3+}$			7.88	
$2M^{2+} + HL^{2-} \rightleftarrows [M_2(HL)]^{2+}$	6.68	5.82	7.26	5.92
$M^{2+} + HL^{2-} + L^{3-} \rightleftarrows [M(HL)L]^{-3}$			10.15	
$M^{2+} + L^{3-} + OH^- \rightleftarrows [M(L)(OH)]^{2-}$	16.49			
$M^{2+} + 2OH^- \rightleftarrows M(OH)_2$		−14.03	−16.61	−17.95

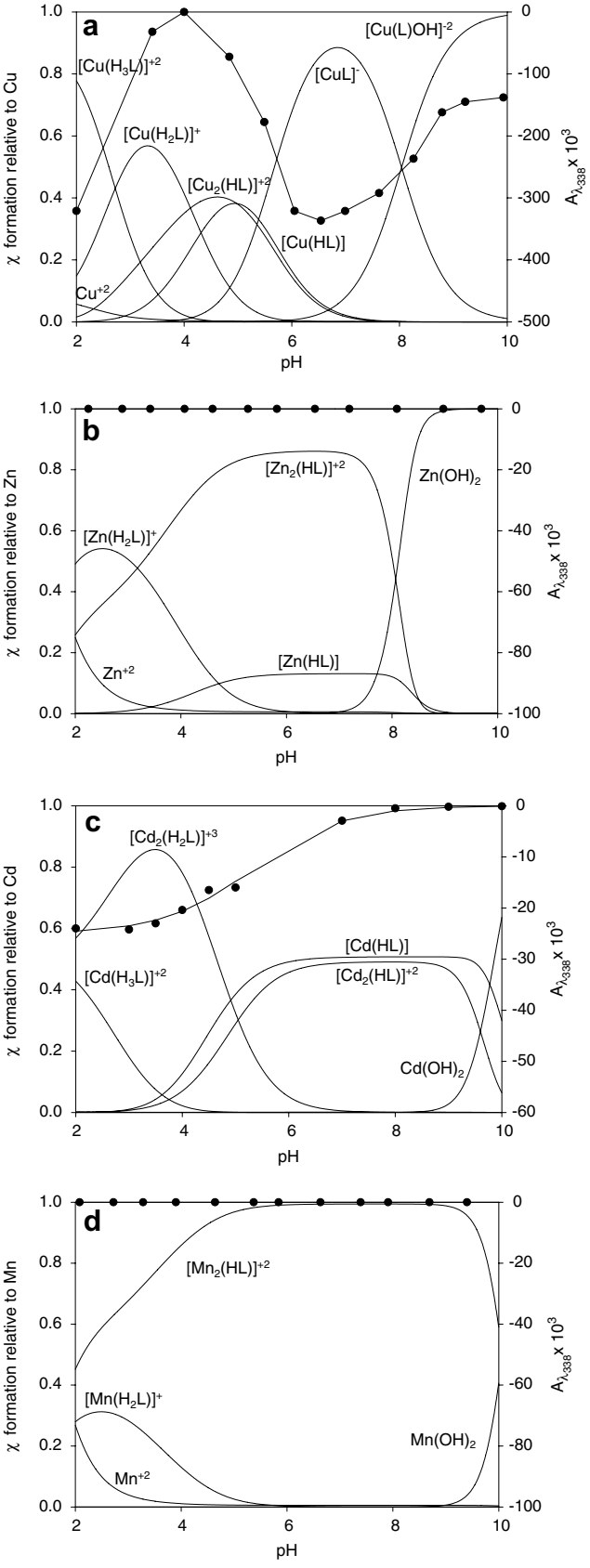


Fig. 4. Distribution species diagrams and absorbance differences at λ = 338 nm (black points, see text) with pH function systems for: (a) H_3L/Cu(II), (b) H_3L/Zn(II), (c) H_3L/Cd(II) and (d) H_3L/Mn(II) (1:1 molar ratio, 0.1 mol dm^{-3} KCl and 298.1 K).

mono-anion, are also detected. Table 2 shows that the highest reactivity corresponds to the Cu^{2+}/ligand system, whereas a poor speciation is found in the Mn^{2+}/ligand system.

Mononuclear complexes containing the fully protonated ligand H_3L are detected in the cases of Cu^{2+} and Cd^{2+} ions. As is expected, it can be seen in Fig. 4 that these complexes are the main species existing in the pH range under 4. Bearing in mind the poor nature of coordination of carboxyl groups and the N3 atom of the pyrimidine to metal–ions [5,13,14,17,18], single positions of the H_3L ligand available for binding to metal ions are the C5NO and C6O groups of the aromatic residue. Thus, it is expected that in complexes of the $[M(H_3L)]^{2+}$ type detected ($M^{2+} = Cu^{2+}$ and Cd^{2+}), H_3L behaves as a chelating bidentate ligand, using the N atom of C5NO and the O atom of C6O as binding positions to the mentioned metal ions. Otherwise, this behaviour is consistent with analogous pyrimidine derivatives, having the substituents –NO and =O at the C5 and C6 positions, respectively. In fact, the stability constants of $[CuH_3L]^{2+}$ and $[CdH_3L]^{2+}$ ($\log K = 3.75$ and 3.76 respectively, see Table 2) are in a similar range to those found for Cu^{2+} and Cd^{2+} complexes, with analogous C5-nitroso C6-oxo derivatives [18].

Deprotonation of H_3L species in the H_3L/metal ion system takes place at slightly lower pH values than in a water solution of the ligand. This fact produces the formation of binuclear $[M_2H_2L]^{3+}$ and/or mononuclear $[MH_2L]^{+}$ species. The former is only detected in the case of the H_3L/Cd^{2+} system (see Fig. 4). In the remaining three systems, these binuclear species are not detected, but mononuclear complexes $[MH_2L]^{+}$ are formed. Log K_{MH2L} values for the association of Cu^{2+}, Zn^{2+}, Cd^{2+} and Mn^{2+} to the carboxylate group in these complexes are similar to those described in the literature for single carboxylate ligands [5,13,14,17–21]. The onset of the deprotonation of the remaining carboxyl functions of H_2L^{-} occurs at higher pH values than the domain of H_2L^{-} complex species, giving rise to mono- and binuclear [MHL] and $[M_2HL]^{2+}$ complexes, respectively. The former is detected in all systems, excluding the Mn^{2+}/ligand system, whereas the second is detected in all systems. The formation of $[M_2HL]^{2+}$ metal complexes suggests that the anchorage of the H_3L ligand on an activated carbon surface would improve the metal–ion capture capacity showed by similar ligands having a C2-substituent with a mono-carboxyl function [6]. In fact, previous results, obtained in the study of the Cu^{2+} adsorption by an H_3L–AC adsorbent, strengthen this hypothesis [15].

It is noteworthy that the calculated $\log K_{MHL}$ values for a given metal ion are very alike to those corresponding to $[MH_2L]^{+}$ complexes (see Table 2), which demonstrate that the coordination of HL^{2-} to the metal–ions in the detected MHL complexes only takes place through one of the two carboxylate groups, whereas the second probably remains uncoordinated. This fact can be due to the low stability of the seven-membered chelate ring, which would result from a cooperative binding of the two carboxylate functions to the same metal ion. However, more stable $[M_2HL]^{2+}$ complexes containing two metal ions coordinated to each of the two carboxylate groups are formed.

Species distribution plots of the Cu^{2+}/ligand system (Fig. 4a) show the formation of CuL^{-} and $CuLOH^{2-}$ metal complexes in the upper pH range, which holds the fully deprotonated L^{3-} anion as a ligand. It is also noteworthy in this system that the onset of the formation of the CuL^{-} species takes place at pH ca. 4, which is a lot lower than that determined for the deprotonation of HL^{2-} in water, which is ca. 10 (Fig. 1). This fact is due to the electron-withdrawing character of Cu^{2+} which induces early deprotonation of the HL^{-} species. The high Log K_{CuL} and $\log K_{CuLOH}$ values probably point out the role of the $C2_{py}N^{-}$ group as a binding site to the metal ion, together with one of the carboxylate groups.

To get further insight into the coordinating behaviour of H_3L, we carried out a spectrophotometric titration in the visible range of an aqueous 1/1 ligand/Cu^{2+} mixture. Fig. 5 shows the spectra obtained at given pH values by

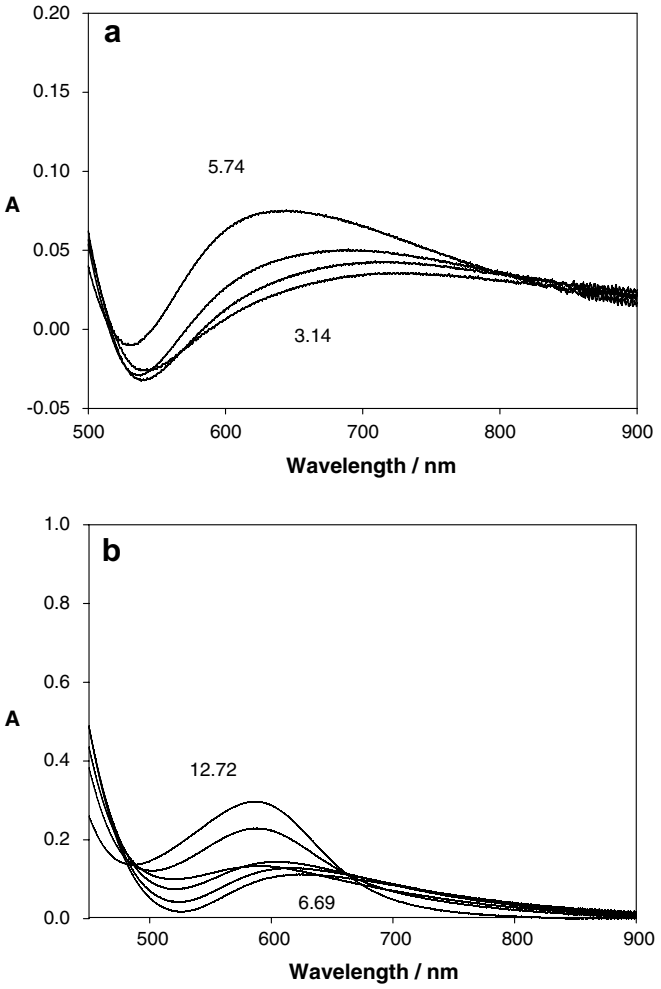


Fig. 5. Spectral curves of the ligand/Cu system in the visible range vs. pH ($[H_3L] = 10^{-3}$ mol dm^{-3}, 0.1 mol dm^{-3} KCl): (a) acidic medium from pH 3.14 to 5.74 (top), (b) basic medium from pH 6.69 to 12.72 (top).

subtracting those of H_3L from the corresponding 1/1 ligand/Cu^{2+} mixtures in aqueous solution.

In the lowest pH range, in which the main complex species existing in solution is $[CuH_3L]^{2+}$, the observed negative absorbance-values at the characteristic wavelength of the forbidden $n_N \rightarrow \pi^*$ transition of the C5NO chromophore ($\lambda_{max} = 524$ nm, see above) point out the blocking of the *n* electron pair of the N atom of such a group. This fact indicates that, in the $[CuH_3L]^{2+}$ complex, the Cu^{2+} ion is coordinated to the nitroso group of the pyrimidine. Moreover, a wide weak band with a λ_{max} value of ca. 700 nm indicates a weak ligand field in this complex.

As the pH increases within the 3–5 range, the concentration of the $[CuH_3L]^{2+}$ complex diminishes until it vanishes at the last pH value, and the $[CuH_2L]^{+}$, $[Cu_2HL]^{2+}$ and CuHL COO^--coordinated complexes increase, becoming the main ones, as Fig. 4 illustrates. The disappearance of the $[CuH_3L]^{2+}$ complex, in which the Cu^{2+} ion is coordinated through the C5NO group, explains the vanishing of the absorbance minimum at 524 nm in the mentioned 3–5 pH range in the spectra of Fig. 5, while the formation of more stable COO^--coordinated complexes explains the shifting of λ_{max} due to the d → d transition to values lower than the above mentioned 700 nm. It can also be seen in Fig. 5 that this shifting continues steadily as pH increases within the 6–12 pH range, reflecting the formation of more stable complexes: $[CuL]^-$ (the only species existing at a pH value of ca. 6.7) and $[CuLOH]^{2-}$, which is the unique complex existing at pH values up to 10.

To get further information on the coordination models of the ligand to the metal ions a series of NMR experiments with various ligand/metal ions mixtures have been performed. As was said above, the metal ions coordination to the N atom of the C5NO group can be enhanced by the disappearance of a characteristic absorption band of this group in the visible range. This weak band, which appears at 525 nm in the H_3L spectrum, is due to a $n \rightarrow \pi$ transition of the σ non-bonding pair of the mentioned N atom [18].

Fig. 6 shows the vanishing of the mentioned 525 nm band with the addition of growing amounts of Cu^{2+} to an H_3L aqueous solution at a constant pH 2.0. This fact proves that the N atom of the C5–NO group act as a binding site in the mononuclear CuH_3L complex formed at this pH value (see Fig. 4a). Due to conjugation of the C5-nitroso group with the pyrimidine moiety, metal coordination to the C5NO group induces electronic changes in the conjugated moiety of the H_3L molecule. These changes explain also the variations observed in the strong intensity bands (which are due to allowed $\pi \rightarrow \pi^*$ transitions) of the UV spectrum of an H_3L water solution (see Fig. 6) under the addition of increasing amounts of Cu^{2+} at a constant pH 2. Thus, it would be expected that the binding of some of the conjugated basic atoms of H_3L to metal ions in the complexes formed in water solution (i.e. in the cases of $[Cu H_3L]^{2+}$, $[Cd H_3L]^{2+}$ and $[CuL]^-$) would be accompanied by clear changes in the UV spectrum. On the contrary the metal ion complexes of H_2L^- and HL^{2-} in which carboxylate anions act as binding sites would not induce such changes in the UV spectrum of the ligand.

Thus, the differences between the UV spectra of a ligand/Cu^{2+} mixture with a 1:1 molar ratio and the ligand alone ($[ligand] = 5 \times 10^{-5}$ mol dm^{-3}) in water solution were obtained at several pH values in the 2.5–10 pH range. The maximum differences in absorbance values are found at a λ value of ca. 338 nm. Insignificant differences in the whole UV range were found in a narrow pH window centred at pH 4. This observation is consistent with the hypothesis established through the potentiometric data, that in the main complex species existing at these pH values ($[CuH_2L]^+$, $[Cu_2HL]^{2+}$ and [CuHL], (see Fig. 4a)) the coordination of the ligands would take place through the carboxylate groups. On the contrary, as the pH values decrease in the 4.0–2.5 pH range, increasing negative differences in the absorbance values at 338 nm are observed in the difference spectra. The last observation is consistent with the fact that the amount of $[CuH_3L]$ (the species in which the H_3L ligand is NO-coordinated) increases with decreasing pH values in that pH range. In the same way the trends of differences in the absorbance values observed in the 4 to 10 pH range, are also consistent with the forma-

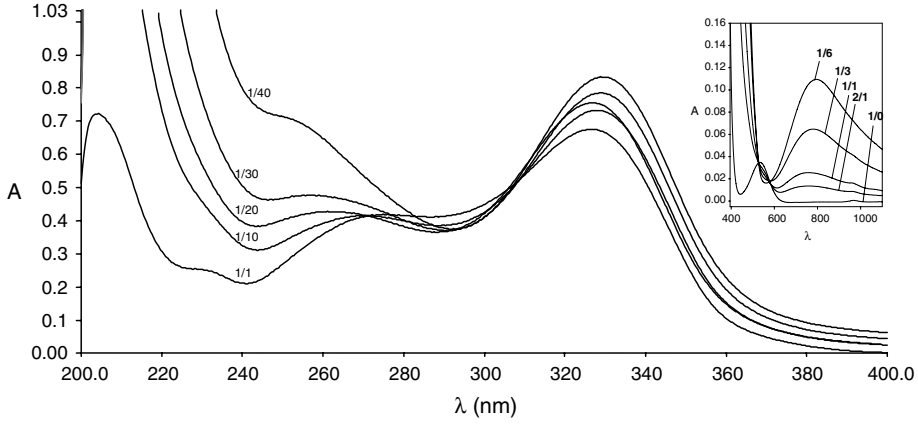


Fig. 6. [Cu] Variations of the visible and UV spectra of an H_3L/Cu^{2+} mixture with variable $H_3L:Cu^{2+}$ molar ratio values at constant pH 2.

tion of $[CuL]^-$ and $[CuLOH]^{2-}$ complexes, which contain the L^{3-} ligand, coordinated through the conjugated N^- atom of the deprotonated amine group attached to $C(2)_{pyr}$.

In the case of the ligand/Cd^{2+} system, the difference spectra shows a negative band at ca. 338 nm in the 2.5–6.0 pH range whereas zero absorbance is obtained in the whole UV region in the 6–10 pH range (see Fig. 6c). The shape of the plot of the absorbance difference values versus pH at the above wavelength is consistent with the potentiometric hypothesis. Thus, the appearance of a band at 338 nm in the UV difference spectra in the low pH range indicates that in the main existing species $[Cd_2(H_2L)]^{3+}$ and $[Cd(H_3L)]^{2+}$the ligand interacts with the metal ion through the N atom of the C(5)NO group. On the contrary, zero absorbance values in the pH range corresponding to values higher than 4 indicate that in [Cd(HL)] and $[Cd(H_2L)]^+$ complexes the ligand is not coordinated to Cd^{2+} through any of the conjugated basic atoms. Fig. 2 shows the plots of the chemical shift values of the carbon signals of the three methylene and the carboxyl groups of the amino acid moiety versus the pH values. These were obtained by the NMR titration of an H_3L/Cd^{2+} mixture as described in the experimental section. Fig. 2 shows that the onset of the formation of [Cd(HL)] and $[Cd(H_2L)]^+$ complexes taking place at a pH value of ca. 3 (see Fig. 4c) is accompanied by the shielding of the methylene carbon atoms and also the carboxyl ones. This indicates the existence of a carboxylate–Cd^{2+} interaction in the above complexes. The observed shielding, which is clearly stronger for the carboxylate groups than for methylene, can be explained by the stronger ionic character of the carboxylate–Cd^{2+} interaction than the carboxylate–proton one.

Very different behaviour is observed in the cases of the H_3L/Zn^{2+} and H_3L/Mn^{2+} systems in aqueous solutions. The difference spectra of both systems, in the 200–400 nm UV region were obtained in the 2.3–10.5 pH range and in the 2.7–10.1 pH range, respectively. The negligible differences in absorbance observed in all of the wavelength range in the two systems prove that complexes having the ligand coordinated through the basic conjugated atoms are not formed in any of the two systems. This proves that complexes detected in the potentiometric studies of these two systems, contains the ligands coordinated through the carboxylate groups (see above).

2.4. Conclusions

The results obtained from the above reactivity studies have provided the needed information (see above) to further interpret the adsorption properties to metal ions of the anchored ligand at the graphitic surface of activated carbon [15]. The whole reactivity data point out that H_3L behaves as a bi-functional ligand. In the low pH range, the only operative function is the C6O–C5NO grouping. This supports the formation of the five-member chelate complexes detected in this pH range with all the studied metal ions, excluding the Mn^{2+} and Zn^{2+} ions. In the last cases, the potentiometric and UV spectroscopic data ruled out the formation of a complex of this type. Nevertheless, the crystal structure of a Mn^{2+} complex with a pyrimidine analogue of H_3L with the methionine residue at the C2 cyclic atom [13], shows a supramolecular assembly in which COO^- coordinated Mn^{2+} ions of each unit interacts with the oxygen atom of the C5NO group of the pyrimidine moiety. All the previous data points out the possibility of the formation of a Mn^{2+} complex in the low pH range (also in the H_3L/Mn^{2+} system), in which the metal ion would be weakly coordinated to the pyrimidine moiety in a similar way. If so, the lack of protic properties of the oxygen atom of the NO group, would be the reason why this complex was not detected with the potentiometric method used in this work.

The deprotonation of the carboxyl functions of the substituent at $C2_{py}$ of the pyrimidine taking place in the intermediate pH range involves the availability of the carboxylate groups as operative basic functions for the binding to metal–ions. This leads to the formation of mono- and binuclear metal complexes within this pH range, in which one or two of the COO^- functions are coordinated to one or two metal ions respectively. Nevertheless, within this pH range, also binuclear complexes of H_2L^- ligand, containing one of the metal ions coordinated to the pyrimidine moiety and the second to a COO^- function, are also formed in the case of the Cd^{2+}/ligand system. Finally, in the highest pH range of all studied systems, the ligand uses one of the two carboxylate groups as a coordinating basic site, although cooperative coordination of both of them to the same metal–ion does not occur. In the case of the Cu^{2+} ion, the ligand also uses the $C2_{py}$-N^- group as a binding site, together with a COO^- group forming chelate complexes. It is noteworthy that the $N3_{py}$ position displays no affinity to any of the studied metal–ions. This fact, which is consistent with previous observations done with other analogous pyrimidine derivatives [5,19], agrees with the typical low electron density existing at the $–NH–(C2–N3–C4)_{py}–NH_2$ moiety [8,10].

In the species distribution diagrams of all the studied systems, it is seen that the deprotonation pH of the most acidic carboxyl groups (those of formation of $[M_2H_2L]^{3+}$ and/or $[M_2HL]^{2+}$ species) takes place at pH values meaningfully lower than those corresponding to the free ligand (see Fig. 1). These results bring up to date the pH values at which the H_3L ligand anchored on the graphite moiety of an AC (the H_3L–AC adsorbent) would be operative for the adsorption of metal ions in aqueous solution, although the expected optimum values would be those corresponding to the maximum of the plots for the metal-complexes with the fully deprotonated carboxyl functions, $[M_2HL]^{2+}$ and [MHL].

3. Crystal structure of $\{[Cd(HL)H_2O]\cdot 3H_2O\}_n$

The crystal structure of the complex $\{[Cd(HL)H_2O]\cdot 3H_2O\}_n$ was solved by single X-ray diffraction methods. A view of the asymmetric unit and the crystal packing is

depicted in Fig. 7, and selected bond and angles are listed in Table 3.

The compound consists of 2D molecules containing equivalent hepta-coordinated Cd^{2+} centres, each of which is coordinated to one water molecule, to two carboxylate groups of two individual HL^{2-} molecules (acting as bidentate chelating ligands with the two oxygen atoms in binding position), and to a third HL^{2-} molecule (also acting as a chelating ligand), using the N atom of the C5NO group and the O atom of the C6O of the pyrimidine moiety as binding sites. Thus, as shown in Fig. 7, HL^{2-} anions act as bridging ligands to three different Cd^{2+} ions using the pyrimidine moiety and the two carboxylate groups as binding moieties, as it has been previously said. The resulting structure around the Cd^{2+} ions can be described as a strongly distorted bipyramid. The distances of the metal ion to the five atoms (the O1, N4, O6, O5 and O3 atoms) in the equatorial plane are similar, and Cd–O3 bonds are widely deviated from the plane. On the other hand, the distances of atoms placed at the apical positions (O4 and O1W), which are also be very alike, are however shorter than the equatorial distances.

The 2D molecules are extended parallel to the *c* axis and are stacked parallel to one another along the *a* axis. Non-coordinated water molecules are placed in the inter-planar space, contributing to the stabilization of the 3D framework through their involvement in hydrogen bonding between neighbour molecular planes.

Concerning the organic ligand, it is noteworthy that the N3 cyclic atom of the pyrimidine does not act as donor atom, as observed in several structures of metal complexes of analogous ligands [14,18,22–25]. This fact is in agreement with the dipolar character of the pyrimidine moiety of the H_3L ligand [8].

Table 3
Selected bond lengths (Å) and bond angles (°) for $\{[Cd(HL)H_2O]\cdot 3H_2O\}_n$

Bond lengths		Bond angles	
$\{[Cd(HL)H_2O]\cdot 3H_2O\}_n$			
O(1)–C(1)	1.218(5)	O(1W)–Cd(1)–O(4)	160.97(7)
O(2)–N(4)	1.277(4)	O(1W)–Cd(1)–O(5)	86.36(9)
N(1)–C(4)	1.371(4)	O(4)–Cd(1)–O(5)	97.02(9)
N(1)–C(1)	1.384(4)	O(1W)–Cd(1)–N(4)	91.85(9)
N(1)–C(5)	1.461(4)	O(4)–Cd(1)–N(4)	99.47(7)
N(2)–C(4)	1.310(5)	O(5)–Cd(1)–N(4)	132.26(7)
N(2)–C(3)	1.333(7)	O(1W)–Cd(1)–O(1)	86.02(11)
N(3)–C(3)	1.328(4)	O(4)–Cd(1)–O(1)	83.94(11)
N(4)–C(2)	1.327(4)	O(5)–Cd(1)–O(1)	157.94(10)
N(5)–C(4)	1.322(5)	N(4)–Cd(1)–O(1)	68.69(11)
N(5)–C(6)	1.465(4)	O(1W)–Cd(1)–O(3)	106.69(9)
C(1)–C(2)	1.462(5)	O(4)–Cd(1)–O(3)	55.42(8)
C(2)–C(3)	1.433(6)	O(5)–Cd(1)–O(3)	83.85(9)
		N(4)–Cd(1)–O(3)	141.07(9)
Cd(1)–O(1W)	2.297(2)	O(1)–Cd(1)–O(3)	78.58(10)
Cd(1)–O(4)	2.299(2)	O(1W)–Cd(1)–O(6)	102.33(9)
Cd(1)–O(5)	2.345(3)	O(4)–Cd(1)–O(6)	94.75(9)
Cd(1)–N(4)	2.383(3)		
Cd(1)–O(1)	2.416(4)		
Cd(1)–O(3)	2.438(2)		
Cd(1)–O(6)	2.456(2)		
Cd(1)–C(7)	2.696(3)		
Cd(1)–C(10)	2.746(5)		

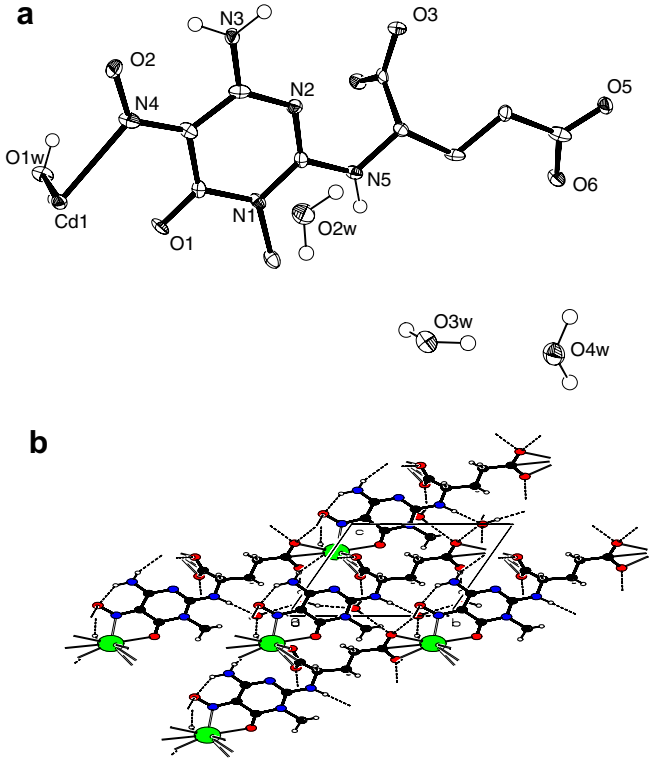


Fig. 7. (a) Drawing of the asymmetric unit, and (b) packing with the view of along arranged planes for $\{[Cd(HL)H_2O]\cdot 3H_2O\}_n$.

4. Experimental

4.1. Reagents

The anhydrous ligand, H_3L ($C_{10}H_{13}N_5O_6$), was obtained by a synthetic method previously reported [8]. Nanopure water was used as the solvent for potentiometric and spectrophotometric measurements. Standardised KOH, HCl, $ZnCl_2$, $CuCl_2$ and $MnCl_2$ aqueous solutions (Merck) were also used. All the potentiometric measurements were carried out in 0.1 mol dm^{-3} KCl as the background electrolyte.

4.2. Synthesis of $\{[Cd(HL)H_2O]\cdot 3H_2O\}_n$

$CdCl_2\cdot 2\cdot 1/2\cdot H_2O$ (114.17 mg, 0.5 mmol) was added to a solution of H_3L (149.5 mg, 0.5 mmol). This solution was left to evaporate over a few days in air until orange crystals suitable for X-ray analysis were formed. *Anal.* Calc. for $C_{10}H_{13}CdN_5O_7$ 3(H_2O): C, 24.94; H, 3.97; N, 14.54. Found: C, 25.20; H, 3.99; N, 14.97%.

4.3. X-ray structure analyses

Details for data collection and structure refinement are summarized in Table 4.

Table 4
Crystal data and structure refinement for $\{[Cd(HL)H_2O]\cdot 3H_2O\}_n$

Empirical formula	$C_{10}H_{13}N_5O_{10}Cd$
Formula weight	481.70
T (K)	293(2)
Wavelength (Å)	0.71073
Space group	$P\bar{1}$
a (Å)	6.4653(12)
b (Å)	8.2956(15)
c (Å)	8.7113(15)
α (°)	65.794(19)
β (°)	73.47(2)
γ (°)	82.88(2)
V (Å^3)	408.51(13)
Z	1
D_{calc} (g cm^{-3})	1.958
μ (cm^{-1})	0.71073
Total reflections	3179
R[a]	0.0288
Rw[b]	0.0203

[a] $R = \sum(|F_o| - |F_c|)\sum|F_o|$.
[b] $Rw = [|\sum w(|F_o| - |F_c|)^2|\sum w|F_o|^2]^{1/2}$.

4.4. X-ray structure of $\{[Cd(HL)H_2O]\cdot 3H_2O\}_n$

Suitable crystals of $\{[Cd(HL)H_2O]\cdot 3H_2O\}_n$ were obtained as orange block-like crystals by slow evaporation of an aqueous solution. The intensity data were collected at 153 K on a Stoe Image Plate Diffraction System [26] using Mo Kα graphite monochromated radiation. Image plate distance 70 mm, ϕ oscillation scans 0–200°, step $\Delta\phi = 2.0°$, 2θ range 3.27–52.1°, d_{min}–d_{max} = 12.45–0.81 Å. The structure was solved by direct methods using the program SHELXS-97 [7]. The refinement and all further calculations were carried out using SHELXL-97 [7]. The NH and NH_2 H atoms were located from difference Fourier maps and refined isotropically. The water molecule H atoms could be located from difference Fourier maps but in the final cycles of refinement they were constrained to be 0.86 Å and their U_{iso} thermal parameters = $1.5U_{eq}$(O atom). The remainder of the H atoms were included in calculated positions and treated as riding atoms using SHELXL default parameters; CH_3 = 0.98 Å, CH_2 = 0.99 Å, CH = 1.00 Å and $U_{iso} = 1.5(CH_3)$ or $1.2U_{eq}$(parent C atom). The non-H atoms were refined anisotropically, using weighted full-matrix least-squares on F^2.

An empirical absorption correction was applied using the DELrefABS subroutine in PLATON [27]; transmission factors $T_{min}/T_{max} = 0.426/0.808$.

The molecular structure and crystallographic numbering scheme are illustrated in the PLATON [27] drawing (see Fig. 6).

4.5. Potentiometric measurements

All potentiometric measurements ($pH = -\log[H^+]$) were carried out in degassed 0.1 mol dm^{-3} KCl solutions at 298.1 ± 0.1 K, with a 713 Methrom pH-mV meter, equipped with a combined glass electrode and connected to a Methron 765 Dosimat autoburette (1 ± 0.001 mL). The experimental procedure used was the same as that described elsewhere [28]. Typically, (1–1.5) × 10^{-3} mol dm^{-3} ligand concentration and 1:1 ligand/metal molar ratios were employed in the potentiometric measurements. At least four titration experiments (150 data points each) were carried out in the pH range between 2.5 and 10.5. The HYPERQUAD software [16], was used to calculate the equilibrium constants from the emf data.

4.6. Spectrophotometric measurements

Adsorption spectra were recorded on a Perkin–Elmer Lambda-19 spectrophotometer. H_3L spectra were obtained from 5×10^{-5} mol dm^{-3} aqueous solutions in the UV range and from 10^{-3} mol dm^{-3} aqueous solutions in the visible range (μ = 0.1 mol dm^{-3} KCl).

UV difference spectra were obtained using metal ion/H_3L mixtures with 1:1 molar ratios in aqueous solutions ($[H_3L] = 5 \times 10^{-5}$ mol dm^{-3}; μ = 0.1 mol dm^{-3} KCl) as samples, and a 5×10^{-5} mol dm^{-3} (μ = 0.1 mol dm^{-3} KCl) solution of the ligand as a reference.

HCl and KOH were used to adjust the pH values in all cases, which were measured on a Crison 2002 micro-pH meter.

4.7. NMR spectroscopy

^{1}H (300.13 MHz) and ^{13}C (75.48 MHz) spectra of H_3L and H_3L/Cd^{2+} mixtures in 1:1 molar ratios ([H_3L = 0.07 mmol dm^{-3}]) in D_2O solution, at several pH values were recorded at 298 K on a Bruker DPX300 spectrometer. ^{1}H–^{1}H and ^{13}C 2D correlation experiments were performed to assign the signals. Small amounts of 0.001 mol dm^{-3} NaOD or DCl solutions were added to a solution of H_3L to adjust the pD. The pH was calculated from the measured pD values using the following relationship pH = pD − 0.40 [29].

Acknowledgement

Financial support from the Spanish Ministerio de Ciencia y Tecnología (CTQ 2004-03332) is gratefully acknowledged.

Appendix A. Supplementary material

CCDC 652099 contains the supplementary crystallographic data for $\{[Cd(HL)H_2O]\cdot 3H_2O\}_n$. These data can be obtained free of charge via http://www.ccdc.cam.ac.uk/conts/retrieving.html, or from the Cambridge Crystallographic Data Centre, 12 Union Road, Cambridge CB2 1EZ, UK; fax: (+44) 1223-336-033; or e-mail: deposit@ccdc.cam.ac.uk.

References

[1] P.M. Cheremisinoff, C. Ellerbusch, Carbon Adsorption Handbook, Ann Arbor Science, Michigan, 1978.

[2] P.A. Brown, S.A. Gill, S.J. Allen, Water Res. 31 (2000) 3907.
[3] K. Csobàn, M. Pàrkànvi-Berka, P. Joo, P. Behra, Colloid Surf. A: Physicochem. Eng. Aspects 111 (1998) 347.
[4] J. García-Martín, R. López-Garzón, M. Luz Godino-Salido, M. Dolores Gutiérrez-Valero, P. Arranz-Mascarós, R. Cuesta, F. Carrasco-Marín, Langmuir 21 (2005) 6908.
[5] Javier García-Martín, Rafael López-Garzón, Maria Luz Godino-Salido, Rafael Cuesta-Martos, Maria Dolores Gutiérrez-Valero, Paloma Arranz-Mascarós, Helen Stoeckli-Evans, Eur. J. Inorg. Chem. (2005) 3093.
[6] M.D. Gutiérrez Valero, M. Luz Godino Salido, Paloma Arranz Mascarós, Rafael López Garzón, Rafael Cuesta, Javier García Martín, Langmuir 23 (2007) 5995.
[7] G.M. Sheldrick, Acta Crystallogr. A46 (1990) 467.
[8] Paloma Arranz Mascarós, M. Dolores Gutiérrez Valero, John N. Low, Christopher Glidewell, Acta Crystallogr. Sect. C 59 (2003) o210.
[9] M. Melguizo, A. Marchal, M. Nogueras, A. Sánchez, J.N. Low, J. Heterocyclic Chem. 39 (2002) 97.
[10] J.N. Low, M.D. López, P. Arranz-Mascarós, R. López-Garzón, M.D. Gutiérrez-Valero, M. Melguizo, G. Ferguson, C. Glidewell, Acta Crystallogr. B56 (2000) 882.
[11] Jussara Lopes de Miranda, Judith Felcman, Polyhedron 22 (2003) 225.
[12] A. Bencini, A. Bianchi, E. García-España, M. Micheloni, J.A. Ramirez, Coord. Chem. Rev. 88 (1999) 97.
[13] R. López Garzón, P. Arranz Mascarós, M.L. Godino Salido, M.D. Gutiérrez Valero, R. Cuesta, J.M. Moreno, Inorg. Chim. Acta 355 (2003) 41.
[14] R. López Garzón, M.L. Godino Salido, P. Arranz Mascarós, M.A. Fontecha Cámara, M.D. Gutiérrez Valero, R. Cuesta, J.M. Moreno, H. Stoekli Evans, Inorg. Chim. Acta 357 (2004) 2007.
[15] M.D. Gutiérrez Valero, R. López Garzón, P. Arranz Mascarós, M.D. López León, M.L. Godino Salido, Carbon (submitted for publication).
[16] P. Gans, A. Sabatini, A. Vacca, Talanta 43 (1996) 1739.
[17] A.E. Martell, R.M. Smith, R.J. Motekaitis, NIST Critically Selected Stability Constants of Metal Complexes Database, Version 7, Texas A&M University, College Station, TX, 2003.
[18] J.M. Moreno, P. Arranz Mascarós, R. López, M.D. Gutiérrez Valero, M.L. Godino Salido, J. Cobo Domingo, Polyhedron 18 (1999) 1635.
[19] C. Kallay, K. Varnagy, G. Micera, D. Scanna, I. Sovago, J. Inorg. Biochem. 99 (2005) 1514.
[20] P. Arranz Mascarós, M.L. Godino Salido, R. López Garzón, M.D. Gutiérrez Valero, J.M. Moreno Sánchez, Polyhedron 18 (1999) 689.
[21] W.J. Puspita, A. Odani, O. Yamauchi, J. Inorg. Biochem. 73 (1999) 203.
[22] R. López Garzón, P. Arranz Mascarós, M.L. Godino Salido, M.D. Gutiérrez Valero, J. Cobo Domingo, J.M. Moreno, Inorg. Chim. Acta 308 (2000) 59.
[23] J.N. Low, Paloma Arranz, Justo Cobo, M. Ángeles Fontecha, M. Luz Godino, Rafael López Garzón, Christopher Glidewell, Acta Crystallogr. C57 (2001) 534.
[24] J.N. Low, Paloma Arranz, Justo Cobo, M. Angeles Fontecha, M. Luz Godino, Rafael López Garzón, Debbie Cannon, Antonio Quesada, Christopher Glidewell, Acta Crystallogr. C57 (2001) 680.
[25] J.M. Salas-Peregrín, M.N. Moreno-Carretero, E. Colacio-Rodriguez, Can. J. Chem./Rev. Can. Chim. 63 (12) (1985) 3573.
[26] Stoe., IPDS Software, Stoe & Cie GmbH, Darmstadt, Germany, 2000.
[27] A.L. Spek, J. Appl. Crystallogr. 36 (2003) 7.
[28] M.L. Godino-Salido, M.D. Gutiérrez-Valero, R. López-Garzón, J.M. Moreno-Sánchez, Inorg. Chim. Acta 221 (1994) 177.
[29] A.K. Covington, M. Paabo, R.A. Robinson, R.G. Bates, Anal. Chem. 40 (1968) 700.

Available online at www.sciencedirect.com
ScienceDirect
Polyhedron 27 (2008) 633–640
POLYHEDRON
www.elsevier.com/locate/poly

Extended structures of copper(II) complexes with 2-di1*H*-2-imidazolylmethylmalonate (DIMMAL), a versatile bis(imidazole)–bis(carboxylate) ligand: Solution studies, crystal structures and spectroscopic characterization

Hugo Núñez [a], Juan Server-Carrió [a,*], Emilio Escrivà [a], Lucía Soto [a], Julia García-Lozano [a], Amparo Sancho [a], Begoña Verdejo [b], Enrique García-España [b]

[a] *Departament de Química Inorgànica, Universitat de València, c/Vicent Andrés Estellés, s/n, 46100 Burjassot, València, Spain*
[b] *Departament de Química Inorgànica, Institut de Ciència Molecular (ICMOL), Universitat de València, Edificio de Institutos de Paterna, Apartado de Correos 22085, 46071 Valencia, Spain*

Received 30 July 2007; accepted 18 October 2007

Abstract

Copper(II) complexes of 2-di1*H*-2-imidazolylmethylmalonate (DIMMAL) have been studied by potentiometric methods. The data revealed that the $CuHL_2^-$ and CuL_2^{2-} species are prevalent in the studied pH range. Moreover, this paper reports the synthesis, structure solution and spectroscopic characterization of two new DIMMAL containing complexes, $(NH_4)_2[Cu(DIMMAL)_2]\cdot 4H_2O$ (**1**) and $[Cu(DIMMAL)(en)(H_2O)]\cdot 5H_2O$ (**2**). The structure of compound **1** consists of centrosymmetric mononuclear anionic $[Cu(DIMMAL)_2]^{2-}$ units, NH_4^+ cations and lattice water molecules, in which $DIMMAL^{2-}$ acts as a tridentate ligand through two imidazole nitrogen atoms and one oxygen atom from a carboxylate group. The crystal structure of compound **2** is built up from mononuclear neutral $[Cu(DIMMAL)(en)(H_2O)]$ and water molecules of crystallization. In both cases the MBBs are interconnected into 3D networks by multiple H-bonding paths and aromatic–aromatic interactions, which play a determinant role in the modulation of the crystal packing. EPR spectra are indicative of an essentially $d_{x^2-y^2}$ ground state for the copper(II) ions in both compounds (CuN_4O_2 chromophores).
© 2007 Elsevier Ltd. All rights reserved.

Keywords: 3D networks; Self-assembly; Imidazole–carboxylate; Copper

1. Introduction

Considerable effort has been spent over the last decade to explore the use of coordination compounds as molecular building blocks (MBBs) that, by an appropriate combination of strong coordinative capacity with weak non-covalent interactions (hydrogen bond and π–π stacking), would provide directional motifs leading to the self-assembling of new network structures [1]. In particular, the understanding of all non-covalent interactions has been shown determinant for the development of inorganic supramolecular chemistry [2].

In recent years, our research interest has focused mainly on the coordinating behaviour of several ligands containing bis(imidazolyl) moieties. These kinds of ligands form very stable complexes with 3d ions *via* the coordination of imidazole nitrogen atoms in six-member chelate rings. In earlier works, we reported the results on the coordination chemistry of several bis(imidazolyl) ligands such as HBIP (3,3-bis(2-imidazolyl)propionic acid) [3], BIBM (bis(2-imidazolyl)bis(methoxycarbonyl)methylmethane) [4], DIMMAL (2-di1*H*-2-imidazolylmethylmalonate) [5] and BIMAM (bis(imidazol-2-yl)methylaminomethane) [6]. As part of our continuing studies on metal complexes of

* Corresponding author. Tel.: +34 963544346; fax: +34 963544960.
E-mail address: juan.server@uv.es (J. Server-Carrió).

0277-5387/$ - see front matter © 2007 Elsevier Ltd. All rights reserved.
doi:10.1016/j.poly.2007.10.026

imidazole–carboxylate-based ligands, we herein report the results of a solution study on the copper(II) complexes of DIMMAL, as well as the molecular and crystal structure and spectroscopic properties of two new DIMMAL derivatives, $(NH_4)_2[Cu(DIMMAL)_2]\cdot 4H_2O$ (**1**) and $[Cu(DIMMAL)(en)(H_2O)]\cdot 5H_2O$ (**2**). DIMMAL is a versatile polyfunctional ligand combining the donor function of the imidazole groups with that of two carboxylic groups, being therefore a potential *N,N,O,O*-tetradentate ligand. These functional groups can undergo acid–base reactions, having in consequence several donor/acceptors centers. In this sense, its efficiency for the build-up of hydrogen-bonded metal coordination network structures has been previously corroborated [5]. Beside this, the imidazole rings are available to generate aromatic–aromatic interactions that would play an important role in the modulation of the crystal packing [7]. Thus the combination of all these multiple simultaneous modes of interactions (coordinative, H-bonding and π–π, i.e., the three driving forces usually involved in the formation of high-dimensional systems [1d,8]) as the directional motifs guiding the self-assembly process, make DIMMAL a particularly attractive structural support that builds interesting supramolecular networks.

2. Experimental

2.1. Materials

The compounds $Na_2(DIMMAL)\cdot 5H_2O$ and $[Cu_2(DIMMAL)_2(H_2O)_2]\cdot 2H_2O$ were prepared as previously described [5] and characterized by elemental analysis and powder X-ray diffraction. All other reagents were used as supplied. Elemental analyses (C, H, N) were performed by the Servei de Microanalisi, Consell Superior d'Investigacions Científiques, Barcelona, Spain. Copper was determined by atomic absorption using a Perkin–Elmer 4100 ZL spectrophotometer.

2.2. Synthesis of the complexes

2.2.1. Synthesis of $(NH_4)_2[Cu(DIMMAL)_2]\cdot 4H_2O$ (*1*)

Aqueous solutions of $Na_2(DIMMAL)\cdot 5H_2O$ (0.5 mmol, 15 mL) and copper(II) chloride (0.25 mmol, 5 mL) were mixed together, resulting in a purple–blue solution. Solid ammonium chloride (1 mmol) was then added with stirring; the final pH value was 7.6. The solution was allowed to stand at a temperature of 4 °C for several days to produce single rectangular purple crystals of (**1**), which were filtered, washed with cold ethanol and dried. *Anal.* Calc. for $C_{20}H_{32}CuN_{10}O_{12}$: C, 35.95; H, 4.83; N, 20.97; Cu, 9.51. Found: C, 35.78; H, 4.97; N, 20.53; Cu, 9.62%.

2.2.2. Synthesis of $[Cu(DIMMAL)(en)(H_2O)]\cdot 5H_2O$ (*2*)

Single crystals of suitable size for X-ray work of compound **2** were obtained according to the following procedure: 0.5 mmol of $[Cu_2(DIMMAL)_2(H_2O)_2]\cdot 2H_2O$ were suspended in water (25 mL) and then ethylenediamine (1 mmol) was added with stirring, producing the redissolution of the blue powder and leading to a purple solution. The solution was left to stand at room temperature, and violet rectangular crystals of **2** formed overnight. The crystals were filtered, washed with cold ethanol and dried. *Anal.* Calc. for $C_{12}H_{28}CuN_6O_{10}$: C, 30.02; H, 5.89; N, 17.51; Cu, 13.24. Found: C, 29.72; H, 5.62; N, 17.79; Cu, 13.31%.

2.3. Physical measurements

Potentiometric titrations were carried out at 298.1 ± 0.1 K using $NaClO_4$ 0.15 M as a supporting electrolyte. The experimental procedure (burette, potentiometer, cell, stirrer, microcomputer, etc.) has been fully described elsewhere [9]. The acquisition of the emf data was performed with the computer program PASAT [10]. The reference electrode was a Ag/AgCl electrode in saturated KCl solution. The glass electrode was calibrated as a hydrogen-ion concentration probe by titration of previously standardized amounts of HCl with CO_2-free NaOH solutions and the equivalent point determined by the Gran's method [11] which gives the standard potential, $E^{\circ\prime}$, and the ionic product of water ($pK_w = 13.73(1)$).

The computer program HYPERQUAD was used to calculate the protonation and stability constants [12]. The pH range investigated was 2.5–11.0 and the concentration of the metal ion and the ligand ranged from 1×10^{-3} to 5×10^{-3} M with 1:1 and 1:2 M:L molar ratio. However, 1:1 M:L ratios gave rise to a non-soluble product not amenable for analysis. The different titration curves for each system (at least two, number of points *ca.* 50 in every titration) were treated either as a single set or as separated curves without significant variations in the values of the stability constants. Finally, the sets of data were merged together and treated simultaneously to give the final stability constants.

Diffuse reflectance spectra were obtained using a Perkin–Elmer Lambda 9 UV/Vis/IR spectrophotometer. Polycrystalline powder EPR spectra were recorded on a Bruker ESP-300 equipped with a variable temperature device.

2.4. X-ray structure determination

X-Ray data sets for compounds **1** and **2** were collected on a Nonius Kappa CCD diffractometer and intensity measurements were carried out at 293 K using graphite-monochromated Mo Kα radiation ($\lambda = 0.71073$ Å). The structures were solved by direct methods using SIR97 [13]. All non-hydrogen atoms were refined anisotropically on F^2 (program SHELXL-97 [14]). Hydrogen atoms from DIMMAL and the ethylenediamine molecule were placed at calculated positions, and hydrogens from water molecules and the ammonium cation were located by difference synthesis. All of them were included using a riding model in

Table 1
Crystallographic data for compounds **1** and **2**

	1	**2**
Chemical formula	$C_{20}H_{32}CuN_{10}O_{12}$	$C_{12}H_{28}CuN_6O_{10}$
Formula weight	668.10	479.95
Space group	$P\bar{1}$	$P2_1/c$
a (Å)	7.4074(3)	8.0564(1)
b (Å)	8.6055(4)	11.8375(2)
c (Å)	10.8248(5)	20.7885(3)
α (°)	83.612(2)	90.00
β (°)	76.127(2)	95.004(1)
γ (°)	83.271(3)	90.00
V (Å^3)	662.80(5)	1974.99(5)
Z	1	4
ρ_{calc} (g cm^{-3})	1.674	1.614
μ (mm^{-1})	0.908	1.170
Reflections collected	4669	8471
Unique reflections [$R_{(int)}$]	2333 [0.073]	4078 [0.025]
R_1^a	0.049	0.0356
wR_2^b	0.123	0.0957

[a] $R_1 = \sum||F_o| - |F_c||/\sum|F_o|$ for reflections with $I > 2\sigma(I)$.
[b] $wR_2 = \{\sum[w(F_o^2 - F_c^2)^2]/\sum[w(F_c^2)^2]\}^{1/2}$ for all reflections; $w = 1/[\sigma^2(F_o^2) + (aP)^2 + bP]$, where $P = [2F_c^2 + F_o^2]/3$ and a and b are constants set by the program.

the final refinement. Molecular representations were produced with ORTEP3 for Windows [15]. Packing figures were produced with Mercury 1.2 [16]. Other relevant data of the crystal structure study are listed in Table 1.

3. Results and discussion

3.1. Potentiometric studies

The stepwise protonation constants of DIMMAL are included in Table 2, along with those previously reported for the related HBIP and BIM (BIM = bis(imidazol-2-yl)methane) ligands [17]. Scheme 1 shows the structure of the H_2DIMMAL molecule in addition to the other two bis(imidazolyl) ligands.

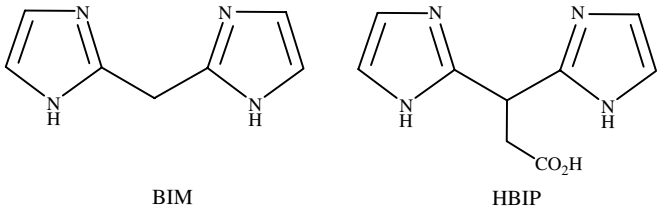
Compared with BIM [17] the two first stepwise constants of DIMMAL and HBIP can be ascribed to the protonation of the imidazole nitrogen atoms while the other two values are associated with the protonation of one (HBIP) or two (DIMMAL) carboxylate groups. The log K values corresponding to the protonation of the imidazole nitrogen atoms are scarcely affected when comparing the HBIP and BIM ligands; on the contrary, when a second carboxylate group is attached to the bis(imidazole) moiety in DIMMAL, although the ionic strength employed is not the same, slight but significant variations are observed: log K shift to higher values by *ca.* 0.6 in HL formation and *ca.* 0.9 in the corresponding H_2L formation.

Stability constants of the copper(II) complexes of all three bis(imidazolyl) ligands are given in Table 3. Speciation studies confirm the presence of 1:2 Cu:DIMMAL species, analogous to those found in the complexes with HBIP and BIM. Early formation of insoluble products in the equilibrium for the Cu:DIMMAL system in a 1:1 molar ratio prevented the acquisition of reliable data.

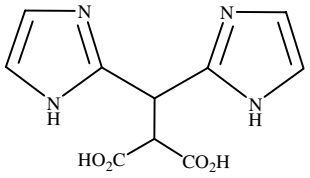
Table 2
Logarithms of the stepwise protonation constants for DIMMAL

Equilibrium[a]	DIMMAL	HBIP[b]	BIM[b]
$L + H \leftrightarrows LH$	7.54(2)[c]	6.90(1)	6.93(1)
$LH + H \leftrightarrows LH_2$	5.54(3)	4.62(1)	4.74(1)
$LH_2 + H \leftrightarrows LH_3$	3.75(4)	2.79(1)	
$LH_3 + H \leftrightarrows LH_4$	2.62(4)		

The corresponding constants for HBIP and BIP have been included for comparison (see text).
[a] Charges omitted.
[b] Taken from Ref. [17].
[c] Values in parentheses are standard deviations in the last significant figure.



BIM HBIP



H_2DIMMAL

Scheme 1.

Table 3
Logarithms of the stability constants for the formation of Cu(II) complexes by DIMMAL

Equilibrium[a]	DIMMAL	HBIP[b]	BIM[b]
$Cu + 2L \leftrightarrows CuL_2$	14.40(4)	17.29(3)	17.03(1)
$Cu + 2L + H \leftrightarrows CuHL_2$	20.44(3)	21.20(3)	
$CuL_2 + H \leftrightarrows CuHL_2$	6.04(4)	3.91(3)	

The corresponding constants for HBIP and BIM have been included for comparison (see text).
Values in parentheses are standard deviations in the last significant figure.
[a] Charges omitted.
[b] Taken from Ref. [17].

The most interesting feature in Table 3 is the lower stability of the 1:2 complex with the DIMMAL ligand in comparison with HBIP and BIM. On the other hand when the considered ligands contain carboxylate groups (DIMMAL and HBIP), protonated $CuHL_2$ species, which likely correspond to the complexes with a protonated carboxylate group, are observed. In the case of DIMMAL, this species is predominant in the pH range 4–6 and the large value for the protonation constant of CuL_2 suggests that it is occurring on a non-coordinated group. However, above pH 7, the CuL_2 complex predominates. So it seems plausible to isolate the dinegative $[Cu(DIMMAL)_2]^{2-}$ anions from 1:2

Cu:DIMMAL solutions at pH $\geqslant$ 7 (see distribution diagram in Fig. 1).

3.2. Description of the structures

3.2.1. Crystal structure of $(NH_4)_2[Cu(DIMMAL)_2]\cdot 4H_2O$ (1)

Compound **1** was obtained at pH > 7, in agreement with the solution data (see above). The structure of compound **1** consists of centrosymmetric mononuclear anionic $[Cu(DIMMAL)_2]^{2-}$ units, NH_4^+ cations and lattice water molecules. Both ionic species are held by extensive hydrogen bonding interactions that involve the water molecules to furnish a three-dimensional network structure. Fig. 2 shows a perspective view of the anionic unit with the atomic numbering scheme. Selected bond distances and angles are listed in Table 4.

The DIMMAL ligands are centrosymmetrically arranged around the copper atoms through two imidazole nitrogen atoms and one carboxylate oxygen atom. Therefore the coordination around the Cu(II) ions adopts a tetragonally elongated octahedral geometry (4 + 2 coordination mode of CuN_4O_2 chromophores). The basal octahedron plane is made up of four nitrogen atoms from four imidazoles rings, with Cu–N bond distances of 1.978(2) and 2.003(2) Å, which are similar to those observed in other *trans*-CuN_4O_2 chromophores with imidazole nitrogen atoms in equatorial positions [3g,5,18]. The axial sites are occupied by oxygen atoms from two carboxylate groups, with a Cu–O distance of 2.773(2) Å, which exceeds the Cu–N_{eq} ones by *ca.* 0.73 Å. According to Hathaway's criterion [19a], the axial oxygen atoms must be considered as semi-coordinated. In fact, the tetragonality parameter, defined as the mean in-plane Cu–N bond length divided by the mean out-of-plane M–O bond length [19b] is $T = 0.72$, similar to those observed in several *trans*-CuN_4O_2 chromophores of imidazole-containing six-coordinate copper(II) complexes with four imidazole rings as strong donor ligands in the basal plane and weaker oxygen donor ligands in apical positions [3g,5,18a,18c,18d].

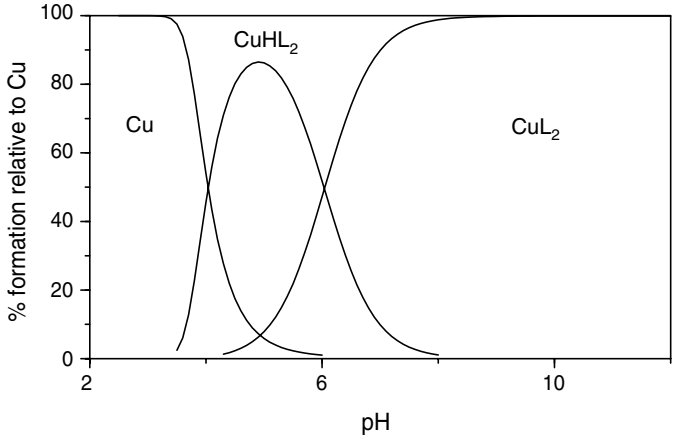


Fig. 1. Distribution diagram for the system Cu(II)–DIMMAL with $[Cu(II)] = 10^{-3}$ M, $[DIMMAL{\equiv}L] = 2\times10^{-3}$ M.

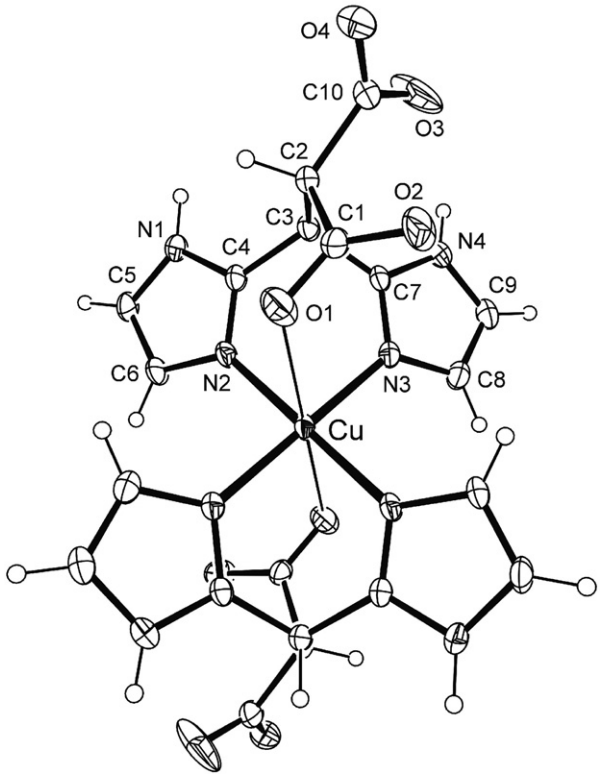


Fig. 2. Structure and atomic numbering scheme of $[Cu(DIMMAL)_2]^{2-}$ units in compound **1**.

Table 4
Selected bond distances (Å) and angles (°) for compound **1**

Cu–N(2)	1.978(2)	N(2)–Cu–N(3)	87.4(1)
Cu–N(3)	2.003(2)	N(2)–Cu–O(1)	81.3(1)
Cu–O(1)	2.773(2)	N(3)–Cu–O(1)	89.6(1)

The interatomic distances and angles within the DIMMAL moieties are similar to those found in the disodium salt as well the two copper(II) complexes previously described [5]. The imidazole rings are planar, with deviations from the mean planes not greater than 0.006(2) Å. The dihedral angle between the two imidazole rings of each ligand is 131.1(1)°.

Both kinds of carboxylate groups (coordinated and non-coordinated) display a similar degree of asymmetry. So the values of the asymmetry parameter [20] δ [$\delta = \{d(C–O_A)–d(C–O_B)\}\times10^3$] are $\delta = 21$ for the coordinated $–CO_2^-$ group and $\delta = 23$ for the uncoordinated one. It must be stressed that in the coordinated $–CO_2^-$ group the $C–O_{uncoord}$ distance is longer than the $C–O_{coord}$ one (1.256(4) and 1.235(4) Å, respectively). The weakness of the interaction Cu–O(1) in addition to the involvement of the uncoordinated O(2) atom in a relatively strong hydrogen bond ($O(6)–H(6B)\cdots O(2^{II})$, $d_{O\cdots O} = 2.596(5)$ Å) may be invoked to explain this behaviour.

Table 5
Hydrogen bonds for compound **1**

X–H···Y (Å)	X–H (Å)	H···Y (Å)	X···Y (Å)	X–H···Y (°)
O(5)–H(5A)···O(1)	0.81	2.828(4)	2.02	178
O(5)–H(5B)···O(4^{I})	0.88	2.707(3)	1.84	168
O(6)–H(6A)···O(5)	0.96	3.229(5)	2.36	151
O(6)–H(6B)···O(2^{II})	0.90	2.596(5)	1.73	159
N(1)–H(1)···O(4^{III})	0.95	2.736(3)	1.79	170
N(4)–H(4)···O(1^{IV})	0.87	3.158(3)	2.36	152
N(5)–H(51)···O(2)	0.92	2.909(4)	2.00	168
N(5)–H(52)···O(3^{V})	0.97	2.666(4)	1.78	150
N(5)–H(53)···O(5^{VI})	0.87	2.829(4)	2.00	158
N(5)–H(54)···O(6^{I})	0.72	2.975(5)	2.32	155

Symmetry operators: I: $-x$, $-y$, $-z+1$; II: x, $y+1$, z; III: $-x-1$, $-y$, $-z+1$; IV: $x-1$, y, z; V: $-x-1$, $-y-1$, $-z+1$; VI: x, $y-1$, z.

Crystal packing is primarily induced by the H-bonds listed in Table 5. As it has been observed in the previously reported DIMMAL derivatives [5] the H-bonding interaction is a determinant force involved in the self-assembly process.

The $[Cu(DIMMAL)_2]^{2-}$ entities, considered as a whole, can behave as hydrogen bond donors (through the protonated imidazole nitrogen atoms) and H-acceptors, by means of the carboxylate groups. The linkage of the $[Cu(DIMMAL)_2]^{2-}$ units by double N(1)–H(1)···O(4^{III}) (d_{O-O} = 2.736(3) Å) hydrogen bonds and aromatic–aromatic interactions generate chains running along the *a* direction with copper–copper distances of 7.4074(3) Å. These chains are linked together into sheets parallel to the *ac* plane by hydrogen bonds of the imidazole N(4) and the crystallization water O(5), both atoms acting as H-donors. Fig. 3 shows the 2D framework originated by these interactions between the chains. The water molecules O(5), which are located between the chains, play a relevant role by taking part in H-bonds with the $[Cu(DIMMAL)_2]^{2-}$ entities. They act as H-donors towards two oxygen atoms, O(1) and O(4^{I}), from two different $[Cu(DIMMAL)_2]^{2-}$ units belonging to neighboring chains. Both interactions should be relatively strong since the O–H···O bridges are nearly linear (angles of 178° for O(1) and 168° for O(4^{I})) and the O···O separations are not far from the range (2.4–2.7 Å) of strong hydrogen-bonded O···O distances [21].

Apart from the hydrogen-bonding set, aromatic–aromatic interactions between the imidazole rings constitute an additional factor in the 2D self-assembly process. The rings containing N(3) and N(4) atoms (in short, [N(3)N(4)] rings) belonging to two neighboring $[Cu(DIMMAL)_2]^{2-}$ units in the same chain interact in a offset face-to-face mode, as usual in observed π–π stacking interactions between imidazole rings [7g]. The geometrical parameters of these interactions are d_c = 3.58 Å, d_p = 3.55 Å and $\gamma = 7.0°$ (d_c being the centroid-to-centroid distance, d_p the plane-to-plane distance and γ the angle between the centroid–centroid vector and the perpendicular to the imidazole nucleus least-square plane [2a,7e]). The key parameters d_c and γ are significantly lower that those observed in other DIMMAL derivatives (mean values of d_c = 3.84 Å and $\gamma = 21.5°$ [5]).

The ammonium cations participate in hydrogen bonds as H-donors towards two carboxylate oxygen atoms and both crystallization water molecules (see Table 5). Every cation is surrounded by four oxygen atoms with N···O distances in the range 2.67–2.98 Å.These set of H-bond contacts, in combination with the π–π interaction between the imidazole rings (the [N(1)N(2)] and [N(3)N(4)] rings are involved in edge-to-edge interactions with d_c = 4.84 Å and a dihedral angle between the imidazole rings of 48.9°), link the above described *ac* layers into an infinite three-dimensional array. Fig. 4 shows the H-bond interactions between adjacent layers along the *b*-axis.

3.2.2. Crystal structure of $[Cu(DIMMAL)(H_2O)(en)]\cdot 5H_2O$ (2)

Compound **2** is the first characterized ternary copper (II) complex containing DIMMAL as a primary ligand. The crystal structure of compound **2** is built up from mononuclear neutral [Cu(DIMMAL)(H_2O)(en)] units (MBBs)

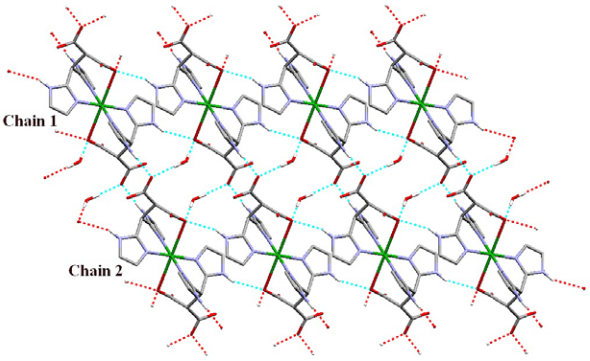


Fig. 3. The two-dimensional network of compound **1** as viewed down the crystallographic *b*-axis, showing the extensive hydrogen bonding in the *ac*-plane.

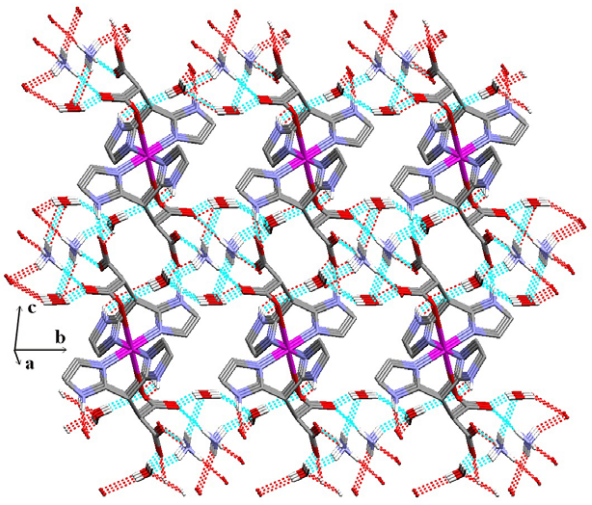


Fig. 4. 3D framework of compound **1**.

which are held by extensive hydrogen bonding interactions that involve the water molecules of crystallization to furnish a three-dimensional network structure. Fig. 5 shows a perspective view of the molecular unit with the atomic numbering scheme. Selected bond distances and angles are listed in Table 6.

The coordination geometry around the metal ion can be described as an elongated distorted octahedron. The equatorial plane comprises four nitrogen atoms, two belonging to the bis(imidazolyl) moiety (N(2) and N(3)) and two from an ethylenediamine molecule (N(5) and N(6)). The hexacoordination is achieved with the participation of two oxygen atoms, O(1) (from a propionate arm of DIMMAL) and O(5) (a water molecule) which occupy the axial positions (O(1)–Cu–O(5) 174.7(1)°), with Cu–O distances near to the borderline to be considered semi-coordinated (see Table 6). Therefore, the coordination mode for the copper atom can thus be viewed as $4+1+1$ (CuN_4OO' chromophore).

Ethylenediamine acts as a chelating ligand, forming five-membered rings with usual Cu–N bond distances. The torsion angle N(5)–C(11)–C(12)–N(6) is 50.7(3)° and the dihedral angle between the C(11)–C(12)–Cu and N(5)–N(6)–Cu planes is 26.5(2)°. Both conformational parameters are similar to those reported for other ethylenediamine–copper(II) complexes [22].

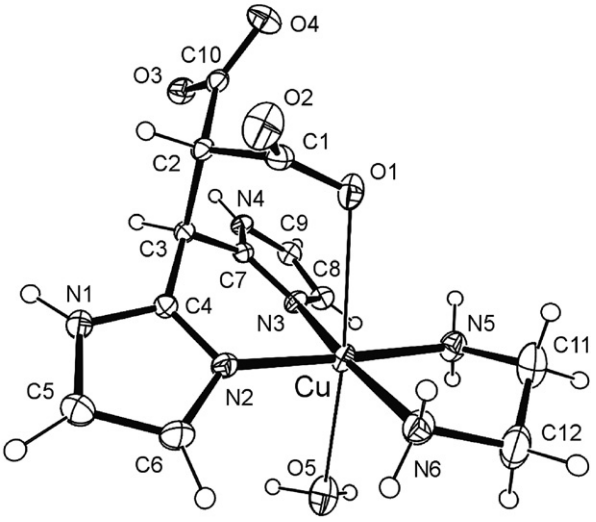


Fig. 5. Molecular structure and atomic numbering scheme of [Cu(DIMMAL)(H_2O)(en)] · $5H_2O$ compound.

Table 6
Selected bond distances (Å) and angles (°) for compound **2**

Cu–N(2)	1.988(2)	Cu–N(6)	2.012(2)
Cu–N(3)	1.980(2)	Cu–O(1)	2.677(2)
Cu–N(5)	2.030(2)	Cu–O(5)	2.596(2)
N(2)–Cu–N(3)	88.9(1)	N(3)–Cu–O(5)	95.7(1)
N(2)–Cu–N(5)	176.1(1)	N(5)–Cu–N(6)	83.6(1)
N(2)–Cu–N(6)	94.7(1)	N(5)–Cu–O(1)	92.0(1)
N(2)–Cu–O(1)	84.7(1)	N(5)–Cu–O(5)	92.8(1)
N(2)–Cu–O(5)	90.6(1)	N(6)–Cu–O(1)	95.5(1)
N(3)–Cu–N(5)	92.5(1)	N(6)–Cu–O(5)	87.4(1)
N(3)–Cu–N(6)	175.2(1)	O(1)–Cu–O(5)	174.7(1)
N(3)–Cu–O(1)	81.8(1)		

The interatomic distances and angles within the DIMMAL moieties are similar to those found in compound **1**. The imidazole rings are planar, with deviations from the mean planes not greater than 0.004(2) Å. The dihedral angle between the two imidazole rings of each ligand is 148.0(1)°. The carboxylate groups (coordinated and non-coordinated) display different degrees of asymmetry. In fact the values of the asymmetry parameter are $\delta = 21$ for the coordinated $-CO_2^-$ group and $\delta = 2$ for the uncoordinated one. Like in compound **1**, in the coordinated $-CO_2^-$ group the C–$O_{uncoord}$ distance is longer than the C–O_{coord} one (1.266(3) and 1.245(3) Å, respectively). Similar arguments (the weakness of the interaction Cu–O(1) together to the greater implication in the hydrogen bonds of the uncoordinated O(2) atom) may be used to explain this similar behaviour.

The existence of several H-donor (NH from the imidazole rings and NH_2 from the ethylenediamine molecule) and H-acceptor (carboxylates) groups confers interesting properties to the [Cu(DIMMAL)(H_2O)(en)] units as potential MBBs for building supramolecular frameworks.

As in compound **1**, the crystal packing is primarily induced by the H-bonds (see Table 7). The [Cu(DIMMAL)(H_2O)(en)] units are linked into a 1D chain structure running along the direction of the *a*-axis by means of O(5)–H(5A)···O(2^{I}) and N(5)–H(5C)···O(2^{I}) hydrogen bonds. In addition, the chains further extend into a double-strand structure based on double N(1)–H(1)···O(3^{VI}) hydrogen-bonds and π–π interactions (see Fig. 6). The latter involve the [N(3)N(4)] imidazole rings of neighboring MBBs in an offset face-to-face mode. The geometrical parameters of such interactions are $d_c = 3.86$ Å, $d_p = 3.44$ Å and $\gamma = 27.1°$. Such a parallel displaced structure agrees with those

Table 7
Hydrogen bonds for compound **2**

X–H···Y (Å)	X–H (Å)	H···Y (Å)	X···Y (Å)	X–H···Y (°)
O(5)–H(5A)···O(2^{I})	0.84	2.872(3)	2.10	153
O(5)–H(5B)···O(6)	0.95	2.835(3)	1.90	168
O(6)–H(6A)···O(7)	0.93	2.858(3)	2.00	153
O(6)–H(6B)···O(8)	0.95	2.824(2)	1.87	172
O(7)–H(7A)···O(9^{II})	0.95	2.758(2)	1.83	164
O(7)–H(7B)···O(5^{III})	1.01	2.972(3)	2.04	154
O(8)–H(8A)···O(9^{IV})	0.91	2.891(2)	1.99	172
O(8)–H(8B)···O(10)	0.90	2.779(3)	1.89	166
O(9)–H(9A)···O(4^{V})	0.95	2.768(2)	1.83	168
O(9)–H(9B)···O(1)	0.84	2.800(2)	1.97	172
O(10)–H(10A)···O(2^{III})	1.01	2.807(3)	1.84	160
O(10)–H(10B)···O(4^{IV})	0.96	2.749(3)	1.86	154
N(1)–H(1)···O(3^{VI})	0.86	2.737(3)	1.93	157
N(4)–H(4)···O(6^{VII})	0.86	2.932(3)	2.23	139
N(5)–H(5C)···O(2^{I})	0.90	3.029(3)	2.15	165
N(6)–H(6C)···O(10^{III})	0.90	3.031(3)	2.18	158
N(6)–H(6D)···O(7^{III})	0.90	2.972(3)	2.13	155

Symmetry operators: I: $x+1$, y, z; II: x, $-y+1/2$, $z-1/2$; III: $-x+1$, $-y$, $-z$; IV: $x+1$, $-y+1/2$, $z-1/2$; V: $-x$, $y-1/2$, $-z+1/2$; VI: $-x$, $-y+1$, $-z$; VII: $-x+1$, $-y+1$, $-z$.

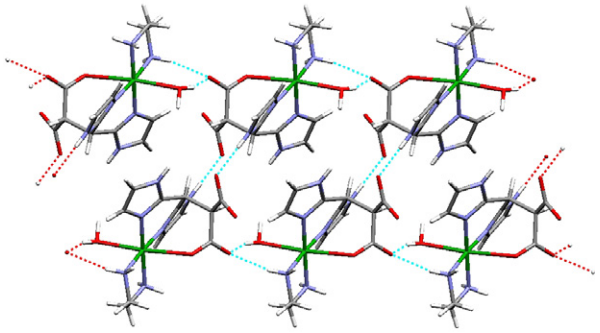


Fig. 6. Double-strand structure of [Cu(DIMMAL)(H_2O)(en)] units generated by hydrogen-bonds and aromatic–aromatic interactions.

reported for π–π interactions between aromatic nitrogen heterocycles and suggest a significant σ,π-contribution to this interaction [2a].

The five water molecules of crystallization (W6–W10) complete an extensive and intricate hydrogen-bond framework through W···W and W···[MBB] interactions (see Table 7), expanding the supramolecular aggregation to a three-dimensional network. In addition, aromatic–aromatic interactions between the imidazole [N(1)N(2)] rings (edge-to-face mode, $d_c = 5.74$ Å) belonging to adjacent double-chains contribute to stabilize the crystal structure.

3.3. Electronic and EPR spectroscopy

The diffuse reflectance spectra of compounds **1** and **2** exhibit very broad absorptions in the visible region with maxima centered at 17400 and 17800 cm^{-1}, respectively. The position of these absorptions, which is consistent with the presence of CuN_4O_2 chromophores with a tetragonally distorted octahedral geometry, is similar to those reported for other imidazole-containing copper(II) complexes exhibiting elongate octahedral *trans*-CuN_4O_2 chromophores [3,5,18].

The room-temperature Q-band EPR spectra of polycrystalline samples of compounds **1** and **2** are very similar (see Fig. 7), showing an axial type signal ($g_{\|} = 2.23_1$, $g_{\perp} = 2.05_1$ for compound **1** and $g_{\|} = 2.24_2$, $g_{\perp} = 2.05_2$ for compound **2**) with resolved hyperfine coupling in the parallel part of the spectrum ($A_{\|} = 186 \times 10^{-4}$ cm^{-1} for compound **1** and $A_{\|} = 184 \times 10^{-4}$ for compound **2**). When the temperature is lowered to 120 K, the signals narrow but the *g* values remain practically unchanged; no half-field signal was detected. These results are consistent with a predominantly $d_{x^2-y^2}$ ground state for the Cu(II) ions in a statically distorted CuN_4O_2 polyhedron in both compounds [23]. On the other hand, the observed set of EPR parameters are similar to those reported for related imidazole-containing copper(II) complexes [3f,5,18].

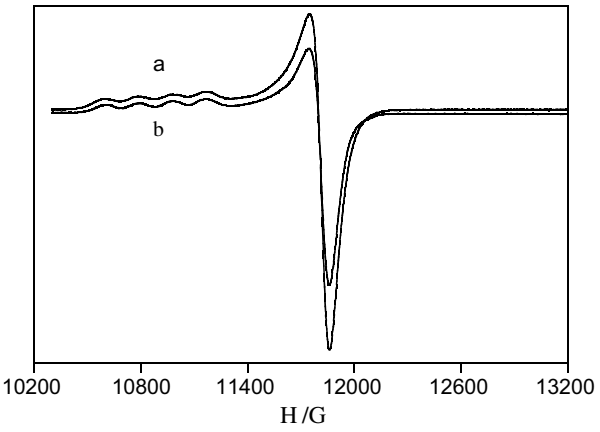


Fig. 7. EPR powder spectra (Q-band) of compounds **1** (a) and **2** (b) at room temperature.

Acknowledgements

We are grateful to the Dirección General de Investigación Científica y Técnica (DGICYT) (Projects BQU2003-01476 and CTQ2006-15672-CO5-01) for financial support.

Appendix A. Supplementary material

CCDC 654606 and 654607 contain the supplementary crystallographic data for compounds **1** and **2**, respectively. These data can be obtained free of charge via http://www.ccdc.cam.ac.uk/conts/retrieving.html, or from the Cambridge Crystallographic Data Centre, 12 Union Road, Cambridge CB2 1EZ, UK; fax: (+44) 1223-336-033; or e-mail: deposit@ccdc.cam.ac.uk. Supplementary data associated with this article can be found, in the online version, at doi:10.1016/j.poly.2007.10.026.

References

[1] (a) J.C. MacDonald, P.C.D. Malissa, M. Pilley, M.M. Foote, J.L. Lundburg, R.W. Henning, A.J. Schultz, J.L. Mansonpp, J. Am. Chem. Soc. 47 (2000) 122;
(b) D. Braga, L. Maini, M. Polito, L. Scaccianoce, G. Cojazzi, F. Greponi, Coord. Chem. Rev. 216 (2001) 225;
(c) B.J. Holliday, C.A. Mirkin, Angew. Chem. Int. Ed. 40 (2001) 2022;
(d) B. Moulton, M.J. Zaworotko, Chem. Rev. 101 (2001) 1629;
(e) Y. Sunatsuki, Y. Motoda, N. Matsumoto, Coord. Chem. Rev. 226 (2002) 199;
(f) O.M. Yaghi, M.L. O'Keeffe, N.W. Ockwig, H.K. Chae, M. Eddaoudi, J. Kim, Nature 42 (2003) 705;
(g) B. Lee, Chem. Soc. Rev. 33 (2004) 476;
(h) G.-H. Cui, J.-R. Li, J.-L Tian, X.-H. Bu, S.R. Batten, Cryst. Growth Des. 5 (2005) 1775.
[2] (a) C. Janiak, J. Chem. Soc., Dalton Trans. (2000) 3885;
(b) L. Brammer, J.C. Mareque Rivas, R. Atencio, S. Fang, F.C. Pigge, J. Chem. Soc., Dalton Trans. (2000) 3855;
(c) H.W. Roesky, M. Andruh, Coord. Chem. Rev. 236 (2003) 91;
(d) J.C. Noveron, M.S. Lah, R.E. Del Sesto, A.M. Arif, J.S. Miller, P.J. Stang, J. Am. Chem. Soc. 124 (2002) 6613.
[3] (a) B. Gimeno, L. Soto, A. Sancho, F. Dahan, J.-P. Legros, Acta Crystallogr. C 48 (1992) 1671;
(b) B. Gimeno, A. Sancho, L. Soto, J.-P. Legros, Acta Crystallogr. C 52 (1996) 1226;
(c) A. Sancho, B. Gimeno, J.M. Amigó, L.E. Ochando, T. Debaerdemaeker, J.V. Folgado, L. Soto, Inorg. Chim. Acta 248 (1996) 153;
(d) Y. Akhriff, J. Server-Carrió, A. Sancho, J. García-Lozano, E. Escrivá, J.V. Folgado, L. Soto, Inorg. Chem. 38 (1999) 1174;

(e) Y. Akhriff, J. Server-Carrió, A. Sancho, J. García-Lozano, E. Escrivá, L. Soto, Inorg. Chem. 40 (2001) 6832;
(f) H. Núñez, E. Escrivà, J. Server-Carrió, A. Sancho, J. García-Lozano, L. Soto, Inorg. Chim. Acta 324 (2001) 117;
(g) Y. Akhriff, J. Server-Carrió, J. García-Lozano, J.V. Folgado, A. Sancho, E. Escrivà, P. Vitoria, L. Soto, Cryst. Growth Des. 6 (2006) 1124.

[4] H. Nuñez, J.-J. Timor, J. Server-Carrió, L. Soto, E. Escrivà, Inorg. Chim. Acta 318 (2001) 8.

[5] H. Nuñez, L. Soto, J. Server-Carrió, J. García-Lozano, A. Sancho, R. Acerete, E. Escrivà, Inorg. Chem. 44 (2005) 4644.

[6] L. Soto, N. Ruiz, H. Nuñez, J. Server-Carrió, E. Escrivà, J. García-Lozano, A. Sancho, Inorg. Chim. Acta 359 (2006) 3221.

[7] (a) D. Cheng, M.A. Khan, R.P. Houser, Inorg. Chem. 40 (2001) 6858;
(b) A. Cammers, S. Parkin, Cryst. Eng. Commun. 6 (2004) 168;
(c) P. Mignon, S. Loverix, P. Geerlings, Chem. Phys. Lett. 401 (2005) 40;
(d) L.E. Cheruzel, M. S Mashuta, R.M. Buchanan, Chem. Commun. (2005) 2223;
(e) M. Kubicki, J Mol. Struct. 743 (2005) 209;
(f) A.K. Ghosh, A.D. Jana, D. Ghoshal, G. Mostafa, N. R Chaudhuri, Cryst. Growth Des. 6 (2006) 701;
(g) S.M. Malathy Sony, M.N. Ponnuswamy, Cryst. Growth Des. 6 (2006) 736.

[8] (a) G.R. Desiraju, Nature 412 (2001) 399;
(b) H.W. Roesky, M. Andruh, Coord. Chem. Rev. 236 (2003) 91;
(c) M.W. Hosseini, Coord. Chem. Rev. 240 (2003) 157.

[9] E. García-España, M.J. Ballester, F. Lloret, J.M. Moratal, J. Faus, A. Bianchi, J. Chem. Soc., Dalton Trans. (1988) 101.

[10] M. Fontanelli, M. Micheloni, in: Proceedings of the I Spanish–Italian Congress on Thermodynamics of Metal Complexes, Peñíscola, Castellón, 1990, Program for the Automatic Control of the Microburette and the Acquisition of the Electromotive Force Readings.

[11] (a) G. Gran, Analyst 77 (1952) 661;
(b) F.J. Rossotti, H. Rossotti, J. Chem. Educ. 42 (1965) 375.

[12] P. Gans, A. Sabatini, A. Vacca, Talanta 43 (1996) 1739.

[13] A. Altomare, M.C. Burla, M. Camalli, G.L. Cascarano, C. Giacovazzo, A. Guagliardi, A.G.G. Moliterni, G. Polidori, R.J. Spagna, J. Appl. Crystallogr. 32 (1999) 115.

[14] G.M. Sheldrick, SHELXL97, University of Göttingen, Göttingen, Germany, 1997.

[15] L.J. Farrugia, J. Appl. Crystallogr. 30 (1997) 565.

[16] I.J. Bruno, J.C. Cole, P.R. Edgington, M.K. Kessler, C.F. Macrae, P. McCabe, J. Pearson, R. Taylor, Acta Crystallogr. B 58 (2002) 389.

[17] K. Várnagy, I. Sóvágó, K. Ágoston, Z. Likó, H. Süli Vargha, D. Sanna, G. Micera, J. Chem. Soc., Dalton Trans. (1994) 2939.

[18] (a) W. Vreugdenhil, P.J.M.W.L. Birker, R.W.M. ten Hoedt, G.C. Verschoor, J. Reedijk, J. Chem. Soc., Dalton Trans. (1984) 429;
(b) A. Ozarowski, D. Reinen, Inorg. Chem. 2 (1985) 3860;
(c) A.L. Abuhijleh, C. Woods, Inorg. Chim. Acta 194 (1992) 9;
(d) C. Place, J.-L. Zimmermann, E. Mulliez, G. Guillot, C. Bois, J.-C. Chottard, Inorg. Chem. 37 (1998) 4030;
(e) B. Barszcz, T. Glowiak, J. Jezierska, Polyhedron 18 (1999) 3713;
(f) K. Kurdziel, T. Glowiak, J. Jezierska, Polyhedron 21 (2002) 1857;
(g) P.C.A. Bruijnincx, M. Lutz, A.L. Spek, E.E. van Faassen, B.M. Weckhuysen, G. van Koten, R.J.M. Klein Gebbink, Eur. J. Inorg. Chem. (2005) 779.

[19] (a) B.J. Hathaway, G. Wilkinson (Eds.), Comprehensive Coordination Chemistry, vol. 5, Pergamon, Oxford, 1985, p. 604;
(b) B.J. Hathaway, G. Wilkinson (Eds.), Comprehensive Coordination Chemistry, vol. 5, Pergamon, Oxford, 1985, p. 603.

[20] A. Fuertes, C.Miravitlles;E. Escrivá, E. Coronado, D. Beltrán, J. Chem. Soc., Dalton Trans. (1986) 1795.

[21] (a) T. Steiner, W. Saenger, Acta Crystallogr. B 50 (1994) 348;
(b) I.D. Brown, Acta Crystallogr. A 32 (1976) 24.

[22] E. Escriva, J. Server-Carrio, J. Garcia-Lozano, J.-V. Folgado, F. Sapina, L. Lezama, Inorg. Chim. Acta 279 (1998) 58, and references therein.

[23] (a) B.J. Hathaway, D.E. Billing, Coord. Chem. Rev. 5 (1970) 143;
(b) B.J. Hathaway, Struct. Bond. 57 (1984) 55.

Available online at www.sciencedirect.com
ScienceDirect
Polyhedron 27 (2008) 641–647
POLYHEDRON
www.elsevier.com/locate/poly

Synthesis, X-ray crystal structure and thermal decomposition of two peroxovanadium complexes with coordinated ammonia molecules: $[\{VO(O_2)_2(NH_3)\}_2\{\mu\text{-}Cu(NH_3)_4\}]$ and $[Zn(NH_3)_4][VO(O_2)_2(NH_3)]_2$

Jana Chrappová [a], Peter Schwendt [a,*], Dorota Dudášová [a], Jozef Tatiersky [a], Jaromír Marek [b]

[a] Department of Inorganic Chemistry, Faculty of Natural Sciences, Comenius University, Mlynská Dolina, 842 15 Bratislava, Slovak Republic
[b] Laboratory of Functional Genomics and Proteomics, Institute of Experimental Biology, Faculty of Sciences, Masaryk University, Kamenice 5, 625 00 Brno, Czech Republic

Received 4 September 2007; accepted 18 October 2007
Available online 26 November 2007

Abstract

The compounds $[\{VO(O_2)_2(NH_3)\}_2\{\mu\text{-}Cu(NH_3)_4\}]$ (**1**) and $[Zn(NH_3)_4][VO(O_2)_2(NH_3)]_2$ (**2**) were prepared and characterized by elemental analysis and infrared spectra. The single crystal X-ray study revealed that the structure of **1** consists of trinuclear complex molecules $[(NH_3)OV(O_2)_2\{\mu\text{-}Cu(NH_3)_4\}(O_2)_2VO(NH_3)]$ with a rare heterobimetalic peroxo bridge: copper(II)–peroxo ligand–vanadium(V). The structure of **2** is composed of tetraamminezinc(II) cations and ammineoxodiperoxovanadate(V) anions. In course of thermal decomposition of **1** performed up to 620 °C, the following intermediate products: $[Cu(NH_3)_2(VO_3)_2]$, and subsequently a mixture of V_2O_5 with monoclinic $\beta\text{-}Cu_2V_2O_7$, were gradually formed. The final product of decomposition is $Cu(VO_3)_2$. The thermal decomposition of **2** is a two-step process. In the first stage, $[Zn(NH_3)_3(VO_3)_2]$ as supposed intermediate was formed, which transformed at higher temperatures by release of ammonia molecules to the monoclinic modification of $Zn(VO_3)_2$.
© 2007 Elsevier Ltd. All rights reserved.

Keywords: Peroxovanadium complexes; Ammine complexes; X-ray structure; IR spectra; Thermal decomposition

1. Introduction

The study of interactions of the $[VO(O_2)_2(NH_3)]^-$ ions with transition metal ammine complexes is attractive from several points of view.

First, the pentagonal pyramidal diperoxovanadium(V) complexes exhibit a certain tendency towards completion of the coordination sphere to pentagonal bipyramidal. This completion proceeds in several stereochemically interesting ways, due to the different bonding interaction between the central atom and a donor atom coordinated in the axial position *trans* to the oxo ligand. These interactions range from normal covalent bonds, as it was observed in the $[VO(O_2)_2F_2]^{3-}$ ion [1], to very weak interactions of non-covalent character, e.g. of the V···O=V type [2]. These different interactions also have an influence on the spectral properties of complexes [3]. The presence of a complex cation in the structure of peroxovanadates provides further possibilities for the completion of the coordination sphere of vanadium. A similar tendency of weakly bonded atoms to occupy the axial positions is obvious for square planar complexes of Cu(II),

* Corresponding author. Tel.: +421 2 602 96 346; fax: +421 2 602 96 273.
E-mail address: schwendt@fns.uniba.sk (P. Schwendt).

0277-5387/$ - see front matter © 2007 Elsevier Ltd. All rights reserved.
doi:10.1016/j.poly.2007.10.016

and complexes with 4 + 1 or 4 + 2 coordinations are thus formed. In complexes with the 4 + 2 coordination, the axial Cu–O bonds are typically longer by several tenths of angström when compared with the equatorial bond lengths [4].

Second, the interactions between the $[VO(O_2)_2NH_3]^-$ ion and transition metal complexes provide a possibility for formation of a peroxo bridge between the vanadium atom and the other transition metal atom. The reactions based on the formation of peroxo bridges are "responsible" for catalytic properties of many important catalysts for oxygen transfer reactions [5]. Moreover, heterobimetallic peroxo-bridged complexes are extremely rare: to the best of our knowledge, only one such example is known for copper(II) (Fe(III)–O_2–Cu(II), Chart 1g).

Third, increasing attention has been recently paid to vanadium based oxide materials due to their impressive structural variability and potential applications in areas of catalysis, sorption, electrochemistry and photochemistry [7]. These oxide materials are often prepared by solid state reactions of the oxides (carbonates, sulfates and hydroxides). Thus, $Cu(VO_3)_2$ obtained by Mocala et al. [8] is a very promising material for lithium batteries [9]. The second way for preparation of these materials is the thermal decomposition of precursors. As suitable precursors, coordination compounds with molecular or anionic ligands which are easily released or decomposed on heating (e.g. H_2O, NH_3, O_2^{2-} and $C_2O_4^{2-}$) can be used. The peroxo complexes of transition metals are often used for such purposes [10,11].

In this paper, we present the results of the study of the $CuSO_4$–NH_4VO_3–NH_3–H_2O_2–H_2O and $ZnSO_4$–NH_4VO_3–NH_3–H_2O_2–H_2O–ethanol reaction systems. Two new ammine complexes were prepared and characterized, including the X-ray structure. For $[\{VO(O_2)_2(NH_3)\}_2\{\mu\text{-}Cu(NH_3)_4\}]$, the unique Cu-μ-$\eta^1$:$\eta^2$-($O_2$)–V bridge was observed.

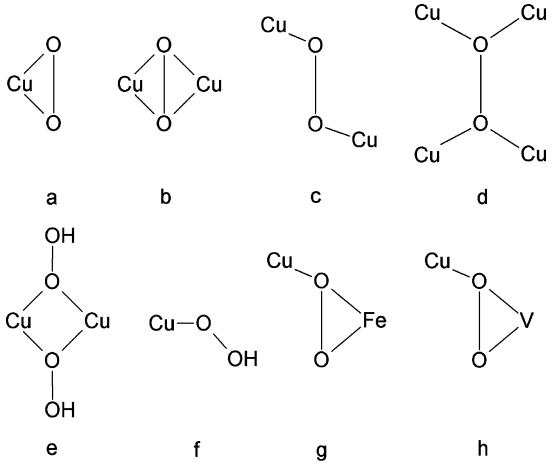


Chart 1. The copper atom–peroxo ligand coordination modes [6] (h – this work).

2. Experimental

2.1. Materials, analyses and measurements

All chemicals were of analytical grade and used as received, except for V_2O_5, which was prepared by thermal decomposition (at 500 °C) of previously purified NH_4VO_3. Vanadium(V) was determined by titration with aqueous solution of $FeSO_4$ in presence of H_3PO_4 and diphenylamine as indicator in a sample previously heated to decompose the peroxidic oxygen. The peroxide content was determined by potentiometric titration with an aqueous solution of $KMnO_4$ in presence of H_2SO_4. Nitrogen was determined on a CHN analyzer 1106 (Carlo Erba).

The IR spectra in nujol mulls were recorded on a FT IR Nicolet Magna 750 spectrometer. The thermal analysis and interrupted thermal treatment were accomplished on a Derivatograph Q 1500 D (MOM, Hungary). The experimental parameters: air atmosphere, sample mass 100 mg, heating rate 10 °C min^{-1}, Pt crucible. The temperature intervals were 20–450 °C for **1** and 20–550 °C for **2**. The mixture of β-$Cu_2V_2O_7$ and V_2O_5, obtained as decomposition product of **1** at 450 °C was annealed at 620 °C for 2 h to induce the mutual reaction of the components. The X-ray powder diffraction patterns were obtained on a Philips PW 1050 diffractometer using Cu Kα radiation.

The single crystal diffraction data were collected with a KM4 CCD four-circle diffractometer with an area-detector (KUMA Diffraction, Poland), and equipped with an Oxford Cryostream Cooler (Oxford Cryosystems, UK). Mo Kα radiation ($\lambda = 0.71073$ Å, monochromator Enhance, Oxford Diffraction, UK) was used in all measurements. The ω scan technique with different κ and φ offsets for covering a whole independent part of reflections in the 2–25° θ range was performed. The cell parameters were refined from all strong reflections. The data reductions were carried out using the CRYSALIS RED (Oxford Diffraction, UK) program. The structures were determined by SHELXS-97 [12] and refined by SHELXL-97, [13] the data for publication were prepared by SHELXL and PARST [14] and the figures by DIAMOND [15]. All H atoms were located in a difference map and refined as riding, with d(N–H) = 0.91 Å, and with U_{iso}(H) = 1.5U_{eq}(N). The crystal data and refinement details are given in Table 1.

2.2. Syntheses

2.2.1. Preparation of $[\{VO(O_2)_2(NH_3)\}_2\{\mu\text{-}Cu(NH_3)_4\}]$ (1)

$CuSO_4$ (0.200 g; 1.25 mmol) was dissolved in aqueous solution of NH_3 (15.0 ml; $w = 25\%$; 200 mmol) and the solution of H_2O_2 (0.50 ml; $w = 30\%$; 5.0 mmol) was added. In the obtained solution, NH_4VO_3 (0.290 g; 2.48 mmol) was dissolved. The resulting solution was cooled in an ice bath, and H_2O_2 (2.0 ml; $w = 30\%$; 20 mmol) was dropwise added. The obtained blue solution was stored at −5 °C. The dark blue crystals formed were isolated after 24 h,

Table 1
Crystallographic data and refinement details for [{$VO(O_2)_2(NH_3)$}$_2$-{μ-$Cu(NH_3)_4$}] (**1**) and $[Zn(NH_3)_4][VO(O_2)_2(NH_3)]_2$ (**2**)

	(**1**)	(**2**)
CSD entry number	417860	417861
Empirical formula	$H_{18}CuN_6O_{10}V_2$	$H_{18}N_6O_{10}V_2Zn$
M_r	427.62	429.45
Crystal	dark blue prism	yellow plate like
Crystal size (mm)	$0.40 \times 0.35 \times 0.30$	$0.50 \times 0.45 \times 0.40$
Crystal system	triclinic	monoclinic
Space group	$P\bar{1}$ (no. 2)	$P2_1/n$ (no. 14)
a (Å)	7.1281(12)	7.7135(5)
b (Å)	7.4249(11)	12.1428(8)
c (Å)	7.5267(11)	14.5206(10)
α (°)	61.425(15)	90
β (°)	75.224(13)	93.242(6)
γ (°)	73.171(14)	90
Volume (Å^3)	331.61(10)	1357.87(16)
Z	1	4
T (K)	110(2)	120(2)
D_{calc} (g/cm^3)	2.141	2.101
μ (mm^{-1})	3.026	3.156
Reflections collected	1905	7544
Reflections unique [R(int)]	1151 [0.0666]	2378 [0.0558]
Goodness-of-fit on F^2	1.117	1.028
R_1 [$I > 2\sigma(I)$][a]	0.0287	0.0271
wR_2 [$I > 2\sigma(I)$][b]	0.0793[c]	0.0689[d]
R_1 (all data)	0.0299	0.0295
wR_2 (all data)	0.0802[c]	0.0703[d]
F(000)	215	864

[a] $R = \Sigma(|F_o| - |F_c|)/\Sigma|F_o|$.
[b] $wR_2 = [\Sigma w(|F_o| - |F_c|)^2/\Sigma(F_o)^2]^{1/2}$.
[c] $w = 1/[\sigma^2(F_o) + (0.05P)^2 + 0.2P]$.
[d] $w = 1/[\sigma^2(F_o) + (0.0375P)^2 + 2.0P]$, $P = (F_o^2 - 2F_c)^2/3$.

washed with ethanol and dried at 5 °C. *Anal.* Calc. for $H_{18}CuN_6O_{10}V_2$: N, 19.7; O_2^{2-}, 29.9; V, 23.8. Found: N, 18.8; O_2^{2-}, 28.2; V, 23.4%. The analyses are not satisfactory due to the instability of the compound. IR (cm^{-1}): 3556 sh, 3330 vs, 3223 s, 3178 vs, 3096 vs ($\nu_{as} + \nu_s(NH_3)$); 1647 m, 1616 s, 1589 s ($\delta_{as}(NH_3)$); 1253 s, 1225 vs, 1210 vs ($\delta_s(NH_3)$); 946 vs (ν(V=O)); 874 vs ($\nu(O_p–O_p)$); 781 s ($\rho_r(NH_3)$); 640 vs, 613 vs, 524 m, 500 m ($\nu(V–O_p)$); 451 vw, 428 w ($\nu(M–N)$, M = V, Cu).

2.2.2. Preparation of $[Zn(NH_3)_4][VO(O_2)_2(NH_3)]_2$ (2)

NH_4VO_3 (0.580 g; 5.00 mmol) was added to an aqueous solution of NH_3 (30 ml; w = 25%; 400 mmol) and the mixture was stirred for 30 min. $ZnSO_4 \cdot 7H_2O$ (2.15 g; 7.50 mmol) was then added and dissolved. To the solution obtained, H_2O_2 (5.0 ml; w = 30%; 50 mmol) was dropwise added. The green solution formed was cooled for 5 min at −30 °C and stored at −5 °C. Within 45 min, the colour of the solution changed to yellow. After 48 h, ethanol (10 ml, φ = 96%) was added. Yellow crystalline products was isolated after 24 h, washed with ethanol and dried at 5 °C. *Anal.* Calc. for $H_{18}N_6O_{10}V_2Zn$: N, 19.6; O_2^{2-}, 29.8; V, 23.7. Found: N, 19.5; O_2^{2-}, 29.8; V, 23.5%. IR: 3553 sh, 3318 s, 3223 s, 3157 vs ($\nu_{as} + \nu_s(NH_3)$); 1615 s, 1597 sh ($\delta_{as}(NH_3)$); 1252 vs, 1242 vs, 1225 s ($\delta_s(NH_3)$); 990 vs, 975 vs (ν(V=O)); 881 vs ($\nu(O_p–O_p)$); 740 s ($\rho_r(NH_3)$); 631 vs, 612 vs, 529 m, 496 m ($\nu(V–O_p)$); 449 vw, 416 w ($\nu(M–N)$, M = V, Zn).

2.2.3. Hydrothermal synthesis of $[Cu(NH_3)_2(VO_3)_2]$ (3)

The compound $[Cu(NH_3)_2(VO_3)_2]$ (**3**) was previously prepared by heating of a mixture of NH_4VO_3–Cu–H_2O at 50 °C for six weeks, and also structurally characterized [16]. We describe here its synthesis by hydrothermal method.

NH_4VO_3 (0.190 g; 1.62 mmol), $CuSO_4$ (0.130 g; 0.814 mmol) and a solution of NH_3 (5.0 ml; w = 25%; 66 mmol) were mixed, placed to a teflon container and heated at 120 °C under autogeneous pressure for 3 days. After cooling to the room temperature, dark green crystals were isolated, washed and dried at room temperature. *Anal.* Calc. for $CuH_6N_2O_6V_2$: N, 9.5. Found: N, 9.4%. IR: 3332 s, 3253 s, 3163 s ($\nu_{as} + \nu_s(NH_3)$); 1597 s ($\delta_{as}(NH_3)$); 1226 vs ($\delta_s(NH_3)$); 969 vs, 937 s (ν(V=O)); 897 vs, 853 vs, 684 b (ν(V–O–V)); 554 s, 469 m ($\nu(M–N)$, M = V, Cu). The X-ray diffraction pattern of **3** corresponds to the pattern calculated from the structure [16].

3. Results and discussion

3.1. Synthesis

Compounds **1** and **2** were prepared by crystallization from the NH_4VO_3–MSO_4–NH_3–H_2O_2–H_2O–(ethanol) systems (M = Cu, Zn). It is recommended to follow exactly the given preparation procedure as under changed conditions, different products, mainly $NH_4[VO(O_2)_2(NH_3)]$, can crystallize out.

Compound **3** was obtained by hydrothermal reaction and also by interrupted thermal decomposition (*vide infra*). While compounds **2** and **3** are stable at room temperature, the crystals of **1** undergo weathering accompanied by their destruction.

3.2. Crystal structures

Despite the similar composition, compounds **1** and **2** possess significantly different structures.

The crystal structure of **1** consists of trinuclear [(NH_3)O-$V(O_2)_2${μ-$Cu(NH_3)_4$}$(O_2)_2VO(NH_3)$] complex molecules with a C_i symmetry. The copper(II) atom is octahedrally coordinated by four ammonia molecules in the equatorial positions and two peroxo oxygen atoms originating from the $[VO(O_2)_2(NH_3)]^-$ anions in axial positions (Fig. 1): the Cu1–O5 bond length (2.484 Å) can be considered as a normal one for the 4 + 2 coordination of the copper atom [4,17]. All other bond lengths are within the expected intervals. The geometry of the $[VO(O_2)_2(NH_3)]^-$ ion is pentagonal pyramidal: the four peroxo oxygen atoms and the nitrogen atom form the base of the distorted pyramid and the oxygen atom of the V=O moiety occupies the apical position. The structure of this ion is similar to the structure of the $[VO(O_2)_2(NH_3)]^-$ ion in $NH_4[VO(O_2)_2(NH_3)]$

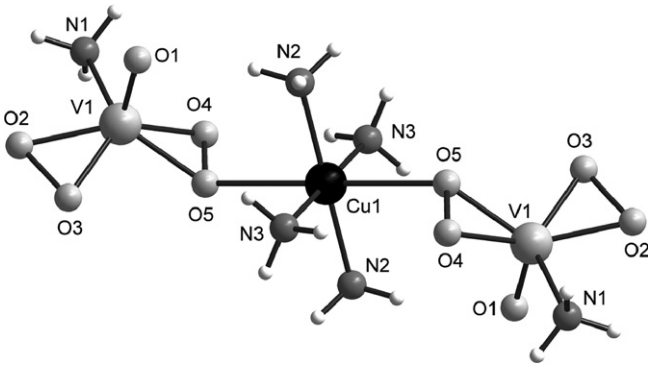


Fig. 1. Molecular structure of **1**. Selected interatomic distances (Å) and angles (°): Cu(1)–N(2) 2.0255(19), Cu(1)–N(3) 2.0269(19), Cu(1)–O(5) 2.4839(14), V(1)–O(1) 1.6227(17), V(1)–O(3) 1.8798(16), V(1)–O(4) 1.8937(17), V(1)–O(5) 1.8948(17), V(1)–O(2) 1.8950(18), V(1)–N(1) 2.1017(19), O(2)–O(3) 1.483(2), O(4)–O(5) 1.476(2), N(2)–Cu(1)–N(3) 90.26(8), O(1)–V(1)–O(3) 107.35(8), O(1)–V(1)–O(4) 107.30(8), O(1)–V(1)–O(5) 103.22(8), O(1)–V(1)–O(2) 105.83(9), O(1)–V(1)–N(1) 94.17(8).

[18]. The vanadium atom is considerably displaced by 0.4475(4) Å from the pentagonal plane towards the oxo ligand. The supramolecular 3D structure of **1** is formed by four types of hydrogen bonds formed between the molecules of $[\{VO(O_2)_2(NH_3)\}_2\{\mu\text{-}Cu(NH_3)_4\}]$: N1–H···O2*, N1–H···O5*, N2–H···O3*, N3–H···O3*; *d*(N···O): 2.789–3.034 Å (* denotes symmetry equivalent atoms).

The crystal structure of **2** consists of slightly distorted tetrahedral $[Zn(NH_3)_4]^{2+}$ cations and two crystallographically independent $[VO(O_2)_2(NH_3)]^-$ anions with an approximate C_s symmetry (Fig. 2).

The structure of the $[VO(O_2)_2(NH_3)]^-$ ion is similar to that found in the structure of **1**; the deviations of the vanadium atoms from the pentagonal plane are: 0.5077(5) (for V1) and 0.5218(4) (for V2) Å. The anions are arranged into chains of two types, A and B, oriented along the *a*-axis (Fig. 3).

The chain A is constructed by anions of the first crystallographic type (V1) and consists of pairs of antiparallely oriented anions. These anions form hydrogen bonds between the atoms N1 and O2* ($d(N1\cdots O2^*) = 2.896$ Å) and a weak contacts between the atoms V1 and O3* in axial position ($d(V1\cdots O3^*) = 3.245$ Å) (Fig. 4). Though very weak, they give an evidence for a tendency of the vanadium atom to complete its coordination sphere [19]. The pairs of anions are mutually connected into chains by hydrogen bonds between the N1 and O5* (peroxo) atoms ($d(N1\cdots O5^*) = 3.079$ Å) (Fig. 4).

In the chain B, the anions of the second type (V2) have an antiparallel orientation too. A very weak axial interaction in which the oxo ligands from the anions of the first type are involved, ($d(V2\cdots O1(V1)) = 3.565$ Å), can be recognized. The hydrogen bonds between the O9 and N6* atoms ($d(O9\cdots N6^*) = 2.972$ Å), respectively, O11 and N6* ($d(O11\cdots N6^*) = 2.931$ Å) connect the anions into a zig-zag chain (Fig. 5). The whole crystal structure is also stabilized by numerous hydrogen bonds between the chains and $[Zn(NH_3)_4]^{2+}$ cations.

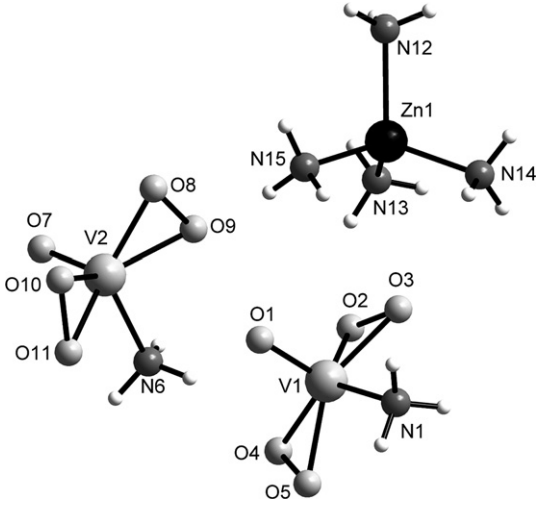


Fig. 2. Part of the crystal structure of **2**. Selected interatomic distances (Å) and angles (°): V(1)–O(1) 1.6003(19), V(1)–O(2) 1.8698(19), V(1)–O(3) 1.8847(18), V(1)–O(5) 1.8995(18), V(1)–O(4) 1.9079(19), V(1)–N(1) 2.102(2), V(2)–O(7) 1.5993(19), V(2)–O(9) 1.8698(19), V(2)–O(11) 1.8748(19), V(2)–O(8) 1.875(2), V(2)–O(10) 1.8947(19), V(2)–N(6) 2.094(2), O(2)–O(3) 1.473(3), O(4)–O(5) 1.478(2), O(8)–O(9) 1.457(3), O(10)–O(11) 1.472(3), Zn(1)–N(13) 1.996(2), Zn(1)–N(15) 2.024(2), O(1)–V(1)–O(2) 108.37(9), O(1)–V(1)–O(3) 106.90(10), O(1)–V(1)–O(5) 107.20(9), O(1)–V(1)–O(4) 104.22(9), O(1)–V(1)–N(1) 99.90(10), O(7)–V(2)–O(9) 108.53(10), O(7)–V(2)–O(11) 109.32(10), O(7)–V(2)–O(8) 106.04(10), O(7)–V(2)–O(10) 106.53(10), O(7)–V(2)–N(6) 98.24(10), N(13)–Zn(1)–N(15) 117.24(10).

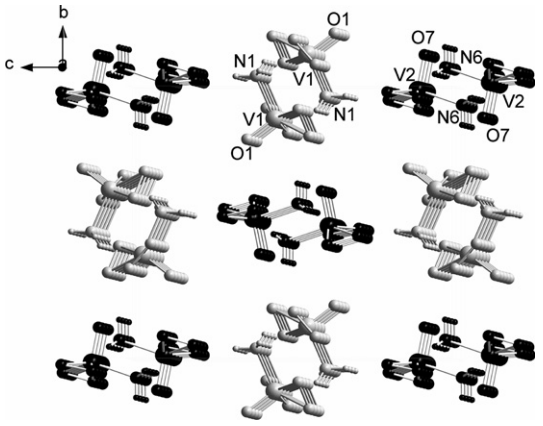


Fig. 3. Packing of the anionic chains along the *a*-axis in the crystal structure of **2** (in grey or black two crystallographically different types of anions).

3.3. IR spectra and thermal analysis

The IR spectrum of compound **1** (see Section 2 and Fig. 6a) exhibits the characteristic bands of coordinated ammonia molecules but the vibrations corresponding to the Cu–NH_3 or to the V–NH_3 groups cannot be distinguished [20]. The intensive splitting of these bands is in accordance with the three different *M*–NH_3 bond lengths in the unit cell (Fig. 1). The bands assigned to the $VO(O_2)_2$ group are similar to those observed for $NH_4[VO(O_2)_2(NH_3)]$ [21].

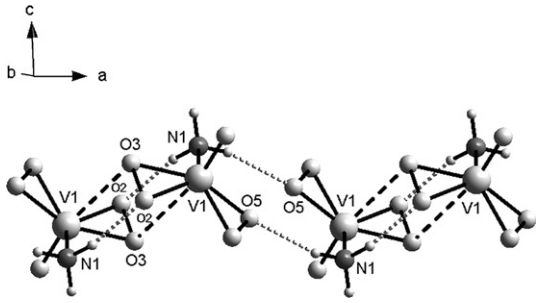


Fig. 4. Representations of pairs of anions in the chain A in the crystal structure of **2**.

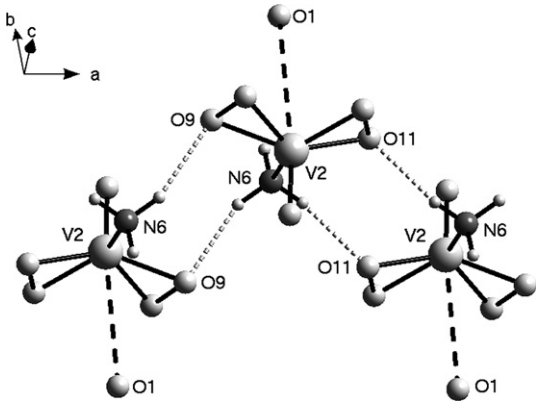


Fig. 5. The chain B in the crystal structure of **2**.

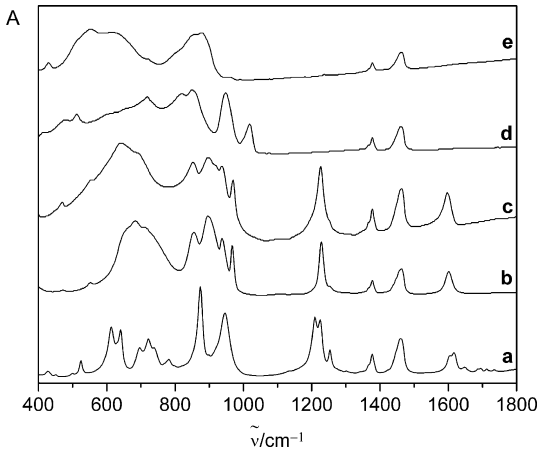


Fig. 6. IR spectra of: (a) **1**; (b) intermediate product obtained by interruption of thermal decomposition of **1** at 150 °C; (c) **3**; (d) intermediate product obtained by interruption of thermal decomposition of **1** at 450 °C and (e) final product of thermal decomposition of **1** at 625 °C.

The thermal decomposition of compound **1** is a two-step process: the individual steps are separated by distinct plateau (Fig. 7).

The first step on the TG curve (20–200 °C) can be described by Eq. (I) (calc. mass loss 30.9, found 30.0%):

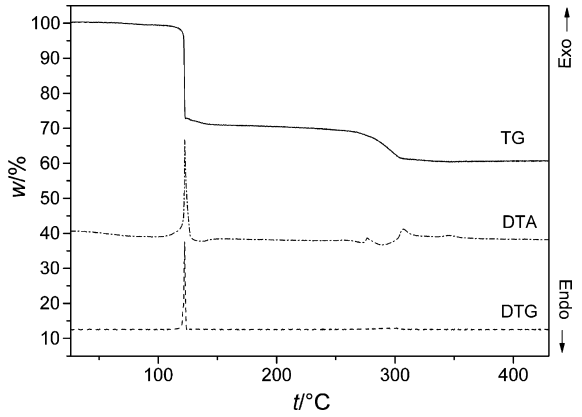


Fig. 7. Thermoanalytical curves of **1**.

$$[\{VO(O_2)_2(NH_3)\}_2\{\mu\text{-}Cu(NH_3)_4\}] \xrightarrow{\Delta t} [Cu(NH_3)_2(VO_3)_2] + 4NH_3 + 2O_2 \quad (I)$$

This reaction is expressed on the DTA curve by the strong exothermic peak at 126 °C. The X-ray powder pattern (Fig. 8c) and the IR spectrum of the product obtained by interruption of thermal decomposition at 150 °C (Fig. 6b) fully correspond to the X-ray powder pattern (Fig. 8b), and the IR spectrum of the hydrothermally prepared compound **3** (Fig. 6c). The IR spectrum of **3** exhibits all characteristic bands of the coordinated ammonia molecule. The broad band at 684 cm^{-1}, which can be assigned to ν_{as}(VOV), gives evidence of a polymeric character of compound **3** [22].

In the second step of decomposition (200–450 °C) accompanied by two exothermic effects on the DTA curve at 269 and 300 °C, the ammonia molecules are released (Eq. II).

$$2[Cu(NH_3)_2(VO_3)_2] \xrightarrow{\Delta t} Cu_2V_2O_7 + V_2O_5 + 4NH_3 \quad (II)$$

This process is manifested by disappearance of IR bands corresponding to the vibrations of the M–NH_3 groups (Fig. 6d). As can be seen from the X-ray powder diffraction

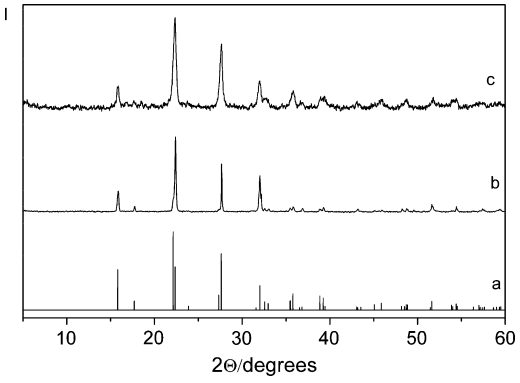


Fig. 8. X-ray powder diffraction patterns: (a) $[Cu(NH_3)_2(VO_3)_2]$ – pattern according the data in Ref. [16]; (b) **3**; (c) intermediate product obtained by interruption of thermal decomposition of **1** at 150 °C.

patterns, the product obtained at 450 °C is a mixture of V_2O_5 and monoclinic β-$Cu_2V_2O_7$ (Fig. 9a–c).

This mixture was annealed for two hours at 620 °C to prepare pure triclinic $Cu(VO_3)_2$ as the only product (Eq. III):

$$Cu_2V_2O_7 + V_2O_5 \xrightarrow{\Delta t} 2Cu(VO_3)_2 \quad \text{(III)}$$

The X-ray diffraction pattern of the annealed product (Fig. 9d) is fully in accordance with the published data on $Cu(VO_3)_2$ [8,9,23].

The IR spectrum of compound **2** exhibits bands which can be assigned to the vibrations of the M–NH_3 (M = Zn, V) and $VO(O_2)_2$ groups (Section 2 and Fig. 10a).

In the first step of thermal decomposition of compound **2** (20–170 °C, Fig. 11), three molecules of ammonia and two molecules of oxygen are released (calc. mass loss 26.8, found 27.2%) and an intermediate with proposed composition $[Zn(NH_3)_3(VO_3)_2]$ is formed (Eq. IV):

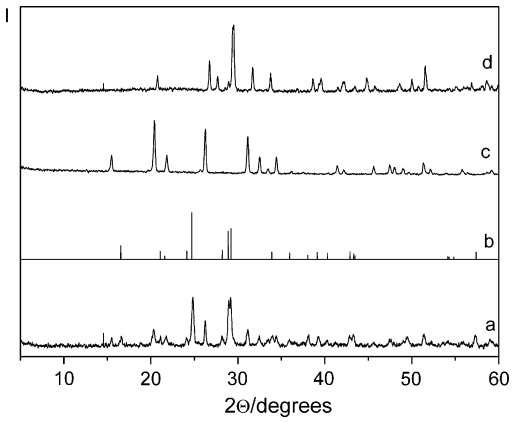


Fig. 9. X-ray powder diffraction patterns: (a) intermediate product obtained by interruption of thermal decomposition of **1** at 450 °C; (b) β-$Cu_2V_2O_7$ – pattern according the data in Ref. [24]; (c) V_2O_5; (d) $Cu(VO_3)_2$ obtained by annealing the mixture of β-$Cu_2V_2O_7$ and V_2O_5 at 620 °C.

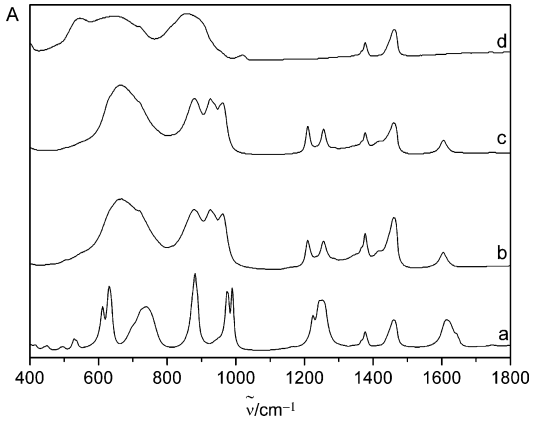


Fig. 10. IR spectra of: (a) **2**; (b) intermediate product obtained by interruption of thermal decomposition of **2** at 130 °C; (c) at 170 °C and (d) at 550 °C.

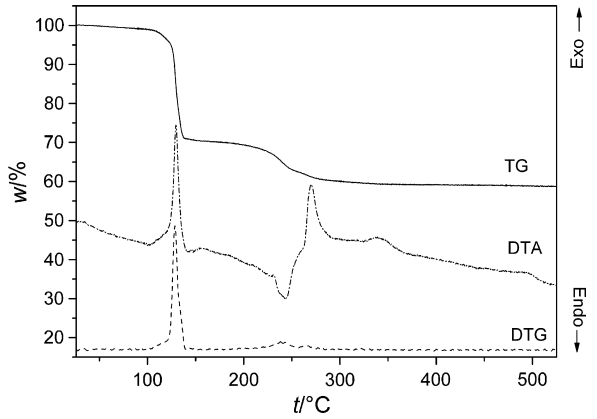


Fig. 11. Thermoanalytical curves of **2**.

$$[Zn(NH_3)_4][VO(O_2)_2(NH_3)]_2 \xrightarrow{\Delta t} [Zn(NH_3)_3(VO_3)_2] + 3NH_3 + 2O_2 \quad \text{(IV)}$$

This process is manifested on the DTA curve by the strong exothermic peak at 126 °C. The X-ray powder diffraction patterns of the decomposition products obtained at 130 and 170 °C and their IR spectra are identical (Figs. 12a and b and 10b and c). The IR spectra exhibit bands corresponding to vibrations of two differently bonded ammine ligands (see e.g. bands corresponding to $\delta_s(NH_3)$ at 1256 and 1210 cm^{-1}). The broad band at 665 cm^{-1}, which can be assigned to ν_{as}(VOV) and which is typical for the $(VO_3)_n^{n-}$ chains [22], may be considered as an evidence for a polymeric structure of the intermediate.

The unusual stoichiometry of $[Zn(NH_3)_3(VO_3)_2]$ raises questions about the structure of this compound. Unfortunately, our attempts to prepare crystals of this compound under hydrothermal conditions were unsuccessful.

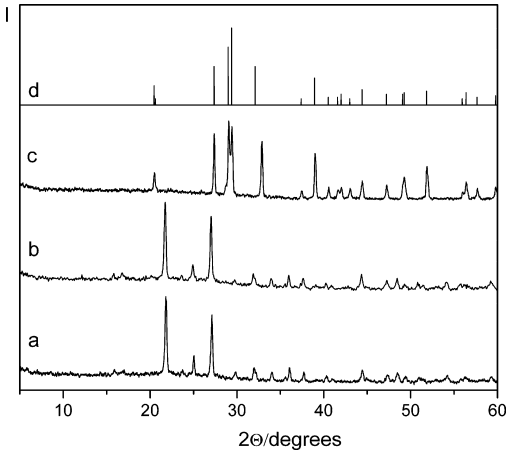


Fig. 12. X-ray powder diffraction patterns: (a) intermediate product obtained by interruption of thermal decomposition of **2** at 130 °C; (b) at 170 °C; (c) at 550 °C; (d) monoclinic $Zn(VO_3)_2$ – pattern according the data in Ref. [25].

The second step of thermal decomposition of **2** (170–550 °C) is described by Eq. (V) (calc. mass loss 11.9, found 10.9%):

$$[Zn(NH_3)_3(VO_3)_2] \xrightarrow{\Delta t} Zn(VO_3)_2 + 3NH_3 \quad (V)$$

On the DTA curve, this process is expressed by the endothermic effect at 236 °C and ensuing exothermic peak at 262 °C. The exothermic peak at 350 °C is not accompanied by any mass loss and corresponds probably to a phase transition. The X-ray diffraction pattern of the final product obtained at 550 °C (Fig. 12c) corresponds to the diffraction pattern of monoclinic modification of $Zn(VO_3)_2$ (Fig. 12d). The IR spectrum of this compound (Fig. 10d) exhibits characteristic bands of polymeric metavanadate chain [22].

Acknowledgements

This work was supported by the Ministry of Education of the Slovak Republic (Grant VEGA 1/4462/07), Comenius University in Bratislava (Grant No. UK/144/2006) and the Ministry of Education of the Czech Republic (Grant MSM0021622415).

Appendix A. Supplementary material

Further details of the crystal structure investigations may be obtained from Fachinformationszentrum Karlsruhe, 76344 Eggenstein-Leopoldshafen, Germany (fax: +49 7247 808 666; e-mail: crysdata@fiz-karlsruhe.de, http://www.fiz-karlsruhe.de/ecid/Internet/en/DB/icsd/depot_anforderung.html), on quoting the deposition number CSD-417860 for $H_{18}CuN_6O_{10}V_2$ and CSD-417861 for $H_{18}N_6O_{10}V_2Zn$. Supplementary data associated with this article can be found, in the online version, at doi:10.1016/j.poly.2007.10.016.

References

[1] R. Stomberg, Acta Chem. Scand. A 38 (1984) 541.
[2] R. Stomberg, S. Olson, Acta Chem. Scand. A 38 (1984) 801.
[3] P. Schwendt, J. Tyršelová, F. Pavelčík, Inorg. Chem. 34 (1995) 1964.
[4] F.A. Cotton, G. Wilkinson, C.A. Murillo, M. Bochmann, Advanced Inorganic Chemistry, John Wiley and Sons, New York, 1999, p. 865.
[5] J.M. Bregeault, M. Vennat, L. Salles, J.I. Piquemal, I. Mahha, E. Briot, P.C. Bakala, A. Atlamsani, R. Thouvenot, J. Mol. Catal. A – Chem. 250 (2006) 177.
[6] (a) A.M. Reynolds, B.F. Gherman, C.J. Cramer, W.B. Tolman, Inorg. Chem. 44 (2005) 6989;
(b) M. Kodera, Y. Kajita, Y. Tachi, K. Katayama, K. Kano, S. Hirota, S. Fujinami, M. Suzuki, Angew. Chem., Int. Ed. 43 (2004) 334;
(c) K. Komiyama, H. Furutachi, S. Nagatomo, A. Hashimoto, H. Hayashi, S. Fujinami, M. Suzuki, T. Kitagawa, Bull. Chem. Soc. Jpn. 77 (2004) 59;
(d) F. Meyer, H. Pritzkow, Angew. Chem., Int. Ed. 39 (2000) 2112;
(e) K. Itoh, H. Hayashi, H. Furutachi, T. Matsumoto, S. Nagatomo, T. Tosha, S. Terada, S. Fujinami, M. Suzuki, T. Kitagawa, J. Am. Chem. Soc. 127 (2005) 5212;
(f) A. Wada, M. Harata, K. Hasegawa, K. Jitsukawa, H. Masuda, M. Mukai, T. Kitagawa, H. Einaga, Angew. Chem., Int. Ed. 37 (1998) 798;
(g) T. Chishiro, Y. Shimazaki, F. Tani, Y. Tachi, Y. Naruta, S. Karasawa, S. Hayami, Y. Maeda, Angew. Chem., Int. Ed. 42 (2003) 2788.
[7] D.J. Hagrman, R.C. Finn, J. Zubieta, Solid State Sci. 3 (2001) 745.
[8] K. Mocala, J. Ziolkowski, J. Solid State Chem. 69 (1987) 299.
[9] (a) X. Cao, J. Xie, H. Zhan, Y. Zhou, Mater. Chem. Phys. 98 (2006) 71;
(b) K. Nanjundaswamy, T. Bofinger, I. Chi, G. Cintra, Lithium cell with improved cathode, United States Patent 7045249.
[10] D. Bayot, B. Tinant, M. Devillers, Inorg. Chem. 43 (2004) 5999.
[11] D. Bayot, B. Tinant, M. Devillers, Catal. Today 78 (2003) 437.
[12] G.M. Sheldrick, SHELXS-97, Program for crystal structure determination, University of Göttingen, Germany, 1997.
[13] G.M. Sheldrick, SHELXL-97, Program for crystal structure refinement, University of Göttingen, Germany, 1997.
[14] M. Nardelli, J. Appl. Cryst. 28 (1995) 659, Release 1999.
[15] DIAMOND, Version 3.1d, Crystal Impact, Postfach 1251, 53002 Bonn, Germany, http://www.crystalimpact.com/diamond.
[16] S. Aschwanden, H.W. Schmalle, A. Reller, H.R. Oswald, Mater. Res. Bull. 28 (1993) 45.
[17] (a) T. Dorn, A.-C. Chamayov, C. Janiak, New J. Chem. 30 (2006) 156;
(b) K. Prout, V.S.B. Mtetwa, F.J.C. Rossotti, Acta Crystallogr., Sect. B 49 (1993) 73;
(c) A.N. Chekhlov, A.I. Yurtanov, I.V. Martynov, Koord. Khim. (Russ.) (Coord. Chem.) 13 (1987) 1541.
[18] R.E. Drew, F.W.B. Einstein, Inorg. Chem. 11 (1972) 1079.
[19] J. Chrappová, P. Schwendt, J. Marek, J. Fluorine Chem. 126 (2005) 1297, and citations therein.
[20] K. Nakamoto, Infrared and Raman spectra of Inorganic and Coordination Compounds, John Wiley and Sons, New York, 1986, p. 192.
[21] P. Schwendt, M. Pisarčík, Collect. Czech. Chem. Commun. 47 (1982) 1549.
[22] (a) D. Joniaková, R. Gyepes, E. Rakovský, P. Schwendt, L'. Žúrková, J. Marek, Z. Mička, Polyhedron 25 (2006) 2491;
(b) R. Kucsera, D. Joniaková, L'. Žúrková, J. Therm. Anal. Calorim. 78 (2004) 263;
(c) L'. Žúrková, J. Tatiersky, P. Fejdi, Monatsh. Chem. 129 (1998) 577;
(d) V. Suchá, M. Sivák, Monatsh. Chem. 127 (1996) 1.
[23] JCPDS card 30-0513.
[24] JCPDS card 73-1032.
[25] JCPDS card 23-757.

Available online at www.sciencedirect.com
ScienceDirect
Polyhedron 27 (2008) 648–654
POLYHEDRON
www.elsevier.com/locate/poly

Synthesis and characterization of three Cd(II) Schiff-base macrocyclic N_3O_2 complexes

Hassan Keypour [a,*], Reza Azadbakht [a], Hamidreza Khavasi [b]

[a] Faculty of Chemistry, Bu-ali Sina University, Hamadan, Iran
[b] Department of Chemistry, Shahid beheshti University, Tehran, Iran

Received 5 June 2007; accepted 25 October 2007

Abstract

Three polyamine ligands of N1-(2-nitrobenzyl)-N1-(2-aminoethyl)ethane-1,2-diamine (L_1), N1-(2-nitrobenzyl)-N1-(2-aminoethyl)-propane-1,3-diamine (L_2) and N1-(2-nitrobenzyl)-N1-(3-aminopropyl)propane-1,3-diamine (L_3) were synthesized and their cyclocondensation with 2-[2-(2-formyl phenoxy)ethoxy]benzaldehyde (L_4) in the presence of various metal(II) ions was examined. These reactions only in the presence of a stoichiometric amount of cadmium(II) nitrate gave the related cadmium(II) macrocyclic Schiff-base complexes. In all the other cases no cyclic complexes have been obtained and metal(II) polyamines were the only products. The complexes have been studied with IR, ^{1}H NMR, ^{13}C NMR, DEPT, COSY, HMQC and microanalysis. The crystal structures of $[Cd(NO_3)(L_5)$-$(\mu$-$NO_3)Cd(NO_3)(L_5)]0.5Cd(NO_3)_4$ (**1**) and $[CdL_5(NO_3)(CH_3OH)]ClO_4$ (**2**) have been also determined.
© 2007 Elsevier Ltd. All rights reserved.

Keywords: Macrocyclic complexes; Schiff-base; Crystal structure; NMR spectroscopy

1. Introduction

Macrocyclic Schiff-base complexes have attracted much attention since the early 1980s, and several reviews covering this area of research have appeared [1–7]. Template Schiff-base condensations between dicarbonyl compounds and diamines are among the simplest and most popular methods for macrocycle synthesis. The size and preferred coordination geometry of the metal ion control the structure of the condensation products [8,9]. We have been interested during the last three decades in the design and synthesis of a range of amines, both for their own intrinsic interest and also because of the possibilities of extending them by the formation of open-chain and macrocyclic Schiff-bases complexes [10]. We have developed a general method for synthesis of [1 + 1] macrocyclic complexes with a single or double alkylamine pendant arm via cyclocondensation of 2,6-diacetalpyridine with appropriate polyamines in the presence of the required metal ions. This allows the preparation of new macrocyclic complexes having one or two 2-aminoethyl pendant arms [11,13–15]. As an extension of this idea, in this work we have synthesized three new Cd(II) macrocyclic complexes by the metal ion templated [1 + 1] cyclocondensation of 2-[2-(2-formyl phenoxy)ethoxy]benzaldehyde (L_4) instead of 2,6-diacetylpyridine and different newly prepared polyamines (L_1, L_2 and L_3). The main purpose of the present work is to study the effect of addition of the 2-nitrobenzyl arm on the formation of macrocycles and their corresponding metal complexes. However, in the presence of the 2-nitrobenzyl arm and in the absence of metal ion, ring closure does not occur. In the presence of metal ions only Cd(II) was effective as a template and attempts for synthesizing the macrocycle using some other metal ions such as Mn(II), Cu(II), Ni(II), Zn(II) and Hg(II) were unsuccessful.

* Corresponding author. Tel.: +98 811 8272044; fax: +98 811 8272404.
E-mail address: keypour@basu.ac.ir (H. Keypour).

0277-5387/$ - see front matter © 2007 Elsevier Ltd. All rights reserved.
doi:10.1016/j.poly.2007.10.029

2. Experimental

2.1. Starting materials

All solvents were of reagent grade quality and purchased commercially. N-(2-aminoethyl)ethane-1,2-diamine, N-(2-aminoethyl)propane-1,3-diamine, N-(3-aminopropyl)propane-1,3-diamine and 2-nitrobenzylcholoride were obtained from Merck and were used without further purification.

2.2. Instrumentation

NMR spectra were obtained using a Bruker A V 300 MHz spectrometer. Infrared spectra were recorded in KBr pellets using a BIO-RAD FTS-40A spectrophotometer (4000–400 cm^{-1}).

2.3. X-ray crystal structure determination

Vapour diffusion of ether into a solution of $[Cd(NO_3)(L_5)(\mu\text{-}NO_3)Cd(NO_3)(L_5)]0.5Cd(NO_3)_4$ in acetonitrile and $[CdL_5(NO_3)(CH_3OH)]ClO_4$ in methanol afforded pale yellow crystalline needles. X-ray data were measured on a STOE IPDS-II two circle diffractometer, using graphite-monochromated Mo Kα X-ray radiation ($\lambda = 0.7107$ nm). Other crystallographic data are summarized in Table 1.

2.4. Synthesis

2.4.1. Ligand synthesis

*2.4.1.1. N1-(2-nitrobenzyl)-N1-(2-aminoethyl)ethane-1,2-diamine threehydrochloride (**I**).* 2,2′-Diphthalimidodiethylamine (3.63 g, 10 mmol) [12] and 2-nitrobenzylcholoride (2 g, 12 mmol) and potassium carbonate (1.38, 10 mmole) were fused together at 160 °C with constant stirring for 1 h. The resulting solid was pulverized and stirred in boiling 1:3 ethanol–water for about 20 min. The insoluble materials were filtered off and then heated under reflux with HCl (200 cm^3, 25%w/w) for 12 h. The phthalic acid which formed on cooling was removed by filtration, and the filtrate was evaporated to small bulk and poured into absolute EtOH. The residue was washed several times with small amounts of cooled absolute EtOH, and dried in vacuo; Yield (70%) [16], Scheme 1.

Anal. Calc. for $C_{11}H_{21}Cl_3N_4O_2$: C, 38.00; H, 6.09; N, 16.11. Found: C, 38.22; H, 6.23; N, 16.31%. IR (KBr, cm^{-1}) 1343, 1527 $\nu(NO_2)$, 2710–3428 $\nu(NH_3Cl)$; ^1H NMR δ_H (D_2O, ppm) 3.57 (m, 8H), 4.48 (s, 2H), 7.84 (m, 3H), 8.26 (d, 1H); ^{13}C NMR δ_C (D_2O, ppm) 33.82, 50.13, 56.76, 123.67, 126.50, 132.32, 135.03, 135.51, 147.91.

*2.4.1.2. N1-(2-nitrobenzyl)-N1-(2-aminoethyl)propane-1,3-diamine threehydrochloride (**II**) and N1-(2-nitrobenzyl)-N1-(3-aminopropyl)propane-1,3-diamine threehydrochloride (**III**).* The compounds (**II**) and (**III**) can be readily prepared by the above procedure except using 2,3′-diphthalimidoethylpropylamine (3.77 g, 10 mmol) and/or 3,3′-diphthalimidodipropylamine (3.91 g, 10 mmol) instead of 2,2′-diphthalimidodiethylamine (3.63 g, 10 mmol).

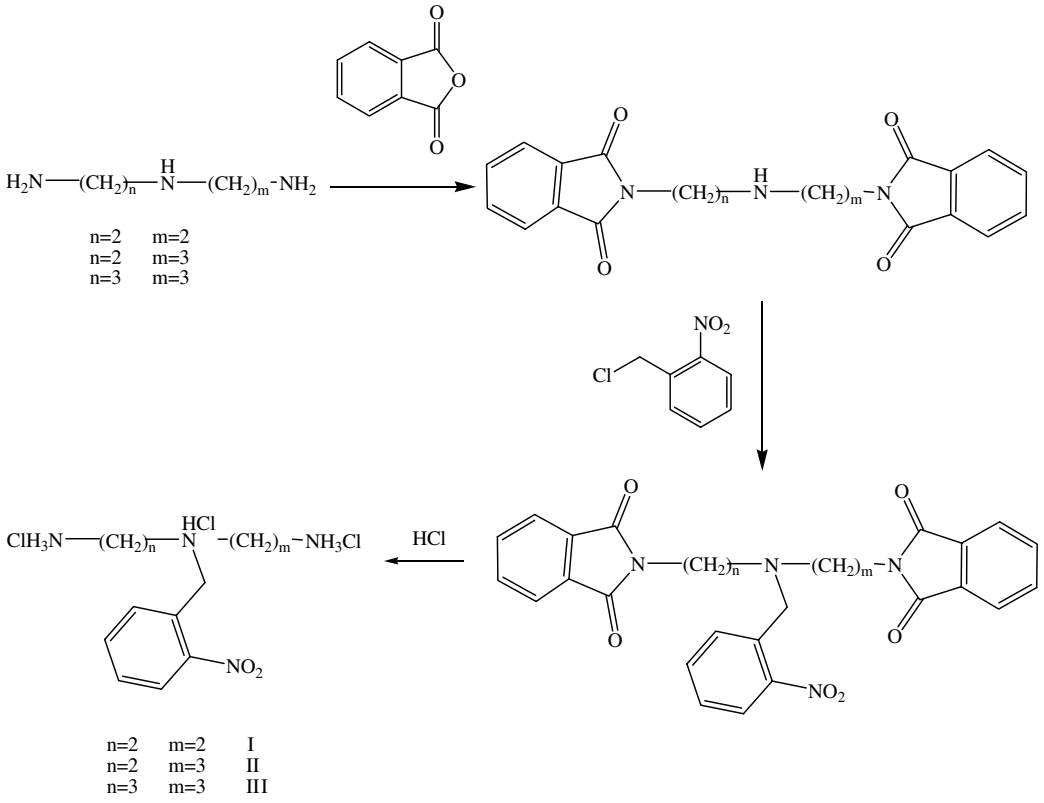
(**II**): Yield (65%). *Anal.* Calc. for $C_{12}H_{23}Cl_3N_4O_2$: C, 39.85; H, 6.41; N, 15.49. Found: C, 40.01; H, 6.32; N, 15.40%. IR (KBr, cm^{-1}) 1344, 1530 $\nu(NO_2)$, 2700–3418 $\nu(NH_3Cl)$; ^1H NMR δ_H (D_2O, ppm) 2.65 (s, 2H), 3.50 (m, 4H), 3.94 (m, 4H), 4.48 (s, 2H), 7.82 (m, 3H), 8.25 (d, 1H); ^{13}C NMR δ_C (D_2O, ppm) 21.13, 33.50, 36.27, 46.49, 51.01, 56.23, 123.23, 126.54, 132.42, 135.13, 135.53, 148.00.

(**III**): Yield (61%). *Anal.* Calc. for $C_{13}H_{25}Cl_3N_4O_2$: C, 41.56; H, 6.71; N, 14.91. Found: C, 41.89; H, 6.62; N, 14.77%. IR (KBr,cm^{-1}) 1354, 1529 $\nu(NO_2)$, 2690–3420 $\nu(NH_3Cl)$; ^1H NMR δ_H (D_2O, ppm) 3.57 (m, 8H), 4.48

Table 1
Crystal data and structure refinement for $[Cd(NO_3)(L_5)(\mu\text{-}NO_3)Cd(NO_3)(L_5)]0.5Cd(NO_3)_4$ (**1**) and $[CdL_5(NO_3)(CH_3OH)]ClO_4 \cdot C_2H_6O$ (**2**)

Compound	**1**	**2**
Empirical formula	$C_{54}H_{58}Cd_{2.5}N_{13}O_{23}$	$C_{30}H_{38}Cd_1Cl_1N_5O_{13}$
Formula weight	1538.13	824.51
Temperature (K)	293(2)	120(2)
Wavelength (Å)	0.71073	0.71073
Crystal system	monoclinic	monoclinic
Space group	*P*21/*n*	*P*21/*c*
Unit cell dimensions		
a (Å)	15.0527(7)	20.2986(11)
b (Å)	27.3030(12)	7.9217(3)
c (Å)	15.3542(7)	21.0413(11)
α (°)	90	90
β (°)	94.871(4)	107.319(4)
γ (°)	90	90
Volume ($Å^3$)	6287.5(5)	3230.0(3)
Z	4	4
D_{calc} (Mg/m^{-3})	1.815	1.696
Absorption coefficient (mm^{-1})	1.109	0.836
F(000)	3452	1688
Crystal size (mm)	0.50 × 0.35 × 0.08	0.50 × 0.40 × 0.30
θ Range for data collection (°)	1.53–26.77	1.99–29.21
Limiting indices	$-19 \leqslant h \leqslant 19$, $-34 \leqslant k \leqslant 29$, $-19 \leqslant l \leqslant 16$	$-22 \leqslant h \leqslant 27$, $-10 \leqslant k \leqslant 9$, $-28 \leqslant l \leqslant 28$
Reflections collected/ unique [R_{int}]	38906/13237 [0.0346]	22132/8615 [0.0323]
Completeness to *θ* (%)	26.77, 98.70	29.21, 98.5
Absorption correction	numerical	numerical
Maximum and minimum transmission	0.920 and 0.640	0.780 and 0.675
Refinement method	full-matrix least-squares on F^2	full-matrix least-squares on F^2
Data/restraints/ parameters	13237/0/905	8615/0/455
Goodness-of-fit on F^2	1.183	1.067
Final *R* indices [$I > 2\sigma(I)$]	[c] $R_1 = 0.0768$, $wR_2 = 0.1874$	$R_1 = 0.0499$, $wR_2 = 0.1331$
R indices (all data)	$R_1 = 0.0786$, $wR_2 = 0.1881$	$R_1 = 0.0520$, $wR_2 = 0.1347$
Largest difference in peak and hole (e A^{-3})	2.187 and −4.669	0.925 and −0.710

[c] Acceptable refinement not achieved (see text).



Scheme 1.

(s, 2H), 7.84 (m, 3H), 8.26 (d,1H); ^{13}C NMR δ_C (D_2O, ppm) 21.22, 36.56, 50.40, 55.53, 123.67, 126,67, 132.27, 135.21, 135.56, 147.88.

2.5. Preparation of the complexes

2.5.1. General synthesis

A solution of NaOH (1.5 mmol) in methanol (10 cm^3) was added to a suspension of the appropriate triamine trihydrochloride (0.5 mmol) in methanol (10 cm^3). The mixture was stirred at room temperature for a few minutes then filtered, and the precipitate was washed well with methanol (10 cm^3). The washings and the filtrate were combined and this solution was added dropwise to a hot solution of $Cd(NO_3)_2 \cdot 6H_2O$ (0.5 mmol) and L_4 (0.5 mmol) in methanol (20 cm^3) over a period of 2 h. After refluxing the solution for 24 h on cooling the product was recovered as a white powder, which was recrystallized from methanol/ethanol [17].

2.5.2. $[Cd(NO_3)(L_5)(\mu\text{-}NO_3)Cd(NO_3)(L_5)]0.5Cd(NO_3)_4$ or $[Cd(L_5)]^{2+}$ (1)

Yield 66%. *Anal.* Calc. for $C_{108}H_{112}Cd_5N_{26}O_{46}$: C, 44.94; H, 3.91; N, 11.16. Found: C, 44.51; H, 4.01; N, 11.31%. IR (KBr) 3060, 2923, 1644, 1360, 1601, 1527 cm^{-1}.

2.5.3. $[Cd(NO_3)(CH_3OH)L_5]ClO_4 \cdot C_2H_6O$ (2)

0.122 g (1 mmol) of $NaClO_4$ was added to a solution of $[Cd(NO_3)(L_5)(\mu\text{-}NO_3)Cd(NO_3)(L_5)]0.5Cd(NO_3)_4$ (0.5 mmol) in methanol and was stirred for 15 min. The solution volume was then reduced to 10 ml by roto-evaporation and a yellow precipitate was formed. This was filtered off, washed with ether and dried in vacuo. Vapour diffusion of ether into a solution of the powder in methanol afforded pale yellow crystalline needles. Yield 55%. *Anal.* Calc. for $C_{30}H_{38}CdClN_5O_{13}$: C, 43.70; H, 4.65; N, 8.49. Found: C, 43.61; H, 4.57; N, 8.52%. IR (KBr) 3060, 2923, 1644, 1360, 1601, 1527, 1090, 624 cm^{-1}.

2.5.4. $[CdL_6](NO_3)_2$ (3)

Yield 55%. *Anal.* Calc. for $C_{28}H_{30}CdN_6O_{10}$: C, 46.52; H, 4.18; N, 11.62. Found: C, 46.61; H, 4.32; N, 11.72%. IR (KBr) 3070, 2871, 2918, 1636, 1523, 1356 cm^{-1}.

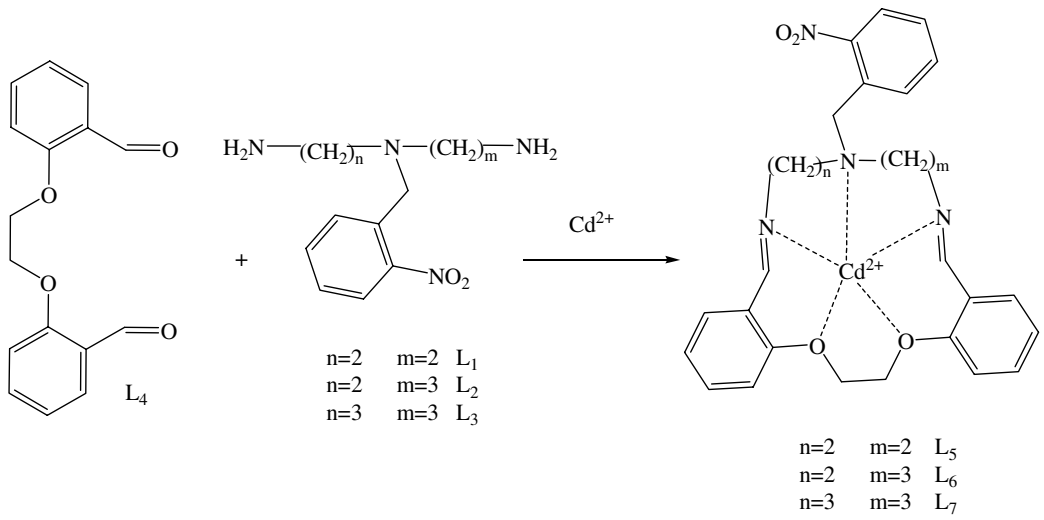
2.5.5. $[CdL_7](NO_3)_2$ (4)

Yield 53%. *Anal.* Calc. for $C_{29}H_{32}CdN_6O_{10}$: C, 47.26; H, 4.38; N, 11.40. Found: C, 47.31; H, 4.44; N, 11.45%. IR (KBr) 3088, 2900, 1645, 1523, 1352 cm^{-1}.

3. Results and discussion

3.1. Synthesis and characterization

The Schiff-base condensation of L_4 and (L_1, L_2 or L_3) in methanol in the presence of the appropriate hydrated Cd(II) salt and in a 1:1:1 mole ratio gave good yields of the analytically pure products $[CdL_5]^{2+}$, $[CdL_6]^{2+}$ and $[CdL_7]^{2+}$, respectively (Scheme 2). All of the complexes



Scheme 2.

were characterized by spectroscopic methods and furthermore by using different counter ions two types of crystalline $[CdL_5]^{2+}$ were isolated and characterized by X-ray crystallography. All the complexes are pale yellow, air-stable solids, moderately soluble in CH_3CN and DMSO. Our attempt to synthesize macrocyclic ligands in the absence of various metal ions were unsuccessful and cyclocondensation reactions did not occur, therefore we tried different metal ions in order to examine the effect of the template reaction on the occurrence of ring closure. Our results clearly demonstrate that the nature of the metal template determines the outcome of the Schiff-base condensation between the difunctional carbonyl component 2-[2-(2-formyl phenoxy)ethoxy]benzaldehyde (L_4) and a difunctional amine component.

Cd(II) facilitates the formation of macrocyclic products in 50-60% yield, attempts to obtain these macrocyclic compounds in the presence of Zn(II), Ni(II), Ag(II) and Cu(II) metal ions were unsuccessful and metal(II) polyamine complexes were the only final products (in high yield). The infrared spectra of the complexes confirm the formation of the macrocyclic compounds by the absence of bands characteristic of carbonyl and primary amine groups of the starting materials. The complexes exhibit a Schiff-base ν(C=N) vibration in the range 1636–1644 cm^{-1} and also bands at approximately 1524–1527 and 1353–1360 cm^{-1} associated with nitro groups. The shift of the imine band to higher wavenumbers upon complexation suggests coordination through the imine nitrogen atoms [21,22].

The NMR study of the cadmium nitrate complexes also provides strong evidence for the formation of the macrocyclic complexes. In order to obtain a suitable crystal for crystal structure determination we simply added $NaClO_4$ to the solution of $[Cd(NO_3)(L_5)(\mu\text{-}NO_3)\ Cd(NO_3)(L_5)]\text{-}0.5Cd(NO_3)_4$ and we observed the replacement of the counter ion by the perchlorate ion and the disappearance of the nitrate bridge.

3.2. X-ray crystal structure

The molecular structures of $[Cd(NO_3)(L_5)(\mu\text{-}NO_3)Cd(NO_3)(L_5)]0.5Cd(NO_3)_4$ (**1**) and $[Cd(NO_3)(CH_3OH)L_5]ClO_4$ (**2**) are shown in Figs. 1 and 2. Selected bond lengths and angles of **2** are given in Table 2. Although the crystal structure of $[Cd(NO_3)(L_5)(\mu\text{-}NO_3)Cd(NO_3)(L_5)]0.5Cd(NO_3)_4$ (**1**) could not be refined to publication standard, the general features of the molecule were obvious from the direct methods solution (Fig. 1). However, the situation for the cadmium complex (**1**) is not straightforward owing to the presence of a $[Cd(NO_3)_4]^{2-}$ ion for each four complex cations in the solid state. Similar structures have been observed for other cadmium complexes [19,20]. The geometry of the complex is best considered as a slightly distorted triangular face dodecahedron structure. In complex **2** (Fig. 2), the Cd^{2+} ion is eight coordinate, being bonded to three nitrogen and two oxygen atoms, lying in an approximately pentagonal plane (N_3O_2), in addition the oxygen atom of methanol and two oxygen atoms of a terminal nitrate ion are also coordinated. The coordination of the nitrate group is asymmetric, with metal to oxygen distances of 2.322(3) and 2.776(3) Å. The only nearest structure to the L_5 complex which has been reported so far is a diamine macrocycle having no side chain [21]. The structure of this complex shows a distorted pentagonal bi-pyramidal coordination geometry with a N_3O_2pentagonal plane (**5**). Comparing the bond lengths for complexes **2** and **5** reveals a small (but significant) increase in bond lengths of the latter complex. Inspection of molecular models suggested that this increase may reflect a slightly poorer fit of the Cd(II) ion for the donor cavity of this larger ring size of macrocycle **5** (two C–N instead of two C=N). This contention is supported by X-ray structure analysis: bond lengths Cd(1)–O(3) and Cd(1)–O(4) of complex **2** are 0.291 and 0.057 Å shorter than those of complex **5**, respectively [21]. Charge balance for complex **2** is provided by a

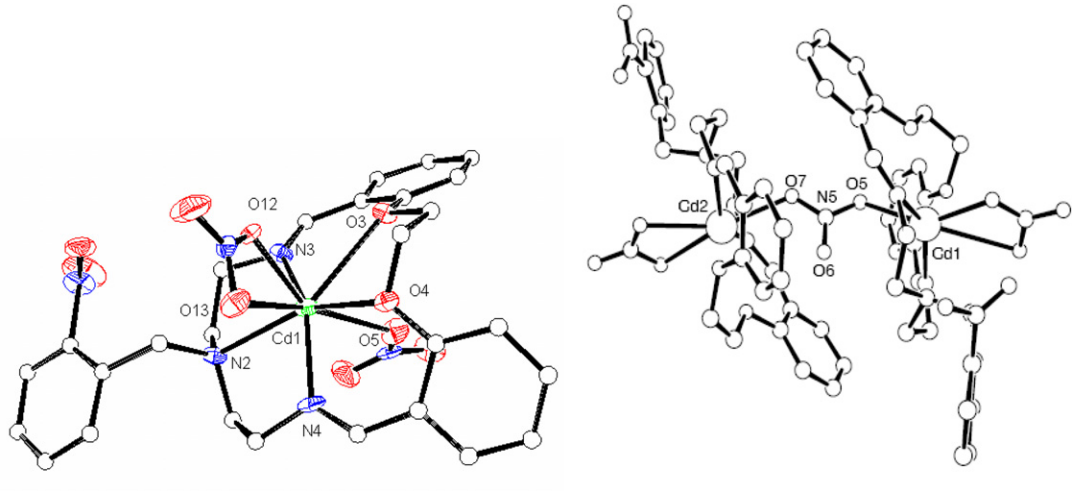


Fig. 1. Structure of the cation $[Cd(NO_3)(L_5)(\mu\text{-}NO_3)Cd(NO_3)(L_5)]0.5Cd(NO_3)_4$.

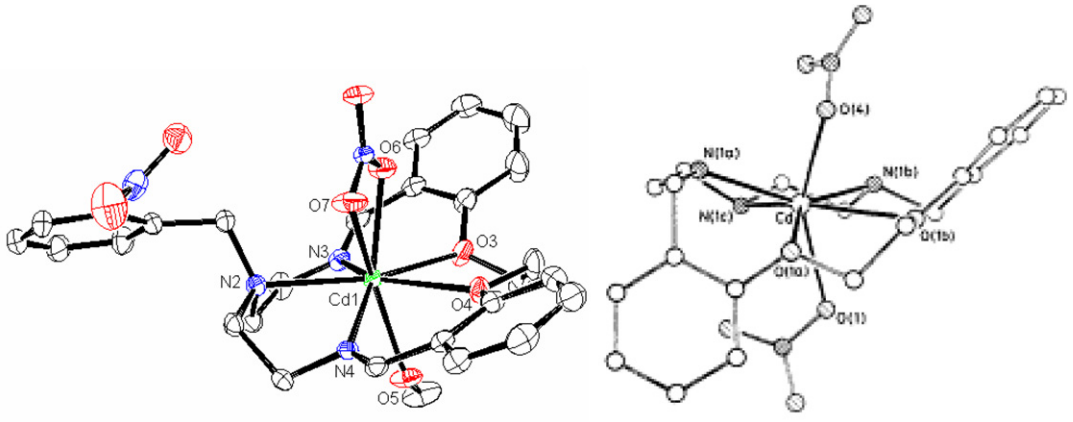


Fig. 2. ORTEP depiction of $[Cd(NO_3)(CH_3OH)\ L_5]^+$ (**2**) and a similar complex (**5**) [21].

Table 2
Important bond lengths (Å) and bond angles (°) for $[Cd(NO_3)(CH_3OH)\ L_5]ClO_4$

Bond	Bond length (Å)	Bond	Bond length (Å)
Cd(1)–N(2)	2.440(3)	Cd(1)–O(4)	2.557(2)
Cd(1)–N(3)	2.333(3)	Cd(1)–O(5)	2.380(3)
Cd(1)–N(4)	2.290(3)	Cd(1)–O(6)	2.322(3)
Cd(1)–O(3)	2.441(2)	Cd(1)–O(7)	2.776(3)
Bond	**Bond angle (°)**	**Bond**	**Bond angle (°)**
O(3)–Cd(1)–N(3)	71.76(10)	O(5)–Cd(1)–N(2)	104.09(10)
N(3)–Cd(1)–N(2)	71.53(9)	O(5)–Cd(1)–O(4)	80.96(10)
N(2)–Cd(1)–N(4)	76.01(9)	O(6)–Cd(1)–O(3)	78.58(10)
N(4)–Cd(1)–O(4)	74.28(8)	O(6)–Cd(1)–N(3)	90.64(10)
O(4)–Cd(1)–O(3)	69.18(8)	O(6)–Cd(1)–N(4)	120.31(9)
O(5)–Cd(1)–O(3)	76.89(10)	O(6)–Cd(1)–N(2)	98.31(9)
O(5)–Cd(1)–N(3)	86.16(10)	O(6)–Cd(1)–O(4)	86.02(9)
O(5)–Cd(1)–N(4)	76.44(9)	O(6)–Cd(1)–O(5)	155.02(10)

coordinated nitrate ion and a ClO_4^- ion. Bond lengths and angles are shown in Table 2. The sum of the angles subtended by the donor atoms at Cd is 362.76° and the plane containing N(4), N(2), N(3), O(3) and O(4) has a r.m.s. of 0.2684 and the metal atom is displaced from this towards the nitrate oxygen atoms, O(8) and O(7), by 0.204 Å. The r.m.s. values of the aromatic rings are 0.0079 and 0.0023 and the angle between their planes is 33.58°.

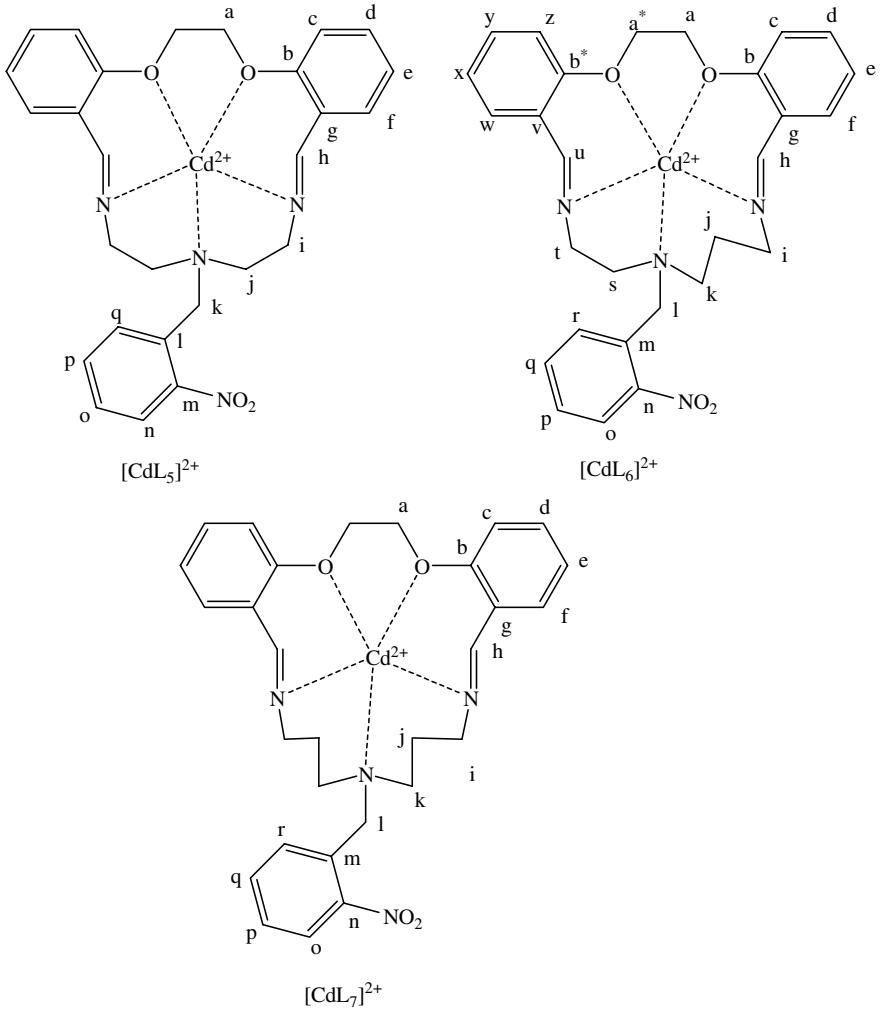
3.3. NMR studies

The ^1H as well as $^{13}C\{1H\}$ NMR data for $[CdL_n]^{2+}$ ($n = 5$, 6 and 7) dissolved in DMSO-d_6 are surveyed, using the lettering scheme shown in Scheme 3. The ^1H and ^{13}C signals were assigned using one- and two-dimensional ^1H–^1H COSY, ^1H–^{13}C HMQC and DEPT spectra.

The ^1H NMR spectrum of the complex $[CdL_6]^{2+}(C_1)$ shows a signal due to the H_j resonance at ca. 1.75 ppm, a signal due to the H_k resonance at ca. 2.38 ppm, a signal due to the H_s resonance at ca. 2.59 ppm, a signal due to the H_l resonance at ca. 3.77 ppm and a signal due to the H_a and $H_a{}^*$ resonances at ca. 4.43 ppm, also the related signals due to H_t and H_i are under the DMSO signal, identified using the HMQC spectrum. Two signals due to the ^1H imine resonance at ca. 8.63 and 8.76 ppm demonstrate the non-equivalence of the two imine (H_h and Hu) environments [18]. In the region characteristic of aromatic protons (6.99–7.83 ppm) five signals were found. Unfortunately, since the protons do not show scalar-coupling, we were not able to assign explicitly the signals to each of the aromatic systems present in the molecule. The ^{13}C NMR spectrum shows that the imine carbon atoms C_h and C_u (156.47, 156.76 ppm) and C_a and C_{a^*} (156.48, 156.76 ppm) are chemically non-equivalent. In the region corresponding to the signals of aromatic ring carbons (113.92–158.09 ppm), 17 peaks are observed, and two aromatic carbon atoms are equivalent, also in the region corresponding to the signals of aliphatic carbons (28.36 – 67.61 ppm), eight peaks are observed.

The ^1H NMR spectrum of the complex $[CdL_5]^{2+}(C_{2v})$ shows a signal due to the H_j resonance at ca. 2.66 ppm, a signal due to the H_i resonance at ca. 3.56, a signal due to the H_k resonance at ca. 3.83 ppm, a signal due to the H_a resonance at ca. 4.43 pm, and also only a single ^1H imine resonance at ca. 8.72 ppm, demonstrating the equivalence of the two imine environments. In the aromatic region (6.98–7.82 ppm) five signals were found, and since the protons do not show scalar-coupling we were not able to assign explicitly the signals to each of the aromatic systems present in the molecule.

The ^{13}C NMR spectrum shows that the imine carbon atoms, C_h (159.0 ppm) are equivalent. Also twelve lines are observed for the carbon atoms of the aromatic rings



Scheme 3.

(114.08–158.05 ppm). The ^{1}H NMR and ^{13}C NMR spectra of the complex $[CdL_7]^{2+}$ resemble those of complex $[CdL_5]^{2+}$.

Acknowledgements

We are grateful to the Faculty of Chemistry of Bu – Ali Sina Universities and the Ministry of Science Research and Technology for financial support.

Appendix A. Supplementary material

CCDC 647082 and 663126 contain the supplementary crystallographic data for this paper. These data can be obtained free of charge via http://www.ccdc.cam.ac.uk/conts/retrieving.html, or from the Cambridge Crystallographic Data Center, 12 Union Road, Cambridge CB2.1EZ, UK; fax: (+44) 1223-336-033; or e-mail: deposit@ccdc.cam.ac.uk. Supplementary data associated with this article can be found, in the online version, at doi:10.1016/j.poly.2007.10.029.

References

[1] H. Okawa, H. Furutachi, D.E. Fenton, Coord. Chem. Rev. 174 (1998) 5175.
[2] P. Guerreiro, S. Tamburini, V.A. Vigato, Coord. Chem. Rev. 139 (1995) 17.
[3] P.A. Vigato, S. Tamburini, D.E. Fenton, Coord. Chem. Rev. 106 (1990) 25.
[4] S.R. Collinson, D.E. Fenton, Coord. Chem. Rev. 148 (1996) 19.
[5] D.E. Fenton, P.A. Vigato, Chem. Soc. Rev. 17 (1988) 69.
[6] P. Zanello, S. Tamburini, P.A. Vigato, G.A. Mazzocchin, Coord. Chem. Rev. 77 (1987) 165.
[7] S. Brooker, Coord. Chem. Rev. 222 (2001) 33.
[8] D.H. Busch, A.L. Vance, A.G. Kolchinski, Comprehensive Supramolecular Chemistry, vol. 9, Pergamon, New York, 1996, pp. 1–42.
[9] J.S. Bradshaw, K.E. Krakowiak, R.M. Izatt, Aza-Crown Macrocycles, Wiley, New York, 1993.
[10] H. Keypour, S. Salehzadeh, Trans. Met. Chem. 25 (2000) 205.
[11] H. Keypour, S. Salehzadeh, R.G. Pritchard, R.V. Parish, Inorg. Chem. 9 (2000) 5787.
[12] H. Keypour, R.G. Pritchard, R.V. Parish, Trans. Met. Chem. 23 (1998) 609.
[13] H. Keypour, H. Khanmohammadi, K.P. Wainwright, M.R. Taylor, J. Iranian Chem. Soc. 1 (2004) 53.
[14] H. Keypour, H. Khanmohammadi, K.P. Wainwright, M.R. Taylor, Inorg. Chim. Acta 355 (2003) 286.
[15] H. Keypour, H. Khanmohammadi, K.P. Wainwright, M.R. Taylor, Inorg. Chim. Acta 357 (2004) 1283.
[16] H. Keypour, S. Salehzadeh, R.G. Pritchard, R.V. Parish, Polyhedron 19 (2000) 1633.
[17] H. Keypour, H. Goudarziafshar, A.K. Brisdon, R.G. Pritchard, Inorg. Chim. Acta 360 (2007) 2298.
[18] H. Keypour, H. Khanmohammadi, K.P. Wainwright, Saeed Jamehbozorgi, Trans. Met. Chem. 29 (2004) 523.
[19] R.R. Fenton, R. Gauci, P.C. Junk, L.F. Lindoy, R.C. Luckay, G.V. Meehan, J.R. Price, P. Turner, G. Wei, J. Chem. Soc., Dalton Trans. (2002) 2185.
[20] P.J. Baillie, N. Choi, L.F. Lindoy, M. McPartlin, H.R. Powell, P.A. Tasker, J. Chem. Soc., Dalton Trans. (1996) 3039.
[21] Kenneth R. Adam, Keith P. Dancey, Barbara A. Harrison, Anthony J. Leong, Leonard F. Lindoy, Mary McPartlin, Peter A. Tasker, J. Chem. Soc., Chem. Commun. (1983) 1351.
[22] S.M. Peng, G.C. Gordon, V.L. Goedken, Inorg. Chem. 17 (1978) 119.

Available online at www.sciencedirect.com
ScienceDirect
Polyhedron 27 (2008) 655–662
POLYHEDRON
www.elsevier.com/locate/poly

Ruthenium(III) complexes with *N*-(acetyl)-*N*′-(5-*R*-salicylidene)hydrazines: Syntheses, structures and properties

Raji Raveendran, Samudranil Pal *

School of Chemistry, University of Hyderabad, Hyderabad 500 046, India

Received 26 September 2007; accepted 19 October 2007
Available online 19 December 2007

Abstract

The reactions of 1 mol equiv. each of $[Ru(PPh_3)_3Cl_2]$ and *N*-(acetyl)-*N*′-(5-*R*-salicylidene)hydrazines (H_2ahsR, R = H, OCH_3, Cl, Br and NO_2) in alcoholic media afford simultaneously two types of complexes having the general formulae $[Ru(HahsR)(PPh_3)_2Cl_2]$ and $[Ru(ahsR)(PPh_3)_2Cl]$. The complexes have been characterized by elemental analysis, magnetic, spectroscopic and electrochemical measurements. Molecular structures of $[Ru(HahsH)(PPh_3)_2Cl_2]$ and $[Ru(ahsH)(PPh_3)_2Cl]$ have been confirmed by X-ray crystallography. In both species, the PPh_3 ligands are *trans* to each other. The bidentate $HahsH^-$ coordinates to the metal ion via the O atom of the deprotonated amide and the imine–N atom in $[Ru(HahsH)(PPh_3)_2Cl_2]$. In $HahsH^-$, the phenolic OH is involved in a strong intramolecular hydrogen bond with the uncoordinated amide N atom forming a seven-membered ring. In $[Ru(ahsH)(PPh_3)_2Cl]$, the tridentate $ahsH^{2-}$ binds to the metal ion via the deprotonated amide O, the imine N and the phenolate O atoms. In the electronic spectra, the green $[Ru(HahsR)(PPh_3)_2Cl_2]$ and brown $[Ru(ahsR)(PPh_3)_2Cl]$ complexes display several absorptions in the ranges 385–283 and 457–269 nm, respectively. Both complexes are low-spin and display rhombic EPR spectra in frozen solutions. Both types of complexes are redox active and display a quasi-reversible ruthenium(III) to ruthenium(II) reduction which is sensitive to the polar effect of the substituent on the chelating ligand. The reduction potentials are in the ranges −0.21 to −0.12 and −0.42 to −0.21 V (versus Ag/AgCl) for $[Ru(HahsR)(PPh_3)_2Cl_2]$ and $[Ru(ahsR)(PPh_3)_2Cl]$, respectively.
© 2007 Elsevier Ltd. All rights reserved.

Keywords: Ruthenium(III) complexes; Acetylhydrazones; Crystal structures; Intramolecular hydrogen bond; Redox properties

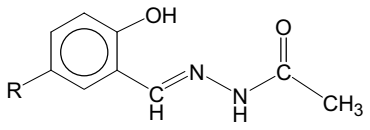
1. Introduction

Coordination complexes of ruthenium are well known for their versatile electron-transfer and energy-transfer properties [1–21]. These characteristics enable ruthenium complexes to exhibit a wide range of reactivities. As a result a large variety of ruthenium complexes have found applications in various research areas, such as artificial photosynthesis, photomolecular devices, probes for biological macromolecules, oxidation catalysts and organic synthesis [8–21]. The continuing quest for new complexes of ruthenium is primarily due to their efficacy in such a broad range of applications. We have been working on organometallic and coordination complexes of ruthenium with amide–O coordinating acid hydrazide based Schiff bases [22–26]. Recently we have reported a diruthenium(III) complex $[Ru_2(\mu\text{-}OCH_3)_2(bhsH)_2(PPh_3)_2]$ and some mononuclear mixed-ligand ruthenium(III) complexes $[Ru(bhsR)(PPh_3)_2Cl]$ with *N*-(benzoyl)-*N*′-(5-*R*-salicylidene)hydrazines (H_2bhsR) [25]. The diruthenium(III) species could be isolated only for the unsubstituted ligand (R = H) due to its poor solubility in the methanolic reaction mixture. The cryomagnetic measurements revealed the antiferromagnetic nature of this diruthenium(III) complex. Scrutiny of the magnetic data and EPR features

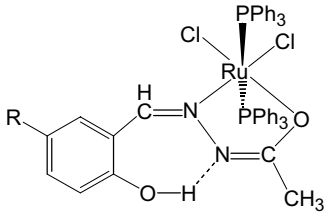
* Corresponding author. Tel.: +91 40 2313 4756; fax: +91 40 2301 2460.
E-mail address: spsc@uohyd.ernet.in (S. Pal).

0277-5387/$ - see front matter © 2007 Elsevier Ltd. All rights reserved.
doi:10.1016/j.poly.2007.10.027

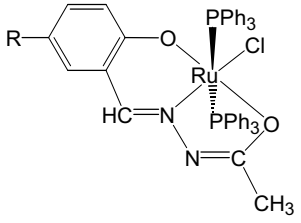
indicate that intermolecular rather than intramolecular metal ion spin-exchange is responsible for the antiferromagnetic behaviour of this complex. In search of similar unusual diruthenium(III) species, we have examined the ruthenium chemistry with *N*-(acetyl)-*N*′-(5-*R*-salicylidene) hydrazines (H_2ahsR), which are sterically less bulky analogues of H_2bhsR. However, instead of dinuclear species, two types of mononuclear ruthenium(III) complexes [Ru(HahsR)$(PPh_3)_2Cl_2$] and [Ru(ahsR)$(PPh_3)_2$Cl] have been obtained. Interestingly in the first type of species, the phenolic OH of $HahsR^-$ remains protonated and the ligand acts as a bidentate imine–N and deprotonated amide–O donor. In the second type of complex, $ahsR^{2-}$ is a typical tridentate phenolate–O, imine–N and deprotonated amide–O donor ligand. In the following account, we have described the syntheses, characterization and physical properties of these complexes. Molecular structures of representative complexes determined by X-ray crystallography have been reported.



H_2ahsR (R = H, Cl, Br, OCH_3, NO_2)



[Ru(HahsR)$(PPh_3)_2Cl_2$]



[Ru(ahsR)$(PPh_3)_2$Cl]

2. Experimental

2.1. Materials

The Schiff bases were synthesized in ~80% yield by condensation of 1 mol equiv. of acetylhydrazine and 1 mol. equiv. of the corresponding 5-substituted salicylaldehyde by following a reported procedure [27]. [Ru$(PPh_3)_3Cl_2$] was prepared using the method reported before [28]. All other chemicals and solvents were of analytical grade available commercially and were used as received.

2.2. Physical measurements

A Thermo Finnigon Flash EA1112 series elemental analyzer was used for the elemental (C, H, N) analysis data. Infrared spectra were recorded by using KBr pellets on a Jasco-5300 FT-IR spectrophotometer. A Cary 100 Bio UV/Vis spectrophotometer was used to record the electronic spectra. The X-band EPR spectra of the complexes in frozen (110 K) dichloromethane–toluene (1:1) solutions were recorded on a Jeol JES-FA200 spectrometer. Room temperature (300 K) magnetic susceptibilities were measured using a Sherwood Scientific balance. Diamagnetic corrections calculated from Pascal's constants [29] were used to obtain the molar paramagnetic susceptibilities. A Digisun DI-909 conductivity meter was used to measure the solution electrical conductivities. Cyclic voltammetric experiments with dichloromethane solutions of the complexes containing tetrabutylammonium perchlorate (TBAP) as the supporting electrolyte were performed using a CH-Instruments model 620A electrochemical analyzer. The three electrode measurements were carried out at 298 K under a dinitrogen atmosphere with a platinum disk working electrode, a platinum wire auxiliary electrode and an Ag/AgCl reference electrode. The potentials reported in this work are uncorrected for junction contributions.

2.3. Synthesis of [Ru(HahsH)$(PPh_3)_2Cl_2$] (1) and [Ru(ahsH)$(PPh_3)_2$Cl] (6)

Solid [Ru$(PPh_3)_3Cl_2$] (260 mg, 0.28 mmol) was added to an ethanol solution (30 ml) of H_2ahsH (50 mg, 0.28 mmol) and stirred in air at room temperature for 8 h. The green solid that precipitated was collected by filtration, washed with *n*-hexane and dried in air. This solid was dissolved in a minimum amount of dichloromethane and transferred to a neutral aluminium oxide column (15 cm length). Elution with dichloromethane–*n*-hexane mixture (2:1) provided complex **1**. It was recrystallized from the same solvent mixture. Yield: 90 mg (37%).

The brown filtrate containing complex **6** was evaporated to dryness on a rotary evaporator. The solid obtained was dissolved in a minimum amount of dichloromethane, transferred to a neutral aluminium oxide column, eluted with dichloromethane and finally recrystallized from dichloromethane–*n*-hexane mixture (1:1). Yield: 115 mg (49%).

These complexes can also be synthesized in methanol instead of ethanol. However, the yields vary significantly due to the change of the solvent. In methanol the yield of **1** was 57% and that of **6** was 22%.

The other complexes [Ru(HahsR)$(PPh_3)_2Cl_2$] (R = OCH_3 (**2**), R = Cl (**3**), R = Br (**4**) and R = NO_2 (**5**)) and [Ru(ahsR)$(PPh_3)_2$Cl] (R = OCH_3 (**7**), R = Cl (**8**), R = Br (**9**) and R = NO_2 (**10**)) reported in this work were synthesized from [Ru$(PPh_3)_3Cl_2$] and the corresponding H_2ahsR (1:1 mol ratio) by following similar procedures as described above. In ethanol, the yields of **2**–**5** and **7**–**10** were in the ranges 24–35% and 44–50%, respectively. On the other hand, the yields of **2**–**5** and **7**–**10** in methanol were in the ranges 44–58% and 16–21%, respectively.

2.4. X-ray crystallography

Single crystals of **1** and **6** were grown by slow evaporation of their solutions in dichloromethane–acetonitrile–

n-hexane (1:1:1) mixture. In each case, unit cell parameters and the intensity data were obtained on a Bruker-Nonius SMART APEX CCD single crystal diffractometer, equipped with a graphite monochromator and a Mo Kα fine-focus sealed tube ($\lambda = 0.71073$ Å) operated at 2.0 kW. The detector was placed at a distance of 6.0 cm from the crystal. Data were collected at 298 K with a scan width of 0.3° in ω and an exposure time of 15 s/frame. SMART software was used for data acquisition and SAINT-PLUS software was used for data extraction [30]. The absorption corrections were performed with the help of the SADABS program [31]. Complex **1** crystallizes as **1**·$2CH_2Cl_2$ in the space group $P2_1/m$, while complex **6** crystallizes as **6**·CH_3CN in the space group $P2_1/n$. The structures were solved by direct methods and refined on F^2 by full-matrix least-squares procedures. All non-hydrogen atoms in both structures were refined using anisotropic thermal parameters. The positional parameters of the methyl group hydrogen atoms in **1**·$2CH_2Cl_2$ located in a difference Fourier map were refined with geometric restraints and $U_{iso}(H) = 1.5U_{eq}(C)$. The remaining hydrogen atoms in **1**·$2CH_2Cl_2$ and all the hydrogen atoms in **6**·CH_3CN were included in the structure factor calculations at idealized positions by using a riding model. The SHELX-97 programs [32] were used for structure solution and refinement. The ORTEX6A package [33] was used for molecular graphics. Selected crystallographic data are listed in Table 1.

Table 1
Crystallographic data for [Ru(HahsH)(PPh_3)$_2Cl_2$]·$2CH_2Cl_2$ (**1**·$2CH_2Cl_2$) and [Ru(ahsH)(PPh_3)$_2$Cl]·CH_3CN (**6**·CH_3CN)

	1·$2CH_2Cl_2$	**6**·CH_3CN
Empirical formula	$C_{47}H_{43}Cl_6N_2O_2P_2Ru$	$C_{47}H_{41}ClN_3O_2P_2Ru$
Formula weight	1043.54	878.29
Crystal size (mm)	0.32 × 0.07 × 0.04	0.31 × 0.11 × 0.05
Crystal system	monoclinic	monoclinic
Space group	$P2_1/m$	$P2_1/n$
a (Å)	9.840(2)	10.538(4)
b (Å)	22.564(5)	18.457(7)
c (Å)	11.247(3)	21.520(8)
β (°)	110.017(3)	94.782(6)
V (Å^3)	2346.4(9)	4171(3)
Z	2	4
$\rho_{calc.}$ (g/cm^3)	1.477	1.399
μ (mm^{-1})	0.784	0.559
$F(000)$	1062	1804
Reflections collected	23844	42714
Unique reflections	4696	8240
Observed reflections ($I \geqslant 2\sigma(I)$)	4033	6132
Data/restraints/parameters	4696/5/300	8240/0/507
Goodness-of-fit on F^2	1.029	1.144
R_1, wR_2 ($I \geqslant 2\sigma(I)$)	0.0455, 0.1216	0.0768, 0.1457
R_1, wR_2 (all data)	0.0534, 0.1287	0.1068, 0.1578
Largest peak and hole (e Å^{-3})	0.620, −0.898	1.288, −0.561

3. Results and discussion

3.1. Synthesis and characterization

Two types of complexes are produced in the reactions of [Ru(PPh_3)$_3Cl_2$] with *N*-(acetyl)-*N*′-(5-*R*-salicylidene) hydrazines (H_2ahsR, R = H, OCH_3, Cl, Br and NO_2) in ethanol or methanol. Elemental analysis data (Table 2) for these two varieties of complexes are consistent with the general formulae [Ru(HahsR)(PPh_3)$_2Cl_2$] and [Ru(ahsR)(PPh_3)$_2$Cl]. Each of the complexes having the formula [Ru(HahsR)(PPh_3)$_2Cl_2$] precipitates from the reaction mixture as a green solid due to its poor solubility, while the brown species of formula [Ru(ahsR)-(PPh_3)$_2$Cl] remain in solution. In ethanol, the yields (24–37%) of [Ru(HahsR)(PPh_3)$_2Cl_2$] were less than the yields (44–50%) of [Ru(ahsR)(PPh_3)$_2$Cl]. In contrast, [Ru(HahsR)(PPh_3)$_2Cl_2$] were obtained in significantly larger yields (44–58%) compared to the yields (16–22%) of [Ru(ahsR)(PPh_3)$_2$Cl] in methanol. All the complexes are electrically non-conducting in solution. The room temperature (298 K) magnetic moments of the complexes are within 1.80–2.01 μ_B (Table 2). Thus the oxidation state of the metal ion in each complex is +3 and it is low-spin. In all likelihood atmospheric oxygen is responsible for the oxidation of the metal ion during the synthesis of all these complexes.

3.2. Spectroscopic features

None of the infrared spectra of the complexes display the characteristic bands associated with the C=O and N–H stretches of the amide functionality, indicating the enolate form of it in the metal coordinated Schiff base [34,35]. All the spectra are also devoid of any band assignable to the phenolic OH stretch. Although deprotonation of phenolic OH is expected for [Ru(ahsR)(PPh_3)$_2$Cl] (**6**–**10**), it should be protonated in [Ru(HahsR)(PPh_3)$_2Cl_2$] (**1**–**5**) as the amide functionality in $HahsR^-$ is in the enolate form. Perhaps involvement of the phenolic OH in strong intramolecular hydrogen bonding (vide infra) is the primary reason for the absence of the OH stretch in the spectra of **1**–**5**. All the complexes display a medium to strong band in the range 1578–1595 cm^{-1}. This band is assigned to the conjugated –C=N–N=C– fragment of the tridentate ligand [22–26]. The presence of ruthenium bound PPh_3 is indicated by three strong bands at ~745, ~694 and ~516 cm^{-1}. [Ru(PPh_3)$_3Cl_2$] and complexes containing {Ru(PPh_3)$_2$} are known to display similar bands [24–26,36].

Dichloromethane solutions of the complexes were used to record the electronic spectra. The spectral data are listed in Table 2. The spectra of the green complexes (**1**–**5**) display primarily three strong absorptions in the wavelength ranges 385–358, 340–300 and 288–283 nm. The spectral profiles of the brown complexes (**6**–**10**) are also very similar. Four strong absorptions are observed in the wavelength ranges 457–413, 375–354, 329–213 and

Table 2
Elemental analysis, electronic spectroscopic[a] and magnetic susceptibility[b] data

Complex	Found (Calc.) (%)			λ_{max} (nm) ($10^{-3} \times \varepsilon$ (M^{-1} cm^{-1}))	μ_{eff} (μ_B)
	C	H	N		
1	61.63 (61.86)	4.39 (4.50)	3.13 (3.21)	358 (16.5), 300 (32.8), 285 (33.3)	2.01
2	60.95 (61.13)	4.42 (4.57)	3.03 (3.10)	385 (11.8), 340[c] (11.3), 303[c] (26.5), 283 (29.3)	1.98
3	59.38 (59.51)	4.09 (4.22)	2.95 (3.08)	368 (15.3), 301 (32.2), 285 (32.0)	1.96
4	56.53 (56.74)	3.97 (4.02)	2.76 (2.94)	368 (17.6), 303 (38.2), 288 (37.8)	1.81
5	58.59 (58.83)	4.05 (4.17)	4.36 (4.57)	360 (15.9), 300 (32.7), 286[c] (30.6)	1.90
6	64.43 (64.55)	4.39 (4.57)	3.21 (3.35)	413[c] (3.5), 354[c] (8.0), 315 (14.9), 270 (30.8)	1.88
7	63.58 (63.70)	4.52 (4.65)	3.10 (3.23)	457[c] (2.7), 375[c] (7.9), 329[c] (15.0), 276 (34.6)	1.80
8	61.82 (62.00)	4.14 (4.28)	2.98 (3.21)	435[c] (2.7), 362[c] (8.1), 318 (16.0), 269 (36.7)	1.98
9	58.68 (58.99)	3.95 (4.07)	2.85 (3.06)	415[c] (4.5), 362[c] (8.9), 319 (18.7), 270 (39.5)	1.99
10	61.07 (61.26)	4.17 (4.23)	4.63 (4.76)	415[c] (16.0), 358 (21.8), 313 (27.9), 271 (33.9)	1.81

[a] In dichloromethane solution.
[b] At 298 K.
[c] Shoulder.

269–276 nm. In both cases, the low-energy absorptions are likely to be due to the ligand-to-metal charge transfer transitions and the high-energy absorptions are possibly due to ligand centred transitions [23,25,26,36].

The EPR spectral profiles of **1**–**10** in frozen (110 K) dichloromethane–toluene (1:1) solutions are very similar. The EPR data are listed in Table 3 and representative spectra are shown in Fig. 1. The complexes display three distinct signals indicating the distortion of the $NOCl_2P_2$ (in **1**–**5**) and the NO_2ClP_2 (in **6**–**10**) coordination spheres around the metal centres from octahedral symmetry. These distortions can be calculated in terms of axial (Δ) and rhombic (V) components. The axial distortion splits the t_2 level into "a" and "e" and the rhombic component again splits "e" into non-degenerate components (Fig. 1). In addition to Δ and V, spin–orbit coupling also affects the energies of these levels. Thus two ligand-field transitions of energies ΔE_1 and ΔE_2 ($\Delta E_1 < \Delta E_2$) are possible within these three levels. The distortion parameters and the transition energies have been calculated with the help of the EPR g-values and the g tensor theory for low-spin d^5 metal ion complexes [37]. In all the complexes, the axial distortion is larger than the rhombic distortion (Table 3). Thus

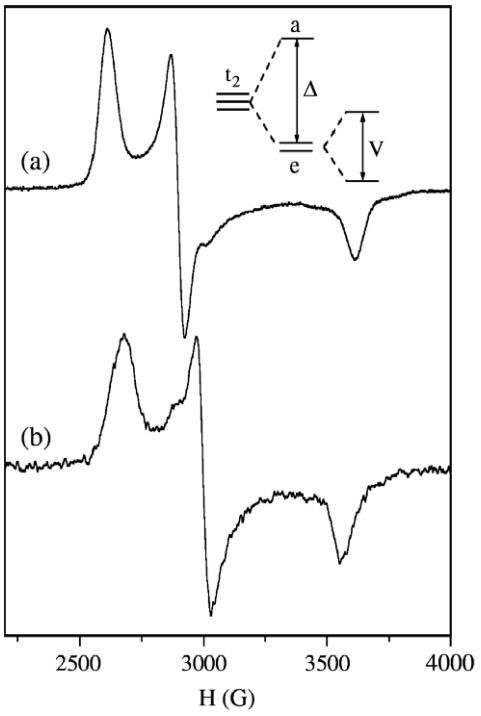


Fig. 1. EPR spectra of: (a) [Ru(HahsNO$_2$)(PPh$_3$)$_2$Cl$_2$] (**5**) and (b) [Ru(ahsNO$_2$)(PPh$_3$)$_2$Cl] (**10**) in frozen (110 K) dichloromethane–toluene (1:1) solutions and the t_2 splitting pattern.

Table 3
EPR g-values,[a] distortion parameters and near-IR transitions[b]

Complex	g_1	g_2	g_3	Δ/λ	V/λ	$\Delta E_1/\lambda$	$\Delta E_2/\lambda$
1	2.51	2.25	1.79	4.252	−2.121	3.324	5.587
2	2.50	2.26	1.80	4.329	−2.026	3.440	5.619
3	2.50	2.25	1.80	4.348	−2.135	3.409	5.687
4	2.51	2.25	1.80	4.374	−2.216	3.398	5.749
5	2.50	2.27	1.80	4.313	−1.921	3.470	5.554
6	2.40	2.15	1.86	5.360	−3.504	3.737	7.320
7	2.37	2.13	1.87	5.578	−3.787	3.812	7.670
8	2.39	2.15	1.86	5.310	−3.369	3.752	7.206
9	2.39	2.15	1.85	5.091	−3.158	3.643	6.891
10	2.43	2.18	1.83	4.756	−2.758	3.511	6.374

[a] In 1:1 dichloromethane–toluene at 110 K.
[b] The calculations are based on the spin–orbit coupling constant (λ) = 1000 cm^{-1}.

the energy-level order is $d_{xy} > d_{xz}$, d_{yz} with the unpaired electron in d_{xy}. Presumably the *trans* binding of the two PPh_3 ligands is primarily responsible for the large and positive axial distortion [24–26,36,38] in these complexes. Such axial distortion is clearly evident in the X-ray structures of **1** and **6** (vide infra). Interestingly there are small but definite differences in the g-values and hence in the Δ, V, ΔE_1 and ΔE_2 values (Fig. 1 and Table 3) for each pair of [Ru(HahsR)(PPh$_3$)$_2$Cl$_2$] and [Ru(ahsR)(PPh$_3$)$_2$Cl] complexes. In general, these values suggest that the extent of distortion is less in **1**–**5** in comparison with that in **6**–**10**. The ΔE_1 and ΔE_2 transitions for [Ru(HahsR)(PPh$_3$)$_2$Cl$_2$]

(**1**–**5**) are expected to occur in the ranges 3324–3470 cm^{-1} (3008–2882 nm) and 5554–5749 cm^{-1} (1800–1739 nm), respectively. On the other hand, for $[Ru(ahsR)(PPh_3)_2Cl]$ (**6**–**10**) the ΔE_1 transition is predicted within 3511–3812 cm^{-1} (2848–2623 nm) and the ΔE_2 transition should appear in the range 6374–7670 cm^{-1} (1568–1304 nm). Further scrutiny of the Δ/V ratios (1.97–2.24 for **1**–**5** and 1.47–1.72 for **6**–**10**) reveals that the rhombic component (V) of the distortion is less in **1**–**5** when compared with that in **6**–**10**. It is very likely that the larger constraint imposed by the rigid tridentate [39] $ahsR^{2-}$ in **6**–**10** compared to the constraint imposed by the bidentate $HahsR^-$ in **1**–**5** is the main reason for the observed differences in the extent of distortions and its rhombic components in these two types of complexes.

3.3. Description of the molecular structures

The molecular structures of **1** and **6** determined by X-ray crystallography are depicted in Figs. 2 and 3, respectively. The bond parameters associated with the metal centres are listed in Table 4. In **1**, the metal centre is in a distorted octahedral $NOCl_2P_2$ coordination sphere assembled by the bidentate deprotonated amide–O and the imine–N donor $HahsH^-$, two mutually *cis* oriented chlorides and two bulky PPh_3 molecules which are *trans* to each other. The asymmetric unit of **1**·$2CH_2Cl_2$ contains half of the complex molecule and a CH_2Cl_2 molecule. Both halves of **1** are related by a crystallographic mirror plane. The *cis*-$\{Ru(HahsH)Cl_2\}$ moiety is perfectly planar as it resides on the mirror plane. There is a strong intramolecular hydrogen bond involving the phenolic-OH and the uncoordinated amide–N atom of $HahsH^-$ (Fig. 2). The O2···N1 distance and the O2–H2···N1 angle are 2.502(6) Å and 171°, respectively. In the case of **6**, the asymmetric unit contains a full complex molecule and a CH_3CN molecule. The meridionally

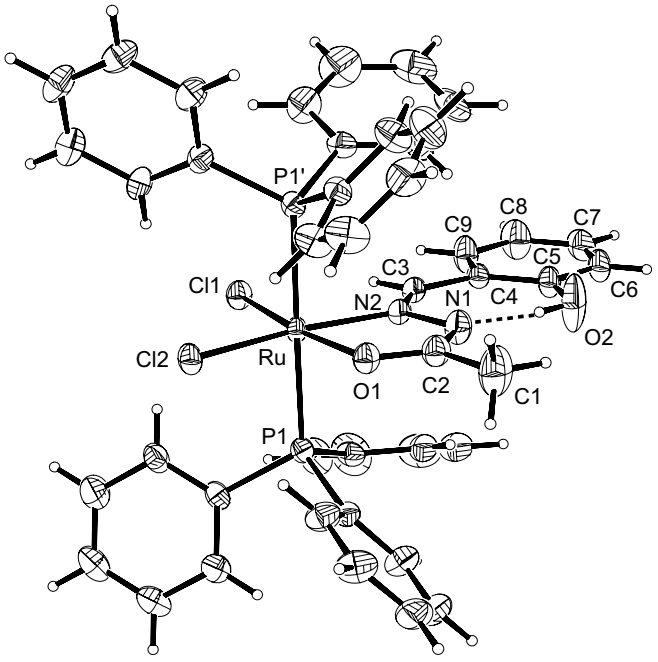


Fig. 2. Molecular structure of $[Ru(HahsH)(PPh_3)_2Cl_2]$ (**1**). All non-hydrogen atoms are represented by their 30% probability thermal ellipsoids. PPh_3 phenyl ring carbon atoms are not labelled for clarity.

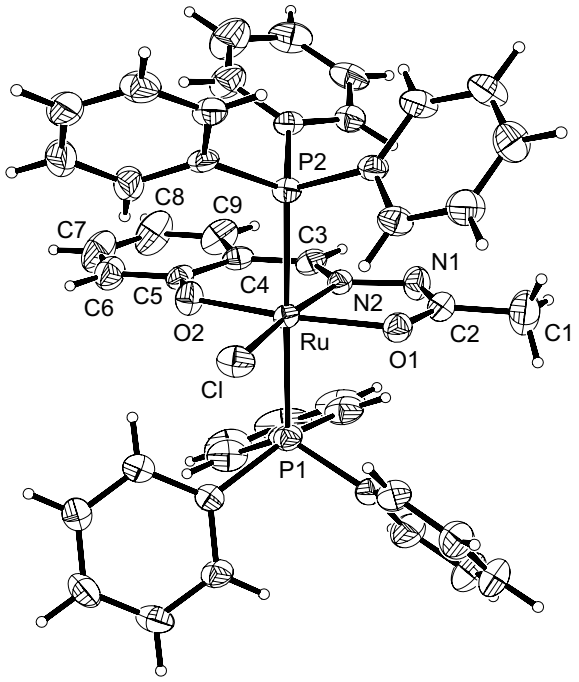


Fig. 3. Molecular structure of $[Ru(ahsH)(PPh_3)_2Cl]$ (**6**). All non-hydrogen atoms are represented by their 30% probability thermal ellipsoids. PPh_3 phenyl ring carbon atoms are not labelled for clarity.

Table 4
Selected bond lengths (Å) and angles (°) for **1**·$2CH_2Cl_2$ and **6**·CH_3CN

*[Ru(HahsH)(PPh$_3$)$_2$Cl$_2$]·2CH$_2$Cl$_2$ (**1**·2CH$_2$Cl$_2$)*[a]			
Ru–O(1)	2.023(3)	Ru–N(2)	2.072(4)
Ru–P(1)	2.4094(10)	Ru–P(1)′	2.4094(10)
Ru–Cl(1)	2.3289(13)	Ru–Cl(2)	2.3282(13)
O(1)–Ru–N(2)	76.92(14)	N(2)–Ru–Cl(2)	167.28(11)
O(1)–Ru–P(1)	89.40(2)	P(1)–Ru–P(1)′	178.73(4)
O(1)–Ru–P(1)′	89.40(2)	P(1)–Ru–Cl(1)	90.56(2)
O(1)–Ru–Cl(1)	170.45(10)	P(1)–Ru–Cl(2)	90.20(2)
O(1)–Ru–Cl(2)	90.36(10)	P(1)′–Ru–Cl(1)	90.56(2)
N(2)–Ru–P(1)	89.67(2)	P(1)′–Ru–Cl(2)	90.20(2)
N(2)–Ru–P(1)′	89.67(2)	Cl(1)–Ru–Cl(2)	99.18(4)
N(2)–Ru–Cl(1)	93.54(11)		
*[Ru(ahsH)(PPh$_3$)$_2$Cl]·CH$_3$CN (**6**·CH$_3$CN)*			
Ru–O(1)	2.028(4)	Ru–O(2)	1.988(4)
Ru–N(2)	2.005(4)	Ru–P(1)	2.4020(16)
Ru–P(2)	2.4078(16)	Ru–Cl	2.3630(16)
O(1)–Ru–O(2)	168.43(14)	O(2)–Ru–Cl	97.18(11)
O(1)–Ru–N(2)	77.56(16)	N(2)–Ru–P(1)	90.00(12)
O(1)–Ru–P(1)	89.79(11)	N(2)–Ru–P(2)	89.85(12)
O(1)–Ru–P(2)	89.38(11)	N(2)–Ru–Cl	171.92(12)
O(1)–Ru–Cl	94.38(11)	P(1)–Ru–P(2)	179.16(5)
O(2)–Ru–N(2)	90.87(16)	P(1)–Ru–Cl	90.61(5)
O(2)–Ru–P(1)	90.28(12)	P(2)–Ru–Cl	89.43(5)
O(2)–Ru–P(2)	90.54(12)		

[a] Symmetry transformation used to generate the equivalent atom P(1)′: $x, -y + 3/2, z$.

spanning tridentate phenolate–O, imine–N and deprotonated amide–O donor $ahsH^{2-}$ and the chloride form an NO_2Cl square-plane around the metal centre in **6**. The bulky PPh_3 molecules occupy the remaining two axial positions. The *trans* P–Ru–P bond angles (Table 4) in **1** and **6** are very close to the ideal value of 180°. All other *trans* bond angles in **1** and **6** are in the range 167.28(11)–171.92(12)°. In both complexes, the chelate bite angles for the five-membered ring formed by the amide–O and the imine–N centres are unexceptional and very similar (76.92(14)° for **1** and 77.56(16)° for **6**). The chelate bite angle (90.87(16)°) for the six-membered ring formed by the phenolate–O and the imine–N centres in **6** is very close to the ideal value for a *cis* bond angle. The remaining *cis* bond angles in **1** and **6** are within 89.2(3)–99.18(4)°. As expected, the two *trans* Ru–P bond lengths are significantly longer than the four equatorial bond lengths, indicating a large axial distortion in both complexes (Table 4). The Ru–O(amide) bond lengths in **1** (2.023(3) Å) and **6** (2.028(4) Å) are essentially identical. However, the Ru–N(imine) bond, which is *trans* to the chloride in both **1** and **6**, is significantly longer (2.072(4) Å) in **1**, containing the bidentate $HahsH^-$, than that (2.005(4) Å) in **6**, containing the tridentate $ahsH^{2-}$. Most likely the rigid tridentate binding mode of $ahsH^{2-}$ and hence the constraint imposed on the imine–N is the main factor for shortening of the Ru–N(imine) bond in **6**. The more effective *trans* influence of the chloride due to the less rigid bidentate binding mode of $HahsH^-$ and the participation of the adjacent amide–N in a strong intramolecular O–H···N hydrogen bond in **1** may also contribute to the observed difference in the Ru–N(imine) bond lengths. Both Ru–Cl bond lengths (2.3289(13) and 2.3282(13) Å) in **1** are very similar but shorter than the Ru–Cl bond length (2.3630(16) Å) in **6**. This is perhaps due to the stronger binding of the imine–N *trans* to the chloride in **6** in comparison with that in **1**. In general, all the bond lengths in both complexes are comparable with the bond lengths reported for ruthenium(III) complexes having the same coordinating atoms [23,25,26,36,38,40,41].

3.4. Electrochemical properties

Cyclic voltammetric measurements with dichloromethane solutions of **1**–**10** have been used to study the electron transfer properties. The potential data are listed in Table 5. Representative cyclic voltammograms are shown in Fig. 4. All the complexes display a quasi-reversible ruthenium(III) to ruthenium(II) reduction in the potential range −0.42 to −0.12 V. In each case, the one-electron stoichiometry of the observed response is confirmed by comparing the current heights with known one-electron redox processes under identical experimental conditions [22–26,36]. The ruthenium(III) to ruthenium(II) reduction potential for $[Ru(HahsR)(PPh_3)_2Cl_2]$ is higher than that for the corresponding $[Ru(ahsR)(PPh_3)_2Cl]$. The potentials for complexes **1**–**5** are in the range −0.21 to −0.12 V, while those for complexes **6**–**10** are within −0.42 to −0.21 V (Table 5). Most likely the more basic phenolate–O coordination in **6**–**10** (NO_2ClP_2 coordination sphere) instead of the less basic chloride coordination in **1**–**5** ($NOCl_2P_2$ coordination sphere) is the primary reason for the observed differences in potentials for these two types of complexes.

In both types of complexes, the trend in the ruthenium(III) to ruthenium(II) reduction potentials reflects the effect of the electronic nature of the substituents (R) on the salicylidene moieties of $HahsR^-$ and $ahsR^{2-}$. In the case of $[Ru(HahsR)(PPh_3)_2Cl_2]$ (**1**–**5**), the $E_{1/2}$ values

Table 5
Cyclic voltammetric[a,b] data

Complex	$E_{1/2}$ (V) (ΔE_p (mV))
$[Ru(HahsH)(PPh_3)_2Cl_2]$ (**1**)	−0.18 (90)
$[Ru(HahsOCH_3)(PPh_3)_2Cl_2]$ (**2**)	−0.21 (140)
$[Ru(HahsCl)(PPh_3)_2Cl_2]$ (**3**)	−0.16 (110)
$[Ru(HahsBr)(PPh_3)_2Cl_2]$ (**4**)	−0.15 (100)
$[Ru(HahsNO_2)(PPh_3)_2Cl_2]$ (**5**)	−0.12 (150)
$[Ru(ahsH)(PPh_3)_2Cl]$ (**6**)	−0.28 (160)
$[Ru(ahsOCH_3)(PPh_3)_2Cl]$ (**7**)	−0.42 (180)
$[Ru(ahsCl)(PPh_3)_2Cl]$ (**8**)	−0.27 (150)
$[Ru(ahsBr)(PPh_3)_2Cl]$ (**9**)	−0.26 (130)
$[Ru(ahsNO_2)(PPh_3)_2Cl]$ (**10**)	−0.21 (160)

[a] In dichloromethane solution (298 K) at a scan rate of 50 mV s^{-1}.
[b] $E_{1/2} = (E_{pa} + E_{pc})/2$, where E_{pa} and E_{pc} are anodic and cathodic peak potentials, respectively; $\Delta E_p = E_{pa} - E_{pc}$.

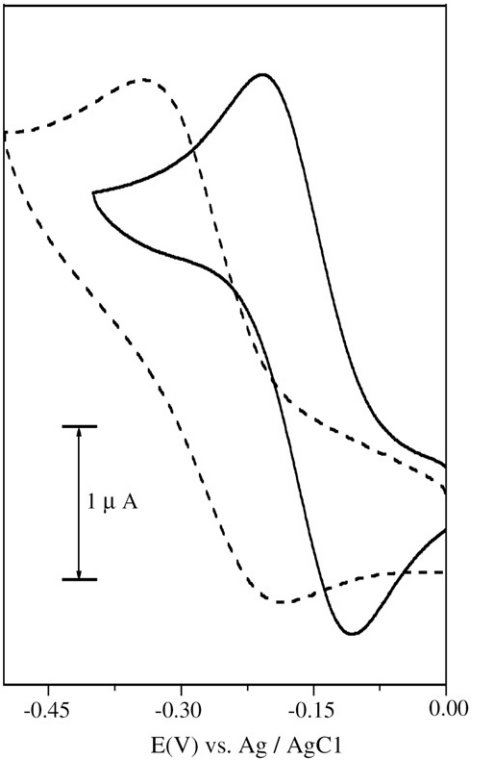


Fig. 4. Cyclic voltammograms (scan rate 50 mV s^{-1}) of $[Ru(HahsBr)(PPh_3)_2Cl_2]$ (**4**) (—) and $[Ru(ahsBr)(PPh_3)_2Cl]$ (**9**) (---). In each case, the solvent is dichloromethane (0.1 M TBAP) and the electrode is platinum.

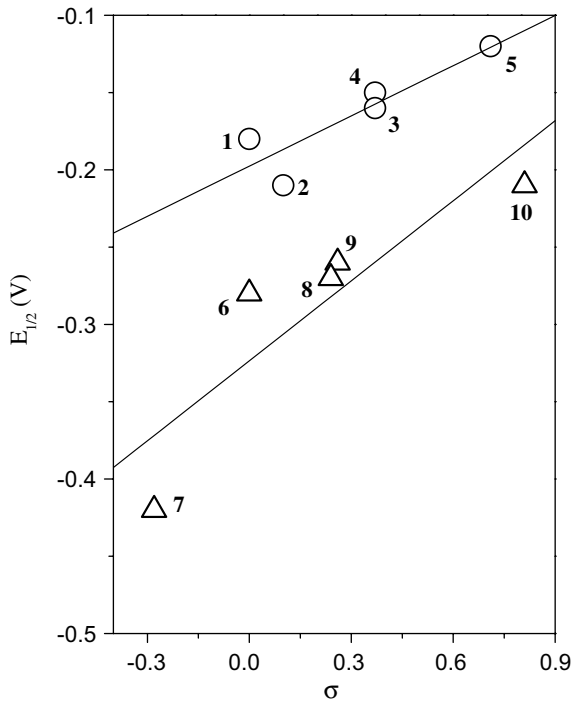


Fig. 5. Correlations between the $E_{1/2}$ values for the ruthenium(III) to ruthenium(II) reductions and the Hammett substituent constants for [Ru(HahsR)$(PPh_3)_2Cl_2$] (○) and [Ru(ahsR)$(PPh_3)_2Cl$] (△). The straight lines represent the linear least-squares fits.

are plotted against the Hammett constants (σ_m) [42] for the substituents (R) which are at the *meta*-position with respect to the metal coordinated azomethine (–CH=N–) group. On the other hand, the $E_{1/2}$ values of [Ru(ahsR)$(PPh_3)_2Cl$] (**6**–**10**) are plotted against the Hammett constants (σ_p) [42] for the substituents (R) which are *para* to the metal coordinated phenolate–O. In both cases, reasonable linear relationships ($R = 0.89$ and 0.88) are observed (Fig. 5). We have also plotted the $E_{1/2}$ values of **6**–**10** against the σ_m values as the substituent is *meta* to the coordinated azomethine–N. However, the linear least-squares fit of this plot is poor ($R = 0.68$) in comparison with that of the $E_{1/2}$ against σ_p plot. It may be noted that the two lines in Fig. 5 are not parallel. This indicates that there is a difference in the reaction constants (ρ). To calculate the values of ρ, we have used the relation $\Delta E_{1/2} = \rho\sigma$ where $\Delta E_{1/2}$ is the shift of $E_{1/2}$ of a particular complex from the $E_{1/2}$ of the complex having R = H [43]. The ρ values are 0.14(3) and 0.19(5) V for [Ru(HahsR)$(PPh_3)_2Cl_2$] and [Ru(ahsR)$(PPh_3)_2Cl$], respectively. Thus the ruthenium(III) to ruthenium(II) reduction in [Ru(ahsR)$(PPh_3)_2Cl$] is slightly more susceptible to the polar effects of the substituents compared to that in [Ru(HahsR)$(PPh_3)_2Cl_2$].

4. Conclusion

Formation of two types of ruthenium(III) complexes [Ru(HahsR)$(PPh_3)_2Cl_2$] ($HahsR^-$ is N,O-donor) and [Ru(ahsR)$(PPh_3)_2Cl$] ($ahsR^{2-}$ is O,N,O-donor) in the reactions of [Ru$(PPh_3)_3Cl_2$] with *N*-(acetyl)-*N*′-(5-*R*-salicylidene)hydrazines (H_2ahsR) in alcohol has been demonstrated. It is very likely that [Ru(HahsR)$(PPh_3)_2Cl_2$] is the intermediate during the formation of [Ru(ahsR)-$(PPh_3)_2Cl$]. Interestingly in [Ru(HahsR)$(PPh_3)_2Cl_2$] the less acidic amide functionality is deprotonated and coordinated through the O-atom while the more acidic phenol remains protonated. Earlier we have observed that in complexes of monoanionic tridentate acid hydrazide based Schiff bases, the more acidic functionality such as phenol or enol is deprotonated and bonded to the metal ion while the protonated amide functionality binds the metal ion through its O-atom [23,44,45]. It may be noted that these complexes do not contain bulky ancillary ligands. Perhaps during the formation of [Ru(HahsR)$(PPh_3)_2Cl_2$] from [Ru$(PPh_3)_3Cl_2$] the ligand first binds the metal centre through the acetyl end instead of the salicylaldimine end due to the steric constraints imposed by the bulky phosphine ligands of the starting material. The strong intramolecular phenolic-OH···N(deprotonated amide) hydrogen bond may also have a partial role in the observed binding mode of $HahsR^-$ in [Ru(HahsR)$(PPh_3)_2Cl_2$].

The one-electron paramagnetic complexes in frozen (110 K) dichloromethane–toluene (1:1) solutions display rhombic EPR spectra. Analysis of the EPR data shows that the rhombic component of the distortion in [Ru-(HahsR)$(PPh_3)_2Cl_2$] is significantly less than that in [Ru(ahsR)$(PPh_3)_2Cl$]. In the cyclic voltammetry, all the complexes display a ruthenium(III) to ruthenium(II) reduction response. The reduction potentials indicate that the reduction of the metal centre in [Ru(ahsR)$(PPh_3)_2Cl$] is difficult and more susceptible to the polar effects of the substituents (R) in comparison with that in [Ru(HahsR)$(PPh_3)_2Cl_2$].

5. Supplementary material

CCDC 661515 and 661516 contain the supplementary crystallographic data for **1**·$2CH_2Cl_2$ and **6**·CH_3CN. These data can be obtained free of charge via http://www.ccdc.cam.ac.uk/conts/retrieving.html, or from the Cambridge Crystallographic Data Centre, 12 Union Road, Cambridge CB2 1EZ, UK; fax: (+44) 1223-336-033; or e-mail: deposit@ccdc.cam.ac.uk.

Acknowledgements

Financial support for this work was provided by the Council of Scientific and Industrial Research, New Delhi (Grant No. 01(1880)/03/EMR-II). X-ray crystal structures were determined at the National Single Crystal Diffractometer Facility, School of Chemistry, University of Hyderabad (established by the Department of Science and Technology, New Delhi). We thank the University Grants Commission, New Delhi for the facilities provided under the UPE and CAS programs.

References

[1] E.A. Seddon, K.R. Seddon, The Chemistry of Ruthenium, Elsevier, New York, 1984.
[2] G. Wilkinson, R.D. Gillard, J.A. McCleverty, Comprehensive Coordination Chemistry, vol. 4, Pergamon, Oxford, 1987, pp. 277.
[3] B.K. Ghosh, A. Chakravorty, Coord. Chem. Rev. 95 (1989) 239.
[4] S.-M. Lee, W.-T. Wong, Coord. Chem. Rev. 164 (1997) 415.
[5] B.-Z. Shan, Q. Zhao, N. Goswami, D.M. Eichhorn, D.P. Rillema, Coord. Chem. Rev. 211 (2001) 117.
[6] C.E. Housecroft, Comprehensive Coordination Chemistry II, vol. 5, Elsevier Pergamon, Amsterdam, 2004, pp. 555.
[7] C.-M. Che, T.-C. Lau, Comprehensive Coordination Chemistry II, vol. 5, Elsevier Pergamon, Amsterdam, 2004, pp. 733.
[8] L. Sun, L. Hammarström, B. Åkermark, S. Styring, Chem. Soc. Rev. 30 (2001) 36.
[9] J.N. Demas, B.A. DeGraff, Coord. Chem. Rev. 211 (2001) 317.
[10] S.E. Angell, C.W. Rogers, Y. Zhang, M.O. Wolf, W.E. Jones Jr., Coord. Chem. Rev. 250 (2006) 1829.
[11] C. Joachim, J.K. Gimzewski, A. Aviram, Nature 408 (2000) 541.
[12] H. Tributsch, Coord. Chem. Rev. 248 (2004) 1511.
[13] N. Sardesai, S.C. Lin, K. Zimmermann, J.K. Barton, Bioconjugate Chem. 6 (1995) 302.
[14] H.B. Gray, J.R. Winkler, Annu. Rev. Biochem. 65 (1996) 537.
[15] D.B. Grotjahn, Coord. Chem. Rev. 190–192 (1999) 1125.
[16] M.J. Clarke, Coord. Chem. Rev. 236 (2003) 209.
[17] J.K. Hurst, Coord. Chem. Rev. 249 (2005) 313.
[18] C.-M. Che, Pure Appl. Chem. 67 (1995) 225.
[19] R. Zong, R.P. Thummel, J. Am. Chem. Soc. 127 (2005) 12802.
[20] T. Naota, H. Takaya, S.-I. Murahashi, Chem. Rev. 98 (1998) 2599.
[21] R. Drozdzak, B. Allaert, N. Ledoux, I. Dragutan, V. Dargutan, F. Verpoort, Coord. Chem. Rev. 249 (2005) 3055.
[22] S.N. Pal, S. Pal, J. Chem. Soc., Dalton Trans. (2002) 2102.
[23] S.N. Pal, S. Pal, Eur. J. Inorg. Chem. (2003) 4244.
[24] R. Raveendran, S. Pal, Polyhedron 24 (2005) 57.
[25] R. Raveendran, S. Pal, Inorg. Chim. Acta 359 (2006) 3212.
[26] R. Raveendran, S. Pal, J. Organomet. Chem. 692 (2007) 824.
[27] S.C. Chan, L.L. Koh, P.-H. Leung, J.D. Ranford, K.Y. Sim, Inorg. Chim. Acta 236 (1995) 101.
[28] T.A. Stephenson, G. Wilkinson, J. Inorg. Nucl. Chem. 28 (1966) 945.
[29] W.E. Hatfield, in: E.A. Boudreaux, L.N. Mulay (Eds.), Theory and Applications of Molecular Paramagnetism, Wiley, New York, 1976, p. 491.
[30] SMART Version 5.630 and SAINT-PLUS Version 6.45, Bruker-Nonius Analytical X-ray Systems Inc., Madison, WI, USA, 2003.
[31] G.M. Sheldrick, SADABS, Empirical Absorption Correction Program, University of Göttingen, Göttingen, Germany, 1997.
[32] G.M. Sheldrick, SHELX-97, Structure Determination Software, University of Göttingen, Göttingen, Germany, 1997.
[33] P. McArdle, J. Appl. Crystallogr. 28 (1995) 65.
[34] W. Kemp, in: Organic Spectroscopy, Macmillan, Hampshire, 1987, pp. 62–65.
[35] K. Nakamoto, in: Infrared and Raman Spectra of Inorganic and Coordination Compounds, Wiley, New York, 1986, pp. 241–244.
[36] F. Basuli, A.K. Das, G. Mostafa, S.-M. Peng, S. Bhattacharya, Polyhedron 19 (2000) 1663.
[37] S. Bhattacharya, A. Chakravorty, Proc. Indian Acad. Sci. (Chem. Sci.) 95 (1985) 159.
[38] S. Chattopadhyay, N. Bag, P. Basu, G.K. Lahiri, A. Chakravorty, J. Chem. Soc., Dalton Trans. (1990) 3389.
[39] S. Das, S. Pal, J. Organomet. Chem. 689 (2004) 352.
[40] S. Bhattacharya, C.G. Pierpont, Inorg. Chem. 30 (1991) 1511.
[41] M. Menon, A. Pramanik, N. Bag, A. Chakravorty, J. Chem. Soc., Dalton Trans. (1995) 1417.
[42] J. March, in: Advanced Organic Chemistry, 4th ed., Wiley, New York, 1992, p. 280.
[43] R.N. Mukherjee, O.A. Rajan, A. Chakravorty, Inorg. Chem. 21 (1982) 785.
[44] N.R. Sangeetha, S. Pal, J. Chem. Crystallogr. 29 (1999) 287.
[45] N.R. Sangeetha, C.K. Pal, P. Ghosh, S. Pal, J. Chem. Soc., Dalton Trans. (1996) 3293.

Available online at www.sciencedirect.com
ScienceDirect
Polyhedron 27 (2008) 663–670
POLYHEDRON
www.elsevier.com/locate/poly

Synthesis, characterizations and crystal structures of new antimony (III) complexes with dithiocarbamate ligands

Han-Dong Yin [a,*], Jun Zhai [a], Yu-Ying Sun [b], Da-Qi Wang [a]

[a] *Department of Chemistry, Liaocheng University, Liaocheng 252059, China*
[b] *Analytical and Testing Center of Beihua University, Beijing, China*

Received 25 September 2007; accepted 21 October 2007
Available online 3 December 2007

Abstract

Eight new antimony (III) complexes containing dithiocarbamate ligands $(R_2NCS_2)_2SbBr$ [$R_2NCS_2 = OC_4H_8NCS_2$ (**1**), $C_2H_5NC_4H_8NCS_2$ (**2**), Me_2NCS_2 (**3**), $C_4H_8NCS_2$ (**4**)] and $(R_2NCS_2)_3Sb$[$R_2NCS_2 = C_5H_{10}NCS_2$ (**5**), Bz_2NCS_2 (**6**), Et_2NCS_2 (**7**), $(HOCH_2CH_2)_2NCS_2$ (**8**)] have been synthesized by the reactions of antimony (III) halides with dithiocarbamate ligands in 1:2 or 1:3 stoichiometries. All the complexes have been characterized by elemental analysis, melting point as well as spectral [IR and NMR (^1H and ^{13}C)] studies. The crystal structures of complexes **1**, **5** and **8** have been determined by X-ray single crystal diffraction, and their electrochemical character has also been studied.

The structure of complex **1** shows that the five-coordinated antimony (III) atom adopts a distorted trigonal bipyramidal geometry. Furthermore, the supramolecular structure of **1** consists of a one-dimensional linear molecular chain which is built up by intermolecular Sb···S and S···S weak interactions. In complex **5**, the central antimony atom is six-coordinated with a distorted octahedral geometry and the supramolecular structure is constructed by C–H···S weak hydrogen bonds. The structure of complex **8** is stabilized by strong intermolecular hydrogen bonds between the ethanolic hydrogens (O–H).
© 2007 Elsevier Ltd. All rights reserved.

Keywords: Antimony (III) complexes; Dithiocarbamate; Crystal structure; X-ray diffraction

1. Introduction

Dialkyl-substituted dithiocarbamate anions have been proved to be highly versatile chelating agents for the separation of metals as metal chelates using gas chromatography [1]. Their performance in liquid–liquid extraction and other analytical procedures [2] make them attractive for the determination of metals using gas chromatography [3]. Some dialkyl-substituted dithiocarbamate salts have also shown interesting biological effects which include anti-alkylation [4,5] or anti-HIV properties [6,7]. With regard to structural studies, dithiocarbamate ligands often display unsymmetrical bidentate coordination patterns. Besides that, the ability of dithiocarbamate ligands to bind to metals has been known for many years [8], forming chelates with virtually all transition elements [9]. However, the chemistry of 1,1,-dithiochelates of main group elements is less widely explored than that of transition metals [8], especially the synthesis and structures of antimony (III) complexes with dithiocarbamate.

On the other hand, antimony complexes have been reported with good cytotoxicity and antitumor activities [10], especially Takahashi et al. have reported some antimony complexes can affect the repair of a DNA-double strand break [10c]. As a continuation of our interest in sulfur-containing ligands, we have synthesized eight new antimony (III) complexes with dithiocarbamates. All the complexes have been characterized by elemental analyses, IR spectra and NMR (^1H and ^{13}C). The crystal structures of complexes **1**, **5** and **8** have been determined by X-ray diffraction and their electrochemical character has also been studied.

* Corresponding author. Tel./fax: +86 6358239121.
E-mail address: handongyin@163.com (H.-D. Yin).

0277-5387/$ - see front matter © 2007 Elsevier Ltd. All rights reserved.
doi:10.1016/j.poly.2007.10.019

2. Experimental

2.1. Materials and instrumentation

Solvents were dried and distilled before use. The elemental analyses were performed on a PE-2400-II elemental analyzer. IR spectra were recorded on a Nicolet-460 spectrophotometer as KBr discs. X-ray measurements were made on a Bruker Smart-1000 CCD diffractometer with graphite monochromated Mo Kα ($\lambda = 0.71073$ Å) radiation. ^{1}H and ^{13}C NMR spectra were recorded on a Varian Mercury Plus-400 NMR spectrometer and the chemical shifts were reported in ppm relative to tetramethylsilane (TMS) in $CDCl_3$. The electrochemical characterisation was carried out on CHI900B.

2.2. Syntheses of dithiocarbamate

To a stirred solution of dialkyl-secondary amine (0.05 mol) in ethanol or methanol (5 ml) was added, at less than 4 °C, carbon disulfide (3.1 ml, 0.052 mol) and sodium hydroxide (50% aqueous solution, 4 ml). After stirring for 4–5 h, evaporation of volatiles was performed without heating. Pure [Na(R_2dtc)] was obtained by recrystallization from ethanol (or methanol). Yield: 80–90%:

$$CS_2 + R_2NH + NaOH \xrightarrow[\text{or } CH_3OH]{CH_3CH_2OH} R_2NCS_2Na + H_2O$$

where $R_2NCS_2Na = OC_4H_8NCS_2Na$, $C_2H_5NC_4H_8NCS_2Na$, Me_2NCS_2Na, $C_4H_8NCS_2Na$, $C_5H_{10}NCS_2Na$, Bz_2NCS_2Na, Et_2NCS_2Na $(HOCH_2CH_2)_2NCS_2K$.

2.3. Syntheses of complexes *1–8*

2.3.1. Preparation of $(OC_4H_8NCS_2)_2SbBr$ (*1*)

Morpholinyldithiocarbamate (74.2 mg, 0.4 mmol) was added to a stirring solution containing $SbBr_3$ (72.3 mg, 0.2 mmol) in acetone (25 ml). After stirring for 5 h at room temperature a yellow solution was obtained and then filtered. The solvent was gradually removed by evaporation under vacuum until a yellow solid was obtained. The solid was recrystallized from ethanol/dichloromethane (1:1) to give yellow crystals, yield 80%, m.p. 235 °C. *Anal.* Calc. for $C_{10}H_{16}BrN_2O_2S_4Sb$ (Mw = 526.15): C, 22.83; H, 3.06; N, 5.32. Found: C, 22.67; H, 3.17; N, 5.43%. IR (KBr) ν(cm^{-1}): 3431, 2973, 2927, 1634, 1569, 1495, 1383, 1353, 1295, 1266, 1203, 1140, 1091, 987, 880, 776, 564, 412. ^{1}H NMR ($CDCl_3$) δ: 4.08 (8H, t, OCH_2), 3.68 (8H, s, NCH_2). ^{13}C NMR ($CDCl_3$) δ: 198.43 (CS_2), 61.01 (CH_2N), 45.21 (CH_2O).

2.3.2. Preparation of $(C_2H_5NC_4H_8NCS_2)_2SbBr$ (*2*)

Complex **2** was prepared in the same way as **1**. The yellow solid was recrystallized from chloroform to give yellow crystals, yield 85%, m.p. 240 °C. *Anal.* Calc. for $C_{14}H_{26}BrN_6S_4Sb$ (Mw = 608.32): C, 27.64; H, 4.31; N, 13.82; S, 21.08. Found: C, 27.51; H, 4.50; N, 13.96; S, 21.25%. IR (KBr) ν(cm^{-1}): 3415, 2961, 2930, 1645, 1548, 1479, 1375, 1310, 1132, 1071, 994, 839, 619, 545, 419. ^{1}H NMR ($CDCl_3$) δ: 3.76 (16H, t, NCH_2CH_2N), 2.52 (4H, m, NCH_2), 2.76 (6H, t, CH_3). ^{13}C NMR ($CDCl_3$) δ: 197.13 (CS_2), 51.96, 51.62 (NCH_2CH_2N), 43.59, 11.92 (NCH_2CH_3).

2.3.3. Preparation of $(Me_2NCS_2)_2SbBr$ (*3*)

Complex **3** was prepared in the same way as **1**. The yellow solid was recrystallized from ethanol to give yellow crystals, yield 85%, m.p. 258 °C. *Anal.* Calc. for $C_6H_{12}BrN_2S_4$ Sb (Mw = 442.10): C, 16.30; H, 2.74; N, 6.34; S, 29.01. Found: C, 16.42; H, 2.63; N, 6.26; S, 29.12%. IR (KBr) ν(cm^{-1}): 3420, 2968, 2920, 1630, 1562, 1485, 1379, 1342, 1135, 985, 850, 530, 415. ^{1}H NMR ($CDCl_3$) δ: 3.02 (12H, s, NCH_3). ^{13}C NMR ($CDCl_3$) δ: 196.70 (CS_2), 46.45 (NCH_3).

2.3.4. Preparation of $(CH_3NC_4H_8NCS_2)_2SbBr$ (*4*)

Complex **4** was prepared in the same way as **1**. The yellow solid was recrystallized from ethanol to give yellow crystals, yield 85%, m.p. 250 °C. *Anal.* Calc. for $C_{12}H_{22}BrN_6S_4Sb$ (Mw = 580.27): C, 24.84; H, 3.82; N, 14.48; S, 22.10. Found: C, 24.70; H, 3.69; N, 14.59; S, 21.95%. IR (KBr) ν(cm^{-1}): 3426, 2964, 2923, 1640, 1546, 1481, 1385, 1329, 1141, 991, 842, 560, 416. ^{1}H NMR ($CDCl_3$) δ: 2.72 (6H, s, NCH_3), 4.08, 4.22 (16H, t, NCH_2CH_2N). ^{13}C NMR ($CDCl_3$) δ: 198.61 (CS_2), 53.52, 50.64, 47.60 (NCH_2, NCH_3).

2.3.5. Preparation of $[(C_5H_{10}NCS_2)_3Sb]_2 \cdot CH_2Cl_2$ (*5*)

Dithiopiperidylcarbamate (109 mg, 0.6 mmol) was dissolved in 10 ml of acetone. $SbCl_3$(45.6 mg, 0.2 mmol) dissolved in acetone (5 ml) was added dropwise to the complex in solution with continuous stirring. The reaction mixture was stirred for 5 h at room temperature. Then the solvent was gradually removed by evaporation under vacuum until a yellow solid was obtained. Single crystals suitable for X-ray diffraction analysis were obtained from ethanol/dichloromethane (1:1) solution, yield 90%, m.p. 258 °C. *Anal.* Calc. for $C_{37}H_{62}C_{l2}N_6S_{12}Sb_2$ (Mw = 1290.05): C, 34.44; H, 4.84; N, 6.51; S, 29.82. Found: C, 34.59; H, 4.68; N, 6.70; S, 29.67%. IR (KBr) ν(cm^{-1}): 3423, 2970, 2918, 1635, 1543, 1495, 1468, 1380, 1334, 1137, 1058, 992, 975, 846, 546, 423. ^{1}H NMR ($CDCl_3$) δ: 1.69, 1.56 (18H, t, CH_2), 3.63 (12H, m, NCH_2). ^{13}C NMR ($CDCl_3$) δ: 198.06 (CS_2), 51.93 (NCH_2), 29.71, 24.82 (CH_2).

2.3.6. Preparation of $(Bz_2NCS_2)_3Sb$ (*6*)

Complex **6** was prepared in the same way as **5**. The yellow solid was recrystallized from acetonitrile to give yellow crystals, yield 85%, m.p. 285 °C. *Anal.* Calc. for $C_{45}H_{42}N_3S_6$ Sb (Mw = 938.98): C, 57.56; H, 4.51; N, 4.48; S, 20.49. Found: C, 57.41; H, 4.68; N, 4.56; S, 20.63%. IR (KBr) ν(cm^{-1}): 3424, 2965, 2925, 1630, 1556, 1483, 1372, 1325, 1136, 996, 871, 556, 420. ^{1}H NMR

Table 1
Crystal data and structure refinement details for complexes **1**, **5** and **8**

Complex	**1**	**5**	**8**
Empirical formula	$C_{10}H_{16}BrN_2O_2S_4Sb$	$C_{37}H_{62}C_{12}N_6S_{12}Sb_2$	$C_{15}H_{30}N_3O_6$ S_6Sb
Formula weight	526.15	1290.05	662.53
T (K)	293(2)	298(2)	298(2)
Crystal system	triclinic	triclinic	triclinic
Space group	$P\bar{1}$	$P\bar{1}$	$P\bar{1}$
a (Å)	6.428(2)	10.785(2)	9.983(3)
b (Å)	11.175(4)	15.345(3)	11.115(3)
c (Å)	13.241(4)	16.999(3)	12.502(4)
α (°)	71.060(4)	72.545(2)	104.339(4)
β (°)	81.796(4)	88.870(2)	105.043(4)
γ (°)	76.924(3)	83.336(2)	94.037(4)
V (Å^3)	873.8(5)	2665.3(9)	1284.4(7)
Z	2	2	2
$F(000)$	512	1308	672
D_{calc} (g cm^{-3})	2.000	1.607	1.713
Crystal dimensions (mm)	$0.48 \times 0.46 \times 0.43$	$0.39 \times 0.37 \times 0.35$	$0.43 \times 0.25 \times 0.11$
θ Range (°)	2.14–25.01	1.26–25.01	2.13–25.01
Reflections collected	4592	13914	6658
Independent reflections	3044	9232	4444
R_{int}	0.0221	0.0192	0.0246
Maximum and minimum transmission	0.2567 and 0.2296	0.6013 and 0.5710	0.8439 and 0.5467
Data/restraints/parameters	3044/0/ 181	9232/1/532	4444/0/280
Goodness-of-fit on F^2	1.035	1.014	1.005
Final R indices	$R_1 = 0.0516$	$R_1 = 0.0381$	$R_1 = 0.0407$
$[I > 2\sigma(I)]$	$wR_2 = 0.1557$	$wR_2 = 0.0985$	$wR_2 = 0.1062$
R indices (all date)	$R_1 = 0.0590$	$R_1 = 0.0611$	$R_1 = 0.0509$
	$wR_2 = 0.1602$	$wR_2 = 0.1174$	$wR_2 = 0.1165$
Largest difference in peak/hole (e A^{-3})	2.018 and −1.039	0.850 and −0.604	1.499 and −1.000

($CDCl_3$) δ: 6.92–7.24 (30 H, m, Ar-H), 3.96 (12H, t, NCH_2). ^{13}C NMR ($CDCl_3$) δ: 198.94 (CS_2), 54.42, 141.01, 137.53, 130.26, 124.75 ($NCH_2C_6H_5$).

2.3.7. Preparation of $(Et_2NCS_2)_3Sb$ (7)

Complex **7** was prepared in the same way as **5**. The yellow solid was recrystallized from acetonitrile to give yellow crystals, yield 85%, m.p. 270 °C. *Anal.* Calc. for $C_{15}H_{30}N_3S_6Sb$ (Mw = 566.57): C, 31.80; H, 5.34; N, 7.42; S, 33.96. Found: C, 31.97; H, 5.18; N, 7.56; S, 34.12%. IR (KBr) ν(cm^{-1}): 3428, 2967, 2923, 1632, 1558, 1492, 1379, 1346, 1269, 1148, 983, 884, 845, 562, 425. ^{1}H NMR ($CDCl_3$) δ: 1.23 (18H, t, CH_3), 3.68 (12H, m, NCH_2). ^{13}C NMR ($CDCl_3$) δ: 197.19 (CS_2), 49.69, 43.61 (NCH_2CH_3).

2.3.8. Preparation of $[(HOCH_2CH_2)_2NCS_2]_3Sb$ (8)

N,*N*′-Iminodiethanoldithiocarbamate (133 mg, 0.6 mmol) was dissolved in 10 ml of THF. $SbBr_3$ (72.3 mg, 0.2 mmol) dissolved in tetrahydrofuran (5 ml) was added dropwise to the complex in solution with continuous stirring. The reaction mixture was stirred for 5 h at room temperature. Then the solvent was gradually removed by evaporation under vacuum until a yellow solid was obtained. Single crystals suitable for X-ray diffraction analysis were grown by recrystallization from ethanol/dichloromethane (1:1) solution, yield 80%, m.p. 260 °C. *Anal.* Calc. for $C_{15}H_{36}N_3O_6S_6Sb$ (Mw = 662.53): C, 26.94; H, 5.43; N, 6.28; S, 28.77. Found: C, 27.05; H, 5.31; N, 6.38; S, 38.62%. IR (KBr) ν(cm^{-1}): 3429, 2975, 2931, 1615, 1572, 1486, 1378, 1352, 1271, 1134, 1086, 995, 876, 775, 558, 416. ^{1} NMR ($CDCl_3$) δ: 3.72 (12H, t, NCH_2), 4.06 (12H, m, OCH_2), 4.5 (OH). ^{13}C NMR ($CDCl_3$) δ: 197.86 (CS_2), 54.36 (NCH_2), 46.32 (OCH_2).

2.4. Crystal structure determination and refinement

Single crystals suitable for X-ray analysis were mounted on a fiber. All measurements were made on a Bruker Smart-1000 CCD diffractometer with graphite monochromated Mo Kα ($\lambda = 0.71073$ Å) radiation at 298(2) K using the Φ/ω scan technique. The structures were solved by the direct method and different Fourier syntheses using the SHELXL-97 program, and refined by full-matrix least-squares on F^2. All non-hydrogen atoms were refined anisotropically. Hydrogen atoms were placed at calculated positions with C–H distances of 0.96 Å and riding on carrier atoms. In the refinement of compound **5**, the restraint we used was delu 0.001 0.0005 Sb2 S10. Crystallographic data and experimental details of the structure determinations are listed in Table 1.

3. Results and discussion

3.1. IR spectra

The explicit feature in the IR spectra compared with sodium dithiocarbamate is the new absorption at around 420 cm^{-1}, which may be assigned to the Sb–S stretching

mode of the vibration. The strong bands at about 1480–1500 cm^{-1} are attributed to the ν(C–N) stretching vibration, which shift to higher frequencies than the free ligands (1450–1476 cm^{-1}). It is suggested that the coordination mode of the dithiocarbamate ligands with antimony ions is bidentate by the sulfur atom. In addition, it is worthy to note that besides the absorption at 1495 cm^{-1}, belonging to C–N, there is another strong band at 1468 cm^{-1} in complex **5**. The shift to higher frequency is only 10–20 cm^{-1}, which is smaller than the shift above. It is shown that there is another coordination mode of dithiopiperidylcarbamate, a unidentate form, which is consistent with the crystal structure of complex **5**.

Furthermore, $\Delta\nu[\nu(CS_2)_{asym}-\nu(CS_2)_{sym}]$ can also illuminate the coordination fashion of these complexes. $\nu(CS_2)_{asym}$ and $\nu(CS_2)_{sym}$ appear at 1132–1152 cm^{-1} and 980–998 cm^{-1}, respectively. The $\Delta\nu$ values $[\nu(CS_2)_{asym}-\nu(CS_2)_{sym}]$ are 110–153 cm^{-1}, which are much smaller than the $\Delta\nu$ values for R_2NCS_2R' [11], but are much larger than the corresponding sodium dithiocarbamate values [12]. All of the above show that the dithiocarbamate groups are coordinated to the Sb atom in an anisobidentate fashion. In complex **5**, however, the C–S stretching vibration also appears at 1058 cm^{-1} and 975 cm^{-1}. The $\Delta\nu$ value is 83 cm^{-1}, almost the same as the corresponding sodium dithiocarbamate value ($\Delta\nu = 90$ cm^{-1}), which suggests that some of the dithiocarbamate ligands adopt a unidentate coordination mode in this complex.

3.2. ^1H and ^{13}C NMR

The ^1H NMR chemical shifts at 2.9 and 3.6 ppm are ascribed to methyl and methylene linked directly with N atoms contained in dithiocarbamate, respectively. They shift downfield by δ 0.4–0.9 ppm as compared to the salts of the appropriate acid. It is shown that the coordinated dithiocarbamate group is more electronegative than in the case of no coordination [13]. The multiple signals observed in the region δ 6.72–7.41 ppm are attributed to the protons of phenyl rings. The methylene protons connected with the O atom in complexes **1** and **8** appear at around 4.10 ppm.

The ^{13}C NMR spectra of these complexes show one sharp singlet signal in the region about δ 196 ppm which may be attributed to the carbon of CS_2. In addition, the signals for the carbons of methyl and methylene groups connected directly to the N atoms appear at about 50 ppm. Additionally, these derivatives also exhibit the expected signals due to the carbons of aryl groups at 120–150 ppm and the carbons of methylene linked directly with the O atoms appear at about 46 ppm.

3.3. Electrochemical properties

The cyclic voltammetric studies were carried out with a glassy carbon electrode as the working electrode, a saturated calomel electrode (SCE) as the reference electrode, and a platinum slice as the counter electrode. Typical voltamograms of complexes **1**, **5** and **8** are shown in Fig. 1. All three complexes show two completely irreversible oxidation responses around −0.6 V and −0.2 V, which are attributed to Sb^{3+}/Sb^{4+} and Sb^{4+}/Sb^{5+}, respectively. That is to say, all the oxidation processes for the complexes involve the transfer of one electron. Compared with complexes **5** and **8**, there is also an irreversible oxidation response at about +0.85 V in complex **1**, which may be due to Br^-/Br_2. Owing to the insolubility of the complexes, the peak current is very weak.

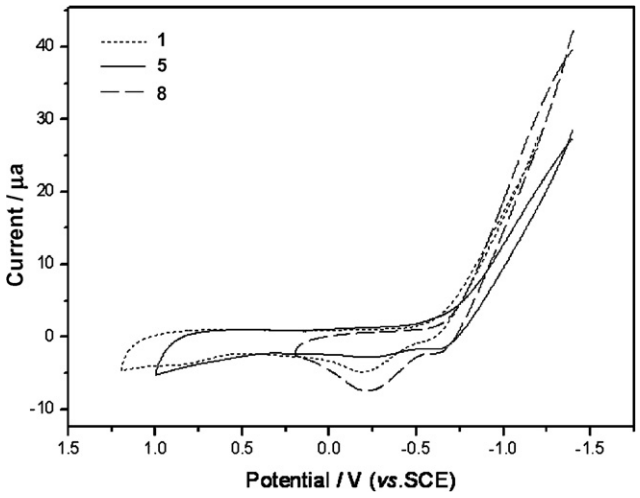


Fig. 1. Voltammograms of complexes **1**, **5** and **8**.

3.4. Crystal structure of complex *1*

Selected bond distances and angles of complex **1** are given in Table 2 and the molecular structure is shown in Fig. 2. The two-dimensional network is displayed in Fig. 3.

As is shown in Fig. 2, the coordination environment of the central antimony atom is five-coordinated with a dis-

Table 2
Selected bond lengths (Å) and angles (°) for complex **1**

Sb(1)–S(3)	2.469(2)	S(4)–S(3)#3	3.564(3)
Sb(1)–S(1)	2.542(2)	N(1)–C(1)	1.32(1)
Sb(1)–S(2)	2.621(2)	N(2)–C(6)	1.33(1)
Sb(1)–Br(1)	2.809(1)	S(1)–C(1)	1.748(9)
Sb(1)–S(4)	2.909(2)	S(2)–C(1)	1.716(9)
Sb(1)–S(1)#1	3.647(2)	S(3)–C(6)	1.740(8)
S(3)–S(4)#2	3.564(3)	S(4)–C(6)	1.702(8)
S(3)–Sb(1)–S(1)	89.32(8)	S(2)–Sb(1)–S(4)	79.63(7)
S(3)–Sb(1)–S(2)	92.18(8)	Br(1)–Sb(1)–S(4)	124.28(6)
S(1)–Sb(1)–S(2)	69.49(7)	S(3)–Sb(1)–S(1)#1	159.42(6)
S(3)–Sb(1)–Br(1)	83.76(6)	S(1)–Sb(1)–S(1)#1	77.14(8)
S(1)–Sb(1)–Br(1)	80.99(6)	S(2)–Sb(1)–S(1)#1	97.36(7)
S(2)–Sb(1)–Br(1)	150.27(6)	Br(1)–Sb(1)–S(1)#1	78.90(5)
S(3)–Sb(1)–S(4)	66.17(7)	S(4)–Sb(1)–S(1)#1	133.49(6)
S(1)–Sb(1)–S(4)	139.75(7)	N(1)–C(1)–S(2)	122.9(6)
N(1)–C(1)–S(1)	120.7(6)	S(2)–C(1)–S(1)	116.3(5)
N(2)–C(6)–S(4)	123.2(6)	N(2)–C(6)–S(3)	118.3(6)

Symmetry code: #1 $-x,-y+1,-z+1$; #2 $x+1, y, z$; #3 $x-1, y, z$.

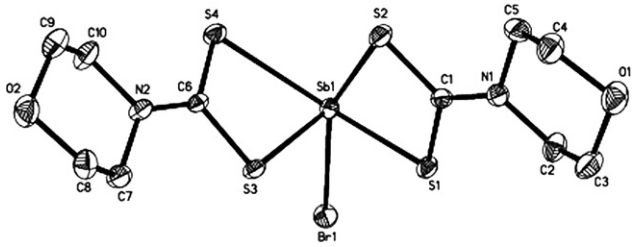


Fig. 2. The molecular structure of complex **1**.

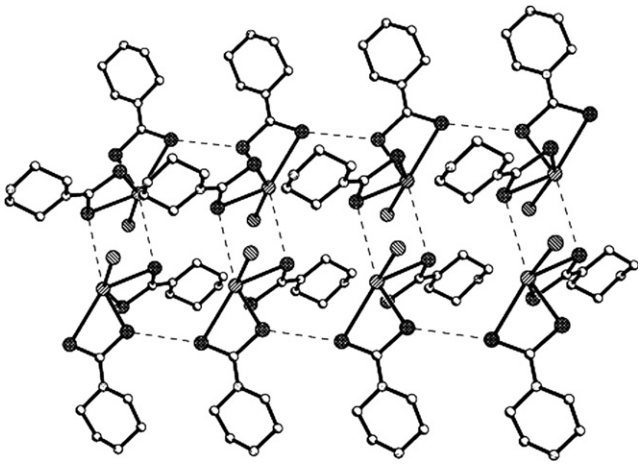


Fig. 3. The supramolecular structure of complex **1**, showing a 2D network linked by intermolecular Sb···S and S···S contacts.

torted trigonal bipyramidal geometry. Around the central Sb atom, S(1), S(3) and S(4) occupy the equatorial plane, while Br(1) and S(2) lie in axial sites. The sum of the equatorial angles is 295.24° ((S(3)–Sb(1)–S(1) 89.32(8)°, S(3)–Sb(1)–S(4) 66.17(7)°, S(1)–Sb(1) –S(4) 139.75(7)°) and the corresponding axial–Sb–axial angle is 150.27(6)°, which suggests that it has large deviations from an ideal trigonal bipyramidal geometry. Among the four Sb–S bond lengths, two of them are short (Sb1–S3 2.469(2) Å, Sb1–S1 2.542(2) Å), which form strong bonds. While the other two are long (Sb1–S2 2.621(2) Å, Sb1–S4 2.909(2) Å), forming weak bonds.

The C–S bonds associated with the strong Sb–S bonds are significantly longer (mean = 1.744(9) Å) than those associated with the weak Sb–S bonds (mean = 1.709(9) Å) [14,15], suggesting some delocation in the system. The N–C bond distances in this complex (mean = 1.33(1)) are manifestations of the presence of a partial double bond. The IR spectrum of the above complex shows a ν(C–N) value of 1490 cm^{-1}, which lies between the single and double bond values, indicating contribution of the thioureide form to the dithiocarbamate [8].

In this complex, the N–C═S angles (mean 123.1(6)°) are considerably larger than the N–C–S angles (mean 119.5(6)°), as expected due to the mutual repulsion between the double bond and the adjacent electronegative atom.

Interestingly, there is a two-dimensional network in the crystal lattice of the complex, which is linked by intermolecular weak Sb···S and S···S contacts of 3.647(2) and 3.564(3) Å, respectively.

3.5. Crystal structure of complex 5

Selected bond distances and angles of complex **5** are given in Table 3. The molecular structure and two-dimensional network are shown in Figs. 4 and 5.

As shown in Fig. 4, the asymmetric unit contains two crystallographically independent molecules A and B, together with a dichloromethane solvent molecule. Between the independent molecules, there is an intramolecular weak hydrogen bond C26–H26A···S4 (C26···S4 3.737(8) Å, H26A···S4 2.79 Å, C26–H26A···S4 166.3°), which links them together. Conformations of the two independent molecules are almost the same, with only a few differences in bond lengths and angles. From Table 3 we can see that around the Sb atom there are three short Sb–S bonds and three long ones, indicating strong coordinations and weak interactions, for Sb(1) as well as for Sb(2). The distances of the long Sb–S bonds are much shorter than the sum of the van der Waals radii of the Sb and S atom, 3.92 Å[16]. Obviously, there are apparent weak intramolecular Sb···S interactions in this complex. Therefore, the Sb atom could be described as six-coordinated with a distorted octahedral geometry, if the weak Sb···S interactions are also taken into consideration.

The central Sb1 atom is surrounded axially by S2 and S5 atoms and equatorially by S1, S3, S4 and S6. The sum of the equatorial angles are 355.97(5)° (S(1)–Sb(1)–S(3) 86.68(5)°, S(1)–Sb(1)–S(6) 86.82(5)°, S(3)–Sb(1)–S(4) 64.47(4)°, S(6)–Sb(1)–S(4) 118.0(5)°), which show that these atoms are not coplanar. Furthermore, the angle of

Table 3
Selected bond lengths (Å) and angles (°) for complex **5**

Sb(1)–S(5)	2.538(1)	Sb(2)–S(9)	2.517(2)
Sb(1)–S(1)	2.537(2)	Sb(2)–S(11)	2.519(2)
Sb(1)–S(3)	2.542(1)	Sb(2)–S(7)	2.545(2)
Sb(1)–S(6)	2.928(2)	Sb(2)–S(10)	2.895(2)
Sb(1)–S(2)	2.933(2)	Sb(2)–S(12)	2.993(2)
Sb(1)–S(4)	2.975(2)	Sb(2)–S(8)	3.013(2)
S(5)–Sb(1)–S(1)	89.25(5)	S(9)–Sb(2)–S(11)	87.96(5)
S(5)–Sb(1)–S(3)	84.70(4)	S(9)–Sb(2)–S(7)	84.49(5)
S(1)–Sb(1)–S(3)	86.68(5)	S(11)–Sb(2)–S(7)	81.60(5)
S(5)–Sb(1)–S(6)	64.95(4)	S(9)–Sb(2)–S(10)	65.65(5)
S(1)–Sb(1)–S(6)	86.82(6)	S(11)–Sb(2)–S(10)	85.61(6)
S(3)–Sb(1)–S(6)	149.01(5)	S(7)–Sb(2)–S(10)	147.88(5)
S(5)–Sb(1)–S(2)	153.53(5)	S(9)–Sb(2)–S(12)	149.42(5)
S(1)–Sb(1)–S(2)	65.15(4)	S(11)–Sb(2)–S(12)	64.22(4)
S(3)–Sb(1)–S(2)	87.08(5)	S(7)–Sb(2)–S(12)	102.58(6)
S(6)–Sb(1)–S(2)	117.18(4)	S(10)–Sb(2)–S(12)	98.05(6)
S(5)–Sb(1)–S(4)	88.68(5)	S(9)–Sb(2)–S(8)	86.53(5)
S(1)–Sb(1)–S(4)	151.14(5)	S(11)–Sb(2)–S(8)	145.37(5)
S(3)–Sb(1)–S(4)	64.47(4)	S(7)–Sb(2)–S(8)	63.86(5)
S(6)–Sb(1)–S(4)	118.00(5)	S(10)–Sb(2)–S(8)	122.42(5)
S(2)–Sb(1)–S(4)	110.26(5)	S(12)–Sb(2)–S(8)	123.47(5)

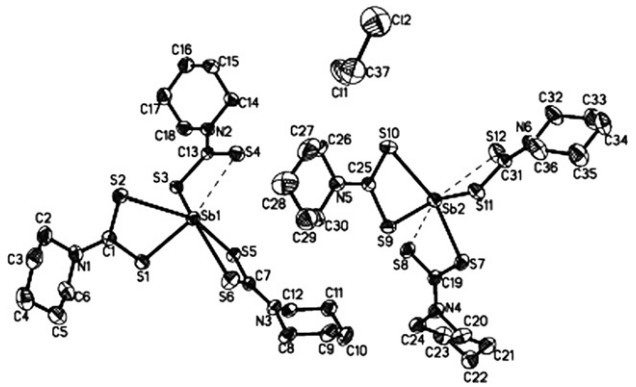


Fig. 4. The molecular structure of complex **5**.

axial S2–Sb1–S5 is 153.53(5)°, deviating from 180°. The conformation of Sb2 is almost the same as Sb1, with only a few differences in bond lengths and bond angles.

The supramolecular structure of complex **5** is dominated by a two-dimensional network connected by intramolecular C–H···S (C26···S4 3.737(8) Å, H26A···S4, 2.79 Å, C26–H26A···S4 166.3°) and intermolecular C–H···S (C3···S6 3.710(6) Å, H3B···S6 2.83 Å, C3–H3B···S6 152.1°, C36···S6 3.821(7) Å , H36B···S6 2.94 Å, C36–H36B···S6 151.5°) weak hydrogen bonds.

3.6. Crystal structure of complex *8*

Selected bond distances and angles of complex **8** are given in Table 4 and hydrogen bonds in Table 5. The molecular structure, projections of the unit cell and the 3D framework are depicted in Figs. 6–8, respectively.

A similar molecular structure of this complex has been reported, which was prepared by the reaction of $SbCl_3$ with the corresponding dithiocarbamate ligand [17].

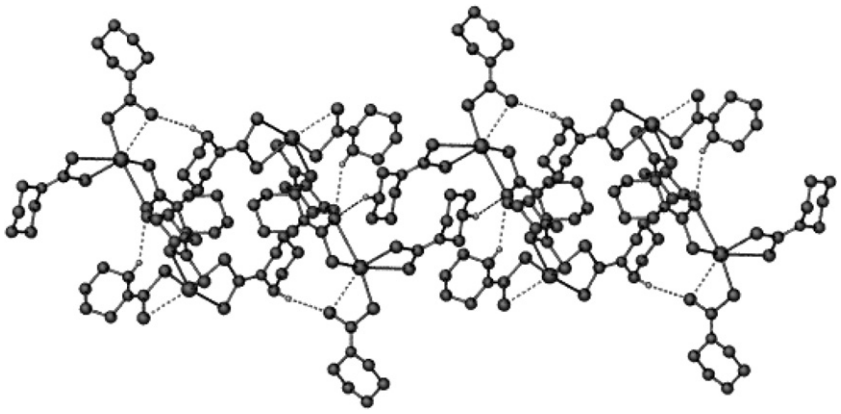


Fig. 5. Supramolecular structure of complex **5**, showing a 2D network linked by C–H···S weak hydrogen bonds.

Table 4
Selected bond lengths (Å) and angles (°) for complex **8**

Sb(1)–S(3)	2.464(1)	S(3)–C(6)	1.765(4)
Sb(1)–S(1)	2.645(1)	S(4)–C(6)	1.695(4)
Sb(1)–S(6)	2.677(1)	S(5)–C(11)	1.701(5)
Sb(1)–S(2)	2.759(1)	S(6)–C(11)	1.717(5)
Sb(1)–S(5)	2.843(1)	N(1)–C(1)	1.345(6)
Sb(1)–S(4)	2.876(1)	N(2)–C(6)	1.315(6)
S(1)–C(1)	1.732(4)	N(3)–C(11)	1.345(6)
S(2)–C(1)	1.703(4)		
S(3)–Sb(1)–S(1)	91.38(4)	S(6)–Sb(1)–S(5)	64.52(4)
S(3)–Sb(1)–S(6)	92.90(5)	S(2)–Sb(1)–S(5)	152.66(4)
S(1)–Sb(1)–S(6)	76.79(4)	S(3)–Sb(1)–S(4)	67.06(4)
S(3)–Sb(1)–S(2)	90.16(4)	S(1)–Sb(1)–S(4)	138.61(4)
S(1)–Sb(1)–S(2)	66.05(4)	S(6)–Sb(1)–S(4)	136.05(4)
S(6)–Sb(1)–S(2)	142.78(4)	S(2)–Sb(1)–S(4)	78.59(4)
S(3)–Sb(1)–S(5)	85.69(5)	S(5)–Sb(1)–S(4)	74.90(4) 113.2(4)
S(1)–Sb(1)–S(5)	140.95(4)	O(1)–C(3)–C(2)	
O(2)–C(5)–C(4)	112.5(4)	O(3)–C(8)–C(7)	112.2(4)
O(4)–C(10)–C(9)	111.9(4)	O(5)–C(13)–C(12)	110.0(4) 124.0(3)
O(6)–C(15)–C(14)	110.2(4)	N(2)–C(6)–S(4)	
N(1)–C(1)–S(2)	122.0(3)	N(2)–C(6)–S(3)	117.8(3)
N(1)–C(1)–S(1)	119.8(3)	N(3)–C(11)–S(6)	119.8(4)
N(3)–C(11)–S(5)	120.9(4)		

Table 5
Hydrogen bonds (Å, °) for complex **8**

D–H	*d*(D–H)	*d*(H···A)	∠DHA	*d*(D···A)	A
O1–H1	0.820	2.026	149.19	2.763	O5 #1
O2–H2	0.820	1.936	155.82	2.705	O6 #2
O3–H3	0.820	1.872	171.38	2.685	O2 #3
O4–H4	0.820	2.329	110.36	2.725	O1 #4
O4–H4	0.820	2.431	113.22	2.855	O5 #5
O5–H5	0.820	2.044	170.41	2.855	O4 #5
O6–H6	0.820	1.986	150.58	2.730	O3 #6

Symmetry code: #1 $-x+1, -y+1, -z+1$; #2 $-x+1, -y, -z+1$; #3 $-x, -y, -z$; #4 $-x+1, -y, -z$; #5 $-x, -y+1, -z$; #6 $-x, -y+1, -z+1$.

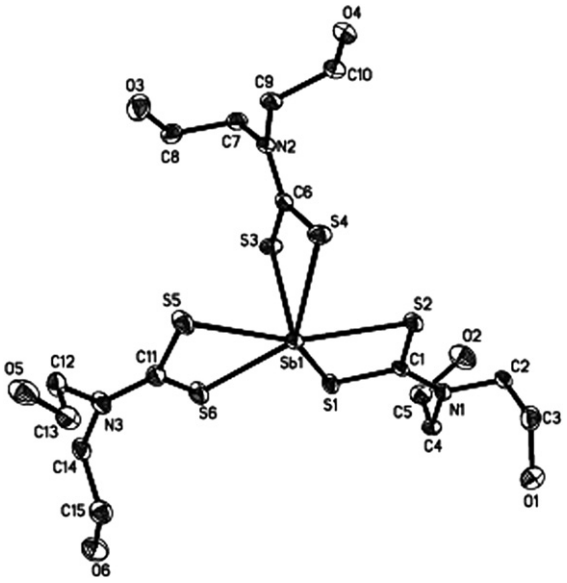


Fig. 6. The molecular structure of complex **8**.

In this complex the Sb atom is coordinated by six S atoms belonging to three *N*,*N*′-iminodiethanoldithiocarbamate ligands. The resulting SbS_6 coordination polyhedron approximates a pentagonal pyramid with S3 in the apical position and the other five atoms (Sb1, S1, S2, S4, S5, S6) occupying the equatorial position, which is similar to the structure reported earlier, with only some differences in bond lengths and bond angles.

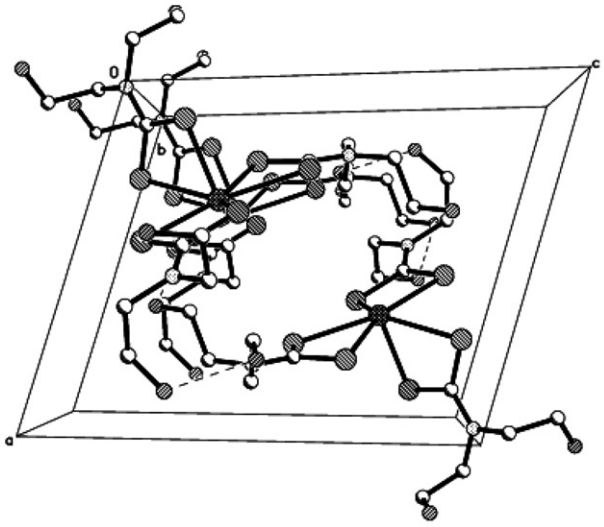


Fig. 7. Projection of the unit cell of complex **8**.

The molecules are held together by strong intermolecular hydrogen bonds between the ethanolic hydrogens (O–H). As a result, the supermolecular structure of this complex can be described as 3D network structure, which is shown in Fig. 8, built up by intermolecular O–H···O hydrogen bonds.

Acknowledgements

We acknowledge the National Natural Science Foundation of China (Grant #20771053) and the Natural Science Foundation of Shandong Province (2005ZX09) for financial support.

Appendix A. Supplementary material

CCDC 601742, 652968 and 601743 contain the supplementary crystallographic data for **1**, **5** and **8**, respectively. These data can be obtained free of charge via http://www.ccdc.cam.ac.uk/conts/retrieving.html, or from the Cambridge Crystallographic Data Centre, 12 Union Road, Cambridge CB2 1EZ, UK; fax: (+44) 1223-336-033; or e-mail: deposit@ccdc.cam.ac.uk. Supplementary data

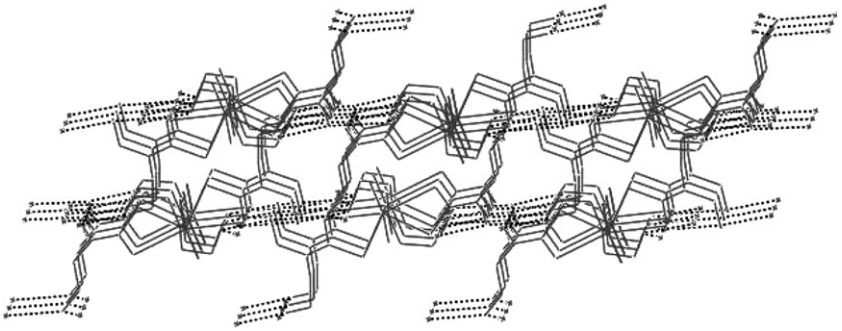


Fig. 8. Supramolecular structure of complex **8**, showing a 3D framework connected by O–H···O hydrogen bonds.

associated with this article can be found, in the online version, at doi:10.1016/j.poly.2007.10.019.

References

[1] M.L. Riekkola, O. Makitie, M. Sundberg, Kem. Kemi. 6 (1979) 523.
[2] G.D. Thorn, R.A. Ludwig, The Dithiocarbamate and Related Complexes, Elsevier, Amsterdam, 1962, p. 1.
[3] M.L. Riekkola, T. Pakkanen, L. Niinisto, Acta Chim. Scand. A37 (1983) 807.
[4] A. Gringeri, P.C. Keng, R.F. Borch, Cancer Res. 48 (1988) 5708.
[5] M.H. Zeng, H. Liang, R.X. Hu. Chinese, J. Appl. Chem. 8 (2001) 837.
[6] T.L. Sheng, X.T. Wu, P. Lin, Polyhedron 18 (1999) 1049.
[7] L.J. Farrugia, F.J. Lawlor, N.C. Norman, J. Chem. Soc., Dalton Trans. (1995) 1163.
[8] D. Coucouvanis, Prog. Inorg. Chem. 11 (1970) 233.
[9] L.Z. Xu, P.S. Zhao, S.S. Zhang, Chin. J. Chem. 19 (2001) 436.
[10] (a) E.R.T. Tiekink, Crit. Rev. Oncol./Hematol. 42 (2002) 21;
(b) G.C. Wang, Y.N. Lua, J. Xiao, L. Yu, H.B. Song, J.S. Li, J.R. Cui, R.Q. Wang, F.X. Ran, J. Organomet. Chem. 690 (2005) 51;
(c) S. Takahashi, H. Sato, Y. Kubota, H. Utsumi, J.S. Bedford, R. Okayasu, Toxicology 180 (2002) 249.
[11] H.D. Yin, C.H. Wang, S.C. Xue, Chin. J. Struct. Chem. 23 (2004) 1356.
[12] F. Bonozi, J. Organomet. Chem. 9 (1967) 395.
[13] H.D. Yin, R.F. Zhang, C.L. Ma, J. Liaocheng Teachers Univ. (Nat. Sci.) 12 (1999) 38.
[14] C.L. Raston, A.H. White, J. Chem. Soc., Dalton Trans. (1976) 791.
[15] M. Ali, W.R. McWhinnie, A.A. West, T.A. Hamour, J. Chem. Soc., Dalton Trans. (1990) 899.
[16] J.G. Alvarado-Rodríguez, S. González-Montiel, N. Andrade-López, L.B. López-Feliciano, Polyhedron 26 (2007) 2929.
[17] V. Venkatachalam, K. Ramalingam, U. Casellato, R. Graziani, Polyhedron 16 (1997) 1211.

Available online at www.sciencedirect.com
ScienceDirect
Polyhedron 27 (2008) 671–678
POLYHEDRON
www.elsevier.com/locate/poly

Structural and magnetic properties of one-dimensional polymeric Co^{II} complexes

Shu-Xin Cui [a], Yu-Long Zhao [a], Bo Li [a], Jing-Ping Zhang [a,*], Qun Liu [a,*], Yan Zhang [b]

[a] *Faculty of Chemistry, Northeast Normal University, Changchun 130024, China*
[b] *Department of Physics, Peking University, Beijing 100871, China*

Received 20 September 2007; accepted 24 October 2007

Abstract

Pyridine-2,6-dicarboxylic acid reacts as the first ligand under hydrothermal conditions with divalent cobalt ions to form three 1D polymeric complexes in the presence of 2,4′-bipyridine as well as its derivatives 5-phenyl-2,4′-bipyridine or 5-(4-bromophenyl)-2,4′-bipyridine as the second ligands. The structures and properties of these complexes are characterized by X-ray crystallography, variable temperature magnetic measurements, infrared and thermal gravimetric analyses. It was found that the antiferromagnetic interactions between the Co^{II} ions can be tuned by the substituent on the second ligand.
© 2007 Elsevier Ltd. All rights reserved.

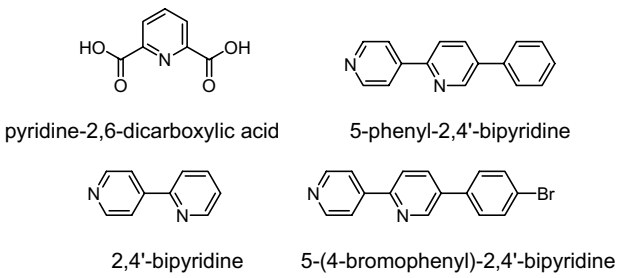
Keywords: Crystal structure; Cobalt complex; Coordination polymer; 1D chain; Magnetic property

1. Introduction

Coordination metal complexes have been the subject of intensive investigation because of their potential applications to material science as catalytic, conductive, luminescent, magnetic, porous, chiral or non-linear optical materials [1–4]. The chemistry of coordination polymers containing paramagnetic metal ions and exhibiting extended structures is at the forefront of modern research, due to these compounds' potential applications in molecular magnetism [3–8]. The most useful strategy to construct such one dimensionally extended systems is to employ appropriate bridging ligands, carboxylate for example, capable of binding metal centers through direct bond formation, promoting magnetic interactions. Pyridine-2,6-dicarboxylate (pdc^{2-}), which has been used as a ligand in homoleptic coordination polymers and coordination complexes, is a suitable building block for two-dimensional arrays [9–14]. Previous studies showed that the magnetic behaviors of a carboxylate bridging complex relate to the planarity of the M–O–C–O–M skeleton, characterized by the dihedral angles between the two adjacent metal center planes [15,16]. It is known that at 180° the interaction is antiferromagnetic, but it is ferromagnetic when this angle is close to 90° [17]. Therefore, we are interested in the design of a 1D magnetic coordination polymeric complex containing transition metals with a twisted skeleton for tuning the magnetic property by crystal engineering of the second ligand. Our studies here aimed at constructing such a 1D cobalt polymeric chain using pdc^{2-} as the first ligand and 2,4′-bipyridine (2,4′-bpy) as well as its derivatives 5-phenyl-2,4′-bipyridine (5-ph-2,4′-bpy) or 5-(4-bromophenyl)-2,4′-bipyridine (5-(4-Br-ph)-2,4′-bpy) as the second ligands (see Scheme 1). The 2,4′-bpy ligand has been employed for the construction of organic solid materials [18,19]. The 5-ph-2,4′-bpy and 5-(4-Br-ph)-2,4′-bpy molecules, with very good π-electron conjugated systems, have been extensively used for functionalized polyoxometallates [20]. The incorporation of paramagnetic cobalt centers with strong anisotropy in extended systems has the potential to afford important new magnetic materials. While, there are only a few reports of 1D coordination polymeric

* Corresponding authors. Tel.: +86 431 85099372; fax: +86 431 85684937.
E-mail address: zhangjingping66@yahoo.com.cn (J.-P. Zhang).

0277-5387/$ - see front matter © 2007 Elsevier Ltd. All rights reserved.
doi:10.1016/j.poly.2007.10.030



Scheme 1.

cobalt complexes [21–24], we have isolated three families of 1D polymeric cobalt complexes successfully. In this article we will report the structural and magnetic characterization of $[Co(pdc)L_2 \cdot H_2O]_n$ (L = 2,4′-bpy (**1**), 5-ph-2,4′-bpy (**2**), 5-(4-Br-ph)-2,4′-bpy (**3**)) polymeric complexes which were obtained in the reaction of pyridine-2,6-dicarboxylic acid (H_2pdc) with divalent cobalt ions under hydrothermal conditions in the presence of the second bipyridyl ligands. Antiferromagnetic coupling between the Co^{II} ions in these complexes has been observed.

2. Experimental

2.1. Reagents and physical measurements

All chemicals purchased were of reagent grade and were used without further purification. 2,4′-Bpy, 5-phenyl-2,4′-bipyridine, and 5-(4-bromophenyl)-2,4′-bipyridine were synthesized in the laboratory and were characterized by their NMR spectra. The IR spectra were obtained on a Nicolet, Magana 560 spectrometer with the samples prepared as KBr pellets. A PE TGA thermogravimetric analyzer was used to obtain TGA curves at a heating rate of 10 °C min^{-1}. Elemental analyses were carried out using a Perkin–Elmer elemental analyzer 2400CHN. The magnetic susceptibilities of **1**–**3** were measured in the temperature range 2–300 K with an applied field of 1000 Oe on a SQUID magnetometer by using polycrystalline samples. Experimental data were corrected for diamagnetic contributions employing both subtraction of the sample holder and Pascal's constants [25]. The temperature-independent paramagnetism (TIP) of the sample was taken into account as well.

2.2. Synthesis

2.2.1. $[Co(pdc)(2,4'\text{-bpy})_2 \cdot H_2O]_n$ (**1**)

Standard hydrothermal conditions used for the synthesis of **1** did not afforded solids suitable for X-ray crystallography. H_2pdc (0.084 g, 0.5 mmol) in an aqueous solution (3 mL) of NaOH (0.080 g, 2 mmol) was mixed with 2,4′-bpy (0.0156 g, 0.1 mmol) in EtOH (2 mL). The mixture was then added to an aqueous solution (2 mL) of $Co(NO_3)_2 \cdot 6H_2O$ (0.145 g, 0.5 mmol). The new mixture was placed in a 15 mL Teflon-lined autoclave and heated at 150 °C for 4 d and then left to cool to room temperature (RT). On allowing the filtrate from the reaction to evaporate at RT, red blocks of **1** could be isolated in ~41% yield. *Anal.* Calc. for $C_{27}H_{21}N_5O_5Co$ (**1**): C, 58.36; H, 3.21; N, 12.41. Found: C, 58.49; H, 3.82; N, 12.63%. IR (KBr, cm^{-1}): 3406 s, 3067 vs, 1610 s, 1586 m, 1573 m, 1548 m, 1505 m, 1466 m.

Table 1
Crystallographic data for complexes **1**–**3**

	1	**2**	**3**
Empirical formula	$C_{27}H_{21}CoN_5O_5$	$C_{39}H_{29}CoN_5O_5$	$C_{39}H_{29}Br_2CoN_5O_5$
Formula weight	554.42	706.6	864.41
Temperature (K)	293(2)	293(2)	293(2)
Crystal system	monoclinic	monoclinic	monoclinic
Space group	*P*2(1)/*c*	*P*2(1)/*c*	*P*2(1)/*c*
a (Å)	12.996(6)	19.146(3)	17.658(4)
b (Å)	10.451(5)	9.944(1)	10.454(2)
c (Å)	18.165(8)	18.194(3)	38.572(9)
β (°)	97.081(1)	113.042(2)	102.99(0)
V (Å^3)	2448.3(2)	3187.5(8)	6938.0(3)
Z	4	4	8
D_{calc} (Mg m^{-3})	1.504	1.472	1.651
μ (mm^{-1})	0.751	0.594	2.852
F(000)	1140	1460	3448
Reflections collected	12606	16859	23620
Independent reflections	4809	6326	7275
Refined parameters	427	559	937
Goodness-of-fit (F^2)	1.046	1.039	0.973
R indices [$I > 2\sigma(I)$]	$R_1 = 0.0397$, $wR_2 = 0.0901$	$R_1 = 0.0348$, $wR_2 = 0.0960$	$R_1 = 0.0537$, $wR_2 = 0.1131$
R indices (all data)	$R_1 = 0.0518$, $wR_2 = 0.0976$	$R_1 = 0.0430$, $wR_2 = 0.1011$	$R_1 = 0.1038$, $wR_2 = 0.1428$
Largest difference in peak/hole (e Å^3)	0.316/–0.238	0.290/–0.217	0.932/–0.321

*2.2.2. [Co(pdc)(5-ph-2,4′-bpy)$_2$ · H_2O]$_n$ (**2**)*

In a typical experiment, H_2pdc (0.042 g, 0.25 mmol) in an aqueous solution (3 mL) of NaOH (0.040 g, 1 mmol) was mixed with 5-ph-2,4′-bpy (0.0231 g, 0.1 mmol) in EtOH (2 mL). The mixture was then added to an aqueous solution (2 mL) of $Co(NO_3)_2 \cdot 6H_2O$ (0.145 g, 0.5 mmol). The new mixture was placed in a 15 mL Teflon-lined autoclave and heated at 150 °C for 4 d. The autoclave was then cooled over a period of 12 h at a rate of 4 K h^{-1}. Red block crystals of **2** that were deposited on the wall of the container were collected and air-dried. Yield: ~40%. *Anal.* Calc. for $C_{39}H_{29}N_5O_5Co$ (**2**): C, 66.30; H, 3.81; N, 9.76. Found: C, 66.29; H, 4.14; N, 9.91%. IR (KBr, cm^{-1}): 3426 s, 3062 vs, 1649 s, 1608 s, 1567 m, 1465 m.

*2.2.3. [Co_2(pdc)$_2$(5-(4-Br-ph)-2,4′-bpy)$_4$ · 2H_2O]$_n$ (**3**)*

H_2pdc (0.042 g, 0.25 mmol) in an aqueous solution (3 mL) of NaOH (0.040 g, 1 mmol) was mixed with 5-(4-Br-ph)-2,4′-bpy (0.0331 g, 0.1 mmol) in EtOH (2 mL). The mixture was then added to an aqueous solution (2 mL) of $CoSO_4 \cdot 7H_2O$ (0.140 g, 0.5 mmol). The new mixture was placed in a 15 mL Teflon-lined autoclave and heated at 150 °C for 4 d. The autoclave was then cooled over a period of 12 h at a rate of 4 K h^{-1}. Red block crystals of **3** that were deposited on the wall of the container were collected and air-dried. Yield: ~43%. *Anal.* Calc. for $C_{78}H_{54}Br_4N_{10}O_{10}Co_2$ (**3**): C, 54.19; H, 3.15; N, 8.10. Found: C, 54.01; H, 2.98; N, 7.89%. IR (KBr, cm^{-1}): 3525 s, 3305 vs, 1677 s, 1648 s, 1538 m, 1464 m.

2.3. X-ray crystallography

All diffraction data were collected at room temperature on a Siemens SMART APEX CCD area detector diffractometer using graphite monochromated Mo Kα radiation ($\lambda = 0.71073$ Å) [26]. Intensity data were collected by the

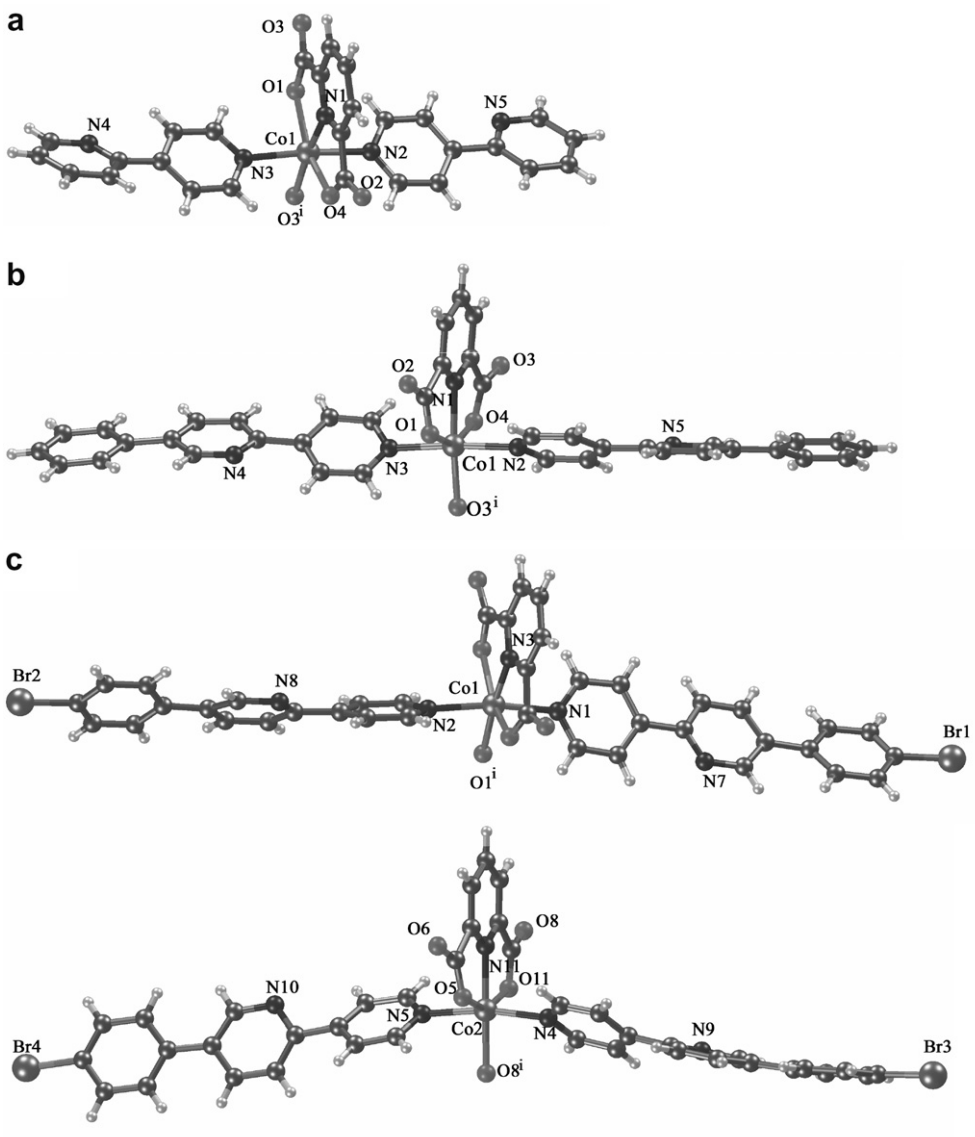


Fig. 1. View illustrating the coordination geometry around the metal ions in complexes **1** (a), **2** (b) and **3** (c) (left: Co1 chain; right: Co2 chain).

ω scan technique. Data were corrected for Lorentz polarization effects [27]. The structures were solved by the direct method using SHELXS-97 [28] and were refined on F^2 by full-matrix least-squares using the SHELXL-97 [28] program package. The non-hydrogen atoms were refined anisotropically. Hydrogen atoms on the water molecule of complex **1** were found in electron-density difference Fourier maps and were refined freely. In **2** and **3**, it was not practical to assign hydrogen atoms on the disordered water molecules. The other H atoms were added in ideal positions (C–H = 0.93 Å, $U_{iso}(H) = 1.2U_{eq}(C)$) and were not refined. The main crystallographic data of these compounds are listed in Table 1.

3. Results and discussion

3.1. Crystal structure

In complex **1**, the Co^{II} ions are bridged by pdc^{2-} anions to form 1D coordination zigzag polymeric chains along the *b*-axis. The metal atoms exist in distorted octahedral coordination environments. The equatorial sites are occupied by one N and two O atoms offered by one pdc^{2-} and one O atom from a neighboring pdc^{2-} in the trans position of the N atom (Figs. 1a and 2a), with normal Co–N (2.071(2) Å) and Co–O (2.019(2)–2.227(2) Å) bond distances (Table 2) [29]. The two axial sites are occupied by two N atoms of the second ligand, 2,4′-bpy. Furthermore, the two Co–N bonds are almost the same length (2.172 (2) and 2.177(2) Å), which are longer than those of other reported cobalt complexes containing 4-pyridyl ligands (2.12–2.15 Å) [21–24,30,31].

In complex **2**, a 1D coordination polymer could be engineered with the same first ligand as in **1** along the *b*-axis, in the presence of the second ligand 5-ph-2,4′-bpy (Figs. 1b and 2b). The two axial sites are occupied by two 5-ph-2,4′-bpy molecules. The equatorial Co–N (2.075(1) Å) and Co–O (2.043(1)–2.201 (1) Å) bond distances are similar to those found in related structures [29]. The two axial Co–N distances are unequal (2.155(2) and 2.175 (2) Å), which is different from that of **1**.

Complex **3** can be engineered with the same first ligand as in **1** or **2** along the *b*-axis, in the presence of the second ligand 5-(4-Br-ph)-2,4′-bpy (Figs. 1c and 2c). Interestingly, there are two crystallographically independent cobalt ions in complex **3**, which is different from complexes **1** and **2**. Each cobalt atom exists in a distorted octahedral coordination environment. The Co^{II} ions are bridged by pdc^{2-} anions to form 1D coordination zigzag polymeric chains along the *b*-axis. Thus, two kinds of 1D coordination zigzag polymeric chains (the Co1 chain and the Co2 chain) occur in complex **3**. In the Co1 chain, the equatorial Co–N (2.062(6) Å) and Co–O (2.039(6)–2.218(5) Å) bond distances are slightly different (±0.03 Å) from those of complexes **1** and **2**, although they are within the range of normal distances as found in related literature [29], the two axial Co–N distances (2.146(6) and 2.152(6) Å) are shorter than those in the former complexes. For the Co2 chain, the equatorial Co–N bond distance is 2.069(6) Å, and the equatorial Co–O bond distances are in the range

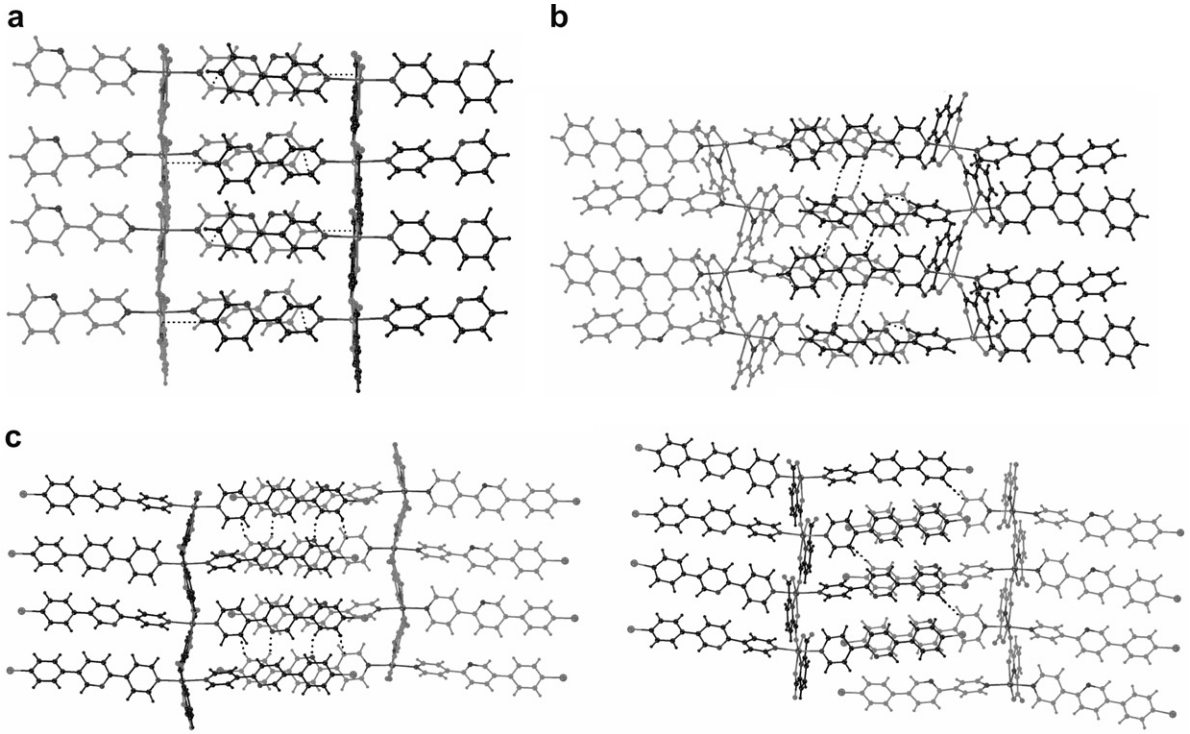


Fig. 2. The crystal packing along the *c*-axis for complex **1** (a), complex **2** (b) and complex **3** (c) (left: Co1 chain; right: Co2 chain). Hydrogen bonds are shown as black dashed lines.

Table 2
Selected bond lengths (Å) and angles (°) for complexes **1**, **2** and **3**

1			
Co1–O3^{i}	2.019(2)	Co1–N3	2.172(2)
Co1–N1	2.071(2)	Co1–N2	2.177(2)
Co1–O4	2.116(2)	Co1–O1	2.227(1)
O3^{i}–Co1–N1	170.8(6)	O4–Co1–N2	92.6(6)
O3^{i}–Co1–O4	113.9(6)	N3–Co1–N2	174.1(7)
N1–Co1–O4	75.3(6)	O3^{i}–Co1–O1	96.9(6)
O3^{i}–Co1–N3	87.7(7)	N1–Co1–O1	73.9(6)
N1–Co1–N3	93.2(6)	O4–Co1–O1	149.3(6)
O4–Co1–N3	90.3(6)	N3–Co1–O1	91.1(6)
O3^{i}–Co1–N2	86.5(7)	N2–Co1–O1	89.1(6)
N1–Co1–N2	92.6(7)		
2			
Co1–O3^{i}	2.042(2)	Co1–N2	2.155(3)
Co1–N1	2.074(2)	Co1–N3	2.175(3)
Co1–O1	2.121(2)	Co1–O4	2.201(1)
O3^{i}–Co1–N1	171.1(6)	O1–Co1–N3	85.7(6)
O3^{i}–Co1–O1	113.2(6)	N2–Co1–N3	175.9(7)
N1–Co1–O1	75.6(5)	O3^{i}–Co1–O4	97.3(5)
O3^{i}–Co1–N2	88.4(6)	N1–Co1–O4	73.9(5)
N1–Co1–N2	89.5(6)	O1–Co1–O4	149.3(5)
O1–Co1–N2	96.2(6)	N2–Co1–O4	87.7(5)
O3^{i}–Co1–N3	87.6(6)	N3–Co1–O4	92.5(5)
N1–Co1–N3	94.5(6)		
3			
Co1–O1^{i}	2.039(6)	Co2–O5	2.110(6)
Co1–N3	2.062(7)	Co2–N4	2.147(7)
Co1–O2	2.123(7)	Co2–N5	2.158(8)
Co1–N1	2.146(7)	Co2–O11	2.194(5)
Co1–N2	2.152(7)	Co2–O8^{ii}	2.055(6)
Co1–O4	2.219(5)	Co2–N11	2.069(7)
O1^{i}–Co1–N3	174.8 (2)	N11–Co2–N4	95.9(3)
O1^{i}–Co1–O2	107.9(2)	O5–Co2–N4	92.2(2)
N3–Co1–O2	75.5(3)	O8^{ii}–Co2–N5	84.1(3)
O1^{i}–Co1–N1	85.6(2)	N11–Co2–N5	94.2(3)
N3–Co1–N1	90.1(2)	O5–Co2–N5	89.5(3)
O2–Co1–N1	96.6(2)	N4–Co2–N5	169.9(3)
O1^{i}–Co1–N2	83.9(2)	O8^{ii}–Co2–O11	99.4(2)
N3–Co1–N2	100.2(2)	N11–Co2–O11	74.3(3)
O2–Co1–N2	87.8(2)	O5–Co2–O11	150.4(2)
N1–Co1–N2	169.5(2)	N4–Co2–O11	91.0(2)
O1^{i}–Co1–O4	102.8(2)	N5–Co2–O11	92.4(3)
N3–Co1–O4	74.1(3)	O8^{ii}–Co2–N11	173.5(3)
O2–Co1–O4	149.3(2)	O8^{ii}–Co2–O5	110.2(2)
N1–Co1–O4	87.9(2)	N11–Co2–O5	76.0(3)
N2–Co1–O4	93.2(2)	O8^{ii}–Co2–N4	86.0(2)

Symmetry codes for complex **1**: (i) $1-x, -0.5+y, 0.5-z$. For complex **2**: (i) $1-x, -0.5+y, 0.5-z$. For complex **3**: (i) $-x, -0.5+y, 0.5-z$; (ii) $1-x, 0.5+y, 0.5-z$.

2.055(6)–2.194(4) Å. The two axial Co–N distances are 2.147(6) and 2.158(7) Å, which are similar to those of the Co1 chain.

The crystal packing patterns along the *c*-axes of the three complexes are shown in Fig. 2. For complexes **1** and **2**, the neighboring zigzag chains are assembled into two-dimensional layers *via* interdigitation involving C–H···π hydrogen bonds [32]. The C–H groups form structural hydrogen bonds in **1** (H···π, *ca.* 2.84 Å, C–H···π, *ca.* 151.1°), both C–H groups and uncoordinated nitrogen atoms contribute to the hydrogen bond formation in **2** (H···π, *ca.* 2.71 Å, C–H···π, *ca.* 140.4°). While for complex **3**, each Co1 or Co2 neighboring chains associate into a 2D layer by hydrogen bond interactions, and the Co1 and Co2 layers are alternately arranged. Interestingly, in the Co1 layer of complex **3**, C–H groups and uncoordinated nitrogen atoms contribute to the hydrogen bond formation (H···π, *ca.* 2.78 Å, C–H···π, *ca.* 151.4°), which is similar to the feature of complex **2**, whereas in the Co2 layer only C–H groups form hydrogen bonds (H···π, *ca.* 2.86 Å, C–H···π, *ca.* 166.8°), which is similar to that of complex **1**. The intra-chain metal–metal distances are 5.64 and 5.43 Å for **1** and **2**, respectively. For complex **3**, the intra-chain Co1–Co1 and Co2–Co2 distances are 5.62 and 5.57 Å, respectively. The neighboring polymer backbones can superpose by a shift in **1**, whereas the backbones of **2** and **3** in neighboring sheets cannot superpose (Fig. 3) with each other. In complex **1**, the torsion angles Co1–O1–C24–O3 and O1–C24–O3–Co1^{ii} are 173.3° and 7.2°, respectively, while the torsion angles Co1–O4–C1–O3 and O4–C1–O3–Co1^{ii} are 168.3° and 12.1° for **2**, respectively. Therefore, the polymeric cobalt chains of **2** are severely twisted compared to those of **1** by the introduction of a phenyl substituent on the second ligand in **2**. In complex **3** the torsion angles Co1–O4–C4–O1, O4–C4–O1–Co1^{iii}, Co2–O5–C8–O8 and O5–C8–O8–Co2^{iv} are 166.9°, 9.7°, 179.5° and −3.9°, respectively. Similarly, the Co1 chains of **3** are more twisted compared to those of **1** by the introduction of the bromophenyl substituent on the second ligand, though the Co2 chains are less twisted in **3**.

3.2. Thermal properties

Thermal gravimetric analysis shows that the coordination polymers **1**–**3** normally begin to lose their uncoordinated water molecules at a low temperature, ranging from 100 to 170 °C (Fig. 4). Complex **1** is the least stable and decomposes at 175 °C, and the weight loss of 52.5% (calc. ~56%) corresponds to the loss of the 2,4′-bpy ligand in the temperature range 175–225 °C. The pdc^{2-} anion begins to decompose at 250 °C. The molecular structure of **2** begins to collapse at 250 °C, and the weight loss of 63.9% in the range 250–325 °C corresponds to the loss of 5-ph-2,4′-bpy (calc. ~65%), and another weight loss of 22.5% (calc. ~23%) corresponds to the loss of one pdc^{2-} anion in the range 325–580 °C. Complex **3** begins its decomposition at 210 °C. The weight loss between 210 and 380 °C is attributed to the loss of the 5-(4-Br)-ph-2,4′-bpy ligand (obsd. 73.7%, calc. ~72%), and another weight loss between 380 and 600 °C is attributed to the loss of pdc^{2-}(obsd. 21.2%, calc. ~19%). The above data clearly demonstrate that the introduction of a substituent on the second ligand is responsible for the increase of the stability of the coordination complexes.

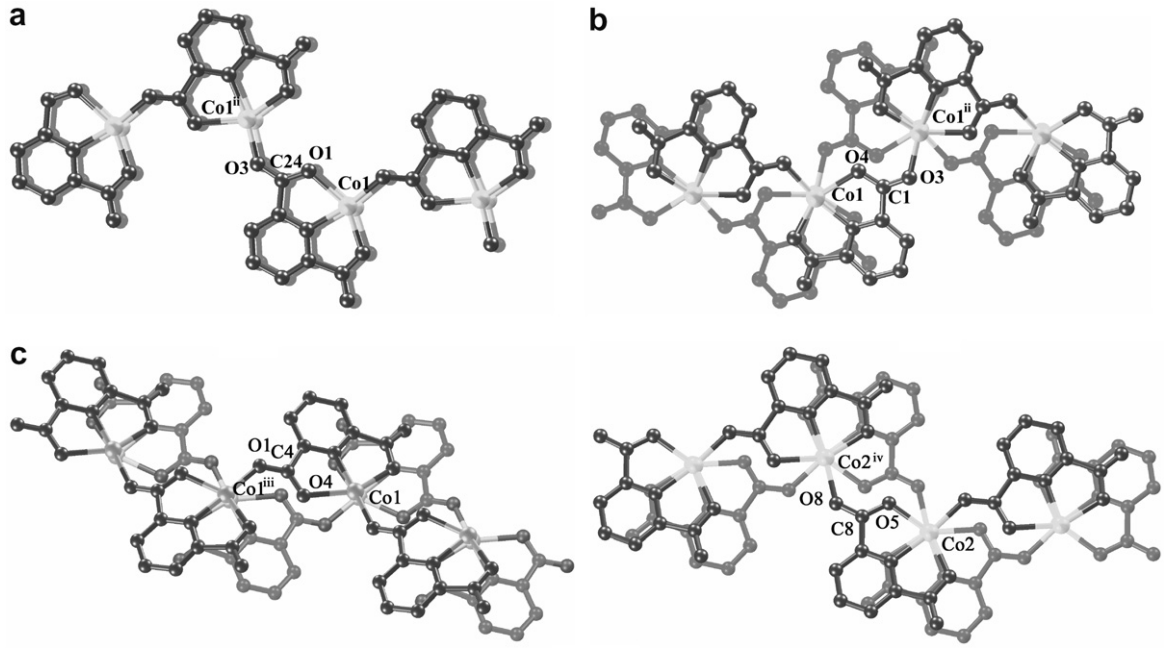


Fig. 3. A top view of the polymer backbones in Fig. 2. Symmetry codes for complex **1**: (ii) $1-x$, $0.5+y$, $0.5-z$. Symmetry codes for complex **2**: (ii) $1-x$, $0.5+y$, $0.5-z$. Symmetry codes for complex **3**: (iii) $-x$, $0.5+y$, $0.5-z$; (iv) $1-x$, $-0.5+y$, $0.5-z$.

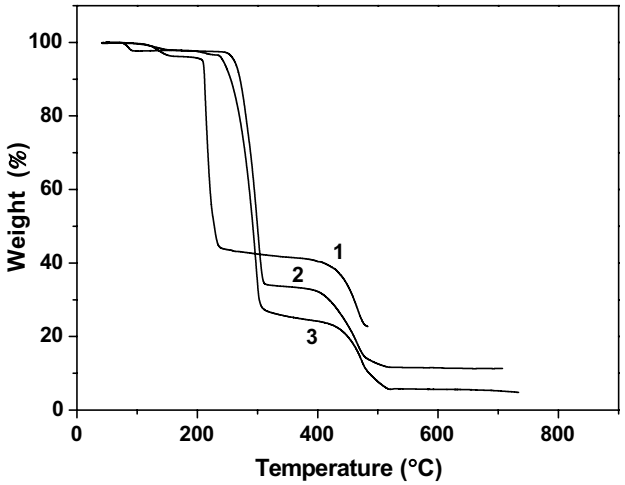


Fig. 4. TGA curves of complexes **1**–**3**.

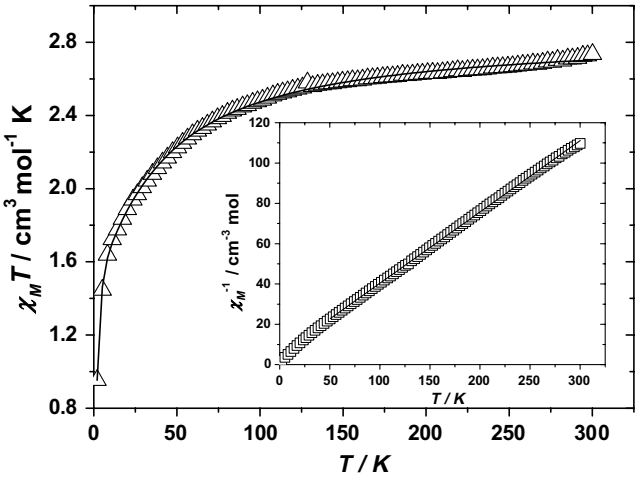


Fig. 5. Plots of $\chi_M T$ vs. T and χ_M^{-1} vs. T (insert) for complex **1**. Solid lines show the best fits to the model (see text).

3.3. Magnetic properties

The magnetic behaviors for complexes **1**–**3** are shown in Figs. 5–7. The global feature of the $\chi_M T$ versus T curve of **1** is a weak intramolecular antiferromagnetic interaction between the Co(II) ions, as shown in Fig. 5. The value of $\chi_M T$ at 300 K is 2.734 $cm^3\ mol^{-1}$ K and thus is higher than the spin-only value of 1.875 $cm^3\ mol^{-1}$ K expected for an uncoupled high-spin Co^{II} ion ($S = 3/2$, $g = 2$), in accordance with the well-documented orbital contribution of the octahedral Co^{II} ion [33,34].As the sample is cooled from room temperature, the $\chi_M T$ value smoothly decreases from 2.734 $cm^3\ mol^{-1}$ K to 2.530 $cm^3\ mol^{-1}$ K at 120 K and then decreases more rapidly at low temperatures, reaching a value of 0.953 $cm^3\ mol^{-1}$ K at 2 K. Fig. 6 shows the temperature dependence of the $\chi_M T$ product for complex **2**. The $\chi_M T$ value at 300 K for **2** is 2.616 $cm^3\ mol^{-1}$ K, and the global feature of the $\chi_M T$ versus T curve for **2** suggests a weak intramolecular antiferromagnetic interaction, the same as that of **1**. Similarly, the global feature of the $\chi_M T$ versus T curve of **3** is a weak intramolecular antiferromagnetic interaction between the Co(II) ions (Fig. 7). As the sample is cooled from room temperature, the $\chi_M T$ value smoothly decreases from 3.214 $cm^3\ mol^{-1}$ K to 2.701 $cm^3\ mol^{-1}$ K at 50 K and then decreases more rapidly at low temperatures, reaching a value of

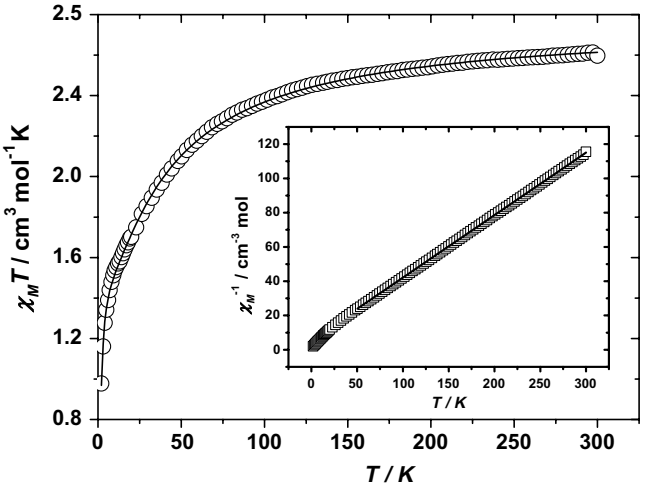


Fig. 6. Plots of $\chi_M T$ vs. T and $\chi_M{}^{-1}$ vs. T (insert) for complex **2**. Solid lines show the best fits to the model (see text).

1.405 $cm^3\ mol^{-1}$ K at 2 K. The high-temperature data (above 50 K) for **1**–**3** can be fitted to the Curie–Weiss law with $C = 2.82$, 2.74 and 3.35 $cm^3\ mol^{-1}$ K, $\theta = -12.85$, −11.06 and −11.79 K, respectively. These values are typical of uncoupled high-spin Co^{II} ions [33]. The high value of C (for a spin-only system with $S = 3/2$ and $g = 2$, the calculated Curie constant is $C = 1.88$ $cm^3\ mol^{-1}$ K) emphasizes a significant orbital contribution to the susceptibility. The θ values of complexes **2** and **3** are less negative than that for complex **1**. This indicates that the antiferromagnetic interactions between the Co^{II} ions can be decreased by the substituent on the second ligand, introducing a larger twisting for the 1 D chain.

To obtain an estimate of the strength of the antiferromagnetic coupling, we used a simple phenomenological equation, which is proposed by Masciocchi and his coworkers [35], $\chi T = A\exp(-E_1/kT) + B\exp(-E_2/kT)$, to fit the magnetic data. Here, $A + B$ equals the Curie constant, E_1 and E_2 represent the "activation energy" corresponding to the spin–orbit coupling and the antiferromagnetic exchange interaction, respectively. This equation adequately describes the spin–orbit coupling, which results in a splitting between discrete levels, and the exponential low-temperature divergence of the susceptibility [$\chi T \propto \exp(\alpha J/2kT)$]. The fitted parameters for complexes **1**, **2** and **3** are $A + B = 2.83$, 2.76 and 3.38 $cm^3\ mol^{-1}$ K, $E_1/k = 46.4$, 42.5 and 42.9 K, $E_2/k = -1.40$, −1.09 and −1.12 K, $R = 1.3 \times 10^{-4}$, 5×10^{-5} and 6.8×10^{-4}, respectively, where $R = \sum[(\chi_M T)_{obs} - (\chi_M T)_{calcd}]^2 / \sum[(\chi_M T)_{obs}]^2$. The $A + B$ and E_1/k values of complexes **1**–**3** are consistent with those reported in the literature for the Curie constant and the effect of spin–orbit coupling [35,24]. E_2/k values of −1.40, −1.09 and −1.12 correspond to $J = -2.80$, −2.18 and −2.24 K according to the Ising chain approximation [$\chi T \propto \exp(J/2kT)$]. The J value of complex **1** is more negative than the values for complexes **2** and **3**. This also demonstrates that the antiferromagnetic interactions between the Co^{II} ions can be decreased by the substituent on the second ligand, introducing a larger twisting for the 1D chain.

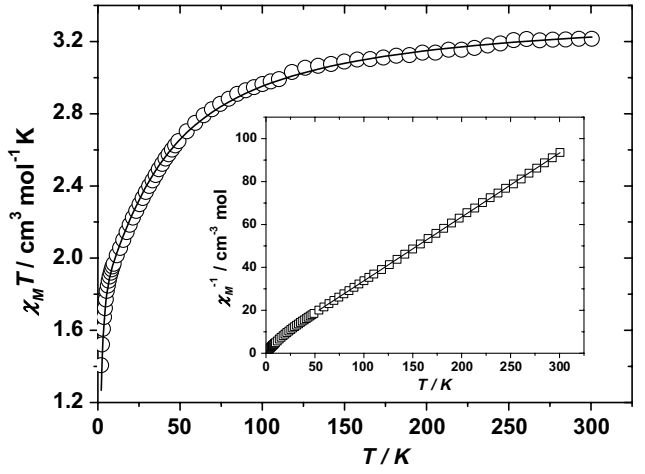


Fig. 7. Plots of $\chi_M T$ vs. T and $\chi_M{}^{-1}$ vs. T (insert) for complex **3**. Solid lines show the best fits to the model (see text).

4. Conclusions

In summary, we have synthesized three new complexes $[Co(pdc)(2,4'\text{-bpy})_2 \cdot H_2O]_n$ (**1**), $[Co(pdc)(5\text{-ph-}2,4'\text{-bpy})_2 \cdot H_2O]_n$ (**2**) and $[Co_2(pdc)_2(5\text{-(4-Br-ph)-}2,4'\text{-bpy})_4 \cdot 2H_2O]_n$ (**3**). Complexes **1**–**3** show antiferromagnetic interactions between the Co^{II} centers bridged by the O–C–O bridge in a trans mode. The polymeric cobalt chains of **2** are severely twisted compared to those of **1** by the introduction of a phenyl substituent on the second ligand, while for **3** half severely and half less twisted polymeric cobalt chains are ascribed to the bromophenyl substituent of the second ligand. As a result, the steric hindrance of the substituent groups from neighboring chains results in the distorted structure of the polymeric chains. The antiferromagnetic interactions between Co^{II} ions are decreased in the order of **1** > **3** > **2**, corresponding to the increasing distorted structure for the polymeric chains. Furthermore, the thermal stability of the coordination complexes is increased by the introduction of substituent groups on the second ligand. This report may provide a promising strategy for the design and exploitation of new polymeric coordination compounds for useful applications.

Acknowledgements

We thank the Natural Science Foundation of China (No. 20274006), NCET-06-0321, NENU-STB07007, and analysis and testing foundation of Northeast Normal University for financial support.

Appendix A. Supplementary material

CCDC 285362, 285361 and 652699 contain the supplementary crystallographic data for **1**, **2** and **3**. These data

can be obtained free of charge via http://www.ccdc.cam.ac.uk/conts/retrieving.html, or from the Cambridge Crystallographic Data Centre, 12 Union Road, Cambridge CB2 1EZ, UK; fax: (+44) 1223-336-033; or e-mail:deposit@ccdc.cam.ac.uk. Supplementary data associated with this article can be found, in the online version, at doi:10.1016/j.poly.2007.10.030.

References

[1] C. Janiak, J. Chem. Soc., Dalton Trans. (2003) 2781.
[2] S.L. James, Chem. Soc. Rev. 32 (2003) 276.
[3] D. Maspoch, D. Ruiz-Molina, J. Veciana, J. Mater. Chem. 14 (2004) 2713.
[4] S.R. Batten, K.S. Murray, Coord. Chem. Rev. 246 (2003) 103.
[5] S. Subramanian, M.J. Zaworotko, Angew. Chem., Int. Ed. 34 (1995) 2127.
[6] P. Losier, M.J. Zaworotko, Angew. Chem., Int. Ed. 35 (1996) 2779.
[7] M. Fujita, J. Yazaki, K. Ogura, Tetrahedron Lett. 32 (1991) 5589.
[8] R.H. Groeneman, L.R. MacGillivray, J.L. Atwood, Inorg. Chem. 38 (1999) 208.
[9] S.K. Ghosh, P.K. Bharadwaj, Inorg. Chem. 42 (2003) 8250.
[10] S.K. Ghosh, J. Ribas, P.K. Bharadwaj, CrystEngComm 6 (2004) 250.
[11] S.K. Ghosh, J. Ribas, P.K. Bharadwaj, Cryst. Growth Des. 5 (2005) 623.
[12] B. Zhao, P. Cheng, Y. Dai, C. Cheng, D.-Z. Liao, S.-P. Yan, Z.-H. Jiang, G.-L. Wang, Angew. Chem., Int. Ed. 42 (2003) 934.
[13] B. Zhao, P. Cheng, X. Chen, C. Cheng, W. Shi, D.-Z. Liao, S.-P. Yan, Z.-H. Jiang, J. Am. Chem. Soc. 126 (2004) 3012.
[14] H.-L. Gao, L. Yi, B. Zhao, X.-Q. Zhao, P. Cheng, D.-Z. Liao, S.-P. Yan, Inorg. Chem. 45 (2006) 5980.
[15] A. Rodríguez-Fortea, P. Alemany, S. Alvarez, E. Ruiz, Chem. Eur. J. 7 (2001) 627.
[16] S.K. Dey, B. Bag, K.M. Abdul-Malik, M.S. El Fallah, J. Ribas, S. Mitra, Inorg. Chem. 42 (2003) 4209.
[17] M.S. Ray, A. Ghosh, A. Das, M.G.B. Drew, J. Ribas-Ariño, J. Novoa, J. Ribas, Chem. Commun. (2004) 1102.
[18] M.B. Zaman, M. Tomura, Y. Yamashita, J. Org. Chem. 66 (2001) 5987.
[19] S.-X. Cui, J.-P. Zhang, L. Wang, Y.-L. Zhao, Acta Crystallogr. E61 (2005) o2193.
[20] Z.-G. Han, Y.-L. Zhao, J. Peng, Y. Feng, J.-H. Yin, Q. Liu, Electroanalysis 17 (2005) 1097.
[21] A. Caneschi, D. Gatteschi, N. Lalioti, C. Sangregorio, R. Sessoli, G. Venturi, A. Vindigni, A. Rettori, M.G. Pini, M.A. Novak, Angew. Chem., Int. Ed. 40 (2001) 1760.
[22] C. Hong, J. Koo, S. Son, Y. Lee, Y. Kim, Y. Do, Chem. Eur. J. 7 (2001) 4243.
[23] L.M. Field, M.C. Morón, P.M. Lahti, F. Palacio, A. Paduan-Filho, N.F. Oliveira Jr., Inorg. Chem. 45 (2006) 2562.
[24] J.-M. Rueff, N. Masciocchi, P. Rabu, A. Sironi, A. Skoulios, Chem. Eur. J. 8 (2002) 1813.
[25] O. Kahn, Molecular Magnetism, VCH, New York, 1993.
[26] Siemens, SMART, Version 5.05, Siemens Analytical X-ray Instruments Inc., Madison, WI, USA, 1995.
[27] P. Starynowicz, COSABS99, Program for Absorption Correction, University of Wroclaw, Wroclaw, Poland, 1999.
[28] G.M. Sheldrick, SHELXS97 and SHELXL97, University of Göttingen, Germany, 1997.
[29] L.C. Nathan, T.D. Mai, J. Chem. Crystallogr. 30 (2000) 509.
[30] K.N. Power, T.L. Hennigar, M.J. Zaworotko, New J. Chem. (1998) 177.
[31] M. Kondo, T. Yoshitomi, K. Seki, H. Matsuzaka, S. Kitagawa, Angew. Chem., Int. Ed. 36 (1997) 1725.
[32] C. Janiak, J. Chem. Soc., Dalton Trans. (2000) 3885.
[33] F.E. Mabbs, D.J. Machin, Magnetism and Transition Metal Complexes, Chapman and Hall, London, 1973.
[34] B.N. Figgis, M.A. Hitchman, Ligand Field Theory and Its Applications, Wiley-VCH, New York, 2000.
[35] J.-M. Rueff, N. Masciocchi, P. Rabu, A. Sironi, A. Skoulios, Eur. J. Inorg. Chem. (2001) 2843.

Available online at www.sciencedirect.com
ScienceDirect
Polyhedron 27 (2008) 679–687
POLYHEDRON
www.elsevier.com/locate/poly

Cascade dicopper architectures of a dibenzodioxatetraazamacrocycle

Sílvia Carvalho [a], Rita Delgado [a,b,*], Michael G.B. Drew [c], Vítor Félix [d], Mauro Figueira [e], Rui T. Henriques [b,f]

[a] Instituto de Tecnologia Química e Biológica, UNL, Apartado 127, 2781-901 Oeiras, Portugal
[b] Instituto Superior Técnico, Av. Rovisco Pais, 1049-001 Lisboa, Portugal
[c] School of Chemistry, University of Reading, Whiteknights, Reading RG6 6AD, UK
[d] Departamento de Química, CICECO, Universidade de Aveiro, 3810-193 Aveiro, Portugal
[e] Instituto Tecnológico e Nuclear, Departamento de Química, 2686 Sacavém Codex, Portugal
[f] Instituto de Telecomunicações, Polo de Lisboa, P1049-001 Lisboa, Portugal

Received 25 July 2007; accepted 26 October 2007
Available online 4 December 2007

Abstract

The dibenzodioxatetraazamacrocycle [26]*p*$bz_2N_4O_2$ was characterised by single crystal X-ray diffraction and the protonation constants of this compound and the stability constants of its copper(II) and lead(II) complexes were determined by potentiometry in water at 298.2 K in 0.10 mol dm^{-3} in KNO_3. Mono- and dinuclear complexes were found for both metal ions, the dinuclear complexes being the main species in the 5–7.5 pH range for copper(II) and 7.5–8.5 for lead(II). As expected the values of the stability constants for the copper(II) complexes are lower than those for related macrocycles containing only nitrogen atoms. The presence of mono- and dinuclear copper complexes was also confirmed by electrospray ionization mass spectrometry. These results suggest that the symmetric macrocyclic cavity of [26]*p*$bz_2N_4O_2$ has enough space for the coordination of two metal ions. Additionally, NMR spectroscopy showed that the dinuclear complex of lead(II) has high symmetry. The equilibrium constants of the dinuclear copper(II) complexes and dicarboxylate anions (oxalate, malonate and succinate) were also determined in 0.10 mol dm^{-3} aqueous KNO_3 solution. Only species containing one anion, $Cu_2H_hLA^{(2+h)}$, were found, strongly suggesting that the anion bridges the two copper(II) ions. The binding constants of the cascade species formed by $[Cu_2[26]pbz_2N_4O_2(H_2O)_x]^{4+}$ with dicarboxylate anions decrease with the increase in length of the alkyl chain of the anion, a fact which was attributed to a higher conformational energy necessary for the rearrangement of the macrocycle to accommodate the larger anions bridging the two copper(II) centres. The variation of the magnetic susceptibility with temperature of $[Cu_2(H_2[26]pbz_2N_4O_2)(oxa)_3]\cdot 4H_2O$ and $[Cu_2([26]pbz_2N_4O_2)(suc)Cl_2]$ were measured and the two complexes showed different behaviour.
© 2007 Elsevier Ltd. All rights reserved.

Keywords: Dibenzodioxatetraazamacrocycle; Cascade species; Stability constants; Magnetic susceptibility

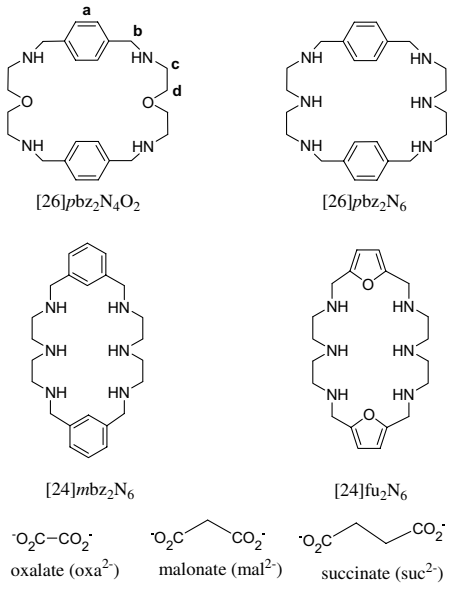
1. Introduction

The growing interest in symmetrical and large polyazamacrocycles mainly results from their ability to form stable dinuclear metal complexes. The capacity of these complexes to interact with additional species can also be used to modulate their physical, chemical and magnetic properties giving rise to new species that can be of great significance as models for interacting paramagnetic centres, catalysts and new molecular materials [1,2]. On the other hand, carboxylate groups as the interacting moieties of a guest can assume many types of bridging conformations, leading to different magnetic properties and making them interesting to be studied from a chemical point of view [2].

The ability of copper complexes of related macrocycles, [24]*m*bz_2N_6 and [24]fu_2N_6 (see Scheme 1 for the abbreviations), to interact with different anions, such as oxalate

* Corresponding author. Address: Instituto de Tecnologia Química e Biológica, UNL, Apartado 127, 2781-901 Oeiras, Portugal. Tel.: +351 214 46 97 37/38; fax: +351 214 41 12 77.
E-mail address: delgado@itqb.unl.pt (R. Delgado).

0277-5387/$ - see front matter © 2007 Elsevier Ltd. All rights reserved.
doi:10.1016/j.poly.2007.10.023



Scheme 1.

[3], malonate [3], phosphate [4], acetate [5] and various amino acids [6] has been reported. The stability of the formed supramolecular species was explained by cooperative electrostatic forces and hydrogen bonds [3,4]. Following these achievements, in the present work we investigated the ability of a 26-membered macrocycle containing *p*-xylyl and oxodiamine motifs to form homodinuclear copper(II) and lead(II) complexes in aqueous solution. Additionally, the ability of the dicopper complex to form cascade species with dicarboxylate anions with alkyl chains of different sizes (oxalate, malonate and succinate) was also evaluated under the same experimental conditions. The variation of the magnetic moment with temperature was also measured in order to study the modulation effect of the magnetic properties by the guests in the dicopper complex. In a study reported before a similar investigation was carried out, but using DMSO as solvent and UV–Vis and EPR spectroscopic techniques to characterise the dicopper interaction mediated by the different anions [7]. The present study complements the former one because in aqueous solution more information can be obtained by potentiometric techniques.

2. Results and discussion

2.1. Acid–base behaviour

The acid–base reactions of [26]*p*$bz_2N_4O_2$ were studied by potentiometric methods in water at 298.2 K, in 0.10 mol dm^{-3} KNO_3. The protonation constants determined are collected in Table 1, together with the values for the related compounds [26]*p*bz_2N_6, and [24]*m*bz_2N_6 for comparison (see Scheme 1).

The protonation constants of all the basic centres of [26]*p*$bz_2N_4O_2$ could be determined by potentiometric techniques. The four protonation constants are of comparable magnitude, because they correspond to amine centres at alternating positions in the macrocycle, far from each other, and therefore the values are only affected by statistical factors, and are of the same order as those found for linear amines [13]. The formation of intramolecular hydrogen bonds between protonated nitrogen and ether oxygen atoms eventually stabilise the first two protonated species, contributing also for their high basicity.

A lower overall basicity would be expected for [26]*p*$bz_2N_4O_2$ when compared to that of [26]*p*bz_2N_6 or [24]*m*bz_2N_6, however only slightly differences were observed for the three compounds, see Table 1. This indicates that the inductive effect of the ether oxygen in close proximity to the basic centres of [26]*p*$bz_2N_4O_2$ is probably compensated by the contribution of intramolecular N–H···O hydrogen bonds, which is in agreement with the X-ray structure of [26]*p*$bz_2N_4O_2$ presented in Fig. 1.

The macrocycle presents a ladder type conformation with an inversion crystallographic centre. This conformation is stabilised by four N–H···O short intermolecular bonding contacts with H···O distances of 2.58(4) and 2.53(3) Å and corresponding N–H···O angles of 106(3)° and 105(2)°. Bond lengths and angles found for [26]*p*$bz_2N_4O_2$ are within the expected values.

The effect of the electrostatic repulsion between contiguous protonated amine centres, resulting in very low protonation constant values, is only observed for the last two values of [26]*p*bz_2N_6 and [24]*m*bz_2N_6.

2.2. Metal complexes studies

The stability constants of the complexes of [26]*p*$bz_2N_4O_2$ with Cu^{2+} and Pb^{2+} were also determined and the results are collected in Table 2, together with the values of the Cu^{2+} complexes of [26]*p*bz_2N_6 for comparison.

Mono- and dinuclear complexes were found for both metal ions. The dinuclear complexes are the main species in the pH range 7.5–8.5 for lead(II) and 5–7.5 for copper(II), see Figs. 2 and 3. These results suggest that the symmetric macrocyclic cavity of [26]*p*$bz_2N_4O_2$ has enough space for the coordination of two metal ions and that the coordination of the second metal centre should lead to a lower energy conformation of the macrocycle. This tendency to form dinuclear complexes was also verified for the related macrocycle [26]*p*bz_2N_6 [8].

The protonated Cu_2HL complex is the main species in the 5–7.5 pH range, and at pH $\geqslant$ 8 the hydrolysis of water molecules directly coordinated to the metal centre gives rise to hydroxocomplexes. The stability of the Cu_2HL complex and the easy formation of hydrolysed species leave the dinuclear complex Cu_2L as the main species in a short pH range around pH 8, see Fig. 3.

The intriguing stability of the asymmetric Cu_2HL species, particularly from a symmetric ligand, requires that one of the amine centres remains protonated before the final rearrangement of the macrocycle in the dinuclear

Table 1
Protonation constants ($\log K_i^H$)[a] for [26]*p*bz$_2$N$_4$O$_2$, [26]*p*bz$_2$N$_6$ and [24]*m*bz$_2$N$_6$ ($T = 298.2$ K; $I = 0.10$ mol dm^{-3} in KNO_3)

Reaction equilibrium	[26]*p*bz$_2$N$_4$O$_2$[b]	[26]*p*bz$_2$N$_6$	[24]*m*bz$_2$N$_6$
$L + H^+ \rightleftharpoons HL^+$	9.36(1)	9.52,[c] 9.54,[d] 9.48,[e] 9.73[f]	9.49,[g] 9.51,[h] 9.43,[i] 9.58,[j] 9.49[k]
$HL^+ + H^+ \rightleftharpoons H_2L^{2+}$	8.75(1)	8.57,[c] 8.76,[d] 8.88,[e] 9.05[f]	8.73,[g] 8.77,[h] 8.68,[i] 8.79,[j] 8.77[k]
$H_2L^{2+} + H^+ \rightleftharpoons H_3L^{3+}$	7.94(1)	7.96,[c] 8.16,[d] 8.23,[e] 8.33[f]	8.03,[g] 7.97,[h] 7.94,[i] 8.08,[j] 8.04[k]
$H_3L^{3+} + H^+ \rightleftharpoons H_4L^{4+}$	7.30(1)	7.06,[c] 7.26,[d] 7.37,[e] 7.64[f]	7.29,[g] 7.09,[h] 7.07,[i] 7.34,[j] 7.18[k]
$H_4L^{4+} + H^+ \rightleftharpoons H_5L^{5+}$		3.2,[c] 3.3,[d] 2.92,[e] 3.68[f]	3.64,[g] 3.79,[h] 3.77,[i] 3.70,[j] 3.51[k]
$H_5L^{5+} + H^+ \rightleftharpoons H_6L^{6+}$		[c], 2.5,[d] 3.57,[e] 2.90[f]	3.45,[g] 3.27,[h] 3.36,[i] 3.37,[j] 3.09[k]
$L + 4\ H^+ \rightleftharpoons H_4L^{4+}$	33.35(1)	33.11[c] – 34.75 [f]	33.12[i] –33.79[j]

[a] Values in parentheses are standard deviations on the last significant figure.
[b] This work.
[c] Ref. [1].
[d] $I = 0.10$ mol dm^{-3} in KCl, Ref. [1].
[e] $I = 0.1$ mol dm^{-3} in KCl, Ref. [8].
[f] $I = 0.100$ mol dm^{-3} in KCl, Ref. [9].
[g] $I = 0.100$ mol dm^{-3} in KNO_3, Ref. [10].
[h] $I = 0.10$ mol dm^{-3} in KCl, Ref. [11].
[i] $I = 0.10$ mol dm^{-3} in KCl, Ref. [12].
[j] $I = 0.1$ mol dm^{-3} in KNO_3, Ref. [5].
[k] $I = 0.10$ mol dm^{-3} in $NaClO_4$, Ref. [6].

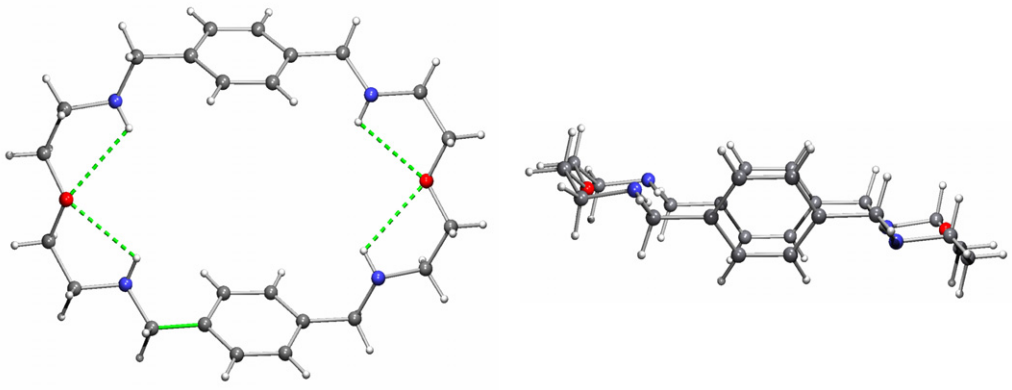


Fig. 1. Molecular structure of [26]*p*bz$_2$N$_4$O$_2$ in two different views, showing the N–H···O intramolecular hydrogen bonding interactions (left) and macrocyclic conformation (right).

complex. This implies that the second copper centre has a NO coordination sphere from donors of the macrocycle, with the remaining positions occupied by solvent molecules or nitrate anions, and the amine not involved in the coordination being still protonated. The proximity of this second copper centre to the positive ammonium cation implies a conformation of the macrocycle minimizing electrostatic repulsion, and a further macrocyclic rearrangement upon deprotonation of the last ammonium group.

The stability constants of the complexes of [26]*p*bz$_2$N$_6$ with Cu^{2+} are about ten log units larger than those of [26]*p*bz$_2$N$_4$O$_2$. This implies that the replacement of the middle nitrogen atom of the diethylenetriamine chain by an oxygen atom has chemical and structural implications. Indeed, the log K_{CuL} corresponding to the replacement of L = diethylenetriamine by 1,5-diamino-3-oxapentane is about 8 units [13], and can reach 10 log units for macrocycles [14]. Therefore the drop found for the constants of the copper(II) complexes of [26]*p*bz$_2$N$_4$O$_2$ when compared with those of [26]*p*bz$_2$N$_6$ is the expected one.

On the other hand, the stability constant obtained for the formation of Pb_2L is relatively high when compared to that of Cu_2L, which can be explained by a better accommodation of lead into the cage formed by the three donor atoms of the macrocycle. However at higher pH values (pH > 7.5), the dinuclear complex gives rise to the mononuclear one in spite of the fact that the large ionic radii of this metal ion does not make good use of all the donor atoms of the macrocycle, giving a small stability constant.

2.3. Cascade species formed by the dinuclear copper(II) complex as the receptor for dicarboxylate substrates

Taking advantage of the tendency of the macrocycle [26]*p*bz$_2$N$_4$O$_2$ to form dinuclear complexes with copper(II), this complex was used as the receptor for anion recognition. Dicarboxylate anions were chosen as the substrates, as indicated in Scheme 1.

The association constants of the cascade species were also determined in aqueous solution by potentiometric

Table 2
Stability constants ($\log \beta_{M_mH_hL_l}$ and $\log K_{M_mH_hL_l}$)[a] for the complexes of [26]*p*bz$_2$N$_4$O$_2$ with Cu^{2+} and Pb^{2+}, and of [26]*p*bz$_2$N$_6$ with Cu^{2+} at $T = 298.2 \pm 0.1$ K and $I = 0.10$ mol dm^{-3} in KNO_3

	[26]*p*bz$_2$N$_4$O$_2$		[26]*p*bz$_2$N$_6$
	M = Cu^{2+}[b]	M = Pb^{2+}	M = Cu^{2+}
Reaction equilibrium			
$M^{2+} + L \rightleftharpoons ML^{2+}$	8.28(2)	5.85(3)	17.50,[c] 18.41,[d] ,[e]
$M^{2+} + H^+ + L \rightleftharpoons MHL^{3+}$			24.97,[c] 26.24,[d] ,[e]
$M^{2+} + 2\ H^+ + L \rightleftharpoons MH_2L^{4+}$		21.46(5)	29.36,[c] 30.41,[d] 29.75[e]
$M^{2+} + L \rightleftharpoons ML(OH)^+ + H^+$	−0.78(2)	−3.25(3)	[c, d, e]
$M^{2+} + L \rightleftharpoons ML(OH)_2 + 2H^+$	−10.95(4)	−12.97(3)	[c, d, e]
$2\ M^{2+} + L \rightleftharpoons M_2L^{4+}$	14.82(3)	9.99(2)	24.12,[c] 25.98,[d] 25.24[e]
$2\ M^{2+} + H^+ + L \rightleftharpoons M_2HL^{5+}$	22.22(1)		[c, d, e]
$2\ M^{2+} + L \rightleftharpoons M_2L(OH)^{3+} + H^+$			[c, d], 16.96[e]
$2\ M^{2+} + L \rightleftharpoons M_2L(OH)_2^{2+} + 2\ H^+$			[c, d], 8.13[e]
Stepwise constants			
$M^{2+} + L \rightleftharpoons ML^{2+}$	8.28	5.85	17.50,[c]18.41,[d, e]
$ML^{2+} + H^+ \rightleftharpoons MHL^{3+}$			7.47,[c] 7.83,[d, e]
$MHL^{3+} + H^+ \rightleftharpoons MH_2L^{4+}$			4.39,[c] 4.17,[d, e]
$ML^{2+} \rightleftharpoons ML(OH)^+ + H^+$	−9.06	−9.10	[c, d, e]
$ML(OH)^+ \rightleftharpoons ML(OH)_2^{2+} + H^+$	−10.17	−9.72	[c, d, e]
$ML^{2+} + M^{2+} \rightleftharpoons M_2L^{4+}$	6.54	4.14	[c, d, e]
$M_2L^{4+} + H^+ \rightleftharpoons M_2HL^{5+}$	7.40		6.62,[c] 7.57,[d, e]
$M_2L^{4+} \rightleftharpoons M_2L(OH)^{3+} + H^+$			[c, d], −8.28[e]
$M_2L(OH)^{3+} \rightleftharpoons M_2L(OH)_2^{2+} + H^+$			[c, d], −8.83[e]

[a] In parentheses are standard deviations on the last significant figures. L = [26]*p*bz$_2$N$_4$O$_2$.
[b] This work.
[c] Ref. [1].
[d] $I = 0.10$ mol dm^{-3} KCl, Ref. [1].
[e] $I = 0.1$ mol dm^{-3} KCl, Ref. [8].

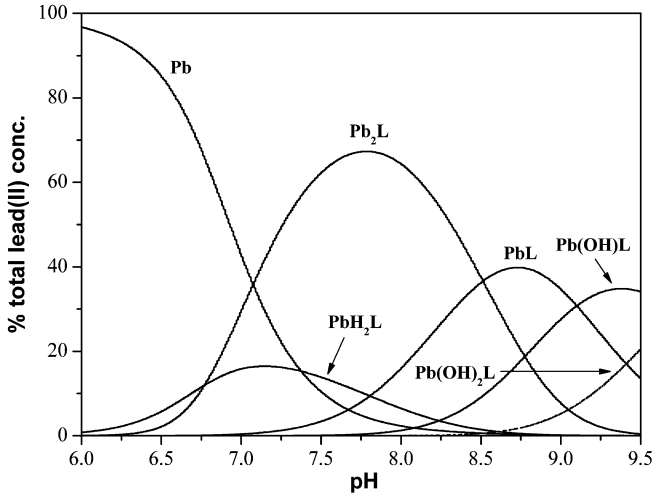


Fig. 2. Species distribution curves calculated for Pb^{2+}:[26]*p*bz$_2$N$_4$O$_2$ at a 1:1 ratio. $C_{Pb} = C_L = 6.0 \times 10^{-3}$ mol dm^{-3}. L = [26]*p*bz$_2$N$_4$O$_2$.

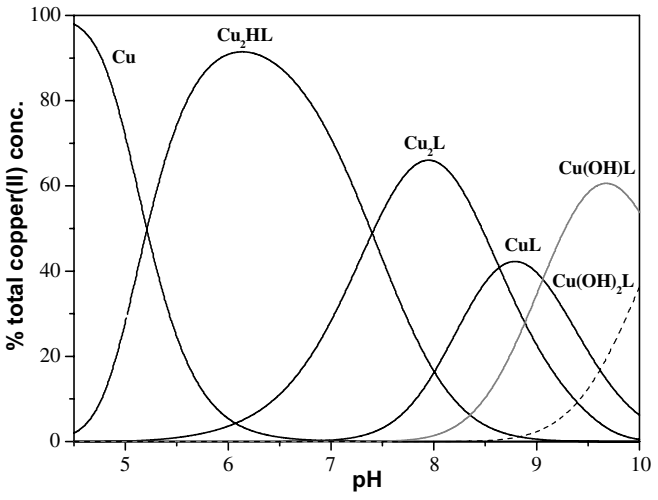


Fig. 3. Species distribution curves calculated for Cu^{2+}:[26]*p*bz$_2$N$_4$O$_2$ at a 1:1 ratio. $C_{Cu} = C_L = 6.0 \times 10^{-3}$ mol dm^{-3}. L = [26]*p*bz$_2$N$_4$O$_2$.

measurements at 298.2 K and 0.10 mol dm^{-3} KNO_3. For solubility reasons the association constants with glutarate could not be determined by this technique. The results are compiled in Table 3 and the distribution curves for the system with oxa^{2-} is shown in Fig. 4.

The values of the protonation constants of the anions were previously determined [15] and the stability constants of their copper(II) complexes are presented in Table 4.

Only species containing one anion, $Cu_2H_hLA^{(2+h)}$, were found, strongly suggesting that the anion bridges the two copper(II) ions. Supporting this suggestion, cascade species with bridging oxa^{2-} and suc^{2-} were found in the solid state by X-ray determination [7].

The $Cu_2H_2LA^{4+}$ species, which can be formed by the reaction of Cu_2HL^{5+} with HA^- or by Cu_2L^{4+} with H_2A, is the main species at low pH (5–7.5). All these species

Table 3
Overall stability constants (log $\beta_{Cu_mH_hL_lA_a}$) for the equilibrium of $[Cu_2([26]pbz_2N_4O_2)](NO_3)_4$ with oxa^{2-}, mal^{2-}, and suc^{2-}

	[26]$pbz_2N_4O_2$[a]	[24]fu_2N_6[b]	[26]$pbz_2N_4O_2$[a]	[24]fu_2N_6[b]	[26]$pbz_2N_4O_2$[a]
	oxa^{2-}		mal^{2-}		suc^{2-}
Equilibrium reaction					
$Cu^{2+} + L + A^{2-} \rightleftharpoons CuLA$				16.97	
$Cu^{2+} + H^+ + L + A^{2-} \rightleftharpoons CuHLA^+$				25.77	
$Cu^{2+} + 2H^+ + L + A^{2-} \rightleftharpoons CuH_2LA^{2+}$		34.75		33.80	
$Cu^{2+} + 3H^+ + L + A^{2-} \rightleftharpoons CuH_3LA^{3+}$		38.42		38.61	
$Cu^{2+} + 4H^+ + L + A^{2-} \rightleftharpoons CuH_4LA^{4+}$		41.92			
$2\,Cu^{2+} + 2H^+ + L + A^{2-} \rightleftharpoons Cu_2H_2LA^{4+}$	34.47(2)		33.14(6)		
$2\,Cu^{2+} + H^+ + L + A^{2-} \rightleftharpoons Cu_2HLA^{3+}$	27.14(4)		26.61(3)		25.63(2)
$2\,Cu^{2+} + L + A^{2-} \rightleftharpoons Cu_2LA^{2+}$	19.45(3)	33.69	18.82(4)	31.54	18.39(5)
$2\,Cu^{2+} + L + A^{2-} \rightleftharpoons Cu_2L(OH)A^+ + H^+$	10.88(5)	23.88	10.73(3)	22.06	10.69(3)
$2\,Cu^{2+} + L + A^{2-} \rightleftharpoons Cu_2L(OH)_2A + 2\,H^+$	2.36(3)		1.81(3)		1.79(5)
$2\,Cu^{2+} + L + A^{2-} \rightleftharpoons Cu_2L(OH)_3A^- + 3H^+$					−7.50(6)
Stepwise constants					
$CuL^{2+} + A^{2-} \rightleftharpoons CuLA$				2.27	
$CuHL^{3+} + A^{2-} \rightleftharpoons CuHLA^+$				2.56	
$CuH_2L^{4+} + A^{2-} \rightleftharpoons CuH_2LA^{2+}$		4.82		3.87	
$CuH_3L^{5+} + A^{2-} \rightleftharpoons CuH_3LA^{3+}$		5.10		5.29	
$CuH_4L^{6+} + A^{2-} \rightleftharpoons CuH_4LA^{6+}$		3.50			
$Cu_2HL^{5+} + HA^- \rightleftharpoons Cu_2H_2LA^{4+}$	8.44		5.69		
$Cu_2HL^{5+} + A^{2-} \rightleftharpoons Cu_2HLA^{3+}$	4.92		4.39		3.41
$Cu_2L^{4+} + A^{2-} \rightleftharpoons Cu_2LA^{2+}$	4.62	6.39	3.99	4.24	3.56
$Cu_2L(OH)^{3+} + A^{2-} \rightleftharpoons Cu_2L(OH)A^+$		4.86		3.04	
$Cu_2L(OH)A^+ \rightleftharpoons Cu_2L(OH)_2A + H^+$	−8.52		−8.92		−8.90
$Cu_2L(OH)_2A \rightleftharpoons Cu_2L(OH)_3A^- + H^+$					−9.29

$T = 298.2 \pm 0.1$ K and $I = 0.10$ mol dm^{-3} in KNO_3.
[a] In parentheses are indicated the standard deviations on the last significant figure. L denotes the macrocycles [26]$pbz_2N_4O_2$ and [24]fu_2N_6, and A the anion.
[b] $I = 0.1$ mol dm^{-3} KCl, Ref. [3].

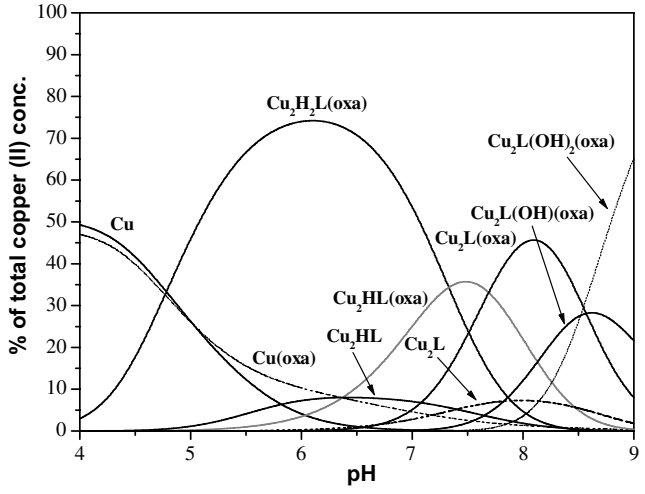


Fig. 4. Species distribution curves calculated for the system $[Cu_2([26]pbz_2N_4O_2)(H_2O)_x]^{4+}$: oxa^{2-} for a 1:1 ratio. $2C_{Cu} = C_L = C_{oxa^{2-}} = 6.0 \times 10^{-3}$ mol dm^{-3} and L = [26]$pbz_2N_4O_2$.

(Cu_2HL^{5+}, Cu_2L^{4+}, HA^- and A^{2-}) exist in this pH range, therefore the $Cu_2H_2LA^{4+}$ species is the result of both reactions. However for practical reasons, in Table 3, the stepwise constant was determined considering only the first reaction. The remaining species are formed from the reaction of the corresponding copper(II) complex with A^{2-}. At pH 9.5, $Cu_2L(OH)_2A$ is the main species, formed by the hydrolysis of two water molecules directly bound to copper(II), indicating that at this pH the anion bridges the two metal centres and in addition to the coordination of donor atoms of the ligand, one OH^- anion is also in the coordination sphere of each metal centre.

Table 4
Stability constants (log units) of the copper(II) complexes with oxa^{2-}, mal^{2-} and suc^{2-}[a]

Reaction equilibrium	oxa^{2-}[a,b]	mal^{2-}[a,b]	suc^{2-}[a,b]
$Cu^{2+} + A^{2-} \rightleftharpoons CuA$	5.64(1)	4.952(3)	2.742(5)
$Cu^{2+} + 2A^{2-} \rightleftharpoons CuA_2^{2-}$	9.50(1)	7.73(1)	4.43(3)
$Cu^{2+} + A^{2-} + H^+ \rightleftharpoons CuHA$		6.98(1)	

$T = 298.2 \pm 0.1$ K and $I = 0.10$ mol dm^{-3} in KNO_3.
[a] In parentheses are indicated the standard deviations on the last significant figure. A denotes the anion.
[b] The protonation constants of the anions determined before [15].

$Cu_2HL(suc)^{3+}$ was the only species found at low pH for this system, which is probably formed by the reaction of Cu_2L^{4+} and $Hsuc^-$ or Cu_2HL^{5+} and suc^{2-}, due to the highest basicity of this anion (Table 4).

A decrease of the association constant with an increase of the alkyl chain of the anion is verified (see Table 3). The basicity of the anion does not seem to be responsible for the strength of the association, as the increase of basicity is opposite to the strength of the association. These results indicate that the energy required to adjust the

macrocycle in the complex to the size and geometry of the bridging substrate is larger for suc^{2-} than for oxa^{2-}. Additionally the methylene groups of mal^{2-} and suc^{2-} are considerably hydrophobic and are poorly accommodated in the aqueous environment [3].

The related macrocycle [24]fu_2N_6 (see Scheme 1) presents a slightly higher value of the binding constant with oxa^{2-}, and a similar one for mal^{2-} [2,3]. The crystal X-ray structure of the cascade species confirms that the oxa^{2-} anion bridges both metal centres [3]. This can be an indication that the oxa^{2-} anion adjusts better to the Cu···Cu distance of the [24]fu_2N_6 complex than to the one of [26]*p*$bz_2N_4O_2$.

2.4. Electrospray ionization mass spectrometry (ESI-MS)

The ESI-MS of methanol solutions of the copper(II) complex gives the cations $[Cu_2LCl_3]^+$ at $m/z = 644.9$ and $[Cu_2LCl]^+$ at $m/z = 573.1$. Peaks corresponding to the free ligand $m/z = 413.3$ $[LH]^+$ and $m/z = 429.3$ $[L(H_2O)H]^+$ could also be found, confirming the low stability constant of the complex of this ligand with copper(II). Additionally, the mononuclear species $[CuL]^+$ at $m/z = 473.4$ and 509.2 and $[CuLCl]^+$ at $m/z = 509.2$ could also be found.

2.5. ^1H NMR spectroscopic data of the lead(II) complexes in D_2O

The ^1H NMR spectra of the lead(II) complexes show four resonances (Table 5): a singlet for H_a protons of the benzene ring, one singlet for the H_b protons and two triplets for the H_c and H_d protons (for labelling see Scheme 1), confirming the high symmetry of the dinuclear complexes. The exchange of NH for ND in D_2O is complete and the N–H resonances could not be seen. Lead satellites could not be observed (^{207}Pb, $I = 1/2$, natural abundance 22.6%). All the geminal protons show chemical and magnetic equivalence that can be explained by considering a dynamic process between two energetically favoured conformations.

The spectra performed at 0.5:1, 1:1 and 2:1 Pb^{2+}:[26]*p*$bz_2N_4O_2$ ratios present the resonances downfield shifted in comparison with those of the free ligand, at the same pD values. At the pD values used and even at a low Pb^{2+} ratio there is a significant amount of the dinuclear complex, and the amount of free ligand is high in comparison with the mononuclear complexes formed. This is the reason why the chemical shifts observed for the 0.5:1 ratio are close to those for the free ligand. Unfortunately due to solubility reasons it was not possible to reach high pD values.

Table 5
^1H NMR data for [26]*p*$bz_2N_4O_2$ and its Pb^{2+} complexes in D_2O (δ, ppm) at 300 K

Compound or complex	pD	**a** (s)	**b** (s)	**c** (t)	**d** (t)
[26]*p*$bz_2N_4O_2$	7.67	7.371	4.042	3.225	3.794
	8.20	7.382	4.068	3.252	3.803
Pb/[26]*p*$bz_2N_4O_2$ (0.5:1)	8.28	7.388	4.090	3.277	3.809
Pb/[26]*p*$bz_2N_4O_2$ (1:1)	8.10	7.400	4.116	3.303	3.819
Pb/[26]*p*$bz_2N_4O_2$ (2:1)	7.60	7.433	4.204	3.390	3.850

[a] For numbering of the atoms see Scheme 1.

2.6. Variation of the magnetic moments with temperature

The temperature dependence of the effective magnetic moment, obtained from molar paramagnetic susceptibility measurements of $[Cu_2(H_2[26]pbz_2N_4O_2)(oxa)_3]\cdot 4H_2O$ and $[Cu_2([26]pbz_2N_4O_2)(suc)Cl_2]$, is presented in Fig. 5.

The behaviour of the two compounds is significantly different, clearly putting into evidence much stronger antiferromagnetic interactions in the succinate compound. In fact, the oxalate-bridged dicopper complex behaviour can be fairly described by a Curie–Weiss law with $\theta = -12.8$ K and the effective magnetic moment in the high temperature range is *ca.* 2.5 μ_B, close to the theoretical value for non-interacting species. On the other hand, for the succinate compound the μ_{eff} at room temperature is *ca.* 1 μ_B and is already temperature dependent. We attempted to fit the susceptibility by the Bleany–Bowers formula [16] for antiferromagnetic coupled copper ions in a dimer, yielding $2J/k = -576$ K, plus a Curie tail to account for impurities and defects. This fraction is unrealistically high (0.17 for $S = 1/2$ impurities), meaning that probably this is not the best model, but it must be stressed that the magnetic moments are significantly damped in this compound from the non-interacting case. At first sight it may appear strange to find a much stronger antiferromagnetic coupling for the succinate compound where the Cu···Cu distances are larger than for the oxalate one, 6.442 Å and 5.484 Å, respectively [7]. However, as pointed out by Carlin [17], the Cu···Cu interaction depends on the superexchange mechanism rather than the distance between the two metal

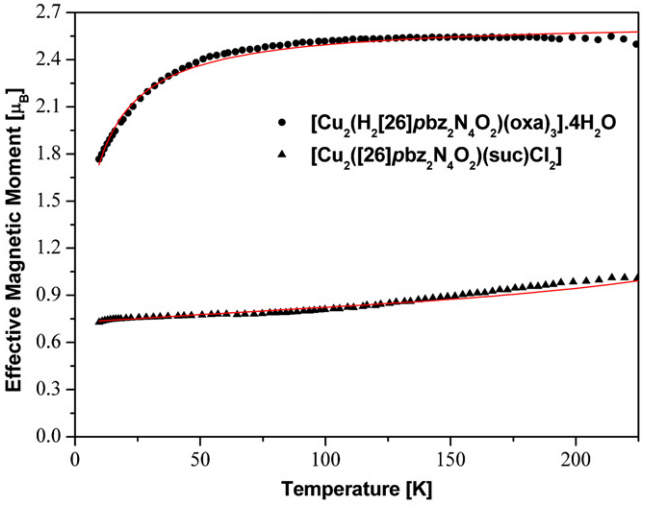


Fig. 5. Thermal dependence of the effective magnetic moment for $[Cu_2(H_2[26]pbz_2N_4O_2)(oxa)_3]\cdot 4H_2O$ and $[Cu_2([26]pbz_2N_4O_2)(suc)Cl_2]$. Solid lines represent fits as described in the text.

ions. This mechanism is provided by the coordinated, highly polarizable, chlorine atoms which are present in the succinate adduct but not in the oxalate one.

3. Conclusions

The presence of mono- and dinuclear copper(II) and lead(II) complexes were confirmed by different techniques (potentiometry, mass spectra and NMR). The presence of oxygen atoms in the macrocyclic backbone lead to a decrease in the stability constants of the copper(II) complex when compared to related macrocycles containing only nitrogen donor atoms.

The high stability constant values of the Pb^{2+} complexes of [26]*p*$bz_2N_4O_2$ when compared with that of the Cu^{2+} one suggest a good fit of lead(II) into the macrocyclic cavity. Even though mononuclear complexes were found, dinuclear ones are the main species even at low metal:ligand ratios, confirming the high tendency of this macrocycle to form dinuclear complexes.

The binding constants of the cascade species formed by $[Cu_2[26]pbz_2N_4O_2(H_2O)_x]^{4+}$ with dicarboxylate anions decrease with the increase in length of the alkyl chain of the anion, a fact that was attributed to a higher conformational energy necessary for the rearrangement of the macrocycle to accommodate the larger anions bridging the two copper(II) centres. The fact that only species with one anion ($Cu_2H_hLA^{(2+h)}$) were found suggest the bridging position for the anion.

In the solid state, the role of the dicarboxylate anions appears to be not very important to mediate the Cu···Cu interaction. In fact the highly polarizable chlorine atoms, when present, provide a superexchange mechanism that couples metallic ions antiferromagnetically, even when the distance between the ions is larger, as was observed in the cases of oxa^{2-} and suc^{2-} for which the crystalline structures were determined [7].

3.1. Experimental

Terephthaldialdehyde and 1,5-diamino-3-oxapentane were obtained from Aldrich, and from Acros Organics, respectively. Oxalic acid (99.5%), malonic acid (>99%) and succinic acid (99%) were purchased from Merck. All the chemicals were of reagent grade and were used as supplied without further purification. The reference used for the ^1H NMR measurements in D_2O was 3-(trimethylsilyl)propanoic acid-d_4 sodium salt, and for ^{13}C NMR spectra dioxane was used as an internal reference. The compound [26]*p*$bz_2N_4O_2$ was synthesised according to the literature [7]. Crystals of quality suitable for X-ray analysis were obtained in four days at room temperature from an ethanol/acetonitrile (1:1 v/v) solution. ^1H NMR (D_2O, ppm): δ 7.26 (8H, s), 3.77 (8H, s), 3.70 (8H, t), 2.91 (8H, t). ^{13}C NMR (D_2O, ppm) δ 138.8, 129.1, 113.3, 79.9, 52.6, 48.0. *Anal.* Calc. for $C_{24}H_{36}N_4O_2$: C 69.87; H, 8.80; N, 13.58. Found: C 69.38; H, 9.25; N, 13.20%.

3.2. Potentiometric measurements

3.2.1. Reagents and solutions

Metal ion solutions were prepared from the nitrate salts, and were standardised as described [18]. A carbonate-free solution of the titrant, KOH, was freshly prepared, maintained in a closed bottle, and discarded when the percentage of carbonate was about 0.5% of the total amount of base (tested by the Gran method) [19,20]. The demineralised water used was obtained from a Millipore/Milli-Q system.

3.2.2. Equipment and working conditions

The equipment used has been described before [15]. The temperature was kept at 298.0 ± 0.1 K; atmospheric CO_2 was excluded from the cell during the titration by passing purified argon across the top of the solution in the reaction cell. The ionic strength of the solutions was kept at 0.10 mol dm^{-3} KNO_3.

3.2.3. Measurements

The $[H^+]$ of the solutions was determined by the measurement of the electromotive force of the cell, $E = E'^{\circ} + Q\log[H^+] + E_j$. E'°, Q, E_j and $K_w = ([H^+][OH^-])$ were obtained as described previously [15]. The term pH is defined as $-\log [H^+]$. The value of K_w was found to be equal to $10^{-13.76}$ mol^2 dm^{-6}.

The potentiometric equilibrium measurements were carried out using 15.00 cm^3 of 2.69×10^{-3} mol dm^{-3} [26]*p*$bz_2N_4O_2$ solutions diluted to a final volume of 32.00 cm^3, in the absence of copper(II) or lead(II), in the presence of metal ions, and in the simultaneous presence of copper(II) and dicarboxylate anions for 1:1:1 and 1:1:2 C_{Cu}:C_L:C_A ratios. A minimum of two replicates was undertaken. All the anions were independently titrated, alone and in the presence of copper(II) ion at 1:1 and 2:1 C_M:C_A ratios.

Only 0.5:1, 1:1 and 1.5:1 Cu^{2+}:L molar ratios were used to determine the stability constants of the complexes, due to precipitation for higher metal ratios. For lead, 1:1 and 2:1 Pb^{2+}:L ratios were used, but for the latter ratio precipitation occurred at pH 8.5.

3.3. Calculation of equilibrium constants

The overall protonation constants, β_i^H, were calculated by fitting the potentiometric data obtained for all the performed titrations with the HYPERQUAD program [21]. The protonation constants of the studied anions (oxa^{2-}, mal^{2-} and suc^{2-}) were also determined from the experimental data under the same experimental conditions, also using the HYPERQUAD program. The stability constants with the copper(II) ion were determined for the ligand and also for the studied anions. All these constants were taken as fixed values to obtain the equilibrium constants of the new species from the experimental data corresponding to all the titrations in different Cu:L:A stoichiometries, also using the HYPERQUAD program. The initial computations

were obtained in the form of overall stability constants, $\beta_{M_mH_hL_lA_a}$ values, $\beta_{M_mH_hLA} = [M_mH_hLA]/([M]^m[H]^h[L][A])$. The species considered in a particular model were those that could be justified by the principles of coordination and supramolecular chemistry. The errors quoted are the standard deviations of the overall stability constants given directly by the program for the input data, which include all the experimental points of all titration curves.

The protonation constants of [26]*p*bz$_2$N$_4$O$_2$ were determined from a minimum of 276 points and the stability constants were determined from a minimum of 138 points. The association constants between the dicopper complex and the different anions were determined from a minimum of 89, 84 and 88 experimental points for oxa^{2-}, mal^{2-} and suc^{2-}, respectively, and a minimum of two titration curves.

3.4. Magnetic susceptibility measurements

The magnetic susceptibility measurements were carried out with a Faraday-type magnetometer (Oxford Instruments) in the range 9–225 K. A magnetic field of 5 T was applied to the polycrystalline powder samples and a gradient of 1 T m^{-1} alternatively in the forward and reverse directions. The force was measured with a Sartorius S3D-V microbalance with powdered samples weighting 10–15 mg placed inside a previous calibrated Teflon bucket. The molar susceptibilities were corrected for the diamagnetism of the constituent atoms by using Pascal constants to give molar paramagnetic susceptibilities.

3.4.1. Preparation of complexes

The dinuclear copper(II) complexes were prepared as described before [7]. The cascade complexes were prepared by addition of 6 equiv. of oxalate or 1 equiv. of succinate potassium salt, dissolved in water, to the dicopper complex dissolved in a mixture of water/ethanol. The mixtures were left stirring overnight and the solvent was removed to dryness. The solid obtained was recrystallised from ethanol to obtain crystals. Yield: 90 % for the copper(II) complexes and 30% for the cascade complexes. [Cu$_2$(H$_2$L)(oxa)$_3$]: C, 41.33; H, 5.43; N, 6.17. *Anal.* Calc. for C$_{30}$H$_{46}$Cu$_2$N$_4$O$_{18}$: C, 41.05; H, 5.28; N, 6.38. [Cu$_2$LCl$_2$(suc)]: C, 43.17; H, 6.11; N, 7.45. *Anal.* Calc. for C$_{28}$H$_{46}$Cl$_2$Cu$_2$N$_4$O$_9$: C, 43.08; H, 5.94; N, 7.18.

3.5. X-ray determination of [26]*pbz*$_2$*N*$_4$*O*$_2$

Crystal data: C$_{12}$H$_{18}$N$_2$O, $M = 206.28$; triclinic $P2_1/a$, $a = 9.300(11)$ Å, $b = 10.590(11)$ Å, $c = 12.270(14)$ Å, $\beta = 97.22(1)$ $V = 1199(2)$ Å^3, $Z = 4$, $D_{calc} = 1.143$ Mg/m^3, $\mu = 0.074$ mm^{-1}, 6494 reflections collected were merged to 2258 independent reflections giving $R_{int} = 0.0747$. The refinement of 143 parameters converged to R indices$R_1 = 0.0980$, $wR_2 = 0.1770$ for all data and $R_1 = 0.1301$, $wR_2 = 0.1908$ for 1672 reflections with $I > 2\sigma(I)$. The X-ray data were collected with a MAR research image plate system with Mo Kα radiation, ($\lambda = 0.71073$ Å) at room temperature. Data analysis was performed with the XDS program [22]. The structure was solved by direct methods and subsequently refined by full-matrix least squares methods on F^2 using the SHELX-97 suite of programs [23]. Anisotropic thermal parameters were used for all non-hydrogen atoms. C–H hydrogen atoms were placed at calculated positions with $U_{iso} = 1.2\ U_{eq}$ of the parent atom refined with individual isotropic thermal parameters. The atomic positions of the hydrogen atoms of the water solvent were not apparent from final difference Fourier maps and they were not included in the refinement of the structure. Molecular diagrams were drawn with PLATON [24].

Acknowledgements

The authors acknowledge the financial support from Fundação para a Ciência e a Tecnologia (FCT) and POCI, with co-participation of the European Community fund FEDER (Project No. POCI/QUI/56569/2004). Sílvia Carvalho and Mauro Figueira also acknowledge FCT for the Grants SFRH/BD/13793/2003 and SFRH/BD/21802/2005 respectively. We also thank EPSRC and the University of Reading for funds for the Image Plate.

Appendix A. Supplementary material

CCDC 655574 contains the supplementary crystallographic data for this paper. These data can be obtained free of charge via http://www.ccdc.cam.ac.uk/conts/retrieving.html, or from the Cambridge Crystallographic Data Centre, 12 Union Road, Cambridge CB2 1EZ, UK; fax: (+44) 1223-336-033; or e-mail: deposit@ccdc.cam.ac.uk. Supplementary data associated with this article can be found, in the online version, at doi:10.1016/j.poly.2007.10.023.

References

[1] M.G. Basallote, J. Durán, M.J. Fernández-Trujillo, M.A. Máñez, M. Quíros, J.M. Salas, Polyhedron 20 (2001) 297.
[2] E. Colacio, M. Ghazi, R. Kivekäs, J.M. Moreno, Inorg. Chem. 39 (2000) 2882.
[3] Q. Lu, J. Reibenspies, A.E. Martell, R.J. Motekaitis, Inorg. Chem. 35 (1996) 2630.
[4] D.A. Nation, A.E. Martell, R.I. Carroll, A. Clearfield, Inorg. Chem. 35 (1996) 7246.
[5] M.G. Basallote, J. Durán, M.J. Fernández-Trujillo, M.A. Máñez, J. Chem, Soc., Dalton. Trans. (1999) 1093.
[6] T.F. Pauwels, W. Lippens, P.W. Smet, G.G. Herman, A.M. Goemine, Polyhedron 18 (1999) 1029.
[7] S. Carvalho, R. Delgado, M.G.B. Drew, V. Félix, Dalton Trans. (2007) 2431.
[8] T. Clifford, A.M. Danby, P. Lightfoot, D.T. Richens, R.W. Hay, J. Chem. Soc., Dalton Trans. (2001) 240.
[9] J. Gao, J.H. Reibenspies, A.E. Martell, Inorg. Chim. Acta 35 (2002) 125.
[10] R. Menif, A.E. Martell, P.J. Squattrito, A. Clearfield, Inorg. Chem. 29 (1990) 4723.

[11] D.A. Nation, J. Reibenspies, A.E. Martell, Inorg. Chem. 35 (1996) 4597.
[12] D.A. Nation, Q. Lu, A.E. Martell, Inorg. Chim. Acta 263 (1997) 209.
[13] L.D. Pettit, H.K.J. Powell, IUPAC Stability Constants Database, Academic Software, Timble, 2003.
[14] L.F. Lindoy, Pure Appl. Chem. 69 (1997) 2179.
[15] S. Carvalho, R. Delgado, N. Fonseca, V. Félix, New J. Chem. 30 (2006) 247.
[16] B. Bleany, K.D. Bowers, Proc. Roy. Soc. London A 214 (1952) 451.
[17] R.L. Carlin, Magnetochemistry, Springer Verlag, Berlin, 1986, p. 82.
[18] G. Schwarzenbach, H. Flaschka, Complexometeric Titrations, Methuen & Co., London, 1969.
[19] G. Gran, Analyst (London) 77 (1952) 661.
[20] F.J. Rossotti, H.J. Rossotti, J. Chem. Educ. 42 (1965) 375.
[21] P. Gans, A. Sabattini, A. Vacca, Talanta 43 (1996) 1739.
[22] W.J. Kabsch, Appl. Crystallogr. 21 (1988) 916.
[23] G.M. Sheldrick, SHELX-97, University of Göttingen, 1997.
[24] L. Spek, PLATON, a Multipurpose Crystallographic Tool, Utrecht University, Utrecht, The Netherlands, 1999.

Available online at www.sciencedirect.com
ScienceDirect
Polyhedron 27 (2008) 688–692
POLYHEDRON
www.elsevier.com/locate/poly

Redox properties of hybrid Dawson type polyoxometalates disubstituted with organo-silyl or organo-phosphoryl moieties

Mohammed Boujtita [a,1], Julien Boixel [c], Errol Blart [c], Cédric R. Mayer [b,*], Fabrice Odobel [c,*]

[a] Université de Nantes, Nantes Atlantique Universités, CNRS, Faculté des Sciences et des Techniques, Laboratoire d'Analyse, Isotopique et Electrochimique, de Métabolismes (LAIEM), UMR CNRS 6006, 2, rue de la, Houssinière, BP 92208, 44322 NANTES Cedex 3, France
[b] Institut Lavoisier de Versailles, UMR-CNRS 8180, Université de Versailles St-Quentin, Bâtiment Lavoisier, 45 avenue des Etats Unis, 78035 Versailles Cedex, France
[c] Université de Nantes, Nantes Atlantique Universités, CNRS, Faculté des Sciences et des Techniques, Laboratoire de Synthèse Organique (LSO), UMR CNRS 6513, 2, rue de la, Houssinière, BP 92208, 44322 NANTES Cedex 3, France

Received 24 July 2007; accepted 30 October 2007
Available online 11 December 2007

Abstract

This paper reports on the electrochemical study of Dawson-type polyoxometalates (POMs) disubstituted with phenyl-phosphonate, phenyl silyl or tertbutylsilyl moieties. The polyanions were studied by cyclic voltammetry and on rotating disk electrode in acetonitrile with tetraphenylphosphonium chloride as supporting electrolyte. We found that these hybrid polyoxometalates can accept up to five electrons and that the organic substituents modify the first and second reduction potential of the POM compared to the unsubstituted POM $[P_2W_{18}O_{62}]^{6-}$. Phenyl-phosphonate lowers the reduction potential, whereas the phenyl silyl or tertbutylsilyl moieties shift them cathodically. We also recorded by spectroelectrochemistry the spectrum of the monoreduced and the bisreduced species of the polyoxometalate disubstituted with phenyl-phosphonate.
© 2007 Elsevier Ltd. All rights reserved.

Keywords: Dawson-type polyoxometalate; Functionalization; Phosphoryl; Silyl; Electrochemical study; Spectroelectrochemistry

1. Introduction

Polyoxometalates (POMs) are large inorganic polyanions generally based on oxides of molybdenum or tungsten. Each metal is located at the center of an octahedron, MO_6, and these octahedra are all bonded together through their corners or their edges and are assembled around an internal tetrahedrally coordinated heteroatom, typically PO_4^{3-} or SiO_4^{4-}. Polyoxometalates are a valuable class of compounds because they span a wide range of potential applications in material science, medicine, catalysis and pigments owing to their rich electrochemical, photochemical and catalytic properties [1–4]. One appealing characteristic of POMs is their capacity to accept several electrons [3,5], which makes them particularly well-suited to act as electron reservoirs. As a result, POMs are attractive candidates to be used as multielectron acceptors for the development of photochemical devices aiming at photocumulative electron transfer and as electrocatalysts for multielectron reduction processes such as the reduction of water into hydrogen gas. Indeed, there are several reports showing that some POMs can act as homogenous catalysts for the reduction of water into dihydrogen from aqueous solution [3,6–9].

The possibility to covalently connect POMs to organic molecules *via* phosphonates [10–13], silanes [14–16], imido [17–21] or other binding units [22,23] opens up the possibil-

* Corresponding authors. Tel.: +33 1 39 25 43 97; fax: +33 1 39 25 43 81 (C.R. Mayer); tel.: +33 2 51 12 54 29; fax: +33 2 51 12 54 02 (F. Odobel).
E-mail address: Fabrice.Odobel@chimie.univ-nantes.fr (F. Odobel).
[1] Tel.: +33 2 51 12 57 23; fax: +33 2 51 12 57 12.

0277-5387/$ - see front matter © 2007 Elsevier Ltd. All rights reserved.
doi:10.1016/j.poly.2007.10.022

ity to prepare inorganic/organic hybrid devices and consequently to merge the intrinsic properties of each fragment. In this context, we are interested to use POMs as electron reservoirs for the construction of photochemical molecular devices in view of water splitting. More precisely, we wish to use the POM as an electron sink that would eventually accept several electrons coming from several multi-component photochemical systems featuring photoinduced electron transfers. Towards this end, we were interested to explore the redox potentials of Dawson type POMs substituted with organic moieties. It was indeed anticipated that the electrochemical properties of the substituted POMs may differ from the unsubstituted parent POM. There is a large amount of information about the electrochemical properties of unsubstituted POMs [3,24–27], but there is almost no report about POMs substituted by an organic group [28] and particularly with Dawson type POMs functionalized with organo-silyl or organo-phosphoryl moieties. The knowledge of the redox potentials of these covalently functionalized POMs is however of a crucial importance to predict the feasibility of a photoinduced electron transfer process with a given sensitizer and therefore for the rational design of a photochemical device relying on POM as terminal electron acceptor, but also in view of other applications since the POMs are often used for their electrochemical properties. The aim of the present paper is therefore to fill this gap by investigating the electrochemical properties of the three functionalized polyoxometalates, α_2-$[P_2W_{17}O_{61}(RPO)_2]^{6-}$ (R = Ph, **1**) and α_2-$[P_2W_{17}O_{61}(RSi)_2O]^{6-}$ (R = Ph, **2** and *ter*-But, **3**) (Fig. 1). More precisely, we have determined the impact of organo-silyl or organo-phosphonate substituents on the reduction potentials of the monovacant Dawson polyoxometalate $[P_2W_{17}O_{61}]^{10-}$ framework and compared to saturated Dawson POM $[P_2W_{18}O_{62}]^{6-}$. We found that the functionalized polyoxometalates **1**–**3** can still receive up to 4 or 5 electrons and that the position of their reduction potentials can be tuned by the nature of the anchoring groups (phosphonate or silyl) used to connect the organic moiety to the POM.

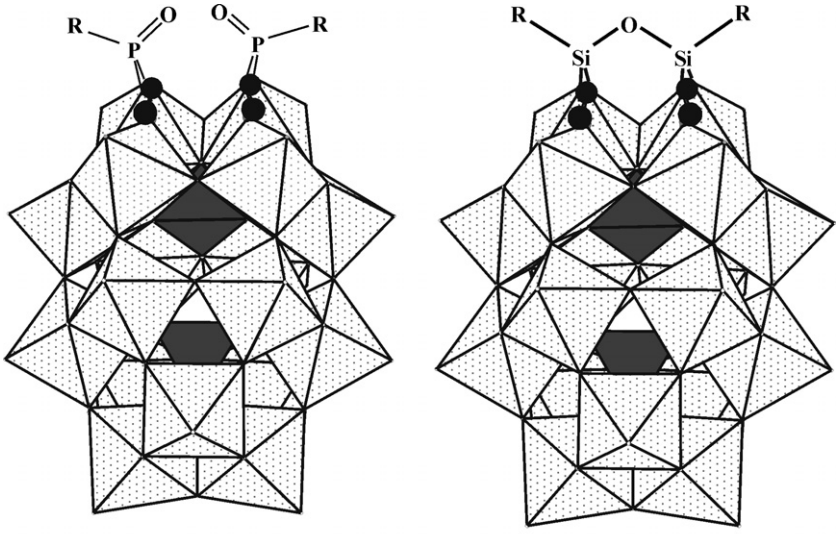
2. Experimental

The polyoxometalates **1**–**3** were prepared as described in the literature [14,29]. The electrochemical measurements were performed with a potentiostat–galvanostat MacLab model ML160 controlled by resident software (Echem v1.5.2 for Windows) using a conventional single-compartment three-electrode cell. The working electrode was a glassy carbon disk of 4 mm^2 area, the auxiliary was a Pt wire and the reference electrode was the saturated potassium chloride calomel electrode (SCE). The solvents used in these studies were distilled prior use following usual drying procedures; however the presence of traces of water in the electrolyte can not be excluded since the POMs themselves are certainly hydrated compounds. All potentials are quoted relative to SCE. In all the experiments the scan rate was 100 mV/s for the cyclic voltammetry and 15 Hz for pulse voltammetry. Spectroelectrochemical spectra were recorded in a thin quartz UV–Vis cell (0.5 mm) surmounted with a reference electrode (SCE) and a platinum wire as counter electrode. The working electrode was a platinum grid inserted within the quartz cell and the other conditions are the same as those for the cyclic voltammetry. UV–Vis absorption spectra were recorded on a UV-2401PC Shimadzu spectrophotometer.

3. Result and discussion

3.1. Electrochemical study

The cyclic voltammograms of the polyoxometalates **1**–**3** are shown in Figs. 2–5 and the half-wave potentials are gathered in Table 1. Since, we were interested to study



1 **2** or **3**

Fig. 1. Schematic drawing of the polyoxometalates studied in this work. **1**: R = Ph; **2**: R = Ph; and **3**: R = tertBu.

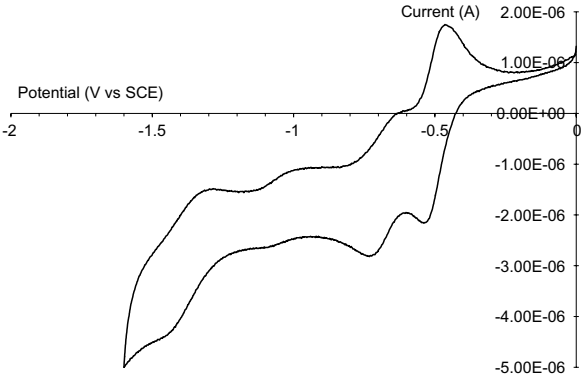


Fig. 2. Cyclic voltammogram of 5×10^{-4} M of $P_2W_{18}O_{62}(Bu_4N)_6$ in DMSO containing 0.1 M of Bu_4NPF_6, scan rate: 100 mV/s, working electrode: glassy carbon, reference electrode: SCE.

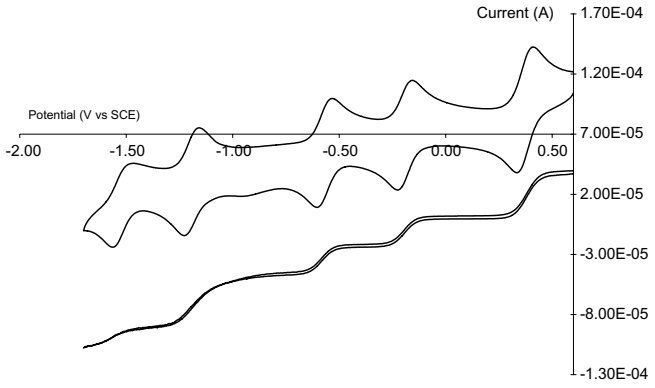


Fig. 3. Overlay of the cyclic voltammogram (upper part) of 5×10^{-4} M of $[P_2W_{17}O_{61}(C_6H_5PO)_2](Bu_4N)_6$ (**1**) in CH_3CN containing 0.1 M of PPh_4Cl, scan rate: 100 mV/s, working electrode: glassy carbon with the voltammogram recorded with the rotating disc-electrode (using the same conditions as above but with the spinning frequency of 4500 rpm). The process in the anodic region is due to ferrocene internal reference.

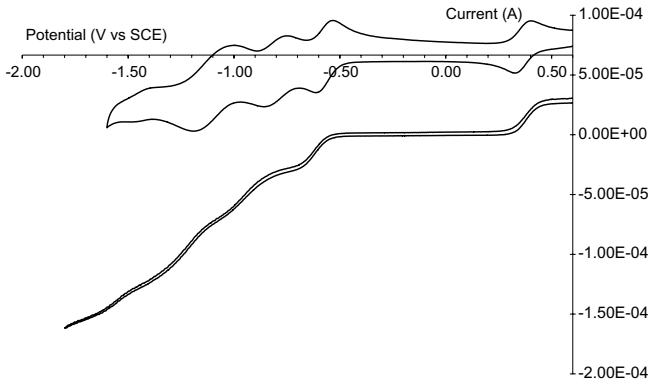


Fig. 4. Overlay of the cyclic voltammogram (upper part) of 5×10^{-4} M of $[P_2W_{17}O_{62}(C_6H_5Si)_2](Bu_4N)_6$ (**2**) in CH_3CN containing 0.1 M of PPh_4Cl, scan rate: 100 mV/s, working electrode: glassy carbon with the voltammogram recorded with the rotating disc-electrode (using the same conditions as above but with the spinning frequency of 4500 rpm). The process in the anodic region is due to ferrocene internal reference.

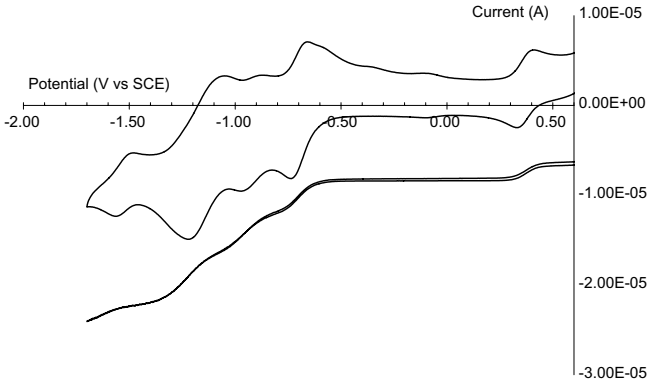


Fig. 5. Overlay of the cyclic voltammogram (upper part) of 5×10^{-4} M of $[P_2W_{17}O_{62}(tC_4H_9Si)_2](Bu_4N)_6$ (**3**) in CH_3CN containing 0.1 M of PPh_4Cl, scan rate: 100 mV/s, working electrode: glassy carbon with the voltammogram recorded with the rotating disc-electrode (using the same conditions as above but with the spinning frequency of 4500 rpm). The process in the anodic region is due to ferrocene internal reference.

the influence of the organic substituent on the redox potential values of the polyoxometalates, we therefore started by examining the electrochemical behaviour of the unsubtituted and saturated polyoxometalate $[P_2W_{18}O_{62}]^{6-}$. The latter can take as a reference and could be considered as the parent compound from which the polyanions **1**–**3** are derived, in which the lacunar surface was saturated by both electrophilic groups. The electrochemistry of $[P_2W_{18}O_{62}]^{6-}$ has already been reported several times in the literature, but it was essentially investigated in buffered aqueous solution [3,24–27] and more rarely in an organic solvent [30]. As expected, our results showed both the solubility and the electrochemical behaviour of the reference $[P_2W_{18}O_{62}]^{6-}$ were found poor in acetonitrile compared with the other substituted polyoxometalates **1**–**3**. Herein, DMSO with Bu_4NPF_6 was used as supporting electrolyte solution and showed a good compromise between the solubility and the electrochemical behaviour of $[P_2W_{18}O_{62}]^{6-}$.

The cyclic voltammogram of $[P_2W_{18}O_{62}]^{6-}$ shows four successive reduction waves up to −1.5 V versus SCE, but only the first process displays a well-resolved voltammogram with the peak-to-peak separation ΔE of 70 mV (Fig. 2). This latter process is consistent with the addition of one electron on the polyoxometalate that resides most probably in a tungsten empty d^0 orbital [3–5,26]. The other reduction waves are relatively well-defined but their intensities decreases steadily with a significant increase in the ΔE values. Such electrochemical behaviour could be attributed to the precipitation of the reduced species generated at the electrode surface due to their low solubility in DMSO + Bu_4NPF_6 electrolyte,

Fig. 3 shows the cyclic voltammogram of the polyoxometalate **1** disubstituted by two phenyl phosphonic acid units that displays four quasi-reversible reduction processes. The comparison of the magnitude of the three first processes to the known Fc^+/Fc one-electron process using the rotating electrode reflects a similar height characteristic

Table 1
Redox potentials of the polyoxometalates **1**–**3** along with those of the parent $P_2W_{18}O_{62}(Bu_4N)_6$

	E_{Red1}/V (ΔE/mV)	E_{Red2}/V (ΔE/mV)	E_{Red3}/V (ΔE/mV)	E_{Red4}/V (ΔE/mV)
$[P_2W_{18}O_{62}]^{6-}$[a]	−0.50 (70)	− 0.68 (86)	−1.03 (112)	1.37 (144)
$[P_2W_{17}O_{61}(PhPO)_2]^{6-}$ (**1**)[b]	−0.20 (66)	−0.58 (66)	−1.20 (68)	−1.54 (90)
$[P_2W_{17}O_{62}(PhSi)_2]^{6-}$ (**2**)[b]	−0.62 (70)	−0.92 (90)	−1.17 (134)	−1.17 (134)
$[P_2W_{17}O_{62}(tBuSi)_2]^{6-}$ (**3**)[b]	−0.70 (70)	−0.91 (90)	−1.19[c]	−1.24[c]

All potentials are referred vs. SCE. In these conditions $E_{1/2}(Fc^{+/0}) = 0.37$ V. Working electrode: glassy carbon.
[a] Recorded in DMSO + Bu_4NPF_6 0.1 M.
[b] Recorded in CH_3CN with Ph_4PCl 0.1 M as supporting electrolyte.
[c] Determined by differential pulse stripping voltammetry.

of one-electron process. In contrast, the last wave seems ill-defined with a height value probably less than one electron. It is interesting to note that, the first reduction potential of the compound **1** is anodically shifted by 300 mV compared to that of the parent $[P_2W_{18}O_{62}]^{6-}$ whereas the second potential is shifted by 110 mV (Table 1). This reflects the known electron-withdrawing property of the phosphonate group that pumps up a certain amount of the electronic density on the negatively charged polyoxometalate. However, this effect becomes less pronounced as the number of injected electrons on the polyoxometalate increases, this is probably due to the fact that the first injected electron is trapped close to the metals directly bound to the phosphonate. The other reduction processes involve electrons that reside on the other metals, that are further away and therefore less influence by phosphonate group.

When, the organic moiety is grafted through a silyl anchoring group a different electrochemical behaviour can be observed. The cyclic voltammogram of **2** and **3** exhibits four distinct waves (Figs. 4 and 5). Both the first and second waves can be considered as a monoelectronic and reversible electrochemical process, but the third corresponds to the exchange of about two electrons as determined with the rotating disk electrode and the last process accounts for less than one electron probably due to the precipitation of the preceding reduced species (Figs. 4 and 5). In compound **3**, the potentials of third and fourth reduction process are sufficiently different to be determined by differential pulse voltammetry, but in POM **2** they merge to give a single bielectronic wave. The comparison of the redox potentials of both polyoxometalate **2** and polyoxometalate **3** with those of the reference and of the polyoxometalate **1**, indicates that the silyl group exhibits an opposite effect compared to that observed with the phosphonate group. With the silyl anchoring group, the first reduction process becomes more difficult than that of **1** and that of the unsubstituted polyoxometalate $[P_2W_{18}O_{62}]^{6-}$ (Table 1). Besides, the inspection of the values of the first reduction potential between **2** and **3** shows that the *tert*butyl group renders the silyl moiety more electron rich than the phenyl one and hence destabilizes greater the reduced polyoxometalate. This is perfectly consistent with the known electron releasing property of alkyl chains compare to the weak electron accepting character of phenyl. As a consequence, the first reduction potential of **3** is cathodically shifted with respect of that of **2** (Table 1). Overall, the nature of the anchoring moiety (silyl or phosphonate) and the organic substituent modify the reduction potentials of the substituted Dawson type polyoxometalates.

3.2. Spectroelectrochemical study

The limited number of spectroelectrochemical studies with organo-functionalized POMs[28] prompted us to determine the spectrum of the monoreduced and the bireduced species of POM **1**. The utilization of POMs as electron acceptors in a photochemical molecular device will inevitably requires the knowledge of the spectroscopic signature of the reduced species in order to be able to monitor their formations by time-resolved transient absorption spectroscopy. We chose to study POM **1** by spectroelectrochemistry because it exhibits the most reversible and the most distinct reduction processes within the series. The spectra of the POM **1** were recorded during the course of the electrolysis of a thin layer of a solution of **1** (Fig. 6).

Before reduction, the spectrum of POM **1** exhibits an intense absorbance in the UV region (below 290 nm). It is attributed to a ligand-to-metal-charge-transfer transition (LMCT) and corresponds to a shift of the electronic density from the oxygen to the tungsten atoms [3,4]. Upon

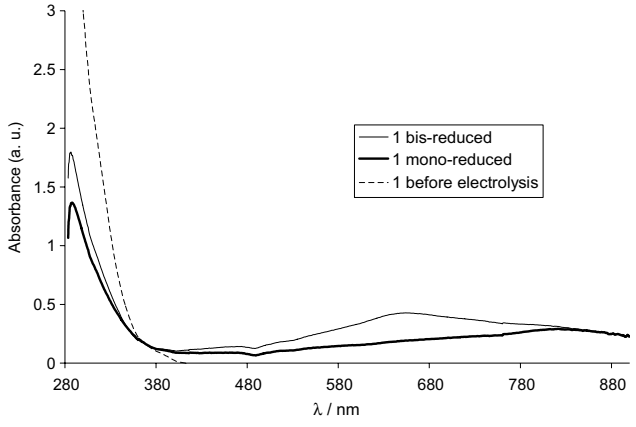


Fig. 6. Electronic absorption spectra of POM **1** (0.3 mM) recorded in CH_3CN with Ph_4PCl (0.1 M) as supporting electrolyte; before electrolysis (dashed line); after one-electron reduction (bold solid line); after two-electron reduction (thin solid line).

one-electron reduction, the colorless solution turned blue evidencing the formation of the expected so-called "heteropoly blue" well-characterized with unsubstituted POMs that were reduced by electrochemical or photochemical means [3–5,30,31]. The one-electron reduction of POM **1** induces a decrease of the absorbance in the far UV region and the formation of a new broad absorption band in the visible region between 500 and 900 nm with a maximum absorption located at 822 nm (Fig. 6). This new band is assigned to an intervalence charge transfer transition between the d^1 reduced-tungsten metal and one of the other d^0 tungsten metals or a metal centered d–d transition [5,30]. Further electrolysis of the solution induces a drop of the absorbance at 822 nm and the formation of a new band localized at 655 nm (Fig. 6). This latter band most probably also corresponds to an intervalence charge-transfer and a tungsten-centered d–d transition, but whose energies has been increased due to the modification of the energy levels of the HOMO and LUMO frontier molecular orbitals of the doubly reduced POM. The spectroscopic features measured here upon reduction of POM **1** are in good agreement with the results of Pope and coworkers on the spectroelectrochemical study of $[P_2W_{18}O_{62}]^{6-}$ [5]. It is worthy of noticing that the application of a positive bias to the grid electrode, after the formation of the doubly reduced species, allows for the retrieval of the initial spectrum recorded before electrolysis. This result clearly demonstrates the chemical stability of the reduced species and the electrochemical reversibility of the two first reduction processes. Overall, we can observe that the monoreduced and bisreduced species exhibit clear and distinct spectroscopic signature that will make the formation of these species easily detected by transient absorption spectroscopy.

4. Conclusions

The electrochemical characterizations of three Dawson POMs substituted by organic phosphonate or silyl moieties are reported for the first time. We demonstrated the influence of organo-phosphonate and organo-silyl groups on the reduction potentials on substituted Dawson type POMs. Compared to the parent unsubstituted $[P_2W_{18}O_{62}]^{6-}$, the phosphonate induces an anodic shift of the first and the second half-wave reduction potential, whereas the silyl group has an inverse effect. The ability to tune the reduction potential of POMs, through the choice of the organic substituent, can be used to alter the electrochemical properties of a specific POM and to engineer new molecular function. Finally, we determined by spectroelectrochemistry the specific fingerprint of the monoreduced and bisreduced species of POM **1** functionalized by two phenyl phosphonic acid groups.

In conclusion, the functionalization of a Dawson type-POM with a phosphonate or silyl groups appears to be an effective mean to prepare electrochemically active hybrid POMs, because the functionalized systems can still undergo several electron reductions at low potentials and they also lead to stable reduced species that can be easily identified by absorption spectroscopy. Therefore, the as-functionalized POMs represent suitable compounds to be used as electron reservoirs for cumulative electron transfers or for other applications such as covalent functionalization of electrodes with POMs for catalysis.

Acknowledgement

The French Research Ministry is gratefully acknowledged for the financial support of these researches through the program ANR blanc "PhotoCumElec".

References

[1] D.E. Katsoulis, Chem. Rev. 98 (1998) 359.
[2] N. Mizuno, M. Misono, Chem. Rev. 98 (1998) 199.
[3] M. Sadakane, E. Steckhan, Chem. Rev. 98 (1998) 219.
[4] T. Yamase, Chem. Rev. 98 (1998) 307.
[5] E. Papaconstantinou, M.T. Pope, Inorg. Chem. 9 (1970) 667.
[6] J.R. Darwent, Chem. Commun. (1982) 798.
[7] H. Hori, K. Koike, Y. Sakai, H. Murakami, K. Hayashi, K. Nomiya, Energy Fuel 19 (2005) 2209.
[8] A. Ioannidis, E. Papaconstantinou, Inorg. Chem. 24 (1985) 439.
[9] P.D. Prenzler, C. Boskovic, A.M. Bond, A.G. Wedd, Anal. Chem. 71 (1999) 3133.
[10] U. Kortz, M.T. Pope, Inorg. Chem. 34 (1995) 3848.
[11] C.R. Mayer, M. Herve, H. Lavanant, J.-C. Blais, F. Sécheresse, Eur. J. Inorg. Chem. (2004) 973.
[12] C.R. Mayer, P. Herson, R. Thouvenot, Inorg. Chem. 38 (1999) 6152.
[13] C.R. Mayer, R. Thouvenot, J. Chem. Soc., Dalton (1998) 7.
[14] C.R. Mayer, C. Roch-Marchal, H. Lavanant, R. Thouvenot, N. Sellier, J.-C. Blais, F. Sécheresse, Chem. – Eur. J. 10 (2004) 5517.
[15] C.R. Mayer, I. Fournier, R. Thouvenot, Chem. – Eur. J. 6 (2000) 105.
[16] C.N. Kato, Y. Kasahara, K. Hayashi, A. Yamaguchi, T. Hasegawa, K. Nomiya, Eur. J. Inorg. Chem. (2006) 4834.
[17] B. Xu, M. Lu, J. Kang, D. Wang, J. Brown, Z. Peng, Chem. Mater. 17 (2005) 2841.
[18] Z. Peng, Angew. Chem., Int. Ed. 43 (2004) 930.
[19] B. Xu, Z. Peng, Y. Wei, D.R. Powell, Chem. Commun. (2003) 2562.
[20] Y. Wei, M. Lu, C.F. Cheung, C.L. Barnes, Z. Peng, Inorg. Chem. 40 (2001) 5489.
[21] B. Xu, Y. Wei, C.L. Barnes, Z. Peng, Angew. Chem., Int. Ed. 40 (2001) 2290.
[22] S. Bareyt, S. Piligkos, B. Hasenknopf, P. Gouzerh, E. Lacote, S. Thorimbert, M. Malacria, J. Am. Chem. Soc. 127 (2005) 6788.
[23] S. Bareyt, S. Piligkos, B. Hasenknopf, P. Gouzerh, E. Lacote, S. Thorimbert, M. Malacria, Angew. Chem., Int. Ed. 42 (2003) 3404.
[24] M.T. Pope, E. Papaconstantinou, Inorg. Chem. 6 (1967) 1147.
[25] I.-M. Mbomekalle, B. Keita, Y.W. Lu, L. Nadjo, R. Contant, N. Belai, M.T. Pope, Eur. J. Inorg. Chem. (2004) 276.
[26] B. Keita, Y. Jean, B. Levy, L. Nadjo, R. Contant, New J. Chem. 26 (2002) 1314.
[27] B. Keita, Y.W. Lu, L. Nadjo, R. Contant, Eur. J. Inorg. Chem. (2000) 2463.
[28] D. Agustin, J. Dallery, C. Coelho, A. Proust, R. Thouvenot, J. Organomet. Chem. 692 (2007) 746.
[29] Z.-G. Sun, Q. Liu, J.-F. Liu, Inorg. Chem. Commun. 3 (2000) 328.
[30] C. Baffert, J.F. Boas, A.M. Bond, P. Koegerler, D.-L. Long, J.R. Pilbrow, L. Cronin, Chem. – Eur. J. 12 (2006) 8472.
[31] N. Fay, V.M. Hultgren, A.G. Wedd, T.E. Keyes, R.J. Forster, D. Leane, A.M. Bond, J. Chem. Soc., Dalton (2006) 4218.

Available online at www.sciencedirect.com
ScienceDirect
Polyhedron 27 (2008) 693–700
POLYHEDRON
www.elsevier.com/locate/poly

Copper(II) complexes of symmetrical and unsymmetrical tetradentate Schiff base ligands incorporating 1-benzoylacetone: Synthesis, crystal structures and electrochemical behavior

Biswarup Sarkar [a,b], Gabriele Bocelli [c], Andrea Cantoni [c], Ashutosh Ghosh [a,*]

[a] Department of Chemistry, University College of Science, University of Calcutta, 92, A.P.C. Road, Kolkata 700 009, India
[b] Bolpur College, Bolpur 731 204, Birbhum, West Bengal, India
[c] IMEM-CNR, Parceo Area delle scienze 37a, I-43100 Fontanini-Parma, Italy

Received 31 July 2007; accepted 29 October 2007

Abstract

Three new copper(II) complexes $[CuL^1]_2(ClO_4)_2$ (**1**), $[CuL^2]ClO_4$ (**2**) and $[CuL^3]$ (**3**) with three Schiff base ligands [HL^1 = 1-phenyl-3-{3-[(pyridin-2-ylmethylene)-amino]-propylimino}-butan-1-one, HL^2 = 1-phenyl-3-[3-(1-pyridin-2-yl-ethylideneamino)-propylimino]-butan-1-one and H_2L^3 = 3-[3-(1-methyl-3-oxo-3-phenyl-propylideneamino)-propylimino]-1-phenyl-butan-1-one] have been synthesized and structurally characterized by X-ray crystallography. The mono-negative tetradentate asymmetric Schiff base ligands $(L^1)^-$ and $(L^2)^-$ are chelated in complexes **1** and **2** to form square planar copper(II) complexes. In complex **1**, the two units are associated weakly through ketonic oxygen of benzoylacetone fragment to form the dimeric entity. The square planar geometry of complex **3** is unusually distorted towards tetrahedral one. All three complexes exhibit reversible cyclic voltammetric responses in acetonitrile solution corresponding to the Cu^{II}/Cu^{I} redox process. The $E_{1/2}$ (−0.47 V versus SCE) of **3** shows significant anodic shift due to the tetrahedral distortion around Cu(II) compare to that of **1** and **2** (−0.82 and −0.87 V versus SCE, respectively).
© 2007 Elsevier Ltd. All rights reserved.

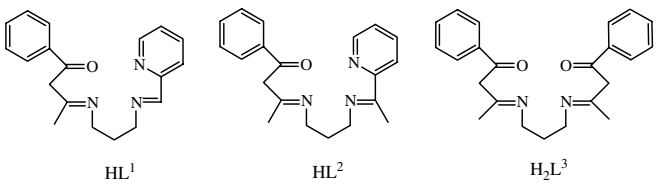
Keywords: Copper(II); Unsymmetrical Schiff base; 1-Benzoylacetone; Crystal structure; Electrochemical behavior

1. Introduction

The interest in the design, synthesis and characterization of the transition metal complexes of unsymmetrical Schiff base ligands has come from the realization that coordinated ligands around central metal ions in natural systems are unsymmetrical [1]. Recently, this class of compounds has also attracted much attention in the field of optoelectronic technologies for their large nonlinear responses [2]. Compare to their symmetrical counterpart, syntheses of such ligands are rather difficult because simple condensation methodology with three components is no longer applied. However, since the first reports on the synthesis of 7-amino-4-methyl-5-azahept-3-en-2-one (AMAH) [3] and 8-amino-4-methyl-5-azaoct-3-en-2-one (AMAO) [4], the monocondensation products of 2,4-pentanedione with 1,2-ethanediamine and or 1,3-propanediamine, respectively, these 'half units' have been used extensively as precursors for the preparation of unsymmetrical quadridentate Schiff base ligands [2,5]. In most of the ligands reported so far, the acetylacetoneiminato side is usually kept unchanged and the other side of the diamine is condensed with various aromatic carbonyl compounds to study the variation and fine tuning of stability, reactivity and electronic properties of such complexes [5,6]. The apparent reason for keeping the acetylacetoneiminato fixed, seems to be the facile synthesis of the 'half unit' by high dilution method [3,4]. Recently, we successfully synthesized the analogous tridentate Schiff base by monocondensation of 1-benzoylacetone

* Corresponding author.
E-mail address: ghosh_59@yahoo.com (A. Ghosh).

0277-5387/$ - see front matter © 2007 Elsevier Ltd. All rights reserved.
doi:10.1016/j.poly.2007.10.021



Scheme 1.

with 1,2-ethanediamine or 1,2-propanediamine under the similar conditions and used those ligands to synthesize trinuclear Cu(II) complexes with a μ_3-OH core [7]. On the contrary, the corresponding 'half unit' of 1,3-propanediamine did not result the similar trinuclear complex, instead underwent hydrolysis during complex formation indicating its lower stability [7]. This encourages us to synthesize tetradentate Schiff base using the precursor 7-amino-3-methyl-1-phenyl-4-azahept-1,3-dien-1-ol (HAMPA, the monocondensation product of 1,3-diaminopropane and 1-benzoylacetone) and to explore if the double condensed ligands are stable enough to result in the formation of complexes with copper(II).

In this paper, we report synthesis, spectral characterization, crystal structures and electrochemical behavior of three Cu(II) complexes. Two of them are derived from the unsymmetrical tetradentate Schiff bases HL^1 and HL^2 formed by the condensation of free amine group of HAMPA with pyridine-2-carboxaldehyde and 2-acetylpyridine, respectively, and the other one from symmetrical Schiff base H_2L^3 containing 1-benzoylacetone at the both ends of 1,3-diaminopropane (Scheme 1). The significant structural differences of these complexes from their acetylacetone analogs are also discussed here.

2. Experimental

All chemicals were of reagent grade and used without further purification.

2.1. Synthesis of the precursor tridentate ligand, HAMPA

The precursor mono-condensed Schiff base, HAMPA was synthesized by high dilution technique [7,8]. 1-Benzoylacetone (10 mmol, 1.6 g) in chloroform (50 cm^3) was added drop wise to a solution of 1,3-propanediamine (10 mmol, 0.76 cm^3) in chloroform (50 cm^3). After completion of the addition, the solution was stirred for an additional 3 h and then chloroform was evaporated under reduced pressure, yielding HAMPA as a viscous liquid.

2.2. Synthesis of the ligands, 1-phenyl-3-{3-[(pyridin-2-ylmethylene)-amino]-propylimino}-butan-1-one (HL^1) and 1-phenyl-3-[3-(1-pyridin-2-yl-ethylideneamino)-propylimino]-butan-1-one (HL^2)

To synthesize HL^1, a methanolic solution (15 cm^3) of pyridine-2-carboxaldehyde (10 mmol, 0.95 cm^3) was added to a methanolic solution (25 cm^3) of HAMPA (10 mmol). The mixture was warmed at 50 °C for 1 h and cooled to room temperature. HL^2 was prepared in the same way as HL^1 using 2-acetyl pyridine (10 mmol, 1.12 cm^3) instead of pyridine-2-carboxaldehyde. The tetradentate ligands HL^1 and HL^2 were not isolated and the methanol solutions were used for the synthesis of the complexes.

2.3. Synthesis of complex $[CuL^1ClO_4]_2$ (1), $[CuL^2ClO_4]$ (2)

A solution of $Cu(ClO_4)_2 \cdot 6H_2O$ (10 mmol, 3.7 g) in methanol (20 cm^3) was added to the resulting methanol solution of each tetradentate ligands HL^1 and HL^2 with continuous stirring. Brown colored solid of complex **1** separated immediately. The dark brown single crystal of **1**, suitable for X- ray diffraction was obtained on dissolving it in acetonitrile. In case of complex **2**, separation of brown mass took place on keeping the mixture overnight in a refrigerator. The reddish-brown single crystal for suitable for X- ray diffraction was obtained on dissolving the mass in a mixture of acetonitrile and methanol (1:2).

Complex **1**: Yield: 1.9 g (57%). *Anal.* Calc. for $C_{38}H_{40}Cl_2Cu_2N_6O_{10}$: C, 48.62; H, 4.29; N, 8.95; Cu, 13.54. Found: C, 48.74; H, 4.12; N, 8.87; Cu, 13.46%. λ_{max}/nm (ε_{max}/$dm^3\ mol^{-1}\ cm^{-1}$) (acetonitrile), 631 (144); IR: ν(C=N), 1525, 1572 cm^{-1}, $\nu(ClO_4^-)$, 1086 cm^{-1}.

Complex **2**: Yield: 2.0 g (55%). *Anal.* Calc. for $C_{20}H_{22}ClCuN_3O_5$: C, 49.69; H, 4.59; N, 8.69; Cu, 13.15. Found: C, 49.86; H, 4.61; N, 8.53; Cu, 13.19%. λ_{max}/nm (ε_{max}/$dm^3\ mol^{-1}\ cm^{-1}$) (methanol), 607 (152); IR: ν(C=N), 1522 and 1557 cm^{-1}, $\nu(ClO_4^-)$, 1091 cm^{-1}.

2.4. Synthesis of complex $[CuL^3]$ (3)

The symmetrical Schiff base in complex **3** was formed by the condensation of 1-benzoylacetone at both end of 1,3-propanediamine. To synthesize H_2L^3, a methanolic solution (15 cm^3) of 1-benzoylacetone (10 mmol, 1.6 g) was added to a methanolic solution (20 cm^3) of HAMPA (10 mmol). The mixture was warmed at 50 °C for 1 h and cooled to room temperature. A solution of $Cu(ClO_4)_2 \cdot 6H_2O$ (10 mmol, 3.7 g) in methanol (20 cm^3) was added to the resulting solution of the tetradentate ligand with continuous stirring. The resulting solution was left overnight when greenish blue crystalline compound suitable for X-ray analysis were separated out.

Complex **3**: Yield: 1.7 g (45%). *Anal.* Calc. for $C_{12}H_{15}CuN_3O_3$: C, 65.15; H, 5.71; N, 6.61; Cu, 14.99. Found: C, 65.32; H, 5.66; N, 6.57; Cu, 14.87%. λ_{max}/nm (ε_{max}/$dm^3\ mol^{-1}\ cm^{-1}$) (methanol), 568(159); IR: ν(C=N), 1520 cm^{-1}.

2.5. Physical measurements

Elemental analyses (carbon, hydrogen and nitrogen) were performed using a Perkin–Elmer 240C elemental ana-

lyzer and the copper contents in all the complexes were estimated spectrophotometrically. The IR spectra in KBr (4500–500 cm^{-1}) were recorded using a Perkin–Elmer RXI FT-IR spectrophotometer. The electronic spectra in methanol (1200–350 nm) were recorded in a Hitachi U-3501 spectrophotometer. Cyclic voltammetry was carried out using Sycopel model AEW2 1820F/S instrument. The measurements were performed at 300 K in acetonitrile solutions containing 0.2 M TEAP and 10^{-3} M Cu(II) complex deoxygenated by bubbling with nitrogen. The working, counter, and reference electrodes used were a platinum wire, a platinum coil, and an SCE.

2.6. Crystallographic studies

The data for complex **1** were collected at room temperature with Mo Kα radiation on Bruker AXS Smart single crystal diffractometer with CCD (area detector).The absorption correction was performed with the method inserted in SHELXTL-NT V5.1 [9]. The structure was solved by direct methods with the software SHELXTL-NT V5.1 inserted in the Bruker AXS software [9].

The data for complexes **2** and **3** were collected at room temperature with Cu Kα radiation on Siemens AED single crystal diffractometer with a local program [10]. The preliminary cell parameters were obtained from least squares of the (θ, χ, ϕ) angular values of 3897 and 1948 reflections (θ range = 4–70° and 5.5–70°) respectively for complexes **2** and **3**, accurately well centered on the diffractometer. The intensity of one standard reflection, recorded for every 100 reflections, showed no significant changes. The recorded data were corrected for polarization and Lorentz effects. The absorption correction was performed with the method of Walker and Stuart [11] with a program written by Gluzinski [12].

The crystal structures of the three complexes were solved by direct methods using SHELXS-97 [13] program and refined by using SHELXL-97 [13]. The nonhydrogen atoms were refined anisotropically while the hydrogen atoms were located from difference Fourier map. The positional and thermal parameters were kept fixed during refinement. Neutral atom scattering factors were taken from Cromer and Weber [14] and anomalous dispersion effects were included in F_{calc} [15]. In complex **2** there are disordered carbon atoms in the diamine fragments. The site occupation factors of the disordered pairs of atoms (C3A and C3B; C4A and C4B) were constrained to be unity and were tied to FVAR. The crystallographic illustrations were prepared using ORTEP-3 [16]. Significant crystallographic data are summarized in Table 1.

3. Results and discussion

3.1. IR and electronic spectra

All these compounds contain no significant peak in the region of 3100–3250 cm^{-1}, which clearly indicates that there is no free $-NH_2$ group i.e. all are the quadridentate ligands that form the complexes. The bands corresponding to azomethylene group (C=N) are distinct in all three complexes and appear within 1572–1520 cm^{-1}. The sharp, strong, single peak at 1086 and 1091 cm^{-1} for complexes **1** and **2** clearly indicates the presence of anionic perchlorate group. As expected, complex **3** does not show any such peak.

The electronic spectral data in acetonitrile solution suggest basically square planar geometry for **1** and **2**. In general square-planar complexes are known to exhibit one or two bands [17]. Complexes **1** and **2** show a broad band at 631 and 607 nm, respectively, as was also observed for

Table 1
Crystal data and structure refinement of complexes **1**–**3**

	1	**2**	**3**
Formula	$C_{38}H_{40}Cl_2Cu_2N_6O_{10}$	$C_{20}H_{22}ClCuN_3O_5$	$C_{46}H_{48}Cu_2N_4O_4$
M	938.76	483.41	847.96
Crystal System	triclinic	monoclinic	monoclinic
Space group	$P\bar{1}$	$P21/c$	Cc
a (Å)	7.627(3)	7.525(2)	12.188(2)
b (Å)	11.847(3)	12.372(3)	20.503(2)
c (Å)	12.263(3)	21.807(2)	9.154(2)
α (°)	67.11(2)	90	90.00
β (°)	75.75(2)	96.070(2)	116.97(3)
γ (°)	85.14(2)	90	90.00
V (Å^3)	989.3(5)	2018.8(7)	2038.7(6)
Z	1	4	4
D_{calc} (g cm^{-3})	1.576	1.590	1.381
μ (mm^{-1})	1.276 [Mo Kα]	3.083 [Cu Kα]	1.669 [Cu Kα]
R_{int}	0.026	0.019	0.218
Number of unique data	4561	3806	1948
Number of data with $I > 2\sigma(I)$	3412	3231	1842
R_1, wR_2	0.0562, 0.1872	0.0463, 0.1475	0.0512, 0.1750
Goodness-of-fit on F^2	0.930	1.000	1.155

the complexes of similar asymmetric ligands [5,18,19]. The appearance of similar d-d transition in both **1** and **2** confirms the semi-coordinated character of the ketonic oxygen of the ligand in **1**, which does not significantly affect the square planar geometry around the Cu(II) ions of the complex. At the higher energy region, the ligand to metal charge transfer bands were located for both the complexes (319 and 281 nm for complex **1** and 345 and 284 nm for complex **2**). Complex **3** also shows a broad band centering at 568 nm for the d-d transition and 341 and 301 nm for ligand to metal charge transfer transitions.

3.2. Description of structures of complexes *1*, *2* and *3*

3.2.1. Complexes *1* and *2*

The structures of the complexes **1** and **2** are shown in Figs. 1 and 2, respectively, with common atom numbering scheme. For both compounds, the structures consist of $[CuL]^+$ cation together with perchlorate anion. In complex **1**, two symmetry related $(1-x, -y, 1-z)$ cations are joined together through very weak interaction from the oxygen atom of the benzoylacetone moiety to the axial position of copper atom at a distance of 2.767(3) (Fig. 3). Although the distance is very long but is less than the sum of the van der Waals radii for copper(II) and oxygen (2.92 Å) [20]. Therefore, a weak bond is considered to be formed between the two. Comparable distances have been regarded as bond in several other reported systems [21]. In **2**, the complex cations are discrete; the closest copper–oxygen distance between the two neighboring units is 3.029 Å. In both complexes, the deprotonated ligands L^1 and L^2 are quadridentate forming two adjacent six-membered and one five-membered chelate rings (6-6-5). The copper(II) ions have square-planar co-ordination with a slight tetrahedral distortion in both the complexes.

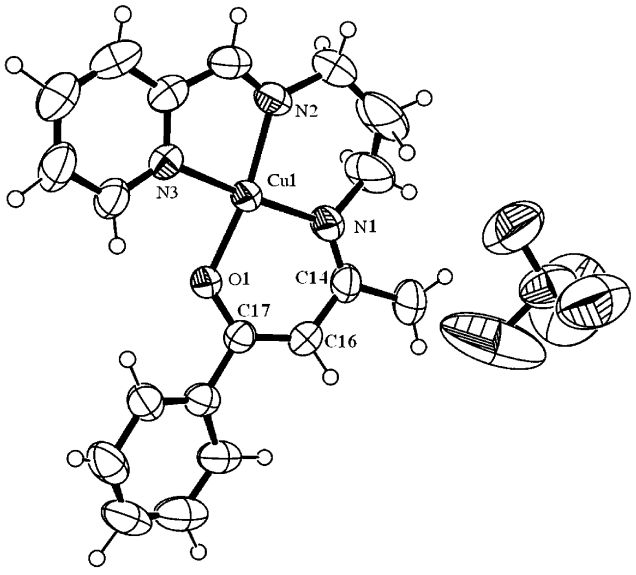


Fig. 1. ORTEP plot of **1** with atom-numbering scheme; ellipsoids at 50% probability.

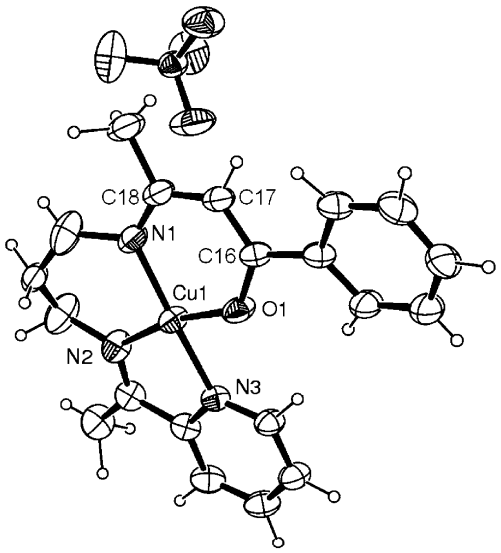


Fig. 2. ORTEP plot of **2** with atom-numbering scheme; ellipsoids at 50% probability.

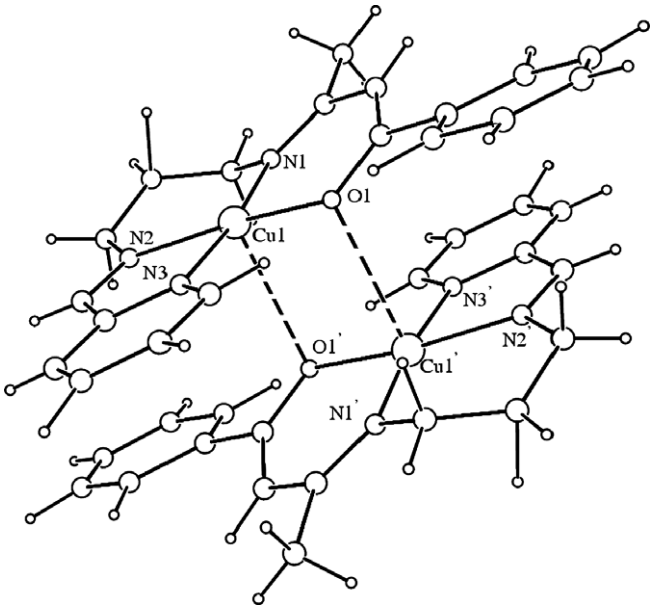


Fig. 3. A view (PLUTO) of the dimer of **1**. Perchlorate ions are not shown for clarity. Symmetry transformation: $' = (1-x, -y, 1-z)$. Dashed bonds represent the weak axial bond.

Deviations of donor atoms O(1), N(1), N(2) and N(3) from the mean plane passing through them are −0.057(2), 0.054(4), −0.059(3) and 0.062(3) Å, respectively, for **1** and −0.047(2), 0.043(3), −0.047(3) and 0.051(2) Å, respectively, for **2**. The central Cu(II) atom deviates negligibly (0.0037(3) Å) in complex **1** and slightly more (0.0274(4) Å) in complex **2** from the same plane. The tetrahedral distortion is apparent since one pair of diagonal donor atoms clearly lies below the plane while the other pair is above the plane with the metal ion in the mean plane. The dihedral angles between the two planes [N(l)–Cu–O(1) and N(2)–Cu–N(3)] is 6.09° for complex **1** and 4.82° for complex **2**

compares with 0° for a perfectly square-planar arrangement and 90° for a perfect tetrahedral arrangement. The two diagonal N–Cu–O and N–Cu–N angles of complex **1** [169.3(1) and 172.8(1)°] and **2** [168.0(1) and 174.7(1)°] are less than 180° as a result of this tetrahedral distortion. The metal ion is not perfectly centered, and the four bond distances between donor atoms to metal ion are significantly different as shown in Table 2. In both the complexes, the mean Cu–N distances (1.999 and 1.988 Å for **1** and **2**, respectively) are slightly longer than that of Cu-O (1.916 and 1.906 Å for **1** and **2**, respectively). This elongated Cu–N bond than the Cu–O is also observed for similar Schiff bases [5,19]. It is worth mentioning that, the Cu–O(1) bonds in complexes **1** and **2** are slightly greater than the similar known copper systems having acetylacetone residue [5].

The six-membered chelate ring incorporating the benzoylacetone moiety is delocalized by the influence of coordination to the metal. In complex **1**, this ring containing Cu(1), N(1), C(14), C(16), C(17) and O(1); the C(16)–C(17) distance of 1.379 Å is much shorter than the normal sp^2–sp^2 C–C single bond (1.51 Å), the C(14)–N(1) distance of 1.288 Å is a little longer than normal imine C=N double bond (1.28 Å) and the C(17)–O(1) bond length of 1.299 Å is shorter than normal sp^2 C–O single bond (1.34 Å). All these changes in bond length indicate delocalization of the chelating ring containing the benzoylacetone fragment. The same trend in bond lengths is also found in the ring of the benzoylacetone fragment in complex **2** with the C(16)–C(17), C(18)–N(1) and C(16)–O(1) distances of 1.370, 1.301 and 1.302 Å, respectively. It is clear that the replacement of acetylacetone residue by a benzoylacetone, slightly increases the C–O (ketonic) and C(16)–C(17) bond distances (1.280 and 1.342 Å, respectively, in the acetylacetone derived complex [5]). However, other bond distances (C–C and C=N) do not show significant changes.

The chelating ring tends to remain planar as a result of this delocalization to form a stable conjugation structure with no atoms deviating from the least square plane by 0.021 and 0.026 Å for complexes **1** and **2**, respectively. It is interesting to note that the mean plane of this ring is not coplanar with the benzene plane, the angles between the two planes are 17.27° and 17.91° for complexes **1** and **2**, respectively. The other six-membered ring incorporating the diamine fragment is not planar as all the carbon atoms are sp^3 hybridized. Two of the carbon atoms (C3 and C4) in **2** are disordered (occupancy of C3b is 0.59(7) and that for C4b is 0.60(1)). Therefore, we perform the conformational analysis with C3b and C4b. The conformation of the chelate ring is intermediate between chair and half-chair conformation for both complexes **1** ($Q = 0.258$ Å, $\theta = 47.7°$ and $\phi = 147.1°$) and **2** ($Q = 0.273$ Å, $\theta = 36.7°$ and $\phi = 17°$) [22]. The bond distances and bond angles of this part of Schiff base are comparable with those of related Cu(II) complexes with other nonsymmetrical Schiff base ligands [5].

The dimerization of **1** through the ketonic oxygen bridge seems to be a noteworthy phenomenon for this type of complexes as the acetylacetone analogue of complex **1** is a discrete monomer [5]. The similar bridging property of phenoxo group is well documented in the literature [23] but the ketonic oxygen of acetylacetone or its derivatives is considered as nonbridging in asymmetrical or symmetrical tetradentate ligands. Till date, the bridging property of such ketonic oxygen is illustrated only in conjunction with other stronger bridging group e.g. hydroxo, oximato, etc. [7,8a,8d,24]. Therefore, to our knowledge, complex **1** is the first example of dimerization in Cu(II) complexes containing tetradentate Schiff base ligand via solely ketonic oxygen bridges.

In both complexes the intermolecular packing is controlled by π-stacking interaction between the aromatic rings. In **1**, there is a strong π–π interaction between the phenyl ring and the pyridyl ring of a neighboring ($2 - x$, $-y$, $1 - z$) dimer with a slip angle of 28.87°, dihedral angle of 5.93° and centroids separation of 3.863(3) Å to form a one-dimensional chain along the a axis as illustrated in Fig. 4. In **2** also there is similar π–π interaction between the phenyl ring and the pyridyl ring of a neighboring ($2 - x$, $-y$, $1 - z$) units (slip angle = 31.71°, dihedral angle = 4.65° and centroid separation = 4.145(2) Å) resulting the stack of molecule along the *a*-axis (Fig S1).

Table 2
Selected bond lengths (Å) and bond angles (°) for complexes **1** and **2**

	1	**2**
Cu(1)–O(1)	1.916(2)	1.906(2)
Cu(1)–N(1)	1.948(4)	1.945(2)
Cu(1)–N(2)	2.017(3)	2.007(3)
Cu(1)–N(3)	2.032(4)	2.012(2)
Cu(1)–O(1)′	2.767(3)	
O(1)–Cu(1)–N(1)	94.50(13)	94.21(9)
O(1)–Cu(1)–N(2)	169.29(14)	167.95(10)
O(1)–Cu(1)–N(3)	89.49(12)	88.38(8)
O(1)–Cu(1)–O(1)′	85.34(9)	
N(1)–Cu(1)–N(2)	96.21(15)	97.85(11)
N(1)–Cu(1)–N(3)	172.83(14)	174.65(10)
N(1)–Cu(1)–O(1)′	100.59(13)	
N(2)–Cu(1)–N(3)	79.88(14)	79.63(10)
N(2)–Cu(1)–O(1)′	92.53(11)	
N(3)–Cu(1)–O(1)′	85.65(11)	

Symmetry transformations: $' = 1 - x, -y, 1 - z$.

3.2.2. Complex 3

The structure of complex **3** with atomic numbering scheme is shown in Fig. 5. The structure consists of discrete four coordinate copper(II) complex having quadridentate symmetrical Schiff base ligand. Selected bond distances and bond angles given in Table 3. The chelated deprotonated ligand, $(L^3)^{2-}$ forms three adjacent six-membered rings (6-6-6); the two terminal rings are consist of benzoylacetone fragments and the one at the middle by the starting diamine. The central Cu(II) atom has a distorted square planer coordination with a significant tetrahedral distortion. The coordinating atoms N1, N2, O1 and O2 deviates

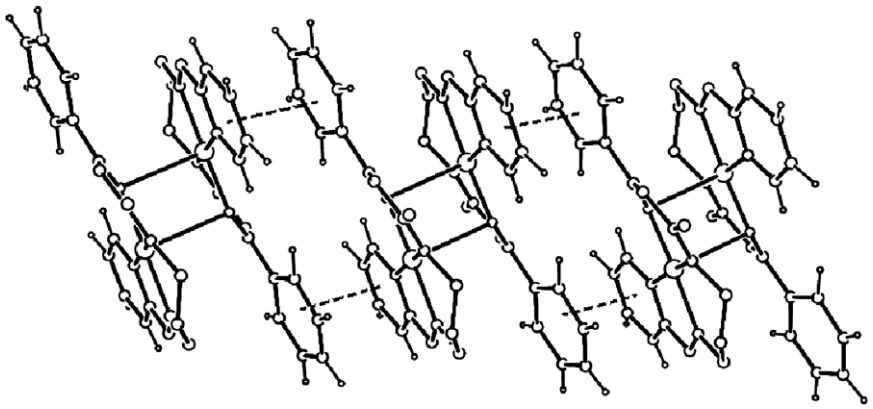


Fig. 4. One-dimensional π–π interactions shown in the dotted lines in complex **1**. Hydrogen atoms of the diamine fragments are not shown for clarity.

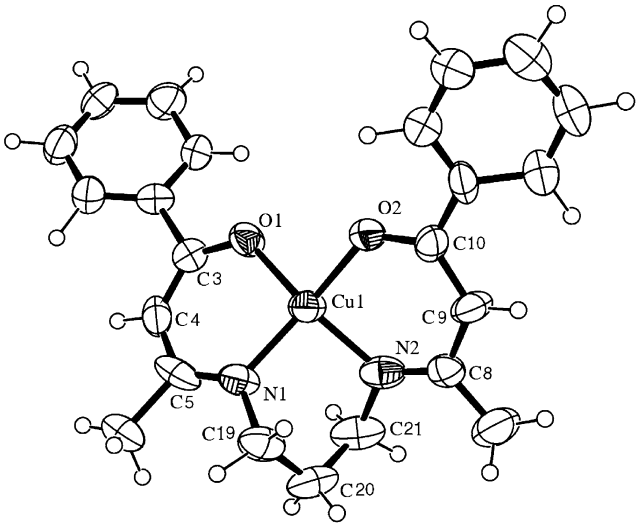


Fig. 5. ORTEP plot of **3** with atom-numbering scheme; ellipsoids at 50% probability.

Table 3
Selected bond lengths (Å) and bond angles (°) for complex **3**

Cu(1)–O(1)	1.898(9)
Cu(1)–O(2)	1.924(9)
Cu(1)–N(1)	1.928(11)
Cu(1)–N(2)	1.955(12)
O(1)–Cu(1)–O(2)	90.7(4)
O(1)–Cu(1)–N(1)	95.4(4)
O(1)–Cu(1)–N(2)	151.5(4)
O(2)–Cu(1)–N(1)	156.3(4)
O(2)–Cu(1)–N(2)	93.5(5)
N(1)–Cu(1)–N(2)	92.0(5)

from the least-square mean plane through them by – 0.442(3), 0.427(3), −0.427(3), 0.442(3) Å. The Cu atom is located 0.039 Å from the same plane. The dihedral angles between the two planes [N(l)–Cu–O(1) and N(2)–Cu–O(2)] is 35.98°, which is much greater than that in the similar tetracoordinated copper(II) complexes like bis-(benzoylacetone)-ethylenediiminato-*N*,*N*′copper(II) complex (3.73°) [25], $[Cu(acactn)H_2O]_2$ (7.77°) and $[Cu_2(acactn)2KClO_4]_2$ (10.85° and 4.6°) where H_2acactn is bis(acetylacetone)-trimethylenediimine [6a] and also than the two asymmetric complexes **1** (6.09°) and **2** (4.82°) reported here. The only known tetradentate copper(II) complex having much distorted system is Cu(sa$l_2$tmput) [26] (H_2sa$l_2$tmput is 2,5-bis(salicylaldimino)-2,5-dimethylhexane (48.5°)) where the diamine (2,5-dimethylhexane-2,5-diamine) fragment produces a more flexible seven membered chelate ring.

These six-membered chelate rings derived from benzoylacetone are not identical with respect to bond distances and bond angles though both the chelating rings are delocalized by the influence of the metal, which is comparable to complexes **1** and **2**. In complex **3**, the first ring containing Cu(1), O(1), C(3), C(4), C(5) and N(1), the C(3)–C(4) distance of 1.379 Å, the C(5)–N(1) distance of 1.294 Å and the C (17)-O(1) bond length of 1.283 Å. Whereas in the second, the chelate ring containing Cu(1), O(2), C(10), C(9), C(8) and N(2), the C(9)–C(10), C(8)–N(2) and C(10)–O(2) distances are 1.427, 1.294 and 1.291 Å, respectively. The angles between the mean plane of these rings with the benzene plane are 24.57° and 24.77° indicating greater nonplanarity compare to that in complexes **1** and **2**. The conformation of six-membered chelate ring incorporating the diamine is an intermediate between boat and twist-boat confirmation [22] ($Q = 0.858$ Å, $\theta = 88.7°$ and $\phi = 265.4°$). Unlike **1** and **2** there is no significant π–π interaction between the molecules in complex **3**. A comparison of the structure of **3** with its acetylacetone analogue [6a] reveal that although the bond angles and distances do not show any significant change, the geometry around the copper atom shows unusually high tetrahedral distortion in **3**.

3.3. Electrochemical study

The cyclic voltammograms of the complexes are recorded in acetonitrile solvent and the diagrams are shown in Fig. 6. As is evident from Fig. 6, all three complexes show reversible reductive responses. The reduction potentials for **1** and **2** are observed at −0.86 and −0.90 V

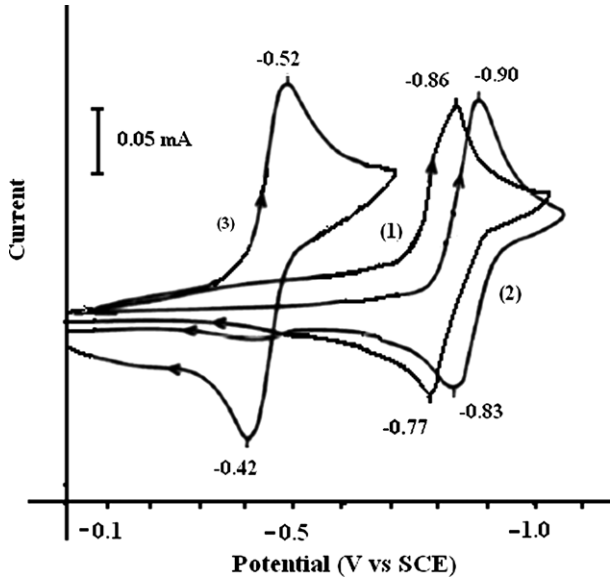


Fig. 6. The cyclic voltammogram of **1**, **2** and **3** in acetonitrile solution (scan rate 100 mV/s).

(E_{pc}). The corresponding E_{pa} values are observed at −0.77 and −0.83 V. The $E_{1/2}$ values of **1** and **2** are −0.82 and −0.87 V (versus SCE), respectively. Under identical experimental conditions the potential values for **3** are −0.52 V (E_{pc}), −0.42 V (E_{pa}) and −0.47 V ($E_{1/2}$) (versus SCE). It is well known that in four-coordinate systems, Cu(II) and Cu(I) have very distinct preference for square-based and tetrahedral geometry, respectively [27]. This preference is well reflected in the redox behavior of these systems. More is the distortion in the coordination geometry around the metal towards tetrahedral arrangement, higher is the anodic shift of the Cu^{II}/Cu^{I} redox potentials [27]. Thus the anodic shift of the potential of **3** compared to **1** and **2** and also to other similar systems corroborates the severe tetrahedral distortion of the copper atom from square planar geometry as observed in the X-ray structural analysis. A similar shift of the potential value and distortion were also observed earlier [26,28].

4. Conclusion

The inability of complex formation of 7-amino-3-methyl-1-phenyl-4-azahept-1,3-dien-1-ol (HAMPA) with Cu(II) but facile synthesis of Cu(II) complexes with three tetradentate ligands, HL^1, HL^2, and HL^3 derived from HAMPA reveals that the singly condensed Schiff bases are more prone to hydrolysis. The successful syntheses of complexes **1** and **2** are significant as they prove that 1-benzoylacetone can also be used like acetylacetone for the synthesis of complexes with unsymmetrical ligands. The crystal structure determination of the complexes shows for the first time that dimerization can occur in this type of systems only through ketonic oxygen bridges. The remarkably different molecular structures of the complexes from their acetylacetone analogues opens up a scope for their potential use in understanding the intricate differences that occur in NLO responses or in natural systems with slight variations in the ligand fragments.

Acknowledgements

We like to thank Dr. G. Mostafa, Jadavpur University, Kolkata, India, for his help and valuable discussions regarding the crystal structures of the compounds.

Appendix A. Supplementary material

CCDC 655614, 655615 and 655616 contain the supplementary crystallographic data for **1**, **2** and **3**. These data can be obtained free of charge via www.ccdc.ac.uk/conts/retrieving.html, or from the Cambridge Crystallographic Data Centre, 12 Union Road, Cambridge CB2 1EZ, UK; fax: (+44) 1223-336-033; or e-mail: deposit@ccdc.cam.ac.uk. Supplementary data associated with this article can be found, in the online version, at doi:10.1016/j.poly.2007.10.021.

References

[1] (a) R. Atkins, G. Brewer, E. Kokot, G.M. Mockler, E. Sinn, Inorg. Chem. 24 (1985) 127;
(b) E. Kwiatkowski, M. Kwiatkowski, J. Chem. Soc., Dalton Trans. (1985) 803;
(c) E. Kwiatkowski, M. Kwiatkowski, Inorg. Chim. Acta 117 (1986) 145.
[2] (a) J. Gradinaru, A. Forni, V. Druta, F. Tessore, S. Zecchin, S. Quici, N. Garbalau, Inorg. Chem. 46 (2007) 884;
(b) D.R. Kanis, M. A Ratner, T.J. Marks, J. Am. Chem. Soc. 114 (1992) 10338;
(c) B.J. Coe, N.R.M. Curati, Inorg. Chem. 25 (2004) 147;
(d) W. Chiang, D. Vanengen, M.E. Thompson, Polyhedron 15 (1996) 2369.
[3] (a) J.P. Costes, G. Cros, M.H. Darbieu, J.P. Laurent, Inorg. Chim. Acta 60 (1982) 111;
(b) G. Cros, J.P. Costes, CR Acad. Sci. II 294 (1982) 173.
[4] E. Kwiatkowski, M. Kwiatkowski, A. Olechnowiez, Inorg. Chim. Acta 90 (1984) 145.
[5] M.S. Ray, R. Bhattacharya, S. Chaudhuri, L. Righi, G. Bocelli, G. Mukhopadhyay, A. Ghosh, Polyhedron 22 (2003) 617, and the references therein.
[6] (a) Y.P. Cai, C.Y. Su, A. Xu, B.S. Kang, YX. Tong, H.Q. Liu, S. Jie, Polyhedron 20 (2001) 657;
(b) M. Kwiatkowski, G. Bandoli, J. Chem. Soc., Dalton Trans. (1992) 372;
(c) M. Kwiatkowski, E. Kwiatkowski, A. Olechnowicz, D.M. Ho, E. Deutsch, J. Chem. Soc., Dalton Trans. (1990) 2497;
(d) C. Li, N. Kanehisa, Y. Miyagi, Y. Nakao, S. Takamizawa, W. Mori, Y. Kai, Bull. Chem. Soc. Jpn. 70 (1997) 2429;
(e) E. Kwiatkowski, M. Klein, G. Romanowski, Inorg. Chim. Acta 293 (1999) 115;
(f) S. Chattopadhyay, G. Bocelli, A. Cantoni, A. Ghosh, Inorg. Chim. Acta 359 (2006) 4441;
(g) J.P. Costes, Inorg. Chim. Acta 130 (1987) 17.
[7] B. Sarkar, M.S. Ray, M.G.B. Drew, A. Figuerola, C. Diaz, A. Ghosh, Polyhedron 25 (2006) 3084.
[8] (a) J.P. Costes, F. Dahan, J.P. Laurent, Inorg. Chem. 25 (1986) 413;
(b) M. Kwiatkowski, E. Kwiatkowski, A. Olechnowicz, D.M. Ho, E. Deutsch, Inorg. Chim. Acta 150 (1988) 65;

(c) H.D. Bian, J.Y. Xu, W. Gu, S.P. Yan, P. Cheng, D.Z. Liao, Z.H. Jiang, Polyhedron 22 (2003) 2927;
(d) M.S. Ray, S. Chattopadhyay, M.G.B. Drew, A. Figuerola, J. Ribas, C. Diaz, A. Ghosh, Eur. J. Inorg. Chem. (2005) 4562, and references therein.
[9] Bruker Axs Inc., 6300 Enterprise Lane, Madison, WI 53719-1173, USA.
[10] D. Belletti, A. Cantoni, G. Pasquinelli, Gestione on Line di Diffrattometro a Cristallo Singolo Siemens AED con Personal Computer, Centro di Studio per la Strutturistica Diffrattometrica del CNR, Parma, Italy, Internal Report 1–93, 1993.
[11] N. Walker, D. Stuart, Acta Crystallogr. A39 (1983) 158.
[12] P. Gluzinski, Set of Programs for X-ray Structural Calculations. IchO, Polish Academy of Sciences, Warszawa, Poland, 1989.
[13] G.M. Sheldrick, in: SHELX-97, Program for the Refinement of Crystal Structure, University of Göttingen, Germany, 1997.
[14] D.T. Cromer, J.T. Weber, International Tables for X-ray Crystallography, vol. IV (Table 2.2A), The Kynoch Press, Birmingham, UK, 1994, p. 2.
[15] J.A. Ibers, W.C. Hamilton, Acta Crystallogr. 17 (1964) 781.
[16] L.J. Farrugia, ORTEP-3 for WINDOWS, University of Glasgow, Scotland, UK, 1999.
[17] (a) F.A. Cotton, J.J. Wise, Inorg. Chem. 5 (1967) 1200;
(b) B.J. Hathaway, D.E. Billing, R.J. Dudly, J. Chem. Soc. A (1970) 1420.
[18] W.N. Wallis, S.C. Cumming, Inorg. Chem. 13 (1974) 991.
[19] X.R. Bu, C.R. Jackson, D. Van Derveer, X.Z. You, Q.J. Meng, R.X. Wang, Polyhedron 16 (1997) 2991, and references therein.
[20] A. Bondi, J. Phys. Chem. 68 (1964) 441.
[21] O.D. Fox, N.K. Dalley, R.G. Harrison, Inorg. Chem. 39 (2000) 620, and references therein.
[22] (a) D. Cremer, J.A. Pople, J. Am. Chem. Soc. 97 (1975) 1354;
(b) J.C.A. Boyens, J. Cryst. Mol. Struct. 8 (1978) 31.
[23] C.K. Lai, A.G. Serrette, T.M. Swager, J. Am. Chem. Soc. 114 (1992) 7948.
[24] J.P. Costes, F. Dahan, A. Dupuis, J.P. Laurent, J. Chem. Soc., Dalton Trans (1998) 1307.
[25] S. Dehghanpour, F. Mojahed, F. Farzaneh, Z. Kristallogr. NCS 220 (2005) 1.
[26] R.C. Elder, M.C. Hill, Inorg. Chem. 18 (1979) 729.
[27] S. Itoh, N. Kishikawa, T. Suzuki, H.D. Takagi, Dalton Trans. (2005) 1066, and references therein.
[28] (a) C. Belle, C. Beguin, I. Gautier-Luneau, S. Hamman, C. Philouze, J.L. Pierre, F. Thomas, S. Torelli, Inorg. Chem. 41 (2002) 479;
(b) J.M. Fernandez-G, E.A. Arauz, R.C. Rosado, R.A. Toscano, N.M. Ruvalcaba, M.A. Martinez, Trans. Met. Chem. 24 (1999) 18, and references therein.

Available online at www.sciencedirect.com
ScienceDirect
Polyhedron 27 (2008) 701–708
POLYHEDRON
www.elsevier.com/locate/poly

Ruthenium(III) complexes of amine-bis(phenolate) ligands as catalysts for transfer hydrogenation of ketones

Sethuraman Kannan, K. Naresh Kumar, Rengan Ramesh *

School of Chemistry, Bharathidasan University, Tiruchirappalli 620 024, India

Received 15 October 2007; accepted 30 October 2007
Available online 3 December 2007

Abstract

Twelve ruthenium(III) complexes bearing amine-bis(phenolate) tripodal ligands of general formula $[Ru(L^1–L^3)(X)(EPh_3)_2]$ (where $L^1–L^3$ are dianionic tridentate chelator) have been synthesized by the reaction of ruthenium(III) precursors $[RuX_3(EPh_3)_3]$ (where E = P, X = Cl; E = As, X = Cl or Br) and $[RuBr_3(PPh_3)_2(CH_3OH)]$ with the tripodal tridentate ligands H_2L^1, H_2L^2 and H_2L^3 in benzene in 1:1 molar ratio. The newly synthesized complexes have been characterized by analytical (elemental and magnetic susceptibility) and spectral methods. The complexes are one electron paramagnetic (low-spin, d^5) in nature. The EPR spectra of the powdered samples at RT and the liquid samples at LNT shows the presence of three different '*g*' values ($g_x \neq g_y \neq g_z$) indicate a rhombic distortion around the ruthenium ion. The redox potentials indicate that all the complexes undergo one electron transfer process. The catalytic activity of one of the complexes $[Ru(pcr\text{-}chx)Br(AsPh_3)_2]$ was examined in the transfer hydrogenation of ketones and was found to be efficient with conversion up to 99% in the presence of isopropanol/KOH.
© 2007 Elsevier Ltd. All rights reserved.

Keywords: Synthesis; Ruthenium(III); Symmetrical tripodal chelator; Characterization; Catalytic transfer hydrogenation

1. Introduction

Even though highly efficient catalytic systems for selective transformations are known [1–3], the design of efficient catalysts for large-scale applications is still a challenging problem. Noteworthy, a prerequisite for achieving high activity and selectivity is the fine tuning of the metal by introduction of ligands. With the high activity, ruthenium complexes play a central role in many organic transformations as versatile catalyst due to its reversible and accessible oxidation states [4]. Many research groups are developing the synthetic chemistry related to ruthenium complexes because of their multiple applications in many different scientific fields [5]. Ruthenium complexes have been used as catalysts or catalyst precursors for a variety of purposes including hydrogenation, oxidation, isomerisation, polymerization, nucleophilic addition to multiple bonds and carbon–carbon bond formation [6]. The ability of transition metal catalysts to add or remove hydrogen from organic substrates by either direct or transfer hydrogenation process is a valuable synthetic tool [7]. Ruthenium complexes have a long pedigree as catalysts for transfer hydrogenation reactions in the presence of 2-propanol as hydrogen source [8,9]. Several recent examples of ruthenium N-heterocyclic carbene complexes [10–12], Ru(arene)-(diamine) [13] and Ru(BINAP)(diamine) [14] catalysts have become the most prominent members for the reduction of ketones in high yields. Pincer-type arylruthenium(II) complexes containing the monoanionic terdentate NCN and PCP ligands have been reported by van Koten as active catalysts for the transfer hydrogenation of ketones in the presence of *i*-PrOH and KOH [15]. A number of other groups have followed Noyori's work using XylBinap [16] and have demonstrated the use of other diphosphines that give rise to high activities and selectivities when used in this catalyst system [17]. Ruthenium(II) complex bearing the

* Corresponding author. Tel.: +91 431 2407053; fax: + 91 431 2407045/2407020.
E-mail address: ramesh_bdu@yahoo.com (R. Ramesh).

0277-5387/$ - see front matter © 2007 Elsevier Ltd. All rights reserved.
doi:10.1016/j.poly.2007.10.024

ligand 2,6-bis(3,5-dimethylpyrazol-1-yl)pyridine in isopropanol [18] has been proved to be an efficient catalyst for the transfer hydrogenation of ketones. The diversity of tertiary phosphines in terms of their Lewis basicity and bulkiness render them excellent candidates to tune the reactivity of octahedral complexes towards a variety of chemical processes, such as oxidative addition and substitution reactions [19]. Even though there are number of reports available on the transfer hydrogenation of ketones, to the best of our knowledge, there are no reports available for catalytic transfer hydrogenation of ketones by ruthenium tripodal complexes.

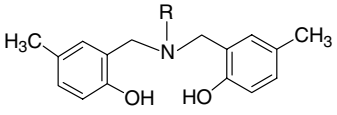
Tripodal ligands are in general facially coordinating tridentate chelate ligands which have received considerable attention in both coordination and organometallic chemistry. Over the past 20 years, there have been hundreds of published reports concerning various aspects of metal complexes which contain tripod ligands. Although the coordination properties of tripodal ligand have been extensively investigated using first row transition metals [20], few second and third row transition metals have been the target of studies with this kind of ligand. Tripodal complexes are of considerable interest as they find application in catalytic processes such as polymerization [21], epoxidation [22], enantioselective hydrogenation of olefins [23], Diels–Alder reaction [24], addition of TMS-CN to carbonyl compounds [25].

In view of the growing interest in the catalytic activity of ruthenium complexes to act as an efficient catalyst in transfer hydrogenation of ketones, we herein report the synthesis of a series of hexacoordinated ruthenium(III) tripodal complexes containing PPh_3/$AsPh_3$. The characterization of the complexes were accomplished by analytical and spectral (FT-IR, UV–Vis and EPR) methods. The redox properties of the complexes have been studied by cyclic voltammetric technique. Further, one of the synthesized complexes has been effectively used as catalyst in transfer hydrogenation of ketones in the presence of isopropanol and KOH as base. The following symmetrical amine-bis(phenolate) tripodal ligands have been used to synthesis the ruthenium(III) complexes (Scheme 1).

2. Experimental

2.1. Reagents and materials

All the reagents used were chemically pure and AR grade. Solvents were purified and dried according to standard procedures [26]. $RuCl_3 \cdot 3H_2O$ was purchased from Loba Chemie Pvt. Ltd. and was used without further purification. The primary amines and *p*-cresol were purchased from Aldrich. The supporting electrolyte tetrabutyl ammonium perchlorate (TBAP) was dried in vacuum prior to use. The ketones and their corresponding alcohols, which were used in the catalytic studies, were purchased from Merck and Aldrich.



Where R = -CH_3 : H_2L1 (pcr-me);
-C_6H_{11} : H_2L2 (pcr-chx);
-C_5H_4N : H_2L3 (pcr-ampy)

Scheme 1. Structure of tripodal ligands.

2.2. Physical measurements

The analysis of carbon, hydrogen and nitrogen were performed by analytic function testing VarioEL III CHNS elemental analyzer at STIC, Cochin University of Science and Technology, Cochin, India. FT-IR spectra were recorded in KBr pellets with a JASCO 460 plus spectrophotometer in the range 4000–400 cm^{-1}. A Cary 300 Bio UV–Vis Varian spectrophotometer was used to record the electronic spectra. Room temperature solid-state magnetic susceptibility measurements were carried out by EG and G model 155 vibrating sample magnetometer at IIT, Chennai. EPR spectra were recorded on JEOL JES-FA 200 EPR spectrometer at X-band frequencies for powder samples at 278 K and solution at 77 K (liquid nitrogen) with microwave power 1.00 mW, modulation amplitude 125 and the field being calibrated with diphenylpicryl hydrazyl (DPPH, $g = 2.0037$) at Pondicherry University, India. Electrochemical studies were performed using a Princeton EG and G-PARC model potentiostat with 0.05 M dichloromethane solutions of $[(n\text{-}C_4H_9)_4N]ClO_4$ (TBAP) as supporting electrolyte under a nitrogen atmosphere. A three-electrode cell was employed with glassy carbon working electrode, a platinum wire auxiliary electrode and an Ag/AgCl reference electrode. Melting points were recorded with a Boetius micro-heating table and are uncorrected. The conversion of products from the catalytic reactions was determined using HP 6890 series GC-FID with a DP-5 column of 30 m length, 0.32 mm diameter and 0.25 μm film thickness. The ruthenium(III) complexes $[RuCl_3(PPh_3)_3]$, $[RuCl_3(AsPh_3)_3]$, $[RuBr_3(AsPh_3)_3]$, $[RuBr_3(PPh_3)_2(CH_3OH)]$ [27–30] were prepared according to the literature reports.

2.3. Preparation of amine-bis(phenolate) tripodal ligands

A solution of *p*-cresol (20.0 mmol, 2.16 g), primary amines such as methylamine, cyclohexylamine and 2-aminopyridine (10.0 mmol, 0.31–0.99 g) and aqueous formaldehyde (1.15 g, 38.4 mmol) in methanol (5 mL) was stirred and refluxed for 18 h. The mixture was cooled in freezer overnight and the supernatant solution was decanted. The solid residue was washed with ice cold methanol, filtered, and washed thoroughly with cold methanol. The solid residue was then again washed with acetonitrile for recrystallization to give a colorless product [31].

Spectral and analytical data for ligands: H_2L1 (pcr-me) (white solid): M.p.: 58 °C. IR (KBr, cm^{-1}): 3442, 1260. ^1H NMR (400 MHz, $CDCl_3$): δ 10.6(s, 2H, OH), δ 6.9–8.0 (m, 6H, Ar–H), δ 3.3 (s, 4H, benzylic protons), δ 2.3 (s, 9H,

CH_3). *Anal.* Calc. for $C_{17}H_{21}NO_2$: C, 75.24; H, 7.80; N, 5.16. Found: C, 74.95; H, 7.68; N, 4.98%.

H_2L2 (pcr-chx) (white solid): M.p.: 157 °C. IR (KBr, cm^{-1}): 3440, 1274. ^1H NMR (400 MHz, $CDCl_3$): δ 10.5 (s, 2H, OH), δ 7.0–7.8 (m, 6H, Ar–H), δ 3.6 (s, 4H, benzylic protons), δ 2.2 (s, 6H, CH_3), δ 1.0–2.0 (br multiplets, 11 H). *Anal.* Calc. for $C_{22}H_{29}NO_2$: C, 77.83; H, 8.61; N, 4.12. Found: C, 77.61; H, 8.46; N, 3.88%.

H_2L3 (pcr-ampy) (white solid): M.p.: 150 °C. IR (KBr, cm^{-1}): 3445, 1251. ^1H NMR (400 MHz, $CDCl_3$): δ 9.8 (s, 2H, OH), δ 6.9–7.5 (m, 10H, Ar–H), δ 3.7 (s, 4H, benzylic protons), δ 2.2 (s, 6H, Ar–CH_3). *Anal.* Calc. for $C_{21}H_{22}N_2O_2$: C, 75.42; H, 6.53; N, 8.37. Found: C, 75.20; H, 6.34; N, 8.04%.

2.4. Synthesis of ruthenium(III) tripodal complexes

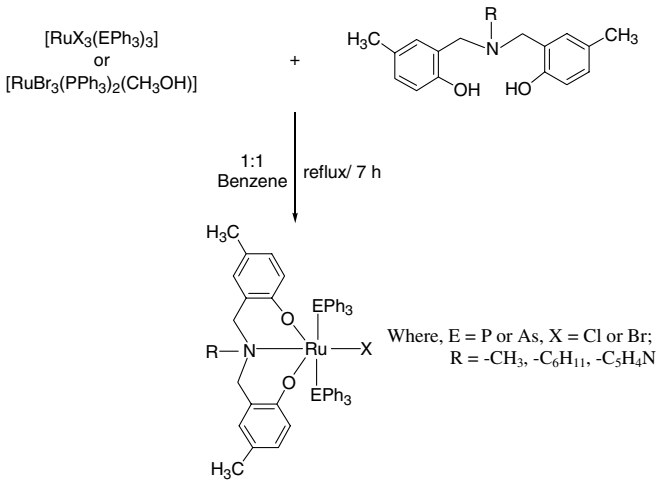
All the reactions were carried out under anhydrous conditions and were prepared by the following general procedure. To a benzene (20 cm^3) solution of the ruthenium(III) precursors $[RuX_3(EPh_3)_3]$ (0.120–0.157 g; 0.125 mmol) (E = P, X = Cl; E = As, X = Cl or Br) or $[RuBr_3(PPh_3)_2(CH_3OH)]$ (0.112 g; 0.125 mmol) was added the appropriate tripodal ligands (0.030–0.032 g; 0.125 mmol) (H_2L1–H_2L3). The solution was allowed to heat under reflux for 7–8 h. The reactions were monitored by TLC. The reaction mixture gradually changed to deep color and the solvent was removed under reduced pressure. The residue was precipitated by addition of light petroleum ether (60–80 °C) and recrystallized from CH_2Cl_2/pet. ether (60–80 °C). The compounds were dried under vacuum (yield: 58–72%).

2.5. Procedure for catalytic transfer hydrogenation

Under an inert atmosphere a mixture containing ketones (3.75 mmol), the ruthenium catalyst (0.0125 mmol) and (0.0625 mmol) KOH was heated to reflux in 10 ml of *i*-PrOH for appropriate period of time as mentioned. The catalyst was removed as precipitate from the reaction mixture by the addition of diethyl ether followed by filtration and subsequent neutralization with 5 ml of 1 M HCl. Then the ether layer was passed through a short path of silica gel and the filtrate was subjected to GC analysis. The hydrogenated product was identified and was determined with authentic sample.

3. Results and discussions

Ruthenium(III) precursors of the type $[RuX_3(EPh_3)_3]$ (E = P, X = Cl; E = As, X = Cl or Br) or $[RuBr_3(PPh_3)_2(CH_3OH)]$ were allowed to react with the tripodal ligands (L1–L3) in 1:1 molar ratio in dry benzene resulting in the formation of low-spin ruthenium(III) complexes (Scheme 2). In all the reactions, the ligands replace two chlorides/bromides, one triphenylphosphine or triphenylarsine and a methanol molecule from the precursor complexes (see Table 1).



Scheme 2. Structure of Ru(III) tripodal complexes.

3.1. Spectroscopic characterization

Infrared spectra of the complexes show many sharp and strong vibrations within 400–1600 cm^{-1} and the assignment of all these vibrations has not been attempted. However, the ligands exhibit bands in the region 1251–1274 cm^{-1} corresponding to phenolic ν_{C-O} stretching vibration. The coordination through phenolic oxygen is confirmed by the increase of ν_{C-O} stretching at higher frequencies in the region 1258–1304 cm^{-1} in all the complexes (Table 2). This was further supported by the disappearance of ν_{OH} band in the range 3440–3445 cm^{-1} in all the complexes. Further, the complexes show a strong band near 530, 690, 740 and 1556 cm^{-1}, which are due to PPh_3/$AsPh_3$ ligands. Besides, all the complexes show strong bands corresponding to ν_{M-N} and ν_{M-O} in the region 400–450 cm^{-1} and 500–550 cm^{-1}, respectively [32,33].

The electronic spectra of all the complexes were recorded in dichloromethane solution in the range 800–200 nm. All the complexes exhibit three to four absorption bands in the region 754–231 nm and are listed in Table 2. The ground state of ruthenium(III) is $^2T_{2g}$ and the first excited doublet levels in the order of increasing energy are $^2A_{2g}$ and $^2A_{1g}$, both arise from $t_{2g}^4e_g^1$ configuration. The bands observed in the region of 754–600 nm are attributable to d–d transitions and the absorptions observed in the region of 575–403 nm are probably due to charge transfer transitions taking place from the filled ligand (HOMO) orbital to the singly-occupied ruthenium t_2 orbital (LUMO). In most of the ruthenium(III) complexes the charge transfer bands of the type $L_{\pi y} \rightarrow T_{2g}$ are prominent in the low energy region, which obscures the weaker bands due to d–d transitions [34]. It is therefore difficult to assign conclusively the bands of ruthenium(III) complexes that appear in the visible region. However, the extinction

Table 1
Analytical data of ruthenium(III) tripodal complexes

S. no.	Complexes	Empirical formula	Color	Melting point (°C)	Elemental analysis		
					Found (calculated) (%)		
					C	H	N
1	[Ru(pcr-me)Cl(PPh_3)$_2$]	$C_{53}H_{49}NO_2ClP_2Ru$	brown	172	68.13 (68.41)	4.88 (5.27)	1.79 (1.50)
2	[Ru(pcr-me)Cl($AsPh_3$)$_2$]	$C_{53}H_{49}NO_2ClAs_2Ru$	brown	164	62.16 (62.50)	4.68 (4.81)	1.25 (1.37)
3	[Ru(pcr-me)Br($AsPh_3$)$_2$]	$C_{53}H_{49}NO_2BrAs_2Ru$	brown	186	59.58 (59.88)	4.46 (4.61)	1.19 (1.32)
4	[Ru(pcr-me)Br(PPh_3)$_2$]	$C_{53}H_{49}NO_2BrP_2Ru$	brown	178	65.65 (65.30)	4.88 (5.03)	1.20 (1.44)
5	[Ru(pcr-chx)Cl(PPh_3)$_2$]	$C_{58}H_{57}NO_2ClP_2Ru$	green	192	69.44 (69.77)	5.52 (5.71)	1.43 (1.40)
6	[Ru(pcr-chx)Cl($AsPh_3$)$_2$]	$C_{58}H_{57}NO_2ClAs_2Ru$	brown	182	63.82 (64.11)	5.05 (5.25)	1.60 (1.29)
7	[Ru(pcr-chx)Br($AsPh_3$)$_2$]	$C_{58}H_{57}NO_2BrAs_2Ru$	brown	165	61.22 (61.59)	4.98 (5.04)	1.04 (1.24)
8	[Ru(pcr-chx)Br(PPh_3)$_2$]	$C_{58}H_{57}NO_2BrP_2Ru$	brown	192	66.39 (66.79)	5.45 (5.47)	1.08 (1.34)
9	[Ru(pcr-ampy)Cl(PPh_3)$_2$]	$C_{57}H_{50}NO_2ClP_2Ru$	brown	188	68.64 (68.91)	4.89 (5.03)	2.69 (2.82)
10	[Ru(pcr-ampy)Cl($AsPh_3$)$_2$]	$C_{57}H_{50}NO_2ClAs_2Ru$	brown	189	63.03 (63.30)	4.72 (4.62)	2.48 (2.59)
11	[Ru(pcr-ampy)Br($AsPh_3$)$_2$]	$C_{57}H_{50}NO_2BrAs_2Ru$	brown	178	60.46 (60.79)	4.41 (4.44)	2.22 (2.48)
12	[Ru(pcr-ampy)Br(PPh_3)$_2$]	$C_{57}H_{50}NO_2BrP_2Ru$	brown	182	65.64 (65.95)	4.72 (4.82)	2.34 (2.69)

co-efficient for the bands in the 754–600 nm region are found to be very low as compared to that of charge transfer bands. Hence, the band around 754–600 nm have been assigned to $^2T_{2g} \rightarrow {}^2A_{2g}$ transition. The absorptions in the ultraviolet region below 400 nm are due to the intraligand transitions (n–π^*, π–π^*). The pattern of the electronic spectra of all the complexes indicate the presence of an octahedral environment around ruthenium(III) ion similar to that of other ruthenium(III) octahedral complexes [35–37].

3.2. Magnetic moments and EPR spectra

The complexes are uniformly paramagnetic with magnetic moments in the range of 1.81–1.93 BM, corresponds to one unpaired electron at 298 K (low-spin Ru^{III}, $t_{2g}{}^5$) in an octahedral environment. In a low-spin d^5 system the $^2T_{2g}$ (octahedral) ground state is orbitally degenerate and will be affected by spin–orbit coupling and low-symmetry ligand-field effects, both of which will remove this degeneracy and influence the temperature dependence of the moment. The theory appropriate to such a situation has been described [38,39]. From powder susceptibility data alone it is not possible to accurately determine the symmetry or the magnitude of the low-symmetry ligand-field component.

However, epr measurements clearly demonstrate, at least in frozen solution, the presence of a rhombic ligand-field component, as one might expect from the nature of the ligands around the metal ion. The distortion of the pseudooctahedral complexes can be expressed as the sum of axial (Δ) and rhombic (V) components. The theory of EPR spectra of distorted octahedral low-spin d^5 (idealized $t_{2g}{}^5$ ground term from $^2T_{2g}$) complexes is documented in the literature [40]. The gyromagnetic tensor 'g' values are given in Table 3. The low-spin d^5 configuration is a good probe of molecular structure and bonding since the observed g values are very sensitive to small changes in the structure and to metal-ligand covalency. The EPR spectra of the powdered ruthenium(III) complexes have been recorded at room temperature which shows the presence of three different 'g' ($g_x = 2.29$–2.43, $g_y = 2.00$–2.16, $g_z = 1.84$–1.92) values indicate a rhombic distortion [41,42] in the complexes and the trans position are assigned for triphenylphosphine/arsine. A similar pattern has been observed in the solution spectra of the complexes [Ru(pcr-me)Br($AsPh_3$)$_2$] (**3**) and [Ru(pcr-ampy)Br(PPh_3)$_2$]

Table 2
IR and electronic spectral data of ruthenium(III) tripodal complexes[A]

Complexes	$\nu_{(C-O)}$	λ_{max} (ε)
1	1258	600[a] (367), 350 (13444), 240 (17220)
2	1264	611[a] (337), 427[b] (1684), 263 (21492)
3	1270	740[a] (207), 502[b] (1505), 286 (12276), 237 (16412)
4	1274	540[b] (2356), 270 (12160), 245 (16544)
5	1304	635[a] (344), 426[b] (2140), 353 (13476), 265 (18256)
6	1294	754[a] (640), 562[b] (2684), 394 (12342), 252 (18234)
7	1308	667[b] (129), 403[b] (2690), 248 (13248)
8	1292	575[b] (1245), 274 (9160), 235 (14288)
9	1265	647[a] (486), 439[b] (4452), 356 (11652), 235 (17084)
10	1274	667[a] (245), 445[b] (3936), 307 (14756), 231 (14668)
11	1272	625[a] (554), 446[b] (3154), 275 (16436)
12	1286	604 (586)[a], 564 (2562)[b], 235 (20132)

[A] Where ν in cm^{-1}, λ_{max} in nm, ε in $dm^3\,mol^{-1}\,cm^{-1}$.
[a] $^2T_{2g} \rightarrow {}^2A_{2g}$.
[b] Charge transfer (LMCT).

Table 3
EPR data of ruthenium(III) tripodal complexes

Complexes	g_x	g_y	g_z	$\langle g \rangle$[a]
1	2.34	2.06	1.87	2.09
2	2.43	2.14	1.86	2.14
3	2.36	2.02	1.86	2.08
4	2.40	2.01	1.88	2.09
5	2.36	2.02	1.92	2.10
6	2.37	2.01	1.84	2.07
7	2.40	2.16	1.90	2.15
8	2.42	2.10	1.89	2.13
9	2.30	2.04	1.90	2.08
10	2.34	2.00	1.87	2.07
11	2.29	2.03	1.86	2.06
12	2.35	2.10	1.90	2.11

[a] $[1/3g_x^2 + 1/3g_y^2 + 1/3g_z^2]^{1/2}$.

(**12**) at LNT and the '*g*' values $g_x = 2.47$, $g_y = 2.30$, $g_z = 1.99$ and $g_x = 2.40$, $g_y = 2.06$, $g_z = 1.92$ for the complexes (**3**) and (**12**), respectively. These values fit very well with the values obtained for other similar ruthenium(III) complexes [42–44]. Further, we have simulated the EPR spectra of both powder (Fig. 1a) and liquid (Fig. 1b) samples. It has been observed that both the experimental and the simulated '*g*' values are very close to each other.

3.3. Redox properties

The electrochemical properties of all the complexes have been examined cyclic voltametrically under N_2 atmosphere at glassy carbon working electrode in dichloromethane solution (0.05 M: NBu_4ClO_4) and the redox potentials are expressed with reference to Ag/AgCl. All the complexes (1×10^{-3} M) are electroactive with respect to the metal centers and exhibited two redox processes in the potential range +1.5 V to −1.5 V. The complexes display a reversible oxidative (Ru^{IV}/Ru^{III}) and an irreversible reductive responses (Ru^{III}/Ru^{II}) at the scan rate of 100 mV s^{-1}. The potentials are summarized in Table 4 and a representative voltamogram of a complex **6** is shown in Fig. 2. All the complexes showed well defined waves in the range 0.60–1.12 V (Ru^{IV}/Ru^{III}) and −0.67 to −0.77 V (Ru^{III}/Ru^{II}). The oxidation potentials are reversible with peak-to-peak separation (ΔE_p) values ranging from 60 to 80 mV corresponding to one electron process. The one electron process of the oxidation has been verified by comparing its current height (i_{pa}) with that of ferrocene/ferrocenium couple under identical experimental conditions [45]. The irreversibility observed for the reductive response may be due to the short live reduced state of the metal ion [46] or probably due to the fast dissociation of chloride or bromide ligand from the ruthenium(III) complexes [47]. There is not much variation in the potentials due to replacement of chlorides by bromides and triphenylphosphine by triphenylarsine.

Table 4
Electrochemical data of ruthenium(III) tripodal complexes

Complexes	Ru^{IV}/Ru^{III}				Ru^{III}/Ru^{II}
	E_{pa}	E_{pa}	ΔE_P (mV)	$E_{1/2}$ (V)	E_{pc}
1	0.60	0.67	70	0.63	−0.77
2	0.64	0.72	80	0.68	−0.70
3	0.56	0.64	80	0.60	−0.72
4	0.75	0.83	80	0.79	−0.73
5	1.14	1.06	80	1.10	−0.76
6	0.98	0.90	80	0.94	−0.72
7	0.86	0.80	60	0.83	−0.75
8	0.90	0.98	80	0.94	−0.67
9	1.08	1.16	80	1.12	−0.72
10	0.63	0.71	80	0.67	−0.74
11	0.93	0.87	60	0.90	−0.75
12	0.91	0.84	70	0.87	−0.77

Supporting electrolyte: NBu_4ClO_4 (0.05 M); complex: 0.001 M; solvent: CH_2Cl_2 where E_{pa} and E_{pc} are anodic and cathodic potentials, respectively; scan rate: 100 mV s^{-1}.

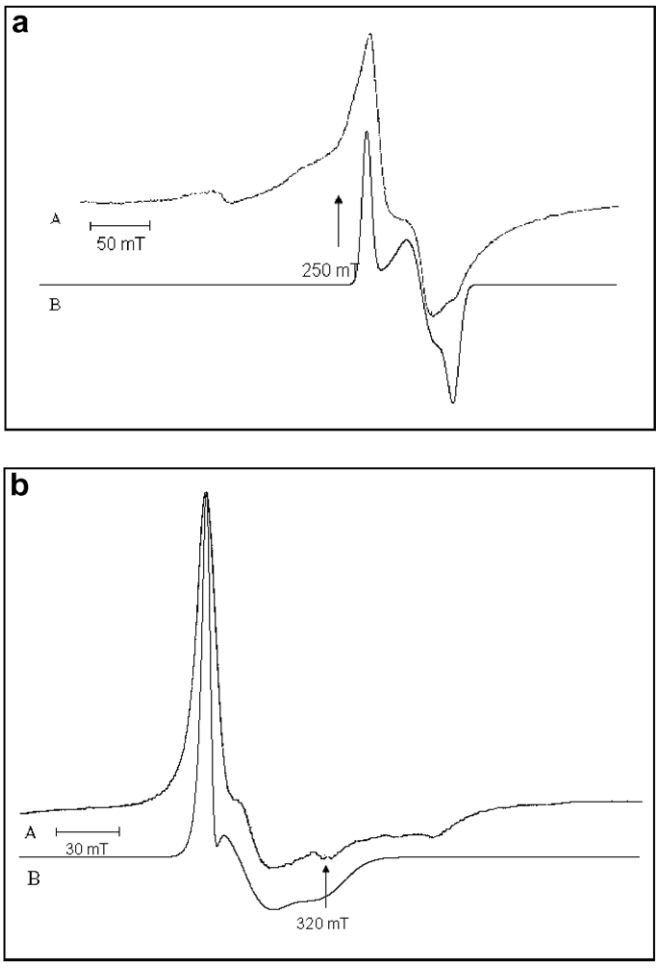


Fig. 1. (a) EPR spectrum of [Ru(pcr-me)Br($AsPh_3$)$_2$] (**3**) at RT (A, experimental and B, simulated). (b) EPR spectrum of [Ru(pcr-me)-Br(AsPh3)$_2$] (**3**) at LNT (A, experimental and B, simulated).

3.4. Catalytic transfer hydrogenation of ketones

Ruthenium mediated transfer hydrogenation reactions are found to be effective catalytic systems in which hydrogen is transferred from one organic molecule to another and this made us to carry out this type of reactions. One

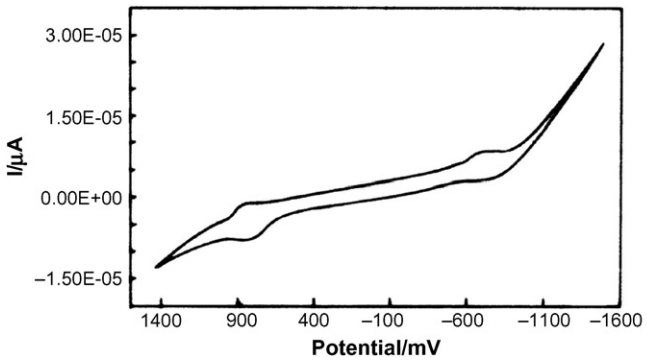
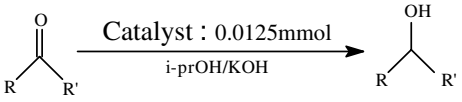


Fig. 2. Cyclic voltammogram of [Ru(pcr-chx)Cl($AsPh_3$)$_2$].

of the complexes [Ru(pcr-chx)Br($AsPh_3$)$_2$] (**7**) is taken as model catalyst and the catalytic activity in the transfer hydrogenation of various aliphatic and aromatic ketones in the presence of isopropanol and KOH as promoter has been explored. The complex catalyzes the reduction of ketones to corresponding alcohols with >90% conversions in all cases and the results are listed in Table 5.

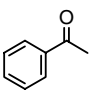
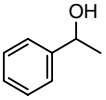
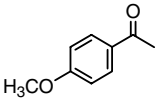
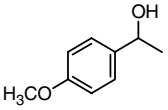
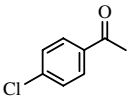
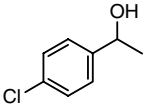
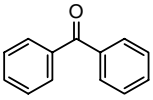
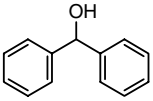
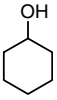
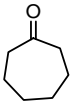
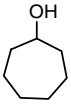
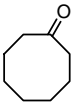
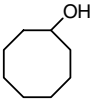
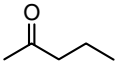
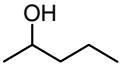
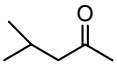
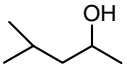
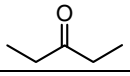
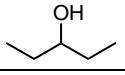


R, R' = alkyl (or) aryl

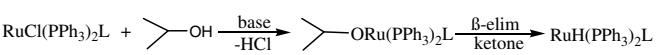
The necessity of the ruthenium complex to observe the ensuing transfer hydrogenation was ascertained by carrying out a series of blank or control experiments suggest that none of $RuCl_3 \cdot 3H_2O$, Ru(III) precursors or tripodal ligands alone or as a mixture causes these transformations under identical reaction conditions. The alcohols formed after the reflux was determined by GC with authentic samples. In this method, the base facilitates the formation of a ruthenium alkoxide by abstracting the proton of the alcohol, which then undergoes β-elimination to give a ruthenium-hydride which is the active catalyst (Scheme 3). This classical mechanism is proposed by several workers on the studies of ruthenium complexes catalyzed transfer hydrogenation reaction by metal hydrides [48,49].

Excellent conversions are obtained for both aliphatic and aromatic ketones. Benzophenone was converted to benzhydrol in >98%. The complex efficiently catalyzed the reduction of aliphatic ketones such as methyl ethyl ketone, methyl propyl ketone, isobutyl methyl ketone and diethyl ketone to their corresponding alcohols with 99.6%, 98.8%, 97.8% and 90.5% conversions, respectively. The conversion in case of acetophenone is 90.8%. The presence of electron donating (OCH_3) and electron withdrawing (Cl) substituents on the substrates (entries 2 and 3) has marginal effect on the catalytic transfer hydrogenation of ketones. 4-Chloro acetophenone is converted to corresponding alcohol in 93.9% and in case of 4-methoxy acetophenone the conversion is 90.7%. Though the effect is minimal, the greater conversion in case of **3** compared to **2** may be due to the fact that reduction involves the substrate gaining electrons and this would be more facile at an electron deficient center [50]. Moreover, this catalyst efficiently catalyzes the reduction of cyclopentanone and cyclohexanone to corresponding alcohols cyclopentanol and cyclohexanol with 99.3% and 90.8% conversions, respectively. The complex showed also good catalytic activity for seven and eight membered cyclic ketones cycloheptanone and cyclooctanone with 99.3% and 97.9% conversions, respectively. The presence of a catalytic amount of base is necessary for the transfer hydrogenation of ketones. Though no mechanistic study has been carried out, the catalytic transformation is supposed to follow the classical pathway in which the ketone coordinates to hydride-ruthenium intermediates, the observed effects seem to indicate that the hydride transfer from the metal to the coordinated ketone is the turnover-limiting step (rather than the ketone complexation) in the catalytic cycle [51].

Table 5
Catalytic transfer hydrogenation of ketones by [Ru(pcr-chx)Br($AsPh_3$)$_2$]/*i*-PrOH/KOH[a]

Entry	Substrates	Products	Time (h)	Conversion[b]	TON[c]
1			1	90.8	272
2			1	90.7	272
3			1	93.9	281
4			1	98.9	296
5			1	99.3	297
6			1	90.8	272
7			1	99.3	297
8			1	97.9	293
9			1	99.6	298
10			1	98.8	296
11			1	97.8	293
12			1	90.5	271

[a] Conditions: reactions were carried out at 80 °C using 3.75 mmol of ketone (5 ml isopropanol); catalyst/ketone/KOH ratio 1:300:2.5.
[b] Yield of product was determined using a HP 6890 series GC-FID with DP-5 column of 30 m length, 0.32 mm diameter and 0.25 μm film thickness and by comparison with authentic samples.
[c] Ratio of moles of product obtained to the moles of catalyst used.



Scheme 3. The role of base (L = arylazo ligand).

The only byproduct acetone was identified in all the cases. As the catalyst is stable in all organic solvents and it can be recovered and the work up process is also very simple for this catalytic system. Although several catalytic systems have been reported to support transfer hydrogenation reactions of ketones, ruthenium(III) tripodal complexes have been exploited for first time towards the catalytic transfer hydrogenation reactions.

4. Conclusions

In conclusion, we have synthesized and characterized a series of ruthenium(III) tripodal complexes. One of the complexes (**7**) has been found to be an efficient catalyst in transfer hydrogenation of both aliphatic as well as aromatic ketones in the presence of isopropanol/KOH. We are currently perusing development of some new chiral ruthenium complexes for asymmetric catalysis.

Acknowledgements

We express our sincere thanks to Professor P. Sambasiva Rao, Department of Chemistry, Pondicherry University for providing the EPR facility. We express sincere thanks to Prof. P.R. Athappan, School of Chemistry, Madurai Kamaraj University, for cyclic voltammetric facility.

References

[1] H.-U. Blaser, B. Pugin, F. Spindler, J. Mol. Catal. A: Chem. 231 (2005) 1.
[2] H.-U. Blaser, C. Malan, B. Pugin, F. Spindler, H. Steiner, M. Studer, Adv. Synth. Catal. 345 (2003) 103.
[3] M.J. Palmer, M. Wills, Tetrahedron Asymm. 10 (1999) 2045.
[4] (a) B. De Clercq, F. Verpoort, Tetrahedron Lett. 42 (2001) 8959;
(b) E.A. Seddon, K.R. Seddon, The Chemistry of Ruthenium, Elsevier, New York, 1984.
[5] (a) D. Chatterjee, Coord. Chem. Rev., in press;
(b) M.D. Ward, Coord. Chem. Rev. 250 (2006) 3128;
(c) E. Peris, R.H. Crabtree, Coord. Chem. Rev. 248 (2004) 2239.
[6] R. Drozdzak, B. Allaert, N. Ledoux, I. Dragutan, V. Dragutan, F. Verpoort, Coord. Chem. Rev. 249 (2005) 3055, and references therein.
[7] S. Burling, Adv. Synth. Catal. 347 (2005) 591.
[8] (a) R. Noyori, S. Hashiguchi, Acc. Chem. Res. 30 (1997) 97;
(b) H.-U. Blaser, B. Pugin, F. Spindler, J. Mol. Catal. A: Chem. 231 (2005) 1;
(c) H.-U. Blaser, E. Schmidt, in: H.-U. Blaser, E. Schmidt (Eds.), Asymmetric Catalysis on Industrial Scale, Wiley-VCH, Weinheim, 2004, p. 1.
[9] (a) K. Everaere, A. Mortreux, J.F. Carpentier, Adv. Synth. Catal. 345 (2003) 67;
(b) M. Wills, M. Palmer, A. Smith, J. Kenny, T. Walsgrove, Molecules 5 (2000) 4;
(c) J.- E. Backvall, J. Organomet. Chem. 652 (2002) 105.
[10] M. Poyatos, J.A. Mata, E. Falomir, R.H. Crabtree, E. Peris, Organometallics 22 (2003) 1110.
[11] A.A. Danopoulus, S. Winston, W.B. Motherwell, Chem. Commun. (2002) 1376.
[12] J. Louie, C.W. Bielawski, R.H. Grubbs, J. Am. Chem. Soc. 123 (2001) 11312.
[13] R. Noyori, T. Okhuma, Angew. Chem., Int. Ed. 40 (2001) 40, and references therein.
[14] (a) T. Ohkuma, H. Ooka, S. Harshiguchi, T. Ikariya, R. Noyori, J. Am. Chem. Soc. 117 (1995) 2675;
(b) T. Okhuma, H. Takeno, R. Noyori, Adv. Synth. Catal. 343 (2001) 369.
[15] (a) M. Albrecht, B.M. Kocks, A.L. Spek, G. van Koten, J. Organomet. Chem. 624 (2001) 271;
(a) P. Dani, T. Karlen, R.A. Gossage, S. Gladiali, G. van Koten, Angew. Chem. 112 (2000) 759.
[16] (a) T. Ohkuma, M. Koizumi, H. Doucet, T. Pham, M. Kozawa, K. Murata, E. Katayama, T. Yokozawa, T. Ikariya, R. Noyori, J. Am. Chem. Soc. 120 (1998) 13529;
(b) T. Ohkuma, D. Ishii, H. Takeno, R. Noyori, J. Am. Chem. Soc. 122 (2000) 6510;
(c) T. Ohkuma, M. Koizumi, H. Ikehira, T. Yokozawa, R. Noyori, Org. Lett. 2 (2000) 659.
[17] (a) A. Dominguez, A. Zanotti-Gerosa, W. Hems, Org. Lett. 6 (2004) 1927;
(b) J.W.H. Chen, W. Kwok, R. Guo, Z. Zhou, C.-H. Yeung, A.S.C. Chan, J. Org. Chem. 67 (2002) 7908;
(c) J. Xie, L. Wang, Y. Fu, S. Zhu, B. Fan, H. Duan, Q. Zhou, J. Am. Chem. Soc. 125 (2003) 4404.
[18] H. Deng, Z. Yu, J. Dong, S. Wu, Organometallics 24 (2005) 4110.
[19] W.A. Herrmann, B. Cornils, W.A. Herrmann (Eds.), Applied Homogeneous Catalysis with Organometallic Compounds, VCH, Weinheim, 1995.
[20] (a) L.F. Szczepura, L.M. Witham, K.J. Takeuchi, Coord. Chem. Rev. 174 (1998) 5;
(b) A.G. Blackman, Polyhedron 24 (2005) 1.
[21] E.Y. Tshuva, I. Goldberg, M. Kol, Z. Goldschmidt, Organometallics 20 (2001) 3017.
[22] (a) J. Chen, K.L. Woo, J. Organomet. Chem. 601 (2000) 57;
(b) K. Jitsukawa, Y. Oka, S. Yamaguchi, H. Masuda, Inorg. Chem. 43 (2004) 8119.
[23] J. Scherer, G. Huttner, M. Buchner, J. Bakes, J. Organomet. Chem. 520 (1996) 45.
[24] J.W. Faller, Y. Ma, J. Am. Chem. Soc. 113 (1991) 1579.
[25] J.W. Faller, L.L. Gundersen, Tetrahedron Lett. 34 (1973) 2275.
[26] A.I. Vogel, Text Book of Practical Organic Chemistry, fifth ed., Longman, London, 1989, 43.
[27] J. Chatt, G.J. Leigh, D.M.P. Mingos, R.J. Paske, J. Chem. Soc. A (1968) 2636.
[28] R.K. Poddar, I.P. Khullar, U. Agarwala, J. Inorg. Nucl. Chem. Lett. 10 (1974) 221.
[29] K. Natarajan, R.K. Poddar, U. Agarwala, J. Inorg. Nucl. Chem. 39 (1977) 431.
[30] T.A. Stephenson, G. Wilkinson, J. Inorg. Nucl. Chem. 28 (1966) 954.
[31] M.-H. Wu, W.-J. Liu, W.-D. Zou, H.-Y. Wang, Acta Crystallogr., Sect. E 62 (2006) o2949.
[32] K. Nakamato, Infrared and Raman Spectra of Inorganic and Coordination Compounds, Wiley Intersceience, New York, 1971.
[33] (a) P. Byabartta, P.K. Santra, T.K. Mishra, C. Sinha, C.H.L. Kennard, Polyhedron 20 (2001) 905;
(b) S. Goswami, R. Mukherjee, A. Chakravorty, Inorg. Chem. 22 (1983) 2825.
[34] K. Natarajan, U. Agarwala, Bull. Chem. Soc. Jpn. 49 (1976) 2877.
[35] A.B.P. Lever, Inorganic Electronic Spectroscopy, second ed., Elsevier, New York, 1984.
[36] M.M.T. Khan, D. Srinivas, R.I. Khureshy, N.H. Khan, Inorg. Chem. 29 (1990) 2320.
[37] S. Pal, S. Pal, Eur. J. Inorg. Chem. (2003) 4244.
[38] B.N. Figgis, Trans. Faraday Soc. 57 (1961) 198.
[39] M. Gerloch, J. Chem. Soc. (1968) 2028.
[40] P. Munshi, R. Samanta, G.K. Lahiri, J. Organomet. Chem. 586 (1999) 176, and references therein.
[41] (a) R. Ramesh, S. Maheswaran, J. Inorg. Biochem. 96 (2003) 457;
(b) S. Kannan, R. Ramesh, Y. Liu, J. Organomet. Chem. 692 (2007) 3380;
(c) S. Kannan, R. Ramesh, Polyhedron 25 (2006) 3095.

[42] O.K. Medhi, U. Agarwala, Inorg. Chem. 19 (1980) 1381.
[43] A.A. Batista, E.A. Polato, S.L. Queiroz, O.R. Nascimento, B.R. James, S.J. Rettig, Inorg. Chim. Acta 230 (1995) 111.
[44] L.R. Dinelli, A.A. Batista, K. Wohnrath, M.P. de Araujo, S.L. Queiroz, M.R. Bonfadini, G. Oliva, O.R. Nascimento, P.W. Cyr, K.S. MacFarlane, B.R. James, Inorg. Chem. 38 (1999) 5341.
[45] S. Dutta, S. Peng, S. Bhattachrya, J. Chem. Soc., Dalton Trans. (2000) 4623.
[46] A.M. Bond, R. Colton, D.R. Mann, Inorg. Chem. 29 (1990) 4665.
[47] M.C. Barral, S. Herrero, J.J. Aparicio, M.R. Torres, F.A. Urbanos, Inorg. Chem. Commun. 7 (2004) 4.
[48] (a) R. Noyori, Asymmetric Catalysis in Organic Synthesis, Wiley, New York, 1994;
(b) I. Ojima, Catalytic Asymmetric Synthesis, second ed., Wiley, New York, 2000;
(c) R. Noyori, S. Hashiguchi, Acc. Chem. Res. 30 (1997) 97;
H. Doucet, T. Ohkuma, K. Murata, T. Yokozawa, M. Kozawa, E. Katayama, F.A. England, T. Ikariya, R. Noyori, Angew. Chem., Int. Ed. 37 (1998) 1703.
[49] (a) E.P. Kelson, P.P. Phengsy, J. Chem. Soc., Dalton Trans. (2000) 4023;
(b) H. Zhang, B.C. Yang, Y.Y. Li, Z.R. Donga, J.X. Gao, H. Nakamura, K. Murata, T. Ikariya, Chem. Commun. (2003) 142;
(c) J. Hannedouche, G.J. Clarkson, M. Wills, J. Am. Chem. Soc. 126 (2004) 986.
[50] J. Soleimannejad, A. Sisson, C. White, Inorg. Chim. Acta 352 (2003) 121.
[51] (a) J.W. Faller, A.R. Lavoie, Organometallics 20 (2001) 5245;
(b) J.W. Faller, A.R. Lavoie, Organometallics 21 (2002) 3493.

Available online at www.sciencedirect.com
ScienceDirect
Polyhedron 27 (2008) 709–716
POLYHEDRON
www.elsevier.com/locate/poly

Synthesis, reactivity and structural characterization of sodium and ytterbium complexes stabilized by a tridentate [*N*,*N*,*O*] Schiff base ligand

Bang-Yu Li [a], Ying-Ming Yao [a,*], Yao-Rong Wang [b], Yong Zhang [a], Qi Shen [a,*]

[a] *Key Laboratory of Organic Synthesis of Jiangsu Province, Department of Chemistry and Chemical Engineering, Dushu Lake Campus, Suzhou University, Suzhou 215123, PR China*
[b] *College of Material Engineering, Suzhou University, Suzhou 215123, PR China*

Received 16 October 2007; accepted 30 October 2007
Available online 4 December 2007

Abstract

A tridentate [*N*,*N*,*O*] Schiff base [3,5-Bu^t_2-2-(OH)-C_6H_2CH=N-8-C_9H_6N(LH)] was prepared, and the corresponding sodium and ytterbium complexes were synthesized and characterized. Reaction of LH with NaH in THF at room temperature afforded the sodium salt of the Schiff base as a dimer [{LNa(THF)}$_2$] (**1**). Complex **1** reacted with anhydrous $YbCl_3$ in THF, after workup, to give the monomeric ytterbium Schiff base dichloride complex, [$LYbCl_2$(DME)] (**2**). Complex **2** is a good precursor for the synthesis of the corresponding ytterbium derivatives. Reaction of complex **2** with 1 equiv. of $NaCH_3C_5H_4$ in THF gave the expected product [Yb($CH_3C_5H_4$)Cl(THF)] (**3**) in a good isolated yield. Similar reaction of complex **2** with 2 equiv. of ArONa (ArO=OC_6H_3-Bu^t_2-2,6) in THF afforded the desired solvent-free ytterbium aryloxide [Yb(OAr)$_2$] (**4**). Complex **4** can also be prepared by the protolytic exchange reaction of LH with $(ArO)_3Yb$ in a 1:1 molar ratio. All of these complexes were well characterized including X-ray structure determination.
© 2007 Published by Elsevier Ltd.

Keywords: Alkali metal; Lanthanide; Schiff base; Synthesis; Crystal structure

1. Introduction

Over the past decade, significant efforts to explore ligands other than traditional ancillary ligand cyclopentadienyl set in organolanthanide chemistry have led to the fruitful design of new non-lanthanocene complexes [1–4]. Of these alternatives, Schiff base ligands, that have hard donor-atom frameworks, are attractive due to their stability and the ease by which modified variations can be obtained. Moreover, these lanthanide complexes are known to serve as precatalysts in homogeneous catalysis, such as asymmetric ring opening reaction of epoxide, ring opening polymerization of lactide and related cyclic esters [5–7], as the materials for the potential applications in biology, medicine as well as high-technology fields [8–12]. Generally, the tridentate Schiff base ligands with a flexible donor atom, in comparison with the bidentate ligands, can provide the protective shields for catalytically active metal centers leading to a ''more stable'' active species via the coordination of the additional donor atom. As a result, the activity of the complex with a tridentate Schiff base ligand is much higher than that of the complex with a bidentate ligand [13,14]. However, anhydrous preparation and reactivity of lanthanide complexes with a tridentate Schiff base ligand still remains poorly explored. Recently, monomeric lanthanocene aryloxide complexes with a tridentate Schiff base ligand *N*-1-(*ortho*-methoxyphenyl) salicylideneamine was synthesized and structurally characterized [15].

* Corresponding authors. Tel.: +86 512 65880306; fax: +86 512 65880305 (Q. Shen).
E-mail addresses: yaoym@suda.edu.cn (Y.-M. Yao), qshen@suda.edu.cn (Q. Shen).

0277-5387/$ - see front matter © 2007 Published by Elsevier Ltd.
doi:10.1016/j.poly.2007.10.025

Herein, we report the synthesis and molecular structure of a series of sodium and ytterbium complexes supported by a tridentate Schiff base ligand including the complexes of formulae $[\{LNa(THF)\}_2]$, $[LYbCl_2(DME)]$, $[LYb(CH_3C_5H_4)Cl(THF)]$ and $[LYb(OAr)_2]$, where L = [3,5-Bc_2^t-2-(O)C_6H_2CH=N-8-C_9H_6N]; ArO=$OC_6H_3Bu_2^t$-2,6. To our best knowledge, $[LYbCl_2(DME)]$ is the first structurally characterized lanthanide dichloride complex stabilized by Schiff base ligand.

2. Results and discussion

2.1. Synthesis and characterization of $[\{LNa(THF)\}_2]$ (1)

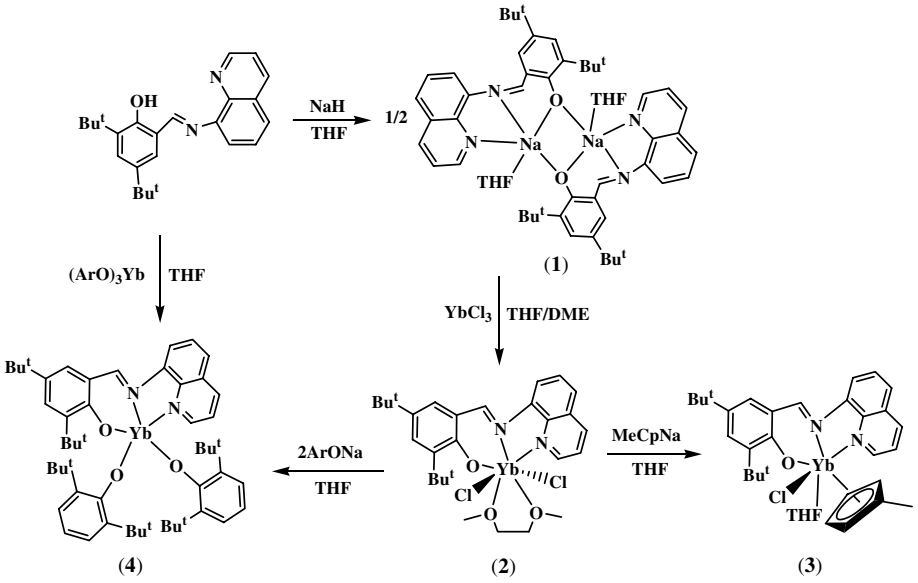
Alkali metal salts of Schiff base are known to be the starting reagents for the anhydrous preparation of lanthanide Schiff base complexes. It may be very informative to know the structure of these starting reagents. However, few structurally characterized Schiff base sodium complexes were reported in the literatures [16,17]. Thus, the sodium salt of the tridentate Schiff base HL, which was synthesized by the condensation reaction of 8-aminoquinoline with 3,5-di-*tert*-butyl-2-hydroxylbenzaldehyde [13], was synthesized and characterized. Reaction of NaH with HL in THF, after workup, afforded $[\{LNa(THF)\}_2]$ (**1**) as yellow crystals as shown in Scheme 1. Complex **1** gave satisfactory elemental analysis results, and its IR spectrum shows the characteristic absorption bands of aromatic rings in the region 1400–1600 cm^{-1} (skeletal vibrations), and of the C=N stretching vibration at 1613 cm^{-1} and of the phenolic C–O bond at 1242 cm^{-1}. The definitive molecular structure was determined by single-crystal X-ray diffraction.

The molecular structure of complex **1** is shown in Fig. 1, and its selected bond lengths and angles are listed in Table 1. Complex **1** has a dimeric structure, and two molecules are connected together by two bridged oxygen atoms. The molecules have approximate C_2 symmetry. Each sodium atom is five-coordinated with one oxygen atom, two nitrogen atoms from one Schiff base ligand, one oxygen atom from another ligand and one oxygen atom from a THF molecule. The coordination geometry at sodium atom can be described as a distorted trigonal bipyramid, in which O(2), O(3) and N(1) can be considered to occupy the equatorial positions, and O(1) and N(2) to occupy the apical positions.

The average Na–O(Ar) bond lengths of 2.279(4) Å falls in the range of Na–O(Ar) bond lengths in $[Na_4(salphen)_2(DME)_2]$ (salphen = *N*,*N*′-*o*-phenylenebis(salicylideneimine), 2.252(9)–2.291(9) Å) [16] and $[Na(18\text{-crown-}6)(THF)_2]_2[Na_2(OC_6H_4\text{-}2\text{-}C{=}NCH_2CH_2OH)]_4$ (2.221(3)–2.235(4) Å) [17]. The Na–N(imine) bond lengths of 2.407(3) (Na(1)–N(1)) and 2.388(3) Å (Na(2)–N(3)) are comparable with those found in $[Na_4(salphen)_2(DME)_2]$ (2.38(1) and 2.37(1) Å) [16], but are smaller than those in $[Na(18\text{-crown-}6)(THF)_2]_2[Na_2(OC_6H_4\text{-}2\text{-}C{=}NCH_2CH_2OH)]_4$ (2.492(4) and 2.570(4) Å) [17]. The bond lengths of Na–N(quinoline) are 2.550(3) (Na(1)–N(2)) and 2.403(3) Å (Na(2)–N(4)), respectively, which are larger than the Na–N(imine) bond lengths.

2.2. Synthesis and characterization of ytterbium complexes

Although lanthanide dichloride complex supported by a Schiff base ligand might be an important precursor for the synthesis of the corresponding lanthanide derivatives via metathesis reactions, no example of such lanthanide dichloride was reported up to date. Thus, we intend to synthesize the ytterbium dichloride complex with the bulky tridentate Schiff base group L as an ancillary ligand. Reaction of



Scheme 1.

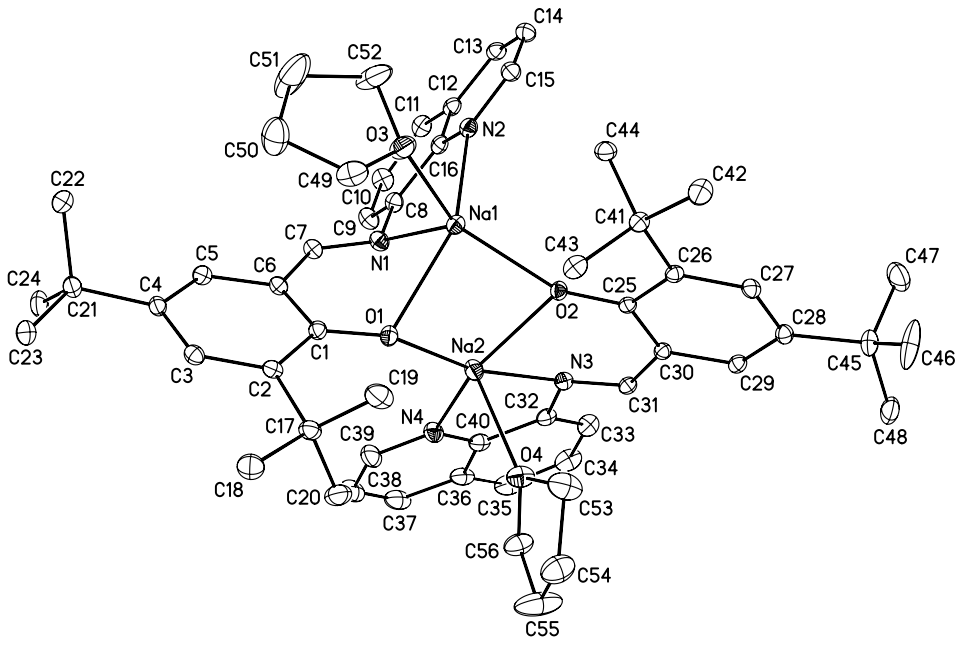


Fig. 1. ORTEP diagram of complex **1** showing atom-numbering scheme. Thermal ellipsoids are drawn at the 20% probability level. Hydrogen atoms are omitted for clarity.

Table 1
Selected bond distances (Å) and angles (°) for complexes **1**–**4**

	1	**2**	**3**	**4**
Bond distances				
M(1)–O(1)	2.365(2)	2.115(2)	2.116(3)	2.104(2)
M(1)–O(2)	2.274(2)	2.526(2)	2.450(3)	2.089(2)
M(1)–O(3)	2.341(3)	2.417(2)		2.082(2)
M(1)–N(1)	2.407(3)	2.386(3)	2.400(3)	2.359(3)
M(1)–N(2)	2.550(3)	2.470(3)	2.436(4)	2.410(3)
Yb(1)–Cl(1)		2.5934(8)	2.594(1)	
Yb(1)–Cl(2)		2.5654(9)		
Yb(1)–C(8)				3.197(3)
Yb(1)–C(25)			2.675(5)	
Yb(1)–C(26)			2.644(5)	
Yb(1)–C(27)			2.636(5)	
Yb(1)–C(28)			2.640(5)	
Yb(1)–C(29)			2.645(4)	
Bond angles				
O(1)–M(1)–O(2)	89.83(8)	151.59(8)	78.8(1)	96.25(9)
N(1)–M(1)–N(2)	67.01(8)	66.40(9)	67.5(1)	68.50(9)
N(1)–M(1)–O(2)	108.36(9)	130.53(8)	73.7(1)	132.39(9)
O(1)–M(1)–N(2)	140.10(9)	135.70(9)	142.4(1)	135.22(9)
N(1)–M(1)–O(1)	73.11(8)	75.96(9)	77.2(1)	76.73(8)
O(2)–M(1)–N(2)	101.46(8)	72.18(8)	79.2(1)	87.45(9)

anhydrous $YbCl_3$ with complex **1** in THF, after workup, gave the first Schiff base lanthanide dichloride complex [$LYbCl_2$(DME)] (**2**) in high isolated yield from toluene/DME mixed solvent as shown in Scheme 1. Complex **2** was characterized by elemental analysis and IR spectrum, and its definitive molecular structure was provided by single-crystal X-ray diffraction. Complex **2** is soluble in THF and DME, and slightly soluble in toluene.

The molecular structure of complex **2** is shown in Fig. 2, and the selected bond lengths and angles are provided in Table 1. Complex **2** has a solvated monomeric structure, and the central metal ytterbium atom is seven-coordinated by one oxygen atom and two nitrogen atoms from one Schiff base ligand, and two chlorine atoms and two oxygen atoms from one DME molecule. The coordination geometry around ytterbium atom can be described as a distorted pentagonal bipyramid, in which O(1), N(1), N(2) (from Schiff base ligand), O(2) and O(3) (from DME) can be considered to occupy the equatorial positions with the sum of the bond angles of 366° and Cl(1) and Cl(2) to occupy the axis positions. The bond angle of Cl(1)–Yb–Cl(2) is slightly distorted away from the ideal value of 180° to 162.29(3)°. The Yb–O(Ar) bond distance is 2.115(2) Å, which is very close to those observed in related ytterbium Schiff base complexes [{2-OC_6H_4CH=(2,6-$^iPr_2C_6H_3$)}$_2$YbCl(THF)] (2.110(7) and 2.10(1) Å) [6], [{(η^5-C_5H_5)Yb(μ-$OC_{20}H_{20}N_2$-O)}$_2$(μ-THF)(THF)] (2.15(2) Å) [18]. The Yb–N(imine) bond distance is 2.386(3) Å, which is slightly smaller than those found in the ytterbium Schiff base complexes mentioned above. The Yb–N(quinoline) bond distance of 2.470(3) Å is apparently larger than the Yb–N(imine) bond distance, indicating the bond strength being somewhat weaker than that of the Yb–N(imine) bond.

Generally, organolanthanide or organolanthanoid chlorides are useful precursors for the synthesis of lanthanide derivatives. Thus, the chloride substitution reactions of complex **2** with other reagents were studied. The reaction of complex **2** with 1 equiv. of $NaCH_3C_5H_4$ in THF went smoothly and, after workup, afforded the desired lanthanide complex [$LYb(CH_3C_5H_4)Cl$(THF)] (**3**) in good

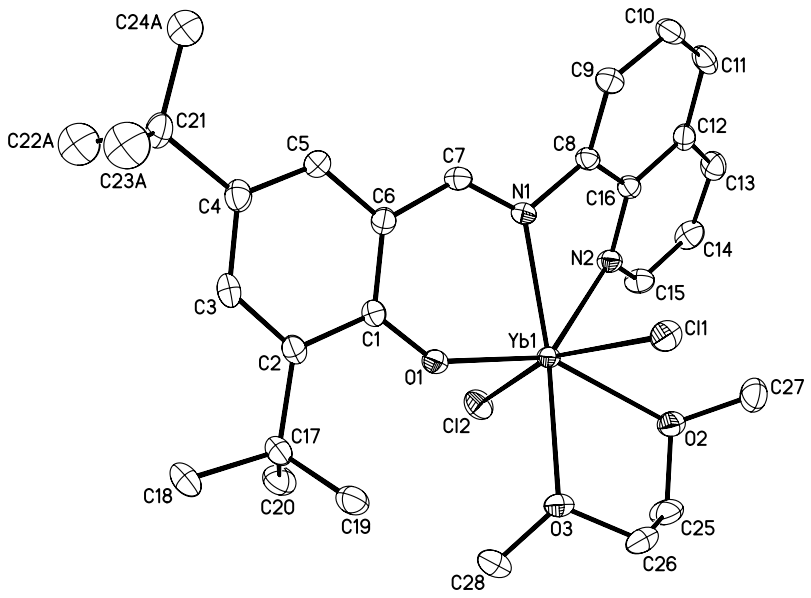


Fig. 2. ORTEP diagram of complex **2** showing atom-numbering scheme. Thermal ellipsoids are drawn at the 40% probability level. Hydrogen atoms are omitted for clarity.

isolated yield (Scheme 1). Similar reaction of complex **2** with 2 equiv. of ArONa in THF, after workup, gave the solvent-free ytterbium aryloxide [$LYb(ArO)_2$] (**4**) as orange-yellow crystals in high yield. Further study revealed that complex **4** can also be conveniently prepared by the direct protolytic exchange reaction of Schiff base LH with $Yb(ArO)_3$ in a 1:1 molar ratio in THF. The compositions of complexes **3** and **4** were confirmed with elemental analysis, and there are characteristic absorption bands of the aryloxo group in their IR spectra. The definitive molecular structures of complexes **3** and **4** were determined by single-crystal structure analysis. Complexes **3** and **4** are well soluble in THF and diethyl ether, and soluble in toluene.

Crystals of complex **3** suitable for an X-ray diffraction study were obtained from THF/Et_2O solution at low temperature. An ORTEP diagram of the molecular structure of complex **3** is shown in Fig. 3, and the selected bond lengths and angles are listed in Table 1. Complex **3** has a monomeric structure. The ytterbium atom is coordinated by two nitrogen atoms and one oxygen atom from the Schiff base ligand, one Cp ring, one chlorine atom and another oxygen atom from THF molecule to form a distorted octahedral geometry, when the Cp ring was considered to occupy one coordination site. Two nitrogen atoms, one oxygen atom of the Schiff base ligand and one chlorine atom can be considered to occupy the equatorial positions with the sum of the bond angles of 359.4°, and the centroid

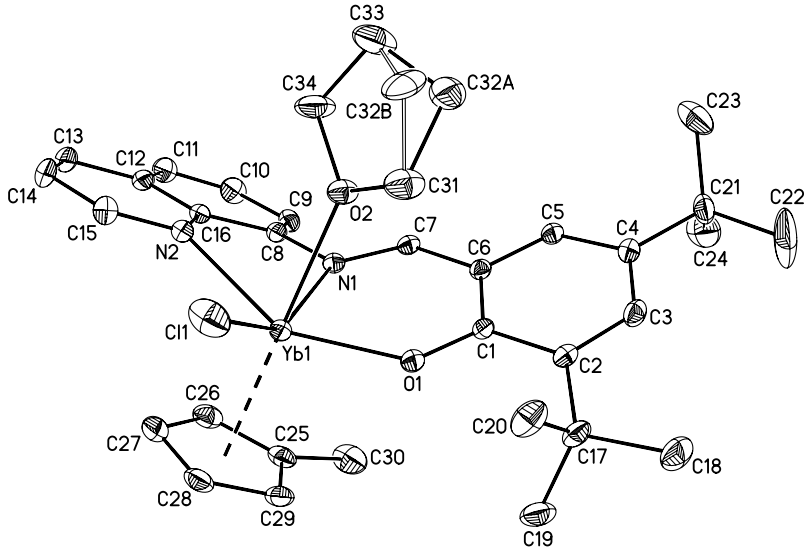


Fig. 3. ORTEP diagram of complex **3** showing atom-numbering scheme. Thermal ellipsoids are drawn at the 30% probability level. Hydrogen atoms are omitted for clarity. Disordered THF molecule is shown in two possible orientations.

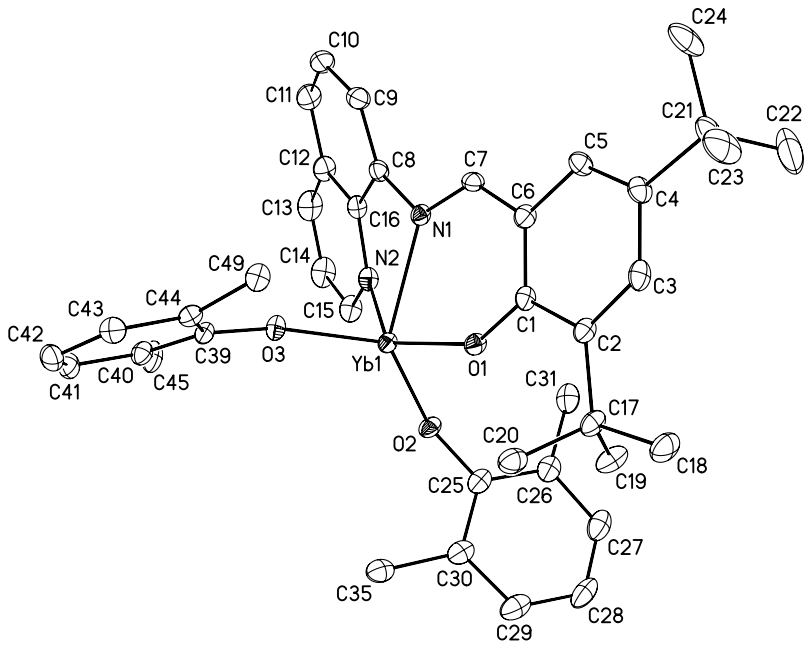


Fig. 4. ORTEP diagram of complex **4** showing atom-numbering scheme. Thermal ellipsoids are drawn at the 30% probability level. Methyl groups of the *tert*-butyl groups of aryloxides and hydrogen atoms are omitted for clarity.

of the Cp ring and the oxygen atom of the THF molecule occupy the apical positions.

The Ln–C(Cp) bond distances range from 2.636(5) to 2.675(5) Å, giving the average 2.648(5) Å, which is slightly smaller than that in lanthanide cyclopentadienyl Schiff base complexes $[\{(\eta^5\text{-}C_5H_5)Ln(\mu\text{-}OC_{20}H_{20}N_2O)\}_2(\mu\text{-THF})(THF)]$ (Ln = Yb, 2.70(3) Å [18]; Ln = Sm, 2.778 Å [19]), and $[(\eta^5\text{-}C_5H_5)_2Sm(OC_{14}H_{13}ON)]$ (2.723 Å) [15], when the difference in ionic radius is considered. The Yb–O(Ar) bond distance of 2.116(3) Å is well comparable with those values in $[\{2\text{-}OC_6H_4CH{=}NC_6H_3\text{-}^iPr_2\text{-}2,6\}_2YbCl(THF)]$ (2.107(7) Å) [6], and other lanthanide Schiff base complexes mentioned above. The Yb–N(imine) bond distance of 2.400(3) Å is comparable with the Yb–N(quinoline) bond distance (2.436(4) Å), which is different from that in complex **2**. The Yb–Cl bond distance of 2.594(1) Å is apparently larger than the corresponding value in $[\{2\text{-}OC_6H_4CH{=}N(2,6\text{-}^iPr_2C_6H_3)\}_2YbCl(THF)]$ (2.497(2) Å) [6], whereas this bond distance is comparable with that in complex **2**.

Crystals of complex **4** suitable for X-ray diffraction were obtained by recrystallization from toluene. The molecular structure diagram with atom-numbering scheme is presented in Fig. 4, and its selected bond lengths and angles are listed in Table 1. The ytterbium atom is coordinated by one oxygen atom, two nitrogen atoms from the Schiff base ligand and two oxygen atoms from two aryloxo groups to form a five-coordinated highly distorted trigonal bipyramidal geometry. O(2), O(3) and N(1) can be considered to occupy the equatorial positions with the sum of the angles of 355.47°, and O(1) and N(2) to occupy the apical positions. Usually, lanthanide Schiff base complexes have high coordination numbers (>6) via oligomerisation or solvent stabilization, these is few structurally characterized five-coordinated mononuclear lanthanide complexes bearing Schiff base ligands in the literatures [20–23].

The Yb–O(Schiff base), Yb–N(imine) and Yb–N(quinoline) bond distances in complex **4** are 2.104(2), 2.359(3) and 2.410(3) Å, respectively, which are in accordance with the corresponding values in complexes **2** and **3**. The bond distances of Yb–O(Ar) of 2.082(2) and 2.089(2) Å, respectively, compare well with the corresponding value in $[(ArO)_2YbCl(THF)_2]$ (2.080(1) Å) [24], but are slightly larger than that in $[\{(DIPPh)_2nacnac\}Yb(ArO)Cl(THF)]$ [2.024(2) Å, $(DIPPh)_2$nacnac=*N*,*N*-diisopropylphenyl-2,4-pentanediimine anion] [25]. In addition, remote π interaction of C(8) with Yb(1) was observed in complex **4**. The bond distance of Yb(1)–C(8) is 3.197(3) Å, which is comparable to those of 3.207(9) and 3.179(10) Å for imidazolidine-bridged bis(phenolate) ytterbium dichloride [26], and 2.814(4) to 3.148(6) Å for chelating η^6-,η^1-Ph–Yb bonding in $[\{Yb(Odpp)_3\}_2]$ (Odpp=2,6-diphenylphenolate) [27].

3. Conclusion

A bulky tridentate Schiff base was prepared, and this compound can be used as an ancillary ligand for a series of sodium and ytterbium complexes. The Schiff base reacted with NaH to give the corresponding sodium salt as a dimeric complex, which reacted with anhydrous $YbCl_3$ to produce the first structurally characterized soluble ytterbium dichloride bearing Schiff base ligand. It was found that this ytterbium dichloride can be used as a useful precursor for the synthesis of the corresponding ytterbium derivatives by direct salt metathesis reactions. All of these complexes were well characterized, and their molecular structures were determined by X-ray diffraction.

4. Experimental

4.1. Materials and methods

All of the manipulations described below were performed under an argon atmosphere, using the standard Schlenk techniques. Solvents were dried and freed of oxygen by refluxing over sodium or sodium benzophenone ketyl and distilled under argon prior to use. Schiff base ligand HL [3,5-Bu^t_2-2-(OH)C_6H_2CH=N-8-C_9H_6N] [13], anhydrous $YbCl_3$ [28] and $Yb(OAr)_3$ [29] were prepared according to the literature methods. $NaCH_3C_5H_4$ was prepared by the reaction of $CH_3C_5H_5$ with sodium in THF. The other reagents were purchased from Acros and used as received without further purification. Metal analyses were carried out using complexometric titration. Carbon, hydrogen, and nitrogen analyses were performed by direct combustion on a Carlo Erba-1110 instrument; Quoted data are the average of at least two independent determinations. IR spectra were recorded on a Nicolet-550 FTIR spectrometer as KBr pellets. ^{1}H NMR spectrum was obtained on an INOVA-400 MHz apparatus. The uncorrected melting points of crystalline samples in sealed capillaries (under argon) are reported as ranges.

4.2. Synthesis of [{NaL(THF)}$_2$] (1)

A solution of HL (1.80 g, 5.0 mmol) in THF (20 mL) was added dropwise to a NaH suspension (1.5 equiv.) in THF at room temperature. The mixture was stirred for 14 h, and then was filtered. The resulting dark red solution was concentrated. Yellow crystals were obtained from the mixture of THF and toluene (6:1) at room temperature in a few days (3.87 g, 85%), m.p.: 279–281 °C (dec). *Anal.* Calc. for $C_{56}H_{70}N_4Na_2O_4$: C, 73.97; H, 7.76; N, 6.16. Found: C, 73.58; H, 7.95; N, 5.76%. IR (KBr pellet, cm^{-1}): 2956(vs), 2909(m), 2871(m), 1613(vs), 1458(vs), 1389(m), 1366(m), 1242(s), 1157(s), 1088(w), 1057(w), 1026(w), 980(w), 880(m), 826(m), 795(m), 640(w), 502(m). ^{1}H NMR (400 MHz, C_6H_6): 8.50–8.48 (m, 1H, C_9H_6N), 8.43 (s, 1H, CH=N), 7.43–7.40 (m, 1H, C_9H_6N), 7.30–7.25 (m, 3H, C_9H_6N), 6.98 (d, 2H, J = 2.6 Hz, C_6H_2), 6.65–6.60 (m, 1H, C_9H_6N), 4.06 (m, 4H, THF), 2.09 (m, 4H, THF), 1.79 (s, 9H, $C(CH_3)_3$), 1.33 (s, 9H, $C(CH_3)_3$).

4.3. Synthesis of [LYbCl$_2$(DME)] (2)

A THF solution (10 mL) of complex **1** (0.91 g, 1.0 mmol) was added to a suspension of anhydrous $YbCl_3$ (0.56 mg, 2.0 mmol) in THF (20 mL) at room temperature. After the solution was stirred overnight, the precipitate was separated from the reaction mixture by centrifugation. The solution was concentrated, and then DME (0.5 mL) was added. Yellow crystals were obtained at room temperature in a few days (1.10 g, 80%), m.p.: 266–268 °C (dec). *Anal.* Calc. for $C_{28}H_{37}Cl_2N_2O_3Yb$: C, 48.49; H, 5.38; N, 4.04; Yb, 24.95. Found: C, 48.87; H, 5.67; N, 3.98; Yb, 24.87%. IR (KBr, cm^{-1}): 2956(m), 2928(m), 1613(s), 1535(m), 1498(m), 1427(m),1319(m), 1234(vs), 1158(vs), 833(m),787(m), 633(m), 556(m), 509(s). The crystals suitable for an X-ray crystal structure determination were obtained by recrystallization from THF–DME solution at room temperature.

4.4. Synthesis of [(CH$_3$C$_5$H$_4$)YbLCl(THF) · THF] (3 · THF)

A Schlenk flask was charged with complex **2** (0.69 g, 1.0 mmol) and THF (20 mL). A THF solution of $NaCH_3C_5H_4$ (1.0 mL, 1.0 mmol) was added by syringe. The reaction mixture was stirred overnight at room temperature. After removed the volatiles in vacuum, the yellow residue was extracted with Et_2O, and NaCl was removed by centrifugation. Orange-yellow crystals were obtained at room temperature, (0.47 g, 60%), m.p.: 158–160 °C (dec). *Anal.* Calc. for $C_{38}H_{50}ClN_2O_3Yb$ (**3** · THF): C, 57.68; H, 6.37; N, 3.54; Yb, 21.87. Found: C, 57.45; H, 6.63; N, 3.57; Yb, 21.51%. IR (KBr, cm^{-1}): 2956(s), 2905(m), 1608 (s), 1534(m), 1503(m), 1463(m), 1425(m), 1330(m), 1223(vs), 1159(vs), 1086(m), 835(m), 792(m), 506(s).

4.5. Synthesis of [LYb(OAr)$_2$] (4)

4.5.1. Method A

A Schlenk flask was charged with complex **2** (0.69 g, 1.0 mmol) and THF (20 mL). A THF solution of NaOAr (2.0 mL, 2.00 mmol) was added by syringe. The reaction mixture was stirred overnight at room temperature. After removed the volatiles in vacuum, the yellow residue was extracted with toluene, and the precipitate was removed by centrifugation. Complex **4** was obtained as yellow crystals at room temperature (0.56 g. 60%), m.p.: 189–191 °C (dec). *Anal.* Calc. for $C_{52}H_{69}N_2O_3Yb$: C, 66.22; H, 7.37; N, 2.97; Yb, 18.35. Found: C, 66.38; H, 7.53; N, 2.91; Yb, 18.27%. IR (KBr, cm^{-1}): 2956(vs), 2909(s), 2871(s), 1613(s), 1528(s), 1505(s), 1466(s), 1428(vs), 1235(s), 1196(s), 1165(s), 1088(m), 1065(m), 833(m), 795(m), 748(m), 656(w), 594(w), 509(w).

4.5.2. Method B

$Yb(OAr)_3$ (0.81 g, 1.0 mmol) in toluene was added dropwise to a THF solution of HL (0.36 g, 1.0 mmol) (30 mL). The reaction mixture was stirred at room temperature for 12 h, and then concentrated in vacuum. Orange-yellow crystals obtained after 4 days at room temperature, (0.66 g. 70%).

4.6. X-ray structures determination

Suitable single crystals of complexes **1**–**4** were sealed in a thin-walled glass capillary for determining the single-crystal structure. Intensity data were collected with a Rigaku Mercury CCD area detector in ω scan mode using Mo

Table 2
Details of the crystallographic data and refinements for complexes **1**–**4**

Compound	**1** · THF	**2**	**3** · **THF**	**4**
Formula	$C_{60}H_{78}N_4Na_2O_5$	$C_{28}H_{37}Cl_2N_2O_3Yb$	$C_{38}H_{50}ClN_2O_3Yb$	$C_{52}H_{69}N_2O_3Yb$
F_w	981.24	693.54	791.29	943.13
T (K)	153(2)	193(2)	193(2)	193(2)
Crystal system	monoclinic	monoclinic	monoclinic	triclinic
Space group	$P2_1/c$	$P2_1/c$	$P2_1/c$	$P\bar{1}$
a (Å)	12.824(1)	13.680(1)	13.509(2)	10.5557(6)
b (Å)	24.651(2)	21.014(1)	15.101(1)	14.1107(9)
c (Å)	18.352(2)	10.5822(9)	18.660(2)	16.980(1)
α (°)				84.492(4)
β (°)	107.192(2)	105.830(3)	109.404(3)	84.294(4)
γ (°)				76.306(3)
V (Å^3)	5542.0(10)	2926.8(4)	3590.5(7)	2438.2(3)
Z	4	4	4	2
D_{calc} (g/cm^{-3})	1.176	1.574	1.464	1.285
μ (mm^{-1})	0.087	3.408	2.716	1.959
$F(000)$	2112	1388	1612	978
Crystal size (mm)	$0.45 \times 0.37 \times 0.20$	$0.55 \times 0.30 \times 0.28$	$0.25 \times 0.20 \times 0.12$	$0.78 \times 0.42 \times 0.20$
2θ Range (°)	50.7	50.7	50.7	50.7
Reflections collected	54227	28349	35016	23349
Independent reflections	10128	5351	6566	8818
Reflections with $I \geqslant 2.0\sigma(I)$	7968	5105	5815	8272
Parameters refined	653	340	414	542
Goodness-of-fit	1.129	1.066	1.149	1.108
R	0.0778	0.0233	0.0369	0.0316
wR	0.1677	0.0569	0.0765	0.0757

Kα radiation ($\lambda = 0.71070$ Å). The diffracted intensities were corrected for Lorentz polarization effects and empirical absorption corrections. Details of the intensity data collection and crystal data are given in Table 2.

The structures were solved by direct methods and refined by full-matrix least-squares procedures based on $|F|^2$. All of the non-hydrogen atoms were refined anisotropically. All of the hydrogen atoms were held stationary and included in the structure factor calculation in the final stage of full-matrix least-squares refinement. The structures were solved and refined using SHELEXL-97 programs.

Acknowledgements

The financial support from the National Natural Science Foundation of China (Grants 20632040 and 20771078), the Natural Science Foundation of Jiangsu province (BK2007505), the Major Basic Research Project of the Natural Science Foundation of the Jiangsu Higher Education Institutions (07KJA15014), and Key Laboratory of Organic Synthesis of Jiangsu Province is gratefully acknowledged.

Appendix A. Supplementary material

CCDC 662844, 662845, 662846 and 662847 contain the supplementary crystallographic data for **1**, **2**, **3** and **4**. These data can be obtained free of charge via www.ccdc.ac.uk/conts/retrieving.html, or from the Cambridge Crystallographic Data Centre, 12 Union Road, Cambridge CB2 1EZ, UK; fax: (+44) 1223-336-033; or e-mail: deposit@ccdc.cam.ac.uk. Supplementary data associated with this article can be found, in the online version, at doi:10.1016/j.poly.2007.10.025.

References

[1] K. Dehnicke, A. Greiner, Angew. Chem., Int. Ed. 42 (2003) 1340.
[2] W.E. Piers, J.J.H. Emslie, Coord. Chem. Rev. 131 (2002) 233.
[3] H.C. Aspinall, Chem. Rev. 102 (2002) 1807.
[4] P.W. Roesky, Chem. Soc. Rev. 29 (2000) 335.
[5] M.O. Tina, W.C. Geoffrey, J. Am. Chem. Soc. 121 (1999) 4072.
[6] L.B. Yu, Y.M. Yao, Q. Shen, J. Zhang, L.X. Wu, L. Ye, Chin. J. Chem. 1 (2003) 442.
[7] S.A. Schuetz, C.M. Silvernail, C.D. Incarvito, A.L. Rheingold, J.L. Clark, V.W. Day, J.A. Belot, Inorg. Chem. 43 (2004) 6203.
[8] V. Patroniak, A.R. Stefankiewicz, J.M. Lehn, M. Kubicki, M. Hoffmann, Eur. J. Inorg. Chem. (2006) 144.
[9] R.D. Archer, H.Y. Chen, L.C. Thompson, Inorg. Chem. 37 (1998) 2089.
[10] R.D. Jones, D.A. Summerville, F. Basalo, Chem. Rev. 79 (1979) 139.
[11] R. Rodriguez-Cortinas, F. Avecilla, C. Platas-Iglesias, D. Imbert, J.-C.G. Bunzli, A. Blas, T. Rodriguez-Blas, Inorg. Chem. 41 (2002) 5336.
[12] M. Gonza'lez-Lorenzo, C. Platas-Iglesias, F. Avecilla, C.F.G.C. Geraldes, D. Imbert, J.-C.G. Bunzli, A. Blas, T.R. Blas, Inorg. Chem. 42 (2003) 6946.
[13] P.A. Cameron, V.C. Gibson, C. Redshaw, J.A. Segal, A.J.P. White, D.J. Williams, J. Chem. Soc., Dalton Trans. (2002) 415.
[14] R.K. O'Reilly, V.C. Gibson, A.J.P. White, D.J. Williams, J. Am. Chem. Soc. 125 (2003) 8450.
[15] M. Yousaf, Q.C. Liu, J.L. Huang, Y.L. Qian, A.S.-C. Chan, Inorg. Chem. Commun. 3 (2000) 105.
[16] E. Solari, S. De Angelis, C. Floriani, A. Chiesi-Villa, C. Rizzoli, J. Chem. Soc., Dalton. Trans. (1991) 2471.
[17] R. Fisher, H. Gorls, D. Walther, Z. Anorg. Allg. Chem. 630 (2004) 1387.
[18] Q.C. Liu, M.X. Ding, J. Organomet. Chem. 553 (1998) 179.

[19] Q.C. Liu, M.X. Ding, Y.H. Lin, Y. Xing, Polyhedron 17 (1998) 555.
[20] Y.P. Cai, H.Z. Ma, B.S. Kang, C.Y. Su, W. Zhang, J. Sun, Y.L. Xiong, J. Organomet. Chem. 628 (2001) 99.
[21] P. Blech, C. Floriani, A. Chiesivilla, C. Guastini, J. Chem. Soc., Dalton Trans. (1990) 3557.
[22] S.A. Schuetz, V.W. Day, A.L. Rheingold, J.A. Belot, J. Chem. Soc., Dalton Trans. (2003) 4303.
[23] W.J. Evans, C.H. Fujimoto, J.W. Ziller, Polyhedron 21 (2002) 1683.
[24] Y.M. Yao, Q. Shen, Y. Zhang, M.Q. Xue, J. Sun, Polyhedron 20 (2001) 3201.
[25] Y. Zhang, Y.M. Yao, Y.J. Luo, Q. Shen, Y. Cui, K.B. Yu, Polyhedron 22 (2003) 1241.
[26] X.P. Xu, Y.M. Yao, Y. Zhang, Q. Shen, Inorg. Chem. 46 (2007) 3743.
[27] G.B. Deacon, S. Nickle, P.I. Mackinnon, E.R.T. Tiekink, Aust. J. Chem. 43 (1990) 1245.
[28] M.D. Taylor, C.P. Carter, J. Inorg. Nucl. Chem. 24 (1962) 387.
[29] P.B. Hitchcock, M.F. Lappert, R.G. Smith, Inorg. Chim. Acta 139 (1987) 183.

Available online at www.sciencedirect.com
ScienceDirect
Polyhedron 27 (2008) 717–726
POLYHEDRON
www.elsevier.com/locate/poly

Architecture of zero-, one-, two- and three-dimensional structures based on metal ions and pyrazine-2,6-dicarboxylic acid

Feng-Qin Wang [a,b], Xiang-Jun Zheng [a], Yong-Hong Wan [a], Ke-Zhi Wang [a], Lin-Pei Jin [a,*]

[a] College of Chemistry, Beijing Normal University, Beijing 100875, PR China
[b] Faculty of Materials Science and Engineering, Tianjin Polytechnic University, Tianjin 300160, PR China

Received 9 July 2007; accepted 1 November 2007
Available online 21 December 2007

Abstract

Six new complexes: $[Ln_2(pzda)_3(H_2O)_2]\cdot 2.5H_2O$ (Ln = Nd, (**1**); Eu, (**2**)), $[Co(pzda)(bpe)]\cdot 0.125(bpe)\cdot 1.75H_2O$ (**3**), $[Mn(pzda)(H_2O)_{1.5}]$ (**4**), $[Co_2(pzda)_2(bpe)(H_2O)_4]\cdot 0.5(CH_3OH)\cdot H_2O$ (**5**) and $[Co(pzda)(2,2'\text{-bpy})(H_2O)]\cdot 0.5H_2O$ (**6**) (H_2pzda = pyrazine-2,6-dicarboxylic acid, bpe = 1,2-bis(4-pyridyl)ethane, 2,2′-bpy = 2,2′-bipyridine) were obtained from metal salts and H_2pzda under hydro(solvo)thermal conditions. The single crystal X-ray structural analysis reveals that the title complexes have different structures, ranging from zero- to three- dimensions, which are mainly due to the different metal ions, and especially the coordination modes of the pzda ligands. Complexes **1** and **2** have 3D metal-organic frameworks containing a 1D tri-strand array, in which the pzda ligand adopts a pentadentate mode to link lanthanide ions. Complex **3** has a 2D metal-organic framework, in which the pzda ligand acts in a tetradentate mode to connect Co(II) ions into 1D chains, which are further connected by bpe spacers into a 2D framework. While in **4**, both of the two carboxylate groups of the pzda ligand adopt μ_2-O bridging modes to link Mn(II) ions into a 1D coordination polymer, which is further assembled into a 2D supramolecular network containing double-stranded hydrogen-bonded helical chains. In both **5** and **6**, the pzda ligand binds metal ions as a tridentate ligand (ONO mode) to form zero dimensional structures. Complex **5** is a binuclear molecule, while **6** is a mononuclear complex, which can be attributed to the bridging ligand bpe for **5** and the terminal auxiliary ligand 2,2′-bpy for **6**.
© 2007 Elsevier Ltd. All rights reserved.

Keywords: Pyrazine-2,6-dicarboxylic acid; Metal ions; Structural versatility; Coordination modes

1. Introduction

Over the past few decades, the design and synthesis of metal-organic frameworks (MOFs) have received much attention not only because of the fascinating structural diversities but also for their useful properties and potential applications as functional materials in molecular adsorption, separation and magnetism [1–3]. From the viewpoint of crystal engineering, one of the most effective approaches to synthesize MOFs is hydro(solvo)thermal controlled assembly of the organic ligands and metal ions. The construction of multidimensional architectures depends mainly on the combination of several factors, including the metal ions, the type of organic ligand and the coordination modes, the auxiliary ligands and the pH value, etc. [4]. Among these factors, the selection or design of a suitable ligand containing appropriate coordination sites is crucial for the construction of coordination polymers or supramolecular architectures [5].

Multidentate N- and O-donor ligands, such as pyridine- [6] or imidazole- [7] carboxylic acids have drawn extensive attention in the construction of coordination polymers or metal-organic frameworks. Among them, pyridine-2,6-dicarboxylic acid has been proved to be effective for the construction of 3d, 4f or 3d–4f MOFs and multidimensional supramolecular networks because it has many coordination modes. Compared with pyridine-2,6-dicarboxylic

* Corresponding author.
E-mail address: lpjin@bnu.edu.cn (L.-P. Jin).

0277-5387/$ - see front matter © 2007 Elsevier Ltd. All rights reserved.
doi:10.1016/j.poly.2007.11.012

acid, pyrazine-2,6-dicarboxylic acid has a similar geometry configuration but one more nitrogen atom in the 4-position of the pyrazine ring, and thus is of particular interest because: (a) it has two carboxylate groups and two nitrogen atoms which can coordinate to metal ions in a variety of coordination modes leading to different topologies for the structures of the complexes, and its diversity of coordination modes in the complexes is depicted in Scheme 1, in which a and c are first reported in this paper; (b) the COOH groups and nitrogen atoms can act as hydrogen bond donors and/or hydrogen bond acceptors, favoring the formation of supramolecular structures; and (c) the COOH groups can be tilted from the pyrazine ring plane and coordinate to metal ions in a different direction, allowing for formation of desirable frameworks. However, the construction of MOFs from the pzda ligand has been rarely reported [8]. Further study is still necessary to understand the coordination chemistry of H_2pzda. In addition, auxiliary ligands such as 2,2′-bpy and bpe often have a significant effect on the formation and structure of metal N-containing polycarboxylate complexes [9].

On the basis of above mentioned points, we synthesized six metal complexes with H_2pzda and auxiliary ligands. Herein, we report the syntheses and crystal structures of six new complexes: $[Ln_2(pzda)_3(H_2O)_2]\cdot 2.5H_2O$ (Ln = Nd, (**1**); Eu, (**2**)), $[Co(pzda)(bpe)]\cdot 0.125(bpe)\cdot 1.75H_2O$ (**3**), $[Mn(pzda)(H_2O)_{1.5}]$ (**4**), $[Co_2(pzda)_2(bpe)(H_2O)_4]\cdot 0.5(CH_3OH)\cdot H_2O$ (**5**) and $[Co(pzda)(2,2'\text{-bpy})\ (H_2O)]\cdot 0.5H_2O$ (**6**). In these complexes, the pzda ligands are able to link metal ions in various modes giving rise to zero-, one-, two- and three-dimensional complexes.

2. Experimental

2.1. Materials and apparatus

Pyrazine-2,6-dicarboxylic acid dihydrate was synthesized according to the literature [10]. All the other reagents were used as received without further purification. The C, H, N microanalyses were carried out with a Vario EL elemental analyzer. The IR spectra were recorded with a Nicolet Avatar 360 FT-IR spectrometer using the KBr pellet technique. The TG experiments for the complexes **1**, **2** and **5** were performed using a Perkin–Elmer TGA7 thermogravimetric analyzer under atmosphere. The heating rate used was 5 °C min^{-1} from ambient temperature to 900 °C.

2.2. Synthesis

2.2.1. Synthesis of $[Nd_2(pzda)_3(H_2O)_2]\cdot 2.5H_2O$ (*1*)

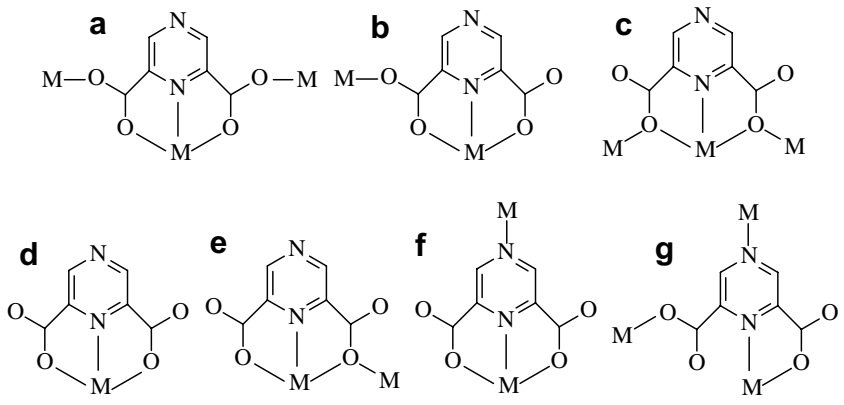
Nd_2O_3 (0.0168 g, 0.05 mmol), H_2pzda (0.0306 g, 0.15 mmol), 4,4′-bpy · $2H_2O$ (0.0192 g, 0.1 mmol), water (3 mL) and isopropyl alcohol (3 mL) were sealed in a Teflon-lined stainless steel vessel (25 mL) and heated at 180 °C for 5 days under autogenous pressure and then cooled slowly to room temperature. Purple plate-like crystals were obtained. Yield: 45%. *Anal.* Calc. for $C_{18}H_{15}Nd_2N_6O_{16.5}$: C, 24.91; H, 1.74; N, 9.69. Found: C, 25.05; H, 1.75; N, 9.60%. IR (KBr pellet, cm^{-1}): 3422br, 1618vs, 1458s, 1406w, 1191m, 1129w,1044m, 946w, 820w, 795m, 746m.

2.2.2. Synthesis of $[Eu_2(pzda)_3(H_2O)_2]\cdot 2.5H_2O$ (*2*)

Eu_2O_3 (0.0176 g, 0.05 mmol), H_2pzda (0.0306 g, 0.15 mmol), 4,4′-bpy · $2H_2O$ (0.0192 g, 0.1 mmol), water (3 mL) and ethanol (3 mL) were sealed in a Teflon-lined stainless steel vessel (25 mL) and heated at 180 °C for 5 days under autogenous pressure and then cooled slowly to room temperature. Colorless crystals were obtained. Yield: 43%. *Anal.* Calc. for $C_{18}H_{15}Eu_2N_6O_{16.5}$: C, 24.47; H, 1.71; N, 9.52. Found: C, 24.61; H, 1.81; N, 9.50%. IR (KBr pellet, cm^{-1}): 3421br, 1617vs, 1459s, 1406w, 1193m, 1130w, 1046m, 796m, 746m.

2.2.3. Synthesis of $[Co(pzda)(bpe)]\cdot 0.125(bpe)\cdot 1.75H_2O$ (*3*)

A mixture of H_2pzda (0.0204 g, 0.1 mmol), $Co(OAc)_2\cdot 4H_2O$ (0.0249 g, 0.1 mmol), 1,2-bis(4-pyridyl)ethane (0.0184 g, 0.1 mmol), NaOH aqueous solution (0.15 mL, 0.65 mol/L) and deionized water (5 mL) was sealed in a Teflon-lined stainless steel vessel (25 mL) and heated at 100 °C for 4 days under autogeneous pressure and then cooled slowly to room temperature. The solution



Scheme 1. The coordination modes of the pzda ligand in the metal complexes.

was filtered and allowed to stand for two months at room temperature. Orange-yellow block crystals were obtained. Yield: 31%. *Anal.* Calc. for $C_{19.5}H_{19}CoN_{4.25}O_{5.75}$: C, 50.45; H, 4.09; N, 12.82. Found: C, 50.58; H, 3.25; N, 13.11%. IR (KBr pellet, cm^{-1}): 3423br, 1646vs, 1613vs, 1559w, 1428m, 1384s, 1364m, 1225m, 1195m, 1116w, 1057m, 814m, 745w.

2.2.4. Synthesis of [Mn(pzda)(H$_2$O)$_{1.5}$] (**4**)

A mixture of $MnCO_3 \cdot H_2O$(0.004 g, 0.03 mmol), H_2pzda (0.0224 g, 0.11 mmol), $Yb(NO_3)_3 \cdot 6H_2O$ (0.009 g, 0.02 mmol), H_2O (1 mL), a drop of NaOH (0.65 mol/L) was sealed in a 25 mL stainless steel reactor with a Teflon liner and heated at 160 °C for 96 h, then cooled to room temperature. Light-yellow crystals were obtained, washed with deionized water and dried in air. Yield: 26%. *Anal.* Calc. for $C_6H_5MnN_2O_{5.5}$: C, 29.02; H, 2.02; N, 11.28. Found: C, 28.94; H, 2.27; N, 11.20%. IR data (KBr pellet cm^{-1}): 3444br, 1621vs, 1454m, 1402s, 1384s 1348m, 1213m, 1188m, 1043 w, 810w, 735w.

2.2.5. Synthesis of [Co$_2$(pzda)$_2$(bpe)(H$_2$O)$_4$] · 0.5(CH$_3$OH) · H$_2$O (**5**)

A mixture of H_2pzda (0.0204 g, 0.1 mmol), $Co(OAc)_2 \cdot 4H_2O$ (0.0249 g, 0.1 mmol), 1,2-bis(4-pyridyl)ethane (0.0184 g, 0.1 mmol), NaOH aqueous solution, (0.3 mL, 0.65 mol/L), deionized water (5 mL) and 0.5 mL methanol was sealed in a Teflon-lined stainless steel vessel (25 mL) and heated at 100 °C for 4 days under autogeneous pressure and then cooled slowly to room temperature. The solution was filtered and allowed to stand for two months at room temperature. Orange-yellow needle crystals were obtained. Yield: 37%. *Anal.* Calc. for $C_{24.5}H_{28}Co_2N_6O_{13.5}$: C, 39.70; H, 3.78; N, 11.34. Found: C, 38.87; H, 4.23; N, 11.21%. IR (KBr pellet, cm^{-1}): 3446br, 1635vs, 1616vs, 1558m, 1541m, 1507w, 1448m, 1335s, 1195m, 1124m, 1062m, 935w, 788w.

2.2.6. Synthesis of [Co(pzda)(2,2′-bpy)(H$_2$O)] · 0.5H$_2$O (**6**)

A mixture of H_2pzda (0.0204 g, 0.1 mmol), $Co(OAc)_2 \cdot 4H_2O$ (0.0249 g, 0.1 mmol), 2,2′-bpy (0.0156 g, 0.1 mmol), deionized water (5 mL) and isopropyl alcohol (1 mL) was sealed in a Teflon-lined stainless steel vessel (25 mL) and heated at 140 °C for 4 days under autogenous pressure and then cooled slowly to room temperature. The solution was filtered and allowed to stand for four weeks at room temperature. Orange-red block crystals were obtained. Yield: 39%. *Anal.* Calc. for $C_{16}H_{13}CoN_4O_{5.50}$: C, 47.07; H, 3.21; N, 13.73. Found: C, 47.03; H, 3.24; N, 13.64%. IR (KBr pellet, cm^{-1}): 3425br, 1613vs, 1474m, 1442s, 1383s, 1193w, 1121m, 1058m, 1024w, 769m.

2.3. X-ray crystallography

Single-crystal X-ray diffraction measurements for the title complexes were carried out on a Bruker Smart 1000 CCD diffractometer, using graphite-monochromatized

Table 1
Crystallographic data and structure refinement for complexes **1**–**6**

	1	**2**	**3**	**4**	**5**	**6**
Chemical formula	$C_{18}H_{15}Nd_2N_6O_{16.5}$	$C_{18}H_{15}Eu_2N_6O_{16.5}$	$C_{19.5}H_{19}CoN_{4.25}O_{5.75}$	$C_{12}H_{10}Mn_2N_4O_{11}$	$C_{24.5}H_{28}Co_2N_6O_{13.5}$	$C_{16}H_{13}CoN_4O_{5.50}$
Formula weight	867.84	881.26	463.82	496.12	740.39	408.23
Temperature (K)	293(2)	293(2)	294(2)	294(2)	293(2)	293(2)
Crystal system	monoclinic	monoclinic	monoclinic	monoclinic	monoclinic	triclinic
Space group	$P2_1/n$	$P2_1/n$	$P2_1/c$	$C2/c$	$P2_1/c$	$P\bar{1}$
a (Å)	14.028(2)	13.898(19)	13.598(3)	19.214(9)	6.937(19)	7.083(12)
b (Å)	10.483 (15)	10.375(15)	16.375(4)	8.652(4)	18.474(5)	9.656(17)
c (Å)	18.144(3)	17.946(3)	10.267(2)	13.266(6)	24.379(7)	12.368(2)
α (°)	90	90	90	90	90	95.803(3)
β (°)	100.028(2)	99.717(2)	96.639(4)	132.06(3)	106.163(8)	94.547(3)
γ (°)	90	90	90	90	90	108.676(3)
V (Å^3)	2627.4(7)	2550.6(6)	2270.8(9)	1637.3(13)	3000.7(14)	791.6(2)
Z	4	4	4	4	4	2
F(000)	1668	1692	955	992	1516	416
ρ (Mg m^{-3})	2.194	2.300	1.357	2.013	1.639	1.713
μ (mm^{-1})	3.999	4.967	0.796	1.617	1.183	1.127
θ Range (°)	1.70–25.01	1.72–25.01	1.95–25.02	2.75–25.01	1.40–25.02	1.67–25.01
Reflections collected	13024	12306	10904	3944	14848	4067
Total independent, R_{int}	4625, 0.0670	4499, 0.0421	3954, 0.0873	1445, 0.0472	5296, 0.1114	2782, 0.0176
Goodness-of-fit on F^2	1.079	1.063	1.032	1.057	1.009	1.121
R indices [$I > 2\sigma(I)$]	$R_1 = 0.0439$, $wR_2 = 0.1139$	$R_1 = 0.0445$, $wR_2 = 0.1347$	$R_1 = 0.0641$, $wR_2 = 0.1435$	$R_1 = 0.0413$, $wR_2 = 0.1071$	$R_1 = 0.0604$, $wR_2 = 0.1126$	$R_1 = 0.0317$, $wR_2 = 0.0821$

Table 2
Selected bond lengths (Å) for complexes **1**–**6**

1					
Nd(1)–O(1)	2.573(5)	Nd(1)–O(13)	2.470(5)	Nd(2)–O(12)#4	2.423(5)
Nd(1)–O(3)	2.494(5)	Nd(1)–N(1)	2.616(6)	Nd(2)–O(4)#3	2.389(5)
Nd(1)–O(5)	2.516(5)	Nd(1)–N(3)	2.625(5)	Nd(2)–O(6)#2	2.381(5)
Nd(1)–O(7)	2.546(5)	Nd(2)–O(9)	2.501(5)	Nd(2)–O(14)	2.473(5)
Nd(1)–O(8)#1	2.464(5)	Nd(2)–O(11)	2.469(5)	Nd(2)–N(5)	2.577(6)
Nd(1)–O(10)	2.416(5)	Nd(2)–O(2)#5	2.478(4)		
2					
Eu(1)–O(1)	2.527(4)	Eu(1)–O(8)#1	2.439(5)	Eu(2)–O(2)#5	2.428(4)
Eu(1)–O(3)	2.454(5)	Eu(1)–N(1)	2.566(6)	Eu(2)–O(4)#3	2.348(4)
Eu(1)–O(5)	2.473(5)	Eu(1)–N(3)	2.561(5)	Eu(2)–O(6)#2	2.333(4)
Eu(1)–O(7)	2.489(5)	Eu(2)–O(9)	2.463(5)	Eu(2)–O(12)#4	2.380(4)
Eu(1)–O(10)	2.362(5)	Eu(2)–O(11)	2.430(5)	Eu(2)–N(5)	2.525(5)
Eu(1)–O(13)	2.420(5)	Eu(2)–O(14)	2.421(4)		
3					
Co(1)–O(1)	2.254(4)	Co(1)–O(2)#1	2.053(5)	Co(1)–N(3)	2.160(6)
Co(1)–O(3)	2.124(5)	Co(1)–N(1)	2.069(5)	Co(1)–N(4)#2	2.140(5)
4					
Mn(1)–O(1)	2.309(2)	Mn(1)–O(5)	2.317(2)	Mn(1)–O(1)#2	2.227(2)
Mn(1)–O(3)	2.463(2)	Mn(1)–O(6)	2.160(3)	Mn(1)–O(3)#1	2.138(2)
Mn(1)–N(1)	2.291(3)				
5					
Co(1)–O(7)	2.208(5)	Co(1)–N(4)	2.093(6)	Co(2)–O(5)	2.069(5)
Co(1)–O(9)	2.207(5)	Co(1)–N(5)	2.028(6)	Co(2)–O(6)	2.065(5)
Co(1)–O(11)	2.066(5)	Co(2)–O(3)	2.197(5)	Co(2)–N(1)	2.041(6)
Co(1)–O(12)	2.056(5)	Co(2)–O(1)	2.221(5)	Co(2)–N(3)	2.105(6)
6					
Co(1)–O(1)	2.22(2)	Co(1)–O(5)	2.15(2)	Co(1)–N(3)	2.10(2)
Co(1)–O(3)	2.15(2)	Co(1)–N(1)	2.06(2)	Co(1)–N(4)	2.10(2)

Symmetry transformations used to generate equivalent atoms. For **1** and **2**: #1 $-x+3/2, y-1/2, -z+1/2$; #2 $x+1/2, -y+1/2, z+1/2$; #3 $-x+1, -y, -z+1$; #4 $-x+3/2, y-1/2, -z+3/2$; #5 $-x+1, -y+1, -z+1$. For **3**: #1 $x, -y+3/2, z+1/2$; #2 $x+1, y, z$. For **4**: #1 $-x, y, -z+1/2$; #2 $-x, -y, -z+1$.

Mo Kα radiation ($\lambda = 0.7107$ Å). Semi-empirical absorption corrections were applied using the SADABS program [11]. All the structures were solved by direct methods and refined by full-matrix least squares on F^2 using the SHELXL-97 program [12]. All non-hydrogen atoms were refined anisotropically. The hydrogen atoms were generated geometrically and treated by a mixture of independent and or constrained refinement. The crystallographic data for **1**–**6** are listed in Table 1, and selected bond lengths (Å) are listed in Table 2.

3. Results and discussion

3.1. Description of the structures

3.1.1. Structural description of $[Nd_2(pzda)_3(H_2O)_2] \cdot 2.5H_2O$ (**1**) and $[Eu_2(pzda)_3(H_2O)_2] \cdot 2.5H_2O$ (**2**)

The single crystal X-ray diffraction determinations show that complexes **1** and **2** are isostructural. So only the structure of complex **2** will be discussed in detail. Complex **2** has a novel 3D metal-organic framework built up from a 1D tri-strand array which is a novel structural motif. In the asymmetric unit of **2**, there are two crystallographically independent Eu(III) ions, three pzda ligands and four and half water molecules. The extended asymmetric unit of Eu(III) ions is shown in Fig. 1. Eu1 is nine-coordinated with a N_2O_7 donor set; six oxygen atoms coming from the carboxylate groups of four different pzda ligands, the remaining oxygen atom from one coordinated water molecule, and two nitrogen atoms from two pzda ligands. The coordination environment of Eu1 can be described as distorted monocapped square-antiprismatic geometry. The Eu1–O bond lengths are in the range 2.362(5)–2.527(4) Å, and the Eu1–N bond lengths are 2.561(5) and 2.566(6) Å. Eu2 displays a distorted dodecahedral geometry with a NO_7 donor set; six oxygen atoms from five pzda ligands, one oxygen atom from one coordinated water molecule, and one nitrogen atom from a pzda ligand. The Eu2–O distances range from 2.333(4) to 2.463(5) Å, and the Eu2–N distance is 2.525(5) Å.

In complex **2**, each pzda ligand adopts a pentadentate mode to connect three Eu(III) ions (see Scheme 1a). One pyrazine nitrogen atom together with two adjacent carboxylate oxygen atoms are coordinated to one Eu(III) ion in a tridentate chelating mode (ONO), forming two five-membered rings. The remaining two oxygen atoms of the pzda ligand coordinate with other two Eu(III) ions, this kind of coordination mode has not been reported before.

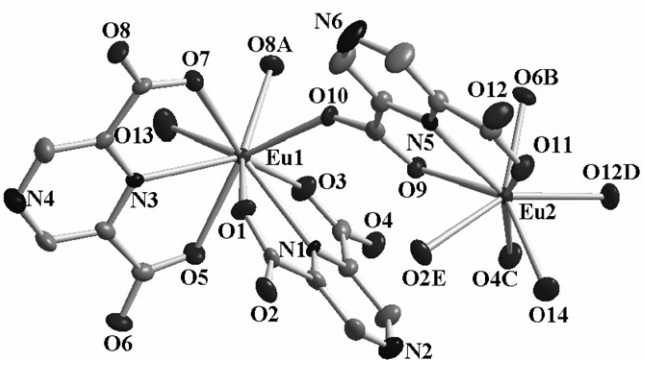


Fig. 1. Extended asymmetric unit of Eu(III) ions in **2** with 30% probability thermal ellipsoids. All the hydrogen atoms are omitted for clarity.

Based on this connection mode, each pzda ligand links three Eu(III) ions, and along the $[10\bar{1}]$ direction, the Eu(III) ions are bridged by pzda ligands to form a Eu–pzda–Eu chain. It is worth noticing that such single chains are interwoven to form a 1D tri-strand array in which the Eu(III) ions are the nodes. This may be contributed to the symmetric coordination mode of the pzda ligand coordinating to the lanthanide ion (see Fig. 2a). Such 1D tri-strand arrays are further connected by bridging carboxylates of the pzda ligands to generate a 3D coordination polymer (see Fig. 2b). To the best of our knowledge, this is the first example of a lanthanide-organic framework constructed from such a unique structural motif.

In complex **2**, there are various hydrogen bonds between the coordinated water and the free water molecules, between the water molecules and the carboxylate oxygen atoms, and between the water molecules and the pyrazine nitrogen atoms, further stabilizing the lanthanide-organic framework of **2**.

*3.1.2. Structural description of [Co(pzda)(bpe)] · 0.125(bpe) · 1.75H_2O (**3**)*

X-ray diffraction analysis shows that complex **3** crystallizes in the monoclinic $P2_1/c$ space group and has a 2D metal-organic framework. There is only one kind of metal

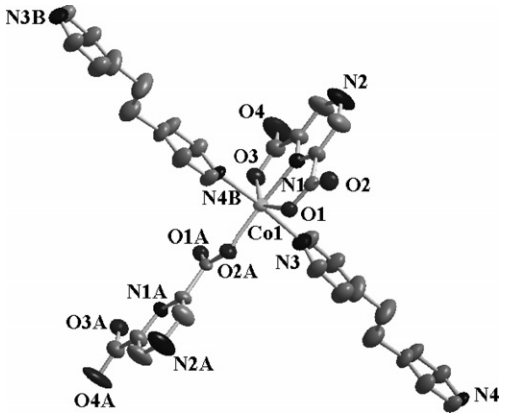


Fig. 3. The coordination environment of the Co(II) ion in complex **3** with 30% probability thermal ellipsoids. All hydrogen atoms are omitted for clarity.

environment in the complex. Each Co(II) ion is coordinated by three oxygen atoms and one nitrogen atom from two pzda ligands, and two nitrogen atoms from two bpe molecules. The coordination environment of the Co(II) ion is shown in Fig. 3.

In complex **3**, each pzda ligand adopts a tetradentate mode to connect two Co(II) ions, as shown in Scheme 1b. In this way, the pzda ligands bridge Co(II) metal centers to form an extended 1D Co–pzda polymeric chain along the *b*-axis. In the crystal of **3**, most bpe molecules are coordinated to Co(II) ions. Also two unit cells share one free bpe molecule. The coordinated bpe molecules are in the *trans*-mode and act as bridging ligands to join these 1D polymeric chains into a 2D rectangular grid-like layer structure with (4,4) topology and the dimension of the rectangular voids is about 5.520×13.598 Å^2, based on Co–Co distances (see Fig. 4a). In the same layer, the Co–pzda chains are arranged in the same fashion, while in the adjacent layers the Co–pzda chains are arranged in another fashion. Such 2D layers are arranged in an alternative sequence along the *c*-axis. The lattice water molecules link free bpe molecules via hydrogen bonds to form hydrogen-bonded chains and these are located between the layers

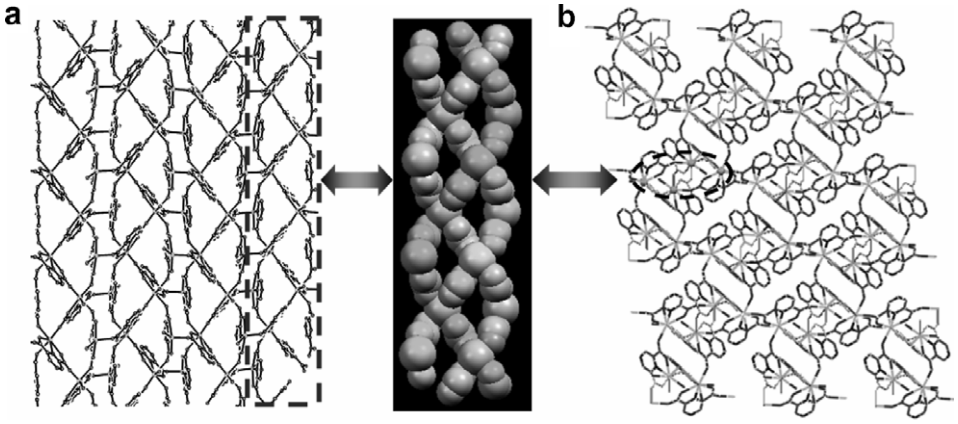


Fig. 2. (a) The 1D tri-strand array of **2** along the $[10\bar{1}]$ direction; (b) 3D metal-organic framework of **2** viewed along the *b*-axis.

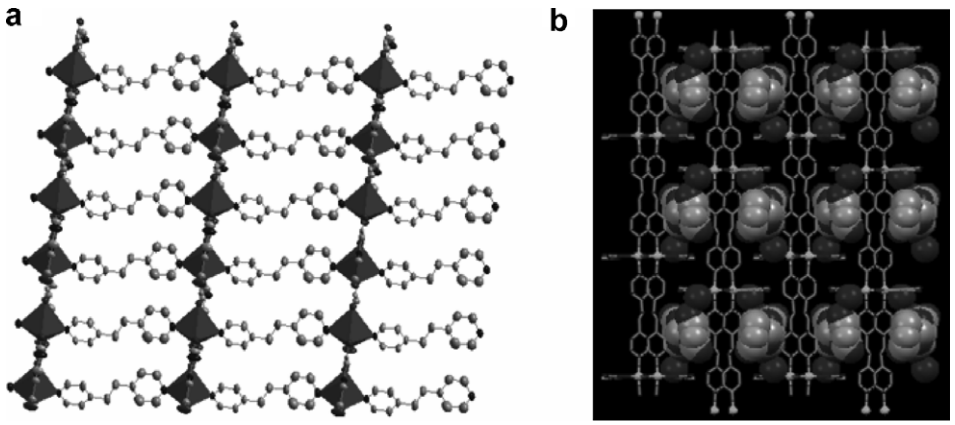


Fig. 4. (a) The 2D rectangular grid-like layer framework of **3** viewed along the *b*-axis; (b) 3D stacking diagram of **3** viewed along the *c*-axis. The space-filling models represent free water and free bpe molecules.

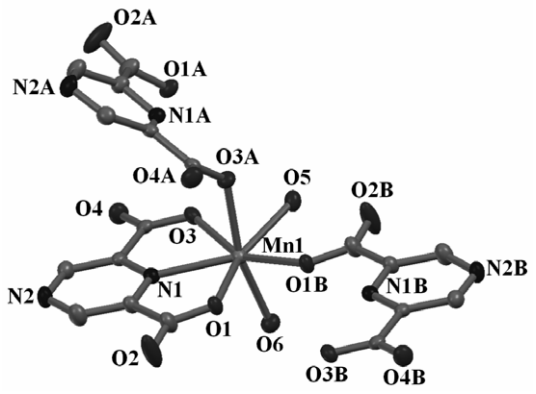


Fig. 5. The coordination environment of the Mn(II) ion in **4** with 30% probability thermal ellipsoids. All hydrogen atoms are omitted for clarity.

(see Fig. 4b). The lattice water molecules are also connected to the 2D metal-organic framework through hydrogen bonds with the coordinated or uncoordinated carboxylate oxygen atoms, and thus a 3D supramolecular network is formed.

3.1.3. Structural description of $[Mn(pzda)(H_2O)_{1.5}]$ (**4**)

The crystal structure of **4** reveals that the complex crystallizes in the monoclinic $C2/c$ space group and consists of 1D Mn–pzda chains. The Mn(II) ion is seven-coordinated to four oxygen atoms and one nitrogen atom from three pzda ligands, and two oxygen atoms from two water molecules (see Fig. 5), displaying a distorted pentagonal bipyramidal geometry. The equatorial plane is occupied by four oxygen atoms and one nitrogen atom, with a maximum deviation of 0.0085 Å. The axial sites are occupied by two oxygen atoms (O3A, O6), the angle O3A–Mn1–O6 being 164.04(9)°.

In **4**, the pzda ligand adopts another pentadentate mode (see Scheme 1c) to link three Mn(II) ions. One pyrazine nitrogen atom together with two adjacent carboxylate oxygen atoms coordinate one Mn(II) ion in the ONO mode. Simultaneously, both the two oxygen atoms act as μ_2-O bridges to connect the other two Mn(II) ions, the other oxygen atom of each carboxylate group of the pzda ligand remains uncoordinated. This is the first example of this kind of coordination mode for the pzda ligand. In this way, Mn(II) ions are linked to form a 1D polymeric $(–Mn–O–)_n$ zigzag chain via oxygen bridges (see Fig. 6a), which is different from the reported 1D coordination polymer featuring a head-to-tail arrangement of the pzda ligand bound to Zn(II) or Cu(II) ions, reported by Leciejewic [8f] and MacDonald. [8i] In these chains of **4**, apart from the carboxylate μ_2-O bridge (the Mn···Mn distance is 3.718 Å), there is a water μ_2-O bridge (the Mn···Mn distance is 3.340 Å), which locates the pzda ligands in different planes.

It is worth noting that in **4** the N atom in the 4-position of the pyrazine ring of the pzda ligand is not coordinated to the Mn(II) ion, which leads to the formation of hydrogen bonds with water molecules. The hydrogen bonds present strong intermolecular interactions to link these 1D polymeric chains into a 2D supramolecular layer structure, which consists of hydrogen-bonded double-stranded helical chains, as shown in Fig. 6b.

3.1.4. Structural description of $[Co_2(pzda)_2(bpe)(H_2O)_4] \cdot 0.5(CH_3OH) \cdot H_2O$ (**5**)

Under similar reaction conditions to complex **3**, except that the amount of NaOH added was different, complex **5** was obtained, but the structures of **3** and **5** are different. Complex **5** crystallizes in the monoclinic $P2_1/c$ space group and is a 0D binuclear molecule. There are two crystallographically independent Co(II) ions in the asymmetric unit and the two Co(II) ions are bridged by the bpe spacer and blocked by the pzda ligand, forming a dimeric unit. The coordination environments of the Co(II) ions are shown in Fig. 7. The two Co(II) ions are both six-coordinated and each Co(II) ion links one pzda ligand, two water molecules and one bpe molecule. The average Co–O distance is 2.134(5) Å for Co1 and 2.138(5) Å for Co2. The average Co–N distance is 2.061(6) Å for Co1 and 2.073(6) Å for Co2. The O(11)–Co(1)–O(12) angle is 177.3(2)°, and the

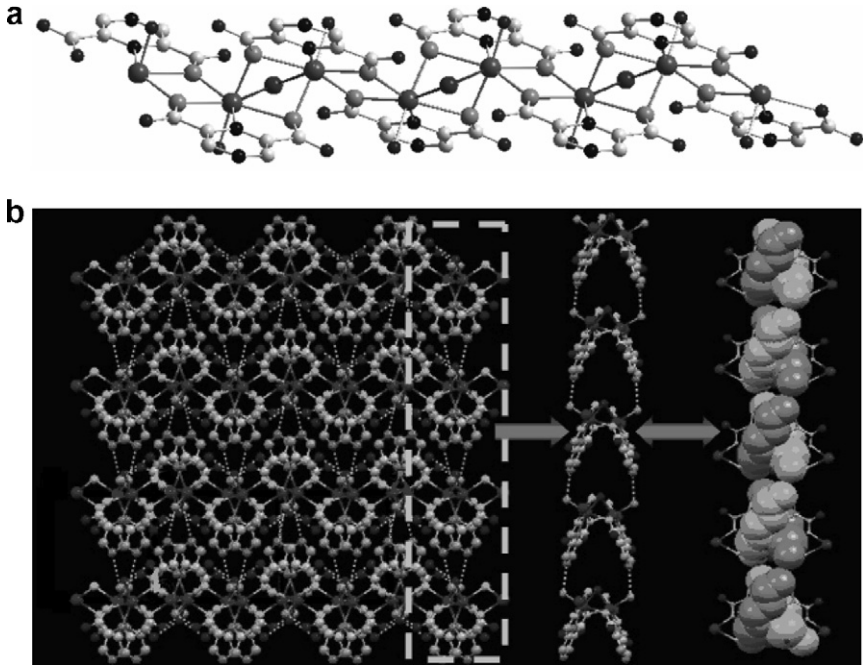


Fig. 6. (a) 1D chain structure of **4** viewed along the *b*-axis; (b) 2D supramolecular layer network of **4** and the hydrogen-bonded double-stranded helical chain.

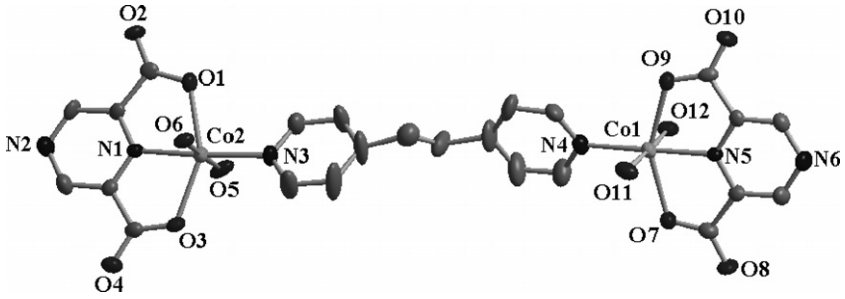


Fig. 7. The coordination environment of Co(II) ions in **5** with 30% probability thermal ellipsoids. All hydrogen atoms are omitted for clarity.

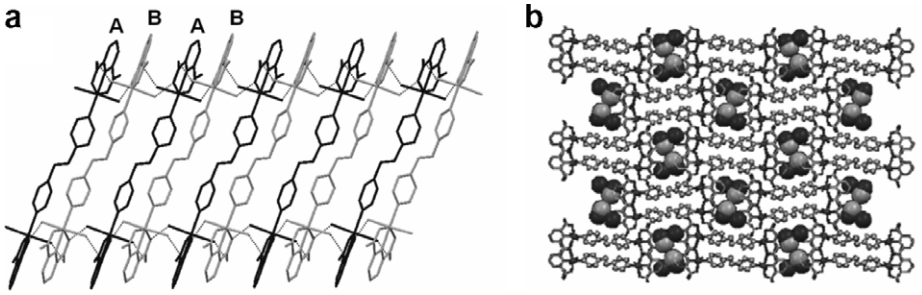


Fig. 8. (a) 1D supramolecular chain of **5** formed via hydrogen bonding along the *b*-axis; (b) 3D supramolecular structure viewed along the *a*-axis. The space-filling models represent free water and methanol molecules.

O(5)–Co(2)–O(6) angle is 177.1(2)°. So the coordination environments of the two Co(II) ions are slightly different.

In the dimer of **5**, two pzda ligands both adopt a tridentate mode (ONO) to coordinate Co(II) ions (see Scheme 1d), the bpe molecule adopts a trans configuration to bridge the two Co(II) ions and the dihedral angle of the two pyridine rings is 74.1°. Each dimer unit is linked with two neighbors by hydrogen bonds between the coordinated water molecules and the carboxylate oxygen atoms of the pzda ligand to afford a 1D hydrogen-bonded chain along the *b*-axis (see Fig. 8a). In these chains, two adjacent binuclear units are in two different layers which are labelled as A and B. These chains are packed alternatively by the hydrogen bonds between the coordinated water molecules

and the coordinated carboxylate oxygen atoms or the uncoordinated carboxylate oxygen atoms of the pzda ligand to afford a 3D supramolecular architecture, as shown in Fig. 8b. Free water and methanol molecules reside in the lattices and form hydrogen bonds with the uncoordinated carboxylate oxygen atoms or uncoordinated nitrogen atoms of the pyrazine ring, which stabilizes the structure of **5**.

3.1.5. Structural description of $[Co(pzda)(2,2'\text{-bpy})(H_2O)]\cdot 0.5H_2O$ (6)

To compare with the binuclear structure of **5**, we replaced the bridging ligand bpe by the terminal ligand 2,2′-bpy, and the mononuclear molecule **6** was obtained. Complex **6** crystallizes in the triclinic $P\bar{1}$ space group and consists of one crystallographically independent Co(II) ion, which is bonded to two oxygen atoms and one nitrogen atom from one pzda ligand, two nitrogen atoms of one 2,2′-bpy molecule, and one oxygen atom from one water molecule. The coordination environment of Co(II) ion is shown in Fig. 9a. The Co–O distances range from 2.150(16) to 2.215(17) Å, and the Co–N distances range from 2.056(18) to 2.103(19) Å.

In complex **6**, the pzda ligand adopts a tridentate mode (ONO) (see Scheme 1d), which is coordinated to one Co(II) ion to form a mononuclear unit. There are two different kinds of interactions that lead to the formation of a 3D supramolecular architecture: hydrogen bonds and π–π stacking interactions. The water molecules form three kinds of hydrogen bonds. The first involves hydrogen bonds between the coordinated water molecules and the uncoordinated carboxylate oxygen atoms such as (O5–H5···O2). The second involves hydrogen bonds between the coordinated water molecules and the uncoordinated pyrazine nitrogen atoms such as (O5–H5···N2). Finally, the lattice water molecules form hydrogen bonds with the uncoordinated carboxylate oxygen atoms such as (O6–H6···O4), which act as hydrogen-bonded bridges together with the former two kinds of hydrogen bonds. Together with the π–π stacking interactions between the 2,2′-bpy molecules, with distances of 3.405 and 3.463 Å, these make the mononuclear units form a 3D supramolecular structure (see Fig. 9b). Free water molecules reside in the voids and connect the network via hydrogen bonds.

3.2. Thermal stability of the complexes

The thermal stability of complexes **1**, **2** and **5** was investigated by thermogravimetric analysis. As observed from the TG curves, the thermal decomposition processes of **1** and **2** are similar. Taking **1** as an example, a weight loss of 9.76% occurred between 53 and 183 °C, corresponding to the release of four and half water molecules (calculated: 9.19%). Then no weight loss occurred until ca. 426 °C, showing a plateau, which indicates that the metal-organic framework is thermally stable. The framework collapsed above the temperature 426 °C. The TG curve of **5** revealed a weight loss of 14.31% between 48 and 149 °C, corresponding to the loss of five water molecules and half a methanol molecule (calculated: 13.28%). A plateau was observed from 149 to 258 °C, indicating no further weight loss, and above 258 °C the complex started to decompose rapidly.

4. Comparison of structures

Six new metal complexes with the pzda ligand were obtained by the hydro(solvo)thermal method. The X-ray crystallographic analyses indicate that these complexes have different structures. They span zero-, one-, two- and three-dimensions. In a comparison of the structures of **1**–**6**, it is found that because of the versatile coordination sites, there are several coordination modes for the pzda ligand to bind the metal ions. Also the coordination modes of the pzda ligand have a very significant effect on the formation and structure of the complexes. In complexes **1** and **2**, in order to meet the requirements of larger radii and higher coordination number of the lanthanide ions, the

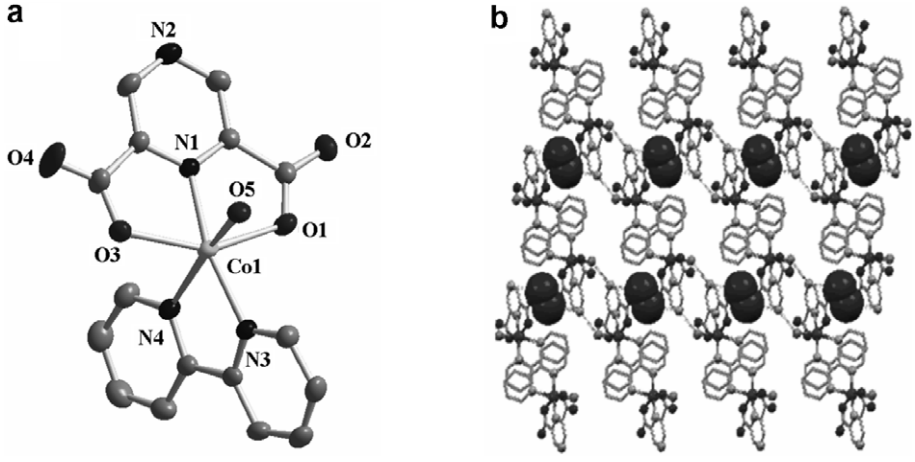


Fig. 9. (a) The coordination environment of the Co(II) ion in **6** with 30% probability thermal ellipsoids. All hydrogen atoms are omitted for clarity; (b) 3D supramolecular network of **6** viewed along the *a*-axis. The space-filling models represent free water molecules.

pzda ligand adopts a pentadentate mode to link the Nd(III) ion (or Eu(III) ion) into a 3D metal-organic framework containing a 1D tri-strand array. In complex **3**, the pzda ligand adopts a tetradentate mode to bind the Co(II) ion cooperatively with a bpe ligand to form a 2D metal-organic framework with (4,4) topology. In complex **4**, the pzda ligand adopts another pentadentate mode to link a Mn(II) ion, which is different from that of **1** and **2**, as shown in Scheme 1c. Two μ_2-O atoms of the carboxylate groups of pzda together with water μ_2-O link three Mn(II) ions into a 1D coordination polymer. It is different from the previously reported Mn–pzda complex ($[Mn(pzda)(H_2O)_2]$),[8b] in which the coordination mode is shown in Scheme 1g. In complexes **5** and **6**, the pzda ligand adopts a tridentate chelating (ONO) mode to coordinate metal ions, forming 0D structures in which the pzda ligand acts as a terminal ligand, but because of the existence of different auxiliary ligands, the structures of **5** and **6** are also different. For complex **5**, bpe is a bridging ligand, connecting Co–pzda units into a binuclear structure. While in **6**, 2,2′-bpy is a terminal ligand, which results in the formation of a mononuclear molecule.

The pH of the reaction mixture also plays an important role in the architectures of complexes **3** and **5**. **3** has a 2D metal-organic framework with (4, 4) topology in which the pzda ligand adopts a tetradentate mode. While **5** is a binuclear molecule, which is further assembled by hydrogen bonds to form a 3D supramolecular structure. This may be attributed to the different pH value, resulting in the different roles for water molecules in **3** and **5**, and thus different coordination modes of pzda, making the coordination number for the Co(II) ions the same. From the above discussion, we can conclude that the higher multidentate modes of the pzda ligand benefit the formation of higher dimensional metal-organic frameworks, while the single tridentate chelating ONO mode of the pzda ligand favors the formation of the 0D structure.

5. Conclusions

Six new complexes with 0D, 1D, 2D and 3D structures using the pzda ligand were obtained under hydro(solvo)thermal conditions. The assembly of structural versatility for the title complexes reveals that the metal ions and the coordination modes of the pzda ligand have a significant effect on the formation and dimensionality of the resulting complexes. The single ONO mode benefits the formation of a 0D structure and the uncoordinated oxygen and nitrogen atoms of the pzda ligand tend to form hydrogen bonds, resulting in a higher dimensional supramolecular structure. The higher multiple dentate mode of pzda together with a larger radius and high coordination number of metal ions, such as the lanthanide (III) ions in complexes **1** and **2**, is available to form 3D MOFs.

Compared with metal pyridine-2,6-dicarboxylate complexes, which show interesting structures and unique properties [6a,6b,6c], metal complexes of pyrazine-2,6-dicarboxylic acid are underdeveloped. Also, the latter ligand has more coordination sites than the former due to the nitrogen atom at the 4-position of the pyrazine ring. Therefore the chemistry of metal pyrazine-2,6-dicarboxylate complexes is a challenge and thus is promising.

Acknowledgements

The authors gratefully acknowledge the financial support from the National Natural Science Foundation of China (20331010, 20501003) and the Natural Science Foundation of Beijing (2073022).

Appendix A. Supplementary material

CCDC 652218, 652219, 652220, 652221, 652222, and 652223 contain the supplementary crystallographic data for **1**, **2**, **6**, **4**, **3**, and **5**. These data can be obtained free of charge via http://www.ccdc.cam.ac.uk/conts/retrieving.html, or from the Cambridge Crystallographic Data Centre, 12 Union Road, Cambridge CB2 1EZ, UK; fax: (+44) 1223-336-033; or e-mail: deposit@ccdc.cam.ac.uk. Supplementary data associated with this article can be found, in the online version, at doi:10.1016/j.poly.2007.11.012.

References

[1] (a) M. Eddaoudi, J. Kim, N. Rosi, D. Vodak, J. Wachter, M. O'Keeffe, O.M. Yaghi, Science 295 (2002) 469;
(b) O.M. Yaghi, H. Li, C. Davis, D. Richardson, T.L. Groy, Acc. Chem. Res. 31 (1998) 474.
[2] (a) K.S. Min, M.P. Suh, Chem. Eur. J. 7 (2001) 303;
(b) K. Uemura, S. Kitagawa, M. Kondo, K. Fukui, R. Kitaura, H.C. Chang, T. Mizutani, Chem. Eur. J. 8 (2002) 3586;
(c) D.N. Dybtsev, H. Chun, S.H. Yoon, D. Kim, K. Kim, J. Am. Chem. Soc. 126 (2004) 32.
[3] (a) O. Kahn, Acc. Chem. Res. 33 (2000) 647;
(b) Y.G. Li, N. Hao, E.B. Wang, Y. Lu, C.W. Hu, L. Xu, Eur. J. Inorg. Chem. (2003) 2567;
(c) E.Q. Gao, S.Q. Bai, Z. He, C.H. Yan, Inorg. Chem. 44 (2005) 677;
(d) H. Oshio, M. Nihei, S. Koizumi, T. Shiga, H. Nojiri, M. Nakano, N. Shirakawa, M. Akatsu, J. Am. Chem. Soc. 127 (2005) 4568;
(e) A.J. Tasiopoulos, W. Wernsdorfer, K.A. Abboud, G. Christou, Angew. Chem., Int. Ed. 43 (2004) 6338;
(f) G. Rajaraman, M. Musugesu, E.C. Sanudo, M. Soler, W. Wernsdorfer, M. Helliwell, C. Muryn, J. Raftery, S.J. Teat, G. Christou, E.K. Brechin, J. Am. Chem. Soc. 126 (2004) 15445;
(g) D.J. Price, S.R. Batten, B. Moubaraki, K.S. Murray, Chem. Commun. (2002) 762;
(h) S. Wang, M.S. Wemple, H.L. Tsai, K. Folting, J.C. Huffman, K.S. Hagen, D.N. Hendrickson, G. Christou, Inorg. Chem. 39 (2000) 1501;
(i) H. Andres, R. Basler, H.U. Gudel, G. Aromi, G. Christou, H. Buttner, B. Ruffle, J. Am. Chem. Soc. 122 (2000) 12469.
[4] (a) A.Y. Robin, K.M. Fromm, Coord. Chem. Rev. 250 (2006) 2127;
(b) M.W. Hosseini, Acc. Chem. Res. 38 (2005) 313;
(c) M.W. Hosseini, Coord. Chem. Rev. 240 (2003) 157;
(d) R.Q. Fang, X.M. Zhang, Inorg. Chem. 45 (2006) 4801;
(e) J.N. Mathur, P. Thakur, C.J. Dodge, A.J. Francis, G.R. Choppin, Inorg. Chem. 45 (2006) 8026;
(f) P. Kitiphaisalnont, S. Thohinung, P. Hanmungtum, N. Chaichit, S. Patrarakorn, S. Siripaisarnpipat, Polyhedron 25 (2006) 2710;

(g) M. Remko, B.M. Rode, J. Phys. Chem. A 110 (2006) 960;
(h) M. Matzapetakis, M. Kourgiantakis, M. Dakanali, C.P. Raptopoulou, A. Terzis, A. Lakatos, T. Kiss, I. Banyai, L. Iordanidis, T. Mavromoustakos, A. Salifoglou, Inorg. Chem. 40 (2001) 1734;
(i) M. Tsaramyrsi, M. Kaliva, A. Salifoglou, C.P. Raptopoulou, A. Terzis, V. Tangoulis, J. Giapintzakis, Inorg. Chem. 40 (2001) 5772;
(j) Y.B. Go, X.Q. Wang, E.V. Anokhina, A.J. Jacobson, Inorg. Chem. 44 (2005) 8265;
(k) L. Pan, T. Frydel, M.B. Sander, X.Y. Huang, J. Li, Inorg. Chem. 40 (2001) 1271.

[5] (a) S.R. Batten, B.F. Hoskins, R. Robson, J. Am. Chem. Soc. 117 (1995) 5385;
(b) G.B. Gardner, D. Venkataraman, J.S. Moore, S. Lee, Science 374 (1995) 792;
(c) B.F. Hoskins, R. Robson, J. Am. Chem. Soc. 112 (1990) 1546;
(d) C.S. Liu, X.S. Shi, J.R. Li, J.J. Wang, X.H. Bu, Cryst. Growth Des. 6 (2006) 656.

[6] (a) B. Zhao, P. Cheng, Y. Dai, C. Cheng, D.Z. Liao, S.P. Yan, Z.H. Jiang, G.L. Wang, Angew. Chem., Int. Ed. 42 (2003) 934;
(b) B. Zhao, P. Cheng, X.Y. Chen, C. Cheng, W. Shi, D.Z. Liao, S.P. Yan, Z.H. Jiang, J. Am. Chem. Soc. 126 (2004) 3012;
(c) B. Zhao, H.L. Gao, X.Y. Chen, P. Cheng, W. Shi, D.Z. Liao, S.P. Yan, Z.H. Jiang, Chem. Eur. J. 12 (2006) 149;
(d) S.O.H. Gutschke, A.M.Z. Slawin, P.T. Wood, Chem. Commun. (1995) 2179;
(e) D.W. Min, S.S. Yoon, D.Y. Lee, Y.J. Kim, W.S. Han, S.W. Lee, Inorg. Chim. Acta 324 (2001) 293;
(f) Y.L. Wei, H.W. Hou, L.K. Li, Y.T. Fan, Y. Zhu, Cryst. Growth Des. 5 (2005) 1405;
(g) M.B. Zhang, J. Zhang, S.T. Zheng, G.Y. Yang, Angew. Chem., Int. Ed. 44 (2005) 1385.

[7] (a) P. Mahata, S. Natarajan, Eur. J. Inorg. Chem. (2005) 2156;
(b) Y.L. Wang, D.Q. Yuan, W.H. Bi, X. Li, X.J. Li, F. Li, R. Cao, Cryst. Growth Des. 5 (2005) 1849;
(c) R.Q. Zou, L. Jiang, H. Senoh, N. Takeichi, Q. Xu, Chem. Commun. (2005) 3526.

[8] (a) F.Q. Wang, X.J. Zheng, Y.H. Wan, C.Y. Sun, Z.M. Wang, K.Z. Wang, L.P. Jin, Inorg. Chem. 46 (2007) 2956;
(b) F.Q. Wang, X.J. Zheng, Y.H. Wan, K.Z. Wang, L.P. Jin, J. Mol. Struct. 798 (2006) 155;
(c) F.Q. Wang, W.J. Zhuang, L.P. Jin, J. Mol. Struct. 83 (2007) 48;
(d) F.Q. Wang, D.F. Weng, X.J. Zheng, J.J. Zhang, H. Ma, L.P. Jin, Inorg. Chim. Acta 360 (2007) 29;
(e) W. Starosta, H. Ptasiewicz-Bak, J. Leciejewicz, J. Coord. Chem. 57 (2004) 167;
(f) M. Gryz, W. Starosta, J. Leciejewicz, J. Coord. Chem. 56 (2003) 1575;
(g) W. Starosta, H. Ptasiewicz-Bak, J. Leciejewicz, J. Coord. Chem. 56 (2003) 677;
(h) H. Ptasiewicz-Bak, J. Leciejewicz, J. Coord. Chem. 56 (2003) 173;
(i) M.V. Yigit, Y. Wang, B. Moulton, J.C. MacDonald, Cryst. Growth Des. 6 (2006) 829.

[9] (a) C.Y. Sun, S. Gao, L.P. Jin, Eur. J. Inorg. Chem. (2006) 2411;
(b) B. Gómez-Lor, M. Gutiérrez-Puebla, M.A. Iglesias, E. Monge, C. Ruiz-Valero, N. Snejko, Chem. Mater. 17 (2005) 2568;
(c) F. Li, Z. Ma, Y.L. Wang, R. Cao, W.H. Bi, X. Li, CrystEngComm 7 (2005) 569;
(d) B.H. Ye, M.L. Tong, X.M. Chen, Coord. Chem. Rev. 249 (2005) 545;
(e) X.L. Wang, C. Qin, E.B. Wang, L. Xu, Z.M. Su, C.W. Hu, Angew. Chem., Int. Ed. 43 (2004) 5036;
(f) N. Hao, E.H. Shen, Y.G. Li, E.B. Wang, C.W. Hu, L. Xu, Eur. J. Inorg. Chem. (2004) 4102;
(g) L.Y. Zhang, G.F. Liu, S.L. Zheng, B.H. Ye, X.M. Zhang, X.M. Chen, Eur. J. Inorg. Chem. (2003) 2965;
(h) T.K. Maji, M. Ohba, S. Kitagawa, Inorg. Chem. 44 (2005) 9225.

[10] (a) F. Weygand, Chem. Ber. 73 (1940) 1259;
(b) F. Weygand, C. Bergmann, Chem. Ber. 80 (1947) 255;
(c) H.I.X. Mager, W. Berends, Recueil 77 (1958) 827.

[11] G.M. Sheldrick, SADABS, Program for Empirical Absorption Correction of the Area Detector Data, University of Göttingen, Germany, 1997.

[12] (a) G.M. Sheldrick, SHELXS-97, Program for Crystal Structure Solution, University of Göttingen, Germany, 1997;
(b) G.M. Sheldrick, SHELXL-97, Program for Crystal Structure Refinement, University of Göttingen, Germany, 1997.

Available online at www.sciencedirect.com
ScienceDirect
Polyhedron 27 (2008) 727–733
POLYHEDRON
www.elsevier.com/locate/poly

Syntheses, crystal structure and spectroscopic characterization of novel 1,2-bis(diphenylphosphine)ethane-(*N*-R-sulfonyldithiocarbimato)nickel(II) complexes

Marcelo R.L. Oliveira [a,*], Jorge Amim Jr [a], Ivan A. Soares [a], Vito M. De Bellis [b], Carlos Alberto de Simone [c], Celice Novais [d], Silvana Guilardi [d]

[a] *Departamento de Química, Universidade Federal de Viçosa, Viçosa MG, CEP 36571-000, Brazil*
[b] *Departamento de Química, Instituto de Ciências Exatas, Universidade Federal de Minas Gerais, Belo Horizonte MG, CEP 31270-901, Brazil*
[c] *Departamento de Química, Universidade Federal de Alagoas, Maceió AL, CEP 57072-970, Brazil*
[d] *Instituto de Química, Universidade Federal de Uberlândia, Uberlândia MG, CEP 38408-100, Brazil*

Received 26 July 2007; accepted 1 November 2007

Abstract

Three new complexes of the general formula: [Ni($RSO_2N{=}CS_2$)(dppe)], where R = CH_3 (**1**), CH_3CH_2 (**2**), 2-$CH_3C_6H_4$ (**3**) and dppe = 1,2-bis(diphenylphosphine)ethane, were obtained in crystalline form by the one-pot reaction of the appropriate potassium *N*-R-sulfonyldithiocarbimate: $RSO_2N{=}CS_2K_2 \cdot 2H_2O$ and 1,2-bis(diphenylphosphine)ethane with nickel(II) chloride hexahydrate in ethanol/water mixture. The complex **1** forms monoclinic crystals ($P2_1/c$) with two molecules in the asymmetric unit ($Z = 8$), while the crystals of the complexes **2** and **3** are orthorhombic, *Pbca* ($Z = 8$) and $P2_12_12_1$ ($Z = 4$) respectively, with one molecule in the asymmetric unit. All complexes present a distorted square-planar environment around the Ni atom. The elemental analyses and the IR, ^{1}H NMR, ^{13}C NMR and ^{31}P NMR spectra are consistent with the formation of the nickel(II) complexes with mixed ligands.
© 2007 Elsevier Ltd. All rights reserved.

Keywords: Dithiocarbimates; 1,2-bis(Diphenylphosphine)ethane; Nickel complexes; Crystal structure

1. Introduction

Dithiocarbamate derivatives show a wide range of applications. For example, they are very active accelerators in vulcanization [1–3] and many dithiocarbamates, anions and complexes, show biological activity and are used as fungicides [1,4].

Many authors have investigated complexes of nickel(II) with diphosphines. These systems are quite attractive in view of their importance as precursors in catalytic reactions [5]. Complexes containing the $NiXS_2P$ chromophore (X = halide, S_2 = dithiocarbamate, P = phosphine) are usually obtained by reacting NiX_2 with dithiocarbamates and PR_3 (R = alkyl/aryl) [6]. Nickel(II) dithiocarbamates normally react with phosphines to form complexes with the NiS_2P_2 chromophore [7–12].

Some nickel complexes with dithiocarbimates and phosphines with general formulae [Ni(R′N=CS_2)(PR_3)$_2$] (R and R′ = alkyl/aryl) have been obtained [13]. However, only the nickel complexes with general formulae [Ni($RSO_2N{=}CS_2$)(PPh_3)$_2$] with R = 2-$CH_3C_6H_4$, 4-$CH_3C_6H_4$ and 4-BrC_6H_4 [14] and with R = 2,5-$Cl_2C_6H_3$ [15] have had their structures determined by X-ray diffraction techniques.

We decided to study dithiocarbimato complexes due to their similarities with the dithiocarbamate compounds. As part of these studies three new nickel(II)-dithiocarbimato-diphosphine complexes of the general formula: [Ni($RSO_2N{=}CS_2$)(dppe)], where R = CH_3 (**1**), CH_3CH_2

* Corresponding author. Tel.: +55 31 3899 3059; fax: +55 31 3899 3065.
E-mail address: marcelor@ufv.br (M.R.L. Oliveira).

0277-5387/$ - see front matter © 2007 Elsevier Ltd. All rights reserved.
doi:10.1016/j.poly.2007.11.001

(**2**), 2-$CH_3C_6H_4$(**3**) and dppe = 1,2-bis(diphenylphosphine)-ethane, were obtained in crystalline form by the reaction of $NiCl_2 \cdot 6H_2O$ with the diphosphine and dithiocarbimate anions derived from sulfonamides. The complexes here studied are the first examples of nickel(II)–sulfonyldithiocarbimato–diphosphine complexes prepared and characterized by single crystal X-ray diffraction techniques. The compounds were also characterized by IR, ^1H, ^{13}C and ^{31}P NMR and elemental analyses for C, H, N and Ni.

2. Experimental

2.1. Methods and materials

The solvents were purchased from Merck and used without further purification. The sulfonamides, nickel(II) chloride hexahydrate and 1,2-bis(diphenylphosphine)ethane were purchased from Aldrich. Carbon disulfide and potassium hydroxide were purchased from Vetec. The *N*-R-sulfonyldithiocarbimate potassium salts dihydrate were prepared in dimethylformamide from sulfonamides analogously as described in the literature [16]. Melting points were determined with a Mettler FP5 equipment. Microanalyses for C, H and N were obtained from a Perkin–Elmer 2400 CHN. Nickel was analysed by atomic absorption with a Hitachi Z-8200 Atomic Absorption Spectrophotometer. The IR spectra were recorded with a Perkin–Elmer 283 B infrared spectrophotometer using KBr pellets and nujol mulls between CsI plates. The ^1H (400 MHz), ^{13}C (100 MHz) and ^{31}P (162 MHz) NMR spectra of the complexes were recorded at 300 K on a Bruker Advance RX-400 spectrophotometer in $CDCl_3$ with TMS (H_3PO_4 for ^{31}P NMR spectra) as internal standard. Additionally, the ^{31}P (162 MHz) NMR spectra were recorded at 240 K.

2.2. Syntheses

The compounds were prepared according to the methodology applied for the syntheses of similar compounds with triphenylphosphine [14] (Scheme 1).

A solution of potassium *N*-R-sulfonyldithiocarbimate dihydrate (1.0 mmol) in water (10 mL) was added to a solution of 1,2-bis(diphenylphosphine)ethane (1.0 mmol) in ethanol (40 mL). Nickel(II) chloride hexahydrate (1.0 mmol) was added to the suspension and the reaction mixture was stirred for 5 h at room temperature. The colour of the suspension changed from green to orange/red. The solid product of the reaction was filtered, washed with distilled water and ethanol, and dried under reduced pressure for one day yielding [Ni($RSO_2N{=}CS_2$)(dppe)] (ca. 70%). Suitable crystals for X-ray structure analysis were obtained after slow evaporation of solutions of the compounds in dichloromethane/ethanol and few drops of water.

2.2.1. [Ni($CH_3SO_2N{=}CS_2$) (dppe)] (**1**)

Elemental *Anal.* Calc. C, 53.69; H, 4.34; N, 2.24; Ni, 9.37. Found C, 53.41; H, 4.46; N, 2.26; Ni, 9.40%. M.p. with decomposition (°C): 227.3–229.5. IR (most important bands) (cm^{-1}): 1463 ν(C=N); 1283 ν_{ass} (SO_2); 1128 ν_{sym} (SO_2); 923 ν_{ass} (CS_2) and 374 ν(NiS). ^1H NMR (δ), *J* (Hz): 7.79–7.69 (m, 8H, H2 and H6 of the aromatic rings); 7.56–7.43 (m, 12H, H3, H4 and H5 of the aromatic rings); 3.03 (s, 3H, CH_3) and 2.36 (d, 4H, $J_{HP} = 17$, CH_2CH_2). $^{13}C\{^1H\}$ NMR (δ), *J*(Hz): 198.67 (N=CS_2); 42.05 (CH_3). dppe signals: 132.91 (t, $J_{CP} = 5.4$, C2 and C6); 131.88 (s, C4); 129.41 (t, $J_{CP} = 5.2$, C3 and C5); 128.23 (t, $J_{CP} = 23$, C1); 26.10 (t, $J_{CP} = 23$, CH_2CH_2). ^{31}P NMR (300 K) (δ): 57.31 (s). ^{31}P NMR (240 K) (δ), *J* (Hz): 58.62 (d, $J_{PP} = 40.5$, P1); 57.78 (d, $J_{PP} = 40.5$, P2).

2.2.2. [Ni($CH_3CH_2SO_2N{=}CS_2$)(dppe)] (**2**)

Elemental *Anal.* Calc. C, 54.39; H, 4.56 N, 2.19; Ni, 9.17. Found: C, 52.49; H, 4.36; N, 2.09; Ni, 9.00%. M.p. with decomposition (°C): 217.0–219.0. IR (most important bands) (cm^{-1}): 1463 ν(C=N); 1275 ν_{ass} (SO_2); 1121 ν_{sym} (SO_2); 920 ν_{ass} (CS_2) and 344 ν(NiS). ^1H NMR (δ), *J* (Hz): 7.78–7.72 (m, 8H, H2 and H6 of the aromatic rings); 7.59–7.44 (m, 12H, H3, H4 and H5 of the aromatic rings); 3.12 (q, 2H, $J = 7.5$ CH_2SO_2); 2.36 (d, 4H, $J_{HP} = 17$, CH_2CH_2); 1.38 (t, 3H, $J = 7.5$ CH_3). $^{13}C\{^1H\}$ NMR (δ), *J* (Hz): 198.32 (N=CS_2); 48.65 (CH_2SO_2); 8.20 (CH_3). dppe signals: 132.88 (t, $J_{CP} = 5.7$, C2 and C6); 131.81 (s, C4); 129.36 (t, $J_{CP} = 5.2$, C3 and C5); 128.21 (t, $J_{CP} = 21$, C1); 25.94 (t, $J_{CP} = 23$, CH_2CH_2). ^{31}P NMR (300 k) (δ): 57.18 (s). ^{31}P NMR (240 k) (δ),*J* (Hz): 58.64 (d, $J_{PP} = 40.5$, P1); 57.75 (d, $J_{PP} = 40.5$, P2).

2.2.3. [Ni(2-$CH_3C_6H_4SO_2N{=}CS_2$)(dppe)] (**3**)

Elemental *Anal.* Calc. C, 58.13; H, 4.45; N, 1.99; Ni, 8.36. Found: C, 57.40; H, 4.51; N, 1.89; Ni, 8.15%. M.p. with decomposition (°C): 230.0–232.0. IR (most important bands) (cm^{-1}): 1459 ν(C=N); 1304 ν_{ass} (SO_2); 1151 ν_{sym} (SO_2); 919 ν_{ass} (CS_2) and 357 ν(NiS). ^1H NMR (δ), *J*(Hz): 8.04 (d, $J = 7.6$, 1H, H6 of the aromatic ring of the dithiocarbimato) 7.76–7.67 (m, 8H, H2 and H6 of the aromatic rings of dppe); 7.51–7.41 (m, 12H, H3, H4 and

$$RSO_2N{=}CS_2K_2.2H_2O \xrightarrow[H_2O/EtOH;\ -8H_2O,\ -2KCl]{NiCl_2.6H_2O,\ dppe} [Ni(RSO_2N{=}CS_2)dppe]$$

1, **2**, **3**

1 (R = CH_3), **2** (R = CH_3CH_2), **3** (R = 2-$CH_3C_6H_4$)

Scheme 1. Syntheses of **1**–**3**.

H5 of the aromatic rings of dppe); 7.36–7.28 (m, 1H, H5 of the aromatic ring of the dithiocarbimato); 7.20–7.13 (m, 2H, H3 and H4 of the aromatic ring of the dithiocarbimato); 2.68 (s, 3H, CH_3); 2.33 (d, 4H $J_{HP} = 17$, CH_2CH_2). $^{13}C\{^1H\}$ NMR (δ), J (Hz): 198.26 (N=CS_2); 140.80 (C1); 137.98 (C2); 131.69 (C4); 128.55 (C5); 125.19 (C6). dppe signals: 132.90 (t, $J_{CP} = 5.4$, C2 and C6); 131.78 (s, C4); 129.36 (t, $J_{CP} = 5.2$, C3 and C5); 128.35 (t, $J_{CP} = 23$, C1); 25.89 (t, $J_{CP} = 23$, CH_2CH_2). ^{31}P NMR (300 k) (δ): 56.80 (s). ^{31}P NMR (240 k) (δ), J (Hz): 58.10 (d, $J_{PP} = 40.5$, P1); 57.43 (d, $J_{PP} = 40.5$, P2).

2.3. X-ray crystallography

X-ray diffraction data collections for all crystals were performed on an Enraf-Nonius Kappa-CCD diffractometer (95 mm CCD camera on κ-goniostat) using graphite monochromated Mo Kα radiation (0.71073 Å), at room temperature for the complex **2** and at lower temperature for the complexes **1** and **3**. Data collections were carried out using the COLLECT software [17] up to 50° in 2θ with a redundancy of four. Final unit cell parameters were based on all reflections. Integration and scaling of the reflections, correction for Lorentz and polarization effects were performed with the *HKL* DENZO-SCALEPACK system of programs [18]. Numerical absorption correction (GAUSSIAN) were applied using the program SORTAV [19].

The structures were solved by direct methods with SHELXS-97 [20]. The models were refined by full-matrix least squares on F^2 using SHELXL-97 [21]. All the hydrogen atoms were stereochemically positioned and refined with the riding model [21]. Data collections and experimental details for the compounds are summarized in Table 1. The program ORTEP-3 [22] was used for graphic representation and the program WINGX [23] to prepare materials for publication. Selected bond and angles are presented in Table 2.

3. Results and discussion

The complexes are quite stable at ambient conditions. They are soluble in acetonitrile, dimethylformamide, dimethylsulfoxide, chloroform and dichloromethane, and insoluble in water, methanol and ethanol. There are no strong or medium bands in the 1400–1600 cm^{-1} region in the IR spectra of the potassium dithiocarbimates related to the complexes **1**–**3**, their $\nu_{C=N}$ band being observed in the 1300–1260 cm^{-1} region [24,25]. These low values point to a great contribution of the canonical forms (a) and (b) for the resonance hybrid of the dithiocarbimate anions (Scheme 2). In the spectra of the bis(dithiocarbimato)

Table 1
Crystal data and structure refinement for the complexes **1**–**3**

Complex	**1**	**2**	**3**
Empirical formula	$C_{28}H_{27}NNiO_2P_2S_3$	$C_{29}H_{29}NNiO_2P_2S_3$	$C_{34}H_{31}NNiO_2P_2S_3$
Formula weight (g mol^{-1})	623.34	640.36	702.43
Temperature (K)	210(2)	293(2)	210(2)
Crystal dimensions (mm)	0.310 × 0.270 × 0.140	0.388 × 0.177 × 0.014	0.407 × 0.149 × 0.117
Crystal system	monoclinic	orthorhombic	orthorhombic
Space group	$P2_1/c$	*Pbca*	$P2_12_12_1$
Unit cell dimensions			
a (Å)	19.3341(2)	16.1991(8)	12.4023(3)
b (Å)	19.1118(4)	15.1391(4)	12.8866(2)
c (Å)	15.9462(3)	23.5503(12)	20.1779(5)
β (°)	104.697(1)		
Volume (Å^3)	5699.48(17)	5775.5(4)	3224.9(1)
Z	8 ($Z' = 4$)	8	4
Calc. density (mg m^{-3})	1.46	1.473	1.447
μ (Mo Kα) (mm^{-1})	1.04	1.028	0.928
F(000)	2592	2656	1456
Transmission factors: minimum, maximum	0.739, 0.864	0.826, 0.986	0.803, 0.900
θ Range for data collection (°)	2.13–27.5	2.98–25.69	1.88–27.44
Index range	$-25 \leqslant h \leqslant 22$, $-22 \leqslant k \leqslant 24$, $-18 \leqslant l \leqslant 20$	$-19 \leqslant h \leqslant 16$, $-14 \leqslant k \leqslant 18$, $-28 \leqslant l \leqslant 28$	$-13 \leqslant h \leqslant 16$, $-15 \leqslant k \leqslant 16$, $-23 \leqslant l \leqslant 26$
Reflections collected	35271	36401	20282
Independent reflections [R_{int}]	13017 [0.0382]	5476 [0.1398]	7322 [0.0445]
Reflections $I > 2\sigma$(I)	9739	2901	6169
Number of parameters refined	667	345	388
Final R for $I > 2\sigma(I)$	$R_1 = 0.0388$, $wR_2 = 0.0779$	$R_1 = 0.0460$, $wR_2 = 0.0774$	$R_1 = 0.0361$, $wR_2 = 0.0793$
R indices [all data]	$R_1 = 0.0628$, $wR_2 = 0.0878$	$R_1 = 0.1285$, $wR_2 = 0.0961$	$R_1 = 0.0479$, $wR_2 = 0.0841$
Goodness-of-fit on F^2	1.011	0.924	1.033
Residual electron density (e Å^{-3})	0.395	0.481	0.332

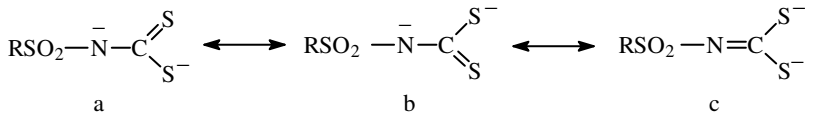
Table 2
Selected bond (Å) and angles (°) for the complexes **1**–**3**

	1		**2**	**3**
	Molecule 1	Molecule 2		
Bond length				
Ni–S1	2.1959(7)	2.1966(6)	2.201(1)	2.1822(7)
Ni–S2	2.1978(7)	2.1979(7)	2.203(1)	2.2065(8)
Ni–P1	2.1562(7)	2.1569(7)	2.171(1)	2.1718(7)
Ni–P2	2.1773(7)	2.1466(6)	2.166(1)	2.1672(7)
P1–C9	1.810(3)	1.821(2)	1.822(4)	1.812(3)
P1–C15	1.816(3)	1.814(2)	1.818(3)	1.818(3)
P1–C33	1.834(3)	1.840(2)	1.823(4)	1.834(3)
P2–C21	1.827(3)	1.813(2)	1.817(4)	1.821(3)
P2–C27	1.813(2)	1.823(2)	1.811(4)	1.819(3)
P2–C34	1.842(2)	1.841(2)	1.835(4)	1.844(3)
C1–S1	1.747(2)	1.744(2)	1.761(4)	1.749(3)
C1–S2	1.742(2)	1.738(2)	1.745(4)	1.745(3)
C1–N	1.286(3)	1.296(3)	1.287(4)	1.280(3)
N–S3	1.638(2)	1.635(2)	1.640(3)	1.641(2)
O1–S3	1.430(2)	1.418(2)	1.445(3)	1.426(2)
O2–S3	1.429(2)	1.433(2)	1.441(3)	1.444(2)
C2–S3	1.757(3)	1.740(3)	1.761(4)	1.776(3)
C2–C3			1.530(5)	1.386(4)
C33–C34	1.521(4)	1.530(3)	1.521(5)	1.526(4)
Bond angles				
S1–Ni–S2	79.14(2)	79.96(2)	79.33(4)	79.21(3)
P1–Ni–P2	86.52(3)	88.47(2)	86.40(4)	86.69(3)
S1–Ni–P1	96.44(3)	96.74(2)	99.31(4)	97.78(3)
S2–Ni–P2	98.89(3)	95.52(2)	95.27(4)	96.32(3)
Ni–P1–C33	109.19(9)	109.09(8)	107.8(1)	106.3(1)
Ni–P2–C34	109.14(9)	108.89(8)	109.7(1)	109.9(1)
S1–C1–S2	106.7(1)	108.4(1)	106.6(2)	106.4(1)
S1–C1–N	132.4(2)	130.6(2)	131.5(3)	132.2(2)
S2–C1–N	120.8(2)	121.0(2)	121.8(3)	121.4(2)
C1–N–S3	121.3(2)	120.2(2)	121.0(3)	124.0(2)
N–S3–O1	112.4(1)	113.7(1)	113.1(2)	105.8(1)
N–S3–O2	109.8(1)	108.7(1)	109.8(2)	107.9(1)
O1–S3–O2	117.5(2)	116.4(2)	116.2(2)	117.4(1)
N–S3–C2	99.3(1)	99.6(1)	99.8(2)	109.4(1)
O1–S3–C2	108.0(2)	108.8(2)	107.6(2)	109.0(1)
O2–S3–C2	108.6(2)	108.2(2)	108.9(2)	107.2(1)
S3–C2–C3			110.2(3)	117.3(2)
C9–P1–C15	107.6(1)	105.8(1)	106.4(2)	104.3(1)
C21–P2–C27	109.3(1)	105.6(1)	106.8(2)	106.7(1)

complexes $[Ni(RSO_2N{=}CS_2)_2]^{2-}$ (R = CH_3, CH_3CH_2 and 2-$CH_3C_6H_4$) this band is observed in the 1400–1360 cm^{-1} region [25–27]. A strong band observed in the 1470–1450 cm^{-1} region in the spectra of the complexes **1**–**3** was assigned to the $\nu_{C=N}$. The mesomeric drift of electrons from the dithiocarbimate moiety towards the metal centre increases the contribution of the canonical form (c) (Scheme 2). This is reflected in the shift in $\nu_{C=N}$ values to higher wavenumbers when compared with those observed in the free ligands and in the analogous bis(dithiocarbimato) complexes spectra. This effect is also observed, for example, when the spectrum of the complex $[Ni(dpdtc)_2]$ (dpdtc = *N*,*N*-propyldithiocarbamato) ($\nu_{C=N}$ band is observed in 1508 cm^{-1}) is compared with the spectrum of $[Ni(dpdtc)(dppe)]^+$ ($\nu_{C=N}$ band is observed in 1526 cm^{-1}) [11]. The ν_{C-S} band were observed at higher frequency in the spectra of the potassium salts of dithiocarbimates (960–940 cm^{-1}) [24,25] than in the spectra of the complexes here studied (925–915 cm^{-1}), and in the spectra of analogous bis(dithiocarbimato) complexes (940–925 cm^{-1}) [25–27]. This band appears without any splitting, confirming the bidentate coordination of the dithiocarbimate moiety. The shifts observed in the ν_{C-S} in the spectra of the complexes are also consistent with the increased importance of the canonical form (c) after complexation (Scheme 2). The spectra of the complexes also show the expected medium band in the 300–400 cm^{-1} range assigned to the NiS vibrations [28]. The *v*NiP bands was not observed above 200 cm^{-1}.

The NMR spectra of **1**–**3** were typical for diamagnetic species supporting the assumption of a square planar geometry around the nickel atom. The ^1H NMR spectra of the complexes showed the signals for the hydrogen atoms of the dppe and the dithiocarbimate moiety. The integration curves on the ^1H NMR spectra were consistent with a 1:1 proportion between the dppe and the dithiocarbimate anion. The signals in the spectra of the free dithiocarbimates [24,25] and in the spectra of the complexes show approximately the same chemical shifts. Nevertheless, the $N{=}CS_2$ (C1) signal is shifted in the spectra of the complexes to higher field if compared to the spectra of the free ligands [24,25] and the correspondent bis(dithiocarbimato) complexes $[Ni(RSO_2N{=}CS_2)_2]^{2-}$ [25–27]. If the canonical form (c) (Scheme 2) is more important for the complexes than for the ligands, then the C1 carbon atom is expected to be more shielded in the complexes here studied.

Most of the diphosphine signals in the ^{13}C NMR spectra appeared as pseudo triplets or doublets. This is consistent with square planar geometry for the complexes. Doublets or pseudo triplets are commonly observed in the ^{13}C NMR spectra of bis(phosphine) transition metal *cis*-complexes [14,29]. The ^{31}P NMR spectra exhibited only one signal (*ca.* 58 δ) at 300 K, but the signal split into two doublets due P–P coupling at 240 K confirming that the phosphorus atoms in the molecules are not magnetically equivalent. Significant changes in the phosphorus chemical shifts in the spectra of the complexes when compared to



Scheme 2. Three canonical forms for *N*-R-sulfonyldithiocarbimate anion.

that of the free diphosphine (*ca.* −12 δ) [5] are caused by the nickel atom that deshields the phosphorus atoms considerably. Similar chemical shifts are also observed in the spectra of many complexes with NiX_2(P–P) chromophores (P–P = 1,2-bis(diphenylphosphine)ethane; X = Cl, Br, I, S) [5,8–12].

The ORTEP-3 view [22] of the solid-state molecular structures of the complexes **1**, **2** and **3** are illustrated in Figs. 1–3. Compound **1** crystallizes in the monoclinic system, space group $P2_1/c$, with two independent molecules in asymmetric unit ($Z = 8$), while the complexes **2** and **3** crystallize in the orthorhombic system, space groups *Pbca* ($Z = 8$) and $P2_12_12_1$ ($Z = 4$), respectively.

In all complexes, the nickel cation is coordinated by the two sulfur atoms of the dithiocarbimato ligand and by two phosphorus atoms of the 1,2-bis(diphenylphosphine)ethane into a distorted square-planar geometry. The P1–Ni–S1 and P2–Ni–S2 angles are more distorted from 90° than the P1–Ni–P2 angles. The S1–Ni–S2 angle is considerably smaller than 90° due to the chelation of the *N*-R-sulfonyldithiocarbimato ligand forming a four membered ring (NiS_2C). When the complex [Ni(2-$CH_3C_6H_4SO_2N{=}CS_2$)-(PPh_3)$_2$] [14] is compared with **3**, some interesting differences can be observed due to the chelation of dppe and its smaller steric effect. The P–Ni–P angle in **3** (86.69°) is smaller than in [Ni(2-$CH_3C_6H_4SO_2N{=}CS_2$)(PPh_3)$_2$] (98.48°). The S–Ni–S angle in **3** (79.21°) is greater than in the bis(triphenylphosphine) complex (77.87°) and the Ni–P bond length in **3** (*ca.* 2.17 Å) is smaller than Ni–P bonding in the bis(triphenylphosphine) complex (*ca.* 2.21 Å).

The Ni–S bonds, in complexes **1** and **2** are symmetric. In **3**, this bond exhibits a small asymmetry, probably due to the repulsive interaction between the S1 atom and the large RSO_2 group. This group, in all complexes, is in *cis* position in relation to the S1 atom. The orientation of the RSO_2 group is also responsible for the difference between the angles S1–C1–N and S2–C1–N.

The C–S bond lengths in complexes **1**–**3** (*ca.* 1.74) are characteristic of partial double bonds (typical bond lengths: 1.81 Å for C–S and 1.69 Å for C=S). The C–N bond distances (*ca.* 1.285) are similar to that of the double bond C=N (1.275–1.300 Å) [30,31]. This behavior indicates that the π electron density is delocalized over S_2CN moiety. The CN bonds in these neutral complexes are shorter than in the bis(dithiocarbimato) complexes (Table 3) [25–27].

The crystallographic data are in accord with the spectroscopic data (Table 3). Both point to an increase on the contribution of the canonical form (c) (Scheme 2) in this sequence: free ligands < bis(dithiocarbimato) complexes < complexes **1**–**3** complexes.

The R-group in complex **3** lies in a significantly different conformation from that observed for the other complexes. The C1–N–S3–C2 torsion angle is 41.8(3)° for the complex **3**, 164.2(2)° for the molecule 1 and −172.0(2)° for the molecule 2 of the complex **1** and 157.0(3)° for the complex **2.**

The P–C_{sp3} and C_{sp3}–C_{sp3} distances in the dppe ligand, in all complexes, are similar to Ni(II) complexes with Ni(S–S)(P–P) chromophores [9,32–34]. The bond lengths and angles in the phenyl rings are in good agreement,

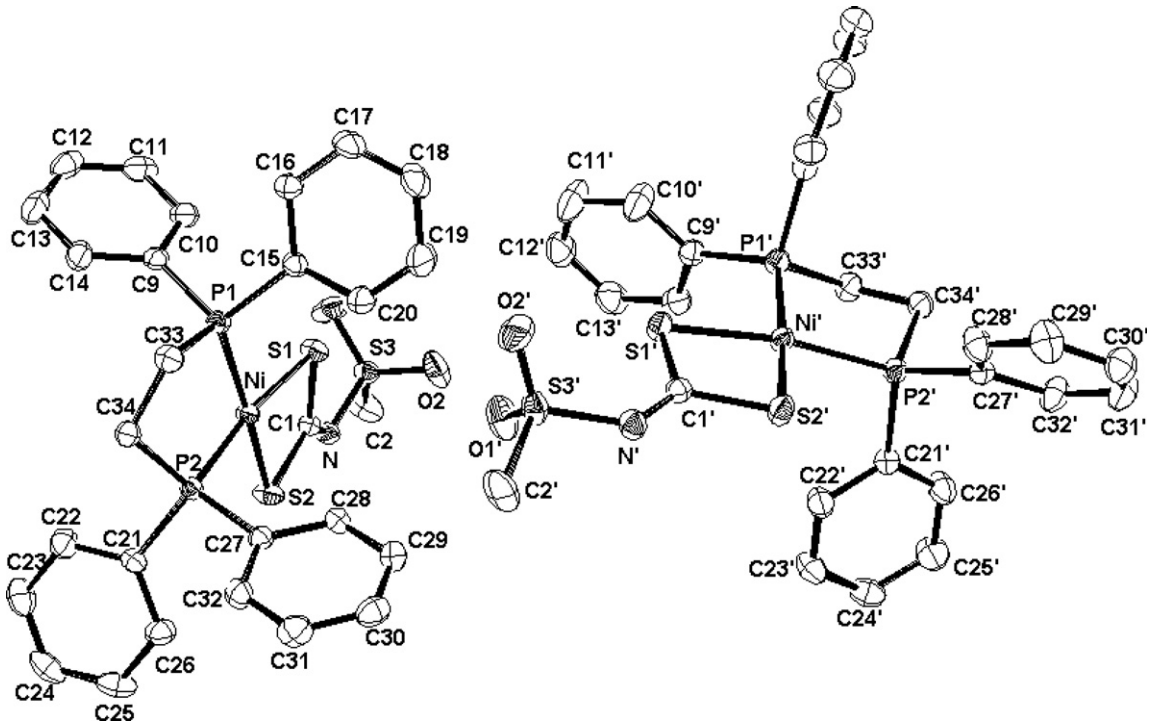


Fig. 1. The molecular structure of **1**. Displacement ellipsoids are drawn at the 30% probability level. H atoms have been omitted for clarity.

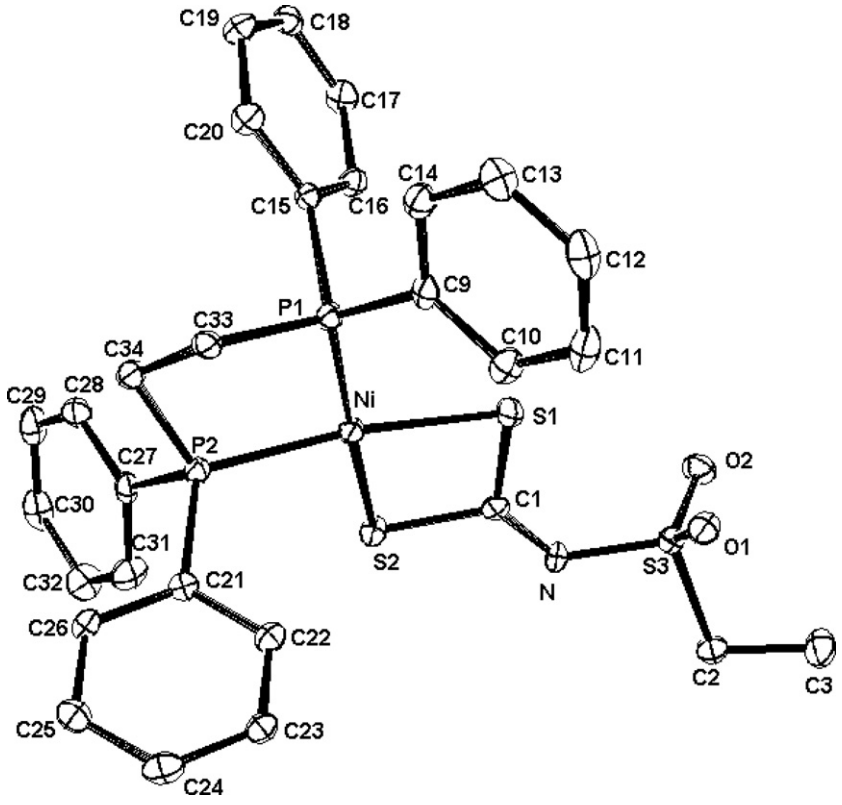


Fig. 2. The molecular structure of **2**. Displacement ellipsoids are drawn at the 30% probability level. H atoms have been omitted for clarity.

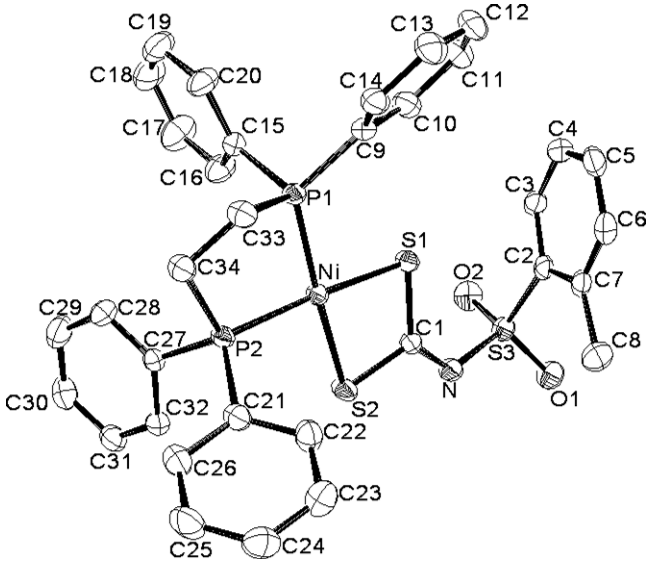


Fig. 3. The molecular structure of **3**. Displacement ellipsoids are drawn at the 30% probability level. H atoms have been omitted for clarity.

Table 3
Comparison between selected crystallographic and spectroscopic data for the CN moiety in the complexes **1**–**3** and related compounds

Compounds	CN length (Å)	νCN (cm^{-1})	^{13}C NMR (δ)
$CH_3SO_2N{=}CS_2K_2$[a]		1260	223
$(Bu_4N)_2[Ni(CH_3SO_2N{=}CS_2)_2]$[b]	1.31(2)	1390	210
$[Ni(CH_3SO_2N{=}CS_2)dppe]$ (**1**)	1.296(3); 1.286(3)	1463	199
$CH_3CH_2SO_2N{=}CS_2K_2$[c]		1300	224
$(Bu_4N)_2[Ni(CH_3CH_2SO_2N{=}CS_2)_2]$[c]	1.309(2)	1399	209
$[Ni(CH_3CH_2SO_2N{=}CS_2)dppe]$ (**2**)	1.287(5)	1463	198
$2\text{-}CH_3C_6H_4SO_2N{=}CS_2K_2$[a]		1280	223
$(Bu_4N)_2[Ni(2\text{-}CH_3C_6H_4SO_2N{=}CS_2)_2]$[d]	1.311(3)	1365	209
$[Ni(2\text{-}CH_3C_6H_4SO_2N{=}CS_2)dppe]$ (**3**)	1.280(3)	1459	198

[a] Ref. [24].
[b] Ref. [27].
[c] Ref. [25].
[d] Ref. [26].

within experimental accuracy, with the values found in the literature [30].

The angles between the planes of the phenyl rings on each phosphorus, P1 and P2 are, respectively: 82.9(1)° and 52.19(8)° (molecule 1) and 63.4(1)° and 61.50(9)° (molecule 2) in complex **1**, 69.7(1)° and 76.4(1) in complex **2** and 87.3(1)° and 68.5(1)° in complex **3**. In all complexes there are weak intermolecular interactions among C33 atom of the ethane group and oxygen, with donor-acceptor distances ranged from 3.209 to 3.405 Å. The complex **2** have another weak interaction [C18–H18...O2 $(-x, -y+1, -z)$] with C...O of 3.409 Å and the complex **1** have two more intermolecular interactions C–H...O involving the carbon atom of the CH_3SO_2 group.

4. Conclusion

Three novel 1,2-bis(diphenylphosphino)ethane(*N*-R-sulfonyldithiocarbimato)nickel(II) complexes were prepared

and characterized by IR, ^{1}H, ^{13}C and ^{31}P NMR, elemental analyses for C, H, N, Ni and by single crystal X-ray diffraction techniques. They are the first examples of nickel(II) complexes with the mixed ligands *N*-R-sulfonyldithiocarbimate and diphosphine.

When the analogous bis(dithiocarbimato) complexes [25–27] are compared with the compounds here studied, the spectroscopic and X-ray data show that the substitution of a dithiocarbimate group by a diphosphine ligand causes a drift of electrons from the dithiocarbimate to the metallic center, increasing the contribution of the canonical form (c) (Scheme 2) to the resonance hybrid, with a consequent increase of the CN double bond character. Therefore, the wavenumbers for the $\nu_{C=N}$ in the IR spectra of **1**–**3** are greater than those in the spectra of the related bis(dithiocarbimato) complexes and this band is observed in smaller wavenumbers in the spectra of the free ligands. Accordingly, the NMR spectra show that the carbon atom of the dithiocarbimate group of **1**–**3** is more shielded than that of the bis(dithiocarbimato) complex and in the parent ligand (see Table 3). Similar behavior is observed for complexes with general formulae $[Ni(RSO_2N{=}CS_2)(PPh_3)_2]$ with R = 2-$CH_3C_6H_4$, 4-$CH_3C_6H_4$ and 4-BrC_6H_4 [14] and with R = 2,5-$Cl_2C_6H_3$ [15].

The comparison between bis(triphenylphosphine)-*N*-R-sulfonyldithiocarbimato-nickel(II) complexes [14,15] and **1**–**3** show that the substitution of two bulky triphenylphosphine ligands by a diphosphine chelating ligand leads to an increase on the S1–C1–S2 angle, and a decrease on the P–Ni–P angle and on the P–Ni bond length.

Acknowledgements

This work has been supported by CNPq, CAPES, FAPEMIG and FAPEAL (Brazil).

Appendix A. Supplementary material

CCDC 653767, 653768 and 653766 contain the supplementary crystallographic data for **1**, **2** and **3**. These data can be obtained free of charge via www.ccdc.cam.ac.uk/conts/retrieving.html, or from the Cambridge Crystallographic Data Centre, 12 Union Road, Cambridge CB2 1EZ, UK; fax: (+44) 1223-336-033; or e-mail: deposit@ccdc.cam.ac.uk. Supplementary data associated with this article can be found, in the online version, at doi:10.1016/j.poly.2007.11.001.

References

[1] D. Hogarth, Prog. Inorg. Chem. 53 (2005) 71.
[2] P.J. Nieuwenhuizen, A.W. Ehlers, J.G. Haasnoot, S.R. Janse, J. Reedijk, E.J. Baerends, J. Am. Chem. Soc. 121 (1999) 163.
[3] P.J. Nieuwenhuizen, J. Reedijk, M. van Duin, W.J. McGill, Ruber Chem. Technol. 70 (1997) 368.
[4] D. Coucouvanis, Prog. Inorg. Chem. 11 (1969) 233.
[5] J.A.S. Bomfim, F.P. de Souza, C.A.L. Filgueiras, A.G. de Sousa, M.T.P. Gambardella, Polyhedron 22 (2003) 1567.
[6] A. Manohar, L. Righi, K. Ramalingan, G. Bocelli, Inorg. Chim. Acta 314 (2001) 172.
[7] S. Thiumaran, K. Ramalingan, Trans. Met. Chem. 25 (2000) 60.
[8] R. Pastorek, J. Kameníček, B. Cvek, V. Slovák, M. Pavlíček , J. Coord. Chem. 59 (8) (2006) 911.
[9] B.A. Prakasam, K. Ramalingam, M. Saravanan, G. Bocelli, A. Cantoni, Polyhedron 23 (2004) 77.
[10] B.A. Prakasam, K. Ramalingam, G. Bocelli, A. Cantoni, Bull. Chem. Soc. Jpn. 79 (1) (2006) 113.
[11] K. Ramalingan, G. Avaramudan, M. Seshasayee, Inorg. Chim. Acta 128 (1987) 231.
[12] R. Pastorek, Z. Trávníček, J. Marek, D. Dastych, Z. Šidelár, Polyhedron 19 (2000) 1713.
[13] C.A. Tsipis, I.P. Meleziadis, D.P. Kessissoglou, G.A. Katsoulos, Inorg. Chim. Acta 90 (1984) L19.
[14] M.R.L. Oliveira, H.P. Vieira, G.J. Perpétuo, J. Janczak, V.M. De Bellis, Polyhedron 21 (2002) 2243.
[15] C. Novais, S. Guilardi, I. Machado Jr., M.R.L. Oliveira, Acta Crystallogr. Sect. E 63 (2007) m1981.
[16] H.U. Hummel, U.Z. Korn, Naturforsch B 44 (1989) 24.
[17] Enraf-Nonius COLLECT, Nonius BV, Delft, The Netherlands (1997-2000).
[18] Z. Otwinowski, W. Minor, in: C.W. CarterJr., R.M. Sweet (Eds.), Methods in Enzymology, vol. 276, Academic Press, New York, 1997, p. 307.
[19] R.H. Blessing, Acta Crystallogr., Sect. A 51 (1995) 33.
[20] G.M. Sheldrick, SHELXS-97 Program for Crystal Structure Resolution, Univ. of Göttingen, Göttingen, Germany, 1997.
[21] G.M. Sheldrick, SHELXL-97 Program for Crystal Structure Refinement, Univ. of Göttingen, Göttingen, Germany, 1997.
[22] L.J. Farrugia, J. Appl. Cryst. 30 (1997) 565.
[23] L.J. Farrugia, J. Appl. Crystallogr. 32 (1999) 837.
[24] M.R.L. Oliveira, V.M. De Bellis, Trans. Met. Chem. 24 (1999) 127.
[25] E.F. Franca, M.R.L. Oliveira, S. Guilardi, R.P. Andrade, R.H. Lindemann, J. Amim Jr., J. Ellena, V.M. De Bellis, M.M.M. Rubinger, Polyhedron 25 (2006) 2119.
[26] M.R.L. Oliveira, R. Diniz, V.M. De Bellis, N.G. Fernandes, Polyhedron 22 (2003) 1561.
[27] M.R.L. Oliveira, V.M. De Bellis, N.G. Fernandes, Struct. Chem. 8 (3) (1997) 205.
[28] K. Nakamoto, Infrared and Raman of Inorganic and Coordination Compounds, 3rd ed., John Wiley & sons, Inc., New York, 1978, p. 339.
[29] D.A. Redfield, L.W. Cary, J.H. Nelson, Inorg. Chem. 14 (1) (1975) 50.
[30] F.H. Allen, O. Kennard, D.G. Watson, L. Brammer, A.G. Orpen, R. Taylor, J. Chem. Soc., Perkin Trans. II (1987) S1.
[31] A.G. Orpen, L. Brammer, F.H. Allen, O. Kennard, D.G. Watson, R. Taylor, J. Chem. Soc., Dalton Trans. (1989) S1.
[32] R. Akilan, K. Sivakumar, V. Venkatachalam, K. Ramalingam, K. Chinnakali, Hoong-Kun Fun, Acta Crystallogr., Sect. C 51 (1995) 368.
[33] A. Manohar, V. Venkatachalam, K. Ramalingam, U. Casellato, R. Graziani, Polyhedron 16 (1997) 1971.
[34] V. Venkatachalam, K. Ramalingam, T.C.W. Mak, Luo Bao-Sheng, Polyhedron 15 (1996) 1295.

Available online at www.sciencedirect.com
ScienceDirect
Polyhedron 27 (2008) 734–738
POLYHEDRON
www.elsevier.com/locate/poly

Synthesis and structural characterization of a coordinatively unsaturated ruthenium complex, $Cp^*Ru(Ph_2nacnac)$, and its CO adduct

Hui Huang [a], Russell P. Hughes [a,*], Arnold L. Rheingold [b]

[a] Departments of Chemistry, 6128 Burke Laboratories, Dartmouth College, Hanover, NH 03755, United States
[b] Department of Chemistry and Biochemistry, University of California at San Diego, San Diego, CA 92093, United States

Received 25 June 2007; accepted 1 November 2007
Available online 11 December 2007

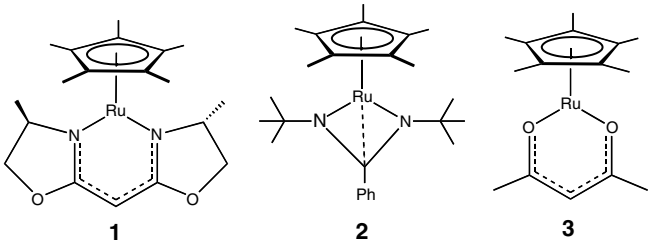
Abstract

Two new half sandwich ruthenium complexes with 2-*N*-phenylamino-4-*N*-phenylimino-2-pentene (Ph_2nacnac) ligands have been synthesized and characterized. Single crystal X-ray diffraction analysis reveals the monomeric, highly air sensitive complex $Cp^*Ru(Ph_2nacnac)$ (**4**) has a coordinatively unsaturated structure and the coordination environment around Ru(II) is effectively a triangle made up of Ct(Cp^*)–N(1)–N(2). An air stable complex $Cp^*Ru(Ph_2nacnac)(CO)$ (**5**) is prepared by reaction of **4** with CO, and has a *pseudo*-tetrahedral geometry around the Ru(II) center, made up of Ct(Cp^*)–N(1)–N(2)–C(28).
© 2007 Elsevier Ltd. All rights reserved.

Keywords: Ruthenium; CO; Nacnac; Synthesis; Crystallography; Structure reactivity

1. Introduction

Half sandwich ruthenium complexes are of considerable interest to coordination chemists since they have been widely used in organometallic synthesis and enantioselective catalysis [1–3]. Clearly it is important to understand any correlations between structure and reactivity of these compounds in order to better understand their behavior as structural templates and catalysts. Coordinatively unsaturated ruthenium complexes of general formula $RuCp^*(X)(PR_3)$ have been obtained previously using bulky phosphine ligands (R = cyclohexyl, *iso*-propyl) [4,5], and analogues of general formula $RuCp(L)^+$ (L = bulky chelating diimine) have also been reported [6–8]. To the best of our knowledge, there are few precedents for neutral, coordinatively unsaturated half sandwich ruthenium complexes stabilized by chelating ligands. One example, **1** reported by Kölle, contains a chiral ligand methyl(bis-5-methyl-tetrahydrooxazol) ligand, but was only characterized by NMR spectroscopy [9]. Yamaguchi et al. reported Cp^*Ru-(amidinate) (**2**) as the first example in which amidinate ligands play an important role in effectively stabilizing a coordinatively unsaturated metal center [10]. An example with a less bulky chelate $Cp^*Ru(acac)$ (**3**), initially reported as a neutral unsaturated monomer [11], was subsequently shown to be a dimer [12].



1 **2** **3**

In recent years, transition metal complexes with β-diketiminate (nacnac) ligands have been the subject of considerable interest [13–18]. Here, we report on a brief

* Corresponding author.
E-mail address: rph@dartmouth.edu (R.P. Hughes).

0277-5387/$ - see front matter © 2007 Elsevier Ltd. All rights reserved.
doi:10.1016/j.poly.2007.11.002

investigation on the synthesis, characterization, and the crystal structure analysis of two half sandwich ruthenium complexes with the "Ph_2nacnac" ligand.

2. Experimental

2.1. General

Air-sensitive reactions were performed in oven-dried glassware, using standard SCHLENK techniques, under an atmosphere of nitrogen, which was deoxygenated over BASF catalyst and dried over Aquasorb, or in a Braun dry-box. Methylene chloride and hexane were dried over an alumina column under nitrogen [19]. Methanol was distilled from Linde type 4 Å molecular sieves. NMR spectra were recorded on a Varian Unity Plus 300 or 500 FT spectrometer. ^{1}H NMR spectra were referenced to the protio impurity in the solvent: C_6D_6 δ (7.16 ppm), CD_2Cl_2 δ (5.32 ppm). Coupling constants are reported as absolute values in units of Hertz. IR spectra were recorded on a Perkin–Elmer FTIR 1600 Series spectrophotometer. Elemental analyses were performed by Schwartzkopf (Woodside, NY).

$RuCl_3 \cdot 3H_2O$ (Johnson Matthey Ltd.) and pentamethylcyclopentadiene (Cp^*H) (Acros) were used without further purification. $[Cp^*RuCl_2]_2$ [20] and Ph_2nacnac [21] were prepared according to published methods.

2.1.1. Synthesis of $Cp^*Ru(Ph_2nacnac)$ (4)

$[Cp^*RuCl_2]_2$ (50 mg, 0.17 mmol) and dry K_2CO_3 (150 mg, 1.15 mmol) were suspended in dry N_2 saturated MeOH (10 mL) and allowed to stir for 6 h to give an intensely red solution with some solid. Ph_2nacnac (41 mg, 0.17 mmol) was added to the solution, which was allowed to react for a half hour to give a red solution. The solvent was removed *in vacuo* to give a dark red solid, which was extracted with hexane (50 mL) and filtered. The solvent was removed from the filtrate to give the product as a dark red solid; 50 mg, 81%. Recrystallization by slow evaporation from hexane gave dark red crystals suitable for X-ray diffraction. *Anal.* Calc. for $C_{27}H_{32}N_2Ru$: C, 66.77; H, 6.64; N, 5.77. Found: C, 66.39; H, 6.94; N, 5.78%. ^{1}H NMR (C_6D_6, 300 MHz, 25 °C) δ 1.08 (15H, s, $C_5(CH_3)_5$); 1.90 (6H, s, CH_3); 5.39 (1H, s, HC); 7.00–7.26 (10H, m, H-Ph).

2.1.2. Synthesis of $Cp^*Ru(Ph_2nacnac)(CO)$ (5)

$Cp^*Ru(Ph_2nacnac)$ (23 mg, 0.047 mmol) was dissolved in hexane (10 mL) to give a red solution. CO (1.0 mL, 0.047 mmol) was added by syringe. The color lightened. CO (3 mL/time × 17 times) was added by syringe and the solution was allowed to react overnight to give a brown yellow solution. The solvent was removed *in vacuo* to give the adduct as yellow solid, with a little brown red tint; 24 mg, 99%. Recrystallization by slow evaporation from hexane gave yellow crystals suitable for X-ray diffraction. *Anal.* Calc. For $C_{28}H_{32}N_2ORu$: C, 65.47; H, 6.28; N, 5.46. Found: C, 65.82; H, 6.81; N, 5.46%. ^{1}H NMR (CD_2Cl_2, 300 MHz, 25 °C) δ 1.23 (1;H, s, $C_5(CH_3)_5$); 1.72 (6H, s, CH_3); 4.50 (1H, s, HC); 6.97 (2H, t, $^3J_{HH} = 7.5$ Hz, *p*-H-Ph); 7.05 (4H, d, $^3J_{HH} = 8.7$ Hz, *o*-H-Ph); 7.26 (4H, t, $^3J_{HH} = 7.5$ Hz, *m*-H-Ph). IR (hexane, cm^{-1}): υ_{CO} 1910 (vs).

2.1.3. X-ray crystallography

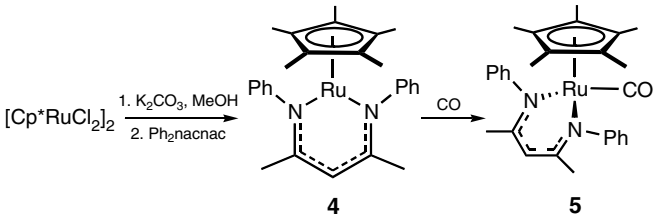
Crystal data and other parameters for complexes **4** and **5** are given in Table 1. Intensity data were collected at 213(2) K, on Bruker Smart CCD diffractometers using graphite-monochromated Mo Kα radiation (k = 0.71073 Å). Of the 17,362 and 7558 reflections that were collected, 5488 ($R_{int} = 0.0413$) and 4186 ($R_{int} = 0.0249$) were unique for complexes **4** and **5**, respectively. Empirical absorption corrections were employed. The structures were solved by direct methods. The final refinement was done by full-matrix least squares based on F^2 with anisotropic thermal parameters for all non-hydrogen atoms, and the hydrogen atoms were generated geometrically.

3. Results and discussion

Complex **4** was obtained via two steps in a one pot reaction with an overall yield of 81%. $[Cp^*RuCl_2]_2$ was stirred with K_2CO_3 in MeOH to give $[Cp^*Ru(OMe)]_2$, which reacted with the Ph_2nacnac ligand to give **4** as a red air-sensitive solid. Reaction of **4** with CO in hexane afforded **5** as a yellow solid in high yield as shown in Scheme 1. This yellow complex is moderately stable in air, unlike its acac analogue [11]. The CO stretching frequency in the IR of **5** is at 1910 cm^{-1} in hexane, while that for the acac analogue $Cp^*Ru(acac)(CO)$ is 1915 cm^{-1} (KBr) [11]. There

Table 1
Crystal data for complexes **4** and **5**

	4	**5**
Formula	$C_{27}H_{32}N_2Ru$	$C_{28}H_{32}N_2ORu$
Formula weight	485.62	513.63
Space group	$P2(1)/n$	$P\bar{1}$
a (Å)	9.363(6)	7.2099(19)
b (Å)	23.983(15)	11.924(3)
c (Å)	11.137(7)	14.596(4)
α (°)		79.706(4)
β (°)	110.285(10)	75.865
γ (°)		81.585
V (Å^3)	2346(3)	1190.4(5)
Z	4	2
D_{calc} (g cm^{-3})	1.375	1.433
μ [Mo Kα] (mm^{-1})	0.684	0.681
Temp. (K)	213(2)	213(2)
Diffractometer	bruker smart apex CCD	bruker smart apex CCD
Radiation	Mo Kα (0.71073 Å)	Mo Kα (0.71073 Å)
Crystal size (mm)	0.30 × 0.20 × 0.10	0.40 × 0.15 × 0.08
F(000)	1008	532
Measured reflections	17362	7558
Independent reflections	5488	4186
R (F), %	0.0446	0.0292
R (wF^2), %	0.0991	0.0769



Scheme 1.

was no reaction when complex **4** was treated with H_2 or ethylene.

The principal structural features of complex **4** are given in Fig. 1, while crystallographic data are summarized in Table 1 and selected bond lengths and angles appear in Table 2. In this complex, the plane of the nacnac ligand (N(2)–Ru(1)–N(1)) is perpendicular to the Cp^* plane, which differs from the dimeric acac analogue **3**, in which the ligand plane is tilted with respect to the Ru–Cp^* by 37.5° [11]. The angle involving the metal center and the bis(ketenimine) ligand deviates significantly from 90°, N(1)–Ru(1)–N(2) = 87.70(9)° and the bond distances Ru(1)–N(1) and Ru(1)–N(2) are 2.053(2) and 2.046(2) Å, respectively. The distance between Ru(1) and the center of the Cp^* ring is 1.800 Å. The five atoms in the bis(ketenimine) ligand and Ru(1) are coplanar. For example, the biggest deviation of C(11) to the least square plane (Ru(1)–N(2)–C(13)–C(12)–C(11)–N(1)) is 0.009 Å. The two C–C distances of 1.388(4) and 1.397(4) Å and the two C–N distances of 1.341(3) and 1.349(4) Å suggest significant delocalization within the π-system of the nacnac ligand. There are no intermolecular interactions in the solid state, consistent with the observation that the red color of **4** observed in the solid state is maintained in hexane solution.

During preparation of this manuscript, two similar complexes were reported. In nickel analogue **6**, reported by Bai et al. [22] the Ni–N distances were found to be 1.937(3) and 1.948(3) Å with a N–Ni–N angle of 94.19(11)°. The angle between the plane of the cyclopentadienyl ligand and NiN_2 plane was 90.8°. When **6** was treated with $[PhMe_2NH][B(C_6F_5)_4]$ a cationic complex **7** was formed by protonation at the CH carbon of the nacnac ligand (Scheme 2). In that structure, the Ni–N distances were found to be 1.928(3) and 1.942(3) Å, a little longer than those reported for **6**, consistent with the poorer donor ability of the protonated nacnac ligand. However, the N–Ni–N bite angle in **7** is 95.50(12)°, similar to that in **6**. Similarly,

Table 2
Selected bond lengths (Å) and angles (°) for **4** and **5**

Complex **4**	
Ru(1)–N(2) 2.046(2)	N(2)–Ru(1)–N(1) 87.70(9)
Ru(1)–N(1) 2.053(2)	N(2)–Ru(1)–C(3) 125.37(10)
Ru(1)–C(3) 2.141(3)	N(1)–Ru(1)–C(3) 128.84(10)
Ru(1)–C(5) 2.159(3)	N(2)–Ru(1)–C(5) 112.13(10)
Ru(1)–C(1) 2.168(3)	N(1)–Ru(1)–C(5) 143.35(9)
Ru(1)–C(2) 2.190(3)	N(2)–Ru(1)–C(1) 146.73(9)
Ru(1)–C(4) 2.199(3)	N(1)–Ru(1)–C(1) 110.40(9)
N(1)–C(11) 1.341(3)	N(2)–Ru(1)–C(2) 164.06(9)
N(2)–C(13) 1.349(4)	N(1)–Ru(1)–C(2) 104.07(10)
C(11)–C(12) 1.388(4)	N(2)–Ru(1)–C(4) 103.14(10)
C(12)–C(13) 1.397(4)	N(1)–Ru(1)–C(4) 166.84(9)
	C(11)–N(1)–Ru(1) 128.78(18)
	C(16)–N(1)–Ru(1) 117.33(17)
	C(13)–N(2)–Ru(1) 129.28(19)
	C(22)–N(2)–Ru(1) 116.99(16)
Complex **5**	
Ru(1)–C(28) 1.837(2)	C(28)–Ru(1)–N(2) 95.25(9)
Ru(1)–N(2) 2.1309(19)	C(28)–Ru(1)–N(1) 94.79(9)
Ru(1)–N(1) 2.1363(19)	N(2)–Ru(1)–N(1) 88.30(7)
Ru(1)–C(22) 2.181(2)	N(2)–Ru(1)–C(22) 134.06(8)
Ru(1)–C(24) 2.214(2)	N(1)–Ru(1)–C(22) 136.60(8)
Ru(1)–C(20) 2.221(2)	N(2)–Ru(1)–C(24) 98.68(8)
Ru(1)–C(26) 2.290(2)	N(1)–Ru(1)–C(24) 153.56(8)
Ru(1)–C(18) 2.299(2)	N(2)–Ru(1)–C(20) 153.88(8)
O(1)–C(28) 1.157(3)	N(1)–Ru(1)–C(20) 100.60(8)
N(1)–C(10) 1.325(3)	N(2)–Ru(1)–C(26) 92.45(8)
N(1)–C(12) 1.429(3)	N(1)–Ru(1)–C(26) 117.42(8)
N(2)–C(7) 1.331(3)	N(2)–Ru(1)–C(18) 118.77(8)
N(2)–C(6) 1.437(3)	N(1)–Ru(1)–C(18) 92.80(8)
C(7)–C(9) 1.399(3)	C(10)–N(1)–Ru(1) 125.37(15)
C(9)–C(10) 1.403(3)	C(12)–N(1)–Ru(1) 116.17(14)
	C(7)–N(2)–Ru(1) 125.94(15)
	C(6)–N(2)–Ru(1) 115.86(14)
	O(1)–C(28)–Ru(1) 173.1(2)

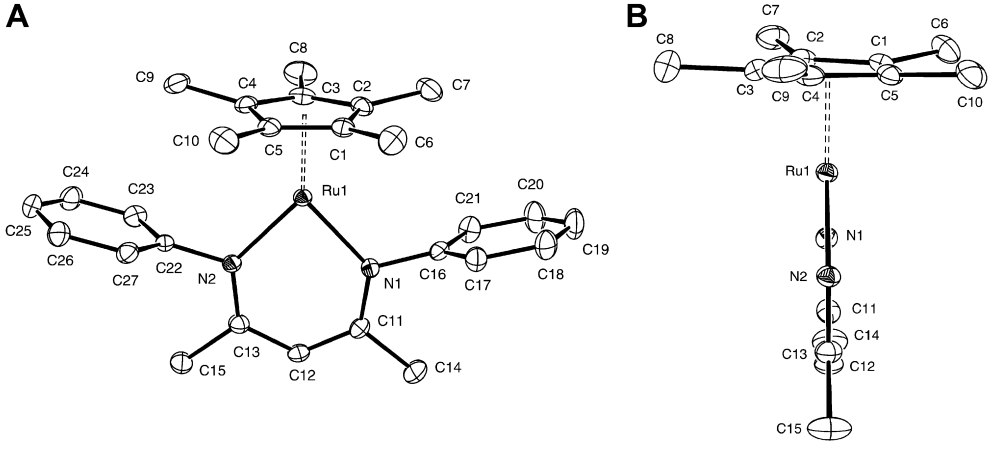
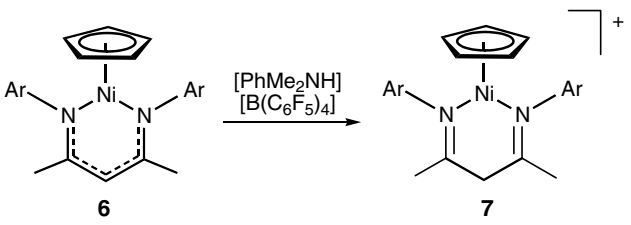


Fig. 1. ORTEP diagram of complex **4** showing atom numbering scheme. (A) Full view; (B) side view (2 Ph groups omitted for clarity).

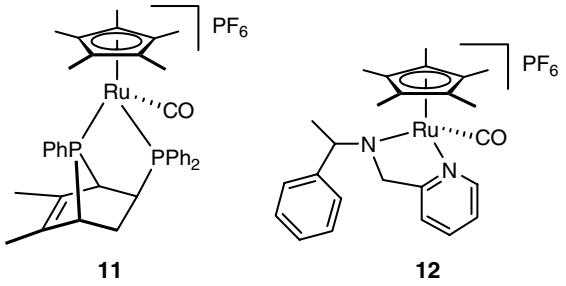


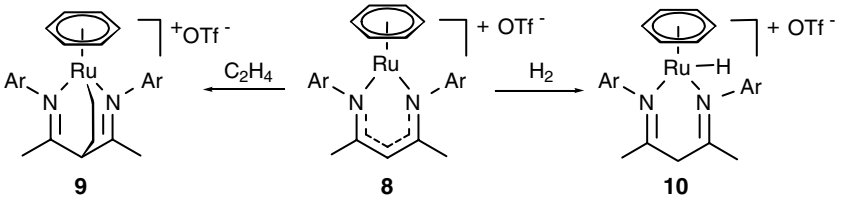
Scheme 2.

the angle between the NiN_2 and Cp^* planes in **7** is 90.5° (see Scheme 3).

A similar 16-electron Ru cationic complex **8** was reported by Phillips et al. [23] The Ru–N bond distances are 1.997(5) and 1.994(5) Å, shorter than those in **4** (2.053(2) and 2.046(2) Å), and the arene centroid to Ru distance is 1.670 Å, also shorter than the Cp^*–Ru distance in **4** (1.800 Å). These differences can perhaps be attributed to the effect of the cationic Ru atom in **8**. The bite angle N–Ru–N is 88.5(2)°, similar to that of **4**. Though neutral complex **4** has no reaction with H_2 and ethylene, **8** can react with H_2 and ethylene in THF to give **9** and **10**, respectively by incorporation of the CH carbon of the nacnac ligand in the reaction chemistry.

In contrast to the lack of reactivity of **4** towards H_2 or ethylene, reaction with CO occurred cleanly to afford adduct **5**, the principal structural features of which are given in Fig. 2. Crystallographic data are summarized in Table 1, and selected bond lengths and angles appear in Table 2. The coordination environment around Ru(1) is *pseudo*-tetrahedral. The angle involving the metal center and the bis(ketenimine) ligand deviates from 90° (N(1)–Ru(1)–N(2) = 88.30(7)°) with bond distances Ru(1)–N(1) and Ru(1)–N(2) of 2.1363(19) and 2.1309(19) Å, respectively. The distance between Ru(1) and the center of the Cp^* ring is 1.885 Å. In this complex, the least squares plane of the nacnac ligand and Ru(1) (Ru(1)–N(2)–C(7)–C(9)–C(10)–N(1)) is tilted toward the Cp^* plane with an interplanar angle of 45.6°. There is still significant delocalization within the π-system of the nacnac ligand, suggested by the two similar C–C distances of 1.399(2) and 1.403(3) Å and the two similar C–N distances of 1.331(3) and 1.325(3) Å. The Ru–nacnac ring itself is, however, less planar than that in **4**, with the largest deviation from the least squares plane of (Ru(1)–N(2)–C(7)–C(9)–C(10)–N(1)) being the Ru atom, which is displaced from the plane by 0.100 Å. The Ru–carbonyl bond distance Ru(1)–C(28) (1.837(2) Å) is shorter than those in two cationic analogues, **11** (1.865(8) Å) [24], and **12**, 1.880(3) Å [25]. The Ru–C(O) bond distance in the analogue Cp^*Ru(amidinate)(CO) is 1.828(7) Å [10] that is identical within experimental error to that of **5**.





Scheme 3.

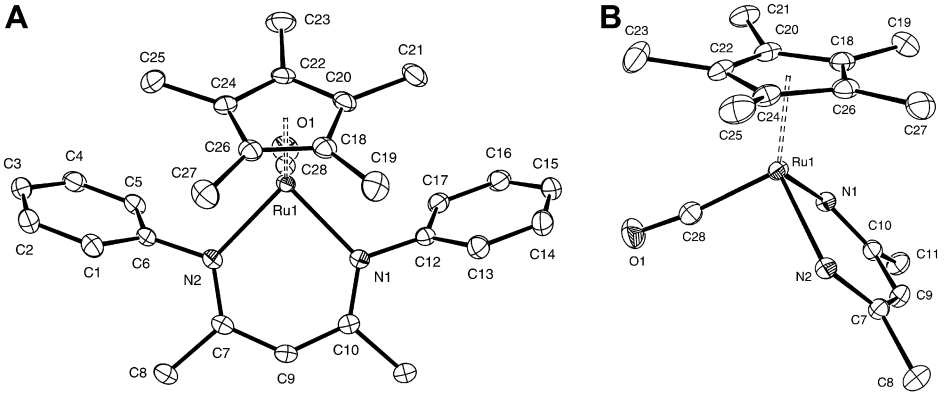


Fig. 2. ORTEP diagram of complex **5** showing atom numbering scheme. (A) Full view; (B) side view (2 Ph groups omitted for clarity).

4. Conclusions

It is evident that the Ru–nacnac complex **4** is disappointingly unreactive with small molecules, unlike some of its cationic analogues. This likely due to decreased Lewis acidity of the metal center in a neutral complex, coupled with the steric effects of the phenyl groups on the α-*N*-atoms.

Acknowledgement

R.P.H. is grateful to the National Science Foundation for generous financial support.

Appendix A. Supplementary material

CCDC 651859 and 651860 contain the contains the supplementary crystallographic data for **4** and **5**. These data can be obtained free of charge via http://www.ccdc.cam.ac.uk/conts/retrieving.html, or from the Cambridge Crystallographic Data Centre, 12 Union Road, Cambridge CB2 1EZ, UK; fax: (+44) 1223-336-033; or e-mail: deposit @ccdc.cam.ac.uk. Supplementary data associated with this article can be found, in the online version, at doi:10.1016/j.poly.2007.11.002.

References

[1] G. Consiglio, F. Morandini, Chem. Rev. 87 (1987) 761.
[2] M. Jiménez-Tenorio, M.C. Puerta, P. Valerga, Eur. J. Inorg. Chem. (2004) 17.
[3] V. Cadierno, M.P. Gamasa, J. Gimeno, Coord. Chem. Rev. 248 (2004) 1627.
[4] B.K. Campion, R.H. Heyn, T.D. Tilley, Organometallics, J. Chem. Soc. Chem. Commun. (1988) 278.
[5] T. Arliguie, C. Border, B. Chaudret, J. Devillers, R. Poilblanc, Organometallics 8 (1989) 1308.
[6] M. Jiménez-Tenorio, M.C. Puerta, P. Valerga, J. Am. Chem. Soc. 115 (1993) 9794.
[7] C. Gemel, K. Mereiter, R. Schmid, K. Kirchner, Organometallics 16 (1997) 5601.
[8] C. Gemel, V.N. Sapunov, K. Mereiter, M. Ferencic, R. Schmid, K. Kirchner, Inorg. Chim. Acta 286 (1999) 114.
[9] U. Koelle, Chem. Rev. 98 (1998) 1313.
[10] Y. Yamaguchi, H. Nagashima, Organometallics 19 (2000) 725.
[11] U. Koelle, J. Kossakowski, G. Raabe, Angew. Chem., Int. Ed. Engl. 29 (1990) 773.
[12] M.E. Smith, F.J. Hollander, R.A. Andersen, Angew. Chem., Int. Ed. Engl. 32 (1993) 1294.
[13] B.C. Bailey, F. Basuli, J.C. Huffman, D.J. Mindiola, Organometallics 25 (2006) 3963.
[14] H. Hamaki, N. Takeda, N. Tokitoh, Organometallics 25 (2006) 2457.
[15] S. Harder, J. Brettar, Angew. Chem., Int. Ed. Engl. 45 (2006) 3474.
[16] G. Bai, P. Wei, A.K. Das, D.W. Stephan, Dalton Trans. (2006) 1141.
[17] G. Bai, P. Wei, D.W. Stephan, Organometallics 25 (2006) 2649.
[18] U.J. Kilgore, F. Basuli, J.C. Huffman, D.J. Mindiola, Inorg. Chem. 45 (2006) 487.
[19] A.B. Pangborn, M.A. Giardello, R.H. Grubbs, R.K. Rosen, F.J. Timmers, Organometallics 15 (1996) 1518.
[20] T.D. Tilley, R.H. Grubbs, J.E. Bercaw, Organometallics 3 (1984) 274.
[21] J.E. Parks, R.H. Holm, Inorg. Chem. 7 (1968) 1408.
[22] G. Bai, P. Wei, A. Das, D.W. Stephan, Organometallics 25 (2006) 5870.
[23] A.d. Phillips, G. Laurenczy, R. Scopelliti, P.J. Dyson, Organometallics 26 (2007) 1120.
[24] D. Duraczynska, J.H. Nelson, Dalton Trans. (2005) 92.
[25] H. Brunner, J. Klankermayer, M. Zabel, Organometallics 21 (2002) 5746.

Available online at www.sciencedirect.com
ScienceDirect
Polyhedron 27 (2008) 739–749
POLYHEDRON
www.elsevier.com/locate/poly

Copper(II) complexes with pyrazolyl-substituted nitronyl and imino nitroxides

Eugene V. Tretyakov, Svyatoslav E. Tolstikov, Elena V. Gorelik, Matvey V. Fedin, Galina V. Romanenko, Artem S. Bogomyakov, Victor I. Ovcharenko *

International Tomography Center, Siberian Branch, Russian Academy of Sciences, Institutskaya Street, 3a, RU-630090 Novosibirsk, Russian Federation

Received 31 August 2007; accepted 2 November 2007

Abstract

It was established that the reactions of pyrazol-3-yl-substituted nitronyl nitroxide ($\mathbf{HL}^1$) and pyrazol-3-yl-substituted imino nitroxide ($\mathbf{HL}^3$) with Cu(II) acetate lead to self-assembly of the $Cu_4(OH)_2(OAc)_4(DMF)_2(L^1)_2$ tetranuclear and $Cu_2(OAc)_2(H_2O)_2(L^3)_2$ dinuclear complexes, respectively. The reaction of Cu(II) acetate with 5-ethoxycarbonyl-pyrazol-3-yl-substituted nitronyl nitroxide ($\mathbf{HL}^2$) gave unexpected solid $Cu_2(H_2O)_2(L^6)_2 \cdot 2DMF$, in which $\mathbf{L}^6$ is a deprotonated 5-carboxy-pyrazol-3-yl-substituted nitronyl nitroxide, formed as a result of cleavage of an ester bond in the starting $\mathbf{HL}^2$. A similar transformation of the paramagnetic ligand was observed in the reaction of Cu(II) acetate with 5-ethoxycarbonyl-pyrazol-3-yl-substituted imino nitroxide ($\mathbf{HL}^4$). It led to the formation of $Cu_2(DMF)_2(L^7)_2$, where $\mathbf{L}^7$ is deprotonated 2-(5-carboxy-1*H*-pyrazol-3-yl)-4,4,5,5-tetramethyl-4,5-dihydro-1*H*-imidazole 3-oxide. An X-ray diffraction study indicated that in $Cu_4(OH)_2(OAc)_4(DMF)_2(L^1)_2$ and $Cu_2(OAc)_2(H_2O)_2(L^3)_2$, the $\mathbf{L}^1$ and $\mathbf{L}^3$ paramagnetic ligands perform the bridging cyclic tridentate function, while in $Cu_2(H_2O)_2(L^6)_2 \cdot 2DMF$ and $Cu_2(DMF)_2(L^7)_2$, the paramagnetic $\mathbf{L}^6$ and diamagnetic $\mathbf{L}^7$ are bridging bicyclic tetradentate ligands. The magnetic behavior of complexes with coordinated nitronyl nitroxide – $Cu_4(OH)_2(OAc)_4(DMF)_2(L^1)_2$ and $Cu_2(H_2O)_2(L^6)_2 \cdot 2DMF$ is dictated by the dominant antiferromagnetic exchange interactions, which is confirmed by quantum-chemical data. The magnetic susceptibility of $Cu_2(OAc)_2(H_2O)_2(L^3)_2$ reflects the competition between the antiferromagnetic and ferromagnetic components, of which the latter is due to electron coupling in the Cu(II) ← N=C–N ÷ O exchange channels. EPR data confirm the results received from static magnetic measurements for multi-spin solids.
© 2007 Elsevier Ltd. All rights reserved.

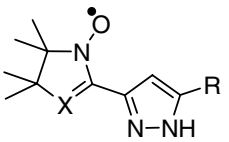
Keywords: Nitronyl nitroxides; Imino nitroxides; Pyrazoles; Copper complexes

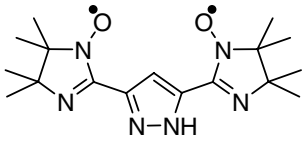
1. Introduction

Pyrazolyl-substituted nitronyl (NN-Pz) and imino nitroxides (IN-Pz) are of particular interest as stable paramagnetic ligands useful in the design of magnetic structures, which stimulates the development of methods for their selective synthesis. A wide range of spin-labeled pyrazoles are now accessible [1], with which mixed-ligand complexes of hexafluoroacetylacetonates [1a,2] and polynuclear metal pivalates [3] have been obtained. At the same time, there are few examples of chelate compounds with deprotonated spin-labeled derivatives NN-Pz and IN-Pz and include only two silver complexes: $[Ag(\mathbf{L}^3)]_6$ and $[Ag(\mathbf{L}^5)]_n$ [1d] and two nickel complexes: $[Ni_3(\mathbf{L}^1)_6]$ and $[Ni_3(\mathbf{L}^3)_6]$ [4]. We have attempted to expand this series of complexes by adding to them Cu(II) compounds with $\mathbf{HL}^1$, $\mathbf{HL}^2$, $\mathbf{HL}^3$, and $\mathbf{HL}^4$. Indeed, we have succeeded in isolating new complexes with spin-labeled pyrazoles and defined their structure. The magnetic properties of these compounds were analyzed using DFT calculations. It has been found that the copper ions are capable of promoting unusual transformations of the paramagnetic ligand.

* Corresponding author. Tel.: +7 383 3331945; fax: +7 383 3331399.
E-mail address: Victor.Ovcharenko@tomo.nsc.ru (V.I. Ovcharenko).

0277-5387/$ - see front matter © 2007 Elsevier Ltd. All rights reserved.
doi:10.1016/j.poly.2007.11.003





HL[5]

HL[1]: R = H, X = $N^+–O^-$
HL[2]: R = CO_2Et, X = $N^+–O^-$
HL[3]: R = H, X = N
HL[4]: R = CO_2Et, X = N

2. Experimental

2.1. Materials and methods

IR spectra were recorded in the 400–4000 cm^{-1} region on a VECTOR 22 Bruker spectrophotometer (KBr pellets). Microanalyses were performed on a Carlo Erba 1106 instrument. The nitroxides **HL**[1], **HL**[2], **HL**[3], and **HL**[4] were prepared by the procedures described in the literature [1e]. All reagents and organic solvents were analytical quality and used as purchased.

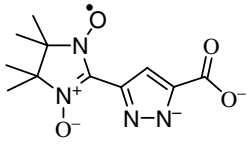
2.2. Syntheses of the complexes

2.2.1. $Cu_4(OH)_2(OAc)_4(DMF)_2(L^1)_2$ (1)

A solution of $Cu(OAc)_2 \cdot H_2O$ (180 mg, 0.9 mmol) in water (1.5 ml) was added to a solution of nitronyl nitroxides **HL**[1] (100 mg, 0.45 mmol) in a mixture of water (1.5 ml) and MeOH (1.5 ml). The resulting solution was kept for 12 h, whereupon the solvent was distilled off in vacuum at room temperature. The residue was dissolved in a minimal amount of DMF (~4 ml). The solution was filtered into a conical flask, which was then connected via a U-tube with a flask containing Et_2O (20 ml). Single crystals of good quality were grown due to gradual dilution of the DMF solution of the complex with diethyl ether that took place under these conditions. After 7 days, the greenish blue crystals were separated by filtration and washed with ether. Yield 200 mg (80%). IR: $\tilde{\nu}_{max} = 415, 485, 546, 614, 672, 699, 790, 872, 972, 1020, 1080, 1103, 1136, 1171, 1211, 1252, 1328, 1382, 1428, 1477, 1576, 1613, 1667, 2928, 2998, 3129, 3436$ cm^{-1}. Elemental *Anal.* Calc. for $C_{34}H_{56}Cu_4N_{10}O_{16}$: C, 36.6; H, 5.1; N, 12.6. Found: C, 36.8; H, 5.3; N, 12.4%. Compound **1** also formed in ~80% yield when the reaction of $Cu(OAc)_2 \cdot H_2O$ (180 mg, 0.9 mmol) with **HL**[1] (100 mg, 0.45 mmol) was conducted in DMF.

2.2.2. $Cu_2(H_2O)_2(L^6)_2 \cdot 2DMF$ (2)

A solution of $Cu(OAc)_2 \cdot H_2O$ (130 mg, 0.66 mmol) in water (2 ml) was added to a solution of nitronyl nitroxide **HL**[2] (100 mg, 0.33 mmol) in MeOH (3 ml). The resulting solution was stored for 12 h; then the solvent was distilled off in vacuum at room temperature. The residue was crystallized as described for **1**. Compound **2** was obtained as greenish blue crystals suitable for an X-ray analysis. Yield 110 mg (77%). IR: $\tilde{\nu}_{max} = 481, 548, 607, 662, 798, 848, 875, 1026, 1074, 1101, 1138, 1170, 1298, 1324, 1351, 1379, 1403, 1467, 1510, 1627, 1666, 2993, 3393$ cm^{-1}. Elemental *Anal.* Calc. for $C_{28}H_{44}Cu_2N_{10}O_{12}$: C, 40.1; H, 5.3; N, 16.7. Found: C, 39.9; H, 5.3; N, 16.7%. When conducted in DMF, the reaction also gave compound **2** in ~85% yield.



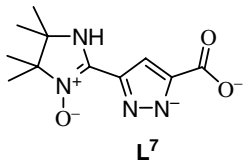
L[6]

2.2.3. $Cu_2(OAc)_2(H_2O)_2(L^3)_2$ (3)

A solution of $Cu(OAc)_2 \cdot H_2O$ (80 mg, 0.39 mmol) in water (1.5 ml) was added to a solution of imino nitroxides **HL**[3] (80 mg, 0.39 mmol) in a mixture of water (1.5 ml), MeOH (1 ml), and EtOH (1.5 ml). The resulting solution was stored for 12 h; then the solvent was distilled off in vacuum at room temperature. The residue was processed as described for **1**. Complex **3** was obtained as dark green crystals suitable for an X-ray analysis. Yield 40 mg (30%). IR: $\tilde{\nu}_{max} = 422, 468, 567, 611, 633, 684, 723, 795, 891, 935, 968, 1020, 1077, 1137, 1188, 1260, 1340, 1369, 1400, 1482, 1593, 1676, 2928, 2972, 3248, 3454$ cm^{-1}. Elemental *Anal.* Calc. for $C_{24}H_{40}Cu_2N_8O_8$: C, 41.4; H, 5.8; N, 16.1. Found: C, 41.6; H, 5.7; N, 16.1%.

2.2.4. $Cu_2(DMF)_2(L^7)_2$ (4)

A solution of $Cu(OAc)_2 \cdot H_2O$ (131 mg, 0.72 mmol) in water (2 ml) was added to a solution of imino nitroxides **HL**[4] (100 mg, 0.36 mmol) in MeOH (1 ml); this immediately resulted in the formation of a brown fine precipitate. Then MeOH (2 ml) was added until the precipitate dissolved. The resulting solution was kept for 15 min; then the solvent was distilled off in vacuum at room temperature. The residue was treated as described for **1**. After 2 days, the solution became greenish blue, and green needles gradually crystallized. After 5 days, the crystals were separated by filtration and washed with ether. Yield 50 mg (36%). IR: $\tilde{\nu}_{max} = 480, 570, 607, 714, 774, 800, 858, 898, 1026, 1074, 1113, 1142, 1202, 1246, 1331, 1348, 1391, 1447, 1544, 1625, 2812, 2885, 2990, 3199, 3454$ cm^{-1}. Elemental *Anal.* Calc. for $C_{28}H_{42}Cu_2N_{10}O_8$: C, 43.5; H, 5.5; N, 18.1. Found: C, 42.5; H, 5.6; N, 16.8%.



L[7]

2.3. X-ray measurement and structure determination

Diffraction reflections were obtained on a SMART APEX CCD (Bruker AXS) diffractometer (Mo Kα, $\lambda = 0.71073$ Å, $T = 295$ K; an absorption correction was applied using the Bruker SADABS program, version 2.10). The structures were solved by direct methods and refined by the full-matrix least-squares method in an anisotropic approximation for all non-hydrogen atoms. Some of the H atoms were located in a difference electron density map, while others were located at calculated positions. The methyl H atoms were refined as a rigid group in an isotropic approximation. All calculations on structure solution and refinement were carried out with a Bruker SHELXTL Version 6.14 program complex. The crystal data for the complexes, details of experiment, and selected bond lengths and angles are given in Tables 1 and 2.

2.4. Magnetic measurements

The magnetic susceptibility of the polycrystalline complexes was measured with a Quantum Design MPMS-5S SQUID magnetometer in the temperature range 2–300 K with magnetic fields of up to 5 kOe. None of the complexes exhibited any field dependence of molar susceptibility at low temperatures. Diamagnetic corrections were made using the Pascal constants. The effective magnetic moment was calculated as $\mu_{\text{eff}}(T) = [(3k/N_A\mu_B{}^2)\ \chi'_M T]^{1/2}$, where χ'_M is corrected molar susceptibility.

Table 1
Crystal data and details of experiment for complexes **1**–**4**

Compound	**1**	**2**	**3**	**4**
Formula	$Cu_4(OH)_2(OAc)_4(DMF)_2(L^1)_2$	$Cu_2(H_2O)_2(L^6)_2 \cdot 2DMF$	$Cu_2(OAc)_2(H_2O)_2(L^3)_2$	$Cu_2(DMF)_2(L^7)_2$
FW	1115.04	839.81	693.70	773.80
Space group	*Pbca*	$P2_1/n$	*Pc*	$P2_1/c$
Z	4	2	2	2
a (Å)	10.936(2)	7.1873(8)	11.504(2)	10.541(2)
b (Å)	20.537(4)	22.521(3)	9.338(2)	15.485(3)
c (Å)	21.349(4)	11.278(1)	14.083(3)	10.527(2)
β (°)		97.529(2)	99.381(3)	107.21(3)
V (Å)^3	4794.6(15)	1809.9(3)	1492.6(5)	1641.3(6)
D_{calc} (g cm^{-3})	1.545	1.541	1.543	1.566
μ (Mo Kα) (cm^{-1})	0.1824	1.248	1.484	1.360
θ (°)	1.91–23.30	1.81–23.31	1.79–29.61	2.02–23.34
I_{hkl} collected/unique	26404/3450	13834/2597	12953/6842	12371/2353
R_{int}	0.0388	0.0918	0.0817	0.2020
N	330	324	428	275
Goodness-of-fit (GOF)	1.296	1.023	0.901	1.204
R_1 for $I > 2\sigma_I$	0.0337	0.0499	0.0480	0.1050
wR_2	0.0960	0.1002	0.1094	0.2058
R_1 for all data	0.0415	0.0725	0.0689	0.1430
wR_2	0.1008	0.1074	0.1203	0.2240

Table 2
Selected bond lengths (Å) and angles (°) for complexes **1**–**4**

Compound	**1**		**2**	**3**		**4**
$Cu–O_L$	2.014(2)		1.974(3)			1.922(5)
$Cu–O_{OAc}$	1.940(2)	1.933(2)	1.958(3)	1.961(4)	1.971(4)	1.963(5)
	2.487(2)	1.956(2)				2.293(7)
$Cu–O_{OH}$	1.943(2)	1.945(2)				
		2.295(2)				
$Cu–O_{DMF}$	2.394(3)					
Cu–Ow			2.282(5)	2.278(5)	2.276(5)	
$Cu–N_L$				2.111(5)	2.088(5)	
$Cu–N_{Pz}$	1.944(3)	1.968(3)	1.935(4)	1.992(5)	1.952(5)	1.942(6)
			1.973(3)	2.049(5)	1.978(5)	1.955(5)
N–O	1.301(4)		1.310(4)	1.294(8)	1.247(8)	1.342(7)
	1.267(4)		1.271(4)			
$\angle CuO_LN$	122.5(2)		124.2(3)			123.7(4)
$\angle CN_2$-Pz	13.0(3)		7.3(3)	5.3(8)	6.8(9)	3(1)
–O···O–	6.246		3.668(5)	4.379(5)		
Cu···O–			3.426(4)			
Cu···Cu	3.3830(8) 3.1217(7) 3.1453(8)		3.919(1)	4.0490(9)		3.921(2)

2.5. EPR measurements

The experiments have been carried out at commercial X-band (9 GHz) continuous wave EPR spectrometer (Bruker EMX) equipped with the homemade cryogenic system. For all studied compounds (**1**–**4**) the powder CW EPR spectra have been recorded within a temperature range 20–300 K in a standard way and then analyzed.

2.6. Computational details

All DFT calculations reported in this paper were performed with the ORCA program package [5]. The exchange correlation was treated in Perdew–Burke–Ernzerhof's (PBE) generalized gradient approximation [6]. An accurate all-electron Gaussian basis set of triple-zeta quality with two sets of polarization functions Wachters + f = (14s11p6d3f)/ [8s6p4d2f] [7] was used for the copper atom. All other (carbon, nitrogen, and hydrogen) atoms were described using the polarized 6-31G(d) basis set [8] of double-zeta quality.

Since our quantum-chemical study aimed at the interpretation of the experimentally observed magnetic properties that were obtained for polycrystalline samples, it dictated the use of X-ray data for electronic structure investigations of the complexes without further geometry optimization.

Molecular orbitals and spin density distributions were plotted using the MOLEKEL program [9]. The broken symmetry (BS) approach [10] was employed to elucidate the magnetic properties of multispin systems under study. The exchange coupling constants were calculated by the generalized spin projection method suggested by Yamaguchi et al. [11].

3. Results and discussion

3.1. Syntheses and structures of the complexes

Interaction of Cu(II) acetate with $\mathbf{HL}^1$ forms a heterospin complex, which crystallizes into perfect single crystals after the DMF solution of the complex has been gradually saturated with diethyl ether. The compound is formed at any ratio of the starting reagents. The optimal ratio, $Cu_2(OAc)_4(H_2O)_2/\mathbf{HL}^1 = 2/1$, leads to at least 80% yield of the product. The yield is drastically reduced when the initial reagent ratio is decreased under the same conditions; for example, the product yield is less than 8% when the ratio is 1/1. An X-ray diffraction study showed that the compound is a tetranuclear complex $Cu_4(OH)_2(OAc)_4(DMF)_2(L^1)_2$ (**1**).

The complex has a centrosymmetric molecule (Fig. 1). The square environment of Cu1, formed by the N3 atom of the pyrazole fragment and by the O atoms of the >N–O and OH groups and bridging bidentate acetate anion, is completed to the elongated bipyramid by the O_{OAc} and O_{DMF} atoms. The O_{OH} atom lies at the apex of the Cu2 square pyramid, while the N4 and O_{OH} atoms and two O_{OAc} atoms lie at its base. The paramagnetic ligand performs the cyclic tridentate bridging function, connecting the two Cu atoms. The planes of the pyrazole ring and the CN_2 fragment of the imidazole ring are

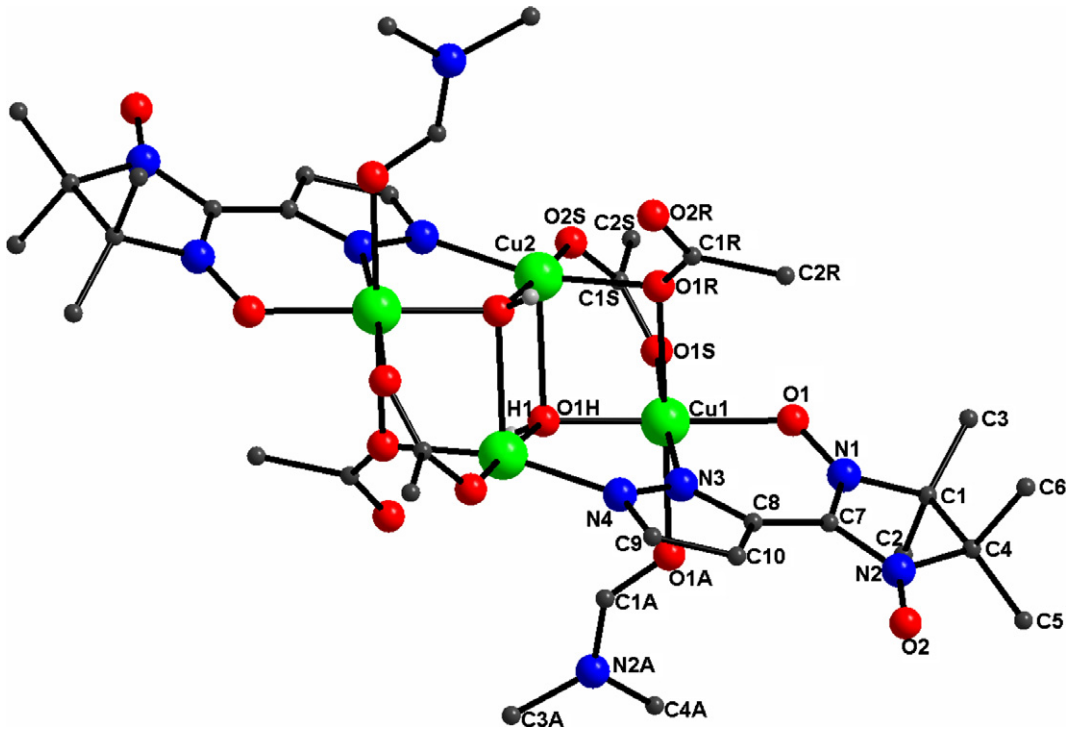


Fig. 1. Structure of molecule **1**.

non-coplanar ($\angle CN_2$-Pz, Table 2). The OH group is coordinated simultaneously by three Cu atoms. The O_{OH} atom lies in the $\{HCu_3\}$ trigonal pyramid. One of the two AcO^- anions is coordinated as a monodentate ligand, while the other, as (μ_2-O,O′), which affects the C–O bond lengths. In the first ligand, these bond lengths are appreciably different (1.272(5) and 1.221(5) Å), while in the second, they are almost the same (1.255(4) and 1.260(4) Å). The N–O distances in the paramagnetic $\mathbf{L}^1$ ligand are non-equivalent: 1.301(4) for the coordinated

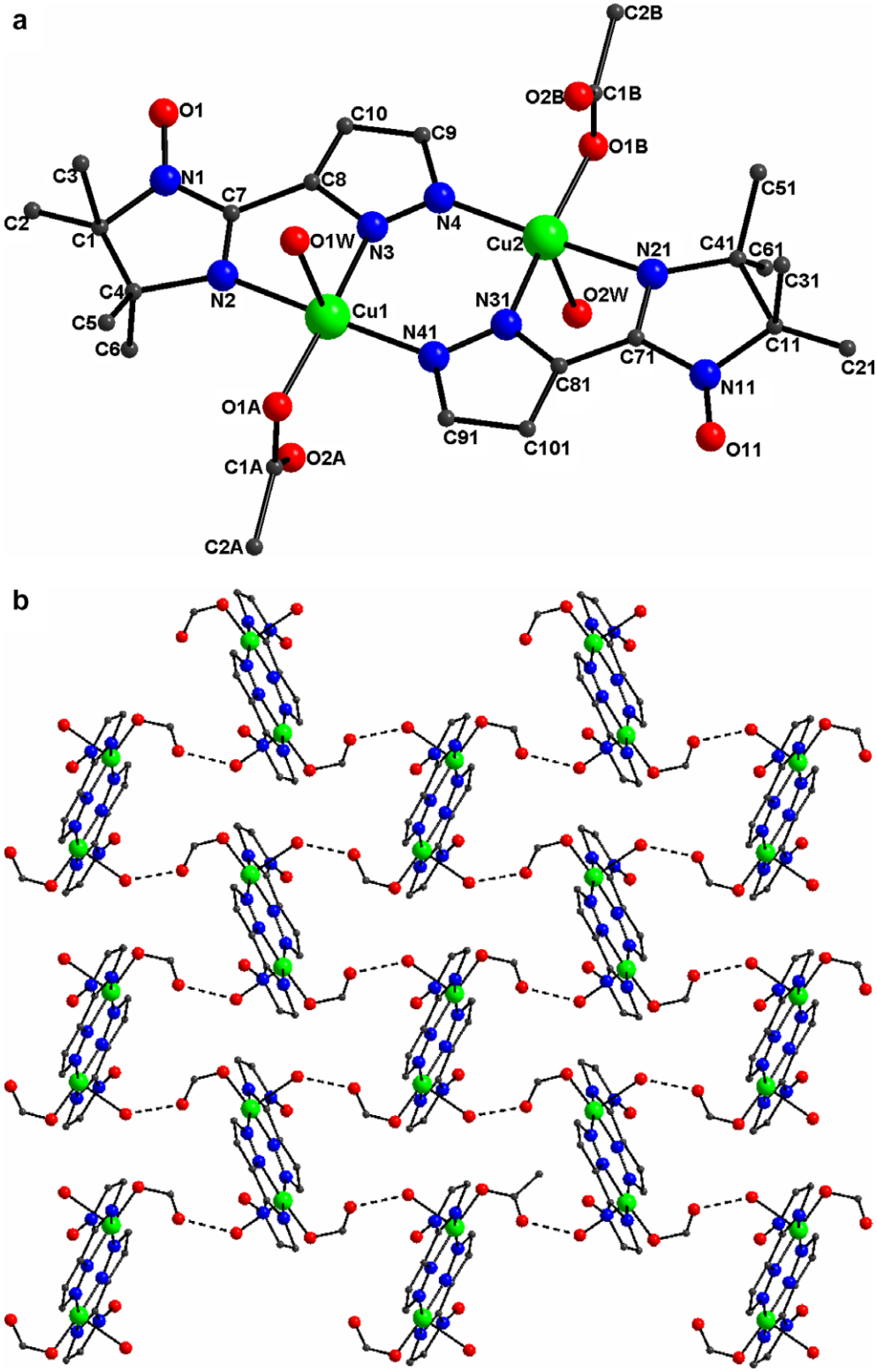


Fig. 2. Structure of the molecule (a) and layer (b, Me groups and H atoms omitted for clarity) in **2**.

NO group versus 1.267(4) Å for the uncoordinated group.

Structure analysis of complex **2**, formed by interaction of Cu(II) acetate with $\mathbf{HL}^3$ (an imine analog of $\mathbf{HL}^1$), showed that this is a dinuclear complex (Fig. 2a). The radical retains its cyclic tridentate bridging function on passing from nitronyl nitroxides to imino nitroxide. In molecule **2**, each of the two Cu atoms is surrounded by a square pyramid with the O atom of the water molecule at the apex. The base of the pyramid is formed by three N atoms of the paramagnetic ligands and the O atom of the acetate anion. The uncoordinated O atoms of the acetate anions form H-bonds with the coordinated water molecules of the neighboring chelates, which leads to the formation of layers in structure **2** (Fig. 2b).

The coordination mode of $\mathbf{L}^3$ was quite predictable; according to the data of the Cambridge Structural Database, this is just the way 3-(2-pyridyl)pyrazole is coordinated to Cu(II) [12,13] to give various products including dinuclear complexes [14]. For $\mathbf{L}^1$, however, the coordination mode cannot be compared with the available data because the database has no structural information for Cu(II) complexes with ligands containing a combination of donor functional groups similar to $\mathbf{L}^1$ [15]. Therefore, one can only assume that the size of the chelate ring that increased from **2** to **1**, as well as the lower donor ability of the O atom of the nitroxyl fragment compared to the imine N atom, enhance dissociation of coordinated water, provoking the condensation of two dinuclear fragments into a tetranuclear fragment in **1** via two μ_3-OH groups.

Based on the data obtained it might be assumed that similar complexes would also be produced from the ester derivatives $\mathbf{HL}^2$ and $\mathbf{HL}^4$. However, the reaction of Cu(II) acetate with $\mathbf{HL}^2$ under conditions similar to the conditions of synthesis of **1** gave the $[CuL^6(H_2O)]_2 \cdot 2DMF$ complex (**3**) as a solid product in a high yield, in which $\mathbf{L}^6$ is the

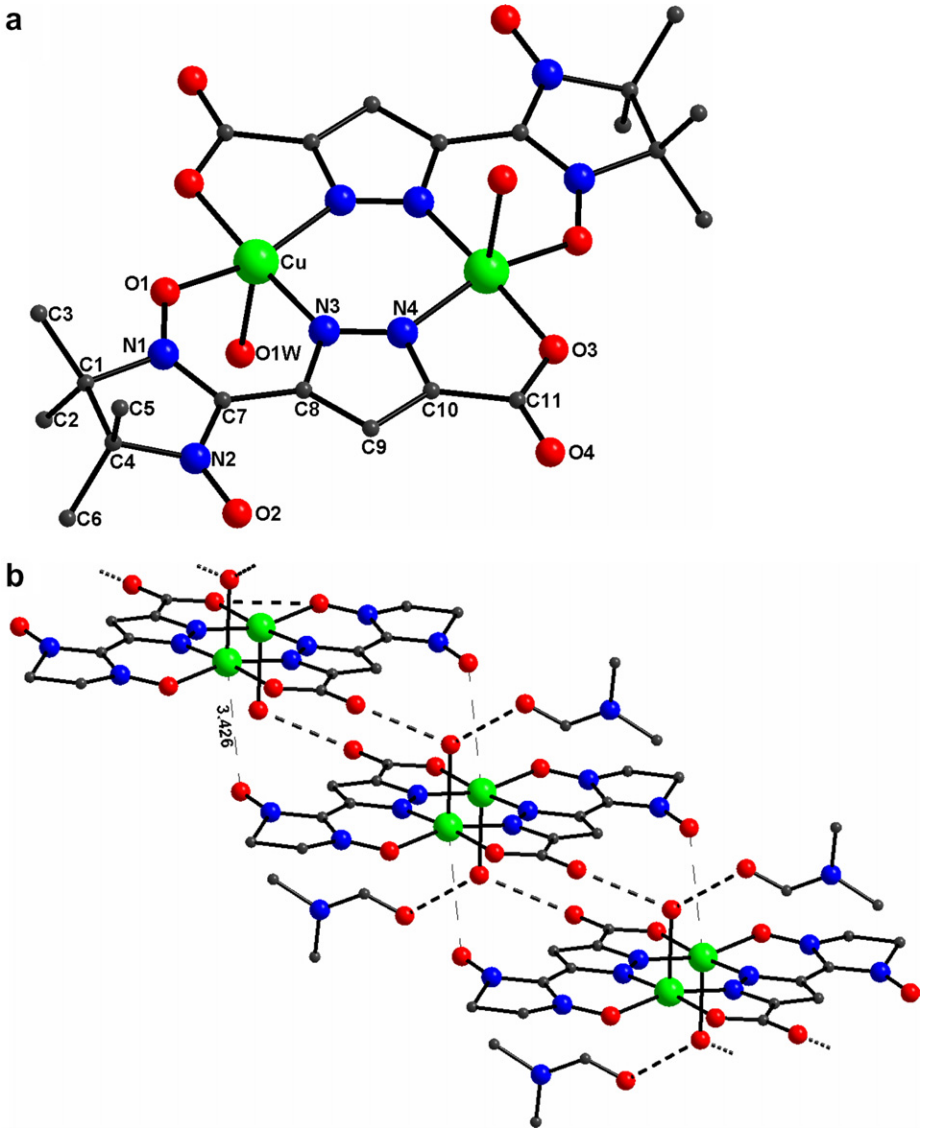


Fig. 3. Structure of the molecule (a) and ribbon (b) in **3**.

product of transformation of the starting nitronyl nitroxide. The complex is the major reaction product that may be reproduced at any starting ratio of reagents. As indicated by the results of X-ray diffraction investigation of **3**, transformation of $\mathbf{L}^2$ into $\mathbf{L}^6$ occurs without affecting the free valence. The structure of the dinuclear compound **3** (Fig. 3a) suggests that the reaction is a cascade process involving the splitting of the O–Et bond in the ester group of $\mathbf{HL}^2$ and further formation of a five-membered metallocycle due to coordination of the O atom of the deprotonated carboxyl group and the N atom of the pyrazole fragment. The structure of the six-membered chelate fragment in **3** is similar to that in **1**. As a result, the $\mathbf{L}^6$ dianion in the dinuclear compound **3** performs the bridging bicyclic tetradentate function.

In the centrosymmetric molecule **3**, the square environment of each Cu atom is completed to pyramidal by the O atoms of the water molecule Å (Fig. 3a), flanking the sides of the chelate plane. The water molecules of the two chelates, in turn, form a couple of contradirectional intermolecular H-bonds with the carboxyl O atoms. This leads to the formation of polymer ribbons in the solid state with short contacts (3.426(4) Å) between the Cu atoms and the N–O groups of the neighboring chelates arising within

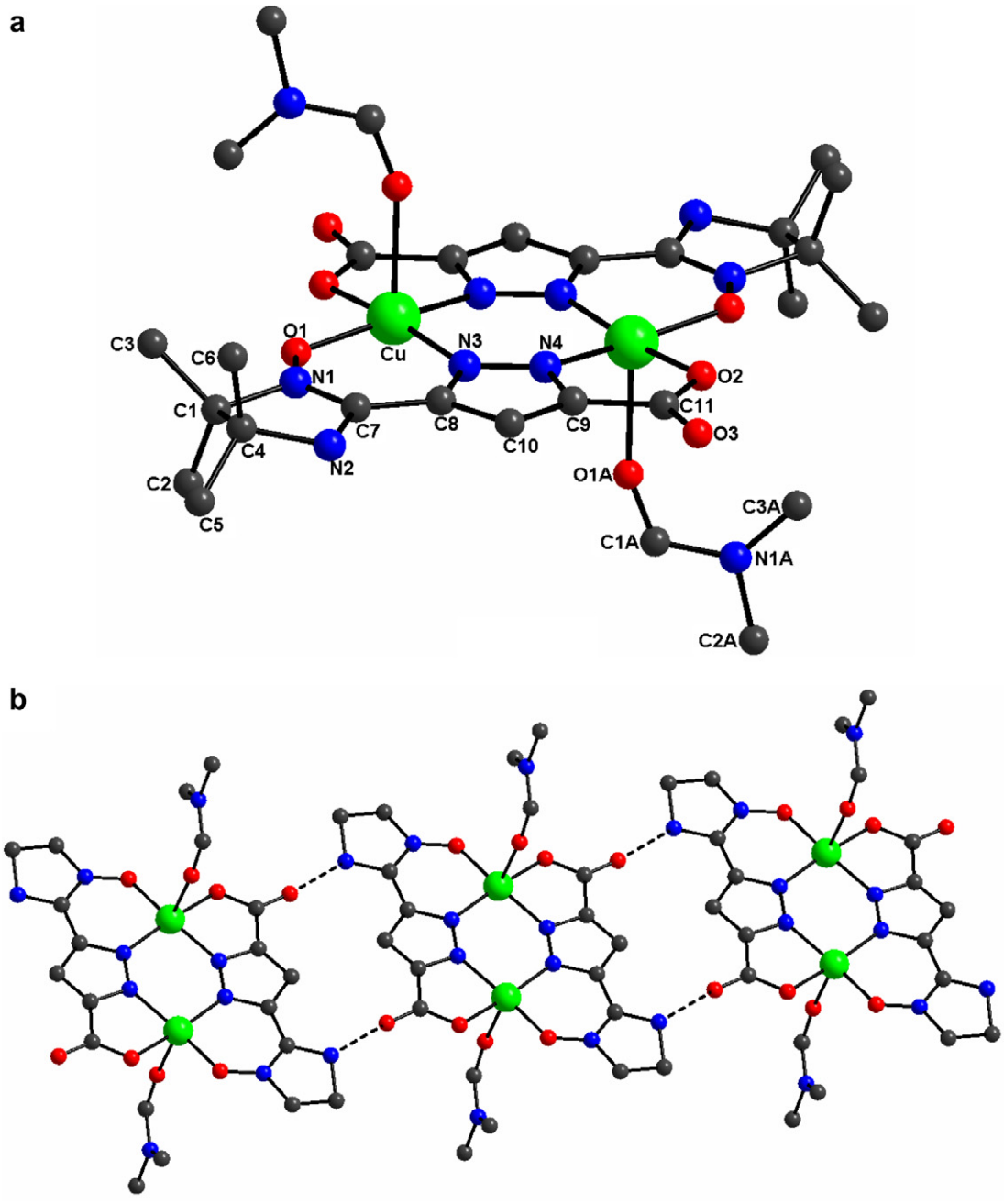


Fig. 4. Structure of the molecule (a) and ribbon (b) in **4**.

the ribbons. The DMF molecules H-bonded with the water molecules lie on the "periphery" of the ribbons (Fig. 3b).

The interaction of the ester derivative of imino nitroxide **HL**[4] with Cu(II) acetate confirmed that a cascade process is the general tendency for the given compounds. The reaction occurred with deprotonation of **HL**[4], cleavage of the C–O ester bond, and reduction of the imino nitroxide fragment to the oxoamidine fragment. The reaction ultimately formed the $Cu_2(DMF)_2(L^7)_2$ complex (**4**) whose structure is similar to that of $Cu_2(H_2O)_2(L^6)_2 \cdot 2DMF$ except that the axial position in the square pyramidal environment of each copper atom is occupied by the O atoms of the DMF molecule (Fig. 4a). In structure **4**, as well as in structure **3**, polymer ribbons are formed, but here they are formed in a different way – via the O···H–N bonds between the uncoordinated O atoms of the carboxyl groups and the NH groups of the neighboring molecules.

3.2. Magnetic properties of the compounds

The temperature dependences of the effective magnetic moment (μ_{eff}) for complexes **1**–**4** are presented in Fig. 5.

It is reasonable to start this section by discussing the magnetic behavior of compound **4**. This will enable us to evaluate the efficiency of the pyrazolate bridges in exchange interactions between the odd electrons of the Cu(II) ions, which are also present in more complex exchange clusters in **1**–**3**. For complex **4**, the high-temperature value of the magnetic moment is about 2.50 β, which is close to the value expected for the non-interacting spins of two copper(II) atoms (spin-only value is 2.45 β). The reduced magnetic moment at lower temperatures points to the antiferromagnetic exchange interactions. To evaluate the optimal parameters for **4** (J_{CuCu}, g_{Cu}) we employed the exchange-coupled dimer model [16]. The resulting parameters are listed in Table 3. Quantum-chemical calculation of the parameter of the exchange interaction gave

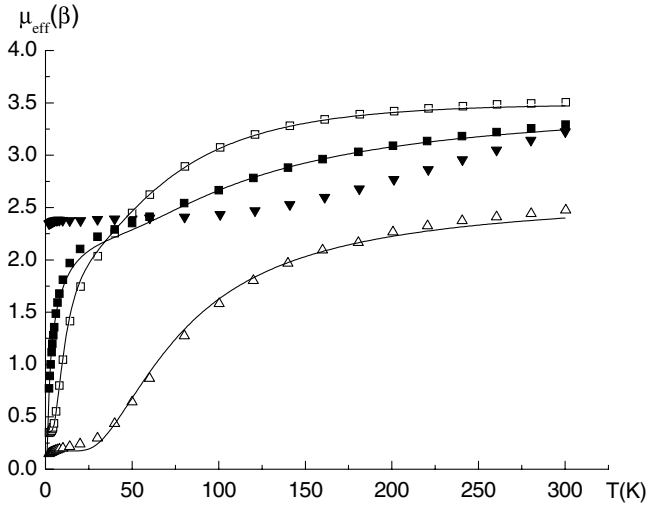


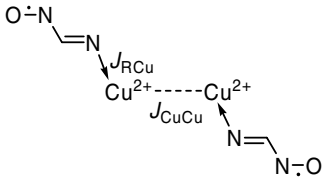
Fig. 5. Dependences $\mu_{eff}(T)$ for **1** (▼), **2** (□), **3** (■), and **4** (Δ). Solid lines – theoretical curves.

Table 3
Experimental and calculated (in parentheses) effective values of exchange interactions (in cm^{-1}) for **2**–**4**

Compound	**2**	**3**	**4**
J_{CuCu}	−72 (−316)	−74 (−120)	−72 (−186)
J_{RCu}	+101 (+174)	−16 (−92)	
g_{Cu}	1.93	2.12	2.19

$J_{CuCu} = -186\ cm^{-1}$ (the calculated values are given in parentheses in Table 3). The calculated value of J coincides (in the order of magnitude and sign) with the experimental value. The slightly overestimated value of J_{CuCu} is explained by the well-known tendency for DFT methods to overstabilize the low-spin states, which generally leads to the parameters of antiferromagnetic exchange exaggerated by a factor of 1.5–2 [17].

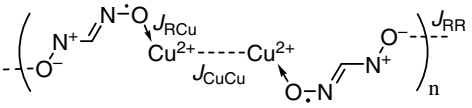
For complex **2**, the μ_{eff} increases at elevated temperatures and approaches 3.46 β, which is the theoretical value for four practically uncoupled spins with $S = 1/2$. From X-ray data for **2** it follows that interaction between the odd electrons of the Cu(II) ion and the N ÷ O group in the molecule occurs via the Cu(II) ← N=C–N ÷ O channel, due to which the interaction is ferromagnetic [18]. As in **4**, the intramolecular interaction between the odd electrons of the two Cu(II) ions occurs via the pyrazolate bridges, owing to which this is a strong antiferromagnetic interaction. Since the intermolecular distances between the paramagnetic centers exceed 4.379 Å in solid **2**, other interactions may be neglected in analysis of the experimental dependence $\mu_{eff}(T)$. Therefore, the exchange structure **2** may be regarded as a system of isolated four-center clusters:



Approximation of the experimental dependence $\mu_{eff}(T)$ by the isotropic spin-Hamiltonian of the cluster [19] allowed us to obtain the optimal values of the parameters g_{Cu} and exchange coupling energies J_{CuCu} and J_{RCu} (Table 3). They show that in solid **2** the antiferromagnetic exchange prevails over the ferromagnetic exchange, which was also confirmed by our quantum-chemical data (Table 3).

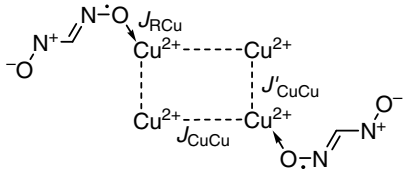
The high-temperature asymptotics of μ_{eff} for **3**, as well as for **2**, tends to reach the value 3.46 β, which is the theoretical value for a system of four spins with $S = 1/2$ provided that $J \ll kT$. Spin coupling gradually takes place at lower temperatures. In molecule **3**, the exchange interaction of the odd electrons of the Cu(II) ions via the pyrazolate bridges should be antiferromagnetic, as in the case of **2** and **4**. Moreover, each of the Cu(II) ions coordinates the O atom

of the nitronyl nitroxyl fragment in the equatorial position, which is known [18] to predetermine the antiferromagnetic character of exchange in the Cu(II)–O ÷ N< cluster. Another possible channel of exchange interactions may be dictated by the short distances (3.426(4) Å) between the O atoms of the >N ÷ O groups of the neighboring molecules. To substantiate the model of dominant exchange interactions, we performed quantum-chemical calculations of J_{CuCu} and J_{RCu} based on the real geometry of molecule **3**. These calculations showed that the intramolecular exchange interactions are antiferromagnetic (Table 3). The efficiency of intermolecular interaction was evaluated based on the calculated data for the cluster that includes two neighboring molecules **3**. According to this estimation, $|J_{RR}|$ is of the order of 1 cm^{-1}. Therefore, exchange structure **3** may be regarded as a system of intramolecular four-center clusters weakly interacting with one another:



The optimal values of the parameters g_{Cu}, J_{CuCu}, and J_{RCu} obtained by approximation of the experimental dependence $\mu_{eff}(T)$ within the framework of the isotropic spin-Hamiltonian are listed in Table 3.

For complex **1**, μ_{eff} decreases at reduced temperatures, and around 100 K the dependence $\mu_{eff}(T)$ becomes a plateau with $\mu_{eff} \approx 2.41$ β, which is close to the theoretical value 2.45 β for two weakly interacting spins $S = 1/2$ with $g = 2$. This behavior of the dependence $\mu_{eff}(T)$ suggests that at $T \leqslant 100$ K the four spins are completely coupled in **1**. Since the X-ray study showed that in solid compound **1** the intermolecular distances between the paramagnetic centers exceed 6 Å, the strong antiferromagnetic interactions are evidently concentrated in the tetranuclear molecules of the complex. In the centrosymmetric molecule **1**, four Cu(II) ions are linked with one another by pairs of various channels, forming an exchange triangle. Moreover, each of the two Cu(II) ions lying at the opposite vertices of an imaginary exchange triangle interacts with the paramagnetic ligand coordinated to it. Thus, exchange structure **1** may be viewed as a system of isolated six-centered clusters:



The optimal values of the parameters g_{Cu}, J_{CuCu}, J'_{CuCu}, and J_{RCu} could not be determined because of the character of the experimental dependence $\mu_{eff}(T)$ for **1**. Our quantum-chemical calculation indicated that the exchange interaction channels J_{CuCu} via the pyrazolate complex and the coordinated OH group and J'_{CuCu} via the acetate bridge differ considerably in intensity. Interaction via the acetate bridge is weak antiferromagnetic; $J'_{CuCu} \sim -11$ cm^{-1}. At the same time, the exchange interaction channel between the Cu(II) ions linked by the pyrazolate bridge and the OH group is characterized as having an unusually high exchange coupling parameter $J_{CuCu} = -938$ cm^{-1}. This may be assumed to be exactly the channel that is responsible for the effective spin coupling in the exchange rectangle. An antiferromagnetic interaction as strong as this is a consequence of direct overlapping of the copper-centered magnetic orbitals on the oxygen atom of the coordinated OH group (Fig. 6). As would be expected for this type of coordination of the nitronyl nitroxyl fragment, the copper–radical interaction is antiferromagnetic with $J_{RCu} = -60$ cm^{-1}.

3.3. EPR characterization of the compounds

The EPR spectrum of complex **4** and its temperature dependence are typical for the two-spin system coupled antiferromagnetically (Fig. 7a). At high temperatures the spectrum consists of the strong absorption band at $g \approx 2.15$ and weaker line at the half-field region of the spectrum ($g \approx 4.2$), characteristic for spin dimers [20,21]. On lowering the temperature, an absolute intensity of the spectrum decreases and spectrum completely disappears below ca. 30 K. At $T = 20$ K only a weak and narrow signal with $g \approx 2.013$ is observed, which is most likely to be assigned to the small admixture of nitroxide radical. Double integration of spectra at $T = 296$ and 20 K allows for the estimate that the concentration of admixture does not exceed 0.4% and thus its influence on the magnetic properties of **4** can be safely neglected.

The room temperature (296 K) EPR spectrum of the compound **1** consists of the single broad line (peak-to-peak width ca. 90 mT) at $g \approx 2.054$ (Fig. 7b). The line shape is close to Lorentzian, implying an assignment to the strongly-coupled exchange cluster. On lowering the temperature, this line gradually transforms into a narrow line with $g \approx 2.008$ observed at $T = 20$ K. The value of the g-

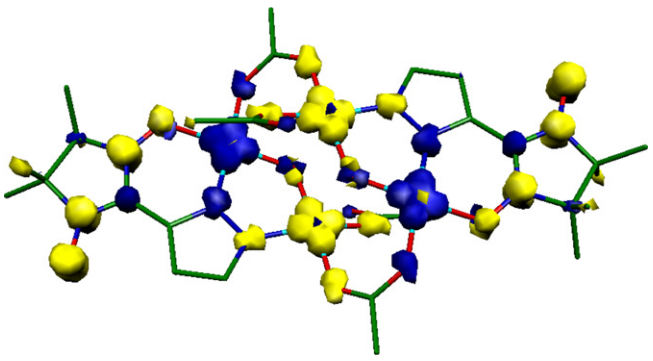


Fig. 6. Spin density in complex **1** for the minimal-energy BS state (H atoms omitted for clarity).

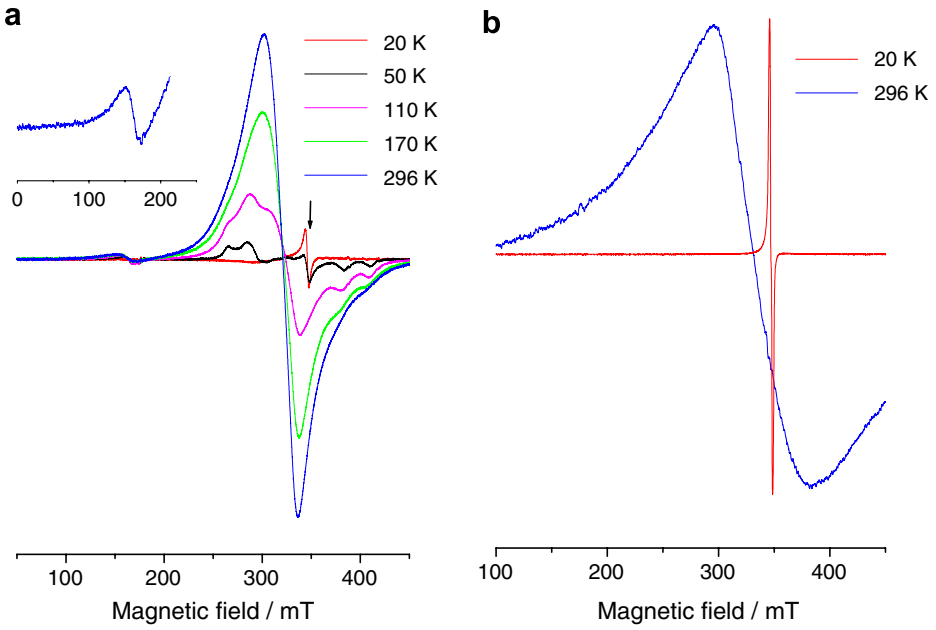


Fig. 7. EPR spectra of **4** at $T = 20$-296 K. The arrow marks the signal of nitroxide admixture. Inset: magnified signal of $\Delta m_s = 2$ transition at $T = 296$ K (a). EPR spectra of **1** at $T = 20$ and 296 K. The intensities are normalized (b).

factor, as well as the width of the line at $T = 20$ K, indicate that at low temperatures the spectrum is dominated by nitroxides and the contribution of copper spins is negligible. This is consistent with the magnetic behavior and the above conclusions, that 4 spins of coppers are strongly-coupled antiferromagnetically and thus virtually do not influence the magnetism below ca. 100 K.

The EPR behavior of the compounds **2** and **3** is rather similar to each other. The spectrum consists of the single broad Lorentzian line (peak-to-peak width ca. 150 mT at room temperature) with no any additional signals. For both compounds, the positions of these lines are temperature dependent. The value $g = 1.969$ is measured for complex **2** at room temperature (296 K), whereas at $T = 20$ K much higher value $g = 2.025$ is observed. For complex **3** the value $g = 1.963$ is found at $T = 296$ K, the value $g = 2.037$ at $T = 120$ K, and at $T = 20$ K the spectrum intensity is too small to be safely detected. The unusual g-values <2 at room temperatures, as well as their temperature dependence, might result from the antiferromagnetic coupling within a four-spin system. Similar effects have been recently observed by us and interpreted for the case of spin triads nitroxide–copper(II)–nitroxide [22–24]. Therefore, these peculiarities are very interesting and will be the future subject of separate investigation beyond this work.

4. Conclusions

Thus our study has shown that the reactions of $\mathbf{HL}^1$ and $\mathbf{HL}^3$ with Cu(II) acetate lead to self-assembly of the $Cu_4(OH)_2(OAc)_4(DMF)_2(L^1)_2$ tetranuclear and $Cu_2(OAc)_2(H_2O)_2(L^3)_2$ dinuclear complexes, respectively, in which $\mathbf{L}^1$ and $\mathbf{L}^3$ perform the bridging cyclic tridentate function by linking the two Cu atoms. The greatest differences between these complexes are due to the character of the intramolecular exchange interactions. The magnetic behavior of $Cu_4(OH)_2(OAc)_4(DMF)_2(L^1)_2$ is dictated by the dominant antiferromagnetic exchange interactions, as confirmed by the results of quantum-chemical analysis of the exchange coupling channels. The magnetic properties of $Cu_2(OAc)_2(H_2O)_2(L^3)_2$ reflect the competition between the antiferromagnetic and ferromagnetic contributions, of which the latter is due to the interaction of electrons in the Cu(II) ← N=C–N ÷ O exchange channels.

It has been found that the reaction of Cu(II) acetate with $\mathbf{HL}^2$ or $\mathbf{HL}^4$ occurs with cleavage of the ester group, resulting in the formation of $Cu_2(H_2O)_2(L^6)_2 \cdot 2DMF$ and $Cu_2(DMF)_2(L^7)_2$ solid dinuclear complexes, where $\mathbf{L}^6$ and $\mathbf{L}^7$ are the products of transformation of the starting nitroxides, which in the case of $\mathbf{HL}^2$ occurs without affecting the free valence. This possibility should be taken into account in designing heterospin systems based on transition metal complexes with polyfunctional nitroxides.

Acknowledgements

This work was supported by the Russian Foundation for Basic Research (Grant Nos. 05-03-32305, 06-03-32157, 06-03-32742, 06-03-04000, 05-03-32264-a), FASI (State Contract No. 02.513.11.3044), CRDF (RUE1-2839-NO-06), President of the RF (Grant NSh-4821.2006.3, MK-4362.2006.3, MK-6673.2006.3), the programs of the Presidium and OKhNM, Russian Academy of Sciences, and the programs of the Siberian (Lavrentiev

Grant SB RAS No. 79) and Ural Branches of the Russian Academy of Sciences.

Appendix A. Supplementary material

CCDC 645063, 645062, 645064 and 645065 contain the supplementary crystallographic data for this paper **1**, **2**, **3** and **4**. These data can be obtained free of charge via http://www.ccdc.cam.ac.uk/conts/retrieving.html, or from the Cambridge Crystallographic Data Centre, 12 Union Road, Cambridge CB2 1EZ, UK; fax: (+44) 1223-336-033; or e-mail: deposit@ccdc.cam.ac.uk. Supplementary data associated with this article can be found, in the online version, at doi:10.1016/j.poly.2007.11.003.

References

[1] (a) S.F. Vasilevsky, E.V. Tretyakov, O.M. Usov, Yu.N. Molin, S.V. Fokin, Yu.G. Shwedenkov, V.N. Ikorskii, G.V. Romanenko, R.Z. Sagdeev, V.I. Ovcharenko, Mendeleev Commun. (1998) 216;
(b) L. Catala, R. Feher, D.B. Amabilino, K. Wurst, J. Vaciana, Polyhedron 20 (2001) 1563;
(c) S.F. Vasilevsky, E.V. Tretyakov, V.N. Ikorskii, G.V. Romanenko, S.V. Fokin, Y.G. Shwedenkov, V.I. Ovcharenko, Arkivoc ix (2001) 55;
(d) S. Yamada, T. Ishida, T. Nogami, Dalton Trans. 6 (2004) 898;
(e) E.V. Tretyakov, S.E. Tolstikov, G.V. Romanenko, Yu.G. Shvedenkov, R.Z. Sagdeev, V.I. Ovcharenko, Russ. Chem. Bull., Int. Ed. 54 (2005) 2169.

[2] (a) V.I. Ovcharenko, K.Yu. Maryunina, S.V. Fokin, E.V. Tretyakov, G.V. Romanenko, V.N. Ikorskii, Russ. Chem. Bull., Int. Ed. 53 (2004) 2406, and references therein;
(b) E. Tretyakov, S. Fokin, G. Romanenko, V. Ikorskii, S. Vasilevsky, V. Ovcharenko, Inorg. Chem. 45 (2006) 3671;
(c) K. Maryunina, S. Fokin, V. Ovcharenko, G. Romanenko, V. Ikorskii, Polyhedron 24 (2005) 2094;
(d) G.V. Romanenko, S.V. Fokin, S.F. Vasilevsky, E.V. Tretyakov, Yu.G. Shvedenkov, V.I. Ovcharenko, Russ. J. Coord. Chem. 27 (2001) 360;
(e) L. Catala, K. Wurst, D.B. Amabilino, J. Vaciana, J. Mater. Chem. 16 (2006) 2736.

[3] V. Ovcharenko, E. Fursova, G. Romanenko, I. Eremenko, E. Tretyakov, V. Ikorskii, Inorg. Chem. 45 (2006) 5338.

[4] S. Yamada, M. Yasui, T. Nogami, T. Ishida, Dalton Trans. (2006) 1622.

[5] F. Neese, ORCA – An Ab Initio, Density Functional and Semiempirical Program Package, Version 2.5, Revision 20. University of Bonn, 2007.

[6] J.P. Perdew, K. Burke, M. Ernzerhof, Phys. Rev. Lett. 77 (1996) 3865.

[7] (a) A.J.H. Wachters, J. Chem. Phys. 52 (1970) 1033;
(b) C.W. Bauschlicher Jr., S.R. Langhoff, L.A. Barnes, J. Chem. Phys. 91 (1989) 2399.

[8] E.R. Davidson, D. Feller, Chem. Rev. 86 (1986) 681.

[9] S. Portmann, H.P. Lüthi, Chimia 54 (2000) 766.

[10] (a) C.A. Daul, I. Ciofini, A. Bencini, in: K.D. Sen (Ed.), Reviews of Modern Quantum Chemistry. Part II, World Scientific, Singapore, 2002, p. 1247;
(b) L. Noodleman, C.Y. Peng, D.A. Case, J.M. Mouesca, Coord. Chem. Rev. 144 (1995) 199;
(c) L. Noodleman, J.G. Norman Jr., J. Chem. Phys. 70 (1979) 4903.

[11] (a) M. Shoji, K. Koizumi, Y. Kitagawa, T. Kawakami, S. Yamanaka, M. Okumura, K. Yamaguchi, Chem. Phys. Lett. 432 (2006) 343;
(b) T. Soda, Y. Kitagawa, T. Onishi, Y. Takano, Y. Shigeta, H. Nagao, Y. Yoshioka, K. Yamaguchi, Chem. Phys. Lett. 319 (2000) 223;
(c) K. Yamaguchi, F. Jensen, A. Dorigo, K.N. Houk, Chem. Phys. Lett. 149 (1988) 537.

[12] V. Chandrasekhar, L. Nagarajan, K. Gopal, V. Baskar, P. Kogerler, Dalton Trans. (2005) 3143.

[13] J.C. Jeffery, P.L. Jones, K.L.V. Mann, E. Psillakis, J.A. McCleverty, M.D. Ward, C.M. White, Chem. Commun. (1997) 175.

[14] J. Pons, A. Chadghan, A. Alvarez-Larena, J.F. Piniella, J. Ros, Inorg. Chem. Commun. 4 (2001) 610.

[15] Cambridge Structural Database, Version 5.28, November 2006 (Updates May 2007).

[16] B. Bleaney, K.D. Bowers, Proc. Roy. Soc. A 214 (1952) 451.

[17] (a) E. Ruiz, P. Alemany, S. Alvarez, J. Cano, J. Am. Chem. Soc. 119 (1997) 1297;
(b) R. Caballol, O. Castell, F. Illas, I. De P.R. Moreira, J.P. Malrieu, J. Phys. Chem. A 101 (1997) 7860;
(c) A. Bencini, F. Totti, C.A. Daul, K. Doclo, P. Fantucci, V. Barone, Inorg. Chem. 36 (1997) 5022.

[18] F. Lanfranc de Panthou, D. Luneau, R. Musin, L. Öhrström, A. Grand, P. Turek, P. Rey, Inorg. Chem. 35 (1996) 3484.

[19] I.V. Ovcharenko, Yu.G. Shvedenkov, R.N. Musin, V.N. Ikorskii, J. Struct. Chem. 40 (1999) 29.

[20] A. Bencini, D. Gatteschi, EPR of Exchange Coupled Systems, Springer-Verlag, Berlin, 1990.

[21] S. Ferrer, P.J. van Koningsbruggen, J.G. Haasnoot, J. Reedijk, H. Kooijman, A.L. Spek, L. Lezama, A.M. Arif, J.S. Miller, J. Chem. Soc., Dalton Trans. (1999) 4269.

[22] M. Fedin, S. Veber, I. Gromov, V. Ovcharenko, R. Sagdeev, A. Schweiger, E. Bagryanskaya, J. Phys. Chem. A 110 (2006) 2315.

[23] M. Fedin, S. Veber, I. Gromov, V. Ovcharenko, R. Sagdeev, E. Bagryanskaya, J. Phys. Chem. A 111 (2007) 4449.

[24] M. Fedin, S. Veber, I. Gromov, K. Maryunina, S. Fokin, G. Romanenko, R. Sagdeev, V. Ovcharenko, E. Bagryanskaya, Inorg. Chem., in press, doi:10.1021/ic7014385.

Available online at www.sciencedirect.com
ScienceDirect
Polyhedron 27 (2008) 750–758
POLYHEDRON
www.elsevier.com/locate/poly

Supported 12-tungstophosphoric acid as heterogeneous and recoverable catalysts for the synthesis of oxazolines, imidazolines and thiazolines under solvent-free conditions

Iraj Mohammadpoor-Baltork *, Majid Moghadam *, Shahram Tangestaninejad, Valiollah Mirkhani, Seyedeh Fatemeh Hojati

Department of Chemistry, Catalysis Division, University of Isfahan, Isfahan 81746-73441, Iran

Received 1 October 2007; accepted 6 November 2007
Available online 27 December 2007

Abstract

12-Tungstophosphoric acid (TPA) supported on silica, activated carbon and poly(4-styrylmethyl)pyridinium chloride (PMP) were found to be highly efficient catalysts for the synthesis of oxazolines, imidazolines and thiazolines from the condensation of various nitriles with aminoalcohols, ethylenediamine and cisteamine, respectively. In the case of oxazolines, dicyanobenzenes were selectively converted to mono- and bis-oxazolines in the presence of these catalysts. In the reaction of dicyanobenzenes with ethylenediamine, only mono-imidazolines were produced and the remaining cyano group did not react even with long reaction times. In the case of thiazolines, only bis-thiazolines were produced in the reaction of dicyanobenzenes with cysteamine. Furthermore, these catalysts could be recovered and reused without significant loss of their activities.
© 2007 Elsevier Ltd. All rights reserved.

Keywords: Oxazolines; Imidazolines; Thiazolines; Nitrile; 12-Tungstophosphoric acid

1. Introduction

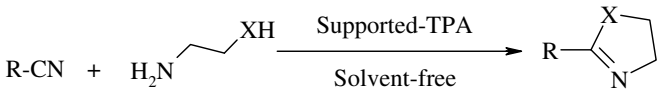
Reusable heterogeneous catalysts have attracted a great deal of interest in recent years [1]. Since most of the catalysts are expensive and contaminate the environment, the development of efficient methods for recovery and reuse of the catalysts is a very important aspect in this chemistry. An easy solution to this problem is to heterogenize the homogeneous catalysts by supporting them on solid materials. The major advantages of solid-supported catalysts are the facile recovery from the reaction mixture and the possibility of reusing them. Furthermore, supporting of the catalysts efficiently increases the surface area and subsequently the reactivity of the catalysts.

Heteropoly acids (HPAs) are an important class of catalysts having both redox and acid properties [2]. Among the heteropoly acids, polytungstic acids are the most widely used catalysts due to their high acid strengths, thermal stability and low reducibility. Heteropoly acid catalysts have many advantages over liquid acid catalysts, being are harmless to the environment with respect to corrosiveness, safety and quantity of waste. Supported heteropoly acids and specially supported 12-tungstophosphoric acid have been known as important classes of supported catalysts that have received much attention in recent publications [3,4]. These catalysts offer several advantages such as high mechanical and thermal stabilities, easy handling, non-toxicity, high reactivity and recyclability.

2-Oxazolines, 2-imidazolines and 2-thiazolines are very important moieties due to their extensive applications in chemistry, biochemistry and pharmacology [5–9]. These heterocycles are found in the structures of many

* Corresponding authors. Tel.: +98 311 7932705; fax: +98 311 6689732.
E-mail addresses: imbaltork@sci.ui.ac.ir (I. Mohammadpoor-Baltork), moghadamm@chem.ui.ac.ir (M. Moghadam).

0277-5387/$ - see front matter © 2007 Elsevier Ltd. All rights reserved.
doi:10.1016/j.poly.2007.11.018



X= S, NH, O

R= Aryl

Scheme 1.

biologically active natural products [10,11]. They also exhibit several pharmaceutical activities such as antidiabetic [12], antihypertensive [13], antidepressive [14], anticancer [15], anti HIV-1 [16], antitumor [17] and antialzimer [18] activities. They are also known as important intermediates in organic transformations [19,20]. Optically active mono- and bis-derivatives of these heterocycles have been widely used as both auxiliaries and ligands in asymmetric synthesis [21–23].

Several publications have been reported for the preparation of 2-substituted oxazolines, imidazolines and thiazolines from different precursors such as carboxylic acids [24], esters [25], nitriles [26,27], amides [28], aziridines [29], hydroxymoyl chlorides [30] and aldehydes [31]. Many of these procedures have several drawbacks such as strong acidic conditions, long reaction times, low yields of the products, use of complex reagents and toxic solvents. Therefore, there is still a need to search for a better catalyst with regards to toxicity, selectivity, availability, reusability and easy work-up conditions for these transformations. Herein we wish to report the use of supported-TPAs as highly efficient catalysts for the clean, suitable and chemoselective synthesis of 2-substituted oxazolines, imidazolines and thiazolines (Scheme 1).

2. Experimental

All materials were commercial reagent grades and were prepared from Merck or Fluka. ^{1}H NMR spectra were recorded on a Bruker-Arance AQS 300 MHz. FT-IR spectra were obtained as potassium bromide pellets in the range 400–4000 cm^{-1} with a Nicolet-Impact 400D instrument. All melting points were obtained by a Stuart Scientific apparatus. All the reactions were monitored by TLC and all yields refer to isolated products. The PMP was prepared by the reaction of chloromethylatedpolystyrene with refluxing pyridine [32]. The silica support was Cab-oSil® M5 and was prepared from Riedel-deHaen. The carbon used was activated carbon, purchased from Merck.

2.1. Preparation of the supported 12-tungstophosphoric acid

The supported TPAs catalysts were prepared by the method of incipient wetness. In a typical process, a 400 mg portion of TPA was dissolved in deionized water (50 mL) and impregnated drop-wise onto 1600 mg poly(4-styrylmethyl)pyridinium chloride (PMP), high surface area SiO_2 (Cabosil 20) and activated carbon supports under constant agitation. The resulting pastes were dried at 110 °C for 4 h and then calcined at 250 °C for 4 h (except for PMP) [33]. The PMP catalyst was dried at 100 °C because the polymer is degraded at 250 °C.

FT-IR spectra have been proven to be a powerful technique for the study of the surface interaction between HPA and organic and inorganic supports. Pure TPA compounds display a characteristic infrared fingerprint in the region of ca. 1100–700 cm^{-1}, attributed to ν_{as}(P=O_a) 1090–1060 cm^{-1}, ν(W=O_d) 1010–930 cm^{-1}, ν_{as}(W–O_b–W) 900–870 cm^{-1} and ν_{as}(W–O_c–W) 850–700 cm^{-1} [34,35] For example, the infrared spectrum of TPA–C exhibited strong vibrations at 1080 (P=O), 973 (W=O), 901 and 814 cm^{-1} (W–O–W). The result suggests that the structure of the 12-tungstophosphoric acid of unit TPA–C was similar to that of TPA. The IR spectrum of PMP–TPA exhibited strong vibrations at 1080 (P=O), 973 (W=O), 900 and 819 cm^{-1}, which confirms that the structure of the 12-tungstophosphoric acid of unit PMP–POM was also similar to that of TPA. In the case of TPA–SiO_2 the IR spectrum shows vibrations at 982 (W=O), 899 and 819 cm^{-1} (W–O–W) and the band assigned to P=O vibrations is masked by SiO_2 broad vibrations. To obtain further information on the structure of the catalysts, we analyzed supported-TPAs by neutron activation analysis (NAA). The content of TPA on all supports, which were calculated from the W content in the supported-TPA catalysts, was determined by neutron activation analysis. The amounts of W loading on the supported catalysts were 29.75 ± 0.9, 28.65 ± 0.9 and 29.53 ± 0.8 for SiO_2–TPA, C–TPA and PMP–TPA, respectively.

The specific surface area for silica was 180 m^2/g. After supporting of TPA, this value reduced to 121 m^2/g, which indicated that HPA has been supported successfully on the silica surface. In the case of carbon the specific surface area was 800 m^2/g which reduced to 720 m^2/g after supporting of TPA on it.

2.2. General procedure for the synthesis of mono- and bis-oxazolines and mono-imidazolines

A mixture of nitrile (1 mmol), aminoalcohols or ethylenediamine (4 mmol per each nitrile group) and supported-tungstophosphoric acids (SiO_2–TPA, C–TPA, PMP–TPA) (30 mg, 0.2 mol% for mononitriles and 45 mg, 0.3 mol% of TPA for dinitriles) was placed in a round bottomed flask and heated at 100 °C (in the case of imidazolines the reactions were performed at 110 °C) for the appropriate time according to Tables 2 and 3. After completion of the reaction, as indicated by TLC, the mixture was cooled to room temperature, diluted with cold ethanol (10 mL) and filtered. The solid material was washed with cold ethanol (10 mL). The solvent was evaporated and the residue was purified by recrystallization in *n*-hexane or by column chromatography (neutral alumina) to afford the pure product.

2.3. General procedure for the conversion of nitriles to thiazolines

Nitrile (1 mmol), 2-aminoethanethiol (1.5 mmol per each nitrile group) and supported catalysts (15 mg, 0.1 mol%) were mixed and heated at 110 °C for the appropriate time (Table 4). At the end of the reaction, as indicated by TLC, the mixture was cooled to room temperature, diluted with cold ethanol (10 mL) and filtered. The solid material was washed with cold ethanol (10 mL). Evaporation of the solvent and purification of the crude product by recrystallization in *n*-hexane or by column chromatography on neutral alumina afforded the desired thiazoline.

2.3.1. Spectroscopic data

2.3.1.1. 3-(4′,5′-Dihydro-1H-imidazol-2′-yl)benzonitrile (Table 3, entry 9). Mp: 133–134 °C, ^{1}H NMR (500 MHz, $CDCl_3$): δ 3.81 (s, 4H, $2CH_2$), 4.2 (br s, 1H, NH), 7.51 (t, $J = 7.8$ Hz, 1H, ArH), 7.71 (d, $J = 7.7$ Hz, 1H, ArH), 8.01 (d, $J = 7.9$ Hz, 1H, ArH), 8.05 (s, 1H, ArH). MS; $m/z = 171$ (M^+, 8.89%), 169 (44.05%), 142 (76.19%), 128 (100%).

2.3.1.2. 2-(4′-Hydroxyphenyl)-4,5-dihydro-1,3-thiazole (Table 4, entry 4). Mp: 176–178 °C, ^{1}H NMR (300 MHz, $CDCl_3$): δ 3.43 (t, $J = 8.3$ Hz, 2H, CH_2–S), 3.85 (br s, 1H, OH), 4.44 (t, $J = 8.3$ Hz, 2H, CH_2–N), 6.84 (d, $J = 8.5$ Hz, 2H, ArH), 7.73 (d, $J = 8.5$ Hz, 2H, ArH). MS; $m/z = 179$ (M^+, 91.33%), 177 (7.33%), 151 (8.06%).

2.3.1.3. 2-(4′-Pyridyl)-4,5-dihydro-1,3-thiazole (Table 4, entry 7). Mp: 74–76 °C, ^{1}H NMR (300 MHz, $CDCl_3$): δ 3.48 (t, $J = 8.5$ Hz, 2H, CH_2–S), 4.51 (t, $J = 8.5$ Hz, 2H, CH_2–N), 7.68 (dd, $J = 1.5$ and 4.5 Hz, 2H, ArH), 8.71 (dd, $J = 1.5$ and 4.5 Hz, 2H, ArH). MS; $m/z = 164$ (M^+, 93.15%), 162 (4.67%), 136 (17.12%).

2.3.1.4. 2-[3′-(4″,5″-Dihydro-1″,3″-thiazol-2″-yl)phenyl]-4,5-dihydro-1,3-thiazole (Table 4, entry 9). Mp: 111–113 °C, ^{1}H NMR (300 MHz, $CDCl_3$): δ 3.46 (t, $J = 8.4$ Hz, 4H, $2CH_2$–S), 4.49 (t, $J = 8.4$ Hz, 4H, $2CH_2$–N), 7.48 (t, $J = 7.8$ Hz, 1H, ArH), 7.95 (dd, $J = 1.5$ and 7.8 Hz, 2H, ArH), 8.27 (s, 1H, ArH). MS; $m/z = 248$ (M^+, 100%), 246 (11.44%), 244 (2.74%), 220 (32.19%), 192 (11.44%).

3. Results and discussion

3.1. Optimization of reaction conditions

First, the ability of the TPA supported on inorganic (high surface area silica-gel and active carbon) and organic (poly-(4-styrylmethyl)pyridinium chloride) supports was investigated with regard to the synthesis of 2-substituted oxazolines. For this aim, the reaction of benzonitrile with 2-aminoethanol in the presence of 0.15–0.25 mol% of supported catalysts was investigated. The reactions were performed in different solvents such as chloroform, dichloromethane, 1,2-dichloroethane and methanol, and in the absence of solvent at room temperature and under reflux conditions. The best results were obtained with molar ratios of benzonitrile/2-aminoethanol/supported catalysts; 1:4:0.002 at 100 °C under solvent-free conditions (Table 1, entries 1–9). 2-Phenyloxazoline was obtained in 90%, 92% and 90% yields using SiO_2–TPA, C–TPA and PMP–TPA as the catalyst, respectively. When the above mentioned reaction was performed with 1, 2 and 3 mol of 2-aminoethanol in the presence of SiO_2–TPA, the product was obtained in 35%, 55% and 72% yields, respectively.

To show the effect of supporting on the catalytic activities of TPA, the reaction of benzonitrile (1 mmol) and 2-aminoethanol (4 mmol) in the presence of the same amounts of non-supported TPA (0.2 mol%) was carried out under the same reaction conditions. The results showed that the catalytic activity of TPA has been increased by supporting on high surface area SiO_2, active carbon and PMP. On the other hand, in the absence of TPA, the supports were less efficient to catalyze the reaction of benzonitrile with 2-aminoethanol. The results are summarized in Table 1.

3.2. Synthesis of 2-oxazolines and bis-oxazolines catalyzed by supported TPA

The chosen reaction conditions have been used for the successful preparation of a series of 2-substituted oxazolines. Various aromatic and heteroaromatic nitriles reacted with 2-aminoethanol and 2-amino-2-methylpropanol to produce the corresponding 2-oxazolines in high to excellent yields (Table 2).

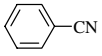
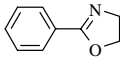
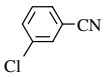
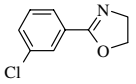
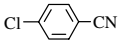
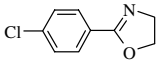
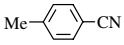
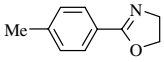
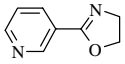
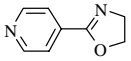
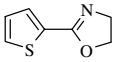
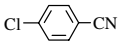
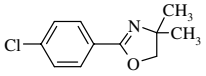
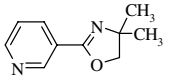
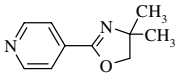
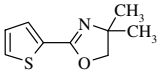
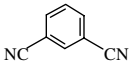
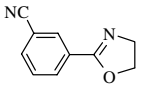
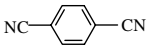
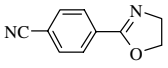
Due to the extensive applications of bis-oxazolines as ligands in chemistry [21–23,34], the reaction of dinitriles with 2-aminoethanol was performed in the presence of

Table 1
Investigation of catalyst effects in the synthesis of 2-phenyloxazoline from benzonitrile and 2-aminoethanol under solvent-free conditions[a]

Entry	Catalyst	TPA (mol%)	Time (h)	Yield[b] (%)
1	SiO_2–TPA	0.15	3	78
2	SiO_2–TPA	0.2	3	90
3	SiO_2–TPA	0.25	3	90
4	C–TPA	0.15	3	80
5	C–TPA	0.2	3	92
6	C–TPA	0.25	3	93
7	PMP–TPA	0.15	2	75
8	PMP–TPA	0.2	2	90
9	PMP–TPA	0.25	2	92
10	TPA	0.2	3	35
11	SiO_2		3	20
12	active carbon		3	12
13	PMP		3	10

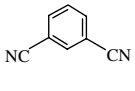
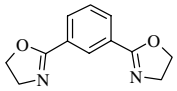
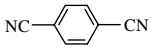
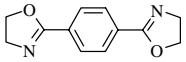
[a] Reaction conditions: benzonitrile (1 mmol), 2-aminoethanol (4 mmol).
[b] Isolated yields.

Table 2
Synthesis of 2-oxazolines and bis-oxazolines catalyzed by supported TPA under solvent-free conditions[a]

Row	Nitrile	Oxazoline[b]	SiO_2–TPA		C–TPA		PMP–TPA		Mp (°C), Ref.
			Time (h)	Yield[c] (%)	Time (h)	Yield (%)[c]	Time (h)	Yield[c] (%)	
1			3	90	3	92	2	90	Oil [36a]
2			2	93	1.5	95	1.5	93	40–42 [27a]
3			2.5	90	3	93	2	95	77–79 [36b]
4			4	80	3	90	3	80	69–71 [36a]
5			2	92	2	95	2	91	66–68 [36a]
6			0.5	94	0.75	95	0.75	96	109–111 [27a]
7			3	88	2.5	90	3	94	58–60 [36c]
8			5.5	70	5.5	75	5	76	78–80 [36d]
9			4	65	5	67	5	75	Oil [26a]
10			3	80	3	82	2.5	85	48–50 [26a]
11			4.5	75	4.5	75	4.5	77	30–32 [27a]
12			0.4	95	0.25	91	0.25	95	98–100 [27a]
13			0.5	90	0.3	90	0.3	93	112–114 [27a]

(*continued on next page*)

Table 2 (*continued*)

Row	Nitrile	Oxazoline[b]	SiO_2–TPA		C–TPA		PMP–TPA		Mp (°C), Ref.
			Time (h)	Yield[c] (%)	Time (h)	Yield (%)[c]	Time (h)	Yield[c] (%)	
14			6	80	6	78	6	80	137–139 [27a]
15			6	75	6	75	6	77	238–240 [36a]

[a] Reaction conditions: nitrile (1 mmol), 2-aminoethanol or 2-amino-2-methylpropanol (4 mmol), catalyst (30 mg; 0.2 mol%) for mononitriles and dinitrile (1 mmol), 2-aminoethanol (8 mmol), catalyst (45 mg; 0.3 mol%) for dinitriles.
[b] All products were identified by comparison with authentic samples (IR, ^{1}H NMR, mp).
[c] Isolated yields.

Table 3
Synthesis of 2-imidazolines catalyzed by supported TPA under solvent-free conditions[a]

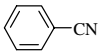
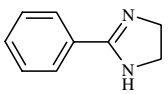
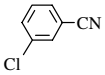
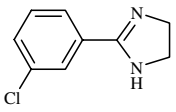
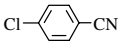
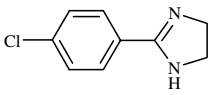
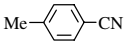
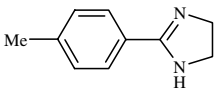
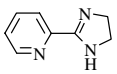
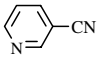
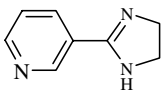
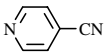
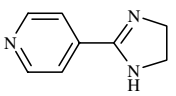
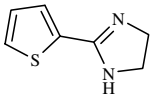
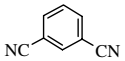
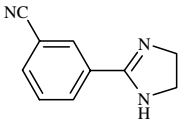
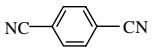
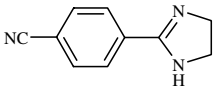
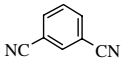
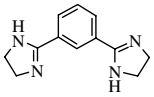
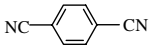
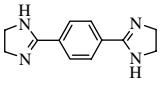
Row	Nitrile	Imidazoline[b]	SiO_2–TPA		C–TPA		PMP–TPA		Mp (°C), Ref.
			Time (h)	Yield[c] (%)	Time (h)	Yield[c] (%)	Time (h)	Yield[c] (%)	
1			4	80	4	88	3.5	80	100–102 [30]
2			3	90	2	95	2	95	134–136 [27f]
3			4	88	4	90	2.5	90	186–188 [30]
4			4.5	80	4	85	4	85	175–177 [27f]
5			0.75	90	0.7	95	0.4	96	100–101 [27f]
6			3	90	4	85	3	91	106–108 [25]
7			3	90	3	90	2.5	93	133–135 [25]
8			3	90	3	90	2	90	174–176 [36e]

Table 3 (*continued*)

Row	Nitrile	Imidazoline[b]	SiO_2–TPA		C–TPA		PMP–TPA		Mp (°C), Ref.
			Time (h)	Yield[c] (%)	Time (h)	Yield[c] (%)	Time (h)	Yield[c] (%)	
9			0.7	95	0.75	93	0.3	95	133–134
10			0.8	90	0.8	90	0.3	92	204–205 [31]
11			12	5	12	6	12	5	242–243 [27e]
12			12	7	12	4	12	7	312–314 [27e]

[a] Reaction conditions: nitrile (1 mmol), ethylenediamine (4 mmol), catalyst (30 mg; 0.2 mol%).
[b] All products were identified by comparison with authentic samples (IR, ^{1}H NMR, mp).
[c] Isolated yields.

supported-TPAs. Surprisingly, it was observed that both mono- and bis-oxazolines can be obtained by this catalytic system. As shown in Table 2, mono-oxazolines were produced from dinitriles in 90–95% yields with shorter reaction times (0.25–0.5 h). Increasing the reaction times to 6 h, produced bis-oxazolines in 75–80% yields. The preparation of mono-oxazolines from dinitrile compounds is of great interest because the remaining nitrile group can be converted to other functional groups [35].

3.3. Synthesis of 2-imidazolines catalyzed by supported TPA

The scope and generality of this catalytic system was shown in the reaction of various types of nitriles with ethylenediamine. Different types of arylnitriles reacted with ethylenediamine under the same reaction conditions used in the synthesis of 2-oxazolines to give the corresponding imidazoline derivatives in good to excellent yields (Table 3). The progress of the reaction was monitored by TLC (eluent: EtOAc/MeOH, 4:1). Work-up of the reaction was very easy. After completion of the reaction, simple filtration of the reaction mixture provided the crude product. Evaporation of the solvent under reduced pressure and recrystallization or chromatography on a neutral alumina column gave the pure product.

Synthesis of bis-imidazolines from the reaction of dinitriles with ethylenediamine catalyzed by supported TPAs failed. Thus, the reaction of 1,3-dicyanobenzene and 1,4-dicyanobenzene with ethylenediamine in the presence of these catalysts afforded 3-(4′,5′-dihydro-1*H*-imidazol-2′-yl)benzonitrile and 4-(4′,5′-dihydro-1*H*-imidazol-2′-yl)benzonitrile in high yields, respectively (Table 3, entries 9 and 10).

3.4. Synthesis of 2-thiazolines and bis-thiazolines catalyzed by supported TPA

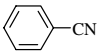
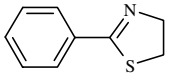
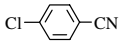
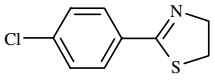
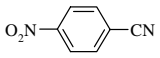
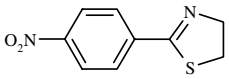
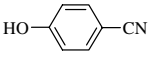
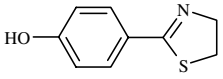
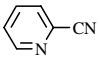
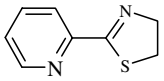
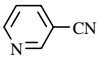
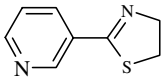
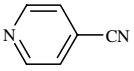
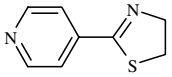
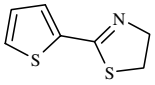
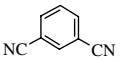
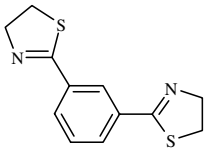
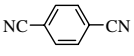
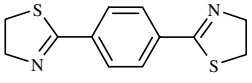
To show the applicability of this catalytic system further, the synthesis of 2-thiazolines was also investigated in the presence of supported TPAs. The reaction of nitriles with 2-aminoethanethiol in the presence of catalytic amounts of supported TPAs (0.1 mol%) produced the corresponding 2-thiazolines in good to excellent yields. The treatment of dinitriles with 2-aminoethanethiol produced bis-thiazolines exclusively (Table 4, entries 9 and 10).

Synthesis of 2-alkyloxazolines, 2-alkylimidazolines and 2-alkylthiazolines with this catalytic system failed. Therefore the chemoselective conversion of arylnitriles to their corresponding 2-aryloxazolines, 2-arylimidazolines and 2-arylthiazolines can be achieved in the presence of alkylnitriles. In this manner, the reaction of an equimolar mixture of some alkyl- and arylnitriles with an excess amount of 2-aminoethanol, ethylenediamine or cysteamine were performed. The results showed that only arylnitriles reacted and the alkylnitriles remained intact in the reaction mixture (Scheme 2).

3.5. Catalyst reuse and stability

The reusability of the catalyst is important for large-scale operation and an industrial point of view. Therefore, the reusability of the catalysts were examined in

Table 4
Synthesis of 2-thiazolines and bis-thiazolines catalyzed by supported TPA under solvent-free conditions[a]

Row	Nitrile	Thiazoline[b]	SiO_2–TPA		C–TPA		PMP–TPA		Mp (°C), Ref.
			Time (min)	Yield[c] (%)	Time (min)	Yield[c] (%)	Time (min)	Yield[c] (%)	
1			5	95	5	95	5	95	126–128 [36e]
2			4	95	5	91	4	95	53–55 [36f]
3			5	80	8	85	5	96	150–152 [36f]
4			5	60	9	65	5	80	176–178
5			15	93	16	93	10	92	92–94 [36g]
6			8	96	7	93	5	97	111–113 [36h]
7			3	97	5	93	5	95	74–76
8			8	95	5	90	6	90	40–42 [36g]
9			10	95	12	95	10	95	111–113
10			12	92	12	87	12	93	105–106 [36f]

[a] Reaction conditions: nitrile (1 mmol), 2-aminoethanethiol (1.5 mmol), catalyst (15 mg; 0.1 mol%).
[b] All products were identified by comparison with authentic samples (IR, ^{1}H NMR, mp).
[c] Isolated yields.

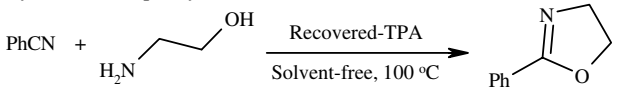
the reaction of benzonitrile with 2-aminoethanol. Since the reaction medium is heterogeneous (solid–liquid), the catalysts can be recovered by simple filtration after dilution of the reaction mixture with EtOH. The recovered catalysts were dried at 100 °C and weighed. Afterwards, according to the catalyst amount, the required amount



Catalyst	X					
	O		N		S	
	Yield (%)	Time (h)	Yield (%)	Time (h)	Yield (%)	Time (min)
SiO_2-TPA	92	2	90	3	96	8
C-TPA	95	2	85	4	93	7
PMP-TPA	91	2	91	3	97	5

Scheme 2.

Table 5
Investigation of catalysts reusability in the synthesis of 2-phenyloxazoline



Run	SiO_2–TPA		C–TPA		PMP–TPA	
	Yield[a] (%)	*W* (%)	Yield[a] (%)	*W* (%)	Yield[b] (%)	*W* (%)
1	90	29.55 ± 0.8	92	28.55 ± 0.9	90	29.45 ± 0.9
2	90	28.78 ± 0.9	90	28.18 ± 0.9	90	28.98 ± 0.8
3	90	28.17 ± 0.8	90	27.12 ± 0.8	88	28.15 ± 0.8
4	85	26.45 ± 0.8	87	26.92 ± 0.8	85	27.35 ± 0.8
5	80	25.01 ± 0.8	85	26.61 ± 0.9	82	26.51 ± 0.8

[a] Reaction time: 3 h.
[b] Reaction time: 2 h.

of fresh nitrile and aminoalcohol were added. The results showed that the catalyst could be reused five consecutive times (Table 5). The amount of catalyst loading after each run was determined by neutron activation analysis (NAA). Addition of fresh nitrile to the filtrates and continuation of the reaction under the same conditions showed that the amounts of 2-phenyloxazoline was about 7–10%, which indicates the catalyst leaching. These data are in agreement with the NAA data about the amount of catalyst loading.

4. Conclusion

In summary, we have demonstrated a simple, efficient and chemoselective catalytic method for the preparation of 2-oxazolines, 2-imidazolines and 2-thiazolines. The use of supported-TPAs as non-toxic, recoverable and reusable heterogeneous catalysts makes this procedure environmentally friendly and economically acceptable. Furthermore, simple work-up, short reaction times, high yields of the products and easy handling of the catalysts are other noteworthy advantages of this catalytic system.

Acknowledgement

The financial support of this work by Center of Excellence of Chemistry of University of Isfahan (Catalyst and Fuel Cell) is acknowledged.

References

[1] (a) H. Firouzabadi, N. Iranpoor, K. Amani, Synthesis (2002) 59;
(b) C.J. Magesh, R. Nagarajan, M. Karthik, P.T. Perumal, Appl. Catal. A: Gen. 266 (2004) 1;
(c) C. Ramesh, G. Mahender, N. Ravindranath, B. Das, Tetrahedron Lett. 44 (2003) 1465;
(d) A.T. Khan, L.H. Choudhury, S. Ghosh, J. Mol. Catal. A: Chem. 255 (2006) 230.
[2] (a) M.T. Pope, Heteropoly and Isopoly Oxometallates, Springer-Verlag, Berlin, 1993;
(b) N. Mizuno, M. Misono, Chem. Rev. 98 (1998) 199;
(c) T. Okuhara, T. Nakato, Catal. Survey Jpn. 2 (1998) 31;
(d) I.V. Kozhevnikov, Chem. Rev. 98 (1998) 171;
(e) I.V. Kozhevnikov, Catalysts for Fine Chemicals, Catalysis by Polyoxometallates, vol. 2, Wiley, Chichester, 2002.
[3] (a) T.-S. Jin, J.-C. Xiao, Z.-H. Wang, T.-S. Li, J. Chem. Res. (S) (2003) 412;
(b) R. Fazaeli, S. Tangestaninejad, H. Aliyan, Appl. Catal. A: Gen. 318 (2007) 218;

(c) R. Fazaeli, S. Tangestaninejad, H. Aliyan, Catal. Commun. 8 (2007) 205;
(d) R. Fazaeli, S. Tangestaninejad, H. Aliyan, M. Moghadam, Appl. Catal. A: Gen. 309 (2006) 44;
(e) H. Firouzabadi, N. Iranpoor, A.A. Jafari, M.R. Jafari, J. Mol. Catal. A: Chem. 247 (2006) 14;
(f) E. Rafiee, S. Rashidzadeh, A. Azad, J. Mol. Catal. A: Chem. 261 (2007) 49.
[4] (a) Y. Izumi, K. Hisano, T. Hida, Appl. Catal. A: Gen. 181 (1999) 277;
(b) Y. Izumi, M. Ono, M. Kitagawa, M. Yoshida, K. Urabe, Micropor. Mater. 5 (1995) 255;
(c) K.A. da Silva Rocha, P.A. Robles-Dutenhefner, E.M.B. Sousa, E.F. Kozhevnikova, I.V. Kozhevnikov, E.V. Gusevskaya, Appl. Catal. A: Gen. 317 (2007) 171;
(d) K.A. da Silva Rocha, I.V. Kozhevnikov, E.V. Gusevskaya, Appl. Catal. A: Gen. 294 (2005) 106;
(e) I.V. Kozhevnikov, Appl. Catal. A: Gen. 256 (2003) 3.
[5] T.G. Gant, A.I. Meyers, Tetrahedron 50 (1994) 2297.
[6] J.A. Frump, Chem. Rev. 71 (1971) 483.
[7] M.R. Grimmett, in: A.R. Katritzky, C.W. Rees, E.F.V. Scriven (Eds.), Comprehensive Heterocyclic Chemistry, vol. 3, Pergamon, Oxford, 1996.
[8] A.G. Gilman, L.S. Goodman, The Pharmacological Basis of Therapeutics, 10th ed., McGraw-Hill, New York, 2001.
[9] A.K. Saxena, S.K. Pandey, P. Seth, M.P. Singh, M. Dikshit, A. Carpy, Bioorg. Med. Chem. 9 (2001) 2025.
[10] R.S. Roy, A.M. Gehring, J.C. Milne, P.J. Belshaw, C.T. Walsh, Nat. Prod. Rep. 16 (1999) 249.
[11] J.V. Greenhill, L. Lue, in: G.P. Ellis, D.K. Luscombe (Eds.), Progress in Medicinal Chemistry, vol. 3, Elsevier, New York, 1993.
[12] F. Rondu, G. Lr Bihan, X. Wang, A. Lamouri, E. Touboul, G. Dive, T. Bellahsene, B. Pfeiffer, P. Renard, B. Guardiola-Lemaître, D. Manéchez, L. Pénicaud, A. Ktorza, J.J. Godfroid, J. Med. Chem. 40 (1997) 3793.
[13] P. Bousquet, J. Feldman, Drugs 58 (1999) 799.
[14] E.S. Vizi, Med. Res. Rev. 6 (1986) 431.
[15] P. Wipf, P.C. Fritch, Tetrahedron Lett. 35 (1994) 5397.
[16] R.J. Boyce, G.C. Mulqueen, G. Pattenden, Tetrahedron Lett. 35 (1994) 5705.
[17] P. Wipf, S. Venkatraman, Synlett (1997) 1.
[18] M. Tomizawa, A. Cowan, J.E. Casida, Toxicol. Appl. Pharmacol. 177 (2001) 77.
[19] D. Yang, Y.-C. Yip, X.-C. Wang, Tetrahedron Lett. 38 (1997) 7083.
[20] K. Puntener, M.D. Hellman, E. Kuester, L.S. Hegedus, J. Org. Chem. 65 (2000) 8301.
[21] (a) G. Desimoni, G. Faita, K.A. Jorgensen, Chem. Rev. 106 (2006) 3561;
(b) K. Matsumoto, K. Jitsukawa, H. Masuda, Tetrahedron Lett. 46 (2005) 5687;
(c) X.-Q. Hao, J.-F. Gong, C.-X. Du, L.-Y. Wu, Y.-J. Wu, M.-P. Song, Tetrahedron Lett. 47 (2006) 5033.
[22] (a) I. Abrunhosa, M. Gulea, J. Levillain, S. Masson, Tetrahedron: Asymmetry 12 (2001) 2851;
(b) A.I. Fernández, J.M. Fraile, J.I. Garcí'a, C.I. Herrerías, J.A. Mayoral, L. Salvatella, Catal. Commun. 2 (2001) 165.
[23] (a) A.K. Ghosh, P. Mathivanan, J. Cappiello, Tetrahedron: Asymmetry 9 (1998) 1;
(b) A. Lee, W. Kim, J. Lee, T. Hyeon, B.M. Kim, Tetrahedron: Asymmetry 15 (2004) 2595.
[24] A. Cwik, Z. Hell, A. Hegedüs, Z. Finta, Z. Horvath, Tetrahedron Lett. 43 (2002) 3985.
[25] G. Neef, U. Eder, G. Sauer, J. Org. Chem. 49 (1981) 2824.
[26] (a) D.S. Clarke, R. Wood, Synth. Commun. 26 (1996) 1335;
(b) G.K. Jnaneshwara, V.H. Deshpande, M. Lalithambika, T. Ravindranathan, A.V. Bedekar, Tetrahedron Lett. 39 (1998) 459.
[27] (a) I. Mohammadpoor-Baltork, A.R. Khosropour, S.F. Hojati, Synlett (2005) 2747;
(b) I. Mohammadpoor-Baltork, A.R. Khosropour, S.F. Hojati, Catal. Commun. 8 (2007) 200;
(c) V. Mirkhani, I. Mohammadpoor-Baltork, M. Moghadam, S. Tangestaninejad, M. Abdollahi-Alibeik, H. Kargar, Appl. Catal. A: Gen. 325 (2007) 99;
(d) M. Moghadam, I. Mohammadpoor-Baltork, V. Mirkhani, S. Tangestaninejad, M. Abdollahi-Alibeik, B.H. Yousefi, H. Kargar, Monatsh. Chem. 138 (2007) 579;
(e) V. Mirkhani, M. Moghadam, S. Tangestaninejad, H. Kargar, Tetrahedron Lett. 47 (2006) 2129;
(f) I. Mohammadpoor-Baltork, M. Abdollahi-Alibeik, Bull. Korean Chem. Soc. 24 (2003) 1354.
[28] C.T. Brain, A. Hallett, S.Y. Ko, Tetrahedron Lett. 39 (1998) 127.
[29] M.K. Ghorai, K. Ghosh, K. Das, Tetrahedron Lett. 47 (2006) 5399.
[30] H. Salgado-Zamora, E. Campos, R. Jimenezourd, H. Cervants, Heterocycles 47 (1998) 1043.
[31] H. Fujioka, K. Murai, O. Kubo, Y. Ohba, Y. Kita, Tetrahedron 63 (2007) 638.
[32] S. Tangestaninejad, M.H. Habibi, V. Mirkhani, M. Moghadam, J. Chem. Res. (S) (2001) 444.
[33] (a) M. Misono, N. Misono, K. Katamura, A. Kasai, Y. Konishi, K. Sakata, T. Okuhara, Y. Yoneda, Bull. Chem. Soc. Jpn. 55 (1982) 400;
(b) T.H. Chang, J. Chem. Soc., Faraday Trans. 91 (2) (1995) 375;
(c) M. Fournier, R. Thouvenot, C. Rocchiccioli-Deltcheff, J. Chem. Soc., Faraday Trans. 87 (2) (1991) 349;
(d) G.D. Yadav, N. Kirthivasan, J. Chem. Soc., Faraday Trans. (1995) 203.
[34] G. Desimoni, G. Faita, K.A. Jorgensen, Chem. Rev. 106 (2006) 3561.
[35] G.K. Jnaneshwara, V.H. Deshpande, A.V. Bedekar, J. Chem. Res. (S) (1999) 252.
[36] (a) H. Witte, W. Seeliger, Liebigs Ann. Chem. (1974) 996;
(b) L.N. Pridgen, J. Org. Chem. 47 (1982) 4319;
(c) B. George, J. Org. Chem. 42 (1977) 441;
(d) B.P. Bandgar, S.S. Pandit, Tetrahedron Lett. 44 (2003) 2331;
(e) N. Suzuki, Y. Fujita, T. Yamabayashi, Y. Deguchi, Y. Izawa, J. Chem. Soc., Perkin Trans. 1 (1976) 1901;
(f) A.R. Katritzky, C. Cai, K. Suzuki, S.K. Singh, J. Org. Chem. 69 (2004) 811;
(g) B. George, E.P. Papadopoulos, J. Org. Chem. 42 (1977) 441;
(h) T. Nakajima, T. Kashiwabara, T. Izawa, S. Nakajima, Bioorg. Med. Chem. Lett. 4 (1994) 2485.

Available online at www.sciencedirect.com
ScienceDirect
Polyhedron 27 (2008) 759–764
POLYHEDRON
www.elsevier.com/locate/poly

Unexpected Schiff-base complex formation from the oxidation reaction of a nickel(II) complex with the *meso*-HMPAO ligand by molecular oxygen

Chomchai Suksai [a,*], Chaveng Pakawatchai [b], Khajadpai Thipyapong [a]

[a] *Department of Chemistry, Faculty of Science, Burapha University, Chonburi 20131, Thailand*
[b] *Department of Chemistry, Faculty of Science, Prince of Songkla University, Songkla 90112, Thailand*

Received 5 June 2007; accepted 4 November 2007
Available online 4 January 2008

Abstract

The synthesis and characterization of the amine–oxime complex [Ni(*meso*-HMPAO)–H] · ClO_4 (**1**) and its oxidized Schiff-base product [Ni(*meso*-HMPAO)-5H] · ClO_4 (**2**), where HMPAO is hexamethyl propylene amine oxime, are presented. Complex **2** results from the oxidation of **1** by molecular oxygen in basic aqueous solution. The structural change of the amine complex **1** to the Schiff-base complex **2** was investigated by the means of NMR spectroscopy and X-ray crystallography.
© 2007 Elsevier Ltd. All rights reserved.

Keywords: *meso*-HMPAO; Nickel(II) complex; Oxidation; Schiff-base complex

1. Introduction

The coordination chemistry of oxime compounds has been increasingly interesting and has been studied from a variety of perspectives by many different research groups [1]. Because of the potential applications of metal oxime complexes, they have been shown to be useful in many research areas such as radiopharmaceutical [2], catalysis [3] and analytical chemistry [4]. It was established that the formation of an intramolecular hydrogen bond between the two oxime oxygen atoms is the most favourable characteristic.

It has long been known that bis(dimethylglyoximato)nickel(II) can be oxidized by molecular oxygen and other oxidizing agents. Moreover, it was found that other amine–oxime complexes exhibit the same oxidation behaviour as well. For example, Schlemper has reported that the [Ni(PnAO)–H]$^+$ complex ion can be easily oxidized to a quasi-aromatic system [Ni(PnAO)–6H] in basic solution [5–7].

In the present paper we report the synthesis, spectroscopic and crystallographic characterization of the new complex [Ni(*meso*-HMPAO)–H] · ClO_4 and its oxidized product [Ni(*meso*-HMPAO)–5H] · ClO_4, where HMPAO is hexamethyl propylene amine oxime.

2. Experimental

2.1. Materials and methods

All reagents were of reagent grade and were used without further purification unless stated otherwise. The ligand *meso*-HMPAO was synthesized according to the method described in the literature [8]. The FT-IR spectra were obtained on a Perkin–Elmer FT-IR spectrophotometer using KBr pellets. The UV–Vis spectra were measured in water solution on a Varian Cary 500 UV–Vis spectrophotometer. ^{1}H NMR, ^{13}C NMR and 2D NMR spectra were record in DMSO-d_6 on a Bruker Avance 400 NMR spec-

* Corresponding author. Tel.: +66 038 745900x3067; fax: +66 038 393494.
E-mail address: jomjai@buu.ac.th (C. Suksai).

0277-5387/$ - see front matter © 2007 Elsevier Ltd. All rights reserved.
doi:10.1016/j.poly.2007.11.014

trometer. Elemental analyses for C, H and N were performed on a Perkin–Elmer 2400 CHN elemental analyzer.

2.2. Syntheses of the complexes

2.2.1. [Ni(meso-HMPAO)-H] · ClO_4 (1)

A solution of $Ni(NO_3)_2 \cdot 6H_2O$ (0.535 g, 1.84 mmol) 2 mL was added to an acidic solution of the ligand *meso*-HMPAO (0.500 g, 1.84 mmol) 10 mL at room temperature. The reaction mixture was adjusted to pH 7.5 by addition of 1 M KOH and the mixture was stirred for 30 min at room temperature under nitrogen atmosphere. Subsequently, 2 M $NaClO_4$ solution was added to the solution, and the obtained amorphous yellow solid was filtered, washed with cold water and dried in vacuo. Yield 0.434 g, (55%). Good quality crystals for X-ray diffraction studies were obtained by recrystallization from methanol. *Anal.* Calc. for $C_{13}H_{27}NiN_4O_6Cl$: C, 36.35; H, 6.34; N, 13.04. Found: C, 36.36; H, 6.37; N, 13.04%. ^{1}H NMR (ppm, DMSO-d_6): δ 0.84 (s, 3H, –C(CH_3)), 0.87 (s, 3H, –C(CH_3)), 1.27 (d, $J = 6.0$, 6H, –CH–(CH_3)$_2$), 1.83 (s, 6H, –N=C–(CH_3)$_2$), 2.22 (m, 4H, –CH_2–), 3.49 (m, 2H, –CH–), 4.43 (s, 2H, *NH*); ^{13}C NMR (DMSO-d_6) δ 13.17, 14.34, 21.52, 26.73, 34.45, 55.95, 62.93, 159.75. ESI: m/z 329.15 $[M]^+$.

Caution! Perchlorate salts are potentially explosive and should be handled with care.

2.2.2. [Ni(meso-HMPAO)–5H] · ClO_4 (2)

The filtrate of compound **1** was kept at room temperature for about one month, giving a solid of orange needles, yield 0.196 g (25%). Recrystallization from ethanol gives intense orange rod crystals suitable for X-ray diffraction studies. *Anal.* Calc. for $C_{13}H_{23}NiN_4O_6Cl$: C, 36.70; H, 5.45; N, 13.17. Found: C, 36.70; H, 5.44; N, 13.18%. ^{1}H NMR (ppm, DMSO-d_6): δ 1.12 (s, 6H, –C(CH_3)$_2$), 2.09 (s, 6H, –N=C–(CH_3)$_2$), 2.27 (s, 6H, OH–N=C–(CH_3)$_2$), 3.08 (s, 4H, –CH_2–); ^{13}C NMR (DMSO-d_6): δ 12.65, 17.15, 24.37, 36.53, 58.33, 155.92, 176.67. ESI: m/z 325.12 $[M]^+$.

2.3. X-ray crystallographic data collection and refinement details

Crystallographic data of **1** and **2** were collected on a BRUKER APEX CCD diffractrometer (graphite-monochromated Mo Kα radiation with $\lambda = 0.71073$ Å). All the structures were solved by direct methods using the program SHLEXS-97 [9] and refined by full-matrix least squares techniques against F^2 using the SHELXL-97 [9] crystallographic software package. Non-hydrogen atoms were refined with anisotropic thermal parameters. During the last stages of refinement some disorder on the perchlorate oxygen atoms of **1** and **2** were evident. Disorder of the oxygen atoms of the perchlorate ion was modelled with two equally weighted sets of oxygen atoms. Detailed crystallographic data and structure refinement parameters for **1** and **2** are summarized in Table 1.

Table 1
Crystallographic data and final refinement parameters for **1** and **2**

	1	**2**
Chemical formula	$C_{13}H_{27}ClN_4NiO_6$	$C_{13}H_{23}ClN_4NiO_6$
Molecular weight	429.55	425.51
Color	yellow	orange
Size (mm)	0.284 × 0.203 × 0.113	0.268 × 0.216 × 0.128
Temperature (K)	293(2)	293(2)
Crystal system	orthorhombic	monoclinic
Space group	*Pbca*	$P2_1/c$
a (Å)	16.2109(8)	7.0705(6)
b (Å)	8.7329(4)	19.0057(15)
c (Å)	27.1331(13)	14.0676(11)
α (°)	90	90
β (°)	90	103.073(2)
γ (°)	90	90
V (Å)^3	3841.2(3)	1841.4(3)
Z	8	4
F(000)	1792	888
D_{calc} (g cm^{-3})	1.479	1.535
μ (mm^{-1})	1.184	1.235
θ Range for data collection (°)	1.50–28.02	1.83–28.06
Index ranges	$-21 \leqslant h \leqslant 21$ $-11 \leqslant k \leqslant 11$ $-35 \leqslant l \leqslant 35$	$-9 \leqslant h \leqslant 9$ $-25 \leqslant k \leqslant 25$ $-18 \leqslant l \leqslant 18$
Reflections collected/ unique [R_{int}]	36657/4646 [0.0411]	21733/4459 [0.0361]
Data/restraints/ parameters	4646/0/265	4459/0/271
Final R indices [$I > 2\sigma(I)$]	$R_1 = 0.0677$, $wR_2 = 0.2008$	$R_1 = 0.0509$, $wR_2 = 0.1252$
R indices (all data)	$R_1 = 0.0867$, $wR_2 = 0.2185$	$R_1 = 0.0678$, $wR_2 = 0.1360$
Goodness-of-fit	1.070	1.063
Maximum, minimum difference (e Å^{-3})	1.066, −0.475	0.568, −0.299

3. Results and discussion

Compounds **1** and **2** are quite stable in the solid state under ambient conditions. They are soluble in water, methanol and ethanol. In the electronic spectra of both complexes in water, weak absorption bands at 435 and 475 nm for complexes **1** and **2** respectively were observed, which are attributed to d–d transitions of square planar nickel(II) complexes [10].

3.1. IR Study

In the IR spectra of the nickel(II) complexes **1** and **2**, displacements of the absorption bands to lower frequencies compare to the free ligand were observed, indicating the coordination of the ligand to the metal ion. In general, the IR spectra of complexes **1** and **2** show the ν(C=N) bands shift to lower frequencies, at 1626 and 1635 cm^{-1} for **1** and **2**, respectively, compared to that of the free ligand at 1690 cm^{-1}, indicating the involvement of the oxime nitrogen atoms in coordination. The oxime hydroxyl stretching of the free ligand is absence, while new vibrational bands of an intermolecular hydrogen bond ν (O–

H–O) between the two oxime groups were observed in the region 1770–1790 cm^{-1} [11,12]. The secondary amine stretching in the region 3151–3269 cm^{-1} for **1**, which are uniquely characteristic and shifted relative to the free ligand (3298 cm^{-1}), suggest the coordination of this group to the metal ion. In contrast, this peak disappears in the spectrum of complex **2**, indicating the deprotonation of the NH group upon coordination. Concerning the ClO_4^- anion, the v_3 mode is around 1121 cm^{-1} for both complexes, but the v_4 band, at 624.01 and 623.76 cm^{-1} respectively, is devoid of any splitting and is consistent with the IR active normal modes for Td symmetry, suggesting that these anions are not coordinated to the nickel ions as is substantiated by the crystal structures of **1** and **2** [13] (see Fig. 1).

3.2. NMR study

The NMR evidence is very useful in distinguishing the two Ni(II) complexes. The sharp NMR peaks in DMSO-d_6 are consistent with planar structures of diamagnetic Ni(II) d^8 complexes. The ^1H NMR and ^{13}C NMR peak assignments are clearly in accordance with the molecular structures determined by X-ray crystal structure analysis, vide infra. The assignments in the 1D spectra were based on additional HMQC and DEPT experiments. The downfield shift of coordinated protons relative to the free ligand can be attributed to the deshielding effect resulting from the coordination of the ligands. However, there are several points of the NMR spectra that merit comment, for example in the ^1H NMR spectrum of compound **2** only four sharp signals appeared, indicating the exclusive formation of a symmetrical complex, which is different from **1**, Fig. 2. In compound **1** the $–CH_2–C–CH_2–$ group must be out of plane of the metal, resulting in the different environments of C7 and C8 atoms and consequently the completely unequivalent positions of their corresponding NMR peaks. In contrast, for compound **2**, these methyl groups are identical, giving a singlet peak, suggesting that the C5 and C9 carbons are essentially in the plane of the rest of the complex, Figs. 2 and 3.

The vic-dioxime carbons peaks appear at 159 and 160 ppm for **1** and **2**, respectively. Interestingly, it is apparent from Fig. 2 that the methane and amine protons of free ligand have moved to downfield positions in complex **1**, whereas these two peaks have disappeared in complex **2**.

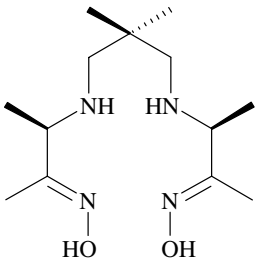


Fig. 1. Structure of *meso*-HMPAO (HL_2).

Moreover, the methine carbons C(3) and C(10) of complex **2** have also disappeared, and simultaneously there is an unexpected signal at 176.6 ppm, Fig. 3. In order to determine the structure of compound **2**, we have used 2D NMR techniques to help analyze the spectrum. It was found that this new peak corresponds to C(3) and C(10) of the double bond –C=N– imine groups, which is in agreement with the conclusion derived from the X-ray crystal structure. It is noteworthy that the NMR data suggests the amine complex can be oxidized to the Schiff-base complex in solution.

3.3. Crystal structures of complexes *1* and *2*

The molecular structures of **1** and **2** are shown in Figs. 4 and 5, respectively and selected bond distances and angles are given in Table 2. The structures consist of discrete $[NiL]^+$ cations together with perchlorate anions. The central Ni(II) atoms in both compounds have a square planar coordination in which the ligand *meso*-HMPAO is coordinated to the nickel atom by four nitrogen atoms. The oxygen atoms O(1) and O(2) of the oximato groups in both complexes are linked by a short hydrogen bond, as in common with oxime–oximate compounds, forming pseudo-macrocyclic complexes.

In compound **1** the deviation of the nickel atom from the basal plane is 0.0198 Å. The six member ring that includes the propylene bridge adopts a chair conformation, which is in agreement with other metal complexes of this ligand type [7,14,15], Fig. 4. The average $Ni–N_{amine}$ distance of 1.882 Å is quite short compared to that found in the $[Ni(PnAO)]^+$ cation (1.937 Å). The N–H group of the *meso*-HMPAO ligand provides no steric hindrance to coordination, and furthermore provides a weak N–H–O hydrogen bond to the perchlorate anion, Table 3. Moreover, the ligand loses one oxime proton on coordinating to nickel(II), forming strong intramolecular hydrogen bonding between the oxime oxygen atoms, in which the O(1)—O(2) distance was found to be 2.413(4) Å, having an asymmetrically disposed hydrogen bond, 1.229(4) Å from O(1) and 1.186(4) Å from O(2).

For compound **2**, the ligand *meso*-HMPAO is coordinated to the nickel atom by four nitrogen atoms, like **1**. The nickel(II) ion sits approximately 0.0481 Å above the plane of the nitrogen atoms. Interestingly, the conformation of the six membered saturated ring of compound **2** present in the asymmetric unit is intermediate between boat and twist boat, Fig. 5. According to the NMR results, not only are the two amine protons are lost by the ligand on coordination, but also the methine protons disappear as well, resulting in the multiple-bond character. Therefore, the average bond length of C(3)–N(1) and C(10)–N(2) is 1.296(4) Å, shorter than the average single bond 1.465(5) Å in complex **1**, but it is in the same range for other Schiff-base complexes (1.27–1.33 Å) [16,17]. The short bond lengths indicate $C(sp^2)–N(sp^2)$ double-bond character and correspondingly the bond angles in the

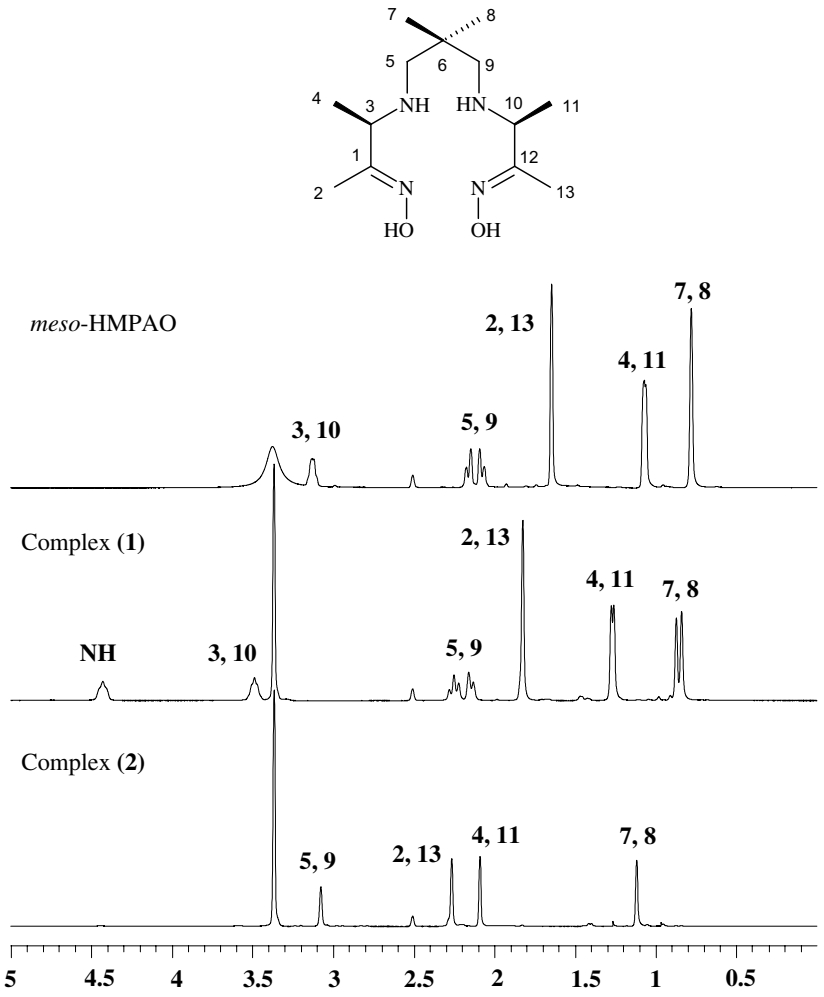


Fig. 2. ^{1}H NMR spectra of the ligand *meso*-HMPAO, and complexes **1** and **2** in DMSO-d_6.

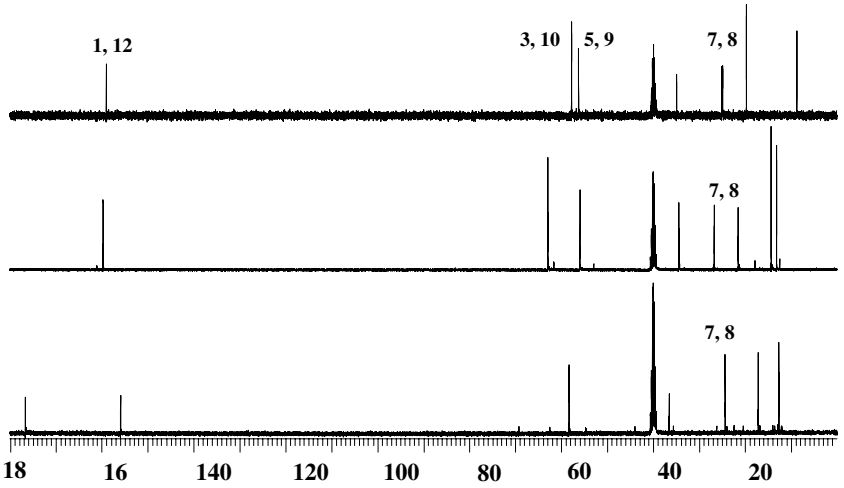


Fig. 3. ^{13}C NMR spectra of the ligand *meso*-HMPAO (top trace), complex **1** (middle trace) and complex **2** (lower trace) in DMSO-d_6.

five-membered ring of complex **2** are very close to coplanar, being of the order of 120° rather than 109°. Moreover, the Ni–N(1) and Ni–N(2) bond distances are considerably shorter than those observed in compound **1**, the average bond distance for the complex reported here is 1.879 Å while in complex **1** the average bond distance of Ni–N(1) and Ni–N(2) is 1.904 Å. The ligand is deprotonated at one of the hydroxyl groups, thereby affording an intramo-

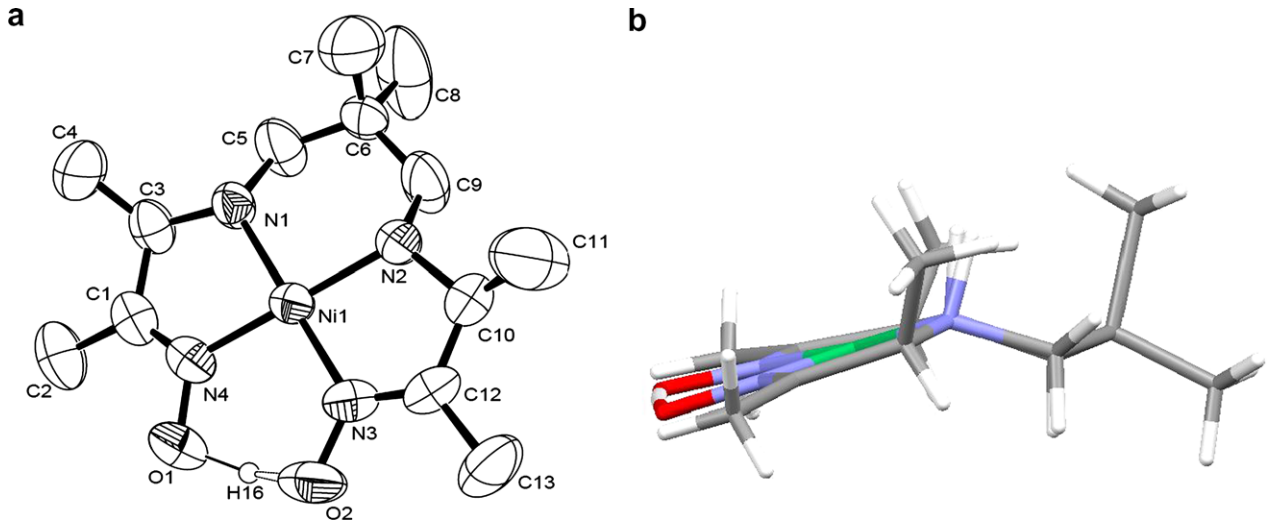


Fig. 4. Molecular structure (a) and side view (b) showing the chair conformation of the complex **1** cation.

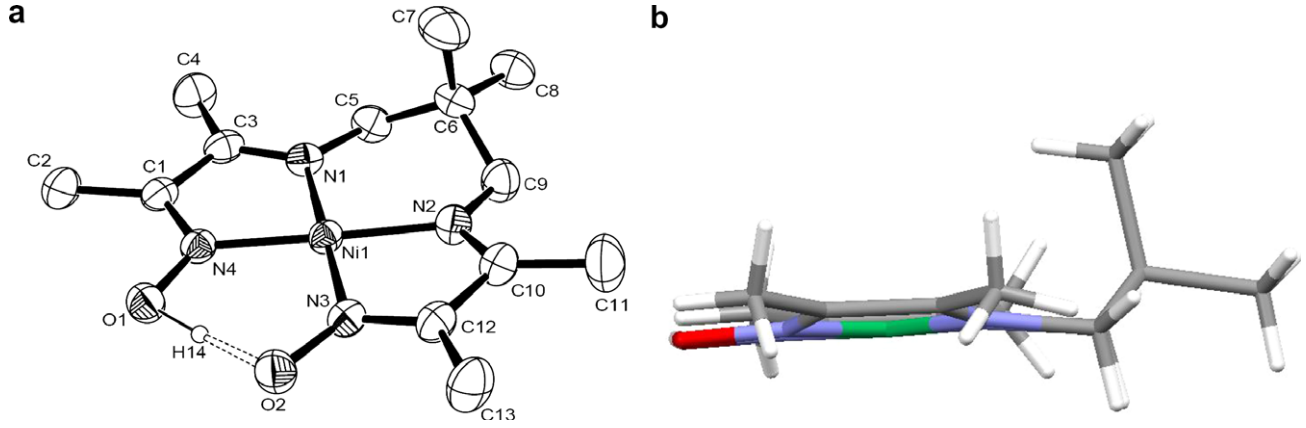


Fig. 5. Molecular structure (a) and side view (b) showing the chair conformation of the complex **2** cation.

Table 2
Selected bond lengths (Å) and angles (°) for complexes **1** and **2**

	1	**2**
Bond lengths		
Ni(1)–N(1)	1.903(4)	1.883(2)
Ni(1)–N(2)	1.905(3)	1.876(3)
Ni(1)–N(3)	1.852(3)	1.867(2)
Ni(1)–N(4)	1.870(4)	1.867(2)
C(1)–N(4)	1.273(6)	1.295(4)
C(12)–N(3)	1.281(6)	1.293(4)
C(3)–N(1)	1.460(5)	1.294(4)
C(10)–N(2)	1.470(5)	1.298(4)
C(5)–N(1)	1.416(6)	1.470(4)
C(9)–N(2)	1.441(5)	1.462(4)
Bond angles		
N(1)–C(3)–C(4)	115.2(6)	125.3(3)
N(1)–C(3)–C(1)	110.2(4)	114.7(2)
C(5)–N(1)–C(3)	116.6(4)	121.6(3)
N(2)–C(10)–C(11)	115.3(5)	126.8(3)
N(2)–C(10)–C(12)	109.6(4)	113.8(3)
C(9)–N(2)–C(10)	113.6(3)	121.7(3)

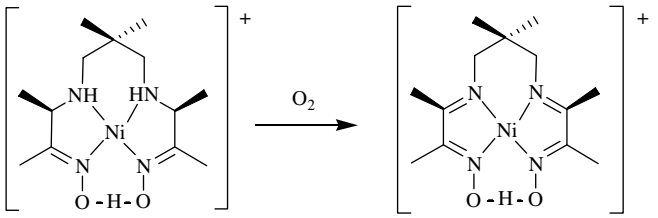
Table 3
Hydrogen bond lengths (Å) and angles (°) for complexes **1** and **2**

D–H···A	*d*(D–H)	*d*(H···A)	*d*(D···A)	∠(DHA)
*Complex **1***				
O(2)–H(16)...O(1)	1.186(4)	1.229(4)	2.413(6)	175.3(2)
N(2)–H(15)···O6A#1	1.108(4)	2.23(3)	3.26(3)	153.0(7)
N(2)–H(15)···O6B#1	1.108(4)	2.211(19)	3.16(2)	141.5(6)
*Complex **2***				
O(1)–H(14)···O(2)	1.18(5)	1.26(5)	2.426(3)	171(4)

lecular hydrogen bond between two oxime oxygen atoms, with the O(1)–O(2) distance being 2.426(3) Å.

4. Conclusion

We have reported that the amine nickel(II) complex [Ni(*meso*-HMPAO)–H]$^{+}$ can be oxidized to the Schiff-base nickel(II) complex [Ni(*meso*-HMPAO)–5H]$^{+}$ in basic



(1) (2)

Fig. 6. Structural formula of complex **1** and its oxidized product **2**.

aqueous solution. This reaction can be rationalized by the oxidation of the amine to the Schiff-base complex by molecular oxygen (Fig. 6), which has been reported previously by Schlemper and co-workers.

Acknowledgements

Financial support from the Centre of Innovation in Chemistry, Postgraduate Education and Research Program in Chemistry (PERCH-CIC) and a Grant from the Faculty of Science, Burapha University, Thailand are gratefully acknowledged.

Appendix A. Supplementary material

CCDC 649427 and 649428 contain the supplementary crystallographic data for **1**) and **2**. These data can be obtained free of charge via http://www.ccdc.cam.ac.uk/conts/retrieving.html, or from the Cambridge Crystallographic Data Centre, 12 Union Road, Cambridge CB2 1EZ, UK; fax: (+44) 1223-336-033; or e-mail: deposit @ccdc.cam.ac.uk. Supplementary data associated with this article can be found, in the online version, at doi:10.1016/j.poly.2007.11.014.

References

[1] (a) S. Akine, T. Taniguchi, T. Nabeshima, Inorg. Chem. 43 (2004) 6142;
(b) C. Baleizao, A. Corma, H. Garcia, A. Leyva, J. Org. Chem. 69 (2004) 439;
(c) B.J. Venhuis, D. Dijkstra, D. Wustrow, L.T. Meltzer, L.D. Wise, S.J. Johnson, J. Med. Chem. 46 (2003) 4136.
[2] (a) S.B. Chaplin, P.A. Oberle, E.H. McKenzie, T.J. Hoffman, W.A. Volkert, R.A. Holmes, L.R. Canning, R.D. Pickett, D.P. Nowotnik, R.D. Neirinckx, Nucl. Med. Biol 13 (1986) 261;
(b) S. Jurrison, E.O. Schlemper, D.E. Troutner, L.R. Canning, D.P. Nowotnik, R.D. Neirinckx, Inorg. Chem. 25 (1986) 543.
[3] (a) V.Y. Kukushkin, A.J.L. Pombeiro, Cood. Chem. Rev. 181 (1999) 147;
(b) A.K. Yatsimirsky, P. Gómez-Tagle, S. Escalante-Tovar, L. Ruiz-Ramírez, Inorg. Chim. Acta 273 (1998) 167.
[4] (a) Karaboöcek, S. Nohut, Ö. Dalman, S. Güner, Anal. Chim. Acta 408 (2000) 163;
(b) N. Chimpalee, D. Chimpalee, S. Lohwithee, L. Nakawatchara, D.T. Burns, Anal. Chim. Acta 329 (1996) 315;
(c) S. Nohut, S. Karaböcek, S. Güner, Y. Gök, J. Pharm. Biomed. Anal. 20 (1999) 309;
(d) Ö. Dalman, S. Karaböcek, M. Tüfecki, S. Nohut, S. Güner, S. Karaböcek, J. Pharm. Biomed. Anal. 27 (2002) 183.
[5] I.O. Urban, E.G. Vassian, Inorg. Chem. 18 (1979) 867.
[6] E.G. Vassian, R.K. Murmann, Inorg. Chem. 6 (1967) 2043.
[7] M.S. Hussain, E.O. Schlemper, Inorg. Chem. 18 (1979) 2275.
[8] P. Pennant, EP Patent, 1985, 8,506,249.
[9] G.M. Sheldrick, SHELXS-97 and SHELXL-97, University of Göttingen, Göttingen, Germany, 1997.
[10] A.B.P. Lever, Inorganic Electronic Spectroscopy, 2nd ed., Elsevier Science Publishers, BV, Netherlands, 1984.
[11] M. Dolaz, M. Tümer, S. Serin, Turk. J. Chem. 25 (2001) 491.
[12] T. Fukuchi, Bull. Chem. Soc. Jpn. 65 (1992) 1807.
[13] K. Nakamoto, in: Infrared and Raman Spectra of Inorganic and Coordination Compounds, fourth ed., John Wiley & Sons, New York, 1986.
[14] S. Jurisson, E.O. Schlemper, D.E. Troutner, L.R. Canning, D.P. Nowotnik, R.D. Neirinckx, Inorg. Chem. 25 (1986) 543.
[15] S. Jurisson, K. Aston, C.K. Fair, E.O. Schlemper, P.R. Sharp, D.E. Troutner, Inorg. Chem. 26 (1987) 3576.
[16] M.I. Fernández-García, B. Fernández-Fernández a, M. Fondo, A.M. García-Deibe, Esther Gómez-Fórneas, M.R. Bermejo, J. Sanmartín, A.M. González, Inorg. Chim. Acta 304 (2000) 144.
[17] J. Gradinaru, A. Forni, V. Druta, S. Quici, A. Britchi, C. Deleanu, N. Gerbeleu, Inorg. Chim. Acta 338 (2002) 169.

Available online at www.sciencedirect.com
ScienceDirect
Polyhedron 27 (2008) 765–776
POLYHEDRON
www.elsevier.com/locate/poly

X-ray crystal structure and nuclear Overhauser effect studies of cerium(IV) complexes with Schiff bases obtained from *N*,*N*′-(1*R*,2*R*)(−)-1,2-cyclohexanediamine and benzaldehyde derivatives

E. Szłyk *, A. Wojtczak, L. Dobrzańska, M. Barwiołek

Faculty of Chemistry, Nicolaus Copernicus University, 87 100 Toruń, Poland

Received 29 August 2007; received in revised form 5 November 2007; accepted 6 November 2007

Abstract

Schiff bases, obtained by condensation of *N*,*N*′-(1*R*,2*R*)-cyclohexanediamine with 2-hydroxy-5-chlorobenzaldehyde or 2-hydroxy-3,5-dichlorobenzaldehyde and of (±)cyclohexanediamine and salicylaldehyde, have been used as ligands for cerium(IV). The complexes were characterized by circular dichroism (CD), ^{1}H NMR,^{13}C NMR and nuclear Overhauser effect (NOE) studies. X-ray crystal structures determined for: [Ce(IV)((1*R*,2*R*)(−)chxn(3,5-diClba)$_2$)$_2$] and [Ce(IV)(±)(chxn(salal)$_2$)$_2$] revealed different orientation of a pair of Schiff base ligands in the coordination sphere. In [Ce(IV)((1*R*,2*R*)(−)chxn(3,5-diClba)$_2$)$_2$] two ligands form a sandwich with the cerium(IV) ion positioned between two layers of dichlorophenolic moieties. CD spectra in acetonitrile solution revealed exciton coupled $\pi \rightarrow \pi^*$ and LMCT transitions. CD data are characteristic for distortion of the chelate ring from planarity and λ conformation of the cyclohexane bridge. NOE difference spectroscopy for the Schiff bases (saturated –**H**C=N–) demonstrate correlations of the azomethine protons with the protons of the phenyl ring and the cyclohexane's CH protons, and a weak correlation with the hydroxyl group. In the case of the cerium(IV) complexes, the strongest NOE (saturated **H**–C=N) was observed with the phenyl ring's hydrogen atoms, a slightly weaker correlation to the cyclohexane's CH_2 protons, and a much weaker NOE to the cyclohexyl's CH_2 protons. Results of spectral analyses suggest central ions in a distorted square antiprism geometry with the two basal N_2O_2 chromophore group. The X-ray crystallography study also confirmed antiprismatic distortion from planarity in obtained complexes.
© 2007 Elsevier Ltd. All rights reserved.

Keywords: Cerium(IV); Schiff base; Noe NMR; X-ray; Circular dichroism

1. Introduction

There are several reports on cerium(IV) complexes with Schiff bases derived from salicylaldehyde (salalH), ethylenediamine (salen) and 1,2-phenyldiamine (salophen) [1–3]. In the latter case, two salophen ligands have perpendicular orientation and cerium(IV) is eight coordinated by four nitrogen and four oxygen atoms. The presence of methoxy groups or fluoride atoms causes the ligand to wrap around the metal ions [1]. Cerium(IV) can also coordinate with Schiff bases to form polymers and has been used as a precursor in MOCVD [4–11]. Transition metal complexes of Schiff bases can be used as catalyst [12–14]. In these systems, stereochemical and electronic effects imposed by the Schiff bases, play an important role. Generally, electron-donating or bulky substituents improve the selectivity of the catalyst, whereas the presence of an electron withdrawing group on the phenyl ring enhances the catalyst's efficiency [15,16]. When benzaldehyde is substituted in position 3, the corresponding Schiff base catalysts are more effective, than those with phenyl ring substituted in position 5.

The electronic structure of a benzylaldimine is less suited for stereochemical studies by means of CD, due to the ligand's low effective symmetry, hence the internal $\pi \rightarrow \pi^*$ transition moments are found to have directions far from the N–O vector. Therefore, in this study, we used

* Corresponding author. Tel.: +48 56 611 43 04; fax: +48 56 654 24 77.
E-mail address: eszlyk@chem.uni.torun.pl (E. Szłyk).

0277-5387/$ - see front matter © 2007 Elsevier Ltd. All rights reserved.
doi:10.1016/j.poly.2007.11.004

cyclohexanediamine and benzaldehyde derivatives which can cause deformation of the Ce(IV) coordination sphere.

To the best of our knowledge, Ce(IV) coordination compounds with Schiff bases, derived from *N*,*N*′-(1*R*,2*R*)-cyclohexanediamine [(1*R*,2*R*)(−)chxn] and salicylaldehyde, 5-chlorobenzaldehyde (5-Clba) or 3,5-dichlorobenzaldehyde (3,5-diClba) have not been studied to date, and it is not possible to predict how the ligands orient themselves around the metal ion. In this work, these new Ce(IV) complexes and their structural features are described. Information, about the stereochemistry of the Schiff base complexes in solution, can be deduced from the analysis of NOE difference ^{1}H NMR spectra.

2. Experimental

2.1. Materials

$Ce(NO)_3 \cdot {}^{\cdot}6H_2O$ (analytical grade) was purchased from POCh (Gliwice, Poland); whereas 2-hydroxy-5-chlorobenzaldehyde (5-ClbaH) (98%), 2-hydroxy-3,5-dichlorobenzaldehyde (3,5-diClbaH) (97%) and salicylaldehyde (salalH) (99%) were purchased from Aldrich. *trans*-(−)-1,2-cyclohexanediammonium $(+)_D$-tartrate [(−)-chxn(+)tart], was prepared according to Galsbol [17], from cyclohexanediamine (Aldrich 96%) and used to isolate (1*R*,2*R*)(−)-cyclohexanediamine, which was used for the synthesis of the Schiff bases.

2.2. Instrumentation

IR spectra were taken on a Spectrum 2000 Perkin–Elmer FT-IR, using KBr pellets in the range 400–4000 cm^{-1} and PE discs in 400–200 cm^{-1}. CD spectra were measured on a JASCO 715 spectropolarimeter in 800–180 nm range in acetonitrile concentration 10^{-4} mol/dm^3. The ^{1}H, ^{13}C NMR, DEPT, HETCOR, and NOE difference spectra were measured with an Avance Bruker 300 MHz, in $CDCl_3$, against TMS, at 297 K. NOE difference spectra were measured, at concentration 0.01 M, using NOE mul sequence. X-ray diffraction data were collected on an Oxford Sapphire CCD diffractometer.

2.3. Synthesis of Schiff bases

A solution of (1*R*,2*R*)(−)chxn (1.14 g, 10 mmol) and 2-hydroxy-5-chlorobenzaldehyde (3.15 g, 20 mmol), 2-hydroxy-3,5-dichlorobenzaldehyde (3.82 g, 20 mmol) or salicylaldehyde (2.44 g, 20 mmol) in EtOH was stirred under reflux for 2 h. The yellow solutions of Schiff bases were evaporated on a rotary evaporator and recrystallized from methanol. In the case of (±)chxn(salalH)$_2$ (±)cyclohexanediamine was used for synthesis. (1*R*,2*R*)(−)chxn(5-ClbaH)$_2$ (**1**): IR: 1624 cm^{-1} (*ν* CN), 3445 (*ν* OH); (1*R*,2*R*)(−)chxn(3,5-diClbaH)$_2$ (**2**), IR: 1631 cm^{-1} (*ν* CN), 3440 cm^{-1} (*ν* OH), (±)chxn(salalH)$_2$ (**3**) IR: 1628 (*ν* CN), 3433 cm^{-1} (*ν* OH).

2.4. Synthesis of complexes

Cerium(IV) complexes were obtained according to the following general procedure: $Ce(NO)_3 \cdot {}^{\cdot}6H_2O$ (0.43 g, 10 mmol) was dissolved in ethanol and stirred for 10 min, followed by the addition of the Schiff base (0.78 g, 20 mmol) **1** or (0.93 g, 20 mmol) **2** or (0.65 g, 20 mmol) **3** in ethanol and the reaction mixture was stirred upon heating for 2 h. The obtained precipitates were filtered, washed with methanol and dried in air. Results of elemental analyses:

Anal. Calc. for [Ce(IV)((1*R*,2*R*)(−)chxn(5-Clba)$_2$)$_2$] (**1a**) ($C_{40}H_{36}N_4O_4Cl_4Ce$): Ce, 15.25; C, 52.29; N, 6.09; H, 3.94. Found: Ce, 15.17; C, 51.96; N, 6.13; H, 3.41%. IR: $\tilde{\nu}_{max}$/cm^{-1} 1616 (CN), 287 (Ce–O), 310 (Ce–O), 428 (Ce–N), 467 (Ce–N).

Anal. Calc. for [Ce(IV)((1*R*,2*R*)(−)chxn(3,5-diClba)$_2$)$_2$] (**2a**) ($C_{40}H_{32}N_4O_4Cl_8Ce$): Ce, 13.26; C, 45.47; N, 5.30; H, 3.05. Found: Ce, 13.42; C, 45.15; N, 5.85; H, 3.15%. IR: $\tilde{\nu}_{max}$/cm^{-1} 1626 (CN), 333 (Ce–O), 312 (Ce–O), 420 (Ce–N), 450 (Ce–N).

Anal. Calc. for [Ce(IV)((±)chxn(salal)$_2$)$_2$] (**3a**) ($C_{40}H_{40}N_4O_4Ce$): Ce, 17.94; C, 61.52; N, 7.17; H, 5.16. Found: Ce, 17.89; C, 60.68; N, 6.93; H, 4.75%. IR $\tilde{\nu}_{max}$/cm^{-1} 1601 (CN), 360 (Ce–O), 270 (Ce–O), 425 (Ce–N), 447 (Ce–N) [18–22].

2.5. Crystal structure determination

The brown crystals of [Ce(IV)((1*R*,2*R*)(−)chxn(3,5-diClba)$_2$)$_2$] (**2a**) crystallized (ethanol) in the tetragonal space group $P4_3$, whereas dark red crystals of [Ce(IV)(±)(chxn(salal)$_2$)$_2$] (**3a**) crystallized (ethanol) in the monoclinic space group $P2_1$. The crystals of **2a** revealed a tendency for twinning. The relatively small crystal selected for the diffraction experiment was also twinned. The diffraction pattern from the main component was isolated and analyzed with the CrysAlis CCD version 1.71 software by Oxford Diffraction. The diffraction data for the studied complexes were measured with an Oxford Sapphire CCD diffractometer and Mo Kα radiation. Structures were solved by the Patterson method and refined to $R_1 = 0.0518$ for **2a** and $R_1 = 0.0821$ for **3a**, using the SHELX-97 program package [23]. The absolute structure was determined by the Flack method [24], with the Flack parameter being 0.02(2) for **2a**, proving the correct enantiomorph, while the value 0.53(4) for **3a** indicated optical twinning (Table 1). Attempts to solve that structure in centrosymmetric space groups were not successful.

3. Results and discussion

3.1. CD absorption spectra

The free ligand absorption spectra in acetonitrile revealed bands below 235 nm, which can be assigned to $\pi \rightarrow \pi^*$ type transitions of the benzene ring. This band in

Table 1
Crystal data and structure refinement for $[Ce(C_{22}H_{23}N_2O_3Cl_4)_2]$ (**2a**) and $[Ce\{C_6H_{10}N_2(C_7H_5O)_2\}_2]$ (**3a**)

	$[Ce\{C_6H_{10}N_2(C_7H_3Cl_2O)_2\}_2]$ (**2a**)	$[CeC_{40}H_{40}N_4O_4]$ (**3a**)
Empirical formula	$C_{40}H_{32}N_4O_4Cl_8Ce$	$C_{40}H_{40}CeN_4O_4$
Formula weight	1056.42	780.88
Temperature (K)	100(2)	293(2)
Wavelength (Å)	0.71073	0.71073
Crystal system	Tetragonal	Monoclinic
Space group	*P*4(3)	*P*2(1)
a (Å)	9.2497(3)	10.147(1)
b (Å)	9.2497(3)	10.846(1)
c (Å)	47.637(3)	15.987(1)
α (°)	90	90
β (°)	90	96.53(1)
γ (°)	90	90
Volume (Å^3)	4075.7(3)	1748.0(3)
Z, D_{calc} (Mg/m^3)	4, 1.722	2, 1.484
Absorption coefficient (mm^{-1})	1.689	1.349
F(000)	2104	796
Crystal size (mm)	0.36 × 0.32 × 0.02	0.33 × 0.33 × 0.14
Θ range for data collection (°)	1.71–28.27	2.94–31.44
Index ranges	$-10 \leqslant h \leqslant 12$, $-12 \leqslant k \leqslant 10$, $-58 \leqslant l \leqslant 63$	$-14 \leqslant h \leqslant 14$, $-15 \leqslant k \leqslant 15$, $-14 \leqslant l \leqslant 23$
Reflections collected/unique [R_{int}]	24682/9063 [0.0642]	17386/10445 [0.0524]
Maximum and minimum transmission	0.9670 and 0.5815	0.8336 and 0.6644
Refinement method	Full-matrix least-squares on F^2	Full-matrix least-squares on F^2
Data/restraints/parameters	9063/61/515	10445/6/436
Goodness-of-fit on F^2	1.082	0.978
Final *R* indices [$I > 2\delta(I)$]	$R_1 = 0.0518$, $wR_2 = 0.0934$	$R_1 = 0.0821$, $wR_2 = 0.2243$
R indices (all data)	$R_1 = 0.0651$, $wR_2 = 0.1006$	$R_1 = 0.1239$, $wR_2 = 0.2618$
Absolute structure parameter	0.02(2)	0.53(4)
Largest difference in peak and hole (e A^{-3})	1.815 and −1.415	1.608 and −0.872

the CD spectra was observed as a maximum at 231 nm (+1421.66) and a minimum at 263 nm (−355.04) for (1*R*,2*R*)(−)chxn(5-ClbaH), and at 234 nm (+552.06) and at 262 nm (−334.41) for (1*R*,2*R*)(−)chxn(3,5-diClbaH)$_2$ (Fig. 1) [25].

The band from the $\pi \rightarrow \pi^*$ transition, which involves a molecular orbital of –C=N– chromophore, was detected for **1** at 335 nm (−198.96) and for **2** at 338 nm (−123.93) [18,19] (Fig. 1). CD spectra of Ce(IV) complexes exhibit bands (below 320 nm), which can be assigned to $\pi \rightarrow \pi^*$ and ligand to metal charge transfer transitions (LMCT). In the spectrum of [Ce(IV)((1*R*,2*R*)(−)chxn(5-Clba)$_2$)$_2$] (**1a**) bands derived from coupled $\pi \rightarrow \pi^*$ type transitions

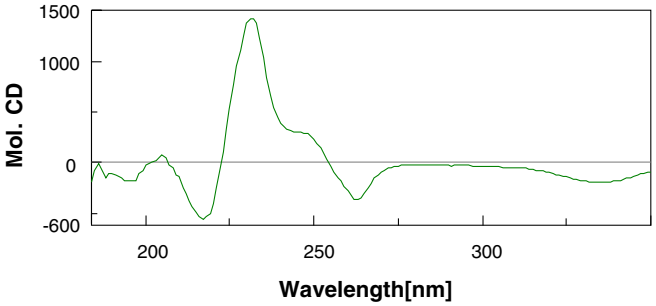


Fig. 1. CD spectrum of (1*R*,2*R*)(−)chxn(5-ClbaH)$_2$.

are splitted: 327 nm (+4.97) and 354 nm (−3.00). The spectrum of [Ce(IV)((1*R*,2*R*)(−)chxn(3,5-diClba)$_2$)$_2$] (**2a**) reveals the band splitted in two components: 320 nm (−24.19) and 343 nm (−37.63), which arise from the exciton coupled $\pi \rightarrow \pi^*$ type transitions. The exciton interaction can be related to the molecular geometry of the complex, where azomethene groups are not planar but produce the square antiprismatic distortion. This band is shifted about 27 nm towards higher energies in comparison to the CD spectrum of the ligand. Besides, the azomethene groups are not planar and 9 nm shift indicates greater distortion of **2a** geometry, than for **1a**. The above results imply, that in Ce(IV) chelates with (1*R*,2*R*)(−)chxn Schiff bases, the cyclohexane ring is *trans* fused to the central chelate ring, forming a rigid structure, in which the metallated ring is locked stereospecifically in λ conformation, as observed previously [26–29].

3.2. NMR spectra

The assignments of hydrogen signals for **1**, **2**, **3**, **1a**, **2a** and **3a** were based on chemical shifts and HETCOR spectra analysis (Table 2).

In the ^{1}H NMR spectra of **1a** and **2a** the OH signals disappeared; indicating Ce–O bond formation. The multiplets from H(1′) in the cyclohexyl ring, centered at 4.38 ppm **1a** and 4.77 ppm **2a**, revealed downfield coordination shifts ($\Delta_{coord} = \delta_{complex} - \delta_{ligand}$) +1.06 ppm for **1a** and +1.2 ppm for **2a**. However, the coordination shift in the case of **2a** is slightly bigger than for **1a**, due to electron withdrawal by 3,5-diCl-benzaldehyde. As the methine hydrogen atoms are three bonds away from the metal center (Ce–N=C(1′)), the coordination shifts are not significant. Then again, the observed coordination shifts are slightly stronger (0.1–0.3 ppm), when compared to those reported for Ni(II) complexes with (1*R*,2*R*)(−)chxn(3-methoxbaH)$_2$] and (1*R*,2*R*)(−)chxn(5-methoxbaH)$_2$] [31]. The latter can be related to the stronger deshielding of the cyclohexyl methine hydrogen, in the presence of chlorine atoms, than in the case of methoxy substituents.

The chemical shifts of H(4′) were detected at 8.44 ppm **1a** and at 8.49 ppm (**2a**), resulting in downfield coordination shifts $\Delta_{coord} = \delta_{complex} - \delta_{ligand} = +0.26$ ppm for **1a**,

Table 2
The ^{1}H NMR chemical shifts (δ, ppm) of the ligands and Ce(IV) complexes

Compound	H(1′)	Δ_{coord}	H(4′)	Δ_{coord}	H(4)	H(3)	H(6)	Δ_{coord}	O*H*	chxn
(1*R*,2*R*)(−)chxn(5-ClbaH)$_2$ (**1**)	3.32(m)		8.18 (s)		7.16(d) $J_{4\text{-}6}$ = 2.7 Hz 7.21(d) J = 2.4 $J_{3\text{-}4}$ = 8.7 Hz	6.84(d) $J_{3\text{-}4}$ = 9 Hz	7.12(d) $J_{4\text{-}6}$ = 2.7 Hz		13.20(s)	1.89(m), 1.73(m), 1.49(m)
[Ce(IV)((1*R*,2*R*)(−)chxn(5-Clba)$_2$)$_2$] (**1a**)	4.38(m)	+1.06	8.44(s)	+0.26	6.96(d) $J_{6\text{-}4}$ = 2.7 Hz 6.98(d) J = 2.7 Hz $J_{3\text{-}4}$ = 7.2 Hz	5.87(d) $J_{3\text{-}4}$ = 8.9 Hz	7.70(d) $J_{6\text{-}4}$ = 2.7 Hz	+0.58		2.41(d), 2.15(d) 1.80(m) 1.55(m)
(1*R*,2*R*)(−)chxn(3,5-diClbaH)$_2$ (**2**)	3.57(m)		8.17(s)		7.34(d) $J_{6\text{-}4}$ = 2.4 Hz		7.07(d) $J_{6\text{-}4}$ = 2.4 Hz		14.19(s)	1.91(m), 1.71(m), 1.48(m)
[Ce(IV)((1*R*,2*R*)(−)chxn(3, 5-diClba)$_2$)$_2$] (**2a**)	4.77(m)	+1.2	8.49(s)	+0.32	7.19(d) $J_{6\text{-}4}$ = 2.7 Hz		7.05(d) $J_{6\text{-}4}$ = 2.7 Hz	+0.02		2.42(d) 2.13(d) 1.82(m), 1.53(m)
(±)chxn(salalH)$_2$ (**3**)	3.40(m) 3.67(m)		8.47(s) 8.56(s)		6.77–7.31	6.77–7.31	6.77–7.31		13.31(s) 13.65(s)	1.44(m) 1.59(m) 1.77(m)
[Ce(IV)((±)chxn(salal)$_2$)$_2$] (**3a**)	4.54(m) 4.74(m)	+1.14[a] +1.07[b]	8.48 8.57	+0.01[a] +0.01[b]	6.01–7.14	6.01–7.14	6.01–7.14			1.24(m) 1.56(s) 1.74(m) 1.86(m) 2.83(m)

$\Delta_{coord} = \Delta_{complex} - \Delta_{ligand}$.
[a] Δ_{coord} for [Ce(IV)(1*R*,2R)(−)chxn(salal)$_2$].
[b] Δ_{coord} for [Ce(IV)(1*S*,2S)(−)chxn(salal)$_2$].

and +0.32 ppm for (**2a**). The magnitude of the H(4′) coordination shift in this case (three bonds distance) can be related to a less effective impact of the dichloro substituted phenyl ring on this hydrogen deshielding. Moreover, the chemical shift of this hydrogen atom is determined mostly by magnetic anisotropy of H–C=N– system, not by electronic effects, explaining why the coordination shift is smaller, than for H(1′). The above can be generalized, that the planarity of the double bond is not changed upon coordination, leaving the hydrogen in the negative sphere of the magnetic anisotropy cone. These coordination shifts are even smaller (*ca.* 0.6 ppm), than those found in the spectra of [Ni(II)(1*R*,2*R*)(−)chxn(3-methoxba)$_2$] and [Ni(II)-(1*R*,2*R*)(−)chxn(5-methoxba)$_2$] complexes [32].

The spectrum of [Ce(IV)((±)chxn(salal)$_2$)$_2$] (**3a**) revealed H(4′) resonances as two singlets at: 8.48 ppm and 8.57 ppm, whereas H(1′) appears as a pair of multiplets centered at 4.54 ppm and 4.74 ppm. When compared to the ^{1}H NMR signals of [Ni(II)(1*R*,2*R*)(−)chxn(salal)$_2$]: (H–C=N′ at 8.15 ppm, H(1′) at 3.16 ppm), the signals found at lower frequencies in **3a**, can be assigned to (1*R*,2*R*)(−)chxn(salal)$_2$ hydrogen atoms. In the case of **3a** the coordination shifts $\Delta_{coord} = \delta_{complex} - \delta_{ligand}$ were: +1.14 ppm and +1.07 ppm for H(1′) and 0.01 ppm and −0.01 ppm for H(4′) for [Ce(IV)(1*R*,2*R*)(−)chxn(salal)$_2$] and [Ce(IV)(1*S*,2*S*)(−)chxn(salal)$_2$] isomers, respectively. The magnitudes of the coordination shifts of both ligand isomers in **3a** are similar or identical, indicating minor distortion of the coordination plane in the chromophore N_2O_2.

^{13}C NMR spectra of **1** and **2** exhibited signals from C(4′) at 163.55 ppm and 163.43 ppm, whereas from C(1′) at 72.65 ppm and 72.23 ppm, respectively. Resonances of the phenyl ring's *ipso* carbons were observed at 159.46 ppm and 156.35 ppm for **1** and **2**. In the spectrum of (±)chxn(salalH)$_2$ (**3**) the doubled number of carbon signals is noted *i.e.*: 72.50 ppm and 69.32 ppm from C(1′), 164.60; 164.03 ppm from C(4′), 118.50; 116.90 ppm from C(1), 161.13 and 160.85 ppm from C(2). In the case of the cyclohexane ring's carbon atoms, resonances were detected in the range 22.38–32.97 ppm. The latter reflects the magnetic unequivalence of two optically active cyclohexane carbons.

^{13}C NMR spectra of [Ce(IV)(1*R*,2*R*)(−)chxn(5-Clba)$_2$] (**1a**) and [Ce(IV)(1*R*,2*R*)(−)chxn(3,5-diClba)$_2$] (**2a**) exhibit signals from C(4′) at 164.64 ppm and 164.40 ppm, shifted downfield $\Delta_{coord} = \delta_{complex} - \delta_{ligand}$ (+0.85 ppm for **1a** and +1.21 ppm for **2a**) in relation to the free bases. These coordination shifts are stronger, than those noted in the proton spectrum, but not distinct enough to be used as unambiguous proof of the coordination sites in the Schiff base.

Resonances of methine C(1′) in the cyclohexyl ring were detected at: 72.66 ppm **1a** and 72.74 ppm **2a**. This carbon atom is two bonds separated from the metal center, same as C(4′), and shifted slightly downfield Δ_{coord}: +0.4 ppm for **1a** and +0.51 ppm **2a**. Surprisingly, *ipso* carbon C(1) in the phenyl ring, which is three bonds apart from Ce(IV), exhibits a stronger coordination shift: −4.43 ppm **1a** (154.97 ppm) and +2.33 ppm **2a** (158.68 ppm). The latter case can be rationalized, as a result of effective deshielding of the *ipso* carbon atom, due to the diamagnetic effect of the deprotonated oxygen atoms involved in M–O σ bond and simultaneous impact of two electron withdrawing chlorine atoms at C(3) and C(5). Another interesting feature is the opposite sign of the C(1) coordination shift in the case of **1a**, when compared to 3,5-dichloro **2a**. The upfield coordination shift of the *ipso* carbon atom in **1a** is in favor of the *para* effect of C(5) chlorine atom. The latter can be generalized, that carbon atom resonances are more sensitive to Ce–O bond formation, than hydrogen atom resonances. The downfield coordination shifts of the *ipso* carbon atom in the 3,5-dichloro derivative can be related to the chlorine atom's strong electron withdrawing properties at C(3). The second interesting feature of the ^{13}C coordination shifts is the bigger magnitude of this effect in three bonds distance from the central ion, than in two bonds. For C(1), the latter can be the result of added effects such as: σ bonds (Ce–O) formation, diamagnetic induction due to the phenyl ring's electrons and deshielding, *via* unsaturated –C=N bond. The stronger coordination shift of C(1) in the discussed complexes, when compared to analogous nickel(II) Schiff base complexes [31–33], can be related to the distance to the central ion, shorter than in the Ni(II) compounds.

3.3. NOE difference measurements

The determination of the structure of the Ce(IV) complex by NMR spectroscopy in solution involves resonance assignment and interpretation of NOE data. The CD exciton chirality method is reliable for determination of the absolute configuration of chiral cyclohexanediamine as was discussed above. The impact of ligand coordination on distances between hydrogen atoms in the nearest proximity to the chelate ring can be evaluated by NOE difference experiment. These NOEs can reveal the whole relative configuration of Schiff bases in solution. In NOE difference experiments, the following protons were saturated: **H**–C=N at 8.18 ppm in **1**; 8.17 ppm in **2**; 8.44 ppm **1a** and 8.49 ppm **2a** and relative enhancements are listed in Table 3 and presented in Fig. 3.

In the spectra of **1** and **2** the strongest enhancements were observed to the methine hydrogen atoms in the cyclohexane ring H(1′) (8.1; 8.50%) and the phenyl ring H(6) (5.1%; 8.54%) respectively. In the case of **2** the enhancements of H(6) are stronger NOE (8.54) than for **1** indicating displacement of H(6) towards the N=C–H plane. Minor enhancements were noted for OH (0.4 in **1** and 1.57% in **2**) and phenyl H(4) in **1** (2.1%). Small but significant difference in NOE of OH signals (**1** and **2**) can be related to deformation of the HOC(1) angle in **2** and a closer distance to the azomethine hydrogen atom. The latter can be caused by the stronger impact of two electronegative chlorine atoms at C(3) and C(5) in **2**, *than in* **1**. The chlorine atoms *can induce* stronger polarization of O–H–N hydrogen bond in **2**, which has further impact on the OH chemical shift (larger for **2**) and displacement of H–O bond from N=C(4′)–H plane. Cyclohexyl CH_2 (C2′, $\delta = 1.9$ ppm) in **1** exhibits low NOE (1.0%) (Figs. 2 and 3), what is in favor of a long distance between the azomethine hydrogen atom and location of CH_2 below azomethine bond plane. In the case of **2**, NOE was not observed for the cyclohexyl CH_2, suggesting even larger distance, than in the case of the monochloro substituted phenyl ring.

The observed NOE enhancements suggest the closest proximity between azomethine hydrogen atom and the cyclohexyl ring H(1′), while the magnitude of the effect in **2** is slightly larger, than in **1** (Table 1). The latter effect can arise from the inclination of N=C–H bond towards C(1′)–H. Moreover, H(1′) in **1** is closer to the azomethine hydrogen, than H(6) due to stronger NOE. From the

Table 3
The results of NOE difference spectra of Schiff bases and cerium(IV) complexes (*H*(4′) saturated)

Compound	*H*(1′)–	(4′)*H*=N (100%)	O*H*	Ar–H	chxn
(1*R*,2*R*)(−)chxn(5-ClbaH)$_2$ (**1**)	3.32(m) (8.1)	8.18(s)	13.20(s) (0.4)	7.21 (2.06)H(4) 7.12 (5.1)H(6)	1.89(m), (1.0)
Ce(IV)(1*R*,2*R*)(−)chxn(5-Clba)$_2$ (**1a**)	4.38(m) (2.49)	8.44(s)		7.07(d) (10.96)H(6)	2.43(d), (6.71)
(1*R*,2*R*)(−)chxn(3,5-diClbaH)$_2$ (**2**)	3.57(m) (8.50)	8.17(s)	14.19(s) (1.57)	7.07(d)H(6) (8.54)	
Ce(IV)(1*R*,2*R*)(−)chxn(3,5-diClba)$_2$ (**2a**)	4.77(m) (2.80)	8.49(s)		7.05(d) (12.79) H(6)	2.39, 2.44 (6.27) 1.85(m), (4.84) 1.54(m)

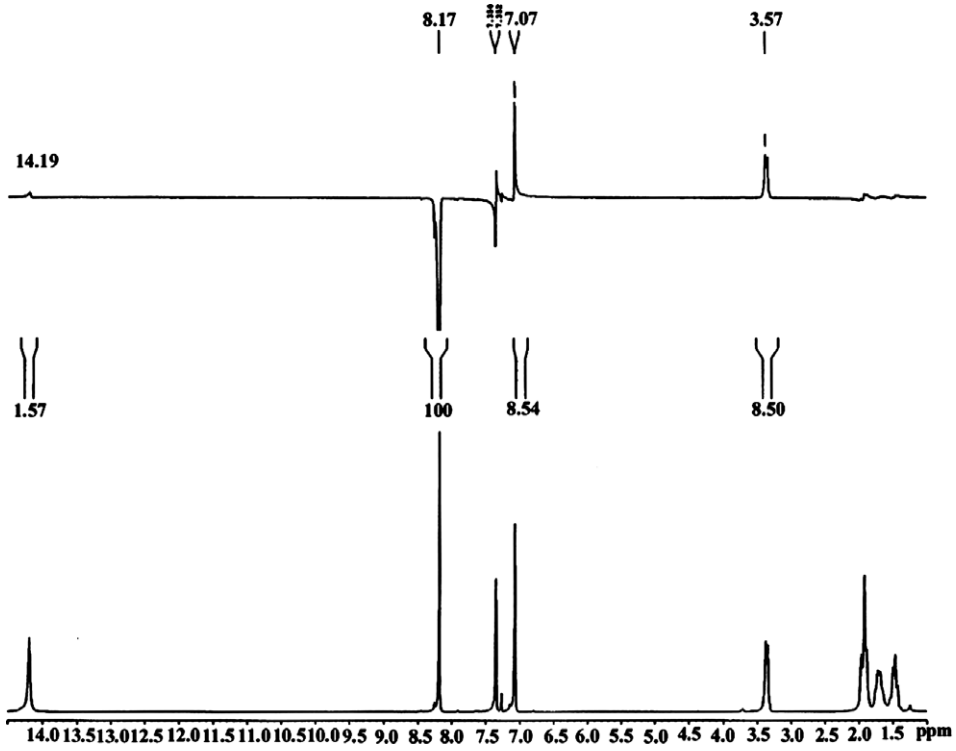


Fig. 2. The NOE spectrum of the ((1*R*,2*R*)(−)chxn(3,5-diClbaH)$_2$) (**2**) – (*H*(4′) saturated).

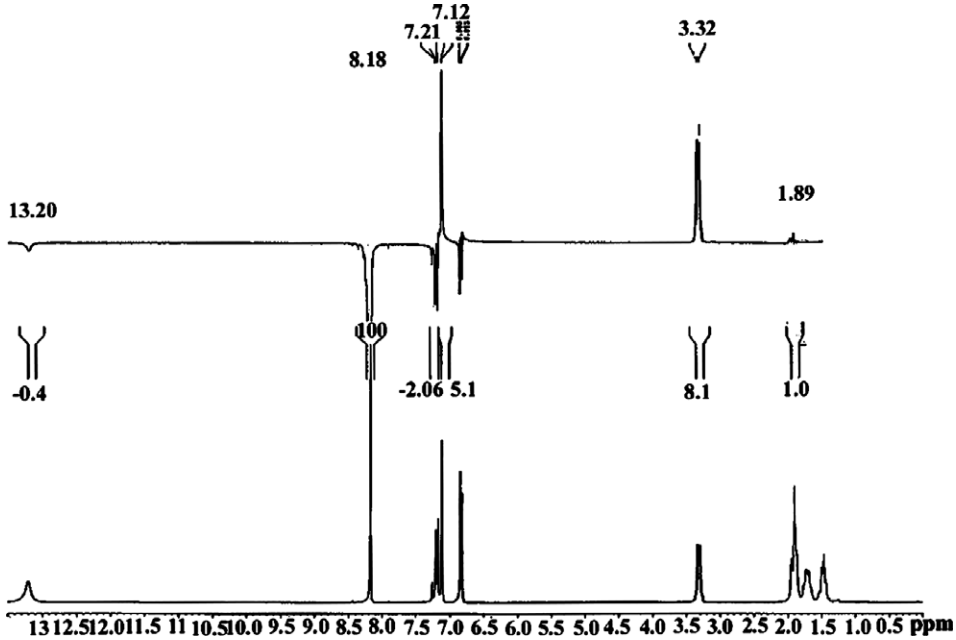


Fig. 3. The NOE spectrum of the ((1*R*,2*R*)(−)chxn(5-ClbaH)$_2$) (**1**) – (*H*(4′) saturated).

discussion above can be concluded, that in solution the cyclohexane ring retains the chair conformation, while there are some changes in position of the benzaldehyde ring. The phenyl ring can rotate along C(4′)–C(1), what may cause the *strongest NOE enhancement of H(6) signal*.

Saturation of **H**C=N in complex **1a** resulted in the following enhancements: H(6) (10.96% – stronger than in **1**), CH_2(2′) (6.71% in **1**) and H(1′) (2.49% *decrease in relation to* **1**) (Fig. 4). The NOE increase observed for H(6) and CH_2(2′), along with the decrease of H(1′) NOE, suggests deformation of the H-C=N bond plane into the direction opposite to H(1′) (Scheme 1). On the other hand, the methine H(1′) is located far from the H–C=N plane. Surprisingly, the enhancement of CH_2(2′) signals observed for **1a**, suggests cyclohexyl ring deformation and/or simultaneous H–C=N– inclination from the coordination plane

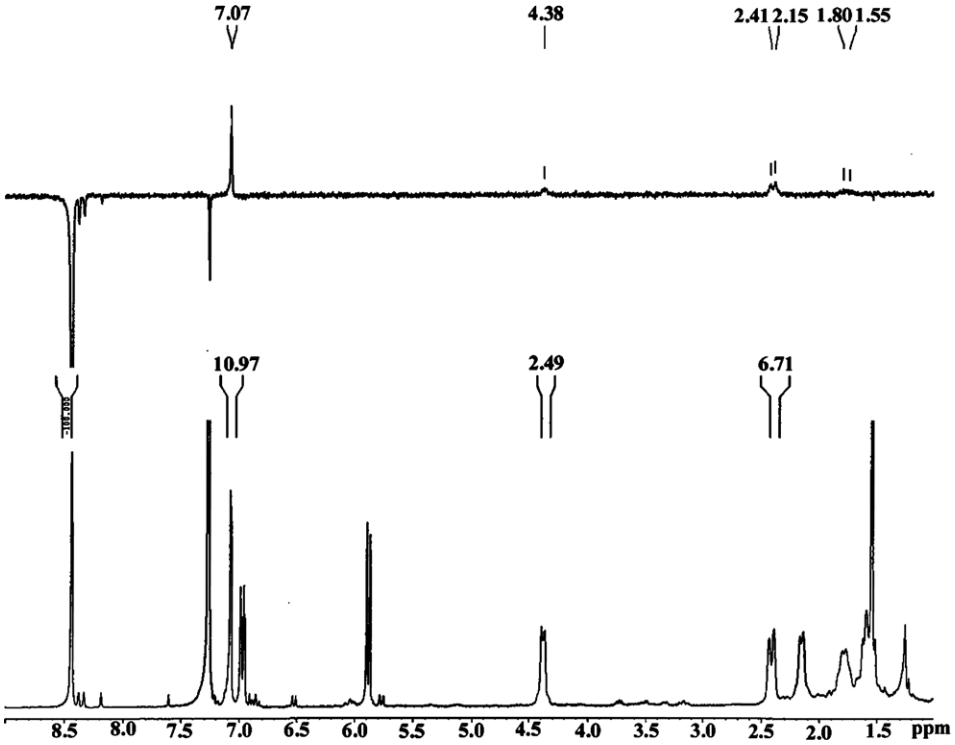
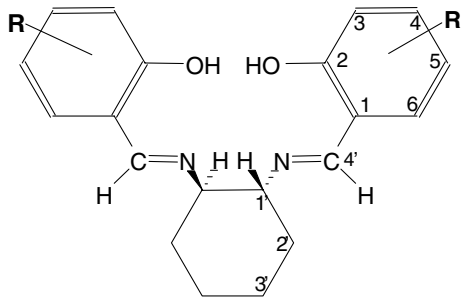


Fig. 4. The NOE spectrum of the [Ce(IV)((1*R*,2*R*)(−)chxn(5-Clba)$_2$)] (**1a**) – (*H*(4′) saturated).



Scheme 1. A schematic representation of (1*R*,2*R*)(−)chxn(**R**-salH)$_2$], **R** = H, or 5-Cl or 3,5-diCl.

towards the cyclohexyl ring. Such effect can be related to deformation of the chelate ring (–Ce–N=C–C(1)–C(2)–O–Ce–), due to molecular packing of two Schiff bases forced by eight coordinated Ce(IV). The electron withdrawing effect of Cl(C5), five bonds away from the donor N atoms, is much less significant.

In the case of **2a** the NOE enhancements were: 12.79% for phenyl H(6), 2.80% for H(1′) and 6.27% for CH_2(2′). The observed NOE correlations suggest stronger interaction between the H(6) hydrogen atom and almost the same for H(1′) (2.49%) and CH_2(C2′) (6.71%) as in the spectrum of **1a**. (Figs. 4 and 5).

The NOEs of **2a** suggest closer distance between H–C=N– and phenyl H(6), due to the influence of the second chlorine atom on conformational changes of the metalloorganic ring. One can assume, that the dihedral angle between the coordination plane and the phenyl ring appears to be smaller, than in the free base and in **1a**. Simultaneous reduction of the C(1)–C(4′)–H angle can be also postulated due to the strongest NOE (12.79%) between H(6) and H(4′). Similar NOE was noted for cyclohexyl –CH_2– (6.27%) in **2a** due to the above mentioned deformations of the coordination ring. These results prompted us to perform a second NOE experiment by saturating the cyclohexane ring's methine H(1′) signals at: 3.32 ppm for (**1**), 3.57 ppm for **2**, 4.38 ppm for **1a** and 4.77 ppm for **2a** (Fig. 6).

The following enhancements were detected for H(4′): (8.65%) in **1**, (2.66%) in **1a**, whereas for **2** and **2a** (8.50%) (2.98%), respectively (Fig. 6). For both complexes, the NOE to azomethine hydrogen is smaller, than in the free bases, what is in accordance with the previous NOE experiment and illustrated at Figs. 7 and 8. There is a small NOE what is in favor of the cyclohexyl chair deformation.

In the Ni(II) complexes with (1*R*,2*R*)(−)chxn(3-methoxbaH)$_2$ and (1*R*,2*R*)(−)chxn(5-methoxbaH)$_2$ when the **H**–C=N protons were saturated, the reported enhancements were as follows: to phenyl ring H(6) (10.68%, 12.28%) and cyclohexyl CH_2 (8.25%, 11.72%) in [Ni(II)(1*R*,2*R*)(−)-chxn(3-methoxba)$_2$] and [Ni(II)(1*R*,2*R*)(−)chxn(5-methoxba)$_2$], respectively [30–33]. However, in these complexes the NOE effect at the H(1′) hydrogen atom was not detected, suggesting different conformational changes due to coordination. Therefore, larger distance between hydrogen atom in the studied cerium(IV), than in nickel(II) complexes can be postulated [30]. In order to correlate

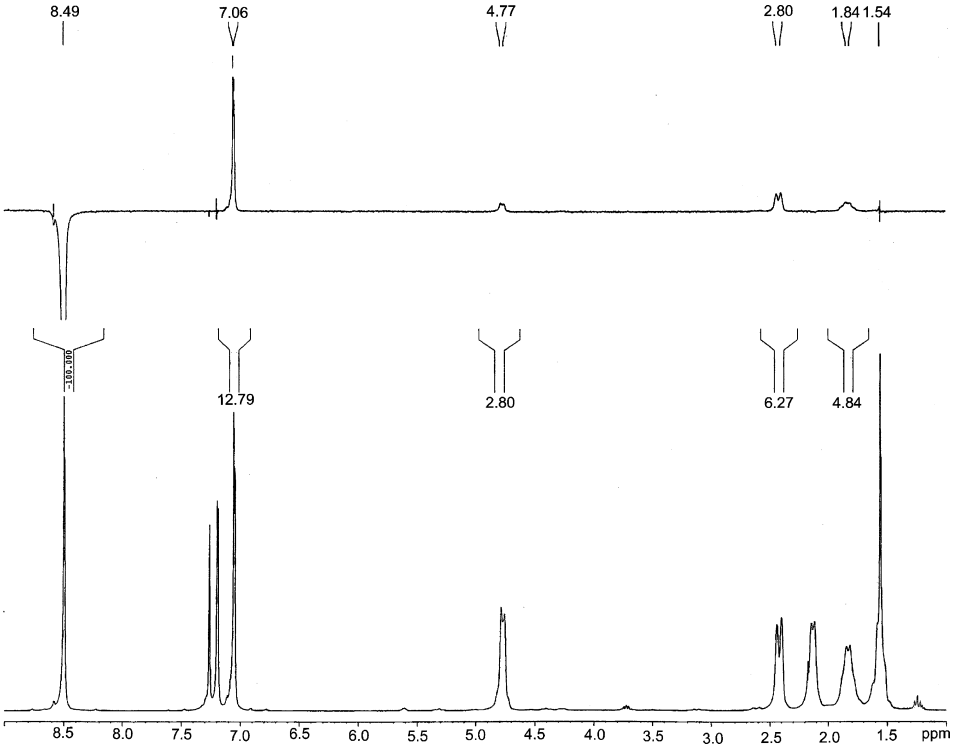


Fig. 5. The NOE spectrum of the [Ce(IV)((1*R*,2*R*)(−)chxn(3,5-diClba)$_2$)] (**2a**) – (*H*(4′) saturated).

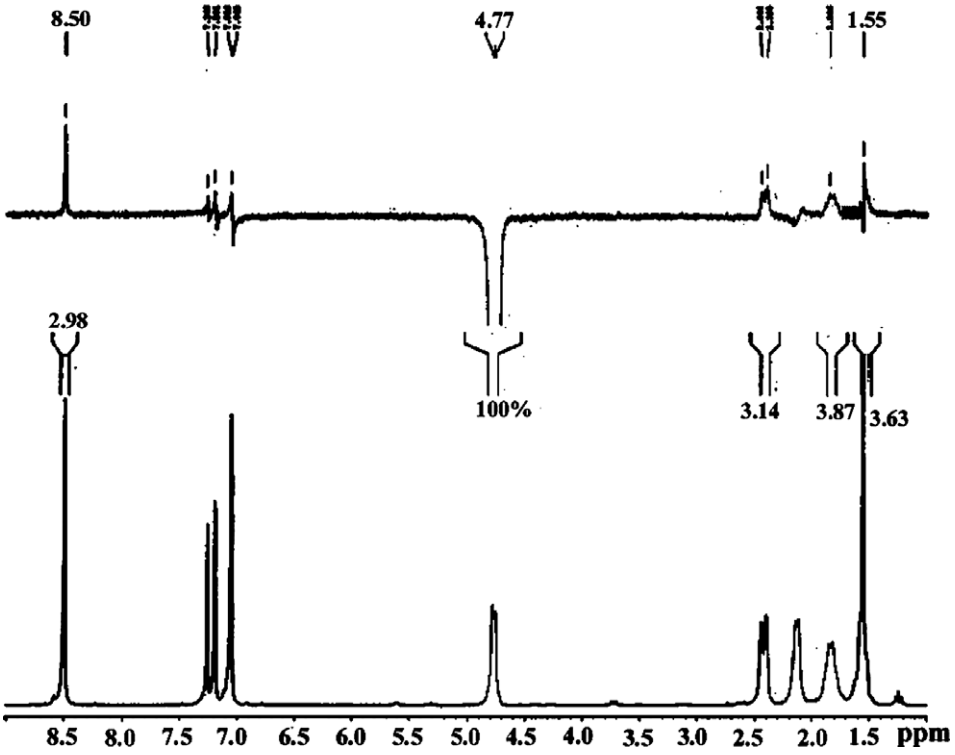


Fig. 6. The NOE spectrum of the [Ce(IV)((1*R*,2*R*)(−)chxn(3,5-diClba)$_2$)] (**2a**) – (*H*(1′) saturated).

solid X-ray data with solution NOE data we have listed these values in Table 4.

Atoms numeration in solution and in the solid state (Schiff bases 1 and 2)

$$\mathbf{C4'} = \mathbf{C7}, \mathbf{C14}, \mathbf{C27}, \mathbf{C34}$$
$$\mathbf{C3'} = \mathbf{C10}, \mathbf{C11}, \mathbf{C31}, \mathbf{C32}$$
$$\mathbf{C2'} = \mathbf{C9}, \mathbf{C12}, \mathbf{C30}, \mathbf{C33}$$

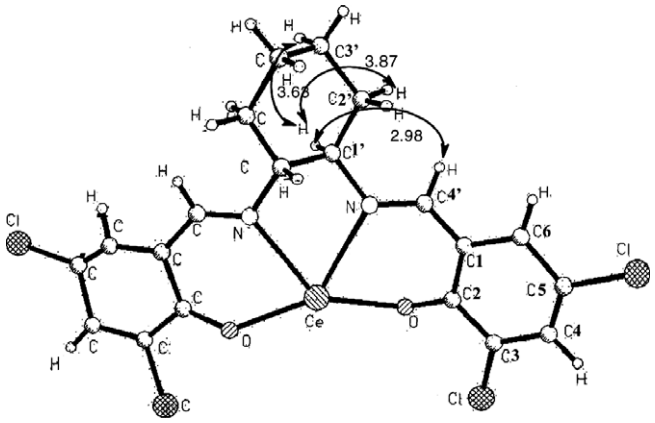


Fig. 7. NOE correlation in $CDCl_3$ in [Ce(IV)((1*R*,2*R*)(−)chxn(3,5-diClba)$_2$)$_2$] (**2a**) – (H(1′) saturated).

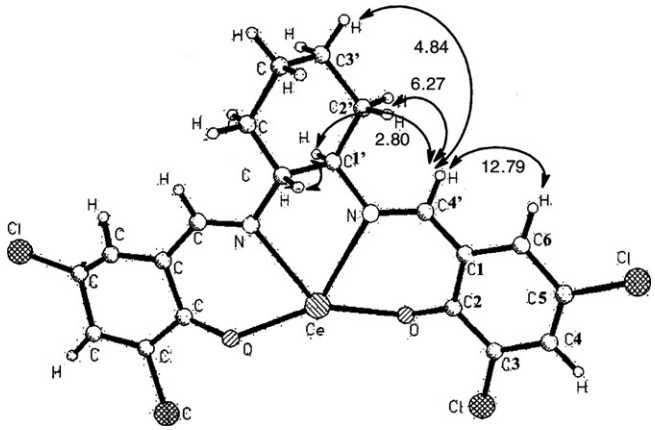


Fig. 8. NOE correlation in $CDCl_3$ in [Ce(IV)((1*R*,2*R*)(−)chxn(3,5-diClba)$_2$)$_2$] (**2a**) – (H(4′) saturated).

$$\mathbf{C1'} = \mathbf{C8}, \mathbf{C13}, \mathbf{C28}, \mathbf{C29}$$
$$\mathbf{C6} = \mathbf{C6}, \mathbf{C20}, \mathbf{C26}, \mathbf{C40}$$

In the crystal structure of complex **2a** positions of the hydrogen and carbon atoms from the two different Schiff bases coordinated to cerium(IV) can be noted, whereas in solution their position in complex molecule is averaged (*vide* numeration). The biggest NOE effect (12.79%) was observed for the phenyl H(6) atoms (Table 4), what can be related to the short distance between hydrogen atoms (H7a–H5a – 2.2958, H14a–H16a – 2.4967) in the solid state. The latter is in favor of the same ligand orientation around metal ion in both states. Second in order NOE effect (6.27) was noted between cyclohexane H(C3′) and azomethine H(4′) atoms (Fig. 8), while in the solid state these two atoms revealed longer distance (about 4 Å) (Table 4). This effect can be related to more pronounced deformation of the cyclohexane ring in solution than in the solid state. NOE effect for other hydrogen atoms in the phenyl ring and cyclohexane ring and corresponding distances in the crystal structure of complex **2a** are comparable.

3.4. Crystal structure description

The details of the diffraction experiment, structure refinement, selected bond distances and angles for the [Ce(IV)((1*R*,2*R*)(−)chxn(3,5-diClba)$_2$)$_2$] are presented in Tables 1 and 5.

Structure **2a** is formed by the molecules of Ce(IV) complex with two Schiff base ligands. The structure revealed the tilt of both dichlorophenolic rings of the Schiff base relative to the coordination plane (Fig. 9).

The aromatic rings are almost parallel to each other, the dihedral angles between their best planes being 6.1(4) and 5.7(5)° for two ligands. The dihedral angles between the CeN_2O_2 coordination plane and the ring planes are 39.3(3) and 33.9(3)° for C1–C6 and C15–C20 rings for the first ligand, and 37.0(4) and 34.0(4)° for C21–C26 and C35–C40 rings of the second ligand. The dihedral angle between the best planes of two ligands, with the cyclohexane's C atoms excluded, is 47.1(2)° In such an arrangement, the aromatic rings forming the double layer are surrounding the central Ce(IV) ion, and the dichlorophenolic moieties of each ligand belong to the different layers (Fig. 9). This is the first report of such an architecture for Schiff base complexes of Ce(IV). This kind of coordination sphere is unique, since in previously reported crystal structures, the Schiff base ligands are always positioned perpendicular to each other [1–3]. The dihedral angle between the best planes of the coordination spheres formed by two ligands is 85.3(3)° and is similar to that of 87.7(3) observed in the complex **3a**.

Each ligand forms four coordination bonds to the central ion. The Ce–O and Ce–N distances vary between 2.212(5) and 2.241(5) Å and between 2.550(7) and 2.570(6) Å, respectively, and are similar to those found in the investigated Ce(IV) complexes of the unsubstituted Schiff ligand **3a**. The angles within the coordination sphere, formed by the atoms of the same Schiff base are similar for both ligands. The O–Ce–O angles are the largest, being 149.7(2) and 149.4(2)° for O(2)–Ce(1)–O(1) and O(3)–Ce(1)–O(4), respectively. The angles formed by the adjacent donor atoms vary between 65.8(2) and 72.7(2)°, while others are between 137.4(2) and 138.5(2)°. Due to the special arrangement of two Schiff base ligands in the sphere, the angles between the coordination bonds formed by the atoms of different ligands vary from 73.0(2) for O(2)–Ce(1)–N(3) to 137.7(2)° for N(1)–Ce(1)–N(3), respectively.

The structure contains two Schiff base ligands, with the absolute configuration of the chiral centers *R*,*R*-(C8,C13) and *R*,*R*-(C28,C29). The torsion angles in the diaminocyclohexane moiety are N(1)–C(8)–C(13)–N(2) −57.0(8)° and N(3)–C(28)–C(33)–N(4) −55.9(8)°.

The cyclohexane ring of the ligand is in the chair conformation. Both the C–N bonds are equatorial. Therefore, the dihedral angle between the plane defined by the central fragment of the cyclohexyl moiety chair and the CeN_2O_2 coordination plane of the ligand are 13.1(9) and 16.6(9)° for C8–C13 and C28–C33 rings, respectively. These values

Table 4
Selected atom distances (Å) and NOE results in the [Ce(IV)((1*R*,2*R*)(−)chxn(3,5-diClba)$_2$)$_2$] (**2a**)

Fig. 7	Schiff base 1		Distance	NOE(H1′) saturated	Schiff base 2		Distance
H1′–H4′	C7–C8	H7a–H8a	3.2862	2.98	C27–C28	H27a–H28a	3.0243
	C13–C14	H13a–H14a	3.2192		C29–C34	H33a–H34a	3.1198
					C33–C34		
H1′–H3′	C8–C10	H8a–H10a	2.5938	3.63	C28–C32	H28a–H30a	3.5423
					C28–C30		
		H8a–H10b	3.6820			H28a–H30b	2.5351
	C13–C11	H13a–H11a	3.7696		C29–C31	H33a–H31a	3.5929
					C33–C31		
		H13a–H11b	2.8221			H33a–H31b	2.6029
H1′–H2′	C8–C9	H8a–H9a	2.9485	3.87	C28–C33	H28a–H29a	2.2402
					C28–C29		
		H8a–H9b	2.5045			H28a–H29b	2.7540
	C12–C13	H13a–h12a	2.3428		C29–C30	H33a–H32a	2.2438
					C33–C32		
		H13a–H12b	2.8404			H33a–H32b	2.7824
Fig. 8	Schiff base 1		Distance	NOE(H1′) saturated	Schiff base 2		Distance
H4′–H6	C6–C7 C5–C7	H7a–H5a	2.2958	12.79	C27–C26	H27a–H25a	2.5817
					C27–C25		
	C14–C20 C14–C16	H14a–H16a	2.4967		C34–C40	H34a–H36a	2.2842
					C34–C36		
H4′–H3′	C7–C10	H7a–H10a	4.3056	4.84	C27–C32	H27a–H30a	4.1143
					C27–C30		
		H7a–H10b	4.1775			H27a–H30b	4.2587
	C14–C11	H14a–H11a	4.0822		C34–C31	H34a–H31a	4.2494
		H14a–H11b	4.3599			H34a–H31b	4.3981
H4′–H2′	C7–C9	H7a–H9a	2.1805	6.27	C27–C33	H27a–H29a	1.9075
					C27–C29		
		H7a–H9b	2.0908			H27a–H29b	2.0851
	C14–C12	H14a–H12a	2.1900		C34–C30	H34a–H32a	2.1959
					C34–C32		
		H14a–H12b	1.9022			H34a–H32b	2.1788
H4′–H1′	C7–C8	H7a–H8a	3.2862	2.80	C27–C28	H27a–H28a	3.0243
	C14–C13	H14a–H13a	3.2192		C34–C29	H34a–H33a	3.1198
					C34–C33		
H1′–H1′	C8–C13	H8a–H13a	2.9446		C28–C29	H28a–H33a	2.7936
					C28–C33		

Table 5
Selected bond lengths and angles (Å) in [(Ce(IV) ((1*R*,2*R*)(−)chxn-(3,5-diClba)$_2$)$_2$)] (**2a**)

Bond	Length	Angle	
Ce(1)–O(3)	2.212(5)	O(3)–Ce(1)–O(2)	90.5(2)
Ce(1)–O(2)	2.241(5)	O(3)–Ce(1)–O(1)	93.9(2)
Ce(1)–O(1)	2.217(5)	O(2)–Ce(1)–O(1)	149.7(2)
Ce(1)–O(4)	2.212(5)	O(3)–Ce(1)–O(4)	149.4(2)
Ce(1)–N(1)	2.570(6)	O(2)–Ce(1)–O(4)	101.8(2)
Ce(1)–N(4)	2.563(5)	O(1)–Ce(1)–O(4)	89.3(2)
Ce(1)–N(2)	2.562(6)	O(3)–Ce(1)–N(1)	78.0(2)
Ce(1)–N(3)	2.550(7)	O(2)–Ce(1)–N(1)	137.4(2)
O(1)–C(1)	1.310(9)	O(1)–Ce(1)–N(1)	72.7(2)
		O(4)–Ce(1)–N(1)	74.0(2)

are similar to those observed for Ni(II) and Zn(II) complexes of Schiff base ligands with (*R*,*R*) configuration of the chiral centers in the analogous ligands [3–5], but are much smaller than the values of almost 90° observed in the Ce complex of the investigated unsubstituted ligand with the (*R*,*S*) chiral centers.

The details of the experiment and structure refinement for **3a** are listed in Table 1. Selected bond lengths and angles are listed in Table 6.

Structure **3a** is formed by complexation of Ce(IV) with two Schiff base ligands. Each ligand forms four coordinate bonds to the central ion. The Ce–O and Ce–N distances vary between 2.148(7) and 2.241(9) Å and between 2.525(11) and 2.619(9) Å, respectively (Fig. 10).

The structure of **3a** contains the Schiff base ligand with the absolute configuration of the chiral centers determined as *R*,*S*-(C8,C13) and *R*,*S*-(C28,C33). However, due to the optical twinning (see Section 2), the *S*,*R*-(C8,C13) and its equivalent also exist in the crystal lattice. This is as a result of the racemic substrate used for the ligand synthesis. The torsion angles in the diaminocyclohexane moiety are N(1)–

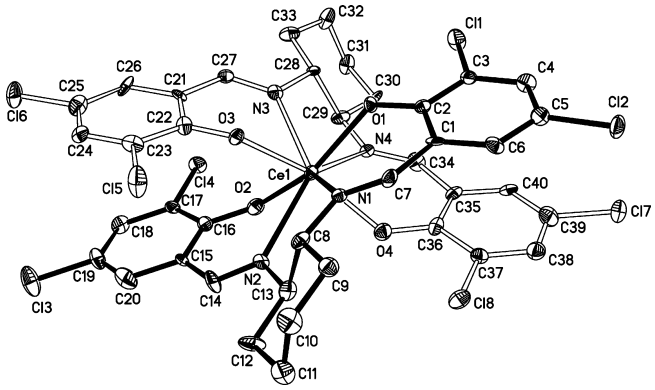


Fig. 9. Molecular diagram with atomic labelling scheme for $[Ce(IV)((1R,2R)(-)chxn(3,5\text{-}diClba)_2)_2]$ (**2a**). The ligands are displayed with filled and open bonds to visualize their spatial arrangement around the central ion (C1–C20 and C21–C40, respectively).

Table 6
Selected bond lengths and angles (Å) for $[(Ce(IV)((\pm)chxn(salal)_2)_2)]$ (**3a**)

Angle		Bond	Length
O(2)–Ce(1)–O(3)	93.9(4)	Ce(1)–O(2)	2.148(7)
O(2)–Ce(1)–O(4)	93.6(5)	Ce(1)–O(3)	2.166(10)
O(3)–Ce(1)–O(4)	151.9(3)	Ce(1)–O(4)	2.239(11)
O(2)–Ce(1)–O(1)	151.1(3)	Ce(1)–O(1)	2.241(9)
O(3)–Ce(1)–O(1)	99.7(6)	Ce(1)–N(4)	2.525(11)
O(4)–Ce(1)–O(1)	86.3(6)	Ce(1)–N(3)	2.590(12)
O(2)–Ce(1)–N(4)	79.0(3)	Ce(1)–N(2)	2.609(10)
O(3)–Ce(1)–N(4)	136.3(4)	Ce(1)–N(1)	2.619(9)
O(4)–Ce(1)–N(4)	71.8(4)		
O(1)–Ce(1)–N(4)	73.6(4)		
O(2)–Ce(1)–N(3)	85.8(3)		
O(3)–Ce(1)–N(3)	68.9(4)		
O(4)–Ce(1)–N(3)	138.7(4)		
O(1)–Ce(1)–N(3)	75.7(4)		
N(4)–Ce(1)–N(3)	67.6(4)		
O(2)–Ce(1)–N(2)	73.4(3)		

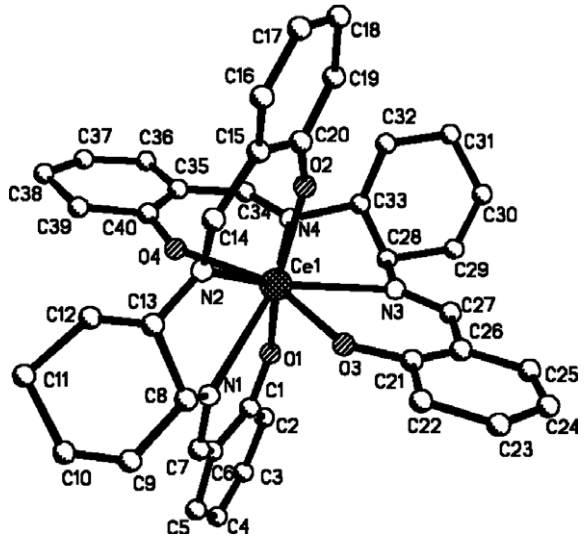


Fig. 10. Molecular diagram with atomic labelling scheme for $[Ce(IV)((\pm)chxn(salal)_2)_2]$ (**3a**).

C(8)–C(13)–N(2) −52.6(14)° and N(3)–C(28)–C(33)–N(4) −64(2)° (Table 6).

The cyclohexane ring of the ligand is in the chair conformation. Since one of the C–N bonds is axial and the other equatorial, the plane defined by the central fragment of the cyclohexyl moiety is almost perpendicular to the coordination plane of the ligand.

This is in contrast to the complexes with the ligands in the (*R*,*R*) configuration of the chiral centers in the Ni(II) complexes of the analogous ligands [31–35] or **2a**, where that angle was below 20°.

Each Schiff base ligand is slightly bent, with the dihedral angles between the phenyl ring planes and the coordination CeN_2O_2 plane being 7.1(8) and 3.8(7)° for the C1–C20 ligand and 5.6(4) and 3.7(5)° for C21–C40 ligand, respectively. In the coordination sphere, two ligands are almost perpendicular to one another, with the dihedral angle between the best CeN_2O_2 planes formed by the two ligands being 87.7(3)°.

4. Conclusions

The present study describes new cerium(IV) complexes with Schiff bases obtained by condensation of *N*,*N*′-(1*R*,2*R*)-cyclohexanediamine with 2-hydroxy-5-chlorobenzaldehyde or 2-hydroxy-3,5-dichlorobenzaldehyde and of (±)cyclohexanediamine with salicylaldehyde.

NOE experiments revealed interactions of the azomethine hydrogen atom with the protons from the cyclohexane ring, phenyl ring and with the hydroxyl group in the case of the Schiff bases, while in the cerium(IV) complexes this proton is in proximity of the phenyl ring hydrogen atom and the cyclohexane CH_2. Results of spectral analyses suggest central ions in a distorted planarity of N_2O_2 chromophore group. The X-ray crystallography study confirmed antiprismatic distortion from planarity in the reported complexes. Different architecture of the coordination sphere is found for **2a** and **3a**. In **2a** the ligand reveals a bent of the chlorophenolic ring relative to the N_2O_2Ce chelate ring. The pair of ligands forms a two-layer environment around the central ion with two phenolic rings of each ligand belonging to a different layer. This type of architecture of the Ce(IV) coordination sphere in Schiff base complexes is reported for the first time. In contrast, in the complex of the unsubstituted ligand **3a**, the coordination N_2O_2 planes of the two ligands are almost perpendicular to each other.

Supplementary material

CCDC 612705 and 612706 contain the supplementary crystallographic data for **2a** and **3a**. These data can be obtained free of charge via http://www.ccdc.cam.ac.uk/conts/retrieving.html, or from the Cambridge Crystallographic Data Centre, 12 Union Road, Cambridge CB2 1EZ, UK; fax: (+44) 1223-336-033; or e-mail: deposit@ccdc.cam.ac.uk.

References

[1] A. Terzis, D. Mentzafos, H.A. Tajmir-Riahi, Inorg. Chim. Acta 84 (1984) 187.
[2] S. Afshar, J.I. Bullock, Inorg. Chim. Acta 38 (1980) 145.
[3] J.A. Bullock, H. Tajmir-Riahi, Inorg. Chim. Acta 38 (1980) 141.
[4] H. Chen, J.A. Cronin, R.D. Archer, Macromolecules 27 (8) (1994) 2174.
[5] H. Chen, J.A. Cronin, R.D. Archer, Inorg. Chem. 34 (9) (1995) 2306.
[6] M. Pan, G.Y. Meng, H.W. Xin, C.S. Chen, D.K. Peng, Y.S. Lin, Thin Solid Films 324 (1998) 89.
[7] M. Becht, T. Gefrin, K.-H. Dahmen, Chem. Mater. 5 (1993) 137.
[8] M. Becht, T. Morishita, Chem. Vap. Depos. 2 (1996) 191.
[9] W.C. Andersen, B.C. Noll, S.P. Sellers, L.L. Whildin, R.E. Sievers, Inorg. Chim. Acta 336 (2002) 105.
[10] J.H. Timmons, J.W.L. Martin, A.E. Martell, P. Rudolf, A. Clearfield, J.H. Arner, S.J. Loeb, C.J. Willis, Inorg. Chem. 19 (12) (1980) 3553.
[11] S. Yamada, A. Takeuchci, H. Yamakita, Inorg. Chim. Acta 2–4 (1968) 425.
[12] W. Zhang, J.L. Leobach, S.R. Wilson, E.N. Jacobsen, J. Am. Chem. Soc. 112 (7) (1990) 2801.
[13] W. Zhang, E.N. Jacobsen, J. Org. Chem. 56 (7) (1991) 2296.
[14] E.N. Jacobsen, W. Zhang, A.R. Muci, J.R. Ecker, L. Deng, J. Am. Chem. Soc. 113 (18) (1991) 7063.
[15] E.G. Samsel, K. Srinivasan, J.K. Kochi, J. Am. Chem. Soc. 107 (25) (1985) 7606.
[16] K. Srinivasan, P. Michaud, J.K. Kochi, J. Am. Chem. Soc. 108 (9) (1986) 2309.
[17] F. Galsbol, P. Steenbol, B.S. Sorensen, Acta Chem. Scand. 26 (1972) 3605.
[18] J.R. Kincaid, K. Nakamoto, Spectrochim. Acta 32A (1976) 277.
[19] P. Teyssie, J.J. Charette, Spectrochim. Acta 19 (1963) 1407.
[20] L.E. Khoo, Spectrochim. Acta 35A (1979) 993.
[21] K. Nakamoto, Infrared and Raman Spectra of Inorganic Compounds, Wiley & Sons, New York, 1997.
[22] P. Gluvchinsky, G.M. Mockler, Spectrochim. Acta 33A (1977) 1073.
[23] G.M. Sheldrick, SHELXS97 and SHELXL97, University of Göttingen, Germany, 1997.
[24] H.D. Flack, Acta Crystallogr. A39 (1983) 876.
[25] M. Gullotti, A. Pasini, P. Fantucci, R. Ugo, R.D. Gillard, Gazz. Chim. Ital. 102 (1972) 855.
[26] Y.L. Bennani, S. Hanessian, Chem. Rev. 97 (8) (1997) 3161.
[27] J. Ferguson, Prog. Inorg. Chem. 12 (1970) 159.
[28] Y. Nishida, S. Kida, Coord. Chem. Rev. 27 (3) (1979) 275.
[29] M.A. Hitchman, Inorg. Chem. 16 (8) (1977) 1985.
[30] E. Szłyk, M. Barwiołek, R. Kruszynski, T.J. Bartczak, Inorg. Chim. Acta 358 (2005) 3642.
[31] E. Szłyk, A. Wojtczak, E. Larsen, A. Surdykowski, J. Neuman, Inorg. Chim. Acta 293 (1999) 239.
[32] A. Wojtczak, E. Szłyk, E. Jaskólski, E. Larsen, Acta Chem. Scand. 51 (1997) 274.
[33] E. Szłyk, A. Surdykowski, M. Barwiołek, E. Larsen, Polyhedron 21 (27-28) (2002) 2711.
[34] E. Szłyk, A. Wojtczak, A. Surdykowski, M. Goździkiewicz, Inorg. Chim. Acta 358 (3) (2004) 467.
[35] F. Azevedo, M.A.A.F. de Carrondo, B. de Castro, M. Convery, D. Domingues, C. Freire, M.T. Duarte, K. Nielsen, Inorg. Chim. Acta 219 (1994) 43.

Available online at www.sciencedirect.com
ScienceDirect
Polyhedron 27 (2008) 777–782
POLYHEDRON
www.elsevier.com/locate/poly

Synthesis and structural characterization of copper–molybdenum–sulfur and copper–tungsten–sulfur cluster complexes (n-Bu_4N)[$OMS_3Cu_3Br_2L_2$] with heterocyclic thiones as ligands

Azizolla Beheshti [a,*], William Clegg [b,*], Sophie H. Dale [b], Ahmad Solimankhani [a]

[a] Department of Chemistry, Faculty of Sciences, Shahid Chamran University, Ahvaz, Iran
[b] School of Natural Sciences (Chemistry), Newcastle University, Newcastle upon Tyne NE1 7RU, United Kingdom

Received 15 June 2007; accepted 6 November 2007

Abstract

Reaction of $(NH_4)_2[WOS_3]$ or $(NH_4)_2[MoO_2S_2]$, n-Bu_4NBr, CuCl and Imt in acetone solvent afforded air- and moisture-stable clusters (n-Bu_4N)[$MOS_3Cu_3(Imt)_2Br_2$] (M = W or Mo, Imt = imidazolidine-2-thione). These compounds have been characterized by IR, UV–Vis, ^1H and ^{13}C NMR spectra and single-crystal X-ray diffraction. They are crystallographically isostructural, with Imt and $[MOS_3]^{2-}$ acting as monodentate and bidentate S-donor ligands, respectively. In the anions, the three Cu atoms have different coordination environments, one being distorted tetrahedral with Imt and Br as terminal ligands, the other two being approximately trigonal planar with Imt as a terminal ligand for one and Br as a terminal ligand for the other. W and Mo have approximately tetrahedral coordination geometry, with a terminal O and three triply-bridging S atoms. The NH groups of the Imt ligands serve as donors in intramolecular N–H···Br and in intermolecular N–H···Br and N–H···O hydrogen bonds, linking the anions to form layers with the cations in cavities.
© 2007 Elsevier Ltd. All rights reserved.

Keywords: Heterocyclic thiones; Heterothiometallic cluster compounds; Hydrogen bonding; Copper(I) complexes; Coordination

1. Introduction

Heterocyclic thiones have attracted considerable interest as ligands in metal complexes because of their relevance in biological systems [1,2]. The chemical interest of heterocyclic thiones is due to the fact that they are potentially ambidentate or multifunctional donors with either the exocyclic sulfur or heterocyclic nitrogen atom available for coordination [3–7]. They are often used for studying binding properties with a soft Lewis acid such as Cu(I) [8–11]. The formation of hydrogen bonds, including both intra- and intermolecular hydrogen bonds, in many thione complexes and biological macromolecules such as azurin and rubredoxin, has been confirmed by X-ray crystallography, vibrational and NMR spectroscopic studies [8]. Tetrathiometallate and oxotrithiometallate anions of molybdenum(VI) and tungsten(VI) have been extensively used as metalloligands for other metal centres, particularly in mixed-metal complexes with copper(I) [12]. We present here two isostructural copper(I) complexes involving the $[MOS_3]^{2-}$ core (M = W, Mo), which display intramolecular and intermolecular N–H···Br and intermolecular N–H···O hydrogen bonds. There are only a few previous examples of crystallographically characterized (oxo)thiometallate–copper complexes with heterocyclic thiones as ligands [13–17]. (Oxo)thiometallate–copper complexes have been investigated in the past because of their biological relevance, including copper–molybdenum antagonism in ruminant animals [18–21].

* Corresponding authors.
E-mail addresses: beheshti_a@hotmail.com (A. Beheshti), w.clegg@ncl.ac.uk (W. Clegg).

0277-5387/$ - see front matter © 2007 Elsevier Ltd. All rights reserved.
doi:10.1016/j.poly.2007.11.005

2. Experimental

2.1. Materials and physical measurements

Starting materials were purchased from commercial sources and used without further purification. Imidazolidine-2-thione (Imt) [22,23], $(NH_4)_2[WOS_3]$ and $(NH_4)_2[MoO_2S_2]$ [24] were prepared from them by published methods. In the case of the thione ligand, a pure sample was obtained by recrystallization from methanol. Infrared spectra (4000–400 cm^{-1}) were recorded from KBr discs with a BOMEN MB102 FT-IR spectrometer. UV–Vis spectra were recorded on a JASCO model 7850 spectrophotometer. ^1H and ^{13}C NMR spectra were obtained using a Bruker DRX 400 AVANCE spectrometer. Microanalysis was carried out by the chemical analysis services of Shiraz University (Iran) and Newcastle University. Melting points could not be determined, as the complexes decomposed on heating.

2.2. Preparation of (n-Bu_4N)[$WOS_3Cu_3(Imt)_2Br_2$] (1)

$(NH_4)_2[WOS_3]$ (0.2 g, 0.60 mmol) was partially dissolved in acetone (50 ml). Solid *n*-Bu_4NBr (0.408 g, 1.27 mmol) was added and the mixture was stirred for ca 10 min, CuCl (0.179 g, 1.8 mmol) was then added and the reaction mixture was stirred for 4 h. The resulting orange solution was filtered to remove the precipitate. After addition of Imt (0.129 g, 1.26 mmol) to the filtrate, the mixture was stirred for another 4 h, the solution was filtered, and the filtrate was evaporated with a vacuum pump. The residue was washed with distilled water (2 × 2 ml), ethanol (2 × 2 ml) and diethyl ether (2 × 5 ml) and dried *in vacuo* to give a yellow powder (0.398 g, 60% based on W). Single crystals were obtained by slow diffusion of diethyl ether into a saturated solution in acetone. On leaving the solution to stand at room temperature overnight, air-stable orange crystals were deposited, which are soluble in common organic solvents. *Anal.* Calc.: C, 24.2; H, 4.4; N, 6.4. Found: C, 23.3; H, 4.0; N, 6.1%.

2.3. Preparation of (n-Bu_4N) [$MoOS_3Cu_3(Imt)_2Br_2$] (2)

The same procedure was employed to synthesize and crystallize the complex (*n*-Bu_4N)[$MoOS_3Cu_3(Imt)_2Br_2$], but using $(NH_4)_2[MoO_2S_2]$ (0.114 g, 0.50 mmol) instead of $(NH_4)_2[WOS_3]$. A red powder was initially obtained (0.217 g, 43% based on Mo), giving red crystals from acetone and diethyl ether. *Anal.* Calc.: C, 26.7; H, 4.8; N, 7.0. Found: C 26.7, H 5.0, N 6.3%. The reaction involves redistribution of O and S atoms at the Mo centre [25].

2.4. X-ray crystallography

Crystal data together with other relevant information on the structure determinations for compounds **1** and **2** are listed in Table 1. All measurements were made on a Nonius KappaCCD diffractometer, with Mo Kα radiation ($\lambda = 0.71073$ Å) at 150 K. Absorption corrections were based on the high redundancy of symmetry-equivalent and repeated reflections. The structures were solved by direct methods and refined by full-matrix least-squares on all F^2 values. Non-hydrogen atoms were refined with anisotropic displacement parameters. Carbon-bound hydrogen atoms were included in calculated positions and refined with isotropic displacement parameters, riding on their parent atoms, while nitrogen-bound hydrogen atoms were refined with a bond-length restraint of 0.88 (1) Å. Programs were standard Nonius control software [26], EvalCCD for data integration [27], SADABS [28] and SHELXTL [29].

Table 1
Crystallographic data

Compound	**1**	**2**
Formula	$C_{16}H_{36}N^+ \cdot C_6H_{12}Br_2Cu_3N_4OS_5W^-$	$C_{16}H_{36}N^+ \cdot C_6H_{12}Br_2Cu_3MoN_4OS_5^-$
Formula weight	1093.2	1005.3
Crystal system	monoclinic	monoclinic
Space group	$P2_1/n$	$P2_1/n$
a (Å)	10.6050(19)	10.6049(15)
b (Å)	11.6715(15)	11.6848(16)
c (Å)	29.637(8)	29.692(3)
β (°)	98.706(18)	98.666(10)
V (Å^3)	3626.1(13)	3637.3(8)
Z	4	4
μ (mm^{-1})	7.41	4.58
Crystal size (mm)	0.45 × 0.21 × 0.20	0.50 × 0.23 × 0.16
Data collected	35 504	42 753
Unique data, R_{int}	6208, 0.087	7023, 0.059
Observed data ($F^2 > 2\sigma$)	4548	5354
R ($F^2 > 2\sigma$)	0.071	0.049
R_w (F^2, all data)	0.197	0.115
Goodness of fit (F^2)	1.05	1.07
Difference map extremes (e Å^{-3})	2.52, −3.78	0.71, −1.91

3. Results and discussion

3.1. Infrared spectra

The most significant FT-IR bands of the ligands and complexes are summarized in Table 2. The bands appearing at 439 and 900 cm^{-1} for complex **1** and 447.7 and 882 cm^{-1} for complex **2** are assigned to the M-μ_3-S and M = O (M = W or Mo) stretching vibrational frequencies of the WOS_3 and $MoOS_3$ groups respectively. The M-μ_3-S stretching vibrational frequencies of $[MOS_3]^{2-}$ are shifted to a lower frequency, while the M = O stretching vibrational frequencies are shifted to a higher frequency relative

Table 2
Selected IR bands (ν, cm^{-1}) of the ligands and complexes

Compounds	C=S	$\Delta\nu_{CS}$	N–H	$\Delta\nu_{NH}$	W–S_t	W-μ_3-S	W=O
$(NH_4)_2[WOS_3]$					459(vs.)		855
$(NH_4)_2[MoO_2S_2]$					483(vs.)		797, 831
Imt	510		3200				
(n-Bu_4N)$[WOS_3Cu_3(Imt)_2Br_2]$ (**1**)	500.9	9.1	3174	26		439	900
(n-Bu_4N)$[MoOS_3Cu_3(Imt)_2Br_2]$ (**2**)	500.6	9.4	3180	20		447.7	882

Abbreviation: vs., very strong; t, terminal.

to those for uncoordinated $[MOS_3]^{2-}$ ligands (see Table 2). This indicates that the $[MOS_3]^{2-}$ metalloligands are coordinated to Cu(I) through sulfur atoms, as is usually the case. The infrared spectra of the complexes display all of the bands due to the presence of the heterocyclic thione ligand. It can be seen from Table 2 that there is a shift of the ν(NH) vibrational frequencies to lower values upon coordination of the Imt ligand to the Cu(I) metal centre. The shift of the ν(NH) vibration to lower frequencies is indicative of the involvement of the H atom in hydrogen-bond formation with the halide ligand and reflects the relative strength of the N–H···X bond formed. The shifts observed for ν(NH) bands due to coordination, in conjunction with the lack of ν(SH) bands at ca. 2500–2600 cm^{-1} indicate the exclusive S-coordination mode of the thione ligand. Upon coordination of the thione ligand to the Cu(I) metal centre in the (n-Bu_4N)$[MOS_3Cu_3(Imt)_2Br_2]$ complexes, no significant structural changes are observed in the heterocycle ring of the thione. However, in both complexes, the coordination of the thione through the S donor atom of the C=S group results in an elongation of the C=S bond (see Table 4). As a consequence, the ν(C=S) band of the free Imt ligand, which appears at 510 cm^{-1}, is shifted to a lower frequency in the complexes (see Table 2).

3.2. Electronic spectra

The electronic absorption spectra of the complexes in DMF solutions appear to be mainly of intraligand character, presenting three broad bands with maxima at 425, 345 and 273 nm for complex **1**, 504, 406 and 271 nm for complex **2**. The first two bands in each complex are derived from sulfur to metal charge-transfer transitions of the MOS_3 (M = W or Mo) group [30]. These bands are red-shifted compared to the free $[MOS_3]^{2-}$ anions (375 nm for W and 457 nm for Mo) [24]. The third band for each complex lies in the region where the free thione absorbs, with a small red shift as a consequence of the coordination to Cu(I), and should, therefore, be considered as a thione intraligand transition which possesses some MLCT character [31,32].

3.3. NMR spectra

The ^1H and ^{13}C NMR spectra of Imt and the complexes in DMSO-d_6 are summarized in Table 3. In the ^1H NMR spectra of the complexes N–H protons of Imt shift downfield with respect to the uncoordinated thione ligand. The deshielding of the N–H proton is related to an increase of the π-electron density in the C–N bond upon coordination of the thione to Cu(I). The absence of a weak S–H signal for the thiol form of Imt and the presence of the N–H proton signal in the ^1H NMR spectra of the complexes indicates that Imt does not bind to Cu(I) via nitrogen, as confirmed by infrared spectroscopy and X-ray crystallography in the solid state. In the ^{13}C NMR spectra of the complexes the main effect observed is the shift in the C_1 signal (using the crystallographic numbering scheme), which is at a higher field than for free Imt. This observation can be rationalized as the reduction of the C=S bond order upon coordination and a shift of electron density, producing partial double-bond character in the C–N bond [33,34].

Table 3
^1H and ^{13}C NMR chemical shifts (δ in ppm referred to TMS) of Imt and the complexes; atoms are numbered as in the crystallographic result

Compounds	NH(1/2)	$\Delta\delta_{NH}$	CH_2(2/3)	C1	$\Delta\delta_{C1}$	C(2/3)
Imt	7.98		3.50	183.35		44.07
Complex **1**	8.56	0.58	3.63	180.01	3.34	44.99
Complex **2**	8.45	0.47	3.61	180.65	2.7	45.01

3.4. Crystal structures

The two complexes **1** and **2** are crystallographically isostructural, with only minor differences in the details of their structures, so the more precise structure of **2** is described here. Selected bond lengths and angles for both complexes are given in Table 4, and hydrogen-bond geometry in Table 5. Fig. 1 shows the structure of the anion of **2**, including intramolecular hydrogen bonds, and Fig. 2 shows the crystal packing with intermolecular hydrogen bonding for the anions.

The asymmetric unit of the crystal structure consists of a discrete monomeric anion and a cation, interacting through normal coulombic forces. The geometry of the cation is unexceptional, with three fully extended alkyl substituents and only one gauche terminal segment for the fourth (this can be seen in Fig. 2).

The anion has a central MoS_3Cu_3 core with an incomplete cubane (or nest-shaped) structure, the cube vertex opposite Mo being unoccupied. This core has a gross structure typical of OMS_3Cu_3 clusters, with acute angles

Table 4
Selected bond lengths (Å) and angles (°) for complexes **1** and **2**

	1 (M = W)	**2** (M = Mo)
M–O(1)	1.724(9)	1.722(4)
M–S(3)	2.264(3)	2.2667(16)
M–S(4)	2.260(3)	2.2677(17)
M–S(5)	2.266(3)	2.2706(15)
Cu(1)–S(3)	2.312(4)	2.2956(18)
Cu(1)–S(4)	2.330(4)	2.3040(16)
Cu(2)–S(4)	2.263(4)	2.2531(17)
Cu(2)–S(5)	2.262(4)	2.2437(18)
Cu(3)–S(3)	2.266(4)	2.2546(17)
Cu(3)–S(5)	2.271(4)	2.2570(17)
Cu(1)–Br(1)	2.611(3)	2.6567(11)
Cu(3)–Br(2)	2.283(2)	2.2914(10)
Cu(1)–S(1)	2.251(4)	2.2504(17)
Cu(3)–S(2)	2.211(4)	2.2106(17)
S(1)–C(1)	1.735(14)	1.711(7)
S(2)–C(4)	1.704(13)	1.712(7)
S(3)–M–S(4)	108.23(12)	107.59(6)
S(3)–M–S(5)	107.73(12)	107.42(6)
S(4)–M–S(5)	107.89(12)	107.28(6)
O(1)–M–S(3)	111.6(4)	112.74(17)
O(1)–M–S(4)	111.7(3)	111.45(17)
O(1)–M–S(5)	109.5(3)	110.13(15)
S(3)–Cu(1)–S(4)	104.31(14)	105.40(6)
S(4)–Cu(2)–S(5)	107.94(14)	108.73(6)
S(3)–Cu(3)–S(5)	107.47(13)	108.32(6)
S(3)–Cu(1)–S(1)	117.73(14)	117.78(6)
S(3)–Cu(1)–Br(1)	103.38(12)	102.80(5)
S(4)–Cu(1)–S(1)	118.72(14)	119.00(7)
S(4)–Cu(1)–Br(1)	98.04(11)	97.89(5)
S(1)–Cu(1)–Br(1)	111.93(12)	111.07(5)
S(4)–Cu(2)–S(2)	128.69(15)	128.45(7)
S(5)–Cu(2)–S(2)	120.65(14)	120.30(7)
S(3)–Cu(3)–Br(2)	126.91(12)	126.48(6)
S(5)–Cu(3)–Br(2)	124.21(12)	123.80(5)
M–S(3)–Cu(1)	73.14(11)	73.00(5)
M–S(3)–Cu(3)	72.32(11)	72.08(5)
Cu(1)–S(3)–Cu(3)	96.33(14)	96.57(7)
M–S(4)–Cu(1)	72.87(11)	72.83(5)
M–S(4)–Cu(2)	72.04(11)	71.89(5)
Cu(1)–S(4)–Cu(2)	97.08(14)	97.70(6)
M–S(5)–Cu(2)	71.96(10)	72.01(5)
M–S(5)–Cu(3)	72.18(11)	71.96(5)
Cu(2)–S(5)–Cu(3)	101.63(14)	101.74(7)
Cu(1)–S(1)–C(1)	107.2(5)	107.0(2)
Cu(2)–S(2)–C(4)	104.4(5)	104.9(2)

Table 5
Hydrogen bonding parameters (Å, °) for complexes **1** and **2**

D–H···A	*d*(D–H)	*d*(H···A)	*d*(D···A)	∠(DHA)
*Complex **1***				
N(1)–H(1)···O(1a)	0.88(1)	2.00(8)	2.792(14)	149(13)
N(2)–H(2)···Br(1)	0.88(1)	2.41(3)	3.284(12)	170(14)
N(3)–H(3)···Br(1)	0.88(1)	2.70(9)	3.449(13)	144(13)
N(4)–H(4)···Br(1b)	0.88(1)	2.51(4)	3.366(13)	166(14)
*Complex **2***				
N(1)–H(1)···O(1a)	0.88(1)	1.93(2)	2.795(7)	167(7)
N(2)–H(2)···Br(1)	0.88(1)	2.44(2)	3.306(5)	169(6)
N(3)–H(3)···Br(1)	0.88(1)	2.65(3)	3.463(6)	155(6)
N(4)–H(4)···Br(1b)	0.88(1)	2.54(2)	3.395(5)	164(6)

Symmetry operators: a, $1/2 - x$, $y - 1/2$, $3/2 - z$; b, $-x$, $2 - y$, $1 - z$.

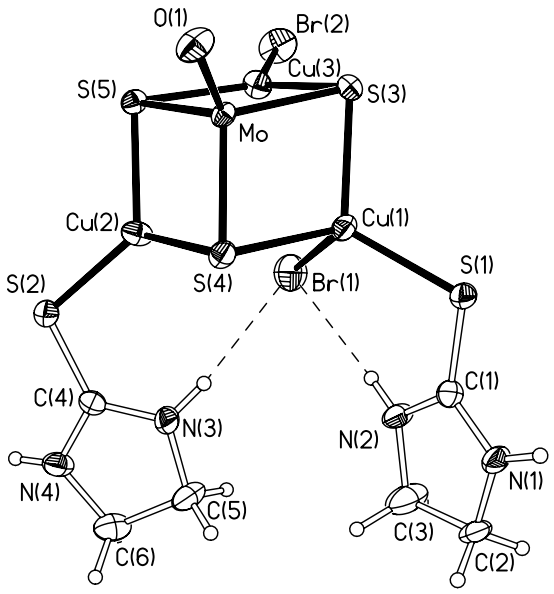


Fig. 1. The structure of the anion of complex **1**, with 50% probability displacement ellipsoids and the numbering scheme for non-hydrogen atoms. Intramolecular hydrogen bonds are shown as dashed lines.

at the S atoms and obtuse angles at the metal atoms. Mo retains the approximate tetrahedral coordination geometry of the parent $[MoOS_3]^{2-}$ anion and deviates only slightly from local C_{3v} symmetry. Each of the Cu atoms has a different coordination environment in this anion. Cu(1), with both thione and bromo substituents, has a distorted tetrahedral geometry; Cu(2) and Cu(3) are both approximately trigonal planar, but Cu(2) has a terminal thione ligand while Cu(3) has a bromo ligand. The source of the bromo ligands is the bromide counterion of (n-Bu_4N)Br used in the synthesis. Bonds to Cu(1) are longer than those to Cu(2) and Cu(3), as expected for the different coordination numbers. The Cu···Mo distances follow the same pattern, with Mo···Cu(2) = 2.6538(1) and Mo···Cu(3) = 2.6600(9) Å, while Mo···Cu(1) = 2.7139(10). Similar trends have been found, for example, for the three- and four-coordinate Cu atoms in polymeric cyano-bridged WS_4Cu_n ($n = 2$, 3) cluster complexes [35] and in $(NEt_4)_3[MoOS_3Cu_3Br_4]\cdot Me_2CO$, which has only halo ligands [36], and is the most similar previously reported structure overall to **1** and **2**. These short Mo···Cu distances do not imply a direct metal–metal bonding interaction, but are a consequence of the incomplete pseudo-cubane cluster structure.

The C–S bond lengths of the coordinated thione ligands are similar to values observed previously for coordinated Imt [13] (the mean for 124 terminally coordinated Imt ligands in the Cambridge Structural Database, Version 5.28 with two updates, is 1.712 Å), and are longer than the distance in the uncoordinated thione (1.688 and 1.692 Å in two independent studies [37,38]). This and the other bond lengths and angles of the ligands are consistent with the thione tautomer having a somewhat weakened C═S double bond on coordination to Cu.

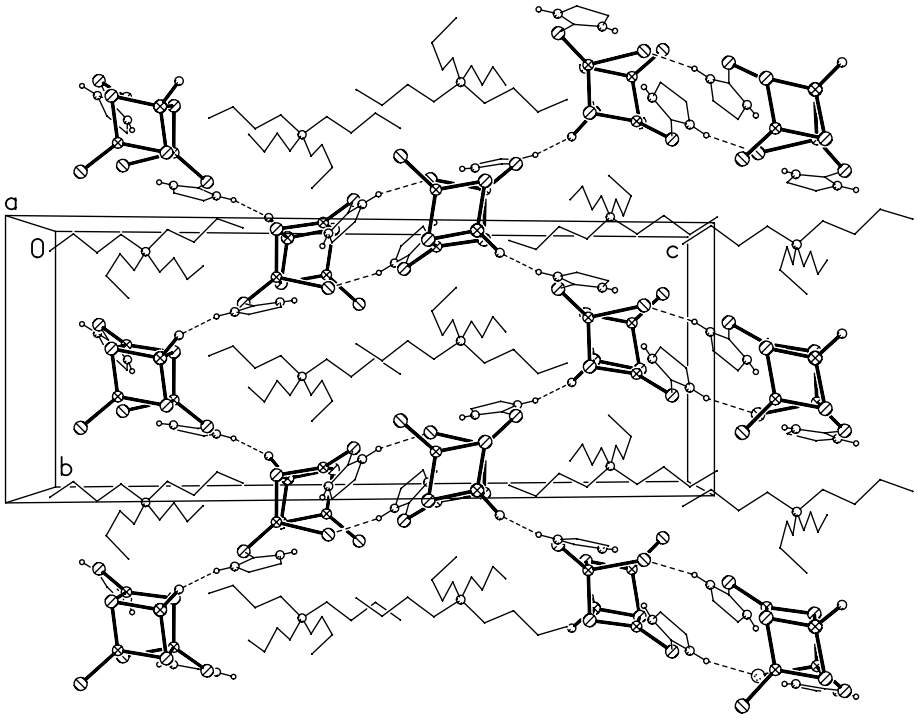


Fig. 2. A packing diagram showing the formation of a layer of anions through intermolecular hydrogen bonds (dashed lines), with cations in the cavities. H atoms bonded to C atoms have been omitted for clarity, and the cations are shown in stick representation.

As shown in Fig. 1, the orientations of the two thione ligands are such that each forms an intramolecular N–H···Br hydrogen bond with Br(1), the bromo ligand attached to Cu(1). The second NH group of each ligand serves as a donor in an intermolecular hydrogen bond to another anion, the two acceptors being O(1) and the same Br atom, which thus acts as a triple acceptor; Br(2) does not take part in hydrogen bonding. The intermolecular hydrogen bonds link anions together in sheets, as shown in Fig. 2, with the cations located in cavities within the sheets. The cavities in successive sheets are aligned above each other to form channels parallel to the *a*-axis, which are occupied by the cations. These channels amount to approximately 50% of the volume of the structure, and it is possible that the particular cations used in this work have a templating effect on the formation of the crystal structure with its hydrogen-bonded network of anions, as a result of their specific size and shape.

Acknowledgements

We thank EPSRC (UK) and Shahid Chamran University (Ahvaz, Iran) for financial support. We also thank Dr. Behroose Zargar and his staff from Shahid Chamran University for recording the NMR spectra.

Appendix A. Supplementary material

CCDC 648641 and 648642 contain the supplementary crystallographic data for **1** and **2**, respectively. These data can be obtained free of charge via http://www.ccdc.cam.ac.uk/conts/retrieving.html, or from the Cambridge Crystallographic Data Centre, 12 Union Road, Cambridge CB2 1EZ, UK; fax: (+44) 1223-336-033; or e-mail: deposit @ccdc.acm.ac.uk. Supplementary data associated with this article can be found, in the online version, at doi:10.1016/j.poly.2007.11.005.

References

[1] S. Oae, Organic Sulfur Chemistry: Structure and Mechanism, CRC Press, Boca Raton, 1992.
[2] B. Krebs, G. Henkel, Angew. Chem., Int. Ed. Engl. 30 (1991) 769.
[3] E.S. Raper, Coord. Chem. Rev. 61 (1985) 115.
[4] E.S. Raper, Coord. Chem. Rev. 153 (1996) 199.
[5] E.S. Raper, Coord. Chem. Rev. 129 (1994) 91.
[6] E.S. Raper, Coord. Chem. Rev. 165 (1997) 475.
[7] P.D. Akrivos, Coord. Chem. Rev. 213 (2001) 181.
[8] D. Li, W.-J. Shi, L. Hou, Inorg. Chem. 44 (2005) 3907.
[9] T.S. Lobana, R. Sharma, R. Sharma, S. Mehra, A. Castineiras, P. Turner, Inorg. Chem. 44 (2005) 1914.
[10] T.S. Lobana, R. Sharma, E. Bermejo, A. Castineiras, Inorg. Chem. 42 (2003) 7728.
[11] P. Aslanidis, P.J. Cox, S. Divanidis, A.C. Tsipis, Inorg. Chem. 41 (2002) 6875.
[12] H.W. Hou, X.Q. Xin, X. Shi, Coord. Chem. Rev. 153 (1996) 25.
[13] A. Beheshti, W. Clegg, S.H. Dale, A. Solimankhani, Acta Crystallogr., Sect. E 61 (2005) m1509.
[14] A. Beheshti, N.R. Brooks, W. Clegg, R. Khorrmdin, Acta Crystallogr., Sect. E 60 (2004) m1923.
[15] Q. Wang, X. Wu, Q. Huang, T. Sheng, Acta Crystallogr., Sect. C 53 (1997) 1220.
[16] Q. Wang, X. Wu, Q. Huang, T. Sheng, P. Lin, Acta Crystallogr., Sect. C 53 (1997) 1542.

[17] Q. Wang, X. Wu, Q. Huang, T. Sheng, Acta Crystallogr., Sect. C 52 (1996) 2738.
[18] J.P. Lang, K. Tatsumi, Inorg. Chem. 37 (1998) 6308.
[19] R.H. Holm, Chem. Soc. Rev. 10 (1981) 455.
[20] C. Zhang, G.C. Jin, J.X. Chen, X.Q. Xin, K.P. Qian, Coord. Chem. Rev. 213 (2000) 51.
[21] D. Coucouvanis, Acc. Chem. Res. 14 (1981) 201.
[22] G.D. Thorn, Can. J. Chem. 33 (1955) 1278.
[23] L. Maier, Helv. Chim. Acta 53 (1970) 1417.
[24] J.W. McDonald, G.D. Friesen, L.D. Rosenhein, W.E. Newton, Inorg. Chim. Acta 72 (1983) 205.
[25] H. Hou, H. Zheng, H.G. Ang, Y. Fan, M.K.M. Low, Y. Zhu, W. Wang, X. Xin, W. Ji, W.-T. Wong, J. Chem. Soc., Dalton Trans. (1999) 2953.
[26] Nonius, COLLECT, Nonius BV, Delft, The Netherlands, 1999.
[27] A.J.M. Duisenberg, L.M.J. Kroon-Batenburg, A.M.M. Schreurs, J. Appl. Crystallogr. 36 (2003) 220.
[28] G.M. Sheldrick, SADABS, University of Göttingen, Germany, 2003.
[29] G.M. Sheldrick, SHELXTL, Version 6, Bruker AXS Inc., Madison, WI, USA, 2001.
[30] H.W. Hou, X.Q. Xin, S. Shi, Coord. Chem. Rev. 153 (1996) 25.
[31] A.A. Del Paggio, D.R. McMillin, Inorg. Chem. 22 (1983) 691.
[32] C. Kutal, Coord. Chem. Rev. 90 (1990) 213.
[33] Z. Popovic, G. Pavlovic, D. Matkovic-Calogovic, Z. Soldin, M. Rajic, D. Vikic-Topic, D. Kovacek, Inorg. Chim. Acta 306 (2000) 142.
[34] U. Bierbach, T.W. Hambly, N. Farrell, Inorg. Chem. 37 (1998) 708.
[35] J.-P. Lang, C.-M. Jiao, S.-B. Qiao, W.-H. Zhang, B.F. Abrahams, Inorg. Chem. 44 (2005) 3664.
[36] A. Beheshti, N.R. Brooks, W. Clegg, R. Khorrmdin, Acta Crystallogr., Sect. E 60 (2004) m231.
[37] T.C.W. Mak, K.S. Jasim, C. Chieh, Can. J. Chem. 62 (1984) 808.
[38] L.P. Battaglia, A.B. Corradi, M. Nardelli, Croat. Chem. Acta 57 (1984) 545.

Available online at www.sciencedirect.com
ScienceDirect
Polyhedron 27 (2008) 783–796
POLYHEDRON
www.elsevier.com/locate/poly

Electrochemical interactions in binuclear molybdenum and tungsten nitrosyl complexes incorporating saturated *n*-alkanediolate bridging ligands. Crystal structures of $[Mo(NO)(Tp^{Me2})I\{O(CH_2)_2OCOCH_3\}]$ and $[W(NO)(Tp^{Me2})I_2]\cdot 0.5I_2\cdot 0.5C_6H_5CH_3$

Andrzej J. Włodarczyk [a,*], Piotr P. Romańczyk [a], Stefan S. Kurek [a], Wojciech Nitek [b], Jon A. McCleverty [c]

[a] *Faculty of Chemical Engineering and Technology, Cracow University of Technology, 31-155 Kraków, Poland*
[b] *Faculty of Chemistry, Jagiellonian University, ul. Ingardena 3, 30-060 Kraków, Poland*
[c] *School of Chemistry, University of Bristol, Cantock's Close, Bristol BS8 1TS, UK*

Received 5 September 2007; accepted 12 November 2007
Available online 26 December 2007

Abstract

A series of bimetallic ($[\{M(NO)(Tp^{Me2})X\}_2(Q)]$ [Tp^{Me2} = tris(3,5-dimethylpyrazolyl)borate; M = Mo, X = Cl, Q = $O(CH_2)_nO$, $n = 3$, 5, 6, or $OCH_2(CF_2)_3CH_2O$; M = Mo, X = I, $n = 3$ or 4; M = W, X = Cl, $n = 3$–6, or $OCH_2(CF_2)_3CH_2O$; M = W, X = Br, $n = 2$]), and a number of monometallic complexes ($[M(NO)(Tp^{Me2})X(QH)]$ [M = Mo, X = Cl, Q = $O(CH_2)_nO$, $n = 3$, or $OCH_2(CF_2)_3CH_2O$; M = W, X = Br, $n = 2$]) were prepared. The heterobimetallic complex $[\{Mo(NO)(Tp^{Me2})Br\}O(CH_2)_2O\{W(NO)(Tp^{Me2})Br\}]$ was also obtained. All compounds were characterised by elemental and mass analyses, ^1H NMR and IR spectroscopy. Electrochemical studies (CV and DPV) of the bimetallic species reveal that the metal–metal interactions decrease by *ca.* 100 mV per CH_2 group with increased length for C_2 to C_4 bridges and become undetectable for complexes with bridges longer than C_4. The substitution of fluorine into the C_5 bridge causes the effect to become measurable due to easier polarisation of the σ-bond framework. The crystal structures of $[Mo(NO)(Tp^{Me2})I\{O(CH_2)_2OCOCH_3\}]$ and $[W(NO)(Tp^{Me2})I_2]\cdot 0.5I_2\cdot 0.5C_6H_5CH_3$ were determined.
© 2007 Elsevier Ltd. All rights reserved.

Keywords: Molybdenum nitrosyl complex; Tungsten nitrosyl complex; Bimetallic complexes; Tris(pyrazolyl)borato complexes; Saturated bridging systems; Electrochemical interactions

1. Introduction

The design and synthesis of redox active binuclear complexes in which metal centres are linked *via* bridging ligands enabling electronic interactions between them are of major interest in the development of models for intramolecular electron transfer over long distances, important for understanding key processes in both chemistry and biology [1–3]. A significant obvious indication of metal–metal interactions is the separation between redox potentials of two redox centres, $\Delta E_{1/2}$, which depends on the metal, its environment, the length and the geometry of the bridge and its electronic properties. The above interactions may be coulombic through-space and through-bond (π-mesomeric effect, σ-inductive effect) in character.

Numerous examples of bimetallic complexes $\{M(NO)(Tp^{Me2})X\}^{+/0}$ [Tp^{Me2} = $HB(3,5\text{-}Me_2C_3HN_2)_3$, X = halide]

* Corresponding author. Tel./fax: +48 126325371.
E-mail address: awlodar@pk.edu.pl (A.J. Włodarczyk).

0277-5387/$ - see front matter © 2007 Elsevier Ltd. All rights reserved.
doi:10.1016/j.poly.2007.11.008

with π-acceptor ligands (e.g. aromatic heterocycles, polyenes) that make the delocalisation of the unpaired electron possible have been reported in the literature. The highest values of $\Delta E_{1/2}$ were obtained for complexes in which Q = pyrazine (1440 mV, $K_c = 2.2 \times 10^{24}$) [4], Q = 1,4-HNC_6H_4NH (920 mV) [5], Q = 4,4′-bipy (765 mV) [6], Q = $OC_6H_4(2,5\text{-}C_4H_2S)_2C_6H_4O$ (670 mV) [7], and Q = pyC≡Cpy (560 mV) [8]. In all these examples, electrochemical interactions were apparently much greater than in the Creutz-Taube ion (390 mV) [9], although the latter measurements were obtained in aqueous conditions, whereas the former were measured in dichloromethane, solvent effects often having a significant influence on $\Delta E_{1/2}$. It is worth mentioning that observable electrochemical interactions and significant magnetic interactions were detected in the complex [{Mo(NO)(Tp^{Me2})Cl}$_2${4,4′-NC_5H_4-$(CH{=}CH)_4C_5H_4N$}], in which the Mo···Mo distance is *ca.* 2 nm [10]. The introduction of a saturated section into the bridge, as, e.g. in Q = 1,2-bi(4-pyridyl)ethane (105 mV) [6], considerably decreases $\Delta E_{1/2}$, but does not exclude electronic and magnetic through-bridge interactions. Electron tunnelling was shown as possible for $\{Ru(NH_3)_5\}^{n+}$ complexes having fully saturated bridging ligands based on a rigid spirane system with the Ru···Ru distance as long as 17.5 Å [11]. Self-arranged monolayers of alkanethiols adsorbed on gold electrodes are also used in the study of electron transfer through the saturated hydrocarbon chains [12]. Merely a few examples of $\{M(NO)(Tp^{Me2})X\}^+$ complexes containing completely saturated bridges have been described in the literature, among them with Q = $NH(CH_2)_nNH$ ($n = 2, 3$) [13], Q = NC_4H_8N (560 mV) [14] and Q = $O(CH_2)_4O$ (100 mV) [15]. The first one shows irreversible reduction processes, because of the presence of N–H protons, which excludes a detailed discussion of metal–metal interactions in these systems, whereas for the species with a cyclic piperazine bridge, the $\Delta E_{1/2}$ value should be treated with caution because of the irreversibility of the second reduction potential.

We showed in our previous paper [16] that despite the presence of a saturated bridge the complexes [{Mo(NO)(Tp^{Me2})X}$_2${$O(CH_2)_2O$}] (X = Cl or Br) exhibit two chemically reversible one-electron reduction processes separated by a potential difference, $\Delta E_{1/2}$, of *ca.* 310 mV, demonstrating thus significant electrochemical interactions comparable to their analogue with the 1,2-$O_2C_6H_{10}$ cyclic bridge ($\Delta E_{1/2}$ 300 mV) [17], and $\{Mo(NO)(Tp^{Me2})Cl\}^{+/0}$ complexes with aromatic bridges, in which mesomeric effects are not possible, e.g. 1,3-$O_2C_6H_4$ ($\Delta E_{1/2}$ 260 mV) [18], 1,3-$(HN)_2C_6H_4$ ($\Delta E_{1/2}$ 370 mV) [19].

In order to determine the magnitude and the range of electrochemical interactions in the molybdenum and tungsten nitrosyls containing *n*-alkanediolate bridging ligands we synthesised a series of complexes with increasing alkyl chain length. The effect of modifying the electronic properties of the alkyl bridge by introducing fluorine atoms into it was also investigated.

2. Results and discussion

2.1. Synthetic and spectroscopic studies

The reactions between [M(NO)(Tp^{Me2})X_2] and the appropriate α,ω-diol afforded mixtures of mono- and bimetallic complexes which are air-stable and the majority of which may be separated by column chromatography on silica gel using CH_2Cl_2 as eluant. When passing the monometallic complexes through the chromatographic column repeatedly, bimetallic complexes were always formed. Bimetallic species were also formed as a result of heating [Mo(NO)(Tp^{Me2})Cl{$O(CH_2)_nOH$}] with acetic acid (*ca.* 0.1 M) in dichloromethane.

The monometallic complex, [Mo(NO)(Tp^{Me2})Cl-{$O(CH_2)_3OH$}] (**18**), could not be isolated in its pure form. Every attempt to isolate it resulted in a mixture of the monometallic in a great excess and corresponding bimetallic complex.[1] A minor product isolated as green crystals from the reaction between [Mo(NO)(Tp^{Me2})I_2] and ethane-1,2-diol in dichloromethane in the presence of silver acetate, was confirmed by X-ray crystallography to be 2-acetoxyethanolate complex **6**. Despite the large number of syntheses of this type of complex described in the literature such a by-product has never been reported. Generally, acetoxy complexes are intermediate products, that easily undergo substitution by alkoxy ligands because of the labile character of acetoxy group [22]. The compounds obtained from the reaction between **17** and ethane-1,2-diol decomposed during column chromatography.

The reaction between [Mo(NO)(Tp^{Me2})Br(OCH_2-CH_2OH)] and [W(NO)(Tp^{Me2})Br_2] afforded the heterobimetallic complex. The ^{1}H NMR spectrum of this compound indicated it to be a mixture of two different diastereoisomers which could not be separated by column chromatography.

As can be seen from Table 1, all new compounds gave satisfactory elemental analyses, and mass spectrometry usually provided parent molecular ions (M^+) in addition to fragment ions consistent with the loss of halide and/or NO.

The infrared spectra of all the complexes exhibited bands typical for $HB(Me_2pz)_3^-$: ν(BH) at *ca.* 2550 cm^{-1}, ν(C–Me) in the range of 1366–1451 cm^{-1} and ν(C=C) at *ca.* 1540 cm^{-1}. The stretching frequency of the nitrosyl group appeared as the most intense, sharp peak, which reflected the fact that the force constant is related to the effective nuclear charge on the metal centre, which in turn depends on the electron properties of co-ligands X, Y. Mono- and bimetallics showed a single ν(N=O) in the

[1] The ^{1}H NMR spectrum of **18** was deducted from the data of the mixture by subtracting the data of the bimetallic in purity: δ_H($CHCl_3$) 5.91, 5.86, 5.76 (1H, s; 1H, s; 1H, s; $Me_2C_3HN_2$); 2.51, 2.45, 2.38, 2.37, 2.35, 2.34 (3H, s; 3H, s; 3H, s; 3H, s; 3H, s; 3H, s; $(CH_3)_2C_3HN_2$); 6.10, 5.96 (1H, m; 1H, m; $OCH_2CH_2CH_2OH$); 3.88 (2H, m; OCH_2CH_2-CH_2OH); 2.20 (2H, m; $OCH_2CH_2CH_2OH$).

Table 1
Characterisation data for [{M(NO)(Tp^{Me2})X}$_2$(Q)], [M(NO)(Tp^{Me2})X(QH)] [Q = O(CH$_2$)$_n$O, OCH$_2$(CF$_2$)$_3$CH$_2$O] and [W(NO)(Tp^{Me2})I$_2$]

{MX}[a]	*n*	Analysis[b] (%)			IR[c] ν(NO) (cm^{-1})	Mass spectrum		^{1}H NMR δ_H/ppm (integral multiplicity)[e]		
		C	H	N		*m*/*z*[d]	Assign.	CH (pz)	Me (pz)	Q
{MoCl}$_2$ (**1**)	3	40.0 (40.0)	5.1 (5.1)	19.5 (19.8)	1673	991.3[f] (991.2)	M$^+$	*Spectrum taken in C$_6$D$_6$*		
								Diastereoisomer I		
								5.43 (2s)	2.73 (6s)	
								5.35 (2s)	2.58 (6s)	
								5.24 (2s)	2.25 (6s)	
									1.99 (6s)	6.23 (2m)
									1.90 (12s)	6.07 (2m)
								Diastereoisomer II		2.61 (2m)
								5.44 (2s)	2.71 (6s)	
								5.35 (2s)	2.59 (6s)	
								5.27 (2s)	2.28 (6s)	
									2.00 (6s)	
									1.88 (12s)	
{MoCl}$_2$ (**2**)	5	41.4 (41.2)	5.2 (5.3)	19.0 (19.2)	1675	985[g] (984.2)	M$^+$−Cl	5.91 (2s)	2.52 (6s)	
								5.86 (2s)	2.43 (6s)	
						525 (527.2)	{Mo(Q)}$^+$	5.75 (2s)	2.38 (6s)	5.91 (4m)
									2.37 (6s)	2.05 (4m)
									2.35 (6s)	1.69 (2m)
									2.34 (3s)	
									2.32 (3s)	
{MoCl} (**3**)	5(F)[i]	35.68 (35.87)	4.01 (4.06)	14.34 (14.64)	1685	674.4[f] (671.1)	M$^+$	5.95 (1s)	2.48 (3s)	6.20 (1m)
								5.89 (1s)	2.40 (3s)	5.80 (1m)
						689.2 (689.1)	M$^+$+NH$_4$	5.75 (1s)	2.38 (3s)	4.07 (2m)
									2.36 (6s)	
						636.3 (636.1)	M$^+$−Cl		2.28 (3s)	
{MoCl}$_2$ (**4**)	5(F)[i]	37.57 (37.29)	4.31 (4.29)	16.81 (17.40)	1684	1125.4[f] (1128.2)	M$^+$	5.95 (2s)	2.48 (6s)	
								5.88 (2s)	2.40 (6s)	
						1147.3 (1146.2)	M$^+$+NH$_4$	5.74 (2s)	2.38 (6s)	6.23 (2m)
									2.36 (12s)	5.83 (2m)
									2.28 (3s)	
									2.28 (3s)	
{MoCl}$_2$ (**5**)	6	41.9 (41.8)	5.8 (5.5)	18.9 (19.0)	1673	1035.4[f] (1034)	M$^+$	5.90 (2s)	2.52 (6s)	
								5.86 (2s)	2.43 (3s)	
						933 (930.3)	M$^+$−2Cl−NO	5.76 (2s)	2.42 (3s)	5.85 (4m)
									2.37 (6s)	1.98 (4m)
									2.36 (6s)	1.56 (4m)
									2.35 (9s)	
									2.33 (3s)	
{MoI} (**6**)	QAc[j]	[k]			1678; 1736 ($\nu_{C=O}$)	[k]		5.88 (1s)	2.49 (3s)	5.70 (2m)
								5.86 (1s)	2.44 (3s)	4.50 (2m)
								5.82 (1s)	2.40 (3s)	2.04 (3s)
									2.37 (3s)	
									2.36 (3s)	
									2.35 (3s)	
{MoI}$_2$ (**7**)	3	33.4 (33.8)	4.7 (4.3)	16.1 (16.7)	1675	1173[h] (1175.1)	M$^+$	*Spectrum taken in C$_6$D$_6$*		
								Diastereoisomer I		
						1047 (1049.2)	M$^+$−I	5.57 (2s)	2.73 (6s)	
								5.40 (2s)	2.21 (6s)	
								5.27 (2s)	2.05 (6s)	
									1.88 (6s)	
									1.87 (12s)	5.79 (4m)
								Diastereoisomer II		
								5.54 (2s)	2.75 (6s)	2.62 (2m)
								5.40 (2s)	2.70 (12s)	
								5.25 (2s)	2.15 (6s)	
									2.04 (6s)	
									1.90 (6s)	

(*continued on next page*)

Table 1 (*continued*)

{MX}[a]	*n*	Analysis[b] (%)			IR[c] ν(NO) (cm^{-1})	Mass spectrum		^{1}H NMR δ_H/ppm (integral multiplicity)[e]		
		C	H	N		*m*/*z*[d]	Assign.	CH (pz)	Me (pz)	Q
$\{MoI\}_2$ (**8**)	4	35.0 (34.4)	4.6 (4.4)	16.0 (16.5)	1675	1191[h] (1189.1)	M^+	*Spectrum taken in C_6D_6*		
						1062 (1063.2)	M^+–I	5.86 (2s)	2.51 (6s)	
								5.83 (2s)	2.42 (3s)	
								5.81 (1s)	2.40 (6s)	
								5.78 (1s)	2.36 (6s)	5.63 (4m)
									2.36 (3s)	2.10 (4m)
									2.35 (6s)	
									2.34 (3s)	
									2.32 (3s)	
{WBr} (**9**)	2	31.34 (31.32)	4.07 (4.17)	15.09 (15.04)	1630	654.3[f] (651.1)	M^+	5.93 (1s)	2.60 (3s)	
								5.89 (1s)	2.53 (3s)	
								5.86 (1s)	2.48 (3s)	5.80 (2m)
									2.37 (6s)	4.05 (2m)
									2.36 (3s)	
$\{WBr\}_2$ (**10**)	2	30.83 (30.95)	3.81 (3.90)	15.61 (15.79)	1634	1243.4[f] (1242.2)	M^+	*Diastereoisomer I*		
								5.85 (2s)	2.56 (6s)	
								5.77 (2s)	2.38 (6s)	
								5.54 (2s)	2.34 (6s)	
									2.33 (6s)	
									2.28 (6s)	
									2.11 (6s)	6.11 (2m)
								Diastereoisomer II		5.66 (2m)
								5.86 (2s)	2.57 (6s)	
								5.75 (2s)	2.37 (12s)	
								5.68 (2s)	2.34 (6s)	
									2.28 (6s)	
									2.17 (6s)	
$\{WCl\}_2$ (**11**)	3	34.2 (34.0)	4.5 (4.3)	16.5 (16.8)	1635	1168[g] (1168.3)	M^+	*Spectrum taken in C_6D_6*		
								5.45 (1s)	2.82 (3s)	
								5.45 (1s)	2.80 (3s)	
								5.29 (1s)	2.65 (3s)	
								5.29 (1s)	2.64 (3s)	
								5.23 (1s)	2.47 (3s)	6.14 (2m)
								5.20 (1s)	2.42 (3s)	6.03 (2m)
									1.94 (3s)	
									1.94 (3s)	
									1.83 (3s)	
									1.83 (6s)	
									1.82 (3s)	
$\{WCl\}_2$ (**12**)	4	34.8 (34.6)	4.6 (4.4)	16.4 (16.6)	1633	1180[g] (1182.3)	M^+	5.92 (2s)	2.59 (6s)	
								5.86 (2s)	2.56 (3s)	
						1145 (1147.3)	M^+–Cl	5.82 (1s)	2.56 (3s)	5.81 (4m)
								5.78 (1s)	2.41 (3s)	1.98 (4m)
									2.36 (6s)	
									2.34 (12s)	
									2.33 (3s)	
$\{WCl\}_2$ (**13**)	5	35.0 (35.2)	4.2 (4.6)	16.1 (16.4)	1633	1194[g] (1196.3)	M^+	5.86 (2s)	2.60 (6s)	5.85 (4m)
								5.81 (2s)	2.56 (6s)	1.91 (4m)
						1094 (1096.4)	M^+–2Cl–NO	5.36 (2s)	2.40 (3s)	1.59 (2m)
									2.40 (3s)	
									2.36 (6s)	
									2.34 (12s)	
$\{WCl\}_2$ (**14**)	5(F)[f]	32.8 (32.3)	3.7 (3.7)	14.8 (15.0)	1641	1302[g] (1302.3)	M^+	5.96 (2s)	2.56 (6s)	
								5.89 (2s)	2.50 (6s)	6.07 (2m)
								5.81 (2s)	2.38 (6s)	5.67 (2m)
									2.36 (6s)	
									2.35 (12s)	

Table 1 (*continued*)

{MX}[a]	*n*	Analysis[b] (%)			IR[c] ν(NO) (cm^{-1})	Mass spectrum		^{1}H NMR δ_H/ppm (integral multiplicity)[e]		
		C	H	N		*m*/*z*[d]	Assign.	CH (pz)	Me (pz)	Q
$\{WCl\}_2$ (**15**)	6	36.1 (35.8)	5.0 (4.7)	16.4 (16.2)	1635	1208[g] (1210.3)	M^+	5.92 (2s) 5.86 (2s) 5.82 (2s)	2.60 (6s) 2.57 (3s) 2.56 (3s) 2.41 (3s) 2.40 (3s) 2.36 (6s) 2.34 (12s)	 5.82 (4m) 1.87 (4m) 1.52 (4m)
{MoBr}–{WBr} (**16**)	2	34.14 (33.30)	4.45 (4.19)	16.40 (16.99)	1673 1635	1155.2[f] (1154) 1075.5 (1075) 570.3 (571)	M^+ M^+-Br $\{W(Q)\}^+$	CH (pz) and Q 6.22–5.52 (10 H)[l]		Me (pz) 2.60–1.93 (36 H)[l]
WI_2[m] (**17**)		25.40 (25.43)	3.12 (2.95)	11.90 (11.98)	1675	670.1[f] (670.0) 640.0 (638.1) 608.1 (608.1)	M^+-Me_2pz M^+-I M^+-I-NO	6.12 (1s) 5.89 (2s)	2.86 (3s) 2.54 (3s) 2.37 (6s) 2.32 (6s)	

[a] {MX} = Mo(NO)(Tp^{Me2})X or W(NO)(Tp^{Me2})X.
[b] Calculated values in parentheses.
[c] Recorded from KBr discs.
[d] Most intense peaks of clusters; values in parentheses based on isotopic distribution calculated by ChemCalc [20].
[e] Spectra were recorded at 300 MHz in $CDCl_3$, if not otherwise stated; s = singlet, m = multiplet.
[f] ESI spectrum.
[g] EI spectrum.
[h] FAB spectrum.
[i] C5(F) = $OCH_2(CF_2)_3CH_2O$.
[j] QAc = 2-acetoxyethanolate.
[k] Not measured; its X-ray structure was determined.
[l] From the ^{1}H NMR spectrum this complex appears to be a mixture of two different diastereoisomers which are inseparable by column chromatography.
[m] WI_2 = [W(NO)(Tp^{Me2})I_2]. Compound was synthesised previously [21], but not fully characterised. The isolated complex contained 1/4 mol $C_6H_5CH_3$ which was also detected in its ^{1}H NMR spectrum.

region 1685–1673 cm^{-1} for molybdenum species and 1630–1641 cm^{-1} for their tungsten counterparts. The IR spectra of **4** and **14**, and their monometallic analogues shows ν(N=O) hypochromically shifted by *ca.* 10 cm^{-1}, relative to the species derived from pentane-1,5-diol, which is consistent with the inductive effect of the fluorine substituents. The heterobimetallic complex exhibited two NO stretching frequencies, at 1673 and 1635 cm^{-1} which are assigned to Mo and W centres, respectively. The ν(OH) could be observed in the range 3350–3450 cm^{-1}. For the 2-acetoxyethanolate complex **6** ν(C=O) occurred at 1736 cm^{-1}.

The bimetallic species can occur as two diastereoisomers (*R*–*R*/*S*–*S* and *R*–*S*/*S*–*R*), which could be seen in the ^{1}H NMR spectra of complexes incorporating shorter bridges ($n = 2$ or 3) exhibiting steric interactions between bulky Tp^{Me2} ligands; for longer bridges they were not observed. It reflects the presence of a lower rotational barrier for longer bridges. The species with short bridges differ in thermodynamic stability and, thus, the mixture of them could be brought to an equilibrium state containing most of the more stable isomer following a thermal treatment of the mixture. For some bimetallics, ^{1}H NMR spectra were recorded both in $CDCl_3$ and C_6D_6. The application of the latter solvent enabled the overlapped signals to be separated. It was also observed that the signals due to protons attached to C^4 of pyrazolyl and methylene bridge protons were shifted significantly to stronger and weaker fields, respectively. This indicates specific orientation of the benzene solvent molecules with respect to those particular parts of the complex molecule; C^4 pyrazolyl protons perhaps being placed somewhere above the centre of the benzene molecule plane and methylene protons outside the edge of it. The ^{1}H NMR spectral pattern observed for most bimetallic complexes, namely of three aromatic proton signals of 2:2:2 integrated intensity ratio, and the presence of a single ν(NO) indicates the equivalence of the metallic centres. A certain differentiation in geometry was noticed in [{Mo(NO)(Tp^{Me2})X}$_2$(μ-O)] (X = Cl, I) [23] and [{Mo(NO)(Tp^{Me2})X}$_2$(μ-NHNH)] (not equal lengths of the Mo-bridge bonds) [24].

2.2. Electrochemical studies

The electrochemical behaviour of both mono- and bimetallic complexes was studied using cyclic voltammetry and differential pulse voltammetry and the results are presented in Table 2.

Table 2
Electrochemical data for the complexes

Complex	$E_{1/2}$[a] (V)	ΔE_p[b] (mV)	$\Delta E_{1/2}$[c] (mV)	ΔE_{dpv}[d] (mV)
$[Mo(NO)(Tp^{Me2})Cl\{O(CH_2)_2OH\}]$[e]	−1.11	97		
$[\{Mo(NO)(Tp^{Me2})Cl\}_2\{O(CH_2)_2O\}]$[e]	−1.17, −1.47	110, 185	300	310
$[Mo(NO)(Tp^{Me2})Cl(OEt)]$	−1.23	90		
$[Mo(NO)(Tp^{Me2})Cl\{O(CH_2)_2OCH_3\}]$	−1.23	169		
$[Mo(NO)(Tp^{Me2})Br\{O(CH_2)_2OH\}]$[e]	−1.09	114		
$[\{Mo(NO)(Tp^{Me2})Br\}_2\{O(CH_2)_2O\}]$[e]	−1.12, −1.44	147, 295	310	320
$[Mo(NO)(Tp^{Me2})Br_2]$	−0.374	90		
$[Mo(NO)(Tp^{Me2})I\{O(CH_2)_2OH\}]$	−1.05[f], −1.57[g]	62, 114		
$[\{Mo(NO)(Tp^{Me2})I\}_2\{O(CH_2)_2O\}]$[e]	−1.11[f,h], −1.36[f,h]	76, 72	250	260
$[Mo(NO)(Tp^{Me2})I\{O(CH_2)_2OCOCH_3\}]$ (**6**)	−1.05[f], −1.70[g]	86, 239		
$[Mo(NO)(Tp^{Me2})I(OEt)]$	−1.15, −1.83[g]	86, 246		
$[Mo(NO)(Tp^{Me2})(OEt)_2]$	−1.90, 0.928[i]	250, 97		
$[Mo(NO)(Tp^{Me2})\{O(CH_2)_2OH\}_2]$[e]	−1.62	258		
$[Mo(NO)(Tp^{Me2})Cl\{O(CH_2)_3OH\}]$ (**18**)	−1.13	100		
$[\{Mo(NO)(Tp^{Me2})Cl\}_2\{O(CH_2)_3O\}]$ (**1**)	−1.16, −1.36	70, 90	200	200
$[\{Mo(NO)(Tp^{Me2})I\}_2\{O(CH_2)_3O\}]$ (**7**)	−1.10[f,j], −1.26[f,j]	60, 60	160[k]	
$[\{Mo(NO)(Tp^{Me2})I\}_2\{O(CH_2)_4O\}]$ (**8**)	−1.07[f,j], −1.22[f,j]	150,	70[k]	
$[Mo(NO)(Tp^{Me2})Cl\{O(CH_2)_4OH\}]$[l]	−1.22	115		
$[\{Mo(NO)(Tp^{Me2})Cl\}_2\{O(CH_2)_4O\}]$[m]	−1.20, −1.27	60, 100	90[k]	90
$[Mo(NO)(Tp^{Me2})Cl\{O(CH_2)_5OH\}]$	−1.24	91		
$[\{Mo(NO)(Tp^{Me2})Cl\}_2\{O(CH_2)_5O\}]$ (**2**)	−1.26	123		
$[Mo(NO)(Tp^{Me2})Cl\{OCH_2(CF_2)_3CH_2OH\}]$ (**3**)	−0.854[n]	27[n]		
$[\{Mo(NO)(Tp^{Me2})Cl\}_2\{OCH_2(CF_2)_3CH_2O\}]$ (**4**)	−0.942[n], −1.01[n]	16[n], 14[n]	68	70
$[Mo(NO)(Tp^{Me2})Cl\{O(CH_2)_6OH\}]$	−1.24	80		
$[\{Mo(NO)(Tp^{Me2})Cl\}_2\{O(CH_2)_6O\}]$ (**5**)	−1.24	95		
$[W(NO)(Tp^{Me2})Cl\{O(CH_2)_2OH\}]$[e]	−1.63	107		
$[\{W(NO)(Tp^{Me2})Cl\}_2\{O(CH_2)_2O\}]$[e]	−1.70, −1.95	121, 213	253	270
$[W(NO)(Tp^{Me2})Br\{O(CH_2)_2OH\}]$ (**9**)	−1.60	80		
$[\{W(NO)(Tp^{Me2})Br\}_2\{O(CH_2)_2O\}]$ (**10**)	−1.64, −1.86	72, 108	225	230
$[W(NO)(Tp^{Me2})Cl\{O(CH_2)_3OH\}]$	−1.66	80		
$[\{W(NO)(Tp^{Me2})Cl\}_2\{O(CH_2)_3O\}]$ (**11**)	−1.68, −1.84	70, 70	160	170
$[\{W(NO)(Tp^{Me2})Cl\}_2\{O(CH_2)_4O\}]$ (**12**)	−1.72, −1.80	120,	80[k]	80
$[\{W(NO)(Tp^{Me2})Cl\}_2\{O(CH_2)_5O\}]$ (**13**)	−1.72, +0.95[i]	100, 110		
$[\{W(NO)(Tp^{Me2})Cl\}_2\{OCH_2(CF_2)_3CH_2O\}]$ (**14**)	−1.46, −1.52; +1.16[o]	60, 70; 70	60	60
$[\{W(NO)(Tp^{Me2})Cl\}_2\{O(CH_2)_6O\}]$ (**15**)	−1.74	100		
$[\{Mo(NO)(Tp^{Me2})Br\}O(CH_2)_2O\{W(NO)(Tp^{Me2})Br\}]$ (**16**)	−1.18, −1.88	82, 114	700	710[q]
$[W(NO)(Tp^{Me2})I_2]$ (**17**)	−0.806	70		

[a] Formal potentials *vs.* ferrocene–ferrocenium couple measured in CH_2Cl_2 with scan rate of 0.1 V s^{-1}; *ca.* 10^{-3} mol dm^{-3} of complex.
[b] Difference between anodic and cathodic peak potentials (for Fc/Fc^+ couple $\Delta E_p = 60$–80 mV).
[c] Separation between two one-electron reduction potentials determined by cyclic voltammetry.
[d] Difference between first and second reduction potentials determined by differential pulse voltammetry; pulse amplitude 50 mV; estimated error 10 mV.
[e] Data from [16].
[f] Practically irreversible ($i_c \gg i_a$).
[g] Quasi-reversible reduction potential of the monoanion degradation product (most probably $[Mo(NO)(Tp^{Me2})Q(solv)]$).
[h] A new anodic wave observed at −0.85 V.
[i] Potential of the quasi-reversible oxidation corresponding to the monocation formation.
[j] A new anodic wave observed at −0.88 V.
[k] Difference between cathodic peaks; only one (or none) anodic wave observed.
[l] Data from [15]; obtained most probably under not exactly the same conditions.
[m] Reexamined.
[n] From deconvoluted voltammogram.
[o] Potential of the irreversible oxidation.
[q] The magnitude of electrochemical interaction was estimated from equation: $\Delta E_{dpv}^{\{Mo-W\}} - (E_{dpv}^{\{Mo\}} - E_{dpv}^{\{W\}}) = 210$ mV.

The monometallic complexes examined, $[M(NO)(Tp^{Me2})X(Y)]$ (M = Mo or W; X = halide, Y = OR; X = Y = OR), underwent one-electron reductions at potentials which were strongly influenced by the nature of M, X and Y (and by the substituents attached to them). Thus, for the Mo complexes the $E_{1/2}$-values become more cathodic in the following order: X = Cl, $Y = OCH_2(CF_2)_3CH_2OH$ < X = I, $Y = O(CH_2)_2OH \approx O(CH_2)_2OCOCH_3$ < X = Cl, $Y = O(CH_2)_2OH$ < X = Cl, $O(CH_2)_3OH$ < X = I, Y = OEt < X = Cl, $Y = O(CH_2)_4OH$ < X = Cl, Y = OEt ≈ X = Cl, $O(CH_2)_2OCH_3$ < X = Cl, $Y = O(CH_2)_5OH \approx$ X = Cl, $O(CH_2)_6OH$ < X = Y = $O(CH_2)_2OH$ < X = Y = OEt, over the range of −0.854 V for the first to −1.90 V for the last complex, which reflects electron

withdrawing/donating capability of the ligands and the inductive effect of their substituents. As expected, the tungsten complexes exhibited reduction potentials of *ca.* 500 mV more cathodic than those of their molybdenum analogues [25]. The complexes in which X is Cl or Br show quasi-reversible behaviour, whereas for [Mo(NO)-(Tp^{Me2})I(Y)] electrochemical reduction is followed by a coupled chemical reaction involving I^- dissociation. Additionally, we observed a quasi-reversible reduction of the degradation product of $[Mo(NO)(Tp^{Me2})I(Y)]^-$ (Y = $O(CH_2)_2OH$, $O(CH_2)_2OCOCH_3$ or OEt), most probably $[Mo(NO)(Tp^{Me2})Y(solv)_n]$, in the region from −1.57 V to −1.83 V. The electronegativity of the halogen is not a determining factor of the redox potentials of [M(NO)-(Tp^{Me2})X(OR)] (X = Cl, Br or I) because the $E_{1/2}$-values for mono- (and the first potential of bi-metallic) complexes become more negative in the sequence I < Br < Cl, which can be explained in terms of $p(\pi) \rightarrow d(\pi)$ donation from X to Mo. At this point it is worth mentioning that for the coordinatively unsaturated boron halides (BX_3) a similar effect is observed, the π character of B–X bond becoming weaker in the sequence $BF_3 > BCl_3 > BBr_3 > BI_3$ [26–28]. The deciding factors of the π-bond strength in these systems are the energy and size of π-donor and π-acceptor orbitals. As the alkyl chain grows, the $E_{1/2}$-values of the complexes $[M(NO)(Tp^{Me2})Cl\{O(CH_2)_nOH\}]$ become more negative and for $n = 5, 6$ assume practically the same value. This is due to a fading induction effect of the hydroxyl group, but other effects like, e.g. torsion angles, could also play a role. In the case of [Mo(NO)-(Tp^{Me2})$(OEt)_2$], quasi-reversible oxidation corresponding to the monocation formation was also observed. Such process is very rarely observed for these type of complexes with anionic X, Y ligands. Correlation analysis of the reduction potentials, which reflects the energy of the LUMO and the nitrosyl stretching frequencies, ν(N=O), has been performed, using the data reported here for the Mo monometallics (Fig. 1).

The linear regression equation obtained reads $\nu(NO) = 1721 + 43E_{1/2}$ with correlation coefficient, R^2, of 0.9779. The inclusion of the point for X = Y = $O(CH_2)_2OH$ reduced the value of R^2 to 0.9563 (perhaps there is some bonding between the two glycol units which forms a chelate). A similar linear dependence has been earlier proposed for the complexes containing aromatic ligands $[M(NO)(Tp^{Me2})X(Y)]$ (M = Mo or W; X = Cl, Y = OPh, NHPh or SPh; X = Y = NC_4H_4, OPh, NHPh or SPh) [29].

The bimetallic {16:16} species exhibited two one-electron reduction processes that lead sequentially to mixed-valence $\{16{:}17\}^-$ and isovalent $\{17{:}17\}^{2-}$ species. The change in the electron density in one of the centres could be sensed by the other centre and, consequently, two signals are observed in the CV. In case of no or negligible interaction, both processes occur as one-electron reductions at virtually the same potential and $\Delta E_{1/2}$ (electrochemical interaction) and corresponding K_c (comproportionation constant) can be calculated from the statistical distribution of products of equal stability with $K_c = 4$ and $\Delta E_{1/2} =$ 35.6 mV consequently.

As can be seen from Fig. 2, the electrochemical interactions decrease by *ca.* 100 mV per CH_2 group with increased length for C_2 to C_4 bridges. Starting with C_5 bridge the electrochemical interactions could not be detected and hence are assumed to be equal to the statistically based value of 35.6 mV. Stabilisation of $\{16{:}17\}^-$ species (K_c range 10 to 10^5) results mainly from through-space coulombic interactions but some polar effects transmitted through σ-bond framework could not be excluded. The replacement of pentane-1,5-diolate bridge by its fluorinated

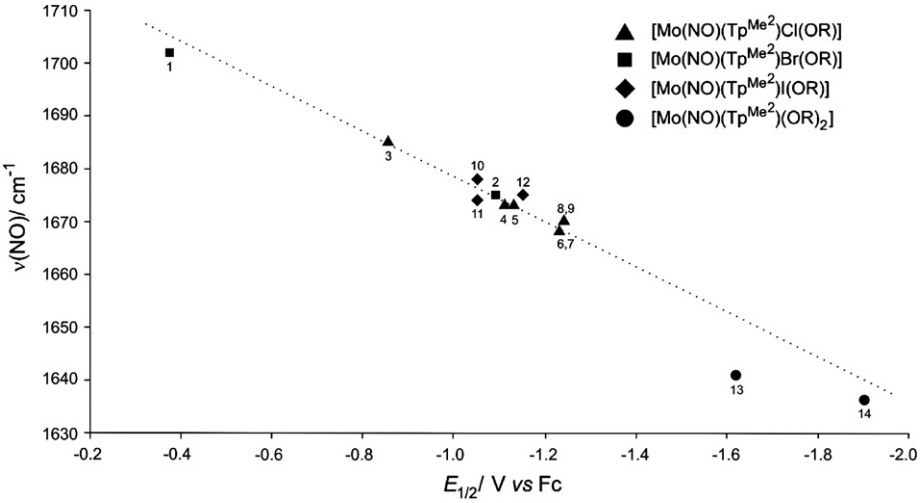


Fig. 1. A plot of ν(N=O) against reduction potentials for $[Mo(NO)(Tp^{Me2})X(Y)]$. Points are labelled as follows: 1 (X = Y = Br), 2 (X = Br, Y = $O(CH_2)_2OH$), 3 (X = Cl, Y = $OCH_2(CF_2)_3CH_2OH$), 4 (X = Cl, Y = $O(CH_2)_2OH$), 5 (X = Cl, Y = $O(CH_2)_3OH$), 6,7 (X = Cl, Y = OEt or $O(CH_2)_2OCH_3$), 8,9 (X = Cl, Y = $O(CH_2)_5OH$ or $O(CH_2)_6OH$), 10 (X = I, Y = $O(CH_2)_2OAc$), 11 (X = I, Y = $O(CH_2)_2OH$), 12 (X = I, Y = OEt), 13 (X = Y = $O(CH_2)_2OH$), and 14 (X = Y = OEt).

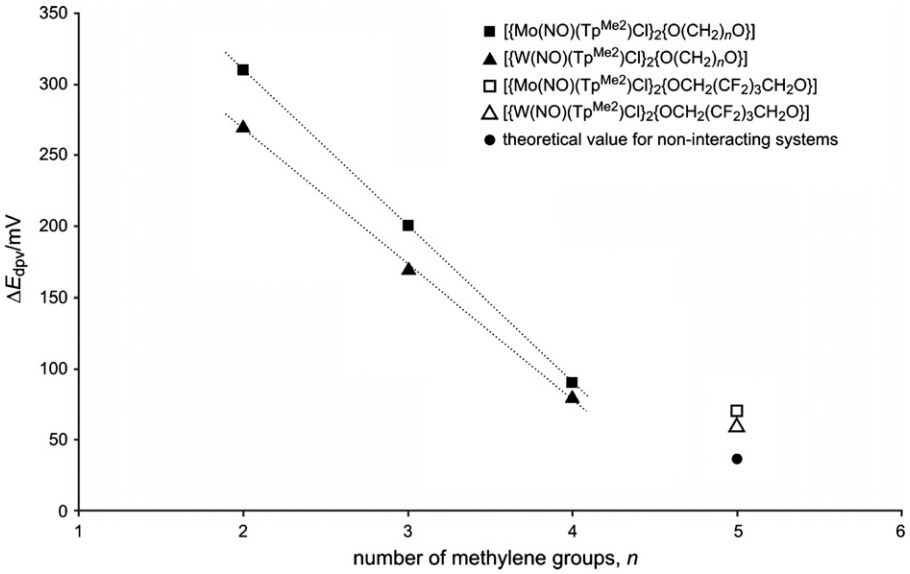


Fig. 2. Dependence of electrochemical interactions, ΔE_{dpv}, on the number of methylene groups in bimetallic Mo and W species. Additionally, for comparison, fluorinated analogues of pentane-1,5-diolate complexes and statistical value for non-interacting systems were included.

analogue causes the appearance of noticeable interactions. As it has been previously noted, interactions between tungsten centres are generally weaker. The heterobimetallic system demonstrates interactions of *ca.* 210 mV that are similar to those observed in the tungsten homobimetallic analogue, which points to mainly through-space coulombic interactions. Bimetallic complexes with C_2 to C_5 bridges undergo the first reduction process at potentials more cathodic by *ca.* 20–70 mV compared with the related monometallic complexes, which seems to be a general rule for the systems with saturated bridges without any significant delocalisation of the unpaired electron [17].

Bimetallic complexes $[\{Mo(NO)(Tp^{Me2})I\}_2\{O(CH_2)_nO\}]$ ($n = 2$–4) show two irreversible reduction waves. The intensity of the cathodic peak for the second reduction process appreciably increases with the scan rate (50–200 mV/s). As was noted above for the monometallic compounds $[Mo(NO)(Tp^{Me2})IQ]$, the signals corresponding to the oxidation of I^-/I_3^- ions were observed. An additional anodic process corresponding to the oxidation of a product of the reaction following the reduction of the complex could also be observed in the range −0.85 V to −0.88 V. It cannot be excluded that the additional wave is associated with the oxidation of the system, in which the I^- ion remains in the proximity of the {17e} centre, and the whole entity is stabilised in the solvent cavity, similar to ion-radical pair in dissociative reduction processes of halogen organic compounds [30,31]. Because of the irreversibility, the $\Delta E_{1/2}$ for these complexes should be taken only as an approximation.

2.3. Crystal and molecular structure of **6**

The molecular structure of **6** is shown in Fig. 3, and selected geometric parameters are listed in Table 3. The asymmetric unit contains two enantiomeric forms (*R* and *S*). The coordination geometry at the molybdenum atoms is distorted octahedral, by a reason of rigid framework of the Tp^{Me2} ligand, which occupies three *fac* sites of the octahedron. The short Mo–O bond lengths (av. 1.88 Å) as well as Mo–O–C angles (130.1°), which reflect a significant degree of $p(\pi) \rightarrow d(\pi)$ donation from O to coordinatively unsaturated Mo, are comparable with those found in $[Mo(NO)(Tp^{Me2})I\{O(CH_2)_3Br\}]$ [32] and $[Mo(NO)(Tp^{*Cl})Cl(OPr^i)]$ (1.86 Å) [33]. For a pure Mo^{II}–O σ bond *ca.* 2.11 Å is expected, as found in $[Mo_2(O_2CCF_3)_4(C_5H_5N)_2]$ [34]. As usually found in this class of complexes, the molybdenum-nitrosyl system is slightly bent from linearity (173.5°, 176.9°), with short Mo–N distance of 1.76 Å. One of the three Mo–N(pyrazolyl) bonds, that lying *trans* to the NO ligand (2.26 Å) is significantly longer than the other two (2.20 Å, 2.22 Å). This has been assigned to the trans influence of the strongly π-accepting nitrosyl group [35]. The Mo–I bond length (2.75 Å) suggests some small degree of π-donor bonding. The pyrazolyl rings of Tp^{Me2} are virtually planar and the N–B–N angles (107.4–109.8°) are close to the tetrahedral value. The boron atom cannot interact with the metal for steric reasons (Mo···B distance 3.29 Å) (see Fig. 4).

2.4. Crystal and molecular structure of ***17*** · $0.5I_2$ · $0.5C_6H_5CH_3$

The complex unit of **17** · $0.5I_2$ · $0.5C_6H_5CH_3$ together with atom numbering is shown in Fig. 5, and its crystal structure is shown in Fig. 6. It contains a molecule of iodine shared between two complex molecules and, as we know from residual electron density and crystallisation conditions, disordered toluene solvates held together by

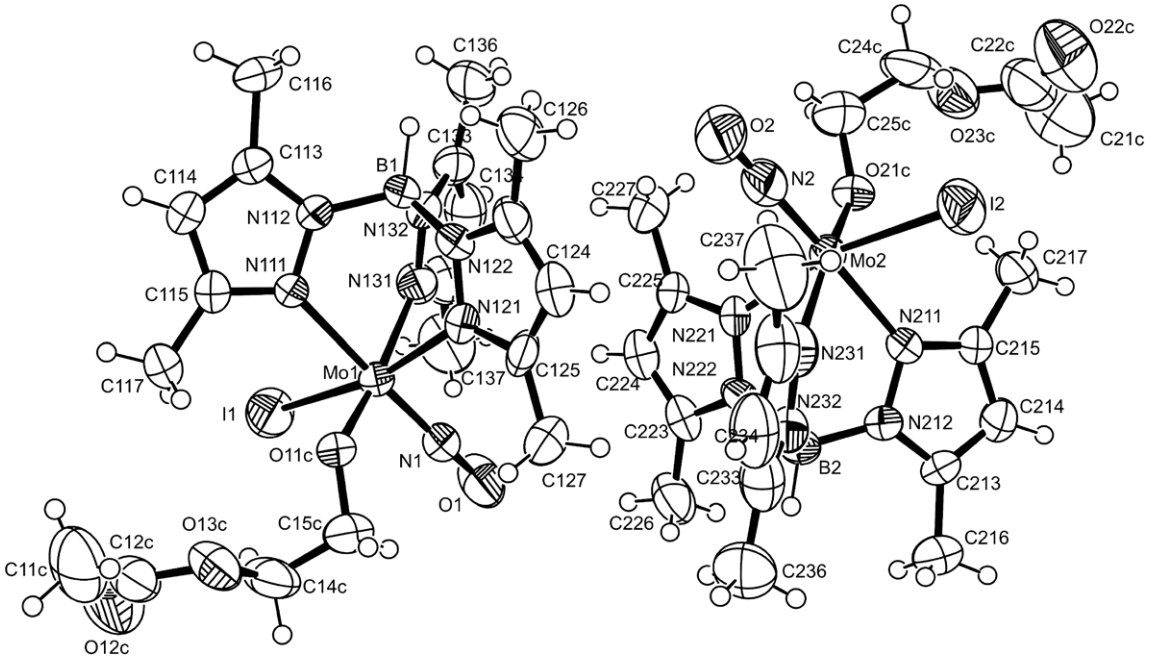


Fig. 3. ORTEP plot of the asymmetric unit of **6** showing thermal ellipsoids at the 50% probability level.

Table 3
Selected bond lengths (Å) and angles (°) for **6**[a]

Mo(1)–N(1)	1.755(9)	Mo(2)–N(2)	1.757(9)
Mo(1)–N(121)	2.160(7)	Mo(2)–N(221)	2.152(7)
Mo(1)–N(131)	2.228(8)	Mo(2)–N(231)	2.230(8)
Mo(1)–N(111)	2.251(6)	Mo(2)–N(211)	2.243(7)
Mo(1)–O(11C)	1.878(6)	Mo(2)–O(21C)	1.881(7)
Mo(1)–I(1)	2.7508(12)	Mo(2)–I(2)	2.7540(12)
N(1)–O(1)	1.173(10)	N(2)–O(2)	1.194(11)
O(11C)–C(15C)	1.410(11)	O(21C)–C(25C)	1.417(13)
C(15C)–C(14C)	1.498(15)	C(25C)–C(24C)	1.470(17)
N(1)–Mo(1)–O(11C)	97.7(3)	N(2)–Mo(2)–O(21C)	96.8(4)
N(1)–Mo(1)–N(121)	96.3(3)	N(2)–Mo(2)–N(221)	95.8(3)
O(11C)–Mo(1)–N(121)	94.7(3)	O(21C)–Mo(2)–N(221)	94.7(3)
N(1)–Mo(1)–N(131)	91.5(3)	N(2)–Mo(2)–N(231)	91.8(4)
O(11C)–Mo(1)–N(131)	169.4(3)	O(21C)–Mo(2)–N(231)	169.9(3)
N(121)–Mo(1)–N(131)	79.0(3)	N(221)–Mo(2)–N(231)	78.9(3)
N(1)–Mo(1)–N(111)	177.0(4)	N(2)–Mo(2)–N(211)	178.0(4)
O(11C)–Mo(1)–N(111)	85.3(3)	O(21C)–Mo(2)–N(211)	85.2(3)
N(121)–Mo(1)–N(111)	84.0(2)	N(221)–Mo(2)–N(211)	83.7(2)
N(131)–Mo(1)–N(111)	85.6(3)	N(231)–Mo(2)–N(211)	86.2(3)
N(1)–Mo(1)–I(1)	90.3(3)	N(2)–Mo(2)–I(2)	91.5(3)
O(11C)–Mo(1)–I(1)	95.8(2)	O(21C)–Mo(2)–I(2)	96.4(2)
N(121)–Mo(1)–I(1)	166.77(19)	N(221)–Mo(2)–I(2)	165.89(19)
N(131)–Mo(1)–I(1)	89.4(2)	N(231)–Mo(2)–I(2)	88.8(2)
N(111)–Mo(1)–I(1)	88.79(17)	N(211)–Mo(2)–I(2)	88.66(18)
Mo(1)–O(11C)–C(15C)	130.1(7)	Mo(2)–O(21C)–C(25C)	130.0(8)
Mo(1)–N(1)–O(1)	173.5(10)	Mo(2)–N(2)–O(2)	176.9(11)

[a] Values in parentheses are estimated standard deviations.

van der Waals forces. The asymmetric unit consists of the complex and half of the iodine molecule (no short contact to the complex). The complex contains a pseudo mirror plane of symmetry passing through W, NO, B and the N(31), N(32), C(33)–C(35) pyrazolyl ring (approximate C_s symmetry which is reflected in ^{1}H NMR spectrum). The co-ordination geometry about tungsten is essentially octahedral. The bond *trans* to the NO group is the longest of the three Mo–N(pyrazolyl) bonds. The tungsten-nitrosyl moiety is slightly bent from linearity (174.8°) with

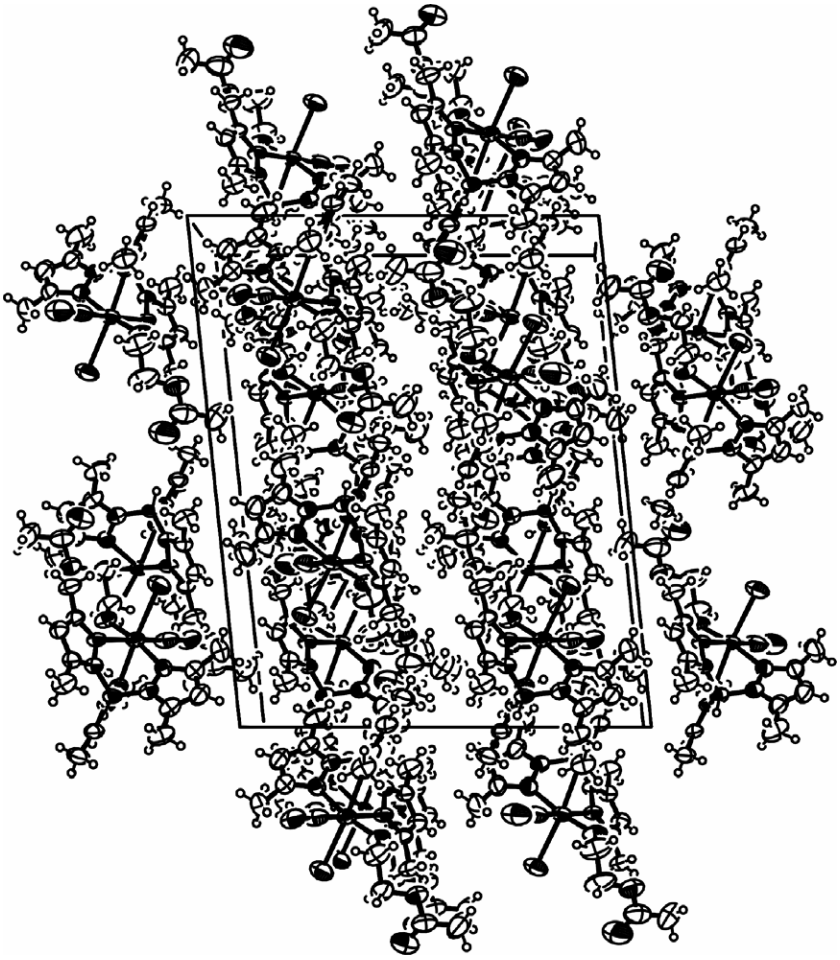


Fig. 4. Packing of molecules in the unit cell of **6** along direct [0 1 0].

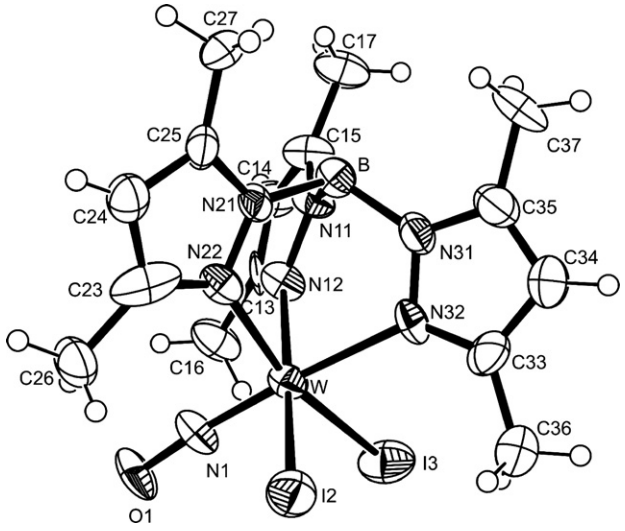


Fig. 5. ORTEP plot of the complex unit of $17 \cdot 0.5I_2 \cdot 0.5\,C_6H_5CH_3$ showing thermal ellipsoids at the 50% probability level.

short W–N distance of 1.75 Å. The W–I distances (2.71, 2.74 Å) are shorter relative to complexes in which formally W^{II} attains normal 18-electron configuration, e.g. $[WI_2(CO)_3(PEt_3)_2]$ (2.85, 2.86 Å) [36], $[Tp^{iPr}WI(CO)_3]$ (2.85 Å) [37]. These distances suggest some degree of $p(\pi) \rightarrow d(\pi)$ donation from I to coordinatively unsaturated W (formally 16-electron). The dimensions of the Tp^{Me2} ligand are as expected with virtually planar pyrazolyl rings and N–B–N angles (106.5–109.8°) close to the tetrahedral value. The boron atom cannot interact with the metal for steric reasons (W···B distance 3.26 Å). The crystal study confirms that iodination of the pyrazolyl rings did not occur.

Selected bond lengths and angles are given in Table 4.

3. Experimental

3.1. Materials and instrumentation

All reactions were carried out under pure argon (BOC, N5.0) using Schlenk techniques and a high-vacuum/gas double line manifold. Commercial solvents and triethylamine were purified by distillation under argon; dichloromethane from calcium hydride, toluene and benzene from sodium-benzophenone and triethylamine from sodium. Anhydrous, 99.8% α,ω-diols were supplied by Aldrich and used directly. The complexes $[M(NO)(Tp^{Me2})X_2]$

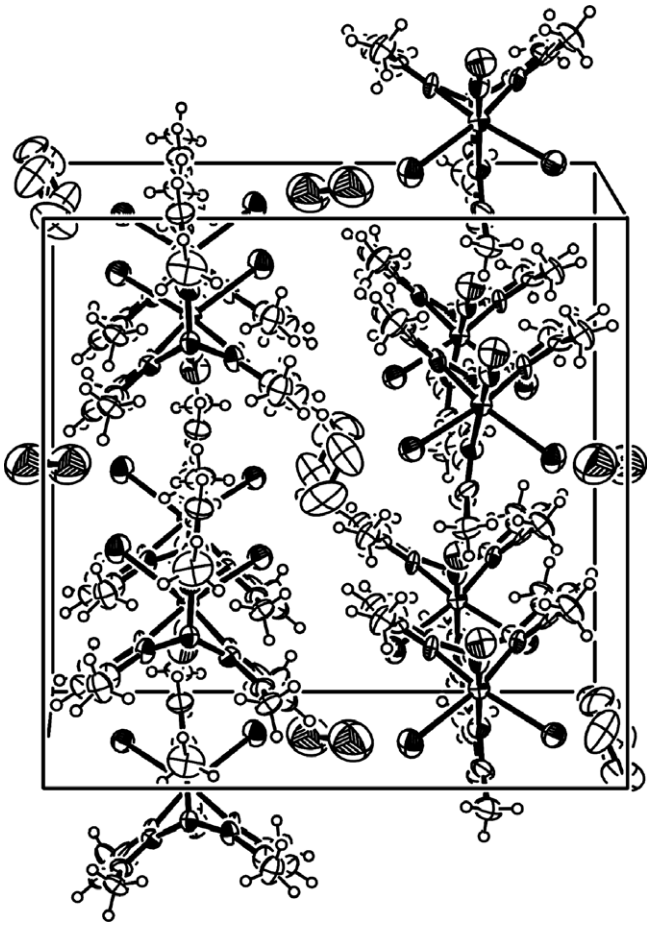


Fig. 6. Packing of molecules in the unit cell of $17 \cdot 0.5I_2 \cdot 0.5C_6H_5CH_3$ along direct [1 0 0].

(M = Mo, X = Cl or I; M = W, X = Cl) were prepared by iodination of $[M(CO)_2(NO)(Tp^{Me2})]$ with (X = Cl) or without (X = I) subsequent addition of benzyl chloride [23]. The monometallic species $[M(NO)(Tp^{Me2})Cl(OR)]$ [M = Mo, $R = (CH_2)_nOH$, $n = 5$, 6; M = W, $R = (CH_2)_nOH$, $n = 2$, 3; M = Mo, $R = (CH_2)_2OMe$] [38], $[Mo(NO)(Tp^{Me2})X(OEt)]$ (X = Cl or I) [33] and $[Mo(NO)(Tp^{Me2})(OEt)_2]$ [21] were prepared according to the literature. Complex **6** was previously obtained as a by-product from the reaction between $[Mo(NO)(Tp^{Me2})I_2]$ and $HOCH_2CH_2OH$ in dichloromethane in the presence of silver acetate [16]. Column chromatography was carried out in glass columns with Merck silica gel 60 (70–230 mesh) as the stationary phase and dichloromethane (to remove bimetallic complexes) or dichloromethane-thf mixtures (to remove monometallic complexes) as elutants. If necessary, fractions were further purified on a second short silica column. The reaction's progress and purity of compounds were monitored by thin-layer chromatography using Merck silica gel (60) F_{254} plates. All yields are based on the starting metal-containing compound. Elemental analyses were performed by the Microanalytical Laboratory of the Faculty of Chemistry at Jagiellonian University or of the Department of Chemistry at the University of Birmingham.

Table 4
Selected bond lengths (Å) and angles (°) for $17 \cdot 0.5I_2 \cdot 0.5C_6H_5CH_3$ [a]

W–N(1)	1.747(16)	W–I(2)	2.707(2)
W–N(32)	2.254(15)	W–I(3)	2.735(2)
W–N(12)	2.090(15)	N(1)–O(1)	1.24(2)
W–N(22)	2.105(18)	I(1)–I(1_3)	2.766(12)
N(1)–W–N(12)	95.7(7)	N(22)–W–I(2)	91.0(4)
N(1)–W–N(22)	96.4(8)	N(32)–W–I(2)	87.2(5)
N(12)–W–N(22)	77.4(6)	N(1)–W–I(3)	91.7(6)
N(1)–W–N(32)	176.7(8)	N(12)–W–I(3)	87.9(5)
N(12)–W–N(32)	87.0(6)	N(22)–W–I(3)	163.8(4)
N(22)–W–N(32)	86.1(6)	N(32)–W–I(3)	86.4(5)
N(1)–W–I(2)	90.6(6)	I(2)–W–I(3)	102.87(6)
N(12)–W–I(2)	167.4(4)	O(1)–N(1)–W	174.7(19)

[a] Values in parentheses are estimated standard deviations.

The infrared spectra were recorded using a Bio-Rad FTS 175C spectrophotometer in KBr pellets and ^1H NMR spectra from solutions in $CDCl_3$ or C_6D_6 using a Varian Mercury-Vx 300 MHz spectrometer. Chemical shifts were referenced to residual $CHCl_3$ or C_6H_6. Mass analyses were performed on a Bruker-Daltonics Esquire 3000 (ESI) spectrometer, VG-Autospec with 3-nitrobenzyl alcohol as matrix (FAB) and Kratos MS80 (EI). Cyclic and differential pulse voltammetry measurements were carried out using a BAS 100B/W electrochemical workstation (Bioanalytical Systems, USA), under argon in *ca.* 10^{-3} M solution of complex in dry dichloromethane containing 0.1 M $[(n\text{-}C_4H_9)_4N][PF_6]$ as base electrolyte at scan rate of 0.1 V s^{-1}. A standard three-electrode cell was used with a platinum disc working electrode, a platinum wire secondary electrode, and a silver–silver chloride reference electrode that was immersed in supporting electrolyte solution and separated from the test solution by a dense ceramic frit. Ferrocene was added at the end of each experiment as an internal standard; all potentials are quoted versus the ferrocene–ferrocenium couple. The data obtained were reproducible, the measurement error in $E_{1/2}$ was estimated at 5 mV. The number of electrons in each transfer was estimated by comparison with $[\{Mo(NO)(Tp^{Me2})Cl\}_2(\mu\text{-}O)]$, for which a one electron process has been shown [23].

3.2. Synthetic procedures

3.2.1. Synthesis of $[\{Mo(NO)(Tp^{Me2})Cl\}_2\{O(CH_2)_3O\}]$ and $[Mo(NO)(Tp^{Me2})Cl\{O(CH_2)_3OH\}]$ (**1**) and (**18**)

To a solution of $[Mo(NO)(Tp^{Me2})Cl_2]$ (0.50 g, 1.0 mmol) in dry dichloromethane (50 cm^3) AgOCOMe (0.19 g, 1.1 mmol) and propane-1,3-diol (0.30 g, 3.9 mmol) were added. The mixture was stirred and refluxed for 8 h, during which time the colour of the solution changed through green to deep blue. The reaction mixture was cooled to r.t., *n*-hexane was added and further cooled to −10 °C. The precipitate of inorganic salts was filtered off. The solvent was then removed *in vacuo* and the solid was dissolved in the minimum volume of dichloromethane and chromatographed on silica

gel using dichloromethane as eluant. The first and the second blue fractions were collected (bi- and monometallic species), partially evaporated *in vacuo* and precipitated from CH_2Cl_2/*n*-hexane. The resulting blue complexes were filtered off, washed with *n*-hexane, dried at *ca.* 80 °C for 1 h and then *in vacuo* for a few hours (0.1 g, 19.9%, mixture of bimetallic diastereoisomers; 0.05 g, 9.3%, monometallic).

*3.2.2. Synthesis of [{Mo(NO)(Tp^{Me2})Cl}$_2${O(CH$_2$)$_5$O}] (**2**)*

This compound was prepared as a blue-green powder according to the procedure described above using [Mo(NO)(Tp^{Me2})Cl$_2$] (0.50 g, 1.0 mmol), pentane-1,5-diol (0.42 g, 4.0 mmol) and AgOCOMe (0.18 g, 1.1 mmol) in dichloromethane (50 cm^3). The first main fraction was collected and precipitated from CH_2Cl_2/*n*-hexane (0.12 g, 23.3%).

*3.2.3. Synthesis of [{Mo(NO)(Tp^{Me2})Cl}$_2${OCH$_2$(CF$_2$)$_3$CH$_2$O}] and Mo(NO)(Tp^{Me2})Cl{OCH$_2$(CF$_2$)$_3$CH$_2$OH}] (**3**) and (**4**)*

A mixture of [Mo(NO)(Tp^{Me2})Cl$_2$] (0.50 g, 1.0 mmol), 2,2,3,3,4,4-hexafluoro-1,5-pentanediol (0.48 g, 2.2 mmol) and hexamethylenetetramine (0.14 g, 1.0 mmol) in dichloromethane (50 cm^3) was stirred and refluxed for 8 h. The solution was then cooled, filtered, evaporated *in vacuo* and the solid so obtained redissolved in CH_2Cl_2 and purified by column chromatography. Two turquoise fractions were separated and precipitated from CH_2Cl_2/*n*-hexane (0.09 g, 15.8%, bimetallic; 0.07 g, 10.3%, monometallic).

*3.2.4. Synthesis of [{Mo(NO)(Tp^{Me2})Cl}$_2${O(CH$_2$)$_6$O}] (**5**)*

[Mo(NO)(Tp^{Me2})Cl$_2$] (0.50 g, 1.0 mmol) together with hexane-1,6-diol (0.39 g, 3.3 mmol) and hexamethylenetetramine (0.22 g, 1.6 mmol) in dichloromethane (50 cm^3) was stirred and refluxed for 7 h. The resulting blue solution was cooled, filtered and evaporated to dryness. The residue was chromatographed on silica gel using dichloromethane as eluant to give a main blue fraction which was collected (0.1 g, 19.1%).

*3.2.5. Synthesis of [{W(NO)(Tp^{Me2})Cl}$_2${O(CH$_2$)$_3$O}] (**11**)*

The complex [W(NO)(Tp^{Me2})Cl$_2$] (0.59 g, 1.0 mmol) was dissolved in warm toluene (100 cm^3) and propane-1,3-diol (1.1 g, 14.5 mmol) were added. The mixture was stirred and refluxed for 8 h, during which time the solution became purple. After cooling to r.t., *n*-hexane was added and the reaction mixture was refrigerated overnight. The supernatant liquid was decanted from an oily deposit and the unreacted [W(NO)(Tp^{Me2})Cl$_2$], and the filtrate evaporated *in vacuo*. The solid obtained was chromatographed on silica gel using dichloromethane as eluant. The first fraction was collected and precipitated from CH_2Cl_2/*n*-hexane as a purple powder (0.09 g, 15.2%).

*3.2.6. Synthesis of [{W(NO)(Tp^{Me2})Cl}$_2${O(CH$_2$)$_n$O}] (n = 4–6) and [{W(NO)(Tp^{Me2})Cl}$_2${OCH$_2$(CF$_2$)$_3$CH$_2$O}] (**12**)–(**15**)*

These complexes were prepared similarly to **11**, which is described immediately above, with yields 15–25%.

*3.2.7. Synthesis of [{Mo(NO)(Tp^{Me2})I}$_2${O(CH$_2$)$_n$O}] (n = 3, 4) (**7**) and (**8**)*

To a solution of [Mo(NO)(Tp^{Me2})I$_2$] (0.50 g, 0.74 mmol) in dichloromethane (50 cm^3) the appropriate *n*-alkanediol (0.1 cm^3) and hexamethylenetetramine (0.12 g, 0.86 mmol) were added. The mixture was stirred and refluxed for 4 h affording a green solution which was cooled to r.t., then *n*-hexane was added and the mixture further was cooled to −10 °C. A precipitate and oily deposit were discarded and the supernatant solution was evaporated to dryness. The residue was purified by chromatography using dichloromethane as eluant. The first fraction was collected and precipitated from CH_2Cl_2/*n*-hexane as a green powder (yields *ca.* 25%).

*3.2.8. Synthesis of [{Mo(NO)(Tp^{Me2})Br}O(CH$_2$)$_2$O-{W(NO)(Tp^{Me2})Br}] (**16**)*

A mixture of [Mo(NO)(Tp^{Me2})Br(OCH$_2$CH$_2$OH)] (0.08 g, 0.14 mmol), [W(NO)(Tp^{Me2})Br$_2$] (0.11 g, 0.16 mmol) and hexamethylenetetramine (0.02 g, 0.14 mmol) was stirred and refluxed in benzene (20 cm^3) for 5 h and then stirred overnight at r.t. The resulting solution was filtered and the filtrate evaporated *in vacuo*. The residue was chromatographed on silica gel using dichloromethane as eluant. The second navy blue fraction was collected and precipitated from CH_2Cl_2/*n*-hexane (mixture of bimetallic diastereoisomers, 0.03 g, 18.3%).

*3.2.9. Synthesis of [{W(NO)(Tp^{Me2})Br}$_2${O(CH$_2$)$_2$O}] and [W(NO)(Tp^{Me2})Br{O(CH$_2$)$_2$OH}] (**9**) and (**10**)*

To a solution of [W(NO)(Tp^{Me2})Br$_2$] (0.50 g, 0.75 mmol) in dry dichloromethane (60 cm^3) ethane-1,2-diol (0.18 g, 2.9 mmol) and hexamethylenetetramine (0.11 g, 0.78 mmol) were added. The mixture was stirred and refluxed for 7 h. The solution was then cooled, filtered, evaporated *in vacuo* and the solid redissolved in CH_2Cl_2 and purified by column chromatography. Two purple fractions were separated and precipitated from CH_2Cl_2/*n*-hexane (0.11 g, 23.8%, mixture bimetallic of diastereoisomers; 0.06 g, 12.4%, monometallic).

*3.3. Crystal structure determination of **6***

The green crystals were obtained from CH_2Cl_2/*n*-hexane mixture. Selected crystal had dimensions 0.18 × 0.08 × 0.03 mm^3. X-ray data were collected on a Nonius Kappa CCD with graphite monochromated Mo Kα radiation

($\lambda = 0.71069$ Å). 11 984 reflections were measured ($2\theta_{max} = 54.9°$) at 293 K. Corrections for Lorentz and polarization were applied. The structure was solved by direct methods and refined by the full-matrix least-squares method on all F^2 data using the SHELXL-97 suite of programs [39]. The model, accepted as the 'correct' structure, gave final R $[= \Sigma(F_o - F_c)/\Sigma(F_o)]$ and $wR[= \Sigma\{w(F_o^2 - F_c^2)^2\}/\Sigma\{w(F_o^2)^2\}]^{1/2}$ values of 0.1300 and 0.2087, respectively for 618 parameters and all 11 984 data. The corresponding R values for 8012 data with $I > 2\sigma(I)$ were 0.0872 and 0.1899. The weighting scheme used was $w = 1/[\sigma^2(F_o^2) + (0.0520P)^2 + 39.1869P]$, where $P = (F_o^2 + 2F_c^2)/3$. All non-hydrogen atoms were refined with anisotropic thermal parameters; hydrogen atoms were included in calculated positions and refined isotropically.

3.3.1. Crystal data

$C_{19}H_{29}BIMoN_7O_4$, $M = 653.14$, monoclinic, space group $P2_1/n$, $a = 17.233(5)$ Å, $b = 14.213(5)$ Å, $c = 21.583(5)$ Å, $\beta = 95.882(5)°$, V=5259(3) Å^3, $Z = 4$, $D_c = 1.650$ g cm^{-3}, $F(0\,0\,0) = 2592$, μ(Mo Kα) = 1.710 mm^{-1}.

3.4. Crystal structure determination of *17 · 0.5I$_2$ · 0.5C$_6$H$_5$CH$_3$*

The dark brown crystals were grown from toluene and then recrystallised from a $CDCl_3$ solution used for the NMR measurement. A crystal ($0.11 \times 0.09 \times 0.08$ mm^3) was mounted on a Nonius Kappa CCD diffractometer with graphite monochromated Mo Kα radiation ($\lambda = 0.71069$ Å). 20 433 reflections were scanned ($2\theta_{max} = 55.0°$) at 293 K. Lorentz and polarization corrections were applied. The structure was determined by direct methods and refined by the full-matrix least-squares method on all F^2 data using the SHELXL-97 suite of programs [39]. The model, accepted as the 'correct' structure, gave final R $[=\Sigma(F_o - F_c)/\Sigma(F_o)]$ and wR $[=\Sigma\{w(F_o^2 - F_c^2)^2\}/\Sigma\{w(F_o^2)^2\}]^{1/2}$ values of 0.1400 and 0.2940, respectively for 287 parameters and all 6080 data. The corresponding R values for 4295 data with $I > 2\sigma(I)$ were 0.1084 and 0.2768. Weighting scheme, $w = 1/[\sigma^2(F_o^2) + (0.0887P)^2 + 175.9498P]$, where $P = (F_o^2 + 2F_c^2)/3$. All non-hydrogen atoms were refined with anisotropic thermal parameters; hydrogen atoms were included in calculated positions and refined isotropically.

3.4.1. Crystal data

$C_{15}H_{22}BI_2WN_7O \cdot 0.5I_2 \cdot 0.5C_6H_5CH_3$, $M = 937.82$, monoclinic, space group $P2_1/c$, $a = 9.336(5)$ Å, $b = 17.409(5)$ Å, $c = 16.989(5)$ Å, $\beta = 105.843(5)°$, $V = 2656.3(18)$ Å^3, $Z = 4$, $D_c = 2.317$ g cm^{-3}, $F(0\,0\,0) = 1696$, μ(Mo Kα) = 7.858 mm^{-1}.

4. Conclusions

A series of bimetallic molybdenum and tungsten complexes with saturated *n*-alkanediolate bridging ligands and their monometallic analogues was synthesised and characterised. The monometallic complexes, [M(NO)(Tp^{Me2})X(Y)] (M = Mo or W; X = halide, Y = OR; X = Y = OR), underwent one-electron reductions at potentials which were strongly influenced by the nature of M, X and Y and substituents attached to them. The redox potentials ($E_{1/2}$-values) of the studied complexes [M(NO)(Tp^{Me2})X(OR)] (X = Cl, Br or I) decrease in the order I > Br > Cl, which can be explained in terms of $p(\pi) \rightarrow d(\pi)$ donation from X to Mo and not the electronegativity of the halogen. The $E_{1/2}$-values of the complexes [M(NO)(Tp^{Me2})Cl{O(CH$_2$)$_n$OH}] become more negative with increasing the length of the alkyl chain, and levelling off for $n = 5, 6$.

The electrochemical interactions in bimetallic complexes, measured as the separation between redox potentials of two redox centres, $\Delta E_{1/2}$, being large for the complex with a C_2 bridge (310 mV, Mo···Mo distance > 6 Å) decrease by *ca.* 100 mV per CH_2 group with increased length for C_2 to C_4 bridges. Starting with C_5 bridge the electrochemical interactions could not be detected and hence are assumed to be equal to the statistically based value of 35.6 mV. Stabilisation of $\{16{:}17\}^-$ species (K_c range 10 to 10^5) results mainly from through-space coulombic interactions but some polar effects transmitted through σ-bond framework could not be excluded.

The occurrence of a measurable separation between the redox potentials in [{M(NO)(Tp^{Me2})Cl}$_2${OCH$_2$(CF$_2$)$_3$CH$_2$O}] (M = Mo or W, $\Delta E_{1/2}$ respectively 70 and 60 mV) can be explained partly by through-bond interactions that may be assumed to occur in these compounds due to easier polarisation of the σ-bond framework containing fluorine.

Spectroscopic studies (UV–Vis–NIR) of the mixed-valence complexes and DFT calculations carried out at present should make it possible to fully explain the mechanism of the electronic interactions.

Appendix A. Supplementary material

CCDC 659506 and 659507 contain the supplementary crystallographic data for this paper. These data can be obtained free of charge via http://www.ccdc.cam.ac.uk/conts/retrieving.html, or from the Cambridge Crystallographic Data Centre, 12 Union Road, Cambridge CB2 1EZ, UK; fax: (+44) 1223-336-033; or e-mail: deposit@ccdc.cam.ac.uk. Supplementary data associated with this article can be found, in the online version, at doi:10.1016/j.poly.2007.11.008.

References

[1] J.A. McCleverty, M.D. Ward, Acc. Chem. Res. 31 (1998) 842.
[2] M.D. Ward, Chem. Soc. Rev. 24 (1995) 121.
[3] P.J.F. de Rege, S.A. Williams, M.J. Therien, Science 269 (1995) 1409.
[4] A. Wlodarczyk, G.A. Doyle, J.P. Maher, J.A. McCleverty, M.D. Ward, Chem. Commun. (1997) 769.

[5] A. Wlodarczyk, J.P. Maher, J.A. McCleverty, M.D. Ward, J. Chem. Soc., Chem. Commun. (1995) 2397.
[6] S.L.W. McWhinnie, C.J. Jones, J.A. McCleverty, D. Collison, F.E. Mabbs, J. Chem. Soc., Chem. Commun. (1990) 940.
[7] J. Hock, A.M.W. Cargill Thompson, J.A. McCleverty, M.D. Ward, J. Chem. Soc., Dalton Trans. (1996) 4257.
[8] A. Das, J.P. Maher, J.A. McCleverty, J.A. Navas Badiola, M.D. Ward, J. Chem. Soc., Dalton Trans. (1993) 681.
[9] C. Creutz, H. Taube, J. Am. Chem. Soc. 95 (1973) 1086.
[10] S.L.W. McWhinnie, J.A. Thomas, T.A. Hamor, C.J. Jones, J.A. McCleverty, David Collison, F.E. Mabbs, C.J. Harding, L.J. Yellowlees, M.G. Hutchings, Inorg. Chem. 35 (1996) 760.
[11] C.A. Stein, Nita A. Lewis, Guenther Seitz, A. David Baker, Inorg. Chem. 22 (1983) 124.
[12] W. Haiss, R.J. Nichols, H. van Zalinge, S.J. Higgins, D. Bethell, D.J. Schiffrin, Phys. Chem. Chem. Phys. 6 (2004) 4330.
[13] N.J. Al Obaidi, C.J. Jones, J.A. McCleverty, Polyhedron 9 (1990) 693.
[14] N. Al Obaidi, T.A. Hamor, C.J. Jones, J.A. McCleverty, K. Paxton, J. Chem. Soc., Dalton Trans. (1987) 2653.
[15] J.A. Thomas, C.J. Jones, J.A. McCleverty, M.G. Hutchings, Polyhedron 15 (1996) 409.
[16] P.P. Romańczyk, M.N. Guzik, A.J. Włodarczyk, Polyhedron 26 (2007) 1182.
[17] S.L.W. McWhinnie, C.J. Jones, J.A. McCleverty, L.J. Yellowlees, J. Chem. Soc., Dalton Trans. (1996) 4401.
[18] S.M. Charsley, C.J. Jones, J.A. McCleverty, Trans. Met. Chem. 11 (1986) 329.
[19] A. Włodarczyk, J.P. Maher, J.A. McCleverty, M.D. Ward, J. Chem. Soc., Dalton Trans. (1997) 3287.
[20] M. Krompiec, L. Patiny, in: Fifth International Electronic Conference on Synthetic Organic Chemistry (ECSOC-5), 2001. <http://www.mdpi.org/ecsoc-5.htm>.
[21] J.A. McCleverty, A.E. Rae, I. Wołochowicz, N.A. Bailey, J.M.A. Smith, J. Chem. Soc., Dalton Trans. (1982) 951.
[22] A. Wlodarczyk, A.J. Edwards, J.A. McCleverty, Polyhedron 7 (1988) 103.
[23] A. Wlodarczyk, J.P. Maher, S. Coles, D.E. Hibbs, M.H.B. Hursthouse, K.M.A. Malik, J. Chem. Soc., Dalton Trans. (1997) 2597.
[24] S.M. Charsley, C.J. Jones, B. D Neaves, R.A. Kresinski, S.L.W. McWhinnie, J.A. McCleverty, L.J. Yellowlees, Polyhedron 21 (2002) 849.
[25] J.A. McCleverty, Chem. Soc. Rev. 3 (1983) 331.
[26] S. Konaka, Y. Murata, K. Kuchitsu, Y. Morino, Bull. Chem. Soc. Jap. 39 (1966) 1134.
[27] S. Konaka, T. Ito, Y. Morino, Bull. Chem. Soc. Jap. 39 (1966) 1146.
[28] M.A. Ring, J.D.H. Donnay, W.S. Koski, Inorg. Chem. 1 (1962) 109.
[29] N. Al Obaidi, M. Chaudhury, D. Clague, C.J. Jones, J.C. Pearson, J.A. McCleverty, S.S. Salam, J. Chem. Soc., Dalton Trans. (1987) 1733.
[30] L. Pause, M. Robert, J.-M. Savéant, J. Am. Chem. Soc. 122 (2000) 9829.
[31] L. Pause, M. Robert, J.-M. Savéant, J. Am. Chem. Soc. 123 (2001) 11908.
[32] C.J. Jones, J.A. McCleverty, B.D. Neaves, S.J. Reynolds, H. Adams, N.A. Bailey, G. Denti, J. Chem. Soc., Dalton Trans. (1986) 733.
[33] J.A. McCleverty, D. Seddon, N.A. Bailey, N.W. 'Joe' Walker, J. Chem. Soc., Dalton Trans. (1976) 898.
[34] F.A. Cotton, J.G. Norman, J. Am. Chem. Soc. 94 (1972) 5697.
[35] J.A. McCleverty, A.E. Rae, I. Wolochowicz, N.A. Bailey, J.M.A. Smith, J. Chem. Soc., Dalton Trans. (1982) 429.
[36] P.K. Baker, A.I. Clark, M.M. Meehan, E.E. Parker, A.E. Underhill, M.G.B. Drew, M.C. Durrant, R.L. Richards, Trans. Met. Chem. 23 (1998) 155.
[37] C.G. Young, S. Thomas, R.W. Gable, Inorg. Chem. 37 (1998) 1299.
[38] J.A. McCleverty, A. Wlodarczyk, Polyhedron 7 (1988) 449.
[39] G.M. Sheldrick, SHELXL-97, Program for Crystal Structure Refinement, University of Göttingen, 1997.

Available online at www.sciencedirect.com
ScienceDirect
Polyhedron 27 (2008) 797–804
POLYHEDRON
www.elsevier.com/locate/poly

Novel dioxorhenium complex with bis(3,5-dimethypyrazol-1-yl)methane ligand – Synthesis, spectroscopic characterization, X-ray structure and DFT calculations

B. Machura [a,*], R. Kruszynski [b], R. Penczek [c], J. Mroziński [d], J. Kusz [e]

[a] Department of Crystallography, Institute of Chemistry, University of Silesia, 9th Szkolna Street, 40-006 Katowice, Poland
[b] Department of X-ray Crystallography and Crystal Chemistry, Institute of General and Ecological Chemistry, Lodz University of Technology, 116 Żeromski Street, 90-924 Łódź, Poland
[c] Department of Inorganic and Coordination Chemistry, Institute of Chemistry, University of Silesia, 9th Szkolna Street, 40-006 Katowice, Poland
[d] Faculty of Chemistry, Wroclaw University, F. Joliot-Curie 14 Street, 50-383 Wrocław, Poland
[e] Institute of Physics, University of Silesia, 4th Uniwersytecka Street, 40-006 Katowice, Poland

Received 21 August 2007; accepted 12 November 2007

Abstract

The reactions of $[ReOBr_3(PPh_3)_2]$ and $[ReOBr_3(AsPh_3)_2]$ with bis(3,5-dimethypyrazol-1-yl)methane (bdmpzm) have been examined and novel dioxorhenium(V) complex $[ReO_2(bdmpzm)_2]Br \cdot HBr \cdot 2H_2O$ has been obtained. The compound has been studied by IR, UV–Vis, ^1H NMR spectroscopy, magnetization measurements and X-ray crystallography. The electronic structure of the $[ReO_2(bdmpzm)_2]^+$ cation has been calculated with the density functional theory (DFT) method. The spin-allowed electronic transitions of $[ReO_2(bdmpzm)_2]^+$ have been calculated with the TDDFT/PCM method, and the UV–Vis spectrum of $[ReO_2(bdmpzm)_2]Br$ has been discussed on this basis.
© 2007 Elsevier Ltd. All rights reserved.

Keywords: Rhenium dioxo complexes; Bis(3,5-dimethypyrazol-1-yl)methane; X-ray and electronic structure; DFT and TDDFT calculations

1. Introduction

For many years, much attention has been focused on the synthesis and study of oxo transition metal complexes. Such compounds can transfer an oxygen atom to reductants such as phosphines, sulfides, and alkenes. Oxygen atom transfer chemistry has been implicated in various reactions of industrial and biological importance [1–3].

Especially interesting properties are observed for $[ReO_2L_4]^+$ complexes with pyridyl-type ligands. These compounds have attracted interest on account of both their electrochemical properties and their photophysical and photochemical reactivity characteristics [4,5].

Recently, related complexes have attracted attention in connection with the utilization of the ^{186}Re and ^{188}Re nuclides for therapeutic purposes in radiopharmacy [6,7]. Consequently, the inorganic chemistry studies with the naturally occurring non-radioactive rhenium isotopes are very attractive in order to clearly establish the molecular structure of ^{99m}Tc- and $^{186/188}Re$-based radiopharmaceuticals. In this context, the design, synthesis and reactivity of the rhenium oxocomplexes has become the aim of several laboratories, including ours.

This work forms part of a program on the synthesis and characterization of new families of oxorhenium compounds with N-donor ligands. In this report we focus on the examinations of the reactions of $[ReOBr_3(AsPh_3)_2]$

* Corresponding author.
E-mail addresses: basia@ich.us.edu.pl (B. Machura), rafal.kruszynski@p.lodz.pl (R. Kruszynski), jmroz@wchuwr.chem.uni.wroc.pl (J. Mroziński).

0277-5387/$ - see front matter © 2007 Elsevier Ltd. All rights reserved.
doi:10.1016/j.poly.2007.11.013

and $[ReOBr_3(PPh_3)_2]$ with bis(3,5-dimethypyrazol-1-yl) methane (bdmpzm).

Bis(pyrazol-1-yl)alkane and its derivatives constitute a family of stable and flexible bidentate ligands, isoelectronic and isosteric with the well-known bis(pyrazolyl)borates. The coordination properties of bis(pyrazol-1-yl)alkanes may be varied in a rather wide range by introducing substituents into the pyrazole rings. Hence, the donor ability of the ligands is determined by the presence of electron-withdrawing or electron-donating functional groups, and steric factors altered by the introduction of bulky alkyl groups into the rings and the alkane bridge between them [8].

These molecules form a variety of coordination compounds with main group and transition metals [9–14], but the rhenium complexes with these ligands have been studied relatively little [15–18].

Here we present synthesis, spectroscopic data and crystal, molecular and electronic structures of $[ReO_2(bdmpzm)_2]Br \cdot HBr \cdot 2H_2O$. The electronic structure of the $[ReO_2(bdmpzm)_2]^+$ cation has been calculated with the density functional theory (DFT) method. The UV–Vis spectrum of the $[ReO_2(bdmpzm)_2]Br$ has been discussed on the basis of time-dependent DFT (TDDFT) calculations.

Recently, some theoretical investigations have been carried out on rhenium compounds. The electronic structures of nitrido, oxo, carbonyl, nitrosyl and nitrile rhenium complexes, as well as their spectroscopic properties, bonding and reactivity have been theoretically studied at the HF, MP2, EHT and DFT levels of theory using various basis sets [19–27]. Gancheff et al. [21] have performed extended tests of the ability of the B3LYP method in LANL2DZ basis set for rhenium compounds in a geometry optimization and calculation of spectral properties. Although this is not a very extended basis set, its use with DFT has shown to be sufficient for the geometry optimization and calculation of spectral properties. It gives good agreement with the experimental data and its use is justified in the case of large molecules.

2. Experimental

2.1. General procedure

All the reagents used to the synthesis were commercially available and were used without further purification. The $[ReOBr_3(PPh_3)_2]$ and $[ReOBr_3(AsPh_3)_2]$ complexes were prepared as reported previously [28], and bis(3,5-dimethypyrazol-1-yl)methane was synthesized according to the modified literature method [29].

IR spectrum was recorded on a Nicolet Magna 560 spectrophotometer in the spectral range 4000–400 cm^{-1} with the samples in the form of KBr pellets. Electronic spectrum was measured on a spectrophotometer Lab Alliance UV–Vis 8500 in the range 1000–200 nm in dichloromethane solution. The ^1H NMR spectrum was recorded with a Bruker AM 400 spectrometer at room temperature using DMSO-d_6 as a solvent. Elemental analyses (C H N) were performed on a Perkin–Elmer CHN-2400 Analyzer.

2.2. Preparation of $[ReO_2(bdmpzm)_2]Br \cdot HBr \cdot 2H_2O$

$[ReOBr_3(PPh_3)_2]$ (0.5 g, 0.52 mmol) and bdmpzm (0.25 g, 1.22 mmol) were refluxed in ethanol (80 ml) for 5 h. The orange–brown solution was cooled and left to slow evaporation. The orange–brown crystals that formed were filtered and recrystallized from slow evaporation of an acetonitrile solution. Yield 60%.

IR (KBr, cm^{-1}) 3454 (m), 3423 (m), 3190 (m), 3118 (m) 3076 (m) 2993 (w), 1643 (w) 1557 (s) 1468 (s) 1425 (s), 1385 (s), 1373 (s), 1276 (s), 1228 (w), 1060 (s), 845 (s) 741 (w), 725 (w), 686 (s), 661 (w), 625 (w), 557 (w), 507 (w).

Anal. Calc. for $C_{22}H_{37}Br_2N_8O_4Re$: C, 32.08; H, 4.53; N, 13.61. Found: C, 32.25; H, 4.50; N, 13.43%.

^1H NMR (400 MHz, DMSO): $\delta = 2.30$ (s, 12H, $-CH_3$), 2.63 (s, 12H, $-CH_3$), 6.37 (s, 4H, $-CH_2-$), 6.58 (s, 1H, H^aC), 6.60 (s, 1H, H^bC), 7.60 (s, 1H, H^cC), 7.64 (s, 1H, H^dC).

2.3. Crystal structures determination and refinement

An orange–brown crystal of $[ReO_2(bdmpzm)_2]Br \cdot HBr \cdot 2H_2O$ was mounted on a KM-4-CCD automatic diffractometer equipped with a CCD detector, and used for data collection. X-ray intensity data were collected with graphite-monochromated Mo Kα radiation ($\lambda = 0.71073$ Å) at temperature of 293(2) K. Details concerning crystal data and refinement are given in Table 1. Lorentz, polarization and empirical absorption correction using spherical harmonics implemented in SCALE3 ABSPACK scaling algorithm [30] were applied. The structure was solved by the Patterson method and subsequently completed by the difference Fourier recycling. All the non-hydrogen atoms were refined anisotropically using full-matrix, least-squares technique. All the hydrogen atoms were found from difference Fourier synthesis after four cycles of anisotropic refinement, and refined as "riding" on the adjacent carbon atom with individual isotropic temperature factor equal 1.2 times the value of equivalent temperature factor of the endocyclic parent atom and equal 1.5 times the value of equivalent temperature factor of the methyl parent carbon atom. During refinement the methyl groups were allowed to rotate about theirs local threefold axes. The HBr hydrogen atom is symmetry disordered over two positions. SHELXS97 [31], SHELXL97 [32] and SHELXTL [33] programs were used for all the calculations. Atomic scattering factors were those incorporated in the computer programs.

2.4. Magnetic measurements

Magnetic measurements in the temperature range 1.8–300 K were performed using a Quantum Design SQUID-

Table 1
Crystal data and structure refinement for $[ReO_2(bdmpzm)_2]Br \cdot HBr \cdot 2H_2O$

Empirical formula	$C_{22}H_{37}Br_2N_8O_4Re$
Formula weight	823.62
Temperature (K)	293(2)
Wavelength (Å)	0.71073
Crystal system	monoclinic
Space group	*C*2/*m*
Unit cell dimensions	
a (Å)	13.257(3)
b (Å)	17.387(4)
c (Å)	8.2880(17)
β (°)	127.73(3)
Volume (Å^3)	1510.9(8)
Z	2
D_{calc} (Mg/m^3)	1.810
Absorption coefficient (mm^{-1})	6.706
F(000)	804
Crystal size (mm)	0.14 × 0.14 × 0.30
θ Range for data collection (°)	3.11–25.00
Index ranges	$-15 \leqslant h \leqslant 15$, $-16 \leqslant k \leqslant 20$, $-9 \leqslant l \leqslant 9$
Reflections collected	4782
Independent reflections [R_{int}]	1367 [0.0219]
Completeness to 2*θ* (%)	99.6
Maximum and minimum transmission	0.421 and 0.283
Data/restraints/parameters	1367/0/93
Goodness-of-fit on F^2	1.046
Final *R* indices [$I > 2\sigma(I)$]	$R_1 = 0.0148$, $wR_2 = 0.0382$
R indices (all data)	$R_1 = 0.0148$, $wR_2 = 0.0382$
Largest difference in peak and hole (e Å^{-3})	0.422 and −0.755

based MPMSXL-5-type magnetometer. The SQUID magnetometer was calibrated with the palladium rod sample (Materials Research Corporation, measured purity 99.9985%). The superconducting magnet was generally operated at a filed strength ranging from 0 to 5 T. Measurements were made at a magnetic field of 0.5 T.

Corrections are based on subtracting the sample – holder signal and contribution χ_D estimated from the Pascal constants [34] and equal -408×10^{-6} cm^3 mol^{-1} for complex $[ReO_2(bdmpzm)_2]Br \cdot HBr \cdot 2H_2O$. The effective magnetic moment was calculated from equation, $\mu_{eff} = 2.83\ (\chi_M T)^{1/2}$ (B.M.).

2.5. Computational details

The gas phase geometry of $[ReO_2(bdmpzm)_2]^+$ was optimized without any symmetry restrictions in the singlet ground-state using the hybrid B3LYP functional of GAUSSIAN-03 [35–37]. The LANL2DZ with additional *d* function with exponent $\alpha = 0.3811$ and *f* function with exponent $\alpha = 2.033$ ECP basis set [38,39] was chosen for the rhenium atom and the standard 6-31G basis set for all the other atoms. For oxygen and nitrogen atoms, diffuse and polarization functions were added [40,41]. The vibrational spectrum was calculated starting from the ground-state geometry optimized in the gas phase. All vibrations were real thus the geometry structure was a true energy minimum. TDDFT/PCM [42] calculations were employed to produce a number (90) of singlet excited-states starting from the ground-state geometry optimized in the gas phase.

3. Results and discussion

3.1. Preparation

Previously, we investigated the reactions of bis(pyrazol-1-yl)methane with $[ReOCl_3(AsPh_3)(OAsPh_3)]$ and $[ReOCl_3(PPh_3)_2]$ in acetone at ambient temperature. In both cases, only neutral turquoise blue $[ReOCl_3(bpzm)]$ complex has been precipitated from the reaction system [18]. The same compound was obtained in the reaction of $[ReOCl_3(PPh_3)_2]$ with bpzm under reflux in THF [17] and in the reaction of $[NBu_4][ReOCl_4]$ with bpzm [16]. Dilworth and co-workers reported also the formation of dimeric $[Re_2O_3Cl_4(bpzm)_2]$ species. The last one was formed slowly on standing the acetonitrile solution of $[ReOCl_3(bpzm)]$ in air [17].

A different course of the reaction is observed for bis(3,5-dimethypyrazol-1-yl)methane with $[ReOBr_3(PPh_3)_2]$ or $[ReOBr_3(AsPh_3)_2]$. The reactions of $[ReOBr_3(PPh_3)_2]$ or $[ReOBr_3(AsPh_3)_2]$ with bdmpzm were carried out in various conditions: at room temperature, under reflux, in acetone, acetonitrile or ethanol. In all the experiments, the orange–brown crystals of $[ReO_2(bdmpzm)_2]Br \cdot HBr \cdot 2H_2O$ complex were formed after a few days from the reaction solutions. Refluxing of $[ReOBr_3(PPh_3)_2]$ with an excess of bis(3,5-dimethypyrazol-1-yl)methane (bdmpzm) in ethanol allows to obtain the title complex with the highest yield. Polar solvents favour the high lability of the bromo and phosphine ligands of the starting material [43].

The new complex has been characterized by IR, UV–Vis and ^{1}H NMR spectroscopy, elemental analysis, magnetic studies and X-ray crystallography, and its formulation $[ReO_2(bdmpzm)_2]Br \cdot HBr \cdot 2H_2O$ is in good accordance with these results.

3.2. IR spectroscopy

The IR spectrum of the title complex displays a single O=Re=O asymmetrical stretching mode at 845 cm^{-1}, consistent with a *trans*-dioxo geometry and within the range accepted for dioxorhenium complexes with pyridyl-type ligands [4]. The characteristic band corresponding to the *ν*(CN), *ν*(C=C) mode of the bdmpzm ligand appears at 1557 cm^{-1} [44].

3.3. ^{1}H NMR spectroscopy

The methyl groups of two bdmpzm ligands appear as two singlets at, respectively, 2.30 and 2.63 ppm. Four singlets corresponding to the pyrazolyl CH protons appear at, respectively, 6.60, 6.58, 7.64 and 7.60 ppm. The singlet at 6.37 ppm is assigned to the protons of the methylene bridge of bdmpzm ligands. Lack of paramagnetic broadening or

shifts of resonances in the ^{1}H NMR spectrum of the title complex confirms its diamagnetism.

3.4. Magnetic properties

Magnetic data of the rhenium complex in the range 1.8–300 K indicated diamagnetism typical for the sample with $5d^2$ electron configuration of the rhenium(V) centers. Relation of the gram magnetic susceptibility in the whole range of measuring temperature characterized the complex as high purity. Also the relation of the magnetization of the sample at 2 K strongly supports this suggestion (0.02 B.M. at $H = 5$ T) (Fig. 2).

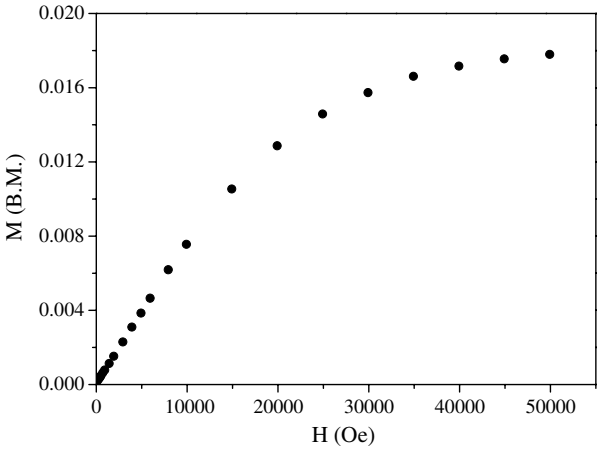


Fig. 2. Field dependence of the magnetization for complex $[ReO_2(bdmpzm)_2]Br \cdot HBr \cdot 2H_2O$ at 2 K.

3.5. Crystal structure

The compound $[ReO_2(bdmpzm)_2]Br$ (Fig. 1) has been obtained in crystalline form as a solvate with two H_2O and one HBr molecules per Re-containing cation. The Br^- ions and HBr molecules occupy alternatively the same crystallographic position. The rhenium atom occupies the special position *a* of *C*2/*m* space group with site symmetry 2/*m* and site multiplicity 2. In consequence the complex cation $[ReO_2(bdmpzm)_2]^+$ occupy four asymmetric units and the O(1)–Re(1)–O(1)#1, N(2)–Re(1)–N(2)#1 and N(2)#2–Re(1)–N(2)#3 bonds angles (symmetry operators used to generate equivalent atoms: #1 $-x$, $-y$, $-z$; #2 x, $-y$, z; #3 $-x$, y, $-z$) are linear by symmetry. The Br(1), C(6), O(1), O(99) atoms also occupy special positions *h* (Br atom) and *i* (C, O atoms) with site symmetry, respectively, 2 and *m* and multiplicity 4. The molecules are linked *via* one medium strength O(99)—H(99P) $\cdots$ Br(1) (D $\cdots$ A distance 3.276(3) Å and D–H $\cdots$ A angle 168.8) and 1 weak C(2)–H(2) $\cdots$ Br(1)#($1/2 - x$, $1/2 - y$, $1 - z$) (D $\cdots$ A distance 3.785(3) Å and D–H $\cdots$ A angle 156.5°) intermolecular hydrogen bonds to the double chain along crystallographic *b*-axis. The weak intramolecular hydrogen bond linking C(6)–H(6A) $\cdots$ O1(1) atoms (D $\cdots$ A distance 2.956(4) Å and D–H $\cdots$ A angle 124.2) provides additional stabilization to the molecule of title compound [45,46]. The crystallographic data for $[ReO_2(bdmpzm)_2]Br \cdot HBr \cdot 2H_2O$ are given in Table 1, and molecular structure of the $[ReO_2(bdmpzm)_2]Br$ complex is presented in Fig. 1. The dioxo complex shows approximately octahedral coordination geometry with the oxo ligands in the axial positions. The equatorial plane of the Re center is occupied by two bidentate bdmpzm molecules. Upon coordination of bis(3,5-dimethypyrazol-1-yl)methane to the rhenium, a

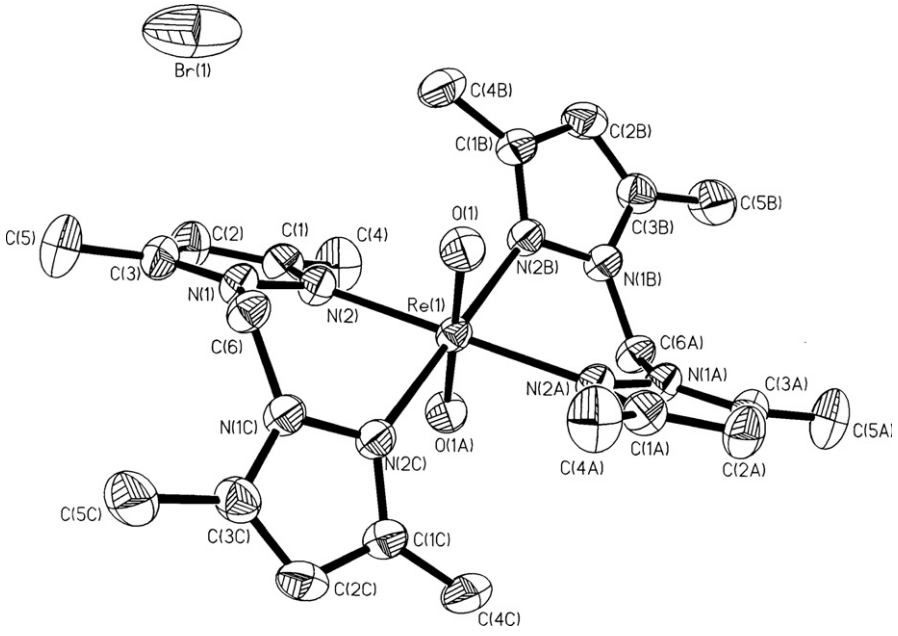


Fig. 1. The molecular structure of $[ReO_2(bdmpzm)_2]Br$.

Table 2
The experimental and optimized bond lengths (Å) and angles (°) for $[ReO_2(bdmpzm)_2]^+$

Bond lengths	Experimental	Optimized	Bond angles	Experimental	Optimized
Re(1)–O(1)	1.779(2)	1.770	O(1)#1–Re(1)–O(1)	180.00(15)	180
Re(1)–N(2)	2.1221(19)	2.169	O(1)–Re(1)–N(2)	91.77(8)	90.46
			O(1)–Re(1)–N(2)#1	88.23(8)	89.54
			N(2)#1–Re(1)–N(2)	180.00(13)	180
			N(2)–Re(1)–N(2)#2	95.91(10)	97.79
			N(2)–Re(1)–N(2)#3	84.09(10)	82.20
			N(2)#2–Re(1)–N(2)#3	180.00(7)	180

Symmetry transformations used to generate equivalent atoms: #1 $-x, -y, -z$; #2 $x, -y, z$; #3 $-x, y, -z$.

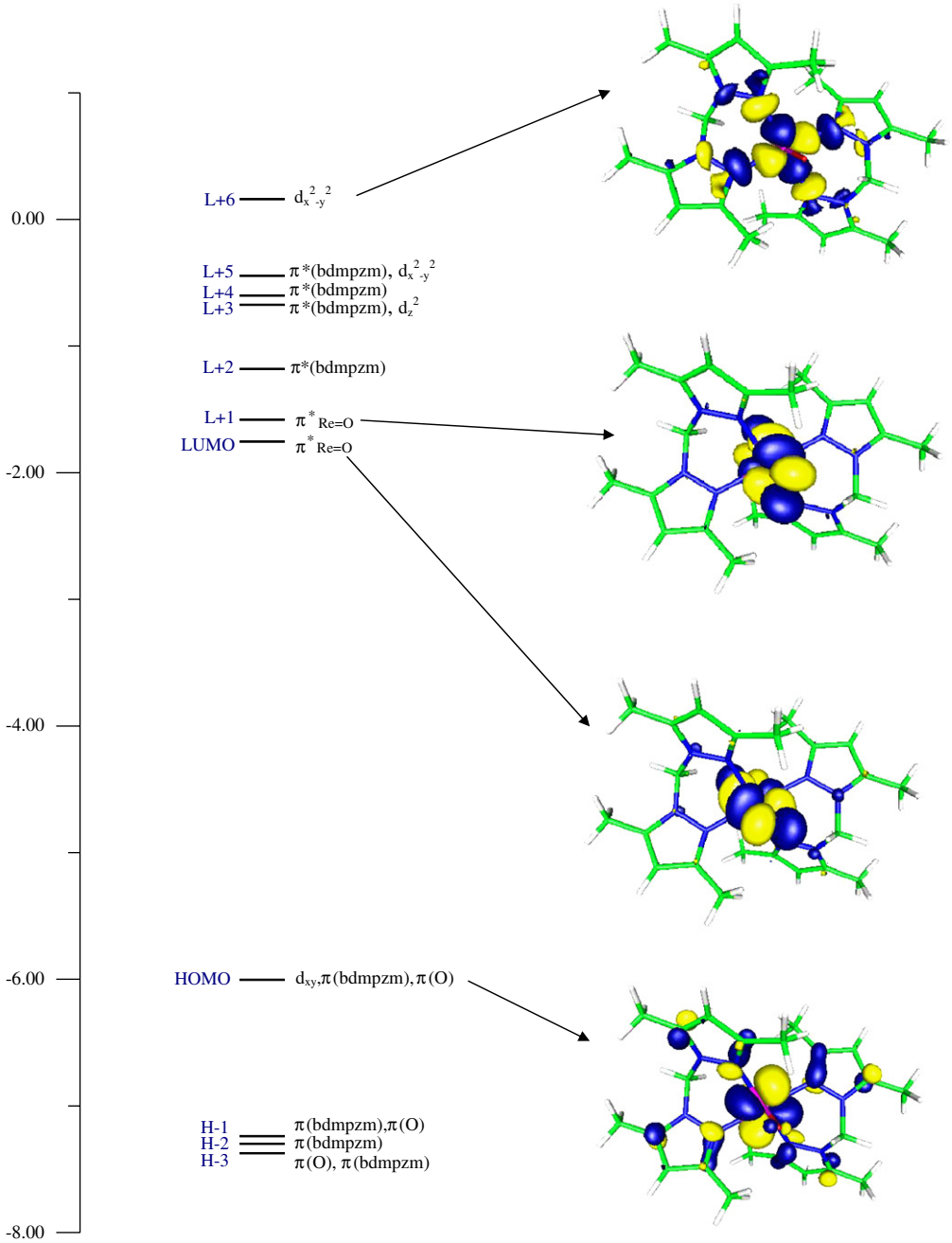


Fig. 3. The energy (eV), character and some contours of the occupied molecular orbitals of the $[ReO_2(bdmpzm)_2]^+$ cation. Positive values of the orbital contour are represented in yellow (0.04 a.u.) and negative values – in blue (−0.04 a.u.). (For interpretation of the references to colour in this figure legend, the reader is referred to see the web version of this article.)

six-membered cycle (made by the four nitrogen atoms, the rhenium atom and the carbon atom) is formed, and the formed ring shows a *boat* conformation with the rhenium and the carbon atoms off the plane defined by the four nitrogen atoms (deviations of 0.809(4) and 0.632(4) Å, respectively, from symmetry planar N_4 moiety). The flapping ReN_2 and CN_2 triangles are inclined to N_4 plane at 30.9(1)° and 49.9(3)°, respectively. The planar in the range of experimental error pyrazole rings are inclined at 63.13(9)°.

The selected bond lengths and angles of the $[ReO_2(bdmpzm)_2]^+$ cation are given in Table 2. The Re–O bond length (1.779(2) Å) falls in the range typical of mononuclear complexes of rhenium(V) having $[ReO_2]^+$ core, but it is one of the longest [47,48].

The Re–N distance, equal 2.1221(19) Å, is also similar to those found in complexes with other N-heterocycles. For $[ReO_2(2\text{-MeImH})_4]^+$, $[ReO_2(py)_4]^+$ and $[ReO_2(en)_2]^+$ cations, average rhenium-oxo distances are 1.766, 1.764 and 1.765 Å, and average Re–N bond lengths are 2.121, 2.148 and 2.162 Å, respectively [5].

3.6. Geometry optimization

The gas phase geometry of $[ReO_2(bdmpzm)_2]^+$ cation was optimized in a singlet state by the DFT method with the hybrid B3LYP functional. The optimized geometric parameters of $[ReO_2(bdmpzm)_2]^+$ are gathered in Table 2. In general, the predicted bond lengths and angles are in agreement with the values based upon the X-ray crystal structure data, and the general trends observed in the experimental data are well reproduced in the calculations.

3.7. Electronic structure

The molecular orbital diagram of the $[ReO_2(bdmpzm)_2]^+$ cation with several highest HOMO and lowest LUMO contours is presented in Fig. 3. The HOMO–LUMO gap equals to 4.25 eV. The highest occupied MO of $[ReO_2(bdmpzm)_2]^+$ is predominantly of d_{xy} type with some contributions from bdmpzm orbitals and p_π oxygen orbitals. The remaining four d-type orbitals of rhenium are found among unoccupied MOs. It confirms d^2 configuration of the rhenium atom.

The rhenium atom uses its six valence orbitals, $5d_{x^2-y^2}$, $5d_{z^2}$, 6s, $6p_x$, $6p_y$ and $6p_z$ to form σ-bonds with the six ligands, empty $5d_{xz}$ and $5d_{yz}$ orbitals are available to overlap with $2p_x$ and $2p_y$ orbitals on the oxygen atoms to form two double bonds in the $[O{=}Re{=}O]^+$ core. The LUMO and LUMO+1 orbitals can be ascribed as π-antibonding rhenium–oxygen interactions (Fig. 3).

3.8. Electronic spectrum

The experimental and calculated electronic spectrum of $[ReO_2(bdmpzm)_2]Br$ are presented in Fig. 4. Each calculated transition is represented by a gaussian function

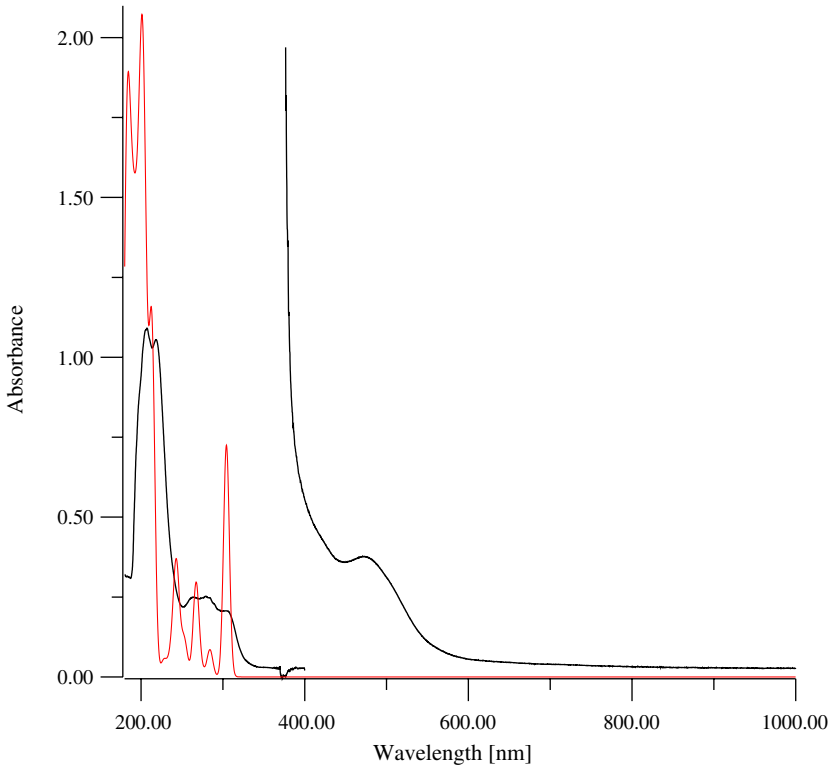


Fig. 4. The experimental (black) and calculated (red) electronic absorption spectrum of $[ReO_2(bdmpzm)_2]Br$. (For interpretation of the references to colour in this figure legend, the reader is referred to see the web version of this article.

Table 3
The energy and molar absorption coefficients of experimental absorption bands and the electronic transitions calculated with the TDDFT method for $[ReO_2(bdmpzm)_2]^+$

The most important orbital excitations	Character	λ (nm)	E (eV)	f	Experimental Λ (nm) (E (eV)) ε
					478.7 (2.59) 140
H → L + 2	d → π*(bdmpzm)	304.3	4.07	*01812*	305.5 (4.06) 5 370
H − 9 → L	π(O)/π(bdmpzm) → d	284.2	4.36	*0.0211*	283.6 (4.37) 6 460
H − 8 → L					
H → L + 4	d → π*(bdmpzm)	267.2	4.64	*0.0730*	
H − 4 → L	π(O)/π(bdmpzm) → d	252.6	4.91	*0.0261*	
H − 4 → L + 1	π (O)/π(bdmpzm) → d	244.0	5.08	*0.0485*	262.0 (4.73) 6 450
H − 9 → L	π(O)/π(bdmpzm) → d	241.7	5.13	*0.0453*	
H − 5 → L + 2	π(bdmpzm) → π*(bdmpzm)	215.1	5.76	*0.0403*	218.5 (5.67) 27 450
H − 7 → L + 2	π(bdmpzm) → π*(bdmpzm)	212.8	5.82	*0.2246*	
H − 2 → L + 3	π(bdmpzm) → π*(bdmpzm)	205.4	6.04	*0.0604*	
H − 1 → L + 4	π(bdmpzm) → π*(bdmpzm)	204.3	6.07	*0.1190*	
H − 6 → L + 5	π(O)/π(bdmpzm) → π*(bdmpzm)	202.7	6.12	*0.1026*	
H − 8 → L + 3	π(O)/π(bdmpzm) → π*(bdmpzm)	201.1	6.17	*0.0839*	208.3 (5.95) 28 250
H − 11 → L + 2	π(bdmpzm)/π(O) → π*(bdmpzm)	199.7	6.21	*0.1228*	
H − 5 → L + 4	π(bdmpzm) → π*(bdmpzm)	197.3	6.28	*0.1010*	
H − 7 → L + 4	π(bdmpzm) → π*(bdmpzm)	192.7	6.43	*0.1782*	
H − 10 → L + 3	π(bdmpzm) → π*(bdmpzm)	187.3	6.62	*0.1896*	

ε: molar absorption coefficient ($dm^3\ mol^{-1}\ cm^{-1}$); f: oscillator strength; H: highest occupied molecular orbital; L: lowest unoccupied molecular orbital.

$y = ce^{-bx^2}$ with the height (c) equal to the oscillator strength and b equal to 0.04 nm^{-2}.

The spin-allowed singlet–singlet electronic transitions calculated with the TDDFT method for $[ReO_2(bdmpzm)_2]^+$ are gathered in Table 3. For the high energy part of the spectrum, only transitions with oscillator strengths larger than 0.020 are listed in Table 3.

The lowest energy electronic transition in the *trans*-dioxo complex (at 478.7 nm) corresponds to $d_{xy} \rightarrow d_{xz/yz}$ orbital excitation and occurs between the $^1A_{1g}$ ground-state and the ^3E_g leading to a spin-forbidden d–d band. The spin-forbidden d–d bands are often observed in the absorption spectra of many dioxo Re(V) complexes, and they indicate that the structural deviations from the expected D_{4h} symmetry have only a minor effect on the energy of electronic states and on the spectra [5].

The intense absorption bands at 305.5, 283.6 and 262.0 nm are assigned to the *Metal–Ligand Charge Transfer* (occurring from the rhenium ion to the π-antibonding orbitals of the bdmpzm ligands) and *Ligand–Metal Charge Transfer* ($\pi_{bdmpzm}/\pi_O \rightarrow d$) transitions. In the experimental spectrum the intensities of the abovementioned bands are very similar, whereas the oscillator strength of the calculated band at 304.4 nm is significantly higher in comparison with the oscillator strengths of the other bands calculated in the region 320–240. These differences between experimental and calculated spectrum can be assigned to intensity borrowing effect or may come from the basis sets which are approximated to a certain extent.

The highest energy experimental absorption bands of $[ReO_2(bdmpzm)_2]Br$ at 218.5 and 208.3 nm result from *Ligand–Ligand Charge Transfer* and interligand (IL) transitions.

4. Supplementary material

CCDC 658076 contains the supplementary crystallographic data for $C_{22}H_{37}Br_2N_8O_4Re$. These data can be obtained free of charge via http://www.ccdc.cam.ac.uk/conts/retrieving.html, or from the Cambridge Crystallographic Data Center, 12 Union Road, Cambridge CB2. 1EZ, UK; fax: (+44) 1223-336-033; or e-mail: deposit@ccdc.cam.ac.uk.

Acknowledgement

The GAUSSIAN-03 calculations were carried out in the Wrocław Centre for Networking and Supercomputing, WCSS, Wrocław, Poland.

References

[1] R.H. Holm, Chem. Rev. 87 (1987) 1401.
[2] C.C. Romão, F.E. Kühn, W.A. Hermann, Chem. Rev. 97 (1997) 3197.
[3] S.B. Seymore, S.N. Brown, Inorg. Chem. 39 (2000) 325.
[4] S. Bélanger, A.L. Beauchamp, Inorg. Chem. 35 (1996) 7836.
[5] C. Savoie, Ch. Reber, Coord. Chem. Rev. 171 (1998) 387.
[6] J.R. Dilworth, S.J. Parrott, Chem. Soc. Rev. 27 (1998) 43.
[7] P. Blower, Dalton Trans. (2006) 1705.
[8] C. Pettinari, R. Pettinari, Coord. Chem. Rev. 249 (2005) 663.
[9] L.-F. Tang, Z.-H. Wang, W.-L. Jia, Y.-M. Xu, J.T. Wang, Polyhedron 19 (2000) 381.
[10] E. Teuma, M. Loy, C. Le Berre, M. Etienne, J.C. Daran, P. Kalck, Organometallics 22 (2003) 5261.
[11] K.A. Van Langenberg, B. Moubaraki, K.S. Murray, E.R.T. Tiekink, Z. Kristallogr, New Cryst. Struct. 218 (2003) 345.
[12] J. Ruiz, V. Rodriguez, C. De Haro, J. Perez, G. Lopez, Inorg. Chim. Acta 357 (2004) 2331.

[13] J. Ruiz, N. Cutillas, C. Vincente, M.D. Villa, G. Lopez, J. Lorenzo, F.X. Aviles, V. Moreno, D. Bautista, Inorg. Chem. 44 (2005) 7365.
[14] A.S. Potapov, A.I. Khlebnikov, Polyhedron 25 (2006) 2683.
[15] D.L. Reger, J.R. Gardinier, P.J. Pellechia, M.D. Smith, K.J. Brown, Inorg. Chem. 42 (2003) 7635.
[16] M. Porchia, G. Papini, C. Santini, G.G. Lobia, M. Pellei, F. Tisato, G. Bandoli, A. Dolmella, Inorg. Chem. 44 (2005) 4045.
[17] A.R. Cowley, J.R. Dilworth, M. Salichou, Dalton Trans. (2007) 1621.
[18] B. Machura, R. Penczek, R. Kruszynski, J. Kusz, Polyhedron 26 (2007) 2581.
[19] A. Voigt, U. Abram, R. Böttcher, U. Richter, J. Reinhold, R. Kirmse, Chem. Phys. 253 (2000) 171.
[20] M. Lipowska, L. Hansen, R. Cini, X. Xu, H. Choi, A.T. Taylor, L.G. Marzilli, Inorg. Chim. Acta 339 (2002) 327.
[21] J. Gancheff, C. Kremer, E. Kremer, O.N. Ventura, J. Mol. Struct. (Theochem.) 580 (2002) 107.
[22] M.L. Kuznestov, E.A. Klestova-Nadeeva, A.I. Dement'ev, J. Mol. Struct. (Theochem.) 671 (2004) 229.
[23] N. Psaroudakis, K. Mertis, D.G. Liakos, E.D. Simandiras, Chem. Phys. Lett. 369 (2003) 490.
[24] X.-Y. Liu, S. Bouherour, H. Jacobsen, H.W. Schmalle, H. Berke, Inorg. Chim. Acta 330 (2002) 250.
[25] É. Bencze, J. Mink, I. Pápai, I.S. Butler, D. Lafleur, D.F.R. Gilson, J. Organomet. Chem. 616 (2000) 1.
[26] W.-Y. Wong, S.-H. Cheung, X. Huang, Z. Lin, J. Organomet. Chem. 655 (2002) 39.
[27] B. Machura, R. Kruszynski, Polyhedron 25 (2006) 1985.
[28] G. Rouschias, G. Wilkinson, J. Chem. Soc. A (1966) 465.
[29] S. Julia, P. Sala, J. del Mazo, M. Sancho, C. Ochoa, J. Elguero, J.P. Fayet, M.C. Vertut, J. Heterocyclic Chem. 19 (1982) 1141.
[30] CrysAlis RED, Oxford Diffraction Ltd., Version 1.171.29.2.
[31] G.M. Sheldrick, Acta Crystallogr. A46 (1990) 467.
[32] G.M. Sheldrick, SHELXL97. Program for the Solution and Refinement of Crystal Structures, University of Göottingen, Germany, 1997.
[33] G.M. Sheldrick, SHELXTL: Release 4.1 for Siemens Crystallographic Research Systems, 1990.
[34] E. König, Magnetic Properties of Coordination and Organometallic Transition Metal Compounds, Springer-Verlag, Berlin, 1966.
[35] GAUSSIAN-03, Revision B.03, M.J. Frisch, G.W. Trucks, H.B. Schlegel, G.E. Scuseria, M.A. Robb, J.R. Cheeseman, J.A. Montgomery, Jr., T. Vreven, K.N. Kudin, J.C. Burant, J.M. Millam, S.S. Iyengar, J. Tomasi, V. Barone, B. Mennucci, M. Cossi, G. Scalmani, N. Rega, G.A. Petersson, H. Nakatsuji, M. Hada, M. Ehara, K. Toyota, R. Fukuda, J. Hasegawa, M. Ishida, T. Nakajima, Y. Honda, O. Kitao, H. Nakai, M. Klene, X. Li, J.E. Knox, H.P. Hratchian, J.B. Cross, C. Adamo, J. Jaramillo, R. Gomperts, R.E. Stratmann, O. Yazyev, A.J. Austin, R. Cammi, C. Pomelli, J.W. Ochterski, P.Y. Ayala, K. Morokuma, G.A. Voth, P. Salvador, J.J. Dannenberg, V.G. Zakrzewski, S. Dapprich, A.D. Daniels, M.C. Strain, O. Farkas, D.K. Malick, A.D. Rabuck, K. Raghavachari, J.B. Foresman, J.V. Ortiz, Q. Cui, A.G. Baboul, S. Clifford, J. Cioslowski, B.B. Stefanov, G. Liu, A. Liashenko, P. Piskorz, I. Komaromi, R.L. Martin, D.J. Fox, T. Keith, M.A. Al-Laham, C.Y. Peng, A. Nanayakkara, M. Challacombe, P.M.W. Gill, B. Johnso, W. Chen, M.W. Wong, C. Gonzalez, J.A. Pople, Gaussian Inc., Pittsburg PA, 2003.
[36] A.D. Becke, J. Chem. Phys. 98 (1993) 5648.
[37] C. Lee, W. Yang, R.G. Parr, Phys. Rev. B 37 (1988) 785.
[38] P.J. Hay, W.R. Wadt, J. Chem. Phys. 82 (1985) 299.
[39] K. Eichkorn, F. Weigend, O. Treutler, R. Ahlrichs, Theor. Chem. Acc. 97 (1997) 119.
[40] P.C. Hariharan, J.A. Pople, Theo. Chim. Acta 28 (1973) 213.
[41] V.A. Rassolov, M.A. Ratner, J.A. Pople, P.C. Redfern, L.A. Curtiss, J. Comp. Chem. 22 (2001) 976.
[42] M.E. Casida, in: J.M. Seminario (Ed.), Recent Developments and Applications in Modern Density Functional Theory, Theoretical and Computational Chemistry, vol. 4, Elsevier, Amsterdam, 1996.
[43] O. Knoesen, H. Görls, S. Lotz, J. Organomet. Chem. 598 (2000) 108.
[44] K. Nakamoto, Infrared and Raman Spectra of Inorganic and Coordination Compounds, 4th ed., Wiley Interscience, New York, 1986.
[45] G.A. Jeffrey, W. Saenger, Hydrogen Bonding in Biological Structures, Springer-Verlag, 1994.
[46] G.R. Desiraju, T. Steiner, The Weak Hydrogen Bond in Structural Chemistry and Biology, Oxford University Press, 1999.
[47] J.M. Mayer, Inorg. Chem. 27 (1988) 3899.
[48] K.R. Reddy, A. Domingos, A. Paulo, I. Santos, Inorg. Chem. 38 (1999) 4278.

Available online at www.sciencedirect.com
ScienceDirect
Polyhedron 27 (2008) 805–811
POLYHEDRON
www.elsevier.com/locate/poly

Synthesis, structure, thermal studies on Zn(II), Cd(II) complexes of N-(2-pyridylmethyl)pyridine-2-carbaldimine and N-(2-pyridylmethyl)pyridine-2-methylketimine

Sumanta Kumar Padhi, Rojalin Sahu, Vadivelu Manivannan *

Department of Chemistry, Indian Institute of Technology Guwahati, Guwahati 781 039, Assam, India

Received 22 September 2007; accepted 12 November 2007
Available online 27 December 2007

Abstract

The bivalent zinc and cadmium complexes of two Schiff bases N-(2-pyridylmethyl)pyridine-2-carbaldimine (**L1**), N-(2-pyridylmethyl)pyridine-2-methylketimine (**L2**), tridentate ligands with an N_3 chromophore and coordinating with two five-membered chelate rings, were synthesized. Complexes $[Zn(\mathbf{L1})(NO_3)_2]$ (**1**), $[Zn(\mathbf{L2})(NO_3)_2]$ (**2**), $[Cd(\mathbf{L1})(NO_3)_2(H_2O)]$ (**3**) and $[Cd(\mathbf{L2})(NO_3)_2(CH_3OH)]$ (**4**) were characterized by X-ray crystallography. In **1** and **2**, Zn(II) has a distorted square-pyramidal geometry where as in **3** and **4**, Cd(II) possesses a pseudo-pentagonal-bipyramidal geometry. The following trends in the bond lengths are observed: $M–N_{im} < M–N_{py}$; Zn–N > Zn–O; Cd–N < Cd–O. The final residues from the thermogravimetric analysis are ZnO and CdO, the SEM studies revealed, respectively, their porous and spherical natures. The average activation energy (E) for the loss of pyridine rings obtained from the Friedman fitting of the DSC data, for **1**, **2**, **3**, and **4** are 193.8(2), 114.5(3), 127.1(4), and 63.7(3) kJ mol^{-1} and their logarithmic pre-exponential factor (A) are 11.22, 5.31, 6.88, and 2.09, respectively.
© 2007 Elsevier Ltd. All rights reserved.

Keywords: Schiff base; Crystal structure; Thermogravimetry; SEM; Thermokinetics

1. Introduction

Self-assembly of coordination compounds to 1D, 2D, and 3D supramolecules is of much interest [1]. Use of $M(NO_3)_2$ fragment in developing supramolecularly assembled materials, which find application in storing small molecules or ions, as chemical sensors, and the use of the channels or cavities as templates for catalysis, is reviewed [1d]. The combination of nitrate anions and pyridyl donor ligands leads to a subtle balance of nitrate *versus* pyridyl coordination resulting in interesting anion effects. Complexes containing aromatic moieties usually exhibit interactions like π–π stacking, C–H···π, D–H···A, and these are important packing forces in the solid state.

Zinc and cadmium oxides have been the subject of intense interest due to their wide ranging applications [2,3]. Synthesis of nano-structured sheets, belts, rods, tubes and wires are being investigated [4]. The controlled growth of ZnO nanobelts exhibiting piezoelectric and ferroelectric properties is reviewed [5a]. One-dimensional ZnO and CdO nanobelts act as semiconductors, which are used for fabrication of field-effect transistors and gas sensors [5]. The preparations of ZnO and CdO nanostructures by thermolysis, their Raman and photoluminescence properties are also reported [5,6].

As a part of our research programme, we have been investigating the coordination chemistry of tridentate Schiff base ligands containing pyridine rings [7]. With Cu^{2+} salts, N-(2-pyridylmethyl)pyridine-2-carbaldimine (**L1**) and N-(2-pyridylmethyl)pyridine-2-methylketimine (**L2**) behave differently: **L1** is oxidized to bis(2-pyridylcarbonyl)amide (bpca), in which both the imine and the methylene groups

* Corresponding author. Tel.: +91 361 258 2306; fax: +91 361 258 2349.
E-mail address: mani@iitg.ernet.in (V. Manivannan).

0277-5387/$ - see front matter © 2007 Elsevier Ltd. All rights reserved.
doi:10.1016/j.poly.2007.11.011

are oxidized; **L2** is converted to 4′-(2-pyridyl)-2,2′:6′,2″-terpyridine, during which the methylene group is oxidized and the methylketimine function involving in a double condensation with 2-acetylpyridine [7a]. As continuation, the complexation behavior of **L1** and **L2** towards d^{10} systems *viz.* Zn(II) and Cd(II) were studied and the nature of the final oxide product of the thermal decomposition are reported in this paper.

2. Experimental

2.1. Instrumentation and materials

FT-IR spectrum in the range 4000–400 cm^{-1} was recorded using Perkin–Elmer Spectrum One. Elemental analysis was performed by Perkin–Elmer Series II CHNS/O Analyzer 2400. $Cd(NO_3)_2 \cdot 4H_2O$, $Zn(NO_3)_2 \cdot 6H_2O$ were

Table 1
Crystal data and refinement

	1	2	3	4
Formula	$C_{12}H_{11}N_5O_6Zn$	$C_{13}H_{13}N_5O_6Zn$	$C_{12}H_{13}N_5O_7Cd$	$C_{14}H_{17}N_5O_7Cd$
CCDC number	659641	659642	659643	659644
M_r	386.63	400.67	451.68	479.74
T (K)	296(2)	296(2)	296(2)	296(2)
Wavelength (Å)	0.71073	0.71073	0.71073	0.71073
Crystal system	monoclinic	hexagonal	monoclinic	orthorhombic
Space group	$P2_1/n$	$P6_5$	$P2_1/n$	$Pbca$
a (Å)	7.922(1)	8.605(1)	10.577(1)	14.002(1)
b (Å)	13.241(2)	8.605(1)	10.972(1)	15.520(1)
c (Å)	14.669(2)	36.933(1)	14.672(1)	16.668(1)
α (°)				
β (°)	103.31(1)		108.64(1)	
γ (°)				
V (Å^3)	1797.4(4)	2368.3(1)	1613.3(2)	3622.2(2)
Z	4	6	4	8
D_{calc} (g cm^{-3})	1.715	1.686	1.860	1759
μ (mm^{-1})	1.682	1.599	1.401	1.254
Goodness-of-fit on F^2[a]	0.928	1.059	1.051	1.083
R [$I > 2\sigma(I)$]	$R_1 = 0.0334$[b], $wR_2 = 0.0756$[c]	$R_1 = 0.0594$[b], $wR_2 = 0.1657$[c]	$R_1 = 0.0418$[b], $wR_2 = 0.1062$[c]	$R_1 = 0.0668$[b], $wR_2 = 0.2062$[c]
R (all data)	$R_1 = 0.0714$[b], $wR_2 = 0.0849$[c]	$R_1 = 0.0869$[b], $wR_2 = 0.1787$[c]	$R_1 = 0.0656$[b], $wR_2 = 0.1189$[c]	$R_1 = 0.1044$[b], $wR_2 = 0.2329$[c]

[a] GOF $= [\sum[w(F_0^2 - F_c^2)^2]/M - N]^{1/2}$ (M = number of reflections, N = number of parameters refined).
[b] $R_1 = \sum||F_o| - |F_c||/\sum|F_o|$.
[c] $wR_2 = [\sum[w(F_o^2 - F_c^2)^2]/\sum[w(F_o^2)^2]]$.

Table 2
Selected bond distances and angles

Bond distances (Å)					Bond angles (°)				
	1	2	3	4		1	2	3	4
M–N1	2.116(2)	2.150(5)	2.403(4)	2.320(6)	N1–M–N2	76.9(1)	76.5(2)	69.8(1)	70.7(2)
M–N2	2.085(2)	2.078(4)	2.333(4)	2.331(7)	N2–M–N3	77.2(1)	77.7(2)	70.0(1)	69.6(2)
M–N3	2.108(2)	2.119(6)	2.366(4)	2.380(7)	N1–M–N3	153.6(1)	154.2(2)	139.9(1)	139.4(3)
M–O1	2.050(2)	2.051(7)	2.541(3)	2.441(7)	O1–M–O2			51.1(1)	51.9(2)
M–O2			2.391(4)	2.414(6)	O1–M–O4	86.7(1)	83.1(3)	114.9(1)	104.4(2)
M–O4	2.024(2)	2.071(7)	2.489(5)	2.376(8)	O1–M–O7			78.0(1)	77.3(3)
M–O7			2.344(4)	2.340(7)	O2–M–O4			103.7(2)	80.2(2)
N1–C5	1.342(3)	1.327(8)	1.314(6)	1.321(11)	O2–M–O7			84.2(1)	89.6(3)
N2–C6	1.366(3)	1.312(10)	1.387(6)	1.459(12)	O4–M–O7			167.1(2)	165.0(3)
N2–C7	1.335(3)	1.380(12)	1.302(6)	1.267(10)	O1–M–N1	97.6(1)	97.9(2)	134.7(1)	132.5(2)
N3–C8	1.339(3)	1.343(8)	1.339(6)	1.339(10)	O1–M–N2	142.2(1)	138.8(3)	149.8(1)	153.1(2)
C5–C6	1.481(3)	1.473(12)	1.477(7)	1.471(13)	O1–M–N3	99.8(1)	100.8(3)	83.5(1)	84.7(2)
C7–C8	1.471(3)	1.493(12)	1.482(7)	1.519(12)	O4–M–N1	97.5(1)	100.1(3)	82.0(2)	85.9(3)
C8–C9	1.375(3)	1.385(11)	1.384(6)	1.365(11)	O4–M–N2	130.9(1)	138.0(3)	81.7(2)	88.8(2)
C7–C13		1.409(13)		1.506(11)	O4–M–N3	103.2(1)	99.7(3)	92.8(2)	101.6(3)
					O7–M–N1			88.7(1)	82.3(3)
					O7–M–N2			86.7(1)	96.0(3)
					O7–M–N3			88.6(1)	93.4(3)
					N2–C7–C8	115.2(2)	113.4(6)	117.9(4)	116.0(7)
					N2–C6–C5	113.5(2)	114.5(6)	115.0(4)	112.8(7)
					C6–N2–C7	125.8(2)	124.9(5)	122.6(4)	121.6(7)

purchased from Merck India Ltd. and pyridine-2-carbaldehyde, 2-acetylpyridine and 2-picolylamine from M/S Aldrich, USA. N-(2-pyridylmethyl)pyridine-2-carbaldimine (**L1**) and N-(2-pyridylmethyl)pyridine-2-methylketimine (**L2**) were prepared as reported earlier [7a]. All the chemical and solvents were of reagent grade and used as received without further purifications.

2.2. X-ray crystallography

Single crystals X-ray crystallographic data were collected using Bruker SMART APEX-CCD diffractometer with Mo Kα radiation ($\lambda = 0.71073$ Å). The intensity data were corrected for Lorentz and polarization effects and empirical absorption corrections was applied using SAINT program [8,9]. All the structures were solved by direct methods using SHELXS-97 [9]. Non-hydrogen atoms located from the difference Fourier maps were refined anisotropically by full-matrix least-squares on F^2, using SHELXL-97 [9]. The hydrogen atoms were included in the calculated positions and refined isotropically using a riding model. Crystal data and bond parameters are listed in Tables 1 and 2, respectively.

2.3. Thermal measurements

Thermogravimetry were studied by a computer controlled METTLER TOLEDO STAR^e system of module TGA/SDTA851^e under static nitrogen atmosphere using platinum pan at a heating rate of 10 °C/min in the temperature range 25–700 °C. The instrument was calibrated using RTypSDTA sensor. Onset temperature obtained from DTG curve is used to evaluate the onset decomposition temperature of the samples. DSC profiles were recorded by a computer controlled METTLER TOLEDO STAR^e system of module DSC821^e under static nitrogen atmosphere. Temperature and energy of the instrument were calibrated by standard indium using the FRS5 ceramic sensor. A 70 μL aluminium pan was used for the temperature range 25–600 °C, for recording the profiles at heating rates of 10, 15, 20, 25, 28, and 30 °C min^{-1}.

2.4. Syntheses

[Zn(**L1**)$(NO_3)_2$] (**1**): To 258 mg (1.31 mmol) of **L1**, dissolved in 25 cm^3 of methanol was added 390 mg (1.31 mmol) of $Zn(NO_3)_2 \cdot 6H_2O$ solid with stirring. A transient violet color disappeared and the solution was left undisturbed after 10 min. Colorless crystals obtained after 3 days were collected after washing with ice-cold methanol. Yield: 0.22 g (43%). IR (KBr, cm^{-1}): 1665 (C=N_{im}), 1602 (C=N_{py}). *Anal.* Calc. for $C_{12}H_{11}N_5O_6Zn$: C, 37.24; H, 2.85; N, 18.11. Found: C, 37.48; H, 2.91; N, 18.35%.

[Zn(**L2**)$(NO_3)_2$] (**2**), [Cd(**L1**)$(H_2O)(NO_3)_2$] (**3**) and [Cd(**L2**)$(CH_3OH)(NO_3)_2$] (**4**) were prepared as described above using 1.31 mmol of respective ligand and metal nitrates.

[Zn(**L2**)$(NO_3)_2$] (**2**): Yield: 0.23 g (43%). IR (KBr, cm^{-1}): 1673 (C=N_{im}), 1610 (C=N_{py}). *Anal.* Calc. for $C_{13}H_{13}N_5O_6Zn$: C, 38.93; H, 3.24; N, 17.47. Found: C, 39.09; H, 3.31; N, 17.55%.

[Cd(**L1**)$(H_2O)(NO_3)_2$] (**3**): Yield: 0.35 g (59%). IR (KBr, cm^{-1}): 1653 (C=N_{im}), 1595 (C=N_{py}). *Anal.* Calc. for $C_{12}H_{13}N_5O_7Cd$: C, 31.88; H, 2.88; N, 15.50. Found: C, 31.99; H, 2.96; N, 15.68%.

[Cd(**L2**)$(CH_3OH)(NO_3)_2$] (**4**): Yield: 0.33 g (40%). IR (KBr, cm^{-1}): 1651 (C=N_{im}), 1590 (C=N_{py}). *Anal.* Calc. for $C_{14}H_{17}N_5O_7Cd$: C, 35.02; H, 3.54; N, 14.59. Found: C, 35.11; H, 3.62; N, 14.70%.

3. Results and discussion

3.1. Molecular structures

Compound **1** crystallized in the space group $P2_1/n$, belong to 2/m Laue symmetry and the asymmetric unit contained one molecule of [Zn(**L1**)$(NO_3)_2$]. Bivalent zinc is pentacoordianted by N_3O_2 chromophore and has a distorted square-pyramidal geometry, as inferred from the τ value of 0.19 [10]. The N1N2N3O1 forms the basal plane with the O4 atom of the monocoordinated NO_3^-, occupying the axial position. A perspective view of **1** is shown in Fig. 1. The Zn–N_{im} distance is shorter than the Zn–N_{py} distances by an average of 0.027(3) Å and the Zn–N bond lengths are longer than the Zn–O distances by 0.066(3) Å. The longer Zn1···O2, 2.626(2) Å and Zn1···O5, 2.723(2) Å contacts are present. The chelate rings, Zn1N2C7C8N3 and Zn1N2C6C5N1 are planar and the inter-plane angle of these two is 4.78(1)°. The plane formed by the chelate and the pyridine rings intercept at ~1.55(1)°. The inner angles at C7 and C6 are, respectively, are 115.22(1)° and 113.44(1)° and are deviating from the ideal values for a sp^2 and sp^3 carbon. The packing diagram of **1** on viewing down the *a*-axis (shown in Fig. 2) reveals the

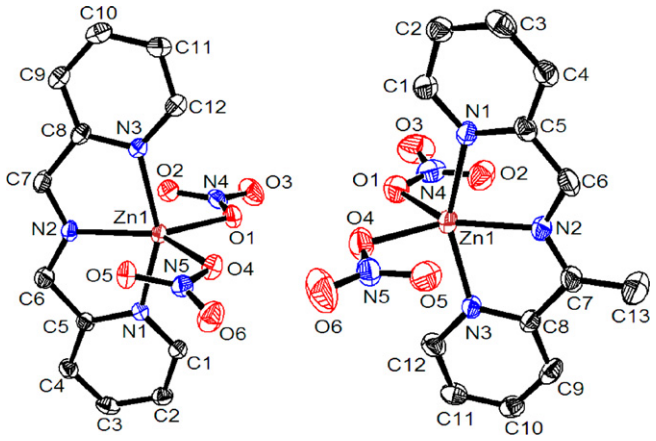


Fig. 1. ORTEP (30% probability) diagram of **1** and **2** (hydrogens are omitted for clarity).

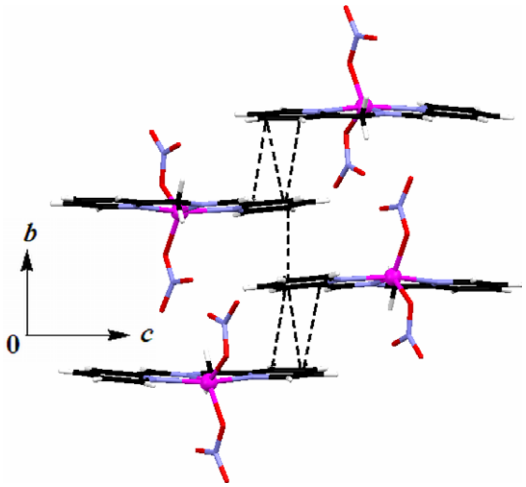


Fig. 2. Packing diagram of **1**.

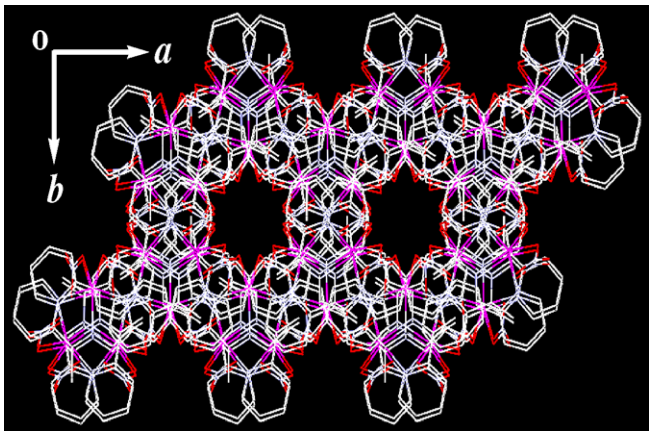


Fig. 3. Packing diagram of **2**.

presence of π–π and C–H···O interactions. The intermolecular π–π contacts are C4···C9 3.287(3) Å, C3···C9 3.348(3) Å, C9···C9 3.361(3) Å and C3···C8 3.379(3) Å.

Compound **2** crystallized in the hexagonal space group $P6_5$, belongs to 6/m Laue symmetry and one molecule of $[Zn(\mathbf{L2})(NO_3)_2]$ is present in the asymmetric unit. The Zn(II) ion has a distorted square-pyramidal geometry with a τ value of 0.26 and has a N_3O_2 coordination environment. In this case also the N1N2N3O1 atoms form the distorted square plane along with O4 at the apical position. A perspective view of **2** is shown in Fig. 1. The following trends are observed: $Zn–N_{im} < Zn–N_{py}$ by an average of 0.057(2) Å and the Zn–N > Zn–O by 0.054(3) Å. The longer Zn1···O2, 2.578(3) Å and Zn1···O5, 2.602(3) Å contacts are present. The chelate rings, Zn1N2C7C8N3 and Zn1N2C6C5N1 are nearly planar and are twisted with respect to each other with the twist angle being 3.37(1)°. The inner angles at sp^2 C7 and sp^3 C6 are, respectively, 113.44(1)° and 114.59(1)°. The packing diagram of **2** on viewing down the *c*-axis is shown in Fig. 3. The predominantly hydrophilic channels of hexagonal cavity of dimension ~4.763 Å containing the O1, O3, O4, and O6 align along *c*-axis. The π–π interactions having intermolecular contacts, C4···C9 3.310(11) Å, C3···C9 3.323(12) Å, C4···C10 3.321(11) Å are dominant in the packing.

The X-ray crystal structure of **3** shows the presence of a discrete mononuclear complex. The Cd(II) is hepta-coordinated by **L1** in a tridentate fashion, one NO_3^- in monodentate and the other in bidentate fashions, and a water molecule. The overall coordination is pseudo-pentagonal-bipyramidal geometry and a perspective view is shown in Fig. 4. The $Cd–N_{im}$ is shorter than the $Cd–N_{py}$ by 0.051(4) Å and the Cd–N bond lengths are shorter than the Cd–O distances by 0.073(5) Å. The chelate rings, Cd1N2C7C8N3 and Cd1N2C6C5N1 are planar and both intercept at an angle 2.21(1)°. The bidentate nitrate ion occupies the pentagonal base and deviates from the plane formed by the two chelate rings by an angle 15.11(1)°. The O2···O7, 2.923(6) Å hydrogen bond and Cd···O6, 2.650(7) Å contact are present.

A discrete mononuclear species of **4** crystallized in an orthorhombic space group *Pbca*, belongs to mmm Laue

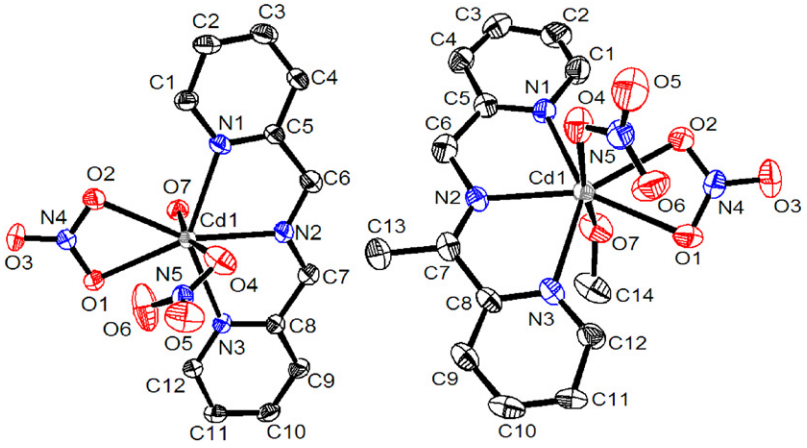


Fig. 4. ORTEP (30% probability) diagram of **3** and **4** (hydrogens are omitted for clarity).

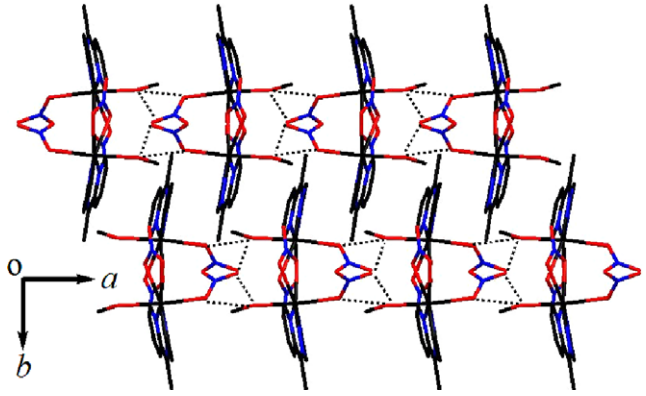


Fig. 5. Packing diagram of **4** viewing down the *c*-axis.

symmetry. The pseudo-pentagonal-bipyramidal geometry around Cd(II) consists of, tridentate **L2**, a monodentate and a bidentate NO_3^- ions, as well as a methanol. A perspective view of **4** is shown in Fig. 4. The Cd–N bond lengths are shorter than the Cd–O distances by 0.050(7) Å. The chelate rings, Cd1N2C7C8N3 and Cd1N2C6C5N1 are planar and both intercept at an angle 7.64(1)°. The plane formed by the chelate and the pyridine rings intercept at ~3.22(1)°. The bidentate nitrate ion occupies the pentagonal base and is twisted with respect to the two chelate rings by an angle 20.50(1)°. The hydrogen bonds, O7···O4, 3.001(10) Å and O7···O5, 2.933(14) Å between the methanol and monodentate nitrate ion dominate the packing diagram, is shown in Fig. 5.

3.2. Thermal decomposition

The thermal decomposition of **1**–**4** was observed using TGA. In **1** and **2** the first step is the loss of $NO_{(g)}$, while in **3** and **4**, coordinated solvent is lost in addition. The volatile components released in step II could not be analyzed and the residue obtained after calcination at respective end-temperatures showed the absence of imine function and the presence of pyridine ring. Loss of two moles of pyridine occur in step III, leaving behind the corresponding metal oxide (ZnO and CdO) as the final residual part. The temperature ranges for the three steps are listed in Table 3.

Table 3
TGA temperature (°C)

Complex	Step I	Step II	Step III
1	35–115	115–280	280–570
2	35–125	125–285	280–580
3	35–120	120–320	320–590
4	35–140	140–280	280–595

The morphology of crystalline samples of **1**–**4** after calcinations at 600 °C, were evaluated by SEM and that from **1** and **4** is shown in Fig. 6. The ZnO obtained from **1** and **2**, are porous in nature having the minimum pore size range of 600–900 nm. Spherical CdO crystalline particles from **3** and **4** are of the size 115–330 nm.

3.3. Kinetics of thermal elimination of pyridine

Thermokinetics of the loss of two moles of pyridine (step III) were analyzed utilizing the DSC data for **1**–**4**. Good analysis was possible with differential iso-conversional method *viz.* Friedman method, which utilizes the differential equation

$$\ln(\mathrm{d}\alpha/\mathrm{d}t)|_{\alpha-\alpha_j} = \ln A - \frac{E}{RT_{kj}} + \ln f(\alpha_j)$$

where α is small ranges of reaction progress, E is the activation energy, A is the pre-exponential factor, R is the universal gas constant [11]. In all the cases, the activation energy remain constant in the region $\alpha = 0.2$–0.9, which is suggestive of a single step reaction. A representative analysis plot of **1** and **3** are displayed in Fig. 7. The average activation energy (E) for **1**, **2**, **3**, and **4** are 193.8(2), 114.5(3), 127.1(4), and 63.7(3) kJ mol^{-1} and their

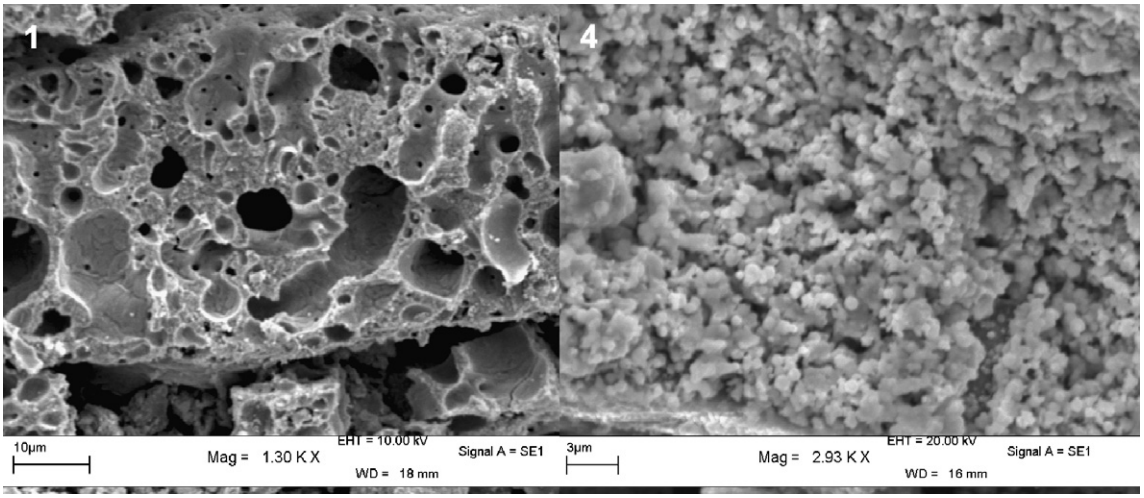


Fig. 6. SEM picture of **1** and **4** calcined at 600 °C.

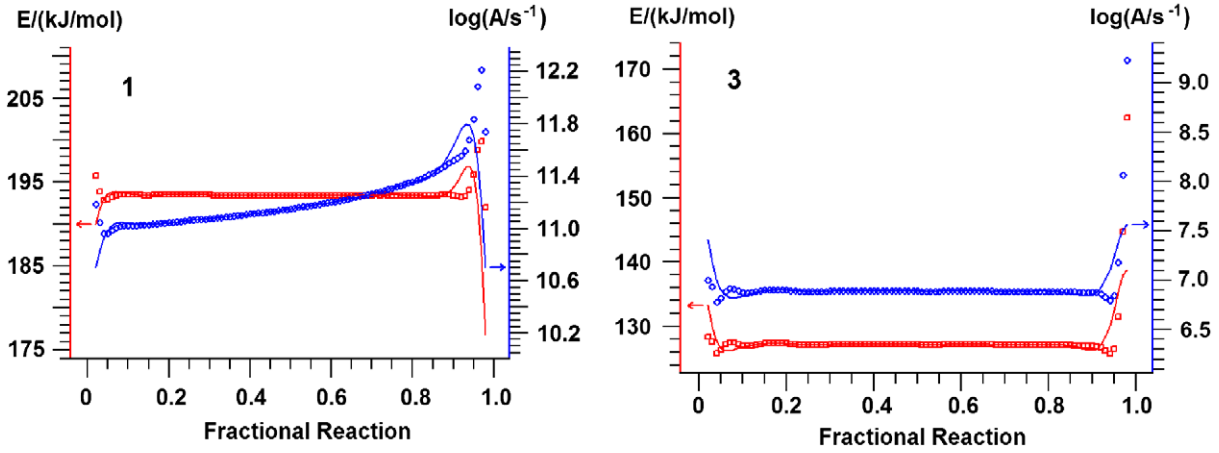


Fig. 7. Friedman plot of **1** and **3** (symbols are the experimental values and lines are simulated).

logarithmic pre-exponential factor (A) are 11.22, 5.31, 6.88, and 2.09, respectively.

4. Conclusion

Four complexes of bivalent zinc and cadmium based on a tridentate-N_3 ligand were synthesized and structurally characterized. Zinc and cadmium complexes, respectively, have pseudo square-pyramidal and pentagonal-bipyramidal geometries. The following trends in the bond lengths are observed: $M–N_{im} < M–N_{py}$; $Zn–N > Zn–O$; $Cd–N < Cd–O$. The final residual part of thermal decompositions are ZnO and CdO, the SEM studies revealed, respectively, their porous and spherical natures. The activation parameters obtained from the Friedman fitting of the DSC profiles for the loss of pyridine rings are reported.

Acknowledgement

We are grateful to the Council of Scientific and Industrial Research for a financial grant, Department of Science and Technology, New Delhi for establishing single crystal X-ray diffractometer facility under FIST scheme and Central Instruments Facility, IIT Guwahati for SEM facility. Authors are thankful to Babulal Das for X-ray data and G. Padmanabhan for providing the NETZSCH TA4 software.

Appendix A. Supplementary material

CCDC 659641, 659642, 659643 and 659644 contain the supplementary crystallographic data for this paper. These data can be obtained free of charge via http://www.ccdc.cam.ac.uk/conts/retrieving.html, or from the Cambridge Crystallographic Data Centre, 12 Union Road, Cambridge CB2 1EZ, UK; fax: (+44) 1223-336-033, or e-mail: deposit@ccdc.cam.ac.uk. Supplementary data associated with this article can be found, in the online version, at doi:10.1016/j.poly.2007.11.011.

References

[1] (a) S.R. Batten, R. Robson, Angew. Chem., Int. Ed. 37 (1998) 1460;
(b) M.J. Plater, M.R.St.J. Foreman, T. Gelbrich, S.J. Coles, M.B. Hursthouse, J. Chem. Soc., Dalton Trans. (2000) 3065;
(c) H.W. Roesky, M. Andruh, Coord. Chem. Rev. 236 (2003) 91;
(d) S.A. Barnett, N.R. Champness, Coord. Chem. Rev. 246 (2003) 145;
(e) B.-H. Ye, M.-L. Tong, X.-M. Chen, Coord. Chem. Rev. 249 (2005) 545.
[2] N. Uekawa, R. Yamashita, Y. Wu, K. Kakegawa, Phys. Chem. Chem. Phys. 6 (2004) 442.
[3] (a) M. Mo, J.C. Yu, L. Zhang, S.A. Li, Adv. Mater. 17 (2005) 756;
(b) H. Wilmer, M. Kurtz, K. Klementiev, O. Tkachenko, W. Grünert, O. Hinrichsen, A. Birkner, S. Rabe, K. Merz, M. Driess, C. Wöll, M. Muhler, Phys. Chem. Chem. Phys. 5 (2003) 4736.
[4] (a) L. Vayssieres, Adv. Mater. 15 (2003) 464;
(b) J.Q. Hu, Y. Bando, J.H. Zhan, Y.B. Li, T. Sekiguchi, Appl. Phys. Lett. 83 (2003) 4414;
(c) J.Q. Hu, Q. Li, X.M. Meng, C.S. Lee, S.T. Lee, Chem. Mater. 15 (2003) 305;
(d) F. Li, Y. Ding, P. Gao, X. Xin, Z.L. Wang, Angew. Chem., Int. Ed. 43 (2004) 5238;
(e) W.I. Park, G.C. Yi, Adv. Mater. 16 (2004) 87;
(f) X.Y. Kong, Y. Ding, R. Yang, Z.L. Wang, Science 303 (2004) 1348;
(g) D. Chen, R. Wang, I. Arachchige, G. Mao, S.L. Brock, J. Am. Chem. Soc. 126 (2004) 16290.
[5] (a) Z.L. Wang, Ann. Rev. Phys. Chem. 55 (2004) 159;
(b) Z.R. Dai, Z.W. Pan, Z.L. Wang, Adv. Funct. Mater. 13 (2003) 9.
[6] (a) A. Umar, Y.B. Hahn, Nanotechnology 17 (2006) 2174;
(b) J.S. Lee, M.S. Islam, S. Kim, Nanoletters 6 (2006) 1487;
(c) Y. Sun, D.J. Riley, M.N.R. Ashfold, J. Phys. Chem. B 110 (2006) 15186;
(d) C. Pacholski, A. Kornowski, H. Weller, Angew. Chem., Int. Ed. 41 (2002) 1188;
(e) X.S. Peng, X.F. Wang, Y.W. Wang, C.Z. Wang, G.W. Meng, L.D. Zhang, J. Phys. D: Appl. Phys. 35 (2002) L101;
(f) B.S. Zou, V.V. Volkov, Z.L. Wang, Chem. Mater. 11 (1999) 3037;
(g) M.-H. Liao, C.-H. Hsu, D.-H. Chen, J. Solid State Chem. 179 (2006) 2020;
(h) X. Wu, R. Wang, B. Zou, L. Wang, S. Liu, J. Xu, W. Huang, J. Mater. Res. 13 (1998) 604;
(i) K.X. Yao, H.C. Zeng, J. Phys. Chem. B 110 (2006) 14736.

[7] (a) S.K. Padhi, V. Manivannan, Inorg. Chem. 45 (2006) 7994;
(b) S.K. Padhi, V. Manivannan, Polyhedron 26 (2007) 1619;
(c) S.K. Padhi, V. Manivannan, Polyhedron 26 (2007) 3092.
[8] SMART and SAINT, Siemens Analytical X-ray Instruments Inc., Madison, WI, 1996.
[9] G.M. Sheldrick, SHELXS-97 and SHELXL-97, University of Göttingen, Göttingen, Germany, 1997.
[10] A.W. Addison, T.N. Rao, J. Reedijk, J. van Rijn, G.C. Verschoor, J. Chem. Soc., Dalton Trans. (1984) 1349.
[11] (a) H.L. Friedman, J. Polymer Lett. 4 (1966) 323;
(b) S.K. Padhi, Thermochim. Acta 448 (2006) 1;
(c) S. Vyazovkin, J. Comput. Chem. 22 (2001) 178;
(d) S. Vyazovkin, Int. J. Chem. Kinet. 28 (1996) 95.

Available online at www.sciencedirect.com
ScienceDirect
Polyhedron 27 (2008) 812–820
POLYHEDRON
www.elsevier.com/locate/poly

Structure modulation of metal–organic frameworks via reaction pH: Self-assembly of a new carboxylate containing ligand *N*-(3-carboxyphenyl)iminodiacetic acid with cadmium(II) and cobalt(II) salts

Qian Chu [a], Guang-Xiang Liu [a], Taka-aki Okamura [b], Yong-Qing Huang [a], Wei-Yin Sun [a,*], Norikazu Ueyama [b]

[a] *State Key Laboratory of Coordination Chemistry, Coordination Chemistry Institute, School of Chemistry and Chemical Engineering, Nanjing University, Nanjing 210093, China*
[b] *Department of Macromolecular Science, Graduate School of Science, Osaka University, Toyonaka, Osaka 560-0043, Japan*

Received 19 July 2007; accepted 12 November 2007
Available online 2 January 2008

Abstract

Self-assembly of a new carboxylate containing ligand, *N*-(3-carboxyphenyl)iminodiacetic acid (H_3L), with Cd(II) and Co(II) salts under different reaction pH results in the formation of four new coordination polymers, namely $[Cd(HL)(H_2O)]$ (**1**), $[Co(HL)(H_2O)]$ (**2**), $[Cd(HL)(H_2O)_4]$ (**3**) and $[Cd_3(L)_2(H_2O)_9]\cdot 7H_2O$ (**4**). Single crystal X-ray diffraction analysis indicates that **1** and **2** are isomorphous and isostructural with a 2D wave-like network structure, while **3** has a 1D zigzag chain structure. The complexes **1**–**3** were obtained at low pH (<7) which makes the ligands only partly deprotonated. However, complex **4**, obtained at pH 7 with all the carboxylate groups deprotonated, exhibits a 2D network structure. The results suggest that the reaction pH is one of the key factors in the formation of the coordination architectures. In addition, the photoluminescence properties of the free ligand (H_3L) and complexes **1**, **3** and **4** were studied in the solid state at room temperature. Moreover, the magnetic property of complex **2** was investigated.
© 2007 Elsevier Ltd. All rights reserved.

Keywords: Coordination polymer; Carboxylate ligand; Cadmium(II); Cobalt(II); Photoluminescence property

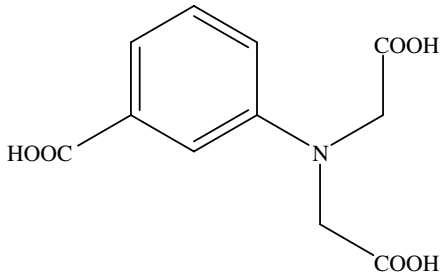
1. Introduction

In recent years, much attention has been focused on metal–organic frameworks (MOFs) due to their fascinating structures such as zero-dimensional (0D) cages, one-dimensional (1D) helical chains, two-dimensional (2D) grids and three-dimensional (3D) frameworks [1], as well as their attractive properties which can be further utilized in the fields of magnetism, catalysis, absorption, optics, etc. [2]. Among them, MOFs with carboxylate containing ligands are especially of great interest in recent years because the carboxylate groups can adopt varied coordination modes such as monodentate, bis-monodentate, chelating, and as a result diverse structures can be obtained [3]. However, it is still a labyrinth because not all of the structures could be generated as predicted, which might be attributed to the factors that influence the formation of the architectures [4]. Particularly, the pH value of the reaction solution and crystallization conditions are crucial parameters, for example, Stock and co-workers have demonstrated the role of the acid/base ratio, temperature, etc., in determining the structure of the complexes [5].

Taking in account of the factors mentioned above, we have focused our attention on the reactions of various metal salts with multi-carboxylate ligands and the influence of reaction pH on the structure of the resultant complexes was investigated. Recently, a new carboxylate containing

* Corresponding author. Fax: +86 25 83314502.
E-mail address: sunwy@nju.edu.cn (W.-Y. Sun).

0277-5387/$ - see front matter © 2007 Elsevier Ltd. All rights reserved.
doi:10.1016/j.poly.2007.11.029



Scheme 1. Schematic drawing structure of the H_3L ligand.

ligand, *N*-(3-carboxyphenyl)iminodiacetic acid (H_3L) (Scheme 1), was obtained, which has remarkable features as follows: (a) it contains three carboxylate groups, therefore quite a lot of bridging modes could be adopted in the formation of MOFs; (b) the three carboxylate groups would be partially or completely deprotonated by tuning the reaction pH; (c) it is a semi-rigid ligand with a carboxyphenyl group fixed and an iminodiacetic moiety which is somewhat flexible, whereby different conformations of the ligand could be achieved which would further generate various architectures; (d) the introduced aromatic and the carboxylate groups could offer additional π–π and hydrogen bonding interactions, respectively, to further consolidate the structure [6].

Herein, we report the synthesis, crystal structure and properties of four new coordination polymers, namely $[Cd(HL)(H_2O)]$ (**1**), $[Co(HL)(H_2O)]$ (**2**), $[Cd(HL)(H_2O)_4]$ (**3**) and $[Cd_3(L)_2(H_2O)_9]\cdot 7H_2O$ (**4**), obtained by the reactions of H_3L with $Cd(NO_3)_2\cdot 4H_2O$ or $CoCl_2\cdot 4H_2O$ under different reaction pH.

2. Experimental

2.1. Materials and methods

All commercially available chemicals and solvents are of reagent grade and were used as received without further purification. Elemental analyses for C, H and N were performed on a Perkin–Elmer 240C Elemental Analyzer at the Analysis Center of Nanjing University. FT-IR spectra were recorded in the range 400–4000 cm^{-1} on a Bruker Vector22 FT-IR spectrophotometer as KBr pellets. ^1H NMR spectra were measured on a Bruker DRX 500 MHz NMR spectrometer at room temperature. Magnetic measurements for complex **2** in the range 1.8–300 K were performed on a MPMS-SQUID magnetometer at a field of 2 kOe on crystalline samples in the temperature settle mode. The diamagnetic contributions of the samples were corrected by using Pascal's constants. The luminescent spectra for the powdered solid samples were recorded at room temperature on an Aminco Bowman Series 2 spectrofluorometer with a Xenon arc lamp as the light source. In the measurements of emission and excitation spectra the pass width was 5.0 nm. All the measurements were carried out under the same experimental conditions.

2.2. Synthesis of the ligand N-(3-carboxyphenyl)iminodiacetic acid (H_3L)

A solution of KOH (33.6 g, 0.6 mol) in water (100 ml) was added dropwise to a solution of monochloroacetic acid (28.4 g, 0.3 mol) in water (100 ml). To the resulting alkaline solution, 3-aminobenzoic acid (13.7 g, 0.1 mol) was added and the mixture was refluxed for 30 h. Then the reaction mixture was cooled to room temperature and a pale brown precipitate appeared, which was collected by filtration, washed by water and recrystallized from water (yield: 52% based on 3-aminobenzoic acid). ^1H NMR (500 MHz, in K_2CO_3, D_2O): δ 7.18 (t, 1H), 7.03 (d, 1H), 6.89 (s, 1H), 6.55 (d, 1H), 3.83 (s, 4H). IR (KBr pellet, cm^{-1}): 3446 (w), 2926 (w), 2552 (w), 1723 (m), 1682 (s), 1603 (m), 1580 (m), 1494 (w), 1465 (m), 1423 (w), 1376 (m), 1361 (m), 1299 (m), 1230 (w), 1183 (w), 1130 (w), 992 (w), 975 (w), 864 (w), 757 (m), 679 (w), 661 (w), 608 (w).

2.3. Synthesis of the complexes

2.3.1. Synthesis of $[Cd(HL)(H_2O)]$ (**1**)

A mixture containing $Cd(NO_3)_2\cdot 4H_2O$ (30.8 mg, 0.1 mmol), H_3L (25.3 mg, 0.1 mmol), KOH (2.8 mg, 0.05 mmol), 6 ml H_2O and 3 ml CH_3OH was sealed in a 16 ml Teflon lined stainless steel container and heated at 140 °C for 3 days. After cooling to room temperature for 12 h, colorless block crystals of **1** suitable for X-ray diffraction analysis were obtained in 68% yield. *Anal.* Calc. for $C_{11}H_{11}CdNO_7$: C, 34.62; H, 2.90; N, 3.67. Found: C, 34.65; H, 2.90; N, 3.70%. IR (KBr pellet, cm^{-1}): 3493 (m), 2917 (w), 1699 (m), 1583 (s), 1439 (m), 1416 (m), 1341 (w), 1313 (m), 1294 (m), 1197 (w), 1135 (w), 992 (w), 971 (w), 931 (w), 878 (w), 809 (w), 774 (w), 756 (w), 720 (w), 690 (w), 664 (w), 620 (w).

2.3.2. Synthesis of $[Co(HL)(H_2O)]$ (**2**)

The preparation of **2** is similar to that of **1** except that $CoCl_2\cdot 4H_2O$ (30.8 mg, 0.1 mmol) was used and that the Teflon container was heated at 120 °C for 3 days. After cooling to room temperature for 12 h, purple block crystals of **2** were collected in 63% yield. *Anal.* Calc. for $C_{11}H_{11}CoNO_7$: C, 40.26; H, 3.38; N, 4.27. Found: C, 40.16; H, 3.27; N, 4.38%. IR (KBr pellet, cm^{-1}): 3474 (m), 2921 (w), 1698 (m), 1586 (s), 1492 (w), 1445 (m), 1419 (m), 1340 (w), 1315 (m), 1295 (m), 1248 (w), 1193 (w), 1175 (w), 1123 (w), 1048 (w), 990 (w), 968 (w), 936 (w), 925 (w), 907 (w), 879 (w), 808 (w), 777 (w), 756 (w), 729 (w), 690 (w), 666 (w), 632 (w).

2.3.3. Synthesis of $[Cd(HL)(H_2O)_4]$ (**3**)

Complex **3** was prepared by a layering method. An aqueous solution (5 ml) of H_3L (25.3 mg, 0.1 mmol) was carefully adjusted to pH 6 by tetrabutylammonium hydroxide (10%) solution and placed at the bottom of a test tube. Then a buffer layer of a solution (5 ml) of

methanol/H_2O 1:1 was layered over it, and afterward, a solution of $Cd(NO_3)_2 \cdot 4H_2O$ (30.8 mg, 0.1 mmol) in methanol (5 ml) was layered over the buffer layer. Colorless block crystals of **3** were collected in 61% yield after several days. *Anal*. Calc. for $C_{11}H_{17}CdNO_{10}$: C, 30.32; H, 3.93; N, 3.22. Found: C, 30.21; H, 3.91; N, 3.29%. IR (KBr pellet, cm^{-1}): 3408 (m), 2930 (w), 1720 (m), 1572 (s), 1535 (s), 1455 (m), 1434 (m), 1413 (m), 1374 (m), 1357 (m), 1317 (m), 1295 (m), 1268 (w), 1234 (w), 1183 (w), 994 (w), 979 (w), 800 (w), 762 (w), 679 (w).

2.3.4. Synthesis of $[Cd_3(L)_2(H_2O)_9] \cdot 7H_2O$ (4)

The preparation of **4** was similar to that described for **3** except that the pH of the bottom solution of H_3L was adjusted to 7 rather than 6. Yield: 53%. *Anal*. Calc. for $C_{22}H_{48}Cd_3N_2O_{28}$: C, 23.47; H, 4.30; N, 2.49. Found: C, 23.59; H, 4.12; N, 2.45%. IR (KBr pellet, cm^{-1}): 3474 (m), 2908 (w), 1597 (s), 1574 (s), 1452 (w), 1402 (s), 1379 (m), 1329 (w), 1297 (m), 1215 (w), 1180 (w), 1135 (w), 987 (w), 933 (w), 891 (w), 800 (w), 762 (w), 681 (w).

2.4. X-ray crystallography

The crystallographic data collections for complexes **1**–**3** were carried out on a Bruker Smart Apex CCD with graphite-monochromated Mo Kα radiation ($\lambda = 0.7107$ Å) at 293(2) K using the ω-scan technique. The data were integrated by using the SAINT program [7], which also used for intensity corrections for Lorentz and polarization effects. An empirical absorption correction was applied using the SADABS program [8]. The structures were solved by direct methods using the program SHELXS-97 [9] and all non-hydrogen atoms were refined anisotropically on F^2 by the full-matrix least-squares technique using the SHELXL-97 crystallographic software package [10]. The hydrogen atoms H2, H3, H5, H6, H7, H7A and H7B in **1**, H7A, H7B and H16 in **2** and all of the hydrogen atoms in **3** were located from difference Fourier maps, and the other hydrogen atoms were generated geometrically. All calculations were performed on a personal computer with the SHELXL-97crystallographic software package. The X-ray diffraction measurement for **4** was carried out on a Rigaku RAXIS-RAPID imaging plate diffractometer at 200 K using graphite-monochromated Mo Kα radiation ($\lambda = 0.7107$ Å). A symmetry-related absorption correction using the program ABSCOR [11] was applied and the data were corrected for Lorentz and polarization effects. The structure was solved by direct methods [11] and expanded using Fourier techniques [12]. The non-hydrogen atoms were refined anisotropically. All calculations for **4** were performed using the TEXSAN crystallographic software package of the Molecular Structure Corporation [13]. Atoms Cd2 and Cd3 in complex **4** are disordered Cd(II) with an occupancy of 0.5, and atoms O3, O4, O10, C13 and C14 in **4** have two positions with site occupancy factors of 0.53(2) and 0.47(2). Atom O17 in **4** is also

Table 1
Crystallographic data for complexes **1**–**4**

Compound	**1**	**2**	**3**	**4**
Empirical formula	$C_{11}H_{11}CdNO_7$	$C_{11}H_{11}CoNO_7$	$C_{11}H_{17}CdNO_{10}$	$C_{22}H_{48}Cd_3N_2O_{28}$
Formula weight	381.61	328.14	435.66	1125.82
Crystal system	monoclinic	monoclinic	monoclinic	monoclinic
Space group	*C*2/c	*C*2/c	$P2_1/n$	*C*2/m
a (Å)	30.192(4)	30.299(7)	5.4335(6)	20.837(3)
b (Å)	9.6582(13)	9.513(2)	25.563(3)	23.271(4)
c (Å)	8.4591(11)	8.3489(18)	10.4650(11)	8.3863(13)
β (°)	93.916(2)	95.395(4)	91.133(2)	97.352(3)
T (K)	293(2)	293(2)	293(2)	200
V (Å^3)	2460.9(6)	2395.8(9)	1453.3(3)	4033.0(11)
Z	8	8	4	4
D_c (g cm^{-3})	2.060	1.820	1.991	1.854
μ (mm^{-1})	1.808	1.466	1.558	1.663
F(000)	1504	1336	872	2248
$2\theta_{max}$ (°)	52.00	50.98	52.00	50.00
Data collected	6436	6099	7750	14335
Independent data	2421	2226	2852	3638
R_{int}	0.0346	0.0528	0.0489	0.0892
Parameters refined	209	193	276	316
Goodness-of-fit	1.011	0.936	1.001	1.075
R_1 [$I > 2\sigma(I)$]	0.0365	0.0426	0.0259	0.0787
wR_2 [$I > 2\sigma(I)$]	0.0884[a]	0.0658[b]	0.0542[c]	0.2046[d]
R_1 (all data)	0.0424	0.0635	0.0318	0.1018
wR_2 (all data)	0.0919	0.0708	0.0562	0.2294

[a] $w = 1/[\sum^2(F_o)^2 + (0.0560P)^2 + 1.7000P]$, where $P = (F_o^2 + 2F_c^2)/3$.
[b] $w = 1/[\sum^2(F_o)^2 + (0.0156P)^2]$, where $P = (F_o^2 + 2F_c^2)/3$.
[c] $w = 1/[\sum^2(F_o)^2 + (0.0208P)^2 + 0.0651P]$, where $P = (F_o^2 + 2F_c^2)/3$.
[d] $w = 1/[\sum^2(F_o)^2 + (0.1006P)^2 + 51.4441P]$, where $P = (F_o^2 + 2F_c^2)/3$.

disordered into two positions with site occupancy factors of 0.63(5) and 0.37(5). The hydrogen atoms of the uncoordinated water molecules O14, O15 and O16 could not be found from the difference Fourier maps. The details of the crystal parameters, data collection and refinements for the complexes are summarized in Table 1, and selected bond lengths and angles with their estimated standard deviations are listed in Table 2.

3. Results and discussion

3.1. Crystal structure of complexes 1–4

3.1.1. [Cd(HL)(H$_2$O)] (1) and [Co(HL)(H$_2$O)] (2)

The result of X-ray crystallographic analysis revealed that complexes **1** and **2** crystallize in the same monoclinic *C*2/*c* space group with similar cell parameters (Table 1), which indicate that they are isomorphous and isostructural. Thus, as a typical example, only the structure of **1** is described here in detail. The asymmetric unit of **1** consists of one Cd(II) atom, one HL^{2-} ligand and one coordinated water molecule. Each Cd(II) atom is six-coordinated with a distorted octahedral geometry, by one nitrogen atom (N1) from the HL^{2-} ligand and five oxygen atoms from one coordinated H_2O molecule (O7) and three different HL^{2-} ligands (O3 and O5, O4A and O6B), as shown in Fig. 1a. The coordination bond lengths and angles around the Cd(II) centre are in the range 2.234(3)–2.556(3) Å and 68.59(10)–159.67(11)°, respectively as listed in Table 2. On the other hand, each HL^{2-} ligand adopts a μ_3 bridging mode to connect three Cd(II) atoms using its iminodiacetate moiety, in which each carboxylate group links two Cd(II) atoms in a *syn–anti* fashion and the central Cd(II) atom is coordinated by two oxygen atoms from two carboxylate groups and the central nitrogen atom (Scheme 2a). In addition, it is noteworthy that the carboxyphenyl group of the ligand, without deprotonation, is free of coordination. The non-deprotonation of the H_3L ligand in **1** and **2** was further confirmed by IR spectral measurements. The IR spectra of complexes **1** and **2** indicate the incomplete deprotonation of the H_3L ligand since vibration bands at 1699 cm^{-1} for **1** and 1698 cm^{-1} for **2** were

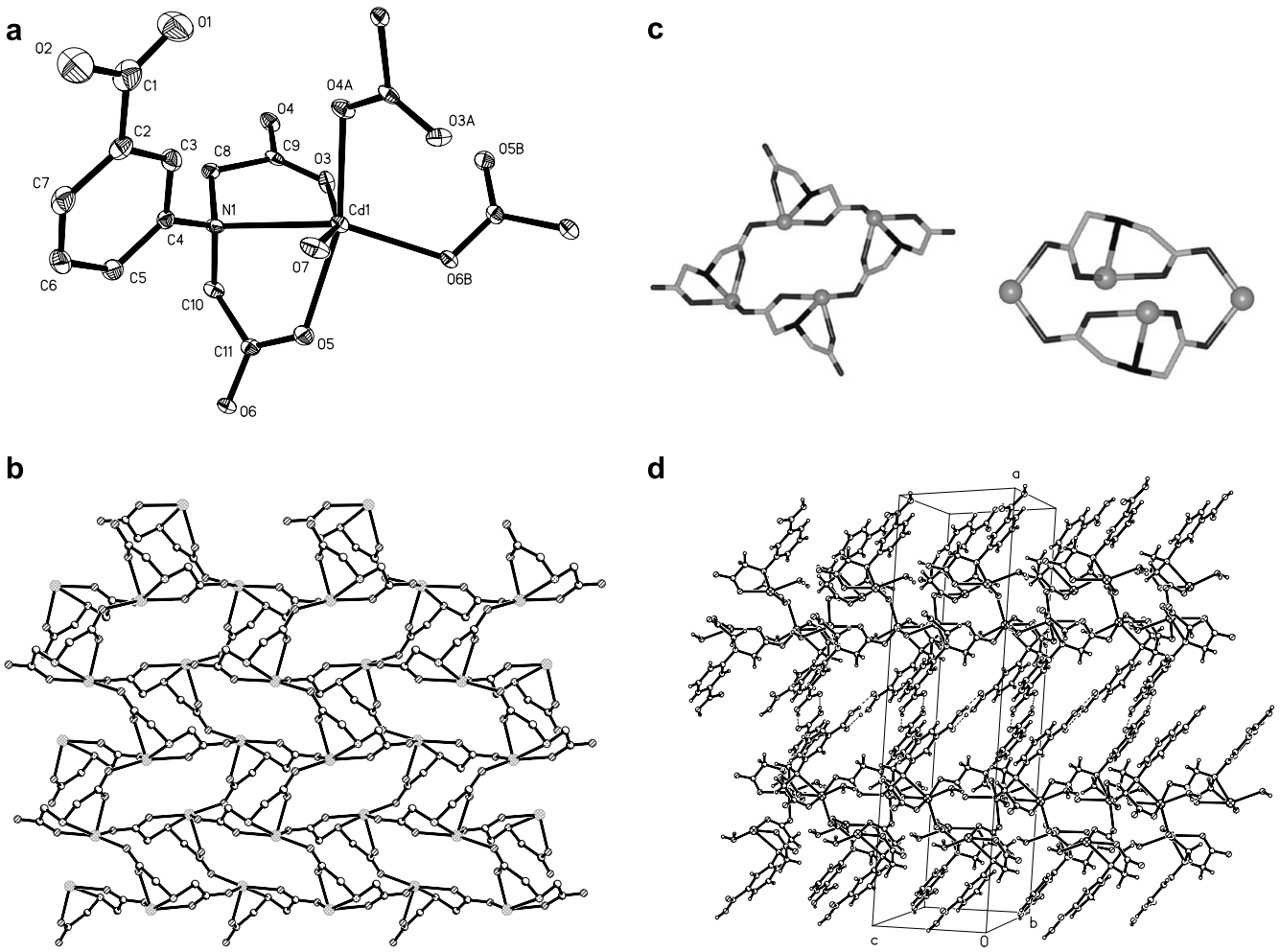
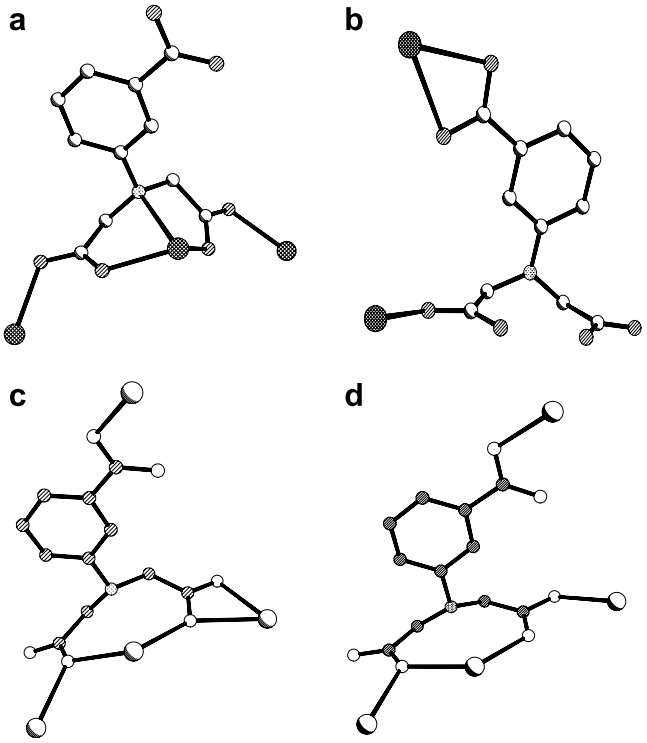


Fig. 1. (a) Coordination environment of the Cd(II) atom in complex **1** with the ellipsoids drawn at the 30% probability level, hydrogen atoms are omitted for clarity. (b) 2D network structure of **1**. (c) Views of the M_4L_4 (left) and M_4L_2 (right) units linked by four and two ligands with the carboxylphenyl groups omitted for clarity. (d) 3D structure of **1** with hydrogen bonds indicated by dashed lines.

Table 2
Selected bond lengths (Å) and angles (°) for complexes **1**–**4**

[*Cd*(*HL*)(*H*$_2$*O*)] (***1***)			
Cd(1)–N(1)	2.556(3)	Cd(1)–O(3)	2.283(3)
Cd(1)–O(4)#1	2.250(3)	Cd(1)–O(5)	2.263(3)
Cd(1)–O(6)#2	2.234(3)	Cd(1)–O(7)	2.306(3)
[*Co*(*HL*)(*H*$_2$*O*)] (***2***)			
Co(1)–N(1)	2.346(3)	Co(1)–O(3)	2.053(2)
Co(1)–O(4)#3	2.086(2)	Co(1)–O(5)	2.067(2)
Co(1)–O(6)#4	2.093(2)	Co(1)–O(7)	2.097(3)
[*Cd*(*HL*)(*H*$_2$*O*)$_4$] (***3***)			
Cd(1)–O(1)	2.435(2)	Cd(1)–O(2)	2.417(2)
Cd(1)–O(3)#5	2.282(2)	Cd(1)–O(7)	2.237(2)
Cd(1)–O(8)	2.383(2)	Cd(1)–O(9)	2.301(2)
Cd(1)–O(10)	2.339(2)		
[*Cd*$_3$(*L*)$_2$(*H*$_2$*O*)$_9$] · 7*H*$_2$*O* (***4***)			
Cd(1)–O(6)#6	2.261(7)	Cd(1)–O(2)	2.333(7)
Cd(1)–O(3)	2.339(17)	Cd(1)–O(7)	2.344(8)
Cd(1)–O(8)	2.380(7)	Cd(1)–O(2)#7	2.446(6)
Cd(2)–O(9)	2.15(2)	Cd(2)–O(10)	2.25(2)
Cd(2)–O(4)	2.339(14)	Cd(2)–O(3)	2.517(15)
Cd(3)–O(10B)	2.30(3)	Cd(3)–O(4B)	2.302(16)
Cd(3)–O(13)	2.335(18)	Cd(3)–O(11)	2.36(2)

Symmetry transformations used to generate equivalent atoms: #1 x, $-y+1$, $z-1/2$; #2 $-x+1/2$, $y+1/2$, $-z+3/2$; #3 x, $-y$, $z+1/2$; #4 $-x+1/2$, $y-1/2$, $-z+1/2$; #5 $x-1/2$, $-y+1/2$, $z-1/2$; #6 $x+1/2$, $-y+1/2$, $z+1$; #7 $-x$, y, $-z+1$.



Scheme 2. Coordination modes of the ligand in complexes **1**–**4**.

observed. Such coordination mode makes a 2D network structure of **1**, as illustrated in Fig. 1b in which the carboxyphenyl groups and coordinated water molecules are omitted for clarity.

It can be seen clearly from Fig. 1b that there are two different macrocyclic rings in the 2D sheet of **1**, namely M_4L_4 and M_4L_2 (Fig. 1c), respectively. In the M_4L_4 ring, each iminodiacetate group of the HL^{2-} ligand coordinates with two Cd(II) atoms using three of its four oxygen atoms and this affords one oxygen atom to link to another Cd(II) atom from a neighbouring ring. While in the case of the M_4L_2 ring, four Cd(II) centers are linked by two HL^{2-} ligands and in turn each HL^{2-} ligand connects three Cd(II) atoms using its four oxygen atoms. These two kinds of macrocyclic rings are arranged alternately to generate a 2D wave-like network. Furthermore, as shown in Fig. 1b, the M_4L_4 and M_4L_2 rings adopt entirely different motifs, i.e. the iminodiacetate moiety of the ligand occupies the space of the M_4L_2 ring whilst there is relatively large cavity in the M_4L_4 ring which is filled by the coordinated water molecules (Fig. S1).

The non-deprotonated carboxyphenyl groups point out of the 2D sheet, up and down alternately, and further connect the 2D network to give a 3D framework through the formation of O–H···O hydrogen bonds between the uncoordinated O atoms of the carboxyphenyl groups from two adjacent layers, with an O···O distance of 2.607(6) Å (Fig. 1d). The hydrogen bonding data are summarized in Table S1. There are other O–H···O and C–H···O hydrogen bonds within the 2D network, which further consolidate the structure [14].

3.1.2. [*Cd*(*HL*)(*H*$_2$*O*)$_4$] (***3***)

When the reaction of ligand H_3L with $Cd(NO_3)_2 \cdot 4H_2O$ was carried out by the layering method instead of a hydrothermal reaction as used for the preparation of **1** and **2**, the new complex **3** was obtained. The crystallographic data showed that complex **3** crystallizes the in monoclinic $P2_1/n$ space group and the Cd(II) atom has a pentagonal bipyramid coordination geometry with an O_7 donor set, as illustrated in Fig. 2a. Two oxygen atoms (O1 and O2) from the carboxyphenyl group of the ligand and three other oxygen atoms (O8, O9 and O10) from coordinated water molecules occupy planar positions with Cd–O bond lengths ranging from 2.301(2) to 2.435(2) Å (Table 2). The axial positions are occupied by one oxygen atom (O3A) from the iminodiacetate group of another ligand and O7 from another coordinated water molecule, with Cd–O bond lengths of 2.282(2) and 2.237(2) Å (Table 2), respectively. As illustrated in Scheme 2b, each HL^{2-} ligand links two Cd(II) atoms in **3**, in which the carboxyphenyl group is in a μ_1–η^1:η^1 chelating mode, and one carboxylate of the iminodiacetate group takes a μ_1–η^1:η^0 monodentate fashion and the other one does not take part in the coordination. It is noteworthy that the coordination mode of the ligand in **3** is quite different from that in **1** and **2**, as discussed above. Firstly, one carboxylate unit from the iminodiacetate group of the ligand remains protonated and is free of coordination in **3**, which was confirmed by the observation of a vibration band at 1720 cm^{-1} in the IR spectrum, however, the one in **1** and **2** non-deprotonated and free of

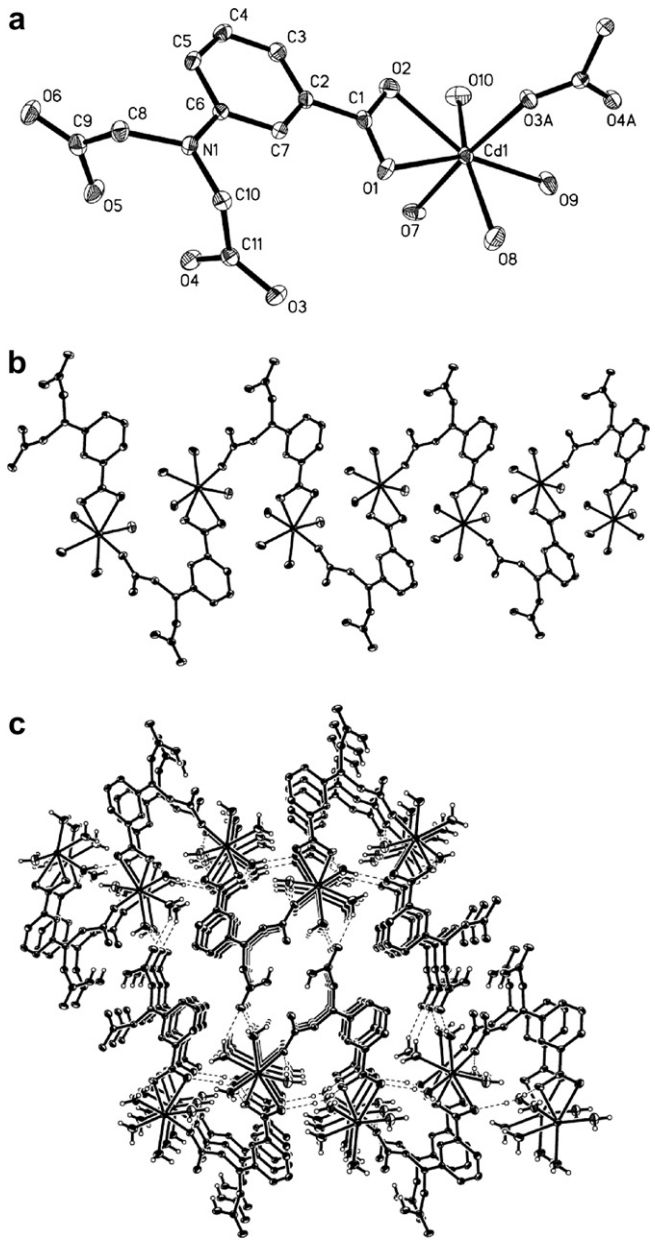


Fig. 2. (a) Coordination environment of the Cd(II) atom in **3** with the ellipsoids drawn at the 30% probability level, hydrogen atoms are omitted for clarity. (b) 1D zigzag chain structure of **3** with hydrogen atoms omitted for clarity. (c) 3D packing structure of **3** with hydrogen bonds indicated by dashed lines.

coordination is the carboxyphenyl group. Moreover, the nitrogen atom of the ligand also does not take part in coordination, and four water molecules participate in coordination to satisfy the coordination need of the Cd(II) atom in **3**. As a result of such differences, a 1D chain-like structure for complex **3** is generated, in which the ligand, utilizing its carboxyphenyl group and one of the iminodiacetate groups, acts as bridge to link the Cd(II) atoms into a zigzag chain structure (Fig. 2b).

In the packing structure of **3**, as shown in Fig. 3c, the 1D chains are firstly linked into a 2D layer by O–H···O hydrogen bonds between the oxygen atoms of the coordinated water molecules (O7 and O10) and carboxyphenyl group from adjacent chains, with O···O distances ranging from 2.707(3) to 3.192(4) Å (Table S1). Then the 2D layers are further connected through O–H···O hydrogen bonds between the oxygen atoms of the coordinated water molecules (O8 and O9) and the free arm of iminodiacetate group from an adjacent layer with O···O distances of 2.814(3) and 2.946(3) Å (Table S1).

3.1.3. $[Cd_3(L)_2(H_2O)_9] \cdot 7H_2O$ (**4**)

In order to further investigate the pH influence on the formation and structure of the complex, the pH value of the ligand solution was carefully adjusted to 7.0, while the other experiment conditions remained the same as those used for the preparation of **3**. As a result, complex **4**, with an entirely different structure, was obtained and the result of crystallographic analysis confirmed that all the carboxylate groups of the ligand are deprotonated and coordinated with the metal atoms in **4**. The complete deprotonation of all three carboxylate groups in **4** was also confirmed by IR spectroscopy since no vibration band around 1700 cm^{-1} for a protonated carboxylate group was observed in the IR spectrum of **4**. The complex crystallizes in the monoclinic *C*2/*m* space group, and in the repeat unit there are two Cd(II) atoms (Cd2 and Cd3) sitting on a symmetry plane with a separation of 2.44 Å and one disordered carboxylate group of the iminodiacetate of the L^{3-} ligand was found near these two Cd(II) atoms. Thus Cd2 and Cd3 are disordered Cd(II) with an occupancy of 0.5. As shown in Fig. 3a, Cd1 is six coordinated by four oxygen atoms (O2, O3, O2A and O6A) from three different L^{3-} ligands, and two oxygen atoms (O7, O8) from two coordinated water molecules, with Cd–O bond lengths ranging from 2.261(7) to 2.446(6) Å (Table 2). While Cd2 and Cd3 are also six coordinated, it is with four oxygen atoms (O3, O4, O3A and O4A) from two L^{3-} ligands and two oxygen atoms (O9, O10) from two coordinated water molecules for Cd2, and two oxygen atoms (O4B and O4BA) from two L^{3-} ligands, and four oxygen atoms (O10B, O11, O13 and O13A) from four coordinated water molecules for Cd3. In addition, two Cd1 atoms (e.g. Cd1 and Cd1A in Fig. 3a) are bridged by two carboxylate oxygen atoms (O2 and O2A) to form a Cd_2O_2 rhombic ring. Therefore, each L^{3-} ligand connects four Cd(II) atoms in two different forms (Scheme 2c and d) in **4** using its three carboxylate groups, and the central nitrogen atom (N1) does not take part in the coordination since the Cd1–N1 distance is 2.70 Å.

The most striking feature of complex **4** is that the Cd(II) centers are connected by the L^{3-} ligand to furnish a 2D network with two different types of cavities filled with water molecules. Firstly, as illustrated in Fig. 3b, six Cd(II) atoms are linked by four L^{3-} ligands to generate a near rectangular ring, and four Cd1 atoms are located at the four corners. Then further connection of the rectangular rings through the Cd_2O_2 rhombic rings results in the formation of an infinite 2D network as

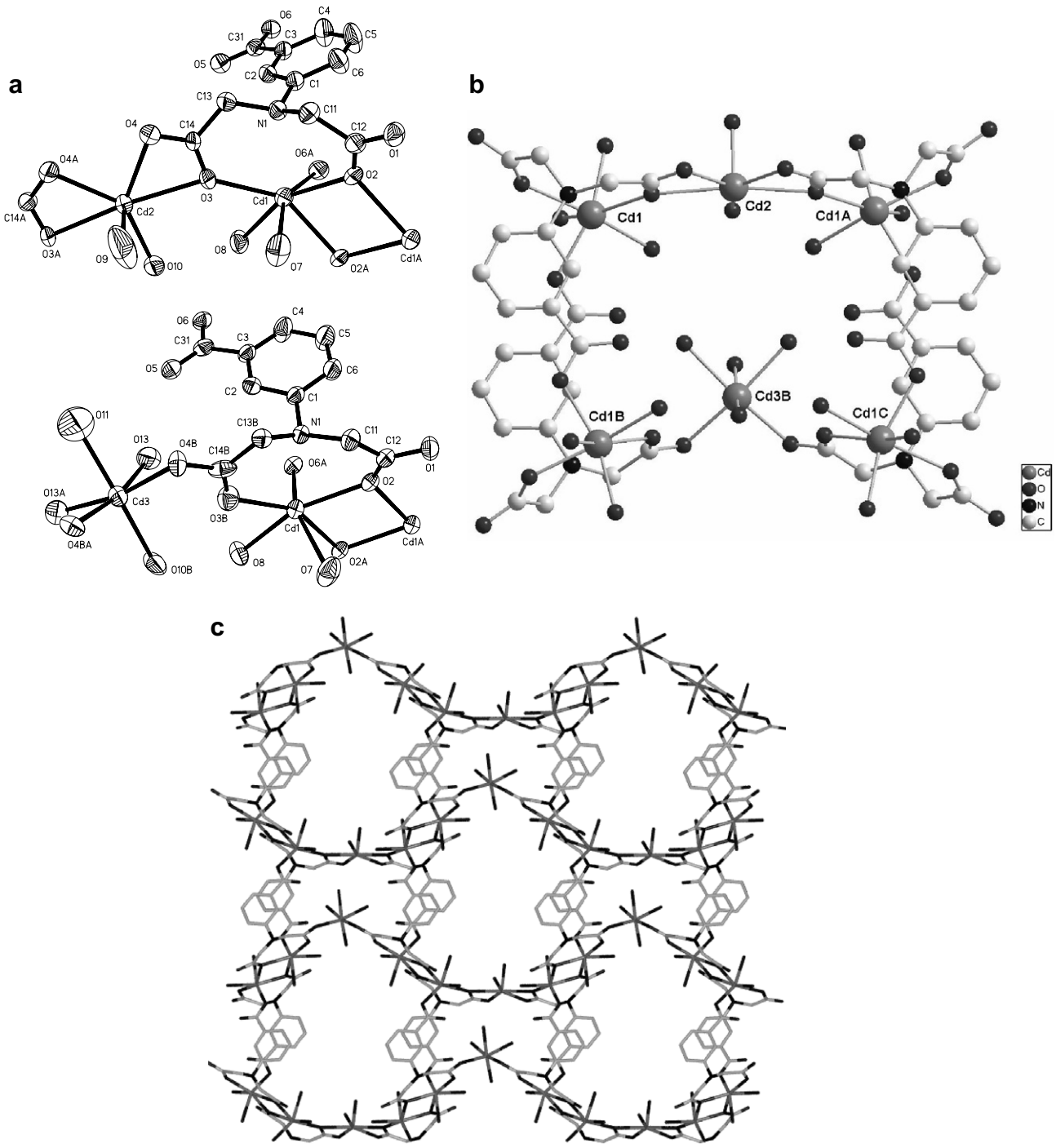


Fig. 3. (a) Coordination environments of the Cd(II) atoms in **4** with the ellipsoids drawn at the 30% probability level, hydrogen atoms and uncoordinated water molecules are omitted for clarity. Top: disordered part with Cd2; bottom: disordered part with Cd3. (b) A near rectangular ring with six Cd(II) atoms linked by four L^{3-} ligands. (c) 2D network structure of **4**. The hydrogen atoms and uncoordinated water molecules are omitted for clarity.

depicted in Fig. 3c. In the crystal packing mode, the 2D sheets are further linked into a 3D structure by C–H···O hydrogen bonds between the C11 atom of an iminodiacetate group and the O1 atom from an adjacent layer, with a C···O distance of 3.552(13) Å, and C–H···O hydrogen bonds also exist in the crystal packing diagram, which further consolidate the structure (Fig. S2, Table S1).

3.2. Effect of synthetic conditions on the structure of the complexes

It has been reported that synthetic conditions, such as pH value, reaction temperature, solvent, etc., are the key factors in assembling MOFs [15,16]. As to the synthesis of **3** and **4**, all the reaction conditions are the same except for the difference of the reaction pH. As a result, complex

3, obtained at a relatively low pH value, is a 1D zigzag chain structure with each Cd(II) center bonded by four water molecules. However in **4**, obtained at a high pH, a more complicated 2D network was generated. Therefore, a rough conclusion could be made that an increase of the pH value in the synthetic process would generate higher dimensionality of the final structure, which is in agreement with the previous reports [17].

In addition, complex **1** was synthesized at a lower pH value and a 2D sheet was obtained rather than a 1D zigzag chain, as in **3**. It might be ascribed to the fact that complex **1** was formed at a high reaction temperature, namely 140 °C under a hydrothermal process, which is considered to be in favor of generating high dimensional structures [18].

From the points discussed above, it is suggested that the increase of reaction pH and temperature may result in a higher connectivity of the carboxylate ligand and further feature a more complicated high dimensional structure.

3.3. Photoluminescence properties of complexes *1*, *3* and *4*

Inorganic–organic hybrid coordination compounds, especially with d^{10} metal centers, have been investigated for fluorescence properties owing to their potential applications as luminescent materials, such as light-emitting diodes (LEDs) [19]. Therefore, in the present study, the photoluminescence properties of **1**, **3** and **4** as well as the free H_3L ligand were investigated in the solid state at room temperature. As shown in Fig. 4, intense emission bands were observed at 407 nm ($\lambda_{ex} = 360$ nm) for the H_3L ligand, 422 nm ($\lambda_{ex} = 350$ nm) for **1**, 414 nm ($\lambda_{ex} = 360$ nm) for **3** and 392 nm ($\lambda_{ex} = 342$ nm) for **4**, respectively. These emissions cannot be attributed to either a metal-to-ligand charge transfer (MLCT) or a ligand-to-metal charge transfer (LMCT) because the Cd(II) ions are in a d^{10} configuration and are difficult to oxidize or to reduce. Therefore,

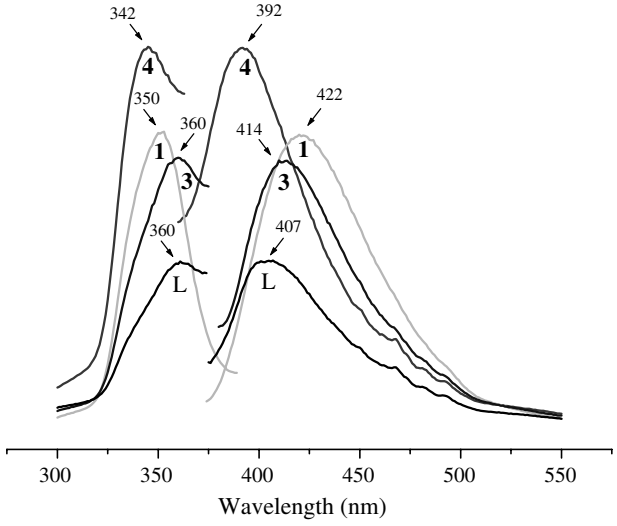


Fig. 4. Excitation and emission spectra of the H_3L ligand and **1**, **3** and **4** in the solid state at room temperature.

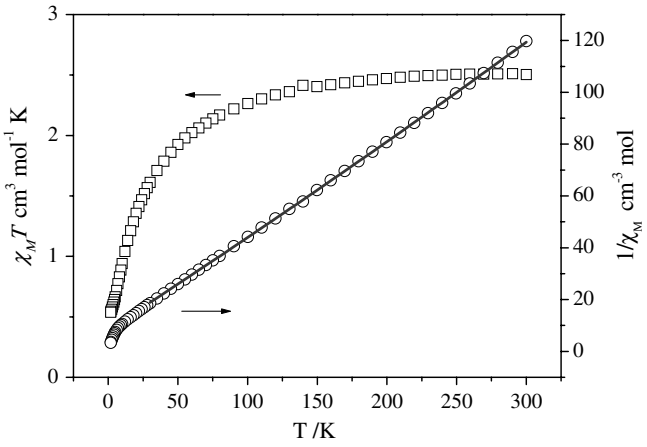


Fig. 5. Temperature dependence of $\chi_M T$ and $1/\chi_M$ for **2**. The solid line shows the Curie–Weiss fitting.

they could be assigned to the π–π^* intraligand fluorescence due to their resemblance to the emission of the H_3L ligand. The enhancement and slight shift of the emissions for **1**, **3** and **4** compared to that of the free ligand probably result from the fact that the coordination of Cd(II) ions increases the ligand conformational rigidity and thus reduces the loss of energy by thermal vibrational decay [20].

3.4. Magnetic properties of complex *2*

The magnetic susceptibility of **2** versus temperature at a field of 2 kOe is shown in Fig. 5, where χ_M is the susceptibility per Co(II) ion. The $\chi_M T$ value is 2.50 cm^3 mol^{-1} K at 300 K, which is significantly larger than the spin-only value of 1.875 cm^3 mol^{-1} K and decreases upon cooling to 0.54 cm^3 mol^{-1} K at 2 K. The magnetic susceptibility above 30 K obeys the Curie–Weiss law with a Weiss constant, $\theta = -24.11$ K, and a Curie constant, $C = 2.88$ cm^3 mol^{-1} K. The high value of C (1.875 cm^3 mol^{-1} K for spin-only Co^{2+}) and negative θ value may be due to the spin–orbit coupling, which is remarkable for the $^4T_{1g}$ state of Co^{2+} in an octahedral ligand field [21].

4. Conclusion

In conclusion, we have successfully synthesized a new carboxylate containing ligand and four new coordination polymers were isolated accordingly under different pH conditions. The results revealed that the reaction pH plays an important role in modulating the architecture of coordination compounds. In addition, complexes **1**, **3** and **4** showed π–π^* intraligand fluorescence in the solid state at room temperature, and the magnetic property of complex **2** was also investigated.

Acknowledgements

This work was supported by the National Basic Research Program of China (Grant No. 2007CB925103)

and the National Science Fund for Distinguished Young Scholars (Grant No. 20425101), which are gratefully acknowledged.

Appendix A. Supplementary material

CCDC 645328, 645329, 645330 and 645331 contain the supplementary crystallographic data for complexes **1**, **2**, **3** and **4**, respectively. These data can be obtained free of charge via http://www.ccdc.cam.ac.uk/conts/retrieving.html, or from the Cambridge Crystallographic Data Centre, 12 Union Road, Cambridge CB2 1EZ, UK; fax: (+44) 1223-336-033; or e-mail: deposit@ccdc.cam.ac.uk. Supplementary data associated with this article can be found, in the online version, at doi:10.1016/j.poly.2007.11.029.

References

[1] (a) L. Carlucci, G. Ciani, D.M. Proserpio, Coord. Chem. Rev. 246 (2003) 247;
(b) H.J. Choi, M.P. Suh, J. Am. Chem. Soc. 126 (2004) 15844;
(c) S.K. Dey, B. Bag, K.M.A. Malik, M.S. El Fallah, J. Ribas, S. Mitra, Inorg. Chem. 42 (2003) 4029;
(d) O. Ohmori, M. Fujita, Chem. Commun. (2004) 1586;
(e) R. Lescouezec, J. Vaissermann, L.M. Toma, R. Carrasco, F. Lloret, M. Julve, Inorg. Chem. 43 (2004) 2234;
(f) T. Kusukawa, M. Fujita, J. Am. Chem. Soc. 124 (2002) 13576.

[2] (a) C. Janiak, J. Chem Soc., Dalton Trans. (2003) 2781;
(b) S.L. James, Chem. Soc. Rev. 32 (2003) 276;
(c) D. Maspoch, D. Ruiz-Molina, J. Veciana, J. Mater. Chem. 14 (2004) 2713;
(d) J.S. Seo, D. Whang, H. Lee, S.I. Jun, J. Oh, Y.J. Jeon, K. Kim, Nature 404 (2000) 982;
(e) B. Chen, N.W. Ockwig, A.R. Millward, D.S. Contreras, O.M. Yaghi, Angew. Chem., Int. Ed. 44 (2005) 4745;
(f) S.-L. Zheng, X.-M. Chen, Aust. J. Chem. 57 (2004) 703.

[3] (a) S.S.Y. Chui, S.M.F. Lo, J.P.H. Charmant, A.G. Orpen, I.D. Williams, Science 283 (1999) 1148;
(b) Z.H. Zhang, Y. Song, T.-a. Okamura, Y. Hasegawa, W.Y. Sun, N. Ueyama, Inorg. Chem. 45 (2006) 2896;
(c) R.Q. Zou, H. Sakurai, Q. Xu, Angew. Chem., Int. Ed. 45 (2006) 2542.

[4] (a) R.B. Walsh, C.W. Padgett, P. Metrangolo, G. Resnati, T.W. Hanks, W.T. Pennington, Cryst. Growth Des. 1 (2001) 165;
(b) J.Y. Zhang, P.W. Miller, M. Nieuwenhuyzen, S.L. James, Chem. Eur. J. 12 (2006) 2448;
(c) H.F. Zhu, W. Zhao, T.-a. Okamura, J. Fan, W.Y. Sun, N. Ueyama, New. J. Chem. 28 (2004) 1010;
(d) R.M. Silva, M.D. Smith, J.R. Gardinier, Inorg. Chem. 45 (2006) 2132;
(e) P.A. Gale, Coord. Chem. Rev. 199 (2000) 181.

[5] P.M. Forster, N. Stock, A.K. Cheetham, Angew. Chem., Int. Ed. 44 (2005) 7608.

[6] (a) T. Steiner, Angew. Chem., Int. Ed. 41 (2002) 48;
(b) C. Janiak, J. Chem. Soc., Dalton Trans. (2000) 3885;
(c) M. Nishio, CrystEngComm 6 (2004) 130.

[7] SAINT, Version 6.02a; Bruker AXS Inc.: Madison, W1, 2002.

[8] G.M. Sheldrick, SADABS, Program for Bruker Area Detector Absorption Correction, University of Göttingen, Göttingen, Germany, 1997.

[9] G.M. Sheldrick, SHELXS-97, Program for Crystal Structure Solution, University of Göttingen, Göttingen, Germany, 1997.

[10] G.M. Sheldrick, SHELXL-97, Program for Crystal Structure Refinement, University of Göttingen, Göttingen, Germany, 1997.

[11] ABSCOR: T. Higashi, Program for Absorption Correction, Rigaku Corporation, Tokyo, Japan, 1995.

[12] DIRDIF-94: P.T. Beurskens, G. Admiraal, G. Beurskens, W.P. Bosman, R. De Gelder, R. Israel, J.M.M. Smits, The DIRDIF-94 program system, Technical Report of the Crystallography Laboratory, University of Nijmegen, The Netherlands, 1994.

[13] TEXSAN: Crystal Structure Analysis Package, Molecular Structure Corporation (1985 and 2004).

[14] (a) G.R. Desiraju, T. Steiner, The Weak Hydrogen Bond, IUCr Monograph on Crystallography, vol. 9, Oxford Science, Oxford, 1999;
(b) C. Janiak, T.G. Scharmann, Polyhedron 22 (2003) 1123, and references therein;
(c) B.R. Bhogala, A. Nangia, Cryst. Growth Des. 3 (2003) 547.

[15] (a) R.Q. Fang, X.M. Zhang, Inorg. Chem. 45 (2006) 4801;
(b) R.S. Rarig, J. Zubieta, J. Chem. Soc., Dalton Trans. (2001) 3446;
(c) M.M. Gomez-Alcantara, A. Cabeza, M.A.G. Aranda, A. Guagliardi, J.G. Mao, A. Clearfield, Solid State Sci. 6 (2004) 479;
(d) Z.G. Guo, R. Cao, X.J. Li, D.Q. Yuan, W.H. Bi, X.D. Zhu, Y.F. Li, Eur. J. Inorg. Chem. (2007) 742.

[16] (a) M. Eddaoudi, J. Kim, N. Rosi, D. Vodak, J. Wachter, M. O'Keefe, O.M. Yaghi, Science 295 (2002) 469;
(b) N. Stock, T. Bein, Angew. Chem., Int. Ed. 43 (2004) 749.

[17] L. Pan, T. Frydel, M.B. Sander, X. Huang, J. Li, Inorg. Chem. 40 (2001) 1271.

[18] J. Chen, M. Ohba, D. Zhao, W. Kaneko, S. Kitagawa, Cryst. Growth Des. 6 (2006) 664.

[19] (a) U.H.F. Bunz, Chem. Rev. 100 (2000) 1605;
(b) W. Wang, H. Schmider, Q. Wu, Y.S. Zhang, S. Wang, Inorg. Chem. 39 (2000) 2397;
(c) Y.B. Chen, J. Zhang, J.K. Cheng, Y. Kang, Z.J. Li, Y.G. Yao, Inorg. Chem. Commun. 7 (2004) 1139.

[20] (a) S.K. Kurtz, T.T. Perry, J. Appl. Phys. 39 (1968) 3798;
(b) A. Vogler, H. Kunkely, Coord. Chem. Rev. 250 (2006) 1622;
(c) R.Q. Fan, D.S. Zhu, Y. Mu, G.H. Li, Y.L. Yang, Q. Su, S.H. Feng, Eur. J. Inorg. Chem. (2004) 4891;
(d) Q. Chu, L.Y. Kong, T.-a. Okamura, H. Kawaguchi, W.L. Meng, W.Y. Sun, N. Ueyama, Z. Anorg. Allg. Chem. 633 (2007) 326;
(e) L. Wen, Y. Li, Z. Lu, J. Lin, C. Duan, Q. Meng, Cryst. Growth Des. 6 (2006) 530.

[21] O. Kahn, Molecular Magnetism, VCH Publishers, Inc., New York, 1993.

Available online at www.sciencedirect.com
ScienceDirect
Polyhedron 27 (2008) 821–834
POLYHEDRON
www.elsevier.com/locate/poly

Two-dimensional divalent metal/pimelate coordination polymers incorporating dipodal organodiimines: Crystal structures, thermal properties, and magnetic studies

Subhashree Mallika Krishnan, Matthew R. Montney, Robert L. LaDuca *

Lyman Briggs College, Department of Chemistry, E-30 Holmes Hall, Michigan State University, East Lansing, MI 48825, USA

Received 10 July 2007; accepted 13 November 2007
Available online 20 December 2007

Abstract

Hydrothermal synthesis has afforded a series of 2-D coordination polymers incorporating the flexible α,ω-dicarboxylate pimelate ligand (pim) and either the kinked organodiimine 4,4′-dipyridylamine (dpa) or its conformationally flexible congener 1,3-di-4-pyridylpropane (dpp).

$[M(pim)(dpa)(H_2O)]_n$ (M = Co, **1-Co**; M = Ni, **1-Ni**) both display puckered (4,4) rhomboid grid-like 2-D layers that aggregate into 3-D through O–H···O hydrogen bonding. $\{[Cu_2(pim)_2(dpa)_2]\cdot 5H_2O\}_n$ (**2**) possesses 2-D slab motifs constructed from the linkage of $[Cu_2(pimelate)_2]_n$ ribbons and $[Cu(pimelate)]_n$ double chains through dpa tethers, entraining discrete water molecule chains with D(8) classification. Employing the longer dpp tether resulted in $[Ni(pim)(dpp)]_n$ (**3**), which manifested a doubly interpenetrated 2-D (4,4) grid layer morphology. Analysis of the variable temperature magnetic susceptibility of **1-Ni** indicated the presence of zero-field splitting as well as possible weak antiferromagnetic coupling between Ni atoms in adjacent layer subunits. In contrast, **2** manifested apparent intra-dimer ferromagnetic interactions with underlying interdimer antiferromagnetic coupling.
© 2007 Elsevier Ltd. All rights reserved.

Keywords: Coordination polymer; Copper; Cobalt; Nickel; Pimelate; Dipyridylamine; Dipyridylpropane; Crystal structure; Antiferromagnetism; Ferromagnetism

1. Introduction

Over the past decade many researchers have undertaken significant effort towards the synthesis and characterization of metal dicarboxylate and tricarboxylate coordination polymers because of the capability of these materials in diverse applications such as gas storage [1], small molecule shape-selectivity [2], ion-exchange [3], catalysis [4], and optical devices [5]. In these phases dianionic dicarboxylate ligands not only serve to link metal cations into higher dimensionalities but also provide necessary charge balance, thereby permitting formation of a large number of neutral coordination polymer frameworks that exclude porosity-curtailing smaller anions. A wide range of structural patterns occurs in these systems, based on the disposition of the donor groups within the dicarboxylate moieties, coordination geometry preferences, and an array of available binding carboxylate modes. While the predominant focus has rested on aromatic dicarboxylates, aliphatic α,ω-dicarboxylate ligands have also shown their utility in the construction of novel coordination polymers due to their ability to undergo facile conformational interconversions [6].

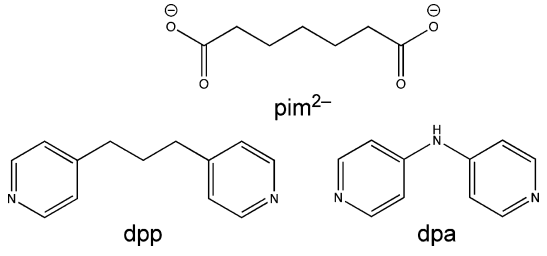
More recently, elaboration of dicarboxylate-containing inorganic/organic hybrid materials has been achieved through the incorporation of neutral organodiimine tethering ligands such as the rigid-rod 4,4′-bipyridine (4,4′-bpy), which can connect metal cations through its distal pyridyl nitrogen donor atoms into a host of structurally interesting

* Corresponding author. Tel.: +1 5174322268.
E-mail address: laduca@msu.edu (R.L. LaDuca).

0277-5387/$ - see front matter © 2007 Elsevier Ltd. All rights reserved.
doi:10.1016/j.poly.2007.11.006

solids with intriguing physicochemical properties [7–10]. For example, the 2-D layered phase {[Zn(isophthalate)(4,4′-bpy)(H_2O)] · 1.5H_2O} manifested intense blue luminescence [8], [Co(thiophene-2,5-dicarboxylate)(4,4′-bipy)] displayed field-dependent spin-flop magnetic behavior at low temperatures [9], and the interpenetrated 3-D material [Zn(terephthalate)(4,4′-bpy)$_{0.5}$] exhibited a remarkable ability to chromatographically separate linear and branched alkanes [10]. This work has been extended to aliphatic α,ω-dicarboxylates, with some divalent metal adipate coordination polymers incorporating 4,4′-bpy or 1,2-di-4-pyridylethane (bpe). In many of these cases doubly interpenetrated 3-D networks were observed [11].

For some time, we have been interested in the synthesis and characterization of coordination polymer materials containing the organodiimine 4,4′-dipyridylamine (dpa, see Scheme 1). Unlike 4,4′-bpy, dpa possesses a kinked disposition of its terminal nitrogen donor atoms as well as a hydrogen bonding locus at its central secondary amine subunit that can assist in the formation of novel structural patterns. Neighboring dpa entities can also interact with each other or with other aromatic subunits through supramolecular π–π stacking interactions. Prior results from our laboratory have shown that coordination polymers with novel structural motifs can result from the hydrothermal combination of metal salts with aliphatic dicarboxylates and dpa [12,13]. Five different divalent metal coordination polymers were prepared utilizing succinate and dpa tethering ligands. Among these, {[Zn(succinate)(dpa)] · H_2O} displayed a rarely seen fourfold interpenetrated $SrAl_2$-type lattice, and {[Ni(dpa)$_2$(succinate)$_{0.5}$]Cl} manifested an unprecedented 5-connected self-penetrated network with 6^{10} topology [12]. [Ni(adipate)(dpa)(H_2O)] exhibited the first-ever example of triple interpenetration within the PtS structure type [13]. In the present study, we have investigated dpa-containing coordination polymers based on pimelate (pim^{2-}), an even longer α,ω-dicarboxylate tethering ligand with enhanced conformational flexibility. Significant differences in their two-dimensional structures were promoted by changes in metal coordination geometry. As the chemistry of dual pimelate/tethering organodiimine coordination polymers remains largely unexplored, we have also investigated the effect of utilizing the more flexible 1,3-dipyridylpropane (dpp) ligand. This change results in interpenetration absent in the dpa cases. Thermal and magnetic properties of these new coordination polymers are also reported herein.



Scheme 1.

2. Experimental

2.1. General considerations

$CoCl_2 \cdot 6H_2O$, $NiCl_2 \cdot 6H_2O$ (Fisher) and pimelic acid (Aldrich) were obtained commercially. The organodiimine 4,4′-dipyridylamine (dpa) was prepared via a published procedure [14]. Water was deionized above 3 MΩ in-house. Thermogravimetric analysis was performed on a TA Instruments TGA 2050 Thermogravimetric Analyzer with a heating rate of 10 °C/min up to 900 °C. Elemental Analysis was carried out using a Perkin–Elmer 2400 Series II CHNS/O Analyzer. IR spectra were recorded on powdered samples on a Perkin–Elmer Spectrum One instrument.

Powder X-ray diffraction patterns were obtained via Θ–2Θ scans performed on a Rigaku Rotaflex instrument. Variable temperature magnetic susceptibility data (2–300 K) was collected on a Quantum Design MPMS SQUID magnetometer at an applied field of 0.1 T. After each temperature change the sample was kept at the new temperature for 5 min before magnetization measurement to ensure thermal equilibrium. The susceptibility data were corrected for diamagnetism using Pascal's constants.

2.2. Preparation of [Ni(pim)(dpa)(H_2O)]$_n$ (**1-Ni**)

$NiCl_2 \cdot 6\,H_2O$ (0.088 g, 0.37 mmol), dpa (0.063 g, 0.37 mmol) and H_2pim (0.059 g, 0.37 mmol) were added to 10 mL of distilled H_2O in a 23 mL Teflon lined Parr acid digestion bomb. The pH was adjusted to 5.7 with 0.7 mL of a 1.0 M NaOH solution. The bomb was sealed, heated to 120 °C for 53 h, and then gradually cooled to ambient temperature. Green plates of **1-Ni** (0.109 g, 73% yield based on Ni) were obtained after filtration, washing with distilled water and acetone, and drying in air. Crystals of **1-Ni** were stable indefinitely in air. *Anal.* Calc. for $C_{17}H_{21}NiN_3O_5$ **1-Ni**: C, 50.28; H, 5.21; N, 10.35. Found: C, 50.30; H, 5.27; N, 10.41%. IR (cm^{-1}): 3250 w br, 2929 w, 1593 s, 1542 m, 1513 s, 1476 m, 1453 w, 1437 m, 1421 m, 1386 s, 1334 s, 1291 w, 1202 m, 1083 w, 1060 m, 1024 m, 904 w, 873 w, 827 s, 764 w, 731 s, 661 m.

2.3. Preparation of [Co(pim)(dpa)(H_2O)]$_n$ (**1-Co**)

The procedure for the synthesis of **1-Ni** was followed with the use of $CoCl_2 \cdot 6H_2O$ (0.088 g, 0.37 mmol) as the metal source. Magenta plates of **1-Co** (0.031 g, 21% yield based on Co) were obtained after filtration, washing with distilled water and acetone, and drying in air. Crystals of **1-Co** were stable indefinitely in air. *Anal.* Calc. for $C_{17}H_{21}CoN_3O_5$ **1-Co**: C, 50.26; H, 5.21; N, 10.34. Found: C, 50.46; H, 4.82; N, 10.36%. IR (cm^{-1}): 3250 w br, 2927 w, 1591 s, 1513 s, 1476 w, 1454 w, 1437 m, 1420 w, 1383

m, 1336 s, 1310 w, 1292 w, 1233 w, 1082 m, 1058 m, 1020 s, 904 m, 873 w, 827 s, 801 w, 732 s, 717 m, 660 s.

2.4. Preparation of $\{[Cu_2(pim)_2(dpa)_2]\cdot 5H_2O\}_n$ (2)

$CuCl_2\cdot 2H_2O$ (0.063 g, 0.37 mmol), H_2pim (0.059 g, 0.37 mmol) and dpa (0.127 g, 0.74 mmol) were placed into 10 g (555 mmol) distilled H_2O in a 23 mL Teflon-lined Parr acid digestion bomb (1:2:1500 mol ratio). The mixture was acidified to pH 4.5 with 0.5 mL of a 1.0 M HCl solution. The bomb was sealed and heated at 150 °C for 24 h, whereupon it was cooled slowly in air to 25 °C. Small blue crystals of **2** (0.089 g, 55% yield based on Cu) were isolated after washing with distilled water. Because the material effuses its waters of crystallization slowly upon standing, it was kept for long-term storage in its mother liquor. *Anal.* Calc. for $C_{34}H_{48}Cu_2N_6O_{13}$ (**2**): C, 46.62; H, 5.52; N, 9.60. Found: C, 43.36; H, 4.92; N, 9.03%. Elemental analyses showed lower than expected values on multiple samples, ascribed to either incomplete combustion or the presence of an amorphous inorganic impurity, as the powder XRD spectrum of freshly prepared **2** coincides exactly with that predicted from the single-crystal X-ray structure. IR (cm^{-1}): 3250 w br, 2927 w, 1593 s, 1526 s, 1445 m, 1394 s, 1358 s, 1291 m, 1256 w, 1205 s, 1062 m, 1026 s, 907 w, 816 s, 760 w, 729 w, 664 w.

2.5. Preparation of $[Ni(pim)(dpp)]_n$ (3)

$NiCl_2\cdot 6H_2O$ (0.088 g, 0.37 mmol), dpp (0.147 g, 0.74 mmol) and H_2pim (0.059 g, 0.37 mmol) were added to 10 mL of distilled H_2O in a 23 mL Teflon lined Parr acid digestion bomb. The bomb was sealed, heated to 150 °C for 44 h, and then gradually cooled to ambient temperature. Green blocks of **3** (0.050 g, 33% yield based on Ni) were obtained after filtration, washing with distilled water and acetone, and drying in air. Crystals of **3** were stable indefinitely in air. *Anal.* Calc. for $C_{20}H_{24}NiN_2O_4$ **3**: C, 57.87; H, 5.83; N, 6.75. Found: C, 57.65; H, 5.74; N, 6.87%. IR (cm^{-1}): 2921 w, 1614 m, 1560 m, 1537 s, 1510 m, 1432 s, 1410 s, 1314 m, 1213 w, 1140 w, 1069 w, 1023 m, 920 w, 894 m, 862 m, 817 m, 808 m, 723 m, 660 m.

3. X-ray crystallography

Single crystals of all materials were subjected to single crystal X-ray diffraction using a Bruker-AXS SMART 1k CCD instrument. Reflection data was acquired using graphite-monochromated Mo Kα radiation ($\lambda = 0.71073$ Å). The data were integrated via SAINT [15]. Lorentz and polarization effect and empirical absorption corrections were applied with SADABS [16]. The structures were solved using direct methods and refined on F^2 using SHELXTL [17]. All non-hydrogen atoms were refined anisotropically. Hydrogen atoms bound to carbon atoms were placed in calculated positions and refined isotropically with a riding model. The hydrogen atoms bound to the central nitrogen of the dpa moieties and all aquo ligands were found via Fourier difference maps, restrained at fixed positions, and then refined isotropically with thermal parameters 1.2 times the average U_{ij} values of the atoms to which they are bound. Distended thermal ellipsoids for some of the pimelate carbon atoms in **2** are indicative of some amount of positional or thermal disorder; however, this could not be successfully modeled. Relevant crystallographic data is listed in Table 1.

4. Results and discussion

4.1. Synthesis and spectral characterization

The coordination polymers **1**–**3** were prepared cleanly under hydrothermal conditions via combination of the appropriate metal chloride, H_2pim, and either dpa (**1**, **2**) or dpp (**3**). The infrared spectra of **1**–**3** were consistent with their formulations. Sharp, medium intensity bands in the range of ~1600 cm^{-1} to ~1200 cm^{-1} were ascribed to stretching modes of the pyridyl rings of the dpa moieties [18]. Features corresponding to pyridyl ring puckering mechanisms were evident in the region between 820 cm^{-1} and 600 cm^{-1}. Asymmetric and symmetric C–O stretching modes of the carboxylate moieties were evidenced by very strong, slightly broadened bands at ~1590 cm^{-1} and ~1340 cm^{-1}. Broad bands in the region of ~3400 cm^{-1} to ~3200 cm^{-1} in all cases represent N–H stretching modes within the dpa ligands and O–H stretching modes within water molecules of crystallization. The broadness of these latter spectral features is caused by significant hydrogen bonding pathways within **1**–**3**. Phase purity was verified with powder XRD by comparison with powder patterns predicted from the single crystal structures.

4.2. Structural description of $[M(pim)(dpa)(H_2O)]_n$ (1-Ni, M = Ni; 1-Co, M = Co)

1-Ni and **1-Co** are isomorphous, both crystallizing in the monoclinic space group $P2_1/c$ and possessing an asymmetric unit consisting of a metal atom, one doubly deprotonated pim^{2-} (pim) moiety, one dpa ligand, and one bound water molecule. The asymmetric unit of **1-Ni** is displayed in Fig. 1; that of **1-Co** is virtually identical. The coordination spheres about the divalent metal ions in these materials are slightly distorted $[MO_4N_2]$ octahedra, with the two nitrogen donors from two different dpa molecules oriented in a *cis* fashion with respect to each other. Two of the oxygen donors (O1, O2) belong to the chelating terminus of a pim^{2-} ligand. The aquo ligand (O5) is disposed in a *cis* manner with respect to the remaining oxygen donor (O3), part of a monodentate carboxylate group of another (but crystallographically identical) pim^{2-} ligand. Bond lengths and angles (Table 2) about the metal ions are standard for distorted octahedral coordination complexes with one chelating ligand. The bond lengths for **1-Ni** are slightly

Table 1
Crystal and structure refinement parameters for **1**–**3**

	1-Ni	**1-Co**	**2**	**3**
Empirical formula	$C_{17}H_{21}NiN_3O_5$	$C_{17}H_{21}CoN_3O_5$	$C_{34}H_{48}Cu_2N_6O_{13}$	$C_{20}H_{24}N_2NiO_4$
Formula weight	406.08	406.30	875.86	415.12
Collection T (K)	173(2)	293(2)	173(2)	173(2)
Color and habit	green plate	magenta plate	blue block	green block
Crystal size (mm)	0.25 × 0.20 × 0.02	0.35 × 0.30 × 0.05	0.20 × 0.18 × 0.12	0.55 × 0.45 × 0.40
λ (Å)	0.71073	0.71073	0.71073	0.71073
Crystal system	monoclinic	monoclinic	triclinic	monoclinic
Space group	$P2_1/c$	$P2_1/c$	$P\bar{1}$	$P2_1/c$
a (Å)	8.6725(15)	8.736(4)	9.9468(17)	7.572(4)
b (Å)	16.176(3)	16.295(7)	10.3520(18)	17.096(9)
c (Å)	13.211(2)	13.337(6)	19.365(3)	15.499(9)
α (°)	90	90	77.728(3)	90
β (°)	104.725(3)	104.513(7)	82.270(3)	93.288(9)
γ (°)	90	90	84.770(3)	90
V (Å^3)	1792.5(5)	1838.0(13)	1926.7(8)	2003.1(19)
Z	4	4	2	4
D_{calc} (g cm^{-3})	1.505	1.468	1.506	1.377
μ (mm^{-1})	1.116	0.966	1.125	0.995
Minimum/maximum, T	0.758	0.878	0.851	0.899
hkl ranges	$-11 \leqslant h \leqslant 11$, $-21 \leqslant k \leqslant 21$, $-17 \leqslant l \leqslant 17$	$-11 \leqslant h \leqslant 11$, $-21 \leqslant k \leqslant 21$, $-17 \leqslant l \leqslant 17$	$-13 \leqslant h \leqslant 13$, $-13 \leqslant k \leqslant 13$, $-25 \leqslant l \leqslant 25$	$-9 \leqslant h \leqslant 9$, $-22 \leqslant k \leqslant 22$, $-20 \leqslant l \leqslant 20$
Total reflections	21 812	20 264	23 946	21 772
Unique reflections	4 410	4274	9214	4581
R_{int}	0.1542	0.0351	0.0772	0.0244
Parameters/restraints	244/4	247/4	525/15	244/0
R_1^a (all data)	0.1363	0.0508	0.1375	0.0329
R_1 ($I > 2\sigma(I)$)	0.0713	0.0360	0.0730	0.0276
wR_2^b (all data)	0.1592	0.0804	0.1678	0.0705
wR_2 ($I > 2\sigma(I)$)	0.1361	0.0745	0.1439	0.0678
Maximum/minimum residual (e$^-$/Å^3)	0.588/−0.756	0.388/−0.256	0.929/−0.578	0.279/−0.180
Goodness-of-fit	1.042	1.036	1.028	1.052

[a] $R_1 = \sum||F_o|-|F_c||/\sum|F_o|$.
[b] $wR_2 = \{\sum[w(F_o^2 - F_c^2)^2]/\sum[wF_o^2]^2\}^{1/2}$.

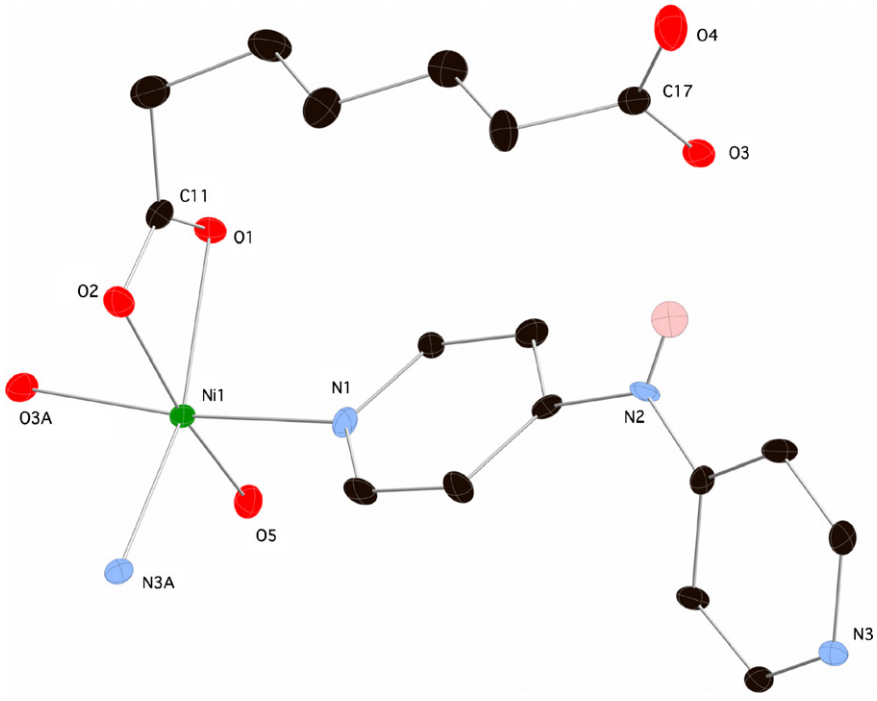


Fig. 1. The asymmetric unit of **1-Ni** with thermal ellipsoids drawn at 50% probability and partial atom numbering scheme.

Table 2
Selected bond distance (Å) and angle (°) data for **1-M**

1-Ni			
Ni1–N3$^{\#1}$	2.053(4)	N3$^{\#1}$–Ni1–O3$^{\#2}$	89.21(14)
Ni1–O3$^{\#2}$	2.068(3)	N3$^{\#1}$–Ni1–O5	90.98(14)
Ni1–O5	2.070(3)	O3$^{\#2}$–Ni1–O5	92.05(13)
Ni1–N1	2.103(4)	N3$^{\#1}$–Ni1–N1	95.93(15)
Ni1–O2	2.121(3)	O3$^{\#2}$–Ni1–N1	172.70(14)
Ni1–O1	2.143(3)	O5–Ni1–N1	93.04(14)
O1–C11	1.267(5)	N3$^{\#1}$–Ni1–O2	98.10(14)
O2–C11	1.264(6)	O3$^{\#2}$–Ni1–O2	85.52(12)
O3–C17	1.274(6)	O5–Ni1–O2	170.55(13)
O4–C17	1.236(6)	N1–Ni1–O2	88.62(14)
		N3$^{\#1}$–Ni1–O1	159.49(14)
		O3$^{\#2}$–Ni1–O1	86.04(12)
		O5–Ni1–O1	109.09(13)
		N1–Ni1–O1	87.35(14)
		O2–Ni1–O1	61.67(12)
1-Co			
Co1–O4$^{\#3}$	2.091(2)	O4$^{\#3}$–Co1–O5	90.44(6)
Co1–O5	2.092(2)	O4$^{\#3}$–Co1–N1	90.50(6)
Co1–N1	2.105(2)	O5–Co1–N1	90.04(6)
Co1–N3$^{\#4}$	2.159(2)	O4$^{\#3}$–Co1–N3$^{\#4}$	172.88(6)
Co1–O2	2.161(2)	O5–Co1–N3$^{\#4}$	93.15(7)
Co1–O1	2.187(2)	N1$^{\#4}$–Co1–N3	95.64(6)
C11–O1	1.268(3)	O4$^{\#3}$–Co1–O2	86.19(6)
C11–O2	1.255(3)	O5–Co1–O2	171.27(6)
C17–O3	1.239(3)	N1–Co1–O2	98.04(6)
C17–O4	1.271(2)	N3$^{\#4}$–Co1–O2	89.38(7)
		O4$^{\#4}$–Co1–O1	86.60(6)
		O5–Co1–O1	111.70(6)
		N1–Co1–O1	158.07(6)
		N3$^{\#2}$–Co1–O1	86.36(6)
		O2–Co1–O1	60.10(6)

Symmetry transformations to generate equivalent atoms: #1 $-x+1$, $y+1/2$, $-z+3/2$; #2 $-x+2$, $y+1/2$, $-z+3/2$; #3 $-x+1$, $y+1/2$, $-z+1/2$; #4 $-x$, $y-1/2$, $-z+1/2$.

shorter than those for **1-Co**, consistent with well-established ionic radius trends [19].

The pim^{2-} ligands adopt a *gauche–anti–anti–anti* conformation (four C-atom torsion angles = 69.19°, 173.08°, 178.17° and 170.39° for **1-Ni**) and bridge neighboring metal atoms in an exobidentate chelating/monodentate fashion to form undulating [M(pim)]$_n$ chain motifs that course parallel to the *b* crystal axis (Fig. 2). While the chelating carboxylates in **1-M** display symmetric binding to the metal, the C–O bond lengths of the monodentate carboxylate termini vary by ~0.40 Å, reflective of enhanced π-type character in the between the carboxylate C atom and the unligated oxygen atoms. The [M(pim)]$_n$ chains in turn are connected through tethering dpa ligands to generate a ruffled [M(pim)(dpa)(H$_2$O)]$_n$ two-dimensional (4,4) layer motif parallel to the *ab* crystal plane (Fig. 3). Each metal ion is covalently connected to four others, with two connections each via pim^{2-} and dpa ligands. The metal–metal contact distances through the pim^{2-} ligands measure 8.988 Å and 9.056 Å for **1-Ni** and **1-Co**, respectively; the corresponding contact distances through the dpa tethers are 11.350 Å and 11.465 Å. In order to accommodate the necessary orientation for appropriate covalent bonding, the dpa molecule undergoes a significant inter-ring torsion (47.1° in **1-Ni** and 46.7° in **1-Co**). The incipient void spaces within the resulting puckered rhomboid circuits in **1-Ni** measure 8.673 and 16.176 Å (via through-space Ni–Ni distances), with Ni–Ni–Ni angles of 48.8°, 48.8°, 90.9° and 128.3°. The corresponding through-space Co–Co distances in **1-Co** are slightly longer at 8.736 and 16.295 Å with virtually identical Co–Co–Co angles.

The covalent connectivity within the layer is supplemented by supramolecular hydrogen bonding donation from the amine functional group of dpa to the oxygen atom O3 within the chelating carboxylate moiety. In addition, the aquo ligand provides a hydrogen bonding point of contact to the unligated oxygen atom of type O4 within the monodentate carboxylate group, possibly preventing a bis-monodentate bis-monodentate binding mode for the pim^{2-} ligand. The puckering of the individual 2-D layers causes an alternation of the position of the pim^{2-} ligands above and below the layer, allowing interlayer hydrogen bonding between the aqua ligands and oxygen atoms of type O1 within the chelating carboxylate groups. These supramolecular interactions result in stacking of the [M(pim)(dpa)(H$_2$O)]$_n$ layers along the *c* crystal direction to establish the pseudo 3-D crystal structures of **1-M** (Fig. 4). The interlayer metal–metal contact distances are 5.113 Å and 5.095 Å in **1-Ni** and **1-Co**, respectively, significantly closer than the intralayer metal–metal distances. Metrical parameters for the classical hydrogen bonding interactions in **1-M** are given in Table 3.

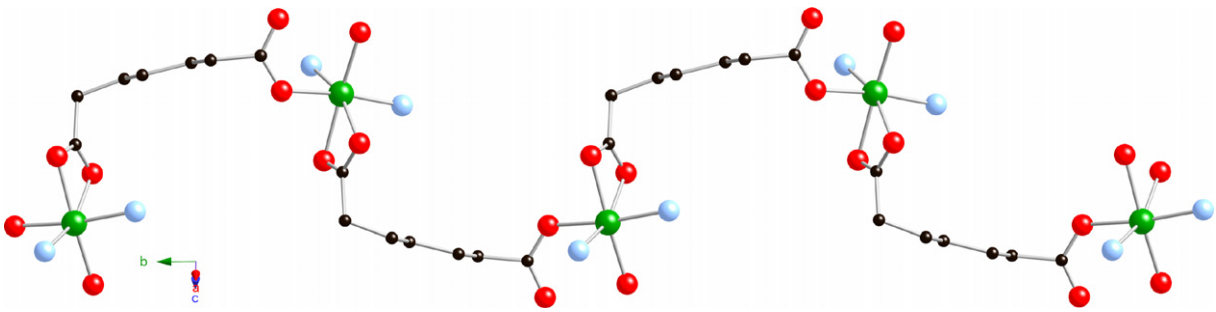


Fig. 2. [Ni(pim)]$_n$ chain motif in **1-Ni**.

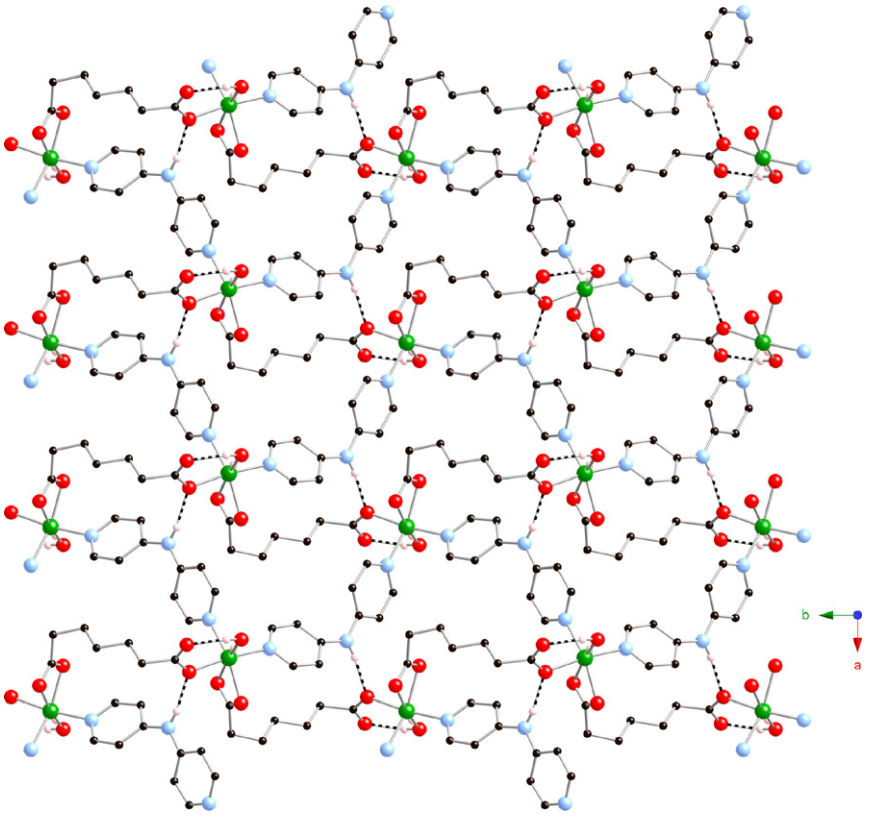


Fig. 3. Face-on view of the $[Ni(pim)(dpa)(H_2O)]_n$ 2-D layers in **1-Ni**. Intralayer hydrogen bonding is shown as dashed lines.

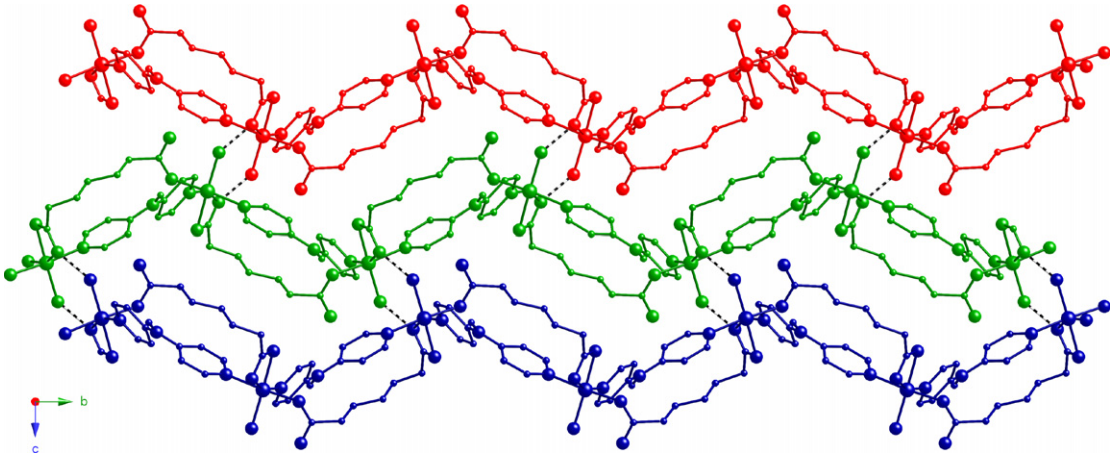


Fig. 4. Stacking of $[M(pim)(dpa)(H_2O)]_n$ layers along the *c* crystal direction by supramolecular interlayer hydrogen bonding (shown as dashed lines).

*4.3. Structural description of $\{[Cu_2(pim)_2(dpa)_2]\cdot 5H_2O\}_n$ (**2**)*

The asymmetric unit of **2** (Fig. 5) was found to contain two crystallographically distinct divalent copper atoms, two fully deprotonated pim^{2-} dianions (C21–C27/O1–O4, *pim-A*; C31–C37/O5–O8, *pim-B*), two dpa ligands (C1–C10/N1–N3, *dpa-A*; C11–C20/N4–N6, *dpa-B*), and five water molecules of crystallization, one of which (O5W) is disordered equally over two positions. One of the copper atoms (Cu1) adopts a virtually perfect $\{CuN_2O_3\}$ square pyramidal coordination geometry ($\tau = 0.01$) [20], with one nitrogen donor from a *dpa-A* ligand, one nitrogen donor from a *dpa-B* ligand, and oxygen donors from two different *pim-B* ligands situated within the basal plane. The nitrogen donors are oriented in a *trans*-fashion within the basal plane, as are the oxygen donors. The coordination sphere about Cu1 is completed by an oxygen donor from a third *pim-B* ligand lying in the axial position. The bond lengths and angles about Cu1 (Table 4) are consistent with the well-known Jahn-Teller distortion for Cu^{2+}. The other crystallographically distinct Cu atom (Cu2) exhibits

Table 3
Hydrogen bonding distance (Å) and angle (°) data for **1**–**2**

D–H···A	*d*(H···A)	∠DHA	*d*(D···A)	Symmetry transformation for A
1-Ni				
O5–H5A···O1	1.87(2)	177(5)	2.707(4)	$-x+2, y+1/2, -z+3/2$
O5–H5B···O4	1.90(3)	142(5)	2.618(5)	$-x+2, -y, -z+1$
N2–H2N···O3	1.93(2)	166(5)	2.799(5)	
1-Co				
O5–H5A···O1	1.88(2)	169(2)	2.711(2)	$-x+1, -y, -z$
O5–H5B···O3	1.79(2)	169(3)	2.623(3)	$-x, y+3/2, -z+1/2$
N2–H2N···O4	1.98(2)	173(2)	2.828(2)	$-x, y+1/2, -z+1/2$
2				
N2–H2N···O1W	2.00(2)	178(5)	2.877(6)	$x-1, y, z$
N5–H5N···O6	2.02(3)	157(5)	2.845(6)	$-x+1, -y+2, -z$
O1W–H1WA···O4	1.96(3)	157(6)	2.768(6)	$-x+1, -y+2, -z$
O1W–H1WB···O6	1.88(3)	164(5)	2.690(5)	
O2W–H2WA···O3W	2.06(2)	143(4)	2.846(7)	$x-1, y-1, z$
O2W–H2WB···O1W	2.08(2)	147(4)	2.926(7)	$-x+1, -y+1, -z$
O3W–H3WA···O3	2.00(3)	163(7)	2.825(6)	
O3W–H3WB···O2	2.16(4)	151(7)	2.921(6)	$x, y+1, z$
O4W–H4WA···O7	2.17(4)	150(7)	2.940(6)	
O4W–H4WB···O5WA	2.07(3)	163(7)	2.905(2)	$x-1, y, z$
O4W–H4WB···O5WB	1.95(6)	128(7)	2.564(2)	$x-1, y, z$

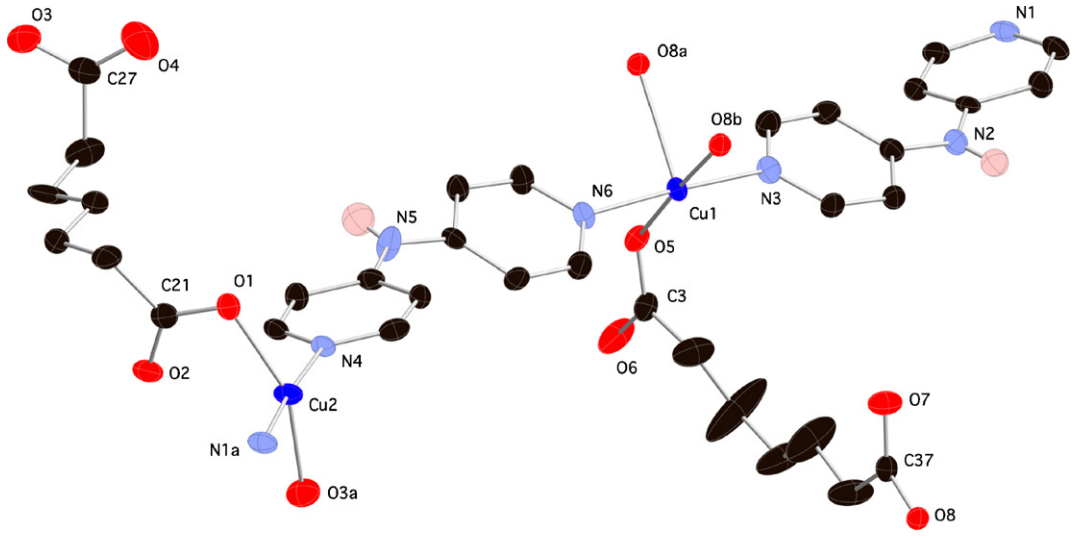


Fig. 5. Asymmetric unit of **2** with thermal ellipsoids shown at 50% probability and partial atom numbering scheme. Most hydrogen atoms have been omitted for clarity.

a {*trans*-CuN_2O_2} square planar coordination environment, with the nitrogen donors belonging to two crystallographically distinct dpa ligands and the oxygen donors provided by two different *pim-A* ligands. The O1–Cu2–O3 bond angle (Table 3) is ~20° narrower than the corresponding trans N1–Cu2–N4 bond angle, a deviation from idealized square planar geometry likely provoked by long range Cu···O interactions and other supramolecular effects (*vide infra*).

Extension of the structure about Cu1 reveals {Cu_2O_2} bimetallic kernels formed by the junction of two adjacent Cu1 atoms by two μ_2-bridging oxygen atoms of type O8 belonging to two different *pim-B* units. Each O8 oxygen atom lies in the basal plane of one Cu1 square pyramid, and is in the axial position of another, resulting in an asymmetric rhomboid four-membered ring. The through-space Cu1–Cu1 and O8–O8 distances are 3.391 Å and 2.796 Å, respectively; the Cu–O–Cu and O–Cu–O angles within the rhomboid {Cu_2O_2} unit subtend 101.2(5)° and 78.8(5)°. Adjacent {Cu_2O_2} units are linked to two others along the *b* crystal direction by means of tethering *pim-B* dianions in an *anti–gauche–anti–anti* conformation (C–C–C–C torsion angles: 177.0°, 25.7°, 175.6°, 174.6°), thereby forming 1-D $[Cu_2(pim)_2]_n$ ribbon motifs (Fig. 6A). The Cu–Cu distance through the kinked *pim-B* ligand is 8.888 Å. The pim^{2-} moieties in this chain are exotridentate,

Table 4
Selected bond distance (Å) and angle (°) data for **2**

Cu1–O5	1.950(3)	O5–Cu1–N3	88.05(15)
Cu1–O8$^{\#1}$	1.991(3)	O8$^{\#1}$–Cu1–N3	92.17(15)
Cu1–N6$^{\#2}$	2.006(4)	N6$^{\#2}$–Cu1–N3	175.65(16)
Cu1–N3	2.006(4)	O5–Cu1–O8$^{\#3}$	104.69(12)
Cu1–O8$^{\#3}$	2.388(3)	O8$^{\#1}$–Cu1–O8$^{\#3}$	78.88(12)
Cu2–O3$^{\#4}$	1.974(4)	N6$^{\#2}$–Cu1–O8$^{\#3}$	91.30(14)
Cu2–N4	1.987(4)	N3–Cu1–O8$^{\#3}$	91.69(14)
Cu2–O1	1.989(3)	O3$^{\#4}$–Cu2–N4	91.67(15)
Cu2–N1	1.996(4)	O3$^{\#4}$–Cu2–O1	154.42(16)
		N4–Cu2–O1	91.86(15)
O5–Cu1–O8$^{\#1}$	176.41(13)	O3$^{\#4}$–Cu2–N1	87.87(16)
O5–Cu1–N6$^{\#2}$	88.13(15)	N4–Cu2–N1	174.69(17)
O8$^{\#1}$–Cu1–N6$^{\#2}$	91.51(14)	O1–Cu2–N1	90.83(15)
		Cu1$^{\#1}$–O8–Cu1$^{\#4}$	101.12(12)

Symmetry transformations to generate equivalent atoms: #1 $-x+1$, $-y$, $-z+1$; #2 $x+1$, $y-1$, $z+1$; #3 x, $y+1$, z; #4 x, $y-1$, z.

binding to Cu in a monodentate fashion at O5, and bridging two Cu atoms via their O8 termini. An interaction between Cu1 and the unligated carboxylate oxygen atom O7 is evident, with a Cu···O distance of 2.783 Å. Such "secondary bonding" interactions are common in Cu^{2+} coordination complexes [21].

In turn, Cu2 atoms are connected into 1-D $[Cu(pim)]_n$ single chains via tethering *pim-A* dianionic units (Fig. 6B), which adopt a spread out *gauche–anti–anti–gauche* conformation (torsion angles = 77.2°, 177.3°, 173.0°, 68.7°) with a bis-monodentate bis-monodentate binding mode. Due to the more open conformation, the Cu2–Cu2 distance through *pim-A* is 10.352 Å, almost 1.5 Å longer than the *pim-B*-bridged corresponding Cu1–Cu1 distance. Abutting $[Cu(pim)]_n$ single chains are weakly conjoined through long "4+1" type Cu2···O1 secondary interactions (2.700 Å, drawn as dashed lines in Fig. 6B). If these interactions are considered "bonds", $\{Cu_2O_2\}$ bimetallic units similar to those within the Cu1-based ribbons can be invoked. However, the Cu2–Cu2 distances within these units are ~0.25 Å longer, at 3.647 Å, with a Cu2–O1···Cu2 angle of 100.99°. It is likely that the conformational flexibility of the pim^{2-} tethers assists in the formation of two different 1-D copper dicarboxylate motifs in **1**.

Alternating $[Cu_2(pim)_2]_n$ ribbons (based on Cu1) and $[Cu(pim)]_n$ double chain subunits (based on Cu2) are subsequently bridged together by tethering dpa ligands to establish a 2-D $[Cu_2(pim)_2(dpa)_2]$ neutral coordination polymer slab that lies parallel to the $(10\bar{1})$ crystal plane (Fig. 7). The Cu1–Cu2 distances measure 11.485 Å (through *dpa-A* with an inter-ring torsion angle of 28.7°) and 11.527 Å (through *dpa-B* with an inter-ring torsion angle of 29.6°). The covalent connectivity within the slab motif is augmented by π–π stacking between *dpa-A* and *dpa-B* ligands (centroid-to-centroid distances 3.647(1) Å and 3.631(1) Å), imposed by the presence of the $\{Cu_2O_2\}$ bimetallic units with similar metal–metal contact distances.

$[Cu_2(pim)_2(dpa)_2]$ slabs stack along the *a* crystal direction via N–H···O hydrogen bonding interactions between the central amine functional groups of *dpa-B* ligands and unligated carboxylate oxygen atoms of type O5 within the *pim-B* dianions, which project into the interlamellar regions (Fig. 8). The closest interlayer Cu–Cu contact distance is 8.549 Å.

Sequestered within and between the coordination polymer layers are discrete hydrogen bonded aqueous chains of eight water molecules each (O3W···O2W···O4W···O5W···O5W···O4W···O2W···O3W), decorated at each

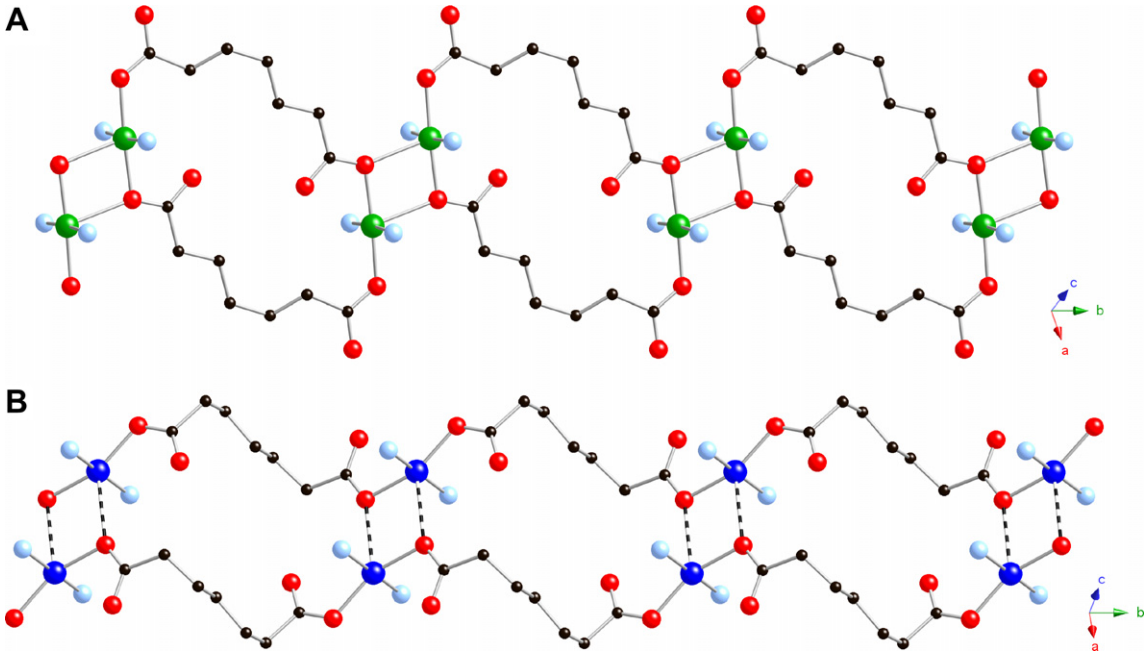


Fig. 6. $[Cu_2(pim)_2]$ ribbons (A) and [Cu(pim)] double chains with long range interactions shown as dashed lines (B) in **2**.

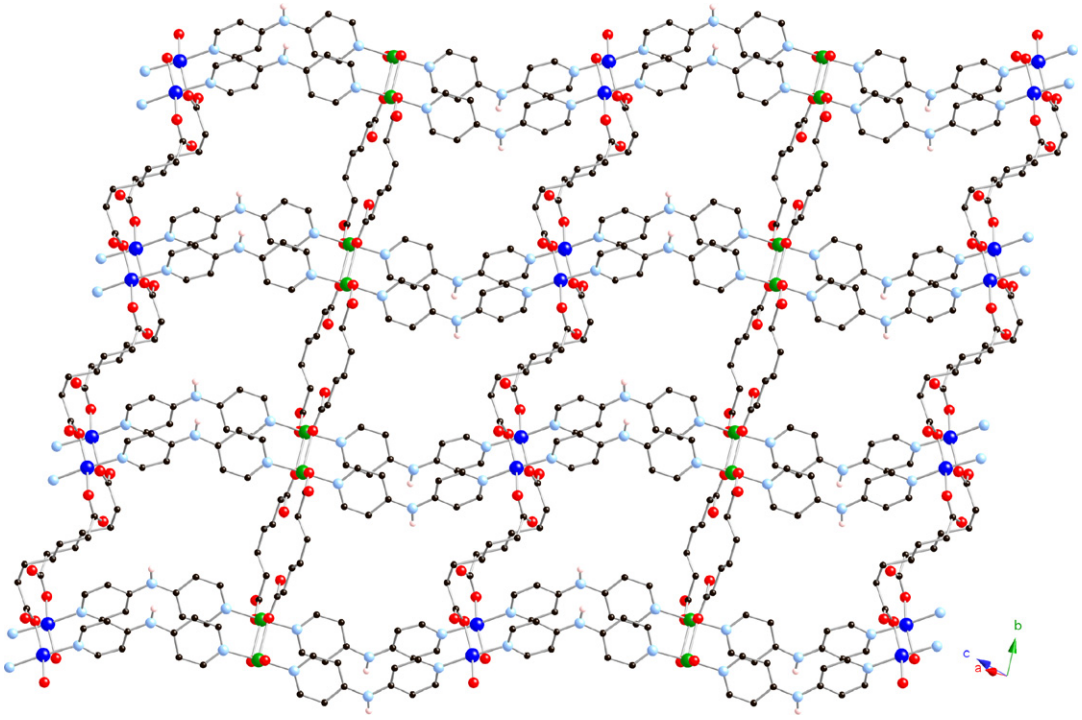


Fig. 7. A 2-D slab motif in **2**, formed from the junction of parallel 1-D $[Cu_2(pim)_2]$ ribbons and [Cu(pim)] double chains through dpa tethers.

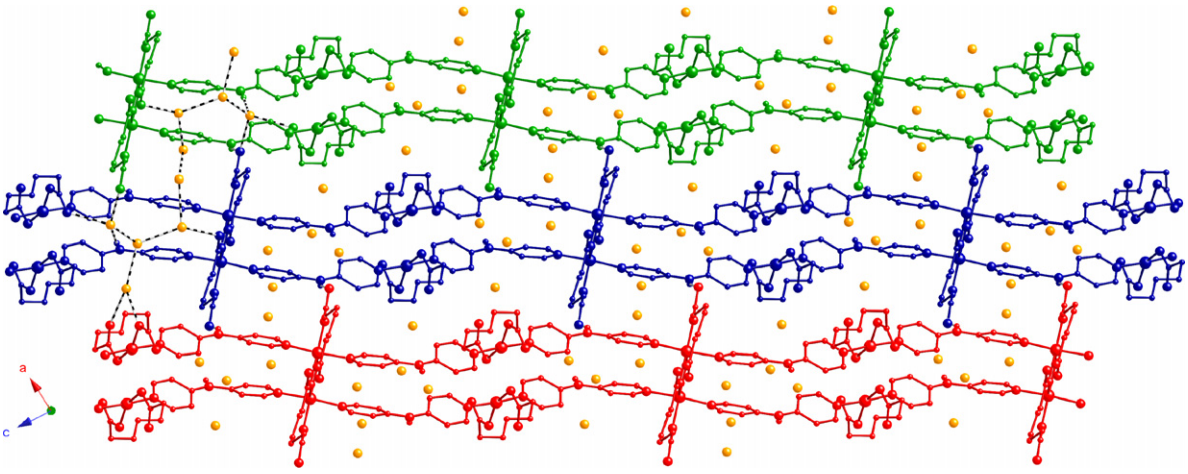


Fig. 8. Stacking of neighboring 2-D slabs in **2**. Discrete water molecule chains can be seen coursing within and between the layers. Hydrogen bonding connectivity for one of these water chains is shown as dashed lines.

O2W position by additional pendant water molecules (type O1W). Therefore the unligated water molecule substructure falls into the uncommonly encountered D(8) morphological classification [22], with a connectivity pattern resembling that of 2,7-dimethyloctane. The uncoordinated water molecules are anchored to the coordination polymer matrix by extensive hydrogen bonding pathways. The water molecules at the chain termini (O3W) engage in hydrogen bonding donation to the ligated and unligated carboxylate oxygen atoms O3 and O2, belonging to two separate *pim-A* ligands. Water molecules of type O1W, serving as "substituents" on the aqueous chain, link to the coordination polymer framework by accepting hydrogen bonds from the amine units of *dpa-A* and donating hydrogen bonds to unligated carboxylate oxygen atoms O4 and O6, belonging to *pim-A* and *pim-B*, respectively. Finally, water molecules of type O4W are held by hydrogen bonding donation to unligated carboxylate oxygen atoms O7, part of *pim-B*. Metrical parameters for the supramolecular hydrogen bonding interactions in **2** are listed in Table 3. According to a calculation performed with PLATON [23], the incipient void spaces occupied by the water molecules of crystallization represent 17.6% of the unit cell volume of **2**.

4.4. Structural description of [Ni(pim)(dpp)] (3)

The asymmetric unit of **3** (Fig. 9) contains one divalent nickel atom, one dpp ligand, and a doubly deprotonated pim^{2-} dianion. Due to the chelation of the pim^{2-} carboxylate termini, the coordination environment about Ni is best described as a distorted $[NiO_4N_2]$ octahedron; bond lengths and angles about Ni are consistent with this description (Table 5). The two nitrogen donors, which belong to two different dpp ligands, are arranged in a *cis* orientation.

Extension of the structure reveals that each Ni atom is linked to four others, two through dpp linkers and two through pim^{2-} dianions, to form a 2-D rhomboid grid coordination polymer morphology. The torsion angles across the trimethylene bridge of the dpp ligand (179.4° and 176.1°) show that the dpp subunit has adopted a splayed-open *anti* conformation, providing a through-ligand Ni–Ni contact distance of 13.42 Å. The bis-bridging bischelating pim^{2-} tethers display a *gauche–anti–anti–anti* conformation (torsion angles 71.6°, 171.2°, 173.6°, and 176.2°), providing a Ni–Ni distance of 10.28 Å, ~3.1 Å shorter than the corresponding through-dpp distance.

The grid apertures in **3**, 17.10 × 15.14 Å as measured by through space Ni–Ni distances, are large enough to accommodate interpenetration of a second identical $[Ni(pim)(dpp)]_n$ 2-D layer (Fig. 10). This stands in marked contrast to **1**, which does not display any interpenetration due to the shorter dpa tethers and resulting smaller grid mesh size. Within a single grid, the Ni–Ni–Ni angles subtend 78.2°, 78.2°, 79.15° and 112.48°. The closest Ni–Ni separation between two independent interpenetrated layers is 7.57 Å. Layer motifs subsequently stack along the *c* crystal direction primarily by means of π–π supramolecular interactions (3.892(2) Å) between dpp pyridyl rings within adjacent layers, thus constructing the pseudo 3-D crystal structure of **3**. The closest interlayer Ni–Ni contact distance is 7.92 Å. Unfortunately, attempts to prepare a copper coordination polymer containing both pim^{2-} and dpp resulted either in amorphous products or the known 1-D chain phase $[CuCl(dpp)]_n$ [24].

Table 5
Selected bond distance (Å) and angle (°) data for **3**

Ni1–O4	2.0675(13)	$N2^{\#1}$–Ni1–N1	92.70(6)
$Ni1–N2^{\#1}$	2.0683(15)	O4–Ni1–$O2^{\#2}$	162.48(4)
Ni1–N1	2.0747(15)	$N2^{\#1}$–Ni1–$O2^{\#2}$	94.25(6)
$Ni1–O2^{\#2}$	2.0761(14)	N1–Ni1–$O2^{\#2}$	97.37(5)
$Ni1–O1^{\#2}$	2.1433(15)	O4–Ni1–$O1^{\#2}$	103.60(5)
Ni1–O3	2.1530(15)	$N2^{\#1}$–Ni1–$O1^{\#2}$	92.74(6)
O1–C21	1.256(2)	N1–Ni1–$O1^{\#2}$	159.22(5)
O2–C21	1.2659(19)	$O2^{\#2}$–Ni1–$O1^{\#2}$	62.22(4)
O3–C27	1.2548(19)	O4–Ni1–O3	62.29(5)
O4–C27	1.2718(18)	$N2^{\#1}$–Ni1–O3	159.02(5)
		N1–Ni1–O3	91.13(6)
$O4–Ni1–N2^{\#1}$	96.80(6)	$O2^{\#2}$–Ni1–O3	105.69(5)
O4–Ni1–N1	95.64(5)	$O1^{\#2}$–Ni1–O3	90.93(6)

Symmetry transformations to generate equivalent atoms: #1 $-x-1$, $y-1/2$, $-z+3/2$; #2 $-x+1$, $y-1/2$, $-z+3/2$.

4.5. Variable temperature magnetism

To probe possible spin communication, samples of **1** and **2** were subjected to variable temperature magnetic study. For **1**, the $\chi_m T$ value at 300 K was 1.23 cm^3 K mol^{-1}. This is slightly higher than predicted for a spin-only uncoupled Ni^{2+} d^8 $S=1$ ion, indicative of anisotropy. The $\chi_m T$ value remained largely constant to 60 K, whereupon it began to decrease, reaching a value of 1.08 cm^3 K mol^{-1} at 12 K. At lower temperatures the $\chi_m T$ product dropped precipitously, a sign of possible antiferromagnetic coupling, zero field splitting, or a cooperative effect of the two phenomena. The magnetic susceptibility of **1** was modeled using Eq. (1) [25], which accounts for both magnetic coupling between Ni centers (Θ) and zero field splitting (D).

$$\chi_m T = \left(\frac{2Ng^2\beta^2}{3k(T-\Theta)}\left(\frac{(2kT/D)-(2kT\exp(x)/D)+\exp(x)}{1+2\exp(x)}\right)T\right) \quad (1)$$

where $x=-D/kT$.

The best fit to the data (Fig. 11) occurred with $g=2.241(2)$, $\Theta=-1.62(4)$ K and $D=4.9(1)$ cm^{-1} with $R=9.55\times10^{-3}=\{\sum[(\chi_m T)_{obs}-(\chi_m T)_{calc}]^2/\sum(\chi_m T)_{obs}]^2\}$. Within the layer structure of **1**, the pimelate and dpa

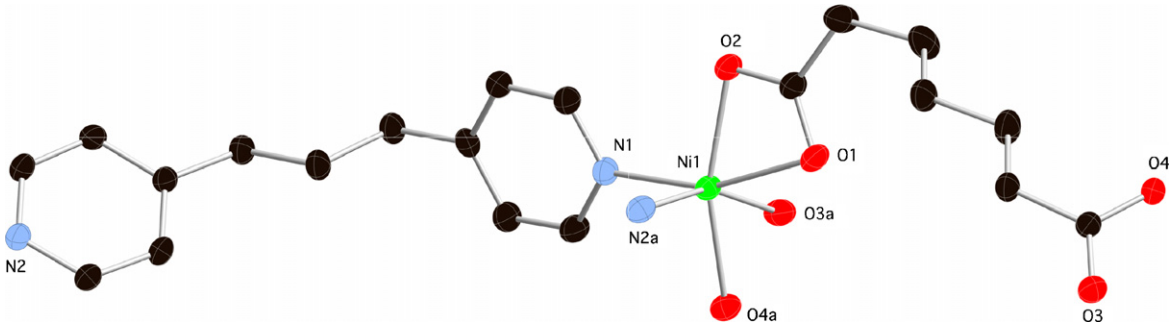


Fig. 9. Asymmetric unit of **3** with thermal ellipsoids shown at 50% probability and partial atom numbering scheme. Most hydrogen atoms have been omitted for clarity.

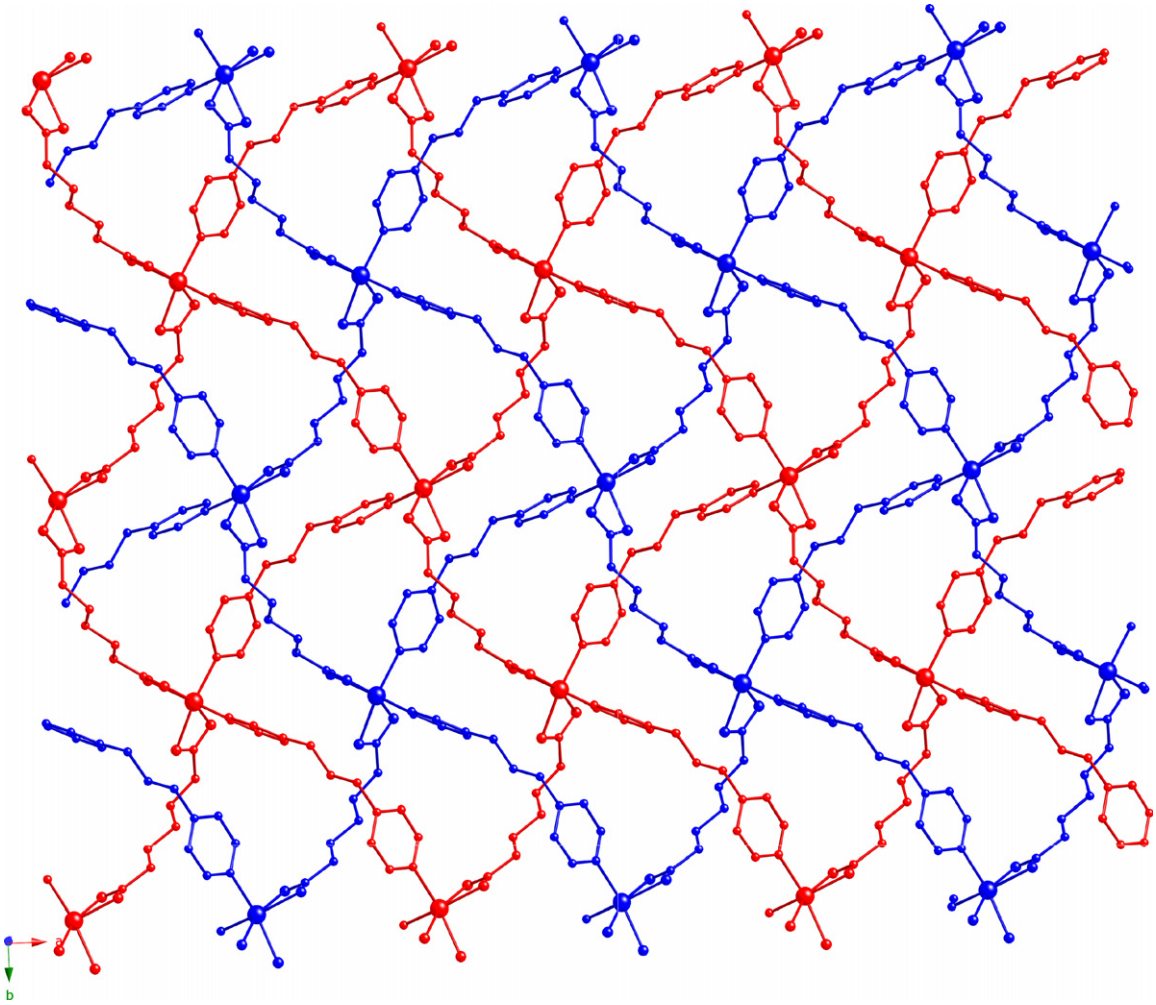


Fig. 10. A view down *c* of doubly interpenetrated (4,4) layers in **3**.

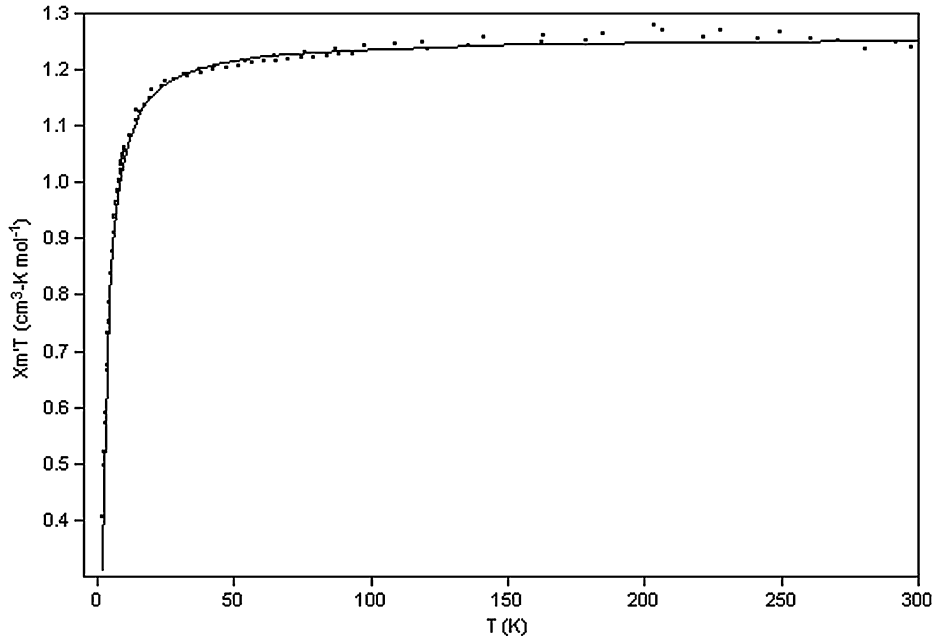


Fig. 11. Plot of $\chi_m T$ vs T for **1-Ni**. The calculated fit to Eq. (1) is indicated as a solid black line.

ligands cause Ni–Ni distances that are likely too long for any significant magnetic communication. Closer Ni–Ni interactions (~5.1 Å), mediated by hydrogen bonding between the aquo ligands and chelating carboxylate moieties in adjacent layers, could be the origin of the observed weak interlayer antiferromagnetic coupling. Attempted fits using models that accounted for either interlayer antiferromagnetic coupling or zero field splitting alone were much less successful. Hydrogen-bonding promoted magnetic communication between paramagnetic metal ions has been reported in other coordination polymer materials [26].

The plot of the $\chi_m T$ product versus T for **2** (Fig. 12) showed an increase in $\chi_m T$ as temperature decreased, a sign of ferromagnetic interactions within one or both types of oxygen bridged dimeric Cu units within the coordination polymer structure. The $\chi_m T$ value reached a maximum of 1.52 cm^3 K mol^{-1} at 5.2 K, below which temperature it began to decrease (see inset of Fig. 12). This low-temperature behavior can be ascribed to weaker antiferromagnetic interactions between adjacent $\{Cu_2O_2\}$ dimeric units through either the pimelate or dpa tethering ligands. Unfortunately no Curie–Weiss regime was found in the variable temperature susceptibility data for **2**, even at higher temperatures. Neither could the data be fit acceptably to the Bleaney–Bowers equation [27] for magnetically interacting Cu(II) dimers, even incorporating an interdimer parameter (Θ). It is possible that the presence of two different types of $\{Cu_2O_2\}$ dimeric units in **2**, with varying Cu···Cu contact distances, results in significant differences in the nature and magnitude of their respective magnetic interactions [28]. Thus, the overall magnetic susceptibility behavior can be ascribed to the simultaneous action of the spin communication within both types of $\{Cu_2O_2\}$ dimer, thereby greatly complicating any attempts at modeling. Nevertheless, it is probable that net intradimer ferromagnetic interactions occur in **2**, with an underlying weak interdimer antiferromagnetic superexchange mechanism.

4.6. Thermal analysis of *1–3*

Compound **1-Ni** underwent loss of its ligated water molecule between 250 °C and 320 °C (4.9% mass loss, 4.4% predicted). Combustion of the organic components ensued, with a series of mass losses between 350 °C and 600 °C. The mass remnant of 21% corresponds roughly with the deposition of NiO (18% calcd.). Compound **2**, which had apparently lost 2 equiv. of unbound water molecules on standing, continued to dehydrate between 45 °C and 115 °C (5.5% mass loss, 6.1% calcd. for 3 equiv. of water). Combustion of organics commenced at ~250 °C, resulting in likely deposition of $CuCO_3$ at 700 °C (29% mass remnant, 30% theoretical). Compound **3** remains stable until ~320 °C at which point rapid expulsion of the organic components occurs. The 22% mass remnant at 600 °C corresponds loosely to NiO (18% calcd.). TGA traces for **1–3** are depicted in Figs. S1–S3.

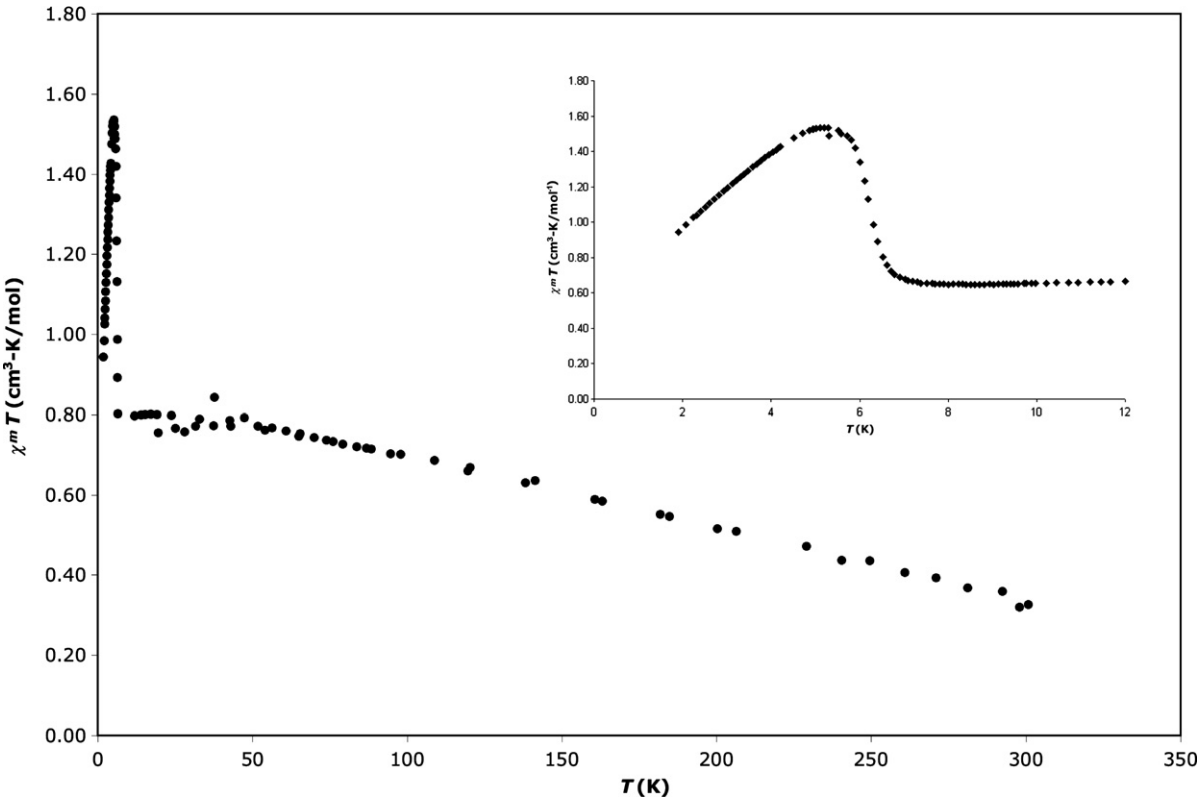


Fig. 12. Plot of $\chi_m T$ vs T for **2** (inset shows low temperature data only).

5. Conclusions

Taking advantage of the conformational flexibility of the α,ω-dicarboxylate pimelate ligand, four two-dimensional organodiimine-containing coordination polymers have been prepared. Both the pimelate conformation and the tether length and hydrogen-bonding capability of the organodiimine component appear to play a significant structure-directing role, in synergy with coordination geometry preferences. Use of a longer tethering organodiimine promotes the formation of rhomboid grids with larger apertures, resulting in an interpenetrated structure. The lowered coordination number at the copper centers in **2**, as opposed to **1** and **3**, promotes a double slab structure with $\{Cu_2O_2\}$ dimers that exhibit apparent ferromagnetic coupling. The differing pimelate conformations observed in these materials reflect this ligand's ability to adjust to the requirements imposed by the metal coordination geometry and the supramolecular environment. Investigation of long-chain α,ω-dicarboxylate coordination polymers incorporating kinked or flexible organodiimines remains a fruitful area of synthetic exploration in our laboratory, and further results will be reported in due course.

Acknowledgements

The authors gratefully acknowledge Michigan State University for financial support of this work.

We thank Dr. Rui Huang for elemental analysis and David Martin and Lindsey Johnston for the acquisition of the infrared spectra. SDG.

Appendix A. Supplementary material

CCDC 652276, 652277, 652278 and 652279 contain the supplementary crystallographic data for compounds **1-Ni**, **1-Co**, **2** and **3**. These data can be obtained free of charge via http://www.ccdc.cam.ac.uk/conts/retrieving.html, or from the Cambridge Crystallographic Data Centre, 12 Union Road, Cambridge CB2 1EZ, UK; fax: (+44) 1223-336-033; or e-mail: deposit@ccdc.cam.ac.uk. Supplementary data associated with this article can be found, in the online version, at doi:10.1016/j.poly.2007.11.006.

References

[1] (a) For example: J.L.C. Roswell, O.M. Yaghi, Angew. Chem., Int. Ed. Engl. 44 (2005) 4670;
(b) M. Kondo, T. Okubo, A. Asami, S.-I. Noro, T. Yoshitomi, S. Kitagawa, T. Ishii, H. Matsuzaka, Angew. Chem., Int. Ed. Engl. 38 (1999) 140;
(c) A.C. Sudik, A.R. Millward, N.W. Ockwig, A.P. Cote, J. Kim, O.M. Yaghi, J. Am. Chem. Soc. 127 (2005) 7110.

[2] (a) For example: J.S. Seo, D. Whang, H. Lee, S.I. Jun, J. Oh, Y.J. Jeon, K. Kim, Nature 404 (2000) 982;
(b) A. Cingolani, S. Galli, N. Masciocchi, L. Pandolfo, C. Pettinari, A. Sironi, J. Am. Chem. Soc. 127 (2005) 6144.

[3] (a) For example: Q.-R. Fang, G.-S. Zhu, M. Xue, J.-Y. Sun, S.-L. Qiu, L. Shi-Lun, Dalton Trans. (2006) 2399;
(b) X.-M. Zhang, M.-L. Tong, H.K. Lee, X.-M. Chen, J. Solid State Chem. (2001) 118;
(c) O.M. Yaghi, H. Li, T.L. Groy, Inorg. Chem. 36 (1997) 4292.

[4] (a) For example: S.G. Baca, M.T. Reetz, R. Goddard, I.G. Filippova, Y.A. Simonov, M. Gdaniec, N. Gerbeleu, Polyhedron 25 (2006) 1215;
(b) H. Han, S. Zhang, H. Hou, Y. Fan, Y. Zhu, Eur. J. Inorg. Chem. 8 (2006) 1594;
(c) W. Mori, S. Takamizawa, C.N. Kato, T. Ohmura, T. Sato, Micropor. Mesopor. Mater. 73 (2004) 15.

[5] (a) For example: S. Zang, Y. Su, Y. Li, Z. Ni, Q. Meng, Inorg. Chem. 45 (2006) 174;
(b) L. Wang, M. Yang, G. Li, Z. Shi, S. Feng, Inorg. Chem. 45 (2006) 2474;
(c) S. Wang, Y. Hou, E. Wang, Y. Li, L. Xu, J. Peng, S. Liu, C. Hu, New J. Chem. 27 (2003) 1144.

[6] (a) For example: D. Ghoshal, A.K. Ghosh, G. Mostafa, J. Ribas, N.R. Chaudhuri, Inorg. Chim. Acta 360 (2007) 1771;
(b) C. Livage, C. Egger, M. Nogues, G. Ferey, Compt. Rend. Acad. Sci. Ser. Chem. 4 (2001) 221.

[7] (a) W.-G. Lu, C.-Y. Su, T.-B. Lu, L. Jiang, J.-M. Chen, J. Am. Chem. Soc. 128 (2006) 34;
(b) S. Horike, R. Matsuda, S. Kitagawa, Stud. Surf. Sci. Cat. 156 (2005) 725;
(c) C. Qin, X.-L. Wang, Y.-G. Li, E.-B. Wang, Z.-M. Su, L. Xu, R. Clerac, Dalton Trans. (2005) 2609;
(d) Y.-Q. Zheng, E.-R. Ying, Polyhedron 24 (2005) 397;
(e) S.K. Ghosh, J. Ribas, P.K. Bharadwaj, Crystal Growth Des. 5 (2005) 623;
(f) X.-Z. Sun, Y.-F. Sun, B.-H. Ye, X.-M. Chen, Inorg. Chem. Commun. 6 (2003) 1412.

[8] L. Xu, G.-C. Guo, B. Liu, M.-S. Wang, J.-S. Huang, Inorg. Chem. Commun. 7 (2004) 1145.

[9] H.-P. Jia, W. Li, Z.-F. Ju, J. Zhang, Eur. J. Inorg. Chem. (2006) 4264.

[10] B. Chen, C. Liang, J. Yang, D.S. Contreras, Y.L. Clancy, E.B. Lobkovsky, O.M. Yaghi, S. Dai, Angew. Chem., Int. Ed. 45 (2006) 1390.

[11] (a) L.-S. Long, Y.-R. Wu, R.-B. Huang, L.-S. Zheng, Inorg. Chem. 43 (2004) 3798;
(b) R.-F. Hu, Y. Kang, J. Zhang, Z.-J. Li, Y.-Y. Qin, Y.-G. Yao, Z. Anorg. Allgem. Chem. 631 (2005) 3053;
(c) Y.-Q. Zheng, J.-L. Lin, Z.-P. Kong, Inorg. Chem. 43 (2004) 2590.

[12] M.R. Montney, S. Mallika Krishnan, N.M. Patel, R.M. Supkowski, R.L. LaDuca, Crystal Growth Des. 7 (2007) 1145.

[13] M.R. Montney, S. Mallika Krishnan, R.M. Supkowski, R.L. LaDuca, Inorg. Chem. 46 (2007) 7362.

[14] P.J. Zapf, R.L. LaDuca, R.S. Rarig, K.M. Johnson, J. Zubieta, Inorg. Chem. 37 (1998) 3411.

[15] SAINT, Software for Data Extraction and Reduction, Version 6.02, Bruker AXS, Inc., Madison, WI, 2002.

[16] SADABS, Software for Empirical Absorption Correction, Version 2.03, Bruker AXS, Inc., Madison, WI, 2002.

[17] G.M. Sheldrick, SHELXTL, Program for Crystal Structure Refinement, University of Gottingen, Gottingen, Germany, 1997.

[18] M. Kurmoo, C. Estournes, Y. Oka, H. Kumagai, K. Inoue, Inorg. Chem. 44 (2005) 217.

[19] R.D. Shannon, Acta Crystallogr., Sect. A 32 (1976) 751.

[20] A.W. Addison, T.N. Rao, J. Chem. Soc. Dalton Trans. (1984) 1349.

[21] L. Yi, L.-N. Zhu, B. Ding, P. Cheng, D.-Z. Liao, Y.-P. Zhai, S.-P. Yan, Z.-H. Jiang, Trans. Met. Chem. 29 (2004) 200.

[22] (a) L. Infantes, S. Motherwell, CrystEngComm 4 (2002) 454;
(b) L. Infantes, J. Chisholm, S. Motherwell, CrystEngComm 5 (2003) 480.

[23] A.L. Spek, PLATON, A Multipurpose Crystallographic Tool, Utrecht University, Utrecht, The Netherlands, 1998.

[24] E. Tang, Y.-M. Dai, S. Lin, Acta Crystallogr., Sect. E 60 (2004) m1095.

[25] B. Chen, F. Jiang, L. Han, B. Wu, D. Yuan, M. Wu, M. Hong, Inorg. Chem. Commun. 9 (2006) 371.

[26] (a) Y. Xie, Q. Liu, H. Jiang, C. Du, X. Xu, M. Yu, Y. Zhu, New J. Chem. 26 (2002) 176;
(b) T.K. Paine, T. Weyhermuller, K. Wieghardt, P. Chaudhuri, Inorg. Chem. 41 (2002) 6538;
(c) C. Desplanches, E. Ruiz, A. Rodriguez-Fortea, S. Alvarez, J. Am. Chem. Soc. 124 (2002) 5197;
(d) X. Ren, Y. Chen, C. He, S. Gao, J. Chem. Soc., Dalton Trans. (2002) 3915;
(e) H. Kumagai, C.J. Kepert, M. Kurmoo, Inorg. Chem. 41 (2002) 3410.
[27] B. Bleaney, K.D. Bowers, Proc. R. Soc. London A 214 (1952) 451.
[28] O. Khan, Molecular Magnetism, VCH Publishers, New York, 1993.

Available online at www.sciencedirect.com
ScienceDirect
Polyhedron 27 (2008) 835–848
POLYHEDRON
www.elsevier.com/locate/poly

X-ray characterization of $Te(S_2CNC_5H_{10})_2$ and $TeI_2[(C_{13}H_{10}N_2S)_2]\cdot 4C_4H_8TeI_2$; the first Te–C bond cleaved products obtained in the substitution reactions of organo(heterocyclic) tellurium(IV) derivatives

Prakash C. Srivastava [a,*], Sangeeta Bajpai [a], Roli Lath [a], Rajesh Kumar [a], Vikas Singh [a], Shrinkhala Dwivedi [a], Ray J. Butcher [b], Satoko Hayashi [c], Waro Nakanishi [c]

[a] Department of Chemistry, Lucknow University, Lucknow 226 007, India
[b] Department of Chemistry, Howard University, Washington, DC 20059, USA
[c] Department of Material Science and Chemistry, Faculty of Systems Engineering, Wakayama University, Wakayama 640-8510, Japan

Received 31 August 2007; accepted 13 November 2007
Available online 20 December 2007

Abstract

The reaction of organo(heterocyclic)tellurium(IV) derivative: $C_8H_8TeI_2$(1,3-dihydro-2λ^4-benzotellurole-2,2-diyl diiodide) with $NH_4S_2CNC_5H_{10}$ (ammonium piperidine dithiocarbamate) gives $C_8H_8Te(S_2CNC_5H_{10})_2$ (**1**) and $Te(S_2CNC_5H_{10})_2$ (**2**) or $C_8H_8TeI(S_2CNC_5H_{10})$ (**5**) according to the reaction conditions. In such type of metathetical reactions, the formation of **2** is unprecedented and it corresponds to the first Te–C cleaved product. The reaction of **2** with CH_3I, yields the oxidative addition product, $CH_3TeI(S_2CNC_5H_{10})_2$ (**8**). The formation of **2** is also supported through Quantum Chemical calculations. Another Te–C bond cleaved product $TeI_2[(C_{13}H_{10}N_2S)_2]\cdot 4C_4H_8TeI_2$ (**9**) is obtained in the reaction of $C_4H_8TeI_2$ (1,1,2,3,4,5-hexahydro-1,1-diiodotellurophene) with $NH_4S_2CNHC_6H_5$ (ammonium aniline dithiocarbamate). The reaction of 1,1,2,3,4,5,6-heptahydro-1-iodo-1-(morpholine dithiocarbamato) tellurane $[C_5H_{10}TeI(S_2CNC_4H_8O)]$ (**10**) with 1,10-phenanthroline gives an unusual product $C_{12}H_8N_2\cdot C_4H_{10}INO$ (**11**). The structures of the new complexes **2**, **8**, **9**, **10** and **11** have been determined by the X-ray analysis.
© 2007 Elsevier Ltd. All rights reserved.

Keywords: Organotellurium; Dithiocarbamates; Cleavage; Quantum Chemical calculations

1. Introduction

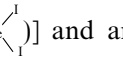
Tellurium organic complexes/organotelluriums have received considerable attention because of (i) the inherent unique tendency of tellurium to be retained in myocardium. Hence tellurium fatty acids have been used as heart imaging agents in nuclear medicine [1] (ii) telluroxanes for tellurite glasses because of their potential applications in non-linear optics and as ionic conductive materials [2] (iii) organotelluriums in organic synthesis [3] and as precursors for (a) semiconductors [4] and (b) optoelectronic materials [5]. On the other hand dithiocarbamate complexes can be used to construct sensors for guest molecules [6]. Further, the chemotherapeutic use of *cis*-diamino dichloro platinum(II) and related drugs often results in some negative side effects including nephrotoxicity which is thought to be caused by the inactivation of enzymes due to the coordination of Pt(II) by thiol groups [7a]. The protection of these thiols is achieved by the use of competitive "rescue agents" such as diethyl dithiocarbamate (Et_2NCS_2) ions [7b,7c,7d] containing soft sulfur atoms. A variety of reactions of organotellurium compounds are known [8a] and organotellurium(IV) dithiocarbamate complexes are generally, prepared by the substitution reactions of organotellurium

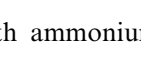
* Corresponding author. Tel.: +91 522 2358473.
E-mail address: pcsrivastava31@rediffmail.com (P.C. Srivastava).

0277-5387/$ - see front matter © 2007 Elsevier Ltd. All rights reserved.
doi:10.1016/j.poly.2007.11.007

(IV) complexes with sodium or ammonium salts of dithiocarbamates [8].

The reactions of organotelluriums involving cleavage of Te–C bonds are known but they are restricted to organotellurium(II) complexes. McWhinnie et al. [9] described the lability of organic groups from tellurium on reaction of organotellurium(II) with a series of metal compounds. Uemura et al. [10] reported a palladium catalysed cross coupling reaction between organic tellurides and alkenes involving cleavage of Te–C bonds. Recently Singh et al. [11] reported Te–C bond cleavage in the reactions of organotellurium(II) compounds with $HgCl_2$ and $Pt(COD)Cl_2$.

So far, we have not come across any metathetical reaction where organo(heterocyclic)tellurium(IV) compounds have undergone cleavage of Te–C bonds along with the substitution reaction. We report in the following unusual Te–C scissions in the reaction between organotellurium(IV) compound: 1,3-dihydro-2λ^4-benzotellurole-2,2-diyl diiodide [$C_8H_8TeI_2$()] and ammonium piperidine dithiocarbamate ($NH_4S_2CNC_5H_{10}$) (1:2 molar ratio) resulting in the cleavage of Te–C bonds to give the $Te(S_2CNC_5H_{10})_2$ (**2**) along with the expected product $C_8H_8Te(S_2CNC_5H_{10})_2$ (**1**). Reaction of $C_8H_8TeI_2$ with $NH_4S_2CNC_5H_{10}$ (1:1 molar ratio) gives $C_8H_8TeI(S_2CNC_5H_{10})$ (**5**). The reaction of $Te(S_2CNC_5H_{10})_2$ (**2**) with CH_3I gives oxidative addition product $CH_3TeI(S_2CNC_5H_{10})_2$ (**8**). Recent studies [12] show that Quantum Chemical calculations are remarkably successful in predicting/justifying a wide range of problems in organometallic chemistry. We have therefore performed Quantum Chemical calculations on a model system to support the formation of **2**. Other reactions of $C_8H_8TeI_2$ with ammonium salts of aniline- and morpholine-dithiocarbamates in (1:1) and (1:2) molar ratio yield the expected $C_8H_8TeL_2$ and C_8H_8TeIL (L = $S_2CNHC_6H_5$, $S_2CNC_4H_8O$) (**3**, **4**, **6**, **7**).

Another Te–C bond cleaved product $TeI_2[(C_{13}H_{10}N_2S_2)_2]\cdot 4C_4H_8TeI_2$ (**9**) is obtained in the reaction of 1,1,2,3,4,5-hexahydro-1,1-diiodotellurophene [$C_4H_8TeI_2$()] with ammonium aniline dithiocarbamate ($NH_4S_2CNHC_6H_5$) (1:2 molar ratio). The reaction of 1,1,2,3,4,5,6-heptahydro-1-iodo-1-(morpholine dithiocarbamato) tellurane [$C_5H_{10}TeI(S_2CNC_4H_8O)$] (**10**) with 1,10-phenanthroline gives an unusual product $C_{12}H_8N_2\cdot C_4H_{10}INO$ (**11**). The structures of the complexes **2**, **8**, **9**, **10** and **11** have been determined by the X-ray analysis.

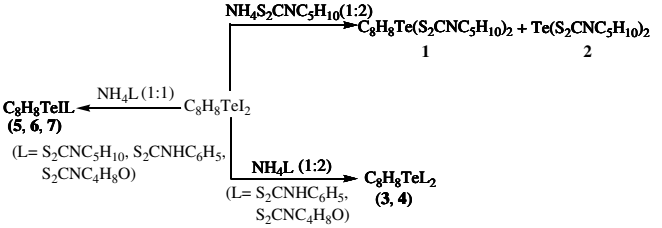
2. Experimental

1,3-Dihydro-2λ^4-benzotellurole-2,2-diyl diiodide ($C_8H_8TeI_2$) was prepared by a modified method (developed in our laboratory) and recrystallized from hot 2-methoxyethanol [13a,13b,13c] to obtain yellow–orange crystals. Te metal, α,α′-dibromoxylene, sodium iodide, iodomethane, 1,4-diiodobutane, 1,5-diiodopentane were obtained from Aldrich and used as received. Piperidine, morpholine, aniline and carbon disulphide (Aldrich) were distilled before use. 2-Methoxy ethanol, solvent ether, petroleum ether, dichloromethane and ethanol were dried by usual methods and distilled before use. Ammonium salts of piperidine-, aniline- and morpholine-dithiocarbamates were freshly prepared. Melting points were recorded in capillary tubes and are uncorrected. Elemental analyses for C, H and N were carried on an Elemental Analyser Heraeus Carlo Erba 1108. Tellurium content was determined volumetrically in the laboratory. IR spectra were recorded using a Shimadzu 8210 PC FTIR spectrometer in the frequency range 4000–350 cm^{-1} with the samples in KBr discs. ^1H and ^{13}C NMR spectra were recorded at 300.13 MHz in $CDCl_3$ solutions containing tetramethyl silane as internal standard on a Varian DRX 300 spectrometer.

2.1. Synthesis of $C_8H_8TeL_2$, C_8H_8TeIL and $Te(S_2CNC_5H_{10})_2$ (L = $S_2CNC_5H_{10}$, $S_2CNC_4H_8O$ and $S_2CNHC_6H_5$)

1,3-Dihydro-2λ^4-benzotellurole-2,2-diyl bis (piperidine dithiocarbamate) $C_8H_8Te(S_2CN\ C_5H_{10})_2$ (**1**), bis(piperidine dithiocarbamato) tellurium(II) $Te(S_2CNC_5H_{10})_2$ (**2**), 1,3-dihydro-2λ^4-benzotellurole-2,2-diyl bis(aniline dithiocarbamate) $C_8H_8Te(S_2CNHC_6H_5)_2$ (**3**), 1,3-dihydro-2λ^4-benzotellurole-2,2-diyl bis(morpholine dithiocarbamate) $C_8H_8Te(S_2CN\text{-}C_4H_8O)_2$ (**4**), 1,3-dihydro-2λ^4-benzotellurole-2,2-diyl-1-iodo-1-piperidine dithiocarbamate $C_8H_8TeI(S_2CNC_5H_{10})$ (**5**), 1,3-dihydro-2λ^4-benzotellurole-2,2-diyl-1-iodo-1-aniline dithiocarbamate $C_8H_8TeI(S_2CNHC_6H_5)$ (**6**), 1,3-dihydro-2λ^4-benzotellurole-2,2-diyl-1-iodo-1-morpholine dithiocarbamate $C_8H_8TeI(S_2CNC_4H_8O)$ (**7**) were prepared by stirring 1,3-dihydro-2λ^4-benzotellurole-2,2-diyl diiodide with freshly prepared ammonium salts of piperidine-, aniline- and morpholine-dithiocarbamates in 1:2 and 1:1 molar ratio in CH_2Cl_2 (Scheme 1).

Complex **1** was prepared by stirring 1,3-dihydro-2λ^4-benzotellurole-2,2-diyl diiodide (2.00 g, 4.12 mmol) in dichloromethane (~25 ml) with freshly prepared ammonium salt of piperidine dithiocarbamate (1.466 g, 8.24 mmol) in 1:2 molar ratio at room temperature (25 °C). After ~6 h the orange colour of the reaction mix-



Scheme 1.

ture changed to a brown colour. The reaction mixture was filtered to eliminate the unidentified material. The filtrate was concentrated to ~10 ml under reduced pressure and kept overnight. A few red crystals were obtained along with an orange solid. The red crystals were separated manually, washed with solvent ether and they were analysed through elemental analysis, FT-IR and single crystal X-ray diffraction studies. These red crystals corresponded to $Te(S_2CNC_5H_{10})_2$ (**2**) (Fig. 1) (Table 2). The orange solid was washed with solvent ether and dried. It was characterized through elemental analysis, FT-IR and (^1H, ^{13}C) NMR spectral data and it corresponded to $C_8H_8Te(S_2CNC_5H_{10})_2$ (**1**). Complexes **3**–**7** were obtained following the same procedure as in **1**. Complex **1** yield: 1.05 g (46%),

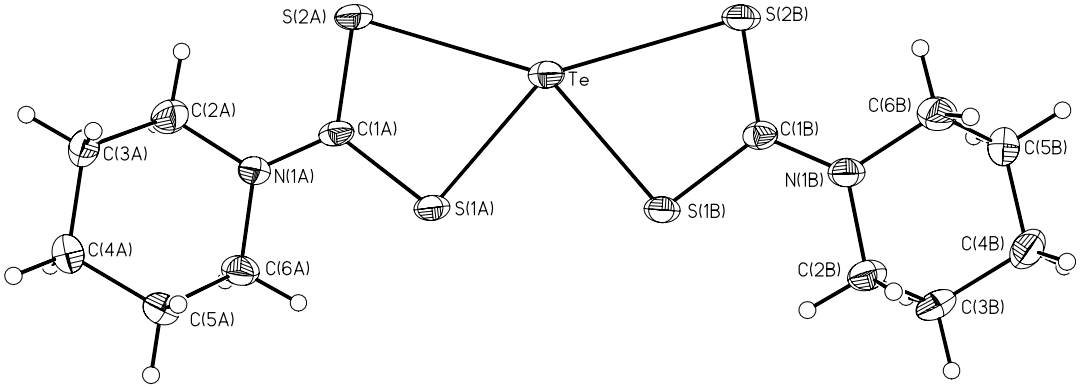


Fig. 1. Crystal structure of $Te(S_2CNC_5H_{10})_2$ (**2**).

Table 1
Crystallographic data and structure parameters for **2**, **8**, **9**, **10** and **11**

Empirical formula	$C_{12}H_{20}N_2S_4Te$ (**2**)	$C_{13}H_{23}IN_2S_4Te$ (**8**)	$C_{42}H_{52}I_{10}N_4S_2Te_5$ (**9**)	$C_{10}H_{18}INOS_2Te$ (**10**)	$C_{16}H_{18}IN_3O$ (**11**)
Formula weight	448.14	590.07	2584.00	486.87	395.23
Temperature (K)	293(2)	93(2)	200(2)	293(2)	293(2)
Wave length (Å)	0.71073	0.71073	0.71073	0.71073	0.71073
Crystal system	monoclinic	triclinic	triclinic	monoclinic	monoclinic
Space group	$P2(1)/n$	$P\bar{1}$	$P\bar{1}$	$P2(1)/n$	$P2(1)/n$
a (Å)	8.8231(5)	8.8171(9)	9.4520(2)	11.0450(5)	11.8066(5)
b (Å)	11.5731(7)	10.7244(11)	9.5955(3)	11.4427(5)	13.2377(6)
c (Å)	16.9103(13)	12.4819(13)	18.5636(6)	12.4484(5)	11.8476(5)
α (°)	90	107.971(2)	91.786(2)	90	90
β (°)	101.940(7)	96.086(2)	99.759(2)	97.0440(10)	113.9010(10)
γ (°)	90	114.278(2)	102.776(2)	90	90
V (Å^3)	1689.36(19)	985.79(18)	1614.07(8)	1561.41(12)	1692.90(13)
Z	4	2	1	4	4
D_{calc} (Mg/m^3)	1.762	1.988	2.658	2.071	1.551
Absorption coefficient (mm^{-1})	2.244	3.494	7.110	4.133	1.894
$F(000)$	888	568	1154	920	784
Crystal size (mm)	0.16 × 0.46 × 0.20	0.35 × 0.55 × 0.95	0.51 × 0.47 × 0.36	0.20 × 0.44 × 0.72	0.55 × 0.8 × 0.85
θ Range for data collection (°)	2.15–27.50	2.26–28.29	4.50–32.54	2.33–28.32	2.05–28.31
Reflection collected/unique (R_{int})	4066	4698	26820	11984	12750
Completeness to θ (°)	99.4%	95.9%	98.9%	98.6%	97.3%
Maximum and minimum transmission	0.8981 and 0.6507	0.8944 and 0.6700	1.00000 and 0.66096	0.928068 and 0.650419	0.928069 and 0.713826
Refinement method	full-matrix least-squares on F^2	full-matrix least-squares on F^2	full-matrix least-squares on F^2	full-matrix least-squares on F^2	full-matrix least-squares on F^2
Data/restraints/parameters	3820/0/193	4698/0/191	10643/0/276	3837/0/145	4101/0/191
Goodness-of fit on F^2	1.032	1.168	0.983	1.066	1.039
Final R indices [$I > 2\sigma(I)$]	$R_1 = 0.0386$, $wR_2 = 0.0773$	$R_1 = 0.0260$, $wR_2 = 0.0672$	$R_1 = 0.0271$, $wR_2 = 0.0593$	$R_1 = 0.0302$, $wR_2 = 0.0799$	$R_1 = 0.0271$, $wR_2 = 0.0693$
R indices (all data)	$R_1 = 0.0750$, $wR_2 = 0.0924$	$R_1 = 0.0274$, $wR_2 = 0.0680$	$R_1 = 0.0467$, $wR_2 = 0.0626$	$R_1 = 0.0393$, $wR_2 = 0.0828$	$R_1 = 0.0336$, $wR_2 = 0.0724$
Largest difference peak and hole (e Å^{-3})	0.463 and −0.384	0.572 and −1.310	1.390 and −1.052	0.962 and −0.728	0.665 and −0.514

Table 2
Bond lengths (Å) and angles (°) for **2**

Bond lengths			
Te–(S1A)	2.505(1)	C(6B)–N(1B)	1.471(7)
Te–(S2A)	2.855(2)	C(2A)–C(3A)	1.502(8)
Te–(S1B)	2.523(1)	C(3A)–C(4A)	1.512(8)
Te–(S2B)	2.858(2)	C(4A)–C(5A)	1.522(8)
S(2A)–C(1A)	1.685(5)	C(5A)–C(6A)	1.491(8)
S(1A)–C(1A)	1.734(5)	C(2B)–C(3B)	1.499(8)
S(1B)–C(1B)	1.740(5)	C(3B)–C(4B)	1.504(8)
S(2B)–C(1B)	1.693(5)	C(4B)–C(5B)	1.515(8)
C(1A)–N(1A)	1.338(6)	C(5B)–C(6B)	1.505(8)
C(2A)–N(1A)	1.456(7)	Te···S(2BA)	3.548(1)
C(6A)–N(1A)	1.479(6)	Te(A)···S(2B)	3.548(1)
C(1B)–N(1B)	1.317(6)	S···S	3.607
C(2B)–N(1B)	1.474(6)		
Bond angles			
S(1A)–Te–S(1B)	80.91(5)	C(2A)–C(3A)–C(4A)	112.2(5)
S(1A)–Te–S(2A)	66.28(4)	C(3A)–C(4A)–C(5A)	110.8(5)
S(1B)–Te–S(2A)	147.17(4)	C(4A)–C(5A)–C(6A)	110.2(5)
S(1A)–Te–S(2B)	146.87(4)	C(5A)–C(6A)–N(1A)	110.8(5)
S(1B)–Te–S(2B)	66.02(4)	C(1B)–N(1B)–C(2B)	124.3(5)
S(2A)–Te–S(2B)	146.71(4)	C(1B)–N(1B)–C(6B)	112.5(4)
S(2B)– C(1B)–S(1B)	118.2(3)	C(2B)–N(1B)–C(6B)	112.8(5)
S(2A)–C(1A)–S(1A)	118.9(3)	N(1B)–C(2B)–C(3B)	111.7(5)
S(2A)–C(1A)–N(1A)	122.9(4)	C(2B)–C(3B)–C(4B)	112.6(5)
S(1A)–C(1A)–N(1A)	118.2(4)	C(3B)–C(4B)–C(5B)	109.6(5)
S(2B)–C(1B)–N(1B)	122.9(4)	C(4B)–C(5B)–C(6B)	111.5(6)
S(1B)–C(1B)–N(1B)	118.9(4)	C(5B)–C(6B)–N(1B)	111.6(5)
C(1A)–N(1A)–C(2A)	123.8(4)	C(1A)–S(2A)···Te	142.4
C(2A)–N(1A)–C(6A)	113.4(5)	C(1B)–S(2B)···Te	142.4
N(1A)–C(2A)–C(3A)	110.8(5)	C–S···S	128.7

m.p. 150 °C. *Anal.* Calc. for $C_{20}H_{28}N_2S_4Te$: C, 43.50; H, 5.08; N, 5.08; Te, 23.13. Found: C, 43.47; H, 5.06%.

N, 5.05; Te, 23.10%. ^{1}H NMR ($CDCl_3$) δ: 7.17 [m, 4H, C_6H_4], 4.74 [s, 4H, (-CH_2)$_2$Te], 3.98 [s, 8H, (-CH_2)$_2$N], 1.65 [d, 8H, (–CH_2)C], 1.93 [s, 4H, (–CH_2)C]. ^{13}C {^{1}H} NMR ($CDCl_3$) δ: 139.20, 129.70, 127.40 (C_6H_4), 44.60 ($TeCH_2$), 52.70 (NCH_2), 21.90(CCH_2). FT-IR (KBr, cm^{-1}): 1475 s, 1429 s (ν CN); 1001 m, 966 m (ν CS); 507 m ($\nu TeCH_2$). Complex **2** yield: 0.06 g (3%), m.p. 180 °C. *Anal.* Calc. for $C_{12}H_{20}N_2S_4Te$: C, 32.17; H, 4.47; N, 6.26; Te, 28.51. Found: C, 32.14; H, 4.42; N, 6.21; Te, 28.50%. FT-IR (KBr, cm^{-1}): 1471s (ν CN); 975 m (ν CS). Complex **3** yield: 1.24 g (53%), m.p. 140 °C. *Anal.* Calc. for $C_{22}H_{20}N_2S_4Te$: C, 46.51; H, 3.52; N, 4.93; Te, 22.48. Found: C, 46.50; H, 3.51; N, 4.88; Te, 22.44%. FT-IR (KBr, cm^{-1}): 1492 m, 1450 s (ν CN); 1020 m, 931 m (ν CS); 549 m ($\nu TeCH_2$). Complex **4** yield: 1.6 g (70%), m.p. 130 °C. *Anal.* Calc. for $C_{18}H_{24}N_2O_2S_4Te$: C, 38.88; H, 4.32; N, 5.04; Te, 22.97. Found: C, 38.84; H, 4.28; N, 5.02; Te, 22.92%. ^{1}H NMR ($CDCl_3$) δ: 7.20 [m, 4H, C_6H_4], 4.69 [s, 4H, (–CH_2)$_2$Te], 4.11[t, 8H, (–CH_2)$_2$N], 3.71 [t, 8H, (–CH_2)O], ^{13}C{^{1}H}NMR ($CDCl_3$) δ: 139.99, 130.41, 128.03 (C_6H_4), 46.33 ($TeCH_2$), 51.50 (NCH_2), 66.61(OCH_2). FT-IR (KBr, cm^{-1}): 1469 s, 1418 s (ν CN); 1020 m, 989 s (ν CS); 538 s ($\nu TeCH_2$). Complex **5** yield: 0.70 g (33%), m.p. 130 °C. *Anal.* Calc. for $C_{14}H_{18}I\,NS_2Te$: C, 32.39; H, 3.47; N, 2.69; Te, 24.60. Found: C, 32.36; H, 3.46; N, 2.64; Te, 24.58%. FT-IR (KBr, cm^{-1}): 1481 s, 1433 s (ν CN); 1005 m, 959 m (ν CS); 546 m ($\nu TeCH_2$). Complex **6** yield: 0.52 g (24%), m.p. 120 °C. *Anal.* Calc. for $C_{15}H_{14}INS_2Te$: C, 34.18; H, 2.66; N, 2.66; Te, 24.23. Found: C, 34.14; H, 2.63; N, 2.62; Te, 24.20%. FT-IR (KBr, cm^{-1}): 1491 m, 1446 m (ν CN); 1022 m, 929 m (ν CS); 502 m ($\nu TeCH_2$). Complex **7** yield: 0.75 g (35%), m.p. 125 °C. *Anal.* Calc. for $C_{13}H_{16}INOS_2Te$: C, 29.96; H, 3.07; N, 2.69; Te, 24.51. Found: C, 29.84; H, 3.05; N, 2.66; Te, 24.50%. ^{1}H NMR ($CDCl_3$) δ: 7.35 [m, 4H, C_6H_4], 4.65 [m, 4H, (–CH_2)$_2$Te], 4.07 [t, 4H, (–CH_2)$_2$N], 3.76 [t, 4H, (–CH_2)-O]. FT-IR (KBr, cm^{-1}): 1472 s, 1421 s (ν CN); 1020 m, 984 m (NCS); 538 s ($\nu TeCH_2$).

2.1.1. Synthesis of $CH_3TeI(S_2CNC_5H_{10})_2$ (**8**)

To the stirred solution of $Te(S_2CNC_5H_{10})$ (**2**) (0.11 g, 0.326 mmol) in dichloromethane (~10 ml) was added (0.10 ml, 1.579 mmol) of CH_3I. It was stirred for 24 h. The solution was filtered and reduced to ~5 ml and then poured in a petri dish. A solid was obtained which on recrystallization with CS_2/ether gave yellow needle shaped crystals of **8** (Fig. 3) (Table 3). Complex **8** yield: 0.10 g (34%), m.p. 120 °C. *Anal.* Calc. for $C_{13}H_{23}IN_2S_4Te$: C, 26.46; H, 3.90; N, 4.75; Te, 21.64. Found: C, 26.44; H, 3.88; N, 4.74; Te, 21.62%. ^{1}H NMR ($CDCl_3$) δ: 3.30 [s, 3H, CH_3], 4.03 [s, 8H, (–CH_2)$_2$N], 1.77[m, 12H, –$C(CH_2)_2$ & –$CC(CH_2)$].

2.2. X-ray measurements

A summary of the crystal data and refinement parameters for $Te(S_2CNC_5H_{10})_2$ (**2**), $CH_3ITe(S_2CNC_5H_{10})_2$ (**8**), $TeI_2[(C_{13}H_{10}N_2S_2)_2]\cdot 4C_4H_8TeI_2$ (**9**), $C_5H_{10}TeI(S_2CNC_4H_8O)$ (**10**) and $C_{12}H_8N_2\cdot C_4H_{10}INO$ (**11**) are given in Table 1. The crystals of **2** were mounted on a Bruker P4 and of **9** on an Oxford Diffraction Gemini while those of **8**, **10** and **11** were mounted on a SMART CCD diffractometer using graphite-monochromated MoKα radiation ($\lambda = 0.71073$ Å). The structure of **2** was solved in space group $P2_1/n$, **8** in space group $P\bar{1}$, **9** in space group $P\bar{1}$, **10** in space group $P2_1/n$ and **11** in space group $P2_1/n$. The data were corrected for Lorentz, polarization and absorption effects. Since, we have been able to grow only large size crystals of complex **9**, hence the crystal placed for single crystal diffraction studies was an irregular chunk cut from the large crystal. As such it did not have faces that could be indexed to allow for a numerical absorption correction. Instead, an absorption correction based on equivalent reflections was applied.

The structures of **2**, **8**, **9**, **10** and **11** were solved by routine heavy atom and Fourier methods (SHELXS-97 [14]). Non-hydrogen atoms were refined anisotropically by full-matrix least squares using the SHELXL-97 program [14] for **2**, **8**, **9**, **10** and **11** with hydrogen atoms in idealized positions (Table 1). Selected bond lengths and bond angles for **2** and **8** are listed in Tables 2 and 3, respec-

Table 3
Selected bond distances (Å) and angles (°) for **8**

Bond lengths			
Te–C	2.122(3)	C(11B)–N(1B)	1.466(4)
Te–I	2.973(4)	C(15A)–N(1A)	1.471(4)
Te–S(1A)	2.681(8)	C(15B)–N(1B)	1.475(4)
Te–S(2A)	2.672(7)	C(11A)–C(12A)	1.520(4)
Te–S(1B)	2.711(7)	C(12A)–C(13A)	1.515(5)
Te–S(2B)	2.722(8)	C(13A)–C(14A)	1.529(5)
S(1A)–C(1A)	1.723(3)	C(14A)–C(15A)	1.517(4)
S(2A)–C(1A)	1.727(3)	C(11B)–C(12B)	1.522(4)
S(1B)–C(1B)	1.725(3)	C(12B)–C(13B)	1.533(5)
S(2B)–C(1B)	1.717(3)	C(13B)–C(14B)	1.521(5)
C(1A)–N(1A)	1.321(4)	C(14B)–C(15B)	1.523(4)
C(1B)–N(1B)	1.325(4)	Te···S(2A)#1	3.549
C(11A)–N(1A)	1.465(4)		
Bond angles			
S(1A)–Te–S(1B)	153.41(2)	C(1A)–N(1A)–C(15A)	123.4(2)
S(2A)–Te–S(2B)	73.66(2)	C(11A)–N(1A)–C(15A)	114.0(2)
S(1A)–Te–S(2A)	66.38(2)	N(1A)–C(11A)–C(12A)	111.0(3)
S(1B)–Te–S(2B)	65.45(2)	C(11A)–C(12A)–C(13A)	110.7(3)
S(1A)–C(1A)–S(2A)	116.26(2)	C(12A)–C(13A)–C(14A)	110.3(3)
S(1B)–C(1B)–S(2B)	117.16(2)	C(13A)–C(14A)–C(15A)	111.3(3)
C–Te–S(1A)	86.51(8)	N(1A)–C(15A)–C(14A)	110.7(2)
C–Te–S(2A)	88.62(8)	S(1B)–C(1B)–N(1B)	121.6(2)
C–Te–S(1B)	86.46(8)	S(2B)–C(1B)–N(2B)	121.2(2)
C–Te–S(2B)	87.48(8)	C(1B)–N(1B)–C(11B)	123.2(3)
S(2A)–Te–I	143.68(17)	C(1B)–N(1B)–C(15B)	123.5(2)
S(1A)–Te–I	77.32(17)	C(11B)–N(1B)–C(15B)	112.1(2)
S(1B)–Te–I	77.08(17)	N(1B)–C(11B)–C(12B)	109.5(2)
S(2B)–Te–I	142.53(16)	C(11B)–C(12B)–C(13B)	110.6(3)
S(1A)–C(1A)–N(1A)	122.5(2)	C(12B)–C(13B)–C(14B)	111.0(3)
S(2A)–C(1A)–N(1A)	121.3(2)	C(13B)–C(14B)–C(15B)	111.5(3)
C(1A)–N(1A)–C(11A)	122.5(2)	N(1B)–C(15B)–C(14B)	108.6(2)
C–H···I hydrogen bonds			
C(12A)–H(12D)···I#1	C–H [0.99], C–H···I [146.5]	H–I [3.24]	C–I [4.098(3)]
C(11B)–H(11A)···I#2	C–H [0.99], C–H···I [140.9]	H–I [3.20]	C–I [4.015(3)]
C(15B)–H(15D)···I#3	C–H [0.99], C–H···I [162.9]	H–I [3.40]	C–I [4.353(3)]
C–H···S hydrogen bonds			
C(15A)–H(15B)···S(1B)#4	C–H [0.99], C–H···S [147.6]	H–S [2.93]	C–S [3.808(3)]
C(14B)–H(14A)···S(2A)#5	C–H [0.99], C–H···S [155.3]	H–S [2.80]	C–S [3.719(3)]

tively, whereas the data for **9**, **11**, **10** are listed in Tables 5–7.

2.3. Quantum Chemical calculations

The core potential basis sets (LANL2DZ) of GAUSSIAN 98 program [15] were employed for the QC calculations, equipped with the extra basis sets of the d-type polarization functions and the sp-type diffusion functions for C, N, S, Te, and I, together with Br and Se. The calculations were performed at the Möller–Plesset second order energy correlation (MP2) level.

3. Results and discussion

The reaction of $C_8H_8TeI_2$ (1,3-dihydro-2λ^4-benzotellurole-2,2-diyl diiodide) with $NH_4S_2CNC_5H_{10}$ (ammonium piperidine dithiocarbamate) in 1:2 molar ratio in CH_2Cl_2 gives the expected product $C_8H_8Te(S_2CNC_5H_{10})_2$ (**1**) as well as the Te–C bond cleaved product $Te(S_2CNC_5H_{10})_2$ (**2**). A detailed investigation of the Te–C bond cleavage processes resulting in formation of **2** has been explained through Quantum Chemical calculations. The complexes (**1**–**8**) are thermally stable and unaffected by atmospheric oxygen and moisture. Spectroscopic data of (**1**–**8**) are given in the experimental section. In the IR spectra of the complexes (**1**–**8**) except **2**, the presence of doublets for ν(CN) and ν(CS) indicates the unidentate nature of the dithiocarbamate ligands. In **2**, single absorptions appear for ν(CN) and ν(CS) indicating the chelating nature of the piperidine dithiocarbamate ligand [16] and [17]. The solution (^{1}H, ^{13}C) NMR data exhibit characteristic signals at their expected positions with expected multiplicity [8d,8f].

When $C_4H_8TeI_2$ is reacted with ammonium aniline dithiocarbamate, one of the products is the Te–C bond cleaved complex $TeI_2[(C_{13}H_{10}N_2S)_2]\cdot 4C_4H_8TeI_2$ (**9**) which results from the cleavage of Te–C bonds from $C_4H_8TeI_2$.

Table 4
QC calculations on $Me_2Te(X,Y)$ and the derivatives for the facile C–Te cleavage[a,b]

Energies of substrates, intermediates, products, and the related species					
Structure	Me_2TeI_2	Me_2TeIY	Me_2TeY_2	Me_2Te^+Y	MeTeY
E (a.u.)	−110.0282	−212.5949	−315.1832	−201.0670	−161.5676
Structure	Me_2Te	$MeTeY_3$	$MeTe^+Y_2$	TeY_2	MeY
E (a.u.)	−87.4401	−389.3107	−275.2006	−235.6930	−153.6070
Structure	I^-	I_2	Y^-	Y_2	MeI
E (a.u.)	−11.3530	−22.5444	−113.9092	−227.7142	−51.0122
Energies of transition states, together with the differences from the corresponding mixtures					
Structure	$Me_2Te^+Y\cdots I^-$ TS_A-1 (I^-)[c]	$Me_2Te^+Y\cdots I^-$ TS_B-1 (I^-)[d]	$Me_2Te^+Y + I^-$	$Me_2Te^+Y\cdots Y^-$ TS-1 (Y^-)	$Me_2Te^+Y + Y^-$
E (a.u.)	−212.5339	−212.5333	−212.4200	−315.1111	−314.9762
ΔE (kJ mol^{-1})	−299.0[e]	−297.5[e]		−354.2[f]	

Energies of the species relative to $Me_2TeI_2 + Y_2 + 3Y^-$			
Compound group	$Me_2TeI_2 + Y_2 + 3Y^-$	$Me_2TeIY + Y_2 + 2Y^- + I^-$	$Me_2TeY_2 + Y_2 + Y^- + 2I^-$
E[g] (a.u.)	−679.4700	−679.4805	679.5126
ΔE[h] (kJ mol^{-1})	As 0.0	−27.6	−111.8
Compound group	$Me_2Te^+Y + Y_2 + 2Y^- + 2I^-$	$MeTeY + MeI + Y_2 + 2Y^- + I^-$	$MeTeY + MeY + Y_2 + Y^- + 2I^-$
E[g] (a.u.)	−679.3056	−679.4654	−679.5040
ΔE[h] (kJ mol^{-1})	431.6	12.1	−89.3
Compound group	$MeTeY_3 + MeY + Y^- + 2I^-$	$TeY_2 + 2MeY + Y^- + 2I^-$	
E[g] (a.u.)	−679.5329	−679.5222	
ΔE[h] (kJ mol^{-1})	−165.14395	−137.0511	

Compound group	Me_2TeIY	$Me_2Te^+Y\cdots I^-$[i]	Me_2TeY_2	$Me_2Te^+Y\cdots Y^-$
E[g] (a.u.)	−212.5949	−212.5339	−315.1832	−315.1111
ΔE (kJ mol^{-1})		160.2[j]		189.3[k]

[a] Calculation method: Core potential basis sets (LANL2DZ) with extra-basis sets of d-type polarization functions and sp-type diffusion functions at the MP2 level.
[b] Y^- is $H_2NCS_2^-$.
[c] Correspond to conformer A.
[d] Correspond to conformer B.
[e] Relative energy based on $Me_2Te^+Y + I^-$.
[f] Relative energy based on $Me_2Te^+Y + Y^-$.
[g] Total energy.
[h] Relative energy based on $Me_2TeI_2 + Y_2 + 3Y^-$.
[i] For TS_A-1 (I^-).
[j] Relative energy based on Me_2TeYI.
[k] Relative energy based on Me_2TeY_2.

The reaction of $C_5H_{10}TeI(S_2CNC_4H_8O)$ (**10**) with 1,10-phenanthroline yields the unusual product $C_{12}H_8N_2 \cdot C_4H_{10}INO$ (**11**). The X-ray structures and the supramolecular associations of **2**, **8**, **9**, **10** and **11** are described in the following pages.

3.1. Description of the structure of $Te(S_2CNC_5H_{10})_2$ (2)

In bis(piperidine dithiocarbamato) tellurium(II) $[Te(S_2CNC_5H_{10})_2]$ (**2**), the tellurium atom is bonded to two piperidine dithiocarbamate ($S_2CNC_5H_{10}$) groups through two sulfur atoms from each $S_2CNC_5H_{10}$ group (Fig. 1) with the bond distances and angles; Te–S(1A) = 2.505(1) Å, Te–S(2A) = 2.855(2) Å, Te–S(1B) = 2.523(1) Å, Te–S(2B) = 2.858(2) Å; ∠ S(1A)–Te–S(1B) = 80.91(5)°, ∠S(1A)–Te–S(2A) = 66.28(4)°, ∠S(1B)–Te–S(2A) = 147.17(4)°, ∠S(1A)–Te–S(2B) = 146.87(4)°, ∠S(1B)–Te–S(2B) = 66.02(4)°, ∠S(2A)–Te–S(2B) = 146.71(4)° (Table 2). Thus tellurium is tetra coordinated and a stereochemically active electron lone pair, apparently, occupies the fifth coordination position.

The $S_2CNC_5H_{10}$ ligands chelate the tellurium atom with asymmetric Te–S bonds (approximately 2.5 and 2.8 Å) and this asymmetry is reflected in the associated C–S bonds. The two sulfur atoms of both $S_2CNC_5H_{10}$ groups are bonded to the carbon atom with the bond length and bond angles, S(2A)–C(1A) = 1.685(5) Å, S(1A)–C(1A) = 1.734 (5) Å, S(1B)–C(1B) = 1.740(5) Å, S(2B)–C(1B) = 1.693 (5) Å; ∠S(2B)–C(1B)–S(1B) = 118.2(3)°, ∠ S(2A)–C(1A)–S(1A) = 118.9(3)°. The C(1A) and C(1B) carbon atoms are bonded to N(1A) and N(1B) with the bond distances 1.338(6) and 1.317(6) Å, respectively. The average C–N and C–C bond length in both $C_5H_{10}N$ rings are 1.422 Å and 1.506 Å, respectively.

Table 5
Bond lengths (Å) and angles (°) for **9**

Bond lengths			
Te(1A)–I(1A)	2.9508(3)	C(2A)–C(3A)	1.519(6)
Te(1A)–I(2A)	2.8721(3)	C(3A)–C(4A)	1.528(5)
Te(1A)–C(1A)	2.151(4)	C(1B)–C(2B)	1.509(5)
Te(1A)–C(4A)	2.149(4)	C(2B)–C(3B)	1.520(5)
Te(1B)–I(1B)	2.8400(3)	C(3B)–C(4B)	1.506(5)
Te(1B)–I(2B)	3.0047(3)	C(11)–C(12)	1.384(5)
Te(1B)–C(1B)	2.154(3)	C(11)–C(16)	1.387(5)
Te(1B)–C(4B)	2.153(3)	C(12)–C(13)	1.375(5)
Te(1C)–I(1C)	2.9659(3)	C(13)–C(14)	1.389(6)
Te(1C)–I(1C)#4	2.9659(3)	C(14)–C(15)	1.381(5)
Te(1C)–S	2.7019(9)	C(15)–C(16)	1.383(5)
Te(1C)–S#4	2.7019(9)	C(21)–C(22)	1.376(5)
S–C	1.714(3)	C(21)–C(26)	1.389(5)
N(1)–C	1.339(4)	C(22)–C(23)	1.383(5)
N(2)–C	1.336(4)	C(23)–C(24)	1.372(5)
N(1)–C(11)	1.429(5)	C(24)–C(25)	1.367(6)
N(2)–C(21)	1.439(4)	C(25)–C(26)	1.400(5)
C(1A)–C(2A)	1.520(6)		
Bond angles			
I(1A)–Te(1A)–I(2A)	179.403(12)	N(2)–C–S	120.7(3)
C(1A)–Te(1A)–I(1A)	87.94(11)	N(1)–C–N(2)	118.6(3)
C(4A)–Te(1A)–I(1A)	91.15(10)	C–N(1)–C(11)	126.0(3)
C(1A)–Te(1A)–C(4A)	84.61(15)	C–N(2)–C(21)	125.3(3)
C(1A)–Te(1A)–I(2A)	91.92(11)	C(12)–C(11)–C(16)	119.9(3)
C(4A)–Te(1A)–I(2A)	89.41(10)	C(12)–C(11)–N(1)	121.8(3)
I(2B)–Te(1B)–I(1B)	175.966(11)	C(16)–C(11)–N(1)	118.1(3)
C(1B)–Te(1B)–I(2B)	88.62(10)	C(13)–C(12)–C(11)	120.1(4)
C(4B)–Te(1B)–I(1B)	93.53(10)	C(12)–C(13)–C(14)	120.1(4)
C(1B)–Te(1B)–I(1B)	87.67(10)	C(15)–C(14)–C(13)	119.9(4)
C(4B)–Te(1B)–I(2B)	87.66(10)	C(14)–C(15)–C(16)	120.0(4)
C(4B)–Te(1B)–C(1B)	84.04(13)	C(15)–C(16)–C(11)	119.9(3)
S–Te(1C)–S#4	180.0	C(22)–C(21)–N(2)	118.6(3)
S–Te(1C)–I(1C)	94.04(2)	C(26)–C(21)–N(2)	120.9(3)
S–Te(1C)–I(1C)#4	85.96(2)	C(22)–C(21)–C(26)	120.5(3)
S#4–Te(1C)–I(1C)	85.96(2)	C(21)–C(22)–C(23)	119.8(3)
S#4–Te(1C)–I(1C)#4	94.04(2)	C(24)–C(23)–C(22)	120.3(4)
I(1C)#4–Te(1C)–I(1C)	180.0	C(23)–C(24)–C(25)	120.2(4)
C–S–Te(1C)	110.38(12)	C(24)–C(25)–C(26)	120.5(3)
N(1)–C–S	120.7(3)	C(25)–C(26)–C(21)	118.6(4)
Te···I and I···I secondary bonds			
Te(1A)···I(1C)	3.8477(4)		
Te(1A)···I(2B)	3.8804(4)		
I(1A)···I(2A)	3.6628(3)		
I(1B)···I(2B)	3.9113(3)		

Table 6
Bond lengths (Å) and bond angles (°) for **11**

Bond lengths			
O–C(4M)	1.405(4)	C(1)–C(2)	1.383(4)
O–C(1M)	1.409(4)	C(2)–C(3)	1.365(4)
N–C(2M)	1.480(3)	C(3)–C(4)	1.406(3)
N–C(3M)	1.482(3)	C(4)–C(5)	1.428(3)
N–H(0A)	0.900	C(4)–C(12)	1.416(3)
N–H(0B)	0.900	C(5)–C(6)	1.342(3)
C(1M)–C(2M)	1.522(4)	C(6)–C(7)	1.436(3)
C(3M)–C(4M)	1.502(4)	C(7)–C(8)	1.405(3)
N(1)–C(1)	1.324(3)	C(7)–C(11)	1.408(3)
N(1)–C(12)	1.358(3)	C(8)–C(9)	1.371(4)
N(2)–C(10)	1.331(3)	C(9)–C(10)	1.392(4)
N(2)–C(11)	1.361(3)	C(11)–C(12)	1.452(3)
Bond angles			
C(4M)–O–C(1M)	109.6(2)	N(2)–C(11)–C(7)	122.69(19)
C(2M)–N–C(3M)	111.5(2)	N(2)–C(10)–C(9)	124.3(2)
C(2M)–N–H(0A)	109.3	N(2)–C(11)–C(12)	118.42(18)
C(3M)–N–H(0A)	109.3	C(3)–C(2)–C(1)	118.6(2)
C(2M)–N–H(0B)	109.3	C(2)–C(3)–C(4)	119.6(2)
C(3M)–N–H(0B)	109.3	C(3)–C(4)–C(5)	122.6(2)
H(0A)–N–H(0B)	108.0	C(6)–C(5)–C(4)	121.2(2)
O–C(1M)–C(2M)	112.0(3)	C(5)–C(6)–C(7)	120.9(2)
O–C(4M)–C(3M)	111.3(3)	C(8)–C(7)–C(6)	122.1(2)
N–C(2M)–C(1M)	109.0(2)	C(9)–C(8)–C(7)	119.5(2)
N–C(3M)–C(4M)	109.8(2)	C(8)–C(9)–C(10)	118.5(2)
C(1)–N(1)–C(12)	117.2(2)	C(4)–C(12)–C(11)	119.02(19)
C(10)–N(2)–C(11)	117.1(2)	C(11)–C(7)–C(6)	120.1(2)
N(1)–C(1)–C(2)	124.8(2)	C(8)–C(7)–C(11)	117.8(2)
N(1)–C(12)–C(4)	122.36(19)	C(7)–C(11)–C(12)	118.89(19)
N(1)–C(12)–C(11)	118.61(19)		
N···H and I···H hydrogen bonds			
N–H(0A)···N(2)	N–H [0.90] N–N [2.918(3)]	N–H···N [157.2]	H···N [2.07]
N–H(0A)···N(1)	N–H [0.90] N–N [2.971(3)]	N–H···N [126.0]	H···N [2.35]
N–H(0B)···I	N–H [0.90] N–I [3.5191(19)]	N–H···I [173.2]	H···I [2.62]

The molecule of $Te(S_2CNC_5H_{10})_2$ is connected to an adjacent molecule by Te···S secondary bonds [Te···S(2-BA) = S(2B)···TeA = 3.548(1) Å, ∠C–S···Te = 142.4°] resulting in a dimer (the sum of covalent radii and van der Waal radii of Te–S are 2.38 Å and 3.86 Å, respectively [8c] and [18] hence Te···S corresponds to a secondary bond). In this dimer each tellurium is surrounded by four sulfur atoms and one stereochemically active electron lone pair and a secondary bond (Te···S). This results in hexa-coordination around each tellurium atom resulting in distorted octahedral geometry. The structure of **2** is similar to the structure of $Te(S_2CNC_4H_8O)_2$ by Husebye [19]. These dimeric units of $Te(S_2CNC_5H_{10})_2$ are interlinked with each other by S···S intermolecular secondary bonds (3.607 Å) [8c] (∠C–S···S = 128.7 Å) resulting in decameric supramolecular association (Fig. 2). Such type of inorganic–organic hybrid polymeric supramolecular associations have attracted considerable attention in recent years because of their interesting molecular topologies and crystal packing motifs along with their potential applications in many areas including catalysis, transport, optics as well as electrical conductivity [20–24].

3.1.1. Description of the structure of $CH_3TeI(S_2CNC_5H_{10})_2$ (**8**)

An ORTEP diagram of iodomethyl bis(piperidine dithiocarbamato) tellurium(IV) $[CH_3TeI(S_2CNC_5H_{10})_2]$ (**8**) is shown in Fig. 3. The selected bond lengths and angles are listed in Table 3. Coordination to the tellurium atom in **8** is from four sulfur atoms, one methyl carbon and an iodine atom. The four sulfur atoms [Te–S(1A) = 2.681(8) Å, Te–S(2A) = 2.672(7) Å, Te–S(1B) = 2.711(7) Å, Te–S(2B) = 2.722(8) Å] and the iodine atom [Te–I = 2.973(4) Å, ∠S(2A)–Te–I = 143.68(17)°, ∠S(1A)–Te–I = 77.32(17)°, ∠S(1B)–Te–I = 77.08(17)°, ∠S(2B)–Te–I =

Table 7
Bond lengths (Å) and bond angles (°) for **10**

Bond lengths			
Te–C(11)	2.151(4)	O–C(3)	1.406(6)
Te–C(15)	2.144(4)	O–C(4)	1.420(6)
Te–S(1)	2.520(10)	C(2)–C(3)	1.473(6)
Te–I	3.042(4)	C(4)–C(5)	1.486(7)
S(1)–C(1)	1.751(3)	C(11)–C(12)	1.480(7)
S(2)–C(1)	1.685(3)	C(12)–C(13)	1.462(8)
N–C(1)	1.316(4)	C(13)–C(14)	1.469(8)
N–C(2)	1.471(5)	C(14)–C(15)	1.479(6)
N–C(5)	1.471(5)		
Bond angles			
C(15)–Te–C(11)	97.82(16)	C(2)–N–C(5)	111.9(3)
C(15)–Te–S(1)	89.92(12)	N–C(2)–C(3)	109.7(4)
C(11)–Te–S(1)	84.98(13)	O–C(3)–C(2)	111.5(4)
C(15)–Te–I	88.00(11)	C(3)–O–C(4)	109.2(4)
C(11)–Te–I	87.57(13)	O–C(4)–C(5)	110.6(4)
S(1)–Te–I	171.92(2)	N–C(5)–C(4)	110.4(4)
C(1)–S(1)–Te	99.20(12)	C(12)–C(11)–Te	116.5(3)
S(2)–C(1)–S(1)	120.7(2)	C(14)–C(15)–Te	115.6(3)
N–C(1)–S(1)	115.5(2)	C(13)–C(12)–C(11)	119.1(5)
N–C(1)–S(2)	123.7(3)	C(12)–C(13)–C(14)	116.8(5)
C(1)–N–C(2)	124.6(3)	C(13)–C(14)–C(15)	118.5(4)
C(1)–N–C(5)	123.2(3)		
C–H···O hydrogen bonds			
C(3)–H(3A)···O#1	C–H [0.97] C–H···O[138.1]	C–O [3.258(5)]	H–O [2.47]

142.53(16)°] are arranged in a pentagonal plane about the tellurium atom. The methyl group is perpendicular to the

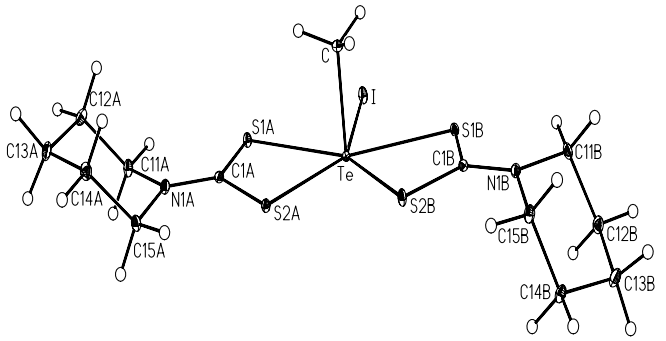


Fig. 3. Crystal structure of $CH_3TeI(S_2CNC_5H_{10})_2$ (**8**).

plane [Te–C = 2.122(3) Å, ∠C–Te–S(1A) = 86.51(8)°, ∠C–Te–S(2A) = 88.62(8)°, ∠C–Te–S(1B) = 86.46(8)°, ∠C–Te–S(2B) = 87.48(8)°] and a sterically active electron lone pair in the opposite side of the plane impart an overall seven coordinated pseudo-pentagonal bipyramidal environment about tellurium atom. The Te–S bond angles are ∠S(1A)–Te–S(IB) = 153.41(2)°, ∠S(2A)–Te–S(2B) = 73.66 (2)°, ∠S(1A)–Te–S(2A) = 66.38(2)° and ∠S(1B)–Te–S(2B) = 65.45(2)°.

The two sulfur atoms of each $S_2CNC_5H_{10}$ group are bonded to the carbon atoms with the bond lengths and bond angles; S(1A)–C(1A) = 1.723(3) Å, S(2A)–C(1A) = 1.727(3) Å, ∠S(1A)–C(1A)–S(2A) = 116.26(2)°, S(1B)–C(1B) = 1.725(3) Å, S(2B)–C(1B) = 1.717(3) Å, ∠S(1B)–C(1B)–S(2B) = 117.16(2)°. The C(1A) and C(1B) carbon

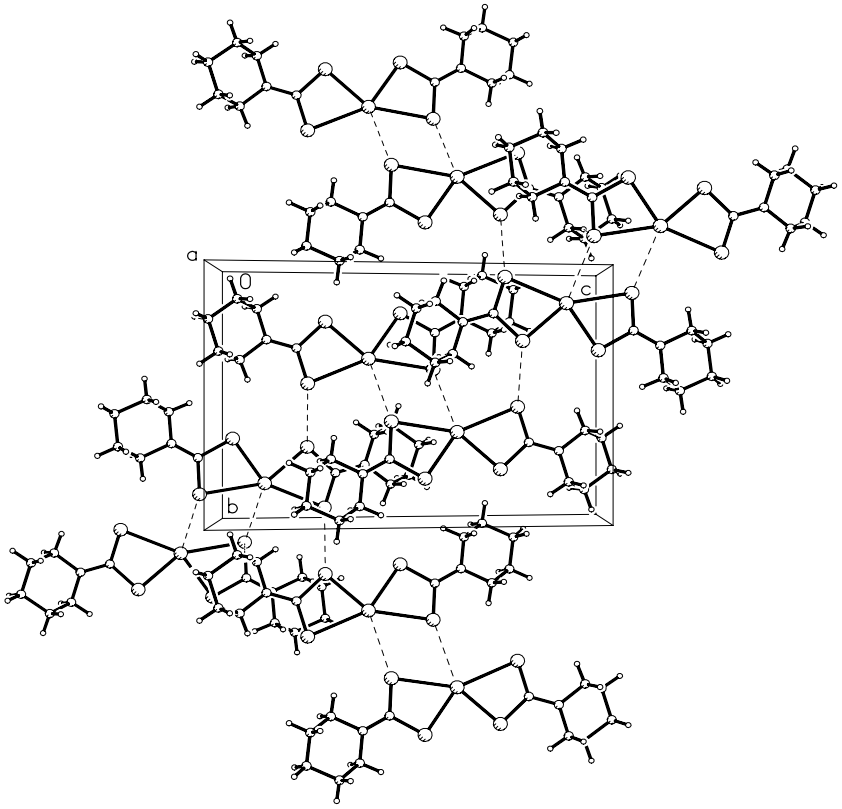


Fig. 2. Decameric supramolecular associations of **2** linked through Te···S and S···S intermolecular secondary bonds.

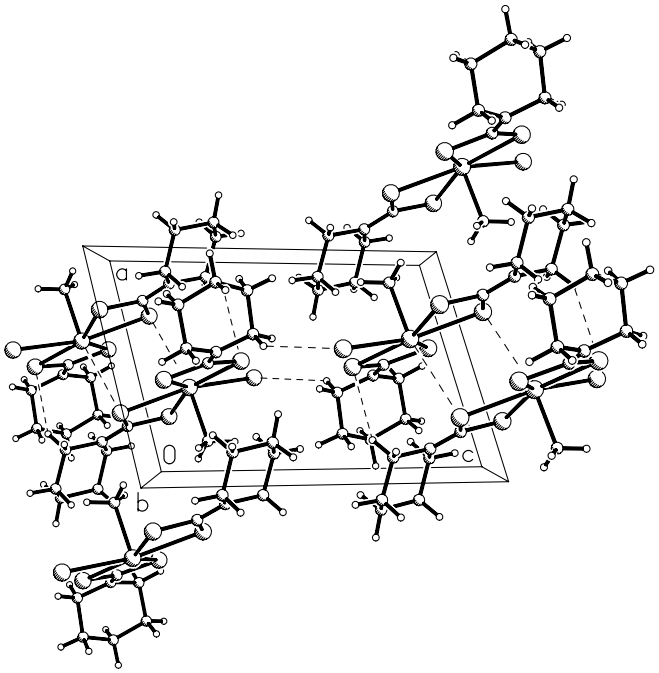


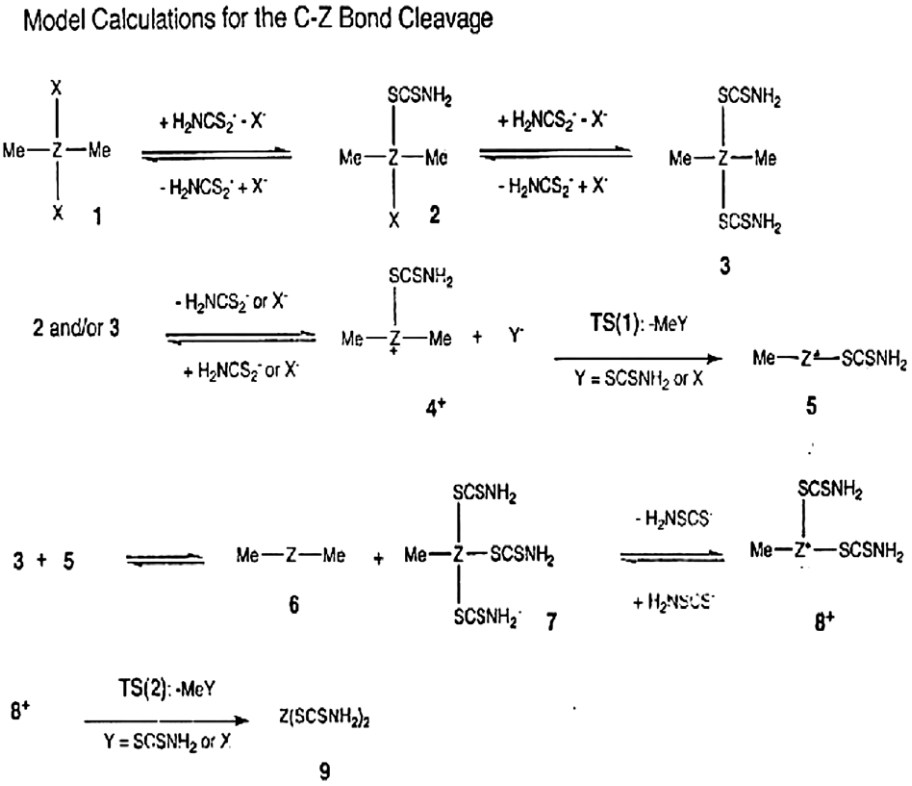
Fig. 4. Tetrameric supramolecular associations of **8** linked through Te···S secondary bonds C–H···I and C–H···S hydrogen bonds.

atoms are bonded to N(1A) and N(1B) with the bond distances 1.321(4) Å, 1.325(4) Å, respectively. The average C–N and C–C bond lengths in both $C_5H_{10}N$ rings are 1.421 Å and 1.523 Å, respectively.

The structure of **8** differs significantly from that of $Te(S_2CNC_5H_{10})_2$ (**2**) where pentacoordination environment about tellurium atom is present. Furthermore, the dithiocarbamate ligands are anisobidentically chelated in $Te(S_2CNC_5H_{10})_2$ (**2**) whereas in $CH_3ITe(S_2CNC_5H_{10})_2$ (**8**) all the tellurium sulfur bonds are close to equivalent and thus dithiocarbamate ligand is symmetrically chelated in the latter case.

It is interesting to note that changing the donor set about the tellurium atom from S_4 in $Te(S_2CNC_5H_{10})_2$ to S_4CI in $CH_3TeI(S_2CNC_5H_{10})_2$ causes the dithiocarbamate ligands to coordinate symmetrically in the latter case. This in turn, implies that the asymmetry observed in the former complex **2** is not a result of steric strain within the four membered (TeS_2C).

In the unit cell (Fig. 4) the molecules of $CH_3TeI(S_2CNC_5H_{10})_2$ are symmetrically connected through Te···S secondary bonds [Te–S(2A) #1 = 3.549 Å] to form dimers. These dimers are connected through C–H···I hydrogen bonds [C(12A)···I#1 = 4.098(3) Å, H(12D)···I#1 = 3.24 Å, ∠C(12A)–H (12D)···I#1 = 146.5°; C(11B)···I#2 = 4.015(3) Å, H(11A)···I#2 = 3.20 Å, ∠C(11B)–H (11A)···I#2 = 140.9°, C(15B)···I#3 = 4.353(3) Å, H(15D)···I#3 = 3.40 Å, ∠C(15B)–H(15D) ···I#3 = 162.9°] to form tetrameric supramolecular association where octa- and heptacoordinated telluriums are present. Apart from these hydrogen bonds, intermolecular C–H···S hydrogen bonds [C(15A)···S(1B)#4 = 3.808(3) Å, H (15B)···S(IB)#4 = 2.93 Å, ∠C(15A)–



Scheme 2.

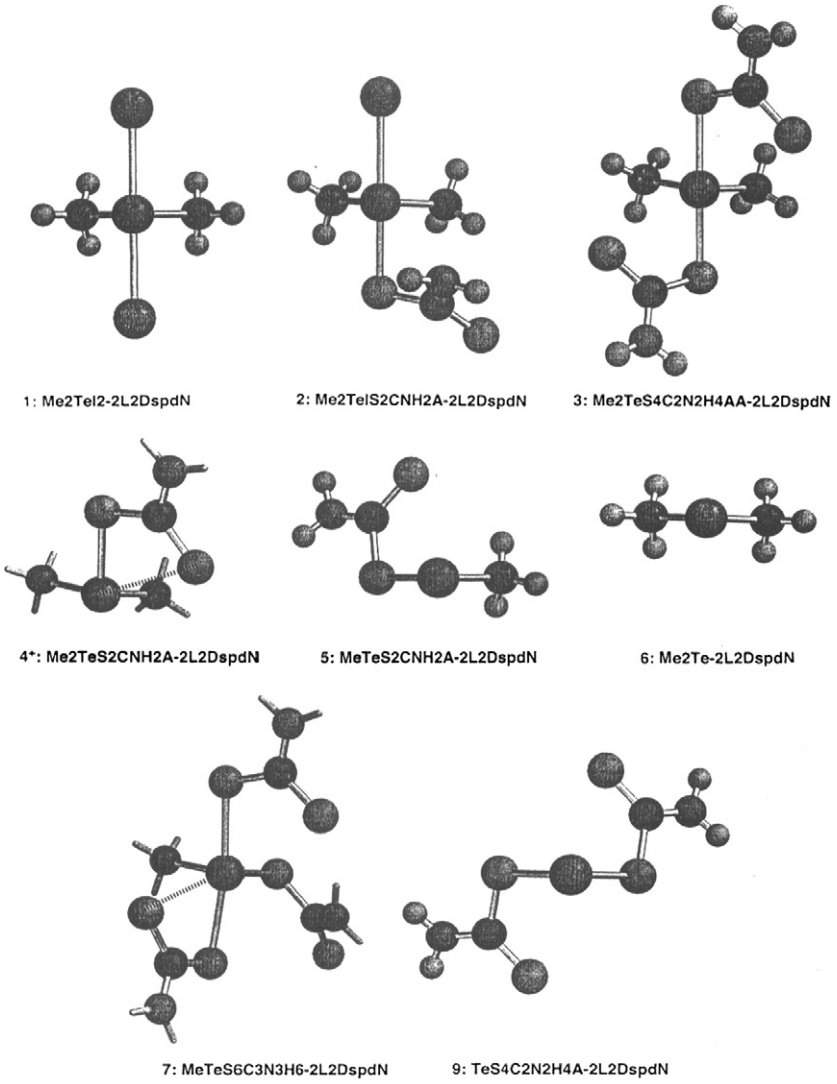


Fig. 5. Optimized structures of substrates, intermediates, products, and transition states of the reaction involved in the formation of $Te(S_2CNC_5H_{10})_2$ (**2**).

H(15B)···S(1B)#4 = 147.6°, C(14B)···S(2A)#5 = 3.719 (3) Å, H (14A)···S(I2A)#5 = 2.80 Å, ∠C(14B)–H(14A) ···S(2A)#5 = 155.3°] are also present.

3.2. Quantum Chemical calculations

The reaction of $C_8H_8TeI_2$ with $NH_4S_2CNC_5H_{10}$ gives $C_8H_8Te(S_2CNC_5H_{10})_2$ (**1**) and $Te(S_2CNC_5H_{10})_2$ (**2**) and/or $C_8H_8TeI(S_2CNC_5H_{10})$ (**5**), according to the reaction conditions. QC calculations were performed on the processes of the reaction, modeled by the reaction Me_2TeI_2 with $H_2NCS_2^-$. The MP2/LANL2 method of the GAUSSIAN 98 program [15] was employed for the calculations, with the extra basis sets of the d-type polarization functions and the sp-type diffusion functions for C, N, S, Te, and I. Scheme 2 shows the postulated processes of the reaction, together with the species produced or intervened in the reaction.

Fig. 5 draws optimized structures of substrates, intermediates, products, and transition states of the reaction.

Table 4 collects the optimized energies of the species. Fig. 6 shows the energy profiles of the reaction, which clarifies the mechanism.

The results strongly support the mechanism shown in Scheme 2. The Te–C bond cleaves by the nucleophilic substitution at C_{Me} of the substrate after ligand exchange with the reagent followed by the partial dissociation, which gives the key substrates ($\mathbf{4}^+$ and $\mathbf{8}^+$) in the reaction. The transition states are also well optimized. However, they are more stable than $\mathbf{4}^+ + I^-$ or $\mathbf{4}^+ + Y^-$, since ionic species are evaluated to be at higher energy.

4. Another Te–C bond cleavage reaction

The reaction of another organo(heterocyclic)tellurium(IV) derivative: 1,1,2,3,4,5-hexahydro-1,1-diiodotel-

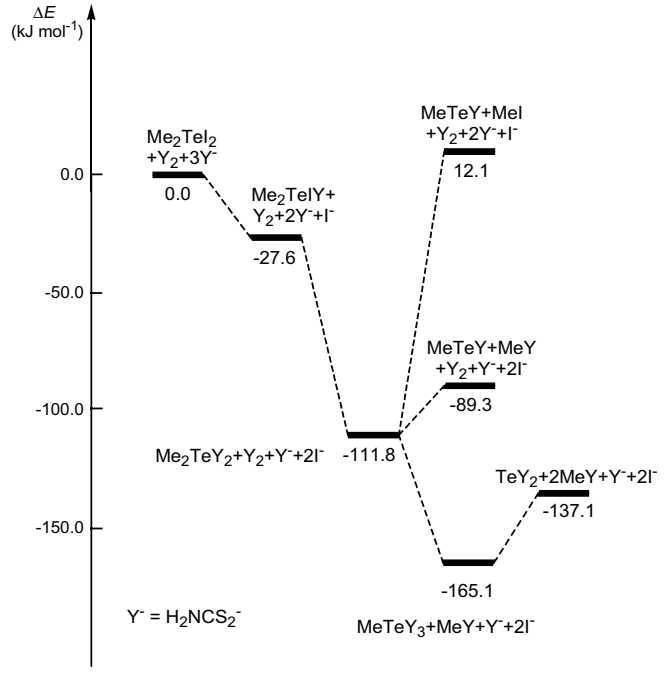


Fig. 6. Calculation on the reaction of Me_2TeI_2 and $H_2NCS_2^-$ (Y^-) with the MP2/LANL2DZ method, containing polarization of d-type and diffusion of sp type functions for non-H atoms.

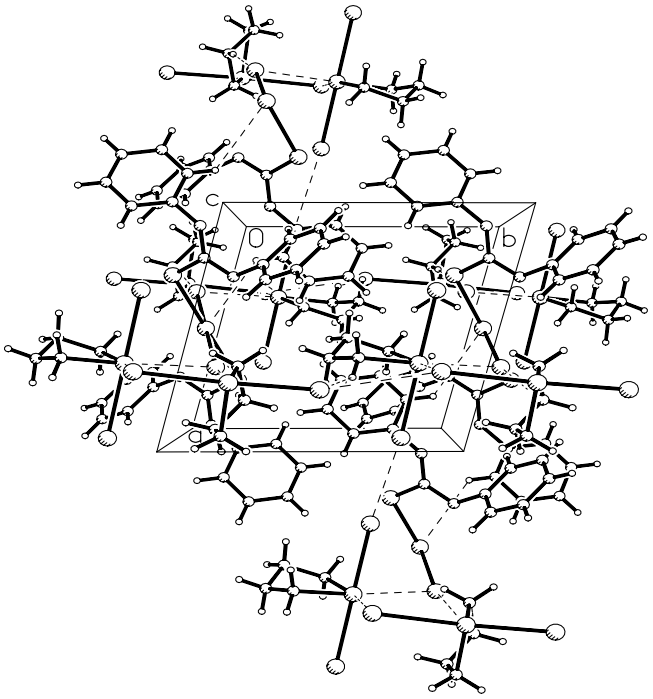


Fig. 8. Crystal structure of $TeI_2[(C_{13}H_{10}N_2S)_2] \cdot 4C_4H_8TeI_2$ (**9**).

lurophene ($C_4H_8TeI_2$) [25] (1.00 g, 2.285 mmol), containing the Te(C_4H_8Te) heterocycle with ammonium aniline dithiocarbamate ($NH_4S_2CNHC_6H_5$) (0.85 g, 4.570 mmol) in 1:2 molar ratio in chloroform gave Te–C bond cleaved product $TeI_2[(C_{13}H_{10}N_2S)_2] \cdot 4C_4H_8TeI_2$ (**9**) with four complete ($C_4H_8TeI_2$) moieties. This has been characterized by single crystal X-ray diffraction studies only (Table 5). A cursory glance at the structure of **9** (Fig. 7) indicates rearrangement of aniline dithiocarbamate groups bound to tellurium of TeI_2 through their S atoms and such system is connected to parent $C_4H_8TeI_2$ moieties through Te···I interactions (Fig. 8).

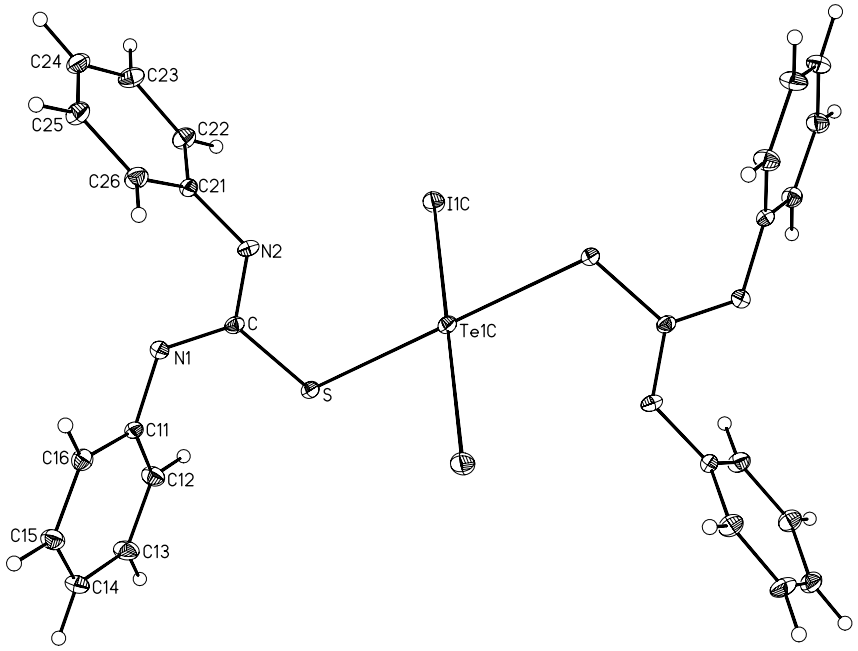


Fig. 7. Crystal structure of $TeI_2[(C_{13}H_{10}N_2S)_2]$.

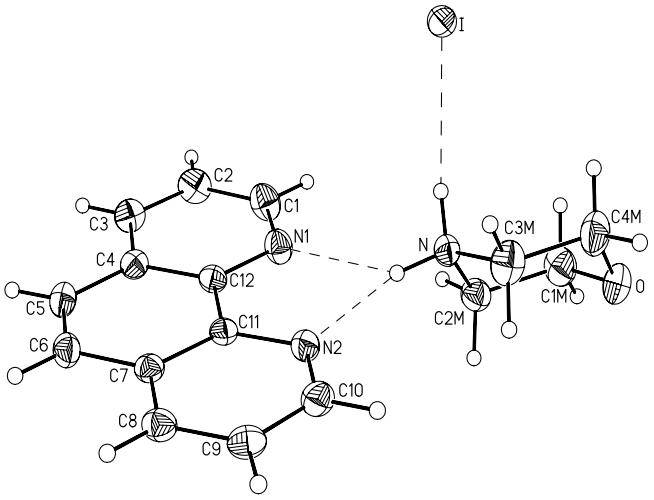


Fig. 9. Crystal structure of $C_{12}H_8N_2 \cdot C_4H_{10}INO$ (**11**).

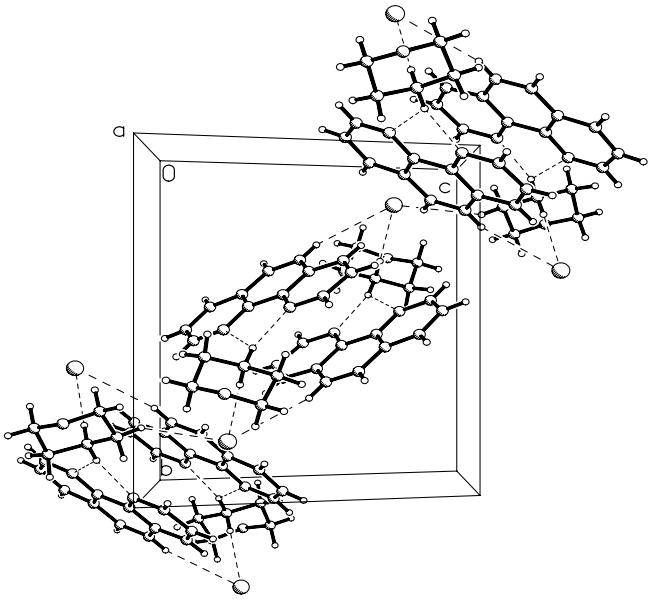


Fig. 10. Hexameric supramolecular associations of **11** linked through N···H and I···H secondary interactions.

4.1. Related reaction

The reaction of 1,1,2,3,4,5,6-heptahydro-1-iodo-1-(morpholine dithiocarbamato) tellurane $[C_5H_{10}TeI(S_2CNC_4H_8O)]$[1] (**10**) (0.50 g, 1.028 mmol) with 1,10-phenanthroline ($C_{12}H_8N_2 \cdot H_2O$) (0.204 g, 1.030 mmol) in 1: 1 molar ratio in dry acetone yielded $C_{12}H_8N_2 \cdot C_4H_{10}INO$ (**11**). The structure of **11** reveals it to contain morpholine connected to 1, 10-phenanthroline through N···H and I···H secondary interactions (Fig. 9) (Table 6).

The dimer of **11** is formed by the association of molecules of **11** connected through I···H (1,10-phenanthroline) secondary interactions and these dimeric units are connected to each other through I···H (morpholine) secondary interactions yielding hexameric supramolecular assembly (Fig. 10).

5. Conclusions

Reaction of $C_8H_8TeI_2$ with $NH_4S_2CNC_5H_{10}$ gives the usual product $C_8H_8Te(S_2CNC_5H_{10})_2$ (**1**) and the Te–C bond cleaved product $Te(S_2CNC_5H_{10})_2$ (**2**). The formation of **2** in such type of metathetical reaction is unprecedented. The reaction of **2** with CH_3I yields the oxidative addition product $CH_3TeI(S_2CNC_5H_{10})$ (**8**). Quantum Chemical calculations also support the formation of **2** (Fig. 11).

The other Te–C cleaved product, **9**, is obtained from the reaction of $C_4H_8TeI_2$ with ammonium aniline dithiocarbamate. The reaction of $C_5H_{10}TeI(S_2CNC_4H_8O)$ (**10**) with 1,10-phenanthroline yields the unusual product **11**.

[1] Yellow crystals of **10** were obtained by the reaction of $C_5H_{10}TeI_2$ [26] (2.00 g, 4.42 mmol) with ammonium salt of morpholine dithiocarbamate (0.79 g, 4.42 mmol) in 1:1 molar ratio in acetone (Yield 1.20 g, 56%, m.p. 186 °C). The X-ray structure determination of $C_5H_{10}TeI(S_2CNC_4H_8O)$ (**10**) reveals it to contain the telluracyclohexane ring which is present in chair conformation in which part of the ring is flattened and a part is considerably puckered. The tellurium atom of this tellurium heterocycle is bonded to one of the sulfur atoms of the morpholine dithiocarbamate group and one I atom by two axial bonds approximately perpendicular to C–Te–C plane with the bond distances Te–I = 3.042(1) Å, Te–S(1)=2.520(10) Å forming bond angle I–Te–S(1) = 171.92(2)° which deviates from linearity with the sulfur and iodine atoms pushed away from the equatorial electron lone pair. This type of geometry has been observed previously in a variety of acyclic- and cyclic-organotellurium complexes [8e,8j,27–36]. The S of morpholine dithiocarbamate is connected to carbon through single bond and the other S of C=S (of CS_2 group) remains free [the bond distances and bond angles are C(1)–S(1) = 1.751(3) Å, C(1)–S(2) = 1.685(3) Å, C(1)–N = 1.316(4) Å, C(2)–N = 1.471(5) Å, ∠S(1)–C(1)–S(2) = 120.7(2)°, ∠S(1)–C(1)–N = 115.5(2)° and ∠N–C(1)–S(2) = 123.7(3)° (Fig. 11) (Table 7)].

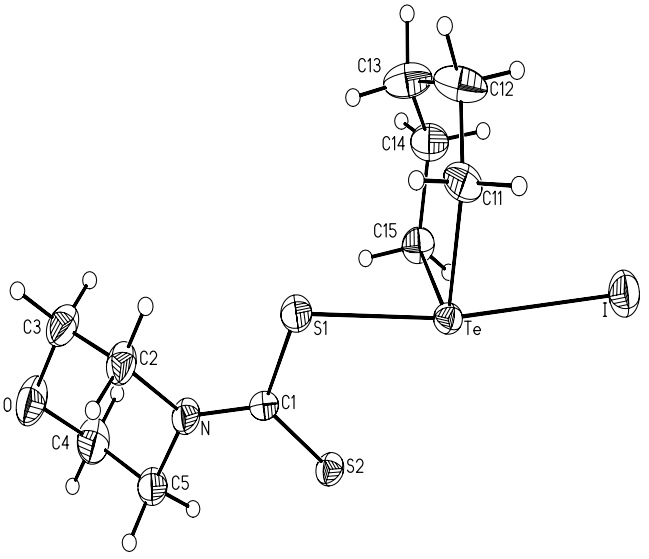


Fig. 11. Crystal structure of **10**.

Acknowledgements

P.C.S. is thankful to Department of Science and Technology (DST), Government of India and Council of Scientific and Industrial Research (CSIR), New Delhi for financial support. R.J.B. wishes to acknowledge the NSF MRI program (Grant No. CHE-0619278) for funds to purchase the X-ray diffractometer. S.B. is thankful to DST for Women Scientist Programme.

Appendix A. Supplementary material

CCDC 238137, 630925, 238136, 654231 and 655107 contain the supplementary crystallographic data for **2**, **8**, **9**, **10** and **11**. These data can be obtained free of charge via http://www.ccdc.cam.ac.uk/conts/retrieving.html, or from the Cambridge Crystallographic Data Center, 12 Union Road, Cambridge CB2.1EZ, UK; fax: (+44) 1223-336-033; or e-mail: deposit@ccdc.cam.ac.uk. Supplementary data associated with this article can be found, in the online version, at doi:10.1016/j.poly.2007.11.007.

References

[1] (a) M.M. Goodman, F.F. Knapp Jr., A.P. Callahan, L.A. Ferren, J. Med. Chem. 25 (1982) 613;
(b) M.M. Goodman, F.F. Knapp Jr., A.P. Callahan, L.A. Ferren, J. Org. Chem. 47 (1982) 3004;
(c) D.R. Elmaleh, F.F. Knapp Jr., T. Yasuda, J.L. Coffey, S. Kopiwada, R.D. Okada, H.W. Strauss, J. Nucl. Med. 22 (1981) 994;
(d) R.D. Okada, F.F. Knapp Jr., D.R. Elmaleh, T. Yasuda, G.M. Pohost, J. Leppo, C.A. Boucher, H.W. Strauss, Circ. Res. 65 (1982) 305;
(e) M.M. Goodman, F.F. Knapp Jr., H.W. Strauss, D.R. Elmaleh, A.P. Callahan, J. Clin. Nucl. Med. 6 (1981) 159.

[2] (a) J.S. Aitchison, J.D. Prohaska, E.M. Vogel, Met. Mater. Process 8 (1996) 277;
(b) J.W. Zwanziger, Int. Rev. Phys. Chem. 17 (1998) 65;
(c) A. Pierre, F. Duboudin, B. Tanguy, J. Portier, Solid State Ionics 53–56 (1992) 1200;
(d) H.W. Roesky, R.J. Butcher, S. Bajpai, P.C. Srivastava, Phosphorus, Sulfur, Silicon Relat. Elem. 161 (2000) 135;
(e) H. Citeau, K. Kirschbaum, O. Conrad, D.M. Giolando, Chem. Commun. (2001) 2006;
(f) P.C. Srivastava, S. Bajpai, C. Ram, R. Kumar, R.J. Butcher, J. Organomet. Chem. 692 (2007) 2482.

[3] (a) L. Engman, Acc. Chem. Res. 18 (1985) 274;
(b) T. Wirth, Angew. Chem., Int. Ed. Engl. 39 (2000) 3740;
(c) L. Uehlin, T. Wirth, Org. Lett. 3 (2001) 2931;
(d) L. Uehlin, G. Fragale, T. Wirth, Chem. Eur. J. 8 (2002) 1125.

[4] (a) M.L. Steigerwald, C.R. Sprinkle, J. Am. Chem. Soc. 109 (1987) 7200;
(b) K.T. Higa, D.C. Harris, Organometallics 8 (1989) 1674;
(c) A.H. Cowley, R. A Jones, Angew. Chem., Int. Ed. Engl. 28 (1989) 1208.

[5] (a) H.B. Singh, N. Sudha, Polyhedron 15 (1996) 745, and references therein;
(b) P.C. Srivastava, S. Bajpai, R. Kumar, S. Srivastava, V. Singh, S. Dwivedi, R.J. Butcher, Can. J. Chem. 85 (2007) 534.

[6] (a) P.D. Beer, N. Berry, M.G.B. Drew, O.D. Fox, M.E.P. Tosta, S. Patell, Chem. Commun. (2001) 199;
(b) O.D. Fox, M.G.B. Drew, E.J.S. Wilkinson, P.D. Beer, Chem. Commun. (2000) 391;
(c) O.D. Fox, M.G.B. Drew, P.D. Beer, Angew. Chem., Int. Ed. Engl. 39 (2000) 136.

[7] (a) J.E. Huheey, E.A. Keiter, R.L. Keiter, Inorganic Chemistry: Principles of Structure and Reactivity, Pearson Education Inc., 2001, pp. 929 and 958;
(b) E.L.M. Lempers, J. Reedjik, Adv. Inorg. Chem. 37 (1991) 175;
(c) R.C. Vallari, R. Pietruszko, Science 216 (1982) 637;
(d) M.S. Wysor, L.A. Zwelling, J.E. Sanders, M.M. Grenan, Science 217 (1982) 454.

[8] (a) S. Patai, Z. Rappoport, The Chemistry of Organic Selenium and Tellurium compounds, vol. 1, John Wiley & Sons, NY, USA, 1986, p. 517;
(b) S. Husebye, K. Maartmann-Moe, W. Steffensen, Acta Chem. Scand. 44 (1990) 579;
(c) I. Haiduc, R.B. King, M.G. Newton, Chem. Rev. 94 (1994) 301, and references therein;
(d) D. Dakternieks, R. Di Giacomo, R.W. Gable, B.F. Hoskins, J. Am. Chem. Soc. 110 (1988) 6753;
(e) D. Dakternieks, R. Di Giacomo, R.W. Gable, B.F. Hoskins, J. Organomet. Chem. 353 (1988) 35;
(f) D. Dakternieks, R. Di Giacomo, R.W. Gable, B.F. Hoskins, J. Organomet. Chem. 349 (1988) 305;
(g) J.H.E. Bailey, J.E. Drake, M.L.Y. Wong, Can. J. Chem. 69 (1991) 1948;
(h) J.H.E. Bailey, J.E. Drake, Can. J. Chem. 71 (1993) 42;
(i) V.G. Montalvo, A.M. Polo, R. Montoya, R.A. Toscano, S.H. Ortega, R. Cea-Olivares, J. Organomet. Chem. 623 (2001) 74;
(j) D. Dakternieks, R.Di. Giacomo, R.W. Gable, B.F. Hoskins, J. Am. Chem. Soc. 110 (1988) 6762.

[9] (a) S.A. Mbogo, W.R. McWhinnie, T.S. Lobana, J. Organomet. Chem. 384 (1990) 115;
(b) M.R. Greaves, T.A. Hamor, B.J. Howlin, T.S. Lobana, S.A. Mbogo, W.R. McWhinnie, D.C. Povey, J. Organomet. Chem. 420 (1991) 327;
(c) S.A. Mbogo, W.R. McWhinnie, T.S. Lobana, Inorg. Chim. Acta 193 (1992) 5;
(d) S.A. Mbogo, W.R. McWhinnie, T.S. Lobana, Inorg. Chim. Acta 172 (1990) 221;
(e) N.I. Al-Salim, W.R. McWhinnie, Polyhedron 8 (1989) 2769.

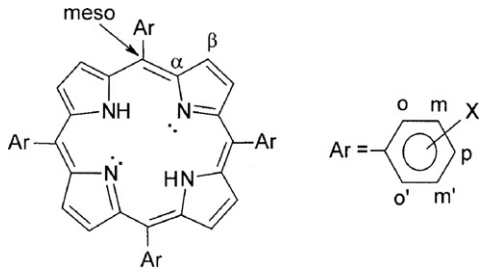
[10] (a) Y. Nishibayashi, C.S. Cho, S. Uemura, J. Organomet. Chem. 507 (1996) 197;
(b) Y. Nishibayashi, C.S. Cho, K. Ohe, S. Uemura, J. Organomet. Chem. 526 (1996) 335.

[11] (a) S.C. Menon, H.B. Singh, R.P. Patel, S.K. Kulshreshtha, J. Chem. Soc., Dalton Trans. (1996) 1203;
(b) S.C. Menon, A. Panda, H.B. Singh, R.J. Butcher, Chem. Commun. (2000) 143;
(c) S.D. Apte, S.S. Zade, H.B. Singh, R.J. Butcher, Organometallics 22 (2003) 5473.

[12] (a) T. Ziegler, Chem. Rev. 91 (1991) 651;
(b) W.M. Davis, J.D. Goddard, Can. J. Chem. 74 (1996) 810;
(c) S. Niu, M.B. Hall, Chem. Rev. 100 (2000) 353;
(d) V.I. Minkin, R.M. Minyaev, Chem. Rev. 101 (2001) 1247;
(e) S. Li, M.B. Hall, Organometallics 20 (2001) 2153;
(f) P. Sanz, M. Yänoez, O. Mo, Chem. Eur. J. 8 (2002) 3999;
(g) M.A. Iron, J.M.L. Martin, M.E. Van der Boom, J. Am. Chem. Soc. 125 (2003) 1702;
(h) D. Conner, K.N. Jayaprakash, T.R. Cundari, T.B. Gunnoe, Organometallics 23 (2004) 2724;
(i) Y. Liao, J.-K. Feng, L. Yang, A.-M. Ren, H.-X. Zhang, Organometallics 24 (2005) 385;
(j) I.D. Sadekov, V.I. Minkin, A.V. Zakharov, A.G. Starikov, G.S. Borodkin, S.M. Aldoshin, V.V. Tkachev, G.V. Shilov, F.J. Berry, J. Organomet. Chem. 690 (2005) 103;
(k) G. Yang, L. Fang, K. Tan, S. Shi, Z. Su, R. Wang, Organometallics 26 (2007) 2082;
(l) K.C. Lam, Z. Lin, T.B. Marder, Organometallics 26 (2007) 3149.

[13] (a) T.N. Srivastava, P.C. Srivastava, R. Kumar, J. Ind. Chem. Soc. 59 (1982) 186;

(b) R. Ziolo, W. Günther, J. Organomet. Chem. 146 (1978) 245;
(c) S. Patai, Z. Rappoport, The Chemistry of Organic Selenium and Tellurium compounds, vol. 1, John Wiley & Sons, NY, USA, 1986, p. 442.
[14] G.M. Sheldrick, SHELXS 86, SHELXS 97 and SHELXL 97, University of Göttingen, 1987 and 1997.
[15] GAUSSIAN 98, Revision A.9; M.J. Frisch, G.W. Trucks, H.B. Schlegel, G.E. Scuseria, M.A. Robb, J.R. Cheeseman, V.G. Zakrzewski, J.A. Montgomery, Jr., R.E. Stratmann, J.C. Burant, S. Dapprich, J.M. Millam, A.D. Daniels, K.N. Kudin, M.C. Strain, O. Farkas, J. Tomasi, V. Barone, M. Cossi, R. Cammi, B. Mennucci, C. Pomelli, C. Adamo, S. Clifford, J. Ochterski, G.A. Petersson, P.Y. Ayala, Q. Cui, K. Morokuma, D.K. Malick, A.D. Rabuck, K. Raghavachari, J.B. Foresman, J. Cioslowski, J.V. Ortiz, A.G. Baboul, B.B. Stefanov, G. Liu, A. Liashenko, P. Piskorz, I. Komaromi, R. Gomperts, R.L. Martin, D.J. Fox, T. Keith, M.A. Al-Laham, C.Y. Peng, A. Nanayakkara, M. Challacombe, P.M.W. Gill, B. Johnson, W. Chen, M.W. Wong, J.L. Andres, C. Gonzalez, M. Head-Gordon, E.S. Replogle, J.A. Pople, Gaussian Inc., Pittsburgh PA, 1998.
[16] (a) C. O'Connor, J.D. Gilbrit, G. Wilkinson, J. Chem. Soc. (1969) 84;
(b) G. St. Nikolov, N. Jordanov, K. Daskslova, Inorg. Nucl. Chem. Lett. 6 (1970) 723.
[17] (a) G.E. Manoussakis, C.A. Tsipis, C.C. Hadjikostus, Can. J. Chem. 53 (1975) 1530;
(b) C.A. Tsipis, G.E. Manoussakis, Inorg. Chim. Acta 18 (1976) 35;
(c) R.K. Kumar, G. Aravamudan, M.R. Udupa, M. Seshasayee, Polyhedron 15 (1996) 3123.
[18] N.W. Alcock, Adv. Inorg. Chem. Radiochem. 15 (1972) 1.
[19] S. Husebye, Acta Chem. Scand. 24 (1970) 2198.
[20] (a) J.-M. Lehn, Angew. Chem., Int. Ed. Engl. 29 (1990) 1304;
(b) O.M. Yaghi, M. O' Keeffe, N.W. Ockwig, H.K. Chae, M. Eddaoudi, J. Kim, Nature 423 (2003) 705.
[21] S. Kitagawa, R. Kitaura, S-i. Noro, Angew. Chem., Int. Ed. Engl. 43 (2004) 2334.
[22] L. Pan, M.B. Sander, X. Huang, J. Li, M. Smith, E. Bittner, B. Bockrath, J.K. Johnson, J. Am. Chem. Soc. 126 (2004) 1308.
[23] M.-L. Tong, S. Kitagawa, H.-C. Chang, M. Ohba, Chem. Commun. (2004) 418.
[24] S.M. Humphrey, P.T. Wood, J. Am. Chem. Soc. 126 (2004) 13236.
[25] G.T. Morgan, F.H. Burstall, J. Chem. Soc. (1931) 180.
[26] W.V. Farrar, J.M. Gulland, J. Chem. Soc. (1945) 11.
[27] S.B. Bulgarevich, B.B. Rivkin, N.G. Furmanova, O.O. Exner, D.Ya. Movshovich, T.A. Yusman, I.D. Sadekov, V.I. Minkin, Zh. Strukt. Khim. 25 (1984) 97.
[28] N.W. Alcock, W.D. Hamson, C. Homes, J. Chem. Soc., Dalton Trans. (1984) 1709.
[29] N.W. Alcock, J. Culver, S.M. Roe, J. Chem. Soc., Dalton Trans. (1992) 1477.
[30] P.C. Srivastava, S. Bajpai, R.J. Butcher, J. Organomet. Chem. 586 (1999) 119.
[31] P.C. Srivastava, A. Sinha, S. Bajpai, H.G. Schmidt, M. Noltemeyer, J. Organomet. Chem. 575 (1999) 261.
[32] P.C. Srivastava, S. Bajpai, R. Lath, C. Ram, Sm. Bajpai, R.J. Butcher, M. Zimmer, M. Veith, J. Organomet. Chem. 649 (2002) 70.
[33] P.C. Srivastava, S. Bajpai, R. Lath, Sm. Bajpai, R. Kumar, R.J. Butcher, Polyhedron 23 (2004) 629.
[34] P.C. Srivastava, S. Bajpai, R. Lath, C. Ram, M. Srivastava, Sm. Bajpai, R.J. Butcher, M. Zimmer, M. Veith, J. Organomet. Chem. 658 (2002) 34.
[35] P.C. Srivastava, S. Bajpai, Sm. Bajpai, R. Kumar, R.J. Butcher, Inorg. Chim. Acta 358 (2005) 227.
[36] P.C. Srivastava, S. Bajpai, Sm. Bajpai, R. Kumar, S. Srivastava, R.J. Butcher, Struct. Chem. 18 (2007) 223.



X = Me, OMe, Cl, Br, H

Fig. 1. *meso*-Tetraarylporphyrins (H_2t(X)pp).

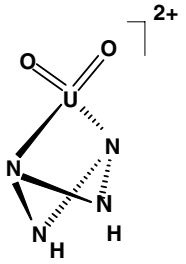


Fig. 2. In the scheme only the tetrahedrally tilted pyrrolenine nitrogens of a porphyrin core are shown. Two nitrogen atoms of pyrrolenine in one side of the porphyrin plane act as the electron donors to the uranium atom of the uranyl.

In this study we present the sitting-atop complex formation of *meso*-tetraarylporphyrins (Fig. 1) with uranyl nitrate hexahydrate. The ionic radius of the uranyl cation is too large so that it is not able to fit into the hole in the center of the macrocycle and it is located out of the ligand plane, distorting it (Fig. 2). Also, the selection of uranyl with a high oxidation number for uranium and using just a small amount of chloroform as a solvent with very weak basicity could be the cause that we successfully prepared the stable sitting-atop complexes as a solid. These conditions determined that the reactions did not progress until the deprotonation of the *meso*-tetraarylporphyrins and they remained at the intermediate step. The similarity of the results of UV–Vis and ^{1}H spectroscopy between the produced complexes and the molecular complexes obtained from the reaction of *meso*-tetraarylporphyrins with 2,3-dichloro-5,6-dicyano-benzoquinone (DDQ) [17], tetracyanoethylene (TCNE) [18], BF_3 [19], SiR_3Cl [20], $BiCl_3$ [21] and $SbCl_3$ [22], suggested saddled porphyrin core structures with one uranyl bonded to only two pyrrolenine nitrogens of the porphyrin, with the pyrrole protons not being released.

2. Experimental

2.1. Material and measurements

Benzaldehyde, various substituted benzaldehydes and uranyl nitrate hexahydrate were obtained from Merck and were used without further purification. Pyrrole, purchased from Merck, was distilled and chloroform (Merck) was dried over anhydrous calcium chloride for 3 days before use. Other solvents that were employed for the synthesis of the porphyrins and sitting-atop complexes were obtained from Merck and Fluka, and were used as received. *meso*-Tetraphenylporphyrin and its substituted derivatives were prepared and purified by the usual methods [23,24]. Alumina and trifluroacetic acid (TFA) were purchased from Merck and were used as received.

The ^{1}H NMR spectra were recorded on a Bruker 400 MHz spectrometer in $CDCl_3$. The residual $CHCl_3$ in the conventional 99.8% atom $CDCl_3$ gives a signal at $\delta = 7.26$ ppm, which was used for calibration of the chemical shift scale. The electronic absorption spectra were obtained in chloroform on an ATI UNICAM-UV\VIS Vision SOFTWARE V-2011 spectrophotometer. The molar conductance of the complexes was measured in acetone on a METROHM 644 conductometer. The FT-IR spectra were recorded on a Magna 550 Nicolet spectrometer using KBr pellets in the range 400–4000 cm^{-1}.

2.2. Preparation of $[(UO_2)H_2t(4\text{-}Me)pp](NO_3)_2$

To an equimolar mixture of *meso*-tetra(4-methylphenyl)porphyrin (0.5 mmol) and $UO_2(NO_3)_2 \cdot 6H_2O$ (0.5 mmol) in a mortar, chloroform (1 ml) was added dropwise, with grinding at ambient temperature for 30 min, until complexation was complete, which was determined by the disappearance of the Soret band of the porphyrin in the UV–Vis spectrum. The sitting-atop complex was obtained as a green solid and dried under vacuum at 50 °C and identified by elemental analysis, molar conductivity and spectroscopic data. *Anal.* Calc. for $C_{48}H_{38}N_6O_8U$: C, 54.1; H, 3.6; N, 7.9. Found: C, 53.5; H, 3.4; N, 7.6%. ^{1}H NMR ($CDCl_3$, δ ppm): ~−0.5 (br, 2H, NH), 2.77 (s, 12H, CH_3), 8.58 (s, 8H, β), 8.50 (d, 8H, o, o′), 7.81 (d, 8H, m, m′). IR (KBr, cm^{-1}): $\upsilon_{NH} \sim 3320$.

2.3. Preparation of $[(UO_2)H_2t(4\text{-}OMe)pp](NO_3)_2$

This complex was synthesized by the method described for $[(UO_2)H_2t(4\text{-}Me)pp](NO_3)_2$. *Anal.* Calc. for $C_{48}H_{38}N_6O_{12}U$: C, 51.1; H, 3.4; N, 7.4. Found: C, 50.5; H, 3.1; N, 7.1%. ^{1}H NMR ($CDCl_3$, δ ppm): ~−0.3 (br, 2H, NH), 4.17 (s, 12H, OCH_3), 8.55 (s, 8H, β), 8.24 (d, 8H, o, o′), 7.55 (d, 8H, m, m′). IR (KBr, cm^{-1}): $\upsilon_{NH} \sim 3320$.

2.4. Preparation of $[(UO_2)H_2t(3\text{-}Me)pp](NO_3)_2$

To a mixture of *meso*-tetra(3-methylphenyl)porphyrin (0.5 mmol) and $UO_2(NO_3)_2 \cdot 6H_2O$ (0.6 mmol) in a mortar, chloroform (1 ml) was added dropwise, with grinding at ambient temperature for 30 min, until complexation was complete, which was determined by the disappearance of the Soret band of the porphyrin in the UV–Vis spectrum. The crude product was washed with diethylether for purification and dried under vacuum at 50 °C. The sitting-atop

complex was obtained as a green solid and identified by elemental analysis, molar conductivity and spectroscopic data. *Anal*. Calc. for $C_{48}H_{38}N_6O_8U$: C, 54.1; H, 3.6; N, 7.9. Found: C, 55.0; H, 3.5; N, 7.7%. ^{1}H NMR ($CDCl_3$, δ ppm): ~−0.5 (br, 2H, NH), 2.87 (s, 12H, CH_3), 8.77 (s, 8H, β), 8.46 (s, 4H, o), 8.46 (d, 4H, o′), 7.95 (t, 4H, m), 7.85 (d, 4H, p). IR (KBr, cm^{-1}): υ_{NH} ~ 3320.

2.5. Preparation of [(UO$_2$)H$_2$t(3-OMe)pp](NO$_3$)$_2$

The procedure was similar to that for [(UO$_2$)H$_2$t(3-Me)pp](NO$_3$)$_2$. *Anal*. Calc. for $C_{48}H_{38}N_6O_{12}U$: C, 51.1; H, 3.4; N, 7.4. Found: C, 50.3; H, 3.3; N, 7.1%. ^{1}H NMR ($CDCl_3$, δ ppm): ~−0.5 (br, 2H, NH), 3.99 (s, 12H, OCH_3), 8.84 (s, 8H, β), 7.87 (s, 4H, o), 7.87 (d, 4H, o′), 7.73 (t, 4H, m), 7.40 (d, 4H, p). IR (KBr, cm^{-1}): υ_{NH} ~ 3320.

2.6. Preparation of [(UO$_2$)H$_2$t(4-Cl)pp](NO$_3$)$_2$

This synthesis was carried out using the above method. *Anal*. Calc. for $C_{44}H_{26}Cl_4N_6O_8U$: C, 46.1; H, 2.3; N, 7.3. Found: C, 45.5; H, 2.0; N, 7.5%. ^{1}H NMR ($CDCl_3$, δ ppm): ~−0.5 (br, 2H, NH), 8.53 (s, 8H, β), 8.37 (d, 8H, o, o′), 7.85 (d, 8H, m, m′). IR (KBr, cm^{-1}): υ_{NH} ~ 3320.

2.7. Preparation of [(UO$_2$)H$_2$t(4-Br)pp](NO$_3$)$_2$

The same procedure was adopted. *Anal*. Calc. for $C_{44}H_{26}Br_4N_6O_8U$: C, 39.9; H, 2.0; N, 6.3. Found: C, 39.5; H, 2.2; N, 6.6%. ^{1}H NMR ($CDCl_3$, δ ppm): ~−0.5 (br, 2H, NH), 8.79 (s, 8H, β), 8.50 (d, 8H, o, o′), 8.24 (d, 8H, m, m′). IR (KBr, cm^{-1}): υ_{NH} ~ 3320.

2.8. Preparation of [(UO$_2$)H$_2$tpp](NO$_3$)$_2$

This complex was synthesized by the method described above. *Anal*. Calc. for $C_{44}H_{30}N_6O_8U$: C, 52.4; H, 3.0; N, 8.3. Found: C, 53.0; H, 3.1; N, 8.1%. ^{1}H NMR ($CDCl_3$, δ ppm): ~−0.5 (br, 2H, NH), 8.64 (s, 8H, β), 8.25 (d, 8H, o, o′), 8.02 (t, 8H, m, m′), 7.71 (d, 4H, p). IR (KBr, cm^{-1}): υ_{NH} ~ 3320.

3. Results and discussion

The ^{1}H NMR spectra obtained for the reactions of different ratios of uranyl nitrate hexahydrate (0.25, 0.5, 0.75, 1.0, 1.5 and 2.0) with *meso*-tetraarylporphyrins (H$_2$t-(4-Me)pp and H$_2$t(4-OMe)pp) showed when the amount of $UO_2(NO_3)_2 \cdot 6H_2O$ was less than a 1:1 mole ratio, we produced a mixture of the porphyrin and the related sitting-atop complex. In presence of excess $UO_2(NO_3)_2 \cdot 6H_2O$ no changes in the spectrum of the 1:1 mixture were observed. Consequently, the sitting-atop complexation between $UO_2(NO_3)_2 \cdot 6H_2O$ and the porphyrins occurred with a 1:1 mole ratio. This was also confirmed by the elemental analysis data.

It is observed that in the free bases H$_2$t(X)pp, the N–H protons are upfield (−2.75 to −2.86 ppm, singlet), and the β-protons appear in the range 8.85–8.90 ppm (singlet). The formation of sitting-atop complexes of *meso*-tetraarylporphyrins with uranyl, similar to the molecular complexation of *meso*-tetraarylporphyrins with various acceptors [17–22], cause downfield shifts for the proton signals of N–H (to a broad peak at about −0.5 ppm for all of the porphyrins in Fig. 1) and aryl rings, and an upfield shift of the β-hydrogens, Table 1. The shifts of the internal N–H (~2.3 ppm downfield) and β-protons (0.06–0.31 upfield) are related to the difference in the ring current between the *meso*-tetraarylporphyrins and the related sitting-atop complexes. The effect of the ring current is lost in the sitting-atop complex. This is because of geometric distortion of the porphyrin macrocycle and the produced positive electric charge in the porphyrin core. The downfield shifts of the aryl ring hydrogens can be related to a direct increase in the ring current of the aryl groups produced by the extension of the aryl π-system. These changes are in the same direction as for molecular complexation of the corresponding *meso*-tetraarylporphyrins with various acceptors [17–22]. The direction of the NH and β-protons shifts of the sitting-atop complexes is similar to the related diprotonated porphyrin species [25], for example, the

Table 1
^{1}H NMR spectral data of different *meso*-tetraarylporphyrins and sitting-atop complexes

Compounds	N–H	H_β
H$_2$t(4-Me)pp	−2.77	8.85
[(UO$_2$)H$_2$t(4-Me)pp](NO$_3$)$_2$	~−0.5	8.58
$\Delta\delta_1^a$	2.27	−0.27
H$_4$t(4-Me)pp^{2+}	−0.65	8.67
$\Delta\delta_2^b$	2.12	−0.18
H$_2$t(4-OMe)pp	−2.75	8.86
[(UO$_2$)H$_2$t(4-OMe)pp](NO$_3$)$_2$	~−0.3	8.55
$\Delta\delta_1^a$	2.45	−0.31
H$_2$t(3-Me)pp	−2.75	8.88
[(UO$_2$)H$_2$t(3-Me)pp](NO$_3$)$_2$	~−0.5	8.77
$\Delta\delta_1^a$	2.25	−0.11
H$_2$t(3-OMe)pp	−2.75	8.90
[(UO$_2$)H$_2$t(3-OMe)pp](NO$_3$)$_2$	~−0.5	8.84
$\Delta\delta_1^a$	2.25	−0.06
H$_2$t(4-Cl)pp	−2.86	8.84
[(UO$_2$)H$_2$t(4-Cl)pp](NO$_3$)$_2$	~−0.5	8.53
$\Delta\delta_1^a$	2.36	−0.31
H$_2$t(4-Br)pp	−2.82	8.89
[(UO$_2$)H$_2$t(4-Br)pp](NO$_3$)$_2$	~−0.5	8.79
$\Delta\delta_1^a$	2.32	−0.10
H$_2$tpp	−2.76	8.85
[(UO$_2$)H$_2$tpp](NO$_3$)$_2$	~−0.5	8.64
$\Delta\delta_1^a$	2.26	−0.21

[a] $\Delta\delta_1$: chemical shifts of the proton signals for the porphyrins upon sitting-atop complexation.
[b] $\Delta\delta_2$: chemical shifts of the proton signals for the H$_2$t(4-Me)pp upon diprotonation with excess TFA.

chemical shifts of the proton signals for $H_2t(4\text{-}CH_3)pp$ upon diprotonation with excess TFA are −0.65 and 8.67 ppm, respectively (Table 1). On the other hand, an excess of uranyl had no effect on the ^1H NMR spectra of the sitting-atop complexes, whereas the ^1H NMR spectrum of $H_4t(4\text{-}CH_3)pp^{2+}$ is quite sensitive to the concentration of trifluoroacetic acid [20,21]. Also, our sitting-atop complexes are rapidly decomposed by alumina or solvents such as DMSO, but their diprotonated porphyrins were quite stable under these conditions. Therefore, the remarkable spectral correspondence between the sitting-atop complexes and the diprotonated species is due to analogous tilted porphyrin core structures in these species, and is not related to the formation of diprotonated porphyrins in our reaction system [20,21].

The results of the UV–Vis spectra for the *meso*-tetraarylporphyrins and related sitting-atop complexes and the diprotonated species are listed in Table 2. The spectra of the porphyrins have five absorption bands (one Soret and four Q bands), whereas the sitting-atop species show two new absorption bands. The observed red shifts for the sitting-atop complexation of *meso*-tetraarylporphyrins with uranyl are similar to the diprotonation of the porphyrins or the molecular complexation with various acceptors [17–22]. The UV–Vis spectra of the diprotonated porphyrins is very like to the related sitting-atop complexes, but, as in the case of NMR spectra, the spectra of the diprotonated species are sensitive to the additional amount of acid added [20,21]. These similarities suggest analogous porphyrin core structures in all of the species (sitting-atop complex, diprotonated porphyrin and molecular complex).

Upon the sitting-atop complexation with uranyl, the UV–Vis spectra of the free base *meso*-tetraarylporphyrins are shifted 24–34 nm to the red. This is interpreted as an evidence for an increased resonance interaction of the aryl ring with the porphyrin nucleus in going from the free base to the sitting-atop complex, which would be allowed by the tilting of the pyrrole groups.

The spectral correspondence (^1H NMR and UV–Vis) between the sitting-atop complexes and the molecular complexes of σ- or π-acceptors with *meso*-tetraarylporphyrins [17–22] proposes a similar structure for the porphyrin core in the two species. Consequently, the non-coplanar pyrrole rings tilted alternatively up and down and the lone pairs of two pyrrolenine nitrogens act as electron donors to the uranium center of the uranyl on one side of the mean plane of the porphyrin, Fig. 2.

The ^1H NMR and UV–Vis spectral shifts for the sitting-atop complexation of various *meso*-tetraarylporphyrins with uranyl showed that the greater steric hindrance of the *meta*-substituents of the aryl rings in the porphyrins decrease the electron donation of those in compare to *para*-substituent (Tables 1 and 2). For *ortho*-substituents this factor make the inconsiderable yield in the reaction of $UO_2(NO_3)_2 \cdot 6H_2O$ with *meso*-tetraarylporphyrins.

Table 2
UV–Vis spectral results of the various *meso*-tetraarylporphyrins, sitting-atop complexes and their diprotonated species in $CHCl_3$

Compounds	λ_{max} (nm)				
$H_2t(4\text{-Me})pp$	418.3(S)	518.4	554.0	593.0	649.0
$[(UO_2)H_2t(4\text{-Me})pp](NO_3)_2$	444.1(S)				668.5
$\Delta\lambda_1^a$	25.8				19.5
$H_4t(4\text{-Me})pp^{2+c}$	442.2(S)				663.4
$\Delta\lambda_2^b$	23.9				14.4
$H_2t(4\text{-OMe})pp$	419.5(S)	520.5	557.1	596.0	653.0
$[(UO_2)H_2t(4\text{-OMe})pp](NO_3)_2$	453.9(S)				687.7
$\Delta\lambda_1^a$	34.4				34.7
$H_4t(4\text{-OMe})pp^{2+c}$	450.0(S)				686.2
$\Delta\lambda_2^b$	30.5				33.2
$H_2t(3\text{-Me})pp$	418.2(S)	517.5	550.6	590.0	647.2
$[(UO_2)H_2t(3\text{-Me})pp](NO_3)_2$	442.2(S)				657.8
$\Delta\lambda_1^a$	24.0				10.6
$H_4t(3\text{-Me})pp^{2+c}$	441.9(S)				657.4
$\Delta\lambda_2^b$	23.7				10.2
$H_2t(3\text{-OMe})pp$	418.9(S)	517.0	550.3	590.3	646.6
$[(UO_2)H_2t(3\text{-OMe})pp](NO_3)_2$	449.6(S)				655.7
$\Delta\lambda_1^a$	30.7				9.1
$H_4t(3\text{-OMe})pp^{2+c}$	448.8(S)				657.8
$\Delta\lambda_2^b$	29.9				11.2
$H_2t(4\text{-Cl})pp$	418.2(S)	517.4	551.0	592.1	649.2
$[(UO_2)H_2t(4\text{-Cl})pp](NO_3)_2$	443.2(S)				660.8
$\Delta\lambda_1^a$	25.0				11.6
$H_4t(4\text{-Cl})pp^{2+c}$	448.2(S)				662.1
$\Delta\lambda_2^b$	30.0				12.9
$H_2t(4\text{-Br})pp$	418.9(S)	515.3	550.7	589.6	645.9
$[(UO_2)H_2t(4\text{-Br})pp](NO_3)_2$	445.4				659.1
$\Delta\lambda_1^a$	26.5				13.2
$H_4t(4\text{-Br})pp^{2+c}$	448.8				665.9
$\Delta\lambda_2^b$	29.9				20.0
H_2tpp	416.7(S)	516.8	551.5	592.0	648.0
$[(UO_2)H_2tpp](NO_3)_2$	441.1				655.7
$\Delta\lambda_1^a$	24.4				7.7
H_4tpp^{2+c}	436.1(S)				652.2
$\Delta\lambda_2^b$	19.4				4.2

(S): Soret band.
[a] $\Delta\lambda_1$: red shifts for the bands of the porphyrins upon sitting-atop complexation.
[b] $\Delta\lambda_2$: red shifts for the bands of the porphyrins upon diprotonation.
[c] The data obtained by the diprotonation with excess of TFA.

The measurements of molar conductivity in methanol solutions indicate the new complexes behave as 1:2 electrolytes [26], completely in accordance with the proposed formula for the sitting-atop complexes, $[(UO_2)H_2t(X)pp](NO_3)_2$. On the other hand, the IR spectra show three bands for NO_3^- anions (for example at 746, 900 and 1476 cm^{-1} for $[(UO_2)H_2t(4\text{-OMe})pp](NO_3)_2$, Fig. 3) that demonstrate these act as counter ions [27]. Also the N–H stretching band, observed at 3320 cm^{-1} for the free base porphyrins [28], does not change upon sitting-atop complexation with uranyl. Furthermore, as mentioned above, the ^1H NMR spectra of the sitting-atop complexes showed that the two protons on the pyrrole nitrogens still remained. Therefore, in our procedure sitting-atop complexation occurred, not metallation.

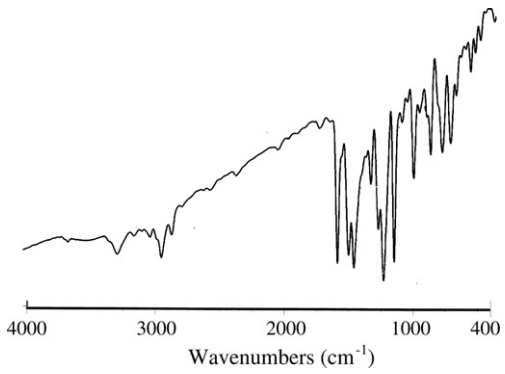


Fig. 3. Infrared spectrum of $[(UO_2)H_2t(4\text{-OMe})pp](NO_3)_2$.

4. Conclusion

Funahashi et al. postulated that in the reaction of copper(II) with H_2tpp in acetonitrile, an intermediate complex species forms, $[Cu(H_2tpp)]^{2+}$, in which the metal stays above the tetraaza plane. We have successfully prepared similar structures from the reaction of uranyl with *meso*-tetraarylporphyrins as a solid, using a little chloroform and grinding. These mild conditions are the reason that the reactions do not progress to the metallation of the porphyrins and remain in the intermediate step (sitting-atop complexes).

Acknowledgements

We are grateful to Kashan University Research Council for their financial support.

References

[1] C.K. Mathews, K.E. Holde, K.G. Ahern, Biochemistry, Addison Wesley Longman, San Francisco, 2000.
[2] G. Knor, Inorg. Chem. Commun. 4 (2001) 160.
[3] P.D. Beer, D.P. Cormode, J.J. Davis, Chem. Commun. (2004) 414.
[4] G.G. Martirosyan, A.S. Azizyan, T.S. Kurtikyan, P.C. Ford, Chem. Commun. (2004) 1488.
[5] G. Knor, A. Strasser, Inorg. Chem. Commun. 9 (2005) 471.
[6] M.D. Lim, I.M. Lorkovic, P.C. Ford, J. Inorg. Biochem. 99 (2005) 151.
[7] E.B. Fleischer, J.H. Wang, J. Am. Chem. Soc. 82 (1960) 498.
[8] J.P. Marquet, T. Theophanides, Can. J. Chem. 51 (1973) 219.
[9] K. Letts, R.A. Mackay, Inorg. Chem. 14 (1975) 2990.
[10] E.B. Fleischer, F. Dixon, Bioinorg. Chem. 7 (1977) 129.
[11] Y. Inada, Y. Sugimoto, Y. Nakano, Y. Itoh, S. Funahashi, Inorg. Chem. 37 (1998) 5519.
[12] Y. Inada, Y. Nakano, M. Inamo, M. Nomura, S. Funahashi, Inorg. Chem. 39 (2000) 4793.
[13] Y. Inada, T. Yamaguchi, H. Satoh, S. Funahashi, Inorg. React. Mech. 2 (2000) 277.
[14] M. Inamo, N. Kamiya, Y. Inada, M. Nomura, S. Funahashi, Inorg. Chem. 40 (2001) 5636.
[15] J.L. Sessler, D. Siedel, A.E. Vivian, V. Lynch, B.L. Scott, D.W. Keogh, Angew. Chem., Int. Ed. Engl. 40 (2001) 591.
[16] J.L. Sessler, P.J. Melfi, G.D. Pantos, Coord. Chem. Rev. 250 (2006) 816.
[17] D. Mohajer, H. Dehghani, J. Chem. Soc., Perkin Trans. 2 (2000) 199.
[18] D. Mohajer, H. Dehghani, Bull. Chem. Soc. Jpn. 73 (2000) 1477.
[19] D. Mohajer, S. Rayati, New J. Chem. 27 (2003) 242.
[20] D. Mohajer, S. Zakavi, S. Rayati, M. Zahedi, N. Safari, H.R. Khavasi, S. Shahbazian, New J. Chem. 28 (2004) 1600.
[21] H. Dehghani, A.R. Ansari Sardrood, Bull. Chem. Soc. Jpn. 80 (2007) 518.
[22] H. Dehghani, A.R. Ansari Sardrood, Polyhedron 26 (2007) 4263.
[23] A.M. d'A. Rocha Gonsalves, J.M.T.B. Varejao, M.M. Pereira, J. Heterocycl. Chem. 28 (1991) 635.
[24] A.D. Adler, J. Org. Chem. 32 (1967) 476.
[25] E.C.A. Ojadi, H. Linschitz, R.I. Walter, J. Phys. Chem. 97 (1993) 13308.
[26] W.J. Geary, Coord. Chem. Rev. 7 (1971) 81.
[27] K. Nakamoto, Infrared and Raman Spectra of Inorganic and Coordination Compounds, fifth ed., John Wiley & Sons Inc., New York, 1997, Part B, p. 124 and 256.
[28] H.H. Limbach, J. Henning, J. Stulz, J. Chem. Phys. 78 (1983) 5432.

Bruker AVANCE 400 spectrometer (400, 100 and 162 MHz, respectively). ^{13}C and ^{31}P NMR resonances were obtained with broad-band proton decoupling. Melting points were measured in capillaries sealed under argon and are uncorrected.

2.2. Synthesis of the complexes

2.2.1. trans-[(1-Carbonyl-2-oxo-cyclohexenediyl)-(2-diphenylphosphanyl)thiophenyl(S,P)]bis-(trimethylphosphine)cobalt(III) (6)

To a suspension of *mer*-hydrido(1-carbonyl-2-oxo-cyclohexenediyl)tris(trimethylphosphine)cobalt(III) (**1**) (1.27 g, 3.07 mmol) in 60 ml of diethyl ether (2-diphenylphosphanyl)thiophenol (0.92 g, 3.12 mmol) dissolved in 20 ml of diethyl ether was added slowly at −80 °C. When the mixture was stirred at ambient temperature for 18 h, the solution changed from yellow to dark-red. After evaporating the volatiles under vacuum, the residue was extracted with pentane and diethyl ether. Both filtrates were crystallized at −27 °C. From pentane solution complex **6** was obtained as dark-red cubic crystals which turned to effloresce under vacuum. Yield: 0.17 g of **6** (9% based on **1**). **17** was also obtained from pentane as brown-yellow cubic crystals suitable for X-ray diffraction analysis. Yield: 0.09 g of **17** (8% based on (2-diphenylphosphanyl)thiophenol). From THF **11** could be obtained as red microcrystals: 0.18 g (yield 25%, based on **1**). From diethyl ether **16** was isolated as brown crystals: 0.61 g (yield 33% based on (2-diphenylphosphanyl)thiophenol). **6**: m.p. (dec.) > 142 °C. *Anal.* Calc. for $C_{31}H_{40}CoO_2P_3S$ (628.57 g/mol): C, 59.23; H, 6.41. Found: C, 59.31; H, 6.38%. IR (Nujol mull, 2600–1550 cm^{-1}): 1608 s, ν(C═O); 1557 s, ν(C═C). ^1H NMR (300 MHz, C_6D_6, 296 K, ppm): $\delta(PCH_3)$ 0.825 (t',$|^2J(PH) + {}^4J(PH)| = 8.1$ Hz, 18H); δ(C–CH_2–CH_2) 1.63 (m, 4H); $\delta(CCH_2)$ 2.37 (s, 2H); $\delta(CCH_2)$ 2.78 (s, 2H); $\delta(CH_{arom})$ 6.93–8.36 (m, 14H). ^{13}C NMR (75 MHz, C_6D_6, 298 K, ppm): $\delta(PCH_3)$ 13.22 (t',$|^1J(PC) + {}^3J(PC)| = 27$ Hz); $\delta(CH_2)$ 23.9, 24.2, 24.4, 33.3; $\delta(C_{arom})$ 113.4, 120.2, 125.6, 129.3, 131.6, 132.2, 133.6, 138.6, 140.5; δ(CO), 165.9; δ(CCO), 189.5. ^{31}P NMR (121 MHz, C_6D_6, 296 K, ppm): $\delta(PCH_3)$ −1.44 (s, 2P); $\delta(PPh_2)$, 32.9 (s, 1P). **11**: m.p. (dec.) > 145 °C. *Anal.* Calc. for $C_{20}H_{35}CoO_4P_2$ (460.37 g/mol): C, 52.18; H, 7.66. Found: C, 52.01; H, 7.72%. IR (Nujol mull, 2600–1500 cm^{-1}): 1592 s, ν(C═O); 1550, 1530 s, ν(C═C). ^1H NMR (300 MHz, $CDCl_3$, 293 K, ppm): *cis*/*trans*-**11** = 2/1. *cis*-**11**: $\delta(PCH_3)$ 1.18 (d, $^2J(PH) = 9.1$ Hz, 18H); δ(CHO) 7.55 (d, $^4J(PH) = 9.6$ Hz, 1H). *trans*-**11**: $\delta(PCH_3)$ 1.15 (s, 18H); δ(CHO) 8.40 (s, 1H); without assignmet: $\delta(CH_2)$ 1.40–2.53 (m, 16H).^{31}P NMR (121 MHz, $CDCl_3$, 294 K, ppm): *cis*-**11**: $\delta(PCH_3)$ 19.0 (s, br); *trans*-**11**: $\delta(PCH_3)$ 12.4 (s, br).

17: m.p. (dec.) > 230 °C. *Anal.* Calc. for $C_{39}H_{37}CoP_3S_2$ (721.7 g/mol): C, 64.91; H, 5.17. Found: C, 64.83; H, 5.24%. IR (Nujol mull, 2600–1500 cm^{-1}): 1575 s, ν(C═C).

2.2.2. [(3,5-Di-tert-butyl-2-oxobenzoyl)(2-diphenylphosphanyl)thiophenyl(S,P)]bis(trimethylphosphine)cobalt(III) (7) and [(3,5-di-tert-butyl-2-oxobenzoyl)(2,4-di-tert-butyl-6-formyl)-phenolato(O,O)]bis(trimethylphosphine)cobalt(III) (12)

A sample of *mer*-hydrido(3,5-di-*tert*-butyl-2-oxobenzoyl) tris(trimethylphosphine)cobalt(III) (**2**) (1.45 g, 2.78 mmol) in 80 ml of diethyl ether and (2-diphenylphosphanyl)thiophenol (0.82 g, 2.79 mmol) in 10 ml of THF after stirring for 18 h at room temperature gave a red-brown suspension. After evaporating the volatiles in vacuo a red-brown residue was obtained. Pentane, diethyl ether, and THF were used in turn to extract the residue, and the three filtrates were crystallized at −27 °C. **7** was collected from pentane as a red needles: 0.10 g, yield 5% (based on **2**) from which some crystals of **17** could be mechanically separated. **16** was obtained from diethyl ether: 0.62 g (yield 38%). From THF **12** was obtained as dark-red cubic crystals: 0.26 g (yield 28% based on **2**). **7**: m.p. (dec.) > 132 °C. *Anal.* Calc. for $C_{39}H_{52}CoO_2P_3S$ (736.75 g/mol): C, 63.58; H, 7.11. Found: C, 63.61; H, 7.08%. IR (Nujol mull, 2600–1500 cm^{-1}): 1620 m, 1593 s ν(C═O); 1526 m, ν(C═C). ^1H NMR (300 MHz, $CDCl_3$, 295 K, ppm): $\delta(CCH_3)$ 1.12 (s, 9H); $\delta(PCH_3)$ 1.24 (t',$|^2J(PH) + {}^4J(PH)| = 8.1$ Hz, 18H); $\delta(CCH_3)$ 1.67 (s, 9H); $\delta(CH_{arom})$ 6.69–8.49 (m, 16H). ^{31}P NMR (121 MHz, CD_3Cl, 295 K, ppm): $\delta(PCH_3)$ 12.1 (s, 2P); $\delta(PPh_2)$ 20.1 (s, 1P). **12**: m.p. (dec.) > 187 °C. *Anal.* Calc. for $C_{36}H_{59}CoO_4P_2$ (676.73 g/mol): C, 63.89; H, 8.79. Found: C, 63.79; H, 8.83%. IR (Nujol mull, 2600–1500 cm^{-1}): 1656 s, 1608 s ν(C═O); 1513 m, ν(C═C). ^1H NMR (300 MHz, C_6D_6, 296 K, ppm): $\delta(PCH_3)$ 0.79 (d,$^2J(PH) = 8.1$ Hz, 18H); $\delta(CCH_3)$ 1.21 (s, 9H); $\delta(CCH_3)$ 1.32 (s, 9H); $\delta(CCH_3)$ 1.55 (s, 9H); $\delta(CCH_3)$ 1.61 (s, 9H); $\delta(CH_{arom})$ 6.96–7.99 (m, 4H); δ(CHO) 9.55 (s, 1H). ^{31}P NMR (121 MHz, C_6D_6, 296 K, ppm): $\delta(PCH_3)$ 14.2 (s).

2.2.3. (2-Oxo-naphthalene-formyl)[(1-formyl)naphtholato-(O,O)]bis(trimethylphosphine)cobalt(III) (13)

A sample of *mer*-hydrido(2-oxo-naphthalene-formyl) tris(trimethylphosphine)cobalt(III) (**3**) (1.49 g, 3.25 mmol) in 60 ml of diethyl ether and (2-diphenylphosphanyl)thiophenol (0.95 g, 3.25 mmol) in 20 ml of diethyl ether after stirring for 18 h at room temperature gave a red-brown suspension. After evaporating the volatiles in vacuo a red-brown residue was obtained. Pentane, diethyl ether and THF were used in turn to extract the residue, and the three filtrates were crystallized at −27 °C. 0.66 g **16** were obtained from diethyl ether (yield 35%). From THF **13** could be obtained as red microcrystals: 0.30 g (yield 33%, based on **3**). **13**: m.p. (dec.) > 257 °C. *Anal.* Calc. for $C_{28}H_{31}CoO_4P_2$ (552.42 g/mol): C, 60.88; H, 5.66. Found: C, 60.92; H, 5.50%. IR (Nujol mull, 2600–1500 cm^{-1}): 1613 s, 1584 s ν(C═O); 1552 m, 1536 m, ν(C═C). ^1H NMR (300 MHz, $CDCl_3$, 295 K, ppm): $\delta(PCH_3)$ 1.25 (t',$|\ {}^2J(PH) + {}^4J(PH)| = 9.4$ Hz, 18H); δ(CH) 6.68–9.51

(m, 12H); δ(C*H*O) 10.37 (s, 1 H). ^{31}P NMR (121 MHz, $CDCl_3$, 295 K, ppm): δ(*P*CH_3) 18.1 (s).

2.2.4. (1-Carbonyl-2-oxo-1,2-diphenylethenyl)[(1-formyl-2-oxo-1,2-diphenylethenyl)(O,O)]bis(trimethylphosphine)-cobalt(III) (*14*)

A sample of *mer*-hydrido(1-carbonyl-2-oxo-1,2-diphenylethenediyl)tris(trimethylphosphine)cobalt(III) (**4**) (0.64 g, 1.25 mmol) in 40 ml of diethyl ether and (2-diphenylphosphanyl)thiophenol (0.37 g, 1.23 mmol) in 10 ml of diethyl ether after stirring for 18 h at 20 °C gave a red-brown suspension. After evaporating the volatiles in vacuo a red-brown residue was obtained. Pentane, diethyl ether and THF were used in turn to extract the residue, and the three filtrates were crystallized at −27 °C. From diethyl ether 0.22 g of 16 were obtained (30% yield). From THF **14** was obtained as yellow powder: 0.10 g (yield 25% based on **4**). **14**: m.p. (dec.) > 168 °C. *Anal.* Calc. for $C_{36}H_{39}CoO_4P_2$ (656.57 g/mol): C, 65.85; H, 5.99. Found: C, 65.53; H, 5.54%. IR (Nujol mull, 2600–1500 cm^{-1}): 1692 s, 1608 s ν(C═O); 1531 m, 1536 s, ν(C═C). ^{1}H NMR (300 MHz, acetone-d_6, 296 K, ppm): δ(PCH_3) 1.37 (dd, ^2J(PH) = 9.9 Hz, ^4J(PH) = 1.8 Hz, 18 H); δ (C*H*) 6.89–7.94 (m, 15H); δ(C*H*O) 9.19 (s, 1H). ^{31}P NMR (121 MHz, acetone-d_6, 296 K, ppm): δ(*P*CH_3) 22.8 (s).

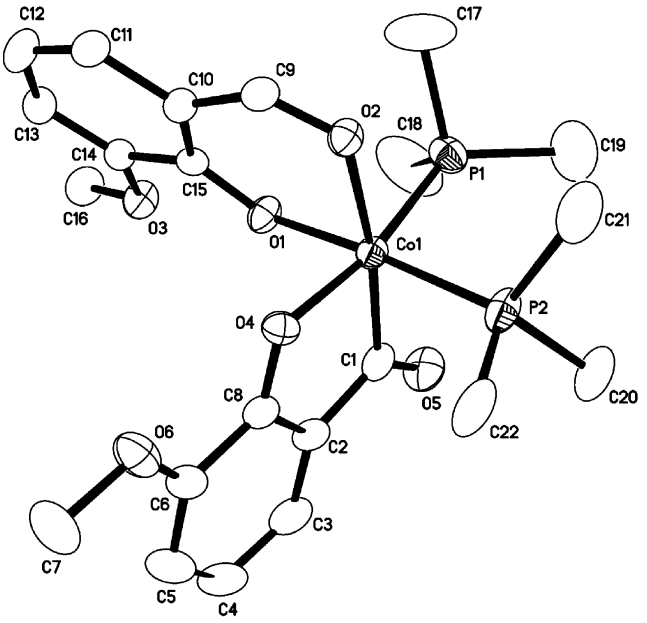


Fig. 1. Molecular structure of *cis*-**15**. Selected distances (Å) and angles (°): Co1–C1 1.914(6), Co1–O1 1.918(3), Co1–O4 1.926(3), Co1–O2 2.071(4), Co1–P2 2.1810(18), Co1–P1 2.2239(18), O2–C9 1.239(6), O5–C1 1.212(6); C1–Co1–O1 87.12(18), C1–Co1–O4 87.1(2), O1–Co1–O4 88.52(15), C1–Co1–O2 169.8(2), O1–Co1–O2 91.77(15), O4–Co1–O2 82.66(14), C1–Co1–P2 88.49(16), O1–Co1–P2 175.54(12), O4–Co1–P2 90.45(11), O2–Co1–P2 92.40(11), C1–Co1–P1 97.69(18), O1–Co1–P1 83.06(12), O4–Co1–P1 170.04(12), O2–Co1–P1 92.26(11), P2–Co1–P1 98.35(7).

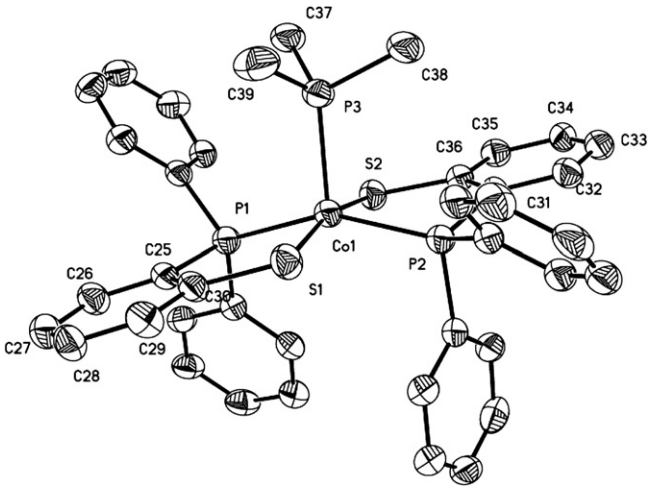


Fig. 2. Molecular structure of **17**. Selected distances (Å) and angles (°): Co1–P2 2.1949(18), Co1–P1 2.2055(18), Co1–S1 2.220(2), Co1–S2 2.70(2), Co1–P3 2.279(2); P2–Co1–P1 152.53(8), P2–Co1–S1 90.49(8), P1–Co1–S1 87.69(7), P2–Co1–S2 84.24(7), P1–Co1–S2 91.34(7), S1–Co1–S2 166.63(8), P2–Co1–P3 103.41(7), P1–Co1–P3 103.94(7), S1–Co1–P3 99.29(9), S2–Co1–P3 93.89(8).

2.2.5. (3-Methoxy-2-oxobenzoyl)[(2-methoxy-6-formyl)phenolato(O,O)]bis(trimethylphosphine)cobalt(III) (*15*)

A sample of *mer*-hydrido(3-methoxy-2-oxobenzoyl)-tris(trimethylphosphine)cobalt(III) (**5**) (1.40 g, 3.20 mmol) in 60 ml of diethyl ether and (2-diphenylphosphanyl)

Table 1
Crystallographic data of complexes **15** and **17**

	15	**17**
Formula	$C_{22}H_{31}CoO_6P_2$	$C_{43}H_{47}CoOP_3S_2$
M_r (g/mol)	512.34	795.77
Color	orange	brown-yellow
Crystal system	triclinic	monoclinic
Space group	$P\bar{1}$	*P2(1)/n*
a (Å)	10.068(4)	15.051(3)
b (Å)	10.785(4)	12.076(2)
c (Å)	11.580(5)	21.916(4)
α (°)	90.701(7)	90
β (°)	107.007(7)	102.16(3)
γ (°)	96.529(7)	90
V (Å^3)	1193.3(8)	3894.0(13)
Z	2	4
$\rho_{calc.}$ (g/cm^3)	1.426	1.357
μ (mm^{-1})	0.888	0.705
Scan range (°)	$1.84 \leqslant \theta \leqslant 25.50$	$1.84 \leqslant \theta \leqslant 25.05$
	$-10 \leqslant h \leqslant 12$,	$-15 \leqslant h \leqslant 17$,
	$-13 \leqslant k \leqslant 13$,	$-12 \leqslant k \leqslant 14$,
	$-11 \leqslant l \leqslant 14$	$-25 \leqslant l \leqslant 25$
Reflections collected	6380	12676
R_{int}	0.0504	0.0857
Independent reflections	4343	6678
Data/restraints/parameters	4343/0/288	6678/0/54
Goodness-of-fit on F_2	0.951	0.811
Final *R* indices [$I > 2\sigma(I)$]	$R_1 = 0.0739$, $wR_2 = 0.1464$	$R_1 = 0.0584$, $wR_2 = 0.1212$
R indices (all data)	$R_1 = 0.1129$, $wR_2 = 0.1643$	$R_1 = 0.1475$, $wR_2 = 0.1473$

thiophenol (0.94 g, 3.20 mmol) in 20 ml of diethyl ether after stirring for 18 h at 20 °C gave a red-brown suspension. After evaporating the volatiles in vacuo a red-brown residue was obtained. Pentane, diethyl ether and THF were used in turn to extract the residue, and the three filtrates were crystallized at −27 °C. From diethyl ether **16** was obtained (0.72 g, yield 40%). From THF **15** was obtained as orange crystals of (0.35 g yield 43% based on **5**). **15**: m.p. (dec.) > 202 °C. *Anal.* Calc. for $C_{22}H_{31}CoO_6P_2$ (512.36 g/mol): C, 51.57; H, 6.10. Found: C, 51.69; H, 6.28%. IR (Nujol mull, 2600–1500 cm^{-1}): 1646 s, 1616 s, ν(C=O); 1579 s, 1537 s, ν(C=C). ^{1}H NMR (400 MHz, $CDCl_3$, 293 K, ppm): *cis*/*trans*-**15** = 1/3. *cis*-**15**: $\delta(PCH_3)$ 1.01 (t',$|^2J(PH) + {}^4J(PH)|$ = 13.4 Hz, 9H); $\delta(PCH_3)$ 1.22 (t',$|\ ^2J(PH) + {}^4J(PH)|$ = 10.9 Hz, 9H); $\delta(OCH_3)$ 3.72 (s, 3H); $\delta(OCH_3)$ 3.77 (s, 3H); δ(CHO) 9.7 (s, 1H). *trans*-**15**: $\delta(PCH_3)$ 1.24 (t',$|^2J(PH) + {}^4J(PH)|$ = 13.7 Hz, 18H); $\delta(OCH_3)$ 3.32 (s, 3H); $\delta(OCH_3)$ 3.57 (s, 3H); δ(CHO) 9.46 (s, 1H), without assignmet: δ(CH) 6.89–7.94 (m, 15H). ^{31}P NMR (121 MHz, $CDCl_3$, 296 K, ppm): *cis*-**15**: $\delta(PCH_3)$ 4.1(s, 1P), 8.1(s, 1P); *trans*-**15**: $\delta(PCH_3)$ 2.3 (s, 1P).

2.3. X-ray diffraction

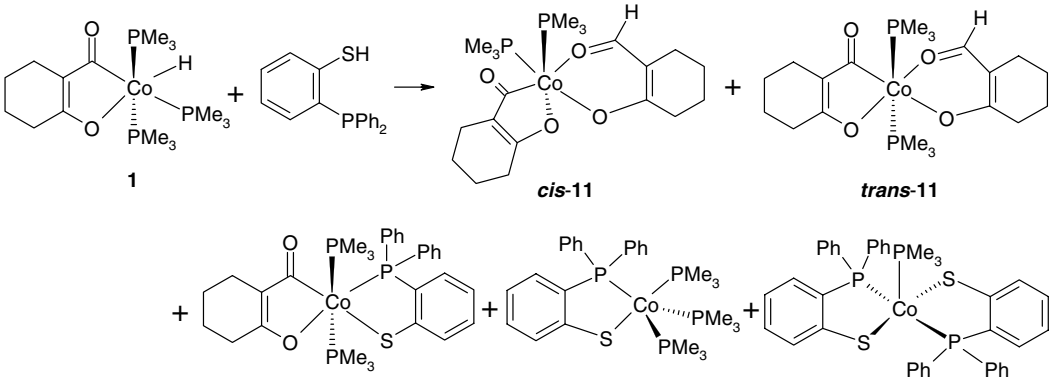
Crystals of complexes **15** and **17** suitable for X-ray diffraction analysis were grown from THF and pentane at 6 °C. The molecular structures are shown in Fig. 1 and Fig. 2, respectively, and related crystallographic data are included in Table 1. The structures were solved by direct methods and refined with full-matrix least-squares on all F^2 (SHELXL-97) with non-hydrogen atoms anisotropically.

3. Results and discussion

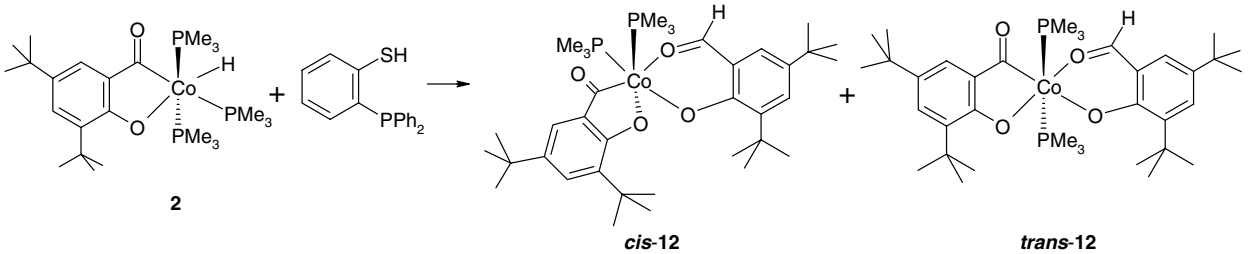
The acyl(hydrido)cobalt complexes **1** and **2** were reacted with (2-diphenylphosphanyl)thiophenol in diethyl ether. After careful work-up, apart from the expected novel cobalt complexes **6** and **7** containing one 2-acylphenolato ligand and one (2-diphenylphosphanyl)thiophenolato ligand, three additional types of cobalt complexes, **11**, **12**, **16**, and **17** were successfully isolated and shown to exist in different formal oxidation states (Eqs. (1) and (2)).

Complexes **6** and **7** are stable below 142 °C and 132 °C under inert atmosphere. In the IR spectra the conspicuous ν(Co–H) absorption of the acyl(hydrido)cobalt complexes (complex **1** and **2**) are absent.

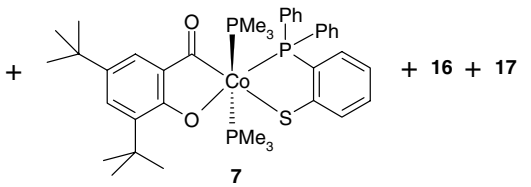
The ^{1}H and ^{31}P NMR spectra of complexes **6** and **7** are well resolved. The pattern of PCH_3 signals as pseudotriplets are is consistent with an octahedral coordination geometry and two *trans*-trimethylphosphine ligands. Two ^{31}P NMR singlets represent one diphenylphosphanyl group and two isochronic trimethylphosphine ligands. Due to

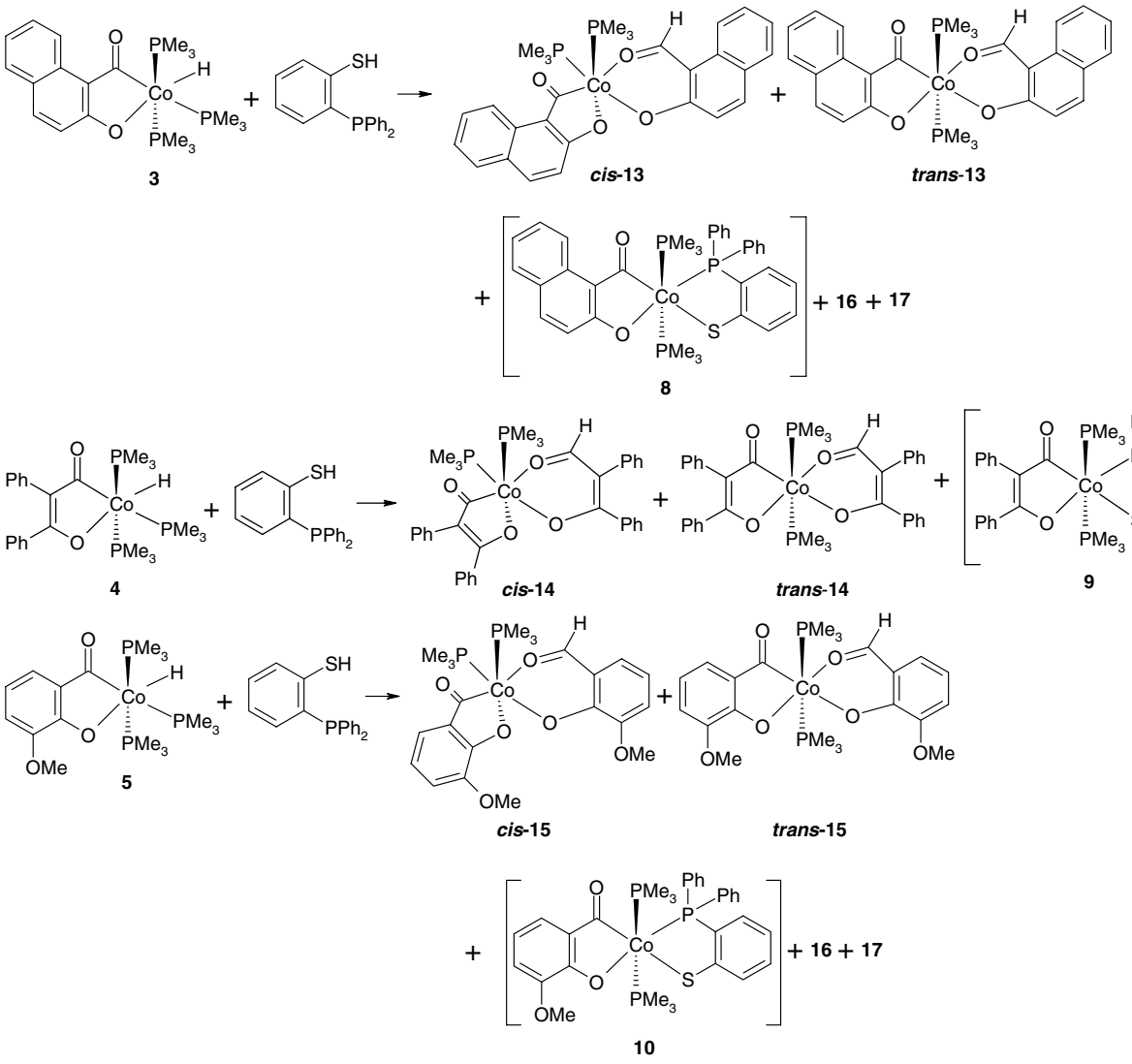


(1)



(2)





(3)

(4)

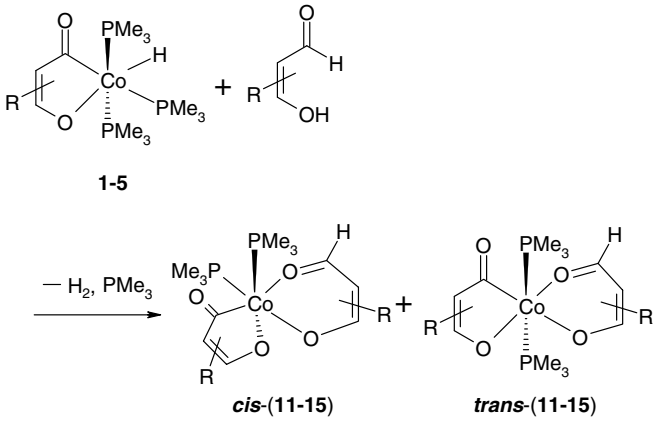
(5)

efflorescence of crystals the crystal structure of complex **6** could not be determined by X-ray diffraction.

In the case of complexes **3**–**5**, the analogous reactions according to Eqs. (3)–(5) have been carried out without successfully isolating the expected complexes **8**, **9**, and **10** due to very low yields of these compounds.

As by-products, the bis-chelate complexes **11**–**15** were obtained from the reactions (Eqs. (1)–(5)) as yellow to orange crystals. In the ^{1}H NMR spectra the aldehyde protons appear between 9 and 10 ppm. X-ray diffraction indicates that complex **15** attains an octahedral configuration with two trimethylphosphine groups in *cis*-positions, while the two 2-acylphenolato ligands are arranged perpendicular to each other (Fig. 1). Complexes **11**–**15** could be isolated as *cis* and *trans* isomers. The ratio of the isomers was determined from ^{1}H NMR and ^{13}P NMR data. Crystalline materials of all these complexes are stable in the air at room temperature.

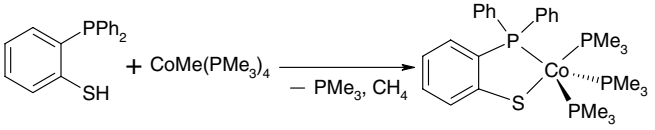
Complexes **11**–**15** can be directly prepared by the reaction of acyl(hydrido)cobalt **1**–**5** with the corresponding β-hydroxy aldehyde (Eq. (6)) [5].



(6)

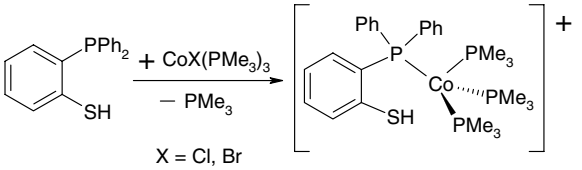
From each reaction in Eqs. (1)–(5) cobalt(I) complex **16** with one [P,S]-chelating ligand was obtained in good yield (>30%). The direct synthesis of complex **16** can be achieved by reaction of (2-diphenylphosphanyl)thiophenol with methyl tetrakis(trimethylphosphine)cobalt(I), $CoMe(PMe_3)_4$, or by reaction of (2-diphenylphosphanyl)thiophenol with

tris(trimethylphosphine)cobalt(I), $CoX(PMe_3)_3$, (Eqs. (7) and (8)) [7].

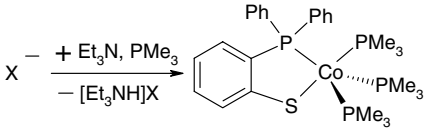


16

(7)



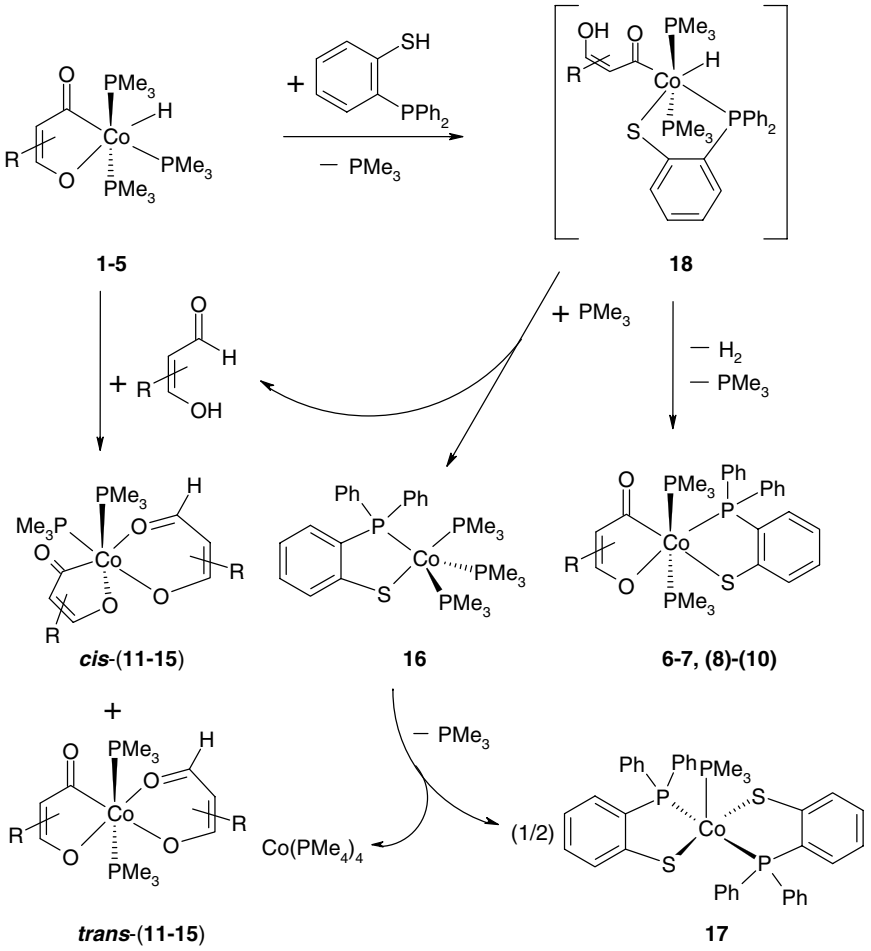
(8)



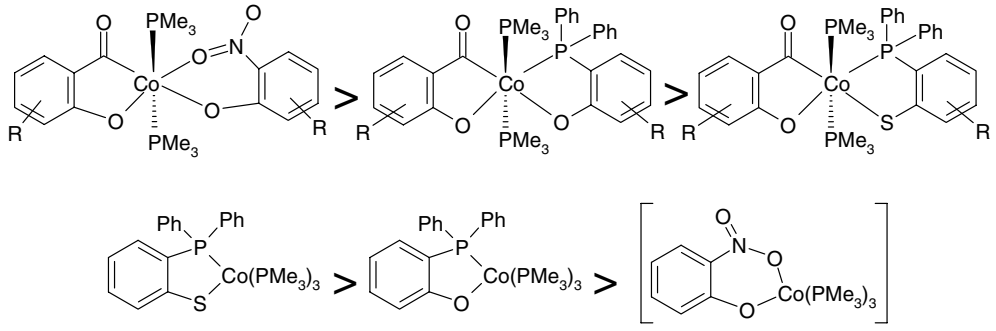
16

At the same time a penta-coordinate cobalt(II) complex with two [P,S]-chelating ligands (**17**) was also isolated from the mother liquor in small amount as tiny brown-yellow cubic crystals. The molecular structure (Fig. 2) shows the expected square-pyramidal geometry of complex **17**. The cobalt atom is located above the center of a plane containing two P-donor and two S-donor atoms of the diphenylphosphanylthiophenolato ligands arranged in mutual *trans*-positions. The P-donor atom of trimethylphosphine is located at the apical point of the pyramid.

Regarding all information obtained from this complicated reaction system (Eqs. (1) and (2)) a mechanism is proposed as given in Scheme 1. In the first step the phenoxy O-donor of the 2-acylphenolato chelating ligand in complexes **1**–**5** is substituted by a (2-diphenylphosphanyl)thiophenolato chelating ligand leading to an intermediate hydridocobalt complex **18**. In the presence of trimethylphosphine, **18** undergoes a reductive elimination to generate the [P,S]-chelate cobalt(I) complex **16** with liberation of a β-hydroxy aldehyde. Subsequently, hydrogen is evolved from the acyl(hydrido)cobalt(III) complexes **1**–**5** and the β-hydroxy aldehyde to afford the bis-chelate cobalt(III) complexes **11**–**15**. Disproportionation of complex **16** gives rise to the bis-chelate complex **17** and tetrakis(trimethylphosphine)cobalt(0). In a parallel reaction of complexes **1**–**5** with 2-diphenylphosphanylthiophenol the bis-chelate complexes **6**–**7** are formed with evolution of hydrogen.



Scheme 1. A proposed mechanism of reaction of acyl(hydrido)cobalt(III) complexes with (2-diphenylphosphanyl)thiophenol.



Scheme 2. Influence of chelating ligands containing hard/soft donor atoms on the stability of cobalt complexes.

According to the earlier work of Klein [1–5] and Sun [8], when reacting an acyl(hydrido)cobalt(III) complex with 2-nitrophenol and (2-diphenylphosphanyl)phenol, respectively, to form cobalt(III) complexes with chelating 2-nitrophenolato ligands, in the light of the HSAB rule, the hard/hard product is expected to be more stable than the hard/soft product with (2-diphenylphosphanyl)phenolato ligands. In combination with our present work, the influence of chelating ligands containing hard/soft donor atoms on the relative stabilities of cobalt complexes can be described as in Scheme 2. In the reaction system with 2-nitrophenol the stable 2-acylphenolato cobalt(III) complex was obtained, while a corresponding cobalt(I) complex could not be experimentally verified [8]. In the present work, the cobalt(I) complex **16** was isolated in high yield, while relatively low yields were attained for complexes **6**–**7** and **8**–**10**. Derivatives of salicylaldehyde released in situ react with starting materials to generate bis-chelate cobalt(III) complexes **11**–**15**, and no formation of salicylalcohol was observed, while salicylalcohol was identified in the reaction system with (2-diphenyl)phosphanylphenol [8]. This result confirms the key role of (2-diphenylphosphanyl)phenol in the formation of salicylalcohol.

4. Conclusions

The reaction of acyl(hydrido)cobalt(III) complexes **1**–**5** with (2-diphenylphosphanyl)thiophenol generated two types of chelate cobalt(III) complexes (**6**–**7**, **8**–**10** and **11**–**15**), one chelate cobalt(I) complex (**16**) and one chelate cobalt(II) complex (**17**). Complex **16** bearing a soft/soft [P,S]-chelate ligand and a soft low-valent cobalt(I) central atom was obtained in the highest yield of about 30–40%, while the expected products with a soft/soft [P,S]-chelate ligand and a hard high-valent cobalt(III) central atom (**6**, **7** and **8**–**10**) show low yields (less than 10%). The by-products **11**–**15** with a hard/hard [O,O]-chelating ligand and a hard cobalt(III) center are very stable. Cobalt(II) complex **17** could be separated as a result of a disproportionation reaction of complex **16**. A possible mechanism is proposed. Coordination of chelating ligands at Co(III) decreases as [N,O] > [P,O] > [P,S], while at Co(I) this order is reversed, which is in accord with the HSAB rule.

Acknowledgements

We gratefully acknowledge support by NSFC China No. 20572062. The Doctoral Program of Ministry of Education of China (MOE) Nos. 20050422010, 20050422011, Natural Science Foundation of Shandon No. Y2006B18 and Shandong Scientific Plan No. 032090105. We also thank the kind assistance from Prof. Dieter Fenske for the X-ray diffraction analysis.

Appendix A. Supplementary material

CCDC 641640 contains the supplementary crystallographic data for **17**. These data can be obtained free of charge via http://www.ccdc.cam.ac.uk/conts/retrieving.html, or from the Cambridge Crystallographic Data Centre, 12 Union Road, Cambridge CB2 1EZ, UK; fax: (+44) 1223-336-033; or e-mail: deposit@ccdc.cam.ac.uk. Supplementary data associated with this article can be found, in the online version, at doi:10.1016/j.poly.2007.11.010.

References

[1] H.-F. Klein, S. Haller, H. Sun, X. Li, T. Jung, C. Röhr, U. Flörke, H.-J. Haupt, Z. Naturforsch. 53b (1998) 587.
[2] H.-F. Klein, S. Haller, H. Sun, X. Li, T. Jung, C. Röhr, U. Flörke, H.-J. Haupt, Z. Naturforsch. 53b (1998) 856.
[3] H.-F. Klein, X. Li, U. Flörke, H.-J. Haupt, Z. Naturforsch. 55b (2000) 707.
[4] H.-F. Klein, X. Li, U. Flörke, H.-J. Haupt, Inorg. Chim. Acta 342 (2003) 179.
[5] X. Li, H. Sun, H.-F. Klein, U. Flörke, Z. Anorg. Allg. Chem. 631 (2005) 1929.
[6] E. Block, G. Ofori-Okai, J. Zubieta, J. Am. Chem. Soc. 111 (1989) 2327.
[7] A. Brand, Doctoral Thesis, Technische Universität Darmstadt, 1998.
[8] H. Sun, X. Li, H.-F. Klein, U. Flörke, H.-J. Haupt, Organometallics 24 (2005) 2612.

behavior of the compounds in various solvents was also investigated.

2. Experimental

2.1. Materials

9-Anthraldehyde (abbreviated as AnthAl; TCI), acetylferrocene (ActFc; Aldrich), ferrocenecarboxaldehyde (FcAl; FC Chiral) and 9-acetylanthracene (ActAnth; Aldrich) were commercially purchased and used as received. The HPLC-grade organic solvents (Aldrich) utilized for column chromatography and crystal growth were used without further purification.

2.2. Measurements

The melting point was measured using an IA 9100 digital melting point apparatus. The high-resolution FAB mass spectra were obtained on a JMS-AX 505 WA mass spectrometer (JEOL). The infrared spectra were recorded by the KBr pellet method on a MIDAC FT-IR spectrophotometer in the range of 4000–400 cm^{-1}. The UV–Vis spectra were obtained at ambient temperature on an HP 8452A diode array spectrophotometer in methanol, ethanol, chloroform, and *n*-hexane. The ^1H NMR measurements were performed at room temperature using an Avance 500 (Bruker, 500 MHz) with the samples dissolved in $CDCl_3$. Tetramethylsilane (TMS) was used as an internal standard. Cyclic voltammetry and differential pulse voltammetry were performed at room temperature with a CHI 620A Electrochemical Analyzer (CHI Instrument Inc.) in 10 mL of acetonitrile solution containing 1.0 mM of the sample, using 0.1 M n-$Bu_4N \cdot BF_4$ as a supporting electrolyte, a Pt-button working electrode ($r = 0.8$ mm), Ag/Ag^+ in CH_3CN as the reference electrode, a Pt wire as the counter electrode and with a scan rate of 50 mV s^{-1}. All redox potentials were referenced against the standard ferrocene/ferrocenium redox couple ($E_{1/2} = +0.136$ V). The fluorescence spectra were measured by a Cary Eclipse fluorescence spectrophotometer (Varian) in methanol, ethanol, chloroform and *n*-hexane. Approximately 3 mL of solutions of the samples at a concentration of 10^{-5}–10^{-6} M in a quartz cell were used to measure the spectra.

2.3. X-ray structure determination

The orange-colored single crystals of Fc–Anth and Anth–Fc suitable for the X-ray structure analysis were obtained by the recrystallization of the purified compounds from CH_2Cl_2/*n*-hexane (needle-shaped Fc–Anth) or CH_2Cl_2/diethyl ether (diamond-shaped Anth–Fc). The X-ray crystallographic data for these compounds were collected on a SMART APEX CCD SYSTEM (Bruker) equipped with graphite-monochromated Mo Kα radiation ($\lambda = 0.71073$ Å). The structures were solved by the direct method and refined by full-matrix least-squares analysis using anisotropic thermal parameters for non-hydrogen atoms with the SHELXL-97 program [24]. The crystallographic data and the details of the data collection are listed in Table 1, and the selected bond distances and angles are summarized in Table 2.

2.4. Synthesis

A mixture of 9-anthraldehyde (5.0 mmol, 1.14 g) and acetylferrocene (5.0 mmol, 1.03 g) or ferrocenecarboxaldehyde(2.0 mmol, 0.43 g) and 9-acetylanthracene(2.0 mmol, 0.44 g) was ground homogeneously in the presence of solid NaOH (at a mole ratio of the mixture to NaOH of 1:5) with a mortar and pestle. The mixture was then allowed to stand in a water bath at 60–70 °C for 24 h, during which time the color of the mixture consistently turned deep red. The product was extracted with CH_2Cl_2 and dried with $MgSO_4$. After filtration, the product was separated by column chromatography (SiO_2, petroleum ether:diethyl ether = 1:1 for Fc–Anth and CH_2Cl_2 for Anth–Fc).

Fc–Anth: yield 57.4% (1.19 g); m.p. 187–188 °C, HR-FABMS Calc. for $C_{27}H_{20}FeO$ 416.0864. Found: 416.0853 (M^+); FT-IR(KBr, cm^{-1}) 3096, 3081, 3050, 3033 (Ar C–H), 1650 (C=O), 1597, 1458 (C=C), 1271, 1088 (Cp C=C), 999, 984 (=C–H), 726 (Ar C–H), 525, 502, 485 (Fe–Cp); ^1H NMR ($CDCl_3$, ppm) 4.30 (5H, CH, s), 4.63 (2H, CH, s), 4.94 (2H, CH, s), 7.18 (1H, CH, s), 7.52 (4H, CH, m), 8.05 (2H, CH, d, $J = 9.4$ Hz), 8.35 (2H, CH, d, $J = 7.7$ Hz), 8.48 (1H, CH, s), 8.76 (1H, CH, s).

Anth–Fc: yield 68.6% (0.57 g); HR-FABMS Calc. for $C_{27}H_{20}FeO$ 416.0864. Found 416.0869 (M^+); m.p. 221–222°C; FT-IR(KBr, cm^{-1}) 3081, 3057 (Ar C–H), 1607 (C=O), 1459 (Ar C=C), 1359, 1224, 1171, 1149 (Cp C=C), 967 (=C–H), 889, 819, 735 (Ar C–H), 488 (Fe–Cp); ^1H NMR ($CDCl_3$, ppm) 4.10 (5H, CH, s), 4.44 (4H, CH, d, $J = 12.4$ Hz), 6.89 (1H, CH, d, $J = 16.0$ Hz), 7.03 (1H, CH, d, $J = 16.0$ Hz), 7.49 (4H, CH, m), 7.93 (2H, CH, d, $J = 8.2$ Hz), 8.06 (2H, CH, d, $J = 8.2$ Hz), 8.54 (1H, CH, s).

Table 1
Crystal data and structure refinement parameters for Fc–Anth and Anth–Fc

	Fc–Anth	Anth–Fc
Empirical formula	$C_{27}H_{20}FeO$	$C_{27}H_{20}FeO$
Formula weight	416.28	416.28
Crystal system	monoclinic	orthorhombic
Space group	*P*2(1)/*c*	*Pbca*
a (Å)	12.728(2)	11.347(1)
b (Å)	19.270(3)	13.088(2)
c (Å)	7.986(1)	26.405(3)
β (°)	95.281(4)	90.00
Volume (Å^3)	1950.5(5)	3921.2(8)
Z	4	8
$R_1(wR_2)$ [$I > 2\sigma(I)$]	0.0525(0.1100)	0.0567(0.1018)

Table 2
Selected bond lengths (Å), bond angles and torsion angles (°) for Fc–Anth and Anth–Fc

Fc–Anth		Anth–Fc	
Bond length			
C10–C11	1.471(5)	C10–C11	1.441(4)
C11–C12	1.485(4)	C11–C12	1.329(4)
C12–C13	1.318(4)	C12–C13	1.441(5)
C13–C14	1.480(4)	C13–C14	1.513(4)
C11–O1	1.226(4)	C13–O1	1.233(4)
C–C(Anth)	1.341(6)–1.438(5)	C–C(Anth)	1.340(5)–1.436(4)
C–C(Fc)	1.391(6)–1.426(5)	C–C(Fc)	1.368(5)–1.430(4)
Bond angle			
C10–C11–C12	118.0(3)	C10–C11–C12	126.1(3)
C11–C12–C13	121.8(3)	C11–C12–C13	125.3(3)
C12–C13–C14	126.1(3)	C12–C13–C14	119.9(3)
C10–C11–O1	121.1(3)	C12–C13–O1	121.8(3)
C12–C11–O1	120.9(3)	C14–C13–O1	118.3(3)
Torsion angle			
C12–C11–C10–C9	9.0(5)	C12–C11–C10–C9	173.6(3)
C13–C12–C11–C10	170.6(3)	C13–C12–C11–C10	176.9(3)
C14–C13–C12–C11	–177.5(3)	C14–C13–C12–C11	−6.4(4)
C12–C13–C14–C27	124.3(4)	C12–C13–C14–C27	−74.9(4)

3. Results and discussion

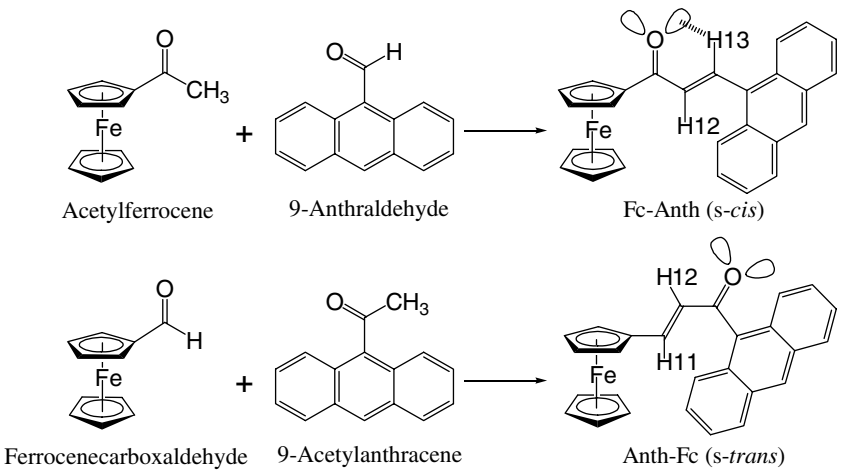
3.1. Synthesis and characterization

The two ferrocenyl chalcones, Fc–Anth and Anth–Fc, were prepared by base-catalyzed solvent-free aldol condensation in 57.4% and 68.6% yields, respectively. These compounds can also be prepared by the reaction method under reflux in CH_2Cl_2 and obtained in yields similar to those of the solvent-free method. However, the solvent-free method is faster, easier and more environmentally friendly than that using an organic solvent. In the high-resolution FAB-MS analysis of Fc–Anth ($m/z = 416$), two main fragments, viz. $[M-Fc]^+$ ($m/z = 231$) and $[FcCO]^+$ ($m/z = 213$), are observed. Also, in the analysis of Anth–Fc ($m/z = 416$), $[M-Anth]^+$ ($m/z = 239$) and $[AnthCO]^+$ ($m/z = 205$) are observed as the two main fragments. These findings indicate that the C–C bonds connected to the C=O bond are susceptible to bond cleavage, resulting in the above fragmentations. The NMR spectrum of Anth–Fc measured at room temperature shows two doublets at 6.89 ppm ($J_{ab} = 16.0$ Hz) and 7.03 ppm ($J_{ab} = 16.0$ Hz), suggesting that the ethylene moiety in the enone linkage is in the *trans*-conformation [25], possibly with an s-*trans* conformation around the C–C bond, as illustrated in Scheme 1. On the other hand, the NMR spectrum of Fc–Anth gives no corresponding peaks in this region, but broad ones at 8.76 ppm and 7.18 ppm. These findings led us to postulate that the ethylene and carbonyl groups are in an s-*cis* conformation and that they cause a significant intramolecular interaction between the lone-pair electrons of the oxygen atom and H13 atom in the solution state, resulting in the up-field shift of the ethylenic protons. This was also supported by the X-ray structural analysis described below.

The UV–Vis spectra of the ferrocenyl chalcones were measured in several solvents of different polarity and compared with those of the AnthAl and FcAl reactants in order to investigate the solvent effect on the electronic transition, or so-called solvatochromic shift, as shown in Table 3. The $\pi \rightarrow \pi^*$ (246–252 nm) and $n \rightarrow \pi^*$ (308–318 nm) transitions of the enone linkage were not significantly influenced by the solvent polarity. However, this was not the case for the d–d transition of the ferrocenyl group which varied from 450 nm (*n*-Hx) to 464 nm (MeOH and EtOH) for FcAl, from 486 nm (*n*-Hx) to 502 nm (EtOH) for Fc–Anth and from 468 nm (*n*-Hx) to 512 nm (EtOH and MeOH) for Anth–Fc. The extent of the solvatochromic shift is only 16 nm for Fc–Anth and 14 nm for FcAl. On the other hand, Anth–Fc shows a strong solvatochromic shift of 44 nm in a lower energy region. Given that a strong solvatochromic shift is a good indication of the potential of a compound to be used as a non-linear optical (NLO) material, Fc–Anth could be a good candidate NLO material, as many chalcones have such properties [6,7].

3.2. X-ray structure analyses

The X-ray structural analyses of the Fc–Anth and Anth–Fc single crystals show that they crystallize in the monoclinic and orthorhombic systems, respectively, with the cell parameters shown in Table 1. The selected bond lengths, bond angles and torsion angles of the compounds are listed in Table 2. The molecular structures of Fc–Anth and Anth–Fc (Fig. 1) and their torsion angles (Table 2) reveal that the Cp ring and enone linkage are almost co-planar with a dihedral angle of less than 9.0(3)°. The planar anthracenyl groups, however, deviate significantly from the plane made by the enone linkage: the dihedral angle between the anthracenyl group and the plane of the enone linkage is



Scheme 1. Solvent-free syntheses of Fc–Anth and Anth–Fc.

Table 3
UV–Vis spectroscopic data for Fc–Anth, Anth–Fc, AnthAl and FcAl dissolved in various solvents

Compound	MeOH	EtOH	$CHCl_3$	*n*-Hx
AnthAl	372 sh, 400 s	372 sh, 400 s	374 sh, 406 s	372 sh, 396 s
Fc–Anth	246 s, 404 m, 500 w	246 s, 404 m, 502 w	252 s, 406 m, 494 w	248 s, 394 m, 486 w
FcAl	244 s, 342 m, 464 w	246 s, 342 m, 464 w	266 s, 342 m, 460 w	238 s, 268 m, 450 w
Anth–Fc	316 s, 364 sh, 512 w	318 s, 364 sh, 512 w	316 s, 366 sh, 506 w	308 s, 346 sh, 468 w

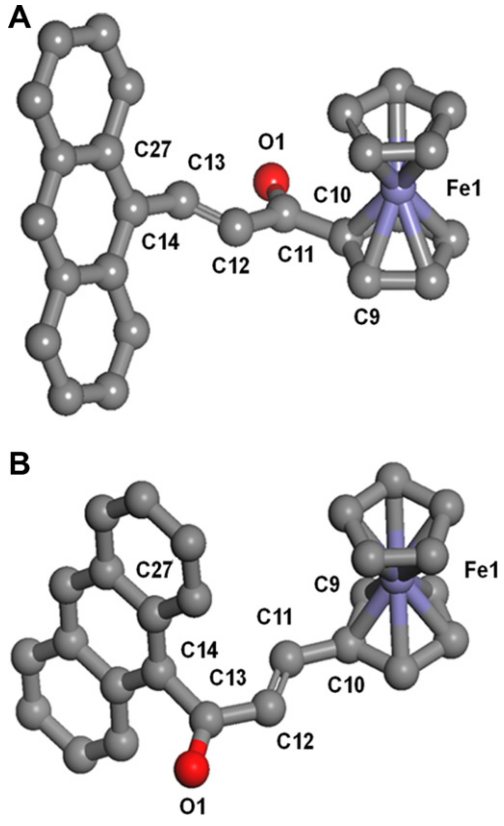


Fig. 1. Molecular structures of Fc–Anth (A) and Anth–Fc (B) with the selected atomic numbering scheme. Hydrogen atoms are omitted for the sake of clarity.

74.9(4)° for Anth–Fc and 55.7(4)° for Fc–Anth. These large dihedral angles indicate that the possibility for electronic communications between the anthracenyl and ferrocenyl groups through the enone linkage is reduced. This is comparable to the case of the ferrocenyl chalcone with naphthalenyl group (Fc–COCH=CH–Naph), in which the naphthalenyl group and the enone linkage are almost coplanar with a dihedral angle of less than 4.4(3)° [23]. It is also noteworthy that the spatial arrangement of the enone part is different in the two compounds. The two double bonds (C=O and C=C) about the intervening C–C single bond are in the s-*cis* conformation for Fc–Anth, while they are in the s-*trans* conformation for Anth–Fc, as clearly shown in Fig. 1. This conformational difference is likely responsible for the significant chemical shift of H13 of up to 8.76 ppm in Fc–Anth due to the intramolecular interaction with the lone-pair electrons of the oxygen atom (Scheme 1), based on the assumption that the solid state X-ray crystal structure is accepted in the solution state. On the other hand, the C=O ⋯ H12–C=C interaction is not probable in Anth–Fc, due to its long distance, as evidenced by the NMR data resulting in the two doublets at 6.89 and 7.03 ppm. This conformational difference together with the positions of the C=O and C=C bonds also influences the oxidation potentials of the ferrocenyl and anthracenyl groups, as will be discussed below.

In the molecular packing of both Fc–Anth (Fig. 2) and Anth–Fc (Fig. 3), the two enantiomers are found to form a racemic mixture: the Fc–Anth enantiomers

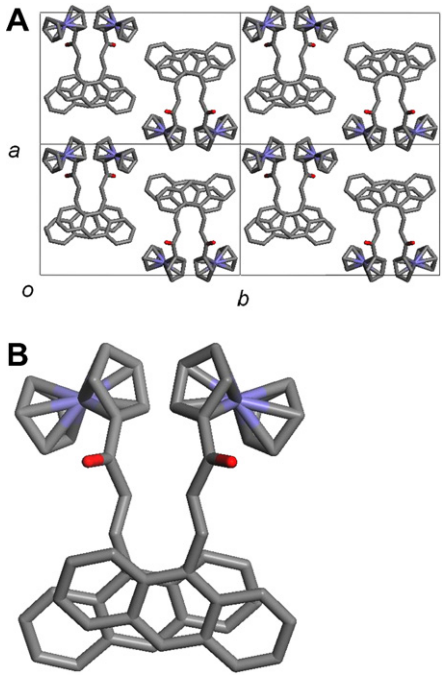


Fig. 2. (A) Crystal structure of Fc–Anth viewed along the *c*-axis. (B) The two enantiomeric molecules are partially overlapped by the anthracene groups. Hydrogen atoms are omitted for the sake of clarity.

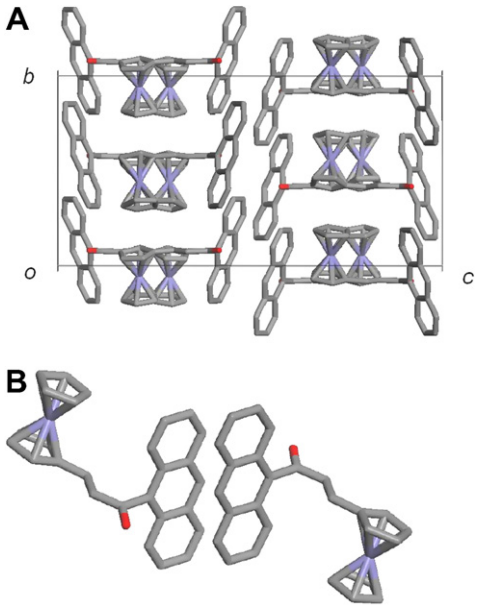


Fig. 3. Crystal structure of Anth–Fc viewed along the *a*-axis (A), and those of the two enantiomeric Anth–Fc molecules (B). Hydrogen atoms are omitted for clarity.

are stacked along the *c*-axis through the partial overlapping of the anthracenyl groups with a long enough separation (3.993(1) Å) for the intermolecular interaction to be ignored. The separation of the anthracenyl groups is longer than the sum of the van der Waals radii of the carbons (3.4 Å). The Anth–Fc crystal is also a racemic mixture, which consists of alternative ferrocene and anthracene layers perpendicular to the *c*-axis. No close intermolecular contacts such as Fe(II)···Fe(II) or anthracene···anthracene interactions are observed in these crystal structures.

3.3. Electrochemical properties

The electrochemical properties of Fc–Anth and Anth–Fc were measured and compared with those of the reactants, as summarized in Table 4. In the cyclic voltammograms (CV) and differential pulse voltammograms (DPV) scanned from 0.0 to +2.0 V and then back to 0.0 V, both compounds exhibit one reversible redox wave in the lower potential region ($E_{1/2} = +0.402$ V for Fc–Anth and +0.277 V for Anth–Fc) and one irreversible oxidation peak in the higher potential region ($E_{pa}{}^2 = +1.073$ V and +1.153 V, respectively), as shown in Fig. 4. These reversible redox peaks can be attributed, without doubt, to the Fc/Fc^+ process. The reversibility of these peaks is more clearly observed in the inset, where the reversible cycles were obtained by scanning within the redox potential region of the ferrocenyl group. The irreversible peaks therefore correspond to the oxidation of the anthracenyl group. The half-wave potential ($E_{1/2}$) for the reversible peak of Fc–Anth (+0.402 V) is slightly higher than that of ActFc (+0.379 V), both of which have a carbonyl group directly connected to a ferrocenyl group. On the other hand, the $E_{1/2}$ value for Anth–Fc (+0.277 V) is much lower than those of the above two compounds. This is ascribed to the functional groups being directly connected to the ferrocenyl group, as can be seen in the comparison of the oxidation potentials of ActFc ($E_{pa}{}^1 = +0.413$ V), vinylferrocene ($E_{pa} = +0.24$ V) [26] and ferrocene ($E_{pa}{}^1 = +0.169$ V). For the same reasons, the second oxidation potential of Anth–Fc ($E_{pa}{}^2 = +1.153$ V) is higher than that of Fc–Anth ($E_{pa}{}^2 = +1.073$ V). Consequently, the potential separation of Fc–Anth ($\Delta E = E_{pa}{}^2 - E_{pa}{}^1 = +0.631$ V) is much smaller than that of Anth–Fc (+0.839 V), suggesting that the magnitude of the on-site Coulomb repulsion in Fc–Anth is smaller than that in Anth–Fc. These results can be explained by the positional difference of the C=O and C=C bonds in the enone linkage.

Table 4
Electrochemical parameters for Fc–Anth and Anth–Fc compared with the reactants[a]

Compounds[b]	E^1_{pa}	E^2_{pa}	E^1_{pc}	E^2_{pc}	$E^c_{1/2}$
Fc	0.169		0.102		0.136
ActFc	0.413		0.345		0.379
ActAnth		1.144		−1.287	
Fc–Anth	0.442	1.073	0.361		0.402
Anth–Fc	0.314	1.153	0.239		0.277

[a] Samples are dissolved in acetonitrile solution containing 0.1 M n-$Bu_4N \cdot BF_4$ electrolyte and measured with a scan rate of 50 mV s^{-1} (ferrocene/ferrocenium: $E_{1/2} = +0.136$ V).
[b] Full names are found in Section 2.
[c] $E_{1/2} = (E_{pa}{}^1 + E_{pc}{}^1)/2$.

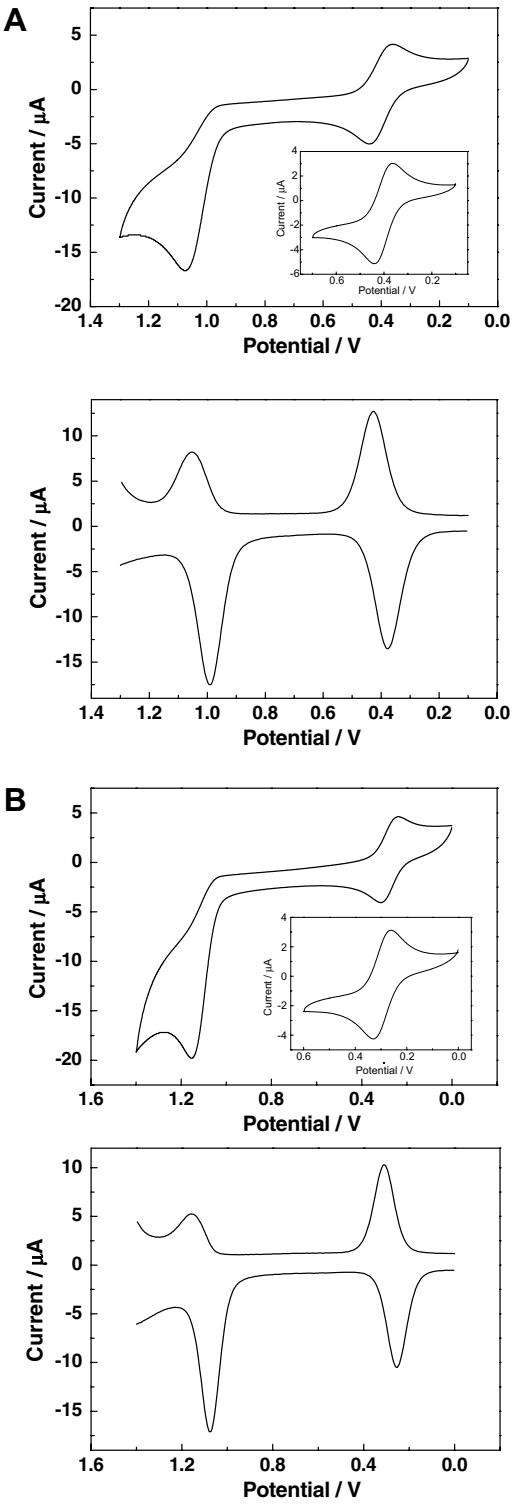


Fig. 4. Cyclic voltammograms (above) and differential pulse voltammograms (below) of Fc–Anth (A) and Anth–Fc (B). The insets show the reversible cycles for the ferrocenyl group in each compound.

3.4. Fluorescence spectroscopy

The fluorescence spectra of the two ferrocenyl chalcones were measured in methanol, ethanol, chloroform, and *n*-hexane with the maximum excitation wavelength. Irrespective of the solvent polarity, the fluorescent properties of Fc–Anth and Anth–Fc are quenched, while those of AnthAl and ActAnth are clearly observed. This is surely due to the quenching of the fluorescence of anthracene by the ferrocenyl group, because ferrocene and its derivatives are known to be effective quenchers of excited states [27,28]. Based on these observations together with the significant deviation of the co-planarity of the ferrocenyl and anthracenyl groups, it can be suggested that the intramolecular fluorescence quenching occurred *via* a through-space process rather than a through-bond process.

4. Conclusion

Two ferrocenyl chalcones with the anthracenyl group, Fc–COCH=CH–Anth (Fc–Anth) and Anth–COCH=CH–Fc (Anth–Fc), synthesized by base-catalyzed solvent-free aldol condensation, were analyzed by X-ray structure determinations. The planar anthracenyl group and the enone linkage are severely distorted from co-planarity with torsion angles of 55.7(4)° for Fc–Anth and 74.9(4)° for Anth–Fc. Also the enone linkages are in the s-*cis* conformation for Fc–Anth, but in the s-*trans* conformation for Anth–Fc. The cyclic voltammetry and differential pulse voltammetry measurements for the compounds exhibit one reversible cycle at $E_{1/2} = +0.402$ V for Fc–Anth and at $E_{1/2} = +0.277$ V for Anth–Fc, corresponding to the Fc/Fc^{+} process, and one irreversible peak attributed to the oxidation of the anthracenyl group at $E_{pa}{}^{2} = +1.073$ V for Fc–Anth and at $E_{pa}{}^{2} = +1.153$ V for Anth–Fc. The potential separations ($\Delta E = E_{pa}{}^{2} - E_{pa}{}^{1}$) of Fc–Anth (+0.631 V) and Anth–Fc (+0.839 V) are closely related to the magnitude of the on-site Coulomb repulsion, and caused by the positional difference of the C=O and C=C bonds in the enone linkage. The fluorescent properties of the anthracenyl group are quenched by the ferrocenyl group.

Acknowledgement

This work was supported by a special research grant from Seoul Women's University (2007).

Appendix A. Supplementary material

CCDC 661664 and 661665 contain the supplementary crystallographic data for Fc–Naph and Naph–Fc. These data can be obtained free of charge via http://www.ccdc.cam.ac.uk/conts/retrieving.html, or from the Cambridge Crystallographic Data Centre, 12 Union Road, Cambridge CB2 1EZ, UK; fax: (+44) 1223-336-033; or e-mail: deposit @ccdc.cam.ac.uk. Supplementary data associated with this article can be found, in the online version, at doi:10.1016/j.poly.2007.11.015.

References

[1] K. Schlogl, H. Egger, Monatsh Chem. 94 (1963) 376.
[2] X. Wu, E.R.T. Tiekink, I. Kostetski, N. Kocherginsky, A.L.C. Tan, S.B. Khoo, P. Wilairat, M.L. Go, Eur. J. Pharm. Sci. 27 (2006) 175.
[3] X. Wu, P. Wilairat, M.L. Go, Bioorg. Med. Chem. Lett. 12 (2002) 2299.
[4] M. Liu, P. Wilairat, M.L. Go, J. Med. Chem. 44 (2001) 4443.
[5] V. Zsoldos-Mady, A. Csampai, R. Szabo, E. Meszaros-Alapi, J. Pasztor, F. Hudecz, P. Sohar, Chem. Med. Chem. 1 (2006) 1119.
[6] B. Zhao, W.Q. Lu, Z.H. Zhou, Y. Wu, J. Mater. Chem. 10 (2000) 1513.
[7] Y. Kawabe, H. Ikeda, T. Sakai, K. Kawasaki, J. Mater. Chem. 2 (1992) 1025.
[8] V. Crasta, V. Ravindrachary, R.F. Bhajantri, R. Gonsalves, J. Cryst. Growth 267 (2004) 129.
[9] S. Shettigar, K. Chandrasekharan, G. Umesh, B.K. Sarojini, B. Narayana, Polymer 47 (2006) 3565.
[10] B. Belavaux-Nicot, J. Maynadie, D. Lavabre, C. Lepetit, B. Donnadieu, Eur. J. Inorg. Chem. (2005) 2493.
[11] B. Belavaux-Nicot, S. Fery-Forgues, Eur. J. Inorg. Chem. (1999) 1821.
[12] J. McMurry, Organic Chemistry, 6th ed., Thomson-Brooks/Cole, NY, 2007.
[13] A. Tarraga, P. Molina, J.L. Lopez, Tetrahedron Lett. 41 (2000) 2479.
[14] A. Tarraga, P. Molina, D. Curiel, J.L. Lopez, M.D. Velasco, Tetrahedron 55 (1999) 14701.
[15] K. Tanaka, F. Tada, Chem. Rev. 100 (2000) 1025.
[16] G. Rothenberg, A.P. Downie, C.L. Raston, J.L. Scott, J. Am. Chem. Soc. 123 (2001) 8701.
[17] W. Liu, Q. Xu, B. Chen, Y. Ma, Synth. Commun. 32 (2002) 171.
[18] W. Liu, Q. Xu, B. Chen, Y. Liang, Y. Ma, W. Liu, J. Organomet. Chem. 637–639 (2001) 782.
[19] W. Liu, T. Xie, Y. Liang, W. Liu, Y. Ma, J. Organomet. Chem. 627 (2001) 93.
[20] S.J. Ji, Z.L. Shen, S.Y. Wang, Chin. Chem. Lett. 14 (2003) 663.
[21] D. Villemin, B. Martin, M. Puciova, S. Toma, J. Organomet. Chem. 484 (1994) 27.
[22] C.L. Raston, J.L. Scott, Green Chem. (2000) 49.
[23] K.I. Son, D.Y. Noh, J. Korean Chem. Soc. 51 (2007) 591.
[24] G.M. Sheldrick, SHELXL-97, Program for the Refinement of Crystal Structures, University of Gottingen, Gottingen, Germany, 1997.
[25] R.M. Silverstein, G.C. Bassler, T.C. Morrill, Spectroscopic Identification of Organic Compounds, 5th ed., John Wiley, Singapore, 1991.
[26] H.J. Lee, D.Y. Noh, A.E. Underhill, C.S. Lee, J. Mater. Chem. 9 (1999) 2359.
[27] S. Fery-Forgues, B. Delavaux-Nicot, J. Photochem. Photobiol. A 132 (2000) 137.
[28] J. Rochford, A.D. Rooney, M.T. Pryce, Inorg. Chem. 46 (2007) 7247.

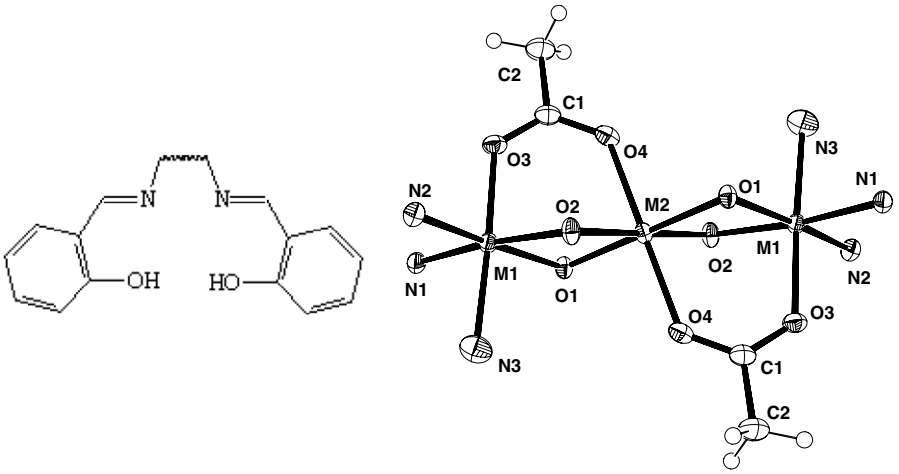


Fig. 1. The common trimetallic motif adopted by tetradentate Schiff base complexes of divalent transition metal acetates. Typically the polymethylene chain (▬▬) between the salicylidene units is either a propane or butane moiety. The sixth coordination site here is filled by a coordinated pyridine (N3) [6].

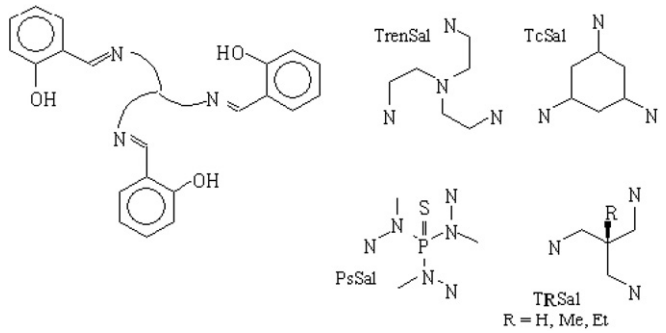


Fig. 2. Commonly used hexadentate and heptadentate Schiff base systems. TrenSal: tris-((2-hydroxybenzylidene)aminoethyl)amine, TcSal: tris(2-oxybenzylidene)-1,3,5-triaminocyclohexane, PsSal: tris-(methyl-(2-hydroxybenzylidene)hydrazono)phosphine sulfide, TRSal (e.g TMeSal and TEtSal, where R = Me and Et respectively): tris-((2-hydroxybenzylidene)-aminomethyl)ethane.

[18–27] and that this combination facilitates the encapsulation of the cation and the formation of simple discrete complexes (Fig. 3). Divalent metals make additional demands on these tri-anionic ligands and an inspection of the small number of complexes derived from these combinations suggest that the trimetallic motif (Fig. 1) will re-establish itself with metals such as nickel and zinc [1,28–30].

As a result of our studies on ligand flexibility [6,12,30,31] we have begun to study the series of multidentate Schiff base species derived from tris-(2-aminoethyl)amine (Fig. 2, Tren) and salicylaldehyde, which potentially offers seven donor atoms [17]. Significantly this motif allows flexibility around the aminoethyl regions in conjunction with the rigidity of the salicylidene units. In our formative study of this ligand system we have elected to revisit the chemistry of nickel and zinc in the expectation that we will expand the catalogue of trimetallic complexes. A comparison is made with the hexadentate ligand system, tris-((2-hydroxybenzylidene)-aminomethyl)propane (TEtSal) which is expected behave in an identical manner to the previously reported TMeSal system [29].

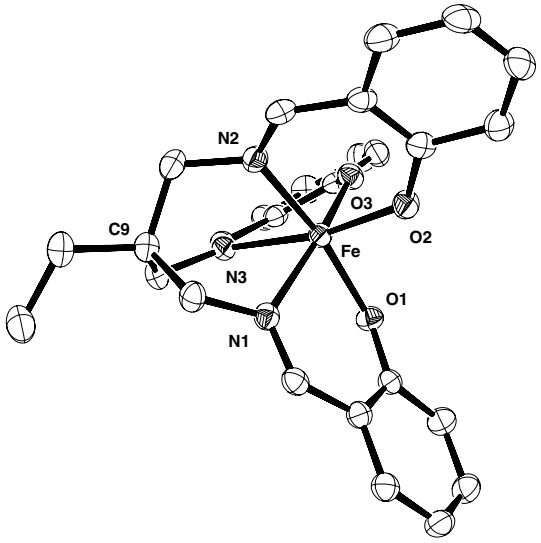


Fig. 3. A typical hexadentate complex of a trivalent metal, [(TEtSal)Fe] (R = Et, Fig. 2), demonstrating how the metal can be fully encapsulated [20].

2. Experimental

All experiments were carried out using standard apparatus and commercially available chemicals apart from 1,1,1-tris(methylamino)propane which was prepared by the combined methods Fleischer [32] and Hellmann [33]. NMR analysis was carried out on either a JEOL EX 270 operating at 270 MHz for ^{1}H and 67.5 MHz for ^{13}C or a Bruker AMX 400 operating at 400 MHz for ^{1}H and 100 MHz for ^{13}C. Solution (solvent) and reflectance (solid, between 350 and 900 nm) spectra were recorded on a Photonics CCD array UV–Vis spectrophotometer. Mass spectra were recorded in house on a Thermo Finnigan LCQDuo by electrospray ion trap apart from $[(TrenSal)_2Ni_3]$ which was recorded at the EPSRC facilities at the University of Wales, Swansea, UK, using a Finnegan MAT95. Infra

red spectra were recorded as potassium bromide discs using a Nicolet Avatar 360 FTIR spectrometer. Magnetic measurements were determined at room temperature in the solid state using an MSB1 magnetic susceptibility balance. Single crystal diffraction data were recorded by Nonius Kappa CCD diffractometers ($\lambda = 0.71073$ Å) except for compound [(Tren5BrSal)$_2$Zn$_3$] where data were obtained at Station 16.2smx of the Daresbury Synchrotron Radiation Source ($\lambda = 0.82520$ Å). All structures were solved and then refined to convergence against F^2 using the SHELXS-97 and SHELXL-97 programs and the WinGX interface [34,35]. Specific crystallographic data and refinement parameters are given in Table 1.

2.1. Preparation of tris-((2-hydroxybenzylidene)-aminoethyl)amine (TrenSal) and tris-((2-hydroxy-5-bromobenzylidene)aminoethyl)amine (Tren5BrSal)

Briefly: 3 mol equiv. of the relevant salicylaldehyde were mixed with 1 mol equivalent of tris(2-aminoethyl)amine (0.9 g; 6.2 mmol) in ethanol (100 ml). The resulting solution was refluxed for 1 h, filtered when hot and allowed to cool whereupon copious amounts of yellow crystals began to form. These were collected and allowed to air dry.

2.2. N,N′,N″-Tris-((2-hydroxybenzylidene)-aminoethyl)amine

Yield 55%. *Anal.* Calc. for $C_{27}H_{30}N_4O_3$: C, 70.72; H, 6.59; N, 12.22. Found: C, 70.64; H, 6.74; N, 12.10%. ^{1}H NMR (400 MHz, $CDCl_3$; δ): 13.7 (br s, 1H, –OH); 7.8 (s, 1H, –HC=N); 7.3 (t, 1H, arom); 6.9 (d, 1H, arom); 6.6 (t, 1H, arom); 6.1 (d, 1H, arom); 3.5 (t, 2H, –CH_2–); 2.8 (t, 2H, –CH_2–). ^{13}C-{^{1}H} NMR (100 MHz $CDCl_3$; δ): 166, 161, 132, 131, 119, 118, 116, 58, 56. FTIR [ν/cm^{-1} (KBr)]: 1634 (C=N); 1500 (C=C); 1275 (C–O); 753, 778 (arom), m.p. 83 °C.

2.3. N,N′,N″-Tris-((2-hydroxy-5-bromobenzylidene)-aminoethyl)amine

Yield 85% *Anal.* Calc. for $C_{27}H_{27}N_4Br_3O_3$: C, 46.64; H, 3.91; N, 8.06. Found: C, 46.65; H, 4.06; N, 7.92%. ^{1}H NMR (400 MHz, $CDCl_3$; δ): 7.9 (s, 1H, –HC=N); 7.4 (dd, 1H, arom); 6.8 (d, 1H, arom); 6.5 (d, 1H, arom); 6.1 (d, 1H, arom); 3.6 (t, 2H, –CH_2–); 2.8 (t, 2H, –CH_2–); 1.6 (br s, 1H, –OH). ^{13}C-{^{1}H} NMR (100 MHz $CDCl_3$; δ): 165, 160, 135, 133, 120, 119, 110, 57, 55. FTIR [ν/cm^{-1} (KBr)]: 1645 (C=N), 1470 (C=C), 1280 (C–O), 819 (arom), m.p. 139 °C.

2.4. Preparation of bis-(tris-((2-hydroxybenzylidene)-aminoethyl)amine nickel)nickel

A methanol solution (100 ml) of TrenSal (0.46 g, 1 mmol) and nickel actetate (0.375 g, 1.5 mmol) was refluxed for 90 min. The solution was allowed to cool and the resulting yellow-green powder collected, washed with water, methanol, dichloromethane and diethyl ether. The product was found to be insoluble in all common solvents. Yield 75%. *Anal.* Calc. for $C_{54}H_{54}N_8Ni_3O_6 \cdot H_2O$[2]C, 58.69; H, 5.65; N, 9.80%. Found: C, 58.78; H, 5.77; N, 9.80%. FTIR [ν/cm^{-1} (KBr)]: 1635 (C=N), 1475 (C=C), 1340, 1321 (C–O), 760 (arom). Mass Spec. (EI) m/z 1084, 1086 $[M]^+/[M-H]^+/[M-2H]^+$. λ_{max} (solid reflectance): 382 nm. μ_{eff}: 4.9 BM (300 K).

2.5. Preparation of bis-(tris-((2-hydroxy-5-bromobenzylidene)aminoethyl)amine nickel)nickel

A methanol solution (100 ml) of Tren5BrSal (0.695 g, 1 mmol) and nickel acetate (0.375, 1.5 mmol) was refluxed for 90 min. The solution was allowed to cool and the resulting green powder collected and recrystallised from dichloromethane: diethyl ether by vapour diffusion. Yield 94%. *Anal.* Calc. for $C_{54}H_{48}N_8Br_6Ni_3O_6 \cdot 2CH_2Cl_2$: C, 38.87; H, 3.03; N, 6.47. Found: C, 38.54; H, 3.17; N, 6.12%. FTIR [ν/cm^{-1} (KBr)]: 1625 (C=N), 1465 (C=C), 1305 (C–O), 820 (arom). Mass Spec. (ESI) m/z 1560 [M+]. λ_{max} (dichloromethane): 382 nm (ε/dm^{3}mol^{-1} cm^{-1}, 1361). μ_{eff}: 6.0 BM (300 K).

2.6. Attempted direct crystallisation of [(TrenSal)$_2$Ni$_3$]

A methanol (20 ml) solution TrenSal (0.131 g, 0.29 mmol) was added to a methanolic solution (30 ml) of nickel bromide trihydrate (0.117 g, 0.43 mmol). The mixture was heated for 90 min and the resulting red solution allowed to cool before being filtered. Excess TMEDA (6 ml, 40 mmol) was introduced into the solution and the mixture allowed to stand, open to the air, for a week during which time the solution slowly changed colour from red to yellow-green. A portion (approx. 50%) of the methanol was allowed to evaporate. Two sets of crystals suitable for X-ray analysis form in the solution which could be manually separated with ease.

Orange crystals: *Anal.* Calc. for $C_{46}H_{64}N_{10}Br_2Ni_3O_4 \cdot MeOH \cdot 3\,H_2O$: C, 45.41; H, 6.00; N, 11.27. Found: C, 45.15; H, 5.76; N, 11.06%. FTIR [ν/cm^{-1} (KBr)]: 1620 (C=N), 1445 (C=C), 775 (arom). Mass Spec. (ESI) m/z 1075 [MBr+].

Green crystals: *Anal.* Calc. for $C_{40}H_{120}N_{12}Br_4Ni_6O_{24} \cdot 2H_2O$: C, 25.81; H, 6.71; N, 9.03. Found: C, 26.20; H,

[2] This compound was obdurately insoluble and could not be recrystallised. Purification was restricted to washing the material with a range of solvents in an attempt to remove the obvious impurities. However, the spectroscopic information obtained from the solid in conjunction with the successful characterisation of the Tren5BrSal below clearly support the formation of the desired compound. The microanalysis consistently returned values somewhat lower than required for an anhydrous product and we resorted to scaling the analysis by adding one or two water molecules to gain agreement. The analysis reported is thus a faithful record of the values one might expect to obtain for this material.

Table 1
Experimental details of the crystallographic determination of $[(Tren5BrSal)_2Ni_3]$, $[(Tren5BrSal)_2Zn_3]$, $[\{(TrenSal\text{-}1)Ni\}_2(TMEDA)Ni]$, $[(TMEDA)Ni_6Br_4(CO_3)_4(H_2O)x]$ (two forms), $[\{(TrenSal)Ni\}Pb(C_5H_5N)Cl]_2$, $[(TEtSal)_2Ni_3]$ and $[\{(TEtSal)Ni\}_2Pb]$

	$1/2[(Tren5BrSal)_2Ni_3]\cdot CH_2Cl_2$	$[(Tren5BrSal)_2Zn_3]\cdot 1.25CHCl_3\cdot 0.5(C_2H_5)_2O$	$[\{(TrenSal\text{-}1)Ni\}_2\cdot (TMEDA)Ni]$	$[(TMEDA)_6Ni_6Br_4(CO_3)_4(H_2O)_{12.3}]$	$[(TMEDA)_6Ni_6Br_4(CO_3)_4(H_2O)_{12}]$	$[\{(TrenSal)Ni\}Pb(C_5H_5N)Cl]_2\cdot$ pyridine	$[(TEtSal)_2Ni_3]\cdot Et_2O$	$[\{(TEtSal)Ni\}_2Pb]\cdot$ pyridine
Formula	$C_{28.25}H_{26.5}Br_3Cl_{2.5}N_4Ni_{1.5}O_{3.25}$	$C_{57.5}H_{54.5}Br_6Cl_4N_8O_{6.5}Zn_3$	$C_{46}H_{60}Br_2N_{10}Ni_3O_{7.75}$	$C_{40}H_{120.6}Br_4N_{12}Ni_6O_{24.3}$	$C_{40}H_{120}Br_4N_{12}N_{i6}O_{24}$	$C_{74}H_{74}Cl_2N_{12}Ni_2O_6Pb_2$	$C_{57.2}H_{60}N_6Ni_3O_{7.2}$	$C_{59}H_{57}N_7Ni_2O_{6.2}Pb_1$
Formula weight	890.45	1778.96	1212.99	1830.78	1825.38	1830.15	1122.84	1287.93
Crystal system	triclinic	triclinic	orthorhombic	cubic	cubic	triclinic	monoclinic	triclinic
Space group	$P\bar{1}$	$P\bar{1}$	*Pbna*	$P\bar{4}3n$	$Pa\bar{3}$	$P\bar{1}$	$C2/c$	$P\bar{1}$
a (Å)	12.8590(3)	12.7720(37)	17.4237(7)	26.5232(4)	25.2840(4)	10.75810(10)	18.7874(5)	11.4329(2)
b (Å)	13.2569(3)	13.5077(39)	17.6974(6)	26.5232(4)	25.2840(4)	12.1227(2)	12.9509(4)	14.2095(3)
c (Å)	19.9401(4)	20.1446(58)	17.8836(5)	26.5232(4)	25.2840(4)	15.2850(3)	20.8500(5)	16.3398(4)
α (°)	82.2470(10)	80.410(3)				107.8160(10)		87.794(1)
β (°)	73.1580(10)	73.275(3)				108.1440(10)	95.786(2)	86.855(1)
γ (°)	88.3810(10)	86.438(3)				99.7570(10)		74.459(1)
Z	4	2	4	8	8	1	4	1
V (Å^3)	3223.45(12)	3281.45(38)	5514.5(3)	18658.54(5)	16163.6(4)	1724.51(5)	5047.2(2)	2552.81(8)
μ_{calc} (mm^{-1})	4.849	7.236	2.510	2.958	3.414	5.545	1.170	4.082
Number of reflections measured	24949	22294	34998	58453	11346	15558	11132	17122
Number of unique reflections	13377	11820	6335	5433	5869	7911	5769	11686
Number of observed reflections	7991	5514	4560	3609	3546	6292	4515	8542
Number of parameters	783	806	316	270	314	442	351	682
R^a ($I > 2\sigma(I)$)	0.0497	0.0733	0.0638	0.0494	0.0388	0.0308	0.0319	0.043
$R_w{}^b$ (all reflections)	0.1165	0.1966	0.1378	0.1193	0.0841	0.0560	0.084	0.076
Goodness-of-Fit	1.005	0.926	1.025	1.004	1.035	1.040	1.052	1.023

6.64; N, 8.23%. FTIR [ν/cm^{-1} (KBr)]: 1635 (C=O), 1450 (TMEDA). Mass Spec. (ESI) m/z 779 (100%), 665 (55%).

2.7. Preparation of bis-(tris-((2-hydroxybenzylidene)-aminoethyl)amine zinc)zinc

A methanolic solution (30 ml) of zinc acetate (0.33 g, 1.5 mmol) was added dropwise to a stirred methanolic (30 ml) solution of TrenSal (0.46 g, 1 mmol). The resulting solution was refluxed for 90 min. The solution was filtered hot and the solvent removed to reveal a gelatinous yellow material. This was recrystallised from pyridine: diethyl ether by vapour diffusion. Yield 75%. *Anal.* Calc. for $C_{54}H_{54}N_8Zn_3O_6$ C, 58.57; H, 4.91; N, 10.12. Found: C, 57.85; H, 4.85; N, 10.71%. ^{1}H NMR (400 MHz, $CDCl_3$; δ): 8.2–8.4 (br m, 3H, –HC=N); 7.1 (br s, 6H, arom); 6.5 (br d, 6H, arom); 3.6–3.8 (m, 6H, –CH_2–); 2.7–2.9 (m, 6H, –CH_2–). FTIR [ν/cm^{-1} (KBr)]: 1630 (C=N), 1470 (C=C), 1150 (C–O), 755 (arom). Mass Spec. (ESI) m/z 521 (70%), [(TrenSal)Zn+2H]$^+$ 587 (40%), [(TrenSal)Zn_2]$^+$.

2.8. Preparation of bis-(tris-((2-hydroxy-5-bromobenzylidene)aminoethyl)amine zinc)zinc

A methanolic solution (30 ml) of zinc acetate (0.33 g, 1.5 mmol) was added dropwise to a stirred methanolic (30 ml) solution of Tren5BrSal (0.70 g, 1 mmol). The resulting solution was refluxed for 90 min. The solution was filtered hot and the bulk (~80%) of the solvent removed to reveal a yellow solid. This was collected and recrystallised from chloroform: diethyl ether by vapour diffusion. Yield 68%. *Anal.* Calc. for $C_{54}H_{48}N_8Br_6O_6Zn_3$: C, 41.04; H, 3.06; N, 7.09. Found: C, 40.99; H, 3.08; N, 7.19%. ^{1}H NMR (400 MHz, $CDCl_3$; δ): 8.3 (br s, 3H, –HC=N); 7.3 (br t, 3H, arom); 7.2 (br d, 3H, arom); 6.5 (br d, 3H, arom); 3.6–3.9 (br m, 6H, –CH_2–); 2.7–2.9 (br m, 6H, –CH_2–). FTIR [ν/cm^{-1} (KBr)]: 1640 (C=N), 1460 (C=C), 1170 (C–O), 830 (arom). Mass Spec. (ESI) m/z 1581, 1582 (55%); [(Tren5BrSal$_2$)Zn_2+H$^+$], 1516, 1518 (100%) [(Tren5BrSal$_2$)Zn_2+2H$^+$], 758, 760 (100%) [(Tren5BrSal)Zn+H$^+$], [(Tren5BrSal)Zn+H$^+$].

2.9. Preparation of bis-(μ-chloro(tris-((2-hydroxy-benzylidene)aminoethyl)amine nickel)pyridino lead)

[(TrenSal)$_2$Ni$_3$] (0.25 g, 0.20 mmol) and lead chloride (0.25 g, 0.9 mmol) were suspended in pyridine (10 ml). The solution was allowed to reflux for 72 h whereupon the colour of the solution darkened. The solution was allowed to cool and then filtered to remove the remaining [(TrenSal)$_2$Ni$_3$] and $PbCl_2$. The solution was re-filtered through celite to leave a dark brown solution which was vapour diffused with diethyl ether to produce a dark brown crystals suitable for X-ray crystallography. Yield 10%. *Anal.* Calc. for $C_{64}H_{64}Cl_2N_{10}Ni_2O_6Pb_2$: C, 45.97; H, 3.86; N, 8.38. Found: C, 45.51; H, 3.58; N, 8.04%. FTIR [ν/cm^{-1} (KBr)]: 1630 (C=N), 1450 (C=C), 1095 (Pb–Cl).

2.10. Preparation of bis-(μ-chloro(tris-((2-hydroxy-5-bromobenzylidene)aminoethyl)amine nickel)pyridino lead)

[(Tren5BrSal)$_2$Ni$_3$] (0.25 g, 0.16 mmol) and lead chloride (0.25 g, 0.9 mmol) were suspended in pyridine (10 ml). The solution was allowed to reflux for 72 h whereupon the colour of the solution darkened. The solution was allowed to cool and then filtered to remove the remaining [(TrenSal)$_2$Ni$_3$] and $PbCl_2$. The solution was taken to dryness and extracted with THF. The resulting brown solution was filtered through celite and taken to dryness again. The resulting gum was re-dissolved in pyridine to form a brown solution, which was filtered through celite. The mixture was crystallised by vapour diffusion with diethyl ether producing a dark brown powder. Yield 20%. *Anal.* Calc. for $C_{64}H_{58}Br_6Cl_2N_{10}Ni_2O_6Pb_2 \cdot$ pyridine: C, 38.58; H, 2.98; N, 7.30. Found: C, 38.88; H, 2.52; N, 6.86%. FTIR [ν/cm^{-1} (KBr)]: 1630 (C=N), 1460 (C=C), 1100 (Pb–Cl).

2.11. Preparation of 1,1,1-tris-((2-hydroxybenzylidene)-aminomethyl)propane (TEtSal)

Briefly: 3 mol equivalents of salicylaldehyde was mixed with 1 mol equivalent of 1,1,1-tris(methylamino)propane [32,33] in chloroform (50 ml). The resulting solution was refluxed for 4 h. The solvent was removed and the resulting dark orange oil recrystallised from chloroform/hexane. Yield 55% *Anal.* Calc. for $C_{27}H_{29}N_3O_3$: C, 73.11; H, 6.59; N, 9.47. Found: C, 72.97; H, 6.55; N, 9.42%. ^{1}H NMR (400 MHz, $CDCl_3$; δ): 13.2 (br s, 3H, –OH); 8.3 (s, 3H, –HC=N); 7.2 (t, 3H, arom); 7.1 (d, 3H, arom); 6.8 (d, 3H, arom); 6.7 (t, 3H, arom); 3.55 (s, 6H, –CH_2–); 1.55 (q, 2H, –CH_2–); 0.95 (t, 3H, –CH_3). ^{13}C-{^{1}H} NMR (100 MHz $CDCl_3$; δ): 166.7, 161.3, 132.8, 131.7, 119.0, 118.9, 117.1, 62.5, 42.6, 25.6, 7.6. FTIR [ν/cm^{-1} (KBr)]: 1635 (C=N); 1490 (C=C); 1275 (C–O); 755 (arom). m.p. 100 °C. Mass Spec (ESI) m/z 444 [M+H$^+$].

2.12. Preparation of bis-((tris-(2-hydroxybenzylidene)-aminomethyl)propane nickel)-μO_6-nickel

TEtSal (0.5 g, 1.1 mmol) and nickel acetate (0.42 g, 1.7 mmol) were mixed in ethanol (50 ml). The resulting solution was refluxed for 4 h. The solvent was removed and the solid recrystallised from chloroform–diethyl ether by vapour diffusion. Yield 60% *Anal.* Calc. for $C_{54}H_{52}N_6Ni_3O_6$ C, 61.35; H, 4.96; N, 7.95. Found: C, 61.57; H, 5.44; N, 7.45%. FTIR [ν/cm^{-1} (KBr)]: 1635 (C=N), 1450 (C=C), 1326 (C–O), 750 (arom). Mass Spec (ESI) m/z 1057 [M+H$^+$]. λ_{max} (solid reflectance): 540 nm. λ_{max} (dichloromethane): 370 nm ($\varepsilon = 97.5$ M^{-1} cm^{-1}). μ_{eff}: 3.6 BM (300 K).

2.13. Preparation of bis-(tris-((2-hydroxybenzylidene)-aminomethyl)propane nickel)lead

$[(TEtSal)_2Ni_3]$ (0.25 g 0.20 mmol) and lead chloride (0.25 g, 0.9 mmol) were suspended in pyridine (10 ml). The solution was allowed to reflux for 72 h whereupon the colour of the solution darkened. The solution was allowed to cool and then filtered to remove the remaining $[(TEtSal)_2Ni_3]$ and $PbCl_2$. The solution was re-filtered through celite to leave a deep orange solution. Vapour diffusion with diethyl ether produced a small number of dark brown crystals suitable for X-ray crystallography distributed amongst the impure powder. These were isolated by Pasteur separation. Yield 5%. *Anal.* Calc. for $C_{64}H_{64}Cl_2N_{10}Ni_2O_6Pb_2$: C, 45.97; H, 3.86; N, 8.38. Found: C, 45.51; H, 3.58; N, 8.04%.

3. Results and discussion

The potentially heptadentate Schiff base ligands, TrenSal and Tren5BrSal can be prepared with ease from tris-(2-aminoethyl)amine and salicylaldehyde and 5-bromo-salicylaldehyde respectively. The reaction of these species with nickel acetate or zinc acetate gives rise to the formation of a homologous series of L_2M_3 complexes (L = TrenSal, Tren5BrSal: M = Ni, Zn). Although the series of complexes $[(TrenSal)_2M_3]$ have proved difficult to properly structurally characterise, the analogous $[(Tren5BrSal)_2M_3]$ species were easily crystallised (Fig. 4). The structures obtained reveal the expected trimetallic motif in which the three metals adopt two different environments. Two metals are fully encapsulated within the Schiff base ligands in an almost symmetric N_3O_3 environment creating two moieties which can be considered as a mono-anionic ligands. Thus the central unique metal (Fig. 4, Ni2) can be described as being effectively coordinated to two facially capping tripodal ligands in an O_6 octahedral motif. This elegant MO_6 core has been observed previously in a limited number of related ligands (Table 2). Consistent with these structures the central metal cations (e.g. nickel, Fig. 4) are found to lie a few degrees off the major axis creating a slight expansion and compression of the metrical parameters about the central O_6–M units (M = Ni, Zn, Table 2). The room temperature magnetic moments of the two nickel complexes are in good agreement with those obtained by Chandrasekar et al. [28] for the phosphotrihydrazone (PsSal, Fig. 2) complex of nickel and Ohta et al. [29] for their tris-((salicylidene)aminomethyl)ethane (TMeSal, Fig. 2) nickel complex both of which contains an iso-struc-

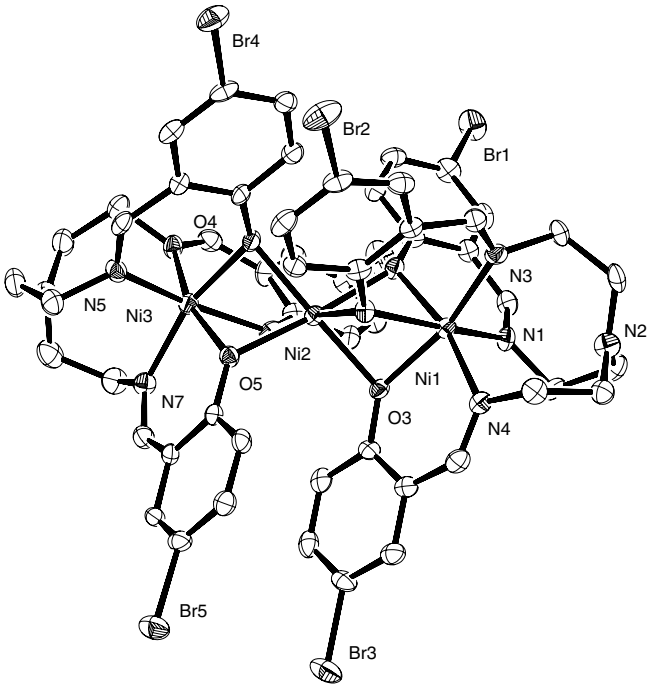


Fig. 4. The X-ray crystal structure of $[(Tren5BrSal)_2Ni_3]$. The thermal ellipsoids are drawn at 50%. The structure of the iso-structural $[(Tren5BrSal)_2Zn_3]$ is not shown. However its metrical parameters are given in Table 2.

Table 2
The key bond angles and bond lengths around the central metal in L_2M_3 complexes of nickel and zinc

	∠O–M_1–O (°) min/max	O–M_2 (Å) min/max	M–M (Å)	<M · M · M (°)
Nickel				
$[(Tren5BrSal)_2Ni_3]$	96.34(13)	2.039(3)	2.8324(10)	176.73(3)
	108.45(14)	2.082(2)	2.8196(10)	
$[(TEtSal)_2Ni_3]$	95.43(7)	2.0578(18)	2.8117(3)	177.80(2)
	109.70(7)	2.0896(18)		
$[(TMeSal)_2Ni_3]$ [29]	95.41	2.077	2.824	178.93
	110.04	2.086		
$[(PsSal)_2Ni_3]$ [28]	93.11	2.045	2.797	174.70
	112.08	2.107		
$[(PsSal)_2Ni_3]$ [1]	74.08	2.060	2.838	176.65
	111.30	2.105		
Zinc				
$[(PsSal)_2Zn_3]$ [28]	95.27	2.097	2.865	174.30
	111.91	2.132	2.882	
$[(Tren5BrSal)_2Zn_3]$	97.6(2)	2.074(6)	2.9458(17)	175.29(5)
	108.1(3)	2.130(6)	2.9513(16)	

tural M_3O_6 motif. These studies suggest that, in the compounds reported here, the two adjacent metal centres (Ni1, Ni2) are ferromagnetic and the two terminal nickels (Ni1, Ni1) antiferromagnetic. As such it was decided that the system was not worthy of deeper study at this time.

There can be some confusion regarding the nature of these species. Although Ohta et al. have produced a trimetallic species similar to $[(TrenSal)_2Ni_3]$ (Table 2) a dimeric species (L_2M_2) and monomeric species have also been isolated [29]. Thus although our data supported the formation of trimetallic motifs from the outset, throughout the study we were driven to conclusively demonstrate this by the isolation of crystals suitable for X-ray analysis. The insolubility of $[(TrenSal)_2Ni_3]$ once formed forced us to investigate more robust crystallisation methods. Within this series of experiments we reluctantly opted to use TMEDA as a chelating agent and base (typically Et_3N is used) in an attempt to slow the rate of complex formation. These reaction mixtures slowly produced two sets of crystals one orange and the other green both of which were identified by X-ray crystallography as TMEDA adducts of nickel.

The orange product was identified as two partially hydrolysed NiTrenSal units coordinated to a Ni(TMEDA) unit (Fig. 5). Imine hydrolysis is not an uncommon consequence of a prolonged "crystallisation" process. Indeed we have previously reported on the X-ray structure of a related partially hydrolysed Schiff base complex [30]. The environment around the three nickels in the compound obtained is unremarkable being comprised of a simple N_4O_2 octahedral motif at TMEDA (Ni1) and two square planar N_3O motifs within the residue of the Schiff base species (Ni2). In contrast to the metal environments the behaviour of the ligand is of more interest. Hydrolysis of the ligand removes one of the phenoxide units and in its absence its function as a donor in the hexadentate motif (c.f. Fig. 4) is replaced by the apical nitrogen of Tren (N2). This modification makes it more difficult for both the remaining salicylidene units to chelate to the same nickel and one of the donor sites is forced to rotate away from nickel (Ni2) and bind to a Ni(TMEDA) moiety which is also present in the solution.

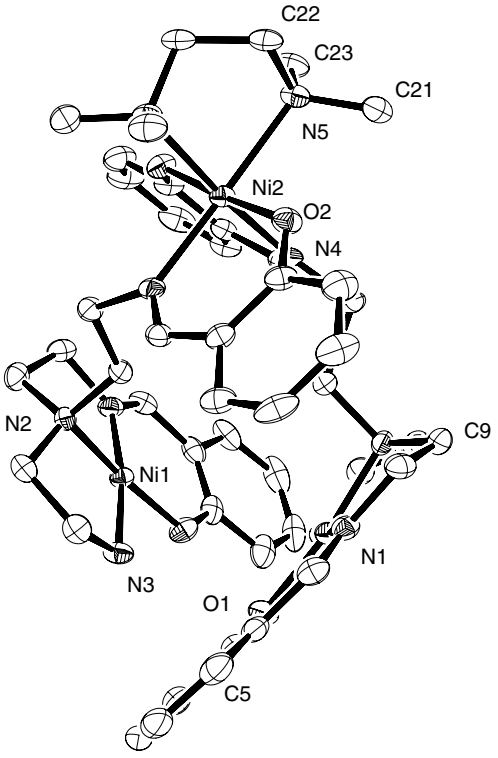


Fig. 5. The X-ray crystal structures of the orange product obtained from the mixture containing TMEDA, nickel bromide and TrenSal: Bis-((bis (2-hydroxybenzylidene)aminoethyl)amine nickel) tetramethylethylenediamine nickel. The thermal ellipsoids are drawn at 50%.

More intriguing was the second green product. These are devoid of the Schiff base ligand and are instead composed of Ni(TMEDA), carbonate and bromide (Fig. 6). There are six Ni(TMEDA) units connected to each other via a carbonate scaffold. Each of the carbonates (e.g. C14) bridge three nickels thus creating a cyclic motif. Water and not bromide fill the remaining coordination sites at nickel. The cyclic Ni(TMEDA) carbonate units stack to form columns. Although the bromides remain in close attention to balance the charge they do not fill the interstitial volumes and the resulting pores are remarkably large −4781 $Å^3$ pore space per unit cell which represents

Table 3
The key bond angles and bond lengths of the trimetallic complexes which employ a TRSalNi metallo-ligand (R = Me, Et), M_c denotes the central metal

	∠O–M_c–O (°) min/max	O–Ni (Å) min/max	N–Ni (Å) min/max	Ni–M (Å)	<Ni · M · Ni (°)
[{(TEtSal)Ni}$_2$Pb]	62.78(9) 69.19(9)	2.042(3) 2.092(3)	2.025(3) 2.057(3)	3.2625(5) 3.3049(6)	144.326(15)
[{(TMeSal)Ni}$_2$Mn] [36]	74.83 76.56	2.065 2.081	2.030 2.056	2.920	177.23
[{(TMeSal)Ni}$_2$Fe] [36]	80.26 80.624	2.090 2.120	2.020 2.047	2.815	180
[(TMeSal)Ni$_3$] [29]	93.11 112.08	2.045 2.107	2.043 2.046	2.797	174.70
[{(TMeSal)Ni}$_2$Gd(NO$_3$)] [37]	64.71 73.240	2.067 2.146	2.037 2.078	3.167 3.170	139.94

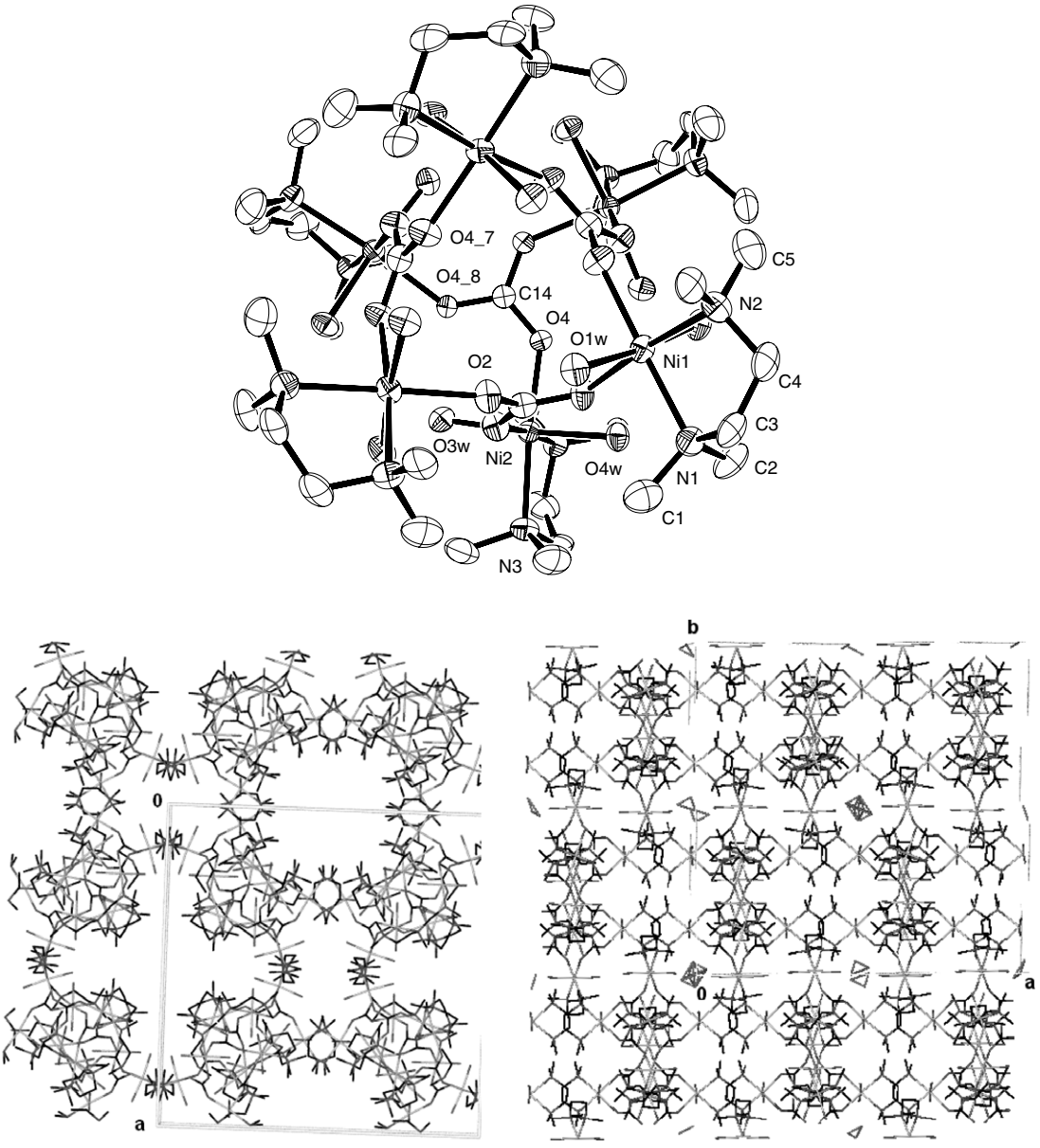


Fig. 6. The X-ray crystal structures of the green product obtained from the mixture containing TMEDA, nickel bromide and TrenSal: TMEDA nickel carbonate bromide. The supramolecular structure of the two crystallographically characterised isoforms of this species are shown which demonstrate the changes in gross structure which were observed. The thermal ellipsoids are drawn at 50%.

25.6% of the structure but contains only small traces of disordered water (Fig. 6 left). Our attempts to synthesis this compound from nickel bromide, TMEDA and sources of carbonate failed. In the absence of TrenSal we only obtained TMEDA · HBr and solvated nickel adducts of TMEDA. The synthesis of the complex from TrenSal is however, highly reproducible including the formation of the crystals. A second sample of these were also crystallographically analysed. Although the coordination environments of the metals and ligands were found to be essentially iso-structural with the species above (Fig. 6, top) with only minor variation in the water balance (Table 1), the supramolecular structures were found to be completely different (Fig. 6, right). The pore network in the second sample would seem to have completely collapsed now only occupying 564 $Å^3$ of space per unit cell which represents only 3.5% of the structure. The variable behaviour of these carbonate structures is in retrospect not surprising. The complex forms slowly under the influence of two rate determining factors *viz* CO_2 diffusion and ligand hydrolysis, which we did not attempt to control. The conditions would seem to allow the reproducible formation of the nickel μ^3-carbonate moiety, in the face of widely variable packing forces.

Our previous studies on trimetallic nickel complexes of tetradentate Schiff base species [6] (Fig. 1) demonstrated that it was possible to replace the central nickel by lead thus generating an interesting heterobimetallic complex.

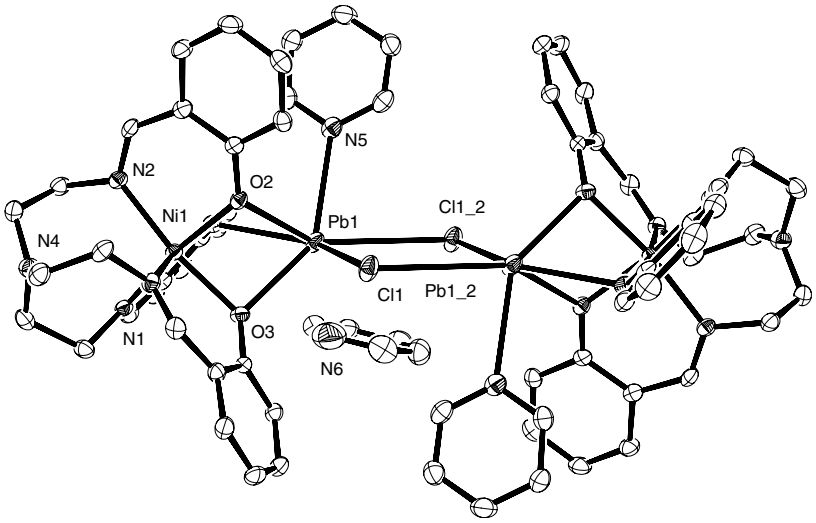


Fig. 7. The X-ray crystal structure of $[\{(TrenSal)Ni\}Pb(NC_5H_5)Cl]_2$ pyridine. Selected bond lengths and angles: Distances (Å): Ni–N1, 2.053(3); Ni–N2, 2.079(3); Ni–O3, 2.075(3); Ni–O1, 2.060(2); Ni–O2, 2.049(2); Ni–O3, 2.078(2); Pb–O1, 2.711(2); Pb–O2, 2.3615(19); Pb–O3, 2.415(2); Pb–Cl, 2.7070(9); Pb–Cl1 3.2719(10): Angles(°): O1–Ni–O2, 81.45(8) O1–Ni–O3, 83.23(8) O2–Ni–O3, 83.93(8) N1–Ni–O2, 168.89(9) N2–Ni–O3, 170.86(9) N3–Ni–O1, 167.91(10); O1–Pb–O2, 63.37(7) O1–Pb–O3, 64.54(7) O2–Pb–O3, 70.58(7). The thermal ellipsoids are drawn at 50%.

A similar reaction was carried out here whereby $[(TrenSal)_2Ni_3]$ and $[(Tren5BrSal)_2Ni_3]$ were refluxed with lead chloride in pyridine. From this mixture containing $[(TrenSal)_2Ni_3]$ we retrieved some X-ray quality crystals that confirm that the replacement reaction proceeds as predicted (Fig. 7). The complex is dimeric containing two bridging chlorides which are not equidistant from the lead centres. The bridge between the two [{(TrenSal)Ni}Pb] units is achieved via a somewhat longer Pb–Cl interaction (3.2719(10) Å). The TrenSal moiety again fully encapsulates the nickel atom holding it in an almost regular octahedral environment. This arrangement again collects the three phenoxide donors such that they generate an O_3 tripodal motif. Thus the [(TrenSal)Ni] moiety can be considered to be a uninegative ligand in its own right. The lead binds at the O_3 cleft in a more asymmetric manner showing a wider variation in bond lengths and angles to that of nickel. The presence of a lone pair on the lead atom can be inferred from the compression of the angles between lead and its six donor atoms.

The manner in which this elegant tetrametallic species forms is in line with the studies of Ohta et al. [29] which suggest that in solution trimetallic species such as TMeSal can also be encouraged to heterometallic species in a similar manner [36,37]. To further investigate this we prepared the related TEtSal ligand which differs from that reported by Ohta et al. [29] only in that it has an ethyl group on the apical carbon. The synthesis of the TEtSal and the respective nickel complex presented no problems. Indeed the nickel complex was isolated in a form that allowed it to be structurally analysed by X-ray crystallography. As expected it is iso-structural with the trimetallic complex previously reported by Ohta et al. (Table 2) where the three nickels lie in octahedral environments two encapsulated within the hexadentate frameworks with the third nickel sandwiched between the O_3 anionic clefts of the folded metallo-ligand ([(TEtSal)Ni], Fig. 8).

The reaction of $[(TEtSal)_2Ni_3]$ with lead chloride was only a partial success in that we only obtained a small number of crystals suitable for X-ray crystallography. However, these revealed that the replacement reaction reported above does proceed and that the nickel Schiff base moiety can be considered to be a ligand capable of being transferred intact. The structure obtained is trimetallic consistent with the studies of Kojima et al. who have recently reported mixed nickel-lanthanide [36] (gadolinium) and nickel-transition metal [37] (iron, manganese) TMeSal complexes. Thus the complex reported here completes the series of trimetallic (Ni–M–Ni) complexes derived from metals located in different parts of the periodic table (f-, d- and p-block). The transition metal complexes form

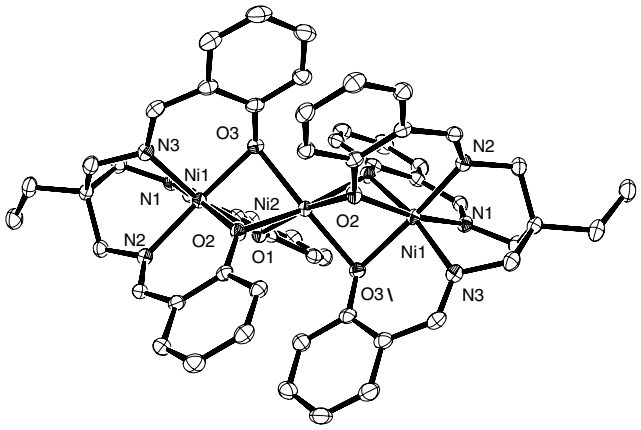


Fig. 8. The X-ray crystal structure of Bis-((tris-(2-hydroxybenzylidene)-aminomethyl)-propane nickel)-μO_6-nickel $[(TEtSal)_2Ni_3]$. The structural homology of $[(TEtSal)_2Ni_3]$ with the previously published structure $[(TMeSal)_2Ni_3]$ should be noted [29]. The key metrical parameters are given in Table 2. The thermal ellipsoids are drawn at 50%.

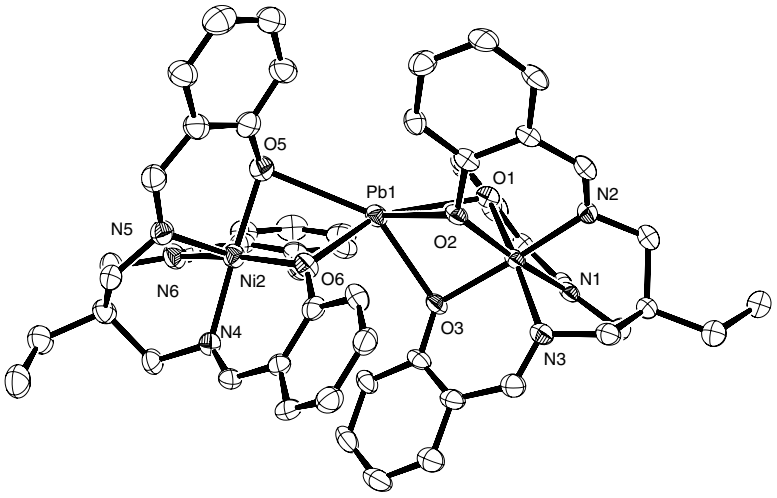


Fig. 9. The X-ray crystal structure of Bis-((tris-(2-hydroxybenzylidene)-aminomethyl)-propane nickel)lead [{(TEtSal)Ni}$_2$Pb]. The key metrical parameters are given in Table 3. The thermal ellipsoids are drawn at 50%.

species that provide an almost regular octahedral environment for the central atom (Fe, Mn, Ni, Table 2) with the three metals adopting a liner arrangement. The lead complex shown here is similar to that of gadolinium in that a significant angle is created between the three metal ions. For gadolinium this angle is created by the presence of the didentate nitrate ligand whereas for lead it arises from the influence of the lone pair on the divalent lead centre (Table 2) Fig. 9.

Of the two NiPb structures reported here that of [{(TEtSal)Ni}$_2$Pb] is consistent with an emerging catalogue of trimetallic complexes where a heteroatom (M = Mn, Fe, Ni, Gd, Pb) is sandwiched between two metallo-ligands. The complex formed from TrenSal [{(TrenSal)Ni}-Pb(NC_5H_5)Cl]$_2$ is in contrast more unique. Kojima et al. have reported a tetrametallic nickel–gadolinium complex that is held together by acetate bridges [36]. However, our ability to produce complexes such as [{(TrenSal)Ni}Pb(NC_5H_5)Cl]$_2$ which contain good leaving groups suggest that even more complex systems can be constructed.

Supplementary material

CCDC 657463, 657464, 657465, 657466, 660524, 661264, 661265, 661266 contain the supplementary crystallographic data for this paper. These data can be obtained free of charge via http://www.ccdc.cam.ac.uk/conts/retrieving.html, or from the Cambridge Crystallographic Data Centre, 12 Union Road, Cambridge CB2 1EZ, UK; fax: (+44) 1223-336-033; or e-mail: deposit@ccdc.cam.ac.uk.

Acknowledgements

AM would like to express his gratitude to Kano University of Science and Technology, Wudil for financial assistance. Thanks are due to the EPSRC National Mass Spectrometry service at the University of Swansea and X-ray Crystallography Service at the University of Southampton for data collection on samples [(TrenSal)$_2$Ni$_3$] and ((TrenSal-1)Ni)$_2$ · (TMEDA)Ni respectively and to the CCLRC for award of beamtime at the Daresbury SRS which allowed us to collect data on [(Tren5BrSal)$_2$-Zn$_3$].

References

[1] D. Colombo-Kather, A.-M. Caminade, R. Kraemer, B. Raynaud, J. Jaud, J.-P. Majoral, Bull. Soc. Chim. Fr. 131 (1994) 733.
[2] A. Elmali, Y. Elerman, I. Svoboda, H. Feuss, K. Griesar, W. Haase, Z. Naturforsch. Teil B 51 (1996) 1882.
[3] D. Ulku, F. Ercan, O. Atakol, F.N. Dincer, Acta Crystallogr. C 53 (1997) 1056.
[4] F. Averseng, P.G. Lacroix, L. Malfant, F. Dahan, K. Nakatani, J. Mater. Chem. 10 (2000) 1013.
[5] E. Kavlakoglu, A. Elmali, Y. Elerman, R. Werner, I. Svoboda, H. Feuss, Z. Naturforsch. Teil B 56 (2001) 43.
[6] J. Reglinski, S. Morris, D.E. Stevenson, Polyhedron 21 (2002) 2167.
[7] S. Akine, T. Nabeshima, Inorg. Chem. 44 (2005) 1205.
[8] O. Atakol, L. Tatar, M.A. Akay, D. Ulku, Anal. Sci. 15 (1999) 199.
[9] D. Ulku, L. Tatar, O. Atakol, M. Aksu, Acta Crystallogr. C57 (2001) 273.
[10] C. Arici, M. Sari, O. Atakol, H. Feuss, I. Svoboda, Main Group. Metal Chem. 24 (2001) 255.
[11] L. Zhang, R.A. Jones, V.M. Lynch, Chem. Commun. (2002) 2986.
[12] J. Reglinski, S. Morris, D.E. Stevenson, Polyhedron 21 (2002) 2175.
[13] S. Akine, T. Taniguchi, T. Nabeshima, Inorg. Chem. 43 (2004) 6142.
[14] O. Atakol, C. Arici, F. Ercan, D. Ulku, Acta Crystallogr. C55 (1999) 511.
[15] F.P. Dwyer, N.S. Gill, E.C. Gyarfas, F. Lions, J. Am. Chem. Soc. 79 (1957) 1269.
[16] F. Lions, K.V. Martin, J. Amer. Chem. Soc. 79 (1957) 1572.
[17] J.A. Broomhead, D.J. Robinson, Aust. J. Chem. 21 (1968) 1365.
[18] M.G.B. Drew, C.J. Harding, V. McKee, G.G. Morgan, J. Nelson, Chem. Commun. (1995) 1035.
[19] F.A. Deeney, C.J. Harding, G.G. Morgan, V. McKee, J. Nelson, S.J. Teat, W. Clegg, Dalton Trans. (1998) 1837.
[20] J. Reglinski, M. Patykiewicz, Acta Crystallogr. E 58 (2002) 543.
[21] E.A. Lewis, J.R. Lindsay Smith, P.H. Walton, S.J. Archibald, S.P. Foxon, G.M.P. Giblin, Dalton Trans. (2001) 1159.

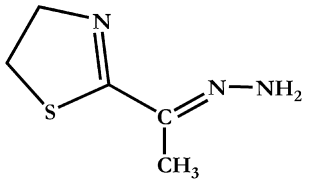
[22] D.A. Rudman, J.C. Huffman, R.F. Childers, W.E. Streib, R.A.D. Wentworth, Inorg. Chem. 14 (1975) 747.
[23] A.K. Nairn, R. Bhalla, S.P. Foxon, X. Liu, L.J. Yellowlees, B.C. Gilbert, P.H. Walton, Dalton Trans. (2002) 1253.
[24] D.F. Cook, D. Cummins, E.D. McKenzie, Dalton Trans. (1976) 1369.
[25] N.W. Alcock, D.F. Cook, E.D. McKenzie, J.M. Worthington, Inorg. Chim. Acta 38 (1980) 107.
[26] Y. Elerman, M. Kabak, I. Svoboda, M. Geselle, Acta Crystallogr. C 50 (1994) 1694.
[27] S. Deoghoria, S. Sain, T.K. Karmaker, S.K. Bera, S.K. Chandra, J. Indian Chem. Soc. 79 (2002) 857.
[28] V. Chandrasekhar, R. Azhakar, G.T.S. Andavan, V. Krishnan, S. Zacchini, J.F. Bickley, A. Steiner, R.J. Butcher, P. Kogerler, Inorg. Chem. 42 (2003) 5989.
[29] H. Ohta, K. Harada, K. Irie, S. Kashino, T. Kambe, G. Sakane, T. Shibahara, S. Takamizawa, W. Mori, M. Nonoyama, M. Hirotsu, M. Kojima, Chem. Lett. (2001) 842.
[30] M.K.T. Taylor, D.E. Stevenson, L.E.A. Berlouis, A.R. Kennedy, J. Reglinski, J. Inorg. Biochem. 100 (2006) 250.
[31] J. Reglinski, M.K.T. Taylor, A.R. Kennedy, Inorg. Chem. Commun. 9 (2006) 776.
[32] E.B. Fleischer, A.E. Gebala, A. Levey, P.A. Tasker, J. Org. Chem. 36 (1971) 3042.
[33] K.W. Hellmann, S. Friedrich, L.H. Gade, W.-S. Li, M. McPartlin, Chem. Ber. 128 (1995) 29.
[34] G.M. Sheldrick, SHELXS-97 and SHELXL-97, Programs for Crystal Structure Analysis (Release 97-2), Institut fur Anorganische Chemie der Universitat, Tammanstrasse 4, D-3400 Gottingen, Germany, 1998.
[35] L.J. Farrugia, J. Appl. Crystallogr. 32 (1999) 837.
[36] T. Kobayashi, T. Yamaguchi, H. Ohta, Y. Sunatsuki, M. Kojima, N. Re, M. Nonoyama, N. Matsumato, Chem Commun. (2006) 1950.
[37] T. Yamaguchi, Y. Sunatsuki, M. Kojima, H. Akashi, M. Tsuchimoto, N. Re, S. Osa, N. Matsumato, Chem Commun. (2004) 1048.

hydrazone (ATH). The Ni(II) and Cu(II) complexes have also been characterized through single crystal X-ray diffraction, as well as electronic paramagnetic resonance (EPR) of the latter.

2. Experimental

2.1. General procedures

All reagents were commercial grade materials and were used without further purification. The ligand 2-acetyl-2-thiazoline hydrazone (ATH) was synthesized according to a reported procedure [17].



ATH

Chemical analyses of carbon, hydrogen, nitrogen and sulphur were performed by means of microanalytical methods using a Perkin–Elmer 240C microanalyser. IR spectra were recorded on a Perkin–Elmer FT-IR 1720 spectrophotometer, from a KBr pellet in the 4000–370 cm^{-1} range and on a Perkin–Elmer FT-IR 1700X spectrophotometer, from a polyethylene pellet in the 500–150 cm^{-1} range. The UV–Vis–NIR reflectance spectra for complexes in the 200–1500 nm range were registered from a pellet of the sample, using a Shimadzu UV-3101 PC spectrophotometer and $BaSO_4$ as reference. Magnetic susceptibility measurements were performed on polycrystalline samples using a magnetometer with pendulum MANICS DSM8, equipped with helium continuous-flow cryostat and an electromagnetometer DRUSCH EAF 16 UE. Data were corrected for temperature-independent paramagnetism and diamagnetic contributions, which were estimated from the Pascal constants. EPR spectra were recorded at room temperature in solid state and at 77 K in methanol solution employing a BRUKER ESP-300E spectrometer using the X band of microwave.

2.2. Synthesis of $[CoCl_2(ATH)_2]$ (1)

This complex was isolated from an ethanol solution (3 mL) of $CoCl_2 \cdot 6H_2O$ (166 mg, 0.7 mmol) that was added to an ethanol solution (25 mL) of ATH (200 mg, 1.4 mmol). After an hour, pink crystalline solid was isolated from the solution at room temperature (104 mg, 36%). Solid was filtered and washed with cold ether and air-dried. *Anal.* Calc. for $C_{10}H_{18}Cl_2CoN_6S_2$: C, 28.85; H, 4.35; N, 20.18; S, 15.40. Found: C, 29.23; H, 3.98; N, 20.45; S, 15.15%. IR(KBr): ν(NH_2) 3367, 3247, 3167; δ(NH_2) 1616; (ring vibration) 1603; ν(C=N) 1546; (ring vibrations) 1000, 950, 734, 682; 653, 602, 564, 448 cm^{-1}.

Table 1
Crystal data, data collection and refinement details for **2** and **3**

	2	**3**
Crystal shape	plate	prism
Colour	green	green
Size (mm)	0.62 × 0.26 × 0.10	0.48 × 0.40 × 0.20
Chemical formula	$C_{10}H_{18}Cl_2N_6NiS_2$	$C_{10}H_{18}Cl_4N_6Cu_2S_2$
Formula weight	416.0	555.3
Crystal system	monoclinic	monoclinic
Space group	$C2/c$	$P2_1/n$
Unit cell dimensions		
a (Å)	16.730(1)	8.645(2)
b (Å)	9.142(1)	12.468(3)
c (Å)	12.053(1)	8.941(2)
β (°)	107.566(1)	93.333(4)
Cell volume (Å^3)	1757.4(2)	962.2(4)
Z	4	2
D_{calc} (g cm^{-3})	1.572	1.917
μ (mm^{-1})	1.646	2.989
$F(000)$	856	556
θ Range	2.6–28.3	2.8–27.5
Index ranges	$-21 \leqslant h \leqslant 21$, $-7 \leqslant k \leqslant 12$, $-15 \leqslant l \leqslant 15$	$-11 \leqslant h \leqslant 11$, $0 \leqslant k \leqslant 16$, $0 \leqslant l \leqslant 11$
Independent reflections	2013	2201
Observed reflections $[F > 4.0\sigma(F)]$	1811	1703
Data completeness	0.921	0.996
Max/min transmission	0.853/0.428	0.542/0.255
Number of refined parameters	97	110
R $[F > 4.0\sigma(F)]$[a]	0.034	0.028
wR $[F > 4.0\sigma(F)]$[b]	0.085	0.067
GOF[c]	1.062	0.974
ρ_{max}, ρ_{min} (e Å^{-3})	0.465, −0.247	0.377, −0.321

[a] $R = \sum \| F_o \| - \| F_c \| / \sum | F_o |$.
[b] $R = \{\sum[w(F_o^2 - F_c^2)^2] / \sum[w(F_o^2)^2]\}^{1/2}$.
[c] The Goodness-of-fit (GOF) equals $\{\sum[w(F_o^2 - F_c^2)^2]/(N_{rf\,ln\,s} - N_{params})\}^{1/2}$.

2.3. Synthesis of $[NiCl_2(ATH)_2]$ (2)

This complex was isolated from an ethanol solution (2 mL) of $NiCl_2 \cdot 6H_2O$ (83 mg, 0.35 mmol) that was added to an ethanol solution (15 mL) of ATH (100 mg, 0.7 mmol). After several hours, 103 mg (71% yield) of a green solid was recovered filtering. This solid was recrystallized from a ethanol/acetonitrile (1:1 v/v) solution, yielding plate dark green crystals, of considerable size, suitable for X-ray diffraction. Anal. Calc. for $C_{10}H_{18}Cl_2NiN_6S_2$: C, 29.01; H, 4.38; N, 20.30; S, 15.49. Found: C, 28.99; H, 4.45; N, 20.35; S, 15.21%. IR(KBr): ν(NH_2) 3335, 3245, 3142; δ(NH_2) 1619; (ring vibration) 1601; ν(C=N) 1546; (ring vibrations) 1001, 954, 741, 683, 642, 602, 562, 435 cm^{-1}.

2.4. Synthesis of $[\{CuCl(ATH)\}_2(\mu\text{-}Cl)_2]$ (3)

This complex was isolated from a methanol solution (2 mL) of $CuCl_2 \cdot 2H_2O$ (119 mg, 0.7 mmol) that was

added to a methanol solution (15 mL) of ATH (100 mg, 0.7 mmol). Green crystals were isolated after a slow evaporation of the solution at room temperature (176 mg, 91%). The crystals were filtered and washed with cold ether and air-dried. *Anal.* Calc. for $C_5H_9Cl_2CuN_3S$: C, 21.63; H, 3.27; N, 15.13; S, 11.55. Found: C, 21.61; H, 3.37; N, 15.11; S, 11.35%. IR(KBr): ν(NH_2) 3364, 3255; δ(NH_2) 1614; (ring vibration) 1581; ν(C=N) 1550; (ring vibrations) 1002, 949, 751, 684, 657, 621, 566, 440 cm^{-1}.

2.5. X-ray determination structure

X-ray diffraction data of **2** and **3** were collected on a Bruker SMART CCD diffractometer with Mo Kα radiation ($\lambda = 0.71073$ Å, graphite monochromator). The first fifty frames were measured at the end of data collection to monitor instrument and crystal stability. The data were empirically corrected for absorption and other effects using the SADABS [19] program. The structures were solved by direct methods and subsequent Fourier differences using the SHELXS-97 [20] program and refined by full-matrix least-squares on F^2 with SHELXL-97 [21], included in WINGX [22] package assuming anisotropic displacement parameters for non-hydrogen atoms. All hydrogen atoms attached to carbon and nitrogen atoms were positioned geometrically, with U_{iso} values derived from U_{eq} values of the corresponding carbon and nitrogen atoms. Diagrams were generated using ORTEP3 for Windows [23]. A summary of the crystal data, experimental details and refinement results are listed in Table 1.

3. Results and discussion

3.1. Description of the crystal structures

The X-ray study of the complex **2** reveals that the crystals are made up of monoclinic unit cells, each containing four $[NiCl_2(ATH)_2]$ molecules. The overall view and labelling of the atoms of complex are displayed in Fig. 1.

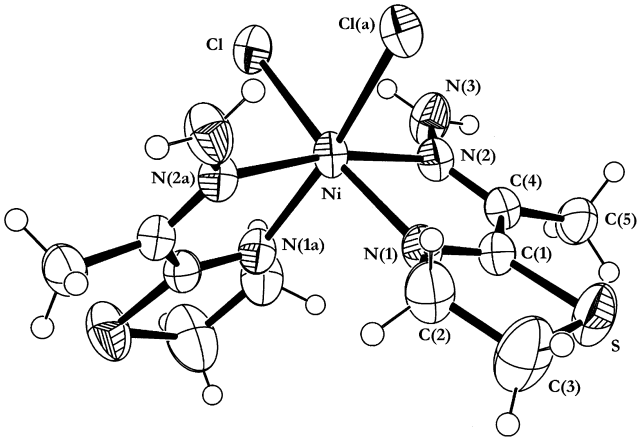


Fig. 1. Molecular structure of **2**, showing the atom-numbering scheme. The thermal ellipsoids are drawn at the 50% probability level.

Table 2
Selected bond lengths (Å), angles (°) and hydrogen-bond parameters for **2**

Ni–Cl	2.4403(6)	Ni–N(1)	2.075(2)
Ni–N(2)	2.089(2)	C(1)–N(1)	1.275(3)
C(1)–C(4)	1.466(3)	N(2)–C(4)	1.290(3)
N(1)–Ni–Cl	169.47(15)	N(1)–Ni–Cl(a)	86.35(6)
N(2)–Ni–Cl	91.83(5)	N(2)–Ni–Cl(a)	95.58(5)
N(1)–Ni–N(2)	77.61(7)	N(1)–Ni–N(1a)	95.26(11)
N(1)–Ni–N(2a)	94.99(7)	N(2)–Ni–N(2a)	169.13(11)
Cl–Ni–Cl(a)	93.99(3)	C(1)–N(1)–Ni	112.52(15)
C(4)–N(2)–Ni	116.47(15)	N(1)–C(1)–C(4)	120.71(19)
N(2)–C(4)–C(1)	112.15(18)		
Bond A···H–D	Position of A	A···D (Å)	A···H–D (°)
N(3)–H(3C)···Cl	$x, -y, z + 1/2$	3.280(2)	146.70(14)

Table 2 lists selected bond lengths, angles and hydrogen-bond parameters.

The complex cation possesses a C_2 symmetry, with the twofold axis placed at the bisector of the Cl–Ni–Cl(a) angle.

The environment around the nickel(II) atom may be described as a slightly distorted octahedral geometry with the ligand-metal-ligand bite angles varying between 77.61(7)° [N(1)–Ni–N(2)] and 95.26(11)° [N(1)–Ni–N(1a)]. The metallic atom is coordinated by two chlorine ligands [Ni–Cl = 2.4403(6) Å], two thiazolinic nitrogen atoms [Ni–N(1) = 2.075(2) Å] and two iminic nitrogen atoms [Ni–N(2) = 2.089(2) Å].

The Ni–Cl bond distance is similar to the average value [2.449(60) Å] calculated using the data of 52 six-coordinated nickel(II) complexes with a chromophore group $NiCl_2N_4$ obtained with CONQUEST software [24] from the Cambridge Structural Database (CSD, Version v5.28, May 2007) [25]. Likewise, the Ni–N_{imine} bond length is comparable to the mean value 2.073(41) Å found for 10 six-coordinated nickel(II) complexes with a Cl_2N_4 environment in CSD. Finally, the Ni–$N_{thiazoline}$ bond length is similar to that found in $[Ni(ATsc)_2](NO_3)_2 \cdot H_2O$ (av. 2.073 Å) [18], $[Ni(PyTT)_2(H_2O)_2]Cl_2 \cdot 3H_2O$ (2.061 Å) [26], $[Ni(L)(H_2O)_2]ClO_4 \cdot H_2O$ (2.057 Å) [27] and $[Ni_4(OH)_4(tzdt)_4(py)_4] \cdot 2py$ (2.106 Å) [28], but somewhat longer to than that observed in $[Ni(TzHy)_2(H_2O)_2]Cl_2 \cdot 2H_2O$ (2.027 Å) [29].

The five-membered chelate ring is essentially planar. The maximum deviation in relation to the corresponding mean plane is produced for C(1) [0.055 Å].

The thiazoline ring shows an intermediate conformation between envelope and half-chair, with C(2) and C(3) deviating 0.095 and 0.116 Å above and below, respectively, the plane formed by S, C(1) and N(1). This geometry is proved by the puckering parameters $q = 0.160$ Å and $\phi = 134.5°$, calculated according to Cremer and Pople [30].

The crystal structure is stabilized by hydrogen-bonds Cl···H(3C)–N(3) of intermolecular type. This hydrogen bonding (Fig. 2) produces an one dimensional chain parallel to the *c*-direction.

The molecular structure of the complex **3** is shown in Fig. 3. Selected interatomic distances and angles are listed

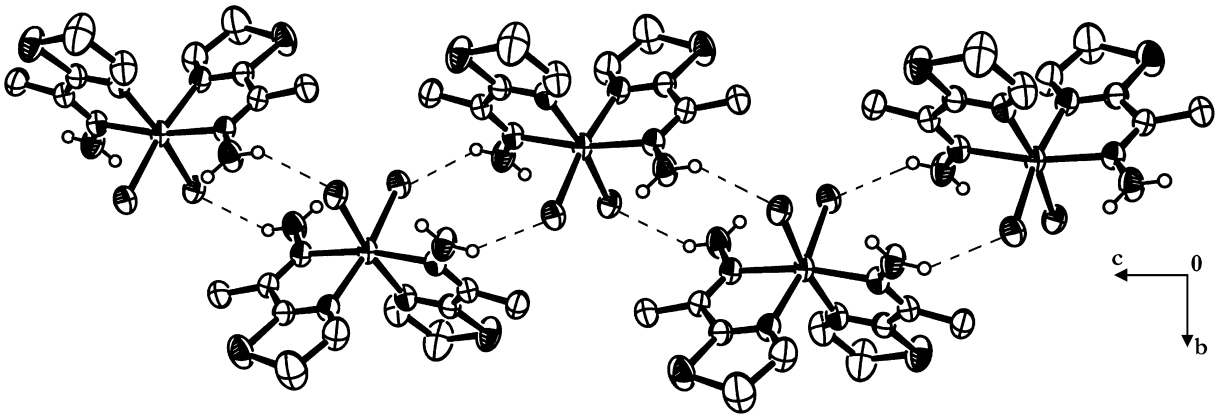


Fig. 2. View of the hydrogen bonds of **2**.

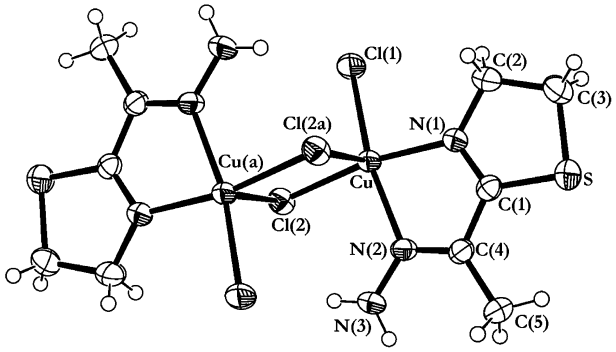


Fig. 3. Molecular structure of **3**, showing the atom-numbering scheme. The thermal ellipsoids are drawn at the 40% probability level.

Table 3
Selected bond lengths (Å) and angles (°) for **3**

Cu–N(1)	1.984(2)	Cu–N(2)	2.077(2)
Cu–Cl(1)	2.2554(9)	Cu–Cl(2)	2.2725(8)
Cu–Cl(2a)	2.6598(8)	C(1)–N(1)	1.280(3)
C(1)–C(4)	1.456(3)	N(2)–C(4)	1.287(3)
N(1)–Cu–N(2)	79.04(8)	N(1)–Cu–Cl(1)	93.35(6)
N(1)–Cu–Cl(2)	169.49(6)	N(1)–Cu–Cl(2a)	94.85(7)
N(2)–Cu–Cl(1)	166.88(6)	N(2)–Cu–Cl(2)	91.46(6)
N(2)–Cu–Cl(2a)	91.22(6)	Cl(1)–Cu–Cl(2)	95.12(3)
Cl(1)–Cu–Cl(2a)	100.13(3)	Cl(2)–Cu–Cl(2a)	89.78(3)
Cu–Cl(2)–Cu(a)	90.22(3)	C(1)–N(1)–Cu	113.90(17)
C(4)–N(2)–Cu	114.78(17)	C(4)–C(1)–N(1)	120.0(2)
N(2)–C(4)–C(1)	112.3(2)		

in Table 3. The structure consists of centrosymmetric dimeric $[\{CuCl(ATH)\}_2(\mu\text{-}Cl)_2]$ units, in which two chlorine ligands bridge the copper atoms forming a four-membered ring; a terminal chlorine ligand and a bidentate chelating molecule of ATH completing five-coordination at each metal. The bridging Cu_2Cl_2 unit is strictly planar by the presence of the crystallographic inversion centre in the middle of the dimer.

The geometry around the copper centres can be described as a slightly distorted tetragonal pyramid with a τ value of 0.04 [31] and a Δ value of 0.86 [32]. The basal plane is made up of one thiazoline nitrogen atom N(1), one imine nitrogen atom N(2), the bridging chlorine ligand Cl(2) and the terminal chlorine ligand Cl(1), while the apical site is occupied by the other bridging chlorine ligand Cl(2a). The Cl(2a)–metal–basal ligand angles differ from the ideal value for a square pyramid, ranging between 100.13(3)° [for Cl(1)–Cu–Cl(2a)] and 89.78(3)° [Cl(2)–Cu–Cl(2a)]. Likewise, the basal ligand–metal–basal ligand angles differ from the ideal value, ranging between 95.12(3)° [Cl(1)–Cu–Cl(2)] and 79.04(8)° [N(1)–Cu–N(2)].

The Cu–Cl and Cu···Cu bond lengths have been compared with the mean value calculated using the data of 65 dichlorine-bridged dimers of copper(II) with a Cl_3N_2 environment obtained from CSD [25]. The $Cu–Cl_{terminal}$ [Cu–Cl(1) = 2.2554(9) Å], the short $Cu–Cl_{bridging}$ [Cu–Cl(2) = 2.2725(8) Å], the long $Cu–Cl_{bridging}$ [Cu–Cl(2a) = 2.6598(8) Å] and the Cu···Cu [Cu···Cu(a) = 3.505(1) Å] distances are similar than the calculated average values [2.257(24) Å], [2.286(33) Å], [2.74(10) Å] and [3.53(14) Å], respectively. The $Cu–N_{imino}$ bond distance is slightly larger than the calculated average value [1.996(33) Å] for 21 copper(II) dimers with this type of unions containing two chlorine bridging ligands and a chromophore group $CuCl_3N_2$ in CSD [25]. Finally, the $Cu–N_{thiazoline}$ bond distance is comparable to the calculated average value [1.960(38) Å] for 16 copper(II) complexes with the 2-thiazoline ligand collected in CSD [25].

The five-membered chelate ring is essentially planar with maximum mean-plane deviation for N(2) [0.059 Å]. The geometry of 2-thiazoline ring is similar to that found in **2**.

Finally, it should be pointed out that the main difference in complexes **2** and **3** with respect to the structure of free ATH [17] is due to the different degree of rotation of the thiazoline ring around the C(1)–C(4) bond, which permits the coordination through thiazoline nitrogen atom [torsion angle S–C(1)–C(4)–N(2) = −169.4° in **2**; 178.0° in **3**; 9.6° in ATH].

3.2. Magnetic susceptibility

The observed molar magnetic susceptibility for complex **1** were corrected for diamagnetism and temperature-inde-

pendent paramagnetism to provide the fully corrected magnetic moment at room temperature, 4.89 BM. This value can be considered in the range 4.7–5.2 BM characteristic of complexes with an high-spin octahedral environment around cobalt(II) [33]. The corrected magnetic moment measured for complex **2** was 3.18 BM, which can be related to an octahedral environment in nickel(II) complexes [34].

The temperature dependence of the molar magnetic susceptibility, χ_M, for complex **3** was measured in 2–300 K temperature range and the plot of χ_M and $\chi_M T$ versus T is shown in Fig. 4. The χ_M value is equal to 2.98×10^{-3} $cm^3\,mol^{-1}\,K$ ($\mu = 1.89$ BM) at room temperature, which is the expected value for two uncoupled copper(II) ions. Upon cooling, the χ_M value for copper(II) firstly increases to a maximum around 10 K, whereupon it decreases. This behaviour is typical for antiferromagnetic interaction between the two Cu(II) centres of the dimer. The fitting of $1/\chi_M$ versus T above 10 K with the Curie–Weiss equation yields $C = 0.95\ cm^3\,mol^{-1}\,K$ and $\theta = -17.2$ K, which clearly indicates that magnetic interaction between copper(II) ions is antiferromagnetic [35].

To estimate the magnitude of the antiferromagnetic coupling the magnetic susceptibility data were fitted to the modified Bleaney–Bowers equation for two interacting copper(II) ions ($S = 1/2$) with the Hamiltonian in the form $H = -2JS_1 \cdot S_2$. The susceptibility equation for such a dimeric system can be written as follows [36]:

$$\chi_M = \frac{2Ng^2\mu_B^2}{K_B T[3 + \exp(-2J/K_B T)]} \quad (1)$$

where χ_M represents the susceptibility per mole of dimer, corrected for diamagnetism and temperature independent paramagnetism, J is the exchange coupling and the other symbols have their usual meaning. The average value got from EPR spectrum (2.14) has been taken as g value.

An attempt to fit the data to the last expression gave a poor fit in the region around the maximum of χ_M.

In a second approach, the possible presence of paramagnetic impurities was considered. These impurities modify extraordinarily the temperature dependence of χ_M at low temperature in complexes with antiferromagnetic coupling, stretching χ_M to infinity at 0 K [37]. The plateau of our experimental data at low temperature (see Fig. 4) confirms this fact. Thus, Bleaney–Bowers expression was modified taking into account the paramagnetic impurities [38]

$$\chi_M = \frac{2Ng^2\mu_B^2}{K_B T[3 + \exp(-2J/K_B T)]}(1 - \rho) + \frac{Ng^2\mu_B^2}{2K_B T}\rho \quad (2)$$

where ρ is the amount of paramagnetic impurities.

The parameters J and ρ were determined as adjustable parameters, in a least-squares fitting procedure that led to the values $J = -7.52(22)\ cm^{-1}$ and $\rho = 0.085(5)$. The agreement factor R, defined as

$$R = \sum \left[\left(\chi_{MJ}^{obs} - \chi_{MJ}^{calc}\right)^2 / \chi_{MJ}^{obs} \right]^2$$

is then equal to 5.58×10^{-4}. The value of J parameter implies weak antiferromagnetic interaction.

Detailed magneto-structural correlations have been carried out on dinuclear copper(II) complexes with a $Cu(\mu\text{-}Cl)_2Cu$

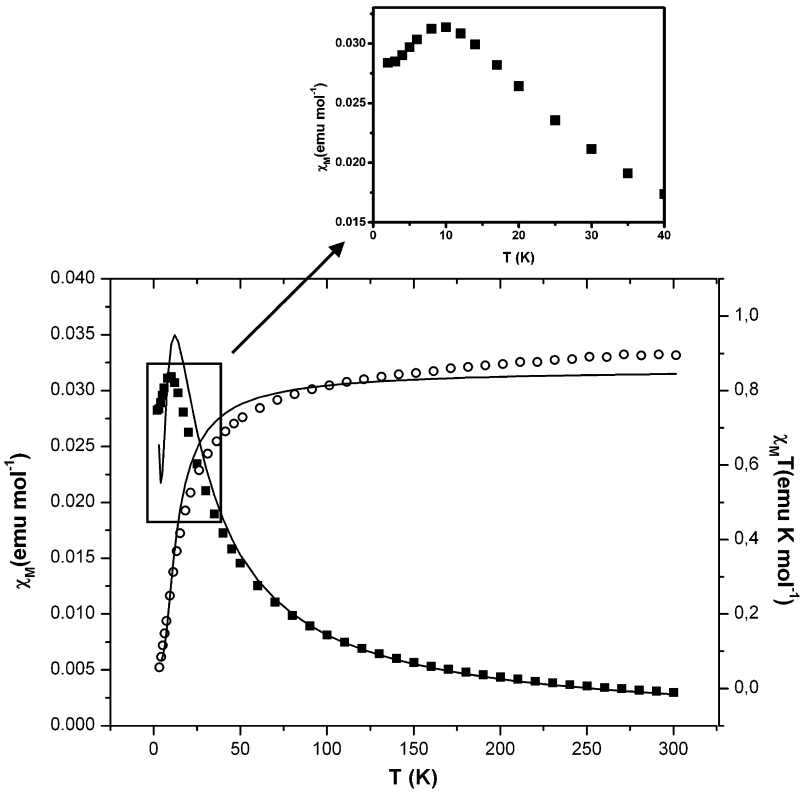


Fig. 4. χ_M vs. T (■) and $\chi_M T$ vs. T (O) plot for **3**. Solid lines represent the best fit of the data with the model described in the text.

motif containing chlorine bridging ligands. In these complexes, the local geometry around the two metal centre is usually a square pyramid with a different degree of distortion towards a trigonal bipyramid. The global arrangement for the square-pyramidal polyhedra can be defined as coplanar, parallel and perpendicular [39]. The extended Hückel calculations performed by Rodríguez et al. [39,40] show that the super exchange pathway with the metal centres will take place mainly through a π^* type interaction between the $d_{x^2-y^2}$ orbitals of Cu(II) ions and the p orbitals of chlorine bridging ligands for square pyramids with parallel basal planes sharing one base-to-apex edge, as it is the case of **3**. For an ideal geometry with a square core, the overlap integral between the former orbitals would be zero. As above, these complexes with parallel arrangement for square pyramids present very small J values, which are due to structural deviations from the ideal square Cu_2Cl_2 core. The small calculated J value for **3** is therefore consistent with the calculations performed by the aforementioned authors.

3.3. Spectroscopic studies

Cobalt(II) complex **1** exhibits a typical electronic spectrum for octahedral species in the solid state [41]. Two main bands are observed in the 7000–25 000 cm^{-1} range, which are assigned to the ν_1 [$^4T_{1g}(F) \rightarrow {}^4T_{2g}(F)$] (9295 cm^{-1}) and ν_3 [$^4T_{1g}(F) \rightarrow {}^4T_{1g}(P)$] (20 160 cm^{-1}) transitions. Moreover, the spectrum shows one intense band at 31 055 cm^{-1} with a shoulder at 34 965 cm^{-1} which are assigned to a charge-transfer band and the $\pi \rightarrow \pi^*$ transition of the organic ligand, respectively. Ligand field parameters, 10Dq and B, were calculated using the following known Konig's equations [42]:

$$\nu_1 = \frac{1}{2}(10Dq - 15B) + \frac{1}{2}[(10Dq + 15B)^2 - 12B \cdot 10Dq]^{\frac{1}{2}}$$

$$\nu_3 = [(10Dq + 15B)^2 - 12B \cdot 10Dq]^{\frac{1}{2}}$$

The calculated values of the ligand field parameters $10Dq = 10\,478\ cm^{-1}$ and $B = 803\ cm^{-1}$ are in good agreement with the predicted values for octahedral complexes of Co(II) [43–45].

Electronic spectrum of the nickel(II) complex **2** shows one intense band at 33 557 cm^{-1}, which is assigned to charger transfer band. Moreover, the spectrum exhibits bands at 10 331 and 16 474 cm^{-1}, all of which were of low intensity. These bands may be assigned as: $\nu_1[{}^3A_{2g}(F) \rightarrow {}^3T_{2g}(F)]$ (10 331 cm^{-1}) and $\nu_2[{}^3A_{2g}(F) \rightarrow {}^3T_{1g}(F)]$ (16 474 cm^{-1}) transitions, in an idealized O_h symmetry. The position of the observed d–d transitions permits to calculate the ligand field parameters, 10Dq and B, using the following known relationships [42]:

$$\nu_1[{}^3A_{2g}(F) \rightarrow {}^3T_{2g}(F)] = 10Dq$$

$$\nu_2[{}^3A_{2g}(F) \rightarrow {}^3T_{1g}(F)] = (1/2)(15B + 30Dq) - (1/2)[(15B - 10Dq)^2 + 12B \cdot 10Dq]^{1/2}$$

The calculated values of the ligand field parameters $10Dq = 10\,331\ cm^{-1}$ and $B = 834\ cm^{-1}$ are consistent with the presence of a chromophore group $[Ni^{II}N_4Cl_2]$ [46,47].

Electronic reflectance spectrum of the copper(II) complex **3** displays one strong band at 26 738 cm^{-1} which can be assigned to Cl → Cu charge transfer transition [48,49]. Moreover, the reflectance spectrum exhibits a broad band centred at 13 850 cm^{-1} with a shoulder at 12 315 cm^{-1}, assigned to the $^2B_1 \rightarrow {}^2A_1$ and $^2B_1 \rightarrow {}^2B_2$, ^2E transitions, respectively, in agreement with the square-pyramidal stereochemistry [50] that presents this complex.

EPR spectra of a polycrystalline sample at 298 K (Fig. 5) and at 77 K (Fig. 6) of complex **3** were recorded in the X-band, using the 100 kHz field modulation. The EPR parameters are presented in Table 4. The spectrum of **3** at 298 K is typically elongated axial with well defined $g_\perp$ and $g_\parallel$ values. The geometric parameter

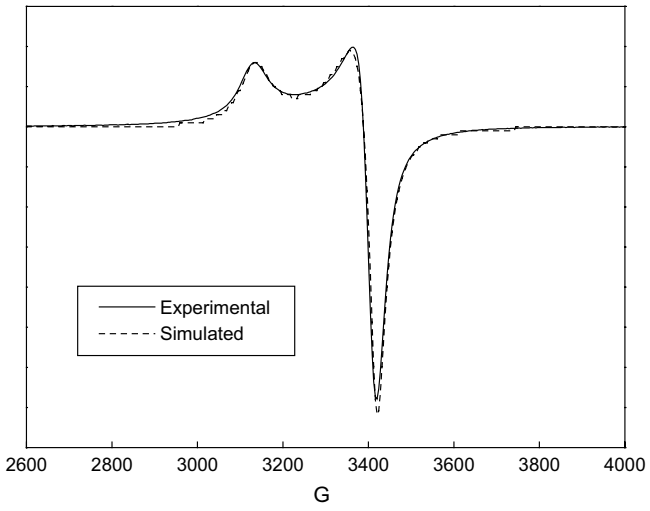


Fig. 5. EPR spectrum of **3** in the polycrystalline state at 298 K.

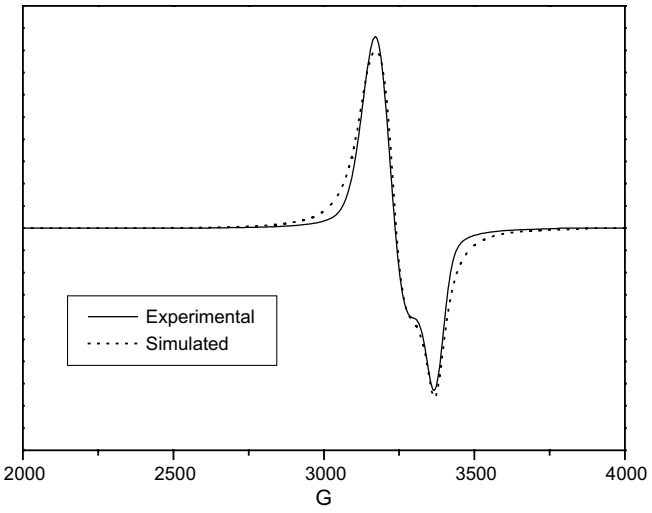


Fig. 6. EPR spectrum of **3** in methanol solution at 77 K.

Table 4
EPR parameters of **3**

Solid (298 K)			Methanol (77 K)			
$g_\perp$	$g_\parallel$	G	g_3	g_2	g_1	R
2.05	2.23	3.80	2.22	2.15	2.08	1.0

Table 5
Far IR bands (cm^{-1}) with tentative assignments

Compound	ν(M–N_{imino})	ν(M–$N_{thiazoline}$)	ν(M–$Cl_{terminal}$)	ν(M–$Cl_{terminal}$), ν(M–Cl_{bridge})
1	325	255	213	
	312			
2	333	271	214	
3	325	253		304
				292

$G = (g_\parallel - 2)/(g_\perp - 2)$ value is found to be in the range 3.5–5.0 and $g_\parallel > g_\perp > 2.0023$, which is consistent with a distorted square-pyramidal geometry with a $(d_{x^2-y^2})^1$ ground state [51,52]. These results are in good accord with the X-ray structural determination data.

With regard to the EPR spectrum in frozen methanol (77 K) is typically compressed rhombic. The geometric parameter $R = (g_2 - g_1)/(g_3 - g_2)$ value is 1, which gives no information indicative to ground state in solution [50–53].

In the low frequency region, the IR spectra of these complexes show bands assignable to metal-ligand stretching vibrations. Tentative assignments are listed in Table 5. Thus, the ν(M–N_{imino}) vibrations [54–56] are registered at 312–333 cm^{-1}, the bands in the region 253–271 cm^{-1} can be attributed to ν(M–$N_{thiazoline}$) vibration [26,44,45,57] and the bands due to ν(M–$Cl_{terminal}$) vibrations [58–63] are found in the range 213–304 cm^{-1}. Finally the bands at 292 and 304 cm^{-1} in the spectrum of Cu(II) complex can also include the ν(M–Cl_{bridge}) vibration according to Refs. [58,59,61].

4. Conclusion

In summary we have synthesized and structurally characterized Co(II), Ni(II) and Cu(II) complexes with 2-acetyl-2-thiazoline hydrazone (ATH). In the same way as that in the cadmium(II) complex preliminary reported [17], it should be pointed out that ATH acts as bidentate ligand coordinating to the metal ion through the imine and thiazoline nitrogen atoms. A study of all the characterization methods applied for complex **1** suggests that cobalt(II) ion presents an octahedral environment. Thus, complex **1** could be formulated as $[CoCl_2(ATH)_2]$. Crystallographic study of **2** shows a distorted octahedral geometry around the nickel(II), meanwhile the structure of complex **3** is consistent with a dimer copper(II) complex doubly bridged by chlorine ligands. The copper centres are penta-coordinated with a slight distortion from square-pyramidal geometry and present a weak ferromagnetic through chlorine-bridge.

[1] The unpaired electron is located in $d_{x^2-y^2}$.

Acknowledgements

We would like to thank the Junta de Extremadura (Consejería de Educación, Ciencia y Tecnología) and the FEDER [Project 2PR04A011] for financial support.

Appendix A. Supplementary material

CCDC 271430 and 663500 contain the supplementary crystallographic data for **2** and **3**. These data can be obtained free of charge via http://www.ccdc.cam.ac.uk/conts/retrieving.html, or from the Cambridge Crystallographic Data Centre, 12 Union Road, Cambridge CB2 1EZ, UK; fax: (+44) 1223-336-033; or e-mail: deposit@ccdc.cam.ac.uk. Supplementary data associated with this article can be found, in the online version, at doi:10.1016/j.poly.2007.11.009.

References

[1] R.A. Sánchez-Delgado, M. Navarro, H. Pérez, J.A. Urbina, J. Med. Chem. 39 (1996) 1095.
[2] M. Navarro, H. Pérez, R.A. Sánchez-Delgado, J. Med. Chem. 40 (1997) 1937.
[3] Z.H. Chohan, A. Rauf, J. Inorg. Biochem. 46 (1992) 41.
[4] R. Malhotra, J.P. Singh, M. Dudeja, K.S. Dhindsa, J. Inorg. Biochem. 46 (1992) 119.
[5] F. Lebon, M. Ledecq, Z. Benatallah, S. Sicsic, R. Lapouyade, O. Kahan, A. Garcon, M. Reboud-Ravaux, F.J. Durant, J. Chem. Soc., Perkin Trans. 2 (1999) 795.
[6] N. Bharti, M.R. Maurya, F. Naqvi, A. Bhattacharya, S. Bhattacharya, A. Azam, Eur. J. Med. Chem. 35 (2000) 481.
[7] A.Y. Louie, T.J. Meade, Chem. Rev. 99 (1999) 2711.
[8] S.K. Sridhar, S.N. Pandeya, J.P. Stables, A. Ramesh, Eur. J. Pharm. Sci. 16 (2002) 129.
[9] P. Vicini, F. Zani, P. Cozzini, I. Doytchinova, Eur. J. Med. Chem. 37 (2002) 553.
[10] B. Kocyigit-Kaymakcioglu, S. Rollas, Farmaco 57 (2002) 595.
[11] J.V. Ragavendran, D. Sriram, S.K. Patel, I.V. Reddy, N. Bharathwajan, J. Stables, P. Yogeeswari, Eur. J. Med. Chem. 42 (2007) 146.
[12] S. Rollas, N. Gulerman, H. Erdeniz, Farmaco 57 (2002) 171.
[13] M. Carcelli, P. Mazza, C. Pelizi, F. Zani, J. Inorg. Biochem. 57 (1995) 43.
[14] D.K. Johnson, T.B. Murphy, N.J. Rose, W.H. Goodwin, L. Pickart, Inorg. Chim. Acta 67 (1982) 159.
[15] J.D. Ranford, J.J. Vittal, Y.M. Wang, Inorg. Chem. 37 (1998) 1226.
[16] J.L. Buss, B.T. Greene, J. Turner, F.M. Torti, S.V. Torti, Curr. Top. Med. Chem. 4 (2004) 1623.
[17] F.J. Barros-García, A. Bernalte-García, F. Luna-Giles, M.A. Maldonado-Rogado, E. Viñuelas-Zahínos, Polyhedron 24 (2005) 1125.
[18] F.J. Barros-García, F. Luna-Giles, M.A. Maldonado-Rogado, E. Viñuelas-Zahínos, Polyhedron 24 (2005) 2972.
[19] SADABS, version 2.03 Bruker AXS Inc., Madison, WI, 2001.
[20] M. Sheldrick, SHELXS-97, Program for Crystal Structures Solution, University of Göttingen, Germany, 1997.
[21] M. Sheldrick, SHELXL-97, Program for Crystal Structures Refinement, University of Göttingen, Germany, 1997.
[22] L.J. Farrugia, J. Appl. Cryst. 32 (1999) 837.
[23] L.J. Farrugia, J. Appl. Cryst. 30 (1997) 565.

[24] F.H. Allen, Acta Crystallogr., Sect. B 58 (2002) 380.
[25] I.J. Bruno, J.C. Cole, P.R. Edington, M. Kessler, C.F. Macrae, P. McCabe, J. Pearson, R. Taylor, Acta Crystallogr., Sect. B 58 (2002) 389.
[26] A. Bernalte-García, F.J. García-Barros, F.J. Higes-Rolando, F. Luna-Giles, Polyhedron 18 (1999) 2907.
[27] K.V. Domasevich, E.B. Rusanov, E.K. Yudin, M.D. Kruglyak, A.A. Mokhir, Russ. J. Inorg. Chem. 40 (1995) 1874.
[28] L. Ballester, E. Coronado, A. Gutiérrez, A. Monge, M.F. Perpiñán, E. Pinilla, T. Rico, Inorg. Chem. 31 (1992) 2053.
[29] A. Bernalte-García, M.A. Díaz-Díez, F.J. García-Barros, F.J. Higes-Rolando, A.M. Pizarro-Galán, J. Romero-Garzón, C. Valenzuela-Calahorro, Polyhedron 15 (1996) 1691.
[30] D. Cremer, J.A. Pople, J. Am. Chem. Soc. 97 (1975) 1354.
[31] A.W. Addison, T.N. Rao, J. Reedijk, J. van Rijn, G.C. Verschorr, J. Chem. Soc., Dalton Trans. (1984) 1349.
[32] E.L. Muetterties, L.J. Guggenberger, J. Am. Chem. Soc. 96 (1974) 1748.
[33] B.N. Figgis, J. Lewis, Prog. Inorg. Chem. 6 (1967) 185.
[34] J. Reedijk, P.W.N.M. van Leeuwen, W.L. Groeneveld, Rec. Trav. Chim. Pays-Bas 87 (1968) 129.
[35] M. Melnik, M. Koman, D. Hudecova, J. Moncol, B. Dudova, T. Glowiak, J. Mrozinski, C.E. Holloway, Inorg. Chim. Acta 308 (2000) 1.
[36] B. Bleaney, K.D. Bowers, Proc. R. Soc. London Ser. A 214 (1952) 451.
[37] J. Ribas Gispert, Química De Coordinación, Omega, Barcelona, 2000.
[38] O. Kahn, Molecular Magnetism, VCH, New York, 1993.
[39] M. Rodríguez, A. Llobet, M. Corbella, A.E. Martell, J. Reibenspies, Inorg. Chem. 38 (1999) 2328.
[40] M. Rodríguez, A. Llobet, M. Corbella, Polyhedron 19 (2000) 2483.
[41] A.B.P. Lever, Inorganic Electronic Spectroscopy, 2nd ed., Elsevier, Amsterdam, 1984.
[42] D.K. Rastogi, K.C. Sharma, S.K. Dua, M.P. Teotia, J. Inorg. Nucl. Chem. 37 (1975) 685.
[43] G. Alzuet, S. Ferrer, J. Borrás, A. Castiñeiras, X. Solans, M. Font-Bardía, Polyhedron 11 (1992) 2849.
[44] A. Bernalte-García, A.M. Lozano-Vila, F. Luna-Giles, R. Pedrero-Marín, Polyhedron 25 (2006) 1399.
[45] A. Bernalte-García, F.J. García-Barros, F.J. Higes-Rolando, F. Luna-Giles, M.M. Pacheco-Rodríguez, E. Viñuelas-Zahínos, Bioinorg. Chem. Appl. 2 (2004) 307.
[46] C. Ochs, F.E. Hahn, T. Lügger, Eur. J. Inorg. Chem. (2001) 1279.
[47] L. Sacconi, F. Mani, A. Bencini, in: G. Wilkinson (Ed.), Comprehensive Coordination Chemistry, vol. 5, Pergamon Press, Oxford, 1987.
[48] S. Menon, M.V. Rajasekharan, Polyhedron 17 (1998) 2463.
[49] A.M. Schuitema, A.F. Stassen, W.L. Driessen, J. Reedijk, Inorg. Chim. Acta 337 (2002) 48.
[50] J. Hathaway, in: G. Wilkinson (Ed.), Comprehensive Coordination Chemistry, vol. 5, Pergamon Press, Oxford, 1987.
[51] B.J. Hathaway, J. Chem. Soc., Dalton Trans. (1972) 1196.
[52] S. Tyagi, B.J. Hathaway, J. Chem. Soc., Dalton Trans. (1981) 2029.
[53] W. Fitzgerald, B.J. Hathaway, J. Chem. Soc., Dalton Trans. (1981) 567.
[54] A. Bernalte-García, F.J. García-Barros, F.J. Higes-Rolando, F. Luna-Giles, Polyhedron 20 (2001) 3315.
[55] M. Shakir, S.P. Varkey, F. Firdaus, P.S. Hamed, Polyhedron 13 (1994) 2319.
[56] F.J. Barros-García, A. Bernalte-García, F.J. Higes-Rolando, F. Luna-Giles, A.M. Pizarro-Galán, E. Viñuelas-Zahínos, Z. Anorg. Allg. Chem. 631 (2005) 1898.
[57] F.J. Barros-García, A. Bernalte-García, F.J. Higes-Rolando, F. Luna-Giles, M.A. Maldonado-Rogado, E. Viñuelas-Zahínos, Inorg. Chim. Acta 357 (2004) 3574.
[58] J.R. Ferraro, Low-frequency Vibrations of Inorganic and Coordination Compounds, Plenum Press, New York, 1971.
[59] K. Nakamoto, Infrared and Raman Spectra of Inorganic and Coordination Compound, 5th ed., Wiley, New York, 1997.
[60] G. Ibrahim, M.A. Khan, P. Richomme, O. Benali-Baitich, G. Bouet, Polyhedron 16 (1997) 3455.
[61] A. Bernalte-García, F.J. García-Barros, F.J. Higes-Rolando, F. Luna-Giles, R. Pedrero-Marín, J. Inorg. Biochem. 98 (2004) 15.
[62] M. Shakir, H.-T.-N. Chishti, P. Chingsubam, Spectrochim. Acta A 64 (2006) 512.
[63] M. Joseph, V. Suni, M.R.P. Kurup, M. Nethaji, A. Kishore, S.G. Bhat, Polyhedron 23 (2004) 3064.

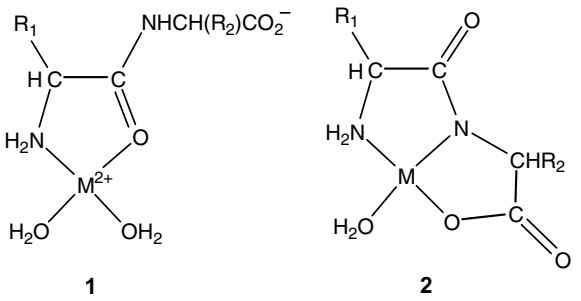


Fig. 1. Structure of dipeptide complexes ML^+ (**1**) and MLH_{-1} (**2**). Central atom (Cu or Ni) is denoted with M.

is denoted as K_a. Ovarall stability constant of the complex MLH_{-1} is β_1 ($=K_1K_a$).

In the Eqs. (1) and (2), L stays for the ionized form of the dipeptide, e.g. $NH_2CH(R_1)CONHCH(R_2)COO^-$. General structure of the ML^+ (**1**) and MLH_{-1} (**2**) complex [26] is given in Fig. 1.

By regarding the formation of the complex MLH_{-1} as a two-step process, enabled us to model Reactions (1) and (2) separately, and to estimate the overall stability constant β_1 from estimates of the K_1 and K_a.

2. Methods

2.1. Calculation of topological indices

The calculations of topological indices were performed with a program system DRAGON 2.1, written by Todeschini and coworkers [28], which is capable to yield 262 topological indices in a single run, along with many other molecular descriptors. The connectivity matrix was constructed with the aid of *Online SMILES Translator and Structure File Generator* [29].

All calculations were done with the Randić index ${}^3\chi^v$ (the valence molecular connectivity index of the 3rd order):

$$ {}^3\chi^v = \sum_{\text{path}} [\delta(i)\delta(j)\delta(k)\delta(l)]^{-0.5} \quad (3)$$

where $\delta(i)$, $\delta(j)$, $\delta(k)$, and $\delta(l)$ are weights (valence-delta values) of vertices (atoms) i, j, k, and l making up the path of length 3 (three consecutive chemical bonds) in a vertex-weighted molecular graph [23,24]. Valence-delta value, $\delta(i)$, of a vertex i is defined by:

$$ \delta(i) = [Z^v(i) - H(i)]/[Z(i) - Z^v(i) - 1] \quad (4)$$

where $Z^v(i)$ is the number of valence electrons belonging to the atom corresponding to vertex i, $Z(i)$ is its atomic number, and $H(i)$ is the number of hydrogen atoms attached to it. For instance, delta values for primary, secondary, tertiary and quaternary carbon atoms are 1, 2, 3, and 4, respectively; for oxygen in OH group is equal to 5, and for NH_2 group $\delta(N) = 3$. (It has to be pointed out that ${}^3\chi^v$ is only a member of the family of valence connectivity indices, ${}^n\chi^v$, which differ each other by path length, i.e. the number of δ's in the summation term, Eq. (3).) The value of ${}^3\chi^v$ index rise with the size (number of atoms) and drops with the branching of molecule.

All the calculations were done on the valence connectivity graph derived from formula of MLH_{-1} complex (**2**, Fig. 1). Application of formula **1** (ML^+) altered results insignificantly.

2.2. Regression calculations

Regression calculations, including the leave-one-out procedure of cross validation, *cv*, were done by CROMRsel program [30]. The standard error of cross validation estimates is defined as:

$$ SE_{cv} = (1/N\Sigma\Delta X^2)^{0.5} \quad (5)$$

where ΔX and N denotes *cv* residuals and number of reference points, respectively.

3. Results

3.1. Estimation of formation constant K_1 (Eq. (1))

The first step in the developing of our model for the estimation of stability constants of copper(II) and nickel(II) complexes with dipeptides is to estimate the formation constant of the ML^+ complex (K_1, Eq. (1), see Table 1). We chose altogether 15 copper(II) and eight nickel(II) complexes (Table 2). All the constants were measured at the same temperature ($T = 25$ °C) and two ionic strengths ($I = 0.1$, 0.16 mol L^{-1}). If more constants for a complex were referred to in the literature, their arithmetic mean is presented in Table 2. The discrepancy between experimental values goes up to 0.86 (for Cu(GG).

Table 1
Linear regressions of $\log K_1$ on the connectivity index ${}^3\chi^v$ of MLH_{-1} complexes (c.f. Table 2)

Model no.	N	Independent variable(s)[a]	Var1 slope (*SE*)	Var2 slope (*SE*)	Intercept (*SE*)	r	*SE*	SE_{cv}
1 (Cu)	15	${}^3\chi^v(r_1)$, ${}^3\chi^v(r_2)$	−0.605(82)	0.149(74)	6.30(24)	0.945	0.13	0.16
2 (Cu)	8	${}^3\chi^v$	0.14(12)		5.14(57)	0.415	0.15	0.21
2 (Ni)	5	${}^3\chi^v$	−0.109(64)		4.68(29)	0.703	0.06	0.12
3 (Cu)	5	${}^3\chi^v$	−0.61(12)		7.82(55)	0.945	0.11	0.15
4 (Cu)	4	${}^3\chi^v$	−0.162(27)		6.10(13)	0.972	0.03	0.05
5 (Cu, Ni)	8	${}^3\chi^v$, In_1	−0.74(18)	−1.55(18)	8.38(79)	0.975	0.19	0.32
6 (Cu, Ni)	23	${}^3\chi^v(r_1)$, In_1	−0.781(74)	−1.673(79)	6.87(14)	0.983	0.17	0.20

[a] $In_1 = 0$ for Cu complexes, $In_1 = 1$ for Ni complexes.

Table 2
Cross-validation estimates of $\log K_1$ for copper(II) and nickel(II) complexes with dipeptides from regression models given in Table 1

	Experimental $\log K_1$ (N)[a]	Estimates						Mean (Models 1–6)	Mean (Models 1–4,6)
		Model 1	Model 2	Model 3	Model 4	Model5	Model 6		
Cu complexes									
Gly–Gly	5.51(6)	5.70	5.81	5.64	5.49	5.80	5.85	5.71	5.70
Gly–Ala	5.73(3)	5.70	5.71				5.82	5.74	5.74
Ala–Gly	5.46(1)	5.29		5.26		5.32	5.41	5.32	5.32
Gly–Val	5.67(3)	5.79	5.77				5.83	5.80	5.80
Val–Gly	4.87(1)	5.11		5.09		5.08	5.11	5.10	5.10
Gly–norVal	5.88(1)	5.75	5.75				5.81	5.77	5.77
Gly–norLeu	5.92(1)	5.79	5.78				5.80	5.79	5.79
Gly–Phe	5.59(2)	5.96	5.99				5.84	5.93	5.93
Phe–Gly	4.66(1)	4.66		4.60		4.41	4.51	4.54	4.59
Ala–Ala	5.37(1)	5.40			5.37		5.41	5.39	5.39
Val–Val	5.20(1)	5.21			5.27		5.07	5.18	5.18
Leu–Leu	5.24(1)	5.13			5.16		4.97	5.09	5.09
Gly–Tyr	5.90(1)	5.88	5.86				5.80	5.85	5.85
Gly–Leu	6.00(2)	5.76	5.75				5.79	5.77	5.77
Leu–Gly	5.05(2)	5.00		4.97		4.94	5.00	4.98	4.99
rms		0.16	0.21	0.15	0.05	0.21	0.17	0.16	0.15
Ni complexes									
Gly–Gly	4.21(2)		4.35			3.76	4.08	4.06	4.21
Gly–Ala	4.23(1)		4.21				4.07	4.14	4.14
Gly–Val	4.18(2)		4.17				4.08	4.13	4.13
Gly–Phe	4.03(1)		4.23				4.11	4.17	4.17
Val–Val	3.12(1)						3.41	3.41	3.41
Gly–Leu	4.25(1)		4.13				4.07	4.10	4.10
Leu–Gly	3.46(2)					3.20	3.24	3.22	3.24
Val–Gly	3.00(1)					3.59	3.44	3.51	3.44
rms			0.12			0.45	0.23	0.25	0.22
SE_{cv}(Cu, Ni)						0.32	0.20	0.19	0.18

[a] Arithmetic mean of N values [26,33–43].

The plot of $\log K_1$ versus connectivity index $^3\chi^v$ (Fig. 2), indicates three subsets of complexes, consisting of YG, GY, and YY type of peptides, where G stays for glycyl and Y for any amino-acid residue. Regression on the subsets (Table 1) gave estimates for copper(II) complexes with SE_{cv} ranging from 0.05 to 0.21 (Models 2–4, Table 2).

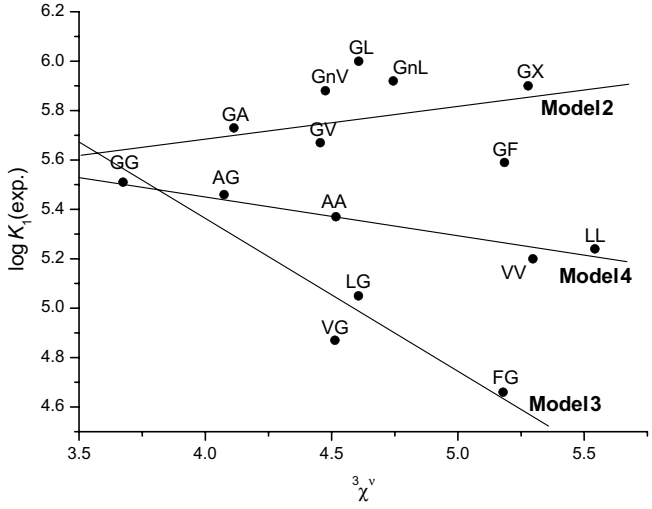


Fig. 2. Regression models for $\log K_1$ of copper(II) complexes with three classes of dipeptides, GY (Model 2), YG (Model 3), and YY (Model 4), Table 1. Dipeptides are denoted by the standard one-letter code, with an exception for norvaline (nV) and norleucine (nL).

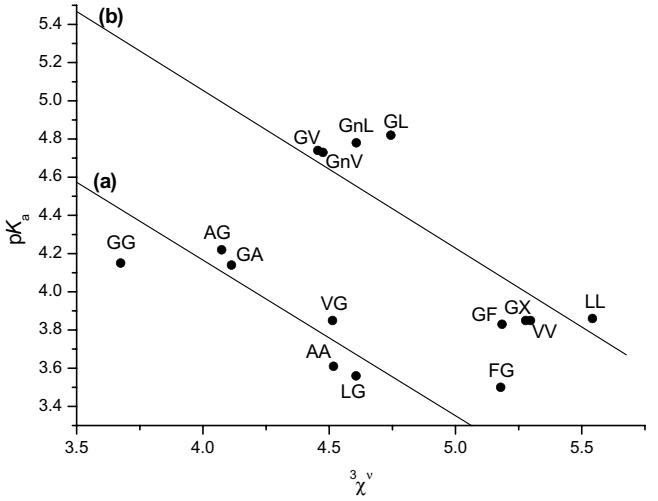


Fig. 3. Regression model for pK_a of copper(II) complexes with two classes of dipeptides, differing in type of the second amino-acid residue (Model 7, Table 3): (a) the second residue is G or A ($In_2 = 0$), (b) the second residue is any other amino-acid residue ($In_2 = 1$). Dipeptides are denoted by the standard one-letter code, with an exception for norvaline (nV) and norleucine (nL).

Unfortunately, paucity of data enabled such kind of estimation only for Ni(GY) complexes, yielding $SE_{cv} = 0.12$.

Other models gave similar results. Model 1 with two variables, where $^3\chi^v(r_1)$ and $^3\chi^v(r_2)$ corresponds to the $^3\chi^v$ index of the first and second chelate ring, respectively, in complex **2** (Fig. 1), yielded $SE_{cv} = 0.16$, and the maximum error of 0.37, for Cu(GF). Introduction of an indicator variable ($In_1 = 0$ for Cu, $In_1 = 1$ for Ni) enabled us to apply the same model along with nickel(II) complexes (Model 6). In this way the results of the same quality were obtained for copper(II) complexes, and $\log K_1$ values for nickel(II) chelates were reproduced with $SE_{cv} = 0.23$. The model with indicator variable was also checked on YG type ligands (Model 5), which enabled estimation of $\log K_1$ for nickel(II) complexes. Averaging all the estimates, as we used to do [21,22], did not alter substantially the results.

3.2. Estimation of dissociation constant K_a (Eq. (2))

For the estimation of deprotonation constant of the complex ML^+ (K_a, Eq. (2)) data from the same papers are subtracted as for the constant K_1. Unfortunately, data for nickel(II) chelates with glycylleucine (GL), and leucylglycine (LG) were missing. Values of constant K_a were determined with lesser accuracy than the values of constant K_1; differences of pK_a for the same chelate span the range from 0.04, for Cu(GL), to 0.5, for Cu(LG), and even 1.0, for Ni(GV).

Table 3
Linear regressions of pK_a on the connectivity index $^3\chi^v$ of MLH_{-1} complexes (c.f. Table 4)

Model no.	N	Independent variable(s)[a]	Var1 slope (*SE*)	Var2 slope (*SE*)	Var3 slope (*SE*)	Intercept (*SE*)	r	*SE*	SE_{cv}
7 (Cu)	15	$^3\chi^v$, In_2	−0.81(13)	0.90(13)		7.41(57)	0.907	0.19	0.25
8 (Cu, Ni)	21	$^3\chi^v$, In_2, In_1	−0.82(13)	0.91(14)	5.07(12)	7.47(57)	0.996	0.22	0.28
9 (Cu)	13	$^3\chi^v$, KD	−0.27(14)	−0.093(26)		5.29(64)	0.799	0.23	0.30
10 (Cu)	13	$^3\chi^v$, C	−0.32(13)	−0.080(20)		5.50(61)	0.824	0.22	0.28
11 (Cu, Ni)	19	$^3\chi^v$, KD, In_1	−0.27(14)	−0.075(27)	5.07(17)	5.28(68)	0.992	0.30	0.39
12 (Cu, Ni)	19	$^3\chi^v$, C, In_1	−0.32(14)	−0.070(22)	5.10(16)	5.48(65)	0.993	0.29	0.37

[a] $In_1 = 0$ for Cu complexes, $In_1 = 1$ for Ni complexes, $In_2 = 0$ for complexes with G or A, $In_2 = 1$ for complexes with other amino acid as the second residue. For the definition of the hydrophobicity parameters KD and C, see Section 3.2.

Table 4
Cross-validation estimates of pK_a for copper(II) and nickel(II) complexes with dipeptides from regression models given in Table 3

	Experimental pK_a (N)[a]	Estimates						Mean (Models 7–12)
		Model 7	Model 8	Model 9	Model 10	Model 11	Model 12	
Cu complexes								
Gly–Gly	4.15(6)	4.58	4.54	4.35	4.39	4.323	4.36	4.42
Gly–Ala	4.14(3)	4.07	4.08	4.42	4.19	4.360	4.18	4.22
Ala–Gly	4.22(1)	4.09	4.1	3.9	4.15	3.961	4.15	4.06
Gly–Val	4.74(3)	4.7	4.71	4.39	4.34	4.314	4.3	4.46
Val–Gly	3.85(1)	3.74	3.74	3.54	3.6	3.669	3.67	3.66
Gly–norVal	4.73(1)	4.68	4.69					4.69
Gly–norLeu	4.82(1)	4.42	4.42					4.42
Gly–Phe	3.83(2)	4.17	4.15	4.27	4.28	4.169	4.2	4.21
Phe–Gly	3.50(1)	3.04	3.07	3.59	3.45	3.659	3.52	3.39
Ala–Ala	3.61(1)	3.78	3.77	4.09	4.07	4.088	4.07	3.98
Val–Val	3.85(1)	4.06	4.04	3.83	3.77	3.835	3.78	3.89
Leu–Leu	3.86(1)	3.82	3.81	3.74	3.64	3.748	3.67	3.74
Gly–Tyr	3.85(1)	4.08	4.06	3.74	4.1	3.763	4.05	3.97
Gly–Leu	4.78(2)	4.54	4.55	4.3	4.34	4.233	4.3	4.38
Leu–Gly	3.56(2)	3.7	3.7	3.66	3.54	3.746	3.62	3.66
rms		0.25	0.23	0.30	0.28	0.29	0.27	0.24
Ni complexes								
Gly–Gly	9.35(1)		9.42			9.283	9.36	0
Gly–Ala	8.79(1)		9.09			9.493	9.34	−0.52
Gly–Val	9.92(2)		9.57			9.270	9.29	0.54
Gly–Phe	8.59(1)		9.21			9.333	9.42	−0.73
Val–Val	9.16(1)		8.89			8.751	8.72	0.37
Val–Gly	9.00(1)		8.61			8.585	8.65	0.38
rms			0.37			0.55	0.53	0.48
SE_{cv} (Cu, Ni)			0.28			0.39	0.37	0.33

[a] Arithmetic mean of N values [26,33–43].

Table 5
The *rms* values for the estimates of the $\log\beta_1$ (=$\log K_1 - pK_a$) for copper(II) complexes with dipeptides from the estimates given in Tables 2 and 4

pK_a	$\log K_1$			
	Model 1	Model 6	Mean (Models 1–6)	Mean (Models 1–4,6)
Model 7	0.21	0.22	0.20	0.21
Model 8	0.20	0.21	0.19	0.20
Model 12	0.25	0.27	0.26	0.25
Mean (Models 7–12)	0.21	0.23	0.21	0.21

The plot of pK_a versus $^3\chi^v$ (Fig. 3) shows two sets of copper(II) chelates of dipeptides. In the first set the second amino-acid residue belongs to an amino acid with a very short side chain, glycyl (–H) or alanyl (–CH_3). The second set consists of all other amino acids. By dividing copper(II) chelates into two subsets, it was possible to apply the regression with an indicator variable In_2 ($In_2 = 0$ for G or A, $In_2 = 1$ for any other amino acid as the second residue, Regr. 7, Table 3). The model yielded very good agreement with experimental data (Table 4), yielding $SE_{cv} = 0.25$ and maximal error = 0.46 (for complex with FG). Unfortunately, such an estimate for nickel(II) complexes was not possible due to paucity of data ($N = 6$), but regression supports general validity of the model (intercept = 12.7(19), slope($^3\chi^v$) = −0.87(45), slope(In_2) = 0.94(51), $r = 0.757$, $SE = 0.28$).

By introduction of indicator variable In_1 (Regr. 8, Table 3) it was possible to obtain even better estimates for copper(II) complexes ($SE_{cv} = 0.23$), and also estimates for nickel(II) complexes, but of lesser quality ($SE_{cv} = 0.37$, max. error = 0.62, for the complex Ni(GF).

Another kind of model checked on copper(II) as well as on nickel(II) chelates were models with hydrophobicity parameters (Regr. 9–12, Table 3). Hydrophobicity parameter of the complex was calculated as the difference of the hydrophobicity parameters (KD [31] or C [32]) of the first and second amino-acid residue with an assumption that this difference reflects dipol momentum of the complex and, accordingly, pK_a of NH group. These models were not shown in any way superior to the previously discussed models (7 and 8, Table 3). Due to lack of data, it was not possible to estimate pK_a of dipeptides with norvaline and norleucine by using such models.

Averaging the results obtained by the all six models for copper(II) and three models for nickel(II) no general improvement was obtained in terms of SE_{cv}. Model 8 proved best in all respects, for both metals.

3.3. Estimation of overall stability constant β_1

The *rms* (root-mean-square) error of estimates of overall stability constant of complex MLH_{-1} (**2**, Fig. 1), $\log\beta_1 = \log K_1 - pK_a$, calculated from the data in Tables 2 and 4 are presented in Table 5. By combining estimates of $\log K_1$ with the estimates of pK_a, *rms* values in the range 0.19–0.27 units were obtained, indicating consistency of all models used.

Close inspection of the results presented in Table 5 reveals, however, that the worst results were obtained with Model 12 ($SE_{cv} = 0.25$–0.27), and the best with model 8 ($SE_{cv} = 0.19$–0.21). The best result ($SE_{cv} = 0.19$) was obtained by the mean value of all models for estimation of $\log K_1$, but the difference to the other estimates with Model 8 is insignificant. By the best model errors of estimates lay in the range from 0.00, for Cu(GL), to 0.34, for Cu(VG).

4. Conclusion

The application of model with the valence connectivity index $^3\chi^v$ on copper(II) and nickel(II) chelates with dipeptides shows its ability to estimate stability of such a complex system (1) if overall stability constant is calculated from the estimations of their constituting constants, and if, subsequently, (2) the set of chelates is divided into subsets or (3) the molecule is divided into constituting parts (chelate rings). (Straight-forward regression of $\log\beta_1$(Cu) versus $^3\chi^v$ yielded $r = 0.26$, $N = 15$.) Consistency of the models (c.f. Table 1) is reflected in fact that the SE_{cv}/SE ratio (1.18–2.00) approaches one for models with higher number of points (N).

Our results are also consistent with the fact that the influence of the first chelate ring is predominant, and the influence of the second one is more dependent on the type of amino-acid residue, than on the specific residue itself. It is noteworthy the separation of pK_a's into two subsets differing in the size of the side chain of the second residue (see Fig. 3 and Section 3.2). Obviously, in the dissociation process $ML^+ \rightarrow MLH_{-1}$ complex ML^+ (**1**, Fig. 1) goes through conformational changes, which are dependent on the size of the side chain of the second residue. Possibly, ML^+ species in two subsets do not exist in the same conformational states – but to discuss this point is beyond the scope of the paper.

References

[1] N. Raos, V. Simeon, Croat. Chem. Acta 56 (1983) 79.
[2] N. Raos, V. Simeon, Croat. Chem. Acta 57 (1984) 1217.
[3] J. Sabolović, N. Raos, Polyhedron 9 (1990) 1277.
[4] J. Sabolović, N. Raos, Polyhedron 9 (1990) 2419.
[5] G.R. Brubaker, D.W. Johnson, Inorg. Chem. 23 (1984) 1591.
[6] B.P. Hay, D. Zhang, J.R. Rustad, Inorg. Chem. 35 (1996) 2650.
[7] A. Fedorowicz, J. Mavri, P. Bala, A. Koll, Chem. Phys. Lett. 289 (1998) 457.

[8] J. Tomasi, M. Persico, Chem. Rev. 94 (1994) 2027.
[9] R. Bonaccorsi, P. Palla, J. Tomasi, J. Am. Chem. Soc. 106 (1984) 1945.
[10] J.R. Rustad, D.A. Dixon, K.M. Rosso, A.R. Felmy, J. Am. Chem. Soc. 121 (1999) 3234.
[11] R.D. Hancock, L.J. Bartolotti, Inorg. Chem. 44 (2005) 7175.
[12] N. Raos, Croat. Chem. Acta 78 (2005) 175.
[13] A. Miličević, N. Raos, Croat. Chem. Acta 78 (2005) 525.
[14] A. Miličević, N. Raos, Croat. Chem. Acta 79 (2006) 281.
[15] N. Raos, Vl. Simeon, J. Inorg. Biochem. 18 (1983) 133.
[16] N. Raos, Croat. Chem. Acta 70 (1997) 913.
[17] B. Grgas, S. Nikolić, N. Paulić, N. Raos, Croat. Chem. Acta 72 (1999) 885.
[18] S. Nikolić, N. Raos, Croat. Chem. Acta 74 (2001) 621.
[19] N. Raos, Croat. Chem. Acta 75 (2002) 117.
[20] A. Miličević, N. Raos, Polyhedron 25 (2006) 2800.
[21] A. Miličević, N. Raos, Polyhedron 26 (2007) 3350.
[22] A. Miličević, N. Raos, Croat. Chem. Acta 80 (2007) 557.
[23] N. Trinajstić, Chemical Graph Theory, 2nd ed., CRC Press, Boca Raton, FL, 1992.
[24] M. Randić, J. Am. Chem. Soc. 97 (1975) 6609.
[25] L.B. Kier, L.H. Hall, Molecular Connectivity in Structure-Activity Analysis, Wiley, New York, 1986.
[26] G. Brookes, L.D. Pettit, J. Chem. Soc. (Dalton) (1975) 2106.
[27] S.H. Laurie, Amino acids, peptides and proteins, Comprehensive Coordination Chemistry, vol. 1, Pergamon Press, Oxford, 1987, p. 739.
[28] http://www.disat.unimib.it/chm/.
[29] http://cactus.nci.nih.gov/services/translate/.
[30] B. Lučić, N. Trinajstić, J. Chem. Inf. Comput. Sci. 39 (1999) 121.
[31] J. Kyte, R.F. Doolittle, J. Mol. Biol. 157 (1982) 105.
[32] J.L. Cornette, K.B. Cease, H. Margalit, J.L. Spouge, J.A. Berzofsky, C. DeLisi, J. Mol. Biol. 195 (1987) 659.
[33] B.R. Rabin, Trans. Faraday Soc. 52 (1956) 1130.
[34] J.L. Biester, P.M. Ruoff, J. Am. Chem. Soc. 81 (1959) 6517.
[35] G.F. Bryce, J.M.H. Pinkerton, L.K. Steinrauf, F.R.N. Gurd, J. Biol. Chem. 240 (1965) 3829.
[36] O. Yamauchi, Y. Hirano, Y. Nakao, A. Nakahara, Canad. J. Chem. 47 (1969) 3441.
[37] W.L. Koltun, M. Fried, F.R.N. Gurd, J. Am. Chem. Soc. 82 (1960) 233.
[38] R.F. Pasternack, L. Gipp, H. Sigel, J. Am. Chem. Soc. 94 (1972) 8031.
[39] S.P. Datta, R. Leberman, B.R. Rabin, Trans. Faraday Soc. 55 (1959) 2141.
[40] R.B. Martin, M. Chamberlin, J.T. Edsall, J. Am. Chem. Soc. 82 (1960) 495.
[41] S.P. Datta, R. Leberman, B.R. Rabin, Trans. Faraday Soc. 55 (1959) 1982.
[42] A.P. Brunetti, E.J. Burke, M.C. Lim, G.H. Nancollas, J. Soln. Chem. 1 (1972) 153.
[43] U.I. Salakhutdinov, A.O. Borisova, Yu. V. Granovskii, I.A. Savich, V.I. Spitsyn, Proc. Acad. Sci. (USSR) 177 (1967) 1039.

site. Thus with the sterically more hindered site, higher branching frequencies are observed [18].

The cationic methallyl complexes with symmetrical β-diimine ($R_1 = R_2 = CH_3$) are excellent catalysts for the oligomerization of the styrene, they yield 1,3-diphenylbut-1-ene with selectivity ⩾98%. However cationic methallyl complexes with α-diimine ligand produce polymer. This reflects the effect of change of rigidity of the ligand toward the catalytic activity of the complex [19]. Different chemistry can be carried out with subtle changes of steric demand in the R_1 and R_2 positions.

The present work is a continuation of our study in β-diimine allylic complexes. In this paper we describe a one-pot synthesis of new η^3-allyl cationic complexes of palladium (II) supported by new ligands, the unsymmetrical β-diimine [20].

2. Results and discussion

These compounds $[(PhCNAr)CH_2(CH_3CNAr)Pd(allyl)]PF_6$ which are isolated as stable salts, can be easily obtained in high yields by an oxidative addition of methallyloxyphosphonium salt **6** to the zerovalent compound $Pd(dba)_2$ **5** in methylene chloride in the presence of a β-iminoamine ligand (Scheme 1).

The new complexes **7**–**10** which are soluble in methylene chloride and sparingly soluble in diethyl ether gave satisfactory analysis and were characterized by ^1H, ^{13}C $\{^1H\}$ NMR and IR spectroscopy.

The NMR data of ligands **1**–**4** are consistent with the hydrogen-bridged β-iminoamine structure [20], although complexes **7**–**10** incorporating these ligands as a β-diimine tautomer.

The ^1H NMR spectra of these compounds show two resonance signals for the allyl protons (H_{syn} and H_{anti}) which appear as a multiplet in contrast with the complexes of the symmetrical β-diimine ($R_1 = R_2 = CH_3$) which appear as a singlet [16]. The multiplicity of these signals is explained by the unsymmetrical diimine backbone and the *syn*/*syn* and *anti*/*anti* interconversion due to the dynamic behaviour of the allyl protons [21].

Thus the two resonances are located, respectively, at 2.19, 2.09, 2.58, 2.54 ppm for H_{anti} and at 2.59, 2.39, 2.88, 2.63 ppm for H_{syn} for complexes **7**–**10**.

In ^{13}C NMR spectra, the allylic carbon C(11) and C(13) appears at (62.51 and 64.54); (63.57 and 64.26); (64.41 and 64.94) and (62.33 and 65.72 ppm), respectively, for complexes **7**–**10**.

The imine carbons show two signals between 172 and 177 ppm.

The IR spectrum of compounds **7**–**10** indicated a shift in the C=N stretching frequency (1645; 1603, 1641; 1623, 1660 and 1616, 1647 cm^{-1}) relative to the respectively corresponding stretching frequency in the free ligands **1**–**4** (1622; 1622; 1610, 1649 and 1615 cm^{-1}). Moreover, the C=N stretching frequency appears at low frequency compared with their value for the compounds with the symmetrical β-diimine.

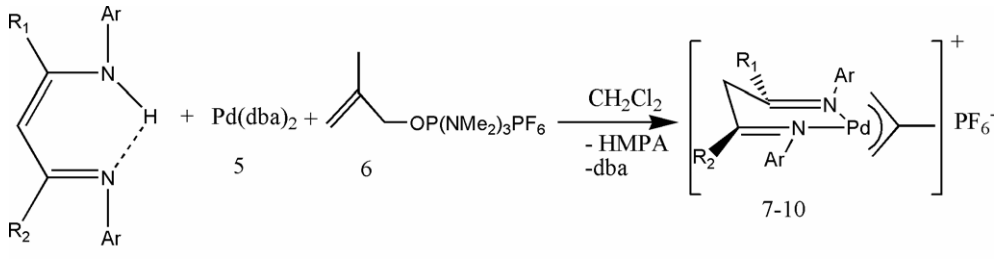
Complexes **7**–**10** exhibit the frequencies of the counter-ion PF_6^- at 838, 846, 832 and 837 cm^{-1}.

X-ray single-crystal analysis reveals that compound **10** exhibits some interesting features compared with the symmetrical β-diimine complexes. Suitable prismatic and colourless single crystals of **10** were obtained by crystallization from CH_2Cl_2/*n*-hexane. Complex **10** crystallizes in the monoclinic unit cell $P2_1/n$ group (Table 1).

An ORTEP-plot shown in Fig. 1 confirms the identity of complex **10**.

The $[(\eta^3\text{-}C_4H_7)Pd(NN)]^+$ cation of **10** adopts the usual slightly distorted square planar arrangement and this distortion is illustrated by the N(1)–Pd–N(2) bond angle equal to 90.9° (Fig. 1b). We note that this distortion is more attenuated than in the complex with the symmetrical β-diimine (N(1)–Pd–N(2) = 90.6°).

Selected bond lengths and angles are listed in Tables 2 and 3.



$R_1 = CH_3$, R_2 = Ph
(7) : Ar = 2-Me-C_6H_4
(8) : Ar = 2-MeO-C_6H_4
(9): Ar = 2,6-Me_2-C_6H_3
(10) : Ar = 2,6-iPr_2-C_6H_3
dba = dibenzylideneacetone
HMPA = Hexamethylphosphotriamide

Scheme 1. Synthesis of $[(\eta^3\text{-}C_4H_7)Pd((PhCNAr)CH_2(MeCNAr))]^+[PF_6]^-$ complexes.

Table 1
Crystallographic data and structure refinement for **10**

Empirical formula	$C_{38}H_{51}F_6N_2PPd$
Formula weight	787.18
Crystal system	monoclinic
Space group	$P2_1/n$
Z	4
a (Å)	12.495(5)
b (Å)	13.697(5)
c (Å)	22.244(5)
α(°)	90.000(5)
β (°)	92.230(5)
γ (°)	90.000(5)
V (Å^3)	3804(2)
D_{calc} (g cm^{-3})	1.374
Crystal size (mm^3)	0.11 × 0.18 × 0.25
Temperature (K)	293(2)
Wavelength (Å)	0.71069
F(000)	1632
Absorption coefficient (mm^{-1})	0.587
θ Range for data collection (°)	1.75–27.03
Limiting indices	$-15 \leqslant h \leqslant 15$, $0 \leqslant k \leqslant 17$, $-2 \leqslant l \leqslant 28$
Reflections collected/unique [R(int)]	9354/ 8271 [0.1933]
Completeness to $\theta = 27.03$	99.2%
Absorption correction	empirical (DIFABS)
Maximum and minimum transmission	0.5729 and 0.1077
Refinement method	full-matrix least-squares on F^2
Data/restraints/parameters	8271/0/433
Goodness-of-fit on F^2	0.941
Final R indices [$I > 2\sigma(I)$]	$R_1 = 0.0907$, $wR_2 = 0.2328$

$R_1 = \sum(||F_o| - |F_c||)/\sum|F_o|$.
$wR_2 = [\sum w(F_o^2 - F_c^2)^2/\sum(F_o^2)^2]^{1/2}$, where $w = 1/[\sigma^2(F_o^2) + (0.17P)^2]$, where $P = (F_o^2 + 2F_c^2)/3$.

Table 2
Selected interatomic distances

	Bond distances (Å) for **10**	Bond distances (Å) for the symmetric complex ($R_1 = R_2 = CH_3$)
Pd–N(1)	2.103(1)	2.105(3)
Pd–N(2)	2.130(1)	2.106(3)
Pd–C(11)	2.091(1)	2.129(4)
Pd–C(13)	2.117(1)	2.115(4)
Pd–C(12)	2.144(1)	2.153(3)
N(2)–C(3)	1.263(1)	1.284(4)
C(1)–N(1)	1.296(1)	1.284(4)
N(2)–C(15)	1.410(1)	1.462(4)
N(1)–C(27)	1.478(1)	1.459(4)
C(1)–C(2)	1.473(1)	1.509(4)
C(3)–C(2)	1.543(1)	1.504(4)

Table 3
Selected angles (°) for **10**

N (1)–Pd–N(2)	90.9(4)	C(11)–Pd–N (1)	101.3(6)
N (1)–Pd–C(13)	166.3(6)	C(11)–Pd–N (2)	166.3(6)
C (13)–Pd–N(2)	101.2(6)	N (1)–Pd–C(12)	133.1(6)
N (2)–Pd–C(12)	133.3(6)	C(11)–Pd–C(13)	66.0(7)
C(11)–Pd–C(12)	37.7(6)	C(11)–Pd–C(12)	37.7(6)
C(13)–Pd–C(12)	38.2(6)	C(3)–N(2)–C(15)	123.3(1)
N(1)–C(1)–C(4)	124.5(1)	N(1)–C(1)–C(2)	123.0(1)
N(2)–C(3)–C(5)	124.1(1)	N(2)–C(3)–C(2)	122.0(1)
C(1)–N(1)–C(27)	120.7(1)	C(3)–N(2)–Pd	123.8(1)
C(15)–N(2)–Pd	112.8(8)	C(1)–N(1)–Pd	123.1(1)
C(27)–N(1)–Pd	116.1(8)	C(16)–C(15)–N	119.3(1)
C(20)–C(15)–N(2)	119.7(1)	C(32)–C(27)–N(1)	120.4(1)
C(28)–C(27)–N(1)	117.4(1)	C(12)–C(11)–Pd	73.2(9)
C(12)–C(13)–Pd	71.9(9)		

If we define a plane containing the Pd and the two nitrogen atoms, then the terminal carbons are 0.24 (C11) and 0.25 Å (C13) below the plane, whereas the central allyl carbon is 0.44 Å above.

The allyl ligand is bonded almost symmetrically to the palladium centre Pd–C(11) = 2.09 Å and Pd–C(13) = 2.11 Å.

The N1–Pd–N2 plane is tilted by 63.74° with regard to the C11–C12–C13 plane. The methyl on the allyl group is slightly tilted out of the allyl plane by about 9.1° as indicated by the torsion angle of 170.1° of C(11)–C(12)–C(13)–C(14). The allyl plane (C(11), C(12), C(13)) makes an angle of 67.65° with the palladium coordinative least-square plane (N(1), N(2), C(11), C(13))

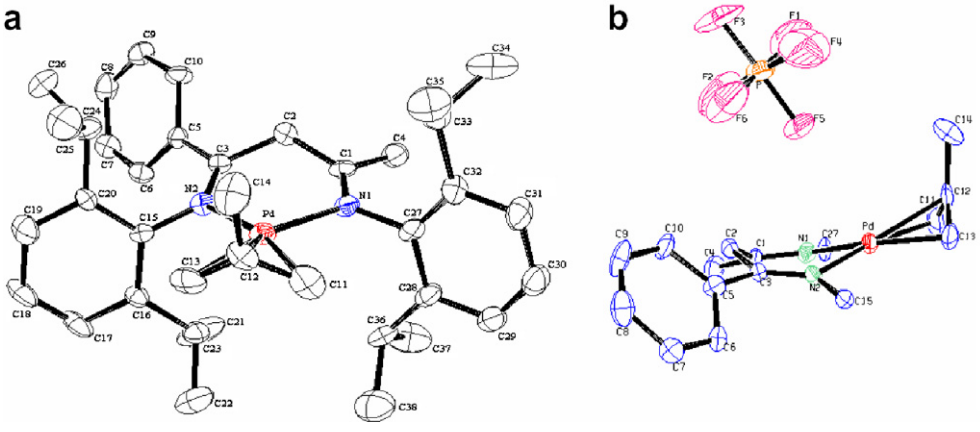


Fig. 1. (a) Perspective ORTEP diagram of the cation of **10**. Thermal ellipsoids are at 30% probability. Hydrogen atoms and anion are omitted for clarity. (b) View of the chelate ring in **10**. Hydrogen atoms and aryl ring are omitted for clarity.

The β-iminoamine ligand is bounded in a unsymmetrical fashion as the β-diimine tautomer, the C(1)–N(1) and C(3)–N(2) distances are 1.29 Å and 1.263 Å, respectively.

This ligand forms a six-membered ring with the palladium atom with Pd–N (sp^2) bond length of 2.10 Å and 2.13 Å in agreement with known values in the literature for related complexes [15,22–24]. Bond distances within the six-member chelate ring are consistent with the localized β-diimine structure drawn in Fig. 1, while the ring itself adopts a boat conformation as indicated in Fig. 1b. The aryl rings C(15–20) and C(27–32) are tilted out of the (N(1), C(1), C(3), N(2)) least-square plane by 70° and 69.49°, respectively.

3. Conclusion

New cationic methallyl palladium complexes supported by unsymmetrical β-diimine have been described. The application of these compounds in catalytic reactions such as dimerization and polymerization of alkenes and functional alkenes is in current study in order to compare them with the symmetric ones.

4. Experimental

4.1. General

All manipulations were carried out under an atmosphere of dry argon using standard Schlenk techniques.

Diethyl ether was distilled from sodium benzophenone; methylene chloride and hexane were distilled over P_2O_5. 2-Methylaniline, 2,6-dimethylaniline, 2-methoxyaniline and 2,6-diisopropylaniline were distilled from potassium hydroxide prior to use. $Pd(dba)_2$ [25,26] methallyloxyphosphonium salt [27] and β-iminoamine ligands [20] were prepared according to literature methods. All other reagents were obtained from standard commercial vendors and used as received. NMR spectra were recorded on a Bruker AC-300 spectrometer. H and C chemical shifts are given in ppm and referenced to the residual solvent resonance relative to TMS. Infrared spectra were recorded on a Bruker Victor 22 (Golden Gate Technique).

4.2. General procedure for the preparation of [(β-diimine)Pd(η^3-C_4H_7)]$^+PF_6^-$ complexes

In an inert atmosphere, $Pd(dba)_2$ complex (1 equiv.) was dissolved in 20 cm^3 anhydrous CH_2Cl_2. Methallyloxyphosphonium salt $C_4H_7OP^+(NMe_2)_3PF_6^-$ and β-iminoamine ligands were added (1 equiv.). The black-red solution was stirred at room temperature for 24 h. The supernatant was separated by filtration through a celite filter, and the solvent was removed under vacuum to afford the oil compound. This was washed with diethyl ether (3×15 cm^3) and dried in vacuum. The solid was crystallized from methylene chloride/*n*-hexane solution. Yields and spectral data of compounds **7**–**10** are reported below.

4.2.1. [(2-CH_3-C_6H_4NC(Ph)CH_2C(Me)NC_6H_4-2-CH_3)Pd(η^3-C_4H_7)]$^+PF_6^-$ (7)

Following the general procedure, from [2-CH_3-C_6H_4-NC(Ph)CHC(Me)NHC_6H_4-2-CH_3] (0.059 g, 0.173 mmol), $Pd(dba)_2$ (0.1 g, 0.173 mmol) and 2-methylallyloxyphosphonium (0.173 mmol, 0.065 g) was obtained 0.097 g of **7** as a pale yellow solid after crystallization from a mixture (CH_2Cl_2/*n*-hexane: 1/1).

Yield 87%. IR (Golden Gate): $\nu_{C=N} = 1645$ cm^{-1}. ^1H NMR (300 MHz, $CDCl_3$, 25 °C, δ [ppm]): $\delta = 1.62$ (s, 3H, Me (allyl)); 1.79 (s, 3H Me on ligand); 1.98 (s, 3H, Me–C_6H_4); 2.11 (s, 3H, Me–C_6H_4); 2.19 (m, 2H, H_{11anti} and H_{13anti}); 2.59 (m, 2H, H_{11syn} and H_{13syn}); 3.83 (m, 2H, ligand–CH_2); 6.97–7.42 (m, 13H, ArH). ^{13}C NMR (75.5 MHz, $CDCl_3$, 25 °C, δ [ppm]): $\delta = 14.25$ (Me (allyl));18.85 (Me on C_6H_4); 19.48 (Me on C_6H_4); 22.31 (Me on ligand); 49.71 (CH_2 on ligand); 62.51 and 64.52 (C(11) and C(13)); 121.37–133.24 (C(ar) and C(12)); 138.13 (C–C on C_6H_5); 148.13 and 150.61 (C–N on C_6H_4); 172.45 and 176.25 (C=N on ligand).

4.2.2. [(2-CH_3O-C_6H_4NC(Ph)CH_2C(Me)NC_6H_4-2-CH_3O)-Pd(η^3-C_4H_7)]$^+PF_6^-$ (8)

Following the general procedure, from [2-CH_3O-C_6H_4NC(Ph)CHC(Me)NHC_6H_4-2-CH_3O] (0.064 g, 0.173 mmol), $Pd(dba)_2$ (0.1 g, 0.173 mmol) and 2-methylallyloxyphosphonium (0.173 mmol, 0.065 g) was obtained 0.104 g of **8** as a pale yellow solid after crystallization from a mixture (CH_2Cl_2/*n*-hexane: 1/1).

Yield = 89%. IR (Golden Gate): $\nu_{C=N} = 1603$ and 1641 cm^{-1}. ^1H NMR (300 MHz, $CDCl_3$, 25 °C, δ [ppm]): $\delta = 1.81$ (s, 3H, Me (allyl)); 2.00 (s, 3H, Me on ligand); 2.09 (m, 2H, H_{11anti} and H_{13anti}); 2.39 (m, 2H, H_{11syn} and H_{13syn}); 3.65–3.80 (m, 2H, ligand–CH_2); 3.85–3.91(m, 6H, H_3CO); 6.77–7.60 (m, 13H, ArH). ^{13}C NMR (75.5 MHz, $CDCl_3$, 25 °C, δ [ppm]): $\delta = 14.18$ (Me (allyl)); 22.75 (Me on ligand); 55.88 (CH_3O); 49.95 (CH_2 on ligand); 62.33 and 65.72 (C(11) and C(13)); 111.52–130.64 (C(ar) and C(12)-allyl); 134.44 (C–C on C_6H_5) 139.58 and 144.42 (C–N on C_6H_4); 177.07 and 177.21 (C=N on ligand).

4.2.3. [2,6-$(CH_3)_2$-C_6H_3NC(Ph)CH_2C(Me)NC_6H_3-2,6-$(CH_3)_2$Pd(η^3-C_4H_7)]$^+PF_6^-$ (9)

Following the general procedure, from [2,6-$(CH_3)_2$-C_6H_3NC(Ph)CHC(Me)NHC_6H_3-2,6-$(CH_3)_2$] (0.063 g, 0.173 mmol), $Pd(dba)_2$ (0.1 g, 0.173 mmol) and 2-methylallyloxyphosphonium (0.173 mmol, 0.065 g) was obtained 0.107 g of **9** as a pale yellow solid after crystallization from a mixture (CH_2Cl_2/*n*-hexane: 1/1).

Yield 92%. IR (Golden Gate): $\nu_{C=N} = 1623$ and 1660 cm^{-1}. ^1H NMR (300 MHz, $CDCl_3$, 25 °C, δ [ppm]): $\delta = 0.87$ (s, 3H, Me (allyl)); 1.56 (s, 3H, Me on ligand); 1.95 (s, 3H, Me on C_6H_3); 2.02 (s, 3H, Me on C_6H_3); 2.19 (s, 3H, Me on C_6H_3); 2.25 (s, 3H, Me on C_6H_3); 2.58 (m, 2H, H_{11anti} and H_{13anti}); 2.88 (m, 2H, H_{11syn} and H_{13syn}); 4.72 (m, 2H, ligand CH_2); 6.92–7.26 (m, 11H, Har). ^{13}C NMR (75.5 MHz, $CDCl_3$, 25 °C, δ [ppm]):

$\delta = 14.20$ (Me (allyl)); 22.72 (Me on ligand); 18.16, 18.37, 18.82 and 19.19(Me on C_6H_3); 49.46 (CH_2 on ligand); 63.57 and 64.26 (C(11) and C(13)); 126.24–135.68 (C(ar) and C(12)); 137.21 (C–C on C_6H_5); 149.84 and 150.51(C–N on C_6H_3); 173.73 and 176.54 (C=N on ligand).

4.2.4. [2,6-(iPr)$_2$-C$_6$H$_3$NC(Ph)CH$_2$C(Me)NC$_6$H$_3$-2,6-(iPr)$_2$Pd(η^3-C$_4$H$_7$)]$^+$PF$_6^-$ (**10**)

Following the general procedure, from [2,6-(iPr)$_2$-$C_6H_3NC(Ph)CHC(Me)NHC_6H_3$-2,6-(iPr)$_2$] (0.083 g, 0.173 mmol), Pd(dba)$_2$ (0.1 g, 0.173 mmol) and 2-methylallyloxyphosphonium (0.173 mmol, 0.065 g) was obtained 0.129 g of **10** as a pale yellow solid after crystallization from a mixture (CH_2Cl_2/*n*-hexane: 1/1).

Yield = 95%. IR (Golden Gate): $\nu_{C=N} = 1616$ and 1647 cm^{-1}. ^{1}H NMR (300 MHz, $CDCl_3$, 25 °C, δ [ppm]): $\delta = 0.88$–1.40 (m, 21 H, Me-iPr and Me on allyl); 1.99 (s, 3H, Me on ligand); 2.17 (d, 6H, $J = 16.8$ Hz, Me-iPr); 2.54 (m, 2H, H_{11anti} and H_{13anti}); 2.63 (m, 2H, H_{11syn} and H_{13syn}); 3.02 (sept, 2H, $J = 7.5$ Hz, H-C-iPr); 3.39 (sept, 1H, $J = 6.9$ Hz, H-C-iPr); 3.76 (sept, 1H, $J = 7.2$ Hz, H-C-iPr); 4.66–5.06 (m, 2H, CH_2 on ligand); 7.02–7.26 (m, 11H, H_{ar}); ^{13}C NMR (75.5 MHz, $CDCl_3$, 25 °C, δ [ppm]): $\delta = 15.87$ (Me-allyl); 22.84 (Me on ligand); 23.84, 23.88, 24.00, 24.21, 24.34, 24.38, 24.71 and 25.66 (Me on iPr group); 28.68, 28.76, 29.20 and 29.43 (CH on iPr group); 49.91 (CH_2 on ligand); 64.41 and 64.9 (C(11) and C(13)); 124.25–138.08 (C(ar) and C(12)); 138.23 (C–C on C_6H_5); 147.26 and 148.14 (C–N on C_6H_3); 172.77 and 177.45 (C=N on ligand).

4.3. X-ray crystallographic study

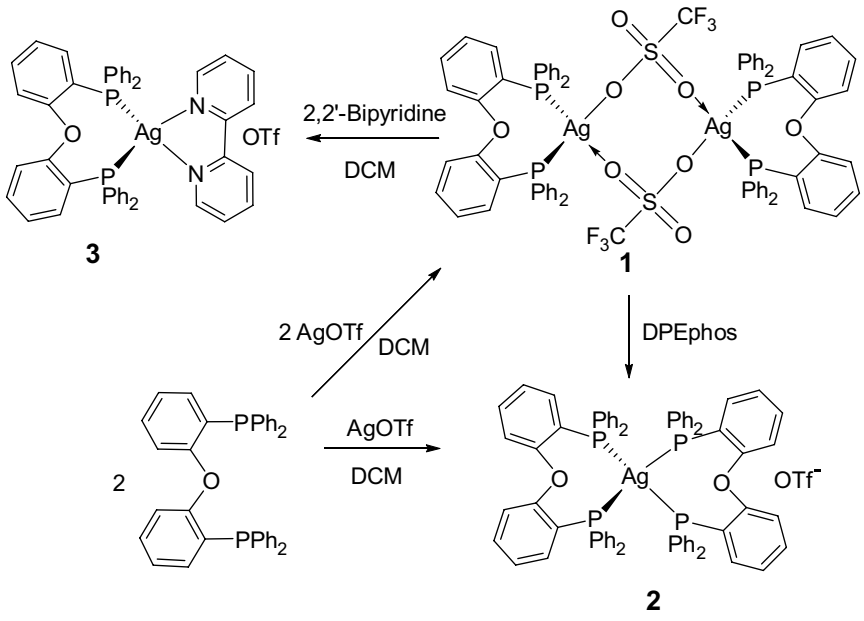
The X-ray crystallographic study of complex **10** was carried out on a CAD4 Enraf-Nonius diffractometer (Mo Kα). Data were collected at 283 K in the range 1–27° and this gave a total of 9354 reflections, yielding 8271 independent values ($R_{int} = 0.1933$). The structure was solved by direct method and difference Fourier techniques and were refined by full-matrix least-squares analysis. Refinements were based on F^2 and were carried out using all the data (SHELXL-97). All of the non-hydrogen atoms were re-fined anisotropically. The hydrogen atoms were fixed geometrically in their idealized positions. The set of physical and crystallographic characteristics as well as the experimental conditions are listed in Table 1.

Appendix A. Supplementary material

CCDC 272962 contains the supplementary crystallographic data for **10**. These data can be obtained free of charge via http://www.ccdc.cam.ac.uk/conts/retrieving.html, or from the Cambridge Crystallographic Data Centre, 12 Union Road, Cambridge CB2 1EZ, UK; fax: (+44) 1223-336-033, or e-mail: deposit@ccdc.cam.ac.uk. Supplementary data associated with this article can be found, in the online version, at doi:10.1016/j.poly.2007.11.026.

References

[1] J.E. Parks, R.H. Holm, Inorg. Chem. 7 (1968) 1408.
[2] A recent review L. Bourget-Merle, Michael F. Lappert, J.R. Severn, Chem. Rev. 102 (2002) 3031.
[3] J. Feldman, S.J. McLain, A. Parthasarathy, W.J. Marshall, J.C. Calabrese, S.D. Arthur, Organometallics 16 (1997) 1514.
[4] W. Clegg, E.K. Cope, A.J. Edwards, F.S. Mair, Inorg. Chem. 37 (1998) 2317.
[5] M. Rahim, N.J. Taylor, S. Xin, S. Collins, Organometallics 17 (1998) 1315.
[6] B. Qian, D.L. Ward, N.R. Smith, Organometallics 17 (1998) 3070.
[7] W.K. Kim, M.J. Fevola, L.M. Liable-Sauds, A.L. Rheingold, K.H. Theopold, Organometallics 17 (1998) 4541.
[8] F. Cosledan, P.B. Hitchcock, M.F. Lappert, Chem. Commun. (1999) 707.
[9] D.L. Reger, S.J. Knox, M.F. Huff, A.L. Rheingold, B.S. Haggerty, Inorg. Chem. 30 (1991) 1754.
[10] C.F. Caro, P.B. Hitchcock, M.F. Lappert, Chem. Commun. (1999) 1433.
[11] P.B. Hitchcock, M.F. Lappert, S. Tian, J. Chem. Soc., Dalton Trans. (1997) 1945.
[12] P.B. Hitchcock, M.F. Lappert, M. Layh, D.-S. Liu, R. Sablong, S. Tian, J. Chem. Soc., Dalton Trans. (2000) 2301 and references quoted therein.
[13] P.B. Hitchcock, J. Hu, M.F. Lappert, M. Layh, D.-S. Liu, J.R. Severn, S. Tian, An. Quim. Int., Ed. Engl. 92 (1996) 186.
[14] K. Landolsi, M. Rzaigui, F. Bouachir, Tetrahedron Lett. 43 (2002) 9463.
[15] E.K. Cope-Eatough, F.S. Mair, R.G. Pritchard, J.E. Warren, R.J. Woods, Polyhedron 22 (2003) 1447.
[16] K. Landolsi, P. Richard, F. Bouachir, J. Organomet. Chem. 690 (2005) 513.
[17] J. Zhang, Z. Ke, F. Bao, J. Long, H. Gao, F. Zhu, Q. Wu, J. Mol. Catal. A: Chem. 249 (2006) 31.
[18] T. Schleis, T.P. Spaniol, J. Okuda, J. Heinemann, R. Mulhaupt, J. Organomet. Chem. 569 (1998) 159.
[19] K. Landolsi, F. Bouachir, E. Bouajila, M. Picquet, D. Poinsot, I. Tkatchenko, in: 1st International Congress on Ionic Liquid, Salzburg/Austria, June 19–22, COIL, 2005, p. 28.
[20] K. Landolsi, N. Belhaj Mbarek Elmkacher, T. Guerfel, F. Bouachir, C.R. Chimie, (2007), doi:10.1016/j.crci.2007.11.005.
[21] Y.-L. Tung, W.-C. Tseng, C.-Y. Lee, P.-F. Hsu, Y. Chi, S.-M. Peng, G.-H. Lee, Organometallics 18 (1999) 864.
[22] D.J. Tempel, L.K. Johnson, R.L. Huff, P.S. White, M. Brookhart, J. Am. Chem. Soc. 122 (2000) 6686.
[23] A. Mechria, M. Rzaigui, F. Bouachir, Tetrahedron Lett. 44 (2003) 6773.
[24] B. Crociani, R. Bertani, G. Bandoli, J. Chem. Soc., Dalton Trans. (1982) 1715.
[25] M.F. Rettig, P.M. Maitlis, Inorg. Synth. 17 (1977) 134.
[26] T. Ukai, H. Kawazura, Y. Ishii, J. Bonnet, J.A. Ibers, J. Organomet. Chem. 65 (1994) 253.
[27] D. Neibecker, B.J. Castro, J. Organomet. Chem. 134 (1977) 105.



Scheme 1.

molecular ion peak corresponding to the cationic complex part at m/z 1185.46 $[M]^+$ with the appropriate isotopic pattern. This evidences that the Ag^I metal center is bis-chelated by DPEphos ligands to form a spirocyclic compound (Fig. 2). The microanalysis supports the structural composition of complex **2**, which is further confirmed by single crystal X-ray data.

The solid state structure of complex **1** shows the presence of a Ag^I complex as a dimer, in which DPEphos binds in a chelating mode whereas the two triflate ions are bridging the two silver atoms *via* O═S–O^- units, thus making a three eight-membered spirocyclic ring structure as shown in Fig. 1. The counter ion plays an important role in coordination with silver atoms, providing stability to complex **1**. Similarly, counter ions such as nitrate, acetate and perchlorate are also known to bridge silver atoms [9–11]. Although the triflate units anchor the silver(I) centers to stabilize complex **1**, they are labile and can be easily substituted with P- and N-donors. The mixed-ligand complex [Ag(κ^2-*P*,*P*′-DPEphos)(2,2′-bpy)][OTf] (**3**) was synthesized in good yield by the reaction of **1** with 2,2′-bipyridine in a 1:2 molar ratio at room temperature. The $^{31}P\{^1H\}$ NMR spectrum of complex **3** at room temperature exhibits a pair of doublets centered at −8.8 ppm with J^{109}_{AgP} and J^{107}_{AgP} values of 426 and 374 Hz, respectively. The ^1H NMR spectrum confirms the presence of 2,2′-bipyridine, which presents peaks at 8.04 and 8.35 ppm. The J_{AgP} values are in the range 370–430 Hz, which is in agreement with those values reported for analogous complexes [10,12].

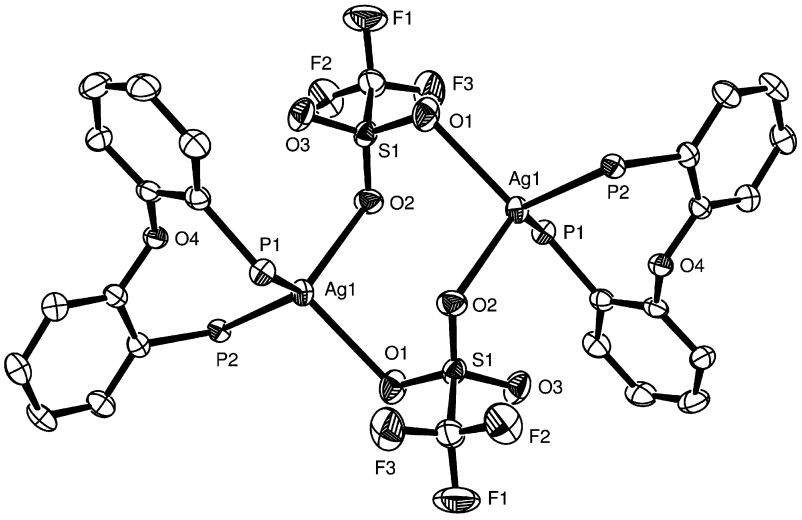


Fig. 1. Molecular structure of complex **1**. Thermal ellipsoids are drawn at the 50% probability level. Hydrogen atoms, phenyl rings attached to phosphorus and uncoordinated solvent molecules have been omitted for clarity.

2.1. Crystal structures of complexes *1–3*

Complexes **1** and **2** were recrystallized from a mixture of CH_2Cl_2/Et_2O, and complex **3** was recrystallized from a $CHCl_3/Et_2O$ mixture. The molecular structures of complexes **1–3** are shown in Figs. 1–3, respectively, and selected bond parameters are displayed in Tables 1 and 2. The crystallographic information is given in Table 3.

Complex **1** crystallizes in the monoclinic crystal system with a center of symmetry and it is dimeric in nature. The Ag^I center possesses a distorted tetrahedral geometry, whose edges are shared by two phosphorus atoms of a DPEphos ligand and two oxygen atoms of triflate ions. Each silver atom is anchored to a chelating DPEphos and bridged by triflate units. The Ag1–O1, Ag1–O2, Ag1–P1 and Ag1–P2 bond distances are 2.553(2),

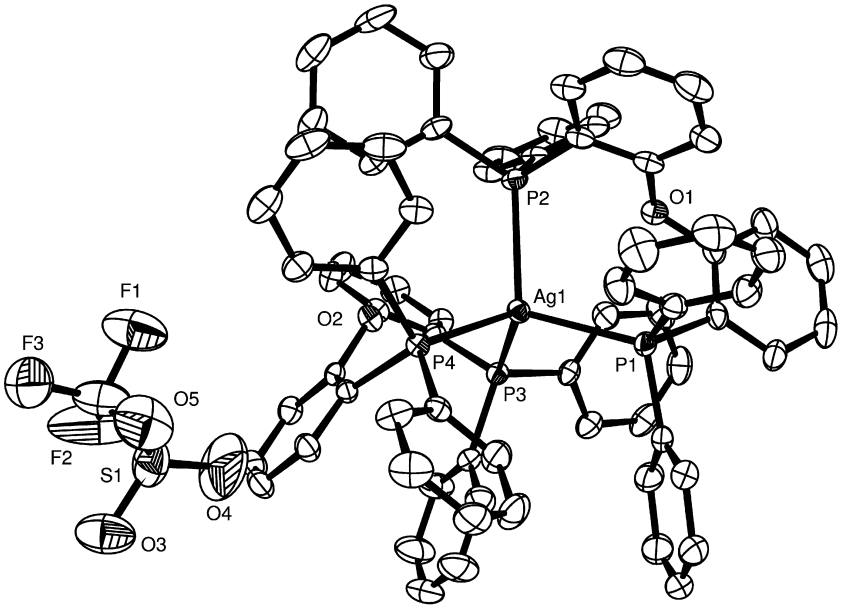


Fig. 2. Molecular structure of complex **2**. Thermal ellipsoids are drawn at the 30% probability level. Hydrogen atoms have been omitted for clarity.

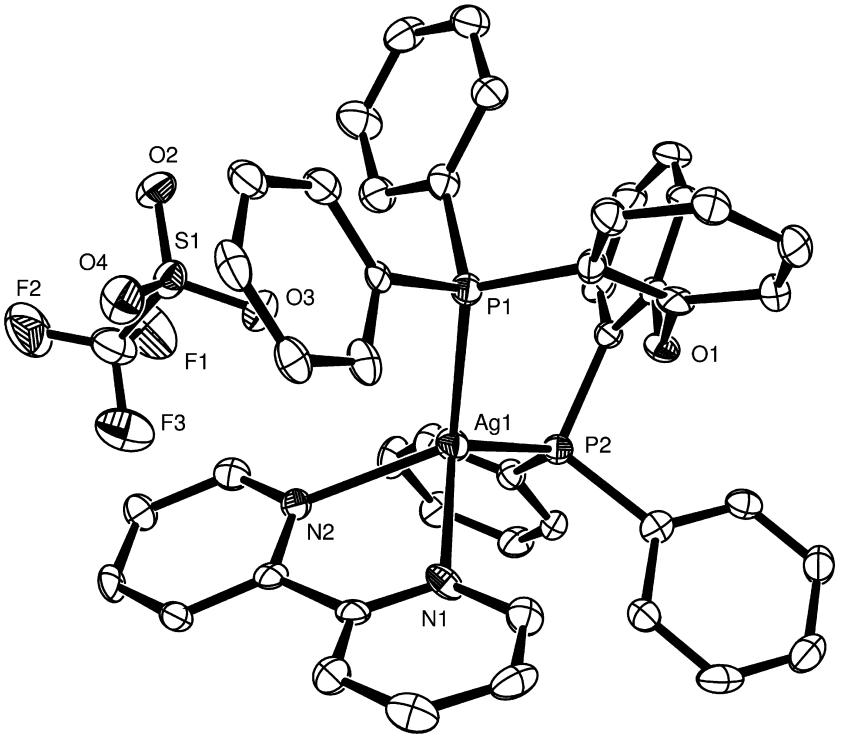


Fig. 3. Molecular structure of complex **3**. Thermal ellipsoids are drawn at the 30% probability level. Hydrogen atoms and uncoordinated solvent molecules have been omitted for clarity.

Table 1
Selected bond distances and bond angles for complexes **1** and **2**

Complex **1**				Complex **2**			
Bond distances (Å)		Bond angles (°)		Bond distances (Å)		Bond angles (°)	
Ag1–O2	2.411(2)	O2–Ag1–P2	111.52(6)	Ag1–P3	2.5385(7)	P3–Ag1–P4	106.37(2)
Ag1–P2	2.4383(9)	O2–Ag1–P1	113.49(6)	Ag1–P4	2.5461(7)	P3–Ag1–P1	107.47(2)
Ag1–P1	2.4521(8)	P2–Ag1–P1	117.40(3)	Ag1–P1	2.6119(7)	P4–Ag1–P1	115.38(2)
Ag1–O1	2.553(2)	O2–Ag1–O1	99.12(8)	Ag1–P2	2.6232(7)	P3–Ag1–P2	107.77(2)
S1–O3	1.426(2)	P2–Ag1–O1	104.07(6)	S1–O3	1.450(3)	P4–Ag1–P2	110.56(2)
S1–O1	1.436(3)	P1–Ag1–O1	109.13(6)	S1–C73	1.786(5)	P1–Ag1–P2	108.96(2)
S1–C1	1.815(3)	O3–S1–O1	115.41(15)	F1–C73	1.338(5)		
F1–C1	1.327(4)	S1–O1–Ag1	112.58(13)				

Table 2
Selected bond distances and bond angles for complex **3**

Complex **3**			
Bond distances (Å)		Bond angles (°)	
Ag1–N2	2.305(6)	N2–Ag1–N1	70.4(2)
Ag1–N1	2.355(6)	N2–Ag1–P2	126.98(16)
Ag1–P2	2.405(2)	N1–Ag1–P2	119.60(17)
Ag1–P1	2.488(2)	N2–Ag1–P1	110.69(15)
S1–O2	1.439(6)	N1–Ag1–P1	107.77(15)
F3–C47	1.317(11)	P2–Ag1–P1	113.51(7)
S1–C49	1.853(11)		

2.411(2), 2.453(3) and 2.438(2) Å, respectively. The Ag1–O2 bond distances of 0.142(2) Å is shorter than Ag1–O1, which indicates that the former one is an ionic bond and the latter one is a covalent bond. The bite angle of the DPEphos ligand is 117.40(3)°, which is 15.4° larger than its natural bite angle (β_n). Complex **2** crystallizes in the monoclinic crystal system and Ag^I exists in a distorted tetrahedral geometry. The silver(I) atom is attached to four phosphorus atoms of two DPEphos ligands. The Ag–P bond distances are 2.5385(7), 2.5460(7), 2.6118(7) and 2.6232(7) Å and are approximately 0.1–0.19 Å longer than the same distances in complex **1**. The bite angles of the two DPEphos ligands are 106.37(2)° and 108.96(2)°, which are 10.73° and 8.44° less when compared with the same angles in complex **1**.

In complex **3**, the Ag^I atom possesses a distorted tetrahedral geometry containing two phosphorus and two nitrogen atoms. The pyridyl units of the 2,2′-bipyridine ligand are not in a plane and are twisted by an angle of 14.50°. The Ag1–P1 bond (2.488(2) Å) is considerably longer than the Ag1–P2 bond (2.405(2) Å). The Ag1–N1 and Ag1–N2 bond distances are 2.305(6) and 2.355(6) Å, respectively. One set of diagonally opposite Ag–N and Ag–P bonds are longer than the other set of Ag–N and Ag–P bonds.

Table 3
Crystallographic data for complexes **1**–**3**

	1	**2**	**3**
Formula	$C_{38}H_{30}AgCl_2F_3O_4P_2S$	$C_{73}H_{56}AgF_3O_5P_4S$	$C_{48}H_{37}AgCl_3F_3N_2O_4P_2S$
F_w	880.39	1333.99	1071.02
Crystal system	monoclinic	monoclinic	triclinic
Space group	$P2_1/a$	$P2_1/c$	$P\bar{1}$
a (Å)	12.2506(15)	14.04760(10)	9.547(5)
b (Å)	26.477(5)	19.0664(2)	13.800(5)
c (Å)	12.5255(6)	23.1718	19.221(5)
α (°)	90	90	107.804(5)
β (°)	115.035(8)	91.6160(10)	94.406(5)
γ (°)	90	90	92.280(5)
V (Å^3)	3681.1(8)	6203.80(10)	2398.6(17)
Z	4	4	2
ρ_{calc} (g cm^{-3})	1.589	1.428	1.483
μ(Mo Kα) (mm^{-1})	0.892	0.524	0.754
F(000)	1776	2736	1084
Crystal size (mm)	0.33 × 0.26 × 0.21	0.26 × 0.21 × 0.18	0.08 × 0.17 × 0.23
T (K)	100(2)	150(2)	150(2)
2θ Range (°)	2.92–25.00	2.90–25.00	3.05–30.00
Total number reflections	20732	60904	8354
Number of independent reflections [R_{int}]	6460 [0.027]	10906 [0.0447]	3817 [0.089]
Goodness-of-fit (F^2)	1.074	1.051	0.842
R_1[a]	0.0332	0.0358	0.0678
wR_2[b]	0.0800	0.0850	0.1705

[a] $R = \sum||F_o| - |F_c||/\sum|F_o|$.
[b] $R_w = \{[\sum w(F_o^2 - F_c^2)/\sum w(F_o^2)^2]\}^{1/2}$ $w = 1/[\sigma^2(F_o^2) + (xP)^2]$ where $P = (F_o^2 + 2F_c^2)/3$.

A similar trend was observed in the analogous copper complex $[Cu(\kappa^2\text{-}P,P'\text{-DPEphos})(\mu\text{-}4,4'\text{-bpy})]_n[BF_4]_n$, but to a lesser extent [5].

3. Conclusion

The silver(I) complexes $[Ag_2(\kappa^2\text{-}P,P'\text{-DPEphos})_2(\mu\text{-}OTf)_2]$ (**1**), $[Ag(\kappa^2\text{-}P,P'\text{-DPEphos})_2][OTf]$ (**2**) and $[Ag(\kappa^2\text{-}P,P'\text{-DPEphos})(2,2'\text{-bpy})][OTf]$ (**3**) have been synthesized and structurally characterized. In all the complexes, the silver(I) atoms exist in a distorted tetrahedral environment and the DPEphos ligand binds in a chelating fashion. The solid state structure of complex **1** evidences the presence of three adjacent eight-membered spirocyclic rings. The triflate ions in complex **1** act as bridging units between the two silver atoms to form a dinuclear complex.

4. Experimental

4.1. General methods

All manipulations were performed under an atmosphere of dry nitrogen using standard Schlenk techniques. All the solvents were purified by conventional procedures and distilled under nitrogen prior to use [13]. The ligand DPEphos was prepared according to the published procedure [14].

4.2. Instrumentation

The ^1H and $^{31}P\{^1H\}$ NMR (δ in ppm) spectra were recorded using a Varian 400 Mercury Plus spectrometer operating at the appropriate frequencies using TMS and 85% H_3PO_4 as internal and external references, respectively. Microanalyses were performed on a Carlo Erba Model 1112 elemental analyzer. Electro-spray ionization (EI) mass spectrometry experiments were carried out using a Waters Q-Tof micro-YA-105.

4.2.1. Synthesis of $[Ag_2(\kappa^2\text{-}P,P'\text{-DPEphos})_2(\mu\text{-}OTf)_2]$ (*1*)

A mixture of DPEphos (0.252 g, 0.467 mmol) and AgOTf (0.120 g, 0.467 mmol) in CH_2Cl_2 (20 mL) was stirred for 4 h at room temperature. All the solvents were dried under vacuum to obtain a white solid, which was recrystallized from CH_2Cl_2/Et_2O as colorless crystals of **1**. Yield: 83% (0.309 g), m.p.: 256–258 °C. ^1H NMR (400 MHz, $CDCl_3$): 6.75–7.46 ppm (m, 56H, Ph). ^{31}P NMR (162 MHz, $CDCl_3$): −10.0 ppm (d, $J_{AgP} = 486.8$ Hz). ^{31}P NMR (162 MHz, 223 K, $CDCl_3$): −10.4 ppm (2d, $J^{109}_{AgP} = 526.8$, $J^{107}_{AgP} = 456.7$). *Anal.* Calc. for $C_{74}H_{56}O_8P_4Ag_2F_6S_2$: C, 55.86; H, 3.55; S, 4.03. Found: C, 55.90; H, 3.56; S, 3.92%.

4.2.2. Synthesis of $[Ag(\kappa^2\text{-}P,P'\text{-DPEphos})_2][OTf]$ (*2*)

The procedure was similar to that of **1**, but using AgOTf (0.025 g, 0.097 mmol) and DPEphos (0.105 g, 0.194 mmol). Yield: 98% (0.127 g), m.p.: >260 °C. ^1H NMR (400 MHz, $CDCl_3$): 6.68–7.21 (m, 56H, Ph). ^{31}P NMR (162 MHz, $CDCl_3$): −10.5 ppm (2d, $J^{109}_{AgP} = 269.7$, $J^{107}_{AgP} = 233.8$). MS (EI): m/z 1185.46 $[M-OTf]^+$. *Anal.* Calc. for $C_{73}H_{56}O_5P_4AgF_3S$: C, 65.72; H, 4.23; S, 2.40. Found: C, 65.74; H, 4.20; S, 2.44%.

4.2.3. Synthesis of $[Ag(\kappa^2\text{-}P,P'\text{-DPEphos})(2,2'\text{-bpy})][OTf]$ (*3*)

A solution of 2,2′-bipyridine (0.010 g, 0.063 mmol) in CH_2Cl_2 (5 mL) was added dropwise to a stirring solution of **1** (0.050 g, 0.031 mmol) also in CH_2Cl_2 (10 mL) at room temperature. After 4 h all the solvents were removed under vacuum and the remaining white solid was recrystallized from a $CHCl_3/Et_2O$ mixture as colorless crystals of **3**. Yield: 88% (0.053 g), m.p.: >260 °C. ^1H NMR (400 MHz, $CDCl_3$): 6.79–7.38 (m, 28H, Ph), 7.00 (t, 2H, bpy), 8.04 (dt, 2H, bpy), 8.35 ppm (m, 4H, bpy). ^{31}P NMR (162 MHz, $CDCl_3$): −8.8 ppm (2d, $J^{109}_{AgP} = 425.6$, $J^{107}_{AgP} = 374.3$). *Anal.* Calc. for $C_{47}H_{36}O_4P_2AgF_3SN_2$: C, 59.32; H, 3.81; N, 2.94; S, 3.37. Found: C, 59.25; H, 3.85; N, 2.86; S, 3.32%.

4.3. X-ray crystallography

A single crystal of each compound **1**–**3** suitable for X-ray crystal analysis was mounted on a glass fiber with epoxy resin. Unit cell determination and data collection of all the compounds were collected on an Oxford Diffraction XCALIBUR-S CCD system using Mo Kα radiation ($\lambda = 0.71073$ Å). The structures were solved and refined by full-matrix least-squares techniques on F^2 using SHELX-97 (SHELXL program package) [15]. The absorption corrections were done by multi-scan and all the data were corrected for Lorentz and polarization effects. The non-hydrogen atoms were refined with anisotropic thermal parameters. All the hydrogen atoms were geometrically fixed and allowed to refine using a riding model.

Acknowledgements

We are grateful to The Department of Science and Technology (DST), New Delhi, for funding. We also thank The Department of Chemistry Instrumentation Facilities, IIT Bombay and The National Single Crystal X-ray Diffraction Facility, IIT Bombay, for instrument facilities.

Appendix A. Supplementary material

CCDC 643885, 643886 and 643887 contain the supplementary crystallographic data for **1**, **2** and **3**. These data can be obtained free of charge via http://www.ccdc.cam.ac.uk/conts/retrieving.html, or from the Cambridge Crystallographic Data Centre, 12 Union Road, Cambridge CB2 1EZ, UK, fax: (+44) 1223-336-033, or e-mail: deposit@ccdc.cam.ac.uk. Supplementary data associated with this article can be found, in the online version, at doi:10.1016/j.poly.2007.11.019.

References

[1] (a) M. Kranenburg, Y.E.M. van der Burgt, P.C.J. Kamer, P.W.N.M. van Leeuwen, K. Goubitz, J. Fraanje, Organometallics 14 (1995) 3081;
(b) R.J. van Haaren, E. Zuidema, J. Fraanje, K. Goubitz, P.C.J. Kamer, P.W.N.M. van Leeuwen, G.P.F. van Strijdonck, Comptes Rendus Chimie 5 (2002) 431;
(c) M.A. Zuideveld, B.H.G. Swennenhuis, M.D.K. Boele, Y. Guari, G.P.F. van Strijdonck, J.N.H. Reek, P.C.J. Kamer, K. Goubitz, J. Fraanje, M. Lutz, A.L. Spek, P.W.N.M. van Leeuwen, J. Chem. Soc., Dalton Trans. (2002) 2308.

[2] (a) D. Kim, B.-M. Park, J. Yun, Chem. Commun. (2005) 1755;
(b) S.-M. Kuang, D.G. Cuttell, D.R. McMillin, P.E. Fanwick, R.A. Walton, Inorg. Chem. 41 (2002) 3313;
(c) S.-M. Kuang, P.E. Fanwick, R.A. Walton, Inorg. Chem. 41 (2002) 405;
(d) J. Wilting, C. Muller, A.C. Hewat, D.D. Ellis, D.M. Tooke, A.L. Spek, D. Vogt, Organometallics 24 (2005) 13;
(e) A. Pintado-Alba, H. de la Riva, M. Nieuwhuyzen, D. Bautista, P.R. Raithby, H.A. Sparkes, S.J. Teat, J.M. López-de-Luzuriagae, M.C. Lagunas, J. Chem. Soc., Dalton Trans. (2004) 3459.

[3] (a) P.W.N.M. van Leeuwen, P.C.J. Kamer, J.N.H. Reek, P. Dierkes, Chem. Rev. 100 (2000) 2741;
(b) M. Ahmed, A.M. Seayad, R. Jackstell, M. Beller, J. Am. Chem. Soc. 125 (2003) 10311;
(c) P.-E. Broutin, I. Cerna, M. Campaniello, F. Leroux, F. Colobert, Org. Lett. 6 (2004) 4419;
(d) Y. Chen, X.P. Zhang, J. Org. Chem. 68 (2003) 4432;
(e) R. Csuk, A. Barthel, C. Raschke, Tetrahedron 60 (2004) 5737;
(f) G.-Y. Gao, A.J. Colvin, Y. Chen, X.P. Zhang, Org. Lett. 5 (2003) 3261;
(g) Y. Kozawa, M. Mori, J. Org. Chem. 68 (2003) 3064;
(h) R. Kuwano, Y. Kondo, Y. Matsuyama, J. Am. Chem. Soc. 125 (2003) 12104;
(i) M. Ogasawara, H. Ikeda, T. Nagano, T. Hayashi, Org. Lett. 3 (2001) 2615;
(j) C.H. Oh, V.R. Reddy, Tetrahedron Lett. 45 (2004) 5221;
(k) M.C. Willis, D. Taylor, A.T. Gillmore, Org. Lett. 6 (2004) 4755;
(l) J.P. Wolfe, M.A. Rossi, J. Am. Chem. Soc. 126 (2004) 1620.

[4] R. Venkateswaran, J.T. Mague, M.S. Balakrishna, Inorg. Chem. 46 (2007) 809.

[5] R. Venkateswaran, M.S. Balakrishna, S.M. Mobin, H.M. Tuononen, Inorg. Chem. 46 (2007) 6335.

[6] (a) M.S. Balakrishna, R. Panda, J.T. Mague, J. Chem. Soc., Dalton Trans. (2002) 4617;
(b) M.S. Balakrishna, R. Panda, J.T. Mague, Polyhedron 22 (2003) 587;
(c) S. Priya, M.S. Balakrishna, S.M. Mobin, R. McDonald, J. Organomet. Chem. 688 (2003) 227;
(d) P. Chandrasekaran, J.T. Mague, M.S. Balakrishna, Inorg. Chem. 44 (2005) 7925;
(e) P. Chandrasekaran, J.T. Mague, M.S. Balakrishna, Organometallics 24 (2005) 3780;
(f) P. Chandrasekaran, J.T. Mague, M.S. Balakrishna, Inorg. Chem. 45 (2006) 5893;
(g) P. Chandrasekaran, J.T. Mague, M.S. Balakrishna, Inorg. Chem. 45 (2006) 6678;
(h) B. Punji, J.T. Mague, M.S. Balakrishna, J. Chem. Soc., Dalton Trans. (2006) 1322;
(i) B. Punji, C. Ganesamoorthy, M.S. Balakrishna, J. Mol. Catal. A: Chem. 259 (2006) 78;
(j) B. Punji, J.T. Mague, M.S. Balakrishna, J. Organomet. Chem. 691 (2006) 4265;
(k) R. Venkateswaran, M.S. Balakrishna, S.M. Mobin, Eur. J. Inorg. Chem. (2007) 1930.

[7] M. Bardaji, O. Crespo, A. Laguna, A.K. Fischer, Inorg. Chim. Acta 304 (2000) 7.

[8] E.J. Sekabunga, M.L. Smith, T.R. Webb, W.E. Hill, Inorg. Chem. 41 (2002) 1205.

[9] P.G. Jones, Acta Crystallogr., Sect. C 49 (1993) 1148.

[10] M.C. Gimeno, P.G. Jones, A. Laguna, C. Sarroca, J. Chem. Soc., Dalton Trans. (1995) 1473.

[11] Effendy, C.D. Nicola, M. Fianchini, C. Pettinari, B.W. Skelton, N. Somers, A.H. White, Inorg. Chim. Acta 358 (2005) 763.

[12] A. Cingolani, Effendy, F. Marchetti, C. Pettinari, R. Pettinari, B.W. Skelton, A.H. White, Inorg. Chim. Acta 329 (2002) 100.

[13] W.L.F. Armarego, D.D. Perrin, Purification of Laboratory Chemicals, IVth ed., Butterworth-Heinemann Linacre House, Jordan Hill, Oxford, UK, 1996.

[14] M. Kranenburg, Y.E.M. van der Burgt, P.C.J. Kamer, P.W.N.M. van Leeuwen, K. Goubitz, J. Fraanje, Organometallics 14 (1995) 3081.

[15] G.M. Sheldrick, SHELXS97 and SHELXL97, University of Gottingen, Gottingen, Germany, 1997.

saccharinate through the *N* atom. The *O*-coordination mode of the saccharinate ligand was found for the complexes $[Cu(sac)_2(pypr)_2]$ [6], $[Ni(sac)_2(dmen)_2]$ [12], $[Cu(sac)(H_2O)(mpy)_4]$ (mpy = 4-methylpyridine) [13], $[Cu(sac)_2(iqn)_4]$ (iqn = isoquinoline) [13] and $[Cu(sac)_2(prz)_4]$ (prz = pyrazole) [14]. Although the literature lists many reports on the coordinating presence of the sac moiety in copper(II) complexes, from an X-ray crystal structure point of view only a limited number of structures with dinuclear copper saccharinate complexes have been obtained to date, $[Cu_2(bipym)_3(sac)_2(H_2O)_2]$ $(sac)_2(H_2O)_4$(bipym = 2,2′-bipyrimidine) [15], $[Cu_2(sac)_2(\mu\text{-}\ dmea)_2(\mu\text{-}\ H_2O)]_n$ (Hdmea = 2-dimethylaminoethanol) [15], $[Cu_2(sac)_2(\mu\text{-}dea)_2]$ (dea = diethanolamine) [16] and $[Cu_2(pypr)_2(sac)_2]$ (pypr = 2-pyridinepropanoxy anion) [17]. An hydroxo-bridged saccharinate complex has not yet been reported.

Square-pyramidal Cu(II)-complexes of the saccharinate ligand with pyridine [18], benzimidazole [19], nicotinamide [20], triethanolaminate [21], *S*-methyl-*N*-(6-methylpyrid-2-yl)methylenedithiocarbazate [22], the pyridine-2-carboxaldehyde Schiff base of the *S*-methyldithiocarbazate anion [23] and 2-formylpyridinethiosemicarbazonate [24] have been reported.

In hydroxo-bridged complexes of transition metals, there is often the possibility of a metal–metal interaction due to the rather small bridging ligands, and these complexes have received much attention because of their interesting magnetic properties [25]. These complexes make interesting model compounds for spin-coupling phenomena.

$[Cu(sac)_2(H_2O)_4]\cdot 2H_2O$ showed a certain inhibitory effect over carbonic anhydrose [26]. $[M(sac)_2(H_2O)_4]\cdot 2H_2O$ (M = Mn(II), Fe(II), Co(II), Ni(II), Cu(II) and Zn(II)) possess the ability to dismutate the O^{2-} anion. The copper(II) complex presents the most important activity [27]. It has also been commented that copper-saccharinate complexes $[Cu(NNS')(sac)(H_2O)]$, $[Cu(NNS'')(sac)(H_2O)]$ and $[Cu(NNS''')(sac)(H_2O)]$ have potent antimicrobial activity against bacteria and yeast [22].

In this paper we describe the syntheses, spectral, thermal, antimicrobial effect and structural characterization of the novel dinuclear di-μ-hydroxo-bis[(*N*,*N*-diethylethylenediamine)(saccharinato-*N*)copper(II)] dihydrate and di-μ-hydroxo-bis[(*N*,*N*,*N*′,*N*′-tetramethylethylenediamine)-(saccharinato- *O*)copper(II)] complexes.

2. Experimental

2.1. Materials and measurements

All chemicals used were analytical reagents and were commercially purchased. IR spectra were obtained with a Bruker Tensor 27 FT-IR spectrometer using KBr pellets in the 4000–400 cm^{-1} range. Elemental analysis for C, H and N were performed using a Carlo Erba 1106 microanalyser. Magnetic susceptibility measurement at room temperature was performed using a Sherwood Scientific MXI model Gouy magnetic balance. The UV–Vis spectra were obtained for aqueous solutions of the complexes (10^{-3} M) with a Unicam UV2 spectrometer in the range 900–190 nm. A Diamond TG/DTA thermal analyzer was used to record simultaneous TG, DTG and DTA curves in static air atmosphere at a heating rate of 10 K min^{-1} in the temperature range 20–600 °C using platinum crucibles.

2.2. Antimicrobial activity studies

The antimicrobial activities were tested against standard strains of Gram-positive (*Stapylococcus aureus* ATCC 6535, *Bacillus cereus* ATCC 7064) and Gram-negative (*Escherichia coli* W3110, *Citrobacter freundii* NRRLB 2643) bacteria and one yeast (*Candida albicans* ATCC 10231) and mould (*Aspergillus niger*) using the disc diffusion method. Antimicrobial studies were performed according to broth microdilution (1 gram + and 1 gram −) and agar diffusion methods.

The agar diffusion experiments were based on the obtained MIC values by broth dilution methods. Stock solutions of the ligand and the new complexes were prepared both in dimethylsulfoxide (DMSO, Merck) and in ultra pure water according to the needed concentrations for the experiments. Nutrient Agar (Merck) plates were prepared and dried for 5 days at room temperature. All the test cultures were grown in 5 ml nutrient broth at 37 °C in a shaker incubator. Then 200 μl cultures were inoculated into 5 ml fresh nutrient broth and the incubation period was 24 h for bacterial strains and 48 h for fungal strains at 37 °C. Test strains were spread on solid nutrient agar surfaces using a sterile glass rod. The final inoculation (inoculums) was approximately 10^5 cfu ml^{-1}. Absorbent paper discs of 6 mm were placed on the agar surface and impregnated with known concentrations (200, 500 and 1000 μg for each disc) determined previously by MIC tests. Antibiotic discs were placed on the same agar plate. Sulfamethoxazole, chloramphenical, streptomycin, tetracyline, neomycin, sulfafurazole, oflaxacin, ceftriaxone were used for antibacterial control while nystatin was used as the antifungal control for test microorganisms. To ensure that the solvent had no effect on bacterial growth, a control test was performed with a test medium supplemented with DMSO following the same procedures as used in the experiments. Incubations were done at 37 °C for 24 h for bacteri and 48 h for fungi after inoculums. The antimicrobial activity was indicated by the presence of clear inhibition zones and cloudiness around the discs, and was measured as diameters in millimeters. All tests were repeated three times and average data were taken as the final result.

2.3. Crystallographic analyses

For the crystal structure determination, single crystals of the compounds $[Cu(\mu\text{-}OH)(sac\text{-}N)(deten)]_2\cdot 2H_2O$ (**1**) and

$[Cu(\mu\text{-}OH)(sac\text{-}O)(tmen)]_2$ **(2)** were used for data collection on a four-circle Rigaku R-AXIS RAPID-S diffractometer equipped with a two-dimensional area IP detector. The cylindrically shaped imaging plate covered the two-theta angular range between −60 and 140° with a crystal-film distance of 127.4 mm. Graphite monochromatized Mo Kα radiation ($\lambda = 0.71073$ Å) and the oscillation scans technique with $\Delta\omega = 5°$ for one image were used for data collection. Images were taken successfully by varying ω with three sets of different χ and ϕ values. One hundred and seven images for three different runs covering about 99.8% of the Ewald spheres were performed. The lattice parameters were determined by least-squares methods on the basis of all reflections with $F^2 > 2\,\sigma\,(F^2)$. Integration of the intensities, correction for Lorentz and polarization effects and cell refinement were performed using CRYSTALCLEAR (Rigaku/MSC Inc., 2005) software [28]. The structures were solved by the direct method using SHELXS [29]. The positional and atomic displacement parameters (ADPs) were refined by the full-matrix least-squares method using SHELXL [29]. The positional and isotropic atomic displacement parameters of hydrogen atoms were refined together with other structural parameters by the full-matrix least-squares procedure based on the squared value of the structure factors. Except for water molecules, hydrogen atomic positions were calculated from assumed geometries. Hydrogen atoms were included in structure factor calculations but they were not refined. The isotropic displacement parameters of the hydrogen atoms were approximated from the *U* (equiv.) value of the atom to which they were bonded. The final difference Fourier maps showed no peaks of chemical significance. Details of the data collection and final refinement parameters are listed in Table 2.

2.4. Preparation of the complexes

A solution of *N*,*N*-diethylethylenediamine (2 mmol, 0.23 g) or *N*,*N*,*N*′,*N*′-tetramethylethylenediamine (2 mmol, 0.23 g) in water (10 mL) was added dropwise to an aqueous solution of $[Cu(sac)_2(H_2O)_4]\cdot 2H_2O$ [30] (1 mmol, 0.54 g) and stirred for 4 h at 50 °C. The reaction mixture was then slowly cooled to room temperature. The violet crystals that formed were filtered and washed with 5 mL of ethanol and dried in air. $[Cu(\mu\text{-}OH)(sac\text{-}N)(deten)]_2\cdot 2H_2O$. Yield *ca.* 76%. *Anal.* Calc. for $C_{26}H_{46}N_6O_{10}S_2Cu_2$(%): C, 39.34; H, 5.84; N, 10.59; S, 8.08. Found: C, 39.57; H, 5.74; N, 10.70; S, 8.32%. $[Cu(\mu\text{-}OH)(sac\text{-}O)(tmen)]_2$ *Anal.* Calc. for $C_{26}H_{42}N_6O_8S_2Cu_2$(%): C, 41.21; H, 5.59; N, 11.09; S, 8.46. Found: C, 40.70; H, 5.07; N, 10.80; S, 8.93%.

3. Results and discussion

3.1. Spectral and magnetic properties

The UV–Vis spectra of the complexes in H_2O display a broad absorption band at 546 nm for **1** ($\varepsilon = 60$ L mol^{-1} cm^{-1}) and 648 nm for **2** ($\varepsilon = 64$ L mol^{-1} cm^{-1}). These observed single broad peaks are consistent with the square pyramidal stereochemistry and are assigned to the $d_{xz}, d_{yz} \rightarrow d_{x^2-y^2}$ transition.

Hydroxo-bridged dinuclear complexes have received a lot of attention due to their different magnetic properties [25]. Di-μ-hydroxo-bridged copper(II) complexes display an antiferromagnetic effect for a Cu–O–Cu angle more than 97.5° [31]. The complexes exhibit magnetic moment values of 2.20 and 2.24 BM which corresponds to two unpaired electrons. However, these magnetic moment values are lower than the spin only value for two unpaired electrons in Cu(II) complexes, indicating an antiferromagnetic effect. These results are surprising because the Cu–O–Cu angles are less than 97.5° in the complexes.

The most important and characteristic absorption bands of both complexes are compared with those of the respective bands of sodium saccharinate [32] in Table 1. The IR spectra of the copper(II) complexes exhibit the characteristic features of OH (hydroxyl), C=O (ketone), symmetric SO_2 and asymmetric SO_2.

The infrared spectra of the copper(II) complexes show a strong and broad band at 3536 cm^{-1}, (water), 3330 cm^{-1} for **1** and 3324 cm^{-1} for **2** due to the bridging hydrogen-bonded OH group [33]. The strong bands in the 3241–3130 cm^{-1} range are attributed to the $\nu(NH_2)$ stretching vibrations of the deten ligand in **1**. The splitting of the CH/CH_2 stretching absorption bands occurs in the 2981–2892 cm^{-1} range as medium bands in the IR spectra of the complexes. The carbonyl (C=O) stretching band of sodium saccharinate (Nasac) appears as one main peak at 1642 cm^{-1} [32], and a comparison between the infrared spectra of Nasac and **1** shows this band is shifted to 1623 cm^{-1}. This shift indicates that the involvement of the *N* atom of the sac ligand in coordination to the metal reduces the electron density in the C=O bond, leading to a downward shift of the related frequencies, whereas the lower band at 1615 cm^{-1} in the IR spectrum of **2** is assigned to the *O*-coordinated sac ligand, *via* the carbonyl group. The very strong bands at 1585 cm^{-1} for **1** and 1582 cm^{-1} for **2** correspond to the ν(CC) vibrations of the sac ligand. The $\nu_{asym}(SO_2)$ and $\nu_{sym}(SO_2)$ modes of sac appear as strong bands at 1275 and 1155 cm^{-1} for **1**

Table 1
Selected IR spectral data[a]

Assignment	Na(sac) · H_2O [48]	**1**	**2**
$\nu(OH)_{water}$	3534 s	3536 s	
$\nu(OH)_{bridge}$		3330 s	3324 s
$\nu(NH_2)$		3241–3130 s	
ν(C=O)	1642 vs	1623 vs	1615 vs
ν(C–C)	1590 s	1585 s	1582 s
ν_s(CNS)	1336 m	1338 m	1335 m
$\nu_{as}(SO_2)$	1258 vs	1275 s	1284 s
$\nu_s(SO_2)$	1150 vs	1155 s	1153 s
Cu–N, Cu–O		469 w, 539 w	471 w, 602 w

[a] Abbreviations: m – medium; s – strong; vs – very strong.

Table 2
Crystal data and structure refinement for complexes **1** and **2**

	1	**2**
Empirical formula	$C_{26}H_{46}N_6O_{10}S_2Cu_2$	$C_{26}H_{42}N_6O_8S_2Cu_2$
Formula weight (g mol^{-1})	397	378.9
Crystal system, space group	monoclinic, $P2_1/c$	triclinic, $P\bar{1}$
Color	violet	violet
Unit cell dimensions		
a (Å)	7.5270(4)	7.9400(4)
b (Å)	24.1190(7)	9.6970(5)
c (Å)	9.9050(5)	10.8020(6)
α (°)	106.15(5)	88.53(5)
β (°)		78.17(5)
γ (°)		84.49(4)
V (Å^3)	1727.2(3)	810.3(8)
Z	4	2
Absorption coefficient (mm^{-1})	1.412	1.497
D (g cm^{-3})	1.527	1.553
Data collection		
T (K)	293(2)	293(2)
Θ Range (°)	2.3–30.6	2.1–30.6
Reflections collected	49 289	24 284
Independent reflections	5282	4922
Reflections with $I > 2\sigma(I)$	3742	4497
Largest difference in peak and hole (e Å^3)	0.980 and −0.92	0.315 and −0.691
Final R indices $I > 2\sigma(I)$	$R_1 = 0.061$, $wR_2 = 0.175$	$R_1 = 0.036$, $wR_2 = 0.108$
R_{int}	0.078	0.038
Goodness-of-fit on F^2	1.033	1.151

$R_1 = \sum ||F_o| - |F_c|| / \sum |F_o|$, $wR_2 = \left\{ \sum [w(F_o^2 - F_c^2)^2] / \sum [w(F_o^2)^2] \right\}^{1/2}$.

and 1284 and 1153 cm^{-1} for **2**, respectively. Additional peaks at *ca.* 1338 cm^{-1} and 944 cm^{-1} may be assigned to the symmetric and asymmetric modes of the CNS moiety of the sac ligand, respectively [34]. The weak bands below 600 cm^{-1} may be attributed to both Cu–N and Cu–O vibrations.

3.2. Thermal analyses

The thermal decomposition behavior of the complexes was followed up to 600 °C in static air atmosphere.

3.2.1. [Cu(μ-OH)(sac-N)(deten)]$_2$ · 2H$_2$O

The first stage in the 99–138 °C range corresponds to the endothermic elimination of crystal water molecules (Found: 4.01, Calc. 4.54%). The second stage between 139 and 175 °C corresponds to the loss of two OH ligands. In the temperature range 176–408 °C, the third and fourth stages of the Cu(II) complex are related to the successively decomposition of the neutral deten and sac ligands, by giving initially an exothermic and then an endothermic contribution ($DTG_{max} = 224$, 386 °C). The following stage involves the extreme burning of organic residue, leading finally to CuO (Found: 79.66, Calc. 79.96%).

3.2.2. [Cu(μ-OH)(sac-O)(tmen)]$_2$

Complex **2** starts to decompose at 106 °C and the endothermic DTA peaks at 171 and 205 °C correspond to removal of the one tmen and two OH ligands (Found: 20.42, Calc. 19.82%). In the second stage, the endothermic elimination of tmen and exothermic decomposition of sac ligands occurs simultaneously between 260 and 386 °C, with a mass loss of 40.34%. In the last stage, the solid residue decomposes in the 385–514 °C range with an extremely exothermic peak at 481 °C. The decomposition product is CuO. The experimental mass loss value of 79.00% is consistent with the calculated value 79.01%. The decomposition product was identified by IR spectroscopy. On the basis of the first DTG_{max}, the thermal stability of the anhydrous complexes follows the order: **1** (224 °C) > **2** (171 °C).

3.3. Crystal structures

The molecular view of [Cu(μ-OH)(sac-*N*)(deten)]$_2$ · 2H$_2$O (**1**) and [Cu(μ-OH)(sac-*O*)(tmen)]$_2$ (**2**) with the atomic numbering scheme are shown in Figs. 1 and 2, respectively. Selected bond lengths and angles together with the hydrogen bonding geometry are given in Tables 3 and 4, respectively. Compound **1** crystallizes in the monoclinic $P21/c$ space group, while **2** crystallizes in the triclinic $P\bar{1}$ space group. Although a lot of saccharinato complexes are well known, quite surprisingly, up until

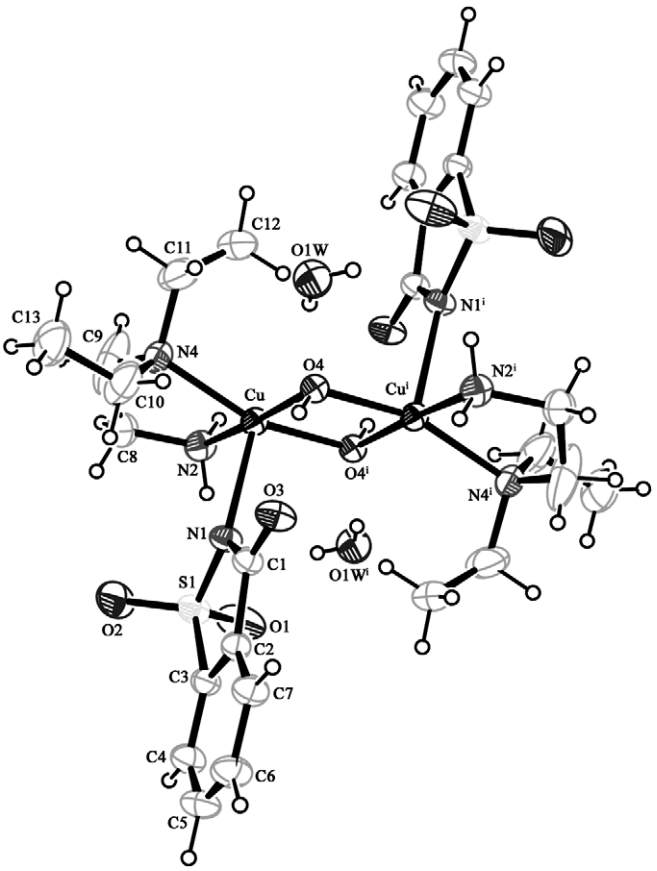


Fig. 1. The molecular structure of [Cu(μ-OH)(sac-*N*)(deten)]$_2$ · 2H$_2$O (**1**) showing the atom numbering scheme. The thermal ellipsoids are plotted at the 50% probability level.

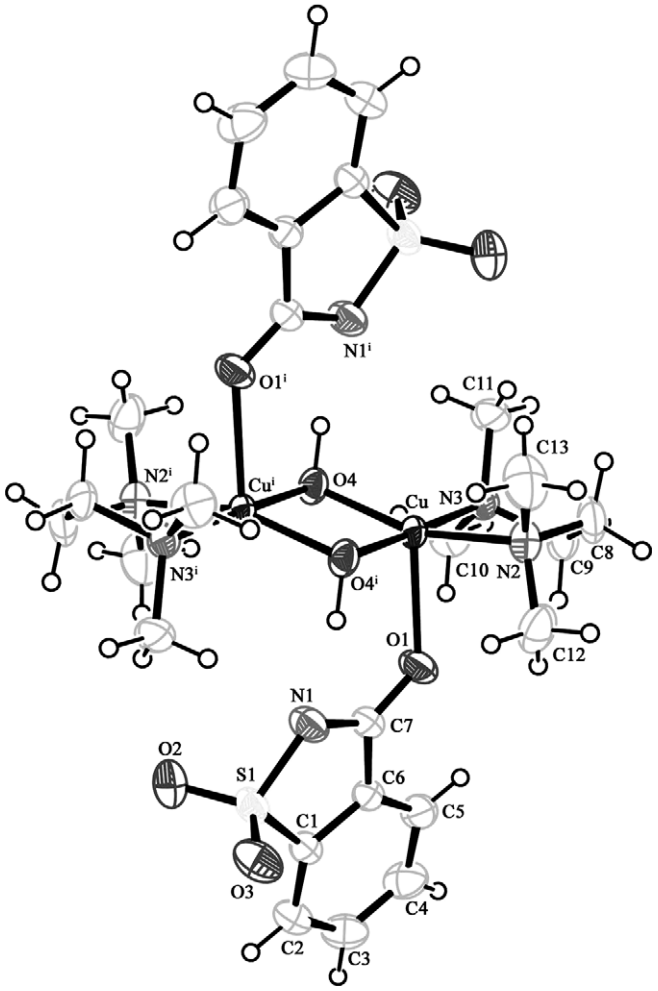


Fig. 2. The molecular structure of [Cu(μ-OH)(sac-*O*)(tmen)]$_2$ (**2**) showing the atom numbering scheme. The thermal ellipsoids are plotted at the 50% probability level.

now hydroxo-bridged dimeric metal complexes of saccharinate have not been reported. In the complexes, the sac ligands exhibit different coordination modes: in **1**, the sac ligand is *N*-bonded, while in the other complex it is *O*-coordinated. Both dinuclear units have a centre of symmetry located in the Cu_2O_2 planes and the copper(II) atoms have a square pyramidal coordination, with the basal plane comprising of two nitrogens atoms from deten or tmen ligands [Cu–N(2) = 2.004(3), Cu–N(4) = 2.098(3) Å] and the oxygen atoms of two hydroxo ligands [Cu–O(4) = 1.951(3), Cu^i–O(4) = 1.972(3) Å, (i) $-x, -y, -z$] for **1** and [Cu–N(2) = 2.076(2), Cu–N(3) = 2.032(2) Å] and [Cu–O(4) 1.951(2), Cu^i–O(4) 1.944(2) Å, (i) $-x+1, -y+2, -z+1$] for **2**. The apical position is occupied by the nitrogen atom of the sac ligand [Cu–N(1) = 2.395(3) Å] for **1** and by the oxygen atom of the sac ligand [Cu–

Table 4
Selected geometric parameters (Å, °) for **2**

Cu–O4	1.9508 (17)	Cu–O1	2.3356 (18)
Cu–N3	2.0317 (18)	Cu–Cu^i	2.8875 (10)
Cu–N2	2.0760 (19)	Cu^i–O4	1.9440 (16)
O4^i–Cu–O4	84.30 (7)	O4^i–Cu–O1	94.71 (6)
O4^i–Cu–N3	178.42 (7)	O4–Cu–O1	105.82 (5)
O4–Cu–N3	95.65 (6)	N3–Cu–O1	86.82 (5)
O4^i–Cu–N2	94.05 (7)	N2–Cu–O1	93.96 (6)
O4–Cu–N2	160.22 (8)	Cu^i–O4–Cu	95.70 (6)
N3–Cu–N2	85.46 (8)		

Hydrogen-bond geometry (Å, °)

D–H···*A*	*D*–H	H···*A*	*D*···*A*	∠*D*–H···*A*
O(4)–H(4O)···N(1)^{ii}	1.01	2.03	2.987 (5)	158

Symmetry code: (ii) $-x+1, -y+2, -z+1$.

Table 3
Selected geometric parameters (Å, °) for **1**

Cu–N4	2.098 (3)	Cu–N2	2.004 (3)
Cu–O4	1.951 (3)	Cu–N1	2.395 (3)
Cu^i–O4	1.972(3)	Cu–Cu^i	2.924(1)
Cu–O4^i	1.972(3)		
Cu–O4–Cu^i	96.40(11)	N2–Cu–N4	83.94(13)
O4–Cu–O4^i	83.60(11)	O4–Cu–N1	89.38(11)
O4–Cu–N2	174.52(12)	O4^i–Cu–N1	98.71(11)
O4^i–Cu–N2	94.28(12)	N2–Cu–N1	95.94(12)
O4–Cu–N4	96.31(12)	N4–Cu–N1	101.43(12)
O4^i–Cu–N4	159.86(12)		

Hydrogen-bond geometry (Å, °)

D–H···*A*	*D*–H	H···*A*	*D*···*A*	∠*D*–H···*A*
O(1w)–H(1O)···O(4)^i	0.95	1.92	2.8087	155
N(2)–H(2A)···O(1w)^i	0.90	2.11	2.9797	162
O(1w)–H(2O)···O(3)	0.70	2.35	3.0167	159
N(2)–H(2B)···O(1)	0.900	2.613	3.372(4)	143
O4–H4O···O3	0.938	2.169	2.816(3)	162

Symmetry code: (i) $-x, -y, -z$.

Table 5
Comparison of the bond distances and angles of hydroxo-bridged copper(II) complexes[a]

Complexes	Cu···Cu	Cu–O_{OH}	O_{OH}–Cu–O_{OH}	Cu–O_{OH}–Cu	Ref.
$[Cu(\mu\text{-}OH)(sac\text{-}N)(deten)]_2 \cdot 2H_2O$	2.924(1)	1.972(3) 1.951(3)	83.6(1)	96.4(1)	this work
$\{[Cu(\mu\text{-}OH)(sac\text{-}O)(tmen)]_2$	2.888(1)	1.951(2) 1.944(2)	83.3(1)	95.7(1)	
$[Cu_2(\mu\text{-}OH)_2(pmdeta)_2]Br_2 \cdot 2CH_3CN$	3.002(1)	1.904(2) 1.988(2)	79.2(1)	100.9(1)	[34]
$[Cu_2(\mu\text{-}OH)_2(dmtac)L1_2](ClO_4)_2$	2.936(1)	1.941(3) 1.952(3)		97.9(1) 97.9(1)	[37]
$[Cu_2(\mu\text{-}OH)_2(dmbtac)_2](ClO_4)_2 \cdot H_2O$	2.89(1)	1.926(3) 1.944(3)		97.0(1) 96.0(1)	
$[Cu_2(\mu\text{-}OH)_2(tcbtac)_2](ClO_4)_2 \cdot 2H_2O$	2.888(1)	1.944(3) 1.945(3)		95.8(1) 96.0(1)	
$[Cu_2(\mu\text{-}OH)_2(phen)_2(H_2O)_2](tpa) \cdot 8H_2O$	2.911	1.925(7)	81.9(3)	98.1	[38]
$[Cu(aprm)_2(\mu\text{-}OH)(CF_3SO_3)]_2 \cdot 2aprm$	2.902(1)	1.929(2)	82.0(1)		[39]
$[Cu_2(\mu\text{-}OH)_2(phen)_2(H_2O)_2][Cu_2(\mu\text{-}OH)_2(HCO_3)_2(phen)_2](3\text{-}pyO)_2 \cdot 10H_2O$	2.894(1) 2.884(1)	1.945(5) 1.953(5)	84.2(2) 83.7(2)	95.8(2) 96.3(2)	[40]
$[Cu_2(phen)_2(OH)_2(H_2O)_2][Cu_2(phen)_2(OH)_2Cl_2]Cl_2{\cdot}6H_2O$	2.933	1.925, 1.949/1.936 1.9504	81.61 82.07		[41]
$[Cu_2(\mu\text{-}OH)_2(acetonitrile)_2(bmpma)_2](ClO_4)_2$	2.952(1)	1.920(3) 1.923(3)	79.6(1)	100.4(1)	[42]

[a] pmdeta = 1,1,4,7,7-pentamethyldiethylenetriamine, dmtac = 1,4-dimethyl-1,4,7-triazacyclononane, dmbtac = 1,4-dimethyl-7-benzyl-1,4,7-triazacyclononane, tcbtac = 1,4,7-tris(3-cyanobenzyl)-1,4,7-triazacyclononane, phen = 1,10-phenanthroline, tpa = terephthalic acid, aprm = 2-aminopyrimidine, bmpma = di-benzyl(6-methyl-2-pyridylmethyl)-amine, 3-pyOH = /3-hydroxypyridine.

O(1) = 2.336(2) Å] for **2**. The Cu···Cu distance within the dinuclear unit is 2.924(1) Å for **1** and 2.888(1) Å for **2**, while the O–Cu–O angle is 83.60(11)° for **1** and 84.30(7)° for **2**. The Cu ··· Cu distances are shorter than that found in $[Cu_2(OH)_2(pmdeta)_2]Br_2 \cdot 2CH_3CN$ [3.0022(7) Å] [35]. Comparison of values of the Cu ··· Cu, Cu–O_{OH} distances and the O_{OH}–Cu–O_{OH} and Cu–O_{OH}-Cu angles for similar hydroxo-bridged complexes can be found in Table 5. The *sac* ligands are essentially planar with a r.m.s. deviation 0.0197 Å for **1** and 0.0204 Å for 2, and the largest deviation from the mean plane is −0.0224 Å for the C2 atom for **1** and −0.0108 Å for the N1 atom for **2**.

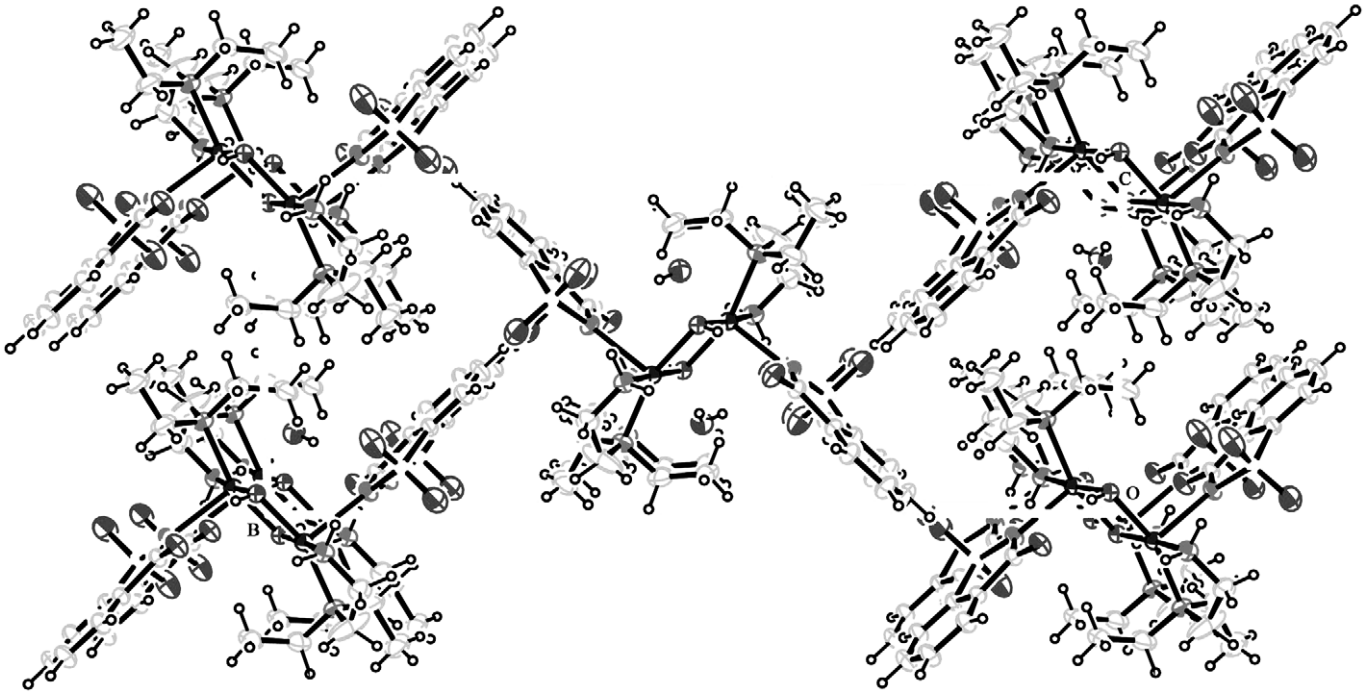


Fig. 3. Packing diagram of **1** viewed along the *a*-axis.

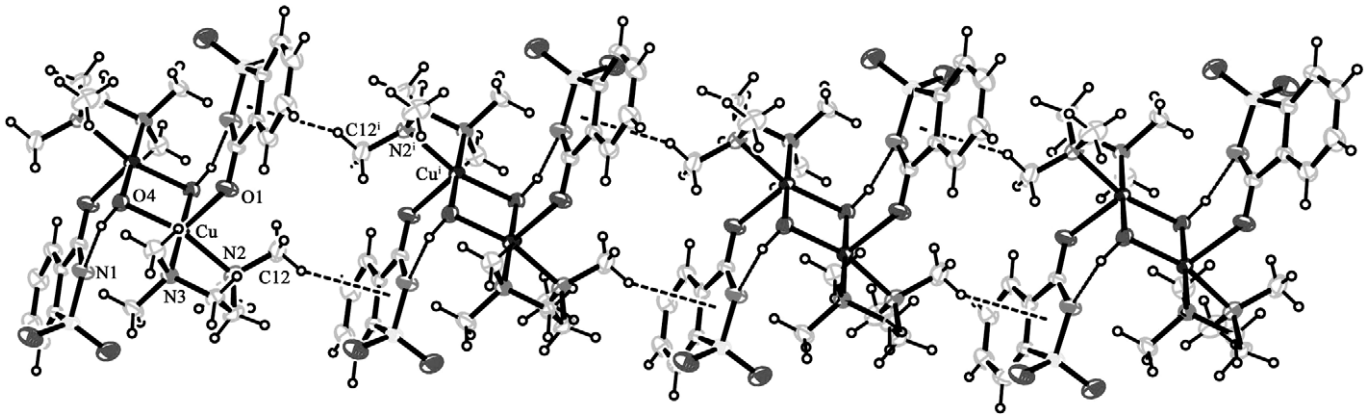


Fig. 4. Intramolecular hydrogen-bonding geometry and C–H···π interactions along the *b*-axis for the complex **2** (i = 1 − *x*, 1 − *y*, 1 − *z*).

The crystal packing is mainly stabilized by hydrogen bonds and van der Waals interactions (Fig. 3). There are also C–H···π interactions between the C(12)–CgA^{i} ring (Cg*A*: Cu, O(4), Cu^{i}, $O(4)^{i}$ for **1** and S(1), N(1), C(7), C(6), C(1) for **2**) (Fig. 4). The nitrogen atom N1 of the sac ligand is also involved in an intramolecular hydrogen bond with the OH group in **2**, N1–H···O4 = 2.9876(6) Å.

3.4. Antimicrobial activity studies

The in vitro antimicrobial activity of saccharin (main matter), $[Cu(sac)_2(H_2O)_4]\cdot 2H_2O$, $[Cu(\mu\text{-}OH)(sac)(deten)]_2\cdot 2H_2O$ and $[Cu(\mu\text{-}OH)(sac)(tmen)]_2$ were tested according to the disc diffusion method, and the results are given in Tables 6 and 7. The compounds were dissolved in DMSO or water. Antimicrobial activity was measured for 200, 500 and 1000 μg concentrations against Gram-positive *Staphylococcus aureus* ATCC 6535, *Bacillus cereus* ATCC 7064, Gram-negative *Escherichia coli* W3110, *Citrobacter freundii* NRRLB 2643 and the yeast *Candida albicans* ATCC 10231 and the mould *Aspergillius niger*. Sulfamethoxazole, chloramphenical, streptomycin, tetracycline, neomycin, sulfafurazole, ceftriaxone, oflaxacin and nystatin antibiotics were also used for comparison. The inhibition zones formed by standard antibiotic discs are shown in Table 8.

The saccharinate complexes (**1** and **2**) showed different antimicrobial activities against test strains. As can clearly be seen from Tables 6 and 7, to dissolve of saccharin and the complexes with different solvents (DMSO or water) did not affect the antimicrobial activity on the tested microorganisms. Furthermore, it appears that the activity of the tested complexes increases as the concentration increases, with the exception of *A. niger*, but it is a well-known fact that the concentration plays a vital role in increasing the degree of inhibition. Saccharin did not show any activity on the bacteria, the fungi or the yeast. Whilst there was no antimicrobial activity of $[Cu(sac)_2(H_2O)_4]\cdot 2H_2O$,

Table 6
Antimicrobial assays of the compounds dissolved in DMSO (diameter in mm)

Compounds	Gram (−)		Gram (+)		Eucaryot	
	Escherichia coli	*Citrobacter freundii*	*Bacillus cereus*	*Staphylococcus aureus*	*Aspergillus niger*	*Candida albicans*
Saccharin 1000 μg						
$[Cu(sac)_2(H_2O)_4]\cdot 2H_2O$						
200 μg	9	8	(14***)			
500 μg	11	10	(20**)	9 (16**)		
1000μg	15	13	10 (23*)	11 (19**)		8
$[Cu(\mu\text{-}OH)(sac)(tmen)]_2$						
200 μg		7		7		
500 μg	10	9	(19**)	9 (14**)		
1000 μg	15	12	(24*)	11 (18**)		7
$[Cu(\mu\text{-}OH)(sac)(deten)]_2\cdot 2H_2O$						
200 μg	8	8	(15***)	9		8
500 μg	12	11	9 (18**)	10 (15**)		9
1000 μg	15	13	10 (23*)	11 (18**)		10

Unclear zone and ***very cloudy **middle cloudy, *slightly cloudy.
Clear zone diameter at outside parentheses, –, no observed activity.
Diameter of 15 mm and above is considered active.

Table 7
Antimicrobial assays of the compounds dissolved in ultra pure water (diameter in mm)

Compounds	Gram (−)		Gram (+)		Eucaryot	
	Escherichia coli	*Citrobacter freundii*	*Bacillus cereus*	*Staphylococcus aureus*	*Aspergillus niger*	*Candida albicans*
Saccharin 1000 μg						
$[Cu(sac)_2(H_2O)_4]\cdot 2H_2O$						
200 μg	9	8	(14***)			
500 μg	12	10	9 (18**)	9 (17**)		
1000μg	15	14	10 (23*)	12 (20**)		8
$[Cu(\mu\text{-}OH)(sac)(deten)]_2\cdot 2H_2O$	N/T	N/T	N/T	N/T	N/T	N/T
$[Cu(\mu\text{-}OH)(sac)(tmen)]_2$						
200 μg	8	8		7		
500 μg	11	10	(18**)	9 (16**)		
1000 μg	14	12	(22*)	11 (18**)		7

N/T = not tested because of very poor solubility in water.
*Unclear zone, cloudiness degree; ***very cloudy **middle cloudy, *slightly cloudy.
Clear zone diameter at outside parentheses, –; no observed activity.
Diameter of 15 mm and above is considered active.

Table 8
Antimicrobial assays of some standard antibiotics (diameter in mm)

	SXT	C	S	TE	N	SF	OFX	CRO	N
	30 μg	30 μg	10 μg	30 μg	30 μg	300 μg	10 μg	10 μg	10 μg
Escherichia coli	24	30	18	25	11		30	30	
Citrobacter freundii	20	26	17	28	10	20	30	21	
Bacillus cereus		25	20	30	16		27		
Staphylococcus aureus	16	21	16	30	11		28	15	
Aspergillus niger									24
Candida albicans									26

SXT: sulfamethoxazole/trimethoprim; C: chloramphenical; S: streptomycin; TE: tetracyline; N: neomycin; SF: sulfafurazole; OFX: oflaxacin; CRO: ceftriaxone; N: nystatin.

$[Cu(\mu\text{-}OH)(sac)(deten)]_2\cdot 2H_2O$ and $[Cu(\mu\text{-}OH)(sac)(tmen)]_2$ on the mould *A. niger*, $[Cu(\mu\text{-}OH)(sac)(tmen)]_2$ and $[Cu(sac)_2(H_2O)_4]\cdot 2H_2O$ show weak antimicrobial activity at 1000 μg concentration against the yeast *C. albicans* used in this study. $[Cu(\mu\text{-}OH)(sac)(deten)]_2\cdot 2H_2O$, dissolved in DMSO, had weak antimicrobial activity on *C. albicans* (inhibitory zone <15 mm), but, this complex is more effective than saccharin and $[Cu(sac)_2(H_2O)_4]\cdot 2H_2O$ on *C. albicans*. Tables 6 and 7 show there is an unclear zone for *S. aureus* and *B. cereus*. This could be due to the relationship with the gram-positive state. It seems that the cloudiness decreases with concentration increases. The compounds are more active against gram-negative than gram-positive bacteria, according to the clear zone. In classifying the antibacterial activity as gram-positive or gram-negative, it would generally be expected that compounds would be more active against gram-positive than gram-negative bacteria, due to the outer membrane layer of these bacteria, which do not allow compounds to enter the cell. According to the clear zone diameter, **1** and **2** at 1000 mg concentration have an antimicrobial activity on only *E. coli* (inhibitory zone ⩾15 mm). Against the other bacteria, they have weak antimicrobial activity (inhibitory zone <15 mm).

It could be said that the Cu(II) complexes **1** and **2** have a lower effect compared to standard antibiotics and they display activity at higher concentrations than antibiotics (Tables 6 and 8). Saccharin metal complexes have been demonstrated to possess antibacterial and antifungal properties [22,27,36,37].

Finally, there are no differences, from the point of view of antimicrobial activity, between $[Cu(sac)_2(H_2O)_4]\cdot 2H_2O$ and the new compounds $[Cu(\mu\text{-}OH)(sac)(deten)]_2\cdot 2H_2O$ and $[Cu(\mu\text{-}OH)(sac)(tmen)]_2$on gram (+), gram (−) bacteria and a mould *A. niger*, but the $[Cu(\mu\text{-}OH)(sac)(deten)]_2\cdot 2H_2O$ complex is more effective than saccharin and $[Cu(sac)_2(H_2O)_4]\cdot 2H_2O$ on *C. albicans*.

4. Supplementary material

CCDC 655440 and 655441 contain the supplementary crystallographic data for $[Cu(\mu\text{-}OH)(sac)(deten)]_2\cdot 2H_2O$ and $[Cu(\mu\text{-}OH)(sac)(tmen)]_2$, respectively. These data can be obtained free of charge via http://www.ccdc.cam.ac.uk/conts/retrieving.html, or from the Cambridge Crystallographic Data Centre, 12 Union Road, Cambridge CB2 1EZ, UK; fax: (+44) 1223-336-033; or e-mail: deposit@ccdc.cam.ac.uk.

References

[1] F.A. Cotton, G.E. Lewis, C.A. Murillo, W. Schwotzer, G. Valle, Inorg. Chem. 23 (1984) 4038.
[2] S.Z. Haider, K.M.A. Malik, K.J. Ahmed, J. Bangladesh Acad. Sci. 5 (1981) 81.
[3] S.Z. Haider, K.M.A. Malik, K.J. Ahmed, Inorg. Synth. 23 (1985) 47.
[4] F.A. Cotton, L.R. Falvello, C.A. Murillo, A.J. Schultz, Eur. J. Solid State Inorg. Chem. 29 (1992) 311.
[5] V.T. Yılmaz, O. Andac, Y. Topcu, W.T.A. Harrison, Acta Crystallogr. C57 (2001) 271.
[6] V.T. Yılmaz, S. Guney, O. Andac, W.T.A. Harrison, Polyhedron 21 (2002) 2393.
[7] V.T. Yilmaz, A. Karadag, C. Thoene, J. Coord. Chem. 55 (2002) 609.
[8] V.T. Yilmaz, S. Caglar, W.T.A. Harrison, J. Coord. Chem. 58 (2005) 549 .
[9] A. Hergold-Brundic, O. Grupce, G. Jovanovski, Acta Crystallogr. C47 (1991) 2659.
[10] O.V. Quinzani, S.H. Tarulli, S. Garcia-Granda, C. Marcos, E.J. Baran, Cryst. Res. Technol. 37 (2002) 1338.
[11] G.V. Bourrouet, L.W. Pineda, L.R. Falvello, R. Lusar, T. Weyhermueller, Polyhedron 26 (2007) 4470.
[12] H. Içbudak, H. Olmez, O.Z. Yesilel, F. Arslan, P. Naumov, G. Jovanovski, A.R. Ibrahim, A. Umsan, H.K. Fun, S. Chantrapromma, S.W. Ng, J. Mol. Struct. 657 (2003) 255.
[13] P. Naumov, G. Jovanovski, M. Ristova, I.A. Razak, S. Çakir, S. Chantapromma, H.K. Fun, S.W. Ng, Z. Anorg. Allg. Chem. 628 (2002) 2930.
[14] P. Naumov, G. Jovanovski, M.G.B. Drew, S.W. Ng, Inorg. Chim. Acta 314 (2001) 154.
[15] V.T. Yılmaz, V. Kars, C. Kazak, Z. Anorg. Allg. Chem. 632 (2006) 505.
[16] V.T. Yılmaz, Y. Topcu, F. Yılmaz, C. Thoene, Polyhedron 20 (2001) 3209.
[17] V.T. Yılmaz, S. Hamamcı, O. Andac, C. Thoene, W.T.A. Harrison, Trans. Met. Chem. 28 (2003) 676.
[18] G. Jovanovski, P. Naumov, O. Grupče, B. Kaitner, Eur. J. Solid State Inorg. Chem. 35 (1998) 231.
[19] P.A.M. Williams, E.G. Ferrer, K.A. Pasquevich, E.J. Baran, Z. Chaia, E.E. Castellano, O.E. Piro, Z. Anorg. Allg. Chem. 626 (2000) 2509.
[20] B.S. Parajon-Costa, E.J. Baran, O.E. Piro, E.E. Castellano, Z. Naturforsch. 57b (2002) 43.
[21] Y. Topcu, O. Andac, V.T. Yılmaz, W.T.A. Harrison, J. Coord. Chem. 55 (2002) 805.
[22] T.B.S.A. Ravoof, K.A. Crouse, M.I.M. Tahir, A.R. Cowley, M.A. Akbar, Polyhedron 23 (2004) 2491.
[23] M.A. Ali, A.H. Mirza, T.B.S.A. Ravoof, P.V. Bernhardt, Polyhedron 23 (2004) 2031.
[24] E.W. Ainscough, E.N. Baker, A.M. Brodie, R.J. Cresswell, J.D. Ranford, J.M. Waters, Inorg. Chim. Acta 172 (1990) 185.
[25] O. Kahn, Molecular Magnetism, VCH, New York, 1993 (Chapter 8.6).
[26] C.T. Supuran, Rev. Roum. Chim. 37 (1992) 849.
[27] E.J. Baran, V.T. Yılmaz, Coord. Chem. Rev. 250 (2006) 1980.
[28] Rigaku, CRYSTALCLEAR, Version 1.3.6. Rigaku American Corporation, 9009 New Trails Drive, The Woodlands, TX, USA, 2005.
[29] G.M. Sheldrick, SHELXS97 and SHELXL97, University of Göttingen, Germany, 1997.
[30] Z. Haider, K.M.A. Malik, K.J. Ahmed, H. Hess, H. Riffel, M.B. Hursthouse, Inorg. Chim. Acta 72 (1983) 21.
[31] H. Crawford, H.W. Richardson, J.R. Wasson, D.J. Hodgson, W.E. Hatfield, Inorg. Chem. 15 (1976) 2107.
[32] O.V. Quinzani, S. Tarulli, O.E. Piro, E.J. Baran, E.E. Castellano, Z. Naturforsch. 52b (1997) 183.
[33] D.L. Lewis, K.T. McGregor, W.E. Hatfield, D.J. Hodgson, Inorg. Chem. 11 (1972) 2216.
[34] O.V. Quinzani, S. Tarulli, C. Marcos, S.G. Granda, E.J. Baran, Z. Anorg. Allg. Chem. 625 (1999) 1848.
[35] G. Kickelbick, Acta Crystallogr. E 57 (2001) m365.
[36] C. Subramanayam, M.R. Bell, P. Carabates, J.J. Court, J.A. Dority Jr., E. Ferguson, R. Gordon, D.J. Hlasta, V. Kumar, J. Med. Chem. 37 (1994) 2623.
[37] T.B.S.A. Ravoof, K.A. Crouse, M.I.M. Tahir, A.R. Cowley, M.A. Akbar, Polyhedron 26 (2007) 1159.
[38] M.J. Belousoff, M.B. Duriska, B. Graham, S.R. Batten, B. Moubaraki, K.S. Murray, L. Spiccia, Inorg. Chem. 45 (2006) 3746.
[39] H.M. Zhang, L.P. Lu, S.S. Feng, S.D. Qin, M.L. Zhu, Acta Crystallogr. E 61 (2005) m1027.
[40] G.A. van Albada, I. Mutikainen, W.J.J. Smeets, A.L. Spek, U. Turpeinen, J. Reedijk, Inorg. Chim. Acta 327 (2002) 134.
[41] S. Iglesias, O. Castillo, A. Luque, P. Roma, Inorg. Chim. Acta 349 (2003) 273.
[42] L.P. Lu, M.L. Zhu, P. Yang, J. Inorg. Biochem. 95 (2003) 31.

describe the syntheses and characterization of dinuclear platinum(IV) complexes with bridging pyrazolato ligands starting from tris(acetone) complex $[PtMe_3(OCMe_2)_3]^+$ and the pyrazole complexes $[PtMe_3(pzH)_3]^+$ and $[PtMe_3I(pzH)_2]$, respectively, as precursor complexes. Due to the advantages of platinum(IV) complexes can have over platinum(II) complexes in chemotherapy, these complexes were investigated with respect to their antitumoral activity.

2. Experimental

2.1. General considerations

Syntheses of complexes were carried out under argon using standard Schlenk techniques whereas the work-up procedures were performed on air. Methylene chloride, acetone, *n*-pentane, benzene and diethyl ether were dried (CH_2Cl_2 over CaH_2, Me_2CO over molecular sieve 3A, *n*-pentane, benzene and Et_2O over Na-benzophenone) and distilled prior to use. $[(PtMe_3I)_4]$ and $[PtMe_3(OCMe_2)_3](BF_4)$ were obtained according to the literature [11,8]. Microanalyses (C, H, N, S) were performed by the microanalytical laboratory of the University of Halle using CHNS-932 (LECO) and Vario EL (elementar Analysensysteme) elemental analyzers. ^1H and ^{13}C NMR spectra were recorded on Varian Gemini 200, VXR 400 and Unity 500 NMR spectrometers. Solvent signals and residual protons of solvent signals were used as internal standard.

2.1.1. Preparation of $[PtMe_3(pzH)_3](BF_4)$ (**1**)

A solution of $[PtMe_3(OCMe_2)_3](BF_4)$ (100 mg, 0.200 mmol) in acetone (10 ml) was added to a solution of pyrazole (40.9 mg, 0.600 mmol) in acetone (10 ml). The solution was evaporated to dryness under vacuum and the residue was extracted with CH_2Cl_2 (10 ml). The colourless product, which was precipitated within 12 h after adding of *n*-pentane (10 ml), was washed with *n*-pentane/CH_2Cl_2 (1:1, 3 × 2 ml) and dried under vacuum. Yield 96 mg, 90%.

Anal. Calc. for $C_{12}H_{21}BF_4N_6Pt$: C, 27.13; H, 3.98; N, 15.82. Found: C, 27.07; H, 4.85; N, 15.77%. ^1H NMR (200 MHz, $(CD_3)_2CO$) δ 1.12 (s + d, $^2J_{Pt,H} = 70.1$ Hz, 9H, PtCH_3), 6.56 (m, 3H, *H*4), 7.70 (m, 3H, *H*5), 8.00 (m, 3H, *H*3), 12.35 (br, 3H, N*H*). ^{13}C NMR (50 MHz, $(CD_3)_2CO$) δ −7.7 (s + d, $^1J_{Pt,C} = 695.8$ Hz, Pt*C*H_3), 107.4 (s + d, $^3J_{Pt,C} = 8.6$ Hz, *C*4), 132.9 (s + d, $^2J_{Pt,C} = 5.3$ Hz, *C*5), 140.4 (s + d, $^3J_{Pt,C} = 8.4$ Hz, *C*3).

2.1.2. Preparation of $[PtMe_3I(pzH)_2]$ (**2**)

A solution of pyrazole (37.7 mg, 0.554 mmol) in acetone (5 ml) was added to a suspension of $[(PtMe_3I)_4]$ (100 mg, 69.2 μmol) in acetone (10 ml). After dissolving the solid (4 h) the solution was evaporated to dryness under vacuum and the solid was extracted with CH_2Cl_2 (10 ml). The product was precipitated within 12 h on addition of *n*-pentane (10 ml) and filtered off. The solid was washed with *n*-pentane/CH_2Cl_2 (1/1, 3 × 2 ml) and dried under vacuum. Yield 41 mg, 90%.

Anal. Calc. for $C_9H_{17}IN_4Pt$: C, 21.48; H, 3.40; N, 11.13. Found: C, 22.00; H, 3.49; N, 11.14%. ^1H NMR (500 MHz, $(CD_3)_2CO$): δ 1.29 (s + d, $^2J_{Pt,H} = 72.9$ Hz, 6H, PtCH_3 *trans* to pzH), 1.33 (s + d, $^2J_{Pt,H} = 71.6$ Hz, 3H, PtCH_3 *trans* to I), 6.43 (m, 2H, *H*4), 7.74 (m, 2H, *H*5), 7.88 (m, 2H, *H*3), 12.09 (br, 2H, N*H*); ^{13}C NMR (126 MHz, $(CD_3)_2CO$): δ −10.5 (s + d, $^1J_{Pt,C} = 682.3$ Hz, Pt*C*H_3 *trans* to pzH), 8.4 (s + d, $^1J_{Pt,C} = 715.9$ Hz, Pt*C*H_3 *trans* to I), 106.4 (s + d, $^3J_{Pt,C} = 8.6$ Hz, *C*4), 131.1 (s + d, $^2J_{Pt,C} = 5.3$ Hz, *C*3), 138.5 (s + d, $^3J_{Pt,C} = 11.5$ Hz, *C*5).

2.1.3. Preparation of $(PPN)[(PtMe_3)_2(\mu\text{-}pz)_3]$ (**3**)

KOAc (118 mg, 1.20 mmol) was added to a solution of $[PtMe_3(OCMe_2)_3](BF_4)$ (100 mg, 0.200 mmol) in acetone (10 ml). A solution of $[PtMe_3(pzH)_3](BF_4)$ (**1**) (106 mg, 0.200 mmol) in acetone (10 ml) was added dropwise to this suspension. After 30 min the suspension was filtered and the filtrate evaporated to dryness under vacuum. The solid was extracted with CH_2Cl_2 (10 ml) and the extract was added to a solution of (PPN)Cl (115 mg, 0.200 mmol) in CH_2Cl_2 (10 ml). After evaporation to 10 ml the KCl was filtered off and the product was precipitated within 12 h by adding of Et_2O (10 ml). The resulting solid was filtered off, washed with *n*-pentane/CH_2Cl_2 (1/1, 3 × 2 ml) and dried under vacuum. Yield 146 mg, 60%.

Anal. Calc. for $C_{51}H_{57}N_7P_2Pt_2$: C, 50.20; H, 4.71; N, 8.04. Found: C, 49.67; H, 5.01; N, 7.77%. ^1H NMR (200 MHz, $(CD_3)_2CO$): δ 0.85 (s + d, $^2J_{Pt,H} = 66.2$ Hz, 18H, PtCH_3), 6.00 (m, 3H, *H*4), 7.31 (m, 6H, *H*3/*H*5), 7.50–7.77 (m, 30H, PPN^+); ^{13}C NMR (126 MHz, $(CD_3)_2CO$): δ −6.7 (s + d, $^1J_{Pt,C} = 675.2$ Hz, Pt*C*H_3), 103.9 (s + d + t, $^3J_{Pt,C} = 15.4$ Hz, *C*4), 127.9/130.2/132.7/134.3 (PPN^+), 134.8 (s + d + d + d · d, $^{2/4}J_{Pt,C} = 25.9/10.6$ Hz, *C*3/*C*5).

2.1.4. Preparation of $(PPN)[(PtMe_3)_2(\mu\text{-}I)(\mu\text{-}pz)_2] \cdot 1/2Et_2O$ (**4**)

The reaction was carried out according to the above procedure. Instead of $[PtMe_3(pzH)_3](BF_4)$ (**1**), $[PtMe_3I(pzH)_2]$ (**2**) (101 mg, 0.200 mmol) was used. Yield 163 mg, 60%.

Anal. Calc. for $C_{100}H_{118}I_2N_{10}OP_4Pt_4$: C, 45.60; H, 4.52; N, 5.32. Found: C, 45.89; H, 4.59; N, 5.75%. ^1H NMR (500 MHz, $(CD_3)_2CO$): δ 1.08 (s + d, $^2J_{Pt,H} = 67.6$ Hz, 12H, PtCH_3 *trans* to pz), 1.10 (t, $^3J_{H,H} = 7.0$ Hz, 3H, OCH_2CH_3), 1.31 (s + d, $^2J_{Pt,H} = 75.7$ Hz, 6H, PtCH_3 *trans* to I), 3.39 (q, $^3J_{H,H} = 7.0$ Hz, 2H, OCH_2CH_3), 5.96 (m, 2H, *H*4), 7.27 (m, 4H, *H*3/*H*5), 7.50–7.77 (m, 30H, PPN); ^{13}C NMR (126 MHz, $(CD_3)_2CO$): δ −11.1 (s + d, $^1J_{Pt,C} = 646.3$ Hz, Pt*C*H_3 *trans* to pz), 7.6 (s + d, $^1J_{Pt,C} = 740.4$ Hz, Pt*C*H_3 *trans* to I), 14.9 (s, OCH_2CH_3), 104.7 (s + d, $^3J_{Pt,C} = 13.6$ Hz, *C*4), 129.1/131.2/134.1/135.4 (PPN^+), 135.8 (s + d + d + d · d, $^{2/4}J_{Pt,C} = 28.2/11.8$ Hz, *C*3/*C*5).

2.1.5. Preparation of [K(18C6)][(PtMe$_3$)$_2$(μ-I)(μ-pz)$_2$] (5)

The reaction was carried out analogously to **4**, but instead of working with a solution of (PPN)Cl in CH_2Cl_2, a solution of 18C6 (52.9 mg, 0.200 mmol) in CH_2Cl_2 (10 ml) was used. Yield 105 mg, 50%.

Anal. Calc for $C_{24}H_{48}IKN_4O_6Pt_2$: C, 27.59; H, 4.63; N, 5.36. Found: C, 27.74; H, 5.08; N, 5.34%. ^{1}H NMR (500 MHz, $(CD_3)_2CO$): δ 1.08 (s + d, $^2J_{Pt,H} = 67.6$ Hz, 12H, PtC*H*$_3$ *trans* to pz), 1.31 (s + d, $^2J_{Pt,H} = 75.7$ Hz, 6H, PtC*H*$_3$ *trans* to I), 3.65 (s, 24H, C*H*$_2$O), 5.96 (m, 2H, *H*4), 7.27 (m, 4H, *H*3/*H*5).

2.1.6. Preparation of [(PtMe$_3$)$_2$(μ-pz)$_2$(μ-Me$_2$S)] (6)

AgO_2CCF_3 (15.5 mg, 70 μmol) was added to a solution of (PPN)[(PtMe$_3$)$_2$(μ-I)(μ-pz)$_2$] · 1/2Et$_2$O (**4**) (92.2 mg, 70 μmol) in acetone (10 ml). After complete precipitation of AgI (12 h) the reaction mixture was filtered. Me_2S (4.9 mg, 78 μmol) was added to the solution and the reaction mixture was evaporated to dryness under vacuum. The residue was extracted in benzene (10 ml) and washed with H_2O (10 ml). The combined organic phases were dried (Na_2SO_4) and concentrated to 5 ml. Then the product was precipitated by adding of *n*-pentane (10 ml), filtered of, washed with *n*-pentane (3 × 2 ml) and dried under vacuum. Yield 28.4 mg, 60%.

Anal. Calc. for $C_{14}H_{30}N_4Pt_2S$: C, 24.85; H, 4.47; N, 8.28; S, 4.74. Found: C, 25.37; H, 4.76; N, 8.38; S, 4.40%. ^{1}H NMR (200 MHz, $(CD_3)_2CO$): δ 0.76 (s + d, $^2J_{Pt,H} = 66.8$ Hz, 12H, PtC*H*$_3$ *trans* to pz), 1.40 (s + d, $^2J_{Pt,H} = 73.0$ Hz, 6H, PtC*H*$_3$ *trans* to S), 2.38 (s + d + t, $^3J_{Pt,H} = 8.7$ Hz, 6H, S(C*H*$_3$)$_2$), 6.18 (m, 2H, *H4*), 7.39 (m, 4H, *H3*/*H5*); ^{13}C NMR (126 MHz, $(CD_3)_2CO$): δ −9.8 (s + d, $^1J_{Pt,C} = 642.1$ Hz, Pt*C*H$_3$ *trans* to pz), 5.2 (s + d, $^1J_{Pt,C} = 694.9$ Hz, Pt*C*H$_3$ *trans* to S), 15.2 (s, S*C*H$_3$, pz), 105.5 (s + d + t, $^3J_{Pt,C} = 14.9$ Hz, *C*4) 136.3 (s + d + d + d · d, $^{2/4}J_{Pt,C} = 27.7/10.3$ Hz, *C*3/*C*5).

2.1.7. Preparation of [(PtMe$_3$)$_2$(μ-pz)$_2$(μ-MeSPh)] (7)

The reaction was carried out according to the above procedure. Instead of Me_2S, MeSPh (9.7 mg, 78 μmol) was used. Yield 31.0 mg, 60%.

Anal. Calc. for $C_{19}H_{32}N_4Pt_2S$: C, 30.89; H, 4.37; N, 7.58; S, 4.34. Found: C, 31.42; H, 4.56; N, 7.65; S, 4.31%. ^{1}H NMR (400 MHz, $(CD_3)_2CO$): δ 0.43 (s + d, $^2J_{Pt,H} = 66.0$, 6H, PtC*H*$_3$ *trans* to pz), 0.74 (s + d, $^2J_{Pt,H} = 66.0$ Hz, 6H, PtC*H*′$_3$ *trans* to pz), 1.50 (s + d, $^2J_{Pt,H} = 74.7$ Hz, 6H, PtC*H*$_3$ *trans* to S), 2.69 (s + d + t, $^3J_{Pt,H} = 7.9$ Hz, 3H, SC*H*$_3$), 6.26 (m, 1H, pz *H*4′), 6.32 (m, 1H, pz *H*4), 6.66 (m, 2H, Ph *o*-*H*), 7.40 (m, 3H, *m*/*p*-*H*), 7.47 (m, 2H, pz *H*3′/*H*5′), 7.51 (m, 2H, pz *H*3/*H*5). ^{13}C NMR (126 MHz, $(CD_3)_2CO$): δ −9.0 (s + d, $^1J_{Pt,C} = 643.9$ Hz, Pt*C*H′$_3$ *trans* to pz), −7.1 (s + d, $^1J_{Pt,C} = 642.0$ Hz, Pt*C*H$_3$ *trans* to pz), 5.3 (s + d, $^1J_{Pt,C} = 704.4$ Hz, Pt*C*H$_3$ *trans* to S), 13.0 (s, S*C*H$_3$), 105.9 (s + d + t, $^3J_{Pt,C} = 14.9$ Hz, pz *C*4′), 106.3 (s + d + t, $^3J_{Pt,C} = 14.9$ Hz, pz *C*4), 122.5/128.4/130.0/130.4 (s, SPh), 136.7 (s + d + d + d · d, $^{2/4}J_{Pt,C} = 10.5/28.4$ Hz, pz *C*3/C3′/C5/C5′), 136.7 (s + d + d + d · d, $^{2/4}J_{Pt,C} = 9.8/24.1$ Hz, pz *C*3/C3′/C5/C5′).

Table 1
Crystal data and structure refinement data for **3** and **4**

	3	**4**
Empirical formula	$C_{51}H_{57}N_7P_2Pt_2$	$C_{50}H_{54}IN_5O_{0.5}P_2Pt_2$
Formula weight	1220.16	1312.00
Crystal system	monoclinic	triclinic
Space group	$P2_1/n$	$P\bar{1}$
a (Å)	17.041(3)	9.830(2)
b (Å)	11.555(2)	15.281(4)
c (Å)	25.675(5)	17.948(4)
α (Å)	90	78.22(3)
β (Å)	105.92(2)	74.32(3)
γ (Å)	90	78.77(3)
V (Å^3)	4862(2)	2513(1)
Z	4	2
D_{calc} (g/cm^3)	1.667	1.734
μ (mm^{-1})	5.856	6.277
F(000)	2392	1264
Independent reflections	9482	9068
Number of observed reflections [$I > 2\sigma(I)$]	6787	7690
Data/restraints/parameters	9482/0/722	9068/0/554
Goodness-of-fit	0.924	1.056
R_1 [$I > 2\sigma(I)$], R_1 (all data)	0.0364, 0.0621	0.0549, 0.0645
wR_2 [$I > 2\sigma(I)$], wR_2 (all data)	0.0723, 0.0790	0.1456, 0.1554

2.2. X-ray crystallography

Single-crystal X-ray diffraction analyses of suitable crystals of complexes **3** and **4** were performed at 220(2) K on a STOE-IPDS diffractometer using Mo Kα radiation (λ = 0.71073 Å, graphite monochromator). A summary of the crystallographic data, the data collection parameters and the refinement parameters is given in Table 1. Absorption correction for **3** was applied numerically ($T_{min}/T_{max} = 0.49/0.60$). The structures were solved by direct methods with SHELXS-97 [12]. The structure refinements were carried out by full-matrix least-square procedures against F^2 (SHELXL-97 [12]) for all reflections. All non-hydrogen atoms were refined with anisotropic displacement parameters. Hydrogen atoms were refined isotropically. In complex **3** all H atoms except those of the methyl ligands were found in the difference Fourier map. The H atoms of the methyl ligands and those of complex **4** were added to the models in their calculated positions using the "riding model". The thermal ellipsoids of the C atoms of the ether molecule in **4** point to a disorder, but refinement in split positions did not succeed.

2.3. Computational details

DFT calculations of compounds **3c**,[1] **4c**, **8c**, **8c′**, pz$^-$ and I$^-$ were carried out by the GAUSSIAN 03 program package [13] using the modified Perdew–Wang 1991 exchange functional

[1] The index "c" denotes calculated equilibrium structures.

by Adamo and Barone [14] plus the Perdew–Wang 1991 correlation functional [15] (MPWPW91). The 6-311G(d,p) [16] basis set as implemented in GAUSSIAN 03 was employed for C, H and N atoms, while the relativistic pseudopotentials of the Ahlrichs group and related basis functions of TZVPP quality [17] were employed for Pt and I atoms. All systems were fully optimized without any symmetry restrictions. The resulting geometries were characterized as equilibrium structures by the analysis of the force constants of normal vibrations. The interaction energies were corrected for basis set superposition errors (BSSE), that were estimated with counterpoise type calculations [18].

2.4. In vitro studies

Stock solutions of investigated platinum complexes and reference compound cisplatin were made in dimethyl sulfoxide (DMSO) at a concentration of 20 mM and diluted by nutrient medium to various working concentrations. Nutrient medium was RPMI-1640 (PAA Laboratories) supplemented with 10% fetal bovine serum (Biochrom AG) and penicillin/streptomycin (PAA Laboratories).

2.4.1. Cell cultures

The human tumor cell lines anaplastic thyroid cancer 8505C, head and neck tumors A253 and FaDu, cervical cancer A431, lung carcinoma A549, ovarian cancer A2780, colon carcinoma DLD-1, HCT-8 and HT-29 were cultivated in the Biocentrum, Martin Luther University Halle-Wittenberg. All cells were maintained as monolayers in nutrient medium in a humidified atmosphere with 5% CO_2.

2.4.2. Cytotoxicity assay

The cytotoxic activity of the platinum compounds was measured by the sulforhodamine-B (SRB) assay [19]. In brief, exponentially growing cells were seeded into 96-well plates and 24 h later, after the cell adherence, nine different concentrations of investigated compounds were added to the wells. The final concentrations were in the range from 0.1 to 100 μM. All experiments were done in triplicate. Nutrient medium with corresponding concentrations of compounds, but void of cells was used as blank. Five days after seeding the cells were fixed with 10% trichloroacetic acid and processed according to the published SRB assay protocol. Absorbance was measured at 570 nm using a 96-well plate reader (SpectraFluor Plus Tecan, Germany) and the percentages of surviving cells relative to untreated controls were determined. The concentration IC_{50}, was defined as the concentration of a drug that inhibited cell survival by 50%, compared with vehicle-treated control.

3. Results and discussion

3.1. Syntheses

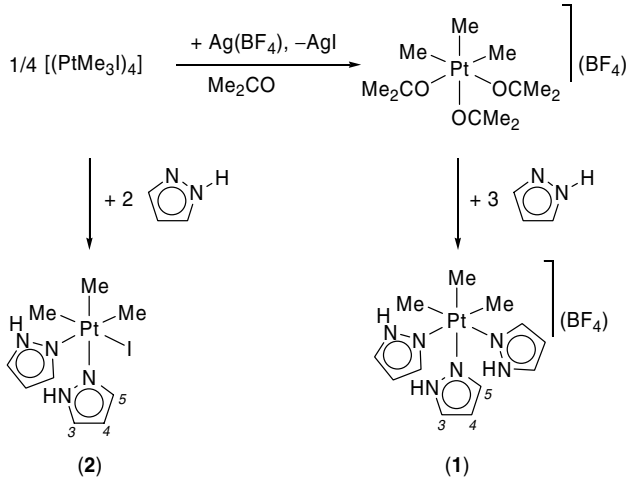
The complex $[PtMe_3(OCMe_2)_3](BF_4)$, obtained by the reaction of $[(PtMe_3I)_4]$ with $Ag(BF_4)$ in acetone [8], was found to react rapidly in acetone with three equivalents of pyrazole yielding the cationic tris(pyrazole) complex **1** (Scheme 1). Furthermore, the tetranuclear platinum complex $[(PtMe_3I)_4]$ was also found to react with pyrazole yielding the neutral bis(pyrazole) complex **2**, but this reaction took one day at room temperature (Scheme 1). Both mononuclear complexes were isolated as airstable colourless (**1**) and pale yellow (**2**) crystals in high yields (ca. 90%). The constitution of both complexes was determined unambiguously by microanalysis and NMR spectroscopy (^1H, ^{13}C).

Deprotonation of the coordinated pyrazole ligand in **1** and **2** afforded μ-pyrazolato complexes. Thus, complexes **1** and **2** reacted with $[PtMe_3(OCMe_2)_3](BF_4)$ in the presence of KOAc yielding dinuclear tris(μ-pyrazolato) and (μ-iodo)bis(μ-pyrazolato) complexes, respectively (Scheme 2). To yield crystalline complexes, the primarily obtained potassium salts were converted in a methatetical reaction to the PPN salts **3** and **4**, respectively. Addition of the crown ether 18C6 to the potassium salt of the (μ-iodo)-bis(μ-pyrazolato) complex resulted in the formation of the [K(18C6)] salt **5**. The colourless, airstable complexes (**3**, **4**, **5**) were obtained in moderate yields (ca. 50–60%) and characterized by microanalysis, NMR spectroscopy (^1H, ^{13}C) and single-crystal X-ray diffraction analyses.

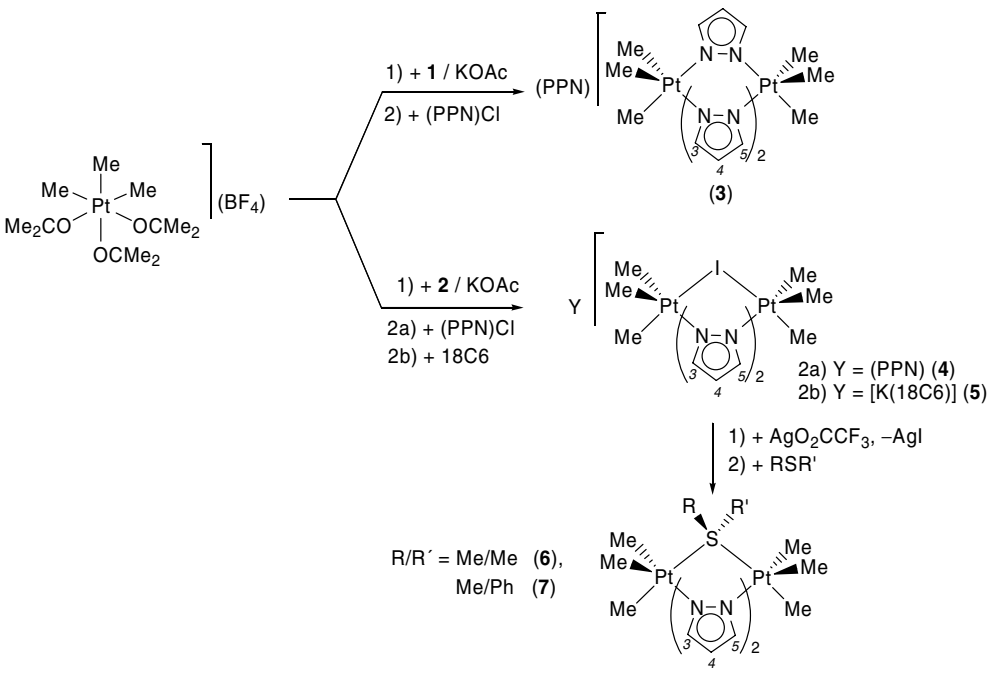
Substitution of the μ-iodo ligand in complex **4** could be achieved by reaction with silver trifluoroacetate followed by addition of thioethers (Scheme 2). Thus, the thioether bridged complexes **6** and **7** were obtained as colourless, airstable crystals in moderate yields (ca. 60%). Their identities have been confirmed by microanalysis and NMR spectroscopy (^1H, ^{13}C).

3.2. Spectral properties

^1H and ^{13}C NMR spectra gave proof that complexes **1** and **2** exhibit (mean) C_{3v} and C_s symmetry, respectively. Thus, in complex **1** all three pyrazole and methyl ligands are chemically equivalent. In complex **2** the two pyrazole



Scheme 1.



Scheme 2.

ligands were found to be equivalent, whereas two different methyl signals were observed. ^{1}H and ^{13}C NMR spectroscopic measurements established the identities of complexes **3**–**7**. In all these complexes the chemical equivalence $\delta(C^3) = \delta(C^5)$ and $\delta(H^3) = \delta(H^5)$[2] indicated a mirror plane perpendicular to the pyrazolato ligands. Furthermore, in accordance with a (mean) D_{3h} symmetry, the anion in **3** showed six and three chemically equivalent methyl and pyrazolato ligands, respectively. In accordance with a (mean) C_{2v} symmetry, in complexes **4**, **5** and **6** two equivalent pyrazolato ligands and two groups of chemically inequivalent methyl ligands (*trans* to pz^- and *trans* to I^-/Me_2S) were observed. On the other hand, in complex **7** (mean C_s symmetry) two inequivalent pyrazolato ligands and three inequivalent methyl ligands were found.

In *fac*-trimethylplatinum(IV) complexes the $^{1}J_{Pt,C}$ and $^{2}J_{Pt,H}$ coupling constants are indicative of the *trans* influence of ligands *trans* to the methyl ligands [20]. The values for dinuclear complexes **3**, **4**, **6** and **7** are given in Table 2. On the basis of the $^{1}J_{Pt,C}$ coupling constants the expected sequence of the *trans* influence was found: 642.0–675.2 Hz (pz^- in **3**–**7**) >694.9 Hz (Me_2S in **6**) ≈ 704.4 Hz (MeSPh in **7**) >740.4 Hz (I^- in **4**). The unusually low *trans* influence of the pyrazolato ligand in complex **3** compared with that in complexes **4**–**7** (675.2 Hz versus 642.0–646.3 Hz) might be reasoned to be due to a different angle strain in the tris- and bis(μ-pyrazolato) complexes as well as a different *cis* influence of the pz^- ligand compared to I^-/MeSR ligands. Principally, the same order of the *trans* influence can be derived from the $^{2}J_{Pt,H}$ coupling constants

Table 2
Selected coupling constants (in Hz) of complexes (PPN)[$(PtMe_3)_2$(μ-pz)$_2$(μ-X)] (**3**, **4**) and [$(PtMe_3)_2$(μ-pz)$_2$(μ-L)] (**6**, **7**)

Compound	X/ L = ligand	$^{1}J_{Pt,C}$ (*trans* N)	$^{1}J_{Pt,C}$ (*trans* X/L)	$^{2}J_{Pt,H}$ (*trans* N)	$^{2}J_{Pt,H}$ (*trans* X/L)
3	$X = pz^-$	675.2		66.2	
4	$X = I^-$	646.3	740.4	67.6	75.7
6	$L = Me_2S$	642.1	694.9	66.8	73.0
7	L = MeSPh	643.9/642.0	704.4	66.0/66.0	74.7

but, as known [21], these are not so sensitive as the $^{1}J_{Pt,C}$ coupling constants are.

In the neutral mononuclear complex [$PtMe_3I(pzH)_2$] (**2**) the magnitude of the $^{1}J_{Pt,C}$ coupling constant *trans* to N (682.3 Hz) demonstrated that, in comparison with the requisite coupling constants in **3**–**7** (642.0–675.2 Hz), pyrazole has a smaller *trans* influence than that of the μ-pyrazolato ligand. Furthermore, the comparison to the $^{1}J_{Pt,C}$ coupling constants in complexes **2** and **4** *trans* to the iodo ligand (715.9 versus 740.4 Hz) showed a *trans* influence $I_{terminal} > I_{bridging}$ as expected.

3.3. Structures

Crystals of complexes **3** and **4** suitable for X-ray diffraction analyses were obtained by recrystallization from CH_2Cl_2/Et_2O. The complexes crystallized as isolated cations and anions without unusual intermolecular interactions. The shortest distances of non-hydrogen atoms between cations and anions are 3.52 Å (C13···C12, **3**) and 3.43 Å (C1···C18, **4**). At distances <3.8 Å from the anion, in complex **3** seven PPN cations are found whereas

[2] Numbering scheme of pzH/pz^- ligands see Schemes 1 and 2.

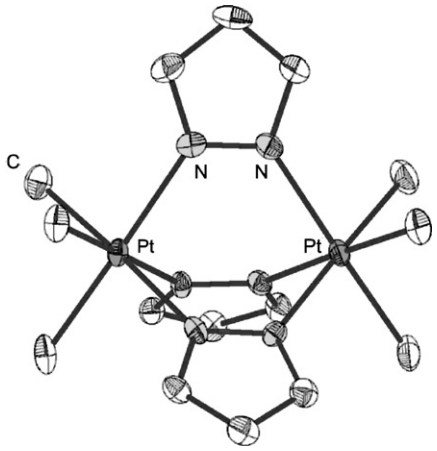


Fig. 1. Molecular structure of $[(PtMe_3)_2(\mu\text{-}pz)_3]^-$ in crystals of **3** (H atoms are omitted for clarity, 30% probability ellipsoids).

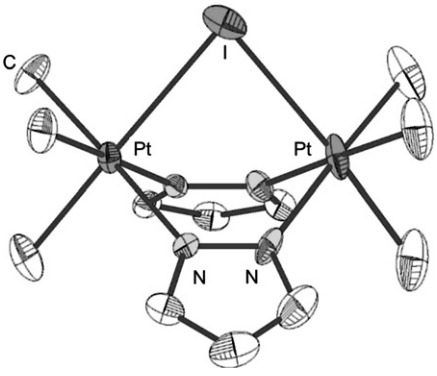


Fig. 2. Molecular structure of $[(PtMe_3)_2(\mu\text{-}I)(\mu\text{-}pz)_2]^-$ in crystals **4** (H atoms are omitted for clarity, 30% probability ellipsoids).

in complex **4** six PPN cations and another anion are found. The molecular structures of the anions are shown in Figs. 1 and 2, selected geometrical parameters are given in Table 3.

The structure of the tris(μ-pyrazolato) bridged dinuclear anion in crystals of **3** is approximately of D_{3h} symmetry (Fig. 1). The platinum atoms exhibit an octahedral coordination (angles between neighbouring ligands: 88.1(3)–91.8(3)°). The Pt···Pt distance amounts to 3.7827(8) Å excluding any direct interaction. The structure of the (μ-iodo)bis(μ-pyrazolato) bridged dinuclear anion $[(PtMe_3)_2(\mu\text{-}I)(\mu\text{-}pz)_2]^-$ in crystals of **4** is very nearly of C_{2v} symmetry (Fig. 2). The platinum atoms are octahedrally coordinated exhibiting a PtC_3N_2I coordination (angles between neighbouring ligands: 87.3(6)–91.4(4)°). The Pt–C bond lengths did not prove to be dependent on the ligand in the *trans* position (Pt–C (*trans* to N): 2.05(2)–2.08(1) Å; Pt–C (*trans* to I): 2.06(2)/2.07(1) Å). The Pt···Pt distance in **4** is significantly shorter than in **3** (3.706(1) versus 3.7827(8) Å).

3.4. DFT calculations

To gain further insight into the strength of the platinum–μ-ligand bonds in the dinuclear platinum(IV) complexes **3** and **4**, quantum chemical calculations were performed on the DFT level. The calculated equilibrium structures of the dinuclear anions $[(PtMe_3)_2(\mu\text{-}pz)_3]^-$ (**3c**) and $[(PtMe_3)_2(\mu\text{-}I)(\mu\text{-}pz)_2]^-$ (**4c**) contained in complexes **3** and **4/5** are illustrated in Fig. 3. Two different diastereoisomers of fragments $[(PtMe_3)_2(\mu\text{-}pz)_2]$ (**8c/8c′**, Fig. 3), with similar energies, were observed in these calculations. Only fragment **8c** is discussed here, because it exhibits a structure close to complexes **3c** and **4c**. Thus, **8c** is expected to be an intermediate in the substitution processes of complex **4**. Selected structural parameters of the equilibrium structures of **3c**, **4c** and **8c** are listed in Table 4. The calculated structures **3c** and **4c** show a good agreement with the experimentally found values. Interestingly, both in the calculated and experimental structures the Pt···Pt distance of the (μ-iodo)-bis(μ-pyrazolato) complex (**4c/4**) was found to be shorter than in the tris(μ-pyrazolato) complex (**3c/3**). An even shorter Pt···Pt distance was found in the complex fragment **8c**. Thus, addition of the μ-pyrazolato (**8c→3c**) and μ-iodo ligand (**8c→4c**) results in a lengthening of the Pt···Pt distance, indicating that the "coordination pocket" of this fragment is too small for both the μ-iodo and the μ-pyrazolato ligand.

Table 3
Selected interatomic distances (in Å) and angles (in °) of complexes $(PPN)[(PtMe_3)_2(\mu\text{-}pz)_3]$ (**3**) and $(PPN)[(PtMe_3)_2(\mu\text{-}I)(\mu\text{-}pz)_2]\cdot 1/2Et_2O$ (**4**)

3		**4**	
Pt–C	2.045(8)–2.085(7)	$Pt–C_{trans\,N}$	2.05(2)–2.08(1)
		$Pt–C_{trans\,I}$	2.06(2)/2.07(1)
Pt–N	2.138(5)–2.157(5)	Pt–N	2.123(8)–2.15(1)
N–N	1.328(8)–1.352(8)	N–N	1.35(1)/1.37(1)
		Pt–I	2.826(1)/2.833(1)
Pt···Pt	3.7827(8)	Pt···Pt	3.706(1)
C–Pt–C	88.1(3)–89.5(3)	$C_{trans\,N}$-Pt-$C_{trans\,N}$	87.3(6)/89.0(5)
		$C_{trans\,N}$-Pt-$C_{trans\,I}$	87.3(5)–89.9(6)
C–Pt–N_{cis}	89.3(3)–91.8(3)	$C_{trans\,I}$–Pt–N_{cis}	88.6(6)–91.4(4)
		$C_{trans\,N}$–Pt–N_{cis}	89.7(4)–91.3(6)
C–Pt–N_{trans}	176.8(2)–179.3(2)	$C_{trans\,N}$ –Pt–N_{trans}	177.4(4)–178.4(4)
		$C_{trans\,I}$–Pt–I	175.9(4)/179.1(4)
N–Pt–N	90.1(2)–91.7(2)	N–Pt–N	90.5(3)/91.0(3)
		Pt–I–Pt	81.83(4)
Pt–N–N	123.9(4)–125.5(4)	Pt–N–N	123.2(5)–123.4(6)
P–N–P	133.7(4)	P–N–P	139.6(6)
Pt–N–N–Pt	2.7(7)–5.9(7)	Pt–N–N–Pt	–1(1)/1(1)
C–C–N–N	–0.3(8)–1.3(8)	N–N–C–C	0(1)–1(1)

On the basis of an energetic approach the strength of metal–ligand interactions can be expressed either as the dissociation energy E_{diss} of the complex into the free fragments in their equilibrium structures or as the interaction energy E_{int} of the "prepared" fragments (isolated fragments having the same geometry as in the complex). For an explanation of these fundamental steps, see Ref. [22]. Thus, the equation

$$-E_{diss} = E_{int} + E_{prep}$$

holds whereas the preparation energy E_{prep} of a bond formation A + B→AB is the energy which is necessary to promote fragments A and B from their equilibrium geometries

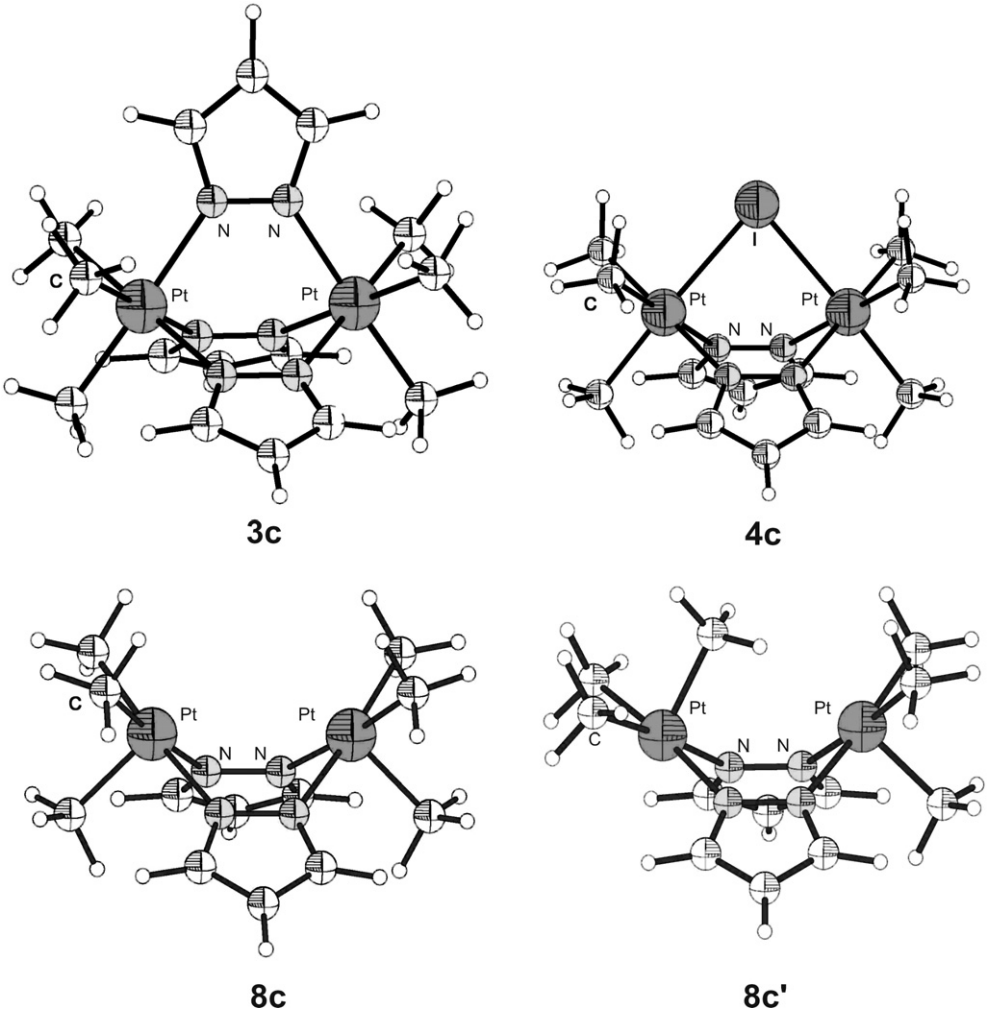


Fig. 3. Calculated equilibrium structures of $[(PtMe_3)_2(\mu\text{-}pz)_3]^-$ (**3c**), $[(PtMe_3)_2(\mu\text{-}I)(\mu\text{-}pz)_2]^-$ (**4c**) and $[(PtMe_3)_2(\mu\text{-}pz)_2]$ (**8c**/**8c′**).

Table 4
Selected interatomic distances (in Å) and angles (in °) of calculated equilibrium structures $[(PtMe_3)_2(\mu\text{-}X)(\mu\text{-}pz)_2]^-$ (μ-X = pz^-, **3c**; I^-, **4c**) and $[(PtMe_3)_2(\mu\text{-}pz)_2]$ (**8c**)

	3c	4c	8c
Pt–$C_{trans\,L}$		2.071	2.043[a]
Pt–$C_{trans\,N}$	2.068–2.070	2.071	2.054
Pt–N	2.168–2.172	2.174	2.161
N–N	1.357–1.358	1.358–1.359	1.363
Pt···Pt	3.830	3.780	3.636
C–Pt–C	88.4–96.2	86.8–89.7	88.7–91.5
C–Pt–N_{cis}	88.9–91.3	89.9–92.5	90.6–92.6
C–Pt–N_{trans}	178.1–179.3	178.9–179.8	175.8–179.8

[a] *trans* to the free coordination site.

to the geometries which they acquire in the complex AB. As shown in Fig. 4, for both processes the μ-pyrazolato ligand in **3c** is more strongly bound ($E_{int} = -80.5$ kcal/mol, $-E_{diss} = -73.7$ kcal/mol) than the μ-iodo ligand in **4c** ($E_{int} = -50.8$ kcal/mol, $-E_{diss} = -46.2$ kcal/mol), which is in accord with the differences in the *trans* influence of the bridging ligands measured by the $^1J_{Pt,C}$ coupling constants. The preparation energy of the platinum fragment in **3c** was found to be larger than that in **4c** (6.3 versus 4.6 kcal/mol) as expected by inspection of the Pt···Pt distances (3.636 Å (**8c**) <3.780 Å (**4c**) <3.830 Å (**3c**)).

3.5. Antitumoral activities

Since the discovery of cisplatin (*cis*-$[PtCl_2(NH_3)_2]$) by Rosenberg [23] the anticancer activity of platinum complexes is well known. In contrast to the large number of platinum(II) complexes, substantially fewer platinum(IV) complexes have been investigated with respect to their cancerostatic properties [24,25]. However, a number of platinum(IV) complexes have been tested in clinical trials. These include iproplatin (*cis*, *trans*, *cis*-$[PtCl_2(OH)_2(NH_2iPr)_2]$) [24] tetraplatin ($[PtCl_4$(D,L-dach)]; dach = 1,2-diaminocyclohexane) [24] and satraplatin (*cis*, *trans*-$[PtCl_2(OAc)_2(NH_3)(NH_2cy)]$) [24,26]. As reported in the literature [27], dinuclear platinum(II) complexes should be able to coordination to DNA in a fashion differing from that observed for mononuclear complexes and thus might show activity against tumor cell lines resistant to cisplatin.

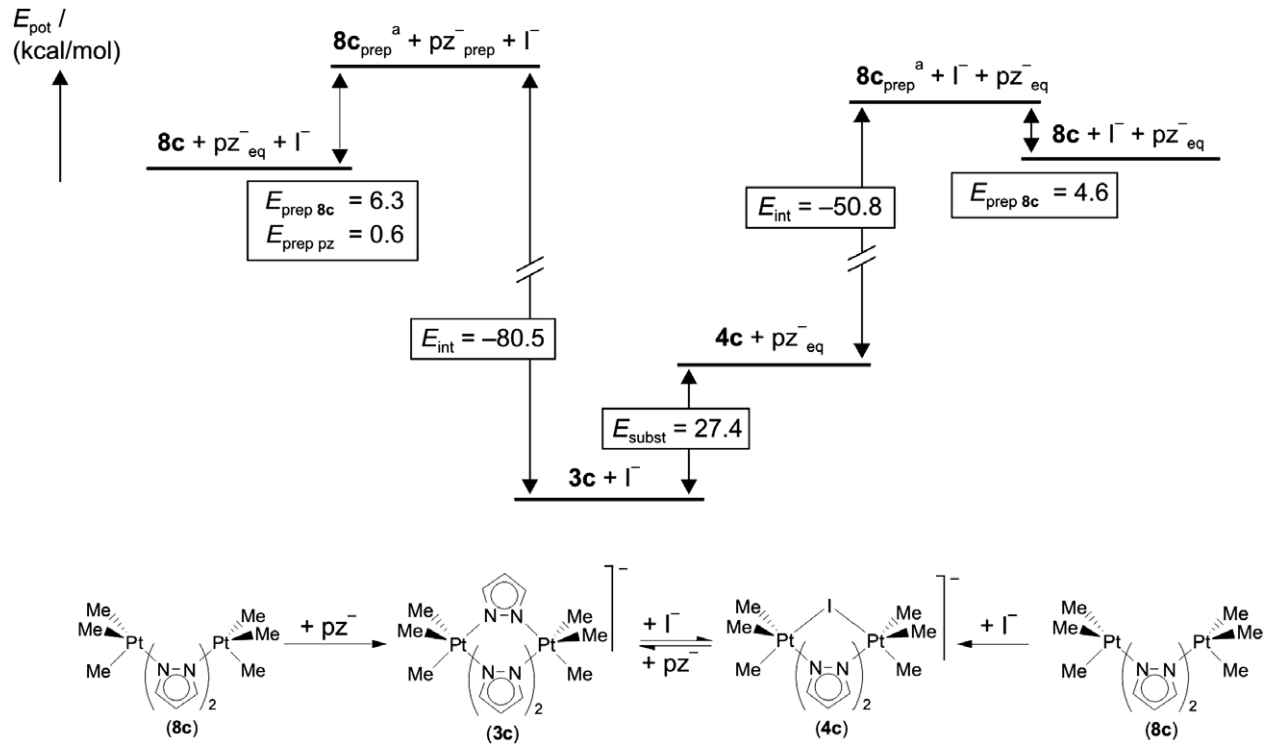


Fig. 4. Energy decomposition analyses of bond formation between fragment **8c** and pz^- and I^-, respectively. Interaction energies include BSSE corrections. (a) $\mathbf{8c}_{prep}$ denotes the fragment **8c** having the geometry as in complex **3c** and **4c**, respectively.

In contrast to the investigation of the anticancer activities of dinuclear platinum(II) complexes, investigations with dinuclear platinum(IV) complexes are lacking. To study the activity of the synthesized trimethylplatinum(IV) complexes two different compounds were chosen (**2**, **5**), exhibiting mono- and dinuclear arrangement, but containing similar (iodo, pyrazole/pyrazolato) ligands.

To investigate the activities of complexes **2** and **5** against various human tumor cell lines, in vitro experiments were carried out. The antitumoral activities of compounds **2** and **5** in comparison to the respective activity of cisplatin are presented in Table 5. The anti-proliferative activity of complex **2** was found to be about one order of magnitude lower than that of cisplatin (IC_{50}(**2**)/IC_{50}(cisplatin) = 7.0–58.4). In contrast, the activity of complex **5** proved to be in the same order than the corresponding activity of cisplatin (IC_{50}(**5**)/IC_{50}(cisplatin) = 0.4–2.7). Two cell lines (8505C, DLD-1), which exhibit low sensitivities against cisplatin, were included in these investigations. On these particular cell lines, complex **5** was found to be more active than cisplatin (IC_{50}(**5**)/IC_{50}(cisplatin) = 0.4–0.5). However, taking into consideration that **5** is a dinuclear complex, roughly the same anti-proliferative activity per Pt atom was observed. The reason for the significantly higher anti-proliferative activity of the dinuclear complex **5** in comparison with the mononuclear complex **2** is not yet clear. It can be speculated that the dinuclear fragment [$(PtMe_3)_2(\mu\text{-pz})_2$] allows a bridging coordination of the nucleobases.

Table 5
IC_{50} values of complexes **2** and **5** against different human tumor cell lines

Cell line	IC_{50} [μM]		
	Complex **2**[a]	Complex **5**[a]	Cisplatin[b]
8505C	35.03 ± 0.86	1.96 ± 0.15	5
A253	20.95 ± 0.94	1.13 ± 0.03	0.8
A431	19.29 ± 0.35	0.95 ± 0.01	0.65
A549	36.22 ± 0.75	2.30 ± 0.03	1.5
A2780	4.82 ± 0.31	1.49 ± 0.07	0.55
DLD-1	37.04 ± 0.56	2.51 ± 0.14	5
FaDu	36.42 ± 0.85	2.32 ± 0.06	1.2
HCT-8	44.97 ± 3.20	3.76 ± 0.13	1.5
HT-29	35.03 ± 1.19	2.18 ± 0.08	0.6

[a] Mean value ± SD from experiments.
[b] Mean value without SD.

To summarize, the investigations showed that dinuclear pyrazolato bridged platinum(IV) complexes can be built up by the synthesis of mononuclear pyrazole precursor complexes followed by controlled deprotonation of the pyrazole ligands. Due to the highly stable *fac*-$PtMe_3$ moiety, threefold bridged dinuclear platinum(IV) complexes were obtained. The substitution lability of the μ-iodo ligand in complex **4**/**5** opened up a way to synthesize and to characterize further complexes having a relatively rigid $Me_3Pt(\mu\text{-pz})_2PtMe_3$ fragment in which to metal centers in high oxidation state are in the vicinity of one another. Furthermore it could be demonstrated that the investigated dinuclear complex **5** exhibited a quite high proliferative activities against a series of human tumor cell lines.

Acknowledgements

The authors gratefully acknowledge financial support by the state of Sachsen-Anhalt (Germany). We also thank Merck (Darmstadt, Germany) for gift of chemicals.

Appendix A. Supplementary material

CCDC 663385 and 663386 contain the supplementary crystallographic data for **3** and **4**. These data can be obtained free of charge via http://www.ccdc.cam.ac.uk/conts/retrieving.html, or from the Cambridge Crystallographic Data Centre, 12 Union Road, Cambridge CB2 1EZ, UK; fax: (+44) 1223-336-033; or e-mail: deposit@ccdc.cam.ac.uk. Energies and Cartesian coordinates of atom positions of the calculated structures **3c**, **4c**, **8c**, **8c′**, pz_{eq}^{-} and I^{-} are available from the authors. Supplementary data associated with this article can be found, in the online version, at doi:10.1016/j.poly.2007.11.020.

References

[1] M. Albrecht, Angew. Chem., Int. Ed. 38 (1999) 3463.
[2] A. Kaiser, P. Bäuerle, Top. Curr. Chem. 249 (2005) 127.
[3] J. Forniés, S. Fuertes, A. Martín, V. Silicia, E. Lalinde, M.T. Moreno, Chem. Eur. J. 12 (2006) 8253.
[4] G. Mezei, M. Rivera-Carrillo, R.G. Raptis, Dalton Trans. (2007) 37.
[5] A. Cingolani, S. Galli, N. Masciocchi, L. Pandolfo, C. Pettinari, A. Sironi, Dalton Trans. (2006) 2479.
[6] S. Bieller, A. Haghiri, M. Bolte, J.W. Bats, M. Wagner, H.W. Lerner, Inorg. Chim. Acta 359 (2006) 1559.
[7] K. Umakoshi, Y. Yamauchi, K. Nakamiya, T. Kojima, M. Yamasaki, H. Kawano, M. Onishi, Inorg. Chem. 42 (2003) 3907.
[8] H. Junicke, C. Bruhn, D. Ströhl, R. Kluge, D. Steinborn, Inorg. Chem. 37 (1998) 4603.
[9] G. Minghetti, G. Banditelli, F. Bonati, J. Chem. Soc., Dalton Trans. (1979) 1851.
[10] D.A. Johnson, A.W. Cordes, B.A. Fithen-Kelley, J. Coord. Chem. 32 (1993) 1.
[11] J.C. Baldwin, W.C. Kaska, Inorg. Chem. 14 (1975) 2020.
[12] G.M. Sheldrick, SHELXS-86, SHELXS-97, Programs for Structure Determinations, University of Gottingen, Germany, 1990, 1997.
[13] M.J. Frisch, G.W. Trucks, H.B. Schlegel, G.E. Scuseria, M.A. Robb, J.R. Cheeseman, J.A. Montgomery Jr., T. Vreven, K.N. Kudin, J.C. Burant, J.M. Millam, S.S. Iyengar, J. Tomasi, V. Barone, B. Mennucci, M. Cossi, G. Scalmani, N. Rega, G.A. Petersson, H. Nakatsuji, M. Hada, M. Ehara, K. Toyota, R. Fukuda, J. Hasegawa, M. Ishida, T. Nakajima, Y. Honda, O. Kitao, H. Nakai, M. Klene, X. Li, J.E. Knox, H.P. Hratchian, J.B. Cross, V. Bakken, C. Adamo, J. Jaramillo, R. Gomperts, R.E. Stratmann, O. Yazyev, A.J. Austin, R. Cammi, C. Pomelli, J.W. Ochterski, P.Y. Ayala, K. Morokuma, G.A. Voth, P. Salvador, J.J. Dannenberg, V.G. Zakrzewski, S. Dapprich, A.D. Daniels, M.C. Strain, O. Farkas, D.K. Malick, A.D. Rabuck, K. Raghavachari, J.B. Foresman, J.V. Ortiz, Q. Cui, A.G. Baboul, S. Clifford, J. Cioslowski, B.B. Stefanov, G. Liu, A. Liashenko, P. Piskorz, I. Komaromi, R.L. Martin, D.J. Fox, T. Keith, M.A. Al-Laham, C.Y. Peng, A. Nanayakkara, M. Challacombe, P.M.W. Gill, B. Johnson, W. Chen, M.W. Wong, C. Gonzalez, J.A. Pople, GAUSSIAN 03, Revision C.02, Gaussian, Inc., Wallingford, CT, 2004.
[14] C. Adamo, V. Barone, J. Chem. Phys. 108 (1998) 664.
[15] (a) K. Burke, J.P. Perdew, Y. Wang, in: J.F. Dobson, G. Vignale, M.P. Das (Eds.), Electronic Density Functional Theory: Recent Progress and New Directions, Plenum Press, New York, 1998;
(b) J.P. Perdew, in: P. Ziesche, H. Eschrig (Eds.), Electronic Structure of Solids'91, Akademie Verlag, Berlin, 1991;
(c) J.P. Perdew, J.A. Chevary, S.H. Vosko, K.A. Jackson, M.R. Pederson, D.J. Singh, C. Fiolhais, Phys. Rev. B 46 (1992) 6671;
(d) J.P. Perdew, J.A. Chevary, S.H. Vosko, K.A. Jackson, M.R. Pederson, D.J. Singh, C. Fiolhais, Phys. Rev. B 48 (1993) 4978;
(e) J.P. Perdew, K. Burke, Y. Wang, Phys. Rev. B 54 (1996) 16533.
[16] (a) M.J.S. Dewar, C.H. Reynolds, J. Comp. Chem. 7 (1986) 140;
(b) K. Raghavachari, J.A. Pople, E.S. Replogle, M. Head-Gordon, J. Phys. Chem. 94 (1990) 5579.
[17] (a) F. Weigend, M. Häser, H. Patzelt, R. Ahlrichs, Chem. Phys. Lett. 294 (1998) 143;
(b) T. Leininger, A. Nicklass, W. Küchle, H. Stoll, M. Dolg, A. Bergner, Chem. Phys. Lett. 255 (1996) 274;
(c) D. Andrae, U. Häußermann, M. Dolg, H. Stoll, H. Preuß, Theor. Chem. Acc. 77 (1990) 123.
[18] (a) S. Simon, M. Duran, J.J. Dannenberg, J. Chem. Phys. 105 (1996) 11024;
(b) S.F. Boys, F. Bernardi, Mol. Phys. 19 (1970) 553.
[19] P. Skehan, R. Storeng, D. Scudiero, A. Monks, J. McMahon, D. Vistica, J.T. Warren, H. Bokesch, S. Kenney, M.R. Boyd, J. Natl. Cancer Inst. 82 (1990) 1107.
[20] T.G. Appleton, H.C. Clark, L.E. Manzer, Coord. Chem. Rev. 10 (1973) 335.
[21] D.E. Clegg, J.R. Hall, G.A. Swile, J. Organomet. Chem. 38 (1972) 403.
[22] (a) G. Frenking, N. Fröhlich, Chem. Rev. 100 (2000) 717;
(b) G. Frenking, K. Wichmann, N. Fröhlich, C. Loschen, M. Lein, J. Frunzke, V.M. Rayón, Coord. Chem. Rev. 238–239 (2003) 55.
[23] B. Rosenberg, L. VanCamp, T. Krigas, Nature 205 (1965) 698.
[24] M.D. Hall, T.W. Hambley, Coord. Chem. Rev. 232 (2002) 49.
[25] (a) M. Galanski, V.B. Arion, M.A. Jakupec, B.K. Keppler, Curr. Pharm. Des. 9 (2003) 2078;
(b) C.X. Zhang, S.J. Lippard, Curr. Opin. Chem. Biol. 7 (2003) 481;
(c) A. Eastman, Pharmacol. Therapeut. 34 (1987) 155;
(d) L. Kelland, Nat. Rev. Cancer 7 (2007) 573.
[26] L.R. Kelland, Exp. Opin. Invest. Drugs 9 (2000) 1373.
[27] (a) S. Komeda, H. Ohishi, H. Yamane, M. Harikawa, K. Sakaguchi, M. Chikuma, J. Chem. Soc., Dalton Trans. (1999) 2959;
(b) N. Farrell, Comments Inorg. Chem. 16 (1995) 373;
(c) E. Wong, C.M. Giandomenico, Chem. Rev. 99 (1999) 2451.

and $[ReOX_3(AsPh_3)(OAsPh_3)]$ (X = Cl or Br) – towards pyrazole, 3,5-dimethylopyrazole, benzotriazole and pyrazine [8]. As an extension of this work, we were keen to examine the reactivity of $[ReOX_3(PPh_3)_2]$ and $[ReOX_3(AsPh_3)_2]$ towards pyrazole ligands containing additional hydrogen-bonding functionality, in addition to the N–H group of the pyrazole ring. 2-(1-H-pyrazol-3-yl)phenol is one such ligand, and is readily available. Furthermore, no other rhenium complexes containing 2-(1-H-pyrazol-3-yl)phenolato ligand have been previously characterized [9].

Here we present synthesis and spectroscopic data for $[ReOCl_2(C_9H_7N_2O)(PPh_3)]\cdot MeCN$ (**1** · MeCN), $[ReOBr_2(C_9H_7N_2O)(PPh_3)]\cdot MeCN$ (**2** · MeCN), $[ReOCl_2(C_9H_7N_2O)(AsPh_3)]\cdot MeCN$ (**3** · MeCN) and $[ReOBr_2(C_9H_7N_2O)(AsPh_3)]\cdot MeCN$ (**4** · MeCN) complexes. X-ray studies have been performed for **1** · MeCN, **3** · MeCN and **4** · MeCN, and electronic structure of **1** has been calculated with the density functional theory (DFT). TD-DFT/PCM calculations have been employed to produce a hundred of singlet excited-states starting from the ground-state geometry optimized in the gas phase, and the UV–Vis spectrum of the complex has been discussed on this basis.

Currently density functional theory (DFT) is commonly used to examine the electronic structure of transition metal complexes. It meets with the requirements of being accurate, easy to use and fast enough to allow the study of relatively large molecules of transition metal complexes [10]. Recent calculations with TD-DFT method for open- and closed-shell of 5d-metal complexes (including rhenium complexes) have also supported the TD-DFT method to be applicable for such systems giving good assignment of experimental spectra [11,12].

Some theoretical investigations have been carried out on rhenium compounds. The electronic structures of nitrido, oxo, carbonyl, nitrosyl and nitrile rhenium complexes, as well as their spectroscopic properties, bonding and reactivity have been theoretically studied at the HF, MP2, EHT and DFT levels of theory using various basis sets [13–22]. Gancheff and co-workers [15] have performed extended tests of the ability of the B3LYP method in LANL2DZ basis set for rhenium compounds in a geometry optimization and calculation of spectral properties. Although this is not a very extended basis set, its use with DFT has shown to be sufficient for the geometry optimization and calculation of spectral properties. It gives good agreement with the experimental data and its use is justified in the case of large molecules.

2. Experimental

2.1. General procedure

The reagents used to the synthesis were commercially available and were used without further purification. The $[ReOX_3(AsPh_3)_2]$ and $[ReOX_3(PPh_3)_2]$ complexes were prepared according to the literature methods [23].

IR spectra were recorded on a Nicolet Magna 560 spectrophotometer in the spectral range 4000–400 cm^{-1} with the samples in the form of KBr pellets. Electronic spectra were measured on a spectrophotometer Lab Alliance UV–Vis 8500 in the range 1000–180 nm in acetonitrile solution. ^1H NMR spectrum was obtained in $CDCl_3$ using Bruker Avance 400 spectrometer. Elemental analyses (C H N) were performed on a Perkin–Elmer CHN-2400 analyzer.

2.2. Preparation of $[ReOCl_2(C_9H_7N_2O)(PPh_3)]\cdot MeCN$

A mixture of $[ReOCl_3(PPh_3)_2]$ (0.50 g, 0.6 mmol), 2-(1-H-pyrazol-3-yl)phenol (0.12 g, 0.75 mmol) and acetone (50 ml) was stirred at room temperature for 3 h. Half of the solvent was removed and diethyl ether (50 ml) was added to precipitate the product as a green solid, which was filtered off, dried and recrystallized from acetonitrile. Yield 85%.

Anal. Calc. for $C_{29}H_{25}Cl_2N_3O_2PRe$: C, 47.35; H, 3.43; N, 5.71. Found: C, 47.60; H, 3.46; N, 5.59%.

IR (KBr; ν/cm^{-1}): 1606 (m), 1581 (w), 1531 (m), 1506 (s) ν_{CN} and $\nu_{C=C}$; 960 (vs) $\nu_{Re=O}$.

^1H NMR (400 MHz; $CDCl_3$) $\delta = 10.61$ (br, 1H, N–H), 7.45-7.36 (m, 10H), 7.34 (dd, 1H, $J = 2.6$ Hz, $J = 1.6$ Hz, H26-pz), 7.29-7.24 (m, 5H), 7.21 (dd, 1H, $J = 7.7$ Hz, $J = 1.6$ Hz, H20–Ar), 6.94 (td, 1H, $J = 7.7$ Hz, $J = 1.6$ Hz, H22–Ar), 6.86 (td, 1H, $^3J = 7.7$ Hz, $J = 1.0$ Hz, H21–Ar), 6.63 (t, 1H, $J = 2.6$ Hz, H27-pz), 6.61 (dd, 1H, $J = 7.7$ Hz, $J = 1.0$ Hz, H23–Ar).

2.3. Preparation of $[ReOBr_2(C_9H_7N_2O)(PPh_3)]\cdot MeCN$

A procedure similar to that for $[ReOCl_2(C_9H_7N_2O)(PPh_3)]\cdot MeCN$ was used with $[ReOBr_3(PPh_3)_2]$ (0.50 g, 0.52 mmol and 2-(1-H-pyrazol-3-yl)phenol (0.11 g, 0.69 mmol). Crystalline precipitate of $[ReOBr_2(C_9H_7N_2O)(PPh_3)]\cdot MeCN$ was collected in 80% yield.

Anal. Calc. for $C_{29}H_{25}Br_2N_3O_2PRe$: C, 42.24; H, 3.06; N, 5.10. Found: C, 42.50; H, 3.16; N, 5.05%.

IR (KBr; ν/cm^{-1}): 1603 (m), 1582 (w), 1531 (m), 1504 (s) ν_{CN} and $\nu_{C=C}$; 963 (vs) $\nu_{Re=O}$.

2.4. Preparation of $[ReOCl_2(C_9H_7N_2O)(AsPh_3)]\cdot MeCN$

A procedure similar to that for $[ReOCl_2(C_9H_7N_2O)(PPh_3)]\cdot MeCN$ was used with $[ReOCl_3(AsPh_3)_2]$ (0.50 g, 0.54 mmol) and 2-(1-H-pyrazol-3-yl)phenol (0.11 g, 0.69 mmol). Crystalline precipitate of $[ReOCl_2(C_9H_7N_2O)(AsPh_3)]\cdot MeCN$ was collected in 85% yield.

Anal. Calc. for $C_{29}H_{25}Cl_2N_3O_2AsRe$: C, 44.68; H, 3.23; N, 5.39. Found: C, 44.77; H, 3.18; N, 5.35%.

IR (KBr; ν/cm^{-1}): 1607 (m), 1581 (w), 1534 (m), 1504 (s) ν_{CN} and $\nu_{C=C}$; 965 (vs) $\nu_{Re=O}$.

2.5. Preparation of $[ReOBr_2(C_9H_7N_2O)(AsPh_3)]\cdot MeCN$

A procedure similar to that for $[ReOCl_2(C_9H_7N_2O)(PPh_3)]$ was used with $[ReOBr_3(AsPh_3)_2]$ (0.50 g,

Table 1
Crystal data and structure refinement for **1** · MeCN, **3** · MeCN and **4** · MeCN complexes

	1 · MeCN	**3** · MeCN	**4** · MeCN
Empirical formula	$C_{29}H_{25}Cl_2N_3O_2PRe$	$C_{29}H_{25}Cl_2N_3O_2AsRe$	$C_{29}H_{25}Br_2N_3O_2AsRe$
Formula weight	735.59	779.54	868.46
Temperature (K)	293(2)	293(2)	293(2)
Wavelength (Å)	0.71073	0.71073	0.71073
Crystal system	monoclinic	monoclinic	monoclinic
Space group	$P2_1/c$	$P2_1/c$	$P2_1/c$
Unit cell dimensions			
a (Å)	10.7513(4)	10.8926(3)	11.0020(5)
b (Å)	14.8900(6)	14.8444(4)	14.9654(5)
c (Å)	17.5981(7)	17.5601(6)	17.6972(6)
β (°)	96.708(4)	97.384(3)	97.295(4)
Volume (Å^3)	2797.94(19)	2815.82(15)	2890.25(19)
Z	4	4	4
D_{calc} (Mg/m^3)	1.746	1.839	1.996
Absorption coefficient (mm^{-1})	4.623	5.703	8.137
$F(000)$	1440	1512	1656
Crystal size (mm)	0.06 × 0.014 × 0.26	0.07 × 0.18 × 0.24	0.06 × 0.16 × 0.22
θ Range for data collection (°)	2.97–25.00	2.98–25.00	2.96–25.00
Index ranges	$-12 \leqslant h \leqslant 9$, $-17 \leqslant k \leqslant 17$, $-20 \leqslant l \leqslant 18$	$-11 \leqslant h \leqslant 12$, $-14 \leqslant k \leqslant 17$, $-20 \leqslant l \leqslant 20$	$-12 \leqslant h \leqslant 13$, $-17 \leqslant k \leqslant 17$, $-14 \leqslant l \leqslant 21$
Reflections collected	16772	17374	17536
Independent reflections (R_{int})	4870 (0.0207)	4932 (0.0208)	5065 (0.0260)
Completeness to $2\theta = 50°$ (%)	99.9	99.6	99.6
Data/restraints/parameters	4870/0/344	4932/0/344	5065/0/344
Goodness-of-fit on F^2	0.976	0.987	1.103
Final R indices [$I > 2\sigma(I)$]	$R_1 = 0.0169$, $wR_2 = 0.0342$	$R_1 = 0.0154$, $wR_2 = 0.0358$	$R_1 = 0.0338$, $wR_2 = 0.1037$
R indices (all data)	$R_1 = 0.0278$, $wR_2 = 0.0357$	$R_1 = 0.0224$, $wR_2 = 0.0366$	$R_1 = 0.0446$, $wR_2 = 0.1077$
Largest difference in peak and hole (e Å^{-3})	0.934 and −0.673	0.607 and −0.498	1.701 and −2.142

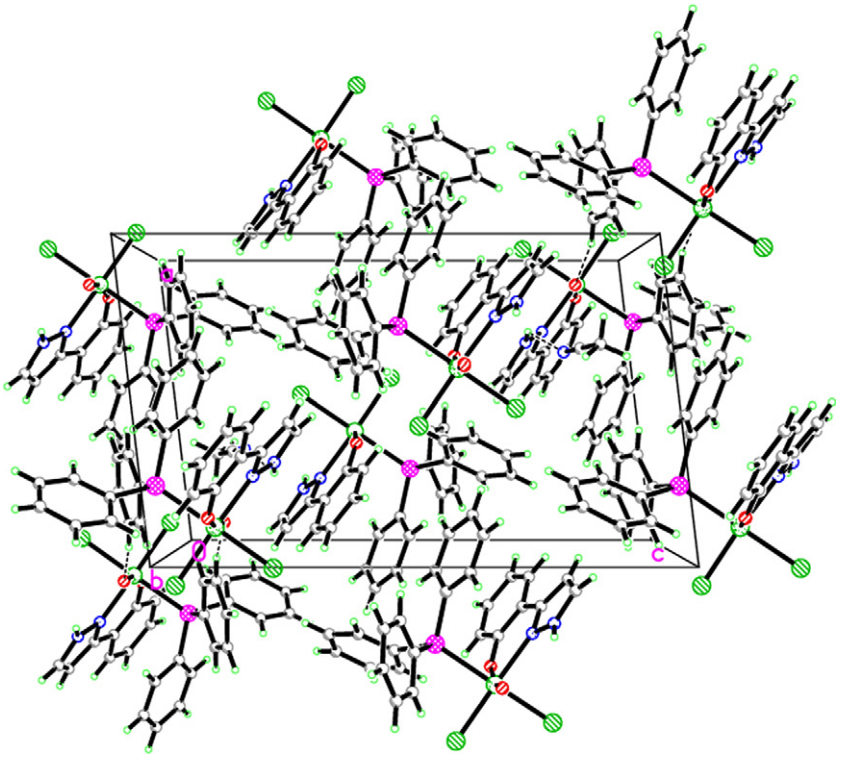


Fig. 1. The cell packing of **1** viewing along the a direction.

0.47 mmol) and 2-(1-H-pyrazol-3-yl)phenol (0.10 g, 0.62 mmol). Crystalline precipitate of $[ReOBr_2(C_9H_7N_2O)(AsPh_3)] \cdot MeCN$ was collected in 90% yield.

Anal. Calc. for $C_{29}H_{25}Br_2N_3O_2AsRe$: C, 40.11; H, 2.90; N, 4.84. Found: C, 40.45; H, 3.01; N, 4.95%.

IR (KBr; ν/cm^{-1}): 1603 (m), 1576 (w), 1531 (m), 1504 (s) ν_{CN} and $\nu_{C=C}$; 962 (vs) $\nu_{Re=O}$.

2.6. Crystal structure determination and refinement

The X-ray intensity data of **1** · MeCN, **3** · MeCN and **4** · MeCN were collected on a KM-4-CCD automatic diffractometer equipped with CCD detector and graphite monochromated Mo Kα radiation ($\lambda = 0.71073$ Å) at room temperature. Details concerning crystal data and refinement are given in Table 1. Lorentz, polarization and absorption correction [24] were applied. The structures were solved by the Patterson method and subsequently completed by the difference Fourier recycling. All the non-hydrogen atoms were refined anisotropically using full-matrix, least-squares technique. The hydrogen atoms were treated as "riding" on their parent carbon atoms and assigned isotropic temperature factors equal 1.2 times the value of equivalent temperature factor of the parent atom.

For structure **4**, a final difference electron density residual peak of 1.701 e Å^{-3} was observed at 0.90 Å of the Re(1) atom, and a hole of −2.142 e Å^{-3} at 0.90 Å of the Br(2) atom. SHELXS97 [25], SHELXL97 [26] and SHELXTL [27] programs were used for all the calculations. Atomic scattering factors were those incorporated in the computer programs.

Table 2
Hydrogen bonds for **1** · MeCN, **3** · MeCN and **4** · MeCN complexes

D	A	H···A	D···A	D–H···A
***1** · MeCN*				
N(2)	O(1)	2.43	2.804(3)	107.2
C(2)	Cl(2)	2.81	3.652(3)	151.3
C(18)	O(2)	2.42	3.155(3)	136.2
***3** · MeCN*				
N(2)	O(1)	2.45	2.815(3)	106.6
C(8)	O(2)	2.53	3.266(3)	136.7
C(17)	O(1)#1	2.52	3.371(3)	153.1
***4** · MeCN*				
N(2)	O(1)	2.44	2.831(8)	108.1
C(2)	O(2)	2.53	3.284(8)	138.1

1: $-x+1, -y+1, -z+1$.

Table 3
Analysis of short contacts between the rings of the 2-(1-H-pyrazol-3-yl)phenolato ligand and triphenyl phospine ring (distances in Å and angles in °)

R(I)	*R*(J)	Cg···Cg	α	β	d_p
***1** · MeCN*					
Cg(1)	Cg(3)	3.6808	16.57	21.24	3.131
Cg(4)	Cg(3)	4.2515	10.69	35.51	3.589
***3** · MeCN*					
Cg(1)	Cg(2)	3.7514	15.47	20.77	3.152
Cg(4)	Cg(2)	4.2960	9.49	35.08	3.634
***4** · MeCN*					
Cg(1)	Cg(3)	3.7960	16.18	22.34	3.136
Cg(4)	Cg(3)	4.2463	8.95	33.71	3.651

The Cg(1), Cg(2), Cg(3), Cg(4) indicates the centroids of aromatic rings containing N(1), C(1), C(7), C(19) atoms respectively; α is a dihedral angle between planes I and J; β is an angle between Cg(I)–Cg(J) vector and normal to plane I and d_p is a perpendicular distance of Cg(I) on ring J plane.

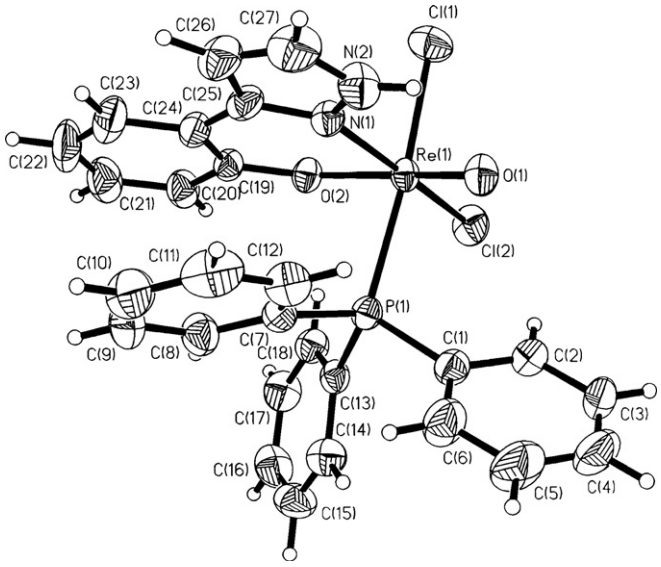


Fig. 2. The molecular structure of **1**. Displacement ellipsoids are drawn at 50% probability.

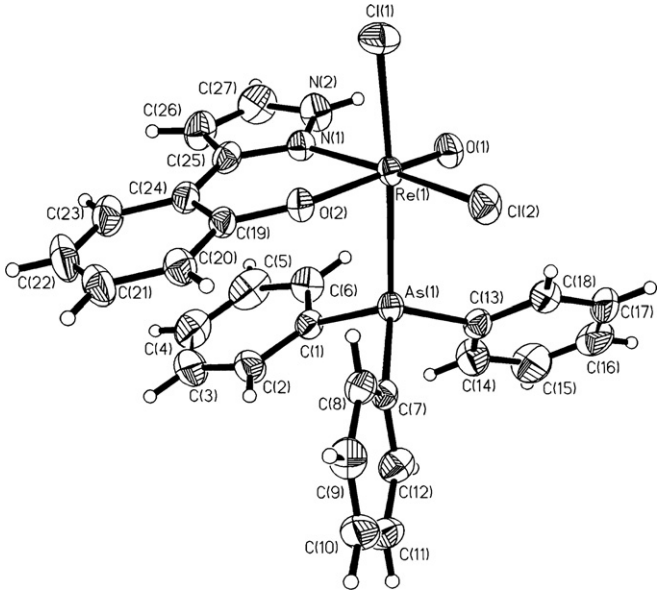


Fig. 3. The molecular structure of **3**. Displacement ellipsoids are drawn at 50% probability.

3. Computational details

The gas phase geometry of **1** was optimized in the singlet ground-state with the DFT method using the hybrid B3LYP [28,29] functional of GAUSSIAN-03 [30]. The LANL2DZ with additional *d* function with exponent $\alpha = 0.3811$ and *f* function with exponent $\alpha = 2.033$ basis set [31,32] was chosen for the rhenium atom and the standard 6-31G basis set for all the other atoms [33,34]. TD-DFT/PCM [35] calculations were employed to produce a hundred singlet excited-states starting from the ground-state geometry optimized in the gas phase.

Natural bond orbital (NBO) calculations were performed with the NBO code [36] included in GAUSSIAN03.

4. Results and discussion

4.1. Preparation and infrared data

The $[ReOX_2(C_9H_7N_2O)(EPh_3)]$ (X = Cl, Br; E = As, P) complexes were prepared in good yields by ligand exchange reactions starting from $[ReOX_3(EPh_3)_2]$ complexes and 2-(1-H-pyrazol-3-yl)phenol in acetone:

$[ReOX_3(EPh_3)_2] + C_9H_8N_2O \rightarrow [ReOX_2(C_9H_7N_2O)(EPh_3)] + HX + EPh_3$ X = Cl, Br; E = As, P.

They were isolated as green microcrystalline solids, soluble in common organic solvents.

The strong ν(Re=O) stretching bands of the $[ReOX_2(C_9H_7N_2O)(EPh_3)]$ compounds are found in the narrow range 960–965 cm^{-1}. They are in the higher end of the range observed for $\{ReO\}^{3+}$ core complexes. It suggests that the Re-hydoxy bond *trans* to the oxo ligand does not compete effectively for the d_{Re} orbitals and indicates the presence of the {O=Re–O} structural subunit in the examined structures. A similar trend is observed for the related Re(V)-oxo complexes with an monoanionic oxygen (RO^- and $R–COO^-$,) *trans* to the oxo group [37].

The H21 and H22 protons (Fig. 2) appear as two doublet of triplets at 6.86 and 6.94 ppm, respectively. Three doublet of doublets at 7.34, 7.21 and 6.61 correspond to H26, H20 and H23, respectively. The H27 proton appears as triplet at 6.63 ppm. The broad singlet at 10.61 ppm is assigned to

Table 4
The experimental and optimized bond lengths (Å) and angles (°) for **1**

Bond lengths	Experimental	Optimized	Bond angles	Experimental	Optimized
Re(1)–O(1)	1.6862(18)	1.699	O(1)–Re(1)–O(2)	164.86(8)	161.26
Re(1)–O(2)	1.9233(17)	1.952	O(1)–Re(1)–N(1)	86.86(8)	84.82
Re(1)–N(1)	2.1442(19)	2.179	O(2)–Re(1)–N(1)	79.45(7)	78.76
Re(1)–Cl(1)	2.4215(7)	2.402	O(1)–Re(1)–Cl(1)	96.46(7)	98.15
Re(1)–Cl(2)	2.3586(6)	2.373	O(2)–Re(1)–Cl(1)	89.46(6)	89.59
Re(1)–P(1)	2.4670(7)	2.551	N(1)–Re(1)–Cl(1)	87.67(6)	85.56
			O(1)–Re(1)–Cl(2)	100.65(6)	102.14
			O(2)–Re(1)–Cl(2)	93.35(5)	94.99
			N(1)–Re(1)–Cl(2)	172.10(6)	171.77
			Cl(1)–Re(1)–Cl(2)	89.00(3)	89.08
			O(1)–Re(1)–P(1)	89.02(6)	87.53
			O(2)–Re(1)–P(1)	85.08(5)	84.84
			N(1)–Re(1)–P(1)	92.03(6)	94.54
			Cl(1)–Re(1)–P(1)	174.49(2)	174.30
			Cl(2)–Re(1)–P(1)	90.59(2)	90.18

Table 5
The experimental bond lengths (Å) and angles (°) for **3** and **4**

Bond lengths	**3** (X = Cl)	**4** (X = Br)	Bond angles	**3** (X = Cl)	**4** (X = Br)
Re(1)–O(1)	1.6827(17)	1.686(5)	O(1)–Re(1)–O(2)	164.62(8)	165.1(2)
Re(1)–O(2)	1.9276(16)	1.924(4)	O(1)–Re(1)–N(1)	86.93(8)	86.8(2)
Re(1)–N(1)	2.134(2)	2.180(6)	O(2)–Re(1)–N(1)	79.87(7)	80.07(19)
Re(1)–X(1)	2.4049(7)	2.5424(8)	O(1)–Re(1)–X(1)	97.46(6)	96.93(16)
Re(1)–X(2)	2.3580(6)	2.4751(9)	O(2)–Re(1)–X(1)	90.19(5)	89.92(13)
Re(1)–As(1)	2.5563(3)	2.5580(7)	N(1)–Re(1)–X(1)	88.91(6)	88.64(14)
			O(1)–Re(1)–X(2)	100.43(6)	99.67(16)
			O(2)–Re(1)–X(2)	92.91(5)	93.58(13)
			N(1)–Re(1)–X(2)	172.62(6)	173.47(14)
			X(1)–Re(1)–X(2)	89.62(2)	89.82(3)
			O(1)–Re(1)–As(1)	87.97(6)	88.74(16)
			O(2)–Re(1)–As(1)	84.36(5)	84.43(13)
			N(1)–Re(1)–As(1)	90.69(6)	91.07(14)
			X(1)–Re(1)–As(1)	174.516(18)	174.30(3)
			X(2)–Re(1)–As(1)	90.075(19)	89.83(3)

the N–H proton of the pyrazole ring. Lack of paramagnetic broadening or shifts of resonances in the ^{1}H NMR spectrum of the title complex confirms its diamagnetism.

Table 6
Atomic charges from the natural population analysis (NPA) for **1**

Atom	Charge
Re(1)	1.020
O(1)	−0.498
O(2)	−0.659
N(1)	−0.313
Cl(1)	−0.447
Cl(2)	−0.393
P(1)	1.376

4.2. Crystal structures

All the complexes crystallise as acetonitrile solvates in the monoclinic space group $P2_1/c$. The cell packing of **1** is shown in Fig. 1. The intra- and intermolecular contacts, which can be considered as weak hydrogen bonds [38,39] are gathered in Table 2. Table 3 presents a short analysis of the π···π stacking interactions between the rings of the 2-(1-H-pyrazol-3-yl)phenolato ligand and one of the triphenyl phospine rings detected in the examined structures [40].

The molecular structures of **1** and **3** are presented in Figs. 2 and 3, and the selected bond distances and angles of **1**, **3** and **4** are collected in Tables 4 and 5.

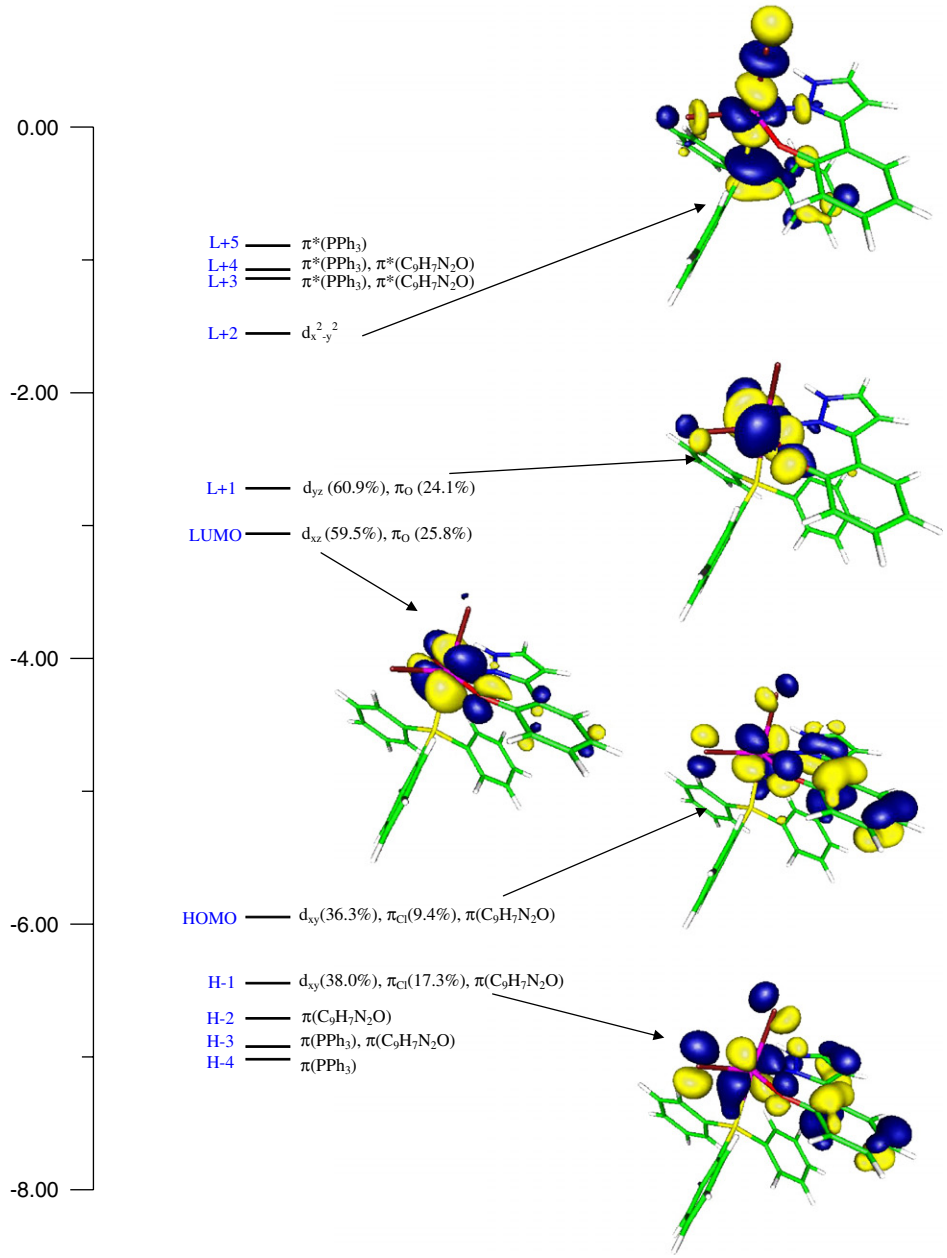


Fig. 4. The energy (eV), character and some contours of the unoccupied molecular orbitals of **1**. Positive values of the orbital contour are represented in blue (0.04 au) and negative values – in yellow (−0.04 au). (For interpretation of the references to colour in this figure legend, the reader is referred to the web version of this article.)

Table 7
The occupancy of the calculated natural bond orbitals (NBOs) between the rhenium and the oxo ligand for **1**

BD	Occupancy	BD	BD*	Occupancy
Re–O_t	1.988	$0.559(d)_{Re} + 0.829(p)_O$	$0.829(d)_{Re} - 0.559(p)_O$	0.285
Re–O_t	1.990	$0.565(d)_{Re} + 0.825(p)_O$	$0.825(d)_{Re} - 0.565(p)_O$	0.305

BD denotes 2-center bond, * denotes antibond NBO.

The geometry of $[ReOX_2(C_9H_7N_2O)(EPh_3)]$ compounds reveals typical features of quasi-octahedral oxorhenium-(V)complexes with oxygenated bidentate ligands. In each complex, the rhenium atom is coordinated by a terminal oxygen atom (O_t), two halide ions in *cis* arrangement, the phosphorus or arsine atom from EPh_3 molecule, and the bidentate N,O donors of the 2-(1-H-pyrazol-3-yl)phenolato ligand. The oxygen atom of 2-(1-H-pyrazol-3-yl)phenolato ligand occupies *trans* position to the terminal oxo ion. The deformation of the octahedron is caused by the presence multiple bonding ligand (terminal oxo) and narrow bite angle of the chelating ligand. The high concentration of electronic density along the Re–O_t axis strongly influences the positions of the adjacent halogen atoms, which are pushed away.

The Re–O_t bond lengths of $[ReOX_2(C_9H_7N_2O)(EPh_3)]$ complexes fall in the range 1.639–1.76 Å, typical of mononuclear complexes of rhenium(V) having $[ReO]^{3+}$ core, and indicate the presence of a triple bond Re≡O [41]. The interatomic distances between the rhenium atom and the oxygen atom of 2-(1-H-pyrazol-3-yl)phenolato ligand are somewhat shorter than an ideal single Re–O bond length (ca. 2.04 Å) [42], It indicates small delocalization in the O(2)–Re(1)–O(1) moiety. The similar trend is observed for many Re(V)-oxo complexes with an monoanionic oxygen *trans* to the oxo group [43].

The Re1–X(1) distances *trans* to the phosphorus or arsine atom of EPh_3 molecule are slightly longer than the Re1–X(2) bonds *trans* to the nitrogen atom of the 2-(1-H-pyrazol-3-yl)phenolato ligand. It is a consequence of *structural trans* effect of the EPh_3 ligands.

4.3. Geometry optimisation, charge distribution, electronic structure and NBO analysis

The geometry of **1** was optimised in a singlet state by the DFT method with the B3LYP functional. The energy of the triplet state is of 15.9 kcal/mol higher. The optimized geometric parameters of **1** are gathered in Table 4. In general, the predicted bond lengths and angles are in agreement with the values based upon the X-ray crystal structure data, and the general trends observed in the experimental data (discussed above) are well reproduced in the calculations.

Table 6 presents the atomic charges from the Natural Population Analysis (NPA) for **1**. The calculated charge on the rhenium atom in **1** is considerable lower than the formal charge +5, corresponding d^2 configuration of the central ion. It results from charge donation from the oxo ligands, halide ions and phosphine molecule. ligands. The P atom is positively charged, and the charges on the terminal oxo, chloride and oxygen atom of 2-(1-H-pyrazol-3-yl)phenolato are significantly smaller than −2, −1 and −1, respectively. The terminal oxo ions are less negative in comparison with the oxygen atoms of 2-(1-H-pyrazol-3-yl)phenolato ligand. It indicates the higher electron density delocalization from the terminal ligand towards the rhenium center and corresponds to differences in the Re–O(1) and Re–O(2) bond lengths.

The energies and characters of several highest occupied and lowest unoccupied molecular orbitals of **1** are presented in Fig. 4. The local symmetry of the rhenium centre

Table 8
Band position (nm) and molar absorption coefficient ($dm^3\ mol^{-1}\ cm^{-1}$) (in brackets) of $[ReOX_2(C_9H_7N_2O)(EPh_3)]$ complexes

1	2	3	4
814.2 (50)	817.1 (50)	809.6 (40)	808.8 (45)
686.8 (115)	684.3 (125)	674.5 (130)	706.0 (100)
401.4 (1165)	401.8 (2750)	397.5 (2780)	400.8 (3020)
283.4 (11 170)	278.0 (12 450)	306.5 (9370)	300.0 (9650)
224.2 (41 800)	224.8 (46 900)	237.3 (47 075)	232.4 (38 350)
208.0 (58 725)	241.5 (62 800)	212.3 (68 600)	208.5 (64 980)

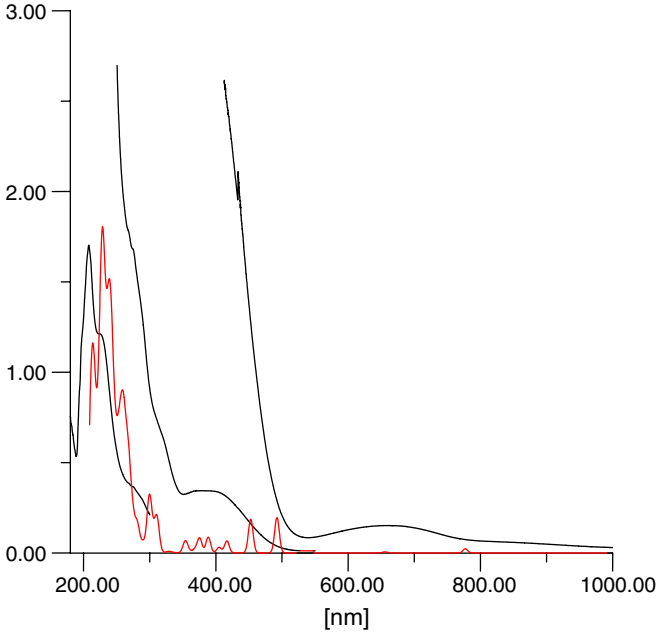


Fig. 5. The experimental (black) and calculated (red) electronic absorption spectra of **1**. (For interpretation of the references to colour in this figure legend, the reader is referred to the web version of this article.)

has been considered in the discussion: z axis goes along the O–Re–O linkage, and x axis – through the P–Re–Cl bonds. The HOMO–LUMO gap of **1** equals to 2.89 eV. Two highest occupied MOs are delocalized among d_{xy} rhenium orbital, chloride and 2-(1-H-pyrazol-3-yl)phenolato orbitals. The LUMO and LUMO + 1 are predominately localized on the rhenium atom (d_{xz} and d_{yz} orbitals) with some contribution of p_π oxygen orbitals. They can be ascribed as π-antibonding rhenium–oxygen molecular orbitals. The LUMO + 2 is of $d_{x^2-y^2}$ character, and d_{z^2} rhenium orbital contributes to the LUMO + 11.

Since the rhenium atom has d^2 electronic configuration, the empty $5d_{xz}$ and $5d_{yz}$ orbitals are available to overlap with $2p_x$ and $2p_y$ orbitals of the terminal oxygen to form an effective triple bond.

The nature of rhenium–terminal oxygen interaction in **1** has been studied by NBO analysis. The occupancy and composition of the calculated Re–O_t natural bond orbitals (NBOs) are given in Table 7.

Each natural bond orbital (NBO) σ_{AB} can be written in terms of two directed valence hybrids (HHOs) h_A and h_B on atoms A and B:

Table 9
The energy and molar absorption coefficients of experimental absorption bands and the electronic transitions calculated with the TD-DFT method for **1**

The most important orbital excitations	Character	λ (nm)	E (eV)	f	Experimental Λ (nm) [E (eV)] ε
H → L	d → d	777.2	1.60	0.0046	814.2 (1.52) 50
H → L + 1	d → d	655.7	1.89	0.0012	686.8 (1.81) 115
H − 1 → L	π(Cl)/π($C_9H_7N_2O$) → d	492.4	2.52	0.0390	401.4 (3.09) 1165
H − 1 → L + 1	π(Cl)/π($C_9H_7N_2O$) → d	452.7	2.74	0.0372	
H − 2 → L	π($C_9H_7N_2O$) → d	416.6	2.98	0.0132	
H → L + 2	d → d	404.8	3.06	0.0062	
H − 3 → L	π(PPh_3)/π($C_9H_7N_2O$) → d	388.5	3.19	0.0174	
H − 2 → L + 1	π($C_9H_7N_2O$) → d	375.5	3.30	*0.0162*	
H − 3 → L + 1	π(PPh_3)/π($C_9H_7N_2O$) → d	353.9	3.50	0.0124	
H − 1 → L + 2	π(Cl)/π($C_9H_7N_2O$) → d	311.5	3.98	0.0223	283.4 (4.37) 11170
H − 9 → L + 1	π(Cl)/π($C_9H_7N_2O$) → d				
H → L + 3	d → π*(PPh_3)/π*($C_9H_7N_2O$)	299.3	4.14	0.0560	
H → L + 2	d → π*(PPh_3)	280.7	4.42	0.0268	
H − 2 → L + 2	π($C_9H_7N_2O$) → d	272.8	4.55	0.0383	224.2 (5.53) 41800
H − 1 → L + 3	π(Cl)/π($C_9H_7N_2O$) → π*(PPh_3)/π*($C_9H_7N_2O$)	267.1	4.64	0.0891	
H − 3 → L + 2	π(PPh_3)/π($C_9H_7N_2O$) → d	261.3	4.75	0.0619	
H − 12 → L + 1	π(Cl)/π(O)/π($C_9H_7N_2O$)/*n*(P) → d	259.6	4.77	0.0427	
H → L + 7	d → π*(PPh_3)	257.1	4.82	0.0204	
H − 4 → L + 2	π(PPh_3) → d	255.3	4.86	0.0565	
H − 13 → L + 1	π(Cl)/π(O)/π($C_9H_7N_2O$) → d				
H − 1 → L + 5	π(Cl)/π($C_9H_7N_2O$) → π*(PPh_3)	251.4	4.93	0.0218	
H − 6 → L + 2	π(PPh_3) → d	250.0	4.96	0.0300	
H − 15 → L + 1	π($C_9H_7N_2O$)/π(Cl)/π(O)/*n*(P) → d	246.5	5.03	0.0546	
H − 15 → L + 1	π($C_9H_7N_2O$)/π(Cl)/π(O)/*n*(P) → d	242.1	5.12	0.0709	
H → L + 8	d → π*(PPh_3)				
H − 4 → L + 3	π(PPh_3) → π*(PPh_3)/π*($C_9H_7N_2O$)	241.8	5.13	0.0609	
H → L + 8	d → π*(PPh_3)				
H − 8 → L + 2	π(PPh_3) → d	238.7	5.20	0.0472	
H − 3 → L + 4	π(PPh_3)/π($C_9H_7N_2O$) → π*(PPh_3)/π*($C_9H_7N_2O$)				
H → L + 9	d → π*(PPh_3)/π*($C_9H_7N_2O$)	237.1	5.23	0.0513	
H − 9 → L + 2	π(Cl)/π($C_9H_7N_2O$)/d → d				
H − 3 → L + 4	π(PPh_3)/π($C_9H_7N_2O$) → π*(PPh_3)/π*($C_9H_7N_2O$)	235.5	5.26	0.0279	
H − 2 → L + 5	π($C_9H_7N_2O$) → π*(PPh_3)	235.1	5.27	0.0337	
H − 8 → L + 2	π(PPh_3) → d	234.3	5.29	0.0278	
H − 2 → L + 5	π($C_9H_7N_2O$) → π*(PPh_3)				
H → L + 10	d → π*(PPh_3)/π*($C_9H_7N_2O$)	230.2	5.38	0.1531	
H − 3 → L + 4	π(PPh_3)/π($C_9H_7N_2O$) → π*(PPh_3)/π*($C_9H_7N_2O$)				
H − 17 → L	n(P) → d	226.6	5.47	0.0330	
H − 5 → L + 4	π(PPh_3) → π*(PPh_3)/π*($C_9H_7N_2O$)	226.5	5.47	0.0808	
H − 10 → L + 2	π(Cl)/*n*(P) → d	225.6	5.49	0.0368	
H − 1 → L + 9	π(Cl)/π($C_9H_7N_2O$) → π*(PPh_3)/π*($C_9H_7N_2O$)	216.7	5.72	0.0349	208.0 (5.96) 58.725
H − 8 → L + 3	π(PPh_3) → π*(PPh_3)/π*($C_9H_7N_2O$)	215.0	5.77	0.0662	
H − 8 → L + 3	π(PPh_3) → π*(PPh_3)/π*($C_9H_7N_2O$)	212.6	5.83	0.0364	

ε – molar absorption coefficient ($dm^3\ mol^{-1}\ cm^{-1}$); f – oscillator strength; H – highest occupied molecular orbital; L – lowest unoccupied molecular orbital.

$$\sigma_{AB} = c_A h_A + c_B h_B$$

where c_A and c_B are polarization coefficients. Each valence bonding NBO must in turn be paired with a corresponding valence *anti*-bonding NBO:

$$\sigma^*_{AB} = c_B h_A - c_A h_B$$

to complete the span of the valence space. The Lewis-type (donor) NBOs are thereby complemented by the non-Lewis-type (acceptor) NBOs that are formally empty in an idealized Lewis picture. The interactions between 'filled' Lewis-type NBOs and 'empty' non-Lewis NBOs lead to loss of occupancy from the localized NBOs of the idealized Lewis structure into the empty non-Lewis orbitals, and they are referred to as 'delocalization' corrections to the zeroth-order natural Lewis structure [36].

Two detected natural Re–O_t bond orbitals of **1** are π orbitals – the p_x and p_y oxygen orbitals and d_{xz} and d_{yz} rhenium orbitals are involved in their formation. Not detected σ_{Re-O_t} bond has character of predominant Coulomb-type interactions between the central ion and ligands [44]. The terminal oxo ligand of **1** has two lone pair orbitals, and electron density from one of them is strongly delocalized into non-Lewis rhenium orbital. Accordingly, NBO analysis confirms a triple bond between the rhenium and the terminal oxygen ligand.

4.4. Electronic spectra

The electronic spectra of $[ReOX_2(C_9H_7N_2O)(EPh_3)]$ complexes are very similar in terms of the position, intensity and shape of the bands in the whole region 1000–180 nm. The positions and molar absorption coefficients of electronic bands for $[ReOX_2(C_9H_7N_2O)(EPh_3)]$ complexes are given in Table 8.

The experimental and calculated electronic spectra of **1** are presented in Fig. 5. Each calculated transition is represented by a gaussian function $y = ce^{-bx^2}$ with the height (c) equal to the oscillator strength and b equal to 0.04 nm^{-2}. Table 9 presents the calculated singlet–singlet electronic transitions of **1** and their assignments to the experimental bands. For the high energy part of the spectrum, only transitions with oscillator strengths larger than 0.020 are listed in Table 9.

The assignment of the calculated transitions to the experimental bands is based on the criterion of the energy and oscillator strength of the calculated transitions. In the description of the electronic transitions the HOMO orbital is described as d_{Re} orbital, whereas the participation of d_{Re} in the H − 1 orbital is omitted.

The longest wavelength experimental bands of **1** at 814.2 and 686.8 nm are attributed to the transitions of d → d character. The *Ligand–Metal Charge Transfer* ($\pi(PPh_3)/\pi(Cl)/\pi(C_9H_7N_2O)$ → d) transitions make the largest contribution into the experimental band at 401.4 nm. The absorption band at 283.4 nm is mainly assigned to *Metal–Ligand Charge Transfer* excitations, whereas the experimental bands at 224.2 and 208.0 nm result mainly from the *Ligand–Ligand Charge Transfer* and interligand (IL) transitions.

5. Supplementary material

CCDC 659177, 659178, and 659179 contain the supplementary crystallographic data for $C_{29}H_{25}Cl_2N_3O_2Pre$, $C_{29}H_{25}Cl_2N_3O_2AsRe$ and $C_{29}H_{25}Br_2N_3O_2AsRe$. These data can be obtained free of charge via http://www.ccdc.cam.ac.uk/conts/retrieving.html, or from the Cambridge Crystallographic Data Centre, 12 Union Road, Cambridge CB2 1EZ, UK; fax: (+44) 1223-336-033; or e-mail: deposit@ccdc.cam.ac.uk.

Acknowledgement

The GAUSSIAN03 calculations were carried out in the Wrocław Centre for Networking and Supercomputing, WCSS, Wrocław, Poland.

References

[1] R.H. Holm, Chem. Rev. 87 (1987) 1401.
[2] C.C. Romão, F.E. Kühn, W.A. Hermann, Chem. Rev. 97 (1997) 3197.
[3] S.B. Seymore, S.N. Brown, Inorg. Chem. 39 (2000) 325.
[4] F.E. Kühn, A. Scherbaum, W.A. Herrmann, J. Organomet. Chem. 689 (2004) 4149.
[5] A.M. Kirillov, M. Haukka, M.V. Kirillova, A.J.L. Pombeiro, Adv. Synth. Catal. 347 (2005) 1435.
[6] W. Volkert, W.F. Goeckeler, G.J. Ehrhardt, A.R. Ketring, J. Nucl. Med. 32 (1991) 174.
[7] E.A. Deutsch, K. Libson, J.L. Vanderheyden, Technetium and Rhenium in Chemistry and Nuclear Medicine, Raven Press, New York, 1990.
[8] B. Machura, Coord. Chem. Rev. 249 (2005) 591.
[9] F.H. Allen, Acta Crystallogr. B 58 (2002) 380.
[10] H. Chermette, Coord. Chem. Rev. 178–180 (1998) 699.
[11] M.C. Aragoni, M. Arca, T. Cassano, C. Denotti, F.A. Devillanova, F. Isaia, V. Lippolis, D. Natali, L. Niti, M. Sampietro, R. Tommasi, G. Verani, Inorg. Chem. Commun. 5 (2002) 869.
[12] P. Romaniello, F. Lelj, Chem. Phys. Lett. 372 (2003) 51.
[13] A. Voigt, U. Abram, R. Böttcher, U. Richter, J. Reinhold, R. Kirmse, Chem. Phys. 253 (2000) 171.
[14] M.L. Kuznestov, A.J. L Pombeiro, Dalton Trans. (2003) 738.
[15] J. Gancheff, C. Kremer, E. Kremer, O.N. Ventura, J. Mol. Struct. (Theochem) 580 (2002) 107.
[16] M.L. Kuznestov, E.A. Klestova-Nadeeva, A.I. Dement'ev, J. Mol. Struct. (Theochem) 671 (2004) 229.
[17] N. Psaroudakis, K. Mertis, D.G. Liakos, E.D. Simandiras, Chem. Phys. Lett. 369 (2003) 490.
[18] X.-Y. Liu, S. Bouherour, H. Jacobsen, H.W. Schmalle, H. Berke, Inorg. Chim. Acta 330 (2002) 250.
[19] M.L. Kuznestov, A.A. Nazarov, A.J.L. Pombeiro, J. Phys. Chem. A 109 (2005) 8187.
[20] W.-Y. Wong, S.-H. Cheung, X. Huang, Z. Lin, J. Organomet. Chem. 655 (2002) 39.
[21] B. Machura, R. Kruszynski, M. Jaworska, Polyhedron 25 (2006) 1111.
[22] B. Machura, R. Kruszynski, Polyhedron 25 (2006) 1985.
[23] G. Rouschias, G. Wilkinson, J. Chem. Soc. A (1966) 465.
[24] STOE & Cie, X-RED, Version 1.18, STOE & Cie GmbH, Darmstadt, Germany, 1999.
[25] G.M. Sheldrick, Acta Cryst. A 46 (1990) 467.

[26] G.M. Sheldrick, SHELXL97, Program for the Refinement of Crystal Structures, University of Göottingen, Germany, 1997.
[27] G.M. Sheldrick, SHELXTL: Release 4.1 for Siemens Crystallographic Research Systems, 1990.
[28] A.D. Becke, J. Chem. Phys. 98 (1993) 5648.
[29] C. Lee, W. Yang, R.G. Parr, Phys. Rev. B 37 (1988) 785.
[30] M.J. Frisch, G.W. Trucks, H.B. Schlegel, G.E. Scuseria, M.A. Robb, J.R. Cheeseman, J.A. Montgomery, Jr., T. Vreven, K.N. Kudin, J.C. Burant, J.M. Millam, S.S. Iyengar, J. Tomasi, V. Barone, B. Mennucci, M. Cossi, G. Scalmani, N. Rega, G.A. Petersson, H. Nakatsuji, M. Hada, M. Ehara, K. Toyota, R. Fukuda, J. Hasegawa, M. Ishida, T. Nakajima, Y. Honda, O. Kitao, H. Nakai, M. Klene, X. Li, J.E. Knox, H.P. Hratchian, J.B. Cross, C. Adamo, J. Jaramillo, R. Gomperts, R.E. Stratmann, O. Yazyev, A.J. Austin, R. Cammi, C. Pomelli, J.W. Ochterski, P.Y. Ayala, K. Morokuma, G.A. Voth, P. Salvador, J.J. Dannenberg, V.G. Zakrzewski, S. Dapprich, A.D. Daniels, M.C. Strain, O. Farkas, D.K. Malick, A.D. Rabuck, K. Raghavachari, J.B. Foresman, J.V. Ortiz, Q. Cui, A.G. Baboul, S. Clifford, J. Cioslowski, B.B. Stefanov, G. Liu, A. Liashenko, P. Piskorz, I. Komaromi, R.L. Martin, D.J. Fox, T. Keith, M.A. Al-Laham, C.Y. Peng, A. Nanayakkara, M. Challacombe, P.M.W. Gill, B. Johnson, W. Chen, M.W. Wong, C. Gonzalez, J.A. Pople, GAUSSIAN 03, Revision B.03, Gaussian, Inc., Pittsburgh, PA, 2003.
[31] P.J. Hay, W.R. Wadt, J. Chem. Phys. 82 (1985) 299.
[32] K. Eichkorn, F. Weigend, O. Treutler, R. Ahlrichs, Theor. Chem. Acc. 97 (1997) 119.
[33] P.C. Hariharan, J.A. Pople, Theor. Chim. Acta 28 (1973) 213.
[34] V.A. Rassolov, M.A. Ratner, J.A. Pople, P.C. Redfern, L.A. Curtiss, J. Comp. Chem. 22 (2001) 976.
[35] M.E. Casida, in: J.M. Seminario (Ed.), Recent Developments and Applications in Modern Density Functional Theory, Theoretical and Computational Chemistry, vol. 4, Elsevier, Amsterdam, 1996.
[36] E.D. Glendening, A.E. Reed, J.E. Carpenter, F. Weinhold, NBO (Version 3.1), A.E. Reed, L.A. Curtiss, F. Weinhold, Chem. Rev. 88 (1988) 899.
[37] L. Wei, J. Babich, J. Zubieta, Inorg. Chim. Acta 358 (2005) 2413.
[38] G.R. Desiraju, T. Steiner, The Weak Hydrogen Bond in Structural Chemistry and Biology, Oxford University Press, 1999.
[39] G.A. Jeffrey, W. Saenger, Hydrogen Bonding in Biological Structures, Springer-Verlag, 1994.
[40] C.A. Hunter, J.K.M. Sanders, J. Am. Chem. Soc. 112 (1990) 5525.
[41] J.M. Mayer, Inorg. Chem. 27 (1988) 3899.
[42] S.R. Fletcher, A.C. Skapski, J. Chem. Soc., Dalton (1972) 1073.
[43] E. Shuter, H.R. Hoveyda, V. Karunaratne, S.J. Retting, C. Orvig, Inorg. Chem. 35 (1996) 368.
[44] M.L. Kuznetsov, A.J.L. Pombeiro, J. Chem. Soc., Dalton Trans. (2003) 738.

property via chelating ability of hydrophilic carboxylate group. Such pronounced effects have already resulted in good dispersibility of CuO nanoparticles in variety of organic solvents such as *n*-octane, *n*-dodecane and *n*-hexadecane [15].

However, we have explored somewhat different approach where in the precursor is devised utilizing the coordination tendency of carboxylate group of oleic acid and the resultant precursor possesses chelated iron center surrounded by hydroxide-gel. This may lead to the generation well segregated iron nuclei in the matrix of oleate groups which upon appropriate chemical treatment may result in small sized, well-dispersed and structurally defined nanoparticles. The present communication describes the nonaqueous synthesis of iron oxide nanoparticles using iron hydroxy-oleate precursor in different organic solvents such as hexadecane, 2-pyrrolidinone and 1-methylnaphthalene generating high-purity iron oxide nanocrystals.

2. Experimental

2.1. Materials

In the present exercise, iron(III) nitrate nonahydrate (99.5%) ammonia (30% v/v) were obtained from Samchun Chemicals while oleic acid, hexadecane, 2-pyrrolidinone and 2-methyl naphthalene were purchased from Aldrich Chemical Co. and were used as received.

2.2. Synthesis of iron hydroxy-oleate precursor

The iron hydroxy-oleate precursor was prepared from iron(III) nitrate and oleic acid. In 200 ml of commercial ethanol, 20.0 g of $Fe(NO_3)_3 \cdot 9H_2O$ was dissolved. To this solution, 7.06 g of oleic acid in 10 ml of ethanol was added with constant stirring followed by a rapid addition of 20 ml of concentrated NH_3 (30%) under vigorous stirring. After the addition of ammonia, the brown colored solution was stirred for 30 min and the as-formed precipitate was filtered, washed well with hot ethanol (5–6 times). The washed precipitate was dried at room temperature overnight.

2.3. Synthesis of iron oxide nanoparticles

In a typical preparation of iron oxide nanocrystal, 2.0 g of iron hydroxy-oleate precursor was suspended in 50 ml of hexadecane and 2.7 g of oleic acid was added at room temperature. The reaction mixture was heated to 250 °C with constant stirring in an oil bath and then kept at that temperature for 2 h. The resulting solution containing nanocrystals was then cooled to room temperature and the excess of ethanol (100 ml) was added to it. A brown precipitate formed immediately, which was isolated by centrifugation at 3000 rpm for 30 min and finally purified with ethanol (3–4 times).

The synthesis was also carried out in two other solvents viz. 2-methylnaphthalene and 2-pyrrolidinone under the similar conditions. The nanoparticles prepared in different solvents are abbreviated as Fe_1 (hexadecane), Fe_2 (2-methylnaphthalene) and Fe_3 (2-pyrrolidinone).

2.4. Characterization

The XRD patterns of as-prepared iron-oxy precursor and iron oxide particles were examined by Rigaku D/MAX IIIB X-ray diffractometer with Cu Kα radiations while FT–IR spectra were recorded on BIO-RAD FT–IR spectrometer (FTS165). The TG/DTA analysis of precursor under N_2 was carried out on Setaram TG 92–12 from 20 to 700 °C at a heating rate of 10 °C/min. The morphological analyses of iron oxide nanomaterial were performed on SEM (Phillips XL30S FEG microscope) and TEM (Model-EM 912Ω, Leo Zeiss Germany). Photoluminescence (PL) emission and excitation spectra of powder sample as well as dispersed solution in $CHCl_3$ were obtained using a Perkin–Elmer LS50B luminescence spectrometer. XPS were recorded with nine channeltron CLAM4 analyzer under vacuum better than 1×10^{-8} Torr using Mg Kα radiation and a constant energy of 50 eV.

3. Results and discussion

The objective of the present work is focused on the nonaqueous synthesis of iron oxide nanoparticles and for this purpose different organic solvents are used. The precursor molecule is designed in such a way that the surfactant molecule will not only function as capping agent but also its coordination tendency will also be effectively utilized for the generation of small sized hydroxide gel. These precursor molecules shall then be decomposed in appropriate organic solvent at elevated temperatures without the loss of capping agent during the synthesis. Being a long chain carboxylic acid, oleic acid is found to possess both these tendencies and its effectiveness has already been explored for CuO nanoparticles [15]. Thus, in the present case, the iron oxide nanoparticles are prepared using oleic acid, which is used both as coordinating and capping agent.

3.1. Thermal studies

In order to determine the decomposition temperature for the formation of iron oxide nanoparticles, the iron hydroxy-oleate precursor was subjected for thermogravimetric studies under N_2 atmosphere at heating rate of 10 °C/min. The thermal pattern exhibits (Fig. 1) two distinct stages of thermal decomposition; the first peak around 100 °C corresponds to desorption of water molecules from the grain surfaces while the other peak centered around 250 °C is probably originating form the onset of thermal decomposition of oleate molecules. Afterwards, there is gradual weight loss with the formation of oxide phase. Similar behavior is also noted for DTA curve with

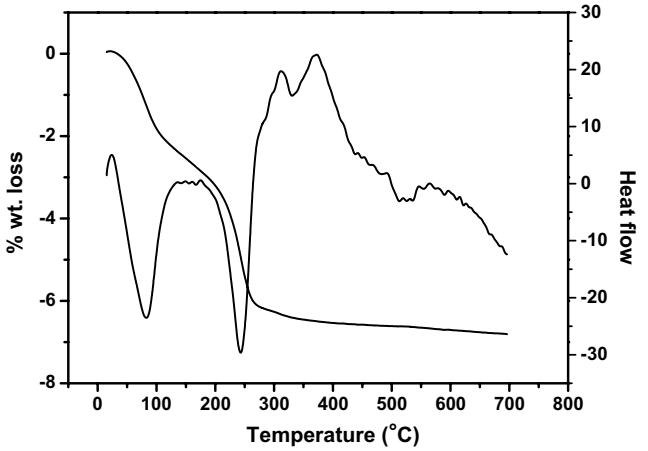


Fig. 1. Thermogravmetric profile of iron hydroxy-oleate precursor.

two endothermic peaks suggesting that the decarboxylation proceeds thorough liberation of oleate fragment from the precursor molecule. From such decomposition patters, it is significant to note that the formation of stable iron oxide phase can be achieved during the thermal decomposition of the iron hydroxy-oleate precursor around 250 °C in various organic solvents thus generating oleate capped iron oxide nanoparticles.

3.2. FT-IR characterization

It is observed that the carboxylate absorption in free oleic acid (1711 cm^{-1}) is considerably shifted towards lower energy side which appears as a doublet for precursor molecule (Fig. 2). Since these two bands are not symmetric in nature as well as they are well separated by almost 150 cm^{-1}, the oleate group is functioning as a bridge (Fig. 2a) between precursor molecules indicating the strong associations through electrostatic interactions [16]. After the thermal treatment of precursor, the presence of splitted absorption at 1534 and 1431 cm^{-1} for Fe_1 (Fig. 2b) reveals the anchoring of the oleate molecules on the surfaces of iron oxide nanoparticles while the bands at 2925 and 2856 cm^{-1} due to $–CH_2$ and $–CH_3$ signify that oleate group still remains as a part of iron oxide nanoparticles. In addition to these changes, the spectrum of capped iron oxide nanoparticles exhibit characteristic Fe–O stretches at 594 and 459 cm^{-1} from iron oxide network.

3.3. XRD analysis

Fig. 3 presents the XRD patterns of iron hydroxy–oleate precursor before (as received) and after thermal treatment in different solvents. It is observed that the precursor material exhibits very broad reflections due to formation small-sized particles (30–40 nm) as evaluated using Scherrer equation showing partial crystallinity. Upon thermal treatment in organic solvents at 250 °C for 2 h, the initial broad signals are replaced with sharp and intense reflections in the 2θ regions 20–80° pointing to the formation of nanocrystalline iron oxide particles. Inspection of these features reveals that iron hydroxy-oleate precursor undergoes structural changes during the thermal decomposition process resulting in the formation of hematite nanoparticles. The characteristic d-spacing values obtained for the reflections due to different planes are in agreement with the reported values (JCPDS No. 33-663) suggesting the presence of α-phase [17,18] of iron oxide (α-Fe_2O_3). The average crystallite sizes evaluated from Scherrer equation for Fe_1–Fe_3 are found to be 32.6, 31.5 and 22.6 nm respectively. However, it is observed that there exists an effect of organic solvent on the morphologies of nanocrystals formed during their synthesis as evidenced from the peak intensities as well as shape of the characteristic oxide phase. For example, the smaller particle size is observed for α-Fe_2O_3 prepared in hexadecane (Fe_1) while for Fe_2 and Fe_3, there seems to be not much of difference in their sizes. Such a size and structural features dependency with the solvent used for synthesis may be originating from the fact that the oleate capping is less effective in hexadecane due to its

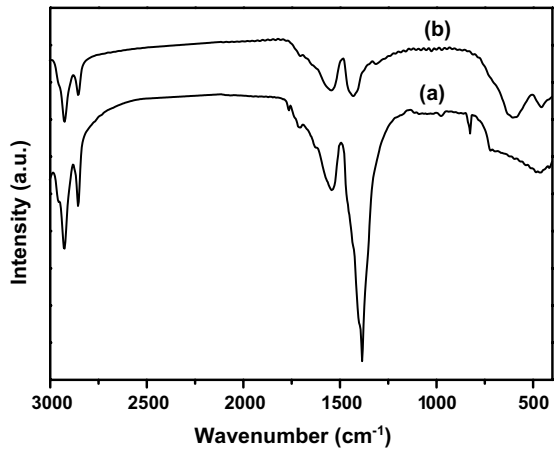


Fig. 2. FT-IR spectra of: (a) iron hydroxy-oleate precursor and (b) Fe_1.

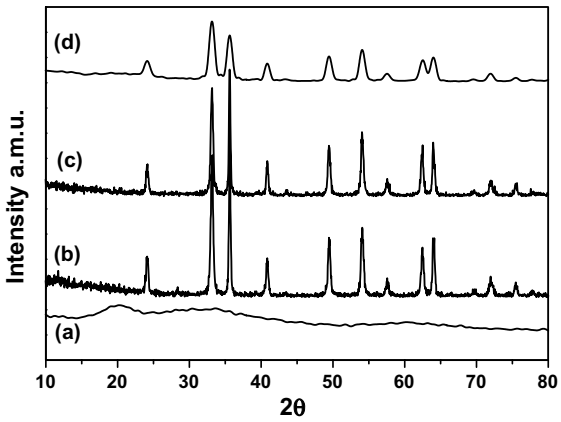


Fig. 3. XRD patterns of: (a) iron hydroxy oleate precursor; (b) Fe_1; (c) Fe_2 and (d) Fe_3.

higher solubility while remaining two solvents have pronounced effect on the crystal growth during the synthesis of iron oxide nanoparticles.

3.4. SEM and TEM analysis

The SEM image of precursor indicates the presence of agglomeration for precursor particles having diameters ranging from 30 to 40 nm. However, the SEM pictures of Fe_2 and Fe_3 (Fig. 4b, c) reveal the spherical-globular clusters with acicular shapes of α-Fe_2O_3 indicating that these particles are agglomerated. On the other hand, TEM photograph of Fe_1 (Fig. 4a) exhibits a cubic shape having particle size of about 30 nm with almost monodisperse phase while Fe_2 and Fe_3 display spherical morphology (Fig. 4b and c) with particle size of about 20 nm. It is evident form this analysis that the morphologies from irregular shape (Fe_2 and Fe_3) transforms into a regular cubic geometry with increase in the particle size (Fe_1). Also, the particle size of Fe_1 observed from TEM measurements is comparable with the one calculated by XRD revealing that the particles are polycrystalline in nature having almost monodisperse phase while Fe_3 consists of a large number of smaller subparticles of tens of nanometers; a feature already been noted by other coworkers [19].

3.5. Photoluminescence studies

It has been reported earlier that bulk hematite exhibits an absorption band around 400 nm attributed to d–d transition [20] while high-energy bands are originating from charge transfer process [21]. However, the criterias are quite different for nanoparticles where the large surface-to-volume ratios induce defects on the surface of particles and bonding of these molecules may result in changes of electronic structures of the particle. It is suggested that localized d–d transition near band-edge as well as other states like 4s or 4p may be involved in the band-edge transition as result of organosol formation between iron oxide nanoparticles and carboxylate groups resulting in a photoluminescent properties for capped iron oxide. Fig. 5 depicts photoluminescence spectra of Fe_1 in solid as well as its dispersion in toluene which are excited at 400 nm. Inspection of this figure reveals that bulk iron oxide (Fe_1) exhibit emission band at lower energy (592 nm) as compared to dispersed organosol (446 nm) indicating that the bulk nanoparticles are agglomerated while they are well dispersed in solution. Red shift of about 55 nm with peak broadening for the bulk is indicative of band-edge emission with decrease in the band-gap. Considering the large Stokes shift of emission peak compared with excitation line, it is attributable to bound-exciton emission, as usually

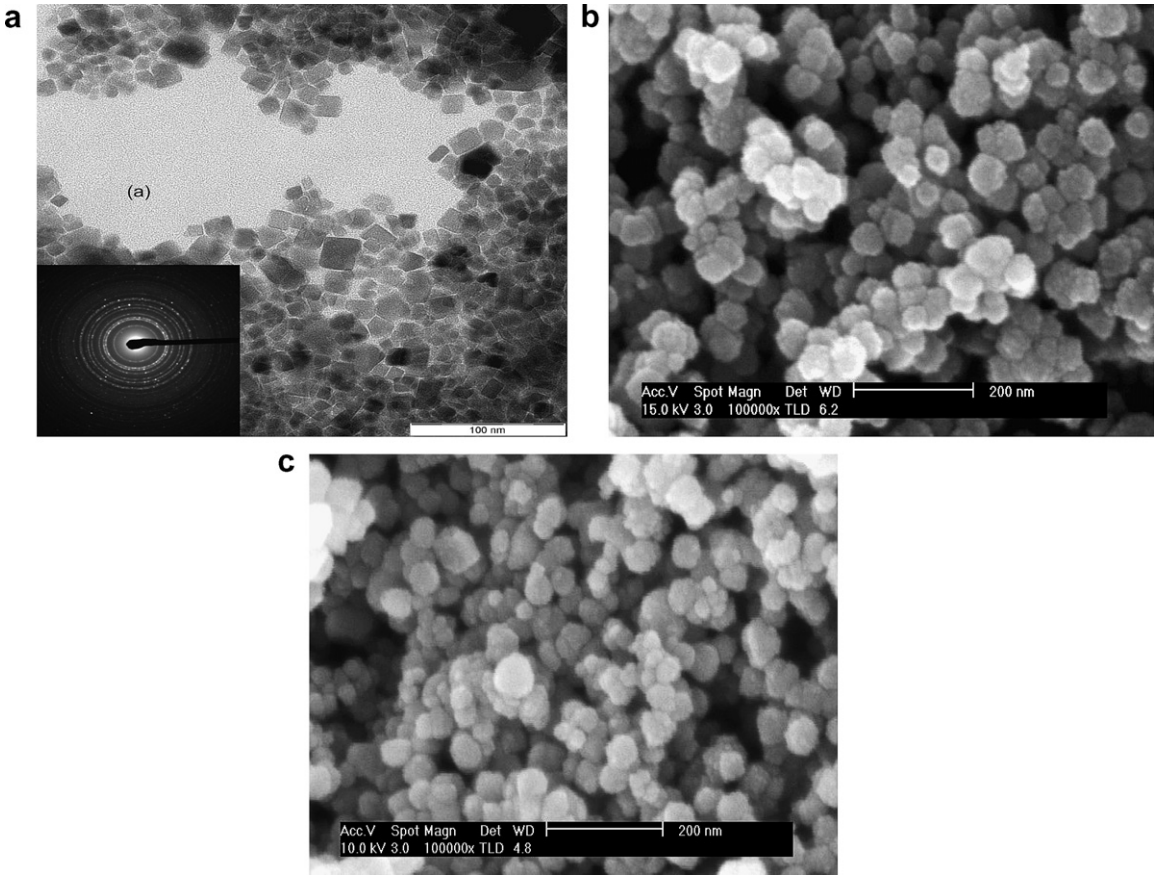


Fig. 4. Morphology of iron oxide nanoparticles: (a) TEM image with SAED pattern of Fe_1, SEM images of Fe_2 (b) and Fe_3 (c).

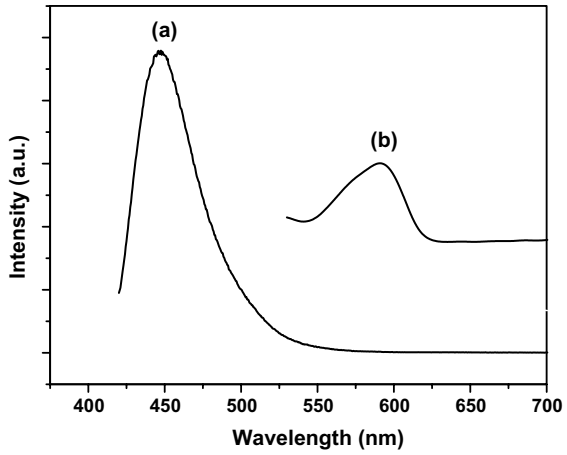


Fig. 5. The photoluminescence spectra of: (a) dispersed solution of Fe_1 in toluene and (b) solid Fe_1 nanocrystals at 400 nm excitation wavelength.

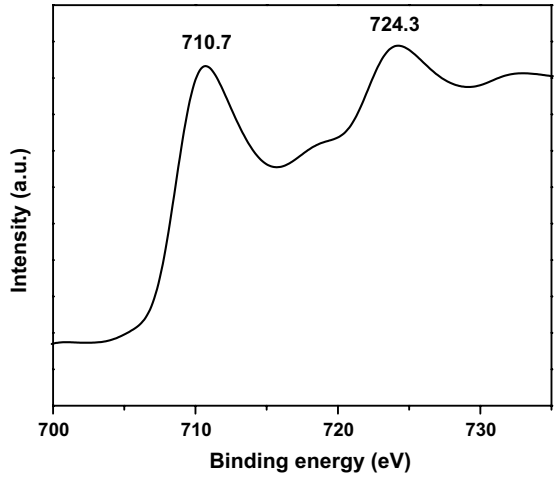


Fig. 6. XPS spectrum for Fe_1.

observed for typical semiconductor nanoparticles. Therefore, it can be argued that the photoluminescence is essentially observed due to the surface modifications of nanoparticles, as observed for hematite nanocrystals with dodecyl benzene sulfonate [22] and pyrene carboxylic acid [23] surfactants.

3.6. XPS measurements

XPS measurements have provided valuable information about the oxidation state as well as surface state of the nanoparticles. The binding energies at 710.7 and 724.3 eV are the characteristic doublet from Fe $2p_{3/2}$ and Fe $2p_{1/2}$ core electrons, respectively (Fig. 6). The spectra of nanoparticles not only matched with the peak positions but also the shapes of the curves reported for α-Fe_2O_3. Moreover, the intensity ratio of the doublet suggests that nanoparticles exclusively exists in the α-form of iron oxide as γ-iron oxide possess difference in the intensity of the doublet with the former peak having about twice the intensity as compared to later peak [24].

4. Conclusion

Solvothermal decomposition of iron hydroxy-oleate precursor in organic solvents in presence of oleic acid can be an effective method for synthesizing iron oxide nanoparticles exhibiting organophilic character. It is observed that these nanocrystals possess cubical as well as spherical morphologies depending upon the solvent employed for synthesis having size of 20–30 nm. Present investigation also highlights an effective way to synthesize surfactant-modified nanoparticles via pre-dispersed precursor molecule thus inferring that dispersibility may be achieved via surface modification technique. The morphology is found to be strongly influenced by the solvents used for the synthesis while the band-edge emission of dispersed nanoparticles is indicative of surface modifications as revealed from the PL measurements. Such modifications bearing the structural network incorporated in functional groups of capping agent possess high technological and biological importance and certainly are the subject of future work in the field of colloidal chemistry.

Acknowledgement

R.C.C. is thankful to KOSEF for Brain-Pool Fellowship and Management and Principal, MES Abasaheb Garware College, Pune, India for grant of study leave.

References

[1] G. Schmid (Ed.), Nanoparticles: From Therapy to Applications, Wiley-VCH, Weinheim, 2004.
[2] D. Pouliquen, C. Chouly, in: R. Arshady (Ed.), Magnetic Microcarriers for Medical Applications, Citus Books, London, 1999, p. 343 (Chapter 12).
[3] J.M. Perez, T. O'Loughin, F.J. Simeone, R. Weissleder, L. Josephson, J. Am. Chem. Soc. 124 (2002) 2856.
[4] M. Zhao, L. Josephson, Y. Tang, R. Weissleder, Angew. Chem., Int. Ed. 42 (2003) 1375.
[5] A.K. Gupta, M. Gupta, Biomaterials 26 (2005) 3995.
[6] L. Shen, P.E. Laibinis, T.A. Hutton, Langmuir 15 (1999) 447.
[7] D.K. Kim, M. Mikhaylova, Y. Zhang, M. Muhammed, Chem. Mater. 15 (2003) 1617.
[8] W. Wang, S. Efrima, O. Regev, Langmuir 14 (1998) 602.
[9] N. Wu, L. Fu, M. Su, M. Aslam, K.C. Wong, V.P. Dravid, Nano Lett. 4 (2004) 383.
[10] J. Rockenberger, E.C. Scher, A.P. Alivisatos, J. Am. Chem. Soc. 121 (1999) 11595.
[11] S. Sun, H. Zeng, D.B. Robinson, R. Raoux, P.M. Rice, S.X. Wang, G. Li, J. Am. Chem. Soc. 126 (2004) 273.
[12] J. Cheon, N.S. Kang, S.M. Lee, J.H. Lee, J.H. Yoon, S.J. Oh, J. Am. Chem. Soc. 126 (2004) 1950.
[13] A.B. Bourlions, A. Simopoulos, D. Petridis, Chem. Mater. 14 (2002) 899.
[14] J. Park, K. An, Y. Hwang, J.E. Park, H.N. Noh, J.Y. Kim, J.H. Park, N.M. Hwang, T. Hyeon, Nat. Mater. 3 (2004) 891.
[15] C.C. Li, M.H. Chang, Mater. Lett. 58 (2004) 3903.
[16] M.R. Alexander, G. Beamson, C.J. Blomfield, G. Leggett, T.M. Duc, J. Electron Spectrosc. 121 (2001) 19.
[17] Z. Li, Y. Zhu, Appl. Surf. Sci. 211 (2003) 315.

[18] Z. Jing, D. Han, S. Wu, Mater. Lett. 59 (2005) 804.
[19] Z. Jing, S. Wu, Mater. Lett. 58 (2004) 3637.
[20] H. Itoh, T. Sugimoto, J. Colloid Interface Sci. 265 (2003) 283.
[21] H. Fei, X. Ai, M. Gao, Y. Yang, Z.T. Zhang, J. Chen, J. Lumin. 66 and 67 (1996) 345.
[22] N.J. Turro, P.H. Lakshminarasimhan, S. Jockusch, S.P. O'Brien, S.G. Grancharov, F.X. Redl, Nano Lett. 2 (2002) 325.
[23] X. Teng, H. Yang, J. Mater. Chem. 14 (2004) 774.
[24] X.C. Shen, X.Z. Fang, Y.H. Zhou, H. Liang, Chem. Lett. 33 (2004) 1468.

A meticulous search on the literature discloses numerous studies on many transition metal complexes with hydroxypyrones but little or no work on Ru thus far [14–17]. Hence, the present work aims at the synthesis and characterization of Ru(II) and Ru(III) complexes of a hydroxypyrone ligand, namely dehydroacetic acid (DHA), in order to explore their biological activities such as DNA-binding and antibacterial activity.

2. Experimental

2.1. Materials and methods

All chemicals were of reagent grade and were used without further purification. Dehydroacetic acid was obtained from Acros organics and solvents were purified following the literature procedures [18]. Protein free Herring Sperm ds DNA obtained from SRL chemicals was stored at 0–4 °C and its purity was checked by measuring the optical density before use. The Tris-buffer solution was prepared with double-distilled water and its pH was adjusted to 7.1 using 0.1 M NaOH solution. DNA stock solutions were freshly prepared with this buffer solution before use. Distilled DMSO (dimethylsulfoxide) was used for the preparation of solutions of the complexes for DNA-binding studies. Commercially available TBAP was properly dried and used as a supporting electrolyte for recording cyclic voltammograms of the complexes (except for DNA-binding studies). The starting complexes $[RuCl_3(PPh_3)_3]$, $[RuCl_3(AsPh_3)_3]$, $[RuBr_3(AsPh_3)_3]$, $[RuHCl(CO)(PPh_3)_3]$, $[RuH_2(CO)(PPh_3)_3]$ and $[RuHCl(CO)(AsPh_3)_3]$ were prepared as described in the literature [19–23].

FT-IR spectra (4000–400 cm^{-1}) of the complexes and the free ligand were recorded as KBr pellets with a Nicolet Avatar Model FT-IR spectrophotometer. Electronic spectra (800–250 nm) of the complexes were obtained on a Systronics 119 UV–Vis spectrophotometer. Room temperature EPR spectra of powdered samples were recorded on an E-112 Varian model instrument in X-band frequencies using DPPH as an internal standard. Magnetic moments were measured on an EG&G-PARC vibrating sample magnetometer at 25 °C. ^1H NMR spectra of the complexes were recorded using a Varian-Australia AMX-400 instrument. Micro analyses (C, H, N and S) were performed on a Vario EL III Elementar analyzer. Cyclic voltammograms were recorded on a CHI 1120A Electrochemical analyzer with a three electrode compartment consisting of a platinum disc working electrode, platinum wire counter electrode and Ag/Ag^+ reference electrode.

2.2. Synthesis of $[RuCl(CO)(PPh_3)_2(L)]$ (1)

$[RuHCl(CO)(PPh_3)_3]$ (0.996 g, 0.1 mmol) was suspended in a mixture of dry ethanol (15 mL) and benzene (10 mL). To this the ligand dehydroacetic acid (0.0168 g, 0.1 mmol) was added. After refluxing the mixture for 10 h, it was cooled and filtered. On evaporation of the solvent to a small volume, the complex separated out. It was filtered and recrystallized from $CHCl_3$/petroleum ether (1:1) mixture. The other Ru(II) complexes, namely $[RuCl(CO)(AsPh_3)_2(L)]$ (**2**) and $[RuH(CO)(PPh_3)_2(L)]$ (**3**), were prepared by the same procedure starting from $[RuHCl(CO)(AsPh_3)_3]$ and $[RuH_2(CO)(PPh_3)_3]$, respectively.

2.3. Synthesis of $[RuCl_2(AsPh_3)_2L]$ (4)

$[RuCl_3(AsPh_3)_3]$ (0.113 g, 0.1 mmol) was suspended in a mixture of dry ethanol (15 mL) and benzene (10 mL). To this the ligand dehydroacetic acid (0.0168 g, 0.1 mmol) was added. The mixture was then refluxed for 10 h, then the solution was filtered and allowed to stand for 3 days whereby a microcrystalline product appeared. Addition of 20 ml of DMF to the solution yielded single crystals suitable for X-ray diffraction. The product was washed with cold methanol and dried.

The other Ru(III) complexes, namely $[RuCl_2(PPh_3)_2L]$(**5**) and $[RuBr_2(AsPh_3)_2L]$(**6**), were synthesized by a similar procedure starting from $[RuCl_3(PPh_3)_3]$ and $[RuBr_3(AsPh_3)_3]$, respectively. However no single crystals could be grown for the products even after several attempts.

Compound **1**: *Anal.* Calc. for $C_{45}H_{37}O_5RuClP_2$: C, 63.15; H, 4.35. Found: C, 62.79; H, 4.39%. IR (KBr, cm^{-1}): ν(C=O) 1652, ν(C–O) 1275, ν(C=O) 1951. ^1H NMR (400 MHz, d_6-DMSO, δ, ppm; s, singlet; m, multiplet): 2.0 (s, 3 H, CH_3), 2.5 (s, 3H, CH_3–CO), 5.72 (s, 1H, HC=C), 7.2–7.6 (m, aromatic). UV–Vis λ (nm) (ε, $mol^{-1}\,cm^{-1}$ L): 359 (10780).

Compound **2**: *Anal.* Calc. for $C_{45}H_{37}O_5RuClAs_2$: C, 57.27; H, 3.95. Found: C, 56.98; H, 3.98%. IR (KBr cm^{-1}): ν(C=O) 1656, ν(C–O) 1272, ν(C=O) 1946. ^1H NMR (400 MHz, d_6-DMSO, δ, ppm; s, singlet; m, multiplet): 2.0 (s, 3H, CH_3), 2.4 (s, 3H, CH_3–CO), 5.70 (s, 1H, HC=C), 7.2-7.54 (m, aromatic). UV–Vis λ (nm) (ε, $mol^{-1}\,cm^{-1}$ L): 335 (9580).

Compound **3**: *Anal.* Calc. for $C_{45}H_{38}O_5RuP_2$: C, 65.80; H, 4.66. Found: C, 64.99; H, 4.02%. IR (KBr cm^{-1}): ν(C=O) 1655, ν(C–O) 1275, ν(C=O) 1956, ν(Ru–H) 2020. ^1H NMR (400 MHz, DMSO-d_6, δ, ppm; s, singlet; m, multiplet): 2.1 (s, 3H, CH_3), 2.4 (s, 3H, CH_3–CO), 5.74 (s, 1H, HC=C), 7.2–7.6 (m, aromatic). UV–Vis λ (nm) (ε, $mol^{-1}\,cm^{-1}$ L): 309 (8560).

Compound **4**: *Anal.* Calc. for $C_{44}H_{37}O_4RuCl_2As_2$: C, 55.51; H, 3.92. Found: C, 55.01; H, 3.72%. IR (KBr cm^{-1}): ν(C=O) 1648, ν(C–O) 1275. UV–Vis λ (nm) (ε, $mol^{-1}\,cm^{-1}$ L):268 (17030), 286 (15730), 326 (15000), 456 (2300).

Compound **5**: *Anal.* Calc. for $C_{44}H_{37}O_4RuCl_2P_2$: C, 61.16; H, 4.31. Found: C, 60.96; H, 4.34%. IR (KBr cm^{-1}): ν(C=O) 1648, ν(C–O) 1273. UV–Vis λ (nm) (ε, $mol^{-1}\,cm^{-1}$ L): 293 (8820), 400 (2540).

Compound **6**: *Anal.* Calc. for $C_{44}H_{37}O_4RuBr_2As_2$: C, 60.53; H, 4.27. Found: C, 60.51; H, 4.24%. IR (KBr cm^{-1}): ν(C=O) 1651, ν(C–O) 1276. UV–Vis λ (nm) (ε, $mol^{-1}\,cm^{-1}$ L): 320 (9680), 359 (6390).

2.4. X-ray structure determination

X-ray diffraction measurements were performed on a Bruker AXS SMART APEX CCD diffractometer with graphite monochromatised Mo Kα radiation. The unit cell was determined using SMART [24a] and SAINT+ [24b], and the data were corrected for absorption using SADABS [24c]. The structure was solved by direct methods and refinements were carried out by full-matrix least-square techniques. The hydrogen atoms were treated by a mixture of independent and constrained refinement. The computer program SHELXTL 6.14 [24d] was used for structure solution, refinement and molecular graphics. Refinement of an extinction coefficient was found to be insignificant. All non-hydrogen atoms were refined anisotropically. The chelating DHA ligand is flip disordered. The occupancy ratio for both moieties refined to 0.732(7) to 0.268(7). For the minor component the following restraints have been applied. The whole ligand was restraint to have the same shape as its major component counterpart (SAME instruction, standard deviation = 0.02). The atoms C5b, C6b, O2b and O3b were restraint to be flat (standard deviation = 0.1), and the atoms C3b, C4b, O2b and C2b were restraint to have similar anisotropic displacement parameters. The following pairs of atoms were restraint to each have identical anisotropic displacement parameters: O1 and O4b, O1b and O4, C6 and C6b, C5 and C5b, C2 and C2b, C8 and C8b, O2 and O3b, C1 and C7b, and C1b and C7. Hydrogen atoms were placed in calculated positions and were refined with an isotropic displacement parameter 1.2 (C–H and CH_2) or 1.5 (CH_3) times that of the adjacent carbon atom.

2.5. Antimicrobial screening and determination of minimum inhibitory concentration

The agar well diffusion method was employed for the determination of antimicrobial activities. MICs (minimum inhibitory concentration) of the compounds against test organisms were determined using the broth micro dilution method [25]. All the tests were performed in duplicate and repeated twice. Modal values were selected. The compounds were weighed and dissolved in DMSO and were filter sterilized using a 0.45 μm membrane filter. Each microorganism was suspended in sterile saline and diluted to ca. 106 colony forming units (cfu/ml). They were flood inoculated on to the surface of Mueller–Hinton Agar (MHA). The wells (8 mm in diameter) were cut from the agar and 0.1 mL of solution was delivered into them. After incubation for 24 h at 37 °C, all plates were examined for any zones of growth inhibition, and the diameter of these zones were measured in millimeters.

A broth microdilution broth susceptibility assay was used as recommended [26] by NCCLS for determination of the MIC. All the tests were performed in Mueller–Hinton Broth (MHB) supplemented with Tween-80 detergent (final concentration of 0.5% (v/v)). Bacterial strains were cultured overnight at 37 °C in MHA. Test strains were suspended in MHB to give a final density of 5×10^5 cfu/ml and these were confirmed by viable counts. Geometric dilutions of the compounds were prepared in a 96-well microtiter plate, including one growth control (MHB + Tween 80) and one sterility control (MHB + Tween 80 + Compound). The plates were incubated under normal atmospheric conditions at 37 °C for 24 h. The MIC of kanamycin and oxytetracycline was individually determined in parallel experiments in order to control the sensitivity of the test organisms. The bacterial growth was indicated by the presence of a white "pellet" on the well bottom.

3. Results and discussion

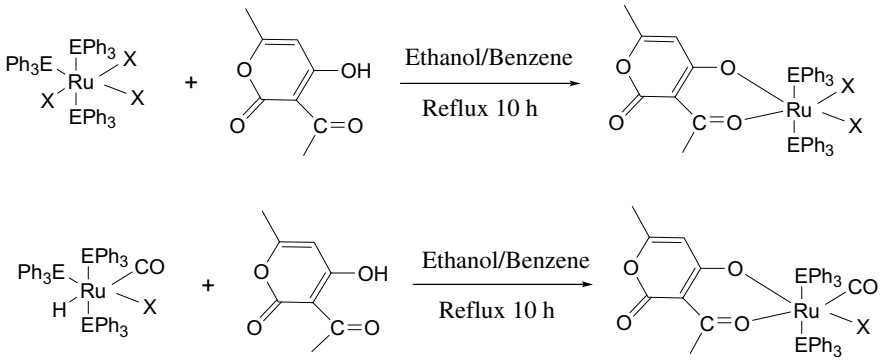
Complexes of the general formulae $[RuX(CO)(EPh_3)_2(L)]$ and $[RuX_2(EPh_3)_2(L)]$ (E = P or As, X = H, Cl or Br and L = monoanion of DHA) were obtained by the reaction of the precursors $[RuX_3(EPh_3)_3]$ and $[RuHX(CO)(EPh_3)_3]$ with the ligand. All the new complexes are stable to air and light and are soluble in most common organic solvents. The analytical data of the metal complexes fit well with the molecular formulae suggested above. The method of synthesis of the complexes is displayed in Scheme 1.

3.1. IR spectra

The new ruthenium complexes were also studied by IR spectroscopy. In the free ligand, three bands at 1713, 1642 and 1252 cm^{-1} have been ascribed to the stretching vibrations of $\nu_{C=O}$(lactone), $\nu_{C=O}$(carbonyl) and ν_{C-O} (phenolic), respectively [27]. In all the complexes $\nu_{C=O}$(lactone) remains unaltered while the other two peaks shift to 1648–1658 cm^{-1} and 1272–1276 cm^{-1}, respectively. The absence of ν_{OH} at 3400 cm^{-1} suggests the deprotonation of the phenolic oxygen prior to coordination [28]. This is further substantiated by the absence of a ^1H NMR signal for the OH group around δ 11.3 ppm for all the complexes. The strong absorption around 1960 cm^{-1} has been assigned to the coordinated terminal carbonyl group and in the hydrido complex ν_{Ru-H} appears at 2010 cm^{-1}. From the IR spectral data, it has been concluded that DHA behaves as a monobasic bidentate ligand coordinating through the deprotonated phenolic oxygen and the carbonyl oxygen.

3.2. Electronic spectra

The electronic spectra of the complexes were recorded in $CHCl_3$ in the 250–800 nm region. For a low-spin d^5 system in an octahedral environment, the ground state is $^2T_{2g}$ arising from a t_{2g}^5 configuration. The next higher energy configuration $t_{2g}^4e_g^1$ gives rise to four states, namely $^2A_{2g}$, $^2A_{1g}$, $^2T_{1g}$ and $^2T_{2g}$, and so four bands are expected. In most Ru(III) complexes, the absorption spectra show only charge transfer bands [29]. In a d^5 system, and especially in Ru(III) which is a relatively good oxidizing agent, the



Scheme 1. Synthesis procedure for the complexes.

charge transfer bands of the type $L_{\pi y} \rightarrow t_{2g}$ are prominent in the low energy region and obscure the weaker bands due to d–d transitions. It, therefore, becomes difficult to conclusively assign bands of Ru(III) complexes which appear in the visible region [30]. The new Ru(III) complexes synthesized in this study showed two to four bands in the region 268–456 nm. The assortment of intense bands exhibited by the complexes in the region 268–359 nm are believed to be ligand centered transitions. In addition, the other bands at 400 and 456 nm have been assigned to charge transfer bands. This is in conformity with the assignments made for other similar Ru(III) octahedral complexes [29]. All the Ru(II) complexes display one intraligand transfer band in the region 309–359 nm, as displayed by other analogous octahedral Ru(II) complexes [29,31].

3.3. ^1H NMR spectra

The ^1H NMR spectra of the Ru(II) complexes were recorded in d_6-DMSO to confirm the binding of DHA to the ruthenium ion. All the complexes showed a sharp peak in the range δ 2.0–2.1 ppm due to the methyl group attached to the pyrone ring. The other peak observed in the range δ 2.4–2.5 ppm is due to the methyl protons of the CH_3–C═O group. A singlet around δ 5.7 ppm was assigned to the vinylic proton. The characteristic multiplets of the PPh_3 or $AsPh_3$ ring protons appear in the range δ 7.2–7.6 ppm. No peak was observed for the OH proton, supporting the assumption that the phenolic group is deprotonated, suggesting coordination through the phenylato oxygen of DHA to the ruthenium.

3.4. Magnetic susceptibility and EPR spectra

Magnetic susceptibility measurements of the Ru(III) complexes showed that they are paramagnetic ($\mu_{eff} = 1.82$–1.93 BM), which corresponds to the +3 state of ruthenium (low-spin d^5, $S = 1/2$) in the complexes. The room temperature EPR spectra of the powdered samples were also recorded at the X-band frequencies. A selected spectrum is shown in Fig. 1. The complexes **5** ($g_\perp = 2.03$, $g_\parallel = 1.95$) and **4** ($g_\perp = 2.38$, $g_\parallel = 2.30$) exhibit two lines indicating a tetragonal distortion and axial symmetry in the complexes. Hence, *trans* positions are assigned for the PPh_3 or $AsPh_3$ groups [32]. On the other hand, complex **6** exhibits a single isotropic line ($g = 2.10$). Such isotropic lines are usually observed either due to intramolecular spin exchange, which can broaden the lines, or due to occupancy of the unpaired electron in a degenerate orbital [33]. The distortion in complex **4** is also supported by its crystal structure.

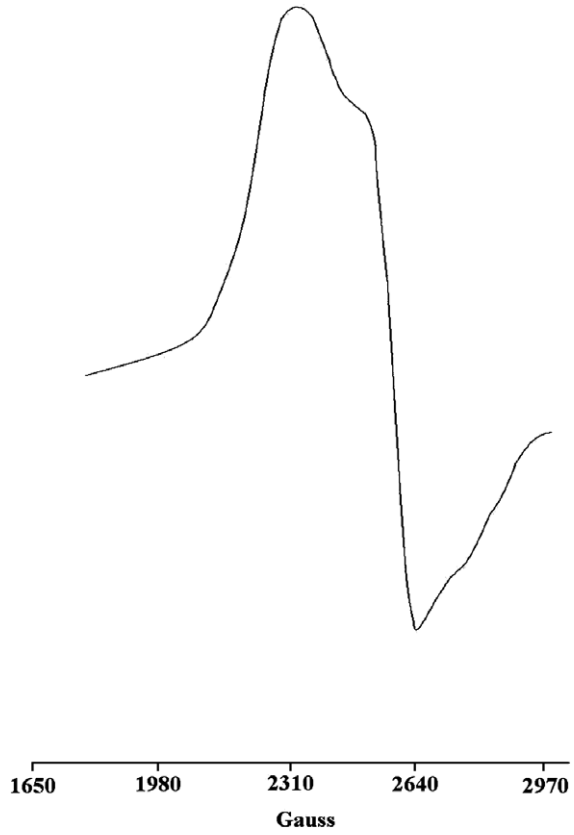


Fig. 1. Powder EPR spectra of **4**.

3.5. Cyclic voltammetry

Cyclic voltammetric experiments were performed with acetonitrile solutions of the complexes. Complexes **4** and

6 showed a quasi-reversible reduction wave (Ru^{III}–Ru^{II}) at −0.71 and −0.69 V, respectively. A close examination of the reduction potentials of the complexes show that the bromo complex is reduced more readily than the corresponding chloro complexes, which is in accordance with a previous study [34]. Similarly the Ru(II) complexes **2** and **3** present a quasi-reversible reduction wave (Ru^{II}–Ru^{I}) at −0.54 V ($\Delta E_p = 910$ mV) and −0.53 V ($\Delta E_p = 830$ mV), respectively. The presence of a π-acidic carbonyl ligand in the Ru(II) complexes helps to stabilize the lower oxidation state of the metal ion. Also, an irreversible oxidation wave ($E_{pa} = 0.64$–0.83 V) is displayed invariably by all the complexes. This may be due to the short lived reduced state of the metal ion [35].

3.6. X-ray crystallography

The molecular structure of complex **4** is shown in Fig. 2. The crystal data are supplied in Table 1 and selected geometrical parameters are listed in Table 2. The coordination sphere around the ruthenium atom consists of two mutually *cis* chloride ligands, an OO chelate of the dehydroacetic acid ligand and two *trans* triphenylarsine ligands. The chelating DHA ligand is flip disordered with a refined occupancy ratio of 0.732(7)–0.268(7). The coordination environment around the ruthenium centre is distorted octahedral in nature. The ligand (DHA) is coordinated to ruthenium as a bidentate OO donor forming a six membered chelate ring with a bite angle (O1–Ru1–O4) of 86.77°. The Ru–As distances (Ru1–As1 = 2.479 and Ru1–As2 = 2.489 Å) are comparable with those of other ruthenium complexes [36,37]. Similarly the two *cis* Ru–Cl distances are almost equal and comparable to those in other Ru(III) complexes [38,39]. However the Ru–Cl distances are shorter than those found in some six coordinated Ru(III) complexes [4,40]. The Ru1–O4(oxy) bond distance of 1.977 Å is significantly shorter than the distance observed in a ruthenium(III)-orthometallated azophenol system [41] (Ru–O = 2.2112 Å), but comparable to Ru–O distances of 1.981 and 1.982 Å found in a ruthenium(III)-salicylaldehydato complex [42] and [Ru(trpy)(L^3)Cl] ClO_4 (L^3 = *o*-$^-OC_6H_3(NO_2)CH{=}NCH_2C_6H_5$) [43], respectively. The Ru–O (keto) bond distance of 2.045 Å agrees well with that reported for other ruthenium(III) complexes [44,45]. From the data, it is obvious that the Ru1–O4 distance is shorter than the Ru1–O1 distance, indicating the stronger preference of the Ru(III) ion for the hydroxyl oxygen than the ketonic oxygen atom. The two chloride ligands bind to ruthenium in a *cis* arrangement (Cl1–Ru1–Cl2 = 95.63), and the Cl anions are opposite to the two oxygen atoms of the chelating ligand. The two axial triphenylarsine ligands are slightly bent towards the *cis* chloride ligands due to the steric bulk of the chelating ligand, causing a slight deviation from a linear *trans* arrangement.

Table 1
Crystal data for **4**

Empirical formula	$C_{44}H_{37}Cl_2As_2O_4Ru$
Formula weight	951.55
Crystal color, habit	purple, plate
Crystal dimensions (mm)	0.60 × 0.23 × 0.10
Crystal system	monoclinic
Lattice type	primitive
Space group	$P2_1/n$
a (Å)	9.6734(6)
b (Å)	24.2371(15)
c (Å)	16.6798(10)
α (°)	90
β (°)	96.5090(10)
γ (°)	90
V (Å^3)	3885.5(4)
Z	4
D_{calc} (Mg m^{-3})	1.627
F_{000}	1908
μ (Mo Kα) (mm^{-1})	2.275
R_{int}	0.0287
Goodness-of-fit (S)	1.148
θ_{max} (°)	30.49

Table 2
Selected bond distances (Å) and angles (°) for **4**

Bond distances			
Ru1–O4	1.977(10)	Ru1–Cl2	2.320(11)
Ru1–O4b	1.990(3)	Ru1–Cl1	2.325(10)
Ru1–O1	2.044(8)	Ru1–As1	2.478(5)
Ru1–O1b	2.160(3)	Ru1–As2	2.480(5)
Bond angles			
O4–Ru1–O1	86.80(3)	O1–Ru1–As2	91.60(13)
O4–Ru1–Cl2	89.40(3)	Cl2–Ru1–Cl1	95.63(4)
O4–Ru1–Cl1	175.0(3)	Cl2–Ru1–As1	87.78(3)
O4–Ru1–As1	92.20(3)	Cl2–Ru1–As2	89.43(3)
O4–Ru1–As2	87.90(3)	Cl1–Ru1–As1	87.89(3)
O1–Ru1–Cl2	176.0(2)	Cl1–Ru1–As2	92.31(3)
O1–Ru1–Cl1	88.20(2)	As1–Ru1–As2	177.21(19)
O1–Ru–As1	91.18(13)		

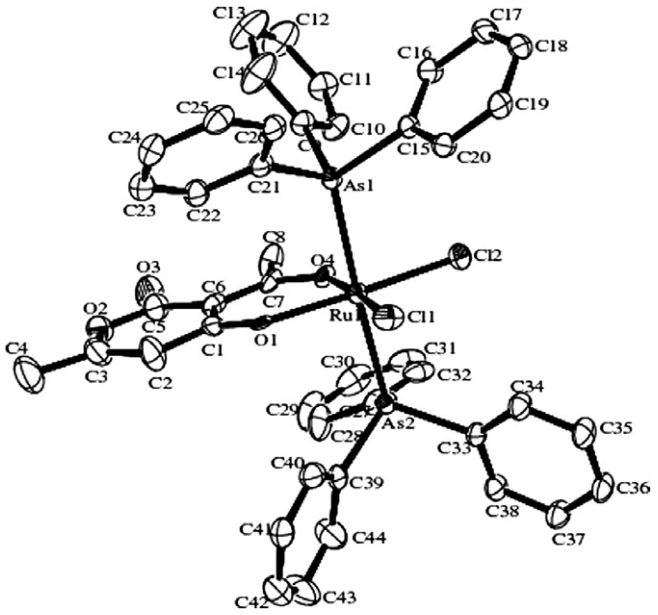


Fig. 2. Perspective view of ORTEP diagram of **4** with thermal ellipsoids of 50% probability. Hydrogen atoms are omitted for clarity.

3.7. Antibacterial study

The ligand DHA and its complexes were found to possess antibacterial activity against both the Gram positive (*S. aureus* and *S. epidermidis*) and Gram negative (*S. sonnei*, *E. coli* and *K. pneumoniae*) strains of bacteria. The zone of inhibition in mm and MIC values in μg/ml are given in Table 3. DHA exhibited an inhibition zone ranging from 13 to 16 mm against the test organisms. Complexes **6** and **1** alone were resistive to all the microorganisms with inhibition zones ranging from 12 to 21 mm. The resistivity of **5** against *E. coli* was fairly comparable with that of the standards used in the study and the activity of the other complexes was only to a lesser extent. The Gram negative bacteria *K. pneumoniae* is sensitive only to complexes **1** and **6**. Another Gram negative bacteria *S. sonnei* is sensitive to all the complexes except **4**. The complexes **5** and **3** were non-resistive to the Gram positive bacteria *S. aureus*. Similarly, **4** and **1** show null activity against another Gram positive bacteria, *S. epidermidis*. In some cases the complexes exhibit better activity than the ligand DHA, which can be explained by the faster diffusion of the metal complexes as a whole through the cell membrane or due to the synergistic effect of the ligand and the metal.

3.8. DNA-binding studies

3.8.1. Absorption spectroscopic studies

The experiments were carried out in Tris–HCl buffer (50 mM, pH 7.2) using a solution of Herring sperm DNA which gave a ratio of UV absorbance at 260 and 280 nm of 1.8:1, indicating that the DNA is sufficiently free from protein. So, no further effort was made to purify the commercially obtained DNA. The concentration of DNA was determined by absorption spectroscopy using the ε value of 6600 mol^{-1} cm^{-1} L^{-1} at 260 nm. Absorption titrations were performed using a fixed ruthenium concentration to which increments of the DNA stock solutions were added in different ratios ranging from 0 to 5 [DNA]/[Ru]. Complex-DNA solutions were allowed to stand for 5 min before recording their absorption. The intrinsic binding constants of the complexes could not be evaluated using the equation valid for perfect intercalators like phenanthroline complexes, due to the random changes in the absorption on the addition of DNA.

The binding of the ruthenium complexes to DNA helices was characterized by following the changes in the absorbance and shift in wavelength on each addition of DNA solution to the complex. A representative absorption spectrum is given in the Fig. 3. The ruthenium(II) complexes in DMSO-buffer mixture exhibit an intense transition in the region around 370–310 nm, which is attributed to a $\pi \rightarrow \pi^*$ intraligand transition. On the titration of Herring sperm DNA with the complexes, a considerable increase or decrease in the absorption along with small red or blue shift was observed. The titration process was repeated until no further change was observed in the spectrum. With increasing concentration of DNA, the absorption bands of the complexes were affected to a considerable extent. There was no appreciable change in the absorption bands of complexes **2** and **3** when they were titrated with DNA. Complexes **1** and **5** exhibit 49% and 42% hypochromicity and 21 and 3 nm bathochromism, respectively in the presence of DNA at saturation. These results indicate the interaction between the complexes and DNA is through the intercalation mode [46]. Based on the percentage of the hypochromism, **1** is thought to bind DNA more strongly than **5**. During the titration the extent of hypochromicity and bathochromism varied. This implies binding of the complexes to DNA through different modes to different extents [47]. As the concentration of the DNA was increased, the absorption bands of **4** showed hyperchromism of 12% initially and on further increment, hypochromism of 21% with a blue shift (20 nm) was observed. This behavior reveals an electrostatic association of the complex with the helix surface [46,48]. The existence of different binding modes between **6** and DNA can be realized by analyzing the spectral data.

3.8.2. Cyclic voltammetry

Since all the new complexes are electroactive, electrochemical methods such as cyclic voltammetry can be used

Table 3
Antibacterial activity of DHA and its ruthenium complexes

Compounds	*Escherichia coli*		*Shigella sonnei*		*Staphylococcus aureus*		*Staphylococcus epidermidis*		*Klebsiella pneumoniae*	
	WD[a]	MIC[b]	WD	MIC	WD	MIC	WD	MIC	WD	MIC
DHA	13	150	13	33	16	150	13	50	15	33
1	15	122	21	100	13	104	18	76	12	140
2	16	250	14	218	16	128	NA	NT	NA	NT
3	14	67	13	112	NA	NT	12	127	NA	NT
4	12	102	NA	NT	20	137	NA	NT	NA	NT
5	25	143	23	261	NA	NT	15	213	NA	NT
6	21	213	18	57	21	43	15	98	14	103
Oxytetracycline	30	15	37	8	32	7	44	8	30	8
Kanamycin	32	18	48	9	40	10	60	11	35	10

[a] WD, disc diffusion method as recommended by NCCLS. Diameter of zone of inhibition (mm) including well diameter 8 mm.100 μg of both compound and antibiotics were used.

[b] MIC, minimum inhibitory concentration. Values given as μg/ml for both compounds and antibiotics. NA – not active; NT – not tested.

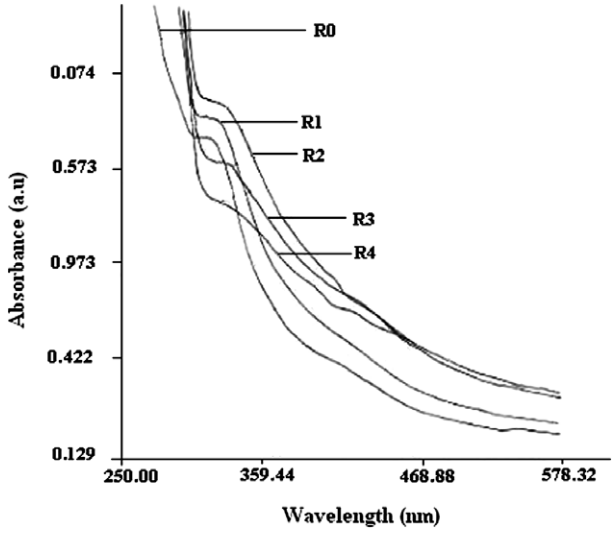


Fig. 3. Change in the absorption of **6** on titration with DNA at different [Ru]/[DNA] ratios (R). R0 = 0, R1 = 1, R2 = 2, R3 = 3, R4 = 4.

effectively to monitor their binding to DNA as a complement to absorption spectroscopic techniques. In a typical cyclic voltammetric titration a fixed concentration of the complex was taken and DNA solution in buffer was added in different ratios as done in the absorption titration, and the voltammetric response was recorded. As observed in the UV experiments, an increase and decrease of the peak current was observed for all the complexes.

Cyclic voltammetric curves were obtained in the absence and in the presence of DNA. The separation of anodic and cathodic peak potentials suggests a quasi-reversible one electron transfer process. The peak-to-peak separation value differed appreciably when DNA was added to the complex in buffer in comparison with that of the solution containing the complex alone. Reversibility of the electron transfer was maintained in the presence of DNA. The positive shift in reduction potential with increase in concentration of DNA suggests a difference in binding properties of the Ru(III), Ru(II) and Ru(I) species [49]. For **1** and **5**, the addition of DNA causes a decrease in the peak current with a slight shift in E_f to less positive potentials. These behaviors are reflective of intercalation of the metal complexes to the DNA double helix. The initial increase in the peak current for **4** and **6** is due to the electrostatic interaction between these complexes and DNA. The intercalation mode of binding is also observed to a small extent in these complexes.

4. Conclusion

A series of Ru(II) and Ru(III) complexes of dehydroacetic acid were prepared and characterized by analytical, magnetic and spectral techniques. The molecular structure of one of the complexes, studied by single crystal X-ray diffraction, shows that the DHA ligand has coordinated to the metal centre as an OO chelate in the equatorial plane. From the data, the geometry around the ruthenium centre is found to be a distorted octahedron. The same observation has also been evidenced by EPR spectroscopy. The redox properties of the complexes studied by cyclic voltammetry show that the presence of the π-acidic carbonyl ligand in the Ru(II) complexes helps to stabilize the lower oxidation state of the metal ion. All of the complexes along with the ligand DHA were tested for their antimicrobial property against five pathogenic bacteria. Since the compounds could interact with DNA they can be used for probing DNA structures.

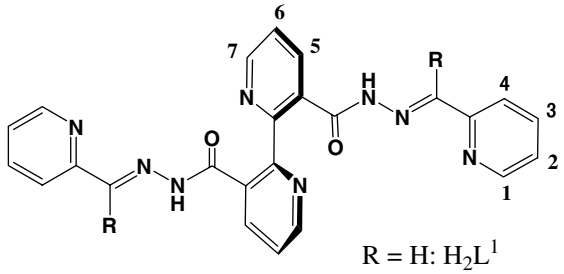
Appendix A. Supplementary material

CCDC 608059 contains the supplementary crystallographic data for complex **4**. These data can be obtained free of charge via http://www.ccdc.cam.ac.uk/conts/retrieving.html, or from the Cambridge Crystallographic Data Centre, 12 Union Road, Cambridge CB2 1EZ, UK; fax: (+44) 1223-336-033; or e-mail: deposit@ccdc.cam.ac.uk. Supplementary data associated with this article can be found, in the online version, at doi:10.1016/j.poly.2007.11.039.

References

[1] J. Reedijk, Curr. Opin. Chem. Biol. 3 (1999) 236.
[2] M. Tolomeo, D. Simoni, Curr. Med. Chem. Anti Cancer Agents 2 (2002) 387.
[3] J.H. Goldie, Cancer Metast. Rev. 20 (2001) 63.
[4] V.V. Arion, E. Reisner, M. Fremuth, M.A. Jakupec, B.K. Keppler, V.Y. Kukushkin, A.J.L. Pombeiro, Inorg. Chem. 42 (2003) 6024.
[5] J.E. Coury, J.R. Anderson, L.M. Isom, L.D. Williams, L.A. Bottomley, J. Am. Chem. Soc. 119 (1997) 3792.
[6] L. Trynda-Lemiesz, Acta Biochim. Pol. 52 (1) (2004) 199.
[7] A. Bergamo, G. Stocco, C. Casarsa, M. Cocchettio, E. Alessio, B. Serli, S. Zorzet, G. Sava, Int. J. Oncol. 24 (2004) 373.
[8] S. Thaisrivongs, D.L. Romero, R.A. Tommasi, M.N. Janakirman, J.W. Strohbach, S.R. Turner, C. Biles, R.R. Morge, P.D. Johnson, P.A. Aristoff, P.K. Tomich, J.C. Lymn, M.M. Horng, K.T. Chong, R.R. Hinshaw, W.J. Howe, B.C. Finzel, K.D. Watenpaugh, J. Med. Chem. 39 (1996) 4630.
[9] P.A. Wolf, W.M. Westveer, Arch. Biochem. 28 (1950) 201.
[10] M. Cindric, V. Vrdoljak, T. Kajfez, P. Novak, A.B. Saranovic, N. Strukan, B. Kamenar, Inorg. Chim. Acta 328 (2002) 23.
[11] M. Rangel, A. Tamura, C. Fukushima, H. Sakurai, J. Biol. Inorg. Chem. 6 (2001) 128.
[12] P. Comba, Coord. Chem. Rev. 123 (1993) 1.
[13] G.R. Hanson, Y. Sun, C. Orvig, Inorg. Chem. 35 (1996) 6507.
[14] J. Casavo, J. Marquet, M.M. Monas, M. Prior, F. Teixidor, F. Florencio, S.M. Carrera, S.G. Blanco, Polyhedron 6 (6) (1987) 1235.
[15] H. Luo, S.J. Retty, C. Orvig, Inorg. Chem. 32 (1993) 4491.
[16] Y. Sun, B.R. James, S.J. Rettig, C. Orvig, Inorg. Chem. 35 (1996) 1667.
[17] O. Carugo, C.B. Castellani, M. Rizzi, Polyhedron 9 (17) (1990) 2061.
[18] A.I. Vogel, Textbook of Practical Organic Chemistry, 5th ed., Longman, London, 1989.
[19] J. Chatt, G.J. Leigh, D.M.P. Mingos, R.J. Paske, J. Chem. Soc. A (1968) 2636.
[20] R.K. Poddar, I.P. Khullar, U. Agarwala, J. Inorg. Nucl. Chem. Lett. 10 (1974) 221.
[21] K. Natarajan, R.K. Poddar, U. Agarwala, J. Inorg. Nucl. Chem. 39 (1997) 431.

[22] N. Ahmed, J.J. Lewison, S.D. Robinson, M.F. Uttley, Inorg. Synth. 15 (1974) 48.
[23] R.A.S. Pelgado, W.Y. Lee, S.R. Choi, Y. Cho, M.J. Jun, Trans. Met. Chem. 16 (1991) 241.
[24] (a) Bruker Advanced X-ray Solutions SMART for WNT/2000 (Version 5.628), Bruker AXS Inc., Madison, WI, USA, 1997–2002;
(b) Bruker Advanced X-ray Solutions SAINT (Version 6.45), Bruker AXS Inc., Madison, WI, USA, 1997–2003;
(c) Bruker Advanced X-ray Solutions SADABS in SAINT (Version 6.45), Bruker AXS Inc., Madison, WI, USA, 1997–2003;
(d) G.M. Sheldrick, SHELXTL v.6.14, Bruker AXS, Inc, Madison, WI, 2003.
[25] NCCLS, National Committee for Clinical Laboratory Standards, Performance Standards for Antimicrobial Disk Susceptibility Test, 6th ed., Approved Standard, Wayne, PA, M2-A6, 1997.
[26] NCCLS, National Committee for Clinical Laboratory Standards, Performance Standards for Antimicrobial Disk Susceptibility Test, 6th ed., Approved Standard, Wayne, PA, M2-A6, 1997.
[27] M.Z. Chalaca, J.D.F. Villar, J.A. Ellena, E.E. Castellano, Inorg. Chim. Acta 328 (2002) 45.
[28] V. Mahalingam, R. Karvembu, V. Chinusamy, K. Natarajan, Spectrochim. Acta, Part A 64 (4) (2006) 886.
[29] A.B.P. Lever, Inorganic Spectroscopy, 2nd ed., Elsevier, New York, 1989.
[30] R. Ramesh, S. Maheswaran, J. Inorg. Biochem. 96 (2003) 457.
[31] K.N. Kumar, R. Ramesh, Y. Liu, J. Inorg. Biochem. 100 (2006) 18.
[32] P.T. Manoharan, P.K. Mehrotra, M.M.T. Khan, R.K. Andal, Inorg. Chem. 12 (1973) 2753.
[33] R. Karvembu, C. Jayabalakrishnan, N. Dharmaraj, S.V. Renukadevi, K. Natarajan, Trans. Met. Chem. 27 (2002) 631.
[34] A.R. Chakravarty, A. Chakravorty, Inorg. Chem. 20 (10) (1981) 3138.
[35] T. Daniel Thangadurai, M. Gowri, K. Natarajan, Synth. React. Inorg. Met-Org. Chem. 32 (2) (2002) 329.
[36] G. Venkatachalam, R. Ramesh, S.M. Mobin, J. Organomet. Chem. 690 (2005) 3937.
[37] G. Venkatachalam, R. Ramesh, Tetrahedron Lett. 46 (2005) 5215.
[38] A.L. Spek, D.M. Tooke, A.G. Ortiz, J. Reedijk, Acta Crystallogr., Sect. E 61 (2005) 2428.
[39] E. Reisner, V.B. Arion, A. Eichinger, N. Kandler, G. Giester, A.J.L. Pombeiro, B.K. Keppler, Inorg. Chem. 44 (2005) 6704.
[40] A.K. Das, S.M. Peng, S. Bhattacharya, J. Chem. Soc., Dalton Trans. (2000) 181.
[41] G.K. Lahiri, S. Bhattacharya, M. Mukherjee, A.K. Mukherjee, A. Chakravorty, Inorg. Chem. 26 (1987) 3359.
[42] N. Bag, G.K. Lahiri, S. Bhattacharya, L.R. Falvello, A. Chakravorty, Inorg. Chem. 27 (1988) 4396.
[43] B. Mondal, S. Chakraborty, P. Munshi, M.G. Walawalker, G.K. Lahiri, J. Chem. Soc., Dalton Trans. (2000) 2327.
[44] J. Comiskey, E. Farkas, K.A.K. Lacina, R.G. Pritchard, C.A. Mcaulifee, K.B. Nolan, J. Chem. Soc., Dalton Trans. (2003) 4243.
[45] J. Jolley, C.J. Campbell, A. Casteneiras, A.I. Yanovsky, K.B. Nolan, Polyhedron 18 (1999) 49.
[46] D. Herebian, W.S. Sheldrick, J. Chem. Soc., Dalton Trans. (2002) 966.
[47] S. Ramakrishnan, M. Palaniandavar, J. Chem. Sci. 117 (2) (2005) 179.
[48] M. Asadi, E. Safaei, B. Ranjbar, L. Hasani, New J. Chem. 28 (2004) 1227.
[49] V.G. Vaidyanathan, B.U. Nair, J. Chem. Soc., Dalton Trans. (2005) 2842.



Scheme 1. The chemical structures of ligand $\mathbf{H_2L^{1-3}}$.

the side chain position can strongly influence the supramolecular structure and the properties of the complexes.

2. Experimental

2.1. Materials and instrumentations

All chemicals were of reagent grade quality obtained from commercial sources and used without further purification. Dicarboxylic acid hydrazide-2,2′-bipyridine is prepared according to the previous work [8]. Elemental analyses (C, H and N) were carried out with a Perkin–Elmer 2400 Analyzer. IR spectra were recorded on a VECTOR 22 Bruker spectrophotometer with KBr pellets in the range of 4000–400 cm^{-1}. ^1H NMR spectra were performed on DRX500 Bruker spectrometer at 298 K with TMS as an internal reference. Electrospray mass spectra were carried out on a LCQ system (Finnigan MAT, USA) with methanol as mobile phase. Solid photoluminescent spectra were performed on AB Series-2 fluorescence spectrometer. Thermogravimetric analyses were carried out with a TA2000/2960 unit at a heating rate of 10 °C/min under nitrogen atmosphere.

Safety note. Perchlorate salts of metal complexes with organic ligands are potentially explosive. Only a small amount of material should be prepared and handled with care.

2.2. Synthesis of the ligand H_2L^{1-3} and cobalt(II) complexes 1–3

2.2.1. Di(2-pyridylcarbaldehyde)-6,6′-dicarboxylic acid hydrazone-2,2′-bipyridine (H_2L^1) and di(2-acetylpyridyl)-6,6′-dicarboxylic acid hydrazone-2,2′-bipyridine (H_2L^2)

Di(2-pyridylcarbaldehyde)-6,6′-dicarboxylic acid hydrazone-2,2′-bipyridine ($\mathbf{H_2L^1}$) and di(2-acetylpyridyl)-6,6′-dicarboxylic acid hydrazone-2,2′-bipyridine ($\mathbf{H_2L^2}$) are prepared and characterized according to the literature method.[9,10] The ligands, $\mathbf{H_2L^1}$ and $\mathbf{H_2L^2}$, are obtained by refluxing a mixed methanol solution of dicarboxylic acid hydrazide-2,2′-bipyridine with pyridyl-2-carbaldehyde and 2-acetylpyridine, respectively, in presence of several drops of acetic acid.

2.2.2. Di(di-2-pyridylketone)-6,6′-dicarboxylic acid hydrazone-2,2′-bipyridine (H_2L^3)

A solution of dicarboxylic acid hydrazide-2,2′-bipyridine (2 mmol, 0.54 g) in methanol (15 mL) was added to a methanol solution (10 mL) containing di-2-pyridylketone (4 mmol, 0.736 g). After 5 drops of acetic acid was added, the yellow mixture was heated at reflux under magnetic stirring for 2 h. During the reaction, a pale yellow precipitate was formed, which was collected by filtration, washed with methanol–ether, and dried in vacuo. Yield: 0.75 g, 62%. ^1H NMR (DMSO-d_6): δ 14.243 (1H, s, NH), 8.624 (1H_7, d, $J = 11.6$ Hz), 8.570 (2H_1, d, $J = 17.6$ Hz), 8.376 (1H_5, d, $J = 32.8$ Hz), 8.126(2H_4, m, $J = 26.4$ Hz), 7.826 (2H_3, t, $J = 12.8$ Hz), 7.743 (2H_2, m, $J = 24.0$ Hz,), 7.641 (1H_6, t, 15.6 Hz). *Anal.* Calc. for $C_{34}H_{24}N_{10}O_2$: H, 4.00; C, 67.54; N, 23.17. Found: H, 4.12; C, 67.34; N, 23.65%. IR (solid KBr pellet, cm^{-1}): 3453.98(m), 1665.27 (s), 1581.78(m), 1432.67(m), 1365.01(m), 1146.87(m), 785.14(m), 674.45(m), 545.45(w). ESI-MS: *m*/*z* 605.58 for $[\mathbf{H_2L^3} + H]^+$, calc. for $[\mathbf{H_2L^3}+H]^+$, 605.21.

2.2.3. Preparation of complex $Co_2(L^1)_2(ClO_4)_2(C_2H_5OH)_2(H_2O)_2$ (1)

$Co(ClO_4)_2 \cdot 6H_2O$ (0.1 mmol, 0.037 g) dissolved in 15 mL ethanol/H_2O (v: v, 95: 5) was added dropwise to a suspension of $\mathbf{H_2L^1}$ (0.1 mmol, 0.045 g) in 10 mL ethanol. The solution was stirred at reflux for 20 min to get dark-red solution. Dark-red block crystals suitable for X-ray diffraction were obtained by evaporating the filtrate after several days (0.051 g, 78.9%). *Anal.* Calc. for $Co_2(C_{24}H_{16}N_8O_2)_2(ClO_4)_2(C_2H_5OH)_2(H_2O)_2$: H, 3.61; C, 46.56; N, 16.72. Found: H, 3.68; C, 46.19; N, 16.41%. ESI-MS: *m*/*z* 1014.3 (calc. for $[Co_2(\mathbf{L^1})_2]^+$, 1014.1) and 507.3 (calc. for $[Co_2(\mathbf{L^1})_2]^{2+}$, 507.1). IR (solid KBr pellet, cm^{-1}): 3425.5 (m), 2442.21(m), 1648.39(m), 1570.89(m), 1502.85(m), 1154.74(s), 1121.06(s), 1094.12(s), 759.13(w), 628.85(w), 576.78(w).

2.2.4. Preparation of compound $Co_2(L^2)(HL^2)(ClO_4)_3(C_2H_5OH)_2(H_2O)_2$ (2)

$Co(ClO_4)_2 \cdot 6H_2O$ (0.1 mmol, 0.037 g) dissolved in 15 mL methanol was added to a suspension of $\mathbf{H_2L^2}$ (0.1 mmol, 0.048 g) in 10 mL methanol. The solution was stirred at reflux for 20 min to obtain a clear solution and allowed to stand at room temperature. After several days, pale-red block microcrystals were obtained (0.042 g, 56.0%). *Anal.* Calc. for $Co_2(C_{26}H_{20}N_8O_2)(C_{26}H_{21}N_8O_2)(ClO_4)_3(C_2H_5OH)_2(H_2O)_2$: H, 3.84; C, 44.91; N, 14.97. Found: H, 3.95; C, 44.79; N, 15.91%. ESI-MS: *m*/*z* 535.4 (calc. for $[Co_2(\mathbf{L^2})_2]^{2+}$, 535.11). IR (solid KBr pellet, cm^{-1}): 3422.42(m), 2443.67(m), 1647.34(m), 1571.76(m), 1507.34(m), 1151.65(s), 1120.43(s), 1090.34(s), 758.67(w), 627.34(w).

2.2.5. Preparation of complex $Co_2(L^3)(HL^3)(ClO_4)_3(H_2O)_4$ (3)

$Co(ClO_4)_2 \cdot 6H_2O$ (0.1 mmol, 0.037 g) dissolved in 15 mL methanol was added to a suspension of H_2L^3 (0.1 mmol, 0.048 g) in 10 mL methanol. The solution was stirred at reflux for 20 min to obtain a clear solution and allowed to stand at room temperature. After several days, dark-red block crystals suitable for X-ray diffraction were obtained (0.064 g, 75.4%). *Anal.* Calc. for $Co_2(C_{34}H_{22}N_{10}O_2)(C_{34}H_{23}N_{10}O_2)(ClO_4)_3(H_2O)_4$: H, 3.27; C, 48.14; N, 16.51. Found: H, 3.35; C, 48.29; N, 16.45%. ESI-MS: *m/z* 1421.69 (calc. for $[Co_2(L^3)_2(ClO_4)]^+$, 1421.20), 660.9 (calc. for $[Co_2(L^3)_2]^{2+}$, 661.1). IR (solid KBr pellet, cm^{-1}): 3423.45(m), 2442.68(m), 1648.24(m), 1571.58(m), 1508.12(m), 1161.25(s), 1125.23(s), 1091.34(s), 757.45(w), 628.04(w).

2.3. X-ray crystallography

Suitable crystals were selected for single-crystal X-ray diffraction structural analysis and the data were collected on a Siemens SMART-CCD diffractometer with graphite-monochromatized Mo Kα radiation ($\lambda = 0.71073$ Å), using the SMART and SAINT programs [11]. Forty-five frames of data were collected at 298 K with an oscillation range of 1°/frame and an exposure time of 10 s/frame. Indexing and unit cell refinement were based on all observed reflections from those 45 frames. The structures were solved by direct method and refined on F^2 by full-matrix least-squares methods with SHELXTL version 5.1 [12]. Anisotropic thermal parameters were refined for non-hydrogen atoms. Hydrogen atoms were localized in their calculated positions and refined by using the riding model. Crystallographic data and parameters for data collection and refinement of the complexes are summarized in Table 1.

Table 1
Crystallographic data and refinement parameters for complexes **1** and **3**

Complex	**1**	**3**
Empirical formula	$C_{52}H_{48}Cl_2Co_2N_{16}O_{16}$	$C_{68}H_{55}Cl_3Co_2N_{20}O_{20}$
Formula weight	1341.82	1696.53
Crystal size (mm)	0.2 × 0.15 × 0.15	0.3 × 0.2 × 0.15
Crystal system	monoclinic	monoclinic
Space group	*C*2/c	*P*2(1)/*n*
a (Å)	22.131(4)	14.6114(2)
b (Å)	22.824(4)	14.2988(2)
c (Å)	15.148(3)	35.371(4)
β (°)	129.584(3)	91.831(2)
V Å^3	5897.1(2)	7386.2(1)
Z, $D_{calc.}$ (Mg/m^3)	4, 1.449	4, 1.519
F(000)	2616	3444
μ (mm^{-1})	0.730	0.645
Reflections measured	5188	12935
Independent reflections (R_{int})	3041 (0.0751)	5588 (0.0871)
Goodness-of-fit (*S*)	1.073	1.018

3. Results and discussion

The ligands H_2L^{1-3} are prepared with a moderate yield and synthesized according to the method in the previous work. [8–10] It should be noted that the construction of metal helicates requires the elaborately designed ligand to transmit the chirality from one metal center to another one. As expected, the designed ligand H_2L^{1-3} can wrap around two metal ions, chiral helices will result only when the two metal centers display the same absolute configurations.

3.1. Crystal structure of complex 1

Interaction of the $Co(ClO_4)_2 \cdot 6H_2O$ with H_2L^1 at reflux gave a dark-red complex whose elemental analysis data for the complex is in good agreement with the general molecular formula $[Co(HL^1)]_n$ as would be expected for a complex consisting of two ligands with two-armed tridentate donor sites and two six-coordination metal ions. As shown in Fig. 1, ESI-MS in acetonitrile/methanol combined solution shows two distinct peaks at 1014.3 and 507.3, corresponding to the species $[Co^{II}Co^{III}(L^1)_2]^+$, calc. 1014.8) and $[Co_2^{III}(L^1)_2]^{2+}$, calc. 507.4), respectively, consistent with formation of a double helical structure. The strongest peak at *m/z* 507.3 corresponds to the most abundant ion $[Co_2(L^1)_2]^{2+}$ with isotopic peaks separated by 0.5, which confirmed the 2+ charge borne by the cation [13]. The presence of one strong $[Co_2(L^1)_2]^{2+}$ peak indicates that this double helical species has high stability even under the electronic spray conditions, which corresponds to the predominant existence of Co(III) species in solution. Considering the easier deprotonation nature and the labile oxidation state of cobalt ion, it is expected that Co(II) is readily oxidised to Co(III) which would account for the intense color and the similarity of the two ends of the ligand. A magnetic susceptibility measurement on the crystal samples showed the room temperature χT value is close to zero, corresponding to the low spin Co(III) species. Figs. 2 and 3 show the molecular structure of metal complex $Co_2(L^1)_2(ClO_4)_2(C_2H_5OH)_2(H_2O)_2$ (**1**). The bis-tridentate ligand H_2L^1 exhibits a *trans* configuration and acts as bridging ligand installed with the pocket-like coordination sites at the terminal. The complex is best described as a double-stranded helicate, and two metal centers occupy the helical axis with the center-to-center separation of 6.077 Å. The complex **1** possesses a crystallographic C_2 axis perpendicular to the helical Co···Co axis. The Co(1) center occupies a six-coordinated pseudooctahedral environment surrounded by two different ligands, each ligand provides a set of N_2O pocket-like coordination sites. Angles O–Co–O, O–Co–N, N–Co–N are all in the range of 82.06(22)–101.69(23)° and 165.09(20)–171.60(0.22)°, respectively, which show a distorted octahedral geometry around two crystallographically equivalent cobalt centers. The Co–O distances of 1.8714–1.8773 Å and Co–N lengths of 1.8467–1.9171 Å agree well with those of the related

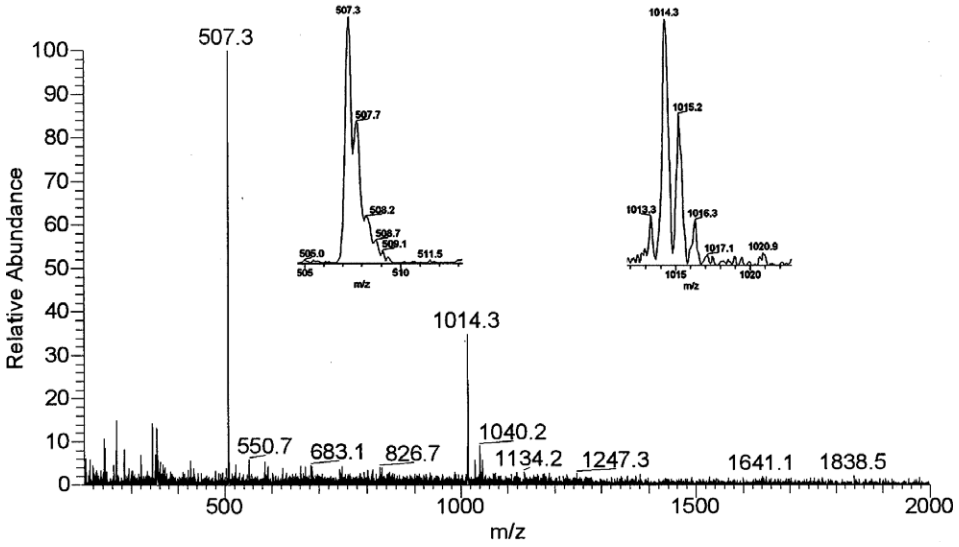


Fig. 1. ESI-MS of compound **1** in CH_3CN/CH_3OH mixed solutions.

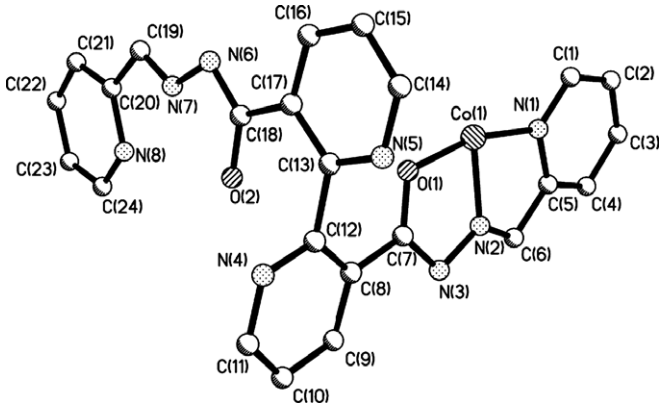


Fig. 2. Atomic numbering scheme for the asymmetric unit of cation of complex **1**. Ellipsoids are represented with 50% probability.

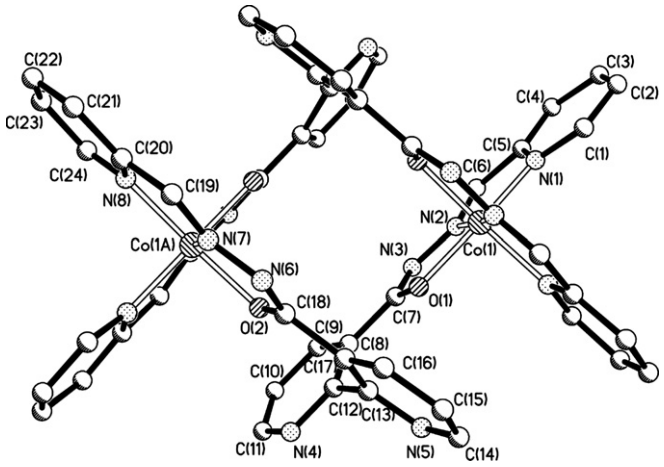


Fig. 3. The helicate structure of complex **1** with the selected atom labels. The hydrogen atoms, anions and solvent molecules are omitted for clarity.

complexes [14]. The presence of two counteranions per helicate suggests the ligand herein lost protons in virtue of coordination to metal ions. As a result, all the bond distances within two arms are intermediate between the normal single bond and double bond, further indicating extensive delocalization over the entire molecular skeleton (Table 2). The coordination to the metal ions also induces the configuration changes within the ligand $\mathbf{H_2L^1}$. The two arms are strongly twisted by the coordination to the metal centers, subsequently resulting in pseudo-perpendicularity each other with the torsion angle of substituted bipyridyl groups being ca. 88.0°.

Since helicate **1** is the molecule possessing true 2-fold symmetry, it is not surprising that the most-frequent space group $C2/c$, a group of maximum density for packing such the molecules, occurs for the complex **1** [15]. The crystal packing structure of helicate **1** can nearly be described as deformed hexagonal unit cells, in fact, the helicates form layers of hexagonal close packed cyclindrical molecules, this leads to pseudohexagonal AB close-packed arrangements [4b]. As in most cases for the helicate structures in monoclinic system, the pseudohexagonal direction is to be found in the *ac* plane. Parallel to the principal axis (H_a) the molecules tend to align themselves to give the densest packing, leaving sufficient space in cavities for the counteranions and solvent molecules (Fig. 4). The observation exactly fit those previously reported by other workers [16]. No obvious weak intermolecular interactions were found in the crystal packing.

3.2. Crystal structure of complex *3*

In acetonitrile-methanol combined solution, ESI-MS studies revealed only one main peak at *m/z* 660.9 corresponds to the species $[\ Co_2^{III}\ (\mathbf{L^3})_2]^{2+}$ (calc. $m/z = 661.5$),

Table 2
The selected bond distances (Å) and bond angles (°)

Complex ***1***	
Co(1)#–N(7)	1.850(4)
Co(1)–N(2)	1.857(4)
Co(1)–O(1)	1.871(4)
Co(1)#–O(2)	1.877(3)
Co(1)–N(1)	1.911(5)
Co(1)#–N(8)	1.924(5)
O(1)–C(7)	1.286(6)
O(2)–C(18)	1.284(6)
N(2)–C(6)	1.272(7)
N(2)–N(3)	1.375(6)
N(3)–C(7)	1.316(6)
N(6)–C(18)	1.316(6)
N(6)–N(7)	1.373(6)
N(7)–C(19)	1.281(7)
N(7)#–Co(1)–N(2)	171.5(2)
N7#–Co1–O1	93.16(18)
N(2)–Co(1)–O(1)	82.1(2)
N(2)–Co(1)#–O(2)	90.9(2)
O(1)–Co(1)#–O(2)	89.9(2)
N(2)–Co(1)–N(1)	82.9(2)
O(1)–Co(1)–N(1)	165.0(2)
N(2)–Co(1)#–N(8)	103.7(2)
O(1)–Co(1)#–N(8)	91.0(2)
N(1)–Co(1)#–N(8)	92.1(2)
Complex ***3***	
Co(1)–N(18)	1.841(5)
Co(1)–N(8)	1.851(5)
Co(1)–O(4)	1.886(4)
Co(1)–O(2)	1.887(4)
Co(1)–N(9)	1.916(5)
Co(1)–N(19)	1.911(6)
C(12)–O(1)	1.298(7)
C(12)–N(4)	1.312(7)
C(23)–O(2)	1.292(7)
C(23)–N(7)	1.313(8)
C(46)–O(3)	1.297(7)
C(46)–N(14)	1.313(8)
C(57)–O(4)	1.292(7)
C(57)–N(17)	1.319(8)
C(58)–N(18)	1.298(8)
N(13)–N(14)	1.366(7)
N(17)–N(18)	1.378(7)
N(3)–N(4)	1.390(7)
N(7)–N(8)	1.361(7)
N(18)–Co(1)–N(8)	172.3(2)
N(18)–Co(1)–O(4)	83.5(2)
N(8)–Co(1)–O(4)	89.5(2)
N(18)–Co(1)–O(2)	93.5(2)
N(8)–Co(1)–O(2)	83.1(2)
N(18)–Co(1)–N(9)	100.4(2)
O(2)–Co(1)–N(9)	166.1(2)

Symmetric code for complex **1**: # $-x+2$, y, $-z+5/2$.

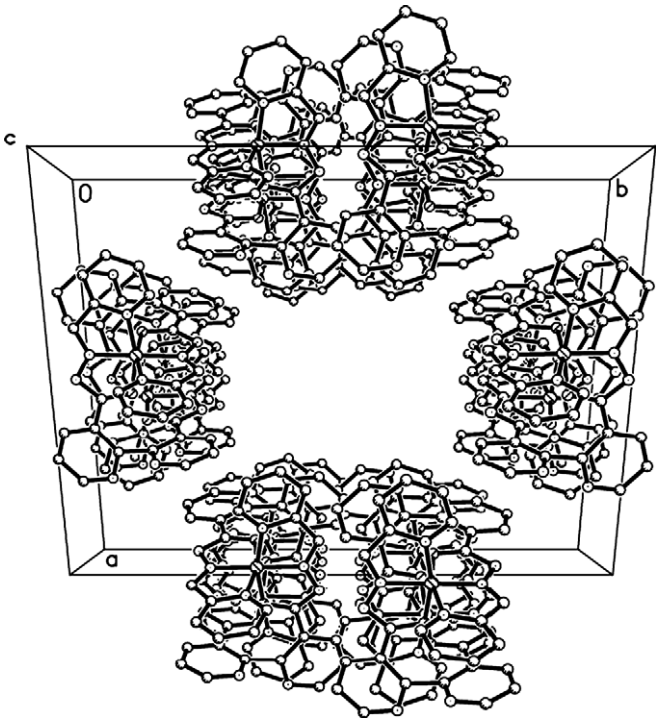


Fig. 4. The crystal packing of complex **1** along the crystallographic *c* axis showing the pore structure, the solvent molecules and anions in the channel are omitted for clarity.

suggesting the helical structure of complex **3** dominantly persists in solution. (Fig. 5) The crystal structure of complex **3** is shown in Fig. 6. The complex **3** crystallizes in the monoclinic crystal system as previously found for the analogous complex **1** but the space group changes from $C2/c$ to $P2(1)/n$. The asymmetric unit contains a dinuclear helicate cation, three anions ClO_4^- and some solvent molecules. The presence of three ClO_4^- anions per helicate indicates that the helicate **3** has trivalent oxidation state. Each Co center adopts pseudo-octahedral configuration and is coordinated by two sets of N_2O unit from the different ligands. The average distances of Co–O and Co–N are consistent with those of complex **1**. The distance between two cobalt centers is 6.156 Å, somewhat longer than that of complex **1**. Two bipyridyl groups are almost perpendicular and the dihedral angles between the substituted pyridyl block is 90.9°. As shown in the complex **1**, the coordination pockets rotate in the opposite direction to assemble as a helicate and the metal center has the homochiral configuration. Based on the fact that the complex **3** crystallized in the achiral space group, the individual helicate, which is inherently chiral, aggregates as a racemate of *P* for right-hand and *M* for left-hand in the solid [17,18].

3.3. Thermogravimetric studies

The TGA curve of the complex **1** showed that the desolvation process takes places beginning at ca. 70 °C. The weight loss is 10.02% in total above 110 °C and slightly greater than the theoretical value (9.54%), corresponding to the loss of all the water and ethanol molecules. As shown in Fig. 7, the desolvated products, $Co_2(C_{24}H_{17}N_8O_2)_2(ClO_4)_2$ are stable enough to ca. 340 °C, on further heating, the complex **1** abruptly begin to decompose. The decomposing curves of complexes **2** and **3** are similar to that of complex **1**.

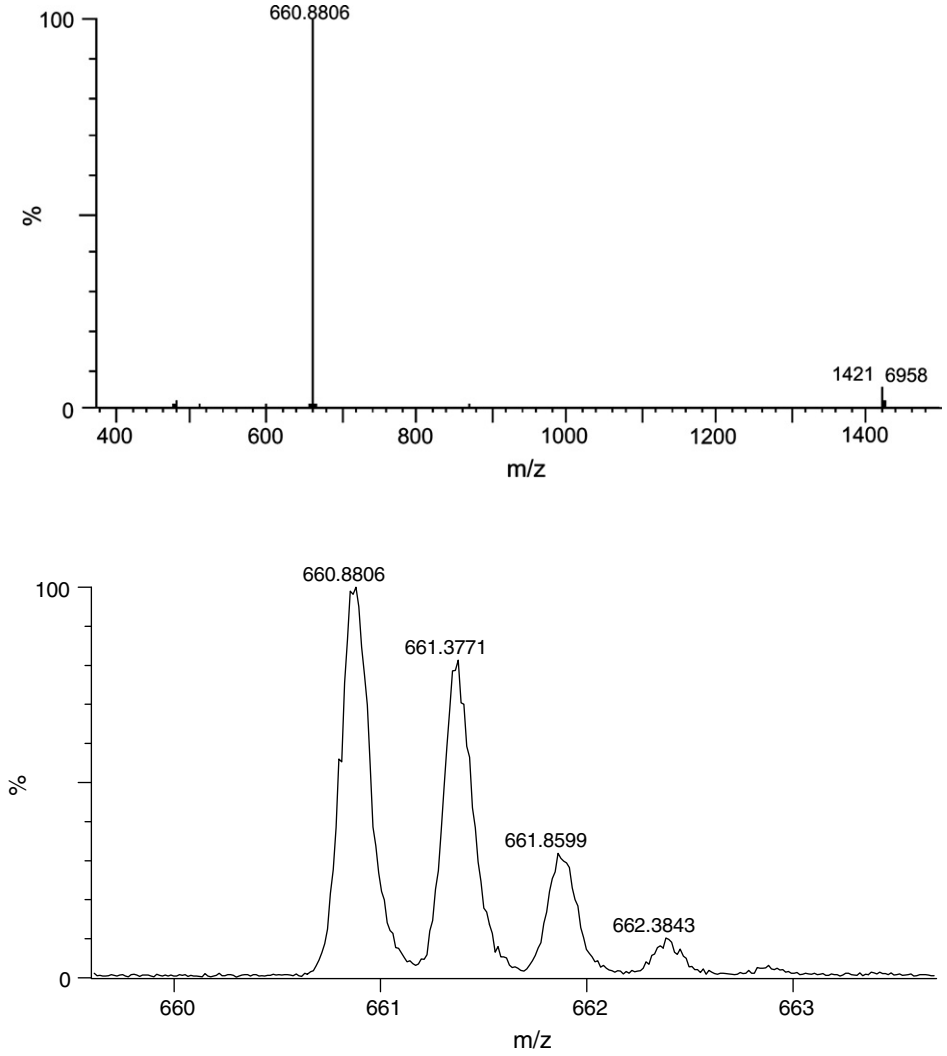


Fig. 5. (a) The ESI-MS of compound **3** in CH_3CN/CH_3OH mixed solution. (b) Isotropic pattern of ESI-MS for compound **3**.

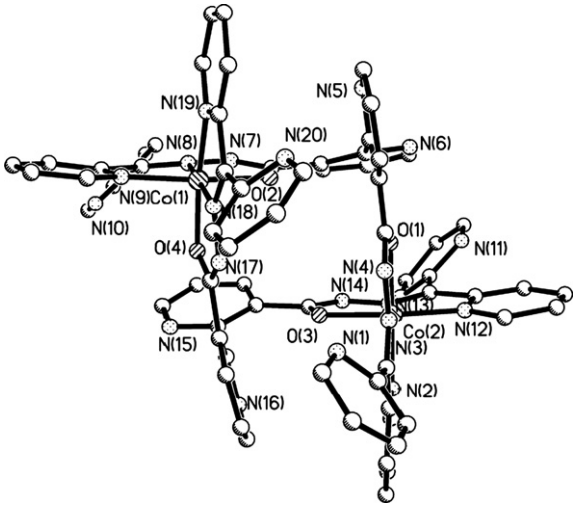


Fig. 6. The crystal structure of complex **3** with the selected atom labels. Hydrogen atoms, anions and solvent molecules are omitted for clarity. Ellipsoids are represented with 50% probability.

3.4. Photoluminescence property

In the solid state, the complex **1** shows photoluminescence at room temperature. Complex **1** exhibits one obvious emission at ca. 530 nm with the excitation at 400 nm at room temperature (Fig. 8). To understand the nature of the emission bands, we analyzed the photoluminescence property of the free $\mathbf{H_2L^1}$ ligand and found that it does not display any emission bands. As well known, cobalt ion is not an excellent metal source for photoluminescence, whereas complex **1** exhibits obvious emission spectrum, which indicates that the photoluminescence property is closely related with the ligand structure in complex **1**. The intense emission at 530 nm of complex **1**, which is different from those of the free $\mathbf{H_2L^1}$ ligand, might be assigned to the intraligand emission excited state [19–21]. It is presumed that the deprotonization of the ligand due to the coordination to metal ion might promote charge delocalization within the whole structure compared to the free ligand,

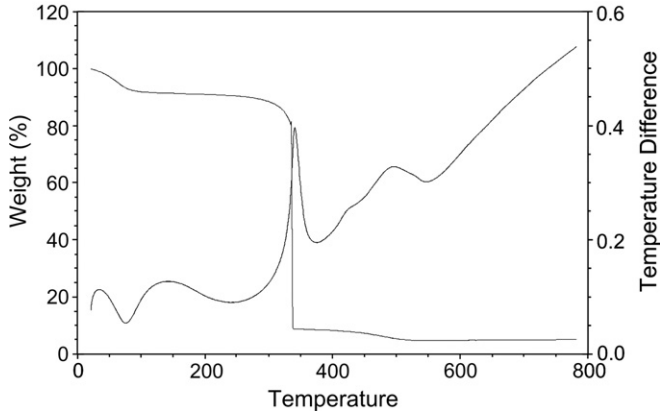


Fig. 7. The TG-DTA curve of complex **1** (T in °C).

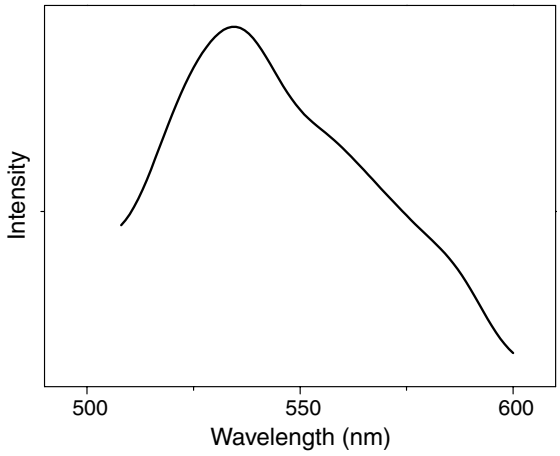


Fig. 8. The emission spectrum of complex **1**. $\lambda_{ex} = 400$ nm.

and thus enhance the photoluminescence of complex **1**. Whereas for the ligand $\mathbf{H_2L^3}$ in complex **3**, in which the ligand can not easily be deprotonated, charge delocalization cannot happen and complex **3** does not exhibit photoluminescence property. This work shows photoluminescence property is closely related with the structure of complex in addition to metal ions.

3.5. Conclusions

In summary, three ligands $\mathbf{H_2L^{1-3}}$ equipped with bipyridine-bridged bis-multidentate coordination pockets have been designed to construct cobalt-containing metallohelicate complexes. Due to the flexible nature and suitable coordination pocket of ligand, the assembly process can produce helicate structure, which can intrinsically transfer the chirality from one metal center to another one. This crystal packing of complex **1** exhibits an interesting pore structure and helicate complex **1** shows photoluminescence at room temperature in the solid state.

Acknowledgement

The authors gratefully acknowledge the financial support of the Natural Science Foundation of Anhui Province.

Appendix A. Supplementary material

CCDC 663029 and 663030 contain the supplementary crystallographic data for **1** and **3**. These data can be obtained free of charge via http://www.ccdc.cam.ac.uk/conts/retrieving.html, or from the Cambridge Crystallographic Data Centre, 12 Union Road, Cambridge CB2 1EZ, UK; fax: (+44) 1223-336-033; or e-mail: deposit@ccdc.cam.ac.uk. Supplementary data associated with this article can be found, in the online version, at doi:10.1016/j.poly.2007.11.025.

References

[1] J.-M. Lehn, Supramolecular Chemistry – Concepts and Perspectives, VCH, Weinheim, 1995.
[2] D. Philp, J.F. Stoddart, Angew. Chem., Ed. Engl. 35 (1996) 1155.
[3] (a) E.C. Constable, Tetrahedron 48 (1992) 10013;
(b) E.C. Constable, Prog. Inorg. Chem. 42 (1994) 67;
(c) E.C. Constable, Nature 346 (1990) 314;
(d) E.C. Constable, in: J.L. Atwood, J.E.D. Davies, D.D. MacNicol, F. Vögtle (Eds.), Comprehensive Supramolecular Chemistry, Pergamon, Oxford, 1996 (Chapter 6).
[4] (a) M. Albrecht, Chem. Rev. 101 (2001) 3457;
(b) C. Piguet, G. Bernardinelli, G. Hopfgartner, Chem. Rev. 97 (1997) 2005;
(c) J. Hamacek, M. Borkovec, C. Piguet, Chem. Eur. J. 11 (2005) 5217.
[5] C. Piguet, G. Bernardinelli, A.F. Williams, Inorg. Chem. 28 (1989) 2920.
[6] S. Riittimann, C. Piguet, G. Bernardinelli, B. Bocquet, A.F. Williams, J. Am. Chem. Soc. 114 (1992) 4230.
[7] (a) O. Mamula, A. von Zelewsky, T. Bark, G. Bernardinelli, Angew. Chem., Int. Ed. 38 (1999) 2945;
(b) M. Albrecht, Chem. Eur. J. 6 (2000) 3485;
(c) C. Piguet, C. Edder, S. Rigault, G. Bernardinelli, J.-C.G. Bunzli, G. Hopfgartner, J. Chem. Soc., Dalton Trans. 375 (2000) 3999;
(d) E.C. Constable, Prog. Inorg. Chem. 42 (1994) 67;
(e) G. Baum, E.C. Constable, D. Fenske, C.E. Housecroft, T. Kulke, Chem. Commun. 2 (1999) 195;
(f) E.C. Constable, M.J. Hannon, P. Harverson, M. Neuburger, D.R. Smith, V.F. Wanner, L.A. Whall, M. Zehnder, Polyhedron 19 (2000) 23;
(g) E.C. Constable, F. Heirlitzer, M. Neuburger, M. Zehnder, J. Am. Chem. Soc. 119 (1997) 5606.
[8] D.-Y. Wu, L.-X. Xie, C.-L. Zhang, C.-Y. Duan, Y.-G. Zhao, Z.-J. Guo, Dalton Trans. 29 (2006) 3528.
[9] L.-X. Xie, D.-Y. Wu, C.-Y. Duan, B.-G. Zhang, Q.-J. Meng, Chin. J. Inorg. Chem. 23 (2007) 191.
[10] D.-Y. Wu, W. Huang, G. Li, L.-X. Xie, C.-Y. Duan, Q.-Z. Sun, Q.-J. Meng, Chin. J. Inorg. Chem. 23 (2007) 1129.
[11] SMART and SAINT, Area Detector Control and Integration Software, Siemens Analytical X-Ray Systems, Inc, Madison, WI, 1996.
[12] G.M. Sheldrick, SHELXTL V5.1, Software Reference Manual, Bruker AXS, Inc, Madison, WI, 1997.
[13] G. Hopfgartner, C. Piguet, J.D. Henion, J. Am. Soc. Mass Spectrom. 5 (1994) 748.

[14] O. Sato, J. Tao, Y.-Z. Zhang, Angew. Chem., Int. Ed. 46 (2007) 152, and references therein.
[15] A.I. Kitaigorodsky, Molecular Crystals and Molecules, Academic Press Inc., London, UK, 1973.
[16] (a) F. Renaud, C. Piguet, G. Bernardinelli, J.-C.G. Bünzli, G. Hopfgartner, Eur. J. Chem. 3 (1997) 1646;
(b) D. Guo, K.-L. Pang, C.-Y. Duan, C. He, Q.-J. Meng, Inorg. Chem. 41 (2002) 5978.
[17] M.H. Hannon, C.L. Painting, W. Errington, Chem. Commun. 3 (1997) 307.
[18] M.J. Hannon, C.L. Painting, N.W. Alcock, Chem. Commun. 20 (1999) 2023.
[19] L.Y. Zhang, G.F. Liu, S.L. Zheng, B.H. Ye, X.M. Zhang, X.M. Chen, Eur. J. Inorg. Chem. 16 (2003) 2965.
[20] Z.Y. Fu, X.T. Wu, J.C. Dai, S.M. Hu, W.X. Du, H.H. Zhang, R.Q. Sun, Eur. J. Inorg. Chem. 10 (2002) 2730.
[21] Y. Gong, T. Wang, M. Zhang, C.W. Hu, J. Mol. Struct. 833 (2007) 1.

ligands were synthesized using metal carbonyls and aziridine by Singh and Angelici [32,33] and also in our group [34] whereas isocyanide complexes were employed by Michelin and co-workers [35]. Beck and co-workers observed the metal-mediated dimerisation of two aziridine ligands forming the chelate *N*-(2-aminoethyl)aziridine ligand [8], and in 1997, Kojima et al. reported the first X-ray structure of a *N*-(2-amino-2-methylethyl)-2-methylaziridine cobalt(III) complex [36].

The tendency towards ring opening of aziridine is mainly a result of Baeyer and Pitzer ring strain [37], especially after NH protonation has occurred and can easily lead to nucleophilic attack. The versatility of the aziridine motif has resulted in widespread interest in this heterocycle [38–40]. Particularly in organic chemistry, aziridine compounds have a variety of synthetic applications, for example, as catalysts in asymmetric synthesis [41–44], synthones in natural product synthesis [45–48], monomers in macromolecular chemistry, [49,50] or target molecules in organic synthesis [51–53]. Another important reason for the increased interest in aziridine chemistry is its biological role, whereby *in vivo* effects of aziridine derivatives are mostly the result of ring opening and alkylation reactions. This results in the carcinogenic activity of natural and synthetic aziridine compounds [54–57]. In this context, the promising cytotoxic and anticancerogenic activities of chelating amine ligands in the coordination sphere of the platinum group metals is also worth mentioning [58]. Biological studies concerning this issue are currently being undertaken, and will be reported in future work. In this communication, the transition metal lewis acid mediated ring opening reaction of aziridine yielding the chelating ligand *N*-(2-aminoethyl)aziridine-*N*,*N*′ is reported.

2. Results and discussion

2.1. Synthesis

Scheme 1 illustrates the reactions of the bis-aziridine complexes $[MCl(Cp^*)(az)_2]Cl$ (M = Rh: **1**, M = Ir: **2**) with first 2.2 equiv. silvertriflate and then with an excess (1:2.5) of aziridine C_2H_4HN (**3**), which leads to the formation of the *N*-(2-aminoethyl)aziridine complexes $[M(Cp^*)(aeaz)(az)](OTf)_2$ (M = Rh: **4**, M = Ir: **5**; aeaz = *N*-(2-aminoethyl)aziridine). Monitoring the first step of this reaction using IR spectroscopy shows that a triflato-*O* ligand is weakly coordinated to the metal centres forming the $[M(Cp^*)(OTf)(az)_2]$ intermediate. For related complexes, we have succeeded in the isolation and structural characterization of triflato-*O* complexes [59].

The same reaction as that described above with the analogous complex $[RuCl(C_6Me_6)(az)_2]Cl$ (**6**) and aziridine **3** did not result in the formation of the analogous complex $[Ru(C_6Me_6)(aeaz)(az)](OTf)_2$ (**7**). Obviously under the reaction conditions applied, **6** appears to be not electrophilic enough to induce the desired ring opening reaction and therefore, an anion exchange reaction occurs yielding the $[RuCl(C_6Me_6)(az)_2]OTf$ (**8**) complex. Nevertheless, even although the preparation of the desired Ru complex was unsuccessful using the mild reaction conditions applied in this work, the synthesis of this complex should be possible.

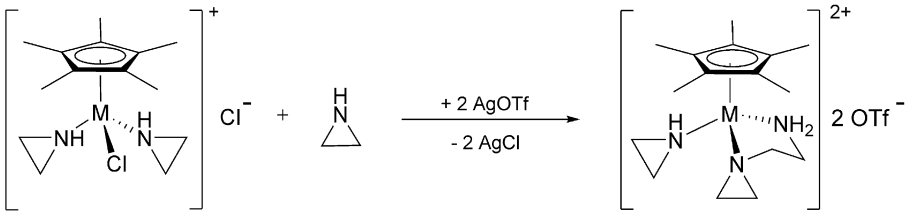
All products were obtained as colourless (**4**) or yellow (**5**, **8**) powders in acceptable yields (60–74%) and are soluble in polar solvents such as acetone, but insoluble in non-polar solvents such as *n*-pentane. Compounds **4**, **5** and **8** can be stored infinitely under an atmosphere of argon.

2.2. X-ray crystal structure analysis

The molecular structures of compounds **4**, **5** and **8** were determined using single crystal X-ray diffraction. Isothermic diffusion of *n*-pentane into solutions of **4** and **5** in acetone or of **8** in dichloromethane resulted in the formation of X-ray quality single crystals. Details of the relevant data collection and refinement are summarised in Table 1. The molecular structures of **4**, **5** and **8** are illustrated in Figs. 1–3. Bond lengths and angles within the coordination sphere of Rh(III), Ir(III) and Ru(II) are listed in Figs. 1–3, respectively.

All three complexes show similar structures with a distorted octahedral geometry as is expected for Rh(III), Ir(III) or Ru(II) transition metal centres. The aromatic ligand L (C_6Me_6 or C_5Me_5) constitutes one octahedral face, while the other three coordinating atoms (Cl or N) form the opposite one.

All of M–N bond lengths (213–218 pm) observed for **4** and **5** lie within a small range and are only slightly elongated in comparison to the M–N bond lengths of the analogous bis-aziridine complexes **1** and **2** [60]. It is worthwhile



1: M = Rh
2: M = Ir

3

4: M = Rh
5: M = Ir

Scheme 1. Synthesis of the cationic *N*-(2-aminoethyl)aziridine complexes **4** and **5**.

Table 1
Crystal data and details of the structure refinement for compounds **4**, **5** and **8**

Compound	**4**	**5**	**8**
Formula	$C_{18}H_{30}F_6N_3O_6RhS_2$	$C_{18}H_{30}F_6N_3O_6IrS_2$	$C_{17}H_{28}ClF_3N_2O_3RuS$
FW	665.48	754.79	534.00
Temperature (K)	200(2)	200(2)	200(2)
Wavelength (Å)	0.71073	0.71073	0.71073
Crystal system	orthorhombic	orthorhombic	monoclinic
Space group	$P2_12_12_1$	$P2_12_12_1$	$P2_1/c$
a (Å)	9.29300(20)	9.3329(19)	14.925(3)
b (Å)	16.26700(29)	16.254(3)	8.9792(18)
c (Å)	17.38730(29)	17.361(4)	19.626(7)
α (°)	90	90	90
β (°)	90	90	126.602(19)
γ (°)	90	90	90
V (Å^3)	2628.425(87)	2633.7(9)	2111.5(10)
Z	4	4	4
ρ_{calc} (g cm^{-1})	1.68171(6)	1.9036(7)	1.6798(8)
μ (mm^{-1})	0.889	5.308	1.014
F(000)	1352	1480	1088
Crystal size (mm)	0.14 × 0.10 × 0.07	0.15 × 0.09 × 0.07	0.19 × 0.10 × 0.02
θ Range (°)	3.21–27.48	3.32–27.48	3.40–27.48
Index range	$-11 \leqslant h \leqslant 12$, $-21 \leqslant k \leqslant 21$, $-22 \leqslant l \leqslant 22$	$-11 \leqslant h \leqslant 12$, $-20 \leqslant k \leqslant 20$, $-22 \leqslant l \leqslant 22$	$-19 \leqslant h \leqslant 19$, $-11 \leqslant k \leqslant 11$, $-25 \leqslant l \leqslant 24$
Reflections collected	38 771	29 248	8823
Independent reflections	6018	5946	4828
R_{int}	0.0659	0.0636	0.0372
Completeness to θ (%)	99.7	99.5	99.6
Refinement method	full-matrix least squares on F^2	full-matrix least squares on F^2	full-matrix least squares on F^2
Data/restraints/parameters	6018/0/326	5946/0/326	4828/0/253
S on F^2	1.076	1.119	1.033
Final R indices [$I > 2\sigma(I)$]	$R_1 = 0.0508$, $wR_2 = 0.1282$	$R_1 = 0.0379$, $wR_2 = 0.0913$	$R_1 = 0.0449$, $wR_2 = 0.1080$
R indices (all data)	$R_1 = 0.0629$, $wR_2 = 0.1347$	$R_1 = 0.0405$, $wR_2 = 0.0924$	$R_1 = 0.0704$, $wR_2 = 0.1204$
Largest difference in peak/hole (e Å^{-3})	2.004 and −0.792	3.828 and −1.775	1.011 and −0.864

to note that in both cases the M–NH bonds (213/214 pm) are significantly shorter than the M–NH_2 bonds (218 pm). The N–C bond lengths within the aziridine ring as well as in the ethane bridge lie in the expected range between 144 and 148 pm, whereas the C–C bond lengths (154/151 pm) within the five-membered ring of the *N*,*N*′-chelate ligand are longer than those in the three-membered aziridine ring (141–147 pm). All of the angles of the intact aziridine rings (58.5–61.5°) are approximately 60° and similar to those observed in free aziridine [61,62]. The N–M–NH_2 angles (78.4°/77.3°) within the five-membered rings are much smaller in comparison with the other N–M–N angles, e.g. the NH–M–NH_2 angles are 91.3° or 90.0° in **4** and **5**, respectively and are larger than the NH–M–N angles (87.0° (**4**)/86.0° (**5**)). This may be constraint due to the five-membered ring that does not allow the opening up to 90°. However, all of the bond lengths and angles mentioned above are found in the expected range and are comparable to those in similar complexes [63–66]. Compound **8** shows Ru–N, Ru–C and Ru–Cl bond lengths in the 213 pm, 216–223 pm ranges and 242 pm range respectively, which are consistent with the corresponding values observed for the analogous bis-aziridine–ruthenium(II) complexes [60]. It is worth mentioning that the angles of the intact aziridine rings (59.5–60.6°) are approximately 60° and similar to those in the uncoordinated aziridine [61,62]. The N–M–N angle is 81.2° and is smaller in comparison with the N–M–Cl angles (88.4° and 88.1°) due to steric reasons. All of the bond lengths and angles mentioned above are within the expected ranges and are comparable to those in similar complexes [60].

2.3. Spectroscopy

The IR, ^{1}H, ^{13}C NMR and mass spectra of compounds **4**, **5** and **8** have been obtained and are consistent with the spectroscopic data expected based on the molecular structures obtained by single crystal X-ray diffraction. The complexes **4** and **5** show two chiral centres at the metal centre and the aziridine–nitrogen atom of the aeaz ligand. Inspite of the potential existence of two diastereomers which should arise a double number of signals in the NMR spectra, only one set of signals for one diastereomer has been observed. In general, the ^{1}H and ^{13}C NMR spectra of **4**, **5** and **8** show signals shifted to lower field in comparison to the signals observed for the free ligand due to deshielding caused by coordination to the transition metal. In particular, in the case of the NH and NH_2 ^{1}H NMR signals for coordinated az and aeaz at 3.55 ppm (NH, **4**), 4.06 ppm (NH, **5**), 3.29–3.39 ppm (NH, **8**), 4.65/5.03 ppm (NH_2, **4**)

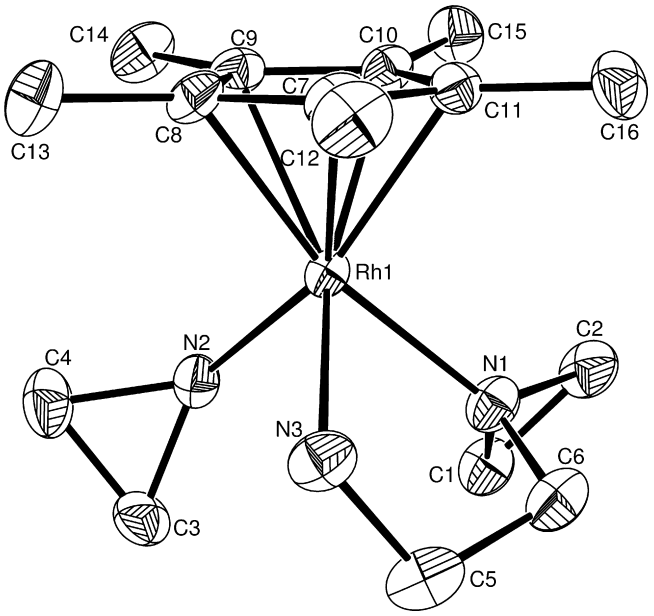


Fig. 1. Molecular structure of 4 with thermal ellipsoids drawn at the 30% probability level. Hydrogen atoms and the two triflate anions are omitted for clarity. Selected bond lengths (Å) and angles (°): Rh(1)–N(1) 2.158(4), Rh(1)–N(2) 2.131(5), Rh(1)–N(3) 2.175(5), N(1)–C(1) 1.447(8), N(1)–C(2) 1.476(9), C(1)–C(2) 1.444(11), N(1)–C(6) 1.467(8), C(5)–C(6) 1.536(11), N(3)–C(5) 1.462(8), N(2)–C(3) 1.456(8), N(2)–C(4) 1.467(8), C(3)–C(4) 1.467(11), N(1)–Rh(1)–N(2) 87.0(2), N(1)–Rh(1)–N(3) 78.4(2), N(2)–Rh(1)–N(3) 91.3(2), N(1)–C(1)–C(2) 61.4(5), N(1)–C(2)–C(1) 59.4(5), C(1)–N(1)–C(2) 59.2(5), N(2)–C(3)–C(4) 60.2(4), N(2)–C(4)–C(3) 59.5(4), C(3)–N(2)–C(4) 60.2(5).

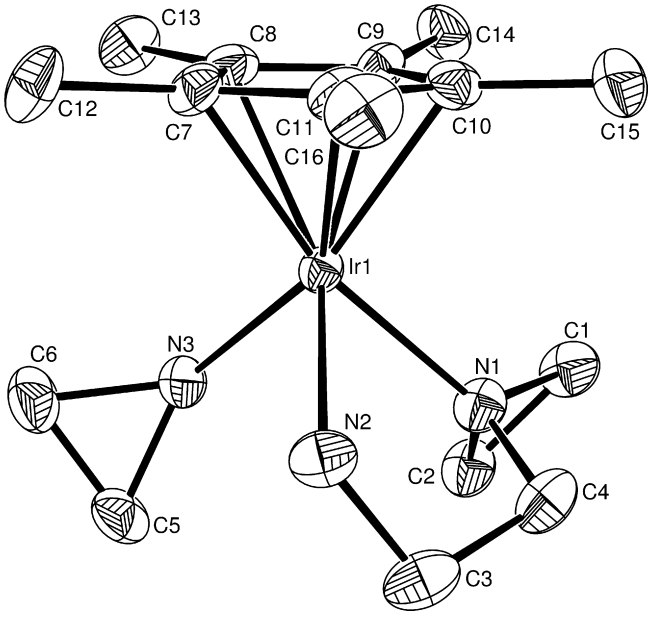


Fig. 2. Molecular structure of **5** with thermal ellipsoids drawn at the 30% probability level. Hydrogen atoms and the two triflate anions are omitted for clarity. Selected bond lengths (Å) and angles (°): Ir(1)–N(1) 2.152(6), Ir(1)–N(2) 2.180(7), Ir(1)–N(3) 2.136(7), N(1)–C(1) 1.473(11), N(1)–C(2) 1.457(10), C(1)–C(2) 1.438(14), N(1)–C(4) 1.460(11), C(3)–C(4) 1.513(15), N(2)–C(3) 1.459(11), N(3)–C(5) 1.435(11), N(3)–C(6) 1.457(11), C(5)–C(6) 1.413(15), N(1)–Ir(1)–N(2) 77.3(3), N(1)–Ir(1)–N(3) 86.0(3), N(2)–Ir(1)–N(3) 90.0(3), N(1)–C(1)–C(2) 60.1(6), N(1)–C(2)–C(1) 61.1(6), C(1)–N(1)–C(2) 58.8(6), N(3)–C(5)–C(6) 60.0(6), N(3)–C(6)–C(5) 61.5(6), C(5)–N(3)–C(6) 58.5(7).

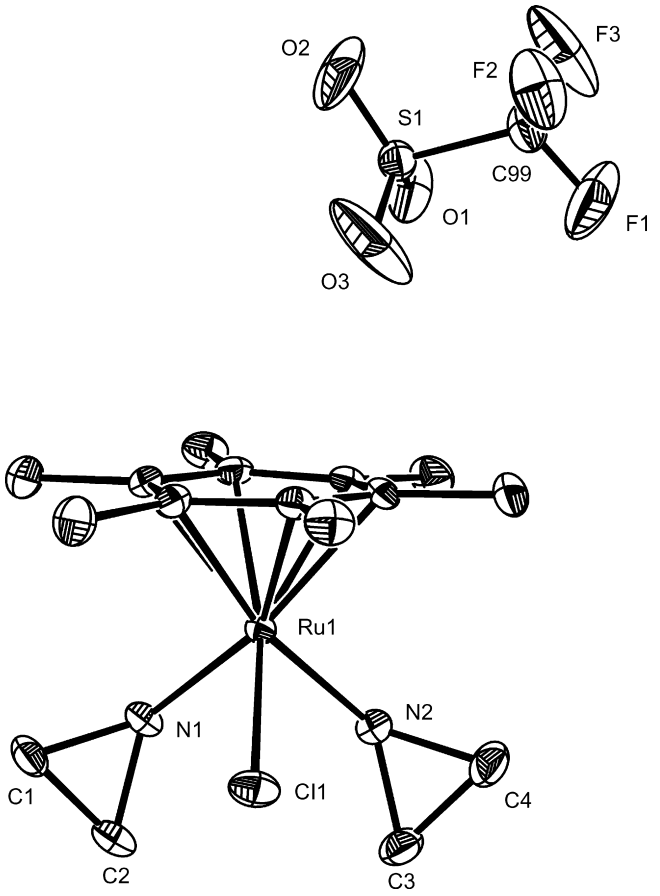


Fig. 3. Molecular structure of **8** with thermal ellipsoids drawn at the 30% probability level. Hydrogen atoms are omitted for clarity. Selected bond lengths (Å) and angles (°): Ru(1)–N(1) 2.125(3), Ru(1)–N(2) 2.133(4), Ru(1)–C(8) 2.162(4), Ru(1)–C(10) 2.226(4), Ru(1)–Cl(1) 2.417(12), N(1)–C(2) 1.471(5), N(1)–C(1) 1.484(5), C(1)–C(2) 1.467(7), N(2)–C(3) 1.470(6), N(2)–C(4) 1.479(6), C(3)–C(4) 1.469(7), N(1)–Ru(1)–N(2) 81.16(14), N(1)–Ru(1)–Cl(1) 88.40(10), N(2)–Ru(1)–Cl(1) 88.12(11), C(2)–N(1)–C(1) 59.54(3), C(1)–C(2)–N(1) 60.66(3), C(2)–C(1)–N(1) 59.80(3), C(3)–N(2)–C(4) 59.75(3), C(3)–C(4)–N(2) 59.81(3), C(4)–C(3)–N(2) 60.43(3).

and 5.22/5.68 ppm (NH_2, **5**), a strong shift to lower field is observed compared to the free ligand with NH (az) and NH_2 (aeaz) ^1H NMR signals at −0.02 ppm (az, $CDCl_3$) and 1.60 ppm (aeaz, CD_3OD). As was noted above, the CH_2 signals for az and aeaz in the ^{13}C NMR spectra are shifted to lower field, for example, whereas the CH_2 groups of the uncoordinated az show a signal at 17.8 ppm, in the coordinated az (**8**) CH_2 signals are detected at 19.6 ppm and 23.8 ppm.

Mass spectrometry was used to investigate the fragmentation of the cationic complexes using positive FAB mode in a nitrobenzylalcohol (NBA) matrix. Compounds **4** and **5** exhibit similar fragmentation patterns with m/z peaks at 516, 266 (**4**) and 607, 457 (**5**) corresponding to M^+ and M^{2+}, respectively. In addition, the fragmentation pattern for complexes **4** and **5** shows the successive loss of the az, aeaz and both ligands for M^+ and az and aeaz for M^{2+}. Compound **8** shows a peak at $m/z = 499$ corresponding to the $M^+ + OTF^- - Cl$ fragment and at $m/z = 385$ for the

M^+ peak. In the fragmentation pattern of M^+ (**8**), the successive loss of one and two az ligands could be identified.

The IR spectra of complexes **4**, **5** and **8** show similar values for the vibrational modes of the transition metal coordinated az and aeaz ligands with those reported for related aziridine complexes [60]. Compounds **4**, **5** and **8** show sharp absorption bands for the aziridine N–H stretching vibrations in the range 3251–3245 cm^{-1} as expected for secondary amines coordinated to transition metals [67]. In addition, typical σ- and δ-ring vibrations in the fingerprint region of az and aeaz were observed [68].

3. Experimental

3.1. Materials and methods

All experiments were performed under a dry argon atmosphere using Schlenk line techniques. Aziridine [69], [RhCl(Cp*)(az)$_2$]Cl, [IrCl(Cp*)(az)$_2$]Cl and [RuCl(Cp*)(az)$_2$]Cl were prepared according to the literature methods [60]. Acetone was distilled from calcium chloride, dichloromethane was distilled from calcium hydride, and *n*-pentane and *n*-hexane were distilled from sodium. All solvents were stored under a dry argon atmosphere over 3 Å molecular sieves. The ^1H and ^{13}C NMR spectra were recorded using a Jeol Eclipse 270 and a Jeol Eclipse 400 instrument operating at 270 MHz (^1H), 400 MHz (^1H) and 68 MHz (^{13}C), 100 MHz (^{13}C). The ^1H and ^{13}C chemical shifts were determined relative to TMS as external standard. IR spectra (KBr) were recorded using a Nicolet 520 FT-IR and Perkin Elmer Spectrum One FT-IR spectrometer. Mass spectra were obtained using a Joel MStation JMS 700, NBA matrix (FAB). Multi-isotope containing fragments refer to the isotope with the highest abundance. Single crystal X-ray diffraction data were collected using a Nonius Kappa CCD diffractometer using graphite-monochromated Mo Kα radiation. Single crystal X-ray structure analyses were performed using direct methods using the SHELXS software and refined by full-matrix least squares with SHELXL-97 [70]. Table 1 contains the crystallographic data and details of the structural refinement of **4**, **5** and **8**. The hydrogen atoms of the C_6Me_6 methyl groups in **8** were found to be disordered in the difference map and were fixed geometrically. Elemental analysis were performed by the Microanalytical Laboratory of the Department of Chemistry and Biochemistry, LMU Munich using a Heraeus Elementar Vario El.

3.2. Synthesis of the aziridine-N-(2-aminoethyl)aziridine complexes *4* and *5*

The bis-aziridine complex (**1** or **2**) was dissolved in 20 mL dichloromethane, together with 2.2 equiv. of AgOTf. After stirring for 1 h and removal of the precipitated AgCl by centrifugation, an excess of 2.5 equiv. of the aziridine **3** was added. The solution was stirred overnight and the precipitate was filtrated through a frit (por. 4). For purification, the powder was stirred in 10 mL *n*-hexane for 12 h. After decantation of the *n*-hexane phase, the product was dried in vacuo.

3.2.1. [Rh(Cp*)(C$_2$H$_4$NC$_2$H$_4$NH$_2$)(C$_2$H$_4$NH)](OTf)$_2$ (*4*)

Reagents: 49.8 mg (0.126 mmol) **1**, 71.2 mg (0.277 mmol) AgOTf, 17.0 μL (0.315 mmol) **3**; Yield: 50.0 mg (0.075 mmol, 60 %) pale yellow powder; decomposition >204 °C. *Anal.* Calc. for $C_{18}H_{30}F_6N_3O_6RhS_2$ (665.48 g/mol): C, 32.49; H, 4.54; N, 6.31. Found: C, 32.23; H, 4.15; N, 6.38%. IR (KBr) [cm^{-1}] 3251 (m), 3175 (m), 1615 (w), 1462 (w), 1385 (w), 1258 (s), 1225 (m), 1171 (s), 1086 (w), 1029 (s), 996 (w), 942 (w), 887 (m), 800 (w), 759 (w), 639 (s), 574 (w), 518 (m), 452 (w), 435 (w). MS-FAB$^+$ *m*/*z* (%) 516 (M^+, 22), 473 (M^+−az, 100), 430 (M^+−aeaz, 23), 387 (M^+−az−aeaz, 35), 266 (M^{2+}, 2), 323 (M^{2+}−az, 77), 280 (M^{2+}−aeaz, 7), 237 (M^{2+}−az−aeaz, 26). ^1H NMR (acetone-d_6) δ 1.82 (s, 15H, Cp*–CH_3), 2.18 (t, $^3J = 6.3$ Hz, 1H, ring–CH_2), 2.26–2.29 (m, 1H, ring–CH_2), 2.30–2.35 (m, 1H, ring–CH_2), 2.41 (t, $^3J = 6.3$ Hz, 2H, ring–CH_2) 2.46–2.50 (m, 1H, ring–CH_2) 2.62–2.75 (m, 2H, ring–CH_2; 2H, ethylene–CH_2), 3.04–3.08 (m, 1H, ethylene–CH_2), 3.19 (dt, $^3J = 3.8$ Hz, $^3J = 12.7$ Hz, 1H, ethylene–CH_2), 3.55 (br, 1H, N*H*), 4.65, 5.03 (br, 2H, NH_2). ^{13}C NMR (acetone-d_6) δ 8.63 (Cp*–*C*H$_3$), 23.17 (d, ^2J(C, Rh) = 12.9 Hz, ring–*C*H$_2$), 23.77 (d, ^2J(C, Rh) = 13.9 Hz, ring–*C*H$_2$), 25.17 (d, ^2J(C, Rh) = 14.4 Hz, ring–*C*H$_2$), 33.97 (ring–*C*H$_2$), 43.19 (d, ^2J(C, Rh) = 11.5 Hz, ethylene–*C*H$_2$), 66.82 (ethylene–*C*H$_2$), 97.68 (d, ^1J(C, Rh) = 7.7 Hz, Cp*–*C*$_q$), 121.8 (q, ^1J(C, F) = 318 Hz, *C*F$_3$).

3.2.2. [Ir(Cp*)(C$_2$H$_4$NC$_2$H$_4$NH$_2$)(C$_2$H$_4$NH)](OTf)$_2$ (*5*)

Reagents: 159 mg (0.328 mmol) **2**, 185 mg (0.722 mmol) AgOTf, 44.3 μL (0.822 mmol) **3**; Yield: 153 mg (0.203 mmol, 62 %) white powder; decomposition >195 °C. *Anal.* Calc. for $C_{18}H_{30}F_6IrN_3O_6S_2$ (665.48 g/mol): C, 28.64; H, 4.01; N, 5.57. Found: C, 28.58; H, 4.02; N, 5.67%. IR (KBr) [cm^{-1}] 3245 (m), 3167 (m), 1618 (w), 1463 (w), 1392 (w), 1269 (s), 1257 (s), 1225 (m), 1173 (m), 1029 (s), 994 (w), 947 (w), 892 (w) 759 (w), 639 (s), 575 (w), 518 (m). MS-FAB$^+$ *m*/*z* (%) 607 (M^+, 41), 563 (M^+−az, 29), 520 (M^+−aeaz, 16), 477 (M^+−az−aeaz, 15), 457 (M^{2+}, 7), 414 (M^{2+}−az, 100), 370 (M^{2+}−aeaz, 10). ^1H NMR (acetone-d_6) δ 1.78 (s, 15H, Cp*–CH_3), 2.11–2.15 (m, 1H, ring–CH_2), 2.26 (ddd, $^2J = 1.0$ Hz, $^3J = 5.9$ Hz, $^3J = 7.0$ Hz, 1H, ring–CH_2), 2.46–2.51 (m, 2H, ring–CH_2), 2.52–2.57 (m, 2H, ring–CH_2), 2.60–2.62 (m, 1H, ring–CH_2), 2.77–2.82 (m, 1H, ring–CH_2; 1H, ethylene–CH_2), 2.93 (ddd, $^2J = 1.9$ Hz, $^3J = 6.1$ Hz, $^3J = 8.2$ Hz, 1H, ethylene–CH_2), 2.98–3.03 (m, 1H, ethylene–CH_2), 3.13 (ddt, 1H, $^2J = 1.0$ Hz, $^3J = 4.0$ Hz, $^3J = 7.9$ Hz, 1H, ethylene–CH_2), 4.06 (br, 1H, N*H*), 5.22, 5.68 (br, 2H, NH_2). ^{13}C NMR (acetone-d_6) δ 8.42 (Cp*–*C*H$_3$), 24.96, 25.43, 27.39, 35.63 (ring–*C*H$_2$), 44.65, 68.37 (ethylene–*C*H$_2$), 89.35 (Cp*–*C*$_q$), 121.95 (q, ^1J(C, F) = 321 Hz, *C*F$_3$).

3.3. Synthesis of [bis(aziridine)-chloro-ruthenium(II)]trifluoromethanesulfonate (8)

The bis-aziridine ruthenium(II) complex **8** was dissolved in 20 mL dichloromethane together with 2.2 equiv. of AgOTf. After stirring for 1.5 h and removal of the precipitated AgCl by centrifugation, an excess of 2.0 equiv. of aziridine (**3**) was added. The solution was stirred over night and the solvent was removed in vacuo. The residue was purified by stirring in 10 mL *n*-hexane for 12 h. After decantation of the *n*-hexane phase, the product was dried in vacuo.

3.3.1. $[RuCl(C_6Me_6)(C_2H_4NH)_2]OTf$ (8)

Reagents: 71 mg (0.169 mmol) **6**, 91 mg (0.354 mmol) AgOTf, 18.2 μL (0.338 mmol) **3**; Yield: 64 mg (0.119 mmol, 70%) yellow powder; decomposition >172 °C. *Anal.* Calc. for $C_{17}H_{28}ClF_3N_2O_3RuS$ (534.00 g/mol): C, 38.24; H, 5.29; N, 5.25. Found: C, 38.65; H, 5.84; N, 4.89. IR (KBr) [cm^{-1}] 3251 (m), 3021 (w), 1437 (w), 1394 (w), 1290 (vs), 1259 (s), 1225 (s), 1157 (s), 1092 (w), 1071 (w), 1032 (vs), 935 (w), 891 (m), 885 (m), 805 (w), 757 (w), 638 (vs), 575 (w), 518 (w), 426 (w). MS-FAB$^+$ *m/z* (%) 499 (M^++OTF^-−Cl, 73), 385 (M^+, 30), 342 (M^+−az, 100), 299 (M^+−2az, 33). ^{1}H NMR (chloroform-*d*) δ 1.54 (ddd, $^3J = 6.8$ Hz, $^3J = 6.8$ Hz, $^3J = 5.5$ Hz, 2H, ring–CH_2), 1.74 (ddd, $^3J = 7.8$ Hz, $^3J = 7.8$ Hz, $^3J = 5.7$ Hz, 2H, ring–CH_2), 1.96 (ddd, $^3J = 7.1$ Hz, $^3J = 7.1$ Hz, $^3J = 5.2$ Hz, 2H, ring–CH_2), 2.16–2.10 (m, 18H, C_6Me_6–*Me*), 2.38 (ddd, $^3J = 7.8$ Hz, $^3J = 7.8$ Hz, $^3J = 5.2$ Hz, 2H, ring–CH_2), 3.39–3.29 (m, 2H, N*H*). ^{13}C NMR (chloroform-*d*) δ 15.51 (C_6Me_6–*Me*), 19.6 (ring–*C*H_2), 23.8 (ring–*C*H_2), 92.2 (C_6Me_6–C_q), 94.5 (C_6Me_6–C_q), 122.9 (q, ^1J(C, F) = 319 Hz, *C*F_3).

Appendix A. Supplementary material

CCDC 665154, 665153 and 665152 contain the supplementary crystallographic data for **4**, **5** and **8**. These data can be obtained free of charge via http://www.ccdc.cam.ac.uk/conts/retrieving.html, or from the Cambridge Crystallographic Data Centre, 12 Union Road, Cambridge CB2 1EZ, UK; fax: (+44) 1223-336-033; or e-mail: deposit@ccdc.cam.ac.uk. Supplementary data associated with this article can be found, in the online version, at doi:10.1016/j.poly.2007.11.023.

References

[1] R.G. Jones, E. Bindschadler, D. Blume, G. Karmas, G.A. Martin Jr., J.R. Thirtle, H. Gilman, J. Am. Chem. Soc. 78 (1956) 6027.
[2] W. Hieber, R. Wiesboeck, Chem. Ber. 91 (1958) 1146.
[3] T.B. Jackson, J.O. Edwards, J. Am. Chem. Soc. 83 (1961) 355.
[4] T.B. Jackson, J.O. Edwards, Inorg. Chem. 1 (1962) 401.
[5] J. Scherzer, P.K. Phillips, L.B. Clapp, J.O. Edwards, Inorg. Chem. 5 (1966) 847.
[6] M.R. Hoffmann, J.O. Edwards, Inorg. Nucl. Chem. Lett. 10 (1974) 837.
[7] R. Lussier, J.O. Edwards, R. Eisenberg, Inorg. Chim. Acta 33 (1969) 468.
[8] R. Höfer, W. Beck, A. Engelmann, Chem. Ber. 106 (1973) 2590.
[9] F. Porta, M. Pizzotti, G. La Monica, L.A. Finessi, S. Cenini, P.L. Bellon, F. Demartin, J. Chem. Soc., Dalton Trans. (1984) 2409.
[10] D.C. Ware, D.S. Mackie, P.J. Brothers, W.A. Denny, Polyhedron 14 (1995) 1641.
[11] S. von Beckerath, I.-P. Lorenz, R. Fawzi, M. Steimann, Z. Naturforsch. 51b (1996) 959.
[12] R. Wilberger, H. Piotrowski, M. Warchhold, I.-P. Lorenz, Z. Anorg. Allg. Chem. 629 (2003) 2485.
[13] R. Wilberger, C. Krinninger, H. Piotrowski, P. Mayer, M. Ossberger, I.-P. Lorenz, Z. Anorg. Allg. Chem. 630 (2004) 1495.
[14] I.-P. Lorenz, C. Krinninger, R. Wilberger, R. Bobka, H. Piotrowski, M. Warchhold, H. Nöth, J. Organomet. Chem. 690 (2005) 1986.
[15] R. Bobb, G. Alhakimi, L. Sudnicki, A. Lough, J. Chin, J. Am. Chem. Soc. 124 (2002) 4544.
[16] R. Ben Cheikh, M.C. Bonnet, R. Chaabouni, F. Dahan, J. Organomet. Chem. 438 (1992) 217.
[17] T. Hauck, K. Sünkel, W. Beck, Inorg. Chim. Acta 235 (1995) 391.
[18] R. Schwesinger, K. Piontek, W. Littke, O. Schweikert, H. Prinzbach, Tetrahedron Lett. 23 (1982) 2427.
[19] R. Aumann, G. Henkel, B. Krebs, Angew. Chem. 94 (1982) 218.
[20] R. Aumann, G. Henkel, B. Krebs, Angew. Chem., Int. Ed. 21 (1982) 204.
[21] E.W. Abel, R.J. Rowley, R. Mason, K.M. Thomas, J. Chem. Soc., Chem. Commun. (1974) 72.
[22] A.J. Conti, R.K. Chadha, K.M. Sena, A.L. Rheingold, D.N. Hendrickson, Inorg. Chem. 32 (1993) 2670.
[23] Y. Zhang, P.H.M. Budzelaar, J.M.M. Smits, R. de Gelder, P.R. Hageman, A.W. Gal, Eur. J. Inorg. Chem. (2003) 656.
[24] W. Beck, W. Danzer, R. Höfer, Angew. Chem. 85 (1973) 87.
[25] W. Beck, W. Danzer, R. Höfer, Angew. Chem., Int. Ed. 12 (1973) 77.
[26] W. Beck, W. Danzer, A.T. Liu, G. Huttner, Angew. Chem. 88 (1976) 511.
[27] W. Beck, W. Danzer, A.T. Liu, G. Huttner, Angew. Chem., Int. Ed. 15 (1976) 495.
[28] A.T. Liu, W. Beck, G. Huttner, H. Lorenz, J. Organomet. Chem. 129 (1977) 91.
[29] W. Danzer, R. Höfer, H. Menzel, B. Olgemöller, W. Beck, Z. Naturforsch. 39b (1984) 167.
[30] I.-P. Lorenz, S. von Beckerath, H. Nöth, Eur. J. Inorg. Chem. (1998) 645.
[31] B.L. Lin, C.R. Clough, G.L. Hillhouse, J. Am. Chem. Soc. 124 (2002) 2890.
[32] M.M. Singh, R.J. Angelici, Inorg. Chem. 23 (1984) 2691.
[33] M.M. Singh, R.J. Angelici, Inorg. Chem. 23 (1984) 2699.
[34] R. Wilberger, Dissertation, LMU Munich, 2002.
[35] R. Bertani, M. Mozzon, R.A. Michelin, Inorg. Chem. 27 (1988) 2809.
[36] M. Kojima, A. Sakurai, M. Murata, K. Nakajima, S. Kashino, Y. Yoshikawa, J. Coord. Chem. 42 (1997) 95.
[37] A. von Baeyer, Ber. Dtsch. Chem. Ges. 18 (1885) 2277.
[38] D. Tanner, Angew. Chem. 106 (1994) 625.
[39] D. Tanner, Angew. Chem., Int. Ed. 33 (1994) 599.
[40] I.D.G. Watson, L. Yu, A.K. Yudin, Acc. Chem. Res. 39 (2006) 194.
[41] D. Tanner, A. Harden, F. Johansson, P. Wyatt, P.G. Andersson, Acta Chem. Scand. 50 (1996) 361.
[42] P.G. Andersson, A. Harden, D. Tanner, P.-O. Norrby, Chem. Eur. J. 1 (1995) 12.
[43] K. Fiore, G. Martelli, M. Monari, D. Savoia, Tetrahedron: Asymmetry 10 (1999) 4803.
[44] F. Ferioli, C. Fiorelli, G. Martelli, M. Monari, D. Savoia, P. Tobaldin, Eur. J. Org. Chem. (2005) 1416.
[45] A.V. Eremeev, I.B. Solodin, F.D. Polyak, Khim. Geterotsikl. Soedin (1980) 1350.
[46] T. Fukuyama, F. Nakatsubo, A.J. Cocuzza, Y. Kishi, Tetrahedron Lett. 49 (1977) 4295.

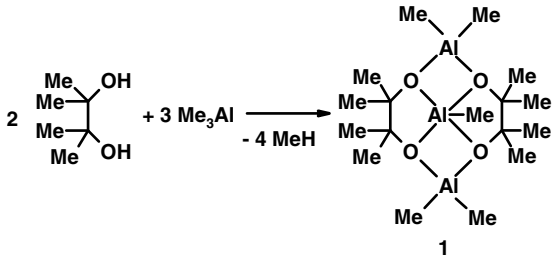
[47] K.M. Goodenough, W.J. Moran, P. Raubo, J.P.A. Harrity, J. Org. Chem. 70 (2005) 207.
[48] O. Ihata, Y. Kayaki, T. Ikariya, Macromolecules 38 (2005) 6429.
[49] J.W. Benbow, G.K. Schulte, S.J. Danishefsky, Angew. Chem. 104 (1992) 934.
[50] J.W. Benbow, G.K. Schulte, S.J. Danishefsky, Angew. Chem., Int. Ed. 31 (1992) 915.
[51] J.W. Benbow, K.F. McClure, S.J. Danishefsky, J. Am. Chem. Soc. 115 (1993) 12305.
[52] Z. Wang, L.S. Jimenez, J. Org. Chem. 61 (1996) 816.
[53] J.B. Sweeney, Chem. Soc. Rev. 31 (2002) 247.
[54] D.M. Noll, T. McGregor Mason, P.S. Miller, Chem. Rev. 106 (2006) 277.
[55] M.M.L. Fiallo, E. Deydier, M. Bracci, A. Garnier-Suillerot, K. Halvorsen, J. Med. Chem. 46 (2003) 1683.
[56] M.M. Paz, G.S. Kumar, M. Glover, M.J. Waring, M. Tomasz, J. Med. Chem. 47 (2004) 3308.
[57] Y.-C. Peng, H.-S. Kuo, H.-D. Tsai, Y.-P. Yang, Y.-L. Lin, Bioorg. Med. Chem. 14 (2006) 263.
[58] Y.K. Yan, M. Melchart, A. Habtemariam, P.J. Sadler, J. Chem. Soc., Chem. Commun. (2005) 4764.
[59] R. Bobka, Dissertation, LMU Munich, 2007.
[60] R. Bobka, J.N. Roedel, B. Neumann, C. Krinninger, P. Mayer, S. Wunderlich, A. Penger, I.-P. Lorenz, Z. Anorg. Allg. Chem. 633 (2007) 1985.
[61] N.W. Mitzel, J. Riede, C. Kiener, Angew. Chem. 109 (1997) 2299.
[62] N.W. Mitzel, J. Riede, C. Kiener, Angew. Chem., Int. Ed. Engl. 36 (1997) 2215.
[63] D.P. Smith, E. Baralt, B. Morales, M.M. Olmstead, M.F. Maestre, R.H. Fish, J. Am. Chem. Soc. 114 (1992) 10647.
[64] R. Krämer, M. Maurus, K. Polborn, K. Sünkel, C. Robl, W. Beck, Chem. Eur. J. 2 (1996) 1518.
[65] G.J. Grant, J.P. Lee, M.L. Helm, D.G. VanDerveer, W.T. Pennington, J.L. Harris, L.F. Mehne, D.W. Klinger, J. Organomet. Chem. 690 (2005) 629.
[66] T. Suzuki, Inorg. Chim. Acta 359 (2006) 2431.
[67] H.P. Fritz, G. Hierl, Z. Anorg. Allg. Chem. 371 (1969) 229.
[68] V.F. Bystrov, R.G. Kostyanovskii, O.A. Pan'skin, A.U. Stepanyants, O.A. Yuzhakova, Opt. Spektrosk. 19 (1965) 217.
[69] H. Wenker, J. Am. Chem. Soc. 57 (1935) 2328.
[70] G.M. Sheldrick, SHELX-97, An Integrated System for Solving and Refining Crystal Structures from Diffraction Data, University of Göttingen, Germany, 1997.

[16,17]. This work is the continuation of our studies on steric repulsion between ligands controlling the formation of group 13 complexes. We report the syntheses and X-ray structure determination of aluminium and gallium alkyl complexes supported by 2,3-dimethylbutane-2,3-diolato (pinacolato) ligands.

2. Results and discussion

Pinacol reacted with Me_3Al in a 2:3 molar ratio to produce the trinuclear aluminium complex $Me_5Al_3[OC(CH_3)_2C(CH_3)_2O]_2$ (**1**), containing two diolate units (Scheme 1).

Compound **1** was sublimed from the post-reaction mixture in 52% yield. The molecular structure of **1** was determined on the basis of an X-ray diffraction study and is shown in Fig. 1. Data collection and structure analysis are listed in Table 1. Crystals of compound **1** contain three kinds of molecules (**A**, **B** and **C**) in a cell differing in bond lengths and angles. The two terminal aluminium atoms, Al(2) and Al(3), are 4-coordinate, residing in the distorted tetrahedrons. The angles O(2A)–Al(1A)–O(4A) 128.5(1)° [O(2B)–Al(1B)–O(4B) 129.2(1)°, O(1C)–Al(1C)–O(3C) 128.4(1)°] and O(1A)–Al(1A)–O(3A) 144.3(1)° [O(1B)–Al(1B)–O(3B) 143.1(1)°, O(2C)–Al(1C)–O(4C) 143.7(1)°] indicate that the coordination sphere geometry of the central aluminium atom Al(1) can be regarded both as a distorted square pyramidal structure with the basal plane consisting of four oxygen atoms and C(5) situated in an apical position and as a distorted trigonal bipyramidal geometry. In **1A** and **1B** molecules, the O(1) and O(3) atoms occupy the axial positions and the C(5), O(2) and O(4) atoms define the equatorial sites of the trigonal bipyramid. In **1C** molecules, the O(2) and O(4) atoms are situated in the axial positions and the O(1), O(2) and C(5) atoms lie in the equatorial sites. The sums of the angles about the oxygen atoms {∑[O(1A)]356.3°; ∑[O(2A)] 351.6°; ∑[O(3 A)]355.4°; ∑[O(4A)351.7°}, {∑[O(1B)] 355.9°; ∑[O(2B)]351.8°; ∑[O(3B)]356.3°; ∑[O(4B)351.7°} and {∑[O(1C)]351.7°; ∑[O(2C)]355.2°; ∑[O(3C)]351.0°; ∑[O(4C)355.8°} are slightly less than 360°, which indicates a small steric strain in the molecule. Bond lengths between the central aluminium atom Al(1) and the oxygen atoms and those between the terminal aluminium atoms Al(2) and Al(3) and the oxygen atoms are very similar. They are situated in the region of 1.84 to 1.86 Å.



Scheme 1.

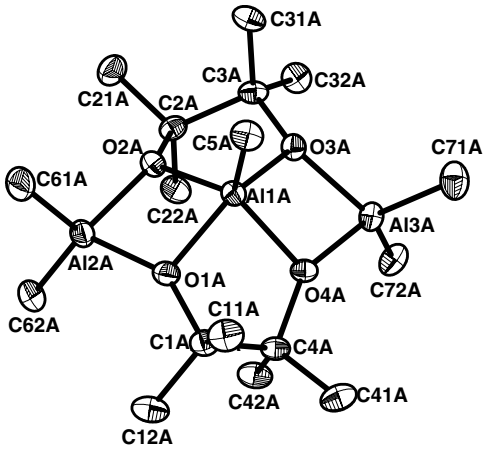


Fig. 1. Molecular structure of $Me_5Al_3[OC(CH_3)_2C(CH_3)_2O]_2$ (**1**). Thermal ellipsoids are shown at the 50% level. Hydrogen atoms are omitted for clarity. The picture shows a molecule of kind A. Selected bond lengths (Å) and bond angles (°) for molecules of **1** of kind A, B and C: Al(1A)–O(2A) 1.866(2) [Al(1B)–O(2B) 1.871(3), Al(1C)–O(2C) 1.876(2)], Al(1A)–O(4A) 1.870(2) [Al(1B)–O(4B) 1.874(2), Al(1C)–O(4C) 1.867(2)], Al(1A)–O(1A) 1.875(2) [Al(1B)–O(1B) 1.875(2), Al(1C)–O(1C) 1.865(2)], Al(1A)–O(3A) 1.876(2) [Al(1B)–O(3B) 1.868(2), Al(1C)–O(3C) 1.877(2)], Al(1A)–C(5A) 1.961(3) [Al(1B)–C(5B) 1.958(4), Al(1C)–C(5C) 1.958(4)], Al(2A)–O(1A) 1.834(2) [Al(2B)–O(1B) 1.833(2), Al(2C)–O(1C) 1.853(3)], Al(2A)–O(2A) 1.858(2) [Al(2B)–O(2B) 1.856(2), Al(2C)–O(2C) 1.835(2)], Al(3A)–O(3A) 1.840(2) [Al(3B)–O(3B) 1.839(2), Al(3C)–O(3C) 1.862(2)], Al(3A)–O(4A) 1.855(2) [Al(3B)–O(4B) 1.855(2), Al(3C)–O(4C) 1.837(2)], O(2A)–Al(1A)–O(4A) 128.5(1) [O(2B)–Al(1B)–O(4B) 129.2(1), O(2C)–Al(1C)–O(4C) 143.7(1)], O(2A)–Al(1A)–O(1A) 80.5(1) [O(2B)–Al(1B)–O(1B) 80.2(1), O(2C)–Al(1C)–O(1C) 80.4(1)], O(4A)–Al(1A)–O(1A) 84.2(1) [O(4B)–Al(1B)–O(1B) 84.2(1), O(4C)–Al(1C)–O(1C) 83.8(1)], O(2A)–Al(1A)–O(3A) 84.1(1) [O(2B)–Al(1B)–O(3B) 84.1(1), O(2C)–Al(1C)–O(3C) 84.2(1)], O(4A)–Al(1A)–O(3A) 80.5(1) [O(4B)–Al(1B)–O(3B) 80.3(1), O(4C)–Al(1C)–O(3C) 80.4(1)], O(1A)–Al(1A)–O(3A) 144.3(1) [O(1B)–Al(1B)–O(3B) 143.1(1), O(1C)–Al(1C)–O(3C) 128.4(1)].

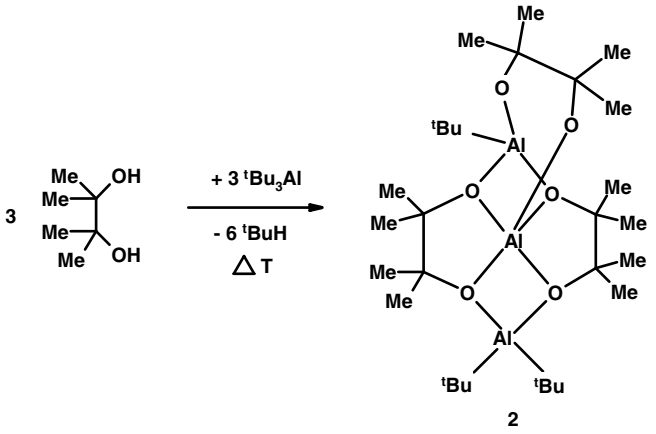
The ^{1}H NMR spectrum of **1** in solution revealed three singlets of CH_3Al group protons (at −0.63, −0.79 and −0.87 ppm) in a 2:1:2 relative intensity ratio. The integration ratio of the signals indicated that protons of the methyl group attached to the central aluminium atom exhibited a singlet at −0.79 ppm. The singlets at −0.63 and −0.87 ppm were assigned to protons of the four CH_3 groups bonded to the terminal aluminium atoms. The presence of these two singlets indicated the equivalence of the two CH_3Al groups positioned *syn* to $CH_3Al_{central}$. The two *anti* CH_3Al groups were also equivalent. Signals of the CCH_3 pinacolate unit protons appeared as two singlets at 1.31 and 1.24 ppm. It indicated that the protons of the four CCH_3 pinacolate units, positioned *anti* to the $CH_3Al_{central}$ group, were magnetically equivalent in solution. Similarly, the protons of *syn* CCH_3 groups were also equivalent. It contrasts with the solid-state structure, in which the CCH_3 groups were inequivalent. The differences between the solid-state structure and the NMR observations are a result of fluxionality phenomena involving transitions between the two non-equivalent antisymmetric structures falling in the fast exchange regime.

Table 1
Crystal data and data collection parameters for **1**, **2** and **3** · $0.5C_6H_{14}O_2$

	1	**2**	**3** · $0.5C_6H_{14}O_2$
Empirical formula	$C_{17}H_{39}Al_3O_4$	$C_{30}H_{63}Al_3O_6$	$C_{24}H_{52}Ga_2O_4 \cdot 0.5C_6H_{14}O_2$
Formula weight	388.42	600.74	603.18
Temperature (K)	100(2)	100(2)	100(2)
Wavelength (Å)	0.71073	0.71073	0.71073
Crystal system	orthorhombic	orthorhombic	monoclinic
Space group	$Pna2_1$	$Pca2_1$	$P2_1/c$
a (Å)	18.534(2)	15.839(1)	18.766(4)
b (Å)	9.815(1)	18.411(2)	14.643(3)
c (Å)	39.233(3)	12.418(1)	11.707(2)
α (°)	90	90	90
β (°)	90	90	101.35(3)
γ (°)	90	90	90
V (Å^3)	7137.1(9)	3621.3(6)	3154.1(1)
Z	12	4	4
D_{calc} (g cm^{-3})	1.084	1.102	1.270
Absorption coefficient (mm^{-1})	0.174	0.140	1.739
$F(000)$	2544	1320	1292
Crystal size (mm)	0.15 × 0.15 × 0.15	0.15 × 0.10 × 0.10	0.15 × 0.15 × 0.10
Θ-range for data collection (°)	3.07–22.50	3.28–25.00	2.99–25.00
Index ranges	$-18 \leqslant h \leqslant 22$, $-11 \leqslant h \leqslant 21$, $-46 \leqslant h \leqslant 46$	$-18 \leqslant h \leqslant 18$, $-21 \leqslant h \leqslant 20$, $-10 \leqslant h \leqslant 14$	$-22 \leqslant h \leqslant 22$, $-17 \leqslant k \leqslant 17$, $-13 \leqslant l \leqslant 13$
Reflections collected	31 507	20 984	35 046
Independent reflections	3742 [$R_{int} = 0.0712$]	5090 [$R_{int} = 0.0612$]	5541 [$R_{int} = 0.1352$]
Refinement method	full-matrix least-squares on F^2	full-matrix least-squares on F^2	full-matrix least-squares on F^2
Data/restraints/parameters	3741/0/343	5090/ 1/374	5541/0/328
Goodness-of-fit on F^2	0.933	1.084	1.002
Final R indices [$I > 2\sigma(I)$]	$R_1 = 0.0515$, $wR_2 = 0.1274$	$R_1 = 0.0590$, $wR_2 = 0.1443$	$R_1 = 0.0555$, $wR_2 = 0.1233$
R indices (all data)	$R_1 = 0.0893$, $wR_2 = 0.1569$	$R_1 = 0.0702$, $wR_2 = 0.1553$	$R_1 = 0.0816$, $wR_2 = 0.1367$
Maximum/minimum of residual electron density	0.151 and −0.158	0.459 and −0.443	1.098 and −0.792

The ^{13}C NMR spectrum of **1** revealed one signal of *C*O carbons at 80.44 ppm. In comparison with the *C*O signals of methyl aluminium benzopinacolate $Me_5Al_3[OC(C_6H_5)_2C(C_6H_5)_2\ O]_2$ (93.31 ppm) [1], the *C*O signal of **1** was shifted upfield. It is the result of the lack of aromatic rings in compound **1**. In the case of benzopinacolates, the electron withdrawing effect of aromatic rings caused a downfield shift of *C*O carbon signals. The presence of one signal of *C*O carbons in the ^{13}C NMR spectrum indicates the equivalence of the four *C*O carbons of the pinacolate units.

The reaction of $^tBu_3Al$ with one equivalent of pinacol in refluxing toluene followed by the removal of the solvent resulted in the pure compound $^tBu_3Al_3[OC(CH_3)_2C(CH_3)_2O]_3$ (**2**) as the only product (Scheme 2). Compound **2** is soluble in most common organic solvents such as pentane, hexane, and toluene. X-ray quality crystals were crystallised from a pentane solution. The molecular structure was determined on the basis of an X-ray diffraction study and is shown in Fig. 2. Data collection and structure analysis are presented in Table 1. The molecule of **2** consists of three aluminium atoms, three diolate units and three *tert*-butyl groups. ^{t}Bu groups are bonded to the terminal 4-coordinate Al(1) and Al(2) metal atoms. The central Al(3) atom is 5-coordinate, residing in a highly distorted square pyramidal geometry with the basal plane consisting


3
Me
OH
Me
Me
Me
OH
+ 3 tBu3Al
- 6 tBuH
T
Me
Me
Me
O
tBu
Al
O
Me
Me
Me

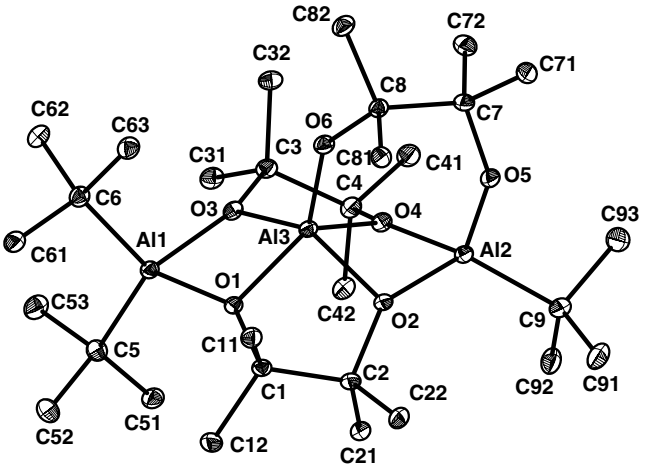


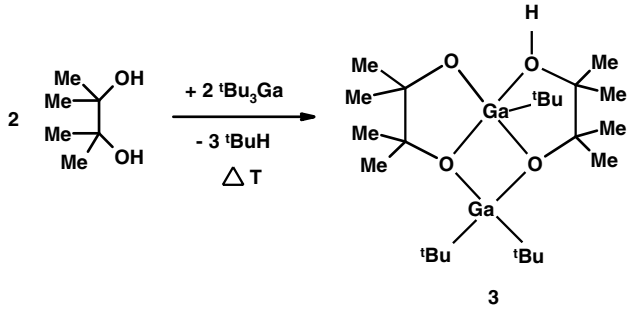
Fig. 2. Molecular structure of $^{t}Bu_3Al_3[OC(CH_3)_2C(CH_3)_2O]_3$ (**2**). Thermal ellipsoids are shown at the 20% level. Hydrogen atoms are omitted for clarity. Selected bond lengths (Å) and bond angles (°): Al(3)–O(6) 1.712(3), Al(3)–O(1) 1.857(3), Al(3)–O(4) 1.861(3), Al(3)–O(3) 1.871(3), Al(3)–O(2) 1.896(3), Al(2)–O(5) 1.708(3), Al(2)–O(4) 1.844(3), Al(2)–O(2) 1.850(3), Al(2)–C(9) 1.993(4), Al(1)–O(3) 1.856(3), Al(1)–O(1) 1.884(3), O(6)–Al(3)–O(1) 124.0(1), O(6)–Al(3)–O(4) 104.0(1), O(1)–Al(3)–O(4) 131.9(1), O(6)–Al(3)–O(3) 110.6(1), O(1)–Al(3)–O(3) 79.6(1), O(4)–Al(3)–O(3) 85.0(1), O(6)–Al(3)–O(2) 104.4(1), O(1)–Al(3)–O(2) 85.3(1), O(4)–Al(3)–O(2) 81.7(1), O(3)–Al(3)–O(2) 144.6(1), C(6)–Al(1)–C(5) 117.8(2), O(5)–Al(2)–C(9) 110.3(2).

They are very similar to the corresponding Al–$O_{3\text{-coord.}}$ bond lengths of compound **1** and longer than the Al(2)–O(5) and Al(3)–O(6) bonds [Al(3)–O(6) 1.712(3) and Al(2)–O(5) 1.708(3) Å].

The ^{1}H NMR spectrum of **2** in solution shows three singlets (at 1.07, 1.03 and 1.02 ppm in a 9:9:9 relative integration ratio) belonging to the hydrogen atoms of the $^{t}BuAl$ groups and five singlets (at 1.59, 1.42, 1.34, 1.28 and 1.14 ppm in a 6:6:6:6:12 integration ratio) of the diolate unit CH_3 protons. The integration ratio of the signals indicates that three $^{t}BuAl$ groups and twelve CH_3 groups of the diolate units are present in the molecule of **2**. The ^{13}C NMR spectrum of **2** exhibits four resonances of *C*O carbons (at 81.20, 80.79, 77.84 and 76.15 ppm). One of them was assigned to the *C*(1) and *C*(3) carbons. The carbons *C*(2) and *C*(4) also gave one signal. The *C*(5) and *C*(6) atoms are magnetically inequivalent and exhibit two signals (numeration of carbons, see Fig. 2).

It is worth noting that compound **2** is the first group 13 diolate with the general formula $R_3M_3[diol\text{-}(2H)]_3$. The presence of three diolate units in the molecule of **2** suggests the formation of the $^{t}Bu_5Al_3[OC(CH_3)_2C(CH_3)_2O]_2$ complex as an intermediate product followed by the reaction of this product with one molecule of pinacol. Unfortunately, the synthesis of $^{t}Bu_5Al_3[OC(CH_3)_2C(CH_3)_2O]_2$ failed. In order to obtain the compound with two pinacolate units, $^{t}Bu_5Al_3[OC(CH_3)_2C(CH_3)_2O]_2$, $^{t}Bu_3Al$ and pinacol were employed in different ratios, ranging from 3:2 to 2:1, under the same reaction conditions. However, compound **2** was the only product of all the reactions, which indicates a reaction course without the intermediate aluminium dipinacolate. On the other hand, the formation of $^{t}Bu_5Al_3[OC(CH_3)_2C(CH_3)_2O]_2$ as a product in the reaction of $^{t}Bu_3Al$ with pinacol cannot be excluded. It is very likely that this compound is formed as an unstable product due to the high steric repulsion of bulky ^{t}Bu and pinacolate ligands, and then it reacts immediately with pinacol, yielding the less sterically crowded compound **2**.

In contrast to the reaction of pinacol with $^{t}Bu_3Al$, a reaction of pinacol with $^{t}Bu_3Ga$ (in a 1:1 molar ratio and with an excess of $^{t}Bu_3Ga$) in refluxing toluene for 3 hours afforded the dinuclear compound $^{t}Bu_3Ga_2[OC(CH_3)_3C(CH_3)_2O][OC(CH_3)_3C(CH_3)_2OH]$ (**3**) (Scheme 3). The compound was isolated as $\mathbf{3}\cdot 0.5C_6H_{14}O_2$ in 40% yield after crystallisation from the post-reaction solution. The molecular structure of **3** is shown in Fig. 3 and selected bond lengths and angles are given in Table 1. One molecule of pinacol per two molecules of **3** is present in the formula unit. The molecule of **3** consists of a tricyclic structure formed from two GaO_2C_2 five-membered rings and one Ga_2O_2 four-membered ring. The two metal atoms are chelated and bridged by mono- and di-deprotonated pinaco-



Scheme 3.

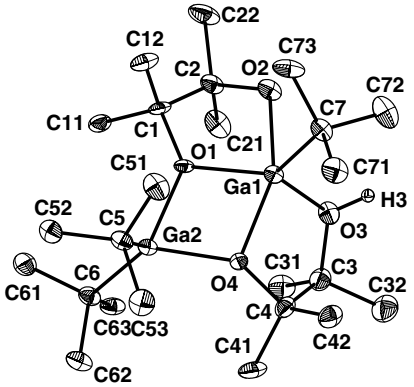


Fig. 3. Molecular structure of $^{t}Bu_3Ga_2[OC(CH_3)_3C(CH_3)_2O][OC(CH_3)_3C(CH_3)_2OH]\cdot 0.5C_6H_{14}O_2$ ($\mathbf{3}\cdot 0.5C_6H_{14}O_2$). Thermal ellipsoids are shown at the 40% level. Hydrogen atoms and a molecule of $C_6H_{14}O_2$ (pinacol) are omitted for clarity. Selected bond lengths (Å) and bond angles (°): Ga(1)–O(3) 1.859(3), Ga(1)–O(1) 1.973(3), Ga(1)–O(4) 2.011(3), Ga(1)–C(7) 2.035(4), Ga(1)–O(2) 2.180(3), Ga(2)–O(4) 1.963(3), Ga(2)–O(1) 1.975(3), O(3)–Ga(1)–O(1) 119.5(1), O(3)–Ga(1)–O(4) 84.7(1), O(1)–Ga(1)–O(4) 75.9(1), O(3)–Ga(1)–C(7) 111.1(2), O(1)–Ga(1)–C(7) 128.1(2), O(4)–Ga(1)–C(7) 121.0(2), O(3)–Ga(1)–O(2) 91.6(1), O(1)–Ga(1)–O(2) 75.6(1), O(4)–Ga(1)–O(2) 144.7(1), C(7)–Ga(1)–O(2) 93.1(2).

late ligands. The molecule adopts a highly distorted trigonal bipyramidal geometry around the Ga(1) atom with the O(2) and O(4) atoms situated in the axial positions and the O(1), C(7) and O(3) atoms placed in the equatorial sites [O(4)–Ga(1)–O(2) 144.7(1)° and O(3)–Ga(1)–O(1) 119.5(1)°].

Potentially possible, intermolecular O–H···O hydrogen bonds between pinacol and **3** or between molecules of **3** were not observed in the crystal structure. Moreover, the signal of O*H* protons at about 4 ppm in the ^{1}H NMR spectrum shows the absence of hydrogen bonds in the solutions. The signals of hydrogen bond protons in complexes of group 13 metals are reported to be shifted downfield (at 14–17 ppm) [15,16,18].

In the ^{1}H NMR spectrum in solution, compound **3** shows three signals (at 1.17, 1.11 and 1.10 ppm) of equal intensity assigned to the protons of the ^{t}Bu groups attached to the gallium atoms. Signals of the CCH_3 protons of the pinacolate units appear as four singlets (at 1.37, 1.29, 1.27 and 1.18 ppm). An integration ratio of the ^{t}Bu and CCH_3 proton signals indicates the presence of three ^{t}Bu and eight CH_3 groups in the molecule. Besides the signals of the CCH_3 protons of **3**, the ^{1}H NMR spectrum reveals a singlet at 1.25 ppm, assigned to the CCH_3 protons of pinacol present in the crystalline compound.

The *C*O carbons of the diolate units of **3** exhibit ^{13}C resonances at 76.49 and 76.39 ppm, indicating two kinds of CO groups. The presence of three inequivalent ^{t}Bu groups attached to the metal atoms is confirmed by three singlets (at 32.69, 31.80 and 31.71 ppm) of GaC(CH_3)$_3$ carbons.

In the literature, a similar structure has been found for the aluminium glycolate ^{t}Bu$_3$Al$_2$(OCH$_2$CH$_2$O)(OCH$_2$CH$_2$OH) [19]. Recently, we have reported that compounds with the formula R_3M_2[diol-(2H)][diol-(H)] (R = alkyl group, M = Al, Ga, In) are intermediate products in reactions of 1,2-diols with group 13 metal trialkyls. These dinuclear intermediate complexes react subsequently with R_3M forming final trinuclear products R_5M_3[diol-(2H)]$_2$ [15]. Presumably, the reaction of ^{t}Bu$_3$Ga with pinacol stopped at the stage of the digallium compound **3** due to the lower reactivity of ^{t}Bu$_3$Ga in comparison with ^{t}Bu$_3$Al. Very recently, ^{t}Bu$_3$Ga has been found unreactive towards benzopinacol, whilst ^{t}Bu$_3$Al reacted with benzopinacol yielding the monomeric compound ^{t}BuAl[OC(C$_6$H$_5$)$_2$C(C$_6$H$_5$)$_2$O](C$_4$H$_8$O) [20].

In summary, we found that the structure of the products of reactions of sterically overcrowded 1,2-diol (pinacol) with aluminium and gallium trialkyls depends on the kind of alkyl group bonded to the metal atoms and on the kind of metal. The reaction of Me_3Al with pinacol afforded the trinuclear complex **1**. We found earlier that Me_3M (M = Al, Ga, In) reacts with sterically overcrowded 1,3-diols resulting in the formation of similar trinuclear diolates. Numerous compounds with structures similar to **1** have been published previously [2].

As was mentioned in Section 1, the interaction of sterically demanding 1,3-diols with aluminium and gallium trialkyls substituted by bulky alkyl groups (i.e., ^{t}Bu) leads to the dimeric complexes ^{t}Bu$_2$M$_2$[OC(CH)$_3$CH$_2$C(CH$_3$)$_2$O]$_2$. In contrast, a sterically overcrowded 1,2-diol (i.e., pinacol) forms the trinuclear complex **2** in reaction with ^{t}Bu$_3$Al. On the other hand, the reaction of pinacol with ^{t}Bu$_3$Ga stopped at the stage of the formation of compound **3**, which is an intermediate product of the reaction of 1,2-diols with group 13 trialkyls. It was presumably caused by the lower reactivity of ^{t}Bu$_3$Ga in comparison with ^{t}Bu$_3$Al.

3. Experimental

All manipulations were carried out using standard Schlenk techniques under an inert gas atmosphere. The solvents were distilled over a blue benzophenone–K complex. Me_3Al and pinacol were purchased from Aldrich. ^{t}Bu$_3$Al and ^{t}Bu$_3$Ga were synthesised as described in the literature [21,22] ^{1}H, ^{13}C and ^{27}Al NMR spectra were obtained on a Mercury-400BB spectrometer. ^{1}H NMR spectra were recorded at 400.09 MHz. Chemical shifts were referenced to the residual proton signals of $CDCl_3$ (7.26 ppm). ^{13}C NMR spectra were acquired at 100.60 MHz (standard: chloroform $^{13}CDCl_3$, 77.20 ppm). Chemical shifts of aluminium signals in ^{27}Al NMR spectra were referenced to the standard Al(acac)$_3$.

Elemental analysis of $\mathbf{3}\cdot 0.5C_6H_{14}O_2$ was obtained on a Perkin–Elmer 2400 analyser. Generally, alkylaluminium complexes are more sensitive to a moisture and oxygen than alkylgallium complexes. Therefore the complexes **1** and **2** were analysed by determination of hydrolysable Me groups and aluminium. The content of carbon and hydrogen in alkylaluminium compounds determined by the analyser was not proper due to a partial decomposition of the compounds during the preparation of samples under air atmosphere. Hydrolysable Me groups for compounds **1** and **2** were determined by hydrolysis of the compound (0.2–0.3 g) under argon using HNO_3 solution (10% concentrated, 5 cm^3) and measurement of the volume of CH_4. Subsequently the sample was transformed into Al_2O_3 by mineralization and the obtained white solid was dissolved in a diluted water solution of HNO_3. The content of aluminium was determined by complexation of Al^{3+} kations with versenate anions using an excess of the titrated solution of calcium disodium versenate. Then the excess of calcium disodium versenate was titrated by $FeCl_3$ according to the procedure described in [23].

Molecular weight of the complexes **1** and **2** was determined by the cryoscopy in benzene. The observed values of the molecular weight are lower than the calculated due to a presence of a small amount of solvents in the solid compounds.

3.1. Synthesis of $Me_5Al_3[OC(CH_3)_2C(CH_3)_2O]_2$ (1)

A solution of pinacol (1.180 g, 10 mmol) in Et_2O (20 cm^3) was added to a stirred solution of Me_3Al

(1.224 g, 17 mmol) in Et_2O (30 cm^3) at −76 °C. A reaction mixture was allowed to warm to room temperature and then filtered. Volatiles were removed *in vacuo* from the filtrate. Compound **1** was sublimed off *in vacuo* from the residue as a white solid (yield 1.009 g, 2.6 mmol, 52%).

^{1}H NMR ($CDCl_3$): δ 1.31 (12H, s, CCH_3), 1.24 (12H, s, CCH_3), −0.63 (6H, s, AlCH_3), −0.79 (3H, s, AlCH_3), −0.87 (6H, s, AlCH_3). ^{13}C NMR ($CDCl_3$): δ 80.44 (*C*O), 26.08 (*C*H_3), 25.97 (*C*H_3), −6,01 (Al*C*H_3, broad), −9.18 (Al*C*H_3, broad). ^{27}Al NMR ($CDCl_3$) δ 148 (Al 4-coord.), 83 (Al 5-coord.) ppm.

Elemental *Anal.* Found: Al, 20.40; hydrolysable methyl groups, 19.92; Calc. for $Me_5Al_3[OC(CH_3)_2C(CH_3)_2O]_2$ Al, 20.85; Me, 19.31 wt.%. Molecular weight: found: 375, calc.: 388.

A solution of **1** in *n*-C_5H_{12} upon cooling to −25 °C furnished X-ray quality crystals. M.p.: 186–190 °C.

3.2. Synthesis of $^tBu_3Al_3[OC(CH_3)_2C(CH_3)_2O]_3$ (2)

A solution of pinacol (1.180 g, 10 mmol) in $C_6H_5CH_3$ (10 cm^3) was added to a stirred solution of $^tBu_3Al \cdot OEt_2$ (2.720 g, 10 mmol) in $C_6H_5CH_3$ (10 cm^3) at room temperature. The reaction mixture was refluxed for 0.5 h. Then volatiles were removed *in vacuo* from the post-reaction mixture resulting in a pure compound **2** as a white solid (yield 1.982 g, 3.3 mmol, 99%).

^{1}H NMR ($CDCl_3$): δ 1.59 (6H, s, CCH_3), 1.42 (6H, s, CCH_3), 1.34 (6H, s, CCH_3), 1.28 (6H, s, CCH_3), 1.14 (12H, s, CCH_3), 1.07 (9H, s, AlCCH_3), 1.03 (9H, s, AlCCH_3), 1.02 (9H, s, AlCCH_3). ^{13}C NMR ($CDCl_3$): δ 81.20, 80.79, 77.84, 76.15 (*C*O), 31.27, 31.16, 30.48 (AlC(*C*H_3)), 29.20, 28.72, 27.92, 27.88, 26.25, 25.65 (C*C*H_3) ppm.

Elemental *Anal.* Found: Al, 13.02; hydrolysable ^{t}Bu groups, 27.98; Calc. for $^tBu_3Al_3[OC(CH_3)_2C(CH_3)_2O]_3$ Al, 13.48; ^{t}Bu, 28.45 wt.%. Molecular weight: found: 570, calc.: 601.

A solution of **2** in *n*-C_5H_{12} upon cooling to −25 °C furnished X-ray quality crystals. M.p.: 213 °C.

3.3. Synthesis of $^tBu_3Ga_2[OC(CH_3)_3C(CH_3)_2O][OC(CH_3)_3C(CH_3)_2OH] \cdot 0.5C_6H_{14}O_2$ (**3** · $0.5C_6H_{14}O_2$)

A solution of pinacol (1.180 g, 10 mmol) in $C_6H_5CH_3$ (10 cm^3) was added to a stirred solution of $^tBu_3Ga$ (2.410 g, 10 mmol) in $C_6H_5CH_3$ (10 cm^3) at room temperature. The reaction mixture was refluxed for 3 h, then filtered. After the filtrate was stored at 5 °C for several days, colourless crystalline **3** · $0.5C_6H_{14}O_2$ was isolated (yield 0.965 g, 1.6 mmol, 40% based on pinacol). M.p.: 150–152 °C.

^{1}H NMR ($CDCl_3$): δ 3.90, [(2H, s, broad, O*H*), The chemical shift of the O*H* group signal depends on the conditions of NMR measurements. In the spectra of different samples we also observed the O*H* signal at 4.24, 3.60 and 3.85 ppm.], 1.37 (6H, s, CCH_3), 1.29 (6H, s, CCH_3), 1.27 (6H, s, CCH_3), 1.25 (6H, s, CCH_3, 0.5 mol of $HOC(CH_3)_2C(CH_3)_3COH$ per 1 mol of **3**), 1.18 (6H, s, CCH_3) 1.17 (9H, s, GaC(CH_3)$_3$) 1.11 (9H, s, GaC(CH_3)$_3$), 1.10 (9H, s, GaC(CH_3)$_3$). ^{13}C NMR ($CDCl_3$): δ 76.49, 76.39 (*C*O), 32.69, 31.80, 31.71 (GaC(*C*H_3)$_3$), 31.70, 31.48, 31.31 (Ga*C*)$(CH_3)_3$ 28.96, 27.74, 27,44, 26.93 (C*C*H_3), 24.88 (C*C*H_3, 0.5 mol of $HOC(CH_3)_2C(CH_3)_3$-COH per 1 mol of **3**).

Anal. Found (Calc.) for $C_{27}H_{59}Ga_2O_5$: C, 53.40 (53.73); H, 9.80 (9.78)%.

3.4. X-ray crystal structure analyses

Crystals of compounds **1**, **2** and **3** · $0.5C_6H_{14}O_2$ were mounted in inert oil and sealed in glass capillaries under argon. Determination of the crystal structures of **1**, **2** and **3** · $0.5C_6H_{14}O_2$ was performed on a KUMA KM4CCD κ-axis diffractometer with graphite-monochromated Mo Kα radiation. The crystal of **1** was positioned at 62.25 mm from the KM4CCD camera and 600 frames were measured at 1.0° intervals with a counting time of 25 s. The crystal of **2** was positioned at 62.25 mm from the KM4CCD camera and 500 frames were measured at 1.2° intervals with a counting time of 35 s. The crystal of **3** · $0.5C_6H_{14}O_2$ was positioned at 62.25 mm from the KM4CCD camera and 900 frames were measured at 1.0° intervals with a counting time of 30 s. All of the data were corrected for Lorentz and polarisation effects. The numeric absorption correction was applied. Data collection, cell refinement and data reduction were carried out with the KUMA diffraction programs [24]. The structure was solved by direct methods [25] and refined using SHELXL [26]. All hydrogen atoms were placed in the calculated positions and their thermal parameters were refined isotropically. Scattering factors were taken from the literature [27, Tables 6.1.1.4 and 4.2.4.2].

The X-ray structures were measured in the Crystallography Unit of the Physical Chemistry Laboratory at the Chemistry Department of the University of Warsaw.

4. Supplementary material

CCDC 662821, 662822, 662821 contain the supplementary crystallographic data for **1**, **2** and **3**. These data can be obtained free of charge via http://www.ccdc.cam.ac.uk/conts/retrieving.html, or from the Cambridge Crystallographic Data Centre, 12 Union Road, Cambridge CB2 1EZ, UK; fax: (+44) 1223-336-033; or e-mail: deposit@ccdc.cam.ac.uk.

Acknowledgement

We thank Warsaw University of Technology for financial support.

References

[1] W. Ziemkowska, Coord. Chem. Rev. 249 (2005) 2176.

[2] C.N. McMahon, S.J. Obrey, A. Keys, S.G. Bott, A.R. Barron, J. Chem. Soc., Dalton Trans. (2000) 2151.
[3] T.A. Zevaco, J.K. Sypień, A. Janssen, O. Walter, E. Dinjus, J. Organomet. Chem. 692 (2007) 1963.
[4] B.-T. Ko, C.-C. Lin, Macromolecules 32 (1999) 8296.
[5] B.-T. Ko, Y.-C. Chao, C.-C. Lin, Inorg. Chem. 39 (2000) 1463.
[6] Y.-C. Liu, B.-T. Ko, C.-C. Lin, Macromolecules 34 (2001) 6196.
[7] H.-L. Chen, B.-T. Ko, B.-H. Huang, C.-C. Lin, Organometallics 20 (2001) 076.
[8] M.H. Chisholm, C.-C. Lin, J.C. Gallucci, B.-T. Ko, Dalton Trans. (2003) 406.
[9] J. Lewiński, P. Horeglad, E. Tratkiewicz, W. Grzenda, J. Lipkowski, E. Kołodziejczyk, Macromol. Rapid Commun. 25 (2004) 1939.
[10] T.A. Zevaco, J. Sypień, A. Janssen, O. Walter, E. Dinjus, Catalysis Today 115 (2006) 151.
[11] I. Taden, H.-C. Kang, W. Massa, T.P. Spaniol, J. Okuda, Eur. J. Inorg. Chem. (2000) 441.
[12] W. Braune, J. Okuda, Angew. Chem., Int. Ed. 42 (2003) 64.
[13] J. Storre, A. Klemp, H.W. Roesky, H.-G. Schmidt, M. Noltemeyer, R. Fleischer, D. Stalke, J. Am. Chem. Soc. 118 (1996) 1380.
[14] C. Schnitter, H.W. Roesky, T. Albers, H.-G. Schmidt, C. Ropken, E. Parisini, G.M. Sheldrick, Chem. Eur. J. 3 (1997) 1783.
[15] W. Ziemkowska, P. Stella, R. Anulewicz-Ostrowska, J. Organomet. Chem. 690 (2005) 722.
[16] W. Ziemkowska, S. Kwaśniewska, R. Wróblewski, R. Anulewicz-Ostrowska, J. Organomet. Chem. 651 (2002) 72.
[17] W. Ziemkowska, R. Anulewicz-Ostrowska, J. Organomet. Chem. 686 (2004) 2056.
[18] W. Ziemkowska, Inorg. Chem. Commun. 4 (2001) 757.
[19] C.N. McMahon, L. Alemany, R.L. Callender, S.G. Bott, A.R. Barron, Chem. Mater. 11 (1999) 3181.
[20] W. Ziemkowska, A. Kubiak, S. Kucharski, R. Woźniak, R. Anulewicz-Ostrowska, Polyhedron 26 (2007) 1436.
[21] W. Uhl, Z. Anorg. Allg. Chem. 570 (1989) 37.
[22] R.A. Kovar, H. Derr, D. Brandau, J.O. Callaway, Inorg. Chem. 14 (1975) 2809.
[23] (a) Z. Marczenko, Odczynniki organiczne w analizie nieorganicznej, PWN, Warszawa, 1959, polish edition;
(b) W.G. Milner, J.L. Woodhead, Anal. Chim. Acta 12 (1955) 127.
[24] Oxford Diffraction. CrysAlis CCD and CrysAlis RED. Oxford Diffraction Poland, Wrocław, Poland 2001.
[25] G.M. Sheldrick, Acta Crystallogr., Sect. A 46 (1990) 467.
[26] G.M. Sheldrick, SHELXL93. Program for the Refinement of Crystal Structures, University of Göttingen, Germany, 1993.
[27] A.I.C. Wilson (Ed.), International Tables for X-ray Crystallography, vol. C15, Kluwer, Dordrecht, 1992.

level were made only for the simplest H_3SiSH/H_3SiS^- case. We decided to asses again the problem of geometry changes using the currently available quantum chemistry tools that focus on the search for anomeric effects.

This work describes a systematic examination of tri-*tert*-butoxysilanethiol and its derivatives by analyzing protonation on the sulfur as well as the oxygen atoms. The study involves density functional theory (DFT) studies on the equilibrium geometry of the species, and the subsequent analysis of the structures by the natural bond orbital (NBO) method. The latter has a unique feature of analyzing the electron density by using sophisticated basis sets and methods in terms that are familiar to a chemist, such as: Lewis structure, lone pairs, bonds, anti-bonds and Rydberg electrons. It also allows the analysis of intramolecular donor–acceptor orbital interactions. Such (anomeric) interactions have successfully explained some of the kinetic characteristics of alcoholysis in silanethiols [6,7].

The results of the study should be applicable for describing and better understanding the chemical reactivity of silicon–sulfur compounds in vacuum and in condensed phases. In addition, the aim of this study was to provide a theoretical basis for rationalizing the geometry changeability found in many metal and ammonium silanethiolates [8] that have been characterized by the X-ray method.

2. Results and discussion

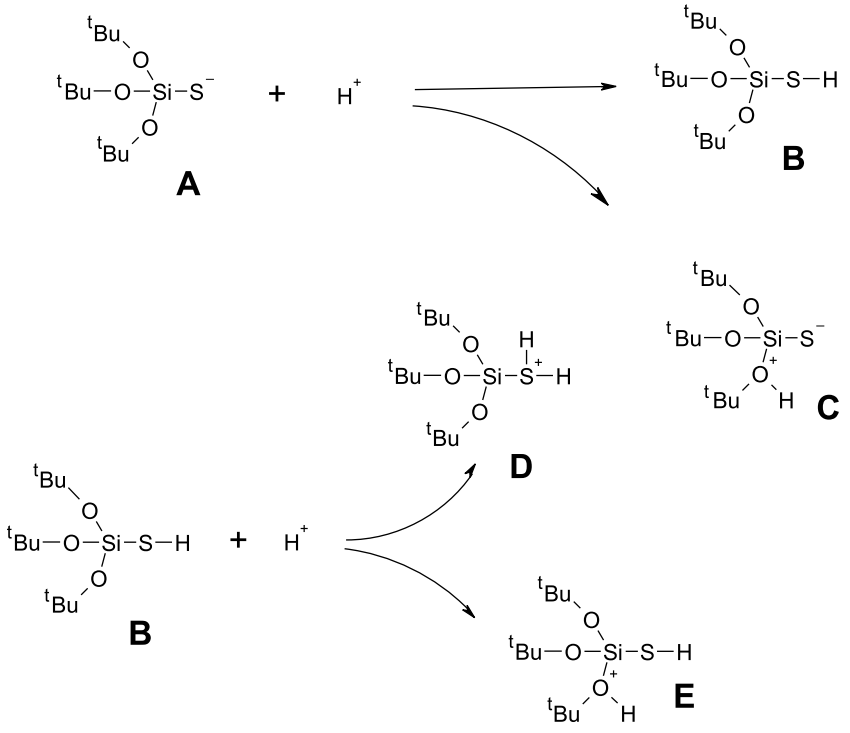
Basic mechanisms of the protonation and deprotonation of tri-*tert*-butoxysilanethiol, and the characterization of the described species are presented in Scheme 1.

Only the processes of proton exchange on the sulfur and oxygen atoms were analyzed as they are presumed to be the most important.

The structure of compounds **A**, **B**, **C**, **D** and **E** (**A**–**E**) were optimized at the B3LYP/6-31+G(d) level. Vibrational frequencies were calculated for all species to determine whether they were minima, transition structures or higher order saddle points. No imaginary frequency mode was found, which is equivalent to classifying all the species as stable compounds, being at the minimum of their potential energy surface. The computed electronic and vibrational energy values for the analyzed species are shown in Table 1.

2.1. Energetics of proton exchange processes

(a) *Reactivity in vacuum.* Protonation of the $(^tBuO)_3SiS^-$ anion **A** on the sulfur atom leads to silanethiol **B**, while its protonation on the oxygen atom gives "zwitterion" **C** with a negative charge on sulfur and a positive charge at the $-OH^+-$ oxonium group. Ground state energy calculations indicate that **B** is the preferred product, and it is *ca.* 100 kJ mol^{-1} more stable than **C**. Further protonation of tri-*tert*-butoxysilanethiol **B** on the sulfur atom yields the $-SH_2^+$ group in compound **D**; when the oxygen atom is attacked, the oxonium group is formed (preserving the –SH residue) in compound **E**. In this case, energy considerations point to compound **E** as being more stable than **D** by *ca.* 17 kJ mol^{-1}. Every protonation decreases the energy. The abovementioned results describe (more or less accurately) acceptance of a



Scheme 1.

Table 1
Overview of electronic DFT (RB + HF–LYP) energies, thermal corrections (zero point energy, ZPE) obtained from geometry optimization, and the results of single point calculations for compounds **A**–**E**

	A	**B**	**C**	**D**	**E**
	Geometry optimization B3LYP/6-31+G(d)				
DFT (a.u.)	−1387.17383	−1387.708633	−1387.671416	−1388.044723	−1388.049933
ZPE, not scaled (a.u.)	0.381778	0.391366	0.394826	0.400962	0.403018
Single point					
B3LYP/6-311++G(d,p) (a.u.)	−1387.40481959	−1387.94610037	−1387.91136276	−1388.28541823	−1388.29386463
B3LYP + scaled ZPE relative to **B** (kJ mol^{-1})	1396.45	0.00	100.11	−866.18	−883.06
Isodensity polarized continuum model for $\varepsilon = 78.38$					
IPCM B3LYP/6−311++G(d,p) (a.u.)	−1387.49249265	−1387.95053269	−1387.92716924	not converged	−1388.36029228

The last but one row lists the differences in the corrected (by subtraction of ZPE scaled by 0.9804) DFT energies in relation to tri-*tert*-butoxysilanethiol **B**. The single point methods included DFT and isodensity polarized continuum model, IPCM [9] computation.

free proton by a single molecule placed in a vacuum. Such an energy gain is usually termed the "proton affinity".

(b) *Protonation in solution.* Considering a real life chemical experiment, the proton source is most often either the hydrated proton $H^+(H_2O)_n$ (from $n = 1$ up to $n \geqslant 6$) from the bulk aqueous phase or the solvated non-ionized acid molecule (or acid oligomer) from an organic phase. Therefore, instead of a simple reaction:

(a) $(^t\mathrm{BuO})_3\mathrm{SiSH} + \mathrm{H}^+ = (^t\mathrm{BuO})_3\mathrm{SiSH_2}^+$

one must regard another reaction scheme:

(b) $(^t\mathrm{BuO})_3\mathrm{SiSH} + \mathrm{H}^+(\mathrm{H_2O})_n = (^t\mathrm{BuO})_3\mathrm{SiSH_2}^+ + (\mathrm{H_2O})_n$

which can be decomposed into the following algebraic sum: (b) = (a)–(c), where

(c) $\mathrm{H}^+ + (\mathrm{H_2O})_n = \mathrm{H}^+(\mathrm{H_2O})_n$.

Heat balance for the aqueous phase was estimated based on this decomposition. The formation energy for water clusters and protonated water clusters (Reaction c) has been the subject of many studies [10,11] as it is important for calorimetric measurements of enthalpy and the Gibbs energy of ion solvation. The absolute hydration enthalpy for a proton was determined with good accuracy [12] to be −1150.1(9) kJ mol^{-1}.

In order to calculate the energy gain in the type (a) reaction, we applied Tomasi's Isodensity Polarized Continuum Model energy values instead of the previously computed energies of molecules in a vacuum. In this approach, we regarded water only as a polarized medium of dielectric constant $\varepsilon = 78.38$, *i.e.* the formation of all additional hydrogen bonds was neglected. The pertinent results have been collated in Table 2. The hydration enthalpy value turned out to be lower than the energy gain for protonation on the sulfur atom in anion **A**, but bigger than the energetic stabilization for protonation on the oxygen atom or any protonation of silanethiol **B**.

Thus, we arrived at the qualitatively correct conclusion about protonation in silanethiol-related systems. Protonation of the anion derived from silanethiol in the aqueous solution of acids is energetically feasible, while further protonation of silanethiol in such medium does not take place (see Table 2). The single point energy calculation using the ICPM method for $(^t\mathrm{BuO})_3\mathrm{SiSH_2}^+$ failed to converge. This might indicate that the compound ionizes in solvents with a higher dielectric constant. Products **C**, **D** or **E** are not stable in the presence of the water phase, however they can be found in the gas phase, *e.g.* during mass spectroscopy experiments.

Table 2
Model of protonation in the aqueous phase

Compound	Protonation site	Protonation energy ICPM (kJ mol^{-1})	Energy gain (a)–(c) (kJ mol^{-1})
A: $(^t\mathrm{BuO})_3\mathrm{SiS}^-$	S	−1177.904	−27.804
	O	−1107.657	42.443
B: $(^t\mathrm{BuO})_3\mathrm{SiSH}$	S	not converged	>104
	O	−1045.831	104.269

The third column lists the energy difference between the protonated and non-protonated species obtained by the IPCM B3LYP/6-311++G(d,p)// B3LYP/6-31+G(d) model, and is corrected for vibrational zero point energy, scaled by 0.9804.

2.2. Geometry of the species

A search of the Cambridge Structural Database (CSD version 5.28, with May 2007 updates [13]) revealed that X-ray structural data are currently available for 61 metal and 7 ammonium tri-*tert*-butoxysilanethiolates. Unfortunately, there are no such data for the species analyzed in this study, except for anion **A** present in ionic compounds, *e.g.* $\{[\mathrm{Co}\{\mathrm{SSi}(\mathrm{OBu}^t)_3\}_2(\mathrm{NH_3})_4]^{(+)}$ and $(\mathrm{Bu}^t\mathrm{O})_3\mathrm{SiS}^{(-)}\}$ [14]. The lack of crystal structures is perhaps due to the limited stability of compounds **C**, **D** and **E**, or, in the case of **B**, due to a low melting point of *ca.* −28 °C which is, of course, only a technical obstacle. The starting geometries were derived from the X-ray structure of **A** by cutting-out from the abovementioned structure. Because the geometries of all the other compounds were optimized by quantum-chemical

Table 3
Selected geometric parameters for the X-ray structure of **A** and DFT B3LYP/6-31+G(d) optimized structures of compounds **A**–**E**

	A (X-ray)	**A**	**B**	**C**	**D**	**E**
Charge	−1	−1	0	0	1	1
S–Si	2.052	2.0435	2.1657	2.0082	2.405	2.1175
Si–O	1.645	1.6878	1.6425	1.9199*	1.6057	1.6112
	1.626	1.7064	1.6455	1.6522	1.6033	1.6115
	1.621	1.6947	1.6442	1.6532	1.6038	1.822*
O–Si–S	106.84	111.6680	104.5185	98.6833*	102.1597	109.7084
	114.35	116.6462	107.8040	124.4499	98.3162	113.7857
	115.14	118.2924	113.8098	123.6784	98.3803	108.4779*
Si–S–H angle			94.9587		98.5204	94.7507
					98.857	
Mean Si–O	1.6307	1.6963	1.6441	1.7418	1.6043	1.6816

* Group with protonated oxygen.

methods [22], *i.e.* by assuming a no-neighbors environment, the same optimization procedure was also applied to the anionic species. Optimization by the B3LYP/6-31+G(d) method gave satisfactory results, especially with regards to the reproduction of the Si–S bond length.

Let us first consider changes in geometry due to protonation on sulfur only, *i.e.* along the pathway from anion **A** through silanethiol **B** to *S*-protonated silanethiol **D**. There is quite a regular trend in the Si–S bond length, namely the more the positive charge on the sulfur atom, the longer the bond. This observation is consistent with the previous findings [5] based on the Si–S bond elongation during transformation from the anion form into silanethiol. It is commonly recognized that the role of the Si d-electrons is marginal in explaining the strength and consequently the length of the Si–S bond. This question will be addressed once more in the section dedicated to NBO analysis.

It is noteworthy that the Si–S–H valence angle is close to a right angle, indicating that the hybridization of the orbitals plays a minor role in the case of sulfur. This is also true for the $-SH_2^+$ groups (see Table 3).

The average Si–O bond length decreases in the series of species arranged according to increasing protonation, *i.e.* **A** → **B** → **D**. Changes in the Si–O bond length can be explained by taking into account the second order perturbation effects, also called the anomeric effect or hyperconjugation. This phenomenon has the character of energetic stabilization due to the donation of electrons from the sulfur lone pair(s) to the anti-bonding σ^*(Si–O) orbitals. Obviously, the donation is more significant for anion **A**, where nominally 3 lone pairs are available (actually, only 2 lone pairs of higher energy are interacting.). In compound **B** only one high energy pair on sulfur is available, while in **D** there are none. As the anti-bonding orbitals become more populated, the Si–O bonds get weaker (and longer too). A detailed discussion on the effects in natural bond orbital (NBO) terms will be presented in a later part of this work.

One more feature can be considered now. The coordination mode of the silicon atom changes from pseudo tetrahedral to pseudo trigonal pyramidal. Changes in the S–Si–O angles are quite substantial, namely from on average *ca.* 116° for **A** to 98° for **D**. On one hand, this indicates that the *S*-protonated silanethiol is ready for cleavage of the Si–S bond with the accompanying release of H_2S and the creation of a flat silicenium cation. On the other hand, such a deformation facilitates nucleophilic attack on the silicon atom from the direction opposite to the SH_2^+ group.

Moreover, a backward shift of the *tert*-butoxy groups in the case of anion **A** leads to greater steric hindrance at the reaction side of the Si atom. This can provide another explanation for the smaller hydrolytic reactivity of **A** in comparison to the respective silanethiol. The described difference has been observed for long time in experimental studies, *e.g.* by Sommer et al. [15,16]. So, the lower reactivity of **A** in nucleophilic attack can be explained in three ways:

(a) The negative charge of the anion slows the reaction down because of electrostatic repulsion.
(b) The Si–S bond to be cleaved is shorter (and stronger) in the anion form than in silanethiol.
(c) For anions, the steric hindrance of the butoxy groups is greater if we assume axial attack of a nucleophile, *e.g.* amongst the three O^{t}Bu groups. Such a geometry facilitates vertical attack of a nucleophile, *e.g.* between the sulfur atom and the O^{t}Bu group which are at a wider angle.

Now, let us turn to the *O*-protonated species. First of all, protonation of anion **A** is preferred on the *S* atom leading to silanethiol **B**. The *O*-protonated species **C** is of higher energy. Nevertheless, the optimal geometry of **C** has some interesting features. Most striking is the shortening of the Si–S bond length. It is even shorter than the corresponding bond in anion **A**. This resembles bond lengths (*ca.* 1.95–2.01 Å) found in silathione [17,18] compounds of the $R_2Si{=}S$ type with the R residues being bulky 2,4,6-substituted (with –*i*Pr or $-CH(SiMe_3)_2$) phenyl groups, or silathiones [19] with additional coordination of nitrogen by silicon. Short Si–S bond can also be found in zwitterions: silatiolato-phosphonic [20] Ph_3P^+–CMe_2–

$SiMe_2S^-$, or silatiolato-arsonic [21] Et_3As^+–$CHSiMe_3$–$SiMe_2$–S^-, or Et_3As^+–CHPh–$SiMe_2$–S^-.

Compound **C** can be regarded as a kind of adduct of $^tBuOH...(^tBuO)_2Si{=}S$ with a separated charge (and ^tBuOH with a long C–O bond) which explains the shortening of the Si–S bond. Additional DFT computations using the same B3LYP/6-31+G(d) method were carried out to calculate the optimized geometry for the molecule of $(^tBuO)_2Si{=}S$ (**F**). The obtained Si–S bond length of 1.963 Å has confirmed the expected shortening for the double bonding. Species **C** can decompose into *tert*-butanol + silathion or into buten+"zwitterionic" di-*tert*-butoxysilanethiolate anion with the OH_2^+ group bound to silicon. Both decompositions are more likely to occur in vacuum at elevated temperatures.

Let us examine the geometry of the *O*-protonated silanethiol **E**. The reason for the shortening of the Si–S bond in **E** in relation to **D** cannot be directly inferred from the above discussion, but the changes are of similar character. In this case, the structure can be regarded as a loose adduct of *tert*-butanol with the silicenium cation: $^tBuOH...(^tBuO)_2Si(+)SH$. The Si–S bond length in the cation is also short. DFT-based geometry optimization carried out for $(^tBuO)_2Si(+)SH$ (**G**) yielded a bond length of 2.077 Å. A qualitative explanation for this effect might be the shrinking of the silicon orbitals resulting in better matching for the size of sulfur, which leads to the higher value of the Si–S bond overlap integral and the consequent shortening of the bond.

Both cases, *i.e.* bond shortening for *O*-protonation and bond elongation for *S*-protonation, show some similarities to the shortening of Si–S bonds found in metal silanethiolates where the ligand acts as a chelating *O,S*-donor for the metal centers. Of course it is not obvious how to separate the shortening of the Si–S bond related to the greater ionic character of the $(^tBuO)_3SiS$ group from shortening due to chelation (which is similar to *O*-protonation).

The Si–O bonds are substantially longer (1.636 and 1.623 Å) in **F** as compared to the respective bonds in **G** (1.577 and 1.579 Å). This phenomenon can be explained in many possible ways. First of all, a positive charge on silicon can result in stronger interactions with the oxygen atoms. It can also be a manifestation of electron donation from the sulfur lone pairs to the anti-bonding Si–O orbitals, which is stronger in the case of silathion **F** than the silicenium cation **G**.

For a more quantitative discussion, we will analyze the NBO orbitals and the second order perturbation energy stabilization due to internal donor–acceptor orbital interactions (principal delocalizations).

2.3. NBO analysis

2.3.1. Anion $(^tBuO)_3SiS^-$ (**A**)

Selected results from the natural population analysis for the compound are presented in Tables 4 and 5. Let us analyze both the occupation and hybridization of the S and O lone pairs. One lone pair on sulfur lp(1) S has mainly s character and it is practically occupied by two electrons. The second and third lone pairs are mainly of p character and their occupation is lower, suggesting the interaction with other, possibly anti-bonding, orbitals. Interestingly, the silicon d orbitals (here RY*(1) Si2) are by far less occupied than the anti-bonding Si–O orbitals. The lone pairs on oxygen are not uniform. Each oxygen atom possesses one pair of p character and one hybrid orbital approximately described as $sp^{2.65}$. Less populated and used as donors in the stabilization of the molecule are mainly the p character lone pairs lp(2) O3, etc. (see Table 5).

Second-order perturbation stabilization (Table 5) is dominated by the donation of electrons from lone pairs (from the sulfur as well as oxygen atoms) to the anti-bonding Si–O orbitals. In turn, the populated, anti-bonding Si–O orbitals behave as electron donors to the Rydberg silicon orbitals, which also results in a stabilizing effect. It is worth noting that in a polarized bond such as Si–O, the anti-bonding σ^*(Si–O) orbital has a greater wavefunction coefficient at the silicon atom as compared to oxygen, so the overlap with the sulfur p-electrons is relatively strong. This σ–π overlap is also effective because the σ^*(Si–O) orbital has three nodal planes so the symmetry of the orbitals is compatible (see Fig. 1). When the aforementioned interaction is analyzed as delocalization, we arrive at the following situation. Two three-centered orbitals are produced from a lone pair and an anti-bond. The lower energy 3c–2e orbital

Table 4
Characteristics of selected orbitals in **A** based on the natural population analysis

Orbital	Occupation	Composition %			
		s	p	d	Contributions of atoms to the orbital
LP(1)S1	1.97102	76.17	23.82	0.01	
LP(2)S1	1.87979	0.12	99.82	0.47	
LP(3)S1	1.85530	0.04	99.89	1.94	
LP(1)O3	1.93702	27.31	72.64	0.05	
LP(2)O3	1.91047	0.03	99.93	0.04	
RY*(1)Si2	0.02935	0.53	11.88	87.59	
BD*(1)S1–Si2	0.06831				32.4%S, 67.6%Si
BD*(1)Si2–O3	0.13495				87.79%Si, 12.21%O
BD*(1)Si2–O4	0.15554				88.04%Si, 11.96%O
BD*(1)Si2–O5	0.14056				87.89%Si, 12.11%O

Abbreviations: LP – lone pair; RY*, BD, BD* – Rydberg, bonding and anti-bonding orbital, respectively.

Table 5
Second order perturbation theory analysis of the Fock matrix for [**A**] based on the NBO method

Donor NBO (*i*)	Acceptor NBO (*j*)	$E^{(2)}$ (kcal/mol)	$E(j) - E(i)$ (a.u.)	$F_{i,j}$ (a.u.)
LP(3)S1	BD*(1)Si2–O5	13.98	0.44	0.070
LP(2)S1	BD*(1)Si2–O4	11.11	0.44	0.063
LP(2)O3	BD*(1)Si2–O4	9.08	0.59	0.067
LP(2)S1	BD*(1)Si2–O3	8.84	0.45	0.056
LP(2)O4	BD*(1)Si2–O3	8.70	0.61	0.066

Items with the highest energy gain were selected.

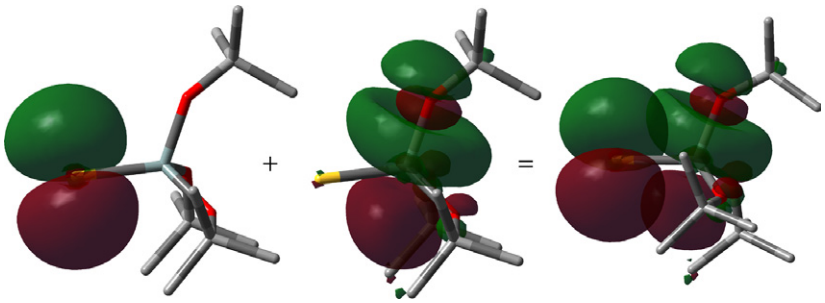


Fig. 1. Geometry of sulfur lone pair overlap with the anti-bonding Si–O orbital generated by GaussView 4.1 (Gaussian, Inc., Pittsburg, PA). Hydrogen atoms are not shown.

increases electron density between the Si and S atoms and decreases electron density between Si and O. This serves as a good explanation for the geometry changeability in **A**, **B** and **D**.

It should be emphasized that the sulfur lone pairs do not act as donors for empty d silicon orbitals (here described as RY* Si), as was initially believed at the earlier developmental stages of silicon chemistry. The energy difference between the two levels is too high to result in important interactions (*e.g.* for lp(2) S1 and RY*(2) Si2, $E(j) - E(i) = 1.03$ a.u.).

2.3.2. Tri-tert-butoxysilanethiol (*B*)

The detailed results of the NBO analysis are given in the Supplementary Materials. This time, the stabilization effects were not reinforcing the Si–S bond so much. As stated previously in qualitative terms, only one lone pair of sulfur gives the second order perturbational stabilization. Lone pairs on oxygen O3 and O4 mutually populate their anti-bonding Si–O orbitals. The third oxygen lone pair lp(2) O5 populates the anti-bonding Si–S orbital, which obviously weakens the bond.

2.3.3. O-protonated anion "zwitterion" (*C*)

The NBO algorithm search for the best Lewis structure returned the structure split into silathion and butanol. Because of that one can find two Si–S bonds, *i.e.* BD(1) S1–Si2 and BD(2) S1–Si2 of σ and π character, respectively, and their anti-bonding partners. Electron density is transferred from one pair LP(2) S1 to the anti-bonding Si2–O5 and Si2–O4 orbitals which, in turn, interact with the anti-bonding C–O orbitals in silathion. The occupation values of the Si–O anti-bonds are quite high. It seems that the orbitals in the vicinity of the silicon atom are indeed highly delocalized.

2.3.4. S-protonated silanethiol (*D*)

Inertness of the lone pair on sulfur is again apparent (see Tables 9 and 10 in the Supplementary Materials); it does not participate in the donation of electrons. This has been confirmed by the high occupancy of the orbital and the pair's absence on the donors list. A relatively high occupation of the anti-bonding Si–S orbital is noteworthy. In this specific compound, the most important second order perturbation effects are generated by lone pairs on the oxygen atoms. In this case, the oxygen pairs that are essentially of p character destabilize the Si–S bond, which results in the greatest energy gain for the system. The process is facilitated by the symmetry of the Si–S anti-bond, namely, sigma symmetry with three nodal planes (Fig. 2). The anti-bonding orbital fits well to the p-type lone pairs on oxygen because SiO_3 is almost a flat system. Again, the lone pairs on oxygen additionally and mutually populate the Si–O anti-bonding orbitals. However, this interaction is not very strong because the energy difference between the levels is high (*ca.* 0.7 a.u.).

2.3.5. O-protonated silanethiol (*E*)

The assignment of double bonds to the two Si–O groups in the best Lewis structure is noteworthy. Inertness of the lone pair on sulfur can be easily seen in Tables 11 and 12 (Supplementary Material). The pair's contribution to donating electrons is not significant. The analysis of the donors and acceptors list points to the high delocalization of the Si–O bonds as being the main stabilizing effect.

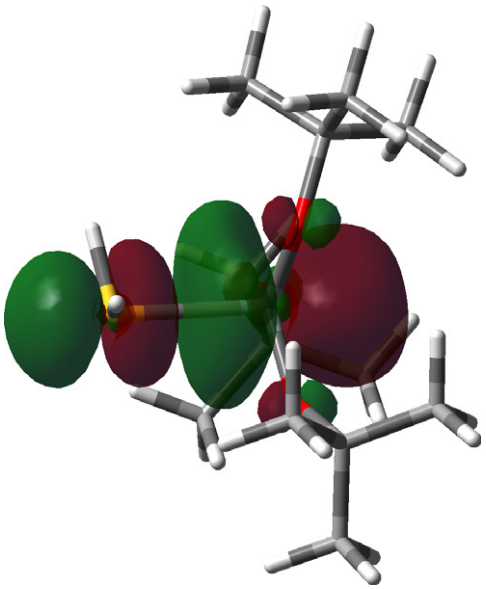


Fig. 2. Shape of the anti-bonding σ*(Si–S) orbital in **D**.

3. Experimental

The quantum mechanical calculations were made using the GAUSSIAN03W [22] package, including NBO [23,24] analysis. Geometry optimizations were performed using the B3LYP/6-31+G(d) method. The starting geometry for **A** was taken from a fragment of the X-ray structure of $[Co(RS)_3(NH_3)_4]^{(+)} \cdot {}^{(-)}SSi(OBu^t)_3$ [14] and later optimized by applying DFT analysis to cancel the effects of packing and hydrogen bonds present in the solid state. This procedure also removed the differences of the C–H bond lengths measured by the X-ray crystallography [25] and set by quantum mechanics. All the other starting geometries were derived from **A** by adding hydrogen atoms and by modifying the total charge of the species. The optimized structures of compounds **A**–**E** are available in PDB format as supplementary material.

Single point ground state energy calculations were carried out on the B3LYP/6-311++G(d,p) and MP2/6-311++G(d,p) level (see Supplementary Materials). The inclusion of solvent effects was performed with a Tomasi IPCM – B3LYP model using the same basis set.

4. Summary

Theoretical considerations of protonation and deprotonation of tri-*tert*-butoxysilanethiol led to the following conclusions:

1. Protonation of the $({}^t BuO)_3SiS^-$ anion is energetically preferred on the sulfur atom and yields tri-*tert*-butoxysilanethiol. Protonation on the oxygen atom also yields a relatively stable product.
2. Protonation of tri-*tert*-butoxysilanethiol can be accomplished by proton acceptance in the gas phase, which yields relatively stable products. Energetically preferred is protonation on the oxygen atom although protonation on the sulfur atom is almost equal in lowering the total energy. These processes do not proceed by transfer of a proton solvated in the aqueous phase or bound in $H^+(H_2O)_n$ clusters with a solvation energy greater than *ca.* 870 kJ mol^{-1} in vacuum.
3. Protonation of both tri-*tert*-butoxysilanethiol and its anion on the sulfur atom results in the elongation of the Si–S bond.
4. Protonation of both tri-*tert*-butoxysilanethiol and its anion on the oxygen atom results in the shortening of the Si–S bond.
5. Delocalization of lone pairs from sulfur proceeds mainly by the interaction with the anti-bonding σ^*_{Si-O} orbitals. It is noteworthy that due to polarization effects these orbitals have greater lobes on the silicon side, which is critical for effective interactions.
6. The numerous values of bond lengths and their changes during transformation can be explained by the intermolecular donor–acceptor orbital interactions. The NBO analysis provides a satisfactory description of the geometry changes in the analyzed class of substances.

The obtained results provide a good basis for a more detailed analysis of geometry changes that have been observed in the structure of metal (or ammonium) silanethiolates.

Acknowledgements

The author wishes to thank Professor Wieslaw Wojnowski for inspiration and encouragement, and Aleksander Herman for helpful discussion. The work was supported by an internal grant from the Gdańsk University of Technology.

Appendix A. Supplementary data

Supplementary data associated with this article can be found, in the online version, at doi:10.1016/j.poly.2007.11.041.

References

[1] R. Piękoś, W. Wojnowski, Z. Anorg. Allg. Chem. 318 (1962) 212.
[2] K. Baranowska, J. Chojnacki, M. Gosiewska, W. Wojnowski, Z. Anorg. Allg. Chem. 632 (2006) 1086.
[3] J. Chojnacki, B. Kasterka, W. Wojnowski, J.F. Biernat, Chem. Anal. (Warsaw) 41 (1996) 347.
[4] M. Cypryk, Y. Apeloig, Organometallics 21 (2002) 2165.
[5] A. Herman, W. Wojnowski, Struct. Chem. 4 (1992) 239.
[6] J. Pikies, W. Wojnowski, J. Organometal. Chem. 386 (1990) 305.
[7] J. Pikies, W. Wojnowski, J. Organometal. Chem. 393 (1990) 187.
[8] K. Baranowska, J. Chojnacki, A. Konitz, W. Wojnowski, B. Becker, Polyhedron 25 (7) (2006) 1555.
[9] M. Cossi, V. Barone, R. Cammi, J. Tomasi, Chem. Phys. Lett. 255 (1996) 327.
[10] J.V. Coe, Int. Rev. Phys. Chem. 20 (2001) 33.
[11] M. Śmiechowski, J. Stangret, J. Chem. Phys. 125 (2006) 204508, pp. 1–14.
[12] M.D. Kissandier, K.A. Cowen, W.Y. Feng, E. Gunglach, M.H. Cohen, A.D. Earhart, V. Coe, T.R. Tuttle Jr., J. Phys. Chem. A 102 (1998) 7787.
[13] F.H. Allen, Acta. Crystallogr., Sect. B 58 (2002) 380.
[14] B. Becker, A. Zalewska, A. Konitz, W. Wojnowski, Z. Anorg. Allg. Chem. 627 (2001) 271.
[15] L. Sommer, J. McLick, J. Am. Chem. Soc. 88 (1966) 5359.
[16] L. Sommer, J. McLick, J. Am. Chem. Soc. 88 (1967) 5806.
[17] H. Suzuki, N. Tokitoh, S. Nagase, R. Okazaki, J. Am. Chem. Soc. 116 (1994) 11578.
[18] H. Suzuki, N. Tokitoh, R. Okazaki, S. Nagase, M. Goto, J. Am. Chem. Soc. 120 (1998) 11096.
[19] P. Arya, J. Boyer, F. Carre, R. Corriu, G. Lanneau, J. Lapasset, M. Perrot, C. Priou, Angew. Chem., Int. Ed. 28 (1989) 1016.
[20] I.V. Borisova, N.N. Zemlyansky, Yu.A. Ustynyuk, V.N. Khrustalev, S.V. Lindeman, Yu.T. Struchkov, Izv. Akad. Nauk SSSR, Ser. Khim. (Russ.) (Russ. Chem. Bull.) (1994) 339.
[21] I.V. Borisova, N.N. Zemlyansky, V.N. Khrustalev, M.S. Nechaev, M.G. Kuznetsova, Yu.A. Ustynyuk, Izv. Akad. Nauk SSSR, Ser. Khim. (Russ.) (Russ. Chem. Bull.) (2002) 627.
[22] M.J. Frisch, G.W. Trucks, H.B. Schlegel, G.E. Scuseria, M.A. Robb, J.R. Cheeseman, J.A. Montgomery Jr., T. Vreven, K.N. Kudin, J.C.

Burant, J.M. Millam, S.S. Iyengar, J. Tomasi, V. Barone, B. Mennucci, M. Cossi, G. Scalmani, N. Rega, G.A. Petersson, H. Nakatsuji, M. Hada, M. Ehara, K. Toyota, R. Fukuda, J. Hasegawa, M. Ishida, T. Nakajima, Y. Honda, O. Kitao, H. Nakai, M. Klene, X. Li, J.E. Knox, H.P. Hratchian, J.B. Cross, V. Bakken, C. Adamo, J. Jaramillo, R. Gomperts, R.E. Stratmann, O. Yazyev, A.J. Austin, R. Cammi, C. Pomelli, J.W. Ochterski, P.Y. Ayala, K. Morokuma, G.A. Voth, P. Salvador, J.J. Dannenberg, V.G. Zakrzewski, S. Dapprich, A.D. Daniels, M.C. Strain, O. Farkas, D.K. Malick, A.D. Rabuck, K. Raghavachari, J.B. Foresman, J.V. Ortiz, Q. Cui, A.G. Baboul, S. Clifford, J. Cioslowski, B.B. Stefanov, G. Liu, A. Liashenko, P. Piskorz, I. Komaromi, R.L. Martin, D.J. Fox, T. Keith, M.A. Al-Laham, C.Y. Peng, A. Nanayakkara, M. Challacombe, P.M.W. Gil, GAUSSIAN 03, Revision D.01.

[23] NBO Version 3.1, E.D. Glendening, A.E. Read, J.E. Carpenter, F. Weinhold, J. Chem. Phys. 78 (1983) 4066.

[24] A.E. Reed, F. Weinhold, J. Chem. Phys. 83 (1985) 1736.

[25] F.H. Allen, Acta Crystallogr., Sect. B 42 (1986) 515.

Although a large amount of work on the synthesis and characterization of transition metal complexes of Schiff bases of *S*-alkyl esters of dithiocarbazic acid have been reported [1–15] very little work has been reported on organometallic complexes of these ligands. In view of very little information available on organotin(IV) complexes of dithiocarbazates and as part of our ongoing work on metal complexes of dithiocarbazic acid and its derivatives, we report here the synthesis, characterization and X-ray crystal and molecular structures of the acetone Schiff bases of *S*-methyl- and *S*-benzyldithiocarbazate together with the structures of their chlorodiphenyltin(IV) complexes.

2. Experimental

2.1. Reagents

Chemicals and solvents used were of analytical reagent grade and used without any further purification. Dichlorodiphenyltin(IV) was purchased from the Aldrich Chemical Company.

2.2. Physical measurements

Microanalyses for C, H & N were performed by the Elemental Analysis Laboratory, National University of Singapore, Singapore. Molar conductivity of *ca.* 10^{-3} M solutions of the complexes in DMSO were measured by means of a Jenway 4310 conductivity meter. The IR spectra were measured as KBr discs on a Perkin–Elmer 2000 FT-IR spectrometer and the electronic spectra were measured as Nujol mulls on a Shimadzu MPC-3100 spectrophotometer. The ^{1}H NMR spectra of the tin(IV) complexes were run in $CDCl_3$ on a Bruker DPX 300 MHz spectrometer using TMS as an internal standard. The Mössbauer spectra were recorded using a Model MS-900 (Ranger Scientific Co., Burleson, TX) spectrometer in the acceleration mode with moving source geometry. A 5-mCi $Ca^{119m}SnO_3$ source was used. The spectra were measured at 80 K using a liquid–nitrogen cryostat (CYRO Industries of America Inc.). The velocity was calibrated at ambient temperature using a composition of $BaSnO_3$ and tin foil (splitting 2.52 mm s^{-1}). The resultant spectra were analyzed by a least-square fit to Lorentzian shaped lines.

2.3. Preparation of the ligands

The Schiff bases were prepared by following procedures reported previously [14,16]. The compounds as isolated from the reaction were suitable for X-ray crystallography.

2.4. General method of preparation of the complexes

To a solution of $SnPh_2Cl_2$ (1 mmol) in boiling abs. ethanol (70 ml) was added a solution of the appropriate Schiff base (1 mmol) in the same solvent (70 ml) and the mixture heated under reflux for 48 h and then left to stand overnight. The product that had formed was filtered off, washed with abs. ethanol and dried in a vacuum desiccator over anhydrous silica gel. These compounds as isolated were suitable for X-ray work. Yield: 50–60%. *Compound* **3** Sn(acsme)Ph_2Cl: *Anal.* Calc. for $C_{17}H_{19}N_2S_2ClSn$: C, 43.48; H, 4.08; N, 5.96. Found: C, 43.40; H, 4.03; N, 5.85%. *Compound* **4** Sn(acsbz)Ph_2Cl: *Anal.* Calc. for $C_{23}H_{23}N_2S_2ClSn$: C, 50.62; H, 4.25; N, 5.13. Found: C, 50.52; H, 4.15; N, 5.46%.

2.5. Crystallography

Cell constants were determined by a least-squares fit to the setting parameters of 25 independent reflections, measured on an Enraf-Nonius CAD 4 four-circle diffractometer using graphite monochromated Mo Kα radiation (0.71073 Å) and operating in the $\omega - 2\theta$ mode within the range $2 < 2\theta < 50°$. Empirical absorption correction (ψ scans) and data reduction were performed with the WINGX [17] suite of programmes. The structures were solved by direct methods with SHELX86 and refined by full-matrix least-squares analysis with SHELXL97 [18]. Non-hydrogen atoms were refined with anisotropic thermal parameters whereas H-atoms were included at estimated positions using a riding model. Drawings of each molecule were produced with ORTEP3 [19]. A summary of the crystal data, structure solution and refinement parameters are given in Table 1 and selected bond lengths appear in Table 6.

3. Results and discussion

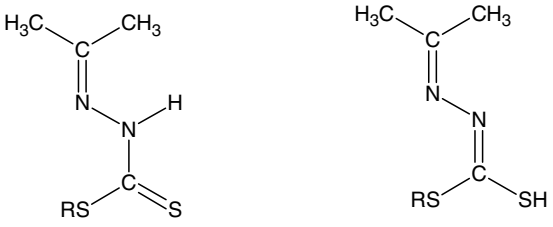
The acetone Schiff bases of *S*-methyldithiocarbazate and *S*-benzyldithiocarbazate have a thioamide (–NH–CS–) functional group and consequently, in principle, they are capable of existing either as the thione form (1a) or the thiol form (1b) or as a mixture of both thione and thiol tautomeric forms (Fig. 1). In the solid state it has been shown that they exist in their thione forms since their IR spectra exhibit the *ν*NH band at *ca.* 3300 cm^{-1} and no *ν*SH band at *ca.* 2600 cm^{-1} [14]. However, in solution they might exist as an equilibrium mixture of both the thione and thiol tautomeric forms. The ^{1}H NMR spectra of the Schiff bases in $CDCl_3$ exhibit a signal at *ca.* 10.15 ppm which is characteristic of an NH as opposed to an SH resonance. No signal at *ca.* 4.00 ppm attributable to the SH proton was detected indicating that even in solution they remain predominantly as the thione tautomer.

3.1. Characterization of the Sn(IV) complexes

In a boiling ethanolic solution the Schiff bases react with $SnPh_2Cl_2$ in their thiol tautomeric forms, deprotonate and coordinate to the tin(IV)ion forming charge neutral complexes of formula, $SnPh_2(NS)Cl$ (NS = deprotonated form of the Schiff bases). The analogous acetone thiosemicarbazone which exhibits a structural backbone very similar to the present compounds, has been shown to react with

Table 1
Crystallographic data

	Hacsme (**1**)	Hacsbz (**2**)	Sn(acsme)Ph_2Cl (**3**)	Sn(acsbz)Ph_2Cl (**4**)
Empirical formula	$C_5H_{10}N_2S_2$	$C_{11}H_{14}N_2S_2$	$C_{17}H_{19}N_2S_2ClSn$	$C_{23}H_{23}N_2S_2ClSn$
Formula weight	162.27	238.36	469.60	545.69
T (K)	293(2)	293(2)	293(2)	293(2)
λ (Å)	0.71073	0.71073	0.71073	0.71073
Crystal system	monoclinic	monoclinic	orthorhombic	monoclinic
Space group	$P2_1/a$	$P2_1/c$	$P2_1cn$	$P2_1/n$
a (Å)	14.58(1)	11.942(1)	9.535(2)	8.2242(9)
b (Å)	11.653(4)	6.163(7)	12.848(2)	13.445(1)
c (Å)	19.41(1)	16.942(3)	16.493(2)	22.187(3)
β (°)	98.58(6)	94.77(1)		92.81(2)
V (Å^3)	3261(3)	1242.2(3)	2020.5(6)	2450.4(5)
D_{calc} (Mg/m^3)	1.322	1.274	1.544	1.479
Z	16	4	4	4
μ (mm^{-1})	0.573	0.399	1.603	1.334
$F(000)$	1376	504	936	1096
Independent reflections [R_{int}]	5702 [0.0523]	2173 [0.0323]	2121 [0]	4309 [0.0155]
Observed reflections ($I > 2\sigma(I)$)	2538	1040	1452	3175
Data/restraint/parameters	5702/0/337	2173/0/138	2121/1/198	4309/0/265
Goodness-of-fit on F^2	1.015	0.997	0.993	1.020
R_1 (observed data) and wR_2 (all data)	0.0539 and 0.1668	0.0430 and 0.1188	0.0830 and 0.2503	0.0273 and 0.0722



(1a; thione form; R = CH_3, CH_2Ph) (1b; thiol form)

Fig. 1. The thione and thiol tautomeric forms of the Schiff base (R = CH_3, Hacsme; R = CH_2Ph, Hacsbz).

$SnPh_2Cl_2$ yielding a diphenyltin(IV) complex containing the neutral form of the ligand [20]. This example illustrates the diversity of reactivity found in these Schiff base ligands in their coordination chemistry with Sn(IV).

The complexes are stable at room temperature and may be kept in a desiccator over anhydrous silica gel for extended periods without any sign of decomposition. The molar conductivities of Sn(acsme)Ph_2Cl and Sn(acsbz)Ph_2Cl in DMF are 11.7 and 11.8 Ω^{-1} cm^2 mol^{-1}, respectively, indicating that even in a polar coordinating solvent like DMF, they behave essentially as non-electrolytes. The conductance data confirm that the Schiff bases coordinate to the tin atom in their monodeprotonated forms.

The IR spectra of the $SnPh_2$(*NS*)Cl complexes when compared with those of the free Schiff bases (Table 2) show that the νNH bands of the free ligands at *ca.* 3300 cm^{-1} are absent in the spectra of the complexes indicating that the ligands are coordinated to the tin atom in their deprotonated mercaptide forms. The shift of the azomethine $\nu_{C=N}$ band in the IR spectra of the free ligands (1634–1628 cm^{-1}) to lower wavenumber (1612–1608 cm^{-1}) in the spectra of complexes support coordination of the azomethine nitrogen atom to the tin atom. This is further supported by the shift of the ν_{N-N} band of the free ligands to higher wavenumbers in the spectra of the complexes.The electronic spectra of the complexes show the intraligand $n \rightarrow \pi^*$ and $\pi \rightarrow \pi^*$ transitions in the ranges 363 and 311–258 nm, respectively. The $n \rightarrow \pi^*$ band of the free ligands is not affected in the electronic spectra of the complexes but there is a hypsochromic shift of the $\pi \rightarrow \pi^*$ band upon coordination to Sn(IV).

The ^{1}H NMR spectra of the complexes do not contain the signal due to the NH proton of the free ligands at 10.15 ppm supporting further the IR evidence presented earlier that the ligands are coordinated to the tin atom in

Table 2
IR and electronic spectra for the ligands and their diphenyltin(IV) chloride complexes

Compound	IR bands				Electronic spectra[b] λ_{max} (nm)
	νNH	νCN	νNN	νCSS	
Hacsme[a]	~3300sh	1634	1064s	998s	364, 293
Hacsbz[a]	~3300sh	1628s	1069	998s	340, 298
[Sn(acsme)(C_6H_5)$_2$Cl]		1608s	1068m	1024, 997m	363sh, 311
[Sn(acsbz)(C_6H_5)$_2$Cl]		1612s	1074m	1011, 996m	362sh, 325sh, 258

[a] Data taken from Ref. [14].
[b] Solid state (Nujol mull).

their deprotonated thiolate forms. The ^{1}H NMR spectra of $SnPh_2(NS)Cl$ show two signals due to two acetone-derived methyl groups due to restricted rotation about the C=N bond. The methyl group, *syn* to the N–N bond resonates at a higher field than the *anti* methyl group [21] (see Table 3).

The Mössbauer spectra of the $Sn(NS)Ph_2Cl$ complexes are shown in Figs. 2 and 3 and the isomer shift (δ), quadrupole splitting (Δ) and ρ values are given in Table 4. The parameters (δ and Δ) are within the range found with Sn (IV) and organotin compounds [22]. The Mössbauer spectra of the tin complexes exhibit identical δ indicating that the substituents (methyl or phenyl) on one of the sulfur atoms of the dithiocarbazate moiety do not have any effect at all on the s-electron density at the tin nucleus. The spectra of the two compounds also exhibit the same values of Δ indicating that they have the same structure. X-ray crystallographic structure determination (see later) confirms this fact. The Mössbauer spectra of the present tin(IV) complexes have lower δ values than the starting tin compound, $SnPh_2Cl_2$ (1.34 mm s^{-1}) [23]. A re-hybridization in the [Sn(NS)Ph_2Cl] complexes (due to higher coordination number of the tin atom in the complexes relative to that in $SnPh_2Cl_2$) accounts for the smaller isomer shift δ value. A greater involvement of the d orbitals in the tin complexes, which take part in the re-hybridization scheme causes a reduction in the s-electron contribution in the complexes relative to that of the starting tin compound [23], thus decreasing the value of the isomer shift. The ρ values, which are used to predict coordination numbers of tin complexes, are found to be 2.02, supporting a coordination number greater than four for the tin ion in the tin complexes [24].

The angle, θ between the axial carbon atoms and tin atom can be obtained from the Mössbauer spectrum using the relationship, $|\Delta| = -4[R](1–0.75\sin^2\theta)^{1/2}$ where Δ is the observed quadrupole splitting, θ is the R–Sn–R angle in the complex and $[R]$ is the partial quadrupole splitting (PQS) of the axial groups [25]. The calculated angle for Sn(acsme)Ph_2Cl is 122.9° using $[R]$ of −0.94 [26] and for Sn(acsbz)Ph_2Cl, 127.3° using $[R]$ of −0.89 [26]. This compares favorably with the values of the angles found by X-ray crystallography; 122.9° and 127.1°, respectively.

3.2. Crystal structures of the free ligands

The structures of Hacsme and Hacsbz are shown in Figs. 4 and 5, respectively, and relevant bond lengths and bond angles are given in Table 5. The asymmetric unit of Hacsme has four crystallographically independent molecules (referred to here as molecules A, B, C and D) which have very similar bond lengths and bond angles. Molecule

Table 3
^{1}H and ^{13}C NMR spectroscopic data

Compound	^{1}H NMR assignments					^{13}C NMR assignments					
	CH_3(*syn*)	CH_3(*anti*)	SCH_3/SCH_2^-	NH	Ar	CH_3(syn)	CH_3(anti)	SCH_3/SCH_2^-	CN	CS	ArC
Hacsme	[1.96][a] 1.95 (s, 3H)	[2.04][a] 2.08 (s, 3H)	[2.57][a] 2.62 (s, 3H)	9.78 (1H)		16.68	17.74	25.28	152.73	200.62	
Hacsbz	1.95 (s, 3H)	2.04 (s, 3H)	4.52 (s, 2H)	9.68 (1H) 7.28–7.32 (m, 2H) 7.40 (d, J = 8 Hz, 2H)		16.79	25.24	39.48	152.81	198.93	127.43 128.57 129.44 136.04
[Sn(acsme)$(C_6H_5)_2$Cl]	1.55 (s, 3H)	2.28 (s, 3H)	2.52 (s, 3H)	7.26 (m, 4H), 7.45 (m, 4H), 7.49 (m,2H)		14.92	22.92	25.65	143.67	174.31	129.09 130.02 134.51 134.90
[Sn(acsbz)$(C_6H_5)_2$Cl]	1.54 (s, 3H)	2.28 (s, 3H)	4.42 (s, 2H)	7.25–7.77 (m, 15H)		23.01	25.67	36.34	143.67	174.54	127.59 128.69 128.54 129.68 128.99 129.10 130.03 134.88

[a] Data reported by [29].

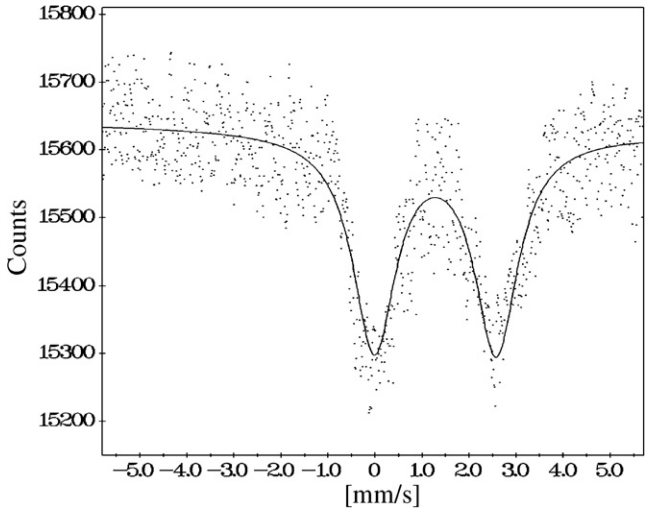


Fig. 2. The Mössbauer spectrum of Sn(acsme)Ph_2Cl.

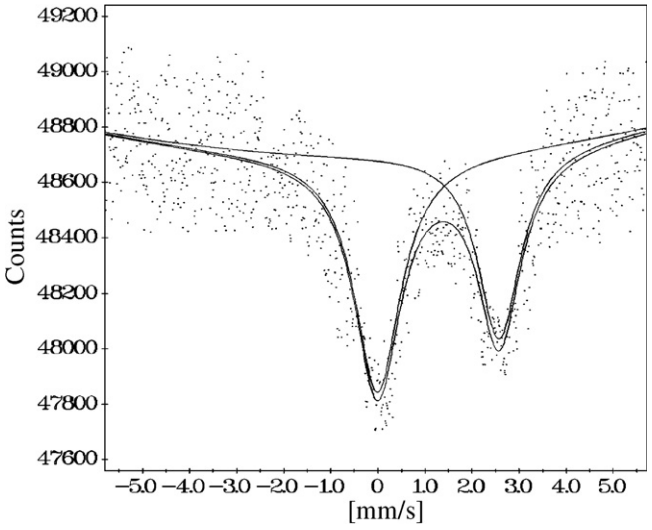


Fig. 3. The Mössbauer spectrum of Sn(acsbz)Ph_2Cl.

Table 4
Mössbauer spectroscopic data for the diphenyltin(IV) complexes

Compound	δ (mms^{-1})	Δ (mms^{-1})	ρ
Sn(acsme)$(C_6H_5)_2Cl$	1.28	2.58	2.02
Sn(acsbz)$(C_6H_5)_2Cl$	1.28	2.59	2.02

'A' is shown in Fig. 4. H-bonding in the structure finds that molecules A and D forms centrosymmetric H-bonded dimers while molecules B and C pair up in a pseudocentrosymmetric arrangement involving N1*n*-H···S2*n* pairs (data not shown).

However, the asymmetric unit of Hacsbz contains only one molecule which too is H-bonded to a centrosymmetri-

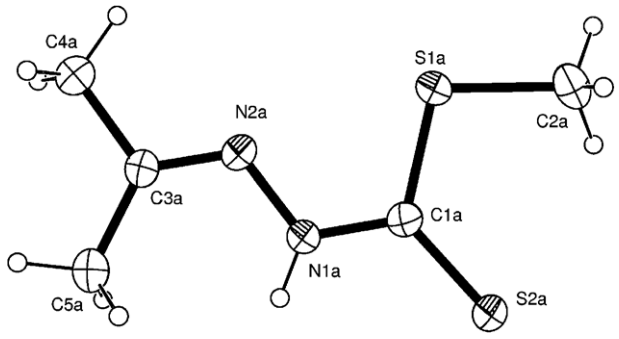


Fig. 4. ORTEP3 view of **1** Hacsme (only one of the four molecules (A) in the asymmetric is shown with 30% probability ellipsoids).

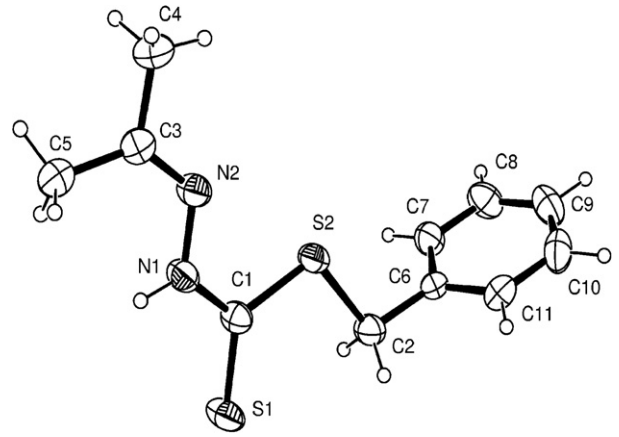


Fig. 5. ORTEP3 view of **2** Hacsbz (30% probability ellipsoids).

Table 5
Selected bond lengths

Bond	1	2	3	4
Sn1–Cl1			2.461(7)	2.465(1)
Sn1–S1			2.431(5)	2.418(1)
Sn1–C6			2.14(2)	2.121(3)
Sn1–C12			2.09(2)	2.122(3)
Sn1–N2			2.35(2)	2.399(3)
C1–S1	1.662(5),1.649(5), 1.663(5),1.652(5)	1.655(4)	1.74(3)	1.752(3)
C1–N1	1.346(6),1.337(6), 1.344(6),1.344(6)	1.332(4) 1.393(4)	1.29(3)	1.272(4)
N1–N2	1.387(5),1.393(5), 1.395(5),1.384(5)	1.393(4)	1.43(3)	1.412(3)

Angles (°)	3	4
C(6)–Sn1– C(12)	129.3(7)	127.1(1)
C(6)–Sn1–N(2)	88.2(7)	88.92(11)
C(12)–Sn1–N(2)	94.2(9)	94.66(11)
C(6)–Sn1–S(1)	115.7(7)	118.29(10)
C(12)–Sn1–S(1)	114.4(4)	113.78(11)
N(2)–Sn1–S(1)	76.8(5)	76.38(7)
C(6)–Sn1–Cl(1)	94.6(6)	94.11(9)
C(12)–Sn1-Cl(1)	96.4(6)	96.02(10)
N(2)–Sn1–Cl(1)	162.3(5)	163.97(7)
S(1)–Sn(1)–Cl(1)	86.2(2)	88.37(4)

cally related molecule in the same manner as molecules A and D in the structure of Hacsme. The crystal structures of the Schiff bases also confirm that both ligands crystallize in their thione tautomeric forms as previously predicted by spectroscopic techniques with the thione sulfur atom *trans* to the azomethine nitrogen atoms. In this conformation these ligands are unable to bind the tin atom as bidentate *NS* chelating ligands but, in solution, a 180° rotation about the C1–N1 bond enables them to act as bidentate chelating agents. The C1–S1 bond lengths (~1.65 Å) indicate that they are essentially double bonds but the length of the C3–N2 bond is intermediate of a single and double bond indicating electron delocalization in the –N–C–S (thioamide) group.

3.3. Crystal structures of the Sn(IV) complexes

The crystal structures of the two Sn complexes are shown in Figs. 6 and 7 and important bond lengths and bond angles are given in Table 5.

The structures show that the tin atom in each compound is five-coordinated with the deprotonated Schiff base chelates the metal ion *via* the azomethine nitrogen atom and the thiolate sulfur atom. The phenyl and chloro ligands occupy the remaining three coordination positions of the coordination polyhedron. The stereochemistry adopted by the metal is intermediate between a trigonal-bipyramid (TBPY) and a square-pyramid (SPY). This may be illustrated by considering distortion from an ideal TBPY geometry. Thus, taking the azomethine nitrogen atom (N2) and the chloro ligand as the axial donor atoms, angles of 163.2(6)° and 163.97(7) are subtended in **3** and **4**, respectively, which are much smaller than the ideal value of 180°. The coordinate angles between the equatorial donors (C6, C12 and S1) also show marked differences from their ideal 120° values. A similar comparison can also be made for an ideal SPY geometry taking S1 as the apical donor and Cl(1), C(6), C(12) and N(2) as donors defining the basal plane.

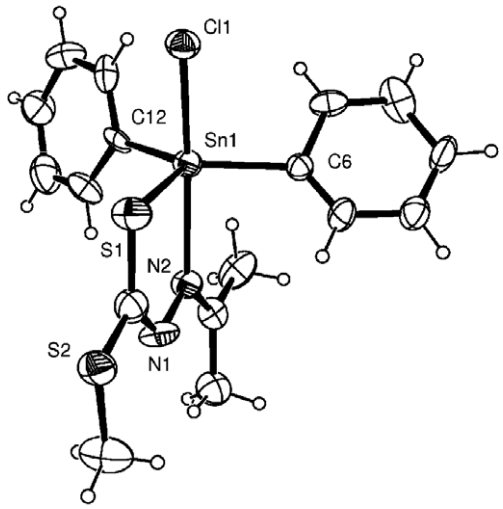


Fig. 6. ORTEP3 view of **3** Sn(acsme)Ph_2Cl (30% probability ellipsoids).

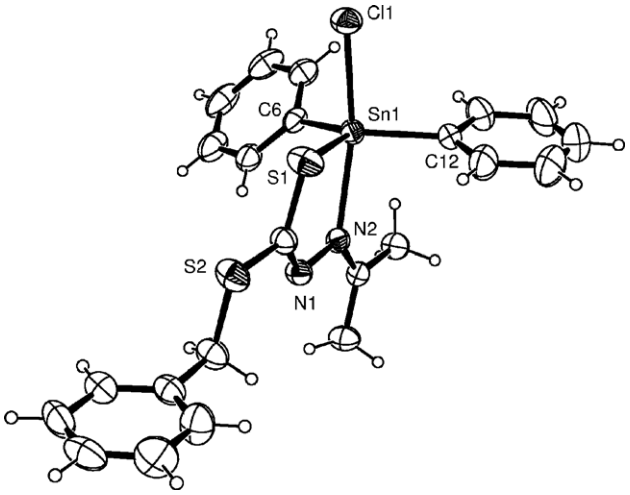


Fig. 7. ORTEP3 view of **4** Sn(acsbz)Ph_2Cl (30% probability ellipsoids).

An angular structural parameter, τ (index of trigonality) has been proposed previously [27] for distinguishing, quantitatively, between a distorted trigonal-bipyramid and a distorted square-pyramid in five-coordinate complexes. The parameter $\tau = \beta - \alpha/60°$ where α and β are the two largest angles; $\tau = 0$ for an ideal SPY geometry (α and $\beta = 180°$) and $\tau = 1$ for an ideal TBPY geometry. Using this criteria the τ values of the present complexes are found to be 0.6 indicating distortion that is somewhere between both extrema, but tending slightly toward TBPY. The largest deviations from ideal geometry are attributable to the restricted bite size of the chelating Schiff base.

The Sn–S distances in both complexes are close to the sum of the covalent radii (2.42 Å) but much shorter than the sum of their van der Waal's radii [4.0 Å] indicating the formation of a genuine Sn–S bond. The Sn–N distances in **3** and **4** are only slightly larger than the sum of the non-polar covalent radius (2.15 Å) again indicating strong Sn–N interactions. A comparison of Sn-donor atom distances in the present diphenyltin(IV) complexes with those of related tin(IV) complexes is presented in Table 6 where the influence of coordination number and ligands is illustrated.

The five-membered chelate ring in **4** adopts an envelope conformation with the atoms C1 and N1 each lying *ca.* 0.3 Å out of the plane defined by Sn1, N2 and S1, while the same chelate ring in **3** is essentially planar within experimental uncertainty. A comparison of the bond distances in the dithiocarbazate chain shows that in both tin complexes the C–S bonds are longer than observed in the respective free ligands but intermediate between those characteristic of single C–S (~1.85 Å) and double bonds (~1.56 Å). Coordination of the ligands to the tin atom in their iminothiolate forms raises the C1–N1 bond order at the expense of the C1–S1 bonds.

Table 6
Comparison of Sn-donor atom distances in some organotin(IV) complexes

	Sn–S	Sn–C	Sn–Cl	Sn–N_{azo}	Ref.
$Sn(actsc)_2Ph_2Cl_2$	2.72	2.142(3)	2.569(1)		[20]
$Sn(acsme)_2Cl_2$	2.457(4)		2.4000(5)	2.313(11)	[29]
$Sn(acsme)Ph_2Cl$	2.431(5)	2.14(2)	2.461(7)	2.35(2)	This work
		2.09(2)			
$Sn(acsbz)Ph_2Cl$	2.418(1)	2.121(3)	2.465(1)	2.399(3)	This work
		2.122(3)			
$[Sn(CH_3)_2(Pytsc)Cl]\cdot 0.5H_2O$	2.478(2)	2.105(7)			[28]
		2.108(7)	2.672(1)	2.359(4)	

3.4. Conclusions

In the solid state, the acetone Schiff bases of *S*-methyl and *S*-benzyldithiocarbazate, like all other Schiff bases derived from *S*-alkyl esters of dithiocarbazic acid, remain in their thione tautomeric forms with the thione sulfur atom *trans* to the azomethine nitrogen atom but in solution they convert to the thiol form accompanied by an inversion of N2 with the concomitant formation of diphenyltin(IV)chloride complexes of the deprotonated Schiff bases. Spectroscopic and X-ray diffraction studies show that the substituents on one of the sulfur atoms of the dithiocarbazate moiety virtually have no effect on the s-electron density at the tin nucleus and on the stereochemistry adopted by the tin complexes.

4. Supplementary material

CCDC 653521, 653522, 653523 and 653524 contain the supplementary crystallographic data for **1**, **2**, **3** and **4**. These data can be obtained free of charge via http://www.ccdc.cam.ac.uk/conts/retrieving.html, or from the Cambridge Crystallographic Data Centre, 12 Union Road, Cambridge CB2 1EZ, UK; fax: (+44) 1223-336-033; or e-mail: deposit@ccdc.cam.ac.uk.

Acknowledgements

M.A.A., A.H.M. and M.H.S.A.H. thank Universiti of Brunei Darussalam for financial support. Thanks are also due to Dk. Misliha Nurhayati Bte Pg. Hj Samsudin and Naziah Bte Sahat for their technical help. O.A., X.S., G.E. and L.M. acknowledge with thanks the financial support for the ^{119}Sn Mössbauer work from the National Institute of Health, Biomedical Research Support Program (MBRS/SCORE, GM08005). P.V.B. acknowledges support from the Australian Research Council and the University of Queensland.

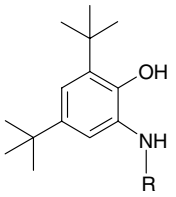
References

[1] D.X. West, S.B. Padhye, P.B. Sonawane, Struct. Bond (Berl.) 76 (1991) 1.
[2] G.F. de Sousa, V.M. Deflon, M.T. do P. Gambardella, R.H.P. Francisco, J.D. Ardisson, E. Niquet, Inorg. Chem. 45 (2006) 4578.
[3] M. Akbar Ali, A.H. Mirza, T.B.S.A. Ravoof, P.V. Bernhardt, Polyhedron 23 (2004) 2031.
[4] M. Akbar Ali, Aminul Huq Mirza, Ray J. Butcher, Karen A. Crouse, Trans. Met. Chem. 31 (2006) 9.
[5] M. Akbar Ali, A.H. Mirza, C.W. Voo, A.L. Tan, P.V. Bernhardt, Polyhedron 22 (2003) 3433.
[6] M. Akbar Ali, A.H. Mirza, M. Nazimuddin, R. Ahmed, L.R. Gahan, P.V. Bernhardt, Polyhedron 22 (2003) 1471.
[7] M. Akbar Ali, A.H. Mirza, See Tho Wai Keng, R.J. Butcher, Trans. Met. Chem. 28 (2003) 241.
[8] (a) M. Akbar Ali, A.H. Mirza, M. Nazimuddin, H. Rahman, R.J. Butcher, Trans. Met. Chem. 27 (2002) 268;
(b) M. Akbar Ali, A.H. Mirza, M. Nazimuddin, P.K. Dhar, R.J. Butcher, Trans. Met. Chem. 27 (2002) 27;
(c) M. Akbar Ali, A.H. Mirza, R.J. Butcher, M.T.H. Tarafder, Manaf A. Ali, Inorg. Chim. Acta 320 (2001) 1.
[9] M. Akbar Ali, S.E. Livingstone, Coord. Chem. Rev. 13 (1974) 101.
[10] T.B.S. Ravoof, K.A. Crouse, M.I.M. Tahir, A.H. Crowley, M.A. Ali, Polyhedron 26 (2007) 1159.
[11] (a) G. Davies, M.A. El-Sayed, A. El-Toukhy, Inorg. Chem. 25 (1986) 2269, and references therein;
(b) S. Al-Sheri, G. Davies, M.A. El-sayed, A. El-Toukhy, Inorg. Chem. 29 (1990) 1198.
[12] K.A. Crouse, Kar-Beng Chew, M.T.H. Tarafder, A. Kasbollah, A.M. Ali, B.M. Yamin, H.-K. Fun, Polyhedron 23 (2004) 161.
[13] M. Das, S.E. Livingstone, Br. J. Cancer 37 (1978) 466.
[14] M. Akbar Ali, A.H. Mirza, R.J. Butcher, M.T.H. Tarafder, Tan Boon Keat, A. Manaf Ali, J. Inorg. Biochem. 92 (2002) 141.
[15] (a) M.T.H. Tarafder, Kar-Beng Chew, K.A. Crouse, A.M. Ali, B.M. Yamin, H.–K. Fun, Polyhedron 21 (2002) 2683;
(b) M.T.H. Tarafder, A. Kasbollah, K.A. Crouse, A.M. Ali, B.M. Yamin, H.-K. Fun, Polyhedron 20 (2001) 2363;
(c) M.E. Hossain, M.N. Alam, J. Begum, M. Akbar Ali, M. Nazimuddin, F.E. Smith, R.C. Hynes, Inorg. Chim. Acta 249 (1996) 207.
[16] M. Akbar Ali, S.E. Livingstone, D.H. Phillips, Inorg. Chim. Acta 5 (1971) 119.
[17] L. Farrugia, J. Appl. Crystallogr. 32 (1999) 837.
[18] G.M. Sheldrick, SHELX86 – Programme for Crystal Structure Solution, Institut für Anorganische Chemie der Universität, Göttingen, Germany, 1986.
[19] G.M. Sheldrick, SHELX86 – Programme for Crystal Structure Solution, Institut für Anorganische Chemie der Universität, Göttingen, Germany, 1998.
[20] Siang-Guan Teoh, Show-Hing Ang, Soon-Beng Teo, Hoong-Kun Fun, Khing-Ling Khew, Chi-Wi Wong, J. Chem. Soc., Dalton Trans. (1997) 465.
[21] S.W. Schneller, Inst. Sulfur Chem. Part B 7 (1972) 295.
[22] J.J. Zuckerman, Adv. Organomet. Chem. 9 (1970) 21.
[23] (a) R.S. Randall, R.W. Wedd, R.J. Sans, J. Organomet. Chem. 30 (1971) 19;
(b) D. Cunningham, M. Little, K. Mcloughlin, J. Organomet. Chem. 165 (1979) 287.

[24] R.H. Herber, A. Stöckler, W.T. Reichle, J. Chem. Phys. 42 (1965) 2447.
[25] R.V. Parish, C.E. Johnson, J. Chem. Soc., Dalton Trans. (1971) 1906.
[26] R.V. Parish, in: G. Long (Ed.), Mössbauer Spectroscopy Applied to Inorganic Chemistry, vol. 1, 1984, p. 542.
[27] A. Addison, T.N. Rao, J. Reedjik, J. Van Rijn, G.C. Serschoor, J. Chem. Soc., Dalton Trans. (1984) 1349.
[28] L. Labib, T.E. Khalil, M.F. Iskander, L.S. Refaat, Polyhedron 15 (1996) 349.
[29] A. Abu-Raqabah, G. Davies, M.A. El-Sayed, A. El-Toukhy, S.N. Shaikh, Z. Zubeita, Inorg. Chim. Acta 193 (1992) 43.

hindered *o*-aminophenols may be assumed to have great potential as ligands in synthesis of new bioactive metal complexes. As for the coordination chemistry of transition metal complexes formed by *O*,*N*-coordinated ligands of this sort, it is quite possible that synthetic difficulties have inhibited the study of metal complexes of sterically hindered *o*-aminophenols, since the attempts to isolate complexes of this type were often unsuccessful and resulted in the ligand being recovered without coordination [21,22]. This has prompted us to investigate the peculiarities of complexation of some di-*tert*-butylated *o*-aminophenolate ligands with transition metal ions [23,24]. Selecting Co(II) and Cu(II) complexes as the main subjects for this study, we had in mind that the antifungal effect of copper(II) and cobalt(II) ions had been known, their complexes still being under study in order to find effective antifungal agents [25–29]. The effect of some transition metal complexes on the structure of fungal and mammalian cell organelles has been studied [25,30–35]. In particular, when administered to some fungal strains, both metal-free 1,10-phenantroline derivatives and the their metal complexes inhibited respiration, reduced the levels of ergosterol in the membrane and altered cytochrome content [25,32–35]. In this connection it may be expected that metal complexes capable of participating in redox processes and of affecting electron-transport cell systems will be promising in the search for antifungal agents. Other papers should be also mentioned, their authors having shown that the bioactivity of metal complexes may be due to their redox effect on electron-transport cell systems, and that a correlation between *in vitro* potency and reduction potential is possible [36,37]. This encouraged us to investigate redox properties of the synthesized *o*-aminophenol derivatives and their Co(II) and Cu(II) complexes by cyclic voltammetry. In so doing we took into account that Co(II) and Cu(II) ions were able to take part in redox processes, thus affecting the properties of the ligands of the phenolic or quinoid types [38]. It was also interesting to find out whether there is any correlation between the antifungal activity of the compounds under study and their redox properties.

Since our earlier work had revealed that Ag(I) and Cu(II) complexation led to an enhancement of the antimicrobial activity of some sterically hindered phenolic derivatives [24,39–41], we were motivated to explore whether there was a similar trend in the case of other transition metal(II) complexes of these organic compounds. We report here the complexation of Co(II) ion with two sterically hindered *o*-aminophenols, namely, 4,6-di(*tert*-butyl)-2-aminophenol (HL^{I}, see the scheme below, R = H) and 2-anilino-4,6-di(*tert*-butyl)phenol (HL^{II}, R = Ph), in order to compare their coordinative behaviour in relation to Co(II) ion with the data obtained previously for their Cu(II) complexes [24] and to assess the influence of complexation on antifungal activities and redox properties of *o*-aminophenols. We have examined the possibility of the formation of *tert*-butyl-substituted *o*-aminophenolates of Cu(II) and Co(II), which may be less toxic than the oxidized (radical) forms of respective ligands [42,43].



HL^{I} – R=H

HL^{II} – R=Ph

2. Experimental

2.1. Materials and methods

Chemicals were purchased from commercial sources and were used without further purification. The two sterically hindered *o*-aminophenols and their Cu(II) complexes were prepared as described elsewhere [24,44,45]. The preparation of Co(II) complexes is described later.

Infrared spectra of solids were recorded with a Spectrum 1000 spectrophotometer in the wavelength range 4000–400 cm^{-1} at room temperature, using nujol mulls of the ligands and their complexes, and polyethylene windows. Thermal analysis was performed with a derivatograph OD-103 MOM. TG/DTA measurements were run in the air between 20 and 450 °C (5 °C min^{-1}). Elemental analyses were carried out according to the standard methods by Microanalytical Laboratory, Bioorganic Chemistry Institute, National Academy of Sciences, Belarus. Metal determination was carried out using an atomic emission spectrometer with an inductively coupled plasma excitation source (Spectroflame Modula). A sample of the Co(II) complex was decomposed on treatment with $HNO_3 + H_2O_2$ using Milestone mls 1200 mega microwave digestion system. After the complex had been decomposed, the content of the metal in the resulting solution was determined. XRD studies were made with an HZG 4 A diffractometer. The UV–Vis absorption spectra were measured in the 220–900 nm range with a Specord M500 spectrophotometer, using acetonitrile solutions of the compounds. Magnetic susceptibility was determined with the use of a Gouy balance at room temperature using $Hg[Co(SCN)_4]$ as a calibrant. ESR spectra of polycrystalline samples were measured with ERS-220 X-band spectrometer (9,45 GHz) at room temperature and at 77 K, using 100-kHz field modulation; *g* factors were quoted relative to the standard marker DPPH ($g = 2.0036$). The molar conductance of 10^{-3} mol L^{-1} solution of the metal(II) complex in acetonitrile was measured at 20 °C using a TESLA BMS91 conductometer (cell constant 1, 0). Electrochemical measurements were performed under dry nitrogen in a three-electrode two-compartment electrochemical cell using a glassy-carbon (GC) working electrode, Pt auxiliary electrode and Ag|AgCl|0.1 mol L^{-1} $(C_2H_5)_4NCl$ reference electrode. The supporting electrolyte was 0.1 mol L^{-1} $(C_2H_5)_4NClO_4$. The Ag|AgCl|0.1 mol L^{-1} $(C_2H_5)_4NCl$ ref-

erence electrode was calibrated with ferricinium|ferrocene redox couple located at $E_{1/2} = +0.52$ V. Acetonitrile was used as a solvent.

2.2. Synthesis of the Co (II) complexes with sterically hindered o-aminophenol derivatives

Based on our previous findings [23], the conditions were created to purposefully provide the preferential formation of the Co(II) complexes, with the composition corresponding to the general formula CoL_2: a solution of Co(II) salt was added in small portions to the ligand solution under continuous stirring, so that the complexation always took place with the excess ligand present. A solution of 0.050 mmol $Co(CH_3COO)_2 \cdot 4H_2O$ in 10 mL of water was added dropwise to a colorless solution of 0.100 mmol of HL^I or HL^{II} dissolved in 10 mL of ethanol (molar ratio Co(II):HL = 1:2). As these ligands can be readily oxidized by oxygen, it is to be taken into account when producing their complexes in order to guard against formation of oxidized ligands (in particular, *o*-iminosemiquinones, as it was shown in some papers [15–21]). To this end, argon was bubbled through the solutions (pH $\leqslant$ 6) during the synthesis. Colored precipitates formed instantaneously. After 1.5–2 h stirring, they were collected on membrane filters (JG 0.2 μm), washed with ethanol and water, and dried *in vacuo* (yield > 70%). It should be specially emphasized that to separate individual $Co(L^I)_2$ complex, the precipitate must be more thoroughly washed with ethanol (5 × 50 mL) in order to eliminate uncoordinated ligand molecules which otherwise could be able to form adducts with the metal complex through hydrogen bonding.

$Co(L^I)_2$ complex. Grey-brown. *Anal.* Calc. for $C_{28}H_{44}N_2O_2Co$: C, 67.29; H, 8.88; N, 5.61; Co, 11.80. Found: C, 67.25; H, 8.83; N, 5.58; Co, 11.75%.

$Co(L^{II})_2$ complex. Blue. *Anal.* Calc. for $C_{40}H_{52}N_2O_2Co$: C, 73.69; H, 8.04; N, 4.30; Co, 9.05. Found: C, 73.61; H, 7.95; N, 4.23; Co, 8.96%.

2.3. Antifungal activities

Antifungal activities of the compounds were tested against the following fungal species (the collection of the Department of Microbiology, The Belarusian State University): *Aspergillus niger*, *Fusarium* spp., *Mucor* spp., *Penicillium lividum*, *Botrytis cinerea*, *Alternaria alternata*, *Sclerotinia sclerotiorum*, *Monilia* spp. Compounds were dissolved in DMSO and diluted in potato dextrose agar medium to yield working solutions of the test compounds with the concentration of 100 μg mL^{-1}. The amount of DMSO in the medium was 1% and did not affect the growth of the tested microorganisms. Antifungal activities of the compounds against moulds and common plant pathogens were checked by the agar plate technique as described elsewhere [41]. The degree of inhibition of radial growth (RI) was calculated as follows [46]: $RI = 100(C - T)/C$ (%), where T is the mean value of the diameter of the fungal colonies in the presence of a given concentration of the compound tested, and C is the mean value of the diameter of the fungal colonies in the absence of the compound, measured under the same conditions.

3. Results and discussion

3.1. Physico-chemical characterization

The stoichiometry of the solid complexes was confirmed by elemental analyses of the isolated chelates. The data show satisfactory agreement with the proposed formulae CoL_2. The complexes demonstrated X-ray patterns of their own, which were significantly different from those of the respective ligands. However, a full structural analysis could not be performed, no crystals suitable for single-crystal X-ray analysis having been obtained, which is not uncommon for compounds with sterically hindered ligands [22]. It is noteworthy that a similar problem when carrying out crystallization of metal complexes of aminophenol derivatives is described in [21,47]. Because of the well-known difficulties in direct X-ray investigations of these complexes, the geometrical arrangement of the ligating atoms in the Co(II) complex has been investigated by several spectroscopic and magnetochemical methods.

Thermal analysis in air flow with identification of the final products by X-ray powder diffraction has shown $Co(L^I)_2$ and $Co(L^{II})_2$ complexes to be anhydrous and unsolvated. No weight loss was observed until decomposition which began about 185 °C (for $Co(L^I)_2$) or 200 °C (for $Co(L^{II})_2$), with exothermic peaks at 190 °C (for $Co(L^I)_2$) or 210 °C (for $Co(L^{II})_2$) without any noticeable weight loss, and at 360 °C (for both complexes), ultimately leaving CoO as the residue. The maximal weight loss (83.72% and 84.1%, respectively, for $Co(L^I)_2$ and $Co(L^{II})_2$) corresponds to the loss of two ligand molecules (Calc. 84.99% and 85.2%, respectively, for $Co(L^I)_2$ and $Co(L^{II})_2$). The agreement between the experimental and theoretical weight losses for the above processes confirms the above-mentioned general formula CoL_2.

The Co(II) complexes are soluble in acetonitrile, acetone, dimethyl formamide, dimethyl sulfoxide, insoluble in nitromethane and ethanol. The conductivity data for the complexes $Co(L^I)_2$ ($\Lambda_{mol} = 11.4\ \Omega^{-1}\ cm^2\ mol^{-1}$) and $Co(L^{II})_2$ ($\Lambda_{mol} = 5.8\ \Omega^{-1}\ cm^2\ mol^{-1}$) indicate their being essentially non-electrolytes in acetonitrile [48], and suggest that the bidentate ligands HL^I and HL^{II} may be coordinated to Co(II) ion as uninegatively charged ligands.

To specify the coordination modes in the Co(II) complexes, we used IR spectroscopy (Table 1).

The IR spectra of the Co(II) complexes as against those of the free ligands are distinguished by the following features: (i) the bands corresponding to ν(OH) vibrations in the free ligands disappear, suggesting the participation of the *o*-OH in complex formation through proton displacement; (ii) the bands at 1230–1140 cm^{-1} assigned to C–I stretching vibrations are shifted towards lower wave num-

Table 1
IR spectral assignments (cm^{-1}) of the ligands and Co(II) complexes

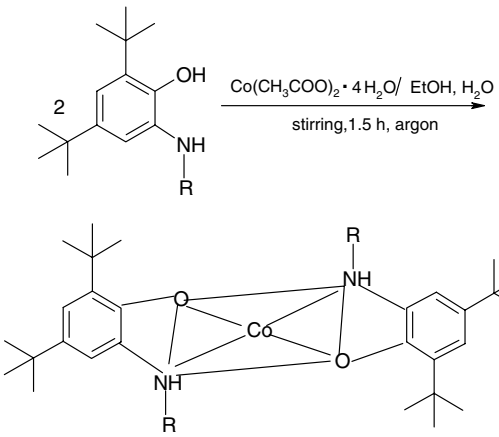
Compound	ν(OH)	ν(C–O)	ν(C–N)	ν(C=C)	ν(N–H)	ν(Co–N)	ν(Co–O)
HL^I	3290m	1235s	1292w	1593m	3366m		
		1204m					
		1142w					
$Co(L^I)_2$		1180s	1300m	1556m	3340w	469w	570w
		1091m				435w	539m
		1044m					514m
		1021m					
HL^{II}	3585m	1202m	1311s	1599s	3352m		
		1150w		1495s			
$Co(L^{II})_2$		1144s	1302m	1537m	3334w	469w	571w
		1106s				424w	545w
		1074w					513m

bers as compared to their positions in the spectra of the ligands; (iii) the positions of the bands assigned to N–H (3352 and 3366 cm^{-1}) and C–N (1292 and 1311 cm^{-1}) stretching vibrations are changed, the presence of the weak bands 3340 and 3334 cm^{-1} in the spectra of the complexes indicating the participation of NH group in coordination without deprotonation; and (iv) bands of moderate intensity appear at 571–424 cm^{-1}, which can be assigned to ν(Co–N) and ν(Co–O). The above-listed facts suggest that NH-groups and deprotonated hydroxyls take part in forming the CoN_2O_2 coordination cores in the Co(II) complexes [49].

The electronic absorption spectra of the free ligands in acetonitrile show characteristic intraligand transition bands at 225 and 280 nm [21,50]. The spectra of the Co(II) complexes in acetonitrile solution exhibit absorption bands in the high-energy region, which can be assigned to intraligand transitions: 230–240 nm ($\log\varepsilon = 4.3$–4.4) and 280–282 nm ($\log\varepsilon = 4.1$–4.2). The bands located in the 305–430 nm region can be attributed to the ligand-to-cobalt(II) charge transfer transitions $N(\sigma) \rightarrow Co^{II}$ and $O_{phenolate} \rightarrow Co^{II}$: respectively, 305 nm ($\log\varepsilon = 4.1$) and 395 ($\log\varepsilon = 3.9$), 430 nm ($\log\varepsilon = 3.7$) [50,51]. The new absorption bands that appeared upwards of 500 nm can be imputed to the d–d transitions of the $Co(L^I)_2$ and $Co(L^{II})_2$ complexes: respectively, 520 nm ($\log\varepsilon = 3.65$) and 640 nm ($\log\varepsilon = 3.69$), characteristic of the low-spin, square planar Co(II) complexes [47,50–58]. This is also corroborated by the effective magnetic moment values: $\mu_{eff} = 2.38$ BM for the $Co(L^I)_2$ complex and $\mu_{eff} = 2.58$ BM $Co(L^{II})_2$ complex, expected for the low-spin square planar geometry around Co(II) ions [47,51–56].

The ESR spectra of Co(II) complexes were obtained in the solid (polycrystalline) state at 77 K and room temperature in order to confirm the geometry of the coordination cores. These spectra are typical axial ones with $g_{\|} = 1.96$ and $g_{\perp} = 2.01$ (for the $Co(L^I)_2$ complex) and $g_{\|} = 1.98$ and $g_{\perp} = 2.07$ (for the $Co(L^{II})_2$ complex), characteristic of low-spin, square-planar Co(II) complexes [47,51,54,55,59–61]. No signal of stabilized radicals present in the ESR spectrum at 77 K, as well as the ν(C=O) and ν(C=N) stretching vibrations lacking in the IR spectrum of Co(II) complex, respectively, in the ranges of 1400–1500 and 1690–1640 cm^{-1}, confirm the phenolate character of the ligand.

In the light of the physico-chemical data and elemental analysis results the mode of bonding in the Co(II) complex can be represented schematically as shown below:



This coordination core agrees with the data obtained by physico-chemical methods for the Cu(II) complex investigated previously [24], where the copper site has the square planar stereochemistry. It should be particularly emphasized that any departure from the specified conditions of the synthesis makes the possibility of separating the individual complex problematic, the free ligands in their oxidized forms being generally obtained in abundance along with it.

3.2. Cyclic voltammetry

Redox properties of the compounds were examined by cyclic voltammetry. Cyclic voltammogram of the ligand HL^I at positive potential shows two anodic peaks at 0.58, 1.72 V, and only one cathodic peak at 0.495 V on the reverse scan (Fig. 1a, solid line). For the ligand HL^{II} a dou-

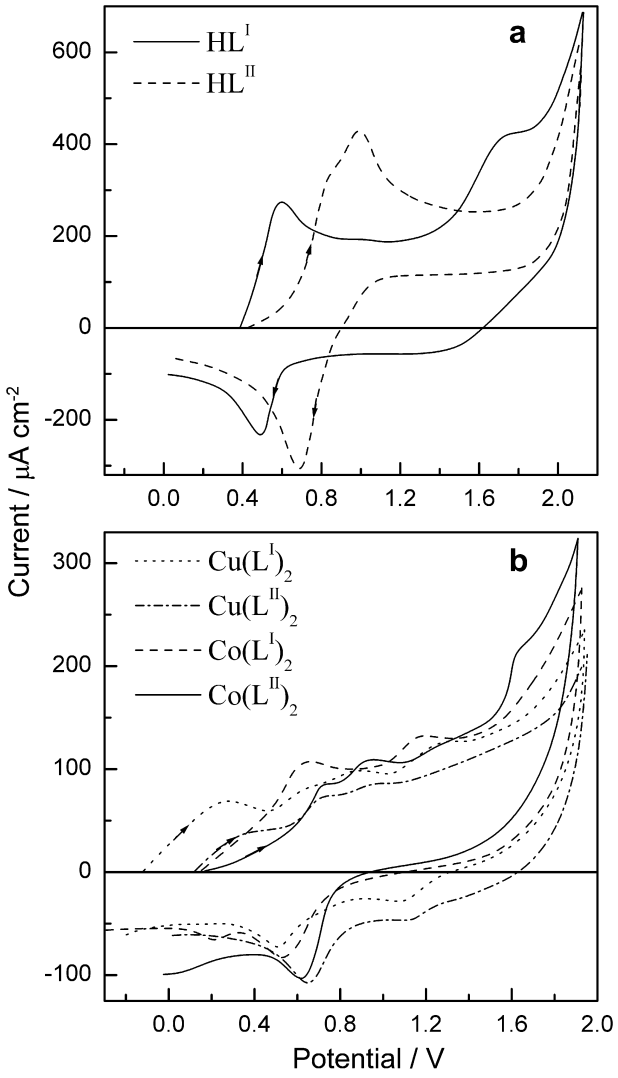


Fig. 1. Cyclic voltammograms (50 mV/s) of the ligands (1.36 mmol L^{-1}) HL^I (solid line), HL^{II} (dashed line) (a) and metal complexes (0.68 mmol L^{-1}) $Cu(L^I)_2$ (dotted line), $Cu(L^{II})_2$ (dashed-dotted line), $Co(L^I)_2$ (dashed line), $Co(L^{II})_2$ (solid line) (b) in 0.1 mol L^{-1} $(C_2H_5)_4NClO_4$ acetonitrile solution on glassy-carbon electrode. (The potentials were measured against Ag|AgCl|0.1 mol dot L^{-1} $(C_2H_5)_4NCl$ reference electrode.)

ble anodic peak is observed at 0.85–0.98 V (is not two overlapping peaks), and a cathodic peak (0.70 V) on the reverse scan (Fig. 1a, dashed line). On cathodic polarization (down to −1.8 V) for HL^I and HL^{II} no peaks are observed. Controlled potential electrolysis carried out for HL^{II} at 1.2 V consumed two electron per molecule. The UV–Vis spectra of the oxidized HL^{II} solution show two broad absorption bands at 400 and 500 nm. These findings agree with the results of electrochemical investigation of HL^{II} compound [16,21], according to which HL^{II} undergoes 2 e-oxidative transformation to give iminobenzoquinone. Controlled potential coulometry for HL^I shows two 1 e-oxidative processes corresponding to anodic peaks at 0.58 and 1.72 V. On the basis of the data on oxidation of *o*-aminophenols [15–19,21] it may be suggested that HL^I is successively oxidized to iminosemiquinone and iminobenzoquinone.

The difficulty of interpreting the electrochemical data for metal complexes of sterically hindered *o*-aminophenol derivatives is caused by the fact that, as noted above, in coordination compounds ligands of this kind can exist in different protonation and redox forms (*o*-aminophenol or *o*-iminosemiquinone). It should be emphasized that the electrochemical properties of the ligands and metal complexes have been studied mainly to compare their reducing power rather than to monitor spectral and structural changes accompanying an electron transfer. The assignment of the redox processes was facilitated by comparison with the literature [16,21,62].

On voltammograms of Cu(II) complexes in the range from −0.1 to +2.1 V anodic peaks are observed: at 0.27, 0.61, 0.89, 1.27 V for $Cu(L^I)_2$ (Fig. 1b, dotted line) and 0.4, 0.7, 0.96 V for $Cu(L^{II})_2$ (Fig. 1b, dashed-dotted line). Cathodic peaks are registered on the reverse scan: at 0.14, 0.51, 1.07 V for $Cu(L^I)_2$ and 0.25, 0.65, 1.12 V for $Cu(L^{II})_2$. Two peaks, at 0.14 and 0.25 V, for Cu(II) complexes are observed in voltammograms on polarization to about 0.6–1.0 V; upon more anodic polarization on the reverse scan they are obscured by the peaks at 0.51 and 0.65 V. On anodic polarization two peaks are observed at 0.65 and 1.19 V for $Co(L^I)_2$ complex, and three peaks are observed at 0.71, 0.94 and 1.63 V for $Co(L^{II})_2$, with cathodic ones on the reverse scan at 0.54, 0.21 V for $Co(L^I)_2$ and 0.62 V for $Co(L^{II})_2$) (Fig. 1b, dashed and solid lines). No prominent cathodic processes are observed on cathodic polarization from the open circuit potential down to −1.8 V.

The cyclic voltammograms of $Cu(L^I)_2$ and $Cu(L^{II})_2$ complexes are more or less similar in their shape, voltammogram of $Cu(L^{II})_2$ being shifted by 0.15–0.20 V into cathodic region because of the influence of phenyl substitute in aminogroup (Fig. 1b). A similar regularity can be observed also for voltammograms of $Co(L^I)_2$ and $Co(L^{II})_2$ complexes. A comparison between cyclic voltammograms of $Cu(L^I)_2$ and $Co(L^I)_2$ complexes shows that common peaks are present at ~0.65 V, and a comparison between voltammograms of $Cu(L^{II})_2$ and $Co(L^{II})_2$ complexes shows that there are common peaks at 0.9 V, corresponding to oxidation of the ligands L^I and L^{II}, as well as cathodic peaks at ~0.5 V (for the complexes of the ligand L^I) and at ~0.65 V (for those of the ligand L^{II}), relating, respectively, to the reduction of the products of L^I and L^{II} oxidation on the reverse scan.

On the basis of the above findings obtained by cyclic voltammetry, and taking into account the data of [62], it may be suggested that Cu(II) and Co(II) ions take part in a sequence of electron transfers; otherwise, whatever the metal (II) ion nature, the redox potentials of the complexes would have differed only slightly in a series of ligands. A comparison between the redox properties of the ligands and those of their metal(II) complexes shows that their reducing ability decreases in the following order: $Cu(L^I)_2 > Cu(L^{II})_2 \geqslant Co(L^I)_2 > Co(L^{II})_2 > HL^I > HL^{II}$ (Fig. 1).

Table 2
Antifungal activities of the compounds tested as evaluated by radial inhibition of mycelial growth (RI, %)

Compound	RI (%)							
	Alternaria alternata	*Sclerotinia sclerotiorum*	*Monilia* spp.	*Aspergillus niger*	*Fusarium* spp.	*Mucor* spp.	*Penicillium lividum*	*Botrytis cinerea*
HL^{I}	60	100	70	55	70	50	40	60
$Cu(L^{I})_2$	100	100	100	65	100	100	80	100
$Co(L^{I})_2$	90	100	55	60	90	80	55	90
HL^{II}	50	90	30	40	60	30	30	50
$Cu(L^{II})_2$	90	100	70	55	90	70	55	100
$Co(L^{II})_2$	90	100	50	50	80	60	50	90
$Cu(CH_3COO)_2$	0	0	0	0	0	0	0	0
$Co(CH_3COO)_2$	0	0	0	0	0	0	0	0
Nistatin	40	50	40	70	90	50	90	60
Terbinafine	50	50	50	100	80	50	60	60
Questiomycin B	40	50	50	30	40	50	40	30

3.3. Antifungal activities

The test microorganisms (the collection of the Department of Microbiology, the Belarusian State University) are listed in Table 1. Inhibition values of the free ligands and their Co(II) and Cu(II) complexes are listed in Table 1. Commonly used antifungal drugs Nystatin, Terbinafine and Questiomycin B were tested as positive controls. The effect of the starting metal(II) acetates is also reported. It should be emphasized that the antifungal tests of these ligands and their Co(II) and Cu(II) complexes were first performed here.

It was found that the inhibitory effects of HL^{I} and HL^{II} ligands and their metal(II) complexes differed with the species of fungi. All of them demonstrate the highest inhibitory properties against *S. sclerotiorum*. A like high activity against *Fusarium* spp., *A. alternata* and *B. cinerea* is characteristic of Co(II) and Cu(II) complexes (Table 1). And it was only $Cu(L^{I})_2$ that showed the highest antifungal activity against *Mucor* spp. and *Monilia* spp. Both the free ligands and Co(II) and Cu(II) complexes exhibit pronounced antifungal activities against some strains, which in a number of cases were comparable with those of Nystatin and Terbinafine or even higher (Table 2).

Antifungal screening *in vitro* indicated that in the cases mentioned above a synergistic effect is present, the antifungal activities of the metal(II) complexes being higher than those of both the ligand and the starting metal salts. This provides reason to believe that antifungal activities of the metal(II) complexes synthesized do not correlate with the toxicity of the metal(II) ions against the fungi tested. It is noteworthy that the two sterically hindered derivatives of *o*-aminophenol synthesized and their metal(II) complexes were more active than Questiomycin B antibiotic tested. In this connection, when estimating the effect of modification of the molecule of *o*-aminophenol by introducing substitutes (two *tert*-butyl ones into the ring and a phenyl one into aminogroup) and complexation with Cu(II) and Co(II) ions on the antifungal activities of the compounds tested, we may suggest that one of the likely reasons for their different activities is related to the nature of the substitute in the ring and to a substitute being present at the nitrogen atom of the amino group. Moreover, the antifungal activities of the complexes exhibit some metal-ion-dependency. By and large the inhibitory effects of the compounds examined decrease in the order: $Cu(L^{I})_2 > Cu(L^{II})_2 \geqslant Co(L^{I})_2 > Co(L^{II})_2 > HL^{I} > HL^{II}$ (Table 1), and their reducing ability declines in the same order, as it was shown above. These data are in accordance with the results of the studies [32–35], where the influence of redox properties of the metal complexes on their antifungal effect was found, and it was shown that this effect appears to be mediated through the disruption of mitochondrial function and uncoupling respiration. These facts may be of interest in designing new antifungal drugs, since this effect is different to the mode of action of the conventional azole and polyene drugs.

Acknowledgement

We are grateful to Dr. R. Zheldakova (The Belarusian State University) for the antifungal testing.

References

[1] K.M. Abu-Salah, Brit. J. Biomed. Sci. 53 (1996) 122.
[2] R.J. Hay, Antimicrob. Chemother. 20 (1987) 1.
[3] N. Singh, Clin. Infect. Dis. 33 (2001) 1692.
[4] K. Asai, N. Tsuchimori, K. Okonogi, J.R. Perfect, O. Gotoh, Y. Yoshida, Antimicrob. Agents Chemother. 43 (1999) 1163.
[5] M. Leeb, Nature 431 (2004) 892.
[6] O.I. Shadyro, G.K. Glushonok, T.G. Glushonok, I.P. Edimecheva, A.G. Moroz, A.A. Sosnovskaya, I.L. Yurkova, G.I. Polozov, Free Radical Res. 36 (2002) 859.
[7] O.I. Shadyro, I.P. Edimecheva, G.K. Glushonok, N.I. Ostrovskaya, G.I. Polozov, H. Murase, T. Kagiya, Free Radical Res. 37 (2003) 1087.
[8] D.K. Petrikevich, V.A. Timoshchuk, O.I. Shadyro, O.T. Andreeva, V.I. Votyakov, V.E. Zhelobkovich, Pharm. Chem. J. 29 (1995) 841.

[9] O.I. Shadyro, V.L. Sorokin, G.A. Ksendzova, S.N. Nikolaeva, N.I. Pavlova, O.V. Savinova, E.I. Boreko, Pharm. Chem. J. 36 (2002) 410.
[10] V.I. Lodyato, I.L. Yurkova, V.L. Sorokin, O.I. Shadyro, V.I. Dolgopalets, M.A. Kisel, Bioorg. Med. Chem. Lett. 13 (2003) 1179.
[11] O.T. Andreeva, L.N. Dunets, P.T. Petrov, O.I. Shadyro, BY Patent 6503 C2, 2004.
[12] O.T. Andreeva, L.N. Dunets, P.T. Petrov, O.I. Shadyro, BY Patent 6594 C2, 2004.
[13] K. Anzai, K. Isono, K. Okuma, S. Suzuki, J. Antibiotics Ser. A 13 (1960) 125.
[14] C.G. Wermuth, The Practice of Medicinal Chemistry, Academic Press, London, 1996.
[15] C.N. Verani, S. Gallert, E. Bill, T. Weyhermuller, K. Wieghardt, P. Chaudhuri, Chem. Commun. (1999) 1747.
[16] P. Chaudhuri, C.N. Verani, E. Bill, E. Bothe, T. Weyhermuller, K. Wieghardt, J. Am. Chem. Soc. 123 (2001) 2213.
[17] H. Chun, C.N. Verani, P. Chaudhuri, E. Bothe, E. Bill, T. Weyhermuller, K. Wieghardt, Inorg. Chem. 40 (2001) 4157.
[18] D. Herebian, P. Ghosh, H. Chun, E. Bothe, T. Weyhermuller, K. Wieghardt, Eur. J. Inorg. Chem. (2002) 1957.
[19] K.S. Min, T. Weyhermuller, K. Wieghardt, Dalton Trans. (2003) 1126.
[20] A.I. Poddel'sky, V.K. Cherkasov, G.K. Fukin, M.P. Bubnov, L.G. Abakumova, G.A. Abakumov, Inorg. Chim. Acta 357 (2004) 3632.
[21] C.N. Verani, Ph.D. Thesis, Ruhr-Universität Bochum, Mülheim an der Ruhr, 2000.
[22] B. Wunderlich, Macromolecular Physics I, Crystal Structure, Morphology, Defects, Academic Press, New York, 1973.
[23] T.V. Koval'chuk, G.A. Ksendzova, Chem. Ser. 5 (2005) 51 (in Russian).
[24] N.V. Loginova, T.V. Koval'chuk, R.A. Zheldakova, N.P. Osipovich, V.L. Sorokin, G.I. Polozov, G.A. Ksendzova, G.K. Glushonok, A.A. Chernyavskaya, O.I. Shadyro, Bioorg. Med. Chem. Lett. 16 (2006) 5403.
[25] B. Coyle, K. Kavanagh, M. McCann, M. Devereux, M. Geraghty, Biometals 16 (2003) 321.
[26] P.R.P. John, A. Sreekanth, V. Rajakannan, T.A. Ajith, M.R. Prathapachandra Kurup, Polyhedron 23 (2004) 2549.
[27] M.C. Rodriguez-Arguelles, E.C. Lopez-Silva, J. Sanmartin, P. Pelagatti, F. Zani, J. Inorg. Biochem. 99 (2005) 2231.
[28] S. Bellu, E.M. Hure, M. Trape, C. Trossero, G. Molina, C. Drogo, P.A.M. Williams, A.M. Atria, .J.C.M. Acevedo, S. Zacchino, M. Sortino, D. Campagnoli, M. Rizzotto, Polyhedron 24 (2005) 501.
[29] R. Del Campo, J.J. Criado, R. Gheorghe, F.J. Gonzalez, M.R. Hermosa, F. Sanz, J.L. Manzano, E. Monte, E. Rodrıguez-Fernandez, J. Inorg. Biochem. 98 (2004) 1307.
[30] M. Geraghty, V. Sheridan, M. McCann, M. Devereux, V. McKee, Polyhedron 18 (1999) 2931.
[31] M. Devereux, M. McCann, D.O. Shea, R. Kelly, D. Egan, C. Deegan, K. Kavanagh, V. McKee, G. Finn, J. Inorg. Biochem. 98 (2004) 1023.
[32] B. Coyle, P. Kinsella, M. McCann, M. Devereux, R.O. Connor, M. Clynes, K. Kavanagh, Toxicol. In Vitro 18 (2004) 63.
[33] A. Eshwika, B. Coyle, M. Devereux, M. McCann, K. Kavanagh, Biometals 17 (2004) 415.
[34] B.S. Creaven, D.A. Egan, D. Karcz, K. Kavanagh, M. McCann, M. Mahon, A. Noble, B. Thati, M. Walsh, J. Inorg. Biochem. 101 (2007) 1108.
[35] M. McCann, B. Coyle, S. McKay, P. McCormack, K. Kavanagh, M. Devereux, V. McKee, P. Kinsella, R. O'Connor, M. Clynes, Biometals 17 (2004) 635.
[36] M.E. Vol'pin, G.N. Novodarova, E.M. Kolosova, N.V. Guzhova, A.A. Kononenko, Yu. N. Lejkin, Inorg. Chim. Acta 50 (1981) 21.
[37] T. Kametani, BR Patent 2002746, 1979.
[38] C.G. Pierpont, Coord. Chem. Rev. 99 (2001) 216.
[39] N.V. Loginova, A.A. Chernyavskaya, G.I. Polozov, T.V. Koval'chuk, E.V. Bondarenko, N.P. Osipovich, A.A. Sheryakov, O.I. Shadyro, Polyhedron 24 (2005) 611.
[40] N.V. Loginova, T.V. Koval'chuk, R.A. Zheldakova, A.A. Chernyavskaya, N.P. Osipovich, G.K. Glushonok, G.I. Polozov, V.L. Sorokin, O.I. Shadyro, Centr. Eur. J. Chem. 4 (2006) 440.
[41] N.V. Loginova, T.V. Koval'chuk, R.A. Zheldakova, A.A. Chernyavskaya, N.P. Osipovich, G.K. Glushonok, G.I. Polozov, V.N. Povalishev, V.L. Sorokin, O.I. Shadyro, Polyhedron 25 (2006) 3603.
[42] N.V.R.R. Urs, J.M. Dunleavy, Phytopathology 65 (1975) 686.
[43] A. Scalbert, Phytochemistry 30 (1991) 3875.
[44] L.A. Maslovskaya, D.K. Petrikevich, V.A. Timoshchuk, O.I. Shadyro, Zhurn. obshchei khimii 66 (1996) 1899 (in Russian).
[45] V.B. Vol'eva, T.I. Prokof'eva, A.I. Prokof'ev, I.S. Belostotskaya, N.L. Komissarova, V.V. Ershov, Izv. AN. Ser. Chim. (1995) 1789 (in Russian).
[46] D.J. Royse, S.M. Ries, Phytopathology 68 (1978) 603.
[47] R.M. Issa, K.Y. El-Baradie, S.A. El-Koni, J. Coord. Chem. 57 (2004) 1611.
[48] W.J. Geary, Coord. Chem. Rev. 7 (1971) 81.
[49] K. Nakamoto (Ed.), Infrared and Raman Spectra of Inorganic and Coordination Compounds. Theory and Applications in Inorganic Chemistry, John Wiley & Sons Inc., New York, 1997.
[50] A.B.P. Lever, E.I. Solomon (Eds.), Inorganic Electronic Structure and Spectroscopy, John Wiley & Sons Inc., New York, 2006.
[51] A. Pui, J.-P. Mahy, Polyhedron 26 (2007) 3143.
[52] B.K. Singh, R.K. Sharma, B.S. Garg, Spectrochim. Acta Part A 63 (2006) 96.
[53] H. Nishikawa, S. Yamada, Bull. Chem. Soc. Jpn. 37 (1964) 8.
[54] Y. Nishida, S. Kida, Bull. Chem. Soc. Jpn. 45 (1972) 461.
[55] F.L. Urbach, R.D. Bereman, J.A. Topich, M. Hariharan, B.J. Kalbacher, J. Am. Chem. Soc. 96 (1974) 5063.
[56] M.J. Carter, D.P. Rillema, F. Basolo, J. Am. Chem. Soc. 96 (1974) 392.
[57] Y. Nishida, K. Hayashida, N. Oishi, S. Kida, Inorg. Chim. Acta 38 (1980) 213.
[58] E.D. McKenzie, R.D. Moore, J.M. Worthington, Inorg. Chim. Acta 14 (1975) 37.
[59] S.M. Abu-El-Wafa, M.A. El-Ries, F.H. Ahmed, Inorg. Chim. Acta 136 (1987) 127.
[60] M. Atanasov, E.J. Baerends, P. Baettig, R. Bruyndonckx, C. Daul, C. Rauzy, M. Zbiri, Chem. Phys. Lett. 399 (2004) 433.
[61] K. Matsumoto, N. Sekine, K. Arimura, M. Ohba, H. Sakiyama, H. Okawa, Bull. Chem. Soc. Jpn. 77 (2004) 1343.
[62] N.T. Berberova, I.V. Smolyaninov, A.O. Ohlobystin, N.N. Letichevskaya, E.V. Shinkar, Ros. him. zh. (Zh. Ros. him. ob-va im. D.I. Mendeleeva) 49 (2004) 67 (in Russian).

In this paper we report upon the first example of an 'empty' dithiophosph(in)ate Cu^{I}_{8} cube, thus showing that so-called templating anions are not prerequisite for Cu^{I}_{8} cube formation with dithio-phosphorus ligands. In addition, the analogous dithiophosphinate Cu^{I}_{8} cube with an encapsulated chloride anion is reported, hence allowing for the first time a direct structural and bonding comparison between a dicationic vacant cube, a mono-cationic chloride centered cube and a neutral sulfide centered cube all with the same ligand system.

2. Experimental

2.1. General procedure

All reactions and manipulations were carried out under an inert atmosphere of dry nitrogen or argon using standard double manifold and glove-box techniques. Purification and drying of the solvents were done using standard methods. Ph_2PH was purchased from Strem and all other chemicals from Sigma–Aldrich. $[Cu(CH_3CN)_4][PF_6]$ was prepared according to known literature procedures [9]. NMR spectra were recorded on a Bruker AV-400 spectrometer. External standards used were TMS (^{1}H) or 85% H_3PO_4 (^{31}P). Mass spectra were recorded on Micromass AutoSpec Premier. Microanalytical data were obtained from the Science Technical Support Unit, London Metropolitan University.

2.2. Preparation of $[Cu_8(S_2PPh_2)_6][PF_6]_2 \cdot 5CH_2Cl_2$ (1)

A solution of Ph_2PH (0.35 mL, 2 mmol) and NEt_3 (0.28 mL, 2 mmol) in CH_3CN (5 mL) was added to a suspension of yellow S_8 (0.128 g, 4 mmol) in CH_3CN (10 mL) and stirred to give a clear solution. $[Cu(CH_3CN)_4][PF_6]$ (0.746 g, 2 mmol) in CH_3CN (10 mL) was then added to yield a yellow precipitate. Ten mL of deoxygenated water were added, the precipitate filtered off and washed with copious amounts of deoxygenated water to give the product **1** in 44% yield (1.01 g). Colorless crystals of $[Cu_8(S_2PPh_2)_6][PF_6]_2 \cdot 5CH_2Cl_2$ suitable for analysis using single crystal X-ray diffraction were obtained by slow diffusion of hexane into a CH_2Cl_2 solution of **1**. M.p. 211–214 °C. *Anal.* Calc. for $C_{72}H_{60}Cu_8P_6S_{12} \cdot 2PF_6$: C, 37.77; H, 2.64. Found: C, 37.83; H, 2.60%. FAB MS [m/z (m/z_{calc})]: 2148.8 (2149.2), $(M-PF_6)^+$; 2003.2 (2004.2), $(M-2PF_6)^+$. ^{1}H NMR (270 MHz, $CDCl_3$): $\delta = 7.3$–7.9 (m, 60H, Ph_2P–). $^{31}P\{^1H\}$ NMR (109 MHz, $CDCl_3$) 59.28 (s), −143.91 (sept, $^1J_{PF} = 763$ Hz, PF_6).

2.3. Preparation of $[Cu_8(\mu_8\text{-}Cl)(S_2PPh_2)_6][PF_6] \cdot 6CH_2Cl_2$ (2)

A solution of Ph_2PH (0.35 mL, 2 mmol) and NEt_3 (0.28 mL, 2 mmol) in CH_3CN (5 mL) was added to a suspension of yellow S_8 (0.128 g, 4 mmol) in CH_3CN (10 mL) and stirred to give a clear solution. $[Cu(CH_3CN)_4][PF_6]$ (0.746 g, 2 mmol) in CH_3CN (10 mL) was then added to yield a yellow precipitate. Ten mL of deoxygenated water were added, the precipitate filtered off and washed with copious amounts of deoxygenated water. The resulting solid was refluxed in CH_2Cl_2 for 30 min to give a pale yellow solution. Slow evaporation of the CH_2Cl_2 solvent from this solution over a period of 8 weeks gave a low yield (0.09 g, 17%) of colorless crystals of $[Cu_8(\mu_8\text{-}Cl)(S_2PPh_2)_6][PF_6] \cdot 6CH_2Cl_2$ (**2**) suitable for analysis using single crystal X-ray diffraction. M.p. 203–206 °C. *Anal.* Calc. for $C_{72}H_{60}Cu_8P_6S_{12}ClPF_6 \cdot 2CH_2Cl_2$: C, 37.86; H, 2.75. Found: C, 37.83; H, 2.60%. ^{1}H NMR (270 MHz, d_6-DMSO): $\delta = 7.5$–7.9 (m, 60H, Ph_2P–). $^{31}P\{^1H\}$ NMR (109 MHz, d_6-DMSO) 58.68 (s, Ph_2P–), −143.56 (sept, $^1J_{PF} = 763$ Hz, PF_6).

2.4. X-ray diffraction studies

Table 1 provides a summary of the crystallographic data for compounds **1** and **2**. Data were collected using a Bruker P4 diffractometer using Mo Kα radiation ($\lambda = 0.71073$ Å), and the structures were refined based on F^2 using the SHELXTL and SHELX-97 program systems [10,11]. All atoms were refined with anisotropic displacement parameters unless stated below and hydrogen atoms were placed in idealized positions and allowed to ride on the relevant carbon atom.

In the structure of **1** the C(31) phenyl ring of the dicationic cluster was found to be disordered. Two orientations were identified of ca. 60% and 40% occupancy, and refined as optimized rigid bodies with only the non-hydrogen atoms of the major occupancy orientation being refined anisotropically. The unique PF_6 anion was found to be disordered and

Table 1
Summary of crystal structure data for **1** and **2**

Data	1	2
Formula	$[C_{72}H_{60}Cu_8P_6S_{12}][PF_6]_2 \cdot 5CH_2Cl_2$	$[C_{72}H_{60}Cu_8P_6S_{12}Cl][PF_6] \cdot 6CH_2Cl_2$
Formula weight	2718.63	2694.04
Crystal size (mm)	0.67 × 0.33 × 0.23	0.67 × 0.53 × 0.47
Temperature (K)	203	203
Crystal system	Monoclinic	Rhombohedral
Space group	$C2/c$ (no. 15)	$R\bar{3}$ (no. 148)
a (Å)	22.187(5)	22.359(5)
b (Å)	20.162(2)	
c (Å)	23.511(3)	
β (°)	102.561(18)	
V (Å^3)	10266(3)	7567.8(15)
Z	4 (C_i symmetry)	3 ($\bar{3}$ symmetry)
D_{calc} (g cm^{-3})	1.759	1.773
Radiation used	Mo Kα	Mo Kα
μ (mm^{-1})	2.316	2.409
2θ max (°)	47	50
Reflections collected, unique	7803, 7580	3120, 2903
R_{int}	0.0417	0.0286
Reflections observed, $\lvert F_o\rvert > 4\sigma(\lvert F_o\rvert)$	5161	2213
Number of parameters	603	232
R_1, wR_2 ($I > 2\sigma I$)[a]	0.0590, 0.1241	0.0369, 0.0742
Residuals (e Å^{-3})	0.776, −0.690	0.388, −0.326

[a] $R_1 = \sum\lvert\lvert F_o\rvert - \lvert F_c\rvert\rvert / \sum\lvert F_o\rvert$; $wR_2 = \{\sum[w(F_o^2 - F_c^2)^2] / \sum[w(F_o^2)^2]\}^{1/2}$; $w^{-1} = \sigma^2(F_o^2) + (aP)^2 + bP$.

two orientations sharing a common phosphorus site were identified of ca. 66% and 34% occupancy. The phosphorus, and the fluorine atoms of the major occupancy orientation, were refined anisotropically, the fluorine atoms of the minor occupancy orientation being refined isotropically. The five included dichloromethane solvent molecules per complex (i.e. 2.5 in the asymmetric unit) were located across three separate sites. At one site the molecule was found to be ordered and so the non-hydrogen atoms were refined anisotropically. At the second site three orientations were identified of ca. 65%, 22% and 13% occupancy; only the chlorine atoms of the two highest occupancy orientations were refined anisotropically, all the other atoms being refined isotropically. At the third site, which is adjacent to a 2-fold axis and so has a maximum occupancy of 50%, two orientations were identified of ca. 29% and 21% occupancy; the chlorine atoms of both orientations were refined anisotropically whilst the carbon atoms were refined isotropically.

In the structure of **2** the C(1) phenyl ring of the cationic cluster was found to be disordered. Two orientations were identified of ca. 81% and 19% occupancy, and refined as optimized rigid bodies with only the non-hydrogen atoms of the major occupancy orientation being refined anisotropically. The unique PF_6 anion, which sits at a $\bar{3}$ position, was found to be disordered and two complete orientations sharing a common phosphorus site (at the $\bar{3}$ position) were identified of ca. 11% and 5% occupancy (totalling the 1/6 occupancy required by the $\bar{3}$ symmetry). The phosphorus atom was refined anisotropically, and all of the fluorine atoms were refined isotropically. Just one unique site was found for the included dichloromethane solvent molecule, and this site was found to be disordered; two orientations were identified of ca. 86% and 14% occupancy with the non-hydrogen atoms of the major occupancy orientation being refined anisotropically, and those of the minor occupancy orientation being refined isotropically.

2.5. Computational details

All calculations were carried out with a GAUSSIAN 03 package [12]. The density functional theory method was employed using the B3LYP hybrid functional [13]. Structures were optimized using a effective core potential with a LanL2DZ basis set for copper and 6-31G(d) for the other atoms. Natural charges were calculated by natural population analysis at the same level used for geometry optimization [14]. Frequency analysis was carried out after geometry optimization to confirm the models were true energy minima with no imaginary frequencies.

3. Results and discussion

3.1. Synthesis and X-ray structure of $[Cu_8(S_2PPh_2)_6][PF_6]_2 \cdot 5CH_2Cl_2$ (1)

In accordance with our recent studies on reactions of elemental chalcogens with phosphines [15–17], reaction of Ph_2PH with 2/8 S_8 in the presence of NEt_3 gave the dithiophosphinate salt $[Ph_2PS_2][HNEt_3]$ in quantitative yields ($^{31}P\{^1H\}$ NMR, d_6-DMSO: $\delta = 60.9$ ppm). Reaction of $[Ph_2PS_2][HNEt_3]$ with $[Cu^I(CH_3CN)_4][PF_6]$ in situ, followed by thorough washing with deoxygenated water to remove the $[PF_6][HNEt_3]$ by-product, and recrystallization from CH_2Cl_2/hexane yielded crystals of the 'empty' cubic cluster $[Cu_8(S_2PPh_2)_6][PF_6]_2 \cdot 5CH_2Cl_2$ (**1**).

Single-crystal X-ray diffraction studies on **1** reveal the octanuclear dication (Fig. 1) to sit on an inversion center and exhibit no significant interactions with either $[PF_6]^-$ or CH_2Cl_2 molecules within the lattice. Each of the faces of the Cu_8 cube in **1** is capped by a μ_4-dithiophosphinate ligand, with Cu–S distances in the range 2.228(2)–2.245(2) Å. The Cu···Cu distances along the edges of the cube are in the range 3.1275(16)–3.2861(14) Å and Cu···Cu···Cu angles lie between 87.82(4)° and 92.97(4)°. Selected unique bond lengths and angles for **1** are given in Table 2.

3.2. Synthesis and X-ray structure of $[Cu_8(\mu_8\text{-}Cl)(S_2PPh_2)_6][PF_6] \cdot 6CH_2Cl_2$ (2)

The analogous mono-cationic chloride centered cluster, $[Cu_8(\mu_8\text{-}Cl)(S_2PPh_2)_6][PF_6] \cdot 6CH_2Cl_2$ (**2**), was also prepared from the reaction of $[Ph_2PS_2][HNEt_3]$ with $[Cu^I(CH_3CN)_4][PF_6]$, but in this case the H_2O-washed product was refluxed in CH_2Cl_2 for 30 min to give a clear solution from which colorless crystals of **2** were grown. These crystals slowly turned blue when exposed to atmospheric oxygen over a period of weeks, presumably due

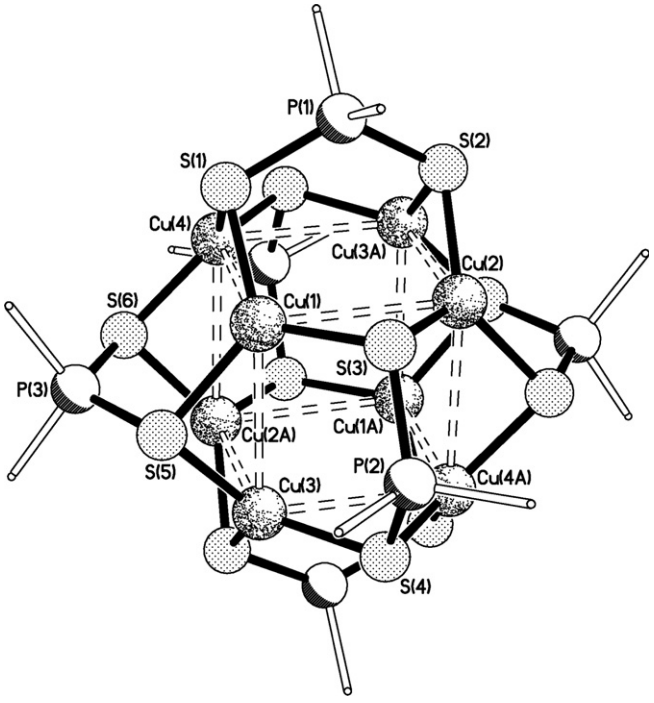


Fig. 1. Molecular structure of the the C_i-symmetric copper(I) cluster dication present in the crystals of **1**. Only the α-carbons of the phenyl rings are shown for clarity.

Table 2
Selected unique bond distances (Å) and angles (°) for **1** and **2**

Complex ***1***			
Cu(1)···Cu(2)	3.1876(16)	Cu(1)···Cu(3)	3.2208(14)
Cu(1)···Cu(4)	3.1596(13)	Cu(2)···Cu(3A)	3.2012(14)
Cu(2)···Cu(4A)	3.2861(14)	Cu(3)···Cu(4A)	3.1275(16)
Cu(2)···Cu(1)···Cu(3)	90.35(4)	Cu(2)···Cu(1)···Cu(4)	87.82(4)
Cu(3)···Cu(1)···Cu(4)	92.59(4)	Cu(1)···Cu(2)···Cu(3A)	91.06(4)
Cu(1)···Cu(2)···Cu(4A)	88.59(4)	Cu(3A)···Cu(2)···Cu(4A)	90.63(4)
Cu(1)···Cu(3)···Cu(2A)	88.59(4)	Cu(1)···Cu(3)···Cu(4A)	90.82(4)
Cu(2A)···Cu(3)···Cu(4A)	88.13(4)	Cu(1)···Cu(4)···Cu(2A)	88.16(4)
Cu(1)···Cu(4)···Cu(3A)	92.97(4)	Cu(2A)···Cu(4)···Cu(3A)	90.23(4)
Complex ***2***			
Cu(1)···Cu(2)	3.0802(7)	Cu(2)···Cu(2C)	3.0770(7)
Cu(1)–Cl	2.6804(9)	Cu(2)–Cl	2.6613(5)
Cu(2)···Cu(1)···Cu(2B)	89.66(2)	Cu(1)···Cu(2)···Cu(2C)	90.279(14)
Cu(2C)···Cu(2)···Cu(2E)	89.78(2)	Cu(1)–Cl–Cu(2)	70.426(11)
Cu(2)–Cl–Cu(2C)	70.632(11)		

to oxidation of one or more of the Cu^{I} centers to Cu^{II}. The source of the chloride anion in **2** is thought to be the dichloromethane solvent: similar chloride abstraction from CH_2Cl_2 has been reported for copper(I) alkoxides [18] and dithiophosphates [19], and CH_2 abstraction from CH_2Cl_2 by copper(I) chalcogenophosphinites is also known [20].

The single-crystal X-ray structure of **2** (Fig. 2) shows the cubic cluster to have $\bar{3}$ symmetry, so only one sixth of the cluster is crystallographically unique. As with **1** no significant intermolecular interactions were observed between the copper cluster and the $[PF_6]^-$ or CH_2Cl_2 molecules. Discounting the central anion, the cubic cluster in **2** is topologically equivalent to that in **1** with Cu–S bonds in the range 2.2800(8)–2.2980(10) Å, Cu···Cu distances in the range 3.0770(7)–3.0802(7) Å and Cu···Cu···Cu angles between 89.66(2)° and 90.279(14)°.

The chloride anion resides almost exactly in the middle of the Cu_8 cube, formally coordinating to all eight metal centers with Cu–Cl distances of 2.6804(9) and 2.6613(5) Å. The Cu–Cl–Cu angles lie in the range 70.44(11)–70.63(11)° which is comparable to the value expected (70.53°) for a perfectly centered cube or the anion site in an anti-fluorite lattice. Selected unique bond lengths and angles for **2** are given in Table 2.

Although this is the first example of a halide-centered copper(I) dithiophosphinate cluster, the related copper(I) dithiophosphate clusters $[Cu_8(\mu_8\text{-}Cl)\{S_2P(OR)_2\}_6][PF_6]$ (R = Me [4], *i*Pr [21]) are known, having been prepared using either $[Bu_4N]Cl$ or $[BzEt_3N]Cl$, respectively, as the chloride anion source. The Cu···Cu distances in these dithiophosphate clusters (mean 3.097 and 3.113 Å, respectively) are comparable to those observed in **2**.

3.3. Comparison of the solid-structures $[Cu_8(\mu_8\text{-}X)(S_2PPh)_6]^{z+}$ (X, z = nothing, 2; Cl, 1; S, 0)

Attempts to prepare the neutral sulfide centered cube $[Cu_8(\mu_8\text{-}S)(S_2PPh_2)_6]$ (**3**) from the reaction of $[Ph_2PS_2][HNEt_3]$ with $[Cu^{I}(CH_3CN)_4][PF_6]$ in the presence of S_8 or Na_2S proved unsuccessful. However, **3** has previously been reported from the reaction of $Ph_2P(S)(SSiMe_3)_2$ with CuO*t*Bu [5]. The key bond lengths for clusters **1**–**3**, as determined from the X-ray diffraction data, is given in Table 3.

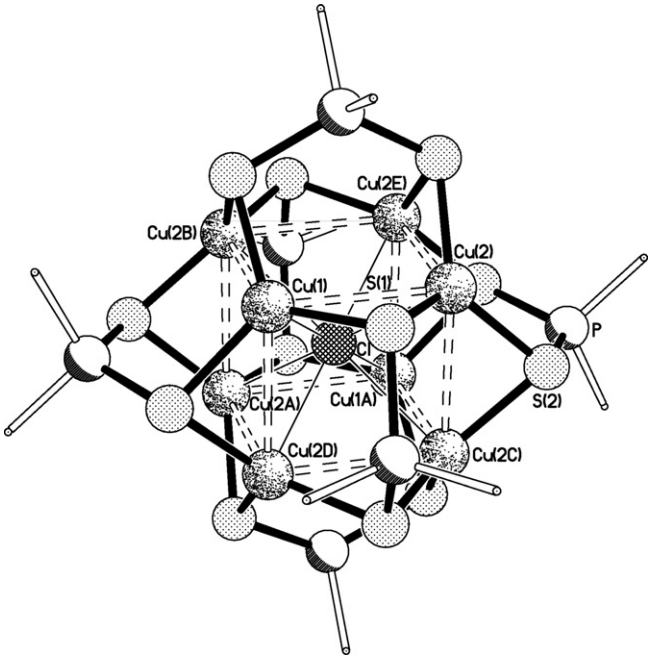


Fig. 2. The molecular structure of the $\bar{3}$-symmetric copper(I) cluster dication present in the crystals of **2** showing the encapsulation of the chloride anion. Only the α-carbons of the phenyl rings are shown for clarity.

The Cu···Cu distances within these clusters increase significantly on going from the sulfide-centered to the chloride-centered to the empty cube. This is also accompanied by a slight decrease in the Cu–S(ligand) distances. Although the large increase in the Cu_8^{I} cube

Table 3
Selected average (mean) bond lengths for the cubic clusters **1**–**3** $[Cu_8(\mu_8\text{-}X)(S_2PPh)_6]^{z+}$

	X	z	Mean bond distance (Å)			Ref.
			Cu···Cu	Cu–S	Cu–X	
1		2	3.197	2.237		
2	Cl	1	3.079	2.289	2.671	
3	S	0	2.824	2.310	2.419	[5]

dimensions for the empty cluster is perhaps at first glance surprising, given that there are no additional steric requirements to fit an anion inside the cube, it can be rationalized by study of the bonding model [22–24]. Each of the copper(I) atoms within the cubic cluster is coordinated in a trigonal planar geometry by three ligand sulfur atoms to give a 16-electron metal center and an overall metal valence electron (MVE) count of 128. This leaves one orbital on each copper not involved in cluster formation – a diffuse $4p_z$ atomic orbital which points towards the center of the cube. Linear combinations of these eight p_z atomic orbitals give a set of $a_{1g} + t_{1u} + t_{2g} + a_{2u}$ orbitals. In the case of the vacant dicationic cube **1** it is expected that these orbitals are empty and lie above the effectively non-bonding Cu···Cu d-orbital overlaps [24].

In the anion centered cubes, the a_{1g} and t_{1u} $Cu(p_z)$ orbital sets overlap with the $3s(a_g)$ and $3p(t_u)$ atomic orbitals of the chloride or sulfide anion to give a 136 MVE cluster with a theoretical $Cu–Cl^-/S^{2-}$ bond order of 0.5 [22,24]. Moreover, the ionic interaction between the negative encapsulated anion and the positive copper cations plays a major role in the overall bonding, and it is this strong ionic interaction that can be used to explain the observed contraction in Cu_8 cube size when the central anion is introduced (**1**–**2**) or when its negative charge is increased (**2**–**3**). It is also likely that the encapsulated anion is responsible for the lengthening of the Cu–S(ligand) distance as a result of its repulsive interaction with the negatively charged dithiophosphinate ligands [24].

3.4. DFT calculations

Theoretical calculations have been carried out by us on the model system $[Cu_8(S_2PMe)_6]^{2+}$ at the B3LYP level of density functional theory to further evaluate the cluster bonding model described above. These calculations reveal the LUMO to contain a strong contribution from the a_{1g} set of $Cu(4p_z)$ orbitals as expected (see Fig. 3). In addition, a small amount of second order mixing between the a_{1g} set and the $Cu(3d_{z^2})$ orbitals is present, which is anticipated to lead to weak net Cu···Cu bonding interactions [24]. This is further backed-up by calculation of the Wiberg bond indexes, which show a small but positive value of 0.027 for the Cu···Cu interaction. However, these Cu···Cu interactions appear too weak to have any significant stabilizing effect on the complex, instead the stability of the dicationic metal cube in the absence of a central 'templating' anion must be attributed almost exclusively to the strength of the metal to dithiophosphinate ligand covalent and ionic interactions.

A comparison of the bonding within dithiophosphinate and dithiophosphate Cu_8 clusters was also undertaken using the optimized model clusters $[Cu_8(\mu_8\text{-}X)(S_2PR_2)_6]^{z+}$ [R = Me, OMe; X(z) = nothing(2), Cl(1), S(0)] – see Table 4. These calculations accurately predict the contraction of Cu···Cu distance and increase in Cu···S(ligand) distance across the series, although all bond lengths are overestimated by approximately 3% when compared to the low-temperature solid-state structural data for the diphenyldithiophosphinate complexes **1**–**3**. Bonding energies were calculated as the difference between the energy of the optimized filled cluster and the sum of the energies of

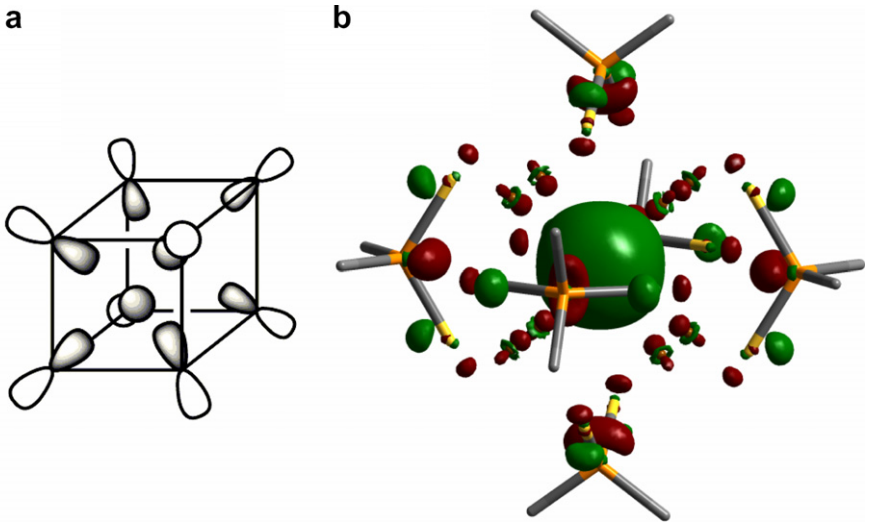


Fig. 3. (a) Schematic diagram of the a_{1g} set of metal orbitals derived from the linear combination of eight $Cu(p_z)$ AOs; (b) calculated surface diagram for the LUMO of $[Cu_8(S_2PMe)_6]^{2+}$.

Table 4
Selected computed data on optimized $[Cu_8(\mu_8\text{-}X)(S_2PR_2)_6]^{z+}$ clusters

R	X	z	Bond distances (Å)			Natural charge			Bonding energy (eV)[a]
			Cu···Cu	Cu···S	Cu···X	Cu	S	X	
Me	S	0	2.92	2.45	2.53	0.74	−0.75	−1.60	−19.95
Me	Cl	1	3.20	2.38	2.78	0.74	−0.76	−0.81	−7.05
Me		2	3.32	2.35		0.72	−0.76		
OMe	S	0	2.91	2.45	2.51	0.74	−0.71	−1.61	−20.08
OMe	Cl	1	3.20	2.38	2.76	0.73	−0.73	−0.81	−7.04
OMe		2	3.33	2.34		0.71	−0.74		

[a] Bonding energy between $X^{-/2-}$ anion and the $[Cu_8(S_2PR_2)]^{2+}$ empty cage.

Cl^-/S^{2-} and the optimized empty cluster. For all the computed complexes this bonding energy is highly negative, indicating a strong thermodynamic preference for anion encapsulation.

As expected these calculations show dithiophosphinate to be more electron rich than dithiophosphate, with a commensurate increased negative natural charge on the ligand sulfur atoms. Although this gives rise to a somewhat larger positive natural charge on the copper centers, overall there is very little difference between the computed bond lengths or bonding energies of the two cluster types. This suggests that empty dicationic clusters with dithiophosphate ligands should also be accessible. The poor solubility of **1** in most solvents is a potential hindrance to its future applications, and hence attempts to prepare the analogous dithiophosphate Cu^I cluster (with a predicted increased solubility) are currently underway. We are particularly interested in the use of these 'empty' Cu^I_8 clusters as coupling catalysts in organic synthesis, where their dipositive charge, and hence increased electrophilicity, could be expected to yield improvements in reactivity over the previously studied mono-cationic halide-centered Cu^I clusters [4].

4. Conclusions

In summary, we have prepared and crystallographically characterized the first example of an 'empty' Cu^I_8 cationic cage with dithio-phosphorus ligands, hence showing that anion templates are not required for the formation of these species. Theoretical calculations show that the stability of this cluster can be attributed to the strong metal–ligand interactions, with no significant contribution from any Cu···Cu bonding interactions. Comparison of the solid-state structures of the empty Cu^I_8 cluster (**1**) with the analogous chloride and sulfide centered clusters (**2** and **3**, respectively) reveals a considerable contraction of the octanuclear cube both on anion encapsulation and when going from a mono- to di-anion. DFT calculations show that this contraction is predominately due to the ionic interactions between the Cu^I cations and the encapsulated anion. Further DFT calculations indicate that similar dicationic empty Cu^I_8 clusters with dithiophosphate ligands should also be accessible, and attempts to prepare these are underway.

Acknowledgement

This work was supported by the EPSRC (Grant EP/E021077/1).

Appendix A. Supplementary material

CCDC 666919 and 666920 contain the supplementary crystallographic data for **1** and **2**. These data can be obtained free of charge via http://www.ccdc.cam.ac.uk/conts/retrieving.html, or from the Cambridge Crystallographic Data Centre, 12 Union Road, Cambridge CB2 1EZ, UK; fax: (+44) 1223-336-033; or e-mail: deposit@ccdc.cam.ac.uk. Supplementary data associated with this article can be found, in the online version, at doi:10.1016/j.poly.2007.11.037.

References

[1] R.P. Davies, in: F.A. Devillanova (Ed.), Handbook of Chalcogen Chemistry: New Perspectives in Sulfur, Selenium and Tellurium, Royal Society of Chemistry, Cambridge, 2007, pp. 286–343.
[2] T.S. Lobana, J.C. Wang, C.W. Liu, Coord. Chem. Rev. 251 (2007) 91.
[3] For recent examples see (a) Y.B. Chen, Z.J. Li, Y.Y. Qin, Y. Kang, J.K. Cheng, R.F. Hu, Y.H. Wen, Y.G. Yao, Inorg. Chem. Commun. 6 (2003) 405;
(b) C.W. Liu, C.M. Hung, B.K. Santra, H.C. Chen, H.H. Hsueh, J.C. Wang, Inorg. Chem. 42 (2003) 3216;
(c) C.W. Liu, C.M. Hung, H.C. Haia, B.J. Liaw, L.S. Liou, Y.F. Tsai, J.C. Wang, Chem. Commun. (2003) 976;
(d) C.W. Liu, H.C. Haia, C.M. Hung, B.K. Santra, B.J. Liaw, Z.Y. Lin, J.C. Wang, Inorg. Chem. 43 (2004) 4464;
(e) C.W. Liu, Phosphorus, Sulfur Silicon Relat. Elem. 180 (2005) 923.
[4] G.F. Manbeck, A.J. Lipman, R.A. Stockland, A.L. Freidl, A.F. Hasler, J.J. Stone, I.A. Guzei, J. Org. Chem. 70 (2005) 244.
[5] D. Fenske, A. Rothenberger, M.S. Fallah, Z. Anorg. Allg. Chem. 630 (2004) 943.
[6] D. Rusanova, K.J. Pike, I. Persson, J.V. Hanna, R. Dupree, W. Forsling, O.N. Antzutkin, Chem. Eur. J. 12 (2006) 5282.
[7] For example see (a) C.W. Liu, R.J. Staples, J.P. Fackler, Coord. Chem. Rev. 174 (1998) 147;
(b) S.A. Baudron, M.W. Hosseini, N. Kyritsakas, New J. Chem. 30 (2006) 1083.
[8] (a) D. Cardell, G. Hogarth, S. Faulkner, Inorg. Chim. Acta 359 (2006) 1321;
(b) G. Hogarth, Prog. Inorg. Chem. 53 (2005) 71.
[9] G.J. Kubas, Inorg. Synth. 28 (1990) 68.

[10] SHELXTL PC Version 5.1, Bruker AXS, Madison, WI, 1997.
[11] SHELX-97 G. Sheldrick, Institut Anorg. Chemie, Tammannstr. 4, D37077 Göttingen, Germany, 1998.
[12] M.J. Frisch, G.W. Trucks, H.B. Schlegel, G.E. Scuseria, M.A. Robb, J.R. Cheeseman, J.A. Montgomery Jr., T. Vreven, K.N. Kudin, J.C. Burant, J.M. Millam, S.S. Iyengar, J. Tomasi, V. Barone, B. Mennucci, M. Cossi, G. Scalmani, N. Rega, G.A. Petersson, H. Nakatsuji, M. Hada, M. Ehara, K. Toyota, R. Fukuda, J. Hasegawa, M. Ishida, T. Nakajima, Y. Honda, O. Kitao, H. Nakai, M. Klene, X. Li, J.E. Knox, H.P. Hratchian, J.B. Cross, V. Bakken, C. Adamo, J. Jaramillo, R. Gomperts, R.E. Stratmann, O. Yazyev, A.J. Austin, R. Cammi, C. Pomelli, J.W. Ochterski, P.Y. Ayala, K. Morokuma, G.A. Voth, P. Salvador, J.J. Dannenberg, V.G. Zakrzewski, S. Dapprich, A.D. Daniels, M.C. Strain, O. Farkas, D.K. Malick, A.D. Rabuck, K. Raghavachari, J.B. Foresman, J.V. Ortiz, Q. Cui, A.G. Baboul, S. Clifford, J. Cioslowski, B.B. Stefanov, G. Liu, A. Liashenko, P. Piskorz, I. Komaromi, R.L. Martin, D.J. Fox, T. Keith, M.A. Al-Laham, C.Y. Peng, A. Nanayakkara, M. Challacombe, P.M.W. Gill, B. Johnson, W. Chen, M.W. Wong, C. Gonzalez, J.A. Pople, GAUSSIAN 03, Revision C.02, Gaussian Inc., Wallingford, CT, 2004.
[13] A.D. Becke, J. Chem. Phys. 98 (1993) 5648.
[14] E.D. Glendening, A.E. Reed, J.E. Carpenter, F. Weinhold, NBO Version 3.1.
[15] R.P. Davies, M.G. Martinelli, Inorg. Chem. 41 (2002) 348.
[16] R.P. Davies, M.G. Martinelli, A.E.H. Wheatley, A.J.P. White, D.J. Williams, Eur. J. Inorg. Chem. (2003) 3409.
[17] J.K. Bjernemose, R.P. Davies, A.P.S. Jurd, M.G. Martinelli, P.R. Raithby, A.J.P. White, Dalton Trans. (2004) 3169.
[18] C.E. Anson, L. Ponikiewski, A. Rothenberger, Z. Anorg. Allg. Chem. 632 (2006) 2402.
[19] B.J. Liaw, T.S. Lobana, Y.W. Lin, J.C. Wang, C.W. Liu, Inorg. Chem. 44 (2005) 9921.
[20] R.P. Davies, M.G. Martinelli, A.J.P. White, Chem. Commun. (2006) 3240.
[21] C.W. Liu, M.D. Irwin, A.A. Mohamed, J.P. Fackler, Inorg. Chim. Acta 357 (2004) 3950.
[22] C.W. Liu, C.M. Hung, B.K. Santra, J.C. Wang, H.M. Kao, Z.Y. Lin, Inorg. Chem. 42 (2003) 8551.
[23] A. Avdeef, J.P. Fackler, Inorg. Chem. 17 (1978) 2182.
[24] M.T. Garland, J.F. Halet, J.Y. Saillard, Inorg. Chem. 40 (2001) 3342.

the Opus V3.3X program package. Melting points were determined on a Meltemp apparatus and were uncorrected. Flash column chromatography was performed on Silica Gel (Merck, 230–400 Mesh ASTM). TLC was done using pre-coated plates with a fluorescent indicator (Merck 5735). The stain solutions of permanganate, *p*-anisaldehyde and iodine were used for visualization of the TLC spots.

Thiophene-2-carboxaldehyde oxime, furan-2-carbaldehydeoxime, thiophene-2-hydroximoyl chloride, 5-chloro-thiophene-2-hydroximoyl chloride, 5-chloro-furan-2-hydroximoyl chloride, *N*-(*p*-methoxyphenyl)thiophene-2-carboxamidoxime and *N*-*p*-tolylthiophene-2-carboxamidoxime were prepared by utilizing literature procedures described previously [12–17].

2.2. Synthesis of N-substituted amidoximes

2.2.1. N-Phenyl-5-chloro-thiophene-2-carboxamidoxime (**3a**)

To a solution of 5-chloro-thiophene-2-hydroximoyl chloride (**2a**) (0.98 g, 6.06 mmol) in chloroform (20 mL) was added dropwise aniline (1.13 g, 12.1 mmol) in chloroform with constant stirring at room temperature. The reaction mixture was stirred for 2 d. The precipitate was filtered and the solution was evaporated under reduced pressure. The residual solid was subjected to flash column chromatography (eluant: hexane:ethyl acetate; 1:3) to give *N*-phenyl-5-chloro-thiophene-2-carboxamidoxime (**3a**), 0.78 g, yield: 65%. M.p. 131–133 °C. R_f: 0.42 (hexane:ethyl acetate; 3:1). IR (KBr, *v*: cm^{-1}): 3368 (N–H), 3204–3099 (broad, NOH), 1630 (C=N). ^1H NMR (400 MHz, $CDCl_3$ + DMSO-d_6): δ 9.98 (broad s, 1H), 7.20 (broad s, 1H), 6.95 (t, 1H), 6.82 (d, $J = 7.4$ Hz, 2H), 6.65 (d, $J = 3.9$ Hz, 1H), 6.61 (d, $J = 3.9$ Hz, 1H). ^{13}C NMR (100 MHz, $CDCl_3$ + DMSO-d_6): δ 145.13, 140.00, 132.62, 130.00, 128.40, 127.06, 125.93, 122.46, 121.20, 119.92. MS (*m*/*z*,%): 252 (M^+,32), 235 (76), 220 (16), 200 (12), 143 (23), 93 (100), 77 (31), 65 (22), 51 (14).

2.2.2. N-(4-Methylphenyl)-5-chloro-thiophene-2-carboxamidoxime (**3c**)

Colourless needles (hexane–ethyl acetate). Yield: 50%. M.p. 132–134 °C. R_f: 0.54 (hexane:ethyl acetate; 3:1). IR (KBr, *v*: cm^{-1}): 3363 (N–H), 3213–3171 (broad, NOH), 1627 (C=N). ^1H NMR (300 MHz, $CDCl_3$ + DMSO-d_6): δ 10.41 (s, 1H, NOH), 7.29 (s, 1H, NH), 6.98 (d, $J = 7.9$ Hz, 2H), 6.78 (d, $J = 7.6$ Hz, 2H), 6.70 (m, 1H), 6.60 (m, 1H), 2.23 (s, 3H). ^{13}C NMR (75 MHz, $CDCl_3$ + DMSO-d_6): δ 146.05, 137.66, 132.98, 130.34, 129.42, 127.46, 126.25, 122.35, 20.83. MS (*m*/*z*,%): M–H_2O, 248 (100), 213 (47), 77 (11).

2.2.3. N-(4-Methoxyphenyl)-5-chloro-thiophene-2-carboxamidoxime (**3e**)

White plates (hexane–ethyl acetate). Yield: 65%. M.p. 140–142 °C. R_f: 0.45 (hexane:ethyl acetate; 3:1). IR (KBr, *v*: cm^{-1}): 3344 (N–H), 3234–3111 (broad, NOH), 1631 (C=N). ^1H NMR (300 MHz, $CDCl_3$ + DMSO-d_6): δ 10.32 (s, 1H, NOH), 7.23 (s, 1H, NH), 6.86 (m, 2H), 6.76 (m, 2H), 6.67 (m, 1H), 6.52 (m, 1H), 3.76 (s, 3H, OCH_3). ^{13}C NMR (75 MHz, $CDCl_3$ + DMSO-d_6): δ 156.37, 146.66, 133.12, 132.87, 130.42, 127.52, 126.21, 124.98, 114.13, 55.49. MS (*m*/*z*,%): M–H_2O, 264 (100), 249 (88), 221 (21).

2.2.4. N-(4-Chlorophenyl)-5-chloro-thiophene-2-carboxamidoxime (**3f**)

Light yellow needles (hexane–ethyl acetate). Yield: 73%. M.p. 97–99 °C. R_f: 0.50 (hexane:ethyl acetate; 3:2). IR (KBr, *v*: cm^{-1}): 3382 (N–H), 3215 (broad, NOH), 1626 (C=N). ^1H NMR (300 MHz, $CDCl_3$ + DMSO-d_6): δ 10.64 (s, 1H, NOH), 7.66 (s, 1H, NH), 7.14 (d, $J = 9.2$ Hz, 2H), 7.03 (d, $J = 9.2$ Hz, 2H), 6.79 (d, $J = 6.7$ Hz, 1H), 6.73 (d, $J = 4.9$ Hz, 1H), 6.66 (d, $J = 4.1$ Hz, 1H), 6.59 (d, $J = 9.1$ Hz, 1H). ^{13}C NMR (75 MHz, $CDCl_3$ + DMSO-d_6): δ 145.80, 145.15, 139.26, 132.74, 130.76, 128.99, 128.78, 127.67, 127.49, 126.41, 122.61, 116.20. MS (*m*/*z*,%): M–H_2O, 268 (100), 233 (40), 198 (5).

2.2.5. N-(4-Bromophenyl)-5-chloro-thiophene-2-carboxamidoxime (**3g**)

Yield: 84%. M.p. 143–145 °C. R_f: 0.61 (hexane:ethyl acetate; 3:2). IR (KBr, *v*: cm^{-1}): 3387 (N–H), 3235 (broad, NOH), 1630 (C=N). ^1H NMR (300 MHz, $CDCl_3$ + DMSO-d_6): δ 10.60 (s, 1H, NOH), 7.54 (d, $J = 7.0$ Hz, 1H, NH), 7.27 (m, 2H), 6.72 (m, 3H). ^{13}C NMR (75 MHz, $CDCl_3$ + DMSO-d_6): δ 145.46, 139.57, 132.35, 131.90, 131.20, 127.74, 126.50, 123.20, 115.73.MS (*m*/*z*,%): M–H_2O, 314 (100), 279 (47), 198 (12).

2.2.6. N-(4-Iodophenyl)-5-chloro-thiophene-2-carboxamidoxime (**3h**)

Yield: 50%. M.p. 141–144 °C. R_f: 0.50 (hexane:ethyl acetate; 3:1). IR (KBr, *v*: cm^{-1}): 3394 (N–H), 3217 (broad, NOH), 1636 (C=N). ^1H NMR (300 MHz, $CDCl_3$ + DMSO-d_6): δ 10.63 (s, 1H, NOH), 7.56 (s, 1H, NH), 7.44 (m, 2H), 6.78–6.61 (m, 4H). ^{13}C NMR (75 MHz, $CDCl_3$ + DMSO-d_6): δ 144.84, 140.48, 137.58, 132.74, 130.76, 127.46, 126.43, 123.06, 122.02, 85.40. MS (*m*/*z*,%): M–H_2O, 362 (100), 346 (14), 219 (35), 144 (16).

2.2.7. N-(1-Naphthyl)-5-chloro-thiophene-2-carboxamidoxime (**3i**)

Yield: 65%. M.p. 168–170 °C. R_f: 0.44 (hexane:ethyl acetate; 3:1). IR (KBr, *v*: cm^{-1}): 3381 (N–H), 3224–3103 (broad, NOH), 1632 (C=N). ^1H NMR (300 MHz, $CDCl_3$ + DMSO-d_6): δ 10.61 (s, 1H, NOH), 8.20 (m, 1H), 7.85 (m, 1H), 7.62–7.26 (m, 5H), 6.95 (d, $J = 7.3$ Hz, 1H), 6.60 (d, $J = 1.1$ Hz, 1H), 6.45 (d, $J = 1.1$ Hz, 1H). ^{13}C NMR (75 MHz, $CDCl_3$ + DMSO-d_6): δ 146.98, 136.14, 134.22, 133.05, 130.18, 128.94, 128.34, 126.91, 126.39, 126.33, 126.17, 125.47, 124.71, 122.25, 121.06. MS (*m*/*z*,%): M–H_2O, 284 (100), 249 (18), 140 (6).

*2.2.8. N-Phenyl-5-chloro-furan-2-carboxamidoxime (**3j**)*

Yield: 20%. M.p. 147–149 °C. R_f: 0.29 (hexane:ethyl acetate; 3:1). IR (KBr, *v*: cm^{-1}): 3384 (N–H), 3119–2945 (broad NOH), 1627 (C=N). ^1H NMR (300 MHz, $CDCl_3$ + DMSO-d_6): δ 10.52 (s, 1H, NOH), 7.47 (s, 1H, NH), 7.18 (m, 2H), 6.97 (m, 1H), 6.75 (d, $J = 8.2$, 6.48 Hz, 1H), 6.21 (m, 1H). ^{13}C NMR (75 MHz, $CDCl_3$ + DMSO-d_6): δ 145.24, 142.39, 140.24, 136.95, 128.85, 122.58, 120.28, 113.44, 107.91. MS (*m*/*z*,%): M–H_2O, 218 (100), 190 (53), 155 (68).

*2.2.9. N-(4-Methylphenyl)-5-chloro-furan-2-carboxamidoxime (**3k**)*

Yield: 40%. M.p. 157–159 °C. R_f: 0.23 (hexane:ethyl acetate; 3:1). IR (KBr, *v*: cm^{-1}): 3384 (N–H), 3089–2970 (broad, NOH), 1624 (C=N). ^1H NMR (300 MHz, $CDCl_3$ + DMSO-d_6): δ 10.31 (s, 1H, NOH), 7.18 (s, 1H, NH), 6.97 (d, $J = 7.9$ Hz, 2H), 6.66 (d, $J = 8.4$ Hz, 2H), 6.40 (d, $J = 1.4$ Hz, 1H), 6.16 (d, $J = 1.6$ Hz, 1H), 2.26 (s, 3H). ^{13}C NMR (75 MHz, $CDCl_3$ + DMSO-d_6): δ 145.23, 142.81, 137.59, 136.82, 132.29, 129.39, 120.89, 113.47, 107.82, 20.75. MS (*m*/*z*,%): M–H_2O, 232 (100), 204 (51), 169 (56).

*2.2.10. N-(4-Methoxyphenyl)-5-chloro-furan-2-carboxamidoxime (**3l**)*

Yield: 22%. M.p. 141–143 °C. R_f: 0.32 (hexane:ethyl acetate; 3:2). IR (KBr, *v*: cm^{-1}): 3363 (N–H), 3191–3155 (broad, NOH), 1641 (C=N). ^1H NMR (300 MHz, $CDCl_3$ + DMSO-d_6): δ 10.34 (s, 1H, NOH), 7.28 (s, 1H, NH), 6.75 (dd, $J = 9.3$ 6.7 Hz, 4H), 6.25 (d, $J = 3.5$ Hz, 1H), 6.16 (d, $J = 3.2$ Hz, 1H), 3.80 (s, 3H, OCH_3). ^{13}C NMR (75 MHz, $CDCl_3$ + DMSO-d_6): δ 155.97, 145.14, 143.39, 136.72, 133.19, 123.56, 114.04, 113.55, 107.74, 55.42. MS (*m*/*z*,%): M–H_2O, 248 (100), 233 (54), 220 (14), 205 (28).

*2.2.11. N-(4-Chlorophenyl)-5-chloro-furan-2-carboxamidoxime (**3m**)*

Yield: 30%. M.p. 142–144 °C. R_f: 0.29 (hexane:ethyl acetate; 3:1). IR (KBr, *v*: cm^{-1}): 3382 (N–H), 3127–3094 (broad, NOH), 1622 (C=N). ^1H NMR (300 MHz, $CDCl_3$ + DMSO-d_6): δ 10.60 (s, br, 1H, NOH), 7.63 (s, 1H, NH), 7.14 (d, $J = 8.7$ Hz, 2H), 6.65 (d, $J = 8.7$ Hz, 2H). ^{13}C NMR (75 MHz, $CDCl_3$ + DMSO-d_6): δ 145.00, 141.81, 139.15, 137.11, 128.67, 127.10, 121.26, 113.59, 108.00. MS (*m*/*z*,%): M–H_2O, 254 (100), 183 (22), 155 (31), 127 (75).

*2.2.12. N-(4-Bromophenyl)-5-chloro-furan-2-carboxamidoxime (**3n**)*

Yield: 44%. M.p. 163–164 °C. R_f: 0.66 (hexane:ethyl acetate; 3:1). IR (KBr, *v*: cm^{-1}): 3382 (N–H), 3087–2970 (broad, NOH), 1625 (C=N). ^1H NMR (300 MHz, $CDCl_3$ + DMSO-d_6): δ 10.57 (s, 1H, NOH), 8.20 (s, 1H, NH), 7.20 (d, $J = 6.4$ Hz, 2H), 6.60 (d, $J = 7.3$ Hz, 2H), 6.55 (dd, $J = 3.5$ 1.1 Hz, 1H), 6.30 (dd, $J = 3.2$, 1.1 Hz, 1H). ^{13}C NMR (75 MHz, $CDCl_3$ + DMSO-d_6): δ 145.10, 141.59, 139.73, 137.06, 131.55, 121.44, 120.21, 114.45, 113.48, 108.00. MS (*m*/*z*,%): M–H_2O, 298 (100), 270 (35), 233 (27), 189 (22).

*2.2.13. N-(4-Iodophenyl)-5-chloro-furan-2-carboxamidoxime (**3o**)*

Yield: 26%. M.p. 165–167 °C. R_f: 0.58 (hexane:ethyl acetate; 3:1). IR (KBr, *v*: cm^{-1}): 3385 (N–H), 3082–2962 (broad, NOH), 1627 (C=N). ^1H NMR (400 MHz, $CDCl_3$ + DMSO-d_6): δ 9.50 (broad s, 1H), 7.48 (d, $J = 8.5$ Hz, 2H), 7.36 (broad s, 1H), 6.50 (d, $J = 8.5$ Hz, 2H), 6.46 (d, $J = 3.3$ Hz, 1H), 6.13 (d, $J = 3.3$ Hz, 1H). ^{13}C NMR (100 MHz, $CDCl_3$ + DMSO-d_6): δ 144.58, 141.56, 140.01, 137.39, 137.17, 121.79, 120.52, 113.61, 107.88, 84.96. MS (*m*/*z*,%): M–H_2O (100), 316 (22), 281 (12), 217 (9), 189 (32), 172 (12), 154 (14), 127 (12).

*2.2.14. N-(1-Naphthyl)-5-chloro-furan-2-carboxamidoxime (**3p**)*

Yield: 30%. M.p. 128–129 °C. R_f: 0.49 (hexane:ethyl acetate; 3:2). IR (KBr, *v*: cm^{-1}): 3365 (N–H), 3143 (broad, NOH), 1636 (C=N). ^1H NMR (300 MHz, $CDCl_3$ + DMSO-d_6): δ 10.56 (s, 1H, NOH), 8.16 (d, $J = 6.7$ Hz, 1H), 7.85 (d, $J = 7.6$ Hz, 1H), 7.60 (d, $J = 8.2$ Hz, 1H), 7.55–7.50 (m, 1H), 7.42 (s, 1H, NH), 7.28 (t, 1H), 6.87 (d, $J = 7.3$ Hz, 1H), 6.21 (d, $J = 3.5$ Hz, 1H), 6.05 (d, $J = 3.5$ Hz, 1H). ^{13}C NMR (75 MHz, $CDCl_3$ + DMSO-d_6):δ 145.10, 141.59, 139.73, 137.06, 131.55, 121.44, 120.21, 114.45, 113.48, 108.00. MS (*m*/*z*,%): M–H_2O, 268 (100), 240 (42), 205 (54), 152 (17).

2.3. Synthesis of oxadiazaboroles

*2.3.1. 4,5-Diphenyl-3-(5-chloro-2-thienyl)-4,5-dihydro-1,2,4,5-oxadiazaborole (**5a**)*

A mixture of *N*-phenyl-(5-chloro-thiophene)-2-carboxamidoxime (**3a**) (150 mg, 0.68 mmol) and phenylboronic acid (**4**) (92 mg, 0.76 mmol) in toluene (10 mL) was refluxed under an inert atmosphere in the presence of molecular sieves (4 Å) overnight. After extracted with acetone and filtering, the solvent was evaporated under reduced pressure. The crude product was crystallized from hexane–ethylacetate mixture to give **5a** as colorless needles, 140 mg, Yield: 67%. M.p. 164–166 °C. R_f: 0.41 (hexane:ethyl acetate; 3:2). IR (KBr, ν_{max}: cm^{-1}): 1601 (C=N), 1452 (B–N), 1372 (B–O), 1109, 767, 701. ^1H NMR ($CDCl_3$, 300 MHz): δ 7.53–7.49 (m, 5H), 7.40–7.38 (m, 2H), 7.34–7.24 (m, 4H), 6.70 (dd, $J = 4.10$ Hz, 2.05 Hz, 1H), 6.53 (dd, $J = 4.10$ Hz, 2.05 Hz, 1H). ^{13}C NMR ($CDCl_3$, 75 MHz) δ: 155.51, 136.92, 134.36, 134.01, 131.44, 130.30, 129.64, 129.05, 128.68, 128.29, 126.68, 125.49. ^{11}B NMR (160.46 MHz, $CDCl_3$–15% $BF_3 \cdot Et_2O$): δ 32.3. MS (*m*/*z*,%): 338 (M^+,100), 234 (15), 179 (20), 103 (11), 91 (7), 77 (15), 51 (6); HRMS calcd for $C_{17}H_{12}BN_2OSCl$: 338.0452; found: 338.0460.

*2.3.2. 5-Phenyl-3-(2-thienyl)-4-(4-methylphenyl)-4,5-dihydro-1,2,4,5-oxadiazaborole (**5b**)*

Yield: 45%. M.p. 222–224 °C (hexane:ethyl acetate). R_f: 0.54 (hexane:ethyl acetate; 3:2). IR (KBr, ν_{max}: cm^{-1}): 1604, 1566, 1514 (C=N), 1444 (B–N), 1369 (B–O), 1121, 1024, 822, 724. ^1H NMR ($CDCl_3$, 300 MHz): δ 7.54 (d, $J = 7.91$ Hz, 2H) 7.43–7.17 (m, 8H), 6.92–6.89 (m, 1H), 6.82 (d, $J = 3.51$ Hz, 1H), 2.46 (s, 3H). ^{13}C NMR (100 MHz, $CDCl_3$): δ 156.31, 138.79, 134.36, 134.16, 131.02, 130.40, 129.36, 128.64, 128.23, 127.99, 127.20, 126.73, 21.33. ^{11}B NMR (160.46 MHz, $CDCl_3$–15% $BF_3 \cdot Et_2O$):δ 32.4. MS (*m*/*z*,%): 318 (M^+,100), 214 (15), 193 (23), 116 (7), 105 (8), 91 (5), 77 (8); HRMS calcd for $C_{18}H_{15}BN_2OS$: 318.0998; found: 318.1002.

*2.3.3. 4-(4-Methylphenyl)-5-phenyl-3-(5-chloro-2-thienyl)-4,5-dihydro-1,2,4,5-oxadiazaborole (**5c**)*

Yield: 65%. M.p. 210–212 °C (hexane). R_f: 0.38 (hexane:ethyl acetate; 2:1). IR (KBr, *v*: cm^{-1}): 1600, 1572, 1514 (C=N), 1452 (B–N), 1369 (B–O), 1111, 823, 698. ^1H NMR (300 MHz, $CDCl_3$): δ 7.98–6.55 (m, 11H), 2.20 (s, 3H). ^{13}C NMR ($CDCl_3$, 75 MHz): δ 155.18, 139.08, 134.18, 133.93, 133.71, 133.20, 131.12, 130.64, 129.25, 128.83, 128.01, 127.95, 127.39, 126.59, 125.24, 122.04, 21.27. ^{11}B NMR (160.46 MHz, $CDCl_3$–15% $BF_3 \cdot Et_2O$): δ 32.2 MS (*m*/*z*,%): 352 (M^+,100), 248 (11), 193 (25), 116 (11), 105 (8), 77 (11). HRMS calcd for $C_{18}H_{14}BN_2OSCl$: 352.0608; found: 352.0626.

*2.3.4. 4-(4-Methoxyphenyl)-5-phenyl-3-(2-thienyl)-4,5-dihydro-1,2,4,5-oxadiazaborole (**5d**)*

Yield: 70%. M.p. 161–163 °C (hexane–ethylacetate). R_f: 0.15 (hexane:ethyl acetate; 3:2). IR (KBr, ν_{max}: cm^{-1}): 1610, 1570, 1515 (C=N), 1444 (B–N), 1370 (B–O), 1256, 1030, 841, 705. ^1H NMR (300 MHz, $CDCl_3$): δ 7.55 (d, $J = 7.32$ Hz, 4H), 7.40–7.21 (m, 4H), 7.00–6.86 (m, 4H), 3.89 (s, 3H). ^{13}C NMR (75 MHz, $CDCl_3$): δ 159.86, 156.70, 134.38, 131.30, 129.79, 129.59, 128.96, 128.26, 127.49, 126.92, 115.15, 55.79. ^{11}B NMR (160.46 MHz, $CDCl_3$–15% $BF_3 \cdot Et_2O$): δ 32.2. MS (*m*/*z*,%): 334 (M^+,100), 230 (6), 216 (25), 209 (30), 194 (12), 121 (15), 77 (9). HRMS calcd for $C_{18}H_{15}BN_2O_2S$: 334.0947; found: 334.0978.

*2.3.5. 4-(4-Methoxyphenyl)-5-phenyl-3-(5-chloro-2-thienyl)-4,5-dihydro-1,2,4,5-oxadiazaborole (**5e**)*

M.p. 169–170 °C (66%) (hexane–ethylacetate). R_f: 0.29 (hexane:ethyl acetate; 2:1). IR (KBr, *v*: cm^{-1}): 1610, 1514 (C=N), 1454 (B–N), 1369 (B–O), 1255, 839, 700. ^1H NMR (300 MHz, $CDCl_3$): δ 7.54–6.60 (m, 11H), 3.84 (s, 3H, OCH_3). ^{13}C NMR (75 MHz, $CDCl_3$): δ 159.82, 155.44, 134.22, 133.99, 134.40, 131.17, 129.38, 128.92, 128.84, 128.07, 127.44, 126.60, 125.28, 115.12, 55.56. ^{11}B NMR (160.46 MHz, $CDCl_3$–15% $BF_3 \cdot Et_2O$): δ 32.2. MS (*m*/*z*,%): 368 (M^+,100), 264 (6), 249 (16), 209 (34), 194 (16), 121 (16), 77 (12). HRMS calcd for $C_{18}H_{14}BN_2O_2SCl$: 368.0558; found: 368.0575.

*2.3.6. 4-(4-Chlorophenyl)-5-phenyl-3-(5-chloro-2-thienyl)-4,5-dihydro-1,2,4,5- oxadiazaborole (**5f**)*

M.p. 158–160 °C (hexane) (75%). R_f: 0.50 (hexane:ethyl acetate; 3:2). IR (KBr, ν_{max}: cm^{-1}): 1600, 1571, 1525 (C=N), 1493, 1449 (B–N), 1370 (B–O), 1093, 829, 701. ^1H NMR (300 MHz, $CDCl_3$): δ 7.49–7.40 (m, 6H), 7.31–7.25 (m, 4H), 6.66 (dd, $J = 5.0$, 1.76 Hz, 1H), 6.58 (dd, $J = 3.9$, 1.46 Hz, 1H). ^{13}C NMR (75 MHz, $CDCl_3$): δ 155.23, 135.51, 135.23, 134.31, 131.61, 130.54, 129.96, 129.19, 128.40, 126.81, 125.08. ^{11}B NMR (160.46 MHz, $CDCl_3$–15% $BF_3 \cdot Et_2O$): δ 32.2. MS (*m*/*z*,%): 372 (M^+,100), 268 (14), 233 (9), 213 (26), 137 (15), 125 (11), 96 (12), 77 (14), 51 (5). HRMS calcd for $C_{17}H_{11}BN_2OSCl_2$: 372.0062; found: 372.0056.

*2.3.7. 4-(4-Bromophenyl)-5-phenyl-3-(5-chloro-2-thienyl)-4,5-dihydro-1,2,4,5-oxadiazaborole (**5g**)*

Yield: 75%. M.p. 177–179 °C (hexane–ethyl acetate). R_f: 0.61 (hexane:ethyl acetate; 3:2). IR (KBr, ν_{max}: cm^{-1}): 1602, 1568, 1510 (C=N), 1488, 1455 (B–N), 1366 (B–O), 1105, 1073, 941, 835, 695. ^1H NMR ($CDCl_3$, 300 MHz): δ 7.65 (d, $J = 0.88$ Hz, 1H), 7.63 (m, 1H), 7.49–7.26 (m, 6H), 7.22 (d, $J = 0.88$ Hz, 1H), 7.20 (m, 1H), 6.74 (dd, $J = 2.34$, 1.17 Hz, 1H), 6.56 (dd, $J = 2.34$, 1.17 Hz, 1H). ^{13}C NMR (75 MHz, $CDCl_3$): δ 155.15, 136.04, 134.32, 133.53, 131.62, 130.28, 129.21, 128.41, 126.84, 125.07, 123.23. ^{11}B NMR (160.46 MHz, $CDCl_3$–15% $BF_3 \cdot Et_2O$): δ 32.3. MS (*m*/*z*,%): 418 (M^+,100), 314 (12), 257 (14), 181 (8), 169 (8), 143 (12), 102 (18), 90 (12), 77 (15), 63 (8), 51 (8). HRMS calcd for $C_{17}H_{11}BN_2OSBrCl$: 415.9557; found: 415.9567.

*2.3.8. 4-(4-Iodophenyl)-5-phenyl-3-(5-chloro-2-thienyl)-4,5-dihydro-1,2,4,5-oxadiazaborole (**5h**)*

Yield: 52%. M.p. 184–186 °C (hexane–ethyl acetate). R_f: 0.50 (hexane:ethyl acetate; 3:2). IR (KBr, ν_{max}: cm^{-1}): 1603, 1597, 1508 (C=N), 1485, 1455 (B–N), 1368 (B–O), 1103, 942, 829, 695. ^1H NMR (300 MHz, $CDCl_3$): δ 7.83 (d, $J = 7.6$ Hz, 2H), 7.49–7.25 (m, 6H), 7.07 (d, $J = 7.6$ Hz, 2H), 6.74 (d, $J = 3.5$ Hz, 1H), 6.55 (d, $J = 3.4$ Hz, 1H). ^{13}C NMR (75 MHz, $CDCl_3$): δ 155.10, 139.49, 136.72, 134.32, 134.27, 131.62, 130.49, 129.23, 128.41, 126.86, 125.05, 94.76. ^{11}B NMR (160.46 MHz, $CDCl_3$–15% $BF_3 \cdot Et_2O$): δ 32.2. MS (*m*/*z*,%): 464 (M^+,100), 360 (12), 305 (26), 229 (7), 198 (7), 151 (9), 102 (15), 90 (17), 77 (11), 63 (7). HRMS calcd for $C_{17}H_{11}BN_2OSClI$: 463.9418; found: 463.9409.

*2.3.9. 4-(1-Naphthyl)-5-phenyl-3-(5-chloro-2-thienyl)-4,5-dihydro-1,2,4,5-oxadiazaborole (**5i**)*

Yield: 46%. M.p. 132–134 °C (hexane–ethyl acetate). R_f: 0.54 (hexane:ethyl acetate; 3:2). IR (KBr, ν_{max}: cm^{-1}): 1599, 1522, 1508 (C=N), 1434 (B–N), 1369 (B–O), 1106, 800, 776, 696. ^1H NMR (300 MHz, $CDCl_3$): δ 8.06 (d, $J = 7.9$ Hz, 1H), 8.00 (d, $J = 7.9$ Hz, 1H), 7.74–7.16 (m, 11H), 6.53 (dd, $J = 1.76$, 0.88 Hz, 1H), 6.39 (dd, $J = 1.76$, 0.88 Hz, 1H). ^{13}C NMR ($CDCl_3$, 75 MHz): δ 156.11,

134.57, 134.22, 133.89, 133.13, 131.48, 131.11, 130.19, 128.90, 128.68, 128.28, 128.24, 127.46, 126.79, 126.62, 125.99, 125.23, 122.52. ^{11}B NMR (160.46 MHz, $CDCl_3$–15% $BF_3 \cdot Et_2O$): δ 32.8. MS (*m*/*z*,%): 388 (M^+,100), 249 (26), 229 (69), 153 (25), 140 (18), 126 (11), 115 (12), 77(9), 51 (5). HRMS calcd for $C_{21}H_{14}BN_2OSCl$: 388.0608; found: 388.0607.

2.3.10. 3-(5-Chloro-2-furyl)-4,5-diphenyl-4,5-dihydro-1,2,4,5-oxadiazaborole (**5j**)

Yield: 50%. M.p. 114–116 °C (benzene–petroleum ether). R_f: 0.29 (hexane:ethyl acetate; 3:1). IR (KBr, ν_{max}: cm^{-1}): 1598, 1534 (C=N), 1498, 1484 (B–N), 1375 (B–O), 1138, 1024, 790, 699. ^{1}H NMR (300 MHz, $CDCl_3$): δ 7.52–7.23 (m, 11H), 6.07 (dd, $J = 2.34$, 1.17 Hz, 1H), 5.87 (dd, $J = 3.66$, 1.17, 0.88 Hz, 1H). ^{13}C NMR (75 MHz, $CDCl_3$): δ 152.63, 140.20, 139.68, 136.99, 134.40, 131.45, 130.15, 129.20, 128.30, 128.27, 115.70, 108.22. MS (*m*/*z*,%): 322 (M^+,100), 285 (15), 258 (31), 179 (18), 166 (35), 154 (44), 128 (15), 103 (35), 77 (34), 64 (10), 51 (13). HRMS calcd for $C_{17}H_{12}BN_2O_2Cl$: 322.0680; found: 322.0709.

2.3.11. 3-(5-Chloro-2-furyl)-5-phenyl-4-(4-methylphenlyl)-4,5-dihydro-1,2,4,5-oxadiazaborole (**5k**)

Yield: 60%. M.p. 167–168 °C (benzene–petroleum ether). R_f: 0.23 (hexane:ethyl acetate; 3:1). IR (KBr, ν_{max}: cm^{-1}): 1611, 1532, 1515 (C=N), 1485 (B–N), 1376 (B–O), 1138, 1028, 831, 794, 707. ^{1}H NMR (300 MHz, $CDCl_3$): δ 7.53 (d, $J = 7.32$ Hz, 2H), 7.41–7.26 (m, 5H), 7.19 (d, $J = 7.32$ Hz, 2H), 7.03 (d, $J = 8.50$ Hz, 1H), 6.77 (d, $J = 8.20$ Hz, 1H) 2.46 (s, 3H). ^{13}C NMR (100 MHz, $CDCl_3$): δ 152.55, 140.15, 139.42, 138.94, 134.19, 134.10, 131.15, 130.49, 129.64, 128.01, 127.79, 122.80, 115.43, 107.93, 21.29. MS (*m*/*z*,%): 336 (M^+,100), 299 (15), 271 (10), 192 (23), 180 (23), 168 (54), 142 (8), 127 (7), 116 (28), 104 (10), 90 (15), 77 (20), 65 (8), 51 (8). HRMS calcd for $C_{18}H_{14}BN_2O_2Cl$: 336.0837; found: 336.0868.

2.3.12. 3-(5-Chloro-2-furyl)-4-(4-methoxyphenyl)-5-phenyl-4,5-dihydro-1,2,4,5-oxadiazaborole (**5l**)

Yield: 65%. M.p. 145–147 °C (hexane–ethyl acetate). R_f: 0.32 (hexane:ethyl acetate; 3:1). IR (KBr, ν_{max}: cm^{-1}): 1612, 1516 (C=N), 1489 (B–N), 1375 (B–O), 1251, 1023, 841, 794, 707. ^{1}H NMR (300 MHz, $CDCl_3$): δ 7.45–6.90 (m, 10H), 6.00 (dd, $J = 3.52$, 1.76 Hz, 1H), 5.70 (dd, $J = 3.52$, 1.76 Hz, 1H) 3.81 (s, 3H). ^{13}C NMR (75 MHz, $CDCl_3$): δ 159.91, 152.92, 140.36, 139.62, 134.40, 131.43, 129.49, 129.34, 128.28, 115.71, 108.26, 55.83. ^{11}B NMR (160.46 MHz, $CDCl_3$–15% $BF_3 \cdot Et_2O$): δ 32.0. MS (*m*/*z*,%): 352 (M^+,100), 209 (27), 194 (16), 184 (30), 133 (21), 121 (10), 103 (11), 90 (13), 77 (15). HRMS calcd for $C_{18}H_{14}BN_2O_3Cl$: 352.0786; found: 352.0800.

2.3.13. 4-(4-Chlorophenyl)-3-(5-chloro-2-furyl)-5-phenyl-4,5-dihydro-1,2,4,5- oxadiazaborole (**5m**)

M.p. 131–133 °C (hexane–dichloroethane) (43%). R_f: 0.29 (hexane:ethyl acetate; 3:1). IR (KBr, ν_{max}: cm^{-1}): 1611, 1530 (C=N), 1496 (B–N), 1373 (B–O), 1139, 1092, 1021, 838, 789, 704. ^{1}H NMR (300 MHz, $CDCl_3$): δ 7.49–7.26 (m, 10H), 6.12 (dd, $J = 3.33$ Hz, 1.76 Hz, 1.46,1H), 5.98 (dd, $J = 3.52$ Hz, 1.76 Hz, 1.46 Hz, 1H). ^{13}C NMR ($CDCl_3$, 75 MHz): δ 152.38, 139.88, 135.60, 135.03, 134.36, 131.63, 130.36, 129.65, 128.39, 115.91, 108.33. ^{11}B NMR (160.46 MHz, $CDCl_3$–15% $BF_3 \cdot Et_2O$): δ 32.1. MS (*m*/*z*,%): 356 (M^+,100), 319 (7), 293 (15), 257 (12), 213 (25), 200 (25), 189 (38), 162 (9), 137 (40), 102 (25), 77 (20), 64 (8), 51(9). HRMS calcd for $C_{17}H_{11}BN_2O_2Cl_2$: 356.0291; found: 356.0270.

2.3.14. 4-(4-Bromophenyl)-3-(5-chloro-2-furyl)-5-phenyl-4,5-dihydro-1,2,4,5-oxadiazaborole (**5n**)

Yield: 72%. M.p. 166–168 °C (hexane–ethyl acetate). R_f: 0.66 (hexane:ethyl acetate; 3:2). IR (KBr, ν_{max}: cm^{-1}): 1610, 1530 (C=N), 1492 (B–N), 1374 (B–O), 1210, 1140, 1020, 789, 704. ^{1}H NMR (300 MHz, $CDCl_3$): δ 7.65 (m, 10H), 6.13 (d, $J = 3.22$ Hz, 1H), 5.99 (dd, $J = 1.76$, 0.88 Hz, 1H). ^{13}C NMR (75 MHz, $CDCl_3$): δ 152.30, 139.92, 139.84, 136.12, 134.37, 133.35, 131.64, 129.96, 128.40, 123.08, 115.90, 108.33. ^{11}B NMR (160.46 MHz, $CDCl_3$–15% $BF_3 \cdot Et_2O$): δ 32.0. MS (*m*/*z*,%): 402 (M^+,100), 257 (29), 244 (15), 232 (26), 181 (18), 154 (8), 127 (15), 102 (40), 90 (12), 77 (26), 63 (9), 51 (9). HRMS calcd for $C_{17}H_{11}BN_2O_2BrCl$: 399.9785; found: 399.9796.

2.3.15. 3-(5-Chloro-2-furyl)-4-(4-iodophenyl)-5-phenyl-4,5-dihydro-1,2,4,5-oxadiazaborole (**5o**)

Yield: 75%. M.p. 203–205 °C (hexane–ethyl acetate). R_f: 0.58 (hexane:ethyl acetate; 3:2). IR (KBr, ν_{max}: cm^{-1}): 1627, 1583 (C=N), 1482 (B–N), 1367 (B–O), 978, 671. ^{1}H NMR (300 MHz, $CDCl_3$): δ 7.83 (d, $J = 1.17$ Hz, 1H), 7.81 (s, 1H), 7.50–7.24 (m, 6H), 7.08 (d, $J = 1.17$ Hz, 1H), 7.06 (s, 1H), 6.13 (dd, $J = 2.34$, 1.17 Hz, 1H), 5.99 (dd, $J = 2.34$, 1.17 Hz, 1H). ^{13}C NMR (75 MHz, $CDCl_3$): δ 152.27, 139.93, 139.83, 139.31, 136.81, 134.37, 131.63, 130.16, 128.39, 115.92, 108.32, 94.45. ^{11}B NMR (160.46 MHz, $CDCl_3$–15% $BF_3 \cdot Et_2O$): δ 32.0. MS (*m*/*z*,%): 448 (M^+,100), 305 (20), 292 (23), 280 (39), 257 (23), 229 (16), 203 (7), 189 (9), 154 (11), 127 (16), 102 (41), 90 (16), 77 (19), 63 (13), 51(9). HRMS calcd for $C_{17}H_{11}BN_2O_2ClI$: 447.9647; found: 447.9683.

2.3.16. 3-(5-Chloro-2-furyl)-4-(1-naphthyl)-5-phenyl-4,5-dihydro-1,2,4,5-oxadiazaborole (**5p**)

Yield: 40%. M.p. 148–150 °C (hexane–dichloroethane). R_f: 0.49 (hexane:ethyl acetate; 3:2). IR (KBr, ν_{max}: cm^{-1}): 1603, 1527 (C=N), 1484 (B–N), 1371 (B–O), 1209, 1143, 1018, 777, 710. ^{1}H NMR (300 MHz, $CDCl_3$): δ 8.03 (d, $J = 8.03$ Hz, 1H), 7.98 (d, $J = 8.03$ Hz, 1H), 7.69–7.12 (m, 11H), 5.87 (s, 1H), 5.39 (s, 1H). ^{13}C NMR (75 MHz, $CDCl_3$): δ 153.08, 140.00, 139.55, 134.49, 134.26, 133.24, 131.50, 130.79, 129.86, 128.79, 128.26, 125.15, 127.41, 126.27, 125.93, 122.52, 115.32, 108.23. MS (*m*/*z*,%): 372 (M^+,69), 336 (92), 308 (42), 292 (15), 259 (34), 233 (48), 216 (54), 204 (100), 189 (15), 178 (17), 153 (54), 140 (34),

126 (29), 115 (23), 77 (18), 51 (8). HRMS calcd for $C_{21}H_{14}BN_2O_2Cl$: 372.0837; found: 372.0824.

2.3.17. 3-(2-Pyridyl)-4-methyl-5-phenyl-4,5-dihydro-1,2,4,5-oxadiazaborole (**5q**)

Yield: 28%. M.p. 76–77 °C hexane–petroleum ether. R_f: 0.18 (hexane:ethyl acetate; 1:3). IR (KBr, *v*: cm^{-1}): 1607, 1587, 1542 (C=N), 1482 (B–N), 1391 (B–O), 1297, 1081, 793, 697. ^1H NMR (300 MHz, $CDCl_3$): δ 8.78–7.44 (m, 9H), 3.67 (s, 3H).^{13}C NMR, (75 MHz, $CDCl_3$) δ: 160.05, 149.24, 147.50, 137.07, 133.88, 130.72, 128.27, 124.76, 124.73, 31.43. ^{11}B NMR (160.46 MHz, $CDCl_3$–15% $BF_3 \cdot Et_2O$): δ 33.2. MS (*m*/*z*,%): 236 (M^+,100), 160 (9), 133 (25), 105 (100), 78 (29), 51(10). HRMS calcd for $C_{13}H_{12}BN_3O$: 237.1073; found: 237.1075.

2.3.18. 3-(2-Pyridyl)-4-ethyl-5-phenyl-4,5-dihydro-1,2,4,5-oxadiazaborole (**5r**)

Yield: 63%. M.p. 82–83 °C (benzene–petroleum ether). R_f: 0.11 (hexane:ethyl acetate; 2:1). IR (KBr, ν_{max}: cm^{-1}): 1600, 1552 (C=N), 1482 (B–N), 1348 (B–O), 1151, 777, 715. ^1H NMR (300 MHz, $CDCl_3$): δ 8.73–8.71 (m, 1H), 7.96–7.79 (m, 4H), 7.51–7.45 (m, 4H), 4.18 (q, 2H), 1.26 (t, 3H). ^{13}C NMR (75 MHz, $CDCl_3$): δ 160.07, 149.54, 147.74, 137.29, 133.94, 130.95, 128.53, 124.96, 124.89, 38.40, 17.85. ^{11}B NMR (160.46 MHz, $CDCl_3$-15% $BF_3 \cdot Et_2O$): δ 33.2. MS (*m*/*z*,%): 250 (M^+,54), 236 (8), 174 (52), 147 (31), 105 (100), 78 (40), 51 (11). HRMS calcd for $C_{14}H_{14}BN_3O$: 251.1230; found: 251.1237.

2.3.19. 3-(2-Pyridyl)-4-(1-naphthyl)-5-phenyl-4,5-dihydro-1,2,4,5-oxadiazaborole (**5s**)

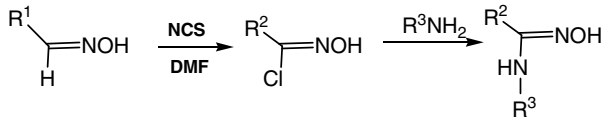
Yield: 51%. M.p. 181–182 °C (hexane–petroleum ether). R_f: 0.31 (hexane:ethyl acetate; 1:3). IR (KBr, *v*: cm^{-1}): 1598, 1525 (C=N), 1473 (B–N), 1374 (B–O), 1151, 824, 768, 694. ^1H NMR (400 MHz, $CDCl_3$): δ 8.20 (d, $J = 4.5$ Hz, 1H), 7.76 (d, $J = 7.7$ Hz, 2H), 7.72 (d, $J = 8.4$ Hz, 1H), 7.62 (d, $J = 7.8$ Hz, 1H), 7.56 (dt, $J = 1.7$, 7.7, 15.5 Hz, 1H), 7.51–7.32 (m, 7H), 7.20 (t, 2H), 7.10 (ddd, $J = 1.0$, 4.8, 7.5 Hz, 1H). ^{13}C NMR (100 MHz, $CDCl_3$): δ 160.30, 149.25, 146.17, 136.32, 134.13, 134.10, 134.08, 131.07, 130.84, 128.44, 128.36, 128.29, 127.96, 127.10, 126.46, 125.87, 125.41, 124.37, 124.12, 122.71. ^{11}B NMR (160.46 MHz, $CDCl_3$–15% $BF_3 \cdot Et_2O$): δ 32.5. MS (*m*/*z*,%): 349 (M^+,100), 318 (11), 272 (19), 244 (27), 229 (10), 141 (27), 115 (8), 78 (9). HRMS calcd for $C_{22}H_{16}BN_3O$: 349.1386; found: 349.1424.

2.3.20. 3-(4-Pyridyl)-4,5-diphenyl-4,5-dihydro-1,2,4,5-oxadiazaborole (**5t**)

Yield: 42%. M.p. 213–215 °C (hexane–ethyl acetate). R_f: 0.08 (hexane:ethyl acetate; 2:1). IR (KBr, ν_{max}: cm^{-1}): 1653, 1599 (C=N), 1516 (B–N), 1373 (B–O), 943, 823, 684. ^1H NMR (300 MHz, $CDCl_3$ + DMSO-d_6): δ 8.22 (d, $J = 5.86$ Hz, 1H), 8.18 (d, $J = 5.56$ Hz, 1H), 7.49 (d, $J = 7.33$ Hz, 1H), 7.24–6.56 (m, 10H), 6.33 (d, $J = 7.62$ Hz, 1H). ^{13}C NMR (75 MHz, $CDCl_3$): δ 149.92, 149.35, 134.20, 134.01, 131.24, 129.94, 128.82, 128.09, 127.57, 127.44, 122.90, 122.40, 120.74. ^{11}B NMR (160.46 MHz, $CDCl_3$–15% $BF_3 \cdot Et_2O$): δ 32.4. MS (*m*/*z*,%): 299 (M^+,100), 222 (8), 195 (11), 179 (31), 118 (8), 91 (11), 77 (15), 51 (9). HRMS calcd for $C_{18}H_{14}BN_3O$: 299.1230; found: 299.1247.

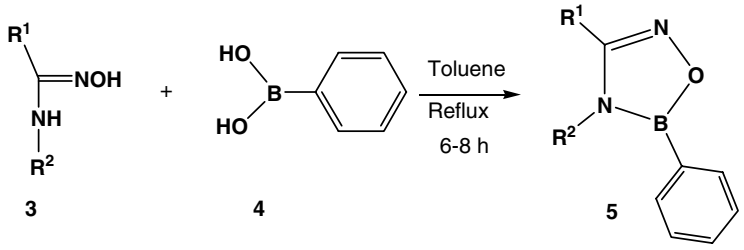
2.3.21. 3-(4-Pyridyl)-4-(4-methylphenyl)-5-phenyl-4,5-dihydro-1,2,4,5-oxadiazaborole (**5u**)

Yield: 80%. M.p. 234–236 °C (hexane–dichloromethane). R_f: 0.18 (hexane:ethyl acetate; 1:2). IR (KBr, ν_{max}: cm^{-1}): 1601, 1587, 1541 (C=N), 1483 (B–N), 1390 (B–O), 1076, 1020, 792, 694. ^1H NMR (400 MHz, DMSO-d_6): δ 8.45 (d, $J = 6.0$ Hz, 1H), 8.12 (s, 1H), 7.84 (s, 1H), 7.76 (d, $J = 6.5$ Hz, 1H), 7.34–7.25 (m, 5H), 6.85 (d, $J = 8.1$ Hz, 1H), 6.54 (d, $J = 8.3$ Hz, 1H), 2.16 (s, 3H).



	1 R^1	2 R^2	3 R^3
a	2-Thienyl	5-Chloro-2-thienyl	Ph
b	2-Thienyl	2-Thienyl	4-Me-C_6H_4
c	2-Thienyl	5-Chloro-2-thienyl	4-Me-C_6H_4
d	2-Thienyl	2-Thienyl	4-MeO-C_6H_4
e	2-Thienyl	5-Chloro-2-thienyl	4-MeO-C_6H_4
f	2-Thienyl	5-Chloro-2-thienyl	4-Cl-C_6H_4
g	2-Thienyl	5-Chloro-2-thienyl	4-Br-C_6H_4
h	2-Thienyl	5-Chloro-2-thienyl	4-I-C_6H_4
i	2-Thienyl	5-Chloro-2-thienyl	1-Naphthyl
j	2-Furyl	5-Chloro-2-furyl	Ph
k	2-Furyl	5-Chloro-2-furyl	4-Me-C_6H_4
l	2-Furyl	5-Chloro-2-furyl	4-MeO-C_6H_4
m	2-Furyl	5-Chloro-2-furyl	4-Cl-C_6H_4
n	2-Furyl	5-Chloro-2-furyl	4-Br-C_6H_4
o	2-Furyl	5-Chloro-2-furyl	4-I-C_6H_4
p	2-Furyl	5-Chloro-2-furyl	1-Naphthyl
q	2-Pyridyl	2-Pyridyl	Me
r	2-Pyridyl	2-Pyridyl	Et
s	2-Pyridyl	2-Pyridyl	1-Naphthyl
t	4-Pyridyl	4-Pyridyl	Ph
u	4-Pyridyl	4-Pyridyl	4-Me-C_6H_4
v	Ph	Ph	4-Me-C_6H_4

Scheme 1. Structure of the *N*-substituted amidoximes.



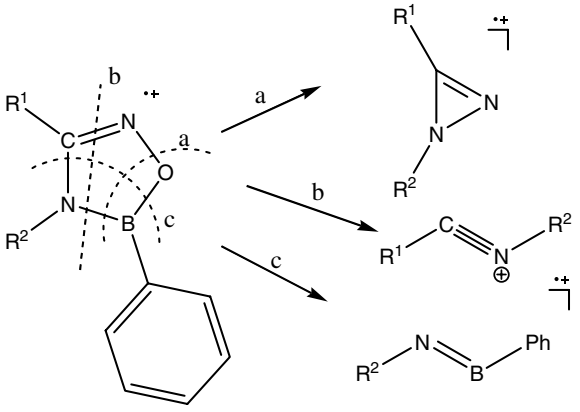
	R^1	R^2		R^1	R^2
5a	5-Chloro-2-thienyl	Ph	**5l**	5-Chloro-2-furyl	4-MeO-C_6H_4
5b	2-Thienyl	4-Me-C_6H_4	**5m**	5-Chloro-2-furyl	4-Cl-C_6H_4
5c	5-Chloro-2-thienyl	4-Me-C_6H_4	**5n**	5-Chloro-2-furyl	4-Br-C_6H_4
5d	2-Thienyl	4-MeO-C_6H_4	**5o**	5-Chloro-2-furyl	4-I-C_6H_4
5e	5-Chloro-2-thienyl	4-MeO-C_6H_4	**5p**	5-Chloro-2-furyl	1-Naphthyl
5f	5-Chloro-2-thienyl	4-Cl-C_6H_4	**5q**	2-Pyridyl	Me
5g	5-Chloro-2-thienyl	4-Br-C_6H_4	**5r**	2-Pyridyl	Et
5h	5-Chloro-2-thienyl	4-I-C_6H_4	**5s**	2-Pyridyl	1-Naphthyl
5i	5-Chloro-2-thienyl	1-Naphthyl	**5t**	4-Pyridyl	Ph
5j	5-Chloro-2-furyl	Ph	**5u**	4-Pyridyl	4-Me-C_6H_4
5k	5-Chloro-2-furyl	4-Me-C_6H_4	**5v**	Ph	4-Me-C_6H_4

Scheme 2. Structure of the 1,2,4,5-oxadiazaboroles.

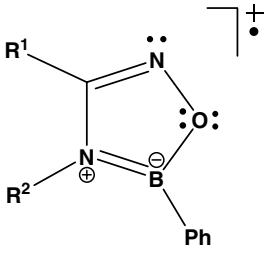
^{13}C NMR (100 MHz, DMSO-d_6): δ 149.85, 148.37, 138.56, 134.45, 130.80, 130.20, 129.32, 128.57, 127.56, 122.45, 120.94, 20.68. ^{11}B NMR (160.46 MHz, $CDCl_3$–15% $BF_3 \cdot Et_2O$): δ 32.2. MS (*m*/*z*,%): 313 (M^+,100), 298 (7), 208 (10), 193 (23), 104 (7), 91(9), 77 (8), 51(6). HRMS calcd for $C_{19}H_{16}BN_3O$: 313.1386; found: 313.1415.

2.3.22. 3,5-Diphenyl-4-(4-methylphenyl)-4,5-dihydro-1,2,4,5-oxadiazaborole (**5v**)

Yield: 85%. M.p. 243–245 °C (hexane–ethyl acetate). R_f: 0.51 (hexane:ethyl acetate; 2:1). IR (KBr, ν_{max}: cm^{-1}): 1600, 1539, 1514 (C=N), 1438 (B–N), 1373 (B–O), 1028, 822, 698. ^{1}H NMR (300 MHz, $CDCl_3$): δ 7.75–6.69 (m, 14H), 2.46 (s, 3H). ^{11}B NMR (160.46 MHz, $CDCl_3$–15% $BF_3 \cdot Et_2O$): δ 32.3. MS (*m*/*z*,%): 312 (M^+,100), 297 (6), 208 (15), 193 (26), 104 (11), 91(12), 77 (15). HRMS calcd for $C_{20}H_{17}BN_2O$: 312.1434; found: 312.1460.



Scheme 3.



Scheme 4.

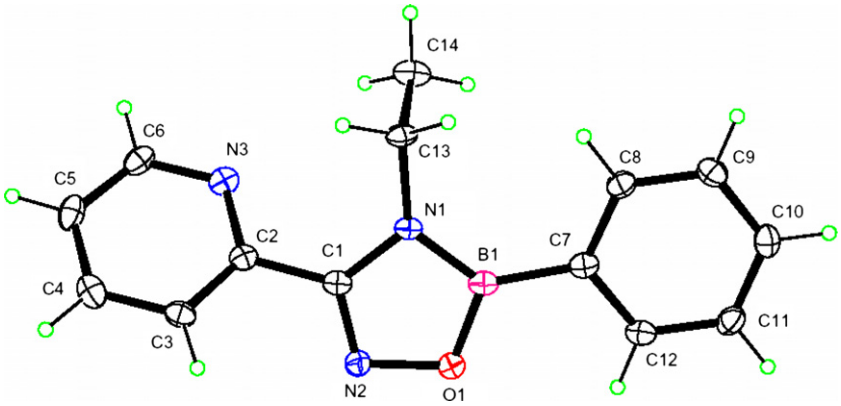


Fig. 1. X-ray ORTEP view of **5r**.

3. Results and discussion

In a recent paper [11] we described the synthesis and protonation equilibria of 4-unsubstituted 1,2,4,5-oxadiazaboroles in non-aqueous media. In the present work we report here the synthesis of some novel 3,4,5-trisubstituted 1,2,4,5-oxadiazaboroles bearing thiophene, furan and pyridine at the 3-position of the heterocyclic ring. The *N*-substituted amidoximes used as the starting compounds were obtained as described in the literature [12–24] (Scheme 1).

The new oxadiazaboroles **5a**–**v** (Scheme 2) show strong absorptions related to the B–N and B–O stretching vibrations in the 1516–1438 and 1391–1348 cm^{-1} regions in their IR spectra, which are remarkably consistent with the reported values for B–O and B–N stretching frequencies [25]. Iminic carbon chemical shifts of the title oxadiazaboroles in their ^{13}C NMR spectra appeared to resonate in the deshielded region at around 160–149 ppm. When there is a 2-pyridyl group on the number three carbon of the heterocycle, the iminic carbon chemical shifts go to more deshielded lowfield regions. In addition, the ^{11}B NMR spectra of these compounds were measured (the conditions are given in Section 2) and the boron chemical shift frequencies appear between 32.0 and 33.2 ppm, which can be considered as an indication of a trigonal planar sp^2 hybridized boron atom [26,27].

As for the electron impact mass spectra of the oxadiazaboroles; peaks related to the following fragmentations: diaziridine cation in route **a**, nitrilium cation in route **b** and borimide cation in route **c**, would occur (Scheme 3).

Except for compounds **5p** and **5r**, all of the molecular ion peaks have relative abundances of 100%, on account of the following structure which has aromatic stability (Scheme 4).

As a representative view, the X-ray crystal structure and selected atomic parameters are given for compound **5r** (Fig. 1, Tables 1 and 2).

Table 1
Crystallographic data for 3-(2-pyridyl)-4-ethyl-5-phenyl-4,5-dihydro-1,2,4,5-oxadiazaborole (**5r**)

Empirical formula	$C_{14}H_{14}BN_3O$
Formula weight (amu)	251.09
Crystal color, habit	colorless, lath fragment
Crystal dimensions (mm)	0.30 × 0.07 × 0.03
Crystal system	Orthorhombic
Space group	*Pbca*
Cell parameters at T (K)	90
α (Å)	11.600 (2)
b (Å)	10.1778 (17)
c (Å)	21.602 (4)
V (Å^3)	2550.4 (8)
Z	8
D_{calc} (Mg m^{-3})	1.308
Absorption correction	none
θ Range for collection (°)	2.5–27.8
Number of reflections measured	23865
Number of independent reflections	3022
Observed reflections	$X = 2$
$[I > X\sigma(I)]$	2142
Refinement method	full matrix least squares on F^2
Final R indices $[I > X\sigma(I)]$	$X = 2$
	$R[F^2 > 2\sigma(F^2)] = 0.049$
	$wR(F^2) = 0.097$

Table 2
Selected bond distances (Å) and bond angles (°) with estimated standard deviations of 3-(2-pyridyl)-4-ethyl-5-phenyl-4,5-dihydro-1,2,4,5-oxadiazaborole (**5r**)

Bond distances		Bond angles	
O1–B1	1.387 (2)	B1–O1–N2	108.70 (11)
O1–N2	1.4370 (16)	O1–B1–N1	106.64 (13)
N1–C1	1.3796 (19)	O1–B1–C7	120.49 (14)
N1–B1	1.430 (2)	N1–B1–C7	132.86 (14)
N1–C13	1.4764 (18)	C1–N1–B1	104.97 (12)
N2–C1	1.3062 (19)	C1–N1–C13	123.75 (13)
N3–C6	1.344 (2)	B1–N1–C13	131.02 (13)
N3–C2	1.3492 (19)	C1–N2–O1	105.38 (11)
		C6–N3–C2	116.65 (13)
		N2–C1–N1	114.32 (13)
		N2–C1–C2	118.96 (13)
		N1–C1–C2	126.69 (13)
		N3–C2–C3	123.57 (14)
		N3–C2–C1	116.29 (13)

Acknowledgements

Abant İzzet Baysal University, Research Fund (BAP Grant No. 2006.03.03.249) for financial assistance and Dr. F.R. Fronczek (Lousiana State University, Baton Rouge, LA, USA) for X-ray diffraction data are gratefully acknowledged.

Appendix A. Supplementary material

CCDC data_MA50 contains the supplementary crystallographic data for **5r**. These data can be obtained free of charge via http://www.ccdc.cam.ac.uk/conts/retrieving.html, or from the Cambridge Crystallographic Data Centre, 12 Union Road, Cambridge CB2 1EZ, UK; fax: (+44) 1223-336-033; or e-mail: deposit@ccdc.cam.ac.uk. Supplementary data associated with this article can be found, in the online version, at doi:10.1016/j.poly.2007.11.043.

References

[1] D.N. Nicolaides, E.A. Varella, in: S. Patai (Ed.), The Chemistry of Acid Derivatives, vol. 2, Suppl. B, John Wiley & Sons Ltd., 1992, p. 875.
[2] F. Eloy, R. Lenaers, Chem. Rev. 62 (1962) 55.
[3] K.S. Webb, D. Levy, Tetrahedron Lett. 36 (1995) 5117.
[4] C. Thiebes, G.K.S. Prakash, N.A. Petasis, G. Olah, Synlett (1998) 141.
[5] A. Suzuki, Pure Appl. Chem. 66 (1994) 213.
[6] N. Miyaura, A. Suzuki, Chem. Rev. 95 (1995) 2457.
[7] A. Dornow, K. Fischer, Chem. Ber. 99 (1966) 68.
[8] A.B. Goel, V.D. Gupta, J. Indian Chem. Soc. 54 (1977) 581.
[9] (a) H.L. Yale, J. Heterocycl. Chem. 8 (1971) 205;
(b) H.L. Yale, J. Heterocycl. Chem. 8 (1971) 193.
[10] P.I. Paetzold, G. Stohr, Chem. Ber. 101 (1968) 2874.
[11] Y. Dürüst, N. Dürüst, M. Akcan, J. Chem. Eng. Data 52 (2007) 718.
[12] Y. Dürüst, C. Altuğ, F. Kılıç, Phosphorus Sulfur Silicon 182 (2007) 299.
[13] N. Dürüst, Y. Dürüst, İ. Meriç, Turk. J. Chem. 26 (2002) 833.
[14] Y. Dürüst, F. Nohut, Synth. Commun. 29 (1999) 1997.
[15] H. Ağırbaş, Y. Dürüst, D. Sümengen, Phosphorus Sulfur Silicon 66 (1992) 321.
[16] Y. Dürüst, N. Dürüst, Synth. Commun. 22 (1992) 209.
[17] Y. Dürüst, H. Ağırbaş, D. Sümengen, Phosphorus Sulfur Silicon 62 (1991) 47.
[18] T.L. Deegan, T.J. Nitz, D. Cebzanov, D.E. Pufko, J.A. Porco Jr., Bioorg. Med Chem. Lett. 9 (1999) 209.
[19] J.B. Hynes, R.F. Gratz, J. Med. Chem. 15 (1972) 198.
[20] H.A. Oskooie, M.M. Heravi, Z. Jaddi, Phosphorus Sulfur Silicon 180 (2005) 1993.
[21] K. Niknam, B. Karami, A.R. Kiasat, Bull. Korean Chem. Soc. 26 (2005) 975.
[22] N. Iranpoor, H. Firouzabadi, G. Aghapour, Synth. Commun. 32 (2002) 2535.
[23] S. Chandrasekhar, K. Gopalaiah, Tetrahedron Lett. 42 (2001) 8123.
[24] T. L Ho, C.M. Wong, Synth. Commun. 5 (1975) 299.
[25] B. Stuart, Infrared Spectroscopy: Fundamentals and Applications, John & Wiley Sons, Inc., Hoboken, NJ, 2004, p. 83.
[26] W. Kliegel, G. Lubkowitz, J.O. Prokriefke, S.J. Rettig, J. Trotter, Can. J. Chem. 79 (2001) 26.
[27] S. Hermanek, Chem. Rev. 92 (1992) 325.

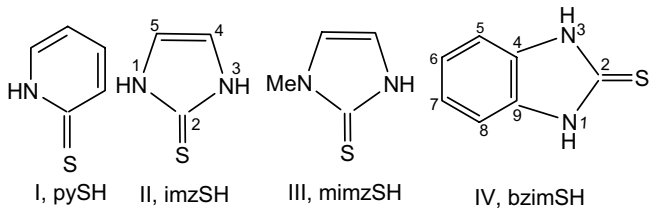


Chart 1.

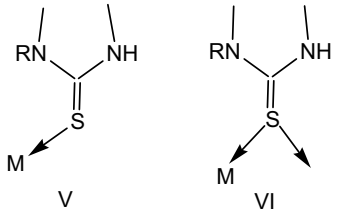


Chart 2. Models of bonding.

neutral ligands, monomers and dimers exhibited modes V (1κS) and VI (μ-1κ^{2}S) modes of bonding (Chart 2).

Recently, we have reported that reaction of 1,3-imidazolidine-2-thione (imzdSH), a saturated analogue of imzSH (II, Chart 1) with copper(I) bromide/iodide (2:1 molar ratio, L:M) has formed novel linear polymers, $\{Cu_6(\mu_3\text{-}1\kappa^3S\text{-imzdSH})_4(\mu\text{-}1\kappa^2S\text{-imzdSH})_2(\mu\text{-}I)_2I_4\}_n$, $\{Cu_6(\mu_3\text{-}1\kappa^3S\text{-imzdSH})_2(\mu\text{-}1\kappa^2S\text{-imzdSH})_4(\mu\text{-}X)_4X_2\}_n$, (X = Br, I), as well as dimers, $\{Cu_2(\mu\text{-}1\kappa^2S\text{-imzdSH})_2(\eta^1\text{-}S\text{-imzdSH})_2Br_2\}$ and $\{Cu_2(\mu\text{-}1\kappa^2S\text{-imzdSH})(1\kappa S\text{-imzdSH})_3Cl_2\}$ [7,8]. It was desired to carry out similar reactions of copper(I) halides with the unsaturated 1,3-imidazoline-2-thione (II, imzSH, Chart 1) and benzimidazoline-2-thione (IV, bzimSH) for obtaining polymeric compounds. The products of these reactions are reported herein.

2. Experimental

2.1. Materials and techniques

Copper(I) halides were prepared by reducing an aqueous solution of $CuSO_4 \cdot 5H_2O$ using SO_2 in the presence of NaX (X = Cl, Br, I) in water [22]. The reagents, 1,3-imidazoline-2-thione, benz-1,3-imidazoline-2-thione and Ph_3P, were procured from Aldrich Chemicals Ltd. and used as such. C, H and N analysis were obtained with Thermoelectron FLASHEA1112 CHNS analyzer. The IR spectra were recorded using KBr pellets in the range 4000–200 cm^{-1} on Pye-Unicam SP-3-300 spectrophotometer. The melting points were determined with a Gallenkamp electrically heated apparatus. ^{1}H NMR spectra were recorded on a JEOL AL-300 FT spectrometer operating at a frequency of 300 MHz in $CDCl_3$ with TMS as the internal reference. The ^{31}P NMR spectra were recorded on a Bruker ACP-300 spectrometer operating at a frequency of 121.5 MHz, using $CDCl_3$ with H_3PO_4 as the external reference.

2.2. Synthesis of complexes

2.2.1. $[Cu_2(1\kappa S\text{-imzSH})(PPh_3)_4Cl_2] \cdot CH_3OH$ (1)

To a solution of copper(I) chloride (0.025 g, 0.25 mmol) in acetonitrile was added a solution of 1,3-imidazoline-2-thione (0.025 g, 0.25 mmol) in acetonitrile, followed by stirring for 1 h at room temperature and to the white precipitates formed was added Ph_3P (0.132 g, 0.50 mmol) and stirred until a clear solution was obtained. The crystalline fibers formed were redissolved in MeOH and a layer of $CHCl_3$ was spread over it. The slow evaporation of solution at room temperature formed colorless crystals of **1**. The complex is soluble in chloroform, dichloromethane and acetonoirile (56%, m.p. 135–138 °C). *Anal.* Calc. for $C_{76}H_{68}Cl_2Cu_2ON_2P_4S$: C, 66.18; H, 4.93; N, 2.03. Found: C, 66.36; H, 4.90; N, 1.63%. Main IR peaks (KBr, cm^{-1}): 3363 s, ν(O–H); 3118–3092 m ν(N–H) + ν(C–H)$_{Ph}$; 2988 w, 2862 m ν(C–H); 1581 s, 1481 s ν(C–N) + δ(C–H); 1217 s ν(C–S); 1093 s ν(P–C$_{Ph}$). ^{1}H NMR data ($CDCl_3$, δ ppm): 7.23 t (C^{4,5}H, imzSH), 7.37 m (*o*-H), 7.33 m (*p*-H), 7.25–7.27 m (*m*-H) (Species **1a**), 7.67 m (*o*-H), 7.55 m (*p*-H), 7.46 m (*m*-H) (Species **1b**). ^{31}P NMR ($CDCl_3$): −3.42 (Species **1a**), 30.74 (Species **1b**) ppm. $\Delta\delta(\delta_{complex} - \delta_{PPh3}) = 1.28$ (Species **1a**); 35.44 (Species **1b**).

Compound **2** was prepared similarly. Here crystals were grown from the reaction solvents (CH_3CN–$CHCl_3$) when allowed to evaporate slowly.

2.2.2. $[CuBr(1\kappa S\text{-imzSH})(PPh_3)_2] \cdot H_2O$ (2)

Complex **2** is soluble in chloroform, dichloromethane and acetonoirile (73%, m.p. 155–157 °C). *Anal.* Calc. for $C_{39}H_{36}BrCuN_2OP_2S$: C, 59.58; H, 4.58; N, 3.56. Found: C, 60.31; H, 4.41; N, 3.12%. Main IR peaks (KBr, cm^{-1}): 3396 s, ν(O–H); 3137 w, 3138 m ν(N–H); 3001–3070 w ν(C–H)$_{Ph}$; 2983 w, 2904 w ν(C–H); 1581 s, 1477 s ν(C–N) + δ(C–H); 1216 s ν(C–S); 1083 s, ν(P–C$_{Ph}$). ^{1}H NMR data ($CDCl_3$, δ ppm): 6.74 t (C^{4,5}H), 10.9 b (NH), 7.66 m (*o*-H), 7.54 m (*p*-H), 7.47 m (*m*-H) [$CuBr(PPh_3)_2$], 7.41 m (*o*-H), 7.33 m (*p*-H), 7.27 m (*m*-H) (**2**). ^{31}P NMR ($CDCl_3$): $\delta = -4.3$, $\Delta\delta(\delta_{complex} - \delta_{PPh3})$, 0.40 (**2**) ppm. Crystals were grown from CH_3CN–$CHCl_3$ mother liquor. Compound **3** was prepared similarly.

2.2.3. $[CuI(1\kappa S\text{-imzSH})(PPh_3)_2]$ (3)

Complex **3** is soluble in chloroform, dichloromethane and chloroform (71%, m.p. 205–207 °C). *Anal.* Calc. for $C_{39}H_{34}ICuN_2P_2S$: C, 57.46; H, 4.17; N, 3.44. Found: C, 57.24; H, 4.15; N, 3.14%. Main IR peaks (KBr, cm^{-1}): 3145 w, ν(N–H); 3070 w, 3051 w ν(C–H)$_{Ph}$; 2981 w, 2958 w ν(C–H); 1577 s, 1473 s ν(C–N) + δ(C–H); 1184 s ν(C–S); 1091 s ν(P–C$_{Ph}$). ^{1}H NMR data ($CDCl_3$, δ ppm): 6.79 t (C^{4,5}H), 7.68 m (*o*-H), 7.64 m (*p*-H), 7.54 m (*m*-H) [$CuI(PPh_3)_2$], 7.47 m (*o*-H), 7.39 m (*p*-H), 7.27 m (*m*-H) (**3**). ^{31}P NMR ($CDCl_3$), −5.1, $\Delta\delta(\delta_{complex} - \delta_{PPh3})$, −0.4 ppm **3**.

Table 1
Crystallographic data for compounds **1**–**4**

	1	**2**	**3**	**4**
Empirical formula	$C_{76}H_{68}C1_2Cu_2N_2OP_4S$	$C_{39}H_{36}BrCuN_2OP_2S$	$C_{39}H_{34}CuIN_2P_2S$	$C_{46}H_{42}BrCuN_2OP_2S$
Formula weight	1379.27	784.13	815.12	874.25
T (K)	295(2)	295(2)	295(2)	295(2)
Wavelength (Å)	0.71073	0.71073	0.71073	0.71073
Crystal system	triclinic	monoclinic	monoclinic	monoclinic
Space group	$P\bar{1}$	$P2_1/n$	$P2_1/n$	$P2_1/c$
a (Å)	9.992(1)	9.623(1)	9.441(2)	13.099(1)
b (Å)	17.6240(10)	22.005(2)	19.554(2)	18.737(2)
c (Å)	19.902(2)	17.6510(10)	19.856(3)	17.407(1)
α (°)	84.18(1)	90	90	90
β (°)	87.50(1)	96.61(1)	92.64 (1)	97.81(9)
γ (°)	78.26(1)	90	90	90
V (Å^3)	3412.8(5)	3712.8(6)	3661.7(1)	4232.6(6)
Z	2	4	4	4
D_{calc} (Mg m^{-3})	1.342	1.403	1.479	1.372
Absorption coefficient (mm^{-1})	0.872	1.839	1.614	1.621
Crystal size (mm)	0.2 × 0.2 × 0.1	0.2 × 0.1 × 0.1	0.2 × 0.1 × 0.1	0.2 × 0.2 × 0.1
θ Range (°)	1.49–29.97	1.48–25.50	1.46–25.50	1.60–25.50
Reflection collected	13816	7105	7258	8235
Unique reflections [R_{int}]	12811 [0.0320]	6674 [0.0383]	6824 [0.0423]	7877 [0.0441]
Final R indices [$I > 2\sigma(I)$]	$R_1 = 0.0452$, $wR_2 = 0.1090$	$R_1 = 0.0535$, $wR_2 = 0.1227$	$R_1 = 0.0529$, $wR_2 = 0.1155$	$R_1 = 0.0698$, $wR_2 = 0.1778$
R indices (all data)	$R_1 = 0.0713$, $wR_2 = 0.1211$	$R_1 = 0.1388$, $wR_2 = 0.1645$	$R_1 = 0.1282$, $wR_2 = 0.1534$	$R_1 = 0.1454$, $wR_2 = 0.2409$

2.2.4. *[CuBr(1κS-bzimSH)(PPh$_3$)$_2$] · CH$_3$COCH$_3$ (**4**)*

To a suspension of copper(I) bromide (0.025 g, 0.17 mmol) in acetone was added a solution of benz-1,3-imidazoline-2-thione (0.026 g, 0.17 mmol) in acetone, followed by stirring for 2 h at room temperature and to the white precipitates formed was added PPh_3 (0.091 g, 0.34 mmol) and contents stirred until a clear solution was obtained. The slow evaporation of solution at room temperature formed colorless crystals of **4**. This complex is soluble in chloroform, acetonitrile and dichloromethane (72%, m.p. 228–231 °C). *Anal.* Calc. for $C_{46}H_{42}BrCuN_2OP_2S$: C, 63.05; H, 4.79; N, 3.20. Found: C, 62.97; H, 4.51; N, 2.90%. Main IR peaks (KBr, cm^{-1}): 3110–3041m, ν(N–H) + ν(C–H)$_{Ph}$; 2958 w, 2854 m ν(C–H);1608 w, 1604 w ν(C–N) + δ(C–H); 1155 s ν(C–S); 1091 m ν(P–C$_{Ph}$). ^{1}H NMR data ($CDCl_3$,δ ppm): 11.2 bs (NH) 7.64–7.71 m (*o*-H, *p*-H), 7.55 m (*m*-H) [$CuBr(PPh_3)_2$], 7.47 m (*o*-H), 7.35 m (*p*-H), 7.22–7.30 m (*m*-H, C$^{4-7}$H, bzimzSH) (**4**). ^{31}P NMR ($CDCl_3$), 30.84 [$CuI(PPh_3)_2$], −3.6 (**4**); $\Delta\delta(\delta_{complex} - \delta_{PPh3})$, 35.54 [$CuI(PPh_3)_2$], 1.10 ppm **4**.

2.3. X- ray crystallography

The data for compounds **1**–**4** were collected at 294(1) K on a Siemens P4 diffractometer. The θ-2θ technique was used to measure the intensities up to a maximum of $2\theta = 5°$, with graphite-monochromatised Mo Kα radiator ($\lambda = 0.71073$ Å). Cell parameters were refined in the θ range, 12–20° using XSCANS [23]. The data were corrected for Lorentz and polarization factors. An empirical psi absorption correction was applied. The structure was solved by the direct methods and refined by full matrix least squares methods based on F^2. All non-hydrogen atoms were refined anisotropically, and hydrogen atoms were assigned calculated positions. Scattering factors from the International Tables for X-ray crystallography were used [24]. Data reduction, structure solution, refinement and molecular graphics were performed using SHELXTL-PC [25] and WINGX [26]. For compound **2**, the imidazole ring showed disorder in terms of having unusual bond distances and slightly higher thermal parameters. The disorder could not be resolved and the structure was refined by adding following restraints on bond distances involving the group (C37–N1, C37–N2 1.373(3), C38–N1, C38–N2 1.440(3), C38–C39 1.336(3) and C37–S1 1.703(3) Å, respectively). Hydrogens of water molecule could not be located from the difference Fourier map and have not been included in the model. All other hydrogens were fixed geometrically and were not refined. The cell and refinement parameters are summarized in Table 1.

3. Results and discussion

3.1. Synthesis and infrared spectroscopy

Reactions of 1,3-imidazoline-2-thione (imzSH) with copper(I) halides in 2:1 molar ratio did not yield polymers similar to that formed by 1,3-imidazolidine-2-thione mentioned in introduction [7,8]. There was a change in color from colorless to green (probably due to Cu^{II}) when solution was left in open for several days and no crystalline product could be isolated. The addition of triphenyl phosphine (Ph_3P) yielded crystalline products. Thus the reaction of copper(I) chloride with imzSH in the presence of Ph_3P in 1:2:2 or 1:1:2 (M:L:PPh_3) molar ratios yielded a compound of unusual composition, $[Cu_2(imzSH)(PPh_3)_4Cl_2] \cdot CH_3OH$

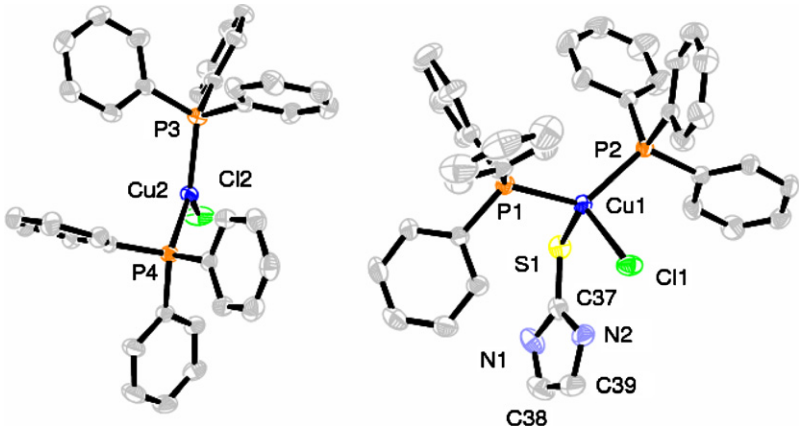


Fig. 1. Two crystallographically independent molecules of $[CuCl(1\kappa S\text{-imzSH})(PPh_3)_2]\cdot[CuCl(PPh_3)_2]$ (**1**) and their partial labeling scheme. Solvent molecule and the hydrogen atoms have been removed for clarity.

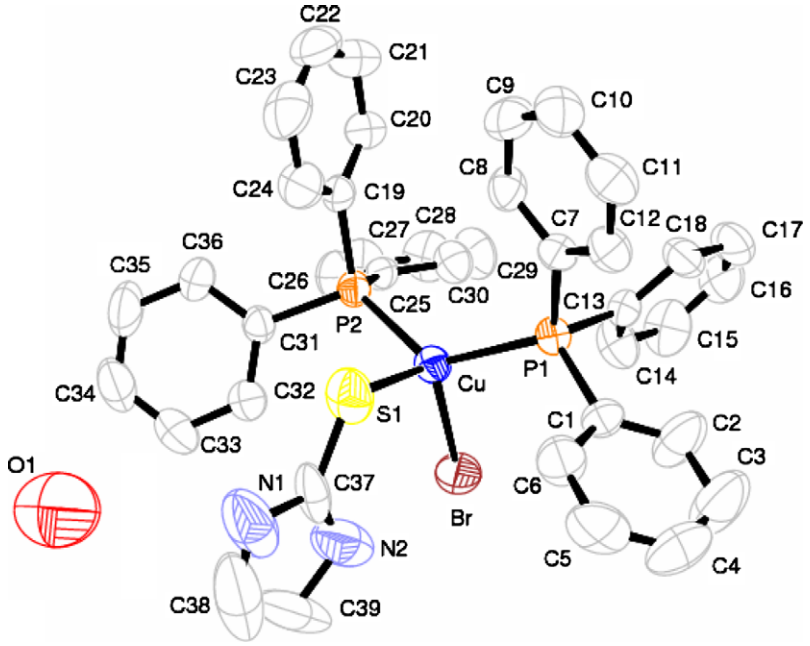


Fig. 2. The structure of $[CuBr(1\kappa S\text{-imzSH})(PPh_3)_2]\cdot H_2O$ (**2**) with numbering scheme.

(**1**), whose X-ray crystallography has shown that its crystals consists of four coordinated $[CuCl(1\kappa S\text{-imzSH})(PPh_3)_2]$ (**1a**) and three coordinated $[Cu(PPh_3)_2Cl]$ (**1b**) independent molecules in the same unit cell (vide infra). In contrast, crystals of complexes of copper(I) bromide/iodide are formed by single molecules of $[CuBr(1\kappa S\text{-imzSH})(PPh_3)_2]\cdot H_2O$ (**2**) and $[CuI(1\kappa S\text{-imzSH})(PPh_3)_2]$ (**3**), respectively, similar to molecule **1a**. A related ligand, 1,3-benzimidazoline-2-thione (bzimSH) formed the complex $[CuBr(1\kappa S\text{-bzimSH})(PPh_3)_2]\cdot CH_3COCH_3$ (**4**), similar to mononuclear complexes, $[Cu(1\kappa S\text{-bzimSH})(PPh_3)_2Cl]\cdot$ acetone and $[Cu(1\kappa S\text{-bzimSH-7-}NO_2)(PPh_3)_2Cl]$ [19a]. In the literature, dealing copper-heterocyclic thioamide chemistry, the only analogous formation of two independent molecules $[Cu(1\kappa S\text{-bztz2SH})_2(PPh_3)_2]$ **A** and][CuCl(1κS-bztz2SH)$(PPh_3)_2$] **B** in the unit cell, resulted from the reaction of $CuCl(PPh_3)_3$ with benzo-1,3-thiazoline-2-thione in 1:2 molar ratio in CH_3CN–MeOH, each having a tetrahedral geometry [27].

The main characteristic IR peaks of complexes of 1,3-imidazoline-2-thione (imzSH) and benz-1,3-imidazoline-2-thione (bzimSH) are listed in the experimental section. The ν(N–H) peak of free imzSH at 3118–3092(m) cm^{-1} undergoes low energy shifts to 3002–3145 cm^{-1} in complexes **1**–**3**. In complex **4**, the ν(N–H) and $\nu(C–H)_{Ph}$ signals merge in the region, 3110–3041 m cm^{-1}. The most significant diagnostic peak due to ν(C=S) in the free imzSH ligand at 1232 cm^{-1} shifts to low energy region 1217–1184 cm^{-1} in its complexes **1**–**3**. Similarly, the ν(C=S) peak of the free bzimSH ligand at 1177 (s) cm^{-1} undergoes low

energy shift to 1155 (s) cm^{-1} in **4**. The shifts in ν(C=S) peaks in all the complexes is attributed to the weakening of C=S bond due to the coordination of thione sulfur to the metal center. In all the complexes, the presence of ν(P–C_{Ph}) occurred in the range, 1083–1093 cm^{-1}. The presence of methanol and water in complexes **1** and **2** has been detected by the presence of ν(O–H) at 3363 (**1**, methanol) and 3396 (**2**, water).

3.2. Crystal structures of complexes 1–4

Complex **1** crystallized in triclinic system with space group $P\bar{1}$, while complexes **2**, **3** and **4** crystallized in monoclinic system with space groups $P2_1/n$ (**2**, **3**) and $P2_1/c$ (**4**). The atomic numbering schemes of complexes **1**, **2**, **3** and **4** are shown in Figs. 1–4, packing diagram in Figs. 5–8 and selected bond lengths and angles are given in Table 2.

3.2.1. Complex [CuCl(1κS-imzSH)(PPh$_3$)$_2$] · [CuCl(PPh$_3$)$_2$] (1)

Complex **1** has four coordinated [CuCl(1κS-imzSH)(PPh$_3$)$_2$] (**1a**) and three coordinated [Cu(PPh$_3$)$_2$Cl] (**1b**) independent molecules in the same unit cell (Fig. 1). In molecule **1a**, Cu is bonded to two P atoms of PPh_3, one S atom of imzSH, and one Cl atom with bond angles around copper in the range, ca. 100–125° (Table 2). It reveals distorted tetrahedral geometry. In molecule **1b**, Cu is bonded to two P atoms of PPh_3, and one Cl atom with bond angles around copper in the range, ca. 114–128° and geometry is distorted trigonal planar. The P–Cu–P angle in **1b** [127.76(3)°] is higher than that in **1a** [124.49(3)°] due to less steric crowding in the trigonal planar geometry. This P–Cu–P angle in **1a** is higher than 122.4° in analogous complex [CuL(PPh$_3$)$_2$Cl] (L = 1, 3- thiazolidine-2-thione) [28]. The Cu–S bond distance, 2.3643(10) Å, in molecule **1a** is comparable with literature values {2.381–2.418 Å} [28,29]. The Cu–Cl bond distance 2.4272(9) Å in complex **1a** is less than sum the of ionic radii of Cu^+ and Cl^-(Cu^+, Cl^-, 2.58 Å) [30]. The Cu–P bond distances, 2.2976(8), 2.2815(9) Å in **1a** are expectedly longer than 2.2695(9), 2.2720(8) Å in three coordinated **1b**, which are similar to Cu–P distances in the analogous complexes [29,31].

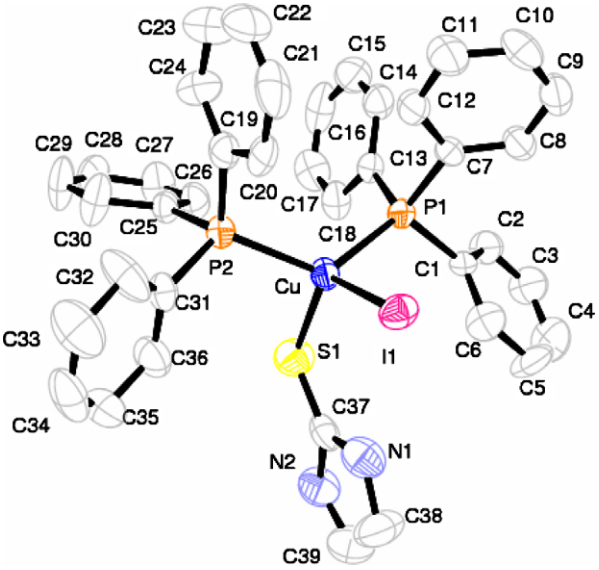


Fig. 3. The structure of [CuI(1κS-imzSH)(PPh$_3$)$_2$] (**3**) with numbering scheme.

3.2.2. Structures of complexes 2–4

In complex **2**, Cu is bonded to two P atoms of Ph_3P ligands, one S atom of the 1,3-imidazoline-2-thione, and one bromine atom. Similar is binding pattern in complexes

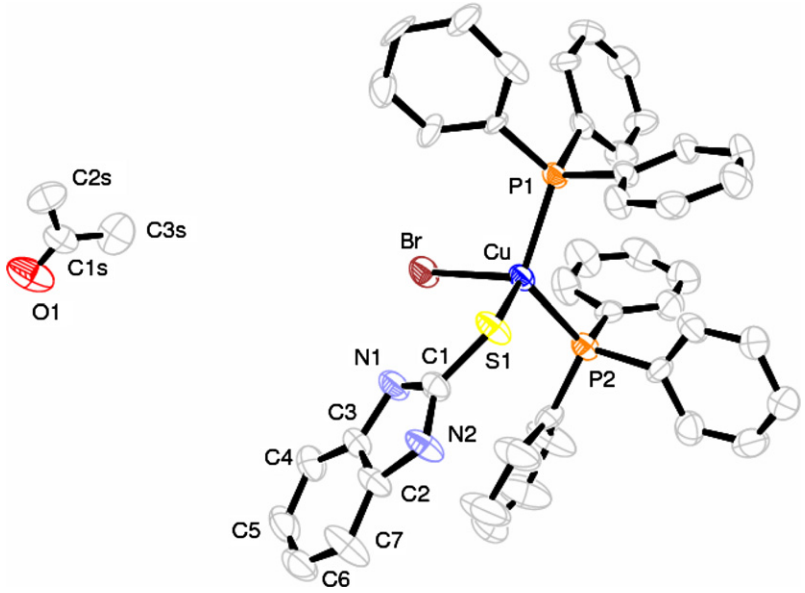


Fig. 4. The structure of [CuBr(1κS-bzimSH)(PPh$_3$)$_2$] · CH_3COCH_3 (**4**) with partial numbering scheme and the solvent.

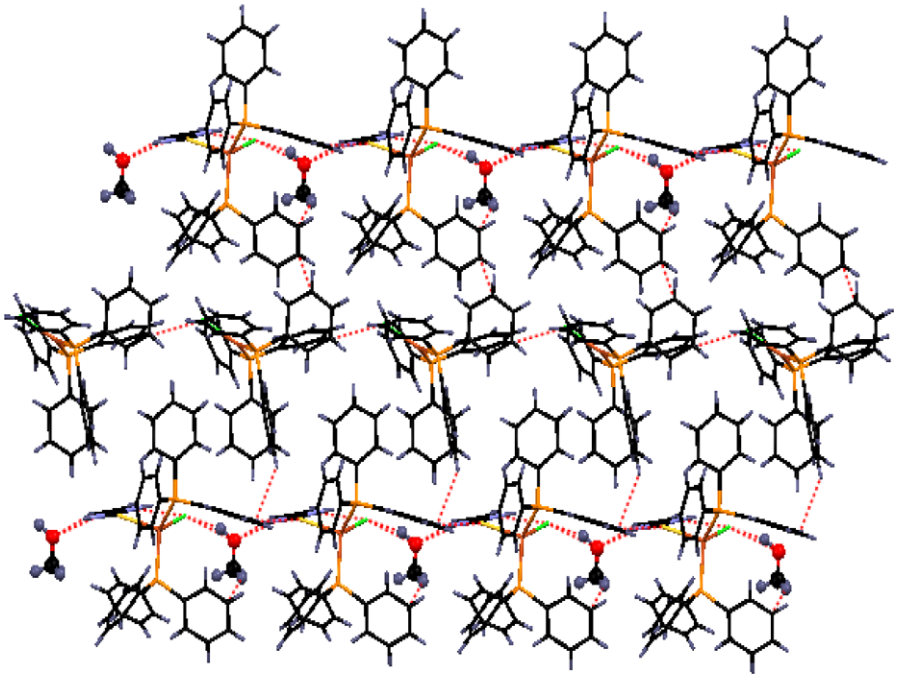


Fig. 5. Crystal structure of complex **1** showing the alternate 1D linear chains of molecule **1a** and molecule **1b**. These two independent chains are further linked to each other due to edge-to-edge π...π and C–H...π interactions forming a 2D network.

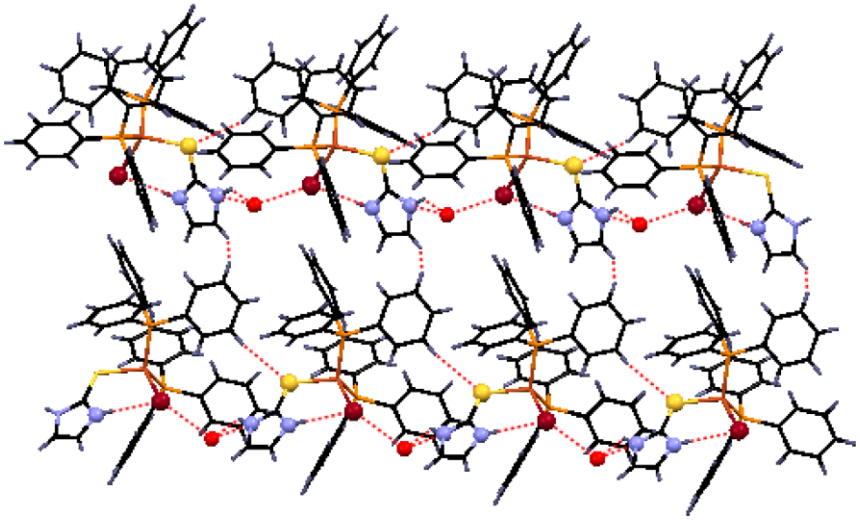


Fig. 6. Packing diagram of compound **2** showing formation 2D structure due to H-bonding and edge-to-edge π...π interactions.

3 and **4** (Figs. 2–4). The angles around Cu lie in the ranges 100.47(7)–128.77(7)°, 102.09(10)–125.06(8)° and 103.64(9)–122.21(8)° in complexes **2**, **3** and **4**, respectively, with P(2)–Cu–P(1) being the largest, and P–Cu–X {X = Br, I} being the smallest. The P–Cu–P angles in complexes **1a**, **2**–**4** are 124.49(3), 128.77(7), 125.06(8) and 122.21(8)°, respectively, and are influenced by the steric and intra- and inter-molecular hydrogen bonding interactions. This reveals a distorted tetrahedral geometry around each copper atom in mononuclear complexes. The Cu–S bond distances lie in close range 2.344(3)–2.373(2) Å in complexes **2**–**4** and are comparable with 2.3643(10) Å in molecule **1a**. The Cu–P distances lie in the range, 2.2819(17)–2.326(3) Å, in complexes **2**–**4**, similar to the distances found in complex **1a**. The Cu–Br and Cu–I bond distances are less than the sum of the ionic radii of Cu^{+} and X^{-} (Cu^{+}, Br^{-}, 2.73; Cu^{+}, I^{-}, 2.97 Å) [30].

3.3. Packing networks of complexes *1–4*

The packing diagram of **1** (Fig. 5) shows alternate 1D linear chains of molecule **1a** and molecule **1b**. Molecule **1a** forms these linear chains due to methanol...chlorine (O1S···Cl 1^{i}) and phenylene C...S (C29...S^{ii}) intermolecu-

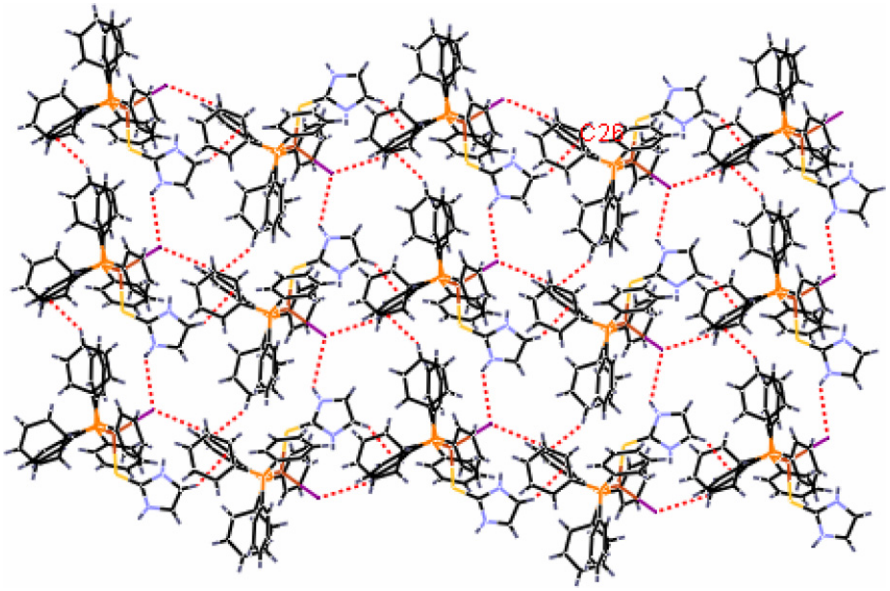


Fig. 7. Crystal structure of compound **3** showing pleated sheet like 2D structure.

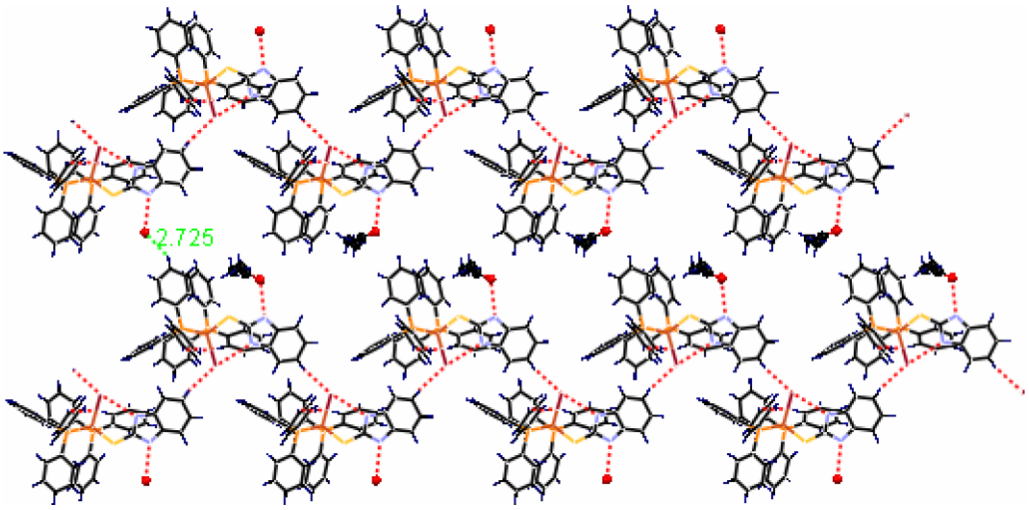


Fig. 8. Packing diagram of compound **4** showing the formation of a 2D H-bonded network in the *bc* plane.

lar and imidazole...methanol (N1···O1S), and imidazole...chlorine (N2···Cl1) intramolecular H-bonding interactions. Molecule 1b is linearly chained due to C74...Cl2 H-bonding interactions. These two independent chains are further linked to each other to form a 2D network due to edge-to-edge π...π interactions between rings **A** (C13–C18) and **I** (C52–C57) and rings **G** (C40–C45) and **E** (C25–C30), with distances of 3.319 and 3.502 Å, respectively, and also due to C–H...π interaction between centroid of ring **C** (C13–C18) and methanol C1S with a distance of 3.688 Å (Table 3).

Complex **2** involves intramolecular H-bonding between imino nitrogen of imidazole and bromine atom (N2···Br) (Fig. 6). Water molecule is present in the crystal lattice and is engaged in intermolecular H-bonding with bromine atom (O1...Br) and with imino nitrogen of imidazole ring (N1···O1) to form the parallel linear chains. These chains are further linked to each other via edge-to-edge π···π interactions (3.582 Å) resulting in 2D structure.

In complex **3**, the terminal iodine atom is engaged in intramolecular H-bonding with imino hydrogen (N1···I1) (Fig. 7). The molecules are linked to each other by means of intermolecular H-bonding, C27···I1^{ii} and C38–H38···ring (C25–C30) (3.858(8) Å) C–H···π interactions to form zig-zag chains. These linear chains are further linked to each other by means of N2···I1^{i} and C–H···π interactions between C22–H22···ring (C25–C30) (3.659(9) Å) to form a pleated sheet like 2D structure.

In complex **4**, there is intramolecular H-bonding between imino hydrogen of imidazole and bromine atom (N1···Br). These molecules are further linked to each other by means of C5–H5···Br H-bonding to form a 1D zig-zag

Table 2
Bond lengths (Å) and bond angles (°) for compounds **1**–**4**

1a			
Cu1–S1	2.3643(10)	S(1)–C(37)	1.703(4)
Cu(1)–P(1)	2.2976(8)	N(2)–C(37)	1.399(5)
Cu(1)–P(2)	2.2815(9)	N(1)–C(37)	1.341(5)
Cu(1)–Cl(1)	2.4272(9)		
P(1)–Cu(1)–S(1)	102.60(4)	S(1)–Cu(1)–Cl(1)	106.43(3)
P(2)–Cu(1)–S(1)	111.40(3)	P(2)–Cu(1)–P(1)	124.49(3)
P(1)–Cu(1)–Cl(1)	110.81(4)	C(37)–S(1)–Cu(1)	109.13(12)
P(2)–Cu(1)–Cl(1)	100.17(3)		
1b			
Cu(2)–Cl(2)	2.2112(10)	Cl(2)–Cu(2)–P(4)	114.41(4)
Cu(2)–P(3)	2.2695(9)	P(3)–Cu(2)–P(4)	127.76(3)
Cu(2)–P(4)	2.2720(8)	Cl(2)–Cu(2)–P(3)	117.80(4)
2			
Cu–S(1)	2.366(2)	S(1)–C(37)	1.703(3)
Cu–P(1)	2.2819(17)	N(2)–C(37)	1.367(3)
Cu–P(2)	2.2862(18)	N(1)–C(37)	1.366(3)
Cu–Br	2.5312(11)		
P(1)–Cu–S(1)	106.06(7)	S(1)–Cu–Br	114.01(7)
P(2)–Cu–S(1)	100.47(7)	P(1)–Cu–P(2)	128.77(7)
P(1)–Cu–Br	103.14(5)	C(37)–S(1)–Cu	108.4(3)
P(2)–Cu–Br	104.80(6)		
3			
Cu–S(1)	2.344(3)	S(1)–C(37)	1.643(10)
Cu–P(1)	2.309(2)	N(2)–C(37)	1.352(10)
Cu–P(2)	2.291(2)	N(1)–C(37)	1.380(11)
Cu–I(1)	2.6729(11)		
P(1)–Cu–S(1)	102.09(10)	S(1)–Cu–(I)	118.30(8)
P(2)–Cu–S(1)	103.61(9)	P(2)–Cu–P(1)	125.06(8)
P(1)–Cu–I(1)	103.54(6)	C(37)–S(1)–Cu	115.3(3)
P(2)–Cu–I(1)	105.44(6)		
4			
Cu–S(1)	2.373(2)	S(1)–C(1)	1.690(8)
Cu–P(1)	2.277(2)	N(1)–C(1)	1.345(11)
Cu–P(2)	2.326(3)	N(1)–C(2)	1.371(10)
Cu–Br	2.5144(13)		
P(1)–Cu–S(1)	103.64(9)	S(1)–Cu–Br	108.05(7)
P(2)–Cu–S(1)	109.42(9)	P(1)–Cu–P(2)	122.21(8)
P(1)–Cu–Br	110.11(7)	C(1)–S(1)–Cu	107.2(3)
P(2)–Cu–Br	102.89(7)		

Table 3
Hydrogen bonds (Å) for complexes **1**–**4**

No.	D–H···A	*d*(D···A) (Å)	*d*(H···A) (Å)	∠D–H...A (°)
1	N2···Cl1	3.080(4)	2.15	156
	N1···OlS	2.711(6)	2.01	159
	O1S···Cl1^{i}	3.035(4)	2.09	160
	C29···S1^{ii}	3.779(4)	2.88	162
	C74···Cl2^{ii}	3.723(4)	2.92	145
2	N1···O1	2.693(12)	2.00	136
	N2···Br	3.228(7)	2.40	162
	C15···S1^{i}	3.801(9)	2.98	148
3	N1···I1	3.744(8)	2.92	162
	N2···I1^{i}	3.809(8)	3.17	132
	C36···S1	3.758(10)	2.92	150
	C27···I1^{ii}	3.909(9)	3.49	136
4	N1···Br	3.218(7)	2.40	159
	C5···Br^{i}	3.664(13)	2.80	154
	C11···O1^{ii}	3.492(13)	2.73	140
	N2···O1^{iii}	2.975(12)	2.21	147

For **1** (i) $x-1, +y, +z$; (ii) $x+1, +y, +z$.
For **2** (i) $x-1, +y, +z$.
For **3** (i) $x-1, y, z$; (ii) $3/2-x, y-1/2, 1/2-z$.
For **4** (i) $x, -y+1/2, +z-1/2$; (ii) $x, -y+1/2, +z+1/2$; (iii) $x, +y-1, +z$.

chain along *c*-axis (Fig. 8). Acetone as a solvent of crystallization is present in crystal lattice and is involved in intermolecular H-bonding N2···O1(solvent) along the chains. C11–H11···O1 weak H-bonds between phenylene C and the solvent helps to form a 2D network in the *bc* plane.

3.4. NMR spectroscopy

The ^{1}H NMR of ligand 1,3-imidazoline-2-thione (imzSH) in DMSO shows a singlet at 6.65 ppm due to equivalent ring ($C^{4}H$, $C^{5}H$) protons. When this ligand coordinates to the metal via its S electrons, ring protons become magnetically inequivalent and thus two expected doublets due to $C^{4}H$, $C^{5}H$ protons merge into an unresolved triplet. Each of complexes **1**–**3** showed a triplet at a low field (7.23, **1**; 6.74, **2**; 6.79 ppm, **3**). Interestingly, NMR spectrum of complex $[CuCl(1\kappa S\text{-imzSH})(PPh_3)_2]\cdot[CuCl(PPh_3)_2]$ (**1**) showed two sets of PPh_3 signals which revealed the formation of $[CuCl(1\kappa S\text{-imzSH})(PPh_3)_2]$ (**1a**) (7.25–7.27 ppm) and $[Cu(PPh_3)_2Cl]$ (**1b**) (7.46–7.67 ppm, PPh_3) in the solution state. Similarly complexes $[CuBr(1\kappa S\text{-imzSH})(PPh_3)_2]\cdot H_2O$ (**2**) and $[CuI(1\kappa S\text{-imzSH})(PPh_3)_2]$ (**3**) showed one set of PPh_3 signals in the regions 7.27–7.41 and 7.27–7.47 ppm, respectively, and another set of weak PPh_3 signals in the regions, 7.47–7.68 ppm showed the formation of compounds, namely, $Cu(PPh_3)_2Br$ and $Cu(PPh_3)_2I$ similar to **1b**. Complex $[CuBr(1\kappa S\text{-bzimSH})(PPh_3)_2]\cdot CH_3COCH_3$ (**4**) showed one set of signals due to PPh_3 in the region, 7.22–7.47 ppm similar to complexes **1a**, **2** and **3** and another set of PPh_3 signals in the region, 7.55–7.64 ppm due to $\{Cu(PPh_3)_2Br\}$. The peaks due to benzimidazoline ring merged with the PPh_3 protons in 7.22–7.64 ppm {cf. peaks due to free bzimSH ligand 7.23 m (2H, $C^{4,7}H$) and 7.15 m (2H, $C^{5,6}H$) in dmso-d_6}. Complexes **2** and **4** showed broad signal due to NH protons (10.2, **2**, 10.4, **4** ppm). The NH proton signals could not be identified in complexes **1** and **3** due to broadening.

The ^{31}P NMR spectra of compounds **1**–**4** showed signals at −3.42 (**1a**), −4.30 (**2**), −5.10 (**3**) and −3.60 ppm (**4**) with coordination shifts ($\Delta\delta$) of 1.28, 0.40, −0.40 and 1.10 3 ppm, respectively. In literature similar shifts in copper(I)–phosphine-heterocyclic thioamide complexes have been observed [29,32]. The signal due to $[CuCl(PPh_3)_2]$ (**1b**) has been identified at 30.74 ppm. Compound **4** showed additional signal at 30.84 ppm, attributed to the formation of species $[Cu(PPh_3)_2Br]$, however, compounds **2** and **3** did not show the formation of similar species $[Cu(PPh_3)_2Br]$ and $[Cu(PPh_3)_2I]$ in solution state.

4. Supplementary material

CCDC 658223, 658224, 658225 and 658226 contain the supplementary crystallographic data for **1**, **2**, **3** and **4**. These data can be obtained free of charge via http://www.ccdc.cam.ac.uk/conts/retrieving.html, or from the Cambridge Crystallographic Data Centre, 12 Union Road, Cambridge CB2 1EZ, UK; fax: (+44) 1223-336-033; or e-mail: deposit@ccdc.cam.ac.uk.

Acknowledgement

Financial assistance (Razia Sultana) from Prof. Harjit Singh Foundation for Promotion of Chemical Sciences, Department of Chemistry, Guru Nanak Dev University, Amritsar is gratefully acknowledged.

References

[1] E.S. Raper, Coord. Chem. Rev. 61 (1985) 115.
[2] E.S. Raper, Coord. Chem. Rev. 153 (1996) 199.
[3] E.S. Raper, Coord. Chem. Rev. 129 (1994) 91.
[4] E.S. Raper, Coord. Chem. Rev. 165 (1997) 475.
[5] (a) P.D. Akrivos, Coord. Chem. Rev. 213 (2001) 181;
(b) J.A. Garcia-Vazquez, J. Romero, A. Sousa, Coord. Chem. Rev. 193 (1999) 691.
[6] (a) S.S. Lemos, M.A. Camargo, Z.Z. Cardoso, V.M. Deflon, F.H. Forsterling, A. Hagenbach, Polyhedron 20 (2001) 849;
(b) P. Aslandis, S.K. Hadjikakou, P. Karagiannidis, Polyhedron 12 (1993) 2221;
(c) M.B. Ferrari, G.G. Fava, C. Pelizzi, P. Tarasconi, Inorg. Chim. Acta 98 (1985) L 49.
[7] T.S. Lobana, Ritu Sharma, Renu Sharma, Sheetal Mehra, A. Castineiras, Peter Turner, Inorg. Chem. 44 (2005) 1914.
[8] T.S. Lobana, Renu Sharma, Geeta Hundal, R.J. Butcher, Inorg. Chem. 45 (2006) 9402.
[9] E.R. Atkinson, D.J. Gardiner, A.R.W. Jackson, E.S. Raper, Inorg. Chim. Acta 98 (1985) 35.
[10] P. Karagiannidis, P. Aslanidis, S. Papastefanou, D. Mentzafos, A. Hountas, A. Terzis, Polyhedron 9 (1990) 981.
[11] J.R. Creighton, D.J. Gardiner, A.C. Gorvin, C. Gutteridge, A.R.W. Jackson, E.S. Raper, P.M.A. Sherwood, Inorg. Chim. Acta 103 (1985) 195.
[12] E.S. Raper, W. Clegg, Inorg. Chim. Acta 180 (1991) 239.
[13] E.S. Raper, J.R. Creighton, D. Robson, J.D. Wilson, W. Clegg, A. Milne, Inorg. Chim. Acta 143 (1988) 95.
[14] E.R. Atkinson, E.S. Raper, D.J. Gardiner, H.M. Dawes, N.P.C. Walker, A.R.W. Jackson, Inorg. Chim. Acta 100 (1985) 285.
[15] E.S. Raper, J.R. Creighton, J.D. Wilson, W. Clegg, A. Milne, Inorg. Chim. Acta 155 (1989) 77.
[16] F. Bonati, A. Burini, B.R. Pietroni, E. Giorgini, F. Bovio, J. Organomet. Chem. 344 (1988) 119.
[17] E.S. Raper, J.R. Creighton, W. Clegg, Inorg. Chim. Acta 183 (1991) 179.
[18] Y. Agnus, R. Louis, R. Weiss, J. Chem. Soc., Chem. Commun. (1980) 867.
[19] (a) S. Skoulika, A. Aubry, P. Karagiannidis, P. Aslanidis, S. Papastefanou, Inorg. Chim. Acta 183 (1991) 207;
(b) P. Aslanidis, P.J. Cox, P. Karagiannidis, S.K. Hadjikakou, C.D. Antoniadis, Eur. J. Inorg. Chem. (2002) 2216.
[20] S.K. Hadjikakou, P. Aslanidis, P.D. Akrivos, P. Karagiannidis, B. Kojic-Prodic, M. Luic, Inorg. Chim. Acta 197 (1992) 31.
[21] E.S. Raper, J.R. Creighton, J.D. Wilson, W. Clegg, A. Milne, Inorg. Chim. Acta 149 (1988) 265.
[22] G. Brauer, Handbook of Preparative Chemistry, 2nd ed., vol. 2, Academic Press, New York, 1965.
[23] XSCANS, Siemens Analytical X-ray Instruments Inc., Madison, WI, USA, 1994.
[24] International Tables for X-ray Crystallography, Kluwer, Dordrecht, The Netherlands, vol. C, 1995.
[25] G.M. Sheldrick, SHELXTL-PC, release 5.03, Siemens Analytical X-ray Instruments Inc., Madison, WI, USA, 1995.
[26] G.X. Win, L.J. Farrugia, J. Appl. Cryst. 32 (1999) 837.
[27] P.J. Cox, P. Aslanidis, P. Karagiannidis, S.K. Hadjikakou, Polyhedron 18 (1999) 1501.
[28] P. Aslanidis, S.K. Hadjikakou, P.J. Cox, Inorg. Chim. Acta 271 (1998) 243.
[29] T.S. Lobana, Alfonso Castineiras, Polyhedron 21 (2002) 1603.
[30] J.E. Huheey, E.A. Keiter, R.L. Keiter, Inorganic Chemistry: Principles of Structure and Reactivity, 4th ed., Harper Collins, New York, 1993.
[31] T.S. Lobana, Rekha, B.S. Sidhu, A. Castineiras, E. Bermejo, T. Nishioka, J. Coord. Chem. 58 (2005) 803.
[32] T.S. Lobana, Seema Paul, A. Castineiras, Polyhedron 16 (1997) 4023.

2. Experimental

2.1. Materials and instrumentation

All reactions were performed under dry deoxygenated nitrogen atmosphere using standard Schlenk techniques. Dichloromethane was dried and distilled over P_2O_5 and acetonitrile was dried over P_2O_5 and stored over molecular sieves. All the catalyst precursors, [{1,3-(3,5-R_2pzCO)$_2$C$_6$H$_4$}Pd$_2$Cl$_2$(μ-Cl)$_2$] (R = ^{t}Bu (**1**) [10], Me (**3**) [10], [{2,6-(3,5-R_2pzCO)$_2$C$_5$H$_3$N)}PdCl$_2$] (R = ^{t}Bu (**4**), Me (**5**)) [11], [(3,5-R_2pz)$_2$PdCl$_2$] (R = H (**6**), Me (**7**), ^{t}Bu (**8**)) [12], [(3,5-^{t}Bu$_2$pz)$_2$PdCl(Me)] (**9**) [12], were prepared by the literature methods, except **2**, which was prepared as described below. Phenylacetylene (98%) was obtained from Merck and used as received. NMR spectra were recorded on a Gemini 2000 instrument at 200 MHz for ^{1}H and 50.3 MHz for ^{13}C. Polymer molecular weights were determined by gel permeation chromatography on a Waters 600E instrument with a Waters 410 differential refractometer detector (THF, at 30 °C, rate = 1.0 mL min^{-1}) and PL-MIXED-C™ columns, using polystyrene as standards.

2.2. Synthesis

2.2.1. 1,3-Bis(3,5-diphenylpyrazolyl-1-carbonyl)benzene (*L1*)

To a solution of isophthaloyl dichloride (0.50 g; 2.46 mmol) in dry toluene (50 mL) was added diphenylpyrazole (1.08 g; 4.92 mmol). The colourless solution turned yellow upon addition of Et_3N (8 mL). The solution was vigorously stirred under nitrogen at room temperature for 24 h. After the specified reaction time, the mixture was filtered and the filtrate evaporated to dryness at reduced pressure to give a yellow solid, which was purified by column chromatography using silica gel and CH_2Cl_2:Et_2O (8:1) as eluent. Yield = 0.64 g, 46%. *Anal.* Calc. for $C_{38}H_{26}N_4O_2$: C, 79.98; H, 4.59; N, 9.82. Found: C, 79.96; H, 4.57; N, 9.65%. ^{1}H NMR ($CDCl_3$): δ 8.95 (s, 1H, Ph); 8.42 (d, 2H, Ph, $^2J_{HH}$ = 10 Hz); 7.69 (t, 1H, Ph); 7.46 (m, 20H, Ph on pz); 6.90 (s, 2H, 4-pz).

2.2.2. Di-μ-chloro-dichloro{1,3-bis(3,5-diphenylpyrazolyl-1-carbonyl)benzene}dipalladium(II) (*2*)

To **L1** (0.33 g, 0.58 mmol) and [PdCl$_2$(NCMe)$_2$] (0.15 g, 0.58 mmol) was added dry dichloromethane (70 mL). The resulting dark red solution was stirred at room temperature under nitrogen for 18 h, turning yellow with formation of small amount of precipitate. The reaction mixture was filtered and the filtrate was evaporated to dryness to give an orange solid. Yield = 0.40 g, 63%. *Anal.* Calc. for $C_{40}H_{30}Cl_8N_4O_2Pd_2$: C, 47.06; H, 2.91; N, 5.78. Found: C, 47.79; H, 2.46; N, 5.78%. ^{1}H NMR ($CDCl_3$): 9.08 (d, 2H, Ph, $^2J_{HH}$ = 4 Hz); 9.05 (d, 2H, Ph, $^2J_{HH}$ = 4 Hz); 8.38 (m, 5H, Ph on pz); 8.31 (t, 1H, Ph); 7.62 (s, 6H, Ph on pz); 7.49 (s, 10H, Ph on pz); 6.79 (s, 2H, 4-pz).

2.3. Polymerization

In a typical experiment a solution of silver triflate (0.078 g, 0.28 mmol) in a 15 mL mixture of CH_2Cl_2 and MeCN (7:1) was added to complex **1** (0.10 g, 0.14 mmol) in 25 mL of CH_2Cl_2 and MeCN (7:1). A white precipitate of AgCl formed immediately and the mixture was stirred for at most 5 min and filtered to give a yellow solution of the active catalyst. To the solution of the active catalyst was added 50 equivalents of phenylacetylene (0.78 mL, 7.0 mmol). The resultant solution changed to dark red immediately. After stirring for 2 min the solution was evaporated to give a dark brown residue, which was dissolved in 10 mL of CH_2Cl_2 followed by the addition of 30 mL of methanol to precipitate a yellowish-orange powder. Yield = (0.58 g, 90%). The product was characterized by a combination of ^{1}H, ^{13}C{^{1}H} NMR spectroscopy and GPC analysis.

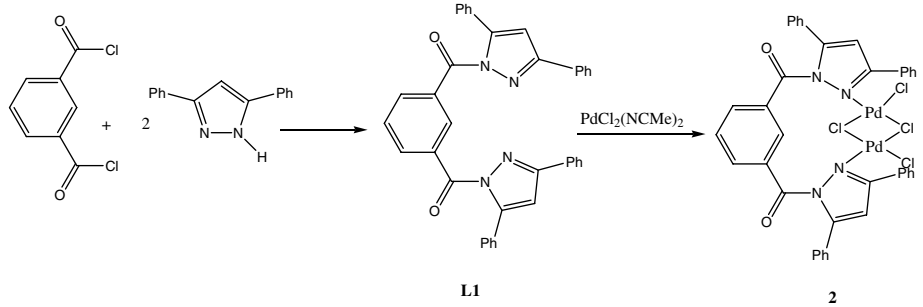
2.4. X-ray crystallography

The crystal evaluation and data collection were performed on a Bruker CCD-1000 diffractometer with Mo Kα (λ = 0.71073 Å) radiation and the diffractometer to crystal distance of 4.9 cm. The initial cell constants were obtained from three series of ω scans at different starting angles. The reflections were successfully indexed by an automated indexing routine built in the SMART program [13]. The absorption correction was based on fitting a function to the empirical transmission surface as sampled by multiple equivalent measurements. A successful solution by the direct methods provided most non-hydrogen atoms from the E-map. The remaining non-hydrogen atoms were located in an alternating series of least-squares cycles and difference Fourier maps. All non-hydrogen atoms were refined with anisotropic displacement coefficients. All hydrogen atoms were included in the structure factor calculation at idealized positions and were allowed to ride on the neighboring atoms with relative isotropic displacement coefficients.

3. Result and discussion

3.1. Synthesis of bis(diphenylpyrazolyl-1-carbonyl)benezene ligand and palladium(II) complex (*2*)

The synthesis of both ligand and complex is similar to the other substituted pyrazolyl compounds and their palladium complexes we reported recently [10]. Scheme 1 shows how **L1** and **2** were prepared. The ^{1}H NMR spectrum of the ligand is typical of other 1,3-benzenedicarbonyl pyrazolyl ligands. The C2, C4 and C5 protons on the benzene appear as a triplet (7.69 ppm), a doublet (8.42 ppm) and doublet of a doublet (8.56 ppm) respectively. The ^{1}H NMR spectrum of **2** suggests that the ligand binds to the Pd in a similar fashion as reported for 1,3-benzenedicarbonyl pyrazolyl ligands [10] to form



Scheme 1.

a dinuclear complex. The structures of the ligand and the dinuclear complex were confirmed by X-ray crystallography.

3.2. Descriptions of the structure of *L1* and *2*

Single crystals of **L1** and **2** were obtained from recrystallization of the respective compounds from CH_2Cl_2 and ether at −15 °C. The crystal quality of **2** was poor and the crystals collapsed once it was dry, but X-ray diffraction analysis could be carried out on the crystals if solvent of crystallization was present; although the quality of data from these crystals was not so good. The refinement was therefore only good to establish the connectivity of atoms, and as such we have not discussed any bond parameters. The structure of **2** was found to be isomorphous with the solid-state structures of **1** and **3** [10]. The molecular structures of **L1** and **2** are shown in Figs. 1 and 2 respectively. Crystallographic information is tabulated in Table 1 while selected bond lengths and angles for **L1** are listed as part of the captions for Fig. 1.

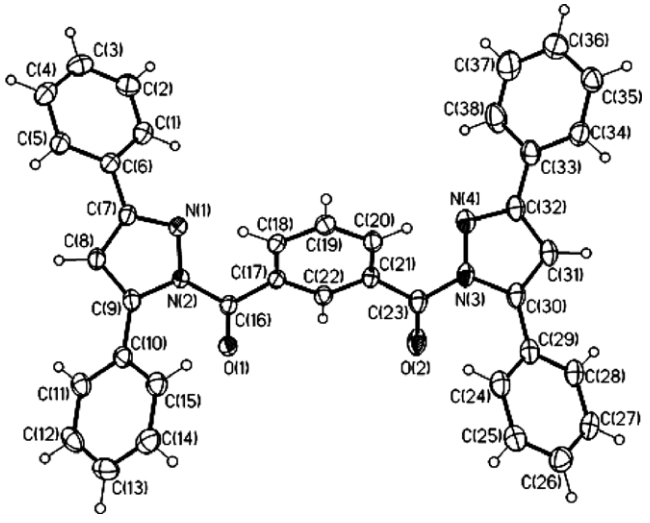


Fig. 1. Molecular structure of 1,3-bis(3,5-diphenylpyrazolyl-1-carbonyl)benzene. Selected bond lengths (Å) and angles (°): N(1)–N(2) 1.374(18), N(2)–C(16) 1.431(19), O(1)–C(16) 1.206(19), C(16)–C(17) 1.485(2). (N91)–N(2)–C(16) 117.31(12), O(1)–C(16)–N(2) 120.03(14), O(1)–C(16)–C(17) 124.22(14).

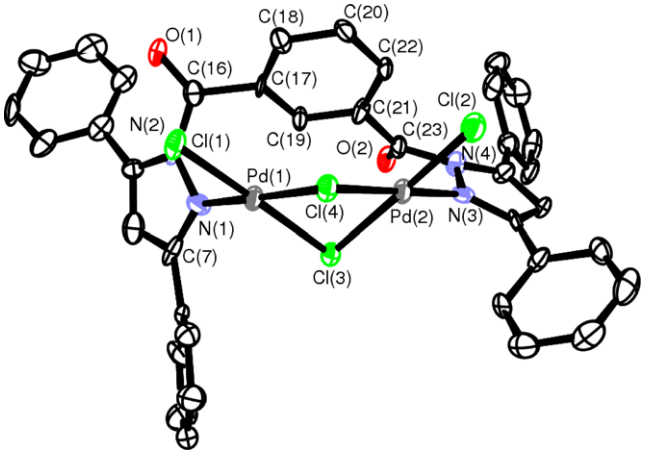


Fig. 2. Molecular structure of **2**. Due to the poor quality of the X-ray data only an ortep drawing is shown to indicate the connectivity of atoms.

Table 1
Crystal data and structure refinement for **L1** and **2**

	L1	**2**
Empirical formula	$C_{38}H_{26}N_4O_2$	$C_{40}H_{30}Cl_8N_4O_2Pd_2$
Formula weight	570.63	1095.08
Temperature (K)	173(2)	100(2)
Wavelength (Å)	0.71073	0.71073
Space group	$P2_1/n$	$P2_1/n$
Crystal system	monoclinic	monoclinic
a (Å)	9.6723(16)	12.819(6)
b (Å)	28.979(5)	16.503(8)
c (Å)	10.1433(17)	19.401(9)
β (°)	92.980(3)	94.703(8)
V (Å)	2839.3(8)	4091(3)
Z	4	4
D_c (Mg m^{-3})	1.335	1.778
μ(Mo K) (mm^{-1})	0.084	1.444
Crystal size	0.44 × 0.34 × 0.17	0.10 × 0.10 × 0.05
Absorption correction/mm	multiscan	
T_{max}/T_{min}	0.9859/0.9640	0.9313/0.8691

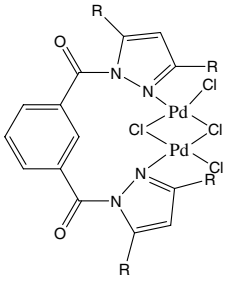
The solid state structure of 1,3-(3,5-R_2pzCO)$_2C_6H_4$ and 1,2-(3,5-R_2pzCO)$_2C_6H_4$ (R = Me, ^{t}Bu) possess either a C_2 or C_s symmetry [10]. These observation can be extended to 1,3-(3,5-Ph_2pzC(O))$_2C_6H_4$. The C_2 symmetry is attained when the pyrazolyl substituents on the benzene ring reside on the opposite sides of its plane. The C_s symmetry is

observed when both substituents are on the same side of the ring with the mirror plane perpendicular to the plane of the ring. Based on the above assessment 1,3-(3,5-$Ph_2pzCO)_2C_6H_4$ has a C_s symmetry. Molecular modeling revealed that the two symmetry conformations are energetically equivalent and are close in energy to a number of calculated energetic minima corresponding to various C_i arrangements. It has also been established that the most energetically favourable conformations are those in which the carbonyl is coplanar with the pyrazole ring.

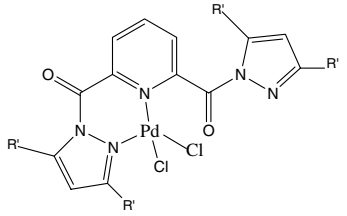
Compound 1,3-$(3,5\text{-}Ph_2pzC(O))_2C_6H_4$ cannot achieve planarity due to either close proximity of the pyrazolyl substituents in the 2-position to the *ortho* hydrogen of the phenyl ring, or due to unfavorable interactions between the nitrogen lone pair and the *ortho* hydrogen. The C=O group can, however, be coplanar with either ring since both pyrazolyl and phenyl groups possess a delocalized π-system, with the preferred ring being the pyrazole. The C–N bond in the O=*C*–*N*–N linkage is shorter than the generic C_{sp2}–N_{sp2} single bond due to electronic resonance. The C–N bond is the shortest when the torsion angle O–C–N–N is 180° and longest when the angle is 90°. The average C–N bond distances in 1,3-$(3,5\text{-}Ph_2pzCO)_2C_6H_4$ averaged 1.4271 Å. This value falls within the range for similar compounds reported by Darkwa et al. [10].

3.3. Polymerization of phenylacetylene

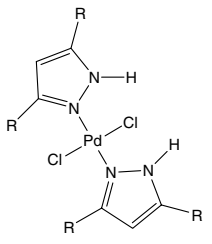
The polymerization of phenylacetylene (PA) was examined with three types of pyrazolyl palladium complexes as catalysts (Scheme 2). These catalysts differ by the nature of the ligand systems, all designed to vary the electron density on the metal centre and the active catalysts were generated *in situ* by reacting each palladium complex with silver triflate in a mixture of CH_2Cl_2 and MeCN. The presence of MeCN is necessary to stabilize the active catalyst, yet the coordination of MeCN has to be weak enough to allow the monomer access to the active centre of the catalysts in order to initiate the polymerization.



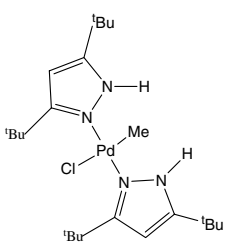
(R = ^{t}Bu (**1**), Ph (**2**), Me (**3**))



(R' = ^{t}Bu (**4**), Me(**5**))



(R = H (**6**), Me (**7**), ^{t}Bu (**8**))



(**9**)

Scheme 2.

The stereochemistry of the polyphenylacetylene produced was determined by ^{1}H NMR spectroscopy. Polymers from solvents mixtures were mainly *cis–transoidal* polyphenylacetylene, which showed a sharp singlet at 5.85 ppm for the vinylic protons in the polymer and broad singlets at 6.66 ppm (*ortho*) 6.97 ppm (*meta* and *para*) protons of the phenyl groups in the polymer. In MeCN and THF the ^{1}H NMR spectra of the polymers produced were very broad and centred at 7.25 ppm typical of *trans–cisoidal* polyphenylacetylene.

Polymerization data, showing the effect of catalysts, solvents and ratio of PA:Pd on polymerization, are listed in Tables 2 and 3. All the catalysts showed moderate to high activity and a general trend where substituents on the pyrazolyl unit or pyrazole determined the molecular weight of polyphenylacetylene formed, was observed. Other factors that affected polymer molecular weights are reaction time and nature of solvent. Polymerization with catalyst **1** resulted in very high conversion, with very little variation in polymers molecular weight when monomer to catalyst ratio was kept at 50:1 and CH_2Cl_2:MeCN ratio of 7:1 (Table 2 (entries 1–4)). Increase in MeCN content of the mixture of solvents, as well as monomer to catalyst ratio (Table 2, entries 5–8) resulted in lower conversion and lower polymer molecular weights. The results suggest that with increased concentration of MeCN, the monomer competes with MeCN for the catalyst. The steric bulk of the catalyst also has profound effect on polymer molecular weight. With bulky substituents on the pyrazolyl ligands (i.e. tertiary butyl and phenyl) and at similar polymerization conditions, high-molecular weight polyphenylactylene were formed (Table 2, entries 4 and 9), but the less bulky methyl substituent only produced oligomers (Table 2, entry 10). Steric bulk of catalyst is a well established property that promotes chain propagation in olefin polymerization reactions; a phenomenon that underlies the success of α-diimine late transition metal complexes as catalysts for the polymerization of olefins [7a].

We also observed that when polymerization reactions were run in neat solvents (MeCN and THF) with the active catalyst generated as described, the polymerization was fast but polymer molecular weights were lower than in the solvent mixtures. Both MeCN and THF are donor solvent and would compete with phenylacetylene for the catalytic centre. It therefore comes as no surprise that reactions in these solvents produced lower molecular weight polymers.

Time dependent polymerization experiments with catalyst **1** showed little variation in monomer conversion, (Table 2, entries 1–4). However, there was no increase in activity with time (Fig. 2) as expected if the catalyst is still

Table 2
Polymerization of phenylacetylene catalyzed by bis(pyrazolyl)Pd(II)[a]

Entry	Catalyst	Solvent[b]	Time (min)	% Con	M_w	M_w/M_n
1	**1**	7:1	2	90	11890	2.36
2	**1**	7:1	30	85	11609	2.25
3	**1**	7:1	60	87	12919	2.20
4	**1**	7:1	120	92	12114	2.12
5	**1**	5:3	1440	86	11521	2.08
6	**1**	1:3	1440	76	8546	1.80
7[c]	**1**	7:1	1440	58	8955	2.99
8[d]	**1**	7:1	1440	60	6444	2.20
9	**2**	7:1	120	100	10237	2.29
10	**3**	7:1	120	45	1203	1.68
11	**2**	MeCN	180	93	5257	1.65
12	**2**	THF	180	100	1610	1.71
13	**3**	MeCN	120	43	1581	2.82
14	**3**	THF	120	50	3949	3.27
15	**4**	7:1	240	96	10119	1.68
16	**4**	5:1	240	82	10831	1.44
17	**4**	3:1	240	87	3798	3.23
18	**5**	7:1	240	73	639	2.32

[a] All reactions were run in 40 mL solvent.
[b] Solvent is a mixture of CH_2Cl_2 and MeCN; [Pd] = 3.5×10^{-3} M; PA:Pd = 50:1.
[c] PA:Pd = 100:1.
[d] PA:Pd = 200:1; temperature = 25 °C.

Table 3
Polymerization of phenylacetylene catalyzed by bis(pyrazole)Pd(II) complexes[a]

Entry	Catalyst	Solvent[b]	Time (min)	% Con	M_w	M_w/M_n
1	**6**	5:3	15	35	13475	2.67
2	**7**	5:3	15	31	16822	2.56
3	**8**	5:3	15	38	15407	3.06
4	**9**	5:3	15	47	23237	2.16
5	**9**	5:3	2	38	26541	2.52
6	**9**	5:3	5	41	27084	2.34
7	**9**	5:3	30	51	22343	2.48
8	**9**	5:3	60	54	24212	2.09
9	**9**	5:3	120	58	26000	2.19
10	**9**	5:3	1440	99	6458	1.81
11[c]	**9**	5:3	15	74	21794	2.84
12[c]	**9**	5:3	30	80	20481	2.84
13[c]	**9**	5:3	60	90	19452	2.82
14[c]	**9**	5:3	120	97	15372	2.66

[a] All reactions were run in 40 mL solvent.
[b] Solvent is a mixture of CH_2Cl_2 and MeCN; [Pd] = 3.5×10^{-3} M; PA:Pd = 50:1.
[c] Reactions run with SO_2; temperature = 25 °C.

active. This is typical of catalyst deactivation, which suggests decomposition of catalyst. Indeed a change in ligand design by using a pyridine linker produced catalysts **4** and **5**; both of which are substantially more stable, albeit less active. Reactions with **4** and **5** took much longer at similar conditions to reach % conversions found for catalysts **1** and **2**; but the steric effect on polymer molecular weight (Table 2, entries 15–18) remained similar to molecular weights observed for catalysts **1**–**3**. It, therefore, appears that upon removal of chloride ligands to give the active catalysts, the uncoordinated pyrazolyl units in **4** and **5** enters the coordination sphere of the palladium and block the coordination site the monomer needs to occupy in order to be polymerized.

In order to establish the full effects of both the carbonyl and pyridine linkers in catalysts **1**–**5**, simple pyrazole palladium complexes (**6**–**9**) were investigated as catalysts for phenylacetylene polymerization. A crucial difference between catalysts **6**–**9** and **1**–**5** is the higher amount of MeCN required to stabilize the active catalysts (i.e. CH_2Cl_2:MeCN = 5:3). Furthermore, % conversion of monomer was generally low with catalysts **6**–**9**, clearly showing that the catalysts centres in **6**–**9** are less electrophilic. Time dependent experiments with **9** showed a gradual increase in % conversion (Table 3, entries 5–9); but never achieved the high conversions observed with **1**–**5**.

We took advantage of the slow kinetics exhibited by catalyst **9** the co-polymerize phenylacetylene and another

monomer. We recently reported the insertion of SO_2 into the Pd–Me bond in **9** [14]. By saturating CH_2Cl_2:MeCN solutions of the active catalyst generated from **9** with SO_2, we could perform time dependent experiments involving the co-polymerization of SO_2 and phenylacetylene. Monomer conversions improved dramatically (Table 3, entries 11–14), but polymer molecular weights decreased with time. Liaw and Lay have co-polymerized CO and phenylacetylene with an *in situ* generated catalyst from 2,2′-bipyridine and $[Pd(MeCN)_4][BF_4]_2$ [15]. The polysulfone formed with catalyst **9** has characteristic ν(SO) peaks at 1259 cm^{-1} in addition to ν(C=C) of the acetylenic functionality at 1550 cm^{-1}.

All the catalysts showed moderate to high activity. The ability of cationic pyrazole palladium catalysts used here to catalyze phenylacetylene polymerization is not surprising. We have observed the formation of linear high density polyethylene catalyzed by bis(pyrazole)nickel(II) [16] and palladium(II) [11] as well as by pyrazolyl palladium(II) [10,12]. This observation confirms the high electrophilicity of these nickel and palladium catalysts, that allows rapid insertion of monomer, gives rise to a much higher rate of chain propagation over chain termination; thus avoiding branching that is common to late transition metal olefin polymerization catalysts. We believe it is this high electrophilicity of the cationic species formed by **1**–**9** that make them active catalysts for phenylacetylene polymerization, when other cationic palladium nitrogen donor compounds [8,7] cannot polymerize acetylenes.

In general complexes **1**, **2** and **4** were the most active, and catalysts with bulky substituents gave high-molecular weight polyphenylacetylene than catalysts that have less bulky substituents. Catalysts with less bulky substituents formed phenylacetylene oligomers. Compared with known Pd(II) catalysts, the (N∧N)Pd(II) catalysts described here are more active, although they produce lower-molecular weight polymers than some of the palladium catalysts reported in the literature. For instance while Pd(II) halide and acetate salts are known to polymerize phenylacetylene to low-molecular weight polymers, the use of Pd(II) acetate is highly exothermic and at times even explosive [3k]. It is also worth noting that the slow conversions by catalyst **9** allowed it to be used as co-polymerization catalyst for SO_2 and phenylacetylene.

4. Conclusions

Pyrazole and pyrazolyl ligands appear to have the right sigma donor ability to produce palladium complexes that catalyze the polymerization of phenylacetylene. This is in contrast to bipyridine and diimine palladium complexes that do not catalyze acetylene polymerization. However, the highly active pyrazolyl palladium catalysts have low stability and gradually deactivates. The lower activity of the pyrazole palladium catalysts allows complexes that have Pd–carbon functionality to be used as co-polymerization catalysts as the slow conversion gives the co-monomer sufficient time to insert to the Pd–C bond, in this case sulfur dioxide, thus enabling chain growth that involves the insertion of sulfur dioxide to produce polyphenylacetylene sulfone.

5. Supplementary material

CCDC 278053 and 275054 contain the supplementary crystallographic data for **L1** and **2**. These data can be obtained free of charge via http://www.ccdc.cam.ac.uk/conts/retrieving.html, or from the Cambridge Crystallographic Data Centre, 12 Union Road, Cambridge CB2 1EZ, UK; fax: (+44) 1223-336-033, or e-mail: deposit@ccdc.cam.ac.uk.

Acknowledgement

This work was funded by a Grant from the National Research Foundation, South Africa.

References

[1] T. Masuda, K. Hasegawa, T. Higashimura, Macromolecules 7 (1974) 728.
[2] (a) T. Masuda, T. Higashimura, Adv. Polym. Sci. 81 (1981) 121;
(b) R.R. Schrock, S. Luo, N.C. Zanetti, H.H. Fox, Organometallics 13 (1994) 3396;
(c) H.H. Fox, R.R. Schrock, Organometallics 11 (1992) 2763;
(d) T. Masuda, T. Higashimura, Acc. Chem. Res. 17 (1984) 51;
(e) S. Hayano, T. Itoh, T. Masuda, Polymer 40 (1999) 4071, and references therein;
(f) R.R. Schrock, S. Luo, J.C. Lee Jr., N.C. Zanetti, W.J. Davis, J. Am. Chem. Soc. 118 (1996) 3883.
[3] (a) A. Furlani, S. Licoccia, M.V. Russo, J. Polym. Sci. A: Polym. Chem. 24 (1986) 991;
(b) A. Furlani, C. Napoletano, M.V. Russo, W.J. Feast, Polym. Bull. 16 (1986) 311;
(c) M. Tabata, W. Yang, K. Yokota, Polym. J. 22 (1990) 1105;
(d) K. Li, G. Wei, J. Darkwa, S.K. Pollack, Macromolecules 35 (2002) 4573;
(e) Y. Goldberg, H. Alper, J. Chem. Soc., Chem. Commun. (1994) 1209;
(f) F.D. Kleist, N.R. Byrd, J. Polym. Sci. A: Polym. Chem. Ed. 7 (1969) 3419;
(g) M. Miyake, Y. Misumi, T. Masuda, Macromolecules 33 (2000) 6636;
(h) K. Kanki, Y. Misumi, T. Masuda, J. Polym. Sci. A: Polym. Chem. 40 (2002) 1075;
(i) B.Z. Tang, W.H. Poon, S.M. Leung, W.H. Leung, H. Peng, Macromolecules 30 (1997) 2209;
(j) K. Tsuchihara, Polymer 41 (2000) 2691;
(k) D.L. Trumbo, C.S. Marvel, J. Polym. Sci. A: Polym. Chem. 25 (1987) 1027;
(l) X. Zhan, M. Yang, J. Mol. Cat. A: Chem. 169 (2001) 27;
(m) L. Weber, M. Barlmeyer, J.-M. Quasdorff, M.L. Sievers, H.-G. Stammler, B. Neumann, Organometallics 18 (1999) 2497;
(n) H.-J. Haupt, U. Ortmann, Z. Anorg. Allg. Chem. 619 (1993) 1209.
[4] Y. Kishimoto, P. Eckerle, T. Miyakate, T. Ikariya, R. Noyori, J. Am. Chem. Soc. 116 (1994) 12131.
[5] P. Mastrorilli, C.F. Nobile, A. Rizzuti, G.P. Suranna, D. Acierno, E. Amendola, J. Mol. Cat. A: Chem. 178 (2002) 35.
[6] M. Tabata, T. Sone, Y. Sadahiro, Macromol. Chem. Phys. 200 (1999) 265.

[7] (a) S.D. Ittel, L.K. Johnson, M. Brookhart, Chem. Rev. 100 (2000) 1169; (b) V.C. Gibson, S.K. Spitzmesser, Chem. Rev. 103 (2003) 283.
[8] A.M. LaPointe, M. Brookhart, Organometallics 17 (1998) 1530.
[9] P. Pelagatti, M. Carcelli, C. Pelizzi, M. Costa, Inorg. Chim. Acta 342 (2003) 323.
[10] I.A. Guzei, K. Li, G.A. Bikzhanova, J. Darkwa, S.F. Mapolie, Dalton Trans. (2003) 715.
[11] M.S. Mohlala, I.A. Guzei, J. Darkwa, S.F. Mapolie, J. Mol. Cat. A: Chem. 241 (2005) 93.
[12] K. Li, J. Darkwa, I.A. Guzei, S.F. Mapolie, J. Organomet. Chem. 660 (2002) 109.
[13] Bruker-AXS, SADABS V.2.05, SAINT V.6.22, SHELXTL V.6.10 & SMART 5.622 Software Reference Manuals, Bruker-AXS, Madison, Wisconsin, USA, 2000–2003.
[14] K. Li, J. Darkwa, I.A. Guzei, Polyhedron 22 (2003) 805.
[15] D.-J. Liaw, B.-F. Lay, J. Mol. Cat. A: Chem. 115 (1997) 107.
[16] S.M. Nelana, J. Darkwa, I.A. Guzei, S.F. Mapolie, J. Organomet. Chem. 689 (2004) 1835.

tion metal complexes of Schiff bases containing tetradentate ligands have anti-microbial activity [8]. Transition metal complexes with redox active ligands bearing sterically hindered salicylaldimines are also reported to undergo one- or two-electron transfer. Sterically hindered ligands bearing salicylaldimines are known to be effective antioxidants and are widely used in rancidification of fats and oils [9]. The copper(II) ions play a central role in biological redox metalenzymes like plastocyanin, hemocyanin, azurin, galactose oxidase an others [10]. In most salicylaldimine, the proton is localized at the oxygen atom and in some cases is attached to the nitrogen atom [11]. Proton transfer can occurs both in solid and solution states, in basic and excited states [11,12].

In recent years, considerable interest has developed in copper complexes with mixed donor ligands as structural models for the active site of copper proteins. In the copper proteins a distorted metal ion environment of low symmetry with a mixed donor sets is present [13]. This information prompted us to synthesize copper(II) metal complexes with a mixed donor atoms environment incorporating nitrogen and oxygen as ligands donor. The present manuscript is devoted to the synthesis and spectroscopic characterization of new salicylideneiminate copper(II) metal complexes containing sterically hindered phenol fragment and electron-donating OH and methylsulfanyl (S–CH_3) substituents, attached to the salicylaldehyde moiety. Here, we report synthesis, characterization and electro-spectrochemical properties of three new dissymmetric bidentate salicylaldimine ligands ($\mathbf{L}_n\mathbf{H}$) ($n = 1$, 2, and 3) (L = *N*-[*m*-(methylmercapto)aniline]-3,5-di-*t*-butylsalicylaldimine, $m = 4$, 3, and 2 positions, respectively) and their copper(II) complexes [$\mathbf{Cu}(\mathbf{L}_n)_2$]. A comparative electro-spectrochemical study was provided an understanding the effect of the position of methylsulfanyl groups attached on the phenol fragment on electron transfer mechanism of the ligands and their copper complexes.

2. Experimental

2.1. Materials and measurements

All reagents and solvents were of reagent-grade quality and obtained from commercial suppliers. (Fluka Chemical Company, Taufkirchen, Germany). 3,5-Di-*t*-butyl-2-hydroxybenzaldehyde (3,5-DTB) was synthesized according to the literature procedure [14]. The elemental analyses were carried out in the Laboratory of the Scientific and Technical Research Council of Turkey (TUBITAK). IR spectra were recorded on a Perkin Elmer Spectrum RXI FT-IR Spectrometer as KBr pellets. ^{1}H NMR spectra were recorded on a Bruker-Avence 400 MHz spectrometers. Magnetic Susceptibilities were determined on a Sherwood Scientific Magnetic Susceptibility Balance (Model MK1) at room temperature (20 °C) using Hg[Co(SCN)$_4$] as a calibrant; diamagnetic corrections were calculated from Pascal's constants [15]. Electronic spectral studies were conducted on a Perkin Elmer model Lambda 25 UV–Vis spectrophotometer in the wavelength 200–900 nm. Molar conductivities (Λ_M) were recorded on a Inolab Terminal 740 WTW Series. Cyclic voltammograms (CV) were carried out using CV measurements with Princeton Applied Research Model 2263 potentiostat controlled by an external PC. A three electrode system (BAS model solid cell stand) was used for CV measurements in DMSO and consisted of a 1.6 mm diameter of platinum disc electrode as working electrode, a platinum wire counter electrode, and an Ag/AgCl reference electrode. Tetra-*n*-butylammonium perchlorate (TBAP) was used as a supporting electrolyte. The reference electrode was separated from the bulk solution by a fritted-glass bridge filled with the solvent/supporting electrolyte mixture. The ferrocene/ferrocenium couple (Fc/Fc^+) was used as an internal standard but all potentials in the paper are referenced to the Ag/AgCl reference electrode. Solutions containing ($\mathbf{L}_n\mathbf{H}$) and [$\mathbf{Cu}(\mathbf{L}_n)_2$] were deoxygenated by a stream of high purity nitrogen for at least 5 min before running the experiment and the solution was protected from air by a blanket of nitrogen during the experiment. Controlled potential electrolysis (CPE) was performed with Princeton Applied Research Model 2263 potentiostat/Galvanostat. An BAS model electrolysis cell with a fritted-glass to separate the cathodic and anodic portions of the cell was used for bulk electrolysis. The sample and solvent were placed into the electrolysis cell under nitrogen. UV–Vis spectroelectrochemical experiments were performed with a home-built thin-layer cell that utilized a light transparent platinum gauze working electrode. A platinum wire counter electrode, and Ag/AgCl reference electrode were used for spectroelectrochemical cell. Potentials were applied and monitored with a Princeton Applied Research Model 2263 potentiostat. Time- and applied-resolved UV–Vis spectra were recorded on Agillent Model 8453 diode array spectrophotometer.

2.2. Synthesis of ligands ($\mathbf{L_1H}$, $\mathbf{L_2H}$ and $\mathbf{L_3H}$)

N-[4-(Methylmercapto)aniline]-3,5-di-*t*-butylsalicylaldimine ($\mathbf{L_1H}$), *N*-[3-(methylmercapto)aniline]-3,5-di-*t*-butylsalicylaldimine ($\mathbf{L_2H}$), and *N*-[2-(methylmercapto)aniline]-3,5-di-*t*-butylsalicylaldimine ($\mathbf{L_3H}$) ligands were synthesized by the reaction of 4.20 mmol (0.98 g) 3,5-di-*t*-butyl-2-hydroxybenzaldehyde in 20 ml absolute ethanol and 4.20 mmol (0.58 g) different marcapto aniline derivative in 10 ml ethanol. Also, 3–4 drops of formic acid were added as catalyst. The mixture was refluxed for 2 h, followed by cooling to room temperature. The crystals were filtered in vacuum. Then the products were recrystallized from methanol. The products are soluble in common solvents such as $CHCl_3$, CH_3CH_2OH, DMF and DMSO.

2.2.1. For ($\mathbf{L_1H}$) ligand

^{1}H NMR (400 MHz, $CDCl_3$, Me_4Si, ppm): δ 13.70 (s, 1H, –O*H*, D-exchangeable), δ 8.64 (s, 1H, *H*C=N), δ 7.45–7.25 (m, 6H, Ar-C*H*), δ 2.51 (s, 3H, S–CH_3), δ 1.47 (s, 9H, C–CH_3) and δ 1.33 (s, 9H, C–CH_3). The ^{13}C NMR results:

16.19; 29.43; 31.49; 34.21; 35.15; 118.31; 121.70; 126.76; 127.57; 128.00; 136.76; 136.96; 140.60; 145.86; 158.22 and 162.98 ppm. IR (KBr pellets, ν_{max}/cm^{-1}): 3641–3173 ν(OH), 2958- 2864 ν(Aliph-H), 1615 ν(C=N), 1490–1440 ν(C=C), 1172 ν(C–O).

2.2.2. For (*L₂H*) ligand

^{1}H NMR (400 MHz, $CDCl_3$, Me_4Si, ppm): δ 13.59 (s, 1H, –O*H*, D-exchangeable), δ 8.63 (s, 1H, *H*C=N), δ 7.52–6.99 (m, 6H, Ar-C*H*), δ 2.53 (s, 3H, S–CH_3), δ 1.49 (s, 9H, C–CH_3) and δ 1.34 (s, 9H, C–CH_3). The ^{13}C NMR results: 14.79; 29.46; 31.49; 34.20; 35.18; 117.48; 118.39; 124.75; 125.24; 126.91; 127.06; 128.28; 134.66; 137.13; 140.51; 145.90; 158.39 and 163.28 ppm. IR (KBr pellets, ν_{max}/cm^{-1}): 3643–3172 ν(OH), 2955–2867 ν(Aliph-H), 1615 ν(C=N), 1467–1440 ν(C=C), 1173 ν(C–O).

2.2.3. For *L₃H* ligand

^{1}H NMR (400 MHz, $CDCl_3$, Me_4Si, ppm): δ 13.43 (s, 1H, –O*H*, D-exchangeable), δ 8.62 (s, 1H, *H*C=N), δ 7.47–6.86 (m, 6H, Ar-C*H*), δ 2.48 (s, 3H, S–CH_3), δ 1.46 (s, 9H, C–CH_3) and δ 1.32 (s, 9H, C–CH_3). The ^{13}C NMR results: 15.73; 29.42; 31.48; 34.21, 35.12; 117.63; 118.20; 119.11; 124.41; 126.31; 128.23; 129.61; 137.02; 139.92; 140.66; 149.30; 158.28 and 164.18 ppm. IR (KBr pellets, ν_{max}/cm^{-1}): 3650–3170 ν(OH), 2957–2869 ν(Aliph-H), 1613 ν(C=N), 1467–1436 ν(C=C), 1169 ν(C–O).

2.3. Synthesis of the Cu(II) metal complexes

(0.53 g, 1.50 mmol), ligands (**L₁H**), (**L₂H**) or (**L₃H**) was dissolved in absolute methanol (45 cm^3). A solution of 0.75 mmol of the metal salt [$Cu(CH_3COO)_2 \cdot H_2O$ (0.15 g)] in absolute methanol (25 cm^3), was added dropwise under a N_2 atmosphere with continuous stirring. The stirred mixtures were then heated to the reflux temperature for 3 h and were maintained at this temperature. Then, the mixture was evaporated to a volume of 15–20 ml in vacuum and left to cool to room temperature. The compounds were precipitated after adding 5 ml ethanol. The products were filtered in vacuum and washed with a small amount of methanol and water. The products were recrystallized from ethanol. Then they were dried at 100 °C. IR (KBr pellets, ν_{max}/cm^{-1}): 2950–2851 ν(Aliph-H), 1600 ν(C=N), 1488–1456 ν(C=C), 1170 ν(C–O), 522 ν(M–O), 478 ν(M–N) for [**Cu**(**L₁**)$_2$], IR (KBr pellets, ν_{max}/cm^{-1}): 2955–2867 ν(Aliph-H), 1593 ν(C=N), 1471–1460 ν(C=C), 1170 ν(C–O), 537 ν(M–O), 482 ν(M–N). for [**Cu**(**L₂**)$_2$], IR (KBr pellets, ν_{max}/cm^{-1}): 2957–2869 ν(Aliph-H), 1594 ν(C=N), 1460–1430 ν(C=C), 1166 ν(C–O), 532 ν(M–O), 487 ν(M–N) for [**Cu**(**L₃**)$_2$].

3. Results and discussion

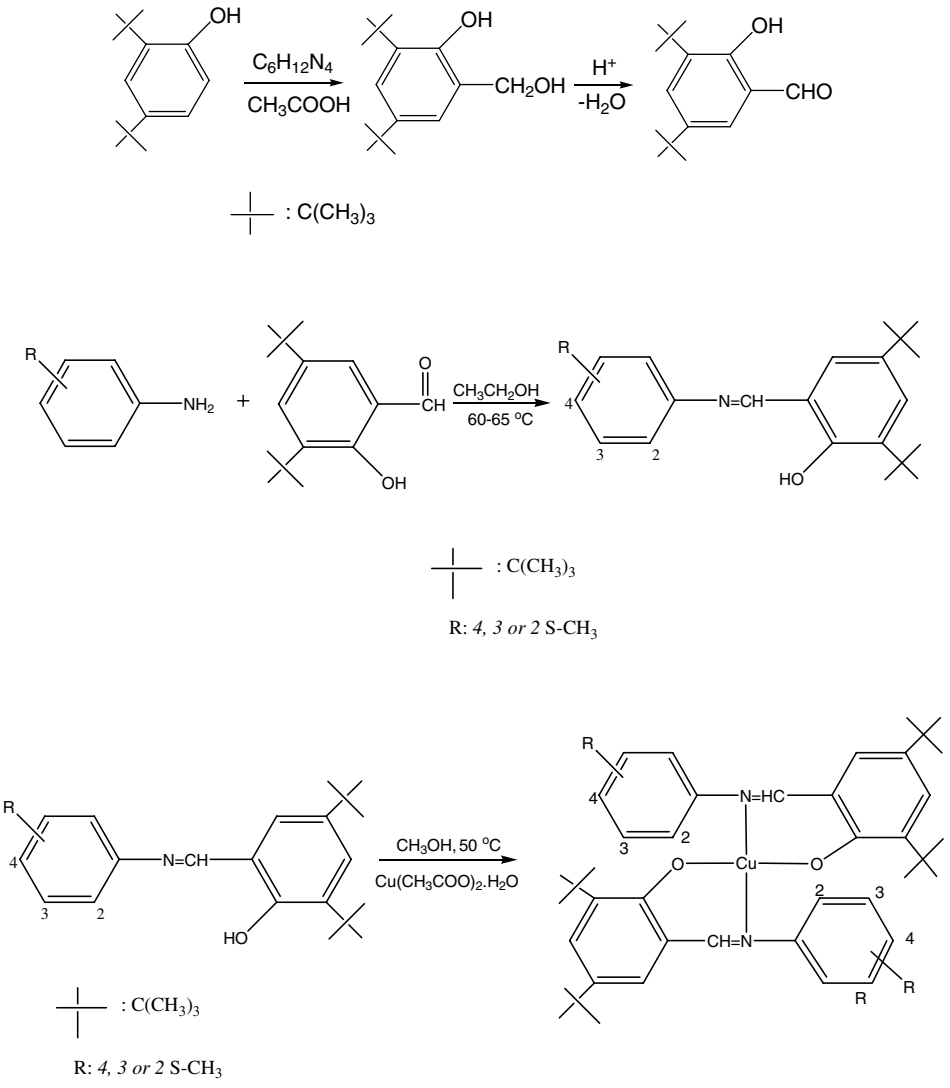
The reaction steps for the synthesis of the ligands and their copper complexes are given in Scheme 1. The first step is the synthesis of 3,5-di-*t*-butyl-2-hydroxybenzaldehyde (3,5-DTB) from the reaction of 2,4-di-*t*-butyl phenol with hexamethylene tetramine. In the second step; the ligands (**L₁H**), (**L₂H**) and (**L₃H**) were synthesized by the condensation of 4, 3 or 2-mercapto aniline with 3,5-di-*t*-butyl-2-hydroxybenzaldehyde. For the structural characterization of ligands (**L₁H**), (**L₂H**) and (**L₃H**) and their Cu(II) complexes [**Cu**(**L**$_n$)$_2$], elemental analysis, IR spectra, UV–Vis spectra, ^{1}H and ^{13}C NMR spectra, magnetic susceptibility measurements, molar conductivity were used and the corresponding data are given in experimental section and Tables 1 and 2. The metal to ligand ratios in the Cu(II) complexes were found to be 1:2. The ligands (**L₁H**), (**L₂H**) and (**L₃H**) on interaction with Cu(II) salt yielded complexes corresponding to the general formula [**M**(**L**$_n$)$_2$].

3.1. NMR results

The ^{1}H NMR spectral results obtained for ligands in $CDCl_3$ together the assignments are given in Section 2. The ^{1}H NMR spectra of the (**L₁H**), (**L₂H**) and (**L₃H**) in the $CDCl_3$ do not give any signal corresponding to mercapto aniline groups protons and 3,5-di-*t*-butyl-2-hydroxybenzaldehyde protons. The proton NMR spectra of the free ligands show a peak at 13.70 ppm for (**L₁H**), at 13.59 ppm for (**L₂H**) and at 13.43 ppm for (**L₃H**), characteristic of intramolecular hydrogen bonded OH proton. The peaks at range 7.45–7.25 ppm for (**L₁H**), at range 7.52–6.99 ppm for (**L₂H**) and at range 7.47–6.86 ppm for (**L₃H**) are assignable to the protons of Ar-CH as multiplet peaks. In the ^{1}H NMR spectra of ligands, the chemical shifts observed at δ 8.64 for (**L₁H**), at δ 8.63 for (**L₂H**) ppm and at δ 8.62 for (**L₃H**) is assigned to the proton of azomethine (CH=N) as singlet [16]. The peak at range 2.53–2.48 ppm for ligands are assignable to the protons of S–CH_3 groups as singlet peaks. Also, the protons of the *t*-butyl groups of ligands exhibit singlet peak at δ 1.47 and 1.33 ppm for (**L₁H**), δ 1.49 and 1.34 ppm for (**L₂H**), and δ 1.46 and 1.32 ppm for (**L₃H**), indicating that the *t*-butyl protons of these compounds are magnetically nonequivalent [17]. ^{1}H NMR and ^{13}C NMR data of the ligands are given in Section 2. The Cu(II) metal complexes are paramagnetic, thus their ^{1}H NMR and ^{13}C NMR spectra could not be obtained.

3.2. IR spectra results

The observed peaks may be classified into those originating from the ligand and those arising from the bonds formed between Cu(II) and coordinating sites. The free salicylaldimine ligands (**L₁H**), (**L₂H**) and (**L₃H**) showed strong peaks at 1615–1613 cm^{-1}, which are characteristic of the azomethine ν(C=N) group [18]. Coordination of the salicylaldimine ligands to the metal through the nitrogen atom is expected to reduce the electron density in the azomethine link and lower the ν(C=N) absorption frequency. The peak due to ν(C=N) is shifted to lower frequencies and appears around 1600–1593 cm^{-1}, indicating



Scheme 1. Synthetic route for preparation of ligands ($\mathbf{L}_n\mathbf{H}$) and their copper complexes [$\mathbf{Cu}(\mathbf{L}_n)_2$].

Table 1
The formula, formula weight, colors, melting points, molar conductivity, yields, magnetic susceptibilities, and elemental analyses results of the compounds

Compounds	F.W. (g/mol)	Color	M.p. (°C)	Λ_M (Ω^{-1} cm^2 mol^{-1})	Yield (%)	μ_{eff} [B.M.]	Elemental analyses % calculated (found)			
							C	H	N	S
$\mathbf{L}_1\mathbf{H}$	355	yellow	113		84		74.37	8.17	3.94	9.01
$C_{22}H_{29}NSO$							(73.83)	(8.43)	(3.72)	(9.06)
$\mathbf{Cu}(\mathbf{L}_1)_2$	771	dark Brown	249	19	42	1.90	68.48	7.26	3.63	8.30
$C_{44}H_{56}N_2S_2O_2Cu$							(68.27)	(7.34)	(3.46)	(8.07)
$\mathbf{L}_2\mathbf{H}$	355	yellow	93		65		74.34	8.17	3.94	9.01
$C_{22}H_{29}NSO$							(74.40)	(8.45)	(3.71)	(9.02)
$\mathbf{Cu}(\mathbf{L}_2)_2$	771	brown-green	244	21	47	1.87	68.48	7.26	3.63	8.30
$C_{44}H_{56}N_2S_2O_2Cu$							(68.21)	(7.33)	(3.46)	(8.06)
$\mathbf{L}_3\mathbf{H}$	355	yellow	135		60		74.37	8.17	3.94	9.01
$C_{22}H_{29}NSO$							(74.13)	(8.46)	(3.71)	(9.03)
$\mathbf{Cu}(\mathbf{L}_3)_2$	771	dark green	258	26	41	1.82	68.48	7.26	3.63	8.30
$C_{44}H_{56}N_2S_2O_2Cu$							(68.32)	(7.29)	(3.52)	(8.09)

coordination of the azomethine nitrogen to the copper metal [19]. A strong peak observed at range 1173–1169 cm^{-1} in the free ligands has been assigned to phenolic C–O stretching. On the complexation this band is shifted to a lower frequency range 1170–1166 cm^{-1}, indicating coordination through the phenolic oxygen. This has been fur-

Table 2
UV–Vis data of the ligands ($\mathbf{L}_n\mathbf{H}$) and their copper complexes [$\mathbf{Cu}(\mathbf{L}_n)_2$]

Compounds	Solvent	Wavelength [λ_{max}/(nm)](log ε)				
($\mathbf{L}_1\mathbf{H}$)	C_2H_5OH	206(3.27)	237(4.22)	276(4.04)	342(4.16)	363(4.20)
	DMSO	253(3.40)	279(3.62)	347(3.88)	365(3.90)	
($\mathbf{L}_2\mathbf{H}$)	C_2H_5OH	206(4.07)	226(4.04)	272(3.96)	305(3.72)	354(3.65)
	DMSO	253(4.20)	274(4.40)	305(4.21)	355(4.14)	
($\mathbf{L}_3\mathbf{H}$)	C_2H_5OH	206(3.61)	221(3.56)	242(3.48)	271(3.46)	365(3.22)
	DMSO	273(4.26)	366(4.10)			
[$\mathbf{Cu}(\mathbf{L}_1)_2$]	C_2H_5OH	213(2.90)	246(3.82)	313(3.84)	415(3.58)	702(2.14)
	DMSO	258(4.18)	317(4.23)	413(4.03)	685(3.18)	
[$\mathbf{Cu}(\mathbf{L}_2)_2$]	C_2H_5OH	216(2.50)	247(3.47)	253(3.36)	292(3.46)	423(3.31), 624(2.21), 803(2.08)
	DMSO	248(3.64)	260(3.87)	292(3.85)	413(3.53)	
[$\mathbf{Cu}(\mathbf{L}_3)_2$]	C_2H_5OH	210(4.22)	238(4.33)	297(4.17)	429(3.85)	695(2.29)
	DMSO	264(4.05)	295(4.03)	426(3.76)	682(2.38)	

ther supported by the disappearance of the broad ν(OH) peak around 3650–3170 cm^{-1} in the Cu(II) metal complexes, indicating deprotonation of the phenolic proton prior to coordination [18]. The coordination of the azomethine nitrogen and phenolic oxygen are further supported by the appearance of two peaks at 537–522 cm^{-1} and 487–478 cm^{-1} due to ν(Cu–O) and ν(Cu–N) stretching vibrations that are not observed in the infrared spectra of the ligands. Thus, it is clear that the ligands ($\mathbf{L}_1\mathbf{H}$), ($\mathbf{L}_2\mathbf{H}$) and ($\mathbf{L}_3\mathbf{H}$) are bonded to the copper metal ion in a ONNO fashion through the deprotonated phenolate oxygen and salicylaldimine nitrogen.

3.3. UV–Vis spectra results

Electronic spectra of ligands ($\mathbf{L}_1\mathbf{H}$), ($\mathbf{L}_2\mathbf{H}$) and ($\mathbf{L}_3\mathbf{H}$) and their copper complexes [$\mathbf{Cu}(\mathbf{L}_n)_2$] have been recorded in the 200–900 nm range in C_2H_5OH and DMSO solutions, and presented in Fig. 1. The corresponding data are also listed in Table 2. Each ligands and their copper complexes show several intense absorptions in the visible and ultraviolet region. The UV–Vis spectra of the ligands in C_2H_5OH and DMSO showed five absorption bands between 206 and 365 nm, and two or four absorption bands between 253 and 366 nm, respectively. The electronic spectra of the Cu(II) metal complexes in C_2H_5OH and DMSO solutions showed four-seven absorption bands between 216 and 698 nm. In the electronic spectra of the ligands and their copper complexes, the wide range bands seem to be due to both the $\pi\rightarrow\pi^*$ and $n\rightarrow\pi^*$ of C=N chromophore or change-transfer transition arising from π electron interactions between the metal and ligand which involves either a metal-to-ligand or ligand-to-metal electron transfer and d–d transitions [20,21]. In the electronic spectra of ligands and their copper complexes, the absorption bands below 366 nm for ligands and the absorption bands below 426 nm for copper complexes have high extinction coefficients in C_2H_5OH and DMSO solutions and are almost certainly associated with intraligand $\pi\rightarrow\pi^*$ and $n\rightarrow\pi^*$ or charge-transfer transitions [22]. The absorption bands below 276 nm in C_2H_5OH are practically identical and can be attributed to $\pi\rightarrow\pi^*$ transitions in the benzene ring or azomethine (–C=N) groups for ligands. The absorption bands observed within the range of 342–365 nm in C_2H_5OH are most probably due to the transition of $n\rightarrow\pi^*$ of imine group corresponding to the ligands [23]. In the spectra of Cu(II) metal complexes the bands observed within the range of 297–317 nm in C_2H_5OH and DMSO solutions are most probably due to the transition of $n\rightarrow\pi^*$ of imine group corresponding to the metal complexes [23]. For copper complexes, the absorption bands in the range of 413–429 nm are assigned to M→L charge-transfer (MLCT) or L→M charge-transfer (LMCT) [24], respectively. The absorption bands observed at lower energy and in lower intensities between 682 and 803 nm may be attributed to the d–d transitions ($d_{xy} \rightarrow d_{x^2-y^2}$ and $d_{z^2} \rightarrow d_{x^2-y^2}$). On complex formation, the electronic spectra of the copper complexes exhibited significantly different absorption bands compared to those of the ligands in C_2H_5OH and DMSO solutions. As expected, the new bands in the range of 413–429 nm arising from M→L charge-transfer (MLCT) or L→M charge-transfer (LMCT) transitions were observed as a result of coordination of copper metal through azomethine nitrogen. Examples of UV–Vis spectra of the ligands and their copper metal complexes were presented in Fig. 1.

3.4. Magnetic moments

Magnetic susceptibility measurements provide sufficient data to characterize the structure of the metal complexes. Magnetic moments measurements of compounds carried out at 25 °C. The room temperature magnetic moments of Cu(II) metal complexes in the range of 1.82–1.90 B.M which were typical for mononuclear of Cu(II) compounds with a $S = 1/2$ spin state and did not indicate antiferromagnetic coupling of spin at this temperature. These results are comparable to the values reported for slightly distorted tetrahedral geometry [25].

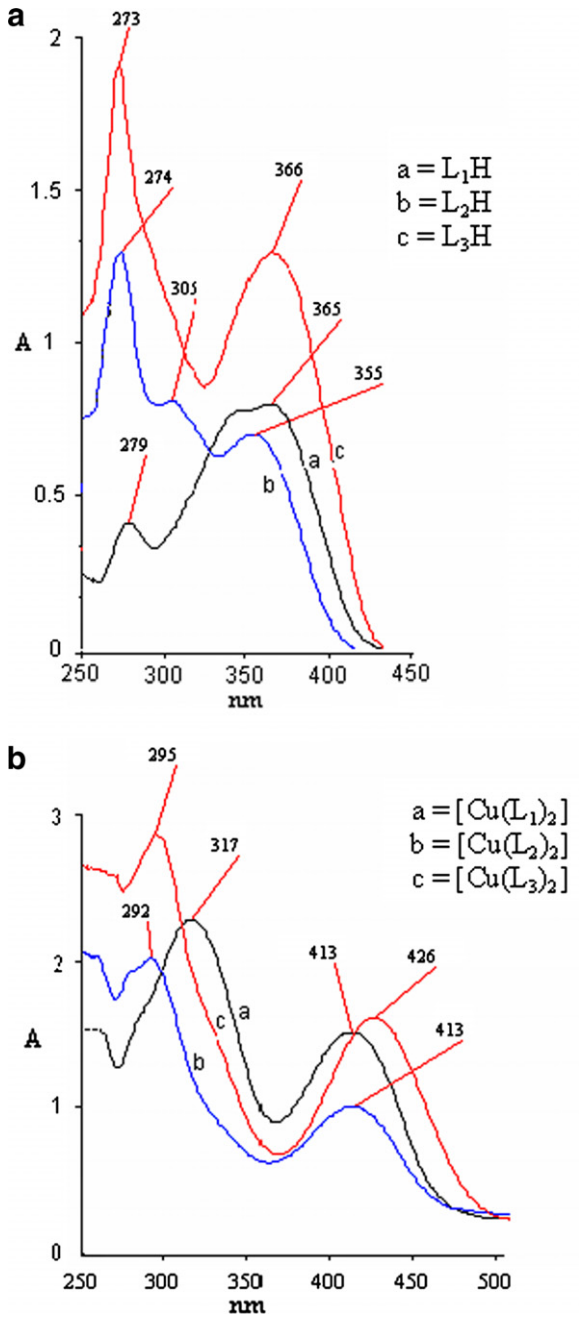


Fig. 1. UV–Vis spectra of ligands ($\mathbf{L}_n\mathbf{H}$) (a); Cu(II) metal complexes $[\mathbf{Cu}(\mathbf{L}_n\mathbf{H})_2]$ in DMSO (b).

3.5. Solubility and molar conductivity

The Ligands ($\mathbf{L}_1\mathbf{H}$), ($\mathbf{L}_2\mathbf{H}$) and ($\mathbf{L}_3\mathbf{H}$), and their Cu(II) metal complexes $[\mathbf{Cu}(\mathbf{L}_n)_2]$ are soluble in C_2H_5OH, CH_3OH, DMSO and DMF solvents. With a view to studying the electrolytic nature of the Cu(II) metal complexes, their molar conductivities were measured in DMF (dimethyl formamide) at 10^{-3} M. The molar conductivities (Λ_M) values of these Cu(II) metal complexes are in the range of 19–26 Ω^{-1} cm^2 mol^{-1} at room temperature [26], indicating their almost non-electrolytic nature. Due to not free ions in Cu(II) metal complexes, the results indicate that Cu(II) metal complexes are very poor in molar conductivity.

3.6. Electrochemistry

The electrochemistry of the ligands ($\mathbf{L}_n\mathbf{H}$) and their copper complexes $[\mathbf{Cu}(\mathbf{L}_n)_2]$ ($n = 1, 2, 3$) were studied by the cyclic voltammetry in the scan rates of 0.025–0.50 V s^{-1} in DMSO solution containing 0.1 M TBAP supporting electrolyte. The cyclic voltammograms (CVs) of the ligands are depicted in Figs. 2 and 3 at 0.025 V s^{-1} scan rate. As seen, all ligands exhibited one irreversible reduction processes without corresponding anodic waves. The redox processes of the ligands are based on the reduction of the azomethine nitrogen in the presence of the phenolic proton in the molecule. Mostly, the process results in the reductive

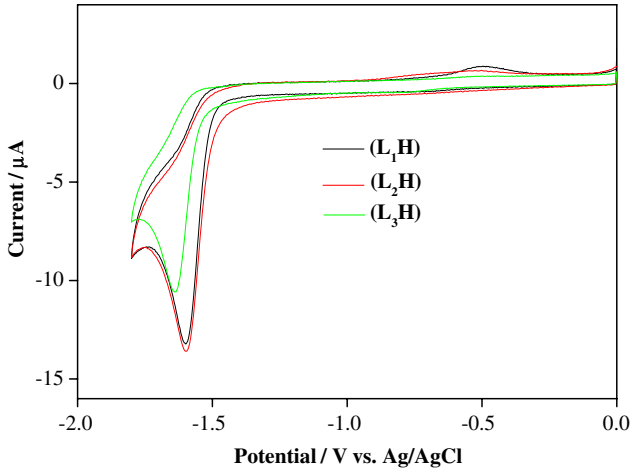


Fig. 2. Cyclic voltammograms (CVs) of the ligands ($\mathbf{L}_n\mathbf{H}$) in DMSO containing 0.1 M TBAP. Scan rates: 0.025 V s^{-1}. Working electrode: a 1.6 mm diameter of platinum disc electrode. $c = 9.4 \times 10^{-3}$ M.

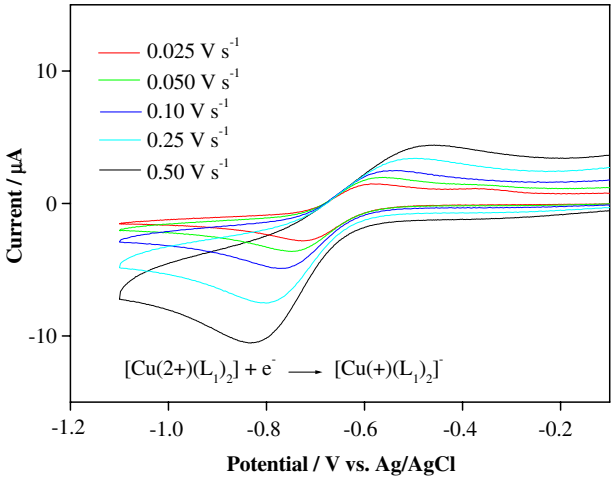


Fig. 3. Cyclic voltammograms (CVs) of the copper complexes $[\mathbf{Cu}(\mathbf{L}_n)_2]$ in DMSO containing 0.1 M TBAP. Scan rates: between 0.025 and 0.50 V s^{-1}. Working electrode: a 1.6 mm diameter of platinum disc electrode. $c = 4.3 \times 10^{-3}$ M.

coupling of the reduced species as previously observed for some Schiff bases such as Salen or its derivatives, indicating irreversible fashion of the processes [27]. However, the reduction process is probably assigned to the electro-deprotonated ligand anion at the platinum surface. The ligands ($\mathbf{L_1H}$), ($\mathbf{L_2H}$), and ($\mathbf{L_3H}$) displayed the cathodic peak potentials at $E_{pc} = -1.60$, -1.60, and -1.64 V versus Ag/AgCl, respectively. It is known that the introduction of electron-donating groups to the electroactive molecules is expected to lead to an increase of electron density in the molecule, thereby making the molecule easier to oxidize and harder to reduce [28–32]. On the other hand, the positions of the substituent on the benzene ring may also effect peak potentials in different extent. This effect was clearly demonstrated by the fact that the cathodic peak potential of ($\mathbf{L_3H}$) was shifted towards more negative potentials compared to those of ($\mathbf{L_1H}$) and ($\mathbf{L_2H}$). It is attributed to the weak-electron-donating methyl sulfanyl group substituted on the *ortho* position of benzene ring. An example of the cyclic voltammograms (CVs) of the copper complexes [$\mathbf{Cu}(\mathbf{L}_n)_2$] in the scan rates of 0.025–0.50 V s^{-1} are exhibited in Fig. 3. The data corresponding to the cyclic voltammograms (CVs) of [$\mathbf{Cu}(\mathbf{L}_n)_2$] are listed in Table 3. All copper complexes showed one quasi-reversible one-electron reduction process in the scan rates of 0.025–0.50 V s^{-1}, which are assigned to simple metal-based one-electron processes; $[Cu(2+)(L_n)_2] + e^- \rightarrow [Cu(1+)(L_n)_2]^-$. The half-wave potentials ($E_{1/2}$) of the reversible Cu(2+)/Cu(1+) redox couples were calculated as the average of the cathodic and anodic peak potentials of the processes. The $E_{1/2}$ of the reduction processes of [$\mathbf{Cu}(\mathbf{L}_1)_2$], [$\mathbf{Cu}(\mathbf{L}_2)_2$], and [$\mathbf{Cu}(\mathbf{L}_3)_2$] are -0.65, -0.65, and -0.68 V versus Ag/AgCl (scan rate 0.025 V s^{-1}), respectively. As seen, $E_{1/2}$ of [$\mathbf{Cu}(\mathbf{L}_3)_2$] was negatively shifted compared to those of [$\mathbf{Cu}(\mathbf{L}_1)_2$], [$\mathbf{Cu}(\mathbf{L}_2)_2$], as observed for the ligands. Although the reduction processes had low ratio of anodic-to-cathodic peak currents (i_{pa}/i_{pc}) (Table 3), the anodic–cathodic peak separations (ΔE) for the Cu(2+)/Cu(1+) couples are 0.100–105 V (scan rate 0.025 V s^{-1}) which assign to the quasi-reversible processes. The slow electron transfer could be associated with a structural rearrangement of the molecule during the reduction process. The reduction processes of ($\mathbf{L}_n\mathbf{H}$) and [$\mathbf{Cu}(\mathbf{L}_n)_2$] are diffusion controlled with the anodic current function ($I_{pa}/v^{1/2}$) independent of the scan rate (v) over the scan range 0.025–0.500 V s^{-1} [33–37].

Table 3
Voltammetric data for the ligands and their copper complexes vs. Ag/AgCl (F_c/F_c^+): values in parentheses vs. F_c/F_c^+ in DMSO–TBAP

Complexes	L/L^- E_{pc}^a (V)	M^{2+}/M^+ $E_{1/2}^b$ (V)	ΔE^c (V)	I_{pa}/I_{pc}^d
($\mathbf{L_1H}$)	−1.60 (−2.10)			
($\mathbf{L_2H}$)	−1.60 (−2.10)			
($\mathbf{L_3H}$)	−1.64 (−2.14)			
[$\mathbf{Cu}(\mathbf{L}_1)_2$]		−0.65 (−1.15)	0.103	0.54
[$\mathbf{Cu}(\mathbf{L}_2)_2$]		−0.65 (−1.15)	0.100	0.60
[$\mathbf{Cu}(\mathbf{L}_3)_2$]		−0.68 (−1.18)	0.105	0.55

[a] E_{pc}: Cathodic peak potential for reduction for irreversible processes.
[b] $E_{1/2} = E_{pc} + E_{pa}/2$.
[c] $\Delta E_p = E_{pc} - E_{pa}$ at 0.025 V s^{-1} scan rate.
[d] i_{pa}/i_{pc} for reduction at 0.025 V s^{-1} scan rate.

3.7. In situ UV–Vis behaviors of the electro-reduced ligands and complexes

"The spectroelectrochemical behaviors of ligands ($\mathbf{L}_n\mathbf{H}$) and their copper complexes [$\mathbf{Cu}(\mathbf{L}_n)_2$] were investigated using a thin-layer UV–Vis spectroelectrochemical technique in DMSO solution containing 0.2 M TBAP. The UV–Vis spectral changes for the reduced species of ($\mathbf{L}_n$) and [$\mathbf{Cu}(\mathbf{L}_n)_2$] were obtained in a thin-layer cell during applied potentials. The absorption spectra of electrochemically generated species, $(\mathbf{L_1H})^-$ and $[\mathbf{Cu}(+)(\mathbf{L}_1)_2]^-$, are given in Figs. 4 and 5. The convenient values of applied potentials for in situ spectroelectrochemical experiment were determined for the reduction processes by taking CVs of the complexes in the thin-layer cell.

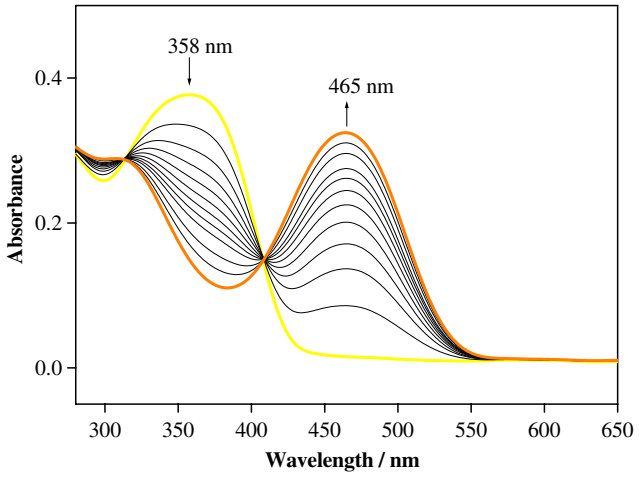


Fig. 4. Time-resolved UV–Vis spectra of ($\mathbf{L_1H}$) during the first reductions at $E_{app} = -1.80$ V in DMSO containing 0.2 M TBAP.

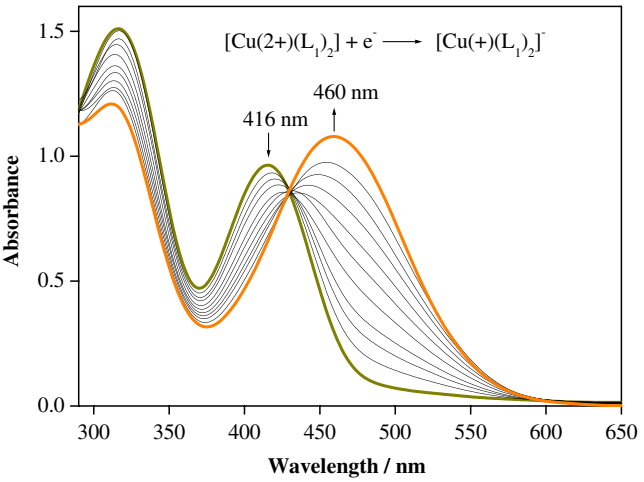


Fig. 5. Time-resolved UV–Vis spectra of [$\mathbf{Cu}(\mathbf{L}_1)_2$] during the first reductions at $E_{app} = -1.00$ V in DMSO containing 0.2 M TBAP.

Fig. 4 shows changes in the electronic spectrum of ($\mathbf{L_1H}$) during reduction process in the thin-layer cell. The well-defined isosbestic point is observed at 408 nm, confirming that the electrode reaction proceeds in a quantitative fashion and therefore the absence of any coupled chemistry [28,29,33,37–39]. When the potential ($E_{app} = -1.80$ V) was applied in the thin-layer cell, the broad band at 358 nm belonging to the $n\rightarrow\pi^*$ transitions of the azomethine (CH=N), disappeared and new bands at 465 and at 315 nm formed during the reduction process. The 465 nm-peak was observed at longer wavelength compared with the neutral ligand, which clearly indicates a reduced product having extended conjugation. The original spectrum corresponding to the neutral ligand was 60% recovered when the potential was applied at $E_{app} = -1.80$ V for the re-oxidation process, indicating decomposition or chemical change of the electro-generated reduced species at the some extent in the time scale of the reduction process. This behavior confirms the irreversible nature of the reduction process observed for the CV of the ligands. Similar spectral changes were observed for ($\mathbf{L_1H}$) and ($\mathbf{L_2H}$) during their reduction processes in the same experimental conditions.

Fig. 5 shows the time-resolved spectra of [$\mathbf{Cu(L_1)_2}$] during the applied potential at $E_{app} = -1.00$ V. The copper complexes showed two main bands at about 316 nm and 416 nm the former of which was referred to the $n\rightarrow\pi^*$ transitions of the azomethine (CH=N) group and the charge-transfer transitions. As expected, the latter band was red-shifted compared to those of the ligands, indicating coordination of the azomethine nitrogen to the copper metal. After reduction, the Cu(II)(d^9)→Cu(I)(d^{10}) process was formed by adding one electron in the metal system. This change resulted in an appearance of the absorption band at 460 nm which was attributed to a metal to ligand charge-transfer transitions (MLCT) in Cu(I) complex. Also, the intensity of the band at 316 nm was decreased during the reduction process. All complexes exhibited similar spectral changes during the reduction processes in the thin-layer cell. The spectral changes were similar to what were observed for a metal-centered reduction Cu(II)→Cu(I) processes in the literature [40–42]. The original spectra of the complexes were obtained upon re-oxidation during spectroelectrochemical measurement. It is concluded that the singly-reduced species remains stable and is not companied by a chemical reaction in the time scale of the spectroelectrochemical measurement. The controlled potential coulometric (CPC) study indicated that the number of electrons transferred for the forward and reverse electrochemical reaction of the complexes was one for the reduction and re-oxidation processes based on the Cu(II)/Cu(I) couples.

4. Conclusion

New sterically constrained Schiff-base ligands ($\mathbf{L_nH}$) ($n = 1$, 2, and 3) (L = *N*-[*m*-(methylmercapto)aniline]-3,5-di-*t*-butylsalicylaldimine, $m = 4$, 3, and 2 positions, respectively) and their copper(II) complexes [$\mathbf{Cu(L_n)_2}$] were synthesized and their electro-spectrochemical properties were investigated using cyclic voltammetric and thin-layer spectroelectrochemical techniques in DMSO. Besides the classical methods such as FT-IR, UV–Vis, ^{1}H and ^{13}C NMR, elemental analysis, magnetic susceptibility, and molar conductivity for structural characterization, the combination of the electrochemical and spectroelectrochemical methods provided a power tool to reveal the complementary nature of the molecular structure and electron-transfer reactions of the reduced species of new electroactive Schiff-bases and their Cu(II) complexes. So the comparative electro-spectrochemical studies revealed that [$\mathbf{Cu(L_n)_2}$] complexes showed four coordination with the ligand ($\mathbf{L_nH}$) having N and O donor sites, and a shift on their half-wave potentials or band positions because of different positions of methylsulfanyl groups attached on benzene ring. The electro-reduced species of [$\mathbf{Cu(L_n)_2}$] complexes remained stable during spectroelectrochemical time scale although the corresponding ligands exhibited an irreversible reduction processes in their CV measurements. Finally, the CVs and the well-defined spectral changes observed during applied potentials in the thin-layer cell spectral data supported the corresponding structures of the copper complexes.

Acknowledgements

This work have been supported, in part, by the HUBAK Fund (Project No. 649) of Harran University (Sanliurfa, Turkey). The supports of State Planning Organization (DPT, Project No. 90177) is gratefully acknowledged. This work has also been supported, in part, by the Turkish Academy of Sciences in the framework of the Young Scientist Award Program (TÜBA-GEBİP).

References

[1] E.J. Cambel, S.T. Nguyen, Tetrahedron 42 (2001) 1221.
[2] A.J. Stemmler, C.T. Burrows, J. Am. Chem. Soc. 121 (1999) 6956.
[3] R. Klement, F. Stock, H. Elias, H. Paulus, M. Valko, M. Mazur, Polyhedron 18 (1999) 3617.
[4] R. Atkins, G. Brewer, E. Kokot, G.M. Mockler, E. Sinn, Inorg. Chem. 24 (1985) 127.
[5] E. Kwiatkowski, M. Kwiatkowski, A. Clechnowicz, Inorg. Chim. Acta 90 (1984) 145.
[6] P.J. Burke, D.R. Mcmillin, J. Chem. Soc., Dalton Trans. (1980) 1794.
[7] X.D. Du, X.D. Yu, J. Mol. Catal. A: Chem. 126 (1997) 109.
[8] N. Raman, A. Kulandaisamy, C. Thangaraja, K. Jeyasubramanian, Transition Met. Chem. 28 (2003) 29.
[9] D. Zurita, S. Menage, J.L. Pierre, E.S. Aman, J. Biol. Inorg. Chem. 2 (1997) 46.
[10] (a) J.A. Halfen, V.G. Toung, W.B. Tolman, Angew. Chem., Int. Ed. Engl. 35 (1996) 1687;
(b) E.I. Solomon, U.M. Sundanam, T.E. Makonkin, Chem. Rev. 96 (1996) 2563;
(c) J.P. Klinman, Chem. Rev. 96 (1996) 2541.
[11] (a) T. Inabe, I. Luneau, T. Mitani, Y. Maruyama, Bull. Chem. Soc. Jpn. 67 (1994) 612;
(b) N. Hoshino, T. Inabe, T. Mitani, Y. Maruyama, Bull. Chem. Soc. Jpn. 61 (1988) 4207.
[12] (a) E. Hadjoudis, M. Vittoakis, I. Moustaki-Mavridis, Tetrahedron 43 (1987) 1345;

(b) T. Kobayahsi, T. Inabe, J. Phys. Chem. A 101 (1997) 644;
(c) M.L. Glowka, D. Martinowski, K. Kozlowska, J. Mol. Struct. 474 (1999) 81;
(d) E. Tas, I. Ucar, V.T. Kasumov, A. Kilic, A. Bulut, Spectrochim. Acta A 68 (2007) 463.
[13] N. Daneshvar, A.E. Entezami, A. Khander, L.A. Saghatforoush, Polyhedron 22 (2003) 1437.
[14] J.F. Larrow, E.N. Jacobsen, Y. Gao, Y. Hong, X. Nie, C.M. Zepp, J. Org. Chem. 59 (1994) 1939.
[15] A. Earnshaw, Introduction to Magnetochemistry, Academic Press, London, 1968, p. 4.
[16] E. Tas, M. Aslanoglu, A. Kilic, O. Kaplan, H. Temel, J. Chem. Res. (S) 4 (2006) 242.
[17] E. Tas, M. Aslanoglu, M. Ulusoy, H. Temel, J. Coord. Chem. 8 (2004) 677.
[18] (a) K.N. Kumar, R. Ramesh, Polyhedron 24 (2005) 1885;
(b) H. Temel, S. Ilhan, M. Aslanoglu, A. Kilic, E. Tas, J. Chin. Chem. Soc. 53 (2006) 1027.
[19] S.A. Ali, A.A. Soliman, M.M. Aboaly, R.M. Ramadan, J. Coord. Chem. 55 (2002) 1161.
[20] L. Sacconi, M. Ciampolini, F. Maffio, F.P. Cavasino, J. Am. Chem. Soc. 84 (1962) 3245.
[21] R.L. Carlin, Transition Met. Chem. 1 (1965).
[22] A. Kilic, E. Tas, B. Gumgum, I. Yilmaz, Chin. J. Chem. 24 (2006) 1599.
[23] C. Fraser, B. Bosnich, Inorg. Chem. 33 (1994) 338.
[24] (a) A.B.P. Lever, Inorganic Electronic Spectroscopy, Elsevier, Amsterdam, 1984;
(b) E. Tas, V.T. Kasumov, O. Sahin, M. Ozdemir, Transition Met. Chem. 27 (2002) 442.
[25] (a) V.T. Kasumov, Spectrochim. Acta A 57 (2003) 1649;
(b) E. Tas, M. Aslanoglu, A. Kilic, Z. Kara, J. Coord. Chem. 59 (8) (2006) 861.
[26] R.L. Dutta, Inorganic Chemistry Part II, 2nd ed., The New Book Stall, Calcutta, 1981, p. 386.
[27] (a) A.A. Isse, A. Gennaro, E. Vianello, Electrochim. Acta 42 (1997) 2065;
(b) T. Shono, N. Kise, E. Shirakawa, H. Matsumoto, E. Okazaki, J. Org. Chem. 56 (1991) 3063;
(c) N. Kise, H. Oike, E. Okazaki, M. Yoshimoto, T. Shono, J. Org. Chem. 60 (1995) 3980.
[28] I. Yilmaz, A.G. Gurek, V. Ahsen, Polyhedron 24 (2005) 791.
[29] I. Yilmaz, M. Kocak, Polyhedron 23 (2004) 1279.
[30] K.M. Kadish, T. Nakanishi, V. Ahsen, I. Yilmaz, J. Phys. Chem. B 105 (2001) 9817.
[31] E. Tas, M. Ulusoy, M. Guler, I. Yilmaz, Transition Met. Chem. 29 (2004) 180.
[32] A. Kilic, E. Tas, B. Gumgum, I. Yilmaz, Transition Met. Chem. 31 (2006) 645.
[33] I. Yilmaz, T. Nakanishi, A. Gürek, K.M. Kadish, J. Porhyrin. Phthalocyan. 7 (2003) 227.
[34] T. Nakanishi, I. Yilmaz, N. Nakashima, K.M. Kadish, J. Phys. Chem. B 107 (2003) 12789.
[35] M. Kandaz, I. Yilmaz, S. Keskin, A. Koca, Polyhedron 21 (2002) 825.
[36] M. Kandaz, S.Z. Coruhlu, I. Yilmaz, A.R. Ozkaya, Transition Met. Chem. 27 (2002) 877.
[37] I. Yilmaz, M. Kandaz, A.R. Ozkaya, A. Koca, Monatsh. Chem. 133 (2002) 609.
[38] S. Arslan, I. Yilmaz, Transition Met. Chem. 32 (2007) 292.
[39] S. Arslan, I. Yilmaz, Inorg. Chem. Commun. 10 (2007) 385.
[40] A. Kilic, E. Tas, B. Deveci, I. Yilmaz, Polyhedron 26 (2007) 4009.
[41] J. Losata, I. Del Peso, L. Beyer, Inorg. Chim. Acta 321 (2001) 107.
[42] D.F. Rohrbach, W.R. Heineman, E. Deutsch, Inorg. Chem. 18 (1979) 2536.

obtain because of its very small interwoven needles which makes the obtainment of single crystal studies difficult [3,7–9]. Harding showed that the positions of Cu in the structure of aurichalcite are octahedrally coordinated [9]. The atom positions occupied by zinc have tetrahedral coordination [9].

Raman spectroscopy has proven very useful for the study of minerals [10–12]. Indeed Raman spectroscopy has proven to be most useful for the study of diagentically related minerals as often occur with carbonate minerals [13–17]. Some previous studies have been undertaken by the authors using Raman spectroscopy to study complex secondary minerals formed by crystallisation from concentrated sulphate solutions [18]. The authors have undertaken some comprehensive studies of selected carbonate minerals [19–23]. The importance of this work rests with the application of Raman spectroscopy to the study of minerals and inorganic compounds which show no or limited symmetry [19,24–31].

As part of our comprehensive research on the molecular structure of secondary minerals, we report the synthesis and characterisation of Ni doped aurichalcite $(Zn^{2+},Cu^{2+},Ni^{2+})_5(CO_3)_2(OH)_6$ using Raman spectroscopy and X-ray diffraction.

2. Experimental

2.1. Synthesis of Ni containing aurichalcite

The mineral $(Cu,Zn,Ni^{2+})_5(CO_3)_2(OH)_6$ was synthesised with a respective metal ratio of 3:16:1. Williams inferred from the studies of natural aurichalcite minerals that the highest ratio of Cu to Zn in aurichalcite is 1:3 [5]. The authors have successfully synthesized aurichalcites with varying Cu/Zn ratios up to Cu:Zn 1:1. A common formula for natural aurichalcite is $Cu_{1.25}Zn_{3.75}(CO_3)_2(OH)_6$. Williams also reported a natural aurichalcite which contained Ni as the dopant ion.

Synthesis of ideal products was modelled on the procedure by Fujita et al. [32]. A solution of metal ions (M^{2+}) was prepared by mixing appropriate concentrations of 1.5 M $Ni(NO_3)_2$, $Cu(NO_3)_2$, and $Zn(NO_3)_2$ that correspond to the desired metal concentrations required in products. Synthesis of the lower nickel concentrations of aurichalcite was carried out by adding dropwise 100 cm^3 of a 1.5 M M^{2+} solution via a peristaltic pump to 1000 cm^3 of 0.2 M HCO_3^- solution at 60 °C. The relatively sensitive nature of aurichalcite to acidic (pH < 6) conditions precluded the use of the depleting methods mentioned in the literature [33] to obtain optimum yields of high phase purity Ni containing aurichalcite. As such, a stream of saturated sodium bicarbonate was added at a quasi-constant rate to maintain a pH ≈7.15. Samples were vacuum filtered and washed with hot, degassed, demineralised water. Samples were then dried overnight at 40 °C. The samples were phase analysed by X-ray diffraction and for chemical composition by EDX measurements.

2.2. X-ray diffraction

Powder X-ray diffraction analyses were performed on a Phillips X-ray diffractometer (radius: 173.0 mm). Incident X-ray radiation was produced from a long fine focused C-Tech PW1050 Co X-ray tube, operating at 40 kV and 32 mA. The incident beam passed through a 1° divergence slit, a 15 mm fixed mask and a 1° fixed anti scatter slit. After interaction with the sample, the diffracted beam was detected by a proportional detector with a 0.2 mm receiving slit fitted to a graphite post-diffraction monochrometer. The detector was set in scanning mode, with an active length of 2.022 mm. Samples were analysed utilising Bragg–Brentano geometry over a range of 3–75° 2θ with a step size of 0.02 ° 2θ, with each step measured for 200 s.

2.3. SEM and EDX

Mineral samples were coated with a thin layer of evaporated carbon and secondary electron images were obtained using an scanning electron microscope (FEI Quanta 200 SEM, FEI Company, Hillsboro, OR, USA). For X-ray microanalysis (EDX), three samples were embedded in Araldite resin and polished with diamond paste on Lamplan 450 polishing cloth using water as a lubricant. The samples were coated with a thin layer of evaporated carbon for conduction and examined in a JEOL 840A analytical SEM (JEOL Ltd., Tokyo, Japan) at 25 kV accelerating voltage. Preliminary analyses of the carbonate mineral samples were carried out on the FEI Quanta SEM using an EDAX X-ray microanalyser, and microanalyses of the clusters of fine crystals were carried out using a full standard quantitative procedure on the JEOL 840 SEM using a JEOL-2300 energy-dispersive X-ray microanalysis system (JEOL Ltd., Tokyo, Japan). Oxygen was not measured directly but was calculated using assumed stoichiometry of the other elements analysed.

2.4. Raman microprobe spectroscopy

The crystals of aurichalcite were placed and oriented on the stage of an Olympus BHSM microscope, equipped with 10× and 50× objectives and part of a Renishaw 1000 Raman microscope system, which also includes a monochromator, a filter system and a Charge Coupled Device (CCD). Raman spectra were excited by a HeNe laser (633 nm) at a resolution of 2 cm^{-1} in the range between 100 and 4000 cm^{-1}. Repeated acquisition using the highest magnification was accumulated to improve the signal to noise ratio. The spectra were calibrated using the 520.5 cm^{-1} line of a silicon wafer. To ensure that the correct spectra are obtained, the incident excitation radiation was scrambled. Details of the technique have been published by the authors.

2.5. Mid-IR spectroscopy

Infrared spectra were obtained using a Nicolet Nexus 870 FTIR spectrometer with a smart endurance single

bounce diamond ATR cell. Spectra over the 4000–525 cm^{-1} range were obtained by the co-addition of 128 scans with a resolution of 4 cm^{-1} and a mirror velocity of 0.6329 cm/s. Spectra were co-added to improve the signal to noise ratio.

Spectral manipulation such as baseline adjustment, smoothing and normalisation was performed using the Spectracalc software package GRAMS (Galactic Industries Corporation, NH, USA). Band component analysis was undertaken using the Jandel Scientific 'Peakfit' software package, which enabled the type of fitting function to be selected and allows specific parameters to be fixed or varied accordingly. Band fitting was done using a Lorentz–Gauss cross-product function with the minimum number of component bands used for the fitting process. The Gauss–Lorentz ratio was maintained at values greater than 0.7 and fitting was undertaken until reproducible results were obtained with squared correlations of r^2 greater than 0.995. The reason for using this type of mathematical function is that this function best fits vibrational spectroscopic data where the central peak is Lorentzian and the wings of the peak are Gaussian. It should be noted that where sharp bands are obtained in the Raman spectra fitting is unique. If one starts with different starting parameters, then the fit will converge to a unique result. When bands are broad the uniqueness of the fit is open to question. Band fitting offers a procedure to determine the exact position of bands.

3. Results and discussion

3.1. X-ray diffraction

The X-ray diffraction patterns of the Ni-aurichalcite together with the reference standard 00-038-0154 are shown in Fig. 1. Clearly, the synthesised mineral is aurichalcite. From the X-ray diffraction data, we can safely assume that the Ni replaces some of the octahedral sites in the crystal structure as the data match so closely with $(Cu_{0.2}Zn_{0.8})_5(CO_3)_2(OH)_6$. At some stage in the future it might be worth another look to see if more nickel can be introduced into the aurichalcite structure by altering the synthesis conditions slightly. The additional peaks in the XRD patterns may be due to the trace of carbonates of zinc and copper.

3.2. Raman spectroscopy

Only a very limited number of Raman studies have been reported on the carbonate anion in hydroxycarbonate type minerals such as hydrozincite and aurichalcite [1,34–39]. When the carbonate species is present as a free ion not involved in any bonding it will exhibit a space group of D_{3h}. In the Raman spectrum, one will observe $\nu_1(A_1')$, $\nu_3(E')$ and $\nu_4(E')$. As a result three bands—the bending non-planar mode $\nu_2(A''2)$, the antisymmetrical stretching mode $\nu_3(E')$ and the bending angular mode $\nu_4(E')$—will be observed in the infrared spectrum around 880, 1415 and 680 cm^{-1}, respectively, while the symmetric stretching mode $\nu_1(A_1')$ is infrared inactive. However, changes can be expected when the carbonate ion is bonded in a mineral structure as it will be affected by interactions with water molecules and OH-groups. In comparison with free CO_3^{2-}, a shift towards lower wavenumbers is generally observed for the carbonate anion in minerals. Interaction between interlayer water molecules and the carbonate ion is reflected by the presence of bands in the OH-stretching region of the infrared spectrum around 3000–3100 cm^{-1}. The shift towards lower wavenumbers indicates a loss of freedom compared to the free CO_3^{2-} and as a consequence, a lowering of the carbonate symmetry from D_{3h} to probably C_{2s} or C_v.

The Raman spectrum of the Ni-aurichalcite is shown in Fig. 2. An intense band at 1070 cm^{-1} is assigned to the ν_1 symmetric stretching mode of the carbonate unit. The band displays some asymmetry on the low wavenumber side of this peak. In the Raman spectrum of natural aurichalcite, two bands were observed at 1060 and 1070 cm^{-1}. The

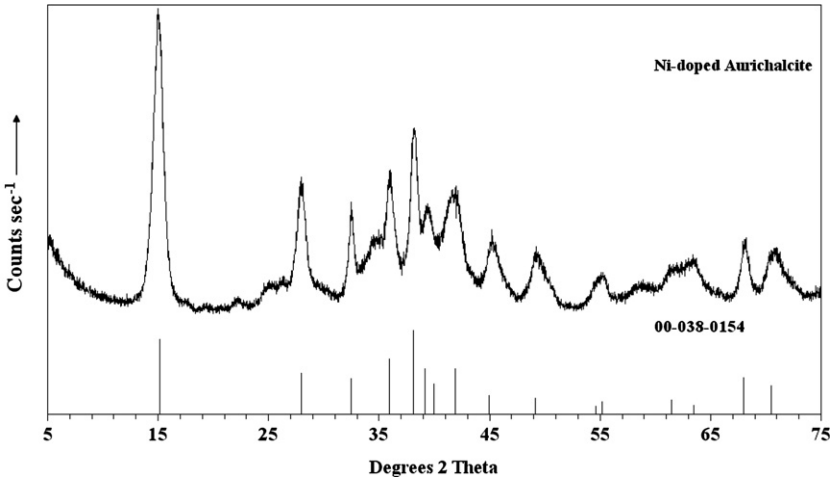


Fig. 1. X-ray diffraction patterns of Ni doped aurichalcite.

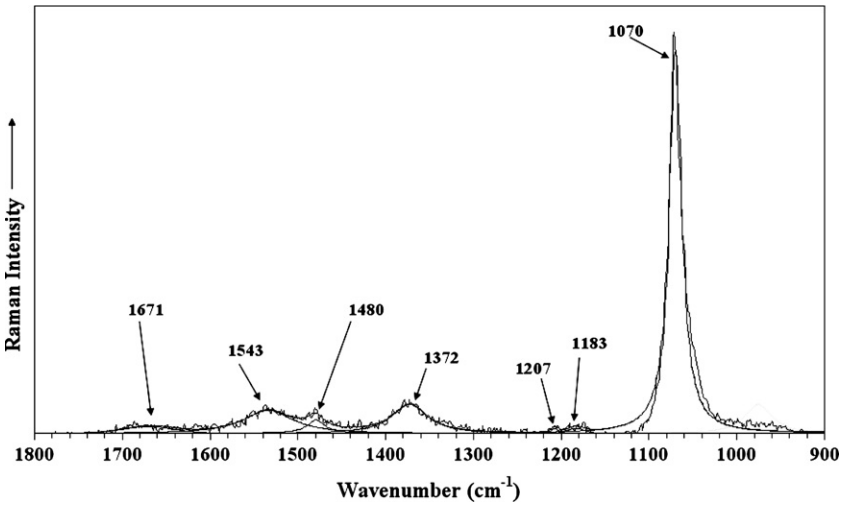


Fig. 2. Raman spectrum of Ni doped aurichalcite in the 900 to 1800 cm^{-1} region.

former band was attributed to the Raman activated δOH deformation mode. It is possible that for the Ni-aurichalcite the two bands overlap and cannot be resolved. Little information on the Raman spectra of aurichalcite is available. Bouchard and Smith published a Raman spectrum of an aurichalcite of unknown origin with an intense peak observed at 1074 cm^{-1} [40]. In the infrared spectrum of the synthesised Ni-aurichalcite (Fig. 3) a low intensity band is resolved at 1049 cm^{-1} whcih may be the infrared activated band equivalent to the Raman v_1 symmetric stretching mode. In the infrared spectrum of natural aurichalcite, a low intensity band is observed at around 1084 cm^{-1} as a shoulder on an infrared spectral profile which is dominated by bands at 1032 cm^{-1} attributed to the δOH deformation mode. The number of bands observed in this spectral region may be attributed to the structural distortion of the mineral. Raman spectra of aurichalcite should be similar to that of the other hydroxy carbonates such as the rosasite mineral group [19,20,28,41]. For rosasite, two intense Raman bands were observed at 1096 and 1056 cm^{-1}. In the infrared spectrum of an aurichalcite from Arizona, two intense bands are observed at 1084 and 1029 cm^{-1} with an additional band at 924 cm^{-1}. The first band at 1084 cm^{-1} is assigned to the v_1 symmetric stretching mode of the carbonate unit. Bands have been observed in the infrared spectra of malachite at 1095 cm^{-1} and for azurite 1090 cm^{-1} [42,43]. The infrared spectrum of hydrocerrusite showed an intense band at 1090 cm^{-1} [44]. Interestingly, the $(CO_3)^{2-}v_1$ band of the aurichalcite mineral should not be infrared active. However, because of symmetry reduction of the carbonate anion the band becomes activated. The intense Raman band observed at 1096 cm^{-1} for rosasite is assigned to the v_1 $(CO_3)^{2-}$ symmetric stretching vibration.

A number of low intensity bands are observed in the 1300–1500 cm^{-1} region (Fig. 2). Bands are observed at 1372, 1480 and 1543 cm^{-1} for the Ni-aurichalcite. These bands may be ascribed to the $v_3(CO_3)^{2-}$ antisymmetric

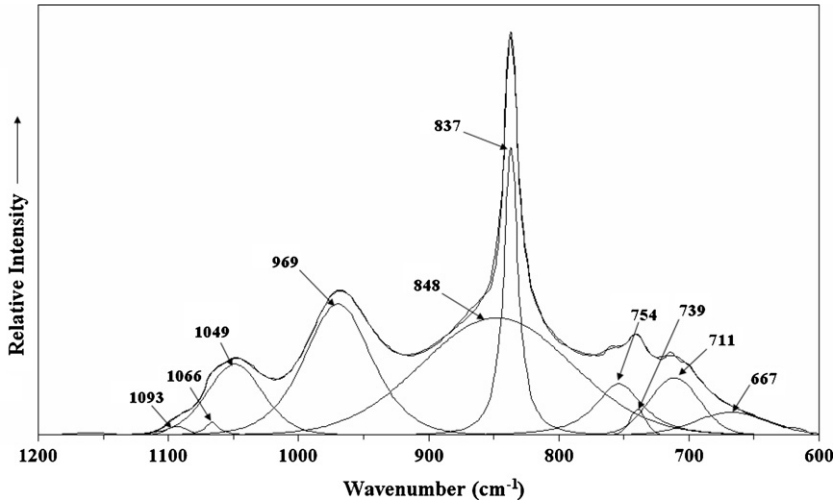


Fig. 3. Infrared spectrum of Ni doped aurichalcite in the 600 to 1200 cm^{-1} region.

stretching modes. Three bands are observed for a natural aurichalcite from Durango at 1506, 1485 and 1337 cm^{-1}. Two very low intensity bands are additionally observed at 1183 and 1207 cm^{-1}. These bands may result from an impurity remaining after the synthesis of the Ni-aurichalcite. The broad band at 1671 cm^{-1} is ascribed to the water bending mode. Such a band for water is found at 1625 cm^{-1}. The observation of the band at 1671 cm^{-1}, a significantly higher wavenumber implies that water is very strongly hydrogen bonded to the aurichalcite surface. In the infrared spectrum in the 1200–1800 cm^{-1} region shown in Fig. 4, intense infrared bands are observed at 1360, 1404, 1482 and 1511 cm^{-1}. These bands are attributed to the v_3 $(CO_3)^{2-}$ antisymmetric stretching modes of the Ni-aurichalcite. The number of bands in this spectral region is attributed to the lack of symmetry of the carbonate anion in the aurichalcite structure. The presence of multiple bands indicates the existence of the carbonate ion in more than one symmetry i.e. two carbonate units exist which are not crystallographically equivalent. In the spectrum reported by Bouchard and Smith, two bands were reported at 1511 and 1479 cm^{-1}. Their spectra showed low signal due to noise, and any low intensity bands would not be observed [40].The observation of multiple sets of bands for the synthetic Ni-aurichalcite suggests that two different carbonate units are in the Ni-aurichalcite structure. A broad band at 1646 cm^{-1} is assigned to the water bending modes. The low intensity of this band suggests that the amount of adsorbed water is low. As for the Raman spectrum the position of the band is higher than that for water. The question arises as to whether water is bonded in the structure of the aurichalcite replacing some of the OH units.

The Raman bands in the low wavenumber region for Ni-aurichalcite are shown in Fig. 5. The v_2 bending modes for carbonates vary from around 890 to 850 cm^{-1}. A single

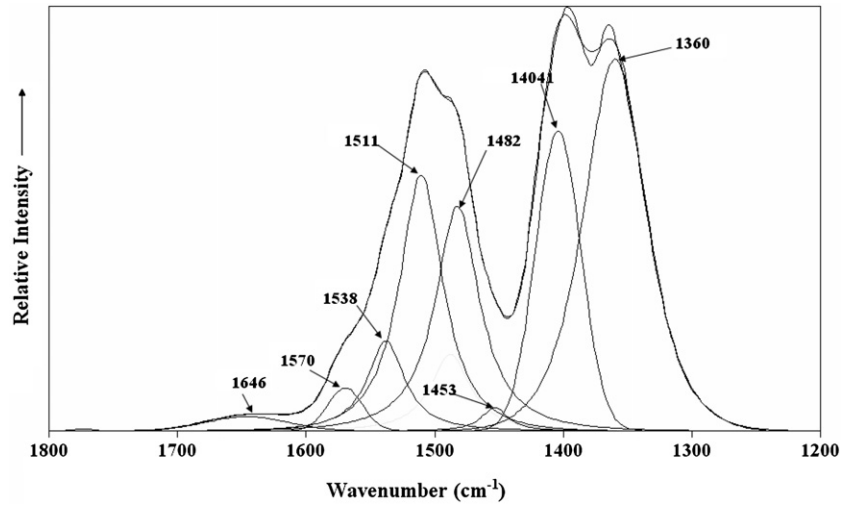


Fig. 4. Infrared spectrum of Ni doped aurichalcite in the 1200 to 1800 cm^{-1} region.

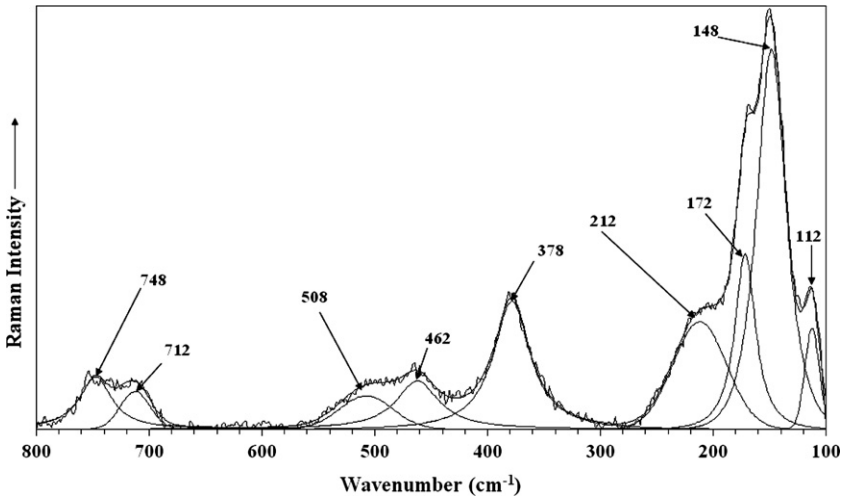


Fig. 5. Raman spectrum of Ni doped aurichalcite in the 100 to 800 cm^{-1} region.

band is observed for Ni-aurichalcite at 855 cm^{-1} assigned to the v_2 bending mode. The band is observed at 860 cm^{-1} for a natural aurichalcite from Arizona. The position of the band for natural aurichalcites appears to vary and probably is a result of crystal strain. It is probable that more than one band is observed in this region; however, the intensity of the band is so low that it makes band fitting difficult. Multiple bands are observed for the carbonate v_4 in phase bending modes in the Raman spectrum of Ni-aurichalcite. Two bands are observed at 712 and 748 cm^{-1}.

A similar result is obtained for natural aurichalcites. For the Durango aurichalcite, three bands are observed at 752, 733 and 708 cm^{-1}; for the Arizona aurichalcite, 748, 737 and 710 cm^{-1}; and for the Chihuahua aurichalcite, 753, 733 and 711 cm^{-1}. The number of bands observed in this spectral region may be attributed to the structural distortion of the mineral. A comparison may be made with other carbonate containing minerals. Only a single band at 817 cm^{-1} is observed in this region for malachite. The infrared spectrum of malachite showed two bands at 879 and 821 cm^{-1} [42]. This infrared spectral region is more complex for azurite with bands observed at 872, 837, 815 and 796 cm^{-1}. This complexity is again ascribed to the loss of degeneracy. The equivalent Raman bands for malachite are observed at 752 and 717 cm^{-1}. In the infrared spectra, bands are observed at 779, 754 and 701 cm^{-1} for azurite and at 780, 750 and 715 cm^{-1} for malachite [42].

The Raman spectra of the low wavenumber region reported in Fig. 5 are expected to show bands associated with CuO and ZnO stretching and bending vibrations. Strong Raman bands for Ni-aurichalcite are observed at 378, 462 and 508 cm^{-1}. Strong bands are observed for auricahlcite at around 498, 460 and 390 cm^{-1}.

In the structure reported by the authors [28], there are three structurally distinct MO stretching vibrations. The M3 site is a solely Zn site. The M1, M2 and M4 sites are shared randomly between Cu and Zn [45]. The above bands are associated with these CuO and ZnO stretching modes. Bouchard and Smith [40] reported the Raman bands at 389, 463 and 503 cm^{-1} which are in agreement with the band positions reported here for Ni-aurchalcite; however no assignments were offered by Bouchard and Smith. The number of bands observed in this spectral region may be attributed to the structural distortion of the mineral. In addition strong Raman bands for Ni-aurichalcite are observed at 112, 148, 172 and 212 cm^{-1}. These bands are attributed to ONiO and OZnO bending vibrations. Two intense bands are observed for natural aurichalcite at around 166 and 142 cm^{-1}. These bands are assigned to the OCuO and OZnO bending vibrations.

The Raman spectra of the OH stretching region of Ni-aurichalcite mineral is shown in Fig. 6. Two broad and quite noisy bands are found at 3362 and 3559 cm^{-1}. The low intensity bands at 2860, 2894 and 2926 cm^{-1} are assigned to CH stretching vibrations of an organic impurity. In the infrared spectrum (Fig. 7) two bands are displayed at 3312 and 3392 cm^{-1}. A comparsion may be made between the spectra of the hydroxyl stretching region of the synthetic Ni-aurichalcite and some selected natural aurichalcites. A single symmetric band is observed for the natural aurichalcite from Durango at 3338 cm^{-1} which may be compared with the value of 3348 cm^{-1} for the Arizona aurichalcite and 3355 cm^{-1} for the aurichalcite from Chihuahua. A comparison can be made with rosasite where two distinct bands are observed at 3387 and 3319 cm^{-1}. The bands are assigned to the OH stretching vibration. Bouchard and Smith reported a noticeably broad band in the Raman spectrum of aurichalcite at 3331 cm^{-1} [40]. This value is in good agreement with the results reported in this work. In the infrared spectra, more complexity is observed. Infrared bands for the Durango aurichalcite are observed at 3491, 3350, 3244 and a broad band at 3173 cm^{-1}. The infrared spectrum of the sample from Chihuahua gave bands at 3359, 3249 and 3106 cm^{-1}. The broad band at around 3002 cm^{-1} may be ascribed to adsorbed water.

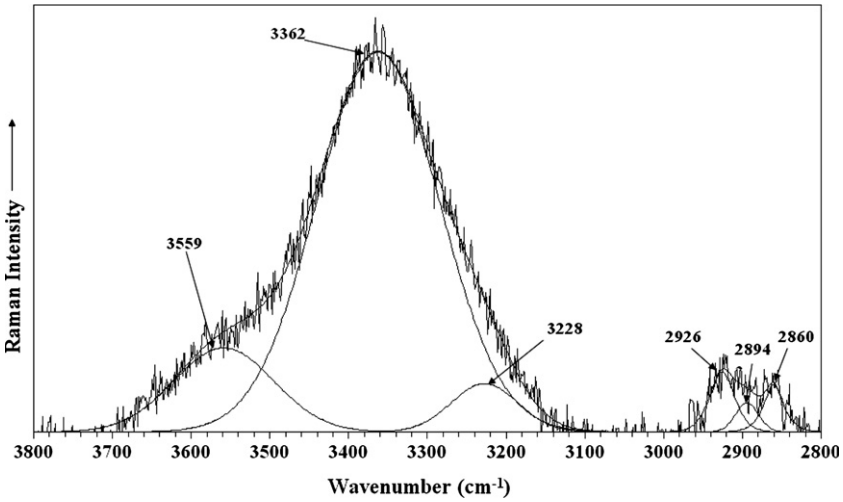


Fig. 6. Raman spectrum of Ni doped aurichalcite in the 2800 to 3800 cm^{-1} region.

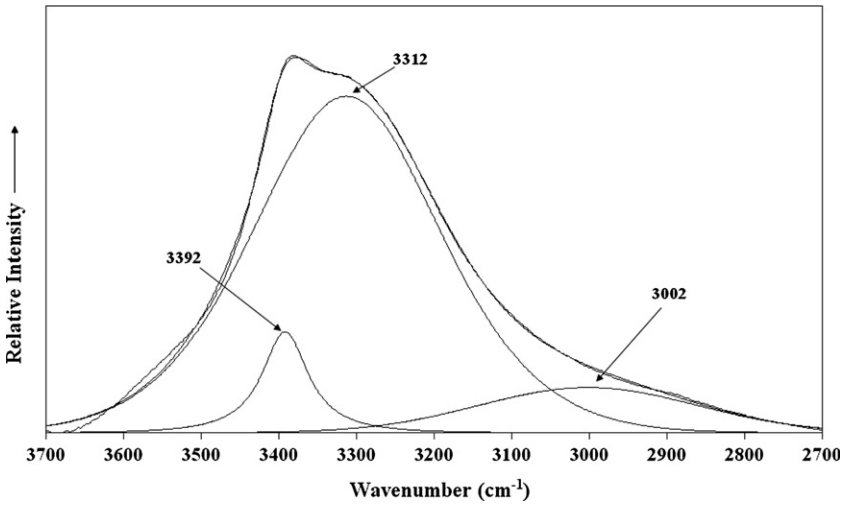


Fig. 7. Infrared spectrum of Ni doped aurichalcite in the 2700 to 3700 cm^{-1} region.

The first two bands are assigned to OH stretching vibrations.

4. Conclusions

Raman spectroscopy complemented with infrared data, X-ray diffraction, electron microscopy and EDAX have been used to characterise the structure and chemical composition of a synthetic aurichalcite. The spectra are correlated with the structure of the mineral. This compositional variation affects the Raman spectral profile. A cation substitution reliance is observed for the hydroxyl stretching vibrational modes. This is related to the hydrogen bond distances of the OH units and the adjacent carbonate units in the aurichalcite structure.

The question arises as to why there are similar Raman spectral patterns for aurichalcite as compared with other hydroxy carbonate minerals such as hydrozincite and members of the rosasite mineral group. The answer must infer that the minerals must have the same structure or at least related structures. Aurichalcite is monoclinic like malachite with point group $2/m$. The rosasite mineral group has spectra similar to that of malcachite. Therefore, it can be suggested that the structure of the rosasite group of minerals is monoclinic, although at this point in time remains unproven. This conclusion is in agreement with the assumptions of Anthony et al. who stated that rosasite and related minerals have monoclinic structure by analogy with malachite [7].

Acknowledgements

The financial and infra-structure support of the Queensland University of Technology, Inorganic Materials Research Program is gratefully acknowledged. The Australian Research Council (ARC) is thanked for funding the instrumentation. Professor B. Jagannadha Reddy wishes to thank the Inorganic materials research program for a QUT visiting professorial fellowship.

References

[1] R.S. Braithwaite, G. Ryback, Mineral. Mag. 33 (1963) 441–449.
[2] R.G. Herman, C.E. Bogdan, P.L. Kumler, D.M. Nuszkowski, Mater. Chem. Phys. 35 (1993) 233–239.
[3] J.L. Jambor, Can. Mineral. 8 (1964) 92–108.
[4] M.W. Pryce, J. Just, Mineral. Mag. 39 (1974) 737–743.
[5] P.A. Williams, Oxide Zone Geochemistry, Ellis Horwood Ltd., Chichester, West Sussex, England, 1990.
[6] G. Sengupta, R.K. Sharma, V.B. Sharma, K.K. Mishra, M.L. Kundu, R.M. Sanyal, S. Dutta, J. Solid State Chem. 115 (1995) 204–207.
[7] J.W. Anthony, R.A. Bideaux, K.W. Bladh, M.C. Nichols, Handbook of Mineralogy, Mineral Data Publishing, Tiscon, AZ, USA, 2003.
[8] J.L. Jambor, I.D. MacGregor, Paper – Geological Survey of Canada 74-1, Pt. B, 1974, pp. 172–174.
[9] M.M. Harding, B.M. Kariuki, R. Cernik, G. Cressey, Acta Crystallogr. Sect. B: Struct. Sci. B50 (1994) 673–676.
[10] R.L. Frost, S.J. Palmer, J.M. Bouzaid, B.J. Reddy, J. Raman Spectrosc. 38 (2007) 68–77.
[11] R.L. Frost, D.A. Henry, M.L. Weier, W. Martens, J. Raman Spectrosc. 37 (2006) 722–732.
[12] R.L. Frost, A.W. Musumeci, J.T. Kloprogge, M.O. Adebajo, W.N. Martens, J. Raman Spectrosc. 37 (2006) 733–741.
[13] R.L. Frost, J. Cejka, M. Weier, W.N. Martens, J. Raman Spectrosc. 37 (2006) 879–891.
[14] R.L. Frost, M.L. Weier, J. Cejka, J.T. Kloprogge, J. Raman Spectrosc. 37 (2006) 585–590.
[15] R.L. Frost, J. Cejka, M.L. Weier, W. Martens, J. Raman Spectrosc. 37 (2006) 538–551.
[16] R.L. Frost, M.L. Weier, B.J. Reddy, J. Cejka, J. Raman Spectrosc. 37 (2006) 816–821.
[17] R.L. Frost, M.L. Weier, W.N. Martens, J.T. Kloprogge, J. Kristof, J. Raman Spectrosc. 36 (2005) 797–805.
[18] R.L. Frost, R.-A. Wills, M.L. Weier, W. Martens, J. Raman Spectrosc. 36 (2005) 435–444.
[19] R.L. Frost, D.L. Wain, W.N. Martens, B.J. Reddy, Polyhedron 26 (2007) 275–283.
[20] R.L. Frost, J. Raman Spectrosc. 37 (2006) 910–921.
[21] R.L. Frost, M.L. Weier, J. Cejka, G.A. Ayoko, Spectrochim. Acta Part A 65 (2006) 529–534.
[22] R.L. Frost, K.L. Erickson, M.L. Weier, O. Carmody, J. Cejka, J. Mol. Struct. 737 (2005) 173–181.
[23] R.L. Frost, B.J. Reddy, D.L. Wain, M.C. Hales, J. Near Infrared Spectrosc. 14 (2006) 317–324.

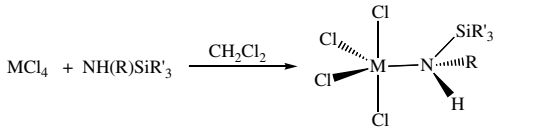
[24] S. Palmer, R.L. Frost, Polyhedron 25 (2006) 3379–3386.
[25] S. Palmer, B.J. Reddy, R.L. Frost, Polyhedron 26 (2007) 524–533.
[26] R.L. Frost, J.M. Bouzaid, B. Jagannadha Reddy, Polyhedron 26 (2007) 2405–2412.
[27] R.L. Frost, J.M. Bouzaid, S. Palmer, Polyhedron 26 (2007) 2964–2970.
[28] R.L. Frost, M.C. Hales, B.J. Reddy, Polyhedron 26 (2007) 3291–3300.
[29] R.L. Frost, S.J. Palmer, Polyhedron 26 (2007) 4533–4541.
[30] R.L. Frost, M. Dickfos, Polyhedron 26 (2007) 4503–4508.
[31] R.L. Frost, J. Cejka, G.A. Ayoko, M.L. Weier, Polyhedron 26 (2007) 3724–3730.
[32] S.-i. Fujita, Y. Kanamori, A.M. Satriyo, N. Takezawa, Catal. Today 45 (1998) 241–244.
[33] G.J. Millar, I.H. Holm, P.J.R. Uwins, J. Drennan, J. Chem. Soc., Faraday Trans. 94 (1998) 593–600.
[34] M. Bouchard, D.C. Smith, Asian Chem. Lett. 5 (2001) 157–170.
[35] J. Kasperek, M. Lenglet, Rev. Metal./Cah. Inform. Tech. 94 (1997) 713–719.
[36] R.L. Frost, P.A. Williams, J.T. Kloprogge, P. Leverett, J. Raman Spectrosc. 32 (2001) 906–911.
[37] B. Lefez, S. Jouen, J. Kasperek, B. Hannoyer, Appl. Spectrosc. 55 (2001) 935–938.
[38] T. Shahwan, B. Zunbul, O. Tunusoglu, A.E. Eroglu, J. Colloid Interf. Sci. 286 (2005) 471–478.
[39] D. Stoilova, V. Koleva, V. Vassileva, Spectrochim. Acta Part A: Mol. Biomol. Spectrosc. 58A (2002) 2051–2059.
[40] M. Bouchard, D.C. Smith, Spectrochim. Acta Part A: Mol. Biomol. Spectrosc. 59A (2003) 2247–2266.
[41] R.L. Frost, B.J. Reddy, D.L. Wain, W.N. Martens, Spectrochim. Acta Part A 66 (2007) 1075–1081.
[42] R.L. Frost, W.N. Martens, L. Rintoul, E. Mahmutagic, J.T. Kloprogge, J. Raman Spectrosc. 33 (2002) 252–259.
[43] R.L. Frost, Z. Ding, J.T. Kloprogge, W.N. Martens, Thermochim. Acta 390 (2002) 133–144.
[44] R.L. Frost, W. Martens, J.T. Kloprogge, Z. Ding, Spectrochim. Acta Part A 59A (2003) 2705–2711.
[45] J.M. Charnock, P.F. Schofield, C.M.B. Henderson, G. Cressey, B.A. Cressey, Mineral. Mag. 60 (1996) 887–896.

atomic layer deposition (ALD) [8]. Several attempts to prepare MN films from $[M(NEt_2)_4]$ and NH_3 by MOCVD have also been reported, however films of composition M_3N_4 were formed [3,9,10]. Crystalline HfN films have been deposited from the MOCVD (metalorganic chemical vapour deposition) of $Hf(NMe_2)_4$ and *N*,*N*-dimethylhydrazine [11].

We have previously shown that dehalosilylation reactions (i.e. the elimination of Me_3SiX; X = halide) can be employed in the synthesis of TiN and GaN [12,13]. The trimethylsilyl group is labile and can lead to materials with no silicon contamination. Furthermore, decomposition of the adduct $[ZrCl_4\{NH(SiMe_3)_2\}]$ has been shown previously to proceed via elimination of Me_3SiCl and HCl, resulting in the formation of ZrN [5]. We were interested in investigating the synthesis and characterization of adducts, of the type $[MCl_4\{NH(R)(SiR'_3)\}]$ (M = Zr, Hf; R = *t*Bu, R′ = Me; R = SiR'_3 = $SiMe_3$, $SiMe_2H$), all of which have a silyl group attached to the nitrogen atom. The decomposition and pyrolysis of the adducts $[MCl_4\{NH(R)(SiR'_3)\}]$ was investigated in order to evaluate complexes of this type as precursors to metal nitrides, the results of which are described herein. Preliminary low pressure CVD of $[MCl_4\{NH(R)(SiR'_3)\}]$ is also discussed.

2. Results and discussion

The Lewis acid/base adducts $[MCl_4\{NH(R)(SiR'_3)\}]$ (M = Zr, R = SiR'_3 = $SiMe_3$ (**1**), $SiMe_2H$ (**2**), R = *t*Bu, R′ = Me (**3**); M = Hf, R = SiR'_3 = $SiMe_3$ (**4**), $SiMe_2H$ (**5**), R = *t*Bu, R′ = Me (**6**)) were formed by the 1: 1 reaction of MCl_4 with $NH(R)(SiR'_3)$ in dichloromethane at room temperature (Scheme 1).



1: M = Zr, R = SiR'_3 = $SiMe_3$
2: M = Zr, R = SiR'_3 = $SiMe_2H$
3: M = Zr, R = *t*Bu, R' = Me
4: M = Hf, R = SiR'_3 = $SiMe_3$
5: M = Hf, R = SiR'_3 = $SiMe_2H$
6: M = Hf, R = *t*Bu, R' = Me

Scheme 1. Preparation of compounds **1**–**6**.

Compounds **1**–**6** were isolated as white/off-white or yellow solids after work-up of the reaction mixture. All the compounds were stable in the solid state at room temperature. Analytical data obtained for compounds **1**–**6** indicated that complexes of formulation $[MCl_4\{NH(R)(SiR'_3)\}]$ had formed. The compounds were also characterized by ^1H and ^{13}C NMR and mass spectroscopy, which provided further support for the formation of the adducts $[MCl_4\{NH(R)(SiR'_3)\}]$. Unfortunately, X-ray quality crystals of **1**–**6** could not be isolated. Lewis base adducts of zirconium tetrachloride are either monomeric, for example $[ZrCl_4\{N(SiMe_3)PPh_3\}]$ [14], or dimeric via chloride bridges such as in $[ZrCl_3(\mu\text{-}Cl)\{N(C_6H_4Cl)H_2\}]_2$ [15]. Only the presence of monomers was observed in the mass spectral data for the adducts $[MCl_4\{NH(R)(SiR'_3)\}]$ and no higher fragments, such as dimers were observed. The structures of **1**–**6** are therefore thought to be monomeric based on mass spectral evidence and so similar to $[ZrCl_4\{N(SiMe_3)PPh_3\}]$, which consists of a central Zr atom adopting a trigonal bipyramidal coordination geometry.

2.1. Thermal analysis and pyrolysis

The thermogravimetric analysis (TGA) of **1**–**6**, under N_2 at atmospheric pressure, shows that at 580 °C, the precursors had lost between 50% and 77% of weight depending on the sample (Table 1) suggesting that carbon or chlorine is retained in the residue (Figs. 1 and 2).

The observed weight loss for **1**, **2** and **5** are in between the calculated values for formation of $[Cl_2MNH]$ and [ClMN] suggesting that these intermediate compounds have been formed. Precursors of the type $[MCl_4\{NH(SiR'_3)_2\}]$ (compounds **1**, **2**, **4** and **5**) are expected to decompose *via* loss of two equivalents of R'_3SiCl to form an intermediate material of formulation $[Cl_2MNH]_n$, with further heating producing [ClMN] and finally the metal nitride (Scheme 2). In general, the elimination of the second equivalent of trialkylchlorosilane begins before complete elimination of the first equivalent of trialkylchlorosilane. It is possible that the required weight loss for the formation of metal nitride from **1**, **2** and **5** would be attained above 600 °C, although the TGA set-up allows analysis only to 600 °C. Note that TGA at atmospheric pressure only gives an indication of the potential of the precursors to form bulk metal nitrides. Any sublimation of the precursor, a desirable characteristic

Table 1
TGA and pyrolysis results of compounds **1**–**6**

Compound number	TGA				Pyrolysis at 620 °C – elemental analysis of resulting powders					
	Calc. weight loss to form MN	Calc. weight loss to form ClMN	Calc. weight loss to form Cl_2MNH	Observed weight loss at 580 °C	%C	%H	%N	%Cl	%Cl Calc. for $[Cl_2MH]$	%Cl Calc. for [ClMN]
1	73	64	55	62	0.65	0.22	7.05	30.46	40.03	25.20
2	71	61	52	59	1.18	0.27	6.83	34.62	40.03	25.20
3	72	62	53	77	3.52	0.60	5.98	35.96	40.03	25.20
4	60	52	45	73	0.80	0.35	4.52	28.65	26.82	15.55
5	58	50	42	50	1.55	0.33	5.86	23.45	26.82	15.55
6	59	51	43	63	1.05	0.10	3.50	22.33	26.82	15.55

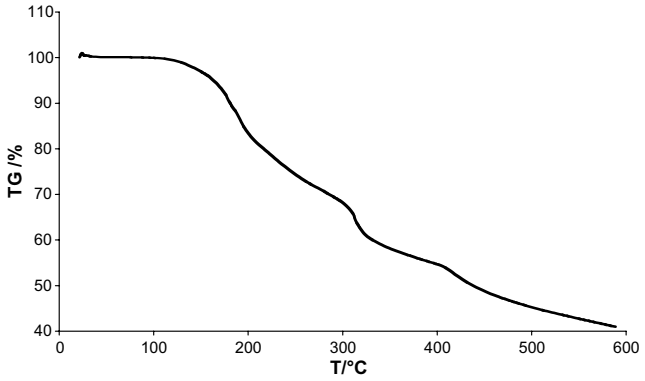


Fig. 1. TGA of $[ZrCl_4\{NH(SiMe_2H)_2\}]$ (**2**).

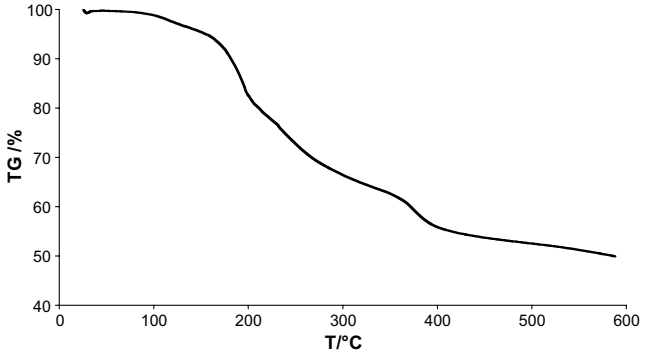
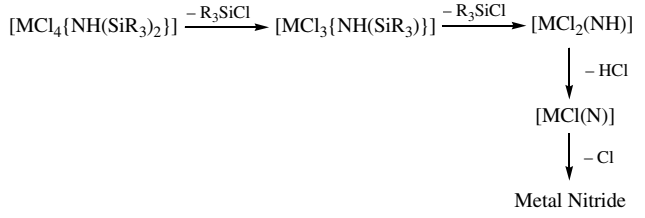


Fig. 2. TGA of $[HfCl_4\{NH(SiMe_2H)_2\}]$ (**5**).



Scheme 2. Proposed decomposition mechanism of $[MCl_4\{NH(SiR_3)_2\}]$.

for low pressure CVD studies would register as a further mass loss, as observed for compounds **3**, **4** and **6**. Nevertheless, the TGA measurements show that all of the complexes decompose at the temperatures of the CVD experiment, probably to form $[Cl_2MNH]$ or [ClMN], but with in some cases sublimation occurring.

The pyrolysis of compounds **1**–**6** was investigated in order to attempt to find the optimum conditions to produce zirconium and hafnium nitride. Based on the TGA results, the compounds were all heated above 600 °C under vacuum to encourage complete decomposition to zirconium or hafnium nitride. Pyrolysis of the zirconium precursors **1**–**3** gave rise to grey–black powders, which were found to contain low levels of carbon (0.65–3.5%) and high levels of chlorine (~30–35%, by elemental analysis). These results support the proposed formation (from the TGA experiments) of the intermediate compound $[Cl_2ZrNH]_n$ (calculated %Cl = 40.03), with the %Cl observed in the pyrolysis products of **1**–**3** suggesting some further decomposition to [ClZrN] (calculated %Cl = 25.20) has occurred. Further support for the proposed decomposition mechanism shown in Scheme 2 was obtained from the ^1H NMR spectrum of the liquid by-products obtained (collected in a liquid N_2 cooled trap) when **1** was thermolysed, which showed resonances assigned to $–SiMe_3$ groups. Compositional analysis by EDAX shows the presence of zirconium and nitrogen in the solids and impurities (Si, Cl by EDAX and C, H and Cl by elemental analysis) were also detected. The grey–black powders did not show any diffraction peaks in their X-ray powder diffraction pattern and are highly sensitive to air/moisture. These results are consistent with those previously reported for **1** [5] and show that compounds **2** and **3** decompose in a similar manner, although %C was higher in the pyrolysed product from **3** probably due to the presence of a *t*Bu group in **3**.

The pyrolysis of **1** and **2** was also carried out under a number of different conditions including vacuum (10^{-3} Torr), under a flow of NH_3 and under N_2. From analytical and XRD data obtained on the powders there was no apparent differences between the products isolated. Compositional analysis by EDAX shows the presence of zirconium and nitrogen in the solids. In addition, significant impurities (Si, Cl by EDAX and C, H and Cl by elemental analysis) were detected and attempts to eliminate these impurities by changing conditions failed.

Pyrolysis of the hafnium nitride precursors **4**–**6** at 650 °C under vacuum, suggest that elimination of the first equivalent of R'_3SiCl has occurred to form $[Cl_2HfNH]$ with some carbon contamination present. These results are in contrast to the TGA of **4**–**6**, which indicated that decomposition to [ClHfN] had occurred. However, the higher weight loss observed in the TGA could be due to sublimation of the precursor. The pyrolysis products from **4**–**6** were also susceptible to oxidation under ambient conditions. Surprisingly, pyrolysis of **5** at 1075 °C under vacuum also produced an air/moisture sensitive solid and did not significantly reduce the %Cl.

2.2. Thin film growth

Low pressure chemical vapour deposition (LPCVD) of **1**–**6** was investigated, the details of which are described in Section 4. Compounds **1**–**3** deposited yellow-coloured films on glass substrates at 620 °C. The films produced were analyzed by EDXA, SEM, powder XRD, XPS and Raman. The films were shown to be amorphous by powder X-ray diffraction. The EDXA data showed the presence of zirconium, nitrogen, carbon and chlorine in the film. Significant breakthrough of the excitation volume through the coating to the underlying glass was observed and so accurate quantitative analysis by EDXA was difficult. By scanning electron microscopy (SEM) the films show the formation of agglomerates of approximately 0.6 μm. All the films were investigated using Raman microscopy. In all cases no

Raman scattering was observed, however, Raman spectroscopy indicated the absence of graphitic carbon in the films. The films passed the Scotch tape test and could not be abraded with a brass stylus but could be marked with a stainless steel scalpel. The films produced showed a maximum transmission in the visible region (450–700 nm) – this behaviour is characteristic of early transition metal nitride films. X-ray photoelectron spectroscopy (XPS) showed the presence of Zr, C, N, O and Cl in the films. The binding energy value for Zr $3d_{5/2}$ for the films deposited from **1**–**3** was measured at 182.1–184.0 eV. These values are close to the Zr $3d_{5/2}$ at 182.2 eV observed in ZrO_2 [16]. However, the Zr $3d_{5/2}$ peak was asymmetrical and the component at 180.3 eV corresponded to zirconium nitride. The N 1s binding energy for the films deposited from **1**–**3** ranged from 396.5–397.5 eV. These values are in agreement with published XPS data for early transition metal nitrides and specifically ZrN_x (396.3–397.5 eV) and Zr_3N_4 (397.2 eV) [3,17]. Thus, XPS indicates that the films comprise of ZrO_2 and ZrN_x, which is supported by the presence of an O 1s peak at 531.0 eV (*cf.* ZrO_2 O 1s 531.1 eV).[18] Significant contamination from chlorine was observed (5–10 atom%), which is consistent with the TGA and pyrolysis experiments. The oxide surface layer was removed by sputtering with the bulk of the films consisting of zirconium nitride and ZrO_2.

Similar results were obtained from the LPCVD of compounds **4**–**6**. Yellow-coloured films were deposited from **4**–**6** on glass substrates at 620 °C. The EDXA data showed the presence of hafnium, nitrogen, carbon and chlorine in the film. Significant breakthrough of the excitation volume through the coating to the underlying glass was observed and so accurate quantitative analysis by EDXA was difficult. By SEM the films show the formation of crystalline-looking agglomerates (Fig. 3). However, the films were shown to be amorphous by powder X-ray diffraction. The films were investigated using Raman microscopy but no Raman scattering was observed. XPS showed the presence of Hf, C, N, O and Cl in the films. Similar to the ZrO_2/Zirconium nitride films, the films produced from **4**–**6** were shown by XPS to comprise of HfO_2 and hafnium nitride. Thus, the N 1s observed at 397.0 eV corresponds well with reported values for Hf_3N_4 (397.8 eV) [3] or HfN_x (397.4 eV) [19] and the O 1s peak at 532.1 eV is close to that expected for HfO_2 (530.7 eV) [20]. The formation of ZrO_2 and HfO_2 indicates that oxidation has occurred either during film deposition or post deposition. Oxidation could occur via diffusion of oxygen from the glass substrates which did not have a barrier layer. However, XPS depth profiling indicated that the amount of zirconium/hafnium and nitrogen increased while oxide decreased with depth in the sample. This suggests that oxidation probably took place after film formation.

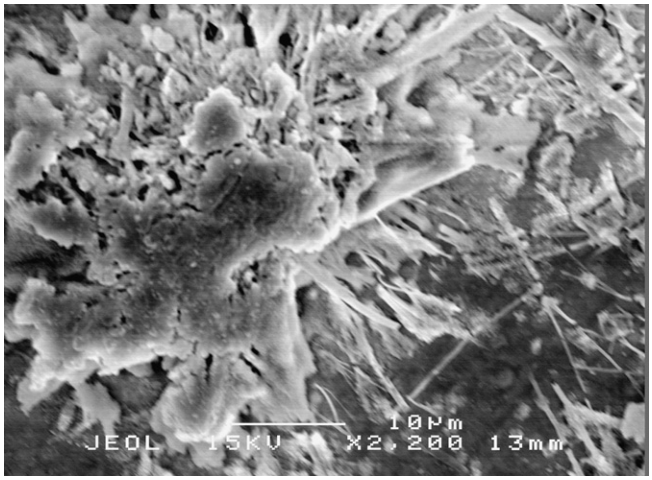


Fig. 3. SEM of a film grown from **6**.

3. Conclusion

The Lewis acid/base adducts $[MCl_4\{NH(R)(SiR'_3)\}]$ (M = Zr, Hf; R = *t*Bu, R′ = Me; R = SiR'_3 = $SiMe_3$, $SiMe_2H$) have been synthesized and characterized. Thermogravimetric analysis and pyrolysis studies showed that $[MCl_4\{NH(R)(SiR'_3)_2\}]$ decomposes via the elimination of R'_3SiCl resulting in the formation of powders of composition [ClMN] or [Cl_2MNH]. Preliminary low pressure CVD studies suggest that $[MCl_4\{NH(R)(SiR'_3)\}]$ is unsuitable as a precursor since amorphous metal oxide/metal nitride films contaminated with carbon and chlorine were obtained.

4. Experimental

4.1. General procedures

All manipulations were performed under a dry, oxygen-free dinitrogen atmosphere using standard Schlenk techniques or in a Mbraun Unilab glove box. Nitrogen (99.99%) was obtained from BOC and used as supplied. Dichloromethane was freshly distilled over CaH_2. The solvents hexane, tetrahydrofuran and toluene were distilled from sodium and benzophenone prior to use. Amines were distilled over 4 Å molecular sieves. All other reagents were procured commercially from Aldrich and used without further purification. Microanalytical data were obtained from University College London (UCL).

4.2. Physical measurements

NMR spectra were recorded on a Bruker AMX400 spectrometer at UCL, referenced to CD_2Cl_2 or $CDCl_3$, which was dried and degassed over molecular sieves prior to use; ^1H and ^{13}C chemical shifts are reported relative to $SiMe_4$ (δ 0.00). Mass spectra (CI) were run on a micromass VG 70-SE spectrometer. IR spectra was collected as nujol and hexachlorobutadiene mulls on a Shimadzu FTIR-8200 instrument. Paraffin oil (nujol) and hexachlorobutadiene was degassed and dried over molecular sieves prior to

use. Melting points were obtained in sealed glass capillaries under nitrogen and are uncorrected. Thermogravimetric analysis (TGA) was performed under a dinitrogen atmosphere with a heating rate of 10 °C min^{-1} and on a Netzsch STA 449C instrument.

X-ray powder diffraction patterns were measured on a Siemens D5000 diffractometer using monochromated Cu $K\alpha_1$ radiation ($\lambda_1 = 1.5406$ Å) with glancing incident radiation (1.5°). EDXA was obtained on a JEOL 35CF and SEM was obtained on a Hitachi S570 instrument using the KEVEX system. X-ray photoelectron spectra were recorded using a VG ESCALAB 220i XL instrument using focused (300 μm spot) monochromatic Al Kα radiation at a pass energy of 20 eV. Scans were acquired with steps of 50 meV. A flood gun was used to control charging and the binding energies were referenced to an adventitious C 1s peak at 284.8 eV. Depth profile measurements were obtained by using argon beam sputtering. Reflectance and transmission spectra were recorded between 300 and 1200 nm by a Zeiss miniature spectrometer. Reflectance measurements were standardized relative to a rhodium mirror and transmission relative to air. Raman spectra were acquired on a Renishaw Raman System 1000 using a helium–neon laser of wavelength 632.8 nm. The Raman system was calibrated against the emission lines of neon.

4.3. Synthesis of [$ZrCl_4${$HN(SiMe_3)_2$}] (1)

$HN(SiMe_3)_2$ (2.2 cm^3, 10 mmol) was added to a suspension of $ZrCl_4$ (2.40 g, 10 mmol) in CH_2Cl_2 (30 cm^3) at room temperature. The reaction mixture was allowed to stir for 72 h to obtain an almost clear solution. The trace amount of insoluble material was filtered out using a filter stick. The filtrate was dried down completely under vacuum yielding a beige coloured powder (1.48 g, 38% yield), m.p. 105 °C. *Anal.* Calc. for $C_6Cl_4H_{19}NSi_2Zr$: C, 18.27; H, 4.86; N, 3.55. Found: C, 18.22; H, 5.00; N, 3.87%. ^{1}H NMR δ/ppm ($CDCl_3$): δ 0.41 (s, SiCH_3), 0.44(s, SiCH_3), 4.3 (s, br, NH). $^{13}C\{^1H\}$ NMR ($CDCl_3$): δ 3.2 (s, SiCH_3), 5.4 (s, SiCH_3). IR (cm^{-1}): 3157 br, 2963 ms, 2905 w, 1402 w, 1266 s, 1155 s, 1072 s, 663 w. Mass Spec. (CI) *m/z* 393, [M]; 392, [M]-H; 320, [M]-$SiMe_3$; 73, Me_3Si.

4.4. Synthesis of [$ZrCl_4${$HN(SiMe_2H)_2$}] (2)

Compound **2** was prepared in the same manner as **1** but using $ZrCl_4$ (4.7 g, 20 mmol), $HN(SiMe_2H)_2$ (3.6 cm^3, 20 mmol), yielding a dark yellow solution. Removal of the solvent *in vacuo* yielded a free flowing white powder (3.08 g, 42% yield), m.p. 150 °C. *Anal.* Calc. for $C_4Cl_4H_{15}NSi_2Zr$: C, 13.11; H, 4.13; N, 3.82. Found: C, 12.95; H, 4.29; N, 3.66%. ^{1}H NMR δ/ppm ($CDCl_3$): δ 0.42 (s, SiCH_3), 0.54 (s, SiCH_3), 4.56 (q, SiH). $^{13}C\{^1H\}$ NMR (CD_2Cl_2): δ 1.3 (s, SiCH_3), 3.7 (s, SiCH_3). IR (cm^{-1}): 3161 br, 1260 s. Mass Spec. (CI) *m/z*: 366, [M]; 315, $ZrCl_3${$N(SiMe_2H)_2$}-Me; 295, [M]-2Cl; 281, [$ZrCl_2$[$HN(SiMe_2H)_2$]-Me+H]; 93, Me_2SiCl; 73, $NSiMe_2H$.

4.5. Synthesis of [$ZrCl_4${$HN(^tBu)SiMe_3$}] (3)

Compound **3** was prepared in the same manner as **1** but using $ZrCl_4$ (1.05 g, 4 mmol), $HN(^tBu)SiMe_3$ (0.8 cm^3, 4 mmol), yielding a pale yellow solution. Removal of the solvent *in vacuo* afforded a pale yellow powder (0.78 g, 46% yield), m.p. 190 °C. *Anal.* Calc. for $C_8Cl_6H_{21}NSiZr(CH_2Cl_2)$: C, 20.74; H, 4.57; N, 3.02. Found: C, 20.70; H, 4.26; N, 3.49%. ^{1}H NMR δ/ppm ($CDCl_3$): δ 0.44 (s, 9H, SiCH_3), 1.39 (s, 9H, C(CH_3)$_3$), 5.28 (s, CH_2Cl_2), 6.42 (s, br, NH). IR (cm^{-1}): 2852 s br, 1556 s, 1463 vs, 1340 w, 1265 vs, 819 w, 775 w, 723 s. Mass Spec. (CI) *m/z*: 378, [M]; 307, $ZrCl_2HN^tBuSiMe_3$; 233, $ZrCl(NH_3)_2$; 118, ^{t}BuSiCl.

4.6. Synthesis of [$HfCl_4${$HN(SiMe_3)_2$}] (4)

Compound **4** was prepared in the same manner as **1** but using $HfCl_4$ (8.52 g, 27 mmol), $HN(SiMe_3)_2$ (5.7 cm^3, 27 mmol), yielding a dull yellow/cloudy solution. Removal of the solvent *in vacuo* afforded a white powder (6.73 g, 53% yield), m.p. 120 °C. *Anal.* Calc. for $C_6Cl_4H_{19}HfNSi_2$: C, 14.96; H, 3.98; N, 2.91. Found: C, 14.03; H, 3.78; N, 2.89%. ^{1}H NMR δ/ppm ($CDCl_3$): δ 0.44 (s, SiCH_3), 0.51 (s, SiCH_3), 4.3 (s, br, NH). $^{13}C\{^1H\}$ NMR ($CDCl_3$): δ 3.26 (s, SiCH_3), 5.43 (s, SiCH_3). IR (cm^{-1}): 3163 s, 2601 w, 1593 m, 1517 s, 1463 s, 1377 s, 1253 s, 1147 s, 1101 s, 1012 m, 920 s, 846 m, 761 w, 719 m, 659 s, 619 w, 607 w, 464 s, 445 w. Mass Spec. (CI) *m/z* 481, [M]; 446, [M]-Cl, 409, [M]-$SiMe_3$; 73, Me_3Si.

4.7. Synthesis of [$HfCl_4${$HN(SiMe_2H)_2$}] (5)

Compound **5** was prepared in the same manner as **1** but using $HfCl_4$ (6.00 g, 19 mmol), $HN(SiMe_2H)_2$ (3.5 cm^3, 19 mmol), yielding a white solution. Removal of the solvent *in vacuo* afforded a white microcrystalline powder (2.22 g, 26% yield), m.p. 91 °C. *Anal.* Calc. for $C_4Cl_4H_{15}HfNSi_2$: C, 10.59; H, 3.33; N, 3.09. Found: C, 10.84; H, 3.71; N, 3.42. ^{1}H NMR δ/ppm (CD_2Cl_2): δ 0.41 (s, SiCH_3) 0.51 (s, SiCH_3), 4.70 (q, SiH) 3.32 (s, br, NH). $^{13}C\{^1H\}$ NMR (CD_2Cl_2): δ 1.3 (s, SiCH_3), 3.7 (s, SiCH_3). Mass Spec. (CI) *m/z* 453, [M]; 417, [M]-HCl; 383, [M]-2Cl; 264, $HfCl_2NH$; 93, Me_2SiCl; 73, $NSiMe_2H$.

4.8. Synthesis of [$HfCl_4${$HN(^tBu)SiMe_3$}] (6)

Compound **6** was prepared in the same manner as **1** but using $HfCl_4$ (0.53 g, 1.66 mmol), $HN(^tBu)SiMe_3$ (0.4 cm^3, 1.6 mmol) yielding a light brown clear solution. Removal of the solvent *in vacuo* yielded a grey coloured powder (0.14 g, 18% yield). *Anal.* Calc. for $C_7Cl_4H_{19}HfNSi$: C, 18.06; H, 4.11; N, 3.01. Found: C, 18.43; H, 4.20; N, 3.28%. ^{1}H NMR δ/ppm (CD_2Cl_2): δ 0.44 (s, SiCH_3), 1.4 (s, C(CH_3)$_3$), 3.69 (s, br, NH). $^{13}C\{^1H\}$ NMR (CD_2Cl_2):

δ 3.3 (s, SiCH_3), 28.3 (s, C(CH_3)$_3$), 30.8 (s, C(CH_3)$_3$). IR (cm^{-1}): 2671 w, 1560 s, 1456 vs, 1344 w, 1263 m, 1161 m, 1028 m, 935 w, 844 w, 723 w.

4.9. Pyrolysis studies

Typically, a sample of precursor (0.30 g) was loaded into a quartz ampoule (30 cm length × 9 mm diameter) in the glove box. The ampoule was then placed in a furnace, which had been pre-heated to the decomposition temperature, such that the sample was in the centre of the furnace. The ampoule was heated for 5 min under a N_2 atmosphere and for a further 4 h under a dynamic vacuum. The furnace was then allowed to cool to room temperature. The powder produced was analyzed by powder XRD and elemental analysis.

4.10. LPCVD studies

The same procedure was followed for all the precursors. Approximately 0.3 g of compound was loaded into the sealed end of a glass tube (400 mm length × 16 mm diameter) in the glovebox. Glass slides (100 mm × 7 mm × 1 mm) were placed carefully along the inside of the tube. The tube was then placed in a furnace such that 30 cm was inside the furnace and the end containing the sample protruded by 4 cm. The tube was heated to a temperature of 620 °C under dynamic vacuum (0.1 Torr, measured by a Hg vacuum gauge). The tube was slowly drawn into the furnace over a period of a few minutes until the sample started to melt. It was then held at that point until all of the precursor had decomposed. Once this had happened, the furnace was allowed to cool to room temperature. The total time taken to complete the whole process was in the region of 120 min. The films deposited on the glass substrates were analyzed by EDAX, SEM, Raman spectroscopy, XPS, and XRD.

Acknowledgement

EPSRC are thanked for a DTA (RP and SEP) and SAFC Hitech for a CASE award (SEP).

References

[1] S.T. Oyama (Ed.), The Chemistry of Transition metal Carbides and Nitrides, Blackie Academic & Professional, London, 1996.
[2] L.E. Toth, Transition metal carbides and nitrides, in: J.L. Margrave (Ed.), Refractory Materials, vol. 7, Academic Press, New York, 1971.
[3] R. Fix, R.G. Gordon, D.M. Hoffman, Chem. Mater. 3 (1991) 1138.
[4] G.R. Fenske, N. Kaugerr, R.H. Lee, B.M. Kramer, R.F. Bunshah, W.D. Sproul, Surf. Coat. Technol. 36 (1988) 791.
[5] C.K. Narula, L.F. Allard, J. Mater. Chem. 8 (1998) 1881.
[6] C.J. Carmalt, A.C. Newport, I.P. Parkin, P. Mountford, A.J. Sealey, S.R. Dubberley, J. Mater. Chem. 13 (2003) 84, and references therein.
[7] G.M. Brown, L. Maya, J. Am. Ceram. Soc. 71 (1988) 78.
[8] J.S. Becker, E. Kim, R.G. Gordon, Chem. Mater. 16 (2004) 3497.
[9] W. Wamg, T. Nabatame, Y. Shimogaki, Jpn. J. Appl. Phys. Part 2 43 (2004) L1445.
[10] D.M. Hoffman, Polyhedron 13 (1994) 1169.
[11] Y. Kim, A. Baunemann, H. Parala, A. Devi, R.A. Fischer, Chem. Vap. Deposit. 11 (2005) 294.
[12] (a) A. Newport, C.J. Carmalt, I.P. Parkin, S. O'Neill, J. Mater. Chem. 12 (2002) 1906;
(b) C.J. Carmalt, A.C. Newport, I.P. Parkin, A.J.P. White, D.J. Williams, Dalton Trans. (2002) 4055.
[13] C.J. Carmalt, J.D. Mileham, A.J.P. White, D.J. Williams, Dalton Trans. (2003) 4255.
[14] M. Grün, F. Weller, K. Dehnicke, Z. Anorg. Allg. Chem. 623 (1997) 224.
[15] H. Wei, Y.-H. Li, Y. Zhang, Acta Crystallogr. E63 (2007) m798.
[16] H. Wiame, M.-A. Centeno, S. Picard, P. Bastians, P. Grange, J. Eur. Cer. Soc. 18 (1998) 1293.
[17] R.P. Netterfield, P.J. Martin, D.R. McKenzie, J. Mater. Sci. Lett. 9 (1990) 972.
[18] M.-S. Kim, Y.-D. Ko, J.-H. Hong, M.-C. Jeong, J.-M. Myoung, I. Yun, Appl. Sur. Sci. 227 (2004) 387.
[19] W.W. Wang, T. Nabatame, Y. Shimogaki, Thin Solid Films 498 (2006) 75.
[20] G. He, M. Liu, L.Q. Zhu, M. Chang, Q. Fang, L.D. Zhang, Surf. Sci. 576 (2005) 67.

measurements, to give ulterior informations about the reactivities of this very important natural compound in the biological processes.

2. Experimental

2.1. Reagents

All chemicals were of analytical-reagent grade and used without further purification. All the solutions were prepared with Milli-Q water. Stock solution of CPI 4.18×10^{-4} mol l^{-1} was prepared by dissolving 76.1 mg of CPI-dihydrochloride in 500 ml of 0.61×10^{-4} mol l^{-1} sodium hydroxide solution. Stock solutions containing 8.90×10^{-3} mol l^{-1} of metal ions were prepared by dissolving weighted suitable quantities of $AgNO_3$ or $AuCl_3$ in water and standardized by Inductively Coupled Plasma (JY24R).

2.2. Methods

For absorbance measurements, all the reactions were studied and monitored, for the required time, by a Hewlett–Packard 8452A diode array spectrophotometer with a 1-cm quartz cell well stoppered and connected to Lauda K2R thermostat. A Metrohm 655 pH meter with a combined electrode (Inlab 413) was used for pH determination.

For the particle size measurements of colloidal metals, transmission electron microscopy (TEM) and electron diffraction studies were carried out on a Philips CM10 instrument operating at 100 kV. The samples were prepared by drying a drop of solution on a carbon-coated Cu grids in air. The film negatives containing the diffraction patterns were scanned at 300 dpi with HP SCANJET 5400C. To eliminate uncertainties in the acceleration voltage and camera length, a standard thallium chloride (TlCl) crystal was used as a reference for the electron diffraction measurements. The morphology of silver and gold colloids was investigated at magnifications up to 73 000.

The diffraction ring in diffraction pattern of TlCl corresponding to the (1 1 1) plane with a lattice spacing $d_{111} = 3.84$ Å, has been obtained according to the ICPDF diffraction data card 06-0486. The camera constant $\lambda \cdot L$ (L in mm and λ in Å) was determined by measuring the radius R of the ring (where R is the distance in mm between the transmitted and diffracted beams), and it was found to be $\lambda \cdot L = 25.92$ Å mm. Provided that diffraction patterns from silver or gold colloids were obtained under the same conditions as the camera constant calibration then the interplanar spacings could be determined using the diffraction relationship: $d_{hkl} = \lambda \cdot L/R$. The particle size distribution in the TEM images was determined using the ImageJ 1.30v Software (The National Institutes of Health, USA) (http://rsb.info.nih.gov/ij).

The scanning electron microscopy (SEM) measurements were carried out on a Leica Cambridge Stereoscan 360 equipped with a backscattered electron detector (4QBSD) at an accelerating voltage of 20 kV. For scanning microscopy, all the samples were prepared by drying 3–5 μl of the solution on aluminum stabs using self-adhesive carbon conductive tabs in a vacuum oven. An X-ray mapping was obtained using an energy dispersive X-ray spectrometer (EDS, Link Analytical) with the SEM. The samples were sputter coated with carbon by Balzers Med 010 to prevent charging when analyzed by the electron beam.

2.3. Gold and silver ions CPI reactions

All the reactions have been carried out from 20 to 60 °C, at pH 6, in the dark because of the photosensitivity of CPI [19]. The value of pH was maintained constant by NaOH addition and determined with a Metrohm 655 pH meter with a combined electrode (Inlab 413).

The reactions of gold ions with CPI were carried out by putting from 100 to 280 μl of the standard solution of CPI and from 104 to 290 μl of the gold stock solution 4.50×10^{-3} mol l^{-1} into 10 ml volumetric flasks.

The reactions of silver ions with CPI were carried out by putting from 100 to 280 μl of the standard solution of CPI and from 50 to 140 μl of the silver(I) 4.68×10^{-3} mol l^{-1} stock solution or from 48 to 135 μl of the silver(II) 4.80×10^{-3} mol l^{-1} stock solution into 10 ml volumetric flasks.

3. Results and discussion

3.1. CPI peculiarity

The CPI is a tetra-anionic porphyrin for the presence of four propionic groups. At pH 6, CPI solution is deep pink with an absorption maximum at 392 nm (Soret band $\varepsilon = 5.98 \pm 0.46 \times 10^4$) and other four weaker bands (Q band) at 500 (IV), 536 (III), 556 (II) and 606 (I) nm (Fig. 1). At this pH, the anionic monomeric form as free-base is prevalent [20].

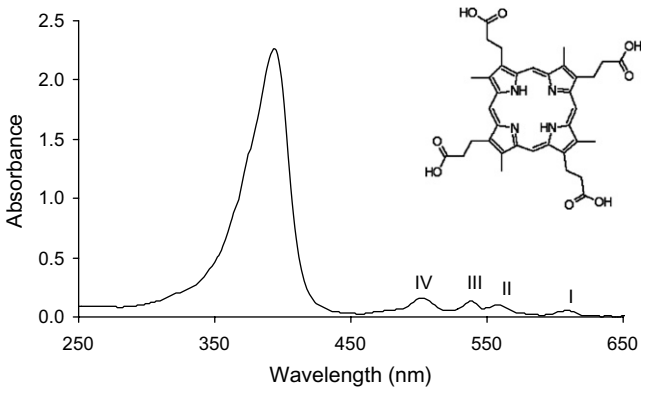


Fig. 1. UV–Vis absorption spectrum of CPI 1.35×10^{-5} mol l^{-1} (pH 6) with inset CPI formula.

3.2. Gold ions reactions

In the reaction of CPI with Au(III), carried out by spectrophotometric measurements, the formation of a plasmon resonance peak at 532 nm attributable of colloidal gold has been previously observed [6].

In this study, the evolution of this reaction has been monitored. At 20 °C, a very slow colour change of the solution was observed: initially it changed from deep pink to grey; after about 2 h it turned to violet and after several days, it changed again from violet to red purple. During this period the UV–Vis absorbance spectra changed in a similar way: the band at 392 nm (corresponding to CPI free-base monomeric form) decreased and the formation of a band at 372 nm (of dimeric form of CPI) that successively reduced with the contemporary increase of a broad band at around 532 nm (red purple solution) was observed (Fig. 2d). Measurements carried out at higher temperatures (up to 50 °C) have immediately shown the formation of the grey colour in the solution that after a week turned to red purple; at temperatures higher than 50 °C, the solution colour changed directly from deep-pink to red purple.

TEM images of the samples of the grey, violet and purple solutions (Fig. 2a–c) showed the initial formation of particles of small sizes (less than 5 nm) in the grey solution, the aggregation of these in the violet solution and the successive increase of particle sizes in purple solution; these particles were of regular distribution, showing several polyhedral structures with sizes ranging from 7 to 60 nm. The change of the colours of the solution (grey, violet and purple) in time was, therefore, due to the coalescence of the colloidal gold particles [21]. The spectrophotometric measurements (Fig. 2d) clearly showed an increase in the plasmon resonance peak at 532 nm with the increase in the particle size. This process involved

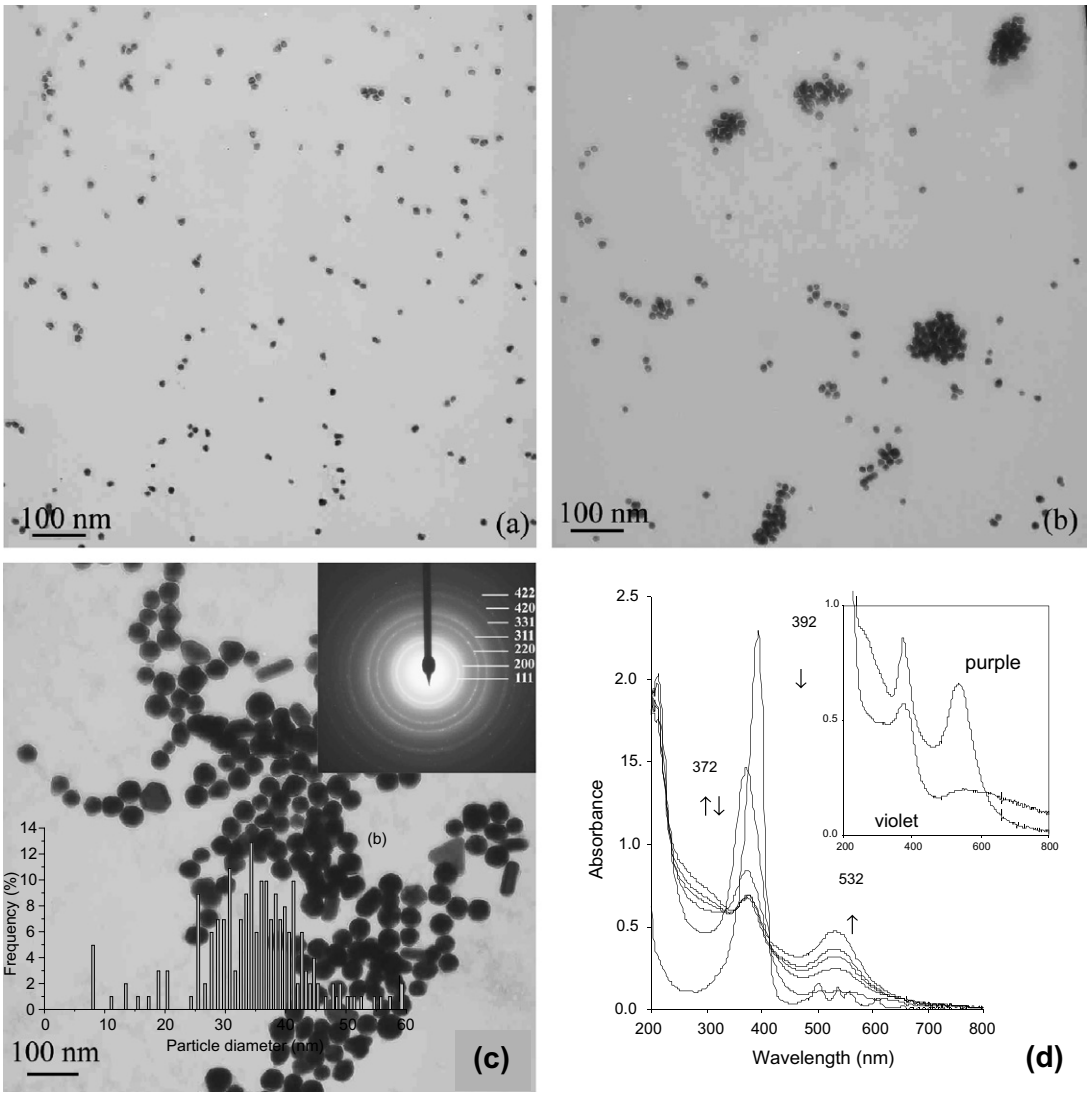


Fig. 2. Reaction at 20 °C of CPI (1.35×10^{-5} mol l^{-1}) with Au(III) (1.35×10^{-4} mol l^{-1}): TEM micrographs (magnification: 73 000×) of gold particles obtained by at once (grey solution) (a), after several days (violet solution) (b) and after several days (purple solution) (c); evolution of UV–Vis spectra during the reaction (up to 120 min) with inset spectra of grey and violet solutions of colloidal gold (d).

three steps: in the first, the metal ions in solution were partially reduced by CPI (Fig. 2a), in the second and third step (Figs. 2b and c), nucleation and successive growth of the particles occurred; the coalescence of atoms leads to the formation of metal clusters and these were stabilized by CPI. In the formation of colloidal gold, the oxidation of CPI occurred by decarboxylation of its propionic groups as previously observed [6]. This provoked the formation of insoluble clotted structure after about one month for the polymerization of neutral decarboxylated CPI. SEM studies of this structure (Fig. 3a) have showed the formation of spheroidal particles of different sizes and twisted into fibrous structures with regular gold distribution as demonstrated by electron backscattered image in Fig. 3c. To explain the nature of these fibrous structures, for comparison, a colloidal gold solution using standard procedure for the reduction with sodium citrate (c.r.) [22] was prepared; this solution was violet and showed an absorption maximum at 548 nm (Fig. 4d). When at pH 6, CPI free-base was added to this solution, a colour intensification was observed and the spectrum showed the presence of the peak at 372 nm (dimeric form of CPI) that decreased in time, and a red shift of the plasmon resonance peak from 548 to 566 nm was observed (Fig. 4d). The red shift arose from the dielectric constant of the CPI capping medium around the gold nanoparticles. This occurred because the negative carboxylic groups of CPI free-base were adsorbed on positive colloidal gold, provoking the initial formation of CPI dimer that decreased in time for gold particles capping proved by the increase of plasmon resonance peak at 566 nm. In fact in Fig. 4a, TEM images showed the gold particles (c.r.) of different sizes and shapes (oval and polygonal structures) that, by CPI addition, changed in agglomerated as well as rodlike fibrous Au-particles, (Fig. 4b and c) indicating the coverage of CPI molecules onto the surface of gold nanoparticles and successive aggregation of these in linear structures.

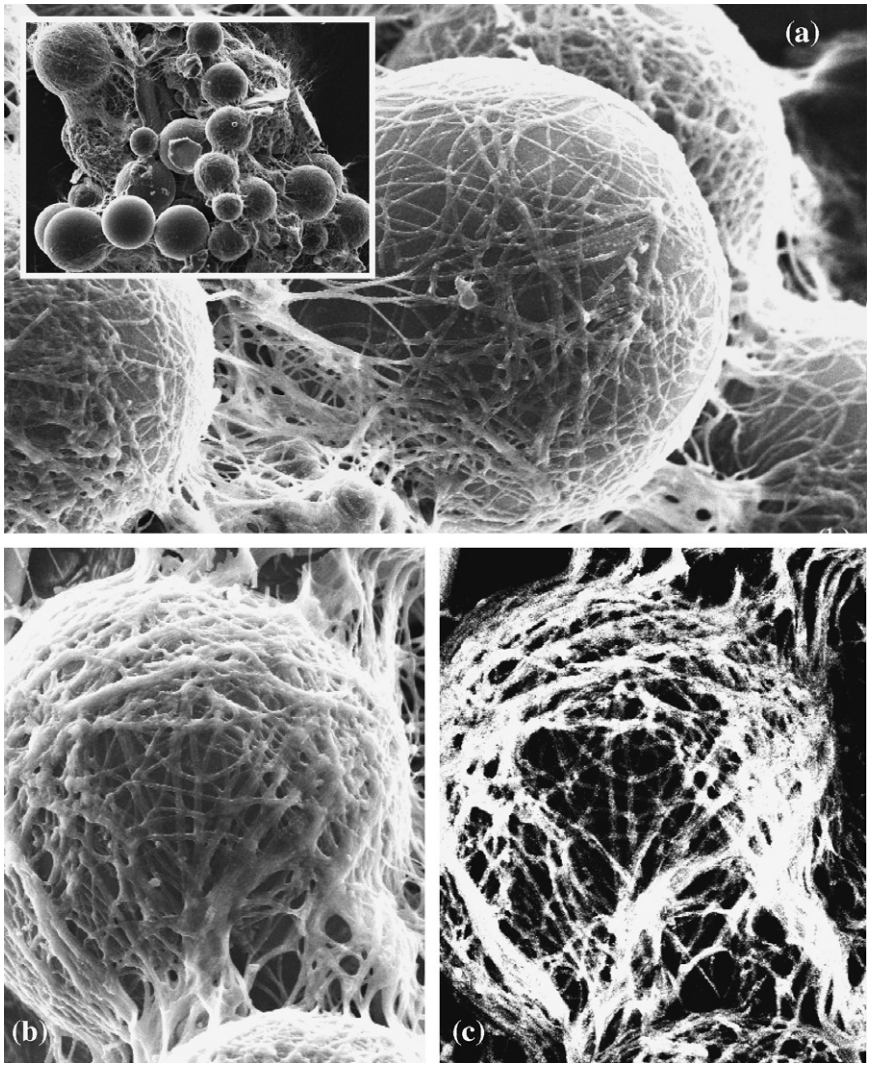


Fig. 3. SEM micrographs of insoluble clotted structure: magnification 809× (a) with inset magnification 205×; magnification 1.00× K (b), electron backscattered image (c).

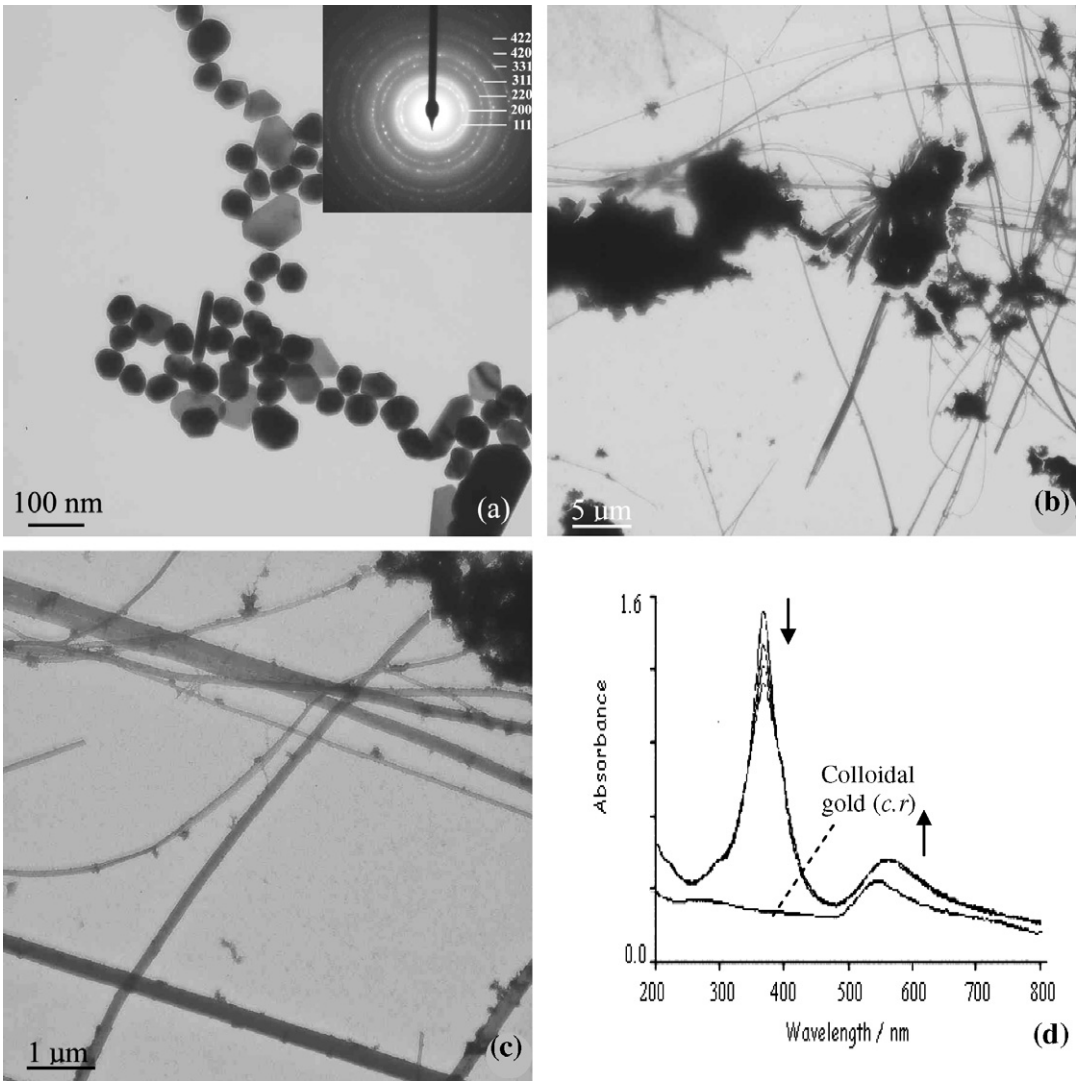


Fig. 4. Reaction at 20 °C of CPI 1.35×10^{-5} mol l^{-1} with gold nanoparticles (c.r.): TEM micrographs and electron diffraction pattern of gold particles (c.r.) at magnification 73000× (a) and in the reaction of CPI at magnifications 1650× (b) and 8900× (c); evolution of UV–Vis spectra during the reaction (d).

3.3. Silver ions reactions

In the reactions of Ag(I) or Ag(II) with CPI, as previously described, Ag^{II}CPI and Ag^{III}CPI complexes with the same absorption maxima (at 260 and 392 nm) were initially formed [6], but the formation of a plasmon resonance peak at 430 nm, with the change of colour solution to deep yellow, attributable to the colloidal silver formation, was observed in time. The spectral evolution of this reaction is reported in Fig. 5a that showed a slight decrease of the absorbance at 260 and 392 nm of silver CPI complexes with a remarkable increase of plasmon resonance peak at 430 nm. The reduction of silver was observed only in the presence of silver CPI complexes, therefore, the formation of colloidal metal must be attributable to the oxidation of Ag^{II}CPI into Ag^{III}CPI. The oxidation of Ag^{II}CPI and the formation of colloidal silver at 20 °C proceeded very slowly and was completed in two days. This reaction was kinetically favoured by higher temperatures, in fact in the same measurements carried out up to 60 °C the formation of the colloid was faster.

TEM images and electron diffraction patterns of these solutions showed silver particles of small sizes (from 4 to 45 nm) and of regular structure, well dispersed and with different spherical shapes (Fig. 5b). In this case, decarboxylated CPI was not formed because the mechanism of silver reduction regarded only the silver CPI complexes.

Neither the spectral change nor the formation of fibrous Ag particles, when CPI was added to colloidal silver solutions prepared by citrate reduction at pH 6, was observed to prove that the adsorption of negative CPI free-base on positive colloidal silver particles did not occur, probably because the surface of colloids was covered by large and strongly attached citrate anions that hindered the absorption of propionic anions of CPI.

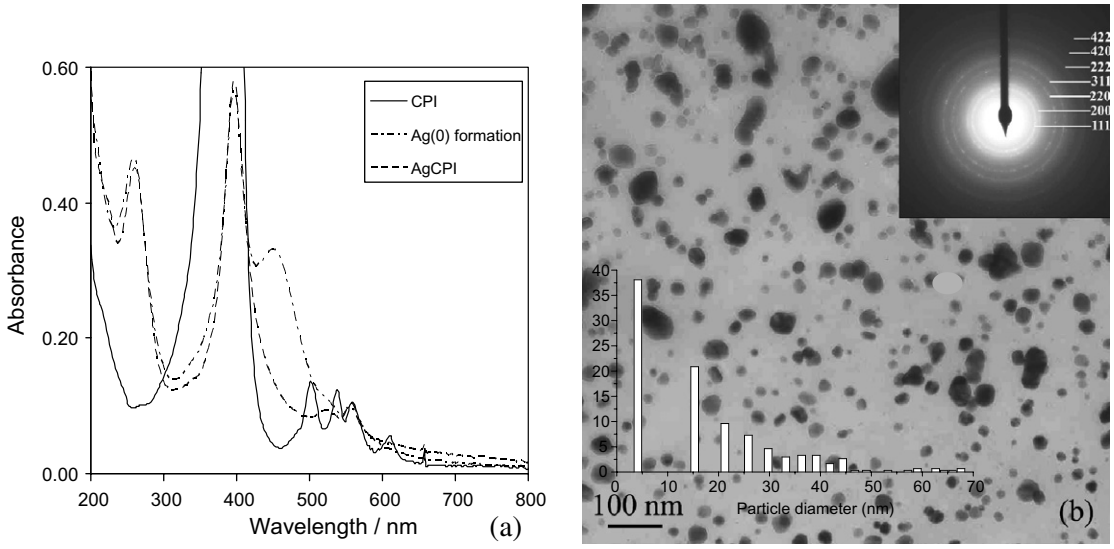


Fig. 5. Reaction at 20 °C of CPI (1.35×10^{-5} mol l^{-1}) with Ag(I) (1.35×10^{-4} mol l^{-1}) after two days: UV–Vis spectrum (a); TEM micrographs (magnification: 73000×) and electron diffraction pattern of silver particles obtained (b).

3.4. Transmission electron diffraction pattern

All samples were examined to determine the structure of the obtained silver and gold nanoparticles. In the insets of Figs. 2c and 4a corresponding to gold nanoparticles obtained by CPI and citrate reduction, respectively, and in Fig. 5b corresponding to silver nanoparticles obtained by CPI reduction, the crystallographic planes for the observed diffraction rings, are identified. The lattice spacing d_{hkl} calculated for silver or gold colloids, compared with theoretical data, according to ICPDF diffraction data, is listed in Tables 1 and 2. The halos of these figures were consistent with cubic-close-packed structure for either silver or gold particles.

Table 1
Silver lattice spacings d_{hkl} values as determined from electron diffraction data and comparison with the corresponding values of the ICPDF diffraction data card no. 04-0783

Theoretical data ICPDF no. 04-0783		Calculated data from TEM
Ag d (Å)	hkl	Ag + CPI d (Å)
2.359	111	2.359
2.044	200	2.049
1.445	220	1.442
1.231	311	1.235
1.1796	222	1.174
0.9375	331	–
0.9137	420	0.9230
0.8341	422	0.8320

Table 2
Gold lattice spacings d_{hkl} values as determined from electron diffraction data and comparison with the corresponding values of the ICPDF diffraction data card no. 04-0784

Theoretical data ICPDF no. 04-0784		Calculated data from TEM	
Au d (Å)	hkl	Au + CPI d (Å)	Au + Citrato d (Å)
2.355	111	2.361	2.357
2.039	200	2.053	2.067
1.442	220	1.433	1.451
1.230	311	1.232	1.231
0.936	331	0.935	0.937
0.910	420	0.913	0.914
0.832	422	0.829	0.836

4. Conclusions

The investigation on the formation of gold and silver colloidal particles in this research fits into a more general study of the reactions of biological compounds or microorganisms with metallic ions.

This work has allowed the characterization of the nanoparticles obtained in the reaction of CPI with silver and gold ions by spectrophotometric, TEM and SEM techniques.

The reaction of silver ions with CPI to form the metal nanoparticles is slow because it occurred after metal complexation and depended on the reduction of $Ag^{III}CPI$. The deep yellow solution, obtained with absorption maximum at 430 nm, corresponded to the nanoparticles of size between 4 and 45 nm.

In the reaction of gold ions with CPI, the spectra, the sizes and the dimensions of the nanoparticles were depending on the formation kinetic, aggregation and coalescence of colloidal gold particles, stabilized by the negative groups of CPI. Very small particles (sizes less than 5 nm) with regular structures were quickly obtained; the aggregation into several polyhedral structures (sizes up to 60 nm) has been observed in time. In this reaction, the decarboxylation of four propionic groups of CPI provoked the polymerization on the neutral decarboxylate CPI for the formation of spheroidal particles; these were twisted into fibres formed for the coverage of no-decarboxylated CPI molecules onto

the surface of gold nanoparticles and aggregated in linear structures with regular gold distribution. It is in fact well-known that carboxylic acid functional groups, which may be ionized by controlling the pH solution, cap the colloidal particles by electrostatic interactions with their stabilization in solution [23].

This behaviour was not observed in the reaction of CPI with colloidal silver particles because the decarboxylation did not occur and, therefore, the polymerization was not observed.

Because the toxicity of metal nanoparticles is known, this study assumes an important meaning to understand the mechanisms on their probable formation in the human metabolism.

References

[1] L.R. Milgrom, The Colours of Life, Oxford University Press, Oxford, 1997.
[2] W.E. Daniell, H.L. Stockbridge, et al., Environmental Health Perspectives 105 (1997) 37.
[3] R. Giovannetti, V. Bartocci, in: S.G. Pandalai (Ed.), Recent Research Developments in Pure and Applied Analytical Chemistry, Transworld Research Network, Trivandrum, India, 1998, pp. 173–185.
[4] R. Giovannetti, V. Bartocci, G. Vitali, J. Chem. Res. (M) (1998) 2958.
[5] R. Giovannetti, V. Bartocci, G. Vitali, J. Chem. Res. (S) (1998) 680.
[6] R. Giovannetti, V. Bartocci, F. Pucciarelli, M. Ricciutelli, Talanta 63 (2004) 857.
[7] S.G. Penn, L. He, M.J. Natan, Curr. Opin. Chem. Biol. 7 (2003) 609.
[8] L. Rivas, S. Sanchez-Cortes, J.W. Garcia-Ramos, G. Morcillo, Langmuir 17 (2001) 574.
[9] I.M. Yakutik, G.P. Shewchenko, S.K. Rakhmanov, Coll. Surf. A 242 (2004) 175.
[10] A.V. Loginov, V.V. Gorbunov, T.V. Boitsova, Russ. J. General Chem. 67 (1997) 189.
[11] A.V. Loginov, V.V. Gorbunov, T.V. Boitsova, J. Nano. Res. 4 (2002) 193.
[12] A. Motoaki, T. Shigeki, O. Kikuo, J. Nano. Res. 5 (2003) 31.
[13] X.Z. Lin, X. Teng, Y. Yang, Langmuir 19 (2003) 10081.
[14] A. Manna, T. Imae, M. Iida, N. Hisamatsu, Langmuir 17 (2001) 6000.
[15] N.V. Loginova, A.A. Chernyavskaya, M.S. Parfenova, N.P. Osipovich, G.I. Polozov, Yu.A. Fedutik, et al., Polyhedron 25 (2006) 1723.
[16] K.L. Kelly, E. Coronado, L.L. Zhao, G.C. Schatz, J. Phys. Chem. B 107 (2003) 668.
[17] J.J. Mock, M. Barbic, D.R. Smith, D.A. Schultz, S. Schultz, J. Chem. Phys. 116 (2002) 6755.
[18] D.-G. Li, S.-H. Chen, S.-Y. Zhao, X.-M. Hou, H.-Y. Ma, X.-G. Yang, Thin Solid Films 460 (2004) 78.
[19] R. Giovannetti, V. Bartocci, S. Ferraro, M. Gusteri, P. Passamonti, Talanta 42 (1995) 1913.
[20] H. Morales-Rojas, A.K. Yatsimirsky, J. Phys. Org. Chem. 12 (1999) 377.
[21] J.A. Creighton, D.G. Eadon, J. Chem. Soc., Faraday Trans. 87 (1991) 3881.
[22] P.C. Lee, D. Meisel, J. Phys. Chem. 86 (1982) 3391, Citrato.
[23] M. Sastry, Curr. Sci. 78 (2000) 1089.

2. Experimental

2.1. Materials and methods

$CuCl_2 \cdot 2H_2O$, KOH, 2-methylimidazole, benzimidazole, CH_3OH, CH_3CN, $C_4H_{10}O$ (S.D. Fine Chem.), 2-ethylimidazole, 2-methylbenzimidazole and $NaClO_4$ (Sigma Aldrich) were used as purchased. The Schiff base ligand was prepared as described in our earlier publication [15]. Elemental analysis was performed on an Elementar vario ELIII Carlo Erba 1108 analyzer. FAB mass spectra were recorded on a Jeol SX-102/DA 6000 mass spectrometer using xenon (6 kV, 10 mA) as the FAB gas. The magnetic susceptibility data were recorded on a Gouy balance at room temperature using mercury(II) tetrathiocyanato cobaltate(II) ($\chi_g = 16.44 \times 10^{-6}$ cgs unit) as the calibrant. The EPR spectra were recorded at room temperature (298 K) and also at liquid nitrogen temperature (77 K) on a Varian E-line Century Series EPR spectrometer operating at 9.4 GHz with TCNE as a calibrant. Electronic spectra were recorded on a Schimadzu UV–Vis 160 spectrophotometer in quartz cells. The IR spectra (400–4000 cm^{-1}) of the complexes were recorded on a Varian 3100 FT IR Excaliber Series spectrophotometer, with samples prepared as KBr pellets. A BAS 100 Epsilon electrochemical analyzer was used for cyclic voltammetric experiments in a DMSO solution of the complex, containing $NaClO_4$ as the supporting electrolyte. The three electrode measurement was carried out at 298 K under a nitrogen atmosphere with a platinum working electrode, a platinum wire auxiliary electrode and a silver/silver chloride reference electrode (Ag/AgCl). The SOD activities were evaluated using alkaline DMSO as a source of superoxide radicals (O_2^-) and nitrobluetetrazolium chloride (NBT) as a scavenger [16].

2.2. Synthesis of the complexes

2.2.1. Synthesis of [Cu(SAA)(H_2O)] (1)

To a methanolic solution (10 mL) of $CuCl_2 \cdot 2H_2O$ (1.0 mmol, 170 mg) a methanolic solution (10 mL) of the potassium salt of the Schiff base (1.0 mmol, 240 mg) was added and the reaction mixture was stirred for 30 min at 25 °C. After completion of the reaction, the dark green precipitate thus formed was collected by filtration and washed with a small amount of methanol and then with diethyl ether successively. The solid was dried in air at room temperature and stored in a $CaCl_2$ desiccator. Yield, 70%. *Anal.* Calc. for $C_{14}H_{11}O_4NCu$ (**1**) C, 52.36; H, 3.42; N, 4.36. Found: C, 51.48; H, 3.94; N, 4.45%. FAB mass (*m*/*z*) Calc.: 321. Found: 320.

2.2.2. Synthesis of [Cu(SAAA)(MeImH)] (2), [Cu(SAA)(EtImH)] (3), [Cu(SAA)(BenzImH)] (4) and [Cu(SAA)(MebenzImH)] (5)

All these ternary complexes were synthesized by following a general procedure. To a methanolic solution (10 mL) of $CuCl_2 \cdot 2H_2O$ (1.0 mmol, 170 mg) a methanolic solution (10 mL) of the potassium salt of the Schiff base (1.0 mmol, 240 mg) was added and the reaction mixture was stirred for 30 min at 25 °C. To the above reaction mixture, a methanolic solution (10 mL) of MeImH (1.0 mmol, 82 mg) was added and the stirring was continued for another 30 min. After completion of the reaction, the light green precipitate thus formed was collected by filtration and washed with a small amount of methanol and then with diethyl ether successively. The solid was dried in air at room temperature and stored in a $CaCl_2$ desiccator. Yield, ~60%. *Anal.* Calc. for $C_{18}H_{15}N_3O_3Cu$ (**2**) C, 56.11; H, 3.89; N, 10.91. Found: C, 56.13; H, 3.75; N, 10.45%. FAB mass (*m*/*z*) Calc.: 385. Found: 384. Complexes **3**, **4** and **5** were synthesized as described above by employing EtImH (1.0 mmol, 96 mg), BenzImH (1.0 mmol, 118 mg) and MeBenzImH (1.0 mmol, 132 mg), respectively, in place of MeImH. *Anal.* Calc. for $C_{19}H_{17}N_3O_3Cu$ (**3**) C, 57.15; H, 4.26; N, 10.53. Found: C, 56.85; H, 4.15; N, 10.50%. FAB mass (*m*/*z*) Calc.: 399. Found: 399. *Anal.* Calc. for $C_{21}H_{15}N_3O_3Cu$ (**4**) C, 59.86; H, 3.56; N, 9.97. Found: C, 59.87; H, 3.50; N, 9.45%. FAB mass (*m*/*z*) Calc.: 421. Found: 420. *Anal.* Calc. for $C_{22}H_{17}N_3O_3Cu$ (**5**) C, 60.69; H, 3.90; N, 9.65. Found: C, 60.56; H, 4.10; N, 9.40%. FAB mass (*m*/*z*) Calc.: 435. Found: 435.

2.3. Crystal structure determination

Crystals suitable for single crystal X-ray analysis for the complexes [Cu(SAA)(MeImH)] (**2**) and [Cu(SAA)(EtImH)] (**3**) were grown by slow evaporation of the CH_3OH:CH_3CN (1:1 V/V) solutions of the complexes at room temperature. The single crystals of **2** and **3** were mounted on a glass fiber and used for data collection. Crystal data were collected on an Oxford Xcalibus-S CCD diffractometer using graphite monochromatized Mo Kα radiation ($\lambda = 0.71073$ Å). The crystal orientation, cell refinement and intensity measurements were made using the program CAD-4PC, performing psi-scan measurements. The structure was solved by the direct methods using the program SHELXS-97 [17] and refined by full-matrix least-squares techniques against F^2 using SHELXL-97 [18]. All the hydrogen atoms were refined anisotropically. All the hydrogen atoms were geometrically fixed and allowed to refine using a riding model.

3. Results and discussion

The reaction of equimolar ratios of the ligands and metal salt yielded the corresponding metal complexes in good yield. All the present complexes prepared were blue in color. They were found to be soluble in DMF, DMSO and in a mixture of CH_3OH:CH_3CN (1:1 V/V) solution, but were only partially soluble in other organic solvents such as $CHCl_3$ and CH_2Cl_2.

3.1. Magnetic measurements

The magnetic susceptibility measurements in the solid state show that the present complexes are paramagnetic

at ambient temperature. The observed magnetic moment values of the complexes are 1.76 for **1**, 1.78 for **2**, 1.82 for **3**, 1.77 for **4** and 1.83 B.M. for **5**. These values are quite close to the values expected for copper(II) complexes [15,19,20] and is in fair agreement with the spin only system $S = 1/2$.

3.2. Crystal structure

Dark blue crystals of the complexes [Cu(SAA)(MeImH)] (**2**) and [Cu(SAA)(EtImH)] (**3**) suitable for X-ray diffraction studies were grown by slow evaporation of a solution of the complexes in CH_3OH:CH_3CN (1:1 V/V). The ORTEP views of the complexes are shown in Figs. 1 and 2. Crystallographic data and structure refinement parameters are given in Table 1 and selected bond angles and bond distances are given in Tables 2 and 3. The structures of the two complexes [Cu(SAA)(MeImH)] (**2**) and [Cu(SAA)(EtImH)] (**3**) are quite similar. The crystal structures of the complexes reveal the presence of ternary copper(II) structures consisting of a tridendate ONO donor Schiff base, a monodentate ligand (MeImH/EtImH) and a copper(II) center in the discrete monomeric species. The coordination geometry in the complexes is distorted square planar. Complex **2** crystallizes in the orthorhombic system with a space group of $Pna2_1$, $a = 9.3715(3)$ Å, $b = 11.0531(4)$ Å, $c = 15.6391(5)$ Å, $\alpha = 90°$, $\beta = 90°$ and $\gamma = 90°$, whereas complex **3** crystallizes in the monoclinic system with a space group of $P2_1/n$, $a = 11.4066(2)$ Å, $b = 9.4081(2)$ Å, $c = 16.3437(3)$ Å, $\alpha = 90°$, $\beta = 97.960(2)°$ and $\gamma = 90°$. The bond distances of the donor atoms of the Schiff base ligand to the central metal atom for these complexes are in the range 1.883(2) to 1.9637(19) Å and the bond distances of the monodentate ligands to the metal atom are 1.991(2) to 1.9827(19) Å. These values are close to ~1.9 Å, typical of similar of copper(II) complexes [15,21].

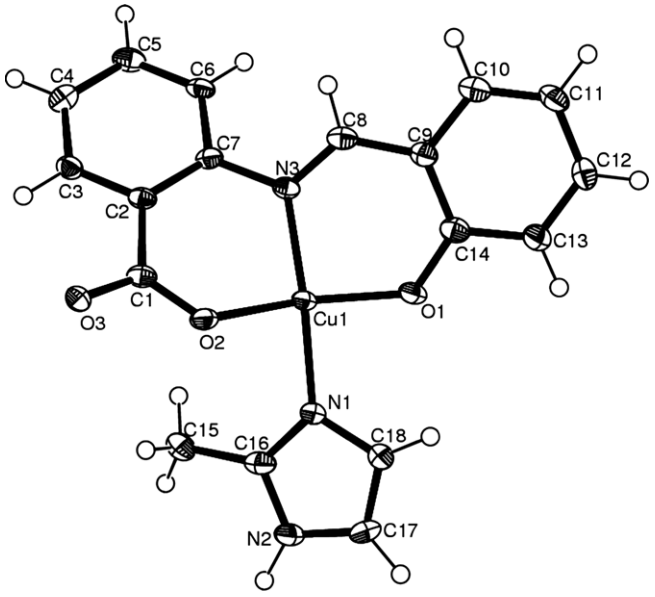


Fig. 1. ORTEP diagram of the complex [Cu(SAA)(MeImH)].

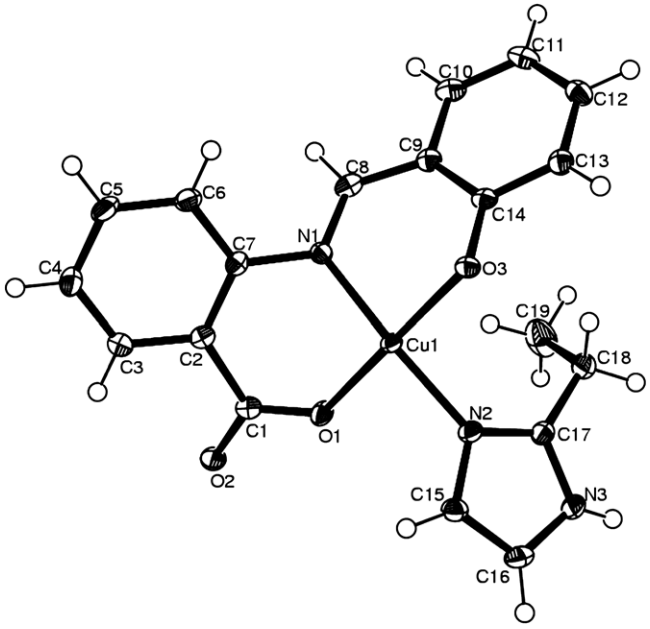


Fig. 2. ORTEP diagram of the complex [Cu(SAA)(EtImH)].

3.3. EPR spectral study

The EPR spectra of the complexes in the polycrystalline state at 298 K and in solution at 77 K were recorded in the X-band region, using 100 KHz field modulation and the g factors were quoted relative to the standard marker TCNE ($g = 2.00277$). EPR spectral assignments of the copper(II) complexes along with the spin Hamiltonian and orbital reduction parameters are given in Table 4. Some representative figures are shown in Figs. 3 and 4.

The EPR spectrum of complex **2** in the polycrystalline state at 298 K shows only one broad signal at $g = 2.110$. Such an isotropic spectrum consisting of a broad signal, and hence only one g value, arises from extensive exchange coupling through misalignment of the local molecular axes between different molecules in the unit cell and enhanced spin lattice relaxation. This type of spectra unfortunately give no information on the electronic ground state of the copper(II) ion present in the complexes. The EPR spectrum of complex **1** in the polycrystalline state at 298 K shows rhombic spectral features with three g values. The EPR spectra of the other complexes in the polycrystalline state at 298 K show axial symmetry with well-defined $g_{\|}$ and $g_{\perp}$ values. The geometric parameter G, which is a measure of the exchange interaction between the copper centers in the polycrystalline compound, is calculated by using the relation [22]: $G = (g_{\|} - 2.0023)/(g_{\perp} - 2.0023)$ for axial spectra and for rhombic spectra $G = (g_3 - 2.0023)/(g_{\perp} - 2.0023)$ and $g_{\perp} = (g_1 + g_2)/2$. The value of G is found to be in the range 2.2–2.9. All the complexes with $g_{\|} > g_{\perp} > 2.0023$ and G values less than 4.0 are consistent

Table 1
Crystal data and structure refinement for [Cu(SAA)(MeImH)] (**2**) and [Cu(SAA)(EtImH)] (**3**)

Empirical formula	$C_{18}H_{15}CuN_3O_3$ (**2**)	$C_{19}H_{17}CuN_3O_3$ (**3**)
Formula weight	384.87	398.90
Temperature (K)	120(2)	120(2)
Wavelength (Å)	0.71073	0.71073
Crystal system	Orthorhombic	Monoclinic
Space group	$Pna2_1$	$P2_1n$
Unit cell dimensions		
a (Å)	9.3715(3)	11.4066(2)
b (Å)	11.0531(4)	9.4081(2)
c (Å)	15.6391(5)	16.3437(3)
α (°)	90	90
β (°)	90	97.960(2)
γ (°)	90	90
Volume (Å^3)	1619.96(9)	1737.02(6)
Z, D_{calc} (Mg/m^3)	4, 1.578	4, 1.525
Absorption coefficient (mm^{-1})	1.371	1.282
$F(000)$	788	820
Crystal size (mm)	0.33 × 0.28 × 0.21	0.33 × 0.26 × 0.21
θ Range for data collection (°)	3.13–24.99	2.98–24.99
Limiting indices	$-11 \leqslant h \leqslant 11$, $-10 \leqslant k \leqslant 13$, $-18 \leqslant l \leqslant 17$	$-13 \leqslant h \leqslant 11$, $-11 \leqslant k \leqslant 11$, $-19 \leqslant l \leqslant 19$
Reflections collected/unique (R_{int})	5353/2452 (0.0278)	15637/3058 (0.0335)
Completeness to $\theta = 24.99$ (%)	99.8	99.8
Absorption correction	Semi-empirical from equivalents	Semi-empirical from equivalents
Maximum and minimum transmission	0.7617 and 0.6604	0.7746 and 0.6771
Refinement method	Full-matrix least-squares on F^2	Full-matrix least-squares on F^2
Data/restraints/parameters	2452/1/231	3058/0/240
Goodness-of-fit on F^2	1.000	1.098
Final R indices [$I > 2\sigma(I)$]	$R_1 = 0.0295$, $wR_2 = 0.0751$	$R_1 = 0.0299$, $wR_2 = 0.0759$
R indices (all data)	$R_1 = 0.0334$, $wR_2 = 0.0776$	$R_1 = 0.0388$, $wR_2 = 0.0813$
Largest difference in peak and hole (e Å^{-3})	0.511 and −0.425	0.470 and −0.317

Table 2
Selected bond lengths (Å) and angles (°) for [Cu(SAA)(MeImH)] (**2**)

Cu(1)–O(1)	1.883(2)	O(1)–C(14)	1.312(4)
Cu(1)–O(2)	1.903(2)	O(2)–C(1)	1.274(4)
Cu(1)–N(3)	1.963(3)	N(3)–C(8)	1.293(4)
Cu(1)–N(1)	1.991(2)	N(3)–C(7)	1.439(4)
C(1)–C(2)	1.503(5)	C(8)–C(9)	1.426(5)
C(2)–C(7)	1.399(5)	C(9)–C(14)	1.417(5)
O(1)–Cu(1)–O(2)	158.29(11)	C(14)–O(1)–Cu(1)	127.0(2)
O(1)–Cu(1)–N(3)	95.05(10)	C(1)–O(2)–Cu(1)	131.0(2)
O(2)–Cu(1)–N(3)	92.12(10)	C(16)–N(1)–Cu(1)	130.4(3)
O(1)–Cu(1)–N(1)	88.51(12)	C(18)–N(1)–Cu(1)	122.7(3)
O(2)–Cu(1)–N(1)	89.00(10)	N(3)–Cu(1)–N(1)	167.15(16)
C(8)–N(3)–Cu(1)	121.9(2)	C(7)–N(3)–Cu(1)	120.5(2)

Table 3
Selected bond lengths (Å) and angles (°) for [Cu(SAA)(EtImH)] (**3**)

Cu(1)–O(1)	1.9328(16)	N(1)–C(8)	1.294(3)
Cu(1)–O(3)	1.9347(16)	N(1)–C(7)	1.428(3)
Cu(1)–N(1)	1.9637(19)	C(1)–C(2)	1.509(3)
Cu(1)–N(2)	1.9827(19)	C(8)–C(9)	1.429(3)
O(1)–C(1)	1.279(3)	C(9)–C(14)	1.428(3)
O(3)–C(14)	1.319(3)		
O(1)–Cu(1)–O(3)	175.39(7)	C(1)–O(1)–Cu(1)	129.13(15)
O(1)–Cu(1)–N(1)	90.25(7)	C(14)–O(3)–Cu(1)	121.65(14)
O(3)–Cu(1)–N(1)	89.24(7)	C(8)–N(1)–Cu(1)	121.93(17)
O(1)–Cu(1)–N(2)	87.04(7)	C(7)–N(1)–Cu(1)	119.10(15)
O(3)–Cu(1)–N(2)	92.51(7)	C(17)–N(2)–Cu(1)	129.37(17)
N(1)–Cu(1)–N(2)	167.82(8)	C(15)–N(2)–Cu(1)	124.37(17)

with a $d_{x^2-y^2}$ ground state in a square planar or square pyramidal geometry [23,24].

The solution EPR spectra of the complexes were recorded in DMSO at 77 K. Frozen solution EPR spectra of the complexes have revealed axial features ($g_\| > g_\perp > 2.0023$) and suggest a $d_{x^2-y^2}$ ground state. These spectral features are characteristic of axial symmetry [21,25]. The EPR parameters $g_\|$, $g_\perp$, $A_\|$ and the energies of the d–d transition were used to evaluate the bonding parameters α^2, β^2 and γ^2, which may be regarded as measures of the covalency of the in-plane σ bonds, in-plane π bonds and out-of plane π bonds, respectively, (Table 4). The value of the in-plane sigma bonding parameter α^2 was calculated using the expression [26]:

$$\alpha^2 = (A_\|/0.036) + (g_\| - 2.0023) + 3/7(g_\perp - 2.0023) + 0.04$$

The orbital reduction factors, $K_\| = \alpha^2\beta^2$ and $K_\perp = \alpha^2\gamma^2$ were calculated using the following expression:

$$K_\|^2 = (g_\| - 2.0023)E_{d\text{–}d}/8\lambda_0$$

$$K_\perp^2 = (g_\perp - 2.0023)E_{d\text{–}d}/2\lambda_0$$

where λ_0 is the spin–orbit coupling constant, with a value of $-828\ cm^{-1}$ for a copper(II) d^9 system. According to

Table 4
EPR spectral parameters of the copper(II) complexes

	1	2	3	4	5
Polycrystalline state (298 K)					
$g_{\parallel}$	2.203 (g_3)		2.203	2.215	2.224
$g_{\perp}$	2.056 (g_1)		2.087	2.087	2.078
	2.127 (g_2)				
g_{iso} or g_{av}	2.128	2.110	2.145	2.151	2.151
DMSO (77 K)					
$g_{\parallel}$	2.225	2.275	2.276	2.285	2.275
$g_{\perp}$	2.046	2.065	2.062	2.058	2.062
$A_{\parallel}$ (G)	160	157	157	160	165
G	2.25		2.35	2.51	2.91
α^2	0.725	0.775	0.775	0.790	0.796
β^2	0.943	0.993	0985	0.939	0.969
γ^2	0.836	0.954	0.920	0.834	0.907
$K_{\parallel}$	0.684	0.772	0.763	0.776	0.758
$K_{\perp}$	0.606	0.740	0.713	0.689	0.710
f (cm^{-1})	139	145	145	142	138

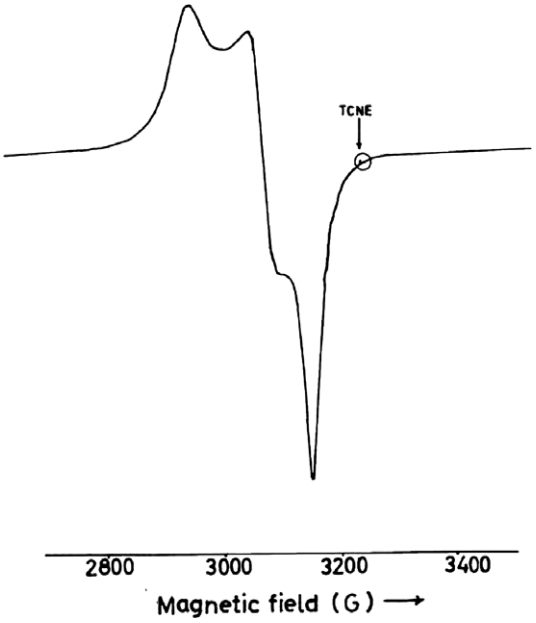


Fig. 3. EPR spectrum of the complex [Cu(SAA)(H_2O)] in powder at 298 K.

Hathaway [23], for pure σ bonding, $K_{\parallel} \approx K_{\perp} \approx 0.77$ and for in-plane π bonding $K_{\parallel} < K_{\perp}$, while for out-of-plane π bonding, $K_{\parallel} > K_{\perp}$.

In all of the present copper(II) complexes, it is observed that $K_{\parallel} > K_{\perp}$, which indicates the presence of significant out-of-plane π bonding. The evaluated values of α^2, β^2 and γ^2 of the complexes are consistent with both strong in-plane σ and out-of-plane π bonding.

The empirical factor $f = g_{\parallel}/A_{\parallel}$ cm^{-1} is an index of tetragonal distortion and its value may vary from 105 to 135 for small to extreme distortions in square planar complexes and it depends on the nature of the coordinated atoms [27]. The f values of these complexes are found to be in the range 138–145, indicating significant distortion from planarity.

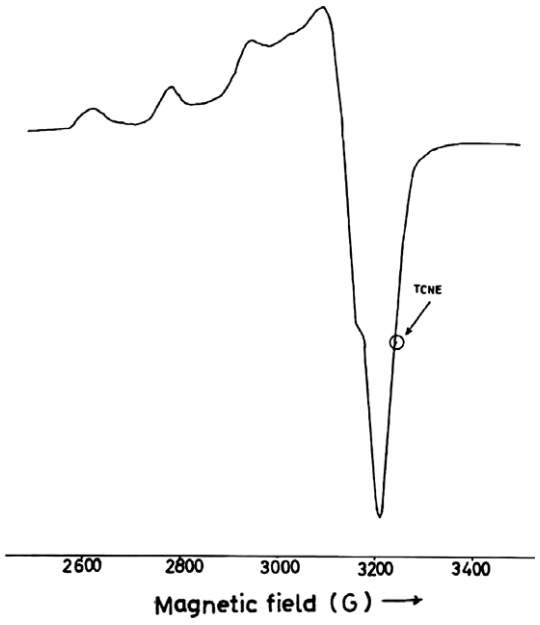


Fig. 4. EPR spectrum of the complex [Cu(SAA)(BenzImH)] (0.003 M) at 77 K in DMSO.

3.4. Electronic spectral study

The significant electronic absorption bands in the spectra of the complexes were recorded in DMSO at 25 °C. For square planar complexes with a $d_{x^2-y^2}$ ground state, three spin allowed transitions are possible, *viz.* $^2B_{1g} \rightarrow {}^2A_{1g}$ $(d_{x^2-y^2} \rightarrow d_z^2)$, $^2B_{1g} \rightarrow {}^2B_{2g}(d_{x^2-y^2} \rightarrow d_{xy})$ and $^2B_{1g} \rightarrow {}^2E_g(d_{x^2-y^2} \rightarrow d_{xz}, d_{yz})$. Since the four d orbitals lie very close together, each transition cannot be distinguished by their energy and hence it is very difficult to resolve the bands into separate components.

The spectra of complexes **1**–**5** each exhibit a broad band centered at 718, 703, 708, 708 and 715 nm, respectively, similar to those reported for copper(II) ions in a square planar environment [28,29]. Due to the broadness of the band, the other expected transitions in this range could not be assigned. The ligand to metal charge transfer band for the complexes appeared at 413–416 nm with a shoulder at 450–461 nm.

3.5. Infrared spectral study

The ν(C=N) band of the ligand at 1621 cm^{-1} is found to be shifted to lower energies (1586–1595 cm^{-1}) in the spectra of the complexes, indicating coordination via the azomethine nitrogen. This is confirmed by bands in the range 459–461 cm^{-1}, which have been assigned to the ν(Cu–N) band [30]. In the IR spectra of the complexes, the replacement of the valence stretching carboxylic vibration $\nu(C{=}O)_{carb}$ of the protonated SAA at 1688 cm^{-1} by the asymmetric, $\nu(CO_2)_{asym}$, at ~1445 cm^{-1} and the asymmetric stretching ν(O–C–O) vibration, $\nu(CO_2)_{syn}$, at ~1381 cm^{-1} as well as the Δ value (~64 cm^{-1}) [$\Delta = \nu(CO_2)_{asym} - \nu(CO_2)_{sym}$] are indicative of a monodentate

coordination mode of the carboxylato group [31]. In the IR spectra of complex **1** a considerable peak observed at 3448 cm^{-1} supports the presence of $\nu(H_2O)$ in the complex. Vibrations at ~460 (weak) (and expected below 400 cm^{-1}, out of our measuring limit) can be attributed to M–O and M–N vibrations [21].

3.6. Cyclic voltammetric measurements

The electrochemical behavior of 1 mM solutions of complexes **1**–**5** have been investigated in DMSO containing 0.1 M $NaClO_4$ as the supporting electrolyte, at a platinum working electrode. The CV results of these complexes are given in Table 5. A representative voltammogram is shown in Fig. 5.

For complexes **1** and **4**, a negative scan initiated at 1000 mV in the potential range 1000 to −1000 mV yielded an irreversible couple corresponding to the Cu(II)/(I) redox process [32]. In these cases the peak potentials difference increases as the scan rate is increased. Constancy of Eo' shows that in all cases both peaks are complementary to each other. The peak current ratio I_{pa}/I_{pc} is less than unity showing that the electron transfer reaction is followed by a chemical reaction (EC mechanism) [33,34].

For complexes **2**, **3** and **5**, a negative scan initiated at 1000 mV in the potential range 1000 to −1000 mV yielded two cathodic peaks at a scan rate 100 mV/s and 200 mV/s (Table 5) but their complementary anodic peaks did not appear, even at higher scan rates. This shows that the Cu(I) state is largely unstable in solution. The E_{pc2} of the corresponding complexes may be due to the Cu(II)/Cu(I) reduction. A perusal of Table 5 shows that the magnitude of the cathodic peak currents I_{pc1} and I_{pc2} differ significantly; I_{pc2} being larger than that of I_{pc1} indicates that the two complex species presumably exist in equilibrium in solution.

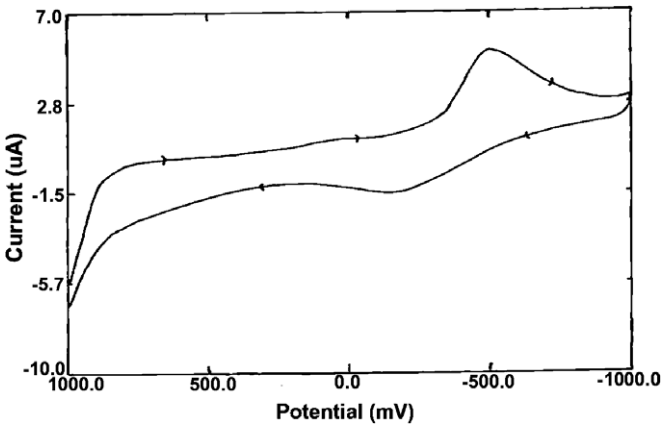


Fig. 5. Cyclic voltammogram of the complex [Cu(SAA)(BenzImH)] in 0.1 M $NaClO_4$ [scan rate: 200 (m V/s)].

3.7. Superoxide dismutase activity

The superoxide dismutase activity (SOD) of the complexes was investigated by the NBT assay method. The SOD activity of the complexes was measured at pH 8.6. The chromophore concentration value required to yield 50% inhibition of the reduction of NBT (IC_{50}) of the present complexes (63 μmol dm^{-3} for **1**, 35 μmol dm^{-3} for **2**, 43 μmol dm^{-3} for **3**, 50 μmol dm^{-3} for **4** and 52 μmol dm^{-3} for **5**) are higher than the value exhibited by the native enzyme ($IC_{50} = 0.04$ μmol dm^{-3}). These higher values may be due to the strong ligand field created by the tridentate Schiff base ligand which opposes the interaction of the complexed copper with the superoxide radical, and another important factor is the ability of the ligand to accommodate the reduced copper(I) center in a tetrahedral-like or linear environment [35].

Table 5
Cyclic voltammetric measurements of copper(II) complexes

Scan rate (mV/s)	E_{pc} (mV)	I_{pc} (μA)	E_{pa} (mV)	I_{pa} (μA)	ΔE_p	E'_o	I_{pa}/I_{pc}
[Cu(SAA)(H₂O)] (*1*)							
100	−656	1.573	−433	0.715	223	−544	0.45
200	−680	2.225	−409	1.012	271	−544	0.45
[Cu(SAA)(BenzImH)] (*4*)							
100	−668	1.404	−385	0.585	283	−526	0.42
200	−693	1.976	−360	0.831	333	−526	0.42

Scan rate (mV/s)	E_{pc1} (mV)	I_{pc1} (μA)	E_{pc2} (mV)	I_{pc2} (μA)
[Cu(SAA)(MeImH)] (*2*)				
100	199	0.327	−692	0.973
200	178	0.473	−721	1.342
[Cu(SAA)(EtImH)] (*3*)				
100	208	0.412	−670	1.014
200	180	0.591	−698	1.442
[Cu(SAA)(MeBenzImH)] (*5*)				
100	228	0.351	−602	1.285
200	205	0.517	−638	1.807

4. Supplementary material

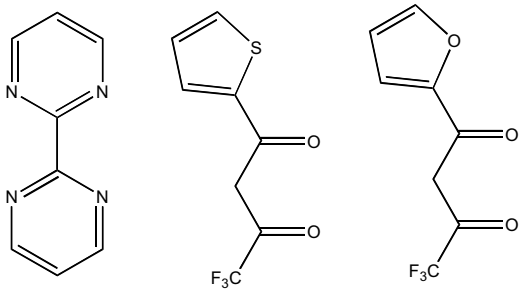
CCDC 661712 and 661713 contain the supplementary crystallographic data for [Cu(SAA)(MeImH)] (**2**) and [Cu(SAA)(EtImH)] (**3**). These data can be obtained free of charge via http://www.ccdc.cam.ac.uk/conts/retrieving.html, or from the Cambridge Crystallographic Data Centre, 12 Union Road, Cambridge CB2 1EZ, UK; fax: (+44) 1223-336-033; or e-mail: deposit@ccdc.cam.ac.uk.

Acknowledgements

V.L.N. Gundla thanks the Council of Scientific & Industrial Research, New Delhi, India, for awarding SRF. Our grateful thanks are due to the National Diffraction Facility, X-ray Division and RSIC (SAIF), IIT Bombai for single crystal data collection and EPR measurements, respectively. The Head RSIC, Central Drug Research Institute, Lucknow is also thankfully acknowledged for providing analytical and spectral facilities.

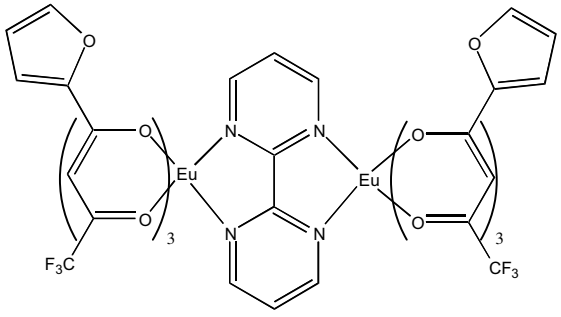
References

[1] H. Sigel (Ed.), Metal Ions in Biological Systems, vol. 12, Marcel Dekker, New York, 1981.
[2] H. Sigel (Ed.), Metal Ions in Biological Systems, vol. 13, Marcel Dekker, New York, 1981.
[3] T. Miura, A. Hori-i, H. Mototani, H. Takeuchi, Biochemistry 38 (1999) 11560.
[4] G.D. Whitener, J.R. Hagadorn, J. Arnold, J. Chem. Soc., Dalton Trans. 1249 (1999).
[5] M.J. Young, D.W. Rosemary, C. Hynes, J. Chin, J. Am. Chem. Soc. 117 (1995) 9441.
[6] I. Que Jr., A.E. True, Prog. Inorg. Chem. 38 (1990) 97.
[7] V.L. Pecoraro (Ed.), Manganese Redox Enzymes, VCH, New York, 1992.
[8] E. Colacio, G. Mustrapha, K. Raikko, J.M. Moreno, Inorg. Chem. 39 (2000) 2882.
[9] S.I. Rethg, R.C. Thompson, J. Trotter, S. Xia, Inorg. Chem. 38 (1999) 360.
[10] V. Tangoulis, G. Psomas, C. Dendrinou-Samara, C.P. Raptopoulous, A. Terzis, D.P. Kessissoglou, Inorg. Chem. 35 (1996) 7655.
[11] J.L. Pierre, P. Chautemps, S. Refaif, C. Beguin, A.E. Marzouki, C. Serratrace, E. Saint-Aman, P. Rey, J. Am. Chem. Soc. 117 (1995) 1965.
[12] R.J. Sundberg, R.B. Martin, Chem. Rev. 74 (1974) 471.
[13] R.N. Preston, Chem. Rev. 74 (1974) 279.
[14] M. Sanchez-Moreno, E. Entrala, D. Janssen, C. Fernandez-Becerra, J.M. Salas-Peregrain, A. Osuma, Pharmacology 52 (1996) 61.
[15] R.N. Patel, N. Singh, V.L.N. Gundla, Polyhedron 25 (2006) 3312.
[16] R.N. Patel, N. Singh, K.K. Shukla, V.L.N. Gundla, U.K. Chauhan, J. Inorg. Biochem. 99 (2005) 651.
[17] G.M. Sheldrick, Acta Crystallogr., Sect. A 46 (1990) 467.
[18] G.M. Sheldrick, SHELXL-97, Program for the Refinement of Crystal Structures, University of Gottingen, Germany, 1997.
[19] K. Skorda, S.P. Perlepes, C.P. Raptopoulou, Transition Met. Chem. 24 (1999) 541.
[20] R.N. Patel, N. Singh, K.K. Shukla, V.L.N. Gundla, U.K. Chauhan, Spectrochim. Acta, Part A 63 (2006) 21.
[21] A. García-Raso, J.J. Fiol, B. Adrover, P. Tauler, A. Pons, I. Mata, E. Espinosa, E. Molins, Polyhedron 22 (2003) 3255.
[22] P.F. Rapheal, E. Manoj, M.R.P. Kurup, Polyhedron 26 (2007) 818.
[23] B.J. Hathaway, G. Wilkinson, R.D. Gillard, J.A. McCleverty (Eds.), Comprehensive Coordination Chemistry II, vol. 5, Pergamon, Oxford, 1987.
[24] V. Philip, V. Suni, M.R.P. Kurup, M. Nethaji, Polyhedron 24 (2005) 1133.
[25] J.P. Klinman, Chem. Rev. 96 (1996) 2541.
[26] G.F. Bryce, J. Phys. Chem. 70 (1966) 3549.
[27] R. Pogni, M.C. Bartoo, A. Diaz, R. Basosi, J. Inorg. Biochem. 79 (2000) 333.
[28] A.B.P. Lever, Inorganic Electronic Spectroscopy, Elsevier, Amsterdam, 1968.
[29] L. Sacconi, M. Ciampolini, J. Chem. Soc. (1964) 276.
[30] K. Nakamoto, Infrared and Raman spectra of Inorganic and Coordination compounds, 5th ed., Wiley, New York, 1997.
[31] C. Dendrinou-Samara, G. Tsotsou, C.P. Raptopoulou, A. Kortsaris, D. Kyriakidis, D.P. Kessissoglou, J. Inorg. Biochem. 71 (1998) 171.
[32] N. Raman, S. Ravichandran, C. Thangaraja, J. Chem. Sci. 116 (4) (2004) 215.
[33] D.H. Evans, Chem. Rev. 90 (1990) 739.
[34] S. Parveen, F. Arjmand, Indian J. Chem. A 44 (2005) 1151.
[35] R.P. Bonono, E. Conte, G. Impellizzer, G. Pappalardo, R. Purrello, E. Rizzarelli, J. Chem. Soc., Dalton Trans. (1996) 100.

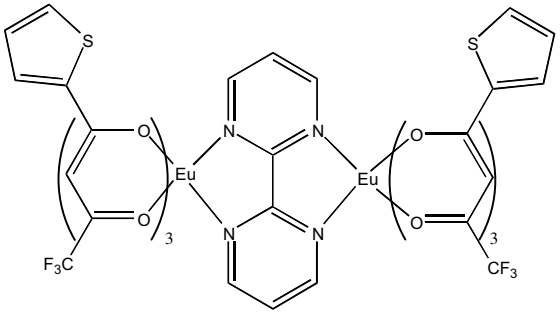


bpm tta tfa

Of the lanthanide metals europium appears to be the most thoroughly studied. This is due in part to the intense luminescence of europium complexes in the visible region of the spectrum. In addition europium complexes display temperature dependent luminescent properties leading to their use as temperature probes. In this report we present the structural and temperature dependent luminescent properties of two homodinuclear europium complexes using tfa and tta as antenna ligands and bridged by bpm, $[Eu(tfa)_3]_2$bpm (**1**) and $[Eu(tta)_3]_2$bpm (**2**).



$[Eu(tfa)_3]_2$bpm (**1**)



$[Eu(tta)_3]_2$bpm (**2**)

2. Experimental

2.1. Materials

All reagents were analytical grade and used without further purification. Europium(III) chloride (Aldrich), 2,2′-bipyrimidine (bpm) (Alfa Aesar), 4,4,4-trifluoro-1-(2-furyl)-1,3-butanedione (tfa), 4,4,4-trifluoro-1-(2-thienyl)-1,3-butanedione (tta), 2,2′-bipyridine (bpy) (ACROS), toluene, ethyl acetate, hexanes and ethanol (Fisher) were used as received. Elemental analysis was performed by Atlantic Microlabs Inc., Norcross Georgia.

2.2. $[Eu(tfa)_3]_2$bpm (*1*)

Synthesis of this bimetallic complex has been previously reported [27]. A solution of bpm (0.055 g, 0.35 mmol) in absolute ethanol (3.0 mL) was added to a basic (2.1 mL of 1.0 M NaOH) solution of tfa (0.433 g, 2.10 mmol) in absolute ethanol (3.0 mL). The mixture was stirred at room temperature for 30 min. To this solution was added an aqueous (3.5 mL) solution of $EuCl_3 \cdot 6H_2O$ (0.26 g, 0.70 mmol) over a 5 min period. The cream colored precipitate was vacuum filtered, washed 3×10 mL with cold absolute ethanol and allowed to air dry. The resulting powder was recrystallized from an ethyl acetate/hexanes mixture to give a white powder (0.59 g, 76%). *Anal.* Calc. for $Eu_2C_{56}H_{30}N_4O_{18}F_{18}$ (1693): C, 39.74; H, 1.79; N, 3.31. Found: C, 39.94; H, 1.71; N, 3.44%. UV–Vis (toluene): λ_{max} (nm) [log ε] = 337 [5.01].

2.3. $[Eu(tta)_3]_2$bpm (*2*)

Synthesis of this bimetallic complex has been previously reported [27]. A solution of bpm (0.055 g, 0.35 mmol) in absolute ethanol (3.0 mL) was added to a basic (2.1 mL of 1.0 M NaOH) solution of tta (0.476 g, 2.10 mmol) in absolute ethanol (3.0 mL). The mixture was stirred at room temperature for 30 min. To this solution was added an aqueous (3.5 mL) solution of $EuCl_3 \cdot 6H_2O$ (0.26 g, 0.70 mmol) over a 5 min period. The cream colored precipitate was vacuum filtered, washed 3×10 mL with cold absolute ethanol and allowed to air dry. The resulting powder was recrystallized from an ethyl acetate/hexanes mixture to give a white powder (0.46 g, 73%). *Anal.* Calc. for $Eu_2C_{56}H_{30}N_4O_{12}F_{18}S_6$ (1789): C, 37.59; H, 1.69; N, 3.13. Found: C, 37.68; H, 1.73; N, 3.23%. UV–Vis (toluene): λ_{max} (nm) [log ε] = 340 [5.16].

2.4. $Eu(tfa)_3$bpy

For spectroscopic comparisons the monometallic analogs of complex **1** and **2** were synthesized. A solution of 2,2′-bipyridine (bpy, 0.51 g, 3.3 mmol) in absolute ethanol (15 mL) was added to a basic (10 mL of 1.0 M NaOH) solution of tfa (2.1 g, 10 mmol) in absolute ethanol (15 mL). The mixture was stirred at room temperature for 45 min. To this solution was added an aqueous (15 mL) solution of $EuCl_3 \cdot 6H_2O$ (1.2 g, 3.3 mmol) over a 5 min period. The white precipitate was vacuum filtered, washed 3×10 mL with cold absolute ethanol and allowed

to air dry. The resulting white powder was recrystallized from an ethyl acetate/hexanes mixture to give a white powder (2.1 g, 69%). *Anal.* Calc. for $EuC_{34}H_{20}N_2O_9F_9$ (923): C, 44.22; H, 2.18; N, 3.03. Found: C, 43.98; H, 2.16; N, 2.99%.

2.5. *Eu(tta)$_3$bpy*

A solution of 2,2′-bipyridine (bpy, 0.21 g, 1.4 mmol) in absolute ethanol (15 mL) was added to a basic (4.2 mL of 1.0 M NaOH) solution of tta (0.93 g, 4.2 mmol) in absolute ethanol (15 mL). The mixture was stirred at room temperature for 45 min. To this solution was added an aqueous (15 mL) solution of $EuCl_3 \cdot 6H_2O$ (0.50 g, 1.4 mmol) over a 5 min period. The white precipitate was vacuum filtered, washed 3 × 10 mL with cold absolute ethanol and allowed to air dry. The resulting white powder was recrystallized from an ethyl acetate/hexanes mixture to give a white powder (0.45 g, 33%). *Anal.* Calc. for $EuC_{34}H_{20}N_2O_6F_9S_3$ (972): C, 42.03; H, 2.07; N, 2.88. Found: C 41.98; H, 2.19; N, 3.08%.

2.6. Physical measurements

Electronic absorption spectroscopy of the europium(III) complexes was run in toluene solutions with a Shimadzu Multispec-1501 diode array spectrophotometer. Luminescence spectra of the europium(III) complexes in a 1 cm quartz spectrophotometer fluorescence cell (Starna) in toluene were run on a Cary Eclipse fluorescence spectrophotometer. Temperature dependent luminescence of the europium(III) complexes in toluene from 5 °C to 55 °C was controlled using a Cary single cell Peltier temperature controller.

2.7. Crystal structure determination of **1** and **2**

For X-ray examination and data collection, suitable crystals of **1** and **2** were mounted in a loop with paratone-N and transferred immediately to the goniostat bathed in a cold stream. Intensity data were collected on a D8 goniostat equipped with a Bruker Platinum200 CCD detector at Beamline 11.3.1 at the Advanced Light Source (Lawrence Berkeley National Laboratory) using synchrotron radiation (**1**: 196 K, $\lambda = 0.7749$ Å; **2**: 193 K, $\lambda = 0.7758$ Å).[1] A series of data frames measured at 0.2° increments of ω were collected to calculate a unit cell. For data collection, frames were measured at 0.3° intervals of ω. Scan durations for both the unit cell and data collection procedures were 4-s for compound **1** and 3-s for compound **2**. The data frames were collected using the program APEX2 and processed using the program SAINT routine within APEX2.[2] The data were corrected for absorption and beam corrections based on the multi-scan technique as implemented in SADABS.[2]

Table 1
Crystal data, collection and structure refinement parameters for complexes **1** and **2**

Parameters	**1**	**2**
Empirical formula	$C_{56}H_{30}Eu_2F_{18}N_4O_{18} \cdot C_4H_8O_2$	$C_{56}H_{30}Eu_2F_{18}N_4O_{12}S_6$
Formula weight	1780.86	1789.12
Crystal system	triclinic	monoclinic
Space group	$P\bar{1}$	$P2_1/c$
Crystal size (mm^3)	0.15 × 0.12 × 0.01	0.05 × 0.04 × 0.02
Temperature (K)	196(2)	193(2)
a (Å)	9.7606(12)	10.400(2)
b (Å)	14.1165(18)	21.726(5)
c (Å)	24.876(3)	14.855(3)
α (°)	87.331(3)	90
β (°)	83.785(3)	106.126(5)
γ (°)	80.672(3)	90
V (Å^3)	3360.9(7)	3224.5(12)
Z	2	2
ρ_{calc} (g cm^{-3})	1.760	1.843
μ (mm^{-1})	2.459	2.799
$F(000)$	1748	1748
R_1 [$I > 2\sigma(I)$]	0.0568	0.0555
wR_2 [$I > 2\sigma(I)$]	0.1243	0.1612
R_1 (all data)	0.0869	0.0587
wR_2 (all data)	0.1350	0.1634
Goodness-of-fit	1.061	1.282

The structure was solved by a combination of direct methods in SHELXTL[2] and the difference Fourier technique and refined by full-matrix least squares on F^2 (**1**: 0.85 Å; **2**: 0.89 Å resolution). Non-hydrogen atoms were refined with anisotropic displacement parameters with the exception of partial-occupancy F-atoms. All H-atom positions were calculated and treated with a riding model. All H-atom isotropic displacement parameters were defined as $1.2U_{eq}$. In the case of compound **1**, F-atoms of the CF_3 groups show disorder as indicated by the enlarged displacement parameters; multi-component conformations are modeled where possible. The refinements converged with crystallographic agreement factors as summarized in Table 1. The selected bond lengths and bond angles for the complexes are listed in Table 2.

[1] Crystallographic data were collected through the SCrALS (Service Crystallography at Advanced Light Source) program at the Small-Crystal Crystallography Beamline 11.3.1 (developed by the Experimental Systems Group) at the Advanced Light Source (ALS). The ALS is supported by the U.S. Department of Energy, Office of Energy Sciences Materials Sciences Division, under contract DE-AC03-76SF00098 at Lawrence Berkeley National Laboratory.

[2] APEX2 v2.0-2 and SAINT v7.23A data collection and data processing programs, respectively. Bruker Analytical X-ray Instruments, Inc., Madison, WI; SADABS v2.10 semi-empirical absorption and beam correction program. G.M. Sheldrick, University of Göttingen, Germany; SHELXTL v6.14 for structure solution, figures and tables, neutral-atom scattering factors as stored in this package. G.M. Sheldrick, University of Göttingen, Germany and Bruker Analytical X-ray Instruments, Inc., Madison, WI.

Table 2
Selected bond lengths (Å) and angles (°) for complexes **1** and **2**

1	**2**		
Eu1–O1	2.344(6)	Eu1–O1	2.406(5)
Eu1–O2	2.343(6)	Eu1–O2	2.335(6)
Eu1–O3	2.366(6)	Eu1–O3	2.349(6)
Eu1–O4	2.324(6)	Eu1–O4	2.391(6)
Eu1–O5	2.363(5)	Eu1–O5	2.386(6)
Eu1–O6	2.355(6)	Eu1–O6	2.354(6)
Eu1–N1	2.612(7)	Eu1–N1	2.635(6)
Eu1–N2	2.597(6)	Eu1–N2	2.657(7)
Eu2–O10	2.356(6)	Eu1′–O1′	2.406(5)
Eu2–O11	2.368(6)	Eu1′–O2′	2.335(6)
Eu2–O12	2.347(6)	Eu1′–O3′	2.349(6)
Eu2–O13	2.375(6)	Eu1′–O4′	2.391(6)
Eu2–O14	2.346(6)	Eu1′–O5′	2.386(6)
Eu2–O15	2.356(6)	Eu1′–O6′	2.354(6)
Eu2–N3	2.652(6)	Eu1′-N1′	2.635(6)
Eu2–N4	2.574(7)	Eu1′-N2′	2.657(7)
O1–Eu1–O2	72.6(2)	O1–Eu1–O2	72.2(2)
O3–Eu1–O4	72.1(2)	O3–Eu1–O4	71.4(2)
O5–Eu1–O6	72.4(2)	O5–Eu1–O6	72.0(2)
N1–Eu1–N2	62.3(2)	N1–Eu1–N2	61.0(2)
O10–Eu2–O11	71.9(2)	O1′–Eu1′–O2′	72.2(2)
O12–Eu2–O13	72.2(2)	O3′–Eu1′–O4′	71.4(2)
O14–Eu2–O15	72.4(2)	O5′–Eu1′–O6′	72.0(2)
N3–Eu2–N4	62.2(2)	N1′–Eu1′–N2′	61.0(2)

3. Results and discussion

3.1. Structural analysis

Synthesis of the homodinuclear europium(III) complexes $[Eu(tfa)_3]_2$bpm (**1**) and $[Eu(tta)_3]_2$bpm (**2**) is accomplished in yields greater than 70% by reacting $EuCl_3$ with tfa or tta and bpm in a 2:6:1 ratio as previously described [27].

The structural analysis of compound **1** indicates that it crystallizes as an ethyl acetate solvate in the triclinic space group $P\bar{1}$. Each Eu^{III} ion in **1** (Fig. 1) is eight-coordinate and the complex is neutral. The coordination sphere around each Eu^{III} ion consists of six O atoms from three tfa ligands and two N atoms from the bpm ligand (average distances: Eu–O = 2.354 Å, Eu–N = 2.609 Å). Both Eu centers are in a distorted square-antiprismatic geometry with the approximate square planes defined as O3–O4–O5–O6 and N1–N2–O1–O2 (mean deviation of 0.275(4) and 0.304(4) Å, respectively, with an angle between the planes of 82.8(1)°) about Eu1 and O12–O13–O14–O15 and N3–N4–O10–O11 about Eu2 (mean deviation of 0.067(4) and 0.103(4) Å, respectively, and an angle of 89.9(1)°). The intramolecular Eu···Eu distance across the bridging bpm ligand is 6.8035(8) Å. The individual bpm rings are planar, with a mean deviation of 0.009(6) and 0.008(7) Å for planes defined by N1–N3–C25–C26–C27–C28 and N2–N4–C29–C30–C31–C32, respectively; they are rotated from planarity by 5.7(5)°.

The structural analysis of compound **2** indicates that it crystallizes without solvent in the lattice in the monoclinic space group $P2_1/c$, with the bpm ligand situated about a crystallographic center of symmetry. As with **1**, each Eu^{III} ion in **2** (Fig. 2) is eight-coordinate, bound by six O atoms from three tta and two N atoms from the bpm ligand. The geometry about the Eu centers can also be described as square-antiprismatic with approximate square planes defined as O3–O4–O5–O6 and N1–N2–O1–O2 (mean deviation of 0.158(4) and 0.056(4) Å, respectively, with an angle between the planes of 89.2(1)°). The average Eu–O and Eu–N distances of 2.370 Å and 2.646 Å, respectively,

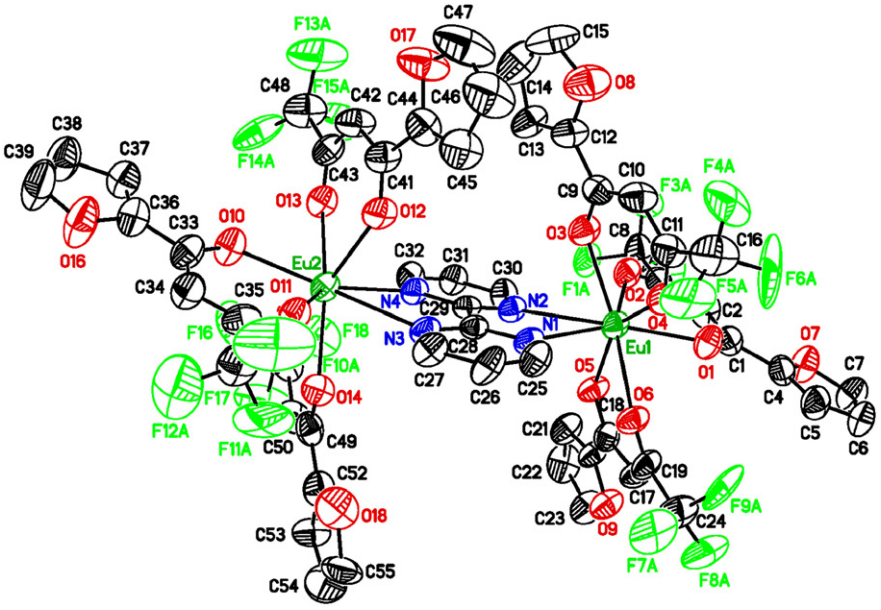


Fig. 1. Molecular structure of $[Eu(tfa)_3]_2$bpm (**1**) showing atomic numbering scheme, 50% thermal ellipsoid probability, only 1 conformation of the disordered CF_3 groups is shown, H-atoms omitted for clarity.

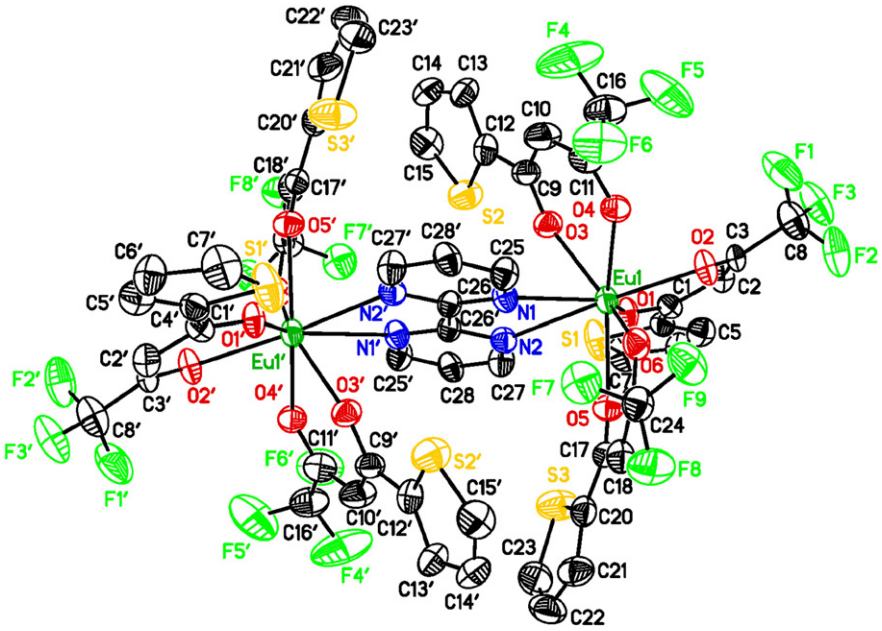


Fig. 2. Molecular structure of $[Eu(tta)_3]_2$bpm (**2**) showing atomic numbering scheme (symmetry-related atoms labeled with a prime), 50% thermal ellipsoid probability, H-atoms omitted for clarity.

are slightly larger than in **1**. The intramolecular Eu···Eu distance (6.9212(15) Å) across the bridging bpm ligand is approximately 0.1 Å longer than that observed in **1**. The individual bpm rings are planar, with a mean deviation of 0.008(6) Å for both rings and a rotation of 0° between the planes.

Simultaneous to our initial report on the synthesis of compound **2**, Shim and co-workers reported an alternate synthetic route to this complex [25]. Their structural analysis of $[Eu(tta)_3]_2$bpm reveals the presence of THF as the solvent of crystallization and a lower overall crystal symmetry of triclinic (space group $P\bar{1}$). They report a 6.3° rotation from planarity for the bpm ligand and a Eu···Eu separation of 6.993 Å. The average Eu–O and Eu–N distances are 2.394 Å and 2.687 Å.

Fernandes and co-workers report the structure of $[Eu(nta)_3]_2$(bpm) (nta = 1-(2-naphthoyl)-3,3,3-trifluoroacetone) [24] where the C_4H_3E (E = O, S) group in compounds **1** and **2** is replaced by a $C_{10}H_7$ group. For this complex, one observes Eu–O and Eu–N distances in the range 2.311(6)–2.384(7) Å and 2.598(8)–2.621(6) Å. The bridging bpm ligand is located on a center of symmetry (rotation from planarity is 0°) and the Eu···Eu distance is 6.856(1) Å.

Replacing both the CF_3 and C_4H_3E (E = O, S) moieties with C_6H_5 groups, Shim and co-workers synthesized and structurally characterized $[Eu(dbm)_3]_2(bpm) \cdot 2Et_2O$ (dbm = dibenzoylmethane) [25]. In this structure, the Eu^{III} sites are eight-coordinate with Eu–O and Eu–N averages distances of 2.343 Å and 2.677 Å. The Eu···Eu separation is 7.011 Å while the bridging bpm ligand is planar and centered about the inversion center.

The metrical details of compounds **1** and **2** also compare favorably with the Tb-containing complex, $[Tb(tta)_3]_2$bpm.EtOAc [26]. The reported Tb···Tb distance across the bridging bpm ligand is 6.7596(5) Å and the bpm ring rotation from planarity is 7.0(2)° (slightly larger than observed in the related structures).

3.2. Electronic and luminescence properties

The UV/Vis spectrum of toluene solutions of $[Eu(tfa)_3]_2$bpm and $[Eu(tta)_3]_2$bpm are dominated by intense broad absorptions associated with the tfa and tta ligands, with the bpm absorption appearing as a weak shoulder near 250 nm. The π–π^* transitions associated with both tfa and tta occur with a $\lambda_{max} = 340$ nm and are responsible for the "antenna" effect leading to the photoluminescence properties of these complexes. The mechanism of energy transfer leading to luminescence is illustrated in Fig. 3. After initial excitation into the ligand singlet excited state intersystem crossing to the ligand triplet state occurs.

This is followed by energy transfer from the ligand triplet state to the ^5D_J manifold of the Eu^{III} ion. All emissions originate from the $^5D_0$ state of the Eu^{III} ion to the ^7F_J manifold, with the $^5D_0 \rightarrow {}^7F_2$ transition being the most intense. This is attributed to the transition becoming allowed due to ligand field effects [29–31]. Due to the symmetry associated with the Eu-bpm-Eu center it is difficult to determine if there is electronic communication between the metal ions via the bpm bridging ligand. The large energy difference between the excited state orbitals associated with the bridging ligand and the metal ions, Fig. 3, suggests that bpm serves only to hold the two Eu(β-diketonate)$_3$ groups together.

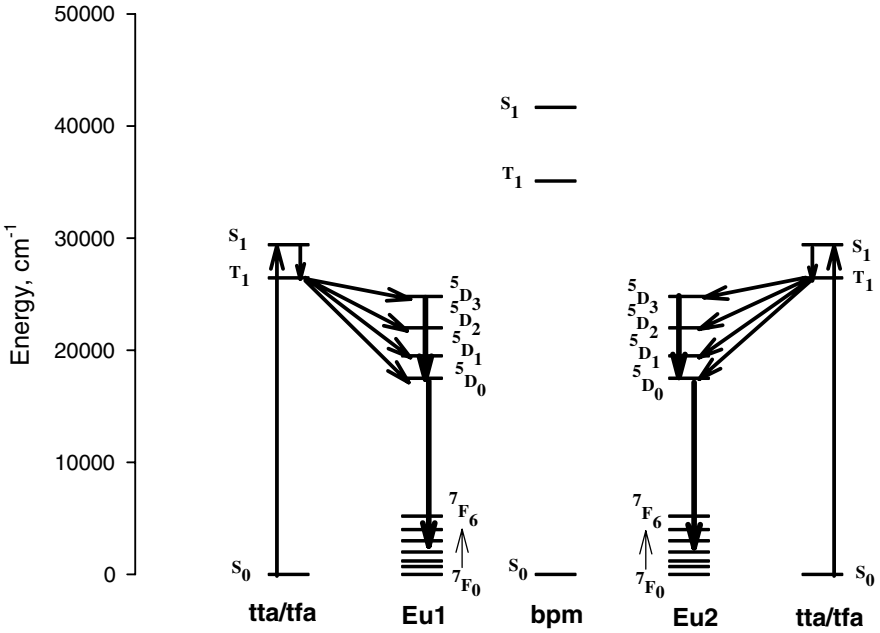


Fig. 3. Schematic energy level diagram and energy transfer process for europium homobimetallic complexes.

The emission spectra of the two europium bimetallic complexes **1** and **2** are very similar, as illustrated in Fig. 4.

The toluene solutions of $[Eu(tta)_3]_2bpm$ (dashed line) and $[Eu(tfa)_3]_2bpm$ (solid line) emit in the visible region when irradiated at 340 nm. The greater intensity observed for $[Eu(tta)_3]_2bpm$ suggests more efficient energy transfer from the triplet state of tta to the europium ^5D_J manifold compared to energy transfer of the triplet state of tfa to the europium ^5D_J manifold. The most intense transition in either complex is $^5D_0 \rightarrow {}^7F_2$ transition at 614 nm due to ligand field effects and the polarizability of the ligand environment around the metal [30].

3.3. Temperature dependent luminescence properties

The use of lanthanide complexes and particularly europium complexes as temperature probes results from the complexes temperature sensitivity. Deactivation of the $^5D_1$ and $^5D_0$ states through thermal quenching is attributed to vibrational interactions with their environment [30]. The

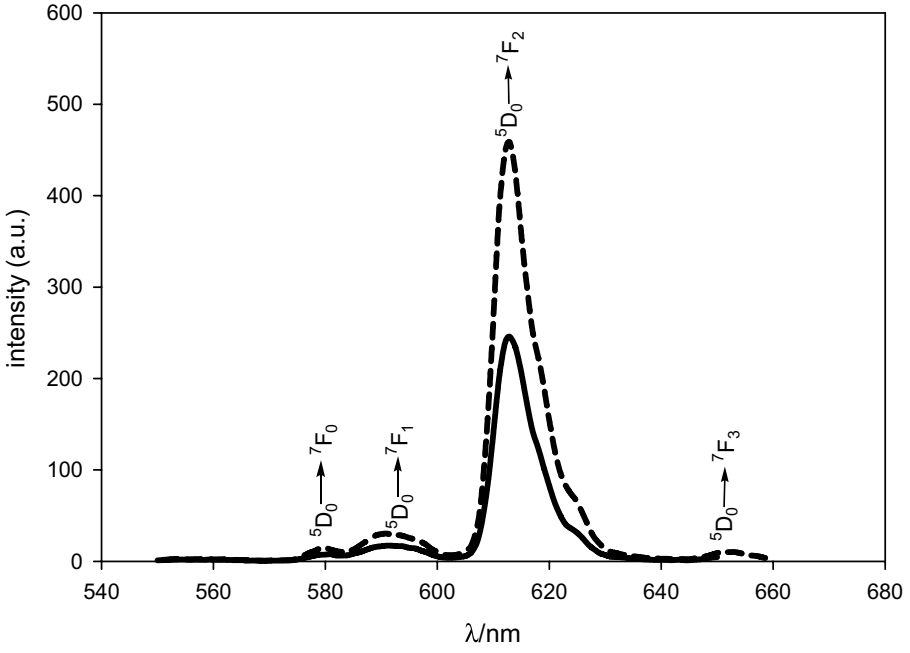


Fig. 4. Emission spectrum of toluene solutions of $[Eu(tta)_3]_2bpm$, dashed line, and $[Eu(tfa)_3]_2bpm$, solid line, at 5 °C. Excitation wavelength was 340 nm.

effect of temperature on the intensity of the emission spectrum and on the lifetime of the emission for $[Eu(tta)_3]_2bpm$ and $[Eu(tfa)_3]_2bpm$ was studied in toluene solutions in the temperature range 5 °C to 55 °C. For comparison similar measurements were made with the monometallic analogs $Eu(tta)_3bpy$ and $Eu(tfa)_3bpy$, where bpy = 2,2′-bipyridine. Fig. 5 illustrates the excitation and emission spectra for toluene solutions of $[Eu(tta)_3]_2bpm$ (Fig. 5A) and $[Eu(tfa)_3]_2bpm$ (Fig. 5B) in the temperature range 5 °C to 55 °C.

As expected the intensity of the $^5D_0 \rightarrow {}^7F_2$ transition at 614 nm decreases with increasing temperature. This is consistent with thermal deactivation of the $^5D_0$ and $^5D_1$ states of the europium [30]. The effect of temperature on the intensity of the 614 nm emission line is similar for the bimetallic ($[Eu(tta)_3]_2bpm$, $[Eu(tfa)_3]_2bpm$) and monometallic ($Eu(tta)_3bpy$, $Eu(tfa)_3bpy$) complexes studied suggesting a similar mechanism of thermal quenching. The monometallic complexes display similar intensity at the 614 nm emission for a given temperature. Intensity of the 614 nm emission for the bimetallic $[Eu(tta)_3]_2bpm$ is similar to that observed for the monometallics but is twice that observed for the tfa bimetallic complex, $[Eu(tfa)_3]_2bpm$.

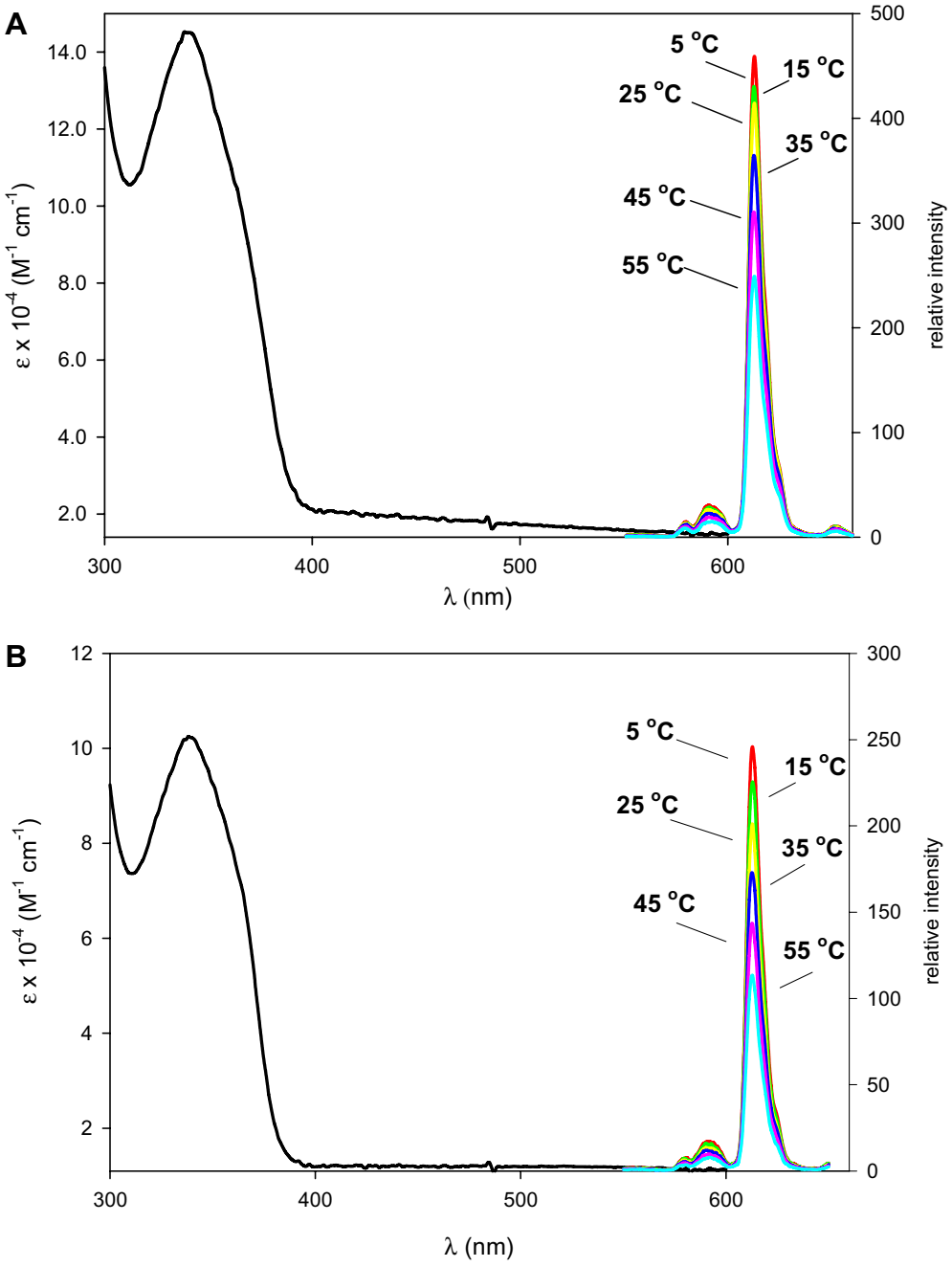


Fig. 5. Absorption and emission spectra in the temperature range 5 °C to 55 °C for toluene solutions of (A) $[Eu(tta)_3]_2bpm$ and (B) $[Eu(tfa)_3]_2bpm$.

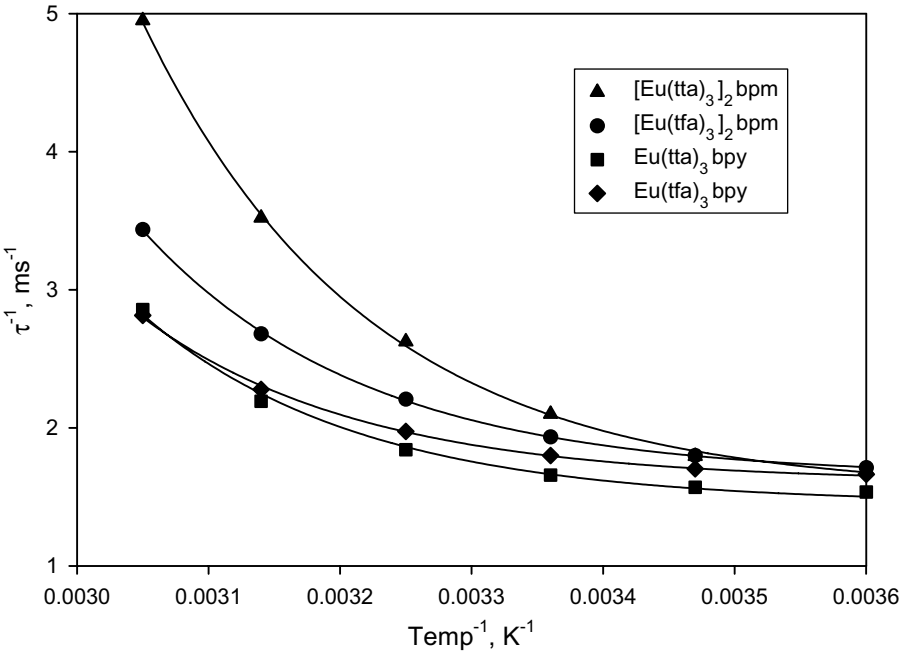


Fig. 6. Arrhenius plots of temperature data.

Table 3
Parameters used to fit the data in Fig. 6 to Eq. (1)

	$[Eu(tta)_3]_2bpm$	$[Eu(tfa)_3]_2bpm$	$Eu(tta)_3bpy$	$Eu(tfa)_3bpy$
k_0 (s^{-1})	1543	1646	1452	1609
k_1 (s^{-1})	2.02×10^{11}	1.10×10^{11}	1.26×10^{11}	9.36×10^{10}
ΔE (kJ mol^{-1})	48.8	48.9	50.0	49.6

Luminescent decay curves of the bimetallic and monometallic europium complexes in toluene fit to a monoexponential. The temperature dependence of the decay times for $[Eu(tta)_3]_2bpm$ (solid triangle), $[Eu(tfa)_3]_2bpm$ (solid circle), $Eu(tta)_3bpy$ (solid square) and $Eu(tfa)_3bpy$ (solid diamond) are illustrated in Fig. 6. These curves can be fit to an Arrhenius-type equation with correlation coefficients $r^2 > 0.9995$ [29–32]

$$1/\tau = k_0 + k_1 \exp(-\Delta E/RT) \quad (1)$$

where k_0 is the temperature independent decay rate, k_1 is the pre-exponential factor, ΔE is the energy gap between the $^5D_0$ state and high energy states and R is the gas constant. Table 3 gives the values for the parameters in equation one used to fit the data for the four europium complexes.

These values are consistent with those observed for $Eu(tta)_3L$, $Eu(fod)_3L$, $Eu(nta)_3L$; where L is a dipyrazolyltriazine derivative, fod is 6,6,7,7,8,8,8-heptafluoro-2,2-dimethyl-3,4-octanedionate and nta is 1-(2-naphthyl)-butane-1,3-dione [7]. From this data it does not appear that the luminescent temperature effects can be related to structural differences in these complexes.

4. Conclusions

The luminescent properties of two new europium homobimetallic complexes, $[Eu(tfa)_3]_2bpm$ (**1**) and $[Eu(tta)_3]_2bpm$ (**2**), and the dependence of the luminescence on temperature were presented. Structural analysis of compound **1**, as an ethyl acetate solvate, was presented for the first time while structural analysis of complex **2**, as a THF solvate, had been previously described in a triclinic space group while our analysis of solvent-free **2** indicates a monoclinic space group. Emission studies of compounds **1** and **2** in toluene solutions are typical of europium complexes containing β-diketonate "antenna" ligands. The intensity of the emission spectra for compounds **1** and **2** is inversely related to temperature. Lifetime measurements in the temperature range of 5 °C to 55 °C fit a monoexponential. Comparison of the luminescence properties and lifetimes of the homodinuclear compounds to their monometallic analogs are very similar. This suggests that there is little electronic communication via the bridging bpm ligand and the two Eu^{III} ions allowing the bimetallic compounds to behave as monometallic compounds in solution. Further studies of heterobimetallic lanthanide complexes bridged by bpm are needed to substantiate this claim.

Acknowledgements

Crystallographic data were collected at Beamline 11.3.1 at the Advanced Light Source (ALS) through the SCrALS (Service Crystallography at Advanced Light Source) program. The ALS is supported by the US Department of Energy, Office of Energy Sciences Materials Sciences Division, under contract DE-AC03-76SF00098 at Lawrence Berkeley National Laboratory.

Appendix A. Supplementary material

CCDC 653085 and 653086 contain the supplementary crystallographic data for compounds **1** and **2**. These data can be obtained free of charge via http://www.ccdc.cam.ac.uk/conts/retrieving.html, or from the Cambridge Crystallographic Data Centre, 12 Union Road, Cambridge CB2 1EZ, UK; fax: (+44) 1223-336-033; or e-mail: deposit@ccdc.cam.ac.uk. Supplementary data associated with this article can be found, in the online version, at doi:10.1016/j.poly.2007.12.001.

References

[1] H.V. Martinus, R.H. Woudenberg, P.G. Emmerink, R. vanGassel, J.H. Hofstraat, J.W. Vernhoeven, Angew. Chem. Int. Ed. 39 (2000) 4542.
[2] X.L. Ji, B. Li, S. Jiang, D. Dong, H.J. Zhang, X.B. Jing, B.Z. Jiang, J. Non-Crystallogr. Solids 52 (2000) 275.
[3] R.F. deFarias, S. Alves Jr., M.F. Belian, G.F. deSa, Opt. Mater. 18 (2002) 431.
[4] J. Sokolnicki, R. Wiglusz, S. Radzki, A. Graczyk, J. Legendziewicz, Opt. Mater. 26 (2004) 199.
[5] A.K. Kewell, G.T. Reed, F. Namavar, Sens. Actuators, Part A 65 (1998) 160.
[6] P.C. Russell, R. Haber, G.R. Jones, W. McGrory, Sens. Actuators, Part A 76 (1999) 231.
[7] S.M. Borisov, O.S. Wolfbeis, Anal. Chem. 78 (2006) 5094.
[8] Y. Liu, G. Qian, Z. Wang, M. Wang, Appl. Phys. Lett. 86 (2005) 071907/1.
[9] B. Isabelle, Handbook Phys. Chem. Rare Earths 33 (2003) 465.
[10] F.S. Richardson, Chem. Rev. 82 (1982) 541.
[11] S. Tamburini, P.A. Vigato, M. Gatos, L. Bertolo, U. Casellato, Inorg. Chim. Acta 359 (2006) 183.
[12] V. Patroniak, A.R. Sefankiewicz, J.-M. Lehn, M. Kubicki, M. Hoffmann, Eur. J. Inorg. Chem. 1 (2006) 144.
[13] M. Volpe, G. Bombieri, N. Marchini, J. Alloys Compd. 408-412 (2006) 1046.
[14] R. Sultan, K. Gadamsetti, S. Swavey, Inorg. Chim. Acta 359 (2006) 1233.
[15] J. Rudovsky, M. Botta, P. Hermann, A. Koridze, S. Aime, Dalton Trans. 19 (2006) 2323.
[16] Y. Li, F.-K. Zheng, X. Liu, W.-Q. Zou, G.-C. Guo, C.-Z. Lu, J.-S. Huang, Inorg. Chem. 45 (2006) 6308.
[17] M. Hunziker, A. Ludi, J. Am. Chem. Soc. 99 (1977) 7370.
[18] D.P. Rillema, K.B. Mack, Inorg. Chem. 21 (1982) 3849.
[19] D.P. Rillema, G. Allen, T.J. Meyer, D. Conrad, Inorg. Chem. 22 (1983) 1617.
[20] R.A. Pavinato, J.A. Walk, M.E. McGuire, Inorg. Chem. 32 (1993) 4982.
[21] S. Swavey, Z. Fang, K.J. Brewer, Inorg. Chem. 41 (2002) 2598.
[22] V. Balzani, S. Campagna, G. Denti, A. Juris, S. Seroni, Chem. Rev. 96 (1996) 759.
[23] N.M. Shavaleev, G. Accors, D. Virgili, Z.R. Bell, T. Lazarides, G. Calogero, N. Armaroli, M.D. Ward, Inorg. Chem. 44 (2005) 61.
[24] J.A. Fernandes, R.A. SaFerreira, M. Pillinger, P. Ribeiro-Claro, I.S. Gonclaves, J. Luminesc. 113 (2005) 50.
[25] H. Jang, C.-H. Shin, B.-J. Jung, D. Kim, H.-K. Shim, Y. Do, Eur. J. Inorg. Chem. (2006) 718.
[26] K. Kirschbaum, A. Fratini, S. Swavey, Acta Crystallogr. C 62 (2006) m186.
[27] D. D'Cunha, D. Collins, G. Richards, G.S. Vincent, S. Swavey, Inorg. Chem. Commun. 9 (2006) 979.
[28] A. Fratini, S. Swavey, Inorg. Chem. Commun. 10 (2007) 636.
[29] G.A. Crosby, Mol. Crystals 1 (1966) 37.
[30] G.E. Khalil, K. Lau, G.D. Phelan, B. Carlson, M. Gouterman, J.B. Callis, L.R. Dalton, Rev. Sci. Instrum. 75 (2004) 192.
[31] S. Biju, D.B. Ambili Raj, M.L.P. Reddy, B.M. Kariuki, Inorg. Chem. 45 (2006) 10651.
[32] L.M. Coyle, M. Gouterman, Sens. Actuators B 61 (1999) 92.

2,4-hexadiene and L6 = 2,5-bis(4-pyridyl)-3,4-diaza-2,4-hexadiene (Fig. 1)}.

In this series of compounds six nitrogen donor-based ligands have been used. These compounds have been selected as they are capable to act as bridging ligands and thus may form polymeric structures. We will show that subtle changes in the use of conformationally flexible ligands as spacers in the design and construction of coordination polymers may lead to new polymeric networks.

As the counter-ion in these Hg(II) coordination polymers I^- anions have been used, which may also be able to act as bridges between the metal centers. With two types of bridging ligands in one coordination system we anticipated that the complexes will be able to form 1D, 2D or 3D coordination polymers either bridged via the iodide or via the nitrogen donor-based ligands, or via both. With such a multifariousness of possibilities it is a challenge to accurately predict the nature of the compounds one will obtain. Despite these challenges the rational construction of new structurally defined metal–organic frameworks using bridging anions as well as bridging nitrogen donor-based ligands promises to be a versatile approach towards the construction of metal coordination polymers of heavy metal ions.

Recent investigations have addressed the use of the ligands L1–L6 [37–43] for the preparation of coordination polymers with other metal ions [37–43]. These studies have demonstrated that the long conjugated rigid ligands L1–L6 are capable of coordinating transition metal centers with both terminal pyridyl and diaza nitrogen donors and generate novel coordination polymers. The relative orientations of the nitrogen donors on the pyridyl rings towards the zig-zag XC=N–N=CX–, X = H or CH_3, and spacer resulted in unusual building blocks, leading to the construction of polymeric motifs that have not been achieved using normal rigid bidentate organic ligands. The soft acid Hg(II) ion, on the other hand, has a versatile coordination chemistry and can serve to link bridging ligands to form polymeric compounds with novel coordination patterns with the ligands L1–L6.

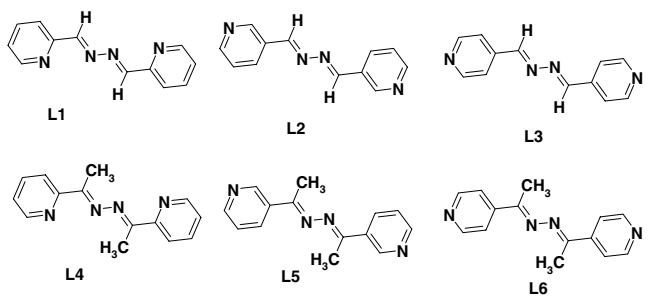


Fig. 1. Organic nitrogen donor-based ligands used in the construction of mercury(II) iodide coordination polymers.

2. Experimental

2.1. Materials and physical techniques

With the exception of the ligands L1–L6 which were prepared according to the literature procedures [44–46], all reagents and solvents for the synthesis and analysis were commercially available and used as received. IR spectra were recorded using Perkin–Elmer 597 and Nicolet 510P spectrophotometers. Microanalyses were carried out using a Heraeus CHN–O– Rapid analyzer. Melting points were measured on an Electrothermal 9100 apparatus and are uncorrected. The thermal behaviour was measured with an PL-STA 1500 apparatus. The luminescent properties were investigated with a Shimadzu RF-5000 spectrofluorophotometer, but the six compounds reported here have not shown luminescent properties.

Crystallographic measurements were made at 293 K for compounds **1**–**6** and 273 K for compound **3** using a Bruker APEX area-detector diffractometer. The intensity data were collected using graphite monochromataed Mo Kα radiation. The structures were solved by direct methods and refined by full-matrix least-squares techniques on F^2. Structure solution and refinement was accomplished using SIR97, SHELXL97 and WINGX [47,48]. The molecular structure plots were prepared using the ORTEPIII [49] and MERCURY [50]. Crystallographic data and details of the data collection and structure refinements are listed in Tables 1 and 2. Bond lengths (Å) and angles (°) for compounds **1**–**6** are reported in Tables 3 and 4. The observed anisotropic thermal parameters, the calculated structure factors, and full lists of bond distances, bond angles and torsion angles are given in the supplementary material.

2.2. Synthesis of $[Hg_2(L1)I_4]_n$ (1)

1,4-Bis(2-pyridyl)-2,3-diaza-1,3-butadiene (L1) (0.5 mmol, 0.105 g) and mercury(II) iodide (0.159 g, 0.5 mmol) were placed in main arm of the branched tube. Methanol was carefully added to fill the arms, the tube was sealed and the ligand-containing arm immersed in an oil bath at 60 °C while the other arm was kept at ambient temperature (Fig. S1). After 2–3 days, yellow crystals (d.p. = 225 °C), had deposited in the cooler arm which were isolated, filtered off, washed with acetone and ether and air dried (0.118 g, yield 85%). *Anal.* Calc. for $C_{12}H_{10}Hg_2I_4N_4$: C, 12.87; H, 0.90; N, 5.00. Found: C, 12.50; H, 0.80; N, 5.10%.

IR (cm^{-1}) bands: 491(w), 627(w), 765(m), 1001 (w), 1149(m), 1213(w), 1410(m), 1568(m), 1619(m), 3040(w).

2.3. Synthesis of $[Hg(L2)I_2]_n$ (2), $[Hg(L3)I_2]_n$ (3), $[Hg_2(L4)I_4]_n$ (4), $[Hg(L5)I_2]_n$ (5), $[Hg(L6)I_3](HL6)$ (6)

The compounds **2**–**6** were prepared using the same the method as for compound **1**.

Table 1
Crystal data and structure refinement $[Hg_2(L1)I_4]_n$ (**1**), $[Hg(L2)I_2]_n$ (**2**) and $[Hg(L3)I_2]_n$ (**3**)

Identification code	**1**	**2**	**3**
Empirical formula	$C_{12}H_{10}Hg_2I_4N_4$	$C_{12}H_8HgI_2N_4$	$C_{12}H_{10}HgI_2N_4$
Formula weight	1119.02	662.61	664.63
Temperature (K)	298(2)	293(2)	273(2)
Wavelength	0.71073	0.71073	0.71073
Crystal system	monoclinic	orthorhombic	monoclinic
Space group	$P2_1/c$	*Pnam*	$P2/c$
Unit cell dimensions			
a (Å)	7.5453(11)	8.5720(11)	8.1267(8)
b (Å)	7.4618(11)	11.8601(15)	6.6414(7)
c (Å)	18.556(3)	15.693(2)	16.3706(14)
α (°)	90	90.00	90.00
β (°)	100.914(2)	90.00	110.209(4)
γ (°)	90	90.00	90.00
Volume (Å^3)	1025.8(3)	1595.5(4)	829.17(14)
Z	2	4	2
D_{calc} (g cm^{-3})	3.623	2.759	2.662
Absorption coefficient (mm^{-1})	20.968	13.509	12.997
$F(000)$	964	1176	592
Crystal size (mm)	0.48 × 0.26 × 0.23	0.40 × 0.30 × 0.20	0.40 × 0.30 × 0.25
θ Range for data collection(°)	2.24–25.10	2.15–25.00	2.65–25.99
Index ranges	$-9 \leqslant h \leqslant 7$, $-7 \leqslant k \leqslant 8$, $-22 \leqslant l \leqslant 20$	$-10 \leqslant h \leqslant 10$, $-14 \leqslant k \leqslant 14$, $-18 \leqslant l \leqslant 18$	$-10 \leqslant h \leqslant 9$, $-4 \leqslant k \leqslant 8$, $-20 \leqslant l \leqslant 20$
Reflections collected	4912	10807	4348
Independent reflections	1796	1462	1617
Absorption correction	multi-scan	multi-scan	multi-scan
Maximum and minimum transmission	0.82 and 0.73	0.1731 and 0.0745	0.80 and 0.70
Refinement method	full-matrix least-squares on F^2	full-matrix least-squares on F^2	full-matrix least-squares on F^2
Data/restraints/parameters	1796/0/100	1462/0/92	1617/0/87
Final R indices [$I > 2\sigma(I)$]	$R_1 = 0.0549$ $wR_2 = 0.1341$	$R_1 = 0.0296$ $wR_2 = 0.1287$	$R_1 = 0.0277$ $wR_2 = 0.0613$
R indices (all data)	$R_1 = 0.0589$ $wR_2 = 0.1376$	$R_1 = 0.0321$ $wR_2 = 0.1361$	$R_1 = 0.0318$ $wR_2 = 0.0629$
Largest difference in peak and hole (e Å^{-3})	3.233 and −2.817	1.224 and −1.457	0.811 and −0.856

Compound 2: Reactant materials: 1,4-bis(3-pyridyl)-2,3-diaza-1,3-butadiene (L2), mercury(II) iodide.

Product: Yellow crystals, d.p. 180 °C. Yield: 0.130 g, 79%. *Anal.* Calc. for $C_{12}H_8HgI_2N_4$: C, 21.73; H, 1.21; N, 8.45. Found: C, 21.60; H, 1.15; N, 8.40%.

IR (cm^{-1}) bands: 494(w), 629(m), 688(vs), 801 (m), 964(m), 1189(s), 1304(s), 1408(s), 1617(vs), 3030(w).

Compound 3: Reactant materials: 1,4-bis(4-pyridyl)-2,3-diaza-1,3-butadiene (L3), mercury(II) iodide.

Product: Yellow crystals, d.p. 246–248 °C. Yield: 0.128 g, 68%. *Anal.* Calc. for $C_{12}H_{10}HgI_2N_4$: C, 21.67; H, 1.51; N, 8.43. Found: C, 21.50; H, 1.58; N, 8.40%.

IR (cm^{-1}) bands: 450(m), 680(s), 808(s), 999 (m), 1054(m), 1236 (m), 1407(s), 1541(s), 1592(vs), 3025(w).

Compound 4: Reactant materials: 2,5-bis(2-pyridyl)-3,4-diaza-2,4-hexadiene (L4), mercury(II) iodide.

Product: Yellow crystals, d.p. 203 °C. Yield: 0.142 g, 58%. *Anal.* Calc. for $C_7H_7HgI_2N_2$: C, 14.65; H, 1.22; N, 4.88. Found: C, 14.60; H, 1.20; N, 4.60%.

IR (cm^{-1}) bands: 555(w), 626(w), 768(s), 1002 (m), 1152(w), 1247(w), 1316(m), 1363(m), 1574(m), 2960(w), 3035(w).

Compound 5: Reactant materials: 2,5-bis(3-pyridyl)-3,4-diaza-2,4-hexadiene (L5), mercury(II) iodide.

Product: Yellow crystals, d.p. 231 °C. Yield: 0.156 g, 65%. *Anal.* Calc. for $C_{14}H_{14}HgI_2N_4$: C, 28.30; H, 2.02; N, 8. 08. Found: C, 28.20; H, 2.15; N, 8.10%.

IR (cm^{-1}) bands: 566(w), 644(m), 689(s), 802 (s), 1036(s), 1113(w), 1192(s), 1357(s), 1601(vs), 2970(w), 3030(w).

Compound 6: Reactant materials: 2,5-bis(4-pyridyl)-3,4-diaza-2,4-hexadiene (L6), mercury(II) iodide.

Product: Yellow crystals, d.p. 220 °C. Yield: 0.156 g, 38%. *Anal.* Calc. for $C_{14}H_{14}HgI_3N_4C_{14}$ $H_{15}N_4$: C, 18.51; H, 1.31; N, 5.29. Found: C, 18.40; H, 1.23; N, 5.44%.

IR (cm^{-1}) selected bands: 472(w), 594(s), 665 (m), 669(m), 733 (m), 821(vs), 1017(m), 1055(m), 1295(m), 1364(s), 1404(s), 1591(vs), 2960(w),.3020(w), 3290(b).

3. Results and discussion

3.1. Synthesis and spectroscopy

Several different synthetic approaches have been offered for the preparation of coordination polymers. Some of

Table 2
Crystal data and structure refinement for $[Hg_2(L4)I_4]_n$ (**4**), $[Hg(L5)I_2]_n$ (**5**) and $[Hg(L6)I_3](HL6)$ (**6**)

Identification code	**4**	**5**	**6**
Empirical formula	$C_7H_7HgI_2N_2$	$C_{14}H_{14}HgI_2N_4$	$C_{28}H_{29}HgI_3N_8$
Formula weight	573.54	692.68	1058.88
Temperature (K)	298(2)	298(2)	298(2)
Wavelength	0.71073	0.71073	0.71073
Crystal system	monoclinic	orthorhombic	triclinic
Space group	*C*2/*c*	*Pnma*	$P\bar{1}$
Unit cell dimensions			
a (Å)	22.352(2)	8.1957(11)	9.6680(13)
b (Å)	7.9064(7)	15.694(2)	12.5730(16)
c (Å)	13.5045(12)	13.6618(18)	15.160(2)
α (°)	90.00	90.00	94.841(2)
β (°)	107.921(2)	90.00	101.324(2)
γ (°)	90.00	90.00	104.902(2)
Volume (Å^3)	2270.8(4)	1757.2(4)	1728.4(4)
Z	8	4	2
D_{calc} (g cm^{-3})	3.355	2.618	2.035
Absorption coefficient (mm^{-1})	18.949	12.271	7.161
F(000)	1992	1248	984
Crystal size (mm)	0.32 × 0.21 × 0.16	0.28 × 0.23 × 0.18	0.44 × 0.21 × 0.18
θ Range for data collection (°)	2.74–24.96	2.61–24.78	2.33–24.94
Index ranges	$-26 \leqslant h \leqslant 22$, $-9 \leqslant k \leqslant 9$, $-16 \leqslant l \leqslant 14$	$-8 \leqslant h \leqslant 9$, $-18 \leqslant k \leqslant 15$, $-15 \leqslant l \leqslant 16$	$-11 \leqslant h \leqslant 10$, $-14 \leqslant k \leqslant 12$, $-17 \leqslant l \leqslant 18$
Reflections collected	5826	8766	6003
Independent reflections	2042	1643	5062
Absorption correction	multi-scan	multi-scan	multi-scan
Maximum and minimum transmission	0.0505 and 0.0141	0.1203 and 0.0482	0.2789 and 0.1807
Refinement method	full-matrix least-squares on F^2	full-matrix least-squares on F^2	full-matrix least-squares on F^2
Data/restraints/parameters	2042/0/111	1643/0/101	6003/0/365
Final *R*indices [$I > 2\sigma(I)$]	$R_1 = 0.0268$ $wR_2 = 0.0615$	$R_1 = 0.0248$ $wR_2 = 0.0562$	$R_1 = 0.0318$ $wR_2 = 0.0740$
R indices (all data)	$R_1 = 0.0299$ $wR_2 = 0.0628$	$R_1 = 0.0271$ $wR_2 = 0.0571$	$R_1 = 0.0388$ $wR_2 = 0.0765$
Largest difference in peak and hole (e Å^{-3})	1.296 and −1.008	1.025 and −0.998	0.695 and −0.822

Table 3
Bond lengths (Å) and angles (°) for $[Hg_2(L1)I_4]_n$ (**1**), $[Hg(L2)I_2]_n$ (**2**) and $[Hg(L3)I_2]_n$ (**3**)

1		**2**		**3**	
Hg(1)–N(1)	2.386(11)	Hg(1)–N(1)	2.471(6)	Hg(1)–N(1)	2.473(4)
Hg(1)–I(1)	2.6418(11)	Hg(1)–N(1)	2.471(6)	Hg(1)–I(1)	2.6395(4)
Hg(1)–I(2)	2.6603(11)	Hg(1)–I(1)	2.6342(8)	N(1)–Hg(1)–N(1)	84.2(2)
Hg(1)–N(2)	2.676(10)	Hg(1)–I2	2.6476(9)	N(1)–Hg(1)– I(1)	98.27(10)
N(1)–Hg(1)–I(1)	129.0(3)	N(1)–Hg(1)–N(1)	85.0(3)	N(1)–Hg(1)– I(1)	105.24(10)
N(1)–Hg(1)–I(2)	96.9(3)	N(1)–Hg(1)–I(1)	102.74(15)	N(1)–Hg(1)– I(1)	105.24(10)
I(1)–Hg(1)–I(2)	133.74(4)	N(1)–Hg(1)–I(1)	102.74(15)	N(1)–Hg(1)– I(1)	98.27(10)
N(1)–Hg(1)–N(2)	64.9(4)	N(1)–Hg(1)–I(2)	100.53(14)	I(1)–Hg(1)– I(1)	148.17(2)
I(1)–Hg(1)–N(2)	93.6(2)	N(1)–Hg(1)–I(2)	100.53(14)		
I(2)–Hg(1)–N(2)	114.1(2)	I(1)–Hg(1)–I(2)	148.25(3)		

them are (1) slow diffusion of the reactants into a polymeric matrix, (2) diffusion from the gas phase, (3) evaporation of the solvent at ambient or reduced temperatures, (4) precipitation or recrystallisation from a mixture of solvents, (5) temperature controlled cooling and (6) hydrothermal synthesis. In this paper, we use another simple method for the construction of multi-dimensional heavy metal ion coordination polymers, the branched tube method [51] (Fig. S1). This method was employed for the synthesis and preparation of large single crystals suitable for single crystal X-ray diffraction for all six new compounds, $[Hg_2(L1)I_4]_n$ (**1**), $[Hg(L2)I_2]_n$ (**2**), $[Hg(L3)I_2]_n$ (**3**), $[Hg_2(L4)I_4]_n$ (**4**), $[Hg(L5)I_2]_n$ (**5**), $[Hg(L6)I_3](HL6)$ (**6**) {L1 = 1,4-bis(2-pyridyl)-2,3-diaza-1,3-butadiene, L2 = 1,4-bis(3-pyridyl)-2,3-diaza-1,3-butadiene, L3 = 1,4-bis(4-pyridyl)-2,3-diaza-1,3-butadiene, L4 = 2,5-bis(2-pyri-

Table 4
Bond lengths (Å) and angles (°) for $[Hg_2(L4)I_4]_n$ (**4**), $[Hg(L5)I_2]_n$ (**5**) and $[Hg(L6)I_3](HL6)$ (**6**)

4		**5**		**6**	
Hg(1)–N(1)	2.437(5)	Hg(1)–N(1)	2.451(4)	Hg(1)–N(1)	2.414(4)
Hg(1)–N(2)	2.480(5)	Hg(1)–N(1)	2.451(4)	Hg(1)–I(1)	2.6913(5)
Hg(1)–I(1)	2.6865(5)	Hg(1)–I(2)	2.6313(6)	Hg(1)–I(3)	2.7497(5)
Hg(1)–I(2)	2.6683(5)	Hg(1)–I(1)	2.6554(7)	Hg(1)–I(2)	2.7561(5)
N(1)–Hg(1)–N(2)	65.56(16)	N(1)–Hg(1)–N(1)	90.61(18)	N(1)–Hg(1)–I(1)	100.58(11)
N(1)–Hg(1)–I(2)	95.94(13)	N(1)–Hg(1)–I(2)	104.51(9)	N(1)–Hg(1)–I(3)	103.72(11)
N(2)–Hg(1)–I(2)	119.83(11)	N(1)–Hg(1)–I(2)	104.51(9)	I(1)–Hg(1)–I(3)	117.131(17)
N(1)–Hg(1)–I(1)	104.58(13)	N(1)–Hg(1)–I(1)	99.37(9)	N(1)–Hg(1)–I(2)	98.92(11)
N(2)–Hg(1)–I(1)	106.62(11)	N(1)–Hg(1)–I(1)	99.37(9)	I(1)–Hg(1)–I(2)	124.558(17)
I(2)–Hg(1)–I(1)	133.524(18)	I(2)–Hg(1)–I(1)	145.74(2)	I(3)–Hg(1)–I(2)	107.530(17)

dyl)-3,4-diaza-2,4-hexadiene, L5 = 2,5-bis(3-pyridyl)-3,4-diaza-2,4-hexadiene and L6 = 2,5-bis(4-pyridyl)-3,4-diaza-2,4-hexadiene}. In preparation of all six new compounds the ratio of metal to ligand was same, as 1:1, but the resulted compounds had the different stoichiometry, M_2L in compounds **1** and **4**, ML in the compounds **2**, **3**, **5** and [ML][HL] in the compound **6**. The relatively weak absorption bands around 3025–3035 cm^{-1} in the IR spectra are due to the C–H modes involving the aromatic ring hydrogen atoms. In the compound **4**–**6** the relatively weak absorption bands around 2940–2960 cm^{-1} in the IR spectra are assigned to the C–H modes of groups of ligands L4-L6. The broad absorption band at 3290 cm^{-1} is assigned to the ν(–NH) modes of HL6 component of compound **6**. The absorption bands with variable intensity in the frequency range 1404–1600 cm^{-1} correspond to vibrations of the pyridyl rings.

3.2. Structure descriptions

3.2.1. $[Hg_2(L1)I_4]_n$ (**1**) and $[Hg_2(L_4)I_4]_n$ (**4**)

Single crystal X-ray analysis reveals that the complexes $[Hg_2(L1)I_4]_n$ (**1**) and $[Hg_2(L4)I_4]_n$ (**4**) (Tables 1–3) crystallize in the monoclinic space groups $P2_1/c$ and $C2/c$, respectively. The crystal structures of **1** and **4** consist of two- and one-dimensional polymers (Figs. 2 and 3). In compounds **1** and **4** the ligands L1 and L4 are chelating with each one nitrogen atom of the pyridyl and diaza groups on one side of the molecule coordinating to a mercury(II) ion. The ligand is located on a crystallographic inversion center, thus forming I_2Hg–(L)– HgI_2 moieties. Of the I^- anions one acts as a monodentate ligand with an Hg–I bond length of 2.6418(11) and 2.6683(5) Å in the compounds **1** and **4**, respectively, whereas the other forms a full halogen bridge to a mercury atom of an adjacent I_2HgL moiety. In the compound **1** two I^- anions bridge between three different Hg atoms, thus building Hg–μI–Hg–μI–Hg bridged two-dimensional polymer as shown in Fig. 3a. In the compound **4** two I^- anions bridge between two different Hg atoms, thus building doubly Hg–$(\mu I)_2$–Hg and the Hg_2I_2 rhombs bridged one-dimensional chains as shown in Fig. 3b. The coordination number in compounds **1** and **4** is five and the geometry can be regarded as a distorted tetragonal pyramid

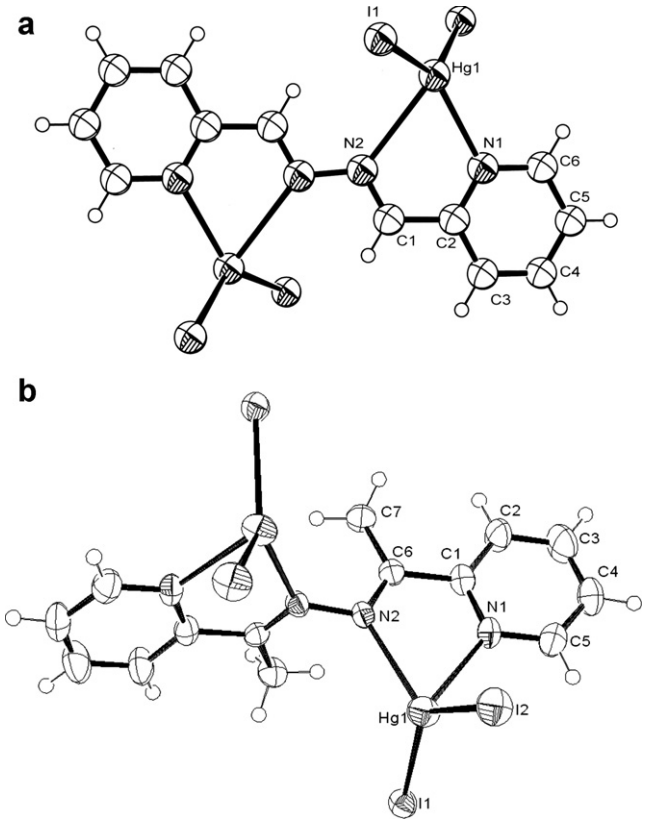


Fig. 2. X-ray crystal structure showing the chelating and bridging coordination of ligands L1 and L4 (a) in compound **1** and (b) in compound **4** (50% thermal displacement ellipsoids).

with two pyridyl nitrogen and two bridging I^- anions in the *basal* positions and one unbridging iodide in the *apical* position. The Hg···Hg distances within the I_2Hg–(L1)–$HgI_2$and I_2Hg–(L4)–HgI_2moieties are 6.372(1) and 5.052(1) Å, those bridged by the I^- anions are 5.039(3) and 4.518(3) Å in the compounds **1** and **4**, respectively. It is interesting that the 2D coordination polymer in compound **1** was changed to 1D one in compound **4** by replacing of methyn hydrogen atoms of ligand L1 with methyl groups in the ligand L4. The main difference of two structure due to the bridging mode of one of I^- anions, as Hg–μI–Hg–μI–Hg in compound **1** and as Hg–$(\mu I)_2$–Hg in compound **4**. However, it seems that the steric effects of methyl groups in the ligand L4 have an effect on

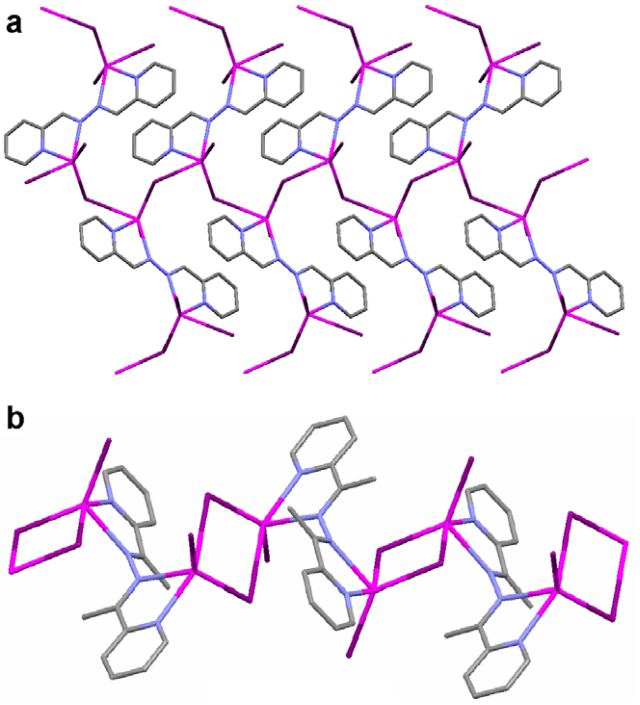


Fig. 3. Showing the 2D and 1D networks (a) in compound **1** and (b) in compound **4**.

the kind of bridging mode of I atoms in the mercury(II) coordination polymers.

3.3. $[Hg(L2)I_2]_n$ (**2**), $[Hg(L3)I_2]_n$ (**3**) and $[Hg(L5)I_2]_n$ (**5**)

Single X-ray crystal analysis reveals that $[Hg(L2)I_2]_n$ (**2**), $[Hg(L3)I_2]_n$ (**3**) and $[Hg(L5)I_2]_n$ (**5**) (Tables 2 and 4) crystallize in orthorhombic, monoclinic and orthorhombic space groups *Pnam*, *P*2/*c* and *Pnma*, respectively. The crystal structures of compounds **2**, **3** and **5** consists of one-dimensional polymeric units of $[Hg(\mu\text{-}L)I_2]$ (L = L2, L3 and L5) (Figs. 4 and 5). The terminal nitrogen atoms of the ligands L2, L3 and L5 are linked to two different mercury atoms, resulting in one-dimensional polymeric units in the solid state. The coordination environments of the Hg ions are distorted tetrahedral with the ligands L2, L3 and L5, thus generating angular nodes at the metal moieties resulting in 1D zig-zag chains. The Hg···Hg distances within the I_2Hg–(L2)–HgI_2, I_2Hg–(L3)–HgI_2 and I_2Hg–(L5)–HgI_2 moieties are 14.90(3), 16.24(2) and 14.90(2) Å in the compounds **2**, **3** and **5**, respectively. The N–Hg1–N and I–Hg1–I angles are 85.0(3) and 148.25(3)° in **2**, 84.2(2) and 148.17(2)° in **3** and 90.61(18) and 145.74(2)° in **5**. The N–Hg1–N angle in the compound **5** is larger than compounds **2** and **3**. This matter may also be related to the presence of methyl groups and increasing of steric effects.

3.4. $[Hg(L6)I_3](HL_6)$ (**6**)

Single X-ray crystal analysis shows that compound **6** (Tables 2 and 4) crystallizes in the triclinic space group $P\bar{1}$. In compounds **1**–**5** the nitrogen of ligands coordinate via both their pyridyl N atoms. In contrast to this the L6 ligand in **6** is linked with only one nitrogen atom of the pyridyl groups on one side of the molecule coordinating to a mercury(II) ion. Determination of the structure of $[Hg(L6)I_3](HL6)$ (**6**) showed the complex in the solid state (Fig. 6) to consists of mononuclear units. The molecular structure of the complex **6** consists of discrete $[Hg(L6)I_3]^-$ anionic and $HL6^+$ cationic compounds. The anionic complex is mononuclear and the mercury atoms are linked by three iodine and one nitrogen atoms and can be considered four-coordinate with I_3N donor atom arrays. The coordination about Hg is distorted tetrahedral and one nitrogen atom of L6 ligands is not coordinated to Hg atoms (Figs. 6 and 7) and thus the L6 acts as a less commonly unidentate ligand.

An interesting point is that the HL_6^+ cations were yielded by resulting in proton–ion transfer between molecular species in the solution. The $HL6^+$ cations are linked by hydrogen bonding (Fig. 7). The hydrogen atom of uncoordinated HL_6^+ cotions are involved in hydrogen bonding, acting as hydrogen-bond donors with N atoms from HL_6^+ cation. The hydrogen bond distances *d*(D–H), *d*(H···A), *d*(D···A), and angle ⟨(DHA)} for N(5)–H(5N)···N(8)[1 + *x*, 1 + *y*, *z*] are 0.86, 1.81, 2.666(6) Å, 177.1°, respectively. As shown in Fig. 6, the hydrogen bonding yields infinite chains of $HL6^+$ relatively perpendicular to mononuclear complex of $[Hg(L6)I_3]^-$ anionic. The other interesting feature complex is that, there are C–H···I interactions, the weak hydrogen bonding, between the hydrogen atoms of $HL6^+$ cations and iodine atoms belonging to adjacent anionic complexes, as shown in Fig. 7. The distance of C–H···I is 4.072 Å and the distances of I···H is 3.167 Å. Indeed, the structure consists an extensive hydrogen-bond network of N–H···N and C–H···I interactions. The reported C–H···I distances range is about 3.20 Å in recent reported species [52,53]. Thus, C–H···I appears to be yet another factor which can make varying contributions to the stability of this complex. Consequently, the two perpendicular anionic and cationic components forms into a two-dimensional network.

4. Thermogravimetric analysis

In order to examine the thermal stabilities of compounds **1**-**6**, thermal gravimetric (TG) and differential thermal analyses (DTA) were carried out between 30 and 700 °C. Compound **1** does not melt and is stable up to 225 °C. The TG curve of compound **1** indicates the decomposition of the compound takes place in one step at 225 °C with two endothermic effects at 250, 304 °C (Fig. S2). The TG curve of compound **2** indicates that this compound does not melt and is stable up to 180 °C at which temperature it begins to decompose. The compound **2** decomposes at 180–600 °C with three exothermic effects at 195, 505 and 610 °C (Fig. S3). The TG curve of compound **3** indicates the release of the L3 molecule to takes place at 175 °C

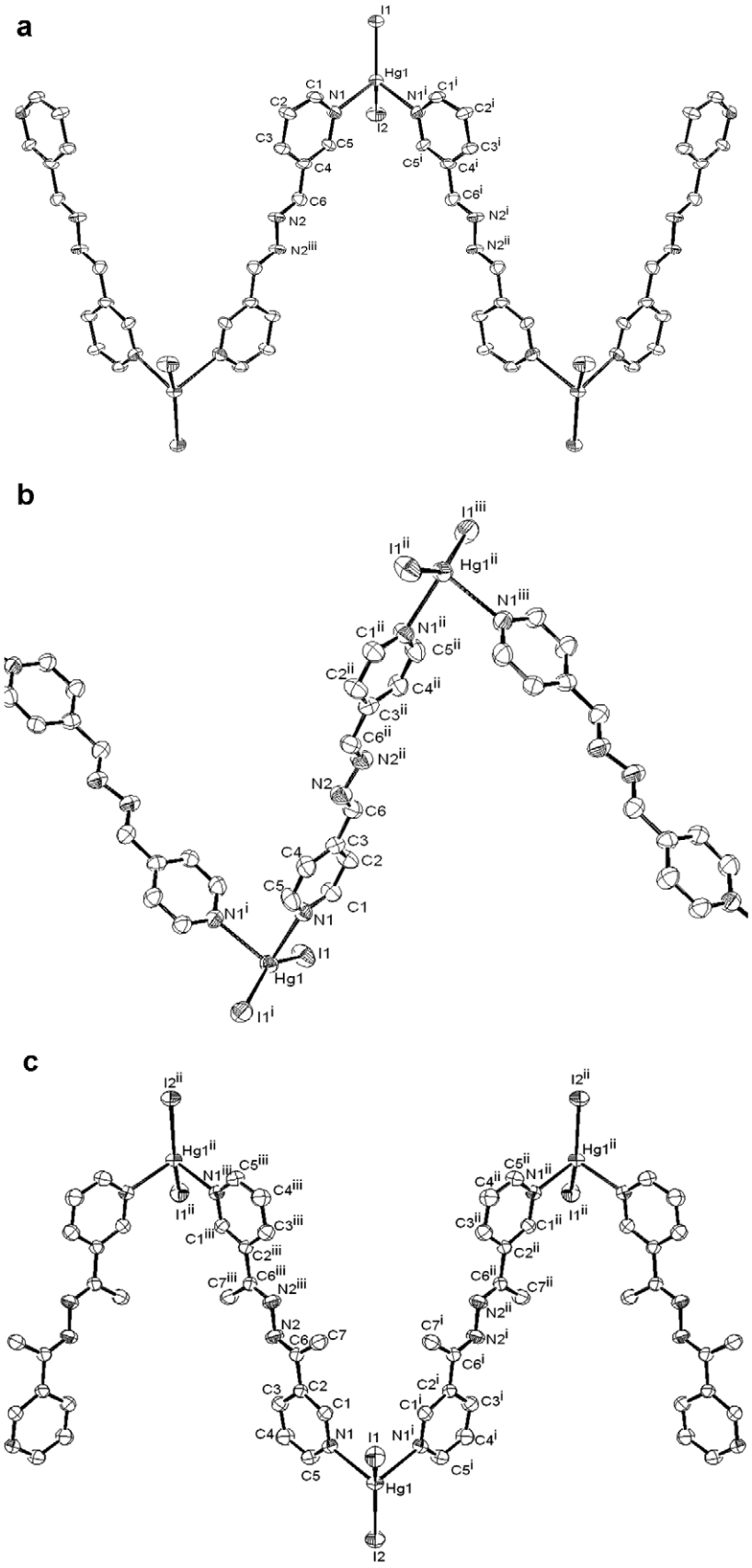


Fig. 4. X-ray crystal structure showing the one-dimensional zig-zag polymer of (a) in compound **2** (i: x, y, $-z+1/2$; ii: $-x$, $-y$, $z+1/2$; iii: $-x$, $-y$, $-z$), (b) in compound **3** (i: $-x$, y, $-z+1/2$; ii: $-x$, y, $-z+1/2$; iii: x, $-y$, $z+1/2$) and (c) in compound **5** (i: $-x$, $y+1/2$, $-z$; ii: x, $-y+1/2$, z; iii: $-x$, $-y$, $-z$). (50% thermal displacement ellipsoids).

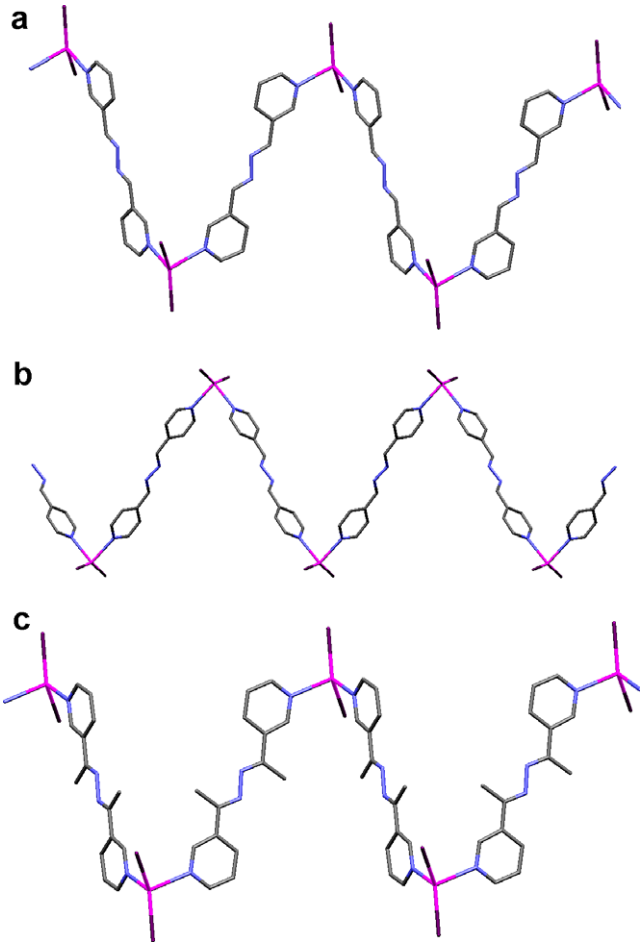


Fig. 5. 1D zig-zag network of the (a) in $[Hg(L2)I_2]_n$ (**2**), (b) in $[Hg(L3)I_2]_n$ (**3**) and (c) in $[Hg(L5)I_2]_n$ (**5**).

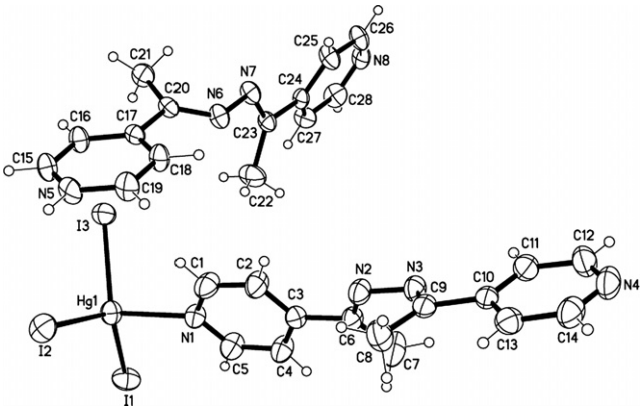


Fig. 6. X-ray crystal structure of compound **6** (50% thermal displacement ellipsoids).

(observed 31.40%, Calc. 31.59%). The solid residue formed at around 180 °C is suggested to be HgI_2. Only at even higher temperatures is it further decomposed, ultimately giving solid that appears to be HgO that under higher temperature is evaporated (Fig. S4). The TG curve of compound **4** indicates the decomposition of compound to

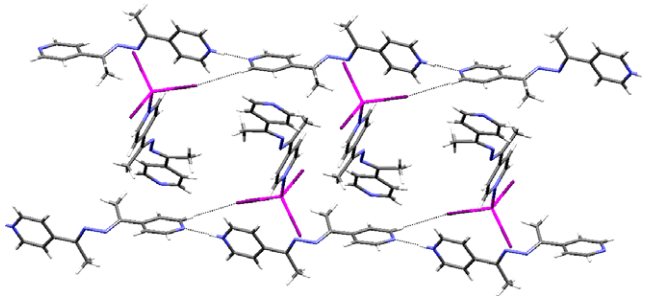


Fig. 7. Depiction of the N···HN hydrogen bonds and weak C–H···I interactions in compound **6**.

take place in the range between 195 and 535 °C with one endothermic effect at 210 and two exothermic effect at 215 and 530 °C (Fig. S5). Compound **5** does not melt and is stable up to 202 °C at which temperature it begins to decompose. The TG curve of compound **5** indicates the decomposition take place between 195 and 540 °C with one endothermic effect at 220 and two exothermic effect at 400 and 535 °C (Fig. S6). The TG curve of compound **6** indicates that the thermal behavior of this compound is different with compounds **1**–**5**. Compound **6** is stable up to 215 °C at which temperature the ligands L6 begins to be removed (Fig. S7). The solid residue formed at around 250 °C is suggested to be the L6-free compound, probability $HHgI_3$ (observed 43.70, Calc. 42.38%), that is stable to 550 °C. In summary, the thermogravimetric analysis shows that all six frameworks have a remarkably thermal stability that they do not melt and only decompose above temperatures of 175–225 °C.

5. Conclusions

Six new mercury(II) coordination polymers with L1 = 1,4-bis(2-pyridyl)-2,3-diaza-1,3-butadiene, L2 = 1,4-bis(3-pyridyl)-2,3-diaza-1,3-butadiene, L3 = 1,4-bis(4-pyridyl)-2,3-diaza-1,3-butadiene, L4 = 2,5-bis(2-pyridyl)-3,4-diaza-2,4-hexadiene, L5 = 2,5-bis(3-pyridyl)-3,4-diaza-2,4-hexadiene and L6 = 2,5-bis(4-pyridyl)-3,4-diaza-2,4-hexadiene, $[Hg_2(L1)I_4]_n$ (**1**), $[Hg(L2)I_2]_n$ (**2**), $[Hg(L3)I_2]_n$ (**3**), $[Hg_2(L4)I_4]_n$ (**4**), $[Hg(L5)I_2]_n$ (**5**), $[Hg(L6)I_3](HL6)$ (**6**), have been synthesized using a thermal gradient approach, the branched tube method. In the assembled processes of compounds **1**–**6**, all factors such as the metal, inorganic anions, solvent medium and metal/ligand ratio are kept constant and the only varied parameter is the ligand, **L1**-**L6** (1,4-bis(X-pyridyl)-2,3-diaza-1,3-butadiene for **1**–**3** and 1,4-bis(X-pyridyl)-2,3-diaza-1,3-hexadiene for **4**–**6**, X = 2, 3 and 4). The compounds are structurally diverse showing three main structural motifs: The coordination polymers obtained from HgI_2 with the ligands L2, L3 and L5 show one-dimensional zig-zag motifs and in these compounds the HgI_2 units are connected to each other by the ligands L2, L3 and L5 through the pyridyl nitrogen atoms. The L1 and L4 ligands in the compounds **1** and **4** act as both a chelating and bridging group by two nitrogen atoms of

the pyridyl groups and two nitrogen atoms of diaza group. The Hg–μI–Hg bridge augments the structures into a two- and one-dimensional coordination polymers, respectively. In the compound **6** the ligand L6 acts as a monodentate ligand, resulting form a discrete compound. This research not only shows the significant influences of the coordination modes and flexibilities of ligands L1–L3 on the structural topology but also illustrates the effect of the substituted methyl on the polymeric components L4–L6, which provides valuable instructions for the rational syntheses of coordination polymers with desired molecular architectures. Also this study demonstrates the capacity of mercury ions as soft lewis acids that are capable to form compounds with coordination numbers of four or five and consequently act in different forms of coordination polymers.

Acknowledgement

This work was supported by the Tarbiat Modares University.

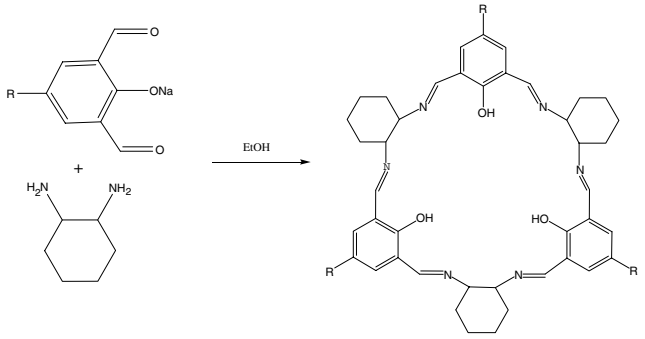
Appendix A. Supplementary material

CCDC 643432, 643426, 643431, 643430, 643429 and 643428 contain the supplementary crystallographic data for **1**, **2**, **3**, **4**, **5** and **6**. These data can be obtained free of charge via http://www.ccdc.cam.ac.uk/conts/retrieving.html, or from the Cambridge Crystallographic Data Centre, 12 Union Road, Cambridge CB2 1EZ, UK; fax: (+44) 1223-336-033; or e-mail: deposit@ccdc.cam.ac.uk. Supplementary data associated with this article can be found, in the online version, at doi:10.1016/j.poly.2007.12.002.

References

[1] H.K. Chae, D.Y. Siberio-Perez, J. Kim, Y. Go, M. Eddaoudi, A.J. Matzger, M.O. Keeffe, O.M. Yaghi, Nature 427 (2004) 523.
[2] Y. Kim, M. Suh, D.Y. Jung, Inorg. Chem. 43 (2004) 245.
[3] Z. Huang, H.-B. Song, M. Du, S.-T. Chen, X.-H. Bu, J. Ribas, Inorg. Chem. 43 (2004) 931.
[4] A.P. Carvalho, C. Castanheira, B. Cardoso, J. Pires, A.R. Silva, C. Freire, B. de Castro, M.B. de Carvalho, J. ZMater. Chem. 14 (2004) 374.
[5] J.Y. Lu, A.M. Babb, Chem. Commun. (2003) 1346.
[6] Y.-G. Li, N. Hao, Y. Lu, E.-B. Wang, Z.-H. Kang, C.-W. Hu, Inorg. Chem. 42 (2003) 3119.
[7] R. Kitaura, S. Kitagawa, Y. Kubota, T.C. Kobayashi, K. Kindo, Y. Mita, A. Matsuo, M. Kobayashi, H.-C. Chang, T.C. Ozawa, M. Suzuki, M. Sakata, M. Takata, Science 298 (2002) 2358.
[8] B. Moulton, M.J. Zaworotko, Chem. Rev. 101 (2001) 1629.
[9] C. Janiak, J. Chem. Soc., Dalton Trans. (2003) 2781.
[10] S.L. James, Chem. Soc. Rev. 32 (2003) 276.
[11] S.-L. Zheng, X.-M. Chen, Aust. J. Chem. 57 (2004) 703.
[12] D. Maspoch, D. Ruiz-Molina, J. Veciana, J. Mater. Chem. (2004) 2713.
[13] S.R. Batten, K.S. Murray, Coord. Chem. Rev. 243 (2003) 103.
[14] Y. Zhou, M. Hong, X. Wu, Chem. Commun. (2006) 135.
[15] S. Kitagawa, R. Kitaura, S. Noro, Angew. Chem., Int. Ed. 116 (2004) 2388.
[16] P.J. Hagrman, D. Hagrman, J. Zubieta, Angew. Chem., Int. Ed. 38 (1999) 2638.
[17] M. Eddaoudi, J. Kim, D. Vodak, A. Sudik, J. Wachter, M. O'Keeffe, O.M. Yaghi, PNAS 99 (2002) 4900.
[18] L. Carlucci, G. Ciani, D. Proserpio, Coord. Chem. Rev. 246 (2003) 247.
[19] M.J. Plater, M.R. St. J. Foreman, T. Gelbrich, S.J. Coles, M.B. Hursthouse, J. Chem. Soc., Dalton Trans. (2000) 3065.
[20] Y.H. Liu, Y.L. Liu, H.C. Wu, J.C. Wang, K.L. Lu, Inorg. Chem. 43 (2002) 2592.
[21] S.M. Kuznicki, V.A. Bell, S. Nair, H.W. Hillhouse, R.M. Jacubinas, C.M. Braunbarth, B.H. Toby, M. Tsapatsis, Nature 412 (2001) 720.
[22] S.A. Bourne, J. Lu, A. Mondal, B. Moulton, M.J. Zaworotko, Angew. Chem., Int. Ed. 40 (2001) 2111.
[23] J. Lu, A. Mondal, B. Moulton, M.J. Zaworotko, Angew. Chem., Int. Ed. 40 (2001) 2113.
[24] M. Aoyagi, K. Biradha, M. Fujita, J. Am. Chem. Soc. 121 (1999) 7457.
[25] C.V.K. Sharma, S. Griffin, T. Rogers, R.D. Chem. Commun. (1998) 215.
[26] S.R. Batten, B.F. Hoskins, R. Robson, J. Am. Chem. Soc. 117 (1995) 5385.
[27] A. Askarinejad, A. Morsali, Helv. Chim. Acta. 89 (2006) 265.
[28] A. Askarinejad, A. Morsali, Inorg. Chem. Commun. 9 (2006) 143.
[29] A. Morsali, L.G. Zhu, Helv. Chim. Acta 89 (2006) 81.
[30] A. Morsali, Solid State Sci. 8 (2006) 82.
[31] A. Morsali, R. Kempe, Helv. Chim. Acta 88 (2005) 2267.
[32] A. Morsali, V.T. Yilmaz, C. Kazak, Z. Anorg. Allg. Chem. 631 (2005) 11577.
[33] A. Morsali, J. Abedini, Inorg. Chem. Commun. 8 (2005) 460.
[34] A. Morsali, A.R. Mahjoub, Polyhedron 23 (2004) 2427.
[35] A. Morsali, L.G. Zhu, Inorg. Chem. Commun. 7 (2004) 1184.
[36] A. Lezzi, S. Cobianco, A. Roggero, J. Polym. Sci. A 32 (1994) 877.
[37] M. Cattaneo, F. Fagalde, E.N. Katz, Inorg. Chem. 45 (2006) 127.
[38] A.E. Dennis, M.H. Grace, F.M. Mary, C.M. Kieran, R.G.R. Guy, Polyhedron 17 (1998) 2321.
[39] Y.-J. Shi, L.-H. Li, Y.-Z. Li, Y. Xu, X.-Tai Chen, Z. Xue, X.-Z. You, Inorg. Chem. Commun. 5 (2002) 1090.
[40] Y.-B. Dong, J.-Y. Cheng, J.-P. Ma, H.-Y. Wang, R.-Q. Huang, D.-S. Guo, M.D. Smith, Solid State Sci. 5 (2003) 1177.
[41] Y.-B. Dong, M.D. Smith, R.C. Layland, H.-C. zur Loye, Inorg. Chem. 39 (2000) 4927.
[42] Y.-B. Dong, J.-P. Ma, R.-Q. Huang, F.-Z. Liang, M.D. Smith, J. Chem. Soc., Dalton Trans. (2003) 1472.
[43] Y.-B. Dong, L. Wang, J.-P. Ma, D.-Y. Zhao, D.-Y. Shen, R. Huang, Cryst. Growth Des. 6 (2006) 2475.
[44] D.M. Ciurtin, Y.-B. Dong, M.D. Smith, T. Barclay, H.-C. zur Loye, Inorg. Chem. 40 (2001) 2825.
[45] Y.-B. Dong, M.D. Smith, R.C. Layland, H.-C. zur Loye, Chem. Mater. 12 (2000) 1156.
[46] E.C. Kesslen, W.B. Euler, Tetrahedron Lett. 36 (1995) 4725.
[47] G. Ferguson, C. Glidewell, E.S. Lavender, Acta Crystallogr. B55 (1999) 591.
[48] G.M. Sheldrick, SHLXTL-97 V5.10, 1997, Bruker AXS Inc., Madison, WI-53719, USA.
[49] L.J. Farrugia, J. Appl. Crystallogr. 30 (1997) 565.
[50] MERCURY 1.4.1, Copyright Cambridge Crystallographic Data Centre, 12 Union Road, Cambridge, CB2 1EZ, UK, 2001–2005.
[51] I. Wharf, T. Gramstad, R. Makhija, M. Onyszchuk, Can. J. Chem. 54 (1976) 3430.
[52] L. Li, J.-X. Yang, H.-P. Zhou, Y.-P. Tian, X.-T. Tao, M.-H. Jiang, Inorg. Chem. Commun. 10 (2007) 163.
[53] M. Kubicki, S.K. Hadjikakou, M.N. Xanthopoulou, Polyhedron 20 (2001) 2179.

[Cu(II), Zn(II), Ni(II), Mn(II)] produces three [2 + 2] dinuclear [Cu(II), Zn(II), Ni(II)] macrocyclic complexes under reflux condition and one [1 + 2] mononuclear Mn(II) complex at room temperature in which the rearrangement of the backbone occurs [10]. In addition, the reduction of chiral (*R*,*R*)-**2** ligand by $NaBH_4$ leads to the amine macrocycle that is able to form mononuclear or multinuclear complexes [11,12]. Until now, most of the studies are focused on (1*R*,2*R*)-diamine derivatives [8–12], however, (1*S*,2*S*)-diamine involved structures are rarely reported. Herein we use chiral [(1*R*,2*R*) and (1*S*,2*S*)] and racemic *trans*-cyclohexane-1,2-diamines to prepare [3 + 3] macrocycles for the sake of comparison. In order to explore the size matching effect of macrocycles and the stereochemical preferences of metal ions, together with the C–H···Cl hydrogen bonding interactions with chlorine acceptors, we focus our attentions on the coordination chemistry of chlorine substituted [3 + 3] macrocycles **1**. In our previous work, we have succeeded in preparing a series of [2 + 2] Schiff-base macrocyclic ligands and their complexes using a sodium template method [13]. Of special emphasis was placed on the self-assembly of macrocyclic dinuclear zinc(II) moiety with diverse architectures and functions [14,15]. By the same method we prepared [3 + 3] Schiff-base macrocycles **1** and **2** (Scheme 1). The treatment of **1** with certain transitional metal salts [Cu(II), Zn(II), Fe(III)] with different counterions under reflux condition led to the cleavage of Schiff-base C=N double bonds and the rearrangement of the macrocycles (Scheme 2). We acquired [2 + 2], [2 + 1], [1 + 2] kinds of ring-contraction metal complexes in the process of bringing up single crystals. Size effect and coordination geometry of the metal centers, the presence of different counterions and solvents play significant roles on the formation of the final products. Herein, we describe the preparation, spectral and crystallographic characterizations of these ring-contraction complexes, where two new sorts of half-macrocyclic complexes **4** and **6** are included, as well as the comparisons between our contribution in this work and previous reports (Scheme 3).

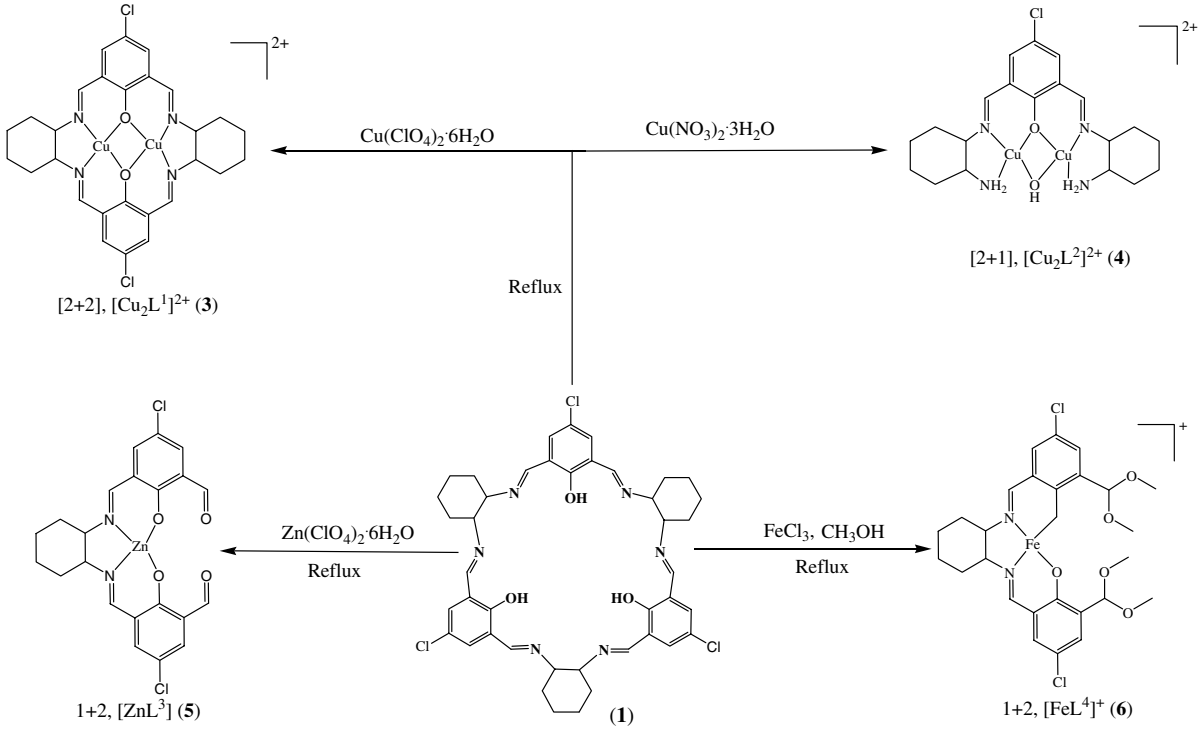


Scheme 1. General synthetic scheme of macrocycles.

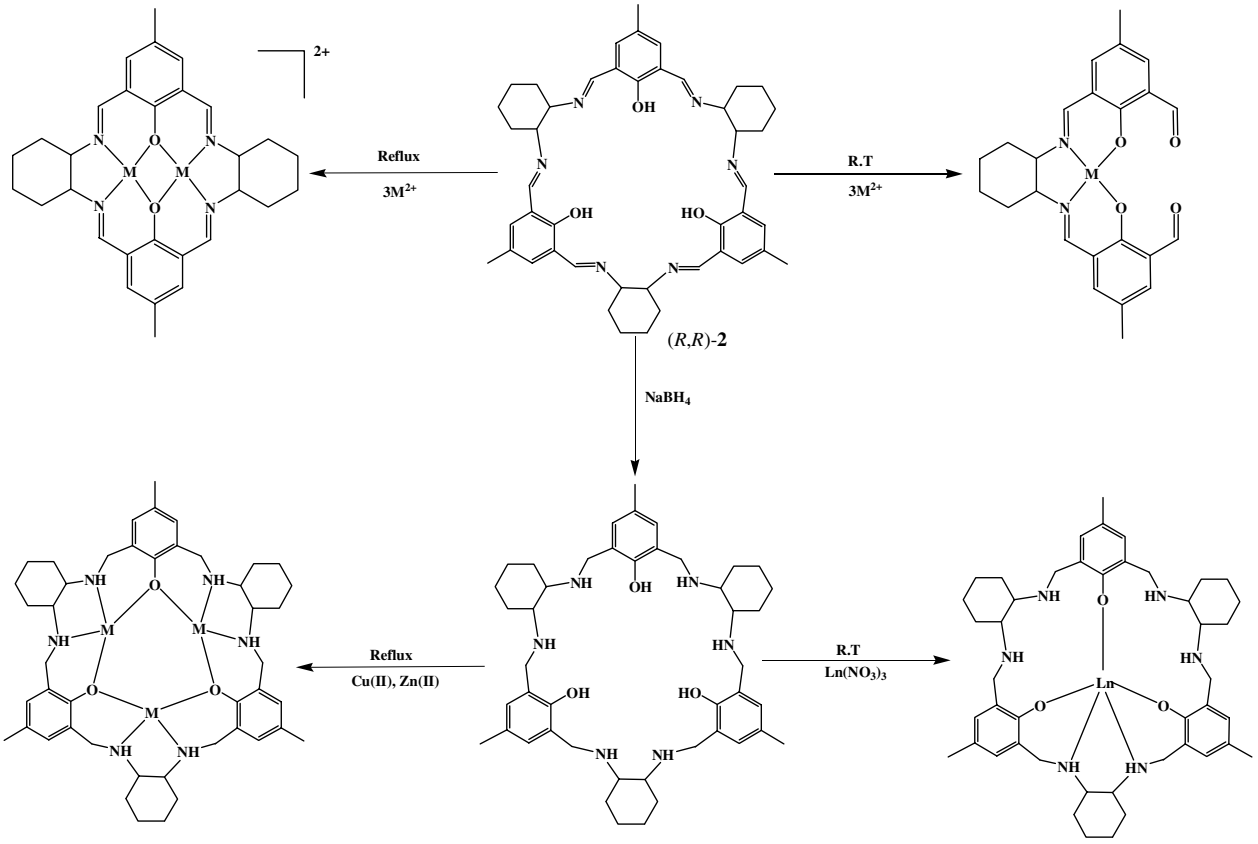
2. Experimental

2.1. Materials and measurements

Chiral [(1*R*,2*R*) and (1*S*,2*S*)] and racemic *trans*-cyclohexane-1,2-diamines were purchased directly from Aldrich. 2,6-Diformyl-4-substituted phenols (R = Cl or CH_3) were pre-



Scheme 2. Schematic illustration for the preparation of complexes **3**–**6**.



Scheme 3. Schematic illustration for Zacharias and Lisowski's work.

pared by an improved oxidation method using active manganese(IV) dioxide [16]. Sodium 2,6-diformyl-4-substituted phenolates were obtained by mixing equimolar amounts of 2,6-diformyl-4-substituted phenols and NaOH in ethanol. The other reagents were of analytical grade from commercial sources and were used without any further purification. Elemental analyses were measured with a Perkin–Elmer 1400C analyzer. Infrared spectra (IR, 4000–400 cm^{-1}) were collected on a Nicolet FTIR 170X spectrophotometer at 25 °C using KBr plates. ^1H NMR spectra were obtained in a Bruker 500 MHz NMR spectrometer. Electrospray ionization (ESI-MS) mass spectra were recorded on a Finnigan MAT SSQ 710 mass spectrometer in a scan range 100–1200 amu. Luminescence spectra were recorded on a Hitachi 850 fluorescence spectrophotometer at room temperature (25 °C). Ultraviolet–Visible (UV–Vis) spectra were recorded on a Shimadzu UV-3100 spectrometer. The circular dichroism spectra were measured with a JASCO J-810 spectopolarimeter using the same solutions as those for the UV–Vis determination. The optical rotation values were determined *via* a WZZ-115 digital auto-polarimeter.

Caution: Perchlorate salts are potentially explosive and should be treated with care and used only in small quantities.

2.2. Synthesis of racemic-*1*

A solution of racemic *trans*-cyclohexane-1,2-diamine (0.57 g, 5 mmol) in ethanol (20 mL) was added dropwise to a suspension of sodium 2,6-diformyl-4-chlorophenolate (1.05 g, 5 mmol) in ethanol (30 mL). The resulting solution was stirred and heated to reflux. As the reaction progressed, the solution became clear quickly. The mixture was kept refluxed for 3 h and concentrated on a rotary evaporator to dry, and then methanol (100 mL) was poured into the residue until yellow microcrystals appeared. The deposits were filtered off and collected in a 70% yield (0.92 g). ESI-MS gave the molecular ion peak at $m/z = 789.2$ (100%), supporting the [3 + 3] condensation. m.p. > 300 °C; ^1H NMR (500 MHz, $CDCl_3$) $\delta =$ 8.68 (3H, s, HC=N), 8.26 (3H, s, HC=N), 7.84 (3H, s, ArH), 7.18 (3H, s, ArH), 3.45 (6H, m, N–CH), 1.93–1.54 (24H, m, CH_2CH_2); UV–Vis (CH_2Cl_2, nm): λ_{max} (ε) = 250, 348; IR data (KBr): $v = 3431$ (w), 2983 (m), 2859 (m), 1637 (s), 1584 (s), 1447 (s), 1374 (m), 1295 (m), 1253 (m), 1143 (w), 1005 (m), 873 (w), 718 cm^{-1} (w). *Anal.* Calc. (%) for $C_{42}H_{45}Cl_3N_6O_3$: C, 64.00; H, 5.75; N, 10.66. Found: C, 63.92; H, 5.83; N, 10.67%. ESI-MS (CH_3OH): m/z 789.2 $[\mathbf{1} + H]^+$.

2.3. Synthesis of (R,R)-*1* and (S,S)-*1*

(*R*,*R*)-**1** and (*S*,*S*)-**1** were prepared by following the procedure similar to that described above. (*R*,*R*)-**1** and (*S*,*S*)-**1** were obtained from the treatment of sodium 2,6-diformyl-4-chlorophenolate (1.05 g, 5 mmol) and (1*R*,2*R*)-cyclohexane-1,2-diamine (0.57 g, 5 mmol) and (1*S*,2*S*)-cyclohex-

ane-1,2-diamine (0.57 g, 5 mmol), respectively. Since (*R*,*R*)-**1**, (*S*,*S*)-**1** and racemic-**1** present identical character of IR, UV–Vis, ESI-MS, only the optical rotation values of these two enantiomers are described simultaneously. (*R*,*R*)-**1**: Yield: 67%, 0.88 g; $[\alpha]_D^{18} = -208$ ($c = 0.1$ g/100 mL in CH_2Cl_2); m.p. > 300 °C; (*S*,*S*)-**1**: Yield: 62%, 0.82 g; $[\alpha]_D^{18} = +210$ ($c = 0.1$ g/100 mL in CH_2Cl_2); m.p. > 300 °C. Single crystals of (*S*,*S*)-**1** suitable for X-ray diffraction were obtained by the diffusion of acetone into a benzene solution of the sample at room temperature.

2.4. Synthesis of (*R*,*R*)-**2** and (*S*,*S*)-**2**

(*R*,*R*)-**2** and (*S*,*S*)-**2** were prepared by following the procedure similar to **1**. (*R*,*R*)-**2**: Yield: 69%, 0.83 g; $[\alpha]_D^{18} = -225$ ($c = 0.1$ g/100 mL in CH_2Cl_2). (*S*,*S*)-**2**: Yield: 71%, 0.86 g; $[\alpha]_D^{18} = +220$ ($c = 0.1$ g/100 mL in CH_2Cl_2); m.p. > 300 °C.

2.5. Synthesis of [(*R*,*R*-L^1)Cu_2(μ-NO_3)] · ClO_4 ((*R*,*R*)-**3**) and [(*S*,*S*-L^1)Cu_2(μ-NO_3)] · ClO_4 ((*S*,*S*)-**3**)

Starting with an ethanol solution (20 mL) of (*R*,*R*)-**1** or (*S*,*S*)-**1** (0.0788 g, 0.1 mmol), $Cu(NO_3)_2 \cdot 3H_2O$ (0.0722 g, 0.3 mmol) in ethanol (10 mL) was added dropwise to the solution. After 2 h′ reflux, an ethanol solution (10 mL) of $Cu(ClO_4)_2 \cdot 6H_2O$ (0.1111 g, 0.3 mmol) was added to replace the anions in order to make it possible to grow high-quality single crystals. The resultant solution was filtered and evaporated slowly at room temperature to give the deep green product. Single crystals of (*R*,*R*)-**3** suitable for X-ray structure analysis were grown by slow evaporation of the mother-liquor over two weeks at room temperature. Since (*R*,*R*)-**3** and (*S*,*S*)-**3** present identical character of IR, UV–Vis, ESI-MS, only the optical rotation values of two enantiomers are described simultaneously. (*R*,*R*)-**3**: Yield: ~32%, 0.047 g; $[\alpha]_D^{10} = -486$ ($c = 0.1$ g/100 mL in ethanol); IR data (KBr): $\nu = 3449$ (w), 2935 (w), 2861 (w), 1632 (s), 1543 (m), 1435 (m), 1384 (m), 1320 (m), 1230 (w), 1117 (s), 1087 (s), 1034 (m), 790 (w), 766 (w), 737 (w), 625 cm^{-1} (m); UV–Vis (ethanol, nm): λ_{max} (ε) = 271, 372. *Anal.* Calc. for $C_{28}H_{28}Cl_4Cu_2N_6O_{16}$: C, 34.55; H, 2.90; N, 8.63. Found: C, 34.63; H, 2.96; N, 8.67%. ESI-MS (CH_3OH): *m*/*z*: 325 [$(Cu_2L^1)^{2+}$/2]. (*S*,*S*)-**3**: Yield: ~35%, 0.051 g; $[\alpha]_D^{10} = +479$ ($c = 0.1$ CH_2Cl_2 in ethanol).

2.6. Synthesis of [(*S*,*S*-L^2)$Cu_2(NO_3)_2(OH)(H_2O)$] (**4**)

Starting with a methanol solution (20 mL) of (*S*,*S*)-**1** (0.0788 g, 0.1 mmol), $Cu(NO_3)_2 \cdot 3H_2O$ (0.0722 g, 0.3 mmol) in methanol (10 mL) was added dropwise to the solution. The resulting mixture was reflux for 5 h, cooled, filtered, and evaporated slowly in the air. Blue crystals **4** were obtained firstly from the mother liquid as the primary product. Single crystals suitable for X-ray analysis were obtained by slow evaporation in methanol at room temperature. Yield: ~37%, 0.038 g; $[\alpha]_D^{18} = +354$ ($c = 0.1$ in ethanol); IR data (KBr): $\nu = 3441$ (s), 3225 (m), 2936 (m), 2860 (m), 1649 (s), 1553 (s), 1448 (m), 1384 (s), 1231 (m), 1120 (w), 1052 (m), 1038 (m), 988 (w), 829 (w), 785 (w), 657 cm^{-1} (w); UV–Vis (ethanol, nm): λ_{max} (ε) = 220, 251, 366. *Anal.* Calc. for $C_{20}H_{33}ClCu_2N_6O_{10}$: C, 35.32; H, 4.89; N, 12.36. Found: C, 35.40; H, 4.97; N, 12.44%. ESI-MS (CH_3OH): *m*/*z*: 618.9 [(**4**–NO_3)$^+$].

2.7. Synthesis of [(*R*,*R*-L^3)$Zn(H_2O)$] (**5**)

A solution of $Zn(ClO_4)_2 \cdot 6H_2O$ (0.112 g, 0.3 mmol) in ethanol was added dropwise to an ethanol solution (20 mL) of (*R*,*R*)-**1** (0.0788 g, 0.1 mmol). After refluxing for 1 h, the solvent was removed by vaporization and the residue was dissolved in methanol. Yellow crystals suitable for X-ray analysis were grown by slow evaporation in methanol at room temperature. Yield: ~63%, 0.050 g; $[\alpha]_D^{18} = -417$ ($c = 0.1$ in ethanol); IR data (KBr): $\nu =$ 3449 (m), 2931 (w), 2856 (w), 1655 (s), 1637 (s), 1543 (m), 1433 (m), 1383 (m), 1223 (w), 1028 (m), 778 (w), 735 (w), 524 cm^{-1} (w); UV–Vis (ethanol, nm): λ_{max} (ε) = 267, 390. *Anal.* Calc. for $C_{22}H_{20}Cl_2ZnN_2O_5$: C, 49.98; H, 3.81; N, 5.30. Found: C, 49.84; H, 3.87; N, 5.25%.

2.8. Synthesis of [(racemic-L^4)Fe(Cl)] (**6**)

To a suspension of racemic-**1** (0.157 g, 0.2 mmol) in hot methanol (20 mL) was added a methanol solution (20 mL) of anhydrous $FeCl_3$ (0.097 g, 0.6 mmol). The solution became brown immediately as $FeCl_3$ was added. The resulting mixture was reflux for 2 h, cooled, filtered, and evaporated slowly at room temperature to give the brown product and the pH value of the mother-liquor is *ca.* 5. Brown crystals suitable for X-ray diffraction studies were directly obtained by slow evaporation of the reaction mixture in this case. Yield: ~57%, 0.107 g; IR data (KBr): $\nu = 3428$ (m), 2927 (s), 2858 (s), 1673 (s), 1628 (s), 1543 (s), 1432 (s), 1384 (s), 1219 (m), 998 (w), 828 (w), 733 (w), 674 cm^{-1} (w). UV–Vis (ethanol, nm): λ_{max} (ε) = 269, 387. *Anal.* Calc. for $C_{26}H_{30}Cl_3FeN_2O_6$: C, 49.67; H, 4.81; N, 4.46. Found: C, 49.58; H, 4.77; N, 4.40%. ESI-MS (CH_3OH): *m*/*z* 591.9 [**6**–Cl]$^+$.

2.9. X-ray crystallographic analysis

Single-crystal X-ray diffraction data were measured on a Siemens SMART CCD diffractometer using graphite-monochromatic Mo Kα radiation ($\lambda = 0.71073$ Å). Data collection was performed by using SMART program and cell refinement and data reduction were made with the SAINT program [17]. The structures were solved by directed method and refined on F^2 by using full-matrix least-squares methods with SHELXTL version 6.10 [18]. All non-hydrogen atoms were refined on F^2 by full-matrix least-squares procedure using anisotropic displacement parameters. Hydrogen atoms were inserted in the calculated positions assigned fixed isotropic thermal parameters at 1.2 times

the equivalent isotropic U of the atoms to which they are attached (1.5 times for the methyl groups, nitrogen and oxygen atoms) and allowed to ride on their respective parent atoms. All calculations were carried out on a PC computer with the SHELXTL PC program package and molecular graphics were drawn by using XP, DIAMOND and CHEM3D softwares. Details of the data collection and refinement for (*S*,*S*)-**1** and complexes (*R*,*R*)-**3** and **4**–**6** are given in Table 1, and the selective bond lengths and angles of these complexes are listed in Table 2 (for (*S*,*S*)-**1**), Table 3 (for (*R*,*R*)-**3**, **4**), and Table 4 (for **5**, **6**), respectively.

The absolute configurations of chiral centers are maintained during all metal complexation, which are proved by the determination of their optical rotation values and circular dichroism spectra. In addition, with regard to chloride substituted (*S*,*S*)-**1**, the reasonable Flack value −0.07(5) demonstrates the right specification of chirality [19]. For [3 + 3] macrocycle (*S*,*S*)-**1** and (*R*,*R*)-**2**, they crystallize in the monoclinic chiral space group $P2_1$ in which all six chiral carbon atoms are in *S* configuration for (*S*,*S*)-**1** and *R* configuration for (*R*,*R*)-**2**, which are in agreement with those of the starting material.

However, for complexes (*R*,*R*)-**3** and **4**–**6**, the absolute configurations of chiral carbon atoms cannot be specified from the crystallographic viewpoint because they crystallize in the centrosymmetric space groups (*C*2/*m*, $P\bar{1}$, $P\bar{1}$ or $P2_1/c$) where all the carbon atoms of cyclohexane-1,2-diamine moieties in the macrocyclic backbones are found disordered at two positions. As for the disorder of *trans*-cyclohexane-1,2-diamines in the metal complexes **4**–**6**, we think the disorder is possible because we use racemic starting material where the same amount of (1*R*,2*R*)-cyclohexane-1,2-diamine and (1*S*,2*S*)-cyclohexane-1,2-diamine are present. When the crystals grow from the mother solution, the same amount of (1*R*,2*R*)-cyclohexane-1,2-diamine and (1*S*,2*S*)-cyclohexane-1,2-diamine are believed to be encapsulated. In the refinement of these complexes, free variable are used to give the site occupancy factors for different carbon atoms. In the case of complex **3**, "add symmetry" is suggested by the Platon check program when a chiral space group *C*2 is assigned and very large thermal parameters for the related carbon atoms are generated. As a result, in complex (*R*,*R*)-**3**, the carbon atoms C6–C8, (C6′–C8′) are refined disordered over two sites in 0.545:0.455 occupancies. For complex **4**, the site occupancy factors for C8–C13 (C8′–C13′) and C14–C19 (C14′–C19′) were fixed at 0.443:0.557 and 0.494:0.506, respectively. In complex **5**, the site occupancy factors for C9–C14 (C9′–C14′) and C31–C36 (C31′–C36′) were fixed at 0.466:0.533 and 0.481:0.519, respectively.

Table 1
Crystallographic data and structure refinements for (*S*,*S*)-**1**, (*R*,*R*)-**3** and **4**–**6**

Compound	(*S*,*S*)-**1**	(*R*,*R*)-**3**	**4**	**5**	**6**
Formula	$C_{42}H_{45}Cl_3N_6O_3$	$Cu_2C_{28}H_{28}Cl_4N_6O_{16}$	$Cu_4C_{40}H_{64}Cl_2N_{12}O_{19}$	$ZnC_{22}H_{20}Cl_2N_2O_5$	$FeC_{26}H_{30}Cl_3N_2O_6$
Formula weight	788.19	973.44	1342.09	528.67	628.72
Crystal size (mm)	0.40 × 0.30 × 0.20	0.40 × 0.30 × 0.20	0.30 × 0.30 × 0.30	0.45 × 0.35 × 0.35	0.50 × 0.20 × 0.20
Crystal system	monoclinic	monoclinic	triclinic	triclinic	monoclinic
Space group	$P2_1$	*C*2/*m*	$P\bar{1}$	$P\bar{1}$	$P2_1/c$
a (Å)	14.667(2)	12.626(2)	8.413(2)	8.484(1)	8.054(1)
b (Å)	18.896(2)	19.103(3)	13.476(3)	13.175(2)	28.668(5)
c (Å)	14.907(2)	9.266(1)	13.701(3)	19.868(3)	12.666(2)
α (°)	90	90	65.921(3)	87.084(3)	90
β (°)	92.904(3)	119.352(2)	72.624(4)	82.291(3)	107.040(4)
γ (°)	90	90	71.908(3)	85.675(3)	90
V (Å^3)	4126.1(9)	1948.0(5)	1321.3(5)	2192.6(5)	2796.3(8)
Z	4	2	1	4	4
ρ_{calc} (g cm^{-3})	1.269	1.660	1.687	1.602	1.493
F(000)	1656	984	700	1080	1300
μ (mm^{-1})	0.268	11.442	1.773	1.402	0.869
Maximum/minimum *h*, *k*, *l*	15/−15, 22/−22, 17/13	15/−15, 21/−23, 11/−7	9/−10, 16/−16, 16/−13	10/−9, 15/−14, 22/−23	9/−9, 33/−34, 15/−14
Maximum/minimum transmission	0.9484/0.9005	0.7480/0.6010	0.6183/0.6183	0.6397/0.5712	0.8454/0.6704
Reflections collected	20643	5298	6549	10974	13839
Reflections unique	14176	1984	4552	7566	4911
Reflections with $I > 2\sigma(I)$	5806	1837	3878	6170	2056
Parameters/restraints	979/13	135/0	390/12	597/18	354/0
Flack parameter	−0.07(5)				
R_1/wR_2 [$I > 2\sigma(I)$]	0.0490/0.0698	0.0494/0.1076	0.0725/0.1495	0.0938/0.2056	0.0834/0.1060
R_1/wR_2 (all data)	0.1474/0.0869	0.0636/0.1175	0.0846/0.1538	0.1112/0.2106	0.2089/0.1356
Goodness-of-fit on F^2	0.707	1.035	1.270	1.264	0.900
Maximum/minimum Δρ (e Å^{-3})	0.20/−0.16	0.24/−0.40	0.50/−0.49	0.48/−0.76	0.31/−0.34

$R_1 = \sum||F_o| - |F_c||/\sum|F_o|$, $wR_2 = [\sum[w(F_o^2 - F_c^2)^2]/\sum w(F_o^2)^2]^{1/2}$.

Table 2
Selected bond lengths (Å) and angles (°) for (*S*,*S*)-**1**

(*S*,*S*)-**1**		(*S*,*S*)-**1**	
Cl(1)–C(4)	1.756(5)	N(2)–C(9)	1.468(6)
Cl(2)–C(19)	1.747(5)	N(3)–C(22)	1.448(6)
Cl(3)–C(33)	1.736(5)	N(3)–C(21)	1.249(6)
O(1)–C(1)	1.352(5)	N(4)–C(23)	1.447(6)
O(2)–C(16)	1.343(6)	N(4)–C(28)	1.273(6)
O(3)–C(30)	1.361(5)	N(5)–C(36)	1.468(6)
N(1)–C(8)	1.459(6)	N(5)–C(35)	1.248(6)
N(1)–C(7)	1.269(5)	N(6)–C(37)	1.454(6)
N(2) –C(14)	1.276(6)	N(6)–C(42)	1.266(6)
O(1)–C(1)–C(6)	120.1(5)	N(1)–C(7)–C(2)	123.0(5)
O(1)–C(1)–C(2)	118.6(5)	N(1)–C(8)–C(9)	108.2(4)
O(2)–C(16)–C(15)	122.1(5)	N(1)–C(8)–C(13)	111.9(5)
O(2)–C(16)–C(17)	117.1(5)	N(2)–C(9)–C(8)	110.7(4)
O(3)–C(30)–C(29)	120.2(6)	N(2)–C(9)–C(10)	108.2(5)
O(3)–C(30)–C(31)	118.5(6)	N(2)–C(14)–C(15)	122.1(5)
Cl(1)–C(4)–C(3)	119.8(5)	N(3)–C(21)–C(17)	123.9(6)
Cl(1)–C(4)–C(5)	119.3(5)	N(3)–C(22)–C(23)	110.8(5)
Cl(2)–C(19)–C(20)	119.6(5)	N(3)–C(22)–C(27)	110.0(5)
Cl(2)–C(19)–C(18)	119.3(5)	N(4)–C(23)–C(22)	109.9(5)
Cl(3)–C(33)–C(32)	118.4(5)	N(4)–C(23)–C(24)	108.7(5)
Cl(3)–C(33)–C(34)	121.2(5)	N(4)–C(28)–C(29)	123.4(6)
C(7)–N(1)–C(8)	116.9(5)	N(5)–C(35)–C(31)	122.5(6)
C(9)–N(2)–C(14)	117.5(5)	N(5)–C(36)–C(41)	106.8(5)
C(21)–N(3)–C(22)	117.8(5)	N(5)–C(36)–C(37)	110.4(5)
C(23)–N(4)–C(28)	120.7(5)	N(6)–C(37)–C(36)	111.0(5)
C(35)–N(5)–C(36)	117.7(5)	N(6)–C(37)–C(38)	108.8(5)
C(37)–N(6)–C(42)	119.9(5)	N(6)–C(42)–C(6)	124.5(5)

For complex **6**, the cyclohexane ring is disordered over two positions C8–C13, (C8′–C13′) in a ratio of 0.745:0.255.

Table 4
Selected bond lengths (Å) and angles (°) for the complexes **5** and **6**

5		**6**	
Zn(1)–O(1)	2.032(6)	Fe(1)–O(1)	1.882(5)
Zn(1)–O(2)	2.009(6)	Fe(1)–O(2)	1.885(5)
Zn(1)–O(5)	2.034(6)	Fe(1)–N(1)	2.094(6)
Zn(1)–N(2)	2.002(8)	Fe(1)–N(2)	2.091(6)
Zn(1)–N(3)	2.075(7)	Fe(1)–Cl(3)	2.208(3)
N(2)–Zn(1)–O(2)	90.1(3)	O(1)–Fe(1)–O(2)	96.1(2)
N(2)–Zn(1)–O(1)	155.5(3)	O(1)–Fe(1)–N(2)	144.6(3)
O(2)–Zn(1)–O(1)	93.7(2)	O(2)–Fe(1)–N(2)	86.8(2)
N(2)–Zn(1)–O(5)	101.3(3)	O(1)–Fe(1)–N(1)	87.1(2)
O(2)–Zn(1)–O(5)	96.2(2)	O(2)–Fe(1)–N(1)	154.3(2)
O(1)–Zn(1)–O(5)	102.3(2)	N(2)–Fe(1)–N(1)	76.4(2)
N(2)–Zn(1)–N(1)	80.5(3)	O(1)–Fe(1)–Cl(3)	107.3(2)
O(2)–Zn(1)–N(1)	160.0(3)	O(2)–Fe(1)–Cl(3)	103.8(2)
O(1)–Zn(1)–N(1)	88.0(3)	N(2)–Fe(1)–Cl(3)	106.1(2)
O(5)–Zn(1)–N(1)	102.9(3)	N(1)–Fe(1)–Cl(3)	99.5(2)

3. Results and discussion

3.1. Syntheses and spectral characterizations

One-step synthesis of 27-membered triphenolic Schiff-base macrocycles (*S*,*S*)-**1** and (*R*,*R*)-**2** has been achieved and characterized by EA, IR, NMR, ESI-MS, UV–Vis, CD and fluorescence spectra as well as X-ray single-crystal diffraction. Though sodium 2,6-diformyl-4-substituted phenolate was used as a starting material because we found the presence of Na(I) ion was helpful for the formation of macrocyclic ligands and their respective complexes by in situ

Table 3
Selected bond lengths (Å) and angles (°) for the complexes (*R*,*R*)-**3** and **4**

(*R*,*R*)-**3**		**4**		**4**	
Cu(1)···Cu(1A)[a]	2.868(1)	Cu(1)···Cu(2)	2.937(1)		
Cu(1)–O(1)	1.878(2)	Cu(1)–O(1)	1.937(4)	Cu(2)–O(1)	1.946(4)
Cu(1)–O(1)[a]	1.878(2)	Cu(1)–O(2)	1.926(4)	Cu(2)–O(2)	1.931(4)
Cu(1)–N(1)	1.884(3)	Cu(1)–O(3)	2.830(7)	Cu(2)–O(4)	2.661(7)
Cu(1)–N(1)[b]	1.884(3)	Cu(1)–O(1W)	2.508(6)	Cu(2)–O(6)	2.577(6)
		Cu(1)–N(1)	1.943(6)	Cu(2)–N(3)	1.950(6)
		Cu(1)–N(2)	1.966(6)	Cu(2)–N(4)	1.978(6)
O(1)–Cu(1)–O(1)[a]	80.4(2)	O(1)–Cu(1)–O(2)	81.4(2)	O(1)–Cu(2)–O(2)	81.1(2)
O(1)–Cu(1)–N(1)[b]	174.8(1)	O(1)–Cu(1)–O(3)	79.4(2)	O(1)–Cu(2)–O(4)	86.1(2)
O(1)–Cu(1)–N(1)[a,b]	94.4(1)	O(1)–Cu(1)–O(1W)	94.2(2)	O(1)–Cu(2)–O(6)	94.0(2)
O(1)–Cu(1)–N(1)	94.4(1)	O(1)–Cu(1)–N(1)	91.3(2)	O(1)–Cu(2)–N(3)	90.7(2)
O(1)–Cu(1)–N(1)[a]	174.8(1)	O(1)–Cu(1)–N(2)	175.2(3)	O(1)–Cu(2)–N(4)	177.0(2)
N(1)–Cu(1)–N(1)[b]	90.7(2)	O(2)–Cu(1)–O(3)	82.0(2)	O(2)–Cu(2)–O(4)	83.6(2)
N(1)–Cu(1)–Cu(1)[a,b]	134.6(1)	O(2)–Cu(1)–O(1W)	91.3(2)	O(2)–Cu(2)–O(6)	89.5(2)
N(1)–Cu(1)–Cu(1)[a]	134.6(1)	O(2)–Cu(1)–N(1)	170.4(3)	O(2)–Cu(2)–N(3)	171.6(2)
C(5)–N(1)–Cu(1)	125.6(3)	O(2)–Cu(1)–N(2)	101.8(2)	O(2)–Cu(2)–N(4)	101.9(2)
C(1)–O(1)–Cu(1)[a,b]	129.5(1)	O(3)–Cu(1)–O(1W)	171.2(2)	O(4)–Cu(2)–O(6)	173.0(2)
Cu(1)–O(1)–Cu(1A)[a]	99.6(2)	O(3)–Cu(1)–N(1)	90.3(3)	O(4)–Cu(2)–N(3)	97.6(3)
C(6)–N(1)–Cu(1)	108.6(3)	O(3)–Cu(1)–N(2)	97.4(3)	O(4)–Cu(2)–N(4)	94.1(3)
C(6′)–N(1)–Cu(1)	107.1(3)	O(1W)–Cu(1)–N(1)	95.7(3)	O(6)–Cu(2)–N(3)	89.4(2)
		O(1W)–Cu(1)–N(2)	89.5(2)	O(6)–Cu(2)–N(4)	86.1(2)
		N(1)–Cu(1)–N(2)	85.1(3)	N(3)–Cu(2)–N(4)	86.4(2)
		Cu(1)–O(1)–Cu(2)	98.3(2)	Cu(1)–O(2)–Cu(2)	99.1(2)

Symmetry operators: (a) $-x$, y, $-z+1$.
(b) $-x$, $-y+1$, $-z+1$.

metal ion replacement [13], the product turned out to be the protonated compounds **1** and **2** instead of deprotonated sodium phenolates. Our synthesis is different from the method of Zacharias et al., where a room temperature condensation between 2,6-diformyl-4-methyl phenol and (1*R*,2*R*)-cyclohexane-1,2-diamine was performed and higher yields of 80% [9] or 90% [10] were reported. Different from the [2 + 2] condensation in the case of 1,3-propanediamine [13], [3 + 3] condensation was proved to be the main reaction for *trans*-cyclohexane-1,2-diamine [9–11]. However, [3 + 3] cyclohexane-1,2-diamine related macrocycles are not stable when treated with transition metal ions mainly due to the size effect and coordination geometric requirements of the metal centers. In most cases, the ring-degradation took place and the products were complicated and hard to isolate. An alternate way to stabilize this kind of macrocycles is to reduce the C=N double bonds by $NaBH_4$. Till now, two trinuclear (Zn_3 and Zn_2Cu) complexes and one mononuclear Eu(III) complex of reduced (*R*,*R*)-**2** ligand have been documented [11,12].

The products of the reaction of Schiff-base macrocycles **1** with $Cu(NO_3)_2 \cdot 3H_2O$ and $Cu(ClO_4)_2 \cdot 6H_2O$ are mixtures of **3** and **4**. However, they can be gradually isolated according to their different solubility in methanol and ethanol. In our experiment, cyclic [2 + 2] dinuclear Cu(II) complex **3** firstly precipitated from ethanol, and then acyclic [2 + 1] dinuclear Cu(II) complex **4**. The treatment of **1** with $Zn(ClO_4)_2 \cdot 6H_2O$ or $FeCl_3$ under reflux condition gave the primary products **5** and **6**, respectively and the impurities were not separated. Zacharias and co-workers concluded that [2 + 2] macrocyclic dinuclear complexes were the main products under reflux condition (~80%) and [1 + 2] products were obtained at room temperature (~70%) [10]. But our experiments demonstrated that the mixtures of several species typically occurred for this kind of reaction and [1 + 2] and [2 + 1] types of complexes could also be yielded under reflux condition. We have isolated and characterized successfully two new sorts of half-macrocyclic complexes **4** and **6**. In addition, five-coordinate Zn(II) complex **5** exhibited a hydrogen-bonded dimeric structure which differed from the six-coordinate Mn(II) complex reported by Zacharias' group [10]. Interestingly, a new type of [1 + 2] dimethyl acetal complex **6** was produced in methanol where $FeCl_3$ is suggested to be a reactive Lewis acid catalyst [20]. The reaction liquor was in a weak acidic condition (pH 5) originated from the hydrolyzation of $FeCl_3$.

In the UV–Vis spectra, **1** and **2** exhibit similar absorption with two intense bands at *ca.* 250 and 348 nm. The strong absorption band at 250 nm is assigned to the π–π* transition of the benzene rings, whereas the intense absorption at 348 nm is attributed to the π–π* transition of the azomethine chromophore. Compared with the positions in free compounds, these bands in complexes **3**–**6** have undergone bathochromic shifts of 10–30 nm. Such shifts are expected due to the contribution from π–π* ligand-to-metal charge transfer (LMCT).

The sign patterns of the CD spectra in macrocycles suggest the intrinsic chiral difference of enantiomers, which have not been systematically studied in literature. It is found that (*S*,*S*)-**1** gives cotton effects that are mirror images of (*R*,*R*)-**1** (Fig. 1). The first cotton effect of (*S*,*S*)-**1** is positive, but for (*R*,*R*)-**1**, it is negative. Moreover, racemic-**1** does not show any remarkable cotton effect and presents as a line. These results clearly indicate that there is no contribution of the phenyl rings to the cotton effects for the macrocycles **1** and that the chiral cyclohexane-1,2-diamine components control the direction of the twist. In contrast to the corresponding electronic absorption band at 348 nm, their CD bands split into 340 nm and 367 nm, which can be attributed to the split π–π* transition of azomethine. On the other hand, one CD peak appears at 273 nm, corresponded to the UV–Vis absorption at 250 nm. The sign patterns of the CD spectra suggest that conformers of negative chirality predominate in the solutions of (*R*,*R*)-macrocycle, whereas conformers of positive chirality predominate in those of (*S*,*S*)-macrocycle. Compared with **1**, **2** exhibits similar but stronger CD and UV–Vis absorptions.

Comparing the CD spectra of (*S*,*S*)-**3** and (*R*,*R*)-**3** (Fig. 2), the enantiomeric pair shows opposite cotton effects. The broad low-energy absorption band at 450–650 nm of CD spectra is ascribed to the d–d transition of copper(II). The higher energy CD components at 400 and 360 nm for **3**, are assigned to π–π* transition of the azomethine and LMCT transitions. The CD spectrum of **4** shows three cotton peaks: 398 (+), 351 (−) and 298 nm (−) (Fig. 3). The broad low-energy absorption band at 450–

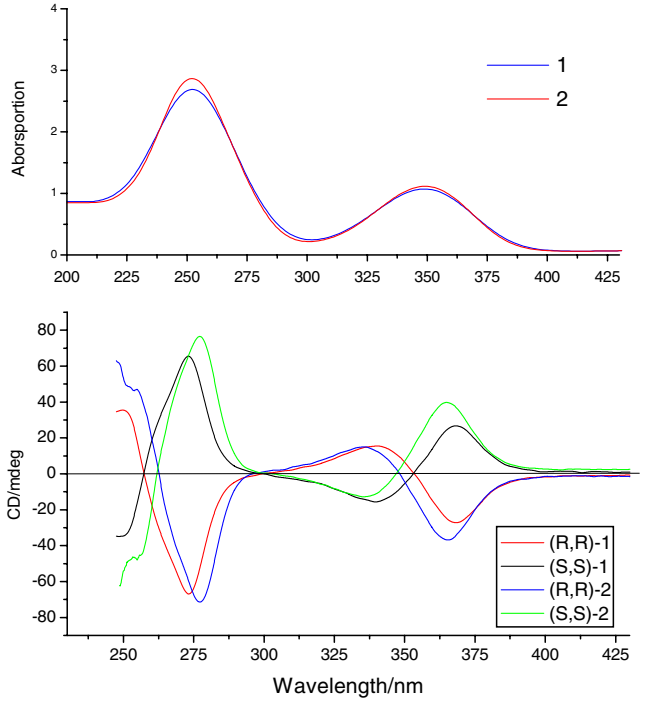


Fig. 1. UV–Vis and CD spectra of (*R*,*R*)-**1**, (*S*,*S*)-**1**, (*R*,*R*)-**2** and (*S*,*S*)-**2** in CH_2Cl_2.

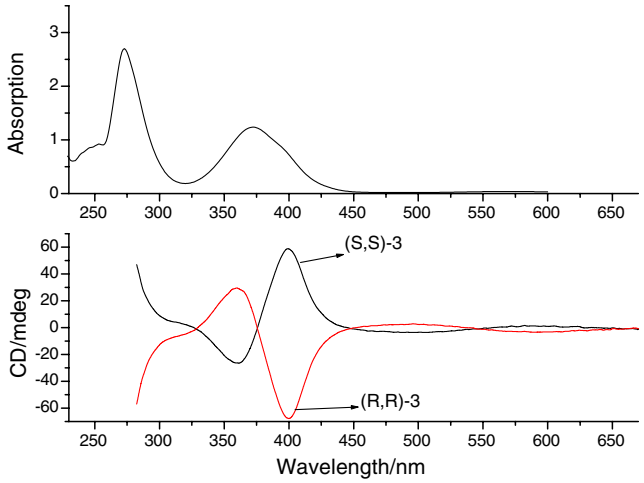


Fig. 2. UV–Vis and CD spectra of (*R*,*R*)-**3** and (*S*,*S*)-**3** in ethanol.

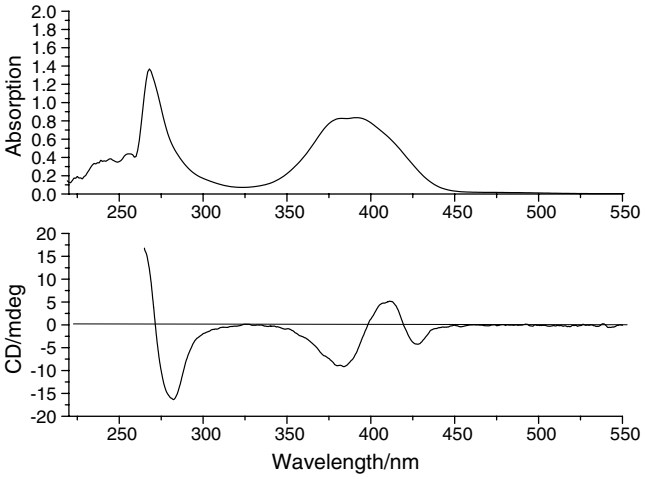


Fig. 4. UV–Vis and CD spectra of (*R*,*R*)-**5** in ethanol.

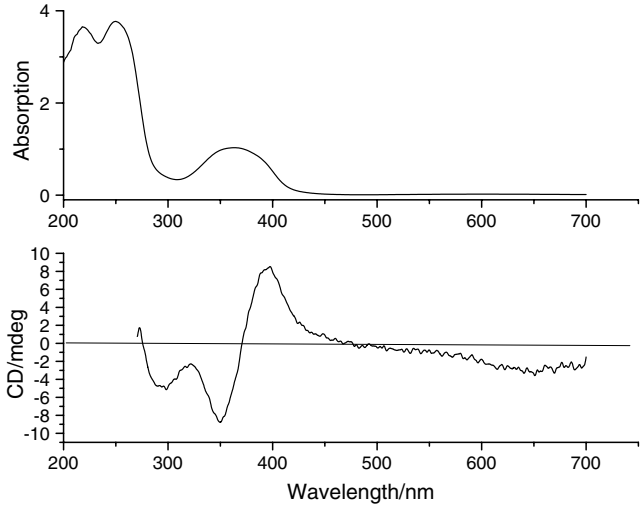


Fig. 3. UV–Vis and CD spectra of **4** in ethanol.

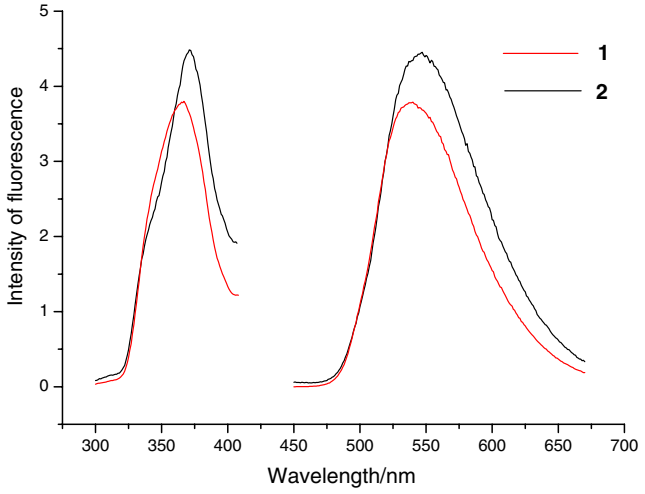


Fig. 5. Fluorescent spectra of **1** and **2** in CH_2Cl_2 solution.

700 nm can be assigned to a d–d transition of metal copper. The CD spectrum of **5** shows four cotton peaks by contrast: 430 (−), 410 (+), 385 (−) and 278 (−) nm (Fig. 4). The studies for the CD spectra of complexes lead us to conclude that the intrinsic chiral difference of the macrocycles can be retained even though the ring-contraction and rearrangement reactions take place.

The fluorescent spectra of **1** and **2** are shown in Fig. 5, with excitation spectra on the left part of the figure and emission spectra on the right part. The maximum excitation bands are located at 371 and 367 nm for **1** and **2**, respectively, whereas the maximum emission bands of them are positioned at 547 and 540 nm, respectively. The yellow fluorescent emission originates from the π–π^* transition of the azomethine chromophore in the compounds. Compare to the macrocycle **1**, metal complexes **3**–**6** quenched the fluorescence in the process of the electron transfer from the chromophore C=N to the metals at the same experimental conditions.

3.2. Crystal structure of (*S*,*S*)-*1* and (*R*,*R*)-*2*

In our experiments, the structures of (*S*,*S*)-**1** and (*R*,*R*)-**2** have been independently determined by X-ray single-crystal diffraction at 298(2) K. However, the crystal structure of (*R*,*R*)-**2** with the data collected at 100(2) K has been newly reported by Lisowski et al. in 2006 [12]. The cell parameters at normal temperature in our case (a = 14.783(1) Å, b = 19.006(1) Å, c = 14.945(1) Å, β = 93.129(1)°, V = 4192.8(4) Å^3) is a little bigger due to the temperature difference (a = 14.650(4) Å, b = 18.789(4) Å, c = 14.803(4) Å, β = 92.56(3)°, V = 4071(2) Å^3). In that paper, the authors simply described the molecular structure of (*R*,*R*)-**2** and did not mention its crystal structure. The CIF of (*R*,*R*)-**2** at 298(2) K, with the final $R_1 = 0.0496$ and $wR_2 = 0.0701$ for intensive data, was attached as the Supporting information of this paper for reference.

(*S*,*S*)-**1** is isomorphous with (*R*,*R*)-**2** although different substituted groups were used. It crystallizes in the chiral

monoclinic space group $P2_1$ with two identical cone-shaped species in each asymmetric unit. The macrocycle contains three tetradentate coordinating sites embedded in a 27-membered cone-like cavity with the dimension of *ca.* 42.36 Å^2 where 21 carbon atoms and six nitrogen atoms are present (Fig. 6). The phenolic hydroxyl groups are positioned at the narrower rim of the cavity, while the chlorine groups form the broader rim. Three phenyl rings in every cavity adopt an analogue equilateral triangle with the corresponding centroid–centroid separations of 6.871, 6.971 and 7.141 Å, and the bite angles between them are 62.1°, 58.3° and 59.6°, respectively.

(*S*,*S*)-**1** and (*R*,*R*)-**2** are stabilized by intramolecular hydrogen bonding interactions (O–H···N and C–H···O) (Table 5). Each hydroxyl group of the phenol unit points to the nitrogen atom of imine moieties with O–H···N distances ranging from 2.57 to 2.62 Å, indicative of strong intramolecular hydrogen-bonding interactions. Hydrogen bonds are also found between the hydrogen atom of CH=N and its neighboring hydroxyl group with the average C–H···O distance of 2.79 Å. In addition, typical intermolecular π–π stacking interactions are observed between the phenyl rings of adjacent macrocycles. As seen in Fig. 7, a vicinal molecule, as a guest by means of π–π stacking interactions with the centroid–centroid separation of 3.599 Å, inserts the triangular hole of the macrocycle forming a dimeric structure. In contrast, π–π stacking interactions between the centroids of contiguous phenyl rings (4.770 Å) of different dimeric pairs are very weak. This kind of packing mode is obviously different from the crystal structure of reduced macrocycle of (*R*,*R*)-**2**, where a channel-like structure governed by the hydrophobic inter-

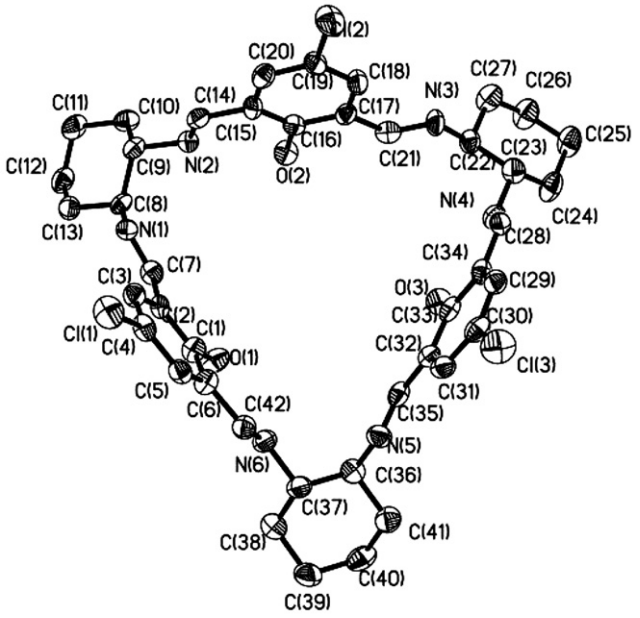


Fig. 6. ORTEP drawing (30% probability displacement ellipsoids) of (*S*,*S*)-**1** with the atom-numbering scheme. Hydrogen atoms are omitted for clarity.

Table 5
Hydrogen-bond parameters (Å, °) in (*S*,*S*)-**1**, complexes (*R*,*R*)-**3** and **4**–**6**

D–H···A	D–H	H···A	D···A	∠DHA
(*S*,*S*)-**1**				
O(1)–H(1)···N(6)	0.82	1.89	2.62(1)	147.0
O(2)–H(2)···N(2)	0.82	1.88	2.60(1)	146.0
O(3)–H(3A)···N(4)	0.82	1.87	2.61(1)	148.0
O(4)–H(4)···N(7)	0.82	1.86	2.59(1)	148.0
O(5)–H(5A)···N(9)	0.82	1.84	2.57(1)	148.0
O(6)–H(6A)···N(11)	0.82	1.86	2.58(1)	146.0
C(35)–H(35)···O(3)	0.93	2.49	2.81(1)	100.0
C(55)–H(55A)···O(1)[a]	0.97	2.53	3.45(1)	159.0
C(70)–H(70)···O(6)	0.93	2.43	2.76(1)	100.0
C(84)–H(84)···O(4)	0.93	2.48	2.80(1)	100.0
(*R*,*R*)-**3**				
C(7)–H(7A)···O(22)[b]	0.97	2.40	3.36(1)	171.0
4				
O(1W)–H(1WA)···O(4)[c]	0.96	1.94	2.82(1)	151.0
O(2)–H(2)···O(1W)[d]	0.85	2.11	2.94(1)	165.0
O(1W)–H(1WB)···O(6)	0.96	2.37	3.08(1)	130.0
O(1W)–H(1WB)···O(8)	0.96	2.10	3.04(1)	167.0
N(2)–H(2B)···O(6)[d]	0.90	2.20	2.92(1)	137.0
O(2W)–H(2WA)···O(1W)[e]	0.85	2.41	3.05(3)	132.0
O(2W)–H(2WA)···O(8)[e]	0.86	2.42	3.07(4)	132.0
O(2W)–H(2WB)···O(5)	0.85	2.46	2.96(3)	118.0
N(4)–H(4A)···O(4)[f]	0.90	2.59	3.07(1)	114.0
N(4)–H(4B)···O(2)[f]	0.90	2.16	3.04(1)	166.0
C(3)–H(3A)···O(3)[g]	0.93	2.55	3.42(1)	155.0
C(5)–H(5A)···O(7)[h]	0.93	2.57	3.41(1)	152.0
C(7)–H(7A)···O(5)[g]	0.93	2.51	3.43(1)	169.0
C(13′)–H(13D)···O(5)[g]	0.97	2.39	3.16(1)	135.0
C(14′)–H(14B)···O(7)	0.98	2.42	3.31(2)	150.0
C(16′)–H(16C)···O(3)[f]	0.97	2.57	3.39(5)	142.0
C(20)–H(20A)···O(7)[h]	0.93	2.57	3.43(1)	154.0
5				
O(5)–H(5A)···O(1)[i]	0.96	1.78	2.71(1)	162.0
O(5)–H(5B)···O(2)[i]	0.96	2.15	2.84(1)	127.0
O(5)–H(5B)···O(4)[i]	0.96	1.78	2.60(1)	141.0
O(10)–H(10A)···O(7)[j]	0.96	1.99	2.94(1)	171.0
O(10)–H(10B)···O(9)[j]	0.96	2.16	2.66(1)	111.0
C(13′)–H(13D)···O(4)[k]	0.97	2.50	3.36(3)	148.0
C(15)–H(15A)···O(8)[j]	0.93	2.36	3.24(1)	159.0
C(29)–H(29)···O(10)[j]	0.93	2.56	3.30(2)	137.0
C(36)–H(36D)···Cl(3)[l]	0.97	2.67	3.63(1)	169.0
C(37)–H(37)···O(3)[i]	0.93	2.39	3.25(1)	154.0
C(43)–H(43)···O(3)[i]	0.93	2.55	3.42(1)	155.0
6				
C(18)–H(18A)···O(6)	0.93	2.35	2.69(1)	101.0
C(18)–H(18A)···Cl(1)[m]	0.93	2.77	3.68(1)	166.0
C(22)–H(22A)···O(1)	0.98	2.41	2.82(1)	104.0
C(25)–H(25A)···Cl(3)[n]	0.96	2.79	3.69(1)	156.0
C(25)–H(25B)···O(2)	0.96	2.48	3.20(1)	132.0

Symmetry operators:
(a) $1-x, -1/2+y, 1-z$.
(b) $-x, y, 1-z$.
(c) $1+x, y, z$.
(d) $2-x, 2-y, 2-z$.
(e) $-1+x, y, z$.
(f) $1-x, 2-y, 2-z$.
(g) $2-x, 2-y, 1-z$.
(h) $2-x, 1-y, 2-z$.
(i) $1-x, 1-y, -z$.
(j) $2-x, 1-y, 1-z$.
(k) $2-x, 1-y, -z$.
(l) $2-x, -y, 1-z$.
(m) $2-x, 1/2+y, 1/2-z$.
(n) $1+x, y, z$.

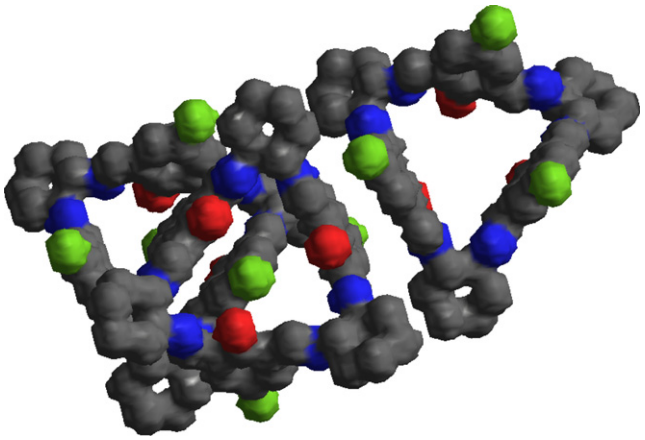


Fig. 7. View of two types of π–π interactions in (*S*,*S*)-**1**.

action and intermolecular N–H···N and C–H···N interactions is generated and π–π stacking interactions are not observed (the shortest separation between the aromatic rings is 5.143 Å) [9].

3.3. Crystal Structure of (*R*,*R*)-3 and 4

The molecular structures of (*R*,*R*)-**3** and **4** with anisotropic displacement ellipsoids and atom-numbering scheme are shown in Figs. 8 and 10, respectively. The distance between Cu(1) and Cu(2) in (*R*,*R*)-**3** is 2.868(1) Å, which is relatively shorter than that in complex **4** (2.937(1) Å) due to the geometric restriction of [2 + 2] macrocyclic ligand. Each Cu(II) center in (*R*,*R*)-**3** and **4** adopts a distorted octahedron geometry. In complex (*R*,*R*)-**3**, the two Cu(II) centers are identical with each being coordinated by two imino nitrogen atoms, two phenoxy bridging oxygen atoms in the basic plane and bridged by two μ_2 bridged nitrate groups above and below the dinuclear skeleton. Perchlorate anion is free from the coordinative bond and is captured in the crystal lattice. To the best of our knowledge, this is the first report on dinuclear Schiff-base complex bridged by two nitrate groups. As for complex **4**, one imine nitrogen atom, one phenol oxygen atom, one amine N-donor from cyclohexanediamine and a μ_2 bridged hydroxyl group form the equatorial plane. Two apical positions are occupied by one μ_2 bridged nitrate ion at one side and one aqua ligand as well as one monodentate nitrate ion at the other side. The slight geometrical differences between Cu(1) and Cu(2) originate from the differences in their axial coordination atoms. That is to say, Cu(1) is bonded to an aqua ligand [Cu(1)–O(1w), 2.508(6) Å], while Cu(2) exhibits a longer bond length with the nitrate donor [Cu(2)–O(6), 2.577(6) Å]. As far as we are aware there is no struc-

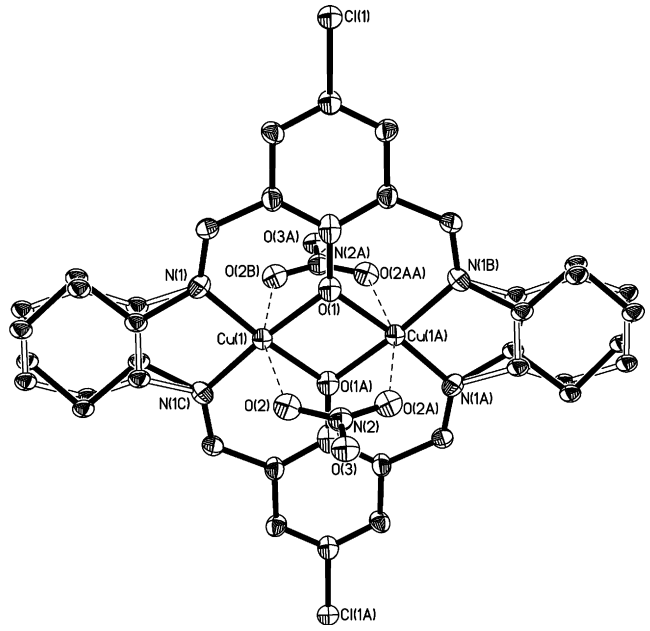


Fig. 8. ORTEP diagram (30% probability displacement ellipsoids) of complex (*R*,*R*)-**3** with the heteroatom-numbering scheme. Hydrogen atoms and perchlorate anion are omitted for clarity.

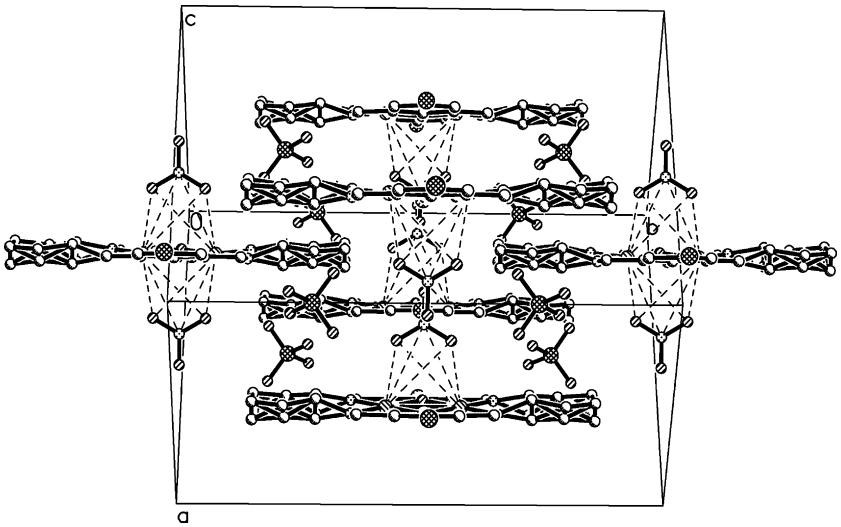


Fig. 9. A perspective view of the crystal packing of (*R*,*R*)-**3** together with the unit cell.

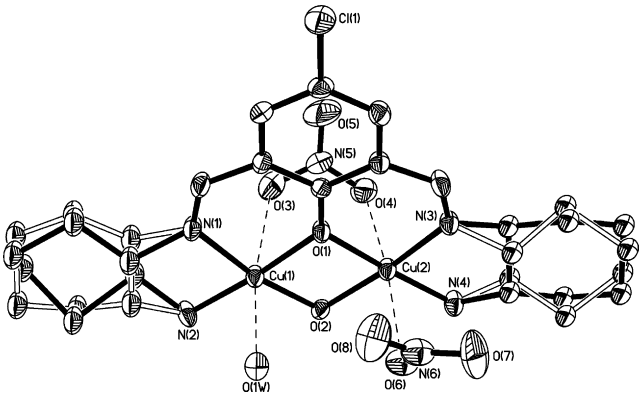


Fig. 10. ORTEP drawing (30% probability displacement ellipsoids) of complex **4** with the heteroatom-numbering scheme, hydrogen atoms and one free water molecule are omitted for clarity.

ture report on dinuclear metal complex of the [2 + 1] chiral Schiff-base macrocycle.

In the crystal structure of complex (*R*,*R*)-**3**, the perchlorate counterions are intercalated between adjacent layers (Fig. 9) forming hydrogen bonds with C–H proton of the cyclohexyl ring with C–H···O distance of 3.36(1) Å. As for complex **4**, hydrogen bonding interactions and π–π stacking interactions are observed to further stabilize the structure. The oxygen atoms of two water molecules are involved in intramolecular O–H···O H-bonds linking to the nitrate groups. The O···O distances vary from 2.94(1) to 3.05(1) Å in this case. Intermolecular O–H···O hydrogen bonds are also present between H_2O and NO_3^- with the O···O distances in the range from 2.82(1) to 3.08(4) Å. The NH_2 groups also participate in the contact of intermolecular N–H···O hydrogen binding interactions with the acceptors as NO_3^- anion and H_2O molecule. In addition, different kinds of weak C–H···O hydrogen bonds are present between the oxygen atoms of NO_3^- and H_2O and the carbon atoms of the phenyl group, cyclohexyl rings and imine C–H units. These connections generate a 2D layer network as illustrated in Fig. 11.

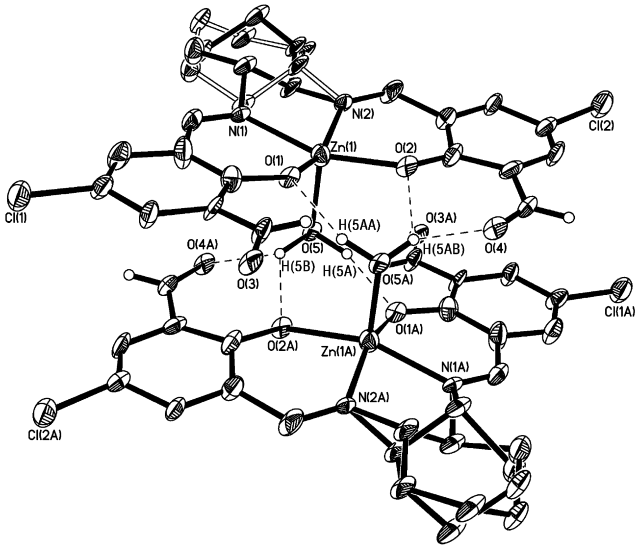


Fig. 12. ORTEP drawing (30% probability displacement ellipsoids) of **5** with the heteroatom-numbering scheme, only molecule **A** related dimeric structure is shown for clarity.

3.4. Crystal Structure of *5*

Complexation of (*R*,*R*)-**1** with $Zn(ClO_4)_2 \cdot 6H_2O$ in a 1:3 ratio in boiling ethanol leads to the formation of [1 + 2] contracted mononuclear complex **5** (Fig. 12). It crystallizes in $P\bar{1}$ space group and the asymmetric unit has two crystallographically independent molecules A and B. The Zn atom has five-coordinate distorted pyramidal geometry supported by a N_2O_3 donor set in molecules A and B. Two phenol oxygen atoms and two C=N nitrogen atoms occupy the equatorial positions and one aqua ligand lies in the axial position. This structure is different from the reported six-coordinate Mn(II) complex packing into a chiral *F*222 space group [10].

It is interesting to mention that hydrogen bonds play a key role in the conformation of a dimeric structure in **5**. As shown in Fig. 13, both of the hydrogen atoms of water

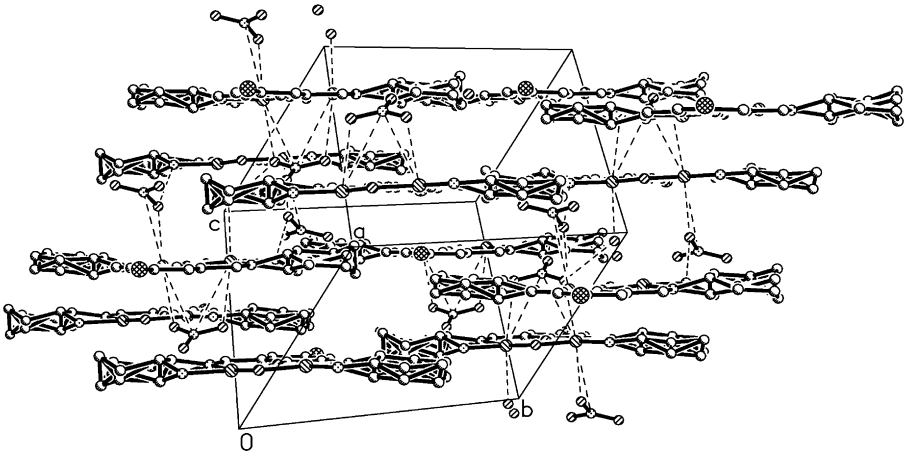


Fig. 11. A crystal packing view of **4** together with the unit cell.

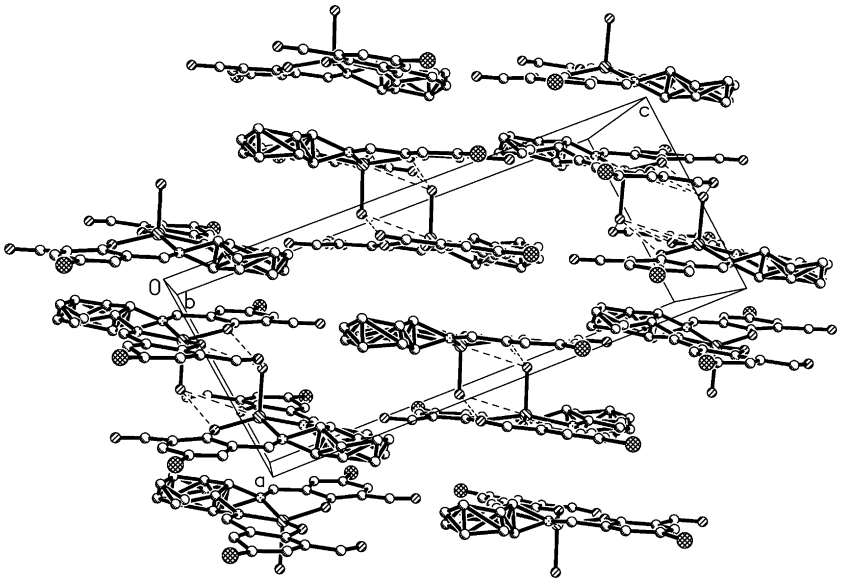


Fig. 13. A crystal packing view of **5** together with the unit cell.

molecule are involved in strong hydrogen bonding interactions with the oxygen atom of phenoxide unit [μ_2 bridging mode: O(5)–H(5A)···O(1) 2.71(1) Å, O(5)–H(5B)···O(2) 2.84(1) Å] and the aldehyde oxygen atom [monodentate mode: O(5)–H(5B)···O(4) 2.60(1) Å] of neighboring molecule. The existence of complementary O–H···O H-contacts stabilizes greatly the half-macrocyclic structure. Furthermore, different kinds of weak C–H···O hydrogen bonding interactions have been observed in the crystal packing. It is noted that intermolecular C–H···Cl interactions are found between the C–H protons of the cyclohexyl ring and the Cl(3) of another molecule with a C···Cl distance of 3.63(1) Å. This non-classical C–H···Cl hydrogen bonding is important in the crystal stacking of **5** [13]. Under the assistance of these above-mentioned weak interactions, a two-dimensional network is constituted.

3.5. Crystal Structure of *6*

It is interesting to find that the reaction of racemic-**1** and anhydrous $FeCl_3$ yields the [1 + 2] type of dimethyl acetal **6** in boiling methanol. Previous reports have demonstrated that Lewis acid $FeCl_3$ can successfully act as a catalyst in organic synthesis especially in strong acidic condition, including a wide range of esterification [21], Friedel–Crafts alkylation and rearrangement reaction [22], and their reaction mechanisms have been fully investigated [23]. In addition, Brooker and co-workers have observed that Fe(III) catalysing changes to [4 + 4] Schiff-base macrocycles where a 1,3-diazacyclopentane ring moiety have been formed [24]. In our reaction, it is suggested that some Schiff-base C=N bonds are broken firstly, coming back to aldehyde, and then the rearrangement intermediate coordinates with

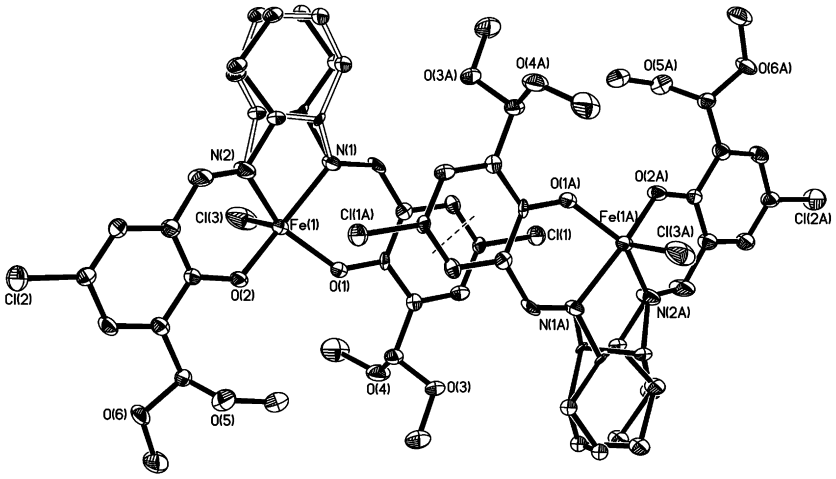


Fig. 14. ORTEP drawing (30% probability displacement ellipsoids) of complex **6** with the heteroatom-numbering scheme.

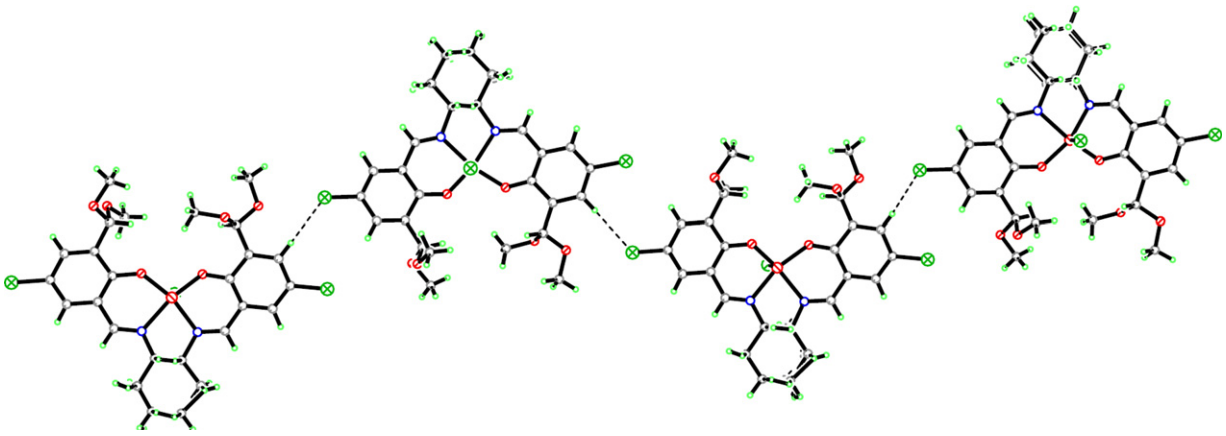


Fig. 15. View of the 1D chain structure of **6** through the C–H···Cl interactions along the *b*-axis.

Fe(III) and the excess $FeCl_3$ as a reactive catalyst and the methanol as nucleophilic reagent to create the acetal **6** simultaneously.

X-ray analyses for **6** indicate that the Fe(III) center adopts the square-pyramidal geometry and is five-coordinated to two imine N-donors, two phenoxy O-donors and one chlorine anion at the axial position (Fig. 14). The dihedral angle between the least-squares plane defined by O(1), Fe(1) and N(1) and the plane defined by O(2), Fe(1) and N(2) is 40.83°. Fe(III) ion deviates from the basal N_2O_2 plane by 0.3888 Å due to the mismatch between the cavity size and the ionic radius of the Fe(III) ion. Complex**6** also consists of dimeric structures stabilized by close intermolecular face-to-face π–π interaction. The centroid–centroid separation between the adjacent parallel aromatic rings is 3.504 Å.

In the crystal packing of **6**, a 1D chain structure along the crystallographic *b*-axis is formed under the assistance of C–H···Cl hydrogen bonds between the chlorine atoms Cl(1) of the aromatic groups and the carbon atoms C(18) of benzene rings (Fig. 15). At the same time, down the direction of the crystallographic *a*-axis, a 1D chain is also observed by the C–H···Cl interactions between the coordinated chlorine atoms Cl(3) and the carbon atoms of methyl C(25) (Fig. 16). The relative H-bond lengths and angles are Cl(1)···C(18) 3.68(1) Å and C(18)–H(18A)···Cl(1) 166.0°, Cl(3)···C(25) 3.69(1) Å and C(25)–H(25A)···Cl(3) 156.0°, respectively. There are two intramolecular C–H···O hydrogen bonds generated between the methyl CH_3 and the oxygen atom of phenol [C(22)–H(22A)···O(1), C(25)–H(25B)···O(2)] and one C–H···O hydrogen bonds formed between C–H of benzene ring and the oxygen atom of dimethyl acetal [C(18)–H(18A)···O(6)].

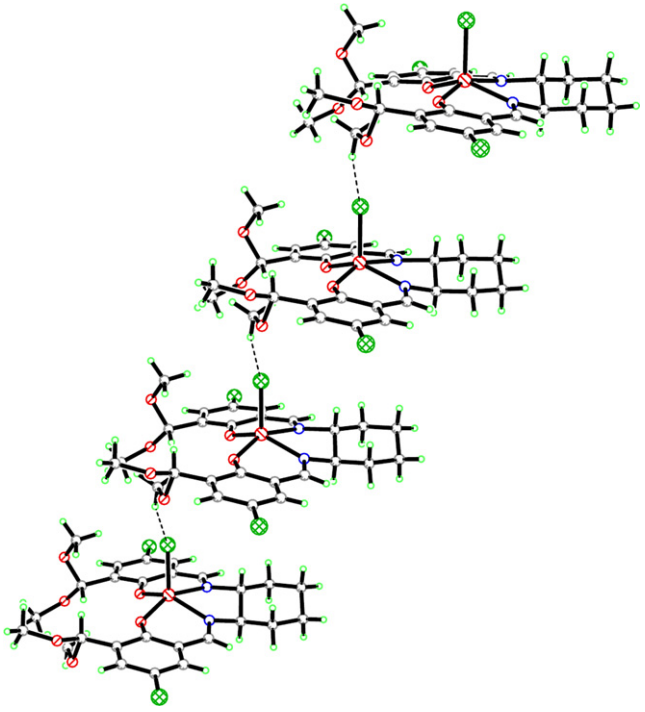


Fig. 16. View of the 1D chain structure of **6** through the C–H···Cl interactions along the *a*-axis.

4. Conclusion

We have reported the syntheses, structural and spectral characterizations of [3 + 3] chiral macrocycles **1** and a series of Cu(II), Zn(II) and Fe(III) ring-contraction complexes. The crystal structures of (*R*,*R*)-**3**, **4**, **5** and **6** demonstrate the formation of corresponding [2 + 2], [2 + 1] and [1 + 2] types of complexes resulting from the cleavage and reorganization of **1** in the course of metal complexation. The reorganization of the macrocycle can be attributed to the planarity and thermodynamic stability of the resulted complexes, namely, the size matching effect of macrocycles as well as the restriction of coordination geometry of the central metals and the counterions used. Specific features of the CD spectra for chiral macrocycles and metal complexes show the asymmetric environment, which will be useful in design of asymmetric catalysis.

Acknowledgements

W.H. would like to acknowledge the Major State Basic Research Development Programs (No. 2006CB806104 and No. 2007CB925101), the National Natural Science Foundation of China (No. 20721002 and No. 20301009) and the Scientific Research Foundation for the Returned Overseas Chinese Scholars, State Education Ministry for financial aid.

Appendix A. Supplementary data

CCDC 638655, 638656, 638657, 638658 and 638659 contain the supplementary crystallographic data for (*S*,*S*)-**1**, (*R*,*R*)-**3**, **4**, **5** and **6**. These data can be obtained free of charge via http://www.ccdc.cam.ac.uk/conts/retrieving.html, or from the Cambridge Crystallographic Data Centre, 12 Union Road, Cambridge CB2 1EZ, UK; fax: (+44) 1223-336-033, or e-mail: deposit@ccdc.cam.ac.uk. Supplementary data associated with this article can be found, in the online version, at doi:10.1016/j.poly.2007.12.003.

References

[1] (a) V. Alexander, Chem. Rev. 95 (1995) 273;
(b) S.M. Nelson, Pure Appl. Chem. 52 (1980) 2461;
(c) D.H. Busch, Science 171 (1971) 241;
(d) N.F. Curtis, Coord. Chem. Rev. 3 (1968) 3.

[2] (a) H. Okawa, H. Furutachi, D.E. Fenton, Coord. Chem. Rev. 17 (1998) 51;
(b) D.E. Fenton, H. Okawa, Chem. Ber. 130 (1997) 433;
(c) S.R. Collinson, D.E. Fenton, Coord. Chem. Rev. 148 (1996) 19;
(d) D.E. Fenton, Pure Appl. Chem. 58 (1986) 1437.

[3] (a) A. Martell, J. Penitka, D. Kong, Coord. Chem. Rev. 55 (2001) 216;
(b) P. Guerriero, S. Tamburini, P.A. Vigato, Coord. Chem. Rev. 139 (1995) 17;
(c) B. Dietrich, P. Viout, J.-M. Lehn, Macrocyclic Chemistry, VCH, Weinheim, 1993;
(d) L.F. Lindoy, The Chemistry of Macrocyclic Ligand Complexes, Cambridge University, Cambridge, UK, 1989;
(e) L.F. Lindoy, Pure Appl. Chem. 61 (1989) 1575;
(f) G.A. Melson, Coordination Chemistry of Macrocyclic Compounds, Plenum Press, New York, 1979.

[4] (a) S. Akine, D. Hashimoto, T. Saiki, T. Nabeshima, Tetrahedron Lett. 45 (2004) 4225;
(b) S. Akine, T. Taniguchi, T. Nabeshima, Tetrahedron Lett. 42 (2001) 8861;
(c) B. Bosnich, Inorg. Chem. 38 (1999) 2554;
(d) R. Das, K. Nag, Inorg. Chem. 30 (1991) 2831;
(e) N.H. Pilkington, R. Robson, Aust. J. Chem. 23 (1970) 2225.

[5] (a) W. Radecka-Paryzek, V. Patroniak, J. Lisowski, Coord. Chem. Rev. 249 (2005) 2156;
(b) J. Gregolinski, J. Lisowski, T. Lis, Org. Biomol. Chem. 3 (2005) 3161;
(c) P.A. Vigato, S. Tamburini, Coord. Chem. Rev. 248 (2004) 1717;
(d) S. Brooker, Coord. Chem. Rev. 222 (2001) 33.

[6] (a) C. Ma, A. Lo, A. Abdolmaleki, M. MacLachlan, J. Org. Lett. 6 (2004) 3841;
(b) N.V. Gerbeleu, V.B. Arion, J. Burges, Template Synthesis of Macrocyclic Compounds, VCH, Weinheim, 1999.

[7] (a) G. Givaja, A.J. Blake, C. Wilson, M. Schroder, J.B. Love, Chem. Commun. (2005) 4423;
(b) S. Brooker, Eur. J. Inorg. Chem. (2002) 2535;
(c) S. Brooker, R.J. Kelly, J. Chem. Soc., Dalton Trans. (1996) 2117;
(d) H. Adams, N.A. Bailey, D.E. Fenton, R.J. Good, R. Moody, C.O. Rodriguez de Barbarin, J. Chem. Soc., Dalton Trans. (1987) 207;
(e) V. Mckee, W.B. Shepard, J. Chem. Soc., Chem. Commun. (1985) 158;
(f) M.G.B. Drew, J. Nelson, S.M. Nelson, J. Chem. Soc., Dalton Trans. (1981) 1678.

[8] (a) J. Gao, J.H. Reibenspies, R.A. Zingaro, F.R. Woolley, A.E. Martell, A. Clearfield, Inorg. Chem. 41 (2005) 232;
(b) J. Gao, R.A. Zingaro, J.H. Reibenspies, A.E. Martell, Org. Lett. 6 (2004) 2453;
(c) J. Gao, A.E. Martell, Org. Biomol. Chem. 1 (2003) 2795;
(d) J. Gao, A.E. Martell, Org. Biomol. Chem. 1 (2003) 2801;
(e) J. Gao, J.H. Reibenspies, A.E. Martell, Angew. Chem., Int. Ed. 42 (2003) 6008.

[9] S.R. Korupoju, P.S. Zacharias, Chem. Commun. (1998) 1267.

[10] S.R. Korupoju, N. Mangayarkarasi, S. Ameerunisha, E.J. Valente, P.S. Zacharias, J. Chem. Soc., Dalton Trans. (2000) 2845.

[11] S.R. Korupoju, N. Mangayarkarasi, P.S. Zacharias, J. Mizuthani, H. Nishihara, Inorg. Chem. 41 (2002) 4099.

[12] M. Paluch, J. Lisowski, T. Lis, Dalton Trans. (2006) 381.

[13] (a) S.H. Gou, W. Huang, M. Qian, Q.D. Zeng, Trends Inorg. Chem. 7 (2001) 15;
(b) H. Adams, N.A. Bailey, P. Bertrand, O.R. Cecilia, D.E. Fenton, S.H. Gou, J. Chem. Soc., Dalton Trans. (1995) 275;
(c) S.H. Gou, D.E. Fenton, Inorg. Chim. Acta 223 (1994) 169.

[14] (a) W. Huang, Z.L. Chu, S.H. Gou, T. Ogawa, Polyhedron 26 (2007) 1483;
(b) W. Huang, H.B. Zhu, S.H. Gou, Coord. Chem. Rev. 250 (2006) 414;
(c) W. Huang, S.H. Gou, D.H. Hu, S. Chantrapromma, H.K. Fun, Q.J. Meng, Inorg. Chem. 41 (2002) 864;
(d) W. Huang, S.H. Gou, D.H. Hu, S. Chantrapromma, H.K. Fun, Q.J. Meng, Inorg. Chem. 40 (2001) 1712.

[15] (a) W. Huang, S.H. Gou, H.F. Qian, D.H. Hu, S. Chantrapromma, H.K. Fun, Q.J. Meng, Eur. J. Inorg. Chem. (2003) 947;
(b) Y.F. Sun, Q.D. Zeng, S.H. Gou, W. Huang, C.Y. Duan, J.C. Yao, J. Inclusion. Phenom. Macrocyclic Chem. 42 (2002) 131;
(c) S.H. Gou, M. Qian, Z. Yu, C.Y. Duan, X.F. Sun, W. Huang, J. Chem. Soc., Dalton Trans. 21 (2001) 3232.

[16] W. Huang, S.H. Gou, D.H. Hu, Q.J. Meng, Synth. Commun. 30 (2000) 1555.

[17] SMART and SAINT, Area Detector Control and Integration Software, Siemens Analytical X-ray Systems Inc., Madison, Wisconsin, USA, 1996.

[18] G.M. Sheldrick, SHELXTL, Version 6.10, Siemens Industrial Automation, Madison, WI, USA, 2000.

[19] H.D. Flack, Acta Crystallogr., Sect. A 39 (1983) 876.

[20] (a) S. Brooker, P.D. Croucher, J. Chem. Soc., Chem. Commun. (1995) 1493;
(b) I.A. Kahwa, F.R. Fronczek, J. Selbin, Inorg. Chim. Acta 126 (1987) 227.

[21] (a) R.G. Mallavarapu, K. Narasimhan, Indian J. Chem., Sect. B. 16 (1978) 725;
(b) A.N. Akopyan, J. Gen. Chem. (USSR) 7 (1937) 1687.

[22] P.A. Sykes, A Guidebook to Mechanism in Organic Chemistry, fourth ed., Longman, 1975, p. 140.

[23] D. Nightingale, R.G. Taylor, H.W. Smelser, J. Am. Chem. Soc. 63 (1941) 258.

[24] I.J. Hewitt, J.-K. Tang, N.T. Madhu, B. Pilawa, C.E. Anson, S. Brooker, A.K. Powell, Dalton Trans. (2005) 429.

2.1. Preparation of $[Sn(CH_2CH_2CN)_3I]$ (1)

A mixture of $[Sn_2(CH_2CH_2CN)_6]$ (0.562 g, 1.0 mmol) and I_2 (0.254 g, 1.0 mmol) in dichloromethane (7 cm^3) was stirred under reflux until the disappearance of iodine was observed. The crystalline solid was filtered off, recrystallized from CH_2Cl_2, washed with cold dichloromethane and dried in vacuo. Yield of the colorless product 0.547 g, 67%. *Anal.* Calc. for $C_9H_{12}N_3ISn$: C, 26.51; H, 2.97; N, 10.30; Sn, 29.11. Found: C, 26.27; H, 2.73; N, 10.15; Sn, 29.40%. IR (KBr, cm^{-1}): 2958 w, 2920 m, 2260 vs (ν_{CN}), 2244 vs (ν_{CN}), 1426 vs, 1417 vs, 1380 w, 1356 vw, 1316 vw, 1283 vw, 1250 vw, 1150 vs, 1140 sh, 1015 m, 1004 s, 912 sh, 890 s, 880 s, 868m, 718 w, 680 vs, 673 vs, 653 s, 632 m, 617 w, 545 vw, 507 vw, 460 m, 440 s, 372 mw. ^{119}Sn NMR (CD_3OD): $\delta = -14.3$ ppm.

Complex $[SnBr(CH_2CH_2CN)_3]$ (**2**) was prepared in a similar manner to $[Sn(CH_2CH_2CN)_3I]$ except for the use 1 mmol of Br_2 instead of I_2. Mass collected 0.527 g, 73%. *Anal.* Calc. for $C_9H_{12}N_3BrSn$: C, 29.96; H, 3.35; N, 11.65; Sn, 32.90. Found: C, 29.79; H, 3.08; N, 11.51; Sn, 32.60%. IR (KBr, cm^{-1}): 2960 w, 2928 m, 2260 vs (ν_{CN}), 2244 vs (ν_{CN}), 1428 vs, 1414 vs, 1382 w, 1310 vw, 1303 vw, 1282 vw, 1268 vw, 1155 vs, 1142 sh, 1015 m, 1003 s, 905 sh, 892 s, 882 s, 870 m, 678 vs, 655 vs, 632 m, 616 w, 508 vw, 460 m, 446 s, 372 mw. ^{119}Sn NMR (CD_3OD): $\delta = -17.5$ ppm.

2.2. Physical measurements

Infrared spectra (KBr pellets and nujol) were recorded on a Bruker IFS 113v, ^{1}H NMR spectra were taken on a Bruker AMX 300 and ^{119}Sn NMR spectra on a Bruker Avance 500. The tin contents were determined using the ICP-AES method on a ARL 3410.

2.3. X-ray crystallographic measurements

All measurements of crystals were performed at low temperature using an Oxford Cryosystem device on a Kuma KM4CCD κ-axis diffractometer with graphite-monochromated Mo Kα radiation. Accurate cell parameters were determined and refined by a least-squares fit of the 4000 strongest reflections. The data were corrected for Lorentz and polarization effects. Absorption correction based on least-squares fitted against $|F_c| - |F_o|$ differences were also applied [15]. Data reduction and analysis were carried out with the Oxford Diffraction (Poland) (formerly Kuma Diffraction Wrocław, Poland) programs. The structure was solved by direct methods (program SHELXS 97 [16]) and refined by the full-matrix least-squares method on all F^2 data using the SHELXL 97 [17] programs. Non-hydrogen atoms were refined with anisotropic vibrational parameters; hydrogen atoms were included from the geometry of the molecules and were refined with isotropic vibrational parameters.

2.4. Computational details

The molecular and electronic structure and IR spectra of the monomer $[SnBr(CH_2CH_2CN)_3]$ and the dimer $[SnBr(CH_2CH_2CN)_3]_2$ of C_1 symmetry have been studied with the GAUSSIAN 03 package of programs [18] using the DFT B3LYP method with the LANL2DZ basis set

3. Results and discussion

Complexes **1** and **2** are colourless, crystalline compounds. An X-ray crystallography study revealed that they are isomorphic and crystallize in the $P2_1/n$ space group. Crystallographic data for complexes **1** and **2** are given in Table 1 and selected bond lengths and angles in Tables 2 and 3. The ORTEP views of the compounds are depicted in Figs. 1 and 2. Both compounds in the solid state consist of zigzag single-strand chains with the bridging 2-cyanoethyl ligand coordinating via the CH_2 group and the N atom (Fig. 3). The tin atoms are in a distorted trigonal bipyramidal environment. In complex **1** axial coordination sites are occupied by the iodo ligand and the N(3) atom of the bridging cyano group; the I(1)–Sn(1)–N(3i) angle is 179.04(5)°. The carbon atoms of the 2-cyanoethyl ligands are coordinated in equatorial positions. The Sn–C distances differ only slightly. The Sn(1)–C(4), Sn(1)–C(1)

Table 1
Crystal data and structure refinement for $[Sn(CH_2CH_2CN)_3I]$ (**1**) and $[SnBr(CH_2CH_2CN)_3]$ (**2**)

Emp. formula	$C_9H_{12}IN_3Sn$	$C_9H_{12}BrN_3Sn$
Formula weight	407.81	360.82
T (K)	100(2)	100(2)
λ (Å)	0.71073	0.71073
Crystal system	monoclinic	monoclinic
Space group	$P2_1/n$	$P2_1/n$
a (Å)	8.4586(5)	8.6507(7)
b (Å)	11.1605(6)	10.7900(10)
c (Å)	13.8541(8)	13.6134(12)
β (°)	103.753(5)	103.744(7)
V (Å^3)	1270.36(13)	1234.30(19)
Z	4	4
D_c (Mg m^{-3})	2.132	1.942
μ (mm^{-1})	4.411	5.276
$F(000)$	760	688
Crystal size (mm)	0.18 × 0.18 × 0.12	0.20 × 0.14 × 0.13
θ Range (°)	3.54–28.47	3.61–28.39
Ranges of h,k,l	−11 → 10,−14 → 14,−18 → 16	−11 → 11,−11 → 14,−15 → 17
Reflections collected	8507	8305
Independent reflections (R_{int})	2964 (0.0404)	2855 (0.0465)
Data/parameters	2964/176	2855/175
Goodness-of-fit (F^2)	1.165	1.116
Final R_1/wR_2 indices ($I > 2\sigma_I$)	0.0205/0.0476	0.0326/0.0700
Largest difference in peak/hole (e Å^{-3})	0.941/−0.599	1.156/−1.408

$w = 1/[\sigma^2(F_o^2) + (a \times P)^2 + b \times P]$, where $P = [\mathrm{Max}(F_o^2, 0) + 2 \times F_c^2]/c$.

Table 2
Selected bond lengths (Å) and angles (°) for $[Sn(CH_2CH_2CN)_3I]$ (**1**)

I(1)–Sn(1)	2.8128(2)	C(8)–C(9)	1.463(3)
Sn(1)–C(4)	2.153(2)	I(1)···I(1iii)	3.997(1)
Sn(1)–C(1)	2.156(2)	C(4)–Sn(1)–C(1)	115.54(9)
Sn(1)–C(7)	2.157(2)	C(4)–Sn(1)–C(7)	123.39(9)
Sn(1)–N(3i)	2.5944(19)	C(1)–Sn(1)–C(7)	113.37(9)
N(1)–C(3)	1.142(3)	C(4)–Sn(1)–N(3i)	78.91(8)
N(2)–C(6)	1.142(3)	C(1)–Sn(1)–N(3i)	84.73(7)
N(3)–C(9)	1.142(3)	C(7)–Sn(1)–N(3i)	78.93(7)
N(3)–Sn(1ii)	2.5944(19)	C(4)–Sn(1)–I(1)	100.48(6)
C(1)–C(2)	1.531(4)	C(1)–Sn(1)–I(1)	94.89(6)
C(2)–C(3)	1.472(4)	C(7)–Sn(1)–I(1)	102.04(6)
C(4)–C(5)	1.527(3)	N(3i)–Sn(1)–I(1)	179.04(5)
C(5)–C(6)	1.474(3)	C(9)–N(3)–Sn(1ii)	162.97(18)
C(7)–C(8)	1.536(3)	Sn(1)–I(1)···I(1iii)	159.36(1)

Symmetry transformations used to generate equivalent atoms: i: $-x+3/2$, $y+1/2$, $-z+1/2$; ii: $-x+3/2$, $y-1/2$, $-z+1/2$.

Table 3
Selected bond lengths (Å) and angles (°) for $[SnBr(CH_2CH_2CN)_3]$ (**2**)

Br(1)–Sn(1)	2.5993(4)	C(5)–C(6)	1.480(3)
Sn(1)–C(4)	2.134(2)	C(7)–C(8)	1.534(3)
Sn(1)–C(7)	2.155(2)	C(8)–C(9)	1.463(3)
Sn(1)–C(1)	2.160(2)	C(4)–Sn(1)–C(7)	121.95(10)
Sn(1)–N(3i)	2.607(2)	C(4)–Sn(1)–C(1)	113.29(9)
N(1)–C(3)	1.142(4)	C(7)–Sn(1)–C(1)	117.29(9)
N(2)–C(6)	1.144(3)	C(4)–Sn(1)–Br(1)	100.80(7)
N(3)–C(9)	1.139(3)	C(7)–Sn(1)–Br(1)	100.92(6)
C(1)–C(2)	1.523(4)	C(1)–Sn(1)–Br(1)	95.44(6)
C(2)–C(3)	1.482(4)	N(3i)–Sn(1)–Br(1)	179.57(6)
C(4)–C(5)	1.534(3)		

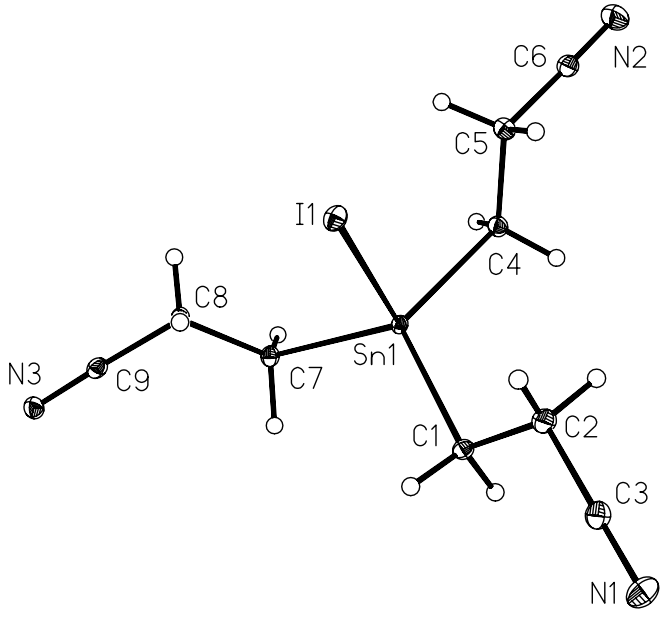


Fig. 1. Molecular structure of complex **1** with crystallographic numbering.

and Sn(1)–C(7) bond lengths are 2.153(2), 2.156(2) and 2.157(2) Å, respectively. The tin-axial ligand bonds are weaker, the Sn(1)–N(3i) (2.5944(19) Å) and Sn(1)–I(1)

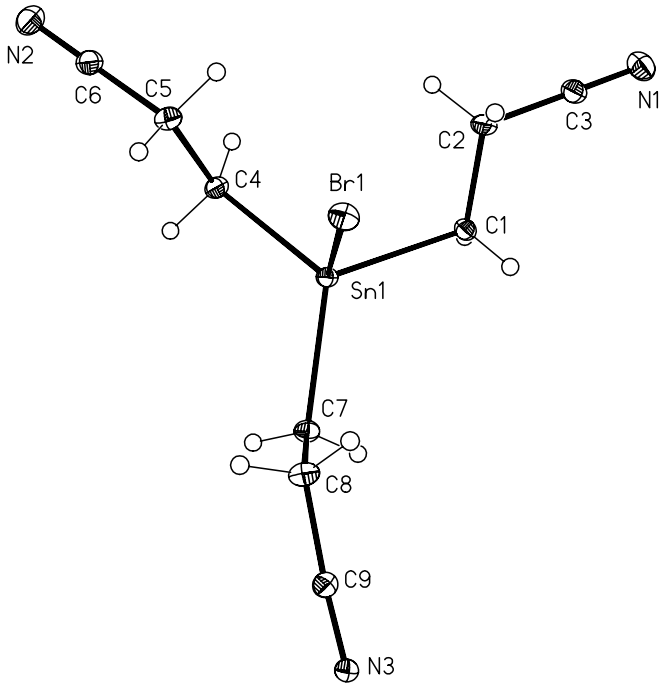


Fig. 2. Molecular structure of complex **2** with crystallographic numbering.

(2.8128(2) Å) distances are considerably longer than those for the equatorial ligands. Considerably weaker bonds of tin with axial ligands in comparison with equatorial ones have been found in many complexes. Thus the Sn–N_{eq} bond in $[Sn(C_4H_9)_2\{OOC(CH_2)_2NCH_2C_6H_5\}]$ is substantially shorter (2.228(3) Å) [19] and in the cationic complex (TBPY-5-12)-$[SnBr_2(C_6H_5)_2(H_2O)]^+$ the Sn–Br_{eq}, Sn–C_{eq}, Sn–Br_{ax} and Sn–O_{ax} bonds are 2.486(1), 2.112(6), 2.599(1) and 2.305(5) Å, respectively [20]. Similarly in the complex with the 2-pyridinecarboxylato ligand, $\{[Bu_2Sn(OOCC_5H_4N)]_2O\}_2$, and in the binuclear pyrazine compound $[Me_2Cl_2Sn(\mu\text{-}NC_4H_4N)SnMe_2Cl_2]$ with the nitrogen ligands coordinated in axial positions, the Sn–N distances are much longer, being 2.550(5) [21] and 2.746(8) Å [22], respectively. It is interesting that there is a weak interaction between iodine atoms of different chains. The I(1)–I(1)#3 distance and Sn(1)–I(1)–I(1)#3 angle are equal to 3.997(1) Å and 159.36(1)°, respectively. Thus, this distance is about 0.3 Å shorter than the sum of the van der Waals radii of iodine atoms. The structure of complex **2** is similar to compound **1**. In the solid state analogous $–(NCCH_2CH_2)_2BrSn(\mu\text{-}NCCH_2CH_2)SnBr(CH_2CH_2CN)_2–$ chains are formed, however, the intermolecular Br–Br distances are larger (4.494 Å) and the Sn–Br–Br angles are smaller (151.66°). Thus in compound **1** there is a weak covalent I–I intermolecular interaction as opposed to complex **2** in which the Br–Br distance is larger than double the van der Waals radius.

The coordination sphere in compound **2** is similar to compound **1**, however in complex **2** there are larger differences between the Sn–C distances. They are equal

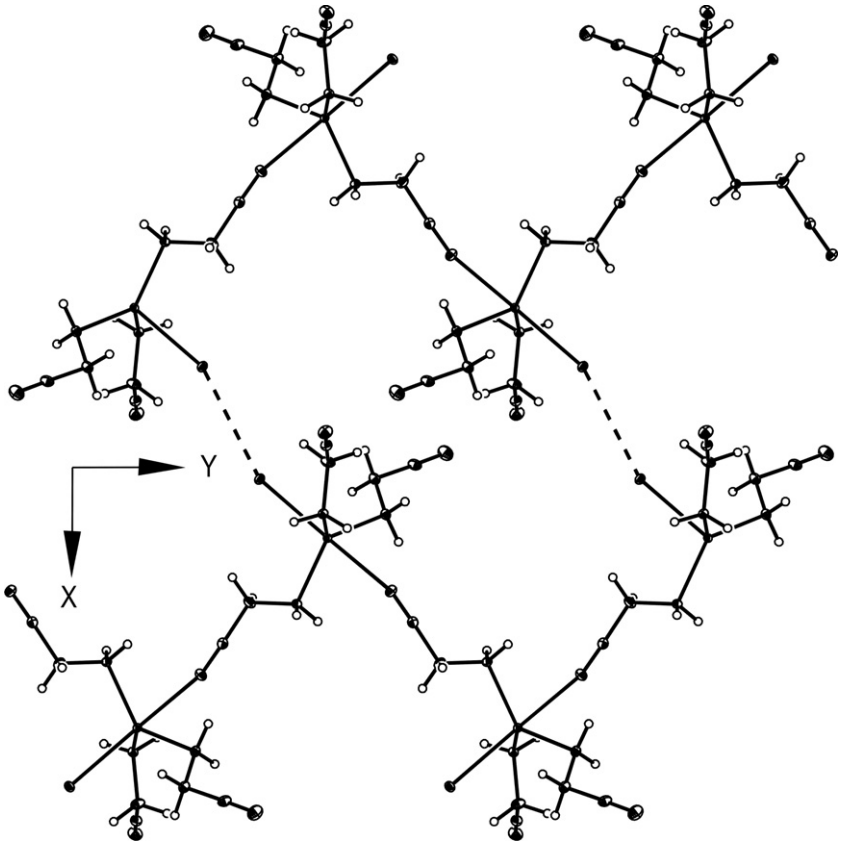


Fig. 3. ORTEP view showing the one-dimensional structure of complex **1**.

to 2.134(2), 2.155(2) and 2.160(2) Å. The Sn(1)–N(3i) bond (2.607(2) Å) is slightly longer than that in complex **1** and the Sn(1)–Br(1) distance (2.5993(4) Å) is almost the same as that in the complex $[SnBr_2(C_6H_5)_2(H_2O)]^+$ [20].

To explain the properties of compounds **1** and **2** and to compare the structures of the isolated $[SnX(CH_2CH_2CN)_3]$ complexes with those in the solid state, the molecular and electronic structure of the $[SnBr(CH_2CH_2CN)_3]$ monomer and $[SnBr(CH_2CH_2CN)_3]_2$ dimer have been studied at the DFT B3LYP level with a LANL2DZ basis set. Calculated interatomic distances and angles agree well with the crystallographic data (Figs. 4 and 5). The calculated coordination sphere of the monomer is pseudotetrahedral with average BrSnC and CSnC angles equal to 105.04° and 113.52°, respectively. As expected, the CSnC angles are smaller and the BrSnC angles are larger than those in compound **2** in the solid state. The calculated interatomic distances and angles for five- and four-coordinated tin atoms are: d(Sn–C) 2.155 and 2.151 Å, ∠CSnC 116.62° and 113.43°, ∠BrSnC 100.72° and 105.13°. Thus the values calculated for a five-coordinated tin atom are similar to those determined for complex **2** (d(SnC) = 2.150 Å, ∠CSnC 117.5° and ∠BrSnC 99.05°). There is a good agreement between the calculated and experimental IR spectra of compound **2** in KBr and nujol as shown in Figs. 6 and 7 and Table 7. The differences between the calculated and experimental values of vibrations are relatively small, especially in the case of bands with great participation of ν(SnBr), ν(SnN), ν(SnC) and ν(CN) stretching vibrations.

Complexes **1** and **2** are soluble in polar organic solvents, e.g. dichloromethane, chloroform, acetone, DMSO and water. The coordination about the tin atom in the complexes in solution can be easily followed using ^{1}H NMR spectroscopy. From the $^2J(^{119}Sn^1H)$ coupling constants calculated from the satellites, it is possible to calculate a value for θ, the C–Sn–C angle in triorganotin compounds, from the following equation [23]:

$$\theta = 0.0161|^2J|^2 - 1.32|^2J| + 133.4$$

The $^2J(^{119}Sn^1H)$ coupling constants for complexes **1** and **2** in $CDCl_3$ are 47.8 and 47.9 Hz, respectively (Table 4). Thus, the θ value for these compounds dissolved in chloroform is 107.1°. Therefore the complexes in chloroform, dichloromethane and other weak coordinating solvents feature four-coordinate Sn atoms with a distorted tetrahedral coordination. However, in solutions of water and other strongly coordinating solvents, substitution of bromo and iodo ligands takes place and five-coordinate complexes are formed:

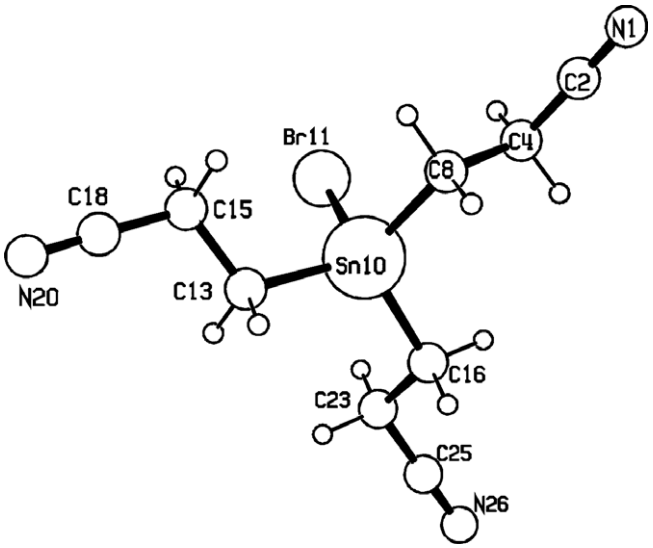


Fig. 4. Molecular structure of $[SnBr(CH_2CH_2CN)_3]$ calculated at the DFT B3LYP level with a LANL2DZ basis set. Selected bond lengths (Å) and angles (°): Sn–C = 2.148–2.149, Sn–Br = 2.602; ⟨CSnC = 113.01–113.95, ⟨CCN = 179.15, ⟨CSnBr = 104.84–105.18.

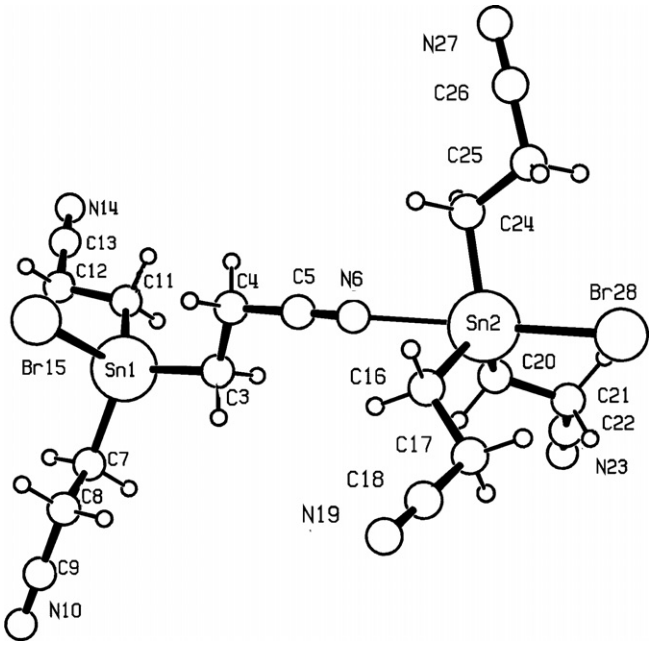


Fig. 5. Molecular structure of $[SnBr(CH_2CH_2CN)_3]_2$ calculated at the DFT B3LYP level with a LANL2DZ basis set. Selected bond lengths (Å) and angles (°): Sn26–C43 = 2.147, Sn26–C16 = 2.148, Sn26–C24 = 2.159, Sn26–Br = 2.601, Sn27–C = 2.154 – 2.157, Sn27–N = 2.682, Sn27–Br = 2.666; ⟨N–Sn27–Br = 178.48, ⟨C–Sn27–C = 116.38–116.99, C–Sn27–Br = 99.71–101.33, ⟨C–Sn26–C = 112.73–114.80, ⟨C–Sn26–Br = 103.73–105.98.

$$[SnBr(CH_2CH_2CN)_3] + 2H_2O \rightarrow [Sn(CH_2CH_2CN)_3(OH)(H_2O)] + H^+ + Br^-$$

Water solutions of these compounds are acidic, the pH of 1 mmol solutions is equal to 3.5. The Br^- and I^- ions are immediately deposited with $AgNO_3$. The $^2J(^{119}Sn^1H)$ coupling constants for complexes **1** and **2** in coordinating solvents are considerably higher than those in $CDCl_3$ (Table 4). In CD_3OD they are equal to 59.2 and 61.4 Hz, respectively, in D_2O 65.9 and 65.8 Hz and in D_2O containing a stoichiometric amount of NaOD 72.4 Hz. Thus the C–Sn–C angles for the complexes in these solutions are about 111.7° and 113.1° in methanol, 116.3° in water and 122.2° in solutions containing sodium hydroxide. In methanol most likely five-coordinate complexes are formed with a relatively strongly distorted trigonal bipyramidal coordination about the tin atoms. Similar C–Sn–C angles (112.7–115.8°) were found for species present in water solutions of $[SnMe_3Cl]$ and for the products of their reactions with glutathione [24]. The presence of the dihydroxo anionic complex $[SnMe_3(OH)_2]^-$ ($\theta = 115.8°$) with a *trans* trigonal pyramidal coordination was suggested for water solutions at a physiological pH value [24]. In acidic water solutions cationic $[Sn(CH_2CH_2CN)_3(H_2O)_2]^+$ or neutral $[Sn(CH_2CH_2CN)_3(OH)(H_2O)]$ complexes are formed with a less distorted trigonal bipyramidal structure, and in slightly basic solutions, obtained by addition of sodium hydroxide (pH 8.0–8.5), the trigonal bipyramidal dihydroxo complex $[Sn(CH_2CH_2CN)_3(OH)_2]^-$ is formed. The interaction of these complexes with adenosine, both in acidic solution obtained by the dissolution of complex **2** in D_2O (pH 3.5) and alkalized with NaOH solution (pH 8–8.5), is weak The ^1H NMR spectra (Tables 4 and 5) of the complexes alone and the complexes in the presence of adenosine are very similar. The chemical shifts as well as the $^2J(^{119}SnH)$ and $^3J(HH)$ coupling constants differ only slightly. However, the interaction of AMP with complex **2**, both in acidic and basic solutions, is relatively strong. The signal of the α-methylene group ($SnCH_2$) is not resolved and the β-methylene groups give two triplets, although the $^2J(^{119}SnH)$ and $^3J(^{119}SnH)$ coupling constants for the **2** + AMP + D_2O and **2** + AMP + D_2O + NaOD systems are similar. The C–Sn–C angles are equal to 115.9° and 122.2°, respectively and differ only slightly from the appropriate values found for solutions of complex **2** without AMP. Two signals were also observed for H^2, H^8 and $H^{1'}$ for the **2** + AMP solution in D_2O. This suggests that in this solution AMP is coordinated via the O atom of the phosphato group, giving two trigonal bipyramidal complexes (Scheme 1), however, the presence of two isomers of one complex cannot be excluded. The ^1H NMR spectra indicate that ATP also interacts with $[Sn(CH_2CH_2CN)_3(OH)(H_2O)]$ and other trigonal bipyramidal complexes, however the changes in the spectra are less pronounced. This results from longer distance of the purine and ribose fragments from the tin atom when ATP is coordinated via the oxygen atom of γ-P.

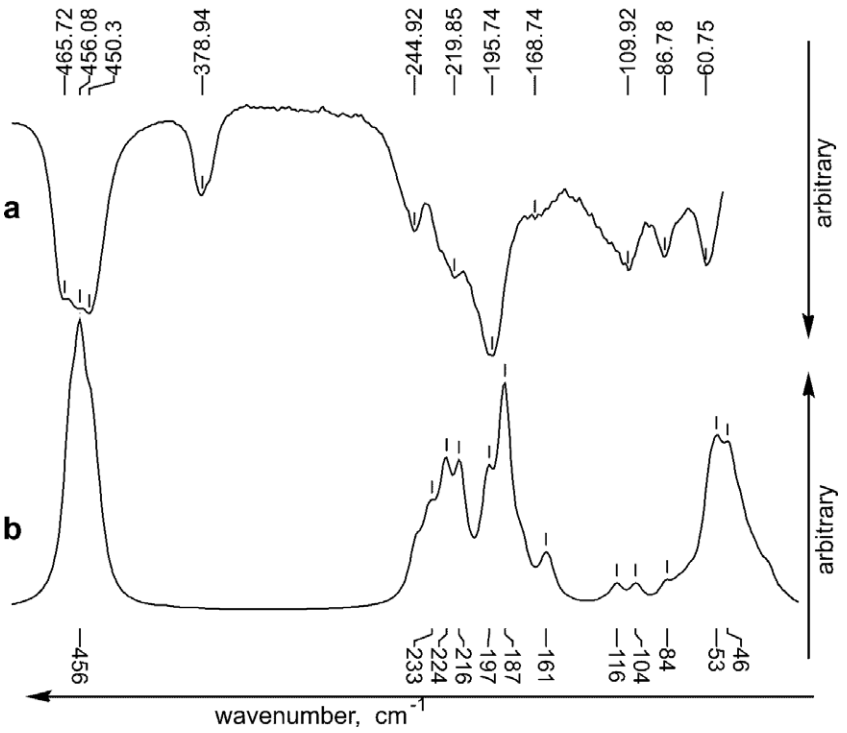


Fig. 6. FI-R spectrum of complex **2**: (a) experimental (in nujol), (b) calculated.

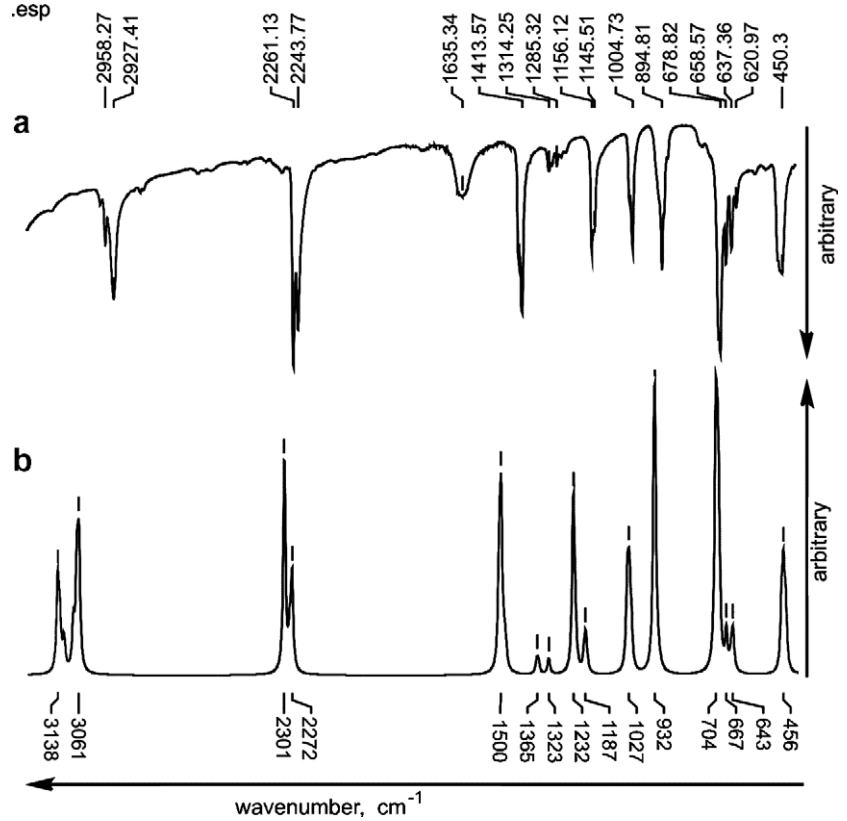


Fig. 7. IR spectrum of complex **2**: (a) experimental (in KBr), (b) calculated.

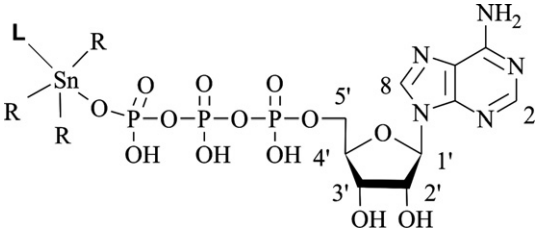
Table 4
^{1}H NMR spectra of complexes **1** and **2**

Compounds	Solvent	NMR data, δ (ppm), J (Hz)	C–Sn–C angle (°)
1	$CDCl_3$	1.83 (t, SnCH_2, $^2J(^{119/117}SnH) = 47.8$ Hz/46.0 Hz, $^3J(HH) = 7.6$ Hz); 2.79 (t, CH_2CN, $^3J(^{119/117}SnH) = 78.7$ Hz/74.9 Hz)	107.1
1	CD_3OD	1.70 (t, SnCH_2, $^2J(^{119/117}SnH) = 59.2$ Hz/57.0 Hz, $^3J(HH) = 8.0$ Hz); 2.84 (t, CH_2CN, $^3J(^{119/117}SnH) = 79.2$ Hz/75.9 Hz)	111.7
1	D_2O	1.66 (t, SnCH_2, $^2J(^{119/117}SnH) = 65.9$ Hz/63.0 Hz, $^3J(HH) = 7.8$ Hz); 2.81 (t, CH_2CN, $^3J(^{119/117}SnH) = 85.7$ Hz/82.0 Hz)	116.3
2	$CDCl_3$	1.83 (t, SnCH_2, $^2J(^{119/117}SnH) = 47.9$ Hz/46.2 Hz, $^3J(HH) = 7.5$ Hz); 2.83 (t, CH_2CN, $^3J(^{119/117}SnH) = 88.4$ Hz/84.4 Hz)	107.1
2	CD_3OD	1.65 (t, SnCH_2, $^2J(^{119/117}SnH) = 61.4$ Hz/58.7 Hz, $^3J(HH) = 8.0$ Hz); 2.83 (t, CH_2CN, $^3J(^{119/117}SnH) = 78.0$ Hz/74.6 Hz)	113.1
2	D_2O	1.61 (t, SnCH_2, $^2J(^{119/117}SnH) = 65.8$ Hz/62.9 Hz, $^3J(HH) = 7.8$ Hz); 2.76 (t. CH_2CN, $^3J(^{119/117}SnH) = 82.2$ Hz/78.6 Hz)	116.3
2	D_2O + NaOD	1.17 (t, SnCH_2, $^2J(^{119/117}SnH) = 72.4$ Hz/ 69.4 Hz, $^3J(HH) = 8.4$ Hz); 2.57 (t, CH_2CN, $^3J(^{119/117}SnH) = 67.1$ Hz/64.2 Hz)	122.2

Table 5
^{1}H NMR spectra adenosine (Ado), AMP, ATP and complex **2** in the presence of Ado, AMP and ATP

Compounds	Solvent	NMR data, δ (ppm), J (Hz)	C–Sn–C angle (°)
Ade	D_2O	3.70 ($H_A^{5'}$, J(AB) = 13.1 Hz); 3.77 ($H_B^{5'}$); 4.17 (m, $H^{4'}$); 4.30 (dd, H^3prime, $^3J(H^{2'}H^{3'}) = 5.0$ Hz, $^3J(H^{3'}H^{4'}) = 3.1$ Hz); 5.93 (d, $H^{1'}$, $^3J(H^{1'}H^{2'}) = 6.2$ Hz); 8.1 (s, H^8); 8.19(s, H^2)	
2 + Ade	D_2O	1.57 (t, SnCH_2, $^2J(^{119/117}SnH) = 65.4$ Hz/ 62.9 Hz, $^3J(HH) = 7.8$ Hz); 2.74 (t, CH_2CN, $^3J(^{119/117}SnH) = 83.5$ Hz/79.7 Hz); 3.72 ($H_A^{5'}$, J(AB) = 13.1 Hz); 3.80 ($H_B^{5'}$); 4.19 (m, $H^{4'}$); 4.31 (dd, $H^{3'}$, $^3J(H^{2'}H^{3'}) = 5.0$ Hz, $^3J(H^{3'}H^{4'}) = 3.7$ Hz); 5.96 (d, $H^{1'}$, $^3J(H^{1'}H^{2'}) = 6.2$ Hz); 8.13 (s, H^8); 8.24(s, H^2)	115.9
Ade	D_2O + NaOD	3.70 ($H_A^{5'}$, J(AB) = 12.8 Hz); 3.75 ($H_B^{5'}$); 4.10 (m, $H^{4'}$); 4.13 (m, $H^{3'}$); 5.77 (d, $H^{1'}$, $^3J(H^{1'}H^{2'}) = 6.3$ Hz); 8.07 (s, H^8); 8.17(s, H^2)	
2 + Ade	D_2O + NaOD	1.14 (t, SnCH_2, $^2J(^{119/117}SnH) = 72.8$ Hz/ 69.9 Hz, $^3J(HH) = 8.4$ Hz); 2.55 (t, CH_2CN, $^3J(^{119/117}SnH) = 67.9$ Hz/64.9 Hz); 3.63 ($H_A^{5'}$, J(AB) = 12.3 Hz); 3.68 ($H_B^{5'}$); 4.02 (m, $H^{4'} + H^{3'}$); 5.67 (d, $H^{1'}$, $^3J(H^{1'}H^{2'}) = 6.9$ Hz); 8.06 (s, H^8); 8.15 (s, H^2)	119.6
AMP	D_2O	4.03 (m, $H^{5'}$); 4.28 (m, $H^{4'}$); 4.40 (t, $H^{3'}$, $^3J(H^{2'}H^{3'}) = {}^3J(H^{3'}H^{4'}) = 4.1$ Hz); 6.08 (d, $H^{1'}$, $^3J(H^{1'}H^{2'}) = 5.7$ Hz); 8.31 (s, H^8); 8.51(s, H^2)	
2 + AMP	D_2O	1.57 (m, SnCH_2, $^2J(^{119/117}SnH) = 65.4$ Hz[a]); 2.78 (two t, CH_2CN, $^3J(^{119/117}SnH) = 80.9$ Hz[a]); 4.02– 4.10 ($H^{5'}$); 4.31 (m, $H^{4'}$); 4.42 (t,$H^{3'}$, $^3J(H^{2'}H^{3'}) = {}^3J(H^{3'}H^{4'}) = 4.4$ Hz); 6.11 (two d, $H^{1'}$, $^3J(H^{1'}H^{2'}) = 5.6$ Hz); 8.350 (s, H^8); 8.353 (s, H^8); 8.531 (s, H^2); 8.538 (s, H^2)	115.9
AMP	D_2O + NaOD	3.81–3.87 ($H^{5'}$); 4.15–4.20 (m, $H^{4'}$); 4.25 (dd, $H^{3\prime}$, $^3J(H^{2'}H^{3'}) = 5.1$ Hz, $^3J(H^{3'}H^{4'}) = 3.3$ Hz); 5.90 (d, $H^{1'}$, $^3J(H^{1'}H^{2'}) = 6.1$ Hz); 8.11 (s, H^8); 8.45 (s, H^2)	
2 + AMP	D_2O + NaOD	1.17 (t, SnCH_2, $^2J(^{119/117}SnH) = 72.3$ Hz/69.4 Hz); 2.57 (t, CH_2CN, $^3J(^{119/117}SnH) = 67.4$ Hz/64.2 Hz); 3.77–3.88 ($H^{5'}$); 4.10–4.17 (m, $H^{3'} + H^{4'}$); 5.81 (d, $H^{1'}$, $^3J(H^{1'}H^{2'}) = 6.1$ Hz); 8.11 (s, H^8); 8.42 (s, H^2)	122.1
ATP	D_2O	4.17 (m, $H^{5'}$); 4.29 (m, $H^{4'}$); 4.44 (m, $H^{3'}$); 6.02 (m, $H^{1'}$); 8.29 (s, H^8); 8.50(s, H^2)	
2 + ATP	D_2O	1.58 (t, SnCH_2, $^2J(^{119/117}SnH) = 67.4$ Hz/ 64.5 Hz, $^3J(HH) = 8.1$ Hz); 2.76 (t, CH_2CN, $^3J(^{119/117}SnH) = 81.6$ Hz/78.5 Hz); 4.19 (m, $H^{5'}$); 4.32 (m, $H^{4'}$), 4.47 (t, $H^{3'}$, $^3J(H^{2'}H^{3'}) = {}^3J(H^{3'}H^{4'}) = 4.4$ Hz); 6.07 (d, $H^{1'}$, $^3J(H^{1'}H^{2'}) = 5.6$ Hz); 8.33 (s, H^8); 8.55(s, H^2)	117.4
ATP	D_2O + NaOD	4.05–4.13 (m, $H^{5'}$); 4.22 (m, $H^{4'}$); 4.44 (dd, $H^{3'}$, $^3J(H^{2'}H^{3'}) = 5.1$ Hz, $^3J(H^{3'}H^{4'}) = 3.4$ Hz); 5.90 (d, $H^{1'}$, $^3J(H^{1'}H^{2'}) = 6,1$ Hz); 8.12 (s, H^8); 8.40 (s, H^2)	
2 + ATP	D_2O + NaOD	1.19 (t, SnCH_2, $^2J(^{119/117}SnH) = 71.8$ Hz/ 68.8 Hz, $^3J(HH) = 8.4$ Hz); 2.58 (t, CH_2CN, $^3J(^{119/117}SnH) = 67.9$ Hz/ 65.2 Hz); 4.07-4.14 (m, $H^{5'}$); 4.2 (m, $H^{4'}$); 4.35 (m, $H^{3'}$); 5.91 (d, $H^{1'}$, $^3J(H^{1'}H^{2'}) = 5.9$ Hz); 8.13 (s, H^8); 8.40(s, H^2)	121.6

[a] The average values of $J(^{119/117}SnH)$ coupling constants, ^{119}Sn and ^{117}Sn satellites are not resolved.



Scheme 1.

4. Conclusion

Organotin complexes with 2-cyanoethyl ligands, $[Sn(CH_2CH_2CN)_3I]$ (**1**) and $[SnBr(CH_2CH_2CN)_3]$ (**2**), have been obtained and characterized by NMR and IR spectroscopy methods and X-ray crystallography. Both compounds crystallize in the $P2_1/n$ space group and in the solid state consist of zigzag single-strand chains with bridging 2-cyanoethyl

Table 6
^{13}C NMR spectra of complexes **1** and **2** and a mixture of **2** with AMP

Compounds	Solvent	NMR data, δ (ppm), J (Hz)
1	CD_3OD	15.43 (Cα, $^1J(^{119}Sn–^{13}C) = 472.3$, $^1J(^{117}Sn–^{13}C) = 451.7$); 15.83 (Cβ, $^2J(^{119/117}Sn–^{13}C) = 19.0$); 121.86 (Cγ, $^3J(^{119/117}Sn–^{13}C) = 81.9$)
2	CD_3OD	15.82 (Cα, $^1J(^{119}Sn–^{13}C) = 495.5$, $^1J(^{117}Sn–^{13}C) = 473.5$); 15.19 (Cβ, $^2J(^{119/117}Sn–^{13}C) = 18.8$); 122.67 (Cγ, $^3J(^{119/117}Sn–^{13}C) = 82.0$)
2 + **AMP**	D_2O + NaOD	14.00 (Cα, $^1J(^{119}Sn–^{13}C) = 545.4.3$, $^1J(^{117}Sn–^{13}C) = 521.8$); 13.08 (Cβ, $^2J(^{119/117}Sn–^{13}C) = 19.6$); 64.43 (C5′); 70.07 (C3′); 74.44 (C2′); 83.85 and 83.92 (C4′); 88.05 (C1′); 118.57 (C5); 122.61(Cγ, $^3J(^{119/117}Sn–^{13}C) = 78.4$); 142.21 (C8); 144.47 (C2); 148.29 (C4); 149.99 (C2);

ligands coordinating via the CH_2 group and the N atom. The tin atoms are in a distorted trigonal bipyramidal environment with bromo or iodo ligands and the nitrogen atom occupying axial coordination sites. The Sn(1)–N(3i) distances in complexes **1** and **2** are considerably longer than the Sn–C equatorial bonds. The molecular and electronic structures and IR spectra of $[SnBr(CH_2CH_2CN)_3]$ mononuclear and $[SnBr(CH_2CH_2CN)_3]_2$ dinuclear fragments of the complex have been studied with the DFT B3LYP method. The calculated interatomic distances for the entity containing a five-coordinate tin atom agree well with those found crystallographically. The compounds in water solutions form trigonal bipyramidal complexes containing aqua and hydroxo axial ligands. The ^1H NMR spectra indicate that complexes **1** and **2** interact with 5′-adenosine monophosphate and 5′-adenosine triphosphate via the oxygen atom of the phosphate group Table 6.

Table 7
IR spectra of $[SnBr(CH_2CH_2CN)_3]$ (**2**)

Wavenumber (cm^{-1})		Assignment
Experimental	Calculated for dimer $(\mathbf{2})_2$	
	46	ρ rocking CH_2^{α}, CH_2^{β}
61	53	ρ rocking CH_2^{α},CH_2^{β}
87	84	$\delta(SnCH_2CH_2)$
	104	$\delta(SnCH_2CH_2)$
110	116	
169	161	$\delta(CH_2SnCH_2) + \delta(CH_2CN)$
196	187	$\nu(SnBr) + \nu(SnN)$
	197	$\delta(CH_2CH_2C) + \delta(CH_2CN)$
	216	$\delta(CH_2SnCH_2)$
220	224	$\nu(SnBr) + \delta(SnCH_2CH_2)$
245	243	$\nu(SnN) + \delta(SnCH_2CH_2)$
450	448	$\nu^s(SnC) + \delta(CH_2CN)$
456	456	$\nu^{as}(SnC)$
466	462	$\nu^s(SnC) + \delta(CH_2CN)$ (bridge)
637	643	$\nu^s(SnC) + \delta(CH_2CH_2C) + \delta(CH_2CN)$
658	667	Rocking CH_2^{α}
679	704	Rocking CH_2^{α}, CH_2^{β}
895	932	$\nu(C^{\alpha}C^{\beta})$ + wagging CH_2^{α} and CH_2^{β}
1005	1027	$\nu^s(CH_2CH_2) + \delta(CH_2CN)$
1146	1187	Twist CH_2^{α} and CH_2^{β}
1156	1232	
1285	1323	Wagging CH_2^{α}
1314	1365	Wagging CH_2^{β}
1414	1500	δ CH_2^{α} and CH_2^{β}
2244	2272	ν(CN)
2261	2301	ν(CN) bridge
2927	3061	$\nu^s(CH_2^{\alpha})$
2958	3138	$\nu^{as}(CH_2^{\alpha}) + \nu^{as}(CH_2^{\beta})$

Acknowledgement

The authors are grateful to the Ministry of Science and Higher Education for support of this work (Grant No. 3 T09A 010 29).

Appendix A. Supplementary data

CCDC 663902 and 663903 contain the supplementary crystallographic data for compounds **1** and **2**. These data can be obtained free of charge via http://www.ccdc.cam.ac.uk/const/retrieving.html or from the Cambridge Crystallographic Data Centre, 12 Union Road, Cambridge CB2 1EZ, UK; fax: (+44) 1223-336-033; or e-mail: deposit@ccdc.cam.ac.uk. Supplementary data associated with this article can be found, in the online version, at doi:10.1016/j.poly.2007.12.012.

References

[1] P.J. Smith, Chemistry of Tin, Blackie Academic & Professional, London, 1998.
[2] A.G. Davies, in: G. Wilkinson, F.G.A. Stone, E.W. Abel (Eds.), Comprehensive Organometallic Chemistry, Pergamon Press, Oxford, 1995 (Chapter 6).
[3] A.J. Crowe, in: B. Keppler (Ed.), Metal Complexes in Cancer Chemotherapy, VCH, Weinheim, New York, 1993, p. 369.
[4] F. Huber, R. Barbieri, in: B. Keppler (Ed.), Metal Complexes in Cancer Chemotherapy, VCH, Weinheim, New York, 1993, p. 351.
[5] M.J. Clarke, F. Zhu, D.R. Frasca, Chem. Rev. 99 (1999) 2511.
[6] M. Gielen, M. Biesemans, D. de Vos, R. Willem, J. Inorg. Biochem. 79 (2000) 139, and references therein.
[7] M. Gielen, E.R.T. Tiekink, in: E.R.T. Tiekink, M. Gielen (Eds.), Metallotherapeutic Drugs and Metal-Based Diagnostic Agents. The Use of Metals in Medicine, J. Wiley, Chichester, 2005, p. 421 (Chapter 22).
[8] J. Koshy, V.G. Kumar Das, S. Balabaskaran, S.W. Ng, N. Wahab, Metal Based-Drugs 7 (2000) 245.
[9] M. Gielen, A. Bouhdid, F. Kayser, M. Biesemans, D. de Vos, B. Mahieu, R. Willem, Appl. Organometal. Chem. 9 (1995) 251.
[10] J. Tao, W. Xiao, Q. Yang, J. Organometal. Chem. 531 (1997) 223.
[11] J.J. Bonire, S.P. Fricker, J. Inorg. Biochem. 83 (2001) 217.
[12] A.P. Tomilov, L.V. Kaabak, Zh. Prikl. Khim. 32 (1959) 2600.
[13] O.R. Brown, E.R. Gonzalez, A.R. Wright, Electrochim. Acta 18 (1973) 555.

[14] F.P. Pruchnik, M. Bańbuła, Z. Ciunik, H. Chojnacki, B. Skop, M. Latocha, T. Wilczok, J. Inorg. Biochem. 90 (2002) 149.
[15] P. Starynowicz, COSABS 99, Program for Absorption Correction, University of Wrocław, 1999.
[16] G.M. Sheldrick, SHELXS 97 Program for Solution of Crystal Structures, University of Göttingen, 1997.
[17] G.M. Sheldrick, SHELXL 97, Program for Crystal Structure Refinement, University of Göttingen, 1997.
[18] M.J. Frisch, G.W. Trucks, H.B. Schlegel, G.E. Scuseria, M.A. Robb, J.R. Cheeseman, J.A. Montgomery, Jr., T. Vreven, K.N. Kudin, J.C. Burant, J.M. Millam, S.S. Iyengar, J. Tomasi, V. Barone, B. Mennucci, M. Cossi, G. Scalmani, N. Rega, G.A. Petersson, H. Nakatsuji, M. Hada, M. Ehara, K. Toyota, R. Fukuda, J. Hasegawa, M. Ishida, T. Nakajima, Y. Honda, O. Kitao, H. Nakai, M. Klene, X. Li, J.E. Knox, H.P. Hratchian, J.B. Cross, C. Adamo, J. Jaramillo, R. Gomperts, R.E. Stratmann, O. Yazyev, A.J. Austin, R. Cammi, C. Pomelli, J.W. Ochterski, P.Y. Ayala, K. Morokuma, G.A. Voth, P. Salvador, J.J. Dannenberg, V.G. Zakrzewski, S. Dapprich, A.D. Daniels, M.C. Strain, O. Farkas, D.K. Malick, A.D. Rabuck, K. Raghavachari, J.B. Foresman, J.V. Ortiz, Q. Cui, A.G. Baboul, S. Clifford, J. Cioslowski, B.B. Stefanov, G. Liu, A. Liashenko, P. Piskorz, I. Komaromi, R.L. Martin, D.J. Fox, T. Keith, M.A. Al-Laham, C.Y. Peng, A. Nanayakkara, M. Challacombe, P.M.W. Gill, B. Johnson, W. Chen, M.W. Wong, C. Gonzalez, J.A. Pople, GAUSSIAN 03, Revision B.04, Gaussian Inc., Pittsburgh, PA, 2003.
[19] T. Mancilla, L. Carrillo, L.S. Zamudio Rivera, C. Camacho, D. de Vos, R. Kiss, F. Darro, B. Mahieu, E.R.T. Tiekink, H. Rahier, M. Gielen, M. Kemmer, M. Biesemans, R. Willem, Appl. Organometal. Chem. 15 (2001) 593.
[20] L.-F. Tang, Z.-H. Wang, J.-F. Chai, W.-L. Jia, Y.-M. Xu, J.-T. Wang, Polyhedron 19 (2000) 1949.
[21] C.S. Parulekar, V.K. Jain, T.K. Das, A.R. Gupta, B.F. Hoskins, E.R.T. Tiekink, J. Organometal. Chem. 372 (1989) 193.
[22] E. Rivarola, M. Camalli, F. Caruso, Inorg. Chim. Acta 126 (1987) 1.
[23] T.P. Lockhart, W.F. Manders, Inorg. Chem. 25 (1986) 892.
[24] F. Capolongo, A.M. Giuliani, M. Giomini, U. Russo, J. Inorg. Biochem. 49 (1993) 275.

to completely enter the central cavity of Pc ring due to its large ionic size. Pb^{2+} has a close shell and is a diamagnetic ion and is expected to enhance intersystem crossing (ISC) and to give Pc complexes with high triplet quantum yields. Lability of lead ion during the work-up of the substituted complex, resulting in regeneration of the starting material, has been reported [22]. Demetallation in PbPc complexes is common [22,28]. There has been less attention paid to non-peripherally [22] substituted compared to peripherally substituted PbPc derivatives. PbPc derivatives have been shown to give good optical limiting properties [29–31] when compared to NiPc and H_2Pc. The study of the photochemical and photophysical behaviour of PbPc complexes has not been fully explored. Polyether peripherally substituted PbPc complex gave a low triplet yield lifetime ($\tau_T = 32$ μs) and about the same triplet quantum ($\Phi_T = 0.30$) compared to the corresponding ZnPc derivative ($\tau_T = 105$ μs, $\Phi_T = 32$) [27]. PbPc derivatives gave large rate constants of intersystem crossing due to the heavy Pb central atom [32]. The lead helicenocyanine derivatives exhibited strong fluorescence when irradiated in the B band region, giving two emission peaks at 500 and 900 nm [33,34].

The development and elucidation of photophysical (triplet yields and lifetimes and fluorescence yields) properties of new phthalocyanine complexes are of fundamental importance, hence this work presents the study of these parameters in different solvents for PbPc derivatives, since solvents affect these parameters.

The complexes studied are: 1,(4)-(tetraphenoxyphthalocyaninato)lead (**7a**), 1,(4)-(tetra-*tert*-butylphenoxyphthalocyaninato)lead (**7b**), 2,(3)-(tetraphenoxyphthalocyaninato) lead (**8a**), 2,(3)-(tetra-*tert*-butylphenoxyphthalocyaninato) lead (**8b**), 2,3-(octaphenoxyphthalocyaninato)lead (**9a**) 2,3-[octakis(4-*t*-butylphenoxyphthalocyaninato)]lead (**9b**), (Scheme 1).

2. Experimental

2.1. Materials

Chloroform ($CHCl_3$), methanol (MeOH), 1-chloronaphthalene (1-CNP), 1-octanol, tetrahydrofuran (THF), dimethylformamide (DMF), hexane and deuterated chloroform ($CDCl_3$) were obtained commercially and dried before use. Potassium carbonate (K_2CO_3), urea, phenol and 4-*tert*-butylphenol were purchased from Aldrich and used as received. Dimethylsulphoxide (DMSO) was purchased from SAARCHEM, and dried in alumina before use. 3-Nitrophthalonitrile (**1**) [11], 4-nitrophthalonitrile (**2**) [35] and 4,5-dichlorophthalonitrile (**3**) [36] were synthesized and purified according to literature procedure. Column chromatography was performed on silica gel 60 (0.04–0.063 mm).

2.2. Equipment

Ground state electronic absorption spectra were performed, on a Varian Cary 500 UV–Vis–NIR spectrophotometer; infra-red spectra (KBr pellets) on Perkin Elmer Spectrum 2000 FT-IR Spectrometer and ^1H nuclear magnetic resonance (^1H NMR) signals on a Bruker EMX 600 NMR spectrometer. Triplet lifetimes (τ_T) and yields were obtained using an Nd-YAG laser providing 400 mJ, 90 ns of laser light at 10 Hz, pumping a Lambda-Physik FL 3002 dye laser. A 300 W xenon arc lamp (Thermo Oriel) provided the analysing light. Kinetic curves were averaged over 256 laser pulses using a Tektronix TDS 360 digital oscilloscope. The τ_T values were obtained by fitting an exponential curve to the kinetic data using ORIGIN Pro 6.0. Elemental analyses were obtained from Carlo Erba 1106 Instrument.

2.3. Photophysical properties

Fluorescence quantum yields (Φ_F) were determined by the comparative method, using Eq. (1) [37,38].

$$\Phi_F = \Phi_F^{std} \frac{F \cdot A_{std} \cdot \eta^2}{F_{std} \cdot A \cdot \eta_{std}^2} \quad (1)$$

where F and F_{std} are the areas under the fluorescence curves of the PbPc derivatives and the standard, respectively. A and A_{std} are the respective absorbances of the sample and standard at the excitation wavelengths (which was ~0.05 in all solvents used), and η and η_{std} are the refractive indices of the solvents used for sample and standard, respectively. ZnPc was employed as a standard in DMSO ($\Phi_F = 0.20$) [37].

The triplet quantum yields were determined using Eq. (2) [39].

$$\Phi_T = \Phi_T^{std} \frac{\Delta A_T \cdot \varepsilon_T^{std}}{\Delta A_T^{std} \cdot \varepsilon_T} \quad (2)$$

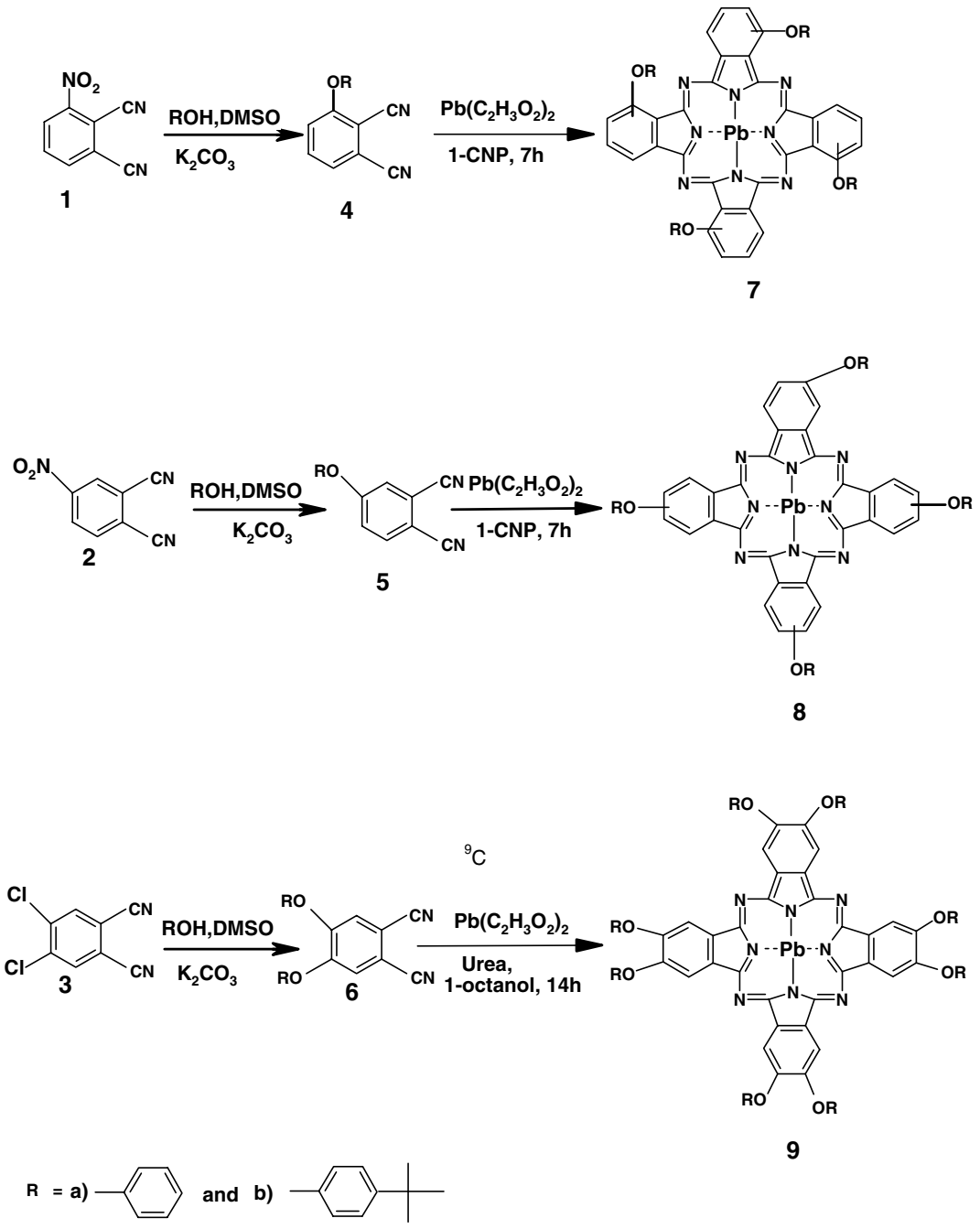
where ΔA_T and ΔA_T^{std} are the changes in triplet state absorbance of PbPc derivatives and the standard, respectively. ε_T and ε_T^{std} are the triplet state molar extinction coefficients for the PbPc derivatives and the standard, respectively. Φ_T^{std} is the triplet quantum yield for the standard, ZnPc ($\Phi_T = 0.65$ in DMSO [40], 0.58 in DMF [41] and 0.65 in toluene [42]).

Quantum yields of internal conversion were obtained from Eq. (3), which assumes that only three processes (fluorescence, intersystem crossing and internal conversion), jointly deactivate the excited singlet state of a PbPc molecule.

$$\Phi_{IC} = 1 - (\Phi_F + \Phi_T) \quad (3)$$

2.4. Synthesis

3-Phenoxyphthalonitrile (**4a**), 3-(4-*t*-butylphenoxy)phthalonitrile (**4b**), 4-phenoxyphthalonitrile (**5a**), 4-(4-*t*-butylphenoxy)phthalonitrile (**5b**), 4,5-diphenoxyphthalonitrile (**6a**), and 4,5-bis(4-*t*-butylphenoxy)phthalonitrile (**6b**) were synthesized and characterized according to reported procedures [43–45].



Scheme 1. Synthesis of phenoxy and 4-*t*-butylphenoxy tetra- and octa-substituted lead phthalocyanines.

*2.4.1. 1,(4)-(Tetraphenoxyphthalocyaninato)lead (**7a**)*

Under a blanket of nitrogen, **4a** (1.60 g, 7.30 mmol) was dissolved in 1-CNP (8 ml). Pb acetate (0.91 g, 2.40 mmol) was then added to the solution and the reaction mixture refluxed at 180 °C for 7 h under nitrogen. After cooling, the solution was chromatographed with hexane as eluent to remove 1-CNP. The column was then eluted with $CHCl_3$ which was evaporated off, thus affording **7a**. Yield: 1.27 g (49%). UV–Vis (DMSO): λ_{max} nm ($\log\varepsilon$) 723 (5.33), 652 (4.65), 460 (4.41), 347 (4.77). IR [(KBr) ν_{max}/cm^{-1}]: 1249(C–O–C), 970, 924, 877, 830, 818, 799, 788, 782, 742, 712, 702 (Pc skeletal). ^1H NMR ($CDCl_3$): δ, ppm 9.04–9.06 (4H, d, Pc–H), 8.89–8.92 (4H, m, Pc–H), 8.60–862 (4H, m, Pc–H), 7.78–8.01 (20H, m, phenyl–H). *Anal*. Calc. for $C_{56}H_{32}N_8O_4Pb$: C, 61.87; H, 2.97; N, 10.31. Found: C, 61.81; H, 3.59; N, 10.07%.

*2.4.2. 1,(4)-(Tetra-tert-butylphenoxyphthalocyaninato)lead (**7b**)*

Synthesis and purification was as outlined for **7a** except **4b** instead of **4a** was employed. The amounts of the reagents employed were as follows: **4b** (1.25 g, 4.55 mmol), lead acetate (0.62 g, 1.65 mmol) and 1-CNP (4.5 ml). Yield: 0.80 g (37%). UV–Vis (DMSO): λ_{max} nm ($\log\varepsilon$) 724 (5.22),

652 (4.64), 460 (4.34), 347 (4.67). IR [(KBr) ν_{max}/cm^{-1}]: 1251 (C–O–C), 999, 970, 944, 869, 827, 750 (Pc skeletal), 2960 (*t*-Butyl-H). ^1H NMR ($CDCl_3$): δ, ppm 8.40–9.06 (12H, m, Pc–H), 7.73–8.00 (16H, m, phenyl–H), 1.27–1.32 (36H, m, ^{t}Bu). *Anal*. Calc. for $C_{56}H_{32}N_8O_4Pb$: C, 65.95; H, 4.92; N, 8.55. Found: C, 67.76; H, 6.14; N, 7.14%.

2.4.3. 2,(3)-(Tetraphenoxyphthalocyaninato)lead (**8a**)

Synthesis and purification was as outlined for **7a** except **5a** instead of **4a** was employed. The amounts of the reagents employed were as follows: **5a** (1.25 g, 5.50 mmol), lead acetate (0.7 g, 1.85 mmol) and 1-CNP (6 ml). Yield: 0.92 g (46%). UV–Vis (DMSO): λ_{max} nm ($\log\varepsilon$) 708 (4.95), 638 (4.26), 346 (4.52). IR [(KBr) ν_{max}/cm^{-1}]: 1229 (C–O–C), 960, 942, 928, 904, 886, 869, 856, 781,759,743, 724 (Pc skeletal). ^1H NMR ($CDCl_3$): δ, ppm 8.69–8.78 (4H, m, Pc–H), 8.48–8.61 (4H, m, Pc–H), 8.26–8.31 (4H, m, Pc–H), 7.73–7.97 (20H, m, phenyl–H). *Anal*. Calc. for $C_{56}H_{32}N_8O_4Pb$.2acetate: C, 59.27; H, 3.23; N, 9.54. Found: C, 57.37; H, 3.04; N, 8.85%.

2.4.4. 2,(3)-(Tetra-tert-butylphenoxyphthalocyaninato)lead (**8b**)

Synthesis and purification was as outlined for **7a** except **5b** instead of **4a** was employed. The amounts of the reagents employed were as follows: **5b** (1.05 g, 3.80 mmol), lead acetate (0.57 g, 1.25 mmol) and 1-CNP (4 ml). Yield: 0.75 g (46%). UV–Vis (DMSO): λ_{max} nm ($\log\varepsilon$) 709 (5.00), 638 (4.37), 347 (4.42) IR [(KBr) ν_{max}/cm^{-1}]: 1240 (C–O–C), 978, 963, 943, 930, 879, 855, 843,828,823, 752, 729 (Pc skeletal), 2967 (*t*-butyl-H). ^1H NMR ($CDCl_3$): δ, ppm 8.43–9.01 (12H, m, Pc–H), 7.52–7.55 (16H, m, phenyl–H), 1.33 (36H, s, ^{t}Bu). *Anal*. Calc. for $C_{56}H_{32}N_8O_4Pb$: C, 65.96; H, 4.92; N, 8.55. Found: C, 67.64; H, 5.90; N, 7.19%.

2.4.5. 2,3-Octaphenoxyphthalocyaninatolead (**9a**)

In 1-octanol (8 ml), compound **6a** (2.00 g, 6.40 mmol), lead acetate (0.85 g, 2.12 mmol) and urea (0.50 g, 8.50 mmol) were stirred under a blanket of nitrogen at 150 °C for 14 h. The reaction mixture was allowed to cool, thereafter, methanol (80 ml) was added and the mixture was refluxed for 2 h. After cooling, the mixture was filtered, and the resulting solid sequentially washed with methanol and water and then dried. The crude product was purified by column chromatography, using $CHCl_3$ as the eluting solvent. After evaporation of solvent, the product was further purified by column chromatography (using chloroform as eluent) to afford the title compound as a dark-green solid. Yield: 1.00 g (32%). UV–Vis (DMSO): λ_{max} nm ($\log\varepsilon$) 707 (5.18), 637 (4.41), 348 (4.65). IR [(KBr) ν_{max}/cm^{-1}]: 1269 (C–O–C), 998, 880, 841, 787, 768, 744, 726 (Pc skeletal). ^1H NMR ($CDCl_3$): δ, ppm 8.50–8.58 (8H, s, Pc–H), 7.23–7.44 (40H, m, phenyl–H). *Anal*. Calc. for $C_{80}H_{48}N_8O_8Pb$: C, 65.91; H, 3.32; N, 7.69. Found: C, 65.44; H, 3.73; N, 8.06%.

2.4.6. 2,3-[Octakis(4-t-butylphenoxyphthalocyaninato)] lead (**9b**)

Synthesis and purification was as outlined for **9a** except **6b** instead of **6a** was employed. The amounts of the reagents employed were: **6b** (2.00 g, 4.75 mmol), lead acetate (0.10 g, 1.19 mmol) and urea (0.285 g, 4.75 mmol) in 1-octanol (8.75 ml). Yield: 1.00 g (44%). UV–Vis (DMSO): λ_{max} nm ($\log\varepsilon$) 709 (4.94), 638 (4.17), 358 (4.41). IR [(KBr) ν_{max}/cm^{-1}]: 1269 (C–O–C), 889, 884, 827, 828, 769, 751,744 (Pc skeletal), 2961 (*t*-butyl-H). ^1H NMR ($CDCl_3$): δ, ppm 8.91 (8H, s, Pc–H), 7.13–7.43 (32H, m, phenyl–H), 1.38 (72H, s, ^{t}Bu). *Anal*. Calc. for $C_{112}H_{112}N_8O_8Pb$: C, 70.68; H, 5.93; N, 5.89. Found: C, 69.88; H, 5.92; N, 5.91%.

3. Results and discussion

3.1. Synthesis and characterization

During synthesis the solvents with high boiling point are used to insert the metal in the central cavity. 3-Nitrophthalonitrile (**1**), 4-nitrophthalonitrile (**2**) and 4,5-dichlorophthalonitrile (**3**) may be employed to prepare 3-monosubstituted, 4-monosubstituted and 4,5-disubstituted phthalonitrile derivatives, respectively, through base catalysed nucleophilic aromatic displacement.

The same route employed for **1**, **2** and **3** was used to prepare complexes **4**, **5** and **6** by reacting phenol or 4-*tert*-butylphenol with complexes **1**, **2** and **3**, respectively (Scheme 1). The reactions were carried out in DMSO at room temperature and gave yields of 57% for compound **4a**, 42% for **4b** and **5a**, 35% for **5b**, 63% for **6a** and 72% for **6b**.

Substituted phthalocyanines are prepared by cyclotetramerization of substituted phthalonitriles. 4-Tetra-substituted phthalocyanines can be synthesized from 4-substituted phthalonitriles while 3-tetra-substituted phthalocyanines are obtained from 3-substituted analogues [46]. Octa-substituted phthalocyanines can be synthesized from 4,5-dichlorophthalonitriles [36].

Tetra-substituted phthalocyanines occur as a mixture of four possible structural isomers, differentiated by their molecular symmetry: C_{4h}, C_{2v}, C_s and D_{2h} [47]. Octa-substituted compounds occur as a single isomer and are easy to be purified than the corresponding tetra-substituted compound.

The syntheses of metallophthalocyanine complexes (**7**, **8** and **9**) were achieved by treatment of phthalonitrile **6** with lead acetate in 1-octanol for octa-substituted and **4** and **5** in 1-CNP for tetra-substituted compounds (Scheme 1). Complex **7** is non-peripherally (α) tetra-substituted, complex **8** is peripherally (β) tetra-substituted and complex **9** is peripherally octa-substituted. Column chromatography with silica gel was employed to obtain the purity of products.

The PbPc derivatives were characterized by UV–Vis, IR and NMR spectroscopies, and elemental analyses. The analyses were consistent with the predicted structures as shown in Section 2. The elemental analyses for complexes **7a**, **9a** and **9b** gave excellent percentage carbon values that

were very close to calculated values. For the rest of the complexes, the elemental analysis values were within 2% of the expected values. It has been reported before that for large Pc molecules, elemental analyses often gives unsatisfactory results [48]. However, we are confident of the purity of the complexes since NMR gave excellent results (see below). The sharp peak for the C≡N vibrations in the IR spectra of phthalonitriles **4a**, **4b**, **5a**, **5b**, **6a** and **6b** at ~2233, 2230, 2233, 2231, 2237 and 2224 cm^{-1}, respectively, disappeared after conversion into lead phthalocyanines. All PbPc derivatives showed absorption peaks between 700 and 1000 cm^{-1} which may be assigned to phthalocyanines skeletal vibrations [49]. The characteristic vibrations corresponding to ether groups (C–O–C) at ca. 1200–1247 cm^{-1} and aliphatic CH stretching at ca. 2900–3000 cm^{-1} were observed for the PbPc derivatives.

The ^1H NMR spectra of diamagnetic lead derivatives in $CDCl_3$ were found to be pure with all the substituent and Pc ring protons observed in their respective regions. Tetra-substituted PbPcs (**7** and **8**) show complex patterns due to the presence of mixed isomers. For complex **7a**, ^1H NMR spectra gave multiplets between 8.60–9.06 ppm for three sets of phthalocyanine ring protons, integrating for a total of 12 protons. The phenyl protons were observed as multiplets between 7.78–8.01 ppm integrating 20 protons. Compound **7b** gave multiplets between 8.40–9.06, 7.73–8.00 and 1.27–1.32 ppm integrating 12 protons for Pc ring, 16 protons for phenyl and 36 protons for methyl protons (*t*-Bu), respectively. The ^1H NMR spectra of **8a** and **8b** show similar spectral features as spectra of **7a** and **7b**. Compound **8a**, showed multiplets between 8.26–8.78 ppm integrating 12 protons for Pc ring and peaks at 7.73–7.97 ppm integrating 20 protons for phenyl rings. The ^1H NMR spectrum of **8b** showed a multiplet at 8.43–9.01 ppm intergrating for 12 Pc ring protons, a multiplet at 7.52–7.55 ppm for 16 phenyl protons and a singlet integrating for 36 methyl protons was observed at 1.33 ppm. Although the presence of isomers for tetra-substituted complexes as well as phthalocyanine aggregation at the concentrations used for the NMR measurements may lead to broadening of the aromatic signals [50], the NMR spectra obtained in this work was relatively well-resolved.

The ^1H NMR spectra for octa-substituted complexes **9** show a singlet integrating for 8 Pc ring protons between 8.50–8.58 ppm (**9a**) and at 8.91 ppm (**9b**). Phenyl protons were observed as multiplets between 7.23–7.44 ppm (**9a**) integrating 40H and 7.13–7.43 ppm (**9b**) representing 32H. Complex **9b** also showed a singlet at 1.38 ppm for 72 methyl protons.

UV/Vis spectra of the complexes showed characteristic absorptions in the Q-band and B-band, Figs. 1 and 2. The peaks obtained in the Q-band region in the range 706–742 nm in five different solvents (Table 1) are responsible for the observed green colour of the complexes. The spectra showed monomeric behaviour, evidenced by a single (narrow) Q-band, typical of unaggregated phthalocyanine complexes in DMSO [51]. The B band region was observed around 345–360 nm in DMSO (Figs. 1 and 2).

The Q-band of the non-peripheral tetra-substituted complexes (**7**) is red-shifted when compared to the corresponding peripherally tetra- and octa-substituted complexes. The observed red spectral shift is typical of phthalocyanines with substituents at the non-peripheral positions and has been explained [52,53] to be due to linear combinations of the atomic orbitals (LCAO) coefficients at the non-peripheral positions of the HOMO being greater than those at the peripheral positions. As a result, the HOMO level is destabilized more at the non-peripheral position that it is at the peripheral position. Essentially, the energy gap (ΔE) between the HOMO and LUMO becomes smaller. Generally, OR groups cause a red shift since they can donate electron density from the lone pair into the π system increasing conjugation, hence lowering HOMO–LUMO gap.

Fig. 3 shows the concentration dependence of complex **9a** in DMSO. As the concentration was increased, the intensity of the Q-band also increased and there were no new bands due to the aggregated species for the complex. The Beer–Lambert's law was obeyed for all of these compounds for concentration less than 1×10^{-5} mol dm^{-3}. Aggregation is also dependent on the nature of the solvent. The aggregation behaviour of PbPc complexes were investigated

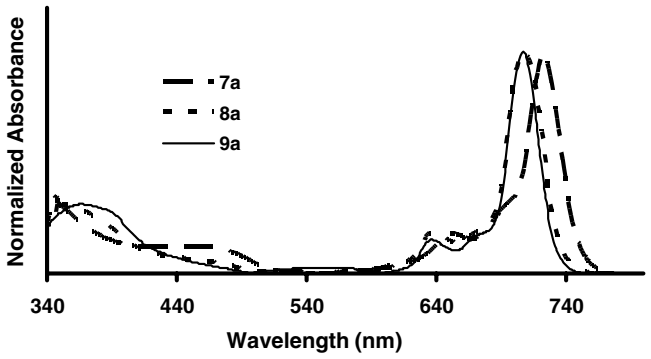


Fig. 1. UV–Vis spectra for tetra- and octa-phenoxy substituted lead phthalocyanines. Solvent = DMSO. Concentration ~2×10^{-6} mol dm^{-3}.

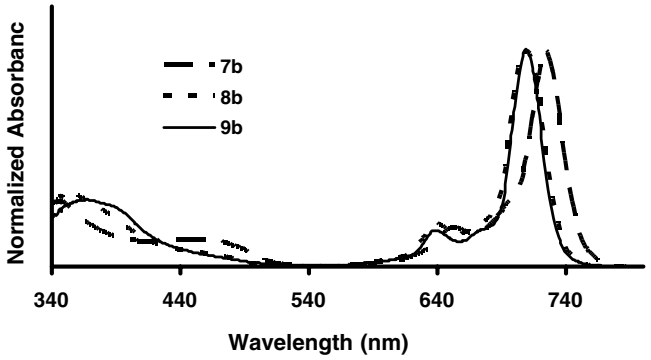


Fig. 2. UV/Vis spectra for tetra- and octa-4-*t*-butylphenoxy substituted lead phthalocyanines. Solvent = DMSO. Concentration ~2×10^{-6} mol dm^{-3}.

Table 1
Spectral, photophysical parameters of PbPc derivatives in various solvents

Solvent	MPc	λ_{max}			Φ_F	Φ_T	Φ_{IC}	τ_T (μs)
		Q_{abs} (nm)	Q_{ems} (nm)	Q_{exc} (nm)				
DMSO	3TPPbPc (**7a**)	723	709	704	<0.01	0.78	0.21	40
	3TTBPPbPc (**7b**)	724	712	702	<0.01	0.80	0.20	30
	4TPPbPPc (**8a**)	708	678	675	<0.01	0.76	0.24	20
	4TTBPPbPPc (**8b**)	709	681	676	<0.01	0.72	0.28	30
	OPPbPc (**9a**)	707	678	672	0.01	0.76	0.23	20
	OTBPPbPc (**9b**)	709	678	673	<0.01	0.88	0.23	50
DMF	3TPPbPc (**7a**)	722	717	708	0.03	0.72	0.25	10
	3TTBPPbPc (**7b**)	724	704	696	0.02	0.82	0.17	9
	4TPPbPPc (**8a**)	706	706	700,669	<0.01	0.75	0.25	9
	4TTBPPbPPc(**8b**)	707	706	700,669	<0.01	0.78	0.21	9
	OPPbPc (**9a**)	706	703	699,668	<0.01	0.78	0.22	5
	OTBPPbPc (**9b**)	707	706	700,669	<0.01	0.74	0.26	5
Toluene	3TPPbPc (**7a**)	732	720	715,685	0.01	0.82	0.17	8
	3TTBPPbPc (**7b**)	734	721	717,687	0.05	0.70	0.25	7
	4TPPbPPc (**8a**)	715	706	701,667	0.02	0.77	0.21	8
	4TTBPPbPPc (**8b**)	716	706	701,667	0.04	0.78	0.18	9
	OPPbPc (**9a**)	716	704	698,667	0.01	0.85	0.14	7
	OTBPPbPc (**9b**)	717	706	702,669	<0.01	0.74	0.26	6
[a] THF	3TPPbPc (**7a**)	724	720	713,685	0.02			10
	3TTBPPbPc (**7b**)	726	723	715,687	0.03			10
	4TPPbPPc (**8a**)	708	703	697,665	<0.01			6
	4TTBPPbPPc(**8b**)	709	704	698,665	0.03			6
	OPPbPc (**9a**)	709	702	697,665	0.01			10
	OTBPPbPc (**9b**)	711	704	698,667	<0.01			9
[a]$CHCl_3$	3TPPbPc (**7a**)	740	723	717,688	0.05			7
	3TTBPPbPc (**7b**)	742	726	720,692	0.08			10
	4TPPbPPc (**8a**)	721	707	701,668	0.04			10
	4TTBPPbPPc(**8b**)	722	708	702,668	0.07			10
	OPPbPc (**9a**)	720	706	700,667	0.07			6
	OTBPPbPc (**9b**)	723	707	702,670	0.03			6

[a] Values of Φ_T and Φ_{ISC} not determined due to lack of standards.

at different solvents (Fig. 4), there were no new band observed in all solvents.

Table 1 shows that the largest red-shift of the Q-band was observed in chloroform. This observation could partly be explained by considering the refractive indices of the solvents. It is known that red-shifting of absorption spectra is a function of the solvent's refractive index [54].

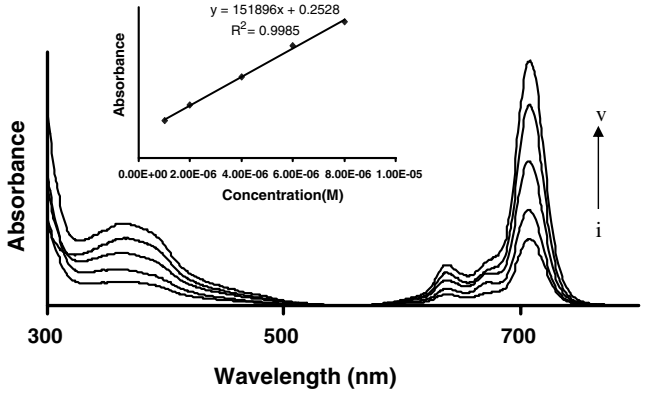


Fig. 3. Absorption spectra of compound **9a** in DMSO at different concentrations: (i) 8×10^{-6}, (ii) 6×10^{-6}, (iii) 4×10^{-6}, (iv) 2×10^{-6}, (v) 1×10^{-6} M.

3.2. Photophysical behaviour

3.2.1. Fluorescence spectra and quantum yields

The values of Φ_F are widely known to be influenced by the factors such as temperature, molecular structure, solvent parameters (polarity, viscosity and refractive index), and the presence of heavy atoms in the solvent and in the molecule itself.

Table 1 shows the Q-band maxima for absorption, emission and excitation spectra. Figs. 5 and 6 show the

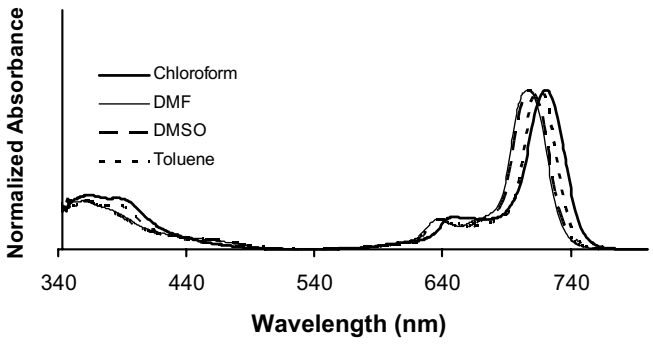


Fig. 4. Absorption spectra of complex **8a** in different solvents. Concentrations ~2×10^{-6} M.

absorption, fluorescence emission and excitation spectra for the complexes in various solvents. The excitation spectra were different from absorption and emission spectra in all solvents shown in Fig. 5 for **7b**. The excitation spectrum shown in Fig. 5a shows demetallation of **7b** in toluene upon excitation, as judged by the blue shifted and split Q band. The excitation spectrum in Fig. 5 was similar to the absorption spectra of the corresponding dematallated H_2Pc derivatives, confirming demetallation upon excitation. Metal free Pcs are known to fluoresce with only one main peak in non-aqueous media which has been assigned as the 0–0 transition of the fluorescence [55]. Complete splitting of the Q band was observed for all complexes in THF, toluene and chloroform. There was broadening in DMSO and partial splitting in DMF of the Q band in the excitation spectra of **7b**. Both DMSO and DMF are basic solvents. It has been documented that in strongly basic solvents, the inner pyrrole hydrogens are acidic enough to dissociate resulting in a charged system (Pc^{-2}) which becomes symmetric and thus possesses an unsplit Q band [51]. This is observed as a partially split Q band in DMF and a broadened Q band in DMSO for **7b**. The lack of split in the Q band in DMSO is more clear in the fluorescence excitation spectra for **9a**, in DMSO (Fig. 5d), which exhibited one band upon excitation. Emission for **9a** was from the demetallated species as evidenced by the red shift observed for emission when compared to the excitation spectra and not the absorption spectra. However, a clear single Q band for the excitation spectra was observed only for complexes **9** in DMSO, Fig. 5d. For other complexes such as **7b** in DMSO, there was broadening of the excitation spectra without showing complete splitting. Thus, the more basic solvents such as DMSO and DMF resulted in a single or broadened excitation spectrum, whereas the less basic solvents (THF, chloroform and toluene) resulted in complete splitting of the Q band of the excitation spectra due to demetallation.

The extent of splitting in the Q band also depended on the nature of the complex considering the same solvent, Fig. 6. For example, the excitation spectrum of **7a** is broadened but not split in DMF (Fig. 6a), while in the same solvent excitation spectrum of **9a** is split. Thus the extent of deprotonation of the ring by the basic solvent depends on the nature of substituents.

The fluorescence quantum yield (Φ_F) values were found to be less than 0.1, hence less than typical values for MPc complexes (e.g. ZnPc in DMSO, $\Phi_F = 0.2$ [37]). Thus, the

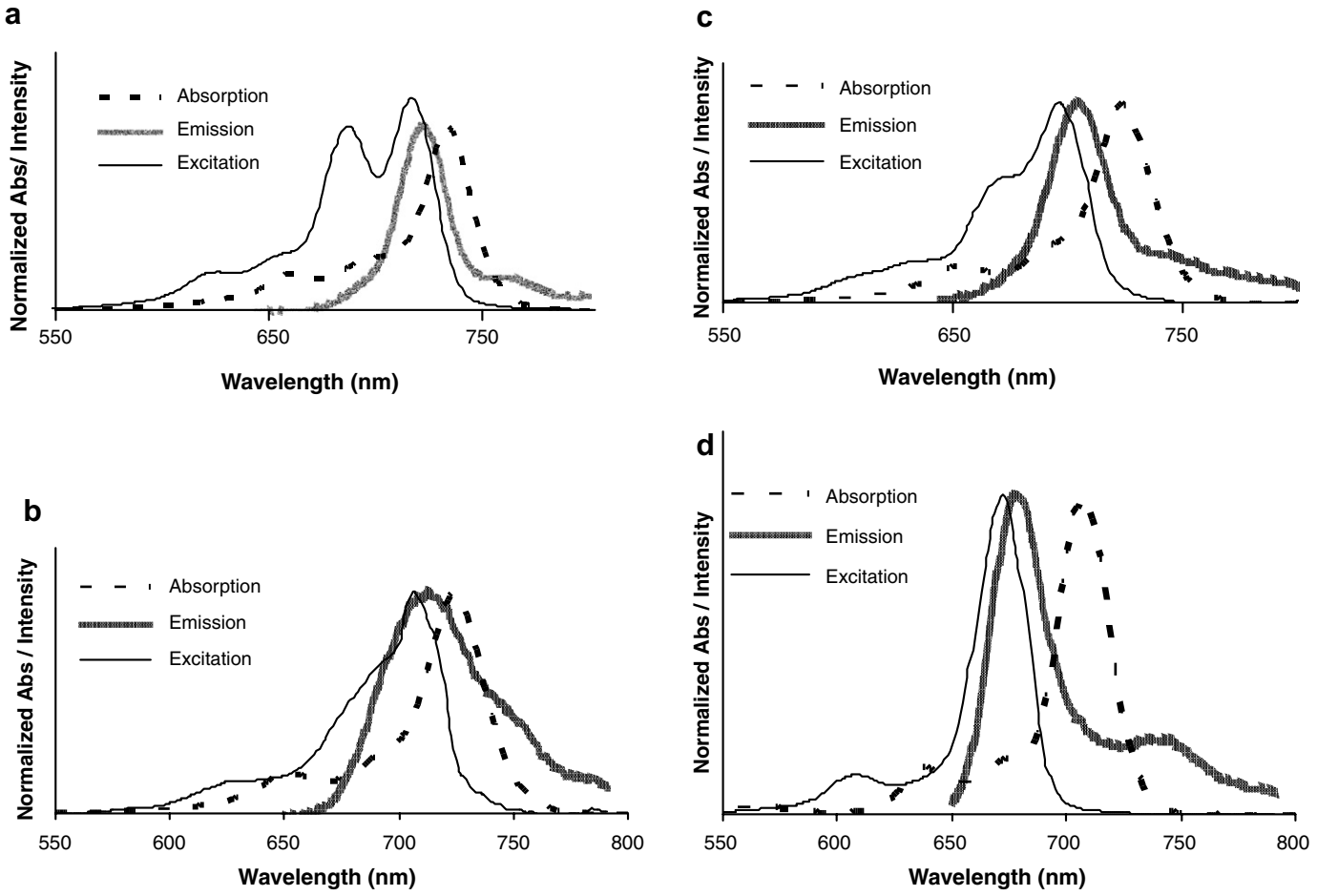


Fig. 5. Absorption, emission and excitation spectra of compound **7b** in (a) toluene, (b) DMSO and (c) DMF. (d) **9a** in DMSO. Concentration $\sim 1 \times 10^{-6}$ mol dm^{-3}.

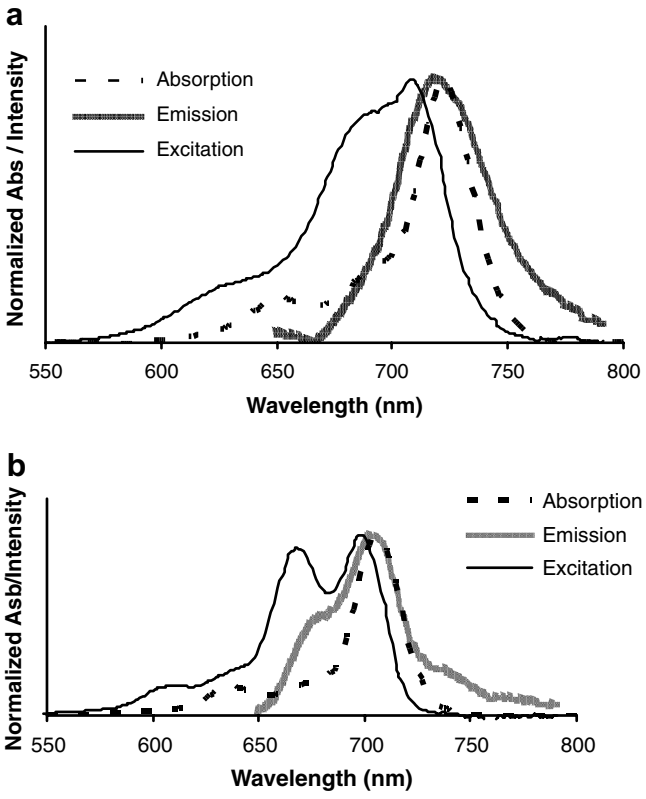


Fig. 6. Absorption, emission and excitation spectra of compound **7a** (a) and **9a** (b) in DMF. Concentration $\sim 1 \times 10^{-6}$ M.

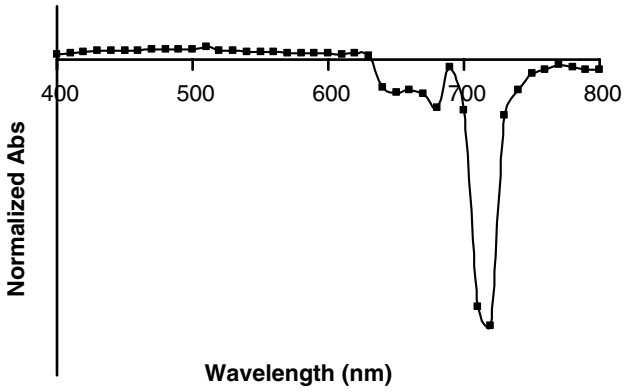


Fig. 7. Transient absorption spectrum for **9a** in DMSO.

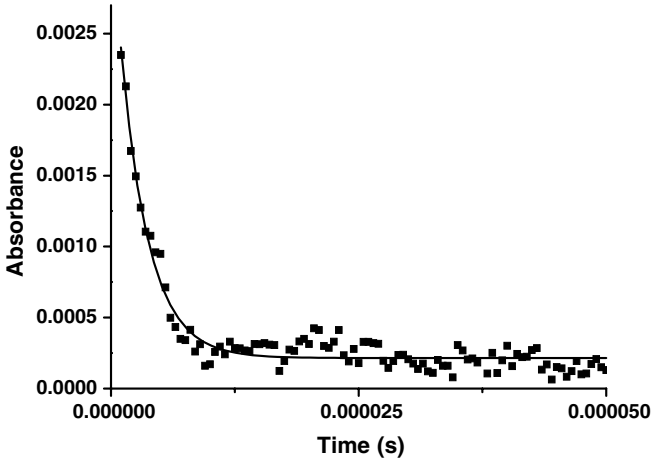


Fig. 8. Triplet decay curve for **9a** in DMF. Excitation wavelength (λ_{exc}) = 706 nm.

Φ_F values are very small due to the presence of heavy atom (Pb) in solution, which enhances intersystem crossing to populate the triplet state, consequently reducing the number of fluorescing molecules. Relatively higher Φ_F values were observed in $CHCl_3$ compared to the rest of the solvents. This contradicts the heavy atom effect of the chlorines in chloroform, which should encourage intersystem crossing resulting in less fluorescence.

The fact that the PbPc complexes become demetallated on excitation suggests that the reported Φ_F values are for the fully or partially dematallated complexes. However the effects of Pb in terms of the heavy atom effect will still influence the values since the Pb is still in solution.

3.2.2. Triplet quantum yields and lifetimes

Both the triplet quantum yield and lifetime were determined by laser photolysis. Transient spectra (Fig. 7) in DMSO showed a single Q band but at a different Q band wavelength from that observed for absorption, thus confirming the changes in the molecule following excitation. As discussed above the molecules demetallate on excitation, but show a single Q band in basic solvents like DMSO. Fig. 8 shows the transient curve for the complexes. Fig. 8 shows a typical triplet decay curve of compound **9a** in DMSO.

Since intersystem crossing and fluorescence are two competing deactivating processes for the excited singlet state, their values for a particular species are expected to be complementary. Thus Table 1 shows high Φ_T values (0.70–0.88) in DMSO, DMF and toluene, corresponding to low Φ_F values of the complexes. These values are high due to the presence of lead. The Φ_T values in $CHCl_3$ and THF could not be determined due to the lack of standard Φ_T values in those solvents. The Φ_T values (Table 1) do not change much with the change of the substituents showing the effect of the phenoxy and *tert*-butylphenoxy substituents on triplet quantum yield was minimal, with Φ_T values ranging between 0.72–0.88 in DMSO, 0.72–0.82 in DMF and 0.70–0.85 in toluene. Thus, the nature of the solvent also has an insignificant effect on the $\Phi_T$values. Again the Φ_T values are for the partially or totally demetallated species since demetallation occurs on excitation, but the Pb is still present in solution.

The triplet curve in Fig. 8 obeyed second order kinetics. This is typical of MPc complexes at high concentrations ($>1 \times 10^{-4}$ M) [56] due to the triplet-triplet recombination. The concentrations employed in this work was in this range hence triplet–triplet recombination is expected.

The triplet lifetime (τ_T) values were found to be low for PbPc complexes compared to ZnPc or AlPc derivatives

[27,57], but are similar to the corresponding InPc derivatives [58], containing a heavy metal, even though the InPc derivatives were not demetallated on excitation. The τ_T values in DMSO were much longer than DMF, chloroform, THF and toluene, which may be attributed to the higher viscosity of DMSO, this has been reported before [45]. Diffusion-like movement that enhance non-radiation deactivation of the excited state are impeded in viscous solvents, resulting in longer excited state lifetimes. The values in DMSO ranged from 20 to 50 μs for PbPc complexes. The triplet lifetimes were very low in the low viscocity solvents DMF, chloroform, THF and toluene, which were less than or equal to 10 μs. Quantum yields of internal conversion (Φ_{IC}) were calculated according to Eq. (3). Table 1 shows that the values of Φ_{IC} were similar.

4. Conclusion

In this study, we synthesized and characterized new non-peripheral and peripheral (phenoxy and 4-*t*-butylphenoxy) tetra-substituted and octa-substituted lead phthalocyanine complexes. The fluorescence spectra were different from absorption spectra due to the loss of symmetry (due to demetallation) upon excitation. The high triplet quantum yields and low triplet lifetimes were observed as the result of heavy atom (Pb).

Acknowledgement

This work has been supported by the National Research Foundation (NRF GUN = 2053657) of South Africa, CSIR, as well as Rhodes University.

References

[1] C.C. Leznoff, A.B.P. Lever (Eds.), Phthalocyanines – Properties and Applications, VCH, New York, 1989–1996.
[2] G. Guillaud, J. Simon, J.P. Germain, Coord. Chem. Rev. 180 (1998) 1433.
[3] J. Simon, C. Sirlin, Pure Appl. Chem. 61 (1989) 1625.
[4] P. Humberstone, G.J. Clarkson, N.B. McKeown, K.E. Treacher, J. Mater. Chem. 6 (1996) 315.
[5] M.J. Cook, N.B. McKeown, J.M. Simmons, A.J. Thomson, M.F. Daniel, K.J. Harrison, R.M. Richardson, S.J. Roser, J. Mater. Chem. 1 (1991) 121.
[6] G. de la Torre, P. Vasquez, F. Agulló-López, Adv. Mater. 9 (1997) 265.
[7] D. Dini, M. Hanack, The Porphyrin Handbook: Physical Properties of Phthalocyanine-based Materials, vol. 17, Academic press, USA, 2003.
[8] F. Gan, Chin. Sci. Bull. 45 (2000) 572.
[9] J.E. Kuder, J. Imag. Sci. 32 (1988) 51.
[10] A.B.P. Lever, M.R. Hempstead, C.C. Leznoff, W. Liu, M. Melnik, W.A. Nevin, P. Seymour, Pure Appl. Chem. 58 (1986) 1467.
[11] R.D. George, A.W. Snow, J. Heterocyclic Chem. 32 (1995) 495.
[12] Y. Chen, M. Hanack, Y. Araki, O. Ito, Chem. Soc. Rev. 34 (2005) 517.
[13] M. Hanack, T. Schneider, M. Barthel, J.S. Shirk, S.R. Flom, R.G.S. Pong, Coord. Chem. Rev. 219–221 (2001) 235.
[14] H.I. Beltra'n, R. Esquivel, A. Sosa-Sa'nchez, Inorg. Chem. 43 (2004) 3555.
[15] Y.Z. Bian, L. Li, K.P.Ng. Dennis, N. Kobayashi, J.Z. Jiang, Inorg. Chem. 43 (2004) 7539.
[16] I. Chambrier, M.J. Cook, P.T. Wood, Chem. Commun. (2000) 2133.
[17] A. Beck, K.M. Mangold, M. Hanack, Chem. Ber. 124 (1991) 2315.
[18] C.C. Leznoff, S.M. Marcuccio, S. Grinberg, A.B.P. Lever, K.B. Tomer, Can. J. Chem. (1985) 623.
[19] W. Eberhardt, M. Hanack, Synthesis (1997) 95.
[20] J.V. Bakboord, M.J. Cook, E. Hamuryudan, J. Porphyr. Phthalocya. 4 (2000) 510.
[21] T.V. Basova, G.A. Guerek, D. Atilla, K. Aseel, V. Ahsen, Polyhedron 26 (2007) 5045.
[22] P.M. Burnham, I. Chabrier, D.L. Hughes, B. Isare, R.J. Poynter, K.A. Powell, M.J. Cook, J. Porphyr. Phthalocya. 10 (2006) 1202.
[23] A. Koca, H.A. Dincer, H. Cerlek, A. Guel, M.B. Kocak, Electrochim. Acta 52 (2006) 1199.
[24] H.A. Dincer, H. Cerlek, A. Gul, M.B. Kocak, Main Group Chem. 4 (2005) 209.
[25] E.M. Maya, A.W. Snow, J.S. Shirk, R.S. Pong, S.R. Flom, G.L. Roberts, J. Mater. Chem. 13 (2003) 1603.
[26] R. Slota, G. Dyrda, Inorg. Chem. 42 (2003) 5743.
[27] S. Foley, G. Jones, R. Liuzzi, D.J. McGarvey, M.H. Perry, T.G. Truscott, J. Chem. Soc., Perkin Trans. 2 (1997) 1725.
[28] H.A. Dincier, H. Cerlek, A. Gul, M.B. Kocak, Main Group Chem. 4 (2005) 209.
[29] H. Zhan, W. Chen, M. Wang, Mater. Lett. 59 (2005) 1395.
[30] W. Sun, C.C. Byeon, M.M. Mckerns, G.M. Gray, D. Wang, C.M. Lawson, SPIE 3472 (1998) 127.
[31] P. Buck, A. Dogariu, D.J. Hagan, E.W. Van Stryland, SPIE 2853 (1996) 12.
[32] C.C. Byeon, M.M. McKerns, W. Sun, T.M. Nordlund, C.M. Lawson, G.M. Gray, Appl. Phys. Lett. 84 (2004) 5174.
[33] T. Sooksimuang, B.K. Mandal, J. Org. Chem. 68 (2003) 652.
[34] B.K. Mandal, T. Sooksimuang, J. Porphyr. Phthalocya. 6 (2002) 666.
[35] J.G. Young, W. Onyebuagu, J. Org. Chem. 55 (1990) 2155.
[36] D. Wöhrle, M. Eskes, K. Shigehara, A. Yamada, Synthesis (1993) 194.
[37] A. Ogunsipe, J.Y. Chen, T. Nyokong, New J. Chem. 28 (2004) 822.
[38] J. Fu, X.Y. Li, D.K.P. Ng, C. Wu, Langmuir 18 (2002) 3843.
[39] P. Kubát, J. Mosinger, J. Photochem. Photobiol. A: Chem. 96 (1996) 93.
[40] T.H. Tran-Thi, C. Desforge, C. Thiec, J. Phys. Chem. 93 (1989) 1226.
[41] J. Kossanyi, O. Chahraoui, Int. J. Photoenerg. 2 (2000) 9.
[42] S.M. Bishop, A. Beeby, A.W. Parker, M.S.C. Foley, D. Phillips, J. Photochem. Photobiol. A: Chem. 90 (1995) 29.
[43] P. Tau, T. Nyokong, Dalton Trans. (2006) 4482.
[44] P. Tau, T. Nyokong, J. Porphyr. Phthalocya. 10 (2006) 1040.
[45] V. Chauke, A. Ogunsipe, M. Durmas, T. Nyokong, Polyhedron 26 (2007) 2666.
[46] C.C. Leznoff, in: C.C. Leznoff, A.B.P. Lever (Eds.), Phthalocyanines, Properties and Applications, vol. 1, VCH Publishers, New York, 1989 (Chapter 1).
[47] M. Durmuş, S. Yeşilot, V. Ahsen, New J. Chem. 30 (2006) 675.
[48] S. Marcuccio, P.I. Svirskaya, S. Greenberg, A.B.P. Lever, Can J. Chem. 63 (1985) 3057.
[49] M.M. El-Nahass, K.F. Abd-El-Rahman, A.A.A. Darwish, Mater. Chem. Phys. 92 (2005) 185.
[50] S. Gaspard, P. Maillard, Tetrahedron 43 (1987) 1083.
[51] M.J. Stillman, T. Nyokong, in: C.C. Leznoff, A.B.P. Lever (Eds.), Phthalocyanines: Properties and Applications, vol. 1, VCH Publishers, New York, 1989 (Chapter 1).
[52] J. Mark, M.J. Stillman, J. Am. Chem. Soc. 116 (1994) 1292.
[53] M. Konami, M. Hatano, A. Tajiri, Chem. Phys. Lett. 166 (1990) 605.
[54] A. Ogunsipe, D. Maree, T. Nyokong, J. Mol. Struct. 650 (2003) 131.
[55] W. Freyer, S. Mueller, K. Teuchner, J. Photochem. Photobiol. A: Chem. 163 (2004) 231.
[56] M.G. Debacker, O. Deleplanque, B. Van Vlieberge, F.X. Sauvage, Laser Chem. 8 (1988) 1.
[57] T. Nyokong, Coord. Chem. Rev. 251 (2007) 1707.
[58] M. Durmus, T. Nyokong, Tetrahedron 63 (2007) 1385.

lines. Generally, cobalt(III) complexes show antitumor activities in vivo [7,8] and, hence recently, the interaction of cobalt complexes with DNA has attracted much attention [9–11]. In a recent report, Shimakoshi et al. have shown that a dicobalt complex was more efficient in cleaving DNA compared to an equivalent monomeric complex [12]. Synthesis of new cobalt(III) complexes enabled chemists to extensively study the ability of these complexes to act as probes in investigating the structure of DNA, when these metal complexes are incorporated with either 1,10-phenanthroline or a modified phenanthroline moiety as one of the ligands.

A polymer–metal complex is composed of a polymeric ligand and metal ion in which the metal ion is attached to the polymer ligand by a coordination bond. In recent years, the chemistry of polymer–metal complexes has been of great interest because these complexes act as excellent models for metalloenzymes [13]. Drug–polymer conjugates are potential candidates for the selective delivery of anticancer agents to tumor tissue and only a very few reports are available for the use of polymer–metal complexes as anticancer drugs [14–16]. Polyethyleneimine (PEI) is a cationic polymer exhibiting the highest positive charge density potential and, recently, PEI has appeared as a possible alternative to viral and liposomal routes of gene delivery [17]. PEI possesses quite a number of advantages as polymer chelating agent, such as good water solubility, high content of functional groups, good physical and chemical stability, and suitable molecular weights [18]. Recently, we have reported our interesting results on the interaction of some polymer–cobalt(III)/copper(II) complexes with DNA [19,20].

In this context, we focused on the development of new water-soluble branched polyethyleneimine–cobalt(III) complex samples with different amounts of cobalt(III) complex (containing 1,10-phenanthroline ligand) moieties bound to the polymer chain and studied the DNA binding properties of these polymer-bound cobalt(III)–phenanthroline complex samples and their antitumor activities on HEp-2 laryngeal cancer cells.

2. Experimental

2.1. Materials and instrumental techniques

Cobalt(II) chloride hexahydrate, 1,10-phenanthroline were purchased from Merck, India. Calf thymus DNA and branched polyethyleneimine (BPEI) (M_w ca. 25000) obtained from Sigma–Aldrich, Germany, were used as such. Plasmid pBR322 DNA was purchased from Genei, India. The spectroscopic titration was carried out in the aqueous buffer solution (50 mM NaCl–5 mM Tris–HCl, pH 7.1) at room temperature. A solution of calf thymus DNA in the buffer gave a ratio of UV absorbance at 260 and 280 nm of (1.8–1.9:1), indicating that the DNA was sufficiently free of protein [21]. Milli-Q water was used to prepare the solutions. The complex, *cis*-$[Co(phen)_2Cl_2]Cl \cdot 3H_2O$, was prepared as reported earlier [22]. Absorption spectra were recorded on a UV–Vis–NIR Cary300 Spectrophotomer using cuvettes of 1-cm path length, and emission spectra were recorded on a JASCO FP 770 spectrofluorimeter. FT-IR spectra were recorded on a FT-IR Perkin–Elmer spectrophotometer with samples prepared as KBr pellets. ^1H NMR spectra were recorded on a BRUKER 400 MHz Spectrometer using D_2O as solvent.

2.2. Synthesis of polymer–cobalt(III) complex samples

A sample of polymer–cobalt(III) complex, *cis*-$[Co(phen)_2(BPEI)Cl]Cl_2 \cdot 4H_2O$, was prepared from *cis*-$[Co(phen)_2Cl_2]Cl \cdot 3H_2O$ by the same method reported earlier for preparing *cis*-$[Co(en)_2(BPEI)Cl]Cl_2$ (en = ethylenediamine) [23] and *cis*-$[Co(en)_2(PVP)Cl]Cl_2 \cdot nH_2O$ [PVP = poly(4-vinylpyridine)] [24]. To a solution of 0.15 g of BPEI dissolved in 15 mL of ethanol, 1.0 g of *cis*-$[Co(phen)_2Cl_2]Cl \cdot 3H_2O$ in 15 mL of water was added slowly with stirring. The mixture was heated between 50 and 60 °C for 12 h in a water bath. The color of the solution changed from violet to reddish brown. After being warmed enough, the dark blue colored mixture was filtered, and the filtrate was dialyzed against cold water for several days. Afterwards, the solvent was evaporated in a rotary evaporator under reduced pressure at room temperature. A dark reddish filmy substance was obtained. It was pulverized and dried. Yield: 0.25 g. *Anal.* Calc.: C, 31.38; H, 7.18; N, 18.85. Found: C, 31.38; H, 7.36; N, 19.13 and $x = 0.245$. (The degree of coordination (x), means the number of moles of cobalt(III) chelate per mole of the repeating unit (imine group) of polymeric ligand. If all the repeating units (imine groups) in the polymer are coordinated to cobalt, then the value of x is 1.) IR (KBr, cm^{-1}): 3433 (ν(N–H), BPEI), 2924, 2853 (C–H asymmetric and symmetric stretching vibration of aliphatic CH_2 of BPEI), 1626 (ν(C=N), phen), 1517 (ν(C=C), phen ring), 849, 725 (ν(C–H), phen). ^1H NMR (D_2O, ppm): δ 8.9 (2H, d, phen), δ 8.3 (2H, s, phen), δ 7.79 (2H, t, phen), δ 7.5 (2H, d, phen), δ 2.5–3.6 (broad, H from N–CH_2–CH_2–N from BPEI).

The polymer–cobalt(III) complex samples with various amounts of cobalt(III) complex units bound to the polymer chain were synthesized by some modifications in the above experimental procedure. That is the amount of *cis*-$[Co(phen)_2(BPEI)Cl]Cl_2 \cdot 4H_2O$ in the reaction solution was varied between 0.6 and 1.0 g. Also the reaction duration has been kept between 6 and 10 h.

2.3. DNA-binding experiments

The DNA-binding experiments were performed at 30.0 ± 0.2 °C. The DNA concentration per nucleotide was determined by electronic absorption spectroscopy using the known molar extinction coefficient value of 6600 $M^{-1}\,cm^{-1}$ at 260 nm [25]. Electronic absorption

titration of the polymer–cobalt(III) complex samples in the aqueous buffer solution (50 mM NaCl–5 mM Tris–HCl, pH 7.1) were performed by using a fixed complex concentration (12 μM) with increasing amounts of DNA over a range of 0.5–2 μM.

The binding constant for the interaction of polymer–cobalt(III) complex samples with DNA was obtained from absorption titration data (at 269 nm where only polymer–cobalt(III) complex absorbs in the concentration range used. No absorption could be observed for DNA). The intrinsic binding constant, K_b, has been determined using the equation [26],

$$[DNA]/(\varepsilon_a - \varepsilon_f) = [DNA]/(\varepsilon_b - \varepsilon_f) + 1/K_b(\varepsilon_b - \varepsilon_f),$$

where [DNA] is the concentration of DNA in base pairs, ε_a, ε_f and ε_b correspond to A_{obsd}/[total cobalt complex units], the extinction coefficient of the complex in its free form and the extinction coefficient of the complex in the fully bound form, respectively. A plot of [DNA]/($\varepsilon_a - \varepsilon_f$) versus [DNA], gives K_b as the ratio of the slope to the intercept (Our attempts to determine the binding constant for the polymer–cobalt(III) complex samples using the visible region of the spectrum were unsuccessful due to the necessity of using very high concentration of the polymer–cobalt(III) complex at which the complex-DNA adduct precipitates out of the solution).

For fluorescence experiments, DNA was pretreated with ethidium bromide (EB) for 30 min. The polymer–cobalt(III) complexes were then added to this mixture and their effect on the emission intensity was measured. The samples were excited at 450 nm and emission was observed between 500 and 700 nm. These experiments were carried out in 50 mM NaCl–5 mM Tris–HCl at pH 7.1 in aqueous media.

For the gel electrophoresis experiments, super-coiled pBR322 DNA (0.1 μg) was treated with the polymer–cobalt(III) complex in 50 mM Tris–HCl, 18 mM NaCl buffer, pH 7.2. The samples were electrophoresed for 3 h at 50 V on a 0.8% agarose gel in Tris–acetic acid–EDTA buffer. The gel was stained with 0.5 μg/mL of ethidium bromide and photographed in UV light.

2.4. Cell culture

HEp-2 human larynx cancer cells were obtained from King's Institute of Preventive Medicine, Chennai, India. The cells were cultured in RPMI 1640 medium (Sigma–Aldrich, St. Louis, MO, USA), supplemented with 10% fetal bovine serum (Sigma, USA) and 100 μg/mL of penicillin and 100 μg/mL of streptomycin as antibiotics (Himedia, Mumbai, India), in 96 well culture plates, at 37 °C, in a humidified atmosphere of 5% CO_2, in a CO_2 incubator (Heraeus, Hanau, Germany). All experiments were performed using cells from passage 15 or less.

2.5. Cytotoxicity assay [27]

The *cis*-$[Co(phen)_2(BPEI)Cl]Cl_2 \cdot 4H_2O$ complex was first dissolved quantitatively in dimethyl sulfoxide (DMSO, Sigma, USA) to make the stock solution. This solution was diluted to get various concentrations of the complex in the range of 25–225 μg/mL. 200 μL of this solution was added to a series of wells containing 5×10^3 HEp-2 cells per well in DMSO medium. DMSO solution was used as the solvent control. After 24 and 48 h of treatment, the gross morphological changes in HEp-2 cells were observed and photographed, using an inverted microscope (Carl Zeiss, Jena, Germany). Immediately thereafter, 20 μL of MTT solution (5 mg/mL in phosphate-buffered saline (PBS)) was added to each well and the plates were wrapped with aluminum foil and incubated for 4 h at 37 °C. The purple formazan product was dissolved by addition of 100 μL of 100% DMSO to each well. The absorbance was monitored at 570 nm (measurement) and 630 nm (reference) using a 96 well plate reader (Bio-Rad, Hercules, CA, USA). Data were collected for four replicates each and used to calculate the respective means. The percentage inhibition was calculated, from this data, using the formula:

$$\frac{\text{Mean absorbance of untreated cells(control)} - \text{Mean absorbance of treated cells} \times 100}{\text{Mean absorbance of untreated cells(control)}}$$

2.6. Hoechst 33258 staining [28]

The cell pathology was detected by staining the nuclear chromatin of trypsinized cells (4.0×10^4/mL) with 1 μL of Hoechst 33258 (1 mg/mL, aqueous) for 10 min at 37 °C. A drop of cell suspension was placed on a glass slide and a cover-slip was laid over to reduce light diffraction. At random 300 cells were observed in a fluorescent microscope (Carl Zeiss, Germany) fitted with a 377–355 nm filter and observed at 400× magnification, and the percentage of cells reflecting pathological changes was calculated. Data were collected for four replicates and used to calculate the mean and the standard deviation.

2.7. Acridine orange (AO) and ethidium bromide (EB) staining

Acridine orange (AO) and ethidium bromide (EB) staining was performed as described by Spector et al. [29]. Cell suspension (25 μL) of each sample (both

attached, released by trypsinization, and floating), containing 5×10^5 cells, was treated with AO and EB solution (1 part of 100 μg/mL AO and 1 part of 100 μg/mL EO in PBS) and examined under a fluorescent microscope (Carl Zeiss, Germany) using an UV filter (450–490 nm). Three hundred cells per sample were counted in tetraplicate for each dose point. Cells were scored as viable, apoptotic or necrotic as judged by the staining, nuclear morphology and membrane integrity, and percentages of apoptotic and necrotic cells were then calculated. Morphological changes were also observed and photographed.

2.8. Leukostat staining

Leukostat staining was performed as described by Spector et al. [29]. Smears of cells (attached, released by trypsinization, and floating were pooled) were fixed by dipping the slide for 10 s in Leukostat fixative solution (2 mg/ml malachite green in 100% methanol). The cytoplasm was stained by dipping for 10 s in Leukostat staining solution 1 (0.1% eosin Y, 0.1% formaldehyde; 0.4% sodium phosphate dibasic, and 0.5% potassium phosphate monobasic) and counterstained by dipping for 10 s in Leukostat staining solution 2 (0.04% azure, 0.04% methylene blue, 0.4% sodium phosphate dibasic, and 0.5% potassium phosphate monobasic). The preparations were examined at 400× magnification in a light microscope (Carl Zeiss, Germany). The cells were scored as normal, apoptotic or necrotic as judged by staining and nuclear/cell morphology. Percentages of apoptotic cells and necrotic cells were then calculated. The morphological changes were also observed and photographed.

3. Results and discussion

3.1. Degree of coordination

The structure of the polymer–cobalt(III) complex is shown in Fig. 1. In this figure 'x' represents degree of coordination. The degree of coordination (x) of the cobalt chelate in the polymer–cobalt(III) complex could be calculated from the carbon content [23,24] or cobalt content [30]. The degree of coordination (x) thus obtained for the polymer–cobalt(III) complexes synthesized were 0.104, 0.125 and 0.245. The x value of the polymer–metal complex was found to reach a constant level of about 0.245. Even if the cobalt chelate was added in large excess or the reaction mixture was warmed for more than 12 h, we could not obtain polymer–cobalt(III) complex samples with degree of coordination more than 0.245. This may be ascribed to the steric hindrance between metal complex units in the polymer chain which prevents further coordination [23].

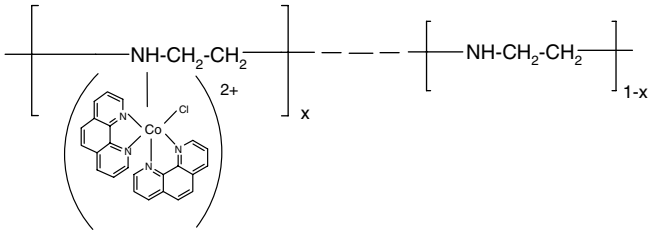


Fig. 1. Structure of *cis*-[Co(phen)$_2$(BPEI)Cl]Cl$_2$ · 4H$_2$O

3.2. Absorption spectroscopic studies

Electronic absorption spectra were initially employed to study the binding of polymer–cobalt(III) complexes with CT-DNA. The absorption spectra in aqueous buffer media of polymer–cobalt(III) complex ($x = 0.245$) in the absence and in the presence of CT DNA are given in Fig. 2. As the concentration of DNA increased, the absorption band of polymer–cobalt(III) complex at 269 nm exhibits hyperchromism and blue shift. A similar hyperchromism has been observed for the soret bands of certain porphyrins when interacted with DNA but has not yet been clearly explained [31].

The polymer–cobalt(III) complex can bind to the double stranded DNA in different binding modes on the basis of their structure and charge and type of ligands. Our polymer–cobalt(III) complex, containing several methylene groups of the branched polyethyleneimine (BPEI) can bind to DNA by van der Waals interactions between these methylene groups and the thymine methyl groups of DNA [32]. On the other hand, since DNA possesses several hydrogen bonding sites which are accessible both in minor and major grooves, it is likely that the amine groups of BPEI forms hydrogen bonds with N-3 of adenine or O-2 of thymine in the DNA, which may contribute to the hyperchromism observed in the absorption spectra. The hyperchromic effect may also be due to the electrostatic interaction between positively charged polymer (BPEI) and the nega-

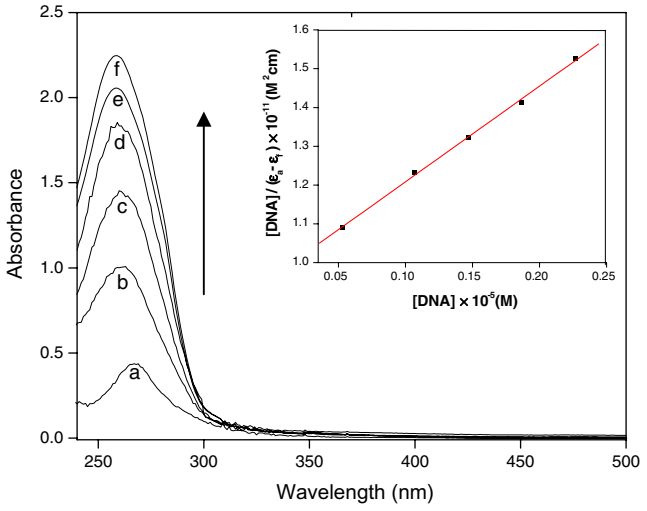


Fig. 2. Absorption spectra of *cis*-[Co(phen)$_2$(BPEI)Cl]Cl$_2$ · 4H$_2$O ($x = 0.245$) in the absence (a) and in the presence of increasing amounts of DNA (b,c,d,e,f), [polymer–cobalt(III) complex] = 12 μM, [DNA] = 0.5–2 μM. Arrow shows the absorbance change upon increasing DNA concentrations. Inset: Plot of [DNA]/($\varepsilon_a - \varepsilon_f$) vs. [DNA].

tively charged phosphate backbone at the periphery of the double helix CT DNA [33]. Structurally, intercalation to DNA may be one of the binding patterns, since our polymer–cobalt(III) complex contains phenanthroline ligands which should provide aromatic moiety extending from the metal center through which overlapping occurs with base pairs of DNA by intercalation. In our complex, the cobalt(III)–phenanthroline chelate moieties are randomly coordinated to the branched polymer, hence complete intercalation of the phenanthroline ligand between a set of adjacent base pairs is sterically impossible, but some type of partial intercalation can be envisioned [34].

Viscosity and circular dichroism measurements could have been helpful to us to confirm the intercalative behaviour. But as our systems are polymeric and DNA being another polymer, we were not able to use viscosity method, because not only changes in the structure of DNA but also the changes in the structure of the polymer–cobalt(III) complex would change the viscosity of the solution. So it will not be possible to resolve the changes in the viscosity behaviour if at all there is a change in the viscosity behaviour. The solubility of polymer–cobalt(III) complex samples are very low, so we could not do circular dichroism measurements also.

The intrinsic binding constant (K_b) values of polymer–cobalt(III) complex with different degrees of cobalt complex content are shown in Table 1 which indicate that complex with higher degree of cobalt complex content has higher K_b value. The significant difference in DNA binding affinity of the three polymer–cobalt(III) complex samples can be understood as a result of the fact that the complex with higher degree of cobalt content shows stronger binding with DNA. Interestingly, the K_b values obtained for our polymer–cobalt(III) complex samples are very much higher than those for the other known ordinary cobalt(III) complexes containing 1,10-phenanthroline and/or modified phenanthroline ligands available in the literature [3–5,35–38]. $[Co(5,6\text{-dmp})_3]^{3+}$ (5,6-dmp = 5,6-dimethyl-1,10-phenanthroline) (K_b, $2.1 \times 10^3\ M^{-1}$), $[Co(phen)_2(bipy)]^{3+}$ (bipy = bipyridine) (K_b, $2.3 \times 10^3\ M^{-1}$), $[Co(phen)_2(imp)]^{3+}$ (imp = imidazo[4,5-*f*][1,10]-phenanthroline) (K_b, $1.2 \times 10^5\ M^{-1}$), $[Co(phen)_2(PIP)]^{3+}$ (PIP = 2-phenylimidazo[4,5-*f*][1,10]-phenanthroline) (K_b, $2.15 \times 10^5\ M^{-1}$), $[Co(phen)_3]^{3+}$ (K_b,$1.6 \times 10^4\ M^{-1}$), $[Co(phen)_2(dicnq)]^{3+}$ (dicnq = dicyanodipyrido quinoxaline) (K_b, $6.0 \times 10^3\ M^{-1}$), $[Co(phen)_2(pdtb)_2]^{3+}$ (pdtb = 3-(pyridine-2-yl)-5,6-diphenyl-as-triazine) (K_b, $8.62 \times 10^3\ M^{-1}$), $[Co(phen)_2(pdta)]^{3+}$ (pdta = 3-(pyridine-2-yl)-as-triazino[5,6-*f*]-acenaphthylene) (K_b, $2.81 \times 10^4\ M^{-1}$), $[Co(phen)_2(HPIP)]^{3+}$ (HPIP = 2-(2-hydroxyphenyl)imidazo[4,5-*f*][1,10]-phenanthroline) (K_b, $4.1 \times 10^5\ M^{-1}$), $[Co(phen)_2(HNAIP)]^{3+}$ (HNAIP = 2-(2-hydroxy-1-naphthyl)imidazo[4,5-*f*][1,10]-phenanthroline) (K_b, $1.8 \times 10^5\ M^{-1}$), $[Co(phen)_2(CNOIP)]^{3+}$ (CNOIP = 2-(2-chloro-5-nitrophenyl)imidazo[4,5-*f*][1,10]-phenanthroline) (K_b, $1.6 \times 10^5\ M^{-1}$), $[Co(en)_2(phen)]^{3+}$ (en = ethylenediamine) (K_b, $1.7 \times 10^3\ M^{-1}$), $[Co(en)_2(dppz)]^{3+}$ (dppz = dipyrido[3,2-*a*:2′,3′-*c*]phenazine) (K_b, $4.3 \times 10^3\ M^{-1}$). Also K_b values for our complex samples are higher than known association constant of PEI to DNA (K_a, $1.2 \times 10^5\ M^{-1}$) [39]. This shows that comparatively our polymer–cobalt(III) complex samples can bind very strongly with DNA.

We have carried out the effect of addition of NaCl salt into the DNA bound polymer–cobalt(III) complex. Fig. 3 shows the changes in the absorption spectra upon addition of increasing amounts of NaCl into the DNA bound polymer–cobalt(III) complex. When increasing the ionic strength of the medium, we observed that the absorbance of the DNA bound polymer–cobalt(III) complex goes on decreasing along with a slight blue shift till the ionic strength reaches sufficiently high value (at 3.2 M). In the case of ordinary cobalt(III)–phenanthroline complex the value is 1.75 M. This implies that electrostatic interaction make significant contribution to the binding between DNA and polymer–cobalt(III) complex.

3.3. Fluorescence studies

No fluorescence was observed for the polymer–cobalt(III) complexes at room temperature in aqueous solution or in any organic solvent examined or in the presence of calf thymus DNA. So the binding of polymer–cobalt(III) complex

Table 1
The intrinsic binding constants (K_b) of polymer–cobalt(III) complex samples with calf thymus DNA

Complex	Degree of coordination (x)	K_b (M^{-1})
cis-$[Co(phen)_2(BPEI)Cl]Cl_2 \cdot 4H_2O$	0.104	1.13×10^6
	0.125	1.54×10^6
	0.245	2.57×10^6

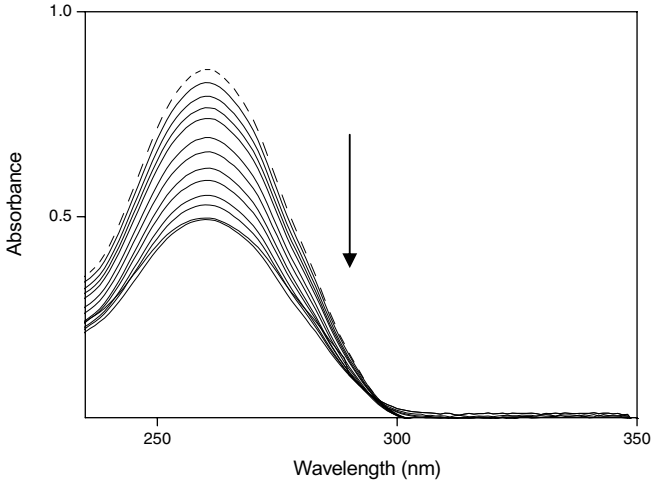


Fig. 3. Influence of the salt concentration on the UV spectra of the DNA bound polymer–cobalt(III) complex ($x = 0.245$) system. Concentrations: [complex] = 12 μM, [DNA] = 0.5 μM. Dashed line: DNA bound polymer–cobalt(III) complex without any salt; solid line: with the addition of 0.1–4 M NaCl.

samples with DNA cannot be directly predicted through the emission spectra. Hence competitive ethidium bromide (EB) binding studies were undertaken to gain support for the extent of binding of polymer–cobalt(III) complex with DNA. The molecular fluorophore, ethidium bromide (EB), emits intense fluorescence light in the presence of CT DNA due to its strong intercalation between the adjacent DNA base pairs [40]. It has been previously reported that the fluorescent light can be reduced by the addition of a second molecule [41], indicating the competition of second molecule with ethidium bromide (EB) in binding to DNA. Recently, Ni et al. [42] found that fluorescence reduction of fluorophore NR (neutral red dye) in the presence of DNA by $Cu(phen)^{2+}$may be due to the replacement of the DNA intercalator, NR. This means that the complex interacts with the same site as NR does. On the other hand, Bronich et al. [43] have reported that the addition of a copolymer (i.e., polyethyleneglycol-polyethyleneimine (PEI)) to ethidium bromide (EB)–DNA complex results in quenching of the fluorescence due to the displacement of ethidium bromide (EB) by the copolymer. Xiao and Zhan [33] have studied the effect of polymeric Schiff base-nickel complexes on the fluorescence of EB-DNA system and they have suggested that a portion of the metal complex, possessing a planar aromatic moiety can intercalate to adjacent base pairs, which can in turn inhibit ethidium bromide (EB) binding to calf thymus DNA competitively. In our studies the addition of the polymer–cobalt(III) complex to DNA pretreated with ethidium bromide (EB) causes appreciable reduction in the emission intensity (Fig. 4), indicating that the replacement of the EB fluorophore by the polymer–cobalt(III) complex, results in decrease in the emission intensity. The polymer–cobalt(III) complex with higher degree of coordination has led to a larger reduction in emission intensity in the presence of DNA. This may be due to the larger number of cobalt(III) chelates (containing phenanthroline ligands) present in the polymer chain which hinders intercalation of ethidium bromide (EB) into DNA and thus decreasing the binding ability between ethidium bromide (EB) and calf thymus DNA.

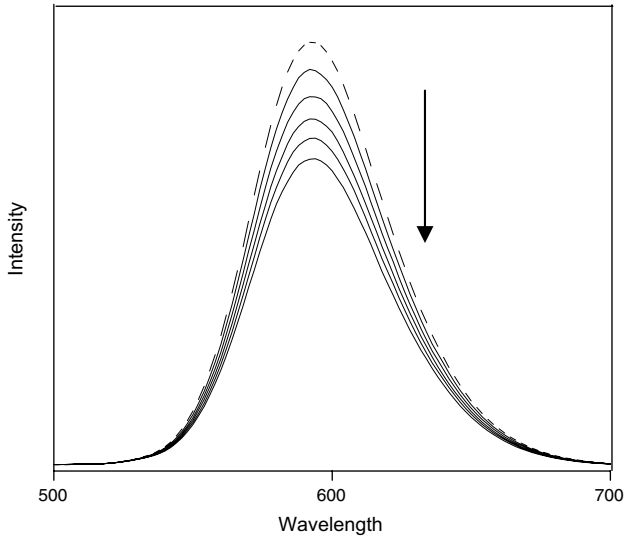


Fig. 4. Emission spectra of EB bound to DNA in the absence (—) and in the presence of *cis*-$[Co(phen)_2(BPEI)Cl]Cl_2 \cdot 4H_2O$ (—) ($x = 0.245$), [EB] = 4 μM, [DNA] = 4 μM, [polymer–cobalt(III) complex] = 0–4 μM.

3.4. Gel electrophoresis studies

Preliminary results from the absorption and fluorescence spectral studies show that the polymer–cobalt(III) complex with high cobalt(III) chelate content binds strongly to DNA. Binding of this complex with DNA was also studied by gel electrophoresis using plasmid pBR 322 DNA. This DNA moves on agarose gel under the influence of electrical field. This movement is retarded when they are bound to other molecules. Many polycationic polymer molecules interact with DNA through electrostatic interactions between phosphate groups of the DNA and oppositely charged groups of polymer [44–46]. Forrest et al. [47] and Vinogradov et al. [48] have reported that the polymer, polyethyleneimine (PEI), retards the DNA migration in agarose gel electrophoresis and they suggest that the binding between DNA and polyethyleneimine (PEI) is thought to occur mainly through electrostatic interactions among the participating species. Recently, Annaraj et al. [49] observed that the phenanthroline containing mixed ligand copper(II) complexes retard the mobility of DNA due to the intercalation of the planar phenanthroline groups. Similar retardation in the DNA mobility has also been observed due to the intercalation by ruthenium complexes [50]. In order to substantiate the ionic binding of our polymer–cobalt(III) complex to DNA, gel retardation assay was performed on pBR322 DNA (Fig. 5). Lane 1 is pure DNA not treated with the complex. Lanes 2–9 represent the DNA treated with increasing amounts of the polymer–cobalt(III) complex and lane 10 is for polymer–cobalt(III) complex alone. As seen from Fig. 5 (lanes 2–5), the DNA band migrates completely with increasing the complex concentration from 5 to 30 μM, but at higher complex concentration (40–50 μM), the migration of DNA band diminishes (lanes 6–8) and in lane 9, due to very high concentration (60 μM), complete retardation of the DNA band has been observed. This demonstrates that the cationic segments of the polyethyleneimine might have neu-

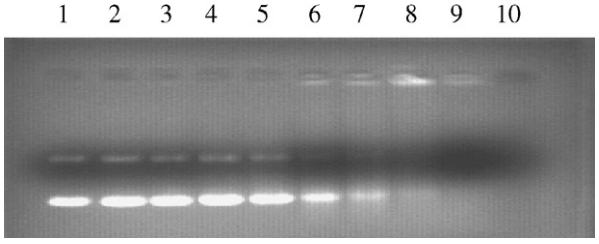


Fig. 5. Gel retardation assay of pBR322 DNA by *cis*-$[Co(phen)_2(BPEI)Cl]Cl_2 \cdot 4H_2O$ ($x = 0.245$). Lane 1: DNA alone, lanes 2–9: DNA + polymer–cobalt(III) complex in the concentration of 5, 10, 15, 20, 30, 40, 50, 60 μM. Lane 10: polymer–cobalt(III) complex alone.

tralized the negative charges of DNA which could have facilitated further due to the increased intercalation of the planar phen groups of cobalt(III) complex moieties. The same behaviour in the electrophoresis has been observed earlier by us in the case of some polyethyleneimine–copper(II)/cobalt(III) complexes [19,20].

3.5. Cytotoxicity assay

We examined the effects of the polymer–cobalt(III) complex ($x = 0.245$) on cultured HEp-2 human larynx cancer cells by exposing cells for 24 h and 48 h to the medium containing the complex at 25–225 μg/mL concentration. Bright field microscopic analysis with control and treated cells revealed that the complex produced dose – as well as duration-dependent cytotoxic effect in the cells (Fig. 6). The results of MTT assay (Fig. 7) indicated that the complex inhibited the growth of the larynx cancer cells significantly in a dose- and duration-dependent manner. For 24 h treatment period, higher concentrations of the complex were required to kill the cells whereas for 48 h treatment the cell killing occurred at lower concentrations. As shown in Table 2, the IC_{50} value of the complex was higher for the 24 h treatment groups, i.e., in the range of 100–140 μg/mL, whereas for the 48 h treatment groups the IC_{50} value fell in the range of 45–65 μg/mL.

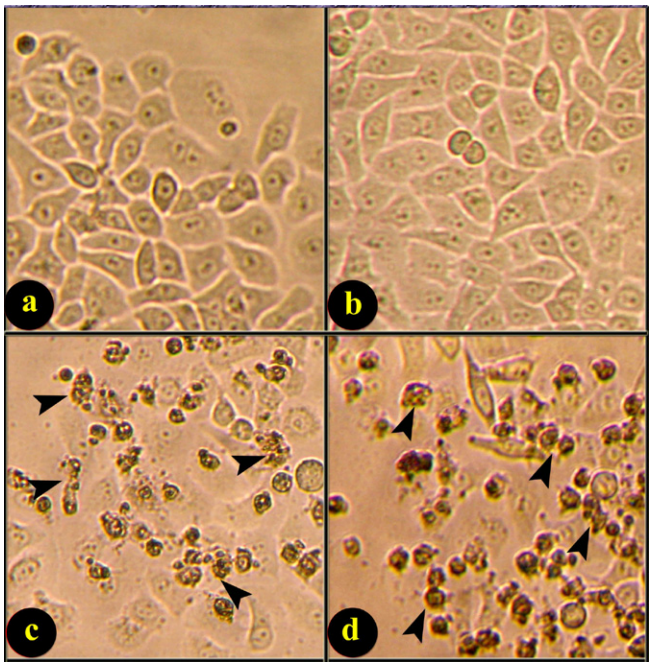


Fig. 6. Bright field microscopic micrographs of HEp-2 cancer cells treated with *cis*-$[Co(phen)_2(BPEI)Cl]Cl_2 \cdot 4H_2O$ ($x = 0.245$). 24 and 48 h 400×. (a,b) Control; (c,d) treated. Arrowheads point to detached abnormal cells.

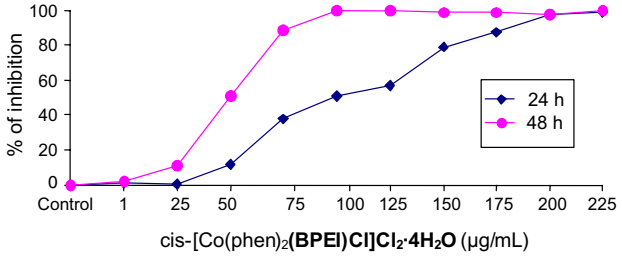


Fig. 7. Graphs showing percentage inhibition vs different concentration for Hep-2 cancer cells exposed to the complex *cis*-$[Co(phen)_2(BPEI)Cl]Cl_2 \cdot 4H_2O$ ($x = 0.245$). Treatment with the complex affects viability of cells in dose- as well as duration dependent manner.

3.6. Hoechst 33258 staining

After the cells were treated with IC_{50} concentrations of polymer–cobalt(III) complex ($x = 0.245$) (100,120,140 μg/mL) for 24 and 48 h the cells were observed for cytological changes adopting Hoechst 33258 staining. The observations revealed that the complex brought about cytological changes such as chromatin fragmentation, binucleation, cytoplasmic vacuolation, nuclear swelling, cytoplasmic blebbing and late apoptosis indication of dot-like chromatin and condensation (Fig. 8). These cytological changes indicated that the cells were committed to death. Data collected from the manual counting of cells with normal and abnormal nuclear features are shown in Fig. 11. Both apoptotic and necrotic cells increased in time-dependent manner with both the complexes.

Table 2
IC_{50} range of *cis*-$[Co(phen)_2(BPEI)Cl]Cl_2 \cdot 4H_2O$ ($x = 0.245$) for HEp-2 cells

Complex	IC_{50} (μg/mL)	
	24 h	48 h
cis-$[Co(phen)_2(BPEI)Cl]Cl_2 \cdot 4H_2O$ ($x = 0.245$)	90–110	45–65

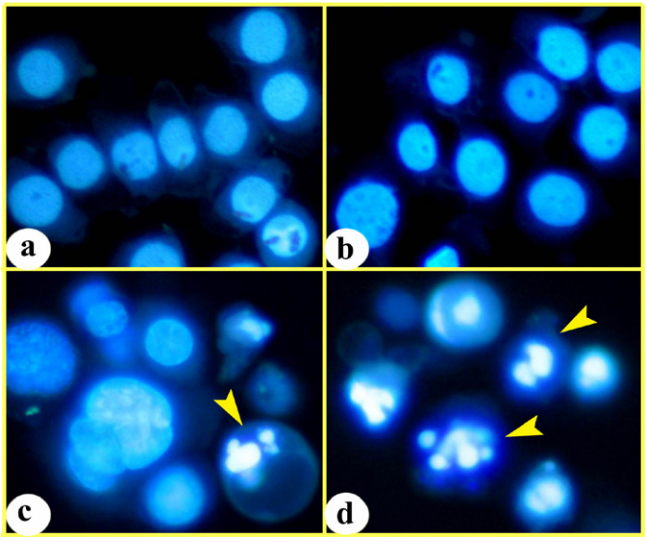


Fig. 8. Hoechst 33258-stained HEp-2 cancer cells treated with *cis*-$[Co(phen)_2(BPEI)Cl]Cl_2 \cdot 4H_2O$ ($x = 0.245$) for 24 and 48 h 400×. (a,b) Control; (c,d) *cis*-$[Co(phen)_2(BPEI)Cl]Cl_2 \cdot 4H_2O$ treated. Arrowheads point to the cells with abnormal nuclei, specially indicating fragmentation of nuclei/chromatin.

3.7. Special staining for apoptosis

To quantify apoptosis, we adopted leukostat as well as AO/EB staining. Treatment of cells with polymer–cobalt(III) complex ($x = 0.245$) for 24 and 48 h induced apoptosis. Using Leukostat triple staining, apoptosis was inferred based on the changes in the overall profile of the cell, and with special reference to chromatin condensation and apoptotic body formation. Normal cells were uniformly stained, both in respect of nuclei and cytoplasm (Fig. 9a and b); cells in early apoptosis had normal profile of the cell membrane but the chromatin was condensed and the nuclei were irregularly shaped (Fig. 9c); cells in late apoptosis had intensely stained cell membrane with blebs and darkly stained highly condensed nuclei (Fig. 9c and d); cells undergoing necrosis had lost the nuclear basophilia and, in their final stage, usually appeared as "ghosts" due to cell lysis (Fig. 9d).

AO/EB staining adopting fluorescence microscopy also revealed apoptosis from the perspective of fluorescence. After HEp-2 cells were exposed to various concentrations of polymer–cobalt(III) complex ($x = 0.245$) for 24 and 48 h, the cells were classified into four types according to the fluorescence emission and the morphological feature of chromatin condensation in the stained nuclei. (1) Viable cells had uniformly green fluorescing nuclei with a highly organized structure (Fig. 10a and b). (2) Early apoptotic cells (which still had intact membranes but had started undergoing DNA fragmentation) had green fluorescing nuclei, but peri-nuclear chromatin condensation was visible as bright green patches or fragments (Fig. 11c and d). (3) Late apoptotic cells had orange to red fluorescing nuclei with condensed or fragmented chromatin (Fig. 10c and d). (4) Necrotic cells had uniformly orange to red fluorescing nuclei with no indication of chromatin fragmentation and the cells were swollen to large size (Fig. 10c and d). The results suggest that polymer–cobalt(III) complex ($x = 0.245$) treatment caused more cells to take to apoptosis in 48 h than 24 h in HEp-2 cells.

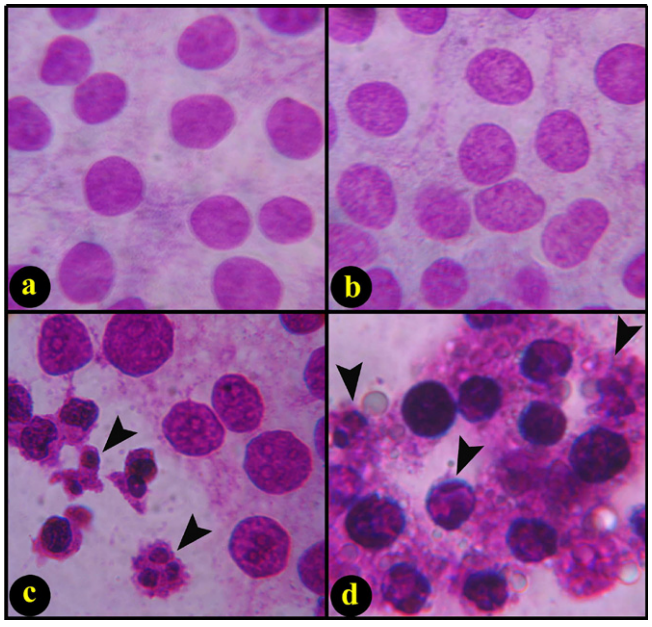


Fig. 9. Leukostat stained HEp-2 cancer cells treated with *cis*-[Co(phen)$_2$(BPEI)Cl]Cl$_2 \cdot 4H_2O$ ($x = 0.245$) 24 and 48 h 400×. (a,b) Control; (c,d) *cis*-[Co(phen)$_2$(BPEI)Cl]Cl$_2 \cdot 4H_2O$ ($x = 0.245$) treated. Arrowheads point to the cells with apoptotic morphologies, specially indicating blebbing.

3.8. Incidence of apoptosis

Data from the three staining methods were compared. Data on cells indicating apoptotic morphologies, induced on treatment with various concentrations of polymer–cobalt(III) complex ($x = 0.245$) for 24 and 48 h, followed by staining with Hoechst 33258, Leukostat and AO/EB, collected from manual counting of cells, are presented in Fig. 10, which indicates that all the three staining methods are efficient in revealing the incidence of apoptosis.

3.9. Efficiency of the complex in killing cancer cells

Thus, polymer–cobalt(III) complex was tested in Hep-2 cancer cell line adopting anti-proliferation and cell morphological assays to find the efficiency in killing the cells and the underlying mechanism. Polymer–cobalt(III) complex has a dose- and duration-dependent relationship in dealing with the cancer cell. Exposing Hep-2 cells to polymer–cobalt(III) complex ($x = 0.245$) led to severe disruption of cellular morphologies such as membrane

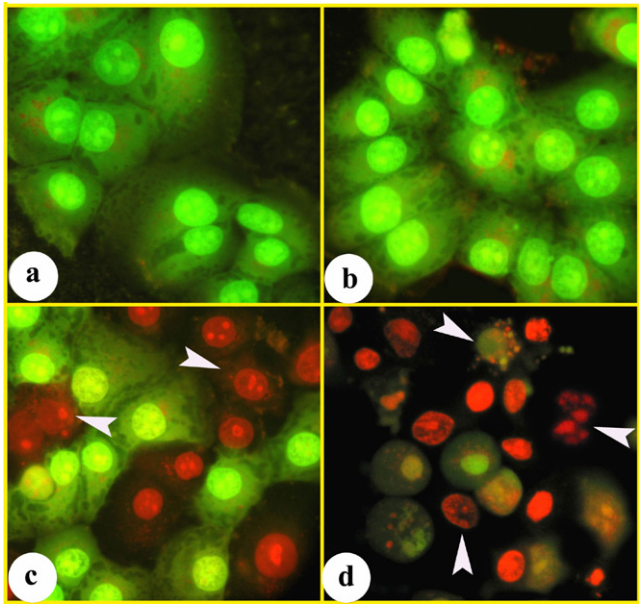


Fig. 10. Photomicrographs of control and AO/EB stained HEp-2 cells incubated for 24 and 48 h, 400×. (a,b) Untreated control cells. The viable cells are uniformly green-fluorescing. (c,d) *cis*-[Co(phen)$_2$(BPEI)Cl]Cl$_2 \cdot 4H_2O$ ($x = 0.245$) treated cells; pre-apoptotic (yellow fluorescing) and apoptotic (red to orange fluorescing) cells were observed. Red to orange fluorescing cells indicate apoptosis. (For interpretation of the references to colour in this figure legend, the reader is referred to the web version of this article.)

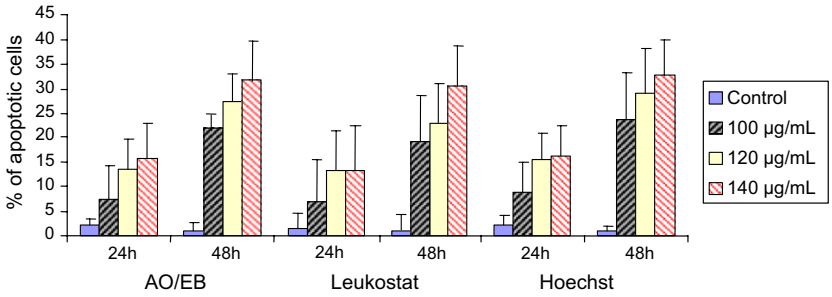


Fig. 11. Bar diagram for comparison of percent cells in apoptosis as revealed by AO/EB, leukostat and Hoechst 33258 staining followed by manual counting. All staining techniques reveal similar data, indicating that all are efficient, though morphological and cytological manifestations differ.

'blebbing' and chromatin fragmentation, which are characteristic of cells dying through apoptotic mechanism. These morphological features were classified based on nuclear as well cytoplasmic features, which reveal that a higher percentage of apoptotic cells is produced in 48 h with a lesser concentration than 24 h.

4. Conclusion

Some new water-soluble polymer–cobalt(III) complexes with different degrees of cobalt(III)–phenanthroline complex moieties on the polymer chain have been synthesized and characterized by Infra-red, UV–Vis, ^{1}H NMR spectral and elemental analysis methods. The DNA binding property of these polymer–cobalt(III) complex samples has been examined by absorption spectroscopy, fluorescence spectroscopy and gel retardation assay. We conclude that many types of interactions like electrostatic interaction, van der Waals interaction, hydrogen bonding and other partial intercalation binding modes exist in this system. The antiproliferative and morphological effects of polymer–cobalt(III) complex sample with high degree of coordination appear to be target-specific killing of cells. In future, this complex might prove to be of application in target-based cancer therapy since the mechanism of cell death appears to be essentially apoptosis but necrosis also is one of the desired endpoints in cancer therapy. From these perspectives, it would be pertinent to confirm the mechanisms of cell killing in the present context by adopting appropriate molecular techniques including expression of pro- and anti-apoptotic genes and caspases in the case of apoptosis, and oxidative damage in the case of necrosis.

Acknowledgements

We are grateful to the UGC-SAP & COSIST and DST-FIST programmes. We thank Dr. L. Uma and Dr. D.Prabhakaran, National Centre for Marine Cyanobacteria, for providing the Gel documentation facility. Council of Scientific and Industrial Research (CSIR), New Delhi is gratefully acknowledged for financial support (Grant no. 01(2075)/06/EMR-II) and a Senior Research Fellowship to R.S.K.

References

[1] M. Demeunynck, C. Bailly, W.D. Wilson (Eds.), DNA and RNA Binders: From Synthesis to Nucleic Acid Complexes, Wiley-VCH, Weinheim, 2003.
[2] M. Gielen, E.R.T. Tiekink (Eds.), Metallotherapeutic Drugs and Metal-based Diagnostic Agents: The Use of Metals in Medicine, John Wiley & Sons, 2005.
[3] X.L. Wang, H. Chao, H. Li, X.L. Hong, Y.J. Liu, L.F. Tan, L.N. Ji, J. Inorg. Biochem. 98 (2004) 1143.
[4] S. Srinivasan, J. Annaraj, P.R. Athappan, J. Inorg. Biochem. 99 (2005) 876.
[5] A.C. Barve, S. Ghosh, A.A. Kumbhar, A.S. Kumbhar, V.G. Puranik, Transit. Met. Chem. 30 (2005) 312.
[6] M. Jung, D.E. Kerr, P.D. Senter, Arch. Pharm. Pharm. Med. Chem. 330 (1997) 173.
[7] B.A. Teicher, M.J. Abrams, K.W. Rosbe, T.S. Herman, Cancer Res. 50 (1990) 971.
[8] S.P. Osinsky, I.Y. Levitin, A.L. Sigan, L.N. Bubnovskaya, I.I. Ganusevich, L. Campanella, P. Wardman, Russ. Chem. Bull. 52 (2003) 2636.
[9] K. Jiao, Q.X. Wang, W. Sun, F.F. Jian, J. Inorg. Biochem. 99 (2005) 1369.
[10] P.T. Selvi, H.S. Evans, M. Palaniandavar, J. Inorg. Biochem. 99 (2005) 2110.
[11] B. Peng, H. Chao, B. Sun, H. Li, F. Gao, L.N. Ji, J. Inorg. Biochem. 101 (2007) 404.
[12] H. Shimakoshi, T. Kaieda, T. Matsuo, H. Sato, Y. Hisaeda, Tetrahedron Lett. 44 (2003) 5197.
[13] M. Kaneko, E.T. Tsuchida, J. Polym. Sci. Macromol. Rev. 16 (1981) 397.
[14] B.A. Howell, E.W. Walls, R. Rashidianfar, Macromol. Chem. Macromol. Symp. 19 (1988) 329.
[15] B. Schechter, R. Arnon, M. Wilchek, React. Polym. 25 (1995) 167.
[16] S. Raja, R. Dhamodharan, J. Macromol. Sci. Part A 41 (2004) 859.
[17] W.T. Godbey, K.K. Wu, A.G. Mikos, J. Control. Release 60 (1999) 149.
[18] K. Geckeler, G. Lange, H. Eberhardt, E. Bayer, Pure Appl. Chem. 52 (1980) 1883.
[19] R.S. Kumar, S. Arunachalam, Polyhedron 25 (2006) 3113.
[20] R.S. Kumar, S. Arunachalam, Polyhedron 26 (2007) 3255.
[21] J. Marmur, J. Mol. Biol. 3 (1961) 208.
[22] A.V. Ablov, Russ. J. Inorg. Chem. 6 (1961) 157.
[23] E. Tsuchida, H. Nishide, T. Ohkawa, Bull. Sci. Res. Lab. 69 (1975) 31.
[24] Y. Kurimura, E. Tsuchida, M. Kaneko, J. Polym. Sci. Part A 9 (1971) 3511.
[25] M.F. Reichmann, S.A. Rice, C.A. Thomas, P. Doty, J. Am. Chem. Soc. 76 (1954) 3047.
[26] A.M. Pyle, J.P. Rehmann, R. Meshoyrer, C.V. Kumar, N.J. Turro, J.K. Barton, J. Am. Chem. Soc. 111 (1989) 3051.
[27] T. Mosmann, J. Immunol. Methods 65 (1983) 55.

[28] H. Kasibhatla, D. Finucane, T. Brunner, E.B. Wetzel, D.R. Green, Cell: a laboratory manual, vol. 1, Protocol: Staining of Suspension Cells with Hoechst 33258 to Detect Apoptosis, Cold Spring Harbor Laboratory Press, Cold Spring Harbor, New York, 2000, pp. 15.5–15.7.
[29] D.L. Spector, R.D. Goldman, L.A. Leinwand, Cell: a laboratory manual, vol. 1, Culture and Biochemical Analysis of Cells, Cold Spring Harbor Laboratory Press, Cold Spring Harbor, New York, 1998, pp. 34.1–34.9.
[30] R.E. Kitson, Anal. Chem. 22 (1950) 664.
[31] R.F. Pasternack, E.J. Gibbs, J.J. Villafranca, Biochemistry 22 (1983) 2406.
[32] C.L. Liu, J.Y. Zhou, Q.X. Li, L.J. Wang, Z.R. Liao, H.B. Xu, J. Inorg. Biochem. 75 (1999) 233.
[33] Y.N. Xiao, C.X. Zhan, J. Appl. Polym. Sci. 84 (2002) 887.
[34] S. Satyanarayana, J.C. Cabrowiak, J.B. Chaires, Biochemistry 32 (1993) 2573.
[35] P.T. Selvi, M. Palaniandavar, Inorg. Chim. Acta 337 (2002) 420.
[36] M. Carter, M. Rodriguez, A.J. Bard, J. Am. Chem. Soc. 111 (1989) 8901.
[37] C.V. Sastri, D. Eswaramoorthy, L. Giribabu, B.G. Maiya, J. Inorg. Biochem. 94 (2003) 138.
[38] Q.L. Zhang, J.G. Liu, J.Z. Liu, H. Li, Y. Yong, H. Xu, H. Chao, L.N. Ji, Inorg. Chim. Acta 339 (2002) 34.
[39] Y.L. Zhou, Y.Z. Li, Spectrochim. Acta Part A 60 (2004) 377.
[40] J. Olmsted, D.R. Kearns, Biochemistry 16 (1977) 3647.
[41] B.C. Baguley, M. Lebret, Biochemistry 23 (1984) 937.
[42] Y. Ni, D. Lin, S. Kokot, Anal. Biochem. 352 (2006) 231.
[43] T.K. Bronich, H.K. Nguyen, A. Eisenberg, A.V. Kabanov, J. Am. Chem. Soc. 122 (2000) 8339.
[44] T.K. Bronich, A.V. Kabanov, L.A. Marky, J. Phys. Chem. B 105 (2001) 6042.
[45] M.X. Tang, F.C. Szoka, Gene Ther. 4 (1997) 823.
[46] A.V. Harpe, H. Petersen, Y. Li, T. Kissel, J. Control. Release 69 (2000) 309.
[47] M.L. Forrest, J.T. Koerber, D.W. Pack, Bioconjugate Chem. 14 (2003) 934.
[48] S.V. Vinogradov, T.K. Bronich, A.V. Kabonov, Bioconjugate Chem. 9 (1998) 805.
[49] J. Annaraj, S. Srinivasan, K.M. Ponvel, P.R. Athappan, J. Inorg. Biochem. 99 (2005) 669.
[50] E.C. Long, J.K. Barton, Acc. Chem. Res. 23 (1990) 271.

the naturally occurring non-radioactive rhenium isotopes are very attractive to clearly establish the molecular structure of ^{99m}Tc- and $^{186/188}$Re-based radiopharmaceuticals. In this context, the design, synthesis and reactivity of novel rhenium oxocomplexes has become the aim of several laboratories, including ours.

Previously, we investigated the reactivity of oxorhenium(V) species – $[ReOX_3(PPh_3)_2]$ and $[ReOX_3(AsPh_3)_2]$ (X = Cl or Br) – towards 8-hydroxyquinoline (Hhqn) and quinoline-2-carboxylic acid [8,9]. As an extension of this work, we were keen to examine the reactivity of $[ReOX_3(PPh_3)_2]$ towards quinoline ligands containing both hydroxy and carboxylate fragments. 8-Hydroxyquinoline-7-carboxylic acid (Hhquin-7-COOH) and 8-hydroxy-2-methylquinoline-7-carboxylic acid (Hhmquin-7-COOH) are such ligands. Additionally, presented here and in previous work [8,9] quinoline derivatives are structural fragments of styryloquinolines, which are important class of compounds in the search for the potential inhibitors of HIV-1 integrase [10].

Here we present synthesis of $[ReOCl_2$(hquin-7-COOH)$(PPh_3)] \cdot OPPh_3$ (**1** · $OPPh_3$), $[ReOBr_2$(hquin-7-COOH)$(PPh_3)]$ (**2**), $[ReOCl_2$(hmquin-7-COOH)$(PPh_3)]$ (**3**) and $[ReOBr_2$(hmquin-2-COOH)$(PPh_3)]$ (**4**) complexes. X-ray studies have been performed for **1** · $OPPh_3$, **2** and **3** and they confirm bidentate coordination mode of the quinoline carboxylic acids. The COOH group of the quinoline carboxylic acids in the examined complexes is potentially available for further conjugation.

The electronic structure of **1** has been calculated with the density functional theory (DFT), and TDDFT/PCM calculations have been employed to produce a hundred of singlet excited-states starting from the ground-state geometry optimized in the gas phase.

Currently density functional theory (DFT) is commonly used to examine the electronic structure of transition metal complexes. It meets with the requirements of being accurate, easy to use and fast enough to allow the study of relatively large molecules of transition metal complexes [11]. Recent calculations with TD-DFT method for open- and closed-shell of 5d-metal complexes (including rhenium complexes) have also supported the TD-DFT method to be applicable for such systems giving good assignment of experimental spectra [12,13].

Some theoretical investigations have been carried out on the rhenium compounds. The electronic structures of nitrido, oxo, carbonyl, nitrosyl and nitrile rhenium complexes, as well as their spectroscopic properties, bonding and reactivity have been theoretically studied at the HF, MP2, EHT and DFT levels of theory using various basis sets [14–22]. Gancheff et al. [16] have performed extended tests of the ability of the B3LYP method in LANL2DZ basis set for rhenium compounds in a geometry optimization and calculation of spectral properties. Although this is not a very extended basis set, its use with DFT has shown to be sufficient for the geometry optimization and calculation of spectral properties. The correctness of B3LYP method with LANL2DZ basis set for rhenium complexes has been also proven in this paper. The experimental geometry of $[ReOCl_2$(hquin-7-COOH)$(PPh_3)]$ is well reproduced and the calculated electronic spectrum is in good accordance with the experimental one.

2. Experimental

2.1. General procedure

The $[ReOX_3(PPh_3)_2]$ complexes were prepared as reported previously [23]. 8-Hydroxyquinoline-7-carboxylic acid and 8-hydroxy-2-methylquinoline-7-carboxylic acid were synthesized according to the literature methods [24]. All the other reagents used to the synthesis were commercially available and were used without further purification.

IR spectra were recorded on a Nicolet Magna 560 spectrophotometer in the spectral range 4000–400 cm^{-1} with the samples in the form of KBr pellets. Electronic spectra were measured on a spectrophotometer Lab Alliance UV–Vis 8500 in the range 1000–180 nm in acetonitrile solution. Elemental analyses (C H N) were performed on a Perkin–Elmer CHN-2400 analyzer. The ^{1}H NMR spectrum was recorded with a Bruker AM 400 spectrometer at room temperature using $CDCl_3$ as a solvent.

2.2. Preparation of $[ReOCl_2$(hquin-7-COOH)$(PPh_3)] \cdot OPPh_3$ (**1** · $OPPh_3$)

A mixture of $[ReOCl_3(PPh_3)_2]$ (0.50 g, 0.60 mmol), 8-hydroxyquinoline-7-carboxylic acid (0.13 g, 0.69 mmol) and acetonitrile (50 ml) was stirred at room temperature for 3 h. The resulting red-brown solution was left to slow evaporation and dark red crystals were obtained after few days. Yield 75%.

Anal. Calc. for $C_{46}H_{36}Cl_2NO_5P_2Re$: C, 55.15; H, 3.62; N, 1.40. Found: C, 55.70; H, 3.66; N, 1.45%.

IR (KBr; ν/cm^{-1}): 1707(s) $\nu_{C=O}$(COOH); 1616(m), 1588(m), 1567(m), ν_{CN} and $\nu_{C=C}$; 978(vs) $\nu_{Re=O}$.

^{1}H NMR (400 MHz; $CDCl_3$) δ = 12.47 (s, 1 H, COOH), 8.17 (dd, 1H), 8.02 (d, 1H), 7.91 (dd, 1H), 7.70–7.25 (m, 31H), 7.16 (d, 1H).

2.3. Preparation of $[ReOBr_2$(hquin-7-COOH)$(PPh_3)]$ (**2**)

A procedure similar to that for $[ReOCl_2$(hquin-7-COOH)$(PPh_3)] \cdot OPPh_3$ was used with $[ReOBr_3(PPh_3)_2]$ (0.50 g, 0.52 mmol) and 8-hydroxyquinoline-7-carboxylic acid (0.12 g, 0.63 mmol). Dark red crystals of $[ReOBr_2$(hquin-7-COOH)$(PPh_3)]$ were collected in 80% yield.

Anal. Calc. for $C_{28}H_{21}Br_2NO_4PRe$: C, 41.39; H, 2.61; N, 1.72. Found: C, 40.90; H, 2.68; N, 1.70%.

IR (KBr; ν/cm^{-1}): 1718(s) $\nu_{C=O}$(COOH); 1612(m), 1592(m), 1570(m), ν_{CN} and $\nu_{C=C}$; 981(vs) $\nu_{Re=O}$.

^{1}H NMR (400 MHz; $CDCl_3$) δ = 12.46 (s, 1H, COOH), 8.15 (dd, 1H), 8.04 (d, 1H), 7.93 (dd, 1H), 7.57 (br, 1H), 7.42–7.28 (m, 15H), 7.20 (d, 1H).

2.4. Preparation of [$ReOCl_2$(hmquin-7-COOH)(PPh_3)] (**3**)

A procedure similar to that for [$ReOCl_2$(hquin-7-COOH)(PPh_3)] · $OPPh_3$ was used with [$ReOCl_3(PPh_3)_2$] (0.50 g, 0.60 mmol) and 8-hydroxy-2-methylquinoline-7-carboxylic acid (0.14 g, 0.69 mmol). Crystalline precipitate of [$ReOCl_2$(hmquin-7-COOH)(PPh_3)] was collected in 70% yield.

Anal. Calc. for $C_{29}H_{23}Cl_2NO_4PRe$: C, 47.22; H, 3.14; N, 1.90. Found: C, 47.50; H, 3.10; N, 1.85%.

IR (KBr; ν/cm^{-1}): 1718(s) $\nu_{C=O}$(COOH); 1616(m), 1550(m), 1513(m), ν_{CN} and $\nu_{C=C}$; 983(vs) $\nu_{Re=O}$.

^{1}H NMR (400 MHz; $CDCl_3$) $\delta = 12.42$ (s, 1H, COOH), 7.91 (d, 1H), 7.84 (d, 1H), 7.55 (d, 1H), 7.44–7.26 (m, 15H), 7.15 (d, 1H), 2.89 (s, 3H).

2.5. Preparation of [$ReOBr_2$(hmquin-7-COOH)(PPh_3)] (**4**)

A procedure similar to that for [$ReOCl_2$(hquin-7-COOH)(PPh_3)] · $OPPh_3$ was used with [$ReOBr_3(PPh_3)_2$] (0.50 g, 0.52 mmol) and 8-hydroxy-2-methylquinoline-7-carboxylic acid (0.13 g, 0.64 mmol). Crystalline precipitate of [$ReOBr_2$(hmquin-7-COOH)(PPh_3)] was collected in 65% yield.

Anal. Calc. for $C_{29}H_{23}Br_2NO_4PRe$: C, 42.14; H, 2.80; N, 1.69. Found: C, 42.37; H, 2.73; N, 1.65%.

IR (KBr; ν/cm^{-1}): 1710(s) $\nu_{C=O}$(COOH); 1620(m), 1559(m), 1513(m), ν_{CN} and $\nu_{C=C}$; 982(vs) $\nu_{Re=O}$.

2.6. Crystal structures determination and refinement

The X-ray intensity data of **1** · $OPPh_3$, **2** and **3** were collected on a KM-4-CCD automatic diffractometer equipped with CCD detector and graphite monochromated Mo Kα radiation ($\lambda = 0.71073$ Å) at room temperature. Details concerning crystal data and refinement are given in Table 1. Lorentz, polarization and empirical absorption correction using spherical harmonics implemented in SCALE3 ABSPACK scaling algorithm [25] were applied. The structures were solved by the Patterson method and subsequently completed by the difference Fourier recycling. All the non-hydrogen atoms were refined anisotropically using full-matrix, least-squares technique. The hydrogen atoms were treated as "riding" on their adjacent atoms and assigned isotropic temperature factors equal 1.2 times the value of equivalent temperature factor of the aromatic parent atoms and equal 1.5 times the value of equivalent temperature factor of the methyl parent carbon atom and oxygen atom (OH). SHELXS97 [26], SHELXL97 [27] and SHELXTL [28] programs were used for all the calculations.

Table 1
Crystal data and structure refinement for **1** · $OPPh_3$, **2** and **3** complexes

	1 · $OPPh_3$	**2**	**3**
Empirical formula	$C_{46}H_{36}Cl_2NO_5P_2Re$	$C_{28}H_{21}Br_2NO_4PRe$	$C_{29}H_{23}Cl_2NO_4PRe$
Formula weight	1001.80	812.45	737.55
Temperature (K)	293(2)	293(2)	293(2)
Wavelength (Å)	0.71073	0.71073	0.71073
Crystal system	monoclinic	monoclinic	monoclinic
Space group	$P2_1/c$	$P2_1/n$	$P2_1/c$
Unit cell dimensions			
a (Å)	10.0349(3)	10.5930(3)	16.6364(9)
b (Å)	20.9077(7)	15.1539(3)	10.4172(4)
c (Å)	20.0326(5)	17.0501(5)	17.5480(9)
β (°)	94.851(2)	104.627(3)	116.327(7)
Volume (Å^3)	4187.9(2)	2648.27(12)	2725.7(2)
Z	4	4	4
D_{calc} (Mg/m^3)	1.589	2.038	1.797
Absorption coefficient (mm^{-1})	3.153	7.702	4.749
$F(000)$	1992	1552	1440
Crystal size (mm)	0.12 × 0.16 × 0.34	0.07 × 0.14 × 0.14	0.01 × 0.14 × 0.32
θ Range for data collection (°)	2.94–25.00	2.92–25.00	2.81–25.05
Index ranges	$-11 \leqslant h \leqslant 11$, $-24 \leqslant k \leqslant 24$, $-19 \leqslant l \leqslant 23$	$-12 \leqslant h \leqslant 12$, $-18 \leqslant k \leqslant 10$, $-20 \leqslant l \leqslant 20$	$-19 \leqslant h \leqslant 19$, $-12 \leqslant k \leqslant 12$, $-20 \leqslant l \leqslant 12$
Reflections collected	25758	16435	16679
Independent reflections (R_{int})	7351 (0.0217)	4639 (0.0223)	4823 (0.0417)
Completeness to $2\theta = 50°$ (%)	99.6	99.7	99.7
Data/restraints/parameters	7351/0/515	4639/0/335	4823/0/345
Goodness-of-fit on F^2	1.024	0.989	0.979
Final R indices [$I > 2\sigma(I)$]	$R_1 = 0.0207$, $wR_2 = 0.0456$	$R_1 = 0.0151$, $wR_2 = 0.0350$	$R_1 = 0.0236$, $wR_2 = 0.0463$
R indices (all data)	$R_1 = 0.0324$, $wR_2 = 0.0474$	$R_1 = 0.0194$, $wR_2 = 0.0356$	$R_1 = 0.0344$, $wR_2 = 0.0479$
Largest difference in peak and hole (e Å^{-3})	0.909 and −0.435	0.679 and −0.520	1.096 and −1.065

Atomic scattering factors were those incorporated in the computer programs.

3. Computational details

The gas phase geometry of **1** was optimized in the singlet ground-state with the DFT method using the hybrid B3LYP [29,30] functional of GAUSSIAN-03 [31]. The LANL2DZ with additional *d* function with exponent $\alpha = 0.3811$ and *f* function with exponent $\alpha = 2.033$ basis set [32,33] was chosen for the rhenium atom and the standard 6-31G basis set for all the other atoms [34,35]. TDDFT calculations were employed to produce a hundred singlet excited-states starting from the ground-state geometry optimized in the gas phase The solvent (acetonitrile) effect was simulated using the polarizable continuum model (PCM) [36].

Natural bond orbital (NBO) calculations were performed with the NBO code [37,38] included in GAUSSIAN03.

4. Results and discussion

4.1. Preparation and infrared data

The $[ReOX_2(hquin\text{-}7\text{-}COOH)(PPh_3)]$ and $[ReOX_2(hmquin\text{-}7\text{-}COOH)(PPh_3)]$ (X = Cl, Br) complexes were prepared in good yields by ligand exchange reactions starting from $[ReOX_3(PPh_3)_2]$ complexes and 8-hydroxyquinoline-7-carboxylic acid or 8-hydroxy-2-methylquinoline-7-carboxylic acid.

$$[ReOX_3(PPh_3)_2] + Hhquin\text{-}7\text{-}COOH \rightarrow [ReOX_2(hquin\text{-}7\text{-}COOH)(PPh_3)] + HX + PPh_3$$

X = Cl, Br

$$[ReOX_3(PPh_3)_2] + Hhmquin\text{-}7\text{-}COOH \rightarrow [ReOX_2(hmquin\text{-}7\text{-}COOH)(PPh_3)] + HX + PPh_3$$

The complexes are air stable and soluble in common organic solvents. The $[ReOCl_2(hquin\text{-}7\text{-}COOH)(PPh_3)]$ complex crystallizes as the $[ReOCl_2(hquin\text{-}7\text{-}COOH)(PPh_3)] \cdot OPPh_3$ adduct. The starting oxo complexes are synthesized by the reduction of ammonium perrhenate:

$$ReO_4^- + 3X^- + 4H^+ + 3PPh_3 \rightarrow [ReOX_3(PPh_3)_2] + OPPh_3 + 2H_2O$$

and $[ReOX_3(PPh_3)_2]$ compounds can be impure with $OPPh_3$.

The selected frequencies observed in the IR spectra of $[ReOX_2(hquin\text{-}7\text{-}COOH)(PPh_3)]$ and $[ReOX_2(hmquin\text{-}7\text{-}COOH)(PPh_3)]$ complexes are given in Section 2. The carboxylic acid group of the *hquin-7-COOH* and *hmquin-7-COOH* ligand is characterized by the $\nu_{C=O}$ absorption observed in the range 1700–1720 cm^{-1} [39,40].

The strong ν(Re=O) stretching bands of $[ReOX_2(hquin\text{-}7\text{-}COOH)(PPh_3)]$ and $[ReOX_2(hmquin\text{-}7\text{-}COOH)(PPh_3)]$ compounds are in the higher end of the range observed for $\{ReO\}^{3+}$ core complexes. Similar to the reported previously $[ReOX_2(hqn)(PPh_3)]$ and $[ReOX_2(quin\text{-}2\text{-}c)(PPh_3)]$ complexes, the Re–hydroxy bond *trans* to the oxo ligand does not compete effectively for the d_{Re} orbitals. Moreover,

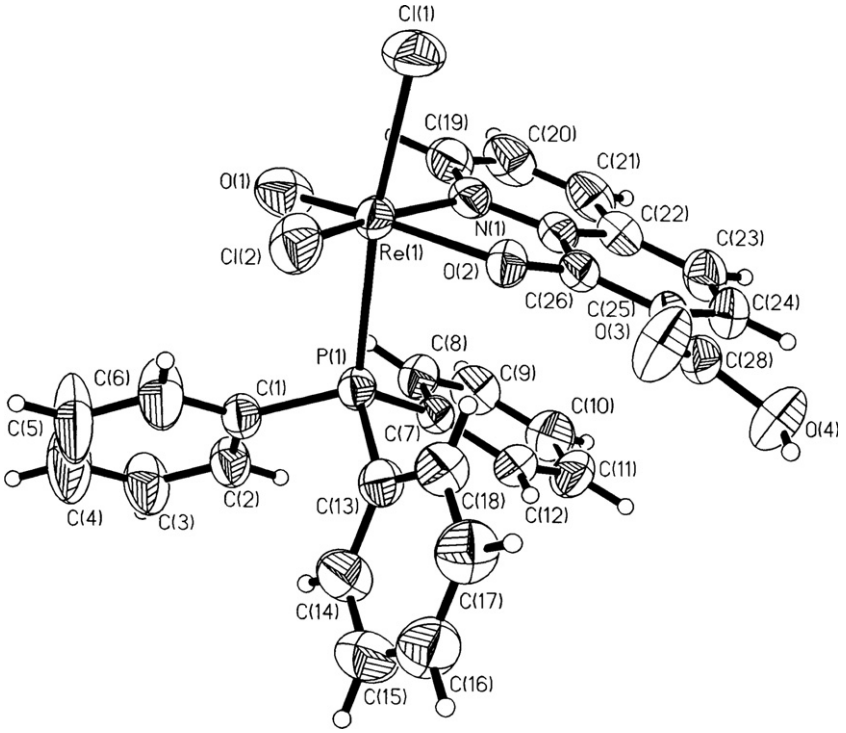


Fig. 1. The molecular structure of **1**. Displacement ellipsoids are drawn at 50% probability.

the narrow range in which the ν(Re=O) bands appear is very similar to those observed for Re(V)-oxo complexes with 8-quinolinolato or quinoline-2-carboxylate ligands [8,9].

4.2. Crystal structures

The crystallographic data for **1** · $OPPh_3$, **2** and **3** are given in Table 1, and molecular structures of the $ReOCl_2$(hquin-7-COOH)(PPh_3)] and [$ReOCl_2$(hmquin-7-COOH)(PPh_3)] complexes are presented in Figs. 1 and 2, respectively. The intermolecular interactions found in the examined structures are shown in Table 2 [41,42]. Additionally in the examined structures exist π···π stacking interactions between the rings of the *hquin-7-COOH* or *hmquin-7-COOH* ligands and one of the triphenylphospine rings. (Table 3) [43]. Presence of the methyl group in the quinoline ring significantly decreases π···π stacking interactions.

The geometry of [$ReOX_2$(hquin-7-COOH)(PPh_3)] and [$ReOX_2$(hmquin-7-COOH)(PPh_3)] compounds reveal typical features of quasi-octahedral oxorhenium(V)complexes with oxygenated bidentate ligands. The deformation of the octahedron is caused by the presence multiple bonding ligand (terminal oxo) and narrow bite angle of the chelating ligand. The high concentration of electronic density along the Re–O_t axis strongly influences the positions of the adjacent halogen atoms, which are pushed away. The presence of the methyl group attached to the quinoline ring in **3** seems to be responsible for significant increase in the Cl(1)–Re(1)–P(1) angle and decrease in the O(1)–Re(1)–P(1) one. In each complex, the rhenium atom is coordinated by a terminal oxygen atom (O_t), two halide ions in *cis* arrangement, the phosphorus atom of PPh_3 molecule, and the bidentate N,O donors of the *hquin-7-COOH* or *hmquin-7-COOH* ligand. The oxygen atom of the quinoline derivative lies in *trans* position to the terminal oxo ion.

Table 2
Hydrogen bonds for **1** · $OPPh_3$, **2** and **3** complexes

D	A	H···A (Å)	D···A (Å)	D—H···A (°)
***1** · OPPh₃*				
O(4)	O(5)	1.83	2.629(3)	165.9
C(32)	O(3)	2.57	3.489(4)	169.6
C(18)	O(2)	2.32	3.084(3)	139.4
C(24)	O(4)	2.41	2.735(4)	100.4
*Complex **2***				
C(16)	Br(1)#1	2.82	3.747(3)	171.8
O(4)	Br(2)#2	2.57	3.377(2)	166.9
C(4)	O(1)#3	2.47	3.314(3)	151.0
C(14)	O(2)	2.49	3.243(3)	137.9
C(19)	O(1)	2.49	2.913(3)	107.8
C(24)	O(4)	2.38	2.720(3)	101.3
*Complex **3***				
C(2)	O(2)	2.52	3.067(5)	117.7
C(18)	O(1)	2.40	3.066(4)	129.0

#1 $0.5+x$, $1.5-y$, $-0.5+z$; #2 $-0.5+x$, $1.5-y$, $-0.5+z$; #3: $-x+2$, $-y+1$, $-z+1$.

The selected bond distances and angles of [$ReOX_2$(hquin-7-COOH)(PPh_3)] and [$ReOX_2$(hmquin-7-COOH)(PPh_3)] complexes are collected in Tables 4 and 5.

The Re–O_t bond lengths of [$ReOX_2$(hquin-7-COOH)-(PPh_3)] and [$ReOX_2$(hmquin-7-COOH)(PPh_3)] fall in the range 1.639–1.76 Å, typical of mononuclear complexes of rhenium(V) having $[ReO]^{3+}$ core, and indicate the presence of a triple bond Re≡O [44]. The elongation of Re–O_t distance in **1** · $OPPh_3$ seems to be results of the crystal packing

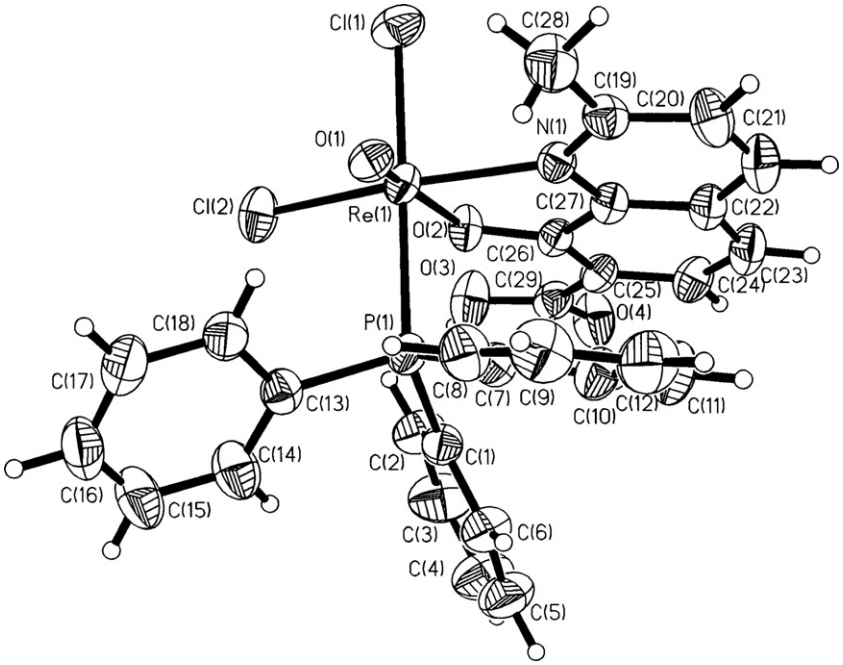


Fig. 2. The molecular structure of **4**. Displacement ellipsoids are drawn at 50% probability.

Table 3
Analysis of short contacts between the *hquin-7-COOH* and *hmquin-7-COOH* rings and triphenylphospine ring (distances in Å and angles in °)

R(I)	R(J)	Cg···Cg	α	β	d_p
1 · *OPPh*$_3$					
Cg(2)	Cg(1)	3.5208	10.74	18.27	3.264
Cg(3)	Cg(1)	3.6021	9.68	21.25	3.385
Complex ***2***					
Cg(2)	Cg(1)	3.6675	16.42	22.00	3.084
Cg(3)	Cg(1)	3.6123	16.19	19.58	3.591
Complex ***3***					
Cg(2)	Cg(1)	4.0621	21.21	24.36	3.075
Cg(3)	Cg(1)	5.3487	17.81	47.74	2.282

R1, R2, R3 indicates the centroids of aromatic rings containing C(7), N(1), C(24) atoms, respectively, α is a dihedral angle between planes *I* and *J*, β is an angle between Cg(I)–Cg(*J*) vector and normal to plane *I* and d_p is a perpendicular distance of Cg(*I*) on ring *J* plane.

caused by the presence of triphenylphosphine oxide in the lattice. The interatomic distances between the rhenium atom and the oxygen atom of bidentate ligand are somewhat shorter than an ideal single Re–O bond length (*ca.* 2.04 Å) [45], and indicates small delocalization in the O(2)–Re(1)–O(1) moiety. The similar trend is observed for many Re(V)-oxo complexes with an monoanionic oxygen *trans* to the oxo group [46].

The Re1–X(1) distances *trans* to the phosphorus atom of PPh_3 molecule are slightly longer than the Re1–X(1) bonds *trans* to the nitrogen atom of the *hquin-7-COOH* or *hmquin-7-COOH* ligand. It is a consequence of *structural trans* effect of the phosphine ligand.

4.3. Geometry optimization, charge distribution, electronic structure and NBO analysis

The geometry of **1** was optimized in a singlet state by the DFT method with the B3LYP functional. The optimized geometric parameters of **1** are gathered in Table 4. In general, the predicted bond lengths and angles are in agreement with the values based upon the X-ray crystal structure data, and the general trends observed in the experimental data (discussed above) are well reproduced in the calculations.

Table 4
The experimental and optimized bond lengths (Å) and angles (°) for **1**

Bond lengths	Experimental	Optimized	Bond angles	Experimental	Optimized
Re(1)–O(1)	1.7197(19)	1.678	O(1)–Re(1)–O(2)	161.91(9)	157.88
Re(1)–O(2)	2.0106(16)	2.043	O(1)–Re(1)–N(1)	89.34(9)	86.23
Re(1)–N(1)	2.139(2)	2.170	O(2)–Re(1)–N(1)	75.00(8)	74.26
Re(1)–Cl(1)	2.3816(7)	2.436	O(1)–Re(1)–Cl(1)	98.96(7)	101.76
Re(1)–Cl(2)	2.3325(8)	2.396	O(2)–Re(1)–Cl(1)	89.49(5)	86.91
Re(1)–P(1)	2.4891(7)	2.541	N(1)–Re(1)–Cl(1)	87.45(6)	84.59
			O(1)–Re(1)–Cl(2)	104.03(8)	105.24
			O(2)–Re(1)–Cl(2)	92.11(5)	95.19
			N(1)–Re(1)–Cl(2)	166.47(6)	167.64
			Cl(1)–Re(1)–Cl(2)	88.37(3)	88.49
			O(1)–Re(1)–P(1)	89.37(7)	91.07
			O(2)–Re(1)–P(1)	82.29(5)	81.50
			N(1)–Re(1)–P(1)	91.92(6)	97.62
			Cl(1)–Re(1)–P(1)	171.63(3)	167.09
			Cl(2)–Re(1)–P(1)	90.35(2)	86.93

Table 5
The experimental bond lengths (Å) and angles (°) for **2** and **3**

Bond lengths	**2** X = Br	**3** X = Cl	Bond angles	**2**	**3**
Re(1)–O(1)	1.6742(17)	1.673(2)	O(1)–Re(1)–O(2)	160.60(7)	163.62(10)
Re(1)–O(2)	2.0044(17)	1.986(2)	O(1)–Re(1)–N(1)	87.02(8)	92.07(10)
Re(1)–N(1)	2.139(2)	2.183(3)	O(2)–Re(1)–N(1)	75.39(7)	75.58(9)
Re(1)–X(1)	2.5444(3)	2.3922(10)	O(1)–Re(1)–X(1)	99.16(6)	100.26(9)
Re(1)–X(2)	2.4950(3)	2.3393(9)	O(2)–Re(1)–X(1)	87.61(5)	90.28(7)
Re(1)–P(1)	2.4702(7)	2.4773(9)	N(1)–Re(1)–X(1)	85.12(5)	88.46(8)
			O(1)–Re(1)–X(2)	103.88(6)	104.24(8)
			O(2)–Re(1)–X(2)	94.28(4)	88.29(7)
			N(1)–Re(1)–X(2)	168.51(5)	163.68(8)
			X(1)–Re(1)–X(2)	89.502(9)	89.17(4)
			O(1)–Re(1)–P(1)	90.68(6)	81.05(8)
			O(2)–Re(1)–P(1)	82.09(5)	88.58(7)
			N(1)–Re(1)–P(1)	92.40(6)	92.12(8)
			X(1)–Re(1)–P(1)	169.694(17)	178.55(3)
			X(2)–Re(1)–P(1)	91.100(16)	89.90(3)

Table 6
Atomic charges from the Natural Population Analysis (NPA) for **1**

Atom	Charge
Re(1)	1.012
O(1)	−0.440
O(2)	−0.659
N(1)	−0.466
Cl(1)	−0.391
Cl(2)	−0.337
P(1)	1.270

Table 6 presents the atomic charges from the Natural Population Analysis (NPA) for **1**. The calculated charge on the rhenium atom in **1** is considerable lower than the formal charge +5, corresponding d^2 configuration of the central ion. It results from charge donation from the oxo ligands, halide ions and PPh_3 molecule. The P atom is positively charged, and the charges on the terminal oxo, chloride and oxygen atom of *hquin-7-COOH* are significantly smaller than −2, −1 and −1, respectively. The terminal oxo ions are less negative in comparison with the oxygen atoms of *hquin-7-COOH* ligand. It confirms the higher electron density delocalization from the terminal ligand towards the rhenium center and corresponds to differences in the Re–O(1) and Re–O(2) bond lengths.

The molecular orbital diagram of **1** with several occupied and unoccupied molecular orbital contours is presented in Fig. 3. The local symmetry of the rhenium center has been considered in the discussion: *z* axis goes

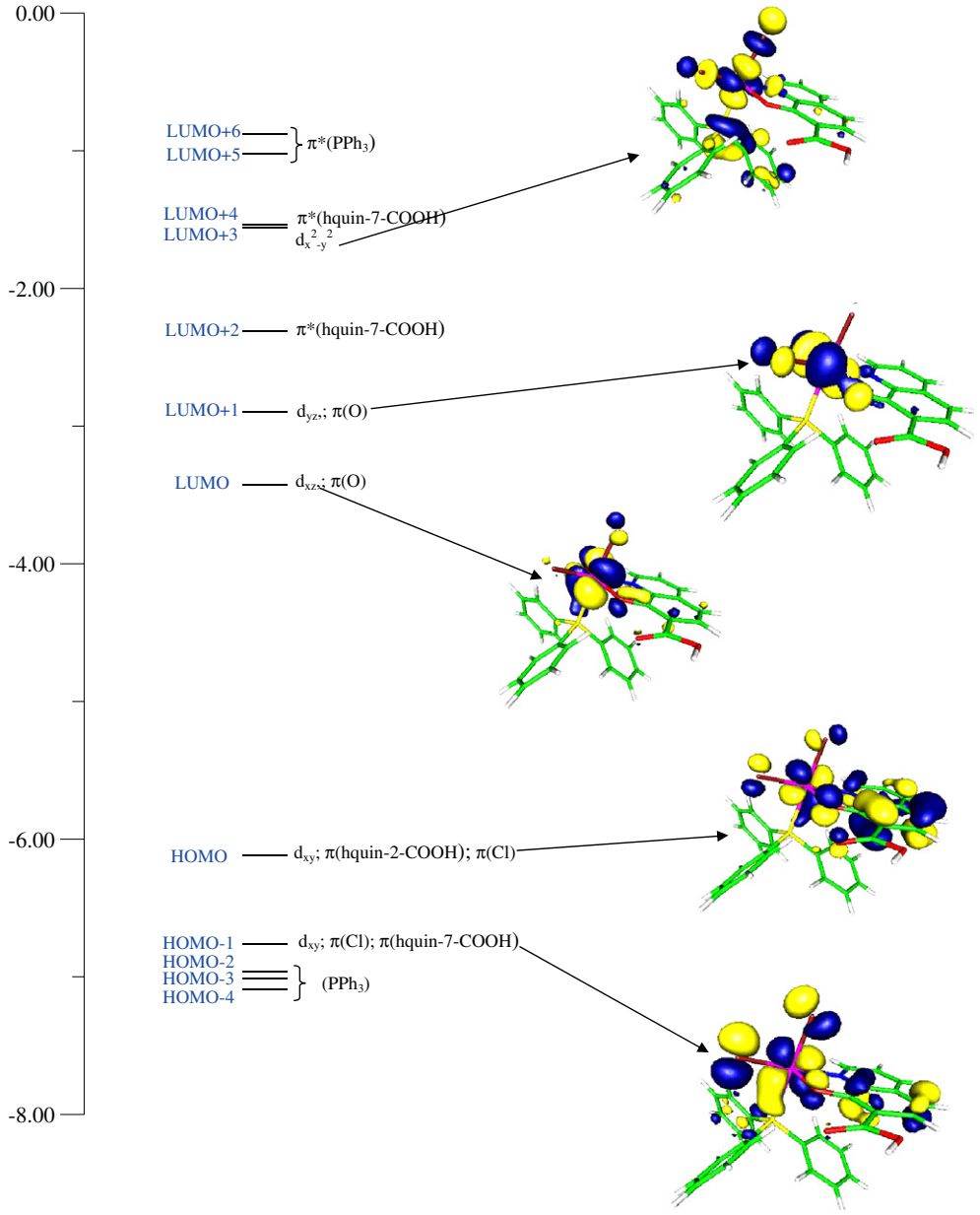


Fig. 3. The energy (eV), character and some contours of the occupied and unoccupied molecular orbitals of **1**. Positive values of the orbital contour are represented in blue (0.04 au) and negative values – in yellow (−0.04 au). (For interpretation of the references in colour in this figure legend, the reader is referred to the web version of this article.)

along the O–Re–O linkage, and *x* axis – through the P–Re–Cl bonds.

The value of the energy separation between the highest occupied molecular orbital (HOMO) and the lowest unoccupied molecular orbital (LUMO) equals to 2.67 eV. This value is lower in comparison with the HOMO–LUMO gap calculated for the related Re(V)-oxo complexes with 8-quinolinolato or quinoline-2-carboxylate ligands [8,9]. The lower absolute value of the gap energies means lower stability and higher reactivity of the title complex.

Two highest occupied MOs are delocalized among d_{xy} rhenium orbital, chloride and *hquin-7-COOH* orbitals. The LUMO and LUMO + 1 are predominately localized on the rhenium atom (d_{xz} and d_{yz} orbitals) with some contribution of p_π oxygen orbitals. They can be ascribed as π-antibonding rhenium–oxygen molecular orbitals. The LUMO + 3 is of $d_{x^2-y^2}$ character, and d_{z^2} rhenium orbital contributes to the LUMO + 13.

Since the rhenium atom has d^2 electronic configuration, the empty $5d_{xz}$ and $5d_{yz}$ orbitals are available to overlap with $2p_x$ and $2p_y$ orbitals of the terminal oxygen to form an effective triple bond.

The nature of rhenium–terminal oxygen interaction in **1** has been studied by NBO analysis. The occupancy and composition of the calculated Re–O_t natural bond orbitals (NBOs) are given in Table 7. Two detected natural Re–O_t bond orbitals of **1** are of π character – they arise from overlap of the two occupied oxygen p_π orbitals with the empty d_{xz} and d_{yz} metal orbitals. Not detected $\sigma_{Re–Ot}$ bond has character of predominant Coulomb-type interactions between the central ion and ligands [47]. The terminal oxo ligand of **1** has two lone pair orbitals, and electron density from one of them is strongly delocalized into non-Lewis rhenium orbital. Accordingly, NBO analysis confirms a triple bond between the rhenium and the terminal oxygen ligand.

4.4. Electronic spectra

The electronic spectra of [$ReOX_2$(hquin-7-COOH)(PPh_3)] and [$ReOX_2$(hmquin-7-COOH)(PPh_3)] complexes are very similar in terms of the position, intensity and shape of the bands in the whole region 1000–180 nm. The positions and molar absorption coefficients of electronic bands for [$ReOX_2$(hquin-7-COOH)(PPh_3)] and [$ReOX_2$(hmquin-7-COOH)(PPh_3)] complexes are given in Table 8.

The experimental and calculated electronic spectra of **1** are presented in Fig. 4. Each calculated transition is represented by a gaussian function $y = ce^{-bx^2}$ with the height (c) equal to the oscillator strength and *b* equal to 0.04 nm^{-2}. Table 9 presents the calculated singlet–singlet electronic transitions of **1** and their assignments to the experimental bands. For the high energy part of the spectrum, only transitions with oscillator strengths larger than 0.015 are listed in Table 9.

The assignment of the calculated transitions to the experimental bands is based on the criterion of the energy and oscillator strength of the calculated transitions. In the description of the electronic transitions the HOMO orbital is described as d_{Re} orbital, whereas the participation of d_{Re} in the H − 1 orbital is omitted.

Table 8
Band position (nm) and molar absorption coefficient [$dm^3\ mol^{-1}\ cm^{-1}$] (in brackets) of [$ReOX_2$(hquin-7-COOH)(PPh_3)] and [$ReOX_2$(hmquin-7-COOH)(PPh_3)] complexes

1	2	3	4
835.0 (125)	815.6 (170)	805.0 (150)	799.5 (175)
691.4 (335)	687.0 (360)	682.0 (350)	685.5 (360)
481.6 (920)	475.4 (1100)	456.3 (990)	456.3 (1050)
402.2 (8090)	405.5 (10160)	387.5 (9100)	392.0 (9500)
264.6 (48800)	264.0 (54600)	271.0 (47600)	262.5 (49200)
221.8 (94400)	225.1 (96700)	218.5 (89900)	221.6 (97800)
209.4 (122600)	208.0 (130900)	205.5 (115700)	204.5 (128400)

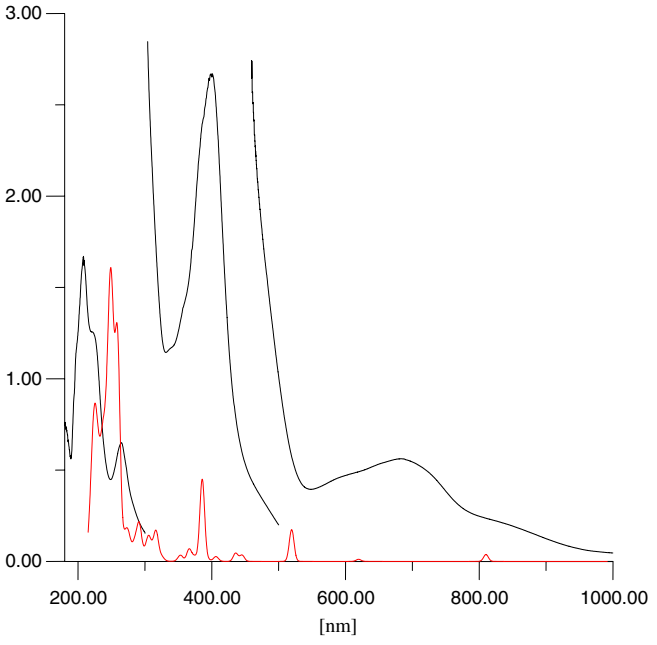


Fig. 4. The experimental (black) and calculated (red) electronic absorption spectra of **1**. (For interpretation of the references in colour in this figure legend, the reader is referred to the web version of this article.)

Table 7
The occupancy of the calculated natural bond orbitals (NBOs) between the rhenium and the oxo ligand for **1**

BD	Occupancy	BD	BD*	Occupancy
Re–O_t	1.993	$0.570(d)_{Re} + 0.821(p)_O$	$0.821(d)_{Re} - 0.570(p)_O$	0.316
Re–O_t	1.984	$0.583(d)_{Re} + 0.813(p)_O$	$0.\ 813(d)_{Re} - 0.583(p)_O$	0.302

BD denotes 2-center bond, * – denotes antibond NBO.

Table 9
The energy and molar absorption coefficients of experimental absorption bands and the electronic transitions calculated with the TDDFT method for **1**

The most important orbital excitations	Character	λ (nm)	E (eV)	f	Experimental Λ (nm) (E (eV)) ε
H → L	d → d	810.2	1.53	*0.0093*	835.0 (1.48) 125
H → L + 1	d → d	619.6	2.00	*0.0028*	691.4 (1.79) 335
H − 1 → L	π(Cl)/π(hquin-7-COOH) → d	519.4	2.39	*0.0434*	481.6 (2.57) 920
H − 1 → L + 1	π(Cl)/π(hquin-7-COOH) → d	445.2	2.78	*0.0085*	402.2 (3.08) 8090
H − 2 → L	π(PPh_3) → d				
H − 2 → L	π(PPh_3) → d	435.6	2.85	*0.0112*	
H → L + 2	d → π*(hquin-7-COOH)	385.7	3.21	*0.1122*	
H → L	d → d	365.9	3.39	*0.0155*	
H → L + 4	d → π*(hquin-7-COOH)	316.6	3.92	*0.0331*	264.6 (4.69) 48 800
H − 8 → L + 1	π(hquin-7-COOH) → d	305.8	4.05	*0.0228*	
H − 1 → L + 3	π(Cl)/π(hquin-7-COOH) → d	291.5	4.25	*0.0456*	
H − 10 → L + 1	π(Cl)/π(hquin-7-COOH) → d	284.9	4.35	*0.0228*	
H − 13 → L	π(Cl)/π(O)/π(hquin-7-COOH) → d	276.0	4.49	*0.0169*	
H − 10 → L + 2	π(Cl)/π(hquin-2-COOH) → π*(hquin-7-COOH)	260.9	4.75	*0.0419*	221.8 (5.59) 94 400
H − 2 → L + 3	π(PPh_3) → d	259.5	4.78	*0.1535*	
H − 2 → L + 4	π(PPh_3) → π*(hquin-7-COOH)	257.4	4.82	*0.1065*	
H − 9 → L + 2	π(Cl) → π*(hquin-7-COOH)	252.6	4.91	*0.0188*	
H − 4 → L + 3	π(PPh_3) → d	252.0	4.92	*0.0205*	
H − 5 → L + 2	π(PPh_3) → d	250.5	4.95	*0.0293*	
H → L + 8	d → π*(PPh_3)				
H − 2 → L + 4	π(PPh_3) → π*(hquin-7-COOH)	249.7	4.97	*0.1939*	
H − 5 → L + 3	π(PPh_3) → d	247.4	5.24	*0.0359*	
H → L + 8	d → π*(PPh_3)				
H − 14 → L	π(Cl)/π(O)/π(hquin-7-COOH) → d	246.1	5.04	*0.0987*	
H − 3 → L + 4	π(PPh_3) → π*(hquin-7-COOH)				
H − 4 → L + 4	π(PPh_3) → π*(hquin-7-COOH)	243.7	5.09	*0.0627*	
H − 1 → L + 5	π(Cl)/π(hquin-7-COOH) → π*(PPh_3)				
H − 1 → L + 5	π(Cl)/π(hquin-7-COOH) → π*(PPh_3)	241.8	5.13	*0.0177*	
H − 6 → L + 3	π(PPh_3) → d				
H − 15 → L + 1	π(Cl)/π(O)/π(hquin-7-COOH) → d	239.1	5.19	*0.0343*	
H − 18 → L	n(PPh_3) → d	237.0	5.23	*0.0376*	
H − 1 → L + 6	π(Cl)/π(hquin-7-COOH) → π*(PPh_3)				
H − 1 → L + 6	π(Cl)/π(hquin-7-COOH) → π*(PPh_3)	236.6	5.24	*0.0323*	
H − 7 → L + 3	π(PPh_3) → d				
H − 2 → L + 5	π(PPh_3) → π*(PPh_3)	231.6	5.35	*0.0445*	
H − 2 → L + 5	π(PPh_3) → π*(PPh_3)	228.5	5.42	*0.0248*	
H − 2 → L + 5	π(PPh_3) → π*(PPh_3)	227.0	5.46	*0.0387*	
H − 12 → L + 2	π(Cl)/π(O)/π(hquin-7-COOH) → π*(hquin-7-COOH)	224.8	5.51	*0.0411*	
H − 5 → L + 5	π(PPh_3) → π*(PPh_3)	223.2	5.55	*0.0269*	
H − 1 → L + 7	π(Cl)/π(hquin-7-COOH) → π*(PPh_3)	222.2	5.58	*0.0293*	
H − 4 → L + 6	π(PPh_3) → π*(PPh_3)	220.8	5.61	*0.0235*	
					209.4 (5.92) 122600

ε – molar absorption coefficient ($dm^3\ mol^{-1}\ cm^{-1}$); f – oscillator strength; H – highest occupied molecular orbital; L – lowest unoccupied molecular orbital.

Two longest wavelength experimental bands at 835.0 and 691.4 nm are attributed to the transitions of d → d character. The *ligand–metal charge transfer* (π(Cl)/π(hquin-7-COOH) → d) transitions make the largest contribution into the experimental band at 481.6 nm.

The intense absorption band with maximum at 402.2 nm results mainly from *metal–ligand charge transfer* (d → π*(hquin-7-COOH)). However the contribution of the *ligand–metal charge transfer* excitations (π(Cl)/π(PPh_3)/π(hquin-7-COOH) → d) into this band is also confirmed by the calculations. The experimental band at 264.8 nm can be asigned the *ligand–metal charge transfer* (π(Cl)/π(hquin-7-COOH) → d) transitions. The absorption bands at 221.8 and 209.4 nm are assigned mainly to *ligand–ligand charge transfer* and interligand (*IL*) transitions. However some contribution of the *ligand–metal charge transfer* from the triphenylphosphine orbitals to the *d* rhenium orbitals in the band at 221.8 nm is also confirmed by the calculations.

As can be seen from Fig. 3 and Table 9, most occupied molecular orbitals are delocalized of the π(Cl)/π(hquin-7-COOH) unit. It seems to explain lack of any differences in the LMCT bands between Cl and Br complexes. Furthermore, the LMCT absorption bands of the examined complexes are broad and overlap.

5. Supplementary material

CCDC 665000, 665001 and 665002 contain the supplementary crystallographic data for $C_{46}H_{36}Cl_2NO_5P_2Re$, $C_{28}H_{21}Br_2NO_4PRe$ and $C_{29}H_{23}Cl_2NO_4PRe$. These data can be obtained free of charge via http://www.ccdc.cam.ac.uk/conts/retrieving.html, or from the Cambridge Crystallographic Data Centre, 12 Union Road, Cambridge CB2 1EZ, UK; fax: (+44) 1223-336-033; or e-mail: deposit@ccdc.cam.ac.uk.

Acknowledgements

The GAUSSIAN03 calculations were carried out in the Wrocław Centre for Networking and Supercomputing, WCSS, Wrocław, Poland.

References

[1] R.H. Holm, Chem. Rev. 87 (1987) 1401.
[2] C.C. Romão, F.E. Kühn, W.A. Hermann, Chem. Rev. 97 (1997) 3197.
[3] S.B. Seymore, S.N. Brown, Inorg. Chem. 39 (2000) 325.
[4] F.E. Kühn, A. Scherbaum, W.A. Herrmann, J. Organomet. Chem. 689 (2004) 4149.
[5] A.M. Kirillov, M. Haukka, M.V. Kirillova, A.J.L. Pombeiro, Adv. Synth. Catal. 347 (2005) 1435.
[6] W. Volkert, W.F. Goeckeler, G.J. Ehrhardt, A.R. Ketring, J. Nucl. Med. 32 (1991) 174.
[7] E.A. Deutsch, K. Libson, J.L. Vanderheyden, Technetium and Rhenium in Chemistry and Nuclear Medicine, Raven Press, New York, 1990.
[8] B. Machura, S. Michalik, R. Kruszynski, J. Kusz, Polyhedron 26 (2007) 2837.
[9] B. Machura, R. Kruszynski, Polyhedron 26 (2007) 3686.
[10] F. Zouhiri, J.-F. Mouscadet, K. Mekouar, D. Desmaele, D. Savoure, H. Leh, F. Subra, M.L. Bret, Ch. Auclair, J. d'Angelo, J. Med. Chem. 43 (2000) 1533.
[11] H. Chermette, Coord. Chem. Rev. 178–180 (1998) 699.
[12] M.C. Aragoni, M. Arca, T. Cassano, C. Denotti, F.A. Devillanova, F. Isaia, V. Lippolis, D. Natali, L. Niti, M. Sampietro, R. Tommasi, G. Verani, Inorg. Chem. Commun. 5 (2002) 869.
[13] P. Romaniello, F. Lelj, Chem. Phys. Lett. 372 (2003) 51.
[14] A. Voigt, U. Abram, R. Böttcher, U. Richter, J. Reinhold, R. Kirmse, Chem. Phys. 253 (2000) 171.
[15] M. Lipowska, L. Hansen, R. Cini, X. Xu, H. Choi, A.T. Taylor, L.G. Marzilli, Inorg. Chim. Acta 339 (2002) 327.
[16] J. Gancheff, C. Kremer, E. Kremer, O.N. Ventura, J. Mol. Struct. (Theochem) 580 (2002) 107.
[17] M.L. Kuznestov, E.A. Klestova-Nadeeva, A.I. Dement'ev, J. Mol. Struct. (Theochem) 671 (2004) 229.
[18] N. Psaroudakis, K. Mertis, D.G. Liakos, E.D. Simandiras, Chem. Phys. Lett. 369 (2003) 490.
[19] X.-Y. Liu, S. Bouherour, H. Jacobsen, H.W. Schmalle, H. Berke, Inorg. Chim. Acta 330 (2002) 250.
[20] É. Bencze, J. Mink, I. Pápai, I.S. Butler, D. Lafleur, D.F.R. Gilson, J. Organomet. Chem. 616 (2000) 1.
[21] W.-Y. Wong, S.-H. Cheung, X. Huang, Z. Lin, J. Organomet. Chem. 655 (2002) 39.
[22] B. Machura, R. Kruszynski, Polyhedron 25 (2006) 1985.
[23] G. Rouschias, G. Wilkinson, J. Chem. Soc. A (1966) 465.
[24] K. Mekouar, J. Med. Chem. 41 (1998) 2846.
[25] STOE & Cie, X-RED. Version 1.18, STOE & Cie GmbH, Darmstadt, Germany, 1999.
[26] G.M. Sheldrick, Acta Crystallogr., Sect. A 46 (1990) 467.
[27] G.M. Sheldrick, SHELXL97. Program for the Refinement of Crystal Structures, University of Göttingen, Germany, 1997.
[28] G.M. Sheldrick, shelxtl: Release 4.1 for Siemens Crystallographic Research Systems, Siemens Analytical X-ray Instruments Inc., Madison, Wisconsin, USA, 1990.
[29] A.D. Becke, J. Chem. Phys. 98 (1993) 5648.
[30] C. Lee, W. Yang, R.G. Parr, Phys. Rev. B 37 (1988) 785.
[31] M.J. Frisch, G.W. Trucks, H.B. Schlegel, G.E. Scuseria, M.A. Robb, J.R. Cheeseman, J.A. Montgomery, Jr., T. Vreven, K.N. Kudin, J.C. Burant, J.M. Millam, S.S. Iyengar, J. Tomasi, V. Barone, B. Mennucci, M. Cossi, G. Scalmani, N. Rega, G.A. Petersson, H. Nakatsuji, M. Hada, M. Ehara, K. Toyota, R. Fukuda, J. Hasegawa, M. Ishida, T. Nakajima, Y. Honda, O. Kitao, H. Nakai, M. Klene, X. Li, J.E. Knox, H.P. Hratchian, J.B. Cross, C. Adamo, J. Jaramillo, R. Gomperts, R.E. Stratmann, O. Yazyev, A.J. Austin, R. Cammi, C. Pomelli, J.W. Ochterski, P.Y. Ayala, K. Morokuma, G.A. Voth, P. Salvador, J.J. Dannenberg, V.G. Zakrzewski, S. Dapprich, A.D. Daniels, M.C. Strain, O. Farkas, D.K. Malick, A.D. Rabuck, K. Raghavachari, J.B. Foresman, J.V. Ortiz, Q. Cui, A.G. Baboul, S. Clifford, J. Cioslowski, B.B. Stefanov, G. Liu, A. Liashenko, P. Piskorz, I. Komaromi, R.L. Martin, D.J. Fox, T. Keith, M.A. Al-Laham, C.Y. Peng, A. Nanayakkara, M. Challacombe, P.M.W. Gill, B. Johnson, W. Chen, M.W. Wong, C. Gonzalez, and J.A. Pople, GAUSSIAN 03, Revision B.03, Gaussian, Inc., Pittsburgh, PA, 2003.
[32] P.J. Hay, W.R. Wadt, J. Chem. Phys. 82 (1985) 299.
[33] K. Eichkorn, F. Weigend, O. Treutler, R. Ahlrichs, Theor. Chem. Acc. 97 (1997) 119.
[34] P.C. Hariharan, J.A. Pople, Theor. Chim. Acta 28 (1973) 213.
[35] V.A. Rassolov, M.A. Ratner, J.A. Pople, P.C. Redfern, L.A. Curtiss, J. Comp. Chem. 22 (2001) 976.
[36] M.E. Casida, in: J.M. Seminario (Ed.), Recent Developments and Applications in Modern Density Functional Theory, Theoretical and Computational Chemistry, vol. 4, Elsevier, Amsterdam, 1996.
[37] J.E. Carpenter, F. Weinhold, J. Mol. Struct. (Theochem) 169 (1988) 41.
[38] A.E. Reed, L.A. Curtiss, F. Weinhold, Chem. Rev. 88 (1988) 899.
[39] K. Nakamoto, Infrared and Raman Spectra of Inorganic and Coordination Compounds, 4th ed., Wiley-Interscience, New York, 1986.
[40] L. Wei, J. Babich, J. Zubieta, Inorg. Chim. Acta 358 (2005) 2413.
[41] G.R. Desiraju, T. Steiner, The Weak Hydrogen Bond in Structural Chemistry and Biology, Oxford University Press, 1999.
[42] G.A. Jeffrey, W. Saenger, Hydrogen Bonding in Biological Structures, Springer-Verlag, 1994.
[43] C.A. Hunter, J.K.M. Sanders, J. Am. Chem. Soc. 112 (1990) 5525.
[44] J.M. Mayer, Inorg. Chem. 27 (1988) 3899.
[45] S.R. Fletcher, A.C. Skapski, J. Chem. Soc., Dalton Trans. (1972) 1073.
[46] E. Shuter, H.R. Hoveyda, V. Karunaratne, S.J. Retting, C. Orvig, Inorg. Chem. 35 (1996) 368.
[47] M.L. Kuznetsov, A.J.L. Pombeiro, J. Chem. Soc., Dalton Trans. (2003) 738.

has been tested for cytotoxicity against HeLa and multidrug resistant CoLo 320DM human cancer cells [18].

In particular, we are interested in the study of metal–metal bonded complexes of non-steroidal anti-inflammatory drugs (NSAIDs) [19,20]. The widely used popular class of NSAID medications is well known due to inflammatory properties but more recently it has attracted great attention mainly because of the chemopreventive effect in a variety of tumors [21].

The mechanism of action for antitumor effects of NSAIDs has not yet been clearly determined [22,23]. The pharmacological properties of individual NSAIDs vary depending on their inhibitory effects in relation to the COX1 and COX2 isoforms [24]. Cyclooxygenase (COX) is the rate-limiting enzyme in the pathway of arachidonic acid metabolism to prostaglandins and thromboxanes [25,26]. The COX1 isoform (chromosome 9) is constitutively expressed while the COX2 isoform (chromosome 1) is induced particularly in inflammatory processes. COX2 expression is up regulated in gliomas and is correlated with increasing histological grade and poor patient prognosis [27–31]. Clinical trials are currently under way to study the COX2 inhibitor effects on tumor progression in patients with glioblastoma multiforme GBM [32,33]. GBM is a malignant brain glioma (WHO grade IV) that has shown little improvement in patient prognosis in recent years despite improvements in surgical techniques and treatment protocols. This is due in part to their highly invasive nature and to the large percentage exhibiting resistance to conventional chemotherapy and radiotherapy [34].

Since epidemological studies have showed up a 50% reduction in the mortality rate from certain cancers in patient consuming NSAIDs, a great interest in the role of cyclooxygenase in neoplasia has been emerged [35,36]. Several studies have demonstrated that certain NSAIDs cause antiproliferative effects independent of cyclooxygenase activity. The effect of some NSAIDs in the proliferation of glioma cell lines have been investigated showing results that may be clinically important for pharmacological intervention in gliomas [36,37].

The present work reports studies on interactions between diruthenium core and NSAIDs and the investigation of antitumor properties of diruthenium–dNSAID complexes (dNSAID = deprotonated NSAID derived from: ibuprofen (Hibp), aspirin (Hasp), naproxen (Hnpx) and indomethacin (Hind) (Fig. 1)). The antitumor effects of the metal compounds were investigated for C6 rat glioma cell line (used as a model for GBM). Two human tumor cell lines (Hep2 larynx and T24/83 bladder) were also tested.

2. Experimental

2.1. Materials

All the chemicals used, unless specifically stated, were reagent grade supplied by Aldrich or Merck and were used as purchased. Aspirin was purchased from Aldrich. The other drugs were purchased from manipulation pharmacies (São Paulo, Brazil): ibuprofen, from Natural Pharma; naproxen, from Purifarma; and indomethacin, from Henrifarma. Elemental analyses and spectroscopic analyses were carried out to confirm their purity. The diruthenium(II, III) precursor compounds, $[Ru_2(O_2CCH_3)_4Cl]$ [38] and $[Ru_2(O_2CCH_3)_4(H_2O)_2]PF_6$ [39], were synthesized starting from $RuCl_3 \cdot nH_2O$ (Aldrich) according to the literature methods.

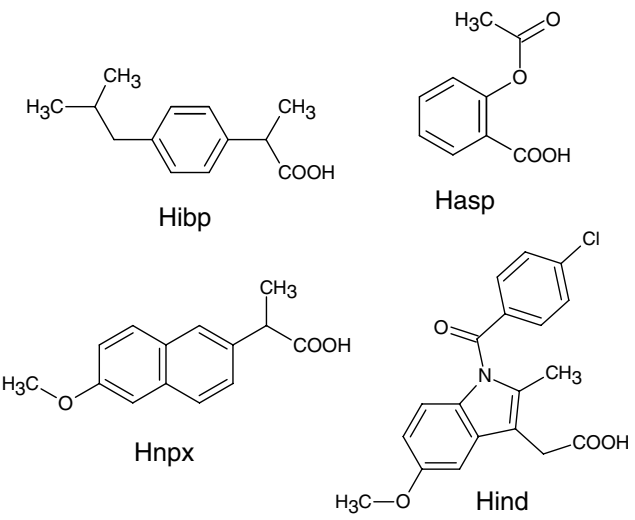


Fig. 1. Structures of Hibp (α-methyl-4-(isobutyl)phenylacetic acid), Hasp (2-(acetyloxy)benzoic acid), Hnpx (2-(6-methoxy-2-naphthyl)propanoic acid), and Hind ([1-(4-chlorobenzoyl)-5-methoxy-2-methyl-1H-indol-3-yl] acetic acid).

2.2. Physical measurements

Elemental analyses were performed on a Perkin–Elmer CHN 2004 Elemental Analyzer, at Instituto de Química (USP). Electronic absorption spectra of ruthenium compounds in solutions, at 200–700 nm (UV–Vis), were recorded on a Shimadzu UV-1650 PC spectrophotometer. The solid reflectance spectra at 350–1400 nm (UV–Vis/NIR), were measured on a Guided Wave model 260 spectrophotometer equipped with optical fiber. Fourier-Transform Infrared (FTIR) spectra of solid samples dispersed in KBr, at 4000–400 cm^{-1}, were recorded on a Bomen MB-102 spectrophotometer coupled to diffuse reflectance accessory (Pike Technologies Inc.). FTIR transmittance spectra of samples in Nujol mulls between CsI pellets, at 400–200 cm^{-1}, were also recorded on the Bomen MB-102 spectrophotometer. Raman spectra of solid samples were carried out on a Micro-Raman RENISHAW System 3000 (laser line = 632.8 nm). The molar magnetic susceptibilities were measured on powdered samples at room temperature by the Faraday method using an electrobalance Cahn DTL 7500; the diamagnetic corrections were made by Pascal's constants and $Hg[Co(SCN)_4]$ was used for calibration. Molar conductance measurements for $\sim 1 \times 10^{-3}$ mol L^{-1} acetonitrile solutions of the compounds were carried out

with a Digimed DM-31 equipment, at 25.0 ± 0.5 °C; KCl aqueous solution, 146.9 μS cm^{-1} at 25 °C, cell constant = 0.1 cm^{-1}, was used for calibration.

2.3. Syntheses of diruthenium compounds with NSAIDs

2.3.1. Synthesis of $[Ru_2(ibp)_4Cl]$ (1)

The complex was synthesized by modified procedure in relation to that previously reported [19]. $[Ru_2(O_2CCH_3)_4Cl]$ (300 mg, 0.63 mmol) was dissolved in 200 mL of water. After rotary evaporation of the solvent to 40 mL, ibuprofen (660 mg, 3.20 mmol) in 40 mL of ethanol and LiCl (370 mg) in 5 mL of water were, separately, added to this solution. The mixture was stirred under nitrogen for 3 h, at 60 °C. The solid product formed on the bottom of the flask was washed with water and then dissolved in ethanol. After filtration, the resulting solution was allowed to evaporate under nitrogen stream and the dark-brown product was dried in a vacuum desiccator over phosphorus pentoxide. Yield = 74%. *Anal.* Calc. for $C_{52}H_{68}O_8ClRu_2 \cdot \frac{1}{2}H_2O$: C, 58.71; H, 6.16. Found: C, 58.39; H, 6.24%. Electronic absorptions at λ_{max} (nm): 483 and 1125 nm (solid phase); 428 nm (in methanol); μ_{eff} = 3.9 B.M.; FTIR major bands, ν (cm^{-1}): 3053sh ($\nu(CH)_{aromatic}$); 2955ms, 2923sh, 2867m ($\nu(CH)_{aliphatic}$); 1513m ($\nu(CC)_{ring}$); 1465s ($\nu_a(COO^-)$); 1409s ($\nu_s(COO^-)$); 1372m ($\delta_s(CH_3)$); 1286m, 1071m, 1019w (region of $\delta_s(CH_3)$, $\delta_{ring\ in\ plane}$, $\rho(CH_3)$); 849m ($\delta_s(CH_3)$, $\delta_{ring\ out\ plane}$); 740 m ($\delta$(OCO)); 555m, 492m ($\nu$(Ru–O)); molar conductance = 2.6 S cm^2 mol^{-1} in acetonitrile.

2.3.2. Synthesis of $[Ru_2(asp)_4Cl]$ (2)

$[Ru_2(O_2CCH_3)_4Cl]$ (300 mg, 0.63 mmol) was dissolved in 200 mL of water. After reducing the volume of this solution to 65 mL by rotary evaporation, 35 mL of ethanol and solutions of aspirin (640 mg, 3.56 mmol) in 50 mL of ethanol and LiCl (270 mg) in 5 mL of water were separately added to it. The mixture was stirred under nitrogen for 2 h, at 60 °C. Then, it was filtered and, after being washed with water and ethanol, the solid product was dried in a vacuum desiccator over phosphorus pentoxide. Yield = 65%. *Anal.* Calc. for $C_{36}H_{28}O_{16}ClRu_2$: C, 45.31; H, 2.96. Found: C, 45.03; H, 2.96%.

2.3.3. Synthesis of $[Ru_2(npx)_4(H_2O)_2]PF_6$ (3)

$[Ru_2(O_2CCH_3)_4(H_2O)_2]PF_6$ (76 mg, 0.12 mmol) was dissolved in 10 mL of water and, then, ethanol (15 mL) followed by naproxen (140 mg, 0.61 mmol) in 10 mL of ethanol and NH_4PF_6 (230 mg) in 3 mL of water were added. The mixture was stirred under nitrogen for 3 h, at 60 °C, and then kept under stirring and nitrogen atmosphere for 18 h, at room temperature. The solid formed was washed with water and dissolved in ethanol. After filtration, the resulting solution was allowed to evaporate under nitrogen stream and the dark-brown product was dried in a vacuum desiccator over phosphorus pentoxide. Yield = 62%. *Anal.* Calc. for $C_{56}H_{56}F_6O_{14}PRu_2$: C, 51.73; H, 4.34; Found: C, 52.10; H, 4.41%.

2.3.4. Synthesis of $[Ru_2(ind)_4(H_2O)_2]PF_6$ (4)

$[Ru_2(O_2CCH_3)_4(H_2O)_2]PF_6$ (80 mg, 0.13 mmol) was dissolved in 10 mL of water and, then, ethanol (15 mL) followed by indomethacin (240 mg, 0.67 mmol) in 20 mL of ethanol and NH_4PF_6 (240 mg) in 3 mL of water were added. The mixture was stirred under nitrogen for 4 h, at 60 °C, in absence of light. The resulting solution was kept under stirring and nitrogen atmosphere for 18 h, at room temperature. The mixture was centrifuged; the solid product was washed with water and small amounts of ethanol and, then, dried in a vacuum desiccator over phosphorus pentoxide. Yield = 26%. *Anal.* Calc. for $C_{76}H_{64}F_6N_4O_{18}PCl_4Ru_2$: C, 50.41; H, 3.57; N, 3.10. Found: C, 50.54; H, 3.87; N, 2.91%.

2.4. Bioassays in vitro

2.4.1. Cell culture

C6 rat glioma cells were obtained from the ATCC, Hep2 cells and T24/83 cells from the ECACC. Stocks were maintained frozen (liquid nitrogen) in Dulbecco's modified Eagle's medium (DMEM) supplemented with 10% foetal calf serum and 20% glycerol. Stock cells were grown in DMEM containing 10% foetal calf serum and antibiotics (penicillin 50 U mL^{-1}, streptomycin 50 μg mL^{-1}). Cells in the exponential phase of growth were used, growing in 75 cm^2 flasks in a humidified atmosphere of 5% CO_2: 95% air at 37 °C.

2.4.2. MTT colorimetric assays

Cells were seeded into 96-well plates at a density of 1–2 × 10^4 cells/well. After overnight incubation the cells were exposed to Ru_2-dNSAID at varying concentrations (1, 10, 100 and 1000 μmol L^{-1}) for 24–72 h, with a change of medium and drug every 24 h. After this growth period, 25 μg of MTT was added to each well and the cells incubated for a further 2–4 h. The medium was removed by aspiration, the cells were re-suspended in 100 μL of 0.04 mol L^{-1} HCl in isopropanol and the reaction product was followed by spectrophotometry at the wavelength of 595 nm. The organic NSAIDs were submitted to the same procedure.

2.4.3. Cell proliferation and viability assay

Cells were seeded into 24-well plates at a density of 1–2 × 10^5 cells/well. After 24, 48 or 72 h cells were harvested by trypsinization (trypsin 0.025%/EDTA 0.02%) before incubating with 0.2% trypan blue solution in PBS for 2 min. Cells were counted using an improved Neubauer counting chamber with cells that did not incorporate the dye considered intact.

2.4.4. mRNA expression analysis of COX-2 by RT-PCR

C6 cells grown *in vitro* and *in vivo* were used for total RNA extraction with Trizol (Life Technologies, USA). The first strand of complementary DNA (cDNA) was generated from 1 μg of RNA, using 2 μL of random

hexamer primer (3 μg μL^{-1}), 1 μL of RNase inhibitor (10 U), 2 μL of deoxynucleoside triphosphate mix (dNTP mix) 10 m mol L^{-1}, and 2 μL moloney murine leukemia virus (M-MLV) reverse transcriptase (200 U μL^{-1}), in a total volume of 20 μL. The reaction was incubated at 21 °C for 10 min, at 42 °C for 50 min and at 99 °C for 10 min in a GeneAmp®PCR System 9700 (PE Applied Biosystems, USA). For amplification of the COX-2 sequence, cDNA was amplified in a 50 μL volume using 0.5 μL (5 U μL^{-1}) platinum Taq DNA polymerase, 1 μL DNTP mix 10 mmol L^{-1}, 1.5 μL $MgCl_2$ 50 mmol L^{-1}, 5 μL PCR buffer 10× and 6 μL of specific primers (3 μL sense + 3 μL antisense). Rat ribosomal L19 (RPL19) gene was amplified as an internal control. The oligonucleotide sequences used for COX-2 and RPL19 were: COX2 sense: 5′-TCAAGACAGATCAGAAG CGA-3′ antisense: 5′-TACCTGAGT GTCTTTGATTG-3′ and RPL19 sense: 5′-TCTCATG GAACACATCCAC AA-3′ antisense: 5′-TGGTCAGCCA GGAGCTTCTT-3′. All reagents used in the reverse transcriptase-polymerase chain reaction (RT-PCR) were purchased from Life Technologies, Brazil. Each cycle of PCR amplification involved denaturing for 1 min at 94 °C, annealing for 1 min at 58 °C and extension for 1 min at 72 °C. To ensure the exponential phase of amplification, the number of PCR cycles was determined and optimized for COX-2 as 38 cycles and RPL19 as 36 cycles. Aliquots of amplified PCR products were fractionated on a 1% agarose gel containing 0.05% ethidium bromide and the image was captured by Foto-Analyst/Archiver^{TM} (Foto-Dyne-Incorporated, USA). Semi-quantitative mRNA expression data was calculated by the ratio of respective mRNA/RPL19 density.

3. Results and discussion

3.1. Diruthenium compounds characterization

Compounds **1** and **2** were prepared by direct reaction between $[Ru_2(O_2CCH_3)_4Cl]$ and the correspondent acidic drug ligands under similar conditions. The $[Ru_2(ibp)_4Cl]$ complex has been obtained by a different method but the characterization data (Section 2) are consistent with those previously reported [19]. Although $[Ru_2(asp)_4Cl]$ has been prepared before [40] no complete characterization of it was found in the literature. Here, the complex was synthesized by a new experimental procedure and its spectroscopic data are presented. The novel compounds, **3** and **4**, were prepared by reactions of $[Ru_2(O_2CCH_3)_4(H_2O)_2]PF_6$with the correspondent acidic drug ligands. Elemental analyses are consistent with complete carboxylate exchange reactions for all the products. The four acetate anions from the precursors chloro-acetate and aqua-acetate are substituted by the deprotonated NSAID (dNSAID) ligands giving the derivatives $[Ru_2(dNSAID)_4Cl]$, with ibp and asp, and $[Ru_2(dNSAID)_4(H_2O)_2]PF_6$, for npx and ind, respectively.

Physicochemical data for compounds **2**, **3** and **4** are shown in Table 1 and they are further discussed along with the data obtained for compound **1** (see Section 2).

Electronic spectra of all diruthenium compounds (in methanol) exhibit absorption bands at about 430 nm which can be ascribed to $\pi(Ru–O, Ru_2) \rightarrow \pi^*(Ru_2)$ electronic transitions. Solid-state λ_{max} shifts to lower energy (470–500 nm) for compounds **1** and **2**, according to observed for analogous diruthenium-tetracarboxylates [41–43]. Broad and low intensity near-IR bands ($\lambda_{max} \sim 1100$ nm) that are characteristics of $\delta(Ru_2) \rightarrow \delta^*(Ru_2)$ electronic transition involving dimetal core δ orbitals were also observed for all solid-state diruthenium compounds. The presence of these UV–Vis and NIR bands is consistent with previously reported spectra for analogous mixed valent diruthenium carboxylates and, consequently, agrees with the existence of metal–metal multiple bonds for the $Ru_2(II,III)$ cores [13,14].

The high effective magnetic moments ($\mu_{eff} = 3.7$–4.1 B.M. per Ru_2 unit) (Table 1) correspond to three unpaired electrons per dinuclear unit according to reported data for analogous complexes and indicate $(\sigma)^2(\pi)^2(\delta)^2(\pi^*\delta^*)^3$ ground state configurations for Ru_2-dNSAIDs complexes [13,14].

Compounds **1** and **2** exhibited low molar conductance values (3.7 S cm^{2}mol^{-1}). The non-electrolyte [44] behavior is consistent with the presence of neutral species in acetonitrile solutions. In contrast, the high values (84 and 65 S cm^2 mol^{-1}, for **3** and **4**, respectively) agree with 1:1 electrolytes according to expected for the presence of $[Ru_2(dNSAID)_4]^+$ cations and PF_6^- anions in solutions of compounds **3** and **4**.

Tentative attributions of most representative FTIR bands for compounds **2**, **3** and **4** are shown in Table 1. No significant spectral changes were observed for the NSAIDs after their coordination to the diruthenium cores, except for the frequencies related to the carboxylic (–COOH) groups [45,46]. The carbonyl stretching, ν(C=O), of the parent acids (1720 cm^{-1}, for Hibp; 1691 cm^{-1}, for Hasp; 1728 cm^{-1}, for Hnpx; 1718 cm^{-1}, for Hind) disappeared in the correspondent metal complexes spectra. Instead, carboxylate (–COO$^-$) typical bands were found at the region of 1480–1400 cm^{-1}. The values for $\Delta\nu$ [ν_a(COO)–ν_s(COO)] are in the range of 40–70 cm^{-1}, corroborating the bridging coordination mode of the carboxylate ligands to the diruthenium cores [14].

The presence of PF_6^- counter-ions in compounds **3** and **4** are confirmed by the bands at ~850 cm^{-1} (ν(PF) stretching, ν_3) and 559 cm^{-1} (δ(FPF), ν_4) [46]. Two relatively intense bands (556 cm^{-1} and 450–490 cm^{-1}), observed for all complexes, might be assigned to ν(Ru–O) stretching modes involving the ruthenium–O(carboxylate) metal-ligand bonds [47].

The Raman bands at 336–357 cm^{-1} can be assigned to ν(Ru–Ru) stretching modes for the two chloro-complexes [47]. The frequencies for compounds **1** (336 cm^{-1}) and **2** (342 cm^{-1}) are shifted to higher energy indicating that

Table 1
Physicochemical data for diruthenium(II, III) compounds **2**, **3** and **4**

Compound	$[Ru_2(asp)_4Cl]$	$[Ru_2(npx)_4(H_2O)_2]PF_6$	$[Ru_2(ind)_4(H_2O)_2]PF_6$
Electronic absorption transitions; λ (nm); ε (mol^{-1} L cm^{-1})			
π(Ru–O, Ru_2) → π^* (Ru_2) (solvent)	439; 976 (in methanol)	429; 770 (in methanol)	430; sh (in methanol)
δ(Ru_2) → δ^* (Ru_2)	1140 (solid)	1112 (solid)	1110 (solid)
Effective magnetic moment per Ru_2; μ_{eff} (B.M.)			
	3.9	4.1	3.7
FTIR major bands; ν (cm^{-1})			
$\nu(CH)_{aromatic}$	3070w	3055vw	3092w
$\nu(CH)_{aliphatic}$	2990w, 2928w, 2882w	2975w, 2939w, 2904sh, 2845w	2993sh, 2962w, 2936w, 2834w
$\nu(C{=}O)_{esther}$	1761ms		
$\nu(C{=}O)_{amide}$			1683s
$\nu(CC)_{ring}$	1606m, 1583sh	1637m, 1604m	1593m
$\nu_a(COO^-)$[a]	1476ms	1459ms	1473s
$\nu_s(COO^-)$[a]	1409s	1410s	1410s, br
$\delta_s(CH_3)$	1374sh	1372m	1360s, br
$\nu(C_{ring}OC)$		1270ms	1227s
ν_a(OCC); ν(CC(O)O)	1191ms		
Region of $\delta_s(CH_3)$; $\delta_{ring\ in\ plane}$; $\rho(CH_3)$	1161sh	1230m, 1214m, 1175m, 1160m, 1069m	1177m, 1147m, 1087m, 1067m, 1033m, z1013m
ν_s(COC)		1029m	
$\delta(CH_3)$; $\delta_{ring\ out\ plane}$	817mw	*	*
$\nu(PF_6^-)$		849vs, br	848vs, br
δ(FPF)		559s	559s
δ(OCO)	712m	711w	718m
ν(Ru–O)	560m, 458m	557m, 474m	557m, 481mw
Raman major bands at low frequency; ν (cm^{-1})			
ν(Ru–Ru)	342s	360m	347s
ν(Ru–O)	367w		
$\nu(PF_6^-)$		760s	749s

Tentative attributions for major bands observed at the correspondent vibrational FTIR and Raman spectra.
[a] $\delta(CH_3)$ is overlapped with these bands; * not identified, overlapped with $\nu_s(PF_6)$; s = strong; m = medium; mw = medium-weak; ms = medium-strong; w = weak; br = broad; sh = shoulder.

the Ru–Ru bond in Ru_2-dNSAID derivatives are slightly shorter than that observed for Ru_2-acetate precursor (327 cm^{-1}). The ν(Ru–O) band was tentatively ascribed for **1** at 374 cm^{-1} and for **2** at 367 cm^{-1}. The aqua-complexes exhibit broad and overlapped bands, mainly due to the presence of axial water molecules, making difficult the attribution at this region of the spectra. The ν(PF) stretching mode, or ν_1 frequency [46], could be observed around 750 cm^{-1} for both $[Ru_2(dNSAID)_4(H_2O)_2]PF_6$ compounds.

Experimental results corroborate the proposition that $[Ru_2(dNSAID)_4Cl]$ and $[Ru_2(dNSAID)_4(H_2O)_2]PF_6$ exhibit mixed valent Ru_2(II, III) cores with Ru–Ru bonds stabilized by four bridging drug ligands in like-paddle-wheel structures (Fig. 2). The coordination of the large dNSAID anions do not show significant influence on the electronic structure of the novel compounds when compared to the correspondent diruthenium-acetate precursors. Compounds **1** and **2** probably exhibit solid-state polymeric structures like other analogous chloro-complexes. In contrast, compounds **3** and **4** have two axially coordinated water molecules, giving positively charged dimeric units that are charge-balanced by the PF_6^- counter-ions.

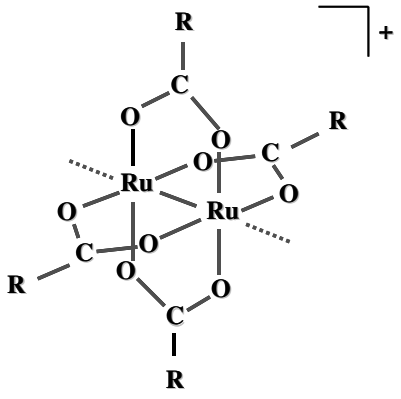


Fig. 2. General structure of the Ru_2-dNSAID compounds.

3.2. In vitro assays

3.2.1. MTT assays

The effects of the four Ru_2–dNSAID complexes and the parent NSAIDs were investigated *in vitro* in the human larynx tumor Hep2, the human bladder tumor T24/83 and the rat glioma C6. Initial experiments found no effects of any drug on the three cell lines at either 1 or 10 μmol L^{-1}, while at 100 μmol L^{-1} the drugs showed some inhibitory effects.

Experiments with 1 mmol L^{-1} complex were discarded as the high concentrations of vehicle (DMSO or ethanol) were cytotoxic to all three cell lines (results not shown). Further experiments were performed at 100 μmol L^{-1}, with no significant effects being found for any of the complexes in the Hep2 human larynx tumor or the T24/83 human bladder tumor (Table 2) after a 24 h incubation period. However, in the C6 rat glioma several drugs were found to inhibit cell proliferation by the MTT assay. The percentages of the control MTT value were: 85.9 ± 6.2 for Hind, 82.7 ± 3.4 for Hnpx, 77.4 ± 5.9 for compound **1** and 72.1 ± 5.5 for compound **3**. Hasp (95.6 ± 4.6) and compound **2** (96.3 ± 7.8) did not exhibit significant values. The high value found for compound **4** (93.1 ± 6.2) could not be explained based on the experiments conducted until the present moment.

3.2.2. Cell proliferation assay

In order to improve the reliability of the MTT data, further experiments for Hibp, Hnpx and their correspondent diruthenium complexes were performed using direct cell counting methods and cell viability analyzed by the trypan blue exclusion method. These experiments were performed on the C6 glioma cell line and involved cell culture in the presence of $[Ru_2(O_2CCH_3)_4Cl]$, Hibp, compound **1**, Hnpx or compound **3** for 24, 48 or 72 h (Table 3). Slight inhibitory effects were found with the Ru_2–dNSAID at 24 h but these were not significant when compared with those obtained by the less accurate MTT assay. Interestingly, inhibition was lost at 48 h but became highly significant at 72 h. In contrast, compound $[Ru_2(O_2CCH_3)_4Cl]$ does not exhibit inhibitory effect at 72 h. These data would suggest that the effects of compounds **1** and **3** are time dependent involving cumulative exposure to the complex to become more anti-proliferative. It is important to note that none of these effects involved direct cytotoxicity as shown by the large percentage of cells which retained their capacity to exclude trypan blue, for example cell viability at 72 h was: 98.5 ± 0.7% for compound **1**; 100 ± 0.1% for compound **3**; and 99.1 ± 0.5% for control (Table 4). Also of note was the inhibitory effect seen after 72 h exposure to the Hibp NSAID alone. Considering that this cell line does not express COX2 under normal culture conditions (Fig. 3) or produce PGE_2 [48] these effects must be through a COX2-independent mechanism.

Compounds **1** and **3** were found to inhibit the proliferation of C6 glioma cells *in vitro* with increasing efficacy correlated to increased time of exposure to the complexes. It is known that the C6 cell line does not express COX2 *in vitro* and therefore any effects of the NSAID component of these complexes must be via either COX1 or non-COX related mechanisms. Coordination of ruthenium to naproxen or ibuprofen, which exhibit antitumor properties alone in C6 cells, had synergistic effects improving their inhibitory properties. Of particular interest is the possibility that these drugs may be even more effective *in vivo* in gliomas where COX2 is expressed by tumor cells, endothelial cells and infiltrating microglial cells. Previous studies with NAMI-A have reported anti-angiogenic and anti-matrix metalloprotease effects [11,12]. The possibility that the complexes

Table 2
MTT assay data

Compound	Hep2	T24/83	C6
$[Ru_2(ibp)_4Cl]$	84.0 ± 7.6	103 ± 9.3	77.4 ± 5.9[a]
Hibp	82.1 ± 5.4	94.3 ± 5.9	94.2 ± 5.3
$[Ru_2(asp)_4Cl]$	83.1 ± 3.9	n.d.	96.3 ± 7.8
Hasp	106 ± 4.3	n.d.	95.6 ± 4.6
$[Ru_2(npx)_4(H_2O)_2]PF_6$	86.7 ± 3.3	138 ± 11.5	72.1 ± 5.5[a]
Hnpx	82.7 ± 8.1	112 ± 9.0	82.7± 3.4[b]
$[Ru_2(ind)_4(H_2O)_2]PF_6$	115 ± 6.3	93.8 ± 6.5	93.1 ± 6.2
Hind	85.8 ± 1.6	94.1 ± 6.5	85.9 ± 6.2[b]

Data are expressed as percentage of optical density of control cells ± SEM, n.d., not determined. Representative data from two separate experiments with $n = 9$–12. Drugs were present at a final concentration of 100 μmol L^{-1}. Statistical analysis used 1-way ANOVA with Tukey's post test, [a]$p < 0.001$; [b]$p < 0.01$.

Table 3
Cell number

Compound	24 h	48 h	72 h
$[Ru_2(O_2CCH_3)_4Cl]$	89.4 ± 4.8	96.2 ± 2.8	93.7 ± 2.4
$[Ru_2(ibp)_4Cl]$	85.5 ± 4.4	99.1 ± 5.7	50.6 ± 1.6[a,b,c]
Hibp	100 ± 3.2	89.8 ± 2.2	74.6 ± 1.7[a]
$[Ru_2(npx)_4(H_2O)_2]PF_6$	88.6 ± 2.0	80.7 ± 6.4	53.2 ± 3.5[a,b,c]
Hnpx	95.6 ± 6.6	81.7 ± 9.5	82.9 ± 2.7[a]

Data are expressed as percentage of control cell number ± SEM. Representative data from three separate experiments with $n = 4$. Drugs were present at a final concentration of 100 μmol L^{-1}. Statistical analysis used 1-way ANOVA with Tukey's post test, $p < 0.05$; [a]versus control; [b]versus ibuprofen; [c]versus naproxen.

Table 4
Cell viability by trypan blue exclusion

	24 h	48 h	72 h
Control	99.5 ± 0.25	99.4 ± 0.39	99.1 ± 0.52
$[Ru_2(O_2CCH_3)_4Cl]$	99.9 ± 0.33	98.5 ± 0.72	98.0 ± 0.41
$[Ru_2(ibp)_4Cl]$	99.8 ± 0.13	98.2 ± 1.10	98.5 ± 0.73
Hibp	99.8 ± 0.11	98.6 ± 0.86	98.4 ± 1.00
$[Ru_2(npx)_4(H_2O)_2]PF_6$	99.8 ± 0.23	98.2 ± 0.84	100 ± 0.10
Hnpx	99.5 ± 0.26	98.3 ± 0.83	99.1 ± 0.45

Viable cell data are expressed as percentage of total cell population ±SEM. Drugs were present at a final concentration of 100 μmol L^{-1}. Cells were incubated with trypan blue prior to counting in a Neubauer chamber. Representative data from three separate experiments with $n = 4$.

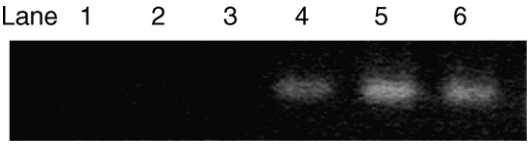


Fig. 3. COX2 mRNA expression in C6 cells *in vitro* lanes 1–3; C6 cells *in vivo* lanes 4–6.

1 and **3** may exert similar effects opens new horizons for studies in the *in vivo* C6 glioma model.

4. Conclusions

Diruthenium compounds of Hipb, Hasp, Hnpx and Hind NSAID drugs exhibited paddlewheel structures with mixed valent $Ru_2(II,III)$ cores containing metal–metal bonds stabilized by four drug-carboxylate bridging ligands. No significant effects were found for the complexes and their parent NSAIDs in the Hep2 human larynx or the T24/83 human bladder tumor. However, the coordination of the $Ru_2(II,III)$ core led to a synergistic effect that increased significantly the C6 rat glioma cell antiproliferative activity of naproxen and ibuprofen drugs. The development of novel drugs with marked effect on glioma cell proliferation, which are also potent inhibitors of COX2, is an important new avenue for future research related to the use of chemotherapy for glioma treatment. The possibility that the diruthenium complexes of ibuprofen and naproxen may exert effects (anti-angiogenic and anti-matrix metalloprotease) that are similar to those exhibited by NAMI-A opens new horizons for *in vivo* C6 glioma model studies.

Investigation about chemical and biological behavior to elucidate the antitumor properties of this kind of compounds is part of our forthcoming work.

Acknowledgements

The authors thank Fundação de Amparo à Pesquisa do Estado de São Paulo (FAPESP) and Conselho Nacional de Desenvolvimento Científico e Tecnológico (CNPq) Brazilian agencies for financial support and fellowships; Instituto do Milênio de Materiais Complexos (IM^2C); Dr. D.L.A. Faria and R. Ando (Laboratório de Espectroscopia Molecular, Instituto de Química, USP) for Raman spectra.

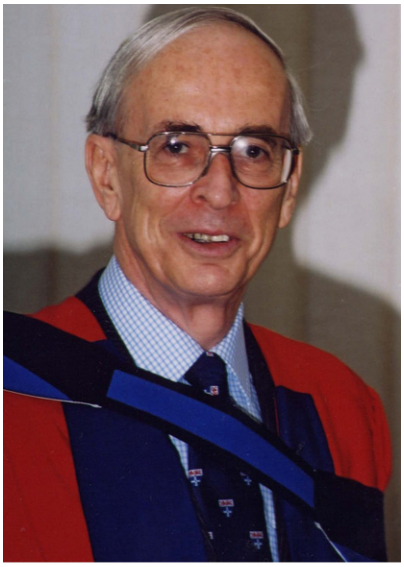
References

[1] M.J. Clarke, Coord. Chem. Rev. 236 (2003) 209.
[2] P.J. Dyson, G. Sava, Dalton Trans. (2006) 1929.
[3] I. Kostova, Curr. Med. Chem. 13 (2006) 1085.
[4] C.X. Zhang, S.J. Lippard, Curr. Opi. Chem. Biol. 7 (2003) 481.
[5] A. Habtemariam, M. Melchart, R. Fernadez, S. Parsons, I.D.H. Oswald, A. Parkin, F.P.A. Fabbiani, J.E. Davidson, A. Dawson, R.E. Aird, D.I. Jodrell, P.J. Sadler, J. Med. Chem. 49 (2006) 6858.
[6] W.H. Ang, P.J. Dyson, Eur. J. Inorg. Chem. 20 (2006) 4003.
[7] C.G. Hartinger, S.Z. Seifred, M.A. Jakupec, B. Kynast, H. Zorbas, B. Keppler, J. Inorg. Biochem. 100 (2006) 891.
[8] S.R. Grguric-Sipka, R.A. Vilaplana, J.M. Pérez, M.A. Fuertes, C. Alonso, Y. Alvarez, T.J. Sabo, F. Vílchez-González, J. Inorg. Biochem. 97 (2003) 215.
[9] A. Bergamo, G. Stocco, B. Gava, M. Cocchietto, E. Alessio, B. Serli, E. Iengo, G. Sava, J. Pharmacol. Expl. Ther. 305 (2003) 725.
[10] V. Djinovíc, M. Momcilovíc, S. Grguric-Sipka, V. Trajkovic, M.M. Stojkovic, D. Miljkovic, T. Sabo, J. Inorg. Biochem. 98 (2004) 2168.
[11] S. Zorzet, A. Bergamo, M. Cocchietto, A. Sorc, B. Gava, E. Alessio, E. Iengo, G. Sava, J. Pharmacol. Expl. Ther. 295 (2000) 927.
[12] G. Sava, S. Zorzet, C. Turrin, F. Vita, M.R. Soranzo, G. Zabucchi, M. Cocchietto, A. Bergamo, S. DiGiovine, G. Pezzoni, L. Sartor, S. Garbisa, Clin. Cancer Res. 9 (2003) 1898.
[13] F.A. Cotton, C.A. Murillo, R.A. Walton (Eds.), Multiple Bonds Between Metal Atoms, 3rd ed., Springer Science and Business Media Inc., New York, 2005.
[14] M.A.S. Aquino, Coord. Chem. Rev. 170 (1998) 141.
[15] M.A.S. Aquino, Coord. Chem. Rev. 248 (2004) 1025.
[16] B.K. Keppler, M. Henn, U.M. Juhl, M.R. Berger, R. Niebl, F.E. Wagner, Prog. Clin. Biochem. Med. 10 (1989) 41.
[17] B.K. Keppler, K. Lipponer, B. Stenzel, F. Kratz, in: B.K. Keppler (Ed.), Metal Complexes in Cancer Chemotherapy, VCH, New York, 1993.
[18] C.E.J. Van Rensburg, E. Kreft, J.C. Swarts, S.R. Dalrymple, D.M. Macdonald, M.W. Cooke, M.A.S. Aquino, Anticancer Res. 22 (2002) 889.
[19] A. Andrade, S.F. Namora, R.G. Woisky, G. Wiezel, R. Najjar, J.A.A. Sertié, D. de Oliveira Silva, J. Inorg. Biochem. 81 (2000) 23.
[20] F.A. Cotton, D. de Oliveira Silva, Inorg. Chim. Acta 249 (1996) 57.
[21] M.J. Thun, S.J. Henley, C. Patrono, J. Nat. Cancer Inst. 94 (2002) 252.
[22] S.J. Shiff, M.I. Koutsos, L. Qiao, B. Rigas, Exptl. Cell Res. 222 (1996) 179.
[23] M.L. Smith, G. Hawcroft, M.A. Hull, Eur. J. Cancer 36 (2000) 664.
[24] G.A. Fitzgerald, Nature Rev. Drug Discovery 2 (2003) 879.
[25] M. Romano, J. Clària, FASEB J. 17 (2003) 1986.
[26] S. Zha, V. Yegnasubramanian, W.G. Nelson, W.B. Isaacs, A.M. De Marzo, Cancer Lett. 213 (2004) 1.
[27] T. Shono, P.J. Tofilon, J.M. Bruner, O. Owolabi, F.F. Lang, Cancer Res. 61 (2001) 4375.
[28] F. Kürzel, C. Hagel, S. Zapf, H. Meissner, M. Westphal, A. Geise, Acta Neurochir. (Wien) 144 (2002) 71.
[29] N. Nathoo, G.H. Barnett, M. Golubic, J. Clin. Pathol. 57 (2004) 6.
[30] P. New, Câncer Control 11 (2004) 152.
[31] M. Wang, D. Yoshida, S. Liu, A. Teramoto, J. Neuro-Oncol. 72 (2005) 1.
[32] J. Drappatz, P. Wen, Curr. Opi. Neur. 17 (2004) 663.
[33] J. Tuettenberg, R. Grobholz, T. Korn, F. Wenz, R. Rever, P. Vajkoczy, J. Cancer Res. Clin. Oncol. 131 (2005) 31.
[34] F. Lefranc, J. Brotchi, R. Kiss, J. Clin. Oncol. 23 (2005) 2411.
[35] N.R. Sivac-Sears, J.A. Schwartzbaum, R. Miike, M. Moghadassi, M. Wrensch, Am. J. Epidemiol. 159 (2004) 1131.
[36] M. Ishibashi, F.G. Bottone Jr., S. Taniura, H. Kamitani, T. Watanabe, T.E. Eling, Exp. Cell Res. 302 (2005) 244.
[37] A. Bernardi, M.C. Jaques-Silva, A. Delgado-Cañedo, G. Lenz, A.M.O. Battastini, Eur. J. Pharm. 532 (2006) 214.
[38] R.W. Mitchell, A. Spencer, G. Wilkinson, J. Chem. Soc., Dalton Trans. (1973) 846.
[39] K.D. Drysdale, E.J. Beck, T.S. Cameron, K.N. Robertson, M.A.S. Aquino, Inorg. Chim. Acta 256 (1997) 243.
[40] A. Carvill, P. Higgins, G.M. McCann, H. Ryan, A. Shiels, J. Chem. Soc., Dalton Trans. (1989) 2435.
[41] J.G. Norman Jr., G.E. Renzoni, D.A. Case, J. Am. Chem. Soc. 101 (1979) 5256.
[42] V.M. Miskowski, H.B. Gray, Inorg. Chem. 27 (1988) 2501.
[43] G. Estiú, F.D. Cukiernik, P. Maldivi, O. Poizat, Inorg. Chem. 38 (1999) 3030.
[44] W.J. Geary, Coord. Chem. Rev. 7 (1971) 81.
[45] R.A. Nyquist, C.L. Putzig, M.A. Leugers, Infrared and Raman Spectral Atlas of Inorganic Compounds and Organic Salts: Text and Explanations, Vol. 1, Academic Press, San Diego, 1996.
[46] K. Nakamoto, Infrared and Raman Spectra of Inorganic and Coordination Compounds. Parts A and B, 5th ed., John Wiley & Sons Inc., New York, 1997.
[47] V.M. Miskowski, T.M. Loehr, H.B. Gray, Inorg. Chem. 26 (1987) 1098.
[48] K.L. Ramos, A. Colquhoun, Glia 43 (2003) 149.

Available online at www.sciencedirect.com
ScienceDirect
Polyhedron 27 (2008) 1139–1140
POLYHEDRON
www.elsevier.com/locate/poly

Obituary

A tribute to Alfred Geoffrey (Geoff) Sykes FRS (1934–2007)



Professor Alfred Geoffrey Sykes FRS
(1934–2007)

With great pleasure I am honoured to write this tribute in honour of Geoff's life and work, and to help summarise his immense contribution to inorganic chemistry and his support for Polyhedron with his loyal service on the editorial board since the initiation of the journal.

Geoff Sykes was appreciated as a good friend by everyone who knew him. He was a loyal supporter, mentor and teacher to all who worked, studied under and collaborated with him over the years, a person who gave of his time generously.

Geoff obtained his B.Sc. in Chemistry from the University of Manchester in 1955, and his Ph.D. (1958) under Bill Higginson. He then began on the many travels around the world that would epitimise his professional life, setting out for a year of post-doctoral work at Princeton University (1958–1959) before moving to the University of Adelaide for a further year of postdoctoral studies in 1959–60. Geoff's first paper was published in 1960, the work presented at a Faraday Society Discussion meeting in Newcastle that year, organised by Professor Lord Wynne-Jones. This meeting attracted not only a galaxy of physical kineticists, but also many associated with the newly emerging area of inorganic reaction mechanisms including A.W. Adamson, F. Basolo, R.W. Dodson, J. Halpern, N. Hush, E.L. King, R.A. Marcus, L.E. Orgel, R.G. Pearson, D.R. Stranks, N. Sutin, H. Taube, R.J.P. Williams, and W.K. Wilmarth.

Geoff's first academic appointment was to a Lectureship in 1961 at the University of Leeds where he was to remain until 1980. Happy and productive times ensued during those early Leeds years both professionally and personally. Geoff's marriage to Elizabeth (Liz) in 1963 gave rise to three children – Richard, Andrew and Caroline. Geoff quickly established a considerable reputation with a series of pioneering studies on peroxo-dicobalt species and in 1964 gained considerable recognition for his seminal text on the 'Kinetics of Inorganic Reactions' published as one of a series of monographs.

Throughout the 1960s and 1970s the Sykes' group thrived as a result of recruiting many of the best Leeds graduates, post-doctoral fellows, and many top visiting scientists. Geoff's research success resulted in his promotion

doi:10.1016/j.poly.2007.12.009

to a Readership in 1970. That same year he became a founder member of the first discussion group (under the Chemical Society as it was then) devoted to research in Inorganic Reaction Mechanisms. The inaugural IMDG meeting was held in Leeds on 20th January 1970 stimulated by the successful International Meeting held the previous year at Bedford College, London with a plenary by Fred Basolo. Other IMDG founder members prominent in those early days were Martin Tobe (the first chairman), Ted Caldin, Ralph Wilkins, Michael Green, Bill Higginson, Martin Twigg, John Burgess and Geoff Stedman. Geoff was the first secretary/treasurer, later to become Martin Tobe's successor as Chairman. The IMDG still thrives today with a meeting held each year either in Europe or in the UK. The 37th meeting of the Group was held in January 2008 at the University of Barcelona, co-organised, like many have in the past, by another of Geoff's former collaborators, Professor Manuel Martinez.

In 1971 Geoff met Karl Wieghardt (then in Heidelberg) who spent a year in Leeds in what proved to be one of the most productive periods. In 1973 Geoff was awarded his D.Sc. from the University of Manchester. Throughout the 1970s many (now well established) scientists spent time with Geoff at Leeds including: Yoichi Sasaki (now Hokkaido), Andreja Bakac (Ames, Iowa), Takashi Shibahara (Okayama), T. Ramasami (Madras), David Weatherburn (Wellington), Graham Lappin (Notre Dame), Richard Henderson (Geoff's successor to the Chair of Inorganic Chemistry at Newcastle) along with Ph.D. students; Roger Thorneley (Norwich) and Fraser Armstrong (Oxford). This helped to establish Geoff's reputation further in the rapidly developing area of Inorganic Reaction Mechanisms.

Towards the end of the 1970s Geoff developed an interest in mechanistic biological inorganic chemistry performing seminal work on the mechanisms underpinning the action of redox proteins such as plastocyanin (Segal) and the ferredoxins (Armstrong).

In 1980, Geoff was appointed to the Established Chair of Inorganic Chemistry at Newcastle. Studies on iridium aqueous chemistry continued (Richens, Castillo-Blum), but soon became focussed almost entirely on Mo and W aqua ions (Richens, Ooi) which led onto extensive work on the chalcogenide-bridged analogues (Ooi, Fedin. Mederos, Hernandez-Molina). This was a highly productive period. Exchanges with the kinetics group at the University of Bloemfontein (Leipoldt, Lamprecht, Roodt, Swarts), and the inorganic groups at Stellenbosch (Cruywagen, Koch) kept the international flavour going throughout the 1980s and into the 1990s.

At Newcastle the metalloprotein studies continued to thrive even further. Work on blue copper proteins (notably Chapman, McGuinnis, Dennison, Kyritsus) and the ferridoxins (Chapman, Im, Worrall) continued, and the attachment of $[Ru(NH_3)_5(H_2O)]^{2+}$ to surface histidine residues provided an opportunity for studying long range intramolecular electron transfer (Jackman, Lloyd-Raven – JACS, 1998). Seminal studies on hemerythrin (Armstrong), hemocyanin (Andrew), aconitase (Faridoon, Zhuang), and the binuclear Fe-enzymes ribonucleotide reductase (Han, Dobbing) and purple acid phosphatase (Aquino, Twichett) and the Cu-enzyme galactose oxidase (Knowles, Phillips and McPherson) provided further important insights.

In 1985, Geoff hosted one of the Climax/Amax Molybdenum Conferences, and in 1992 the first European Bioinorganic Conference (Eurobic), both of them in Newcastle.

The international flavour of Geoff's group was reflected by 40 different nationalities spending time at various stages over the years providing a friendly and productive atmosphere for research. The group produced 53 Ph.Ds, and amassed over 500 publications. Geoff edited 28 books, including Vols. 32–53 of the highly regarded review series; Advances in Inorganic Chemistry.

Throughout his career Geoff thrived on his many visiting appointments around the world which included time spent at the Argonne National Laboratory, USA; University of Heidelberg; University of Leoben, Austria; Northwestern University, USA; University of Berne, Switzerland; Universities of Sydney, Adelaide and Melbourne, Australia; as a JSPS Fellow in Japan, Kuwait University, Memorial University, Newfoundland; University of the West Indies (Barbados, Trinidad, Jamaica); University of Lausanne, Switzerland; Universities of Stellenbosch and Bloemfontein, South Africa; University of La Laguna, Spain, and the City University of Hong Kong.

In 1999, his immense contribution to our present understanding of the mechanisms of metalloprotein reactions and inorganic coordination complexes was recognised by his election to a Fellowship of the Royal Society, possibly the first for contributions to this area of chemistry.

Geoff was undoubtedly one of the most influential British inorganic chemists of his generation. From my own experience he undoubtedly had a unique ability to attract, enthuse, support and inspire young graduates and researchers into the area of Chemistry that he loved.

We all miss him.

David T. Richens
School of Chemistry, University of St. Andrews
North Haugh, St Andrews, Fife KY16 9ST, UK
E-mail address: dtr@st-andrews.ac.uk

Available online 28 January 2008

biological activity of these Schiff bases and their metal complexes may come from their interaction with potential donors of biological heterocycles in vivo [13,14]. The efficiency of the Schiff bases as therapeutic agents has often been enhanced upon coordination with a metal [15,16]. In many cases, the pharmacological activity has been found to be highly dependent on the identity of the metal and the donor sequence of the ligands with different ligands showing widely different biological activities although they may vary only slightly in their molecular structure [7,15,16]; however, the mechanism has yet to be determined. To date, no pattern has emerged to enable the activity to be predicted on the basis of the structure of the dithiocarbazate derivatives. Thus, it is worthwhile to carry out the study of additional isomeric dithiocarbazates and their metal complexes to supplement available information with a view of towards elucidation of the selectivity pattern of this class of compounds. We have previously reported the structure of benzyl *N*-[1-(thiophen-2-yl)ethylidene] hydrazine carbodithioate, SB2ATP [17]. Herein, we examine SB2ATP and benzyl *N*-[1-(thiophen-3-yl)ethylidene] hydrazine carbodithioate (SB3ATP) and their metal complexes of cobalt(II), nickel(II), copper(II), zinc(II)and cadmium(II). Since some of the related heterocyclic thiosemicarbazones and their Schiff bases also possess biochemical and pharmacological properties which may afford potential therapeutic applications [18,19] it is anticipated that continuance of this work may provide some basis for comparison and an understanding of structure–reactivity relationships.

2. Experimental

2.1. Materials

All chemicals were analytical grade and, unless otherwise specified, were used as received. The solvents were purified by conventional methods.

2.2. Preparation of S-benzyldithiocarbazate

This compound was synthesized as reported previously [3]. Potassium hydroxide (11.4 g, 0.2 mol) was dissolved completely in 90% ethanol (70 ml) and the mixture was cooled in an ice bath. To the mixture, hydrazine hydrate (10 g, 0.2 mol) was added slowly with stirring. Carbon disulphide (15.2 g, 0.2 mol) was then added drop-wise with vigorous stirring. The temperature of the reaction mixture was not allowed to rise above 5 °C during the period of addition of carbon disulfide. The resulting brown oil was separated by means of a separating funnel and dissolved in 40% ethanol (60 ml) and the solution was cooled in ice. Benzyl chloride (25.3 g, 0.2 mol) was added slowly with vigorous stirring. The white product was separated by filtration, washed with water and dried in air. The crude product was recrystallized from absolute ethanol; yield, 24.5 g (61.9%); the melting point was 124 °C (Lit. 123–125 °C) [1].

2.3. The preparation of benzyl N-[1-(thiophen-2-yl)ethylidene] hydrazine carbodithioate and benzyl N-[1-(thiophen-3-yl)ethylidene] hydrazine carbodithioate (SB2ATP)

The Schiff base, benzyl *N*-[1-(thiophen-2-yl)ethylidene] hydrazine carbodithioate, SB2ATP, was synthesized as reported previously [17]. *S*-Benzyldithiocarbazate, SBDTC (9.9 g, 0.05 mol) was dissolved in absolute ethanol (35 ml). To this solution was added 2-acetylthiophene (6.3 g, 0.05 mol) also in absolute ethanol (30 ml). The mixture was heated while being stirred for 15 min and later allowed to stand for 20 min whereupon a precipitate formed. This precipitate was filtered and dried over silica gel. Crude products were recrystallized from absolute ethanol.

The Schiff base, benzyl *N*-[1-(thiophen-3-yl)ethylidene] hydrazine carbodithioate, SB3ATP, was synthesized by substituting the 2-acetylthiophene with 3-acetylthiophene.

2.4. General method for preparation of the metal complexes

To 0.005 mol of metal salt dissolved in absolute ethanol (20 ml) was added Schiff base (0.01 mol) in 20 ml of absolute ethanol. The mixture was heated while being stirred. The precipitate was filtered, washed with ice-cold ethanol and dried over silica gel. The yield and melting point were recorded for each product. Metal ions used were cobalt, nickel, copper, zinc and cadmium.

2.5. Physical measurements

IR spectra were recorded on a Perkin–Elmer 1650X FTIR spectrometer using KBr pellets, in the 4000–400 cm^{-1} region. Elemental analyses were carried out using a LECO CHNS-932 and a Perkin–Elmer Plasma 1000 Emission Spectrometer. ^1H NMR spectra were obtained on a JOEL JNM 400 MHz spectrometer. The molar conductance of 10^{-3} M solutions of the metal complexes in DMSO were measured at 30 °C using a Jenway 4310 conductivity meter and a dip-cell with platinized electrode. Electronic absorption spectra were obtained on a Shimadzu UV-2501 PC spectrophotometer using DMSO solutions in the 200–900 nm region. An Electrothermal digital melting point apparatus was used to determine the melting points. Room temperature magnetic susceptibility data were collected with a Sherwood Scientific MSB-AUTO magnetic susceptibility balance at 300 K.

2.6. X-ray structure determination

Dark brown crystals of the Ni(II) complex, Ni(SB2ATP)$_2$, were formed when an acetonitrile solution was allowed to slowly evaporate for a couple of weeks. The selected crystal of the Ni(II) complex was mounted on a glass fiber using perfluropolyether oil and cooled rapidly to 150 K in a stream of cold N_2 using an Oxford Cryosystems CRYOSTREAM unit. Diffraction data were mea-

sured using an Enraf-Nonius Kappa CCD diffractometer (graphite-monochromatic Mo Kα radiation, $\lambda = 0.71073$ Å). Intensity data were processed using the DENZO-SMN package [20]. The crystal was found to be monoclinic with $a = 10.5360(3)$ Å, $b = 8.5915(2)$ Å, $c = 17.0856(5)$ Å and $\beta = 103.6699(11)°$. The structure was solved in the space group $P2/c$ using the direct-methods program SIR92 [21] which located all non-hydrogen atoms. Subsequent full-matrix least-squares refinement of F was carried out using CRYSTALS program suite [22]. Coordinates and anisotropic thermal parameters of all non-hydrogen atoms were refined. Hydrogen atoms were positioned geometrically after each cycle of refinement. A five-term Chebychev polynomial weighting scheme was applied. Refinement converged satisfactorily to give $R = 6.01$ and $R_w = 6.13$ with minimum and maximum residual electron density of -0.74 and 1.07 e Å^{-3}.

2.7. Bioactivity

Antimicrobial assays were carried out at the Laboratory of Molecular and Cell Biology, Institute of Biosciences, Universiti Putra Malaysia while cytotoxic assays were done at the Clinical Genetics Unit, Department of Human Growth and Development, Faculty of Medicine and Health Sciences, Universiti Putra Malaysia.

2.7.1. Qualitative antimicrobial assay

Eight pathogenic microbial strains were used to test the biological potential of the compounds: (i) Methicillin resistant *staphylococcus* (MRSA), (ii) *Bacillus subtilis* wild type (B29), (iii) *Bacillus subtilis* mutant defective DNA repair (B28), (iv) *Pseudomonas aeruginosa* (60690), (v) *Candida albicans* (CA), (vi) *Aspergillus ochraceous* (398), (vii) *Saccharomyces cereviceae* (20341) and (viii) *Candida lypolytica* (2075). The antimicrobial activity of each compound was determined qualitatively through the modified disc diffusion method [23]. A lawn of microorganisms was prepared by pipetting and evenly spreading 10 µl of inocula (adjusted turbid metrically to 10^5–10^6 CFU/cm^3 [CFU = colony forming units]) onto agar set in petri dishes. Nutrient agar (NA) was used for bacteria while potato dextrose agar (PDA) was used for fungi. Filter paper discs (Whatman no. 1) measuring 6 mm in diameter were impregnated with dimethylsulphoxide (DMSO) stock solution of the compounds (100 mg/cm^3) and dried under sterile conditions. The dried discs were then placed on the previously inoculated agar surface. The plates were inverted and incubated for 24 h at 37 °C for the bacteria and 30 °C for the fungi. Antimicrobial activity was indicated by the presence of clear inhibition zones around the discs.

2.7.2. Quantitative antimicrobial assay

Compounds that showed positive antimicrobial activity with the disc diffusion assay were subjected to the broth dilution method for the qualitative measurement of micro biostatic (inhibitory) activity as described by Hufford and Clark [24]. The lowest concentration that completely inhibited visible microbial growth was recorded as the minimum inhibitory concentration (MIC, µg/ml). Streptomycin and nystatin (Sigma, USA) were used as positive controls for bacteria and fungi, respectively.

2.7.3. Cytotoxic assay

2.7.3.1. Cell culture. Five cell lines were used: human myeloid leukemia (HL-60), human ovarian cancer (Caov-3), human cervical cancer (HeLa), human breast carcinoma with positive estrogen receptor (MCF-7) and human breast carcinoma with negative estrogen receptor (MDA-MB-231). All the cell lines were obtained from the National Cancer Institute, USA. HL-60, Caov-3, HeLa and MDA-MB-231 were grown in RPMI-1640 adjusted to contain 0.024 M sodium bicarbonate and 10% fetal calf serum. While MCF-7 was grown in RPMI-1640 containing 0.018 M sodium bicarbonate supplemented with 0.001 M sodium pyruvate, 1 ml of 10 mg/ml bovine insulin and 10% fetal calf serum. All the cells were incubated in an atmosphere of 5% CO_2, 100% relative humidity at 37 °C.

2.7.3.2. Treatments and sample dilutions. Cells from all cell lines were counted, diluted and inoculated on to sterile 96-well microtiter plates. Cells were inoculated in a volume of 100 µl per well at densities between 5000 and 20 000 cells per well (Table 1). The microtiter plates containing the cells were preincubated overnight at 37 °C in an atmosphere of 5% CO_2 and 100% relative humidity to allow stabilization prior to addition of compounds.

Stock solutions of the compounds (10 mg/ml) were prepared using DMSO. The compounds were then diluted with complete medium to concentrations ranging from 100 µg/ml to 0.3 µg/ml. Immediately after preparation of these intermediate dilutions, 100 µl aliquots of each dilution were added to the appropriate microtiter plate wells. The treated cultures were incubated for 4 days in an atmosphere of 5% CO_2 and 100% relative humidity at 37 °C and the end-point was measured using MTT assay as described below.

2.7.3.3. MTT assay. Cytotoxicity was evaluated using MTT (3-[4,5-dimethylthiazo-2-yl]-2,5-diphenyltetrazolium bromide) (Sigma, USA) assay following Mosmann [25] and Monks [26]. The MTT assay was based on metabolic reduction of (3-[4,5-dimethylthiazo-2-yl]-2,5-diphenyltet-

Table 1
Cancer cell lines and inoculation densities used in compound screening

Cell lines	Cells/well
HL-60	20 000
Caov-3	5000
HeLa	5000
MCF-7	5000
MDA-MB-231	7500

razolium bromide) (MTT). A 40 μl aliquot of MTT solution (2.5 mg MTT in 1 ml of PBS solution) was added directly to all the appropriate microtiter plate wells containing cells, complete growth media and test agents as prepared above. The culture was then incubated for 4 h to allow for MTT metabolism to formazan. After this, the supernatant was pipetted out and 200 μl of DMSO was added to dissolve the formazan. The plates were agitated on a plate shaker to ensure a homogeneous solution and the optical densities were read on an automated spectrophotometric plate reader (model MRX II microplate Elisa reader) at a test wavelength of 570 nm and a reference wavelength of 630 nm. Cytotoxicity is shown as the minimum concentration required to reduce the absorbance of treated cells by 50% with reference to the untreated cells (CD_{50}). Tamoxifen and etoposide were used as cytotoxic standards.

3. Results and discussion

3.1. IR spectroscopy and elemental characterization

Table 2 shows the yield, colour, melting points and elemental analysis of the synthesized compounds. All the compounds were synthesized in reasonable yield. The CHNS values of the compounds were determined to be in agreement with the empirical formulae. These dithiocarbazate substituted esters, SB2ATP and SB3ATP, are capable of exhibiting thione–thiol tautomerism existing in either form or as an equilibrium mixture (Fig. 1).

The IR spectra of the free ligands, SB2ATP and SB3ATP, in KBr do not exhibit a ν(S–H) band at around 2700 cm^{-1}, but show a broad and weak band at 3184 cm^{-1} for SB2ATP and 3188 cm^{-1} for SB3ATP attributable to ν(N–H). This indicates that in the solid state, the ligand remains in the thione form. Although an equilibrium mixture of the thione and thiol tautomeric forms may be expected to exist in solution, the ^{1}H NMR spectra of SB2ATP and SB3ATP in DMSO do not exhibit any signal at approximately 4 ppm due to the S–H proton, however, they display signals at 12.51 ppm (SB2ATP) and 12.43 ppm (SB3ATP) due to N–H protons, indicating that even in solution they exist predominantly as the thione tautomers. In the presence of metal salts, they can quickly convert to the thiol form and coordinate to the metal ion in its deprotonated thiolate form.

Both SB2ATP and SB3ATP display a broad and weak band (3184 cm^{-1} and 3188 cm^{-1}, respectively) attributable to ν(N–H). In the spectra of the complexes, this band was not present. This indicates that the ligands were coordinated in their deprotonated form. In the IR spectra of the complexes, the ν(C=N) band is not shifted but the ν(N–N) band of the free ligands shifted to considerably higher wave numbers suggesting coordination *via* the azomethine nitrogen atom. The shift of the ν(C=S) at 914 cm^{-1} (SB2ATP) and 968 cm^{-1} (SB3ATP) to the higher wave numbers for the metal complexes imply coordination through the thiol sulfur. All the significant IR bands of the Schiff bases and their metal complexes are tabulated (Table 3).

3.2. Molar conductivity and magnetic susceptibility

Molar conductivity data are presented in Table 4. All compounds are non-electrolytes in DMSO indicating covalent bonding in each case. Although some dissociation of the complexes seems to occur, the conductance values are much lower than that expected for 1:1 electrolytes in this solvent. All metal complexes were diamagnetic with the exception of CoSB2ATP with $\mu_{eff} = 2.589 \times 10^{-6}$ BM (unfortunately, data are unavailable for the CoSB3ATP complex).

3.3. Electronic spectra

Electronic spectral data of the synthesized compounds are shown in Table 5. The Schiff bases, SB2ATP and SB3ATP, exhibit $(n \rightarrow \pi^*)_{thiophene}$ bands at 357 nm and 337 nm, respectively [18]. The $(n \rightarrow \pi^*)_{dithiocarbazate}$ band was observed at 392 nm for SB2ATP and 337 nm for SB3ATP. Upon coordination with metal complexes, the $(n \rightarrow \pi^*)_{thiophene}$ and $(n \rightarrow \pi^*)_{dithiocarbazate}$ band shifted.

Table 2
Yield, colour, melting point and elemental analysis of synthesized compounds

Compound	Yield (%)	Colour	MP (°C)	Found (calculated) (%)			
				C	H	N	S
SB2ATP	72.6	yellow	131	54.55 (54.87)	4.54 (4.60)	9.38 (9.14)	31.38 (31.28)
$Co(SB2ATP)_2$	51.3	green	181	50.02 (50.21)	3.86 (3.91)	8.77 (8.36)	29.06 (28.71)
$Ni(SB2ATP)_2$	66.3	dark brown	177	49.08 (50.23)	4.03 (3.91)	8.09 (8.37)	32.22 (28.73)
$Cu(SB2ATP)_2$	71.1	dark brown	138	49.88 (49.86)	4.05 (3.89)	8.04 (8.31)	29.43 (28.52)
$Zn(SB2ATP)_2$	59.5	yellow	184	49.51 (49.73)	4.09 (3.88)	8.22 (8.28)	29.82 (28.44)
$Cd(SB2ATP)_2$	70.1	yellow	171	46.32 (46.50)	3.05 (3.62)	7.91 (7.75)	27.61 (26.59)
SB3ATP	80.3	yellow	130	54.01 (54.87)	4.30 (4.60)	9.33 (9.14)	29.23 (31.28)
$Co(SB3ATP)_2$	49.6	dark brown	195	51.03 (50.21)	3.13 (3.91)	7.66 (8.36)	28.45 (28.71)
$Ni(SB3ATP)_2$	62.3	green	217	49.57 (50.23)	3.92 (3.91)	8.91 (8.37)	29.68 (28.73)
$Cu(SB3ATP)_2$	74.3	dark green	169	49.86 (49.86)	3.83 (3.89)	8.56 (8.28)	28.41 (28.44)
$Zn(SB3ATP)_2$	67.3	light yellow	179	49.21 (49.73)	4.01 (3.88)	7.89 (8.28)	28.89 (28.44)
$Cd(SB3ATP)_2$	63.1	light yellow	178	46.41 (46.50)	3.54 (3.62)	8.08 (7.75)	26.77 (26.59)

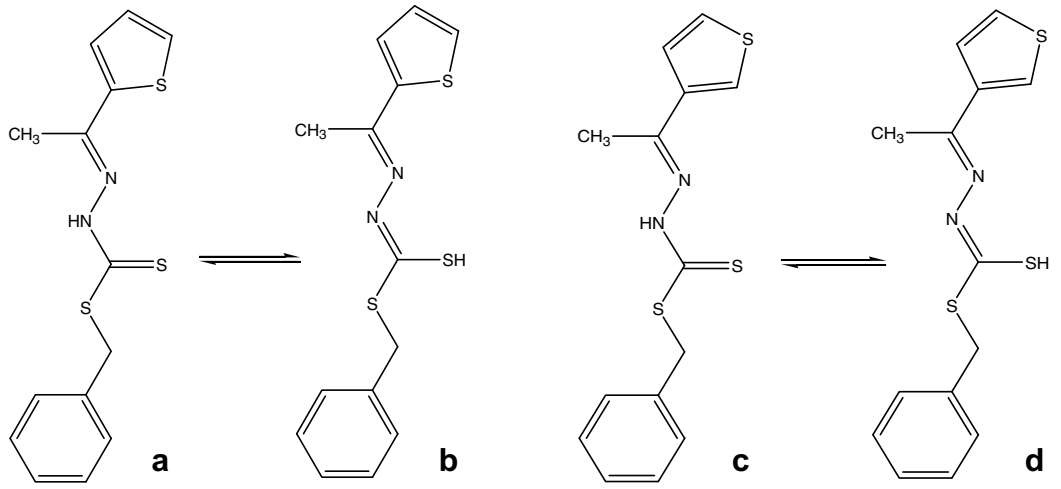


Fig. 1. The thione and thiol form of SB2ATP (a,b) and SB3ATP (c,d).

Table 3
Significant IR bands of the Schiff bases and their metal complexes

Compound	ν(N–H) (cm^{-1})	ν(C=N) (cm^{-1})	ν(N–N) (cm^{-1})	ν(CSS) (cm^{-1})
SB2ATP	3184	1530	1034	914
$Co(SB2ATP)_2$		1552	1030	934
$Ni(SB2ATP)_2$		1552	1070	990
$Cu(SB2ATP)_2$		1556	1072	1026
$Zn(SB2ATP)_2$		1562	1076	1018
$Cd(SB2ATP)_2$		1560	1074	1018
SB3ATP	3188	1526	1056	968
$Co(SB3ATP)_2$		1568	1078	1004
$Ni(SB3ATP)_2$		1572	1076	994
$Cu(SB3ATP)_2$		1574	1080	948
$Zn(SB3ATP)_2$		1572	1072	1006
$Cd(SB3ATP)_2$		1578	1080	1002

Table 4
Molar conductance of the metal complexes

Compound	(Ω^{-1} cm^2 mol^{-1})
$Co(SB2ATP)_2$	25.9
$Ni(SB2ATP)_2$	10.5
$Cu(SB2ATP)_2$	9.7
$Zn(SB2ATP)_2$	11.6
$Cd(SB2ATP)_2$	10.3
$Co(SB3ATP)_2$	20.9
$Ni(SB3ATP)_2$	6.1
$Cu(SB3ATP)_2$	2.7
$Zn(SB3ATP)_2$	12.3
$Cd(SB3ATP)_2$	16.7

The UV–vis spectra of Co(II), d^7, complexes indicate that they are distorted tetrahedral structure. The $^4T_1$ (F) $\rightarrow$ $^4A_2$ bands can be seen at 716 nm and 705 nm for SB2ATP and SB3ATP complexes, respectively [27]. The band at 416 nm for both Co(II) complexes can be assigned to the $^4T_1$ (P) $\rightarrow$ $^4A_2$ transition [27]. The bands at 286 nm (SB2ATP) and 262 nm (SB3ATP) are assigned to the LMCT S $\rightarrow$ d. The $Ni(SB2ATP)_2$ complex adopts a distorted square planar structure with the $^4T_1$ (F) $\rightarrow$ $^4A_2$ band observed at 856 nm [27]. $Ni(SB3ATP)_2$ did not exhibit a band in this region. The $^4T_1$ (P) $\rightarrow$ $^4A_2$ transition can be seen at 416 nm for both of the Ni(II) complexes [27]. The LMCT S $\rightarrow$ d absorption for $Ni(SB3ATP)_2$ is at 281 nm but for $Ni(SB2ATP)_2$ this band was hidden by a strong CT transition.

Cu(II) complexes are usually highly distorted [27]. The $^1A_1 \rightarrow {}^1A_2$ and $^1A_1 \rightarrow {}^1B_1$ transitions can be assigned in the 500 nm and 400 nm region, respectively [3]. The absorption at 262 nm in the $Cu(SB3ATP)_2$ spectrum is expected to be the LMCT S $\rightarrow$ d and the 570 nm can be assigned to the $^1A_1 \rightarrow {}^1E$ transition (see Fig. 1).

3.4. The structure of $[Ni(SB2ATP)_2]$

The molecular structure of $Ni(SB2ATP)_2$ is a distorted square planar monomeric entity with twofold axis running through to the metal ion. A perspective view with the atomic numbering scheme of the complex and its packing arrangement are shown in Figs. 2 and 3, respectively. Selected crystallographic data and refinement data are given in Tables 6 and 7. The nickel(II) ion is coordinated through the azomethine nitrogen atom N(2) and the mercapto-sulfur atom S(12) of the Schiff base ligands at 1.949(2) and 2.148(1) Å, respectively. The nickel atom adopts a distorted square planar geometry with N(2)–N(1)–N(2′), N(2)–Ni(1)–S(12) and S(12)–Ni(1)–S(12′) angles of 104.05°, 86.07° and 87.86°. A weak interaction between thiophenyl sulfur to the nickel ion is reflected by the Ni(1)–S(5) distance of 3.22 Å which could be the cause for the distortion from a perfect square planar geometry.

The N(10)–C(11) distance in the complex is 1.292(4) Å, while for the free ligand it is 1.342(2) Å [17]. The decrease in length of this bond upon complexation through the adjacent N(2) atom. The C(11)–S(12) and N(2)–C(3) bond lengths in the complex are 1.737(3) Å and 1.303(3) Å, respectively. These distances are longer than those observed for the free ligand 1.650(2) Å and 1.276(2) Å

Table 5
Electronic spectral data for synthesized compounds

Compound	$(n \rightarrow \pi^*)_{thiophene}$	$(n \rightarrow \pi^*)_{dithiocarbazate}$		λ_{max} (nm)		
				CT and d–d transitions		
SB2ATP	357 (4.3)	392 (3.5)				
$Co(SB2ATP)_2$	338 (4.1)	384 (3.5)	286 (4.0)	416 (3.6)	716 (1.5)	
$Ni(SB2ATP)_2$	335 (3.5)	383 (3.5)	416 (3.6)	856 (2.3)		
$Cu(SB2ATP)_2$	332 (3.6)	377 (3.4)	405 (3.6)	562 (3.0)		
$Zn(SB2ATP)_2$	363 (3.9)	388 (3.5)	294 (3.6)	411 (3.5)		
$Cd(SB2ATP)_2$	360 (4.2)	389 (3.2)	283 (4.0)	259 (4.0)	470 (3.5)	
SB3ATP	337 (4.1)	364 (3.6)				
$Co(SB3ATP)_2$	344 (4.0)	375 (3.5)	262 (4.2)	416 (3.6)	705 (1.0)	
$Ni(SB3ATP)_2$	340 (3.9)	387 (3.3)	281 (3.8)	416 (3.6)		
$Cu(SB3ATP)_2$	333 (3.5)	376 (3.4)	298 (3.6)	416 (3.6)	563 (3.2)	572 (2.3)
$Zn(SB3ATP)_2$	338 (4.3)	386 (3.5)	260 (4.1)	296 (4.3)		
$Cd(SB3ATP)_2$	332 (4.2)	382 (3.5)	260 (4.1)	294 (4.2)		

Log ε (mol^{-1} cm^{-1}) are in parentheses.

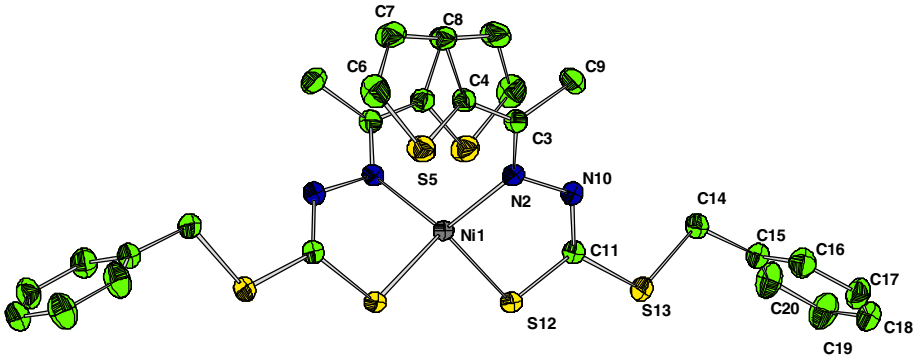


Fig. 2. ORTEP diagram of $Ni(SB2ATP)_2$ with 50% probability displacement ellipsoids showing the distorted square planar arrangement around the metal centre.

[17], as expected and as corroborated by the shifts observed in the infrared spectrum. The C–N bond distances of the complex of the bi-chelated ligands are typical for double bond Schiff base compounds [11]. The C–S bond distances of 1.737(3) Å indicate single bond character which supports the suggestion that the complex formation involves the ligand in its thiol form. The C(3)–N(2)–N(10)–C(11) has a *s*-trans disposition with the benzyl and 1-(thiophene-2-yl)ethylideamine groups nearly orthogonal to each other (79.76°).

3.5. Biological activities

3.5.1. Antimicrobial activity

All compounds were assayed for microbial activity. The disc diffusion technique was employed [23]. The $Cu(SB2ATP)_2$ showed strong activity towards *Candida lypolytica*. SB2ATP, SB3ATP, $Co(SB2ATP)_2$, $Cd(SB2ATP)_2$ and $Cu(SB3ATP)_2$ showed weak microbial activity towards several microbes and fungi while the others showed no activity toward the target microbes and fungi. Quantitative assays were not carried out for these compounds since they showed low activity.

Lead, tin, iron, cobalt and cadmium complexes of *S*-benzyldithiocarbazate Schiff bases formed using 5-methyl-2-furylaldehyde (NS) and 2-furylmethylketone (NS′) did not show not much inhibitory activity against targeted microbes, *Methicillin* resistant *staphylococcus* (MRSA), *Bacillus subtilis*-wild type (B29), *Bacillus subtilis*-mutant defective DNA repair (B28) and *Pseudomonas aeruginosa* (60690) [10]. However, all the compounds showed clear inhibition zones of 10 mm and above against *Aspergillus ochraceous* (398) except the cadmium complex of the 2-furylmethylketone Schiff base [10].

The complexes of the Schiff bases prepared using the same ketone, 2-furylmethylketone, and aldehyde, 5-methyl-2-furylaldehyde, but with different dithiocarbazate moiety, *S*-methyldithiocarbazate, $Cd(NS)_2$, $Sn(NS')_2$ and $Co(NS')_2$ showed clear inhibition of MRSA, B29, B28, 60690, *Candida albicans* (CA), *Aspergillus ochraceous* (398), *Saccharomyces cerevisiae* (20341) and *Candida lypolytica* (2075) with the exceptions that $Cd(NS)_2$ and $Sn(NS')_2$ were inactive towards MRSA and CA, respectively. However, $Cd(NS')_2$, $Fe(NS')Cl_2$ and $Pb(NS')_2$ were inactive towards all target bacteria. $Cd(NS')_2$ was active against CA and 20341, while $Fe(NS')Cl_2$ and $Pb(NS')_2$ showed clear inhibition of 2075 and 398, respectively. $Sn(NS)_2$ showed activity against 60690, MRSA, B29, 2075 and 398. While $Fe(NS)Cl_2$, $Pb(NS)_2$ and $Co(NS)_2$ were inactive towards all target bacteria and fungi [28].

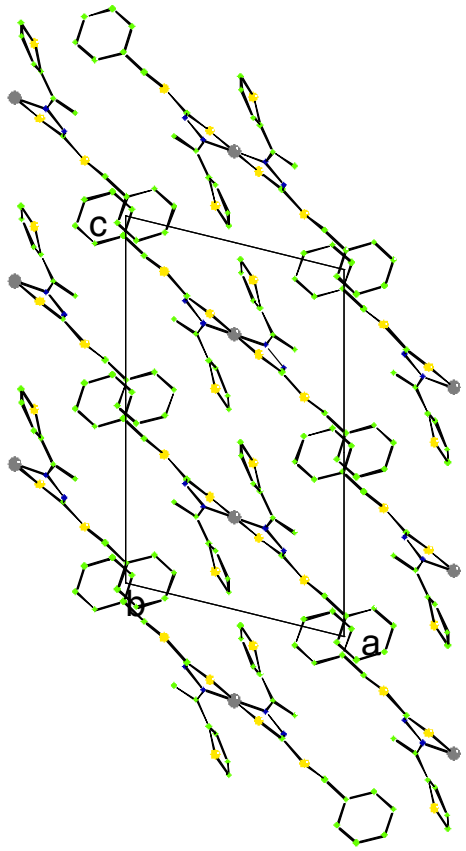


Fig. 3. Packing arrangement of Ni(SB2ATP)$_2$ viewed along the *b* axis.

Table 6
Summary of crystal data and structure refinement parameters for Ni(SB2ATP)$_2$

Chemical formula	$C_{28}H_{26}N_4Ni_1S_6$
Formula weight	669.65
Crystal class	monoclinic
Space group	*P*2/*c*
a (Å)	10.5360(3)
b (Å)	8.5915(2)
c (Å)	17.0856(5)
α (°)	90
β (°)	103.6699(11)
γ (°)	90
V (Å^3)	1502.78(7)
Z	2
Mo Kα (Å)	0.7107
T (K)	150
ρ_{calc} (Mg m^{-3})	1.480
μ (mm^{-1})	1.088
Sample dimension (mm)	0.10 × 0.22 × 0.32
F (000)	692
θ Range for data collection (°)	5–27
Limiting indices	$-13 \leqslant h \leqslant 13$, $-11 \leqslant k \leqslant 11$, $-22 \leqslant l \leqslant 22$
Reflections collected/unique [R_{int}]	6786/3439 [0.02]
Maximum and minimum transmission	0.79 and 0.90
Data/restrains/parameters	2583/0/177
Goodness-of-fit on F^2	1.0294
Minimum and maximum residual electron density (e Å^{-3})	−0.74 and 1.07
R, R_w	6.01, 6.13

Table 7
Selected bond lengths (Å) and bond angles (°) for Ni(SB2ATP)$_2$

Bond lengths			
Ni(1)–N(2)	1.949(2)	S(5)–C(6)	1.683(3)
Ni(1)–N(2)	1.949(2)	N(10)–C(11)	1.292(4)
Ni(1)–S(12)	2.1489(7)	C(11)–S(12)	1.737(3)
Ni(1)–S(12)	2.1489(7)	C(11)–S(13)	1.741(3)
N(2)–C(3)	1.303(3)	S(13)–C(14)	1.822(3)
N(2)–N(10)	1.423(3)	C(14)–C(15)	1.501(4)
C(3)–C(4)	1.452(3)	C(15)–C(16)	1.378(4)
C(3)–C(9)	1.506(4)	C(15)–C(20)	1.397(4)
C(4)–S(5)	1.713(3)		
Bond angles			
N(2)–Ni(1)–N′(2)	104.05(12)	C(3)–C(4)–C(8)	126.1(2)
N(2)–Ni(1)–S(12)	86.07(6)	S(5)–C(4)–C(8)	110.91(19)
N(2)–Ni(1)–S′(12)	162.71(6)	C(4)–S(5)–C(6)	92.87(14)
N′(2)–Ni(1)–S(12)	162.71(6)	S(5)–C(6)–C(7)	112.8(2)
N′(2)–Ni(1)–S′(12)	86.07(6)	N(2)–N(10)–C(11)	111.0(2)
S(12)–Ni(1)–S′(12)	87.87(4)	N(10)–C(11)–S(12)	124.97(19)
Ni(1)–N(2)–C(3)	130.16(17)	N(10)–C(11)–S(13)	121.38(19)
Ni(1)–N(2)–N(10)	118.10(16)	S(12)–C(11)–S(13)	113.63(15)
C(3)–N(2)–N(10)	111.7(2)	NI(1)–S(12)–C(11)	95.50(9)
N(2)–C(3)–C(4)	119.6(2)	C(11)–S(13)–C(14)	103.65(13)
N(2)–C(3)–C(9)	122.1(2)	S(13)–C(14)–C(15)	105.7(2)
C(4)–C(3)–C(9)	118.3(2)	C(14)–C(15)–C(16)	120.2(3)
C(3)–C(4)–S(5)	122.9(2)	C(14)–C(15)–C(20)	121.3(3)

Substitution of the *N* with *S* in the five-membered ring has considerably altered the activity of the compounds towards target microbes and fungi as has substitution of the benzene ring with a methyl group.

3.5.2. Cytotoxic activity

The results of the cytotoxic assays are shown in Table 8. SB2ATP and Cd(SB3ATP)$_2$ showed significant bioactivity towards human myeloid leukemia (HL-60) while Co(SB3ATP)$_2$ showed slight cytotoxic activity towards this cell line. SB2ATP, SB3ATP, Co(SB2ATP)$_2$, Cu(SB2ATP)$_2$, Cu(SB3ATP)$_2$, Zn(SB2ATP)$_2$ and Cd(SB2ATP)$_2$ showed significant chemotherapeutic activity against human breast carcinoma with positive estrogen receptor (MCF-7) while the remainder of the compounds showed significant bioactivity towards this cell line. The Schiff bases show higher cytotoxic activity compared to their metal complexes except for Cu(SB3ATP)$_2$. It can be deduced that metal chelation may slightly inhibit cytotoxic activity. The SB2ATP Schiff bases showed a slightly lower cytotoxic dose concentration than SB3ATP. None of the compounds showed any cytotoxic activity towards human cervical cancer (HeLa) or towards human breast carcinoma with negative estrogen receptors (MDA-MB-231).

Previous studies have shown that bidentate *S*-benzyldithiocarbazate Schiff bases formed using 5-methyl-2-furylaldehyde (NS^a) and 2-furylmethylketone (NS^b) and the Pb(NS^a)$_2$ complex exhibited high cytotoxicity against the Human T-lympho-blastic leukemia (CEM-SS) cell line. The Cd(NS^b)$_2$ complex was inactive towards the CEM-SS cell line in contrast to results reported on other Cd complexes containing similar bidentate ligands [10,11]. *S*-meth-

Table 8
Cytotoxic activity

Compound	IC_{50} (μg/ml)				
	HL-60	Caov-3	HeLa	MCF-7	MDA-MB-231
SB2ATP	13			1.4	
$Co(SB2ATP)_2$				1.8	
$Ni(SB2ATP)_2$					
$Cu(SB2ATP)_2$				4.2	
$Zn(SB2ATP)_2$				3.9	
$Cd(SB2ATP)_2$				4	
SB3ATP				2.8	
$Co(SB3ATP)_2$					
$Ni(SB3ATP)_2$					
$Cu(SB3ATP)_2$				1.6	
$Zn(SB3ATP)_2$					
$Cd(SB3ATP)_2$	9			11.7	
Tamoxifen		3.0	2.7	1.5	5.0
Etoposide	0.5				

Human myeloid leukemia (HL-60); Human ovarian cancer (Caov-3.); Human cervical cancer (HeLa); Human breast carcinoma with positive estrogen receptor (MCF-7); Human breast carcinoma with negative estrogen receptor (MDA-MB-231).
IC_{50} (μg/ml) = inhibition dose at 50%, i.e., the concentration to inhibit growth of cancer cells by 50%.
na, not available.
⩽4 μg/ml = chemotherapeutic significant; 4–30 μg/ml = bioactive significant.
Empty columns indicates ⩾30 μg/ml, i.e. not significant.

yldithiocarbazate Schiff bases prepared using 2-furylmethylketone (NS^c) and 5-methyl-2-furylaldehyde (NS^d), gave complexes, $Cd(NS^c)_2$, $Cd(NS^d)_2$ and $Co(NS^c)_2$, which were very active against CEM-SS and cervical cancer cell (HeLa) lines [28]. The compounds synthesized in this work were not assayed against CEM-SS due to the unavailability of the cell line.

As a general observation, it appears that the complexes of the *S*-benzyldithiocarbazate Schiff base containing the acetylthiophene moiety are not as toxic as the related 2-furylmethylketone and 5-methyl-2-furylaldehyde complexes. It would, therefore, seem that substitution of oxygen by sulfur in the substituent five-membered rings reduces cytotoxicity.

4. Conclusion

The SB2ATP and SB3ATP behave as uninegatively charged bidentate ligands with Co(II), Ni(II), Cu(II), Zn(II) and Cd(II) complexes. The IR spectra of the free ligands indicate that in solid state the ligand remains in the thione form. The thione and thiol tautomeric forms may be expected to exist in solution but the ^1H NMR spectra of SB2ATP and SB3ATP indicates that the ligands, even in solution, exist predominantly as the thione tautomers. All complexes are non-electrolytes in DMSO signifying covalent bonding in each case. The CoSB2ATP complex is paramagnetic with its magnetic moment indicating that it is a square planar structure, the diamagnetic Ni(II) complexes are expected to be in a square planar environment. This has been verified by crystallographic measurements for the NiSB2ATP complex. The diamagnetic Zn(II) and Cd(II) ions are expected to be tetrahedral complexes since they are unlikely to form bridged dimeric square planar structures. The results of magnetic measurements for the Cu complexes may possibly be understood in terms of spin-spin interaction. The thiophenyl substituents displayed lower activity towards target microbes and fungi than the furanyl groups in comparable complexes and also appeared to inhibit the cytotoxicity.

Acknowledgements

We would like to thank the Department of Chemistry, Faculty of Science, Clinical Genetics Unit, Department of Human Growth and Development, Faculty of Medicine and Health Sciences and the Laboratory of Molecular and Cell Biology, Institute of Biosciences, Universiti Putra Malaysia for the provision of laboratory facilities. This research was funded by grants from the Ministry of Science, Technology and Innovation Malaysia, under the Intensification of Research in Priority Areas Scheme (IRPA Grant nos. 09-02-040755 and 09-02-04-0296).

Appendix A. Supplementary material

CCDC 245093 contain the supplementary crystallographic data for complex $Ni(SB2ATP)_2$. These data can be obtained free of charge via http://www.ccdc.cam.ac.uk/conts/retrieving.html, or from the Cambridge Crystallographic Data Centre, 12 Union Road, Cambridge CB2 1EZ, UK; fax: (+44) 1223-336-033; or e-mail: deposit@ccdc.cam.ac.uk. Supplementary data associated with this article can be found, in the online version, at doi:10.1016/j.poly.2007.11.035.

References

[1] M.A. Ali, S.E. Livingstone, Coord. Chem. Rev. 13 (1974) 101.
[2] M.A. Ali, R. Bose, J. Inorg. Nucl. Chem. 39 (1977) 265.
[3] M.A. Ali, M.T.H. Tarafder, J. Inorg. Nucl. Chem. 39 (1977) 1785.
[4] M.T.H. Tarafder, M.A. Jalil Miah, R.N. Bose, M.A. Ali, J. Inorg. Nucl. Chem. 43 (1981) 3151.
[5] M.A. Ali, R.N. Bose, Polyhedron 3 (1984) 517.
[6] Z. Xu, E.C. Alyea, G. Ferguson, M.C. Jennings, Polyhedron 10 (1991) 1625.
[7] M.E. Hossain, M.N. Alam, J. Begum, M. Akbar Ali, M. Nazimuddin, F.E. Smith, R.C. Hynes, Inorg. Chim. Acta 249 (1996) 207.
[8] M. Akbar Ali, A.H. Mirza, R.J. Butcher, M.T.H. Tarafder, M.A. Ali, Inorg. Chim. Acta 320 (2001) 1.
[9] M.T.H. Tarafder, A. Kasbollah, K.A. Crouse, A.M. Ali, B.M. Yamin, H.-K. Fun, Polyhedron 20 (2001) 2363.
[10] M.T.H. Tarafder, T.-J. Khoo, K.A. Crouse, A.M. Ali, B.M. Yamin, H.-K. Fun, Polyhedron 21 (2002) 2691.
[11] M.T.H. Tarafder, T.-J. Khoo, K.A. Crouse, A.M. Ali, B.M. Yamin, H.-K. Fun, Polyhedron 21 (2002) 2547.
[12] Y.-C. Shi, H.-M. Yang, H.-B. Song, C.-G. Yan, X.-Y. Hu, Polyhedron 23 (2004) 567.
[13] S.C. Chan, L.L. Koh, P.-H. Leung, J.D. Ranford, K.Y. Sim, Inorg. Chim. Acta 236 (1995) 101.
[14] X.-H. Zhu, X.-F. Chen, X.-M. Ren, X.-Z. You, S.S.S. Raj, H.-K. Fun, Polyhedron 18 (1999) 3683.

[15] M.A. Ali, C.M. Haroon, M. Nazimuddin, S.M.M.-u.-H. Majumder, Trans. Met. Chem. 17 (1992) 133.
[16] M.E. Hossain, M.N. Alam, M.A. Ali, M. Nazimuddin, F.E. Smith, R.C. Hynes, Polyhedron 15 (1996) 973.
[17] M.-H.E. Chan, K.A. Crouse, M.T.H. Tarafder, B.M. Yamin, Acta Crystallogr., Sect. E 59 (2003) 628.
[18] J. Garcia-Tojal, A. Garcia-Orad, J.L. Serra, J.L. Pizarro, L. Lezama, M.I. Arriortua, T. Rojo, J. Inorg. Biochem. 75 (1999) 45.
[19] J. Garcia-Tojal, J.L. Pizarro, A. Garcia-Orad, A.R. Perez-Sanz, M. Ugalde, A. Alvarez Diaz, J.L. Serra, M.I. Arriortua, T. Rojo, J. Inorg. Biochem. 86 (2001) 627.
[20] Z. Otwinowski, D. Minor, Processing of X-ray diffraction data collected in oscillation mode in methods in enzymology, in: C.W. Carterjr., R.M. Sweet (Eds.), Macromolecular Crystallography, Part A, vol. 276, Academic Press, New York, 1997, p. 307.
[21] A. Altomare, G. Cascarano, G. Giacovazzo, A. Guagliardi, M.C. Burla, G. Polidori, M. Camalli, J. Appl. Cryst. 27 (1994) 435.
[22] D.J. Watkin, C.K. Prout, J.R. Carruthers, P.W. Betteridge, Crystals, 10 ed., Chemical Crystallography Laboratory, University of Oxford, 1996.
[23] A.W. Bauer, M.D.K. Kirny, J.C. Sherries, M. Turck, Am. J. Clin. Pathol. 45 (1966) 493.
[24] C.D. Hufford, A.M. Clark, Elsevier 2 (1988) 421.
[25] T. Mosmann, J. Immunol. Methods 65 (1983) 55.
[26] A. Monks, K. Paull, D. Vistica, C. Hose, J. Langley, P. Cronise, A. Vaigro-Wolff, M. Gray-Goodrich, H. Campbell, J. Mayo, M. Boyd, J. Nat. Cancer Inst. 83 (1991) 757.
[27] A.B.P. Lever, Inorganic Electronic Spectroscopy, 2nd ed., vol. 33, Elsevier Science Publishers, 1984.
[28] K.-B. Chew, M.T.H. Tarafder, K.A. Crouse, A.M. Ali, B.M. Yamin, H.-K. Fun, Polyhedron 23 (2004) 1385.

W, Si and Ge were determined by ICP-AES. C, H and N analyses were determined using a PE-2400 analyzer. ^{183}W NMR spectra of the Me_4N^+ salts were recorded at 16.64 MHz on a Unity-400 spectrometer (solvent D_2O). Chemical shifts were recorded with respect to 2 mol/L Na_2WO_4 in D_2O for ^{183}W NMR. ^1H NMR spectra were recorded on INOVA 500 NMR spectrometer (solvent D_2O). IR spectra were recorded on an Alpha Centauri FTIR spectrometer (4000–200 cm^{-1} range) as KBr pellets.

2.2. Synthesis

2.2.1. $(Me_4N)_4H_5[(HOOCCH_2CH_2Ge)_3(PW_9O_{34})_2]\cdot 1.5DMSO$ (1)

To a mixture of $Na_8H[PW_9O_{34}]\cdot 12H_2O$ (2.7 g, 1 mmol) and Me_4NBr (1.368 g, 9 mmol) in DMSO (10 mL), $HOOCCH_2CH_2GeCl_3$ (1.875 g, 3 mmol) was added with stirring. The mixture turned clear immediately and some HCl gas was released. The solution was stirred for 10 h at room temperature and then filtered. CH_3CH_2OH (100 mL) was added to the filtrate until no more precipitate formed. The white precipitate was recrystallized from hot DMSO–Et_2O and dried under vacuum, yield 46%. *Anal.* Calc. for $(Me_4N)_4H_5[(HOOCCH_2CH_2Ge)_3(PW_9O_{34})_2]\cdot 1.5DMSO$: P, 1.17; W, 62.26; Ge, 4.13; C, 6.32; H, 1.45; N, 1.05. Found: P, 1.02; W, 62.09; Ge, 3.91; C, 6.50; H, 1.79; N, 1.34%.

2.2.2. $(Me_4N)_4H_5[\{HOOCCH_2(m\text{-}NO_2C_6H_4)CHGe\}_3(PW_9O_{34})_2]\cdot 1.5DMSO$ (2)

Compound **2** was prepared analogously using the same quantities as above, yield 46%. *Anal.* Calc. for $(Me_4N)_4H_5[\{HOOCCH_2(m\text{-}NO_2C_6H_4)CHGe\}_3(PW_9O_{34})_2]\cdot 1.5DMSO$: P, 1.09; W, 58.27; Ge, 3.84; C, 7.81; H, 1.51; N, 1.72. Found: P, 1.12; W, 58.40; Ge, 3.64; C, 7.36; H, 1.87; N, 2.05%.

2.2.3. $(Me_4N)_4H_5[(HOOCCH_2\ CH_2Ge)_3(SbW_9\mathbf{O}_{33})_2]\cdot 1.5DMSO$ (3)

Compound **3** was prepared analogously. To a mixture of $Na_9[SbW_9O_{33}]\cdot 19.5\ H_2O$ (2.7 g, 1 mmol) and Me_4NBr (1.368 g, 9 mmol) in DMSO (10 mL), $HOOCCH_2CH_2GeCl_3$ (1.875 g, 3 mmol) was added with stirring. Then CH_3CH_2OH (100 mL) was added to precipitate out $(Me_4N)_4H_5[(HOOCCH_2CH_2Ge)_3(SbW_9O_{33})_2]$. The white precipitate was recrystallized from hot DMSO–Et_2O and dried under vacuum, yield 48%. *Anal.* Calc. for $(Me_4N)_4H_5[(HOOCCH_2CH_2Ge)_3(SbW_9O_{34})_2]\cdot 1.5DMSO$: Sb, 4.46; W, 60.55; Ge, 3.99; C, 6.14; H, 1.41; N, 1.02. Found: Sb, 4.38; W, 61.04; Ge, 3.70; C, 6.50; H, 1.79; N, 1.34%.

2.2.4. $(Me_4N)_4H_5[\{HOOCCH_2(m\text{-}NO_2C_6H_4)CHGe\}_3(SbW_9O_{33})_2]\cdot 1.5DMSO$ (4)

Compound **4** was prepared analogously using the same quantities as above, yield 49%. *Anal.* Calc. for $(Me_4N)_4H_5[\{HOOCCH_2(m\text{-}NO_2C_6H_4)CHGe\}_3(SbW_9O_{33})_2]\cdot 1.5DMSO$: Sb, 4.18; W, 56.78; Ge, 3.74; C, 7.61; H, 1.47; N, 1.68. Found: Sb, 4.25; W, 56.78; Ge, 3.51; C, 7.36; H, 1.87; N, 2.05%.

2.3. The antitumoral activity of the POMs

The antitumoral activity in vitro of the POMs on two of human cancer cells was tested by the MTT experiment [11]. Samples containing the POMs were treated by the following method: the POMs were dissolved by PBS, then autoclaved and diluted by a RPMI 1640 medium with water to final concentrations of 31.3 μg mL^{-1}, 15.6 μg mL^{-1}, 7.8 μg mL^{-1}, 3.9 μg mL^{-1}, 2 μg mL^{-1} and 1 μg mL^{-1}.

The antitumoral activity in vivo was assayed by the animal tumor implantation method. The C57 rats (18–20 g) were supplied by the Changchun Institute of Biological Manufacture. Animals were randomly divided into four treatment groups: control rats, rats bearing with cancer cell and rats receiving compound **3** $(Me_4N)_4H_5[(HOOCCH_2CH_2Ge)_3(SbW_9O_{33})_2]\cdot 1.5DMSO$ (abbreviated as $(C_3H_5O_2Ge)_3(SbW_9)_2$) and positive control compound treatments. Each experimental group consisted of both male and female animals in a 1:1 ratio. The rats bearing cancer were produced by a single subcutaneous inoculation of 5×10^5 mL^{-1} of S180 cancer cells. The rats receiving drug treatments were administered as a single gavage dose orally on days 1–10 and were sacrificed on day 11, then the weight of the tumor and spleen were measured to assay the inhibitory effect and the effect on the immune organ. The control rats were fed with physiological saline.

3. Results and discussion

3.1. IR spectra

The observed frequencies and tentative assignments of the main IR bands of the title complexes are given in Table 1.

Compared with $PW_{12}O_{40}^{4-}$, the IR spectra of the substituted heteropolyanions still have the four characteristic peaks of $\nu_{as(W\text{–}O_d)}$ (O_d, terminal oxygen), $\nu_{as(W\text{–}O_b\text{–}W)}$, $\nu_{as(W\text{–}O_c\text{–}W)}$ (O_b, O_c, bridging oxygen) and $\nu_{as(X\text{–}O_a)}$ (O_a, central oxygen), indicating that the new complexes still retain the basic frame of a Keggin structure. However, the terminal oxygen vibrations for $[(RGe)_3(PW_9O_{34})_2]^{9-}$ are shifted to a lower energy relative to the terminal oxygen vibration

Table 1
IR (cm^{-1}) spectra of the compounds

Anions[a]	$\nu_{as(W\text{–}O_d)}$	$\nu_{as(X\text{–}O_a)}$	$\nu_{as(W\text{–}O_b\text{–}W)}$	$\nu_{as(W\text{–}O_c\text{–}W)}$	ν_{co}
$(PW_9)_2(GeR_1)_3$	962	1085, 1025	832	757	1702
$(PW_9)_2(GeR_2)_3$	958	1085, 1025	834	758	1702
$(SbW_9)_2(GeR_1)_3$	961	775	818	740	1712
$(SbW_9)_2(GeR_2)_3$	961	775	820	742	1712
PW_{12}	977	1080	896	808	
PW_9	931	1057, 1013	821	734	
SbW_9	920	767	890	715	

[a] $R_1 = HOOCCH_2CH_2$, $R_2 = HOOCCH_2(m\text{-}NO_2C_6H_4)CH$.

Table 2
^{1}H NMR data (ppm) of the compounds

Anions[a]	^{1}H				
$(PW_9)_2(GeR_1)_3$	1.38(6)	2.43(6)	3.13(48)	2.54(12H)	
$(PW_9)_2(GeR_2)_3$	2.90–3.10(9)	7.57–8.12(12)	3.11(48)	2.54(12H)	
$(SbW_9)_2(GeR_1)_3$	1.34(6)	2.49(6)	3.14(48)	2.50(12)	12.10(3)
$(SbW_9)_2(GeR_2)_3$	2.85–3.13(9)	7.64–8.07(12)	3.13(48)	2.51(12H)	
R_1GeCl_3	2.19(2)	2.86(2)	9.95(1)		
R_2GeCl_3	3.25(2)	3.98(1)	7.56–8.26(4)	9.74(1)	

[a] $R_1 = HOOCCH_2CH_2$, $R_2 = HOOCCH_2(m\text{-}NO_2C_6H_4)CH$.

for $PW_{12}O_{40}^{4-}$. This is due to an increase of negative charge on the polyanion. The P–O_a bond vibrations of $[(RGe)_3(PW_9O_{34})_2]^{9-}$ split. This fact demonstrates that the $[RGe]^{3+}$ group does not occupy the three vacant sites of the PW_9 anions to give $(RGe)_3PW_9$. The IR spectra are similar to that of $Co_3(PW_9)_2$ [12].

The IR spectra display a single, sharp absorption in the 1700–1712 cm^{-1} region. This feature is characteristic of the C=O stretch. This shows the existence of an organogermanium acid group in the complexes.

3.2. ^{1}H NMR and ^{183}W NMR spectra

The ^{1}H NMR and ^{183}W NMR spectra are given in Table 2 and Fig. 1.

The title complexes gave clear ^{1}H spectra. In $HOOCCH_2CH_2GeCl_3$ (the ^{1}H NMR spectrum contains peaks at 2.19 (t, CH_2COOH), 2.86 (t, CH_2GeCl_3) and 9.95 (s, COOH) ppm), the Ge atom links with three chlorine atoms and the H chemical shift of $GeCH_2$ is 2.86 ppm. When $HOOCCH_2CH_2GeCl_3$ was reacted with PW_9 to form $(HOOCCH_2CH_2Ge)_3(PW_9)_2$, for example, the electron density on Ge was affected by the heteropoly anion, the electron density on Ge increased, and thus the H chemical shift of $GeCH_2$ shifted to a higher magnetic field (1.36 ppm). The other H chemical shifts also changed (the ^{1}H NMR shifts are 12.10 (COOH) and 2.49 (t, $2 \times CH_2COOH$) ppm). This demonstrates that the $[RGe]^{3+}$ group is incorporated with the tungstophosphate and the organic group does not separate from the Ge atom.

The ^{1}H NMR spectrum of $[\{HOOCCH_2(m\text{-}NO_2C_6H_4)CHGe\}_3(PW_9O_{34})_2]^{9-}$ is similar to that of $HOOCCH_2(m\text{-}NO_2C_6H_4)CHGeCl_3$, only some shifts occur, similar to that of $[\{HOOCCH_2(m\text{-}NO_2C_6H_4)CHGe\}_3(PW_9O_{34})_2]^{9-}$, indicating that the polyoxometallate anion $[\{HOOCCH_2(m\text{-}NO_2C_6H_4)CHGe\}_3(PW_9O_{34})_2]^{9-}$ contains the organogermanium group.

The ^{183}W NMR spectrum (Fig. 1) for $(HOOCCH_2CH_2Ge)_3(PW_9)_2$ shows two lines of intensity 1:2, indicating

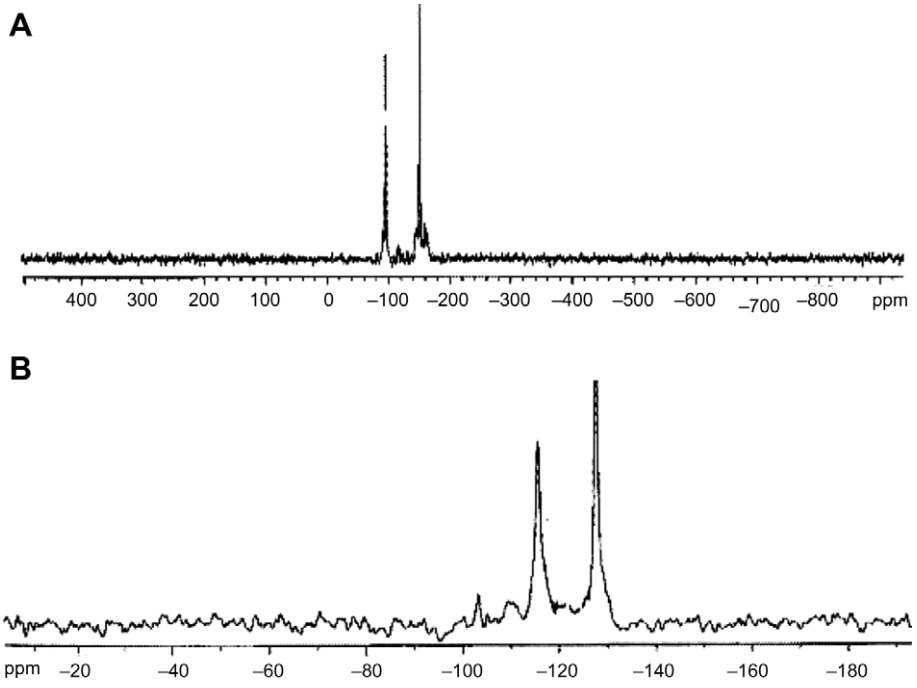


Fig. 1. The ^{183}W NMR spectra of $(HOOCCH_2CH_2Ge)_3(PW_9)_2$ (A) and $(HOOCCH_2CH_2Ge)_3(SbW_9)_2$ (B).

Table 3
Inhibitory effect of the title complexes on two human tumor cell lines in vitro

Anions[a]	Dose (μg mL^{-1})	S180 Inhibitory effect (%)	Hela Inhibitory effect (%)
$(PW_9)_2(GeR_1)_3$	0.246	21.97	11.65
	2.46	25.67	23.40
	24.6	96.69	97.09
$(PW_9)_2(GeR_2)_3$	0.433	9.36	10.75
	4.33	30.26	10.88
	43.30	95.15	98.39
$(SbW_9)_2(GeR_1)_3$	0.522	17.87	25.75
	5.220	75.71	94.76
	52.20	99.30	98.81
$(SbW_9)_2(GeR_2)_3$	0.501	2.73	8.97
	5.010	20.29	11.45
	50.10	96.57	59.22

[a] Me_4N salts dissolved in DMSO.

that there are two kinds of coordination environment for tungsten in the $(HOOCCH_2CH_2Ge)_3(PW_9)_2$ anions. According to the ^{183}W NMR patterns of trisubstituted heteropolyanions, summarized by Pope [13], the ^{183}W NMR spectra of sandwich structures show two lines with an intensity ratio of 1:2. This fact supports the stoichiometry of the new heteropolyanion and demonstrates that $(HOOCCH_2CH_2Ge)_3(PW_9)_2$ has a normal D_{3h} symmetry containing three $[HOOCCH_2CH_2Ge]^{3+}$ groups sandwiched between two PW_9 anions.

The ^{183}W NMR spectrum for $(HOOCCH_2CH_2Ge)_3(SbW_9)_2$ is similar to that of $(HOOCCH_2CH_2Ge)_3(PW_9)_2$, with two lines of relative intensity 1:2, corresponding to the cap tungsten (3W) and belt tungsten atoms (6W), respectively. This also demonstrates that $(HOOCCH_2CH_2Ge)_3(SbW_9)_2$ has a normal D_{3h} symmetry containing three $[HOOCCH_2CH_2Ge]^{3+}$ groups sandwiched between two SbW_9 anions.

3.3. Antitumoral activity

The data summarized in Table 3 show that the title complexes display antiproliferation activity to S180 cancer cells and leucocythemia tumor cells.

From Table 3, we can see that the organogermanium-substituted polyoxotungstates have an inhibitory effect on S180 and leucocythemia tumor cells after being treated for about 4 days. The antitumoral activity increases with the increasing of concentration of the POMs. Compared with the inhibitory effect of $Na_8H[PW_9O_{34}]$, the antitumoral activity of the organogermanium-substituted heteropolyanions $(HOOCCH_2CH_2Ge)_3(PW_9)_2$ was higher at a dose of about 52.20 μg mL^{-1}. This fact shows that the antitumoral activity of the heteropolyanions can be increased by grafting organometallic groups onto the polyoxometallate surface, which can help the POMs cross cell membranes easily. Our experience demonstrates the point of Hill [2]. As for these two kinds of organogermanium substituted heteropolyanion, $(RGe)_3(SbW_9)_2$ exhibits higher antitumoral activity than $(RGe)_3(PW_9)_2$. To investigate the antitumoral activity of $(HOOCCH_2CH_2Ge)_3(SbW_9)_2$, further tests have been carried out and the results are listed in Tables 4 and 5.

Table 4
Inhibitory effect of $(HOOCCH_2CH_2Ge)_3(SbW_9)_2$ on the S180 human tumor cell line in vitro

Dose (μg mL^{-1})	Inhibitory effect (%)
1	2.47
2	16.87
3.9	49.56
7.8	77.83
15.6	88.54
31.3	98.69

Table 5
Inhibitory effect of $(HOOCCH_2CH_2Ge)_3(SbW_9)_2$ and the influence on the spleen of rats bearing the S180 human tumor cell in vivo

Dose (mg kg^{-1})	Mean tumor weight (g)	Splenic index (mg kg^{-1})
Negative control	2.0614 ± 0.3585	7.9494 ± 1.0660
12.5	1.9102 ± 0.3945	8.5828 ± 1.1056
25.0	$0.9922 \pm 0.1751^*$	9.8604 ± 1.0794
75.0	$0.8966 \pm 0.1947^*$	10.5474 ± 1.0892
Positive control	$0.6631 \pm 0.1040^*$	9.2350 ± 1.1631

* $P < 0.05$.

From Table 4 it can be seen that $(HOOCCH_2CH_2Ge)_3(SbW_9)_2$ exhibits a higher inhibitory effect on S180 cancer cell in vitro and the antitumoral activity increases with increasing dosage. The experimental results (Table 5) using the animal tumor implantation method show a decreased tumor weight for the rats bearing S180. It can be seen that $(HOOCCH_2CH_2Ge)_3(SbW_9)_2$ remarkably decreased the tumor weights of the rats bearing S180, which for a dose of 25 mg kg^{-1}, resulted in a tumor weight decrease of 51.9%.

From Table 5 it can be seen that when rats bearing S180 were treated by $(HOOCCH_2CH_2Ge)_3(SbW_9)_2$ (with doses of 25.0 mg kg^{-1} and 75.0 mg kg^{-1}) for about 10 days, the splenic index increases more than the positive group CYT (cyclophosphamide), which means that $(HOOCCH_2CH_2Ge)_3(SbW_9)_2$ can enhance the immune ability of the rats.

To assess the stability of the complexes, they were treated with the same MTT experimental conditions but without adding cancer cells, and the pH of the solution was about 7.2. After evaporation to dryness, IR and ^1H NMR spectra showed that the complexes retained their Keggin structure and the $[RGe]^{3+}$ group was not eliminated from the XW_9 moiety, demonstrating that they are stable under the evaluation conditions.

4. Conclusions

In summary, we have prepared four new organogermanium substituted heteropolytungstates and all the four complexes have showed quite high activity against two of human tumor cell lines in vitro. Unfortunately, all attempts to obtain crystalline materials for X-ray diffraction analysis using variable mixed solutions (e.g. H_2O, H_2O/DMSO and DMSO/Et_2O) were unsuccessful. In addition, compound **4** has exhibited some certain antitumoral activity in vivo and can increase the splenic index.

Acknowledgements

This work was supported by the Postdoctoral Foundation of China (No. 2004036491) and the project was sponsored by the Guangdong Provincial Natural Science Foundation (No. 5301047). This work was also supported by the Analysis and Testing Foundation of Northeast Normal University.

References

[1] M.T. Pope, A. Müller, Angew. Chem., Int. Ed. Engl. 30 (1991) 34.
[2] J.T. Rhule, C.L. Hill, D.A. Judd, Chem. Rev. 98 (1998) 327.
[3] W.H. Knoth, J. Am. Chem. Soc. 101 (1979) 759.
[4] W.H. Knoth, J. Am. Chem. Soc. 101 (1979) 2211.
[5] F. Zonnevijlle, M.T. Pope, J. Am. Chem. Soc. 101 (1979) 2731.
[6] G. Sazani, M.T. Pope, J. Chem. Soc., Dalton Trans. (2004) 1989.
[7] J.X. Li, R.X. Tan, R. Li, X.H. Wang, E.M. Li, F.Y. Zhai, S.D. Zhang, Inorg. Chem. Commun. 10 (2007) 216.
[8] R.Q. Huang, H.L. Wang, J. Zhou, The Preparation of Organic Medium, Chemical and Engineer Press, Beijing, 1997, p. 236.
[9] A. Teze, G. Herve, Inorg. Synth. 27 (1992) 89.
[10] M. Bösing, I. Loose, H. Pohlnann, B. Krebs, Chem. Eur. J. 3 (1997) 1232.
[11] X.H. Wang, J.F. Liu, Y.G. Chen, Q. Liu, J.T. Liu, M.T. Pope, J. Chem. Soc., Dalton Trans. (2000) 1139.
[12] W.H. Knoth, P.J. Domaille, R.L. Harlow, Inorg. Chem. 25 (1986) 1577.
[13] F.B. Xin, M.T. Pope, G.J. Long, U. Russo, Inorg. Chem. 35 (1996) 1207.

[10]. Substitution of various groups on the peripheral positions of porphyrazines has been accomplished either starting with an unsaturated dinitrile precursor with this group attached at the beginning (e.g., dimethylaminoethylthio- [16], tosylaminoethylthio- [17], etc.) or a porphyrazine with reactive functional groups has been prepared at first and then additional groups (e.g., ferrocene [18], benzo-15-crown-5 [19–21], pyridine [13], etc.) have been incorporated by further condensation reactions.

Here in this study, a porphyrazine core with eight 4-*tert*-butylphenyl units attached to the peripheral positions through methylthio bridges was synthesized and metal insertion into the inner core resulted with the corresponding cobalt, zinc, and copper porphyrazines. EPR spectra of paramagnetic Cu–porphyrazine have been investigated in solution and powder form.

2. Experimental

IR spectra were recorded on a Mattson 1000 FT-IR spectrophotometer by using KBr pellets and electronic spectra on an Agile 8453 UV–Vis spectrophotometer. ^{1}H NMR spectra were recorded on Bruker 250 MHz spectrometer using TMS as internal reference. The elemental analyses and mass spectra (LC-MS) were determined in the TUBITAK Laboratory (Center of Science and Technology Research of Turkey). Melting points were obtained with a Gallenkamp CAP MPD-350 apparatus in open capillaries. All reagents and solvents were of reagent grade quality obtained from commercial suppliers. The homogeneity of the products was tested in each step by TLC. Chemicals employed were of the highest grade available. Unless specified other wise, reagent grade reactants and solvents were used as received from chemical suppliers. The solvents were stored over molecular sieves. The disodium salt of dithiomaleonitrile (**1**) was prepared according to the previously reported procedures [24].

Cu^{+2} coordinated metallo-porphyrazine has been investigated by using Electron Paramagnetic Resonance (EPR) technique at room temperature. The EPR spectra of (**3c**) compounds in powder form and in chloroform solution have been recorded by a conventional X-band ($\nu = 9.5$–9.85 GHz) Bruker EMX model spectrometer employing an ac magnetic modulation technique.

2.1. Synthesis of 1,2-bis(4-tert-butylbenzylthio)maleonitrile (2)

Disodium salt of dithiomaleonitrile (**1**) (1.5 g, 8 mmol) and 4-*tert*-butylbenzylbromide (2.94 ml, 10 mmol) in ethanol were mixed under argon at ambient temperature for about 15 min. Then the mixture was heated at 100 °C under argon for about 35 h. The precipitate was settled down from red solution by cooling to room temperature and it was filtered out. The precipitate was dissolved in diethyl ether and filtered to remove any excess disodium salt of dithiomaleonitrile. Finally pale yellow crystals were obtained by evaporation of the solvent under reduced pressure. It was soluble in chloroform, dichloromethane, diethyl ether and acetone. Yield: 2.95 g (85%); m.p. 88 °C. FT-IR (KBr), $\nu_{max}/(cm^{-1})$: 3028 (H–Ar), 2961 C–$(CH_3)_3$, 2209 (C≡N), 1492, 1174, 823, 743, 691. ^{1}H NMR ($CDCl_3$ 250 MHz): $\delta = 7.37$–7.24 (m, 4H, Ar–H), 4.28 (s, 2H, CH_2–S), 1.3 (s, 9H, $(CH_3)_3$–C).

2.2. [2,3,7,8,12,13,17,18-Octakis(4-tert-butylbenzylthio)-porphyrazinato]Mg(II) (3a)

Mg turnings (0.0378 g, 1.575 mmol) and a small I_2 crystal were refluxed in *n*-BuOH (7 ml) for about 20 h to obtain $Mg(BuO)_2$. When 1,2-bis(4-*tert*-butylbenzylthio)maleonitrile (**2**) was added to this suspension and the mixture was refluxed for about 10 h, a dark blue suspension was obtained. The mixture was filtered while hot, washed with *n*-BuOH and the combined filtrates were evaporated under reduced pressure. The remaining oily product was treated with refluxing methanol (30 ml) to dissolve any unreacted maleonitrile and the methanol solution was decanted. The blue–green product was washed with methanol, filtered and dried *in vacuo*. The crude product was purified by column chromatography on silicagel using dichloromethane as the eluent. The pure blue–green porphyrazine was obtained by drying *in vacuo*. Yield: 0.426 g (%81); m.p. >300 °C. FT-IR (KBr), $\nu_{max}/(cm^{-1})$: 3028 (H–Ar), 2978 C–$(CH_3)_3$, 1511, 1462, 1252, 1201, 1105, 1018, 834, 751, 701. ^{1}H NMR ($CDCl_3$ 250 MHz): $\delta = 7.31$–7.10 (m, 4H, Ar–H), 4.91 (s, 2H, CH_2–S), 1.14 (s, 9H, $(CH_3)_3$–C).

2.3. [2,3,7, 8,12,13,17,18-Octakis(4-tert-butylbenzylthio) ^{21}H, ^{23}H porphyrazine] (3b)

Compound **3a** (985 mg, 0.559 mmol) was dissolved in minimum amount of CF_3COOH and stirred overnight at room temperature. The reaction mixture was added into ammonia solution (25%, 7 ml) to neutralize and then cooled overnight at 0 °C. It was treated with chloroform and then the organic phase was washed first with water, then with a solution of 10% Na_2CO_3 and then with water again. The chloroform phase was dried over anhydrous Na_2SO_4 and the solvent was evaporated *in vacuo*. The oily product was treated with a small amount of diethyl ether by cooling in an ice-bath to enhance precipitation. The precipitate formed was filtered when cold. Finally, pure violet colored metal-free porphyrazine was obtained after cooling *in vacuo*. The product was soluble in chloroform, dichloromethane and THF. Yield: 0.341 g (%35). FT-IR (KBr), $\nu_{max}/(cm^{-1})$: 3289 (N–H), 3024 (H–Ar), 2956 C–$(CH_3)_3$, 1513,1461, 1201, 834, 741, 703. ^{1}H NMR ($CDCl_3$ 250 MHz): $\delta = 7.33$–7.17 (m, 4H, Ar–H), 5.18 (s, 2H, CH_2–S), 1.17 (s, 9H, (CH_3)–C), −1.55 (br, 2H, N–H).

2.4. General procedure for metallo-porphyrazines (3c–3e)

To a solution of anhydrous metal salt [$Cu(CH_3COO)_2$ (187 mg, 0.094 mmol), 0.021 g (0.094 mmol) $Zn(CH_3$-

$COO)_2$ or 0.028 g (0.114 mmol) $Co(CH_3COO)_2$] in 10 ml of ethanol was added a solution of **3b** (80 mg, 0.046 mmol) in 10 ml of THF and sealed under Ar. The mixture was stirred and refluxed for 18 h in an oil bath. After cooled to ambient temperature, a precipitate made up of the crude product and the excess metal salt was formed. It was filtered and washed with hot THF. The filtrates were combined and the solvent was evaporated under reduced pressure. The remaining product was first treated with hot water to remove any unreacted metal salt, then washed with methanol and dried *in vacuo*. Finally, pure dark blue porphyrazine derivatives were obtained. The products were very soluble in chloroform, THF and dichloromethane.

*2.4.1. [2,3,7,8,12,13,17,18-Octakis(4-tert-butylbenzylthio)-porphyrazinato]Cu(II) (**3c**)*

Yield: 70 mg (75%). FT-IR (KBr) $\nu_{max}/(cm^{-1})$: 3025 (H–Ar), 2957 C–$(CH_3)_3$, 1511, 1462, 1252, 1201, 1105, 1018, 834, 751, 705.

*2.4.2. [2,3,7,8,12,13,17,18-Octakis(4-tert-butylbenzylthio)-porphyrazinato]Co(II) (**3d**)*

Yield: 96 mg (93%). FT-IR (KBr) $\nu_{max}/(cm^{-1})$: 3025 (H–Ar), 2956 C–$(CH_3)_3$, 1511, 1463, 1253, 1202, 1106, 1025, 835, 752, 705.

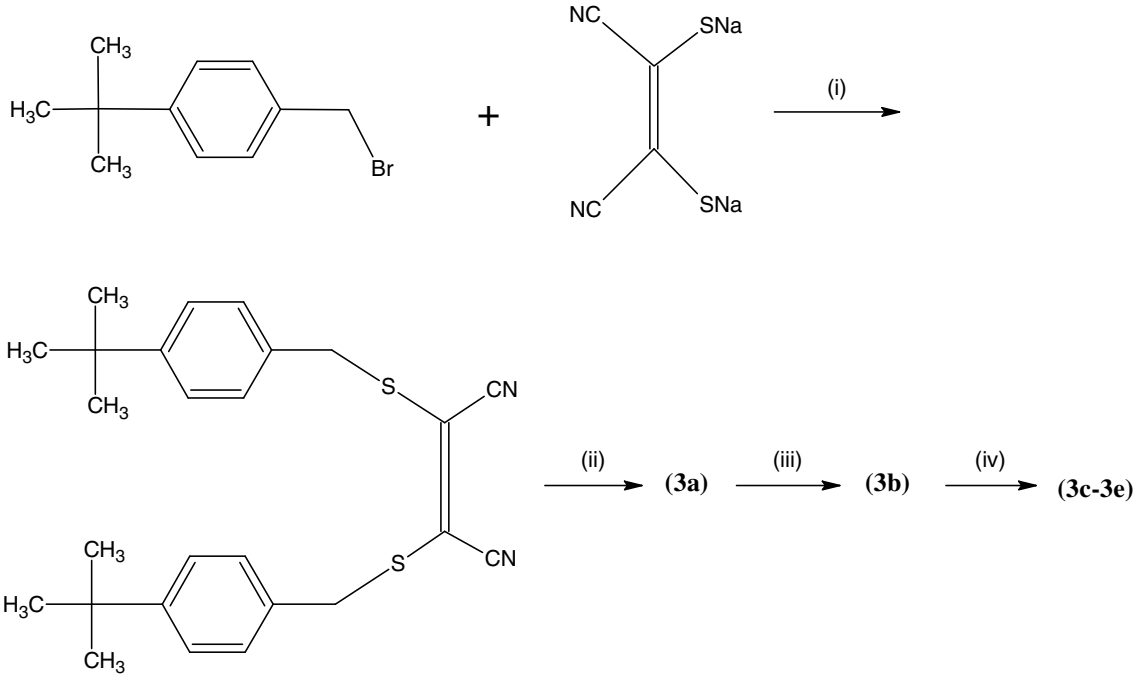
*2.4.3. [2,3,7,8,12,13,17,18-Octakis(4-tert-butylbenzylthio)-porphyrazinato]Zn(II) (**3e**)*

Yield: 66 mg (80%). FT-IR (KBr) $\nu_{max}/(cm^{-1})$: 3023 (H–Ar), 2978 C–$(CH_3)_3$, 1513, 1463, 1201, 1106, 1017, 835, 744, 702. ^1H NMR ($CDCl_3$ 250 MHz): $\delta = 7.17$–7.12 (m, 4H, Ar–H), 4.95 (s, 2H, CH_2–S), 1.16 (s, 9H, (CH_3)–C).

3. Results and discussion

3.1. Synthesis and characterization

The starting point of this new porphyrazine structure with eight (4-*tert*-butylbenzylthio) groups bound to the periphery is 1,2-bis-(4-*tert*-butylbenzylthio)maleonitrile (**2**) which was obtained from disodium salt of dithiomaleonitrile (**1**) and 4-*tert*-butylbenzylbromide (Scheme 1). The solid product (**2**) was obtained in relatively high yield (85%). The presence of electron donating S-groups is expected to shift the absorption range of the porphyrazine Q-band to higher wavelength and *tert*-butyl groups to enhance solubility [25–29]. The cyclotetramerization process of dinitrile derivative (**2**) by the template effect of magnesium butanolate in butanol resulted with the blue–green octakis(4-*tert*-butyl-benzylthio)porphyrazinatomagnesium (**3a**) in 81% yield (Fig. 1). It is very soluble in hexane, chloroform, acetone, dichloromethane and DMF, but in soluble in ethanol, benzene and ether. Treatment of this magnesium compound with a strong organic acid (such as triflouroacetic acid) at room temperature for 8 h afforded the metal-free derivatives (**3b**). Thus, the free base porphyrazine were obtained in a reasonable yield of 30–40%. Apparent differences between magnesium and metal-free derivatives are the change of color from the dark blue–green to purplish blue and lowering in the solubility. Insertion of metal ions into (**3b**) with various metal (II) acetates (M = Cu, Co, Zn) at reflux temperature in THF and ethanol afforded derivatives (**3c**–**3e**) in approximately quantitative yield. Elemental analysis results closely follow the values calculated for (**2**, **3a**–**3e**) (Table 1).



Scheme 1. (i) Methanol; (ii) Mg turnings, I_2, *n*-BuOH; (iii) CF_3CO_2H; (iv) EtOH and $Cu(OAc)_2$, $Co(OAc)_2$, or $Zn(OAc)_2$.

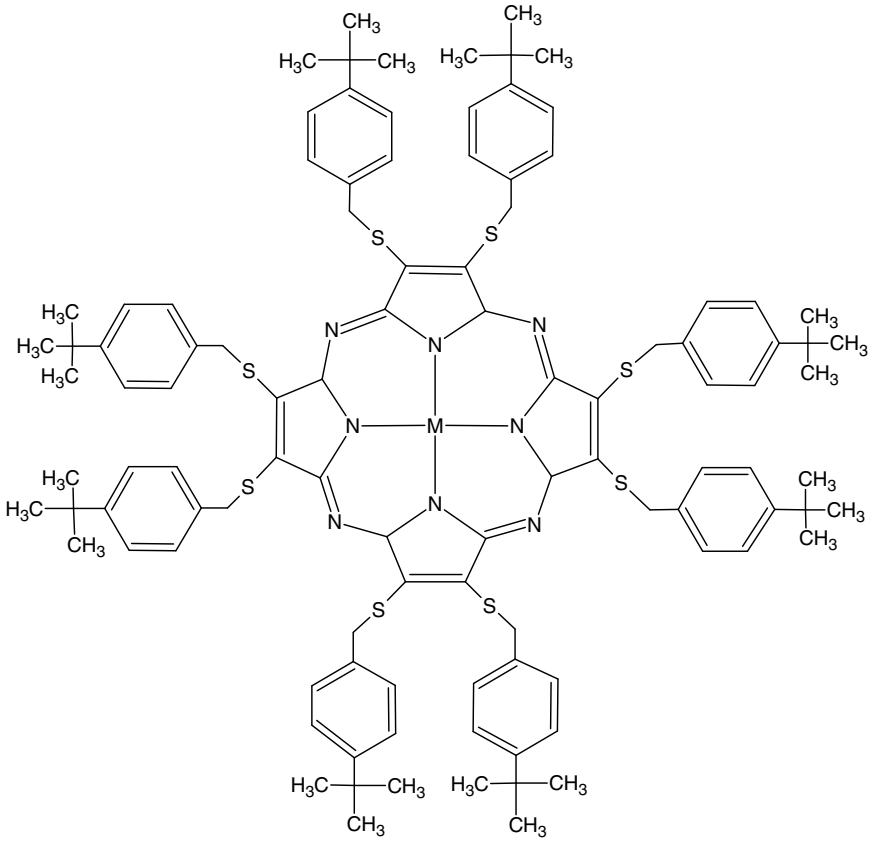


Fig. 1. Octakis(4-*tert*-butylbenzylthio) substituted porphyrazines (M = Mg (**3a**); 2H (**3b**); Cu (**3c**); Co (**3d**); Zn (**3e**)).

Table 1
Elemental analyses results of the porphyrazines[a]

Compound	C	H	N
2	71.84 (71.38)	6.96 (6.98)	6.96 (6.54)
3a	69.55 (69.11)	6.86 (7.13)	6.36 (6.12)
3b	70.48 (70.06)	7.08 (7.57)	6.44 (6.61)
3c	68.61 (68.25)	6.71 (6.57)	6.22 (5.84)
3d	68.49 (68.83)	6.93 (7.44)	6.23 (5.81)
3e	68.94 (68.56)	6.70 (7.12)	6.21 (5.88)

[a] Required values are given in parentheses.

Spectroscopic investigations on the newly synthesized intermediates and porphyrazines are in accordance with the proposed structures. Comparison of the FT-IR spectra of each step gave some hints related to the nature of the product. In the FT-IR spectrum of (**2**) stretching vibration of C≡N is observed at 2213 cm^{-1}, *tert*-butyl peak around 2978 cm^{-1}, S–CH_2 peak around 680 cm^{-1} and aromatic C–H peaks around 3028 cm^{-1}. These values comply with those reported in the literature for similar compounds [30]. The sharp C≡N vibration around 2213 cm^{-1} had disappeared after the formation of porphyrazine (**3a**). After demetalation of (**3a**), the N–H stretching vibration of the inner core of the metal-free porphyrazine (**3b**) was observed around 3289 cm^{-1} as expected [31,32]. The FT-IR spectra of all MPz derivatives (**3a**–**3e**) were very similar (M = Mg, Cu, Co, Zn) as expected [30].

In the ^{1}H NMR spectra of **2**, **3a** and **3b** chemical shifts corresponding to *tert*-butyl protons came out at the expected values: a singlet at 1.3 ppm in (**2**), 1.14 ppm in (**3a**) or 1.17 ppm in (**3b**) corresponding to *tert*-butyl groups. Inner core –NH protons of metal-free porphyrazine (**3b**) appear as a deuterium exchangeable broad chemical shift at −1.55 ppm indicating the typical shielding of inner core protons which is a common feature of the ^{1}H NMR spectra of metal-free porphyrazines [17,31,33,34].

The electronic absorption spectra of all the metallo-porphyrazines (**3a**, **3c**–**3e**) exhibit a strong absorption between 648 and 680 nm which is due to a $\pi \rightarrow \pi^*$ transition and is commonly referred to as Q-band that the first intense bands of porphyrazine core are dominated. A second intense and broad $\pi \rightarrow \pi^*$ transition in the near UV region of the range 343–380 nm which is called soret or B-band is also a characteristic of these tetrapyrole derivatives [16,17]. UV–Vis spectra of metallo-porphyrazines (**3a** in $CHCl_3$, **3c**–**3e** in $CHCl_2$) prepared in the present work exhibited intense single Q-band absorption of the $\pi \rightarrow \pi^*$ transition around 648–679 nm and B-bands in the UV region around 338–382 nm (Fig. 2). As expected the metal-free derivative (**3b**) shows a splitted Q-band at 647 and 714 nm because of the change of symmetry of porphyrazine core from D_{4h} in the case of metallo-species to D_{2h} in the metal-free ones (Table 2) [35–37].

UV–Vis spectra were measured at different levels of concentration to assess whether or not compound **3d** reveals

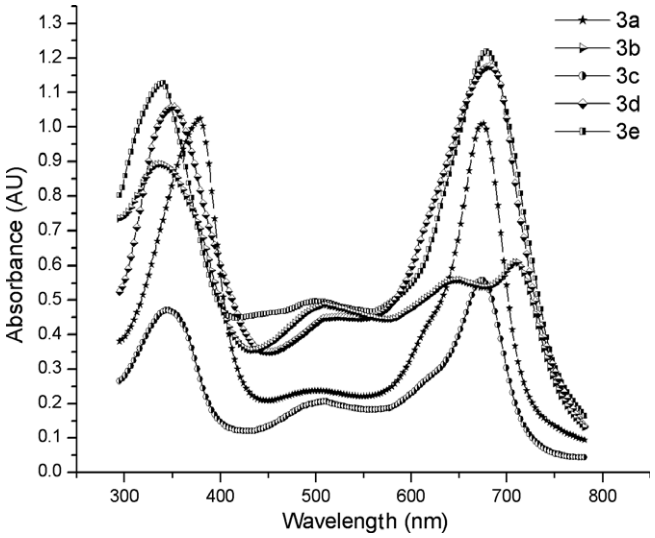


Fig. 2. Electronic spectra of octakis(4-*tert*-butylbenzylthio) substituted porphyrazines **3a**, **3b**, **3c**, **3d** and **3e** as 4×10^{-5} M solutions in dichloromethane.

Table 2
UV–Vis data for the porphyrazines in dichloromethane

Compound	Band λ/nm (log ε/dm^3 mol^{-1} cm^{-1})		
	B	Q	
3a	380 (4.42)	678 (4.38)	
3b	352 (3.97)	653 (3.75)	714 (3.88)
3c	346 (4.24)	674 (4.26)	
3d	352 (4.38)	684 (4.32)	
3e	340 (4.31)	679 (4.35)	

aggregation property. In the light of the results obtained, it was observed that the compound did not show appreciable aggregation in the concentration range of 10^{-3}–10^{-6} M.

3.2. EPR studies for Cu(II) doped porphyrazine

We have tried to measure the room temperature paramagnetic properties of Cu(II) doped porphyrazine sample as powder and solution forms. The first-derivative EPR signals taken from powder and solution forms are shown in Fig. 3. As seen from the figure, the first signal is that of the powder form and it seems to have a single EPR signal with isotropic character and does not contain hyperfine lines. Sometimes, the EPR spectra taken from powder complexes do not exhibit any hyperfine lines at both perpendicular and parallel parts of the spectrum as reported in some Cu(II) complexes [38–40]. The reason must be the exchange-narrowing effect between Cu(II) ions. Therefore, one can expect hyperfine structure in the EPR spectra due to the magnetic interactions between electronic spins ($S = 1/2$) and the nuclear spins ($I = 3/2$). Generally, this interaction can give rise a splitting about a few tens Oersteds which is easily measurable in most of the cases. The absence of hyperfine structure suggests the existence of exchange interactions between electronic spins of Cu(II) ions in the chain. If there is sufficiently strong exchange

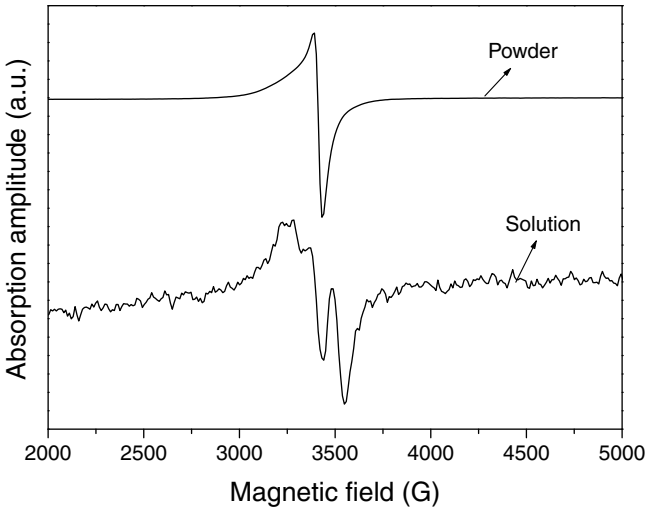


Fig. 3. X-band EPR spectra of (**3c**) as powder form and as chloroform solution at room temperature.

interaction between neighboring electronic spins, then any spin on a particular Cu(II) ion can move around and interact with the nuclear spins of other Cu(II) or nitrogen ions having statistically distributed different nuclear state. The average values of the nuclear spin of different Cu(II) ion cancel out. Thus, the observed EPR spectrum does not exhibit hyperfine features. In this case, the hyperfine structure is completely compressed. That is, the exchange interaction is remarkably strong. The $g_{\|}$ and $g_{\perp}$ values are related by an expression $G = (g_{\|} - 2)/(g_{\perp} - 2)$ and found to be less than 4, which supports the exchange interaction among Cu(II) ions, as well [39].

When we dissolve the powders in chloroform, we can see an EPR spectrum (Fig. 3) for a conventional powdered sample containing a paramagnetic ion with an axially symmetric g factor with $g_{\|} > g_{\perp}$ ($g_{\|} = 2.15$ and $g_{\perp} = 2.04$) and with hyperfine splitting. Namely, the local symmetry of the paramagnetic center giving this signal should be axial. The trend $g_{\|} > g_{\perp} > 2$ indicates that the unpaired electron is located mainly in the $d_{x^2-y^2}$ orbital ($^2B_1$ as ground state) [38]. Here $g_{\|}$ and $g_{\perp}$ denote effective g-values when the applied dc field is parallel ($B_{\|}$) and perpendicular ($B_{\perp}$) to the symmetry axis around the paramagnetic center, respectively. As it is expected, the absorption corresponding to $g_{\perp}$ is more intensive than that of $g_{\|}$ in statistically and randomly oriented solids [40]. Also, the g-value seems to be highly anisotropic.

The Hamiltonian describing an axially symmetric Zeeman interaction can be written as

$$H_{\text{aiso}} = \beta_e(g_{\perp}(B_xS_x + B_yS_y) + g_{II}(B_zS_z)) \quad (1)$$

where β_e and S denote Bohr magneton and the electronic spin angular momentum of the magnetic ion, respectively.

4. Conclusion

In conclusion, we have described the synthesis and spectral characterization of new porphyrazines with bulky

(*tert*-butylphenyl) groups on the periphery. The distinctive property of these compounds is that they have a good solubility in polar organic solvents. The presence of bulky *tert*-butyl groups hindered aggregation at relatively higher concentrations (e.g., 10^{-3} M).

The EPR spectra indicate axial symmetry around paramagnetic Cu^{+2} ion coordinated porphyrazines compounds. Spin Hamiltonian parameters fitted well. Orbital energy levels for magnetic electrons were obtained from Spin Hamiltonian parameters as well. Especially Cu^{+2} coordinated compound shows stronger covalency effects with neighboring N atoms.

Acknowledgement

This work was supported by the Research fund of the Yıldız Technical University. Project No.: 23-01-02-01.

References

[1] N. Kobayashi, K.M. Kadish, K.M. Smith, The Porphyrin Handbook, vol. 2, Academic Press, Newyork, 2000, p. 301.
[2] B.D. Berezin, Coordination Compounds of Porphyrazines and Phthalocyanines, Wiley, Chichester, 1976.
[3] C.C. Leznoff, A.B.P. Lever, Phthalocyanines Properties and Applications, vol. 2, VCH, Weinheim, 1989.
[4] E.A. Ough, K.A.M. Creber, M.J. Stillman, Inorg. Chim. Acta (1996) 361.
[5] N. Kobayashi, C.C. Leznof, A.B.P. Lever (Eds.), Phthalocyanines: Properties and Application, vol. 2, VCH, New York, 1993.
[6] K.K. Dailey, G.P.A. Yap, A.L. Rheingold, T.B. Rauchfuss, Angew. Chem., Int. Ed. Engl. 35 (1996) 1833.
[7] M.J. Crossley, P.L. Burn, S.J. Langford, J.K. Prashar, J. Chem. Soc., Chem. Commun. (1995) 1921.
[8] J.S. Miller, C. Vazquez, J.C. Calabrese, R.S. McLean, A. Epstein, J. Adv. Mater. 6 (1994) 217.
[9] A. Rosa, E. Baerends, J. Inorg. Chem. 33 (1994) 584.
[10] K.I. Ozoemena, T. Nyokong, Inorg. Chem. Commun. 6 (2003) 1192.
[11] J. Leclaire, Y. Coppel, A.M. Caminade, J.P. Majoral, J. Am. Chem. Soc. 126 (2004) 2304.
[12] H. Eichhorn, J. Porphyr. Phthalocya. 4 (2000) 88.
[13] C.G. Claessens, W.J. Blau, M. Cook, M. Hanack, R.J.M. Nolte, T. Torres, D. Wöhrle, Monatsh. Chem. 132 (2001) 3.
[14] E.A. Lukyanets, J. Porphyr. Phthalocya. 3 (1999) 424.
[15] D. Wöhrle, Macromol. Chem. Rapid Commun. 22 (2001) 68.
[16] C.F. van Nostrum, R.J.M. Nolte, Chem. Commun. (1996) 2385.
[17] A.E. Pullen, C. Faulmann, P. Cassoux, Eur. J. Inorg. Chem. (1999) 269.
[18] O.G. Khelevina, N.V. Chizhova, P.A. Stuzhin, J. Porphyr. Phthalocya. 4 (2000) 555.
[19] N.B. McKeown, Phthalocyanine Materials, Cambridge University Press, Cambridge, 1998.
[20] N. Kobayashi, R. Higashi, K. Ishii, K. Ohta, Bull. Chem. Soc. Jpn. 72 (1999) 1263.
[21] G. Gümüş, A. Gül, V. Ahsen, New J. Chem. 21 (1997) 589.
[22] T.F. Baumann, M.S. Nasir, J.W. Sibert, A.J.P. White, M.M. Olmstead, D.J. William, A.G. M Barrett, B.M. Hoffman, J. Am. Chem. Soc. 118 (1996) 10479.
[23] D.P. Goldberg, S.L.J. Michel, A.J.P. White, D.J. Williams, A.G.M. Barrett, B.M. Hoffman, Inorg. Chem. 37 (1998) 2100.
[24] A. Davison, R.H. Holm, Inorg. Synth. 10 (1967) 8.
[25] S. Vagin, M. Barthel, D. Dini, M. Hanack, Inorg. Chem. 42 (2003) 2683.
[26] R. Öztürk, A. Gül, Tetrahedron Lett. 45 (2004) 947.
[27] B. Hasanov, A. Gül, Synth. React., Inorg. Met. Org. Chem. 31 (2001) 673.
[28] R. Öztürk, S. Güner, B. Aktaş, A. Gül, Synth. React. Inorg. Met. Org. Chem. 31 (2001) 1623.
[29] M. Polat, A. Gül, Dyes Pigments 45 (2000) 195.
[30] H.Y. Yenilmez, I. Özçeşmeci, A.I. Okur, A. Gül, Polyhedron 23 (2004) 787.
[31] H. Akkuş, A. Gül, Trans. Met. Chem. 26 (2001) 689.
[32] K.M. Kadish, J. Shao, Z. Ou, C. Comte, C.P. Gros, R. Guilard, J. Porphyr. Phthalocya. 4 (2000) 639.
[33] B.Ş. Sesalan, A. Koca, A. Gül, Polyhedron 22 (2003) 3083.
[34] Ö. Sağlam, A. Gül, Polyhedron 20 (2001) 269.
[35] V.N. Kopranenkov, L.S. Goncharova, E.A. Luk'yanets, J. Org. Chem., USSR 15 (1979) 1076.
[36] P. Doppelt, S. Huille, New J. Chem. 14 (1990) 607.
[37] E. Gonca, A. Gül, Polyhedron 23 (2004) 1845.
[38] A.C. Fabretti, G.C. Franchini, G. Peyronel, Inorg. Chim. Acta 52 (1981) 11.
[39] B.T. Hathaway, Struct. Bond. 14 (1973) 60.
[40] K. Golcuk, A. Altun, S. Guner, M. Kumru, B. Aktaş, Spectrochim. Acta Part A 60 (2004) 303.

HL^2. The mode of coordination of these ligands is determined by the nature of the anion of the parent salt.

2. Experimental

2.1. Materials and instrument

Elemental analyses were performed by atomic absorption spectroscopy (for metals) and with a Perkin–Elmer 2400 CHN Analyzer (for C, H and N). Infrared spectra were recorded as KBr pellets on a UR-20 spectrophotometer in the 4000–400 cm^{-1} region using conventional techniques. Electronic spectra of the compounds in chloroform were recorded on a LOMO MDR-23 spectrophotometer in the 400–800 cm^{-1} region at room temperature. EPR spectra of the powder samples and their solutions in DMF were recorded on a Bruker ESP 300E spectrometer at room temperature and at 77 K. ^1H NMR spectra in DMSO-d^6 solution were recorded on a Varian 400 spectrometer (with Me_4Si as an internal standard) at room temperature.

2.2. X-ray analysis

The crystals of $[CuL_2^1]\cdot H_2O$ are orthorhombic. At 293 K, $a = 13.131(3)$, $b = 14.556(3)$, $c = 13.383(2)$ Å, $V = 2558.4(3)$ Å^3, $M_r = 570.14$, $Z = 8$, space group $Pca2_1$, $d_{calc} = 1.480$ g/m^3, μ(Mo Kα) = 1.060 mm^{-1}, $F(000) = 1172$. Intensities of 25206 reflections (5771 independent, $R_{int} = 0.02$) were measured on an Xcalibur-3 diffractometer (graphite monochromator Mo Kα radiation, CCD detector, ω-scanning, $2\Theta_{max} = 55°$). The absorption correction was made by the semi-empirical method [6] ($T_{min} = 0.475$, $T_{max} = 0.718$). The structure was solved by the direct method using the SHELXTL package [7]. Positions of hydrogen atoms were located from the electron density difference maps and refined by the "riding" model with $U_{iso} = nU_{eq}$ of the non-hydrogen atom bonded with the given hydrogen atom ($n = 1.5$ for methyl and hydroxyl groups and $n = 1.2$ for other hydrogen atoms). Full-matrix least-squares refinement against F^2 in an anisotropic approximation for non-hydrogen atoms using 5753 reflections was converged to $wR_2 = 0.151$ ($R_1 = 0.050$ for 4527 reflections with $F > 4\sigma(F)$, $S = 1.031$).

2.3. Preparations

The ligands HL^1 and HL^2 were prepared as described in the literature [8] according to Scheme 1.

2.3.1. Preparation of $[CuL_2^1]\cdot H_2O$ (1)

To a solution of $Cu(CH_3COO)_2\cdot H_2O$ (1.5 mmol) in 5 ml methanol was added a 10 ml methanol solution of HL^1 (3 mmol). The resulting solution was allowed to stand above $CaCl_2$ at room temperature. Dark violet crystals of **1** suitable for X-ray crystallography were formed after 2 days. The crystals were filtered off, washed with methanol and dried in air. The collected mass was 56 mg, yield: 67%. *Anal.* Calc. for $C_{24}H_{22}N_6O_3S_2Cu$: C, 50.56; H, 3.89; N, 14.74; Cu, 11.15. Found: C, 50.66; H, 3.75; N, 14.68; Cu, 11.23%. IR (KBr pellet, cm^{-1}): $\nu = 1630$ (C=O), 1535 (C=N), 3335 (N–H). The compound is soluble in chloroform, toluene, DMSO and DMF.

2.3.2. Preparation of $[ZnL_2^1]$ (2)

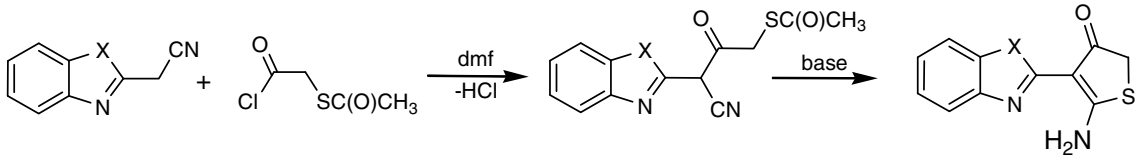
This complex was obtained in a similar manner to **1**, except with the use of $Zn(CH_3COO)_2\cdot 2H_2O$ instead of $Cu(CH_3COO)_2\cdot H_2O$. The collected mass was 54 mg, yield: 65%. *Anal.* Calc. for $C_{24}H_{20}N_6O_2S_2Zn$: C, 52.04; H, 3.64; N, 15.17; Zn, 11.80. Found: C, 52.10; H, 3.57; N, 15.22; Zn, 11.75%. IR (KBr pellet, cm^{-1}): $\nu = 1620$ (C=O), 1530 (C=N), 3345 (N–H). The compound is soluble in DMSO and DMF.

2.3.3. Preparation of $[NiL_2^1]\cdot 2H_2O$ (3)

This complex was obtained in a similar manner to **1**, except with the use of $Ni(CH_3COO)_2\cdot 4H_2O$ instead of $Cu(CH_3COO)_2\cdot H_2O$. The collected mass was 49 mg, yield: 60%. *Anal.* Calc. for $C_{24}H_{22}N_6O_4S_2Ni$: C, 49.42; H, 4.15; N, 14.42; Ni, 10.06. Found: C, 49.32; H, 4.17; N, 14.32; Ni, 9.95%. IR (KBr pellet, cm^{-1}): $\nu = 1640$ (C=O), 1540 (C=N), 3340 (N–H). The compound is soluble in chloroform, toluene, DMSO and DMF.

2.3.4. Preparation of $[CuL_2^2]\cdot H_2O$ (4)

To a solution of $Cu(CH_3COO)_2\cdot H_2O$ (1.5 mmol) in 5 ml methanol was added a 10 ml chloroform solution of HL^2 (3 mmol). The resulting solution was allowed to stand above $CaCl_2$ at room temperature. The crystalline product



X = N-CH$_3$ (HL^1)
X = S (HL^2)

Scheme 1.

of **4** was filtered off, washed with methanol and dried in air. The collected mass was 53 mg, yield: 68%. *Anal.* Calc. for $C_{22}H_{16}N_4O_3S_2Cu$: C, 45.86; H, 2.80; N, 9.72; Cu, 11.03. Found: C, 45.91; H, 2.76; N, 9.74; Cu, 11.10%. IR (KBr pellet, cm^{-1}): $\nu = 1620$ (C=O), 1550 (C=N), 3230 (N–H). The compound is soluble in DMSO and DMF.

*2.3.5. Preparation of $[ZnL^2_2]$ (**5**)*

This complex was obtained in a similar manner to **4**, except with the use of $Zn(CH_3COO)_2 \cdot 2H_2O$ instead of $Cu(CH_3COO)_2 \cdot H_2O$. The collected mass was 61 mg, yield: 73%. *Anal.* Calc. for $C_{22}H_{14}N_4O_2S_2Zn$: C, 47.19; H, 2.52; N, 10.0; Zn, 11.67. Found: C, 48.06; H, 2.61; N, 14.74; Zn, 11.55%. IR (KBr pellet, cm^{-1}): $\nu = 1630$ (C=O), 1530 (C=N), 3340 (N–H). The compound is soluble in DMSO and DMF.

*2.3.6. Preparation of $[NiL^2_2]$ (**6**)*

This complex was obtained in a similar manner to **4**, except with the use of $Ni(CH_3COO)_2 \cdot 4H_2O$ instead of $Cu(CH_3COO)_2 \cdot H_2O$. The collected mass was 49 mg, yield: 60%. *Anal.* Calc. for $C_{22}H_{14}N_4O_2S_2Ni$: C, 47.75; H, 2.55; N, 10.14; Ni, 10.61. Found: C, 47.64; H, 2.53; N, 10.08; Ni, 11.58%. IR (KBr pellet, cm^{-1}): $\nu = 1640$ (C=O), 1535 (C=N), 3335 (N–H). The compound is soluble in chloroform, DMSO and DMF.

*2.3.7. Preparation of $[CoL^2_2] \cdot 2H_2O$ (**7**)*

This complex was obtained in a similar manner to **4**, except with the use of $Co(CH_3COO)_2 \cdot 4H_2O$ instead of $Cu(CH_3COO)_2 \cdot H_2O$. The collected mass was 48 mg, yield: 59%. *Anal.* Calc. for $C_{22}H_{18}N_4O_4S_2Co$: C, 44.82; H, 3.08; N, 9.50; Co, 10.00. Found: C, 44.76; H, 3.13; N, 9.46; Co, 10.03%. IR (KBr pellet, cm^{-1}): $\nu = 1630$ (C=O), 1530 (C=N), 3320 (N–H). The compound is soluble in chloroform, DMSO and DMF.

*2.3.8. Preparation of $[Cu(HL^1)_2Cl_2]$ (**8**)*

To a solution of $CuCl_2$ (1.5 mmol) in 5 ml methanol was added a 10 ml methanol solution of HL^1 (3 mmol). The resulting solution was allowed to stand above $CaCl_2$ at room temperature. The crystalline product of **8** was filtered off, washed with methanol and dried in air. The collected mass was 51 mg, yield: 55%. *Anal.* Calc. for $C_{24}H_{22}N_6O_2S_2Cl_2Cu$: C, 46.12; H, 3.55; N, 13.45; Cu, 10.17. Found: C, 45.99; H, 3.51; N, 13.41; Cu, 10.13%. IR (KBr pellet, cm^{-1}): $\nu = 1630$ (C=O), 1560 (C=N), 3330, 3250 (N–H). The compound is soluble in DMSO and DMF.

*2.3.9. Preparation of $[Zn(HL^1)_2Cl_2]$ (**9**)*

This complex was obtained in a similar manner to **8**, except with the use of $ZnCl_2$ instead of $CuCl_2$. The collected mass was 50 mg, yield: 55%. *Anal.* Calc. for $C_{24}H_{22}N_6O_2S_2Cl_2Zn$: C, 45.98; H, 3.54; N, 13.41; Zn, 10.43. Found: C, 46.21; H, 3.49; N, 13.46; Zn, 10.51%. IR (KBr pellet, cm^{-1}): $\nu = 1625$ (C=O), 1550 (C=N), 3325, 3230 (N–H). The compound is soluble in DMSO and DMF.

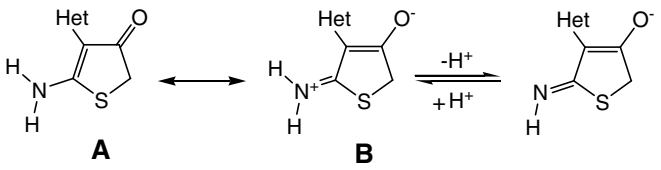
*2.3.10. Preparation of $[Ni(HL^1)_2Cl_2]$ (**10**)*

This complex was obtained in a similar manner to **8**, except with the use of $NiCl_2$ instead of $CuCl_2$. The collected mass was 46 mg, yield: 50%. *Anal.* Calc. for $C_{24}H_{22}N_6O_2S_2Cl_2Ni$: C, 46.48; H, 3.58; N, 13.55; Ni, 9.47. Found: C, 46.51; H, 3.52; N, 13.46; Ni, 9.50%. IR (KBr pellet, cm^{-1}): $\nu = 1640$ (C=O), 1540 (C=N), 3340 (N–H). The compound is soluble in DMSO and DMF.

3. Results and discussions

As was already remarked earlier, 2-amino-4(5H)-ketothiophens can coordinate to metal ions in the neutral and deprotonated forms. The deprotonated form of 2-amino-4(5H)-ketothiophens is realized in those cases where acetate salts are used as a starting reactant. Such behaviour of HL^1 and HL^2 is explained by the acidic nature of the amine hydrogen of these ligands, which is caused by the considerable contribution of the bipolar resonance structure B (see Scheme 2), characteristic for 2-amino-4-keto derivatives of five-membered heterocyclic systems [9]. The complexes with the neutral form of HL^1 are formed on using metal chlorides as the starting salts. These compounds are characterized by considerably less stability on comparison with the complexes with the deprotonated ligand. This behaviour is caused by the low basicity of the amine nitrogen of the ligands. Therefore, coordination compounds with the deprotonated ligand HL^2 cannot be obtained under such conditions.

The structural features of the complexes were determined by IR, electronic, EPR and ^1H NMR spectroscopy and from a single-crystal X-ray study (for **1**). A bidentate coordination of the ligands through the nitrogen atom of the heterocyclic substitute and the amino group of the ketothiophen was proposed based on the IR-spectra. The shift of the absorption band of stretching vibrations ν(C=N) to lower frequencies was used as a criterion of the ligand coordination to the 3d-metal ions. The value of $\Delta\nu$(C=N) for complexes with HL^1 amounted to 60–80 cm^{-1}, while in the case of complexes with HL^2 this value was lower ($\Delta\nu$(C=N) = 50–70 cm^{-1}). The stretching vibrations of the carbonyl group are shifted in the high-frequency region by 5–10 cm^{-1}. This fact can be used as an evidence for the non-participation of the carbonyl oxygen for formation of a coordination bond with the metal ion

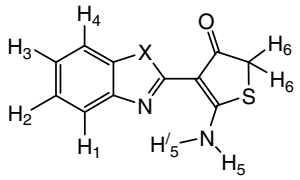


Scheme 2.

[10]. The IR spectra of 2-amino-4(5H)-ketothiophens show, in the 3100–3400 cm^{-1} region, two bands due to symmetric and asymmetric stretching vibrations of the NH_2 group, while complexes **1**–**7** show only one band in this region. The disappearance of one band assigned to the stretching vibrations of the N–H bond is related to the substitution of the amine proton by a metal ion. The values of ν(N–H) for all the complexes lie in the range 3310–3350 cm^{-1}, excluding complex **4** – in this case the value of ν(N–H) is 3270 cm^{-1}. Such a difference in the positions of the absorption bands is probably caused by the formation of hydrogen bonds between the amino group of the ligand and molecules of solvent. The IR spectra of coordination compounds **8**–**10** show stretching vibrations of the amino group ν(N–H) around 3320–3330 cm^{-1} (asymmetrical), 3240–3250 cm^{-1} (symmetrical) and an intense band in the 1550–1560 cm^{-1} region corresponds to ν(C=N).

The coordination compounds of zinc, **2** and **5**, were studied using the method of ^1H NMR spectroscopy. As shown in Table 1, the chemical shifts of the protons of the free ligands differ from the ones for the coordination compounds, which are related with the redistribution of electronic density in organic molecule during coordination to the zinc ion. It is necessary to remark that due to the ligand coordination by the metal ion, the biggest shift value (0.5–0.7 ppm) is observed for the aromatic ring proton H(1), located near the coordination centre (see Scheme 3). The existence of ligands in the deprotonated form is confirmed by the disappearance of a signal from one proton of the amino group H(5′) in the NMR spectra of the complexes. Additionally, the signal of the proton H(5) (singlet at 8.23 ppm for **2** and at 9.04 ppm for **5)** is shifted to higher field on comparison with the free ligands, which proves the coordination of the ligands by the zinc ion through the nitrogen atom of the deprotonated amino group. Consequently it is possible to assert that compounds **2** and **5** have similar structures.

The electronic spectrum of a chloroform solution of nickel complex **3** shows two bands at 21 000 and 16 000 cm^{-1}, which can be reasonably assigned to the $^3A_{2g} \rightarrow {}^3T_{1g}(F)$ and $^3A_{2g} \rightarrow {}^3T_{1g}(P)$ transitions, respectively, suggesting an octahedral geometry of the Ni(II) coordination sphere. In the spectrum of a chloroform solution of complex **6** there is one intensive band at 22 000 cm^{-1}, in contrast to the previous compound. The band in the spectrum of **6** appears due to the electronic transitions typical for a Ni(II) ion in a square-planar surrounding [11]. Such a difference in the structure of coordination compounds **3** and **6** is explained by the different structure of the ligands. It is worth noting that the essential repulsion between the methyl and carbonyl groups induces a significant deviation of the ligand HL^1 from the mean plane passing through the methylbenzoimidazole fragment and thiophene ring. Such a structure of the ligand HL^1 does not provide the possibility of the formation of square-planar complexes. In turn, the ligand HL^2 has a planar structure, which is realized due to the presence of an intramolecular S···O-interaction between the oxygen of the carbonyl group and the sulfur of the benzothiazole substitute. The electronic spectrum of a chloroform solution of complex **7** shows only one band in the visible region at 18 600 cm^{-1}, which can be reasonably assigned to the $^4T_{1g}(F) \rightarrow {}^4T_{1g}(P)$ transition, suggesting an octahedral geometry of the cobalt(II) coordination sphere.



X = N-CH_3 (HL^1)
X = S (HL^2)

Scheme 3.

The EPR spectrum of the polycrystalline complex **4** was recorded at room temperature (see Fig. 1). The form of the spectrum is characteristic for mononuclear complexes of Cu(II) with a square-planar surrounding ($g_\perp = 2.067$, $g_\parallel = 2.232$). Also the spectra of compound **4** were recorded in DMF solution at room temperature and at 77 K. Interpretation of the EPR spectrum at 293 K is not possible because of its low quality, which is related to the significant dissociation of the complex. The EPR spectrum of a frozen solution has an axially symmetric form with a divided hyperfine structure in the region of parallel orientation, which is caused by the interaction of an unpaired electron with the nucleus of copper(II) ($I_{Cu} = 3/2$). The EPR spectrum of compound **4** shows three lines in the region of parallel orientation, the fourth line is overlapped by a more intensive line of perpendicular orientation. It displays the following spin-Hamiltonian parameters $g_\parallel = 2.222$; $g_\perp = 2.069$; $A_\parallel = 162 \times 10^{-4}$ cm^{-1}, which are characteristic for copper complexes with N-donor ligands. The EPR

Table 1
Value of the chemical shifts of protons (ppm) in the NMR spectra for the zinc complexes and free ligands in DMSO solution

Compounds	1-H	2-H	3-H	4-H	5-H	5-H′	CH_2	CH_3
HL^1	7.4d	7.15m	7.15m	7.52d	9.04d	9.04d	3.74s	3.74s
$[ZnL^1_2]$	6.90d	7.02t	7.14t	7.45d	8.23s		3.73s	3.82s
HL^2	7.83d	7.40t	7.28t	7.92d	9.73s	10.08s	3.83s	
$[ZnL^2_2]$	7.13d	7.22m	7.22m	7.90d	9.04s		3.91s	

s, singlet; d, doublet; t, triplet; m, multiplet.

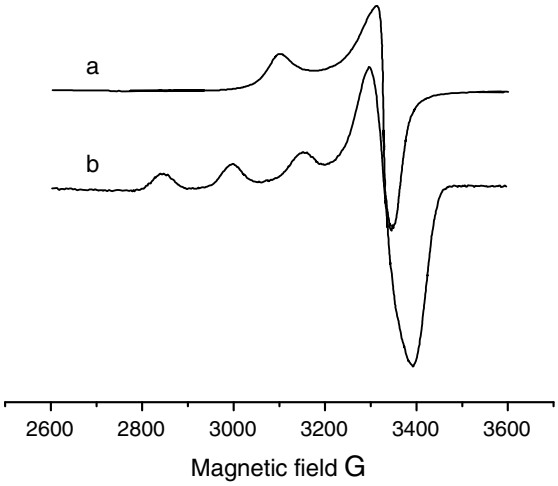


Fig. 1. EPR spectra of $[CuL^2_2] \cdot H_2O$ in the polycrystalline state (a), and in DMF solution (b).

spectrum does not display any superhyperfine features either in the $g_{\|}$ or in the $g_{\perp}$ region, however the large linewidths of the EPR spectra most likely result from the unresolved interaction of the unpaired electron with the nuclear spin of the coordinated nitrogen atoms (^{14}N; $I = 1$), as found for other copper complexes with N-donor ligands [12,13].

An X-ray diffraction study was carried out for compound **1**. In the crystal phase this compound exists as the monohydrate (see Fig. 2). The coordination polyhedron of the Cu(1) atom is formed by four nitrogen atoms of two ligands and the metal has intermediate coordination pattern between tetrahedral and square-planar coordination. The nitrogen atoms of the organic ligands are not coplanar. The angle between the N(1)···N(2) and N(4)···N(5) lines is 38.5°. The nitrogen atoms of the imino group and the heterocyclic substituent of the ligand $(L^1)^-$ are located in *cis*-positions relative to each other. The Cu–N bond lengths (N is the nitrogen of the imino group) are within 1.939–1.959 Å (see Table 2). Such values of the bond lengths are related to the formation of partly covalent bonds, which is typical for amide complexes of copper

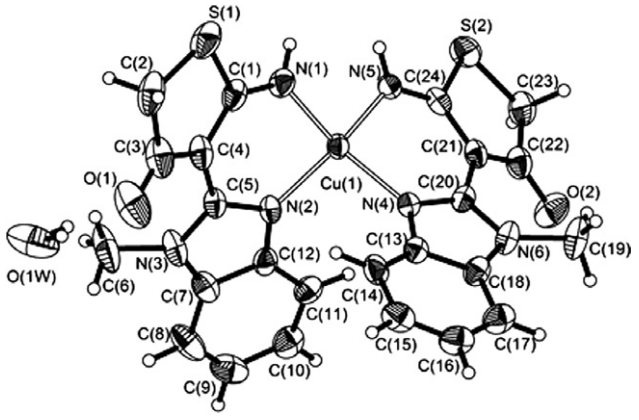


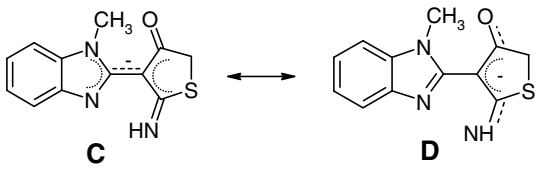
Fig. 2. The molecular structure of the compound $[CuL^1_2] \cdot H_2O$ with 30% probability thermal ellipsoids.

Table 2
Selected interatomic distances (Å) and angles (°) for the compound $[CuL^1_2] \cdot H_2O$

Cu(1)–N(5)	1.939(3)	N(4)–C(13)	1.399(6)
Cu(1)–N(1)	1.959(3)	N(5)–C(24)	1.289(5)
Cu(1)–N(4)	1.970(3)	C(1)–C(4)	1.423(7)
Cu(1)–N(2)	1.979(3)	O(1)–C(3)	1.230(8)
S(1)–C(1)	1.760(4)	O(2)–C(22)	1.259(6)
S(1)–C(2)	1.764(6)	C(2)–C(3)	1.535(8)
S(2)–C(24)	1.772(4)	C(3)–C(4)	1.415(6)
S(2)–C(23)	1.803(5)	C(4)–C(5)	1.451(6)
N(1)–C(1)	1.275(5)	C(20)–C(21)	1.465(6)
N(2)–C(5)	1.343(5)	C(21)–C(24)	1.384(6)
N(2)–C(12)	1.367(6)	C(21)–C(22)	1.407(6)
N(4)–C(20)	1.318(5)	C(22)–C(23)	1.493(8)
N(5)–Cu(1)–N(1)	94.7(4)	C(12)–N(2)–Cu(1)	127.8(3)
N(5)–Cu(1)–N(4)	91.3(4)	C(20)–N(4)–Cu(1)	125.3(3)
N(1)–Cu(1)–N(4)	151.0(2)	C(13)–N(4)–Cu(1)	126.0(3)
N(5)–Cu(1)–N(2)	150.4(3)	C(24)–N(5)–Cu(1)	124.1(3)
N(1)–Cu(1)–N(2)	91.4(4)	N(1)–C(1)–C(4)	126.7(4)
N(4)–Cu(1)–N(2)	97.2(3)	N(1)–C(1)–S(1)	121.2(4)
N(2)–C(5)–C(4)	123.3(4)	C(1)–C(4)–C(5)	120.8(4)
C(24)–S(2)–C(23)	92.3(2)	N(4)–C(20)–C(21)	123.9(4)
C(1)–N(1)–Cu(1)	124.6(3)	C(24)–C(21)–C(20)	119.8(3)
C(5)–N(2)–Cu(1)	125.1(3)	N(5)–C(24)–C(21)	127.9(4)

(with Cu–N bond lengths of 1.91–1.96 Å [14,15]). According to the literature data [16], the length of the Cu···N distance for the coordinated heterocyclic substituent is longer (1.970–1.979 Å). The Cu(1), N(1), C(1), C(4), C(5), N(2) and Cu(1), N(5), C(24), C(21), C(20), N(4) six-membered metallocycles adopt a twist-boat conformation. Deviations of the C(1), N(1) and C(24), N(5) atoms from the mean plane of the remaining atoms of the rings are −0.44, −0.70 and 0.27, 0.54 Å, respectively.

Analysis of the bond lengths within the heterocyclic ligands reveals significant delocalization of the electron density due to the presence of the negative charge. The redistribution of the electron density in the ligands allows the assumption that the structure of these anions can be described as a superposition of two resonance structures C and D (see Scheme 4). The C(1)–N(1) bond (1.275(5) Å) of one of the coordinated ligands is very close to the $C(sp^2)$=N bond length (the mean value is 1.279 Å [17]) and the O(1)–C(3) bond (1.230(8) Å) is close to the C=O bond length (1.210 Å). The C(4)–C(1), C(4)–C(3), C(4)–C(5), N(2)–C(5) and N(3)–C(5) bonds are equalized. Such a distribution of the electron density allows the assumption that the resonance structure C provides the main contribution to the structure of this ligand. In the case of the second ligand, the N(5)–C(24) and O(2)–C(22) bonds



Scheme 4.

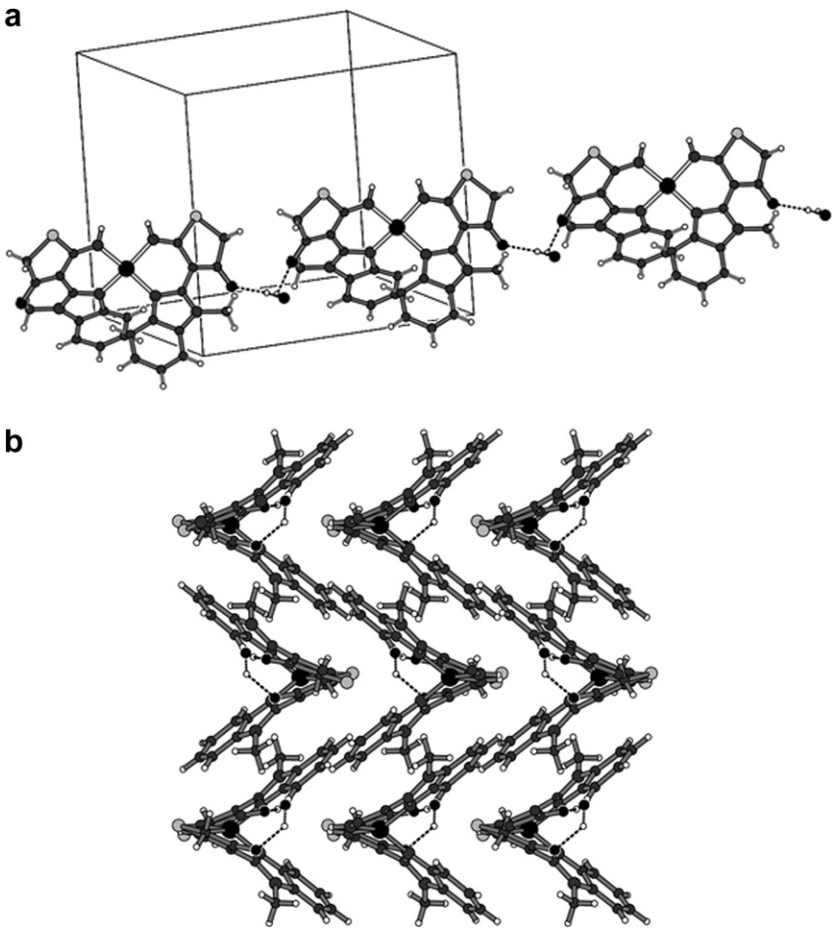


Fig. 3. The infinite chain along the (0 1 0) crystallographic direction (a) and a view of the layer arrangement (b) of complex **1**.

(1.289(5) and 1.259(6) Å) are longer as compared with typical lengths values. The value of the C═O bond length is close to the mean value for a $C(sp^2)$–O^- bond. The C(21)–C(22) and C(21)–C(24) bonds are close enough (1.384(6) and 1.407(6) Å, respectively), but the bond lengths in the imidazole ring are close to their mean value. Therefore the main contribution in the structure of this ligand is provided by the resonance structure D.

The S(1), C(1)···C(4) ring adopts an envelope conformation. Deviation of the C(3) atom from the mean plane of the remaining atoms of the ring is 0.15 Å. The S(2), C(21)···C(24) ring has a twist conformation. Deviations of the S(2) and C(22) atoms from the plane of the remaining atoms of the ring are 0.17 and −0.10 Å, respectively.

The essential repulsion between the methyl and carbonyl groups (shortened intramolecular contacts C(6)···C(3) 3.16 Å (the van der Waals radii sum is 3.42 Å [18]), C(6)···O(1) 2.82 Å (3.00 Å), O(1)···H(6a) 2.13 Å (2.46 Å), C(19)···O(2) 2.85 Å (3.00 Å), C(19)···C(22) 3.21 Å (3.42 Å), O(2)···H(19a) 2.11 Å (2.46 Å)) causes the turn of the methylbenzoimidazole fragment and dihydrothiophene ring relatively to each other (the C(1)–C(4)–C(5)–N(2) and C(24)–C(21)–C(20)–N(4) torsion angles are 24.6(7)° and 22.8(6)°, respectively). The C(6) and C(19) methyl groups are non-coplanar to the plane of the imidazole ring (the C(6)–N(3)–C(7)–C(8) and C(19)–N(6)–C(20)–C(21) torsion angles are −13.3(5)° and 10.3(7)°, respectively). Thus, it is possible to suggest that steric repulsion within the ligands may be responsible for the deformation of the coordination polyhedron of the central atom.

The molecules of **1** form infinite chains along the (0 1 0) crystallographic direction in the crystal (see Fig. 3a) due to intermolecular hydrogen bonds O(1w)–H(1wa)···O(1) (D–H···A = 121°, D–H = 0.91 Å, H···A = 1.90 Å), (x, $1 + y$, z) and O(1w)–H(1wb)···O(2) (D–H···A = 169°, D–H = 0.94 Å, H···A = 2.13 Å). Additionally, an intermolecular association in the structure occurs through π–π stacking interactions (ca. 3.5 Å) between molecules of ligands of adjacent chains. Thereby a layered supramolecular assembly is formed (see Fig. 3b).

4. Conclusions

The present research provides a way of synthesizing 10 novel mononuclear coordination compounds of nickel(II), cobalt(II), zinc(II) and copper(II) with 2-amino-4(5H)-ketothiophens in the neutral and deprotonated forms. Evidently for these compounds, a key difference lies in the nature of the anion in the initial salt and our results

show that complexes of 3d-metal ions with the neutral form of HL^1 were obtained in the case of the usage of metal chlorides as reactants, while complexes with the deprotonated forms of HL^1 and HL^2 were obtained with the use of metal acetates. Thus, the ability of 2-amino-4(5H)-ketothiophens to be deprotonated under soft conditions on coordination by transition metal ions was found. The complexes were unambiguously determined using spectroscopic methods and single crystal X-ray analysis.

Appendix A. Supplementary material

CCDC 659742 contains the supplementary crystallographic data for this paper. These data can be obtained free of charge via http://www.ccdc.cam.ac.uk/conts/retrieving.html, or from the Cambridge Crystallographic Data Centre, 12 Union Road, Cambridge CB2 1EZ, UK; fax: (+44) 1223-336-033; or e-mail: deposit@ccdc.cam.ac.uk. Supplementary data associated with this article can be found, in the online version, at doi:10.1016/j.poly.2007.12.025.

References

[1] E.L. Andronicashvili, V.G. Bregadze, J.R. Monaselidze, Met. Ions Biol. Syst. 23 (1988) 331.
[2] V.G. Karcev, G.A. Tolstikov, Azotic Heterocycles and Alkaloids, Mir, Moskow, 2001.
[3] M. Nakanishi, T. Tahara, K. Araki, J. Med. Chem. 16 (2) (1973) 214.
[4] C. Horig, H. Koch, Pharmazie 28 (9) (1973) 553.
[5] J.D. Ramanathan, D.G. Namboothiri, G.F. Shah, J. Indian Chem. Soc. 55 (8) (1978) 822.
[6] R.H. Blessing, Acta Crystallogr. Sect A 51 (1995) 33.
[7] G.M. Sheldrick, SHELX97 Programs for Crystal Structure Analysis (Release97-2), Institut für Anorganische Chemie der Universität Göttingen, Germany, 1998.
[8] Y.M. Volovenko, T.A. Volovnenko, A.V. Dobridnev, Chem. Heterocycl. Compd. 42 (5) (2006) 594.
[9] Y.M. Volovenko, A.V. Tverdokhlebov, A.P. Gorulya, S.V. Shishkina, R.I. Zubatyuk, O.V. Shishkin, Eur. J. Org. Chem. 4 (2002) 663.
[10] K. Nakamoto, Infrared and Raman Spectra of Inorganic and Coordination Compounds, 4th ed., Wiley, New York, 1986.
[11] A.B.P. Lever, Inorganic Electronic Spectroscopy, second ed., Elsevier, Amsterdam, 1984.
[12] M.C. Mimmi, M. Gullotti, L. Santagostini, G. Battaini, E. Monzani, R. Pagliarin, G. Zoppellarod, L. Casella, J. Chem. Soc., Dalton Trans. (2004) 2192.
[13] L. Siegfried, C.N. McMahon, T.A. Kaden, C. Palivan, G. Gescheidtc, J. Chem. Soc., Dalton Trans. (2004) 2115.
[14] B. Cervera, J.L. Sanz, M.J. Ibanez, G. Vila, F. Lloret, M. Julve, R. Ruiz, X. Ottenwaelder, A. Aukauloo, S. Poussereau, Y. Journaux, M.C. Munoz, J. Chem. Soc., Dalton Trans. 5 (1998) 781.
[15] J.L. Sans, B. Cervera, R. Ruiz, C. Bios, J. Faus, F. Lloret, M.J. Julve, Chem. Soc., Dalton Trans. 7 (1996) 1359.
[16] Z.J. Zhong, N. Matsumoto, H. Okawa, S. Kida, J. Inorg. Chem. 30 (1991) 436.
[17] H.B. Burgi, J.D. Dunitz, Structure Correlation, vol. 2, VCH, Weinheim, 1994, pp. 741.
[18] Yu.V. Zefirov, P.M. Zorky, Usp. Khim. 58 (5) (1989) 713.

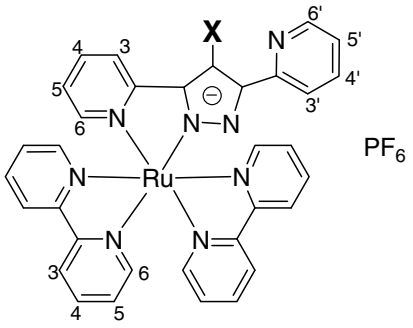


Fig. 1. Structures and labelling scheme for the ^{1}H NMR spectra of complexes **1**–**5**.

research work on functional mimics of the donor side of photosystem II, we have synthesized some new mononuclear ruthenium polypyridyl complexes bearing Hbpp as well as its 4-nitro and 4-halogen substituted analogues. In this paper, we present the synthesis, structure, spectroscopic, electrochemical and acid–base properties of $[Ru(bpy)_2(Xbpp)](PF_6)$. The structures of the mononuclear Ru complexes are showed in Fig. 1.

2. Experimental

2.1. Materials

All chemicals were obtained from commercial sources and were used without further purification. Acetonitrile used in spectroscopic measurements and electrochemistry was of spectroscopy grade. Other solvents were reagent grade. The ligands 3,5-bis(2-pyridyl)-1*H*-pyrazole (Hbpp) [7], 4-chloro-3,5-bis(2-pyridyl)-1*H*-pyrazole (ClHbpp), 4-bromo-3,5-bis(2-pyridyl)-1*H*-pyrazole (BrHbpp), 4-iodo-3,5-bis(2-pyridyl)-1*H*-pyrazole (IHbpp), 4-nitro-3,5-bis (2-pyridyl)-1*H*-pyrazole (NO_2Hbpp) [8] and the complex *cis*-$[Ru(bpy)_2Cl_2]\cdot 2H_2O$ [9] were prepared according to the reported methods.

2.2. Preparation of the complexes

2.2.1. *[Ru(bpy)$_2$(bpp)](PF$_6$) (**1**) (representative procedure)*

111 mg (0.5 mmol) of Hbpp and 260 mg (0.5 mmol) of *cis*-$[Ru(bpy)_2Cl_2]\cdot 2H_2O$ were dissolved in 60 mL of ethanol and the mixture was heated under reflux with stirring for 2 h. Then the solution was evaporated to dryness, and the resulting solid was dissolved in a minimum amount of deionized water. A precipitation was formed by adding an excess of aqueous NH_4PF_6 to the solution. After filtration, the compound was purified over neutral alumina using CH_2Cl_2/CH_3OH (40:1, v/v) as the eluent. The major fraction, corresponding to the target complex, was evaporated to dryness to give dark red microcrystals. Yield: 270 mg (70%). ^{13}C NMR (CD_3CN): $\delta = 158.0$, 157.9, 157.8, 157.6, 156.7, 155.0, 153.8, 152.0, 151.8, 151.7, 151.6, 150.4, 150.0, 149.3, 137.1, 136.6, 136.4, 136.21, 136.18, 136.0, 127.31, 127.27, 126.9, 126.3, 124.0, 123.7, 123.4, 123.1, 122.1, 121.1, 119.7, 118.8, 102.6; HRMS ESI, *m*/*z*: $[M-PF_6]^+$. Calc. for $C_{33}H_{25}N_8Ru$: 635.1246. Measured: 635.1261. *Anal.* Calc. for $C_{33}H_{25}F_6N_8PRu\cdot CH_2Cl_2$: C, 47.23; H, 3.15; N, 12.96. Found: C, 47.29; H, 3.51; N, 13.24%.

2.2.2. *[Ru(bpy)$_2$(Clbpp)](PF$_6$) (**2**)*

This complex was prepared in a similar manner to complex **1** from 130 mg (0.25 mmol) of *cis*-$[Ru(bpy)_2Cl_2]\cdot 2H_2O$ with 64 mg (0.25 mmol) of ClHbpp. Yield: 138 mg (68%). ^{13}C NMR (CD_3CN): $\delta = 157.9$, 157.8, 157.7, 157.5, 155.6, 153.1, 152.0, 151.9, 151.7, 151.6, 150.9, 149.3, 149.0, 144.4, 137.2, 136.8, 136.6, 136.4, 136.3, 136.1, 127.4, 127.3, 127.0, 126.3, 124.0, 123.8, 123.5, 123.2, 122.7, 121.6, 121.3, 119.7, 106.1; HRMS ESI, *m*/*z*: $[M-PF_6]^+$ Calc. for $C_{33}H_{24}ClN_8Ru$: 669.0856. Measured: 669.0879. *Anal.* Calc. for $C_{33}H_{24}ClF_6N_8PRu\cdot CH_3COCH_3$: C, 49.58; H, 3.47; N, 12.85. Found: C, 49.20; H, 3.65; N, 12.75%.

2.2.3. *[Ru(bpy)$_2$(Brbpp)](PF$_6$) (**3**)*

This complex was prepared in a similar manner to complex **1** from 260 mg (0.5 mmol) of *cis*-$[Ru(bpy)_2Cl_2]\cdot 2H_2O$ with 150 mg (0.5 mmol) of BrHbpp. Yield: 320 mg (75%). ^{13}C NMR (CD_3CN): $\delta = 157.9$, 157.8, 157.7, 157.5, 155.9, 153.3, 152.0, 151.9, 151.64, 151.57, 151.0, 148.9, 145.4, 137.1, 136.8, 136.6, 136.4, 136.3, 136.1, 127.4, 127.3, 127.0, 126.3, 124.0, 123.8, 123.5, 123.2, 122.8, 121.8, 121.7, 119.9, 89.8; HRMS ESI, *m*/*z*: $[M-PF_6]^+$. Calc. for $C_{33}H_{24}BrN_8Ru$: 713.0351. Measured: 713.0371. *Anal.* Calc. for $C_{33}H_{24}BrF_6N_8P\ Ru\cdot CH_3COCH_3$: C, 47.17; H, 3.30; N, 12.22. Found: C, 46.94; H, 3.23; N, 12.29%.

2.2.4. *[Ru(bpy)$_2$(Ibpp)](PF$_6$) (**4**)*

120 mg (0.35 mmol) of IHbpp and 180 mg of (0.35 mmol) *cis*-$[Ru(bpy)_2Cl_2]\cdot 2H_2O$ were dissolved in 50 mL of ethanol, and the mixture was stirred for 18 h at 50 °C. After an excess aqueous solution of NH_4PF_6 was added, this solution was stirred for a few minutes and the resulting solution was diluted to 200 mL with water. The aqueous phase was extracted with dichloromethane (2 × 50 mL). The organic phase was evaporated to dryness, and the resulting solid was purified over neutral alumina using CH_2Cl_2/CH_3OH (40:1, v/v) as the eluent. The major fraction, corresponding to the target complex, was obtained as a dark red microcrystal after evaporating the solvent. Yield: 144 mg (46%). ^{13}C NMR (CD_3CN): $\delta = 157.8$, 157.74, 157.70, 157.5, 156.2, 154.1, 153.8, 151.9, 151.8, 151.6, 151.5, 151.1, 148.6, 147.6, 136.8, 136.6, 136.34, 136.29, 136.1, 127.39, 127.36, 127.0, 126.3, 124.1, 123.8, 123.5, 123.2, 123.0, 122.2, 121.8, 120.2, 53.7; HRMS ESI, *m*/*z*: $[M-PF_6]^+$. Calc. for $C_{33}H_{24}IN_8Ru$: 761.0212. Measured: 761.0185. *Anal.* Calc. for $C_{33}H_{24}$-

$F_6IN_8P\ Ru \cdot CH_3COCH_3$: C, 44.87; H, 3.14; N, 11.63. Found: C, 45.07; H, 3.29; N, 11.85%.

2.2.5. *[Ru(bpy)$_2$(NO$_2$bpp)](PF$_6$) (**5**)*

This complex was prepared in a similar manner to complex **1** from 130 mg (0.25 mmol) of *cis*-$[Ru(bpy)_2Cl_2] \cdot 2H_2O$ and 66 mg (0.25 mmol) of NO_2Hbpp. Yield: 160 mg (79%). ^{13}C NMR (CD_3CN): $\delta = 157.64$, 157.62, 157.57, 157.4, 154.1, 152.3, 152.1, 151.8, 151.7, 151.6, 151.5, 151.4, 149.2, 144.3, 137.5, 137.2, 137.0, 136.8, 136.7, 136.4, 131.5, 127.6, 127.5, 127.3, 126.5, 124.6, 124.2, 124.0, 123.6, 123.32, 123.31, 123.2, 123.0; HRMS ESI, *m/z*: $[M-PF_6]^+$. Calc. for $C_{33}H_{24}N_9O_2Ru$: 680.1096; Measured: 680.1116. *Anal.* Calc. for $C_{33}H_{24}F_6N_9\ O_2PRu$: C, 48.06; H, 2.93; N, 15.29. Found. C, 47.84; H, 3.02; N, 15.13%.

2.3. Instrumental methods

^1H and $\{^1H–^1H\}$COSY NMR spectra were recorded on a Varian INOVA spectrometer at 400 MHz and ^{13}C NMR spectra were recorded at 100 MHz. Chemical shifts are given in δ units relative to the tetramethylsilane (TMS) signal as an internal reference. High resolution mass spectra (HRMS) were provided by Q-TOF micro (Micromass Int., Manchester, England). Elemental analyses were carried out on a CARLO ERBA MOD-1106 elemental analyzer. UV–Vis absorption spectra were obtained on a HP8453 spectrophotometer with 1 cm quartz cells. Emission spectra were recorded using a FP-6500 spectrofluorometer with 1 cm quartz cells. Emission/excitation slit widths were 10 nm. The spectra were uncorrected for photomultiplier response. The quantum yields of the complexes at 298 K were determined by a relative method using $Ru(bpy)_3^{2+}$ in the same solvent as the standard. The quantum yields were calculated [9] using the following equation:

$$\varphi = \varphi_{std}(A_{std}/A)(I/I_{std})(\eta^2/\eta^2_{std}) \quad (1)$$

where φ and φ_{std} are the quantum yields of unknown and standard samples, A and A_{std} are the absorbances at the excitation wavelength and η and η_{std} are the refractive indices of the solutions. pK_a values were determined in Britton–Robinson buffer (0.04 M boric acid, 0.04 M acetic acid, 0.04 M phosphoric acid). The pH was adjusted by adding conc. NaOH or conc. H_2SO_4 and was measured using a pHS-25 pH meter. The pK_a values were calculated using custom-written non-linear least-squares curve-fitting programs implemented within SigmaPlot 2000 (SPSS Inc.).

Luminescence lifetime measurements were obtained using a LP920 Flash Photolysis Spectrophotometer. Samples were deaerated for 20 min using N_2 gas before the measurements were carried out. Cyclic voltammetric (CV) experiments were performed in a BAS-100W electrochemical potentiostat using a three electrode cell. A glassy carbon disk electrode (3 mm diameter) was used as the working electrode, a platinum wire was used as the auxiliary electrode and a non-aqueous Ag/Ag^+ electrode (0.01 M $AgNO_3$ in CH_3CN) was used as the reference electrode. All cyclic voltammograms presented in this work were recorded at a scan rate of 100 mV/s under an argon atmosphere and the complex concentration was approximately 1 mM. The complexes were dissolved in previously degassed CH_3CN solution containing 0.1 M Bu_4NPF_6 as a supporting electrolyte. The measured potentials in Table 4 were corrected to the value of SCE by adding 0.30 V. Ferrocene was used as an internal standard for the measurement. Under the experimental conditions used, the $E_{1/2}$

Table 1
Crystal data for complexes **2**–**5**

	2 · 1.5CH_3COCH_3	**3** · CH_3COCH_3	**4** · CH_3COCH_3	**5** · 2CH_3COCH_3
Empirical formula	$C_{37.50}H_{33}ClF_6N_8O_{1.50}PRu$	$C_{36}H_{30}BrF_6N_8OPRu$	$C_{36}H_{30}F_6IN_8OPRu$	$C_{39}H_{36}F_6N_9O_4PRu$
F_w (g mol^{-1})	901.21	916.63	963.62	940.81
Temperature (K)	180(2)	298(2)	180(2)	180(2)
λ(Mo Kα) (Å)	0.71073	0.71073	0.71073	0.71073
Symmetry	orthorhombic	orthorhombic	orthorhombic	triclinic
Space group	*Pbca*	*Pbca*	*Pbcn*	$P\bar{1}$
a (Å)	17.9199(8)	18.007(13)	13.1243(4)	12.3793(9)
b (Å)	17.4283(8)	17.489(13)	18.5460(6)	13.4334(5)
c (Å)	47.743(2)	46.97(3)	30.3816(9)	14.2207(5)
α (°)	90.00	90.00	90.00	113.938(2)
β (°)	90.00	90.00	90.00	101.559(2)
γ (°)	90.00	90.00	90.00	98.615(2)
V (Å^3)	14910.8(11)	14792(19)	7395.0(4)	2045.86(18)
Formula units/cell	16	16	8	2
Number of reflections collected	68710	29522	30160	16736
Independent reflections (R_{int})	0.0784	0.0884	0.0397	0.0221
Goodnes-of-fit F^2	1.142	1.039	1.036	1.095
Final R_1 [$I > 2\sigma(I)$]	0.0885	0.0562	0.0402	0.0372
Final R_1 (all data)	0.1030	0.0892	0.0540	0.0434

value of the ferrocene/ferrocenium couple, which has been corrected, was 0.43 V versus SCE.

2.4. X-ray crystallography

Each of the single crystals was obtained by slow diffusion of *n*-pentane into an acetone solution of the corresponding complexes **2**–**5**. Crystals **2**, **4** and **5** are highly sensitive to losing solvent immediately after removal from their mother liquor, so their measurements were performed at low temperature ($T = 180$ K). Measurements were collected on a Bruker SMART APEXII CCD equipped with Mo Kα radiation. Full-sphere data collection was used with ω and φ scans. Programs used: data collection, Smart V. 5.060 (Bruker AXS 1999); data reduction, Saint+ Version 6.02 (Bruker AXS 1999). Relevant experimental data are presented in Table 1. The structures were solved and refined with the SHELXTL-97 program [10] and the non-hydrogen atoms were refined with anisotropic thermal parameters.

3. Results and discussion

3.1. Preparation

The preparation of these complexes was carried out using standard procedures by the reaction of Hbpp and its derivatives with an equivalent amount of *cis*-$[Ru(bpy)_2Cl_2]$ at reflux [11–13]. In the case of complex **4**, however, the iodine atom on the ligand was found to be partially cleaved producing complex **1**, which was very difficult to separate from the target complex **4**. We optimised the reaction conditions and observed that when the reaction was carried out under mild conditions (at 50 °C for 18 h), no complex **1** was found as a byproduct, and complex **4** was obtained in a 46% yield. All these complexes have been purified by column chromatography. Furthermore, it is worth mentioning that complexes **1**–**5** are all obtained as monocations upon the addition of excess PF_6^-, which has been proved by their HRMS spectra and crystal structures. Therefore, we can conclude that the pyridylpyrazole ligands XHbpp deprotonate easily upon coordination to the metal centre to form $Xbpp^-$ and the valence state of ruthenium is Ru(II).

3.2. ^1H NMR spectra

The ^1H NMR and {H–H}COSY NMR spectra for complexes **1**–**5** have been recorded in CD_3CN solution at room temperature (see supporting information). The numbering scheme used to assign the observed resonances is given in Fig. 1.

Table 2 summarizes the spectral assignments made for complexes **1**–**5**. No complete assignment could be made, but by {H–H}COSY NMR spectra and comparison with the signals of the bipyridine complexes already described [11,14], the major part of the spectrum could be understood. The asymmetric nature of the complexes is evident from the occurrence of a fairly large number of resonances, parts of which are overlapped with each other. The COSY

Table 2
^1H NMR spectral data [a] for complexes **1**–**5** in CD_3CN

Proton [b]	1	2	3	4	5
Xbpp ligand					
3	7.84(d), 1H	8.37(d), 1H	8.59(d), 1H	8.85(d), 1H	8.65(d), 1H
4	7.75(t), 1H	7.83(t),1H	7.83(t), 1H	7.87–7.81(m), 1H	7.90–7.70(m), 1H
5	6.95(t), 1H	7.03(t), 1H	7.05(t), 1H	7.05(t),1H	7.16(t), 1H
6	7.43(d), 1H	7.51(d), 1H	7.53(d), 1H	7.54(d), 1H	7.65(d), 1H
3′	7.62(d), 1H	7.62(d), 1H	7.62(d), 1H	7.63–7.54(m), 1H	7.45–7.35(m), 1H
4′	7.54(t), 1H	7.62(d), 1H	7.62(d), 1H	7.63–7.54(m), 1H	7.68(t), 1H
5′	7.03(t), 1H	7.12(q), 1H	7.13(q), 1H	7.14(t), 1H	7.25–7.19, 1H
6′	8.43–8.39(m), 1H	8.49(d),1H	8.48(d), 1H	8.49(d), 1H	8.47–8.43(m), 1H
pzH_4	7.42(s), 1H				
bpy ligands					
3	8.43–8.39(m), 2H	8.43(t), 2H	8.43(t), 2H	8.43(t), 2H	8.47–8.43(m), 2H
	8.35(d), 1H	8.37(d), 2H	8.35(d), 2H	8.34(d), 2H	8.37(d), 1H
	8.30(d),1H				8.33(d), 1H
4	8.0–7.9(m), 1H	8.0–7.88(m), 4H	8.0–7.84(m), 4H	8.0–7.83(m), 4H	8.01–7.70(m), 4H
	7.89(t), 2H				
	7.81–7.76, 1H				
5	7.36–7.24(m), 4H	7.40(t), 1H	7.40–7.32(m), 3H	7.40–7.31(m), 3H	7.45–7.35(m), 3H
		7.36(t), 2H	7.25(t), 1H	7.24(t), 1H	7.25–7.19(m), 1H
		7.26(t), 1H			
6	8.0–7.9(m), 1H	8.0–7.88(m), 1H	8.0–7.84(m), 2H	8.0–7.83(m), 2H	8.01–7.70(m), 3H
	7.89(t), 1H	7.86(d), 1H	7.77(d), 1H	7.72(t), 2H	7.71(d), 1H
	7.81–7.76(m), 1H	7.79(d), 1H	7.74(d), 1H		
	7.69(d), 1H	7.74(d), 1H			

[a] For ^1H NMR data, respectively: chemical shift (ppm), number of protons.
[b] For proton numbering see Fig. 1.

spectra have been particularly useful in assigning the protons of the pyridine moiety of Xbpp bound to the metal as against the uncoordinated one. The chemical shifts of the protons on the coordinated pyridine ring are noticeably different from those observed for the uncoordinated pyridine of Xbpp, which is mainly caused by the changes in electron density of the ruthenium-bound pyridine ring. But for the H6 proton, the relative higher field shift with respect to the H6′ proton is mainly caused by the maximum diamagnetic shielding by the anisotropic ring current of the adjacent bipyridine rings as can be seen from the structure (see Fig. 1). According to the spectral assignments of complexes **1**–**5**, we can conclude the chemical shifts decrease in the order H3 > H4 > H6 > H5 for the coordinated pyridine ring; H6′ > H3′, H4′ > H5′ for the uncoordinated pyridine ring; H3 > H4, H6 > H5 for the bipyridine ligand. The observation that only H3 of the coordinated pyridine ring among all the protons of Xbpp, at δ 8.37 for **2**, 8.59 for **3**, 8.85 for **4** and 8.65 for **5**, is significantly down field-shifted relative to that of complex **1** (δ 7.84) is of considerable interest. Clearly, the H3 atom is the closest proton to the substituents in the pyrazole ring, which can be confirmed by their crystal structures, so that the electron density around the H3 atom is seriously decreased by their electron-withdrawing effect.

3.3. Crystal structures

ORTEP views of the cationic moieties of complexes **2**–**5** together with the labelling scheme are shown in Fig. 2. All the complexes co-crystallised with acetone molecules. The deprotonation of the pyrazole ring was confirmed by the presence of one PF_6 counter ion per ruthenium centre in the solid-state structures. Selected bond lengths and angles for these complexes are listed in Table 3. The N3–Ru1–N4 bite angles for **2** (78.5(4)°), **3** (77.7(4)°) and **4** (78.28(13)°) correspond well with the bite angle obtained for [Ru(bpy)$_2$(3,5-bis(pyridine-2-yl)-1,2,4-triazole)]PF_6 (78(1)°) [15], [Ru(bpy)$_2$(3-(pyrazin-2′-yl)-5-(pyridine-2″-yl)-1,2,4-triazole)]PF_6 (77.98(6)°) [12] and [Ru(bpy)$_2$(3-(pyrazin-2′-yl)-5-phenyl-1,2,4-triazole)]PF_6 (78.2(4)°) [14]. But for **5** this angle is 76.98(9)°, about 1° smaller than that of the other complexes, attributed to the relatively big steric effect of the nitro group on C7. The bite angles of 78.4(4)° and 78.8(4)° for **2**, 78.9(4)° and 79.0(5)° for **3**, 78.44(13)° and 78.81(14)° for **4**, 78.59(9)° and 78.87(9)°

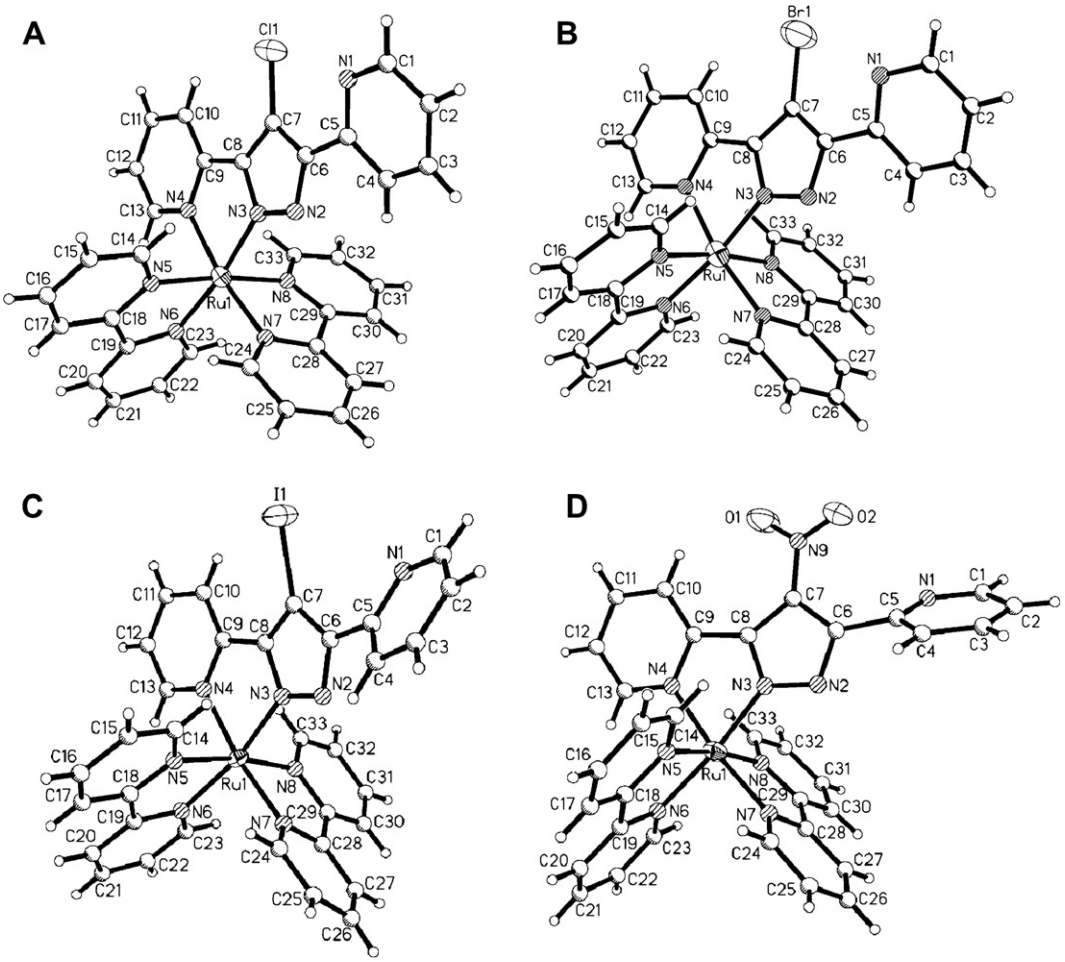


Fig. 2. X-ray structures (ORTEP plots with ellipsoids at the 50% probability level) and labelling scheme for (A) **2**, (B) **3**, (C) **4**, (D) **5**.

Table 3
Selected bond distances (Å) and angles (°) of complexes **2–5**

	2	3	4	5
Bond distances (Å)				
X–C7	1.741(1)	1.864(1)	2.070(4)	1.422(3)
Ru1–N3	2.037(9)	2.012(8)	2.031(3)	2.024(2)
Ru1–N4	2.075(1)	2.083(9)	2.080(3)	2.063(2)
Ru1–N5	2.039(9)	2.034(9)	2.049(3)	2.051(2)
Ru1–N6	2.045(1)	2.043(9)	2.064(3)	2.061(2)
Ru1–N7	2.041(9)	2.028(9)	2.052(3)	2.051(2)
Ru1–N8	2.044(1)	2.036(9)	2.032(3)	2.059(2)
Bond angles (°)				
N3–Ru1–N4	78.5(4)	77.7(4)	78.28(13)	76.98(9)
N3–Ru1–N5	96.4(4)	96.5(4)	93.88(13)	96.82(8)
N3–Ru1–N7	93.3(4)	94.1(4)	95.77(13)	97.24(9)
N3–Ru1–N8	88.2(4)	88.2(3)	92.66(13)	88.65(8)
N4–Ru1–N5	89.3(4)	91.2(3)	90.67(12)	91.43(8)
N4–Ru1–N6	95.5(4)	96.7(4)	94.42(12)	98.07(9)
N4–Ru1–N8	96.5(4)	95.4(4)	95.90(13)	96.31(9)
N5–Ru1–N6	78.4(4)	78.9(4)	78.44(13)	78.59(9)
N7–Ru1–N8	78.8(4)	79.0(5)	78.81(14)	78.87(9)

for **5** for the two bipyridine ligands are typical for this class of complexes. The Ru–N distances 2.037(9)–2.075(1) Å **2**, 2.012(8)–2.083(9) Å **3**, 2.031(3)–2.080(3) Å **4** and 2.024(2)–2.063(2) Å **5** are comparable to those found in other similar complexes [11–14]. Ru1–N4 is the longest and Ru1–N3 is the shortest Ru–N bond in all these complexes. The data show the substituents on the C7 have no obvious effect on the Ru–N distances. The uncoordinated pyridine ring shows a *trans* geometry, i.e., the uncoordinated pyridylic N1 atom is located at the opposite side of the coordinated pyridylic N4 atom, which coincides with the solid-state structure of the ligand Hbpp. The ligand Hbpp is generally planar with two dihedral angles, 3.14° and 9.61°, between one of the two pyridine rings and the central pyrazole pentagon [16]. Due to the existence of the substituents on the C7 in complexes **2–5**, the uncoordinated pyridine rings are twisted out of the plane of the central pyrazole (see Fig. 2). With the increase of the substituents' volume ($NO_2 > I > Br > Cl$), the extent of this twist is bigger, shown by the two dihedral angles: one between the uncoordinated pyridine ring and central pyrazole ring, the other between the coordinated pyridine ring and central pyrazole ring, 56.1° and 7.9° **5**, 38.1° and 8.5° **4**, 25.5° and 4.9° **3**, 15.6° and 1.8° **2**, respectively.

3.4. Electronic properties

The visible absorption and emission data obtained for complexes **1–5**, together with those for $[Ru(bpy)_3]^{2+}$, are listed in Table 4 (also see Fig. 3). The lowest energy absorption feature for these complexes is assigned to several overlapping $d\pi$–π^* transitions due to a series of singlet metal-to-ligand-charge-transfer (^{1}MLCT) transitions ($\log\varepsilon \sim 4$), involving both bpy and Xbpp ligands, by comparison with other ruthenium polypyridyl complexes [11,13,17]. For complex **1**, the absorption and emission maxima are red-shifted with respect to $[Ru(bpy)_3]^{2+}$, which is expected as the π-electron rich pyrazole containing ligand is a stronger σ-donor/weaker π-acceptor than 2,2′-bipyridine and destabilizes the filled metal d-orbitals and hence raises the energy of the ground state of the metal-based orbitals [13,17a]. Additionally, it can be concluded that the introduction of the substituents Cl, Br, I and NO_2 have a blue-shifted effect on the absorption and emission maxima of complex **1**, and among them the influence of NO_2 is the most, whilst Cl, Br and I are similar to each other. Obviously, the greater the electron-withdrawing strength of the substituent, the more the σ-donor ability of the pyrazole ring is reduced.

All the complexes examined are luminescent in the region of 665–715 nm in acetonitrile at room temperature, typical for a ^{3}MLCT emission [11]. The emission lifetimes and quantum yields of these complexes are also listed in Table 4. The emission decay for **1** is double exponential in nature with lifetimes of 44 ns (16%) and 372 ns (84%) (see Fig. 5), but upon the introduction of the Cl, Br, I and NO_2 groups to **1**, an approximate 300 ns decrease in

Table 4
Spectroscopic and electrochemical data for complexes **1–5** and references

Compound	Abs.[a] λ_{max}/nm ($\log\varepsilon$)	Emission[a]/nm ($10^3\varphi$)	Lifetime[b] (ns)	Oxidation[c]	Reduction[c]
				$E_{1/2}$/V(ΔE_p/mV)	$E_{1/2}$/ V
$Ru(bpy)_3^{2+}$	452(4.18)	608(62) [d]	885	1.34(87)	−1.28, −1.46, −1.71
$[Ru(bpy)_2(bpp)]^+$ (**1**)	494(4.05), 447(3.97)	715(3.2)	$\tau_1 = 44(16\%)$ $\tau_2 = 372(84\%)$	0.73(72)	−1.45, −1.71
$[Ru(bpy)_2(Clbpp)]^+$ (**2**)	486(3.95), 440(3.87)	697(3.4)	80	0.80(62)	−1.44, −1.69
$[Ru(bpy)_2(Brbpp)]^+$ (**3**)	487(4.12), 443(4.05)	700(3.9)	70	0.79(72)	−1.44, −1.69
$[Ru(bpy)_2(Ibpp)]^+$ (**4**)	488(4.08), 444(4.02)	702(3.2)	60	0.78(82)	−1.46, −1.69
$[Ru(bpy)_2(NO_2bpp)]^+$ (**5**)	472(4.21)	665(4.8)	70	0.96(78)	−1.49, −1.58(irr), −1.71

[a] All the measurements were made in CH_3CN at 298 K.
[b] Lifetimes measured in deaerated CH_3CN at 298 K.
[c] All redox potentials are measured in 0.1 M $TBAPF_6$–CH_3CN, 100 mV s^{-1} scan rate and corrected relative to SCE.
[d] Value obtained from Ref. [9].

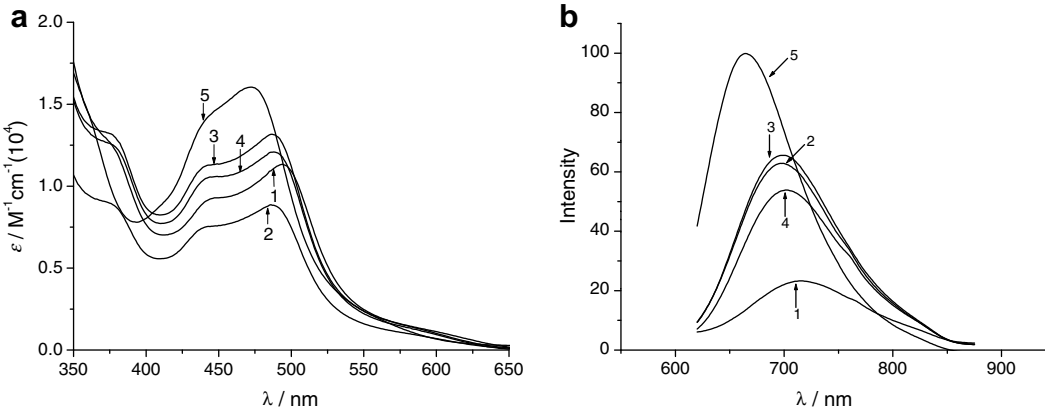


Fig. 3. UV–Vis and emission spectra for complex **1**–**5** (5×10^{-5} M) in CH_3CN at room temperature.

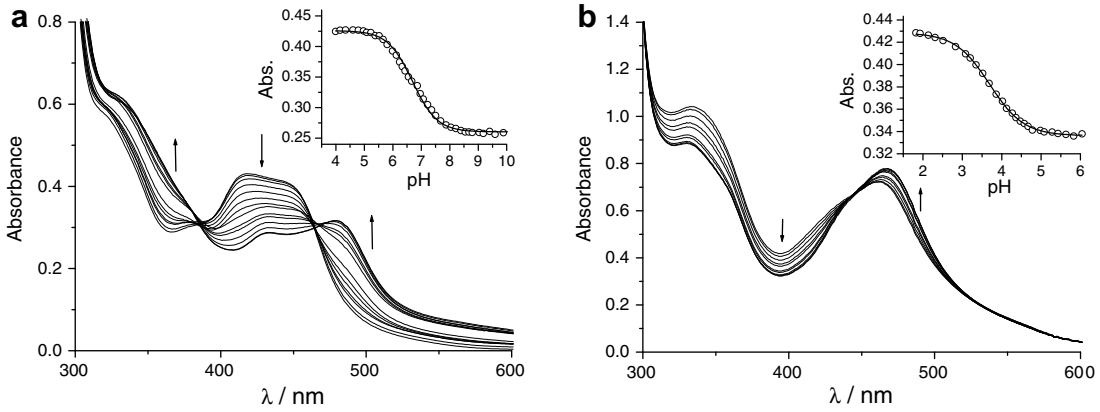


Fig. 4. Changes in the UV–Vis spectra of (a) **1** (5×10^{-5} M) as the pH is varied from 3.99 to 9.88 and (b) **5** (5×10^{-5} M) as the pH is varied from 1.82 to 6.04 in an aqueous Britton–Robinson buffer. The arrows indicate an increase or decrease in band intensity with increasing pH. The insets show the variation of absorbance with pH (418 nm for **1** and 400 nm for **5**).

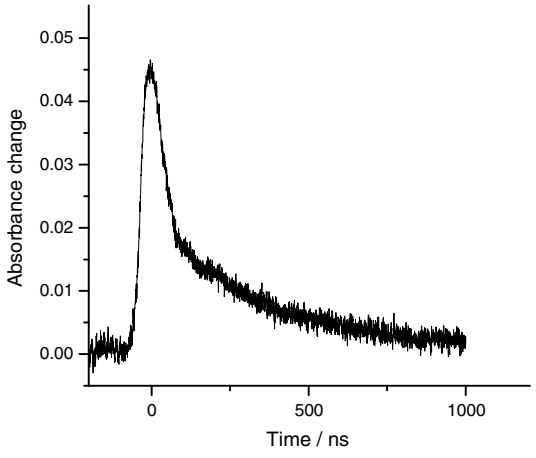


Fig. 5. Kinetic trace for time-resolved emission of complex **1** (50 μM) at 715 nm measured in CH_3CN.

the emission lifetime is observed. This suggests that there is a significant quenching by the substituents Cl, Br, I and NO_2 in the ligands (see Fig. 5).

3.5. Acid–base properties

Complexes **1**–**5** have two sites that can be protonated. One is the uncoordinated pyridylic nitrogen and the other is the pyrazolylic nitrogen on the corresponding $Xbpp^-$ ligand. Therefore, the pK_a values of complexes **1**–**5** can be determined by spectrophotometric acid–base titrations. As expected, the titrations in aqueous Britton–Robinson buffers result in a shift of the lowest energy MLCT band from 418 to 480 nm for **1**, 421 to 474 nm for **2**, 422 to 474 nm for **3**, 422 to 475 nm for **4** and from 460 to 468 nm for **5**. Similar behaviour has been observed for a series of complexes containing imidazole, 1,2,4-triazole and pyrazole moieties and was explained by the increased π-donor capacity of the deprotonated ligand [9,12,17]. According to the pK_a values of those Hbpp containing Ru(II) complexes reported previously [18], the pK_a values at 6.69 ± 0.02 ($R = 0.996$) for **1** (see Fig. 4a, inset), 5.47 ± 0.01 ($R = 0.999$) for **2**, 5.57 ± 0.02 ($R = 0.999$) for **3**, 5.65 ± 0.02 ($R = 0.999$) for **4** (see supporting information) and 3.69 ± 0.01 ($R = 0.999$) for **5** (see Fig. 4b, inset), revealed from the plot of absorbance versus pH, were

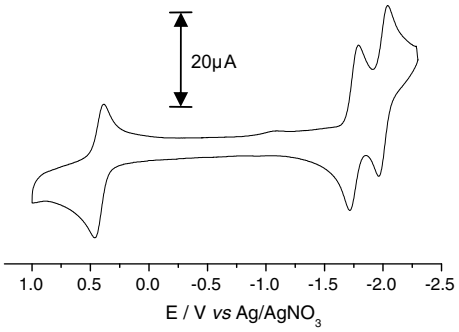


Fig. 6. Cyclic voltammograms of complex **1** (1 mM) in CH_3CN.

assigned to the protonation/deprotonation of the pyrazole moiety as indicated as follows:

$$[Ru(bpy)_2(Xbpp)]^+ \underset{-H^+}{\overset{+H^+}{\rightleftarrows}} [Ru(bpy)_2(XHbpp)]^{2+} \quad (2)$$

With the increase of the electron withdrawing ability of the substituent, the corresponding pK_a value decreased gradually. A comparison of the pK_a values of **5** and **1** showed that the pyrazole ring became more acidic by 3.0 pH units in the presence of the nitro group, which is a strong electron-withdrawing group. As expected, within this framework the pK_a values indicate that the substituents' effect on the acid–base properties of the complexes are substantial. The pK_a values for the protonation/deprotonation of the uncoordinated pyridine moiety in both **1**–**5** were not well determined in the pH range of 1.8–11.

3.6. Electrochemical properties

The redox properties of complexes **1**–**5** have been studied in acetonitrile and the relevant electrochemical data are presented together with $Ru(bpy)_3{}^{2+}$ in Table 4. For each of the complexes a single reversible wave was observed at low oxidation potentials which was assigned to the Ru^{II}/Ru^{III} couple. The metal oxidation potential (0.73 V) for complex **1** (see Fig. 6) is considerably lower than that for $[Ru(bpy)_3]^{2+}$ (1.34 V), owing to the stronger σ-donating pyrazoles. The influences of the substituents Cl, Br and I to the Ru^{II}/Ru^{III} couple are similar and are approximately 50–70 mV higher than that of complex **1**. For **5**, the oxidation wave is observed at a higher potential, 0.96 V (versus SCE), arising from the stronger electron-withdrawing effect of the NO_2 group. All these five complexes undergo two one-electron reversible reductions, similar to those of $[Ru(bpy)_3]^{2+}$, suggesting they are bipyridine-based reductions [11]. In addition, for **5** there is an irreversible reduction peak of the nitro group at −1.58 V (versus SCE).

4. Conclusion

The synthesis, structural, electronic and electrochemical characterization of a new series of $Ru(bpy)_2$ complexes based on the ligand Hbpp are reported. The data presented above indicate that 3,5-bis(2-pyridyl)-1*H*-pyrazole (Hbpp) is a much stronger σ-donor ligand than 2,2′-bipyridine (bpy). On the other hand, the introduction of different substituents such as Cl, Br, I or NO_2 groups to the central pyrazole ring can decrease the ligands σ-donating strength and thereby influence the physico-chemical properties of those complexes to a certain degree. Among them, the effect of the NO_2 group is most obvious and the others complexes with Cl, Br and I show similar properties. The overall effects of these electron-withdrawing groups are in the expected order, making the absorption and emission maxima of complex $[Ru(bpy)_2(bpp)]^+$ (**1**) blue-shifted, the oxidation potential of Ru^{II}/Ru^{III} couple increased and the pK_a value decreased accordingly. In addition, a significant quenching by these groups to the emission of complex $[Ru(bpy)_2(bpp)]^+$ (**1**) was also observed, but the mechanism need to be further investigated. With the relative longer lifetime of 372 ns and the strong absorption in the visible region for complex **1**, it can be potentially used as a photosensitizer to realize light-induced electron transfer to donor–acceptor systems.

Acknowledgements

The authors are grateful to the Natural Science Foundation of China (No. 20633020 and 20672017), the Program of Introducing Talents of Discipline to Universities, the Swedish Research council, the Swedish Energy Agency and K&A Wallenberg Foundation for financial support.

Appendix A. Supplementary data

CCDC 631283, 631284, 631285, 631286 contain the supplementary crystallographic data for **2**, **3**, **4**, **5**. These data can be obtained free of charge via http://www.ccdc.cam.ac.uk/conts/retrieving.html, or from the Cambridge Crystallographic Data Centre, 12 Union Road, Cambridge CB2 1EZ, UK; fax: (+44) 1223-336-033; or e-mail:deposit@ccdc.cam.ac.uk. Supplementary data associated with this article can be found, in the online version, at doi:10.1016/j.poly.2007.12.023.

References

[1] (a) T.J. Mayer, Acc. Chem. Res. 22 (1989) 163;
(b) L. De Cola, P. Belser, Coord. Chem. Rev. 177 (1998) 301;
(c) M.J. Blanco, M.C. Jiménez, J.C. Chambron, V. Heitz, M. Linke, J.P. Sauvage, Chem. Soc. Rev. 28 (1999) 293.
[2] (a) V. Balzani, F. Scandola, Supramolecular Photochemistry, Ellis Horwood, Chichester, 1991;
(b) V. Balzani (Ed.), Supramolecular Photochemistry, Reidel, Dordrecht, 1997.
[3] H. Dürr, S. Bossmann, Acc. Chem. Rev. 34 (2001) 905.
[4] P.R. Rich, Faraday Discuss., Chem. Soc. 75 (1982) 349.
[5] V.J. Catalano, T.J. Craig, Inorg. Chem. 42 (2003) 321.
[6] V.J. Catalano, R.A. Heck, C.E. Immoos, A. Ohman, M. Hill, Inorg. Chem. 37 (1998) 2150.
[7] (a) P.W. Ball, A.B. Blake, J. Chem. Soc. A (1969) 1415;
(b) F. Teixidor, R. Garcia, J. Pons, J. Casabu, Polyhedron 71 (1988) 43.

[8] W. Zhang, J. Liu, K. Jin, L. Sun, J. Heterocyclic Chem. 43 (2006) 1669.
[9] B.P. Sullivan, D.J. Salmon, T.J. Meyer, Inorg. Chem. 17 (1978) 3334.
[10] SHELXS-97 (Sheldrick, 1990) and SHELXL-97 (Sheldrick, 1997), University of Göttingen, Göttingen 1997.
[11] W.R. Browne, C.M. O'Connor, H.P. Hughes, R. Hage, O. Walter, M. Doering, J.F. Gallagher, J.G. Vos, J. Chem. Soc., Dalton Trans. (2002) 4048.
[12] W.R. Browne, D. Hesek, J.F. Gallagher, J.G. Vos, J. Chem. Soc., Dalton Trans. (2003) 2597.
[13] P. Passaniti, W.R. Browne, C. Lynch, D. Hughes, M. Nieuwenhuyzen, P. James, M. Maestri, J.G. Vos, J. Chem. Soc., Dalton Trans. (2002) 1740.
[14] P. Belser, A.V. Zelewsky, Helv. Chim. Acta 63 (1980) 1675.
[15] R. Hage, R.A.G. de Graaff, J.G. Haasnoot, J.P. Turkenburg, J.G. Vos, Acta Crystallogr., Sect. C 45 (1989) 381.
[16] W.S. Yu, C.C. Cheng, Y.M. Cheng, P.C. Wu, Y.H. Song, Y. Chi, P.T. Chou, J. Am. Chem. Soc. 125 (2003) 10800.
[17] (a) R. Hage, A.H.J. Dijkhuis, J.G. Haasnoot, R. Prins, J. Reedijk, B.E. Buchanan, J.G. Vos, Inorg. Chem. 27 (1988) 2185;
(b) R. Hage, J.G. Haasnoot, H.A. Nieuwenhuis, J. Reedijk, D.J.A. De Ridder, J.G. Vos, J. Am. Chem. Soc. 112 (1990) 9245;
(c) L. O'Brien, M. Duati, S. Rau, A.L. Guckian, T.E. Keyes, N.M. O'Boyle, A. Serr, H. Görls, J.G. Vos, J. Chem. Soc., Dalton Trans. (2004) 514.
[18] C. Sens, M. Rodriguez, I. Romero, A. Llobet, Inorg. Chem. 42 (2003) 8385.

state. So far, various ligands, such bipyridine-type and biphenyl cyanide-type ligands, have been used for supramolecular building blocks [12–14]. The affinity of Ag^+ for N-donor ligands is well known. The ligand 1,4-bis(4,5-dihydro-2-oxazolyl)benzene act as bidentate bridging ligand, which may adopts two different forms, namely syn and anti conformation (Fig. 1). The 1,4-bis(4,5-dihydro-2-oxazolyl)benzene ligands in complexes **1**–**4** adopt the different conformations, syn and anti, where syn and anti indicate the relative positions of the nitrogen atoms of the oxazolyl groups. In this paper, the syntheses and structures of Ag(I) complexes of the types $[Ag_2(\mathbf{L})(CH_3COO)_2]_\infty$ (**1**), $[Ag_2(\mathbf{L})_3(ClO_4)_2]_\infty$ (**2**), $[Ag(\mathbf{L})(CF_3SO_3)]_\infty$ (**3**), and $\{[Ag_2(\mathbf{L})_3(H_2O)_3][SO_4]\cdot 9H_2O\}_\infty$ (**4**), form the subject of this report.

2. Experimental

2.1. General procedures

All manipulations were carried out under dry, oxygen-free nitrogen by using Schlenk techniques, unless otherwise noted. Solvents were dried and deoxygenated by refluxing over the appropriate reagents before use. Elemental analyses were obtained from a PE 2400 series II CHNS/O analyzer. IR spectra (KBr disk) were recorded on a Jasco FT/IR-460 plus spectrometer.

2.2. Materials

The reagent 1,4-bis(4,5-dihydro-2-oxazolyl)benzene was purchased from T.C.I. Chemical Co., silver acetate from Wako Chemical Co., silver sulfate from Aldrich Chemical Co. and silver perchlorate and silver trifluoromethane sulfonate from Strem Chemical Co.

Caution: Perchlorate salts are dangerous (especially if they are dry) and should be handled with care.

2.2.1. Preparation of complex *1*

1,4-Bis(4,5-dihydro-2-oxazolyl)benzene (0.216 g, 1 mmol) in 5 ml MeOH was layered onto a solution of $AgCH_3CO_2$ (0.XX g, 0.10 mmol) in 5 ml H_2O. The resulting solution was slowly diffused for several weeks to give colorless crystal. Yield: 0.407 g (74%). *Anal.* Calc. for $C_{16}H_{18}Ag_2N_2O_6$ (MW = 550.06): C, 34.93; H, 3.29; N, 5.09. Found: C, 34.90; H, 3.29; N, 5.12%. IR (cm^{-1}): 3434(m), 1637(m), 1564(m), 1513(m), 1467(m), 1407(m), 1364(m), 1322(m), 1256(m), 1205(m), 1190(m), 1119(m), 1098(m) 1080(m), 1015(m), 973(m), 938(m), 895(m), 869(m), 688(m).

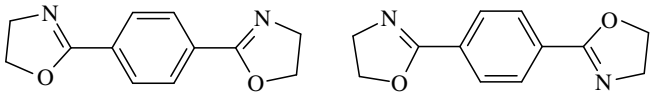


Fig. 1. Possible conformations, syn-(left) and anti-(right), for the 1,4-bis(4,5-dihydro-2-oxazolyl)benzene ligand.

2.2.2. Preparation of complex *2*

Was prepared as for **1**. Yield: 0.414 g (78%). *Anal.* Calc. for $C_{18}H_{18}AgClN_3O_7$ (MW = 531.67): C, 40.66; H, 3.41; N, 7.90. Found: C, 40.68; H, 3.40; N, 7.87%. IR (cm^{-1}): 3498(br), 3048(m), 2982(m), 2933(m), 2912(m), 2877(m), 1637(w), 1512(m), 1478(m), 1407(m), 1365(m), 1324(m), 1256(m) 1143(m), 1081(m), 1071(m), 947(m), 940(m), 896(m), 869(m), 856(m), 688(m), 627(m).

2.2.3. Preparation of complex *3*

Was prepared as for **1**. Yield: 0.395 g (68%). *Anal.* Calc. for $C_{19}H_{18}AgF_3N_3O_6S$ (MW = 581.29): C, 39.25; H, 3.12; N, 7.22. Found: C, 39.22; H, 3.13; N, 7.25%. IR (cm^{-1}): 3447(br), 3048(m), 2978(m), 2932(m), 2875(m), 1642(m), 1514(m), 1476(m), 1413(m), 1364(m), 1322(s), 1256(m), 1176(m) 1118(w), 1081(m), 1035(m), 1017(m), 973(m), 942(m), 896(m) 687(m), 6511(m), 518(m).

2.2.4. Preparation of complex *4*

Was prepared as for **1**. Yield: 0.835 g (71%). *Anal.* Calc. for $C_{36}H_{60}Ag_2N_6O_{22}S$ (MW = 1176.69): C, 36.74; H, 5.14; N, 7.14. Found: C, 36.70; H, 5.10; N, 7.15%. IR (cm^{-1}): 3435(br), 2847(m), 1638(m), 1580(m), 1490(m), 1436(m), 1313(m), 1259(m), 1201(m), 1119(m), 1075(m), 995(m), 944(m), 829(s), 619(m).

2.2.5. X-ray crystallography

The diffraction data of **1**–**4** were collected on a Siemens CCD diffractometer, which were equipped with a graphite-monochromated Mo Kα ($\lambda_\alpha = 0.71073$ Å) radiation. Data reduction was carried by standard methods with use of well-established computational procedures [15]. A colorless crystal of **1** was mounted on the top of a glass fiber with epoxy cement. ω data collection method was used to scan the data points at $4.50° \leqslant 2\theta \leqslant 52.24°$. The structure factors were obtained after Lorentz and polarization correction. The positions of some of the heavier atoms, including the silver atom, were located by the direct method. The remaining atoms were found in a series of alternating difference Fourier maps and least-square refinements [16]. The final residuals of the final refinement were $R_1 = 0.0529$ and $wR_2 = 0.1799$. The crystallographic procedures for the other complexes were similar to those for **1**. Basic information pertaining to crystal parameters and structure refinement are summarized in Table 1. Selected bond distances and angles are listed in Table 2.

3. Results and discussions

3.1. Syntheses

Complexes of the type $[Ag_2(\mathbf{L})(CH_3COO)_2]_\infty$ (**1**), $[Ag_2(\mathbf{L})_3(ClO_4)_2]_\infty$ (**2**), $[Ag(\mathbf{L})(CF_3SO_3)]_\infty$ (**3**), and $\{[Ag_2(\mathbf{L})_3(H_2O)_3][SO_4]\cdot 9H_2O\}_\infty$ (**4**) (**L** = 1,4-bis(4,5-dihydro-2-oxazolyl)benzene) were prepared by reactions of AgX (X = CH_3COO^-, **1**, ClO_4^-, **2**, $CF_3SO_3^-$, **3** and $1/2SO_4^{2-}$, **4**) with 1,4-bis(4,5-dihydro-2-oxazolyl)benzene in

Table 1
Crystal data and structure refinement for complexes **1**–**4**

Complex	**1**	**2**	**3**	**4**
Formula	$C_{16}H_{18}Ag_2N_2O_6$	$C_{18}H_{18}AgClN_3O_7$	$C_{19}H_{18}AgF_3N_3O_6S$	$C_{36}H_{60}Ag_2N_6O_{22}S$
Formula weight	550.06	531.67	581.29	1176.70
Crystal system	triclinic	monoclinic	monoclinic	rhombohedral
Space group	$P\bar{1}$	$P2_1/c$	$P2_1/c$	R-3
a (Å)	5.441(3)	10.1626(11)	10.3714(8)	9.2823(5)
b (Å)	8.743(5)	13.5816(11)	14.1523(11)	9.2823(5)
c (Å)	9.258(5)	14.6658(19)	15.0270(11)	48.735(4)
α (°)	81.143(11)	90	90	90
β (°)	80.835(10)	102.428(8)	100.9560(10)	90
γ°	86.545(11)	90	90	120
V (Å^3)	429.3(4)	1976.8(4)	2165.4(3)	3636.5(4)
Z	1	4	4	3
D_{calc} (g/cm^3)	2.127	1.786	1.783	1.587
$F(000)$	270	1068	1164	1782
Crystal size (mm)	0.33 × 0.31 × 0.21	0.45 × 0.22 × 0.20	0.51 × 0.45 × 0.28	0.61 × 0.55 × 0.24
μ (Mo Kα) (mm^{-1})	2.317	1.202	1.095	0.932
Range(2θ) for data collection (°)	$4.50 \leqslant 2\theta \leqslant 52.24$	$4.10 \leqslant 2\theta \leqslant 55.00$	$3.98 \leqslant 2\theta \leqslant 56.56$	$5.02 \leqslant 2\theta \leqslant 52.00$
Temperature (°C)	22	22	22	22
Reflections collected	2346	5730	13 520	6825
Data/restraints/parameters	1656/0/127	4527/0/271	5225/0/377	1595/0/114
Quality-of-fit indicator[c]	1.302	1.028	1.302	1.563
Final R indices $[I > 2\sigma(I)]$[a,b]	$R_1 = 0.0529$, $wR_2 = 0.1799$	$R_1 = 0.0412$, $wR_2 = 0.0913$	$R_1 = 0.0426$, $wR_2 = 0.1426$	$R_1 = 0.0342$, $wR_2 = 0.1244$
R indices (all data)	$R_1 = 0.0546$, $wR_2 = 0.1812$	$R_1 = 0.0718$, $wR_2 = 0.1034$	$R_1 = 0.0499$, $wR_2 = 0.1483$	$R_1 = 0.0349$, $wR_2 = 0.1254$
Largest difference in peak and hole (e/Å^3)	1.181 and −1.050	0.419 and −0.399	0.802 and −0.770	0.823 and −0.473

[a] $R_1 = \sum||F_o| - |F_c||/\sum|F_o|$.
[b] $wR_2 = [\sum w(F_o^2 - F_c^2)^2/\sum w(F_o^2)^2]^{1/2}$. $w = 1/[\sigma^2(F_o^2) + (ap)^2 + (bp)]$, $p = [\max(F_o^2 \text{ or } 0) + 2(F_c^2)]/3$. $a = 0.0000$, $b = 1.9076$ for **1**; $a = 0.0000$, $b = 1.9076$ for **2**; $a = 0.0850$, $b = 0.0000$ for **3**; $a = 0.0750$, $b = 0.0000$ for **4**.
[c] Quality-of-fit $= [\sum w(|F_o^2| - |F_c^2|)^2/N_{observed} - N_{parameters}]^{1/2}$.

Table 2
Selected bond distances (Å) and angles (°) for complexes **1**–**4**

Complex ***1***[a]			
Ag(1)–N(3)	2.159(3)	Ag(1)–N(1)	2.174(3)
Ag(1)–N(2A)	2.466(3)		
N(3)–Ag(1)–N(1)	158.29(11)	N(3)–Ag(1)–N(2A)	106.78(11)
N(1)–Ag(1)–N(2A)	93.70(11)		
Complex ***2***[a]			
Ag(1)–N(3)	2.159(3)	Ag(1)–N(1)	2.174(3)
Ag(1)–N(2A)	2.466(3)		
N(3)–Ag(1)–N(1)	158.29(11)	N(3)–Ag(1)–N(2A)	106.78(11)
N(1)–Ag(1)–N(2A)	93.70(11)		
Complex ***3***[b]			
Ag–N(3)	2.162(3)	Ag–N(1)	2.175(3)
Ag–N(2A)	2.492(3)		
N(3)–Ag–N(1)	154.78(10)	N(3)–Ag–N(2)#1	109.11(9)
N(1)–Ag–N(2A)	95.57(10)		
Complex ***4***[c]			
Ag–N(A)	2.293(2)	Ag–N	2.293(2)
N(A)–Ag–N	119.411(14)	N(A)–Ag–N(B)	119.411(14)

[a] Symmetry transformations used to generate equivalent atoms: (A) $-x$, $y - 1/2$, $-z + 1/2$.
[b] Symmetry transformations used to generate equivalent atoms: (A) $-x - 1/2$, y, $z + 1/2$.
[c] Symmetry transformations used to generate equivalent atoms: (A) $-x-1/2$, y, $z + 1/2$; (B) $-y + 1$, $x - y$, z.

MeOH/H_2O. Crystals suitable for X-ray diffraction studies were obtained by **L** in methanolic solution was layered onto a solution of AgX (X = CH_3COO^-, **1**, ClO_4^-, **2**, $CF_3SO_3^-$, **3** and $1/2SO_4^{2-}$, **4**) in H_2O. All these complexes were structurally characterized by X-ray crystallography. Complexes **1**–**4** were insoluble in most organic solvents, such as methanol, ethanol, chloroform, benzene, toluene, dichloromethane, acetone, acetonitrile, THF but soluble in DMSO or DMF.

3.1.1. Structure of *1*

The structure of complex **1** was solved in the space group $P\bar{1}$ and Fig. 2 shows the local coordination of the silver center atom in **1**. Table 2 list the selected bond distances and angles around Ag for complex **1**. The silver metal center adopts a slightly distorted tetrahedral coordination geometry. The Ag atom is bonded to one 4,5-dihydro-2-oxazolyl nitrogen atoms (Ag–N = 2.329(5) Å) and three acetate oxygen atoms (Ag–O = 2.289(4), 2.297(4) and 2.460(4) Å) from three different bridging acetate anions. The ligands in complex **1** are almost flat with the dihedral angle between two 4,5-dihydro-2-oxazolyl rings is 0°, while the dihedral angle between the 4,5-dihydro-2-oxazolyl and the phenyl rings is 7.4°.

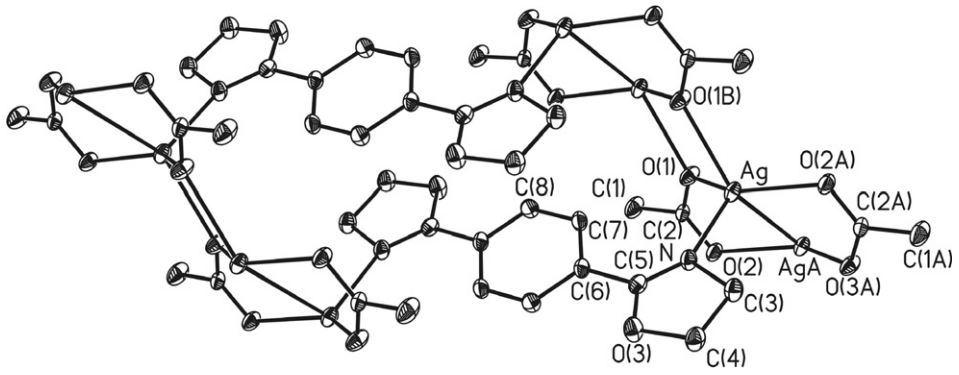


Fig. 2. An ORTEP drawing showing the coordination geometry of the silver metal center of complex **1**.

Complex **1** forms a 2-D pleated coordination polymeric framework, viewing down the *b*-axis (Fig. 3, bottom). Along the *a*-axis, the Ag atoms are linked by the η^1, η^2, μ_3-acetate anions form a 1-D waving $\{Ag_2(OAc)_2\}$ chains which the Ag–Ag separation in the $Ag_2(OAc)_2$ core is 2.985(3) Å and the distance between the cores is 3.698 Å (Fig. 3, top). The acetate anions bridging the silver atoms form an eight-member ring $\{Ag_2O_4C_2\}$, while a four-member ring $\{Ag_2O_2\}$ is formed by two oxygen atoms from the η^2-acetate anions and two silver atoms from two different $Ag_2(OAc)_2$ cores. The dihedral angle between the $\{Ag_2O_4C_2\}$ and $\{Ag_2O_2\}$ rings in 1-D waving chain is

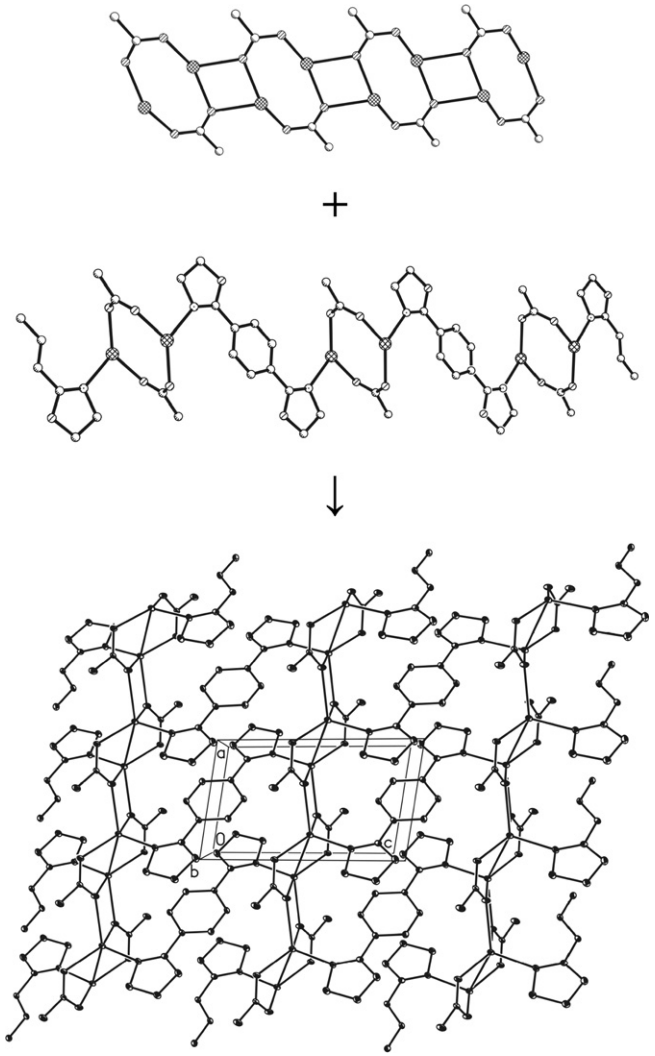


Fig. 3. ORTEP drawings for **1**, showing the waving $\{Ag_2(OAc)_2\}$ chain, top, zig-zag $\{Ag_2(OAc)_2(\mathbf{L})\}$ chain, middle, and the 2-D pleated net, bottom.

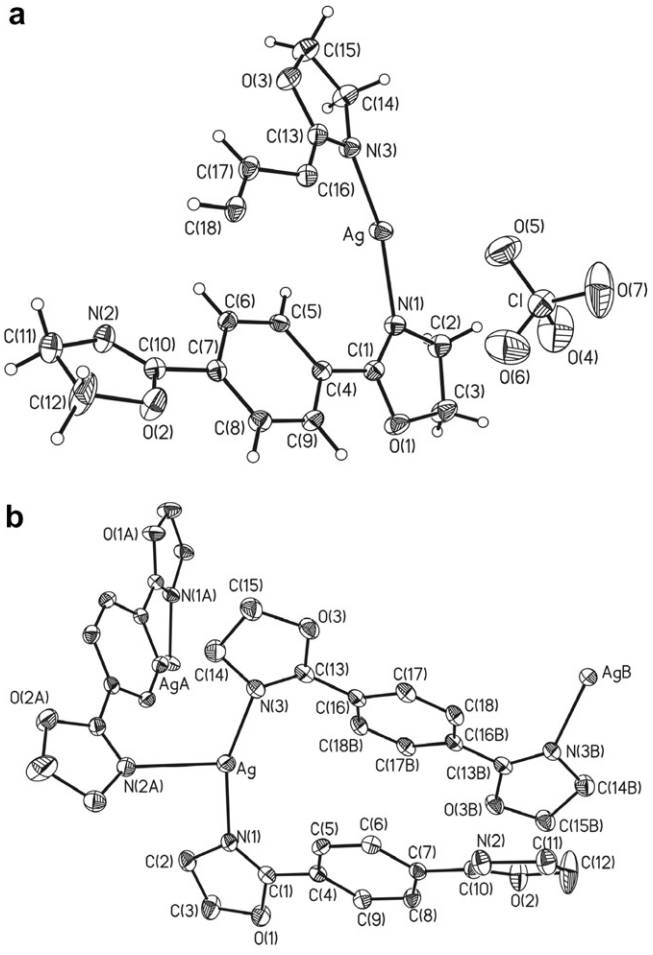


Fig. 4. (a) An ORTEP drawing for the representative asymmetric unit of complexes **2** and **3**. (b) Representative ORTEP diagram showing the coordination arrangement around Ag(I) center of complexes **2** and **3**.

24.0°. Along the *c*-axis, the 1-D zig-zag $\{Ag_2(OAc)_2$ (**L**)$\}$ chains formed by $Ag_2(OAc)_2$ cores and the anti-type bridging ligand, which the Ag–Ag distance in zig-zag chain separated by the bridging **L** is 9.774 Å (Fig. 3, middle) Two anti-type ligands link two $Ag_2(OAc)_2$ cores and two silver atoms into a $\{Ag_6C_{12}N_4O_2\}$ 24-member ring.

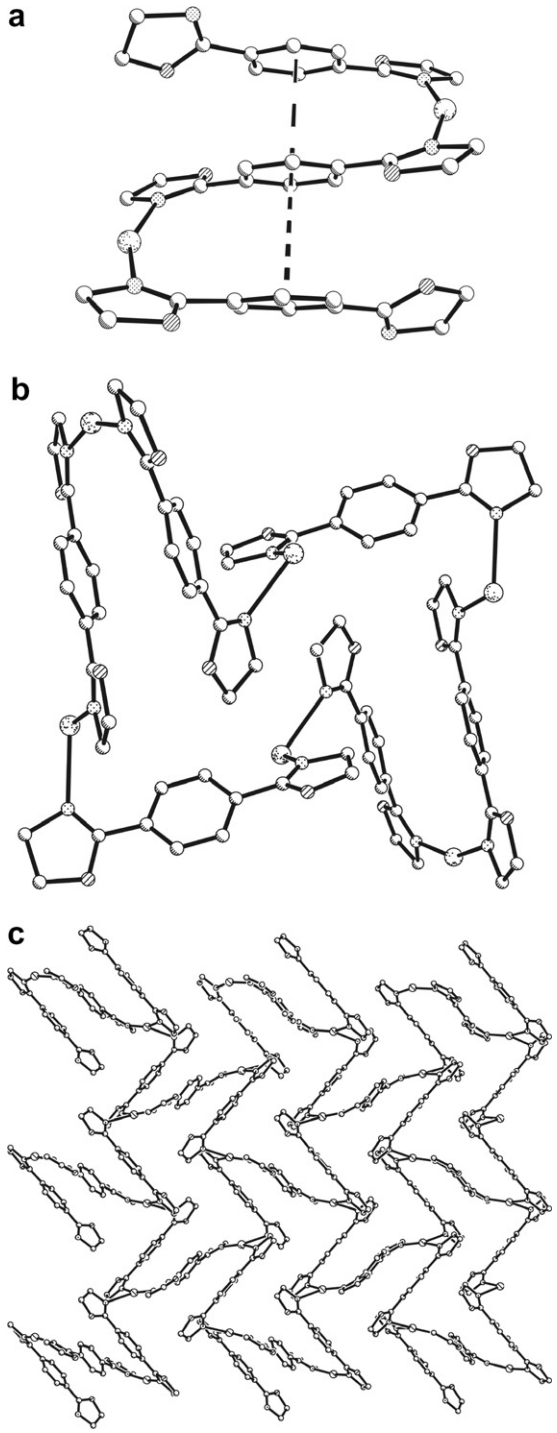


Fig. 5. (a) ORTEP drawing showing the Z-shape building unit in complexes **2** and **3**. (b) Two different conformation ligands form the $\{Ag(L)\}_6$ 54-member ring. (c) Packing diagram showing the cationic 2-D layer for complexes **2** and **3**.

The $\{Ag_6C_{12}N_4O_2\}$ 24-member rings are further extended into a 2-D pleated net, by sharing $Ag_2(OAc)_2$ joints and **L** edges. The complex shows the distorted rectangular pores (5.441×9.774 Å^2), which the length is defined by the distance between Ag(I) atoms linking through **L** ligands and the width is defined by the distance between Ag(I) atoms linking through the η^1, η^2, μ_3-bridging acetate anions.

3.1.2. Structures of 2 and 3

Complexes **2** and **3** are isomorphous and were solved in the same space group $P2_1/c$. Fig. 4a shows a representative asymmetric unit ORTEP diagram for **2**, which containing one silver atom, one and half 1,4-bis(4,5-dihydro-2-oxazol-yl)benzene ligands and an uncoordinated perchlorate anion. The structure of **3** is similar to that of **2** where the ClO_4^- anion is replaced by $CF_3SO_3^-$ anion. Fig. 4b showing the silver metal center is coordinated to three nitrogen atoms from three different 1,4-bis(4,5-dihydro-2-oxazol-yl)benzene ligands (Ag–N(1) = 2.176(3) Å for **2** and 2.175(3) Å for **3**; Ag–N(2A) = 2.466(3) Å for **2** and

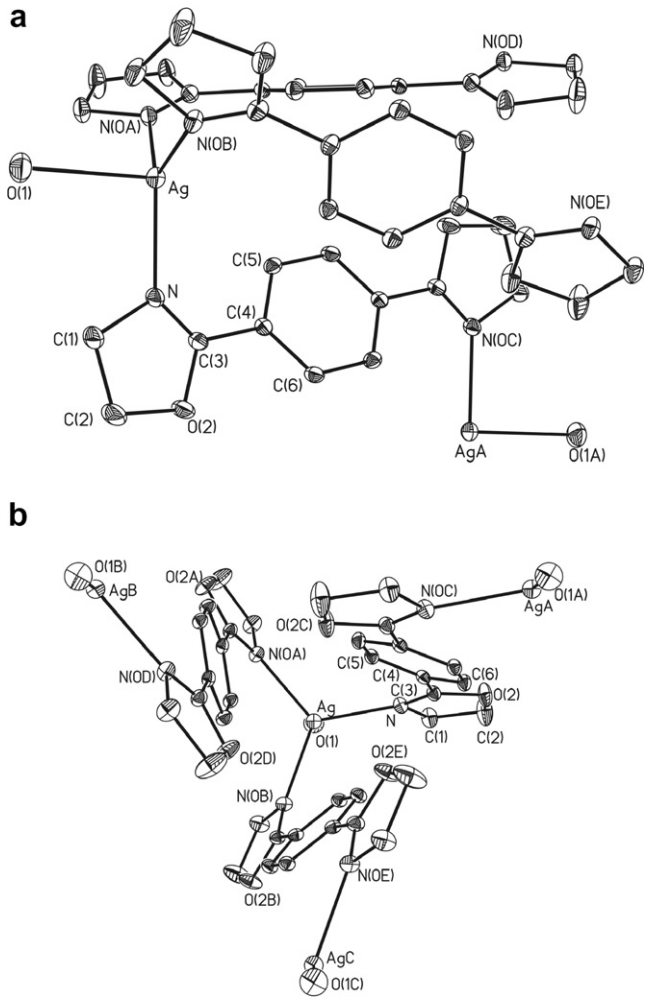


Fig. 6. (a) An ORTEP drawing showing the coordination arrangement around Ag(I) center of complex **4**. (b) An ORTEP drawing showing the three-fold coordination type along the Ag–O axial.

2.492(3) Å for **3**; Ag–N(3) = 2.157(3) Å for **2** and 2.162(3) Å for **3**, respectively) to form a slightly distorted T-shape geometry (∠N(1)–Ag–N(3) = 158.26(11)° for **2** and 154.78(10)° for **3**). Table 2 list the selected bond distances and angles around Ag for complexes **2** and **3**.

In complexes **2** and **3**, three 1,4-bis(4,5-dihydro-2-oxazolyl)benzene ligands link two Ag(I) atoms forming the Z-shape unit as a building block (Fig. 5a). The phenyl groups in the Z-shape building unit interact each through π–π stacking [17], and the distances between the centers of the rings are 3.859 Å for **2** and 3.856 Å for **3**. The bridging ligands in complexes **2** and **3** are not coplanar with the dihedral angels between oxazolyl rings and phenyl rings are 23.2°, 24.4° and 25.7° for complex **2** and 27.8°, 28.0° and 28.5° for complex **3**. The dihedral angles between the oxazolyl rings are 37.4° and 47.5° for complex **2**, and 48.7° and 55.6° for complex **3**, respectively. Fig. 5b showing the six 1,4-bis(4,5-dihydro-2-oxazolyl)benzene ligands link Ag(I) into a $\{Ag(\mathbf{L})\}_6$ 54-member ring. In the $\{Ag(\mathbf{L})\}_6$ ring, the six Ag(I) atoms and six **L** ligands are not coplanar in the chair-form cyclohexane like, which due to the different types of **L** ligands. The Ag–Ag distances separated by the bridging ligands are 6.903 Å and 9.129 Å in complex **2**, and those are 7.202 Å and 9.242 Å in complex **3**, respectively. The $\{Ag(L)\}_6$ rings are further extended into a 2-D layer by sharing Ag(I) joints and **L** edges, Fig. 5c. Complexes **2** and **3** form 3-D supramolecular structures which are interlinked by ClO_4^- and $CF_3SO_3^-$ anions through Ag---O [Ag---O = 3.219(2) Å] interactions and C–H---O [H---O = 2.515–2.547 Å, ∠C–H···O = 133.2 –151.1°] hydrogen bonds for **2**, and through Ag---O [Ag---O = 3.121(3) and 3.546(1) Å] interactions and

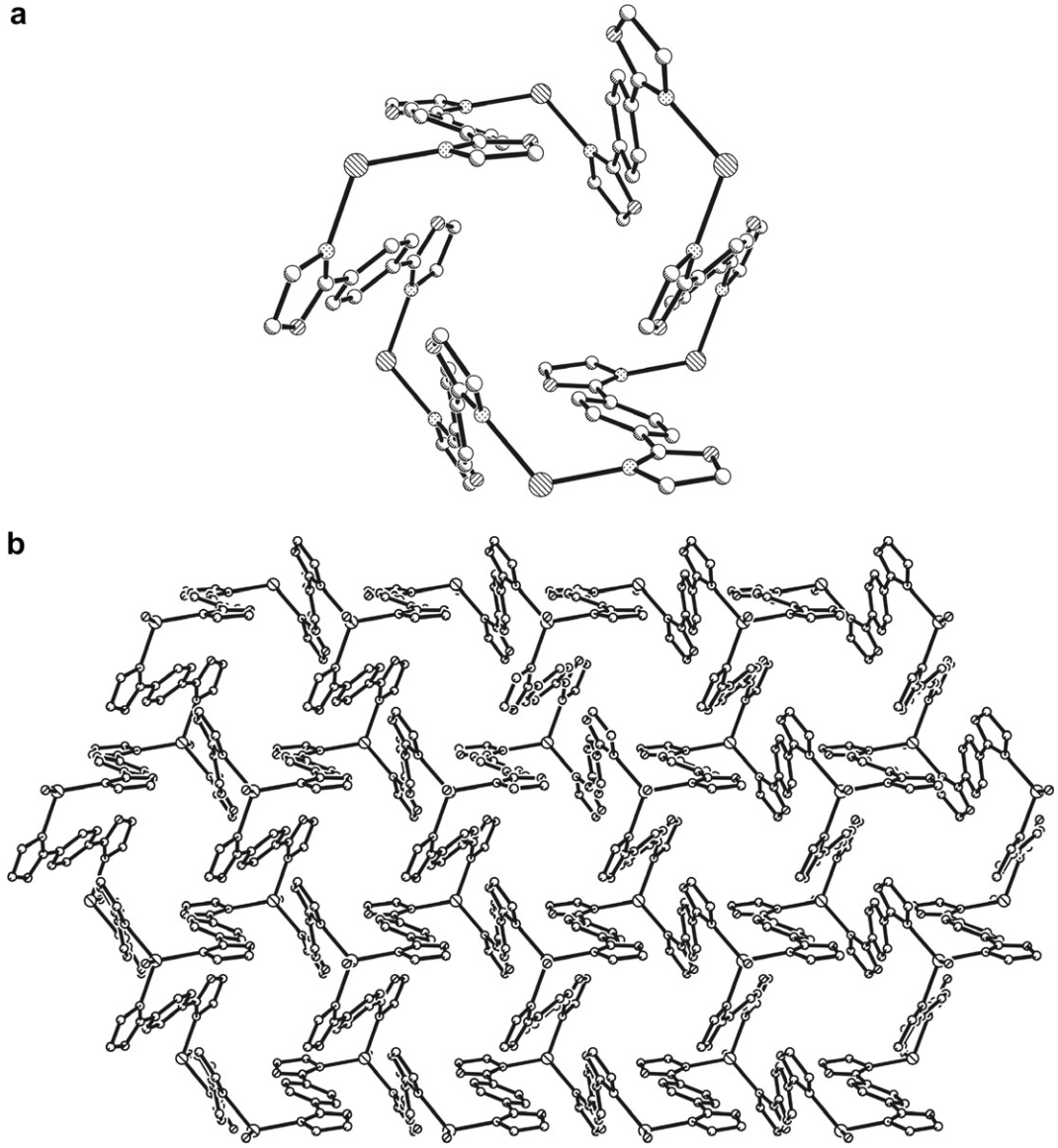


Fig. 7. (a) ORTEP drawing showing the $\{Ag(\mathbf{L})\}_6$ 54-member ring. (b) Packing diagram showing the cationic 2-D layer for complex **4**.

C–H---F [H---F = 2.492 Å, ∠C–H···F = 133.4°] [18] and C–H---O [H---O = 2.524–2.548 Å, ∠C–H···O = 123.9–153.2°] hydrogen bonds for **3**, respectively.

3.1.3. Structures of 4

The structure of complex **4** was solved in the space group *R*-3 and Fig. 6a shows the coordination geometry of the silver metal center. Complex **4** is a four coordinate complex and the coordination geometry of the Ag(I) center adopts a trigonal pyramidal coordination geometry with the bond angles only slightly deviated from 90° and 120° (Table 2). In complex **4**, three 1,4-bis(4,5-dihydro-2-oxazolyl)benzene ligands are each bound via the nitrogen atom of the oxazolyl group (Ag–N = 2.293(2) Å) in the equatorial plane, and the Ag(I) atom also bonded one water molecule (Ag–O(1) = 2.537(4) Å) in a axial position to complete the distorted-trigonal–pyramidal coordination geometry. The silver metal adopts a triangular planar geometry with the bond angles close to 120° (N–Ag–N(A) = 119.411(14)°), and is located only 0.036 Å out of the plane defined by the three nitrogen atoms coordinated the metal atom. Fig. 6b shows the three-fold coordination for Ag(I) center containing 1,4-bis(4,5-dihydro-2-oxazolyl)benzene ligands, viewing along the axial of silver and water bond. The ligands in complex **4** are not flat with the dihedral angle between the oxazolyl group and the phenyl rings is 21.9°.

Fig. 7a showing the six 1,4-bis(4,5-dihydro-2-oxazolyl)benzene ligands link Ag(I) into a $\{Ag(\mathbf{L})\}_6$ 54-member ring, which like as the honey comb pore. The Ag–Ag distance separated by the bridging ligands is 9.347 Å in complex **4**. The $\{Ag(\mathbf{L})\}_6$ rings are further extended into a 2-D layer by sharing Ag(I) joints and **L** edges, Fig. 7b. Complex **4** forms 3-D supramolecular structure which the cationic layers are interlinked by co-crystal water molecules and the sulfate anions through C–H---O [H---O = 2.096–2.558 Å, ∠C–H···O = 105.9–159.4°] hydrogen bonds.

3.1.4. Structural comparisons

The 1,4-bis(4,5-dihydro-2-oxazolyl)benzene ligands in complexes **1**–**4** adopt the different conformations, syn and anti, where syn and anti indicate the relative positions of the nitrogen atoms of the oxazolyl groups. While the **L**'s in **1** and **4** adopt the anti conformation to given the longer Ag–Ag separation, which are 9.774 Å for **1** and 9.347 Å for **4**, those in **2** and **3** adopt both the syn and anti conformations to form coordination polymers with various Ag–Ag distances of 6.903 Å and 9.129 Å in **2** and 7.202 Å and 9.242 Å in **3**, respectively. In complexes **2** and **3**, the ClO_4^- and $CF_3SO_3^-$ anions are not coordinated to the Ag(I) centers, but interact with the Ag(I) metals through the oxygen atom with different Ag–O distances 3.219(2) Å for **2** and 3.121(3) and 3.546(1) Å for **3**, respectively. Fig. 8 shows the schematic drawings for complex **1** (top), **2** and **3** (middle) and **4** (bottom). Complex **1** is a neutral 2-D polymeric layer which formed by Ag(OAc) chains and Ag(**L**)(OAc) chains forming the distorted rectangular net. The cations

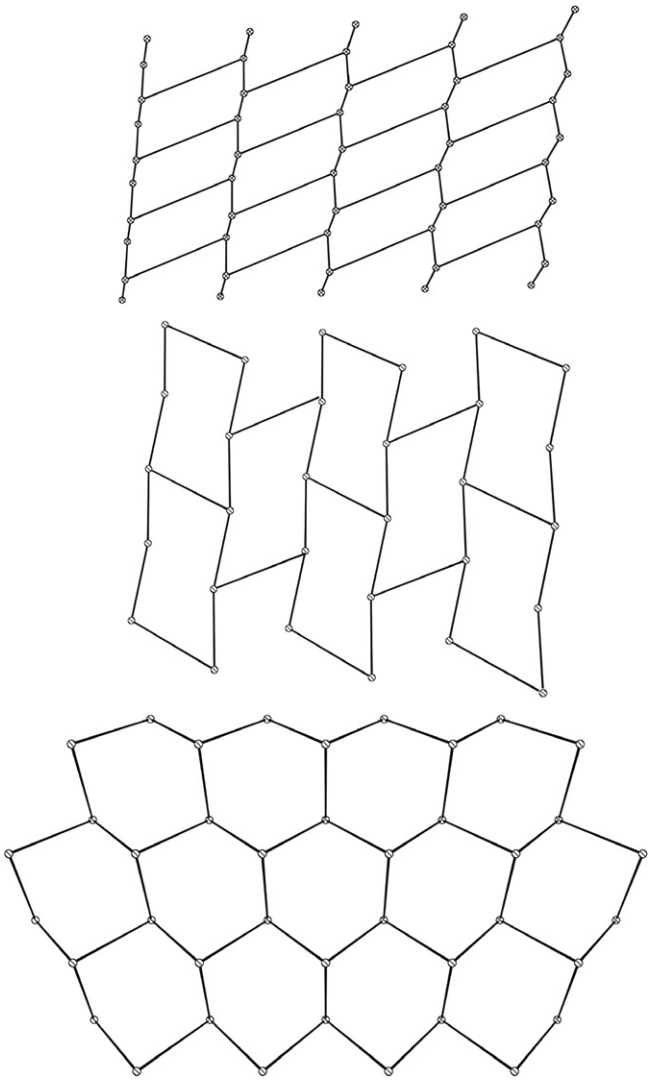


Fig. 8. Schematic drawings for complex **1** (top), **2** and **3** (middle) and **4** (bottom).

of polymeric nets, **2** and **3**, were linking Ag(I) atoms in both syn- and anti-type bridging **L**'s forming the waving 2-D grids, while complex **4** formed 2-D honey comb like framework.

Acknowledgement

We are grateful to the National Science Council of the Republic of China for support.

Appendix A. Supplementary material

CCDC 661925, 661926, 661927 and 661928 contain the supplementary crystallographic data for **1**, **2**, **3** and **4**. These data can be obtained free of charge via http://www.ccdc.cam.ac.uk/conts/retrieving.html, or from the Cambridge Crystallographic Data Centre, 12 Union Road, Cambridge CB2 1EZ, UK; fax: (+44) 1223-336-033; or e-mail: deposit@ccdc.cam.ac.uk. Supplementary data

associated with this article can be found, in the online version, at doi:10.1016/j.poly.2008.01.001.

References

[1] (a) J.M. Lehn, Supramolecular Chemistry, VCH, Weinheim, 1995;
(b) R. Robson, B.E. Abrahams, S.R. Batten, R.W. Gable, B.F. Hoskins, J. Lieu, Supramolecular Architecture, ACS Publications, Washington, DC, 1992.

[2] (a) C. Janiak, Dalton Trans. (2003) 2781;
(b) S.L. James, Chem. Soc. Rev. 32 (2003) 276;
(c) D. Maspoch, D. Ruiz-Molina, J.J. Veciana, Mater. Chem. 14 (2004) 2713;
(d) S.R. Batten, K.S. Murray, Coord. Chem. Rev. 246 (2003) 103;
(e) L. Carlucci, G. Ciani, D. Poserpio, Coord. Chem. Rev. 246 (2003) 247;
(f) C.-L. Chen, B.-S. Kang, C.-Y. Su, Aust. J. Chem. 59 (2006) 3;
(g) M. Munakata, L.P. Wu, T. Kuroda-Sowa, Adv. Inorg. Chem. 46 (1999) 173.

[3] (a) R.P. Sijbesma, E.W. Meijer, Curr. Opin. Colloid Interface Sci. 4 (1999) 24;
(b) S.C. Zimmerman, P.S. Corbin, Struct. Bond. 96 (2000) 63;
(c) D.C. Sherrington, K.A. Taskinen, Chem. Soc. Rev. 30 (2001) 83;
(d) D.S. Lawrence, T. Jiang, M. Levett, Chem. Rev. 95 (1995) 2229.

[4] S. Muthu, J.H.K. Yip, J.J.J. Vittal, Chem. Soc., Dalton Trans. (2002) 4561.

[5] (a) T. Hennigar, D.C. MacQuarrie, P. Loiser, R.D. Rogers, M.J. Zaworotko, Angew. Chem., Int. Ed. Engl. 36 (1997) 972;
(b) L. Carlucci, G. Ciani, D.M. Proserpio, S. Rizzato, Chem. Commun. (2000) 1319.

[6] (a) M.B. Zaman, M.D. Smith, H.-C. zur Loye, Chem. Commun. (2001) 2256;
(b) B. Moulton, E.B. Rather, M.J. Zaworotko, Cryst. Eng. 4 (2001) 309;
(c) M. Du, X.-H. Bu, Y.-M. Guo, H. Liu, S.R. Batten, J. Ribas, T.C.W. Mak, Inorg. Chem. 41 (2002) 4904;
(d) M.-L. Tong, Y.-M. Wu, J. Ru, X.-M. Chen, H.-C. Chang, S. Kitagawa, Inorg. Chem. 41 (2002) 4846;
(e) Z.-Y. Fu, X.-T. Wu, J.-C. Dai, S.-M. Hu, W.-X. Du, New J. Chem. 26 (2002) 978;
(f) M.J. Plater, M.R.St.J. Foreman, T. Gelbrich, M.B.J. Hursthouse, Chem. Soc., Dalton Trans. (2000) 1995.

[7] (a) M.J. Plater, M.R.St.J. Foreman, T. Gelbrich, S.J. Coles, M.B.J. Hursthouse, Chem. Soc., Dalton Trans. (2000) 3065;
(b) M. Fujita, Y.J. Kwon, M. Miyazawa, K.J. Ogure, Chem. Soc., Chem. Commun. (1994) 1977;
(c) M. Fujita, Y.J. Kwon, O. Sasaki, K. Yamaguchi, K.J. Ogura, Am. Chem. Soc. 117 (1995) 7287;
(d) X.-C. Su, S.-R. Zhu, H.-K. Lin, X.-B. Leng, Y.-T.J. Chen, Chem. Soc., Dalton Trans. (2001) 3163;
(e) M.O. Awaleh, A. Badia, F. Brisse, Inorg. Chem. 44 (2005) 7833;
(f) M.O. Awaleh, A. Badia, F. Brisse, Cryst. Growth Des. 5 (2005) 1897;
(g) M. Du, C.-P. Li, X.-J. Zhao, Cryst. Growth Des. 6 (2006) 335.

[8] (a) H.-H. Li, Z.-R. Chen, J.-Q. Li, C.-C. Huang, Y.-F. Zhang, G.-X. Jia, Cryst. Growth Des. 6 (2006) 1813;
(b) M.O. Awaleh, A. Badia, F. Brisse, Cryst. Growth Des. 6 (2006) 2674;
(c) S. Noro, R. Kitaura, M. Kondo, S. Kitagawa, T. Ishii, H. Matsuzaka, M.J. Yamashita, Am. Chem. Soc. 124 (2002) 2568;
(d) Y.-H. Wang, K.-L. Chu, H.-C. Chen, C.-W. Yeh, Z.-K. Chan, M.-C. Suen, J.-D. Chen, CrystEngComm 8 (2006) 84;
(e) C.-Y. Lin, Z.-K. Chan, C.-W. Yeh, C.-J. Wu, J.-D. Chen, J.-C. Wang, CrystEngComm 8 (2006) 841;
(f) Y.-F. Hsu, J.-D. Chen, Eur. J. Inorg. Chem. (2004) 1488;
(g) H.-L. Hu, C.-W. Yeh, J.-D. Chen, Eur. J. Inorg. Chem. (2004) 4696.

[9] X.H. Bu, W. Chen, W.F. Hou, R.H. Zhang, F. Brisse, Inorg. Chem. 41 (2002) 3477.

[10] A.J. Blake, N.R. Champness, P.A. Cooke, P.A. Cooke, J.E.B. Nicolson, C.J.J. Wilson, Chem. Soc., Dalton Trans. (2000) 3811.

[11] (a) E.C. Constable, Aust. J. Chem. 59 (2006) 1;
(b) C.M. Fitchett, P.J. Steel, Aust. J. Chem. 59 (2006) 19;
(c) T. Dorn, K.M. Fromm, C. Janiak, Aust. J. Chem. 59 (2006) 22;
(d) M.B. Duriska, S.R. Batten, D.J. Price, Aust. J. Chem. 59 (2006) 26;
(e) E.C. Constable, C.E. Housecroft, B.M. Kariuki, C.B. Smith, Aust. J. Chem. 59 (2006) 30;
(f) Y.-B. Xie, J.-R. Li, X.-H. Bu, Aust. J. Chem. 59 (2006) 34;
(g) L. Cunha-Silva, R. Ahmad, M.J. Hardie, Aust. J. Chem. 59 (2006) 40;
(h) H.-P. Wu, C. Janiak, G. Rheinwald, H.J. Lang, Chem. Soc., Dalton Trans. (1999) 183;
(i) C. Janiak, L. Uehlin, H.-P. Wu, P. Klufers, H. Piotrowski, T.G.J. Scharmann, Chem. Soc., Dalton Trans. (1999) 3121.

[12] (a) M.-C. Suen, J.-C.J. Wang, Coord. Chem. 60 (2007) 257;
(b) P.J. Hagrman, D. Hagrman, J. Zubieta, Angew. Chem., Int. Ed. Engl. 38 (1999) 2638, and references therein.

[13] (a) S. Batten, R. Robson, Angew. Chem., Int. Ed. Engl. 37 (1998) 1998, and references therein;
(b) Y.-B. Dong, X. Zhao, G.-X. Jin, R.-Q. Huang, M.R. Smith, Eur. J. Inorg. Chem. (2003) 4017;
(c) Y.-B. Dong, J.-P. Ma, X. Zhao, G.-X. Jin, R.-Q. Huang, M.R. Smith, Dalton Trans. (2003) 4324.

[14] (a) M.-C. Suen, H.-A. Tsai, J.-C.J. Wang, Chin. Chem. Soc. 52 (2005) 1085;
(b) M.-C. Suen, Z.-K. Chan, J.-D. Chen, J.-C. Wang, C.-H. Hung, Polyhedron 25 (2006) 2325;
(c) M.-C. Suen, J.-C. Wang, Struct. Chem. 17 (2006) 315;
(d) M.-C. Suen, J.-C. Wang, Inorg. Chem. Commun. 9 (2006) 478;
(e) M.-C. Suen, H.-A. Tsai, J.-C. Wang, J. Chin. Chem. Soc. 53 (2006) 305;
(f) H.-L. Hu, M.-C. Suen, C.-W. Yeh, J.-D. Chen, Polyhedron 24 (2005) 1497;
(g) M.-C. Suen, Y.-H. Wang, Y.-F. Hsu, C.-W. Yeh, J.-D. Chen, J.-C. Wang, Polyhedron 24 (2005) 2913.

[15] XSCANS, Release, 2.1, Siemens Energy & Automation, Inc, Madison, Wisconsin, USA,1995.

[16] SHELXTL 5.10. Bruker Analytical X-ray Instruments Inc., Karlsruche, Germany, 1997.

[17] C.J. Janiak, Chem. Soc., Dalton Trans. (2000) 3885.

[18] G. Althoff, J. Ruiz, V. Rodriguez, G. Lopez, J. Perez, C. Janiak, CrystEngComm 8 (2006) 662.

interactions is an important aspect in supramolecular chemistry and crystal engineering. 4-Terpyridone is known to coordinate to the metal ions in its enolic form (LH) [2]. With an expectation that H–O–pyridine–M–pyridine–O–H fragment in $[M(LH)_2]^{n+}$ species may act as hydrogen bond donor/acceptor and thus may be a potential supramolecular synthon, an enolic 4-terpyridone based nickel(II) dicyanamide supramolecule, $[Ni^{II}(LH)_2](dicyanamide)_2 \cdot 2H_2O$ has been previously reported [2b]. Again, if 4-terpyridone forms 1:1 metal complex $[M(LH)(L^1)_x]^{n+}$ (L^1 is another ligand), it will have H–O–pyridine–M moiety which may also act as a hydrogen bond acceptor and donor due to the presence of O–H functionality. In addition to the importance as a supramolecular synthon, 4-terpyridone containing complexes may also exhibit spin-crossover phenomena due to intermediate field strength of this ligand [2a].

Dicyanamide is known as a versatile inorganic bridging ligand to develop coordination polymers. Five types of bridging modes of dicyanamide have been structurally characterized so far; two connecting ($\mu_{1,5}$- or $\mu_{1,3}$-) [4–10], three connecting ($\mu_{1,3,5}$- or $\mu_{1,1,5}$-) [3,10–13], four connecting ($\mu_{1,1,3,5}$-) [14], and even five connecting ($\mu_{1,1,3,5,5}$-) [15]. Although dicyanamide can mediate only weak interactions between the paramagnetic metal centers [4–15], a few multidimensional dicyanamide-bridged compounds exhibit long range magnetic ordering [3]. Evidently, dicyanamide is also a promising building unit to derive magnetic materials.

To explore further 4-terpyridone (LH) containing complexes, we report herein syntheses, molecular and supramolecular structures, and magnetic properties of a mononuclear manganese(II) compound $[Mn^{II}(LH)_2](ClO_4)_2$ (**1**) and a dicyanamide-bridged one-dimensional copper(II) compound $[Cu^{II}(LH)(\mu_{1,5}\text{-dca})]_n(NO_3)_n$ (**2**).

2. Experimental

2.1. Materials and physical methods

All the reagents and solvents were purchased from the commercial sources and used as received. Elemental (C, H, and N) analyses were performed on a Perkin–Elmer 2400 II analyzer. IR spectra were recorded in the region 400–4000 cm^{-1} on a Bio-Rad FTS40 spectrophotometer with samples as KBr disks. Variable-temperature (2–300 K) magnetic susceptibility measurements were carried out with a Quantum Design MPMS SQUID magnetometer.

2.2. Syntheses

2.2.1. $[Mn^{II}(LH)_2](ClO_4)_2$ (**1**)

A methanol solution (10 mL) of $Mn(ClO_4)_2 \cdot 6H_2O$ (0.18 g, 0.5 mmol) was added to a stirred methanol solution (20 mL) of 4-terpyridone (0.249 g, 1 mmol). A yellow precipitate was started to deposit after a few minutes. After stirring for 1 h, the yellow compound was collected by filtration and washed with methanol. Recrystallization from acetonitrile yielded yellow crystalline compound. Yield: 0.3 g (80%). The single crystals suitable for X-ray diffraction were obtained on diffusing diethylether to an acetonitrile solution of yellow crystalline compound. Anal. Calc. for $C_{30}H_{22}Cl_2MnN_6O_{10}$: C, 47.89; H, 2.95; N, 11.17. Found: C, 47.78; H, 3.02; N, 11.26%. IR (KBr/cm^{-1}): perchlorate: 1116s, 637m.

2.2.2. $[Cu^{II}(LH)(\mu_{1,5}\text{-dca})]_n(NO_3)_n$ (**2**)

A methanol solution (25 mL) of $Cu(NO_3)_2 \cdot 3H_2O$ (0.12 g, 0.5 mmol) and 4-terpyridone (0.125 g, 0.5 mmol) was refluxed for 1 h. The resulting blue solution was cooled to room temperature. To this blue solution, an aqueous solution (5 mL) of sodium dicyanamide (0.178 g, 2 mmol) was dropwise added with stirring. After a few minutes blue precipitate started to deposit. After 1 h stirring, the blue compound was collected by filtration and washed with methanol. Recrystallization on diffusing diethylether to a dimethylformamide solution yielded blue crystalline compound containing diffraction quality single crystals. Yield: 0.11 g (50%). Anal. Calc. for $C_{17}H_{11}CuN_7O_4$: C, 46.31; H, 2.51; N, 22.24. Found: C, 46.40; H, 2.42; N, 22.20%. IR (KBr/cm^{-1}): dicyanamide: 2348w (sh), 2315s, 2251s, 2181vs, 2147m (sh); nitrate: 1384s.

2.3. Crystal structure determination of $[Mn^{II}(LH)_2](ClO_4)_2$ (**1**) and $[Cu^{II}(LH)(\mu_{1,5}\text{-dca})]_n(NO_3)_n$ (**2**)

Pertinent crystallographic data of these two complexes are summarized in Table 1. Diffraction data were collected

Table 1
Crystallographic data for **1** and **2**

	1	**2**
Empirical formula	$C_{30}H_{22}N_6O_{10}Cl_2Mn$	$C_{17}H_{11}N_7O_4Cu$
Formula weight	752.39	440.87
Crystal system	monoclinic	triclinic
Space group	$P2(1)/n$	$P\bar{1}$
a (Å)	8.8281(4)	7.5342(3)
b (Å)	8.7736(4)	8.9307(4)
c (Å)	39.7838(16)	15.0189(8)
α (°)	90.00	73.0032(15)
β (°)	95.719(1)	81.3701(16)
γ (°)	90.00	65.461(2)
V (Å^3)	3066.1(2)	878.65(7)
Z	4	2
T (K)	150(1)	295(2)
λ (Mo Kα) (Å)	0.71073	0.71073
$D_{calc.}$ (g cm^{-3})	1.630	1.666
μ (mm^{-1})	0.675	1.286
$F(000)$	1532	446
2θ range (°)	2.06–55.00	5.18–55.00
Total reflections	27902	19403
Unique reflections	7007	4015
R_1^a/wR_2^b ($I > 2\sigma(I)$ data)	0.0465/0.0931	0.0528/0.1338
R_1^a/wR_2^b (all data)	0.0765/0.0997	0.0815/0.1567

[a] $R_1 = [\Sigma \,||F_o| - |F_c||/\Sigma\,|F_o|]$.
[b] $wR_2 = [\Sigma w(F_o^2 - F_c^2)^2/\Sigma w(F_o^2)^2]^{1/2}$.

on a Bruker SMART CCD (for **1**) and a NONIUS Kappa CCD (for **2**) diffractometer in the ω–2ϑ scan mode at 150 K and 295 K, respectively, using graphite monochromated Mo Kα radiation, having $\lambda = 0.71073$ Å. The accurate unit cells were obtained by means of least-squares fittings of 25 centered reflections. The intensity data were corrected for Lorentz and polarization effects, and semiempirical absorption corrections were made from ψ-scans. A total of 27902 reflections were collected for **1** in the range $2\vartheta = 2.06$–$55.0°$ with $-10 \leqslant h \leqslant 11$, $-11 \leqslant k \leqslant 11$, and $-51 \leqslant l \leqslant 51$, of which 7007 independent reflections ($R_{int} = 0.0526$) were used for structure determination. In the case of **2**, among 19403 of the total reflections collected in 2ϑ range of 5.18–55.0° with $-9 \leqslant h \leqslant 9$, $-10 \leqslant k \leqslant 11$, and $-19 \leqslant l \leqslant 19$, 4015 were independent ($R_{int} = 0.0625$). The structures were solved by direct and Fourier methods and refined by full-matrix least-squares methods based on F^2 using the programs SHELXS-97 and SHELXL-97 [16]. All non-hydrogen atoms were readily located and refined by anisotropic thermal parameters. The final least-squares refinements (R_1) based on $I > 2\sigma(I)$ converged to 0.0465 for **1** and 0.0528 for **2**.

3. Results and discussion

3.1. Description of the structure of $[Mn^{II}(LH)_2](ClO_4)_2$ (1)

Molecular structure of $[Mn^{II}(LH)_2](ClO_4)_2$ (**1**) is shown in Fig. 1, while selected bond lengths and angles are listed in Table 2. The structure of **1** contains three independent units: the dication $[Mn^{II}(4\text{-terpyridone})_2]^{2+}$ and two perchlorate anions. The manganese(II) center in **1** is hexacoordinated. Three nitrogens of each of the two enolic 4-terpyridone chelate to the metal ion. The Mn–N distances fall into two ranges; those involving the central pyridine rings are almost the same (Mn–N(2) = 2.197(2) Å and Mn–N(5) = 2.199(2) Å), while those (Mn–N(1) = 2.256(2) Å, Mn–N(3) = 2.252(2) Å, Mn–N(4) = 2.253(2) Å, and Mn–N(6) = 2.275(2) Å) involving the other four rings are little longer. The stereochemistry of the metal ion, due to the rigidity of the donor environment of 4-terpyridone, deviates appreciably from an ideal octahedron. Among fifteen N–Mn–N bond angles, three (N(1)–Mn–N(3), N(2)–Mn–N(5), and N(4)–Mn–N(6)) are *transoid* angles, while the remaining 12 are *cisoid* angles. In addition to the differences in the metal–ligand bond distances, the *transoid* angles (144.58(8)°, 144.37(8)°, and 177.96(8)°) and the wide range of *cisoid* angles (71.82(8)–109.92(8)°) are indicative of high distortion of the coordination environment. The deviations of the metal ion or the donor centers from N(2)N(4)N(5)N(6) and N(1)N(2)N(3)N(5) coordination planes, the later of which is the best least-squares plane, are not very high (<0.05 Å). However, the fact that the atoms N(1), N(3), N(4), and N(6) practically do not define any plane (average deviation of the nitrogens

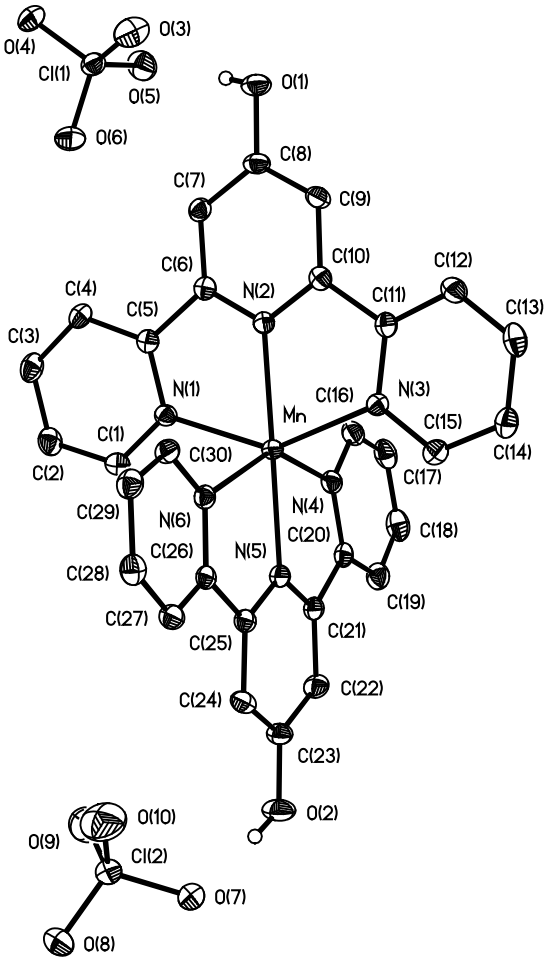


Fig. 1. Crystal structure of $[Mn^{II}(LH)_2](ClO_4)_2$ (**1**) with atom label schemes. C–H hydrogens are omitted for clarity.

Table 2
Selected bond lengths (Å) and angles (°) for **1**

Mn–N(1)	2.256(2)
Mn–N(2)	2.197(2)
Mn–N(3)	2.252(2)
Mn–N(4)	2.253(2)
Mn–N(5)	2.199(2)
Mn–N(6)	2.275(2)
C(8)–O(1)	1.355(3)
N(1)–Mn–N(3)	144.58(8)
N(2)–Mn–N(5)	177.96(8)
N(4)–Mn–N(6)	144.37(8)
N(1)–Mn–N(2)	72.76(8)
N(1)–Mn–N(4)	93.75(8)
N(1)–Mn–N(5)	107.77(8)
N(1)–Mn–N(6)	93.17(8)
N(2)–Mn–N(3)	71.82(8)
N(2)–Mn–N(4)	109.92(8)
N(2)–Mn–N(6)	105.51(8)
N(3)–Mn–N(4)	98.33(8)
N(3)–Mn–N(5)	107.62(8)
N(3)–Mn–N(6)	95.97(8)
N(4)–Mn–N(5)	72.07(8)
N(5)–Mn–N(6)	72.54(8)

is 0.68 Å) is in parallel with the large distortion of the coordination environment.

Eight hydrogen bonds, six of C–H···O types and two of O–H···O types, link the individual components in **1** into a three-dimensional network. The analyses of hydrogen bonds and topology resulted therein can be better understood as fragments. Simplified illustration of hydrogen bonds between perchlorate anions, $Cl(1)O_4$ and $Cl(2)O_4$, and 4-terpyridone moieties are shown in Figs. 2 and 3, respectively, while the hydrogen bond geometries are listed in Table 3. As shown in Fig. 2, $Cl(1)O_4$ anion forms hydrogen bonds with four complex dications to result in the creation of a two-dimensional sheet. One perchlorate oxygen, O(3), is a double acceptor and interacts with hydrogens (H(1) and H(13C)) attached with O(1) and C(13C), respectively. The second oxygen, O(4), forms hydrogen bond with H(16A) linked with C(16A). The third oxygen, O(5), interacts with hydrogen H(12B) which is linked with C(12B). The fourth oxygen, O(6), is a bifurcated acceptor and interacts with C(4)–H(4) and C(7)–H(7) hydrogens. Another perchlorate anion, $Cl(2)O_4$, forms two hydrogen bonds, O(2)–H(2)···O(7) and C(15D)–H(15D)···O(7) (Fig. 3). It may be noted that one manganese(II) center (Mn) in Fig. 3 belongs to the two-dimensional sheet represented in Fig. 2, while the second metal center (MnD) belongs to a second two-dimensional sheet. Evidently, the two-dimensional hydrogen bonded sheets formed due to hydrogen bonds involving $Cl(1)O_4$ are interlinked with each other due to the hydrogen bonds involving the second perchlorate anion, $Cl(2)O_4$. Therefore, the overall topology in compound **1** is three-dimensional.

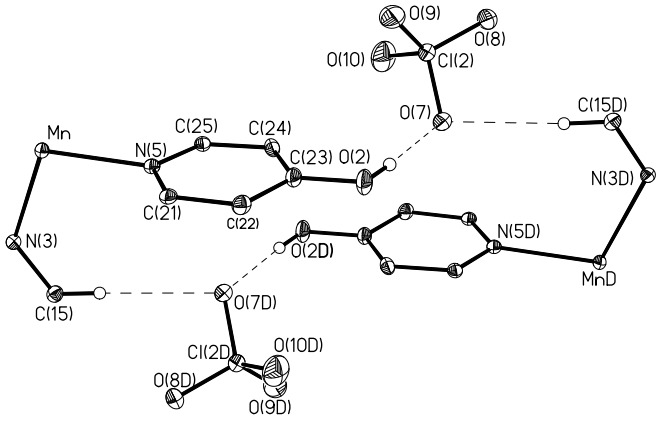


Fig. 3. Perspective view to demonstrate the hydrogen bonds involving one perchlorate anion ($Cl(2)O_4$) and O–H and C–H groups of enolic 4-terpyridones. Except central ring of one 4-terpyridone and except C(15) and N(3) atoms of the second 4-terpyridone, all other atoms have been omitted for clarity. Those hydrogen atoms participating in hydrogen bonds are only shown. Symmetry code: D, $1-x, -1-y, 1-z$.

3.2. Description of the structure of $[Cu^{II}(LH)(\mu_{1,5}\text{-}dca)]_n(NO_3)_n$ (2)

An ORTEP representation of the coordination environment and the formation of one-dimensional infinite chain of **2** is shown in Fig. 4, while the selected bond lengths

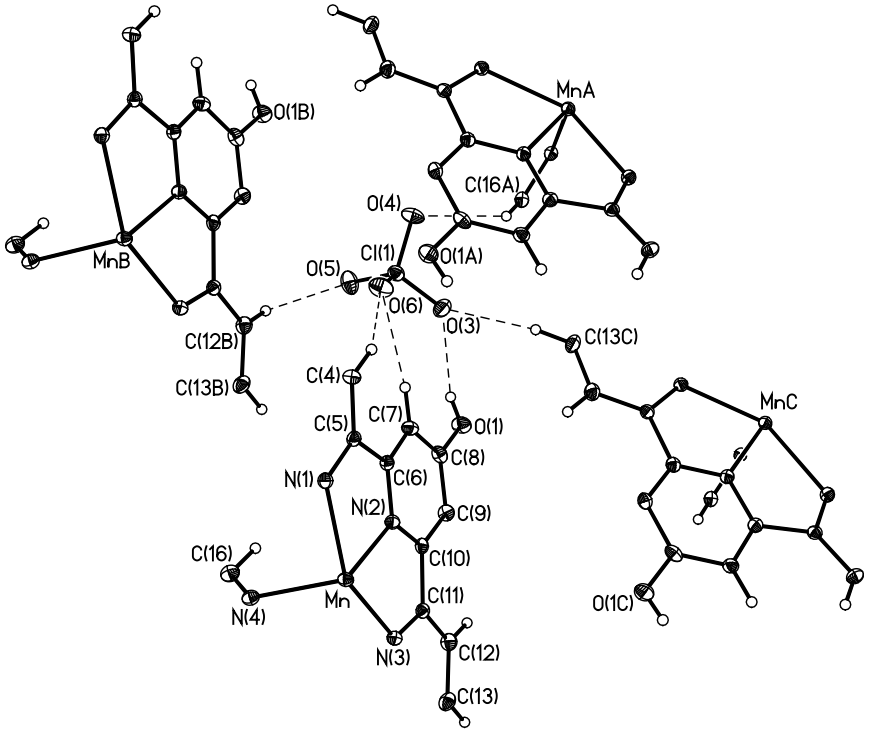


Fig. 2. Perspective view to demonstrate the hydrogen bonds and two-dimensional network resulted due to interactions involving one perchlorate anion ($Cl(1)O_4$) and O–H and C–H groups of enolic 4-terpyridones. C(1), C(2), C(3), C(14), and C(15) atoms of one 4-terpyridone and atoms, except N(14) and C(16), of the second 4-terpyridone have been omitted for clarity. Those hydrogen atoms participating in hydrogen bonds are only shown. Symmetry codes: A, $2.5-x, y+0.5, 1.5-z$; B, $1+x, y, z$; C, $1.5-x, y+0.5, 1.5-z$.

Table 3
Geometries (distances in Å and angles in °) of the hydrogen bonds in **1**

D–H···A	H···A	D···A	D–H···A
O(1)–H(1)···O(3)	2.15	2.85	163.7
C(13C)–H(13C)···O(3)	2.49	3.33	147.9
C(16A)–H(16A)···O(4)	2.47	3.22	135.6
C(12B)–H(12B)···O(5)	2.53	3.43	158.2
C(4)–H(4)···O(6)	2.47	3.36	156.2
C(7)–H(7)···O(6)	2.39	3.33	173.0
O(2)–H(2)···O(7)	1.94	2.74	176.3
C(15D)–H(15D)···O(7)	2.48	3.38	158.0

Symmetry codes: as in Figs. 2 and 3.

Table 4
Selected bond lengths (Å) and angles (°) for **2**

Cu–N(1)	2.038(3)
Cu–N(2)	1.920(3)
Cu–N(3)	2.040(3)
Cu–N(4)	2.207(3)
Cu–N(6B)	1.943(3)
C(8)–O(1)	1.325(5)
C(16)–N(4)	1.140(5)
C(17)–N(6)	1.144(5)
C(16)–N(5)	1.295(5)
C(17)–N(5)	1.290(5)
N(1)–Cu–N(3)	158.52(13)
N(2)–Cu–N(6B)	158.24(14)
N(4)–Cu–N(1)	95.88(13)
N(4)–Cu–N(2)	102.33(12)
N(4)–Cu–N(3)	94.10(13)
N(4)–Cu–N(6B)	99.43(13)
N(1)–Cu–N(2)	79.65(12)
N(1)–Cu–N(6B)	97.83(13)
N(2)–Cu–N(3)	79.66(12)
N(3)–Cu–N(6B)	99.23(14)
C(16)–N(5)–C(17)	122.5(4)
N(4)–C(16)–N(5)	173.4(4)
N(5)–C(17)–N(6)	172.4(4)
Cu–N(4)–C(16)	161.9(3)
CuA–N(6)–C(17)	158.5(3)

Symmetry code: as in Fig. 4.

and angles of this compound are listed in Table 4. As shown in Fig. 4, the metal ion is pentacoordinated by enolic 4-terpyridone, which behaves as a tridented neutral chelating ligand, and nitrile nitrogens of two end-to-end (EE) dicyanamide ligands. The other ends of these two dicyanamides, bonded to a metal ion in *cis* positions (N(4)–Cu–N(6B) = 99.43(13)°), coordinate to two different copper atoms to result in the formation of a one-dimensional chain which propagates along the crystallographic *a* axis.

The coordination geometry around the pentacoordinated metal ion is distorted square pyramidal. The best equatorial plane is defined by three pyridyl nitrogens (N(1), N(2), and N(3)) of 4-terpyridone moiety and one dicyanamide nitrogen (N(6B)), while the axial position is occupied by the second dicyanamide nitrogen (N(4)). The Cu–N distances involving 4-terpyridone fall into two distinct ranges; that (Cu–N(2) = 1.920(3) Å) involving the central pyridine ring is smaller than the bond lengths (Cu–N(1) = 2.038(3) Å and Cu–N(3) = 2.040(3) Å) involving the other two rings. Regarding Cu–N(dicyanamide) bond lengths, while that (Cu–N(6B) = 1.943(3) Å) in the basal plane lie within the range (1.920(3)–2.038(3) Å) of Cu–N(4-terpyridone) distances, the Cu–N(axial) bond length (Cu–N(4) = 2.207(3) Å) is significantly longer due to Jahn–Teller distortion. Among six N–Cu–N bond angles in the equatorial square plane, two (N(1)–Cu–N(3) and N(2)–Cu–N(6B)) are *transoid* angles, while other four are *cisoid* angles. Again, all the four N–Cu–N bond angles involving apical nitrogen (N(4)) are *cisoid* angles. In addition to the differences in the metal–ligand bond distances, the reduction of the *transoid* angles (N(1)–Cu–N(3) = 158.52(13)° and N(2)–Cu–N(6B) = 158.24(14)°) in the basal plane and the wide range of *cisoid* angles (79.65(12)–102.33(12)°) are indicative of high distortion of the coordination environment. The average deviation of the four nitrogen atoms and the displacement of the copper(II) center from the least-squares N(1)N(2)N(3)N(6B) plane are, respectively, 0.096 Å and 0.26 Å, which also

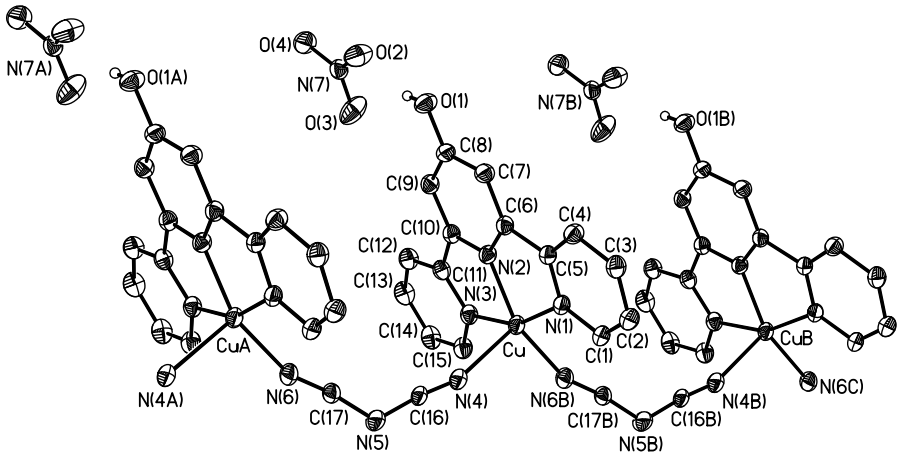


Fig. 4. Crystal structure of $[Cu^{II}(LH)(\mu_{1,5}\text{-dca})]_n(NO_3)_n$ with atom label schemes. C–H hydrogens are omitted for clarity. Symmetry codes: A, $1 + x$, y, z; B, $x - 1$, y, z; C, $x - 2$, y, z.

indicates that the coordination environment around the metal center is highly distorted.

As indicated from the Cu–N–C angles (Cu–N(6B)–C(17B) = 158.5(3)° and Cu–N(4)–C(16) = 161.9(3)°), each EE dca anion coordinates with the metal ion in slightly bent way. The C≡N and C–N distances for the dca anions are in the normal range. In addition, the C–N–C angle of 122.5(4)° indicates the pseudo C_{2v} symmetry of the dicyanamide.

Seven hydrogen bonds, six of C–H···O types and one of O–H···O type, link the dicyanamide-bridged one-dimensional chains into a two-dimensional sheet consisting of interlinked one-dimensional double-chains. A simplified illustration, down the crystallographic *b* axis, of the hydrogen bonds and the topology resulted therein is shown in Fig. 5, while the geometries of hydrogen bonds are listed in Table 5. Parts of four one-dimensional chains (CuA···Cu···CuB, CuD···CuE, CuF···CuG, and CuH···CuI) are shown in Fig. 5. The chains CuA···Cu···CuB and CuF···CuG belong to the same *ac* plane and, in comparison to this *ac* plane, the chains CuD···CuE and CuH···CuI belong to a lower and upper *ac* planes, respectively. Enolic oxygen (O(1)) of CuA···Cu···CuB chain acts as a double acceptor and interacts with two C–H (C(4D)–H(4D) and C(7D)–H(7D)) hydrogens of 4-terpyridone moiety of another chain CuD···CuE. One nitrate oxygen (O(2)) also acts as a double acceptor and interacts with one enolic hydrogen (O(1)–H(1)) and one C–H hydrogen (C(4D)–H(4D)) of two chains, CuA···Cu···CuB and CuD···CuE, respectively. Clearly, these four hydrogen bonds link the one-dimensional chains to result in the generation of one-dimensional double chains. Other two nitrate oxygens (O(3) and O(4)) are hydrogen bonded with two C–H hydrogens, C(13I)–H(13I) and C(14I)–H(14I), of a third one-dimensional chain CuH···CuI to add another dimension in the structure. O(3) acts as a bifurcated acceptor and interacts also with H(9) attached with C(9). In summary, the supramolecular structure in this compound can be considered as a two-dimensional sheet consisting of the hydrogen bonded double chains of interlinked dicyanamide-bridged one-dimensional coordination polymers.

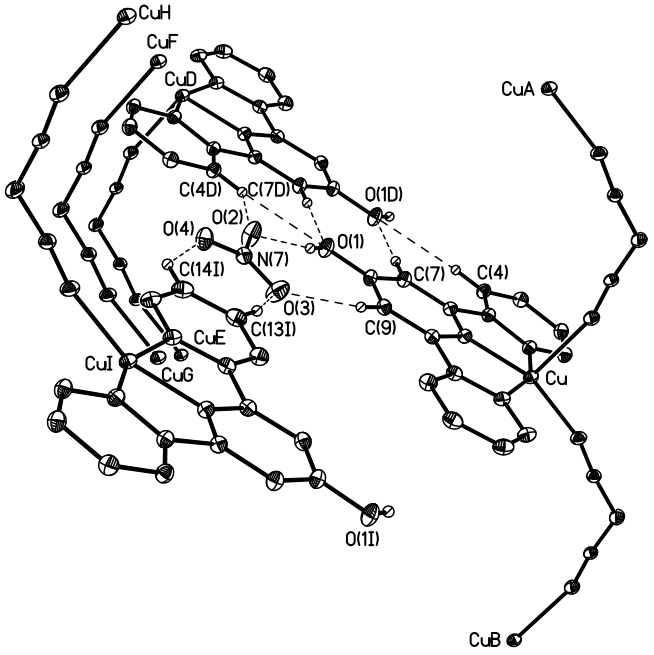


Fig. 5. Perspective view of **1** down the crystallographic *b* axis to show two-dimensional sheet consisting of the hydrogen bonded double chains of interlinked dicyanamide-bridged one-dimensional coordination polymers. C–H hydrogens are omitted for clarity. Symmetry codes: A, $1 + x$, y, z; B, $x - 1$, y, z; C, $x - 2$, y, z; D, $2 - x$, $-y$, $2 - z$; E, $1 - x$, $-y$, $2 - z$; F, $2 - x$, $1 - y$, $2 - z$; G, $1 - x$, $1 - y$, $2 - z$; H, $2 - x$, $2 - y$, $2 - z$; I, $1 - x$, $2 - y$, $2 - z$.

Table 5
Geometries (distances in Å and angles in °) of the hydrogen bonds in **1**

D–H···A	H···A	D···A	D–H···A
O(1)–H(1)···O(2)	1.88	2.54	161.3
C(4D)–H(4D)···O(1)	2.58	3.50	175.7
C(7D)–H(7D)···O(1)	2.51	3.44	177.7
C(4D)–H(4D)···O(2)	2.57	3.18	123.7
C(9)–H(9)···O(3)	2.37	3.26	158.3
C(13I)–H(13I)···O(3)	2.42	3.32	161.7
C(14I)–H(14I)···O(4)	2.57	3.26	131.6

Symmetry codes: as in Fig. 5.

3.3. Magnetic properties

Variable-temperature (2–300 K) magnetic behavior at fixed field strength of 1 T of **1** is shown in Fig. 6 in the form of $\chi_M T$ versus T plots. The $\chi_M T$ value at 300 K is 4.33 $cm^3\ mol^{-1}\ K$, which is almost equal to the spin-only $\chi_M T$ value of high spin Mn^{II}. On lowering of temperature, $\chi_M T$ values remain almost constant upto ~10 K and then decrease rapidly to 2 K where the $\chi_M T$ value is 3.38 $cm^3\ mol^{-1}\ K$. The profile is characteristic of high spin man-

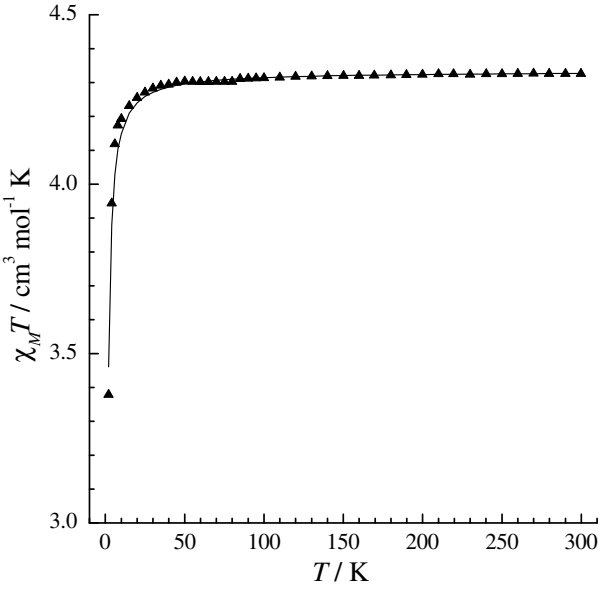


Fig. 6. Experimental (▲) and calculated (—) $\chi_M T$ vs. T plots for **1**.

ganese(II) with zero-field splitting. As shown in Fig. 6, experimental data are well matched with single-ion expression derived from $\mathbf{H} = D(\mathbf{S}_Z^2 - 1/3S(S+1))$ with $g = 1.99$ and $|D| = 0.14\ \mathrm{cm}^{-1}$; the agreement factor ($R$) defined as $\sum\{(\chi_M T)_{obs} - (\chi_M T)_{calc}\}^2/\sum(\chi_M T)^2_{obs}$ being 5.88×10^{-3}. It may be mentioned that, unlike in mononuclear cobalt(II) complexes, $[Co^{II}(LH)_2]X_2 \cdot nH_2O$ (X = Cl, ClO_4) [2a], spin crossover does not occur in the mononuclear manganese(II) compound **1**.

As shown in Fig. 7, $\chi_M T$ values for **2** are almost constant (*ca.* 0.41 $\mathrm{cm^3\ mol^{-1}\ K}$) throughout the temperature range 2–300 K indicating that copper(II) centers in this compound are noninteracting ($J = 0$). It is known from previous studies that copper(II) centers in dicyanamide-bridged compounds are either weakly antiferromagnetic, weakly ferromagnetic or noninteracting and the range of J values is from $-0.35\ \mathrm{cm}^{-1}$ to $0.20\ \mathrm{cm}^{-1}$ [4]. Therefore, $J = 0$ in **2** is in the range observed in reported compounds. Although the interaction in dicyanamide-bridged copper(II) complexes is very weak, the nature of interaction has been explained previously on the basis of equatorial-equatorial (usually short–short) and equatorial-axial (usually short–long) linkage of dicyanamide ligands to copper(II) centers [4a,4b]. According to this hypothesis, if the difference between Cu–N(equatorial) and Cu–N(axial) bond lengths is small and the coordination geometry is less distorted, the interaction should be ferromagnetic for the axial-equatorial case because of accidental orthogonality between the magnetic orbitals. In **2**, the difference between the Cu–N(equatorial) and Cu–N(axial) bond lengths (1.943(3) versus 2.207(3)) is not large. Again, the τ parameter in the square pyramidal coordination geometry is only 0.004, which apparently indicates an almost ideal environment around the metal center in **2**. However, as discussed above, the coordination geometry is actually highly distorted. $J = 0$ in **2** indicates that accidental orthogonality, which is strongly dependent on the structural features, does not take place in **2** probably due to large distortion in the coordination environment.

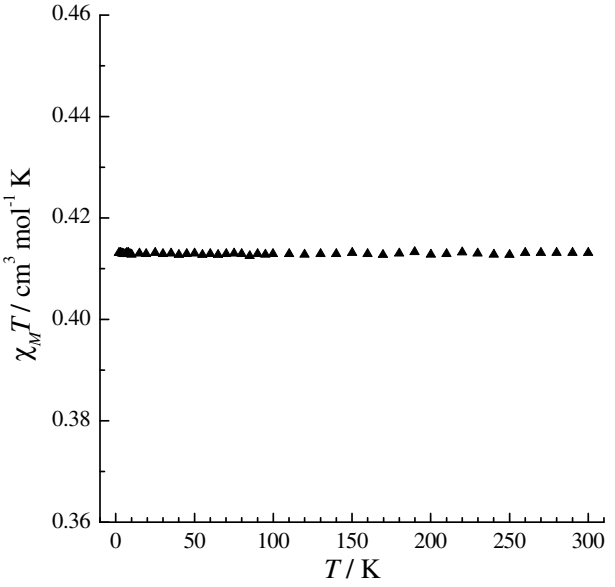


Fig. 7. Experimental (▲) $\chi_M T$ vs. T plots for **2**.

4. Conclusions

The main objective of the present investigation has been isolation and determination of structures of complexes derived from 4-terpyridone with an expectation that 4-terpyridone containing metal compounds may be good building unit to develop hydrogen bonded supramolecular structures. Accordingly, syntheses and structures of two 4-terpyridone containing compounds **1** and **2** have been described in this investigation. In both the compounds, partiticipation of enolic O–H group is observed to generate hydrogen bonded two- or three-dimensional supramolecular structure. Dicyanamide-bridged one-dimensional polymer, **2**, is a new addition in the family of dicyamide-metal systems. Magnetic studies of **1** reveal that, unlike in mononuclear cobalt(II)-4-terpyridone complexes, $[Co^{II}(LH)_2]X_2 \cdot nH_2O$ (X = Cl, ClO_4) [2a], spin-crossover does not take place in the manganese(II) compound **1**. Dicyanamide-bridged copper(II) centers in **2** are practically noninteracting, which is related to the highly distorted coordination environment of the metal centers.

Acknowledgement

Financial support from National Science Council, Taiwan (NSC95-2113-M032-005) and Department of Science and Technology, the Government of India (SR/S1/IC–27/2002), is gratefully acknowledged.

Appendix A. Supplementary data

CCDC 665479 and 665478 contain the supplementary crystallographic data for **1** and **2**. These data can be obtained free of charge via http://www.ccdc.cam.ac.uk/conts/retrieving.html, or from the Cambridge Crystallographic Data Centre, 12 Union Road, Cambridge CB2 1EZ, UK; fax: (+44) 1223-336-033; or e-mail: deposit@ccdc.cam.ac.uk. Supplementary data associated with this article can be found, in the online version, at doi:10.1016/j.poly.2007.12.017.

References

[1] (a) R. Robson, in: J.L. Atwood, J.E.D. Davies, D.D. MacNicol, F. Vögtle, R.B. Toda (Eds.), Comprehensive Supramolecular Chemistry, vol. 6, Pergamon, Oxford, 1996, pp. 733–755;
(b) A.J. Blake, N.R. Champness, P. Hubberstey, M.A. Withersby, M. Schröder, Coord. Chem. Rev. 183 (1999) 117;
(c) J.-P. Sauvage (Ed.), Transition Metals in Supramolecular Chemistry (Perspectives in Supramolecular Chemistry), vol. 5, Willey, England, 1999;
(d) G.R. Desiraju (Ed.), The Crystal as a Supramolecular Entity (Perspectives in Supramolecular Chemistry), vol. 2, Willey, England, 1996;

(e) D. Braga, F. Grepioni, A.G. Orpen, Crystal Engineering: from Molecules and Crystals to Materials, Kluwer Academic Publishers, Dordrecht, 1999;
(f) D. Braga, L. Maini, M. Polito, L. Scaccianoce, G. Cojazzi, F. Grepioni, Coord. Chem. Rev. 216 (2001) 225;
(g) B. Moulton, M.J. Zaworotko, Chem. Rev. 101 (2001) 1629.

[2] (a) A.B. Gaspar, M.C. Munoz, V. Niel, J.A. Real, Inorg. Chem. 40 (2001) 9;
(b) M. Nayak, R. Koner, S. Evans, S. Mohanta, Cryst. Growth Des. 5 (2005) 1907.

[3] (a) S.R. Batten, P. Jensen, B. Moubaraki, K.S. Murray, R. Robson, J. Chem. Soc., Chem. Commun. (1998) 439;
(b) J.L. Manson, C.R. Kmety, Q.-Z. Huang, J.W. Lynn, G.M. Bendele, S. Pagola, P.W. Stephens, L.M. Liable-Sands, A.L. Rheingold, A.J. Epstein, J.S. Miller, Chem. Mater. 10 (1998) 2552;
(c) M. Kurmoo, C.J. Kepert, New J. Chem. (1998) 1515;
(d) S.R. Batten, K.S. Murray, Coord. Chem. Rev. 246 (2003) 103.

[4] (a) B. Vangdal, J. Carranza, F. Lloret, M. Julve, J. Sletten, J. Chem. Soc., Dalton Trans. (2002) 566;
(b) M. Du, X.-J. Zhao, S.R. Batten, J. Ribas, Cryst. Growth Des. 5 (2005) 901;
(c) J.L. Manson, J. Gu, J.A. Schlueter, H.-H. Wang, Inorg. Chem. 42 (2003) 3950;
(d) P. Jensen, D.J. Price, S.R. Batten, B. Moubaraki, K.S. Murray, Chem. Eur. J. 6 (2000) 3186;
(e) H.J. Luo, M.C. Hong, J.B. Weng, J.Y. Zhao, R. Cao, Inorg. Chim. Acta 329 (2002) 59;
(f) W. Gu, H.-D. Bian, J.-Y. Xu, Z.-Q. Liu, P. Cheng, S.-P. Yan, D.-Z. Liao, Z.H. Jiang, Inorg. Chem. Commun. 6 (2003) 966.

[5] G.-Y. Hsu, P. Misra, S.-C. Cheng, H.-H. Wei, S. Mohanta, Polyhedron 25 (2006) 3393.

[6] (a) G.A. van Albada, M.E. Quiroz-Castro, I. Mutikainen, U. Turpeinen, J. Reedijk, Inorg. Chim. Acta 298 (2000) 221;
(b) A. Escuer, F.A. Mautner, N. Sanz, R. Vicente, Inorg. Chem. 39 (2000) 1668;
(c) S. Martin, M.G. Barandika, J.I.R. de Larramendi, R. Cortés, M. Font-Bardia, L. Lezama, Z.E. Serna, S. Solans, T. Rojo, Inorg. Chem. 40 (2001) 3687.

[7] (a) I. Riggio, G.A. van Albada, D.D. Ellis, A.L. Spek, J. Reedijk, Inorg. Chim. Acta 313 (2001) 120;
(b) S.R. Batten, A.R. Harris, P. Jensen, K.S. Murray, A. Ziebell, J. Chem. Soc., Dalton Trans. (2000) 3829;
(c) B.-W. Sun, S. Gao, B.-Q. Ma, Z.-M. Wang, New J. Chem. 24 (2000) 953;
(d) I. Dasna, S. Golhen, L. Ouahab, M. Fettouhi, O. Peña, N. Daro, J.-P. Sutter, Inorg. Chim. Acta 326 (2001) 37.

[8] (a) H.-H. Lin, S. Mohanta, C.-J. Lee, H.-H. Wei, Inorg. Chem. 42 (2003) 1584;
(b) B.-W. Sun, S. Gao, B.-Q. Ma, D.-Z. Niu, Z.-M. Wang, J. Chem. Soc., Dalton Trans. (2000) 4187;
(c) C. Paraschiv, J.-P. Sutter, M. Schmidtmann, A. Müller, M. Andruh, Polyhedron 22 (2003) 1611.

[9] (a) P.M. van der Werff, S.R. Batten, P. Jensen, B. Moubaraki, K.S. Murray, Inorg. Chem. 40 (2001) 1718;
(b) S. Triki, F. Thétiot, J.-R. Galán-Mascaros, J. Sala Pala, K. Dunbar, New J. Chem. 25 (2001) 954;
(c) S.R. Marshall, C.D. Incarvito, J.L. Manson, A.L. Rheingold, J.S. Miller, Inorg. Chem. 39 (2000) 1969.

[10] J.L. Manson, J.A. Schlueter, U. Geiser, M.B. Stone, D.H. Reich, Polyhedron 20 (2001) 1423.

[11] A.M. Kutasi, S.R. Batten, B. Moubaraki, K.S. Murray, J. Chem. Soc., Dalton Trans. (2002) 819.

[12] S.R. Batten, P. Jensen, B. Moubaraki, K.S. Murray, R. Robson, J. Chem. Soc., Chem. Commun. (2000) 793.

[13] (a) Y.-J. Shi, L.-H. Li, Y.-Z. Li, X.-T. Chen, Z. Xue, X.-Z. You, Polyhedron 22 (2003) 917;
(b) H.-L. Sun, S. Gao, B.-Q. Ma, G. Su, Inorg. Chem. 42 (2003) 5399.

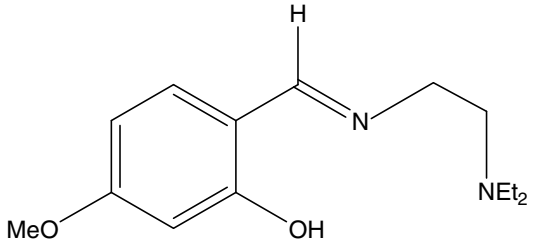
[14] Y.M. Chow, D. Britton, Acta Crystallogr., Sect. B 31 (1975) 1934.

[15] Y.-J. Shi, X.-T. Chen, Y.-Z. Li, Z. Xue, X.-Z. You, New J. Chem. 26 (2002) 1711.

[16] (a) G.M. Sheldrick, SHELXL-97: A Program for Crystal Structure Solution, University of Göttingen, Germany, 1990;
(b) G.M. Sheldrick, SHELXL-97: A Program for Crystal Structure Refinement, University of Göttingen, Germany, 1997.

derived from and based upon metal-coordination networks, ranging from simple chains to ladders, sheets, diamondoid nets, and other fascinating architectures [5]. Azide ion is known for its versatility as bridging ligand since it can bind two metal centers in *end-on* and/or *end-to-end* fashions [6,7]. Among the various transition and non-transition metal atoms cadmium is an extremely toxic element that is naturally present in the environment and also as a result of human activities. Recently, in living organisms the concentration of this metal has been increased gradually. The development of chelating agents is essential for the treatment of cadmium intoxication [8]. The practical importance of Cd(II) coordination chemistry results from the mobilization and immobilization of this metal in the environment, in organisms, and in some technical processes which depend significantly on the complexation of the metal center by chelating organic molecules containing nitrogen and/or sulfur donor atoms. Complexes of Cd(II) with nitrogen-containing ligands have also been used successfully in ligand exchange chromatography [9]. Though cadmium has been known as a toxic metal and is often associated with Hg and Pb as one of the biologically harmful metal ions, recently it has been found that Cd(II) ion can serve as the catalytic center in a newly discovered carbonic anhydrase [10]. Cd(II) ion is capable of adopting a wide variety of geometries and coordination numbers permitted by its d^{10} configuration [11]. Most Cd(II) complexes are octahedral [12] while four- and five-coordinated complexes are limited to few cases imposed either by bulkiness of the donor atoms [13–16] or by steric requirements of the ligands [17]. Moreover, the d^{10} center metals like Zn(II) and Cd(II) associated with the conjugated π systems containing aromatic rings favor the development of fluorescent materials [18–20].

Our research group has already reported some mono-, di-, tri- and polynuclear Cd(II) complexes with different Schiff base ligands or various bidentate chelating diamines in presence of pseudohalides [3,8,9,21–25]. Recently, we also reported three new pseudohalide bridged dinuclear Zn(II) complexes [26] of a potentially tetradentate Schiff base ligand which is the condensation product of *o*-vanillin and 2-dimethylaminoethylamine. In continuation, using a N_2O donor tridentate Schiff base ligand **LH** (Scheme 1) obtained by condensing 2-hydroxy-4-methoxybenzaldehyde and 2-diethylaminoethylamine, we have reported synthetic details, spectral characterizations, thermal investigation, along with X-ray crystal structures and fluorescence studies of two new di- and polynuclear Cd(II) complexes, $[Cd_2(L)_2(Cl)_2]$ (**1**) and $[Cd_3(\mu_{1,1}\text{-}N_3)_4(L)_2\{H_2N(CH_2)_2N(C_2H_5)_2\}\cdot H_2O]_n$ (**2**), respectively, in the present paper.



Scheme 1. **LH**.

2. Experimental

2.1. Materials

2-Diethylaminoethylamine, 2-hydroxy-4-methoxybenzaldehyde (Aldrich, Germany), cadmium(II) acetate dihydrate, cadmium(II) chloride dihydrate, sodium azide (E. Merck, India) were used as received. All the solvents were of AR grade and used as received.

Caution! Azido compounds of metal ions are potentially explosive especially in presence of organic ligands. Only a small amount of material should be prepared and it must be handled with care.

2.2. Physical measurements

The infrared spectra of the complexes were recorded on a Perkin–Elmer RX I FT-IR spectrophotometer with KBr discs (4000–300 cm^{-1}). Elemental analyses (C, H, N) were carried out using a Perkin–Elmer 2400 II elemental analyzer. ^1H NMR spectra were recorded on a Bruker 300 MHz FT-NMR spectrometer using trimethylsilane as internal standard in $CDCl_3$ for complexes **1** and **2**. The thermal analysis of **1** was done on a Mettler Toledo TGA/SDTA-851e thermal analyzer system in a dynamic atmosphere of dinitrogen (flow rate: 30 cm^3 min^{-1}) in alumina crucible at a heating rate of 10 °C min^{-1}. Ground state absorptions for the ligand and the complexes were made with a Perkin–Elmer Lambda 40 (UV–Vis) spectrophotometer in methanol. Perkin–Elmer LS50B spectrofluorimeter model was used for the steady state fluorescence measurements of the complexes and Schiff base ligand at room temperature (298 K). The solutions of the ligand and complexes **1** and **2** were prepared in methanol medium.

2.3. Synthesis of the Schiff base ligand and metal complexes

2.3.1. Schiff base $[(C_2H_5)_2NCH_2CH_2N{=}CHC_6H_3(OH)(OMe)]$ (**LH**)

The Schiff base was obtained by refluxing a methanolic solution (50 ml) of 2-hydroxy-4-methoxybenzaldehyde (10 mmol) and 2-diethylaminoethylamine (10 mmol) for 30 min. The resulting orange yellow solution containing the required product was used without further purification.

2.3.2. $[Cd_2(L)_2(Cl)_2]$ (**1**)

To a methanolic solution (20 ml) of cadmium chloride dihydrate (0.200 g, 1 mmol), the solution of Schiff base (1 mmol) was added with constant stirring for 10 min. Colourless, block shaped crystals suitable for X-ray diffraction were obtained after 5 days. Crystals were collected by filtra-

tion and air-dried. Yield: 53%. *Anal.* Calc. for $C_{28}H_{42}N_4O_4Cl_2Cd_2$: C, 42.33; H, 5.33; N, 7.05. Found: C, 42.09; H, 5.25; N, 7.01%.

2.3.3. $[Cd_3(\mu_{1,1}\text{-}N_3)_4(L)_2\{H_2N(CH_2)_2N(C_2H_5)_2\}\cdot H_2O]_n$ (2)

To the aqueous methanolic solution (30 ml) of cadmium acetate dihydrate (0.266 g, 1 mmol), the solution of Schiff base **LH** (1 mmol) was added followed by mixing a solution of sodium azide (0.065 g, 1 mmol) in minimum volume of methanol with constant stirring for 10 min. This mixture was kept at room temperature yielding red, block shaped crystals suitable for X-ray diffraction after 10 days. Crystals were isolated by filtration and air-dried. Yield: 61%. *Anal.* Calc. for $C_{68}H_{120}N_{36}O_9Cd_6$: C, 36.13; H, 5.35; N, 22.31. Found: C, 35.98; H, 5.21; N, 22.25%.

2.4. Crystallographic data collection and structure refinements

Intensity data for crystals of **1** and **2** were collected on Bruker X8 Apex II CCD diffractometer and Bruker SMART Apex CCD diffractometer, respectively. Data were corrected for absorption empirically by means of multi-scans (SADABS) for both **1** and **2**. The structures were solved by direct and difference Fourier methods and refined by full-matrix least-squares on F^2. All non-hydrogen atoms were refined with anisotropic displacement parameters. The crystallographic computing was performed using SHELXTL [27] programs. Further details have been given in Table 1. Complex **1** crystallises in the non-centrosymmetric space group $P2_1$ and was refined as a racemic twin. No higher symmetry could be found and there are no significant correlation matrix elements to suggest higher molecular symmetry.

Table 1
Experimental, crystallographic and refinement data for complexes **1** and **2**

Complex	1	2
Empirical formula	$C_{28}H_{42}N_4O_4Cl_2Cd_2$	$C_{68}H_{120}N_{36}O_9Cd_6$
Formula weight	794.36	2260.40
Temperature (K)	123(1)	100(2)
Wavelength (Å)	0.71073	0.71073
Crystal system	monoclinic	triclinic
Space group	$P2_1$	$P\bar{1}$
Unit cell dimensions		
a (Å)	10.4879(2)	11.809(2)
b (Å)	12.9687(4)	12.869(3)
c (Å)	12.1802(3)	17.996(4)
α (°)	90	99.26(3)
β (°)	108.8950(10)	102.77(3)
γ (°)	90	116.57(3)
Volume (Å^3)	1567.41(7)	2277.3(13)
Z	2	1
D_{calc} (Mg/m^3)	1.683	1.648
Absorption coefficient (mm^{-1})	1.566	1.446
$F(000)$	800	1140
Crystal size (mm)	0.16 × 0.14 × 0.10	0.34 × 0.28 × 0.20
θ range for data collection (°)	1.77–27.50	1.22–26.37
Reflections collected	12228	18080
Independent reflections [R_{int}]	5121 [0.1278]	9159 [0.0542]
Goodness-of-fit on F^2	1.074	1.078
Final R indices [$I > 2\sigma(I)$]	$R_1 = 0.0453$, $wR_2 = 0.1233$	$R_1 = 0.0665$, $wR_2 = 0.1710$
R indices (all data)	$R_1 = 0.0483$, $wR_2 = 0.1273$	$R_1 = 0.0771$, $wR_2 = 0.1795$
Largest difference in peak and hole (e Å^{-3})	1.287 and −1.974	2.460 and −1.362

3. Results and discussion

3.0.1. Description of crystal structure of 1

An ORTEP representation of the binuclear unit for complex **1** is shown in Fig. 1 with dimensions about the Cd atoms in Table 2. The structure is a dimer, comprising two essentially equivalent cadmium(II) centers, each with a terminal chloride ligand and the deprotonated tridentate

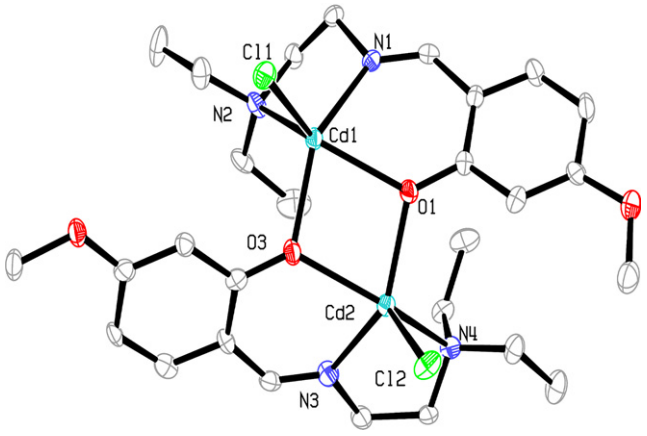


Fig. 1. ORTEP view of the dimeric unit of complex **1**, with atom labels. Displacement ellipsoids are shown at 50% probability level. The hydrogen atoms are omitted for clarity.

Table 2
Selected molecular dimensions (bond lengths in Å and angles in °) for **1**

Bond lengths			
Cd(1)–Cl(1)	2.4357(16)	Cd(2)–Cl(2)	2.4418(18)
Cd(1)–O(3)	2.227(5)	Cd(2)–O(3)	2.284(4)
Cd(1)–N(1)	2.230(6)	Cd(2)–N(3)	2.277(6)
Cd(1)–N(2)	2.428(6)	Cd(2)–N(4)	2.412(6)
Cd(1)–O(1)	2.294(4)	Cd(2)–O(1)	2.242(5)
Bond angles			
O(3)–Cd(1)–Cl(1)	108.84(15)	O(3)–Cd(2)–Cl(2)	115.79(15)
N(1)–Cd(1)–Cl(1)	105.14(16)	N(3)–Cd(2)–Cl(2)	113.52(17)
N(2)–Cd(1)–Cl(1)	104.81(16)	N(4)–Cd(2)–Cl(2)	102.99(14)
O(1)–Cd(1)–Cl(1)	121.00(13)	O(1)–Cd(2)–Cl(2)	105.04(14)
N(1)–Cd(1)–O(3)	145.2(2)	O(3)–Cd(2)–N(4)	139.2(2)
O(3)–Cd(1)–N(2)	102.1(2)	O(1)–Cd(2)–N(3)	140.2(2)
O(3)–Cd(1)–O(1)	75.86(16)	O(1)–Cd(2)–O(3)	75.76(16)
N(1)–Cd(1)–N(2)	76.0(2)	N(3)–Cd(2)–N(4)	74.1(2)
O(1)–Cd(1)–N(1)	80.34(18)	O(3)–Cd(2)–N(3)	78.95(19)
O(1)–Cd(1)–N(2)	132.5(2)	O(1)–Cd(2)–N(4)	107.06(19)
Cd(2)–O(1)–Cd(1)	103.34(18)	Cd(1)–O(3)–Cd(2)	104.13(18)

Schiff base ligand $\mathbf{L}^-$ bonded through the imine nitrogen, amine nitrogen and phenolato oxygen (N,N,O) atoms. Two phenolato O atoms O(1) and O(3) of two molecules of deprotonated Schiff base ligand bridge the two cadmium(II) centers and link the two halves of the dimer about a pseudo two fold symmetry axis which lies normal to the almost planar Cd_2O_2 ring. The geometry about the five-coordinated cadmium centers is approximately square pyramidal with the chlorine atoms occupying the (off-center) apical sites; the basal planes *e.g.* O(1), O(3), N(1) and N(2) about Cd(1), form good mean-planes from which the Cd atoms are displaced by 0.886(7) and 0.893(7) Å towards the chloride ligands. The bridging oxygen atoms form asymmetric linkages to the Cd atoms with a range of Cd–O distances 2.227(5)–2.294(4) Å and Cd(1)–O–Cd(2) bridging angles of 103.34(18) and 104.13(18)°. The long distance (3.558 Å) between two Cd(II) centers suggests that there is no interaction between these two metal centers. The angles around O(1) and O(3) are 359.44 and 359.33°, respectively (almost equals to 360°) indicating no pyramidal distortion at these atoms.

3.0.2. Description of crystal structure of **2**

The trimeric asymmetric unit of the polymeric complex **2** is shown in Fig. 2 with selected bond distances and bond angles listed in Table 3. This trinuclear asymmetric unit of complex **2** forms a zig-zag ladder shaped one-dimensional polymer (Fig. 3) through the doubly *end-on* azido bridging. The non-bonded Cd(1)...Cd(3), Cd(1)...Cd(2), Cd(2)...Cd(2) and Cd(3)...Cd(3) separations are 3.685, 3.692, 3.972 and 3.847 Å, respectively.

As shown in Fig. 3, the Cd(II) atoms are all six coordinated with distorted octahedral geometry having N_4O_2 donor set for each of the central Cd(1) atom, while N_5O donor set for the adjacent Cd(2) and Cd(3) atoms. The distortion in the geometry from regular octahedron is evidenced from the respective *cis*- and *trans*-angles about Cd(1), Cd(2) and Cd(3) centers (Table 3). Such variations in the bond angles are clearly due to the formation of bridges between the Cd atoms and also due to the formation of chelate by the organic amine. The Cd(1) atom is doubly bound together with both the adjacent Cd(2) and Cd(3) centers by μ_2-phenolato oxygen atoms O(2) and O(4), respectively from the two deprotonated Schiff base moieties $\mathbf{L}^-$ and the $\mu_{1,1}$-azido nitrogen atoms N(4) and N(7), respectively, as depicted in Fig. 2. Again, the Cd(2) or Cd(3) atom of one trimeric asymmetric subunit is bridged with the adjacent cadmium(II) atom of the next subunit via doubly *end-on* azido groups generating one-dimensional ladder shaped zig-zag polynuclear network (Fig. 3). In this complex the chelating diamine is attached with the Cd(1) centers together with the deproto-

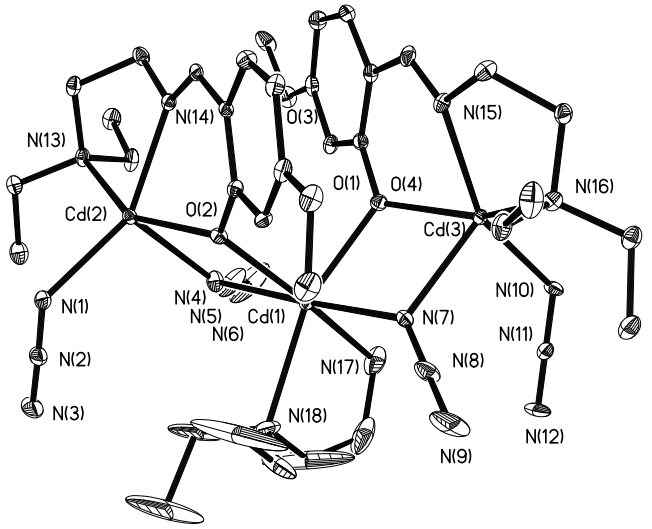


Fig. 2. ORTEP view of the trimeric asymmetric subunit of polymeric complex **2**, with atom labels. Displacement ellipsoids are shown at 50% probability level. The hydrogen atoms are omitted for clarity.

Table 3
Selected molecular dimensions (bond lengths in Å and angles in °) for **2**

Bond lengths			
Cd(1)–O(2)	2.272(5)	Cd(2)–N(1)	2.255(6)
Cd(1)–O(4)	2.301(5)	Cd(2)–N(14)	2.272(6)
Cd(1)–N(17)	2.338(7)	Cd(2)–O(2)	2.304(5)
Cd(1)–N(4)	2.412(6)	Cd(2)–N(4)	2.323(6)
Cd(1)–N(7)	2.418(6)	Cd(2)–N(13)	2.437(6)
Cd(1)–N(18)	2.459(7)	Cd(2)–N(1)#1	2.609(6)
Cd(3)–O(4)	2.265(5)	Cd(3)–N(10)	2.277(6)
Cd(3)–N(15)	2.288(6)	Cd(3)–N(7)	2.337(6)
Cd(3)–N(16)	2.433(6)	Cd(3)–N(10)#2	2.470(6)
N(1)–Cd(2)#1	2.609(6)	N(10)–Cd(3)#2	2.470(6)
Bond angles			
O(2)–Cd(1)–O(4)	91.01(17)	N(1)–Cd(2)–N(14)	149.40(2)
N(17)–Cd(1)–O(2)	167.10(2)	N(1)–Cd(2)–O(2)	107.10(2)
N(17)–Cd(1)–O(4)	91.50(3)	N(14)–Cd(2)–O(2)	80.96(18)
O(2)–Cd(1)–N(4)	74.40(2)	N(1)–Cd(2)–N(4)	101.10(2)
N(4)–Cd(1)–O(4)	104.30(2)	N(4)–Cd(2)–N(14)	109.50(2)
N(17)–Cd(1)–N(4)	92.70(3)	O(2)–Cd(2)–N(4)	75.50(2)
O(2)–Cd(1)–N(7)	103.65 (19)	N(1)–Cd(2)–N(13)	99.80(2)
N(7)–Cd(1)–O(4)	74.05(19)	N(14)–Cd(2)–N(13)	76.20(2)
N(17)–Cd(1)–N(7)	89.20(2)	O(2)–Cd(2)–N(13)	153.11(18)
N(4)–Cd(1)–N(7)	177.50(2)	N(13)–Cd(2)–N(4)	98.80(2)
O(2)–Cd(1)–N(18)	104.30(2)	N(1)–Cd(2)–N(1)#1	70.70(3)
O(4)–Cd(1)–N(18)	161.70(2)	N(14)–Cd(2)–N(1)#1	79.10(2)
N(17)–Cd(1)–N(18)	75.70(3)	O(2)–Cd(2)–N(1)#1	97.39(18)
N(4)–Cd(1)–N(18)	89.60(2)	N(4)–Cd(2)–N(1)#1	167.40(2)
N(7)–Cd(1)–N(18)	92.50(2)	N(13)–Cd(2)–N(1)#1	92.10(2)
O(4)–Cd(3)–N(10)	105.50(2)	N(7)–Cd(3)–N(16)	98.70(2)
O(4)–Cd(3)–N(15)	80.80(19)	O(4)–Cd(3)–N(10)#2	96.20(2)
N(10)–Cd(3)–N(15)	152.70(2)	N(10)–Cd(3)–N(10)#2	71.80(2)
O(4)–Cd(3)–N(7)	76.28(19)	N(15)–Cd(3)–N(10)#2	81.20(2)
N(10)–Cd(3)–N(7)	91.80(2)	N(7)–Cd(3)–N(10)#2	159.60(2)
N(7)–Cd(3)–N(15)	115.50(2)	N(16)–Cd(3)–N(10)#2	96.90(2)
O(4)–Cd(3)–N(16)	150.58(19)	Cd(2)–N(1)–Cd(2)#1	109.30(3)
N(10)–Cd(3)–N(16)	103.70(2)	Cd(1)–O(4)–Cd(3)	107.60(2)
N(16)–Cd(3)–N(15)	75.30(2)	Cd(1)–N(7)–Cd(3)	101.60(2)
Cd(2)–O(2)–Cd(1)	107.66(19)	Cd(3)–N(10)–Cd(3)#2	108.20(2)
Cd(2)–N(4)–Cd(1)	102.50(2)	N(9)–N(8)–N(7)	178.50(12)
N(3)–N(2)–N(1)	178.0(8)	N(12)–N(11)–N(10)	178.0(8)
N(6)–N(5)–N(4)	177.90(13)		

Symmetry transformations used to generate equivalent atoms: #1 $-x$, $-y+1$, $-z$; #2 $-x+1$, $-y+1$, $-z+1$.

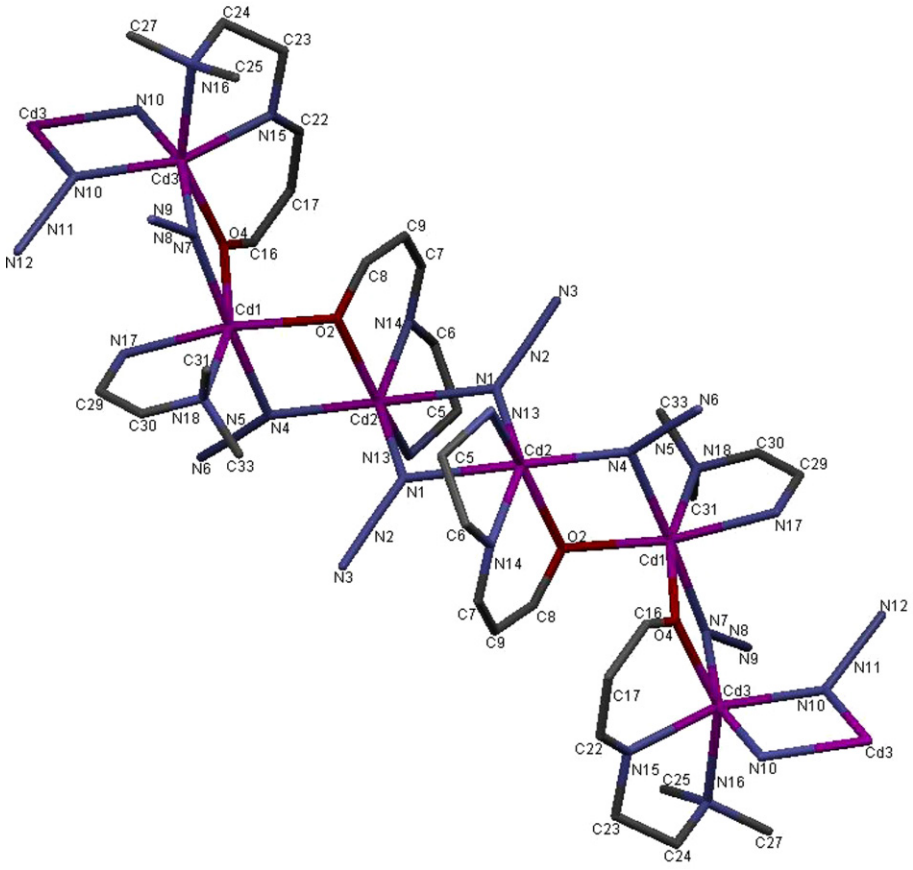


Fig. 3. View of the longer part of zig-zag ladder shaped polymeric chain of the core complex **2** in Mercury, with atom labels (all pendant groups such as the aryl and ethyl moieties are omitted for clarity).

nated bridging Schiff base ligands $\mathbf{L}^-$. The reason behind this may be the partial hydrolysis of the Schiff base ligand in the presence of the azide anion bridged with the metal centers to generate the free amine moiety. The square base around the Cd(1) is formed by phenolato oxygen atoms [O(4) and O(2)] from the two bridging $\mathbf{L}^-$, amino nitrogen atoms N(17) and N(18) from the chelating diamine $H_2N(CH_2)_2N(C_2H_5)_2$, where as the axial sites are occupied by the N(4) and N(7) atoms of the two $\mu_{1,1}$-azido groups with a *trans* angle, N(4)–Cd(1)–N(7), of 177.5(2)°. On the other side the N_2O donor set [imino nitrogen N(14), amino nitrogen N(13) and the bridging phenolato oxygen O(2)] from the bridging $\mathbf{L}^-$ and the *end-on* bridging azido nitrogen N(1) form the square base around Cd(2) and other two $\mu_{1,1}$-azido nitrogen atoms N(4) and N(1)#1 take up two axial positions with respect to the equatorial plane of the pseudooctahedral geometry, with a *trans* angle, N(4)–Cd(2)–N(1)#1, of 167.4(2)°. The environment around the Cd(3) atom is identical with the Cd(2) center. For Cd(3), we define the equatorial plane comprising of imino nitrogen N(15), amino nitrogen N(16), the bridging phenolato oxygen O(4) (coming from the bridging $\mathbf{L}^-$) and the *end-on* bridging azido nitrogen N(10). The N(7) and N(10)#2 are in the axial positions with respect to this plane, with a *trans* angle, N(7)–Cd(3)–N(10)#2, of 159.6(2)°. The bridging angles Cd–O–Cd and Cd–N(azido)–Cd vary from 107.6(2) to 107.66(19)° and 101.6(2)–109.3(3)°, respectively. The N–N–N bond angles in the $\mu_{1,1}$-azido groups are 177.9(13)–178.5(12)°, slightly deviated from the linearity.

3.1. Infrared spectra

The infrared spectra of the complexes are consistent with their structural data given in this paper. The trifurcated bands at 2095, 2067 and 2038 cm^{-1} for **2** are attributed for the bridging azido (N_3^-) groups in **2** [28]. The strong $\nu_{C=N}$ bands occurring at 1625 and 1602 cm^{-1} for **1** and **2**, respectively, are shifted considerably towards lower frequencies compared to that of the free Schiff base ligand (1635 cm^{-1}) indicating the coordination of the imino nitrogen atoms with the metal centers [29]. Ligand coordination to metal centers is substantiated by two bands appearing for ν_{M-N} at 425, 460 cm^{-1} and for ν_{M-O} at 375, 370 cm^{-1} for **1** and **2**, respectively.

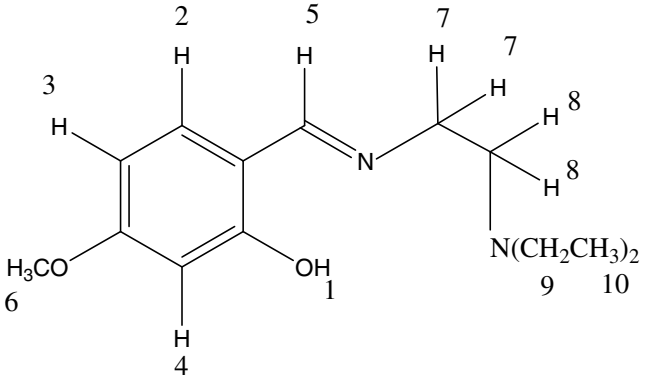
3.2. ^1H NMR spectra

The ^1H NMR spectroscopy has been used to extract information regarding the coordination mode of the ligand with metal ions for the complexes **1** and **2**; the NMR data

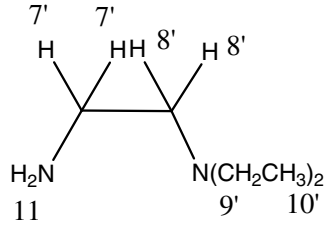
Table 4
^{1}H NMR spectral data with assignments for the Schiff base **LH** and complexes **1** and **2**

Schiff base/ Complex	δ (in ppm)
LH	2.01 (6H, t, $J = 2.1$ Hz, H10); 2.06 (4H, q, $J = 2.4$ Hz, H9); 2.64 (2H, t, $J = 3.4$ Hz, H8); 3.42 (2H, t, $J = 4.5$ Hz, H7); 3.86 (3H, s, H6); 5.26 (1H, s, H1); 6.35 (1H, d, $J = 7.2$ Hz, H2); 6.61 (1H, s, H4); 8.01 (1H, d, $J = 7.8$ Hz, H3); 8.30 (1H, s, H5)
1	2.04 (12H, t, $J = 2.1$ Hz, H10); 2.12 (8H, q, $J = 2.4$ Hz, H9); 2.66 (4H, t, $J = 3.4$ Hz, H8); 3.48 (4H, t, $J = 4.2$ Hz, H7); 3.87 (6H, s, H6); 6.44 (2H, d, $J = 7.2$ Hz, H2); 6.82 (2H, s, H4); 8.05 (2H, d, $J = 7.6$ Hz, H3); 8.33 (2H, s, H5)
2	2.04 (12H, t, $J = 2.1$ Hz, H10); 2.14 (8H, q, $J = 2.4$ Hz, H9); 2.65 (4H, t, $J = 3.2$ Hz, H8); 3.46 (4H, t, $J = 3.9$ Hz, H7); 4.03 (6H, s, H6); 6.51 (2H, d, $J = 6.8$ Hz, H2); 6.83 (2H, s, H4); 8.13 (2H, d, $J = 7.8$ Hz, H3); 8.35 (2H, s, H5); 2.06 (6H, t, $J = 2.1$ Hz, H10′); 2.15 (4H, q, $J = 2.4$ Hz, H9′); 2.63 (4H, t, $J = 3.2$ Hz, H8′); 3.40 (4H, t, $J = 3.9$ Hz, H7′); 5.65 (2H, s, H11)

are summarized in Table 4 showing the proton numbering Schemes 2 and 3. In the ^{1}H NMR spectra of **1** and **2**, the signal due to the phenolic hydrogen (H1) of the free **LH** molecule (5.26 ppm) is absent, indicating the coordination of the deprotonated ligands ($\mathbf{L}^-$) in these complexes. The signals for the amino ethyl groups (H9 and H10) show down-field shifts (0.08 ppm) in their position from those of the free molecule due to the coordination of the amino nitrogen atom with the metal centers. The singlet due to the proton (H5) attached to the imino (–C=N) group shows a down-field shift (0.03–0.05 ppm) compared to its position in the free molecule, reflecting the coordination of the deprtonated Schiff base ligand ($\mathbf{L}^-$) to the metal centers through the imine nitrogen atom. The phenyl hydrogens show significant shifts [0.15–0.16 ppm (H2), 0.22 ppm (H4), 0.12 ppm (H3)] indicating the involvement of phenolato oxygen in coordination with the metal centers. For the complexes, the protons (H7) of the CH_2 group attached to the imine nitrogen and the protons (H8) of the CH_2 group associated with the amine nitrogen atoms show down field shifts from 0.04 ppm and 0.01 ppm, respectively, from that of the free ligand. For complex **2** five additional NMR signals are observed due to the protons (H10′, H9′, H8′, H7′ and H11) of chelating diamine $H_2N(CH_2)_2N(C_2H_5)_2$ attached with the Cd(1) center. Hydrogen atoms attached to the amino nitrogen atoms show increase in the chemical shift value from the free diamine ligand due to the coordination to the Cd(II) ion. The results obtained from the ^{1}H NMR spectra support the structures obtained from X-ray analysis and suggest that the structures of the complexes **1** and **2** are retained in $CDCl_3$ solution.



Scheme 2. Schiff base ligand.



Scheme 3. Free diamine ligand.

3.3. Thermogravimetric analysis

The thermal study of complex **2** was not carried out in order to avoid the explosion of the azide compound. The thermal analysis of complex **1** was performed in the temperature range 28.3–800 °C in dynamic nitrogen atmosphere. It shows a gradual weight loss indicating decomposition in fragment with increasing temperature. The thermogram exhibits the weight loss between 240.5 and 800 °C corresponding to about 76.24% and its stability upto 240.5 °C. The complete decomposition of the complex **1** occurs in three steps. The first step occurs between 240.5 and 487.1 °C, while the second and the third steps take place between 499.1–590.3 °C and 624.3–800 °C, respectively. The mass loss for **1** is due to the elimination of two molecules of the coordinating ligand $\mathbf{L}^-$ and the remaining residue at 800 °C corresponds to cadmium oxide which is confirmed by quantitative estimation.

3.4. Fluorescence spectral studies

The fluorescence properties of the Schiff base ligand (**LH**) and its Cd(II) complexes (**1** and **2**) were studied at room temperature (298 K) in methanol–water solutions (Fig. 4). Complex **1** displays emission spectrum at 410 nm while **2** has a band at 419 nm. Complex **1** shows very weak fluorescence. Complex **2** exhibits strong fluorescence in comparison to **LH** and complex **1**. For Cd(II) complex, no emission originating from metal-centered MLCT/LMCT excited states are expected, since Cd(II) ion is difficult to oxidize or reduce due to its stable d^{10} configuration.

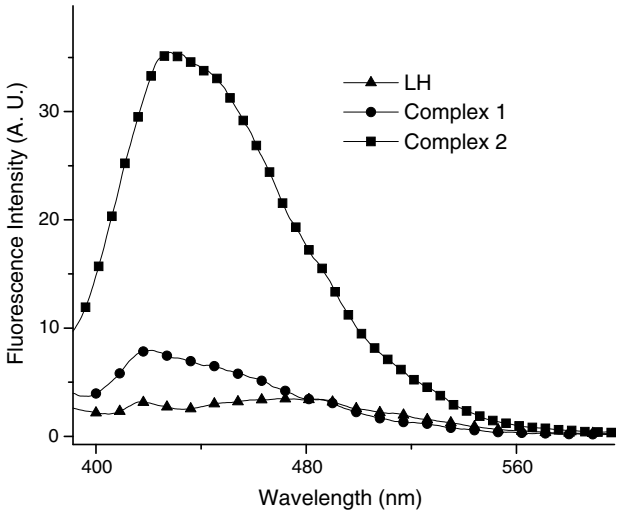


Fig. 4. Fluorescence spectra of LH, complexes **1** and **2** in methanol–water medium ($\lambda_{exc} = 370$ nm).

Thus, the emission observed in the complex is tentatively assigned to the $^1(\pi–\pi^*)$ intraligand fluorescence. It is interesting that the Cd(II) complexes show higher intensity than that of the free ligand. Metal ions can enhance or quench the fluorescence emission of some Schiff base ligands containing aromatic ring. Quenching of fluorescence of a ligand by transition metal ions during complexation is a rather common phenomenon which is explained by processes such as magnetic perturbation, redox activity and electronic energy transfer. Enhancement of fluorescence through complexation is, however, of much interest as it opens up the opportunity for photochemical applications of these complexes [30]. In the absence of metal ions the fluorescence of the ligand is probably quenched by the occurrence of a photoinduced electron transfer (PET) process due to the presence of lone pairs of electrons of the donor atoms in the ligand. Such a PET process is prevented by the complexation of **LH** with metal ions; thus the fluorescence intensity may be greatly enhanced by the coordination of Cd(II). This is defined as chelation enhanced fluorescence intensity. The chelation of the ligand to Cd(II) increases the rigidity of the ligand and thus reduces the loss of energy by thermal vibrational decay [31].

4. Conclusion

In this paper it has been shown that the geometry about the Cd(II) centers in the dinuclear complex **1** and polynuclear complex **2** are square pyramidal and distorted octahedral, respectively. The two Cd(II) centers in **1** are held together by two μ_2-phenolato oxygen atoms with the two terminal chlorine atoms occupying the apical sites of the square pyramidal environment of both the metal centers. On the other hand complex **2** is the one-dimensional ladder shaped zig-zag polymer having six-coordinated Cd(II) centers linked via $\mu_{1,1}$-azido and μ_2-phenolato bridges. In this complex also the chelating diamine is attached with the Cd(1) centers together with the deprotonated bridging Schiff base ligands $\mathbf{L}^-$. This may be due to the partial hydrolysis of the Schiff base ligand in presence of the azide anion bridged with the metal centers.

Acknowledgements

We gratefully acknowledge Jadavpur University, Kolkata, India for providing Laboratory facilities. We are thankful to Dr. N. Gucchait and Ms. A. Chakraborty, Department of Chemistry, University College of Science and Technology, Kolkata, India for recording the fluorescence spectra.

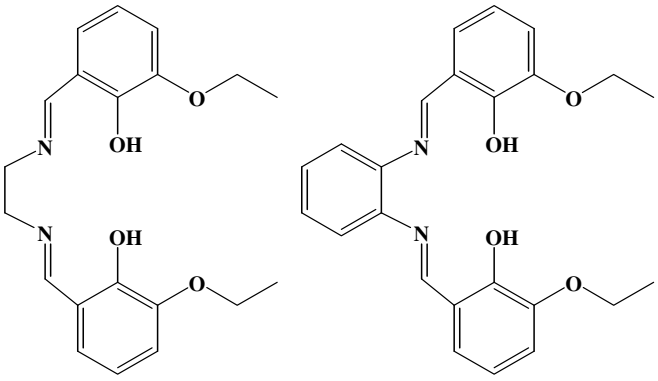
Appendix A. Supplementary material

CCDC 649492 and 649491 contain the supplementary crystallographic data for **1** and **2**, respectively. These data can be obtained free of charge via http://www.ccdc.cam.ac.uk/conts/retrieving.html, or from the Cambridge Crystallographic Data Center, 12, Union Road, Cambridge CB2 1EZ, UK; fax: (+44) 1223-336-033; or e-mail: deposit@ccdc.cam.ac.uk. Supplementary data associated with this article can be found, in the online version, at doi:10.1016/j.poly.2007.12.005.

References

[1] B. Xiao, H. Hou, Y. Fan, M. Tang, Inorg. Chim. Acta 360 (2007) 3019, and references therein.
[2] D. Bose, J. Banerjee, S.H. Rahaman, G. Mostafa, H.-K. Fun, R.D.B. Walsh, M.J. Zaworotko, B.K. Ghosh, Polyhedron 23 (2004) 2045.
[3] S. Sen, P. Talukder, S.K. Dey, S. Mitra, G. Rosair, D.L. Hughes, G.P.A. Yap, G. Pilet, V. Gramlich, T. Matsushita, Dalton Trans. (2006) 1758, and references therein.
[4] S. Jin, D. Wang, W. Chen, Inorg. Chem. Commun. 10 (2007) 685, and references therein.
[5] M.A. Withersby, A.J. Blake, N.R. Champness, P.A. Cooke, P. Hubberstey, M. Schröder, J. Am. Chem. Soc. 122 (2000) 4044.
[6] J. Ribas, M. Monfort, B.K. Ghosh, X. Solans, M.F. Bardía, J. Chem. Soc., Chem. Commun. (1995) 2375.
[7] A. Escuer, M. Font-Bardía, E. Penalba, X. Solans, R. Vicente, Polyhedron 18 (1998) 211.
[8] S. Sen, P. Talukder, G. Rosair, S. Mitra, Struct. Chem. 16 (2005) 605.
[9] R. Karmakar, C.R. Choudhury, D.L. Hughes, S. Mitra, Inorg. Chim. Acta 360 (2007) 2631, and references therein.
[10] T.W. Lane, F.M.M. Morel, Proc. Natl. Acad. Sci. USA 97 (2000) 4627.
[11] H. Strasdeit, W. Saak, S. Pohl, W.L. Driessen, J. Reedjik, Inorg. Chem. 27 (1988) 1557.
[12] Specialist Periodical Report, The Chemical Society, London, vols. 1–5, 1973–1977.
[13] M. Nardelli, L. Cavalca, A. Braibanti, Gazetta 87 (1957) 137.
[14] A. Domenicano, L. Torelli, A. Vaciago, L. Zambonelli, J. Chem. Soc. A (1968) 1351.
[15] B.F. Hoskins, B.P. Kelly, Inorg. Nucl. Chem. Lett. 8 (1972) 875.
[16] E.F. Epstein, I. Bernel, J. Chem. Soc. A (1971) 3628.
[17] M. Cannas, G. Carta, A. Cristini, G. Marongiu, J. Chem. Soc., Dalton Trans. (1976) 210, and references therein.
[18] L.L. Wen, D.B. Dang, C.Y. Duan, Y.Z. Li, Z.F. Tian, Q.J. Meng, Inorg. Chem. 44 (2005) 7161.

[19] L.L. Wen, Y.Z. Li, Z.D. Lu, J.G. Lin, C.Y. Duan, Q.J. Meng, Cryst. Growth Des. 6 (2006) 530.
[20] L.L. Wen, Z.D. Lu, J.G. Lin, Z.F. Tian, H.Z. Zhu, Q.J. Meng, Cryst. Growth Des. 7 (2007) 93.
[21] J. Chakraborty, B. Samanta, G. Pilet, S. Mitra, Inorg. Chem. Commun. 10 (2007) 40.
[22] J. Chakraborty, S. Thakurta, B. Samanta, A. Ray, G. Pilet, S.R. Batten, P. Jensen, S. Mitra, Polyhedron 26 (2007) 5139.
[23] N. Mondal, M.K. Saha, S. Mitra, V. Gramlich, J. Chem. Soc., Dalton Trans. (2000) 3218.
[24] C.R. Choudhury, S.K. Dey, N. Mondal, S. Mitra, S.O.G. Mahalli, K.M.A. Malik, Inorg. Chem. Commun. 4 (2001) 419.
[25] C.R. Choudhury, S.K. Dey, N. Mondal, S. Mitra, V. Gramlich, Inorg. Chim. Acta 353 (2003) 217.
[26] S. Basak, S. Sen, S. Banerjee, S. Mitra, G. Rosair, M.T.G. Rodriguez, Polyhedron 26 (2007) 5104.
[27] G.M. Sheldrick, Programs for the Solution and Refinement of Crystal Structures, SHELXTL version 5.1. Bruker AXS P4 Inc., Madison, Wisconsin, USA, 1999.
[28] K. Nakamoto, Infrared and Raman Spectra of Inorganic and Coordination Compounds, 5th ed., Wiley & Sons Interscience Publication, New York, 1997.
[29] M. Tanaka, M. Kitaoka, H. Ökawa, S. Kida, Bull. Chem. Soc. Jpn. 42 (1976) 677.
[30] A. Majumder, G.M. Rosair, A. Mallick, N. Chattopadhyay, S. Mitra, Polyhedron 25 (2006) 1753, and references therein.
[31] D. Das, B.G. Chand, K.K. Sarker, J. Dinda, C. Sinha, Polyhedron 25 (2006) 2333.



H_2L H_2L^1

Chart 1. Chemical structures of H_2L and H_2L^1.

diamines, we have reported that the potential encapsulation of water in the vacant O_4 ligand compartment results in the formation of an inclusion compound $[Cu^{II}L\subset(H_2O)]$ and tetrametallic compounds $[\{Cu^{II}LM^{II}(H_2O)_3\}\{Cu^{II}L\}_2](ClO_4)_2$ (M = Cu, Co, or Mn) consisting of cocrystals of one dinuclear $[Cu^{II}LM^{II}(H_2O)_3]^{2+}$ cationic unit and two mononuclear $[Cu^{II}L]$ moieties (H_2L = *N*,*N*′-ethylenebis(3-ethoxysalicylaldimine); Chart 1) [2]. The reason for cocrystallization in these compounds is clearly understood from the hydrogen bonding interactions. This observation indicates that designed syntheses of dinuclear–mononuclear cocrystals may be possible in similar ligand environments. In order to further explore this possibility, we report here the syntheses, structures, and magnetic properties of an inclusion compound $[Cu^{II}L^1\subset(H_2O)]$ (**1**) as well as self-assembled heptacopper(II) compound $[\{Cu^{II}L^1Cu^{II}(H_2O)_3\}_2\{Cu^{II}L^1\}_3](ClO_4)_4\cdot 2CH_3COCH_3$ (**2**), and tetrametallic compounds $[\{Cu^{II}L^1M^{II}(H_2O)_3\}\{Cu^{II}L^1\}_2](ClO_4)_2\cdot H_2O\cdot CH_3COCH_3$ (M = Co (**3**), M = Mn (**4**)) derived from the ligand *N*,*N*′-*o*-phenylenebis(3-ethoxysalicylaldimine) (H_2L^1; Chart 1).

2. Experimental

2.1. Materials and physical methods

All the reagents and solvents were purchased from commercial sources and used as received. The Schiff base ligand H_2L^1 was prepared by 2:1 condensation of 3-ethoxysalicylaldehyde and *o*-phenylenediamine in methanol. Elemental (C, H, and N) analyses were performed on a Perkin–Elmer 2400 II analyzer. IR spectra were recorded in the region 400–4000 cm^{-1} on a Perkin–Elmer RXIFT spectrophotometer with samples as KBr disks. Magnetic susceptibility measurements of **1** at 300 K were carried out with a Sherwood Scientific Co., UK magnetic susceptibility balance. Variable-temperature (2–300 K) magnetic susceptibility measurements at a fixed field strength of 1 T were carried out with a Quantum Design MPMS SQUID magnetometer. Diamagnetic corrections were estimated from the Pascal constants [8].

2.2. Syntheses

2.2.1. $[Cu^{II}L^1\subset(H_2O)]$ (**1**) [9]

An aqueous solution (10 mL) of copper(II) acetate monohydrate (1.0 g, 5 mmol) was dropwise added to a suspension of H_2L^1 (2.02 g, 5 mmol) in methanol (30 mL). A reddish brown precipitate started to deposit. After one hour stirring, the compound was collected by filtration and air dried. Dimethylformamide was used for recrystallization. Yield: 1.94 g (80%). Anal. Calc. for $C_{24}H_{24}N_2O_5Cu$: C, 59.56; H, 4.99; N, 5.79. Found: C, 59.65; H, 4.92; N, 5.70%. IR (cm^{-1}, KBr): $\nu_{as}(H_2O)$, 3506w; $\nu_s(H_2O)$, 3468w; ν(C=N), 1606s; $\delta(H_2O)$, 1541m; ν(C–OEt), 1244s. μ_{eff} = 1.71 BM (bohr magneton).

2.2.2. $[\{Cu^{II}L^1Cu^{II}(H_2O)_3\}_2\{Cu^{II}L^1\}_3](ClO_4)_4\cdot 2CH_3COCH_3$ (**2**) and $[\{Cu^{II}L^1M^{II}(H_2O)_3\}\{Cu^{II}L^1\}_2](ClO_4)_2\cdot H_2O\cdot CH_3COCH_3$ (M = Co (**3**), M = Mn (**4**))

These three compounds were prepared in the same way as described below for **2** using the appropriate $M(ClO_4)_2\cdot 6H_2O$.

To a suspension of **1** (0.121 g, 0.25 mmol) in acetone (20 mL) was added dropwise with stirring a acetone solution (5 mL) of copper(II) perchlorate hexahydrate (0.093 g, 0.25 mmol). Immediately, a brown solution formed which was filtered after 0.5 h to remove any suspended particles. The filtrate was then kept at room temperature for slow evaporation. After a few days, diffraction quality brown crystals that deposited were collected and washed with cold acetone. Yield: 0.125 g (82%). Anal. Calc. for $C_{126}H_{134}N_{10}O_{44}Cl_4Cu_7$: C, 49.10; H, 4.38; N, 4.55. Found: C, 49.08; H, 4.34; N, 4.47%. IR (KBr/cm^{-1}): $\nu(H_2O)$, 3402w; ν(C=N), 1609s; $\nu(ClO_4)$, 1088vs, 621w.

Data for **3**: Color: brown. Yield: 75%. Anal. Calc. for $C_{75}H_{80}N_6O_{25}Cl_2Cu_3Co$: C, 50.44; H, 4.52; N, 4.71. Found: C, 50.53; H, 4.49; N, 4.76%. IR (KBr/cm^{-1}): $\nu(H_2O)$, 3408w; ν(C=N), 1605s; $\nu(ClO_4)$, 1089vs, 622w.

Data for **4**: Color: red. Yield: 85%. Anal. Calc. for $C_{75}H_{80}N_6O_{25}Cl_2Cu_3Mn$: C, 50.55; H, 4.53; N, 4.72. Found: C, 50.57; H, 4.46; N, 4.66%. IR (KBr/cm^{-1}): $\nu(H_2O)$, 3398w; ν(C=N), 1607vs; $\nu(ClO_4)$, 1094s, 621w.

2.3. Crystal structure determination of $[\{Cu^{II}L^1Cu^{II}(H_2O)_3\}_2\{Cu^{II}L^1\}_3](ClO_4)_4\cdot 2CH_3COCH_3$ (**2**) and $[\{Cu^{II}L^1Mn^{II}(H_2O)_3\}\{Cu^{II}L^1\}_2](ClO_4)_2\cdot H_2O\cdot CH_3COCH_3$ (**4**)

The crystallographic data of these two compounds are summarized in Table 1. Diffraction data for **2** were collected on an Enraf-Nonius CAD4 diffractometer at 293 K. The data collection and reduction were carried out with CAD4 Express Enraf-Nonius CAD4 programs package. Data for **4** were collected at 293 K on a XCALI-

Table 1
Crystallographic data for **2** and **4**

	2	**4**
Empirical formula	$C_{126}H_{134}N_{10}O_{44}Cl_4Cu_7$	$C_{75}H_{78}N_6O_{25}Cl_2Cu_3Mn$
Formula weight	3079.08	1779.96
Crystal system	monoclinic	monoclinic
Space group	*C*2/*c*	*P*21/*n*
a (Å)	32.846(8)	14.205(6)
b (Å)	14.816(9)	27.060(9)
c (Å)	29.213(9)	20.451(6)
β (°)	113.35(5)	107.17(4)
V (Å^3)	13053(9)	7511(5)
Z	4	4
T (K)	293(2)	293(2)
λ (Mo Kα) (Å)	0.71073	0.71073
Crystal dimension (mm)	0.20 × 0.18 × 0.12	0.25 × 0.20 × 0.15
D_{calc} (g cm^{-3})	1.567	1.574
μ (mm^{-1})	1.291	1.159
F(000)	6332	3664
2θ Range (°)	4.62–60.06	6.02–55.00
Total reflections	74534	58137
Unique reflections (R_{int})	19031 (0.2580)	17242 (0.0484)
Index ranges	$-46 \leqslant h \leqslant 46$, $-20 \leqslant k \leqslant 20$, $-41 \leqslant l \leqslant 41$,	$-14 \leqslant h \leqslant 18$, $-34 \leqslant k \leqslant 35$, $-26 \leqslant l \leqslant 25$,
R_1^a/wR_2^b ($I > 2\sigma(I)$)	0.0576/0.1366	0.0551/0.1451
R_1^a/wR_2^b (all data)	0.2270/0.1966	0.0829/0.1614

[a] $R_1 = [\sum ||F_o| - |F_c|| / \sum |F_o|]$.
[b] $wR_2 = [\sum w(F_o^2 - F_c^2)^2 / \sum w(F_o^2)^2]^{1/2}$.

BUR diffractometer in the ω/ϕ scan mode using CrysAlis, Oxford Diffraction programs package. All data were corrected for Lorentz-polarization effects and analytical absorption corrections were made for **4**. Both the structures were solved by direct and Fourier methods and refined by full-matrix least-squares methods based on F^2 with the programs SIR92 and SHELXL-97 [10]. The two perchlorates in the asymmetric unit of **2** are statically disordered (occupancy 0.5) situated in O(16), O(17) and O(19), O(20), O(21). Hydrogen atoms were inserted at calculated positions with isotropic parameters constrained to be 1.2 times the U_{eq} of the carrier atoms (1.5 times for hydrogen atoms of methyl groups) and refined except for hydrogen atoms of water molecules which were located from a difference Fourier map. The same isotropic thermal parameters were used for these hydrogen atoms and they were then refined. The final least-squares refinements (R_1) based on $I > 2\sigma(I)$ converged to 0.0576 and 0.0551 for **2** and **4**, respectively.

3. Results and discussion

3.1. Syntheses and characterization

Reaction of copper(II) acetate and H_2L^1 produces the mononuclear copper(II) complex $[Cu^{II}L^1 \subset (H_2O)]$ (**1**). The IR spectrum (Fig. S1) of compound **1** exhibits two weak but sharp bands at 3506 and 3468 cm^{-1} due to the O–H stretching vibration of the water molecule and one medium intensity band at 1541 cm^{-1} due to the bending vibration mode of water. These indicate that the water molecule in **1** is encapsulated in the O_4 compartment of the ligand resulting in the formation of an inclusion product (Chart 2) [2,11]. When **1** is treated with $Cu(ClO_4)_2 \cdot 6H_2O$ in acetone, the heptanuclear compound $[\{Cu^{II}L^1Cu^{II}(H_2O)_3\}_2\{Cu^{II}L^1\}_3](ClO_4)_4 \cdot 2CH_3COCH_3$ (**2**) separates from the solution as brown crystals. On the other hand, the reaction of **1** either with $Co(ClO_4)_2 \cdot 6H_2O$ or $Mn(ClO_4)_2 \cdot 6H_2O$ leads to the formation of the heterotetranuclear complexes $[\{Cu^{II}L^1Co^{II}(H_2O)_3\}\{Cu^{II}L^1\}_2](ClO_4)_2 \cdot H_2O \cdot CH_3COCH_3$ (**3**) or $[\{Cu^{II}L^1Mn^{II}(H_2O)_3\}\{Cu^{II}L^1\}_2](ClO_4)_2 \cdot H_2O \cdot CH_3COCH_3$ (**4**), respectively. Surprisingly, no such compound could be isolated with nickel(II) perchlorate. Compared to the $\nu_{C=N}$ vibration observed in the free ligand H_2L^1 at 1615 cm^{-1}, this vibration is shifted slightly to lower frequency at *ca.* 1606 cm^{-1} in complexes **1**–**4**.

3.2. Description of the structures

3.2.1. $[\{Cu^{II}L^1Cu^{II}(H_2O)_3\}_2\{Cu^{II}L^1\}_3](ClO_4)_4 \cdot 2CH_3COCH_3$ (2)

One-half of the structure of **2** is symmetry related to the other half because of the presence of a crystallographic twofold axis. The asymmetric unit, $[\{Cu^{II}L^1Cu^{II}(H_2O)_3\}](ClO_4)_2 \cdot 1.5[Cu^{II}L^1] \cdot CH_3COCH_3$, in this compound consists of one dinuclear cationic unit $[\{Cu^{II}L^1Cu^{II}(H_2O)_3\}]^{2+}$, one and a half mononuclear $[Cu^{II}L^1]$ moieties, two perchlorate anions, and one acetone molecule as solvent of crystallization. Evidently, the overall composition of **2** is $[\{Cu^{II}L^1Cu^{II}(H_2O)_3\}_2\{Cu^{II}L^1\}_3](ClO_4)_4 \cdot 2CH_3COCH_3$. In the dicopper(II) core, one copper(II) ion occupies the N_2O_2 cavity, and the second compartment of $[L^1]^{2-}$ is occupied by the second metal ion. As will be discussed below, the dinuclear cation is interlinked with the mononuclear moieties to result in the formation of the heptanuclear assembly in this compound. The structure and interlinking of the dinuclear moiety with the mononuclear fragments are shown in Fig. 1, while the heptanuclear assembly is in Fig. 2.

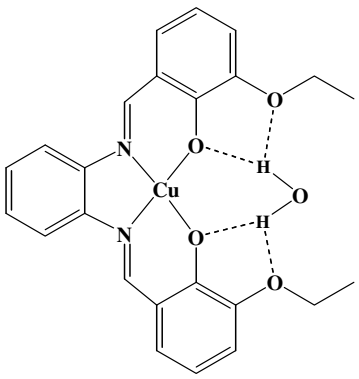


Chart 2. Chemical structure of $[Cu^{II}L^1 \subset (H_2O)]$ (**1**).

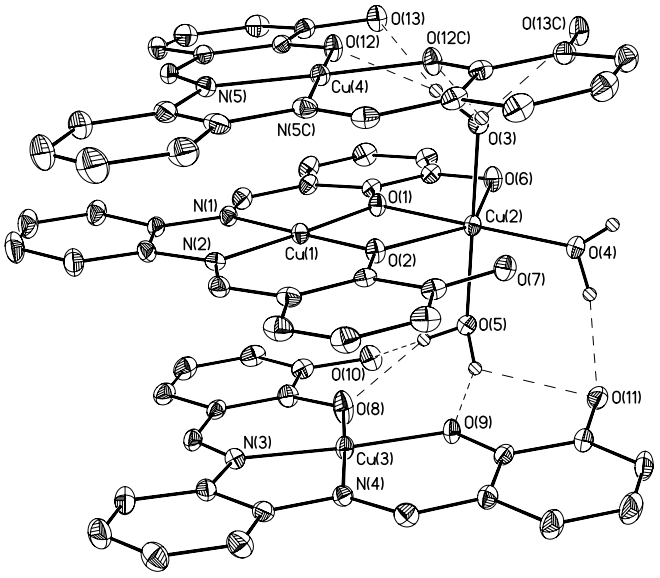


Fig. 1. Structure of **2** representing the dinuclear $\left[Cu^{II}L^{1}Cu^{II}(H_2O)_3\}\right]^{2+}$ cationic unit and two mononuclear $[Cu^{II}L^{1}]$ moieties. Only those hydrogens participating in hydrogen bonds are shown. Except oxygens, other atoms of the ethoxy groups are also omitted for clarity. Cu(2)–O(2) bond is shown to demonstrate an alternate CuO_6 coordination geometry of Cu(2).

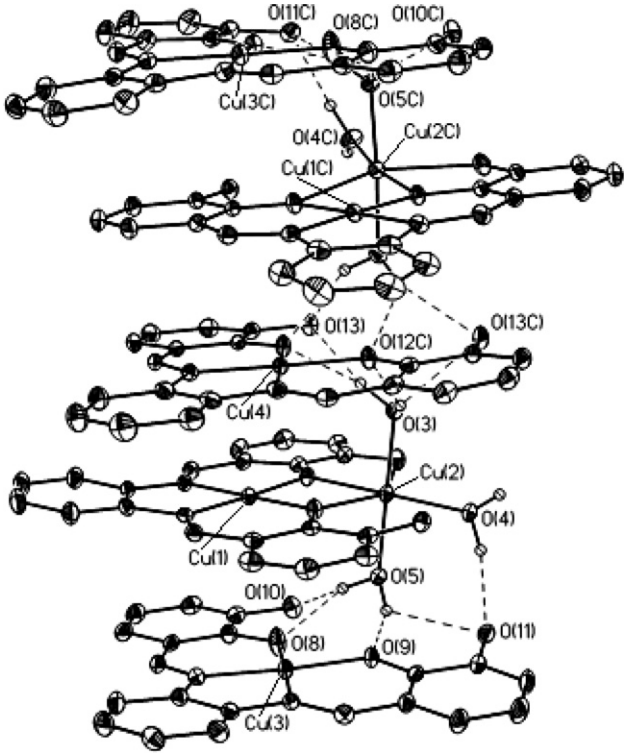


Fig. 2. Structure of **2** representing the interlinking of two dinuclear $[Cu^{II}L^{1}Cu^{II}(H_2O)_3\}]^{2+}$ cationic units and three mononuclear $[Cu^{II}L^{1}]$ moieties to result in the formation of self-assembled heptacopper(II) system. Only those hydrogens participating in hydrogen bonds are shown. Except oxygens, other atoms of the ethoxy groups are also omitted for clarity. Cu(2)–O(2) bond is shown to demonstrate an alternate CuO_6 coordination geometry of Cu(2).

The selected bond lengths and angles of the coordination environments of the three copper(II) centers (Cu(1), Cu(3), and Cu(4)) in the N_2O_2 compartment are in the usual range (Table 2) [2]. The coordination environments of these metal centers are very close to square planar as evidenced by the ranges of the *cisoid* (84.51(18)–95.32(16)°) and *transoid* (175.98(17)–179.40(17)°) angles, the average deviation (0.003–0.043 Å) of the donor atoms, and the displacement (0.000–0.023 Å) of the copper(II) center from the corresponding least-squares N_2O_2 plane.

There are two possibilities regarding the coordination environment of the second metal center (Cu(2)) in the dinuclear core; five-coordinate CuO_5 and six-coordinate CuO_6. In the former case, dinuclear core is monophenoxo-bridged; the second metal center (Cu(2)) is coordinated to one bridging phenoxo oxygen (O(1)), one ethoxy oxygen (O(6)), and three water oxygens (O(3), O(4), and O(5)), while one ethoxy oxygen (O(7)) and one phenoxo oxygen (O(2)) of the ligand remain uncoordinated. The coordination geometry of this pentacoordinated copper(II) is slightly distorted square pyramidal. The bridging phenoxo oxygen (O(1)) and three water oxygens (O(3), O(4), and O(5)) define the basal plane, while the ethoxy oxygen O(6) occupies the apical position. The average deviation

Table 2
Selected bond lengths (Å) and angles (°) of **2**

Cu(1)–N(1)	1.940(4)	N(1)–Cu(1)–O(2)	179.40(17)
Cu(1)–N(2)	1.919(4)	N(2)–Cu(1)–O(1)	177.64(17)
Cu(1)–O(1)	1.917(3)	N(1)–Cu(1)–O(1)	93.32(16)
Cu(1)–O(2)	1.909(3)	N(2)–Cu(1)–O(2)	95.32(16)
		N(1)–Cu(1)–N(2)	84.51(18)
		O(1)–Cu(1)–O(2)	86.85(14)
Cu(3)–N(3)	1.952(4)	N(3)–Cu(3)–O(9)	175.98(17)
Cu(3)–N(4)	1.927(4)	N(4)–Cu(3)–O(8)	177.68(17)
Cu(3)–O(8)	1.884(4)	N(3)–Cu(3)–O(8)	92.41(18)
Cu(3)–O(9)	1.914(3)	N(4)–Cu(3)–O(9)	94.38(16)
		N(3)–Cu(3)–N(4)	84.62(18)
		O(8)–Cu(3)–O(9)	87.67(16)
Cu(4)–N(5)	1.936(4)	N(5)–Cu(4)–O(12C)	178.90(18)
Cu(4)–O(12)	1.892(3)	N(5)–Cu(4)–O(12)	94.25(17)
		N(5)–Cu(4)–N(5C)	85.6(3)
		O(12)–Cu(4)–O(12C)	85.9(2)
Cu(2)–O(2)	2.487(4)	O(1)–Cu(2)–O(4)	169.81(16)
Cu(2)–O(6)	2.358(4)	O(2)–Cu(2)–O(6)	145.89(12)
Cu(2)–O(1)	1.954(3)	O(3)–Cu(2)–O(5)	177.00(15)
Cu(2)–O(3)	1.979(4)	O(6)–Cu(2)–O(1)	74.82(13)
Cu(2)–O(4)	1.937(4)	O(6)–Cu(2)–O(3)	88.23(14)
Cu(2)–O(5)	1.964(4)	O(6)–Cu(2)–O(4)	95.79(16)
		O(6)–Cu(2)–O(5)	94.73(14)
		O(1)–Cu(2)–O(3)	89.99(14)
		O(1)–Cu(2)–O(5)	91.23(15)
		O(3)–Cu(2)–O(4)	93.72(16)
		O(4)–Cu(2)–O(5)	85.54(15)
		O(2)–Cu(2)–O(1)	71.46(12)
		O(2)–Cu(2)–O(3)	86.78(13)
		O(2)–Cu(2)–O(4)	118.19(15)
		O(2)–Cu(2)–O(5)	91.01(13)
		Cu(1)–O(1)–Cu(2)	109.73(16)
		Cu(1)–O(2)–Cu(2)	91.15(12)

Symmetry: C, $1-x$, y, $0.5-z$.

of the four oxygens and the displacement of the metal center from the least-squares O_4 plane are 0.106 Å and 0.057 Å, respectively. The *transoid* and *cisoid* angles in the O(1)O(3)O(4)O(5) basal plane lie in the ranges 169.81(16)–177.00(15)° and 85.54(15)–93.72(16)°, respectively, while the range of the bond angles involving the apical oxygen is 74.82(13)–95.79(16)°. These values along with the τ [12] value of 0.12 indicate that the coordination geometry of Cu(2) is slightly distorted square pyramidal. In the basal O_4 plane of Cu(2), the Cu–O bond distances lie in the ranges 1.937(4)–1.979(4)Å. By comparison, the apical Cu–O(ethoxy) bond distance is 2.358(4) Å. The Cu···Cu intramolecular distance and Cu–O(phenoxo)–Cu bridge angle are 3.165 Å and 109.73(16)°, respectively. The bridging moiety is appreciably twisted as evidenced by the dihedral angle (90.9°) between the basal planes of the two copper(II) centers.

For the CuO_6 coordination environment, dinuclear core is diphenoxo-bridged (Figs. 1 and 2, Table 2). In addition to the five oxygens in CuO_5 environment, the second phenoxo oxygen (O(2)) is also coordinated in this case. The coordination geometry for this CuO_6 environment is Jahn–Teller distorted tetragonal with the ethoxy oxygen (O(6)) and the second bridging phenoxo oxygen (O(2)) occupying the axial positions. *Transoid* angle and the ranges of *cisoid* angles involving O(2) are 145.89(12)° and 71.46(12)–118.19(15)°, respectively, and the apical Cu(2)–O(2) distance is 2.487(4) Å. If O(2) is considered as a coordinating center, Cu(2)–O(2) bond length should be smaller than the Cu(2)–O(6) bond distance because O(2) and O(6) are anionic and neutral centers, respectively. However, the apical bond length involving anionic center (O(2)) is longer than that involving neutral center (O(6)). Again, in comparison to the *transoid* angles (169.81(16)° and 177.00(15)°) in the O_4 basal plane and the range of all the *cisoid* angles (74.82(13)–95.79(16)°) in CuO_5 environment, the *transoid* angle (O(2)–Cu(2)–O(6) = 145.89(12)°) and the ranges of *cisoid* angles (71.46(12)–118.19(15)°) involving O(2) is significantly deviated from the ideal values. Evidently, coordination of O(2) to Cu(2) results in a tetragonal geometry which is much more distorted than that expected for Jahn–Teller effect, while CuO_5 environment is only slightly distorted from square pyramidal geometry. Therefore, among the two possibilities (CuO_5 and CuO_6), slightly distorted square pyramidal CuO_5 coordination environment is a better choice for Cu(2) center.

As shown in Fig. 1, the hydrogen bonding interactions between coordinated water molecules of the dinuclear $[\{Cu^{II}L^1Cu^{II}(H_2O)_3\}]^{2+}$ cation and phenoxo/ethoxy oxygens of the mononuclear $[Cu^{II}L^1]$ moieties result in the dinuclear–mononuclear interlinking in this compound. Among three coordinated water molecules, two ($H_2O(3)$ and $H_2O(5)$) interact and are encapsulated in the O_4 cavity of two $[Cu^{II}L^1]$ species, $[Cu^{II}(4)L^1]$ and $[Cu^{II}(3)L^1]$, respectively. Each of the water hydrogens of these two water molecules form bifurcated hydrogen bonds with two oxygens, one of which is a phenoxo and the second is an ethoxy oxygen. The geometries of these hydrogen bonds are summarized in Table 3. The donor···acceptor contacts for the $H_2O(3)$···phenoxo and $H_2O(5)$···phenoxo hydrogen bonds lie in the ranges 2.921(5)–2.982(5) Å and 2.669(5)–2.762(6) Å, respectively, while the ranges of the donor···acceptor contacts for the $H_2O(3)$···ethoxy and $H_2O(5)$···ethoxy hydrogen bonds are 3.151(5)–3.160(5) Å and 2.913(4)–2.972(5) Å, respectively. Evidently, the hydrogen bonds involving phenoxo oxygens are stronger. Again, the hydrogen bonds involving $H_2O(5)$ are stronger than those involving $H_2O(3)$. In addition to the bifurcated hydrogen bonds between phenoxo/ethoxy oxygens and two coordinated water molecules discussed above, there exists another hydrogen bond between one hydrogen (H(4A)) of the third coordinated water molecule ($H_2O(4)$) and one ethoxy oxygen (O(11)) of the mononuclear $[Cu^{II}(3)L^1]$ unit (Figs. 1 and 2, Table 3). The O(water)···O(ethoxy) contact in this case is 2.751(6) Å.

As already mentioned, one-half of compound **2** is symmetry related to the other half because of the presence of a crystallographic twofold axis. This twofold axis passes through the $[Cu^{II}(4)L^1]$ mononuclear unit. As shown in Fig. 2, the acyclic O_4 compartment of $[Cu^{II}(4)L^1]$ interacts with $H_2O(3)$ and another coordinated water molecule ($H_2O(3C)$; C, $1-x, y, 0.5-z$) of a different dinuclear unit to result in the self-assembled $[2\times2+1\times3]$ heptanuclear Cu^{II}_7 compound containing cocrystallized two dinuclear $[\{Cu^{II}L^1Cu^{II}(H_2O)_3\}]^{2+}$ cationic units and three mononuclear $[Cu^{II}L^1]$ moieties.

3.2.2. Description of the structure of $[\{Cu^{II}L^1Mn^{II}(H_2O)_3\}\{Cu^{II}L^1\}_2](ClO_4)_2\cdot H_2O\cdot CH_3COCH_3$ (4)

The structure of **4** consists of the heterotetranuclear $[\{Cu^{II}L^1Mn^{II}(H_2O)_3\}\{Cu^{II}L^1\}_2]^{2+}$ cation (Fig. 3, Table 4),

Table 3
Geometries (distances in (Å) and angles in (°)) of the hydrogen bonds in **2** and **4**

Compound	D–H···A	D···A	H···A	D–H···A
2	O(3)–H(3B)···O(12)	2.982(5)	2.208	132.1
	O(3)–H(3B)···O(13)	3.160(5)	2.202	157.3
	O(3)–H(3A)···O(12C)	2.921(5)	2.192	146.8
	O(3)–H(3A)···O(13C)	3.151(5)	2.563	129.0
	O(4)–H(4A)···O(11)	2.751(6)	1.870	167.3
	O(5)–H(5A)···O(9)	2.669(5)	1.812	149.5
	O(5)–H(5A)···O(11)	2.972(5)	2.381	120.3
	O(5)–H(5B)···O(8)	2.762(6)	2.014	139.7
	O(5)–H(5B)···O(10)	2.913(4)	2.157	141.3
4	O(3)–H(3A)···O(12)	2.795(4)	2.358	126.1
	O(3)–H(3A)···O(14)	2.971(4)	2.329	166.6
	O(3)–H(3B)···O(13)	2.714(4)	2.011	156.7
	O(3)–H(3B)···O(15)	2.943(4)	2.421	128.3
	O(4)–H(4A)···O(15)	2.822(4)	1.998	161.5
	O(5)–H(5A)···O(8)	2.851(4)	2.186	136.6
	O(5)–H(5A)···O(10)	3.030(4)	2.279	149.8
	O(5)–H(5B)···O(9)	2.863(4)	2.128	147.9
	O(5)–H(5B)···O(11)	3.023(4)	2.379	135.3

Symmetry: C, $1-x, y, 0.5-z$.

two perchlorate anions, and one water and one acetone molecule as solvent of crystallization. In **4**, as in **2**, the dinuclear $[Cu^{II}L^{1}Mn^{II}(H_2O)_3]^{2+}$ core is interlinked with mononuclear $[Cu^{II}L^{1}]$ moiety by hydrogen bonding interactions. In this case, the interlinking of one dinuclear $[Cu^{II}L^{1}Mn^{II}(H_2O)_3]^{2+}$ core with two mononuclear $[Cu^{II}\ L^{1}]$ moieties generates tetranuclear $Cu^{II}_3Mn^{II}$ assembly. In the dinuclear $[Cu^{II}L^{1}Mn^{II}(H_2O)_3]^{2+}$ core, copper(II) occupies the N_2O_2 compartment, and the second compartment of $[L^{1}]^{2-}$ is occupied by manganese(II). The structural parameters in the planar N_2O_2 coordination environment of the three different copper(II) centers (Cu(1), Cu(2), and Cu(3)) are similar to those in compound **2** (Table 4).

There are two possibilities regarding the coordination environment of manganese(II); five-coordinate MnO_5 involving two phenoxo oxygens (O(1) and O(2)) and three water oxygens (O(3), O(4), and O(5)) and seven-coordinate MnO_7 involving additional coordination by two ethoxy oxygens (O(6) and O(7)). The MnO_5 coordination environment (Fig. 3, Table 4) in **4** is highly distorted. The value of τ [12] in this case is 0.38, indicating that the geometry is highly distorted square pyramidal. In this square pyramidal environment, one phenoxo oxygen (O(1)) and three water oxygens (O(3), O(4), and O(5)) define the basal plane, while the second bridging phenoxo oxygen (O(2)) occupies the apical position. The average deviation of O(1), O(3), O(4), and O(5) from the least-squares O_4 plane is 0.183 Å, and the manganese(II) center is displaced by 0.312 Å from this plane. These deviations and displacement along with the range of *transoid* angles (150.42(10)–173.09(11)°) in the basal O_4 plane and the range of all the 10 *cisoid* angles (69.38(9)–135.97(10)°) indicate significant distortion of the coordination environment of manganese(II). The metal–ligand bond distances in the basal plane (Mn(1)–O(1) = 2.169(2) Å, Mn(1)–O(3) = 2.152(3) Å, Mn(1)–O(4) = 2.171(3) Å, Mn(1)–O(5) = 2.149(3) Å) are slightly shorter than the Mn–O(apical) bond length (Mn(1)–O(2) = 2.249(2) Å). The Cu(1)–O(1)–Mn(1) and Cu(1)–O(2)–Mn(1) bridge angles and the Cu(1)···Mn(1) distance in the dinuclear core are 105.23(10)°, 101.62(10)°, and 3.221 Å, respectively. As in **2**, the bridging moiety in the dinuclear core is highly twisted, as evidenced by the dihedral angles (91.1°) between the N_2O_2 plane of the copper(II) center and the basal O_4 plane of the manganese(II) environment.

If coordination of two ethoxy oxygens are also considered, the coordination environment of manganese(II) is distorted pentagonal bipyramidal; two phenoxo oxygens (O(1) and O(2)), two ethoxy oxygens (O(6) and O(7)), and one water oxygen (O(4)) define the basal pentagonal

Table 4
Selected bond lengths (Å) and angles (°) of **4**

Cu(1)–N(1)	1.919(3)	N(1)–Cu(1)–O(2)	178.52(11)
Cu(1)–N(2)	1.922(3)	N(2)–Cu(1)–O(1)	178.68(11)
Cu(1)–O(1)	1.878(2)	N(1)–Cu(1)–O(1)	94.97(12)
Cu(1)–O(2)	1.897(2)	N(2)–Cu(1)–O(2)	95.35(12)
		N(1)–Cu(1)–N(2)	86.12(13)
		O(1)–Cu(1)–O(2)	83.56(10)
Cu(2)–N(3)	1.947(3)	N(3)–Cu(2)–O(9)	175.79(11)
Cu(2)–N(4)	1.949(3)	N(4)–Cu(2)–O(8)	176.40(12)
Cu(2)–O(8)	1.916(3)	N(3)–Cu(2)–O(8)	94.05(12)
Cu(2)–O(9)	1.907(3)	N(4)–Cu(2)–O(9)	93.62(12)
		N(3)–Cu(2)–N(4)	83.40(13)
		O(8)–Cu(2)–O(9)	89.06(10)
Cu(3)–N(5)	1.953(3)	N(5)–Cu(3)–O(13)	176.91(11)
Cu(3)–N(6)	1.938(3)	N(6)–Cu(3)–O(12)	176.95(12)
Cu(3)–O(12)	1.881(2)	N(5)–Cu(3)–O(12)	93.15(12)
Cu(3)–O(13)	1.910(2)	N(6)–Cu(3)–O(13)	93.85(11)
		N(5)–Cu(3)–N(6)	84.55(13)
		O(12)–Cu(3)–O(13)	88.36(10)
Mn(1)–O(1)	2.169(2)	O(3)–Mn(1)–O(5)	173.09(11)
Mn(1)–O(2)	2.249(2)	O(1)–Mn(1)–O(4)	150.42(10)
Mn(1)–O(3)	2.152(3)	O(1)–Mn(1)–O(2)	69.38(9)
Mn(1)–O(4)	2.171(3)	O(1)–Mn(1)–O(3)	85.00(11)
Mn(1)–O(5)	2.149(3)	O(1)–Mn(1)–O(5)	92.94(10)
Mn(1)–O(6)	2.511(3)	O(2)–Mn(1)–O(3)	90.69(10)
Mn(1)–O(7)	2.691(3)	O(2)–Mn(1)–O(4)	135.97(10)
		O(2)–Mn(1)–O(5)	94.76(10)
		O(3)–Mn(1)–O(4)	80.49(12)
		O(4)–Mn(1)–O(5)	98.39(12)
		O(6)–Mn(1)–O(1)	66.26(8)
		O(6)–Mn(1)–O(2)	135.50(8)
		O(6)–Mn(1)–O(3)	88.83(10)
		O(6)–Mn(1)–O(4)	87.71(10)
		O(6)–Mn(1)–O(5)	84.31(10)
		O(6)–Mn(1)–O(7)	162.09(8)
		O(7)–Mn(1)–O(1)	130.99(8)
		O(7)–Mn(1)–O(2)	61.65(8)
		O(7)–Mn(1)–O(3)	96.93(11)
		O(7)–Mn(1)–O(4)	76.61(10)
		O(7)–Mn(1)–O(5)	89.41(10)
		Cu(1)–O(1)–Mn(1)	105.23(10)
		Cu(1)–O(2)–Mn(1)	101.62(10)

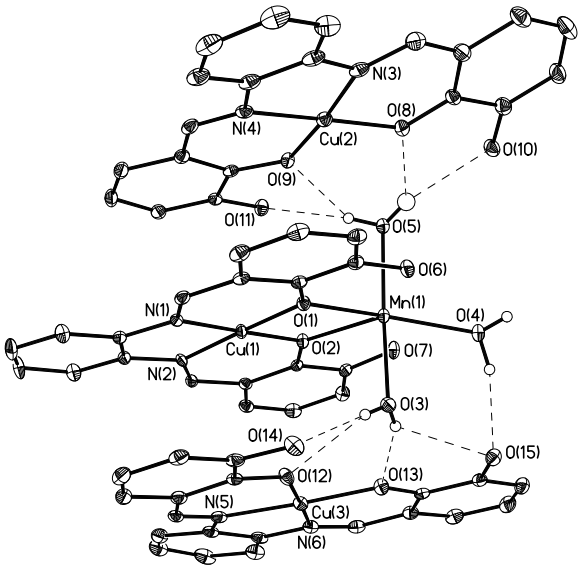


Fig. 3. Structure of the heterotetrametallic unit of composition $[\{Cu^{II}L^{1}Mn^{II}(H_2O)_3\}\{Cu^{II}L^{1}\}_2]^{2+}$ consisting of one dinuclear $[Cu^{II}L^{1}$-$Mn^{II}(H_2O)_3\}]^{2+}$ cationic unit and two mononuclear $[Cu^{II}L^{1}]$ moieties in **4**. Only those hydrogens participating in hydrogen bonds are shown. Except oxygens, other atoms of the ethoxy groups are also omitted for clarity.

plane, while other two water oxygens (O(3) and O(5)) occupy the axial positions. The average deviation of O(1), O(2), O(4), O(6), and O(7) and the displacement of the metal center from the least-squares O_5 plane are 0.17 Å and 0.06 Å, respectively. Mn(1)–O(ethoxy) bond distances (2.511(3) Å and 2.691(3) Å) are much longer than the other five bond lengths (2.169(2)–2.249(2) Å). Due to this difference in bond lengths, the pentagonal plane is significantly distorted as evidenced by the ranges of the apex···apex (O···O) distances (2.515–3.254 Å) and the internal O···O···O angles (91.4–121.5°). Evidently, both the MnO_5 and MnO_7 environments are significantly distorted. However, unlike in copper(II) center, there is no metal-center origin of the difference in bond distances in high spin manganese(II). Due to anionic versus neutral nature of the phenoxo and ethoxy/water oxygens, difference in metal–O(phenoxo) and metal–O(ethoxy/water) bond lengths may take place. However, much longer Mn–O(ethoxy) bond distances in comparison to the Mn–O(water) bond lengths is not usual. Therefore, coordination by two ethoxy oxygens should be discarded and the coordination environment of manganese (II) center should be considered as highly distorted square pyramidal MnO_5.

As in **2**, water encapsulation through bifurcated hydrogen bonds occurs also in **4** to result in the self-assembled $[2 \times 1 + 1 \times 2]$ heterotetranuclear $Cu^{II}_3Mn^{II}$ compound composed of one cocrystallized dinuclear $[\{Cu^{II}L^1Mn^{II}(H_2O)_3\}]^{2+}$ cationic unit and two mononuclear $[Cu^{II}L^1]$ moieties. Among the three coordinated water molecules two are encapsulated in the O_4 cavity of two $[Cu^{II}L^1]$ species. As demonstrated in Fig. 3, $H_2O(3)$ is encapsulated in the O(12)O(13)O(14)O(15) compartment of the $[Cu^{II}(3)L^1]$ moiety, and $H_2O(5)$ is encapsulated in the O(8)O(9)O(10)O(11) compartment of the $[Cu^{II}(2)L^1]$ fragment. The geometries of the hydrogen bonds are summarized in Table 3. The donor···acceptor contacts for the $H_2O(3)$···phenoxo and $H_2O(5)$···phenoxo hydrogen bonds lie in the ranges 2.714(4)–2.795(4) Å and 2.851(4)–2.863(4) Å, respectively, while the ranges of the donor···acceptor contacts for the $H_2O(3)$···ethoxy and $H_2O(5)$···ethoxy hydrogen bonds are 2.943(4)–2.971(4) Å and 3.023(4)–3.030(4) Å, respectively. Evidently, as in **2**, the hydrogen bonds involving phenoxo oxygens are stronger. In this compound also, the third water molecule ($H_2O(4)$) interacts with one ethoxy oxygen with an O(water)···O(ethoxy) distance of 2.822(4) Å (Fig. 3, Table 3).

3.3. Composition of *3*

It has not been possible to grow a diffraction quality crystal of the $Cu^{II}_3Co^{II}$ compound **3**. However, as mentioned in the Section 2, elemental analyses of **3** and **4** are well matched with the similar compositions $C_{75}H_{80}N_6O_{25}Cl_2Cu_3Co$ and $C_{75}H_{80}N_6O_{25}Cl_2Cu_3Mn$, respectively. Again, IR spectra of these two compounds are also similar (Section 2). The similarity in the composition of **3** and **4** as well as the similarity of the structures of the related $Cu^{II}_3Mn^{II}$ and $Cu^{II}_3Co^{II}$ compounds [2] derived from *N*,*N*′ -ethylenebis(3-ethoxysalicylaldimine) (H_2L) suggest that compounds **3** and **4** should have similar structure.

3.4. Comparison of the compositions of *1*–*4* with the related compounds derived from *N*,*N*′-ethylenebis(3-ethoxysalicylaldimine) (H_2L)

The mononuclear copper(II) compounds $[Cu^{II}L^1\subset(H_2O)]$ (**1**) and $[Cu^{II}L\subset(H_2O)]$ (**5**) [2] derived from *N*,*N*′-*o*-phenylenebis(3-ethoxysalicylaldimine) (H_2L^1) and *N*,*N*′-ethylenebis(3-ethoxysalicylaldimine) (H_2L), respectively, are inclusion products. The treatment of perchlorate salts of copper(II), cobalt(II), and manganese(II) with **5** results in the self-assembled $[2 \times 1 + 1 \times 2]$ heterotetranuclear $Cu^{II}_3M^{II}$ compounds $[\{Cu^{II}LM^{II}(H_2O)_3\}\{Cu^{II}L\}_2](ClO_4)_2$ (M^{II} = Cu (**6**), Co (**7**), M^{II} = Mn (**8**)) containing self-assembled and cocrystallized single dinuclear $[\{Cu^{II}LM^{II}(H_2O)_3\}]^{2+}$ cationic and two mononuclear $[Cu^{II}L]$ units [2]. Cocrystals of similar composition, $[\{Cu^{II}L^1M^{II}(H_2O)_3\}\{Cu^{II}L^1\}_2](ClO_4)_2 \cdot CH_3COCH_3$ (M^{II} = Co (**3**), M^{II} = Mn (**4**)), are also obtained from the reaction of **1** with the perchlorate salts of cobalt(II) and manganese(II) in the H_2L^1 ligand system. However, the composition of the cocrystal $[\{Cu^{II}L^1Cu^{II}(H_2O)_3\}_2\{Cu^{II}L^1\}_3](ClO_4)_4 \cdot 2CH_3COCH_3$ (**2**) produced from the reaction of **1** with copper(II) perchlorate is different. In this case, two dinuclear $[\{Cu^{II}L^1Cu^{II}(H_2O)_3\}]^{2+}$ cationic units are self-assembled and cocrystallized with three mononuclear $[Cu^{II}L^1]$ moieties.

As discussed earlier, the second metal center in the dinuclear cores in **2** and **4** adopts slightly distorted square pyramidal CuO_5 and appreciably distorted square pyramidal MnO_5 coordination environment, respectively. The coordination environment of the second metal center in the dinuclear cores in **6**–**8** was also described previously as five-coordinate MO_5 involving coordination by two phenoxo and three water oxygens [2]. However, it may be relevant to discuss other possibilities of coordination environment in **6**–**8**. There are two independent dinuclear units (unit I and unit II) in **6**. The τ [12] values of the CuO_5 environment in these two units are 0.04 and 0.37 indicating almost ideal and appreciably distorted square pyramidal geometry, respectively. The second possibility of coordination environment of the second metal centers in unit I and unit II is Jahn–Teller distorted tetragonal. In these cases, coordination by the ethoxy oxygens O(6) and O(21) to Cu(1) and Cu(5), respectively, should also be considered (Fig. 4). For both the units, two Cu–O(apical) bond distances (Cu(1)–O(5) = 2.37 Å, Cu(1)–O(6) = 2.50 Å, Cu(5)–O(20) = 2.29 Å, Cu(5)–O(21) = 2.55 Å) are significantly different. Again, while the *transoid* angles (174.97° and 177.6°) in the O_4 basal plane of unit I are very close to 180°, the *transoid* angle (145.3°) involving O(6) is deviated significantly from the ideal value indicating significant distortion of the tetragonal geometry. Therefore, as τ is only 0.04 for the CuO_5 environment in unit I, coordina-

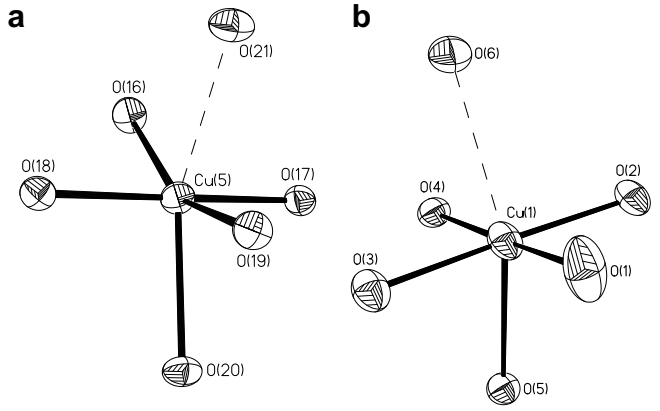


Fig. 4. CuO_5 (solid bonds) and CuO_6 (solid and dotted bonds) coordination environment of copper(II) centers in the O_4 compartment of the two units (a: unit I. b: unit II) in $[\{Cu^{II}LCu^{II}(H_2O)_3\}\{Cu^{II}L\}_2](ClO_4)_2$.

tion geometry of Cu(1) should be better described as slightly distorted square pyramidal. In the case of unit II, both the two possible geometries are significantly distorted as evidenced by the τ value (0.37) in CuO_5 environment, *transoid* angles (153.8° and 176.0°) in the O_4 basal plane, and the *transoid* angle (140.2°) involving O(21). Evidently, it is difficult to judge the nature of coordination environment of Cu(5). However, as the two Cu–O(apical) bond lengths in CuO_6 environment differs significantly (2.29 Å versus 2.55 Å), it may be better to discard the hexacoordinated case and to describe the geometry of Cu(5) as significantly distorted square pyramidal.

The second possibility of the coordination geometry for the cobalt(II) and manganese(II) centers in **7** and **8**, respectively, is pentagonal bipyramidal which involves additional coordination by two ethoxy oxygens (O(2) and O(2A); Fig. 5). However, the bond distances (2.63 Å for **7** and 2.61 Å for **8**) involving the ethoxy oxygens are much longer than the lengths of other five bonds (2.05–2.12 Å for **7** and 2.15–2.20 Å for **8**). As explained earlier, such differences in bond lengths for high spin manganese(II) are not usual. For high spin cobalt(II) also, such differences are not usual because metal-center distortion originates from t_{2g} orbitals. Therefore, five-coordinate MO_5 coordination environment, as described previously [2], should be better choice in these two cases also.

The noteworthy aspect is the remarkable difference between the dinuclear cores in **2** and those of the other compounds **3**–**8**. The dinuclear cores in **3**–**8** are diphenoxo-bridged; the second metal center is coordinated to the two phenoxo oxygens and three water oxygens, while the two ethoxy oxygens are noncoordinated. In contrast, the dinuclear core in **2** is monophenoxo-bridged; the second metal center in this case is coordinated to one phenoxo oxygen, one ethoxy oxygen, and three water oxygens, while one phenoxo and one ethoxy oxygen is noncoordinated to the second metal center. Thus, it appears that the coordination of the ethoxy oxygen to the second metal center is the major factor contributing to the emergence of a new structural motif for **2**.

The relative extent of the encapsulation of water may be understood from the displacement (d_O) of the water oxygen from the least-squares $O(phenoxo)_2O(ethoxy)_2$ plane. In the case of **5**, the oxygen atom of the encapsulated water lies on the least-squares $O(phenoxo)_2O(ethoxy)_2$ plane, and the oxygen atoms of the encapsulated water molecules in **6**–**8** are displaced by 0.92–1.23 Å from the corresponding $O(phenoxo)_2O(ethoxy)_2$ plane, indicating that the extent of encapsulation in **5** is much greater than that in the compounds **6**–**8** [2]. The values of d_O for the two water oxygens O(3) and O(5) in the $Cu^{II}_3Mn^{II}$ compound **4** are 1.10 and 1.16 Å, respectively, indicating that the extent of encapsulation in this compound is similar to that in the compounds **6**–**8**. In the case of the Cu^{II}_7 compound **2**, while the d_O value (1.08 Å) for O(5) is in the range observed in **4**–**8**, the second water oxygen is significantly displaced ($d_O = 1.77$ Å) from the corresponding $O(phenoxo)_2O(ethoxy)_2$ plane indicating that this water molecule is poorly encapsulated.

It should be noted that treatment of compounds **2**–**4** and **6**–**8** with dimethylformamide results in the formation of compound **1** and **5**, respectively, indicating that the O_4

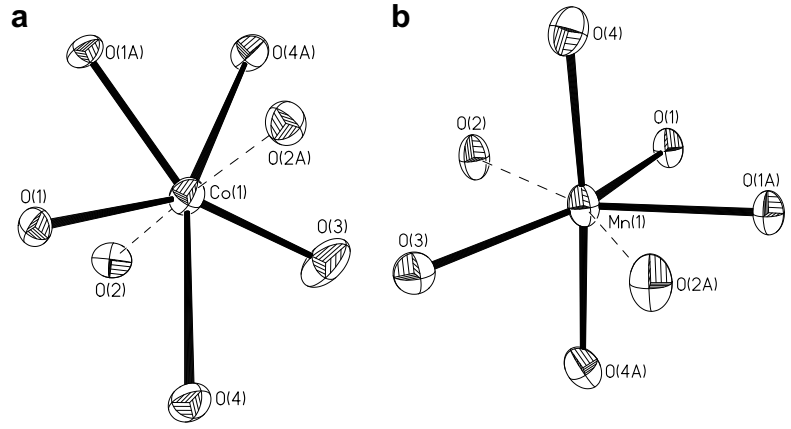


Fig. 5. MO_5 (solid bonds) and MO_7 (solid and dotted bonds) coordination environment of cobalt(II) and manganese(II) centers in $[\{Cu^{II}LM^{II}(H_2O)_3\}\{Cu^{II}L\}_2](ClO_4)_2$ (a: M = Co (**7**). b: M = Mn (**8**)).

compartment is more preferable for water in both the systems [2]. Again, in both the systems, the formation of a 3d–4f or 3d–3d bimetallic core from the mononuclear inclusion product and the decomposition of the former to the latter by dimethylformamide resemble the transmetallation reaction. This behavior can be considered as the resemblance of water with metal ions.

3.5. Magnetic properties

The cryomagnetic behavior of **2** is shown in Fig. 6 in terms of $\chi_M T$ versus T and χ_M versus T plots. The $\chi_M T$ value (2.76 $cm^3\ mol^{-1}\ K$) at 300 K of **2** is slightly greater than the theoretical value (2.62 $cm^3\ mol^{-1}\ K$) for seven isolated copper(II) ions with $g = 2$. On lowering of temperatures, $\chi_M T$ decreases very slowly to 2.43 $cm^3\ mol^{-1}\ K$ at 80 K. On further lowering of temperatures, $\chi_M T$ diminishes rapidly to a narrow plateau (*ca.* 1.13 $cm^3\ mol^{-1}\ K$) in the temperature range 8–6 K. Below 6 K, $\chi_M T$ decreases sharply to reach a value of 0.93 $cm^3\ mol^{-1}\ K$ at 2 K. The profile indicates that there exists a moderate antiferromagnetic interaction in this molecule. The magnetic exchange between the metal ions in the mononuclear species with the pentacoordinated metal center in the dinuclear cores should be very small because these metal ions are separated as Cu(mononuclear)–O(phenoxo)···H–O(water)–Cu(pentacoordinated) and the Cu(pentacoordinated)···Cu(mononuclear) separations lie in the range 4.78–4.91 Å. Therefore, the two copper(II) centers in the $[Cu^{II}L^1]$ moieties should only influence the $\chi_M T$ values as a known amount of paramagnetic impurity. The rapid increase of the χ_M values at lower temperatures (Fig. 6) is indicative of such an assumption. Again, the absence of a maximum in the χ_M versus T plots is also indicative of the influence of the paramagnetic contribution of the two isolated $s = 1/2$ centers. Considering molecular field approximation (zJ') for the possible very weak Cu(mononuclear)–O(phenoxo)···H–O(water)–Cu(pentacoordinated) interaction and the same value for the magnetic moment (μ_{Cu}) of the copper(II) centers in the mononuclear fragments, the theoretical expression for the molar magnetic susceptibility (χ_M) of a system of two exchange-coupled dicopper(II) ($\mathbf{H} = -2J\mathbf{S}_1 \cdot \mathbf{S}_2$) and three mononuclear copper(II) moieties can be derived as [2]

$$\chi_M = \frac{\chi_M^1}{1 - 2zJ'\chi_M^1/N\beta^2 g^2} \quad (1)$$

where

$$\chi_M^1 = \frac{15.995\chi_D T + 3\mu_{Cu}^2}{7.997T}$$

with

$$\chi_D = \frac{N\beta^2 g^2}{kT}\,\frac{2e^{2J/kT}}{1 + 3e^{2J/kT}}$$

Least-squares fitting (Fig. 6) of the experimental data with Eq. (1) leads to $J = -22.2\ cm^{-1}$, $zJ' = -0.12\ cm^{-1}$, $g = 2.146$, and μ_{Cu} (fixed) = 1.73 BM; the agreement factor (R) defined as $[\sum\{(\chi_M T)_{obs} - (\chi_M T)_{calc}\}^2 / \sum(\chi_M T)_{obs}^2]$ is 1.37×10^{-2}. It may be mentioned that simulation (Fig. S2) of almost similar quality is obtained without considering molecular field approximation ($J = -22.7\ cm^{-1}$, $zJ' = 0\ cm^{-1}$ (fixed), $g = 2.143$, μ_{Cu} (fixed) = 1.73 BM, and $R = 1.89 \times 10^{-2}$). In this case divergence between the observed and calculated profiles occurs only for the data below 6 K. Comparison of the simulated curves in Fig. 6 and Fig. S2 indicates that very rapid decrease of $\chi_M T$ below 6 K takes place due to very weak ($zJ' = -0.12\ cm^{-1}$) Cu(mononuclear)–O(phenoxo)···H–O(water)–Cu(pentacoordinated) interaction. Again, it is obvious that sharp decrease of $\chi_M T$ below 80 K is related to moderate antiferromagnetic interaction ($J = -22.2\ cm^{-1}$) because more the extent of antiferromagnetic interaction higher the temperature below which $\chi_M T$ rapidly diminishes and vice versa. For example, if J values are $-40\ cm^{-1}$ and $-5\ cm^{-1}$ for a system like **2**, $\chi_M T$ should rapidly diminish below 120 K and 30 K, respectively.

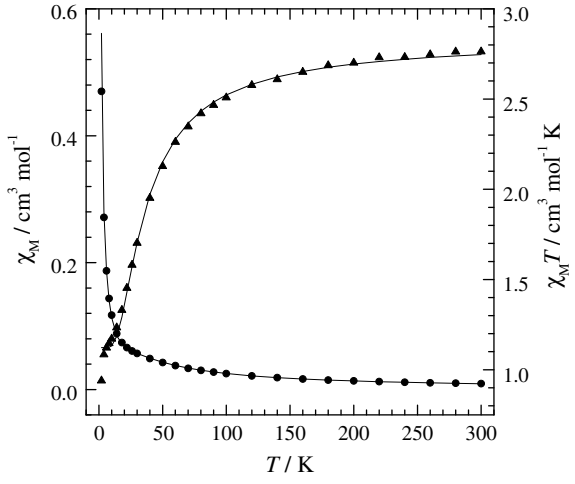


Fig. 6. χ_M (circles) versus T and $\chi_M T$ (triangles) versus T plots for **2**. The solid lines represent the simulated curves with $J = -22.2\ cm^{-1}$, $zJ' = -0.12\ cm^{-1}$, $g = 2.146$, and μ_{Cu} (fixed) = 1.73 BM.

As shown in Fig. 7, the $\chi_M T$ value (5.52 $cm^3\ mol^{-1}\ K$) at 300 K of **4** is almost equal to the theoretical value (5.50 $cm^3\ mol^{-1}\ K$) for the isolated one Mn^{II} ($s = 5/2$) and three Cu^{II} ($s = 1/2$) ions with $g = 2$. In this case, $\chi_M T$ gradually decreases on lowering of temperatures to reach a plateau (3.95 $cm^3\ mol^{-1}\ K$) in the temperature range 22–10 K. Below 10 K, $\chi_M T$ decreases sharply to reach a value of 3.62 $cm^3\ mol^{-1}\ K$ at 2 K. Clearly, the nature of interaction between the copper(II) and manganese(II) centers in the dinuclear core is antiferromagnetic. The absence of a maximum in the χ_M versus T plots as well as the observation of a rapid increase in the χ_M values at lower temperatures (Fig. 7) indicate that the Cu(mononuclear)–O(phenoxo)···H–O(water)–Cu(pentacoordinated) interaction is very weak. Considering molecular field approximation for the possible weak Cu(mononuclear)–O(phenoxo)···H–O(water)–Mn(pentacoordinated) interac-

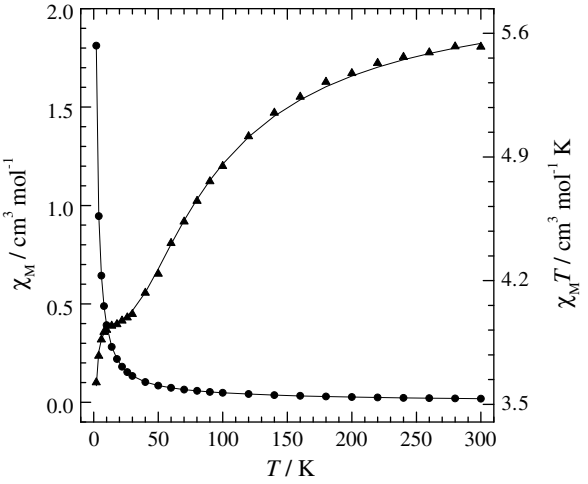


Fig. 7. χ_M (circles) versus T and $\chi_M T$ (triangles) versus T plots for **4**. The solid lines represent the simulated curves with $J = -15.9\ cm^{-1}$, $zJ' = -0.032\ cm^{-1}$, $g = 2.086$, μ_{Cu} (fixed) = 1.73 BM.

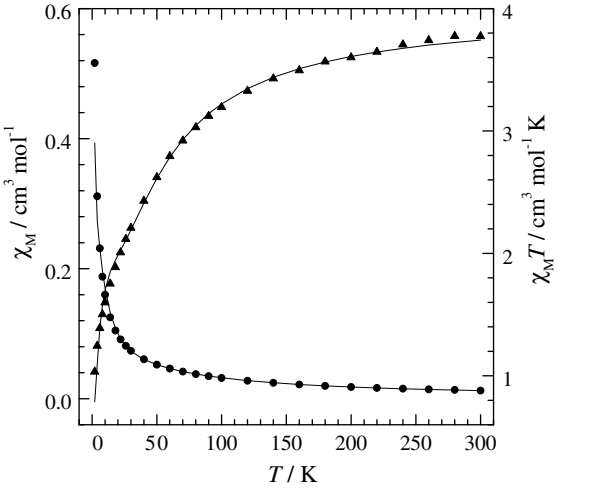


Fig. 8. χ_M (circles) versus T and $\chi_M T$ (triangles) versus T plots for **3**. The solid lines represent the simulated curves with $J = -16.7\ cm^{-1}$, $g = 2.408$, $|D| = 4.53\ cm^{-1}$, μ_{Cu} (fixed) = 1.73 BM.

tion, the theoretical equation of susceptibility one dinuclear $Cu^{II}Mn^{II}$ core and two noninteracting Cu^{II} centers can be derived as [2]

$$\chi_M = \frac{\chi_M^1}{1 - 2zJ'\chi_M^1/N\beta^2 g^2} \quad (2)$$

where

$$\chi_M^1 = \frac{7.997\chi_D T + 2\mu_{Cu}^2}{7.997T}$$

with

$$\chi_D = \frac{N\beta^2 g^2}{kT}\,\frac{10 + 28\,e^{6J/kT}}{5 + 7\,e^{6J/kT}}$$

In this case, global minimization (Fig. 7) takes place with $J = -15.9\ cm^{-1}$, $zJ' = -0.032\ cm^{-1}$, $g = 2.086$, μ_{Cu} (fixed) = 1.73 BM, and $R = 3.15 \times 10^{-3}$. It may be mentioned that slight divergence between the observed and calculated profiles occurs throughout the temperature range for the simulation (Fig. S3) without considering molecular field approximation ($J = -13.6\ cm^{-1}$, $zJ' = 0\ cm^{-1}$ (fixed), $g = 2.057$, μ_{Cu} (fixed) = 1.73 BM, and $R = 1.69 \times 10^{-2}$). Comparison of the simulated curves in Fig. 7 and Fig. S3 indicates that very rapid decrease of $\chi_M T$ below 10 K takes place due to very weak ($zJ' = -0.032\ cm^{-1}$) Cu(mononuclear)–O(phenoxo)···H–O(water)–Mn(pentacoordinated) interaction.

The cryomagnetic behavior of **3** is shown in Fig. 8. In this case, the $\chi_M T$ value (3.77 $cm^3\ mol^{-1}$ K) at 300 K is much greater than the theoretical value for the isolated one Co^{II} ($s = 3/2$) and three Cu^{II} ($s = 1/2$) ions with $g = 2$. On lowering of temperatures, $\chi_M T$ value gradually decreases to 3.12 $cm^3\ mol^{-1}$ K at 90 K. Further lowering of temperatures results in rapid decrease of $\chi_M T$ to 1.03 $cm^3\ mol^{-1}$ K at 2 K. Simulation of the experimental data with Eq. (3) [2], which accounts for the exchange coupling in the dinuclear core, molecular field approximation for the possible weak Cu(mononuclear)–O(phenoxo)···H–O(water)–Co(pentacoordinated) interaction, and magnetic moment for the two mononuclear copper(II) centers, is converged with $J = -15.8\ cm^{-1}$, $zJ' = -1.09\ cm^{-1}$, $g = 2.416$, μ_{Cu} (fixed) = 1.73 BM, and $R = 1.68 \times 10^{-2}$ (Fig. S4). On fixing $zJ' = 0\ cm^{-1}$, simulation (Fig. S5) of very poor quality is obtained with $J = -13.1\ cm^{-1}$, $zJ' = 0\ cm^{-1}$ (fixed), $g = 2.26$, μ_{Cu} (fixed) = 1.73 BM, and $R = 1.21 \times 10^{-1}$. In **2** and **4**, Cu(mononuclear)–O(phenoxo)···H–O(water)–M(pentacoordinated) distances lie in the range 4.78–4.91 Å and 4.85–4.90 Å, respectively, indicating that the similar magnitude of the Cu(mononuclear)–O(phenoxo)···H–O(water)–Co(pentacoordinated) distances in **3**. The similar values of the Cu(mononuclear)–O(phenoxo)···H–O(water)–M(pentacoordinated) distances (Cu_4^{II} (**6**), 4.86–5.04 Å; $Cu_3^{II}Co^{II}$ (**7**), 4.965 Å; $Cu_3^{II}Mn^{II}$ (**8**), 5.034 Å) in the cocrystals derived from H_2L support this assumption. Therefore, as observed for **2** and **4** ($zJ' = -0.12\ cm^{-1}$ and $-0.032\ cm^{-1}$, respectively), the values of zJ' should be small for **3** also. Evidently, the zJ' value of $-1.09\ cm^{-1}$ as well as its significant role in the susceptibility data throughout the temperature range (Fig. S4 versus Fig. S5) should be discarded. It may also be mentioned that the magnetic properties of the systems containing high spin cobalt(II) ion is associated with the first-order orbital angular momentum of the metal center. In **3**, this can be evidenced by the high value of $\chi_M T$ at 300 K. Therefore, the susceptibility data of **3** have been simulated with Eq. (4) [2,13] which considers the exchange coupling between cobalt(II) and copper(II) centers in the dinuclear core, single-ion zero-field parameter (D) of the cobalt(II) ion, and the contribution of the two isolated $s = 1/2$ spins. The simulation (Fig. 8) in this case is converged with $J = -16.7\ cm^{-1}$, $g = 2.408$, $|D| = 4.53\ cm^{-1}$, μ_{Cu} (fixed) = 1.73 BM, and $R = 2.36 \times 10^{-2}$. Comparison of the simulated curves in Fig. 8 and Fig. S5 indicates that rapid decrease of $\chi_M T$

below 90 K is associated with zero-field effect of cobalt(II). It may be noted that g value of 2.408 in **3** is in the usual range (2.2–2.5) of g values in previously reported systems containing cobalt(II) [13–19]. It may also be mentioned that, although simulations of magnetic susceptibility data in some cobalt(II) compounds have been performed without considering D [14], zero-field effect is known to govern the magnetic behavior of many cobalt(II) compounds [13,15–17] and the range of D in reported compounds is much wider; small value of *ca.* 0.1 cm^{-1} [13,15] and large value of *ca.* 10.5 cm^{-1} [16] and even *ca.* 145 cm^{-1} [17] are known. Again, large θ values (*ca.* 30 K or 70 K) taken in the simulation process in some cases [18] might be replaced by large D values (as described above, Fig. 8 versus Fig. S4). It may also be mentioned that magnetic behavior of cobalt(II) containing compounds may be so complicated that even the consideration of zero-field effect results in only poor quality simulation [19].

$$\chi_M = \frac{\chi_M^1}{1 - 2zJ'\chi_M^1/N\beta^2 g^2} \tag{3}$$

where

$$\chi_M^1 = \frac{7.997\chi_D T + 2\mu_{Cu}^2}{7.997T}$$

with

$$\chi_D = \frac{N\beta^2 g^2}{kT}\frac{2 + 10\,e^{4J/kT}}{3 + 5\,e^{4J/kT}}$$

$$\chi_M = \frac{7.997\chi_D T + 2\mu_{Cu}^2}{7.997T} \tag{4}$$

where

$$\chi_D = \frac{2N\beta^2 g^2}{kT}\frac{e^A + 4e^C + e^E}{2e^A + e^B + e^F + e^E}$$

with

$$A = \left[4J + \frac{5}{4}D - (4J^2 - 2DJ + D^2)^{1/2}\right]\Big/kT$$

$$B = \left[2J + \frac{1}{4}D\right]\Big/kT$$

$$C = \left[6J + \frac{9}{4}D\right]\Big/kT$$

$$F = \left[6J + \frac{1}{4}D\right]\Big/kT$$

$$E = \left[\left(4J + \frac{5}{4}D\right) + (4J^2 - 2DJ + D^2)^{1/2}\right]\Big/kT$$

A major emphasis to study the magnetic properties of exchange-coupled complexes is to find out the relationships between structural parameters and magnetic coupling. Based on such correlations one can predict and analyze the magnetic behavior of new systems more easily. Several magneto-structural correlations in different types of systems have been obtained either from experimental results or from theoretical study [13,20–25].

The first and perhaps the most elegant of these correlations was established by Hatfield and Hodgson [20,22] who demonstrated linear dependence of exchange-coupling constant (J) on the Cu–O–Cu bridge angle (θ) in planar dihydroxo-bridged dinuclear copper(II) complexes. Subsequently, similar linear correlations between J and θ have been reported for the alkoxo-bridged tetrameric copper(II) clusters of the cubane type [23] and diphenoxo-bridged macrocyclic dicopper(II) systems [24]. For dihydroxo-bridged and alkoxo-bridged systems, $J = 0$ at bridge angles 97.5° and 95.7°, respectively. These are the angles of accidental orthogonality or cross-over angles below which the interaction is ferromagnetic and above which antiferromagnetic interaction predominates. For diphenoxo-bridged dimmers, $J = 0$ at $\theta \approx 77°$, indicating that antiferromagnetic exchange dominates in these complexes at angles well below the angle for accidental orthogonality established in above two cases. The involvement of an additional exchange pathway through the conjugated double bonds in the phenoxo-bridged systems has been proposed to explain the observed difference in magnetic behavior [24]. Evidently, in dihydroxo, alkoxo, and diphenoxo-bridged copper(II) systems, the range of 95–98° should be considered as cross-over angle. Kahn et al. have examined roof-shaped dihydroxo-bridged copper(II) dimmers [20,25]. Theoretically they have shown that as the dihedral angle (δ) between the two CuO_2 planes decreases from 180°, antiferromagnetic contribution to superexchange decrease and a cross-over is attained at $\delta = 130°$.

The origin of the observed moderate antiferromagnetic interaction ($J = -22.2\ cm^{-1}$) in the dinuclear core in **2** can be understood from the relative orientation of the magnetic orbitals as well as from the above mentioned magneto-structural correlations. In the dinuclear core, two phenoxo oxygens occupy the square plane of the metal ion in the salen-type cavity indicating that the lobes of the $d_{x^2-y^2}$ orbital of this metal ion are directed towards both the bridging atoms. In contrast, for the more probable CuO_5 coordination environment of the second metal center (Cu(2)), one phenoxo oxygen occupies an equatorial position, while the second phenoxo oxygen is noncoordinated. Again, for the less probable CuO_6 coordination environment of Cu(2), two phenoxo oxygens occupy an equatorial and axial positions, respectively. Therefore, the lobes of $d_{x^2-y^2}$ orbital of Cu(2) are directed only towards one phenoxo oxygen. As a matter of fact, only one phenoxo oxygen of the dinuclear core participates in the superexchange interaction, which, in turn, should result in reduced antiferromagnetic interaction. Again, the Cu–O–Cu bridge angle (*ca.* 110°) involving the phenoxo oxygen participating in the exchange pathway is only slightly larger than the cross-over angle (95–98°), proposed in the related systems. Evidently, the moderate antiferromagnetic interaction between the metal centers in the dinuclear core in **2** is related to the participation of only one bridging phenoxo oxygen as well as the value of this bridge angle. It may be noted that the participation of only one phenoxo oxygen

in the exchange interaction as well as the value of Cu–O–Cu bridge angle (*ca.* 105°) are responsible for the similar moderate antiferromagnetic interaction ($-17.4\ cm^{-1}$) in the previously reported compound $[\{Cu^{II}L^{1}Cu^{II}(H_2O)_3\}\{Cu^{II}L^{1}\}_2](ClO_4)_2$ (**6**) [2]. However, slightly greater magnitude ($-22.2\ cm^{-1}$ versus $-17.4\ cm^{-1}$) can be rationalized from the slightly larger value of the Cu–O–Cu bridge angle (110° in **2** versus 105° in **6**).

The exchange interaction between the metal centers in the $Cu^{II}Mn^{II}$ dinuclear core in **4** is also moderately antiferromagnetic ($J = -15.9\ cm^{-1}$). In this case, the extent of interaction is a little less than that between the copper(II) centers in the dinuclear core in **2**. In this compound, all the five d orbitals of manganese(II) are occupied by unpaired electrons. Although the $d_{x^2-y^2} \leftrightarrow d_{x^2-y^2}$ pathway gives rise to an antiferromagnetic interaction, the other four routes provide a ferromagnetic contribution to the overall magnetic coupling. These two opposite effects result in, in comparison to the coupling in the dicopper(II) core in **2**, a reduction in the strength of the net antiferromagnetic interaction between the copper(II) and manganese(II) centers in **4**. It may be mentioned that similar moderate antiferromagnetic interaction ($J = -14\ cm^{-1}$) has been observed in the $Cu^{II}Mn^{II}$ dinuclear core in analogues $Cu^{II}_3Mn^{II}$ compound (**8**) derived from *N*,*N*′ -ethylenebis(3-ethoxysalicylaldimine) (H_2L).

4. Conclusions

The present study is concerned with the designed syntheses of inclusion compound and of dinuclear–mononuclear cocrystals involving the encapsulation of a water molecule. The formation of the inclusion product (**1**) and the dinuclear–mononuclear cocrystals (**2**–**4**) derived from *N*,*N*′-*o*-phenylenebis(3-ethoxysalicylaldimine) (H_2L^1) have been the major outcome of the present investigation. The most interesting aspect of this study is the emergence of a heptanuclear copper(II) compound $[\{Cu^{II}L^{1}Cu^{II}(H_2O)_3\}_2\{Cu^{II}L^{1}\}_3](ClO_4)_4 \cdot 2CH_3COCH_3$ (**2**) in which two monophenoxo-bridged dinuclear $[Cu^{II}L^{1}Cu^{II}(H_2O)_3]^{2+}$ cationic units are self-assembled and cocrystallized with three mononuclear $[Cu^{II}L^{1}]$ complex units. The composition of **2** is in sharp contrast to those of the heterotetranuclear complexes $[\{Cu^{II}L^{1}M^{II}(H_2O)_3\}\{Cu^{II}L^{1}\}_2](ClO_4)_2 \cdot H_2O \cdot CH_3COCH_3$ (M = Co (**3**), M = Mn (**4**)) as well as to those of the tetranuclear compounds $[\{Cu^{II}LM^{II}(H_2O)_3\}\{Cu^{II}L\}_2](ClO_4)_2$ (M^{II} = Cu (**6**), Co (**7**), M^{II} = Mn (**8**)) derived from *N*,*N*′-ethylenebis(3-ethoxysalicylaldimine) (H_2L). In these compounds, one diphenoxo-bridged heterodinuclear $[Cu^{II}(L^{1}/L)M^{II}(H_2O)_3]^{2+}$ cationic unit is self-assembled and cocrystallized with two mononuclear $[Cu^{II}(L^{1}/L)]$ moieties. In the $Cu^{II}_3M^{II}$ compounds **3**, **4**, and **6**–**8**, the $Cu^{II}M^{II}$ dinuclear cores are diphenoxo-bridged and the ethoxy oxygens are noncoordinated. In contrast, the dinuclear cores in the heptacopper(II) compound **2** are monophenoxo-bridged and one ethoxy oxygen coordinates to the second metal center. Thus, it appears that the formation of the heptanuclear self-assembly in **2** is related to the coordination of the ethoxy oxygen.

Acknowledgements

Financial support from the Department of Science and Technology, the Government of India (SR/S1/IC-27/2002), Council for Scientific and Industrial Research (Fellowship to M.N., S.H., and R.K.) is gratefully acknowledged. P.L. thanks Université Paris Descartes, Laboratoire de Cristallographie et RMN biologiques UMR 8015, Faculté de Pharmacie for single crystal X-ray data collection. Dr. Tareque Abedin, Memorial University of Newfoundland is acknowledged for variable-temperature magnetic data collection.

Appendix A. Supplementary material

Crystallographic data and Figs. S1–S5. CCDC 649248 and 649249 contain the supplementary crystallographic data for compounds **2** and **4**. These data can be obtained free of charge via http://www.ccdc.cam.ac.uk/conts/retrieving.html, or from the Cambridge Crystallographic Data Centre, 12 Union Road, Cambridge CB2 1EZ, UK; fax: (+44) 1223-336-033; or e-mail: deposit@ccdc.cam.ac.uk. Supplementary data associated with this article can be found, in the online version, at doi:10.1016/j.poly.2007.12.010.

References

[1] (a) R. Robson, in: J.L. Atwood, J.E.D. Davies, D.D. MacNicol, F. Vögtle, R.B. Toda (Eds.), Comprehensive Supramolecular Chemistry, vol. 6, Pergamon, Oxford, 1996, pp. 733–755;
(b) A.J. Blake, N.R. Champness, P. Hubberstey, M.A. Withersby, M. Schröder, Coord. Chem. Rev. 183 (1999) 117;
(c) J.-P. Sauvage (Ed.), Transition Metals in Supramolecular Chemistry (Perspectives in Supramolecular Chemistry), vol. 5, Wiley, England, 1999;
(d) G.R. Desiraju (Ed.), The Crystal as a Supramolecular Entity (Perspectives in Supramolecular Chemistry), vol. 2, Wiley, England, 1996;
(e) D. Braga, F. Grepioni, A.G. Orpen, Crystal Engineering: From Molecules and Crystals to Materials, Kluwer Academic Publishers, Dordrecht, 1999;
(f) D. Braga, L. Maini, M. Polito, L. Scaccianoce, G. Cojazzi, F. Grepioni, Coord. Chem. Rev. 216 (2001) 225;
(g) B. Moulton, M.J. Zaworotko, Chem. Rev. 101 (2001) 1629.
[2] M. Nayak, R. Koner, H.-H. Lin, U. Flörke, H.-H. Wei, S. Mohanta, Inorg. Chem. 45 (2006) 10764.
[3] (a) H. Koshima, M. Nagano, T. Asahi, J. Am. Chem. Soc. 127 (2005) 2455;
(b) S.L. Childs, L.J. Chyall, J.T. Dunlap, V.N. Smolenskaya, B.C. Stahly, G.P. Stahly, J. Am. Chem. Soc. 126 (2004) 13335;
(c) J.F. Remenar, S.L. Morissette, M.L. Peterson, B. Moulton, J.M. MacPhee, H.R. Guzman, O. Almarsson, J. Am. Chem. Soc. 125 (2003) 8456;
(d) X.-L. Zhang, X.-M. Chen, Cryst. Growth Des. 5 (2005) 617.
[4] (a) T.E. Keyes, R.J. Forster, A.M. Bond, W. Miao, J. Am. Chem. Soc. 123 (2001) 2877;

(b) U. Geiser, S.K. Kumar, B.M. Savall, S.S. Harried, K.D. Carlson, P.R. Mobley, H.-H. Wang, J.M. Williams, R.E. Botto, Chem. Mater. 4 (1992) 1077;
(c) B. Olenik, R. Boese, R. Sustmann, Cryst. Growth Des. 3 (2003) 175;
(d) F. Pan, M.S. Wong, V. Gramlich, C. Bosshard, P. Gunter, J. Am. Chem. Soc. 118 (1996) 6315.

[5] (a) H. Koshima, H. Miyamoto, I. Yagi, K. Uosaki, Cryst. Growth Des. 4 (2004) 807;
(b) S. Ohba, H. Hosomi, Y. Ito, J. Am. Chem. Soc. 123 (2001) 6349;
(c) J.H. Loehlin, M.C. Etter, C. Gendreau, E. Erika Cervasio, Chem. Mater. 6 (1994) 1218;
(d) B.R. Bhogala, A. Nangia, Cryst. Growth Des. 3 (2003) 547.

[6] (a) H.M. Lee, M.M. Olmstead, G.G. Gross, A.L. Balch, Cryst. Growth Des. 3 (2003) 691;
(b) M.M. Olmstead, P. Wei, A.S. Ginwalla, A.L. Balch, Inorg. Chem. 39 (2000) 4555;
(c) P. Le Magueres, S.M. Hubig, S.V. Lindeman, P. Veya, J.K. Kochi, J. Am. Chem. Soc. 122 (2000) 10073;
(d) I. Ara, J. Fornies, J. Gomez, E. Lalinde, M.T. Moreno, Organometallics 19 (2000) 3137;
(e) D. Wiechert, D. Mootz, T. Dahlems, J. Am. Chem. Soc. 119 (1997) 12665;
(f) R. Koner, M.G.B. Drew, A. Figuerola, C. Diaz, S. Mohanta, Inorg. Chim. Acta 358 (2005) 3041.

[7] (a) C.-C. Chou, C.-C. Su, H.-L. Tsai, K.-H. Lii, Inorg. Chem. 44 (2005) 628;
(b) M. Palaniandavar, R.J. Butcher, A.W. Addison, Inorg. Chem. 35 (1996) 467;
(c) R.C. Holz, L.C. Thompson, Inorg. Chem. 32 (1993) 5251;
(d) P. Jones, R.S. Vagg, P.A. Williams, Inorg. Chem. 23 (1984) 4110;
(e) W.J. Evans, T.J. Boyle, J.W. Ziller, Inorg. Chem. 31 (1992) 1120.

[8] E. König, Magnetic Properties of Transition Metal Compounds, Springer-Verlag, Berlin, 1966.

[9] R. Koner, G.-H. Lee, Y. Wang, H.-H. Wei, S. Mohanta, Eur. J. Inorg. Chem. (2005) 1500.

[10] (a) A. Altomare, G. Cascarano, C. Giacovazzo, A. Guagliardi, J. Appl. Crystallogr. 26 (1993) 343;
(b) G.M. Sheldrick, SHELXS-97: A Program for Crystal Structure Solution, University of Göttingen, Göttingen, Germany, 1997;
(c) G.M. Sheldrick, SHELXL-97: A Program for Crystal Structure Refinement, University of Göttingen, Göttingen, Germany, 1993.

[11] (a) G. Hoshina, M. Tsuchimoto, S. Ohba, Bull. Chem. Soc. Jpn. 73 (2000) 369;
(b) D. Cunningham, J.F. Gallagher, T. Higgins, P. McArdle, J. McGinley, M. O'Gara, J. Chem. Soc., Dalton Trans. (1993) 2183;
(c) J.R. Zamian, E.R. Dockal, G. Castellano, G. Oliva, Polyhedron 14 (1995) 2411.

[12] A.W. Addison, T.N. Rao, J. Reedijk, J. van Rijn, G.C. Verschoor, J. Chem. Soc. Dalton Trans. (1984) 1349.

[13] S. Mohanta, K.K. Nanda, L.K. Thompson, U. Flörke, K. Nag, Inorg. Chem. 37 (1998) 1465.

[14] (a) Y. Nakamura, M. Yonemura, K. Arimura, N. Usuki, M. Ohba, H. Ōkawa, Inorg. Chem. 40 (2001) 3739;
(b) M. Yonemura, K. Arimura, K. Inoue, N. Usuki, M. Ohba, H. Ōkawa, Inorg. Chem. 41 (2002) 582;
(c) A. Escuer, R. Vicente, B. Mernari, A.El. Gueddi, M. Pierrot, Inorg. Chem. 36 (1997) 2511.

[15] J.-P. Costes, R. Gheorghe, M. Andruh, S. Shova, J.-M.C. Juan, New J. Chem. (2006) 572.

[16] D. Nelson, L.W. ter Haar, Inorg. Chem. 32 (1993) 182.

[17] Md. J. Hossain, M. Yamasaki, M. Mikuriya, A. Kuribayashi, H. Sakiyama, Inorg. Chem. 41 (2002) 4058.

[18] M.A.M. Abu-Youssef, F.A. Mautner, R. Vicente, Inorg. Chem. 46 (2007) 4654.

[19] S. Osa, Y. Sunatsuki, Y. Yamamoto, M. Nakamura, T. Shimamoto, N. Matsumoto, N. Re, Inorg. Chem. 42 (2003) 5507.

[20] O. Kahn, Molecular Magnetism, VCH Publications, New York, 1993, see also references therein.

[21] R.D. Willett, D. Gatteschi, O. Kahn (Eds.), Magneto-Structural Correlations in Exchange Coupled Systems, Kluwer Academic Publishers, Dordrecht, The Netherlands, 1985.

[22] V.M. Crawford, M.W. Richardson, J.R. Wasson, D.J. Hodgson, W.E. Hatfield, Inorg. Chem. 15 (1976) 2107.

[23] L. Merz, W. Haase, J. Chem. Soc., Dalton Trans. (1980) 875.

[24] L.K. Thompson, S.K. Mandal, S.K. Tandon, J.N. Bridson, M.K. Park, Inorg. Chem. 35 (1996) 3117.

[25] M.F. Charlot, O. Kahn, S. Jeannin, Y. Jeanin, Inorg. Chem. 19 (1980) 1410.

ligands with hydrophilic properties. Among water-soluble phosphanes, particular attention has recently been paid to the cage-like tertiary phosphane 1,3,5-triaza-7-phosphaadamantane (PTA) [7] (Fig. 1) whose high solubility in water has been ascribed to the extensive participation of its three nitrogen atoms in hydrogen bonding interactions with water molecules.

Many PTA metal complexes have been synthesized [8] and utilized in aqueous catalysis, particularly hydrogenation of C=C and C=O bonds, that are useful in fine chemicals synthesis [9]. Ruthenium half-sandwich complexes containing the PTA ligand are also known for their catalytic [10] and biochemical implications [11–13].

In this context, a wide variety of half-sandwich ruthenium(II) complexes with PTA ligands have been reported including cyclopentadienyl (Cp) [11], indenyl [10], and arene [12] complexes; however, despite the similarities between the isoelectronic Cp and Tp (Tp = hydridotris(pyrazolyl)borate) complexes, to the best of our knowledge, no Tp–ruthenium(II) complexes containing PTA ligands have been described to date.

Furthermore, differences in size and electronic properties between Cp and Tp ligands [14] prompted us to explore the synthesis and reactivity of the first water-soluble ruthenium complexes containing a hydridotris(pyrazolyl)borate ligand. Moreover, the presence of nitrogen atoms in the pyrazol groups constitutes a new potential active site for interactions with hydrogen atoms, not only in water but in biological molecules as well.

Recently, we have published a series of ruthenium(II) complexes containing the water-soluble sulfonated phosphane TPPMS [15]. Continuing in line with our interest in the area of water-soluble metal complexes, in this work we report the synthesis of numerous ruthenium(II) complexes containing the cage-like phosphanes PTA or m-PTA and hydridotris(pyrazolyl)borate as ligands. Studies on their DNA binding properties and antimicrobial activity are also reported.

2. Experimental

All manipulations were performed under an atmosphere of dry nitrogen using vacuum-line and standard Schlenk techniques. All reagents were obtained from commercial suppliers and used without further purification. Solvents were dried by standard methods and distilled under nitrogen before use. The compounds [RuCl{κ^3(*N*,*N*,*N*)-Tp}(PPh_3)$_2$] [16], [RuCl(η^5-C_9H_7)(PPh_3)$_2$] [17] and PTA phosphane [18] were prepared by previously reported methods. Infrared spectra were recorded on a Perkin–Elmer FT-IR Paragon 1000 spectrometer. The C, H, and N analyses were carried out with a Perkin–Elmer 240-B microanalyzer. NMR spectra were recorded on a Bruker 300DPX instrument at 300.1 MHz (^{1}H), 121.5 MHz (^{31}P), or 75.4 MHz (^{13}C) and on a Bruker AC-400 instrument at 400.1 MHz (^{1}H), 161.9 (^{31}P) or 100.6 MHz (^{13}C) using $SiMe_4$ or 85% H_3PO_4 as standards. DEPT experiments were carried out for all the compounds. Coupling constants *J* are given in Hertzs. Resonances due to the Tp ligand are reported by chemical shift and multiplicity only, since all $^3J_{H,H}$ values for pyrazolyl rings are 2 Hz. Abbreviations used: br, broad signal; s, singlet; d, doublet; vt, virtual triplet; sept, septuplet; m, multiplet. For indenyl ligand the atom labels used for the ^{1}H and ^{13}C{^{1}H} are as in previous papers [19].

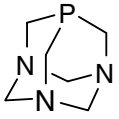


Fig. 1. 1,3,5-Triaza-7-phosphaadamantane (PTA) ligand.

2.1. Synthesis of the complexes

2.1.1. Synthesis of [RuCl{κ^3(*N*,*N*,*N*)-Tp}(*PTA*)$_2$] (*1*)

Method A: To a solution of complex [RuCl{κ^3(*N*,*N*,*N*)-Tp}(PPh_3)$_2$] (100 mg, 0.11 mmol) in toluene (1.5 mL) was added PTA (53 mg, 0.34 mmol). The reaction mixture was refluxed for 5 h and a yellow precipitate was formed. The solid was filtered off, washed with hexane and dried under vacuum to give compound **1**. Yield: 98% (72 mg).

Method B: To a solution of complex [RuCl{κ^3(*N*,*N*,*N*)-Tp}(PPh_3)(PTA)] (100 mg, 0.13 mmol) in toluene (3 mL) was added PTA (20 mg, 0.13 mmol). The reaction mixture was refluxed for 5 h and a yellow precipitate was formed. The solid was filtered off, washed with hexane and dried under vacuum to give compound **1**. Yield: 99% (85 mg). $S_{20\,°C}$ (H_2O) = 9.0 mg/mL. IR (KBr, cm^{-1}): ν(BH) = 2489. ^{1}H NMR (300.1 MHz, CD_2Cl_2, 20 °C): δ = 7.94 (d, 2H, H^{3,5} (pz)), 7.77 (d, 1H, H^{3,5} (pz)), 7.70 (d, 2H, H^{3,5} (pz)), 7.21 (d, 1H, H^{3,5} (pz)), 6.25 (br, 3H, H^4 (pz)), 4.56 (AB spin system, $J_{HA,HB}$ = 16 Hz, 6H, NCH_2N), 4.47 (AB spin system, $J_{HA,HB}$ = 16 Hz, 6H, NCH_2N), 4.13 (s, 12H, NCH_2P) ppm. ^{13}C{^{1}H} NMR (100.6 MHz, CD_2Cl_2, 20 °C): δ = 147.1 (s, C-3 (pz)), 143.2 (s, 2C, C-3 (pz)), 136.5 (s, C-5 (pz)), 135.1 (s, 2C, C-5 (pz)), 106.1 (s, C-4 (pz)), 105.3 (s, 2C, C-4 (pz)), 73.2 (s, 6C, N*C*H_2N), 53.7 (s, 6C, N*C*H_2P) ppm. ^{31}P{^{1}H} NMR (161.9 MHz, CD_2Cl_2, 20 °C): δ = −29.2 (s, PTA) ppm. *Anal.* Calc. for $C_{21}H_{34}BClN_{12}P_2Ru$: C, 37.99; H, 5.16; N, 25.32. Found: C, 38.05; H, 5.36; N, 25.16%.

2.1.2. Synthesis of [RuCl{κ^3(*N*,*N*,*N*)-Tp}(*PPh*$_3$)(*PTA*)] (*2*)

To a solution of complex [RuCl{κ^3(*N*,*N*,*N*)-Tp}(PPh_3)$_2$] (1000 mg, 1.14 mmol) in toluene (70 mL) was added PTA (179 mg, 1.14 mmol). The reaction mixture was refluxed for 4 h. After this, volatiles were removed in vacuum. The crude product was recrystallized from dichloromethane/acetone and compound **2** was obtained as a microcrystalline yellow solid. Yield: 96% (842 mg). $S_{20\,°C}$ (H_2O) = 3.0 mg/mL. IR (KBr, cm^{-1}): ν(BH) = 2476. ^{1}H NMR (400.1 MHz, CD_2Cl_2, 20 °C):

$\delta = 8.18$ (d, 1H, $H^{3,5}$ (pz)), 7.70 (d, 1H, $H^{3,5}$ (pz)), 7.69 (d, 1H, $H^{3,5}$ (pz)), 7.68–7.60 (m, 6H, PPh_3), 7.38–7.29 (m, 10H, PPh_3 and $H^{3,5}$ (pz)), 6.68 (d, 1H, $H^{3,5}$ (pz)), 6.28 (t, 1H, H^4 (pz)), 6.02 (d, 1H, $H^{3,5}$ (pz)), 5.83 (t, 1H, H^4 (pz)), 5.73 (t, 1H, H^4 (pz)), 4.34 (AB spin system, $J_{HA,HB} = 13$ Hz, 3H, NCH_2N), 4.31 (AB spin system, $J_{HA,HB} = 13$ Hz, 3H, NCH_2N), 3.90 (AB spin system, $J_{HA,HB} = 16$ Hz, 3H, NCH_2P), 3.86 (AB spin system, $J_{HA,HB} = 16$ Hz, 3H, NCH_2P) ppm. $^{13}C\{^1H\}$ NMR (100.6 MHz, CD_2Cl_2, 20 °C): $\delta = 146.5$ (s, C-3 (pz)), 143.8 (s, C-3 (pz)), 143.3 (s, C-3 (pz)), 136.1 (d, $J_{C,P} = 39$ Hz, 3C, C-1 PPh_3), 135.8 (s, C-5 (pz)), 135. 4 (s, C-5 (pz)), 135.0 (s, C-5 (pz), 134.2 (d, $^2J_{C,P} = 9$ Hz, 6C, C-2,6 PPh_3)), 129.2 (s, 3C, C-4 PPh_3), 127.8 (d, $^3J_{C,P} = 9$ Hz, 6C, C-3,5 PPh_3), 105.7 (s, C-4 (pz)), 105.3 (s, C-4 (pz)), 104.7 (s, C-4 (pz)), 73.2 (d, $^3J_{C,P} = 6$ Hz, 3C, NCH_2N), 51.8 (d, $J_{C,P} = 14$ Hz, 3C, NCH_2P) ppm. $^{31}P\{^1H\}$ NMR (161.9 MHz, 20 °C, CD_2Cl_2): $\delta = 47.1$ (d, $^2J_{P,P} = 32$ Hz, PPh_3), −35.6 (d, $^2J_{P,P} = 32$ Hz, PTA) ppm. *Anal.* Calc. for $C_{33}H_{37}BClN_9P_2Ru$: C, 51.54; H, 4.85; N, 16.39. Found: C, 51.36; H, 4.52; N, 16.69%.

2.1.3. Synthesis of [RuI{κ³(N,N,N)-Tp}(PPh₃)(PTA)] (3)

To a solution of complex **2** (100 mg, 0.13 mmol) in methanol (80 mL) was added sodium iodide (206 mg, 1.37 mmol). The reaction mixture was stirred at room temperature for 24 h. After this, volatiles were removed in vacuum. The solid residue was extracted with dichloromethane and the resultant solution was filtered through kieselguhr and concentrated under vacuum to a volume of approx. 1 mL. Addition of hexane afforded an orange precipitate. The solvents were decanted and the solid residue was washed with hexane (3 × 10 mL) and dried under reduced pressure to afford complex **3**. Yield: 76% (85 mg). $S_{20\,°C}$ (H_2O) = 0.5 mg/mL. IR (KBr, cm^{-1}): ν(BH) = 2466. ^1H NMR (400.1 MHz, CD_2Cl_2, 20 °C): $\delta = 8.48$ (s, 1H, $H^{3,5}$ (pz)), 7.67 (s, 3H, $H^{3,5}$ (pz)), 7.62–7.58 (m, 6H, PPh_3), 7.39–7.36 (m, 3H, PPh_3), 7.30–7.26 (m, 6H, PPh_3), 6.65 (s, 1H, $H^{3,5}$ (pz)), 6.25 (t, 1H, H^4 (pz)), 5.91 (s, 1H, $H^{3,5}$ (pz)), 5.80 (t, 1H, H^4 (pz)), 5.72 (t, 1H, H^4 (pz)), 4.42 (AB spin system, $J_{HA,HB} = 13$ Hz, 3H, NCH_2N), 4.26 (AB spin system, $J_{HA,HB} = 13$ Hz, 3H, NCH_2N), 3.92 (s, 6H, NCH_2P) ppm. $^{13}C\{^1H\}$ (100.6 MHz, CD_2Cl_2, 20 °C): $\delta = 147.0$ (s, C-3 (pz)), 146.6 (s, C-3 (pz)), 146.2 (s, C-3 (pz)), 135.8 (d, $J_{C,P} = 30$ Hz, 3C, C-1 PPh_3), 135.7 (s, C-5 (pz)), 135.6 (s, C-5 (pz)), 135.0 (d, $^2J_{C,P} = 9$ Hz, 6C, C-2,6 PPh_3 and s, C-5 (pz) (masked)), 129.3 (s, 3C, C-4 PPh_3), 127.5 (d, $^3J_{C,P} = 9$ Hz, 6C, C-3,5 PPh_3), 105.7 (s, C-4 (pz)), 105.3 (s, C-4 (pz)), 104.5 (s, C-4 (pz)), 73.2 (d, $^3J_{C,P} = 6$ Hz, 3C, NCH_2N), 53.9 (d, $J_{C,P} = 15$ Hz, 3C, NCH_2P) ppm. $^{31}P\{^1H\}$ NMR (161.9 MHz, CD_2Cl_2, 20 °C): $\delta = 50.4$ (d, $^2J_{P,P} = 32$ Hz, PPh_3), −40.2 (d, $^2J_{P,P} = 32$ Hz, PTA) ppm. *Anal.* Calc. for $C_{33}H_{37}BIN_9P_2Ru$: C, 46.06; H, 4.33; N, 14.65. Found: C, 46.15; H, 4.40; N, 14.15%.

2.1.4. Synthesis of [Ru(NCS){κ³(N,N,N)-Tp}(PPh₃)(PTA)] (4)

To a solution of complex **2** (100 mg, 0.13 mmol) in methanol (10 mL) was added potassium thiocyanate (KSCN) (40 mg, 0.42 mmol). The reaction mixture was refluxed for 6 h. The solution was cooled to room temperature and the solvent was removed under vacuum. The solid residue was extracted with dichloromethane and the resultant solution was filtered through kieselguhr and concentrated under vacuum to a volume of approx. 1 mL. Addition of hexane afforded a yellow precipitate. The solvents were decanted, the solid residue was washed with hexane (3 × 5 mL) and dried under reduced pressure to afford complex **4**. Yield: 68% (70 mg). $S_{20\,°C}$(H_2O) = 2.0 mg/mL. IR (KBr, cm^{-1}): ν(BH) = 2485, ν(SCN) = 2113. ^1H (400.1 MHz, CD_2Cl_2, 20 °C): $\delta = 7.96$ (s, 1H, $H^{3,5}$ (pz)), 7.80 (s, 1H, $H^{3,5}$ (pz)), 7.72 (br, 2H, $H^{3,5}$ (pz)), 7.43–7.28 (m, 15H, PPh_3), 6.68 (s, 1H, $H^{3,5}$ (pz)), 6.42 (s, 1H, $H^{3,5}$ (pz)), 6.32 (s, 1H, H^4 (pz)), 5.97 (s, 1H, $H^{3,5}$ (pz)), 5.87 (s, 1H, H^4 (pz)), 4.41 (AB spin system, $J_{HA,HB} = 13$ Hz, 3H, NCH_2N), 4.23 (AB spin system, $J_{HA,HB} = 13$ Hz, 3H, NCH_2N), 3.85 (s, 3H, NCH_2P) ppm. $^{13}C\{^1H\}$ (100.6 MHz, CD_2Cl_2, 20 °C): $\delta = 146.7$ (s, C-3 (pz)), 143.7 (s, C-3 (pz)), 143.5 (s, C-3 (pz)), 136.5 (s, C-5 (pz)), 136.3 (s, SCN), 135. 7 (s, C-5 (pz)), 135.6 (s, C-5 (pz), 135.1 (d, $J_{C,P} = 40$ Hz, 3C, C-1 PPh_3)), 134.1 (d, $^2J_{C,P} = 9$ Hz, 6C, C-2,6 PPh_3), 129.7 (s, 3C, C-4 PPh_3), 128.2 (d, $^3J_{C,P} = 9$ Hz, 6C, C-3,5 PPh_3), 106.1 (s, C-4 (pz)), 105.8 (s, C-4 (pz)), 105.4 (s, C-4 (pz)), 73.0 (d, $^3J_{C,P} = 6$ Hz, 3C, NCH_2N), 51.5 (d, $J_{C,P} = 13$ Hz, 3C, NCH_2P) ppm. $^{31}P\{^1H\}$ NMR (161.9 MHz, CD_2Cl_2, 20 °C): $\delta = 47.8$ (d, $^2J_{P,P} = 31$ Hz, PPh_3), −35.6 (d, $^2J_{P,P} = 31$ Hz, PTA) ppm. *Anal.* Calc. for $C_{34}H_{37}BN_{10}P_2RuS$: C, 51.59; H, 4.71; N, 17.69. Found: C, 51.38; H, 5.21; N, 17.25%.

2.1.5. Synthesis of [RuH(κ³(N,N,N)-Tp)(PPh₃)(PTA)] (5)

To a solution of NaOMe (56 mg, 1.04 mmol) in methanol (10 mL) was added the complex **2** (100 mg, 0.13 mmol). The resulting solution was refluxed for 4 h. The solution was cooled to room temperature and volatiles were removed in vacuum and the solid residue was extracted with dichloromethane. The resultant solution was filtered through kieselguhr and concentrated under vacuum to a volume of approx. 0.5 mL. Addition of hexane afforded a yellow precipitate. The solvents were decanted and the solid was dried under reduced pressure to afford complex **5**. Yield: 53% (51 mg). $S_{20\,°C}$ (H_2O) = 1.7 mg/mL. IR (KBr, cm^{-1}): ν(BH) = 2457, ν(Ru–H) = 1923. ^1H NMR (300.1 MHz, CD_2Cl_2, 20 °C): $\delta = 7.91$ (d, 1H, $H^{3,5}$ (pz)), 7.86 (d, 1H, $H^{3,5}$ (pz)), 7.68 (d, 1H, $H^{3,5}$ (pz)), 7.58 (d, 1H, $H^{3,5}$ (pz)), 7.50–7.44 (m, 5H, PPh_3), 7.36–7.29 (m, 10H, PPh_3), 7.27 (d, 1H, $H^{3,5}$ (pz)), 6.49 (d, 1H, $H^{3,5}$ (pz)), 6.22 (t, 1H, H^4 (pz)), 6.17 (t, 1H, H^4 (pz)), 5.64 (t, 1H, H^4 (pz)), 4.34 (AB spin system, $J_{HA,HB} = 13$ Hz, 3H, NCH_2N), 4.14 (AB spin

system, $J_{HA,HB} = 13$ Hz, 3H, NCH_2N), 3.76 (AB spin system, $J_{HA,HB} = 15$ Hz, 3H, NCH_2P), 3.51 (AB spin system, $J_{HA,HB} = 15$ Hz, 3H, NCH_2P), −14.71 (dd, $^2J_{H,P} = 31$ Hz and $^2J_{H,P} = 26$ Hz, 1H, Ru–H) ppm. $^{13}C\{^1H\}$ NMR (100.6 MHz, CD_2Cl_2, 20 °C): $\delta = 147.6$ (s, C-3 (pz)), 145.6 (s, C-3 (pz)), 144.8 (s, C-3 (pz)), 139.8 (d, $J_{C,P} = 36$ Hz, 3C, C-1 PPh_3), 135.4 (s, C-5 (pz)), 135.2 (s, C-5 (pz)), 134.9 (s, C-5 (pz), 134.7 (d, $^2J_{C,P} = 10$ Hz, 6C, C-2,6 PPh_3)), 129.1 (s, 3C, C-4 PPh_3), 127.9 (d, $^3J_{C,P} = 10$ Hz, 6C, C-3,5 PPh_3), 105.3 (s, C-4 (pz)), 105.0 (s, C-4 (pz)), 104.6 (s, C-4 (pz)), 73.4 (d, $^3J_{C,P} = 6$ Hz, 3C, NCH_2N), 55.7 (d, $J_{C,P} = 14$ Hz, 3C, NCH_2P) ppm. $^{31}P\{^1H\}$ (161.9 MHz, CD_2Cl_2, 20 °C): $\delta = 70.4$ (d, $^2J_{P,P} = 36$ Hz, PPh_3), −23.4 (d, $^2J_{P,P} = 36$ Hz, PTA) ppm. *Anal.* Calc. for $C_{33}H_{38}BN_9P_2Ru$: C, 53.96; H, 5.21; N, 17.16. Found: C, 53.72; H, 5.69; N, 16.98%.

2.1.6. Synthesis of [Ru(κ³(N,N,N)-Tp)(NCMe)(PPh₃)(PTA)][PF₆] (6)

To a solution of complex **2** (100 mg, 0.13 mmol) in a mixture acetonitrile (2 mL)/methanol (10 mL) was added $NaPF_6$ (67 mg, 0.39 mmol). The reaction mixture was refluxed for 7 h. The solution was cooled to room temperature and the solvent was removed under vacuum. The solid residue was extracted with dichloromethane, filtered through kieselguhr and the resultant solution was concentrated under vacuum to a volume of approx. 1 mL. Addition of diethyl ether afforded a white precipitate. The solvents were decanted and the solid residue was washed with diethyl ether (2 × 5 mL) and dried under reduced pressure to afford complex **6**. Incomplete combustion for this complex prevented us from obtaining any satisfactory analysis. Yield: 82% (98 mg). $S_{20\,°C}$ (H_2O) = 0.4 mg/mL. IR (KBr, cm^{-1}): ν(BH) = 2491, $\nu(PF_6) = 840$. ^1H NMR (300.1 MHz, CD_2Cl_2, 20 °C): $\delta = 8.01$ (d, 1H, $H^{3,5}$ (pz)), 7.97 (d, 1H, $H^{3,5}$ (pz)), 7.87 (d, 1H, $H^{3,5}$ (pz)), 7.81 (d, 1H, $H^{3,5}$ (pz)), 7.49–7.34 (m, 10H, Ph and $H^{3,5}$ (pz)), 7.21–7.17 (m, 6H, Ph), 6.65 (d, 1H, $H^{3,5}$ (pz)), 6.39 (t, 1H, H^4 (pz)), 6.27 (t, 1H, H^4 (pz)), 6.03 (t, 1H, H^4 (pz)), 4.43 (AB spin system, $J_{HA,HB} = 13$ Hz, 3H, NCH_2N), 4.30 (AB spin system, $J_{HA,HB} = 13$ Hz, 3H, NCH_2N), 3.82 (AB spin system, $J_{HA,HB} = 15$ Hz, 3H, NCH_2P), 3.71 (AB spin system, $J_{HA,\ HB} = 15$ Hz, 3H, NCH_2P), 2.19 (s, 3H, NCCH_3) ppm. $^{13}C\{^1H\}$ NMR (100.6 MHz, CD_2Cl_2, 20 °C): $\delta = 147.1$ (s, C-3 (pz)), 143.8 (s, C-3 (pz)), 142.5 (s, C-3 (pz)), 137.8 (s, C-5 (pz)), 136.5 (s, C-5 (pz)), 134. 3 (s, C-5 (pz)), 134.1 (d, $^2J_{C,P} = 9$ Hz, 6C, C-2,6 PPh_3), 133.9 (d, $J_{C,P} = 32$ Hz, 3C, C-1 PPh_3), 130.4 (s, 3C, C-4 PPh_3), 128.5 (d, $^3J_{C,P} = 9$ Hz, 6C, C-3,5 PPh_3), 125.7 (s, NCCH_3), 107.1 (s, C-4 (pz)), 106.7 (s, C-4 (pz)), 106.5 (s, C-4 (pz)), 72.7 (d, $^3J_{C,P} = 6$ Hz, 3C, NCH_2N), 50.8 (d, $J_{C,P} = 14$ Hz, 3C, NCH_2P), 4.0 (s, NCCH_3) ppm. $^{31}P\{^1H\}$ NMR (161.9 MHz, CD_2Cl_2, 20 °C): $\delta = 43.9$ (d, $^2J_{P,P} = 29$ Hz, PPh_3), −42.4 (d, $^2J_{P,P} = 29$ Hz, PTA), −144.1 (sept, $J_{F,P} = 707$ Hz, PF_6) ppm.

2.1.7. Synthesis of [Ru(κ³(N,N,N)-Tp)(PPh₃)(PTA)₂][PF₆] (7)

To a solution of complex **2** (100 mg, 0.13 mmol) in methanol (20 mL) was added $NaPF_6$ (67 mg, 0.39 mmol) and the phosphane PTA (20 mg, 0.13 mmol). The reaction mixture was refluxed for 6 h. The solution was cooled to room temperature and the solvent was removed under vacuum. The solid residue was extracted with dichloromethane and the resultant solution was filtered through kieselguhr and concentrated under vacuum to a volume of approx. 1 mL. Addition of hexane afforded a white precipitate. The solvents were decanted and the solid residue was washed with hexane (3 × 5 mL) and dried under reduced pressure to afford complex **7**. Yield: 73% (98 mg). $S_{20\,°C}$ (H_2O) = 2.5 mg/mL. IR (KBr, cm^{-1}): ν(BH) = 2488, $\nu(PF_6) = 842$. ^1H NMR (400.1 MHz, CD_2Cl_2, 20 °C): $\delta = 8.00$ (s, 1H, $H^{3,5}$ (pz)), 7.89–7.86 (m, 3H, $H^{3,5}$ (pz)), 7.61 (br, 3H, PPh_3), 7.47–7.35 (m, 12H, PPh_3), 6.55 (s, 1H, $H^{3,5}$ (pz)), 6.12–6.06 (m, 4H, $H^{3,5}$ (pz) and H^4 (pz)), 4.40 (AB spin system, $J_{HA,HB} = 13$ Hz, 6H, NCH_2N), 4.26 (AB spin system, $J_{HA,HB} = 13$ Hz, 6H, NCH_2N), 3.75 (s, 12H, NCH_2P) ppm. $^{13}C\{^1H\}$ NMR (100.6 MHz, CD_2Cl_2, 20 °C): $\delta = 146.5$ (s, 2C, C-3 (pz)), 145.9 (s, C-3 (pz)), 137.7 (s, 2C, C-5 (pz)), 137.3 (s, C-5 (pz)), 135.7 (d, $^2J_{C,P} = 7$ Hz, 6C, C-2,6 PPh_3), 132.8 (d, $J_{C,P} = 40$ Hz, 3C, C-1 PPh_3), 131.4 (s, 3C, C-4 PPh_3), 128.3 (d, $^3J_{C,P} = 9$ Hz, 6C, C-3,5 PPh_3), 107.9 (s, C-4 (pz)), 105.9 (s, 2C, C-4 (pz)), 72.6 (s, 6C, NCH_2N), 53.0 (s, 6C, NCH_2P) ppm. $^{31}P\{^1H\}$ NMR (161.9 MHz, CD_2Cl_2, 20 °C): $\delta = 48.6$ (t, $^2J_{P,P} = 31$ Hz, PPh_3), −49.1 (d, $^2J_{P,P} = 31$ Hz, PTA), −144.3 (sept, $J_{F,P} = 712$ Hz, PF_6) ppm. *Anal.* Calc. for $C_{39}H_{49}BF_6N_{12}P_4Ru \cdot CH_2Cl_2$: C, 42.87; H, 4.59; N, 15.00. Found: C, 42.16; H, 4.60; N, 14.94%.

2.1.8. Synthesis of [RuCl(κ³(N,N,N)-Tp)(m-PTA)₂][CF₃SO₃]₂ (8)

Complex **1** (100 mg, 0.13 mmol) was dissolved in 2 mL of dichloromethane. The yellow solution was stirred at −30 °C during 15 min. After this time period, methyl trifluoromethanesulfonate (32 μL, 0.26 mmol) was added and the reaction mixture was stirred at −30 °C during 40 min. Addition of hexane afforded a white precipitate. The solvents were decanted and the solid residue was washed with hexane (2 × 5 mL) and dried under reduced pressure to afford complex **8**. Yield: 31% (40 mg). $S_{20\,°C}$ (H_2O) = 4.5 mg/mL. IR (KBr, cm^{-1}): ν(BH) = 2485, ν(OSO) = 1259. ^1H NMR (400.1 MHz, NCMe-d_3, 20 °C): $\delta = 8.01$ (d, 2H, $H^{3,5}$ (pz)), 7.91 (d, 1H, $H^{3,5}$ (pz)), 7.83 (d, 2H, $H^{3,5}$ (pz)), 7.40 (d, 1H, $H^{3,5}$ (pz)), 6.36 (t, 1H, H^4 (pz)), 6.33 (t, 2H, H^4 (pz)), 5.12 (AB spin system, $J_{HA,HB} = 12$ Hz, 2H, NCH_2N), 4.92 (AB spin system, $J_{HA,HB} = 12$ Hz, 2H, NCH_2N), 4.83–4.77 (m, 4H, NCH_2N), 4.50–4.36 (m, 8H, 4H NCH_2N and 4H NCH_2P), 4.18 (s, 4H, NCH_2P), 3.83 (AB spin system, $J_{HA,HB}$ = 16 Hz, 2H, NCH_2P), 3.69 (AB spin system, $J_{HA,HB}$ = 16 Hz, 2H, NCH_2P), 2.80 (s, 6H, CH_3N) ppm. $^{13}C\{^1H\}$

NMR (100.6 MHz, NCMe-d_3, 20 °C): $\delta = 148.7$ (s, C-3 (pz)), 144.5 (s, 2C, C-3 (pz)), 137.8 (s, C-5 (pz)), 136.3 (s, 2C, C-5 (pz)), 121.1 (q, $J_{C,F} = 322$ Hz, CF_3SO_3), 107.7 (s, C-4 (pz)), 106.2 (s, 2C, C-4 (pz)), 79.8 (s, 2C, CH_3NCH_2N), 79.6 (s, 2C, CH_3NCH_2N), 69.0 (s, 2C, NCH_2N), 57.2 (s, 2C, CH_3NCH_2P), 49.5 (vt, $J = 8$ Hz, 2C, NCH_2P), 48.9 (s, 2C, CH_3N), 48.6 (vt, $J = 8$ Hz, 2C, NCH_2P) ppm. $^{31}P\{^1H\}$ NMR (161.9 MHz, NCMe-d_3, 20 °C): $\delta = -9.8$ (s, m-PTA) ppm. *Anal.* Calc. for $C_{25}H_{40}BClF_6N_{12}O_6P_2RuS_2$: C, 30.27; H, 4.06; N, 16.94; S, 6.46. Found: C, 30.29; H, 4.02; N, 16.11; S, 6.03%.

2.1.9. Synthesis of [RuCl(κ³(N,N,N)-Tp)(PPh₃)(m-PTA)][CF₃SO₃] (9)

Complex **2** (100 mg, 0.13 mmol) was dissolved in 2 mL of dichloromethane. The yellow solution was stirred at −30 °C during 15 min. After this time period, methyl trifluoromethanesulfonate (16 μL, 0.13 mmol) was added and the reaction mixture was stirred at −30 °C during 40 min. The yellow precipitate thus formed was filtered off and washed with hexane (3 × 10 mL). The product was dried under vacuum to give compound **9**. Yield: 71% (86 mg). $S_{20\,°C}$ (H_2O) = 0.8 mg/mL. IR (KBr, cm^{-1}): ν(BH) = 2483, ν(OSO) = 1258. ^1H NMR (400.1 MHz, NCMe-d_3, 20 °C): $\delta = 8.11$ (d, 1H, $H^{3,5}$ (pz)), 7.85 (d, 1H, $H^{3,5}$ (pz)), 7.83 (d, 1H, $H^{3,5}$ (pz)), 7.80 (d, 1H, $H^{3,5}$ (pz)), 7.45–7.35 (m, 15H, PPh_3), 6.82 (d, 1H, $H^{3,5}$ (pz)), 6.66 (d, 1H, $H^{3,5}$ (pz)), 6.30 (t, 1H, H^4 (pz)), 5.93 (t, 1H, H^4 (pz)), 5.89 (t, 1H, H^4 (pz)), 4.72–4.67 (m, 2H, NCH_2N), 4.60–4.52 (m, 2H, NCH_2N), 4.24 (AB spin system, $J_{HA,HB} = 14$ Hz, 1H, NCH_2N), 4.12 (AB spin system, $J_{HA,HB} = 14$ Hz, 1H, NCH_2N), 4.02 (AB spin system, $J_{HA,HB} = 14$ Hz, 1H, NCH_2P), 3.93 (AB spin system, $J_{HA,HB} = 14$ Hz, 1H, NCH_2P), 3.77–3.73 (m, 1H, NCH_2P), 3.66 (br, 3H, NCH_2P), 2.60 (s, 3H, NCH_3) ppm. $^{13}C\{^1H\}$ NMR (100.6 MHz, NCMe-d_3, 20 °C): $\delta = 148.3$ (s, C-3 (pz)), 144.4 (s, C-3 (pz)), 143.8 (s, C-3 (pz)), 136.9 (s, C-5 (pz)), 136.2 (s, C-5 (pz)), 136.1 (s, C-5 (pz)), 135.3 (d, 3C, $J_{C,P} = 40$ Hz, C-1 PPh_3), 134.2 (d, $^2J_{C,P} = 9$ Hz, 6C, C-2,6 PPh_3), 129.9 (s, 3C, C-4 PPh_3), 128.1 (d, $^3J_{C,P} = 9$ Hz, 6C, C-3,5 PPh_3), 119.6 (q, $J_{C,F} = 314$ Hz, CF_3SO_3), 106.7 (s, C-4 (pz)), 105.7 (s, C-4 (pz)), 105.3 (s, C-4 (pz)), 80.5 (d, $^3J_{C,P} = 9$ Hz, 2C, CH_3NCH_2N), 68.8 (d, $^3J_{C,P} = 5$ Hz, NCH_2N), 57.2 (d, $^3J_{C,P} = 7$ Hz, CH_3NCH_2P), 49.2 (s, NCH_3), 47.9 (d, $J_{C,P} = 15$ Hz, NCH_2P), 47.5 (d, $J_{C,P} = 15$ Hz, NCH_2P) ppm. $^{31}P\{^1H\}$ NMR (161.9 MHz, NCMe-d_3, 20 °C): $\delta = 42.0$ (d, $^2J_{P,P} = 31$ Hz, PPh_3), −13.6 (d, $^2J_{P,P} = 31$ Hz, m-PTA) ppm. *Anal.* Calc. for $C_{35}H_{40}BClF_3N_9O_3P_2RuS \cdot 1/2\ CH_2Cl_2$: C, 43.71; H, 4.24; N, 12.92; S, 3.29. Found: C, 43.52; H, 4.53; N, 12.68; S, 3.03%.

2.1.10. Synthesis of [RuH(κ³(N,N,N)-Tp)(PPh₃)(m- PTA)][CF₃SO₃] (10)

Complex **4** (100 mg, 0.14 mmol) was dissolved in 2 mL of dichloromethane. The yellow solution was stirred at −30 °C during 15 min. After this time period, methyl trifluoromethanesulfonate (17 μL, 0.14 mmol) was added and the reaction mixture was stirred at −30 °C during 40 min. The yellow precipitate thus formed was filtered off and washed with hexane (3 × 10 mL). The product was dried under vacuum to give compound **10**. Yield: 64% (80 mg). $S_{20\,°C}$ (H_2O) = 0.4 mg/mL. IR (KBr, cm^{-1}): ν(BH) = 2476, ν(Ru–H) = 1931, ν(OSO) = 1258. ^1H NMR (400.1 MHz, NCMe-d_3, −10 °C): $\delta = 7.96$ (d, 1H, $H^{3,5}$ (pz)), 7.82 (d, 1H, $H^{3,5}$ (pz)), 7.72 (d, 1H, $H^{3,5}$ (pz)), 7.66 (d, 1H, $H^{3,5}$ (pz)), 7.54 (d, 1H, $H^{3,5}$ (pz)), 7.37–7.10 (m, 15H, PPh_3), 6.25–6.23 (m, 2H, $H^{3,5}$ and H^4 (pz)), 6.14 (t, 1H, H^4 (pz)), 5.62 (t, 1H, H^4 (pz)), 4.54–3.96 (m, 6H, NCH_2N), 3.79–3.17 (m, 6H, NCH_2P), 2.43 (s, 3H, CH_3N), −14.46 (dd, $^2J_{H,P} = 33$ Hz and $^2J_{H,P} = 25$ Hz, 1H, Ru–H) ppm. $^{13}C\{^1H\}$ NMR (100.6 MHz, NCMe-d_3, −10 °C): $\delta = 147.6$ (s, C-3 (pz)), 145.9 (s, C-3 (pz)), 143.9 (s, C-3 (pz)), 138.3 (d, $J_{C,P} = 38$ Hz, 3C, C-1 PPh_3), 136.0 (s, C-5 (pz)), 135.5 (s, 2C, C-5 (pz)), 134.3 (d, $^2J_{C,P} = 10$ Hz, 6C, C-2,6 PPh_3), 129.6 (s, 3C, C-4 PPh_3), 128.0 (d, $^3J_{C,P} = 9$ Hz, 6C, C-3,5 PPh_3), 120.9 (q, $J_{C,F} = 320$ Hz, CF_3SO_3), 105.7 (s, C-4 (pz)), 105.4 (s, C-4 (pz)), 104.9 (s, C-4 (pz)), 79.6 (s, $^3J_{C,P} = 6$ Hz, 2C, NCH_2NCH_3), 68.5 (d, $^3J_{C,P} = 6$ Hz, NCH_2N), 59.2 (s, CH_3NCH_2P), 50.8 (vt, $J_{C,P} = 12$ Hz, 2C, NCH_2P), 49.0 (s, CH_3N) ppm. $^{31}P\{^1H\}$ NMR (161.9 MHz, NCMe-d_3, −10 °C): $\delta = 64.5$ (d, $^2J_{P,P} = 34$ Hz, PPh_3), −4.7 (d, $^2J_{P,P} = 34$Hz, m-PTA) ppm. *Anal.* Calc. for $C_{35}H_{41}BF_3N_9O_3P_2RuS \cdot CH_2Cl_2$: C, 43.96; H, 4.41; N, 12.82; S, 3.26. Found: C, 43.72; H, 4.12; N, 12.67; S, 3.84%.

2.1.11. Synthesis of [Ru(η⁵-C₉H₇)(PTA)₃][Cl] (11)

To a solution of $[Ru(\eta^5\text{-}C_9H_7)Cl(PPh_3)_2]$ (100 mg, 0.13 mmol) in toluene (3 mL) was added PTA (72 mg, 0.46 mmol). The reaction mixture was heated at reflux during 6 h. The precipitate thus formed was filtered off and dried under vacuum. The solid residue was extracted with water and filtered through kieselguhr. The solvent was evaporated under vacuum and the yellow solid obtained was recrystallized in a mixture dichloromethane/hexane. Yield: 53% (50 mg). $S_{20\,°C}$ (H_2O) = 20.0 mg/mL. ^1H NMR (400.1 MHz, D_2O, 20 °C): $\delta = 7.75$ (d, $J_{H,H} = 8$ Hz, 2H, Ind_6), 7.38 (d, $J_{H,H} = 8$ Hz, 2H, Ind_6), 5.58 (br, 2H, H-1 and H-3 Ind), 5.41 (br, 1H, H-2 Ind), 4.46 (m, 18H, NCH_2N), 3.83 (s, 18H, NCH_2P) ppm. $^{13}C\{^1H\}$ NMR (100.6 MHz, D_2O, 20 °C): $\delta = 128.9$ (s), 124.2 (s) (C-4, C-5, C-6, C-7 Ind), 108.1 (s, 2C, C-3a and C-7a Ind), 91.4 (s, C-2 Ind), 70.5 (s, 9C, NCH_2N), 68.8 (s, 2C, C-1 and C-3 Ind), 55.4 (s, 9C, NCH_2P) ppm. $^{31}P\{^1H\}$ NMR (161.9 MHz, D_2O, 20 °C): $\delta = -26.7$ (s, PTA) ppm. *Anal.* Calc. for $C_{27}H_{43}ClN_9P_3Ru$: C, 44.84; H, 5.99; N, 17.43. Found: C, 44.78; H, 5.91; N, 16.00%.

2.2. DNA mobility shift assays

Reactions between DNA and the ruthenium complexes were performed in 10 mM sodium phosphate buffer at physiological pH 7.0, containing 0.05 μg/μL of the

pBR322 plasmid (4361 base pairs, from Fermentas) and appropriate amounts of freshly prepared solutions of the Ru complexes also dissolved in phosphate buffer. Reaction mixtures were incubated for 14 h at 37 °C. Ten microliters of the reactions were mixed with 1 μL dye (0.025 mg bromophenol blue, 1 mL glycerol and 1 mL distilled water) and they were analyzed by electrophoresis in 0.8% agarose gels in TBE (Tris–Borate–EDTA) buffer. Gel running was conducted at a constant voltage of 3 V/cm. DNA bands were visualized by incubation of the gel with 1 μg/mL ethidium bromide in TBE buffer for 10 min and photographed under UV light.

2.3. Antimicrobial activity

Microbial cytotoxicity of ruthenium compounds was measured against three yeasts (*Candida albicans* ATCC 14053, *Candida parapsilosis* and *Rhodosporidium toruloides*), and different bacteria: *Micrococcus luteus* ATCC 9341, *Bacillus subtilis* ATCC 19659, *Escherichia coli* C600 ATCC 23724, *Streptomyces coelicolor* A3(2), *Streptomyces antibioticus* ATCC 11891, *Streptomyces glaucescens* DSM 40716 and *Pseudomonas aeruginosa* PAO1 ATCC 15692. The antimicrobial activity was tested according to the Kirby Bauer disc diffusion method [20]. The microorganisms were mixed at known concentrations with Mueller Hinton and poured into petri dishes (9 cm in diameter; 10 mL of culture medium per plate). The ruthenium complex was pipetted onto sterile filter paper disks (0.5 cm in diameter) and the solvent evaporated before placing them on the cultures. Plates were maintained at 4 °C during 1 h, and then incubated at 30 °C for the yeasts and *Streptomyces*, and 37 °C for the rest of bacteria. Different amounts per disc were used depending of the compound solubility [450 μg (**1**), 150 μg (**2**), 25 μg (**3**), 100 μg (**4**), 85 μg (**5**), 20 μg (**6**), 125 μg (**7**), 225 μg (**8**), 40 μg (**9**), 20 μg (**10**), 1000 μg (**11**) and 225 μg (**12**)]. For the compounds that were effective against microbes the size of the growth inhibition holes was measured in mm.

2.4. X-ray crystal structure determination of complexes $1 \cdot 2CH_2Cl_2$, $2 \cdot 1.5\ CH_2Cl_2$ and $4 \cdot CH_2Cl_2 \cdot C_6H_{14}$

Crystals suitable for X-ray diffraction analysis were obtained by slow evaporation of a saturated dichloromethane (**1** and **2**) or dichloromethane/ hexane (**4**) solutions. The most relevant crystal and refinement data are collected in Table 1.

Table 1
Crystal data and structure refinement for compounds $[RuCl\{\kappa^3(N,N,N)\text{-Tp}\}(PTA)_2] \cdot 2CH_2Cl_2$, $[RuCl\{\kappa^3(N,N,N)\text{-Tp}\}(PPh_3)(PTA)] \cdot 1.5CH_2Cl_2$ and $[Ru(NCS)\{\kappa^3(N,N,N)\text{-Tp}\}(PPh_3)\ (PTA)] \cdot CH_2Cl_2 \cdot C_6H_{14}$

	1 · **2CH_2Cl_2**	**2** · **1.5CH_2Cl_2**	**4** · **CH_2Cl_2** · **C_6H_{14}**
Empirical formula	$C_{21}H_{34}BClN_{12}P_2Ru$, $2(CH_2Cl_2)$	$2(C_{33}H_{37}BClN_9P_2Ru)$, $3(CH_2Cl_2)$	$C_{34}H_{37}BN_{10}P_2RuS$, CH_2Cl_2, C_6H_{14}
Fw	833.72	1792.75	962.71
T (K)	120(2)	293(2)	293(2)
Wavelength (Å)	0.71073	1.54180	1.54180
Crystal system	monoclinic	monoclinic	orthorhombic
Space group	$P21/c$	$P21/c$	$Fdd2$
a (Å)	10.0150(1)	10.1023(2)	42.7124(6)
b (Å)	12.7840(2)	19.9273(6)	40.5949(7)
c (Å)	26.1510(4)	20.6059(5)	10.2229(2)
α (°)	90	90	90
β (°)	96.668(1)	113.119(13)	90
γ (°)	90	90	90
Z	4	2	16
Volume (Å)^3	3325.51(8)	3815.1(4)	17725.5(5)
ρ_{calc} (g cm^3)	1.665	1.561	1.443
μ (mm)	1.008	7.019	5.434
$F(000)$	1696	1828	7968
Crystal size (mm)	0.20 × 0.20 × 0.17	0.10 × 0.05 × 0.05	0.26 × 0.03 × 0.03
θ Range (°)	1.57–25.24	3.22–67.69	3.00–75.04
Number of reflections collected	27156	31615	22483
Number of unique reflections (R_{int})	6009 (0.0518)	6361 (0.098)	6885 (0.0397)
Completeness to θ_{max} (%)	99.9	92.3	97.9
Number of parameters/restraints	401/0	482/39	492/18
Goodness-of-fit on F^2	1.184	1.106	1.041
Weight function (a, b)	0.1401, 6.2660	0.1084, 1.3684	0.1296, 0
R_1 $[I > 2\sigma(I)]$[a]	0.0691	0.0622	0.0579
wR_2 $[I > 2\sigma(I)]$[a]	0.1853	0.1606	0.1531
R_1 (all data)	0.0906	0.0977	0.0638
wR_2 (all data)	0.2336	0.1958	0.1614
Largest difference in peak and hole (e Å^{-3})	4.443 and −2.048	0.955 and −0.901	1.629 and −0.704

[a] $R_1 = \Sigma(|F_o| - |F_c|)/\Sigma|F_o|$; $wR_2 = \{\Sigma[w(F_o^2 - F_c^2)^2]/\Sigma[w(F_o^2)^2]\}^{1/2}$.

Diffraction data were recorded on a Nonius KappaCCD single crystal diffractometer using Mo Kα radiation, $\lambda = 0.71073$ Å (**1**) and Cu Kα radiation, $\lambda = 1.5418$ Å (**2**). Crystal-detector distance was fixed at 40 mm and using the oscillation method, with 1° oscillation and 30 s exposure time per frame for **1** and crystal-detector distance was fixed at 29 mm and using the oscillation method, with 2° oscillation and 100 s exposure time per frame for **2**. Data collection strategy was calculated with the program COLLECT [21]. Data reduction and cell refinement were performed using the programs HKL DENZO and SCALEPACK [22] and absorption correction was applied by means of Sortav [23]. For **4** data collection was performed at 120(2) K on a Oxford Diffraction Xcalibur Nova single crystal diffractometer, using Cu Kα radiation ($\lambda = 1.5418$ Å). Images were collected at a 65 mm fixed crystal-detector distance, using the oscillation method, with 1° oscillation and variable exposure time per image (7–25 s). Data collection strategy was calculated with the program CRYSALIS PRO CCD [24]. Data reduction and cell refinement was performed with the program CRYSALIS PRO RED [25]. An empirical absorption correction was applied using the Scale3 Abspack algorithm as implemented in the program CRYSALIS PRO RED [25].

The software package WINGX was used for space group determination, structure solution and refinement [26]. The structures were solved by Patterson interpretation and phase expansion using DIRDIF [27]. Isotropic least-squares refinement on F^2 using SHELXL97 was performed [28]. In the crystal of **2** three dichloromethane molecules of solvation per two formula units of the complex were found. A molecule was disordered over two positions, with 0.5 site occupancy factors. All non-hydrogen atoms were anisotropically refined, (except the C atoms of the highly disordered hexane solvent molecule in **4**, which was found and isotropically refined). The coordinates of the H atoms bonded to the boron, in all cases were found from difference Fourier maps and included in the refinement with isotropic parameters. The other hydrogen atoms were geometrically placed riding on their parent atoms with isotropic displacement parameters set to 1.2 times the U_{eq} of the atoms to which they are attached (1.5 for methyl groups). In all cases, the maximum residual electron density is located near the disordered solvent molecules.

The function minimized was $[\Sigma w(F_o^2 - F_c^2)/\Sigma w(F_o^2)]^{1/2}$ where $w = 1/[\sigma^2(F_o^2) + (aP)^2 + bP]$ (a and b values are collected in Table 1) with $\sigma^2(F_o^2)$ from counting statistics and $P = \text{Max}\ (F_o^2 + 2F_c^2)/3$.

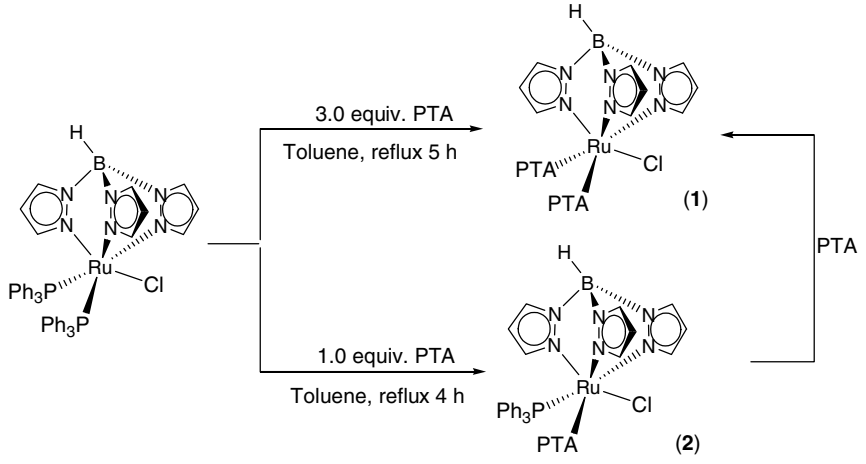
Atomic scattering factors were taken from the International Tables for X-ray Crystallography [29]. Geometrical calculations were made with Parst [30]. The crystallographic plots were made with Platon [31].

3. Results and discussion

3.1. Synthesis of half-sandwich ruthenium(II) complexes $[RuCl\{\kappa^3(N,N,N)\text{-}Tp\}(PTA)_2]$ (1) and $[RuCl\{\kappa^3(N,N,N)\text{-}Tp\}(PPh_3)(PTA)]$ (2)

Complex $[RuCl\{\kappa^3(N,N,N)\text{-Tp}\}(PPh_3)_2]$ undergoes phosphane substitution with adamantane phosphane PTA under different reaction conditions which leads to complexes $[RuCl\{\kappa^3(N,N,N)\text{-Tp}\}(PTA)_2]$ (**1**) and $[RuCl\{\kappa^3(N,N,N)\text{-Tp}\}(PPh_3)(PTA)]$ (**2**). Thus, the reaction of the complex $[RuCl\{\kappa^3(N,N,N)\text{-Tp}\}(PPh_3)_2]$ with an excess of PTA (1:3) in refluxing toluene produces the complex $[RuCl\{\kappa^3(N,N,N)\text{-Tp}\}(PTA)_2]$ (**1**), which precipitates from hot, concentrated solutions and can be isolated as a yellow solid with a 98% yield. When the same reaction is carried out using a stoichiometric amount of PTA and more diluted solutions in refluxing toluene, the complex $[RuCl\{\kappa^3(N,N,N)\text{-Tp}\}(PPh_3)(PTA)]$ (**2**) is isolated as an air-stable, yellow solid with a 96% yield (Scheme 1). Moreover, complex **2** reacts with an excess of PTA, giving rise to complex **1**.

Complexes **1** and **2** are soluble in water (9 and 3 mg/mL, respectively) and in common organic solvents such as methanol, chloroform, and dichloromethane and insoluble



Scheme 1.

in acetone, diethyl ether, and hexane. Both complexes have been analytically and spectroscopically characterized (IR and ^{1}H, ^{13}C{^{1}H} and ^{31}P{^{1}H} NMR). In particular, it must be noted that: (i) the IR spectra (KBr) show the characteristic ν(BH) absorption for the Tp ligand at 2489 (**1**) and 2476 (**2**) cm^{-1}; (ii) ^{31}P{^{1}H} spectrum exhibits a singlet at −29.2 ppm for complex **1** and two doublet resonances at $\delta = 47.1$ and −35.6 ppm ($J_{P,P} = 32$ Hz) for the PPh_3 and the PTA ligands, respectively, for complex **2**; (iii) the ^{1}H NMR spectra show the signals for the two hydrogen atoms of the NCH_2N group of the PTA ligand, which appear as AB spin systems at 4.56 and 4.47 ($J_{HA,HB} = 16$ Hz) for complex **1** and at 4.34 and 4.31 ($J_{HA,HB} = 13$ Hz) for complex **2**. The NCH_2P protons appear as a singlet at 4.13 in complex **1** and as two doublets at 3.90 and 3.86 ($J_{HA,HB} = 16$ Hz) for complex **2**. Assignments of the ^{1}H NMR data were made by comparison with data derived from the literature. The different multiplicity that CH_2 groups of PTA exhibit upon solvent change are noteworthy. These data are consistent with those reported for ruthenium complexes containing the PTA ligand [10–13]; (iv) ^{13}C{^{1}H} NMR spectra reveal the CH_2 groups of the PTA ligand as singlets at 73.2 ppm (NCH_2N) and 53.7 ppm (NCH_2P) for complex **1** and as two doublets at 73.2 ppm ($^3J_{C,P} = 6$ Hz) (NCH_2N) and 51.8 ($J_{C,P} = 14$ Hz) ppm (NCH_2P) for complex **2**.

Slow evaporation of complexes **1** and **2** in CH_2Cl_2 solutions enable crystals to be obtained that are suitable for X-ray diffraction studies of **1** · **2CH$_2$Cl$_2$** and **2** · **1.5 CH$_2$Cl$_2$**. ORTEP type representations are shown in Figs 2 and 3. Selected bonding data are collected in Table 2.

For both complexes, the ruthenium atom exhibits a distorted octahedral coordination geometry bonded $\kappa^3(N,N,N)$ to the hydridotris(pyrazolyl)borate ligand, to

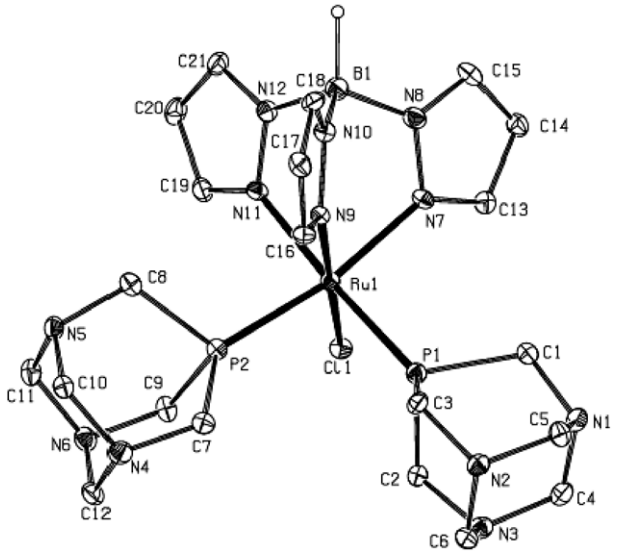


Fig. 2. Molecular structure and atom-labelling scheme for complex **1** · **2CH$_2$Cl$_2$**. Except for B–H, hydrogen atoms have been omitted for clarity as well as solvent molecules. Non-hydrogen atoms are represented by their 10% probability ellipsoids.

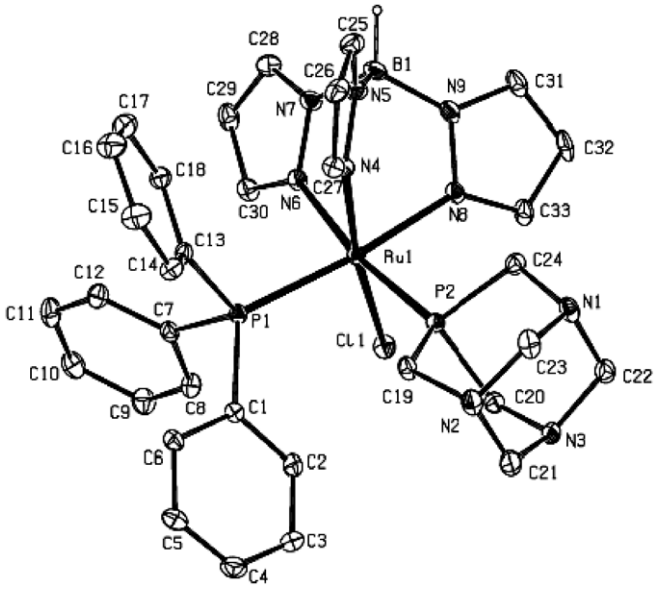


Fig. 3. Molecular structure and atom-labelling scheme for complex **2** · **1.5CH$_2$Cl$_2$**. Except for B–H, hydrogen atoms have been omitted for clarity as well as solvent molecules. Non-hydrogen atoms are represented by their 10% probability ellipsoids.

one chlorine atom and to two phosphorous atoms of the PTA ligands in complex **1** and of PTA and PPh_3 in complex **2**. For both complexes, the interligand N–Ru–N angles are in the range of 80.40–88.57 due to the constraints of the chelation of the Tp scorpionate ligand. Ru–N bond distances are typical for divalent ruthenium complexes [RuCl{κ^3(*N*,*N*,*N*)-Tp}(NCMe)(PPh_3)] [32] with Ru–N bond distances in the range of 2.088–2.159. For both complexes, the Ru–N bond distances trans to the phosphane ligands (in the range 2.148(6)–2.159(6)) are significatively longer than those trans to the chlorine atom (Ru(1)–N(9) = 2.088(5) for complex **1** and Ru(1)–N(4) = 2.102(7) for complex **2**) according with the higher trans influence for the phosphane ligands [33,34].

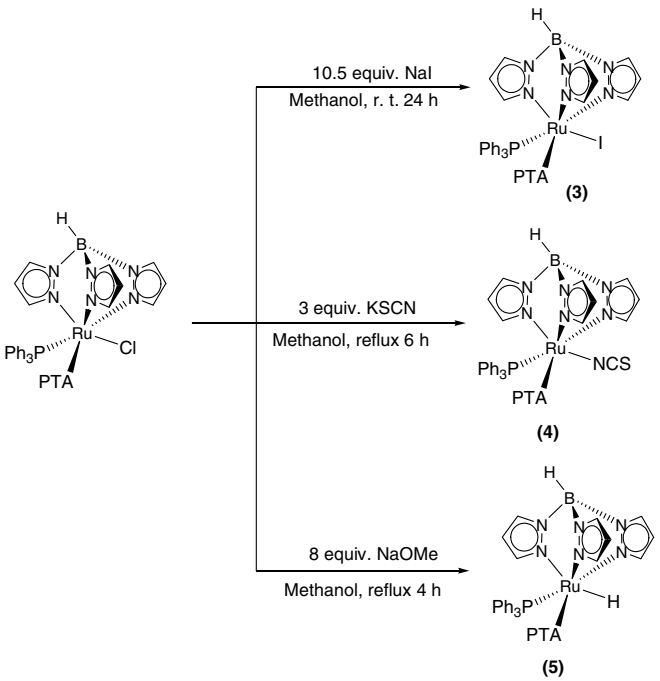
3.2. Chloride metathesis on complex 2: Synthesis of [RuX{κ^3(N,N,N)-Tp}(PPh$_3$)(PTA)] (X = I (3), NCS (4), H (5))

Reaction of complex [RuCl{κ^3(*N*,*N*,*N*)-Tp}(PPh_3)-(PTA)] (**2**) with an excess of sodium iodide or potassium thiocyanate in methanol leads to the synthesis of the corresponding metathesis complexes [RuX{κ^3(*N*,*N*,*N*)-Tp}-(PPh_3)(PTA)] (X = I (**3**), NCS (**4**)) respectively (Scheme 2). When the reagent was NaMeO, a β-elimination in the intermediate complex [Ru(OMe){κ^3(*N*,*N*,*N*)-Tp}(PPh_3)-(PTA)] produces the hydride complex [RuH{κ^3(*N*,*N*,*N*)-Tp}(PPh_3)(PTA)] (**5**).

Complexes **3**–**5** are soluble in water ($S_{20\,°C} = 0.5$ (**3**), 2.0 (**4**) and 1.7 (**5**) mg/mL), alcohols, and dichloromethane and are insoluble in hexane. Elemental analyses corroborate the proposed stoichiometry and ^{1}H, ^{31}P{^{1}H} and ^{13}C{^{1}H} NMR spectra support the proposed structure. The most

Table 2
Selected bond lengths (Å) and bond angles (°) for $[RuCl\{\kappa^3(N,N,N)\text{-Tp}\}(PTA)_2]\cdot 2CH_2Cl_2$ and $[RuCl\{\kappa^3(N,N,N)\text{-Tp}\}(PPh_3)(PTA)]\cdot 1.5CH_2Cl_2$

Bond lengths (Å) for $[RuCl\{\kappa^3(N,N,N)\text{-Tp}\}(PTA)_2]\cdot 2CH_2Cl_2$			
Ru(1)–N(7)	2.157(5)	Ru(1)–P(1)	2.2674(15)
Ru(1)–N(9)	2.088(5)	Ru(1)–P(2)	2.2605(15)
Ru(1)–N(11)	2.152(5)	Ru(1)–Cl(1)	2.4265(15)
Bond angles (°) for $[RuCl\{\kappa^3(N,N,N)\text{-Tp}\}(PTA)_2]\cdot 2CH_2Cl_2$			
N(7)–Ru(1)–N(9)	88.57(18)	N(9)–Ru(1)–N(11)	88.09(17)
N(7)–Ru(1)–N(11)	80.40(17)	N(7)–Ru(1)–P(1)	95.05(13)
N(7)–Ru(1)–P(2)	169.34(13)	N(9)–Ru(1)–P(1)	94.78(13)
N(9)–Ru(1)–P(2)	89.67(14)	N(11)–Ru(1)–P(1)	174.58(12)
N(11)–Ru(1)–P(2)	89.03(13)	N(7)–Ru(1)–Cl(1)	88.91(13)
N(9)–Ru(1)–Cl(1)	175.93(14)	N(11)–Ru(1)–Cl(1)	88.34(12)
P(1)–Ru(1)–Cl(1)	88.62(5)	P(2)–Ru(1)–Cl(1)	92.22(5)
P(1)–Ru(1)–P(2)	95.57(5)		
Bond lengths (Å) for $[RuCl\{\kappa^3(N,N,N)\text{-Tp}\}(PPh_3)(PTA)]\cdot 1.5CH_2Cl_2$			
Ru(1)–N(4)	2.102(7)	Ru(1)–P(1)	2.3314(18)
Ru(1)–N(6)	2.159(6)	Ru(1)–P(2)	2.2888(18)
Ru(1)–N(8)	2.148(6)	Ru(1)–Cl(1)	2.428(2)
Bond angles (°) for $[RuCl\{\kappa^3(N,N,N)\text{-Tp}\}(PPh_3)(PTA)]\cdot 1.5CH_2Cl_2$			
N(4)–Ru(1)–N(6)	88.4(2)	N(6)–Ru(1)–N(8)	82.3(2)
N(4)–Ru(1)–N(8)	85.9(2)	N(4)–Ru(1)–P(1)	93.78(17)
N(4)–Ru(1)–P(2)	89.26(17)	N(6)–Ru(1)–P(1)	90.11(16)
N(6)–Ru(1)–P(2)	171.04(16)	N(8)–Ru(1)–P(1)	172.41(17)
N(8)–Ru(1)–P(2)	88.90(17)	N(4)–Ru(1)–Cl(1)	172.04(17)
N(6)–Ru(1)–Cl(1)	90.30(18)	N(8)–Ru(1)–Cl(1)	86.10(19)
P(1)–Ru(1)–Cl(1)	94.08(7)	P(2)–Ru(1)–Cl(1)	90.80(7)
P(1)–Ru(1)–P(2)	98.69(6)		



Scheme 2.

remarkable features of these complexes are (i) the high field doublet of doublets at −14.71 ppm ($^2J_{H,P} = 31$ Hz and $^2J_{H,P} = 26$ Hz) corresponding to the hydride atom in complex **5**. This datum is consistent with the one reported for recently described PTA hydride complexes [35]; (ii) the IR spectra (KBr) exhibit the characteristic ν(BH) absorption of the Tp ligand at 2466 (**3**), 2485 (**4**), and 2457 (**5**) cm^{-1}, ν(RuH) absorption at 1923 cm^{-1} in complex **5**, and the band at 2113 cm^{-1} due to the NCS ligand in complex **4**. The C–N stretching band of the thiocyanate group appears at a lower frequency for N-bonded than for S-bonded complexes (around 2050 cm^{-1} versus 2100 cm^{-1}, respectively) [36]. However, the ν(CN) frequency is sensitive to other factors and assignments should be applied with caution, as described for iron thiocyanates [37].

To ascertain the coordination mode of the thiocyanate group in complex **4**, an X-ray study was performed. Slow evaporation of the solvent in a CH_2Cl_2/hexane solution of complex **4** allows suitable crystals for X-ray diffraction studies to be obtained. The asymmetric unit consists of a $[Ru(NCS)\{\kappa^3(N,N,N)\text{-Tp}\}(PPh_3)(PTA)]$ (**4**) molecule, a dichloromethane molecule and a hexane molecule.

An ORTEP type representation is shown in Fig. 4. Selected bonding data are presented in the caption.

As for complexes **1** and **2**, the ruthenium atom exhibits a distorted octahedral coordination geometry bonded $\kappa^3(N,N,N)$ to the hydridotris(pyrazolyl)borate ligand, to two phosphorous atoms of the PTA and PPh_3 ligands and to the nitrogen atom of the NCS group. The Ru–N(Tp) bond distances are in the range of the obtained for complexes **1** and **2**. Again, the Ru–N bond distance trans to the NCS group (Ru(1)–N(8) 2.089(5) Å) is shorter than the other two Ru–N bond distances (2.132(7) and 2.161(6)) in accord with the similar trans influence of Cl and NCS ligands [38].

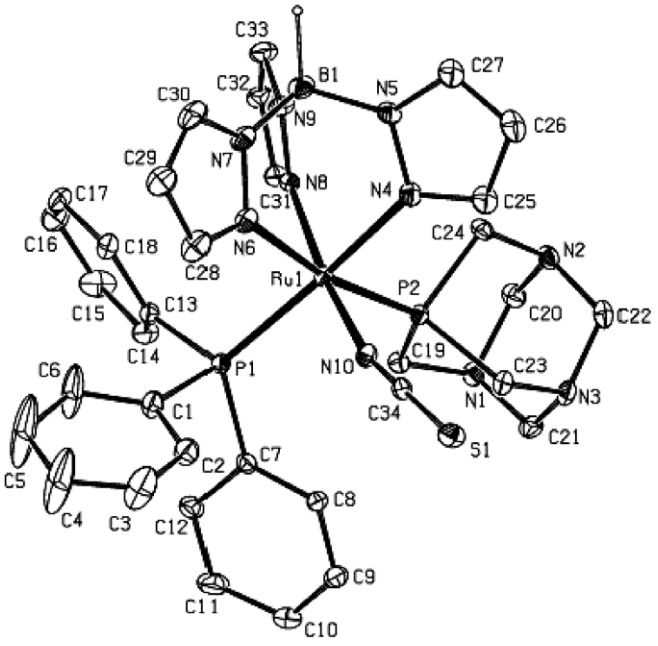


Fig. 4. Molecular structure and atom-labelling scheme for complex $\mathbf{4}\cdot\mathbf{CH_2Cl_2}\cdot\mathbf{C_6H_{14}}$. Except for B–H, hydrogen atoms have been omitted for clarity as well as solvent molecules. Non-hydrogen atoms are represented by their 10% probability ellipsoids. Selected bond lengths (Å): Ru(1)–N(4) = 2.132(7), Ru(1)–N(6) = 2.161(6), Ru(1)–N(8) = 2.089(5), Ru(1)–N(10) = 2.033(6), Ru(1)–P(1) = 2.3294(18), Ru(1)–P(2) = 2.2894(15), N(10)–C(34) = 1.161(9), C(34)–S(1) = 1.631(7). Selected bond angles (°): N(4)–Ru(1)–N(6) = 81.9(3), N(6)–Ru(1)–N(8) = 87.2(2), N(4)–Ru(1)–N(8) = 87.1(3), N(4)–Ru(1)–N(10) = 84.9(3), N(6)–Ru(1)–N(10) = 90.1(2), N(8)–Ru(1)–N(10) = 171.8(3), N(4)–Ru(1)–P(1) = 174.10(17), N(4)–Ru(1)–P(2) = 88.66(16), N(6)–Ru(1)–P(1) = 92.4(2), N(6)–Ru(1)–P(2) = 169.9(2), N(8)–Ru(1)–P(1) = 94.21(18), N(8)–Ru(1)–P(2) = 88.72(16), P(1)–Ru(1)–N(10) = 93.64(19), P(2)–Ru(1)–N(10) = 92.64(16), P(1)–Ru(1)-P(2) = 97.12(6), Ru(1)–N(10)–C(34) = 166.9(6), N(10)–C(34)–S(1) = 179.1(8).

The thiocyanate group is N-bonded and displays a linear NCS arrangement (Ru–N–C and N–C–S angles 166.9(6)° and 179.1(8)°, respectively) as found for analogous ruthenium N-bonded derivatives [39]. The Ru–N(10) bond distance of 2.033(6) Å is consistent with a donation of d_π electron density from ruthenium to the π-accepting thiocyanate group.

3.3. Synthesis of the cationic complexes $[Ru\{\kappa^3(N,N,N)\text{-}Tp\}(NCMe)(PPh_3)(PTA)][PF_6]$ (6) and $[Ru\{\kappa^3(N,N,N)\text{-}Tp\}(PPh_3)(PTA)_2][PF_6]$ (7)

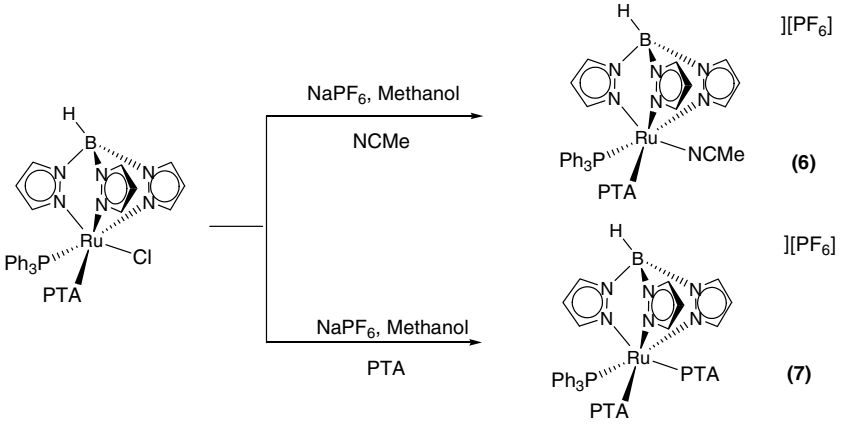
Reaction of complex $[RuCl\{\kappa^3(N,N,N)\text{-}Tp\}(PPh_3)(PTA)]$ (**2**) with an appropriate chloride abstractor such as $NaPF_6$ in the presence of acetonitrile, allows the cationic complex $[Ru\{\kappa^3(N,N,N)\text{-}Tp\}(NCMe)(PPh_3)(PTA)][PF_6]$ (**6**) to be synthesized. When the reaction is carried out in the presence of PTA, the complex $[Ru\{\kappa^3(N,N,N)\text{-}Tp\}(PPh_3)(PTA)_2][PF_6]$ (**7**) is obtained (Scheme 3).

Complexes **6** and **7** are soluble in water (0.4 and 2.5 mg/mL, respectively), alcohols, and dichloromethane and insoluble in diethyl ether and hexane. Analytical and spectroscopic data are consistent with the proposed structure. Thus, the IR spectra for complexes **6** and **7** are characterized by ν(BH) at 2491 and 2488 cm^{-1} and by $\nu(PF_6)$ at 840 and 842 cm^{-1}, respectively. $^{31}P\{^1H\}$ spectra show two doublets at $\delta = 43.9$ (PPh_3) and −42.4 (PTA) ($J_{P,P} = 29$ Hz) for complex **6** and one triplet $\delta = 48.6$ (PPh_3) and one doublet at $\delta = -49.1$ (PTA) ($J_{P,P} = 31$ Hz) for complex **7**. For complex **6,** the methyl group of the NCMe ligand appears as a singlet at 2.19 ppm in the ^1H NMR and at 4.0 ppm in the $^{13}C\{^1H\}$ spectra.

Attempts to synthesize complexes $[Ru\{\kappa^3(N,N,N)\text{-}Tp\}(NCMe)(PTA)_2][PF_6]$ and $[Ru\{\kappa^3(N,N,N)\text{-}Tp\}(PTA)_3][PF_6]$ from $[RuCl\{\kappa^3(N,N,N)\text{-}Tp\}(PTA)_2]$ (**1**) failed and the starting material was recovered.

3.4. Methylation reactions: Synthesis of $[RuCl\{\kappa^3(N,N,N)\text{-}Tp\}(m\text{-}PTA)_2][CF_3SO_3]_2$ (8) and $[RuX\{\kappa^3(N,N,N)\text{-}Tp\}(PPh_3)(m\text{-}PTA)][CF_3SO_3]$ (X = Cl (9), H (10))

Treatment of complexes **1**, **2**, and **5** at −30 °C with MeOTf in CH_2Cl_2 leads to the methylation of one of the nitrogen atoms of the PTA ligand resulting in the



Scheme 3.

complexes containing the 1-methyl-3,5-diaza-1-azonia-7-phosphaadamantane (m-PTA) triflate ligand. Thus, the complexes $[RuCl\{\kappa^3(N,N,N)\text{-Tp}\}(\text{m-PTA})_2][CF_3SO_3]_2$ (**8**), $[RuCl\{\kappa^3(N,N,N)\text{-Tp}\}(PPh_3)(\text{m-PTA})][CF_3SO_3]$ (**9**), and $[RuH\{\kappa^3(N,N,N)\text{-Tp}\}(PPh_3)(\text{m-PTA})][CF_3SO_3]$ (**10**) have been isolated as yellow solids (Scheme 4).

Water solubility decreases with respect to the parent compounds (4.5 mg/mL (**8**), 0.8 mg/mL (**9**), 0.4 mg/mL (**10**) versus 9 mg/mL (**1**), 3 mg/mL (**2**), and 1.7 mg/mL (**5**)).

Elemental analysis and spectroscopic data agree with the proposed formulations. Thus, the chemical shift of the phosphorous atom of the m-PTA ligand in the $^{31}P\{^1H\}$ NMR spectra ($\delta = -9.8$ (**8**), -13.6 (**9**), -4.7 (**10**)) appears in all cases at lower fields than the PTA ligand in the former complexes spectra ($\delta = -29.2$ (**1**), -35.6 (**9**), -23.4 (**10**)). The typical AB spin system for the NCH_2N groups observed in the ^1H NMR spectra of complexes **1**, **2**, and **5** disappears and a large number of doublets and triplets in the range of 4.12–5.12 ppm appear for complexes **8**–**10**. The methyl group of the m-PTA ligand for complexes **8**–**10** appears as a singlet in the range of 2.43–2.80 in the ^1H NMR spectra and 48.9–49.2 in the $^{13}C\{^1H\}$ NMR spectra.

3.5. Synthesis of $[Ru(\eta^5\text{-}C_9H_7)(PTA)_3][Cl]$

For comparative purposes, the synthesis of complex $[Ru(\eta^5\text{-}C_9H_7)(PTA)_3][Cl]$ (**11**) was carried out. Hence, the treatment of $[RuCl(\eta^5\text{-}C_9H_7)(PPh_3)_2]$ with PTA ligand in refluxing toluene allows the synthesis of complex **11** as a yellow solid with a 53% yield. It has been analytically and spectroscopically characterized and its water solubility has been quantified as 20 mg/mL.

The indenyl complex $[Ru(\eta^5\text{-}C_9H_7)(PTA)_3][Cl]$ (**11**) exhibits a single resonance in the $^{31}P\{^1H\}$ NMR spectrum at $\delta = -26.7$ ppm. The ^1H NMR spectrum reveals the presence of the indenyl group and the PTA ligands. Accordingly, the spectrum shows a NCH_2N multiplet at 4.46 ppm and a singlet at 3.83 ppm for the NCH_2P protons of the PTA ligand. Complex $[RuCl(\eta^5\text{-}C_9H_7)(PPh_3)(PTA)]$ (**12**) has also been used in this work and has been synthesized as previously reported [10a].

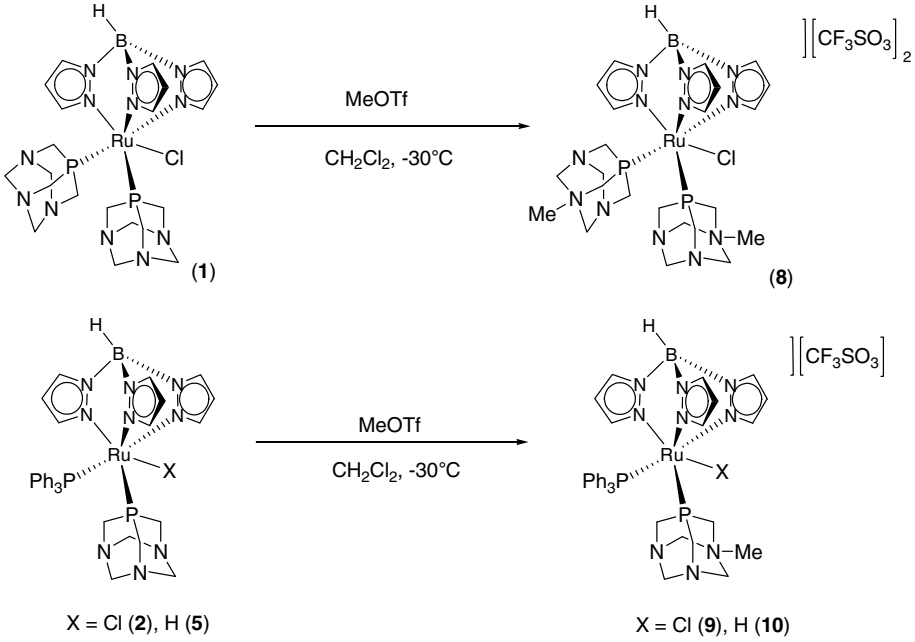
3.6. Chemical behavior in aqueous solution

Stability of complexes **2**, **5**, **6**, **9**, and **10** under physiological conditions was tested by heating samples of complexes in phosphate buffer solutions at pH 7 to 37 °C. After 14 h, no appreciable decomposition was observed in any of the complexes tested. The experiments were conducted both in the presence and in absence of oxygen and no significant differences were found.

Conductivity measurements in water (5×10^{-4} M) for complexes **1**–**3** confirm that these complexes are neutral in aqueous solution, ruling out potential halide dissociation.

3.7. DNA binding properties and cytotoxicity of ruthenium complexes

The reported complexes **1**–**10** present in their structures a hydridotris(pyrazolyl)borate ligand which contain three pyrazol groups and PTA or m-PTA ligands conferring water solubility to the complexes by virtue of hydrogen bonding to the tertiary amine nitrogen atoms. The new synthesized complexes are appealing for the study of their



Scheme 4.

DNA binding properties, since it is well known that the most advanced as antitumoral ruthenium complexes are those with N-donor ligands [40]. Furthermore, the hydride ligand in complexes **5** and **10** constitutes an additional site for hydrogen bonding.

The interaction of new ruthenium complexes with supercoiled DNA (SC) was tested by shift mobility assay on agarose gels. Alteration of the mobility of SC DNA and/ or open circular DNA (OC) indicates a disturbance of the DNA structure by the ruthenium compounds. Retardation of SC DNA was observed for complexes containing the PTA ligand, namely [RuCl{κ^3(*N*,*N*,*N*)-Tp}(PPh_3)(PTA)] (**2**), [RuH{κ^3(*N*,*N*,*N*)-Tp}(PPh_3)(PTA)] (**5**), [Ru{κ^3(*N*,*N*,*N*)-Tp}(NCMe)(PPh_3)(PTA)][PF_6] (**6**), and [Ru{κ^3(*N*,*N*,*N*)-Tp}(PPh_3)$(PTA)_2$][PF_6] (**7**), and with m-PTA [RuCl{κ^3(*N*,*N*,*N*)-Tp}$(m\text{-}PTA)_2$][CF_3SO_3]$_2$ (**8**), [RuCl{κ^3(*N*,*N*,*N*)-Tp}(PPh_3)(m-PTA)][CF_3SO_3] (**9**), and [RuH{κ^3(*N*,*N*,*N*)-Tp}(PPh_3)(m-PTA)][CF_3SO_3] (**10**). The indenyl complexes [Ru(η^5-C_9H_7)$(PTA)_3$][Cl] (**11**) and [RuCl(η^5-C_9H_7)-(PTA)(PPh_3)] (**12**) were also found to be active (Fig. 5).

No interaction with the plasmid was detected for complexes [RuCl{κ^3(*N*,*N*,*N*)-Tp}$(PTA)_2$] (**1**), [RuI{κ^3(*N*,*N*,*N*)-Tp}(PPh_3)(PTA)] (**3**), and [Ru(NCS){κ^3(*N*,*N*,*N*)-Tp}-(PPh_3)(PTA)] (**4**). Given that complex **1**, which does not exhibit any effect, is the most soluble of the pyrazolyl borate complexes described, we can state that solubility of the complex is not the only important factor. On the other hand, even though complex **2** binds to DNA, the replacement of chloride by iodide or NCS in complexes **3** and **4**, respectively, results in the loss of DNA binding and biological activity (see below), probably due to a stronger Ru–I or Ru–N–C–S bonding which prevents the coordination of nucleophiles from the DNA bases to the ruthenium atom.

To perform an initial analysis of the *in vivo* activity of the novel ruthenium complexes, we have used the Kirby Bauer disc diffusion method described by Biemer [20]. This classical assay has been widely used for screening new antimicrobial compounds, as well as for their quantification by using logarithmic calibration curves [20]. Seven different bacteria (*M. luteus*, *B. subtilis*, *E. coli* C600, *S. coelicolor*, *S. antibioticus*, *S. glaucescens,* and *P. aeruginosa*) and three eukaryotic microorganisms (*C. albicans*, *C. parapsilosis,* and *R. toruloides*) were used (see Section 2 and Fig. 6). Complexes [Ru{κ^3(*N*,*N*,*N*)-Tp}(NCMe)(PPh_3)(PTA)][PF_6] (**6**), [RuCl{κ^3(*N*,*N*,*N*)-Tp}(PPh_3)(m-PTA)][CF_3SO_3] (**9**), and [RuH{κ^3(*N*,*N*,*N*)-Tp}(PPh_3)(m-PTA)][CF_3SO_3] (**10**) proved to be the most biologically active compounds. They were active against most of the microorganisms tested and showed the largest inhibition halos (for *M. luteus*, inhibition growth halo of 15 mm (**6**), 21 mm (**9**) and 17 mm (**10**), for *S. antibioticus* inhibition growth halo of 11 mm for each one, *S. coelicolor* inhibition growth halos of 14 (**6**), 13 (**9**) and 10 mm (**10**), and for *S. glaucescens* inhibition

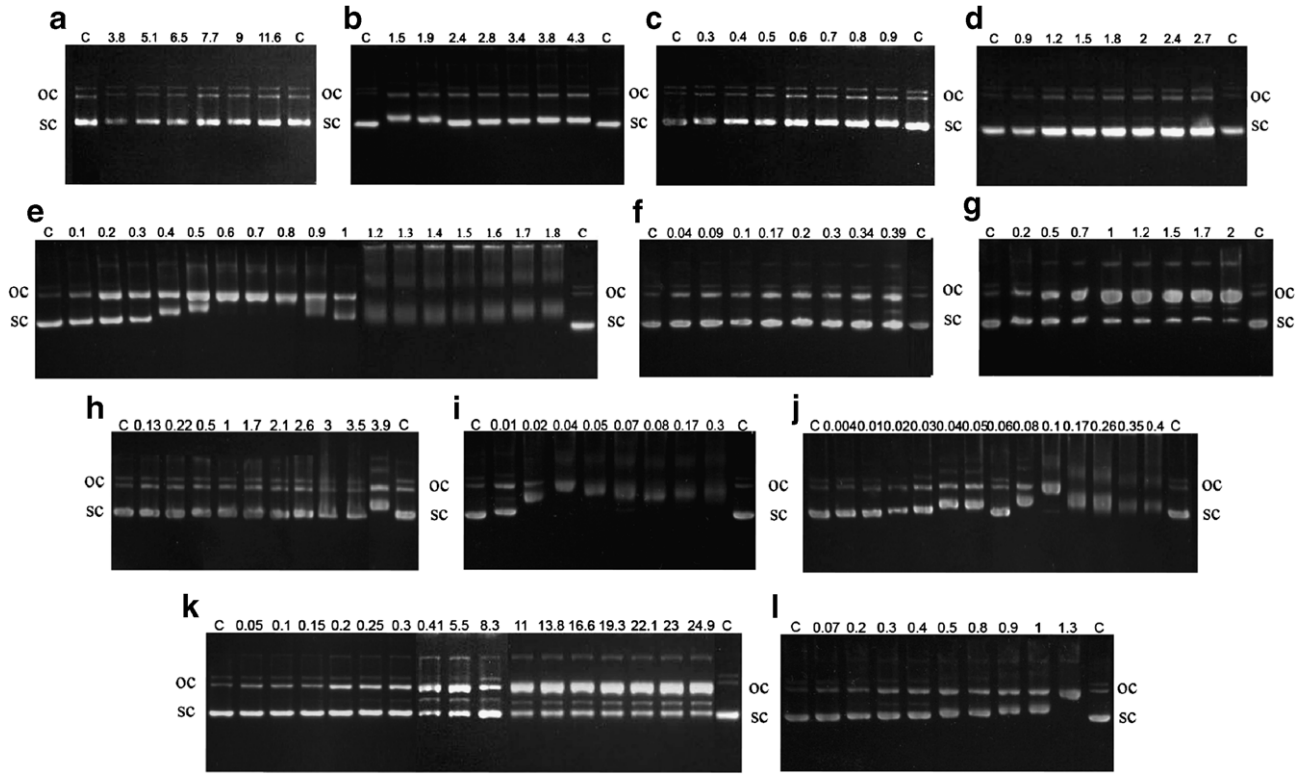


Fig. 5. DNA mobility shift assay for the water-soluble ruthenium complexes: (a) **1**, (b) **2**, (c) **3**, (d) **4**, (e) **5**, (f) **6**, (g) **7**, (h) **8**, (i) **9**, (j) **10**, (k) **11**, (l) **12**. The range of ruthenium complex concentrations used were (top of the panels, mM): **1** (3.8–11.6), **2** (1.5–4.3), **3** (0.3–0.9), **4** (0.9–2.7), **5** (0.1–1.8), **6** (0.04–0.39), **7** (0.2–2), **8** (0.13–3.9), **9** (0.01–0.3), **10** (0.004–0.4), **11** (0.05–24.9), **12** (0.07–1.3). C is the control lane without the ruthenium complex. OC, open circular plasmidic DNA; SC, supercoiled DNA.

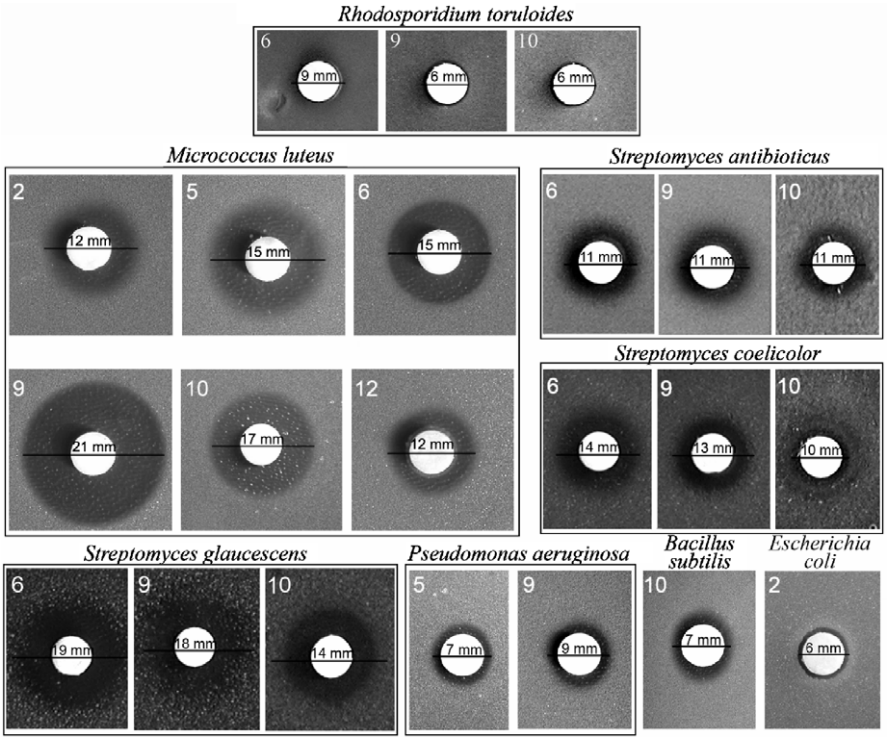


Fig. 6. DNA antimicrobial activity of the ruthenium complexes. The compounds (numbers), inhibition halos (mm), and the microorganism tested are indicated. Ruthenium complex used per disc: 450 μg (**1**), 150 μg (**2**), 25 μg (**3**), 100 μg (**4**), 85 μg (**5**), 20 μg (**6**), 125 μg (**7**), 225 μg (**8**), 40 μg (**9**), 20 μg (**10**), 1000 μg (**11**), and 225 μg (**12**).

growth halos of 19 (**6**), 18 (**9**) and 14 mm (**10**)) (Fig. 6). Their antimicrobial activity, however, is relatively low when compared to that of antibiotic compounds: for example, erythromycin A (0.6 μg) or mitramycin (1 μg) give inhibition halos against *M. luteus* of 21 mm in diameter (not shown), whereas the most active ruthenium compound **9** displayed the same inhibition growth halo diameter at 20 μg concentration.

The activity results revealed important differences among the microorganisms tested. *M. luteus* and *Streptomyces* species were the most sensitive microorganisms (Fig. 6). These two genera have high guanine and cytosine content in their genomes [41] (60–70%), which could explain their high sensitivity to the complexes analyzed, since guanine residues have been described as preferential binding sites when DNA is modified with ruthenium(II) [42]. In accordance with this hypothesis, the other less sensitive bacteria assayed have lower guanine and cytosine percentages [41]. On the other hand, *M. luteus* and *Streptomyces* differ in their sensitivity to ruthenium complexes; also, differences in sensitivity were observed among the three *Streptomyces* species analyzed (Fig. 6). This suggests that additional factors other than guanine and cytosine content affect the biological activity of the ruthenium complexes, and the cellular permeability could be one of them. The assayed yeasts were strongly resistant to the ruthenium complexes: only *R. toruloides* was sensible to complexes **6**, **9** and **10**, while *C. albicans* and *C. parapsilosis* were resistant to the twelve tested compounds (not shown), stressing again the importance of the particular microorganism with respect to the cytotoxicity results. Complexes **6**, **9**, and **10** were the most biologically active compounds. Interestingly, they correspond to the lower water-soluble compounds (see Section 2), suggesting that the solubility could be an important factor determining cellular activity. An underlying explanation for this might be related to the hydrophobic nature of the biological cell membranes, which are more permeable to the less water-soluble complexes. This would explain also the high resistance of yeasts, since in this case chromosomal DNA is additionally protected by the nuclear membrane.

In summary, we have described the first examples of hydridotris(pyrazolyl)borate ruthenium complexes containing the water-soluble PTA phosphane, their interaction with plasmidic DNA, and also their antimicrobial activity. Future experiments will be necessary to test the putative effect of these compounds against tumoral eukaryotic cells, their primary targets and the mechanism involved, including those hypothetically related with their DNA binding properties.

4. Conclusion

The ruthenium(II) complexes reported here constitute the first examples of water-soluble hydridotris(pyrazolyl)borate complexes. The presence of 1,3,5-triaza-7-phosphaadamantane (PTA) and 1-methyl-3,5-diaza-1-azonia-7-phosphaadamantane (m-PTA) triflate induce hydrophilicity in the complexes. Compounds with the m-PTA ligand have been

selectively synthesized by direct methylation of PTA complexes with methyl triflate in mild conditions. Moreover, hydride complexes **5** and **10** are interesting for their potential use in synthesis, either catalytic or stoichiometric processes that are currently under research.

Several of the ruthenium(II) complexes tested show DNA binding and antimicrobial activity. Among the compounds used, complexes with the methylated PTA phosphane ligand **9** and **10** were the most active against prokaryotic microorganisms, in spite of the low water solubility found in these derivatives. On the other hand, derivatives **5** and **10** showed a high interaction capability with DNA, probably due to their ability for establish hydrogen bonding. Although they have not been tested yet against mammalian cells, they constitute an interesting subject for research as potential antitumor agents.

The precise mechanisms involved in DNA coordination of these complexes remain unclear. Current development of new metal complexes and subsequent analysis of DNA coordination will undoubtedly clarify this point, thereby facilitating the synthesis of more active drugs.

Appendix A. Supplementary material

CCDC 649219, 649220 and 649221 contain the supplementary crystallographic data for ($\mathbf{1 \cdot 2CH_2Cl_2}$), ($\mathbf{2 \cdot 1.5CH_2Cl_2}$) and ($\mathbf{4 \cdot CH_2Cl_2 \cdot C_6H_{14}}$). These data can be obtained free of charge via http://www.ccdc.cam.ac.uk/conts/retrieving.html, or from the Cambridge Crystallographic Data Centre, 12 Union Road, Cambridge CB2 1EZ, UK; fax: (+44) 1223-336-033; or e-mail: deposit@ccdc.cam.ac.uk. Supplementary data associated with this article can be found, in the online version, at doi:10.1016/j.poly.2007.12.013.

References

[1] (a) P.J. Dyson, G. Sava, Dalton Trans. (2006) 1929;
(b) W.H. Ang, P.J. Dyson, Eur. J. Inorg. Chem. (2006) 4003;
(c) C.S. Allardyce, A. Dorcier, C. Scolaro, P.J. Dyson, Appl. Organometal. Chem. 19 (2005) 1.

[2] (a) Y.K. Yan, M. Melchart, A. Habtemarian, P.J. Sadler, Chem. Commun. (2005) 4764;
(b) M.J. Clarke, F. Zhu, D.R. Frasca, Chem. Rev. 99 (1999) 2511.

[3] (a) For recent examples of ruthenium complexes with antitumoral activity see for example: R.E. Aird, J. Cummings, A.A. Ritchie, M. Muir, R.E. Morris, H. Chen, P.J. Sadler, D.I. Jodrell, Brit. J. Cancer 86 (2002) 1652;
(b) R.E. Morris, R.E. Aird, P.S. Murdoch, H. Chen, J. Cummings, N.D. Hughes, S. Parsons, A. Parkin, G. Boyd, D.I. Joderell, P.J. Sadler, J. Med. Chem. 44 (2001) 3616;
(c) H. Chen, J.A. Parkinson, R.E. Morris, P.J. Sadler, J. Am. Chem. Soc. 125 (2003) 173;
(d) H. Chen, J.A. Parkinson, S. Parsons, R.A. Coxall, R.O. Gould, P.J. Sadler, J. Am. Chem. Soc. 124 (2002) 3064;
(e) I. Bratsos, B. Serli, E. Zangrando, N. Katsaros, E. Alessio, Inorg. Chem. 46 (2007) 975;
(f) A. Egger, V.B. Arion, E. Reisner, B. Cebrián-Losantos, S. Shova, G. Trettenhahn, B.K. Keppler, Inorg. Chem. 44 (2005) 122;
(g) E. Reisner, V.B. Arion, M.F.C. Guedes da Silva, R. Lichtenecker, A. Eichinger, B.K. Keppler, V.Y. Kukushkin, A.J.L. Pombeiro, Inorg. Chem. 43 (2004) 7083;
(h) J.M. Redemaker-Lakhai, D. van den Bongard, D. Pluim, J.H. Beijnen, J.H.M. Schellens, Clin. Cancer Res. 10 (2004) 3717;
(i) G. Sava, I. Capozzi, A. Bergamo, R. Gagliardi, M. Cocchietto, L. Masiero, M. Onisto, E. Alessio, G. Mestroni, S. Garbisa, Int. J. Cancer 68 (1996) 60.

[4] (a) M. Coluccia, G. Sava, F. Loseto, A. Nassi, A. Boccarelli, D. Giordano, E. Alessio, G. Mestroni, Eur. J. Cancer 29A (1993) 1873;
(b) W.J. Zeller, S. Fruhauf, G. Chen, B.K. Keppler, E. Frei, M. Kaufmann, Eur. J. Cancer 27 (1991) 62.

[5] M.J. Clarke, Coord. Chem. Rev. 236 (2003) 209.

[6] C.S. Allardyce, P.J. Dyson, Platinum Met. Rev. 45 (2001) 62.

[7] A.D. Phillips, L. Gonsalvi, A. Romerosa, F. Vizza, M. Peruzzini, Coord. Chem. Rev. 248 (2004) 955.

[8] (a) For recent examples see: M = Re: S. Bolaño, L. Gonsalvi, P. Barbaro, A. Albinati, S. Rizzato, E. Gutsul, N. Belkova, L. Epstein, E. Shubina, M. Peruzzini, J. Organomet. Chem. 691 (2006) 629;
(b) M = Mo:B.J. Frost, S.B. Millar, K.O. Rove, D.M. Pearson, J.D. Korinek, J.L. Harkreader, C.A. Mebi, J. Shearer, Inorg. Chim. Acta 359 (2006) 283;
(c) M = Ag, Au:F. Mohr, S. Sanz, E.R.T. Tiekink, M. Laguna, Organometallics 25 (2006) 3084;
(d) F. Mohr, E. Cerrada, M. Laguna, Organometallics 25 (2006) 644;
(e) F. Mohr, L.R. Falvello, M. Laguna, Eur. J. Inorg. Chem. (2006) 3152;
(f) M = Ni, Pd and Pt:P. Bergamini, V. Bertolasi, L. Marvelli, A. Canella, R. Gavioli, N. Mantovani, S. Mañas, A. Romerosa, Inorg. Chem. 46 (2007) 4267;
(g) D.J. Darensbourg, J.B. Robertson, D.L. Larkins, J.H. Reibenspies, Inorg. Chem. 38 (1999) 2473.

[9] (a) S. Bolaño, L. Gonsalvi, F. Zanobini, F. Vizza, V. Bertolasi, A. Romerosa, M. Peruzzini, J. Mol. Catal. A: Chem. 224 (2004) 61;
(b) D.J. Darensbourg, J.C. Yarbrough, S.J. Lewis, Organometallics 22 (2003) 2050;
(c) J. Kovacs, T.D. Todd, J.H. Reibenspies, F. Joó, D.J. Darensbourg, Organometallics 19 (2000) 3963;
(d) D.J. Darensbourg, N.W. Staford, F. Joó, J.H. Reibenspies, J. Organomet. Chem. 488 (1995) 99;
(e) D.J. Darensbourg, T.J. Decuir, J.H. Reibenspies, NATO ASI Series, Series 3: High Technology 5 (1995) 61.

[10] (a) C.A. Mebi, P.N. Radhika, B.J. Frost, Organometallics 26 (2007) 429;
(b) C.A. Mebi, B.J. Frost, Organometallics 24 (2005) 2339.

[11] (a) A. Romerosa, M. Saoud, T. Campos-Malpartida, C. Lidrissi, M. Serrano-Ruiz, M. Peruzzini, J.A. Garrido-Cárdenas, F. García-Maroto, Eur. J. Inorg. Chem. 45 (2007) 2803;
(b) A. Romerosa, T. Campos-Malpartida, C. Lidrissi, M. Saoud, M. Serrano-Ruiz, M. Peruzzini, J.A. Garrido-Cárdenas, F. García-Maroto, Inorg. Chem. 45 (2006) 1289.

[12] (a) C. Gossens, A. Dorcier, P.J. Dyson, U. Rothlisberger, Organometallics 26 (2007) 3969;
(b) C. Scolaro, T.J. Geldbach, S. Rochat, A. Dorcier, C. Gossens, A. Bergamo, M. Cocchietto, I. Tavernelli, G. Sava, U. Rothlisberger, P.J. Dyson, Organometallics 25 (2006) 756;
(c) C. Scolaro, A. Bergamo, L. Brescacin, R. Delfino, M. Cocchietto, G. Laurenczy, T.J. Geldbach, G. Sava, P.J. Dyson, J. Med. Chem. 48 (2005) 4161;
(d) C.S. Allardyce, P.J. Dyson, D.J. Ellis, P.A. Salter, R. Scopelliti, J. Organomet. Chem. 668 (2003) 35;
(e) C.S. Allardyce, P.J. Dyson, D.J. Ellis, S.L. Heath, Chem. Commun. (2001) 1396.

[13] B. Serli, E. Zangrando, T. Gianferrara, C. Scolaro, P.J. Dyson, A. Bergamo, E. Alessio, Eur. J. Inorg. Chem. (2005) 3423.

[14] (a) S. Pavlik, K. Mereiter, M. Puchberger, K. Kirchner, Organometallics 24 (2005) 3561;
(b) C.M. Standfest-Hauser, K. Mereiter, R. Schmid, K. Kirchner, Organometallics 23 (2004) 2194;
(c) C.M. Standfest-Hauser, K. Mereiter, R. Schmid, K. Kirchner,

Eur. J. Inorg.Chem. (2003) 1883;
(d) C. Slugvoc, R. Schmid, K. Kirchner, Coord. Chem. Rev. 185–186 (1999) 109, and references cited therein.
[15] J. Díez, M.P. Gamasa, E. Lastra, A. García-Fernández, M.P. Tarazona, Eur. J. Inorg. Chem. (2006) 2855.
[16] N.W. Alcock, I.D. Burns, K.S. Claire, A.F. Hill, Inorg. Chem. 31 (1992) 2906.
[17] L.A. Oro, M.A. Ciriano, M. Campo, C. Foces-Foces, F.H. Cano, J. Organomet. Chem. 289 (1985) 117.
[18] D.J. Daigle, Inorg. Synth. 32 (1998) 40.
[19] J. Díez, M.P. Gamasa, J. Gimeno, E. Lastra, A. Villar, Organometallics 24 (2005) 1410.
[20] J.J. Biemer, Ann. Clin. Lab. Sci. 3 (1973) 135.
[21] Collect, Nonius BV, Delft, 1997, p. 2000.
[22] Z. Otwinowski, W. Minor, Methods Enzymol. 276 (1997) 307.
[23] R.H. Blessing, Acta Crystallogr., Sect. A 51 (1995) 33.
[24] CRYSALIS PRO CCD, Oxford Diffraction Ltd., 2007.
[25] CRYSALIS PRO RED, Oxford Diffraction Ltd., 2007.
[26] L.J. Farrugia, J. Appl. Crystallogr. 32 (1999) 837.
[27] P.T. Beurskens, G. Admiraal, G. Beurskens, W.P. Bosman, S. García-Granda, R.O. Gould, J.M.M. Smits, C. Smykalla, The DIRDIF Program System, Technical Report of the Crystallographic Laboratory, University of Nijimegen, Nijimegen, The Netherlands, 1999; L.J. Farrugia, J. Appl. Crystallogr. 32 (1999) 837.
[28] G.M. Sheldrick, SHELXL-97, Program for the Refinement of Crystal Structures, University of Göttingen, 1997.
[29] International Tables for X-ray crystallography, vol. IV, Kynoch Press, Birmingham (Present distributor: Kluwer Academic Publishers, Dordrecht), 1974.
[30] M. Nardelli, Comput. Chem. 7 (1983) 95.
[31] A.L. Spek, PLATON, A Multipurpose Crystallographic Tool, Utrecht University, Utrecht, The Netherlands, 2006.
[32] B. Buriez, I.D. Burns, A.F. Hill, A.J.P. White, D.J. Williams, J.D.E.T. Wilton-Ely, Organometallics 18 (1999) 1504.
[33] (a) S. Pavlik, K. Mereiter, M. Puchberger, K. Kirchner, J. Organomet. Chem. 690 (2005) 5497, and references cited therein;
(b) M. Jiménez-Tenorio, M.D. Palacios, M.C. Puerta, P. Valerga, Organometallics 24 (2005) 3088, and references cited therein.
[34] T.G. Appleton, H.C. Clark, L.E. Manzer, Coord. Chem. Rev. 10 (1973) 335.
[35] (a) B.J. Frost, C.A. Mebi, Organometallics 23 (2004) 5317;
(b) G. Laurenczy, S. Jedner, E. Alessio, P.J. Dyson, Inorg. Chem. Commun. 10 (2007) 558.
[36] K. Nakamoto, in: Infrared Raman Spectra of Inorganic Coordination Compounds, 4th ed., Wiley-Interscience, New York, 1986.
[37] M.J. Maroney, E.O. Fey, D.A. Balwin, R.E. Stenkamp, L.H. Jensen, N.J. Rose, Inorg. Chem. 25 (1986) 1409.
[38] (a) A.R. Khan, S.M. Zoclo, D.W. Meek, R. Yasmeen, Inorg. Chim. Acta 234 (1995) 109;
(b) K.D. Tau, D.W. Meek, Inorg. Chem. 18 (1979) 3574.
[39] (a) H. Nagao, D. Ooyama, T. Hirano, H. Naoi, M. Shimada, S. Sasaki, N. Nagao, M. Mukaida, T. Oi, Inorg. Chim. Acta 320 (2001) 60;
(b) P. Homanen, M. Haukka, T.A. Pakkanan, J. Pursiainen, R.H. Laitinen, Organometallics 15 (1996) 4081.
[40] (a) V. Brabec, O. Novakova, Drug Resist. Updates 9 (2006) 111;
(b) O. Novakova, J. Kasparkova, V. Bursova, C. Hofr, M. Vojtiskova, H. Chen, P.J. Sadler, V. Brabec, Chem. Biol. 12 (2005) 121.
[41] R.G.E. Murray, D.J. Brenner, M.P. Bryant, H.G. Holt, N.R. Krieg, J.W. Moulder, N. Pfenning, P.H.A. Sneath, J.T. Staley, Bergey's Manual of Systematic Bacteriology, Williams and Wilkins, Baltimore, 1984.
[42] (a) H.-K. Liu, S.J. Berners-Price, F. Wang, J.X. Parkinson, J. Bella, P.J. Sadler, Angew. Chem., Int. Ed. 45 (2006) 8153;
(b) O. Novakova, H. Chen, O. Vrana, A. Rodger, P.J. Sadler, V. Brabec, Biochemistry 42 (2003) 11544.

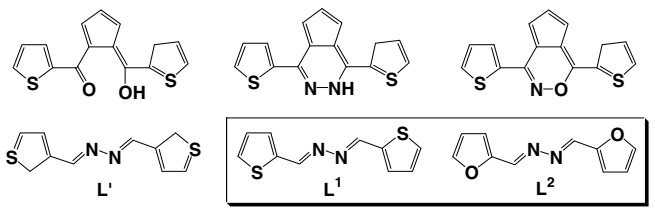


Chart 1.

terminal heterocyclic rings with sulfurs and oxygens, respectively, with an emphasis to investigate the variation in topology of the resulting compounds with the counterions used. We report herein the preparation and structures of five silver compounds, $[AgL^1_2](PF_6)$ (**1**), $[Ag_2L^2_3](PF_6)_2$ (**2**), $[Ag_2L^2_3](ClO_4)_2$ (**3**), $[Ag_2L^2_2](BF_4)_2$ (**4**), and $[Ag_2L^2(NO_3)_2]$ (**5**). X-ray structure analysis of these compounds revealed that compound **1** is a discrete molecule, whereas compounds **2**–**5** are coordination polymers or networks constructed by either covalent bonds or van der Waals contacts.

2. Experimental

All solid chemicals were purified by recrystallization, and all solvents were distilled and stored over molecular sieves. Ligands L^1 (1,2-bis(thiophen-2-ylmethylene)hydrazine) [19] and L^2 (1,2-bis(furan-2-ylmethylene)hydrazine) [33] were prepared by the literature methods. IR spectra were recorded with a Nicolet 320 FTIR spectrophotometer. Elemental analyses were performed with EA1110 (CE instrument, Italy) at the Korea Basic Science Institute. Photoluminescence (PL) experiments were performed with an AB2 spectrophotometer (Amico Bowmann).

2.1. Preparation of $[AgL^1_2](PF_6)$ (1)

A dichloromethane solution (4 ml) of L^1 (61.0 mg, 0.280 mmol) was allowed to diffuse slowly into a methanol solution (3 ml) of $AgPF_6$ (35.0 mg, 0.139 mmol). Yellow crystals of compound **1** formed in 5 days (62 mg, 0.089 mmol, 64%). *Anal.* Calc. for $C_{20}H_{16}F_6N_4PS_4Ag$ ($M_r = 693.45$): C, 34.64; H, 2.31; N, 8.08. Found: C, 33.89; H, 2.51; N, 7.85%. IR (KBr, cm^{-1}): 1603 (s), 1420 (m), 1212 (m), 1050 (m), 838 (s), 714 (m).

2.2. Preparation of $[Ag_2L^2_3](PF_6)_2$ (2), $[Ag_2L^2_3](ClO_4)_2$ (3), $[Ag_2L^2_2](BF_4)_2$ (4), and $[Ag_2L^2(NO_3)_2]$ (5)

Polymers **2**–**5** were prepared in the same way. A dichloromethane solution (4 ml) of L^2 (46.0 mg, 0.250 mmol) was layered on the top of a methanol solution (6 ml) of $AgPF_6$ (43.0 mg, 0.169 mmol). Yellow crystals of compound **2** formed in 5 days (70 mg, 0.065 mmol, 76%). *Anal.* Calc. for $C_{30}H_{24}F_{12}N_6O_6P_2Ag_2$ ($M_r = 1070.23$): C, 33.67; H, 2.24; N, 7.85. Found: C, 33.96; H, 2.52; N, 7.67%. IR (KBr, cm^{-1}): 1637 (s), 1465 (m), 1289 (m), 1021 (m), 842 (s), 756 (m).

Data for polymer **3**: 68% yield. *Anal.* Calc. for $C_{30}H_{24}N_6O_{14}Cl_2Ag_2$ ($M_r = 979.19$): C, 36.80; H, 2.45; N, 8.58. Found: C, 37.05; H, 2.39; N, 7.85%. IR (KBr, cm^{-1}): 1637 (s), 1465 (m), 1288 (m), 1093 (s), 1016 (m), 935 (m), 756 (m).

Data for polymer **4**: 80% yield. *Anal.* Calc. for $C_{20}H_{16}B_2F_8N_4Ag_2$ ($M_r = 765.73$): C, 31.37; H, 2.09; N, 7.31. Found: C, 31.10; H, 2.18; N, 7.38. IR (KBr, cm^{-1}): 1636 (s), 1461 (m), 1391 (m), 1294 (m), 1054 (s), 935 (m), 769 (m).

Data for polymer **5**: 72% yield. *Anal.* Calc. for $C_{10}H_8N_4O_8Ag_2$ ($M_r = 527.94$): C, 22.75; H, 1.52; N, 7.58. Found: C, 22.46; H, 1.55; N, 7.58. IR (KBr, cm^{-1}): 1634 (s), 1447 (m), 1357 (s), 1273 (s), 1014 (m), 936 (m), 761 (m).

2.3. X-ray structure determination

X-ray data were collected with a Siemens P4 diffractometer (**1**) or a Bruker Smart APEX2 diffractometer (**2**–**5**) equipped with a Mo X-ray tube. Absorption corrections were made with ψ-scan data (**1**) or SADABS (**2**–**5**) [34]. All calculations were carried out with SHELXTL programs [35]. All structures were solved by direct methods. All non-hydrogen atoms were refined anisotropically. All hydrogen atoms were generated in idealized positions and refined in a riding model. Details on crystal data, intensity collection, and refinement details are given in Table 1.

3. Results and discussion

3.1. Preparation

In this study, all compounds $[AgL^1_2](PF_6)$ (**1**), $[Ag_2L^2_3](PF_6)_2$ (**2**), $[Ag_2L^2_3](ClO_4)_2$ (**3**), $[Ag_2L^2_2](BF_4)_2$ (**4**), and $[Ag_2L^2(NO_3)_2]$ (**5**) were prepared by layer diffusion, in which a dichloromethane solution containing a ligand was layered on the top of a methanol solution containing a silver salt. All products were characterized by elemental analysis, IR spectroscopy, and X-ray diffraction, and their IR spectra display the C=N stretches in the range 1603–1636 cm^{-1}, which is consistent with the fact that C=N stretches of Schiff bases appear in the range 1603–1680 cm^{-1} [36–38].

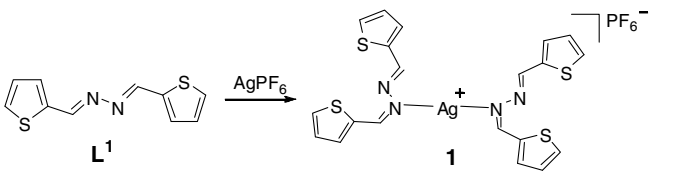
Our initial goal was to prepare silver coordination polymers by treating silver salts (AgX) with ligand L^1, which contains terminal thiophene rings (sulfur donors). For this purpose, $AgPF_6$ was selected, because it possesses a labile PF_6^- ion and a soft Ag metal. Inconsistent with our expectation, however, an ionic Ag compound $[AgL^1_2](PF_6)$ (**1**) was produced from the reaction (Eq. (1)). In the cationic part of compound **1**, the Ag metal is bonded to the harder imine nitrogen atoms in the Schiff-base fragments in the ligand (L^1), not to the softer sulfur atoms in the terminal thiophene rings, which are *cisoid* to each other. In the free form of ligand L^1, the terminal thiophene rings are in a *transoid* conformation [19]. It would be meaningful to compare compound **1** with $[AgL'_2](PF_6)$, which contains an iso-

Table 1
X-ray data collection and structure refinement details

	1	2	3	4	5
Empirical formula	$C_{20}H_{16}F_6N_4PS_4Ag$	$C_{30}H_{24}F_{12}N_6O_6P_2Ag_2$	$C_{30}H_{24}N_6O_{14}Cl_2Ag_2$	$C_{20}H_{16}B_2F_8N_4O_4Ag_2$	$C_{10}H_8N_4O_8Ag_2$
Formula weight	693.45	1070.23	979.19	765.73	527.94
Temperature (K)	293(2)	296(2)	296(2)	296(2)	296(2)
Crystal system	monoclinic	triclinic	triclinic	orthorhombic	triclinic
Space group	$P2_1/n$	$P\bar{1}$	$P\bar{1}$	$Pna2_1$	$P\bar{1}$
Color	yellow	yellow	yellow	yellow	yellow
Crystal size (mm)	0.24 × 0.20 × 0.16	0.20 × 0.16 × 0.12	0.38 × 0.26 × 0.22	0.32 × 0.24 × 0.14	0.30 × 0.24 × 0.16
Crystal shape	block	block	block	block	block
a (Å)	10.045(3)	9.417(2)	9.2583(1)	17.572(1)	8.0207(4)
b (Å)	16.875(4)	9.939(2)	9.7346(1)	18.289(1)	8.5569(4)
c (Å)	15.634(3)	11.377(3)	11.1080(2)	7.9771(6)	11.4218(5)
α (°)		94.66(1)	95.804(1)		72.396(2)
β (°)	92.31(2)	98.10(1)	99.113(1)		82.019(2)
γ (°)		117.41(1)	116.278(1)		70.683(2)
V (Å^3)	2647.9(11)	922.8(4)	869.59(2)	2563.6(3)	704.47(6)
Z	4	1	1	4	2
D_{cal} (g cm^{-3})	1.740	1.926	1.870	1.984	2.489
μ (mm)	1.197	1.260	1.358	1.622	2.833
$F(000)$	1376	526	486	1488	508
T_{min}	0.4881	0.7866	0.6264	0.6249	0.4837
T_{max}	0.5698	0.8635	0.7543	0.8048	0.6600
Number of reflections measured	4872	14088	14432	9607	9103
Number of reflections unique	4590	4414	4248	4468	3450
Number of reflections with $I > 2\sigma(I)$	2461	3128	3754	3436	3092
Number of parameters refined	325	263	245	362	218
Maximum, in $\Delta\rho$ (e Å^{-3})	0.647	0.668	0.935	0.396	0.876
Minimum, in $\Delta\rho$ (e Å^{-3})	−0.534	−0.712	−0.549	−0.999	−0.719
Goodness-of-fit on F^2	1.017	1.013	1.053	1.026	1.036
$R1$[a]	0.0644	0.0434	0.0327	0.0437	0.0221
wR_2[b]	0.1316	0.1026	0.0903	0.1059	0.0528

[a] $R_1 = \sum[|F_o| - |F_c|]/\sum|F_o|]$.
[b] $wR_2 = \sum[w(F_o^2 - F_c^2)^2]/\sum[w(F_o^2)^2]^{1/2}$.

meric ligand of $\mathbf{L}^1$. Unlike polymer **1**, $[Ag\mathbf{L}'_2](PF_6)$ formed a 2D network in which the sulfur donors participated in the Ag···S contacts and two F atoms of the counterion PF_6^- participated in the Ag···F contacts [20]. It should be pointed out that we previously obtained silver coordination polymers $\{[Ag\mathbf{L}^1_{0.5}(NO_3)]$ and $[Ag\mathbf{L}^1_2](ClO_4)\}$ by treating $AgNO_3$ and $AgClO_4$ with ligand $\mathbf{L}^1$ [19]. We believe that the different reactivity between these two silver salts and $AgPF_6$ is primarily due to the different counterions in the starting silver salts.



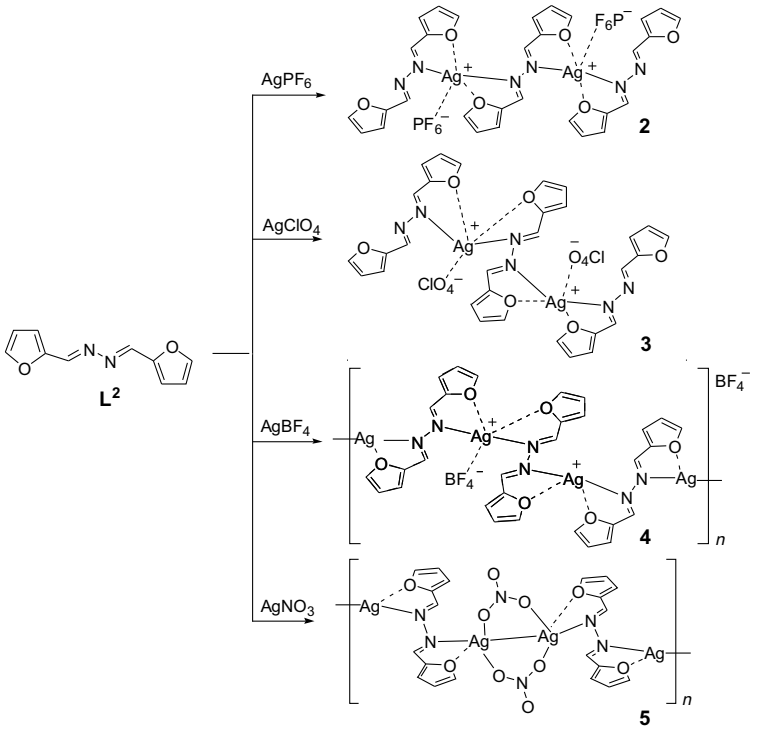
(1)

In contrast with the above results, the corresponding reactions of silver salts (AgX: X = PF_6^-, ClO_4^-, BF_4^-, NO_3^-) with ligand $\mathbf{L}^2$, which contains terminal furan rings (oxygen donors), produced silver coordination networks based on covalent bonds or van der Waals contacts: $[Ag_2\mathbf{L}^2_3](PF_6)_2$ (**2**), $[Ag_2\mathbf{L}^2_3](ClO_4)_2$ (**3**), $[Ag_2\mathbf{L}^2_2](BF_4)_2$ (**4**), and $[Ag_2\mathbf{L}^2(NO_3)_2]$ (**5**) (Scheme 1, where intermolecular van der Waals contacts are omitted for clarity). In all these polymers or networks, the imine nitrogen atoms are bonded to the Ag ions, and the furan rings in each $\mathbf{L}^2$ are *transoid*. Interestingly, all the furan oxygen atoms are in van der Waals contacts with the silver ions to form five-membered pseudo-chelates in these coordination polymers.

3.2. Structures

The structure of compound **1** with the atom-numbering scheme is shown in Fig. 1. This ionic compound consists of one Ag(I) metal, two $\mathbf{L}^1$ ligands, and one PF_6^- ion that is not bound to the Ag metal and simply behaves as a counterion. The central silver atom is covalently bonded to two nitrogen atoms of two different $\mathbf{L}^1$ ligands.

A monomer unit of compound **2** is given in Fig. 2, which shows an asymmetric unit consisting of one Ag, one and half $\mathbf{L}^2$, and one PF_6^-. The Ag–N bond lengths (2.200(3) and 2.244(3) Å) indicate normal covalent bonds, and therefore the Ag metal is 2-coordinate. The Ag metal is further bound to three oxygen (O1–O3) and two fluorine (F3 and F6) atoms via van der Waals contacts: Ag···O (2.705(3)–3.091(3) Å) and Ag···F (3.049(3)–3.144(4) Å). Considering



Scheme 1.

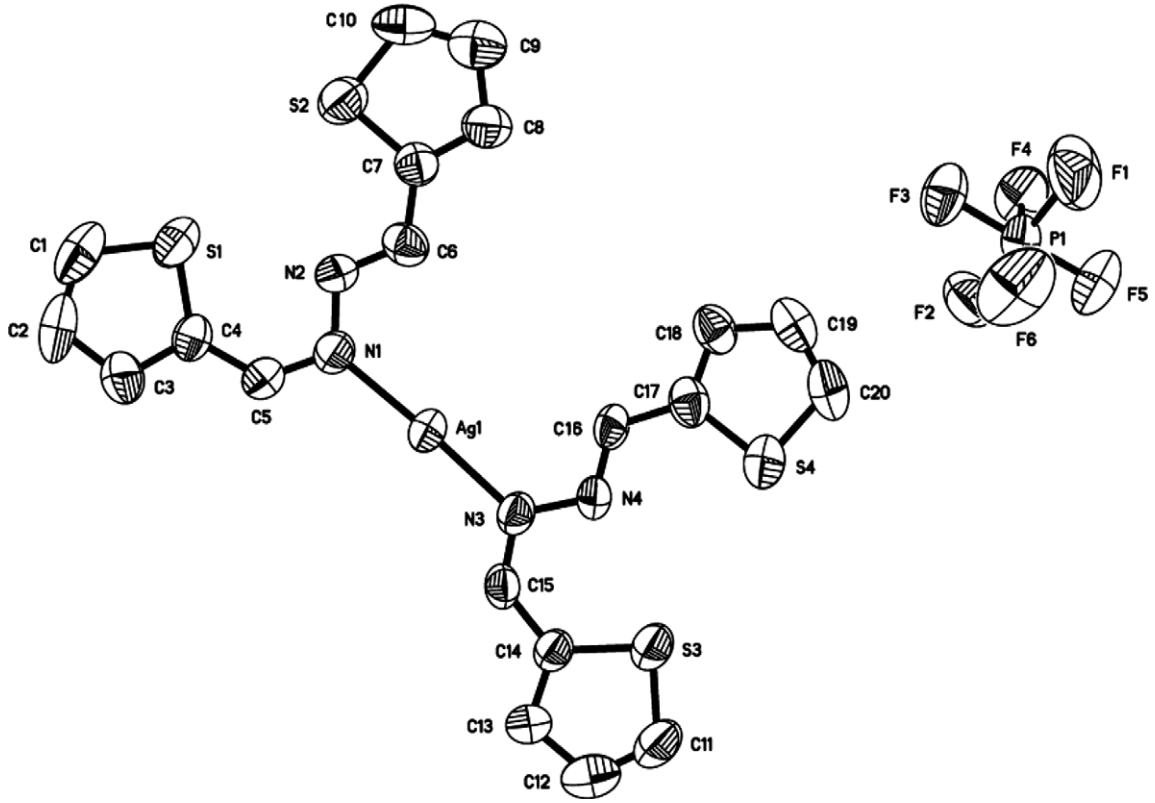


Fig. 1. ORTEP drawing of compound **1** with 50% probability thermal ellipsoids. Selected bond distances (Å) and angles (°): Ag1–N1 2.141(7), Ag1–N3 2.141(6), N1–N2 1.386(9), N3–N4 1.405(9); N1–Ag1–N3 176.6(3), C5–N1–Ag 1119.7(6), N4–N3–Ag1, 125.2(5).

these van der Waals contacts, the Ag metal may now be thought of as being 7-coordinate. For comparison, the van der Waals radii of Ag, O, and F atoms are 1.72, 1.50, and 1.55 Å, respectively. Fig. 3 demonstrates a 2D

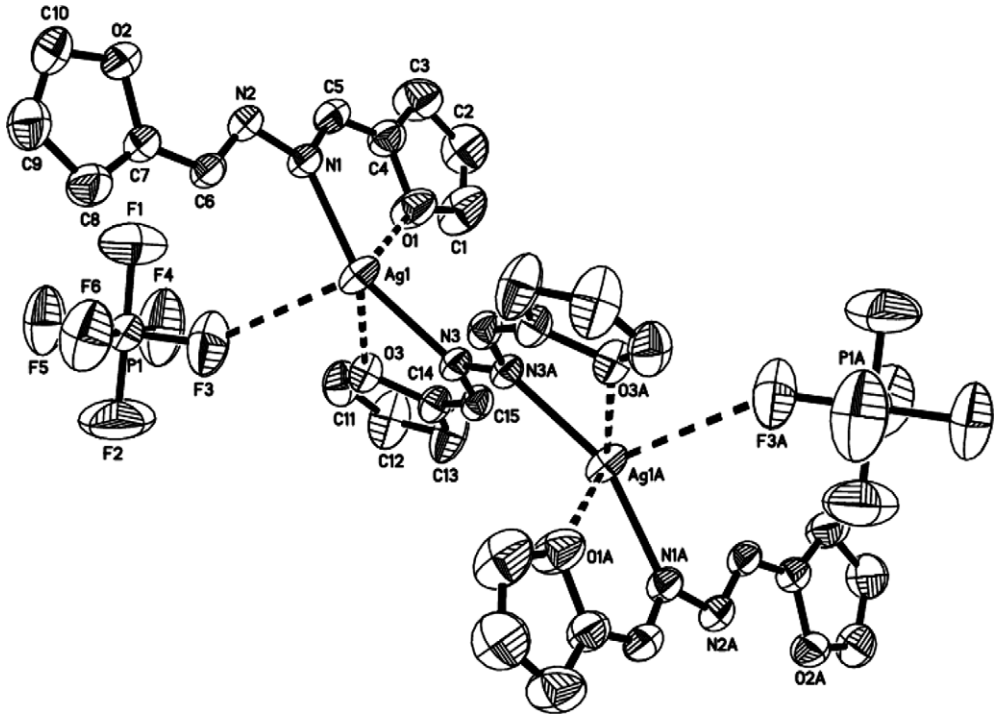


Fig. 2. Monomer unit of compound **2** showing van der Waals contacts (dashed lines). Selected bond distances (Å) and angles (°): Ag1–N1 2.200(3), Ag1–N3 2.244(3), N1–N2 1.401(4); N1–Ag1–N3 158.2(1), C5–N1–Ag1 122.5(2), N2–N1–Ag1 124.3(2).

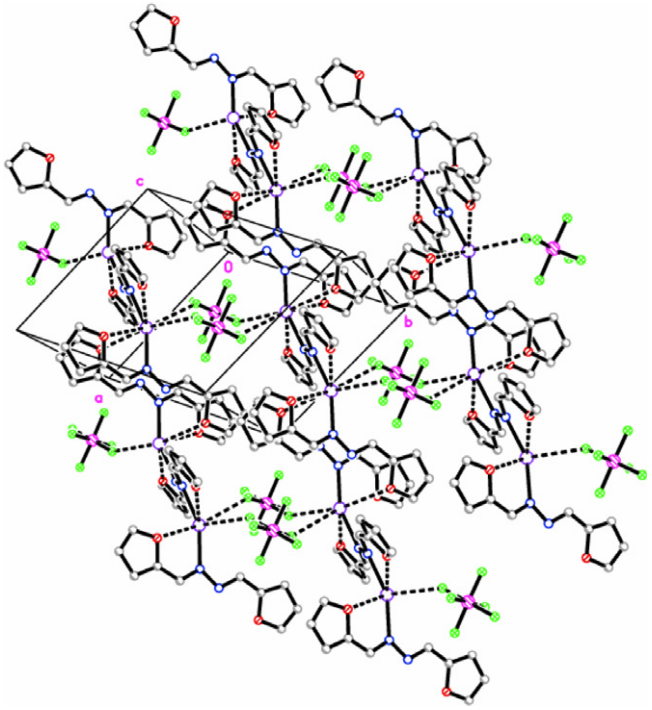


Fig. 3. Packing diagram of compound **2** along the *c*-axis showing a 2D network.

network of compound **2**, in which the Ag_2L_3 repeating units are connected by the PF_6^- ions (in the [0 1 1] direction) as well as by the ligands (in the diagonal direction of the unit cell). In other words, the 2D network is constructed by two types of intermolecular van der Waals contacts of Ag···F (PF_6^-; Ag···F–P–F···Ag connectivity) and Ag···O (furan). The Ag···F interactions lead to the formation of cyclohexane-like connectors between arrays forms by the Ag···O interactions.

A monomer unit of compound **3** is presented in Fig. 4, which is isostructural with compound **2**, except for the counterion (PF_6^- versus ClO_4^-). The Ag metal is also 2-coordinate. Each Ag metal is in van der Waals contacts (Ag···O = 2.680(2)–3.200(2) Å) with five oxygen atoms (O1–O3 (furan); O4 and O6) (ClO_4^-), and therefore its coordination sphere may also be considered as 7-coordinate. As consistent with our expectation, like compound **2**, compound **3** has a 2D network form, in which the ClO_4^- counterions play the same role as the PF_6^- counterions in compound **2** (Fig. 5).

A dinuclear monomer unit of compound **4** is given in Fig. 6, which shows two Ag metals, two $\mathbf{L}^2$ ligands, and two BF_4^- ions. Two Ag metals have distinct coordination environments due to van der Waals contacts, explaining a dimeric chemical formula $[Ag_2\mathbf{L}^2_2](BF_4)_2$, not $[Ag\mathbf{L}^2](BF_4)$. The Ag1 atom is bound to two oxygen (O2 and O3) and one fluorine (F7) atoms via van der Waals contacts: Ag···O (2.713(5) and 2.787(6) Å) and Ag···F (2.931(9) Å). On the other hand, the Ag2 atom is in van der Waals contacts with two oxygen (O1 and O4) atoms only: Ag···O (2.613(5) and 2.700(5) Å). Considering these van der Waals contacts, the Ag1 metal may be regarded as 5-coordinate and the Ag2 metal as 4-coordinate. Fig. 7 is a packing diagram of compound

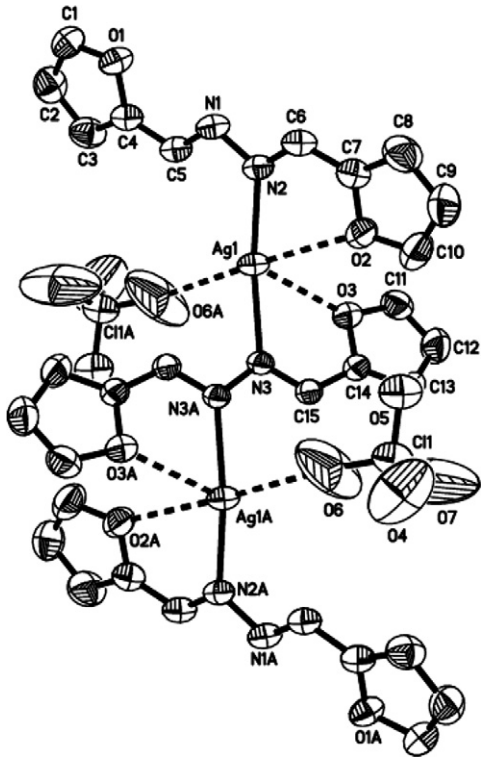


Fig. 4. Monomer unit of compound **3** showing van der Waals contacts. Selected bond distances (Å) and angles (°): Ag1–N2 2.217(2), Ag1–N3 2.268(2), N1–N2 1.401(3); N2–Ag1–N3 151.4(1), C6–N2–Ag1 124.0(2), N1–N2–Ag1 123.5(2).

4, which shows a 1D chain. The monomer units are covalently connected in the atom-connectivity manner of –N–N–Ag–N–N–Ag–N–N– to give a 1D chain. It is worth noting that only one (F7) out of eight F atoms participates in the van der Waals contacts.

Compound **5** also has a dinuclear monomer unit consisting of two Ag metals, one $\mathbf{L}^2$, and two NO_3^- ligands (Fig. 8). The Ag–N (2.288(2) and 2.359(2) Å) and Ag–O (NO_3^-) bond lengths (2.419(2) and 2.472(2) Å) indicate normal covalent bonds. Two Ag metals are distinct. Besides the Ag1–N1, Ag1–O3, and Ag1–O6#1 bonds, the Ag1 metal is further bound to three oxygen atoms (O1, O4#2, and O7#1) via van der Waals contacts (Ag···O = 2.668(2)–2.716(3) Å). On the other hand, the Ag2 metal is covalently bonded to the N2, O5#3, O6, and O4#4 atoms, and it is further in van der Waals contacts with two oxygen atoms (O2 and O6#5; Ag···O = 2.745(2) and 2.845(2) Å) and another Ag2 metal (Ag···Ag = 3.3510(4) Å) In this manner, the Ag2 metal can now be thought of having a 7-coordinate environment. Fig. 9 shows a packing diagram of compound **5**. The $Ag_2\mathbf{L}^2$ units are connected by the NO_3^- ions along the *a*-axis and by the ligands along [110] direction to form a 2D network, in which two NO_3^- ions are distinct. One NO_3^- ion (N3, O3–O5) links four Ag metals via four Ag–O covalent bonds (Ag1–O3, Ag1#7–O4, Ag2#1–O4, Ag2#8–O5) and one Ag···O van der Waals contact (Ag1···O5). The other NO_3^- ion (N4, O6–O8) links three Ag metals via two Ag–O covalent bonds (Ag1#3–O6, Ag2–O6) as well as two Ag···O van der Waals contact (Ag1#3–O7, Ag2#10···O6). The ligands are oriented approximately along the *c*-axis, and the $Ag_2(NO_3)_2$ fragments along the *a*-axis.

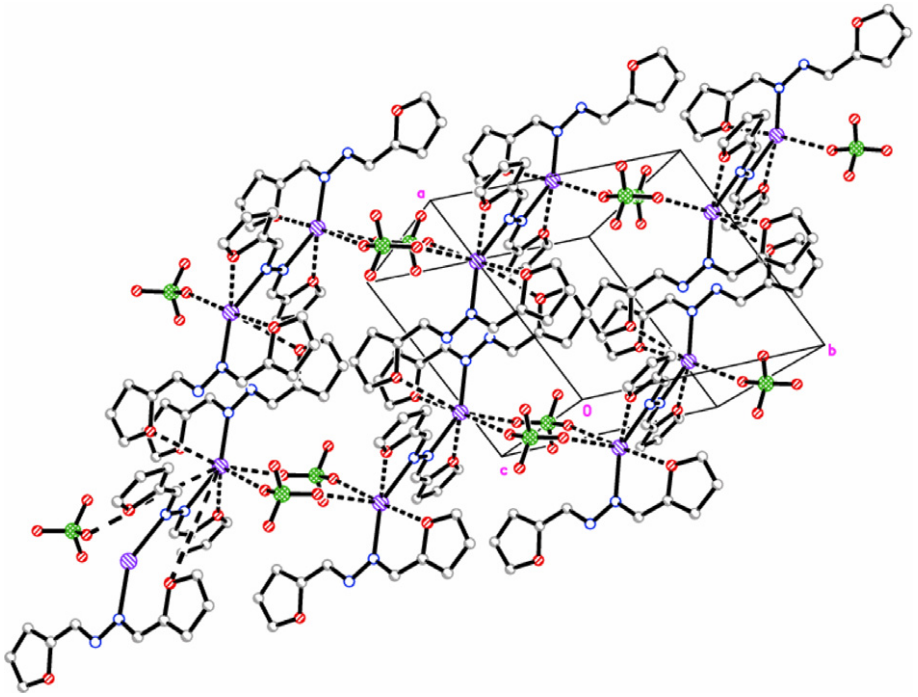


Fig. 5. Packing diagram of compound **3** showing a 2D network.

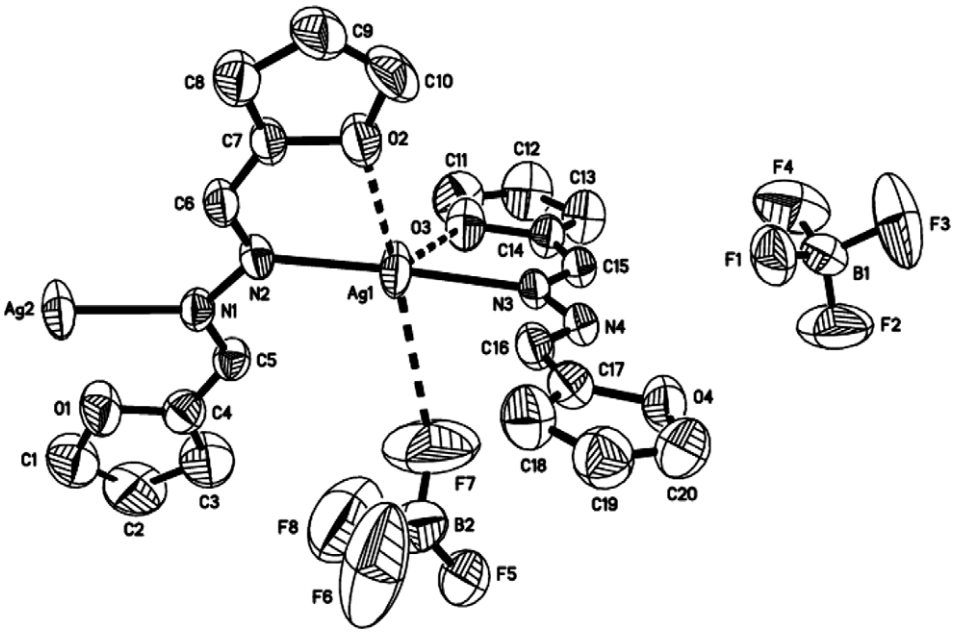


Fig. 6. Monomer unit of compound **4** showing van der Waals contacts (dashed lines). Selected bond distances (Å) and angles (°): Ag1–N2 2.177(5), Ag1–N3 2.187(5), Ag2–N1 2.168(5); Ag2–N4#1 2.181(5), N2–Ag1–N3 170.8(2), N1–Ag2–N4#1 175.8(2). Symmetry transformations used to generate equivalent atoms: #1 $-x+1/2$, $y-1/2$, $z+1/2$.

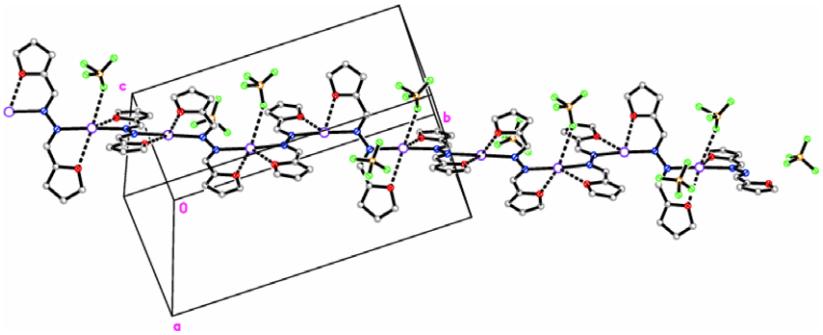


Fig. 7. Packing diagram of compound **4** showing a 1D chain.

3.3. Photoluminescence (PL) property of compound 5

Recently, much research has been focused on coordination polymers exhibiting photoluminescence due to their potential application as light emitting diodes [5,39–41]. Of five compounds in this study, only compound **5** exhibits green photoluminescence in the solid state at room temperature. Fig. 10 shows its photoluminescence emission spectrum, which displays a single well-defined maximum at 480 nm ($\lambda_{excitation} = 290$ nm). Photoluminescent silver coordination polymers commonly exhibit weak blue emission at low temperature that depends on the nature of ligands [18,19,26,29,31], and therefore the room-temperature photoluminescence of compound **5** is somewhat interesting, considering the lack of photoluminescence of ligand $\mathbf{L}^2$.

In summary, we prepared five silver compounds, $[Ag\mathbf{L}^1_2](PF_6)$ (**1**), $[Ag_2\mathbf{L}^2_3](PF_6)_2$ (**2**), $[Ag_2\mathbf{L}^2_3](ClO_4)_2$ (**3**), $[Ag_2\mathbf{L}^2_2](BF_4)_2$ (**4**), and $[Ag_2\mathbf{L}^2(NO_3)_2]$ (**5**) by layer diffusion (dichloromethane–methanol). All compounds were structurally characterized by X-ray diffraction. Compound **1** is a discrete compound. Whereas compounds **2** and **3** form 2D networks by van der Waals contacts, compounds **4** and **5** are a 1D and a 2D coordination polymer, respectively, formed by covalent bonds. The structural variation in the polymeric compounds **2**–**5** depended on the counter-ion used. Compound **5** exhibited blue-green photoluminescence at room temperature in the solid state.

4. Supplementary material

CCDC 654198, 654199, 654200, 654201, and 654202 contain the supplementary crystallographic data for **1**, **2**, **3**, **4**, and **5**. These data can be obtained free of charge via http://www.ccdc.cam.ac.uk/conts/retrieving.html, or from

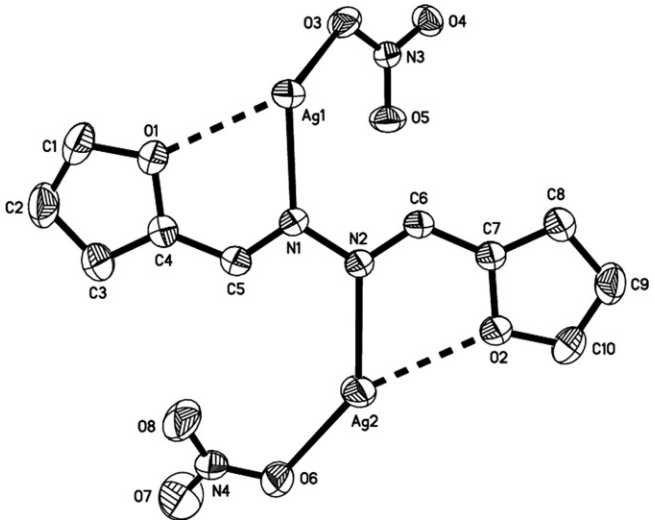


Fig. 8. Monomer unit of compound **5** showing van der Waals contacts. Selected bond distances (Å) and angles (°): Ag1–N1 2.288(2), Ag1–O3 2.419(2), Ag1–O6#1 2.472(2), Ag1–O4#2 2.668(2), Ag1–O1 2.676(2), Ag1–O7#1 2.716(3), Ag2–N2 2.359(2), Ag2–O5#3 2.414(2), Ag2–O6 2.421(2), Ag2–O4#4 2.536(2), Ag2–O2 2.745(2), Ag2–O6#5 2.845(2), Ag2–Ag2#5 3.3510(4); N1–Ag1–O3 120.40(6), N1–Ag1–O1 67.27(6), O3–Ag1–O1 127.16(6), N2–Ag2–O6 138.65(6), N2–Ag2–O2 64.95(5), O6–Ag2–O2 152.64(6). Symmetry transformations used to generate equivalent atoms: #1 $x+1, y-1, z$; #2 $-x, -y, -z+1$; #3 $-x-1, -y+1, -z+1$; #4 $x, y+1, z$; #5 $-x-1, -y+2, -z+1$.

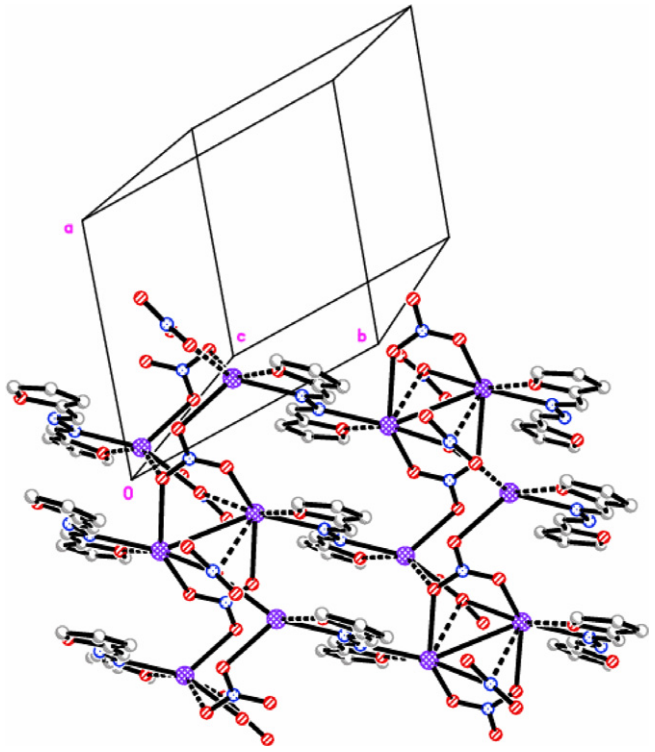


Fig. 9. Packing diagram of compound **5** showing a 2D polymeric structure.

the Cambridge Crystallographic Data Centre, 12 Union Road, Cambridge CB2 1EZ, UK; fax: (+44) 1223-336-033; or e-mail: deposit@ccdc.cam.ac.uk.

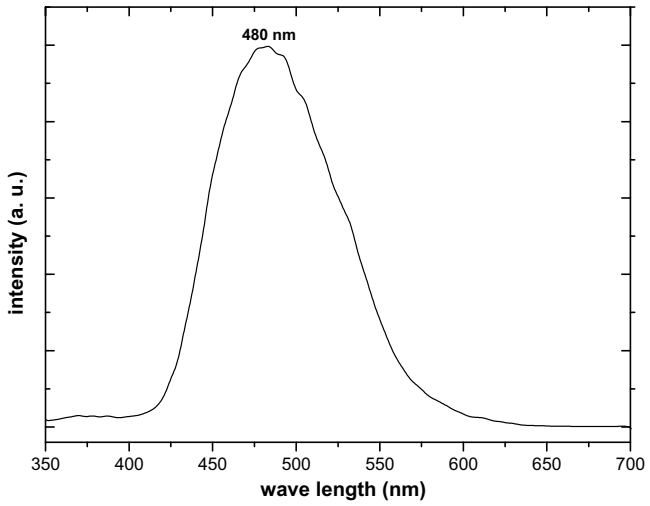


Fig. 10. Solid state photoluminescence emission spectrum for compound **5** at room temperature (excitation at 290 nm).

Acknowledgement

This work was supported by the 63 Research Fund of Sungkyunkwan University (2004–2005).

References

[1] G.F. Swiergers, T.J. Malefetse, Chem. Rev. 100 (2000) 3483.
[2] B. Moulton, M.J. Zaworotko, Chem. Rev. 101 (2001) 1629.
[3] M. Eddaoudi, D.B. Moler, H. Li, B. Chen, T.M. Reineke, M. O'Keeffe, O.M. Yaghi, Acc. Chem. Res. 319 (2001) 34.
[4] M. Eddaoudi, J. Kim, N. Rosi, D. Vodak, J. Wachter, M. O'Keeffe, O.M. Yaghi, Science 295 (2002) 469.
[5] C. Janiak, Dalton Trans. (2003) 2781.
[6] B. Kesanli, W. Lin, Coord. Chem. Rev. 246 (2003) 305.
[7] S.A. Barnett, N.R. Champness, Coord. Chem. Rev. 246 (2003) 145.
[8] J.L.C. Rowsell, O.M. Yaghi, Micropor. Mesopor. Mater. 73 (2004) 3.
[9] N.W. Ockwig, O.D. Friedrichs, M. O'Keeffe, O.M. Yaghi, Acc. Chem. Res. 38 (2005) 176.
[10] A.Y. Robin, K.M. Fromm, Coord. Chem. Rev. 250 (2006) 2127.
[11] H.K. Chae, J. Kim, O.D. Friedrichs, M. O'Keeffe, O.M. Yaghi, Angew. Chem., Int. Ed. 42 (2003) 3907.
[12] H.K. Chae, D.Y. Siverio-Perez, J. Kim, Y.B. Go, M. Eddaoudi, A.J. Matzger, M. O'Keeffe, O.M. Yaghi, Nature 427 (2004) 523.
[13] N.L. Rosi, J. Kim, M. Eddaoudi, B. Chen, M. O'Keeffe, O.M. Yaghi, J. Am. Chem. Soc. 127 (2005) 1504.
[14] A.C. Sudik, A.R. Millward, N.W. Ockwig, A.P. Cote, J. Kim, O.M. Yaghi, J. Am. Chem. Soc. 127 (2005) 7110.
[15] Y.-B. Dong, M.D. Smith, R.C. Layland, H.-C. zur Loye, Chem. Mater. 12 (2000) 1156.
[16] Y.-B. Dong, M.D. Smith, H.-C. zur Loye, Inorg. Chem. 39 (2000) 4927.
[17] D.M. Ciurtin, Y.-B. Dong, M.D. Smith, T. Barclay, H.-C. zur Loye, Inorg. Chem. 40 (2001) 2825.
[18] Y.-B. Dong, Y. Geng, J.-P. Ma, R.-Q. Huang, Organometallics 25 (2006) 447.
[19] H.K. Lee, S.W. Lee, Bull. Korean Chem. Soc. 28 (2007) 421.
[20] S.H. Kim, S.W. Lee, Inorg. Chim. Acta 361 (2008) 137.
[21] M. Hong, Y. Zhao, W. Su, R. Cao, M. Fujita, Z. Zhou, A.S.C. Chan, Angew. Chem., Int. Ed. 39 (2000) 2468.
[22] C. He, B.-G. Zhang, C.-Y. Duan, J.-H. Li, Q.-J. Meng, Eur. J. Inorg. Chem. (2000) 2549.

[23] A.N. Khlobystov, A.J. Blake, N.R. Champness, D.A. Lemenovskii, A.G. Majouga, N.V. Zyk, M. Schröder, Coord. Chem. Rev. 222 (2001) 155.
[24] M.-L. Tong, Y.-M. Wu, J. Ru, X.-M. Chen, H.-C. Chang, S. Kitazawa, Inorg. Chem. 41 (2002) 4846.
[25] Y.-B. Dong, J.-Y. Cheng, R.-Q. Huang, M.D. Smith, H.-C. zur Loye, Inorg. Chem. 42 (2003) 5699.
[26] Y.-B. Dong, J.-Y. Cheng, J.-P. Ma, H.-Y. Wang, R.-Q. Huang, D.-S. Guo, M.D. Smith, Solid State Sci. 5 (2003) 1177.
[27] H.-F. Zhu, L.-Y. Kong, T.-A. Okamura, J.F. Bu, W.-Y. Sun, N. Ueyama, Eur. J. Inorg. Chem. (2004) 1465.
[28] Y.-B. Dong, X. Zhao, B. Tang, H.-Y. Wang, R.-Q. Huang, M.D. Smith, H.-C. zur Loye, Chem. Commun. (2004) 220.
[29] Y.-B. Dong, X. Zhao, R.-Q. Huang, M.D. Smith, H.-C. zur Loye, Inorg. Chem. 43 (2004) 5603.
[30] M. Oh, C.L. Stern, C.A. Mirkin, Inorg. Chem. 44 (2005) 2647.
[31] H.-C. Wu, P. Thanasekaran, C.-H. Tsai, J.-Y. Wu, S.-M. Huang, Y.-S. Wen, K.-L. Lu, Inorg. Chem. 45 (2006) 295.
[32] D.B. Cordes, L.R. Hanton, Inorg. Chem. 46 (2007) 1634.
[33] H.K. Lee, S.W. Lee, J. Korean Chem. Soc. 50 (2006) 420.
[34] G.M. Sheldrick, SADABS, Program for Absorption Correction, University of Göttingen, 1996.
[35] Bruker, SHELXTL, Structure Determination Software Programs, Bruker Analytical X-ray Instruments Inc., Madison, Wisconsin, USA, 1997.
[36] M. Calligaris, L. Randaccio, in: G. Wilikinson, R.D. Gillard, J.A. McCleverty (Eds.), Comprehensive Coordination Chemistry, vol. 2, Pergamon Press, New York, 1987, pp. 715–738.
[37] P.A. Vigato, S. Tanburini, Coord. Chem. Rev. 248 (2004) 1717.
[38] R. Hernanddez-Molina, A. Mederos, in: J.A. McCleverty, T.J. Meyer (Eds.), Comprehensive Coordination Chemistry II, vol. 2, Pergamon Press, New York, 2004, pp. 411–446.
[39] E. Cariati, X. Bu, P.C. Ford, Chem. Mater. 12 (2000) 3385.
[40] F. Würthner, A. Sautter, Chem. Commun. (2000) 445.
[41] D.M. Ciurtin, N.G. Pschirer, M.D. Smith, U.H.F. Bunz, H.-C. zur Loye, Chem. Mater. 13 (2001) 2743.

Mn^{II}–Mn^{II} → Mn^{III}–Mn^{III} redox cycle similar to the catalase enzyme. X-ray structure diffraction shows that in *Thermus thermophilus* catalase the Mn···Mn separation is 3.18 Å in the reduced Mn^{II}–Mn^{II} form and 3.14 Å in the oxidized Mn^{III}–Mn^{III} form [18]. The *T. thermophilus* catalase contains a $\mu_{1,3}$-carboxylate ligand as a bridge. During hydrogen peroxide dismutation, it is believed that these bridges undergo changes, but their functional significance remains unidentified. In the literature, there are three systems based on a series of dinuclear complexes; the first system, the functionalized Schiff base $[Mn(2\text{-}OHsalpn)]_2$, is an excellent peroxide disproportionation catalyst in acetonitrile [19–21]. The second system, that shows moderate activity, contains a septadentate ligand with a benzimidazole group and a single bridging alkoxide [22–25]. The third model complexes (only three in the literature), using dicarboxylic acid as a bridge, have been reported as efficient catalysts [26,27]. Some mononuclear manganese(II) complexes are also reported to show catalase activity. However, the best chemical mimics of manganese catalase are 10^3–10^5 times slower than the enzymes.

In this work, as part of our continuing interest to synthesize and structurally characterize cobalt(III) [28] and zinc(II) complexes [29] of mixed ligands, long chain α,ω-dicarboxylic acid and 1,10-phenanthroline, we report here the preparation and characterization of a manganese(II) complex of perfluorosebacic acid ($HO_2C(CF)_8CO_2H$) and 1,10-phenanthroline. Besides, we examined its catalytic activity on H_2O_2 disproportionation. It is known that manganese(II) carboxylate complexes with added phenanthroline are particularly active catalysts for the disproportionation of hydrogen peroxide in the presence of the added base imidazoyl [30]. Here, we will report on the catalytic activity of the polymeric Mn(II) complex with a dicarboxylate bridge and a long Mn–Mn distance.

2. Experimental

All chemicals were commercially available in p.a. grade and were used without further purification. Elemental analysis was performed on a VARIO EL*III* CHNOS Elemental Analyzer. FT-IR spectra were recorded on a JASSCO FT/IR-300E spectrophotometer using the KBr pellet technique in the range 4000–400 cm^{-1}. The electronic spectra were recorded on a SHIMADZU UV-2450 spectrophotometer. Conductometric measurement was carried out on a Thermo-Orion Aplus 145A with an Orion electrode 011510. Thermogravimetric Analysis (TG) was taken on a SETERAM LabsysDTA 1600:amb 1600 °C unit at a heating rate of 5 °C/min under an argon atmosphere.

2.1. Synthesis of the catalyst

Addition of 0.5 ml (1M) Na_2CO_3 to a stirred solution of $MnSO_4 \cdot H_2O$ (200 mg, 0.985 mmol) in 10 ml of H_2O yielded a precipitate, which was separated by filtration, washed with distilled water several times and finally added to a stirred solution of phenanthroline monohydrate (195 mg, 0.985 mmol) and perfluorosebacic acid (483 mg, 0.985 mmol) dissolved in 20 ml of EtOH/H_2O (1:1 v/v). The mixture was stirred for *ca.* 2 h. The colorless solution was allowed to stand at room temperature. Slow evaporation for 2 days afforded light green crystals. Decomp. point 225–227 °C, yield 436 mg (49%). *Anal.* Calc. for $C_{34}H_{18}N_4O_5F_{16}Mn$ (921.45): C, 44.32; H, 1.97; N, 6.08. Found: C, 44.13; H, 1.74; N, 5.93%. FT-IR (KBr): 3434, 3066, 1705, 1693, 1592, 1518, 1496, 1428, 1381, 1345, 1304, 1213, 1148, 847, 807, 727, 655, 639, 555 cm^{-1}.

2.2. Crystallography

A light green color crystal of the manganese complex, $\{[Mn(O_2C(CF_2)_8CO_2)(phen)_2]H_2O\}_n$, suitable for data collection was mounted on a glass fiber and data collection was performed on a STOE IPDS IIdiffractometer with graphite monochromated Mo Kα radiation at 296 K. Details of crystal data, data collection and refinement are given in Table 2.

The structure was solved by direct-methods using SHELXS-97 [31] and refined by full-matrix least-squares methods on F^2 using SHELXL-97 from within the WINGX [32,33] suite of software. All non-hydrogen atoms were refined with anisotropic parameters. Hydrogen atoms bonded to carbon were placed in calculated positions (C–H = 0.93 Å) and refined using a riding model with U = 1.2U of the parent atom for C–H. The H atoms of the water oxygen atom were located in difference maps and refined subject to a DFIX restraint of O–H = 0.83 Å (U = 1.5U of the parent atom). The large s.u. values and displacement parameters of some F atoms in the molecule are caused by disorder of the perfluorosebacate group. The refinement of the disordered perfluorosebacate group was made anisotropically using PART and EADP restrictions. This disorder was modelled as two different orientations as Fa and Fb groups [hereafter Fa = F1a, F2a, F3a, F4a, F5a, F6a, F9a, F10a and Fb = F1b, F2b, F3b, F4b, F5b, F6b F9b, F10b], seen in Fig. 1, with occupancy factors of 0.267(6) and 0.733(6), respectively. The molecular drawing was obtained using ORTEP-III [34] and MERCURY [35]. Geometric calculations were performed on PLATON [36].

2.3. Hydrogen peroxide disproportionation studies

Volumetric measurements of evolved dioxygen during the reaction of the manganese(II) complex with H_2O_2 were carried out as follows: A 50 ml two-necked round-bottom flask containing a solution of the complex in organic solvents was placed in a water bath (±0.2 °C). One of the necks was connected to a graduated burette filled with water and the other was stoppered by a rubber septum. The solution was stirred for 20 min to reach a stable temperature. While the solution was stirring, a chosen volume of H_2O_2 stock solution was injected into it through the rubber septum using a syringe, and the volume of evolved

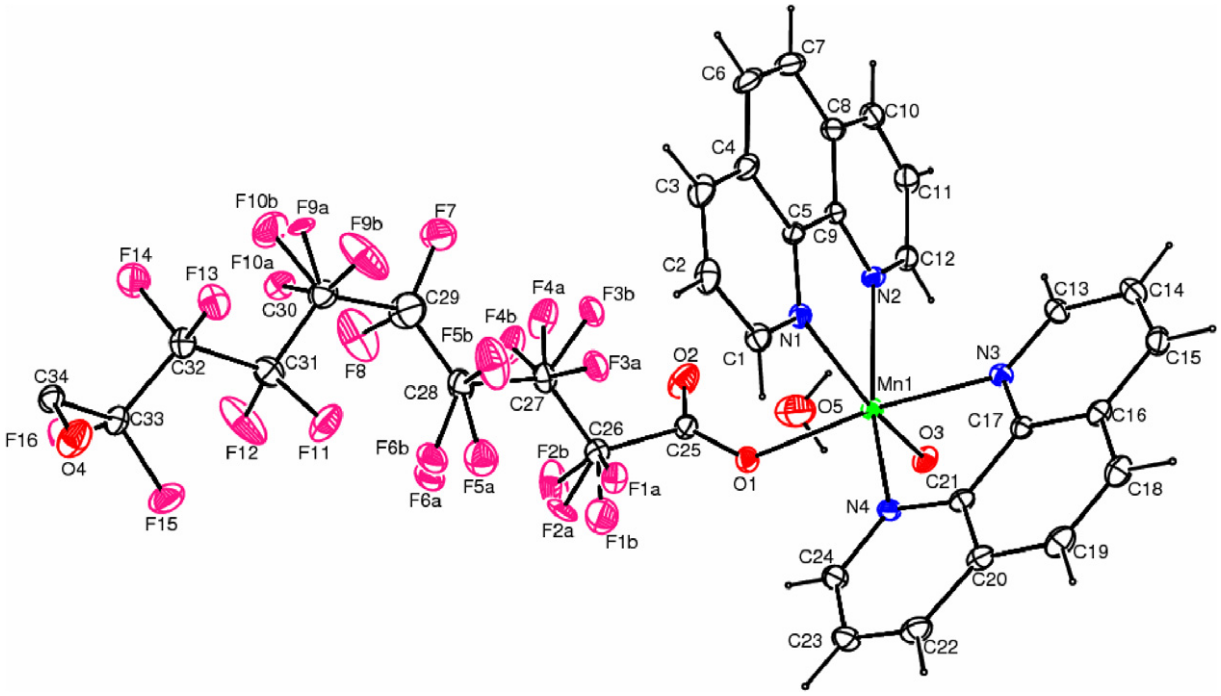


Fig. 1. Molecular structure of $\{[Mn(O_2C(CF_2)_8CO_2)(phen)_2]H_2O\}_n$, asymmetric unit.

dioxygen was measured with a burette as a function of time.

3. Results and discussion

$\{[Mn(O_2C(CF_2)_8CO_2)(phen)_2]H_2O\}_n$ was prepared in high yield reacting $MnCO_3 \cdot H_2O$ with perfluorosebacic acid and 1,10-phenanthroline in a water–ethanol mixture. Crystallization was done by evaporation at room temperature. The complex is soluble in methanol and insoluble in acetone, toluene and hexane. The molar conductivity of the complex is 20 S cm^2 mol^{-1} in methanol.

The ORTEP view of the manganese(II) complex with an asymmetric unit is shown in Fig. 1 and important interatomic data are listed in Table 1. The crystallographic data are summarized in Table 2. The structure of the complex consists of a one-dimensional neutral coordination chain $\{[Mn(O_2C(CF_2)_8CO_2)(phen)_2]H_2O\}_n$ with one guest H_2O molecule. The manganese atom is six-coordinate by two bidentate phen ligands via N1–N2 and N3–N4, and half of the two dicarboxylate ligands, both of them monodentate via O1 and O3 atoms. The manganese ion has an irregular six-coordinate geometry, principally due to the acute bite binding angle required by the phenanthroline ligands ((N4–Mn1–N3) 72.39(18)° to (N2–Mn1–N1) 72.52(2)°). The largest single deviation from octahedral geometry, however, is 158.04(19)° (O1–Mn1–N3), this may be due to steric interference between the perfluorosebacate ion and the phenanthroline ring. As would be expected, the non-coordinating oxygens of the perfluorosebacate ligand are involved in extensive hydrogen-bonding (Table 3). It can be seen from Fig. 2 that the uncoordinated oxygen (O4) is involved in hydrogen-bonding with the atoms C15 and C18, resulting in $R_1^2(6)R_2^2(62)R_1^2(6)R_2^2(18)$ motifs parallel to the ab plane. In the extended structure, the water oxygen (O5) is involved in interchain hydrogen-bonding; the one-dimensional polymer chains are connected by interchain O5–H5A···F14 ($x-1$, $-y+1/2+1$, $z-1/2$),

Table 1
Selected bond lengths (Å) and angles (°) for the manganese complex with e.s.d.s. in parameters

N4–Mn1	2.260 (5)	C21–N4–Mn1	117.2 (4)	O3–Mn1–N	90.3 (2)
N3–Mn1	2.325 (5)	C13–N3–Mn1	128.4 (5)	O1–Mn1–N2	106.8 (2)
N2–Mn1	2.284 (5)	C17–N3–Mn1	114.8 (4)	N4–Mn1–N2	155.72 (19)
N1–Mn1	2.306 (5)	C12–N2–Mn1	127.0 (5)	O3–Mn1–N1	161.7 (2)
O1–Mn1	2.139 (5)	C9–N2–Mn1	115.6 (4)	O1–Mn1–N1	83.21 (19)
O3–Mn1	2.122 (5)	C1–N1–Mn1	126.3 (5)	N4–Mn1–N1	90.5 (2)
		C5–N1–Mn1	115.5(4)	N2–Mn1–N1	72.5 (2)
		C25–O1–Mn1	130.0 (5)	O3–Mn1–N3	98.66 (19)
		O3–Mn1–O1	96.1 (2)	O1–Mn1–N3	158.04 (19)
		O3–Mn1–N4	107.7 (2)	N4–Mn1–N3	72.39 (18)
		O1–Mn1–N4	87.7 (2)	N2–Mn1–N3	89.31 (19)

Table 2
Crystal data and structure refinement parameters for $\{[Mn(O_2C(CF_2)_8CO_2)(phen)_2]H_2O\}_n$

Empirical formula	$C_{34}H_{18}F_{16}MnN_4O_5$
Formula weight	921.44
Temperature (K)	296
Wavelength (Å)	0.71073
Crystal system	monoclinic
Space group	$P2_1/c$
Unit cell dimensions	
a (Å)	13.5283(8)
b (Å)	21.9792(9)
c (Å)	11.6110(6)
α (°)	90
β (°)	94.026(5)
γ (°)	90
Volume (Å^3)	3443.9(3)
Z	4
D_{calc} (Mg/m^{-3})	2.134
Absorption coefficient (mm^{-1})	0.579
$F(000)$	2187
Crystal size (mm)	0.36 × 0.22 × 0.08
θ Range for data collection (°)	1.77–28.05
Independent reflections	6773
Collected reflections	34032
Absorption correction	integration
T_{min}	0.4996
T_{max}	0.9049
R_{int}	0.0921
θ_{max} (°)	26
h	−16→16
k	−26→27
l	−14→14
Refinement method	full-matrix least-squares on F^2
$wR(F^2)$	0.2936
Goodness-of-fit on F^2	1.015
Final R indices [$I > 2\sigma(I)$]	0.0934
R indices (all data)	0.146
$(\Delta/\sigma)_{max}$	0.00
$\Delta\rho_{max}$ (e Å^{-3})	1.50
$\Delta\rho_{min}$ (e Å^{-3})	−0.86

O5–H5B···O2 and C7–H7···O5 ($-x+1$, $-y+1$, $-z$) interactions (Fig. 2), which forms a $R_4^4(63)$ motif parallel to the ab plane. The ring atom C13 in the reference molecule at (x, y, z) acts as a hydrogen-bond donor, via atom H13, to atom F12 ($-x+1$, $y-1/2$, $-z+1/2$), thus forming a C(14) chain running parallel to the [0 1 0] direction. At the same time, atom C10 in the reference molecule at (x, y, z) acts as a hydrogen-bond donor, via atom H10, to atom O2 ($-x+1$, $-y+1$, $-z$), thus forming $R_2^2(18)$ rings running parallel to the [0 0 1] direction and centrosymmetric $R_2^2(18)$ rings centred at (1/2, 1/2, n) (n = zero or integer). The structure also contains two intermolecular C–H···π interactions. The first is from C6 in the phenyl ring of the reference molecule to the centroid of the Cg(7) ($1-x$, $-y$, $-z$) ring [C6···Cg(7) = 3.67(3) Å, H6···Cg(7) = 2.7701 Å, C6–H6···Cg(7) = 164.75°]. The second C–H···π contact is between C3 in the phenanthroline ring to the centroid of the Cg(4) ($1-x$, $-y$, $-z$) ring [C3···Cg(4) = 3.50(3) Å, H3···Cg(4) = 2.6049 Å, C3–H3···Cg(4) = 164.14°]. The C–H···π interactions produce a chain running parallel to the [1 0 0] direction. There are also π···π interactions [Cg(4)–Cg(7) ($2-x$, $-y$, $-z$), Cg(6-)-Cg(6) ($1-x$, $-y$, $-z$) and Cg(7)–Cg(4) ($2-x$, $-y$, $-z$)] with the geometric parameters as given in Table 3. The intrachain Mn1···Mn1 ($1+x$, $3/2-y$, $1/2+z$) distance is 15.830(5) Å, whereas the shortest interchain distance is 21.475(4) Å for Mn1···Mn1 ($1+x$, $1/2-y$, $-1/2+z$). The Mn–N bond lengths in apical positions are slightly shorter, Mn1–N4 = 2.26(5) Å, Mn1–N2 = 2.284(5) Å, than the Mn–N bond lengths in the equatorial plane, Mn1–N3 = 2.325(5) Å, Mn1–N1 = 2.306(5) Å. The equatorial plane is constituted by two nitrogen atoms (Mn1–N3 and Mn1–N1), belonging to two different phen ligands, while the other positions are occupied by two oxygen atoms (Mn1–O1 = 2.139(5) Å and Mn1–O3 = 2.122(5) Å) of two coordinated perfluorosebacate ligands.

Table 3
Hydrogen bonds, π···π and π···ring interactions for $\{[Mn(O_2C(CF_2)_8CO_2)(phen)_2]H_2O\}_n$

D–H···A	D–H (Å)	H···A (Å)	D···A (Å)	D–H···A (°)
O5–H5A···F14^{i}	0.83(2)	2.17(3)	2.996(12)	173(8)
C13–H13···F12^{ii}	0.93	2.49	3.218(9)	135.7
C15–H15···O4^{iii}	0.93	2.60	3.402(10)	144.2
C18–H18···O4^{iii}	0.93	2.55	3.362(11)	145.6
C7–H7···O5^{iv}	0.93	2.53	3.384(14)	153.5
C10–H10···O2^{iv}	0.93	2.53	3.426(12)	160.8
O5–H5B···O2	0.84(2)	3.051	2.753	61.7
Cg(I)	Cg(J)	Cg–Cg (Å)	Perpendicular distance (Å)	
Cg(4)	Cg(7)^{v}	4.055(13)	3.565	
Cg(6)	Cg(6)^{vi}	3.544(15)	3.317	
Cg(7)	Cg(4)^{v}	4.054(13)	3.579	
X···H(I)	Cg(J)	H···Cg (Å)	X–H···Cg (°)	
C(6)–H(6)	Cg(7)^{vi}	2.7701	164.75	
C(3)–H(3)	Cg(4)^{vi}	2.6049	164.14	

Cg(4): N3–C13–C14–C15–C16–C17, Cg(6): N1–C1–C2–C3–C4–C5, Cg(7): C16–C17–C18–C19–C20–C21.
Symmetry codes: $^{(i)}x-1$, $3/2-y$, z; $^{(ii)}1-x$, $y-1/2$, $1/2-z$; $^{(iii)}1-x$, $y-1/2$, $3/2-z$; $^{(iv)}1-x$, $1-y$, $-z$; $^{(v)}2-x$, $-y$, $-z$; $^{(vi)}1-x$, $-y$, $-z$.

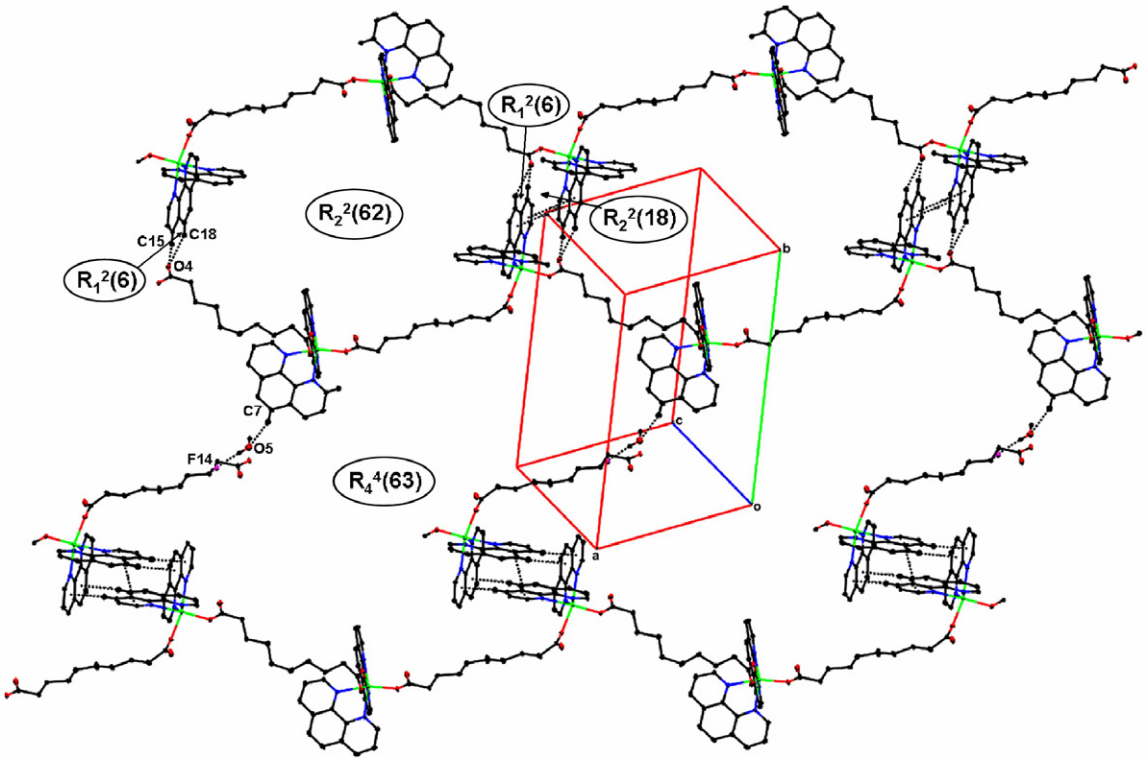


Fig. 2. Supramolecular assembly of the $\{[Mn(O_2C(CF_2)_8CO_2)(phen)_2]H_2O\}_n$ complex into a 2D layer based on intermolecular hydrogen bonds, π–π and π-ring interactions.

The unique structural feature of complex focuses on the role of the perfluorosebacate ligands which directly bridges manganese atoms forming an infinite linear coordination chain along the a axis (Fig. 2). The packing diagram of the complex is also shown in Fig 3.

3.1. IR and UV–Vis spectroscopic studies

The FT-IR spectrum of the title compound show characteristic bands of C–F stretching in the 1213–1148 cm^{-1} region. Bands due to vibrations of the carboxylate ligand are broad strong peaks at 1693 cm^{-1} for antisymmetric and 1381 cm^{-1} for symmetric stretching. These values are quite a bit higher than the literature values because of the high electronegativity of the fluorine atoms in the long chain. The separation (Δ) between $\nu_{as}(COO^-)$ and $\nu_s(COO^-)$ is 312 cm^{-1}, indicating a monodentate coordination mode for the coordinated carboxylate group [37,38]. The absorption at 1760 cm^{-1}, assigned to the asymmetrical stretching of free carboxyl groups, shows a shift towards a relatively low frequency when compared to $\nu_{as}(COO^-)$ (1693 cm^{-1}) of coordinated carboxylic acid in which intermolecular hydrogen-bonding possibly weakens the C=O bond in the carboxyl group. The stretching vibrations corresponding to those typical of coordinated 1,10-phenanthroline occur at 727, 847 and 1518 cm^{-1}.

The ground state term of the high spin octahedrally coordinated Mn(II) ion is $^6A_{1g}$. It is known that all d–d transitions in high spin d^5 complexes have extremely low intensity and in the presence of organic ligands they can rarely be detected not only because they are Laporte forbidden but also spin forbidden. This is also case of the title Mn(II) complex. Nevertheless, the electronic spectrum of the manganese complex exhibits three weak intensity absorption bands at ca. 322, 447 and 597 nm, which could be tentatively assigned to $^6A_{1g} \rightarrow {}^4T_{1g}(^4P)$, $^6A_{1g} \rightarrow {}^4E_g$, $^4A_{1g}(^4G)$ and $^6A_{1g} \rightarrow {}^4T_{1g}$ (^4G), respectively [39]. In the high energy region, very intense multiple absorption bands (204, 223 and 264 nm) are observed for $\pi \rightarrow \pi^*$ and/or $n \rightarrow \pi^*$ charge transitions of the coordinated groups.

3.2. Thermal analysis of the complex

The thermal decomposition of the Mn(II) complex was studied by thermogravimetry (TG) under argon atmosphere from 50 to 800 °C (Fig. 4). The manganese complex decomposes via an endothermic solid state reaction. The TG data shows that the decomposition mainly occurs in two steps. The complex does not decompose up to 200 °C. In the first step, a sharp drop corresponds to the lost of phenanthroline ligands at 198–219 °C (weight loss 39.87%, calculated 39.94%). The second decomposition step corresponds to release of the coordinated perfluorosebacate ligands (weight loss 54.1%, calculated 54.02%).

3.3. Catalysis studies

All the reactions were carried out in a 50 ml round-bottom flask which was thermostatically controlled. To methanol (5 ml) was added the manganese(II) complex and the

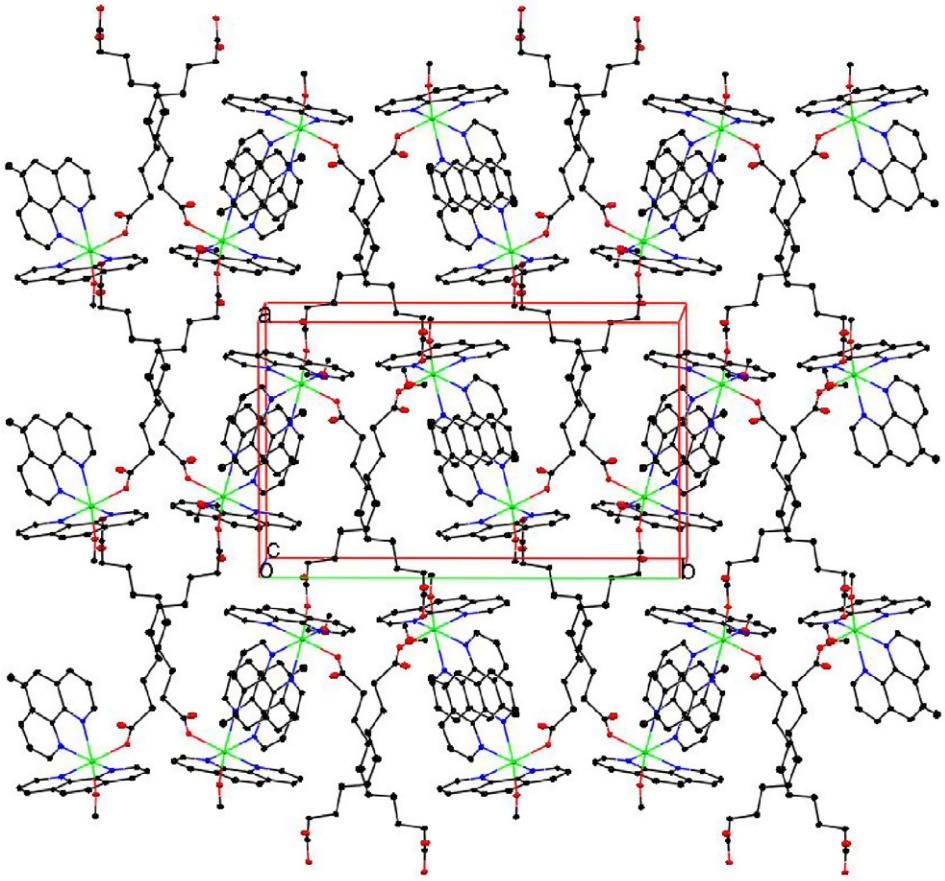


Fig. 3. Packing arrangement of the molecules in the unit cell.

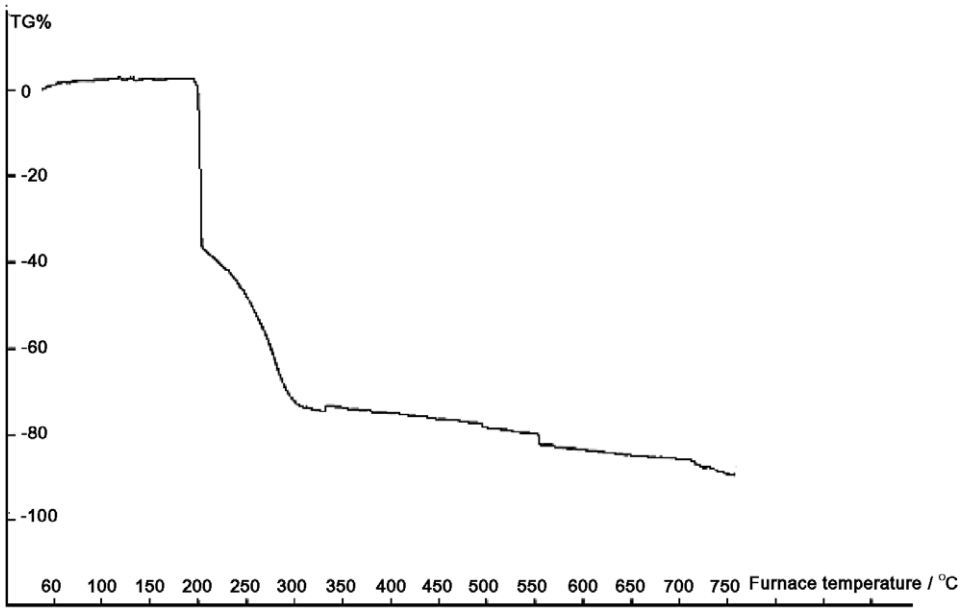


Fig. 4. The TG curve for the manganese complex in the range 50–800 °C (weight taken = 12.0 mg).

flask closed with a rubber septum. After hydrogen peroxide addition, dioxygen evolution was measured at time intervals, volumetrically. The observed initial rates were expressed in M s^{-1} and were calculated from the maximum slope of curve describing evolution of O_2 versus time. We did not observe a brown precipitate that is insoluble in

many solvents, characteristic of MnO_2, at the end of the reaction.

3.3.1. Solvent influence

Many different solvents have been used in previous studies on the catalase-like reaction. It was reported that the mechanism of the reaction can change between DMF and acetonitrile [7,10]. In our studies we also observed that the decomposition rate of H_2O_2 by the manganese complex has been found to depend strongly on the solvents used. Fig. 5 illustrates the data obtained in methanol, acetonitrile, DMF and water. In the inset of Fig. 5, an induction period to reach rigorous evolution of dioxygen was observed in DMF and in water, but no induction period has been observed in methanol and acetonitrile. The reaction rate was the slowest (2.27×10^{-5} M s^{-1}) and only a small part (4.3% at 150 min) of hydrogen peroxide was disproportionated in water. The reaction in methanol has the best results (22.1×10^{-5} M s^{-1}, ten times faster than in water, 46% disproportionation at 150 min). For this reason all subsequent measurements were performed in methanol. The experimental initial rates were calculated as 9.19×10^{-5} and 4.13×10^{-5} M s^{-1} for acetonitrile and DMF, respectively.

3.3.2. Kinetics

The dependence of the initial rates of dioxygen evolution was examined with varying concentrations of H_2O_2 and the manganese(II) complex. In the first experimental series, the hydrogen peroxide concentration was kept constant and the concentration of the complex was varied ($2.21–17.7 \times 10^{-4}$ M). Fig. 6 shows the first-order dependence of the H_2O_2 disproportionation rate with respect to catalyst concentration. The order of reaction calculated from the plot of $\ln(v_0)$ versus ln[catalyst] was found to be unity ($-\ln v_0 = 1.39 \ln[\text{catalyst}] - 1.231$; $R^2 = 0.956$) (Fig. 6b). Under the conditions studied in this set of kinetic measurements, the linear dependence of the rate is also evidence that the reaction is first order with respect to the catalyst concentration (Fig. 6c), and the rate constant ($k_{cat} = 0.214$ s^{-1}) was obtained from the slope of this line. In the second experimental series, the catalyst concentration was kept constant and the H_2O_2 concentration was varied (0.09–3.14 M). For the a constant initial concentration of Mn(II) (0.26×10^{-4} M), Fig. 7 demonstrates the effect of the initial concentration of H_2O_2 on the initial rate, v_0. For $[H_2O_2]$ lower than 0.357 M, which corresponds to $[H_2O_2]/Mn(II) = 74.5$, the initial rate increased with increasing $[H_2O_2]$. During this period, depending on the extent of electron transfer within the complex, the resulting active intermediate species can be regarded as Mn(II) coordinated with H_2O_2 and Mn(III) coordinated with peroxo, hydroperoxo or hydroxo complexes. All these intermediate complexes decompose with an excess amount of H_2O_2 by cycling their oxidation states, probably between Mn(II) and Mn(III), without any significant decomposition of the complexes themselves. On further addition of H_2O_2 after this point, the initial rate decreased rapidly with increasing $[H_2O_2]$. The exact reason for the non-linear catalytic behavior with the further addition of

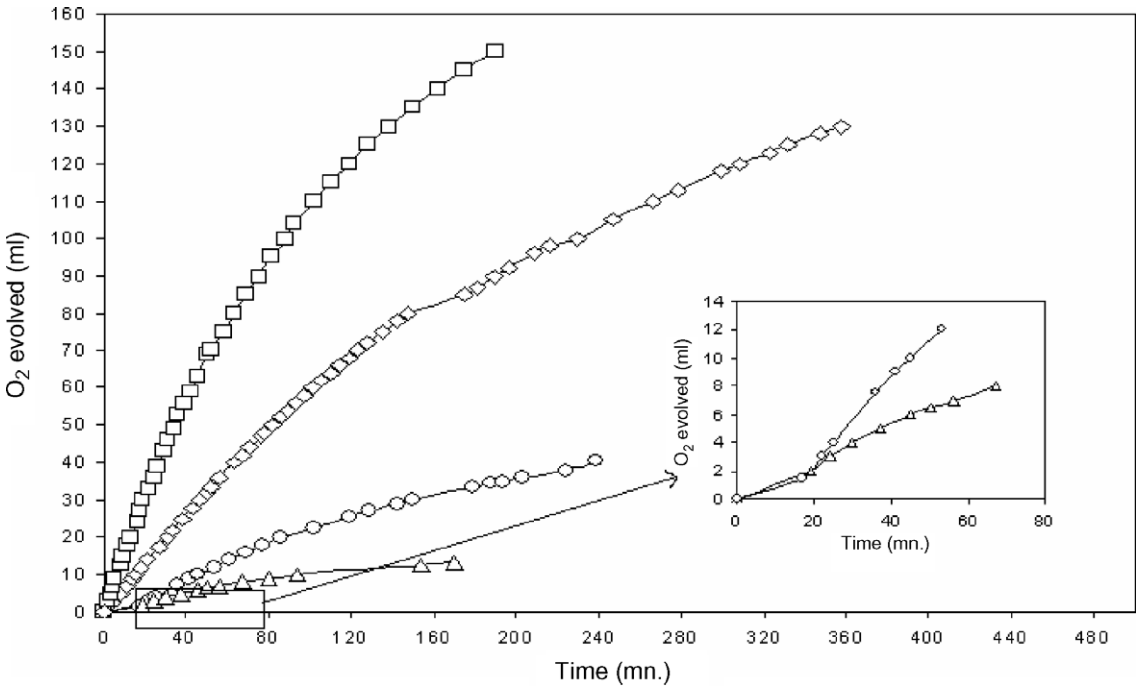


Fig. 5. Time dependence of dioxygen evolution upon reaction of the manganese complex with H_2O_2 in different solvents: methanol (□), acetonitrile (♦), DMF (○) and water (△). Conditions; [catalyst] = 0.886 M, $[H_2O_2]$ = 4.850 M at 295 K. The inset shows the induction time for disproportionation of H_2O_2 in DMF and water.

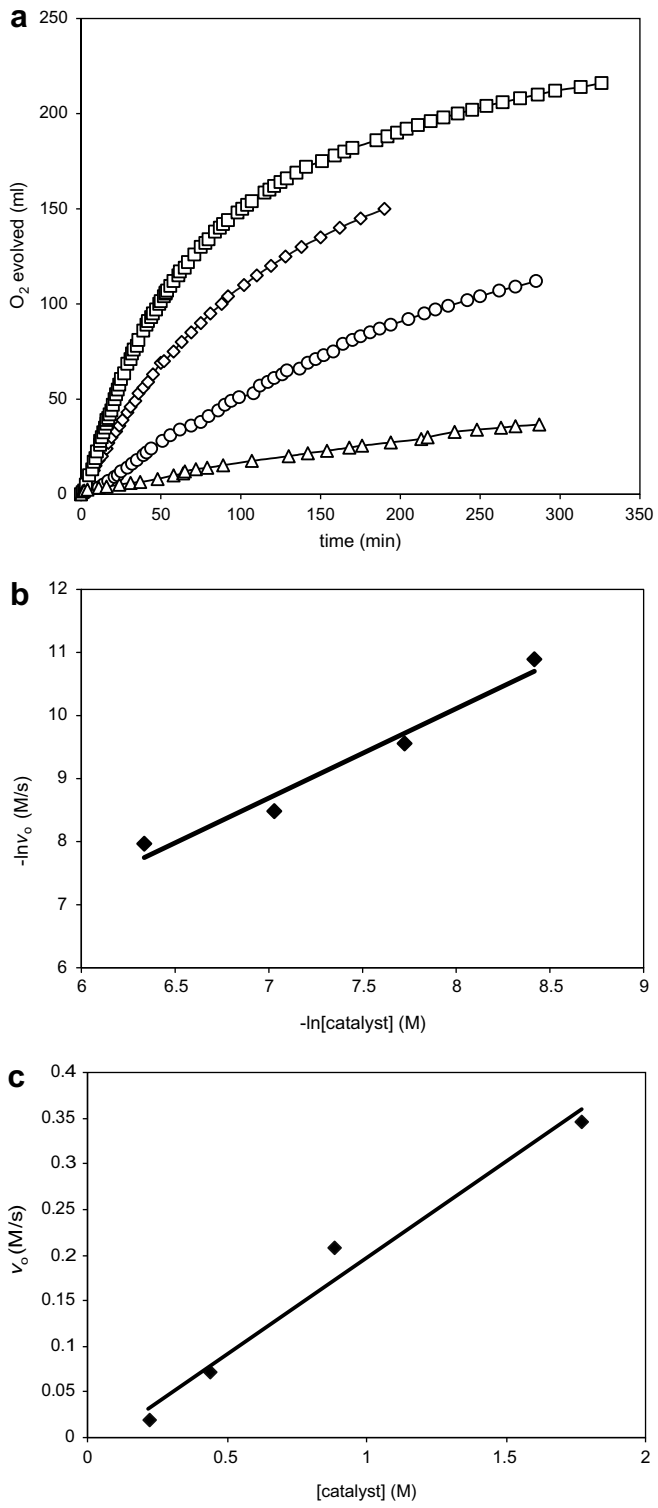


Fig. 6. Effect of catalyst concentration on the initial rate of H_2O_2 disproportionation: (a) Evolution of O_2 formation at constant H_2O_2 ($[H_2O_2] = 4.85$ M) concentrations with different concentrations of catalyst in methanol at 298 K: 2.21×10^{-4} (□), 4.42×10^{-4} (♦), 8.84×10^{-4} (○) and 17.70×10^{-4} (△). (b) $-\ln v_0$ vs. $-\ln$[catalyst]. (c) v_0 vs. [catalyst].

H_2O_2 is difficult to assess without detailed mechanistic studies. The decrease of the initial rate is probably attributed to the decomposition of the active intermediate species, being reduced to an inactive Mn(II) complex, or the decrease of the molar fraction of the active intermediate complex with increasing H_2O_2 concentration.

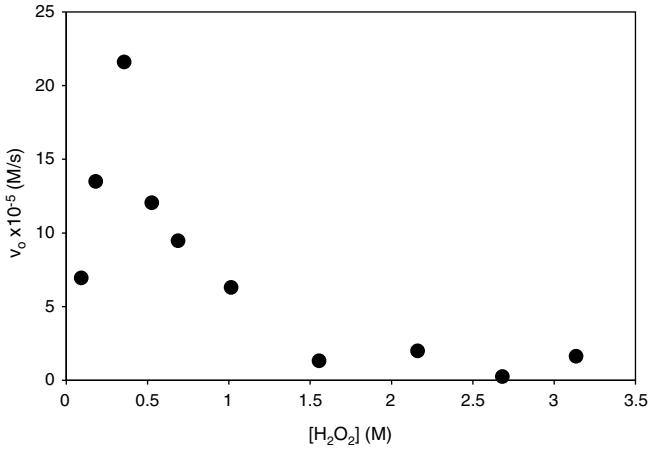


Fig. 7. Effect of H_2O_2 concentration on the initial rate of H_2O_2disproportionation at 299 K and [catalyst] $= 0.26 \times 10^{-4}$ M in methanol.

At constant catalyst concentration, Michaelis–Menten parameters could not be determined since it does not give saturation kinetics. This result shows that the catalytic activity of the present compound is not similar to related dinuclear model compounds with Mn–Mn distances similar with that of catalase enzyme [40], since the Mn–Mn distance of about 15.8 Å in the solid state may be different in the solution phase and the chain structure probably does not allow a similar mechanism for the disproportionation of H_2O_2.

The calculated initial rate constant ($k_{cat} = 0.214\ s^{-1}$) is within the range of values, $k_{cat} = 0.18$–$0.40\ s^{-1}$, obtained for dinuclear Mn complexes having (μ-AcO)(μ-MeO) bridges (reaction cond.: solvent = methanol, acetonitrile at 25 °C) [11]. The present model system gives higher catalytic activity than that of $k_{cat} = 0.027\ s^{-1}$ for [(tol)Mn(bbml)$_2$Mn(tol)](ClO$_4$)$_2 \cdot H_2O \cdot 0.5$EtOH (bbml = 2-[bis(2-benzimidazoylmethyl)-amino]ethanol; tol = toluic acid; reaction cond.: solvent = acetonitrile, at 13 °C) [41] and $k_{cat} = 0.013\ s^{-1}$ for [Mn(III)(TTP)] (TTP = meso-tetraphenylporphyrin; reaction cond.: solvent = methanol, acetonitrile at 25 °C) [19]. Additionally, we tested the activity of manganese(II) nitrate, manganese(II) perchlorate and manganese(II) carbonate under identical conditions as in the case of the present compound. As shown in Fig. 8, 25% of H_2O_2 decomposed using the present polymeric compound whereas 0.2% of H_2O_2 decomposed using the other manganese(II) compounds.

3.3.3. Temperature dependence

The determination of thermodynamic parameters of the hydrogen peroxide disproportionation reaction with the manganese complex was carried out by investigating the rate of oxygen evolution with [catalyst]=48.5×10^{-4} M, $[H_2O_2] =$ 0.34 M at different temperatures over the range 285–328 K. The plot of $-\ln v_0$ versus $1/T$ yields straight line

($-\ln v_0 = 6015/T - 12.365$; $R^2 = 0.966$) (Fig. 9). The value of the enthalpy, entropy and free energy of activation have been calculated from the known equations $\Delta H = E_a - RT$, $\Delta S = Rln(hA/e^2K_BT)$ and $\Delta G = \Delta H - T\Delta S$, respectively. The Arrhenius plot, constructed from the obtained kinetic data, yielded the following activation parameters at 301 K; $E_a = 50.0$ kJ mol^{-1}; $\Delta H^{\ddagger} = 47.5$ kJ mol^{-1}; $\Delta S^{\ddagger} = -153.8$ J K^{-1} mol^{-1}; $\Delta G^{\ddagger} = 96.3$ kJ mol^{-1}.

3.3.4. Effect of base addition

The rate of H_2O_2 disproportionation in our studies was significantly affected by addition of a strong base (NaOH). Such an enhancement of the rate of hydrogen peroxide disproportionation by added base has also been reported by other workers [17,25]. In control experiments, we observed a very slow disproportionation of H_2O_2 on the addition of NaOH to H_2O_2 in the absence of catalyst. No lag phase was observed for the reaction with or without addition of NaOH. The initial rates of H_2O_2 disproportionation in the presence and absence of NaOH are compared in Fig. 10. The maximum effect was observed upon addition of 2 eqiuv. of NaOH (per complex) at which point the rate of dioxygen evolution (1.25×10^{-3} M s^{-1}) was *ca.* 4 times higher than in the absence of NaOH under identical conditions. Further addition of NaOH caused a decrease of the initial rate. When 7 equiv. of NaOH were added, the initial rate was 22 times slower (5.07×10^{-4} M s^{-1}) than 2 equiv. of NaOH, but the catalyst was still active for a long time. The role of NaOH is not clear in the catalytic cycle with the Mn(II) complex at this moment, but the function of the hydroxide is probably related to its ability to bind to the Mn(II) ion. Stability of the one electron oxidized mixed-valence state Mn_2(II,III) is probably caused by binding of the hydroxide ligand on addition of 2 equiv. of NaOH. Upon addition of more than 2 equiv. of base, it is possible that the coordination around the manganese ion may change and produce inactive intermediate species.

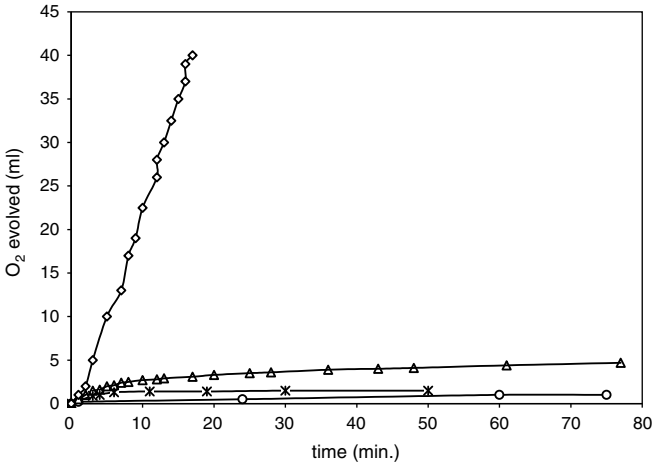


Fig. 8. Time dependence of dioxygen evolution upon reaction of different manganese compounds with H_2O_2 in methanol: {[$Mn(O_2C(CF_2)_8CO_2)$-$(phen)_2$]H_2O}$_n$ (♦), $MnCO_3$ (△), $Mn(ClO_4)_2 \cdot 6H_2O$ (∗) and $Mn(NO_3)_2$ (○). Reaction conditions: Substrate/catalyst = 2750 at 298 K.

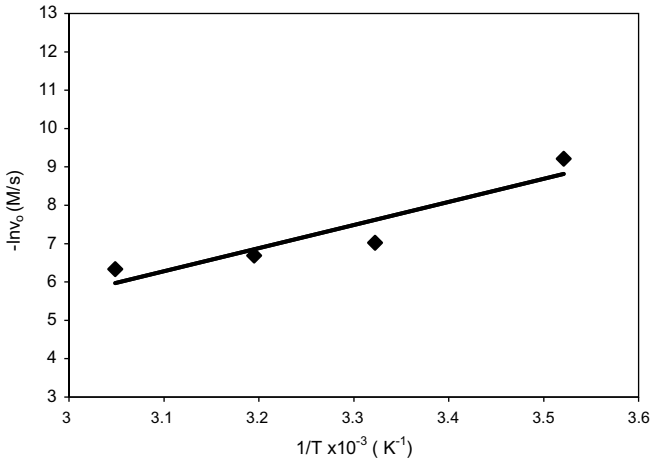


Fig. 9. The rate of O_2 formation at constant [catalyst] (48.5×10^{-4} M) and [H_2O_2] (0.34 M) at different temperatures in methanol.

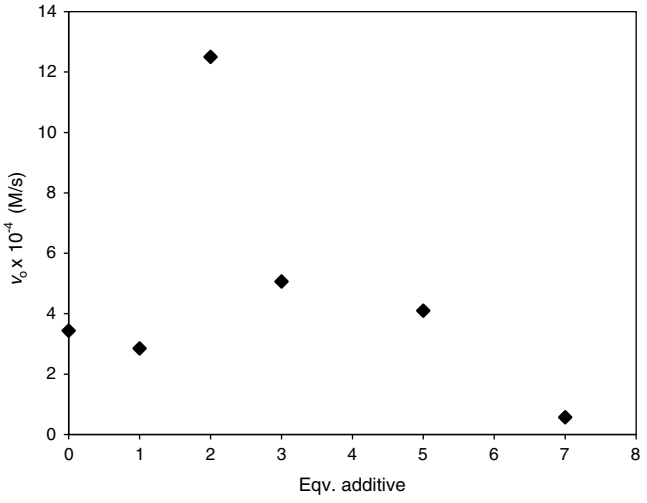


Fig. 10. Effect of base addition on the initial rate of H_2O_2 disproportionation at 300 K. Conditions: catalyst = 5.53×10^{-7} mol, H_2O_2 = 5.48×10^{-3} mol in methanol (5 ml).

3.3.5. UV–Vis monitoring of the catalase reaction

UV–Vis absorption spectra were taken during the progress of the reaction of the manganese complex with H_2O_2 in the presence of NaOH in methanol at room temperature. After addition of the substrate and base, the spectra reveal four weak absorption bands at 487, 622, 745 and 890 nm, which may be accounted for by the formation of a catalyst–substrate intermediate complex. The optical transitions are consistent with d–d transitions of Mn(III) or Mn_2(III,III) species, as previously reported [42,43].

4. Conclusion

In this study, the synthesis, full characterization and the catalytic activity of a one-dimensional polymeric manganese(II) complex with a long Mn–Mn distance have

been presented. The disproportionation of H_2O_2 by the present compound does not exhibit saturation kinetics with the substrate, but there is first-order dependence of the reaction rate on the catalyst and it proceeds without an initial time-lag in methanol. The turnover and the rate of reaction increase remarkably with the addition of two equivalents of NaOH to the catalyst solution, but the initial rate of O_2 evolution gradually decreases as more than two equivalents of NaOH are added. The kinetic and spectroscopic evidence suggest that the catalytic activity of the compound is not similar to catalase enzyme. The exact nature of the active species participating during the turnover could not be confirmed at the present moment.

Acknowledgements

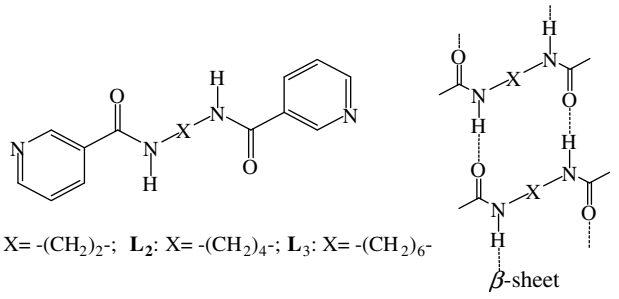
The authors wish to acknowledge Anadolu University, Commission of Scientific Research Projects for financial support (Project No. 031036) and the Faculty of Arts and Sciences, Ondokuz Mayis University, Turkey, for the use of the STOE IPDS IIdiffractometer (purchased under Grant F.279 of the University Research Fund).

Appendix A. Supplementary material

CCDC 627710 contains the supplementary crystallographic data for this paper. These data can be obtained free of charge via http://www.ccdc.cam.ac.uk/conts/retrieving.html, or from the Cambridge Crystallographic Data Centre, 12 Union Road, Cambridge CB2 1EZ, UK; fax: (+44) 1223-336-033; or e-mail: deposit@ccdc.cam.ac.uk. Supplementary data associated with this article can be found, in the online version, at doi:10.1016/j.poly.2007.12.032.

References

[1] (a) R.J. Hill, D.L. Long, N.R. Champness, P. Huberstey, M. Schröder, Chem.-A Eur. J. 11 (5) (2005) 1384;
(b) O.M. Yaghi, H. Li, J. Am. Chem. Soc. 118 (1996) 295;
(c) X.X. Zhang, S.S.-Y. Chui, I.D. Williams, J. Appl. Phys. 87 (2000) 6007.
[2] (a) S. Kitagawa, R. Kitaura, S. Noro, Angew. Chem., Int. Ed. 43 (2004) 2334;
(b) F.S. Delgado, J. Sanchiz, C. Ruiz-Pérez, F. Lloret, M. Julve, Inorg. Chem. 42 (2003) 5938.
[3] A. Gelasco, V. Pecoraro, J. Am. Chem. Soc. 115 (1993) 7928.
[4] M.P. Mathur, M. Crowder, G.C. Dismukes, J. Am. Chem. Soc. 109 (1987) 5227.
[5] M. Devereux, M. McCann, M.T. Casey, M. Curan, G. Ferguson, C. Cardin, M. Convery, V. Quillet, J. Chem. Soc., Dalton Trans. (1995) 771.
[6] A. Gelasco, M.L. Kirk, J.W. Kampf, V.L. Pecoraro, Inorg. Chem. 36 (1997) 1829.
[7] Y. Sasaki, T. Akamatsu, K. Tsuchiya, S. Ohba, M. Sakamoto, Y. Nishida, Polyhedron 17 (1998) 235.
[8] M. Manerio, M.R. Bermejo, A. Sousa, M. Fonda, A.M. Gonzlez, A. Sousa-Pedrares, C.A. McAuliffe, Polyhedron 19 (2000) 47.
[9] C. Palopoli, B. Chansou, J.P. Tuchagues, S. Signorella, Inorg. Chem. 39 (2000) 1458.
[10] T. Nakamura, N. Kenshin, S. Usugi, H. Asada, M. Fujiwara, T. Matsushita, Polyhedron 20 (2001) 191.
[11] D. Verónica, B. Hernán, C. Palopoli, S. Sergiu, J.P. Tuchagues, S. Signorella, J. Inorg. Biochem. 98 (2004) 1806.
[12] L. Dubois, D.F. Xiang, X.S. Tan, J.M. Latour, Eur. J. Inorg. Chem. (2005) 1565.
[13] P.J. Pessiki, G.C. Dismukes, J. Am. Chem. Soc. 116 (1994) 898.
[14] A.E.M. Boelrijk, S.V. Khangulov, G.C. Dismukes, Inorg. Chem. 39 (2000) 3009.
[15] M.U. Triller, W.Y. Hsieh, V.L. Pecoraro, A. Rompel, B. Krebs, Inorg. Chem. 41 (2002) 5544.
[16] I. Romero, L. Dubois, M.N. Collomb, A. Deronzier, J.M. Latour, J. Pécaut, Inorg. Chem. 41 (2002) 1795.
[17] (a) M.D. Godbole, M. Kloskowski, R. Hage, A. Rompel, A.M. Mills, A.L. Spek, E. Bouwman, Eur. J. Inorg. Chem. (2005) 305;
(b) U.P. Singh, P. Tyagi, S. Upreti, Polyhedron 26 (2007) 3625;
(c) M. Geraghty, M. McCann, M.T. Casey, M. Curran, M. Devereux, V. McKee, J. McCrea, Inorg. Chim. Acta 277 (1998) 257.
[18] V.V. Barynin, P.D. Hempstead, A.A. Vagin, S.V. Antonyuk, W.R. Melik-Adamyan, V.S. Lamzin, P.M. Harrison, P.J. Artymiuk, J. Inorg. Biochem. 67 (1997) 196.
[19] V.L. Pecorarro, M.J. Baldwin, A. Gelasco, Chem. Rev. 94 (1994) 807.
[20] A. Gelasco, A. Askenas, V.L. Pecoraro, Inorg. Chem. 35 (1996) 1419.
[21] A. Gelasco, S. Bensink, V.L. Pecoraro, Inorg. Chem. 37 (1998) 3301.
[22] P.J. Pessiki, S.V. Khangulov, D.M. Ho, G.C. Dismukes, J. Am. Chem. Soc. 116 (1994) 891.
[23] P.J. Pessiki, G.C. Dismukes, J. Am. Chem. Soc. 116 (1994) 898.
[24] N. Aurangzeb, C.E. Hulme, C.A. McAuliffe, R.G. Pritchard, M. Watkinson, M.R. Bermejo, A. Garcia-Deibe, M. Rey, J. Sanmartin, A. Sousa, J. Chem. Soc., Chem. Commun. (1994) 1153.
[25] A.E.M. Boelrijk, G.C. Dismukes, Inorg. Chem. 39 (2000) 3020.
[26] (a) D.F. Xiang, C.Y. Duan, X.S. Tan, Y.J. Liu, W.X. Tang, Polyhedron 17 (1998) 2647;
(b) M.T. Casey, M. McCann, M. Devereux, M. Curran, C. Cardin, M. Convery, V. Quillet, C. Harding, J. Chem. Soc., Chem. Commun. (1994) 2643.
[27] D.F. Xiang, X.S. Tan, W.X. Tang, F. Xue, T.C.W. Mak, Polyhedron 17 (1998) 1375.
[28] I. Kani, O. Büyükgüngör, F. Şişman, Z. Naturforsch. B-Chem. Sci. 61b (2006) 1198.
[29] I. Kani, O. Şahin, F. Yılmaz, O. Büyükgüngör, Acta Crystallogr., Sect. E 62 (2006) m1909.
[30] M. Devereux, M. Curran, M.M. Michael, T. Casey, V. McKee, Polyhedron 15 (1996) 2029.
[31] G.M. Sheldrick, SHELXS-97 – A Program for Automatic Solution of Crystal Structures, University of Gottingen, Germany, 1997.
[32] L.J. Farrugia, WINGX – A Windows Program for Crystal Structure Analysis, University of Glasgow, 1998.
[33] L.J. Farrugia, J. Appl. Crystallogr. 30 (1999) 837.
[34] L.J. Farrugia, Appl. Crystallogr. 30 (1997) 565.
[35] C.F. Macrae, P.R. Edgington, P. McCabe, E. Pidcock, G.P. Shields, R. Taylor, M. Towler, J. van de Streek, J. Appl. Crystallogr. 39 (2006) 453.
[36] A.L. Spek, PLATON – A Multipurpose Crystallographic Tool, Utrecht University, Utrecht, The Netherlands, 2005.
[37] G.B. Deacon, R.J. Phillips, Coord. Chem. Rev. 33 (1980) 227.
[38] K. Nakamoto, Infrared and Raman Spectra of Inorganic and Coordination Compounds, Wiley, New York, 1986.
[39] A.B.P. Lever, Inorganic Electronic Spectroscopy, Elsevier, Amsterdam, 1968.
[40] J.E. Penner-Hahn, V.L. Pecoraro (Eds.), Manganese Redox Enzymes, VCH Publishers, New York, 1992, p. 29.
[41] J.J. Zhang, Y.Y. Tang, Q.H. Luo, C.Y. Duan, Z.L. Wang, Y.H. Mei, Polyhedron 20 (2001) 2285.
[42] J.E. Sheats, R. Czernuziewicz, G.C. Dismukes, A. Rheingold, V. Petronleas, J. Stubbe, W.H. Armstrong, R. Beer, S.J. Lippard, J. Am. Chem. Soc. 109 (1987) 1435.
[43] J. Gao, S.H. Zhong, J. Mol. Catal. A: Chem. 186 (2002) 25.



Scheme 1. Exo bidentate ligands with a bis(amido)alkane spacer; β-sheet.

1–**5**. The crystal structures of these complexes reveal that **1**–**3** exhibit a 1D-coordination network, **4** is a 0D-complex and **5** exhibits a doubly interpenetrated 2D-network containing 4,4-topology. The crystallographic parameters are given in Table 1, bond lengths around Cu(II) in complexes **1**–**5** are given in Table 2 and parameters for hydrogen bonding are given in Table 3.

$Cu(L_1)(NBA)_2(H_2O)_2 \cdot (HNBA) \cdot 2H_2O$ (**1**)
$Cu(L_2)(NBA)_2(H_2O)_2 \cdot (HNBA) \cdot EtOH$ (**2**)
$Cu(L_3)(NBA)_2(H_2O)_2 \cdot 2H_2O$ (**3**)
$Cu(L_1)_2(HIPA)_2 \cdot 6H_2O$ (**4**)
$Cu(L_1)(SA)(H_2O)_2 \cdot H_2O$ (**5**)

2.1. Coordination geometry around the Cu(II) ions

In all the complexes the Cu(II) ions have an octahedral coordination geometry with two pyridine N atoms of the ligands, two water molecules and two O atoms of carboxylates, and it also sits on an inversion center. The Cu–O (carboxylate) distances are somewhat shorter (1.954(3)–1.980(3) Å) than the Cu–N(pyridine) distances (2.020(4)–2.052(4) Å). The Cu–O(aqua) distances (2.466(2)–2.680(5) Å) are much longer than those of Cu–O(carboxylate) and Cu–N(pyridine). Therefore, the coordination geometry around Cu(II) can be best described as a "Jahn–Teller" distorted octahedron with elongated axial distances. Only one O-atom of the carboxylates coordinates to Cu(II) in a monodentate fashion while the other uncoordinated O-atom of the carboxylates is involve in intramolecular

Table 2
Bond lengths around the Cu(II) centre in the crystal structures of **1**–**5**

Complex	1	2	3	4	5
Cu–O(carboxylate)	1.961(3)	1.974(2)	1.954(3)	1.980(3)	1.960(3)
Cu–N(pyridine)	2.043(5)	2.030(2)	2.020(4)	2.043(3)	2.052(4)
Cu–O(water)	2.680(5)	2.466(2)	2.676(5)	2.494(4)	2.519(4)

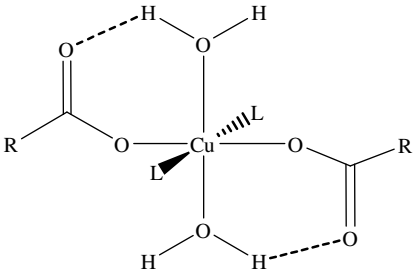
Table 3
Hydrogen bonds formed between water and amide functionalities in the crystal structures of **1**–**5**

	D–H···A	D···A (Å)	D–H···A (°)
1	N(21)–H(21)···O(1W)[a]	2.997(3)	165
	O(1W)···O(2W)[b]	2.700(4)	
	O(2W)···O(16)[c]	2.810(3)	
	O(2W)···O(16)[c]	2.861(3)	
2	O(1W)[a]···O(16)[b]	2.686(3)	
3	O(1W)–H(1A)···O(12A)	2.754(8)	107
	O(1W)–H(1B)···O(16)[c]	2.684(7)	174
	O(2W)–H(2A)···O(1W)[b]	2.748(7)	167
	N(21)–H(21)···O(2W)[a]	2.939(7)	163
4	O(1W)–H(1A)···O(2W)[b]	2.882(5)	169(5)
	O(2W)–H(2A)···O(26)[c]	2.720(5)	171(4)
	O(2W)–H(2B)···O(3W)[b]	2.789(6)	175(5)
	O(3W)–H(3A)···O(41)	2.786(5)	163(6)
	O(3W)–H(3B)···O(16)[c]	2.787(5)	173(5)
	N(31)–H(31)···O(3W)[b]	2.979(5)	156
	N(32)–H(32)···O(2W)[b]	2.880(5)	157
	O(42)–H(42O)···N(11)py	2.609(5)	173(6)
5	N(12)–H(12)···O(2W)[a]	2.846(5)	155
	O(2W)···O(1W)[b]	2.817(5)	
	O(16)···O(1W)[b]	2.746(5)	

[a] Coordinated water.
[b] Free water.
[c] Amide O-atom.

Table 1
Crystallographic parameters for the crystal structures of complexes **1**–**5**

Compound	1	2	3	4	5
Formula	$C_{35}H_{35}N_7O_{18}Cu$	$C_{39}H_{41}N_7O_{17}Cu$	$C_{32}H_{38}N_6O_{14}Cu$	$C_{44}H_{50}N_8O_{18}Cu$	$C_{18}H_{24}N_4O_9Cu$
Molecular weight	905.24	943.33	794.22	1042.47	503.95
T (K)	293(2)	293(2)	293(2)	293(2)	293(2)
System	triclinic	triclinic	triclinic	triclinic	monoclinic
Space group	$P\bar{1}$	$P\bar{1}$	$P\bar{1}$	$P\bar{1}$	$C2/c$
a (Å)	8.6530(2)	8.7310(2)	8.6297(2)	7.0130(1)	10.196(2)
b (Å)	11.355(2)	11.137(2)	8.9671(2)	10.660(2)	16.435(3)
c (Å)	11.945(2)	12.603(3)	12.467(3)	16.628(3)	12.705(3)
α (°)	111.36(3)	106.51(3)	93.51(3)	98.21(3)	90.00
β (°)	102.79(3)	90.29(3)	106.47(3)	92.96(3)	97.14(3)
γ (°)	100.55(3)	98.08(3)	96.74(3)	108.14(3)	90.00
V (Å^3)	1020.0(4)	1162.0(4)	914.2(4)	1163.1(5)	2112.5(8)
Z	1	1	1	1	4
D_{calc} (Mg/m^3)	1.474	1.348	1.443	1.488	1.585
R_1 ($I > 2\sigma(I)$)	0.0757	0.0454	0.0648	0.0497	0.0497
wR_2 (on F^2, all data)	0.2006	0.1298	0.2011	0.1544	0.1672



Scheme 2. Coordination geometry around Cu(II) and intramolecular hydrogen bonding observed in the crystal structures of **1**–**5**.

hydrogen bonds with coordinated water molecules to form a cyclic ring containing Cu(II) (Scheme 2). In these six membered rings the O···O distances of intramolecular hydrogen bonds are 2.676(4), 2.694(3), 2.705(7), 2.688(5) and 2.614(6) Å in the structures of **1**–**5**, respectively.

2.2. One-dimensional networks in complexes *1*–*3*

In the crystal structures of **1**–**3**, the ligands L_1, L_2 and L_3 exhibit the lengths of 12.850, 14.146 and 16.629 Å, respectively.[1] However, the separation of the Cu(II) atoms by the ligand in the crystal structures does not follow a similar trend; the separation distances are 16.227, 15.839 and 19.153 Å in **1**–**3**, respectively (Fig. 1). In all the three structures, the interplanar angles between the amide and pyridine are quite similar (22–25°). However, the interplanar angles between the pyridine and alkyl chain (3.4°) and the amide and alkyl chain (19.7°) of **2** differ significantly from those of **1** (81.3° and 86°) and **3** (97.8° and 58.2°).

Moreover, complexes **1** and **2** include HNBA and water or EtOH as guest molecules. The available guest volume in the structures of **1** and **2** accounts for 31.5% and 39.5% of the crystal volume respectively. In contrast, complex **3** includes water but not HNBA. In all the three structures the 1D-chains are assembled into two-dimensional layers. However, the compositions of the layers differ significantly from each other (Fig. 2). In **1**, hydrogen bonding between coordinated water molecules and N–H groups and also between CO groups and uncoordinated water molecules join the chains. Two water molecules indeed form an eight membered ring with amide CO groups, which comprises of four O-atoms and four H-atoms. The shortest interchain separation of Cu(II) atoms in the layer is 8.653 Å. The nitro benzoate groups are positioned above and below the layer in a perpendicular fashion.

In complex **2** the chains are joined together by hydrogen bonding between coordinated water and CO groups. The NBA moieties are positioned above and below the layer with some inclination towards plane of the layer. The shortest interchain separation of the Cu(II) atoms in the layers is 8.731 Å. Within the layer there exist rectangular cavities which are occupied by EtOH molecules (not located).

The 1D-chains in complex **3** also form a layer via O–H···O hydrogen bonds between water molecules and benzoates. Further, the joining of these chains occurs through the formation of a cyclic hydrogen bond aggregate comprising of six O-atoms and six H-atoms. The amide CO is also involved in O–H···O hydrogen bonding with a free water molecule.

In complexes **1** and **2**, the layers pack on each other such that channels are formed parallel to the layers. These channels are occupied by HNBA molecules which have a disorder in both the complexes. In both cases each moiety of HNBA (guest) is surrounded by the six coordinated NBA moieties (Fig. 3). In short, these structures can be described as bilayer architectures in which the layer of metal ion and ligand alternates with the layer of coordinated and uncoordinated NBA moieties.

2.3. 0D and interpenetrated 2D networks containing dicarboxylate moieties (*4* and *5*)

As the usage of monocarboxylic acid in **1**–**3** resulted in 1D-chains, we considered dicarboxylic acids (H_2IPA and H_2SA) in anticipation of forming higher dimensional coordination networks. As anticipated, complex **5** formed a 2D network whereas complex **4** differed from our expectations and formed a 0D species. The 0D complex results as only one carboxylate of HIPA and one pyridine moiety of L_1 coordinates with Cu(II). The second –COOH of H_2IPA does not lose a proton and exhibits C–O and C=O bond lengths of 1.309(5) and 1.216(5) Å, respectively, while the deprotonated –COOH has C–O bond lengths of 1.273(5) and 1.248(5) Å.[2]

The –COOH of HIPA and the uncoordinated pyridine group of L_1 interact with each other via an O–H···N hydrogen bond (Fig. 4). Differing from all the structures reported here, the metal to ligand ratio in this complex is 1:2. The O–H···N hydrogen bond between the pyridine and COOH group assembles the aggregates into 1D-chains which are further linked into a 2D layer *via* hydrogen bonds between water molecules and amide functional groups.

In complex **5**, the coordination environment is similar to the above complex but both the carboxylates of SA and both the pyridines of L_1 coordinates to Cu(II) to form a (4,4)-layer containing rectangular cavities of the dimension 9.67×16.46 Å^2 (see Fig. 5). The diagonal-to-diagonal distances are 17.25 and 20.77 Å, which confirm the rectangular nature of the cavities. The layers are interpenetrated in a 2-fold fashion with an inclined orientation in the diagonal-to-diagonal mode, the Cu(II) planes of these layers exhibit an interplanar angle of 48.8°. The $Cu(OH_2)_2$ moieties of

[1] The length of the ligand has been considered as the distance between the two pyridine N-atoms of the ligand.

[2] The deprotonation might have occurred by the ligand which is present in excess or by the presence of counter anions of the Cu(II) salts ClO_4^-.

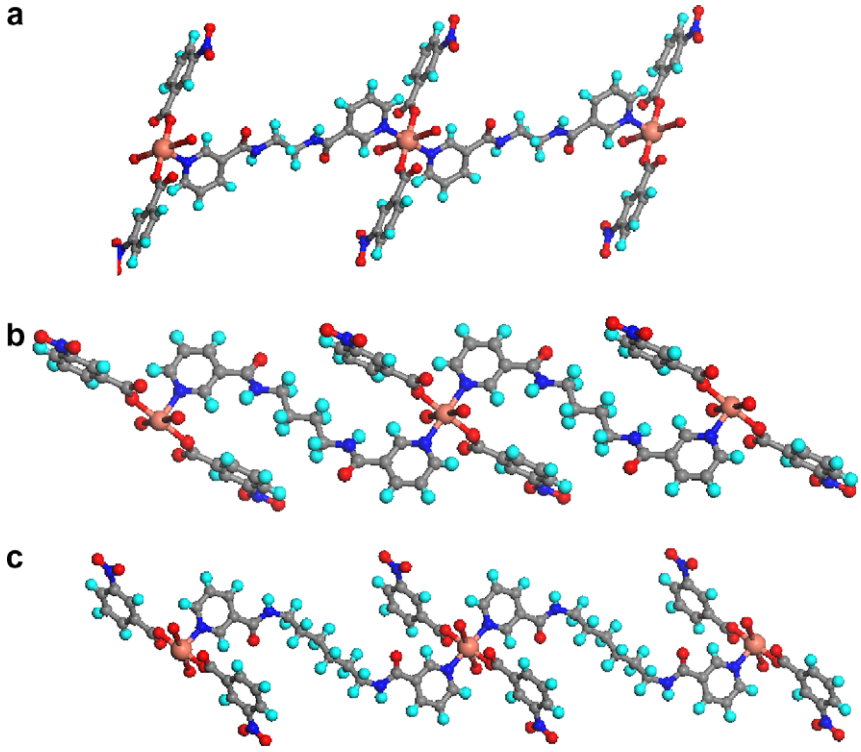


Fig. 1. One-dimensional coordination networks exhibited by crystal structures: (a) **1**, (b) **2**; and (c) **3**. Compare the network in **1** with those in **2** and **3**.

one network fit into the cavities of the other network by the formation of N–H···O hydrogen bonding between amide N–H and coordinated water molecules. Also the CO of the amide forms a hydrogen bond with a free water molecule.

2.4. Thermogravometric analysis for complexes *1* and *2*

The TGA of complexes **1** and **2** were analyzed, and both complexes show differences in the loss of solvent molecules. Complex **1** loses all four water molecules (two loosely coordinated and two uncoordinated) at 78 °C (weight loss: expt. 7.94% and calc.7.96%) and loses guest HNBA by 239 °C (weight loss: expt. 17.85% and calc.18.46%). Whereas complex **2** loses EtOH at room temperature as the crystals were taken out of the mother liquor and kept at room temperature for a week. Complex **2** without EtOH loses coordinated water molecules by 179 °C.

3. Conclusion

The ligands L_1, L_2 and L_3 were shown to form coordination networks in the presence of carboxylic acids HNBA, H_2IPA and H_2SA. The presence of HNBA resulted in 1D networks with the inclusion of HNBA itself as guest molecules in complexes **1** and **2**. Although H_2IPA is a diacid under the given conditions, it exhibits mono deprotonation and forms discrete species as one of the pyridine groups of the ligand is occupied by the –COOH group of HIPA. In contrast, H_2SA forms a dianion and acts as a spacer between Cu(II) ions to form a higher dimensional coordination network. The resultant network contains rectangular grids of dimension 9.7×16.5 Å^2 and doubly interpenetrates in an inclined mode. In all the complexes, due to the presence of coordinated and free water molecules, amide-to-amide hydrogen bonds were not observed.

4. Experimental

4.1. Synthesis of complex *1*

An ethanolic solution (10.0 mL) of $Cu(ClO_4)_2$ (370.15 mg, 1.0 mmol) was added to a solution of 3-nitrobenzoic acid (668.0 mg, 4.0 mmol) in EtOH (10.0 mL). The resultant solution was added to a stirred solution of the ligand L_1 (540 mg, 2.0 mmol) in 30 mL of EtOH, which resulted in the formation of a blue precipitate. The precipitate was dissolved by adding 20.0 mL of water and the clear solution was kept for slow evaporation. Complexes **2**–**5** were synthesized in a similar way by taking the corresponding ligand and carboxylic acids.

4.2. Elemental analysis

1 *Anal.* Calc. for $C_{35}H_{35}CuN_7O_{18}$: C, 46.43; H, 3.87; N, 10.83. Found: C, 45.95; H, 4.05; N, 11.24%.

2 *Anal.* Calc. for $C_{39}H_{41}CuN_7O_{17}$: C, 49.75; H, 4.36; N, 10.42. Found: C, 49.86; H, 4.33; N, 10.07%.

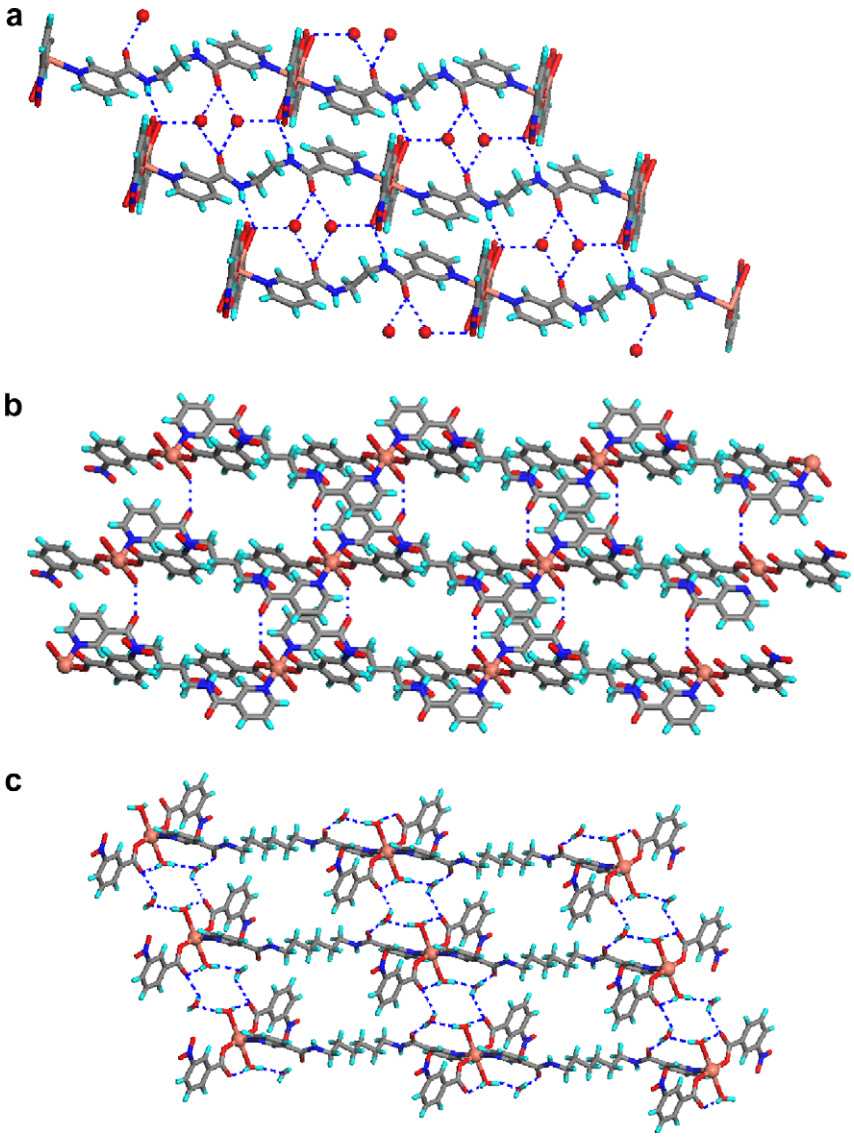


Fig. 2. Assembling of one-dimensional networks into two-dimensional layers via hydrogen bonds in the crystal structures: (a) **1**, (b) **2**, and (c) **3**. Notice the differences in the assembling.

3 *Anal.* Calc. for $C_{32}H_{38}CuN_6O_{14}$: C, 48.51; H, 4.80; N, 10.61. Found: C, 47.90; H, 4.52; N, 10.34%.

4 *Anal.* Calc. for $C_{44}H_{50}CuN_8O_{18}$: C, 50.69; H, 4.80; N, 10.75. Found: C, 51.12; H, 4.64; N, 10.63%.

5 *Anal.* Calc. for $C_{18}H_{24}CuN_4O_9$: C, 42.90; H, 4.77; N, 11.12. Found: C, 43.40; H, 4.88; N, 10.99%.

4.3. X-ray crystal structure determination

The single crystal data were collected on a Bruker-Nonius Mach3 CAD4 X-ray diffractometer using graphite monochromated Mo Kα radiation ($\mu = 0.71073$ Å) by the ω-scan method. The structures were solved by direct methods and refined by least square methods on F^2 using SHELX-97 [7]. Non-hydrogen atoms were refined anisotropically and hydrogen atoms were fixed at calculated positions and refined using a riding model. The hydrogen atoms of water molecules were located and refined with afix-2 instruction in the complexes of **3** and **4**. PLATON was used for the calculation of available guest volumes [8]. The HNBA moieties were disordered in both complexes **1** and **2** and were modelled as shown in Scheme 3.

Acknowledgements

We gratefully acknowledge financial support from the Council of Scientific and Industrial Research, India (CSIR, 01(2114)/07/EMR-II) and DST-FIST for the single crystal X-ray facility. L.R. thanks IIT (Kharagpur) for a research fellowship.

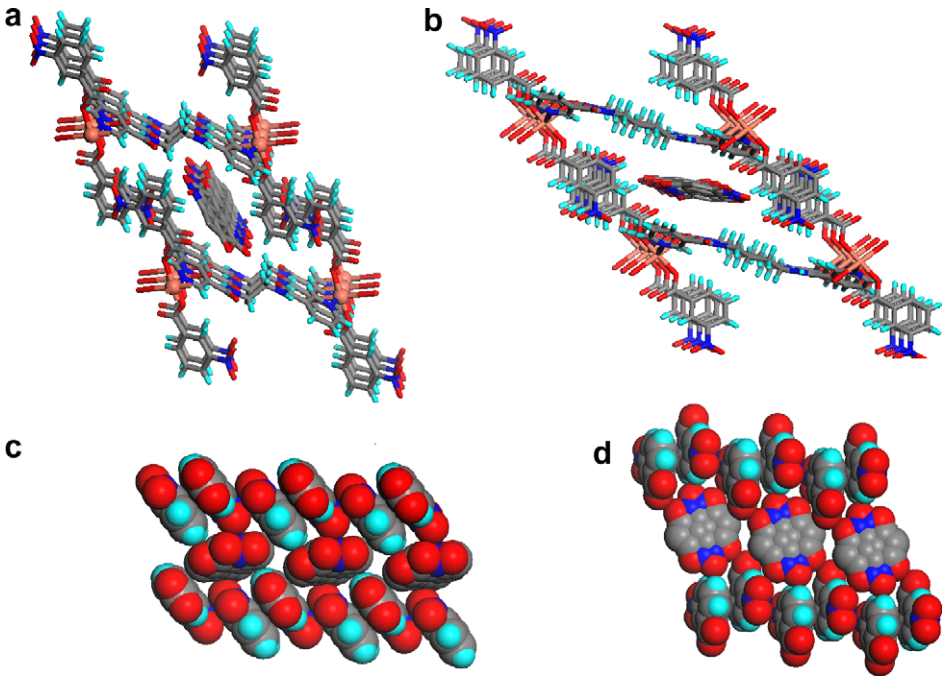


Fig. 3. Encapsulation of HNBA molecules between hydrogen bonded layers in the crystal structures of: (a) **1** and (b) **2**. Illustrations of the middle layer constituted by coordinated NBA and guest HNBA in (c) **1** and (d) **2**.

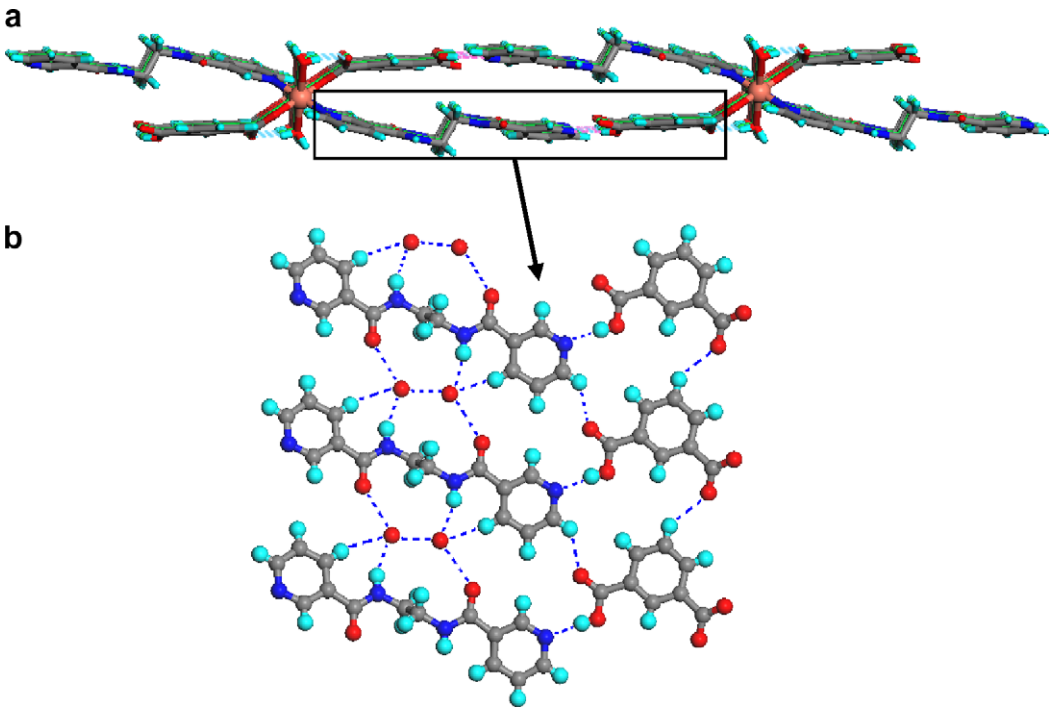


Fig. 4. Illustrations for the crystal structure **4**: (a) side view of the hydrogen bonded 2D layer of the discrete complex and (b) illustration of hydrogen bonds between L_1 and HIPA.

Appendix A. Supplementary material

CCDC 664688, 664689, 664690, 664691 and 664692 contain the supplementary crystallographic data for **1**, **2**, **3**, **4** and **5**. These data can be obtained free of charge via http://www.ccdc.cam.ac.uk/conts/retrieving.html, or from the Cambridge Crystallographic Data Centre, 12 Union Road, Cambridge CB2 1EZ, UK; fax: (+44) 1223-336-033; or e-mail: deposit@ccdc.cam.ac.uk. Supplementary data associated with this article can be found, in the online version, at doi:10.1016/j.poly.2007.12.027.

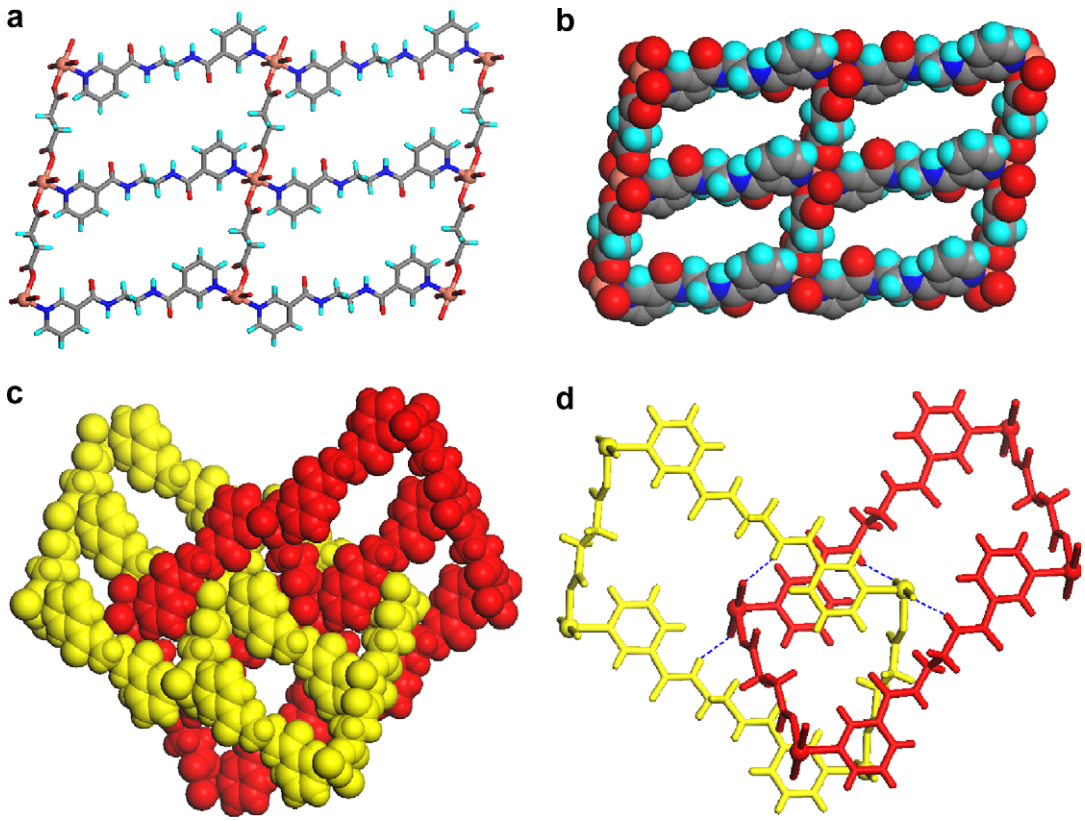
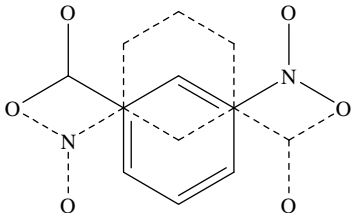


Fig. 5. Illustrations for the crystal structure of **5**. Two-dimensional layer containing rectangular cavities: (a) cylinder mode and (b) space-filling mode; (c) 2-fold interpenetration of two-dimensional layers in an inclined fashion in the space-filling mode and (d) hydrogen bonds between coordinated water molecules and amide N–H groups of interpenetrated layers.



Scheme 3. The disorder of HNBA moieties in **1** and **2**.

References

[1] (a) G.R. Desiraju, Angew. Chem., Int. Ed. Engl. 34 (1995) 2311;
(b) M. O'Keeffe, O.M. Yaghi, Acc. Chem. Res. 34 (2001) 319;
(c) S.R. Batten, R. Robson, Angew. Chem., Int. Ed. 37 (1998) 1460;
(d) B. Moulton, M.J. Zaworotko, Chem. Rev. 101 (2001) 1629;
(e) S. Kitagawa, R. Kitaura, S. Noro, Angew. Chem., Int. Ed. 43 (2004) 2334;
(f) W. Lin, O.R. Evans, Acc. Chem. Res. 35 (2002) 511;
(g) K. Biradha, M. Fujita, Angew. Chem., Int. Ed. 41 (2002) 3392;
(h) G.S. Papaefstathiou, L.R. MacGillivray, Coord. Chem. Rev. 246 (2003) 169;
(i) J.S. Seo, D. Whang, H. Lee, S.I. Jun, J. Oh, Y.J. Jeon, K. Kim, Nature 404 (2000) 982;
(j) M. Lahav, R. Gabai, A.N. Shipway, I. Willner, Chem. Commun. (1999) 1937;
(k) K. Biradha, Cryst. Eng. Commun. 5 (2003) 374;
(l) O. Ohmori, M. Kawano, M. Fujita, J. Am. Chem. Soc. 126 (2004) 6292;
(m) D. Sun, S. Ma, Y. Ke, D.J. Collins, H.-C. Zhou, J. Am. Chem. Soc. 128 (2006) 3896;
(n) S. Hasegawa, S. Horike, R. Matsuda, S. Furukawa, K. Mochizuki, Y. Kinoshita, S. Kitagawa, J. Am. Chem. Soc. 129 (2007) 2607.

[2] (a) D. Braga, J. Chem. Soc., Dalton. Trans. (2000) 3705;
(b) S. Kitagawa, M. Kondo, Bull. Chem. Soc. Jpn. 71 (1998) 1739;
(c) O.M. Yaghi, H. Li, C. Davis, D. Richardson, T.L. Groy, Acc. Chem. Res. 31 (1998) 474;
(d) R. Robson, J. Chem. Soc., Dalton. Trans. (2000) 3735;
(e) D.-L. Long, A.J. Blake, N.R. Champness, C. Wilson, M. Schröder, Angew. Chem., Int. Ed. 113 (2001) 2510;
(f) S.A. Boume, J. Lu, A. Mondal, B. Moulton, M.J. Zawarotko, Angew. Chem., Int. Ed. 113 (2001) 2169;
(g) A.G. Wong-Foy, A.J. Matzger, O.M. Yaghi, J. Am. Chem. Soc. 128 (2006) 3494;
(h) Y.Q. Lan, X.L. Wang, S.L. Li, Z.M. Su, K.Z. Shao, E.B. Wang, Chem. Commun. (2007) 4863.

[3] (a) S. Horike, D. Tanaka, K. Nakagawa, S. Kitagawa, Chem. Commun. (2007) 3395;
(b) L.R. MacGillivray, R.H. Groeneman, J.L. Atwood, J. Am. Chem. Soc. 120 (1998) 2676;
(c) F. Luo, J.-m. Zheng, S.R. Batten, Chem. Commun. (2007) 3744;
(d) K. Biradha, M. Sarkar, L. Rajput, Chem. Commun. (2006) 4169;
(e) K. Biradha, C. Seward, M.J. Zaworotko, Angew. Chem., Int. Ed. 38 (1999) 492;
(f) Z. Lin, D.S. Wragg, J.E. Warren, R.E. Morris, J. Am. Chem. Soc. 129 (2007) 10334.

[4] (a) M. Sarkar, K. Biradha, Cryst. Growth Des. 7 (2007) 1318;
(b) M. Sarkar, K. Biradha, Cryst. Growth Des. 6 (2006) 1742;
(c) M. Sarkar, K. Biradha, Chem. Commun. (2005) 2229;
(d) M. Sarkar, K. Biradha, Eur. J. Inorg. Chem. (2006) 531.

[5] F.H. Allen, O. Kennard, Chem. Des. Automat. News 8 (1993) 31.
[6] (a) J. Tao, X. Yin, R. Huang, L. Zheng, Inorg. Chem. Commun. 5 (2002) 1000;
(b) J. Tao, M.-L. Tong, J.-X. Shi, X.-M. Chen, S.W. Ng, Chem. Commun. (2000) 2043;
(c) S.G. Ang, B.W. Sun, Cryst. Growth Des. 5 (2005) 383;
(d) J. Zhang, Y. Kang, R.-B. Zhang, Z.-J. Li, J.-K. Chang, Cryst. Eng. Commun. 7 (2005) 177;
(e) S.-M. Ying, J.-G. Mao, Y.-Q. Sun, H.-Y. Zeng, Z.-C. Dong, Polyhedron 22 (2003) 3097;
(f) L.-S. Long, Y.-R. wu, R.-B. Huang, L.-S. Zheng, Inorg. Chem. 43 (2004) 3798;
(g) M. Du, X.-J. Zhao, H. Cai, J. Ribas, Eur. J. Inorg. Chem. (2006) 1245.
[7] G.M. Sheldrick, SHELX-97, Program for the Solution and Refinement of Crystal Structures, University of Göttingen, Germany, 1997.
[8] A.L. Spek, PLATON – A Multi Purpose Crystallographic Tool, Utrecht University, Utrecht, The Netherlands, 2002.

2. Experimental

All solvents were HPLC grade and used without further purification. Melting points were determined using Kofler hot stage melting point apparatus. IR spectra were recorded on Shimadzu Fourier Transform Infrared Spectrometer FTIR-400 using KBr disks. ^{1}H NMR spectra were recorded on a Bruker AVANCE 400 MHz in the deuterated solvents specified, and are reported in parts per million (ppm, δ).

The films were deposited onto standard microscope slide substrates of thickness 1 mm at room temperature. The slide substrates were cleaned ultrasonically in acetone and then rinsed with deionized water. The films were deposited using spin coating technique (Specialty Coating Systems G3P-8 Spin Coater) under nitrogen flow at 2000 rpm for 2 min. The surface microstructure was measured by atomic force microscopy (AFM; Veeco CP-II) in non-contact mode with Si tips at a scan rate of 1 Hz. The film thickness of 45–50 nm was estimated from AFM measurements. Transmittance $T(\lambda)$, and reflectance, $R(\lambda)$ spectra of the films were measured at normal incidence and at an incident angle of 5°. The measurements were acquired at room temperature in the spectral range 190–3000 nm by using a computer-aided double-beam spectrophotometer Shimadzu 3150 UV–VIS–NIR with a resolution of 0.1 nm. Phthalocyanine diffraction pattern was examined using Shimadzu XRD-6000 X-ray diffractometer using Cu Kα radiation ($\lambda = 1.5418$ Å). The X-ray tube voltage and current were 40 kV and 30 mA, respectively.

2.1. Preparation of 4,5-dichloro-3,6-dihexyloxyphthalonitrile (2)

The compound was synthesized as reported before [13].

2.2. Preparation of 4,5-bis(3,5-dichlorophenoxy)-3,6-bis(hexyloxy)phthalonitrile (3)

The compound was synthesized following the procedure reported before [13]. The resulting product was purified by column chromatography (silica gel, eluent: *n*-hexane:THF, 5:1) to yield 4,5-bis(3,5-dichlorophenoxy)-3,6-bis(hexyloxy)phthalonitrile (**3**) as a white solid (280 mg, Yield 85 %). IR (KBr): ν_{max} cm^{-1} 2933, 2851, 1596, 2220 (C≡N), 1604 (C=C), 1468, 1315, 1263, 1125 (C–O–C), 963, 832. MS (GC–MS): *m*/*z* (CI) 650. δ_H (400 MHz; $CDCl_3$): δ_H, ppm 7.09 (2H, t, Ar–**H**), 6.71 (4H, d, Ar–**H**), 4.16 (4H, t, **OCH**$_2$), 1.67 (4H, quint, –CH$_2$**CH**$_2$(CH$_2$)$_3$CH$_3$), 1.2–1.48 (12H, m, –CH$_2$CH$_2$(**CH**$_2$)$_3$CH$_3$), 0.82 (6H, t, 2 × **CH**$_3$).

2.3. Preparation of 1,4,8,11,15,18,22,25-octahexyloxy-2,3,9,10,16,17,23,24-octa-(3,5-dichlorophenoxy)phthalocyaninato zinc(II) (4)

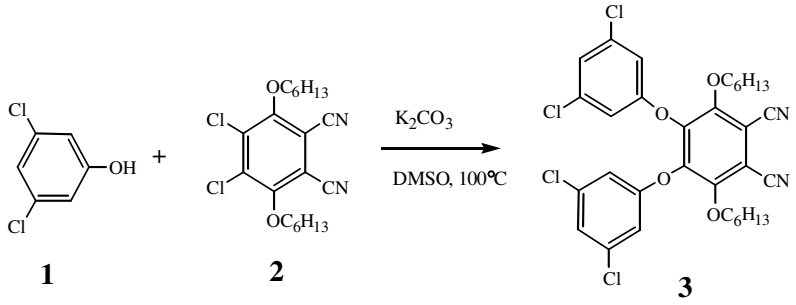
A mixture of 3,6-didecylphthalonitrile (40 mg 0.095 mmol), 4,5-bis(3,5-dichlorophenoxy)-3,6-bis(hexyloxy)phthalonitrile (127 mg, 0.196 mmol), zinc acetate dihydrate 99.999% (excess) and two drops of 1,8-diazabicyclo[5,4,0]undec-7-ene (DBU) in dry n-pentanol (10 mL) was heated to reflux for 12 h under an argon atmosphere. The reaction mixture was cooled down to room temperature and the solvent was rotaevaporated under reduced pressure. The resulting dark green compound was separated by silica gel column chromatography using the appropriate eluent. Column chromatography on silica gel with *n*-hexane/DCM 4:1 gave five bands. The required 1,4,8,11,15,18,22,25-octahexyloxy-2,3,9,10,16,17,23,24-octa-(*3,5-dichloro*phenoxy)phthalocyaninato zinc(II) (**4**) was collected as the final fraction by changing the eluent to (*n*-hexane/DCM 3:2) and it was further purified by column chromatography (silica gel, eluent: petroleum ether (bp 40–60 °C)/THF 10:1) to afford a waxy green product (70 mg, Yield 9%). IR(KBr): ν, cm^{-1}, 3052 (Ar–CH), 2940 and 2850 (CH_2). δ_H (400 MHz, $CDCl_3$): δ_H, ppm 6.90 (8H, t, Ar–H), 6.65 (16H, d, Ar–H), 4.17 (16H, t, 8 × OC**H**$_2$), 1.02–1.60 (64H, m), 0.81 (24H, t, 8 × –C**H**$_3$). δ_C (400 MHz, $CDCl_3$) ppm 14.0 (**C**H$_3$), 22.5 (CH_2), 25.3 (**C**H$_2$), 29.9 (**C**H$_2$), 31.4 (**C**H$_2$), 76.6 (O**C**H$_2$), 114.4 (2 × **C**H), 120.4 (C), 123.6 (**C**H), 135.6 (**C**), 146.1 (**C**), 146.9 (**C**), 157.8 (**C**), 164.3 (**C**). MS (GC–FAB): *m*/*z* (%) 2668 $[M+H]^+$, MS (GC–FAB): *m*/*z* (%) 2668 $[M+H]^+$.

3. Results and discussion

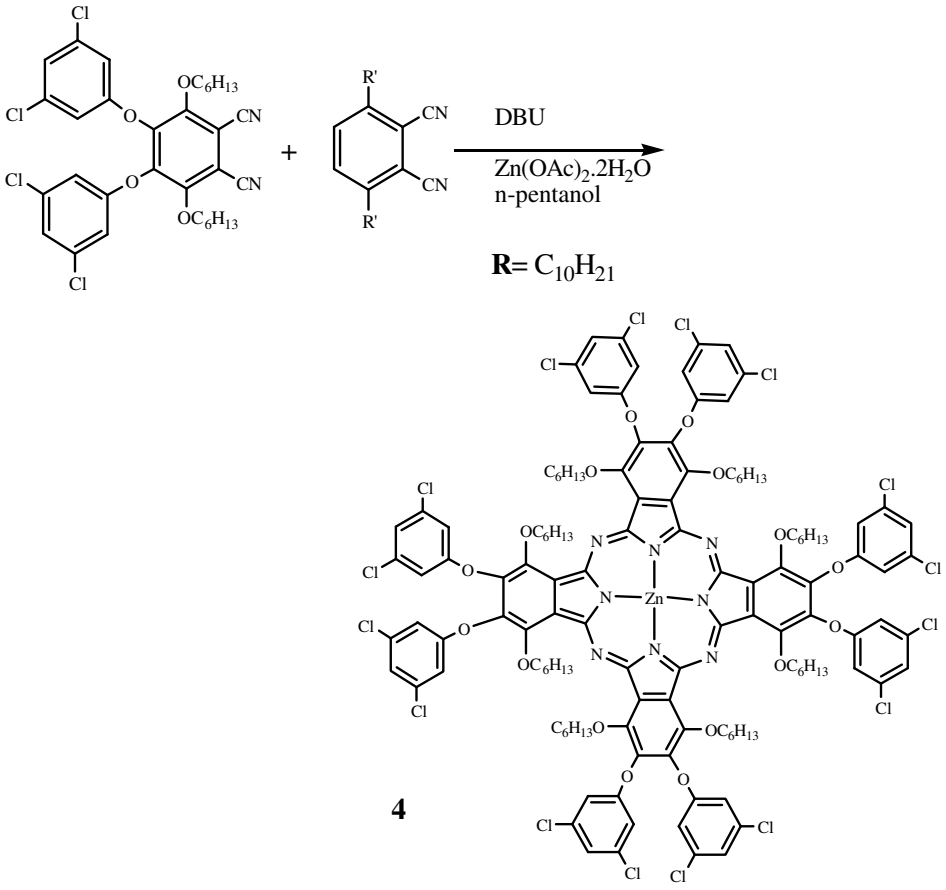
3.1. Synthesis

Preparation of the phthalonitrile derivative with the desired substituents is a critical step in phthalocyanine synthesis. In the key intermediate, aryloxy groups substituted with chlorine atoms were incorporated to increase the solubility of the resulting phthalocyanine. The oxygen atoms in the non-peripheral and peripheral positions cause a bathochromic shift of the long wavelength absorption maximum which helps to widen the visible window of the target ZnPc. Therefore, 4,5-bis(3,5-dichlorophenoxy)-3,6-bis(hexyloxy)phthalonitrile was prepared by the treatment of 4,5-dichloro-3,6-dihexyloxyphthalonitrile with 3,5-dichlorophenol, **1**, and K_2CO_3 in DMSO, Scheme 1.

It is difficult to synthesize the target ZnPc complex by direct cylotetramerization of 4,5-bis(dichlorophenoxy)-3,6-dihexyloxyphthalonitrile in the presence of a catalytic amount of 1,8-diazabicyclo[5.4.0]undec-7-ene (DBU) [14]. The steric effect of the bulky substituents on the phthalonitrile probably is the reason for the slow reaction progress. The target ZnPc complex was synthesized according to the statistical condensation of two different phthalonitriles procedure [13,15]. The procedure involves the reaction of 4,5-bis(3,5-dichlordphenoxy)-3,6-dihexyloxyphthalonitrile (**3**) and 3,6-didecylphthalonitrile (2:1 ratio) in *n*-pentanol in the presence of $Zn(OAc)_2 \cdot 2H_2O$ and a catalytic amount of 1,8-diazabicyclo[5.4.0]undec-7-ene (DBU) at 140 °C under argon atmosphere for 12 h (Scheme 2). The resulting crude product was subjected to TLC using *n*-hexane/DCM (3:2)



Scheme 1. Synthesis of 4,5-bis(dichlorophenoxy)-3,6-dihexyloxyphthalonitrile (**3**).



Scheme 2. Synthesis of 1,4,8,11,15,18,22,25-octahexyloxy-2,3,9,10,16,17,23,24-octa-(3,5-dichlorophenoxy)phthalocyaninato zinc(II) (**4**).

as eluent and showed five bands. The first fraction contained the undesired symmetrical octadecylphthalocyanine (AAAA) compound. The following three bands were possibly AAAB, AABB and ABBB which can be isolated in a very small quantity. The final separable green fraction was the symmetrical phthalocyanine derivative (BBBB), **4**, which was further purified by a new column using petroleum ether (bp 40–60 °C)/THF 10:1 as eluent to yield 60 mg (8.4%) as green waxy product. The aromatic region showed two broad signals integrated for 24 protons and assigned to the phenoxy ring protons. A triplet at 4.17 ppm was assigned to the 16 methylenoxy protons. The FAB–MS showed an isotopic cluster at 2668 m/e corresponding to the expected structure.

Attaching the chlorinated pheneoxy groups to the peripheral position and hexyloxy groups to the non-peripheral position of phthalocyanines enhanced the solubility in organic solvents [16]. The increased solubility might be due to that the steric hindrance of peripheral 3,5-dichlorophenoxy substituents makes it harder to form dimers of **4**. The prepared ZnPcs show high solubility in various organic solvents such as acetone, benzene, toluene, dichloromethane, ethyl acetate and tetrahydrofuran.

3.2. Electronic absorption spectrometry

The UV–Vis spectrum of **4** in THF solution is typical of phthalocyanine compound, having a soret and Q-bands

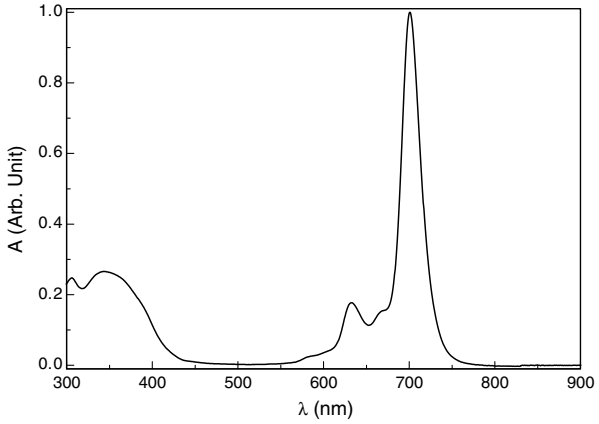


Fig. 1. UV–Vis absorption spectrum of **4** in THF solution at room temperature.

(Fig. 1). The introduction of dichlorphenoxy groups onto the phthalocynine periphary increases the Q-band absorption wavelength of these molecules. The absorption spectrum of **4** is characterized by a strong absorption in the red region and a weaker absorption in the blue region. It is clear that the absorption bands of the chlorinated phenoxy phthalocyanine **4** are shifted to a longer wavelength compared with the unsubstituted Pc. The spectral shift is attributed to the distortion of the ZnPc macrocycle and the electron withdrawing chlorine substituents on the phenyl rings. It is possible that the high electron withdrawing character of chlorine atoms tends to depopulate the π-systems, which would lead from a highly symmetrical planar state to low symmetry state molecule. However, there is no apparent change in the spectral features by comparing the chlorinated-phenoxy with the fluorine substituted phthalocyanines [13].

3.3. Structural studies

The structure and morphology of phthalocyanine thin film was examined by using AFM. Many investigations on the morphology of metal–phthalocyanine have been reported especially CuPc complexes [17–19]. The molecular orientation strongly depends on the growth conditions and substrates. The regular structure of phthalocyanine thin films is described as a stack of needle-like molecules with alternating tilt angles so that the molecules are arranged in zig-zag chains. The growth direction of the molecule columns (*b*-axis) is normally found either with the *b*-axis parallel to the surface or standing up from the substrate face with an angle of about 32° from the surface plane [17–19].

Fig. 2a and b shows 5 × 5 μm 2D and 3D AFM images of the thin film surface. The molecular arrangement of the ZnPc crystallites is visible. The phthalocyanine molecules are growing in aggregation rows rather in the parallel or in the zig-zag arrangement. The roughness of the films was estimated to be about 4.2 nm.

The XRD results of the as-deposited ZnPc film are shown in Fig. 3. The film showed a low degree of crystallinity as indicated by the small intensity of the diffraction peak at $2\theta = 5.08°$. The pattern shows the α form because it does not show the characteristic double intense peak that is observed with the β form. The individual crystallite grain size was determined using Scherrer's relation [20] and was found in the order of 16.56 nm.

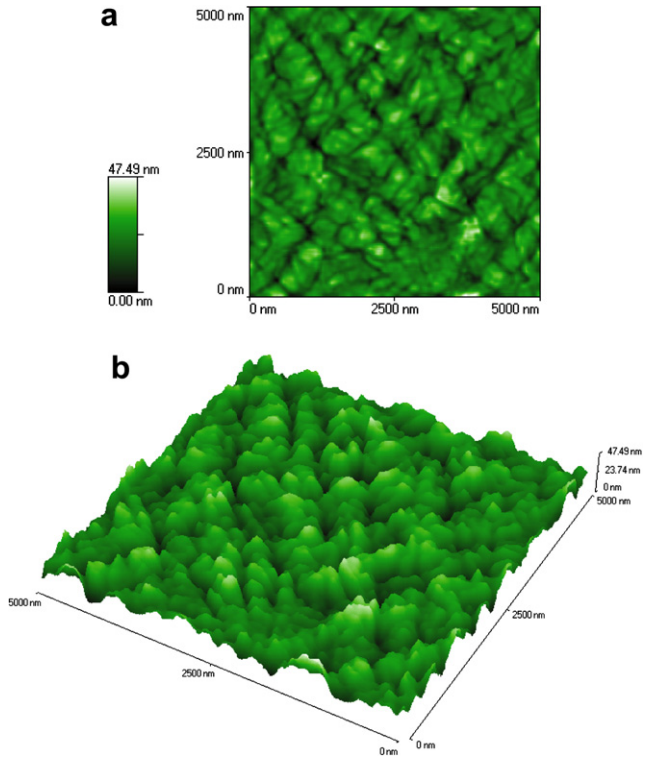


Fig. 2. 5 μm × 5 μm AFM surface pattern of thin film of **4**: (a) 2-D as-deposited and (b) 3-D as-deposited.

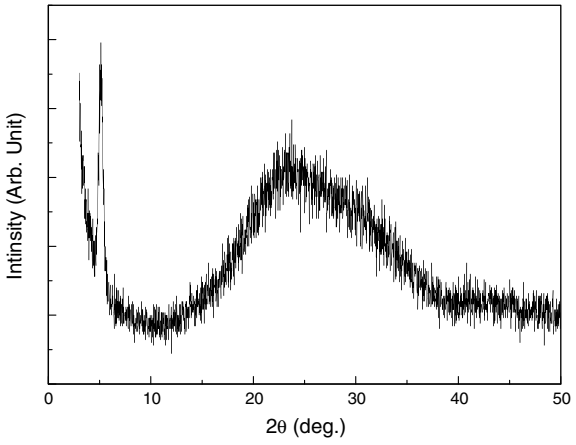


Fig. 3. X-ray diffraction pattern of as-deposited thin film of **4**.

3.4. Optical studies

Fig. 4 shows the UV-near infrared spectral behavior of transmittance $T(\lambda)$ and reflectance $R(\lambda)$ of the as-deposited ZnPc thin film. In Fig. 5, we report the absorption spectra

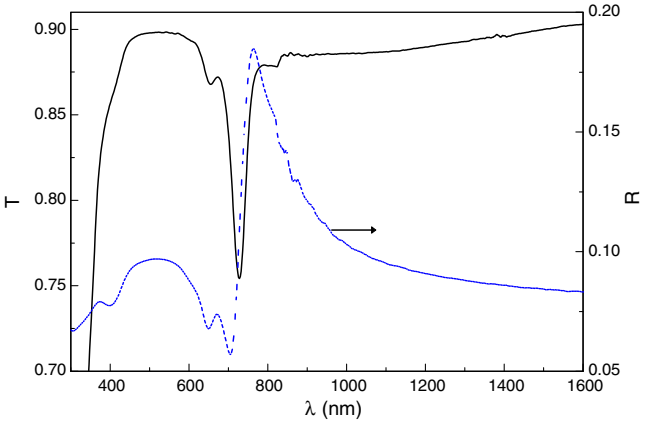


Fig. 4. Spectral behavior of transmittance $T(\lambda)$ and reflectance $R(\lambda)$ of thin film of **4**.

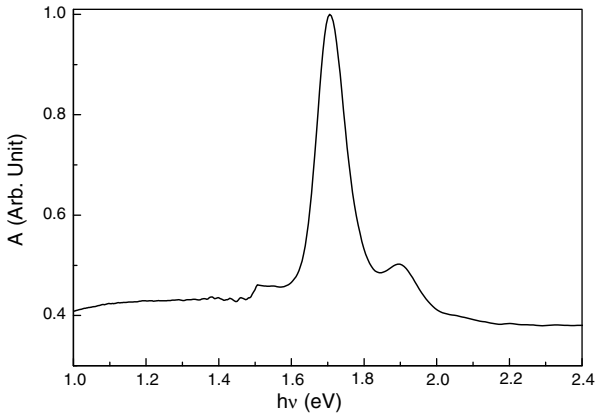


Fig. 5. Spectral distribution of absorbance A (v) of thin film of **4**.

of ZnPc thin film as a function of photon energy, hv. There are two main absorption bands: Q_I at about 728 and Q_{II} at about 655 nm and identified as the Q-band and attributed to the monomer and dimer, respectively [21].

The optical parameters were calculated from the transmission, absorption, and reflectivity data. The average transmission of a thin film on a substrate is given by [20]:

$$T = \frac{(1-R)^2(1+k^2/n^2)}{\exp(\alpha d) - R^2\exp(-\alpha d)} \tag{1}$$

where

$$k = \frac{\alpha\lambda}{4\pi} \tag{2}$$

The parameters α, k, d, n, and λ are the absorption coefficient, absorption index, thin-film thickness, refractive index, and wavelength of the incident light in air, respectively. In any practical experiments, where $k^2 \ll n^2$, the average transmission is simplified as

$$T = \frac{(1-R)^2\exp(-\alpha d)}{1 - R^2\exp(-2\alpha d)} \tag{3}$$

The reflectivity of an absorbing medium of indices n and k in air for normal incidence is given by:

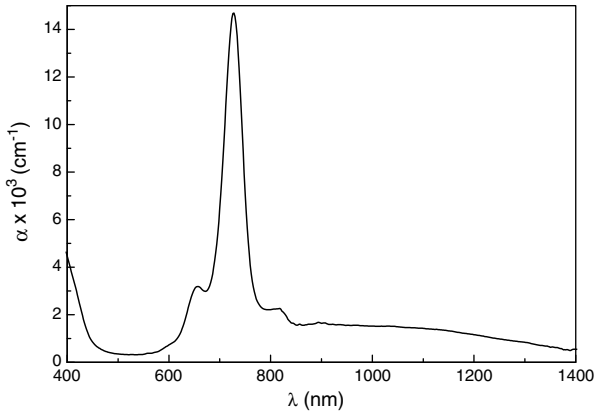


Fig. 6. The variation of absorption coefficient α as a function of wavelength of thin film of **4**.

$$R = \frac{(n-1)^2 + k^2}{(n+1)^2 + k^2} \tag{4}$$

where n is the refractive index.

Using Eqs. (2) and (3), the variation of absorption coefficient, α, with the wavelength was calculated as shown in Fig. 6.

The spectral distribution of refractive index $n(\lambda)$ for **4** in the range 200–2800 nm is shown in Fig. 7. The spectrum shows an anomalous scattering in the range 300–760 nm with various peaks and a normal dispersion in the wavelength range 760–2700 nm. A very high rate of decrease is seen the refractive index in the range of wavelength 760–1400 nm followed by a very low rate of decrease until about 2550 nm whereas the refractive index becomes wavelength-independent. Finally a sudden drop around ~2700 nm occurs.

The variation of absorption coefficient α with photon energy hv and the optical energy gap E_g is obtained from the following formula [20]:

$$\alpha = \alpha_0(hv - E_g)^S \tag{5}$$

where α_0 is a constant

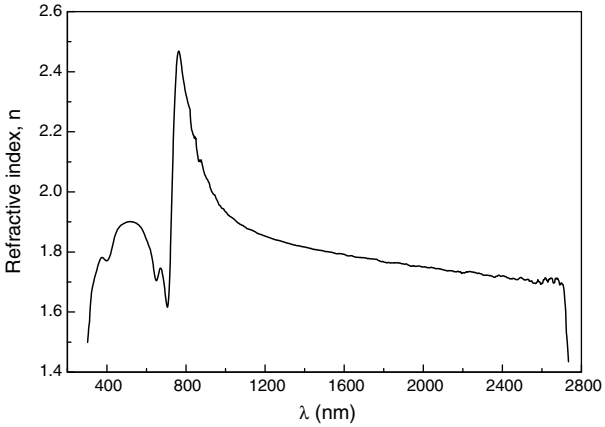


Fig. 7. Spectral distribution of refractive index $n(\lambda)$ of thin film of **4** in the range 200–2800 nm.

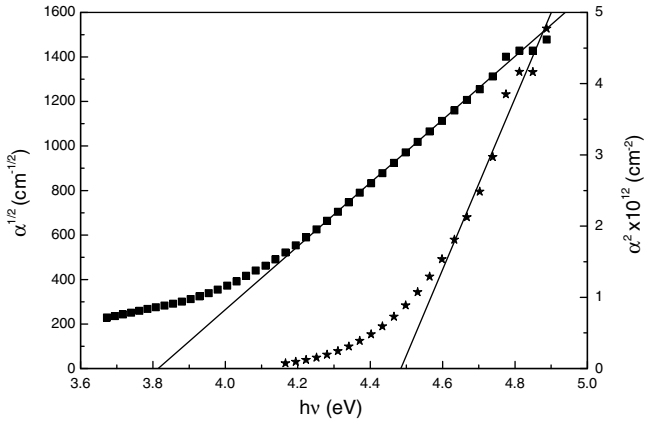


Fig. 8. Variation of $\alpha^{1/2}$ and α^2 with photon energy $h\nu$ of as-deposited thin film of **4**.

The exponent S determines the type of transition and can take the values 1/2, 2, or 3/2 for direct, indirect, and forbidden transitions, respectively [20]. A satisfactory fit was obtained for $\alpha^{1/2}$ and α^2 as a function of $h\nu$, Fig. 8. This indicates that the absorption mechanism is due to both the indirect and direct transitions. The optical band gap of the indirect and direct transitions (E_{gi}, E_{gd}) can be obtained from the intercept of $\alpha^{1/2}$ versus $h\nu$ plots with the energy axis and α^2 versus $h\nu$, respectively (Fig. 8). The results obtained for indirect and direct optical band gaps for the as-deposited **4** thin film were determined as 3.81 and 4.48 eV, respectively.

4. Conclusions

The present work describes the preparation, characterization and spin coated film of novel hexadecachlorinatedphthalocyaninato zinc(II), which have been peripherally substituted with eight chlorinated-phenoxy groups and non-peripherally substituted with eight hexyloxy groups. The synthesized complex possesses excellent solubility in various organic solvents such as CH_2Cl_2, THF, acetone and ethyl acetate.

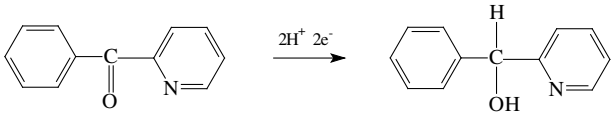
The structure and optical properties of the spin coated ZnPc thin films of thickness about 45–50 nm have been studied. X-ray studies revealed the typical structure of phthalocyanines with the diffraction peak at $2\theta = 5.08°$. Studies using AFM showed that the phthalocyanine molecules are growing in aggregation rows.

The optical properties of the ZnPc thin film were studied in the range 200–2800 nm. The absorption spectra recorded show two main Q-bands: Q_I at about 728 and Q_{II} at about 655 nm. The spectral distribution of refractive index $n(\lambda)$, was obtained. The optical band gap of the indirect and direct transitions were found to be equal to 3.81 and 4.48 eV, respectively.

References

[1] C.C. Leznoff, A.B.P. Lever, Phthalocyanine-Properties and Applications, vol. 3, VCH, New York, 1993.
[2] G. Winter, H. Heckmann, P. Haisch, W. Eberhard, M. Hanack, J. Am. Chem. Soc. 120 (1998) 11663.
[3] Z.L. Yang, H.Z. Chen, L. Cao, H.Y. Li, M. Wang, Mater. Sci. Eng. B 106 (2004) 73.
[4] D.A. Evans, H.J. Steiner, R. Middleton, T.S. Jones, C.H. Chen, K. Horn, S. Park, T.U. Kampen, D. Tenne, D.R.T. Zahn, A. Patchett, I.T. McGovern, Appl. Surf. Sci. 175-176 (2001) 374.
[5] R. Rella, A. Serra, P. Siciliano, A. Tepore, L. Valli, A. Zocco, Supramol. Sci. 4 (1997) 461.
[6] M.J. Cook, J. Mater. Chem. 6 (1996) 677.
[7] B.M. Hassan, H. Li, N.B. McKeown, J. Mater. Chem. 10 (2000) 39.
[8] Z. Ali-Adib, G.J. Clarkson, N.B. McKeown, K.E. Treacher, H.F. Gleeson, A.S. Stennett, J. Mater. Chem. 8 (1998) 2371.
[9] H. Nakahara, K.Z. Sun, K. Fukuda, N. Azuma, H. Nishi, H. Uchida, T. Katsube, J. Mater. Chem. 5 (1995) 395.
[10] T. Kudo, M. Kimura, K. Hanabusa, H. Shirai, T. Sakaguchim, J. Porphyr. Phthalocya. 3 (1999) 65.
[11] R.M. Christie, Dyes Pigments 27 (1995) 35.
[12] N.B. McKeown, Phthalocyanine Materials, Synthesis Structure and Function, Cambridge University Press, 1998.
[13] S.Y. Al-Raqa, Dyes Pigments 77 (2008) 259.
[14] H. Tomoda, S. Saito, S. Ogawa, S. Shiraishi, Chem. Lett. (1980) 1277.
[15] S.Y. Al-Raqa, J. Porphyr. Phthalocya. 10 (2006) 55.
[16] S. Wie, D. Huang, L. Li, Q. Meng, Dyes Pigments 56 (2003) 1.
[17] R. Hiesgen, M. Rabisch, H. Bottcher, D. Meissner, Solar Energy Mater. Solar Cell 61 (2000) 73.
[18] S. Zhu, C.E. Banks, D.O. Frazier, B. Penn, H. Abdeldayem, R. Hicks, H.D. Burns, G.W. Thompson, J. Crystal Growth 211 (2000) 308.
[19] M.J. Cook, I. Chambrier, in: K.M. Kadish, K.M. Smith, R. Guilard (Eds.), Phthalocyanine Thin Films: Deposition and Structural Studies, The Porphyrin Handbook, vol. 17, Academic Press, 2003.
[20] S.N. Alamri, A.A. Joraid, S.Y. Al-Raqa, Thin Solid Films 510 (2006) 265.
[21] R. Rella, J. Spadavecchia, G. Ciccarella, P. Siciliano, G. Vasapollo, L. Valli, Sensors Actuators B 89 (2003) 86.

through the N–O chelating site. This coordination produces a five-membered ring containing an unsaturated α-iminoketo function which can act as a π acceptor towards a bound π electron-rich metal center. The α-iminoketo chelation plays an important role in the biosynthesis of the pterins, lumazines, and flavins coenzymes [9,10]. This type coordination has been confirmed for $[ReCl(CO)_3(bopy)]$ complex [11], whereas in the examined structures two-electron reduced form is coordinated to the central ion.



Here we present synthesis, spectroscopic data and X-ray structures of $[ReOCl_2(bopyH)(PPh_3)]$ (**1**) and $[ReOBr_2(bopyH)(PPh_3)]$ (**2**). In addition, the paper includes density functional theory (DFT) and time-dependent DFT (TD-DFT) calculations for chloride complex. Recently, the electronic structures of nitrido, oxo, carbonyl, nitrosyl and nitrile rhenium complexes, as well as their spectroscopic properties, bonding and reactivity have been theoretically studied at the HF, MP2, EHT and DFT levels of theory using various basis sets [12–20]. Gancheff and co-workers [14] have performed extended tests of the ability of the B3LYP method in LANL2DZ basis set for rhenium compounds in a geometry optimization and calculation of spectral properties. Although this is not a very extended basis set, its use with DFT has shown to be sufficient for the geometry optimization and calculation of spectral properties. The correctness of B3LYP method with LANL2DZ basis set for rhenium complexes has been also proven in this paper. The experimental geometry of **1** is well reproduced and the calculated electronic spectrum is in good accordance with the experimental one.

2. Experimental

2.1. General procedure

All the reagents used to the synthesis were commercially available and were used without further purification. The $[ReOX_3(PPh_3)_2]$ (X = Cl, Br) complexes were prepared according to the literature methods [21].

IR spectra were recorded on a Nicolet Magna 560 spectrophotometer in the spectral range 4000–400 cm^{-1} with the samples in the form of KBr pellets. Electronic spectra were measured on a spectrophotometer Lab Alliance UV–Vis 8500 in the range 1000–200 nm in acetonirile solution. ^1H NMR spectrum was obtained in $CDCl_3$ using Bruker Avance 400 spectrometer. Elemental analyses (CHN) were performed on a Perkin–Elmer CHN-2400 analyzer.

2.2. Preparation of $[ReOCl_2(bopyH)(PPh_3)]$

A mixture of $[ReOCl_3(PPh_3)_2]$ (0.50 g, 0.6 mmol), benzoylpyridine (0.15 g, 0.8 mmol), ethanol (80 ml) and two drops of concentrated HCl was refluxed for 5 h. The blue-violet solution was cooled and left to slow evaporation. The violet crystals that formed were filtered and recrystallized from slow evaporation of an acetonitrile solution. Yield 75%.

IR (KBr; ν/cm^{-1}): 1600 (m), 1567 (w) ν_{CN} and $\nu_{C=C}$; 945 (vs) $\nu_{Re=O}$.

^1H NMR (400 MHz; $CDCl_3$) $\delta = 4.72$ (s, 1H), 6.70 (d, 1H), 7.22–752 (m, 20H), 7.69 (br, 2H), 8.25 (d, 1H).

Anal. Calc. for $C_{30}H_{25}Cl_2NO_2PRe$: C, 50.07; H, 3.50; N, 1.95. Found: C, 50.85; H, 3.73; N, 1.77%.

2.3. Preparation of $[ReOBr_2(bopyH)(PPh_3)]$

A procedure similar to that for $[ReOCl_2(bopyH)(PPh_3)]$ was used with $[ReOBr_3(PPh_3)_2]$ (0.5 g, 0.52 mmol), benzoylpyridine (0.14 g, 0.76 mmol) and two drops of HBr. Crystalline violet precipitate of $[ReOBr_2(bopyH)(PPh_3)]$ was collected in 80% yield.

IR (KBr; ν/cm^{-1}): 1599 (m), 1571 (w) ν_{CN} and $\nu_{C=C}$; 945 (vs) $\nu_{Re=O}$.

Anal. Calc. for $C_{30}H_{25}Br_2NO_2PRe$: C, 44.57; H, 3.12; N, 1.73. Found: C, 44.18; H, 3.25; N, 1.89%.

2.4. Crystal structures determination and refinement

The X-ray intensity data of $[ReOX_2(bopyH)(PPh_3)]$ (X = Cl, Br) were collected on a KM-4-CCD automatic diffractometer equipped with CCD detector and graphite monochromated Mo Kα radiation ($\lambda = 0.71073$ Å). Details concerning crystal data and refinement are given in Table 1. Lorentz, polarization and absorption correction [22,22] were applied. The structures were solved by the Patterson method and subsequently completed by the difference Fourier recycling. All the non-hydrogen atoms were refined anisotropically using full-matrix, least-squares technique. The hydrogen atoms were treated as "riding" on their parent carbon atoms and assigned isotropic temperature factors equal 1.2 times the value of equivalent temperature factor of the parent atom. SHELXS97 [23], SHELXL97 [24] and SHELXTL [25] programs were used for all the calculations. Atomic scattering factors were those incorporated in the computer programs.

2.5. Magnetic measurements

The magnetic measurements of the powdered samples were measured over the temperature range 1,8–300 K using a quantum design SQUID-based MPMSXL-5-type magnetometer. The superconducting magnet was generally operated at a field strength ranging from 0 to 5 T. Measurements of a sample of the compound were made at a magnetic field of 0.5 T.

The SQUID magnetometer was calibrated with the palladium rod sample (Materials research corporation, measured purity 99.9985%). Corrections are based on subtracting the sample-holder signal.

Table 1
Crystal data and structure refinement for $[ReOX_2(bopyH)(PPh_3)]$ complexes

	1	2
Empirical formula	$C_{30}H_{25}Cl_2NO_2PRe$	$C_{30}H_{25}Br_2NO_2PRe$
Formula weight	719.58	808.50
Temperature (K)		291.0(3) K
Wavelength		0.71073 Å
Crystal system	Monoclinic	
Space group	$P2_1/n$	
Unit cell dimensions		
a (Å)	17.3226(9)	7.6094(9)
b (Å)	8.8066(4)	8.9241(3)
c (Å)	19.5869(12)	19.3411(12)
β (°)	112.643(6)	112.292(7)
Volume (Å^3)	2757.7(3)	2812.3(2)
Z		4
$F(000)$	1408	1552
D_{calc} (Mg/m^3)	1.733	1.910
Absorption coefficient (mm^{-1})	4.687	7.248
Crystal size (mm)	0.020 × 0.023 × 0.027	0.02 × 0.08 × 0.20
Transmission factors (min., max.)	0.887, 0.909	0.487, 0.860
θ Range for data collection (°)	2.00–25.05	3.02–25.00
Index ranges	$-20 \leqslant h \leqslant 20$ $-9 \leqslant k \leqslant 10$ $-23 \leqslant l \leqslant 23$	$-20 \leqslant h \leqslant 19$ $-10 \leqslant k \leqslant 8$ $-20 \leqslant l \leqslant 23$
Reflections collected	26 204	17 171
Independent reflections (R_{int})	4894 (0.0751)	4931 (0.0275)
Completeness to $2\theta = 50°$ (%)	100	99.5
Data/restraints/parameters	4894/0/334	4931/0/334
Goodness-of-fit on F^2	1.143	0.969
Final R indices [$I > 2\sigma(I)$]	$R_1 = 0.0420$ $wR_2 = 0.1168$	$R_1 = 0.0227$ $wR_2 = 0.0511$
R indices (all data)	$R_1 = 0.0545$ $wR_2 = 0.1296$	$R_1 = 0.0349$ $wR_2 = 0.0528$
Largest difference peak and hole (e Å^{-3})	2.986 and −2.234	0.765 and −0.844

2.6. Computational details

The gas phase geometry of **1** was optimized without any symmetry restrictions in the singlet ground-state with the DFT method using the hybrid B3LYP functional of GAUSSIAN-03 [26–28]. The calculations were performed by using ECP basis set on the rhenium atom, the standard 6-31+G** basis for chlorine, phosphorous, oxygen and nitrogen, 6-31G* for carbon and 6-31G for hydrogen atoms [29,30]. The Xe core electrons of Re were replaced by an effective core potential and DZ quality Hay and Wadt Los Alamos ECP basis set (LANL2DZ) [31] was used for the valence electrons. Additional d function with exponent $\alpha = 0.3811$ and f function with exponent $\alpha = 2.033$ on the rhenium atom were added [32]. All vibrations in the calculated vibrational spectrum of **1** were real thus the geometry structure was a true energy minimum.

The electronic spectrum of **1** was calculated with the TDDFT method, and the solvent effect was simulated using the polarizable continuum model with the integral equation formalism (IEF-PCM) [33].

Natural bond orbital (NBO) calculations were performed with the NBO code [34,35] included in GAUSSIAN03.

3. Results and discussion

3.1. Preparation and infrared data

The $[ReOX_2(bopyH)(PPh_3)]$ (X = Cl, Br) complexes were prepared by refluxing of $[ReOX_3(PPh_3)_2]$ with a small excess of benzoylpyridine in ethanol. In the both structures two-electron reduced form of benzoylpyridine is coordinated to the central ion. Addition of two drops of HX acid allows obtaining the title complexes in higher yield.

The strong ν(Re=O) stretching bands of the $[ReOX_2(bopyH)(PPh_3)]$ compounds are found in at ~945 cm^{-1}, at a relatively high wavenumber, which suggests that the Re–hydroxy bond *trans* to the oxo ligand does not compete effectively for the Re_d orbitals and indicates the presence of the {O=Re–O} structural subunit in the examined structures.

3.2. Crystal structures

The both complexes are isostructural, they crystallise in the monoclinic space group $P2_1/n$ and their structures consist of discrete and well-separated monomers.

The molecular structure of **1** is presented in Fig. 1 and the selected bond distances and angles of $[ReOX_2(bopyH)(PPh_3)]$ (X = Cl, Br) complexes are collected in Tables 2 and 3, respectively.

The geometry of $[ReOX_2(bopyH)(PPh_3)]$ compounds reveals typical features of quasi-octahedral oxorhenium(V)complexes with oxygenated bidentate ligands. In the both complexes, the rhenium atom is coordinated by a terminal oxygen atom (O_t), two halide ions in *cis* arrangement, the phosphorus atom from PPh_3 molecule, and the bidentate N, O donors of the reduced form of benzoylpyridine. The oxygen atom of the bopyH occupies *trans* position to the terminal oxo ion. The deformation of the octahedron is caused by the presence multiple bonding ligand (terminal oxo) and narrow bite angle of the chelating ligand. The high concentration of electronic density along the Re–O_t axis strongly influences the positions of the adjacent halogen atoms, which are pushed away.

For complex **1** the rhenium atom is displaced 0.1804(16) Å from the equatorial plane formed by the two chlorine, one nitrogen and one phosphorous atoms (plane A) and 0.0001(23) and 0.1222(19) Å from the axial planes formed respectively by the two oxygen, one chlorine and one nitrogen atoms (plane B) and two oxygen, one chlorine and one phosphorous atoms (plane C). Least squares plane A is inclined at 88.10(13)° to plane B and at 89.89(13)° to plane C. Planes B and C are inclined at 88.24(9)°. These values for bromide analogue are,

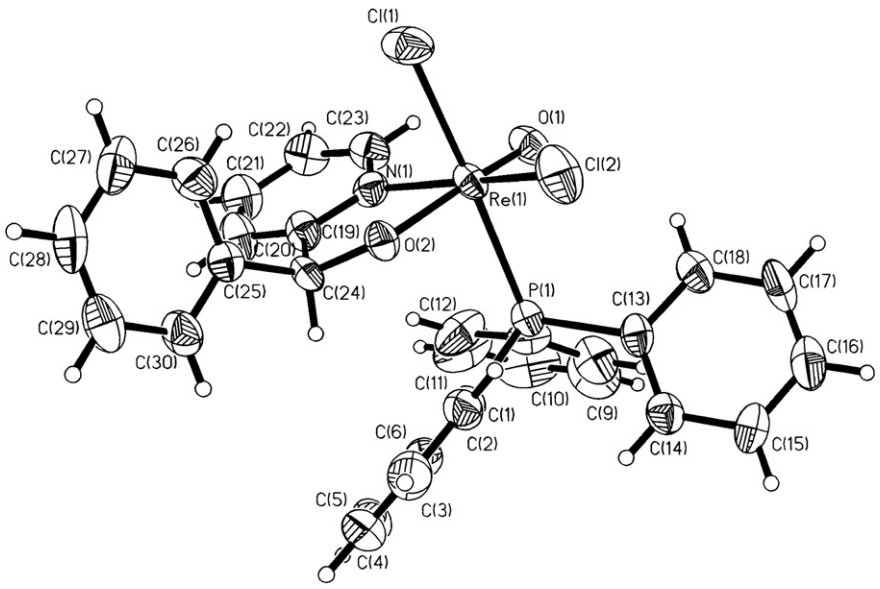


Fig. 1. The molecular structure of **1**. Displacement ellipsoids are drawn at 50% probability.

respectively, 0.1787(9), 0.0101(12) and 0.1299(9) Å, 88.35(7)°, 89.90(6)° and 89.90(4)°.

In compound **1**, the planar in the experimental error pyridine and phenyl rings are inclined at 81.1(2)° and the spacer C(24) atom derive 0.054(11) and 0.052(12) Å, respectively, from these planes. These values in **2** are, respectively, 82.26(12)°, 0.025(6) and 0.069(6) Å.

The Re–O_t bond lengths fall in the range 1.639–1.76 Å, which is typical of mononuclear complexes of rhenium(V) having $[ReO]^{3+}$ core, and indicates the presence of a triple bond Re≡O [36]. The interatomic distance between the rhenium atom and the oxygen atom of bopyH in *trans* position to the terminal oxo ion, is only somewhat shorter than an ideal single Re–O bond length (*ca.* 2.04 Å) [37]. It indicates small delocalization in the O(2)–Re(1)–O(1) moiety. The similar trend is observed for many Re(V)-oxo complexes with an monoanionic oxygen *trans* to the oxo

Table 3
The experimental bond lengths (Å) and angles (°) for **2**

Bond lengths	Experimental	Bond angles	Experimental
Re(1)–O(1)	1.684(3)	O(1)–Re(1)–O(2)	162.75(11)
Re(1)–O(2)	1.921(2)	O(1)–Re(1)–N(1)	89.95(12)
Re(1)–N(1)	2.155(3)	O(2)–Re(1)–N(1)	74.75(11)
Re(1)–Br(1)	2.5585(5)	O(1)–Re(1)–Br(2)	105.15(9)
Re(1)–Br(2)	2.4918(5)	O(2)–Re(1)–Br(2)	90.96(7)
Re(1)–P(1)	2.4780(11)	N(1)–Re(1)–Br(2)	163.90(8)
		O(1)–Re(1)–Br(1)	96.04(10)
		O(2)–Re(1)–Br(1)	90.38(8)
		N(1)–Re(1)–Br(1)	84.10(8)
		Br(2)–Re(1)–Br(1)	88.702(19)
		O(1)–Re(1)–P(1)	86.84(10)
		O(2)–Re(1)–P(1)	86.60(8)
		N(1)–Re(1)–P(1)	94.98(8)
		Br(2)–Re(1)–P(1)	91.46(3)
		Br(1)–Re(1)–P(1)	176.97(3)

Table 2
The selected experimental and optimized bond lengths (Å), bond angles (°) for **1**

Bond lengths	Experimental	Optimized	Bond angles	Experimental	Optimized
Re(1)–O(1)	1.697(5)	1.694	O(1)–Re(1)–O(2)	162.4(2)	159.22
Re(1)–O(2)	1.921(4)	1.944	O(1)–Re(1)–N(1)	89.5(2)	87.11
Re(1)–N(1)	2.146(6)	2.173	O(2)–Re(1)–N(1)	75.0(2)	74.54
Re(1)–Cl(1)	2.4198(19)	2.471	O(1)–Re(1)–Cl(2)	105.76(19)	105.53
Re(1)–Cl(2)	2.355(2)	2.409	O(2)–Re(1)–Cl(2)	90.53(15)	93.58
Re(1)–P(1)	2.4760(18)	2.544	N(1)–Re(1)–Cl(2)	163.98(15)	166.79
			O(1)–Re(1)–Cl(1)	96.64(19)	97.28
			O(2)–Re(1)–Cl(1)	90.06(15)	90.73
			N(1)–Re(1)–Cl(1)	84.41(16)	84.62
			Cl(2)–Re(1)–Cl(1)	88.89(8)	89.87
			O(1)–Re(1)–P(1)	86.83(18)	85.51
			O(2)–Re(1)–P(1)	86.59(15)	86.83
			N(1)–Re(1)–P(1)	95.57(15)	96.16
			Cl(2)–Re(1)–P(1)	90.25(7)	88.78
			Cl(1)–Re(1)–P(1)	176.54(6)	177.14

group [38]. The Re1–X(1) distances *trans* to the phosphorus atom of the triphenylphosphine molecule are slightly longer than the Re1–X(2) bonds *trans* to the nitrogen atom of the bopyH ligand. It is a consequence of structural *trans* effect of the PPh_3 ligands.

3.3. Geometry optimisation, charge distribution and NBO analysis

Complex **1** indicated diamagnetic properties in the whole measuring temperature range from values $-0.60 \times 10^{-6}\,cm^3\,g^{-1}$ at 1.8 K to $-0.32 \times 10^{-6}\,cm^3\,g^{-1}$ at 300 K. The geometry of **1** was optimised in a singlet state by the DFT method with the B3LYP functional. The optimized geometric parameters of **1** are gathered in Table 2. In general, the predicted bond lengths and angles are in agreement with the values based upon the X-ray crystal structure data, and the general trends observed in the experimental data are well reproduced in the calculations.

Table 4 presents the atomic charges from the Natural Population Analysis (NPA) for **1**. The calculated charge on the rhenium atom is considerable lower than the formal charge +5, corresponding d^2 configuration of the central ion. It results from significant charge donation from the ligands. The charges on the terminal oxo, chloride and oxygen atom of bopyH are significantly smaller than −2, −1 and −1, respectively. The terminal oxo ion is less negative in comparison with the oxygen atom of bopyH ligand. It indicates the higher electron density delocalization from the O_t ligand towards the central ion and corresponds to differences in the Re–O_{hydoxy} and Re–$O_{terminal}$ bonds lengths.

The nature of rhenium–terminal oxygen interaction in **1** has been studied by NBO analysis. The occupancy and composition of the calculated Re–O_t natural bond orbitals (NBOs) are given in Table 5. Each natural bond orbital (NBO) σ_{AB} can be written in terms of two directed valence hybrids (NHOs) h_A and h_B on atoms A and B:

$$\sigma_{AB} = c_A h_A + c_B h_B$$

where c_A and c_B are polarization coefficients. Each valence bonding NBO must in turn be paired with a corresponding valence *anti*-bonding NBO:

$$\sigma^*_{AB} = c_B h_A - c_A h_B$$

to complete the span of the valence space. The Lewis-type (donor) NBOs are thereby complemented by the non-Lewis-type (acceptor) NBOs that are formally empty in an idealized Lewis picture. The interactions between 'filled' Lewis-type NBOs and 'empty' non-Lewis NBOs lead to loss of occupancy from the localized NBOs of the idealized Lewis structure into the empty non-Lewis orbitals, and they are referred to as 'delocalization' corrections to the zeroth-order natural Lewis structure [34,35].

The detected natural Re–O_t bond orbitals of **1** are π orbitals – the p_x and p_y oxygen orbitals and d_{xz} and d_{yz} rhenium orbitals are involved in their formation. Not detected $\sigma_{Re–Ot}$ bond has character of predominant Coulomb-type interactions between the central ion and ligands [39]. The

Table 4
Atomic charges from the Natural Population Analysis (NPA) for **1**

Atom	Charge
Re(1)	1.046
O(1)	−0.489
O(2)	−0.686
N(1)	−0.479
P(1)	1.273
Cl(1)	−0.469
Cl(2)	−0.392

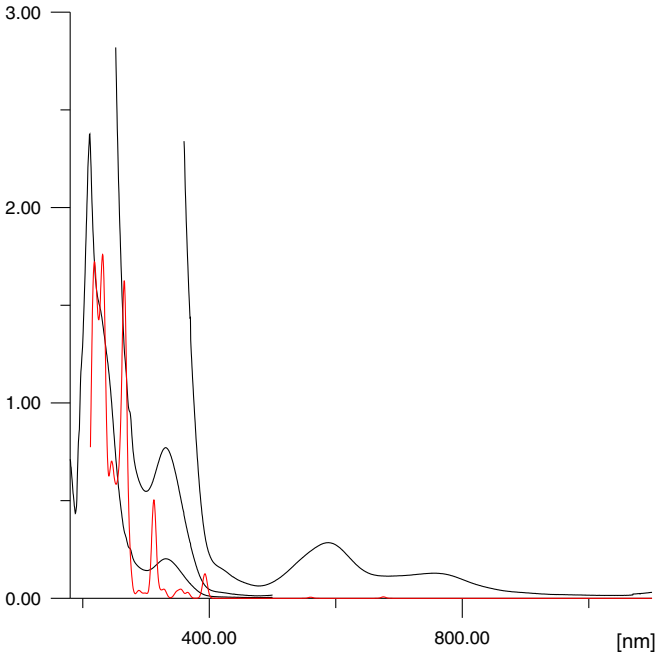


Fig. 2. The experimental (black) and calculated (red) electronic absorption spectra of **1**. (For interpretation of the references to colour in this figure legend, the reader is referred to the web version of this article.)

Table 5
The occupancy of the calculated natural bond orbitals (NBOs) between the rhenium and the oxo ligand for **1**

BD	Occupancy	Composition of NBO	BD[a]	Occupancy
Re–O_t	1.988	$0.564(d)_{Re} + 0.826(p)_O$	$0.826(d)_{Re} - 0.564(p)_O$	0.294
Re–O_t	1.986	$0.573(d)_{Re} + 0.819(p)_O$	$0.819(d)_{Re} - 0.573(p)_O$	0.317

BD denotes 2-center bond.
[a] Antibond NBO.

terminal oxo ligand of **1** has two lone pair orbitals, and electron density from one of them is strongly delocalized into non-Lewis rhenium orbital. Accordingly, NBO analysis confirms a triple bond between the rhenium and the terminal oxygen ligand.

3.4. Electronic spectra

The experimental and calculated electronic spectra of **1** are presented in Fig. 2. Each calculated transition is represented by a gaussian function $y = ce^{-bx^2}$ with the height (c) equal to the oscillator strength and b equal to 0.04 nm^{-2}. In general, the electronic spectrum of **1** is well reproduced by the calculations. Some shifts between the experimental and calculated absorption bands may come from the basis sets which are approximated to a certain extent.

The shape of the UV–Vis spectrum of **2** is the same as for the chloride analogue; the absorption bands of the bromide complex were recorded at 746.0, 607.0, 332.5, 249.5 and 208.0 nm.

Table 6 presents the most important electronic transitions calculated with the TDDFT method assigned to the observed absorption bands of **1**. The assignment of the calculated orbital excitations to the experimental bands was based on an overview of the contour plots and relative energy to the orbitals HOMO and LUMO involved in the electronic transitions. Contour plots and energy of the selected HOMO and LUMO orbitals active in the electronic transitions are depicted in Fig. 3.

The TDDFT/PCM calculations show that the two longest wavelength experimental bands of **1** at 767.0 and 589.5 nm originate in the HOMO → LUMO and HOMO → LUMO + 1 transitions, respectively. As d_{Re} orbitals take main part in the HOMO, LUMO and LUMO + 1 orbitals, the HOMO → LUMO and HOMO → LUMO + 1 transitions may be attributed to the transitions of d → d character. However, as it can be seen from Fig. 3, the HOMO, LUMO and LUMO + 1 orbitals are delocalized among rhenium ion, chloride, oxo and bopyH ligands so a delocalized MLLCT (metal–ligand-to-ligand CT) description also can be used.

The absorption band at 330.5 nm can be related to a metal-to-bopyH ligand charge transfer (MLCT) with a certain contribution of ligand–metal charge transfer (π_{PPh3}/π_{bopyH}/π_{Cl} → d) transitions.

The experimental bands below 300 nm result mainly from ligand–ligand charge transfer and interligand (IL) transitions.

Table 6
The energy and molar absorption coefficients of experimental absorption bands and the electronic transitions calculated with the TDDFT method for **1**

The most important orbital excitations	Character	λ (nm)	E (eV)	f	Experimental Λ (nm) (E (eV)) ε
H → L	d → d	675.4	1.84	0.0012	767.0 (1.62) 190
H → L + 1	d → d	560.2	2.21	0.0009	589.5 (2.07) 435
H-1 → L	π(bopyH)/n(PPh_3) → d	393.7	3.15	0.0154	330.5 (3.75) 5880
H → L + 3	d → d/π*(bopyH)	391.4	3.17	0.0064	
H-1 → L + 1	π(bopyH)/n(PPh_3) → d	355.9	3.48	0.0064	
H-10 → L	π(Cl) → d	313.2	3.96	0.0134	
H-8 → L	π(PPh_3) → d				
H → L + 2	d → d/π*(bopyH)	312.2	3.97	0.0671	
H-1 → L + 2	π(bopyH)/n(PPh_3) → d/π*(bopyH)	269.8	4.60	0.0248	260.0 (4.77) 65200
H → L + 6	d → π*(PPh_3)/π*(bopyH)	266.5	4.65	0.0208	
H-1 → L + 3	π(bopyH)/n(PPh_3) → d/π*(bopyH)	266.6	4.67	0.2147	
H-4 → L + 3	π(PPh_3) → d/π*(bopyH)	254.4	4.87	0.0404	
H-1 → L + 4	π(bopyH)/n(PPh_3) → π*(PPh_3)	244.1	5.08	0.0397	
H-2 → L + 5	π(PPh_3)/π(bopyH) → π*(bopyH)	234.7	5.28	0.0393	211.0 (5.88) 91065
H-9 → L + 3	π(bopyH)/π(Cl) → d/π*(bopyH)				
H-9 → L + 3	π(bopyH)/π(Cl) → d/π*(bopyH)	233.7	5.31	0.0347	
H-8 → L + 2	π(PPh_3) → d/π*(bopyH)				
H-3 → L + 5	π(bopyH) → π*(bopyH)	232.3	5.34	*0.0526*	
H-10 → L + 3	π(Cl) → d/π*(bopyH)	231.8	5.35	0.0358	
H-6 → L + 4	π(PPh_3) → π*(PPh_3)	229.3	5.41	0.0306	
H → L + 11	d → π*(PPh_3)				
H-12 → L + 2	π(Cl)/π(bopyH) → d/π*(bopyH)	223.7	5.54	0.0412	
H-1 → L + 7	π(bopyH)/n(PPh_3) → π*(PPh_3)	220.9	5.61	0.0412	
H-11 → L + 2	π(Cl)/π(bopyH)/π(O_t) → d/π*(bopyH)	217.3	5.71	0.0600	
H-12 → L + 3	π(Cl)/π(bopyH) → d/π*(bopyH)	216.9	5.72	0.0368	
H-1 → L + 7	π(bopyH)/n(PPh_3) → π*(PPh_3)	215.3	5.76	0.0581	

ε – molar absorption coefficient ($dm^3\ mol^{-1}\ cm^{-1}$).
f – oscillator strength.
H – highest occupied molecular orbital.
L – lowest unoccupied molecular orbital.

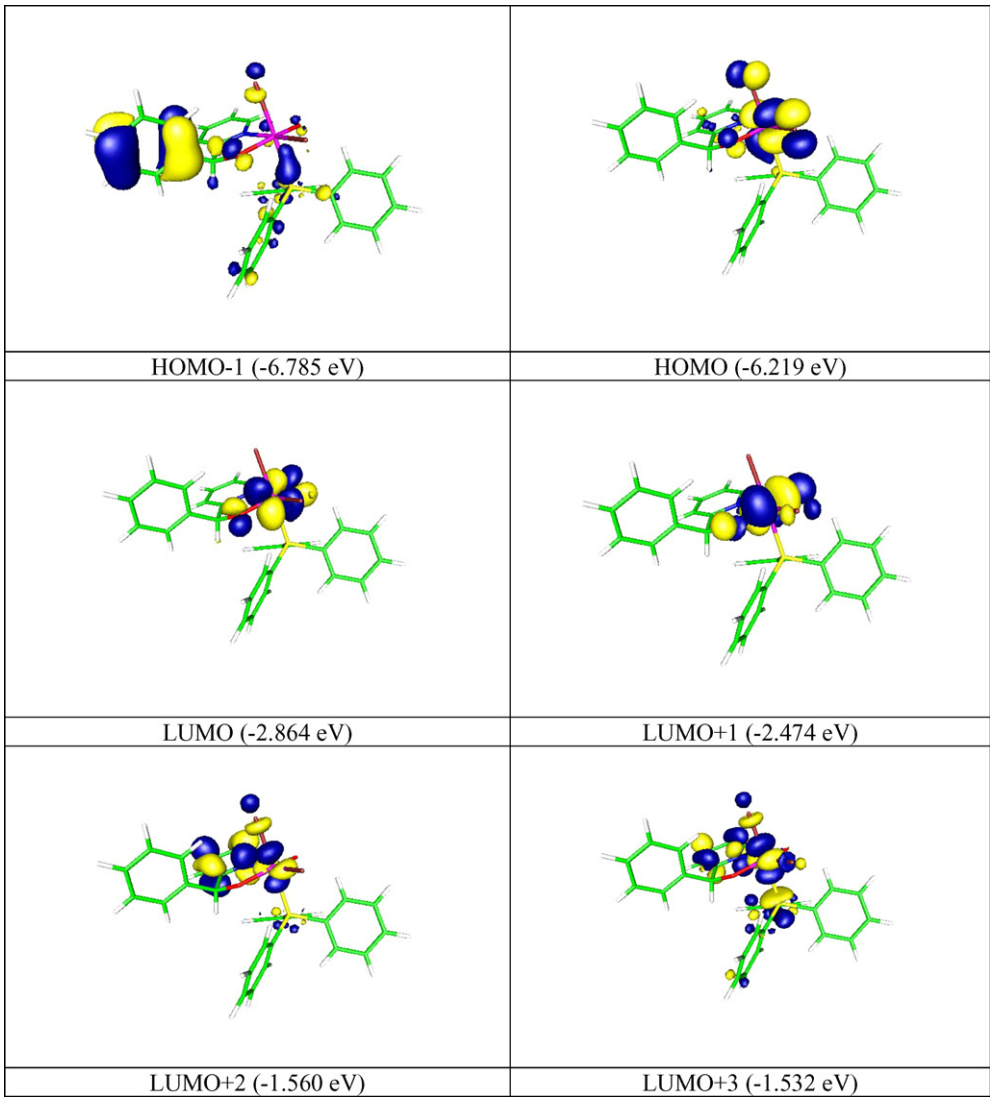


Fig. 3. Contour plots and energy of the selected HOMO and LUMO orbitals active in the electronic transitions. The orbitals were plotted with contour values −0.04 (yellow) and 0.04 au (blue) and referred to the *z*-axis along the O–Re–O linkage, and *x*-axis – through the N(2)–Re–Cl(2) bonds. (For interpretation of the references to colour in this figure legend, the reader is referred to the web version of this article.)

Supplementary data

CCDC 668975 and 668976 contain the supplementary crystallographic data for $C_{30}H_{25}Br_2NO_2PRe$ and $C_{30}H_{25}Cl_2NO_2PRe$. These data can be obtained free of charge via http://www.ccdc.cam.ac.uk/conts/retrieving.html, or from the Cambridge Crystallographic Data Centre, 12 Union Road, Cambridge CB2 1EZ, UK; fax: (+44) 1223-336-033, or e-mail: deposit@ccdc.cam.ac.uk.

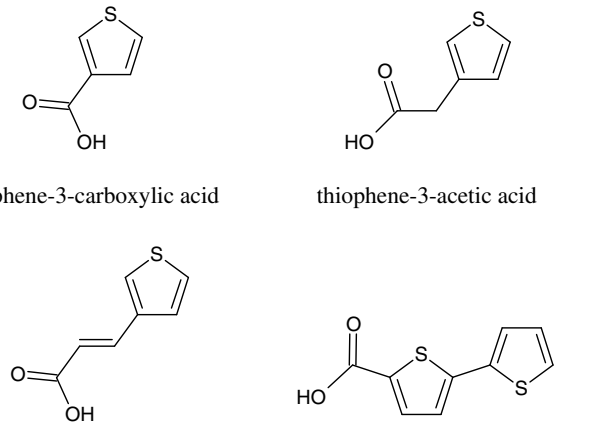
Acknowledgement

The GAUSSIAN03 calculations were carried out in the Wrocław Centre for Networking and Supercomputing, WCSS, Wrocław, Poland.

References

[1] C.C. Romão, F.E. Kühn, W.A. Hermann, Chem. Rev. 97 (1997) 3197.
[2] A.A. Shteinman, Russ. Chem. Bull., Int. Ed. 50 (2001) 1795.
[3] F.E. Kühn, A. Scherbaum, W.A. Herrmann, J. Organomet. Chem. 689 (2004) 4149.
[4] G.S. Owens, J. Arias, M.M. Abu-Omar, Catal. Today 55 (2000) 317.
[5] A.M. Kirillov, M. Haukka, M.V. Kirillova, A.J.L. Pombeiro, Adv. Synth. Catal. 347 (2005) 1435.
[6] A. Deloffre, S. Halut, L. Salles, J.-M. Brégeault, J.R. Gregorio, B. Denise, H. Rudler, J. Chem. Soc., Dalton Trans. (1999) 2897.
[7] J.R. Dilworth, S.J. Parrott, Chem. Soc. Rev. 27 (1998) 43.
[8] P. Blower, Dalton Trans. (2006) 1705.
[9] W. Kaim, B. Schwederski, O. Heilmann, F.M. Hornung, Coord. Chem. Rev. 182 (1999) 323.
[10] S.B. Jiménez-Pulido, M. Sieger, A. Knödler, O. Heilmann, M. Wanner, B. Schwederski, J. Fiedler, M.N. Moreno-Carretero, W. Kaim, Inorg. Chim. Acta 325 (2001) 65.

[11] B. Machura, R. Kruszynski, J. Organomet. Chem. 692 (2007) 4161.
[12] A. Voigt, U. Abram, R. Böttcher, U. Richter, J. Reinhold, R. Kirmse, Chem. Phys. 253 (2000) 171.
[13] M. Lipowska, L. Hansen, R. Cini, X. Xu, H. Choi, A.T. Taylor, L.G. Marzilli, Inorg. Chim. Acta 339 (2002) 327.
[14] J. Gancheff, C. Kremer, E. Kremer, O.N. Ventura, J. Mol. Struct. (Theochem) 580 (2002) 107.
[15] M.L. Kuznestov, E.A. Klestova-Nadeeva, A.I. Dement'ev, J. Mol. Struct. (Theochem) 671 (2004) 229.
[16] N. Psaroudakis, K. Mertis, D.G. Liakos, E.D. Simandiras, Chem. Phys. Lett. 369 (2003) 490.
[17] X.-Y. Liu, S. Bouherour, H. Jacobsen, H.W. Schmalle, H. Berke, Inorg. Chim. Acta 330 (2002) 250.
[18] É. Bencze, J. Mink, I. Pápai, I.S. Butler, D. Lafleur, D.F.R. Gilson, J. Organomet. Chem. 616 (2000) 1.
[19] W.-Y. Wong, S.-H. Cheung, X. Huang, Z. Lin, J. Organomet. Chem. 655 (2002) 39.
[20] B. Machura, R. Kruszynski, Polyhedron 25 (2006) 1985.
[21] G. Rouschias, G. Wilkinson, J. Chem. Soc. A (1966) 465.
[22] CrysAlis Red, Oxford Diffraction Ltd., Version 1.171.29.2.
[23] G.M. Sheldrick, Acta Crystallogr., Sect. A 46 (1990) 467.
[24] G.M. Sheldrick, SHELXL97. Program for the Refinement of Crystal Structures, University of Göttingen, Germany, 1997.
[25] G.M. Sheldrick, SHELXTL: release 4.1 for Siemens Crystallographic Research Systems, 1990.
[26] GAUSSIAN 03, Revision B.03, M.J. Frisch, G.W. Trucks, H.B. Schlegel, G.E. Scuseria, M.A. Robb, J.R. Cheeseman, J.A. Montgomery, Jr., T. Vreven, K.N. Kudin, J.C. Burant, J.M. Millam, S.S. Iyengar, J. Tomasi, V. Barone, B. Mennucci, M. Cossi, G. Scalmani, N. Rega, G.A. Petersson, H. Nakatsuji, M. Hada, M. Ehara, K. Toyota, R. Fukuda, J. Hasegawa, M. Ishida, T. Nakajima, Y. Honda, O. Kitao, H. Nakai, M. Klene, X. Li, J.E. Knox, H.P. Hratchian, J.B. Cross, C. Adamo, J. Jaramillo, R. Gomperts, R.E. Stratmann, O. Yazyev, A.J. Austin, R. Cammi, C. Pomelli, J.W. Ochterski, P.Y. Ayala, K. Morokuma, G.A. Voth, P. Salvador, J.J. Dannenberg, V.G. Zakrzewski, S. Dapprich, A.D. Daniels, M.C. Strain, O. Farkas, D.K. Malick, A.D. Rabuck, K. Raghavachari, J.B. Foresman, J.V. Ortiz, Q. Cui, A.G. Baboul, S. Clifford, J. Cioslowski, B.B. Stefanov, G. Liu, A. Liashenko, P. Piskorz, I. Komaromi, R.L. Martin, D.J. Fox, T. Keith, M.A. Al-Laham, C.Y. Peng, A. Nanayakkara, M. Challacombe, P.M.W. Gill, B. Johnson, W. Chen, M.W. Wong, C. Gonzalez, J.A. Pople, Gaussian Inc., Pittsburgh, PA, 2003.
[27] A.D. Becke, J. Chem. Phys. 98 (1993) 5648.
[28] C. Lee, W. Yang, R.G. Parr, Phys. Rev. B 37 (1988) 785.
[29] P.C. Hariharan, J.A. Pople, Theor. Chim. Acta 28 (1973) 213.
[30] V.A. Rassolov, M.A. Ratner, J.A. Pople, P.C. Redfern, L.A. Curtiss, J. Comput. Chem. 22 (2001) 976.
[31] P.J. Hay, W.R. Wadt, J. Chem. Phys. 82 (1985) 299.
[32] K. Eichkorn, F. Weigend, O. Treutler, R. Ahlrichs, Theor. Chem. Acc. 97 (1997) 119.
[33] M.E. Casida, in: J.M. Seminario (Ed.), Recent Developments and Applications in Modern Density Functional Theory, Theoretical and Computational Chemistry, vol. 4, Elsevier, Amsterdam, 1996.
[34] E.D. Glendening, A.E. Reed, J.E. Carpenter, F. Weinhold, NBO (version 3.1).
[35] E. Reed, L.A. Curtiss, F. Weinhold, Chem. Rev. 88 (1988) 899.
[36] J.M. Mayer, Inorg. Chem. 27 (1988) 3899.
[37] S.R. Fletcher, A.C. Skapski, J. Chem. Soc., Dalton (1972) 1073.
[38] E. Shuter, H.R. Hoveyda, V. Karunaratne, S.J. Retting, C. Orvig, Inorg. Chem. 35 (1996) 368.
[39] M.L. Kuznetsov, A.J.L. Pombeiro, J. Chem. Soc., Dalton Trans. (2003) 738.



Scheme 1.

ferrocenyl) the latter reaction's yields suffer significantly and long reaction times are required. The former method produces, in most cases, yields in excess of 80% in 2–3 h [9]. The disassembly of a tetrathiophenecarboxylate derivative would be a prime candidate for such a reaction, as both the di- and mononuclear thiophene containing complexes would have the potential to be electrochemically polymerized.

Herein we report the synthesis and characterization as well as electrochemical behaviour of both diruthenium(II,III) and monoruthenium(II) complexes incorporating the thiophene-containing ligands 3-thiophene carboxylate, 3-thiophene acetate, *trans*-3-(3-thienyl)acrylate and 2,2′-bithiophene-5-carboxylate (Scheme 1).

2. Experimental

2.1. Equipment

Cyclic voltammetry studies were performed on dry dichloromethane solutions (approx. 1 mM) containing 0.1 M tetrabutylammonium hexafluorophosphate ($TBAPF_6$) that were placed in a standard three-neck cell with Luggin-Haber capillary, with an Analytical Sensors Inc. Pt button working electrode, a saturated calomel reference electrode (SCE) and a platinum wire counter electrode. The potential applied to the working electrode was controlled by a Pine Instruments bipotentiostat (model AFCBP1) interfaced to a PC through a PINECHEM 2.7.9 software package. Cyclic voltammetry scans were conducted at a scan rate of 0.100 V/s. The working electrode was polished prior to each scan using Buehler Alpha Micropolish I alumina (5.0 μm) followed by Buehler Gamma Micropolish II deagglomerated alumina (0.05 μm) on a Buehler microcloth. Infrared spectra were performed on KBr discs using a Bio-Rad FTS-175 spectrophotometer. NMR measurements were carried out on a Bruker Avance II 400 MHz spectrophotometer using Norell sample tubes. Elemental analysis was performed by Canadian MicroAnalytical Services Ltd., Delta, BC.

2.2. Materials

Most of the reagents and solvents were purchased from commercial sources and used as received. $Ru_2(\mu\text{-}O_2CCH_3)_4Cl$ was prepared by the method of Mitchell et al. [12]. Dichloromethane was distilled over CaH_2 and stored under argon prior to use. Tetrabutylammonium hexafluorophosphate ($TBAPF_6$) was recrystallized three times from ethanol and thoroughly dried before use. All of the synthetic procedures were carried out under an atmosphere of argon.

2.3. Syntheses

2.3.1. Preparation of $[Ru_2(\mu\text{-}O_2CR)_4(MeOH)_2]PF_6$ complexes, O_2CR^- = thiophene-3-carboxylato **1**, thiophene-3-acetato **2**, and trans-3-(3-thienyl)acrylato **3**

$Ru_2(\mu\text{-}O_2CCH_3)_4Cl$ (0.100 g, 0.21 mmol) and a 6-fold molar excess (1.26 mmol) of the appropriate thiophene-3-carboxylic acid were dissolved in 50 ml of a 1:1 water/methanol solution. The brown solution was then refluxed under argon for 8 h over which time it lightened somewhat to an orange or yellow-brown. The solution was placed in the fridge overnight, the resulting brown solid of $Ru_2(\mu\text{-}O_2CR)_4Cl$ collected, washed with methanol and diethyl ether and dried in vacuo. Further purification of these $Ru_2(\mu\text{-}O_2CR)_4Cl$ derivatives was not carried not. Subsequent dechlorination was typically carried out by dissolving 0.100 g (0.13 mmol) of the $Ru_2(\mu\text{-}O_2CR)_4Cl$ in 50 ml of methanol (0.080 g (0.010 mmol) of the acrylato derivative in 90 ml of methanol). To this solution was added a solution of 0.033 g (0.13 mmol) of silver hexafluorophosphate in 10 ml of methanol (0.025 g (0.10 mmol) in 10 ml for the acrylato derivative). These solutions were heated in the dark, with stirring, at 40–50 °C for 1 h. The AgCl that formed was then filtered off over a bed of Celite. The orange/brown filtrate was collected and concentrated under vacuum to precipitate a dark brown solid which was collected and washed with a small amount of cold methanol. Yields: **1**: 0.063 g (51%); **2**: 0.060 g (46%); **3**: 0.062 g (60%). Elem. *Anal.* Calc. for **1**, $C_{22}H_{20}O_{10}S_4Ru_2PF_6$: C, 28.73; H, 2.19. Found: C, 28.62; H, 2.29%. Elem. *Anal.* Calc. for **2**, $C_{26}H_{28}O_{10}S_4Ru_2PF_6$: C, 32.00; H, 2.89. Found: C, 32.11; H, 2.71%. Elem. *Anal.* Calc. for **3**, $C_{30}H_{28}O_{10}S_4Ru_2PF_6$: C, 36.04; H, 2.82. Found: C, 35.88; H, 2.99%. IR (cm^{-1}) for **1**: 3448 (m), 3115 (w), 1526 (s), 1441 (s), 1393 (m), 1349 (s), 1045 (w), 865 (s). For **2**: 3498 (m), 3109 (w), 2923 (m), 2859 (w), 1465 (s), 1436 (s), 1394 (s), 1292 (s), 1043 (w), 839 (s). For **3**: 3448 (m), 3101 (w), 3023 (w), 1628 (s), 1426 (s), 1384 (s), 1294 (m), 1248 (m), 990 (m), 845 (s).

*2.3.2. Preparation of $[Ru_2(\mu\text{-}O_2CC_8H_5S_2)_4(EtOH)_2](PF_6)$, $O_2CC_8H_5S_2^- = 2,2'$-bithiophene-5-carboxylato **4***

$Ru_2(\mu\text{-}O_2CCH_3)_4Cl$ (0.100 g, 0.21 mmol) and 6-fold molar excess of 2,2′-bithiophene-5-carboxylic acid (0.266 g, 1.26 mmol) were dissolved into 25 ml of argon-purged methanol. This brown solution was then refluxed under argon for 8 h, over which time the solution lightened slightly. Upon completion of the reflux, the solution was placed in the fridge overnight. The resulting brown solid was collected via suction filtration, and washed successively with methanol and diethyl ether. Dechlorination of the product was then carried out by dissolving 0.100 g of the product into 50 ml of argon-purged ethanol. To this, a solution of silver hexafluorophosphate (0.030 g, 0.11 mmol) in 10 ml of argon purged ethanol was added. The combined solution was heated to 40–50 °C and stirred for 1 h in the dark. The solution was then filtered through a bed of Celite to remove the precipitated AgCl, and washed with 20 ml of ethanol. The red-brown filtrate was collected and reduced in volume, precipitating a dark brown solid. This solid was collected via suction filtration. Yield: **4**: 0.107 g (91%). Elem. *Anal.* Calc. for **4**, $C_{40}H_{32}O_{10}S_8Ru_2PF_6$: C, 37.64; H, 2.53. Found: C, 37.39; H, 2.54%. IR (cm^{-1}): 3470 (m), 3109 (w), 2969 (w), 2937 (w), 1515 (m), 1447 (s), 1404 (s), 1125 (m), 850 (s), 746 (m).

*2.3.3. Preparation of $[Ru(\eta^2\text{-}O_2CR)(dppe)_2]PF_6$ complexes, O_2CR^- = thiophene-3-carboxylato **5**, thiophene-3-acetato **6**, and trans-3-(3-thienyl)acrylato 7*

About 0.050 g of the appropriate $[Ru_2(\mu\text{-}O_2CR)_4(MeOH)_2]PF_6$ derivative was dissolved under argon in 100 ml of methanol. To this was added four molar equivalents of 1,2-bis(diphenylphosphino)ethane (dppe) and the resulting solution refluxed for 8 h during which time the solution changed colour from red-brown to bright yellow. The solution was cooled, reduced in volume to 30 ml and placed in the fridge overnight. The resulting yellow crystalline solid was collected by suction filtration and dried in vacuo. Yields: **5**: 0.095 g (67%); **6**: 0.129 g (89%); **7**: 0.105 g (72%). Elem. *Anal.* Calc. for $\mathbf{5}\cdot CH_3OH$, $C_{58}H_{55}O_3F_6P_5RuS$: C, 57.95; H, 4.61. Found: C, 58.29; H, 4.50%. Elem. *Anal.* Calc. for **6**, $C_{58}H_{53}O_2F_6P_5RuS$: C, 58.83; H, 4.51. Found: C, 58.75; H, 4.67%. Elem. *Anal.* Calc. for $\mathbf{7}\cdot 0.5CH_3OH$, $C_{59.5}H_{55}O_{2.5}F_6P_5RuS$: C, 58.96; H, 4.57. Found: C, 58.71; H, 4.39%. IR (cm^{-1}) for **5**: 3448 (w), 3056 (m), 1544 (m), 1455 (s), 1436 (s), 1358(m), 1099 (m), 841 (s). For **6**: 3060 (w), 1515 (m), 1448 (s), 1437 (s), 1409 (m), 1098 (m), 839 (s). For **7**: 3062 (w), 1638 (m), 1483 (m), 1438 (s), 1408 (s), 1097 (m), 840 (s). ^1H NMR (400 MHz, $CDCl_3$) δ (ppm) for **5**: 5.94–7.81 (m, 40H, dppe phenyl protons); 6.67 (m, 1H, thiophene proton); 7.15 (m, 2H, thiophene proton); 1.52, 2.15, 2.33, 2.93 (4m, 8H, methylene protons). ^{31}P NMR (400 MHz, $CDCl_3$) δ (ppm): 58.80 (m (b), 4P, probably two overlapping triplets). For **6**: (^1H): 5.90–7.76 (m, 40H, dppe phenyl protons); 6.44 (d, 2H, thiophene proton); 7.16 (s, 1H, thiophene proton); 1.52, 2.00, 2.36, 2.89 (m, 8H, methylene protons). (^{31}P): 58.08 (t, 2P) and 58.13 (t, 2P). For **7**: (^1H): 5.92–7.82 (m, 40H, dppe phenyl protons); 6.90 (m, 1H, thiophene proton); 7.15 (m, 2H, thiophene proton); 4.91 (d, 1H, acrylic proton); 6.51 (d, 1H, acrylic proton); 1.53, 2.09, 2.30, 2.93 (m, 8H, methylene protons). (^{31}P): 58.02 (t, 2P) and 58.72 (t, 2P).

*2.3.4. Preparation of $[Ru(\eta^2\text{-}O_2CC_8H_5S_2)(dppe)_2](PF_6)$, $O_2CC_8H_5S_2^- = 2,2'$-bithiophene-5-carboxylato **8***

About 0.125 g, (0.1 mmol) of $[Ru_2(\mu\text{-}O_2CC_8H_5S_2)_4(EtOH)_2](PF_6)$ and four molar equivalents of bis-1,2-(diphenylphosphino)ethane (160 mg, 0.4 mmol) were dissolved in 150 ml of argon-purged ethanol. The dark brown solution was refluxed for 8 h, during which time the solution changed to a cloudy yellow. The solution was removed from heat and allowed to cool to room temperature. Potassium hexafluorophosphate (20 mg, 1.1 mmol) was added to the solution with stirring. The volume of the solution was then reduced using rotary evaporation to approximately 40 ml. The solution was then placed in the fridge overnight. The resulting orange-yellow crystalline solid that precipitated from solution was collected using suction filtration and dried under vacuum. Yield: **8**: 0.160 g (79%). Elem. *Anal.* Calc. for **8**: C, 58.51; H, 4.27; P, 12.37. Found: C, 58.29; H, 4.32; P, 12.51%. IR (cm^{-1}): 3430 (m), 3064 (w), 1518 (m), 1432 (s), 1414 (s), 1384 (m), 1097 (m), 841 (s), 747 (m), 695 (s). ^1H NMR (400 MHz, $CDCl_3$) δ (ppm): 5.91–7.78 (m, 40H, dppe phenyl protons); 7.65 (d, 1H, bithiophene proton); 7.34 (d, 2H, bithiophene protons); 7.22 (d, 1H, bithiophene proton); 7.05 (m, 1H, bithiophene proton); 1.53, 2.11, 2.35, 2.91 (m, 8H, methylene protons). ^{31}P NMR (400 MHz, $CDCl_3$) δ (ppm): 58.15 (t, 2P) and 58.48 (t, 2P).

2.4. X-ray crystallography

Crystals were mounted on a glass fiber and all measurements were made on a Rigaku AFC5R diffractometer (or Rigaku RAXIS RAPID imaging plate area detector for **8**) with either graphite monochromated Mo Kα (complexes **5** and **8**) or Cu Kα (complexes **6** and **7**) radiation and a rotating anode generator. The structures were solved by direct methods [13,14] and expanded using Fourier techniques [15]. For complexes **5**, **6** and **8** the non-hydrogen atoms were refined anisotropically and some of the hydrogen atoms were refined isotropically with the rest included in fixed positions. For complex **7** some non-hydrogen atoms were refined anisotropically, while the rest were refined isotropically. Hydrogen atoms were included but not refined. Neutral atom scattering factors were taken from Cromer and Waber [16]. Anomalous dispersion effects were included in F_{calc} [17]; the values of $\Delta f'$ and $\Delta f''$ were those of Creagh and McAuley [18]. The values for the mass attenuation coefficients are those of Creagh and Hubbell [19]. All calculations were performed using the CRYSTALSTRUCTURE [20,21] crystallographic software package. A full listing of crystal parameters is given in Table 1.

Table 1
Crystal and structure refinement data for complexes (**5**)–(**8**)

Compound	(**5**) · MeOH	(**6**)	(**7**) · 0.5MeOH	(**8**)
Formula	$C_{58}H_{54}O_3P_5F_6RuS$	$C_{58}H_{53}O_2P_5F_6RuS$	$C_{59.5}H_{54.5}O_{2.5}P_5F_6RuS$	$C_{60}H_{53}O_2P_5F_6RuS_2$
Formula weight	1201.05	1184.04	1211.57	1252.14
Temperature (°C)	−100	23.0	23.0	−150
Wavelength (Å)	0.71069	1.54178	1.54178	0.71069
Crystal system	monoclinic	monoclinic	orthorhombic	orthorhombic
Space group	*C*2/*c*	$P2_1$	*Pbca*	*Pbca*
a (Å)	24.35(2)	12.621(3)	25.328(4)	20.5509(2)
b (Å)	12.275(9)	14.816(6)	28.395(4)	22.5442(3)
c (Å)	36.959(7)	14.431(3)	15.250(5)	24.0774(3)
α (°)	90.00	90.00	90.00	90.00
β (°)	103.57(3)	100.80(2)	90.00	90.00
γ (°)	90.00	90.00	90.00	90.00
V (Å^3)	10739(13)	2650(1)	10967(3)	11155.1(2)
Z	8	2	8	8
D_{calc} (g/cm^3)	1.485	1.483	1.467	1.491
μ (mm^{-1})	0.546	4.736	4.600	0.5638
F(000)	4920.00	1212.00	4964.00	5120.00
Crystal size (mm)	0.03 × 0.17 × 0.34	0.27 × 0.32 × 0.13	0.19 × 0.23 × 0.24	0.44 × 0.38 × 0.17
$2\theta_{max}$ (°)	60.2	127.5	127.7	71.3
Index ranges	$0 \leqslant h \leqslant 29$, $0 \leqslant k \leqslant 17$, $-52 \leqslant l \leqslant 50$	$0 \leqslant h \leqslant 14$, $0 \leqslant k \leqslant 17$, $-16 \leqslant l \leqslant 16$	$0 \leqslant h \leqslant 29$, $0 \leqslant k \leqslant 33$, $-17 \leqslant l \leqslant 17$	$-31 \leqslant h \leqslant 31$, $-34 \leqslant k \leqslant 34$, $-33 \leqslant l \leqslant 38$
Reflections collected	16230	4736	18766	67057
Independent reflections	15575	3939	11016	20502
R_{int}	0.066	0.067	0.077	0.045
Data/restraints/parameters	6800/0/670	3342/0/658	7024/0/692	9306/0/747
Goodness of fit on F^2	1.124	1.148	0.999	1.025
R [$I > 3\sigma(I)$]	0.054	0.066	0.064	0.0428
R_w [$I > 3\sigma(I)$]	0.064	0.083	0.083	0.0481

3. Results and discussion

3.1. Synthesis

The synthesis of the tetracarboxylate derivatives (**1**–**4**) was carried using a standard carboxylate exchange reaction in 1:1 (v/v) methanol/water, using an excess of the desired carboxylic acid (HO_2CR), followed by dechlorination of the $Ru_2(\mu\text{-}O_2CR)_4Cl$ intermediate in methanol or ethanol to get the desired solvent diadducts as PF_6^- salts (Eqs. (1) and (2)) [5]. The diadducts are easier to work with than the chloride derivatives as they are soluble in a wider variety of solvents.

$$Ru_2(\mu\text{-}O_2CCH_3)_4Cl + \text{excess } HO_2CR \rightarrow Ru_2(\mu\text{-}O_2CR)_4Cl + \text{free } HO_2CCH_3 \quad (1)$$

$$Ru_2(\mu\text{-}O_2CR)_4Cl + AgPF_6 \xrightarrow{MeOH} [Ru_2(\mu\text{-}O_2CR)_4(MeOH)_2]PF_6 + AgCl \quad (2)$$

The "disassembly" of complexes **1**–**4** to form the mononuclear ruthenium derivatives of the form $[Ru(\eta^2\text{-}O_2CR)(dppe)_2]PF_6$ (complexes **5**–**8**) was achieved by a method we [9–11] and others [22] have used in which the dimer is reacted with a π-acid ligand such as a phosphine; bis(1,3-diphenylphophino)ethane (dppe) in our case (Eq. (3)). The advantage of using this method, as was mentioned in the Introduction, is the ability to synthesize complexes containing relatively bulky R groups in good yields.

$$[Ru_2(\mu\text{-}O_2CR)_4(MeOH)_2]PF_6 + 4dppe \xrightarrow{PF_6^-} 2[Ru(\eta^2\text{-}O_2CR)(dppe)_2]PF_6 + \text{free } {}^-O_2CR \text{ and oxidation products} \quad (3)$$

All complexes gave satisfactory elemental analyses.

3.2. Infrared and NMR properties

Complexes **1**–**4** show infrared spectra typical of this class of compounds with C–H stretching modes at 2850–3150 cm^{-1}, symmetric and asymmetric O–C–O stretches in the range 1384–1441 cm^{-1}, thiophene ring modes at 1000–1300 cm^{-1} and a strong P–F stretching mode around 840 cm^{-1} [23]. In addition, the O–H stretching mode due to the axially coordinated methanol or ethanol is seen around 3450 cm^{-1}. Similar infrared bands are seen for the mononuclear complexes **5**–**8**. The only difference of note is that the separation between the symmetric and asymmetric O–C–O stretching modes is somewhat smaller due to the η^2 versus μ_2 coordination of the carboxylate.

^{1}H NMR (400 MHz) was performed on complexes **5**–**8** (complexes **1**–**4** are paramagnetic with three unpaired elec-

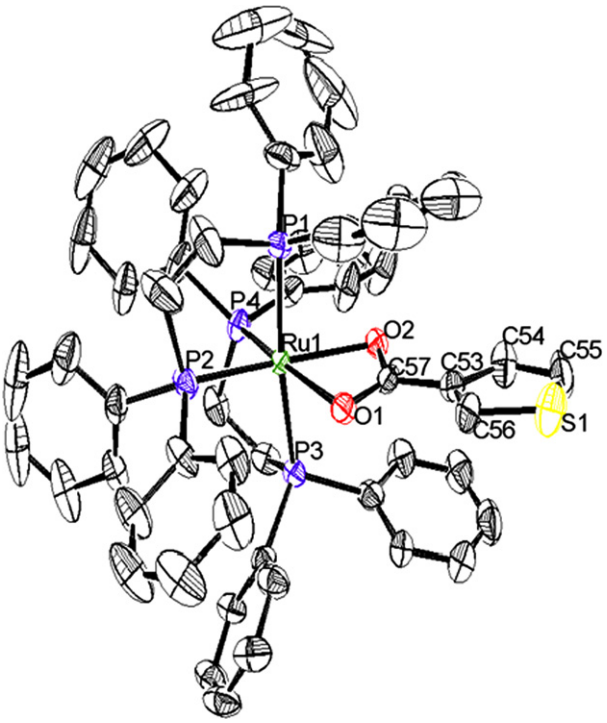


Fig. 1. Molecular structure of the $[Ru(\eta^2\text{-}O_2CC_4H_3S)(dppe)_2]^+$ cation, **5**. Hydrogen atoms, the hexafluorophosphate anion and the methanol molecule of solvation have been omitted for clarity.

trons per dimer) and gave limited information. The phenyl and thiophene protons are seen in the 5.9–7.9 ppm range with the methylene protons at 1.5–3.0 ppm which is similar to what we have seen previously for $[Ru(\eta^2\text{-}O_2CCH_3)(dppe)_2]PF_6$ [9]. In complex **7** the *trans* –HC=CH– protons are clearly discernible as a pair of doublets at 4.91 and 6.51 ppm. The ^{31}P NMR spectra for all three complexes show the characteristic doublet of triplets around 58 ppm which have been reported in an earlier study [9]. The splitting between the triplets in all three cases is very small which is consistent with the A_2B_2 splitting pattern seen in $[Ru(\eta^2\text{-}O_2CCH_3)(dppe)_2]PF_6$ [9].

3.3. X-ray structures

Complexes **5**–**8** were also characterized by X-ray diffraction and the relevant crystal data is reported in Table 1. Complex **5** crystallizes in the $C2/c$ space group with a molecule of methanol in the unit cell. An ORTEP diagram is shown in Fig. 1 and selected bond lengths and angles are given in Table 2. The three bidentate ligands (two dppe's and a carboxylate) assume a distorted octahedral geometry about the Ru center with P–Ru–P and P–Ru–O bond angles in the range 82.4–106.6° and the O–P–O bond angle a more restrictive 60.0°. The Ru–P bond lengths are 2.290(2) and 2.303(1) Å for those *trans* to a carboxylate oxygen and 2.360(1) and 2.372(1) Å for those *trans* to another phosphorous, a clear illustration of the greater *trans*-influence of P versus O. The Ru–O bond lengths

Table 2
Selected bond lengths (Å) and angles (°) for complex **5** · MeOH

Bond distances			
Ru(1)–P(1)	2.360(1)	Ru(1)–P(2)	2.303(1)
Ru(1)–P(3)	2.372(1)	Ru(1)–P(4)	2.290(2)
Ru(1)–O(1)	2.180(4)	Ru(1)–O(2)	2.192(3)
O(1)–C(57)	1.262(7)	O(2)–C(57)	1.276(7)
C(53)–C(57)	1.464(8)	C(53)–C(54)	1.43(1)
C(53)–C(56)	1.37(1)	C(54)–C(55)	1.43(1)
S(1)–C(55)	1.67(1)	S(1)–C(56)	1.706(7)
Bond angles			
P(1)–Ru(1)–P(2)	84.15(5)	P(1)–Ru(1)–P(3)	172.79(5)
P(1)–Ru(1)–P(4)	100.86(5)	P(1)–Ru(1)–O(1)	88.1(1)
P(1)–Ru(1)–O(2)	85.7(1)	P(2)–Ru(1)–P(3)	102.10(5)
P(2)–Ru(1)–P(4)	93.63(6)	P(2)–Ru(1)–O(1)	101.1(1)
P(2)–Ru(1)–O(2)	158.8(1)	P(3)–Ru(1)–P(4)	82.46(5)
P(3)–Ru(1)–O(1)	87.2(1)	P(3)–Ru(1)–O(2)	87.2(1)
P(4)–Ru(1)–O(1)	163.5(1)	P(4)–Ru(1)–O(2)	106.6(1)
O(1)–Ru(1)–O(2)	60.0(1)	Ru(1)–O(1)–C(57)	91.0(3)
Ru(1)–O(2)–C(57)	90.1(3)	O(1)–C(57)–O(2)	118.9(5)

are 2.180(4) and 2.192(3) Å showing relatively symmetrical binding to the Ru. All of the bond lengths and angles are similar to those of the previously reported structures of $[Ru(\eta^2\text{-}O_2CR)(dppe)_2]PF_6$ with $R = CH_3$ and ferrocenyl [9].

Complex **6** crystallized in the $P2_1$ space group and displays very similar bond lengths and angles to those in complex **5** except that the carboxylate group binds less symmetrically with Ru–O bonds of 2.138(8) and 2.202(8) Å. As well, the thiophene ring is significantly bent out of plane with respect to the Ru–O–C–O plane with an angle of 79(1)°! Fig. 2 gives an ORTEP diagram of complex **5** and Table 3 summarizes the bond lengths and angles.

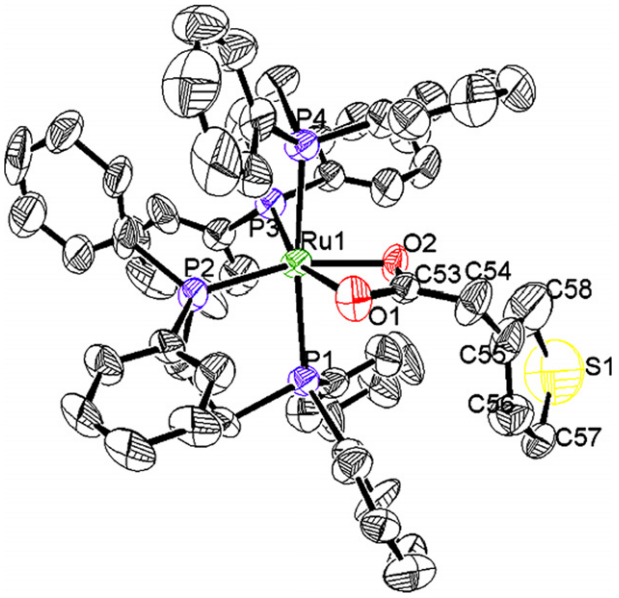


Fig. 2. Molecular structure of the $[Ru(\eta^2\text{-}O_2CCH_2C_4H_3S)(dppe)_2]^+$ cation, **6**. Hydrogen atoms and the hexafluorophosphate anion have been omitted for clarity.

Table 3
Selected bond lengths (Å) and angles (°) for complex **6**

Bond distances			
Ru(1)–P(1)	2.397(3)	Ru(1)–P(2)	2.306(3)
Ru(1)–P(3)	2.294(3)	Ru(1)–P(4)	2.370(3)
Ru(1)–O(1)	2.202(8)	Ru(1)–O(2)	2.138(8)
O(1)–C(53)	1.29(1)	O(2)–C(53)	1.26(1)
C(53)–C(54)	1.51(2)	C(54)–C(55)	1.47(2)
C(55)–C(56)	1.40(2)	C(55)–C(58)	1.34(2)
C(56)–C(57)	1.42(2)	S(1)–C(57)	1.60(2)
S(1)–C(58)	1.69(2)		
Bond angles			
P(1)–Ru(1)–P(2)	83.2(1)	P(1)–Ru(1)–P(3)	101.8(1)
P(1)–Ru(1)–P(4)	172.3(1)	P(1)–Ru(1)–O(1)	88.6(2)
P(1)–Ru(1)–O(2)	85.2(2)	P(2)–Ru(1)–P(3)	89.8(1)
P(2)–Ru(1)–P(4)	103.0(1)	P(2)–Ru(1)–O(1)	110.0(2)
P(2)–Ru(1)–O(2)	164.4(2)	P(3)–Ru(1)–P(4)	82.9(1)
P(3)–Ru(1)–O(1)	158.7(3)	P(3)–Ru(1)–O(2)	102.8(2)
P(4)–Ru(1)–O(1)	85.0(2)	P(4)–Ru(1)–O(2)	87.8(2)
O(1)–Ru(1)–O(2)	59.2(3)	Ru(1)–O(1)–C(53)	91.3(7)
Ru(1)–O(2)–C(53)	95.2(7)	O(1)–C(53)–O(2)	114(1)

Table 4
Selected bond lengths (Å) and angles (°) for complex **7** · 0.5MeOH

Bond distances			
Ru(1)–P(1)	2.298(1)	Ru(1)–P(2)	2.382(1)
Ru(1)–P(3)	2.292(1)	Ru(1)–P(4)	2.376(1)
Ru(1)–O(1)	2.166(3)	Ru(1)–O(2)	2.211(3)
O(1)–C(59)	1.268(6)	O(2)–C(59)	1.264(6)
C(58)–C(59)	1.454(8)	C(57)–C(58)	1.320(8)
C(55)–C(57)	1.455(8)	C(54)–C(55)	1.40(1)
C(55)–C(56)	1.36(1)	C(53)–C(54)	1.41(1)
S(1)–C(53)	1.684(9)	S(1)–C(56)	1.694(8)
Bond angles			
P(1)–Ru(1)–P(2)	83.00(5)	P(1)–Ru(1)–P(3)	90.55(5)
P(1)–Ru(1)–P(4)	101.01(5)	P(1)–Ru(1)–O(1)	104.86(9)
P(1)–Ru(1)–O(2)	161.55(9)	P(2)–Ru(1)–P(3)	103.83(4)
P(2)–Ru(1)–P(4)	172.27(5)	P(2)–Ru(1)–O(1)	86.72(9)
P(2)–Ru(1)–O(2)	86.4(1)	P(3)–Ru(1)–P(4)	82.85(5)
P(3)–Ru(1)–O(1)	162.41(9)	P(3)–Ru(1)–O(2)	106.66(9)
P(4)–Ru(1)–O(1)	85.86(9)	P(4)–Ru(1)–O(2)	88.0(1)
O(1)–Ru(1)–O(2)	59.4(1)	Ru(1)–O(1)–C(59)	92.4(3)
Ru(1)–O(2)–C(59)	90.5(3)	O(1)–C(59)–O(2)	117.7(4)

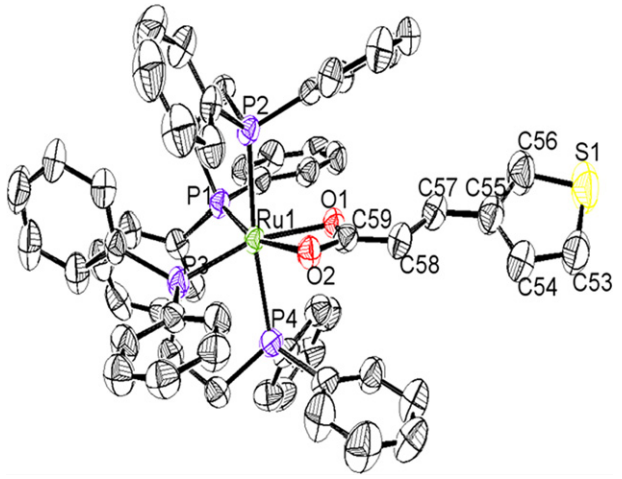


Fig. 3. Molecular structure of the $[Ru(\eta^2\text{-}O_2CCH{=}CHC_4H_3S)(dppe)_2]^+$ cation, **7**. Hydrogen atoms, the hexafluorophosphate anion and the methanol molecule of solvation have been omitted for clarity.

Complex **7** crystallized in the *Pbca* space group with a half molecule of methanol in the unit cell. An ORTEP diagram is seen in Fig. 3 and bond lengths and angles given in Table 4. The corresponding bond lengths and angles are, again, similar to those in complexes **5** and **6** and to those previously reported [9]. The asymmetry of the carboxylate binding is somewhere between that seen in complexes **5** and **6** with Ru–O bond lengths of 2.166(3) and 2.211(3) Å. The thiophene–CH=CH– moiety extends relatively straight out from the Ru core with an *anti* arrangement about the double bond. The dihedral angle between the Ru–O(1)–C(59)–O(2) plane and the thiophene ring is 33°. The C(55)–C(57), C(57)–C(58) and C(58)–C(59) bond lengths are 1.454(8), 1.320(8) and 1.455(8) Å, respectively, indicating limited, if any, conjugation.

Complex **8** also crystallized in the orthorhombic Pbca space group and an ORTEP diagram is shown in Fig. 4 with selected bond lengths and angles listed in Table 5. The key bond lengths and angles are again similar to those of complexes **5**–**7**. The two thiophene rings are close to being coplanar with a dihedral angle of 9.1(2)°.

3.4. Electrochemistry

3.4.1. Diruthenium(II,III) tetra-(3-thiophencarboxylates) and tetra-(2,2′-bithiophene-5-carboxylate), *1*–*4*

The cyclic voltammetry of the diruthenium(II,III) tetra-(3-thiophenecarboxylates) and tetra-(2,2′-bithiophene-5-carboxylate), **1**–**4**, were performed on 1mM solutions in the presence of 0.1 M $TBAPF_6$ in dry dichloromethane. Full details are given in Section 2. A typical experiment consisted of 6–10 consecutive scans run at 100 mV/s. It should be noted that thiophene-3-carboxylates were employed, rather than the thiophene-2-carboxylates such as those synthesized by Jimenez-Aparicio and coworkers [8], since they are better candidates for polymerization as the position of the carboxylate at the 3-position leaves both α sites on the ring available for coupling. The scans for diruthenium(II,III) tetra-3-thiophenecarboxylate, **1**, are shown in Fig. 5. Similar scans are seen for complexes **2** and **3** with E_{pa} values greater than 1.5 V. In fact, there are no clearly distinguishable oxidation waves in most cases, only shoulders on the more intense solvent oxidation wave.

Estimates of the E_{pa} values from these shoulders are given in Table 6. There is no evidence of oxidative polymerization of the thiophene rings in any of the three single ring thiophene carboxylates as the scans *diminish* somewhat in intensity (rather than increasing as a polymer film grows) which is likely due to passivation of the electrode surface which deposits an electronically insulating film. The high oxidation potential of these complexes reflects the electron-withdrawing nature of the carboxylate group attached

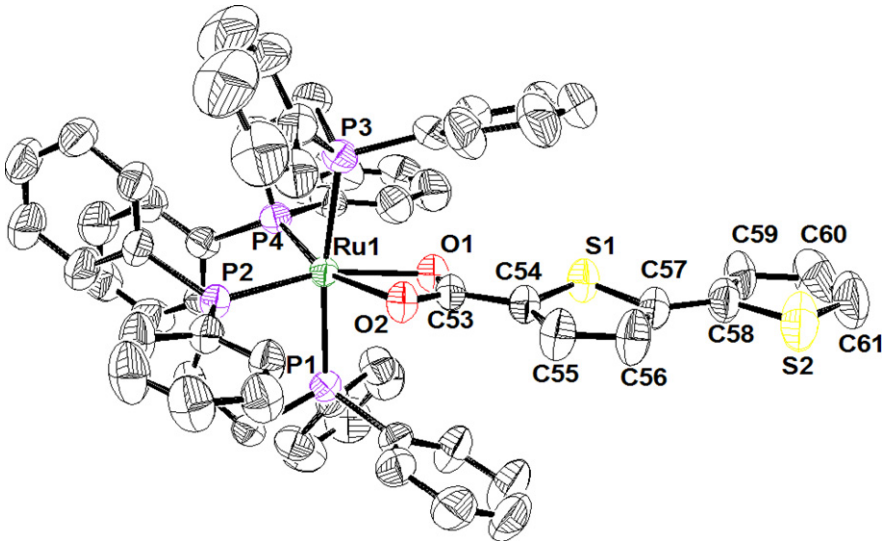


Fig. 4. Molecular structure of the $[Ru(\eta^2\text{-}O_2CC_8H_5S_2)(dppe)_2]^+$ cation, **8**. Hydrogen atoms and the hexafluorophosphate anion have been omitted for clarity.

Table 5
Selected bond lengths (Å) and angles (°) for complex **8**

Bond distances			
Ru(1)–P(1)	2.3846(8)	Ru(1)–P(2)	2.3044(7)
Ru(1)–P(3)	2.3803(8)	Ru(1)–P(4)	2.3078(7)
Ru(1)–O(1)	2.193(2)	Ru(1)–O(2)	2.223(2)
O(1)–C(53)	1.277(3)	O(2)–C(53)	1.263(3)
C(53)–C(54)	1.465(4)	C(54)–C(55)	1.362(4)
C(55)–C(56)	1.418(4)	C(56)–C(57)	1.364(4)
C(57)–C(58)	1.457(4)	C(58)–C(59)	1.382(5)
C(59)–C(60)	1.430(5)	C(60)–C(61)	1.343(6)
S(1)–C(54)	1.725(3)	S(1)–C(57)	1.727(3)
S(2)–C(58)	1.723(3)	S(2)–C(61)	1.709(4)
Bond angles			
P(1)–Ru(1)–P(2)	83.03(2)	P(1)–Ru(1)–P(3)	171.28(2)
P(1)–Ru(1)–P(4)	103.17(2)	P(1)–Ru(1)–O(1)	84.73(5)
P(1)–Ru(1)–O(2)	87.18(5)	P(2)–Ru(1)–P(3)	103.33(2)
P(2)–Ru(1)–P(4)	89.28(2)	P(2)–Ru(1)–O(1)	162.44(5)
P(2)–Ru(1)–O(2)	107.53(5)	P(3)–Ru(1)–P(4)	83.07(2)
P(3)–Ru(1)–O(1)	87.72(5)	P(3)–Ru(1)–O(2)	85.21(5)
P(4)–Ru(1)–O(1)	105.78(6)	P(4)–Ru(1)–O(2)	161.37(5)
O(1)–Ru(1)–O(2)	59.22(7)	Ru(1)–O(1)–C(53)	91.68(16)
Ru(1)–O(2)–C(53)	90.69(17)	O(1)–C(53)–O(2)	118.4(2)

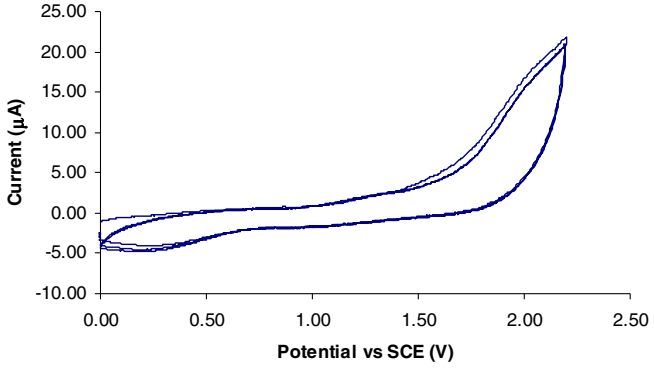


Fig. 5. Consecutive cyclic voltammetry scans for complex **1** in dichloromethane (scan rate = 100 mV/s).

Table 6
Cyclic voltammetry data for complexes **1**–**8**[a,b]

Complex	E_{pa} (V)	E_{pc} (V)	$E_{1/2}$ (ΔE) (V)	i_a/i_c
1	~2.0			
2	~2.1			
3	~1.8			
4	1.55			
5	1.68	1.62	1.65	1.12
6	1.75	1.59	1.67	1.01
7	1.65	1.54	1.60	1.37
8	1.51	1.03?[c]		

[a] 1 mM solutions in dry dichloromethane and 0.1 M $TBAPF_6$, scan rate = 100 mV/s.
[b] Thiophene oxidation process for complexes **1**–**4**, $Ru^{3+/2+}$ couple for complexes **5**–**8**.
[c] Most likely due to a small amount of impurity.

to the thiophene ring which serves to destabilize any radical cation intermediate and thus inhibit oxidative polymerization. It should be noted that the oxidation is unlikely to be due to the $Ru_2^{6+/5+}$ couple as this couple has never been seen inside the solvent front in any diruthenium(II,III) tetracarboxylate adducts with modest axial Lewis base donors (such as methanol in these cases) [5,6]. Only in strong axial donor adducts, such as phosphines, does this wave become accessible [24].

The behaviour of the bithiophene complex, **4**, is, on the other hand, distinctly different. Inspection of the voltammogram (see Fig. 6) shows an E_{pa} value for the initial scan at 1.55 V. This clear oxidation wave is much lower than those of the mono-thiophene systems, which indicates that the radical cation intermediate is more accessible. For this compound, the terminal thiophene ring is presumably far enough removed from the carboxylate group to permit cation formation and subsequent coupling. This value lowers somewhat with each subsequent scan, indicative of poly-

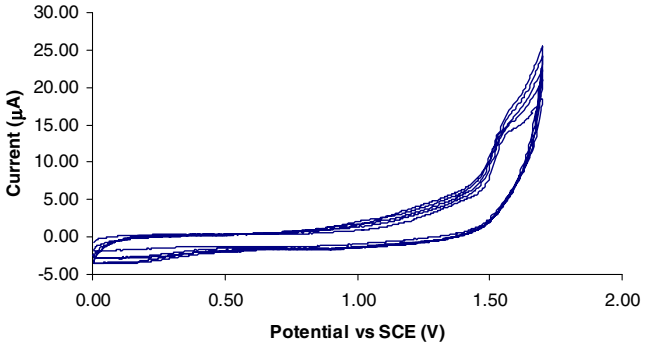


Fig. 6. Consecutive cyclic voltammetry scans for complex **4** in dichloromethane (scan rate = 100 mV/s).

merization. In addition, a distinct *growth* in the current is seen on successive scans, which again is strong evidence for the occurrence of oxidative polymerization. This was further confirmed by the appearance of a transparent yellow film on the platinum surface of the working electrode.

It should be noted here that in all cases the free ligands (see Scheme 1) do not show any evidence of polymerization, only a large oxidation wave, E_{pa}, at greater than 1.5 V for the single-ring thiophenes and an $E_{pa} = 1.45$ V for the 2,2′-bithiophene-5-carboxylic acid. The latter case shows a dramatic drop and deterioration in current on the second scan that indicates potential dimerization and precipitation from solution. On subsequent scans dimerization is inhibited by the newly-deposited film, and the observed current drops off noticeably (see Fig. S1). This suggests that 2,2′-bithiophene-5-carboxylic acid is also not capable of polymerizing in its free acid form.

3.4.2. Mononuclear ruthenium(II) 3-thiophenecarboxylates and 2,2′-bithiophene-5-carboxylate, 5–8

The "diphosphine-disassembled" mononuclear ruthenium(II) 3-thiophene-carboxylate and 2,2′-bithiophene-5-carboxylate derivatives, **5**–**8**, were studied under identical conditions to their dinuclear precursors. Fig. 7 shows a set of consecutive cyclic voltammetry scans on complex **6** and while the oxidation potentials, E_{pa}, seem somewhat better resolved and lie at slightly lower potentials, than in the dinuclear derivatives, there does not appear to be any polymerization taking place.

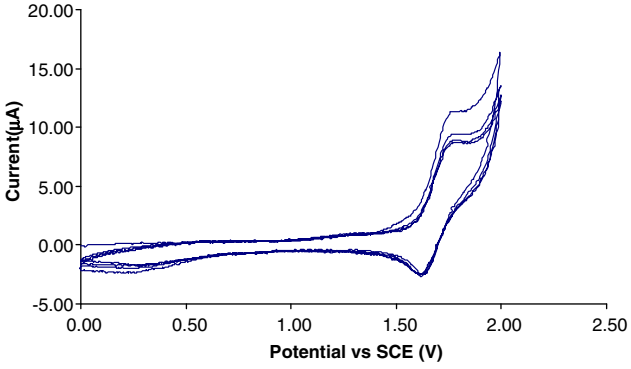


Fig. 7. Consecutive cyclic voltammetry scans for complex **6** in dichloromethane (scan rate = 100 mV/s).

A $Ru^{3+/2+}$ process is evident, centered around 1.65 V. This potential is somewhat high due to the presence of the two π-acidic diphosphine ligands. A thiophene oxidation process is not observed before the upper potential limit (~2 V) is reached. Repeated potential cycling of complexes **5** and **7** also yielded no evidence of polymerization. Presumably, the inductive nature of the carboxylate group is sufficient to elevate thiophene's oxidation potential beyond the point at which it can effectively undergo coupling. It is also possible, particularly for complexes **5** and **6**, that the degree of steric crowding imparted by the diphosphines inhibits access to the thiophene thereby preventing any possible coupling reaction.

Contrary to the behaviour of complex **4**, the "disassembled" 2,2′-bithiophene-5-carboxylato derivative, **8**, shows no evidence of polymerization either and its profile looks similar to those of complexes **5**–**7** (see Fig. S2). The inability of complex **8** to polymerize was not a surprise. The dinuclear ruthenium complex, **4**, has four available thiophene groups for coupling reactions. In the disassembled monoruthenium product, there is only one available carboxylate ligand but because of the substituents in the 2-position with respect to the sulfur (as in 2-thiophenecarboxylate), the structure allows for, at most, dimerization. The potential values for **5**–**8** are summarized in Table 6 and compare well with those previously measured in our lab for the complex $[Ru(\eta^2\text{-}O_2CCH_3)\text{-}(dppe)_2]PF_6$ which displays $E_{pa} = 1.70$ V versus SCE and $E_{pc} = 1.60$ V ($E_{1/2} = 1.65$ V) [9].

3.5. Further polymer characterization

Due to the aforementioned polymerization of complex **4**, further electrochemical and spectral studies were performed. Additional polymer films were synthesized *via* electrochemical polymerization of the complex in boron trifluoride diethyl etherate ($BF_3 \cdot OEt_2$) without added electrolyte. The use of this solvent has been reported in the preparation of several different metallopolymers involving thiophene-substituted transition metal complexes, in part due to its ability to stabilize radical cation intermediates formed during oxidation, as evidenced by lower E_{pa} potentials [25–27]. A cyclic voltammogram showing the electropolymerization of complex **4** in $BF_3 \cdot OEt_2$ is shown in Fig. 8 (top). The polymer was also grown on an indium tin oxide (ITO) transparent electrode from this same solution in order to perform UV–Vis spectroscopy on the film. This can be seen in Fig. 8 (bottom) where the much larger current is due to this electrodes' substantially larger surface area. In both figures, a growth in current with increasing scan number is evident, reflecting the deposition of a thicker electroactive polymer film onto the electrode surface with each scan [28].

The polymer-coated electrode was then removed from the polymerization medium and placed into a fresh solution of 0.10 M Bu_4NPF_6 in dichloromethane. A series of potential scans was performed in order to probe the elec-

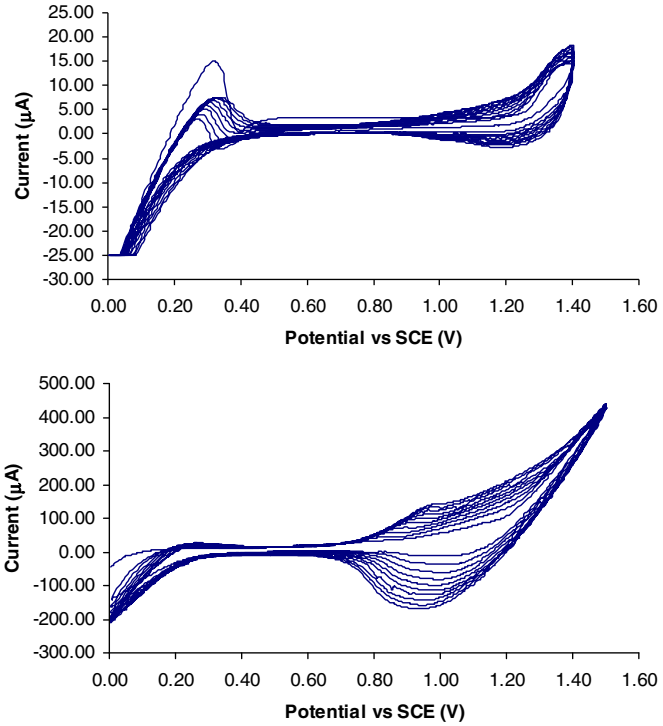


Fig. 8. Consecutive cyclic voltammetry scans for complex **4** in $BF_3 \cdot OEt_3$ on a (top) Pt electrode and (bottom) ITO electrode.

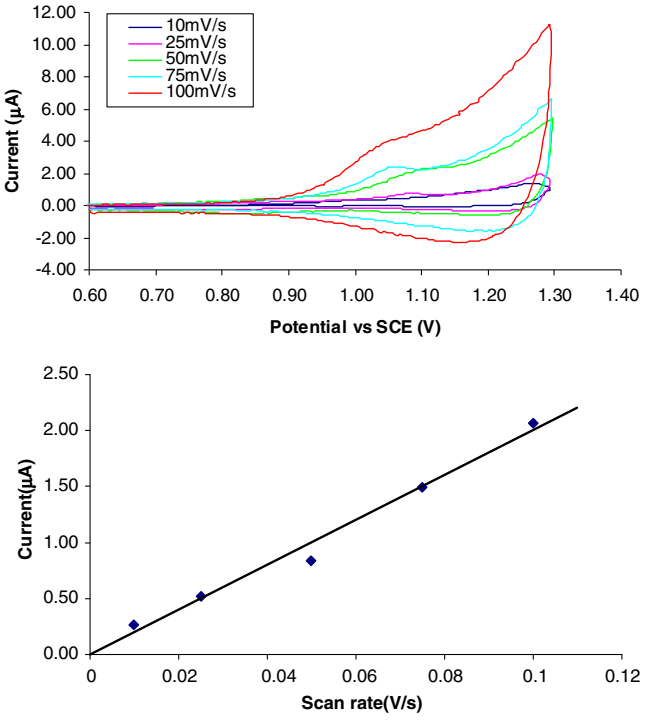


Fig. 9. (Top) Cyclic voltammograms for a "poly[Ru_2(μ-2,2′-bithiophene-5-carboxylate)$_4$(EtOH)$_2$]"-coated Pt electrode at varying scan rates in dichloromethane. (Bottom) Plot of peak current vs. scan rate for the system above.

trochemistry of the newly-formed polymer. Studies carried out over a range of scans speeds (Fig. 9, top) demonstrate a linear relationship between current and scan rate, confirming that the observed electrochemistry results from surface-confined sites [29,30]. The Randles–Sevcik equation describes diffusional behaviour for a species in solution ($i_p = 2.69 \times 10^5 n^{3/2} A D^{1/2} C \upsilon^{1/2}$, where n is the number of electrons transferred, A is the area of electrode, D is the diffusion coefficient, C is the concentration and υ is the scan rate). Since this is clearly not the case for our system (Fig. 9, bottom) this result, in conjunction with the results of the above polymerization experiment, suggest an electroactive polymer coating. Visual inspection of the electrode revealed a dark, insoluble film on its surface.

Fig. 10 shows the UV–Vis spectra for complex **4** and its polymer. The peak at 354 nm arises from what is likely a π–π* charge-transfer transition within the bithiophene ring system. The molar absorptivity (ε) for this transition is $4.0 \times 10^4\ M^{-1}\ cm^{-1}$. The two smaller peaks at 237 and 255 nm are also most likely due to weaker π–π* charge transfer processes occurring within the bithiophene ring with absorptivities of 1.45×10^4 and $1.42 \times 10^4\ M^{-1}\ cm^{-1}$, respectively. The spectrum of the polymer (Fig. 10, bottom) was performed using a transparent ITO coated glass electrode, upon which the polymer was grown. In this spectrum the primary charge-transfer band is shifted to 393 nm. The red shift is attributed to the longer conjugation path in the polymerized form. As the monomer units link together, the π orbital system becomes further delocalized, lowering the energy of the system, and thus lowering

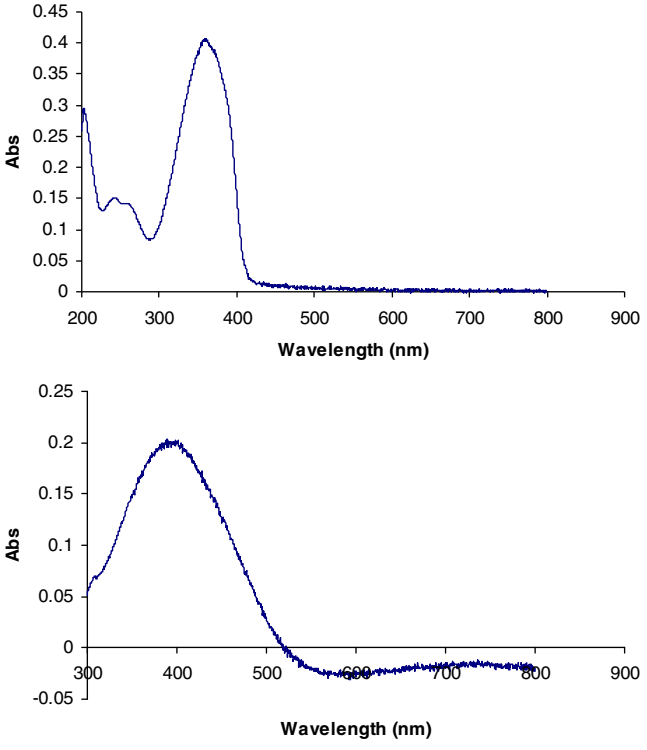


Fig. 10. (Top) UV–Vis spectrum of [Ru_2(μ-2,2′-bithiophene-5-carboxylate)$_4$-(EtOH)$_2$](PF$_6$), **4**, in ethanol (1.00×10^{-5} M, 20 °C). (Bottom) UV–Vis spectrum of "poly[Ru_2(μ-2,2′-bithiophene-5-carboxylate)$_4$(EtOH)$_2$]" on an ITO electrode at 20 °C.

the energy of the absorption process. The broadening of the peak can be explained by cross-linking reactions. The molar absorptivities for the polymer could not be determined as the spectrum was taken of a transparent solid of unknown concentration. The wavelength of this transition is close to the data reported for a solution-phase study for tetrathiophene (394 nm) [31]. It is expected that tetrathiophene linkages will be formed during anodic polymerization. It is acknowledged here that comparisons between solution-phase data and solid-state data must be made with caution, due to differences in solvent-chromophore interactions and the presence of counterions in the polymer film.

4. Conclusion

We have synthesized and characterized eight thiophene-carboxylate-containing complexes; four dimers of the form $[Ru_2(\mu\text{-}O_2CR)_4(alcohol)_2]PF_6$ which were made via a facile carboxylate exchange reaction and four monomers of the form $[Ru(\eta^2\text{-}O_2CR)(dppe)_2]PF_6$ which can be synthesized in moderate to high yield by a disassembly process (R = $-C_4H_3S$, $-CH_2C_4H_3S$, $-CH{=}CHC_4H_3S$ and $-C_8H_5S_2$). All complexes were characterized by IR and elemental analysis and the four monomers were also characterized by NMR and X-ray crystallography. In the six compounds containing mono-thiophene ring systems, cyclic voltammetry scans showed no evidence of oxidative polymerization of the attached thiophene groups possibly due to the very high thiophene oxidation potential in the dinuclear derivatives and a combination of high oxidation potential and steric hindrance in the mononuclear disassembled products. Interestingly, the dimer complex containing the bithiophene ring system, 2,2′-bithiophen-5-carboxylate, was able to be polymerized by anodic polymerization and thin films were produced in both dichloromethane and $BF_3 \cdot OEt_2$. The ability of **4** to undergo polymerization is presumably due to the lower oxidation potential of its bithiophene substituents compared to those present in **1**–**3**. The availability of four polymerization sites in the lantern complex, **4**, permits multiple linking reactions, contrary to its mono-ruthenium analogue, **8**.

Acknowledgements

We thank the Natural Sciences and Engineering Research Council (NSERC) (Canada) and the Canadian Foundation for Innovation (CFI) for financial support.

Appendix A. Supplementary material

CCDC 652956, 652957, 652958 and 668226 contain the supplementary crystallographic data for **5**, **6**, **7** and **8**. These data can be obtained free of charge via http://www.ccdc.cam.ac.uk/conts/retrieving.html, or from the Cambridge Crystallographic Data Centre, 12 Union Road, Cambridge CB2 1EZ, UK; fax: (+44) 1223-336-033; or e-mail: deposit@ccdc.cam.ac.uk. Supplementary data associated with this article can be found, in the online version, at doi:10.1016/j.poly.2007.12.015.

References

[1] A.F. Diaz, K.K. Kanazawa, G.P. Gardini, J. Chem. Soc., Chem. Commun. (1979) 635.
[2] A.F. Diaz, J.A. Logan, J. Electroanal. Chem. 111 (1980) 111.
[3] J. Roncalli, Chem. Rev. 92 (1992) 711.
[4] M.O. Wolf, Adv. Mater. 13 (2001) 545.
[5] M.A.S. Aquino, Coord. Chem. Rev. 170 (1998) 141.
[6] M.A.S. Aquino, Coord. Chem. Rev. 248 (2004) 1025.
[7] P. Angaridis, in: F.A. Cotton, C.A. Murillo, R.A. Walton (Eds.), Multiple-Bonds Between Metal Atoms, Springer Science and Business Media, Inc., New York, 2005, pp. 45–58.
[8] M.C. Barral, R. Jimenez-Aparicio, J.L. Priego, E.C. Royer, M.J. Saucedo, F.A. Urbanos, U. Amador, Polyhedron 14 (1995) 2427.
[9] I.W. Wyman, T.J. Burchell, K.N. Robertson, T.S. Cameron, M.A.S. Aquino, Organometallics 23 (2004) 5353.
[10] I.W. Wyman, K.N. Robertson, T.S. Cameron, J.C. Swarts, M.A.S. Aquino, Organometallics 24 (2005) 6055.
[11] I.W. Wyman, K.N. Robertson, T.S. Cameron, J.C. Swarts, M.A.S. Aquino, Inorg. Chim. Acta 359 (2006) 3092.
[12] R.W. Mitchell, G. Wilkinson, J. Chem. Soc., Dalton Trans. (1973) 846.
[13] SIR92: A. Altomare, G. Cascarano, C. Giacovazzo, A. Guagliardi, M. Burla, G. Polidori, M. Camalli, J. Appl. Cryst. 27 (1994) 435.
[14] SHELXL97: G.M. Sheldrick, 1997.
[15] DIRDIF99: P.T. Beurskens, G. Admiraal, G. Beurskens, W.P. Bosman, R. de Gelder, R. Israel, J.M.M. Smits, The DIRDIF-99 Program System, Technical Report of the Crystallography Laboratory, University of Nijmegan, Netherlands, 1999.
[16] D.T. Cromer, J.T. Waber, International Tables for X-ray Crystallography, vol. IV, The Kynoch Press, Birmingham, England, 1974 (Table 2.2A).
[17] J.A. Ibers, W.C. Hamilton, Acta Crystallogr. 17 (1964) 781.
[18] D.C. Creagh, W.J. McAuley, in: A.J.C. Wilson (Ed.), International Tables for Crystallography, vol. C, Kluwer Academic Publishers, Boston, 1992, p. 219 (Table 4.2.6.8).
[19] D.C. Creagh, J.H. Hubbell, in: A.J.C. Wilson (Ed.), International Tables of Crystallography, vol. C, Kluwer Academic Publishers, Boston, 1992, p. 200 (Table 4.2.4.3).
[20] CRYSTALSTRUCTURE 3.6.0: Crystal Structure Analysis Package, Rigaku and Rigaku/MSC, 9009 New Trails Dr., The Woodlands, TX 77381, USA, 2000–2004.
[21] CRYSTALS Issue 10: D.J. Watkin, C.K. Prout, J.R. Carruthers, P.W. Betteridge, Chemical Crystallography Laboratory, Oxford, UK, 1996.
[22] E.B. Boyar, P.A. Harding, S.D. Robinson, C.P. Brock, J. Chem. Soc., Dalton Trans. (1986) 1771.
[23] K. Nakamoto, Infrared and Raman Spectra of Inorganic and Coordination Compounds, 5th ed., John Wiley and Sons, New York, 1997.
[24] G.G. Briand, M.W. Cooke, T.S. Cameron, H.M. Farrell, T.J. Burchell, M.A.S. Aquino, Inorg. Chem. 40 (2001) 3267.
[25] J. Hjelm, R.W. Handel, A. Hagsfeldt, E.C. Constable, C.E. Housecroft, R.J. Forster, J. Phys. Chem. B 107 (2003) 10431.
[26] B.J. MacLean, P.G. Pickup, J. Mater. Chem. 11 (2001) 1357.
[27] B.J. MacLean, P.G. Pickup, Chem. Commun. (1999) 2471.
[28] P. Denisevich, H.D. Abruna, C.R. Leidner, T.J. Meyer, R.W. Murray, Inorg. Chem. 21 (1982) 2153.
[29] L.F. Schweiger, K.S. Ryder, D.G. Morris, A. Glidle, J.M. Cooper, J. Mater. Chem. 10 (2000) 107.
[30] T.A. Skotheim, R.L. Elsebaumer, J.R. Reynolds (Eds.), Handbook of Conducting Polymers, 2nd ed., revised and expanded., Marcel Dekker, New York, 1986.
[31] A. Yang, M. Kuroda, Y. Shiraishi, T. Kobayashi, J. Phys. Chem. B 102 (1998) 3706.

clear species with four pendent SCN^- and two ppz coordinating Co(II) center through N atoms resulting an octahedral coordination environment, to the contrary of our expectation. Interestingly here ppz gets protonated owing to charge neutrality and debars SCN^- bridging resulting a supramolecular network. Assuming the source of the proton as NH_4^+ ions in the solution we have planned to prevent the protonation using NaSCN instead of NH_4SCN. A similar reaction in the identical condition leads **II**, a polymorph of **I** (Fig. 1).

2. Experimental

2.1. Materials

All the chemicals used were of AR grade.

2.2. Physical measurements

Elemental analyses (carbon, hydrogen and nitrogen) were performed using a Perkin–Elmer 240C elemental analyzer. IR spectra were measured from KBr pellets on a Nicolet 520 FT-IR spectrometer. Thermal analyses were carried out on SDT Q600 TA instrument.

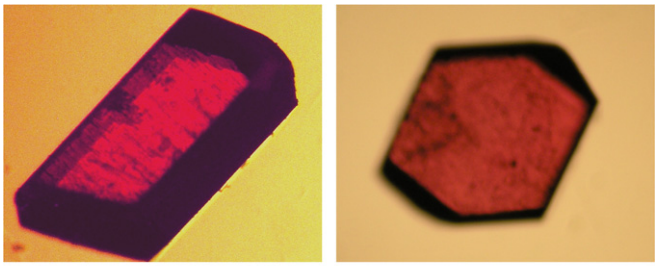


Fig. 1. Polymorphs **I** and **II** with distinct morphology.

2.3. Synthesis

Polymorph **I** was prepared using diffusion technique. A methanolic solution (10 mL) of ppz (1 mmol, 0.086 g) was diffused on an aqueous layer (10 mL) of $Co(NO_3)_2 \cdot 6H_2O$ (1 mol, 0.291 g) and NH_4SCN (2 mmol, 0.152 g) in a tube. Pink crystals suitable for X-ray analysis were obtained at the junction of the two solutions after a few days. Polymorph **II** was synthesized adopting the same reaction procedure as in **I** using NaSCN instead of NH_4SCN. Yield: 75% for **I** and 72% for **II**. *Anal.* Calc. for $C_{12}H_{22}CoN_8S_4$: C, 30.93; H, 4.72; N, 24.05. Found: C, 30.44; H, 4.63; N, 24.39% for **I** and C, 30.42; H, 4.62; N, 24.37% for **II**.

2.4. Crystallographic data collection and refinement

Single crystals of the polymorphs were mounted on a Bruker Smart and Crysalis (Oxford Diffraction) diffractometer for polymorphs **I** and **II**, respectively, equipped with a graphite monochromator and Mo Kα ($\lambda = 0.71073$ Å) radiation. The structure was solved using Patterson method with the help of SHELXL software package. The correct position for the cobalt atom was deduced from an E-map. Subsequent difference Fourier synthesis and least-square refinement revealed the positions of the remaining non-hydrogen atoms. At this point, a calculation by PLATON showed that there was no missed crystallographic symmetry. Non-hydrogen atoms were refined with independent anisotropic displacement parameters. Hydrogen atoms were placed in "idealized positions" and their

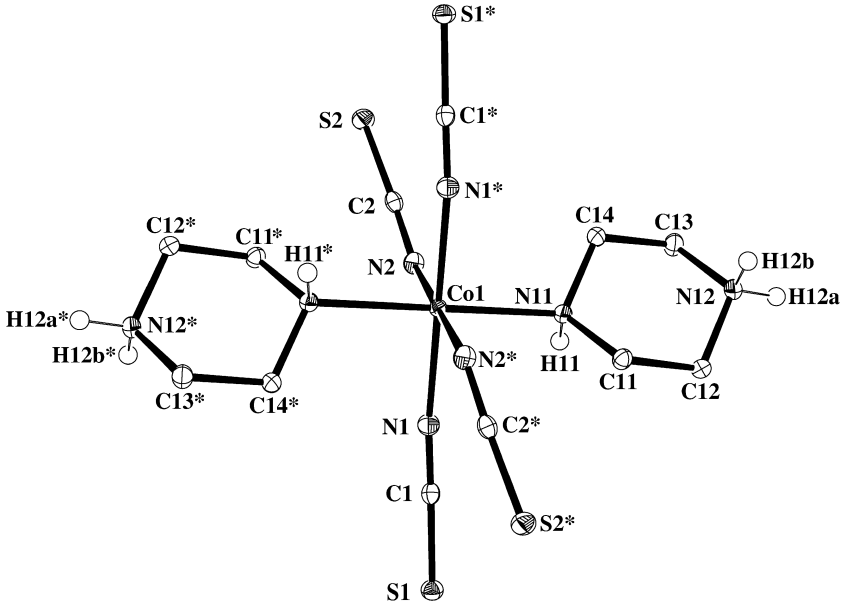


Fig. 2. The ORTEP diagram with 50% ellipsoidal probability for **I**.

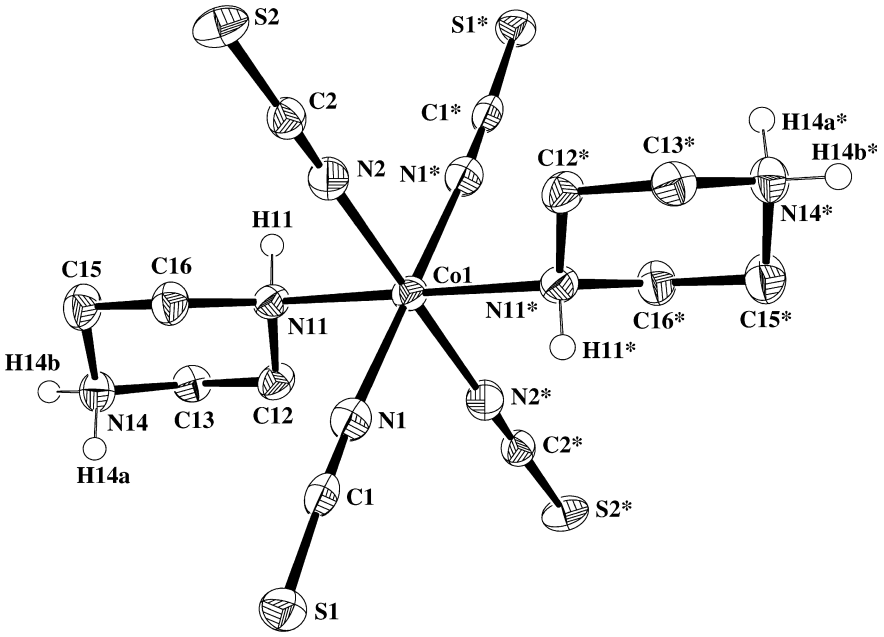


Fig. 3. The ORTEP diagram with 50% ellipsoidal probability for **II**.

displacement parameters were fixed to be 25% larger than those of the attached non-hydrogen atom. Successful convergence was indicated by the maximum shift/error of 0.001 for the last cycle of the least-squares refinement. All calculations were carried out using SHELXL 97 [12], SHELXS 97 [13], PLATON 99 [14], ORTEP-32 [15] and WINGX system Ver-1.64 [16].

3. Results and discussion

3.1. Structural description

ORTEP diagrams for the two polymorphs have been depicted in Figs. 2 and 3. Co(II) centers assume octahedral coordination environments with Co(II) atoms occupying the inversion center in both of them. Interestingly they have the same space group but the unit cell dimensions are slightly different (Table 1) from each other. Four SCN^- molecules and two ppz molecules bind the Co(II) center through their N terminals. SCN^- molecules form the equatorial plane of the Co(II) octahedron and ppz molecules occupy the *trans* axial positions. It is to note that ppz molecules get protonated in both the cases to maintain charge neutrality and this helps in building the supramolecular networks. In **I**, Co(II)–N distances for the equatorial plane are 2.08 Å and 2.18 Å whereas the axial Co(II)–N distance is 2.21 Å. In case of **II**, Co(II)–N distances of the equatorial plane are 2.11 Å and 2.14 Å whereas the axial Co(II)–N distance is 2.25 Å (Table 2). Octahedral geometry of **I** is observed to be more distorted than that of **II**, reflected from the bond angles (Table 2). The angles, N–Co–N′ vary in the range 86.33–92.15° for **I** and 88.76–90.56° for **II**. Most prominent distinction between **I** and **II** is the angle of SCN^- alignment with respect to the *trans* equatorial line passing through N–Co–N′ (Scheme 1) of the Co(II) octahedral coordination environment. Two SCN^- ions make 15.41° and 50.39° angles with this direction in **I** but these

Table 1
Crystallographic data and details of structure refinement for polymorphs **I** and **II**

Polymorph	I	II
Empirical formula	$C_{12}H_{22}CoN_8S_4$	$C_{12}H_{22}CoN_8S_4$
M	465.55	465.55
Crystal system	monoclinic	monoclinic
Space group	$P2_1/n$ (no. 14)	$P2_1/n$ (no. 14)
a (Å)	6.7162(3)	7.4350(12)
b (Å)	11.8350(6)	11.115(2)
c (Å)	11.9941(6)	12.413(3)
β (°)	101.8020(10)	96.844(15)
V (Å^3)	933.21(8)	1018.4(3)
Z	2	2
D_{calc} (g/cm^3)	1.657	1.518
μ (mm^{-1})	1.382	1.266
$F(000)$	482	482
Crystal size (mm)	0.16 × 0.20 × 0.28	0.02 × 0.03 × 0.25
T (K)	100	150
Mo Kα (Å)	0.71073	0.71073
θ_{Min}, θ_{Max} (°)	2.4, 36.3	2.5, 30.2
Data total, unique, R_{int}	16695, 4474, 0.019	6700, 2963, 0.052
Observed data [$I > 2\sigma(I)$]	3946	1532
N_{ref}, N_{par}	4474, 115	2963, 115
R, wR_2, S	0.0226, 0.0657, 1.14	0.0394, 0.0789, 0.80
Maximum and average shift/error	0.00/0.00	0.00/0.00
Minimum and maximum residual density (e/Å^3)	−0.35 and 0.99	−0.56 and 0.57

$w = 1/[\sigma^2(F_o^2) + (0.0384P)^2 + 0.0376P]$ where $P = (F_o^2 + 2F_c^2)/3$.

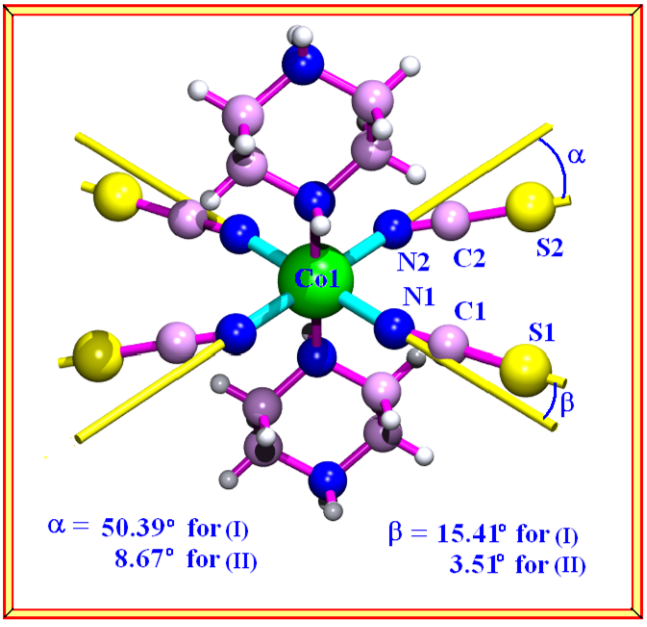
Table 2
Selected bond distances (Å) and angles (°) of polymorphs **I** and **II**

	I	II
Co1–N1	2.0811(7)	2.113(2)
Co1–N2	2.1816(7)	2.136(2)
Co1–N11	2.2076(7)	2.2504(18)
N1–C1	1.1698(10)	1.170(3)
N2–C2	1.1825(10)	1.169(3)
S1–C1	1.6414(7)	1.660(3)
S2–C2	1.6246(7)	1.660(2)
N1–Co1–N2	92.15(3)	90.54(8)
N1–Co1–N11	86.64(2)	90.56(7)
N2–Co1–N11	86.33(2)	88.76(7)
S1–C1–N1	178.73(7)	178.2(2)
S2–C2–N2	176.83(7)	178.6(2)
Co1–N1–C1	164.59(6)	176.49(18)
Co1–N2–C2	129.61(6)	171.33(19)

Table 3
Hydrogen bonding interaction in the polymorphs **I** and **II**

D–H···A	D–H (Å)	H···A (Å)	D–A (Å)	∠D–H···A (°)
I				
N11–H11···S2[a]	0.91	2.68	3.57(7)	167
N12–H12A···S1[b]	0.90	2.86	3.37(8)	117
N12–H12A···S2[c]	0.90	2.86	3.43(7)	123
N12–H12A···S1[d]	0.90	2.73	3.40(8)	132
N12–H12B···N2[e]	0.90	2.08	2.96(10)	167
II				
N11–H11···S2[f]	0.91	2.63	3.526(2)	168
N14–H14A···S2[g]	0.90	2.43	3.301(2)	164
N14–H14B···S1[h]	0.90	2.55	3.328(2)	145
C16–H16A···N2	0.97	2.58	3.154(3)	118

Symmetry code: a = $5/2 - x$, $-/2 + y$, $1/2 - z$; b = $3/2 - x$, $1/2 + y$, $1/2 - z$; c = $3/2 - x$, $-1/2 + y$, $1/2 - z$; d = $-1/2 + x$, $3/2 - y$, $1/2 + z$; e = $-1 + x$, y, z; f = $1/2 - x$, $-1/2 + y$, $1/2 - z$; g = $1 - x$, $1 - y$, $-z$; h = $1/2 + x$, $1/2 - y$, $1/2 + z$.



Scheme 1.

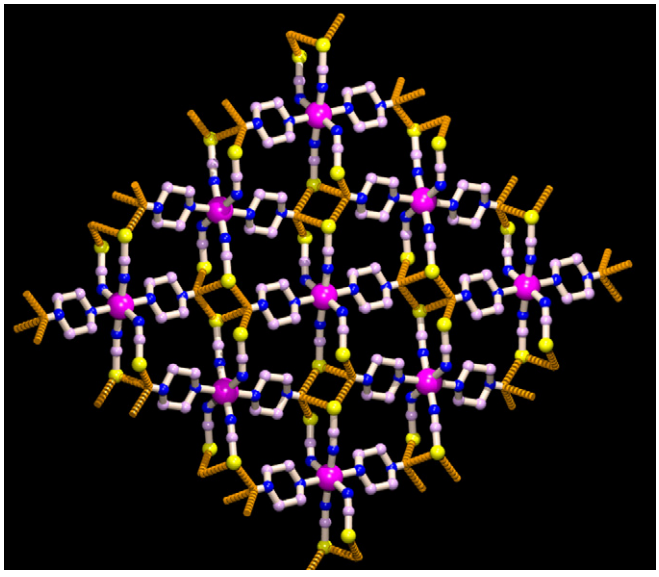


Fig. 4. Trifurcated N–H···S hydrogen bonds form 2D layers (1 0 1) in **I**.

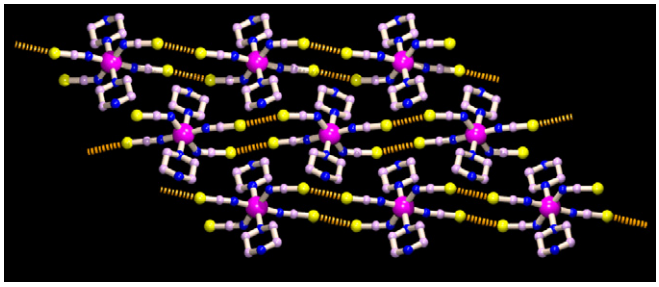


Fig. 5. 2D layers (1 0 1) of **I** viewed as side-by-side alignment of S···S interaction mediated supramolecular 1D ribbons.

are very small, i.e. 3.51° and 8.67° in **II** (Table 2). The angular differences produce a near parallel alignment of coordinated SCN^- ions in **I**, and nearly perpendicular alignment in **II**.

Occurrence of two supramolecular assemblies in case of polymorphs **I** and **II** are due to difference of SCN^- alignment in the outer coordination sphere. In **I** the monomer fragments interact with each other through rarely observed trifurcated hydrogen bonding (N12–H12A···S1; N12–H12A···S2; N12–H12A···S1; Table 3) leading to 2D supramolecular sheet (Fig. 4). The sheets are in (1 0 1) planes. This hydrogen bonding cooperation has been reinforced by S···S interactions, operating between SCN^- ions of adjacent Co(II) centers. The 2D sheet can be viewed as the parallel alignment of 1D supramolecular chains, generated through S···S weak forces (Fig. 5). The S···S distances are 3.6032(4) Å for S1···S2* (* = x, $-1 + y$, z) and 3.6033(4) for S2···S1** (** = x, $1 + y$, z) which are less than the sum of the van der Waals radii of S atoms [17]. Due to the relative angular alignment of successive Co(II) centers, the 2D sheet is actually a thick layer with the

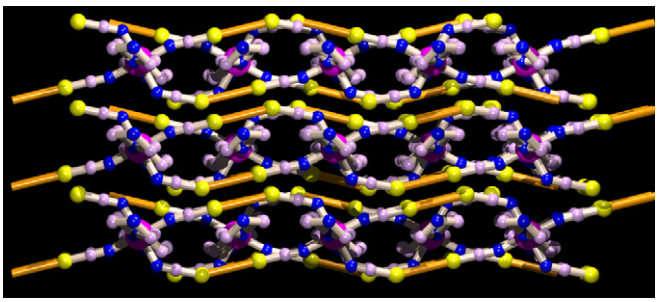


Fig. 6. Stacking of 2D layers in **I** along [1 0 1] (S atoms lie on the edges of the layers with boundaries demarcated by S···S interaction).

SCN^- ligands from adjacent units interacting through S···S interactions and remains nearly parallelly aligned on the two faces of this layer (Fig. 6). The thick layers are stacked along [1 0 1] direction facilitated by inter layer N–H···S and N–H···N hydrogen bonding (Table 3, Fig. S1).

Nearly perpendicular alignment of SCN^- in the outer coordination sphere generates a distinctly different supramolecular assembly in case of **II**. N–H···S hydrogen bonds between adjacent monomers lead to a (4, 4) net topology of the supramolecular 2D sheets (in 1 1 0 plane) parallelly linked through N–H···S hydrogen bond resulting a 3D supramolecular network (Table 3, Figs. 7 and 8).

3.2. Thermal analysis

The thermogravimetric analyses of **I** and **II** (Figs. 9 and 10) reveal that both the polymorphs have identical

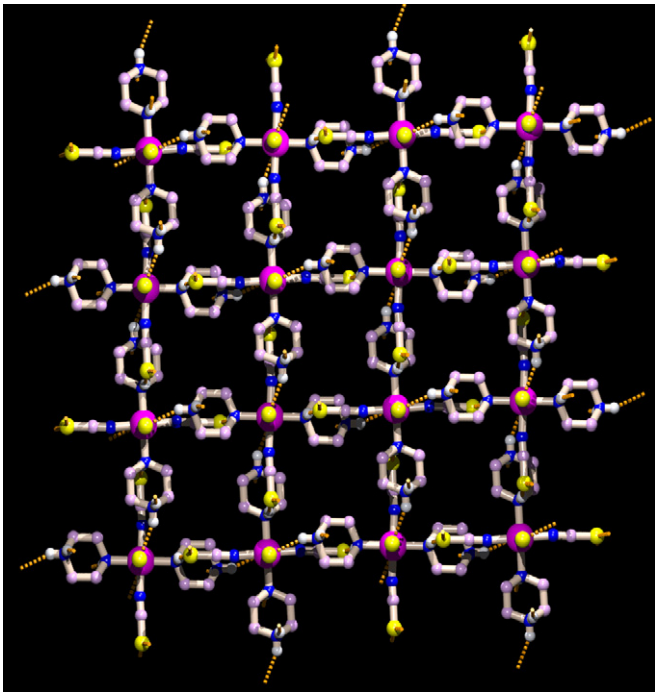


Fig. 7. Supramolecular arrangement leading to assembly in (1 1 0) plane with (4, 4) net topology through N–H···S hydrogen bonding in **I**.

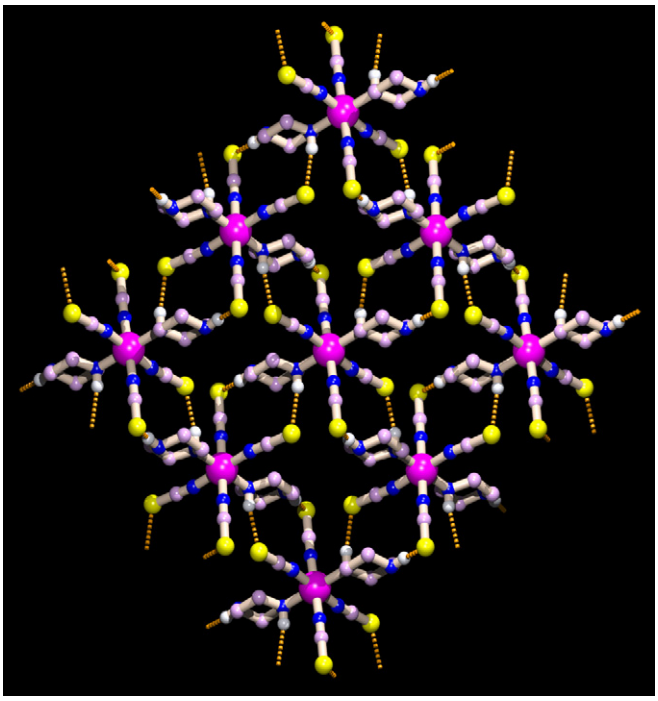


Fig. 8. Details of N–H···S hydrogen bonding between adjacent monomers in **II** (viewed along *a* axis).

decomposition pattern but **I** has slightly higher decomposition temperature (~260 °C) than that of **II** (~282 °C). The DSC curve of **I** does not show any phase transition before decomposition whereas, **II** shows small endothermic pick ($\Delta H = 5.228\ J\ g^{-1}$) in the temperature range, 208–228 °C indicating **II** → **I** transformation. We have run the cooling curve which does not show any phase transition. The room temperature IR spectra of **I** and **II** (Figs. S2 and S3) show a noticeable difference in the ν_{CN} band of SCN^-. There is only one band at 2100.34 cm^{-1} in **I** but **II** shows two bands at 2086.84 cm^{-1} and 2021.26 cm^{-1}. The thermally induced transition [**II** → **I**] is also corroborated by the IR spectra. The room temperature IR spectra immediately after heating **II** at 222 °C show (Fig. S4) only one band at 2108.05 cm^{-1} in the 1900–2300 cm^{-1} region, which is nearly identical to that of **I**. We have also recorded the same spectrum at room temperature after storing the above heated sample at open atmosphere for ~50 days, which shows the reappearance of the IR band at 2023.19 cm^{-1} (Fig. S5) close to the original band at 2021.26 cm^{-1}, showing time dependent reversibility. The foregoing facts suggests polymorph (II) reverts slowly. Thereby we can assume that the polymorphs are enantiotropically related and polymorph **II** is the thermodynamicly stable form at temperatures below the phase transition. This is a counter intuitive considering the higher decomposition temperature and higher density of **I** with respect to **II**, but this kind of anomaly is not uncommon [18] and deserves further investigation.

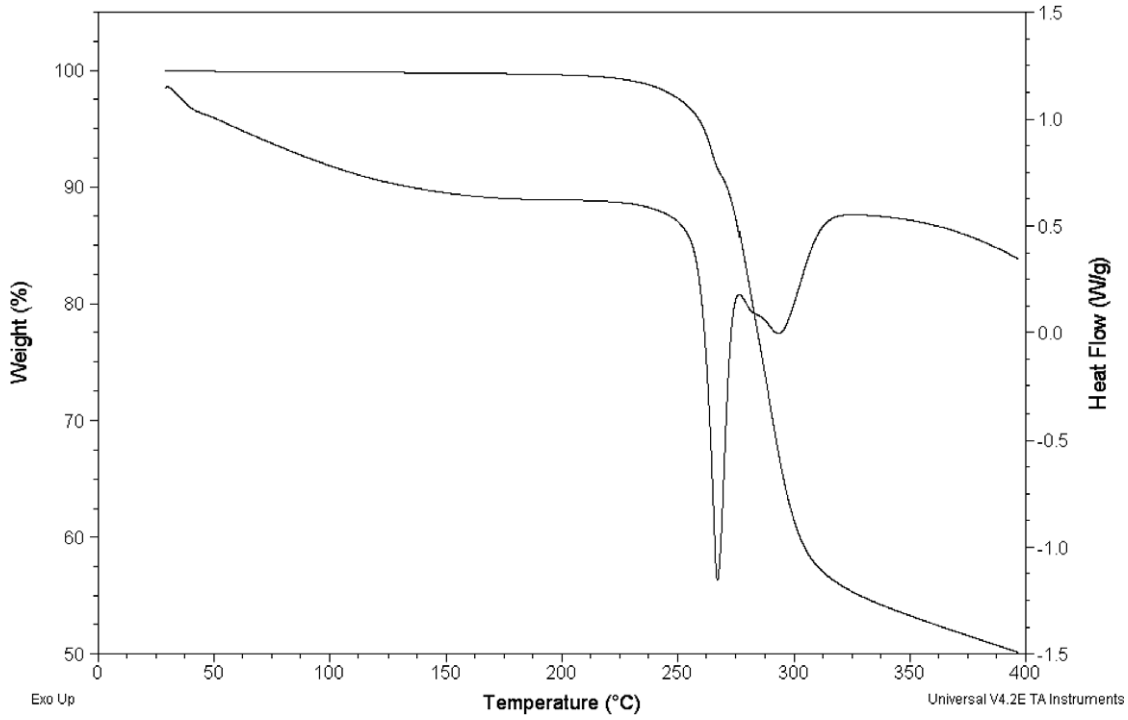


Fig. 9. TG and DSC curves of polymorph **I**.

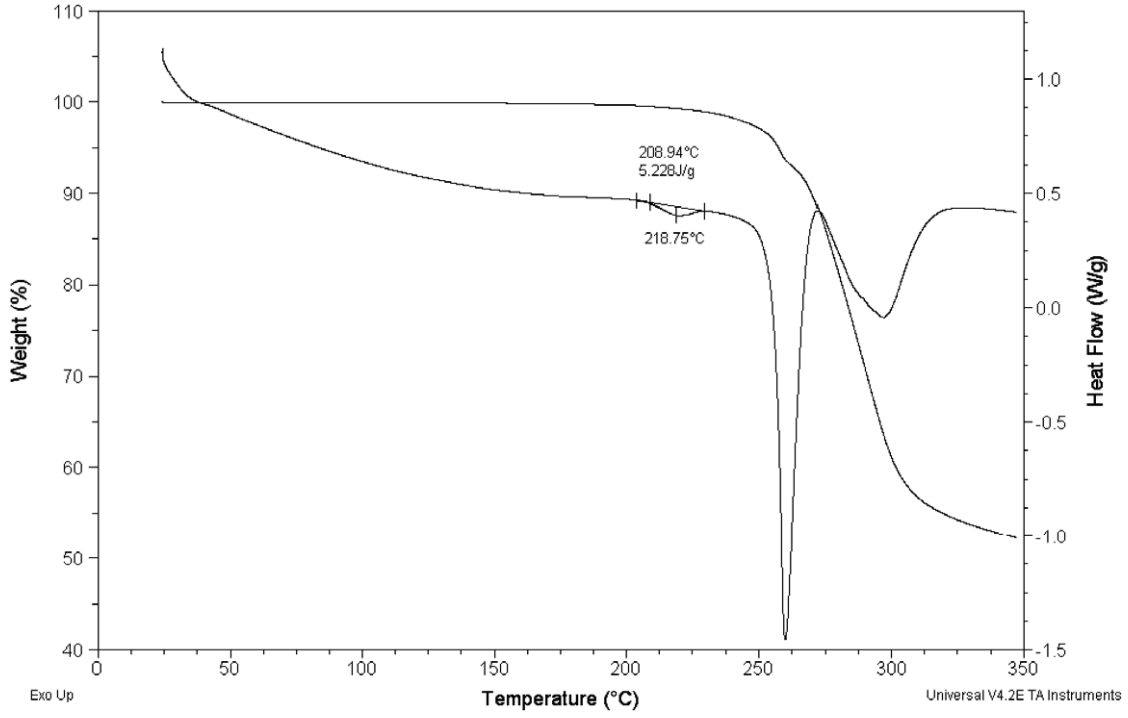


Fig. 10. TG and DSC curves of polymorph **II**.

4. Conclusion

The study shows that for coordination complexes, flexible alignment of pendant ligands is an important fact that needs to be considered which is often overlooked. In the present case the flexible alignment of pendant SCN ligands in the outer coordination sphere is probably the root for the appearance of two polymorphs. The polymorphism phenomenon shows how relatively weaker forces, i.e. S···S interactions cooperate with rare trifurcated hydrogen bond and produce distinctly different packing pattern indicating the urgency of understanding as well as controlling

such weak forces in any successful crystal engineering endeavor.

Acknowledgements

The authors are thankful to Dr. Georgina M. Rosair (Heriot-Watt University) for structural data collection of one complex. A.D.J. acknowledges UGC (India) for granting a leave under the FIP programme. G.M. acknowledges Jadavpur University for a research grant under the "Nano Science and Technology Programme" with the University with Potential for Excellence Scheme of UGC (India).

Appendix A. Supplementary data

CCDC 638125 and 638126 contain the supplementary crystallographic data for yyyy. These data can be obtained free of charge via http://www.ccdc.cam.ac.uk/conts/retrieving.html, or from the Cambridge Crystallographic Data Centre, 12 Union Road, Cambridge CB2 1EZ, UK; fax: (+44) 1223-336-033, or e-mail: deposit@ccdc.cam.ac.uk. Supplementary data associated with this article can be found, in the online version, at doi:10.1016/j.poly.2007.12.016.

References

[1] P. Munshi, T.N. Guru Row, Cryst. Growth Des. 6 (2006) 708.
[2] (a) Z.-Q. Zhang, J.M. Njus, D.J. Sandman, C. Guo, B.M. Foxman, P. Erkm, R. Gelder, Chem. Commun. (2004) 886;
(b) G.Y. Ciftci, Inorg. Chem. Commun. 7 (2004) 1258;
(c) L. Yu, G.A. Stephenson, C.A. Mitchell, C.A. Bunnell, S.V. Snorek, J.J. Bowyer, T.B. Borchardt, J.G. Stowell, S.R. Byrn, J. Am. Chem. Soc. 122 (2000) 585.
[3] L. Fabian, A. Kalman, G. Argay, G. Bernath, Z.C. Gyarmati, Chem. Commun. (2004) 2114.
[4] (a) J.D. Dunitz, J. Bernstein, Acc. Chem. Res. 28 (1995) 193;
(b) T.V. Timofeeva, T. Kinnibrugh, O.Y. Borbulevych, B.B. Averkiev, V.N. Nesterov, A. Sloan, M.Y. Antipin, Cryst. Growth Des. 4 (2004) 1265.
[5] (a) J. Bernstein, R.J. Davey, J.-O. Henck, Angew. Chem., Int. Ed. 38 (1999) 3440;
(b) P. Raiteri, R. Martonk, M. Parrinello, Angew. Chem., Int. Ed. 44 (2005) 3769;
(c) J. Bernstein, Polymorphism in Molecular Crystals, Oxford University Press, New York, 2002.
[6] (a) M. Mirmehrabi, S. Rohani, K.S.K. Murthy, B. Radatus, Cryst. Growth Des. 6 (2006) 141;
(b) V. Suitchmezian, I. Jess, C. Nather, Cryst. Growth Des. 7 (2007) 69;
(c) L.M. Nagao, S. Lyapustina, M.K. Munos, M.D. Capizzi, Cryst. Growth Des. 5 (2005) 2261;
(d) S. Desikan, R.L. Parsons Jr., W.P. Davis, J.E. Ward, W.J. Marshall, P.H. Toma, Org. Proc. Res. Dev. 9 (2005) 933.
[7] (a) M.A. Deij, E. Aret, S.X.M. Boerrigter, L. Meervelt, G. Deroover, H. Meekes, E. Vlieg, Langmuir 21 (2005) 3831;
(b) M.A. Deij, J.H. Horst, H. Meekes, P. Jansens, E. Vlieg, J. Phys. Chem. B 111 (2007) 1523.
[8] G. Mazzanti, S.E. Guthrie, E.B. Sirota, A.G. Marangoni, S.H.J. Idziak, Cryst. Growth Des. 6 (2004) 1303.
[9] (a) R.M. Vrcelj, H.G. Gallagher, J.N. Sherwood, J. Am. Chem. Soc. 123 (2001) 2291;
(b) R.M. Vrcelj, J.N. Sherwood, A.R. Kennedy, H.G. Gallagher, T. Gelbrich, Cryst. Growth Des. 3 (2003) 1027.
[10] (a) D. Braga, F. Grepioni, Chem. Commun. (2005) 3635;
(b) D.M. Shin, I.S. Lee, Y.K. Chung, M.S. Lah, Chem. Commun. (2003) 1036;
(c) C.-F. Wang, Z.-Y. Zhu, X.-G. Zhou, L.-H. Weng, Q.-S. Shen, Y.-G. Yan, Inorg. Chem. Commun. 9 (2006) 1326;
(d) D.A. Pantazis, J.E. McGrady, J. Am. Chem. Soc. 128 (2006) 4128.
[11] R. Hiremath, J.A. Basile, S.W. Varney, J.A. Swift, J. Am. Chem. Soc. 127 (2005) 18321.
[12] G.M. Sheldrick, SHELXS 97, Program for Structure Solution, University of Göttingen, Germany, 1997.
[13] G.M. Sheldrick, SHELXL 97, Program for Crystal Structure Refinement, University of Göttingen, Germany, 1997.
[14] A.L. Spek, PLATON, Molecular Geometry Program, J. Appl. Crystallogr. 36 (2003) 7.
[15] L.J. Farrugia, J. Appl. Crystallogr. 30 (1997) 565.
[16] L.J. Farrugia, J. Appl. Crystallogr. 32 (1999) 837.
[17] S.C. Nyburg, C.H. Faerman, Acta Crystallogr., Sect. B 41 (1985) 274.
[18] P. Bombicz, M. Czugler, R. Tellgren, A. Kálmán, Angew. Chem., Int. Ed. 42 (2003) 1957.

copper(I)–polypyridine type complexes, the absorption characteristics of the MLCT band depends on the symmetry of the ground state, whereas the properties of the excited state strongly depend on the structural distortions following the change in the formal oxidation state after excitation. Different structural and chemical properties, and the coordination ability of the solvents, have been used to modulate the geometry distortions of the ground and excited state [2–6]. This line of research on the Cu–polypyridine family has been reviewed by Meyer et al. up to 1999 [7]. More recently, the dynamics of the distortion process on the photo excited MLCT state of the $[Cu(I)(dmp)_2]^+$, dmp = dimethylphenanthroline, has been investigated both experimentally and theoretically [8]. Using pulsed X-Ray, a transient five-coordinated MLCT state was proposed to have the coordination geometry of a distorted trigonal bipyramid [8a].

The plasticity of the coordination sphere in copper complexes has also been used to investigate specific changes in the microenvironments of electroactive and/or photoactive cores, by studying the size effect of the dendritic core in Cu(I)–polypyridine dendrimers [9].

Coppens et al. [10] with the aim to quantify the Cu coordination environment distortion, defined a distortion parameter ξ_{CD} and found an inverse correlation between the ξ_{CD} value for the ground-state geometry of $[Cu(bfp)_2]^+$ complex, bfp = 2,9-bis(trifluoromethyl)-1,10-phenanthroline, and its ^{3}MLCT excited-state lifetime. A more quantified relationship between structural changes and oxidation state has also been established [11]. Very recently, in order to further elucidate the role of the ligand structure in defining the photophysical properties of $[Cu(NN)_2]^+$ type complexes, Armaroli et al. [12], synthesized two novel phenanthroline ligands characterized by the presence of bulky aryl substituents in the 2,9-positions. The Cu(I) homoleptic complex with the most bulky substituent, shows an unusual absorption spectrum since the intensities of the characteristic band in the range 440–470 nm and the low lying shoulder (500–600 nm) are inverted, so the most prominent band is centered at 560 nm while that at 444 nm appears as a weak shoulder. This spectrum is similar to that of a Cu(I)–catenate complex, which presents a low symmetry, that is, a strongly distorted tetrahedral geometry.

In this context, the present work reports the synthesis, and the spectroscopic and electrochemical characterization of homoleptic copper(I) complexes with substituted pyrazino[2,3-*f*]-1,10-phenanthroline, RpplR′ (R = H, Me, COOMe, and R′ = H, Me) as ligand (Scheme 1).

The ligand ppl (which can be seen as a "fusion" of a bipyridine and a quinoxaline moiety or a phenanthroline and a pyrazino moiety) has been formerly reported by our research group and others [13]. It works as an acceptor of electronic density, which is delocalized mainly on the quinoxaline ring of its structure [13]. This fact should improve the directionality of the electron transfer of the MLCT excited state in the copper complexes. The use of a substituent (R) in the quinoxaline moiety was in order to evaluate its effect on the ground and excited state properties; in the case of R = COOH, the group was envisioned as an anchoring group to a semiconductor oxide electrode, in a potential application of the complex as dye in a solar conversion cell. On the other hand, R′ = Me in the phenanthroline moiety of the ligand is used in order to evaluate comparatively the steric effect on the symmetry of the metal center and to avoid the possibility of exciplex quenching of the excited state [7].

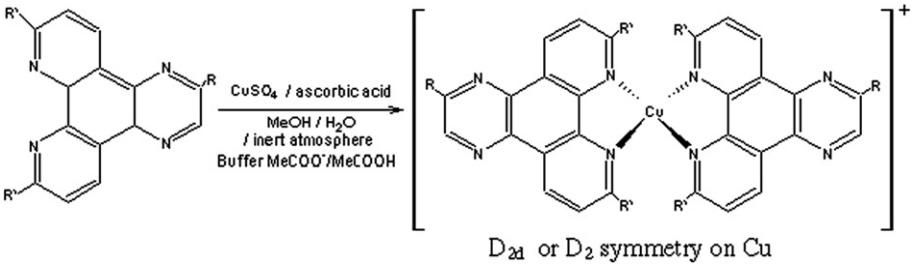
2. Experimental

2.1. Materials

1,10-Phenantroline (hydrate), 2,9-dimethyl-1,10-phenantroline and NH_4PF_6 were p.a. Sigma–Aldrich. The rest of the solids were Merck p.a. chemicals; all of them were used as purchased. All solvents were Merck p.a.; when needed, they were purified and dried by standard methods [13]. The precursors 1,10-phenanthroline-5,6-dione and 2,9-dimethyl-1,10-phenantroline-5,6-dione were synthesized following reported procedures. The corresponding elemental analysis and ^{1}H NMR spectra were in agreement with the published results [14].

2.2. Physical measurements

Elemental analyses were performed on a Fisons Instruments Analyzer, model EA 1108/CHNS-O with PC NCR system 3225. UV–Vis spectra were recorded on a Shimadzu, UV-3101 PC Spectrophotometer, IR Spectra on Bruker Vector-22FTIR spectrometer using KBr pellets and ^{1}H NMR Spectra on a Bruker AC/200 (200 MHz) or Bruker



Scheme 1.

Aspect 400 MHz spectrometer, using CD_3CN or CD_3Cl as solvent and TMS as reference. ESR spectra were recorded in the X band (9.7 GHz) using a Bruker ECS 106 spectrometer with a rectangular cavity and 50 kHz field modulation.

Cyclic voltammetry experiments were carried out using a Bas CV-50W-2,3-MF-9093 equipment with a three-electrode arrangement with a platinum wire, a platinum coil and a Ag/AgCl electrode (in a tetra butyl ammonium chloride solution and adjusted to SCE) as working, auxiliary and reference electrodes, respectively. Experiments were carried out under argon atmosphere, with (TFBTBA) 0.1 M as supporting electrolyte and a scan speed of 200 mV s^{-1}. Emission measurements were carried out in an Aminco SLM-C spectrofluorimeter, at room temperature in Ar atmosphere.

2.3. Synthesis

2.3.1. Ligands

The synthesis of the pyrazino[2,3-*f*]-1,10-phenanthroline (ppl), 2-methylpyrazino[2,3-*f*]-1,10-phenanthroline (Meppl) and 2-carboxylic acid methyl ester pyrazino[2,3-*f*]-1,10-phenanthroline (COOMeppl) were carried out according to Ref. [13]. The pyrazino[2,3-*f*]-2,9-dimethyl-1,10-phenantroline ($pplMe_2$) was synthesized following the same procedure as for the ppl ligand but using 2,9-dimethyl-1,10-phenantroline as starting material. 2-Carboxylic acid pyrazino[2,3-*f*]-1,10-phenanthroline was synthesized as described in Ref. [13], but with the following modifications: after the green solution was poured over ice, the green solid obtained was filtered off and thoroughly washed with water. KOH (1 M) was added to a suspension of the green solid in water until complete dissolution. The solution was filtered and HCl (1:1) added to the supernatant. The white precipitate was filtered off, washed and dried in vacuum. Elemental analysis and ^1H NMR spectra for all the ligands were in agreement with the published results [13]. For pyrazino[2,3-*f*]-2,9-dimethyl-1,10-phenantroline ($pplMe_2$) the results are: Yield: 26.9% *Anal*. Calc. for $C_{16}H_{12}N_4$: C, 73.83; H, 4.65; N, 21.52. Found: C, 72.70; H, 4.67; N, 21.00%. IR (ν_{max}/cm^{-1}): 750, 1391, 1362, 1362. ^1H NMR ($CDCl_3$ as solvent, δ in ppm, J in Hz): 7.64 (d, 2H, H_2, $H_{2''}$, $J_{2,3} = 8.32$), 9.35 (d, 2H, H_3, H_3', $J_{3,2} = 8.32$), 8.90 (s, 2H, H_4, H_4), 2.98 (s, 6H; methyl).

2.3.2. *[Cu(RpplR′)$_2$] PF$_6$ type copper complexes*

General method: The syntheses were carried out following the McMillin general procedure [15]. In a typical synthesis, two degassed solutions, one contains 0.64 mmol of the ligand in 20 ml of methanol and the other one containing 80 mg (0.32 mmol) of $CuSO_4 \cdot 5H_2O$ and 52 mg (0.32 mmol) of NH_4PF_6 dissolved in 10 ml of acetate/acetic acid buffer (0.05 M) were mixed. A green solution was obtained. The solution was degassed and the system maintained in Ar atmosphere. Excess of ascorbic acid (0.48 mmol) was added to the mixture and a reddish-violet solid suddenly precipitated. The solid was collected by vacuum filtration, washed with degassed water, methanol and finally with ethyl ether. The solid was then dried in vacuum and kept under nitrogen or argon. All the steps were carried out under an inert atmosphere.

Bis(pyrazino[2,3-*f*]-1,10-phenanthroline)copper(I) hexafluorophosphate, $[Cu(I)(ppl)_2]$ PF_6 (**1**) Yield: 96.5%. *Anal*. Calc. for $[Cu(I)(C_{14}H_8N_4)_2]PF_6$: C, 49.92; H, 2.39; N, 16.64. Found: C, 49.96; H, 2.16; N, 16.96%. IR (ν_{max}/cm^{-1}): 740, 841, 1391, 1467, 1581.

Bis(2-methylpyrazino[2,3-*f*]-1,10-phenanthroline) copper(I) hexafluorophosphate, $[Cu(I)(Meppl)_2]PF_6$ (**2**): Yield: 93.0%. *Anal*. Calc. for $[Cu(I)$ $(C_{15}H_{10}$ $N_4)_2]PF_6$: C, 51.40; H, 2.87; N, 15.98. Found: C, 50.62; H, 2.80; N, 15.50%. IR (ν_{max}/cm^{-1}), 735, 841, 1370, 1407, 1474, 1578.

Bis(pyrazino[2,3-*f*]-1,10-phenanthroline-2-carboxylic acid methyl ester)copper(I) hexafluorophosphate, $[Cu(I)(MeCOOppl)_2]$ PF_6 (**3**): Yield: 96.5%. *Anal*. Calc. for $[Cu(I)(C_{16}H_{10}N_4O_2)_2]PF_6$: C, 48.64; H, 2.55; N, 14.18. Found: C, 48.59; H, 2.39; N, 14.40%. IR (ν_{max}/cm^{-1}), 794, 841, 1366, 1726, 1745.

bis(Pyrazino[2,3-*f*]-2,9-dimethyl 1,10-phenanthroline)copper(I) hexafluorophosphate, $[Cu(I)(pplMe_2)_2]$ PF_6 (**4**): Yield: 69.0%. *Anal*. Calc. for $[Cu(I)$ $(C_{16}H_{12}N_4)_2]PF_6$: C, 52.71; H, 3.32; N, 15.37. Found: C, 52.62; H, 3.27; N, 15.25%. IR (ν_{max}/cm^{-1}), 745, 840, 1363, 1389, 1584.

3. Results and discussion

Following McMillin's general procedure [15], it was possible to synthesize four new homoleptic complexes of Cu(I) with substituted pyrazino[2,3-*f*]-1,10-phenanthroline, RpplR′, as ligand. Elemental analysis results were in good agreement with the proposed formula for the complexes giving therefore evidence of their purity. The IR spectra of the complexes exhibit the characteristic bands of the corresponding free ligands, except for showing the effect of coordination to the metal. All the metal-complexes display a strong band at 841 cm^{-1} characteristic of the PF_6^- ion.

The ^1H NMR spectra of the complexes display signals at the same region than that for the corresponding free ligands; nevertheless, since the signals are wide, no unambiguous assignment was possible. Initially we supposed that, although the species were manipulated under inert atmosphere, it was not possible to discard the presence of paramagnetic Cu(II) species as an explanation of the low resolution of the spectra; *nevertheless, a silent EPR*[1] for the complexes (not shown) indicated the definitive absence of Cu(II) species. This result was in agreement with the fact that on the NMR spectra, although the signals corresponding to the complexes are wide, the ones corresponding to the solvent were not. A fluxional process as the reason for the observed NMR behavior was postulated. To prove

[1] EPR spectra conditions: Center field: 3250.500 G; sweep width: 1000.000 G; frequency: 9.750 GHz; receiver gain: 74 dB; modulation amplitude: 0.87 G; sweep time: 41.943 s.

this possibility, a VT NMR study was accomplished. Fig. 1 shows the results for the [Cu(I)(Meppl)] PF_6 compound.

The figure shows that at low temperature the signals sharpen, some of them resolve given support to the fluxionally hypothesis. Added to this fact (or maybe related with it) and considering that the RpplR′ ligands have an acceptor character, and that the experimental evidence indicates that even in the ground state (at room temperature) the Cu(I) geometry is distorted towards the Cu(II) preferred geometry, our interpretation is that it is possible to think that the complex presents a type of "internal paramagnetism" due to the presence of a more deshielded Cu(I) as consequence of the displacement of the electronic density towards the acceptor RpplR′ ligand.

Fig. 2 shows the electronic absorption spectra of the complexes. All of them display bands in the 400–650 nm range, which are of MLCT character.

According to the analysis of McMillin et al. [16] for similar complexes of $Cu(NN)_2^+$ type, the shoulder around 500 nm should be assigned to the band named as band I. The assignment of this electronic transition is still controversial [17], but it is related to either a static or dynamic flattening distortion ($D_{2d} \rightarrow D_2$ symmetry). The band centered around 450 nm, named as band II, is associated to an $e(xz, yz) \rightarrow e(\pi^*L)$ excitation on a D_{2d} symmetry or $b(yz) \rightarrow b_2(\pi^*L)$ on D_2 symmetry. The band named as band III, which appears around 380 nm in other polypyridine systems, seems to be, in our case, overlapped with a LC band in the proximity of 350 nm. The UV zone shows ligand centered $\pi \rightarrow \pi^*$ and $n \rightarrow \pi^*$ bands around 250, 300 and 350 nm. Table 1 summarizes the λ_m absorption data for band II.

As in the case of homoleptic and heteroleptic complexes of Ru (II) with Rppl as ligand, the λ_{max} of the MLCT band around 450 nm and the LC bands in the copper complexes, do not change significantly with the R substituent [13]; the tendency of the small changes observed cannot be explained in terms of its donor/acceptor character. The changes are minor also at the shoulder around 350 nm, but the red or blue shift is in agreement with the acceptor or donor properties of the substituents respect to the ppl

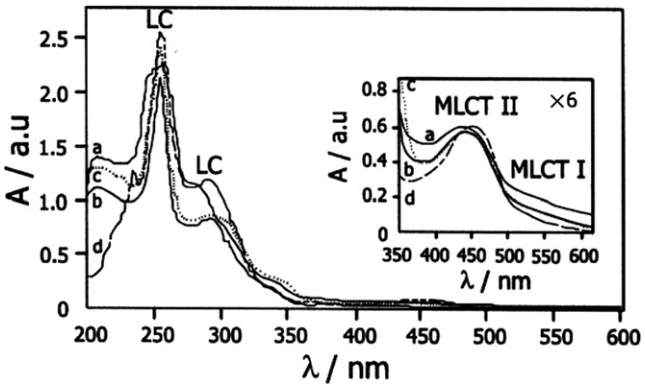


Fig. 2. Electronic absorption spectra of 1.7×10^{-5} M copper complexes solution in CH_3CN as solvent: [Cu(I) (ppl)] PF_6 (a), [Cu(I)(Meppl)] PF_6, (b), [Cu(I)(COOMeppl)]PF_6 (c), [Cu(I)(pplMe)]PF_6 (d); LC ligand centered, MLCT ligand to metal charge transfer.

Table 1
Absorption data for band II of [(RpplR′)$_2$ Cu]PF_6 complexes

Complex	λ_m (nm)[a]
R′ = –H, R = –H	439
R′ = –H, R = –CH_3	440
R′ = –H, R = –$COOCH_3$	443
R′ = –CH_3, R = –H	457

[a] CH_3CN as solvent.

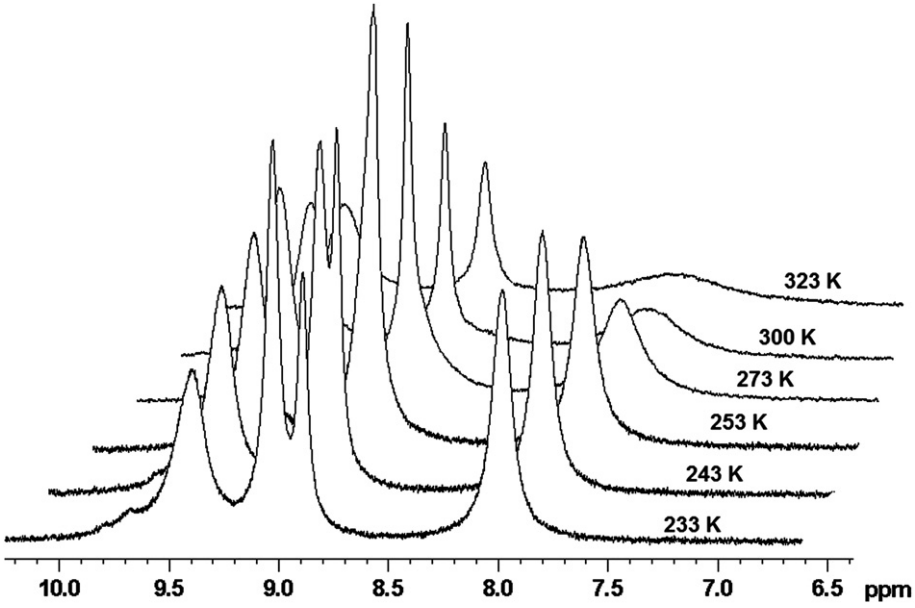


Fig. 1. NMR spectra as a function of the temperature of a [Cu(I)(Meppl)] PF_6, solution in CH_3CN as solvent.

ligand. Changes in the R′ substituents produce a more significant change in the λ_{max} of band II, although not in the way expected for the donor character of the methyl group.

The spectral characteristics of the complexes in Fig. 1, point to a certain degree of D_2 flattened symmetry distortion on the metal center [7,9,12]. If the intensity of the shoulder around 500 nm is taken as a measure of such distortion in the ground state, the observed order for the degree of distortion is $[Cu(I)(ppl)_2]PF_6 > [Cu(I)(Meppl)_2]PF_6 \cong [Cu(I)(COOMeppl)_2]PF_6 > [Cu(I)(pplMe_2)_2]PF_6$.

The above mentioned similar tendency in the electronic absorption spectra of copper complexes and ruthenium complexes with ppl type ligands is less evident when the redox properties are analyzed, since the redox potential of the copper center on the complexes reported herein is affected by the electronic character of R and R′, although the corresponding Ru(II) complexes do not show this behavior [13]; Table 2 shows the electrochemical potentials for the series of complexes.

The redox potentials values do not show the expected correlation with the acceptor or donor electronic character of the substituents on the ligands, *e.g.* the Cu(I)/Cu(II) potential for $[Cu(I)(Meppl)_2]PF_6$ shows a more positive value than that for $[Cu(I)(ppl)_2]PF_6$ or, more surprising, the oxidation process for $[Cu(I)(ppl(Me)_2)_2]PF_6$ is energetically much more disfavored than the same process for $[Cu(I)(COOMeppl)_2]PF_6$. These results, as well as the irreversibility of the redox couples, are not unexpected taking into account the inner-sphere geometric change associated with the change in oxidation state. The relation of the irreversibility of the redox process with the distortion had also been observed electrochemically for some Cu(II) complexes [18]. Karpishin et al. [5a] reported that the absorption spectra of $[Cu(II)(dpp)]^{2+}$ ion, dpp = 2,9-diphenyl-1,10-phenanthroline, shows a low energy shoulder at 750 nm, assigned to a d–d transition and a 575 nm band, assigned to a LMCT. They concluded that $[Cu(II)(dpp)]^{2+}$ remains four-coordinated in solution as it was in the solid states indicated by the X-ray structure. In our case, the electronic absorption spectra of the Cu(II) complexes (not shown)[2] show a visible band centered at ~680 nm with a low extinction coefficient (≈70 cm^{-1} M^{-1}). Although it is difficult to establish the coordination symmetry around copper using visible absorption spectra, the characteristics of this band resembles the band for five or six-coordinated species of Cu(II), giving support to a distortion following the oxidation state change [19,20].

In order to model the solvent dependence of the redox potentials of $[Cu(I)(dmp)_2](PF_6)$, Meyer et al. [7] consider solvent binding equilibrium, following the flattened distortion after the Cu(I)/Cu(II) oxidation. This effect lowers the free energy, making the overall redox process (electron transfer process, distortion of the metal center and coordination of the solvent) more favorable. Therefore, the redox potential values must reflect the balance of the energies associated to all factors affecting the redox process. Consequently, the greater distortion of the Cu(I) site in $[Cu(I)(ppl)_2]PF_6$ ground state relative to $[Cu(I)(Meppl)_2]PF_6$, as seen by absorption spectroscopy, reduces the positive ΔG value associated to the distortion process in the excited state, but not the negative ΔG of the solvent coordination. The effect of both facts favoring the oxidation process, could exceed the effect of the good donor character of the methyl in $[Cu(I)(Meppl)_2]PF_6$, explaining the less positive oxidation potential in the first complex. Otherwise, in the case of $[Cu(I)(ppl(Me)_2)_2]PF_6$ the distortion in the ground state of the Cu(I) center is partially hindered, as well as the distortion after the oxidation process. Consequently the good solvent coordination process and the donor character of the methyl group would not be compensated, explaining its more positive oxidation potential. On the other hand, as expected, the presence of an attractor group produces a change on the redox potentials disfavoring the copper oxidation process and favoring the reduction of the ligand, $E_{pc_{(1)}}$, (*e.g.*: free ppl < -1.5 V; $pplCH_3 < -1.5$ V and COOMeppl $= -1.1$ V). In the same solvent, the Cu(II)/Cu(I) processes for $[Cu(I)(phen)_2]^+$ and $[Cu(I)(dmp)_2]^+$ have a potential of 0.04 V and 0.68 V, respectively [21], as compared with E_{pa} (V) values 0.03 V and 0.4 V values for $[Cu(I)(ppl)_2]^+$ and $[Cu(I)(ppl(Me)_2)_2]^+$, respectively. Therefore, Cu(I) is more unstable with the ppl and $ppl(Me)_2$ ligand. This fact cannot be explained by the acceptor character of the ppl ligand; thus structural effects that would favor Cu(II) type geometry in the ground state should be responsible for this result.

The effect of the solvent on the redox potential values can be seen by comparing the values in two different solvents for the complex with ppl as ligand; as expected from the model described above, the oxidation is more favored in DMSO than in CH_3CN, in accordance with the greater coordination power of the latter solvent.

All complexes studied in this work showed no emission in acetonitrile at room temperature. Although starting

Table 2
Electrochemical properties of $[Cu(I)(RpplR)_2]PF_6$ complexes, vs. SCE in CH_3CN as solvent

Compounds	E_{pa} (V)	E_{pc} (V)	$E_{pc_{(1)}}$ (V)
$[Cu(I)(ppl)]_2PF_6$	0.14	0.03	$\geqslant -1.5$
	0.10[a]	0.05[a]	
$[Cu(I)(Meppl)_2]PF_6$	0.18	0.07	$\geqslant -1.5$
$[Cu(I)(COOMeppl)_2]PF_6$	0.31	0.15	−1.1
$[Cu(I)(ppl(Me)_2)_2]PF_6$	0.59	0.40	$\geqslant -1.5$

[a] In DMSO as solvent; −1.5 is the cathodic limit of the solvent. E_{pa} is assigned to Cu(I)/Cu(II) oxidation. E_{pc} is the corresponding Cu(II)/Cu(I) back process. $E_{pc_{(1)}}$ corresponds to ligand reduction.

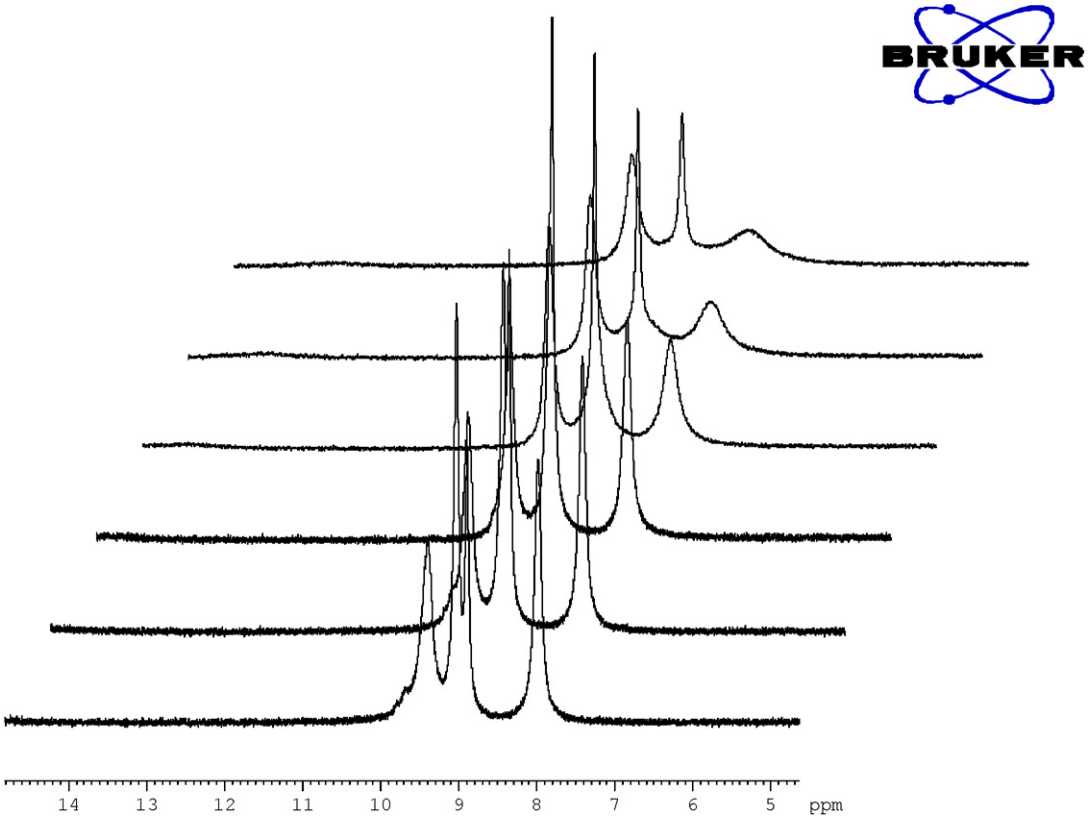
[2] $[Cu(II)(ppl)_2](PF_6)_2$ copper complex: the synthesis was carried out following the same procedure as synthesis (b) in Section 2, except for the addition of the ascorbic acid reductor; the solid was precipitated by the addition of NH_4PF_6.

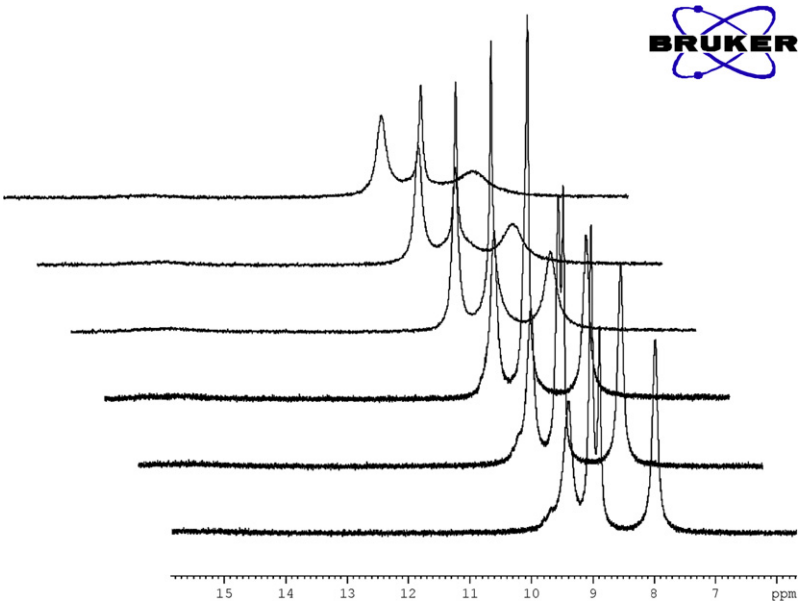
from a distorted ground state, the geometrical change to a more flattened coordination geometry in going to the Franck–Condon state, produced after light absorption (MLTC band), allows the exciplexes quenching process [22]; this explains the non emissive character of the complexes. In this context it was expected that this excited state distortion should be avoided by the steric effect produced by the dimethyl substitution in the 2 and 9 positions in the phenanthroline moiety of the ppl ligand, permitting in this way the $[Cu(I)(ppl(Me)_2)_2]PF_6$ complex to photoluminesce. Nevertheless, no emission was observed even in a less coordinant solvent such as dichloromethane. The excited state behaviour of $[Cu(I)(Meppl)_2]PF_6$ can be compared with the observed for $[Cu(I)(dmp)_2]^+$. In the latter, emission is observed, although with a low quantum yield even in rigid media at low temperature [23]. In spite of the fact that ligand delocalization arguments would predict longer lifetimes and a better excited emissive state [24], the absence of emission in $[Cu(I)(Meppl)_2]PF_6$ is not unreasonable because, as shown above, even in the ground state the geometry of the Cu(I) center in $[Cu(I)(Meppl)_2]PF_6$ is distorted toward the Cu(II) geometry. In general, the photophysical properties of the excited state of some metal polypyridinic type complexes [5b,24,25] reflect the mixture of a variety of electronic (basicity of the donor, electron delocalization) and structural factors (changes in metal-ligand distances, distortion on the metal geometry, change of the coordination number, fluxionally of the ligands). In contrast to ruthenium complexes, structural factors are predominant in the case of copper complexes, influencing even properties related to the ground state, as shown in this work.

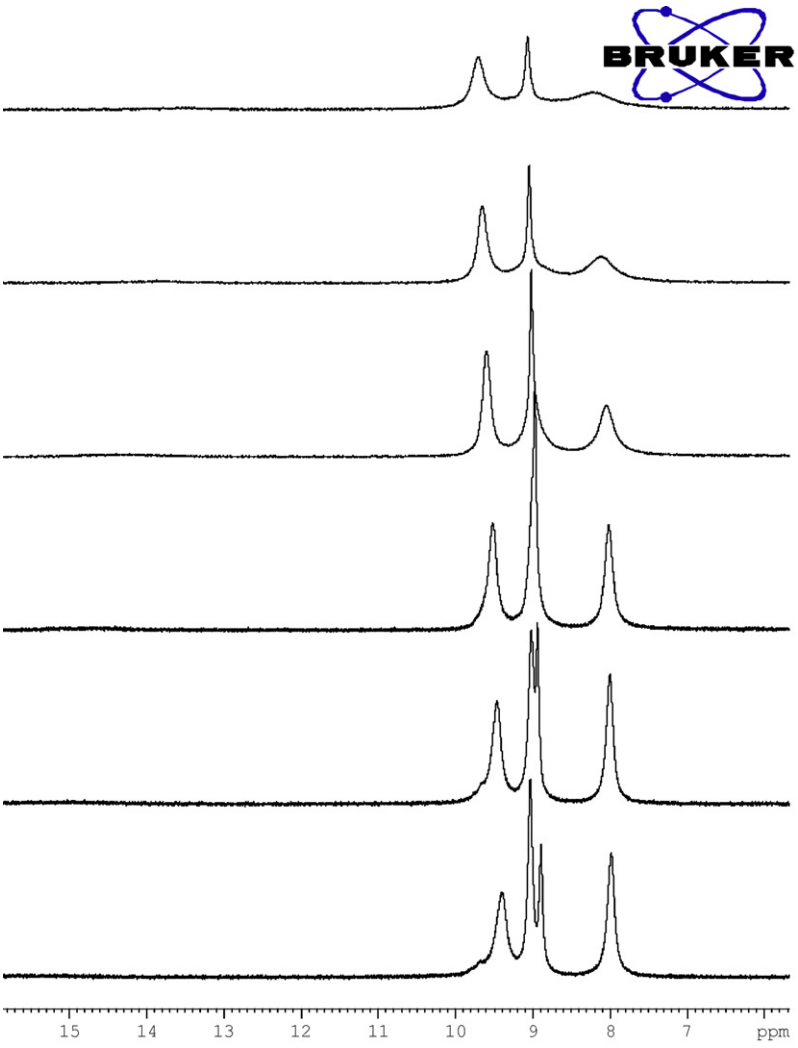
Acknowledgements

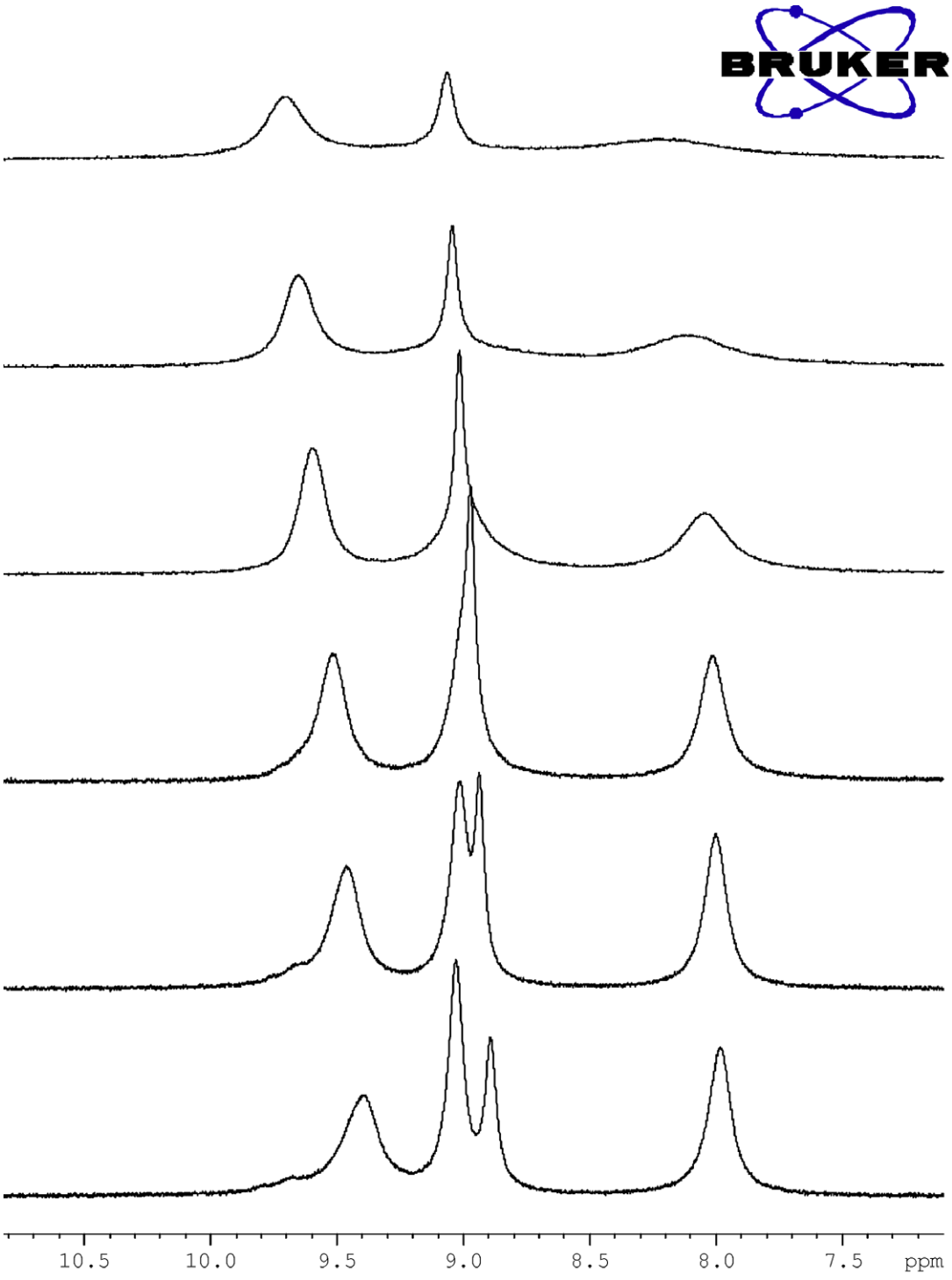
FONDECYT Grant 1020517 and 1070799 is gratefully acknowledged. We thank Mr. Jorge Rodriguez for the EPR spectra and Mr. Sergio Alegria for the VT NMR Spectra.

Appendix




BRUKER
15
14
13
12
11
10
9
8
7
ppm

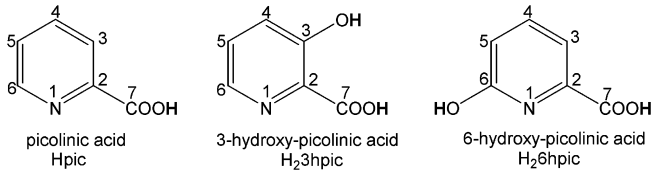

BRUKER
15
14
13
12
11
10
9
8
7
ppm



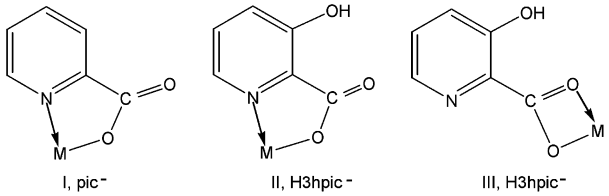
References

[1] (a) F. Barigelleti, L. Flamigni, Chem. Soc. Rev. 29 (2000) 1;
(b) M.K. Nazeruddin, L. Rodicio, R. Humphrey-Baker, E. Müller, N. Vlauchopoulos, M.J. Grätzel, J. Am. Chem. Soc. 115 (1993) 6382.
[2] M. Ruthkosky, F. Castellano, G.M. Meyer, Inorg. Chem. 35 (1996) 6406.
[3] N. Armaroli, Chem. Soc. Rev. 30 (2001) 13.
[4] M. Miller, T.B. Karpishin, Inorg. Chem. 38 (1999) 5246.
[5] (a) M.T. Miller, P.T. Gantzel, T.B. Karpishin, Inorg. Chem. 37 (1998) 2285;
(b) M.T. Miller, P.T. Gantzel, T.B. Karpishin, Inorg. Chem. 38 (1999) 3414.
[6] D.R. Mc Millin, K.M. McNett, Chem. Rev. 98 (1998) 1201.
[7] D.V. Scaltrito, D.W. Thompson, J.A. Callaghan, G.M. Meyer, Coord. Chem. Rev. 208 (2000) 243, and references therein.
[8] (a) C.G. Jennings, D.J. Gosztola, J.P. Hessler, D.V. Scaltrito, G.J. Meyer, J. Am. Chem. Soc. 124 (2002) 10861;
(b) L.X. Chen, G.B. Shaw, I. Novozhilova, T. Liu, G. Jennings, K.

Attonkofer, G. Meyer, P. Coppens, J. Am. Chem. Soc. 125 (2003) 7022.
[9] (a) Y. Rio, G. Accorsi, N. Armaroli, D. Felder, E. Levillain, J.F. Nierengarden, Chem. Commun. (2002) 1830;
(b) E.g. Kontekca, Y. Río, C. Bourgogne, M. Elhabiri, R. Louis, A.M. Albrecht-Gary, J.F. Nierengarden, Inorg. Chem. 43 (2004) 3200.
[10] A.Y. Kovalewky, M. Gembicky, P. Coppens, Inorg. Chem. 43 (2004) 828.
[11] S. Zahn, D. Das, J.W. Canary, Inorg. Chem. 45 (2006) 6056.
[12] V. Kalsani, M. Schmittel, A. Listorti, G. Accorsi, N. Armaroli, Inorg. Chem. 45 (2006) 2062.
[13] A. Delgadillo, P. Romo, A.M. Leiva, B. Loeb, Hel. Chim. Acta 83 (2003) 2110.
[14] W. Paw, R. Eisenberg, Inorg. Chem. 36 (1997) 2287.
[15] D. Mc Millin, T. Bucker, B. Tae Ahn. Inorg. Chem. 16 (1977) 943.
[16] R.M. Everly, D. McMillin, J. Phys. Chem. 95 (1991) 9071.
[17] M. Eggleston, D. McMillin, K. Koeng, D.A. Pallenberg, Inorg. Chem. 36 (1997) 172.
[18] I. Toledo, M. Arancibia, C. Andrade, I. Crivelli, Polyhedron 17 (1998) 73.
[19] W.M.E. Koomen van Oudenniel, R.A.G. de Graaff, R. Prins, J. Reedijk, Inorg. Chem. 28 (1989) 1128.
[20] Y. Oh, J. Korean Chem. Soc. 44 (2000) 507.
[21] P. Federlin, J.M. Kern, A. Rastegar, C.P. Dietrich-Bruchecker, A. Marnot, J.P. Sauvage, New J. Chem. 14 (1999) 9.
[22] R.M. Everly, D. McMillin, Photochem. Photobiol. 6 (1989) 711.
[23] R.M. Everly, R. Ziessel, J. Suffert, D. McMillin, Inorg. Chem. 30 (1991) 559.
[24] J.A. Treadway, B. Loeb, R. López, P.A. Anderson, F.R. Keene, T.J. Mayer, Inorg. Chem. 35 (1996) 2242.
[25] M.H. Damrauer, T. Boussie, M. Devenney, J.K. McKusker, J. Am. Chem. Soc. 119 (1997) 8253.



Scheme 1. Structural formulae of the ligands.



Scheme 2. Most common coordination modes of picolinato and 3-hydroxypicolinato ligands.

X-ray diffraction in the solid state [17,18]. In accordance with this expectation, two of the picolinate derivatives prepared in present work were isolated as crystalline solids and were studied by diffractometry. Attempts to recrystallize the complex of **3** unexpectedly gave rise to a new derivative containing both $TlMe_2^+$ and Na^+. This new product is, as far as we know, the first heterobimetallic compound of H6hpic$^-$ to be prepared and identified by X-ray diffraction.

2. Experimental

2.1. Materials

Hpic, $H_2$3hpic and $H_2$6hpic were commercial products (Merck, Fluka, Aldrich). $TlMe_2I$ and $TlMe_2(OH)$ were obtained according to the methods reported in the literature [19,20]. All other chemicals were AR grade and were used without further purification.

2.2. Measurements

Elemental analysis (C, H, N) was performed using Fisons 1108 and Perkin-Elmer analyzers. Melting points were determined with a Büchi apparatus and were not corrected. IR [KBr pellets (4000–500 cm^{-1}) and Nujol mulls between polyethylene pellets (500–100 cm^{-1})] and Raman (polycrystalline samples) spectra were recorded on a Bruker IFS-66V spectrometer equipped with an FRA 106 module. ^{1}H and ^{13}C NMR spectra were measured at room temperature on Bruker AMX 300 (operating at 300.14 and 75.48 MHz, respectively) and AMX 500 (operating at 500.14 and 125.77 MHz, respectively) spectrometers using sample solutions in DMSO-d_6. Chemical shifts are reported in ppm and referred to TMS using the solvent signal for ^{1}H and ^{13}C spectra (^{1}H: 2.50 ppm, ^{13}C: 39.50 ppm). Chemical shifts were considered positive at lower applied field.

2.3. Synthesis and characterization

2.3.1. *[$TlMe_2$(pic)]* ***(1)***

An aqueous solution of dimethylthallium hydroxide, prepared from $TlMe_2I$ (0.462 g, 1.28 mmol), was added dropwise to a stirred solution of picolinic acid (0.156 g, 1.28 mmol) in methanol (20 mL). The mixture was stirred for about 8 h and then concentrated with a rotary evaporator until a solid product was formed. Yield: 79%. M.p. 230 °C. *Anal.* Calc. for $C_8H_{10}NO_2Tl$ (356.56): C, 26.95; H, 2.83; N, 3.93. Found: C, 27.02; H, 2.79; N, 3.93%. IR (cm^{-1}): $\nu_s(CO_2)$ 1364 s, ν_{ring}(Py) 1608 m, 1587 m, 1563 m, 1469 w, ν(Tl–C) 525 w, ν(Tl–O) 411 s, ν(Tl–N) 208 w. Raman (cm^{-1}): ν(Tl–C) 497 s, ν(Tl–O) 411 w. ^{1}H NMR $\delta = 0.73$ (d, 6H, $TlMe_2^+$, $^2J_{H-Tl} = 429.5$ Hz), 7.58 (dd, 1H, H^5, $^3J_{H-H} = 7.12$ Hz, $^4J_{H-H} = 1.23$ Hz), 7.95 (td, 1H, H^4, $^3J_{H-H} = 7.64$ Hz, $^4J_{H-H} = 1.64$ Hz), 8.04 (d, 1H, H^3, $^3J_{H-H} = 7.70$ Hz), 8.66 (d, 1H, H^6, $^3J_{H-H} = 4.49$ Hz). ^{13}C NMR $\delta = 124.4$ (C^3), 124.7 (C^5), 137.4 (C^4), 147.6 (C^6), 155.0 (C^2), 167.8 (C^7). The carbon signal of the $TlMe_2^+$ moiety was not observed.

Crystals suitable for single-crystal X-ray diffraction studies were obtained by recrystallization from the methanol solution of the crude product.

2.3.2. *[$TlMe_2$(H3hpic)]* ***(2)***

An aqueous solution of dimethylthallium hydroxide, prepared from $TlMe_2I$ (0.460 g, 1.30 mmol), was added dropwise to a stirred solution of 3-hydroxypicolinic acid (0.180 g, 1.30 mmol) in methanol (25 mL). The final mixture was stirred for about 8 h and then concentrated with a rotary evaporator until a solid product was formed. Yield: 70%. M.p. 270 °C. *Anal.* Calc. for $C_8H_{10}NO_3Tl$ (372.56): C, 25.79; H, 2.71; N, 3.76. Found: C, 25.78; H, 2.66; N, 3.71%. IR (cm^{-1}): $\nu_s(CO_2)$ 1385 m, ν_{ring}(Py) 1620 m, 1568 w, 1531 w, 1460 s, $\nu(C_{Py}–OH)$ 1256 m, 1227 m, ν(Tl–C) 510 vw, ν(Tl–O) 393 s, ν(Tl–N) 208 w. Raman (cm^{-1}): ν(Tl–C) 501 s, ν(Tl–O) 394 w. ^{1}H NMR $\delta = 0.74$ (d, 6H, $TlMe_2^+$, $^2J_{H-Tl} = 433.7$ Hz), 7.43 (dd, 1H, H^5, $^3J_{H-H} = 8.36$ Hz, $^3J_{H-H} = 4.50$ Hz), 7.34 (dd, 1H, H^4, $^3J_{H-H} = 8.35$ Hz, $^4J_{H-H} = 1.37$ Hz), 8.13 (dd, 1H, H^6, $^3J_{H-H} = 4.51$ Hz, $^4J_{H-H} = 1.35$ Hz), 15.53 (s, 1H, OH). ^{13}C NMR $\delta = 22.5$ (d, $TlMe_2^+$, $^1J_{C-Tl} = 3127$ Hz), 125.6 (C^4), 127.5 (C^5), 135.0 (C^2), 137.3 (C^6), 159.5 (C^3), 171.4 (C^7).

Crystals suitable for X-ray diffraction studies were obtained by recrystallization of the crude product from methanol.

2.3.3. *[$TlMe_2$(H6hpic)]* ***(3)***

An aqueous solution of dimethylthallium hydroxide, prepared from $TlMe_2I$ (0.469 g, 1.27 mmol), was added dropwise to a stirred solution of 6-hydroxypicolinic acid (0.177 g, 1.27 mmol) in methanol (30 mL). The final mixture was stirred for about 8 h and then concentrated with a rotary evaporator until a solid product was formed. Yield: 63%. M.p. 241°C. *Anal.* Calc. for $C_8H_{10}NO_3Tl$

(372.56): C, 25.79; H, 2.71; N, 3.76%. Found: C, 26.24; H, 2.58; N, 4.07%. IR (cm^{-1}): $\nu_s(CO_2)$ 1385s, ν_{ring}(Py) 1592 m, 1556 m, 1520 m, $\nu(C_{Py}–OH)$ 1240 m, ν(Tl–C) 520 sh, ν(Tl–O) 342 m. Raman (cm^{-1}): ν(Tl–C) 487 s. The poor solubility of this complex in DMSO prevented the measurement of its NMR spectra.

When the crude product was recrystallized from methanol, a few single crystals of $[NaTlMe_2(H6hpic)_2]$ (**3′**) were obtained after a very slow solvent evaporation of almost a year being one of which suitable for X-ray diffraction studies. It is plausible that the Na^+ cation present in the compound comes from the NaOH solution used in the preparation of Me_2TlOH.

2.4. Crystallographic data collection and structure determination

Data collection and processing were carried out using an Enraf-Nonius CAD 4 diffractometer with a graphite-monochromated Mo Kα radiation source ($\lambda = 0.71073$ Å). Details of the crystal structure determination and refinement for all three compounds are given in Table 1. The intensities were corrected for Lorentz polarization factors. The structures were solved using a Patterson method for heavy atoms and refined by full matrix least-squares methods for the location of the remaining non-hydrogen atoms (SHELX 97 [21]). All of the non-hydrogen atoms were treated anisotropically. All hydrogen atoms were included in the model at geometrically calculated positions. The maximum height around Tl atom in the final ΔF map was 6.4 e $Å^{-3}$ at a distance of 0.30 Å of the heavy atom. The drawings were obtained using the ORTEP [22] and MERCURY [23] programs.

3. Results and discussion

3.1. Crystal structures

The crystal structures of compounds **1** and **2** are shown in Fig. 1 and their bond distances and angles are listed in Table 2.

The asymmetric unit of compound **1** consists of two independent molecules associated as a dimer. In the asymmetric unit of compound **2** there is only one molecule but this is also associated with a neighbouring one (i = $-x$, $-y$, $-z$). In both compounds the ligands are N,O-chelated with the monodentate deprotonated carboxylate groups bridging two dimethylthallium(III) units. In this way, each ligand coordinates one $TlMe_2^+$ unit through a pyridine nitrogen (N11/N21 in **1**, N in **2**) and one carboxylate

Table 1
Crystal data and experimental details of the structure refinement for **1**, **2** and **3′**

	1	**2**	**3′**
Molecular formula	$C_{16}H_{20}N_2O_4Tl_2$	$C_{16}H_{20}N_2O_6Tl_2$	$C_{14}H_{14}N_2NaO_6Tl$
Formula weight	713.08	745.1	533.65
Temperature (K)	100(2)	100(2)	120(2)
λ (Å)	0.71073	0.71073	0.71073
Crystal size (mm)	0.20 × 0.10 × 0.06	0.20 × 0.16 × 0.12	0.28 × 0.23 × 0.08
Crystal system	Triclinic	Triclinic	Tetragonal
Space group	$P\bar{1}$	$P\bar{1}$	$P4_12_12$
Unit cell dimension			
a (Å)	6.7500(2)	7.2520(2)	10.4821(3)
b (Å)	10.4020(3)	7.6840 (2)	10.4821(3)
c (Å)	13.6360(4)	9.3970(3)	13.9283(4)
α (°)	85.869(1)	107.428(1)	
β (°)	81.669(1)	99.353(1)	
γ (°)	83.555(1)	96.445(2)	
V ($Å^3$)	939.83(5)	485.71(2)	1530.36(8)
Z	2	1	4
D_{calc} (g cm^{-3})	2.520	2.554	2.316
F(000)	648	342	1004
μ (Mo Kα) (mm^{-1})	17.145	16.601	7.402
θ Range for data collection (°)	1.51–25.00	2.32–25.00	3.5–27.5
Limiting indices (h,k,l)	(−7, 8); (−12, 12); (−16,16)	(−8,8); (−9,9); (−11,11)	(−12,13); (−11,13); (−18,14)
Reflections collected	9867	6601	6938
Independent reflections [$R_{(int)}$]	3288 [0.1088]	1912 [0.0652]	1762 [0.0591]
Maximum and minimum transmissions	0.357 and 0.110	0.137 and 0.077	0.4110 and 0.1133
Refinement method		Full-matrix least-squares on F^2	
Diffractometer		Enraf Nonius CAD 4	
Goodness-of-fit on F^2	1.106	1.100	1.001
Final R indices [$I > 2\sigma(I)$]	$R_1 = 0.0524$, $wR_2 = 0.1482$	$R_1 = 0.0260$, $wR_2 = 0.0642$	$R_1 = 0.0459$, $wR_2 = 0.1058$
R indices (all data)	$R_1 = 0.0548$, $wR_2 = 0.1504$	$R_1 = 0.0283$, $wR_2 = 0.646$	$R_1 = 0.0467$, $wR_2 = 0.1064$
Largest difference in peak and hole, e $Å^{-3}$	2.383 and −3.127	1.110 and −2.311	6.422 and −6.515
Programs used		SHELX 97, ORTEP, PLATON	

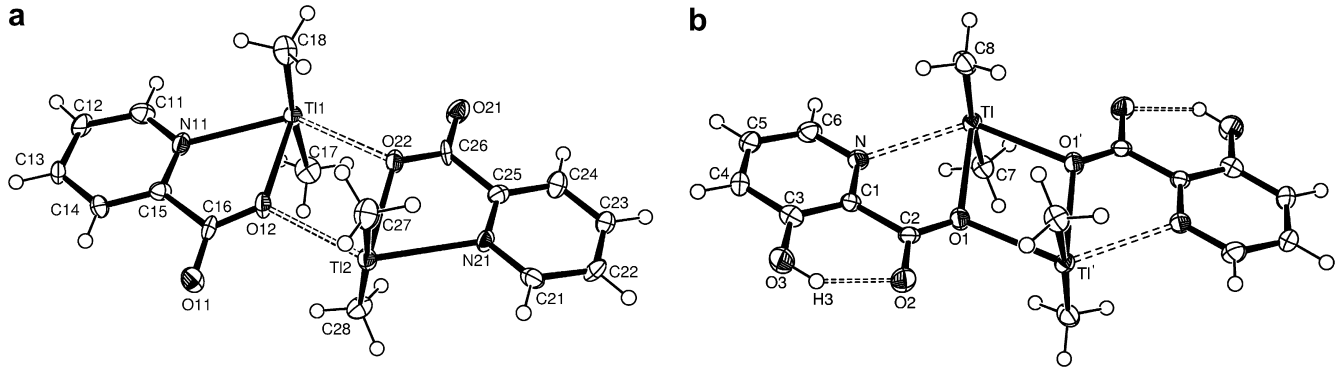


Fig. 1. ORTEP plots of: **1** (a) and **2** (b) showing the numbering scheme in the asymmetric unit, the dimer association and the intramolecular hydrogen bonds for **2**.

Table 2
Selected bond lengths (Å) and angles (°) for **1**, **2** and **3′**

1		**2**		**3′**	
Tl(1)–C(18)	2.106(13)	Tl–C(8)	2.105(6)	Tl–C(7)	2.124(9)
Tl(1)–C(17)	2.127(13)	Tl–C(7)	2.125(6)	Tl–O(1)	2.615(7)
Tl(1)–N(11)	2.567(11)	Tl–N	2.678(5)	Tl–O(2)	2.789(7)
Tl(1)–O(12)	2.532(9)	Tl–O(1)	2.502(4)	Tl–O(3)^{ii}	3.203(7)
Tl(1)–O(22)	2.665(8)	Tl–O(1)^{i}	2.555(4)	Na–O(1)	2.443(7)
Tl(1)–O(11)^{i}	2.788(9)	Tl–O(2)^{ii}	2.966(4)	Na–O(2)^{vi}	2.483(7)
Tl(2)–C(28)	2.116(12)			Na–O(3)^{iv}	2.354(7)
Tl(2)–C(27)	2.120(14)			Tl–Na	3.70583(11)
Tl(2)–N(21)	2.586(10)				
Tl(2)–O(12)	2.625(8)				
Tl(2)–O(22)	2.501(9)				
Tl(2)–O(21)^{ii}	2.825(9)				
C(18)–Tl(1)–C(17)	172.6(6)	C(8)–Tl–C(7)	171.4(2)	C(7)–Tl–C(7)^{i}	179.1(6)
N(11)–Tl(1)–O(12)	64.0(3)	N–Tl–O(1)	63.06(13)	O(1)–Tl–O(1)^{i}	82.2(3)
O(12)–Tl(1)–O(22)	71.6(3)	O(1)–Tl–O(1)^{i}	67.16(15)	O(1)–Tl–O(2)	48.9(2)
C(28)–Tl(2)–C(27)	173.0(6)	N–Tl–O(2)^{ii}	98.47(13)	O(2)–Tl–O(3)^{iii}	61.8(2)
N(21)–Tl(2)–O(22)	64.4(3)	O(1)^{i}–Tl–O(2)^{ii}	130.72(12)	O(3)^{ii}–Tl–O(3)^{iii}	61.5(2)
O(12)–Tl(2)–O(22)	72.8(3)			O(1)–Na–O(1)^{i}	89.5(3)
				O(1) –Na–O(3)^{v}	170.5(3)
				O(1) –Na–O(3)^{iv}	81.2(4)
				O(2)^{vi}–Na–O(2)^{vii}	164.0(4)
				O(3)^{iv}–Na–O(3)^{v}	108.2(4)

Symmetry transformation used to generate equivalent atoms: **1**: (i) = $x+1, y, z$; (ii) = $x-1, y, z$; **2**: (i) = $-x, -y, -z$; (ii) = $x-1, y, z$; **3′**: (i) = $x, y, -z$; (ii) = $-x+1/2, y-1/2, -z+1/4$; (iii) = $y-1/2, -x+1/2, z-1/4$; (iv) = $-y+1/2, -x+1, -z+1/2$; (v) = $-x+1, -y+1, z-1/2$; (vi) = $-x+1/2, y+1/2, z+1/4$; (vii) = $y+1/2, -x+1/2, z-1/4$.

oxygen (O12/O22 in **1**, O1 in **2**), with the latter also binding to a second $TlMe_2^+$ unit.

These two complexes exhibit some common features: (a) the structural parameters of the $[TlMe_2]^+$ unit [Tl–C = 2.105(6)–2.127(13) Å, C–Tl–C = 171.4(2)–173.0(6)°] are similar to those found in other $[TlMe_2]^+$ complexes with N,O or O,O donor ligands [17,24,25]; (b) the Tl–N distances [2.567(11), 2.586(10) and 2.678(5) Å] are close to or shorter than those found in $[TlMe_2(phen)](ClO_4)$ [2.75(2) Å] [26] and $[TlMe_2(Py)_2CH_2]NO_3$ [2.658(9), 2.666(9) Å] [27] although they are longer than those in $TlMe_2^+$ complexes with other hydroxy pyridine carboxylic acids [11,18]; (c) the Tl–O bond lengths in the dimers, in the range 2.501(9)–2.665(8) Å, are comparable with those in other $TlMe_2^+$ carboxylate complexes [17,18]; (d) the weak interactions between the metal and the second atom of the $-COO^-$ group (O11/O21 in **1** and O2 in **2**) associate the dimers to give a polymeric chain along the *x*-axis (see Fig. 2 for compound **1**). The distance between Tl and O(2)^{i} [3.462(5) Å] in **2** is too close to the sum of the van der Waals radii {Tl–O = 3.50 Å [28]} to be considered a significant bonding interaction. The resulting $[C_2NO_3]$ coordination sphere can be described as a very distorted octahedron with the methyl groups in the apical positions (Fig. 2).

In **2** there are also intramolecular hydrogen bonds formed between the hydroxyl O(3)–H(3) group and the oxygen O(2) of the COO^- (Fig. 1b, Table 3).

Despite the structural similarity between the complexes, some small differences between the two compounds are

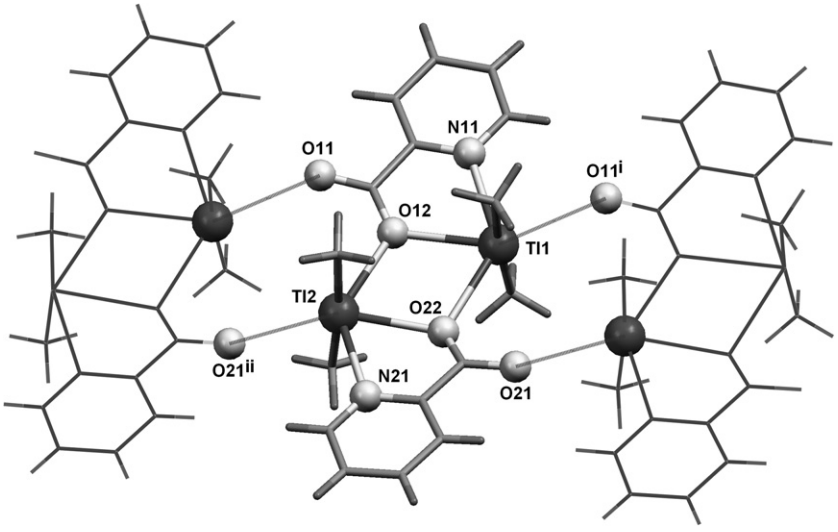


Fig. 2. Fragment of the polymeric chain in **1**.

Table 3
Hydrogen bonds (Å, °) parameters for **2** and **3′**

Compound	D–H···A	D–H	H···A	D···A	DHA
2	O(3)–H(3)···O(2)	0.8400	1.8230	2.5549	144.67
3′	N–H···O(1)	0.8800	2.3353	2.7010	105.05
	N–H···O(3)^{iv}	0.8800	1.9711	2.8148	160.20

(iv) $= -y + 1/2, -x + 1, -z + 1/2$.

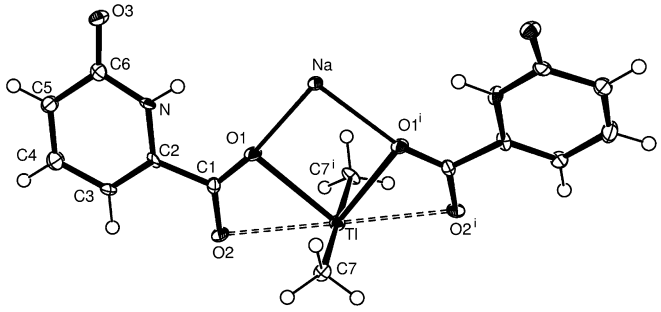


Fig. 3. Asymmetric unit and numbering scheme used for **3′**.

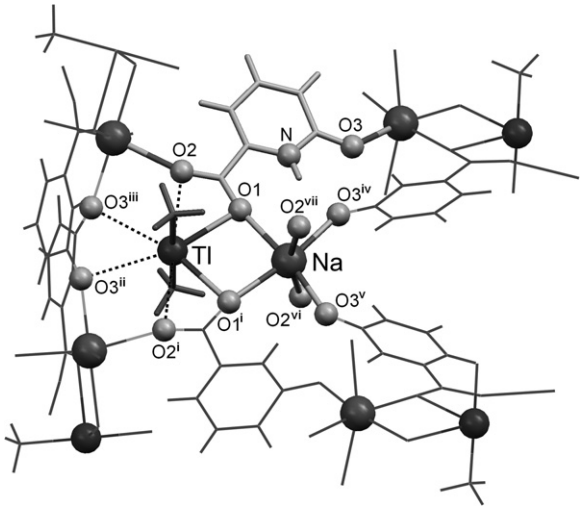


Fig. 4. MERCURY plot showing a fragment of the 3D polymeric arrangement and all the metal–ligand interactions in **3′**.

evident concerning the strength of the primary and secondary M–L bonds. For example, while the Tl–N interaction is significantly shorter in **1**, the intramolecular and intradimer Tl–O bonds are longer. These differences are highlighted in Fig. 1a and b. It is also worth noting that the interdimer secondary Tl···O interactions are shorter in **1**.

The X-ray crystal structure of **3′** is presented in Fig. 3. The asymmetric unit of this compound consists of an H6hpic$^-$ anion (occupation 1) and dimethylthallium(III) and Na^+ cations (occupation 0.5 each). The derivative is a three-dimensional polymer in which the H6hpic$^-$ anions interact with cations through bonding forces that probably have a significant ionic character, at least in the Na^+ case. The picolinate anion with the deprotonated carboxylate group is in the keto form and the presence of a proton on the N atom rules out its involvement in the coordination. As in **1** and **2**, O1 oxygens from the carboxylate groups of two ligands bridge between the two, in this case, heterobimetallic cations to give a four-membered Tl–O1–Na–O1 ring (see Figs. 3 and 4), which in turn leads to a Tl···Na distance [3.70585(11) Å] shorter than the sum of the van der Waals radii (Tl–Na = 4.30 Å) [29,30]. Additionally, the O2 (carboxylate) and O3 (carbonyl) oxygen atoms both interact with Na^+ and, more weakly, with Me_2Tl^+, so all three oxygens of the picolinate ligand are simultaneously in close, and probably ionic, contact with both metallic cations (see Fig. 4). The C_2O_6 atoms around the thallium form a distorted hexagonal bipyramid with the apical methyl groups [C–Tl–C = 179.0(6)°], while the six oxygen atoms surrounding the sodium ion form a distorted octahedron [O(1)^i–Na–O(3)^{iv} = 170.5(3)°].

Comparison of the ligand moiety with free $H_2$6hpic [31] highlights the following structural changes: (i) deprotonation of the –COOH group leads to the expected modification in the carbon–oxygen bond distances (two unequal distances belonging to the C=O and C–OH fragments in the free acid become two almost equal C–O distances in the complex); (ii) the distances in the N–C(6)–O(3) fragment evolve in the complex to the "normal" distances for the keto form [N–C(6) distance increases with respect to the free ligand, which is in an intermediate keto-enol form, while C–O(3) diminishes].

In the lattice, adjacent units of **3′** are also connected through NH···O(1) and NH···O(3)^{iv} hydrogen bonding interactions (see Table 3), which reinforce the three-dimensional network.

3.2. IR and Raman spectra

The main IR (1800–100 cm^{-1}) and Raman (600–100 cm^{-1}) frequencies for complexes **1**–**3** are listed in the Section 2. Assignments were made by comparison with the IR spectra of the free acids and literature data [12,32,33]. The spectra of the complexes lack a band that can be ascribed to the stretching vibration of the C=O bond, an observation consistent with deprotonation of the COOH group and the presence of the enolic form of both H3hpic$^-$ and H6hpic$^-$ ligands. Note that this means that the latter adopts a different tautomeric form in **3** than in **3′**, suggesting that the coordination mode of H6hpic$^-$ in **3** may be similar to that of H3hpic$^-$ in **2** (see Fig. 1). The absorption bands in the 1620–1460 cm^{-1} range in the spectra of the complexes correspond to the strongly mixed [ν(C=N), δ(CN), δ(NH) and ν_{ring}(Py)] modes and these are labelled in Section 2 as ν_{ring}(Py). The difference $\Delta\nu = [\nu(CO_2)_{asym} - \nu(CO_2)_{symm}]$, which correlates with the coordination pattern of the carboxylate group, could not be determined due to overlap of $\nu(CO_2)_{asym}$ with ν_{ring}(Py) in the spectra of the complexes.

Stretching vibrations for the Tl–C, Tl–O and Tl–N bonds in the IR and Raman spectra of all three complexes (see Section 2) are within the range for the $[TlMe_2]^+$ complexes with (N,O)/(O,O) donor ligands [33].

3.3. NMR study

Due to its low solubility in non polar solvents, the NMR spectra of compounds **1** and **2** were recorded in DMSO-d_6. Compound **3**, which is not soluble in this solvent, was not investigated. The assignment of the ^{1}H and ^{13}C resonances listed in Section 2 was carried out with the aid of the ligand spectra, ^{1}H–^{13}C heteronuclear correlations (HMQC and HMBC) and literature data [12]. For the atomic numbering used see Scheme 1.

In the proton spectra of the compounds, the presence of a broad doublet at high field centred at 0.74 ppm for compounds **1** and **2** indicates the presence of the organometallic moiety and the expected 1:1 (ligand/Me_2Tl) molar ratio.

In compound **1**, the absence of a broad signal at 12.40 ppm indicates deprotonation of the ligand. The singlet observed at 15.53 ppm in the spectrum of compound **2**, which accounts for one proton, is displaced 2 ppm downfield with respect to that in the free ligand. The observed connectivity of this signal with C^4, C^2 and C^3 in a HMBC experiment shows that, as in the solid state (see Fig. 1b), in DMSO solution the ligand in **2** is in the enol form.

Analysis of the ^{13}C data and comparison with those of the free acids [34] shows that C^2 experiences a deshielding effect (+6.6 ppm) in **1** and the same occurs with C^7 (+1.6 ppm). Other carbons are shielded (C^6 −1.8, C^5 −2.3 ppm) or are unchanged (C^4 and C^3). In complex **2** the changes observed in the spectrum of the ligand are similar but are more marked than those observed in previously studied complexes of H3hpic$^-$ with the same coordination mode [12]: C^7, C^6 and C^2 are strongly deshielded (+5.9, +3.9 and +5.6 ppm, respectively) and the other carbons, particularly C^4, are shielded (C^4 −6.5, C^5 −2.1, C^3 −0.7 ppm) with respect to those in the acid.

The ^{1}H and ^{13}C chemical shifts of the organometallic moiety, together with the values of the coupling constants $^1J(^{13}C–^{205}Tl)$ and $^2J(^1H–^{205}Tl)$, are in the range found for other dimethylthallium compounds with (N,O)/(O,O) donor atoms [18,33–36].

4. Conclusion

The work described here concerns the synthesis and characterization of dimethylthallium(III) complexes with picolinic, 3-hydroxypicolinic and 6-hydroxypicolinic acids. The compounds were characterized by elemental analysis and vibrational spectroscopy in the solid state. X-ray diffraction studies of compounds **1** and **2** show a distorted octahedral environment, with the metal atom coordinated to the methyl groups and the N and O atoms of the monodeprotonated acid. The thallium coordination is completed by the O atom of a neighbouring ligand, leading to the formation of a polymeric chain in compound **1** and a dimeric association in compound **2**. The latter complex contains intramolecular hydrogen bonds between the remaining hydroxylic hydrogen and one of the oxygen atoms of the carboxylate group.

The solubility of compounds **1** and **2** in DMSO facilitated its study in solution by ^{1}H and ^{13}C NMR spectroscopy. In complex **2** the singlet observed at 15.53 ppm indicates that the enol form of the ligand is present in the solid state remains in solution.

When we attempted to recrystallize compound **3**, only a few crystals of **3′** were serendipitously obtained after very slow evaporation of the solvent. This derivative is a three-dimensional polymer in which the monodeprotonated ligand interacts with the cations through bonding forces that probably have significant ionic character. The coordination sphere around the thallium atom is a distorted hexagonal bipyramid with the methyl groups apical and six

oxygen atoms of four different ligands equatorial. The distorted octahedron that surrounds the sodium ions is formed by six oxygen atoms of six different ligands.

Acknowledgements

M. Toma gratefully acknowledges Agencia Española de Cooperación Internacional and The Department of Inorganic Chemistry, University of Santiago de Compostela, Spain.

Appendix A. Supplementary material

CCDC 662834, 662835, 662836 contain the supplementary crystallographic data for compound **1**, **2**, **3′**. These data can be obtained free of charge via http://www.ccdc.cam.ac.uk/conts/retrieving.html, or from the Cambridge Crystallographic Data Centre, 12 Union Road, Cambridge CB2 1EZ, UK; fax: (+44) 1223-336-033; or e-mail: deposit@ccdc.cam.ac.uk. Supplementary data associated with this article can be found, in the online version, at doi:10.1016/j.poly.2007.12.021.

References

[1] D.M. Stearns, W.H. Armstrong, Inorg. Chem. 31 (1992) 5178.
[2] M. Jian-Fang, J. Zhong-Sheng, N. Jia-Zuan, Polyhedron 14 (1995) 563.
[3] M. Chatterjee, S. Ghosh, A.K. Nandi, Polyhedron 16 (1997) 2917.
[4] P.C.R. Soares-Santos, H.I.S. Nogueira, V. Felix, M.G.B. Drew, R.A. Sa Ferreira, L.D. Carlos, T. Trindalde, Inorg. Chem. Commun. 6 (2003) 1234.
[5] D. Dakternieks, A. Duthie, D.R. Smyth, C.P.D. Stapleton, E.R.T. Tiekink, Appl. Organomet. Chem. 18 (2004) 53.
[6] S. Basu, S.M. Peng, G.H. Lee, S. Bhattacharya, Polyhedron 24 (2005) 157.
[7] C. Sun, X. Zheng, L. Jin, J. Mol. Struct. 646 (2003) 201.
[8] S.M.O. Quintal, H.I.S. Nogueira, V. Felix, M.G.B. Drew, New J. Chem. 24 (2000) 511.
[9] S.M.O. Quintal, H.I.S. Nogueira, H.M. Carapuça, V. Felix, M.G.B. Drew, J. Chem. Soc., Dalton Trans. (2001) 3196.
[10] S. Gato, T.I.A. Gerber, G. Bandol, J. Perils, J.G.H. Du Preez, Inorg. Chim. Acta 269 (1998) 235.
[11] M. Toma, A. Sánchez, M.S. García-Tasende, J.S. Casas, J. Sordo, E.E. Castellano, J. Ellena, Centr. Eur. J. Chem. 2 (2004) 534.
[12] Z. Popović, G. Pavlović, M. Vinković, D. Vikić-Topć, M. Rajić Linarić, Polyhedron 25 (2006) 2353.
[13] U.A. Shinde, G. Sharma, Y.I. Xu, N.S. Dhalla, R.K. Goyal, J. Trace Elem. Med. Biol. 18 (2004) 23.
[14] D. Rehder, Inorg. Chem. Commun. 6 (2003) 604.
[15] (a) M. Nakai, M. Obata, C. Orvig, J. Inorg. Biochem. 98 (2004) 105;
(b) H. Yasui, A. Tamura, H. Sakurai, J. Inorg. Biochem. 91 (2002) 327.
[16] (a) A. Sengüi, O. Büyükgüngör, Acta Crystallogr. C61 (2005) m119;
(b) S. Chattopadhyay, P.E. Fanwick, R.A. Walton, Dalton Trans. (2003) 3617;
(c) G.Q. Bian, T. Kuroda-Sowa, H. Konaka, M. Maekawa, M. Munakata, Acta Crystallogr. C60 (2004) m338;
(d) C.Y. Sun, X.J. Zheng, L.P. Jin, Z. Anorg. Allg. Chem. 630 (2004) 1342;
(e) C.Y. Sun, L.P. Jin, J. Mol. Struct. 741 (2005) 241;
(f) G.Q. Bian, T. Kuroda-Sowa, S. Sigimoto, M. Maekawa, M. Munakata, Acta Crystallogr. C61 (2005) m144.
[17] J.S. Casas, M.S. García-Tasende, J. Sordo, Coord. Chem. Rev. 193-195 (1999) 287.
[18] M. Toma, Ph.D. Thesis, Univ. "Al.I.Cuza", Iasi, 2003.
[19] H. Gilman, R.G. Jones, J. Am. Chem. Soc. 68 (1946) 517.
[20] M.V. Castaño, A. Sánchez, J.S. Casas, J. Sordo, J.L. Briansó, J.F. Piniella, X. Solans, G. Germain, T. Debaerdemaeker, J. Glaser, Organometallics 7 (1998) 1897.
[21] G.M. Sheldrick, SHELX 97, An integrated system for solving and refining crystal structures from diffraction data, University of Göttingen, 1997.
[22] J.L. Farrugia, J. Appl. Crystallogr. 30 (1997) 565.
[23] I.J. Bruno, J.C. Cole, P.R. Edgington, M.K. Kessler, C.F. Macrae, P. McCabe, J. Pearson, R. Taylor, Acta Crystallogr. B58 (2002) 389.
[24] M. Toma, A. Sánchez, M.S. García-Tasende, J.S. Casas, J. Sordo, E.E. Castellano, J. Ellena, Revista Chimie (Bucharest) 56 (2005) 1149.
[25] M. Toma, A. Sánchez, M.S. García-Tasende, J.S. Casas, J. Sordo, E.E. Castellano, J. Ellena, Appl. Organomet. Chem. 18 (2004) 302.
[26] T.L. Blundell, H.M. Powell, Chem. Commun. 1 (1967) 54.
[27] A.J. Canty, K. Mills, B.W. Skelton, A.H. White, J. Chem. Soc., Dalton Trans. (1986) 939.
[28] A. Bondi, J. Phys. Chem. 68 (1964) 441.
[29] J. Emsley, in: The Elements, Oxford University Press, New York, 1998.
[30] J.E. Huheey, E.A. Keiter, R.L. Keiter, Inorganic Chemistry, fourth ed., Harper Collins College Publishers, New York, 1993.
[31] K. Sawada, Y. Ohashi, Acta Crystallogr. C54 (1998) 1491.
[32] S. Teoh, D. Tan, G. Yeap, H. Fun, J. Coord. Chem. 48 (1999) 53.
[33] M.S. García-Tasende, B.E. Rivero, A. Castiñeiras, A. Sánchez, J.S. Casas, J. Sordo, W. Hiller, J. Strahler, Inorg. Chim. Acta 181 (1991) 43.
[34] M. Toma, A. Sánchez, J.S. Casas, J. Sordo, M.S. García Tasende, E.E. Castellano, J. Ellena, I. Berdan, Centr. Eur. J. Chem. 1 (2003) 441.
[35] M.V. Castaño, A. Macías, A. Castiñeiras, A. Sánchez González, E. García Martínez, J.S. Casas, J. Sordo, E.E. Castellano, J. Chem. Soc., Dalton Trans. (1990) 1001.
[36] M.S. García-Tasende, M.I. Suárez, A. Sánchez, J.S. Casas, J. Sordo, E.E. Castellano, Y.P. Mascarenhas, Inorg. Chem. 26 (1987) 3818.

is necessary for the synthesis of the later complexes. As a result, coordination of the carbonate anion is not reversible and decomposition of the complexes takes place by loss of it. These complexes are similar to the previously reported $[(A\text{-}\alpha\text{-}AsW_9O_{34})_2(OCe^{IV}OH_2)_3]^{12-}$[16]. The carbonate anion makes a well-defined bonding interaction with the internal cavity of the sandwich-type complex and on this basis Pope and Müller define these complexes as *cryptates* [3].

2. Experimental

2.1. Chemical and apparatus

All reagents were commercially obtained and were used without further purification. $Na_8H[A\text{-}\alpha\text{-}AsW_9O_{34}]\cdot xH_2O$ was prepared according to the literature [17,18]. Infrared spectra were recorded in KBr disks on a Thermo Nicolet FT-IR model Nexus-670 and NMR spectra were recorded on a BRX-500 AVANCE spectrometer. The resonance frequency is 125.75 MHz for ^{13}C and the chemical shift is given with respect to chloroform as an external standard.

Thermogravimetric Analysis (TGA) and Differential Scanning Calorimetry were carried out using PL-1500 TGA and NETZSCH DSC 200 F3 apparatus, respectively. The electronic spectra were recorded on a Varian, CARY 1E UV–Vis spectrophotometer.

2.2. Complex preparation

2.2.1. $K_{10}Na[(A\text{-}\alpha\text{-}AsW_9O_{34})_2(YOH_2)_3(CO_3)]\cdot 19H_2O$ (**1**)

A 0.45 g (1.5 mmol) sample of $YCl_3\cdot 6H_2O$ was dissolved in 20 mL of twice distilled water, and 2 mL of 1 M Na_2CO_3 was slowly added to the solution with stirring. The slurry was heated to 80 °C, and then solid $Na_8H[A\text{-}\alpha\text{-}AsW_9O_{34}]\cdot xH_2O$ (2.1 g, 0.8 mmol) was quickly added with vigorous stirring. The solution was maintained at 80 °C for 30 min and then cooled to room temperature. Any insoluble material was removed by centrifugation and then solid KCl (3 g) was added to the solution. The solution was cooled in an ice water bath and then filtered off. The crude product was dissolved in a minimal amount of hot water and cooled to 5 °C. This procedure was repeated at least twice (yield: 1.2 g, 37%). Single crystals suitable for X-ray crystallography were obtained from the filtrate of the second recrystallization at 5 °C by slow evaporation. *Anal.* Calc. for $K_{10}Na[(A\text{-}\alpha\text{-}AsW_9O_{34})_2(YOH_2)_3(CO_3)]\cdot 19H_2O$: C, 0.20; K, 6.66; Na, 0.39; As, 2.55; W, 56.4; Y, 4.54; H_2O, 6.96. Found: C, 0.22; K, 6.50; Na, 0.35; As, 2.40; W, 57.0; Y, 4.63; H_2O, 6.80%.

2.2.2. $K_{10}Na[(A\text{-}\alpha\text{-}AsW_9O_{34})_2(YbOH_2)_3(CO_3)]\cdot 17H_2O$ (**2**)

The procedure for **1** was repeated, but $YbCl_3\cdot 6H_2O$ (0.57 g) was used instead of $YCl_3.H_2O$ (yield: 1.3 g, 38%). *Anal.* Calc. for $K_{10}Na[(A\text{-}\alpha\text{-}AsW_9O_{34})_2(YbOH_2)_3(CO_3)]\cdot 17H_2O$: C, 0.2; K, 6.63; Na, 0.39; As, 2.54; W, 56.1; Yb, 8.80; H_2O, 6.10. Found: C, 0.22; K, 6.56; Na, 0.35; As, 2.38; W, 55.1; Yb, 9.54; H_2O, 6.00%.

2.2.3. $K_{10}Na[(A\text{-}\alpha\text{-}AsW_9O_{34})_2(SmOH_2)_3(CO_3)]\cdot 18H_2O$ (**3**)

A 0.55 g (1.5 mmol) sample of $SmCl_3\cdot 6H_2O$ was dissolved in 20 mL of twice distilled water, and 2 mL of 1 M Na_2CO_3 was slowly added to the solution with stirring. Solid $Na_8H[A\text{-}\alpha\text{-}AsW_9O_{34}]\cdot xH_2O$ (2.1 g, 0.8 mmol) was quickly added with vigorous stirring. The solution was maintained at room temperature (30 °C) for 60 min. Any insoluble material was removed by centrifugation and then solid KCl (3 g) was added to the solution. The solution was cooled in an ice water bath and then filtered off. The crude product was dissolved in a minimal amount of warm water and cooled to 5 °C. This procedure was repeated at least twice (yield: 1.1 g, 35%). Single crystals suitable for X-ray crystallography were obtained from the filtrate of the second recrystallization at 5 °C by slow evaporation. *Anal.* Calc. For $K_{10}Na[(A\text{-}\alpha\text{-}AsW_9O_{34})_2(SmOH_2)_3(CO_3)]\cdot 18H_2O$: C, 0.21; K, 6.68; Na, 0.39; As, 2.56; W, 56.6; Sm, 7.71; H_2O, 6.46. Found: C, 0.19; K, 6.59; Na, 0.36; As, 2.37; W, 56.2; Sm, 7.78; H_2O, 6.40%.

2.3. X-ray crystallographic structure determination

Crystal data collection and refinement parameters for **1** and **3** are given in Table 1. The data were collected at 100 K on a Bruker APEX 1000 CCD area detector single crystal diffractometer with graphite-monochoromated Mo Kα radiation ($\lambda = 0.71073$ Å). Data collection, indexing and initial cell refinements were all handled using APEX2 software [19]. The final cell parameters were determined from least-squares refinement on 8521 and 8889 reflections for **1** and **3**, respectively. The multi-scan method was used to carry out absorption corrections. The structures were solved using direct methods and difference Maps techniques (SHELXTL, V5.1) [20]. All metal atoms were refined anisotropically. Scattering factors and anomalous dispersion corrections were taken from the International Tables for X-ray Crystallography [21]. Structure solution, refinement and generation of publication materials were performed by using SHELXTL V5.1 software. Selected bond lengths and bonds angles of **1** and **3** are given in Table 2.

3. Result and discussion

3.1. Syntheses and stabilities

$A\text{-}\alpha\text{-}[AsW_9O_{34}]^{9-}$ reacts with MCl_3 (M = Y, Yb and Sm) in an aqueous Na_2CO_3 solution (0.09 M) to form **1**, **2** and **3** in modest yields, respectively. Monitoring of the reaction solution by pH shows that the pH of the carbonate solution decreases (5.5) with addition of MCl_3 (M = Y,

Table 1
Crystal data and structure refinement for **1** and **3**

	1	**3**
Empirical formula	$CH_{44}AsK_{10}NaO_{93}W_{18}Y_3$	$CH_{50}As_2K_{10}NaO_{96}Sm_3W_{18}$
Formula weight	5687.21	5922.59
Crystal system	cubic	cubic
Space group	$P2_13$	$P2_13$
Unit cell dimensions		
a (Å)	20.7572(3)	20.8529(4)
α (°)	90	90
Volume (Å^3)	8943.5(2)	9067.7(3)
Z	4	4
D_{calc} (Mg/m^3)	4.242	4.338
Absorption coefficient (mm^{-1})	26.293	25.948
$F(000)$	10100	10436
$2\theta_{max}$ (°)	60.96	63.96
Reflections collected	122038	132973
Crystal size (mm)	0.12 × 0.08 × 0.05	0.36 × 0.30 × 0.21
Crystal description	prism	prism
Independent reflections [R_{int}]	9104 [0.0953]	10468 [0.1235]
Absorption correction	semi-empirical from equivalents	integration
Refinement method	full-matrix least-squares on F^2	full-matrix least-squares on F^2
Data/restraints/parameters	9104/12/394	10468/30/413
Goodness-of-fit on F^2	1.021	1.056
Final R indices with $I > 2\sigma(I)$]	$R_1 = 0.0323$, $wR_2 = 0.0695$ [for 8521 reflections]	$R_1 = 0.0423$, $wR_2 = 0.0783$ [for 8889 reflections]
R indices (all data)	$R_1 = 0.0369$, $wR_2 = 0.0712$	$R_1 = 0.0583$, $wR_2 = 0.0852$
Largest difference in peak and hole (e Å^{-3})	3.163 and −1.501	2.670 and −1.751

Table 2
Selected bond lengths and angles for **1** and **3**

1		VBV	**3**		VBV
Bond lengths (Å)					
Y1–O8A	2.300(7)	0.47	Sm1–O4	2.340(9)	0.47
Y1–O12	2.270(7)	0.51	Sm1–O9	2.335(10)	0.48
Y1–O15	2.288(7)	0.48	Sm1–O16	2.341(10)	0.47
Y1–O16	2.265(7)	0.51	Sm1–O21	2.366(9)	0.44
Y1–O13	2.436(6).	0.32	Sm1–O1CB	2.471(9)	0.33
Y1–O13A	2.452(6)	0.31	Sm1–O1C	2.473(9)	0.33
Y1–O14(1W)	2.369(6)	0.39	Sm1–O1W	2.426(10)	0.38
C1–O13	1.279(6)	1.35	C1–O1C	1.285(9)	1.33
W2–O12(Y)	1.790(7)	1.38	W1–O4(Sm)	1.802(9)	1.32
W3–O8(Y)	1.770(7)	1.48	W2–O9(Sm)	1.791(9)	1.36
W4–O15(Y)	1.789(7)	1.34	W4–O16(Sm)	1.789(10)	1.36
W5–O16(Y)	1.790(7)	1.35	W5–O21(Sm)	1.794(10)	1.35
W1–O1d*	1.710(7)	1.65	W1–O1d	1.694(9)	1.72
W2–O11d	1.731(7)	1.51	W2–O6d	1.732(9)	1.57
W3–O7d	1.727(7)	1.59	W3–O10d	1.694(9)	1.72
W4–O18d	1.740(7)	1.54	W4–O13d	1.725(10)	1.59
W5–O20d	1.719(7)	1.62	W5–O18d	1.702(10)	1.68
W6–O25d	1.717(6)	1.62	W6–O22d	1.707(10)	1.66
Bond angles (°)					
O13A–Y1–O8	81.3(2)		O4–Sm1–O1C	80.8(3)	
O13A–Y1–16	83.9(2)		O16–Sm1–O1C	83.7(3)	
O8–Y1–O16	85.1(2)		O4–Sm1–O16	83.3(3)	
O13–Y1–O12	82.2(2)		O9–Sm1–O21	83.4(3)	
O13–Y1–O15	82.5(2)		O9–Sm1–O1CB	81.9(3)	
O15–Y1–O12	84.4(3)		O21–Sm1–O1CB	81.9(3)	
O12–Y1–13A	120.4(2)		O9–Sm1–O1C	120.3(3)	
O12–Y1–O8A	91.5(2)		O21–Sm1–O16	90.5(3)	
O16–Y1–O12	154.5(2)		O9–Sm1–O1CB	154.9(3)	
O13–Y1–13A	53.9(3)		O1CB–Sm1–O1C	53.5(4)	

Symmetry transformations used to generate equivalent atoms for **1**: 1A: $y + 1/2$, $-z + 3/2$, $-x + 2$ and 1B: $-z + 2$, $x - 1/2$, $-y + 3/2$.
Symmetry transformations used to generate equivalent atoms for **3**: 1A: z, x, y and 1B: y, z, x.

Yb and Sm) and increases with addition of A-α-$[AsW_9O_{34}]^{9-}$. The trivalent metals react with the carbonate ion to form the corresponding insoluble metal carbonate (the solution becomes turbid) and then A-α-$[AsW_9O_{34}]^{9-}$ reacts with metal carbonate (the solution becomes clearer). In order to establish the compositions of the complexes in

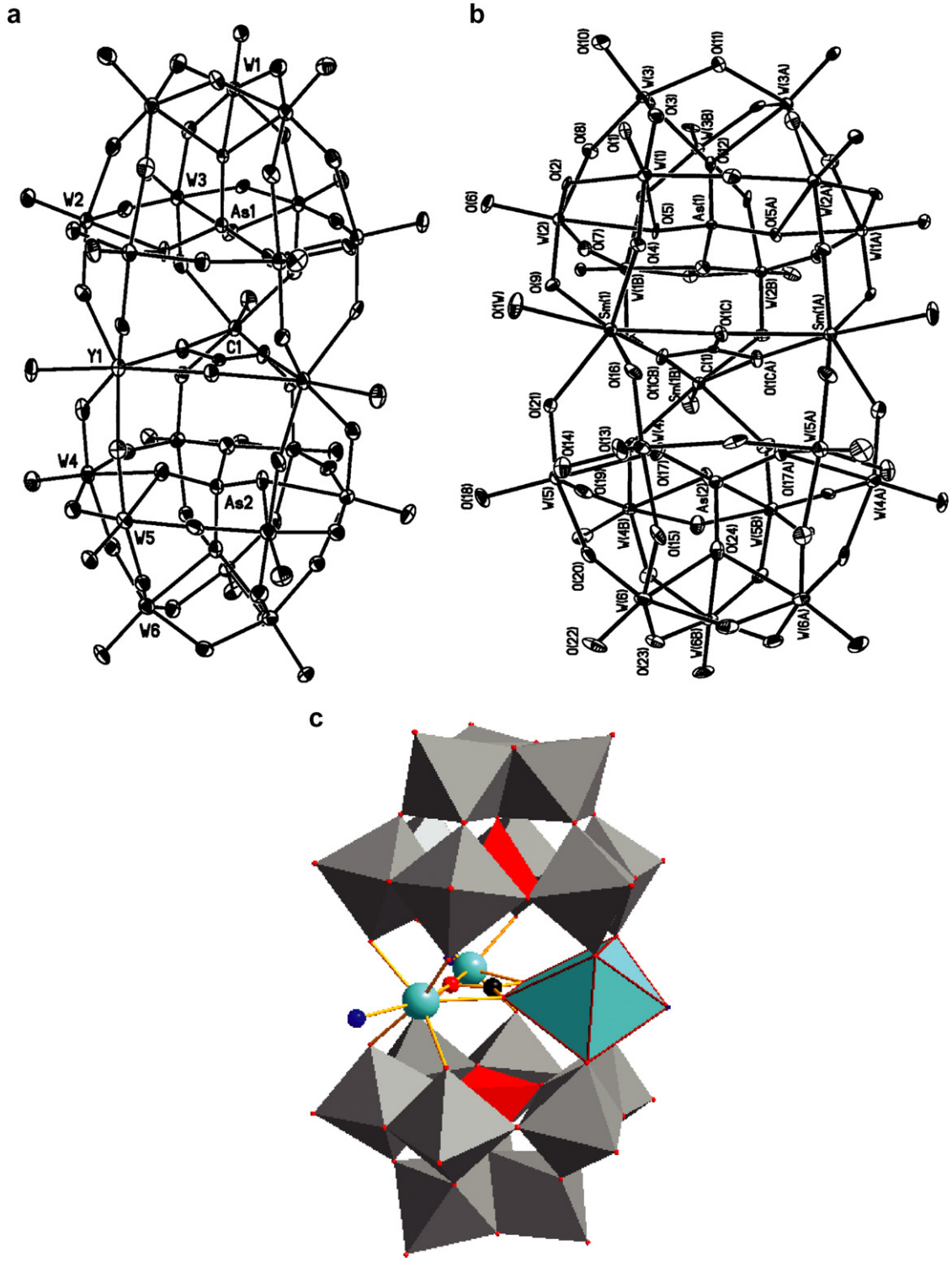


Fig. 1. Thermal ellipsoid plot of: (a) $[(A\text{-}\alpha\text{-}sW_9O_{34})_2(YOH_2)_3(CO_3)]^{11-}$ (**1**), (b) $[(A\text{-}\alpha\text{-}AsW_9O_{34})_2(SmOH_2)_3(CO_3)]^{11-}$ (**3**) set at the 50% probability level and (c) combination ball-and-stick/polyhedral representation of **1** and **3**. The W, As, M (Y, Sm), C, O atoms and water molecule are shown in grey, orange, aqua, black, red and blue, respectively. (For interpretation of the references to colour in this figure legend, the reader is referred to the web version of this article.)

solution, turbidity variation of the solution as a function of addition of A-α-$[AsW_9O_{34}]^{9-}$, which is due to the formation of the complexes in solution, were performed. The titration results show a breakpoint near to the 2:3 L:M^{III} (L = A-α-$[AsW_9O_{34}]^{9-}$) ratio. The syntheses of **1**, **2** and **3** require the presence of CO_3^{2-}. **1**, **2** and **3** are also synthesized in the presence of HCO_3^-. It has been demonstrated that the starting material A-α-$[AsW_9O_{34}]^{9-}$ can be transformed to B-α-$[AsW_9O_{34}]^{9-}$ simply by heating the solid. The reaction of 2 mmol of B-$[AsW_9O_{34}]^{9-}$ prepared in this way with an aqueous carbonate solution of 3 mmol of YCl_3 generated anion **1** directly. The crystal structure (see below) reveals that anion **1** contains two A-α-$[AsW_9O_{34}]^{9-}$ units, which indicates that the synthesis involves a structural rearrangement of the starting material B-α-$[AsW_9O_{34}]^{9-}$. Preparation of the samarium derivative at 80 °C is not favored because of the formation of an unknown suspended solid on recrystallization, which is followed by a decrease of the product yield.

Unlike the A-type sandwiches based on divalent d-block metals [14,17,18,22,23], the complexes of **1**, **2** and **3** are stable in unbuffered H_2O. The experimental results suggest that**1** and **2** are stable in the pH range of 5–10 for long time. **3** is not stable in the above conditions. The best stability condition for **3** is the pH range 6–9. When complexes **1**, **2** and **3** are passed through a strongly acidic ion exchange (Dowex-50W-X8) column, the product is the Dawson anion, $[As_2W_{18}O_{68}]^{6-}$, which is isolated as $H_6[As_2W_{18}O_{68}]$. This observation confirms that the $AsW_9O_{34}^{9-}$ units in the complexes are the A-isomer [24–26].

3.2. Structures

Single crystal analysis was carried out on **1** and **3**, which are isostructural with **2**. The complexes crystallize in the cubic space group $P2_13$, with a total number of 37 atoms in the anion part containing 6W (W1–W6), 2As (As1–As2), 1Y (Y1), 26O (O1–O26), 1C (C1) and 1H_2O (O1W) atoms for **1** and 36 atoms containing 6W (W1–W6), 2As (As1–As2), 1Sm (Sm1), 25O (O1–O26, O1C), 1C (C1) and 1H_2O (O1W) atoms for **3** in the asymmetric unit. The structures of **1**and**3** consist of two lacunary A-α-$[AsW_9O_{34}]^{9-}$ Keggin moieties which are linked by an equatorial M_3CO_3 (M = Y^{III} or Sm^{III}) belt into an assembly of virtual C_{3v} symmetry (Fig. 1). The metal ions (M^{III}) form a regular triangle and are fixed together by oxygen atoms of a carbonate anion lying in the center and coplanar to the metal ions (Fig. 2). The C_3 axis of the anionic complexes is perpendicular to the equatorial belt and involves the carbon atom of the carbonate anion. The oxygen atoms of the carbonate anion lie on the midpoint of the side of the regular triangle. On the basis of valance bond sum (VBS) calculations, derived by Brown and Altermatt [27,28], the oxygen atoms of the belt are oxides and not hydroxides (Table 2).The encapsulated CO_3^{2-} still displays D_{3h} symmetry and as a special feature

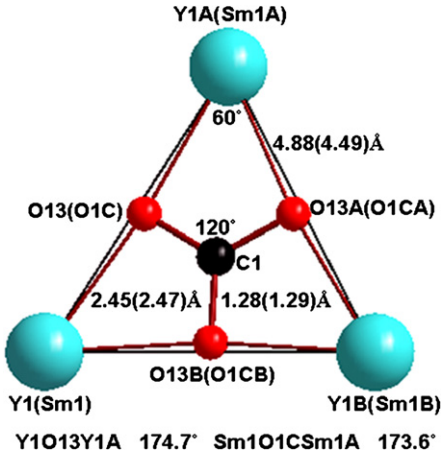


Fig. 2. The relevant distances (Å) and angles (°) for the M_3CO_3 belt arrangement in **1** and **3**.

acts as a tridentate ligand, which is unusual in metallocarbonate complexes. The VBS for the carbon and oxygen atoms is 4.02(3) and 1.98(1), respectively. Each M^{III} ion adopts a mono-capped trigonal-prismatic coordination, the local 3-fold axis of the MO_6 group lying in the regular triangular M_3CO_3 plane. The trigonal prismatic geometry is achieved by two terminal oxygen atoms of an edge shared pair of WO_6 octahedra to each A-α-$[AsW_9O_{34}]^{9-}$ moiety and two oxygen from the belt. The cap is achieved by one external water ligand. The M–O bond lengths in the MO_6 group and M–O(nW) are in the range 2.265(7)–2.452(6) Å, average 2.335(8) Å, and 2.369(6) Å for **1** and 2.335(10)–2.473(10) Å, average 2.388(6) Å, and 2.426(10) Å for **3**, respectively (Table 2). The VBS for the yttrium, samarium, tungsten and arsenic atoms is 2.96, 2.90, 6.08(6) and 4.96(15), respectively.

3.3. IR and NMR spectroscopy

As expected, the IR spectra of the A-type sandwich complex anions are very similar to that of the trivalant lacunary A-$[XW_9O_{34}]^{9-}$. The IR spectra of **1**, **2** and **3** are very similar and are also similar to that of A-$[AsW_9O_{34}]^{9-}$, except for the splitting of the asymmetry stretching vibration of W–Oc–W (Oc is the edge sharing oxygen) (Fig. 3). This splitting is attributed to the presence of the trivalent cations (directly bound to the terminal oxygen of an edge shared pair of WO_6) [29,30]. The IR spectra of **1**, **2** and **3** show bands in the region 1491–1465 cm^{-1}, which is assigned to the doubly degenerate ν_3 vibrational mode of CO_3^{2-} with a small splitting of 10 cm^{-1} [31]. This splitting is attributed to distortion of the CO_3^{2-} group (Fig. 3). The other two infrared active modes, ν_2 and ν_4, overlap with the W–O stretching bands.

The ^{13}C NMR spectrum of **1** (0.1 mM) shows one peak at 171.32 ppm which is attributed to the encapsulated CO_3^{2-} anion (Fig. 4). In order to obtain a solution of **1** that was concentrated enough for ^{13}C NMR spectroscopy it



Fig. 3. IR spectra of **1** (upper), **2** (inner) and **3** (lower).

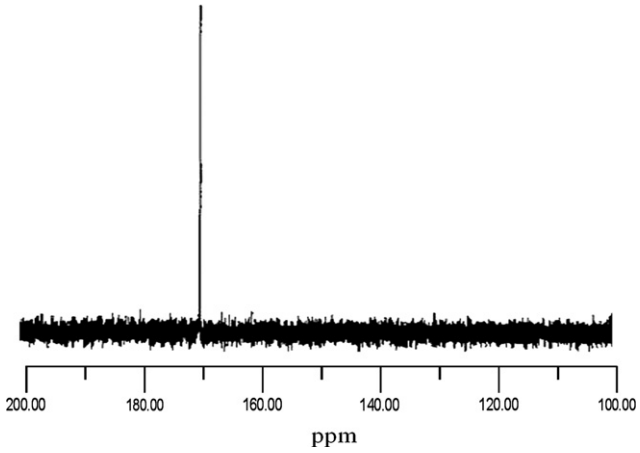


Fig. 4. ^{13}C NMR spectrum of **1**.

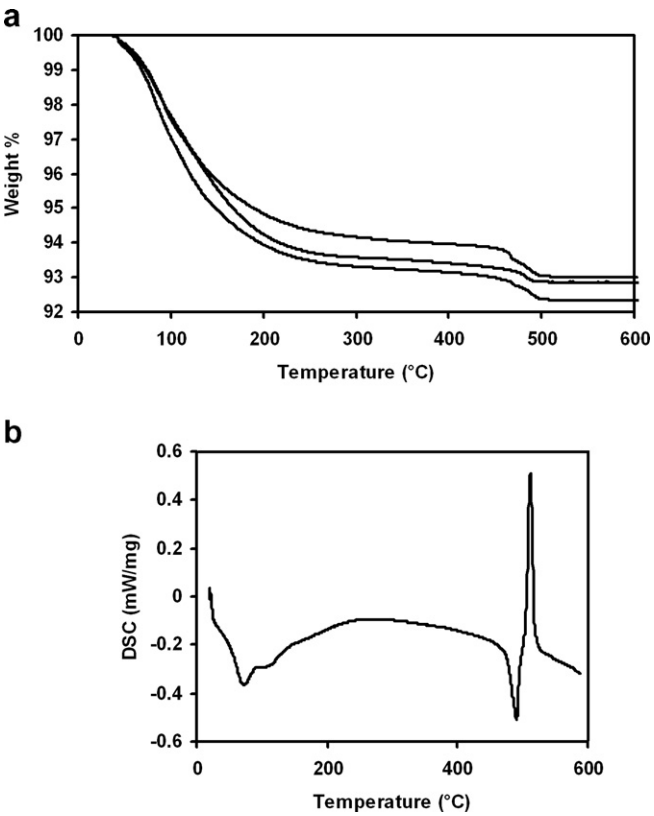


Fig. 5. (a) Thermogravimetric curve of **1** (lower), **2** (upper) and **3** (inner) and (b) differential scanning calorimetric curve of **2**.

was necessary to convert the potassium salt to the lithium salt by addition of $LiCLO_4$. The lithium salt of **1** is stable for several months and its solution (during NMR scanning) is stable.

3.4. Thermal properties TGA and DSC

Thermogravimetric analysis (TGA) curves of **1**, **2** and **3** show two mass loss regions below 500 °C. The first, 30–300 °C with 6.8%, 6.0% and 6.4% weight loss, is assigned to lattice and coordinated water (bonded to $M^{(III)}$) loss, equal to 22 (19 + 3), 20 (17 + 3) and 21 (18 + 3) molecules for **1**, **2** and **3**, respectively. The second region, 430–500 °C, with approximately 0.8%, 0.8% and 0.71% weight loss for **1**, **2** and **3**, respectively, are assigned to the loss of one molecule of CO_2 from the decomposition of CO_3^{2-} (Fig. 5a). Differential scanning calorimetry (DSC) curves of **2** show two endothermal and one exothermal process. The endothermal processes at 80–120 °C and 491 °C are attributed to exit of the water contents of the complex and CO_2, respectively, and the exothermal process at 510 °C is attributed to the decomposition of the structure (Fig. 5b). On the basis of the TGA and DSC studies it can be thus concluded that **1** and **2** are thermally stable up to 490 °C but, **3** decomposes from 440 °C.

3.5. Electronic spectroscopy

The UV-electronic spectra of the complexes **1**, **2** and **3** exhibit two characteristic bands at/200 and/257 nm ($\varepsilon = 55200$), assigned to W-/Od and W-/Ob-/W transitions, respectively (Od is a terminal oxygen and Ob is a bridging oxygen [1]) (Fig. 6a). These bands are shifted to lower frequencies on comparison with the A-$[AsW_9O_{34}]^{9-}$ ligand, due to the coordination of the lanthanide cations.

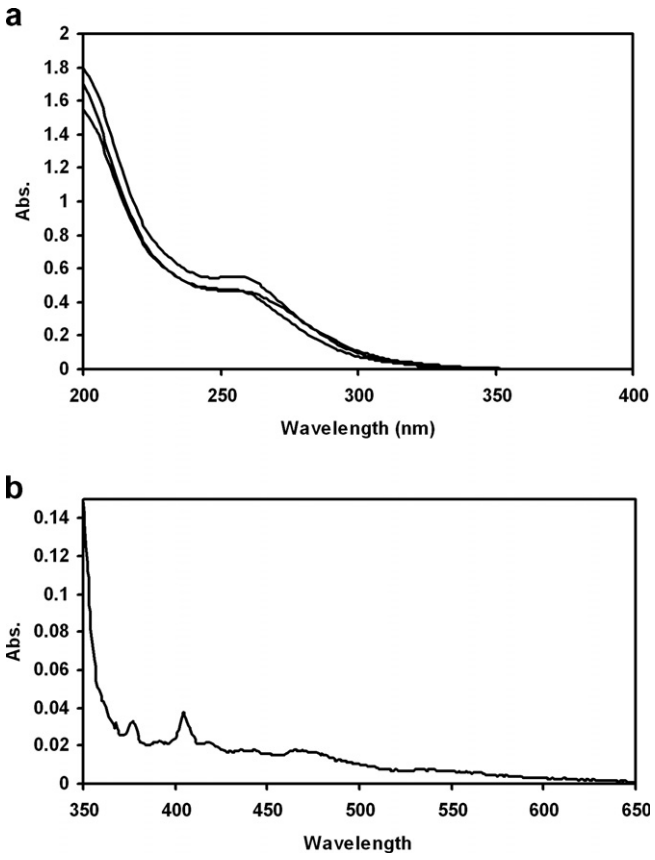


Fig. 6. (a) UV spectra of (1×10^{-5}M) **1** (lower), **2** (upper) and **3** (inner) and (b) visible spectrum of (5×10^{-3} M) **3**.

Complex **3** exhibits an additional metal-to-ligand charge transfer band at 350–400 nm ($\varepsilon_{max} = 7$) (Fig. 6b).

4. Conclusion

Three new sandwich-type polyoxometallate complexes $[(A\text{-}\alpha\text{-}AsW_9O_{34})_2(MOH_2)_3(CO_3)]^{11-}$ ($M = Y^{(III)}$, $Yb^{(III)}$ and $Sm^{(III)}$) were synthesized by the reaction of $M^{(III)}$ ions with $A\text{-}\alpha\text{-}[AsW_9O_{34}]^{9-}$ in carbonate solution. The experimental results show that the synthesis of the complexes requires the presence of the carbonate anion. The crystal structure of complexes consist of two lacunary $A\text{-}\alpha\text{-}[AsW_9O_{34}]^{9-}$ Keggin moieties which are linked by a M_3CO_3 belt into an assembly of virtual C_{3v} symmetry. The complexes are stable up to ~490 °C, and the decomposition of the complexes is followed by the loss of a carbonate anion. Other tools such as IR, ^{13}C NMR, UV–Vis spectroscopy, TGA and DSC confirm the structures.

5. Supplementary material

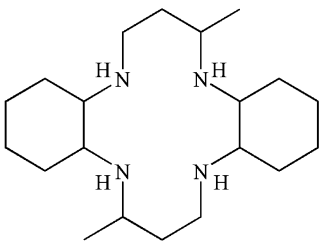
Crystallographic data (CIF file) for the structural analysis have been deposited with the Fachinformationszentium Karlsruhe (FIZ), CSD-number 391424 and 391425. These data can be obtained free of charge via E-mail: crysdata@FIZ-Karsruhe.de.

Acknowledgement

We gratefully acknowledge the Research Council of the University of Kurdistan for partial support of this work.

References

[1] M.T. Pope, Heteropoly and Isopoly Oxometallates, Springer-Verlag, New York, 1983.
[2] M.T. Pope, in: G. Wilkinson, R.D. Gillard, J.A. McCleverty (Eds.), Comprehensive Coordination Chemistry, vol. 3, Pergamon Press, 1987, pp. 1023–1058.
[3] M.T. Pope, A. Müller, Angew. Chem., Int. Ed. Engl. 30 (1991) 34.
[4] M.T. Pope, A. Müller (Eds.), Polyoxometallates. From Platonic Solids to Anti-Retroviral Activity, Kluwer Academic Publishers, Dordrecht, The Netherlands, 1994.
[5] C.L. Hill (Ed.), Chem. Rev. 98 (1998) (special edition on polyoxometallates).
[6] M.T. Pope, A. Müller (Eds.), Polyoxometallate Chemistry: From Topology via Self-assembly to Applications, Kluwer Academic Publishers, Dordrecht, 2001.
[7] J. Fischer, L. Ricard, R. Weiss, J. Am. Chem. Soc. 98 (1976) 3050.
[8] M. Michelon, G. Hervé, M. Leyrie, J. Inorg. Nucl. Chem. 42 (1980) 1583.
[9] M. Leyrie, G. Hervé, Nouu. J. Chim. 2 (1978) 233.
[10] F. Robert, M. Leyrie, G. Hervé, A. Tézé, Y. Jeannin, Inorg. Chem. 19 (1980) 1746.
[11] M.H. Chiang, M.R. Antonio, C.W. Williams, L. Soderholm, J. Chem Soc., Dalton Trans. (2004) 801.
[12] L. Soderholm, M.R. Antonio, S. Skanthakumar, C.W. Williams, J. Am. Chem. Soc. 124 (2002) 7290.
[13] F. Hussain, U. Kortz, B. Keita, L. Nadjo, M.T. Pope, Inorg. Chem. 45 (2006) 761.
[14] W.H. Knoth, P.J. Domaille, R.L. Harlow, Inorg. Chem. 25 (1986) 1577.
[15] X. Fang, T.M. Anderson, W.A. Neiwert, C.L. Hill, Inorg. Chem. 42 (26) (2003) 8600.
[16] M.H. Alizadeh, H. Eshtiagh-Hosseini, R. Khoshnavazi, J. Mol. Str. 688 (2004) 33.
[17] L.H. Bi, R.D. Hung, J. Peng, E.B. Wang, Y.H. Wang, C.W. Hu, J. Chem. Soc., Dalton Trans. (2001) 21.
[18] W.H. Knoth, P.J. Domaille, R.D. Farlee, Organometallics 4 (1985) 62.
[19] Bruker, APEX2 Software Package, Bruker AXS Inc., 5465, East Cheryl Parkway, Madison, WI 5317, 2005.
[20] G.M. Sheldrick, SHELXTL v. 5.10, Structure Determination Software Suite, Bruker AXS, 1998, Madison, WI, USA.
[21] A.J.C. Wilson (Ed.), International Tables for X-ray Crystallography, vol. C, Kluwer Academic, Dordrecht, 1992, Tables 4.2.6.8 (pp. 219–222) and 6.1.1.4 (pp. 500–502).
[22] N. Laronze, J. Marrot, G. Herve', Inorg. Chem. 42 (2003) 5857.
[23] K.-C. Kim, M.T. Pope, J. Am. Chem. Soc. 121 (1999) 8512.
[24] R. Contant, R. Thouvenot, Inorg. Chim. Acta 212 (1993) 41.
[25] R. Khoshnavazi, H. Eshtiagh-hossieni, M.H. Alizadeh, M.T. Pope, Polyhedron 25 (2006) 1921.
[26] R. Khoshnavazi, H. Eshtiagh-hossieni, M.H. Alizadeh, M.T. Pope, Inorg. Chim. Acta 360 (2) (2007) 686.
[27] I.D. Brown, D. Altermatt, Acta Crystallogr. Sect. B 41 (1985) 244.
[28] http//www.ccp14.ac.uk/ccp/web-mirrors/i_d_brown/bond_valence_param/.
[29] R. Contant, R. Thouvenot, Can. J. Chem. 69 (1991) 1498.
[30] C. Rocchiccioli-Deltcheff, M. Fournier, R. Franck, Inorg. Chem. 22 (1983) 207.
[31] K. Nakamoto (Ed.), Infrared and Raman Spectra of Inorganic and Coordination Compounds, Part B, 4th ed., Wiley-Interscience, New York, 1986, Planar XY_3 Molecules, pp. 121–125; Carbonate Complexes, pp. 252–254.



L

2. Experimental

2.1. Materials and physical methods

All chemicals used in syntheses were of reagent grade and were used without further purification. The macrocycle 3,14-dimethyl-2,6,13,17-tetraazatricyclo[14,4,$0^{1.18}$,$0^{7.12}$] docosane (L) and $[Ni(L)]Cl_2 \cdot 2H_2O$ were prepared according to the literature methods [19,20]. Infrared spectra were recorded as KBr pellets on a Perkin–Elmer Paragon 1000 FT-IR spectrometer. The solution electronic and diffuse reflectance spectra were obtained on a Jasco V-550 spectrophotometer. Magnetic susceptibility data were collected in the temperature range 5.0–300 K in an applied field of 1.0 T with the use of a Quantum Design MPMS7 SQUID magnetometer. The diamagnetic corrections were calculated from Pascal's constants. Elemental analyses (C, H, N) were performed on a Perkin–Elmer CHN-2400 analyzer.

2.2. Synthesis of $\{[Ni(L)(isoph)] \cdot 3H_2O\}_n$ (1)

An aqueous solution (10 ml) of $[Ni(L)]Cl_2 \cdot 2H_2O$ (251 mg, 0.5 mmol) was added to an aqueous solution (10 ml) of sodium isophthalate (105 mg, 0.5 mmol) and the mixture was stirred for 30 min at room temperature. The solution was filtered and left at room temperature until the violet crystals formed. The product was recrystallized from a hot water/acetonitrile (1:1 v/v, 10 ml) mixture. Yield: 65%. *Anal.* Calc. for $C_{28}H_{50}N_4NiO_7$: C, 54.82; H, 8.22; N, 9.13. Found: C, 54.93; H, 8.31; N, 9.04%. IR (KBr, cm^{-1}): ν(NH) 3210, ν_{as}(COO) 1717, 1606, 1560, ν_{sym}(COO) 1425, 1381.

2.3. Syntheses of $\{[Ni(L)(H\text{-}chtc)] \cdot H_2O\}_n$ (2)

This compound was prepared as violet crystals in a reaction similar to that of **1**, using sodium 1,3,5-cyclohexanetricarboxylate (140 mg, 0.5 mmol) instead of sodium isophthalate. Yield: 68%. *Anal.* Calc. for $C_{29}H_{52}N_4NiO_7$: C, 55.51; H, 8.35; N, 8.93. Found: C, 55.42; H, 8.43; N, 8.86%. IR (KBr, cm^{-1}): ν(OH) 3405, ν(NH) 3205, ν_{as}(COO) 1690, 1560, ν_{sym}(COO) 1449, 1394.

2.4. X-ray crystal structure analysis

Intensity data collected on a Bruker SMART 1000 CCD (**1**) and an Enraf-Nonius CAD4 (**2**) diffractometer using graphite-monochromated Mo Kα radiation ($\lambda = 0.71073$ Å). Accurate cell parameters and an orientation matrix were determined by the least-squares fit of 25 reflections. The intensity data were collected by the ω-2θ technique and corrected for Lorentz and polarization effects. An empirical absorption correction was applied with the SADABS program [21] for **1** and φ-scan [22] for **2**. The structure was solved by direct methods [23] and the least-squares refinement of the structure was performed by the SHELXL-97 program [24]. All atoms except for all hydrogen atoms were refined anisotropically. Hydrogen atoms were placed in calculated positions, allowing them to ride on their parent C or N atoms with $U_{iso}(H) = 1.2U_{eq}$(C or N). For **1**, the

Table 1
Crystallographic data

	1	2
Empirical formula	$C_{28}H_{50}N_4NiO_7$	$C_{29}H_{52}N_4NiO_7$
Formula weight	613.43	627.46
Temperature (K)	293(2)	293(2)
Crystal color/habit	violet/plate	violet/prism
Crystal system	monoclinic	triclinic
Space group	$P2_1/c$	$P\bar{1}$
Unit cell dimensions		
a (Å)	16.0642(11)	9.9995(18)
b (Å)	19.6800(13)	12.755(2)
c (Å)	10.1155(7)	12.8119(18)
α (°)		93.00(2)
β (°)	103.717(2)	102.16(2)
γ (°)		106.77(2)
V (Å^3)	3106.7(4)	1518.3(4)
Z	4	2
D_{calc} (Mg m^{-3})	1.312	1.372
Absorption coefficient (mm^{-1})	0.673	0.690
F(000)	1320	676
Crystal size (mm)	0.22 × 0.11 × 0.07	0.20 × 0.10 × 0.10
θ Range (°)	1.30 to 28.31	1.64 to 24.98
Limiting indices	$-9 \leqslant h \leqslant 21$, $-26 \leqslant k \leqslant 25$, $-13 \leqslant l \leqslant 12$	$-11 \leqslant h \leqslant 11$, $-15 \leqslant k \leqslant 15$, $-1 \leqslant l \leqslant 15$
Reflection collected/ unique (R_{int})	22 688/7713 (0.0603)	6112/5326 (0.1011)
Absorption correction	SADABS	φ-scan
Maximum and minimum transmission	0.9553 and 0.6541	0.9331 and 0.7569
Data/restraints/ parameters	7713/0/387	5326/0/388
Goodness-of-fit on F^2	0.932	0.955
Final R indices ($I > 2\sigma(I)$)	$R_1^a = 0.0545$, $wR_2^b = 0.1379$	$R_1 = 0.0797$, $wR_2 = 0.1404$
R indices (all data)	$R_1 = 0.1218$, $wR_2 = 0.1902$	$R_1 = 0.2871$, $wR_2 = 0.1923$
Largest difference in peak and hole (e Å^{-3})	0.597 and −0.574	0.449 and −0.822

[a] $R_1 = \|F_o| - |F_c\|/\sum|F_o|$.
[b] $wR_2 = [\sum[w(F_o^2 - F_c^2)^2]/\sum[w(F_o^2)^2]]^{1/2}$.

hydrogen atoms of Ow(3) were not found. Crystal parameters and details of the data collections and refinement are summarized in Table 1.

3. Results and discussion

3.1. Crystal structures

An ORTEP drawing of $\{[Ni(L)(isoph)]\cdot 3H_2O\}_n$ (**1**) with the atomic numbering scheme is shown in Fig. 1 and the selected bond lengths and angles are listed in Table 2. The ligand skeleton of the present compound takes the *trans*-III(*R,R,S,S*) configuration with two chair six-membered and two gauche five-membered chelate rings. The crystal structure of **1** has cationic $[Ni(L)]^{2+}$ units, $isoph^{2-}$ anion, and water molecules. An inversion center exists on the central nickel(II) ion. In the chain structure, the nickel(II) reveals a distorted octahedral coordination environment in which the macrocycle and carboxylate oxygen atoms of the two $isoph^{2-}$ ligands have assembled around the nickel(II) center. Thus, one-dimensional coordination polymers have formed. The Ni···Ni distance across the polymer backbone is 11.327(1) Å, whereas the closest Ni···Ni distance between neighboring stands is 8.032(1) Å. The Ni–N (secondary amine) distances vary from 2.057(3) to 2.091(3) Å and the Ni–O (carboxylate oxygen) distances vary from 2.128(2) to 2.140(2) Å, giving an axially elongated octahedron in the 1D chain direction. The average Ni–N distance of 2.075(3) Å is significantly longer than in the square-planar geometry of $[Ni(L)]Cl_2\cdot 2H_2O$ [1.948(4) Å] [20], but is similar to that observed for high-spin octahedral nickel(II) complexes with 14-membered tetraaza macrocyclic ligands [25–27]. The average Ni–O distance of 2.134(2) Å is comparable to the previously reported values in the related systems $\{[Ni(L)(tp)]\cdot 2H_2O$ [17]: Ni–O = 2.116(3) Å; $[Ni(L)(pdc)]\cdot H_2O$ [17]: Ni–O = 2.121(9) and 2.137(10) Å; $[Ni(cyclam)(tp)]\cdot 4H_2O$ [28]: Ni–O = 2.129(5) Å}, which have a tetragonally distorted octahedral geometry. The N–Ni–N angles of the six-membered chelate rings are larger than those of the five-membered chelate rings. The axial Ni(1)–O(1) and Ni(2)–O(3) linkages are bent slightly off the perpendicular

Table 2
Selected bond lengths (Å) and angles (°) for $\{[Ni(L)(isoph)]\cdot 3H_2O\}_n$ (**1**)

Bond lengths (Å)			
Ni(1)–N(1)	2.061(3)	Ni(2)–N(3)	2.057(3)
Ni(1)–N(2)	2.089(3)	Ni(2)–N(4)	2.091(3)
Ni(1)–O(1)	2.140(2)	Ni(2)–O(3)	2.128(2)
C(22)–O(1)	1.267(4)	C(27)–O(3)	1.255(4)
C(22)–O(2)	1.241(4)	C(27)–O(4)	1.249(4)
Ni(1)···Ni(2)^{i}	8.032(1)	Ni(1)···Ni(2)	11.327(1)
Bond angles (°)			
N(1)–Ni(1)–N(2)	84.2(1)	N(3)–Ni(2)–N(4)	84.5(1)
N(1)–Ni(1)–N(2)^{ii}	95.8(1)	N(3)–Ni(2)–N(4)^{ii}	95.5(1)
N(1)–Ni(1)–O(1)	90.2(1)	N(3)–Ni(2)–O(3)	89.0(1)
N(1)^{ii}–Ni(1)–O(1)	89.8(1)	N(3)^{ii}–Ni(2)–O(3)	91.0(1)
N(2)–Ni(1)–O(1)	82.85(11)	N(4)–Ni(2)–O(3)	83.2(1)
N(2)^{ii}–Ni(1)–O(1)	97.15(11)	N(4)^{ii}–Ni(2)–O(3)	96.8(1)
Ni(1)–O(1)–C(22)	135.6(2)	Ni(2)–O(3)–C(27)	136.5(2)
O(1)–C(22)–O(2)	125.7(3)	O(3)–C(27)–O(4)	125.8(3)

Symmetry codes: (i) $x+1, y, z+1$; (ii) $-x+1, -y+1, -z+1$.

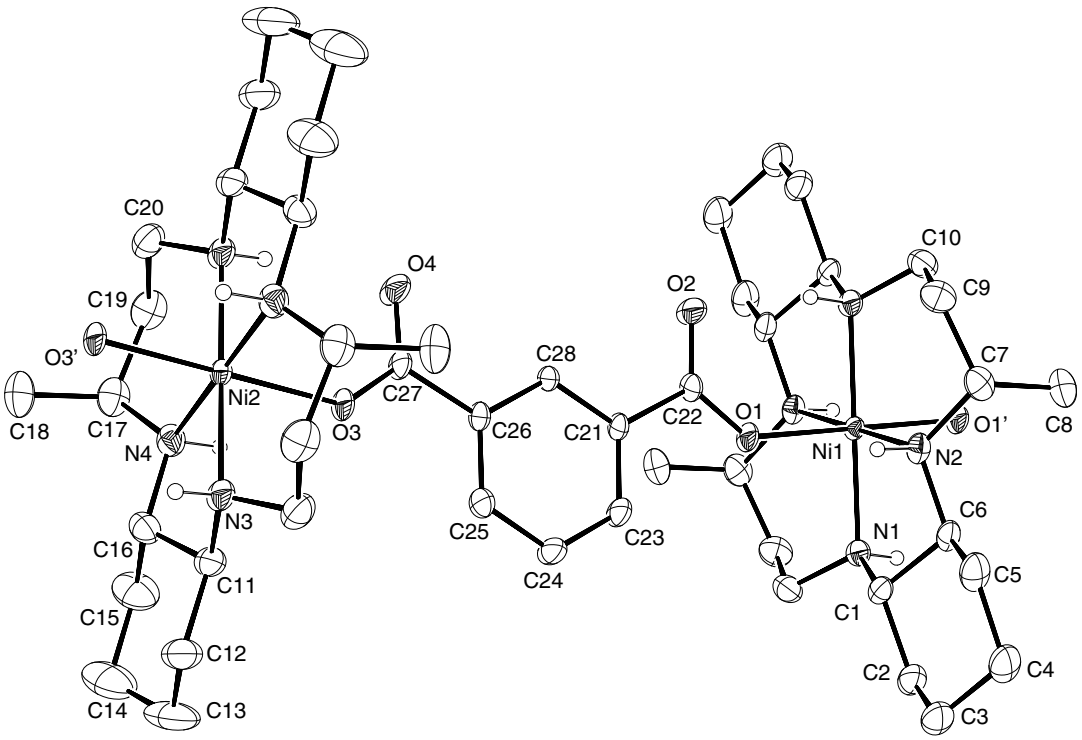


Fig. 1. An ORTEP diagram of $\{[Ni(L)(isoph)]\cdot 3H_2O\}_n$ (**1**) with the atom-numbering scheme (30% probability ellipsoids shown). The hydrogen atoms and water molecules are omitted for clarity.

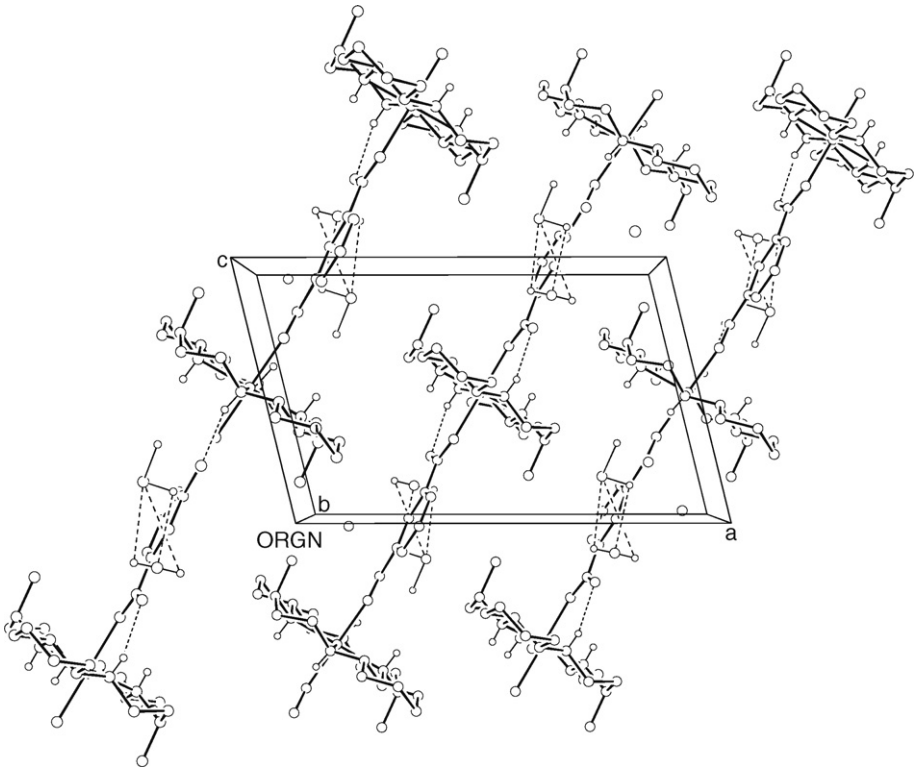


Fig. 2. Crystal packing of $\{[Ni(L)(isoph)] \cdot 3H_2O\}_n$ (**1**), showing the hydrogen bonds as dotted lines.

to the NiN_4 plane by 0.2–7.2° and 1.0–6.8°, respectively. The dihedral angles (α) between the plane of the carboxylate group and benzene ring involving Ni(1) and Ni(2) are 4.0(5) and 7.2(6)°. Moreover, the dihedral angles (β) between the plane of the carboxylate group and NiN_2O_2 plane involving Ni(1) and Ni(2) are 11.2(5) and 78.2(3)°. The Ni(1)–O(1)–

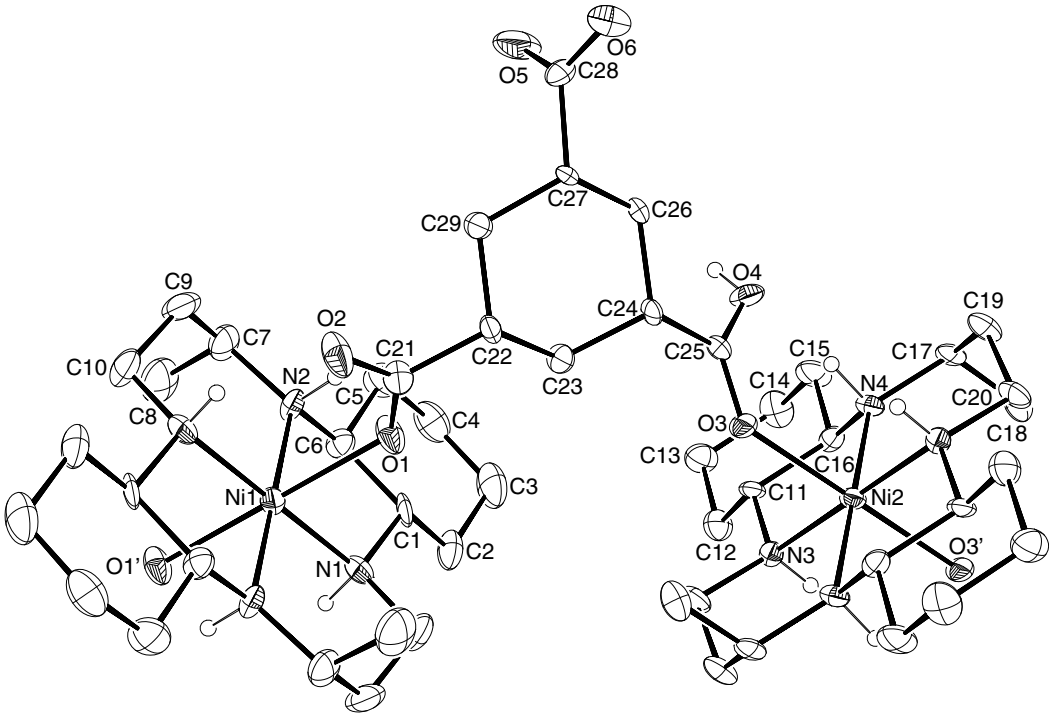


Fig. 3. An ORTEP diagram of $\{[Ni(L)(H\text{-}chtc)] \cdot H_2O\}_n$ (**2**) with the atom-numbering scheme (30% probability ellipsoids shown). The hydrogen atoms and water molecules are omitted for clarity.

Table 3
Selected bond lengths (Å) and angles (°) for $\{[Ni(L)(H\text{-}chtc)]\cdot H_2O\}_n$ (**2**)

Bond lengths (Å)			
Ni(1)–N(1)	2.038(8)	Ni(2)–N(3)	2.063(7)
Ni(1)–N(2)	2.075(8)	Ni(2)–N(4)	2.068(7)
Ni(1)–O(1)	2.176(6)	Ni(2)–O(3)	2.152(6)
C(21)–O(1)	1.245(10)	C(25)–O(3)	1.230(10)
C(21)–O(2)	1.232(10)	C(25)–O(4)	1.258(10)
Ni(1)···Ni(2)^{i}	8.800(2)	Ni(1)···Ni(2)^{ii}	9.273(1)
Bond angles (°)			
N(1)–Ni(1)–N(2)	83.5(3)	N(3)–Ni(2)–N(4)	84.1(3)
N(1)–Ni(1)–N(2)^{iii}	96.5(3)	N(3)–Ni(2)–N(4)^{iv}	95.9(3)
N(1)–Ni(1)–O(1)	86.2(3)	N(3)–Ni(2)–O(3)	90.8(3)
N(1)^{iii}–Ni(1)–O(1)	93.8(3)	N(3)^{iv}–Ni(2)–O(3)	89.2(3)
N(2)–Ni(1)–O(1)	80.4(3)	N(4)–Ni(2)–O(3)	91.6(3)
N(2)^{iii}–Ni(1)–O(1)	99.6(3)	N(4)^{iv}–Ni(2)–O(3)	88.4(3)
Ni(1)–O(1)–C(21)	130.6(6)	Ni(2)–O(3)–C(25)	133.7(6)
O(1)–C(21)–O(2)	125.9(9)	O(3)–C(25)–O(4)	124.5(9)

Symmetry codes: (i) $x, y-1, z-1$; (ii) $x, y-1, z$; (iii) $-x+1, -y-1, -z$; (iv) $-x+1, -y, -z+1$.

C(22) and Ni(2)–O(3)–C(27) angles and C(22)–O(1) and C(27)–O(3) distances relative to the isoph^{2-} ligand are 135.6(2)–136.5(2)° and 1.267(4)–1.255(4) Å, respectively. Interestingly, the secondary amines of the macrocycle are hydrogen bonded to the carboxylate oxygen atoms of the isoph^{2-} ligand [N(1)···O(2)^{ii} 2.886(4) Å, 160(4)°; N(3)···O(4)^{iii} 2.930(4) Å, 154(4)°; symmetry codes: (ii) $-x+1, -y+1, -z+1$; (iii) $-x, -y+1, -z-1$]. Furthermore, the water molecules found in the lattice also form hydrogen bonds with other water inclusions [Ow(1)···Ow(2)^{iv} 2.839(8) Å, 89(2)°; Ow(1)···Ow(2) 2.969(8) Å, 95(2)°; Ow(1)···Ow(3)^{v} 3.087(11) Å, 122(2)°; Ow(2)···Ow(1) 2.969(8) Å, 94(2)°; symmetry codes: (iv) $x, -y+3/2, z+1/2$; (v) $x, y, z-1$] (Fig. 3).

An ORTEP drawing of $\{[Ni(L)(H\text{-}chtc)]\cdot H_2O\}_n$ (**2**) with the atomic numbering scheme is shown in Fig. 2 and the selected bond lengths and angles are listed in Table 3. The structure of **2** consists of $[Ni(L)]^{2+}$ units, H-chtc^{2-} anion, and water molecule. The nickel(II) ion occupies a distorted octahedral coordination environment in which the macrocycle, two H-chtc^{2-} ions, and water molecule have assembled around each nickel center. Consequently, a 1D coordination polymer has formed. The intramolecular Ni···Ni distance is 8.800(1) Å, whereas the shorter intermolecular Ni···Ni distance is 9.273(2) Å. The two average Ni–N (secondary amine) distances [Ni(1)–N_4 = 2.057(8) and Ni(2)–N_4 = 2.066(7) Å] are shorter than the two Ni–O (carboxylate oxygen) distances [Ni(1)-O(1) = 2.176(6) and Ni(2)–O(3) = 2.152(6) Å], which is similar to that observed for complex **1**. The axial Ni(1)–

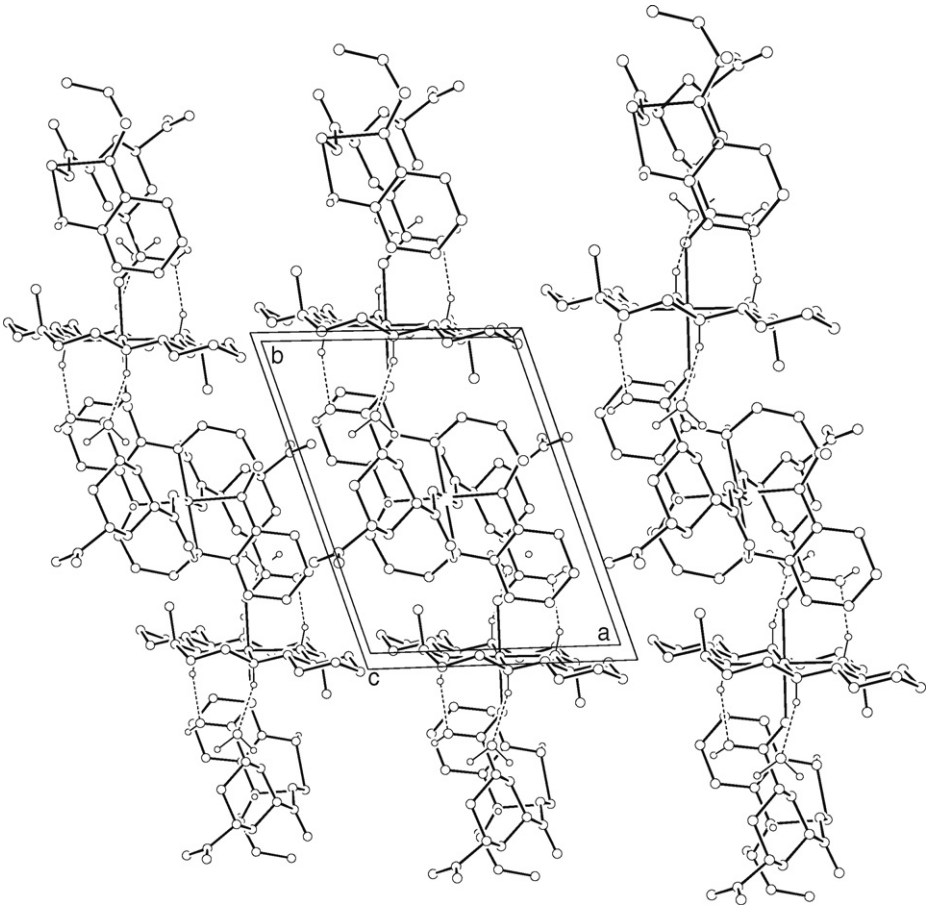


Fig. 4. Crystal packing of $\{[Ni(L)(H\text{-}chtc)]\cdot H_2O\}_n$ (**2**), showing the hydrogen bonds as dotted lines.

O(1) and Ni(2)–O(3) bonds are bent slightly off the perpendicular to the NiN_4 plane by 3.8–9.6° and 0.8–1.6°, respectively. The dihedral angles (β) between the plane of the carboxylate group and NiN_2O_2 plane involving Ni(1) and Ni(2) are 70.0(5) and 19.0(2)°. The coordination of the H-chtc^{2-} bridge is slightly asymmetrical; the two Ni(1)–O(1)–C(21) and Ni(2)–O(3)–C(25) angles are 130.6(6) and 133.7(6)°, the larger angle corresponding to the shorter bond distance. In contrast to complex **1**, the COO^- and COOH groups of the H-chtc^{2-} ligand coordinate to the nickel(II) ion but the other COO^- group is not coordinated to the metal ion. Interestingly, the protonated carboxylate oxygen atom of the H-chtc^{2-} ligand is hydrogen-bonded to the carboxylate oxygen atom [O(4)···O(6)^{viii} 2.577(9) Å, 104(9)°; symmetry code: (viii) $-x, -y-1, -z+1$]. Furthermore, the secondary amines of the macrocycle are hydrogen bonded to the carboxylic and carboxylate oxygen atoms of the H-chtc^{2-} ligand and water molecule [N(1)···O(2)^{v} 2.870(10) Å, 152.9°; N(4)···O(4)^{vii} 2.862(10) Å, 159.7°; N(3)···Ow(1)^{vi} 2.941(10) Å, 143(7)°; symmetry codes: (v) $-x+1, -y-1, -z$; (vi) $-x+1, -y, -z-1$; (vii) x, y, z]. Similar result was observed for the related macrocyclic complex *trans*-[Ni(*O*-benzoato)$_2$(cyclam)] [29]. The water molecules found in the lattice also form hydrogen bonds with the carboxylate oxygen atoms of the H-chtc^{2-} ligand [Ow(1)···O(5)^{viii} 2.857 (10) Å, 142(8)°; Ow(1)···O(2)^{viii} 2.721(10) Å, 155(10)°; symmetry code: (viii) $-x+1, -y-1, -z+1$] (Fig. 4).

3.2. Characterization of the complexes

The spectroscopic data of the complexes are listed in Table 4. The solid reflectance and MeCN solution spectra of **1** and **2** show an absorption maximum in the region 268–270 and 270–272 nm attributed to ligand–metal charge-transfer transitions associated with the nitrogen and oxygen donors [30]. The visible absorption spectra of the complexes in the solid and solution show that d–d transition $^3A_{2g} \rightarrow {}^3T_{1g}(F)$ [31] occurs at 523–532 (solid), 520–524 nm (MeCN), which are ca. 60–70 nm longer than that of the square-planar complex $[Ni(L)](ClO_4)_2 \cdot 2H_2O$ (459–465 nm) [19]. This fact indicates that the nickel(II) ion has a high-spin octahedral coordination environment [32]. However, all compounds dissolve in water and decompose into the original building block $[Ni(L)]Cl_2 \cdot 2H_2O$ ($\lambda_{max} = 463$ nm) [20], indicating that the square-planar species is predominant over octahedral species in aqueous solution.

Table 4
Electronic spectral data[a]

Complex	State	λ_{max}/nm (ε/M^{-1} cm^{-1})
$[Ni(L)](ClO_4)_2$[b]	CH_3CN	465 (66)
	H_2O	459 (70)
$\{[Ni(L)(isoph)] \cdot 3H_2O\}_n$ (**1**)	Solid	268, 523
	CH_3CN	270 (7.2×10^2), 524 (8.2)
	H_2O	257 (6.6×10^3), 462 (75)
$\{[Ni(L)(H\text{-}chtc)] \cdot H_2O\}_n$ (**2**)	Solid	270, 532
	CH_3CN	272 (2.6×10^3), 531 (94)
	H_2O	258 (6.2×10^3), 460 (81)

[a] Solution = CH_3CN and H_2O at 20 ± 0.1 °C; Solid = diffuse reflectance.
[b] Ref. [19].

The magnetic susceptibilities (χ_m) of **1** and **2** were measured in the range of 5.0–300 K. The χ_m and effective magnetic moment (μ_{eff}) versus temperature plots for the compounds **1** and **2** are shown in Figs. 5 and 6. The room temperature magnetic moments (μ_B) are 2.89 for **1** and 3.19 for **2**, respectively. For all compounds the μ_{eff} values gradually decrease with decreasing temperature, indicating the presence of an antiferromagnetic interaction between the nickel(II) centers. The magnetic susceptibility data are interpreted with Fisher's model for the classical-spin chain system ($S = 1$ and $H_{chain} = -J \sum S_i \cdot S_{i+1}$) [33,34]. The χ_m data can be expressed as

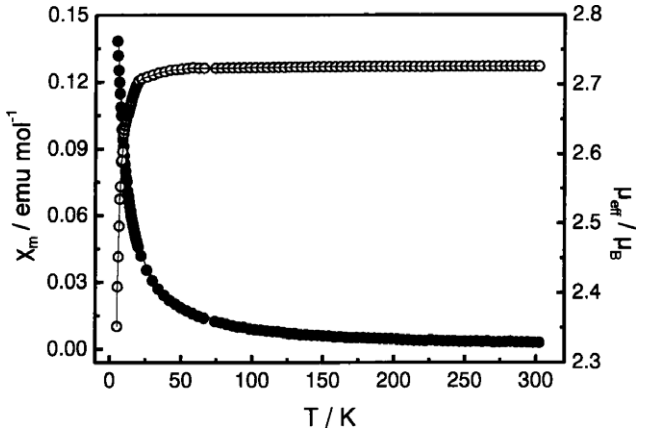


Fig. 5. Plots of χ_m vs. T (●) and μ_{eff} vs. T (○) for $\{[Ni(L)(isoph)] \cdot 3H_2O\}_n$ (**1**). The solid line represents the best fit of the experimental data to Eq. (1).

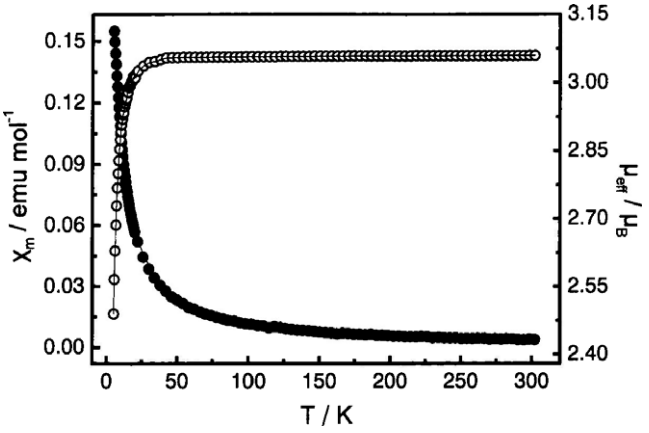


Fig. 6. Plots of χ_m vs. T (●) and μ_{eff} vs. T (○) for $\{[Ni(L)(H\text{-}chtc)] \cdot H_2O\}_n$ (**2**). The solid line represents the best fit of the experimental data to Eq. (1).

Table 5
Structural and magnetic data of nickel(II) complexes

Complex	g	J (cm^{-1})	α (°)	β (°)	d_{intra} (Å)	d_{inter} (Å)
{[Ni(Me_4cyclam)(pdc)] · H_2O}$_n$[a]	2.26	−1.04	4.0, 4.5	3.7, 38.5	11.2	7.9
{[Ni(L)(isoph)] · $3H_2O$}$_n$ (**1**)	2.02	−0.93	4.0, 7.1	11.2, 78.1	11.3	8.0
{[Ni(L)(H-chtc)] · H_2O}$_n$ (**2**)	2.28	−1.28		19.0, 70.5	8.8	9.3

Me_4cyclam = 2,5,9,12-tetramethyl-1,4,8,-11-tetraazacyclotetradecane; pdc = 2,6-pyridinedicarboxylate.
[a] Ref. [35].

$$\chi_m = \frac{N\beta^2 g^2 S(S+1)}{3kT}\frac{(1+\mu)}{(1-\mu)} \quad (1)$$

$$\text{with} \quad \mu = \coth\left[\frac{JS(S+1)}{kT}\right] - \left[\frac{kT}{JS(S+1)}\right]$$

The best fitting of the variable-temperature data to Eq. (1) gives $J = -0.93\ cm^{-1}$ with $g = 2.02$ for **1** and $J = -1.28\ cm^{-1}$ with $g = 2.28$ for **2**, suggesting the existence of very weak antiferromagnetic interactions between the nickel(II) ions. The structural and magnetic data for complexes **1** and **2** are given in Table 5 along with the other carboxylate-bridged nickel(II) complexes. The value of J for **1** is smaller than that of **2**, but is similar to that observed in {[Ni(Me_4cyclam)(pdc)] · H_2O}$_n$ (Me_4cyclam = 2,5,9,12-tetramethyl-1,4,8,-11-tetraazacyclotetradecane; pdc = 2,6-pyridinedicarboxylate) [35], which reveals 1D coordination polymer with the distorted octahedral geometry. An increase in the intramolecular distances slightly leads to a decrease in the antiferromagnetic coupling constant with carboxylate-bridged nickel(II) complexes. However, the intermolecular distances and dihedral angles do not follow the expected trend, which may not play a significant role.

4. Supplementary material

CCDC 668949 and 668950 contain the supplementary crystallographic data for **1** and **2**. These data can be obtained free of charge via http://www.ccdc.cam.ac.uk/conts/retrieving.html, or from the Cambridge Crystallographic Data Centre, 12 Union Road, Cambridge CB2 1EZ, UK; fax: (+44) 1223-336-033; or e-mail: deposit@ccdc.cam.ac.uk.

Acknowledgement

This study was financially supported by Kongju National University in the 2007 Star Project Program.

References

[1] J.-M. Lehn, Supuramolecular Chemistry, VCH, Weinheim, Germany, 1995.
[2] V. Vogtle, Supuramolecular Chemistry, Wiley, New York, 1991.
[3] M.J. Zaworotko, Angew. Chem., Int. Ed. 39 (2000) 3052.
[4] B. Moulton, M.J. Zaworotko, Chem. Rev. 101 (2001) 1629.
[5] P.J. Stang, B. Olenyuk, Acc. Chem. Res. 30 (1997) 502.
[6] S. Leininger, B. Olenyuk, P.J. Stang, Chem. Rev. 100 (2000) 853.
[7] L. Pan, E.B. Woodlock, X. Wang, Inorg. Chem. 39 (2000) 4174.
[8] S. Noro, S. Kitazawa, M. Kondo, K. Seki, Angew. Chem., Int. Ed. 39 (2000) 2082.
[9] O. Kahn, Molecular Magnetism, VCH, Weinheim, Germany, 1993.
[10] O. Kahn, C.J. Martinez, Science 279 (1998) 44.
[11] O. Kahn, Acc. Chem. Res. 33 (2000) 647.
[12] W. Lin, Z. Wang, L. Ma, J. Am. Chem. Soc. 121 (1999) 11249.
[13] O.R. Evans, R. Xiong, Z. Wang, G.K. Wong, W. Lin, Angew. Chem., Int. Ed. 38 (1999) 536.
[14] T. Kuroda-Sowa, T. Horrino, M. Yamamoto, Y. Ohno, M. Maekawa, M. Munakata, Inorg. Chem. 36 (1997) 6382.
[15] M. Fujita, Y.J. Kwon, S. Washizu, K. Ogura, J. Am. Chem. Soc. 116 (1994) 1151.
[16] J. Lu, T. Paliwala, S.C. Lim, C. Yu, T. Niu, A.J. Jacobson, Inorg. Chem. 36 (1997) 923.
[17] K.-Y. Choi, K.M. Chun, I.-H. Suh, Polyhedron 20 (2001) 57.
[18] H.J. Choi, M.P. Suh, J. Am. Chem. Soc. 120 (1998) 10622.
[19] S.-G. Kang, J.K. Kweon, S.-K. Jung, Bull. Korean Chem. Soc. 12 (1991) 483.
[20] K.-Y. Choi, J.C. Kim, W.P. Jensen, I.-H. Suh, S.-S. Choi, Acta Crystallogr., Sect. C 52 (1996) 2166.
[21] G.M. Sheldrick, SADABS, University of Göttingen, Germany, 1996.
[22] A.C.T. North, D. C Phillips, F.S. Mathews, Acta Crystallogr., Sect. A 24 (1968) 351.
[23] G.M. Sheldrick, Acta Crystallogr., Sect. A 46 (1990) 467.
[24] G.M. Sheldrick, SHELXL-97, Program for the Refinement of Crystal Structures, University of Göttingen, Germany, 1997.
[25] R. Vicente, A. Escuer, M.S. El Fallah, X. Solans, M.J. Font-Bardia, Inorg. Chim. Acta 261 (1997) 227.
[26] K. Mochizuki, T. Kondo, Inorg. Chem. 34 (1995) 6241.
[27] K.-Y. Choi, H. Ryu, I.-H. Suh, Polyhedron 17 (1998) 1241.
[28] H.J. Choi, M.P. Suh, Inorg. Chem. 38 (1999) 6309.
[29] L.F. Lindoy, M.S. Mahinay, B.W. Skelton, H. White, J. Coord. Chem. 56 (2003) 1203.
[30] T.M. Donlevy, L.R. Gahan, T.W. Hambley, G.R. Hanson, K.L. McMahon, R. Stranger, Inorg. Chem. 33 (1994) 5131.
[31] E. Konig, in: Structure and Bonding, Springer, New York, 1971, p. 175.
[32] G.A. Melson, Coordination Chemistry of Macrocyclic Compounds, Plenum Press, New York, 1979.
[33] M.E. Fisher, Am. J. Phys. 32 (1964) 343.
[34] H. Oshio, H. Okamoto, T. Kikuchi, T. Ito, Inorg. Chem. 36 (1997) 3201.
[35] K.-Y. Choi, H. Ryu, Y.-M. Lim, N.D. Sung, U.S. Shin, M. Suh, Inorg. Chem. Commun. 6 (2003) 412.

overcome by introduction of the bulky heterocyclic ligands. As a result, some palladium complexes with aromatic N-containing ligands, e.g. derivatives of pyridine, quinoline, pyrazole and 1,10-phenanthroline, have shown very promising antitumor characteristics [4–9]. As the biological activity of a complex strongly depends on the nature of the ligands and on the metal coordination pattern, the recent research has been directed to synthesis and evaluation of complexes with biologically interesting ligands with the aim of widening spectrum of complex activity. The combination of metallic and organic activity may reveal new modes of action. These findings have stimulated investigation of complexes with the aminophosphonate derivatives because of their relevance to the natural systems and important biological and pharmacological properties [10,11]. Our research in this area is focused on complexes with the aromatic aminophosphonates and we have designed and structurally characterized a series of palladium and platinum complexes which demonstrated notable *in vitro* cytostatic activity against various tumor cell lines [7–9,12,13]. It is interesting to note that in some cases palladium complexes were more active than their platinum analogues [13].

As a continuation of our study on this class of organophosphorus compounds which might be of interest as antitumor agents, in the present work we describe the synthesis as well as spectroscopic properties and thermal analysis of palladium(II) complexes with monoethyl 8-quinolylmethylphosphonate. The antitumor activity *in vitro* of complexes was investigated against the epidermoid human KB and murine leukemia L1210 cell lines. In the course of investigations, the obtained results were compared with those previously reported for the palladium complexes of the corresponding diethyl 8-quinolylmethylphosphonate and the monoethyl 2-quinolylmethylphosphonate [7,8], and are discussed in terms of their coordination behaviour and structure–activity relationships.

2. Experimental

2.1. Materials and methods

Monoethyl 8-quinolylmethylphosphonate hydrochloride monohydrate (8-Hmqmp · HCl · H_2O) and sodium 8-quinolylmethylphosphonate dihydrate (Na(8-mqmp) · $2H_2O$), prepared as previously described [14], were purified prior to use by recrystallization from absolute ethanol. Palladium reagents (Aldrich) were high purity products and used as received. Solvents were purified and dried according to standard procedures.

Melting points were determined on a hot stage microscope and are uncorrected. Infrared spectra were recorded on an ABB Bomen MB102 spectrometer using KBr (4000–250 cm^{-1}) and polyethylene (400–200 cm^{-1}) pellets. Mass spectrometric measurements were performed on a double-focusing reverse-geometry VG ZAB 2F instrument operating under FAB conditions using the 8 keV Xe atoms. Glycerol or 3-nitrobenzyl alcohol were employed as the matrix for recording the positive-ion mass spectra. Negative-ion spectra were obtained with the 3-nitrobenzyl alcohol liquid matrix. The UV–Vis spectra were obtained in DMF solution with a Perkin–Elmer 124-spectrophotometer in the 250–600 nm range. The ^1H NMR spectra were recorded with Varian Gemini 300 Fourier-transform spectrometer in DMF-d_7 at 300 K with $SiMe_4$ as an internal reference. The two-dimensional experiments were performed by standard pulse sequences, using GEMINI DATA SYSTEM software Version 6.3 Revision A. The ^1H–^1H COSY spectra were obtained in the magnitude mode, while NOESY spectra in the phase-sensitive mode. Conductance measurements were carried out at room temperature using a CD 7A Tacussel conductance bridge for 10^{-3} mol^{-1} solutions in DMF and methanol. Magnetic susceptibilities were determined at the room temperature by the standard Gauy method using a Cahn-Ventron RM-2 balance and $CuSO_4 \cdot 5H_2O$ as the susceptibility standard. The thermogravimetric analyses (TG) were carried out on a Cahn RG electromicrobalance in an air atmosphere at a heating rate of 4 °C min^{-1} up to 850 °C. Differential thermal analyses (DTA) were performed with a Netzsch 406 differential thermal analyzer applying a heating rate of 5 °C min^{-1} in static air atmosphere. The reference substance was pure alumina. The samples were diluted with the reference substance in the ratio 1:1 by weight. The X-ray powder diffraction patterns were taken with a Philips counter diffractometer (monochromatized Cu Kα radiation). Elemental analyses (C, H and N) were performed on a Perkin–Elmer Analyser PE 2400 Series 2 in the Ruđer Bošković Institute. The chlorine and bromine content was determined by the Schöninger method, phosphorus by the vanadomolybdatophosphoric acid spectrophotometric method, and water by the thermogravimetric analysis.

2.2. Synthesis of the complexes

The complexes of 8-Hmqmp were prepared either by reaction of 8-Hmqmp · HCl · H_2O or Na(8-mqmp) · $2H_2O$ with palladium(II) halide compounds.

2.2.1. [8-H_2mqmp]$_2$[$PdCl_4$] (**1**)

(a) A concentrated aqueous solution of $K_2[PdCl_4]$ (0.146 g, 0.45 mmol) was added dropwise to a stirred solution of 8-Hmqmp · HCl · H_2O (0.255 g, 0.84 mmol) in water (3 ml). The reaction mixture was continuously stirred for 24 h at room temperature. The hazel precipitate that gradually formed was filtered off, washed with ice-cold water and methanol, and dried *in vacuo* over P_2O_5. Yield 0.205 g, 65%.

(b) $PdCl_2$ (0.090 g, 0.48 mmol) was dissolved in water (3 ml) by addition of 1:1 HCl (0.5 ml) and heating for 30 min at 50 °C. After filtration to remove any impurities, the cooled solution was added dropwise to a concentrated solution of Na(8-mqmp) · $2H_2O$ (0.240 g, 0.877 mmol) in water (3 ml). An additional constant stirring for 12 h at 4 °C yielded precipitate which was separated, washed and

dried as described. Yield 0.203 g, 64%; m.p. 182–183 °C. *Anal*. Calc. for $C_{24}H_{30}Cl_4N_2O_6P_2Pd$: C, 38.30; H, 4.02; N, 3.72; Cl, 18.84; P, 8.23; Pd, 14.19. Found: C, 38.12; H, 4.14; N, 3.58; Cl, 18.51; P, 8.54; Pd, 14.14%. Molar conductance Λ_M (DMF; MeOH, 22 °C) 72.4; 209.2 S cm^2 mol^{-1}. UV–Vis (λ_{max}, nm (ε, dm^3 mol^{-1} cm^{-1}), DMF): 276 (33 110); 300 (sh); 314 (6310); 332 (1660); 426 (210).

2.2.2. [8-H_2mqmp]$_2$[$PdBr_4$] · 2H_2O (2)

(a) A mixture of $PdBr_2$ (0.146 g, 0.55 mmol) and 1:1 HBr (1.3 ml) in water (3 ml) was stirred for 1 h, filtered and then was slowly added to a solution of Na(8-mqmp) · 2H_2O (0.249 g, 0.912 mmol) in water (3 ml). After vigorous stirring for 4 h, the reddish brown precipitate that formed was separated, washed with cold water and dried under vacuum. Yield 0.347 g, 80%.

(b) A mixture of $K_2[PdBr_4]$ (0.216 g, 0.43 mmol) and 1:1 HBr (0.9 ml) in water (4 ml) was added to a concentrated aqueous solution of 8-Hmqmp · HCl · H_2O (0.255 g, 0.84 mmol). The reaction mixture was stirred for 24 h at room temperature, the formed precipitate was isolated, washed and dried as described. Yield 0.292 g, 72%; m.p. 171–173 °C. *Anal*. Calc. for $C_{24}H_{34}Br_4N_2O_8P_2Pd$: C, 29.82; H, 3.55; N, 2.90; Br, 33.07; P, 6.41; Pd, 11.01; H_2O, 3.72. Found: C, 29.59; H, 3.81; N, 2.78; Br, 32.82; P, 6.36; Pd, 10.96; H_2O, 3.78%. Molar conductance Λ_M (DMF, MeOH, 22 °C) 70.1, 206.8 S cm^2 mol^{-1}. UV–Vis (λ_{max}, nm (ε, dm^3 mol^{-1} cm^{-1}), DMF): 278 (13 180); 300 (sh); 315 (7760); 412 (1990); 510 (320).

2.2.3. [8-H_2mqmp]$_2$[Pd_2Cl_6] (3)

A mixture of $K_2[PdCl_4]$ (0.247 g, 0.76 mmol) and 1:1 HCl (0.5 ml) in water (4 ml) was added to a concentrated aqueous solution of Na(8-mqmp) · 2H_2O (0.202 g, 0.74 mmol). The hazel precipitate that formed after stirring the reaction mixture for 24 h at room temperature was filtered off, washed with cold water and acetone, and dried under vacuum over P_2O_5. Yield 0.220 g, 64%; m.p. >180 °C (decomp.). *Anal*. Calc. for $C_{24}H_{30}Cl_6N_2O_6P_2Pd_2$: C, 31.00; H, 3.25; N, 3.01; Cl, 22.87; P, 6.66; Pd, 22.88. Found: C, 30.91; H, 3.12; N, 2.96; Cl, 22.75; P, 6.42; Pd, 22.69%. Molar conductance Λ_M (DMF, MeOH, 22 °C) 81.4, 175.2 S cm^2 mol^{-1}. UV–Vis (λ_{max}, nm (ε, dm^3 mol^{-1} cm^{-1}), DMF): 280 (17 920); 312 (sh); 338 (2820); 436 (340).

2.2.4. [8-H_2mqmp]$_2$[Pd_2Br_6] · 2H_2O (4)

A mixture of $K_2[PdBr_4]$ (0.418 g, 0.83 mmol) and 1:1 HBr (1.3 ml) in water (5 ml) was added dropwise to a stirred solution of Na(8-mqmp) · 2H_2O (0.221 g, 0.81 mmol) in water (3 ml). The reaction mixture was stirred for 4 h at 4 °C. The reddish brown precipitate that formed was filtered off, washed with minimum ice-cold water and dried under vacuum overnight at ambient temperature. Yield 0.345 g, 70%; m.p. >160 °C (decomp.). *Anal*. Calc. for $C_{24}H_{34}Br_6N_2O_8P_2Pd_2$: C, 23.38; H, 2.78; N, 2.27; Br, 38.90; P, 5.03; Pd, 17.26; H_2O, 2.92. Found: C, 23.02; H, 2.72; N, 2.18; Br, 38.71; P, 5.18; Pd, 16.98; H_2O, 3.15%. Molar conductance Λ_M (DMF, MeOH, 22 °C) 79.8, 171.1 S cm^2 mol^{-1}. UV–Vis (λ_{max}, nm (ε, dm^3 mol^{-1} cm^{-1}), DMF): 283 (19 950); 314 (sh); 419 (3310); 514 (490).

2.2.5. [8-H_2mqmp] [Pd(8-Hmqmp)Cl_3] (5)

This complex could be prepared either by heating the tetrachloropalladium complex **1** or hexachlorodipalladium complex **3** in methanol at reflux temperature for 30 min under a stream of nitrogen. The hot solution was filtered to remove some black decomposition products. The brown precipitate that gradually formed on cooling was isolated, washed with cold methanol and dried under vacuum at room temperature. M.p. 170–172 °C. *Anal*. Calc. for $C_{24}H_{29}Cl_3N_2O_6P_2Pd$: C, 40.25; H, 4.08; N, 3.91; Cl, 14.85; P, 8.65; Pd, 14.86. Found: C, 40.01; H, 3.96; N, 3.75; Cl, 14.62; P, 8.72; Pd, 14.75%. Molar conductance Λ_M (DMF, MeOH, 22 °C) 49.2, 126.1 S cm^2 mol^{-1}. UV–Vis (λ_{max}, nm (ε, dm^3 mol^{-1} cm^{-1}), DMF): 275 (11 120); 292 (9890); 314 (5980); 334 (1590); 428 (190).

2.2.6. [8-H_2mqmp] [Pd(8-Hmqmp)Br_3] (6)

This complex was prepared as a dark brown compound by the similar procedure as its chloro analogue **5**, by heating the tetrabromopalladium complex **2** or hexabromodipalladium complex **4** in methanol at reflux temperature under an inert atmosphere. M.p. 162–164 °C. *Anal*. Calc. for $C_{24}H_{29}Br_3N_2O_6P_2Pd$: C, 33.93; H, 3.44; N, 3.30; Br, 28.22; P, 7.29; Pd, 12.52. Found: C, 33.69; H, 3.52; N, 3.18; Br, 28.35; P, 7.18; Pd, 12.64%. Molar conductance Λ_M (DMF, MeOH, 22 °C) 48.7, 124.0 S cm^2 mol^{-1}. UV–Vis (λ_{max}, nm (ε, dm^3 mol^{-1} cm^{-1}), DMF): 277 (13 420); 290 (10 230); 303 (sh); 316 (6610); 419 (1740); 520 (260).

2.2.7. [Pd(8-mqmp)$_2$] · 2H_2O (7)

(a) A concentrated aqueous solution of $K_2[PdCl_4]$ (0.130 g, 0.40 mmol) was added to a stirred solution of 8-Hmqmp · HCl · H_2O (0.240 g, 0.79 mmol) in water (2 ml) adjusted to pH 6 by addition of dilute sodium hydroxide. An additional stirring of 48 h yielded pale yellow precipitate which was filtered off, washed with minimum cold water and absolute ethanol, and dried under vacuum over P_2O_5. Yield 0.172 g, 68%.

(b) A concentrated aqueous solution of $K_2[PdCl_4]$ (0.163 g, 0.50 mmol) was added dropwise to a stirred solution of Na(8-mqmp) · 2H_2O (0.256 g, 0.94 mmol) in water (3 ml). The reaction mixture was continuously stirred for 48 h at room temperature. The precipitate that formed was separated, washed and dried as described. Because of its hygroscopity, the handling of this complex was performed under nitrogen in a dry-box. Yield 0.213 g, 70%; m.p. >200 °C (decomp.). *Anal*. Calc. for $C_{24}H_{30}N_2O_8P_2Pd$: C, 44.84; H, 4.70; N, 4.36; P, 9.64; Pd, 16.55; H_2O, 5.61. Found: C, 44.72; H, 4.59; N, 4.16; P, 9.38; Pd, 16.42; H_2O, 5.99%. Molar conductance Λ_M (DMF, 22 °C) 0.6 S cm^2 mol^{-1}. UV–Vis (λ_{max}, nm (ε, dm^3 mol^{-1} cm^{-1}), DMF): 311 (13 070); 317 (13 490).

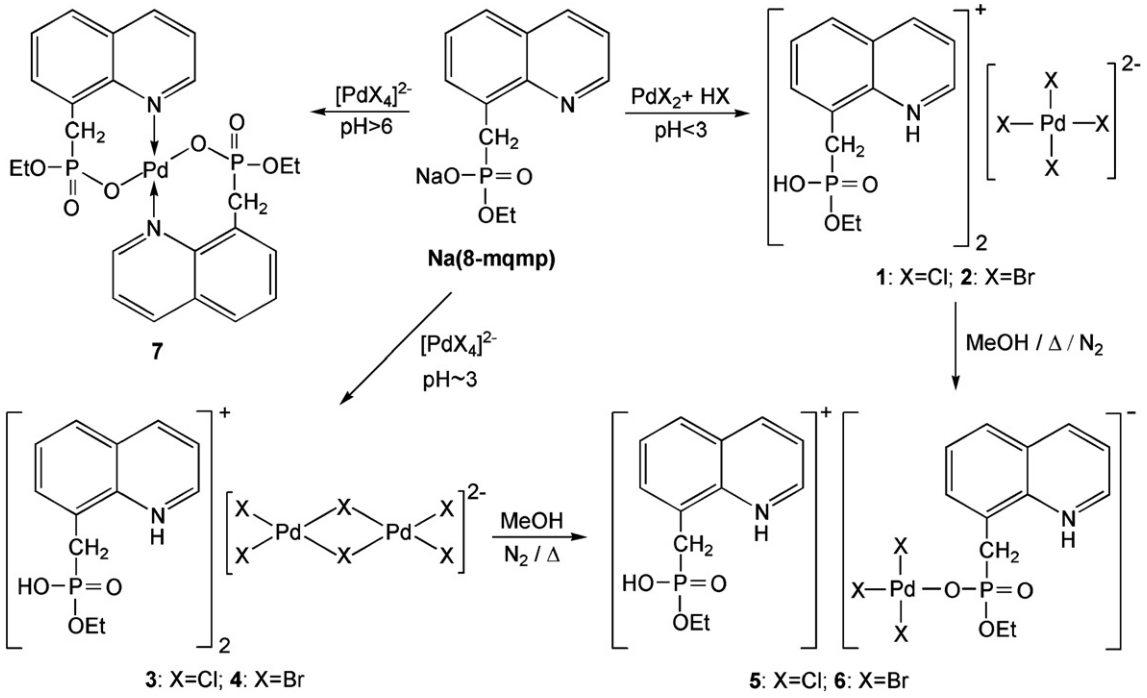
2.3. In vitro antitumor assays

In vitro antitumor activity of the complexes was evaluated against KB cell line derived from an oral epidermoid human carcinoma and murine leukemia L1210 cell line according to previously described methods [9]. The KB cells were maintained in Eagle's Minimum Essential Medium (MEM) supplemented with 10% newborn calf serum and 1% non-essential amino acids. The cell population doubling time was ca. 24 h. The L1210 cells were maintained in RPMI 1640 medium, supplemented by 10% fetal calf serum. Under these conditions the doubling time was 12 h. The complexes were dissolved immediately before use in sterile DMSO, and these solutions were diluted with the growth medium to the desired concentrations. The final DMSO concentration in the culture medium, 0.5%, showed no cytostatic effect in preliminary tests. At least five concentrations of each compound were used and each concentration was tested in triplicate on at least two separate occasions. Cytostatic activity was valued as percentage of the cellular growth inhibition in culture treated with complex compounds with respect to the growth observed in the control culture. Data were analyzed using Student unpaired *t*-test and significance was accepted at which tumor cell growth showed 50% inhibition (IC_{50}), and was calculated by linear regression analysis [15].

3. Results and discussion

3.1. Synthesis and properties

The complex-forming behaviour of monoethyl 8-quinolylmethylphosphonate towards palladium(II) ion has been investigated by reactions of the hydrochloride, 8-Hmqmp · $HCl \cdot H_2O$, and sodium salt, Na(8-mqmp) · $2H_2O$, of this monoester with palladium(II) halide compounds in aqueous solution over a wide pH range. It is interesting to note that while preparing monoalkyl esters of the aniline- and quinoline-based phosphonic acids under the same experimental conditions, by acidification of the corresponding sodium salts with diluted hydrochloric acid, the obtained monoesters exhibit great differences in their structural properties. Thus, it was shown that the monoalkyl (α-anilinobenzyl)phosphonates have inner-salt character, with the aniline group being protonated and the phosphonic acid group being ionized, which was confirmed by the spectroscopic and X-ray crystallographic studies [16,17]. In the case of benzeneazoanilino derivatives in which the basicity of the aniline N atom is reduced by participation of its electron pair in resonance with the adjacent azobenzene π-system, the isolated monoesters have a neutral molecular form [17–19]. Monoethyl ester of 2-quinolylmethylphosphonic acid exhibits also a zwitterion structure [20] similar to a large number of various alkyl α-aminophosphonic acids and their monoesters [21,22]. On the other hand, the corresponding monoethyl 8-quinolylmethylphosphonate was isolated as the hydrochloride with a water of crystallization [14]. For this reason, comparing the complex forming ability of these two monoesters with respect to the Pd(II) ion, the great differences could be observed. The former ligand depending on pH exhibits either the molecular, zwitterion or the anionic form, and therefore according to the acidity of the reaction solution forms three types of palladium(II) complexes; dihalide adducts *trans*-$[Pd(2\text{-}Hmqmp)_2X_2]$ ($pH \sim 3.5$), ion-pair salt complexes $[2\text{-}H_2mqmp][Pd(2\text{-}$



Scheme 1. Synthesis of the complexes by reaction of sodium 8-quinolylmethylphosphonate with palladium(II) halide compounds.

Hmqmp)X_3] (pH < 3) (X = Cl, Br) and chelate complex [Pd(2-mqmp)$_2$] (pH > 6) [9,20]. Monoethyl 8-quinolylmethylphosphonate at various reaction conditions could form four types of palladium complexes (see Section 2). Reactions of sodium salt are presented in Scheme 1. Generally, under acidic solution were isolated the ion-pair salt complexes [8-H_2mqmp]$_2$[PdX_4] (**1** and **2**, pH < 3) and [8-H_2mqmp]$_2$[Pd_2X_6] (**3** and **4**, pH ~ 3), containing the protonated quinoline ligand as cation and tetrahalopalladate or hexahalodipalladate complex as anion. By heating in methanol the chloro complexes **1** and **3** as well as bromo complexes **2** and **4** were converted into the quinolinium salt complexes [8-H_2mqmp][Pd(8-Hmqmp)X_3] (**5** and **6**), containing as anion the quinoliniummethylphosphonatetrihalopalladate complex with palladium bonded at the phosphonic acid moiety while the quinoline nitrogen is protonated. In neutral and basic media 8-Hmqmp acts as a bidentate chelate ligand through the quinoline nitrogen and the deprotonated phosphonic acid group giving complex **7**, [Pd(8-mqmp)$_2$] · $2H_2O$, with two seven-membered {N,O} chelate rings [23]. All attempts to prepare dihalide adducts with ligand bonded only through the quinoline nitrogen were unsuccessful.

The prepared complexes are microcrystalline or powder like diamagnetic compounds, coloured yellow to brown, and are stable in the solid state under normal laboratory conditions. The molar conductance data in DMF and methanol are consistent with the proposed structure of complexes; complexes **1**, **2**, **3** and **4** exhibit conductivities comparable to those of 2:1 electrolytes (Λ_M = 70–82 in DMF and 171–209 in methanol), **5** and **6** to those of 1:1 electrolytes ($\Lambda_M \approx 49$ in DMF and 125 in methanol), while the very low conductance of complex **7** ($\Lambda_M < 1$ in DMF) confirms the presence of deprotonated phosphonic acid group in this chelate complex. In general, complexes are only slightly soluble or insoluble in all common solvents, and slightly soluble or soluble in DMF and DMSO. The structure of the complexes, as well as their stability and mode of decomposition, were deduced mainly from their spectral and thermal studies. The relevant spectral data are summarized in Tables 1–4, while results of antitumor assays are listed in Table 5.

Table 1
Selected infrared spectroscopic data for 8-Hmqmp and its palladium complexes (cm^{-1})[a]

Compound	ν(OH)[b], (H_2O)	ν(NH^+),ν[P(O)OH]	ν(C=C), ν(C=N)	ν(P=O), $\nu_{as}(PO_2^-)$	ν(PO–C), $\nu_{sym}(PO_2^-)$, ν(PO–H)	ν(Pd–X)[b]	ν(Pd–N)
(8-Hmqmp) · HCl · H_2O	3250 w–m, br	2900–2400 m, br 2050–1750 w, br 1630 m–s	1598 s 1560 s	1234 vs 1220 s 1210 sh	1040 sh 1035 s, br 994 vs, br		
Na(8-mqmp) · $2H_2O$	3400 w–m br		1598 w 1575 m	1250 sh 1225 s 1200 s	1055 vs, br		
1		2900–2500 m, br 2360 w, br 1635 s	1598 s 1568 s	1235 m, br 1228 sh	1039 m–s 1020 s 1002 vs 989 vs	329 m–s	
2	3358 m 3280 m	2900–2400 m–br 2330 w, br 1630 s	1596 s 1568 s	1220 m 1192 vs 1170 s	1032 vs 1021 vs 967 s	243 m	
3		2900–2500 m, br 2350 m, br 1637 s	1603 s 1571 s	1248 m–s 1230 s 1200 s	1041 vs 1030 vs 967 s	326 m 240 m	
4	3505 s, br 3450 m–s	2920–2400 s, br 2340 w, br 1635 s	1602 s 1568 s	1250 m 1220 m–s 1200 vs	1035 sh 1028 s 987 s	246 m	
5		2900–2500 m, br 2380 w, br 1635 s	1599 s 1567 s	1238 m 1224 m–s 1190 m–s	1044 vs 965 s 950 sh	345 sh 334 w–m 285 w	
6		2900–2500 m, br 2350 w, br 1630 s	1598 s 1568 s	1236 m 1220 m-s 1196 m–s	1042 vs 960 s 937 sh	248 w	
7	3385 m–s, br		1598 w 1513 m–s	1225 m–s 1217 vs 1196 s	1044 vs 1032 vs 1015 s–vs 991 m–s		260 w

[a] As KBr pellets. Abbreviations: vs, very strong; s, strong; m, medium; w, weak; br, broad; vbr, very broad; sh, shoulder.
[b] X = Cl, Br.

3.2. IR spectra

The IR spectra of the complexes are very complicated due to extensive vibrational coupling and overlapping of the absorption bands, so the proposed assignments given in Table 1 must be regarded as approximate description of the vibrations.

All the ionic complexes **1**–**6**, which contain the protonated quinoline nitrogen, show the characteristic bands attributed to the $\nu(NH^+)$ vibration, similarly as the hydro-

Table 2
^{1}H NMR data [δ (ppm), J (Hz)][a]

Proton	Na(8-mqmp) · $2H_2O$	**1**	**2**	**4**	**6**	**7**[b]
H2	9.10 dd $^3J_{HH}$ = 4.6, 1.6	9.41 dd $^3J_{HH}$ = 4.9, 1.4	9.49 dd $^3J_{HH}$ = 5.1, 1.4	9.36 dd $^3J_{HH}$ = 4.9, 1.5	9.42 d $^3J_{HH}$ = 4.5	9.62 s br
H3	7.59 dd $^3J_{HH}$ = 7.5, 3.6	8.13 dd $^3J_{HH}$ = 8.4, 4.8	8.23 dd $^3J_{HH}$ = 8.3, 4.9	8.06 dd $^3J_{HH}$ = 8.4, 4.8	8.15 dd $^3J_{HH}$ = 8.4, 4.8	7.98[c]
H4	8.45 dd $^3J_{HH}$ = 8.4, 1.6	9.11 dd $^3J_{HH}$ = 8.0, 1.4	9.28 dd $^3J_{HH}$ = 7.9, 1.4	9.04 dd $^3J_{HH}$ = 8.4, 1.5	9.16 d $^3J_{HH}$ = 8.1	8.92 d (8.82–9.00) $^3J_{HH}$ = 8.0
H5	7.88 d $^3J_{HH}$ = 8.1	8.34 d $^3J_{HH}$ = 8.0	8.43 d $^3J_{HH}$ = 8.3	8.31 d $^3J_{HH}$ = 8.1	8.37 d $^3J_{HH}$ = 7.8	8.23 s br
H6	7.60 t $^3J_{HH}$ = 7.5	7.98 t $^3J_{HH}$ = 7.6	8.05 t $^3J_{HH}$ = 7.6	7.96 t $^3J_{HH}$ = 7.5	8.01 t $^3J_{HH}$ = 7.5	7.86 t (7.82–7.89)[c] $^3J_{HH}$ = 7.5
H7	8.22 d $^3J_{HH}$ = 7.5	8.23 dd $^3J_{HH}$ = 6.7, 3.5	8.29 dd $^3J_{HH}$ = 6.8, 3.5	8.21 dd $^3J_{HH}$ = 6.7, 3.3	8.24 dd $^3J_{HH}$ = 6.6, 3.0	8.14[d]
PCH_2	3.94 d[e] $^2J_{PH}$ = 20.1	4.22 d[e] $^2J_{PH}$ = 21.8	4.21 d[e] $^2J_{PH}$ = 21.3	4.15 d[e] $^2J_{PH}$ = 21.6	4.16 d[e] $^2J_{PH}$ = 20.1	6.80 d (6.58–6.92) $^2J_{PH}$ = 20
OCH_2	3.93 m[e]	4.21 m[e]	4.24 m[e]	4.19 m[e]	4.20 m[e]	3.78–4.13 m
CH_3	0.98 t $^3J_{HH}$ = 6.9	1.30 t $^3J_{HH}$ = 7.1	1.32 t $^3J_{HH}$ = 7.1	1.31 t $^3J_{HH}$ = 7.0	1.31 t $^3J_{HH}$ = 7.0	0.74 s br
NH^+, OH	3.70 s br	6.70 s br	6.60 s br	7.43 s br	6.08 s br	3.60 s br

[a] Spectra recorded in DMF-d_7 at room temperature: s, singlet; d, doublet; t, triplet; dd, doublet of doublets; m, multiplet; br, broad signal.
[b] Data for the most abundant isomer. Presence of more isomeric species in complex brings about multiple signals in the region given in parentheses.
[c] Partly overlapped H3 and H6. Tentative value obtained from a COSY experiment.
[d] Partly overlapped with DMF-d_7 absorption. Tentative value obtained from a COSY experiment.
[e] Overlapped PCH_2 and OCH_2.

Table 3
Major fragments in positive-ion mass spectra[a]

Ionic species[b]	Compound m/z (rel. int. %)[c]								
	1	**2**	**3**	**4**	**5**	**6**	**7**	8-Hmqmp · HCl	Na(8-mqmp)
$[M+H]^+$	752 (–)	930 (–)	930 (–)	1191 (–)	715 (–)	847 (–)	607 (6)	287 (30)	274 (65)
$[(M+Na)-X]^+$					702 (1)	790 (1)			
$[(M+Na)-2X]^+$					667 (1.5)	712 (1)			
$[(M+H)-2X]^+$					645 (3)	689 (1)			
$[(M+Na)-3X]^+$					632 (2.5)	632 (1)			
$[(M+H)-3X]^+$					610 (10)	610 (2.5)			
$[Pd(L-H)_2+H]^+$	607 (1)	607 (9)	607 (4)		607 (4)	607 (3)	[d]		
$[Pd(QCH_2)_2]^+$							390 (6)		
$[L_2+Na]^+$	525 (4)	525 (50)	525 (22)	525 (3)	525 (22)	525 (14)			
$[L_2+H]^+$	503 (30)	503 (68)	503 (86)	503 (28)	503 (85)	503 (52)	503 (5)		
$[Q]_2^+$	260 (25)	260 (28)	260 (55)	260 (68)	260 (33)	260 (24)	260 (18)		
$[Pd(L-H)+H]^+$	357 (5)		357 (17)	357 (8)	357 (22)	357 (7)	357 (10)		
$[Pd(QCH_2)PO_2OH]^+$	328 (4)	328 (5)	328 (4)	328 (7)	328 (15)	328 (20)	328 (6)		
$[Pd(QCH_2)]^+$	248 (8)	248 (7)	248 (45)	248 (18)	248 (38)	248 (37)	248 (18)		
$[PdQ]^+$	236 (12)	236 (8)	236 (60)	236 (22)	236 (64)	236 (72)	236 (6)		
$[L+Na]^+$	274 (92)	274 (95)	274 (48)	274 (95)	274 (38)	274 (39)	274 (68)	274 (9)	274 (65)
$[L+H]^+$	252 (100)	252 (100)	252 (100)	252 (100)	252 (100)	252 (100)	252 (100)	252 (69)	252 (56)
$[L+H-C_2H_4]^+$	224 (42)	224 (58)	224 (30)	224 (95)	224 (35)	224 (68)	224 (18)	224 (100)	224 (100)
$[L+H-EtOH]^+$	206 (62)	206 (68)	206 (50)	206 (60)	206 (55)	206 (58)	206 (27)		

[a] FAB matrix 3-nitrobenzyl alcohol for complexes **1**–**7** and Na(8-mqmp), and glycerol for 8-Hmqmp · HCl.
[b] X = Cl, Br; L = 8-Hmqmp, Q = quinolyl.
[c] Ion masses referenced to isotopes ^{106}Pd, ^{35}Cl and ^{79}Br.
[d] See $[M+H]^+$ ion.

Table 4
Major ion fragments in negative-ion mass spectra of the ionic Pd(II) complexes[a]

Ionic species[b]	Compound m/z (rel. int. %)[c]					
	1	**2**	**3**	**4**	**5**	**6**
$[M-H]^-$	749 (–)	925 (–)	925 (–)	1189 (–)	713 (–)	845 (–)
$[(M-H)-X]^-$					678 (7)	766 (2)
$[(M-H)-2X]^-$					643 (2.5)	687 (2)
$[(M-H)-3X]^-$					608 (7)	608 (12)
$[LPd_2X_6]^-$			673 (4)	935 (7)		
$[Pd_2X_6+Na]^-$	445 (3)	709 (4) A	445 (9)	709 (8)		
$[Pd_2X_6]^{2-}$	422 (5)	686 (2.5) B	422 (10)	686 (5)		
$[Pd_2X_5]^-$	387 (4)	607 (14) C	387 (25)	607 (40)		
$[LPdX_3]^-$					462 (3)	594 (3)
$[(L-H)PdX_2]^-$					426 (5)	514 (2)
$[(L-H)PdX]^-$					391 (4)	435 (2)
$[Pd_2X_4]^-$	352 (35)	528 (17) D	352 (45)	528 (40)	352 (8)	528 (16)
$[Pd_2X_3]^-$	317 (13)	449 (12) E	317 (20)	449 (34)	317 (32)	449 (18)
$[PdX_3]^-$	211 (43)	343 (42) F	211 (80)	343 (52)	211 (62)	343 (36)
$[PdX_2]^-$	176 (25)	264 (54) G	176 (90)	264 (100)	176 (17)	264 (57)
$[L-H]^-$	250 (100)	250 (35) H	250 (100)	250 (33)	250 (100)	250 (55)
$[(L-H)-H_2O]^-$	232 (24)	232 (100) I	232 (18)	232 (38)	232 (12)	232 (33)
$[L-H-C_2H_4]^-$	223 (38)	223 (12) J	223 (16)	223 (17)	223 (18)	223 (26)
$[L-H-EtOH]^-$	204 (22)	204 (18) K	204 (15)	204 (21)	204 (15)	204 (9)

[a] FAB matrix 3-nitrobenzyl alcohol.
[b] X = Cl, Br; L = 8-Hmqmp.
[c] Ion masses referenced to isotopes ^{106}Pd, ^{35}Cl and ^{79}Br.

Table 5
In vitro cytostatic activity of Pd(II) complexes with quinolylmethylphosphonates

Complex[a]		IC_{50} (μg/mL)[b]			
		KB cells[c]		L1210 cells[d]	
1	$[8\text{-}H_2mqmp]_2[PdCl_4]$	>50		15.32	(20.35)
2	$[8\text{-}H_2mqmp]_2[PdBr_4]\cdot 2H_2O$	41.01	(42.42)	12.31	(12.74)
3	$[8\text{-}H_2mqmp]_2[Pd_2Cl_6]$	>50		18.25	(19.62)
4	$[8\text{-}H_2mqmp]_2[Pd_2Br_6]\cdot 2H_2O$	31.40	(25.30)	10.03	(8.14)
	$[2\text{-}H_2mqmp]_2[Pd_2Br_6]\cdot 2H_2O$	18.26	(15.30)[e]	12.60	(10.50)[e]
5	$[8\text{-}H_2mqmp][Pd(8\text{-}Hmqmp)Cl_3]$	45.34	(63.39)	17.23	(24.05)
	$[2\text{-}H_2mqmp][Pd(2\text{-}Hmqmp)Cl_3]$	43.60	(61.11)[e]	22.11	(30.91)[e]
6	$[8\text{-}H_2mqmp][Pd(8\text{-}Hmqmp)Br_3]$	32.00	(37.66)	11.80	(13.88)
	$[2\text{-}H_2mqmp][Pd(2\text{-}Hmqmp)Br_3]$	27.20	(32.02)[e]	15.90	(18.73)[e]
7	$[Pd(8\text{-}mqmp)_2]\cdot 2H_2O$	18.40	(28.62)	17.30	(26.91)
	$[Pd(2\text{-}mqmp)_2]\cdot 2H_2O$	25.40	(42.04)[e]	15.81	(25.93)[e]
	$[Pd(8\text{-}dqmp)_2Cl_2]$	6.65	(9.03)[f]	7.92	(10.76)[f]
	$[Pd(8\text{-}dqmp)_2Br_2]$	10.03	(12.12)[f]	12.72	(15.42)[f]
	$[8\text{-}Hdqmp]_2[PdCl_4]\cdot 2H_2O$	16.00	(18.98)[f]	11.51	(13.65)[f]
	$[8\text{-}Hdqmp]_2[PdBr_4]\cdot 2H_2O$	9.89	(10.04)[f]	9.83	(9.98)[f]
	$[8\text{-}Hdqmp]_2[Pd_2Cl_6]$	18.72	(18.98)	16.12	(16.33)
	$[8\text{-}Hdqmp]_2[Pd_2Br_6]$	17.61	(14.04)[f]	14.79	(11.80)[f]

[a] Monoethyl 8- and 2-quinolylmethylphosphonates (8-Hmqmp and 2-Hmqmp), and diethyl 8-quinolylmethylphosphonate (8-dqmp).
[b] Molar concentration of the complexes are given in the parentheses (mol dm^{-3}).
[c] KB – epidermoid human carcinoma cell line.
[d] L1210 – murine leukemia cell line.
[e] Data taken from Ref. [9].
[f] Data taken from Ref. [8].

chloride salt of the 8-mqmp, but their position is a bit different [14,24]. In the complexes a very broad complex progression of absorptions mostly of medium intensity is between 2900 and 2400 cm^{-1}, less intense absorption is centered within 2380 and 2320 cm^{-1}, and a medium to strong sharp band is at about 1635 cm^{-1} (see Fig. 1a). The variation in their position may arise from the weak hydrogen bonding between the NH^+ and the phosphoryl oxygen or that of the lattice water present in some of the complexes. In addition, in these regions also occur the less intense absorptions characteristic for the hydrogen bonded phosphonic acidic P(O)OH group [19,25]. The absorption over 1600 cm^{-1} contributes to deformation modes of the lattice water present in the hydrated complexes. It is worth noting that in the non-hydrated phosphonic acid compounds there is no evidence of band at about 3500 cm^{-1} normally ascribed to the absorption of the OH group alone. The hydrated complexes **2** and **4** in the ν(OH) region show two rather intense bands in the range 3550–3400 cm^{-1}, while in the hydrochloride salt is present only one broad ν(OH) absorption around 3250 cm^{-1}, indicating a strong hydrogen bonding in this salt. All complexes show also a great complexity of the spectra in the region of 1250–950 cm^{-1} where bands arising from the stretching modes of the P=O, P–O–C and PO–H vibrations, along with those of the ionized PO_2^- group, give a series of medium to very strong absorption bands. The variation in position and complexity of these absorptions is arising from their sensitivity to the hydrogen bonding, as well as to the nature of the metal ion [19,26]. Coordination of single oxygen of a PO_2^- group would result in considerably different P–O bond orders arising from a combination of bond polarization and covalence effects.

The far-IR spectra of the ionic complexes are consistent with the spectral data obtained for complexes containing the square-planar monomeric $[PdX_4]^{2-}$, dimeric halobrid-

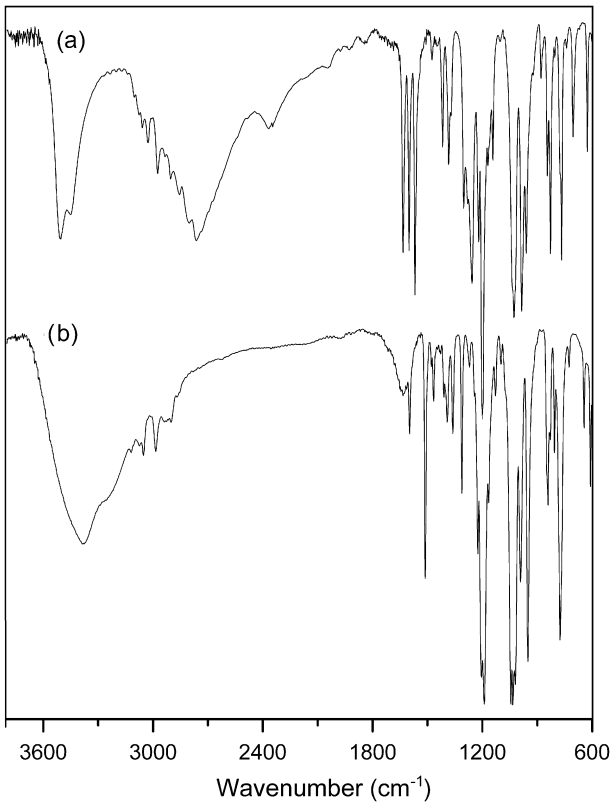


Fig. 1. Infrared spectra of complexes (a) **4** and (b) **7**.

ged $[Pd_2X_6]^{2-}$ anions as well as complexes having the form $[PdLX_3]^-$ for which the C_{2v} symmetry is a reasonable approximation [8,27]. Thus, one ν(Pd–X) band is visible in the complexes **1** and **2**, two bands in the chloride complex **3**, while complicated absorption is present in complex **5** in the examined region. In the case of bromo complexes **4** and **6** only one band is found in the examined range, as the other bands are expected to be at the lower frequencies [27,28].

In the spectrum of complex **7** there is no evidence of the bands associated with the NH^+ and P–O–H absorptions (see Fig. 1b), since in this complex the deprotonated phosphonate ligand acts as a N,O-bidentate ligand in the ionic form. Its spectrum is characterized by a series of complex bands of medium to very strong intensity between 1230 and 1190 cm^{-1} for the antisymmetric and between 1045 and 1015 cm^{-1} for the symmetric mode of the PO_2^- vibration. In the latter frequency region also occurs a strong ν(PO–C) absorption. One ν(Pd–N) band at 260 cm^{-1} confirms palladium coordination through the quinoline nitrogen in a *trans*-orientation. The presence of the lattice water in this complex is confirmed by a very broad ν(OH) absorption around 3400 cm^{-1}.

3.3. ^1H NMR spectra

While all bromopalladium complexes are sufficiently soluble in DMF for the ^1H NMR spectral analysis, among the chloro complexes only for the tetrachloropalladium complex **1** a satisfactory spectrum could be obtained. The spectral data are given in Table 2 and the numbering scheme is shown in Scheme 1.

In the spectra of complexes the resonances of most of protons show a certain downfield shift with respect to the sodium salt of the quinoline ligand. These changes could be explained by decrease in the electron density in the heterocyclic aromatic ring caused by the protonation of the quinoline nitrogen in the ionic complexes or by its coordination to palladium atom in the chelate complex, as well as by the proximity of the palladium atom which is known to be magnetically anisotropic bringing about deshielding effects [29]. In general, the magnitude of the shift changes decreases with the distance from the protonation or coordination site. Therefore, in the ionic complexes the most pronounced downfield shift could be observed for the aromatic protons and there are no significant differences in the spectra between three types of palladium complexes. The signal of OH and NH^+ protons gives a broad singlet between 6 and 7.5 ppm. The situation is more complicated in the chelate complex **7**, which spectrum shows a great complexity arising from the existence of more isomeric species with different magnetic environment in dynamic equilibrium. This can be interpreted by the restricted rotation around the metal–ligand bond due to the proximity of the bulky phosphonate ligand group and the formation of the asymmetric center on the phosphorus atom as a result of the N,O-ligand bonding to palladium. As a consequence either the broadening or the presence of few sets of signals could be observed. The connectivities from 2D NMR experiments corroborate the tentative assignments of all protons in the major isomer, which are given in Table 2 along with the tentative spectral range covering absorption of all isomers of each proton. The greatest downfield shift was observed for the aromatic H-2 proton (0.52 ppm) and for the PCH_2 protons (2.64–2.98 ppm). The similar spectroscopic feature has been reported for some palladium(II) and platinum(II) complexes of various quinoline derivatives [13,16,30], which was confirmed by variable temperature measurements.

3.4. UV–Vis spectra

All palladium(II) complexes are diamagnetic with a square-planar geometry, for which three spin-allowed d–d transitions corresponding to transitions from the three lower lying d levels to the empty $d_{x^2-y^2}$ orbitals, are expected [31]. The ground state is $^1A_{2g}$ and the excited states related to these transitions are $^1A_{2g}$, $^1B_{1g}$ and ^1E_g in order of increased energy. Overlapping of the strong absorptions from the charge-transfer or intraligand transitions (π–π^* transitions in quinoline) prevents the observation and detection of the expected bands [32]. The relatively dark colour of the ionic complexes (**1**–**6**) indicates strong charge-transfer absorptions originating in the ultraviolet and trailing off into the visible region. The most prominent absorption in all three types of ionic complexes

is in the visible region around 430 nm for the chloro and about 515 nm for the corresponding bromo complexes, which could be ascribed to the metal-to-ligand charge-transfer transitions. The absorption at lower energies in bromide complexes than in their chloride analogues is due to the lower position of bromide in the spectrochemical series, and their various optical electronegativity [33]. In addition, the intensity of absorption bands is generally higher for the bromide complexes, which could be ascribed to the increased ligand participation in the occupied MO-levels, derived mainly from the metal d-levels. The relatively pale colour of the chelate complex **7** indicates that the quinoline ligand has a low ligand field strength in forming this complex.

3.5. Mass spectra

All palladium complexes have been investigated by positive/negative FAB mass spectrometric measurements, giving valuable structural information of these compounds. The fragment ions containing palladium and halide atoms are identified by the presence of the characteristic clusters of isotopic peaks corresponding to the relative abundances of the palladium and halide isotopes. The major structurally informative fragment ions in the positive-ion mode of all the complexes are given in Table 3, while those obtained in the negative-ion mode of the ionic complexes **1**–**6** are summarized in Table 4.

In the positive-ion mass spectra of all the palladium complexes, the protonated ligand molecule [8-Hmqmp+H]$^+$ as the intact cation is the base peak (*m*/*z* 252). The loss of the C_2H_4 according to six-membered McLafferty-type rearrangement yields the $[QCH_2PO\text{-}(OH)_3]^+$ ion at *m*/*z* 224 [34]. This fragment ion is dominant in the spectra of the free ligand, both, in the form of hydrochloride and sodium salt. In addition, all compounds show ions obtained by loss of a water molecule as well as the ethanol loss from the protonated ligand, which is often observed in the mass spectrometry of the ethyl esters [35,36], and ions obtained by FAB-induced dimerization of the organophosphorus ligand at *m*/*z* 503. In the complexes the first point to be noted is that only complex **7** exhibits the protonated molecular ion. Its intensity (6%) is much lower than that obtained for the corresponding chelate complex of 2-Hmqmp (37%), indicating less stability of the former complex with bidentate N,O-bonded ligand forming seven-membered chelate ring with respect to the second one with the six-membered chelate ring [20]. Complexes **5** and **6** contain structurally relevant fragment ions that allow also the anion characterization by the small abundant fragment ions formed by the successive loss of the three halide ions from the anionic trihalide palladium complex. The predominant peaks corresponding to ions containing palladium in the complexes are those with metal bonded to one or two ligand molecules at *m*/*z* 357 and *m*/*z* 607, respectively, as well as to those with palladium bonded to some ligand fragments $[Pd(QCH_2)PO_2OH]^+$, $[Pd(QCH_2)]^+$ and $[PdQ]^+$ at *m*/*z* 328, *m*/*z* 248 and *m*/*z* 236, respectively. It may be presumed that these ions contain the bidentate N,O-bonded organophosphorus ligand while in the ion at *m*/*z* 248 the quinolylmethyl fragment may undergo palladation at the quinoline nitrogen and the quinolylmethyl carbon atom. It is worth noting that the spectra show also some sodium adduct ions based on addition of sodium ion presumably either to halides or to phosphonate oxygen atoms as well as are present NBA matrix ions and their sodium adducts.

In the negative-ion mass spectrometry the palladium halide fragment ions are more stable and abundant than in the positive-ion mode [37], giving more structural information of the anionic part of the ionic complexes. The spectra of all the complexes show the palladium halide $[PdX_n]^-$, $n = 2$, 3 and dipalladium halide adduct ions $[Pd_2X_n]^-$, $n = 2$–6. As expected, the latter fragment ions are much more abundant in hexahalodipalladium complexes **3** and **4**, which show also the structure specific $[LPd_2X_6]^-$ ion at *m*/*z* 673 and *m*/*z* 935, respectively. Palladium trihalide and dihalide adduct ions are the most abundant palladium-containing peaks in tetrahalopalladium complexes **1** and **2**, and a spectrum of bromide complex with fragment ion assignation is presented in Fig. 2. In trihalide palladium complexes **5** and **6**, the important diagnostic fragment ions are those of small abundance obtained by sequential loss of halide radicals from the deprotonated molecular ion as well as those related to the intact complex anion $[PdLX_3]^-$ at *m*/*z* 462 and *m*/*z*

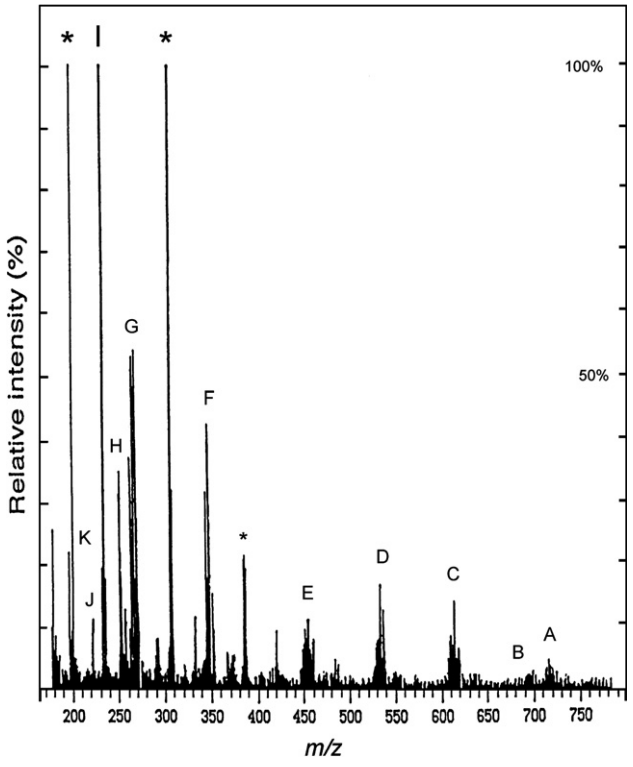


Fig. 2. Negative-ion FAB mass spectrum of complex **2** with NBA matrix. Matrix ions are indicated by an asterisk.

594, respectively, and those obtained by subtracting one and two halide radicals from these ionic species. The fragmentation pattern of the ligand molecule is similar to that obtained in the positive-ion mode including C_2H_4, H_2O and EtOH loss from the deprotonated ligand molecular ion.

3.6. Thermal data

Decomposition behaviour of the complexes was investigated also by thermal analyses, and examples of the appropriate TG-DTA plots for complexes **1**, **4** and **7**, are presented in Fig. 3. Although no stable intermediate products, except the corresponding anhydrous compounds in the case of the hydrated complexes **2** and **4**, were found owing to the complexity and the overlap of the degradation processes, thermal analysis subsequently followed by the IR study provides valuable information about decomposition properties of the complexes. IR spectra were recorded every 50 °C and are compared with the corresponding spectra at room temperature. The hydrated complexes **2** and **4** exhibit a single dehydration step between 80–140 °C with the mass loss close to evolution of two molecules of water. Degradation of the ionic halide complexes begins by a dehalogenation process overlapped with the ligand deesterification, and is influenced by the type of complex. Dehalogenation occurs in two steps, as revealed by the very distinct inflections in the TG curves, although well-defined

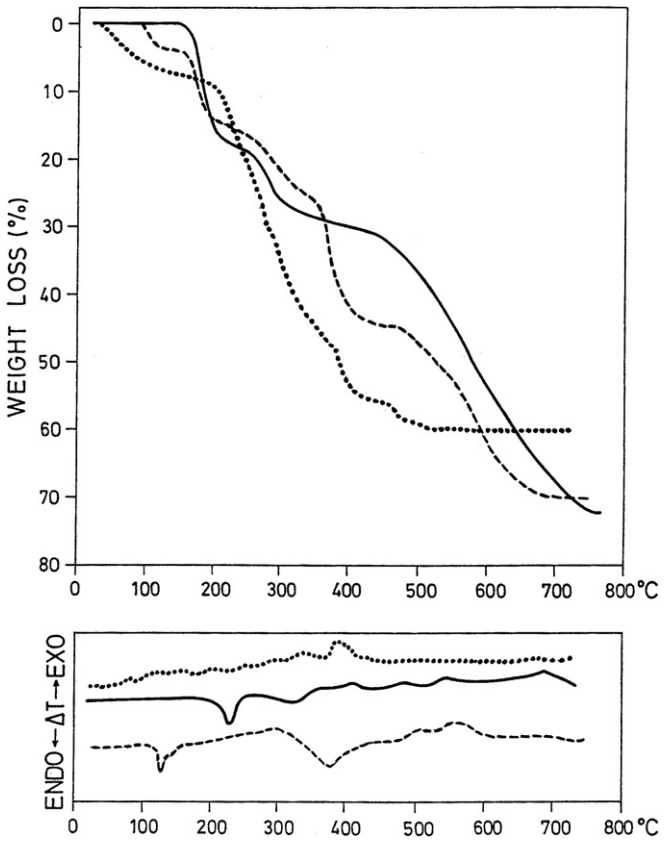


Fig. 3. TG-DTA curves for complexes: **1** (___); **4** (– – – –) and **7** (· · · · · ·).

TG plateaus are not reached. In tetrahalopalladium and hexahalodipalladium complexes, the first step ranged up to 220–240 °C and 210–220 °C, respectively, corresponds to the loss of two halogens and two ethyl ester groups (found mass loss: 19.1, 24.4, 19.2 and 21.7%; calc. 21.4, 25.9, 17.3 and 20.3% for **1**, **2**, **3** and **4**, respectively). The mass loss in the second step which ranged up to ca. 300–320 °C corresponds approximately to the release of two and four, respectively, remaining halogens (found mass loss: 10.7, 15.3, 13.5 and 20.8%; calc. 9.4, 16.5, 15.3 and 25.9%). In the quinolinium trihalopalladium complexes the first step between 165 °C and 185 °C for the chloride and between 190 °C and 210 °C for the bromide complex corresponds approximately to the loss of one halide ion (found mass loss: 5.4 and 10.6%; calc. 4.9 and 9.4%, respectively). The mass loss in the second step, which ends at ca. 300 °C, of ca. 20% (calc. 22.5) for **5** and ca. 27% (calc. 29.4) for **6** corresponds approximately to two halide ions and two ethyl ester groups. In the DTA curves these processes are visible as two endothermic peaks between 210 °C and 290 °C. The complete dehalogenation and deesterification of the complexes is confirmed by the absence of the *ν*(Pd–Cl/Br), P–O–Et and C–C ethyl absorptions in the IR spectra. The pyrolytic decomposition of the ligand is followed by a continuous mass loss with several mostly endothermic or unclear peaks in the DTA curves. In the chelate complex **7** a broad dehydration step between 40 and 160 °C, which indicates that two water molecules are lattice-held [38], is followed by decomposition of the complex including deesterification and other ligand degradation processes in the 200–500 °C region. The pyrolytic residue in all the complexes is a mixture of Pd and P_2O_5, which was confirmed by the IR and X-ray data. Difference obtained between the calculated and found residue value could be ascribed to partial sublimation of P_2O_5, which takes place at higher temperatures [39].

It was shown that dehalogenation of the complexes is the main process in the course of decomposition of the halide complexes, what is in agreement with the FAB-mass spectroscopy data, in which the main fragment ions are those obtained by the sequential loss of halide ions.

3.7. Antitumor activity

The antitumor activity of the complexes **1**–**7** was assayed *in vitro* on the human epidermoid KB and the murine leukemia L1210 cell lines as a preliminary screening for their biological activity. The results, expressed as concentration of the complex required to inhibit the tumor cell growth by 50% (IC_{50}), are summarized in Table 5. Reported data of the molecular and ionic palladium complexes with diethyl 8-quinolylmethylphosphonate (8-dqmp) and monoethyl 2-quinolylmethylphosphonate (2-Hmqmp) are given for comparative purposes [8,9]. In general, it was shown that the L1210 line was more responsive than the KB cell line and that the bromo complexes were slightly more effective than their chloro analogues in the case of monoester 8-

Hmqmp derivatives. However, for complexes of diester 8-dqmp there is no significant difference in response between the two cell lines, neither between the chloro and bromo complexes. Complexes of diester were a bit more effective than those of monoesters, especially against the KB cell line, which may be partly ascribed to the greater solubility and lypophilicity of the former complexes. Fairly good relationship generally could be seen between activity and solubility of the complexes. The lypophilicity of the complexes increases with increasing bulkiness from monoester to diester derivatives and may facilitate transport through the cellular membranes [40]. On the other hand, the presence of the acidic phosphonate group in monoester may cause the opposite effect. It is interesting to note that there are no significant differences in antitumor activity between various types of complexes with 8-Hmqmp (ca. 18–50 in KB and 10–18 μM in L1210 cells) and 2-Hmqmp (ca. 18–44 in KB and 16–22 μM in L1210 cells), as well as between neutral and ionic complexes of 8-dqmp (ca. 7–18 in KB and 8–16 μM in L1210 cells), in spite of their different structural properties and presumably different properties in hydrolysis, transport mechanism inside the cells and different mode of DNA binding and nicking ability [41]. Cytotoxicity in the case of ionic complexes most probably reflects the combined activity of the protonated ligand and the anionic metal complex. Further studies on the potential mechanism of antitumor action of complexes are needed for a better understanding how chemical properties of complexes impact their biological activity.

4. Conclusion

With the aim of preparing new complexes which might be of interest as antitumor agents, a series of palladium(II) complexes of monoethyl 8-quinolylmethylphosphonate has been prepared and studied. Depending on the reaction conditions (pH and initial quinolinium and palladium salts) four types of complexes were isolated, which structure as well as stability and mode of decomposition were determined by spectral and thermal studies. The biological properties of the complexes were investigated by evaluation of their antitumor activity. In general, it may be concluded that the quinoline-based aminophoshonates and their palladium(II) complexes represent an interesting family of compounds with regard to their physicochemical, structural and biological properties. Although none of the complexes were found to exhibit cytostatic activity with potential therapeutic applicability, the present results obtained by studying the chemical characteristics that mold biological activity of the complexes could help in design of the novel compounds with potent biological activity.

Acknowledgement

The financial support of the Croatian Ministry of Science, Education and Sports (Grant No. 098-0982915-2950) is gratefully acknowledged. The authors would like to thank Mr. Ž. Marinić for recording the NMR spectra and Dr. R. Trojko for some TG/DTA measurements.

Appendix A. Supplementary data

Supplementary data associated with this article can be found, in the online version, at doi:10.1016/j.poly.2008.01.002.

References

[1] P.J. O'Dwyer, P. Stevenson, S.W. Johnson, Clinical status of cisplatin, carboplatin, and other platinum-based antitumor drugs, in: B. Lippert (Ed.), Chemistry and Biochemistry of a Leading Anticancer Drug, Verlag Helvetica Chimica Acta, Zurich, 1999, pp. 31–72.

[2] (a) G. Sava, E. Alessio, A. Bergamo, G. Mestroni, Sulphoxide ruthenium complexes: non-toxic tools for the selective treatment of solid tumour metastases, in: M.J. Clarke, P.J. Sadler (Eds.), Topics in Biological Inorganic Chemistry-Metallopharmaceuticals I, Springer, Berlin, 1999, pp. 143–169;
(b) M. Groessl, E. Reisner, C.G. Hartinger, R. Eichinger, O. Semenova, A.R. Timerbaev, M.A. Jakupec, V.B. Arion, B.K. Keppler, J. Med. Chem. 50 (2007) 2185;
(c) Y.K. Yan, M. Melchart, A. Habtemariam, P.J. Sadler, Chem. Commun. (2005) 4764;
(d) H.-K. Liu, S.J. Berners-Price, F. Wang, J.A. Parkinson, J. Xu, J. Bella, P.J. Sadler, Angew. Chem., Int. Ed. 45 (2006) 8153.

[3] D.S. Gill, in: M.P. Hacker, E.B. Douplr, I.H. Krakoff (Eds.), Platinum Coordination Complexes in Cancer Chemotherapy, Nijhoff, Boston, 1984, pp. 267–278.

[4] (a) L.S. Hollis, in: S.B. Howell (Ed.), Platinum and Other Metal Coordination Compounds in Cancer Chemotherapy, Plenum Press, New York, 1991, pp. 115–125;
(b) F.L. Wimmer, S. Wimmer, P. Castan, S. Cros, N. Johnson, E. Colacio-Rodrigez, Anticancer Res. 9 (1989) 791;
(c) J.D. Higgins III, L. Neely, S. Fricker, J. Inorg. Biochem. 49 (1993) 149.

[5] (a) D. Kovala-Demertzi, M.A. Demertzis, E. Filiou, A.A. Pantazaki, P.N. Yadav, J.R. Miller, Y. Zheng, D.A. Kyriakidis, Biometals 16 (2003) 411;
(b) E. Budizisz, U. Krajewska, M. Rozalski, A. Szulawska, M. Czyz, B. Nawrot, Eur. J. Pharmacol. 502 (2004) 59;
(c) J. Kuduk-Jaworska, A. Puszko, M. Kibiak, M. Pelczynska, J. Inorg. Biochem. 98 (2004) 1447.

[6] (a) G. Zhao, H. Lin, Curr. Med. Chem. – Anticancer Agents 5 (2005) 137;
(b) D. Kovala-Demertzi, A. Bocarelli, M.A. Demertzis, M. Coluccia, Chemotherapy 53 (2007) 148.

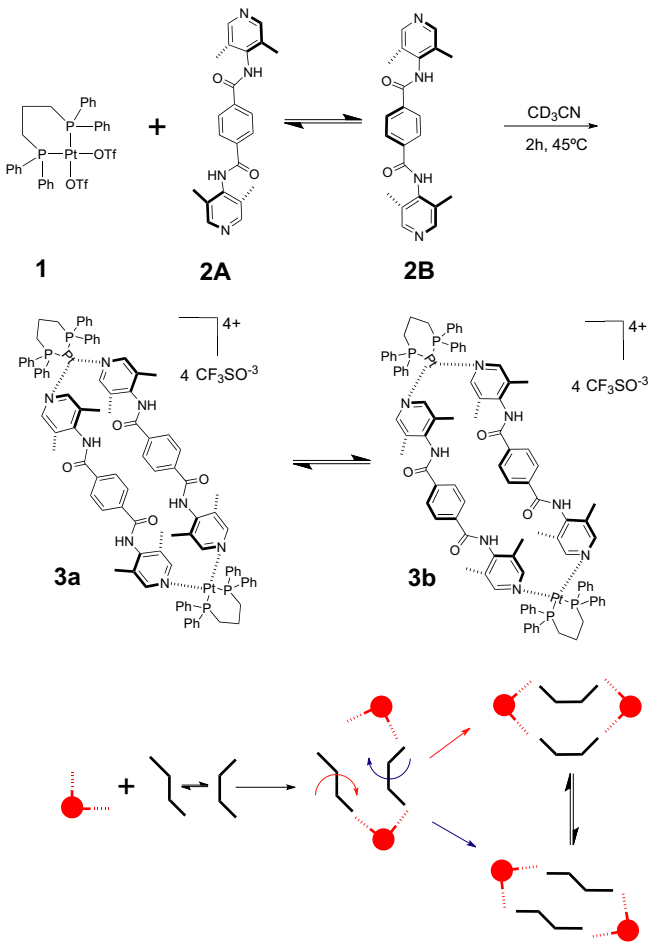
[7] (a) Lj. Tušek-Božić, I. Matijašić, G. Bocelli, G. Calestani, A. Furlani, V. Scarcia, A. Papaioannou, J. Chem. Soc., Dalton Trans. (1991) 195;
(b) Lj. Tušek-Božić, M. Komac, M. Ćurić, A. Lyčka, M. D'Alpaos, V. Scarcia, A. Furlani, Polyhedron 19 (2000) 937;
(c) Lj. Tušek-Božić, V. Cmrečki, J. Balzarini, E. De Clercq, Lett. Drug Des. Discov. 3 (2006) 528.

[8] Lj. Tušek-Božić, I. Matijašić, G. Bocelli, G. Sgarabotto, A. Furlani, V. Scarcia, A. Papaioannou, Inorg. Chim. Acta 185 (1991) 229.

[9] Lj. Tušek-Božić, A. Furlani, V. Scarcia, E. De Clercq, J. Balzarini, J. Inorg. Biochem. 72 (1998) 201.

[10] (a) P. Kafarski, B. Lejczak, in: V.P. Kukhar, H.R. Hudson (Eds.), Aminophosphonic and Aminophosphinic Acids. Chemistry and Biological Activity, John Wiley & Sons, Chichester, 2000, pp. 407–442;
(b) F.R. Atherton, C.H. Hassall, R.W. Lambert, J. Med. Chem. 29 (1986) 29;

(c) S. Du, H. Faiger, V. Belakhov, T. Baasov, Bioorg. Med. Chem. 7 (1999) 2671.
[11] (a) T. Klenner, P. Valenzuela-Paz, F. Amelung, H. Münch, H. Zahn, B.K. Keppler, H. Blum, Platinum phosphonato complexes with particular activity against bone malignancies. An evaluation of an experimental model highly predictive for the clinical situation, in: B.K. Keppler (Ed.), Metal Complexes in Cancer Chemotherapy, VCH, Weinheim, 1993, pp. 85–127;
(b) E. Brzezinska-Blaszczyk, M. Mincikiewicz, J. Ochocki, Eur. J. Pharmacol. 298 (1996) 155;
(c) M.J. Bloemink, J.H. Diederen, J.P. Dorenbos, R.J. Heeterbij, B.K. Keppler, J. Reedijk, Eur. J. Inorg. Chem. 10 (1999) 1655.
[12] M. Ćurić, Lj. Tušek-Božić, D. Vikić-Topić, V. Scarcia, A. Furlani, J. Balzarini, E. De Clercq, J. Inorg. Biochem. 63 (1996) 125.
[13] Lj. Tušek-Božić, F. Frausin, V. Scarcia, A. Furlani, J. Inorg. Biochem. 95 (2003) 259.
[14] V. Jagodić, B. Božić, Lj. Tušek-Božić, M.J. Herak, J. Heterocycl. Chem. 17 (1980) 685.
[15] R.J. Tallarida, R.B. Murray, Manual of Pharmacological Calculations with Computer Programs, Springer, New York, 1987.
[16] Lj. Tušek-Božić, A. Lyčka, Magn. Reson. Chem. 40 (2002) 175.
[17] A. Višnjevac, Lj. Tušek-Božić, Acta Crystallogr. C60 (2004) o434.
[18] V. Jagodić, Lj. Tušek, J. Org. Chem. 37 (1972) 1222.
[19] Lj. Tušek-Božić, Vib. Spectrosc. 28 (2002) 235.
[20] Lj. Tušek-Božić, M. D'Alpaos, Polyhedron 17 (1998) 1481.
[21] (a) T.G. Appleton, J.R. Hall, I.J. McMahon, Inorg. Chem. 25 (1986) 720;
(b) Z. Galdecki, W.M. Wolf, Acta Crystallogr. C46 (1990) 271;
(c) J. Ochocki, K. Kostka, B. Zurowska, J. Mrozinski, E. Galdecka, Z. Galdecki, J. Reedijk, J. Chem. Soc., Dalton Trans. (1992) 2955.
[22] (a) D. Fernandez, D. Vega, Acta Crystallogr. C59 (2003) o228;
(b) D. Fernandez, D. Vega, J.A. Ellena, Acta Crystallogr. C59 (2003) o289.
[23] I. Matijašić, G. Bocelli, Lj. Tušek-Božić, in: Third Slovenian-Croatian-Crystallographic Meeting, Kranjska gora, Slovenia, 1994, p. 20.
[24] R.M. Silverstein, F.X. Webster, Spectrometric Identification of Organic Compounds, 6th ed., John Wiley & Sons, New York, 1998.
[25] L.C. Thomas, Interpretation of Infrared Spectra of Organophosphorus Compounds, Plenum Press, New York, 1974, pp. 39–45.
[26] A.W. Herlinger, J.R. Ferraro, R. Chiarizia, E.P. Horwitz, Polyhedron 16 (1997) 1843.
[27] K. Nakamoto, Infrared and Raman Spectra of Inorganic and Coordination Compounds, Part B: Applications in Coordination Organometallic and Bioinorganic Chemistry, 5th ed., Wiley-Interscience, 1997.
[28] M.I. Moreno-Vida, E. Colacio-Rodrigues, M.N. Moreno-Carretero, J. Salas-Peregrin, M. Simard, A.L. Beauchamp, Inorg. Chim. Acta 157 (1989) 201.
[29] A. Albinati, P.S. Pregosin, F. Wombacher, Inorg. Chem. 29 (1990) 1812.
[30] (a) P.J. Stang, B. Olenyuk, A.M. Arif, Organometallics 14 (1995) 5281;
(b) U. Bierbach, N. Farrell, Inorg. Chem. 36 (1997) 3657;
(c) R.M. Scolaro, A. Mazzaglia, A. Romeo, M.R. Plutino, M. Castriciano, R. Romeo, Inorg. Chim. Acta 330 (2002) 189.
[31] S.E. Livingstone, The Chemistry of Ruthenium, Rhodium, Palladium, Osmium, Iridium and Platinum, Pergamon Press, Oxford, 1973.
[32] J. Onyang, Z. Tai, C. Jiang, W. Tang, Spectrosc. Lett. 29 (1996) 763.
[33] J. Sola, R. Yanez, J. Chem. Soc., Dalton Trans. (1986) 2021.
[34] F.W. McLafferty, Interpretation of Mass Spectra, 3rd ed., University Science Books, CA, 1980, p. 65.
[35] P. Caliceti, F.M. Veronese, F. Marsilio, S. Lora, R. Seraglia, P. Traldi, Org. Mass Spectrom. 27 (1992) 1199.
[36] C.S. Harden, A.P. Snyder, G.A. Eiceman, Org. Mass Spectrom. 28 (1993) 585.
[37] E. De Hoffmann, V. Stroobant, Mass Spectrometry, Principles and Applications, 2nd ed., John Wiley & Sons Ltd., Baffins Lane, Chichester, 2002.
[38] S.P. Perleps, P. Jacops, H.O. Desseyn, J.M. Tsangaris, Spectrochim. Acta 43A (1987) 771.
[39] D.R. Lide (Ed.), Handbook of Chemistry and Physics, The Chemical Rubber Co., Boca Raton, Florida, 1998, p. 76.
[40] (a) J.P. Souchard, T.T.B. Ha, S. Cros, N.P. Johnson, J. Med. Chem. 34 (1991) 863;
(b) J. Reedijk, Chem. Commun. (1996) 801.
[41] Y.A. Lee, Y.K. Chung, Y.S. Sohn, J. Inorg. Biochem. 68 (1997) 289.



Scheme 1. Formation of self-assembled macrocycles **3a** and **3b**.

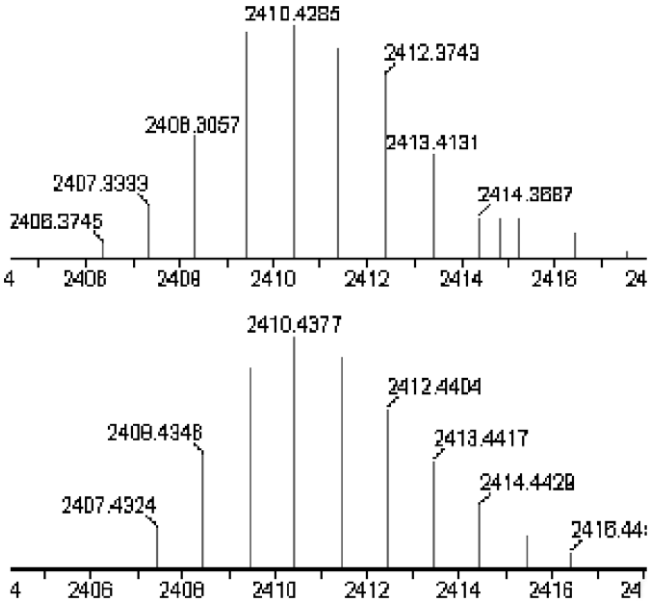


Figure 2. ESI-MS spectrum of **3a**–**3b**, in acetonitrile. Isotopic distribution for $[M_2L_2]^+$, found (top) and calculated (bottom).

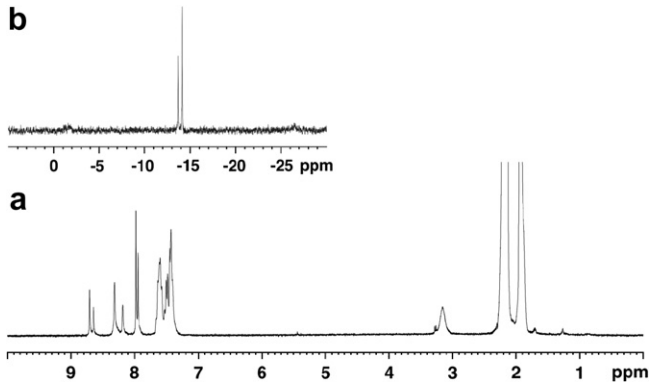


Figure 1. (a) ^{1}H NMR (CD_3CN, 25 °C), and (b) ^{31}P NMR (CD_3CN, 25 °C) of macrocycles **3a**–**3b.**

changes that make pyridil groups non-equivalents. The ^{31}P NMR spectrum also contains two singlets, at −13.72 and −14.16 ppm indicative of the presence of two isomers with equivalent corners and phosphine ligands. The presence of a *syn*/*anti* isomer due to two inequivalent phosphorus centres, coordinated to platinum in cis position must show an AB pattern with a J_{P1-P2} coupling constant in the ^{31}P NMR spectrum. No P–P coupling was observed, in ^{31}P NMR spectrum, that means that the two phosphorus atoms remained equivalents for the isomer presents *syn*/*syn* **3b** and *anti*/*anti* **3a**.

The integration ratio of the ^{31}P NMR signals was found to be temperature-dependent, changing from 1:2 at room temperature over 2.5:1 at 258 K, and 1:5 at 338 K. This, strongly supports the presence of two different conformers in equilibrium (Fig. 3). As suitable X-ray quality crystals for **3** could not be obtained, MM2 force field simulation

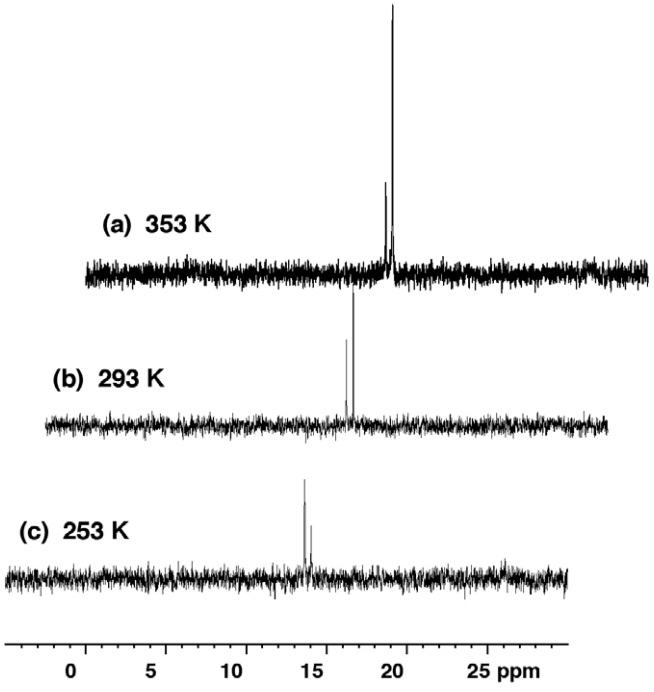


Figure 3. ^{31}P NMR (81 MHz) spectrum of isomers **3a** and **3b**. Variable temperature ^{31}P NMR spectra recorded in CD_3CN at (a) 353 K; (b) 293 K; (c) 253 K.

was employed to visualize the shape and size of **3a**–3b [5]. A view of the molecules is shown in Fig. 4.

The structure establishes the formation of a 34-membered macrocycles, containing two identical platinum atoms, separated by 17.16 and 17.27 Å, respectively. Size estimation using MM2 simulations shows the assemblies are almost 25 Å in length and 8 Å wide. N–Pt–N angle values for **3a**–b are given in Table 1.

Simulation studies are in agreement with the experimental NMR data (Table 1) showing an upfield displacement of the ^{31}P NMR signal when N–Pt–N angle close to 90° increase, while the opposite behavior is found for ^{1}H NMR shifts corresponding to protons orto to the pyridyl–nitrogen atom. In order to corroborate this, the bipyridin Pt complex $[Pt(dppp)(Py)_2][OTf]_2$ (**4**) [6] (Fig. 5) was prepared and the upfield shift of the ^{31}P NMR signals $\partial = -14.86$ ppm was found to be in accordance with the N–Pt–N angle value 90.73° obtained from the theoretical simulation (Table 1).

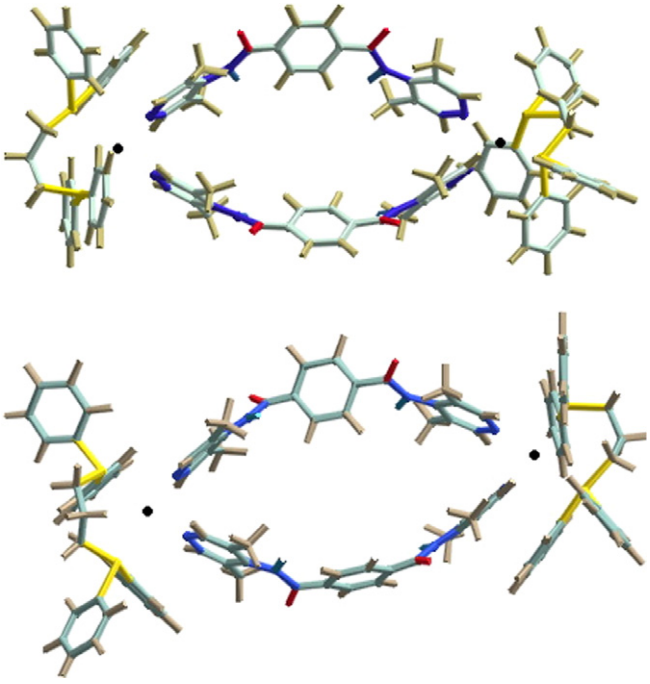


Figure 4. Optimized structures corresponding to the **3a** *anti* and **3b** *syn* compounds obtained from CAChe.

Table 1
Experimental ^{31}P NMR coordination shifts in $[Pt(dppp)(L)_2][OTf]_2$ and calculated N–Pt–N angle values

Solvent	Ligand $(L)_2$	$[Pt(dppp)(L)_2][OTf]_2$ ∂^{31}P (ppm)	N–Pt–N (°)	Pt1–Pt2 (Å)
$CDCl_3$	H_2O	−12.60		
$CDCl_3$	CD_3CN	−16.12		
CD_3CN	CD_3CN	−15.10		
CD_3CN	Py	−14.86	90.73	
CD_3CN	2B (3b)	−14.16	83.77	17.16
CD_3CN	2A (3a)	−13.72	83.28	17.27

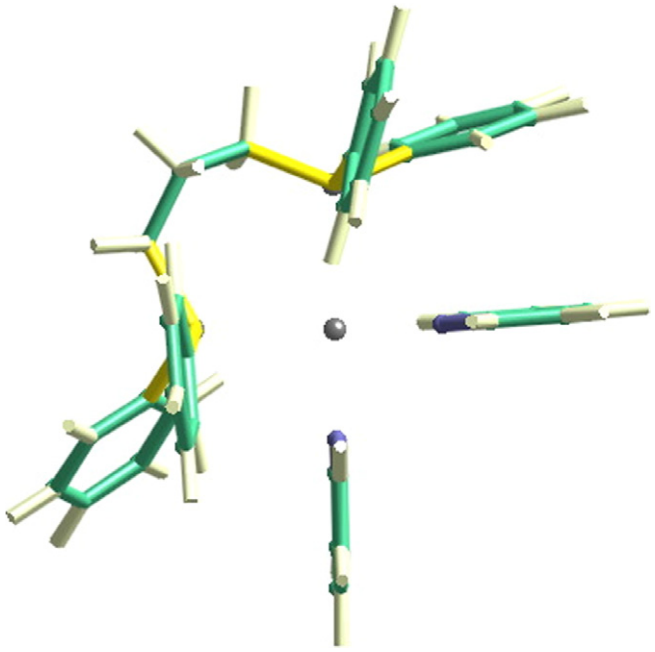


Figure 5. $[Pt(dppp)(Py)_2][OTf]_2$ (**4**) optimized structure obtained from CAChe.

Based on the results summarized in Table 1, that an upfield displacement of the ^{31}P NMR signals correspond to an increase of the N–Pt–N angle values, the signal at $\partial = -13.72$ ppm on the ^{31}P NMR spectra was assigned to the *anti* arrangement **3a** with a N–Pt–N angle of 83.28°, while the signal at $\partial = -14.16$ ppm correspond to the *syn* arrangement **3b** with a N–Pt–N angle of 83.77°.

3. Conclusions

The bis(amidopyridine) ligands combine easily with *cis*-protected square planar platinum (II) corners to form M_2L_2 macrocycles. The bridging coordination of the bis(amidopyridine) ligand **2** can occur with different ligand conformations **A** or **B** in witch the NH groups have a *syn* or an *anti* arrangement. The distinctive $\Delta\partial$ values, 0.22 ppm for the alfa pyridil hydrogens, and 0.44 ppm for the diphosphine ligand (^{31}P NMR shifts) produced from differences in the chemical environment of the **3a**–**b** isomers, have been found to be closely related with the N–Pt–N angle aperture of the complexes, and used to the assignment.

In summary, a new rhomboid was isolated, as two different geometric isomers **3a** *anti* and **3b** *syn*.

4. Experimental

^{1}H NMR and ^{31}P NMR spectra were obtained using a Bruker AMX 300 NMR and were recorded at 300 and 81 MHz, respectively. All reagents and chemicals were obtained from the Aldrich Chemical Company and were used as received unless otherwise noted.

Syntheses of [Pt(dppp)(O_3SCF_3)$_2$] (**1**) was prepared according to literature procedures [3e]. ^{1}H NMR (300 MHz, CD_3Cl) $\delta = 7.72$–7.65 (m, 8H), 7.49–7.40 (m, 12H), 2.93 (m, 4H), 2.17 (m, 2H); ^{31}P {^{1}H NMR} (CD_3Cl, 81 MHz) $\delta = -12.6$ (s, ^{195}Pt satellite, $J_{Pt-P} = 3789.8$ Hz); ^{19}F NMR (188.6 MHz, CD_3Cl) $\delta = -77.0$ ppm. ^{1}H NMR (300 MHz, CD_3CN) $\delta = 7.62$–7.50 (m, 8H), 7.49–7.39 (m, 12H), 2.85–2.60 (m, 6H); ^{31}P {^{1}H NMR} (CD_3CN, 81 MHz) $\delta = -15.1$ (s, ^{195}Pt satellite, $J_{Pt-P} = 3789.8$ Hz).

4.1. *N,N′-Bis(3,5-dimethyl-4-pyridinyl)-1,4-benzene-dicarboxamide (**2**)*

To a CH_2Cl_2 (10 ml) solution of 1,4 benzene-dicarbonyl dichloride (235 mg, 1 mmol) at 0 °C was added 4-amino-3,5-lutidine (285 mg, 2.1 mmol) and N,N-diisopropylethylamine (420 μl, 2.5 mmol). The solution was stirred at room temperature for 2 h and subsequently heated at reflux for 2 h. The reaction mixture was diluted with CH_2Cl_2(10 mL), washed with saturated $NaHCO_3$ and brine, dried over anhydrous $MgSO_4$, and evaporated. The solid residue was washed with diethyl ether and recrystallized in CH_2Cl_2/EtOAc solvent to provide **2** as a white solid (190 mg, 50%). ^{1}H NMR (300 MHz, CD_3CN) $\delta = 9.78$(s, NH, 2H), 8.25 (s, 4H), 8.16 (s, 4H), 2.26 (s, 12H); ESI-MS *m/z* 375.1814 $[M+H]^+$ (calc. mass), Found (375.1821).

4.2. *Macrocycles **3a**–**3b***

To a solution of **2** (3.7 mg, 1 mmol) in CD_3CN 500 μl was slowly added [Pt(dppp)(O_3SCF_3)$_2$] (**1**) (9.1 mg, 1 mmol) and heated at 45 °C for 2 h. **3a** *anti* ^{1}H NMR (300 MHz, CD_3CN) $\delta = 8.71$ (s, NH, 4H), 8.31 (s, 8H), 7.98 (s, 4H), 7.61 (brs, 8H), 7.98 (brs, 16H), 3.16 (brs, 8H), 2.17(brs, 4H), 1,89 (s, 24H); ^{31}P {^{1}H NMR} (CD_3CN, 81 MHz) $\delta = -14.16$ (s, ^{195}Pt satellite, $J_{Pt-P} = 1508$ Hz); **3b***syn*; ^{1}H NMR (300 MHz, CD_3CN) $\delta = 8.64$ (s, NH, 4H), 8.19 (s, 8H), 7.95 (s, 4H), 7.61 (brs, 8H), 7.44 (brs, 16H), 3.16 (brs, 8H), 2.17 (brs, 4H), 1,89 (s, 24H); ^{31}P {^{1}H NMR} (CD_3CN, 81 MHz) $\delta = -13.72$ (s, ^{195}Pt satellite, $J_{Pt-P} = 1510$ Hz). ESI/MS: *m/z* 2410.4766 (M-OTf) found; 2410.4377 (M-OTf) calc. Elemental analysis Found: C, 47.32; H, 3.74; N,4.48. Calculated for $C_{102}H_{96}F_{12}O_{16}P_4Pt_2S_4$: C, 47.85; H, 3.78; N,4.38. IR (*ν* (BrK)): 3483.84 (N–H), 2960.45, 2928.04 (aliphatic C–H), 1662.91 (C=O), 1492.91, 1278.59, 1157.82, 1030.40 ($CF_3SO_3^-$), 693.80, 637.76, 516.95.

Acknowledgement

I thank the DGICYT of Spain (Project CTQ2005-08989) for financial support.

References

[1] (a) S. Leininger, B. Olenyuk, P.J. Stang, Chem. Rev. 100 (2000) 853;
(b) M. Fujita, Chem. Soc. Rev. 27 (1998) 417;
(c) B.J. Holliday, Ch.A. Mirkin, Angew. Chem., Int. Ed. 40 (2001) 2022;
(d) G.F. Swiegers, T.J. Malefetse, Chem. Rev. 100 (2000) 3483;
(e) O.D. Fox, M.G.B. Drew, E.J.S. Wilkinson, P.D. Beer, Chem. Commun. (2000) 391;
(f) A. Ikeda, M. Yoshimura, H.C. Fukuhara, S. Shinkai, J. Am. Chem. Soc. 121 (1999) 4296;
(g) P. Jacopozzi, E. Dalcanale, Angew. Chem., Int. Ed. Engl. 36 (1997) 613;
(h) Z. Zhong, A. Ikeda, S. Shinkai, Sh. Sakamoto, K. Yamaguchi, Org. Lett. 3 (2001) 1085;
(i) S.J. Park, J.-I. Hong, Chem. Commun. (2001) 1554.

[2] (a) M. Fujita, S. Nagao, K. Ogura, J. Am. Chem. Soc. 117 (1995) 1649;
(b) M. Fujita, D. Oguro, M. Miyazawa, H. Oka, K. Yamaguchi, K. Ogura, Nature 378 (1995) 469;
(c) M. Fujita, N. Fujita, K. Ogura, K. Yamaguchi, Nature 400 (1999) 52;
(d) D.K. Chand, K. Biradha, M. Fujita, Chem. Commun. (2001) 1652;
(e) M. Fujita, K. Umemoto, M. Yoshizawa, N. Fujita, T. Kusukawa, K. Biradha, Chem. Commun. (2001) 509;
(f) M. Fujita, M. Tominaga, A. Hori, B. Therrien, Acc. Chem. Res. 38 (2005) 371;
(g) N.C. Giannaneschi, M.S. Masar III, C.A. Mirkin, Acc. Chem. Res. 38 (2005) 825;
(h) C. Schalley, A. Lützen, M. Albrecht, Chem.-Eur. J. 10 (2004) 1072.

[3] (a) U. Radhakrishnan, M. Schweiger, P.J. Stang, Org. Lett. 3 (2001) 3141;
(b) M. Schweiger, S.R. Seidel, A.M. Arif, P.J. Stang, Angew. Chem., Int. Ed. 40 (2001) 3467;
(c) B. Olenyuk, J.A. Whiteford, A. Fechtenkötter, P.J. Stang, Nature 398 (1999) 796;
(d) P.J. Stang, J. Fan, B. Olenyuk, Chem. Commun. (1997) 1453;
(e) P.J. Stang, D.H. Cao, Sh. Saito, M.A. Arif, J. Am. Chem. Soc. 117 (1995) 6273.

[4] (a) Z. Qin, M.C. Jenning, R.J. Puddephatt, Inorg. Chem. 42 (2003) 1956;
(b) P. Ballester, M. Capó, A. Costa, P.M. Deyà, A. Frontera, R. Gomila, Molecules 9 (2004) 278;
(c) P.S. Mukherjee, N. Das, P.J. Stang, J. Org. Chem. 69 (2004) 3526;
(d) P. Diaz, J.A. Tovilla, P. Ballester, J. Benet-Buchholz, R. Vilar, Dalton Trans. (2007) 3516.

[5] CAChe 6.0 program, Fujitsu.

[6] X. Xu, S.L. James, M.P. Mingos, A.J.P. White, D.J. Williams, J. Chem. Soc., Dalton Trans. (2000) 3783.

stoichiometry is found for the acetate type $[Cu_2(RCOO)_4(denia)_2]$ dimeric complexes [3–7]. The 1:2 stoichiometry can be found in monomeric complexes of $Cu(RCOO)_2(denia)_2(H_2O)_x$, where $x = 0$, [8–10], $x = 2$ [11–15], $x = 4$ [16] or in $Cu(RCOO)_2(denia)_2(CH_3OH)$ [17], and in all those complexes the denia molecules are unidentate N donor ligands. Recently the first polymeric complex with bridging denia molecules, of the composition $[Cu_2(ClCH_2COO)_4(denia)_1]_n$, has been structurally characterized [18]. In this paper we report on the preparation, spectral and magnetic properties, and X-ray structures of two new copper(II) complexes containing the denia ligand – one is a polymeric complex of an unusual stoichiometry containing denia bridges, $[Cu_2(2\text{-}NO_2Bz)_4(denia)_1]_n$ (**1**), and its molecular counterpart with the same 2-nitrobenzoato-ligand showing the usual and most frequent stoichiometry, $[Cu(2\text{-}NO_2Bz)_2(denia)_2(H_2O)_2]$ (**2**), together with the complex $[Cu_2(2\text{-}NO_2Bz)_4(DMF)_2]$ (**3**), that was obtained as a byproduct by recrystallization of (**1**) using dimethylformamide solvent.

2. Experimental

2.1. Synthesis

Both complexes (**1**) and (**2**) could be obtained from the same reaction mixture at different temperatures.

2.1.1. Preparation of $[Cu_2(2\text{-}NO_2Bz)_4(denia)_1]_n$ (1)

An ethanolic solution of copper(II) acetate (1 mmol in cca 20 mL of ethanol) was stirred with *N*,*N*-diethylnicotinamide (2 mmol), then 2-nitrobenzoic acid (2 mmol) was added and the reaction mixture was stirred until the precipitation of the green product finished (about 20 min). The microcrystalline green product (**1**) was filtered off, washed with a small portion of ethanol and dried at ambient temperature. The light blue mother liquid obtained after filtration was left for crystallization. Blue crystals of complex (**2**) were obtained from mother liquid. Crystals of (**1**) suitable for X-ray structure determination were obtained by recrystallization of (**1**) from an ethanolic solution.

Calc. for $C_{38}H_{30}N_6O_{17}Cu_2$ Cu, 13.10; C, 47.06; H, 3.12; N, 8.67. Found: Cu, 13.37; C, 46.86; H, 3.21; N, 9.41%.

2.1.2. Preparation of $[Cu(2\text{-}NO_2Bz)_2(denia)_2(H_2O)_2]$ (2)

An ethanolic solution of copper(II) acetate (1 mmol in cca 20 mL of ethanol) was stirred with *N*,*N*-diethylnicotinamide (2 mmol), then 2-nitrobenzoic acid (2 mmol) was added and the reaction mixture was stirred under heating until the green microcrystalline solid dissolved and a dark blue solution was obtained. The obtained solution was left to stand for slow crystallization and the obtained blue crystalline product (including crystals suitable for X-ray structure determination) was filtered off, washed with a small amount of ethanol and dried at ambient temperature.

Calc. for $C_{34}H_{44}N_6O_{12}Cu$: Cu, 8.06; C, 51.81; H, 5.12; N, 10.66. Found: Cu, 8.82; C, 51.99; H, 5.24; N, 11.71%.

2.1.3. Preparation of $[Cu_2(2\text{-}NO_2Bz)_4(DMF)_2]$ (3)

Crystals for X-ray structure determination were obtained by recrystallization of (**1**) from dimethylformamide.

Calc. for $C_{34}H_{30}N_6O_{18}Cu_2$: Cu, 13.22; C, 44.96; H, 3.14; N, 8.74. Found: Cu, 13.00; C, 44.90; H, 3.20; N, 8.95%.

2.2. Analytical measurements

Carbon, hydrogen and nitrogen analysis were carried out on a CHNSO FlashEA 1112 (ThermoFinnigan) elemental analyzer. Copper was determined by electrolysis of a water solution obtained by sample mineralization with a mixture of sulfuric acid and potassium peroxodisulfate.

2.3. Physical measurements

Electronic spectra (190–1100 nm) of the complexes were measured in Nujol suspensions with a SPECORD 200 (Carl Zeiss Jena) spectrophotometer, and infrared spectra in the region 4000–100 cm^{-1} were measured with a Nicolet MAGNA 750 IR spectrometer using both KBr pellet and Nujol suspension techniques for the 4000–400 cm^{-1} region and polyethylene pellets for the 400–100 cm^{-1} region.

EPR spectra of powdered samples were recorded at room temperature and at 77 K, on a Bruker ESP 300 spectrometer, operating at the X-band and equipped with an ER 035M Bruker NMR gaussmeter and a HP 5350B Hewlett Packard microwave frequency counter.

Data collection and cell refinement of complex (**1**) were carried out using a Siemens P4 diffractometer [19], data for complex (**2**) were collected using a Nonius kappaCCD diffractometer [20], and for complex (**3**) using an Xcalibur PX kappa-geometry diffractometer with a CCD Onyx camera with graphite monochromated Mo Kα radiation, using the CRYSALIS software package [21]. Intensity data were corrected for Lorenz and polarization factors and absorption corrections of (**1**) were made [22]. The structures were solved by the direct atom method with SHELXS-97 [23], and refined by the full-matrix least squares procedure with SHELXL-97 [24]. Geometrical analyses were performed using SHELXL-97 [24] and the structures were drawn using the ORTEP-3 for Windows program [25]. Final crystal data and structure refinement parameters are given in Table 1.

Magnetization measurements of all the samples in the temperature range 1.8–300 K were carried out on powdered samples of the complexes, at a magnetic field of 5 kG, using a Quantum Design SQUID Magnetometer (type MPMS-XL5). Corrections for diamagnetism of the constituent atoms were calculated using Pascal constants [26], the value of 60×10^{-6} cm^3 mol^{-1} was used as the temperature-independent paramagnetism of the Cu^{2+} ion. The effective magnetic moments were calculated from the expression:

$$\mu_{eff} = 2.83\sqrt{\chi_m^{corr} \cdot T}\ (\text{B.M.})$$

Table 1
Crystal data and structure refinement for complexes **1**, **2** and **3**

	1	**2**	**3**
Chemical formula	$C_{38}H_{30}Cu_2N_6O_{17}$	$C_{34}H_{40}CuN_6O_{12}$	$C_{34}H_{30}Cu_2N_6O_{18}$
M_r	969.76	788.26	937.72
Crystal system	monoclinic	monoclinic	monoclinic
Space group	$P2_1/n$	$P2_1/n$	$P2_1/n$
T (K)	298(2)	173(2)	100(2)
a (Å)	10.685(3)	12.5476(2)	10.196(3)
b (Å)	21.913(5)	10.7613(2)	10.562(3)
c (Å)	17.094(4)	14.5198(3)	17.638(5)
β (°)	92.25(2)	110.972(1)	95.86(3)
V (Å^3)	3999.3(17)	1830.71(6)	1889.5(9)
Z	4	2	2
D_x (Mg m^{-3})	1.611	1.430	1.648
Radiation type	Mo Kα	Mo Kα	Mo Kα
μ (mm^{-1})	1.15	0.67	1.21
Crystal form, colour	prism, green	block, blue	parallelepiped, blue
Crystal size (mm)	0.50 × 0.35 × 0.30	0.26 × 0.24 × 0.16	0.20 × 0.20 × 0.15
$h/k/l$	−1,13/−1,27/−21,21	−14,14/−12,11/−17,17	−16,15/−17,13/−28,28
Data/restrains/parameters	8170/76/604	3111/3/249	5481/0/273
$F(000)$	1976	822	956
θ Range (°)	2.12–26.5	3.00–24.7	4.84–35.0
R, wR	0.058, 0.150	0.032, 0.077	0.048, 0.080
S	1.06	1.07	1.01
$\Delta\rho_{max}$, $\Delta\rho_{min}$ (e Å^{-3})	0.70, −0.67	0.24, −0.29	0.72, −0.39

3. Results and discussion

3.1. Complex preparation

The present study of *N*,*N*-diethylnicotinamidecopper(II) complexes with 2-nitrobenzoate anions is based on a knowledge that the 2-nitrobenzoate anion in comparison to other isomeric nitrobenzoate anions exhibits variable bonding modes, due to the presence of a nitro-substituent in the *ortho*-position. The formation of a dimeric complex, $[Cu_2(2\text{-}NO_2bz)_4(H_2O)_2]\cdot 2H_2O$, has been observed [27]. On the other hand, $[Cu(2\text{-}NO_2bz)_2(3\text{-pyme})_2(H_2O)_2]$ (where 3-pyme=3-pyridylmethanol) is the first complex with the 3-pyme ligand that exhibits a molecular monomeric structure [28], while all other carboxylatocopper(II) complexes with the 3-pyme ligand have a polymeric structure with 3-pyme as a bridging ligand. A monomeric structure was also observed in the $[Cu(2\text{-}NO_2bz)_2(nia)_2(H_2O)_2]$ complex [29]. However, the reaction conditions (solvent used, stoichiometry and temperature) can play a significant role in such syntheses, and therefore we performed the syntheses under different conditions. The reactions done in water solutions gave $[Cu_2(2\text{-}NO_2Bz)_4(denia)_1]_n$ (**1**) only at lower copper(II):denia molar ratios (1:0.5 or 1:1), whilst with copper(II):denia ratios higher than 1:1 blue solutions were obtained and blue crystals of $[Cu(2\text{-}NO_2Bz)_2(denia)_2(H_2O)_2]$ (**2**) crystallized after solvent evaporation. Less polar solvents that shift equilibria towards dimeric species

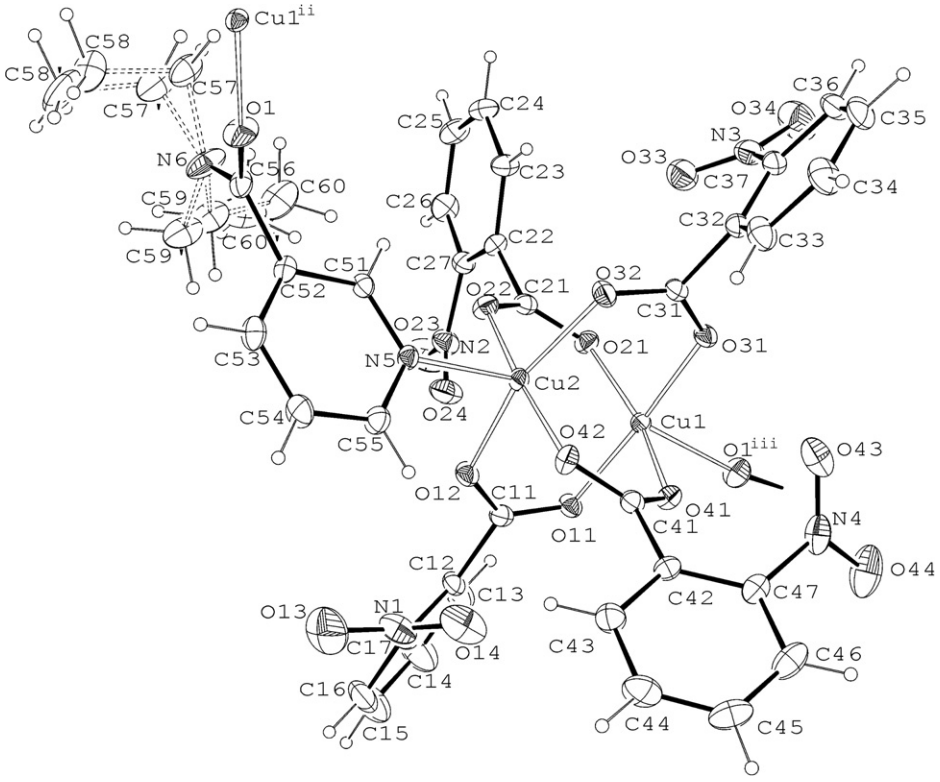


Fig. 1. Perspective view of $[Cu_2(2\text{-}NO_2bz)_4(denia)_1]_n$ (**1**) with the non-hydrogen atom numbering scheme. The disordered ethyl groups of the complex are drawn in open dashed lines.

in solution (acetone and/or toluene) give preferential complex (**1**) formation even at copper(II):denia molar ratios of 1:2 or 1:4. However, recrystallizations from different solvents have shown that the acidity of the reaction mixture (presence of acetic acid) after the reaction probably plays a significant role in transformation of $[Cu_2(2\text{-}NO_2Bz)_4(denia)_1]_n$ (**1**) to $[Cu(2\text{-}NO_2Bz)_2(denia)_2(H_2O)_2]$ (**2**) during heating of the reaction mixture.

3.2. Structure, spectral and magnetic properties of $[Cu_2(2\text{-}NO_2Bz)_4(denia)_1]_n$ (1)

The principal structural features and atom numbering scheme of complex (**1**) are depicted in Fig. 1 and selected bond distances and angles are listed in Table 2. The independent part of the structure consists of the dimeric $Cu_2(2\text{-}NO_2Bz)_4$ unit and one molecule of a denia ligand that is bonded to the Cu2 atom of the dimeric unit *via* the pyridine N5 nitrogen atom (with a Cu2–N5 distance of 2.145(4) Å) and bonded *via* the carbonyl O1 oxygen atom to the Cu1^{ii} [(ii) $= x + 0.5, -y + 0.5, z - 0.5$] atom of a neighbouring dimeric unit (with a Cu1–O1 distance of 2.137(4) Å), thus forming a *zig-zag* chain parallel to the *ac* plane. The square-pyramidal coordination polyhedron of the Cu1 atom has the base formed by the O11, O21, O31 and O41 atoms of carboxylate groups (average Cu1–O_{base} distance 1.968 Å) and the O1 atom of the bridging denia molecule in the apical position. Similarly, the square pyramid of the Cu2 atom consists of O12, O22, O32 and O42 oxygen atoms (average Cu2–O_{base} distance 1.972 Å) within the basal plane and the N5 nitrogen atom in the apical position. The Cu1···Cu2 distance within the dimeric $Cu_2(2\text{-}NO_2bz)_4$ unit is 2.6990(9) Å and both copper atoms are shifted from the basal planes towards the apical position, showing a Cu1–O_4(basal plane) distance of 0.209 Å and Cu2–O_4(basal plane) distance of 0.238 Å, confirming the greater shift of the copper atom from the basal plane towards the apical nitrogen atom in comparison to that towards the apical O-donor [30]. The distance between the Cu atoms bridged by the denia molecule, Cu2···Cu1^{ii} [(ii) $= x + 0.5, -y + 0.5, z - 0.5$], is 7.980(3) Å.

An interesting feature of this structure is that all four 2-nitrobenzoato anions are crystallographically independent, thus all of them exhibit different space orientations. The dihedral angles between the Cu_2O_2C plane (bridging carboxylato group with both copper atoms) and the corresponding phenyl ring plane are 40.4° for the C12–C17 ring, 69.1° for the C22–C27 ring, 61.6° in the case of the C32–C37 ring and finally 35.2 for the C42–C47 ring. Consequently these different space orientations of the phenyl rings lead to the conclusion that to name this structure as a "paddle-wheel" like structure is inadequate because the C12–C17 phenyl ring shows an opposite space orientation in comparison to the three other rings. Similarly different values were found for the "nitro group-to-benzene ring" with a dihedral angle of 49.4° for the C12–C17 ring, 14.3° for the C22–C27 ring, 26.0° for the C32–C37 ring and 52.2° for the C42–C47 ring.

The published structure of $[Cu_2(ClCH_2COO)_4(denia)]_n$, the only one containing a bridging denia ligand [18], differs from our one by having an "antiparallel denia bridge orientation" which results in alternation of two different dimeric units $\{-[Cu_2(RCOO)_4]-N(\mu\text{-denia})O-[Cu_2(RCOO)_4]-O(\mu\text{-denia})N-\}_n$, while the "similar denia bridge orientation" in our case leads to the formation of dimeric units with two different apical donor atoms. It should be stressed that this is the second example in which two Cu(II) atoms within one dimeric unit are different from each other by their coordination polyhedra (Cu^1O_4O' and Cu^2O_4N). The first one was the $[Cu_2(Cl_3CCOO)_4(caf)]_n \cdot 2n(CH_3C_6H_5)$ polymeric complex [31] with a caffeine molecule as the bridging ligand between the dimeric units. Similarly, different chromophores were observed [32] for the molecular complex $[Cu_2(fluf)_4(caf)(H_2O)]$ where caf = caffeine and fluf = flufenamate. On the other hand, the alternation of two different dimeric units were found for the $[Cu_2(CH_3COO)_4(nia)]$ [33] (where nia = nicotinamide) and $[Cu_2(Me_3CCOO)_4(NITpPY)]_n$ complexes [34] (where NITpPY = 2-(3-pyridyl)-4,4,5,5-tetramethyl-1*H*-imidazolyl-1-oxyl-3-oxide). The polymeric chains of complexes $[Cu_2(2\text{-}O_2Nbz)_4(denia)]_n$ (a) and $[Cu_2(ClCH_2COO)_4(denia)]_n$ (b) are given in Fig. S1 in the Supplementary material.

Both magnetic susceptibility measurements, Fig. 2, and EPR spectra, Fig. 3, have proved the presence of a dimeric moiety within the crystal structure of $[Cu_2(2\text{-}NO_2Bz)_4(denia)_1]_n$ (**1**). Magnetic susceptibility, measured in the temperature range 1.8–300 K, has shown that complex (**1**) is diamagnetic in the temperature region 1.8–75 K, then the magnetic susceptibility increases systematically with increasing temperature, from 80 K to 300 K, and a reaches maximum at about room temperature. At 300 K the observed value of the effective magnetic moment is equal to 1.33 B.M. and at a temperature of 80 K $\mu_{eff} \cong 0.08$ B.M. This trend indicates an exchange antiferromagnetic interac-

Table 2
Selected distances (Å) and angles (°) for complex **1**

Cu1–O11	1.943(3)	Cu1–O21	1.986(3)
Cu1–O31	1.943(3)	Cu1–O41	1.998(3)
Cu1–O1^{i}	2.137(4)	Cu1···Cu2	2.6990(9)
Cu2–O12	2.022(3)	Cu2–O22	1.947(3)
Cu2–O32	1.995(3)	Cu2–O42	1.953(3)
Cu2–N5	2.145(4)	O1–Cu1^{ii}	2.137(4)
O11–Cu1–O21	90.20(15)	O11–Cu1–O31	174.11(14)
O11–Cu1–O41	89.06(14)	O21–Cu1–O31	90.12(15)
O21–Cu1–O41	161.61(14)	O31–Cu1–O41	88.78(15)
O11–Cu1–O1^{i}	89.44(15)	O21–Cu1–O1^{i}	108.18(16)
O31–Cu1–O1^{i}	96.05(15)	O41–Cu1–O1^{i}	90.19(15)
O12–Cu2–O22	88.45(15)	O12–Cu2–O32	159.92(14)
O12–Cu2–O42	90.76(15)	O22–Cu2–O32	89.38(15)
O22–Cu2–O42	172.51(15)	O32–Cu2–O42	88.81(15)
O12–Cu2–N5	94.15(14)	O22–Cu2–N5	95.81(15)
O32–Cu2–N5	105.92(14)	O42–Cu2–N5	91.68(15)

Symmetry codes: (i) $x - 1/2, -y + 1/2, z + 1/2$; (ii) $x + 1/2, -y + 1/2, z - 1/2$.

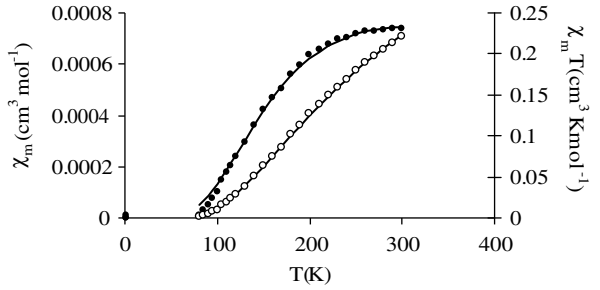


Fig. 2. The plot of χ_m (•) and the $\chi_m T$ (○) product vs. temperature for complex (**1**) (χ_m – the molar magnetic susceptibility calculated per one copper(II) center). The solid line was generated from the best-fit magnetic parameters, $g = 2.20$, $2J = -340\ cm^{-1}$ $zJ' = -0.10\ cm^{-1}$, $R = 2.00 \times 10^{-4}$.

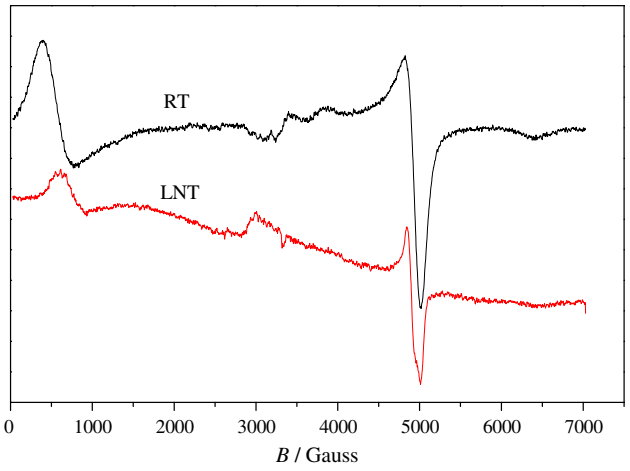


Fig. 3. EPR spectra of a powdered sample of complex (**1**) at room (RT) and at liquid nitrogen temperature (LNT). Parameters obtained from the spectra: $g_\perp = 2.07$, $g_\parallel = 2.35$, $D = 0.380\ cm^{-1}$.

tion between the copper(II) magnetic centers like in the other dimeric Cu^{II} tetracarboxylates [35,36]. Similar magnetic properties were observed in the dihydrate tetrakis(2-nitrobenzoato)di(aqua)dicopper(II) complex [27]. The magnetic data of the complex were fitted to a susceptibility equation derived from the spin Hamiltonian $H = -2JS_1S_2$, with the Bleaney–Bowers equation [37], to characterize the intradimer interaction:

$$\chi_{Cu} = \frac{N\beta^2 g^2}{3kT}\left[1 + \frac{1}{3}\exp\left(\frac{-2J}{kT}\right)\right]^{-1} + N\alpha$$

(where N is the Avogadro number, g – the spectroscopic splitting factor, β – the Bohr magneton, k – the Boltzmann constant and J – the exchange parameter), together with the application of a molecular field model for the calculation of the present magnetic data of complex (**1**) to obtain characteristics of the interdimer magnetic interactions, the zJ' parameter (z is the number of nearest neighbours) [42].

$$\chi_m^{corr} = \frac{\chi_m}{1 - \frac{2zJ'\chi_m}{Ng^2\beta^2}}$$

The best fitting parameters: singlet–triplet energy gap $2J = -340\ cm^{-1}$, $zJ' = -0.1\ cm^{-1}$, $g = 2.20$, were obtained with a good agreement factor $R = 1.99\ 10^{-4}$, R is the agreement factor, defined by

$$R = \frac{\sum_{i=1}^{n}(\chi_i^{exp}T - \chi_i^{calc}T)^2}{\sum_{i=1}^{n}(\chi_i^{exp}T)^2}$$

The results are presented in Fig. 2. The calculation procedure shows that the main factor determining the magnetic properties of the polymeric complex **1** is the antiferromagnetic coupling between the Cu^{2+} ions in the dimeric subunits. The magnetic interactions through diethylnicotinamide are very weak ($zJ' = -0.1\ cm^{-1}$), comparable to nicotinamide bridges [38]. The $2J$ value exceeding $300\ cm^{-1}$ is in good relation [39] to the coplanarity of all four carboxylato groups with the corresponding Cu_2O_2 planes. The greatest deviation from coplanarity was found between the O11–C11–O12 plane and the corresponding O11–Cu1–Cu2–O12 plane, where the φ_{bend} dihedral angle is 2.90°.

The EPR spectra, Fig. 3, of complex (**1**) shows the typical features of dimeric "acetate type" copper(II) complexes. The signal of complex (**1**) is very weak at liquid nitrogen temperature and that is consistent with the magnetic susceptibility measurements and raising a singlet state population with decreasing temperature. It is worth noting that no signal of a paramagnetic monomeric impurity is observed in this case, thus the dimeric units are connected and form a polymeric structure.

This structural observation is also supported by the IR spectrum data. The spectrum of complex (**1**) contains peaks of COO^- vibrations at 1579 (ν_{as}) and 1411 cm^{-1} (ν_s). The $\Delta\nu$ value ($\Delta\nu = \nu_{as} - \nu_s$) of 168 cm^{-1} is consistent with a bridging mode of bonding of the 2-NO_2-benzoate anion [40] and our previous results [27]. The electronic spectrum of (**1**) exhibits a broad asymmetric band with a maximum at 733 nm, that could be assigned to a d ← d transition, and a shoulder at about 375 nm, which is typical for a dimeric "acetate type" structure.

3.3. Structure, spectral and magnetic properties of [Cu(2-NO_2Bz)$_2$(denia)$_2$(H_2O)$_2$] (2)

The structure of (**2**) consists of centrosymmetric molecules, Figs. 4 and 5, with an elongated tetragonal-bipyramidal coordination polyhedron around the Cu atom (Table 3). The coordination sphere of the copper(II) atom in the *trans*-basal plane is formed by two 2-nitrobenzoate anions bonded *via* O1 atoms (the Cu–O1 distance is 1.958(2) Å) and two denia molecules bonded *via* N2 atoms (the Cu–N2 distance is 2.042(2) Å), and in the apical positions are two water molecules (the Cu–O1W distance is 2.462(2) Å). The water molecules, due to an intramolecular hydrogen bond (O1W–H2W···O2^{iii} with O1W···O2^{iii} [symmetry code: (iii) $-x+1$, $-y$, $-z$] at a distance of 2.770(2) Å) are slightly shifted from a precise apical posi-

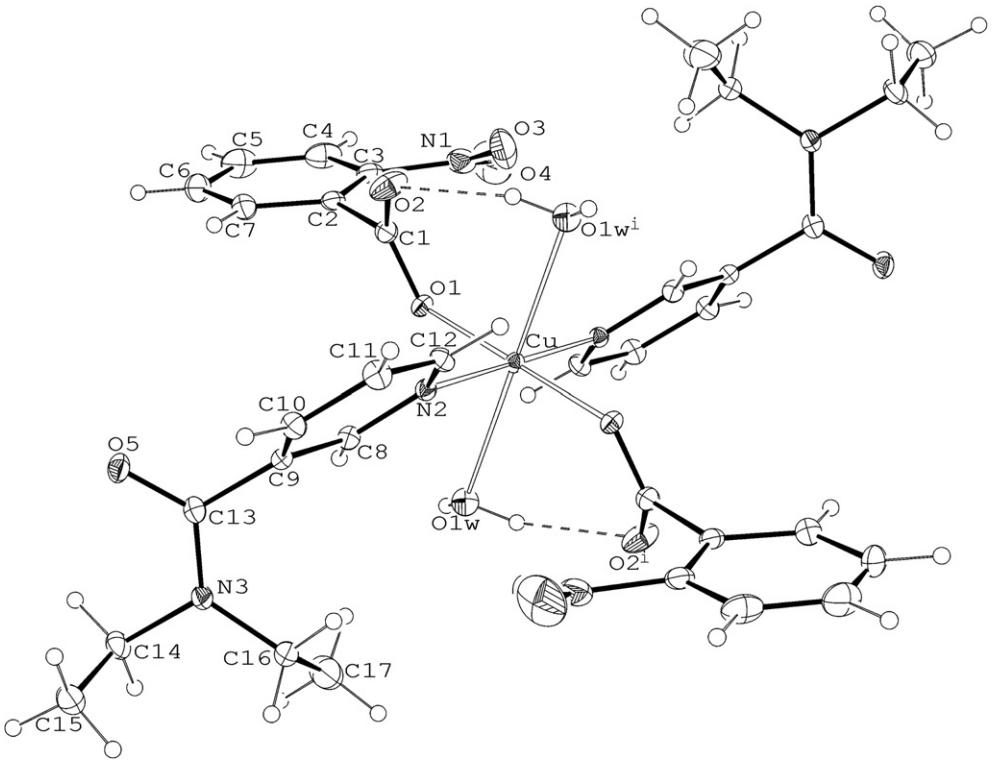


Fig. 4. Perspective view of $[Cu(2\text{-}NO_2bz)_2(denia)_2(H_2O)_2]$ (**2**) with the non-hydrogen atom numbering scheme.

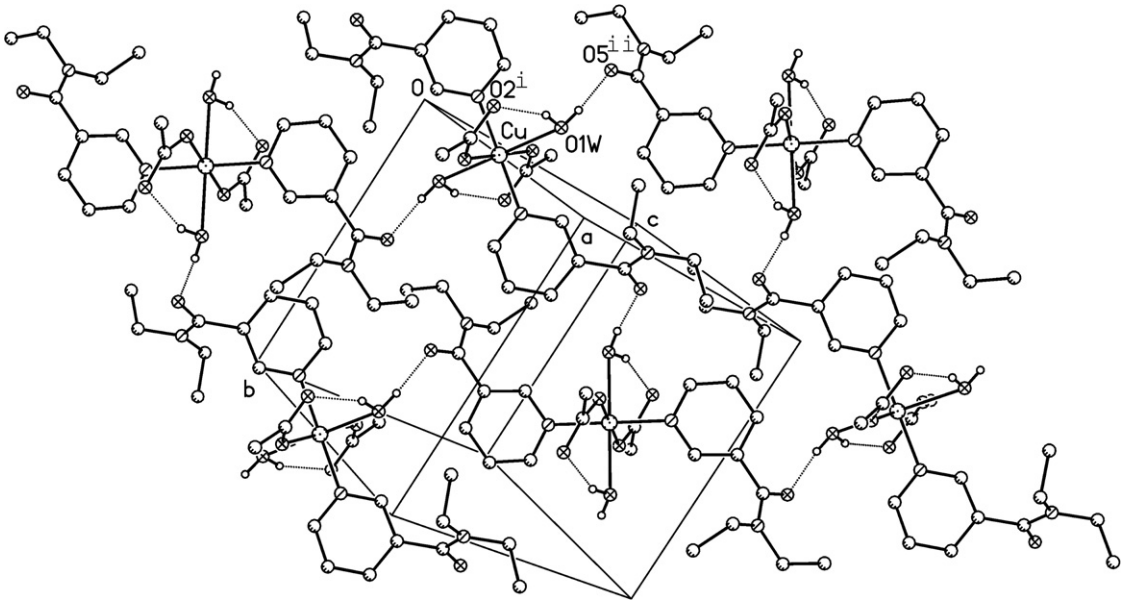


Fig. 5. View of the two-dimensional sheet of complex (**2**). Dashed lines indicate O–H···O hydrogen bonds. The 2-nitrophenyl groups are omitted for clarity.

Table 3
Selected distances (Å) and angles (°) for complex **2**

Cu–O1	1.9579(13)	O1–Cu–O1W	86.52(6)
Cu–N2	2.0415(16)	O1–Cu–N2	92.17(6)
Cu–O1W	2.4622(16)	N2–Cu–O1W	87.46(6)

tion towards the uncoordinated O2 carboxylato oxygen atom and the O1–Cu–O1W angle is 86.52(6)° (Table 4). The molecules of (**2**) are linked to adjacent molecules by O1W–H1W···O5^{iv} [symmetry code: (iv) $x+3/2$, $y1/2$, $z+1/2$] hydrogen bonds with a O1W···O5^{iv} distance of 2.810(2) Å into 2-D hydrogen bonding sheets with a Cu···Cu distance of 9.403(3) Å (Fig. 5).

The structure of (**2**) can be compared to other complexes of the general formula $[Cu(RCOO)_2(denia)_2(H_2O)_2]$ [11–15]. The Cu–O distances (Cu–O_{eq} where O_{eq} is the oxygen of a carboxylate group, and Cu–O_{ax} where O_{ax} stands for water oxygen) for complex (**2**) were found within the range

Table 4
Parameters in (Å) and (°) of hydrogen bonds within the structure of complex **2**

D–H···O	d(D···O)	∠(DHO)	Symmetry code
O1W–H1W···O5^{iv}	2.810 (2)	168 (4)	$-x+3/2$, $y-1/2$, $-z+1/2$
O1W–H2W···O2^{iii}	2.770 (2)	155 (4)	$-x+1$, $-y$, $-z$

of those distances for other known complexes 1.936(3) and 2.557(3) Å for RCOO = mefenamate [11], 1.961(2) and 2.449(2) Å for RCOO = flufenamate [12], 1.959(2) and 2.485(2) Å for RCOO = 4-nitrobenzoate [13], 1.965(2) and 2.503(2) Å for RCOO = 2-chloronicotinate [14] and 1.960(1) and 2.440(2) Å for RCOO = 2-chlorobenzoate [15]. On the other hand, the Cu–N_{eq} distance (N_{eq} is the pyridine nitrogen atom of the denia ligand) for complex (**2**) is the longest one in comparison to 2.027(3) Å for RCOO = mefenamate [11], 2.001(2) Å for RCOO = flufenamate [12], 2.019(2) Å for RCOO = 4-nitrobenzoate [13], 2.015(2) Å for RCOO = 2-chloronicotinate [14] and 2.031(2) for RCOO = 2-chlorobenzoate [15]. The value of the τ parameter ($\tau = R_S/R_L$), indicating [41] the degree of tetragonal elongation of the octahedron, increases in the order 0.775 (mefenamate) [11] <0.795 (2-chloronicotinate) [14] <0.800 (4-nitrobenzoate) [13] <0.809 (flufenamate) [12] <0.813 for complex (**2**) <0.818 (2-chlorobenzoate) [15]. All the complexes $[Cu(RCOO)_2(denia)_2(H_2O)_2]$ have a similar molecular structure, but only $[Cu(2\text{-}ClBz)_2(denia)_2(H_2O)_2]$ [15] is isostructural with complex (**2**).

The magnetic data of $Cu(2\text{-}NO_2bz)_2(denia)_2(H_2O)_2$ are shown in Fig. 6. At 300 K $\chi_m T$ is equal to 0.417 cm^3 K mol^{-1} ($\mu_{eff} = 1.83$ B.M.) and it is characteristic for non-coupled, $S = 1/2$ Cu^{II} centers. With a lowering of a temperature, the $\chi_m T$ value and the magnetic moment smoothly, but systematically, increase to $\chi_m T = 0.431$ cm^3 K mol^{-1} ($\mu_{eff} = 1.86$ B.M.) at 1.8 K. It suggests a very weak ferromagnetic interaction between the Cu^{II} centers, similar to those observed for the polymeric, $[Cu\{3,5\text{-}(NO_2)_2bz\}_2(ron)_2]_n$ complex [28]. Very weak but antiferromagnetic interactions were also observed in the similar monomeric complex $[Cu(2\text{-}NO_2Bz)_2(nia)_2(H_2O)_2]$ [29]. This similarity is probably based on similar weak intermolecular hydrogen bonds (Table 4) in the crystal lattice. The π–π stacking between the aromatic rings of complex **1** molecules was not observed in the crystal structure. In order to obtain a value of the exchange interactions parameter, the present magnetic data of (**2**) have been fitted using magnetic centers ($S = 1/2$) in the molecular field model of magnetic interactions [42]:

$$\chi_m = \frac{N\beta^2 g^2}{3kT} S(S+1), \quad \chi_m^{corr} = \frac{\chi_m}{1 - \frac{2zJ'\chi_m}{Ng^2\beta^2}}$$

where zJ' is the molecular exchange parameter, z is number of the nearest neighbours. The R is the agreement factor defined as

$$R = \sum_{i=1}^{n} \frac{(\chi_i^{exp} T - \chi_i^{calc} T)^2}{(\chi_i^{exp} T)^2}.$$

The magnitude of the magnetic exchange between the ions obtained from these calculations, $zJ' = 0.05$ cm^{-1}, $R = 4.99 \cdot 10^{-5}$ confirm only very weak ferromagnetic interactions in the crystal lattice of complex **2**.

The EPR spectrum, Fig. 7, of complex (**2**) is different from the previous one and is of the axial type with hyperfine splitting in the parallel area that was detected at room and even at liquid nitrogen temperature. Hyperfine splitting of polycrystalline samples of Cu(II) complexes is observed when the copper centers are isolated in the crystal lattice [29], in this case by 2-nitrobenzoate anions and denia molecules.

This conclusion is supported by the IR spectrum of $Cu(2\text{-}NO_2Bz)_2(denia)_2(H_2O)_2$ where the COO^- vibrations at 1607 (ν_{as}), and 1375 cm^{-1} (ν_s), giving a difference between asymmetric and symmetric vibration of 232 cm^{-1}, confirms the monodentate bonding mode of the 2-NO_2-benzoate anion [40]. The electronic spectrum of this monomeric complex also differs from the dimeric

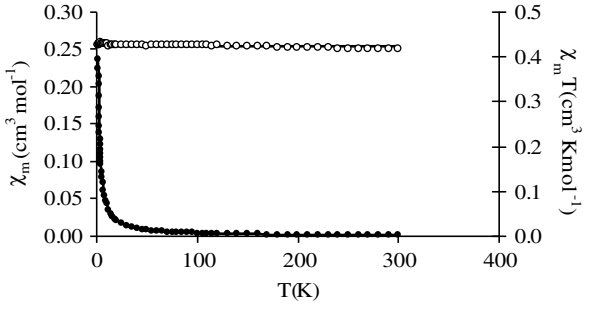


Fig. 6. Plots of the magnetic data versus temperature; χ_m (●), $\chi_m \cdot T$ (○) for complex (**2**). Solid lines present calculated curves using magnetic centers ($S = 1/2$) in the molecular field model of the magnetic interactions (parameters in the text).

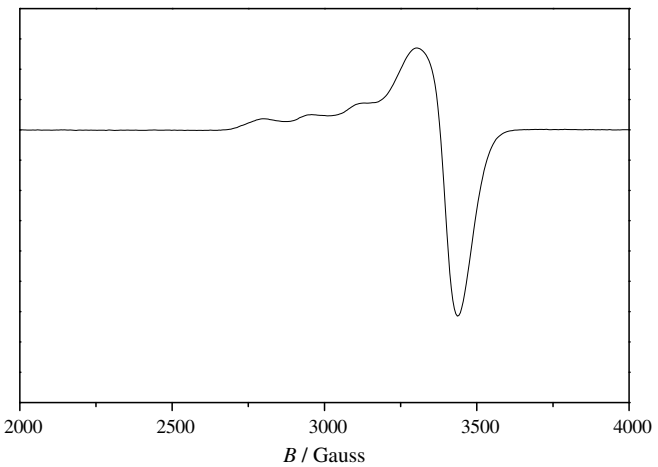


Fig. 7. The EPR spectrum of a powdered sample of complex (**2**) at room temperature: $g_\perp = 2.05$, $g_\parallel = 2.30$, $A_\parallel = 160$ G.

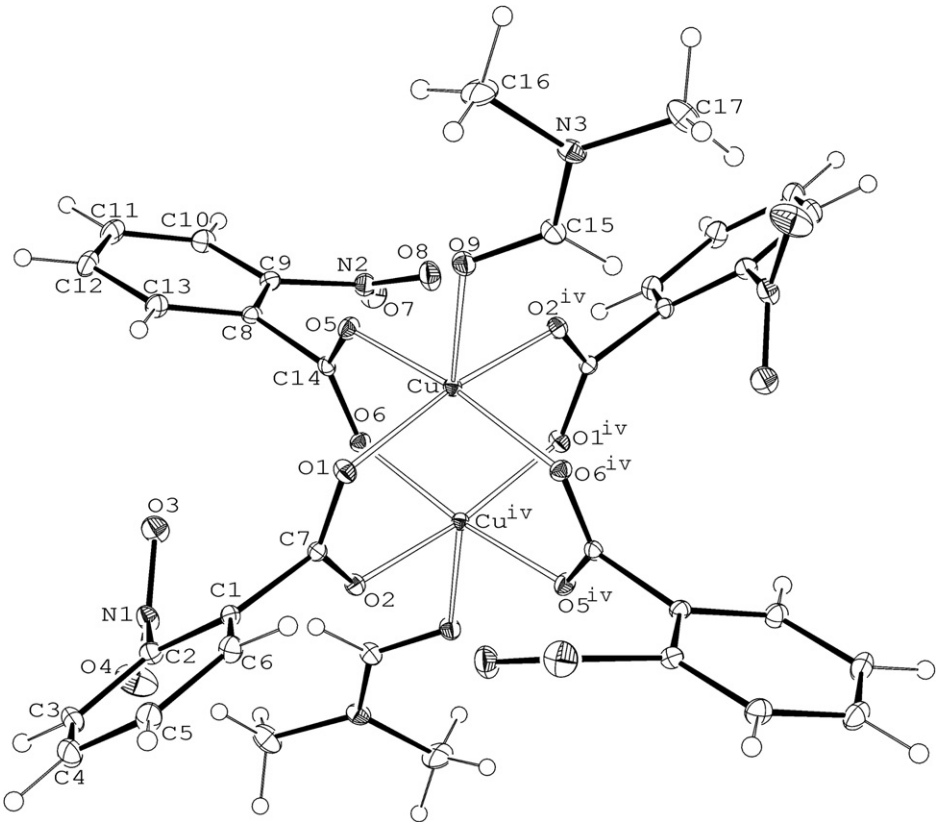


Fig. 8. Perspective view of $[Cu_2(2\text{-}NO_2bz)_4(DMF)_2]$ (**3**) with the non-hydrogen atom numbering scheme.

ones and the d ← d transition for complex (**2**) was found at 634 nm as a broad asymmetric band.

3.4. Structure, spectral and magnetic properties of $[Cu_2(2\text{-}NO_2Bz)_4(DMF)_2]$ (3)

The molecular structure and the numbering scheme are shown in Fig. 8. The structure consists of the centrosymmetric dimeric molecule $[Cu_2(2\text{-}NO_2bz)_4(DMF)_2]$, in which two copper(II) atoms are bridged *via* four carboxylato anions thus forming a square base of four oxygen atoms (Table 5) around each copper (the average Cu–O distance is 1.97(2) Å). The apical position of the square-pyramidal coordination polyhedron is occupied by the oxygen atom O9 of a DMF molecule (the Cu–O9 distance is 2.127(2) Å). The copper atoms are displaced from the respective basal planes towards the apical oxygen atoms by 0.19(1) Å, and the Cu–Cu separation within the dimer was found to be 2.633(1) Å. The crystal structure of (**3**) can be compared with the other dimeric copper(II) aromatic carboxylates with DMF ligands in apical positions [43–53]. It is interesting that the Cu···Cu intradimer distances vary within a narrow region from 2.598 to 2.641 Å, and this variation is caused mainly by moving the copper atom from the basal plane towards the apical ligand (correlation coefficient $R = 0.90$, Table S1 and Fig. S2), and this movement must be related to the anionic bridging ligand nature[1], because the apical ligands are DMF. Similarly, the Cu–DMF distances vary from 2.097 to 2.207 Å and there is a very weak relationship between this distance and the displacement of the copper atom from the basal plane. Comparison of similar complexes containing the moiety $[Cu_2(2\text{-}NO_2bz)_4(L)_2]$ (where $L = H_2O$ [27] or L = DMSO [54]) with complex (**3**) shows that the nature of the apical ligand exhibits a greater influence on all the Cu···Cu, the Cu–basal plane and $Cu\text{–}O_{apic}$ distances.

The magnetic properties of complex (**3**) (Fig. 9) are shown as plots of χ_m and the $\chi_m T$ product versus T (χ_m – the molar magnetic susceptibility calculated per one copper(II) center). The magnetic susceptibility reaches a maximum at room temperature and the value of $\chi_m T$ continuously decreases on lowering of the temperature. At 300 K the observed value of $\chi_m T$ is 0.238 cm^3 K mol^{-1} and the effective magnetic moment is equal to 1.38 B.M. At the temperature 50 K, $\chi_m T$ reaches a minimum (about 0.002 cm^3 K mol^{-1}, which corresponds to $\mu_{eff} \cong 0.13$ B.M). This trend indicates an antiferromagnetic exchange interaction between the two copper(II) magnetic centers of the dimeric unit and depopulation of the excited triplet ($S = 1$) state. Further temperature decreasing results in an increase of $\chi_m T$, probably due to the presence of mono-

[1] For data see Supplementary material Table S1.

Table 5
Selected distances (Å) and angles (°) for complex **3**

Cu–O1	1.9702(12)	Cu–O2^{v}	1.9797(12)
Cu–O5	1.9666(12)	Cu–O6^{v}	1.9690(12)
Cu–O9	2.1272(12)	Cu–Cu^{v}	2.6334(7)
O1–Cu–O2^{v}	168.89(4)	O1–Cu–O5	89.19(5)
O1–Cu–O6^{v}	89.66(5)	O2^{v}–Cu–O5	90.53(5)
O2^{v}–Cu–O6^{v}	88.49(5)	O5–Cu–O6^{v}	168.93(5)
O1–Cu–O9	98.48(5)	O2^{v}–Cu–O9	92.55(5)
O5–Cu–O9	98.20(5)	O6^{v}–Cu–O9	92.86(5)

Symmetry codes: (v) $-x+1, -y+1, -z+1$.

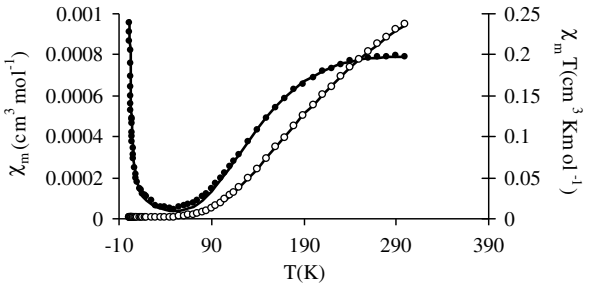


Fig. 9. The plot of χ_m and the $\chi_m T$ product vs. temperature for complex (**3**) (χ_m – the molar magnetic susceptibility calculated per one copper(II) center). The solid line was generated from the best-fit parameters $g_{dim} = 2.20$, $g_{mon} = 2.16$, $2J = -320\ cm^{-1}$, $R = 9.97 \times 10^{-6}$.

meric impurities present in this sample. The magnetic data of the complex were fitting using the modified Bleaney–Bower's equation [42]:

$$\chi_m = \left\{ \frac{Ng_{dim}^2\beta^2}{3kT}\left[1 + \frac{1}{3}(e^{-2J/kT})\right]^{-1} \right\}(1-x) + \left(\frac{Ng_{mon}^2\beta^2}{4kT}\right)x$$

where x is the mole fraction of the monomeric form, and g_{mon} and g_{dim} are spectroscopic splitting factors of the monomer and dimer forms, respectively, and the other symbols have their usual meaning. The magnetic parameters: $g_{dim} = 2.20$, $g_{mon} = 2.16$, $2J = -320\ cm^{-1}$ and monomeric impurities at the 0.38% level were obtained, $R = 9.97 \times 10^{-6}$

$$R = \sum_{i=1}^{n} \frac{(\chi_i^{exp}T - \chi_i^{calc}T)^2}{(\chi_i^{exp}T)^2}$$

The "normal" $-2J$ value for complex (**3**) is a proof of the mutual relation between the $-2J$ value and the φ_{bend} angle. Both structurally independent bridges are nearly planar and exhibit small values of the φ_{bend} angle 1.1(2)° and 3.2(2)°. The orientation of the benzene rings with respect to the carboxylate bridge probably has no influence on the magnetic interaction between the copper centers.

The EPR spectra of the powdered sample of complex (**3**) were measured at room temperature and liquid nitrogen temperature (Fig. 10). The spectra exhibit features typical of those for dimeric carboxylatocopper(II) complexes, absorptions at low and high field (at room temperature $H_{z1} \approx 415$ G and $H_{z2} \approx 6280$ G, respectively) and the line $H_{\perp 2} \approx 4900$ G. At liquid nitrogen temperature the signal of the dimeric species becomes weaker, but hyperfine splitting was observed in the H_{z1} region (Fig. 10). At room temperature as well as at liquid nitrogen temperature a monomeric impurity was observed at about 3380 G.

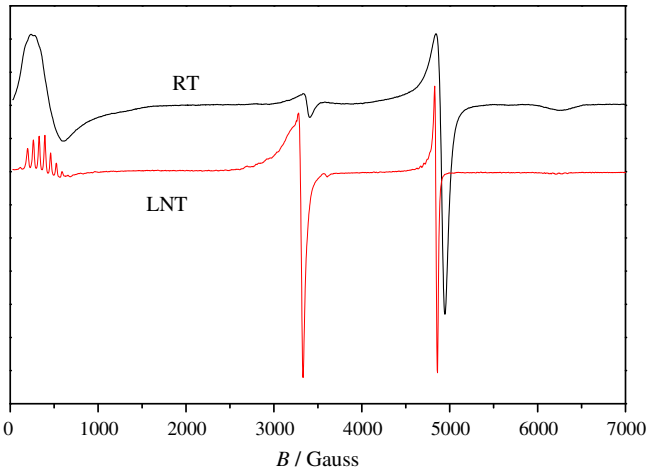


Fig. 10. EPR spectra of a powdered sample of complex (**3**) at room (RT) and at liquid nitrogen temperature (LNT). The amount of monomeric impurity, calculated from magnetic measurements equal ~0.4%, and 7 lines observed at H_{z1} lines correspond to $A = 65$ G. Remaining EPR parameters are: $g_{\perp} = 2.06$, $g_{\parallel} = 2.28$, $D = 0{,}346\ cm^{-1}$, $g_{mon} = 2.06$.

The spectrum of (**3**) contains peaks of COO^{-} vibrations at 1577 (ν_{as}) and 1412 cm^{-1} (ν_s), and the $\Delta\nu$ value ($\Delta\nu = \nu_{as} - \nu_s$) of 168 cm^{-1} is similar to that for complex (**1**). Similarly the electronic spectrum of (**3**) exhibits a broad asymmetric band with a maximum at 718 nm (d ← d transition) and a shoulder at about 400 nm.

Acknowledgements

We thank the Scientific Grant Agency of the Ministry of Education of Slovak Republic and the Slovak Academy of Sciences (1/2452/05), Research and Development Support Agency (APVT-20-005504) and the Polish Ministry of Science and Higher Education – Grant No. 1T09A 12430, for financial support.

Appendix A. Supplementary material

CCDC 667553, 667554 and 667555 contain the supplementary crystallographic data for **1**, **2** and **3**. These data can be obtained free of charge via http://www.ccdc.cam.ac.uk/conts/retrieving.html, or from the Cambridge Crystallographic Data Centre, 12 Union Road, Cambridge CB2 1EZ, UK; fax: (+44) 1223-336-033; or e-mail: deposit@ccdc.cam.ac.uk. Supplementary data associated with this article can be found, in the online version, at doi:10.1016/j.poly.2007.12.030.

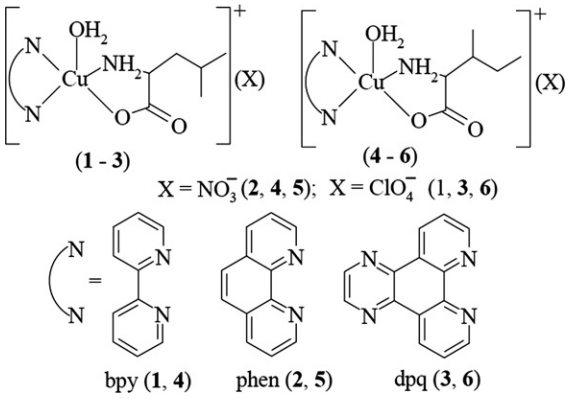
References

[1] L.B. Zavodnik, V.M. Tsyrkumov, M.I. Bushma, P.I. Lukienko, L.F. Legon'kova, Farmakolo. Toksikol. 54 (1991) 69.
[2] A.A. Rasool, J. Pharm. Sci. 80 (1991) 387.
[3] B. Kozlevcar, N. Lah, I. Leban, F. Pohleven, P. Segedin, Croat. Chem. Acta 73 (2000) 733.
[4] (a) F.A. Allen, Acta Crystallogr., Sect. B 58 (2002) 380;
(b) F.A. Allen, O. Kennard, Chem. Des. Autom. News 8 (1993) 31, Searches of CSD version 5.28 (November 2006) plus two updates (January 2007 and May 2007) were conducted using the CONQUEST software..
[5] L. Kh. Minacheva, T.S. Khodashova, M.A. Porai-Koshits, A. Yu. Tsivadze, Koord. Khim. 7 (1981) 455.
[6] T. Hokelek, H. Necefoglu, M. Balci, Acta Crystallogr., Sect. C 51 (1995) 2020.
[7] J. Moncol, B. Kalinaková, J. Švorec, M. Kleinová, M. Koman, D. Hudecová, M. Melník, M. Mazúr, M. Valko, Inorg. Chim Acta 357 (2004) 3211.
[8] F. Valach, M. Dunaj-Jurčo, M. Melník, N.N. Hoang, Z. Kristallogr. 209 (1994) 267.
[9] T. Hokelek, H. Gunduz, H. Necefoglu, Acta Crystallogr., Sect. C 52 (1996) 2470.
[10] M. Koman, M. Melník, T. Glowiak, J. Coord. Chem. 44 (1998) 133.
[11] M. Melník, M. Koman, Macášková, T. Glowiak, J. Coord. Chem. 44 (1998) 163.
[12] M. Melník, I. Potočňák, Macášková, D. Mikloš, C.E. Holloway, Polyhedron 15 (1996) 2159.
[13] T. Hokelek, K. Budak, H. Necefoglu, Acta Crystallogr., Sect. C 53 (1997) 1049.
[14] J. Moncol, M. Palicová, P. Segl'a, M. Koman, M. Melník, M. Valko, T. Glowiak, Polyhedron 21 (2002) 365.
[15] J. Moncol, M. Koman, M. Melník, D. Mikloš, T. Głowiak, Challenges for Coordination Chemistry in the New Century, vol. 5, Slovak Technical University Press, Bratislava, 2001.
[16] J. Moncol, Z. Púčeková, T. Lis, D. Valigura, Acta Crystallogr., Sect. E 62 (2006) m448.
[17] M. Koman, M. Melník, J. Moncol, S. Lörinc, T. Glowiak, in: M. Melnik, A. Sirota (Eds.), Progress in Coordination and Bioinorganic Chemistry, vol. 6, Slovak Technical University Press, Bratislava, 2003, p. 121.
[18] J. Moncol, M. Múdra, P. Lönnecke, M. Hewitt, M. Valko, H. Morris, J. Švorec, M. Melník, M. Mazúr, M. Koman, Inorg. Chim. Acta 360 (2007) 3213.
[19] XSCANS, Siemens Analytical X-ray Instruments Inc., Madison, Wisconsin, USA 1994.
[20] (a) Nonius, COLLECT, Nonius BV, Delft, The Netherlands, 2000;
(b) Z. Otwinowski, W. Minor, Methods in enzymology, in: C.W. CarterJr., R.M. Sweet (Eds.), Macromolecular Crystallography, Part A, vol. 276, Academic Press, New York, 1997, pp. 307–326.
[21] Oxford Diffraction, CRYSALIS CCD and CRYSALIS RED Versions 1.171, Oxford Diffraction Poland, Wroclaw, Poland, 2003.
[22] XEMP, Version 4.2. Siemens Analytical X-ray Instruments Inc., Madison, Wisconsin, USA, 1990.
[23] G.M. Sheldrick, Acta Crystallogr., Sect. A 46 (1990) 467.
[24] G.M. Sheldrick, SHELXL97, University of Gőttingen, Germany, 1997.
[25] L.J. Farrugia, J. Appl. Crystallogr. 30 (1997) 565.
[26] E. Kőnig, Magnetic Properties of Coordination and Organometallic Transition Metal Compounds, Springer, Berlin, 1996.
[27] P. Stachová, D. Valigura, M. Koman, M. Melník, M. Korabik, J. Mrozinski, T. Glowiak, Polyhedron 23 (2004) 1303.
[28] P. Stachová, M. Korabik, M. Koman, M. Melník, J. Mrozinski, T. Glowiak, M. Mazúr, D. Valigura, Inorg. Chim. Acta 359 (2006) 1275.
[29] P. Stachová, M. Melnik, M. Korabik, J. Mrozinski, M. Koman, T. Glowiak, D. Valigura, Inorg. Chim. Acta 360 (2007) 1517.
[30] M. Melník, Coord. Chem. Rev. 42 (1982) 259.
[31] H. Uekusa, S. Ohba, T. Tokii, Y. Muto, M. Kato, S. Husebye, O.W. Steward, Shih-Chi Chang, J.P. Rose, J.F. Pletcher, I. Suzuki, Acta Crystallogr., Sect. B 48 (1992) 650.
[32] M. Melník, M. Koman, T. Glowiak, Polyhedron 17 (1998) 1767.
[33] B. Kozlevcar, I. Leban, I. Turel, P. Segedin, M. Petric, A.J.P. White, D.J. Williams, J. Sieler, Polyhedron 18 (1999) 755.
[34] Y.-H. Chung, H.-H. Wei, Inorg. Chem. Commun. 2 (1999) 267.
[35] M. Melník, Coord. Chem. Rev. 36 (1981) 287.
[36] M. Melník, Coord. Chem. Rev. 42 (1982) 259.
[37] B. Bleaney, K.D. Bowers, Proc. Roy. Chem. London A 214 (1952) 451.
[38] D. Valigura, J. Moncol, M. Korabik, Z. Púčeková, T. Lis, J. Mroziński, M. Melnik, Eur. J. Inorg. Chem. (2006) 3813.
[39] T. Kawata, H. Uekusa, S. Ohba, Acta Crystallogr., Sect. B 48 (1992) 253.
[40] K. Nakamoto, Infrared and Raman Spectra of Inorganic and Coordination Compounds, Part B, 5th ed., Wiley, New York, 1997.
[41] J. Gažo, I.B. Bersuker, J. Garaj, M. Kabešová, J. Kohout, H. Langfelderová, M. Melník, M. Serátor, F. Valach, Coord. Chem. Rev. 19 (1976) 253.
[42] O. Kahn, Molecular Magnetism, VCV Publishers, New York, 1993.
[43] S. Batsanov, Yu. T. Struchkov, A.S. Grigor'eva, E.E. Kriss, N.F. Konakhovich, Yu. A. Fialkov, Koord. Khim. 7 (1981) 784. ANTHCU and ANTHCU01.
[44] D. Kovala-Demertzi, A. Galani, M.A. Demertzis, S. Skoulika, C. Kotoglou, J. Inorg. Biochem. 98 (2004) 358. ARALUA.
[45] M.G. Mys'kiv, V.V. Olijnik, E.E. Kriss, N.F. Konakhovich, A.S. Grigor'eva, Koord. Khim. 8 (1982) 1415, BOTXUD.
[46] G. Facchin, M.H. Torre, E. Kremer, O.E. Piro, E.J. Baran, Z. Anorg. Allg. Chem. 624 (1998) 2025, BOTXUD01.
[47] V. Kh. Sabirov, A.S. Batsanov, Yu. T. Struchkov, A.S. Grigor'eva, E.E. Kriss, N.F. Konakhovich, Yu. A. Fialkov, Koord. Khim. 10 (1984) 1474, COZBEY.
[48] Y.-L. Zhang, S.-W. Chen, W.-S. Liu, D.-Q. Wang, Acta Crystallogr., Sect. E 60 (2004) m196, ETEJIW.
[49] Y. Xiufen, H. Zhongle, Z. Hanhui, Chin. J. Struct. Chem. 7 (1988) 124, cited from CSD as GEXPOO and GEXPUU.
[50] G. Morgant, N.-H. Dung, J.-C. Daran, B. Viossat, X. Labouze, M. Roch-Arveiller, F.T. Greenaway, W. Cordes, J.R.J. Sorenson, J. Inorg. Biochem. 81 (2000) 11, MIWDUR.
[51] B. Viossat, J.-C. Daran, G. Savouret, G. Morgant, F.T. Greenaway, N.-H. Dung, V.A. Pham-Tran, J.R.J. Sorenson, J. Inorg. Biochem. 96 (2003) 375, OKEZUZ.
[52] R.E. Del Sesto, A.M. Arif, J.S. Miller, Inorg. Chem. 39 (2000) 4894, QALZEI.
[53] J. Yang, L. Li, J.-F. Ma, Y.-Y. Liu, Acta Crystallogr., Sect. E 61 (2005) m237, FAYLUN.
[54] M. Klinga, M.R. Sundberg, M. Melnik, J. Mrozinski, Inorg. Chim. Acta 162 (1989) 39.

generate fragments those could be subsequently relegated. Zn(II), being a strong Lewis acid, exchanges ligands very rapidly. Several Zn(II) complexes are well-known for their hydrolase activity [7c]. Hydrolytic cleavage active species mimic restriction enzymes. The oxidative DNA cleavage involves either oxidation of the deoxyribose moiety by abstraction of sugar hydrogen or oxidation of nucleobases. Oxidative DNA cleavage by redox-active metal complexes, like $[Fe(edta)]^{2-}$ or Cu(1,10-phenanthroline)$_2$Cl$_2$, is mediated by the production of reactive oxygen species, like HO$^{\cdot}$, through a Fenton-type mechanism [10]. These free radicals abstract the most accessible and exposed sugar hydrogens and initiate the oxidative cleavage, leading to DNA-cleavage products. The purine base guanine is most susceptible for oxidation among the four nucleobases. The role of ternary copper(II) complexes in biological systems is well known [11]. Among the transition metal based DNA cleaving agents, copper phenanthroline complexes are particularly primarily sugar directed. They are responsible for direct strand scission by hydrogen atom abstraction from the deoxyribose moiety. Sigman and coworkers have reported that the bis-(1,10-phenanthroline)copper(I) complex in the presence of H_2O_2 act as a 'chemical nuclease' that efficiently nicks DNA [1,2]. Recently there have been several reports of copper(II) complexes showing efficient chemical nuclease activity [12–17]. Recent reports have shown that amino acid/peptide based copper(II) complexes show efficient DNA cleavage activity by oxidative and hydrolytic pathways [17–22]. Such complexes may show DNA cleavage both in the presence (chemical nuclease) or absence (hydrolytic) of a reducing agent. The favored pathway depends on several factors, viz. Lewis acidity, accessible redox potential and rate of ligand exchange.

The present work stems from our interest to explore the structural and functional properties of redox active ternary copper(II) complexes having bioessential α-amino acids L-leucine or L-isoleucine and *N*,*N*-donor heterocyclic bases as a DNA groove binder. The efficiency of the DNA strand scission can be enhanced by increasing the binding affinity of the metal complex for DNA. Typically such coordination complexes contain a DNA-binding moiety that binds either at a groove, or act as an intercalator, thereby increasing the DNA-targeting ability of the metal complex. Our choice of 2,2′-bipyridine (bpy), 1,10-phenanthroline (phen) and dipyridoquinoxaline (dpq) are based on their differences in DNA binding ability. Both L-leucine and L-isoleucine are essential for development of skeletal muscle tissue and preserve muscle glycogen levels [24].

Herein, we report the syntheses, structure, DNA binding and oxidative DNA cleavage properties of ternary copper(II) complexes of the general formula [Cu(L-leu/ile)(B)(H$_2$O)](X) (**1**–**6**) where B is a *N*,*N*-donor heterocyclic base, viz. 2,2′ -bipyridine (bpy, **1**, **4**); 1,10-phenanthroline (phen, **2**, **5**) and dipyrido[3,2-*d*:2′,3′-*f*]quinoxaline (dpq, **3**, **6**), L-leu = L-leucine and L-ile = L-isoleucine (Scheme 1). The bpy and dpq complexes of L-ile (**4**, **6**) have been structurally characterized by X-ray crystallography. Studies have been made to explore the role of DNA binder and amino acid along with mechanistic pathways involved in the 'chemical nuclease' activity.



Scheme 1. Complexes **1**–**6** and the heterocyclic bases.

2. Experimental

2.1. Materials

All products were obtained from commercial sources and were used without further purification. Solvents used for electrochemical and spectroscopic studies were purified by standard procedures [25]. The supercoiled pUC19 DNA (CsCl purified) was purchased from Bangalore Genei (India). Calf thymus (CT) DNA, agarose (molecular biology grade), distamycin-A, catalase, superoxide dismutase (SOD) and ethidium bromide (EB) were obtained from Sigma (USA). Tris(hydroxymethyl)aminomethane–HCl (Tris–HCl) buffer solution was prepared by using deionized, sonicated triple distilled water. The *N*,*N*-donor heterocyclic base dipyrido[3,2-*d*:2′,3′-*f*]quinoxaline (dpq) was prepared by the literature procedure using 1,10-phenanthroline-5,6-dione as a precursor and reacting it with ethylenediamine [26]. The complexes **2** and **5** were prepared by literature procedures [27].

2.2. Preparation of [Cu(AA)(B)(H$_2$O)](X) (1–6) (AA = L-leu (1–3) or L-ile (4–6); B = bpy, phen, dpq); X = NO$_3^-$ (2, 4, 5); ClO$_4^-$ (1, 3, 6)

The complexes were prepared by following a modified reported [27] synthetic procedure in which a 10 ml aqueous solution of Cu(NO$_3$)$_2$ · 3H$_2$O (0.48 g) or Cu(ClO$_4$) · 6H$_2$O (0.75 g) (2.0 mmol) was reacted with L-leucine or L-isoleucine (0.27 g, 2.1 mmol) treated with NaOH (0.08 g, 2.0 mmol) in water (10 ml) under magnetic stirring at room temperature. Slow evaporation of the solution at room temperature yielded a crystalline material. Crystals of complexes **4** and **6** were suitable for X-ray diffraction studies. After 30 min, a 20 ml methanolic solution of the heterocyclic base [bpy (0.28 g), phen (0.35 g), dpq (0.42 g) (1.8 mmol)] was added to the solution and the resulting

mixture was stirred for 2 h at room temperature. On cooling the solution to an ambient temperature, it was filtered and the filtrate on slow concentration yielded a crystalline solid of the product. The solid was isolated and washed with cold aqueous methanol and finally dried over P_4O_{10} (Yield: ~75%). *Anal*. Calc. for $C_{16}H_{22}CuN_3O_7Cl$ (**1**): C, 41.12; H, 4.74; N, 8.99. Found: C, 41.32; H, 4.88; N, 8.85%. λ_{max}, nm (ε, M^{-1} cm^{-1}) in water: 604 (50), 310 (12560), 300 (12700), 242 (10,020). FT-IR, cm^{-1} (KBr disc): 3486br, 3340br, 3092m, 2953m, 2873w, 1633s, 1606s, 1498m, 1474m, 1446m, 1385s, 1316m, 1250m, 1110vs (ClO_4^-), 1067s, 976m, 833m, 770s, 731m, 652w, 620m, 553m, 416m (s, strong; m, medium; w, weak; br, broad; vs, very strong). Λ_M (Ω^{-1} cm^2 M^{-1}) in water at 25 °C: 104. μ_{eff} (solid, 298 K): 1.78 μ_B. *Anal.* Calc. for $C_{18}H_{22}CuN_4O_6$ (**2**): C, 47.61; H, 4.88; N, 12.34. Found: C, 47.35; H, 4.47; N, 12.18%. λ_{max}, nm (ε, M^{-1} cm^{-1}) in water: 610 (55), 293 (9,640), 272 (31380), 204 (43860). FT-IR, cm^{-1} (KBr disc): 3385br, 3219br, 2953m, 1634s, 1585s, 1520m, 1430s, 1384vs (NO_3^-), 1315s, 1154m, 1130w, 1109w, 1041m, 984m, 918w, 857s, 826m, 782m, 723s, 649m, 559m, 429m. Λ_M (Ω^{-1} cm^2 M^{-1}) in water at 25 °C: 122. μ_{eff} (solid, 298 K): 1.74 μ_B. *Anal.* Calc. for $C_{20}H_{22}CuN_5O_7Cl$ (**3**): C, 44.20; H, 4.08; N, 12.89. Found: C, 44.13; H, 4.03; N, 12.78%. λ_{max}, nm (ε, M^{-1} cm^{-1}) in water: 608 (74), 293 (15000), 257 (47600), 208 (31540). FT-IR, cm^{-1} (KBr disc): 3499br, 3293br, 2957m, 1594s, 1531w, 1486s, 1470m, 1407s, 1386s, 1215m, 1114s, 1084vs (ClO_4^-), 879w, 824m, 732s, 625s, 576m, 438m. Λ_M (Ω^{-1} cm^2 M^{-1}) in water at 25 °C: 115. μ_{eff} (solid, 298 K): 1.76 μ_B. *Anal.* Calc. for $C_{16}H_{22}CuN_4O_6$ (**4**): C, 44.68; H, 5.16; N, 13.03. Found: C, 44.56; H, 5.20; N, 12.78%. λ_{max}, nm (ε, M^{-1} cm^{-1}) in water: 604 (55), 310 (13420), 300 (13620), 243 (10220). FT-IR, cm^{-1} (KBr disc): 3500br, 3287br, 3026m, 2959m, 2875m, 1654s, 1601s, 1497m, 1479m, 1383vs (NO_3^-), 1255m, 1159s, 1134m, 1086m, 1063m, 1033m, 1019m, 989m, 897m, 825w, 806w, 774s, 731s, 662w, 584w, 417m. Λ_M (Ω^{-1} cm^2 M^{-1}) in water at 25 °C: 138. *Anal.* Calc. for $C_{18}H_{22}CuN_4O_6$ (**5**): C, 47.61; H, 4.88; N, 12.34. Found: C, 47.43; H, 4.53; N, 12.43%. λ_{max}, nm (ε, M^{-1} cm^{-1}) in water: 611 (55), 293 (8320), 272 (27620), 204 (38660). FT-IR, cm^{-1} (KBr disc): 3444br, 3252br, 3133m, 3056w, 2956m, 2874m, 1644s, 1586m, 1518m, 1432m, 1382vs (NO_3^-), 1332m, 1225w, 1158m, 1108w, 1007m, 873w, 856s, 825m, 781m, 737w, 723s, 648m, 567m, 489w, 429m. Λ_M (Ω^{-1} cm^2 M^{-1}) in water at 25 °C: 127. μ_{eff} (solid, 298 K): 1.80 μ_B. *Anal.* Calc. for $C_{20}H_{22}CuN_5O_7Cl$ (**6**): C, 44.20; H, 4.08; N, 12.89. Found: C, 44.33; H, 4.05; N, 12.93%. λ_{max}, nm (ε, M^{-1} cm^{-1}) in water: 609 (80), 295 (14400), 257 (45840), 208 (26260). FT-IR, cm^{-1} (KBr disc): 3433br, 3286br, 3086m, 2961m, 1637s, 1582m, 1532m, 1487s, 1460m, 1407s, 1387s, 1213m, 1087vs (ClO_4^-), 873m, 823m, 733s, 625s, 568m, 431m. Λ_M (Ω^{-1} cm^2 M^{-1}) in water at 25 °C: 106. μ_{eff} (solid, 298 K): 1.77 μ_B.

Solubility and stability. The complexes showed high solubility in water, methanol, dimethylformamide (DMF) and dimethyl sulfoxide (DMSO) and are insoluble in hydrocarbons. They are stable in the solid and in solution phases.

Caution! Perchlorate salts are potentially explosive and only small quantities were handled with care.

2.3. General methods

The elemental analysis was done using a Thermo Finnigan FLASH EA 1112 CHNS analyzer. The infrared and electronic spectra were recorded on Perkin–Elmer Lambda 35 and Perkin–Elmer spectrum one 55 spectrophotometers, respectively. DNA melting experiments were carried out on a Varian Cary 300 Bio UV–Vis spectrophotometer attached to a Cary Peltier temperature controller. Molar conductivity measurements were done using a Control Dynamics (India) conductivity meter. Electrochemical measurements were made at 25 °C on an EG&G PAR model 253 VersaStat potentiostat/galvanostat with electrochemical analysis software 270 using a three electrode setup consisting of a glassy carbon working, platinum wire auxiliary and a saturated calomel reference electrode (SCE) in DMF containing 0.1 M TBAP. The electrochemical data were uncorrected for junction potentials. Magnetic susceptibility data at 298 K were obtained using Model 300 Lewis-coil-force magnetometer of George Associates Inc. (Berkley, USA) make.

2.4. X-ray crystallographic procedures

Single crystals of [Cu(L-ile)(bpy)(H_2O)](NO_3) · H_2O (**4** · H_2O) and [Cu(L-ile)(dpq)(H_2O)](ClO_4) (**6**) were obtained by slow evaporation of an aqueous-methanolic solution of the complexes. A rectangular single crystal was mounted on a glass fiber and used for data collection. All geometric and intensity data were collected at 293 K using an automated Bruker SMART APEX CCD diffractometer equipped with a fine focus 1.75 kW sealed tube Mo Kα X-ray source ($\lambda = 0.71073$ Å), with increasing ω (width of 0.3°/frame) at a scan speed of 5 and 2 s/frame for complexes **4** and **6**, respectively. Intensity data, collected using the ω–2θ scan mode, were corrected for Lorentz-polarization effects and for absorption [28]. SMART software was used for data acquisition and SAINT software for data extraction [29]. Absorption corrections were made using SADABS [30]. The structures were solved and refined by the full-matrix least-squares method using the SHELX system of programs [31]. All non-hydrogen atoms were refined anisotropically. All hydrogen atoms attached to the heteroatoms were in their calculated positions and refined using a riding model. Perspective views of the complexes were obtained by ORTEP [32].

2.5. DNA binding experiments

The UV absorbance at 260 and 280 nm of the CT-DNA solution in 5 mM Tris–HCl buffer (pH 7.2) gave a ratio of 1.9, indicating the DNA was free of protein [33]. The

concentration of CT DNA was measured from the band intensity at 260 nm with a known ε value (6600 M^{-1} cm^{-1}) [34]. Absorption titration measurements were done by varying the concentration of CT DNA, keeping the metal complex concentration constant in 5 mM Tris–HCl/5 mM NaCl buffer (pH 7.2). Samples were kept for equilibrium before recording each spectrum. The intrinsic binding constant (K_b) for the interaction of the complexes with CT-DNA were determined from a plot of [DNA]/($\varepsilon_a - \varepsilon_f$) vs. [DNA] using absorption spectral titration data and the following equation:

$$[DNA]/(\varepsilon_a - \varepsilon_f) = [DNA]/(\varepsilon_b - \varepsilon_f) + [K_b(\varepsilon_b - \varepsilon_f)]^{-1},$$

where [DNA] is the concentration of DNA in base pairs. The apparent absorption coefficients ε_a, ε_f and ε_b correspond to $A_{obsd.}$/[Cu], the extinction coefficient for the free copper(II) complex and extinction coefficient for the copper(II) complex in the fully bound form, respectively [35]. K_b is given by the ratio of the slope to the intercept.

The apparent binding constant (K_{app}) values of the complexes were determined by a fluorescence spectral technique using ethidium bromide (EB) bound CT DNA solution in Tris–HCl/NaCl buffer (pH, 7.2). The emission intensities of EB at 600 nm (546 nm excitation) with an increasing amount of the ternary complex concentration were recorded. Ethidium bromide was non-emissive in Tris–buffer medium due to fluorescence quenching of the free EB by the solvent molecules [36]. In the presence of DNA, EB showed enhanced emission intensity due to its intercalative binding to DNA. A competitive binding of the copper complexes to CT DNA could result in the displacement of EB or quenching of the bound EB by the paramagnetic copper(II) species, decreasing its emission intensity.

DNA-melting experiments were carried out by monitoring the absorbance of CT-DNA (200 μM NP) at 260 nm with varying temperature in the absence and presence of the complexes in a 2:1 ratio of DNA to complex with a ramp rate of 0.5 °C min^{-1} in phosphate buffer (pH 6.85) using a Peltier system attached to the UV–Vis spectrophotometer.

Viscometric titrations were performed with a Schott Gerate AVS 310 Automated Viscometer. The viscometer was thermostated at 37 °C in a constant temperature bath. The concentration of DNA was 200 μM in NP and the flow times were measured with an automated timer, each sample was measured three times and an average flow time was calculated. Data were presented as $(\eta/\eta_0)^{1/3}$ vs. [complex]/[DNA], where η is the viscosity of DNA in the presence of complex and η_0 was the viscosity of DNA alone. Viscosity values were calculated from the observed flowing time of DNA-containing solutions (t) corrected for that of buffer alone (t_0), $\eta = (t - t_0)$ [37].

2.6. DNA cleavage experiments

The extent of cleavage of supercoiled (SC) DNA in the presence of the complex and reducing agent MPA was determined by agarose gel electrophoresis. In a typical reaction, supercoiled pUC19 DNA (0.2 μg), taken in 50 mM Tris–HCl buffer (pH 7.2) containing 50 mM NaCl, was treated with the complex. The extent of cleavage was measured from the intensities of the bands using the UVITEC Gel Documentation System.

For mechanistic investigations, inhibition reactions were carried out by adding the reagents prior to the addition of the complex. The solutions were incubated for 1 h in a dark chamber at 37 °C, followed by addition to the loading buffer containing 25% bromophenol blue, 0.25% xylene cyanol and 30% glycerol (2 μL), and the solution was finally loaded on 1.0% agarose gel containing 1.0 μg/ml ethidium bromide (EB). Electrophoresis was carried out for 2 h at 60 V in tris–acetate–EDTA (TAE) buffer. Bands were visualized by UV light and photographed for analysis. Due corrections were made to the observed intensities for the low level of NC form present in the original sample of SC DNA and for the low affinity of EB binding to SC in comparison to nicked circular (NC) and linear forms of DNA [38]. The concentration of the complexes or the additives mentioned corresponded to the quantity of the sample in 2 μL stock solution prior to dilution to the 20 μL final volume by Tris–HCl buffer.

3. Results and discussion

3.1. Synthesis and general aspects

The ternary copper(II) complexes are prepared in high yield from the reaction of $Cu(NO_3)_2 \cdot 3H_2O$ or $Cu(ClO_4)_2 \cdot 6H_2O$ with L-leucine/L-isoleucine and heterocyclic bases. The complexes are stable and soluble in water and common polar organic solvents. They are characterized from the analytical and physicochemical data (Table 1). The complexes display an intense charge transfer (CT) band in the range 200–310 nm, that can be attributed to the $\pi \rightarrow \pi^*$ transition of the coordinated *N*,*N*-donor heterocyclic base. The d–d band is observed at ~600 nm in aqueous medium and is in agreement with a square-pyramidal geometry (Fig. 1). The complexes are redox active and display a cyclic voltammetric response near −0.1 V vs. SCE in DMF-0.1 M TBAP. The redox process is assignable to the Cu(II)/Cu(I) couple. The complexes show 1:1 electrolytic behavior in solution.

3.2. Crystal structures

The bpy and dpq complexes of L-isoleucine (**4** · H_2O, **6**) are structurally characterized using the single-crystal X-ray diffraction technique. Selected crystallographic data are summarized in Table 2. The ORTEP views of the complexes are shown in Figs. 2 and 3. Selected bond distances and angles are given in Table 3. The crystal structures of [Cu(L-leu)(phen)(H_2O)](NO_3) (**2**) and [Cu(L-ile)(phen)(H_2O)](NO_3) (**5**) are known [27]. Both the complexes show distorted (4 + 1) square-pyramidal geometry, in which Cu^{2+} coordinates with two nitrogen atoms of 1,10-phenanthroline, the amino nitrogen atom and one carboxylate oxygen atom of

Table 1
Physicochemical data for the ternary copper(II) complexes **1**–**6**

Complex	**1**	**2**	**3**	**4**	**5**	**6**
IR[a]: [ν (NO_3^-/ClO_4^-)/cm^{-1}]	1110 (ClO_4^-)	1384 (NO_3^-)	1084 (ClO_4^-)	1383 (NO_3^-)	1382 (NO_3^-)	1087 (ClO_4^-)
d–d band: λ_{max}/nm (ε/M^{-1} cm^{-1})[b]	604 (50)	610 (55)	608 (74)	604 (55)	611 (55)	609 (80)
CV: $E_{1/2}$/V (ΔE_p/mV)[c]	−0.13 (430)	−0.10 (330)	−0.06 (390)	−0.13 (440)	−0.12 (340)	−0.10 (360)
Λ_M^d (Ω^{-1} cm^2 M^{-1})	104	122	115	138	127	106
K_a^e (M^{-1})	1.06×10^4	4.66×10^5	1.15×10^6	1.66×10^4	5.75×10^5	9.8×10^5
K_b^f (M^{-1})		5.1×10^3	1.05×10^4		2.24×10^3	1.92×10^4
ΔT_m^g (°C)	1.0 (±0.2)	2.4 (±0.2)	3.2 (±0.2)	1.3 (±0.3)	2.7 (±0.2)	3.0 (±0.3)

[a] KBr phase.
[b] In aqueous medium.
[c] Cu(II)/Cu(I) couple in DMF–0.1 M TBAP. $E_{1/2} = 0.5(E_{pa} + E_{pc})$, $\Delta E_p = |E_{pa} - E_{pc}|$, where E_{pa} and E_{pc} are the anodic and cathodic peak potentials, respectively. Scan rate: 50 mV s^{-1}.
[d] In aqueous medium at 25 °C.
[e] Apparent DNA binding constant from competitive binding assay by the emission method.
[f] Intrinsic DNA binding constant (K_b) from the absorption spectral method.
[g] Changes in melting temperature of CT DNA.

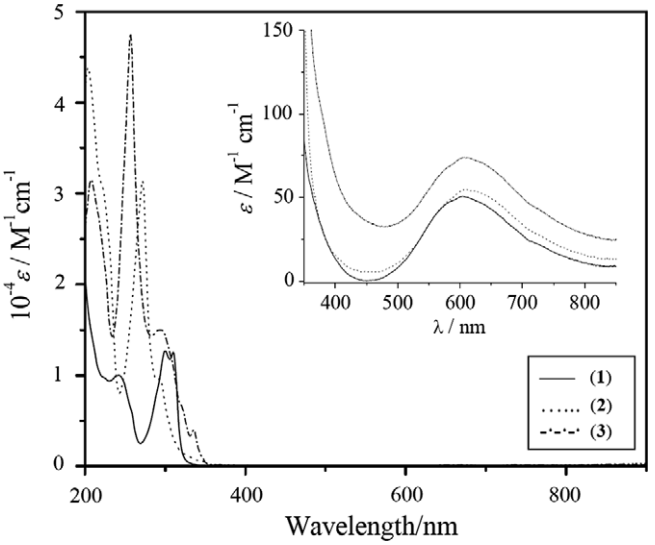


Fig. 1. Electronic spectra of complexes **1** (—), **2** (···) and **3** (-···-) in water. The inset shows the d–d band of complexes **1**–**3**.

L-Leu/Ile in equatorial positions, and an oxygen atom of water in the elongated axial position. Complexes **4** and **6** crystallize in the non-centrosymmetric $P2_1$ (monoclinic) and $P\bar{1}$ (triclinic) space groups, having one and two independent molecules in the crystallographic asymmetric unit respectively. The copper(II) ion is coordinated in a distorted square-pyramidal (4 + 1) coordination geometry through the carboxylate oxygen atom O(1) and the amino nitrogen atom N(3) of L-isoleucine and two N-atoms of 2,2′-bipyridine/dpq and a weakly bound apical water molecule (average trigonal distortion parameter, τ (**4** · H_2O) = 0.268; τ_{av} (**6**) = 0.087) [39]. Both the structures resemble the corresponding known structure of [Cu(L-leu/L-ile)(phen)(H_2O)](NO_3) [27]. The configuration at the isoleucine chiral α-carbon is *S* in both complexes. The copper atom is displaced by ~0.15 and ~0.19 Å from the mean plane through its basal atoms in the direction towards the apical water molecule for complexes **4** and **6**, respectively.

Table 2
Selected crystallographic data for **4** · H_2O and **6**

	4 · H_2O	**6**
Formula	$C_{16}H_{24}CuN_4O_7$	$C_{20}H_{22}ClCuN_5O_7$
Crystal size (mm)	0.26 × 0.18 × 0.12	0.65 × 0.30 × 0.20
Formula weight (g M^{-1})	447.93	543.42
Crystal system	monoclinic	triclinic
Space group (no.)	$P2_1$ (no. 4)	$P\bar{1}$ (no. 1)
a (Å)	11.559(4)	8.2524(19)
b (Å)	6.659(2)	11.940(3)
c (Å)	13.226(5)	13.440(3)
α (°)	90.0	109.257(4)
β (°)	92.777(6)	101.000(4)
γ (°)	90.0	106.193(4)
V (Å^3)	1016.8(6)	1140.7(5)
Z	2	2
T (K)	293(2)	293(2)
D_{calc} (g cm^{-3})	1.463	1.582
λ (Å) (Mo Kα)	0.71073	0.71073
Absorption coefficient (cm^{-1})	11.18	11.27
Data/restraints/parameters	3885/1/253	8546/3/613
Goodness-of-fit on F^2	1.130	1.025
R (F_o)[a] [$I > 2\sigma(I)$] (R [all data])	0.0404 (0.0448)	0.0547 (0.0882)
wR (F_o)[b] [$I > 2\sigma(I)$] (wR [all data])	0.1138 (0.1166)	0.1198 (0.1378)
Largest difference in peak and hole (e Å^{-3})	0.679 and −0.266	0.485 and −0.273
$w = 1/[\sigma^2(F_o^2) + (AP)^2 + (BP)]$	$A = 0.0595$; $B = 0.1680$	$A = 0.0640$; $B = 0.0000$

[a] $R = \sum||F_o| - |F_c||/\sum|F_o|$.
[b] $wR = \{\sum[w(F_o^2 - F_c^2)^2]/\sum[w(F_o)^2]\}^{1/2}$; $w = [\sigma^2(F_o)^2 + (AP)^2 + BP]^{-1}$, $P = (F_o^2 + 2F_c^2)/3$.

Both the bpy (**4**) and dpq (**6**) structures show extensive intermolecular non-covalent interactions. While one hydrogen atom of the axial water ligand is hydrogen-bonded to the carboxylate oxygen atom belonging to the neighbouring molecule (distances: 2.678 and 2.819 Å), the other hydrogen atom is H-bonded with the oxygen atom of the lattice NO_3^-/ClO_4^- anion (distances: 2.776 and 2.851 Å). The unit cell packing diagrams and intermolecular hydrogen bonding interactions present in **4** · H_2O and **6** are shown in Figs. S1–S4 (see supporting information).

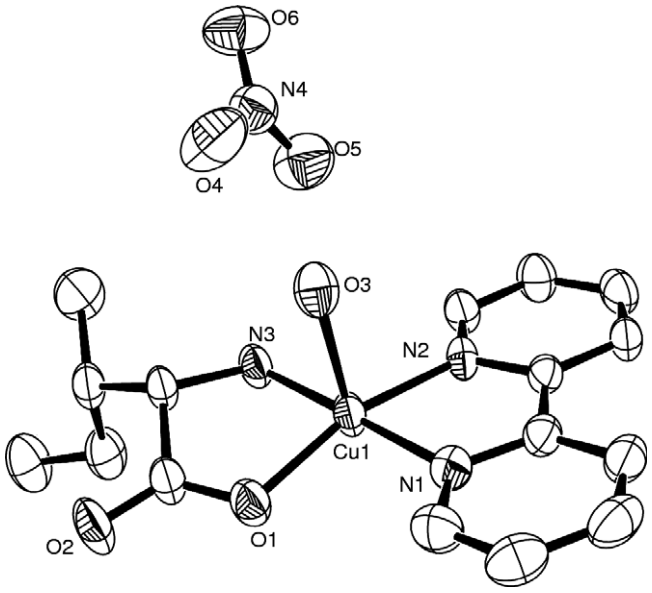


Fig. 2. ORTEP diagram of complex **4** showing 50% probability thermal ellipsoids with the atom labelling scheme for the metal and heteroatoms.

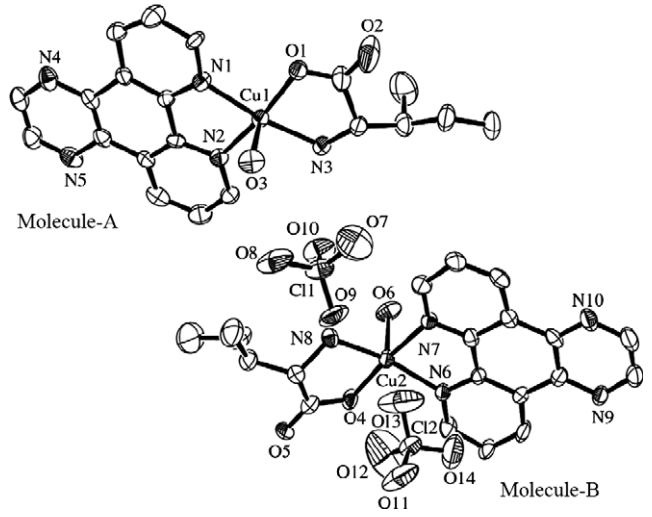


Fig. 3. ORTEP diagram of two independent molecules of complex **6** showing 30% probability thermal ellipsoids with the atom labelling scheme for the metal and heteroatoms.

3.3. DNA binding properties

The binding of complexes **1**–**6** to calf thymus (CT) DNA has been studied by electronic absorption spectral techniques. The interaction of complex **5** with DNA had been reported earlier [27d]. We have studied this complex for comparison with the other analogous complexes here. The absorption spectral traces of complex **3** with increasing concentration of CT DNA are shown in Fig. 4. We have observed a minor bathochromic shift of ~3 nm along with significant hypochromicity for the phen and dpq complexes. The intrinsic DNA binding constants (K_b) of the complexes to CT DNA are obtained by monitoring the change of the absorption intensity of the spectral bands with increasing concentration of CT DNA, keeping the complex concentration constant. The bpy complexes show weak binding to the DNA due to less extended planarity compared to phen or dpq, which is consistent with the observed trend in hypochromism. The K_b values for complexes **2** and **3** are 5.1×10^3 and 1.05×10^4 M^{-1}, respectively. The higher binding propensity of the phen and dpq complexes in comparison to their bpy analogues could be due to the presence of extended planar aromatic rings facilitating non-covalent interactions with the DNA molecule. Earlier studies on bis-phen copper complex have shown that this complex binds to DNA either by partial intercalation or by binding of one phen ligand to the minor groove while the other phen making favourable contacts within the groove [40–43]. The nature of binding of the phen complex is proposed to be similar as observed for the bis-phen species.

The emission spectral method is used to study the relative binding of the complexes to calf thymus-DNA. The emission intensity of ethidium bromide (EB) is used as a spectral probe as EB shows no apparent emission intensity in buffer solution because of solvent quenching and shows an enhancement of the emission intensity when intercalatively bound to DNA [44]. The binding of the complexes to DNA decreases the emission intensity of EB. The relative binding propensity of the complexes to DNA is measured from the extent of reduction of the emission intensity (Fig. 5, Table 1). The reduction of the emission intensity of EB on increasing the complex concentration could be caused due to displacement of the DNA bound EB by the ternary copper(II) complexes.

The denaturation of DNA from double-strand to single strand results in absorption hyperchromism at 260 nm. The binding of metal complexes to the double-stranded DNA usually stabilizes the duplex structure to some extent, depending on the strength of the interaction with the nucleic acid [45]. The binding should lead to an increase in the melting temperature (T_m) of DNA as compared to DNA itself. The binding of the phen and dpq complexes results in a moderate increase (~2 °C) in the melting temperatures (ΔT_m) of CT-DNA suggesting primarily an electrostatic and/or groove binding nature of the complexes (Table 1, Fig. 6a).

To investigate further the binding modes of the complexes viscosity measurements on solutions of calf thymus DNA incubated with the complexes were carried out. Because the viscosity of a DNA solution is sensitive to the addition of organic drugs and metal complexes bound by intercalation, we examined the effect on the specific relative viscosity of DNA upon addition of complexes. The relative specific viscosity (η/η_0), (η and η_0 are the specific viscosities of DNA in the presence and absence of a complex, respectively) of DNA reflects the increase in contour length associated with the separation of DNA base pairs caused by intercalation. The relative viscosity of DNA and contour length follows the equation: $(\eta/\eta_0) = (L/L_0)^{1/3}$,

Table 3
Selected bond distances (Å) and angles (°) for [Cu(L-ile)(bpy)(H_2O)](NO_3) · H_2O (**4** · H_2O) and for the two molecules of [Cu(L-ile)(dpq)(H_2O)](ClO_4) (**6**)

4 · H_2O	**6**			
	Molecule A		Molecule B	
Cu(1)–N(1)	1.991(3)	1.997(7)	Cu(2)–N(6)	2.023(7)
Cu(1)–N(2)	2.014(3)	2.013(7)	Cu(2)–N(7)	2.014(6)
Cu(1)–N(3)	1.972(3	2.008(7)	Cu(2)–N(8)	1.978(7)
Cu(1)–O(1)	1.930(3)	1.953(6)	Cu(2)–O(4)	1.894(6)
Cu(1)–O(3)	2.297(3)	2.281(6)	Cu(2)–O(6)	2.294(7)
N(1)–Cu(1)–N(2)	81.11(13)	81.8(3)	N(6)–Cu(2)–N(7)	82.3(3)
N(1)–Cu(1)–N(3)	179.24(13)	169.5(3)	N(6)–Cu(2)–N(8)	163.0(3)
N(1)–Cu(1)–O(1)	95.09(12)	92.8(3)	N(6)–Cu(2)–O(4)	94.3(3)
N(1)–Cu(1)–O(3)	90.22(13)	95.0(3)	N(6)–Cu(2)–O(6)	99.2(3)
N(2)–Cu(1)–N(3)	99.59(12)	100.2(3)	N(7)–Cu(2)–N(8)	97.6(3)
N(2)–Cu(1)–O(1)	163.10(15)	170.1(3)	N(7)–Cu(2)–O(4)	172.9(3)
N(2)–Cu(1)–O(3)	97.78(14)	96.2(3)	N(7)–Cu(2)–O(6)	91.7(3)
N(3)–Cu(1)–O(1)	84.15(12)	83.7(3)	N(8)–Cu(2)–O(4)	83.9(3)
N(3)–Cu(1)–O(3)	90.00(14)	94.9(3)	N(8)–Cu(2)–O(6)	97.9(3)
O(1)–Cu(1)–O(3)	98.69(12)	92.5(3)	O(4)–Cu(2)–O(6)	95.0(3)

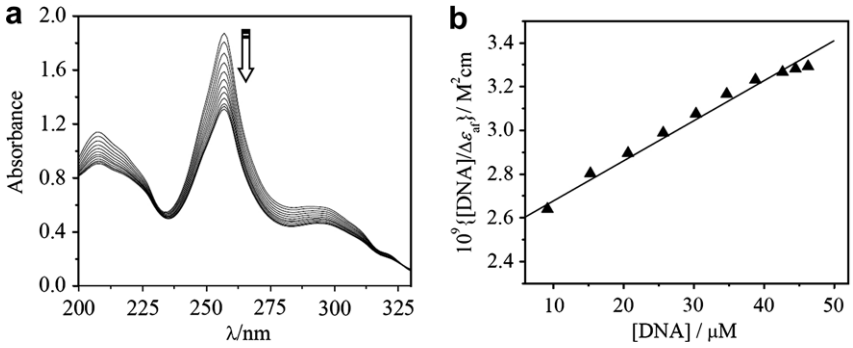


Fig. 4. (a) Absorption spectral traces on addition of CT DNA to a solution of **3** (shown by arrow). (b) Plot of $[DNA]/(\varepsilon_a - \varepsilon_f)$ vs. [DNA] for the absorption titration of CT-DNA with complex **3**.

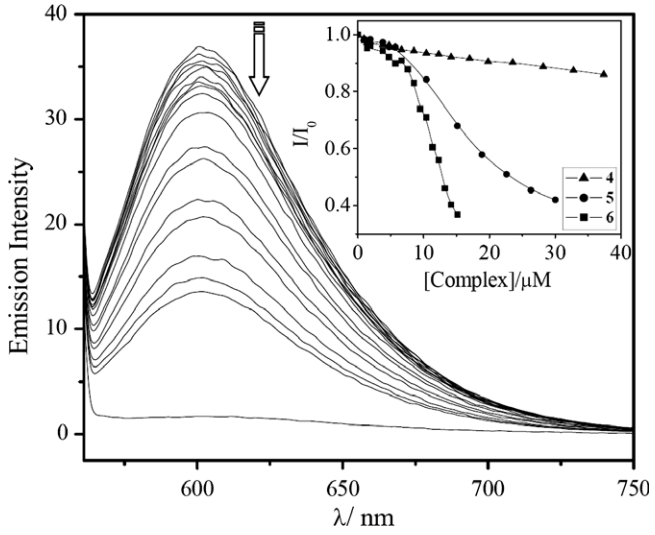


Fig. 5. Emission spectral changes on addition of [Cu(L-ile)(dpq)(H_2O)](ClO_4) (**6**) to CT-DNA bound to ethidium bromide (shown by arrow). Inset: Effect of addition of [Cu(L-ile)(B)(H_2O)](X) [B = bpy (**4**, ▲); phen (**5**, ●); dpq (**6**, ■)] to the emission intensity CT DNA-bound ethidium bromide in a 5 mM Tris–HCl/5 mM NaCl buffer (pH 7.2) at 25 °C.

where L and L_0 are the contour length of DNA in the presence and absence of complex respectively [37]. A classical intercalator such as EtBr could cause a significant increase in the viscosity of DNA solutions, in contrast, a partial and/or non-classical intercalation of the ligand could bend or kink DNA resulting in a decrease in its effective length with a concomitant increase in its viscosity [46,47]. The plots of relative viscosities with R = [Cu]/[DNA] are shown in Fig. 6(b). The change in relative viscosity for the dpq complexes are more than that for the phen or bpy analogues suggesting greater DNA binding propensity of the dpq complexes in comparison to the phen or bpy analogues, but this change is less compared to that of potential classical intercalators, e.g. ethidium bromide. This is consistent with the observed trend shown by other optical methods and suggests primarily an electrostatic and/or groove binding nature of the complex.

3.4. DNA cleavage studies

The oxidative DNA cleavage activity of the complexes in the presence of the reducing agent 3-mercaptopropionic acid (MPA, 5 mM) was studied by agarose gel electrophoresis

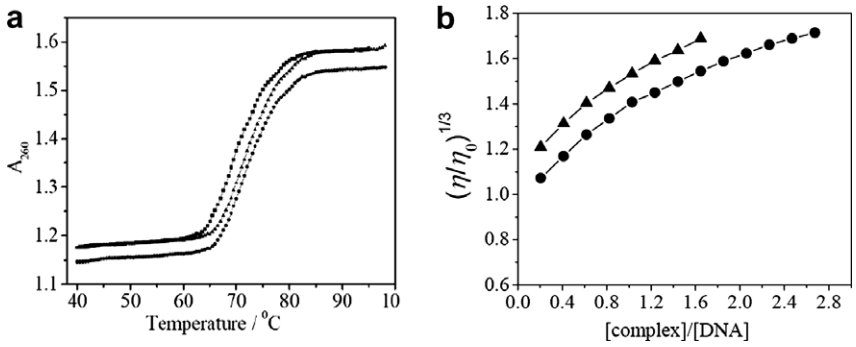


Fig. 6. (a) Effect of addition of complexes **3** (●) and (**6**) (▲) (50 μM) on the melting temperature of CT- DNA (■) (200 μM) in 5 mM Phosphate buffer (pH 6.85) with a ramp rate of 0.5 °C/min. (b) Change in relative specific viscosity of CT-DNA (150 μM) with addition complexes **2** (●) and **3** (▲) in 5 mM Tris–Cl buffer medium at 37 ± 0.1 °C.

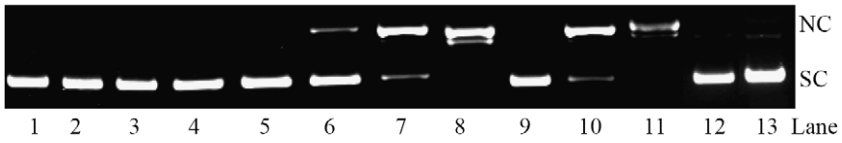


Fig. 7. Gel electrophoresis diagram showing the cleavage of SC pUC19 DNA (0.2 μg, 30 μM) by complexes **1**–**6** (30 μM) in 50 mM Tris–HCl/50 mM NaCl buffer (pH 7.2) in the presence of MPA (5 mM): Lane 1, DNA + MPA; Lane 2, DNA + L-leu (30 μM) + MPA; Lane 3, DNA + L-ile (30 μM) + MPA; Lane 4, DNA + **2**; Lane 5, DNA + **5** + MPA; Lane 6, DNA + **1** + MPA; Lane 7, DNA + **2** + MPA; Lane 8, DNA + **3** + MPA; Lane 9, DNA + **4** + MPA; Lane 10, DNA + **5**; Lane 11, DNA + **6** + MPA; Lane 12, DNA + distamycin-A (100 μM) + **2** + MPA; Lane 13, DNA + distamycin-A (100 μM) + **6** + MPA.

using supercoiled (SC) plasmid pUC19 DNA (0.2 μg, 30 μM NP) in 50 mM Tris–HCl/50 mM NaCl buffer (pH, 7.2) and the copper(II) complexes (Fig. 7). Selected DNA cleavage data are given in Table 4. The phen and dpq complexes show significant "chemical nuclease" activity. 30 μM of complexes **3** and **6** show almost complete conversion of the SC (form I) to its nicked circular form (NC, form II) of DNA. Control experiments using only MPA or the ternary complexes alone do not show any apparent conversion of SC to its nicked-circular (NC) form. The DNA cleavage activity order for the complexes follows the relative binding propensities of the complexes to DNA. The bpy complexes are cleavage inactive due to their poor binding ability to ds-DNA. This may be attributed to ROS forms which may not be able to reach the SC-DNA by diffusion and consequently are quenched by solvent molecules. To determine the groove binding preference of the complexes, control experiments have been carried out in the presence of the minor groove binder distamycin-A [48]. Inhibition of cleavage in the presence of distamycin-A for both the phen and dpq complexes suggest their minor groove binding nature.

Mechanistic aspects of the chemical nuclease reactions were investigated using various control experiments (Fig. 8). The addition of hydroxyl radical scavengers, [49] like DMSO, catalase and KI, shows significant inhibition of the DNA cleavage activity of the complexes, indicating the possibility of the involvement of the hydroxyl radical and/or a "copper-oxo" intermediate as the reactive species. Addition of superoxide dismutase (SOD) does not show any apparent effect on the DNA cleavage activity, suggesting the non-involvement of $O_2^{\cdot -}$ in the cleavage reaction

Table 4
Selected cleavage data of SC pUC19 (0.2 μg, 30 μM NP) by complexes **1**–**6**[a]

Sl. no	Reaction condition	[Complex]/μM	% SC	% NC
1	DNA + MPA		97	3
2	DNA + L-leucine (30 μM) + MPA		95	5
3	DNA + L-isoleucine (30 μM) + MPA		96	4
4	DNA + **2**	30	92	8
5	DNA + **5**	30	94	6
6	DNA + **1** + MPA	30	86	14
7	DNA + **2** + MPA	30	24	76
8	DNA + **3** + MPA	30	10	90[b]
9	DNA + **4** + MPA	30	88	12
10	DNA + **5** + MPA	30	28	72
11	DNA + **6** + MPA	30	11	89[b]
12	DNA + distamycin-A[c] + **2** + MPA	30	74	26
13	DNA + distamycin-A + **6** + MPA	30	70	30
14	DNA + DMSO[d] + **2** + MPA	30	90	10
15	DNA + catalase[e] + **2** + MPA	30	84	16
16	DNA + KI[f] + **2** + MPA	30	86	14
17	DNA + mannitol[g] + **2** + MPA	30	88	12
18	DNA + SOD[h] + **2** + MPA	30	30	70

[a] SC and NC are supercoiled and nicked circular forms of DNA. [MPA] = 5 mM.
[b] Including ~15–20% linear form.
[c] 100 μM.
[d] 4 μL.
[e] 4 units.
[f] 1 mM.
[g] 1 mM.
[h] 4 units.

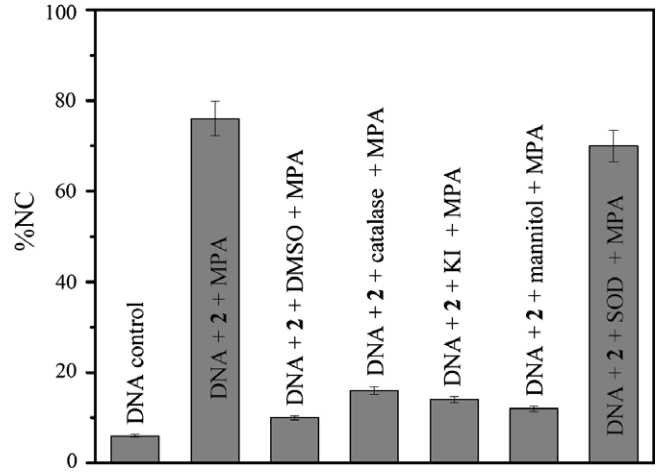
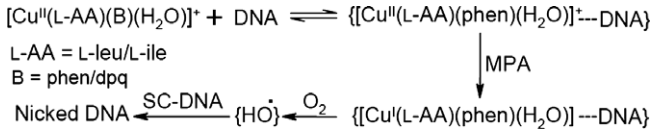


Fig. 8. Cleavage of SC pUC19 DNA (30 μM) by [Cu(L-leu)(phen)(H_2O)](NO_3) (**2**) in the presence of MPA (5 mM) with various additives in Tris buffer (pH 7.2) medium. The additive concentrations/quantity are: DMSO (4 μL), catalase (4 U), KI (1 mM), mannitol (1 mM), SOD (4 U).



Scheme 2. Proposed mechanistic pathway for the chemical nuclease activity of the complexes in Tris–buffer medium.

[50]. The pathways involved in the DNA cleavage reactions are believed to be analogous to those proposed by Sigman and coworkers for the chemical nuclease activity of bis(phen)copper species (Scheme 2) [1,43,44].

4. Conclusions

Ternary redox active copper(II) complexes having N,O-donor α-amino acid L-leucine or L-isoleucine and *N*,*N*-donor heterocyclic bases have been prepared and characterized. The copper(II) complexes with planar phenanthroline bases, with a CuN_3O_2 coordination geometry, show efficient DNA binding ability. The phen and dpq complexes were shown to be DNA minor groove binders. The study also confirms that the binding ability of the complexes is an important precondition to show efficient DNA cleavage activity. Efficient chemical nuclease activity is observed for the redox active phen and dpq complexes under physiological reaction conditions via a mechanistic pathway involving formation of hydroxyl radicals in the presence of the reducing agent MPA.

Acknowledgements

The authors gratefully acknowledge the support of Prof. Akhil R. Chakravarty, Department of Inorganic and Physical Chemistry, Indian Institute of Science, Bangalore, India, in providing facilities and useful discussions. Financial support received from the Department of Science and Technology (DST, SR/S5/BC-14/2006), Government of India, is gratefully acknowledged. R.K. is thankful to DST for a fellowship. A.K.P is thankful to CSIR for a fellowship. Thanks are due to the Alexander von Humboldt Foundation, Germany, for donation of an electroanalytical system; the Convener, Bioinformatics Center, Indian Institute of Science, Bangalore, for a database search; and the DST for the CCD single crystal X-ray diffractometer facility.

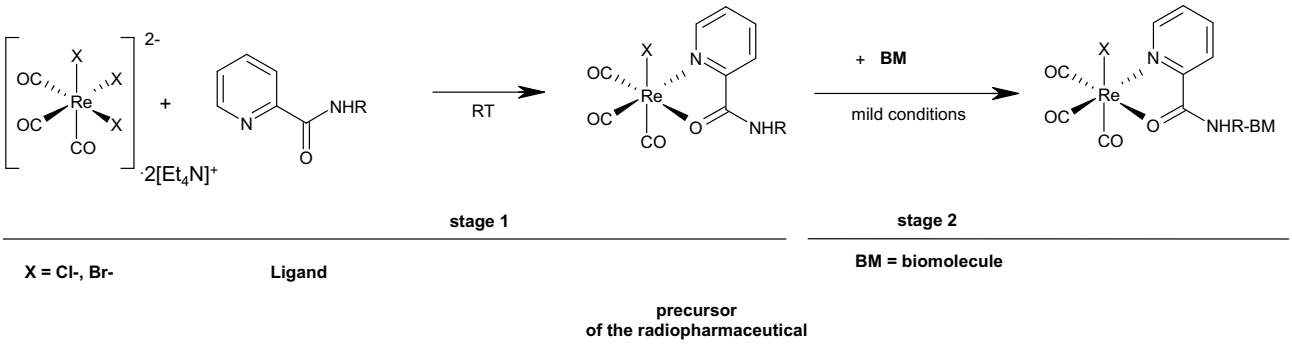
Appendix A. Supplementary material

CCDC 662368 and 662369 contain the supplementary crystallographic data for **4** · H_2O and **6**. These data can be obtained free of charge via http://www.ccdc.cam.ac.uk/conts/retrieving.html, or from the Cambridge Crystallographic Data Centre, 12 Union Road, Cambridge CB2 1EZ, UK; fax: (+44) 1223-336-033; or e-mail: deposit@ccdc.cam.ac.uk. Supplementary data associated with this article can be found, in the online version, at doi:10.1016/j.poly.2007.12.026.

References

[1] (a) D.S. Sigman, A. Mazumder, D.M. Perrin, Chem. Rev. 93 (1993) 2295;
(b) D.S. Sigman, Acc. Chem. Res. 19 (1986) 180;
(c) K.A. Reich, L.E. Marshall, D.R. Graham, D.S. Sigman, J. Am. Chem. Soc. 103 (1981) 3582.
[2] (a) B. Meunier, Chem. Rev. 92 (1992) 1411;
(b) G. Pratviel, J. Bernadou, B. Meunier, Adv. Inorg. Chem. 45 (1998) 251;
(c) G. Pratviel, J. Bernadou, B. Meunier, Angew. Chem., Int. Ed. Engl. 34 (1995) 746.
[3] M. Pyle, J.K. Barton, Prog. Inorg. Chem. 38 (1990) 413.
[4] K.E. Erkkila, D.T. Odom, J.K. Barton, Chem. Rev. 99 (1999) 2777.
[5] B. Armitage, Chem. Rev. 98 (1998) 1171.
[6] (a) D.R. McMillin, K.M. McNett, Chem. Rev. 98 (1998) 1201;
(b) F. Mancin, P. Scrimin, P. Tecilla, U. Tonellato, Chem. Commun. (2005) 2540.
[7] (a) W.K. Pogozelski, T.D. Tullius, Chem. Rev. 98 (1998) 1089;
(b) T.D. Tullius, J.A. Greenbaum, Curr. Opin. Chem. Biol. 9 (2005) 127;
(c) E. Boseggia, M. Gatos, L. Lucatello, F. Mancin, S. Moro, M. Palumbo, C. Sissi, P. Tecilla, U. Tonellato, G. Zagotto, J. Am. Chem. Soc. 126 (2004) 4543.
[8] H.T. Chifotides, K.R. Dunbar, Acc. Chem. Res. 38 (2005) 146.
[9] E.R. Jamieson, S.J. Lippard, Chem. Rev. 99 (1999) 2467.
[10] W.S. Bowen, W.E. Hill, J.S. Lodmell, Methods Enzymol. 25 (2001) 344.
[11] (a) M. Sabat, in: A. Sigel, H. Sigel (Eds.), Metal ions in Biological Systems, vol. 32, Marcel Dekker, New York, Basel, 1996;
(b) R.N. Mukherjee, Indian J. Chem. 42A (2003) 2175.
[12] (a) A.R. Chakravarty, P.A.N. Reddy, B.K. Santra, A.M. Thomas, Proc. Ind. Acad. Sci (Chem. Sci.) 114 (2002) 391;
(b) B.K. Santra, P.A.N. Reddy, G. Neelkanta, S. Mahadevan, M. Nethaji, A.R. Chakravarty, J. Inorg. Biochem. 89 (2002) 191;
(c) A.M. Thomas, G. Neelkanta, S. Mahadevan, M. Nethaji, A.R. Chakravarty, Eur. J. Inorg. Chem. (2002) 2720;
(d) A.M. Thomas, M. Nethaji, S. Mahadevan, A.R. Chakravarty, J. Inorg. Biochem. 94 (2003) 171;
(e) P.A.N. Reddy, M. Nethaji, A.R. Chakravarty, Eur. J. Inorg. Chem. (2004) 1440.

[13] S. Dhar, P.A.N. Reddy, M. Nethaji, S. Mahadevan, M.K. Saha, A.R. Chakravarty, Inorg. Chem. 41 (2002) 3469.
[14] R. Pradhan, A.M. Thomas, A. Mukherjee, S. Dhar, M. Nethai, A.R. Chakravarty, Indian J. Chem. 44A (2005) 18.
[15] P.U. Maheswari, K. Lappalainen, M. Sfregola, S. Barends, P. Gamez, U. Turpeinen, I. Mutikainen, G.P. van Wezel, J. Reedijk, J. Chem. Soc., Dalton Trans. (2007) 3676.
[16] P.D. Hoog, C. Boldron, P. Gamez, K. S.-Bol, I. Roland, M. Pitie, R. Kiss, B. Meunier, J. Reedijk, J. Med. Chem. 50 (2007) 3148.
[17] (a) A.K. Patra, S. Dhar, M. Nethaji, A.R. Chakravarty, Chem. Commun. (2003) 1562;
(b) A.K. Patra, S. Dhar, M. Nethaji, A.R. Chakravarty, J. Chem. Soc., Dalton Trans. (2005) 896;
(c) A.K. Patra, M. Nethaji, A.R. Chakravarty, J. Chem. Soc., Dalton Trans. (2005) 2798;
(d) A.K. Patra, M. Nethaji, A.R. Cakravarty, J. Inorg. Biochem. 101 (2007) 233;
(e) R. Rao, A.K. Patra, P.R. Chetana, Polyhedron 26 (2007) 5331.
[18] H. Li, X.-Y. Le, D.-W. Pang, H. Deng, Z.-H. Xu, Z.-H. Lin, J. Inorg. Biochem. 99 (2005) 2240.
[19] S. Zhang, Y. Zhu, C. Tu, H. Wei, Z. Yang, L. Lin, J. Ding, J. Zhang, Z. Guo, J. Inorg. Biochem. 98 (2004) 2099.
[20] Y. Jin, J. Cowan, J. Am. Chem. Soc. 127 (2005) 8408.
[21] F.V. Pamatong, C.A. Detmer III, R. Bocarsly, J. Am. Chem. Soc. 118 (1996) 5339.
[22] R. Ren, P. Yang, W. Zheng, Z. Hua, Inorg. Chem. 39 (2000) 5454.
[23] A. García-Raso, J.J. Fiol, B. Adrover, V. Moreno, I. Mata, E. Espinosa, E. Molins, J. Inorg. Biochem. 95 (2003) 77.
[24] D.L. Nelson, M.M. Cox, in: Lehninger, Principles of Biochemistry, 3rd ed., Worth Publishing, New York, 2000.
[25] D.D. Perrin, W.L.F. Armarego, D.R. Perrin, Purification of Laboratory Chemicals, Pergamon Press, Oxford, UK, 1980.
[26] E. Amouyal, A. Homsi, J.-C. Chaambron, J.-P. Sauvage, J. Chem. Soc., Dalton Trans. (1990) 1841.
[27] (a) N. Hu, K. Aoki, H. Yamazaki, Inorg. Chim. Acta 163 (1989) 105;
(b) X. Le, X. Zhou, C. Huang, X. Feng, J. Coord. Chem. 56 (2003) 861;
(c) S. Chen, X. Le, X. Zhou, X. Liu, G. Liu, Huaxue Tongbao 67 (2004) 461;
(d) Q. Gu, X.-Y. Le, Y. Xie, L.-F. Hong, C.-X. Zhuang, Chin. J. Inorg. Chem. 22 (2006) 757.
[28] N. Walker, D. Stuart, Acta Crystallogr. A39 (1993) 158.
[29] (a) SMART, Siemens Energy & Automation, Inc., Madison, WI, 1996.;
(b) SAINT Version 4 Software Reference Manual, Siemens Energy & Automation, Inc., Madison, WI, 1996.
[30] G.M. Sheldrick, SADABS Version 2 Multi-Scan Absorption Correction Program, University of Göttingen, Germany, 2001.
[31] G.M. Sheldrick, SHELX 97 Programs for Crystal Structure Solution and Refinement, University of Göttingen, Göttingen, Germany, 1997.
[32] M.N. Burnett, C.K. Johnson, ORTEP-III Report ORNL-6895, Oak Ridge National Laboratory, Oak Ridge, TN, 1996.
[33] J. Marmur, J. Mol. Biol. 3 (1961) 208.
[34] M.E. Reichmann, S.A. Rice, C.A. Thomas, P. Doty, J. Am. Chem. Soc. 76 (1954) 3047.
[35] A. Wolfe, G.H. Shimer, T. Meehan, Biochemistry 26 (1987) 6392.
[36] (a) J.-B. LePecq, C. Paoletti, J. Mol. Biol. 27 (1967) 87;
(b) S. Neidle, Nat. Prod. Rep. 18 (2001) 291.
[37] G. Cohen, H. Eisenberg, Biopolymers 8 (1969) 45.
[38] J. Bernadou, G. Pratviel, F. Bennis, M. Girardet, B. Meunier, Biochemistry 28 (1989) 7268.
[39] A.W. Addison, T.N. Rao, J.V. Reedijk, G.C. Verschoor, J. Chem. Soc., Dalton Trans. (1984) 1349.
[40] J.M. Veal, R.L. Rill, Biochemistry 30 (1991) 132.
[41] J.M. Veal, K. Merchant, R.L. Rill, Nucleic Acids Res. 19 (1991) 3383.
[42] O. Zelenko, J. Gallagher, D.S. Sigman, Angew. Chem. Int. Ed. Engl. 36 (1997) 2776.
[43] D.S. Sigman, Biochemistry 29 (1990) 9097.
[44] J.M. Kelly, A.B. Tossi, D.J. McConnel, C. OhUigin, Nucleic Acids Res. 13 (1985) 6017.
[45] M. Lee, A.L. Rhodes, M.D. Wyatt, S. Forrow, J.A. Hartley, Biochemistry 32 (1993) 4237.
[46] S. Satyanarayana, J.C. Dabrowiak, J.B. Chaires, Biochemistry 31 (1992) 9319.
[47] T. Hirohama, Y. Kuranuki, E. Ebina, T. Sugizaki, H. Arii, M. Chikira, P.T. Selvi, M. Palaniandavar, J. Inorg. Biochem. 99 (2005) 1205.
[48] (a) C. Bailly, J.B. Chaires, Bioconjugate Chem. 9 (1998) 513;
(b) M. Coll, C.A. Frederick, A.H.-J. Wang, A. Rich, Porc. Natl. Acad. Sci. USA 84 (1987) 8385.
[49] (a) O.I. Aruoma, B. Halliwell, M. Dizdaroglu, J. Biol. Chem. 264 (1989) 13024;
(b) S.M. Klein, G. Cohen, A.I. Cederbaum, Biochemistry 20 (1981) 6006.
[50] S. Inoue, S. Kawanishi, Cancer Res. 47 (1987) 6522.

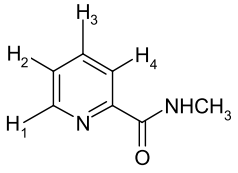


Scheme 1. Labeling of biomolecules with rhenium tricarbonyl complex [9].

The presented work is involved in a series of studies on coordination chemistry of rhenium(I) tricarbonyl complexes with the goal of searching new ^{186}Re and ^{188}Re radiopharmaceuticals. Data, Publisher already, on coordination chemistry of numerous monovalent rhenium tricarbonyl compounds allow the preparation of a number of water-soluble carbonyl complexes with various donor-active species. These complexes have attracted interest as precursors for the labeling of the tumor cells targeting biomolecules [7], because such labeling requires existence of a bifunctional chelator [8]. This can be presented in Scheme 1.

2. Experimental

The work was performed with macroamounts of natural, non-radioactive rhenium. To synthesize the complex, we adopted procedure described by Schöster and Zeisler [10]. Because it had originally been established for obtaining the technetium compounds, detailed experimental conditions were slightly changed. To characterize the obtained compounds, we used conventional analytical methods: elemental analysis, X-ray diffraction, IR spectroscopy, NMR and HPLC.



2.1. Synthesis

N-Methylpyridine-2-carboxyamide (ligand, **1**) was obtained according to the general procedure [11]: 4 g (0.0325 mol) of the 2-picolinic acid was dissolved in 100 cm^3 of toluene and 10 cm^3 of oxalyl chloride was added. A reaction mixture was heated under reflux for 10 h, the solvents and the unreacted substrates were then evaporated. The solid product was washed with hexane, dissolved in 20 cm^3 of 25% solution methylamine in methanol and stirred overnight in a RT. The crude product was purified on a silica gel column (chloroform–methanol; 98:2 vol/vol). 2.1 g of pure product was obtained. (Yield: 43.7%).

Calc.: C, 64.86; H, 5.40; N, 20.05. Found: C, 64.75; H, 5.50; N, 19.89%. ^{1}H NMR ($CDCl_3$, 200 MHz, δ [Hz]): 8.51 (1H, dd, $J_1 = 0.8$, $J_2 = 7.8$, H-1), 8.20 (1H, d, $J = 8.0$, H-4); 7.82 (1H, dt, $J_1 = 1.8$, $J_2 = 7.8$, H-2), 7.40 (1H, dq, $J_1 = 1.4$, $J_2 = 5.0$, $J_3 = 7.3$, H-3), 3.05, 3.021 (3H, 2 × s, HNCH_3) ^{13}C NMR ($CDCl_3$, 50 MHz): 164.55, 149.40, 147.52, 186.76, 124.54, 212.43, 25.55. IR (film): 3050, 2944, 1590, 1530, 1470, 1405, 1398, 1300, 1150, 792.

[Re(CO)$_3$L]Cl (complex, **2**) was obtained as follows: Re(CO)$_5$Cl (170 mg, 0.470 mmol) was dissolved in 13 mL THF. On addition of **1** (62 mg, 0.455 mmol) the solution turned yellow and intensity of the color gradually increased. After 16 h of stirring under Ar at ambient temperature, a light yellow substance started to precipitate. Progress of the reaction was checked by TLC analysis. The reaction was completed after 48 h, the solvent was evaporated and the residue extracted with pentane. Then, the solution was separated, solvent evaporated and solid residue was isolated as an air-stable, microcrystalline phase, soluble in common organic solvents. Its IR spectrum (KBr pellets) displays three bands in the carbonyl stretching region: a sharp intense band at 2085 cm^{-1} and two lower-energy bands closely spaced (1998 and 1879 cm^{-1}), typical for the tricarbonyl Re^{I} complexes. Single crystals of the title complex [Re^{I}(CO)$_3$L]Cl suitable for the X-ray studies were grown from the dichloromethane/hexane (vol:vol = 2:1). Yield: ca. 25%.

M.p.: 97–101 °C. Calc.: C, 27.18; H, 1.81; N, 5.34. Found: C, 26.98; H, 1.93; N, 5.21%. ^{1}HNMR (DMSO-d^6, δ): 10.60 (1H, broad s, *H*–N–CH$_3$), 8.99 (1H, d, $J = 5.0$ Hz, H-1), 8.53 (1H, d, $J = 8.0$ Hz, H-4), 8.41 (1H, dd, $J_1 = 1.5$ Hz, $J_2 = 8.0$ Hz, H-2), 7.91 (1H, dq, $J_1 = 1.0$ Hz, $J_2 = 5.0$ Hz, H-3), 3.033 (3H, s, HN–*CH*$_3$). IR (KBr): 3320, 3094, 2947, **2085**, **1998**, **1879**[1], 1639, 1475, 1186, 530, 510, 482.

[1] Bold letters mean fingerprint positions of the Re-(CO) vibrations in the IR spectra.

2.2. X-ray studies

Data were collected on the KUMA KM4 four-circle diffractometer operating in the ω–2θ mode. Structure was solved by direct method [12] and refined by full-matrix least-squares method [13]. The reflections were processed using profile analysis and corrected for the Lorentz factor and polarization effect. The heavy atom i.e. Re was located by applying Patterson's method and the positions of other non-hydrogen atoms were determined in the course of successive refinement using SHELXLS program. Final refinement on F^2 by full-matrix least-squares method was performed on positional parameters of all atoms, anisotropic temperature factors of all non-hydrogen atoms and isotropic temperature factors of hydrogen atoms. Weighting scheme was used in the following form: $w = 1/[\sigma^2(F_o^2) + (A \cdot P)^2 + B \cdot P]$, where $P = [\mathrm{Max}(F_o^2, 0) + 2F_c^2]/3$. Values of the parameters A and B are given in Table 1. Calculations were carried out using the SHELXL97 program [12,13]. A summary of the experimental details is presented in Table 1.

IR spectra of **1** or **2** in solid KBr pellets (investigated species being about 1% of the pellet; 4000–600 cm^{-1}) were recorded using Bruker Equinox 55 FT-IR spectrophotometer. FIR spectra (600–200 cm^{-1}) were recorded in the solid CsI pellets. All spectra were registered for at least three pellets with 50 scans each and with spectral resolution of 1 cm^{-1}.

Table 1
Summary of the structure refinement parameters for **2**

Empirical formula	$C_{10}H_8ClN_2O_4Re$
Formula weight	441.84
Temperature (K)	293(2)
Wavelength (Å)	0.71073
Crystal system	orthorhombic
Space group	$P\bar{1}$
Unit cell dimensions	
a (Å)	7.6635(15)
b (Å)	7.8340(16)
c (Å)	10.650(2)
α (°)	77.72(3)
β (°)	85.48(3)
γ (°)	88.63(3)
V (Å^3)	622.8(2)
Z	2
D_{calc} (g cm$_{-3}$)	2.356
μ (Mo Kα) (mm^{-1})	2.01
F(000)	412
Crystal size (mm)	0.30 × 0.12 × 0.10
Maximum 2θ for data collection (°)	70.54
Index range	$-10 \leqslant h \leqslant 0$, $-11 \leqslant k \leqslant 11$, $-15 \leqslant l \leqslant 14$
Number of measured reflections	3918
Number of unique reflections with $F_o > 4\sigma(F_o)$	3348
R_{int}	0.0214
Method of structure solution	Patterson method
Method of structure refinement	full-matrix least-squares on F^2
Number of parameters refined	164
Goodness-of-fit on F^2	1.142

2.3. ^1H NMR

^{1}H NMR spectra were recorded on the Varian Unity Plus Spectrometer operating at 500 MHz. Tetramethylsilane was used as an internal standard. Chemical shifts are reported in ppm.

2.4. HPLC

HPLC analyses were performed on the Merck L7100 system equipped with the Supelcosil LC-C_{18} HPLC column and Shimadzu UV–Vis SPD-10AVP detector. HPLC solvents were TEAP buffer, 25 mM, pH 2.25 (solvent A) and MeOH (HPLC grade; solvent B). Elutions were made in the gradients: 0–3 min: 100% A, 3–6 min: to 75% A; 6–9 min: to 66% A; 9–20 min to 0% A; 20–25 min: 0% A; 25–30 min: to 100% A. Flow rate: 1 mL/min.

2.5. Quantum chemical investigation

Initial three-dimensional structure of the compound was built using the SPARTANPRO 5.0 software [14] and as the first step, semiempirical geometry optimization was performed at the PM3 level.

It has already been demonstrated that quantum chemical investigations using the MPW1PW/LanL2DZ method within the density functional theory (DFT) framework yielded the geometry and vibrational frequencies for heavy metal complexes in good agreement with the experimental data [15]. Taking this into consideration, final calculations of the **2** structural parameters and vibrational frequencies have been performed by two independent DFT methods: MPW1PW/LanL2DZ and B3LYP/LanL2DZ using the GAUSSIAN 98 program package [16], running on the Silicon Graphics IRIS Indigo workstation with the processor RISC 10000.

3. Results and discussion

All analytical methods (elemental analysis, NMR spectra, sharp melting of the complex) demonstrate that both **1** and **2** were obtained and purified properly. Integration of the peaks area in ^{1}H NMR spectra gives result adequate to the numbers of protons, both in **1** and **2**. The most distinct difference between the ^{1}H NMR spectra of **1** and **2** is the absence of the H–N–CH_3 peak in the spectrum of ligand, which is present in the spectrum of complex at 10.60 ppm. This can be attributed to the analytical conditions – possible presence of small amount of the $CDCl_3$ hydrolysis products and the isotopic exchange appearing on the aforementioned group.

It is well known fact that Re^I complexes are easily oxidized in aerated aqueous solutions, i.e. under real conditions. So, stability of **2** towards oxidation was checked in aqueous solution by registering UV–Vis spectra and by performing the HPLC analyses as a function of time. A slight decrease in the absorption was observed in the region

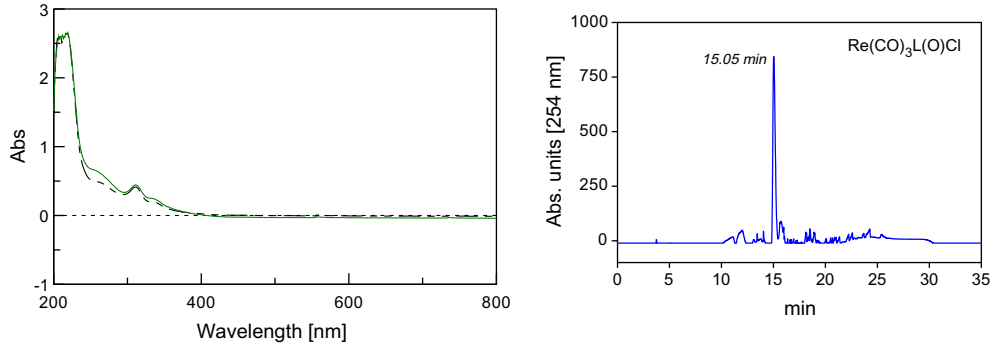


Fig. 1. Left: UV–Vis spectra of the title complex **2** registered in the beginning of the experiment (solid line) and after a week (dotted line); right: HPLC of **2**.

of 250 nm (generally assigned to the d → π^*_{CO} transitions in the Re^I complexes [17]) after a few days only. Nevertheless, within time required for preparing and medical application of the ^{188}Re-radiopharmaceuticals, i.e. several hours, no distinct change in the spectrum was detected (see, left part of Fig. 1). Also, area of the HPLC peak characteristic for **2** (retention time $R_t = 15.05$ min) remained constant.

An essential point in structural considerations was checking the chemical form of the free ligand. It is a textbook knowledge that amides and thioamides may exist in the keto- or enol-forms. Quantum chemical calculations have shown that energy of *N*-methylpyridine-2-carboxyamide in the keto-form is about 15.62 kcal/mol lower than the enol-. For *N*-methyl-2-pyridinethioamide the difference is 10.99 kcal/mol. These large values suggest that both ligands exist predominantly in the keto-form and the thio compound may be more easily converted into the enol-form. Unfortunately ligand **1** is an oily species and its X-ray diffraction studies appeared to be impossible.

Luckily in order to compare molecular structure of **2** with its thio-analogue studied already [18], both X-ray diffraction studies and quantum chemical calculations appeared to be possible to realize. In the first step using semiempirical calculations on the PM3 level we optimized structure of **2** containing ligand in the conformation proposed by Mueller as the most probable [20]. Next, the conformer exhibiting the lowest PM3 energy was optimized using the DFT procedure. Both experimental and theoretical results show that **2** exhibits similar structure to this with *N*-methylpyridine-2-thiocarboxyamide [18].

Molecular structure of the title complex together with atom labeling is shown in Fig. 2. Selected bond lengths and bond angles (both experimental values and found theoretically) are listed in Table 2.

The main results obtained in the structural investigations may be summarized as follows:

- We expected that three CO molecules form a Re^I octahedron together with donor nitrogen and oxygen atoms from the bidentate ligand (**1**), and one chloride anion. However, we have found that Re^I cation adopts a slightly distorted octahedral geometry with C(1)–Re–O(11) = 170.7(2)°, C(2)–Re–N(11) = 172.4(2)° and Cl–Re–C(3) 177.7(23)°. The N–Re^I–O angle of 75.25° (bite angle) is smaller than 90° in the regular octahedron. This small bite angle is, however, typical for 5-membered chelate rings. The bond distances of Re–C 1.881(7)–1.912(7) Å are in the range of these in numerous known $Re^I(CO)_3^+$ complexes [20]. Finally, the Re–N and Re–O bond distances in **2** are 2.176(5) and 2.163(4) Å, respectively. Summarizing – planar 5-membered ring as well as picoline ring are nearly perpendicular to the Cl–Re^I–C(3) axis. The corresponding dihedrals are inserted into Table 1.
- The MPW1PW/LanL2DZ and B3LYP/LanL2DZ procedures result in very similar structures of **2**. What is more, the parameters calculated at the initial PM3 level were also very similar to those DFT ones and also to the experimental values.
- In spite of the fact that several possible rotamers of free ligand may exist (in the case of picolinamide, see [19]), because of their stabilization by the intramolecular hydrogen bonds, only one complex structure has been

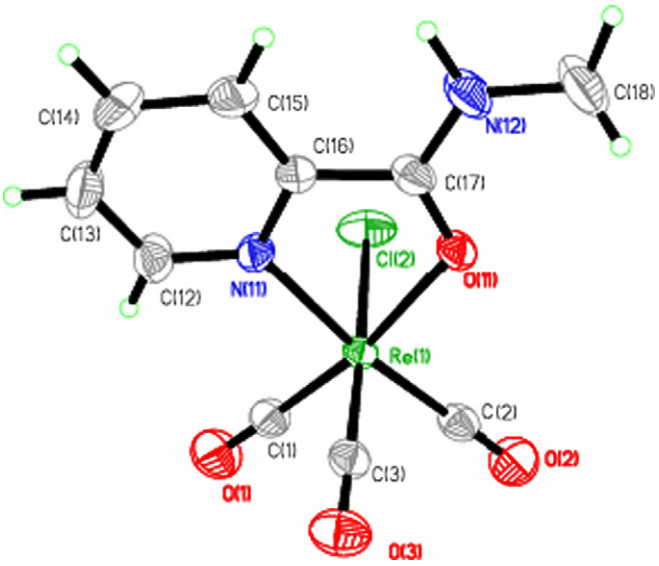


Fig. 2. Molecular structure of the title complex **2**.

Table 2
Selected bond lengths (Å) and angles (°) in the $Re(CO)_3LCl$ complex **2**

	Exp.	Calc.[a]
Bond lengths		
Re–N(11)	2.176 (5)	2.153
Re–O(11)	2.163 (4)	2.017
Re–Cl	2.457 (2)	2.469
Re–C(1)	1.881 (7)	1.929
Re–C(2)	1.912 (7)	1.928
Re–C(3)	1.886 (7)	1.948
C(16)–N(11)	1.334 (8)	1.363
C(16)–C(17)	1.334 (8)	1.482
O(11)–C(17)	1.251 (7)	1.356
C(17)–N(12)	1.304 (8)	1.293
N(12)–C(18)	1.446 (1)	1.460
Angles		
N(11)–Re–O(11)	73.99 (0.19)	76.97
N(11)–C(16)–C(17)	113.22 (0.52)	114.7
C(17)–O(11)–Re	117.02 (0.42)	119.93
C(16)–C(17)–O(11)	118.82 (0.55)	113.77
C(16)–N(11)–Re	116.61 (0.42)	114.43
N(12)–C(17)–C(16)	119.67 (0.60)	120.19
N(12)–C(17)–O(11)	118.82 (0.55)	126.05
Cl–Re–C(3)	177.72 (0.52)	173.02
Dihedrals		
C(12)–C(16)–Re–C(3)		91.23
C(16)–C(17)–Re–C(3)		95.42

[a] MPW1PW/LanL2DZ procedure.

confirmed crystallographically. Also quantum chemical calculations have not shown the existence of other structures with comparable energies.

- All the intramolecular Cl···H distances, both placed in the pyridine ring and in the –HN–CH_3 group are too long to suggest formation of the hydrogen bonds. The experimental nearest C–H···Cl^- distance is equal to 4.02 Å, while the respective value calculated from the literature data is equal to [21] −3.77 Å. On the other hand, the experimental Cl···H–C(15) distance between the neighboring molecules, equal to 2.82 Å, does not exclude the existence of intramolecular hydrogen bonds which stabilize the molecular packing (see, Fig. 3).

Infrared spectra of the species are shown in Fig. 4. Detailed assignment of the peaks was made according to our previous paper [14], the references cited therein and to [22]. The most important IR bands of **1** and **2**, are listed in Table 3 together the proposition of their assignment. As one can see, all main bands of the pyridinecarboxyamide vibrations can be found in both spectra. Also three characteristic peaks of the Re^I–(CO) vibrations (≈2000 cm^{-1}), which appear only in the spectrum of the complex, confirm the existence of the typical rhenium-tricarbonyl core. It has been shown that a region of 2000 cm^{-1} can be treated as a fingerprint region for the $Re(CO)_3^+$ core [23]. For some complexes, however, only two peaks are observed. It can be seen that their frequencies, $\nu_{CO(Re)}$, are lower than the corresponding values for the pyridinethiocarboxyamide complex [18]. Therefore we may deduce that the ionicity

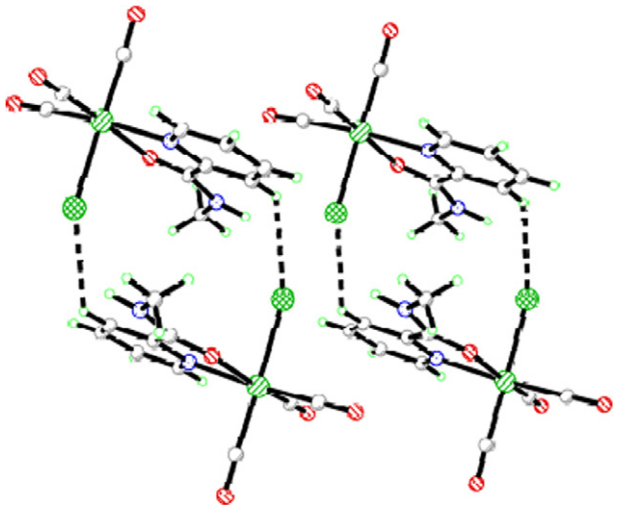


Fig. 3. A part of the molecular packing of **2** showing intermolecular hydrogen bonds creating a dimer structure. Hydrogen bonds are indicated by dashed lines.

of the Re^I-pyridinecarboxyamide bond is greater than that of its thio-analogue. Mullikan charges on the atoms in the analogous Tc^I N,O- and N,S-chelates, reported by Narbutt [24] are consistent this observation. Theoretical calculations of the molecular vibrations also generate bands situated in the region of 2000 cm^{-1}, close to the experimental peaks. Furthermore, the region of 520 cm^{-1} spectra of **2** exhibit three distinct peaks (namely, at 530, 510 and 482 cm^{-1}), which can be attributed to the Re–C vibrations. Appearance of three separate peaks in both regions (2000 and 520 cm^{-1}) may be interpreted in terms of the inequality of the CO groups forming the $Re(CO)_3^+$ core.

The comparison of the calculated and experimental frequencies found for the three $\nu_{CO(Re)}$ and the $\nu_{C=O,(amide)}$ vibrations (see, Table 3) shows that the mean ratio of the calculated to experimental values is 0.9928 ± 0.0180. This agreement correlates well with the similarity of the experimental and calculated structures (Table 3).

The experimental value for the Re^I–O bond in (**2**), of 2.16 Å, is by 0.28 Å shorter than that for Re^I–S (2.44 Å [18]) and nearly equal to that of Re^I–N in the Re^I tricarbonyl *N*-(2-pyridinylmethylene)phenylamine complex (2.19 Å [25]). Therefore, if we assume that the radius of the Re^I cation is the same in all the three complexes, we could have suggested that the oxygen radius is also smaller than that of sulfur by about 0.28 Å. However, both differences between the ionic radii of the dinegative oxygen and sulfur ions and between the radii of the *2p* and *3p* orbitals in the oxygen and sulfur atoms (responsible for the covalent bonds) are close to 0.45 Å [27]. Let us discuss the different values of 0.28 and 0.45 Å in terms of different contributions from ionicity and covalency in the Re^I–X bonds (Fig. 5):

- It is well known, that coordination bonds are formed by electron pairs which come from the donor atoms of ligands. The difference in Pauling electronegativity

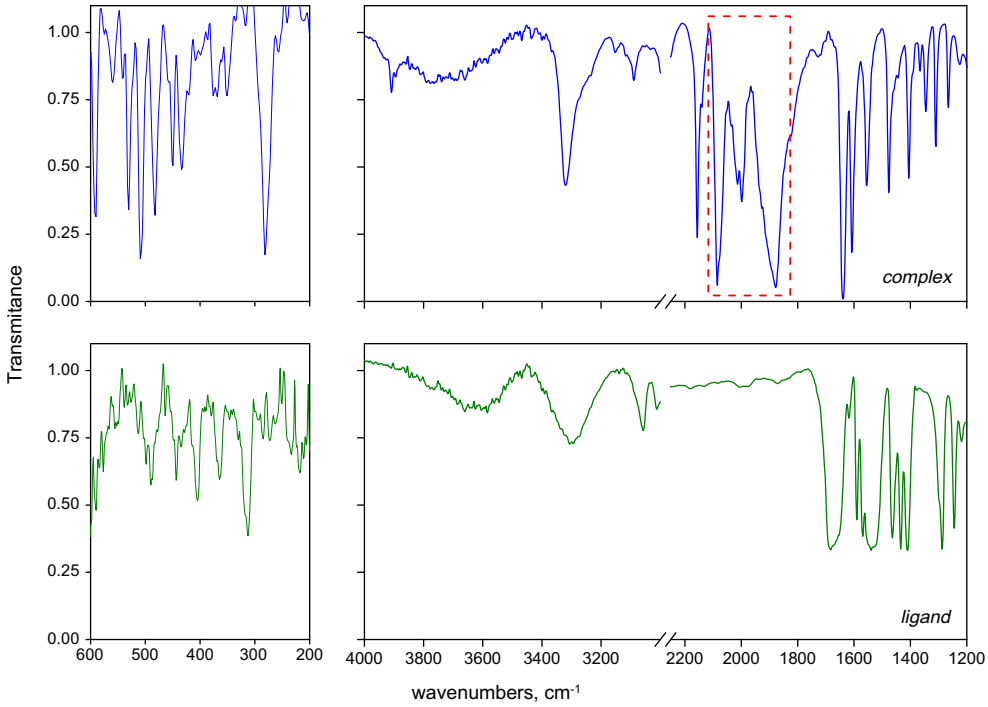


Fig. 4. FT-MIR (right, KBr pellets) and FT-FIR (left, CsI pellets) spectra of ligand **1** and complex **2**.

between two atoms in a chemical bond, e.g. Re^{I}–X, is the measure of its ionic/covalent character: $\Delta\chi \leqslant 1$, for mainly covalent bond [26]. The increase in the difference ($\Delta\chi = \chi_X - \chi_{Re}$) makes the ionic character of the bond stronger. The plot of the length of the Re^{I}–X against $\Delta\chi_{Re-X}$ is nearly linear (Fig. 5, left). Assuming that the radius of the Re^{I} cation in the N,O and N,S complexes is constant ($\chi_{(Re)} \sim 1.9$ [26]), a greater shift of electron density towards electronegative atom (O,S: ~3.5 and ~2.5, respectively [26]) takes place in the Re^{I}–O bond. Therefore, the ionicity of the Re^{I}–O bond is greater than that of the Re^{I}–S one (Fig. 5, right part).

- The ratio of the ionic/covalent bond character can also be discussed in terms of the "hard and soft acids and bases" concept [28]. In the complex studied, Re^{I} cation acts as a soft acid because of low positive charge and relatively large size. Comparing the electronegativity of the S and O donor atoms ($\chi_{(O)} > \chi_{(S)}$) and their radii (oxygen being smaller than sulfur, i.e. $\langle r_{cov} \rangle$ are ~0.65 and ~1.10 Å, respectively) we may assume that pyridinethioamide is softer base than pyridineamide. Because soft–soft combinations form mainly covalent and hard–hard combinations mainly ionic bonding [28], based on the HSAB concept, we may conclude that the covalent character of the Re^{I}–S bond is greater than that of the Re^{I}–O bond.
- To finish, the length of Re–O/S bonds length can be discussed in terms of the free ligands basicity (defined as a propensity to donate an electron pair and forming new bond, which acts in the opposite sense to electronegativity). Because the oxygen and sulfur donor atoms in the pyridineamide and pyridinethioamide are in the same chemical environment, the ligands basicity depends mainly on the properties of the oxygen and sulfur donor atoms (the only two atoms which differentiate both ligands). Based on the experimentally obtained crystallographic data for the $Re^{I}(CO)_3$-pyridine(thio)amides, we may suggest that for the pyridineamide complex electronegativity effect plays a greater role and for pyridinethioamide complex a greater role plays the basicity of the donor atom.

Table 3
Main IR bands (cm^{-1}) of **1** and **2** together with their vibrational assignment

	Ligand **1**	Title complex **2**		
		Exp.	Calc.[a]	Calc./Exp.
$\nu_{as,NH}$	3590 m			
$\nu_{sym,NH}$	3294 sh	3320 m		
$\nu_{CH,(aromatic\ ring)}$	3057 m	3094 m		
$\nu_{as,CH3}$	2943 sh	2947 m		
$\nu_{CO(Re)}$		2085 vs	2043	0.9799
$\nu_{CO(Re)}$		1998 m	1948	0.9750
$\nu_{CO(Re)}$		1879 s	1919	1.0213
$\nu_{C=O,(amide)}$	1591 m	1639 vs	1631	0.9951
ν_{CN}	1463 m	1475 m		
ν_{ring}	1155 m	1186 m		
Re(CO)		530 s		
Re(CO)		510 vs		
Re(CO)		482 s		
Re–N		450 m		
Re–O		433 m		
Re–Cl		281 vs		

ν – stretching, δ – bending vibrations; vs – very strong, s – strong, m – medium, sh – shoulder.

[a] n the gaseous phase.

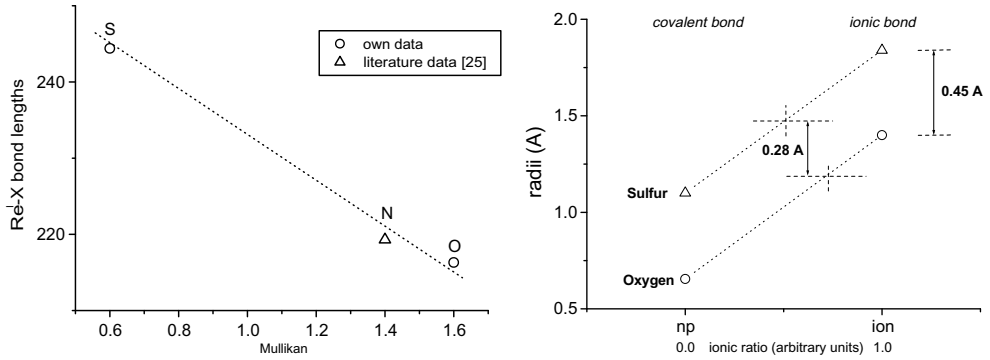


Fig. 5. Re^{I}–X distances found for (**2**) and structurally similar complexes [18,25] (left) and clarification of the distance shortening (right).

Recapitulating, we can conclude that difference in the Re–X bonds length in the $Re(CO)_3$–pyridineamide and –pyridinethioamide (0.28 Å), smaller than expected value (0.45 Å), is caused by higher covalent shortening of the Re–S bond than of the Re^{I}–O one.

Our observation of the ionic/covalent character of the Re^{I}–*N*-methyl-2-pyridine(thio)carboxyamide bonds seems to be consistent with this drawn by Czerwinski and Narbutt from their theoretical calculation of the Mullikan charge distribution in the Tc^{I} complexes formed with the same ligands [24].

4. Conclusions

A novel bidentate ligand with N,O donor atoms, L = *N*-methyl-2-pyridinecarboxyamide (**1**) and the tricarbonyl-chloro-rhenium(I) complex, $[Re(CO)_3L]Cl$ (**2**), have been synthesized. Structural studies of **2** confirm that ligand **1** coordinates the Re^{I} cation bidentatly by O and N atoms. The same can be seen in the most stable structure obtained from the quantum chemical calculations. The investigated complex **2** is not oxidized in aerated solutions within sufficient time for it to be applied in nuclear medicine. As a result of different covalent shortenings of the Re^{I}–S and Re^{I}–O bonds (reflecting their different covalent/ionic contribution) difference in the bond lengths decreases from the theoretical value of 0.45 Å to the value of 0.28 Å.

Acknowledgements

The work was undertaken within the Maria Curie Transfer of Knowledge training contract MTKD-CT-2004-509224 (POL-RAD-PHARM: *Chemical studies for design and production of new radiopharmaceuticals*).

We thank Dr. W. Starosta (INCT) for help in the X-ray studies and Prof. S. Siekierski (INCT) for valuable discussions on structural features of the complexes.

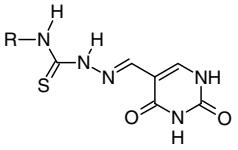
Appendix A. Supplementary material

CCDC 270202 contains the supplementary crystallographic data for $C_{10}H_8ClN_2O_4Re$. These data can be obtained free of charge via http://www.ccdc.cam.ac.uk/conts/retrieving.html, or from the Cambridge Crystallographic Data Centre, 12 Union Road, Cambridge CB2 1EZ, UK; fax: (+44) 1223-336-033; or e-mail: deposit@ccdc.cam.ac.uk. Supplementary data associated with this article can be found, in the online version, at doi:10.1016/j.poly.2007.12.031.

References

[1] W.A. Volkert, T.J. Hoffman, Chem. Rev. 99 (1999) 2269.
[2] R. Alberto, R. Schibli, A. Egli, A. Schubiger, W.A. Herrmann, G. Artus, U. Abram, T.A. Kaden, J. Organomet. Chem. 493 (1995) 119.
[3] N.C. Singa, D.N. Sathyanarayana, Spectrochim. Acta, Part A 54 (1998) 1059.
[4] T. Takano, Y. Sasada, M. Kakudo, Acta Crystallogr. 21 (1966) 514.
[5] A.R. Katritzky, I. Ghiviriga, J. Chem. Soc., Perkin Trans. 2 8 (1995) 1651.
[6] J. Anad, N.C. Singha, D.N. Sathyanarayana, J. Mol. Struct. 412 (1997) 221.
[7] (a) For example: R. Alberto, K. Ortner, N. Wheatley, R. Schibli, A.P. Schubiger, J. Am. Chem. Soc. 123 (2001) 3135;
(b) J. Wald, R. Alberto, K. Ortner, L. Candreia, Angew. Chem., Int. Ed. Engl. 40 (2001) 3062;
(c) R.L. Bella, E. Garcia-Garayoa, M. Bahler, P. Blauenstein, R. Schibli, P. Conrath, D. Tourwe, A.P. Schubiger, Bioconjugate Chem. 13 (2002) 599.
[8] (a) R. Schibli, R. Schwarzbach, R. Alberto, K. Ortner, H. Schmalle, C. Dumas, A. Egli, A.P. Schubiger, Bioconjugate Chem. 13 (2002) 750;
(b) J. Petrig, R. Schibli, C. Dumas, R. Alberto, A.P. Schubiger, Chem. Eur. J. 7 (2001) 1868;
(c) J.D.G. Correia, A. Domingos, I. Santos, R. Alberto, K. Ortner, Inorg. Chem. 40 (2001) 5147.
[9] W. Wang, B. Spingler, R. Alberto, Inorg. Chim. Acta 355 (2003) 386.
[10] F.S. Schoester, S.K. Zeisler, J. Radioanal. Nucl. Chem. 220 (1997) 149.
[11] Neuere Methoden der Präparativen Organischen Chemie, Band III, Verlag Chemie, 1961, p. 30.
[12] G.M. Sheldrick, Acta Crystallogr., Sect. A 46 (1990) 467.
[13] G.M. Sheldrick, SHELXL97, Program for Refinement of Crystal Structure, University of Göttingen, Göttingen, 1997.
[14] PC Spartan Pro Ver. 1, Wavefunction, Inc., Irvine CA, USA, 1999.
[15] For example: R. Wysokinski, D. Michalska, J. Comp. Chem. 22 (2001) 901.
[16] M.J. Frisch, G.W. Trucks, H.B. Schlegel, G.E. Scuseria, M.A. Robb, et al., GAUSSIAN 98 – A.7 Revision, Gaussian, Inc., Pittsburgh PA, USA, 1998.
[17] B. Machura, R. Kruszynski, J. Kusz, Polyhedron 26 (2007) 1590.

[18] L. Fuks, E. Gniazdowska, J. Mieczkowski, J. Narbutt, W. Starosta, M. Zasepa, J. Organomet. Chem. 89 (2004) 4751.
[19] R.A. Olsen, L. Liu, N. Ghaderi, A. Johns, M.E. Hatcher, L.J. Mueller, J. Am. Chem. Soc. 125 (2003) 10125.
[20] (a) For example: K. Yoshihara, T. Omori (Eds.), Topics in Current Chemistry, Technetium and Rhenium, vol. 176, Springer, 1996;
(b) U. Mazzi, M. Nicolini (Eds.), Technetium, Rhenium and Other Metals in Chemistry and Nuclear Medicine, SGEditoriali, Padova, 1995, 1999, 2002, 2006.
[21] A. Kovacs, Z. Varga, Coord. Chem. Rev. 250 (2006) 710.
[22] (a) E. Akalin, S. Akyuz, Vib. Spectrosc. 42 (2006) 333;
(b) M. Bakiler, O. Bolukbasi, A. Yilmaz, J. Mol. Struct. 826 (2007) 6.
[23] For example: P.J. Giordano, M.S. Wrighton, J. Am. Chem. Soc. 101 (1979) 2888.
[24] (a) J. Narbutt, M. Czerwinski, M. Zasepa, Tricarbonyltechnetium(I) complexes with N,O- and N,S-donating ligands-theoretical and radiochemical studies, NUCAR 2005, in: K. Chander, R. Acharya, B.S. Tomar, V. Venugopal (Eds.), Proceedings of the DAE-BRNS Symposium on Nuclear and Radiochemistry, Amritsar, India, March 15–18, 2005, BARC, Trombay, Mumbai, pp. 64–67.;
(b) M. Czerwinski, J. Narbutt, Density functional calculations on tricarbonyltechnetium(I) complexes with amides of picolinic and thiopicolinic acids and related ligands, INCT Annual Report 2004, p. 71.
[25] M.L. Creber, K.G. Orrell, A.G. Osborne, V. Sik, M.B. Hursthouse, M.E. Light, Polyhedron 20 (2001) 1973.
[26] M.S. Silberberg, Chemistry, The Molecular Nature of Matter and Change, 3rd ed., McGraw Hill, NY, 2003.
[27] S. Siekierski, J. Burgess, Concise Chemistry of the Elements, Horwood Publishing, Chichester, 2002, p. 115.
[28] R.G. Pearson, Coord. Chem. Rev. 100 (1990) 403.



R	Compound	
CH_3-CH_2-	Et-H_3ut	(**1**)
CH_2=CH-CH_2-	Allyl-H_3ut	(**2**)
	Ph-H_3ut	(**3**)
	MePh-H_3ut	(**4**)

Scheme 1. Chemical drawing of the R-H_3ut ligands.

Moreover, uracil provides oxygens as additional potential coordinating sites to the thiosemicarbazidic chain.

The present paper deals with the syntheses and characterization of four 5-formyluracil thiosemicarbazones (H_3ut) with substituents on the aminic nitrogen of the thiosemicarbazide chain. The introduction of the different groups: ethyl-, allyl-, phenyl-, methylphenyl-groups (Scheme 1) is made in order to vary the hydrophilic–lipophilic character of the compounds with the aim of increasing the absorption of the drugs in cells.

Substitutions on the terminal N position can also affect the coordination and biological properties [5,6,10,11,24–29]. Moreover, as small molecules, they could react at specific sites along a DNA strand through a series of weak interactions [30]. Many anticancer drugs exert their antitumor effects through binding to DNA in one way or another, thereby blocking the replication of DNA and inhibiting the growth of tumor cells. The understanding of DNA binding and cleavage is the basis for the design of new, efficient antitumor drugs, their effectiveness depending on the binding mode and affinity towards DNA [31,32]. The biological action mechanism of thiosemicarbazone complexes is not clear or well defined so far. One of the proposed pathways is DNA oxidative damage induced by the copper ion [1]. In this view the presence of a moiety with a potential high DNA affinity could act as a Trojan horse in order to anchor the active metal complex to the target site. Copper complexes are also synthesized and identified by means of different spectroscopic and analytical techniques.

To quantify the DNA binding capability in aqueous solution, a spectroscopic investigation with calf thymus DNA has been carried out. Nuclease activity has been verified on plasmid DNA pBR 322 by electrophoresis.

2. Experimental

2.1. Materials and physical measurements

5-Formyluracil (Aldrich, 98%), 4-ethylthiosemicarbazide (Janssen), 4-allylthiosemicarbazide (Janssen), 4-(3-methyl)-phenylthiosemicarbazide (Janssen), 4-phenylthiosemicarbazide (Janssen), $Cu(NO_3)_2 \cdot 3H_2O$ (Carlo-Erba) and $CuCl_2 \cdot 2H_2O$ (Carlo-Erba) were commercially available and were used without further purification. C, H, N and S analyses were obtained with a Carlo-Erba 1108 instrument. IR spectra were recorded using KBr pellets in the 4000–400 cm^{-1} range and using CsI pellets in the 650–150 cm^{-1} range on a Nicolet 5PC FTIR spectrophotometer. Calf thymus (CT) DNA was obtained from Serva and was used as received. DNA samples were dissolved in 50 mM NaCl/5 mM Tris, pH 7.2. A stock solution of CT-DNA was prepared by dissolving the nucleic acid in this buffer in order to obtain a *ca.* 10^{-5} M in base-pair, [bp] solution that gave ratios of UV absorbance at 260 and 280 nm, A_{260}/A_{280}, of *ca.* 1.8, indicating that the CT-DNA was sufficiently protein free. The concentration of the nucleic acid solutions was determined by UV absorbance at 260 nm after 1:100 dilution of the stock solution. The extinction coefficient ε_{260} was taken as 13100 $M^{-1}\,cm^{-1}$ [33]. Stock solutions were stored at 4 °C and used after no more than 4 days. TRIS and TRIS–acetate–EDTA 10× buffers and agarose were purchased from Sigma. pBR322 DNA plasmid (Roche), DirectLoad Wide-Range DNA marker, ethidium bromide and gel loading solution type I 6× concentrate were from Sigma. Chemical ionization-mass (*m*/*z*, 70 eV) fragmentation patterns were obtained, using samples dissolved in methanol, with a Finnegan 1020 6c mass spectrometer equipped with a quadrupole mass selector MATSSQ 710. Melting points were determined with a Gallenkamp instrument. UV measurements were performed on a Perkin–Elmer UV/Vis Lambda 25 spectrometer with quartz cuvettes. Thermogravimetric analyses were performed on a Perkin–Elmer TGA 7 from 30 °C to 450 °C with a 20 °C/min gradient in N_2 atmosphere. Conductivity measurements were performed on a Mayo International Srl digital conductimeter with samples dissolved in absolute EtOH. NMR spectra were recorded on a Bruker AC300 Spectrometer.

2.2. Synthesis of the ligands

5-Formyluracil thiosemicarbazones (**1**), (**3**) and (**4**) (R-H_3ut, Scheme 1) were synthesized by dissolving ca. 0.80 mmol of aldehyde in 20 mL of water at reflux temperature and adding dropwise an equimolar amount of thiosemicarbazide previously dissolved by refluxing in 20 mL of the same solvent. To the 5-formyluracil solution a couple of drops of HCl were added as a catalyst. The mixture was left under magnetic stirring at reflux temperature for 3 h. All compounds afforded shining yellow powders with cooling, which were filtered on Buchner funnel, washed several times with H_2O and allowed to dry in air. The same method has already been used to synthesize ligand **2** [18,34].

2.2.1. Et-H_3ut (*1*)

Yield: 129 mg (67%). *Anal.* Calc. for $C_8H_{11}N_5O_2S$: C, 39.83; H, 4.59; N, 29.03; S, 13.29. Found: C, 40.15; H, 4.46; N, 28.47; S, 13.43%. Main IR peaks (KBr, cm^{-1}): ν(N–H) 3434 m and 3169 w; ν(C–$H_{aliphatic}$) 2973 w;

ν(C=O) 1711 vs and 1675 vs; ν(C=N) 1631 s; ν(C=S) 772 m. UV–Vis (DMF, nm, M^{-1} cm^{-1}) 270 (18900), 334 (21000). MS (*m*/*z*, %) MH^+ (242, 85%); ^{1}H NMR ($CDCl_3$, ppm): 11.55 (CSN*H*, 1H, br s), 9.95 (N3H_{ur}, 1H, s), 9.55 (N1H_{ur}, 1H, s), 8.51 (CH_{ur}, 1H, s), 8.03 (CH_2N*H*, 1H, t), 7.86 (C*H* = N, 1H, s), 3.05 (CH_2, 2H, m), 1.14 (CH_3, 3H, t). ^{13}C NMR ($CDCl_3$, ppm): 178.3 (*C*S), 175.9 (*C*H_2N) 164.0 (*C*4$_{ur}$), 151.4 (*C*2$_{ur}$), 146.5 (*C*6$_{ur}$), 113.7 (*C*5$_{ur}$), 132.2 (*C*HN), 38.1 (*C*H_3). M.p. 185 °C.

2.2.2. Allyl-H_3ut (**2**)

Yield: 135 mg (65%). *Anal.* Calc. for $C_9H_{11}N_5O_2S$: C, 42.68; H, 4.38; N, 27.65; S, 12.66. Found: C, 42.31; H, 4.48; N, 27.54; S, 12.92%. Main IR peaks (KBr, cm^{-1}): ν(N–H) 3163 m; ν(C–H$_{aromatic}$) 3014; ν(C=O) 1713 vs and 1672 vs; ν(C=N) 1630 m; ν(C=S) 793 m. UV–Vis (DMF, nm, $M^{-1}cm^{-1}$) 270 (20800), 335 (23300). MS (*m*/*z*, %) MH^+ (254, 72%); ^{1}H NMR ($CDCl_3$, ppm): 11.61 (CSN*H*, 1H, br s), 10.03 (N3H_{ur}, 1H, s), 9.58 (N1H_{ur}, 1H, s), 8.56 (CH_{ur}, 1H, s), 8.10 (CH_2N*H*, 1H, t), 7.90 (C*H* = N, 1H, s), 5.88 (C*H* gem, 1H, m), 5.12 (CH_2 *cis* + *trans*, 2H, m), 4.22 (CH_2NH, 2H, m). ^{13}C NMR ($CDCl_3$, ppm): 179.1 (*C*S), 164.5 (*C*4$_{ur}$), 152.1 (*C*2$_{ur}$), 147.5 (*C*6$_{ur}$), 135.5 ($CH_2 = CHCH_2$), 115.1 ($CH_2 = CHCH_2$), 113.9 (*C*5$_{ur}$), 134.2 (*C*HN), 45.3 (*C*H_2N). M.p. 192 °C.

2.2.3. Ph-H_3ut (**3**)

Yield: 162 mg (68%). *Anal.* Calc. for $C_{12}H_{11}N_5O_2S$: C, 49.82; H, 3.83; N, 24.21; S, 11.08. Found: C, 50.02; H, 4.03; N, 24.33; S, 10.98%. Main IR peaks (KBr, cm^{-1}): ν(N–H) 3391 s and 3204 w; ν(C–H$_{aromatic}$) 3045; ν(C=O) 1726 mw and 1668 vs; ν(C=N) 1621 m; ν(C=S) 784 m. UV–Vis (DMF, nm, M^{-1} cm^{-1}) 270 (23900), 351 (26010). MS (*m*/*z*, %) MH^+ (290, 78%); ^{1}H NMR ($CDCl_3$, ppm): 11.60 (CSN*H*, 1H, br s), 10.10 (N3H_{ur}, 1H, s), 9.52 (N1H_{ur}, 1H, s), 8.54 (CH_{ur}, 1H, s), 8.10 (Ph-N*H*, 1H, s), 7.85 (C*H* = N, 1H, s), 7.54–7.00 (CH_{ar}, 5H, m). ^{13}C NMR ($CDCl_3$, ppm): 178.8 (*C*S), 165.1 (*C*4$_{ur}$), 151.8 (*C*2$_{ur}$), 146.4 (*C*6$_{ur}$), 114.2 (*C*5$_{ur}$), 126.7–124.8 (*C*$_{ar}$), 134.2 (*C*HN). M.p. 201 °C.

2.2.4. MePh-H_3ut · H_2O (**4**)

Yield: 195 mg (74%). *Anal.* Calc. for $C_{13}H_{15}N_5O_3S$: C, 48.59; H, 4.70; N, 21.79; S, 9.98. Found: C, 48.49; H, 4.68; N, 21.61; S, 10.19%. Main IR peaks (KBr, cm^{-1}): ν(O–H) 3429 bs; ν(N–H) 3251 m and 3200 w; ν(C–H$_{aromatic}$) 3039; ν(C–H$_{aliphatic}$) 2999 w; ν(C=O) 1718 s and 1676 vs; ν(C=N) 1632 m; ν(C=S) 773 m. UV–Vis (DMF, nm, M^{-1} cm^{-1}) 272 (21800), 359 (24300). MS (*m*/*z*, %) $MH^+ - H_2O$ (304, 85%); ^{1}H NMR ($CDCl_3$, ppm): 11.58 (CSN*H*, 1H, br s), 10.10 (N3H_{ur}, 1H, s), 9.54 (N1H_{ur}, 1H, s), 8.54 (CH_{ur}, 1H, s), 8.08 (Ph-N*H*, 1H, s), 7.84 (C*H* = N, 1H, s), 7.55–7.00 (CH_{ar}, 4H, m), 2.31 (CH_3, 3H, s). ^{13}C NMR ($CDCl_3$, ppm): 178.6 (*C*S), 165.4 (*C*4$_{ur}$), 152.0 (*C*2$_{ur}$), 146.5 (*C*6$_{ur}$), 114.2 (*C*5$_{ur}$), 128.0–124.2 (*C*$_{ar}$), 134.2 (*C*HN), 17.9 (*C*H_3). M.p. 210 °C.

2.3. Synthesis of the Cu(II) complexes

The Cu(II) complexes were synthesised following this general procedure: *ca.* 0.30 mmol of the ligands were dissolved in EtOH (40 mL) with gentle heating. An equimolar amount of $Cu(NO_3) \cdot 3H_2O$ or $CuCl_2 \cdot 2H_2O$ was dissolved in the minimum quantity of the same solvent and added dropwise to the pale yellow ligand solutions. All the resulting mixtures slowly became light green coloured and were left under magnetic stirring at reflux temperature for 1 h. By slow solvent evaporation dark green powders were afforded and characterized.

2.3.1. [Cu(Et-H_3ut)$NO_3(OH_2)_2$]$NO_3 \cdot 2H_2O$ (**5**)

Anal. Calc. for $C_8H_{19}CuN_7O_{12}S$: C, 19.18; H, 3.82; N, 19.57; S, 6.40. Found: C, 19.21; H, 3.78; N, 19.48; S, 6.26%. Main IR peaks (KBr, cm^{-1}): ν(O–H) 3583 m; ν(N–H) 3479 m and 3237 m; ν(C–H$_{aromatic}$) 3056; ν(C–H$_{aliphatic}$) 2919 w; ν(C=O) 1731 s and 1643 vs; ν(C=N) 1613 s; ν(NO_3^-) 1385 vs and 1304 s; ν(C=S) 775 m. Main Far IR peaks (CsI, cm^{-1}): ν(Cu–N) 450 m; ν(Cu–O) 417 w; ν(Cu–S) 348 m. UV–Vis (DMF, nm, M^{-1} cm^{-1}) 257 (11700), 286 (13800), 335 (22000), 648 (165). Λ (Ω^{-1} cm^2 mol^{-1}) 50. TGA (°C, % weight loss) 105, 7; 195, 8; 230, 12; 295, 10; 340, 15.6.

2.3.2. [Cu(Et-H_3ut)Cl_2] · $4H_2O$ (**6**)

Anal. Calc. for $C_8H_{19}Cl_2CuN_5O_6S$: C, 21.46; H, 4.28; N, 15.64; S, 7.16. Found: C, 21.85; H, 3.99; N, 15.73; S, 7.31%. Main IR peaks (KBr, cm^{-1}): ν(O–H) 3424 m; ν(N–H) 3344 m sh and 3248 m; ν(C–H$_{aromatic}$) 3050; ν(C–H$_{aliphatic}$) 2938 w; ν(C=O) 1730 s and 1652 vs; ν(C=S) 758 m. Main Far IR peaks (CsI, cm^{-1}): ν(Cu–N) 451 m; ν(Cu–S) 352 m; ν(Cu–Cl) 315 w and 303 s. UV–Vis (DMF, nm, M^{-1} cm^{-1}) 253 (9200), 285 (11700), 335 (20300), 645 (129), 960 (25). Λ (Ω^{-1} cm^2 mol^{-1}) 32. TGA (°C, % weight loss) 220, 12; 260, 11; 290, 20.

2.3.3. [Cu(Allyl-H_3ut)$NO_3(OH_2)_2$]$NO_3 \cdot 3H_2O$ (**7**)

Anal. Calc. for $C_9H_{21}CuN_7O_{13}S$: C, 20.36; H, 3.99; N, 18.47; S, 6.04. Found: C, 20.10; H, 4.17; N, 18.58; S, 6.42%. Main IR peaks (KBr, cm^{-1}): ν(O–H) 3422 m; ν(N–H) 3185 m; ν(C–H$_{aromatic}$) 3024; ν(C–H$_{aliphatic}$) 2948 w; ν(C=O) 1730 s and 1650 s; ν(C=N) 1600 m; ν(NO_3^-) 1385 vs and 1304 s; ν(C=S) 792 w. Main Far IR peaks (CsI, cm^{-1}): ν(Cu–N) 452 m; ν(Cu–O) 418 w; ν(Cu–S) 350 m. UV–Vis (DMF, nm, M^{-1} cm^{-1}) 250 (8950), 279 (12050), 339 (18300), 649 (108). Λ (Ω^{-1} cm^2 mol^{-1}) 54. TGA (°C, % weight loss) 102, 10; 198, 7; 308, 14.

2.3.4. [Cu(Allyl-H_3ut)Cl_2] · $3H_2O$ (**8**)

Anal. Calc. for $C_9H_{17}Cl_2CuN_5O_5S$: C, 24.47; H, 3.88; N, 15.85; S, 7.26. Found: C, 24.18; H, 4.12; N, 15.65; S, 7.17%. Main IR peaks (KBr, cm^{-1}): ν(O–H) 3433 m; ν(N–H) 3250 m; ν(C–H$_{aromatic}$) 3047; ν(C–H$_{aliphatic}$) 2931 w; ν(C=O) 1729 s and 1652 vs; ν(C=N) 1604 m; ν(C=S) 754 m. Main Far IR peaks (CsI, cm^{-1}): ν(Cu–N) 450 m; ν(Cu–S) 355 m;

ν(Cu–Cl) 316 w and 303 s. UV–Vis (DMF, nm, $M^{-1}\,cm^{-1}$) 252 (9500), 278 (11 620), 335 (21 000), 644 (131), 652 (330). Λ ($\Omega^{-1}\,cm^2\,mol^{-1}$) 22. TGA (°C, % weight loss) 103, 12; 258, 8.5; 288, 9.

2.3.5. *[Cu(Ph-H$_3$ut)(NO$_3$)(OH$_2$)$_2$]NO$_3$ (**9**)*

Anal. Calc. for $C_{12}H_{15}CuN_7O_{10}S$: C, 28.10; H, 2.95; N, 19.12; S, 6.25. Found: C, 28.15; H, 2.63; N, 18.87; S, 6.55%. Main IR peaks (KBr, cm^{-1}): ν(O–H) 3475 m; ν(N–H) 3294 m and 3217 m; ν(C–$H_{aromatic}$) 3024; ν(C–$H_{aliphatic}$) 2939 m; ν(C=O) 1739 s and 1639 s; ν(C=N) 1606 m; ν(NO_3^-) 1385 vs; ν(C=S) 769 w. Main Far IR peaks (CsI, cm^{-1}): ν(Cu–N) 452 m; ν(Cu–O) 417 w; ν(Cu–S) 352 m. UV–Vis (DMF, nm, $M^{-1}\,cm^{-1}$) 265 (13 850), 356 (14 200), 630 (110). Λ ($\Omega^{-1}\,cm^2\,mol^{-1}$) 40. TGA (°C, % weight loss) 189, 8; 230, 15.

2.3.6. *[Cu(Ph-H$_3$ut)Cl$_2$] · H$_2$O (**10**)*

Anal. Calc. for $C_{12}H_{13}Cl_2CuN_5O_3S$: C, 32.62; H, 2.96; N, 15.85; S, 7.26. Found: C, 33.06; H, 2.64; N, 15.57; S, 7.47%. Main IR peaks (KBr, cm^{-1}): ν(O–H) 3429 m; ν(N–H) 3309 w and 3200 m; ν(C–$H_{aromatic}$) 3062 m; ν(C–$H_{aliphatic}$) 2935 w; ν(C=O) 1739 s and 1670 vs; ν(C=N) 1597 m; ν(C=S) 762 m. Main Far IR peaks (CsI, cm^{-1}): ν(Cu–N) 448 m; ν(Cu–S) 349 m; ν(Cu–Cl) 318 w and 303 s. UV–Vis (DMF, nm, $M^{-1}\,cm^{-1}$) 273 (12 920), 360 (14 130), 661 (135). Λ ($\Omega^{-1}\,cm^2\,mol^{-1}$) 24. TGA (°C, % weight loss) 105, 4; 255, 8.5; 292, 9.

2.3.7. *[Cu(MePh-H$_3$ut)NO$_3$(OH$_2$)$_2$]NO$_3$ · 3H$_2$O (**11**)*

Anal. Calc. for $C_{13}H_{15}CuN_7O_{13}S$: C, 26.88; H, 3.99; N, 16.88; S, 5.52. Found: C, 27.11; H, 3.87; N, 17.05; S, 5.47%. Main IR peaks (KBr, cm^{-1}): ν(O–H) 3446 m; ν(N–H) 3290 w and 3095 m; ν(C–$H_{aromatic}$) 3032; ν(C–$H_{aliphatic}$) 2947 vw; ν(C=O) 1737 ms and 1642 ms; ν(C=N) 1607 m; ν(NO_3^-) 1385 vs; ν(C=S) 789 w. Main Far IR peaks (CsI, cm^{-1}): ν(Cu–N) 450 m; ν(Cu–O) 419 w; ν(Cu–S) 350 m. UV–Vis (DMF, nm, $M^{-1}\,cm^{-1}$) 264 (13 100), 360 (14 050), 611 (195). Λ ($\Omega^{-1}\,cm^2\,mol^{-1}$) 45. TGA (°C, % weight loss) 105, 10; M.p. (°C) 164.

2.3.8. *[Cu(MePh-H$_3$ut)Cl$_2$] · 3H$_2$O(**12**)*

Anal. Calc. for $C_{13}H_{19}Cl_2CuN_5O_5S$: C, 31.75; H, 3.89; N, 14.24; S, 6.52. Found: C, 32.05; H, 3.75; N, 14.37; S, 6.29%. Main IR peaks (KBr, cm^{-1}): ν(O–H) 3436 br; ν(N–H) 3255 m; ν(C–$H_{aromatic}$) 3057 m; ν(C–$H_{aliphatic}$) 2927 w; ν(C=O) 1723 s and 1650 vs; ν(C=S) 770 w. Main Far IR peaks (CsI, cm^{-1}): ν(Cu–N) 465 w; ν(Cu–S) 351 m; ν(Cu–Cl) 318 w and 303 m. UV–Vis (DMF, nm, $M^{-1}\,cm^{-1}$) 272 (1050), 373 (12 500), 640 (250). Λ ($\Omega^{-1}\,cm^2 mol^{-1}$) 22. TGA (°C, % weight loss) 105–130, 11; 240, 8; 295, 9.

2.4. DNA interaction studies

Binding constants for the interaction of the studied compounds with nucleic acid were determined as described in [35]. These studies were carried out on the ligands and their nitrate complexes because with their ionic character they are expected to show more interactions towards DNA than the neutral chloro complexes. The intrinsic binding constant K_b for the interaction of the studied compounds with CT-DNA was calculated by absorption spectral titration data using the following equation: $1/\Delta\varepsilon_{ap} = 1/(\Delta\varepsilon K_b D) + 1/\Delta\varepsilon$ where $\Delta\varepsilon_{ap} = |\varepsilon_A - \varepsilon_f|$, $\Delta\varepsilon = |\varepsilon_B - \varepsilon_f|$, $D = [DNA]$, and ε_A, ε_B and ε_f are the apparent, bound and free extinction coefficients of the compound, respectively. K_b is given by the ratio of the slope to intercept from the plot of $[DNA]/(\varepsilon_A - \varepsilon_f)$ versus [DNA] and it is expressed in M^{-1}. The previous equation, originally used to calculate the binding constants for hydrophobic derivatives, is now broadly used to investigate a wide variety of metal complexes containing phenanthroline and its derivatives and it has been adopted to obtain binding constant values from metal complexes with different ligands [23,30,36–39]. Fixed amounts of the ligands and of the complexes were dissolved in DMSO because the high solubility of the compounds in this solvent allowed us to prepare concentrated solutions and therefore to utilize reduced volumes (5 μL) for titrations. It was also verified that the DMSO percentage (0.7%) added to the DNA solution did not interfere with the nucleic acid; in fact, the 260 nm absorption band is not subjected to modifications in intensity and position. Concentrated solutions of NaCl, Tris–HCl (pH 7.2) buffer and DNA were prepared. Calculated amounts of the described stock solutions were taken to final concentration values of 50 mM NaCl, 5 mM Tris–HCl and increasing amounts of DNA over a range of DNA concentrations from 10^{-5} to 10^{-3} M. These solutions were then added to the 5 μL solution of the considered compounds in order to maintain the final volume of the solutions as fixed to 700 μL. The compounds were titrated at room temperature. The changes in absorbance of DNA of an intraligand (IL) band upon each addition were monitored at the maximum wavelengths 334, 335, 351 and 359 nm for **1**, **2**, **3** and **4**, respectively for the ligands, and at the maximum wavelengths 336, 339, 356 and 360 nm for complexes **5**, **7**, **9** and **11**, respectively.

2.5. Nuclease activity

The DNA cleavage was carried out on double stranded plasmid DNA pBR 322 by electrophoresis. Buffers were prepared using sterile distilled water. Solutions composed of 1.6 μL of plasmid (40 μg/mL), 4 μL of the studied compounds dissolved in DMSO (0.1 mM) and 8.4 μL Tris buffer solution (10 mM) were incubated for 1 h at 37 °C. This was followed by addition of a gel loading solution, and each sample was loaded directly into different wells on a 1.5% agarose gel for analysis by electrophoresis at 75 V for 3 h. The gel was stained with ethidium bromide and photographed under UV light in a transilluminator.

3. Results and discussion

3.1. Synthesis and spectroscopy

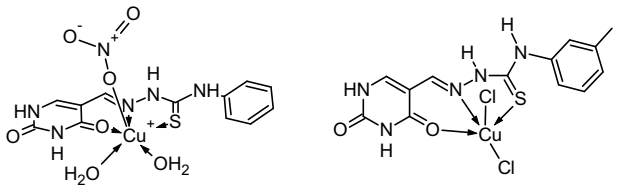
The ligands were synthesised in water in good yields. The products absorbed water giving rise to a gel-like texture and therefore it was necessary to pay attention to the drying step on the Buchner funnel and in air.

The copper complexes were synthesised by the direct reaction of the inorganic salt solutions with the ligand solutions. Under the experimental conditions used both monovalent anions are always present and therefore no ligand deprotonation is observed. The synthesis of the complexes is reproducible and the thiosemicarbazones coordinate as tridentate ligands in their neutral form (H_3ut). The elemental analyses are in agreement with the general formula $M(R\text{-}H_3ut)X_2 \cdot nH_2O$, where X is the counterion. Conductivity measurements show that complexes bearing nitrate as counterions behave as 1:1 electrolyte type compounds and therefore are monocationic [40], while complexes bearing chlorine as counterions behave as neutral molecular complexes. Thermogravimetric analyses show that two water molecules are directly bound to the metal center in the nitrate derivatives. Therefore, as a consequence of the inorganic anionic nature, two types of stoichiometries are exhibited, namely $[Cu(R\text{-}H_3ut)NO_3(OH_2)_2]NO_3$ and $[Cu(R\text{-}H_3ut)Cl_2]$ (see Scheme 2).

These observations agree with previous results [23].

3.2. IR and electronic spectra

The infrared spectral data of the ligands and their metal complexes are reported in Section 2 with their tentative assignments. It is interesting to note that the uracyl moiety owns two carboxyl groups but only the one whose ν(C=O) is assigned at *ca.* 1670 cm^{-1} is involved in coordination. Upon metal binding this carboxyl stretching is shifted downwards by 20–30 cm^{-1} while ν(C=O) not directly linked to the metal is shifted to higher frequencies because of inductive effects arising from the metal coordination. On coordination of the azomethine nitrogen, ν(C=N) shifts to lower wavenumbers by 15–25 cm^{-1}, as the band shifts from *ca.* 1630 cm^{-1} in the uncomplexed thiosemicarbazone spectra to *ca.* 1600 cm^{-1} in the spectra of the complexes. Coordination of the azomethine nitrogen is confirmed with the presence of bands at *ca.* 450 cm^{-1} (at 465 cm^{-1} for complex **12**) assignable to ν(Cu–N) for these complexes. The decrease in the stretching frequency of the C=S bond from *ca.* 770–790 cm^{-1} in the thiosemicarbazones upon complexation indicates coordination *via* the sulfur atom. The presence of a new band in the 345–355 cm^{-1} range assignable to ν(Cu–S), is another indication of the involvement of sulfur coordination. The presence of an absorption at *ca.* 420 cm^{-1} in the spectra of the complexes is assignable to ν(Cu–O). The IR spectra of the chloro complexes also display bands at *ca.* 315 and 300 cm^{-1}, characteristic of coordinated ν(Cu–Cl).



Scheme 2. Hypothesized structure for complex **9** (left) and **10** (right) deduced from spectroscopic data.

The electronic spectra of the complexes in DMF solution are presented in Section 2. Each thiosemicarbazone and its copper(II) complexes have ring $\pi \rightarrow \pi^*$ bands in the range 260–312 nm and $n \rightarrow \pi^*$ bands in the range 312–357 nm. The ligand field strength of the sulfur atom has been found to vary more than that of any other donor atom, with variations of up to 50% being known [40]. This is probably due to the variation in π-bonding effects according to whether the sulfur atom has two or three lone pairs, as in thioketones (>C=S) or mercaptide ions (≡C–S^-), which allows ample scope for M-S π-bonding. The complex spectra have bands in the range 330-357 nm which must be due to L → M transfer from sulfur to copper [41].

3.3. Absorption spectral features of DNA binding

The binding constants obtained for ligands **1**, **2**, **3** and **4** are 2.1×10^3, 1.0×10^3, 2.9×10^2 and 5.6×10^3, respectively. The binding constants obtained for complexes **5**, **7**, **9** and **11** are 2.5×10^2, 5.9×10^2, 2.3×10^1 and 2.3×10^3, respectively. In Fig. 1 the plot of $[DNA]/(\varepsilon_A - \varepsilon_f)$ versus [DNA] for absorption titration of the studied complexes is reported, useful for obtaining K_b by the ratio of the slope to intercept.

Our experimental K_b values are lower than those observed for classical intercalators (ethidium-DNA, 1.4×10^6 in 25 mM Tris–HCl/40 mM NaCl buffer, pH 7.8 [42]; 3.0×10^6 in 5 mM Tris–HCl/50 mM NaCl buffer, pH 7.2 [this work]), indicating that the compounds bind DNA with less affinity, as already noticed for copper(II) complexes with macrocyclic ligands [36]. It is interesting to note that the metal complexes reported in this work bind to DNA with less affinity than copper complexes with aliphatic thiosemicarbazones [37], complexes synthesised with formyluracil thiosemicarbazones bearing less bulky substituents on the side chain [23] and copper complexes with thiosemicarbazide [43]. Since upon complexation no significant increase of K_b was observed, the constant values can probably be related to the role played by the ligand in the binding to DNA. The terminal NH group seems to play an important function in the binding process: as the access to the NH becomes more difficult with the presence of bulky substituents, the association to the nucleic acid becomes weaker. Compounds **4** and **11**, having the bulkier methylphenyl substituent, show a major affinity towards the nucleic acid with respect to the phenyl analogues **3** and **9** (K_b 5.6×10^3 (**4**) versus 2.9×10^2 (**3**) and K_b

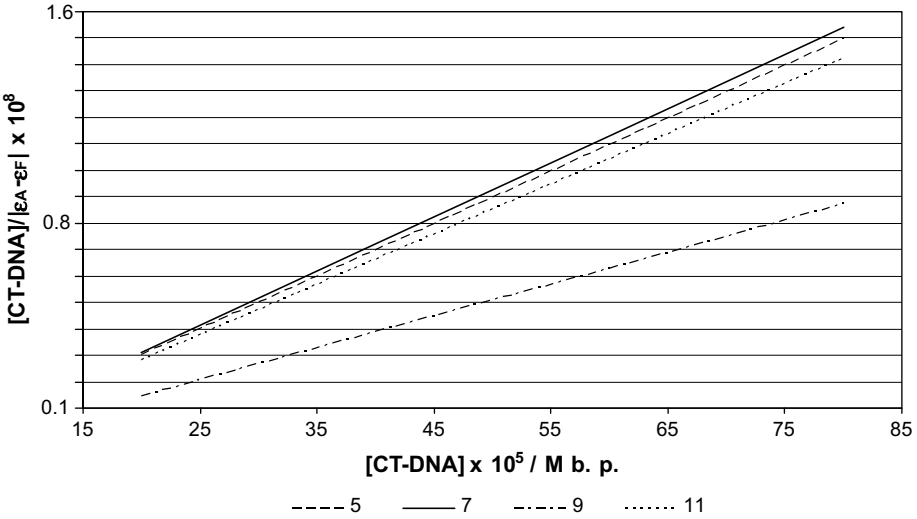


Fig. 1. Typical plots of $[DNA]/(\varepsilon_A - \varepsilon_f)$ vs [CT-DNA] for absorption titration with CT-DNA in 50 mM NaCl/5 mM Tris buffer, pH 7.2 at 25 °C.

2.3×10^3 (**11**) versus 2.3×10^1 (**9**)). This effect can probably be ascribed to the major deviation from planarity of the overall thiosemicarbazonic system due to the methyl substituent on the aromatic ring, as observed in N terminal substituted thiosemicarbazones [28] that decreases the steric hindrance on increasing the accessibility to the aminic group. The weak interactions between our compounds and the nucleic acid are also confirmed by a negligible hypochromism and bathochromism in the electronic absorption spectra of DNA bound to different compounds. These phenomena are generally attributed to intercalation, involving a strong stacking interaction between the aromatic chromophores and the base pairs of DNA. The ratio r ($r = [CT\text{-}DNA]/[complex]$) varied between 0 and 15 in 5 mM Tris–HCl buffer (pH 7.2), 50 mM NaCl at 25 °C. Our results are in agreement with the fact that the glycosidic bond of a formyluracil residue derivative in DNA is about 3 orders of magnitude more labile than that of the parent pyrimidine, thymine and is assignable to the electron-withdrawing effect of the 5-formyl substituent [44]. Additionally, the electron-withdrawing substituent destabilizes the *N*-glycosidic bond, rendering oligonucleotides containing formyluracil, highly susceptible to hydrolysis. The thiosemicarbazidic chain in the five position of the uracil moiety could additionally form potentially irreversible covalent cross-links with an amino group of DNA-binding proteins, resulting in locking the binding instead of blocking binding [44]. The presence of substituents on the terminal nitrogen seems to weaken the capability of bonding towards DNA.

3.4. Nuclease activity

In addition to the studies carried out with CT-DNA, a gel electrophoresis experiment using pBR322, a circular plasmid DNA, was performed with all our compounds. From the results (data not shown) it was verified that at millimolar concentrations for all tested compounds the supercoiled was the predominant form of DNA followed by a slight amount of the open circular form, indicating that there is no significant breaking of plasmid-DNA due to oxidative stress or phosphodiester hydrolysis.

4. Conclusions

As hypothesized in the introduction, the presence of a substituent on the thiosemicarbazidic chain strongly affects the DNA interactions of thiosemicarbazones and their metal complexes. The variation of the hydrophilic/lipophilic character due to the different alkylic or aromatic groups could vary the uptake by the cells but this feature has no consequence on the direct effects of the compounds towards DNA; on the contrary, with respect to the unsubstituted analogous compounds, the free NH_2 thiosemicarbazone moiety seems to play an important role in DNA binding. The presence of the substituents, on the other hand, has no consequence on the coordination mode that, on the contrary, seems to be more influenced by the counterion.

References

[1] R.W. Byrnes, M. Mohan, W.E. Antholine, R.X. Xu, D.H. Petering, Biochemistry 29 (1990) 7046.
[2] K.C. Agrawal, A.C. Sartorelli, J. Med. Chem. 12 (1969) 771.
[3] W.E. Antholine, J. Knight, H. Whelan, D.H. Petering, Mol. Pharm. 13 (1977) 89.
[4] D.L. Klayman, J.F. Bartosovich, T.S. Griffin, C.J. Mason, J.P. Scovill, J. Med. Chem. 22 (1979) 855.
[5] D.L. Klayman, J.P. Scovill, J.F. Bartosovich, C.J. Mason, J. Med. Chem. 22 (1979) 1367.
[6] D. Ronen, L. Sherman, S. Bar-Nun, Y. Teitz, Antimicrob. Agents Chemother. 31 (1987) 1798.
[7] R.C. Condit, R. Easterly, R.F. Pacha, Z. Fathi, R.J. Meis, Virology 185 (1991) 857.
[8] M. Belicchi Ferrari, G. Gasparri Fava, P. Tarasconi, R. Albertini, S. Pinelli, R. Starcich, J. Inorg. Biochem. 53 (1994) 13.

[9] J.G. Cory, A.H. Cory, G. Rappa, A. Lorico, M.-C. Liu, T.-S. Lin, A.C. Sartorelli, Biochem. Pharmacol. 48 (1994) 335.
[10] D. Kovala-Demertzi, P. Nath Yadav, M.A. Demertzis, M. Coluccia, J. Inorg. Biochem. 78 (2000) 347.
[11] J.P. Scovill, D.L. Klayman, C.F. Franchino, J. Med. Chem. 25 (1982) 1261.
[12] Z. Lakovidou, A. Papageorgiou, M.A. Demertzis, E. Mioglou, D. Mourelatos, A. Kotsis, P.N. Yadav, D. Kovala-Demertzi, Anticancer Drugs 12 (2001) 65.
[13] K. Hussain Reddy, P. Sambasiva Reddy, P. Ravindra Babu, Trans. Met. Chem. 25 (2000) 154.
[14] M. Belicchi-Ferrari, F. Bisceglie, C. Casoli, S. Durot, I. Morgenstern-Badarau, G. Pelosi, E. Pilotti, S. Pinelli, P. Tarasconi, J. Med. Chem. 48 (2005) 1671.
[15] S. Adsule, V. Barve, D. Chen, F. Ahmed, Q.P. Dou, S. Padhye, F.H. Sarkar, J. Med. Chem. 49 (2006) 7242.
[16] C.R. Kowol, R. Berger, R. Eichinger, A. Roller, M.A. Jakupec, P.P. Schmidt, V.B. Arion, B.K. Keppler, J. Med. Chem. 50 (2007) 1254.
[17] F. Karatas, M. Koca, H. Kara, S. Servi, Eur. J. Med. Chem. 41 (2006) 664.
[18] J. Boissier, P. Lepine, J. De Rudder, M. Privat de Garilhe, F Patent (1968), 1512549.
[19] N. Wolmark, H. Rockette, J. Clin. Oncol. 17 (1999) 3553.
[20] W.A. Denny, Eur. J. Med. Chem. 36 (2001) 577.
[21] M. Belicchi Ferrari, G. Gasparri Fava, E. Leporati, G. Pelosi, R. Rossi, P. Tarasconi, R. Albertini, A. Bonati, P. Lunghi, S. Pinelli, J. Inorg. Biochem. 70 (1998) 145.
[22] M. Belicchi Ferrari, F. Bisceglie, G. Pelosi, P. Tarasconi, R. Albertini, A. Bonati, P. Lunghi, S. Pinelli, J. Inorg. Biochem. 83 (2001) 169.
[23] M. Baldini, M. Belicchi-Ferrari, F. Bisceglie, G. Pelosi, S. Pinelli, P. Tarasconi, Inorg. Chem. 42 (2003) 2049.
[24] D.X. West, J.K. Swearingen, J. Valdés-Martínez, S. Hernández-Ortega, A.K. El-Sawaf, F. van Meurs, A. Castineiras, I. Garcia, I. Bermejo, Polyhedron 18 (1999) 2919.
[25] M. Belicchi Ferrari, S. Capacchi, G. Reffo, G. Pelosi, P. Tarasconi, R. Albertini, S. Pinelli, P. Lunghi, J. Inorg. Biochem. 81 (2000) 89.
[26] U. Abram, K. Ortner, R. Gust, K. Sommer, J. Chem. Soc., Dalton Trans. (2000) 735.
[27] M. Belicchi Ferrari, S. Capacchi, F. Bisceglie, G. Pelosi, P. Tarasconi, Inorg. Chim. Acta 312 (2001) 81.
[28] M. Belicchi Ferrari, F. Bisceglie, G. Pelosi, P. Tarasconi, R. Albertini, S. Pinelli, J. Inorg. Biochem. 87 (2001) 137.
[29] M. Belicchi Ferrari, F. Bisceglie, E. Leporati, G. Pelosi, P. Tarasconi, S. Pinelli, Bull. Chem. Soc. Jpn. 75 (2002) 781.
[30] Mudasir, N. Yoshioka, H. Inoue, J. Inorg. Biochem. 77 (1999) 239.
[31] A.E. Friedman, C.V. Kumar, N.J. Turro, J.K. Barton, Nucl. Acids Res. 19 (1991) 2595.
[32] A.M. Pyle, T. Morii, J.K. Barton, J. Am. Chem. Soc. 112 (1990) 9432.
[33] M.E. Reichmann, S.A. Rice, C.A. Thomas, P. Doty, J. Am. Chem. Soc. 76 (1954) 3047.
[34] F. Andreeff, M. Privat de Garilhe, Bull. Soc. Chim. Biol. 50 (2) (1968) 435.
[35] A. Wolfe, G.H. Shimer Jr., T. Meehan, Biochemistry 26 (1987) 6392.
[36] J. Liu, T. Zhang, T. Lu, L. Qu, H. Zhou, Q. Zhang, L. Ji, J. Inorg. Biochem. 91 (2002) 269.
[37] F. Bisceglie, M. Baldini, M. Belicchi-Ferrari, E. Buluggiu, M. Careri, G. Pelosi, S. Pinelli, P. Tarasconi, Eur. J. Med. Chem. 42 (2007) 627.
[38] V. Uma, M. Kanthimathi, T. Weyhermuller, Balachandran Unni Nair, J. Inorg. Biochem. 99 (2005) 2299.
[39] M. Baldini, M. Belicchi-Ferrari, F. Bisceglie, S. Capacchi, G. Pelosi, S. Pinelli, P. Tarasconi, J. Inorg. Biochem. 99 (2005) 1504.
[40] W.J. Geary, Coord. Chem. Rev. 7 (1971) 81.
[41] M.J.M. Campbell, Coord. Chem. Rev. 15 (1975) 279.
[42] W.D. Wilson, F.A. Tanious, M. Fernandez-Saiz, C.T. Rigl, in: K.R. Fox (Ed.), Methods in Molecular Biology, vol. 90, Humana, Clifton, NJ, 1997.
[43] P. Murali Krishna, K. Hussain Reddy, P.G. Krishna, G.H. Philip, Indian J. Chem. 46A (2007) 904.
[44] D.K. Rogstad, J. Heo, N. Vaidehi, W.A. Goddard III, A. Burdzy, L.C. Sowers, Biochemistry 43 (2004) 5688.

Another characteristic of an efficient photosensitizer is a Q-band absorption close to 700 nm. The Q-band of octa(thiophen-2-yl) ZnAzaPc was found at 673 nm, whereas unsubstituted AzaPc has a Q-band at 635 nm [5] and both octaphenylZnAzaPc and octa(pyridin-2-yl)ZnAzaPc absorb at 657 nm [4]. In other words, thiophen-2-yl peripheral substituents induce substantially red shifted Q-bands for these macrocycles.

We have reported several investigations on the synthesis [6–8] and photodynamic properties [9–12] of alkylheteroatom (N, O, S) substituted AzaPcs. AzaPcs substituted peripherally with pyridin-2-yl were also investigated by another group from the UV–Vis spectral and electrochemical point of view [13–16]. However, as far as we know, there has been no systematic study of how mixed types of substituents (heteroaromatic and alkylheteroatom) on the AzaPcs influence the Q-band positions, singlet oxygen and fluorescence quantum yields.

Our aim for the present investigation is to extend our knowledge about how various types of substituents on ZnAzaPc influence the three characteristics: Q-band positions, singlet oxygen and fluorescence quantum yields of the complexes. The most interesting substituent among the carbon attached heterocycles, the thiophen-2-yl group, will be compared to thiophen-3-yl and benzo[*b*]thiophen-3-yl groups. However, good solubility and low tendency to aggregate are important for efficient PDT sensitizers as well. Both characteristics are expected to improve for octasubstituted AzaPcs with two different types of peripheral substituents instead of one. Therefore, ZnAzaPcs with a combination of thiophen-2-yl and either sulfur or nitrogen attached substituents, will be synthesized and studied. We have not considered substituents attached through oxygen, since the carbon–oxygen bond is labile during normal reaction conditions for cyclotetramerisations [8,11]. However, an interesting and successful approach to the synthesis of AzaPcs with ether linked substituents has been reported recently [2]. The choice of sulfur attached substituents was made among alkylsulfanyl groups, since arylsulfanyl groups are somewhat labile and may be replaced by nucleophiles. The two nitrogen attached substituents were chosen so that one is electron donating (thiomorpholine), and the other is electron withdrawing (a substituted maleimide). Both the sulfur and nitrogen attached substituents are relatively bulky in order to prevent aggregation.

2. Experimental

2.1. Materials and methods

Electron impact (EI) mass spectra of compounds **2**–**5** were obtained on a Finnigan MAT 95XL spectrometer at 70 eV electron energy and 1.0 mA electron current. MALDI-TOF mass spectra of compounds **6** and **7** were recorded in the negative reflectron mode on a mass spectrometer Voyager-DE STR (Applied Biosystems, Framingham, MA, USA). For each sample, 0.5 μl of the mixture was spotted onto the target plate, air-dried and covered with 0.5 μl of matrix solution consisting of 10 mg of α-cyano-4-hydroxycinnamic acid in 100 μl of 50% ACN in 0.1% TFA. The instrument was calibrated externally with a five-point calibration using Peptide Calibration Mix1 (LaserBio Labs, Sophia-Antipolis, France). IR spectra were obtained on a Nicolet 20-SXC FT IR spectrometer. ^{1}H and ^{13}C NMR spectra were recorded on a Bruker Avance DPX 400 NMR spectrometer or on a Bruker Avance Digital 600 NMR spectrometer at 100.4, 399.65 or 600.18 MHz, respectively. Chemical shifts are given relative to internal tetramethyl silane (TMS). UV–Vis spectra were recorded on a Cary 50 UV–Vis spectrophotometer or a UV-2401PC spectrophotometer from Shimadzu. Fluorescence data were obtained on an AMINCO-Bowman Series 2 luminescence spectrometer. Melting points were obtained on a Büchi 530 melting point apparatus and are uncorrected. The elemental analyses were carried out on an Automatic Microanalyser EA1110CE (Fisons Instruments S.p.A., Milano, Italy). Merck Kieselgel 60F 254 was used for thin layer chromatography (TLC) and Merck silica 63–200 μm was used for column chromatography. Zinc phthalocyanine (ZnPc) was purchased from Eastman Organic Chemicals (New York, USA). 1,3-Diphenylisobenzofuran (DPBF) was obtained from Aldrich.

2.2. Synthesis

The following compounds have been prepared previously in our laboratories and published: **2c** and **6c** [4], **5a** and **7a** [17], **7c** [18] and **7d** [22]. Compound **3** was prepared according to a published procedure [19].

2.2.1. Compounds *2*

*2.2.1.1. General procedure for the synthesis of compounds **2**.* A solution of 3,3′-thenil (**1a**) [20] or 3,3′-benzo[*b*]thenil (**1b**) [21] (10 mmol) and diaminomaleonitrile (15 mmol) in glacial acetic acid (30 ml) was heated under reflux for **2a** 24 h, and for **2b** 3 h. The solvent was removed under reduced pressure and the residue was extracted with dichloromethane (DCM) and chromatographed on silica with DCM.

*2.2.1.2. 5,6-Di(thiophen-3-yl)pyrazine-2,3-dicarbonitrile (**2a**).* Yield: 2.38 g (81%) of a pale yellow powder, m.p. 218–220 °C. EIMS: *m*/*z* (% rel. int.) 295 (22.9), 294 (M, 100), 293 (50.0), 261 (44.3), 250 (15.6). Found 294.00338, calcd. for $C_{14}H_6N_4S_2$ 294.00339. UV–Vis (DCM): λ_{max}, nm (ε, $M^{-1}\,cm^{-1}$) 280 (16000), 350 (17000). ^{1}H NMR ($CDCl_3$): δ, ppm 7.25 (2H, dd, $J_{4,5} = 5$ Hz, $J_{4,2} = 1.3$ Hz), 7.38 (2H, dd, $J_{5,2} = 3$ Hz, $J_{5,4} = 5$ Hz), 7.83 (2H, dd, $J_{2,5} = 3$ Hz, $J_{2,4} = 1.3$ Hz). ^{13}C NMR ($CDCl_3$): δ, ppm 113.17 (CN), 126.94, 127.73, 129.18, 130.61, 136.63, 149.81. IR (KBr): ν, cm^{-1} 3105, 2239 (CN), 1651, 1503, 1387, 1218, 1162, 806, 701.

*2.2.1.3. 5,6-Di(benzo[b]thiophen-3-yl)pyrazine-2,3-dicarbonitrile (**2b**).* Yield: 1.65 g (42%) of a yellow powder, m.p. 254–258 °C (decomp). EIMS: *m/z* (% rel. int.) 395 (21.3), 394 (M, 15.2), 393 (21.2), 362 (26.9), 159 (67.2). Found 394.03447, calc. for $C_{22}H_{10}N_4S_2$ 394.03462. UV–Vis (DCM): λ_{max}, nm (ε, $M^{-1}\,cm^{-1}$) 265 (22000), 362 (15300), 395 (15800). ^1H NMR ($CDCl_3$): δ, ppm 7.36, *H5* (2H, dd, $J_{5,4} = 8$ Hz, $J_{5,6} = 7$ Hz), 7.42, *H6* (2H, dd, $J_{6,7} = 8$ Hz, $J_{6,5} = 7$ Hz), 7.67, *H2* (2H, s), 7.87, *H7* (2H, ddd, $J_{7,6} = 8$ Hz, $J_{7,5} = 2$ Hz, $J_{7,4} = 0.7$ Hz), 7.93, *H4* (2H, ddd, $J_{4,5} = 8$ Hz, $J_{4,6} = 2$ Hz, $J_{4,7} = 0.7$ Hz). ^{13}C NMR ($CDCl_3$): δ, ppm 113 (CN), 122.91, 123.61, 125.60, 125.61, 129.48, 130.96, 132.98, 135.72, 140.08, 151.21 (after 24 h, an orange precipitate separates from the $CDCl_3$ solution). IR (KBr): ν, cm^{-1} 3109(w), 2238 (w, CN), 1500, 1429, 1382, 1246, 1182, 1063, 856, 803, 758, 735.

*2.2.2. Compounds **5***

*2.2.2.1. 5-(tert-Butylsulfanyl)-6-(thiophen-2-yl)pyrazine-2,3-dicarbonitrile (**5b**).* A solution of *tert*-butanethiol (3 mmol, 0.78 g) in 0.1 M NaOH (3.3 mmol, 3.3 ml) was stirred at ambient temperature for 0.5 h. A solution of **3** (3 mmol, 0.74 g) in THF (6 ml) was added with stirring. The reaction mixture was stirred for 15 min, water (25 ml) was added, and the precipitate was collected by filtration and was washed thoroughly with water. Yield: 0.87 g (97%) of a yellow powder, m.p. 184–186 °C (decomp). EIMS: *m/z* (% rel. int.) 300 (M, 4.5), 246 (9.6), 245 (33.5), 244 (84.0), 243 (100). Found 300.04949, calc for $C_{14}H_{12}N_4S_2$ 300.05034. UV–Vis (DCM): λ_{max}, nm (ε, $M^{-1}\,cm^{-1}$) 390 (14100), 345 (16300), 285 (14600). ^1H NMR ($CDCl_3$): δ, ppm 1.69 (9H, s), 7.23, *H4* (1H, dd, $J_{4,3} = 4$ Hz, $J_{4,5} = 5$ Hz), 7.71, *H5* (1H, dd, $J_{5,4} = 5$ Hz, $J_{5,3} = 1$ Hz), 8.22, *H3* (1H, dd, $J_{3,4} = 4$ Hz, $J_{3,5} = 1$ Hz). The pulse techniques HSQC and HMBC were used for identification of the ^{13}C signals. ^{13}C NMR ($CDCl_3$): δ, ppm 29.63 (*CH*$_3$), 52.39 (*C*Me$_3$), 113.33 (*CN*), 113.42 (*CN*), 125.66 (*C2*-pyrazine), 126.74 (*C3*-pyrazine), 128.71 (*C4*-thiophene), 133.03 (*C3*-thiophene), 133.95 (*C5*-thiophene), 138.44 (*C2*-thiophenyl), 148.06 (*C6*-pyrazine), 159.73 (*C5*-pyrazine). IR (KBr): ν, cm^{-1} 2998, 2959, 2232 (w, CN), 1488, 1423, 1326, 1264, 1138, 1092, 1049, 909, 850, 728.

*2.2.3. Compounds **6***

*2.2.3.1. General procedure for the synthesis of compounds **6**.* Compound **2** (1 mmol) and dry zinc(II) acetate (1 mmol) were ground together in a mortar, transferred to a round bottomed flask, quinoline (0.5 ml) was added, and nitrogen was passed over the reaction mixture for 20 min at ambient temperature. The mixture was heated to 155–160 °C for 50 min (**2a**) and 15 min (**2b**). The dark solid that formed was thoroughly washed, using sonification, with water, acetone and a mixture of DCM and acetone.

*2.2.3.2. [Octa(thiophen-3-yl)-(octazaphthalocyaninato)]-zinc(II) (**6a**).* Yield: 0.2 g (64%) of a black powder. UV–Vis (pyridine): λ_{max}, nm (ε, $M^{-1}\,cm^{-1}$) 661 (224000), 599 (26000), 385 (113000). MALDI-TOF MS *m/z* 1240.08 [M+H$^+$]. *Anal.* Calc. for $C_{56}H_{24}N_{16}S_8Zn + 5H_2O$: C, 50.46; H, 2.57; N, 16.81. Found: C, 50.49; H, 2.33; N, 16.74%.

*2.2.3.3. [Octa(benzo[b]thiophen-3-yl)-(octazaphthalocyaninato)]zinc(II) (**6b**).* Yield: 0.18 g (44%) of a black powder. UV–Vis (pyridine): λ_{max}, nm (ε, $M^{-1}\,cm^{-1}$) 664 (187000), 600 (37000), 390 (91000). The DQF-COSY pulse technique was used for identifications of ^1H NMR signals. ^1H NMR (pyridine-d_5): δ, ppm 7.24 *H5* (4H, partly superimposed on the pyridine signal), 7.37, *H6* (4H, m), 8.01, *H7* (4H, d, $J = 7.8$ Hz), 8.17, *H2* (4H, s), 8.53 *H4* (4H, d, $J = 7.8$). The use of the HSQC pulse technique allowed identification of the following ^{13}C NMR signals: ^{13}C NMR (pyridine-d_5): δ, ppm *C7* 123.3, *C4* 124.5, *C5* 125.3, *C6* 125.3, *C2* 131.2. MALDI-TOF MS *m/z* 1641.03 [M+H$^+$]. *Anal.* Calc. for $C_{88}H_{40}N_{16}S_8Zn + 5H_2O$: C, 60.98; H, 2.91; N, 12.93. Found: C, 57.86; H, 2.61; N, 12.33%.

*2.2.4. Compounds **7***

*2.2.4.1. [Tetra(tert-butylsulfanyl)-tetra(thiophen-2-yl)-(octazaphthalocyaninato)]zinc(II) (**7b**).* Compound **7b** was prepared from **5b** and $Zn(OAc)_2$ in quinoline as described for compounds **6**. The crude product was purified as for compounds **6**. The crude product was then chromatographed on silica with pyridine. Yield 40% of a black, shiny solid. UV–Vis (pyridine): λ_{max}, nm (ε, $M^{-1}\,cm^{-1}$) 671 (234000), 605 (47000), 395 (160000). *NMR*: Four different signals were found for each of the three thiophene protons, apparent due to isomers. The corresponding ^{13}C signals were found by HSQC and HMBC pulse techniques. Each isomer is listed separately with the corresponding $^1H/^{13}C$ NMR signals (pyridine-d_5): δ, ppm: *Isomer 1*: *H5*/*C5*, 8.08 (d, $J = 5$ Hz)/131.8, *H4*/*C4*, 7.49 (m)/129.0, *H3*/*C3*, 8,77 (m)/131.5, *C2*, 143.7, *C6-pyrazine*, 147.6. *Isomer 2*: *H5*/*C5*, 8.06 (d, $J = 5$ Hz)/131.8, *H4*/*C4*, 7.48 (m)/129.0, *H3*/*C3*, 8,74 (m)/131.6, *C2*, 143.7, *C6-pyrazine*, covered by the pyridine signal. *Isomer 3*: *H5*/*C5*, 7.87 (d, $J = 5$ Hz)/131.2, *H4*/*C4*, 7.41 (m)/128.6, *H3*/*C3*, 8,66 (m)/131.5, *C2*, 142.8, *C6-pyrazine*, 147.6. *Isomer 4*: *H5*/*C5*, 7.85 (d, $J = 5$ Hz)/131.2, *H4*/*C4*, 7.39 (m)/128.6, *H3*/*C3*, 8,62 (m)/131.6, *C2*, 143.0, *C6-pyrazine*, 147.7. *tert-butyl groups*: ^1H NMR (pyridine-d_5): δ, ppm 2.23–2.32 (broad singlets, several signals). MALDI-TOF MS *m/z* 1265.08 [M+H$^+$]. *Anal.* Calc. for $C_{56}H_{48}N_{16}S_8Zn + 2H_2O$: C, 51.62; H, 4.02; N, 17.20. Found: C, 51.70; H, 3.89; N, 17.05%.

*2.2.5. (Tetra{1-[3-chloro-4-(4-thiomorpholinyl) maleimidyl]}-tetra(thiophen-2-yl)-(octazaphthalocyaninato))zinc(II) (**7d**)*

The previously reported product [22] was further purified by absorbing a DCM solution of the compound on a silica column. Impurities were eluted with DCM, and compound **7d** was eluted with pyridine, which was removed

under reduced pressure. The dark solid residue was triturated with diethyl ether and filtered to give a dark blue to black shiny solid. UV–Vis (pyridine): λ_{max}, nm (ε, $M^{-1}\,cm^{-1}$) 675 (208 000), 615 (49 000), 390 (172 000), 315 (191 000). *NMR*: Two different signals were found for each of the three thiophene protons, apparently due to isomers. The corresponding ^{13}C signals were found by DQF-COSY, HSQC and HMBC pulse techniques. Each isomer is listed separately with the corresponding $^{1}H/^{13}C$ NMR signals (pyridine-d_5): δ, ppm: *Isomer 1*: *H5*/*C5*, 7.84/132.3, *H4*/*C4*, 7.27/129.4, *H3*/*C3*, 8.61/132.2, *C2*, 139.3. *Isomer 2*: *H5*/*C5*, 7.79/132.4, *H4*/*C4*, 7.21/129.3, *H3*/*C3*, 8.48/132.2, *C2*, 139.3. Two isomers were found for thiomorpholine, and they are listed as above. *Isomer 1*: *H2*/*C2*, 2.92/28.4, *H3*/*C3*, 4.33/51.8, *C3-maleimide*, 143.2. *Isomer 2*: *H2*/*C2*, 2.89/28.4, *H3*/*C3*, 4.30/51.8, *C3-maleimide*, 143.3. MALDI-TOF MS *m*/*z* 1832.94 [M+H$^+$]. *Anal*. Calc. for $C_{72}H_{44}Cl_4N_{24}O_8S_8Zn + 5H_2O$: C, 44.78; H, 2.82; N, 17.44. Found: C, 47.25; H, 3.06; N, 17.74%.

2.3. Singlet oxygen measurements

Singlet oxygen production was monitored as DPBF (1,3-diphenylisobenzofuran) decomposition reactions, as reported by us previously [10], but with a slight modification. Pyridine solutions of the metal complexes **6a**–**c** and **7a**–**d** were heated at approximately 115 °C for a few minutes to ensure complete dissolution and monomerisation of possible dimers. The pyridine solutions were cooled to ambient temperature, diluted until the Q-band λ_{max} absorption became 0.1 and then kept strictly in the dark. A 2.4 ml sample of these solutions was transferred into a 10 × 10 mm quartz optical cell, 24 μl of a 5 mM stock solution of DPBF in pyridine was added, and the resulting solution was purged with oxygen for 1 min. A Tip 200 W halogen lamp was used for irradiation of the oxygen purged solution, and exact time intervals were used. The decomposition of DPBF was monitored at 417 nm, and irradiation was stopped before the decomposition of DPBF had reached 15%. Other conditions (filters, etc.) as well as the calculations of Φ_Δ have been described previously [10]. ZnPc in pyridine was used as the standard ($\Phi_\Delta = 0.61$ [23]).

2.4. Fluorescence measurements

Fluorescence quantum yields of the dyes were determined in pyridine and calculated according to following equation (Eq. (1)):

$$\Phi_F^S = \Phi_F^R \frac{AUC^S}{AUC^R} \frac{1 - 10^{-A^R}}{1 - 10^{-A^S}} \quad (1)$$

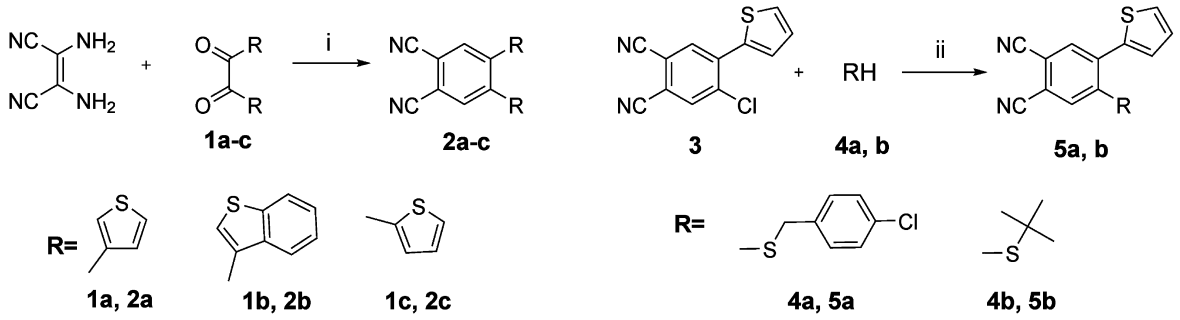
where Φ_F is the fluorescence quantum yield, AUC is the integrated area under the emission spectrum and A is absorbance at the excitation wavelength. Superscripts R and S correspond to reference and sample, respectively. ZnPc in pyridine was used as a reference ($\Phi_F = 0.20$ in pyridine [23]). The dye solutions prepared as mentioned above were used for measurements after the appropriate dilution. In all cases the absorbance at λ_{max} of the Q-band was below 0.04 in order to minimize reabsorption of the emitted light. Fluorescence emission spectra were recorded after excitation at 606 nm. Fluorescence excitation spectra were recorded observing the fluorescence signal at 720 nm.

3. Results and discussion

3.1. Syntheses and characterisation

The syntheses of pyrazine-2,3-dicarbonitriles **2a**–**c**, **3** and **5a**,**b** are shown in Scheme 1. The macrocycles ZnAzaPcs **6a**–**c** and **7a**–**b** were obtained from monomers **2**, **3** and **5** and their structures are shown in Fig. 1. Compounds **2a**, **b** were obtained from a condensation between diaminomaleonitrile and 3,3′-thenil (**1a**) or 3,3′-benzo[*b*]thenil (**1b**) dissolved in acetic acid. The extended conjugation of the benzo[*b*]thiophene group is reflected in the UV–Vis absorption at 395 nm for compound **2b** compared to 350 nm for **2a**. Compound **3** was used for syntheses of the sulfanyl substituted monomers **5a,b**. The zinc complexes **6a**–**c** and **7a**–**d** were obtained from cyclotetramerization with zinc(II) acetate and quinoline. Attempts to tetramerize compound **3** by the same procedure gave an AzaPc macrocycle ($\lambda_{max}(\varepsilon) = 670$ (81 000)) of low solubility. Neither MALDI-TOF nor elemental analyses confirmed the expected structure. The chlorine atom of **3** is most likely labile and was exchanged either during cyclisation or work up procedures.

The thiophen-3-yl substituted compound **6a** has very low solubility in most organic solvents, including pyridine, and therefore NMR spectra could not be properly measured for **6a**. Compounds **6b**–**c** and **7a**–**d** are somewhat more soluble and pyridine-d_5 solutions were used for NMR studies of these substances. ^{1}H NMR spectra of **6b**–**c** and **7a**–**d** were recorded, and the pulse techniques DQF-COSY, HSQC and HMBC were used to correlate proton and carbon signals. NMR spectra of compound **6b**, dissolved in pyridine-d_5, show all the aromatic protons, including the thiophen-2-yl protons, at a higher field than for the corresponding protons of monomer **2b**. Complexation with zinc is expected to have, and indeed it has, the same effect on all these macrocycles. It was noted that the pyridine-d_5 solution of **6b** deposited a dark precipitate after about 24 hours, apparently due to slow aggregation. Complexes **7a**–**d** are expected to be mixtures of four constitutional isomers due to the unsymmetrically substituted monomers. Compound **7b**, with equal numbers of thiophen-2-yl and *tert*-butylsulfanyl groups, gave four different proton signals for each of the three thiophen-2-yl hydrogens. We interpret these as signals from four isomers. The tendency of aggregation plays an important role in the interpretation of NMR spectra. The *tert*-butylsulfanyl groups may cause more steric strain than the 4-chlorobenzylsulfanyl group of **7a** and consequently **7b** is less



Scheme 1. Scheme of the synthesis of the precursors. Reaction conditions: (i) acetic acid, reflux; (ii) pyridine, acetone (for **4a**) or NaOH, water, THF (for **4b**).

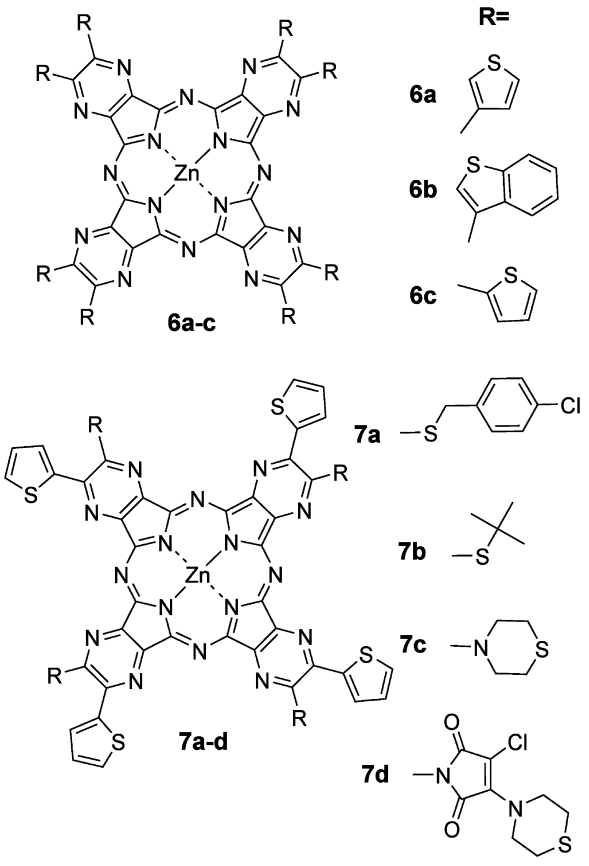


Fig. 1. Structures of the substituted ZnAzaPc systems examined in the study.

aggregated. Only one set of ^{1}H NMR signals were observed for the thiophen-2-yl groups of **7a** [17], indicating one isomer only. However, the presence of other isomers could have been masked by aggregation. Compound **7d**, with a large substituted maleimide group, shows two sets of proton signals for each of the three thiophen-2-yl hydrogen atoms and also for each of the two different kinds of thiomorpholine hydrogen atoms. This indicates that there are at least two different isomers of **7d**. Similarly to the previous compound, the presence of two other isomers may be masked by aggregation.

The mass spectra of the dyes were measured by MALDI-TOF spectrometry. The mass $M+H^+$, as well as the adducts with Na^+ and K^+, were detected for all the new macrocycles, i.e. for compounds **6a**–**b**, **7b** and **7d.** Due to ionisation, a stepwise removal of isobutenes from the *tert*-butylsulfanyl substituents of **7b** was observed in accordance with previous observations [10]. These observations confirm the expected structure of **7b**. No other than the expected molecular ions were detected in the mass spectra of compounds **6a**–**b**, **7b** and **7d**.

Elemental analyses of the dyes were satisfactory for compounds **6a** and **7b**. However the elemental analyses of **6b** and **7d** are not quite satisfactory, and we conclude that these compounds are slightly contaminated. Due to the low solubilities of compounds **6b** and **7d**, further purifications were not successful.

Table 1 summarizes the spectral, photophysical and photochemical data for compounds **6a**–**c** and **7a**–**d**. Complex **6a** with thiophen-3-yl substituents has a Q-band at 661 nm, whereas **6c**, with thiophen-2-yl substituents, has a Q-band at 673 nm. The 12 nm red shift for **6c** is most likely caused by better conjugation, i.e. more resonance forms, between the macrocycle and thiophen-2-yl groups. Compound **6b** shows a 3 nm red shifted Q-band compared to **6a** and this probably reflects the higher aromaticity of benzo[*b*]thiophene compared to thiophene. Compounds **7a**–**d** are substituted with four thiophen-2-yl groups and either four sulfanyl, amino or imido groups. The following Q-band positions were measured for these compounds: 669 (**7a**), 671 (**7b**), 669 (**7c**) and 675 nm (**7d**). Compound **6c** is substituted with eight peripheral thiophen-2-yl groups, and its Q-band position is 673 nm. Therefore it appears that four peripheral thiophen-2-yl substituents will induce almost the same red shift of a Q-band as eight thiophen-2-yl groups. Except for the substituted maleimide group of compound **7d**, the other sulfanyl or amino groups of **7a**–**7c** have negligible effects on the Q-band positions of these compounds. Incidentally, maleimide substituents were originally used in order to facilitate cyclotetramerisations since imido-nitrogens would be electron withdrawing [22]. Electron donating substituents make the cyclization procedure complicated [7] while electron withdrawing groups facilitate macrocycle formation [2,12].

Table 1
Spectral, photophysical and photochemical data of the substituted ZnAzaPc systems in pyridine

	Peripheral substitution		Q-band λ_{max} (nm)	Fluorescence λ_{max} (nm)	Φ_Δ	Φ_F
ZnPc	H	H	674	680	0.61[a]	0.20[a]
6a	thiophen-3-yl	thiophen-3-yl	661	668	0.581	0.235
6b	benzo[*b*]thiophen-3-yl	benzo[*b*]thiophen-3-yl	664	672	0.416	0.102
6c	thiophen-2-yl	thiophen-2-yl	673	680	0.635[b]	0.176[b]
7a	thiophen-2-yl	4-chlorobenzylsulfanyl	669	678	0.695	0.177
7b	thiophen-2-yl	*tert*-butylsulfanyl	671	680	0.672	0.162
7c	thiophen-2-yl	thiomorpholine	669	678	0.107	0.019
7d	thiophen-2-yl	substituted maleimide	675	682	0.103	0.036

[a] Used as reference. See [23].
[b] From Ref. [4].

3.2. Fluorescence and singlet oxygen quantum yields

The quantum yields were measured in pyridine and with zinc phthalocyanine (ZnPc) as the reference. The data obtained are summarized in Table 1. Singlet oxygen quantum yields were determined using a specific chemical trap for singlet oxygen, 1,3-diphenylisobenzofuran (DPBF)[3]. Several other dyes, previously synthesized by us but not characterized from the point of view of quantum yields, were introduced into this study in order to clarify the influence of peripheral substituents on the photophysical and photochemical properties of AzaPc macrocycles. Fluorescence spectra were of a typical shape for AzaPc, with only a small Stokes shift in the range of 7–9 nm (see Table 1). The calculations of quantum yields were based on the absorption of light in the Q-band area. The presence of low mass impurities, without absorption in the Q-band area, will not influence the results obtained for compounds **6b** and **7d**. This was confirmed also by a perfect fit between the absorption and fluorescence excitation spectra (for example see Fig. 2). The possible impurities would modify the absorption spectra but not the fluorescence excitation spectra. The aggregation of the dyes did not influence the results either, because the measurements were performed in very dilute pyridine solutions (below 0.5 μM for Φ_Δ and below 0.2 μM for Φ_F) where the dyes stay almost exclusively in the monomeric form. Also perfect agreement of absorption and excitation spectra (Fig. 2) confirmed the presence of only the monomeric form during measurements.

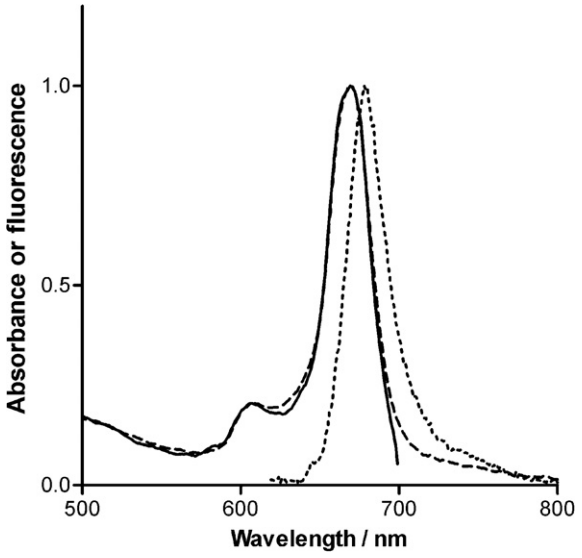


Fig. 2. Normalized absorption (dashed line), fluorescence excitation (full line) and fluorescence emission (dotted line) spectra of compound **7c**.

The sum of the quantum yields ($\Phi_\Delta + \Phi_F$) of the macrocycles with octathiophene substitution (**6c**) and (**6a**) was the same. The change of position of the thiophene substitution (thiophen-2-yl or thiophen-3-yl) led only to differences in the distribution of released energy between fluorescence and photoprocess type II (higher Φ_Δ for **6c** and reversely higher Φ_F for **6a**). An extended conjugation of the benzo[*b*]thiophene group in compound **6b** decreases the overall quantum yields. This is probably due to the larger molecular size, which increases the possibility to release absorbed energy in the form of heat through collision with surrounding molecules. Similarly, larger naphthalocyanines have lower quantum yields compared to Pc [24]. Compounds **7** are unsymmetrically substituted and the influence of the second substituent was also investigated. We have shown previously [11] that alkylsulfanyl substituents have positive effect on Φ_Δ, while the presence of nitrogen connecting peripheral chains with the macrocycle strongly decreases the overall quantum yields [10]. The obtained results confirmed further such formulated structure-activity relationships. Compounds **7a** and **7b** with alkylsulfanyl substituents exerted the highest Φ_Δ value amongst the studied compounds. Their values of Φ_Δ were very close to each other because both substituents (*tert*-butylsulfanyl and 4-chlorobenzylsulfanyl) should influence the macrocycle in the same way. Compounds **7c** and **7d**, with nitrogen atoms connecting the substituents to the macrocycle, showed far lower quantum yields. This is also in good agreement with previously postulated relationships.

4. Conclusion

The present studies have shown that ZnAzaPcs substituted with thiophen-2-yl groups in combination with other

substituents may be of interest for the development of new photosensitizers. The thiophen-2-yl group will, regardless of the presence of other groups, cause a red shift of the Q-band to 670 nm or higher. A combination of imide substituents, attached to the macrocycle through nitrogen atoms, and thiophen-2-yl substituents, is expected to increase the Q-band red shift further, as seen for compound **7d**. However, imide substituents in general are expected to decrease the singlet oxygen quantum yields of ZnAzaPcs, and will be of little interest in our future search for efficient photosensitizers. The thiophen-3-yl substituents are less efficient than thiophen-2-yl groups for inducing red shifted Q-bands, and therefore are less interesting for a future search for photosensitisers. However, the thiophen-3-yl substituents induce a relatively high production of singlet oxygen, which may be of interest for other purposes. The best combination of substituents for the prepared ZnAzaPcs is a mixture of thiophen-2-yl substituents with bulky sulfanyl groups. This combination gives good solubility and little aggregation due to more disorder in these compounds. The bulky *tert*-butylsulfanyl substituents of **7b** inhibit efficiently the aggregation, and together with its high Φ_Δ and absorbance at 671 nm, this compound is promising for future tests as a potential photosensitizer in PDT. The $\Phi_\Delta = 0.67$ of this AzaPc is more than sufficient for efficient sensitization. For comparison, the sulfonated AlPc approved for various cancer treatments under the name Photosens (developed in NIOPIK, Russia) has $\Phi_\Delta = 0.42$ [25].

Acknowledgement

P.Z. would like to thank for financial support to the Research Project MSM 0021620822.

References

[1] B.H. Lee, J.Y. Jaung, S.C. Jang, S.C. Yi, Dyes Pigment. 65 (2005) 159.
[2] S. Makhseed, F. Ibrahim, C.G. Bezzu, N.B. McKeown, Tetrahedron Lett. 48 (2007) 7358.
[3] P. Zimcik, M. Miletin, Z. Musil, K. Kopecky, L. Kubza, D. Brault, J. Photochem. Photobiol. A: Chem. 183 (2006) 59.
[4] E.H. Mørkved, N.K. Afseth, P. Zimcik, J. Porphyr. Phthalocya. 10 (2007) 130.
[5] S.V. Kudrevich, J.E. Van Lier, Coord. Chem. Rev. 156 (1996) 163.
[6] E.H. Mørkved, L.T. Holmaas, H. Kjøsen, G. Hvistendahl, Acta Chem. Scand. 50 (1996) 1153.
[7] E.H. Mørkved, H. Kjøsen, H. Ossletten, N. Erchak, J. Porphyr. Phthalocya. 3 (1999) 417.
[8] E.H. Mørkved, H. Ossletten, H. Kjøsen, Acta Chem. Scand. 53 (1999) 1117.
[9] M. Kostka, P. Zimcik, M. Miletin, P. Klemera, K. Kopecky, Z. Musil, J. Photochem. Photobiol. A: Chem. 178 (2006) 16.
[10] Z. Musil, P. Zimcik, M. Miletin, K. Kopecky, M. Link, P. Petrik, J. Schwarz, J Porphyr. Phthalocya. 10 (2006) 122.
[11] P. Zimcik, M. Miletin, M. Kostka, J. Schwarz, Z. Musil, K. Kopecky, J. Photochem. Photobiol. A: Chem. 163 (2004) 21.
[12] Z. Musil, P. Zimcik, M. Miletin, K. Kopecky, P. Petrik, J. Lenco, J. Photochem. Photobiol. A: Chem. 186 (2007) 316.
[13] M.P. Donzello, Z. Ou, D. Dini, M. Meneghetti, C. Ercolani, K.M. Kadish, Inorg. Chem. 43 (2004) 8637.
[14] M.P. Donzello, Z. Ou, F. Monacelli, G. Ricciardi, C. Rizzoli, C. Ercolani, K.M. Kadish, Inorg. Chem. 43 (2004) 8626.
[15] C. Bergami, M.P. Donzello, C. Ercolani, F. Monacelli, K.M. Kadish, C. Rizzoli, Inorg. Chem. 44 (2005) 9852.
[16] C. Bergami, M.P. Donzello, F. Monacelli, C. Ercolani, K.M. Kadish, Inorg. Chem. 44 (2005) 9862.
[17] E.H. Mørkved, F.M. Pedersen, N.K. Afseth, H. Kjøsen, Dyes Pigment. 77 (2008) 145.
[18] E.H. Mørkved, N.K. Afseth, H. Kjøsen, J. Porphyr. Phthalocya. 10 (2006) 1301.
[19] A. Nakamura, T. Ataka, H. Segawa, Y. Takeuchi, T. Takematsu, Agric. Biol. Chem. 47 (1983) 1561.
[20] J.L. Hyatt, V. Stacy, R.M. Wadkins, K.J.P. Yoon, M. Wierdl, C.C. Edwards, M. Zeller, A.D. Hunter, M.K. Danks, G. Crundwell, P.M. Potter, J. Med. Chem. 48 (2005) 5543.
[21] E. Campaign, E.S. Neiss, J. Heterocycl. Chem. 3 (1966) 46.
[22] E.H. Mørkved, Chem. Heterocycl. Comp. (2007) 1409.
[23] A. Ogunsipe, D. Maree, T. Nyokong, J. Mol. Struct. 650 (2003) 131.
[24] D. Wöhrle, M. Shopova, S. Muller, A.D. Milev, V.N. Mantareva, K.K. Krastev, J. Photochem. Photobiol. B: Biol. 21 (1993) 155.
[25] N.A. Kuznetsova, N.S. Gretsova, V.M. Derkacheva, S.A. Mikhalenko, L.I. Solov'eva, O.A. Yuzhakova, O.L. Kaliya, E.A. Luk'yanets, Russ. J. Gen. Chem. 72 (2002) 300.

While several dimeric complexes of copper(I) halides with heterocyclic thioamides are reported [12], there are only two dimeric complexes of heterocyclic thioamides with silver(I), namely, $[Ag_2Br_2(pymSH)_2(PPh_3)_2]$ (pymSH = pyrimidine-2-thione) [10a] and $[Ag_2(\mu\text{-S-pySH})_2\text{-}(\mu\text{-P,P-dppb})_2](NO_3)_2$ (dppb = $Ph_2P\text{-}(CH_2)_4\text{-}PPh_2$) [10b]. In this paper, dimeric complexes of silver(I) halides with pyridine-2-thione are reported and characterized using analytical data, NMR spectroscopy and single crystal X-ray crystallography.

2. Experimental

2.1. Materials and techniques

Pyridine-2-thione and triphenyl phosphine were procured from Aldrich–Sigma Ltd. Silver(I) halides were freshly prepared from $AgNO_3$ and NaBr, or KCl and dried *in vacuo*. Elemental analysis for C, H and N were carried out using a thermoelectron FLASHEA1112 analyser. The melting points were determined with a Gallenkamp electrically heated apparatus. The IR spectra of the ligands and the complexes were recorded on the FTIR-SHIMADZU 8400 Fourier Transform spectrophotometer in the range, 4000–500 cm^{-1} (using KBr pellets). ^1H NMR spectra were recorded on a JEOL AL300 FT spectrometer at 300 MHz in $CDCl_3$ with TMS as the internal reference. The ^{31}P NMR spectra were recorded at 121.5 MHz with $(CH_3O)_3P$ as the external reference taken as zero position.

2.2. Synthesis of $[Ag_2(\mu\text{-S-pySH})_2(PPh_3)_2Cl_2]$ (1)

To AgCl (0.025 g, 0.17 mmol) suspended in 20 mL of acetonitrile was added solid PPh_3 (0.045 g, 0.17 mmol) and stirring was carried out for 24 h. Acetonitrile was removed from the white colored precipitates and chloroform (15 mL) was added. To these precipitates suspended in chloroform, solid pyridine-2-thione (0.019 g, 0.17 mmol) was added, and the contents stirred for 1 h until clear solution was obtained. Slow evaporation of the solution at room temperature formed a solid mass which was crystallized from methanol–dichloromethane mixture (20 mL, 1:3 v/v). The yellow colored crystals were formed. Yield: 60%; m.p. 155–57 °C. *Anal.* Calc. for $AgClC_{23}H_{20}NSP$: C, 53.43; H, 3.87; N, 2.71. Found: C, 53.78; H, 3.70; N, 3.01%. Main IR peaks (KBr, cm^{-1}), υ(N–H), 3178(m); υ(C–H), 3035–2920(m); υ(C=N) + υ(C–C); 1608(m)–1571(s); δ(N–H) + δ(C–H), 1500(s)–1363(s); υ(C=S), 1130(s); υ(P–C_{Ph}) 1093(m). ^1H NMR (δ, $CDCl_3$), δ = 7.81(d, H^6), 7.26–7.63m (Ph_3P + $C^{3,4}H$); 6.89(t, H^5). ^{31}P NMR ($CDCl_3$), δ = −98.4 ppm, $\Delta\delta(\delta_{complex} - \delta_{PPh_3})$ = 14.8 ppm. δP, –78.63, $\Delta\delta$ = 34.80 ppm.

2.3. Synthesis of $[Ag_2(\mu\text{-S-pySH})_2(PPh_3)_2Br_2]$ (2)

To AgBr (0.025 g, 0.13 mmol) suspended in 20 mL of acetonitrile was added solid PPh_3 (0.070 g, 0.26 mmol) and stirring was carried out for 24 h. Acetonitrile was removed from the white colored precipitates and chloroform (15 mL) was added. To the precipitates suspended in $CHCl_3$ solid pyridine-2-thione (0.019 g, 0.17 mmol) was added and the contents were stirred for 1 h until a clear solution was obtained. Slow evaporation of solution at room temperature formed a solid mass which was treated with diethyl ether to remove any unreacted PPh_3 and then crystallized from methanol–dichloromethane mixture (25:75:v/v). The yellow colored crystals were formed. Yield: 65%; m.p. 190–195 °C. *Anal.* Calc. for $AgBrC_{23}H_{20}NSP$: C, 49.22; H, 3.55; N, 2.49. Found: C, 49.50; H, 3.91; N, 2.49%. Main IR peaks (KBr, cm^{-1}); ν(N–H), 3170(m); υ(C–H) 3058(m)–3035(m); ν(C=N) + υ(C=C); 1608(m)–1569(s); δ(N–H) + δ(C–H) 1498(s)–1361(s); ν(C=N), 1608(w); ν(C=S), 1128(s); ν(P–C_{Ph}), 1093(m). ^1H NMR data (δ, $CDCl_3$): 7.78 (d, H^6); 7.67 (m, H^4); 7.57(d, H^3); 6.91(t, H^5); 7.32–7.53 (PPh_3). ^{31}P NMR ($CDCl_3$), δ = − 100.6, $\Delta\delta(\delta_{complex} - \delta_{PPh_3})$ = 12.6 ppm. δP, −78.29, $\Delta\delta$ = 34.86 ppm.

2.4. Crystallography

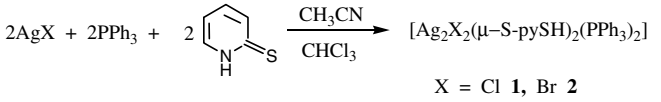
Single crystals of compounds **1** and **2** were mounted on CCD area detector diffractometer, equipped with a graphite monochromator and Mo Kα radiator (λ = 0.71073 Å). The unit cell dimensions and intensity data were measured at 93(2) K. The structures were solved by the direct methods, and refined by the full matrix least square based on F^2 with anisotropic thermal parameters for the non-hydrogen atoms using Bruker SMART (data collection and cell refinement), Bruker SAINT (data reduction) SHELXS-97 (structure solution), and SHELXL-97 (structure refinement) and Bruker SHELXTL (molecular graphics) [13–16]. A multi-scan absorption correction (SADABS) was applied.

3. Results and discussion

3.1. Synthesis and IR spectroscopy

Reaction of silver(I) chloride with PPh_3 in acetonitirile and then with pyridine-2-thione chloroform (1:1:1 molar ratio) yielded compound of stoichiometry, {AgCl(pySH)(PPh_3)} and similar reaction with silver(I) bromide yielded, {AgBr(pySH)(PPh_3)}. The X-ray crystallography has shown both compounds to be dimers, $[Ag_2Cl_2(\mu\text{-S-pySH})_2(PPh_3)_2]$ **1** and $[Ag_2Br_2(\mu\text{-S-pySH})_2(PPh_3)_2]$ **2** (Scheme 1).

Complexes showed ν(N–H) peaks at 3178 cm^{-1} in **1** and at 3170 cm^{-1} in **2**, and it revealed that there is no deprotonation of NH proton of pySH ligand. The diagnostic



Scheme 1.

ν(C=S) peak in free pySH ligand occurs at 1138 cm^{-1} [12], which is shifted to lower energy region in complexes, at 1130 cm^{-1} **1** and 1128 cm^{-1} **2**. These trends in ν(C=S) and ν(N–H) peaks suggest coordination by thione sulfur donor atom. The ν(C–H) peaks fall in the regions 3055–2920 cm^{-1}; while other peaks due to ν(C–C) + ν(C=N) + δ(N–H) + δ(C–H) fall in the region, 1332–1608 cm^{-1}. A characteristic peak due to $\nu(P–C_{Ph})$ at 1093 cm^{-1} indicated the presence of PPh_3 in the complexes.

3.2. Crystal structures of the complexes

Compounds $[Ag_2(\mu\text{-S-pySH})_2Cl_2(PPh_3)_2]$ **1** and $[Ag_2(\mu\text{-S-pySH})_2Br_2(PPh_3)_2]$ **2** crystallized as triclinic crystals in space group $P\bar{1}$. The atomic numbering schemes of complexes **1** and **2** are shown in Figs. 1 and 2, respectively. Crystal data are given in Table 1 and bond lengths and angles are given in Table 2.

In complex **1**, Ag is bonded to one Cl atom, one P atom of Ph_3P and one S atom of pySH forming three coordinate unit, {AgCl(Ph_3P)(pySH)}, and two such units dimerize via the bonded S atoms to yield sulfur-bridged dimer $[Ag_2Cl_2(\mu\text{-S-pySH})_2(PPh_3)_2]$ **(1)** (Fig. 1). The formation of $[Ag_2Br_2(\mu\text{-S-pySH})_2(PPh_3)_2]$ **(2)** (Fig. 2) is similar with Br as the anion. The central Ag_2S_2 core forms a parallelogram with two unequal Ag–S bond distances (2.5832(8), 2.7208(11) Å) in **1** and (2.6306(4), 2.6950(7) Å) in **2**, respectively. These bridging Ag–S bond distances are in the range of terminal Ag–S bond distance, 2.625 Å in [AgCl(pySH)(PPh_3)$_2$] [9a]. The S–Ag–S and Ag–S–Ag bond angles within the {Ag(μ-S)$_2$Ag} core of **1** are 87.190(15)° and, 92.810(15)° **1**, respectively. The similar angles are 87.814(18)° and 92.187(18)° in **2**. The angles around Ag vary in the range 87.19(2)–121.71(2)° in **1**, and 87.81(2)–121.53(2)° in **2**, which indicate highly distorted tetrahedral geometries. Finally the Ag–S–C bond angles are 105.10(6)°,

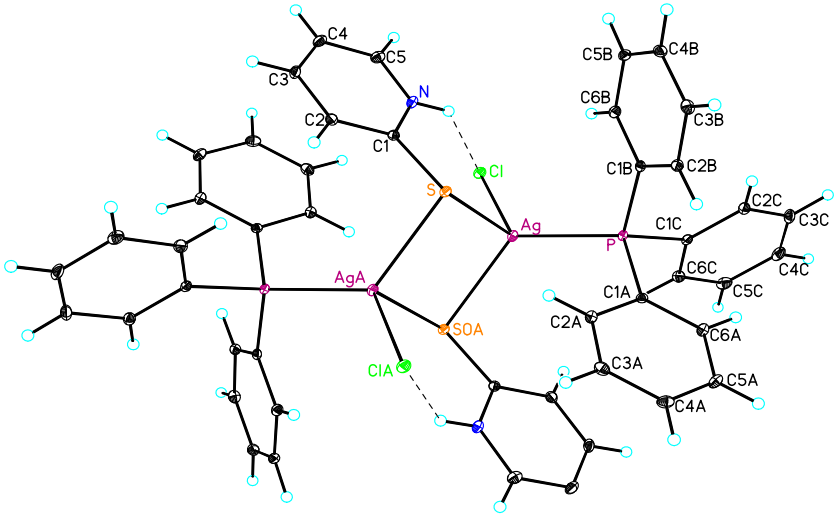


Fig. 1. Structure of complex **1** showing the atomic numbering scheme.

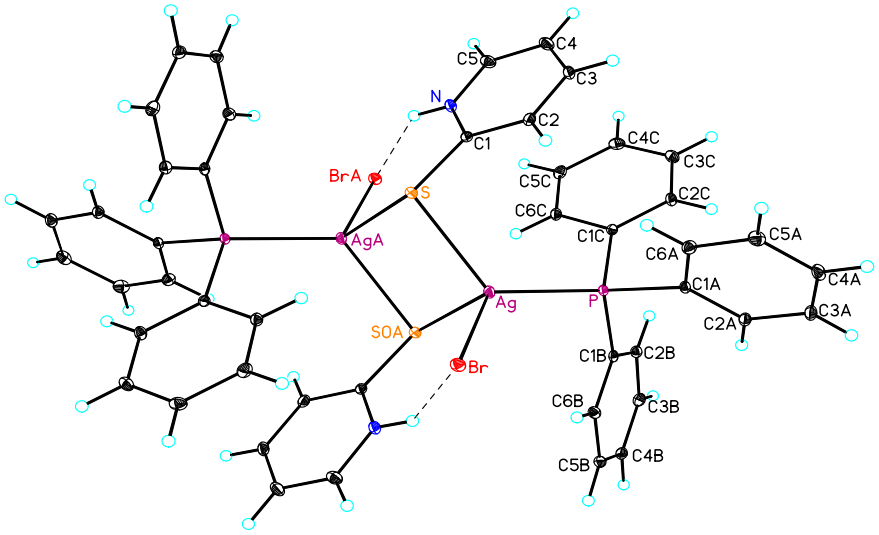


Fig. 2. Structure of complex **2** showing the atomic numbering scheme.

Table 1
Crystal data and refinement details for complexes **1** and **2**

	1	**2**
Empirical formula	$C_{46}H_{40}Ag_2Cl_2N_2P_2S_2$	$C_{46}H_{40}Ag_2Br_2N_2P_2S_2$
M	1033.50	1122.42
T (K)	93(2)	93(2)
Crystal system	triclinic	triclinic
Space group	$P\bar{1}$	$P\bar{1}$
Unit cell dimensions		
a (Å)	9.520(3)	9.526(1)
b (Å)	9.507(3)	9.583(1)
c (Å)	14.014(5)	14.121(2)
α (°)	71.563(5)	77.512(2)
β (°)	77.357(6)	72.176(2)
γ (°)	62.924(5)	63.011(2)°
V (Å^3)	1067.1(6)	1088.9(3)
Z	1	1
D_{calc} (mg m^{-3})	1.608	1.712
μ (mm^{-1})	1.251	2.938
Reflections collected	8376	8192
Unique reflections [R(int)]	5003 [0.0268]	5049 [0.0161]
Reflections with [$I > 2\sigma(I)$]	4807	4438
Final R indices [$I > 2\sigma(I)$]	$R_1 = 0.0254$, $wR_2 = 0.0665$	$R_1 = 0.0235$, $wR_2 = 0.0562$
R indices (all data)	$R_1 = 0.0267$, $wR_2 = 0.0673$	$R_1 = 0.0306$, $wR_2 = 0.0600$

Table 2
Selected bond length (Å) and angles(°) for **1** and **2**

1			
Ag–P	2.435(1)	Ag–S	2.721(1)
Ag–Cl	2.530(1)	Ag–S	2.583(1)$^{\#1}$
S–C(1)	1.722(2)	Ag···Ag	3.8425(8)
P–Ag–Cl	121.71(2)	P–Ag–S	101.35(2)
Cl–Ag–S	103.91(2)	P–Ag–S$^{\#1}$	120.70(2)
Cl–Ag–S$^{\#1}$	112.24(3)	Ag–S–Ag	92.81(2)
Ag–S–C(1)	109.93(6)	S–Ag–S	87.19(2)
Ag$^{\#1}$–S–C(1)	105.10(6)		
2			
Ag–P	2.441(1)	Ag–Br	2.631(1)
Ag–S	2.608(1)	Ag–S$^{\#1}$	2.695(1)
S–C(1)	1.717(2)	Ag···Ag	3.8211(4)
P–Ag–Br	121.53(2)	P–Ag–S	121.16(2)
S–Ag–Br	109.47(2)	P–Ag–S$^{\#1}$	102.44(2)
Br–Ag–S$^{\#1}$	106.98(1)	Ag–S–Ag	92.19(2)
Ag–S–C(1)	103.79(8)	S–Ag–S$^{\#1}$	87.81(2)
Ag$^{\#1}$–S–C(1)	111.62(1)		

109.93(6)° in **1** and 103.79(8)°, 111.62(1)° in **2** and are similar to that reported for $[Ag(pySH)(PPh_3)_2Cl]$ [9a].

The Ag–Cl bond is strong as the bond distance in complex **1**, 2.530(1) Å is less than the sum of the ionic radii of Ag^+ and Cl^-, 2.7501 Å [17]. The Ag–Br bond distance in complex **2**, 2.631(1) Å, is shorter than the Ag–Br bridging bond distance [2.7350(6), 2.8241(5) Å] observed in $[Ag_2Br_2(\mu\text{-S-pymSH})_2(PPh_3)_2]$ [10a]. The S–C bond distance 1.722(2) Å in **1** is slightly larger than 1.717(2) Å in complex **2**. This is due to high electronegativity of Cl^- versus Br^- which weakens C–S bond in the former. The Ag–P bond distances are, 2.4346(10) Å in **1** and 2.4414(6) Å in **2**, which are nearly same. The Ag···Ag contacts of compounds **1** and **2** of 3.8425(8) and 3.8211(4) Å, respectively, are higher than twice the sum of van der Waals radius of Ag atom, 3.40 Å.

There are inter dimer π–π stacking interactions between pyridyl rings. The inter ring distances are 3.498 and 3.510 Å in complexes **1** and **2**, respectively. Packing diagrams are shown in Figs. 3 and 4.

3.3. NMR spectroscopy

Proton NMR spectra of sparingly soluble complexes, $[AgCl(pySH)(PPh_3)]_2$ **1** and $[AgBr(pySH)(PPh_3)]_2$ **2**, in $CDCl_3$ has been recorded. Complexes **1** and **2** show peaks due to H^6 proton at low field, δ 7.81 and 7.78 ppm, respectively, vis-à-vis the free ligand (pySH) at δ 7.56 ppm [12]. Likewise, H^5 proton signals at δ 6.89 (**1**) and 6.91 (**2**) ppm are downfield (free pySH, δ 6.73 ppm). The H^3 and H^4 proton signals for **1** merged with the PPh_3 signals in the region, δ 7.26–7.63 ppm; while in complex **2**, these signals were clearly visible (see Section 2). The ^{31}P NMR spectra showed two peaks for each complex with coordination shifts, 14.8, 34.80 ppm (**1**) and 12.6, 34.86 (**2**) ppm. These data reveal that dimers (δ 34.80, 34.86 ppm **1** and **2**) probably set an equilibrium with monomers (14.8, 12.6 ppm,**1a**, **2a**, respectively) in solution. The monomers are suggested as $AgX(pySH)(PPh_3)_2$ (X = Cl, **1a**; Br, **2a**) formed by rearrangement of dimers in solution, a phenomenon observed in copper(I) halide-thiosemicarbazone chemistry [18].

3.4. Electronic absorption spectroscopy

The electronic absorption spectrum of complex **1** in dichloromethane showed three peaks at λ_{max} values of 238, 270 and 359 nm. Similarly complex **2** has shown two peaks at λ_{max} values of 239, 271 and 359 nm. The peaks

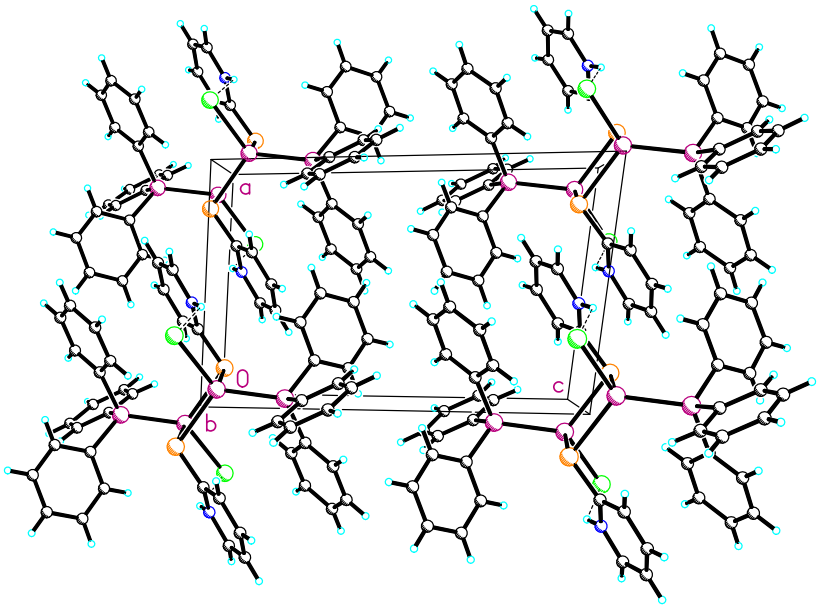


Fig. 3. Packing diagram of complex **1**.

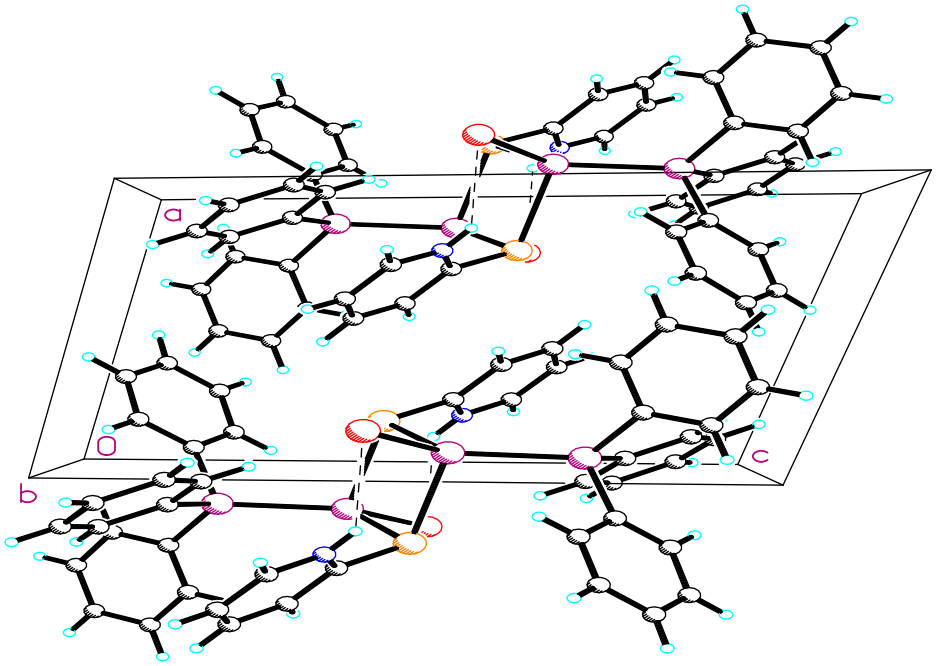


Fig. 4. Packing diagram of complex **2**.

at 359 nm are attributed to –C═S groups due to n → π* transitions while other beaks are due to π → π* transitions based on pyridyl and phenyl rings. Neither of the two compounds exhibited any fluorescence properties.

3.5. Conclusion

Pyridine-2-thione has formed hitherto unknown dimers **1** and **2**. It may be noted that AgCl has formed both previously known monomer, $[Ag(pySH)(PPh_3)_2Cl]$ [9a], and the newly formed dimer $[Ag_2Cl_2(\mu\text{-S-pySH})_2(PPh_3)_2]$ **1**; while for copper(I) chloride only monomer, $[CuCl(pySH)(PPh_3)_2]$ is known to date as all efforts to get a dimer $[Cu_2Cl_2(\mu\text{-S-pySH})_2(PPh_3)_2]$ ended in the formation of only monomer $[CuCl(pySH)(PPh_3)_2]$ due to strong intramolecular –NH···Cl hydrogen bonding in the latter [12].

Acknowledgements

One of us (Rohit) thanks Guru Nanak Dev University for research facilities. The authors also thank Razia Sultana and Sonia Khanna for their help.

Appendix A. Supplementary data

CCDC 657505 and 657504 contain the supplementary crystallographic data for **1** and **2**. These data can be obtained free of charge via http://www.ccdc.cam.ac.uk/conts/retrieving.html, or from the Cambridge Crystallographic Data Centre, 12 Union Road, Cambridge CB2 1EZ, UK; fax: (+44) 1223-336-033, or e-mail: deposit@ccdc.cam.ac.uk. Supplementary data associated with this article can be found, in the online version, at doi:10.1016/j.poly.2008.01.008.

References

[1] E.S. Raper, Coord. Chem. Rev. 61 (1985) 115.
[2] E.S. Raper, Coord. Chem. Rev. 153 (1996) 199.
[3] E.S. Raper, Coord. Chem. Rev. 129 (1994) 91.
[4] E.S. Raper, Coord. Chem. Rev. 165 (1997) 475.
[5] P.D. Akrivos, Coord. Chem. Rev. 213 (2001) 181.
[6] J.A. Garcia-Vazquez, J. Romero, A. Sousa, Coord. Chem. Rev. 193 (1999) 691.
[7] T.S. Lobana, Ritu Sharma, Renu Sharma, Sheetal Mehra, A. Castineiras, Peter Turner, Inorg. Chem. 44 (2005) 1914.
[8] T.S. Lobana, Renu Sharma, Geeta Hundal, R.J. Butcher, Inorg. Chem. 45 (2006) 9402.
[9] (a) P. Karagiannidis, P. Aslanidis, S.C. Kokkou, C.J. Cheer, Inorg. Chim. Acta 172 (1990) 247;
(b) P. Aslanidis, P. Karagiannidis, P.D. Akrivos, B. Krebs, M. Lage, Inorg. Chim. Acta 254 (1997) 277;
(c) G. Giusti, G. Geier, A. Currao, R. Nesper, Acta Crystallogr., Sect. C 52 (1996) 1914;
(d) W. McFarlane, P.D. Akrivos, P. Aslanidis, P. Karagiannidis, C. Hatzisymeon, M. Numan, S. Kokkou, Inorg. Chim. Acta 281 (1998) 121;
(e) M.B. Ferrari, C.G. Fava, M.E.V. Tani, Cryst. Struct. Commun. 10 (1981) 571;
(f) J. Sola, A. Lopez, R.A. Coxall, W. Clegg, Eur. J. Inorg. Chem. (2004) 4871.
[10] (a) P.J. Cox, P. Aslanidis, P. Karagiannidis, S. Hadjikakou, Inorg. Chim. Acta 310 (2000) 268;
(b) P. Aslanidis, P.J. Cox, S. Divanidis, P. Karagiannidis, Inorg. Chim. Acta 357 (2004) 2677;
(c) M. Hong, W. Su, R. Cao, W. Zhang, J. Lu, Inorg. Chem. 38 (1999) 600.
[11] W. Su, M. Hong, J. Weng, Y. Liang, Y. Zhao, R. Cao, Z. Zhou, A.S.C. Chan, Inorg. Chim. Acta 331 (2002) 8.
[12] T.S. Lobana, A. Castineiras, Polyhedron 21 (2002) 1603.
[13] Bruker, SMART, SAINT and XPREP. Area Detector Control and Data Integration and Reduction Software. Bruker Analytical X-ray Instruments Inc., Madison, WI, USA, 1995.
[14] G.M. Sheldrick, SADABS, Program for Empirical Absorption Correction of Area Detector data, University of Gottingen, Gottingen, Germany, 1997.
[15] G.M. Sheldrick, Acta Crystallogr., Sect. A 46 (1990) 467.
[16] G.M. Sheldrick, SHELXL-97, Program for the Refinement of Crystal Structures, University of Gottingen, Gottingen, Germany, 1997.
[17] J.E. Huheey, E.A. Keiter, R.L. Keiter, Inorganic Chemistry: Principles of Structure and Reactivity, 4th ed., Harper Collins College Publishers, New York, 1993.
[18] T.S. Lobana, Rekha, R.J. Butcher, A. Castineiras, E. Bermejo, P.V. Bharatam, Inorg. Chem. 45 (2005) 1535.

stackings responsible for the extended networks are also discussed.

2. Experimental

2.1. Materials and measurements

All reagents were purchased from commercial sources and used as supplied. The elemental analyses (C, H and N) were performed on a Vario EL Elemental Analyser. IR spectra were recorded on a MATTSON 1000 FT/IR spectrophotometer as KBr pellets in the frequency range 4000–400 cm^{-1}. ESR spectra were run on a Varian E-109C model X Band EPR spectrophotometer. Room temperature magnetic susceptibility measurements were carried out using a Sherwood Scientific MXI model Evans magnetic balance. Thermal analysis curves (TG and DTA) were obtained from a Rigaku TG8110 thermal analyzer in a static air atmosphere using a sample size of 5–10 mg.

2.2. Synthesis of the copper(II) complexes

Complexes **1** and **2** were prepared using the same synthesis procedure. Ten millilitres of methanol solution of saccharin (2 mmol, 0.37 g) was mixed with a warm methanol solution of $Cu(OAc)_2 \cdot H_2O$ (1 mmol, 0.20 g) with stirring. To the solution, 2 mmol (0.17 g) ppz or 2 mmol (0.26 g) aeppz dissolved in 10 ml methanol was added drop-wise and the reaction mixtures were stirred for 1 h at room temperature. The resulting solutions were allowed to stand at room temperature and X-ray quality green prisms of **1** and **2** were formed after a day.

$[Cu(sac)_2(ppz)(H_2O)]_n$ (**1**): Yield 70%. *Anal.* Calc. for $C_{18}H_{20}N_4O_7S_2Cu$ (%) C, 40.64; H, 3.79; N, 10.53. Found C, 40.67; H, 3.65; N, 10.63%. (Solid KBr pellet): ν (cm^{-1}) 3417sb, 3342s, 3276m, 3053w, 2927w, 1656vs, 1572vs, 1456m, 1336m, 1288vs, 1153vs, 1103sh, 1034s, 958vs, 748s, 677s, 604s, 521m, 453m.

$[Cu(sac)_2(aeppz)_2]$ (**2**): Yield 90%. *Anal.* Calc. for $C_{26}H_{38}N_8O_6S_2Cu$ (%) C, 40.50; H, 5.58; N, 16.33. Found C, 40.59; H, 5.46; N, 16.44%. (Solid KBr pellet): ν (cm^{-1}) 3444sb, 3300s, 3245s, 3114m, 2939s, 2836m, 1619vs, 1574vs, 1465s, 1366s, 1285vs, 1158vs, 1122vs, 1059w, 951vs, 924s, 842s, 770vs, 734w, 688m, 644m, 608s, 544s, 463w.

2.3. X-ray crystallography

Intensity data for the title complexes were collected using a Stoe-IPDS-2 diffractometer equipped with a graphite monochromated (Mo Kα radiation, $\lambda = 0.71073$ Å) at 293 K. The structure was solved by direct methods using SHELXS-97 [7] and refined by a full-matrix least-squares procedure using the program SHELXL-97 [7]. The value of R_{int} for the structure of **2** is slightly high due to the crystal quality. All non-hydrogen atoms were easily found from the difference Fourier map and refined anisotropically. All carbon and amine hydrogen atoms were included using a riding model, while the water H atoms were refined freely. Details of crystal data, data collection, structure solution and refinement are given in Table 1.

3. Results and discussion

3.1. Synthesis and characterization

The new complexes were prepared by the direct reaction of the ppz or aeppz ligands with a mixture of copper(II) acetate and saccharin in solution. Both complexes were obtained in high yields (over 70%) and the analytical data are consistent with the proposed formulation of the complexes, and also confirmed by X-ray crystallography as reported in this paper. All the complexes are non-hygroscopic and stable in air, and soluble in water, methanol and ethanol.

The FT-IR spectra of all the complexes were recorded in the frequency range 4000–400 cm^{-1}. In the IR spectra of **1**, the strong and broad absorption band centered at around 3417 cm^{-1} are attributed to the ν(OH) vibrations of the aqua ligand. The bands at 3342 and 3276 cm^{-1} are assigned to the ν(NH) vibrations of the ppz ligand. The corresponding vibrations were observed at 3300 and 3245 cm^{-1} for **2**. The weak bands in the range 3115–2835 cm^{-1} are due to the aromatic and aliphatic ν(CH) vibrations. The bands for the carbonyl group of sac appear at *ca.* 1655 and 1620 cm^{-1}, respectively. The carbonyl bands at around 1650 cm^{-1} usually correspond to the monodentate coordination of sac through the deprotonated N-atom [8]. In the

Table 1
Crystallographic data for complexes **1** and **2**

Complex	**1**	**2**
Formula	$C_{18}H_{20}N_4O_7S_2Cu$	$C_{26}H_{38}N_8O_6S_2Cu$
M	532.04	686.30
T (K)	293(2)	293(2)
λ (Å)	0.71073	0.71073
Crystal system	triclinic	triclinic
Space group	$P\bar{1}$	$P\bar{1}$
a (Å)	7.095(3)	8.4301(8)
b (Å)	11.730(4)	9.3493(9)
c (Å)	13.726(3)	11.5495(12)
α (°)	105.95(2)	94.287(8)
β (°)	103.52(2)	109.844(8)
γ (°)	103.78(3)	115.961(7)
V (Å^3)	1010.5(7)	742.49(15)
Z	2	1
D_{calc} (g cm^{-3})	1.749	1.535
μ (mm^{-1})	1.340	0.932
θ Range (°)	1.91–27.12	1.94–27.95
Index range (h,k,l)	−8/9, −14/14, −17/17	−9/10, −12/12, −14/14
Reflections collected	15685	12245
Data/parameters	4322/297	3383/188
Goodness-of-fit on F^2	1.047	1.005
R_1 [$I > 2\sigma$]	0.0284	0.0419
wR_2	0.0755	0.1050

case of the coordination *via* the carbonyl group, a significant shift to lower frequencies occurs due to a weakening of the carbon–oxygen bond. Therefore, the sharp bands at 1655 and 1620 cm^{-1} for complexes **1** and **2**, respectively, clearly indicate that the sac is N-bonded in **1**, but O-bonded in **2**. The stretching vibrations of $\nu_{asym.}(SO_2)$ and $\nu_{sym.}(SO_2)$ were observed as very strong bands at *ca.*1285 and 1155 cm^{-1}, respectively.

The electronic spectra of methanol solutions of **1** and **2** display broad absorption bands at 632 ($\varepsilon = 54$ dm^3 mol^{-1} cm^{-1}) and 623 nm ($\varepsilon = 53$ dm^3 mol^{-1} cm^{-1}), respectively, which are assigned to d–d transitions. The strong absorption bands below 300 nm are due to intra-ligand transitions of ppz, aeppz and sac ligands.

The powder ESR spectra of complexes **1** and **2** were measured at the room temperature. Both complexes display intense spectra with no hyperfine structure. Complex **1** exhibits a broad signal with three g values ($g_z = 2.244$, $g_x = 2.139$ and $g_y = 2.008$). The R factor for complex **1** [defined as $R = (g_x - g_y)/(g_z - g_y)$], is 1.24, which suggests that the 3d unpaired electron of the copper(II) ion occupied the d_{z^2} orbital [9,10]. The ESR spectrum of complex **2** shows a sharp signal with a g value of 2.162. Compared to that of the free electron value ($g = 2.0023$), it can be concluded that in both complexes, the interactions between copper(II) centers in the solid state are negligible.

The room temperature magnetic moments are 1.76 and 1.74 B.M. for complexes **1** and **2**, respectively, and consistent with the calculated value (1.73 B.M.) of the spin-only magnetic moment of the d^9 configuration. As well as ESR spectra, magnetic susceptibility measurements also indicate that the polymeric complex **1** does not exhibit any anti-ferromagnetic interaction at the room temperature.

3.2. Description of the crystal structures

Complex **1** is a 1D helical coordination polymer and the ORTEP view of the building unit with atom labeling is shown in Fig. 1. Selected bond lengths and angles are listed in Table 2. The copper(II) ion is coordinated to an aqua O atom, two imine nitrogen atoms from two sac ions and two N atoms of two symmetry related ppz ligands. The coordination geometry around the Cu^{II} center is described as a trigonal-bipyramidal generated by N1–N2–N3–N4–OW1 atoms with τ value of 0. 61, which is used to describe the degree of distortion for penta-coordinated complexes ($\tau = 0$ for an ideal square-pyramid and $\tau = 1$ for an ideal trigonal-bipyramid) [11]. The sac anions are N-coordinated and their nitrogen atoms act as the axis of trigonal-bipyramid with the mean Cu–N distance of 2.057(2) Å. Two N atoms from two ppz rings together with an aqua O atom are composed of the basal plane and the copper(II) ion is deviated from this coordination plane by 0.068(1) Å. The ppz rings are in normal chair conformation with the puckering parameters $q = 0.550(2)$–$0.561(2)$ Å and $\theta = 0.00(1)$–$3.06(1)°$, and the ring torsion angles lying in the range of 54.1–56.2°. On the other hand, the sac ring system is essentially planar and the dihedral angles between the adjacent sac rings is 14.64(5)°.

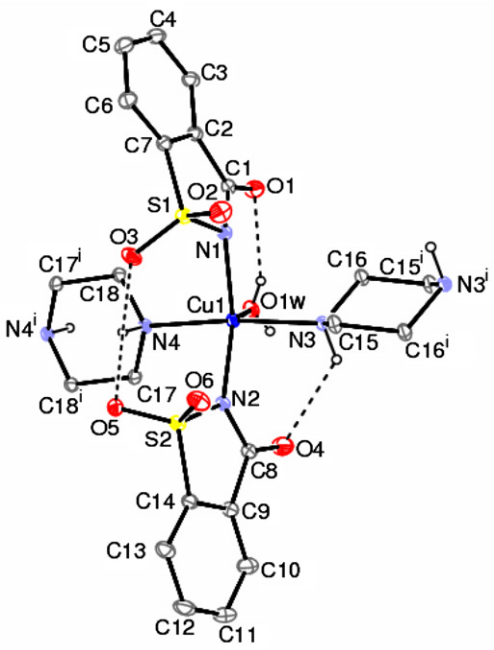


Fig. 1. The building block unit and coordination environment of Cu^{II} in **1** with the atom labeling scheme. CH hydrogen atoms are omitted for clarity. The intramolecular hydrogen bonds are indicated by dashed lines. Symmetry code (i) = $-x + 2$, $-y + 1$, $-z + 1$.

Table 2
Selected bond lengths (Å) and bond angles (°) for **1** and **2**

Complex ***1***			
Cu1–N1	2.063(2)	Cu1–N4	2.075(2)
Cu1–N2	2.051(2)	Cu1–O1W	2.143(2)
Cu1–N3	2.041(2)		
N1–Cu1–N2	137.54(7)	N3–Cu1–N4	173.98(7)
N1–Cu1–N3	92.78(7)	N1–Cu1–O1W	100.31(8)
N1–Cu1–N4	93.21(7)	N2–Cu1–O1W	122.03(8)
N2–Cu1–N3	87.86(7)	N3–Cu1–OW1	93.90(7)
N2–Cu1–N4	88.09(7)	N4 –Cu1– OW1	84.50(7)
Complex ***2***			
Cu1–N2	1.978(2)	Cu1–O1	2.103(2)
Cu1–N3	2.469(2)		
N2–Cu1–N3	81.54(8)	N2–Cu1–$N3^i$	98.46(8)
N2–Cu1–O1	92.74(7)	N2–Cu1–$O1^i$	87.26(7)
N3–Cu1–O1	92.22(6)	N3–Cu1–$O1^i$	87.78(6)

Symmetry operations: (i) $-x$, $-y + 1$, $-z$.

The copper(II) centers are bridged by both nitrogen atoms of ppz ligands leading to a 1D helical chain (Fig. 2). The closest Cu–Cu^i contact is only 6.915 Å (i = $-x + 2$, $-y + 1$, $-z + 1$). Analysis of the crystal packing of complex **1** in the unit cell shows that there exist multiple intra- and intermolecular hydrogen-bonding interactions as listed in Table 3. The individual chains running parallel to the crystallographic axis c are connected by OW–H···O hydrogen bonds into 2D layers running in the

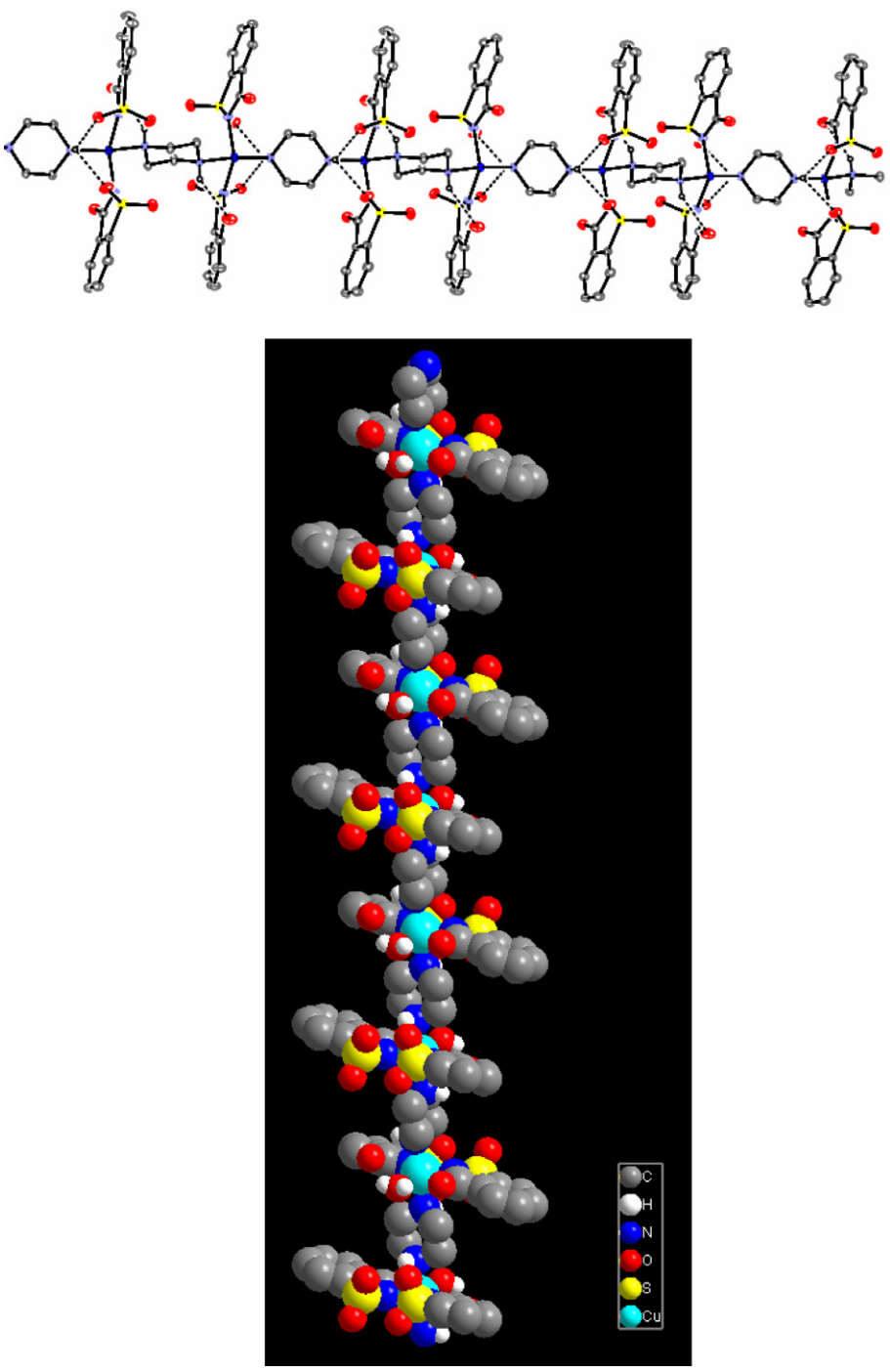


Fig. 2. ORTEP and space-filling views of a fragment of a one-dimensional helical chain in **1**.

ab plane and these layers are further associated by weak π(sac)–π(sac) stacking interactions with the Cg–Cg^{i} separation of 3.923(2) Å (i = $-x$, $-y$, $-z$) to give a 3D network as shown in Fig. 3.

The molecular view of complex **2** is illustrated in Fig. 4. The selected bond lengths and angles are given in Table 2. The crystal structure of **2** consists of isolated centrosymmetric $[Cu(sac)_2(aeppz)_2]$ molecules, in which the Cu^{II} ion lies on a center of inversion and displays a distorted octahedral coordination geometry with two aeppz and two sac ligands at the *trans* positions. In contrast to complex **1**, the sac ion in **2** coordinates to Cu^{II} through to carbonyl O atom, while aeppz acts as an *N*,*N*′-bidentate chelating ligand, creating a five-membered ring around Cu^{II}.

Complex **2** is isostructural with the cobalt(II), nickel(II), zinc(II) and cadmium(II) complexes of sac containing aeppz ligands [12–14]. All complexes show similar structural characteristics and the most interesting feature in these metal complexes is the elongation of the octahedral geometry even in the case of Ni^{II}, Zn^{II} and Cd^{II}. The elon-

Table 3
Hydrogen bond data for complexes **1** and **2**

D–H···A	D–H (Å)	H···A (Å)	D···A (Å)	D–H···A (°)
Complex ***1***				
O1W–H2W···O1	0.73(4)	2.29(4)	2.882(3)	140(4)
N3–H3A···O4	0.91	2.48	3.160(3)	132
N4–H4A···O3	0.91	2.47	2.982(3)	116
N4–H4A···O5	0.91	2.31	3.027(3)	136
O1W–H2W···O3^{i}	0.73(4)	2.28(4)	2.836(3)	134(4)
O1W–H1W···O5^{i}	0.78(4)	2.06(4)	2.839(3)	172(3)
Complex ***2***				
N2–H2A···N1	0.90	2.25	2.955(3)	135
N2–H2B···N4^{ii}	0.90	2.38	3.189(3)	150
N4–H4A···O3^{iii}	0.82(4)	2.27(4)	3.083(4)	169(3)

Symmetry operations: (i) $x+1$, y, z; (ii) $x-1$, y, z; (iii) $-x+1$, $-y+2$, $-z$.

gation occurs along the M–$N_{ppz\ ring}$ bonds and is possibly due to a poor overlap between the orbitals of the metal ions and the sp^3 lone pair of the $N_{ppz\ ring}$ atom. In the series of the isostructural cobalt(II), nickel(II), copper(II) and zinc(II)-sac complexes of aeppz, the elongation is the most pronounced in the case of copper(II) with a Cu–N3 bond distance of 2.469(2) Å. This is clearly as a result of the additional effect of the Jahn–Teller distortion.

Another interesting feature of complex **2** is the O-coordination of the sac ligands *via* the carbonyl oxygen atom, since sac commonly exhibits the N-coordination mode and the O-coordination is rare. In complex **2**, both sac ligands are O-coordinated and it appears that the steric hindrance of the aminoethyl group impedes the coordination of sac through the negatively charged N atom. The Cu–O_{sac} bond distance of 2.103(2) Å is slightly longer than those found in [Cu(dipyr)(sac)$_2$(H_2O)] [15], [Cu(sac)$_2$(py)$_3$] [16], [Cu(pypr)$_2$(sac)$_2$] [17] and ApyH[Cu(sac)$_3$(H_2O)$_2$] [18], where dipyr, py, pypr and ApyH are dipyridylamine, pyridine, 2-pyridinepropanol and 2–aminopyridinium, respectively. Again, as in complex **1**, the sac ring system in **2** is essentially planar. The puckering parameters of the ppz ring system in **2** are $q = 0.535(2)$ Å and $\theta = 174.18(12)°$, and the torsion angles are in the range 52.1–58.2°, suggesting that the ppz rings exhibit an essentially cyclohexane-like chair conformation.

The molecules of **2** in the unit cell are doubly bridged by N–H···N and N–H···O hydrogen bonds, forming a hydrogen bonded chain running along the *a* axis (Fig. 5). These hydrogen bonded chains are extended to a 2D layer by π(sac)–π(sac) stacking interactions with the *Cg*–*Cg*^{i} separation of 3.886(1) Å (i = 2 − *x*, 1 − *y*, 1 − *z*).

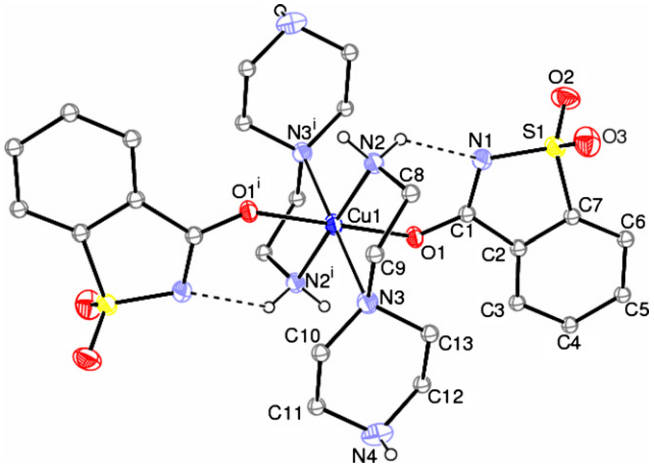


Fig. 4. The molecular structure of **2** with the atom labeling scheme. CH hydrogen atoms are omitted for clarity. The intramolecular hydrogen bonds are indicated by dashed lines. Symmetry code (i) = − *x*, −*y* + 1, −*z*.

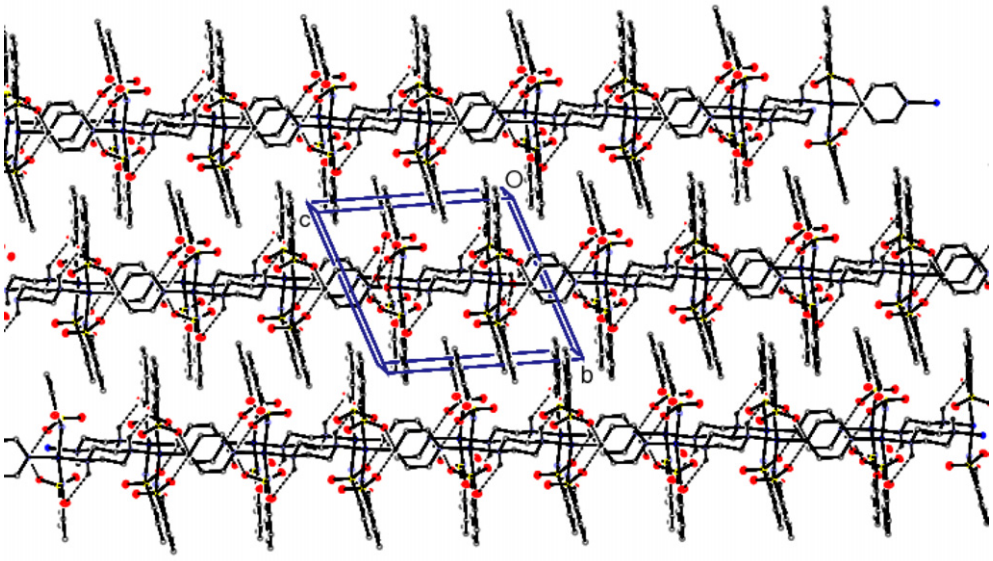


Fig. 3. Packing of 1D chains into 3D network in **1** viewed down the *a* axis, showing aromatic π···π stacking interactions between sac ligands.

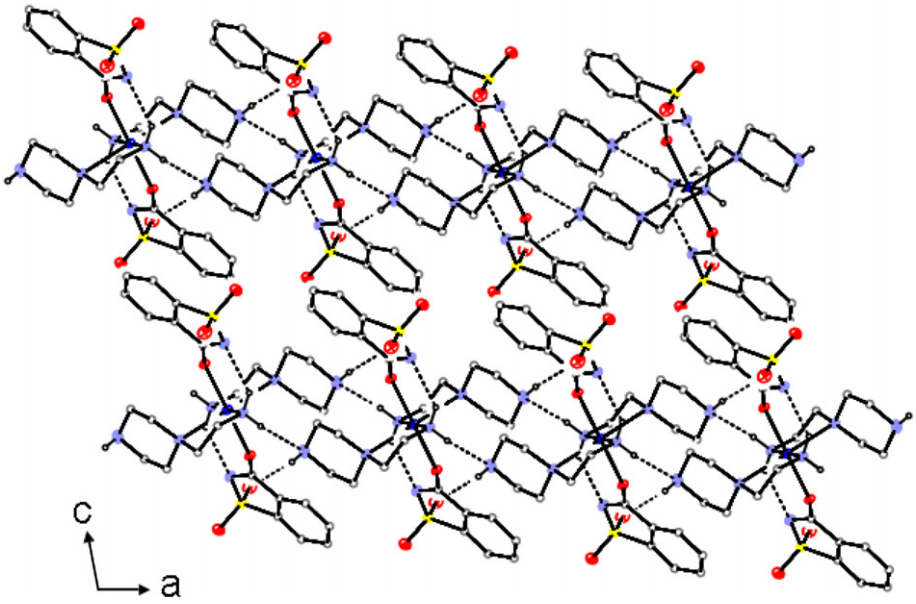


Fig. 5. Packing of hydrogen bonded chains of **2**, viewed down the *b* axis.

3.3. Thermal analysis

Thermal behavior of the complexes was studied by DTA and TG in the temperature range 20–800 °C in the static atmosphere of air. Complex **1** dehydrates between 35 and 103 °C with a mass loss of 3.6% (calc. 3.4%). The elimination of the ppz ligand takes place in the temperature range 162–259 °C, accompanied by a mass loss of 16.0% (calc. 16.2%). The decomposition of the sac moiety occurs between 270 and 474 °C with two extremely exothermic DTA peaks at 401 and 509 °C to give an end product CuO.

Complex **2** is thermally stable up to 143 °C and then begins to decompose. The TGA curve shows that complex **2** exhibits a continuous mass in the temperature range 143–540 °C and therefore, it is difficult to calculate mass loss values. However, the endothermic DTA peaks at 153, 226 and 247 °C correspond to removal of two aeppz molecules, while the highly exothermic peak at 489 °C is characteristic for the degradation of the sac anion [19]. The decomposition ends at 540 °C to give a decomposition product CuO. The total experimental mass loss of 89.0% agrees well with the calculated value of 90.7%.

Acknowledgements

We thank Dr. O. Z. Yesilel and Dr. B. Karabulut for their assistance in obtaining DTA-TG curves and ESR spectra, respectively.

Appendix A. Supplementary material

CCDC 670731 and 670732 contain the supplementary crystallographic data for **1** and **2**. These data can be obtained free of charge via http://www.ccdc.cam.ac.uk/conts/retrieving.html, or from the Cambridge Crystallographic Data Centre, 12 Union Road, Cambridge CB2 1EZ, UK; fax: (+44) 1223-336-033; or e-mail: deposit@ccdc.cam.ac.uk. Supplementary data associated with this article can be found, in the online version, at doi:10.1016/j.poly.2008.01.009.

References

[1] E.J. Baran, V.T. Yilmaz, Coord. Chem. Rev. 250 (2006) 1980.
[2] M.C. Suen, T.C. Keng, J.C. Wang, Polyhedron 21 (2002) 2705.
[3] S.V. Ganesan, S. Natarajan, Inorg. Chem. 43 (2004) 198.
[4] X.-J. Zhao, M. Du, Y. Wang, X.-H. Bu, J. Mol. Struct. 692 (2004) 155.
[5] M. Nolte, I. Pantenburg, G. Meyer, Z. Anorg. Allg. Chem. 631 (2005) 2923.
[6] H. Xu, Y.L. Song, L.W. Mi, H.W. Hou, M.S. Tang, Y.L. Sang, Y.T. Fan, Y. Pan, Dalton Trans. (2006) 838.
[7] G.M. Sheldrick, SHELX-97. Programs for Crystal Structure Analysis, University of Göttingen, Germany, 1997.
[8] P. Naumov, G. Jovanovski, J. Mol. Struct. 563/564 (2001) 335.
[9] R.T. Bhaskar, M. Narayana, Phys. Stat. Sol. 106 (1981) 601.
[10] B. Karabulut, R. Tapramaz, A. Bulut, Z. Naturforsch. 54a (1999) 256.
[11] A.W. Addison, T.N. Rao, J. Reedijk, J. van Rijn, G.C. Verschoor, J. Chem. Soc., Dalton Trans. (1984) 1349.
[12] S. Guney, V.T. Yilmaz, W.T.A. Harrison, J. Coord. Chem. 58 (2005) 1667.
[13] V.T. Yilmaz, S. Guney, W.T.A. Harrison, Z. Naturforsch. 60b (2005) 403.
[14] V.T. Yilmaz, S. Guney, C. Kazak, Acta Crystallogr., Sect. E 64 (2008) m59.
[15] R.M.K. Deng, K.B. Dillon, A.E. Goeta, M. Mapolelo, Inorg. Chim. Acta 315 (2001) 245.
[16] O.V. Quinzani, S.H. Tarulli, S. Garcia-Granda, C. Marcos, E.J. Baran, Cryst. Res. Technol. 37 (2002) 1338.
[17] V.T. Yilmaz, S. Hamamci, O. Andaç, C. Thone, W.T.A. Harrison, Transition Met. Chem. 28 (2003) 676.
[18] V.T. Yilmaz, F. Yilmaz, C. Kazak, Transition Met. Chem. 30 (2005) 95.
[19] H. Icbudak, V.T. Yilmaz, H. Olmez, J. Therm. Anal. 53 (1998) 843.

butyl-hydroperoxide (*t*-BuOOH in dacane, 78%), were purchased from Aldrich Chemical Co. and were used without further purification. HPLC grade acetonitrile obtained from Qualigens Chemicals (Glaxo, India); extra pure dichloromethane (99%) obtained from Merck. All sodium and potassium phosphates (anhydrous) were obtained from Pfizer Chemicals (India) and were further dehydrated by heating at 200 °C under vacuum 6 h and were stored under argon.

Dichloromethane and acetonitrile were dried over $CaCl_2$ and were freshly distilled from P_4O_{10}. Acetonitrile was further distilled, once more from 1:1 mixture of $KMnO_4$ and $LiCO_3$. Cyclohexene was purified by passing through silica gel (120 mesh) column until it was nearly 100% pure (as analyzed by GC) prior to use.

Iron(III) [tetrakis(pentafluorophenyl)] porphyrin triflate was synthesized by stirring silver triflate (9 mg) and iron(III) [tetrakis(pentafluorophenyl)] porphyrin chloride (7 mg) in acetonitrile (CD_3CN, 1.5 mL) for several days. A change from chloride to triflate coordination was evidenced from the expected shift in the β-pyrrole ^1H NMR resonance from 80 to 58 ppm.

2.2. Experimental setup

Each reaction was conducted in 4.0 mL vial fitted with silicone septa. A flow meter (with an outlet) was connected with a 5 mm polyethylene tube with an oxygen cylinder. A sensitive stopper and a needle (0.16 mm, o.d.) were attached between the flow meter and the cylinder. The outlet is first closed with silicone septa and then pierced with the same sized needle to ensure a laminar flow and a pressure of 1 atm of oxygen. To maintain constant temperature the vial was dipped into a paraffin oil bath with a heating coil connected to a dimmerstat. All the reactions were performed at 32 ± 1 °C unless mentioned otherwise.

A Perkin–Elmer (Auto system XL) gas chromatograph fitted with an Carbo Wax (30 m × 0.32 mm × 0.5 μm) capillary column and an FID detector was used to detect the production of oxidation products. Oxidation products were quantified relative to internal standard (C_6F_5I). The identification and quantitation of the products were done from the response factors of standard samples.

Some reactions are strictly maintained in argon atmosphere where the oxygen was removed from solvents and substrates by bubbling with argon. Reaction mixtures of solvent, internal standard, catalyst and substrate were prepared in air-tight, sealed 5.0 mL reaction vials with septa caps. Oxidant was added to the reaction mixture via a gas-tight microsyringe through the septa cap. Samples for GC analysis were removed via a gas-tight microsyringe to prevent exposure to oxygen.

2.3. Spectroscopic measurements

All the electronic spectra were recorded on a Perkin–Elmer UV–Vis spectrophotometer(Model Lambda 2S) interfaced with a computer using PECSS software. The spectrophotometer cell holder was equipped with the outer water-circulating jacket to maintain constant temperature. Constant temperature of 25 °C was maintained by using a Julabo F-30 circulator. Most of the samples were taken in acetonitrile (1 mL) in a 1 cm path-length long-necked cell with air-tight silicon septa. Some samples containing catalyst in acetonitrile (1 mL) were analyzed in presence of solid anhydrous phosphates (5 mg) after shaking.

The ^1H NMR spectra were obtained using a Bruker DPX-300 (300 MHz) spectrometer in acetonitrile (d_3). (i) The ^1H NMR of β-pyrrole protons of catalyst were done in precision NMR tubes by addition of 6.0 mM iron[tetrakis(pentafluorophenyl)] porphyrin chloride in 0.5 mL acetonitrile (d_3). (ii) The same were recorded for iron[tetrakis(pentafluorophenyl)] porphyrin triflate. (iii) In sample (i) 100 μL of D_2O was added and analyzed. (iv) Forth sample was prepared by stirring iron[tetrakis(pentafluorophenyl)] porphyrin triflate (6 mM) and anhydrous K_2HPO_4 (10 mg) in acetonitrile (1.5 mL) in a vial for 5–6 h. After stirring 0.5 mL of the decanted solution were taken for analysis.

3. Result and discussion

3.1. Role of phosphate

The oxidation of cyclohexene with dioxygen in presence of small quantities of *t*-BuOOH and various phosphate salts has been studied. In a typical reaction a mixture of cyclohexene (3.25 M), *t*-BuOOH (5.5 mM), $F_{20}TPPFeCl$ (9.0 ± 1 μM, $F_{20}TPPH_2$ = *meso*tetrakis(pentafluorophenyl)porphyrin) and solid phosphate salt (25 mg) in acetonitrile (1 mL) was stirred at 32 ± 1 °C for 20 min under 1 atm of dioxygen. The organic products formed were analyzed by GC and the results are given in Table 1. The results support the following conclusions: (i) phosphate salts are assisting the dioxygen activation process, (ii) potassium phosphates

Table 1
$F_{20}TPPFe(III)Cl$ catalyzed oxidation of cyclohexene in presence of various phosphates at 32 ± 1 °C where 2-cyclohexen-1-one (**1**) and 2-cyclohexen −1-ol (**2**) were the major products[a]

Entry no.	Phosphate	Product profile (mM)		Total yield (mM)	TOF (min^{-1})	(**1**)/(**2**) ratio
		(**1**)	(**2**)			
1	K_2HPO_4	52.7	27.6	80.3	446	1.9
2	Na_2HPO_4	26.6	11.3	37.9	210	2.3
3	KH_2PO_4	5.4	2.0	7.4	41	2.7
4	NaH_2PO_4	4.6	1.8	6.4	35	2.5
5	K_3PO_4	51.1	29.0	80.1	445	1.8
6	Na_3PO_4	34.5	14.3	48.9	271	2.4

[a] All the reactions were performed at 32 ± 1 °C for 20 min in acetonitrile (1.0 mL) containing cyclohexene (3.25 M) at 1 atm of oxygen. Average results of duplicate sets of experiments are given. Concentrations of catalyst: 9.0–11μM; *tert*-butyl hydroperoxide: 5.5 mM; and phosphate: 25 mg. In all these reactions the yield of cyclohexe oxide was less than 0.5 mM and are not reported here.

are more efficient than the corresponding sodium phosphates (entry: 1 versus 2, 3 versus 4 and 5 versus 6), (iii) among the potassium phosphate salts the order of efficiency is $K_3PO_4 \approx K_2HPO_4 \gg KH_2PO_4$ (entries 1, 3 and 5). In these experiments it has been noted that the variation in the phosphate particle size has no effect on the reaction yield. The phosphate salts were grind into powder so that it can be stirred well. The results have demonstrated that almost all the phosphates included in this study, especially K_2HPO_4 and K_3PO_4 play significant role in dioxygen activation. Secondly, the presence of small quantities of hydroperoxide initiates the oxygenation more efficiently. Similar role of K_2HPO_4 has also been noted in the oxygenation of cyclohexane and cyclooctene. In the following however we present details of the reactions conducted with K_2HPO_4 only.

3.2. Role of catalyst and t-BuOOH

The above noted reaction was when conducted with two different catalyst concentrations and the reactions were monitored for 1 h, 2-cyclohexen-1-one (**1**) and 2-cyclohexen-1-ol (**2**) were the major products and epoxide formation was always very low (below 0.5 mM). The products were formed linearly till about 20 min, and afterwards catalyst decay was noticed, and the non-linear product formation has also been observed. These results are given in Fig. 1A. These reactions were then conducted in absence of *t*-BuOOH and Fig. 1B clearly demonstrates that the presence of *t*-BuOOH initiates the oxygenation process. In order to realize the role of various reagents, the control experiments were then carried out for only 20 min and the results are given in Table 2. The first data set (entries 1–6, Table 2) clearly indicated that: in absence of catalyst there is no reaction (entry 6), dioxygen activation is definitively there (entries 1 and 5), in absence of the hydroperoxide dioxygen activation is quite appreciable (entries 1 and 2), and its presence makes dioxygen activation more efficient. Notable feature in these two reactions is that the product ratio remains the same (1.9), which is indicative of the probable operation of similar mechanism in presence and in absence of *t*-BuOOH in the oxygenation of cyclohexene. The rest of the data reported in Table 2 (entries 7–16) and their comparative analysis support the conclusion that F_{20}TPPFeCl is the best catalyst among the series used in this study. The data also indicate that the role of phosphate in dioxygen activation is not special for only one catalyst, it seems to be a general phenomenon. In fact similar effect has also been observed in TPP and TMP derivatives too, but we have not reported those data here. It has also been noted that among dichloromethane and acetonitrile the latter one is the solvent of better choice (entries 1 and 4).

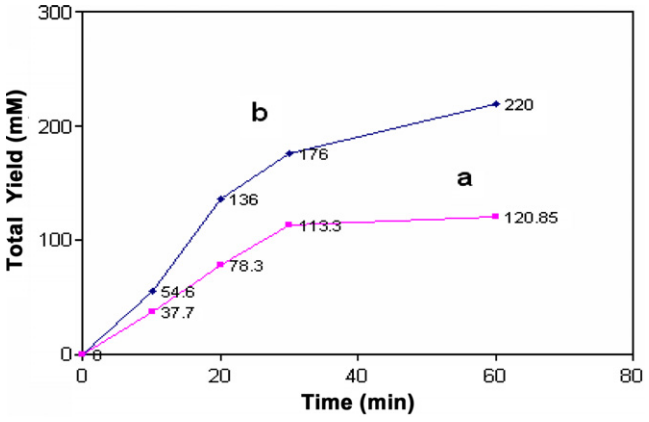


Fig. 1A. Plot of the total yield of cyclohexene oxidation products vs. time, catalyzed by $F_{20}TPPFe^{III}Cl$ in acetonitrile under 1 atm of O_2 at 32 ± 1 °C. Catalyst concentrations were (a) 9 ± 1 μM and (b) 27 ± 1 μM. *tert*-Butyl hydroperoxide: 5.5 mM and phosphate: 25 mg in acetonitrile. Average values of duplicate sets of experiments are used in the plots.

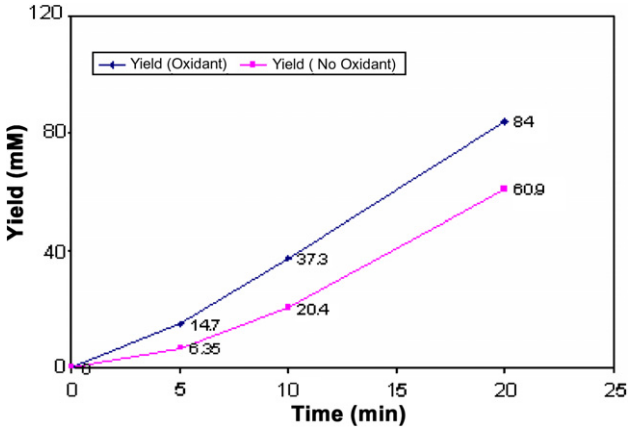


Fig. 1B. Plot of the total yield of cyclohexene oxidation products vs. time, catalyzed by $F_{20}TPPFe^{III}Cl$ in acetonitrile under 1 atm of O_2 at 32 ± 1 °C in presence and absence of oxidant (*t*-BuOOH). Catalyst concentrations being 9 ± 1 μM. *tert*-Butyl hydroperoxide: 5.5 mM and phosphate: 25 mg in acetonitrile.

3.3. Spectral analysis

In presence of only K_2HPO_4 the spectrum of the catalyst was changed continuously till 3.6 h, this is shown in Fig. 2. In presence of K_3PO_4, which is more basic, the spectrum of the catalyst was changed exactly similarly but faster (in 30 min). Such spectral change was not observed in case of KH_2PO_4 up to 4 h. The addition of *t*-BuOOH to a solution of the catalyst already having K_2HPO_4 for 3.6 h evolves another spectrum (Fig. 3). There is also a clear change of the catalyst spectrum in acetonitrile containing excess of cyclohexene (Fig. 4) and this is not the case for either cyclohexane or cyclooctene. This change shown in Fig. 4 has an induction period of 17 min, which shortens to 4 min in presence of K_2HPO_4.

Careful analysis of the spectral changes support that all the four transitions (highest occupied $a_2u(\pi)$ and $a_1u(\pi) \rightarrow$ two degenerate lowest unoccupied $e_g(\pi^*)$) of the catalyst remained intact in all the spectra presented in Figs. 2 and 4, and these bands are only shifted by few

Table 2
Catalytic oxidation of cyclohexene to 2-cyclohexen-1-one (**1**) and 2-cyclohexen-1-ol (**2**)[a]

Entry no.	Catalyst	Products (mM)		Total yield (mM)	TOF (min^{-1})	(**1**)/(**2**) ratio
		(**1**)	(**2**)			
1	$F_{20}TPPFe^{III}Cl$	52.7	27.6	80.3	446	1.9
2[b]	$F_{20}TPPFe^{III}Cl$	40.2	20.7	60.9	338	1.9
3[c]	$F_{20}TPPFe^{III}Cl$	16.0	7.4	23.4	130	2.2
4[d]	$F_{20}TPPFe^{III}Cl$	5.2	1.8	7.0	38	2.9
5[e]	$F_{20}TPPFe^{III}Cl$	0.8	1.1	1.9	11	0.6
6[f]	NIL					
7	$F_8TPPFe^{III}Cl$	40.2	19.2	59.4	285	2.0
8[c]	$F_8TPPFe^{III}Cl$	3.1	1.9	5.0	25	1.6
9	$F_{20}TPPMn^{III}Cl$	34.3	13.3	47.6	267	2.5
10[c]	$F_{20}TPPMn^{III}Cl$	3.9	1.4	5.3	29	2.9
11	$F_8TPPMn^{III}Cl$	26.2	10.2	36.4	202	2.6
12[c]	$F_8TPPMn^{III}Cl$	8.6	2.8	11.4	57	3.0
13	$Cl_8TPPFe^{III}Cl$	19.8	7.5	27.3	125	2.6
14[c]	$Cl_8TPPFe^{III}Cl$	1.6	0.6	2.2	10	2.7
15	$Cl_8TPPMn^{III}Cl$	4.6	1.6	6.2	31	2.9
16[c]	$Cl_8TPPMn^{III}Cl$					

[a] All the reactions were performed at 32 ± 1 °C for 20 min in acetonitrile (1.0 mL) containing cyclohexene (3.25 M) at 1 atm of oxygen. Average results of duplicate sets of experiments are given. Concentrations of catalyst: 9.0–11μM; *tert*-butyl hydroperoxide: 5.5 mM; and phosphate: 25 mg. In all these reactions the yield of cyclohexe oxide was less than 0.5 mM and are not reported here.
[b] In this reaction medium *t*-BuOOH was absent.
[c] These reactions were conducted in absence of phosphate.
[d] This reaction was conducted in dichloromethane.
[e] This reaction was conducted under argon atmosphere.
[f] This reaction was conducted without any catalyst.

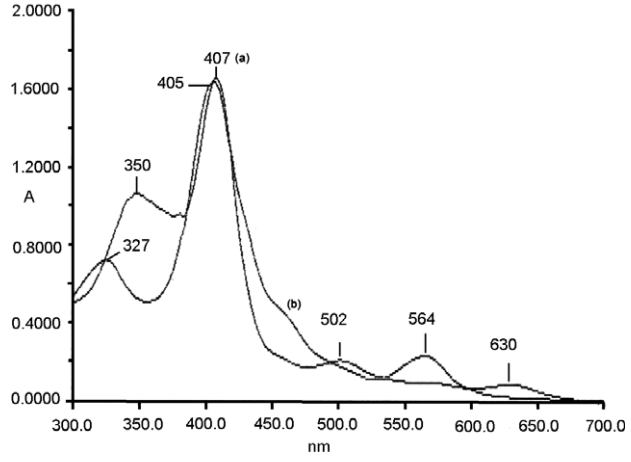


Fig. 2. UV–Vis spectra of (a) $F_{20}TPPFe^{III}Cl$ (16 μM) in acetonitrile and (b) $F_{20}TPPFe^{III}Cl$ (16 μM) in acetonitrile in presence of K_2HPO_4.

nanometers with some changes in the intensities of the transitions only [14]. The most rational proposition for this observation could be the possible exchange of the axial ligand rather than any major change of the spin state of the central metal ion or any modification on the porphyrin periphery during these catalytic reactions. It has been noted that this kind of spectral change is very strongly dependant on the solvent system used. For example the change is very slow in dichloromethane than in acetonitrile.

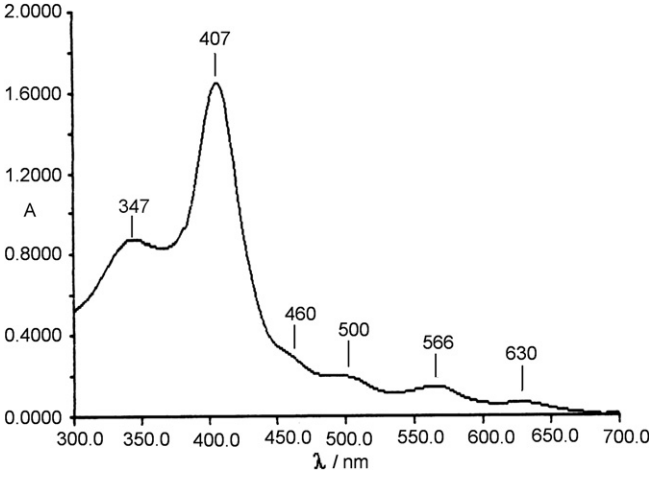


Fig. 3. UV–Vis spectrum of $F_{20}TPPFe^{III}Cl$ (15 μM) on addition of *t*-BuOOH (5.5 mM) to a solution of catalyst solution in acetonitrile containing K_2HPO_4.

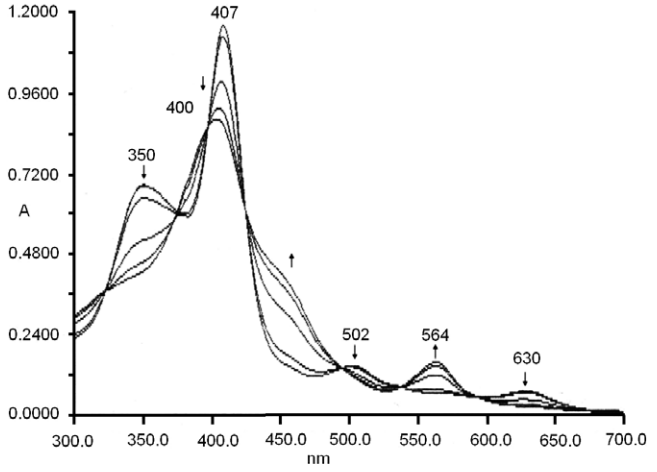
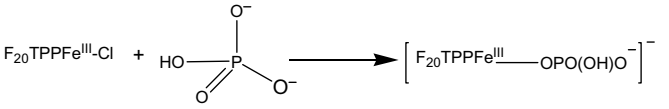
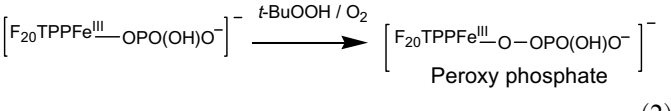


Fig. 4. UV–Vis spectra of $F_{20}TPPFe^{III}Cl$ (9 μM) in acetonitrile in presence of cyclohexene (0.65 M).

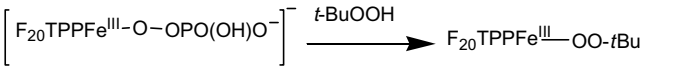
We believe that the change observable in Fig. 2 is due to the exchange of iron(III) bound chloride by HPO_4^{2-} ions (Eq. (1)). Presence of the band at 350 nm in $F_{20}TPPFeCl$ is diagnoistic of the presence of the bound chloride ion to the ferric ion of the catalyst. Addition of phosphate shifts this band to 327 nm. This could be due to the probable displacement of the chloride ligand by the phosphate ion. Among CH_3CN and CH_2Cl_2 the former solvent facilitated this process and this may be owing to the higher polarity and better solubility of the phosphate in CH_3CN.



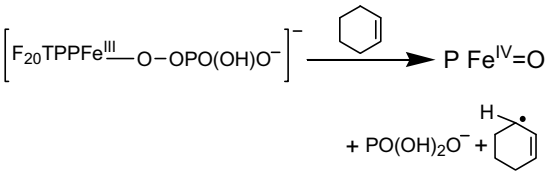
(1)



(2)



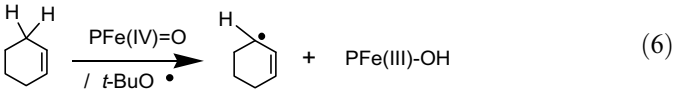
(3)



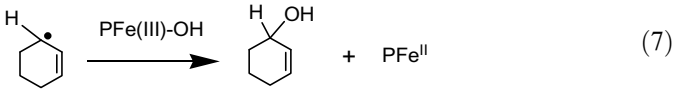
(4)



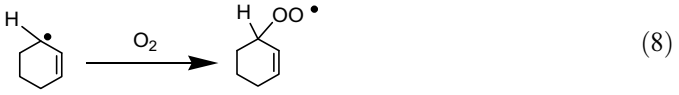
(5)



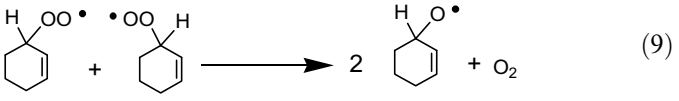
(6)



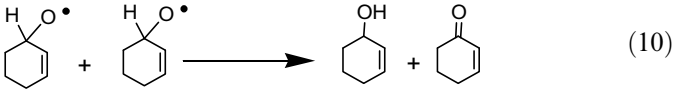
(7)



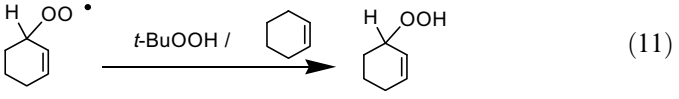
(8)



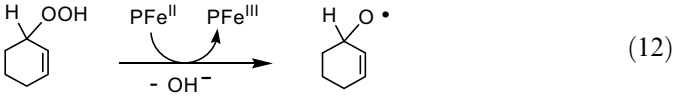
(9)



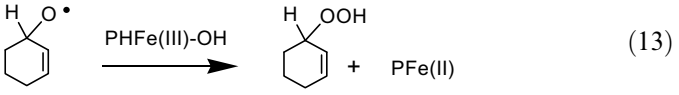
(10)



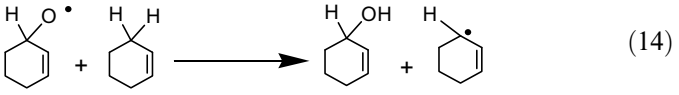
(11)



(12)



(13)



(14)

In an ^{1}H NMR experiment, the catalyst was stirred with silver triflate (trifluoromethanesulfonic acid silver salt, CF_3SO_3Ag) in acetonitrile for several days to remove the chloride ion. The β-pyrrole proton peak of the corresponding catalyst with triflate axial ligand was observed at 58 ppm (Supplementary Figure S1). The β-pyrrole proton peak then shift to 83.03 ppm when the solution was stirred with dry K_2HPO_4 after filtration(Supplementary Figure S2), indicates the phosphate ligation to Fe(III). The salt used is highly anhydrous and ligation through any water molecule may be discarded by the fact that in that case the peak would have shifted to 70 ppm. These results probably indicate the HPO_4^{2-} ion participation in these reactions. Furthermore, the use of KH_2PO_4 and NaH_2PO_4 (Table 1, entries 1–4) decreases the product yields signifying the importance of Eq. (1) and it seems to be expected form the fact that coordination ability of KH_2PO_4 is less than that of K_2HPO_4 and K_3PO_4 and may be due to the dissociation differences. This is again supported by the fact that time taken for the spectral change due to removal of Cl^- ion may be given in order $KH_2PO_4 >> K_2HPO_4 > K_3PO_4$.

The coordinated phosphate must be more electrophilic, so its possible oxidation by *t*-BuOOH/O_2 to give the coordinated peroxy phosphate as represented by Eq. (2) is possible. In presence of excess of *t*-BuOOH with respect to the catalyst the possible replacement (at least partial) of peroxy phosphate by *tert*-butyl hydroperoxide may be anticipated (Eq. (3)) and this could explain the extra peaks (more than four) observed in Fig. 3. We believe that the reaction is going through a radical pathway as indicated by the fact that presence of even 10 mM of 2,4,6-tri-*tertiary*butylphenol ceases the reaction completely.

Here peroxy phosphate probably cleaves homolytically to evolve PFe(IV) = O and the cyclohexene radical (Eq. (4)). The evolution of such oxoiron(IV) species through Eq. (5) cannot also be ignored. Subsequent reaction of oxoiron(IV) and alkoxy radical to evolve the cyclohexene radical (Eq. (6)) will certainly be the next important step for dioxygen activation [6]. This will be followed by the proposed Eqs. (7)–(14). Epoxide is the major product where oxoiron(IV) porphyrin cation radical is the major reactive intermediate [1]. In our system epoxide is not the major product in cyclohexene oxidation, so we do not think heterolytic cleavage of the peroxy phosphate is important here. Slow epoxidation could be possible from the hydroperoxy or peroxy phosphate adduct as has been anticipated recently from the theoretical studies [15]. The homolytic cleavage of peroxy linkage proposed in this study seems to be more appropriate for cyclohexene in particular, because it has the ability to coordinate to iron(III) (Fig. 4).

The above reaction was then tested on cyclohexane and cyclooctene and the results are given in Tables 3 and 4, respectively. In case of cyclohexane oxidation a mixed solvent (acetonitrile:dichloromethane) was used and the reactions were monitored for 2 h. In this reaction cyclohexanol and cyclohexanone were the major products. Secondly in the cyclohexane oxygenation, F_{20}TPPMnCl seems to be the better catalyst than the corresponding iron analogue. The cyclooctene oxidation was carried out in acetonitrile:dichloromethane (2:1) and the reactions were monitored for 4–8 h. It has been established from the independent studies that 2-cyclohexen-1-one and cyclohexanone were not formed from the over oxidation of 2-cyclohexen-1-ol and cyclohexanol, respectively, under our catalytic reaction conditions. The oxygenation reactions of both cyclohexane and cyclooctene were found to be very slow and less efficient with respect to that of cyclohexene. This may be rationalized from the fact that cyclohexene acts as a ligand to Fe(III) center of the catalyst (Fig. 4), which can encourage homolytic cleavage of the peroxyphosphate to

Table 3
Catalytic oxidation of cyclohexane to cyclohexanone (**3**) and cyclohexanol (**4**)[a]

Entry no.	Catalyst (μM)	Product profile (mM)		Total yield (mM)	TOF (min^{-1})	(**3**)/(**4**) ratio
		(**3**)	(**4**)			
1	$F_{20}TPPFe^{III}Cl$	5.06	3.87	8.93	4.7	1.3
2[b]	$F_{20}TPPFe^{III}Cl$					
3[c]	$F_{20}TPPFe^{III}Cl$	1.98	2.93	4.91	2.5	0.67
4[d]	$F_{20}TPPFe^{III}Cl$					
5	$F_{20}TPPMn^{III}Cl$	8.0	10.3	18.3	13.9	0.77
6[d]	$F_{20}TPPMn^{III}Cl$	2.5		2.5	1.8	

[a] All the reactions were performed at 32 ± 1 °C for 2 h in acetonitrile:dichloromethane (1:1) solvent (0.5 mL), containing cyclohexane (6.5 M), catalyst (16 ± 1 μM for $F_{20}TPPFeCl$ and 11 ± 1 μM for $F_{20}TPPMnCl$), *tert*-butyl hydroperoxide (5.5 mM) and K_2HPO_4 (25 mg) in 1 atm of oxygen. Average values of duplicate sets of experiments are given in the table.
[b] No oxidant (*t*-BuOOH) used.
[c] Argon atmosphere, but in presence of 5.5 mM of *t*-BuOOH.
[d] No phosphate.

Table 4
Catalytic oxidation of cyclooctene to cyclooctene oxide[a]

Entry no.	Catalyst (μM)	Product profile (mM) cyclooctene oxide	TOF (min^{-1})
1	$F_{20}TPPFe^{III}Cl$	12	5.5
2[b]	$F_{20}TPPFe^{III}Cl$	28	6.5
3[c]	$F_{20}TPPFe^{III}Cl$		
4[d]	$F_{20}TPPFe^{III}Cl$	1.4	0.6
5	$F_{20}TPPMn^{III}Cl$	8.0	3.7
6[d]	$F_{20}TPPMn^{III}Cl$	0.06	

[a] All the reactions were performed at 32 ± 1 °C for 4 h in acetonitrile:dichloromethane (2:1) solvent (0.5 mL), containing cyclooctene (4.5 M), catalyst (30 ± 2 μM for $F_{20}TPPFeCl$ and 09 ± 1 μM for $F_{20}TPPMnCl$), *tert*-butyl hydroperoxide (5.5 mM) and K_2HPO_4 (25 mg) in 1atmosphere of oxygen. Average values of duplicate sets of experiments are given in the table.
[b] Reaction was performed for 8 h.
[c] No oxidant (*t*-BuOOH) used.
[d] No phosphate.

oxoiron(IV) species, secondly low dissociation of the co-catalyst used for cyclohexane and cyclooctene reaction medium could be the reason for such low yield. It has also been noted that absence of *t*-BuOOH in the oxidation reaction of cyclohexane no product was formed. Thus it is clear from the fact that R· radical formation from R–H is very important for this radical reaction to occur (Eq. (4)). Since cyclohexene radical is stable enough due to conjugation, formation R· radical is easier even in absence of hydroperoxide in such reaction condition which is not possible in case of cyclohexane. Absence of hydroperoxide in cyclohexene thus slows down the product yield (Table 2, entry 2[b]; Fig. 1B) and results no product formation in the oxidation of cyclohexane. Thus simultaneous presence of small *t*-BuOOH is required along with K_2HPO_4 for the oxidation of cyclohexane. In this oxidation possibly the formation of *t*-BuOOH adduct with iron(III) (Eq. (3)) is most important.

We have also observed that presence of even 10 μL/1.5 mL of the anhydrous acetonitrile solvent inhibits the dioxygen activation in presence of phosphate and *t*-BuOOH and the total yield of the oxidized product was noticeably reduced.

4. Conclusions

We have convincingly demonstrated that in the metalloporphyrin catalyzed dioxygen activation anhydrous phosphates play a very significant role. Presence of a small quantity of a hydroperoxide enhances the process appreciably. It has been shown that by appropriate tuning of the reaction medium, the dioxygen activation under ambient conditions is certainly possible. In the oxygenation of cyclohexane manganese porphyrins seem to be more promising. We are in the process of further tuning the solvent, catalyst and co-catalyst to achieve selective products with higher turnovers so that the results could be more useful.

Acknowledgements

We thank the Department of Science and Technology (Project no. SR/S1/IC-04/2007) for funding and CSIR for the fellowship to V.B.

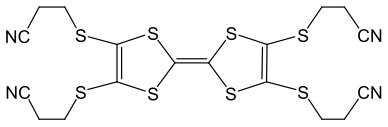
Appendix A. Supplementary data

Supplementary data associated with this article can be found, in the online version, at doi:10.1016/j.poly.2008.01.003.

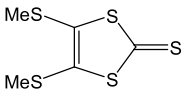
References

[1] J.T. Groves, in: P.R. Ortiz de Montellano (Ed.), Cytochrome P450: Structure, Mechanism and Biochemistry, third ed., Kluwer Academic/Plenum Press, New York, 2005, p. 1.
[2] W. Nam, Acc. Chem. Res. 40 (2007) 522.
[3] R.A. Sheldon, in: Metalloporphyrins in Catalytic Oxidation, Marcel Dekker Inc., New York, 1994.
[4] B. Meunier, Chem. Rev. 92 (1992) 1411.
[5] D. Mansuy, Coord. Chem. Rev. 125 (1993) 129.
[6] A. Bottcher, E.R. Birnbaum, M.W. Day, H.B. Gray, M.W. Grinstaff, J.A. Labinger, J. Mol. Catal. A: Chem. 117 (1997) 229.
[7] J.E. Lyons, P.E. Ellis Jr., Catal. Lett. 8 (1991) 45.
[8] P.S. Traylor, D. Dolphin, T.G. Traylor, J. Chem. Soc., Chem. Commun. (1984) 279.
[9] S. Evans, J.R. Lindsay Smith, J. Chem. Soc., Perkins Trans. 2 (2000) 1541.
[10] M. Takeuchi, M. Kodera, K. Kano, Z. Yoshida, J. Mol. Catal. A: Chem. 113 (1996) 51.
[11] A.D.N. Vaz, D.F. McGinnity, M. Coon, J. Proc. Natl. Acad. Sci. USA 95 (1998) 3555.
[12] S. Jin, T.M. Makris, T.A. Bryson, S.G. Sliger, J.H. Dawson, J. Am. Chem. Soc. 125 (2003) 3406.
[13] M. Sanchez, A. Hadasch, R.T. Fell, B. Meunier, J. Catal. 202 (2001) 177.
[14] P.J. Spellane, M. Gouterman, A. Antipas, S. Kim, Y.C. Liu, Inorg. Chem. 19 (1980) 386.
[15] E. Derat, D. Kumar, H. Hirao, S. Shaik, J. Am. Chem. Soc. 128 (2006) 473.

which TTF ligands act as substituted groups. However, these TTF molecules were excluded from the helices for their rigid backbones, just like that previously reported by Munakata et al. [13d]. It is a challenge to involve TTF motifs into a helix, there is no effective method to predict the final network topology of a self-assembly process for it was highly effected by several factors such as metal centers [19], ligands [20], solvents [21], counterions [22], and so on. Recently, the use of Ag(I) cation was of growing interest for its various coordination modes such as linear, trigonal, tetrahedral, triangle pyramid and T-shaped [23–27]. Although many Ag-coordinated helical structures have been synthesized [28], to our best knowledge, no Ag(I)–TTF helical coordination polymer was reported before. In this paper, two novel 3D coordination polymeric networks $[Ag_4(tces\text{-}TTF)_2(CF_3SO_3)_2](CF_3SO_3)_2$(tces = 2,3,6,7-tetra(cyanoethylsulfanyl)) (**1**) and $[Ag_2(bmdt)_2](SbF_6)_2 \cdot$ acetone(bmdt = 4,5-bis(methylsulfanyl)-1,3-dithiole-2-thione) (**2**) were synthesized, both of them formed 3D networks constructed from coordinate bonds only, axially chiral helical frames were found in **1** and **2**. Details of the preparations, crystal structures, conductive behavior and S···S contacts are discussed.



tces-TTF



bmdt

2. Experimental

2.1. Materials and instrumentation

All the chemicals and solvents used in the syntheses were bought commercially as analytical grade. The tces-TTF and bmdt ligands were prepared according to literature methods [29,30]. Elemental analysis (for C, H, and N) was performed using a ThermoQuest Flash EA1112 elemental analyzer. The IR spectra (400–4000 cm^{-1}) were recorded on a JASCO FT/IR-460 plus spectrometer with the samples prepared as KBr pellets. The UV–Vis spectra were recorded on UV–VIS8500 UV spectrometer with the crystalline samples dissolved in CH_3CN. The conductivities were measured by conventional two-probe technique with compacted pellets.

2.2. Synthesis of the compounds

2.2.1. Synthesis of $[Ag_4(tces\text{-}TTF)_2(CF_3SO_3)_2](CF_3SO_3)_2$ (1)

An acetone solution (2 mL) of $AgCF_3SO_3$ (11.6 mg, 0.045 mmol) was added into an acetone solution (10 mL) in which tces-TTF (12.3 mg, 0.023 mmol) was dissolved. The mixture was stirred at 40 °C for 6 hours and filtered, then the filtrate was introduced into a glass tube and layed with *n*-hexane as a diffusion solvent. The glass tube was sealed, after standing at room temperature for 15 days, orange block crystals of **1** were obtained. *Anal.* Calc. for $C_{40}H_{32}Ag_4F_{12}N_8O_{12}S_{20}$: C, 22.68; H, 1.52; N, 5.29. Found: C, 23.16; H, 1.71; N, 5.42%. IR data (KBr pellet, cm^{-1}): 2953.07(w), 2926.15(w), 2249.56(m), 1625.70(m), 1416.46(s), 1259.29(s), 1033.66(s), 1175.40(s), 647(s) cm^{-1}; UV–Vis: λmax = 390 nm.

2.2.2. Synthesis of $[Ag_2(bmdt)_2](SbF_6)_2 \cdot$ acetone (2)

Bmdt (0.2 mmol, 45.2 mg) was dissolved in the mixture of acetone and CH_3CN (5 mL), $AgSbF_6$ (0.2 mmol, 68.7 mg) was dissolved in acetone (3 mL), these two solutions were mixed together and stirred at 20 °C for 2 h and filtered, the filtrate was introduced into a glass tube and layed with diethyl ether as a diffusion solvent. The glass tube was sealed and made to stand at room temperature for 1 week, then brown block crystals of **2** were obtained. *Anal.* Calc. for $C_{13}H_{18}Ag_2F_{12}OS_{10}Sb_2$: C, 13.03; H, 1.51. Found: C, 12.83; H, 1.45%. IR data (KBr pellet, cm^{-1}): 2911.02(w), 1469.49(m), 1420.32(m), 1315.21(m), 1058.73(s), 1035.59(m), 967.13(w), 900.59(w), 663.30(s). UV–Vis: λmax = 408 nm.

2.3. Crystal structure determination

For complex **1**, data collection ($6.4 < 2\theta < 55.0°$) was performed at 150 K on a Rigaku/MSC Mercury CCD diffractometer ($\lambda = 0.71070$ Å); For complex **2**, data collection ($3.4 < 2\theta < 50.0°$) was performed at 180 K on a Bruker Smart APEX CCD diffractometer ($\lambda = 0.7107$). The two structures were solved using direct methods and refined with full-matrix least-squares (SHELX-97). The crystal data and details of the structure determinations of **1** and **2** are summarized in Table 1, selected bond lengths and angles are listed in Table 2.

Table 1
Crystallographic data for complexes **1** and **2**

	1	**2**
Formula	$C_{40}H_{32}Ag_4F_{12}N_8O_{12}S_{20}$	$C_{13}H_{18}Ag_2F_{12}OS_{10}Sb_2$
Fw	2117.39	1198.11
T (K)	150	183
Space group	*Pnnm*	$P2_1/n$
a (Å)	26.870(7)	18.6584(5)
b (Å)	12.316(3)	8.8969(2)
c (Å)	21.468(6)	20.1351(6)
α (°)	90	90.00
β (°)	90	101.7620(10)
γ (°)	90	90.00
V (Å^3)	7104 (6)	3272.28(15)
Z	4	4
D_{calc} (g cm^{-3})	1.980	2.432
μ (cm^{-1})	17.60	3.532
R	0.073	0.027
wR	0.135	0.068

Table 2
Selected bond lengths (Å) and angles (°) for complex **1** and **2**

Complex ***1***			
Ag(1)–S(5)	2.504(1)	Ag(1)–O(1)	2.420(7)
Ag(2)–S(6)	2.520(1)	Ag(2)–O(3)	2.360(4)
Ag(3)–N(1B)	2.336(6)	Ag(3)–N(2)	2.221(6)
Ag(3)–N(3)	2.213(6)	Ag(3)–N(4C)	2.312(6)
S(5)–Ag(1)–S(5A)	135.14(7)	S(5)–Ag(1)–O(1)	114.5(2)
S(5)–Ag(1)–O(1A)	90.1(2)	O(1)–Ag(1)–O(1A)	113.8(3)
S(6)–Ag(2)–S(6A)	123.62(7)	S(6)–Ag(2)–O(3)	91.7(1)
S(6)–Ag(2)–O(3A)	128.4(1)	O(3)–Ag(2)–O(3A)	93.0(2)
N(1B)–Ag(3)–N(2)	118.9(2)	N(1B)–Ag(3)–N(3)	91.2(2)
N(1B)–Ag(3)–N(4C)	104.2(2)	N(2)–Ag(3)–N(4C)	133.7(2)
N(2)–Ag(3)–N(4C)	93.6(2)	N(3)–Ag(3)–N(4C)	113.2(2)
Complex ***2***			
Ag(1)–S(5)	2.456(1)	Ag(2)–S(2)	2.622(1)
Ag(1)–S(6)	2.571(1)	Ag(1)–S(7)	2.657(1)
Ag(1)–S(5A)	2.881(1)	Ag(2)–S(1)	2.610(1)
Ag(2)–S(10B)	2.632(1)	Ag(2)–S(10C)	2.632(1)
S(5)–Ag(1)–S(6)	148.22(4)	S(10C)–Ag(2)–S(1)	135.77(4)
S(5)–Ag(1)–S(7)	124.63(4)	S(10C)–Ag(2)–S(2)	123.92(3)
S(6)–Ag(1)–S(7)	83.81(4)	S(1)–Ag(2)–S(2)	81.56(3)
S(5)–Ag(1)–S(5A)	85.22(3)	S(10B)–Ag(2)–S(10C)	89.02(3)
S(6)–Ag(1)–S(5A)	95.42(3)	S(1)–Ag(2)–S(10B)	114.22(3)
S(7)–Ag(1)–S(5A)	115.17(5)	S(2)–Ag(2)–S(10B)	114.54(3)

Symmetry operations for **1**: (A) $-x+1$, $-y$, z; (B) $-x+3/2$, $y+1/2$, $-z+1/2$; (C) $-x+3/2$, $y-1/2$, $-z+1/2$; for **2**: (A) $2-x$, $-1-y$, $1-z$; (B) $-1/2+x$, $-3/2-y$, $1/2+z$; (C) $3/2-x$, $-1/2+y$, $1/2-z$.

3. Results and discussions

3.1. Crystal structure of complex *1*

The coordination geometry of silver(I) and partial atom numbering of **1** are shown in Fig. 1. There are three crystallographically independent silver(I) atoms in this network all of which feature a 4-coordinate mode. Ag(3) is coordinated by four N atoms from three different tces-TTF ligands (two are from the same ligand in the diagonal direction). Connected by one Ag(3) atom and C=C bonds on the terminal side of TTF skeleton, these flexible cyanoethylsulfanyl arms form a right-handed helix (Fig. 1). As Ag(3) atoms are located on a infinite wavy line (along *b*-axis) and tces-TTF ligands are alternately arranged on both sides of the line (Fig. 2), the helix is infinitely prolonged on both sides of the wavy line, thus a 1D column is formed by the two orderly arranged helices with the Ag(3) wavy line functioning as a "hinge". This 1D column can also be described as a sandwich structure with extended TTF shells and helical stuffing.

Since all the long flexible nitrile chains of tces-TTF are sandwiched inside the 1D columns, the S atoms of the cyanoethylsulfanyl arms are exposed to each other between adjacent columns. Therefore, Ag(1) and Ag(2) atoms can easily bridge them together to result in a 2D layer extending along *a*-axis. The S–Ag–S angles are 135.14° of S(5)–Ag(1)–S(5) and 123.62(7)° of S(6)–Ag(2)–S(6), respectively. As 4-coordinate metal centers, Ag(1) (or Ag(2)) atom also connects two $CF_3SO_3^-$ anions by O atoms. Two adjacent Ag(1) (or Ag(2)) atoms are double-bridged by $CF_3SO_3^-$ anion through Ag–O bonds (Fig. 3, free $CF_3SO_3^-$ anions are omitted for clarity), therefore these anions stick the 2D layers together to extend infinitely along *c*-axis and

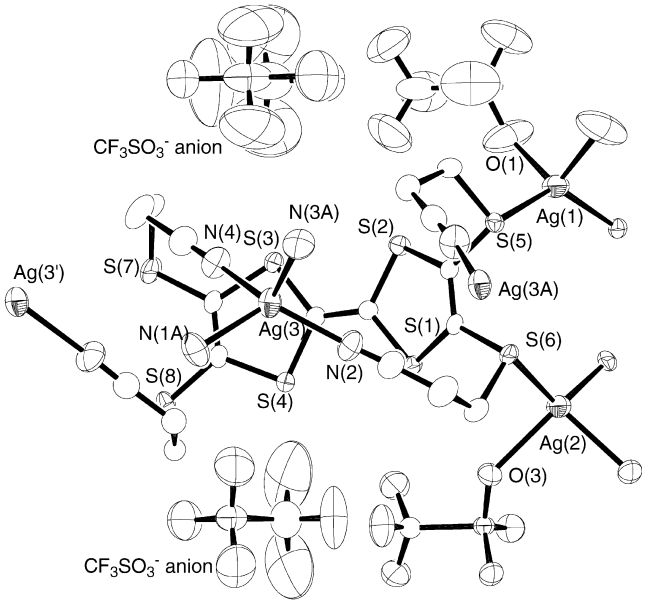


Fig. 1. Coordination geometry of Ag(3) and partial atom numbering of **1**.

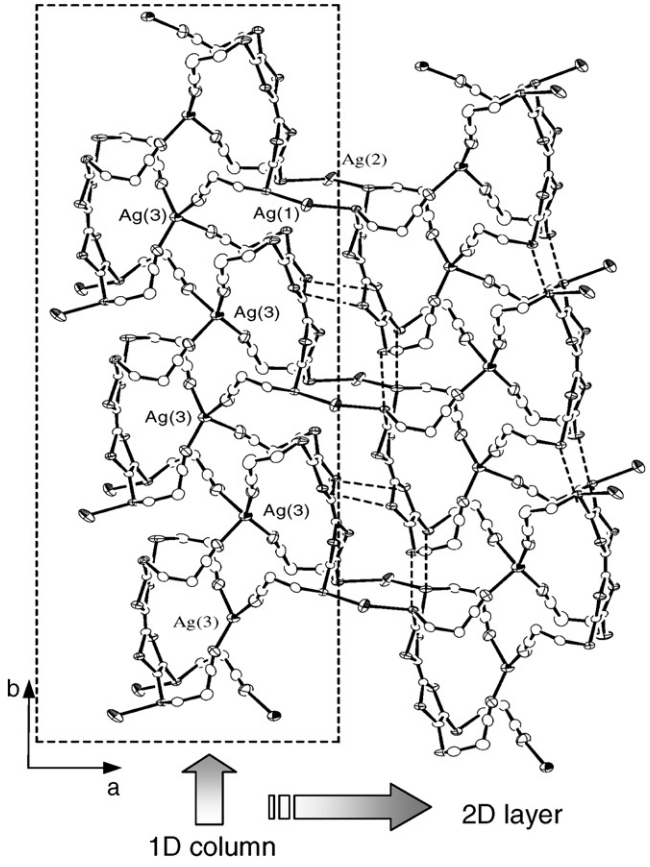


Fig. 2. 1D column, 2D layer and S···S contacts(dashed lines) in polymer **1**.

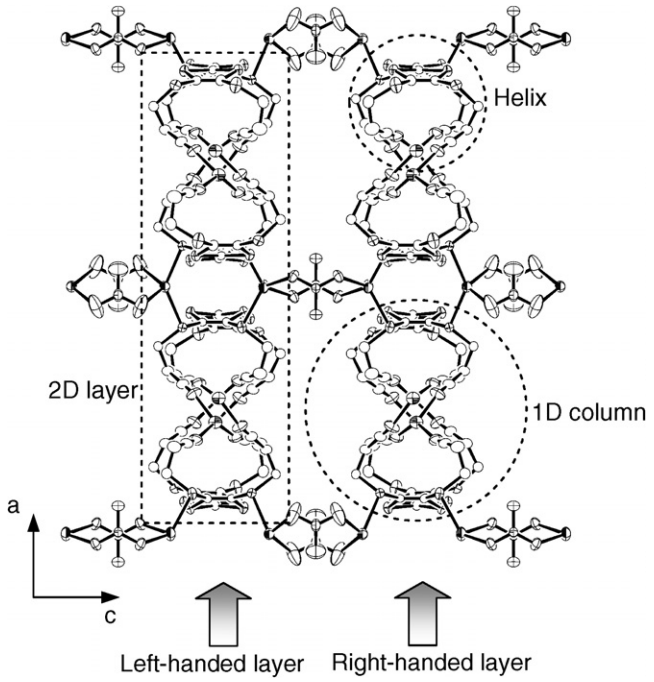


Fig. 3. "8"-shaped channels and axially chiral motifs in polymer **1**.

finally form a 3D network. It is noteworthy that polymer **1** is completely constructed by coordinate bonds, this phenomenon is rare for metal-TTF polymers and gives rise to a stable construction of the polymer. Viewed along *b*-axis, an obvious "8"-shaped channel is found. The vacuities between the "8"-shaped channels are smaller ones which have S···S contacts due to the close face-to-face arrangement of two TTF molecules. The canals between the 2D sheets are separated by $CF_3SO_3^-$ anions to result in the largest channels which are occupied by free $CF_3SO_3^-$ anions. Another coordination polymer with 1D linear structure based on Ag(I) and a TTF derivative bearing two cyanoethylsulfanyl and two methylsulfanyl groups is known [13c], however, for polymer **1**, more flexible cyanoethyl groups help to form helical motifs; various coordination modes of Ag(I) and $CF_3SO_3^-$ anions involved in the coordination system lead to a 3D network.

3.2. Crystal structure of complex *2*

The crystallographic study revealed that complex **2** is also a 3D network with crisscrossed grids assembled orderly by bmdt ligands. Fig. 4 gives the coordination geometry and atom numbering of Ag(I) and bmdt ligands. There are two crystallographically independent silver(I) atoms in the network and both of them are connected with four S atoms from three bmdt ligands. The bond lengths of Ag(1)–S range from 2.456 to 2.881 Å and those of Ag(2)–S from 2.534 to 2.632 Å, while the angles of S–Ag(1)–S and S–Ag(2)–S are within the ranges of 83.81–148.22° and 81.56–135.77°, respectively. Therefore, both Ag(1) and Ag(2) adopt a distorted tetrahedral coordination sphere. Fig. 5 gives the top view of complex **2** (along *b*-axis), Ag(1) and Ag(2) atoms form two kinds of Ag_2S_2 rhombohedra units which connect bmdt ligands regularly and spiral up along *b* axis infinitely, thus a 3D network with helices along *b*-axis is obtained. The SbF_6^- anions were included between the 2D gridding layers.

To better understand the structure conformation of **2**, we simplified the Ag_2S_2 rhombohedra as a 4-connected node. For both $Ag(1)_2S_2$ and $Ag(2)_2S_2$ nodes, the shortest circuits starting and ending on each center are five hexagons and one octagon. Thus the topology type of **2** can be classified as $6^5.8$, and the connection mode of the network can be described as "cds" which is similar to the structure of $CdSO_4$ [31].

3.3. Helical structures of *1* and *2*

Both **1** and **2** formed unusual helical structures albeit complexes **1** and **2** are synthesized from different ligands

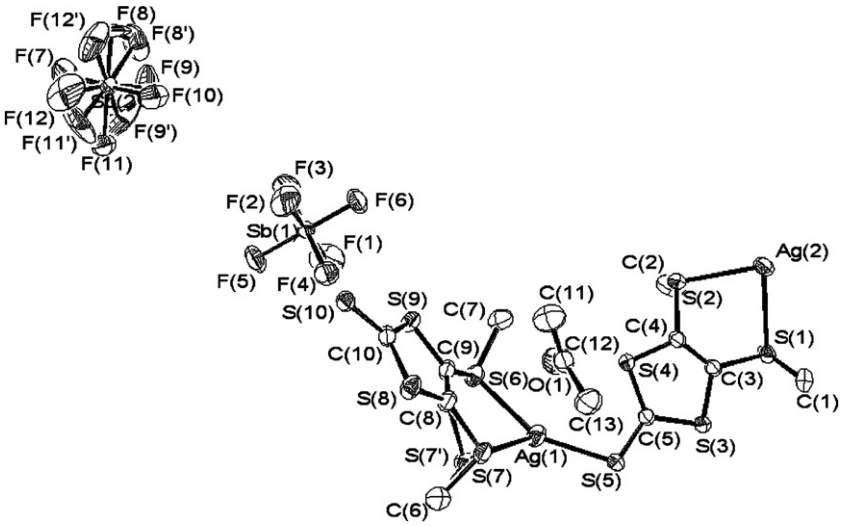


Fig. 4. Structure and labeling of **2** (ORTEP, 50% probability).

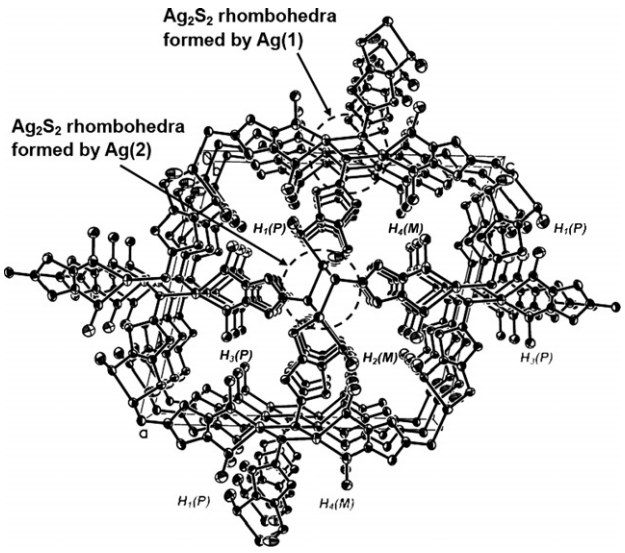


Fig. 5. Overall 3D supramolecular structure with axially chiral griddings for **2** (SbF_6^- anions and acetone were omitted for clarity).

and silver(I) salts. Fig. 6 exhibits the striking feature of polymer **1** with infinite axially chiral double-stranded helix in a space-filling mode. 1D columns on *ab* plane are connected by Ag(1) and Ag(2) atoms to result in a homo-chiral 2D layers, however, the chirality alternates between the layers. In Fig. 6a (left-handed case), the left helix spirals up by sharing the downside C=C bonds of the TTF skeletons, while the right one sharing the upside; It undergoes the same way for the right-handed one (Fig. 6b) except the helix was marked with black and gray. The double-helices feature a twisted geometry because Ag(3) atoms from the wavy lines were arranged on one plane, this was consistent with the formation of "8"-shaped channels which extended infinitely along *b*-axis. The formation of unusual double-stranded helices in complex **1** can be ascribed to the four long flexible arms of ligand tces-TTF and the coordination feature of silver(I). Although some coordination polymers with double-helical frames were reported before [32], it is rare for the case of TTF derivatives, and also, for using coordinate bonds to construct double-helical structures [33].

An overall 3D network structure of **2** is shown in Fig. 5. Four types of helices were found in **2** (Fig. 7), named as H_1, H_2, H_3 and H_4, respectively. These bmdt ligands are connected head to tail by Ag(1) or Ag(2) atoms and spiral up along *b*-axis. A further observation of these helices shows that when they were assembled along *a*-axis, the chirality does not change, while along *c*-axis, it alternates.

Helices with partially shared hinges formed by metal atoms or organic ligands are not rare [34], similar structures with parallel helices were also reported before [35]. To our surprise, complex **2** has entirely shared sides formed by bmdt ligands only, adjacent griddings are not penetrated and feature an approximately identical construction mode. Besides, this 3D network is built up through coordinate bonds only and result in a $6^5.8$ topology, to the best of our knowledge, suchlike TTF-based helical structure was never reported before.

Additionally, the double helix in **1** can also be described as two single stranded helices hinged by the Ag(3) wavy line which have the same chirality, and were enclosed between two rows of TTF skeletons to result in a sandwich structure. In **2**, the shorter skeleton and three coordination sites (S1, S2, S5) of bmdt provide tri-connected assemblies, they were regularly linked by Ag_2S_2 rhombohedra units in a head-to-tail fashion and this made it possible to form an infinite helix.

In this paper, two different types of ligands tces-TTF and bmdt were used for the following reasons: (a) rigid TTF π-backbone (whole for tces-TTF and half for bmdt) may bring potential properties like other TTF polymers; (b) feasible bonding sites (four N atoms on tces-TTF and three S atoms on bmdt) may provide rich coordination modes; (c) tces-TTF possesses flexible cyanoethylsulfanyl arms which are possible to form a helical structure [15e].

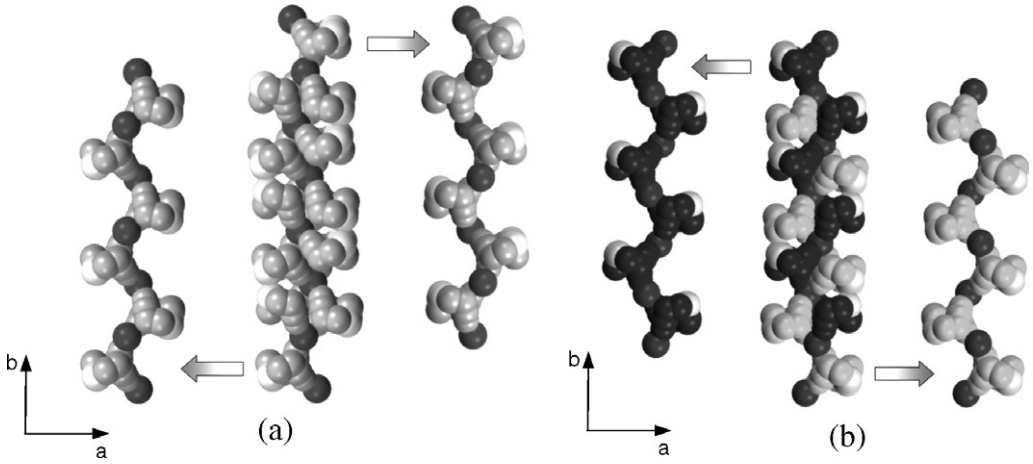


Fig. 6. Space-filling representation of the 1D column in **1** (atoms not involved in the double-stranded helix were omitted for clarity). (a) Left-handed. Ag: black; C: dark gray; S: gray; (b) Right-handed. Black and gray represent the two strands of helices, respectively.

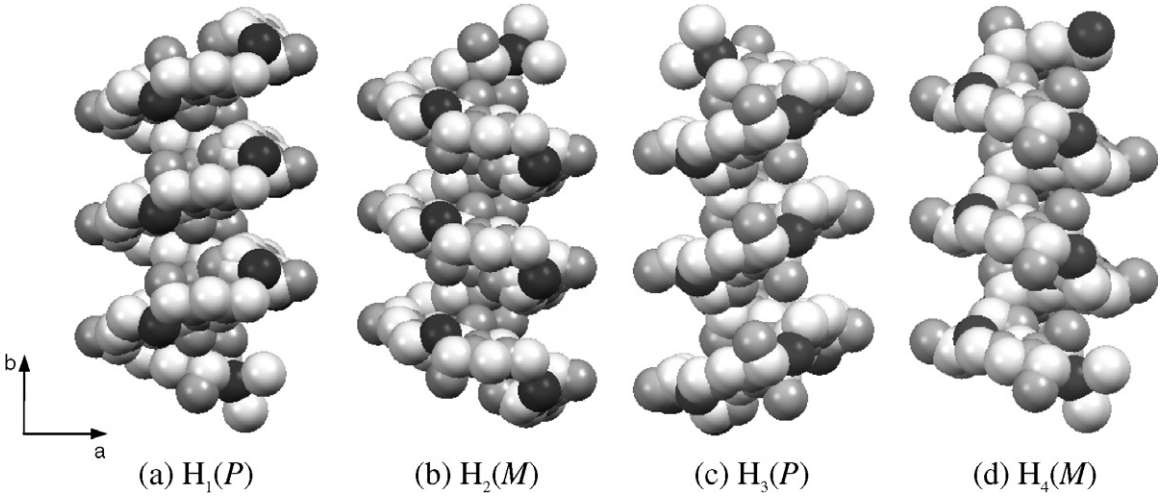


Fig. 7. Four types of axially chiral griddings in **2**. H_1 (a) and H_2 (b) are enantiomorphous as well as H_3 (c) and H_4 (c). Ag: black; C: dark gray; S: gray. (a) $H_1(P)$ (b) $H_2(M)$ (c) $H_3(P)$ (d) $H_4(M)$.

3.4. Spectroscopic properties and conductivity

The IR spectrum of **1** reveals a sharp band at 1416 cm^{-1} which indicates neutral tces-TTF molecules. The UV–Vis spectra of **1** and **2** show a range of absorption from 380 to 430 nm which may be ascribed to local excitations of tces-TTF and bmdt molecules. No spectral information indicating radical cations was found, σ value of polymer **1** is $3.47 \times 10^{-6} S \cdot cm^{-1}$ (measured by conventional two-probe technique under room temperature). It is S···S contacts that contribute to this weak conductive property, Fig. 2 shows the S···S contacts in polymer **1**: 3.397(2) Å of S(5)···S(7) and 3.434(2) Å of S(6)···S(8) which extend infinitely along the 1D column; 3.588(3) Å of S(3)···S(3′) and 3.517(3) Å of S(4)···S(4′) which are approximately perpendicular to the former ones. For complex **2**, it is an insulator, no S···S contact within 3.70 Å (van der Waals radii of two sulfur atoms) was found.

4. Conclusion

Two 3D coordination polymeric networks with axially chiral motifs were synthesized and crystallographically characterized. Complex **1** has novel "8"-shaped channels and twisted double-helical structure. Although the center TTF skeleton of tces-TTF is rigid, those flexible cyanoethylsulfanyl arms contribute to the formation of the helical structure. **1** also exhibits semi-conductive behavior ($\sigma = 3.47 \times 10^{-6} S\ cm^{-1}$) because of extensive intramolecular S ··· S contacts. In polymer **2**, bmdt ligands are linked by Ag_2S_2 analogues and result in an infinite helix which shares its sides with adjacent ones. A tailored building block with multi-coordinate sites helps the formation of this helical structure. In addition, complex **2** is also a "cds" network with a $6^5.8$ topology. It is an insulator for it has not effective S···S contacts. These two 3D polymeric networks are formed by coordinate bonds only, and therefore their stabilities are higher.

Acknowledgement

This work was partly supported by the Scientific Research Foundation for the Returned Overseas Chinese Scholars, State Education Ministry of China, the Scientific Research Foundation, Liaoning Province of China, and Grant-in-Aid for Scientific Research from the Ministry of Education, Science, Sports and Culture of Japan.

Appendix A. Supplementary data

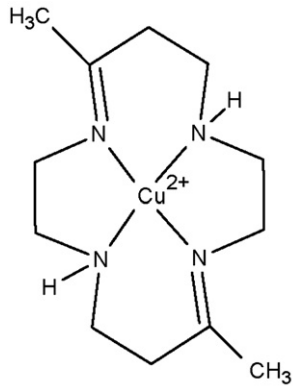
CCDC 615421 and 651218 contain the supplementary crystallographic data for this paper. These data can be obtained free of charge via http://www.ccdc.cam.ac.uk/conts/retrieving.html, or from the Cambridge Crystallographic Data Centre, 12 Union Road, Cambridge CB2 1EZ, UK; fax: (+44) 1223-336-033; or e-mail: deposit@ccdc.cam.ac.uk. Supplementary data associated with this article can be found, in the online version, at doi:10.1016/j.poly.2008.01.010.

References

[1] H. Pninzbach, H. Berger, A. Lüttringhaus, Angew. Chem., Int. Ed. Engl. 4 (1965) 436.
[2] J. Ferraris, D.O. Cowan, V.J. Walatka, H.J. Perlstein, J. Am. Chem. Soc. 95 (1973) 948.
[3] (a) For recent TTF reviews, see: A. Kobayashi, E. Fujiwara, H. Kobayashi, Chem. Rev. 104 (2004) 5243;
(b) J.M. Fabre, Chem. Rev. 104 (2004) 5133.
[4] (a) F. Wudl, Acc. Chem. Res. 17 (1984) 227;
(b) M.R. Bryce, Chem. Soc. Rev. 20 (1991) 355;
(c) J.M. Williams, A.J. Schultz, U. Geiser, K.D. Carlson, A.M. Kini, H.H. Wang, W.K. Kwok, M.H. Whanbo, J.E. Schirber, Science 252 (1991) 1501;

(d) T. Ishiguro, K. Yamaji, G. Saito, Organic Superconductors, 2nd ed., Springer-Verlag, Berlin, Heidelberg, 1998.
[5] (a) J.-M. Lehn, Comprehensive Supramolecular Chemistry, Ed. Pergamon Press, Oxford, UK, 1996;
(b) C. Piguet, G. Bernardinelli, G. Hopfgartner, Chem. Rev. 97 (1997) 2005;
(c) F.J.M. Hoeben, P. Jonkheijm, E.W. Meijer, A.P.H.J. Schenning, Chem. Rev. 105 (2005) 1491.
[6] (a) H.-L. Sun, B.-Q. Ma, S. Gao, S.R. Batten, Cryst. Growth Des. 6 (2006) 1261;
(b) B.F. Abrahams, M.G. Haywood, R. Robson, J. Am. Chem. Soc. 127 (2005) 816;
(c) B.F. Abrahams, S.R. Batten, B.F. Hoskins, R. Robson, Inorg. Chem. 42 (2003) 2654;
(d) A.C. Sudik, A.P. Côté, A.G. Wong-Foy, M. O'Keeffe, O.M. Yaghi, Angew. Chem., Int. Ed. Engl. 45 (2006) 2528;
(e) B.-L. Chen, C.-D. Liang, J. Yang, D.S. Contreras, Y.L. Clancy, E.B. Lobkovsky, O.M. Yaghi, S. Dai, Angew. Chem., Int. Ed. Engl. 45 (2006) 1390;
(f) S. Banfi, L. Carlucci, E. Caruso, G. Ciani, D.M. Proserpio, Cryst. Growth Des. 4 (2004) 29;
(g) L. Carlucci, G. Ciani, M. Moret, D.M. Proserpio, S. Rizzato, Chem. Mater. 14 (2002) 12;
(h) S. Masaoka, D. Tanaka, Y. Nakanishi, S. Kitagawa, Angew. Chem., Int. Ed. Engl. 43 (2004) 2530;
(i) Z.-Q. Wang, V.C. Kravtsov, M.J. Zaworotko, Angew. Chem., Int. Ed. Engl. 44 (2005) 2877;
(j) S.-Q. Liu, T. Kuroda-Sowa, H. Konaka, Y. Suenaga, M. Maekawa, T. Mizutani, G.-L. Ning, M. Munakata, Inorg. Chem. 44 (2005) 1031.
[7] (a) S. Perruchas, K. Boubekeur, P. Batail, Cryst. Growth Des. 5 (2005) 1585;
(b) C. Jia, S.-X. Liu, C. Ambrus, A. Neels, G. Labat, S. Decurtins, Inorg. Chem. 45 (2006) 3152.
[8] (a) M. Mas-Torrent, S.S. Turner, K. Wurst, J. Vidal-Gancedo, X. Ribas, J. Veciana, P. Day, C. Rovira, Inorg. Chem. 42 (2003) 7544;
(b) J. Dai, M. Munakata, L.-P. Wu, T. Kuroda-Sowa, Y. Suenaga, Inorg. Chim. Acta 258 (1997) 65;
(c) J.-C. Zhong, Y. Misaki, M. Munakata, T. Kuroda-Sowa, M. Maekawa, Y. Suenaga, H. Konaka, Inorg. Chem. 40 (2001) 7096.
[9] (a) M. Yuan, B. Ülgüt, M. McGuire, K. Takada, F.J. DiSalvo, S. Lee, H. Abruña, Chem. Mater. 18 (2006) 4296;
(b) S. Ichikawa, S. Kimura, H. Mori, G. Yoshida, H. Tajima, Inorg. Chem. 45 (2006) 7575.
[10] (a) E. Fujiwara, A. Kobayashi, H. Fujiwara, H. Kobayashi, Inorg. Chem. 43 (2004) 1122;
(b) J.-Y. Niu, D.-J. Guo, J.-P. Wang, J.-W. Zhao, Cryst. Growth Des. 4 (2004) 241.
[11] S. Curreli, P. Deplano, M.L. Mercuri, L. Pilia, A. Serpe, J.A. Schlueter, M.A. Whited, U. Geiser, E. Coronado, C.J. Gómez-García, E. Canadell, Inorg. Chem. 43 (2004) 2049.
[12] B.H. Ward, G.E. Granroth, K.A. Abboud, M.W. Meisel, D.R. Talham, Chem. Mater. 10 (1998) 1102.
[13] (a) J. Dai, M. Munakata, T. Kuroda-Sowa, Y. Suenaga, L.-P. Wu, Inorg. Chim. Acta 225 (1997) 163;
(b) J. Dai, T. Kuroda-Sowa, M. Munakata, M. Maekawa, Y. Suenaga, Y. Ohno, J. Chem. Soc., Dalton Trans. 13 (1997) 2363;
(c) L.-P. Wu, J. Dai, M. Munakata, T. Kuroda-Sowa, M. Maekawa, Y. Suenaga, Y. Ohno, J. Chem. Soc., Dalton Trans. 19 (1998) 3255;
(d) M. Munakata, T. Kuroda-Sowa, M. Maekawa, A. Hirota, S. Kitagawa, Inorg. Chem. 34 (1995) 2705.
[14] (a) Y. Ding, J.-C. Zhong, M. Munakata, H. Konaka, G.-L. Ning, H.-Z. Wang, Chem. Lett. 34 (2005) 1632;
(b) C.-Y. Jia, D.-Q. Zhang, C.-M. Liu, W. Xu, H.-M. Hu, D.-B. Zhu, New J. Chem. 26 (2002) 490.
[15] (a) M. Munakata, L.-P. Wu, T. Kuroda-Sowa, Adv. Inorg. Chem. 46 (1998) 173, and references therein;
(b) M. Munakata, G.L. Ning, Y. Suenaga, K. Sugimoto, T. Kuroda-sowa, M. Maekawa, Chem. Commun. 16 (1999) 1545;
(c) O.J. Gelling, B.F. Van, B.L. Feringer, J. Chem. Soc., Chem. Commun. (1991) 917;
(d) S.R. Batten, B.F. Hoskins, R. Robson, Angew. Chem., Int. Ed. Engl. 36 (1997) 636;
(e) L. Han, M.-C. Hong, Inorg. Chem. Commun. 8 (2005) 406;
(f) B. Kesanli, W. Lin, Coord. Chem. Rev. 246 (2003) 305.
[16] (a) C. Janiak, Dalton Trans. (2003) 2781;
(b) S. James, J. Chem. Soc. Rev. 32 (2003) 276;
(c) L.J. Childs, M.J. Hannon, Supramol. Chem. 16 (2004) 7;
(d) M. Pascu, F. Tuna, E. Kolodziejczyk, G.I. Pascu, G. Clarkson, M.J. Hannon, Dalton Trans. (2004) 1546;
(e) T. Nakano, Y. Okamoto, Chem. Rev. 101 (2001) 4013;
(f) M. Albrecht, Chem. Rev. 101 (2001) 3457.
[17] N. Kobayashi, T. Naito, T. Inabe, Adv. Mater. 16 (2004) 1803.
[18] J. Sly, P. Kasák, E. Gomar-Nadal, C. Rovira, L. Górriz, P. Thordarson, D.B. Amabilino, A.E. Rowan, R.J.M. Nolte, Chem. Commun. (2005) 1255.
[19] (a) M.-C. Hong, Y.-J. Zhao, W.-P. Su, R. Cao, M. Fujita, Z.-Y. Zhou, A.S.C. Chan, Angew. Chem., Int. Ed. Engl. 39 (2000) 2468;
(b) H.-P. Wu, C. Janiak, G. Rheinwald, H. Lang, J. Chem. Soc., Dalton Trans. 2 (1999) 183.
[20] S. Lopez, M. Kaharaman, M. Harmata, S.W. Keller, Inorg. Chem. 36 (1997) 961.
[21] T.L. Hennigar, D.C. MacQuarri, P. Losier, R.D. Rogers, J.M. Zaworotko, Angew. Chem., Int. Ed. Engl. 36 (1997) 972.
[22] (a) L. Carlucci, G. Ciani, D.M. Proserpio, S. Rizzato, Chem. Eur. J. 8 (2002) 1519;
(b) L. Carlucci, G. Ciani, P. Macchi, D.M. Proserpio, S. Rizzato, Chem. Eur. J. 8 (1999) 237;
(c) L. Carlucci, G. Ciani, D.M. Proserpio, S. Rizzato, Cryst. Eng. Commun. 4 (2002) 413;
(d) M.A. Withersby, A.J. Blake, N.R. Champness, P. Hubberstey, W.-S. Li, M. Schroder, Angew. Chem., Int. Ed. Engl. 36 (1997) 2327.
[23] (a) T.C.W. Mak, Inorg. Chim. Acta 84 (1984) 19;
(b) W.-H. Bi, D.-F. Sun, R. Cao, M.-C. Hong, Acta Crystallogr. E 58 (2002) 324.
[24] B.-L. Fei, W.-Y. Sun, T. Okamura, W.X. Tang, N. Uegama, New J. Chem. 25 (2001) 210.
[25] D.-F. Sun, R. Cao, J.-B. Weng, M.-C. Hong, Y.-C. Liang, J. Chem. Soc., Dalton Trans. 3 (2002) 291.
[26] D.L. Reger, R.F. Semeniuc, J. Derek Elgin, V. Rassolov, M.D. Smith, Cryst. Growth Des. 6 (2006) 2758.
[27] T.J. Burchell, R.J. Puddephatt, Inorg. Chem. 45 (2006) 650.
[28] (a) L. Carlucci, G. Ciani, D.W.W.v. Gudenberg, D.M. Proserpio, Inorg. Chem. 36 (1997) 3812;
(b) I.G. Dance, L.J. Fitzpatrick, A.D. Rae, M.L. Scudder, Inorg. Chem. 22 (1983) 3785;
(c) M. Munakata, L.-P. Wu, T. Kuroda-Sowa, M. Maekawa, Y. Suenaga, G.L. Ning, T. Kojima, J. Am. Chem. Soc. 120 (1998) 8610;
(d) A. Erxleben, Inorg. Chem. 40 (2001) 2928;
(e) J.-R. Li, X.-H. Bu, J. Jiao, W.-P. Du, X.-H. Xu, R.-H. Zhang, Dalton Trans. 3 (2005) 464;
(f) C.-L. Chen, C.-Y. Su, Y.-P. Cai, H.-X. Zhang, A.-W. Xu, B.-S. Kang, H.C. zur Loye, Inorg. Chem. 42 (2003) 3738.
[29] N. Svenstrup, K.M. Rasmussen, T.K. Hansen, J. Becher, Synthesis (1994) 809.
[30] Y. Misaki, H. Nishikawa, K. Kawakami, S. Koyanagi, T. Yamabe, M. Shiro, Chem. Lett. (1992) 2321.
[31] (a) For "cds" net see: O. Delgado Friedrichs, M. O'Keeffe, O.M. Yaghi, Acta Crystallogr. Sect. A 59 (2003) 22;
(b) O. Delgado Friedrichs, M. O'Keeffe, O.M. Yaghi, Solid State Sci. 5 (2003) 73;
(c) N.L. Rosi, J. Kim, M. Eddaoudi, B.L. Chen, M. O'Keeffe, O.M. Yaghi, J. Am. Chem. Soc. 127 (2005) 1504.
[32] (a) L. Carlucci, G. Ciani, D.W.v. Gudenberg, D.M. Proserpio, Inorg. Chem. 36 (1997) 3812;

(b) S.D. Reid, A.J. Blake, C. Wilson, J.B. Love, Inorg. Chem. 45 (2006) 636;
(c) A. Casnati, R. Liantonio, P. Metrangolo, G. Resnati, R.U. Franco Ungaro, Angew. Chem. 118 (2006) 1949.
[33] (a) J.M. Lehn, A. Rigault, J. Siegel, J. Harrowfield, B. Chevrier, D. Moras, Proc. Natl. Acad. Sci. USA 84 (1987) 2565;
(b) A. Jouaiti, M.W. Hosseini, N. Kyritsakas, Chem. Commun. 3 (2003) 472.
[34] (a) L. Han, M.-C. Hong, R.-H. Wang, J.-H. Luo, Z.-Z. Lin, D.-Q. Yuan, Chem. Commun. 20 (2003) 2580;
(b) Y.-T. Wang, H.-H. Fan, H.-Z. Wang, X.-M. Chen, J. Mol. Struct. 740 (2005) 61;
(c) D. Maspoch, N. Domingo, D. Ruiz-Molina, K. Wurst, J.M. Hernández, G. Vaughan, C. Rovira, F. Lloret, J. Tejada, J. Veciana, Chem. Commun. 40 (2005) 5035.
[35] Y. Cui, S.J. Lee, W. Lin, J. Am. Chem. Soc. 125 (2003) 6014.



Scheme 1. Schematic view of the macrocyclic copper(II) complex.

macrocyclic copper(II) complex $Cu(cyclam)^{2+}$ in order to obtain a heterometallic system $\{[Cu(cyclam)][Co(NCS)_4]\}_n$ bridged by a thiocyanate group. Square-planar macrocyclic complexes of Cu(II) and Ni(II) with two free coordination places at the metal atom can play here the role of the so-called "building blocks". Considering the fact that in unsaturated complexes of the type [14]dieneN$_4$, the N-configuration of the macrocyclic ring influences its conformation, and thus the arrangement of substituents in it [15], an attempt was undertaken to study the relation between the N-configuration and the crystal structure and magnetic properties of the compounds obtained [9]. Previously, we obtained a heterometallic compound of the type $[(CuL_3)[Co(NCS)_4]$ (L_3 = *N-meso*-5,12-Me$_2$-7,14-Et$_2$-[14]-4,11-dieneN$_4$) [9], in which the macrocyclic complexes of Cu(II) forms a linear polymer with the $[Co(NCS)_4]^{2-}$ anion. There are also two known complexes of the general formula $[ML_3]_2[Mn(NCS)_4](ClO_4)_2$ (where M = Cu(II), Ni(II); L_3 = N-dl-5,7,7,12,14,14-hexamethyl-1,4,8,11-tetraazacyclotetradeca-4,11-diene), whose crystal structures are built up by isostructural, trinuclear complex-cations $\{[ML_3]_2[Mn(NCS)_4]\}^{2+}$ (M = Ni^{II}, Cu^{II}) and perchlorate anions [16]. It is shown that the number and size of the substituents in the macrocyclic rings influence the crystal structure and magnetic properties of the compounds. In this paper, we present results concerning a new such system, containing the non-saturated substituted complex CuL_1^{2+} (where L_1 = *N-rac*-5,12-Me$_2$-[14]-4,11-dieneN$_4$) (Scheme 1), as well as the simple ion of the $[Co(NCS)_4]^{2-}$complex.

2. Experimental

2.1. Materials

All materials used in this work were of reagent grade purity and were used as commercially obtained. $[CuL_1](ClO_4)_2$ was prepared as previously reported [17].

2.2. Synthesis of the complex

A solution of $[CuL_1](ClO_4)_2$ (73.02 mg, 0.15 mmol) in CH_3CN (10 mL) was added, dropwise, to a solution containing an aqueous solution of KSCN (58.31 mg, 0.6 mmol) and $CoCl_2 \cdot 6H_2O$ (35.69 mg, 0.15 mmol). The mixture was subsequently stirred. After a few days a dark-blue crystalline solid was formed from the violet solution by slow evaporation. It was filtered and washed using diethyl ether (2 × 10 mL). Yield: 82.53 mg (95%). A blue needle crystal of the compound suitable for X-ray diffraction studies was obtained by slow evaporation of a solution of all the reagents in CH_3CN–H_2O (1:1) at room temperature. *Anal.* Calc. for $C_{16}H_{24}N_8S_4CoCu$ (579.14): C, 33.18; H, 4.18; N, 19.35; S, 22.15. Found: C, 33.20; H, 4.27; N, 19.48; S, 21.78. The copper and cobalt content was determined by the ICP method: Calcd Co, 10.18; Cu, 10.97. Found: Co, 9.88; Cu, 10.12.

2.3. Infrared spectra

The FIR spectrum was measured in Nujoll mulls (500–50 cm^{-1}) and the MIR spectrum in KBr pellets (4000–500 cm^{-1}) with a Brucker IFS 66 spectrophotometer.

The infrared spectrum of the complex exhibits three bands near 2000 cm^{-1} (2121 and 2088 cm^{-1}), which are associated with the ν_{as}(NCS) stretching mode, resulting from a combinations of four effects: (i) the presence of bridging thiocyanate ligands (Co–NCS–Cu); (ii) the presence of non-bridging thiocyanate ligands (Co–NCS); (iii) the distorted octahedral copper(II) environment and (iv) the tetrahedral environment of cobalt(II).

2.4. Magnetic measurements

Magnetic measurements in the temperature range 1.8–300 K were performed using a Quantum Design SQUID-based MPMSXL-5-type magnetometer. The SQUID magnetometer was calibrated with a palladium rod sample (Materials Research Corporation, measured purity 99.9985%). Magnetization measurements of a polycrystalline sample were carried out at a magnetic field of 0.5 T over the temperature range 1.8–300 K and versus a magnetic field from 0 to 5 T at a temperature of 2 K. Corrections are based on subtracting the sample holder signal and the contribution χD estimated from Pascal constants [18].

2.5. EPR spectra

EPR spectra were recorded at room temperature and 77 K on a Bruker ESP 300 spectrometer operating at the X-band frequency, equipped with an ER 035M Bruker NMR gaussmeter and HP 5350B Hewlett–Packard microwave frequency counter. The spectra at 4.5 K temperature were measured with an X-band Radiopan SE/X 2543 spectrometer.

2.6. X-ray crystallographic analysis

A blue needle crystal was mounted on a KM-4-CCD automatic diffractometer equipped with a CCD detector,

and was used for data collection. X-ray intensity data were collected with graphite monochromated Mo Kα radiation with the ω scan mode. A 42 s exposure time was used. The unit cell parameters were determined from 7689 strongest reflections. Details concerning crystal data and refinement are given in Table 1. Examination of reflections on six reference frames monitored after each 10 frames measured showed 9.8% loss of the intensity. During the data reduction the above decay correction coefficient was taken into account. Lorentz, polarization and numerical absorption [19] corrections were applied. The structure was solved by the partial structure expansion procedure. All the non-hydrogen atoms were refined anisotropically using the full-matrix, least-squares technique on F^2. All the hydrogen atoms were found from difference Fourier synthesis after four cycles of anisotropic refinement, and refined as "riding" on the adjacent atom with geometric idealisation after each cycle of refinement and with individual isotropic displacement factors equal to 1.2 times the value of the equivalent displacement factor of the parent non-methyl atom and 1.5 times of the parent methyl group carbon atom. The methyl groups were allowed to rotate about their local threefold axis. The SHELXS97 [20], SHELXL97 [21] and SHELXTL [22] programs were used for all the calculations. Atomic scattering factors were those incorporated in the computer programs. Selected interatomic bond distances and angles are listed in Table 2.

Table 1
Crystal data and structure refinement for {(CuL)[Co(NCS)$_4$]}

Empirical formula	$C_{16}H_{24}CoCuN_8S_4$
Formula weight	579.14
Temperature (K)	291.0(3)
Wavelength (Å)	λ (Mo Kα) = 0.71073
Crystal system, space group	orthorhombic, $P2_12_12_1$
Unit cell dimensions	
a (Å)	8.0207(8)
b (Å)	15.3983(14)
c (Å)	20.2241(17)
V (Å^3)	2497.8(4)
Z	4
D_{calc} (Mg/m^3)	1.540
Absorption coefficient (mm^{-1})	1.869
F(000)	1184
Crystal size (mm)	0.398, 0.151, 0.150
θ Range for data collection	2.65–25.05
Index ranges	$-9 \leqslant h \leqslant 9$, $-18 \leqslant k \leqslant 18$, $-24 \leqslant l \leqslant 22$
Reflections collected/unique (R_{int})	26608/4422 (0.0354)
Completeness to $2\theta = 25.05°$	99.9%
Refinement method	full-matrix least-squares on F^2
Maximum and minimum transmission	0.754 and 0.722
Data/restraints/parameters	4422/0/275
Goodness-of-fit on F^2	1.062
Final *R* indices [$I > 2\sigma(I)$]	$R_1 = 0.0359$, $wR_2 = 0.0846$
R indices (all data)	$R_1 = 0.0536$, $wR_2 = 0.0959$
Absolute structure parameter (Flack [5])	−0.006(19)
Largest difference in peak and hole (e Å^{-3})	0.745 and −0.331

Table 2
Selected structural data for {(CuL)[Co(NCS)$_4$]}

Cu(1)–N(13)	1.981(3)
Cu(1)–N(11)	1.988(4)
Cu(1)–N(12)	1.995(5)
Cu(1)–N(14)	1.999(5)
Co(1)–N(4)	1.948(5)
Co(1)–N(3)	1.947(4)
Co(1)–N(2)	1.960(5)
Co(1)–N(1)	1.960(5)
N(1)–C(1)	1.141(6)
C(1)–S(1)	1.622(6)
N(2)–C(2)	1.160(6)
C(2)–S(2)	1.610(6)
N(3)–C(3)	1.168(6)
C(3)–S(3)	1.624(5)
N(4)–C(4)	1.147(7)
C(4)–S(4)	1.603(7)
Cu(1)–S(2)	2.8761(13)
Cu(1)–S(3)$^{\#1}$	3.1704(13)
N(13)–Cu(1)–N(11)	176.83(16)
N(13)–Cu(1)–N(12)	85.9(2)
N(11)–Cu(1)–N(12)	94.4(2)
N(13)–Cu(1)–N(14)	93.9(2)
N(11)–Cu(1)–N(14)	85.7(2)
N(12)–Cu(1)–N(14)	178.14(18)
N(4)–Co(1)–N(3)	108.0(2)
N(4)–Co(1)–N(2)	113.6(2)
N(3)–Co(1)–N(2)	113.4(2)
N(4)–Co(1)–N(1)	110.1(2)
N(3)–Co(1)–N(1)	107.86(19)
N(2)–Co(1)–N(1)	103.8(2)
C(1)–N(1)–Co(1)	168.3(5)
N(1)–C(1)–S(1)	179.3(5)
C(2)–N(2)–Co(1)	149.1(5)
N(2)–C(2)–S(2)	178.6(5)
C(3)–N(3)–Co(1)	167.2(4)
N(3)–C(3)–S(3)	179.2(4)
C(4)–N(4)–Co(1)	163.6(5)
N(4)–C(4)–S(4)	178.8(6)
S(2)–Cu(1)–S(3)$^{\#1}$	171.63(4)
S(2)–Cu(1)–N(11)	93.27(11)
S(2)–Cu(1)–N(12)	85.86(12)
S(2)–Cu(1)–N(13)	89.90(12)
S(2)–Cu(1)–N(14)	95.99(13)
S(3)$^{\#1}$–Cu(1)–N(11)	82.87(11)
S(3)$^{\#1}$–Cu(1)–N(12)	87.03(12)
S(3)$^{\#1}$–Cu(1)–N(13)	94.00(12)
S(3)$^{\#1}$–Cu(1)–N(14)	91.14(13)
C(2)–S(2)–Cu(1)	104.65(18)
C(3)$^{\#1}$–S(3)$^{\#1}$–Cu(1)	97.76(15)

Symmetry transformations used to generate equivalent atoms: #1: $-x - 1.5$, $-y$, $z - 0.5$.
Distances in Å, angles in °.

3. Results

3.1. Structural description

A perspective view of the structure occupying the asymmetric unit of the unit cell together with the atom numbering scheme is shown in Fig. 1, displacement ellipsoids are plotted with 50% probability. All atoms lie in general positions. The macrocyclic chiral nitrogen atoms have the

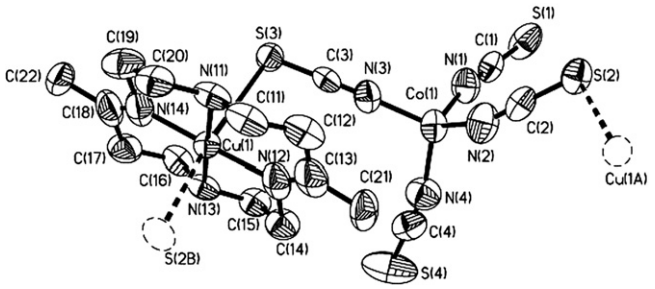


Fig. 1. The molecular conformation of $\{(CuL_1)[Co(NCS)_4]\}$ with the atom numbering, plotted with 50% probability of displacement ellipsoids. The hydrogen atoms are omitted for clarity. Atoms belonging to the asymmetric unit are indicated by full lines. The symmetry generated atoms Cu(1A) and S(2B) are indicated by dashed lines.

configuration R and S for the N(11) and N(13) atoms, respectively, thus the macrocycle does not posses chirality. Despite this fact, the title compound crystallises in the chiral space group $P2_12_12_1$. The copper atom is six coordinated by four macrocyclic nitrogen atoms and two sulfur atoms of bridging thiocyanate groups. The coordination polyhedra of the copper atoms can be described as distorted tetragonal bipyramid with the sulfur atoms in axial positions. The copper atom deviates 0.043(2) Å from the macrocyclic N_4 least squares plane. Adopting a slightly distorted tetrahedral coordination (Table 2), the cobalt atom is four coordinated by the nitrogen atoms of the thiocyanate groups. The bridging thiocyanate groups are located in a facial arrangement. One of the Cu–S distances (Table 2) is distinctly larger than the most common values (2.33–2.95 Å), but still lies in the typical range of 2.2–3.2 Å observed for Cu–SCN bonds in coordination compounds. The macrocycle conformation can be described as sc^-, sc^+, ap^-, ap^-, sc^-, ap^+, ap^+, sc^+, sc^-, ap^-, ap^+, sc^+, ap^-, ap^-. The existence of a twofold screw axis around the copper atom expands the molecules to a one-dimensional zig-zag coordination polymer along the crystallographic *c* axis (Fig. 2). In the structure can be found medium strength N–H···S hydrogen bonds (Table 3) [23] of which one (N(11)–H(11)···S(3)) provides additional stabilisation to the polymer chain and a second (N(13)–H(13)···S(1)) expands the polymer chain to a two-dimensional net along

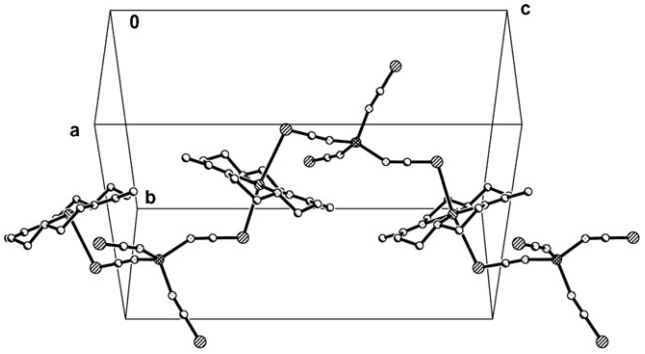


Fig. 2. The coordination polymer of $\{(CuL_1)[Co(NCS)_4]\}$.

Table 3
Hydrogen bonds for $\{(CuL)[Co(NCS)_4]\}$

D–H···A	*d*(D–H)	*d*(H···A)	*d*(D···A)	∠(DHA)
N(11)–H(11)···S(3)$^{\#1}$	0.83	2.99	3.527(4)	123.7
N(13)–H(13)···S(1)$^{\#2}$	0.77	2.82	3.566(4)	162.2

Symmetry transformations used to generate equivalent atoms: #1: $-x-3/2, -y, z-1/2$; #2: $x+1, y, z$.
Distances in Å, angles in °.

the crystallographic *ac* plane. Besides those mentioned above, there are no unusual intermolecular short contacts in the structure. The polymer chain nearest Cu(1)···Co(1) distances are 6.4152(9) and 6.0988(9) Å, and the nearest Cu(1)···Co(1) interchain distances are 6.8609(9), 6.9628(9) and 6.0336(10) Å.

3.2. Magnetic properties

The magnetic behavior of the complex is shown in Fig. 3 in the form of χ_M and $\chi_M T$ versus T plots, where χ_M is the magnetic susceptibility per Cu(II)Co(II). The value of $\chi_M T$ at room temperature for the compound equals 2.78 $cm^3\ mol^{-1}\ K$ (4.72 B.M.), which is larger than the expected value for a magnetically non-interacting Cu(II)-Co(II) entity with local spins $S_{Cu} = 1/2$ and $S_{Co} = 3/2$ (2.25 $cm^3\ mol^{-1}\ K$, $g = 2.0$). This may be due to the contribution of the spin–orbit coupling of the Co^{II} ion. It is also likely that at room temperature we already have ferromagnetic coupling occurring. In this way, the value of $\chi_M T$ is greater than the calculated value. Upon cooling, the $\chi_M T$ value is practically independent of temperature in the temperature range 100–300 K and then increases as the temperature is lowered further to $T_{max} = 10$ K. The $\chi_M T$ values at T_{max} is equal to 2.97 $cm^3\ mol^{-1}\ K$ (4.87 B.M.). The interaction of cobalt(II) with copper(II) gives rise to spin triplet ($S = 1$) and spin quartet ($S = 2$) low lying states, separated by *J*. The increase of $\chi_M T$ upon cooling

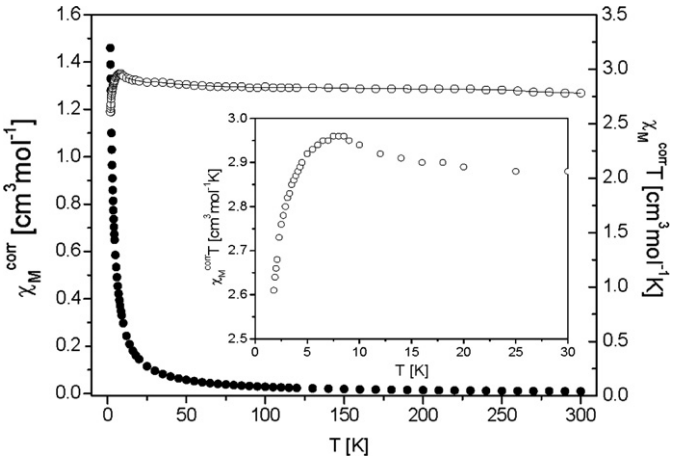


Fig. 3. Thermal dependence of χ_M (●) and $\chi_M T$ (○) for $\{(CuL_1)[Co(NCS)_4]\}$. The solid line is the calculated curve.

indicates that the quartet is the ground state, the interactions between the Cu(II) and Co(II) ions through the thiocyanate bridge being ferromagnetic in the temperature range 10–300 K. Below 10 K, $\chi_M T$ rapidly decreases at the lowest temperatures to 2.61 $cm^3\,mol^{-1}$ K (4.57 B.M.). The lowered $\chi_M T$ value below 10 K indicates the contribution of an antiferromagnetic interaction between the ferromagnetic chains and/or the zero-field splitting effect of Co^{II}.

The values of C and θ, determined from the relation $1/\chi_M = f(T)$ over the 50–300 K range of temperatures, are equal to 2.80 $cm^3\,mol^{-1}$ K and 1.4 K, respectively. The positive value of the Weiss constant confirms that ferromagnetic coupling occurs.

As mentioned in the structural discussion, this complex can be viewed as a heterobimetallic one-dimensional zigzag chain. The problem is why in the examined compound there is no minimum on the $\chi_M T$ versus T curve, which is typical for ferrimagnetic behaviour.

According to Kahn's theory [2b], for a ferrimagnetic chain, $\chi_M T$ first decreases on cooling, reaches a minimum for finite temperatures, then diverges as T approaches zero. The minimum on $\chi_M T$ corresponds to a short range order state where spins S_A and S_B of adjacent magnetic center are antiparallel, but where there is no correlation between the neighboring AB units. Below the temperature of the minimum $\chi_M T$ value, the magnetic behavior is qualitatively equivalent for a chain of n spins $|S_A - S_B|$ which are ferromagnetically coupled. If the intrachain interaction is ferromagnetic ($J > 0$), no extremum of the $\chi_M T$ versus T plot can be observed and $\chi_M T$ increases in the low temperature range. This situation is occured in the examined complex.

The J_{CuCo} parameter can be related to contributions from pairs of magnetic orbitals for copper(II) in octahedral symmetry and cobalt(II) tetrahedral symmetry and is given by

$$J_{CuCo} = \frac{1}{3}(J_{a_1b_1} + J_{a_2b_1} + J_{b_2b_1})$$

which contains only positive terms, of which $J_{a_1b_1}$ is the most important. For the reason of strict orthogonality of the magnetic orbital, the interaction is certainly ferromagnetic with an $S = 2$ ground state well separated in energy from an $S = 1$ excited state.

For magnetic interactions occurring over the whole temperature range, the following equation describing the behavior of a heterometallic chain with F/AF interactions was used [2b]:

$$\chi_{chain} = \frac{N\beta^2}{3kT}\left[g^2\frac{1+u}{1-u} + \delta^2\frac{1-u}{1+u}\right]$$

$$g = (g^e_{Cu} + g^e_{Co})/2$$

$$\delta = (g^e_{Cu} - g^e_{Co})/2$$

$$u = \coth\left(\frac{J^c}{kT}\right) - \left(\frac{kT}{J^c}\right)$$

where:

$$g^c_{Cu} = g_{Cu}[S_{Cu}(S_{Cu}+1)]^{1/2}$$

$$g^c_{Co} = g_{Co}[S_{Co}(S_{Co}+1)]^{1/2}$$

$$J^c = J[S_{Cu}(S_{Cu}+1)S_{Co}(S_{Co}+1)]^{1/2}$$

Taking into consideration the possibility of interchain interactions occurring in the crystal lattice, a correction for a molecular field was also taken into account [24]:

$$\chi_M = \frac{\chi_i}{1 - [(2zJ'/Ng_i^2\mu_B)\chi_i]}$$

The following parameters were obtained from the calculations: $g_{Co} = 2.28$, $g_{Cu} = 2.08$, $J = 1.42\ cm^{-1}$, $zJ' = -0.26\ cm^{-1}$, as indicated by the solid curve in Fig. 3. The agreement factor R, defined as $R = \sum(\chi_{exp}T - \chi_{calc}T)^2/\sum(\chi_{exp}T)^2$, is 2.76×10^{-5}. A positive value of the integral J_{CuCo} witnesses the occurrence of a ferromagnetic interaction between the Co^{II} and Cu^{II} ions. The small value of J_{CuCo} obtained from the calculations follows from the large distances between those ions, amounting to 6.4152(9) and 6.0988(9) Å. The decrease of the value of $\chi_M T$ in the low-temperature range (below 10 K) is thus caused by the occurrence of interchain antiferromagnetic interactions, as well as the parameter D originating from the Co(II) ion, which was not resolved, however, because of too complex mathematical calculations. Interchain interactions in this compound are very weak, of antiferromagnetic character ($zJ' = -0.26\ cm^{-1}$), which is the result of large distances between the metallic ions in the neighboring chains. The nearest Cu(1)···Co(1) interchain distances are 6.8609(9), 6.9628(9) and 6.0336(10) Å.

This suggestion fully confirms the magnetization versus field curve at 2 K. The results are shown in Fig. 4, where the molar magnetization M is expressed in B.M. units and M is expected to have the saturation value M_s, when M/kT becomes very large, according to the equation of $M_s = Ng\mu_B S$. In such a case the ground state

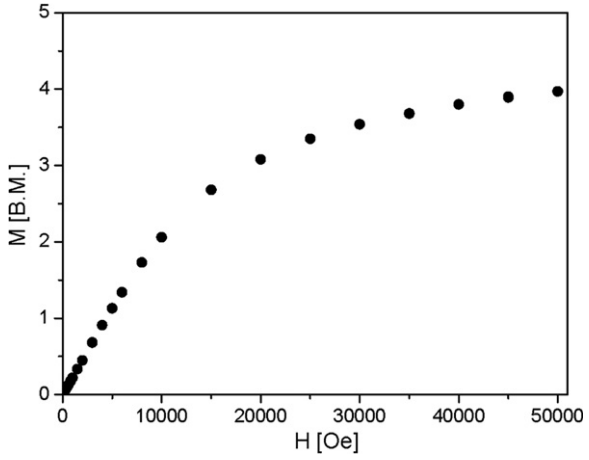


Fig. 4. Field dependence of the magnetization for complex {(CuL$_1$)-[Co(NCS)$_4$]}.

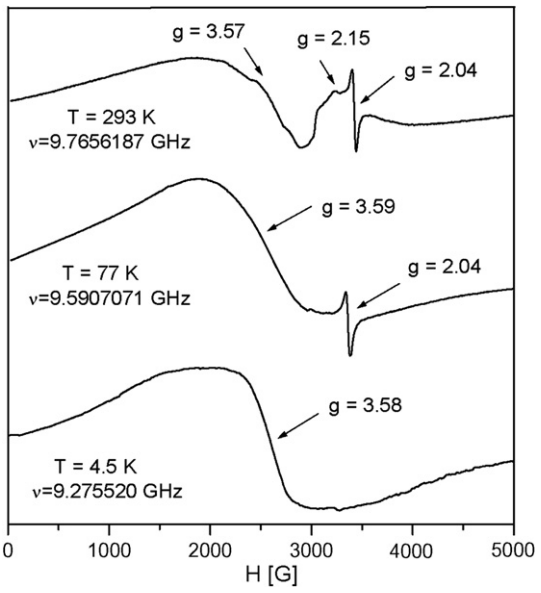


Fig. 5. EPR spectra for $\{(CuL_1)[Co(NCS)_4]\}$ at room temperature, 77 K and 4.5 K.

is $S_{max} = 1/2 + 3/2 = 2$ and the magnetization (per Cu–Co unit) should saturate to the value of $M = 4$ B.M. Experimental data have shown that at the magnetic field $B = 5$ T and with the temperature as low as $T = 2.0$ K the magnetization adopts a value of $M = 3.97\mu_B$, very close to the theoretical value. This fact evidences a very small or absence role of the zero-field splitting effect for the Co(II) ions.

3.3. EPR spectra

X-band EPR spectrum of a powdered sample of the complex $\{(CuL_1)[Co(NCS)_4]\}$ exhibits a broad low-field signal at $g \sim 3.58(10)$ at 293 K. This signal is assigned to a transition within the lowest $|\pm 3/2\rangle$ doublet of the spin state of Co^{II} magnetic center. The spectrum shows also an anisotropic line at $g = 2.04$ (Fig. 5), which is connected only with the electronic configuration ($S = 1/2$) of the copper centers in the octahedral ligand field. The EPR signal of the complex at higher temperatures can indicate superimposing copper(II) and cobalt(II) ground state doublet signals (lines at $g = 2.04$ and 2.15). At 77 and 4.5 K, the spectra display the same isotropic line at $g = 2.04$ ($\delta_{Hpp} = 50$ G) and a more intensive and broad signal at $g \sim 3.59$. The EPR spectrum consists of a few lines, because the investigated complex contains two magnetic centers Cu^{2+} ($S = 1/2$) in a distorted octahedral environment and Co^{II} ($S = 3/2$) with nearly tetrahedral coordination.

4. Discussion

The examined complex has a similar crystalline structure to $(CuL_2)[Co(NCS)_4]$ (L_2 = *N-meso*-5,12-Me_2-7,14-Et_2-[14]-4,11-dieneN$_4$) [9], however the macrocyclic complexes of Cu(II) used for the synthesis differ in the number and size of substituents in the macrocyclic rings. Taking into account the substituents in the macrocyclic rings, the central ion is accessible for the bridging ligands from both sides, due to which it forms a linear polymer with the $[Co(NCS)_4]^{2-}$ anion. For the above reason, the magnetic properties of both complexes are similar, with characteristic weak ferromagnetic interactions. The magnetic properties mainly depend upon the nature of the magnetic orbitals of the metals interacting with each other and the bridge angle [2b]. The bond lengths and the angles of the Cu–S–C bridge in the CuCo unit differ slightly. The bridge angles are equal to 97.86(14)° and 97.92(14)° for $(CuL_2)[Co(NCS)_4]$ (L_2 = *N-meso*-5,12-Me_2-7,14-Et_2-[14]-4,11-dieneN$_4$) [9] and 97.76(15)° and 104.65(18)° for the examined complex. The Cu–S distances are equal to 2.9845(11) and 2.9830(11) Å for the compound investigated earlier and the same distances in the obtained compound are unequivalent and are equal to 2.8761(13) and 3.1704(13) Å. Additionally, the polymer chain nearest Cu(1)···Co(1) distances are 6.4152(9) and 6.0988(9) Å and are larger than in the literature complex (5.93(2) and 5.94(5) Å) [9]. These results suggest that when the distance between the metal ions increase, the magnitude of the exchange coupling constant decreases, as expected for poor overlap of magnetic orbitals, which is a reason for the occurrence of a higher value of the parameter J for compound $(CuL_2)[Co(NCS)_4]$ (L_2 = *N-meso*-5,12-Me_2-7,14-Et_2-[14]-4,11-dieneN$_4$) ($J = 3.07$ cm^{-1}) [9].

On the other hand, by comparing the results obtained for complex $\{(CuL_1)[Co(NCS)_4]\}$ (L_1 = *N-rac*-5,12-Me_2-[14]-4,11-dieneN$_4$) with an appropriate system $\{[Cu(cyclam)][Co(NCS)_4]\}_n$ [13], in which cyclam, being a macrocyclic saturated non-substituted tetra-azo ligand, has greater freedom in adapting itself to the spatial requirements of the anion, it can be seen that substituents that occur at the peripheries of a macrocyclic ligand have significant influence on the properties of the complex obtained. The compound $\{[Cu(cyclam)][Co(NCS)_4]\}_n$, similarly to the examined complex, forms a 1-D polymeric chain, but its magnetic properties are different. Complex $\{(CuL_1)[Co(NCS)_4]\}$ shows the occurrence of weak ferromagnetic interactions between the magnetic centres, while the compound $\{[Cu(cyclam)][Co(NCS)_4]\}_n$ was treated as a ferrimagnetic chain [13], for which there was the occurrence of weak antiferromagnetic interactions in the chain, probably together with an antiferromagnetic coupling between the chains. The authors suggest that the ferrimagnetic character of this compound will likely show itself below 1.7 K. The reason for the differences in the magnetic properties should be looked for in the crystalline structure. Both compounds crystallize with the same crystallographic structure, but in different point groups, which was caused by a different packing in the crystal lattice and a different mutual arrangement of the magnetic centres. In the compound $\{[Cu(cyclam)][Co(NCS)_4]\}_n$, the Cu–S bonds occurring are unequivalent (2.891(3) and 3.160(3) Å) while the bridging angles are equal (111.81(15)° and 111.97(12)°).

Additionally, the Cu···Co distance within the chain is equal to 6.909(3) Å and the same distance between chains is equal to 6.361(2) Å. The intrinsic structural features and larger distance between the copper(II) and cobalt(II) centers leads to a poor overlap of magnetic orbitals. This is probably the main reason for the different magnetic properties. In both compounds the heterogeneous-core character suggests the possibility of the occurrence of both ferro- (F) and antiferromagnetic (AF) interactions. It may be thus supposed that in the complex $\{(CuL_1)[Co(NCS)_4]\}$ that we obtained, the contribution coming from the F interactions is bigger than the contribution from AF interactions, in contrast with the compound $\{[Cu(cyclam)][Co(NCS)_4]\}_n$.

Acknowledgements

This work was supported by the EC 6th NoE Programme "MAGMANet". The crystallographic part was financed by funds allocated by the Ministry of Science and Higher Education to the Institute of General and Ecological Chemistry, Technical University of Lodz.

Appendix A. Supplementary material

CCDC 637546 contains the supplementary crystallographic data for the title compound. These data can be obtained free of charge via http://www.ccdc.cam.ac.uk/conts/retrieving.html, or from the Cambridge Crystallographic Data Centre, 12 Union Road, Cambridge CB2 1EZ, UK; fax: (+44) 1223-336-033; or e-mail: deposit@ccdc.cam.ac.uk.

References

[1] (a) J.M. Lehn, Supramolecular Chemistry, VCH, Weinheim, Germany, 1995;
(b) V. Balzani, F. Scandola, Supramolecular Photochemistry, Horwood, Chichester, UK, 1991.
[2] (a) O. Kahn (Ed.), Molecular Magnetism, A Supramolecular Function, Kluwer, Dordrecht, Netherlands, 1996;
(b) O. Kahn, Molecular Magnetism, VCH, New York, 1993.
[3] H.O. Stumpf, L. Ouahab, Y. Pei, D. Grandjean, O. Kahn, Science 261 (1993) 447.
[4] S. Ferlay, T. Mallah, R. Ouahès, P. Veillet, M. Verdaguer, Nature 378 (1995) 701.
[5] (a) H. Tamaki, Z.J. Zhong, N. Matsumoto, S. Kida, M. Koikawa, N. Achiwa, Y. Hashimoto, H. Okawa, J. Am. Chem. Soc. 114 (1992) 6974;
(b) S. Decurtins, H.W. Schmalle, P. Schneuwly, J. Ensling, P. Gütlich, J. Am. Chem. Soc. 116 (1994) 9521.
[6] (a) G. De Munno, G. Bruno, F. Nicolo, M. Julve, J.A. Real, Acta Crystallogr., Sect. C 49 (1993) 457;
(b) M. Julve, M. Verdaguer, G. De Munno, J.A. Real, G. Bruno, Inorg. Chem. 32 (1993) 795.
[7] J.A.R. Navarro, M.A. Romero, J.M. Salas, M. Quiros, E.R.T. Tiekink, Inorg. Chem. 36 (1997) 4988.
[8] J. Ribas, C. Diaz, X. Solans, M. Font-Bardia, Inorg. Chim. Acta 231 (1995) 229.
[9] A. Skorupa, B. Korybut-Daszkiewicz, J. Mrozinski, Inorg. Chim. Acta 324 (2001) 286.
[10] H.-Z. Kou, D.-Z. Liao, P. Cheng, Z.-H. Jiang, S.-P. Yan, G.-L. Wang, X.-K. Yao, H.-G. Wang, Can. J. Chem. 76 (1998) 1102.
[11] M.C. Burla, B. Chiari, A. Cinti, O. Piovesana, Mol. Cryst. Liq. Cryst. 273 (1995) 211.
[12] M.B. Hursthouse, K.J. Izod, M.A. Thornton, Polyhedron 9 (1990) 535.
[13] G. Francese, S. Ferlay, H.W. Schmalle, S. Decurtins, New J. Chem. 267 (1999).
[14] (a) S. Ferlay, T. Mallah, J. Vaissermann, F. Bartolomé, P. Veillet, M. Verdaguer, Chem. Commun. (1996) 481;
(b) J. Zou, X. Hu, Ch. Duan, Z. Xu, X. You, Transition Met. Chem. 23 (1998) 477;
(c) E. Colacio, J.M. Dominguez-Vera, M. Ghazi, R. Kivekäs, M. Klinga, J.M. Moreno, Chem. Commun. 10 (1998) 1071;
(d) E. Colacio, J.M. Dominguez-Vera, M. Ghazi, R. Kivekäs, F. Lloret, J.M. Moreno, H. Stoeckli-Evans, Chem. Commun. 11 (1999) 987;
(e) H.Z. Kou, S. Gao, W.M. Bu, D.Z. Liao, B.Q. Ma, Z.H. Jiang, S.P. Yan, Y.G. Fan, G.L. Wang, J. Chem. Soc., Dalton Trans. (1999) 2477;
(f) H.Z. Kou, S. Gao, B.Q. Ma, D.Z. Liao, Chem. Commun. (2000) 713;
(g) E. Colacio, J.M. Dominguez-Vera, M. Ghazi, R. Kivekä s, J.M. Moreno, A. Pajunen, J. Chem. Soc., Dalton Trans. (2000) 505.
[15] G.A. Melson, Coordination Chemistry of Macrocyclic Compounds, Plenum Press, New York, 1979.
[16] A. Bieńko, J. Kłak, J. Mroziński, R. Boča, I. Brüdgam, H. Hartl, J. Chem. Soc., Dalton Trans. (2007) 2681.
[17] J. Mrozinski, J. Bull. Acad. Polon.: Chim. 26 (1978) 789.
[18] E. König, Magnetic Properties of Coordination and Organometallic Transition Metal Compounds, Springer-Verlag, Berlin, 1966.
[19] X-RED. Version 1.18. STOE & Cie GmbH, Darmstadt, Germany, 1999.
[20] G.M. Sheldrick, Acta Crystallogr., Sect. A 46 (1990) 467.
[21] G.M. Sheldrick, SHELXL97. Program for the Solution and Refinement of Crystal Structures, University of Göottingen, Germany, 1997.
[22] G.M. Sheldrick, SHELXTL: Release 4.1 for Siemens Crystallographic Research Systems, 1990.
[23] H.D. Flack, Acta Crystallogr., Sect. A 39 (1983) 876.
[24] J. Samuel Smart, Effective Field Theories of Magnetism, W.B. Saunders Comp., Philadelphia and London, 1966.

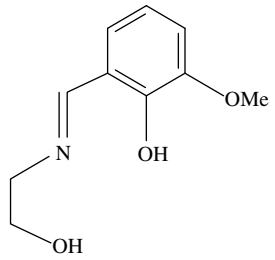


Chart 1. Chemical structure of H_2L.

A few Schiff base ligands have been previously utilized to derive uranium compounds. Salmon et al. have reported a number of mono-, tri-, tetra- and hexanuclear uranium(IV) complexes derived from compartmental Schiff base ligands obtained by the condensation of salicylaldehyde or substituted salicylaldehydes with diamines [14–16]. A mononuclear uranyl(VI) compound in a similar ligand environment has been reported by Ikeda et al. [8]. Using a tridentate ligand obtained by the condensation of 3-methoxysalicylaldehyde and *o*-aminophenol, a diphenoxo-bridged diuranyl(VI) compound has been reported by Reedijk and coworkers [17]. A series of dialkoxo-bridged diuranyl(VI) compounds derived from tridentate ligands obtained by the condensation of salicylaldehyde or substituted salicylaldehydes and substituted 2-aminoethanol have been reported by Rao and coworkers [18]. Herein, we report the synthesis, molecular and supramolecular structure, spectroscopy and electrochemistry of a dialkoxo-bridged diuranyl(VI) compound $[(UO_2)_2(L)_2(dimethylformamide)_2]$ (**1**) derived from the Schiff base ligand (H_2L; Chart 1) obtained by the condensation of 3-methoxysalicylaldehyde with 2-aminoethanol.

2. Experimental

2.1. Materials and physical methods

All the reagents and solvents were purchased from commercial sources and were used as received. The Schiff base ligand H_2L was prepared by condensing 3-methoxysalicylaldehyde with 2-aminoethanol in methanol. The syntheses of the ligand and title compound were performed in open atmosphere. Elemental (C, H and N) analyses were performed on a Perkin–Elmer 2400 II analyzer. IR spectra were recorded in the region 400–4000 cm^{-1} on a Perkin–Elmer RXIFT spectrophotometer with the samples as KBr disks. Electronic spectra were obtained with a Hitachi U-3501 spectrophotometer. The electrospray ionization mass spectra were recorded on a Micromass Qtof YA 263 mass spectrometer. The ^1H NMR (300 MHz) spectra were recorded on a Bruker Avance DPX-300 spectrometer. Cyclic voltammetric (CV) measurement was done using a Bioanalytical System BAS 100B electrochemical analyzer. The concentration of the supporting electrolyte, tetrabutylammonium perchlorate (TBAP), was 0.1 M, while that of the complex was 1 mM. Cyclic voltammetric measurement in dimethylsulfoxide solution was carried out with a three-electrode assembly comprising a glassy carbon disk working electrode, a platinum auxiliary electrode and an aqueous Ag/AgCl reference electrode. The reference electrode was separated from the bulk solution using a TBAP salt bridge in acetonitrile. Under the experimental conditions, the $E_{1/2}$ value of the ferrocene/ferrocenium couple was 400 mV.

Table 1
Crystallographic data for **1**

Formula	$C_{26}H_{36}N_4O_{12}U_2$
Molecular weight	1072.65
Crystal color	red
Crystal system	monoclinic
Space group	$P2_1/n$
a (Å)	10.5713(2)
b (Å)	11.9895(2)
c (Å)	12.9372(2)
β (°)	102.773(3)
V (Å^3)	1599.14(5)
Z	2
Temperature (K)	293(2)
2θ	8.152–69.944
μ (mm^{-1})	10.179
$D_{calc.}$ (g cm^{-3})	2.228
$F(000)$	1000
Scan mode	φ- and ω-scans
Number of frames	510
Scan time per frame (s)	30
Rotation width (°)	2
Crystal-detector-dist. (mm)	28
Absorption-correction	multi-scan
T_{min}	0.7499
T_{max}	0.9051
Index ranges	$-17 \leqslant h \leqslant 17$, $-19 \leqslant k \leqslant 18$, $-20 \leqslant l \leqslant 20$
Reflections collected	12911
Independent reflections ($F_o > 4\sigma(F_o)$)	7002
R_1^a/wR_2^b ($F_o > 4\sigma(F_o)$)	0.0287/0.0706
R_1^a/wR_2^b (for all F_o^2)	0.0412/0.0754

[a] $R_1 = [\sum||F_o| - |F_c||/\sum|F_o|]$.
[b] $wR_2 = [\sum w(F_o^2 - F_c^2)^2/\sum wF_o^4]^{1/2}$.

2.2. Synthesis of $[(UO_2)_2(L)_2(dmf)_2]$ (**1**)

To a stirred dimethylformamide (dmf) solution (40 ml) containing H_2L (0.098 g, 0.5 mmol) and uranyl nitrate hexahydrate (0.251 g, 0.5 mmol) was added a dmf solution (10 mL) of triethylamine (0.101 g, 1 mmol). The resulting red solution was filtered to remove any suspended particles and the filtrate was kept at room temperature. After a few hours a red crystalline compound containing diffractable single crystals were deposited, then collected by filtration and washed with methanol. Yield: 0.24 g (90%). *Anal.* Calc. for $C_{26}H_{36}N_4O_{12}U_2$: C, 29.11; H, 3.38; N, 5.22. Found: C, 29.20; H, 3.46; N, 5.31%. IR (KBr/cm^{-1}): υ(C=N), 1636 vs; υ(O=U=O), 891 m.

2.3. Structure determination and refinement of $[(UO_2)_2(L)_2(dmf)_2]$ (1)

Single-crystal X-ray intensity data of the title compound were collected at 293 K on a Nonius Kappa diffractometer with a CCD area detector, using Mo K_α radiation having $\lambda = 0.71073$ Å. The intensity data were processed with the Nonius program suites DENZO-SMN [39] and corrected for Lorentz, polarisation, background and absorption effects [40]. The crystal structure was determined by direct methods and subsequent Fourier and difference Fourier syntheses, followed by full-matrix least-squares refinements on F^2 [41,42]. All H atoms could be located in the difference Fourier map and refined without constraints, except for the methyl hydrogen atoms, which were treated as "riding". Using anisotropic treatment of the non-H atoms and unrestrained isotropic treatment of the H atoms, the refinement converged at an R value of 2.9%. Crystal data, details of the measurement and refinement are given in Table 1.

3. Results and discussion

3.1. Synthesis

The title compound $[(UO_2)_2(L)_2(dmf)_2]$ (**1**) is readily formed on reacting uranyl nitrate hexahydrate, H_2L, and triethylamine in dimethylformamide. Deprotonation of both the phenolic and alcoholic hydrogens takes place in the reaction mixture. As will be discussed below, two uranyl(VI) species are bridged by two alkoxo oxygen atoms of two deprotonated ligands, while the phenoxo oxygen acts as a terminal donor center. Each of the two uranyl(VI) species are further coordinated to one dmf molecule, resulting in the formation of the title compound.

3.2. IR, UV–Vis, mass and NMR spectra

The IR spectrum of H_2L exhibits one strong absorption at 1644 cm^{-1} due to the stretching vibration of the imine moiety. In the diuranyl(VI) compound **1**, the imine stretching is observed at a slightly lower frequency (1636 cm^{-1}). A medium intensity band at 891 cm^{-1} in the IR spectrum of **1** can be assigned to the stretching vibration of the O=U=O moiety. This assignment is supported by the results of Cattalini et al. and Ikeda and coworkers [19,20].

The UV–Vis spectrum of H_2L exhibits two bands at 261 nm ($\varepsilon = 2497$ L mol^{-1} cm^{-1}) and 418 nm ($\varepsilon = 209$ L mol^{-1} cm^{-1}) and a shoulder at 294 nm ($\varepsilon = 540$ L mol^{-1} cm^{-1}). In the spectrum of **1**, one band at 256 nm ($\varepsilon = 7686$ L mol^{-1} cm^{-1}) and two shoulders at 346 nm ($\varepsilon = 1935$ L mol^{-1} cm^{-1}) and 402 nm ($\varepsilon = 1059$ L mol^{-1} cm^{-1}) appear due to an internal ligand transition. An additional band at 475 nm ($\varepsilon = 349$ L mol^{-1} cm^{-1}) in the spectrum of **1** appears due to a charge transfer from the uranyl oxygens to the uranium (VI) center.

The composition of **1** was further verified by electrospray ionization mass spectroscopy (ESI-MS positive). The ESI-MS spectrum of **1** in dimethylsulfoxide exhibits two peaks at $m/z = 464.17$ and 927.26, which are assignable to $[(UO_2)_2L_2H]^+$ (60%) and $[(UO_2)_2LH]^+$ (100%) cations, respectively. As shown in Fig. 1, the isotopic distribution patterns of the observed peaks and the simulated spectral patterns are in excellent agreement with each other.

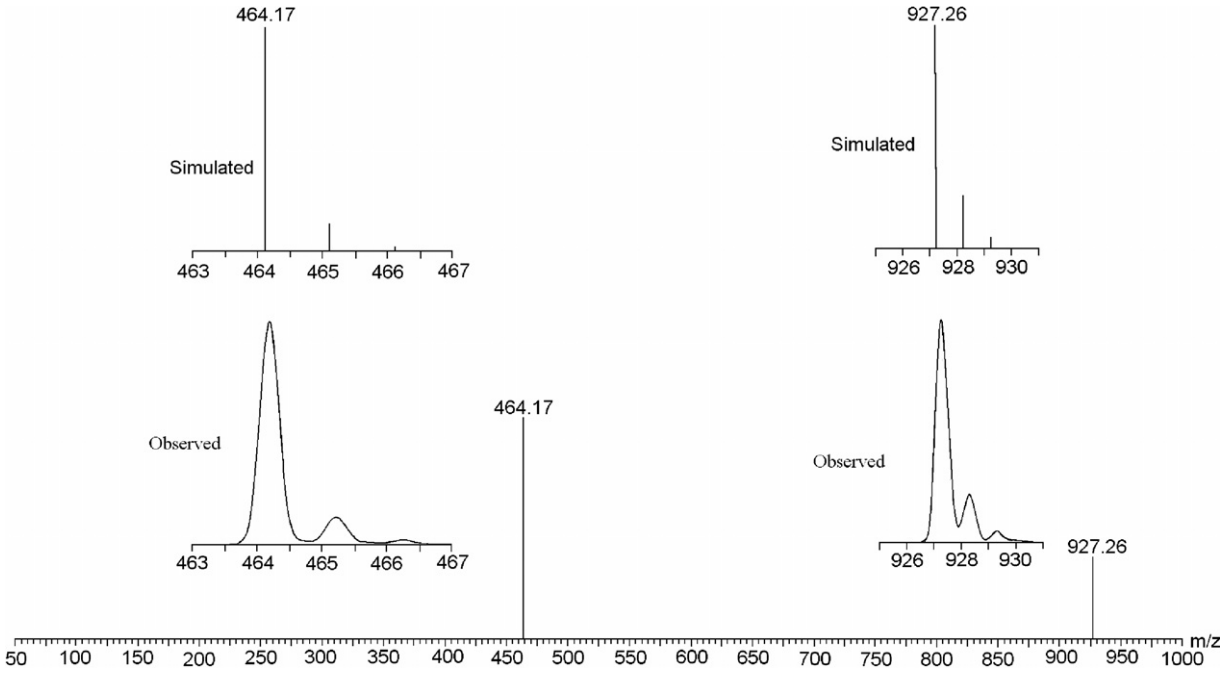


Fig. 1. ESI-MS spectrum of $[(UO_2)_2(L)_2(dmf)_2]$ (**1**) in DMSO.

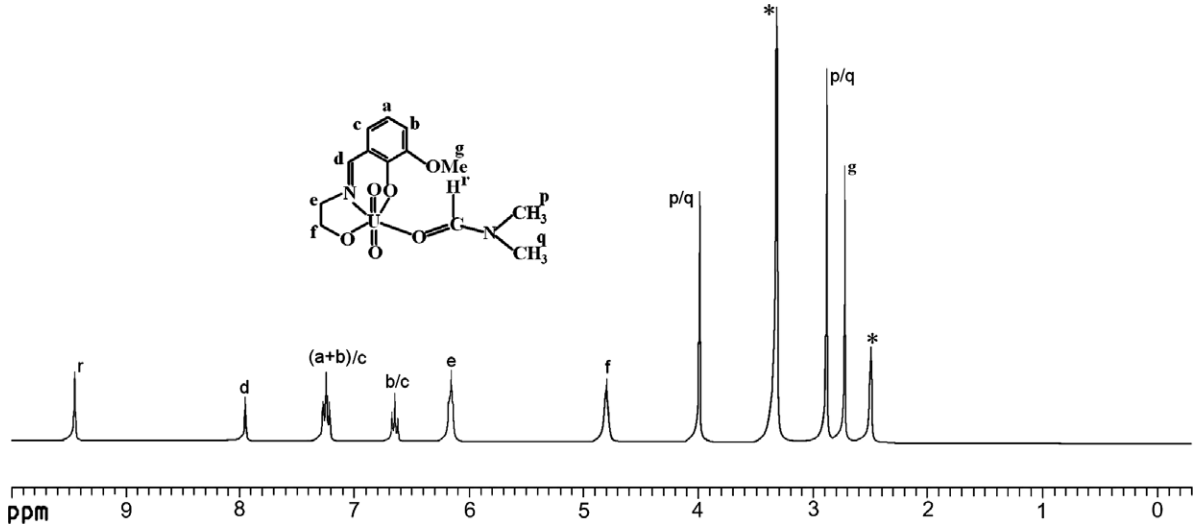


Fig. 2. ^{1}H NMR spectrum of $[(UO_2)_2(L)_2(dmf)_2]$ (**1**) in DMSO-d_6. * marked signals are due to solvent.

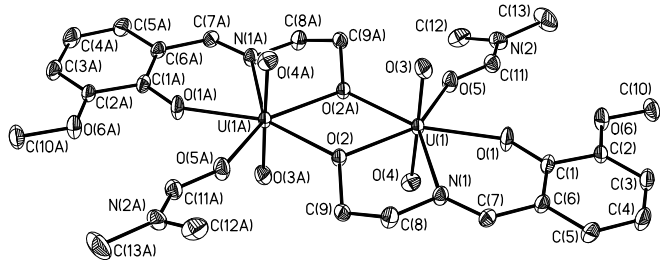


Fig. 3. Crystal structure of $[(UO_2)_2(L)_2(dmf)_2]$ (**1**) with the atom labelling scheme. Hydrogen atoms are omitted for clarity. Symmetry code: A, $1-x$, $1-y$, $-z$.

The proton NMR spectrum (Fig. S1 in supplementary informations) of the ligand H_2L in $CDCl_3$ exhibits six peaks at 13.67 (br, 2H, phenolic OH and alcoholic OH), 8.38 (s, 1H, imine), 6.77–6.96 (m, 3H, aromatic), 3.89–3.93 (t, 2H, CH_2 of $CH_2N{=}CH$), 3.74–3.77 (t, 2H, CH_2 of CH_2OH) and 3.89 ppm (s, 3H, OCH_3). On the other hand, the spectrum of complex **1** in DMSO-d_6 (Fig. 2) is comprised of nine peaks. In comparison to those in H_2L, the methoxy hydrogens (2.73 ppm (s, 3H, OMe)) and imine hydrogen (7.95 ppm (s, 1H, imine)) are a little shielded. Again, splitting of three aromatic hydrogen atoms (6.62–6.67 (t, 1H, aromatic) and 7.21–7.27 ppm (t, 2H, aromatic)) takes place. The presence of the dmf ligand in this complex is evidenced by two singlets (2.88 (s, 3H, CH_3 (DMF)) and 3.99 ppm (s, 3H, CH_3 (DMF))) due to the methyl groups and one singlet at 9.45 ppm (s, 1H, CHO (DMF)) due to the amide moiety. It may be mentioned that both ^{1}H and ^{13}C NMR spectra have been used to characterize uranium(IV) and uranium(VI) compounds [1,8,13,15–19].

3.3. Description of the structure

The crystal structure of **1** is shown in Fig. 3, while selected bond lengths and angles are listed in Table 2.

Table 2
Selected bond lengths (Å) and angles (°) of **1**

U(1)–O(1)	2.254(4)
U(1)–O(2)	2.358(3)
U(1)–O(2A)	2.351(3)
U(1)–O(3)	1.790(4)
U(1)–O(4)	1.786(3)
U(1)–O(5)	2.429(4)
U(1)–N(1)	2.564(4)
U(1)···U(1A)	3.861(4)
O(3)–U(1)–O(4)	178.68(11)
O(3)–U(1)–O(1)	90.23(13)
O(3)–U(1)–O(2)	92.28(10)
O(3)–U(1)–O(2A)	89.56(11)
O(3)–U(1)–O(5)	93.14(11)
O(3)–U(1)–N(1)	93.58(11)
O(4)–U(1)–O(1)	90.73(14)
O(4)–U(1)–O(2)	86.40(10)
O(4)–U(1)–O(2A)	90.02(11)
O(4)–U(1)–O(5)	87.97(10)
O(4)–U(1)–N(1)	85.89(11)
O(1)–U(1)–O(2)	138.07(9)
O(1)–U(1)–O(2A)	152.04(8)
O(1)–U(1)–O(5)	75.83(8)
O(1)–U(1)–N(1)	70.52(9)
O(2)–U(1)–O(2A)	69.86(11)
O(2)–U(1)–O(5)	145.62(7)
O(2)–U(1)–N(1)	67.55(10)
O(2A)–U(1)–O(5)	76.27(9)
O(2A)–U(1)–N(1)	137.38(7)
O(5)–U(1)–N(1)	145.67(9)
U(1)–O(2)–U(1A)	110.14(11)

Symmetry code: A, $1-x$, $1-y$, $-z$.

The structure of **1** reveals that it is a dialkoxo-bridged dinuclear compound of uranyl(VI) containing two deprotonated ligands, $[L]^{2-}$, two dimethylformamide (dmf) molecules and two UO_2^{2+} centers. One half of the molecule is symmetry related to the other half due to the presence of a center of inversion. The uranium(VI) center in this

compound is heptacoordinated by the phenoxo oxygen and imine nitrogen of a $[L]^{2-}$, two uranyl oxygens, two bridging alkoxo oxygens of two $[L]^{2-}$, and one oxygen atom of a dmf molecule. The coordination geometry around the uranium(VI) center is distorted pentagonal bipyramidal; two uranyl oxygens (O(3) and O(4)) occupy the axial positions, while the basal pentagonal plane is defined by the phenoxo oxygen (O(1)), bridging alkoxo oxygens (O(2) and O(2A)), imine nitrogen (N(1)) and dmf oxygen (O(5)). As expected, due to π-back bonding, the U–O bond lengths (U(1)–O(3) = 1.790(4); U(1)–O(4) = 1.786(3) Å) involving uranyl oxygens are much shorter than the U–O(phenoxo), U–O(alkoxo), U–O(dmf) and U–N(imine) bond distances in the basal plane, which lie in the range 2.254(4)–2.564(4) Å. The U–O(phenoxo, terminal), U–O(alkoxo, bridging), U–N(imine) and U–O(dmf) distances in **1** lie in the ranges observed in the previously reported related compounds [17,18,28–30].

The *transoid* angle (178.68(11)°) involving the axial uranyl oxygens as well as the *cisoid* angles (89.56(11)–93.58(11)° for O(3) and 85.89(11)–90.73(14)° for O(4)) involving the axial oxygens and the five donor atoms in the basal plane are close to the ideal values. Again, from the least-squares NO_4 basal plane, the nitrogen or oxygen atoms defining the plane are deviated by only *ca.* 0.06 Å and the metal center is displaced by only 0.07 Å. However, the ranges of apex···apex (O···O or O···N) distances and internal angles (O···O···O, O···N···O or N···O···O) inside the basal pentagonal plane are 2.696–2.952 Å and 100.0–114.7°, respectively, indicating distortion of the coordination geometry from the ideal case. In the dinuclear unit, the metal centers are separated by 3.861(4) Å with a U(1)–O(2)–U(1A) bridge angle of 110.14(11)°.

Three C–H···O type hydrogen bonds involving one uranyl oxygen (O(4)), two dmf hydrogens (H(12B), H(13C)) and the imine hydrogen (H(7)) link the dinuclear units into a two-dimensional network. A simplified illustration of the hydrogen bonded two-dimensional sheet is demonstrated in Fig. 4. As shown in this figure, one uranyl oxygen (O(4)) of a dinuclear unit U(1)···U(1A) acts as a triple acceptor and interacts with the dmf hydrogens H(12BD) and H(13CD) of the dinuclear unit U(1D)···U(1E) as well as with the imine hydrogen H(7F) of the dinuclear unit U(1F)···U(1G). Similarly, another uranyl oxygen O(4A), which is symmetry related to O(4), of the dinuclear unit U(1)···U(1A) interacts with the hydrogens of two other dinuclear units U(1H)···U(1I) and U(1J)···U(1K). Clearly, one dinuclear unit is interlinked with four other units to result in the creation of a two-dimensional sheet (Fig. 4). The geometries of the hydrogen bonds are given in Table 3.

3.4. Electrochemistry

The cyclic voltammetric measurement of complex **1** was carried out in dimethylsulfoxide at 25 °C under a nitrogen

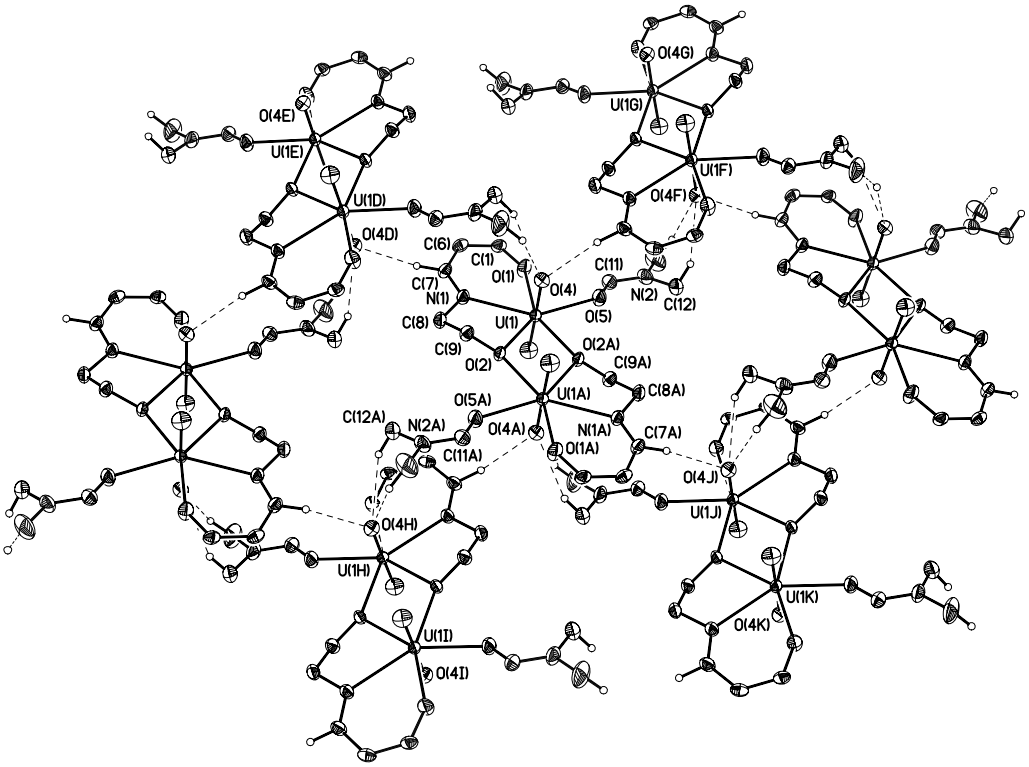


Fig. 4. Perspective view to demonstrate the hydrogen bonding interactions and the resultant two-dimensional topology in $[(UO_2)_2(L)_2(dmf)_2]$ (**1**). The atoms C(2), C(3), C(4), C(5), C(10) and O(6) are omitted for clarity. Among the hydrogen atoms, only three participating in hydrogen bonds are shown. Symmetry codes: D, $1.5 - x$, $y - 0.5$, $0.5 - z$; E, $0.5 + x$, $0.5 - y$, $0.5 + z$; F, $1.5 - x$, $0.5 + y$, $0.5 - z$; G, $0.5 + x$, $1.5 - y$, $0.5 + z$; H, $x - 0.5$, $0.5 - y$, $z - 0.5$; I, $0.5 - x$, $y - 0.5$, $-0.5 - z$; J, $x - 0.5$, $1.5 - y$, $z - 0.5$; K, $0.5 - x$, $0.5 + y$, $-0.5 - z$.

Table 3
Geometries (distances in (Å) and angles in (°)) of the hydrogen bonds in **1**

D–H···A	D···A	H···A	D–H···A
C(12D)–H(12BD)···O(4)	3.272(5)	2.42	147.2
C(13D)–H(13CD)···O(4)	3.463(7)	2.69	137.8
C(7F)–H(7F)··· O(4)	3.270(5)	2.27	171(3)

Symmetry codes: as in Fig. 4.

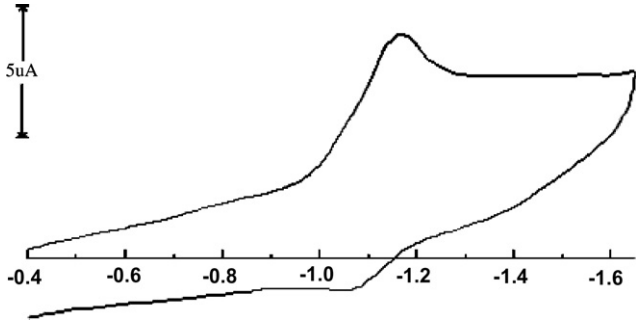


Fig. 5. Part (−400 to −1650 mV) of the cyclic voltammogram of complex **1** in dimethylsulfoxide in the scan range 0 to −1800 mV at a scan rate of 50 mV s^{-1}.

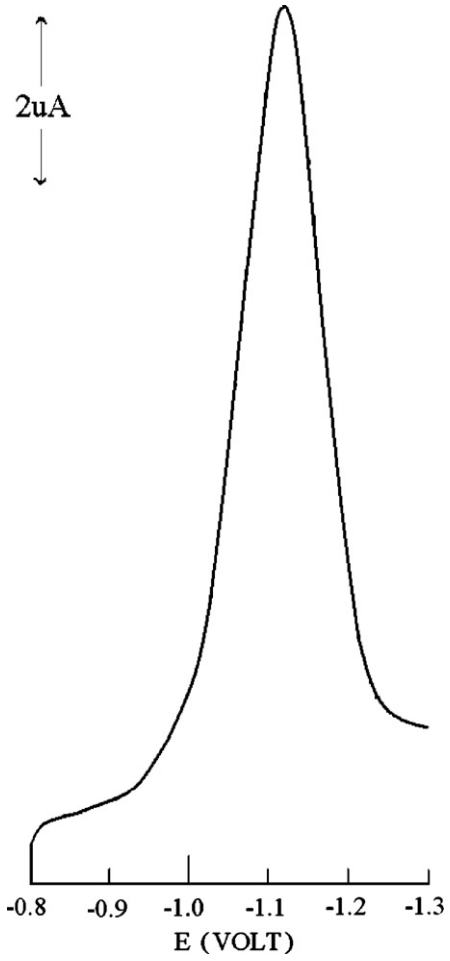


Fig. 6. Square wave voltammogram (−800 to −1300 mV) of complex **1** in dimethylsulfoxide at a scan rate of 50 mV s^{-1}.

atmosphere using glassy carbon as the working electrode and at a scan rate of 50 mV/s. In the potential range of 0 to −1800 mV, one cathodic response at −1160 mV and, in the return sweep, one anodic peak at −1063 mV are observed. The part (*ca.* −400 to −1650 mV) containing the peaks of the cyclic voltammogram for the 0 to −1800 mV scan range is shown in Fig. 5, while the square wave voltammogram (SWV) related to this couple is shown in Fig. 6. The $E_{1/2}$ value of this couple is −1112 mV. It may be noted that the peak position (−1120 mV) in SWV (Fig. 6) is very close to the $E_{1/2}$ value obtained from cyclic voltammogram. Again, the value of the difference (ΔE_P) of the cathodic and anodic peak potentials is 97 mV, indicating the quasireversible nature of the reduction–oxidation process. The observation of only one couple clearly indicates that the 2 equiv. uranium(VI) centers in **1** are reduced (U(VI)U(VI) → U(V)U(V)) at −1160 mV and the reduced uranium(V) centers are oxidized (U(V)U(V) → U(VI)U(VI)) at −1063 mV.

It may be relevant to discuss the electrochemical properties of only a few previously reported results. Ikeda et al. have reported that the quasireversible U(VI) → U(V) reduction of uranium compounds derived from *N*,*N*′-disalicylidene-*o*-phenylenediaminate, dibenzoylmethanate and carbonato ligands takes place at −1550 mV, −1362 mV and *ca.* −751 mV, respectively [12]. Kiplinger and his group have shown that uranium(IV) compounds may exhibit a single reversible reduction (U(IV) → U(III)), a reversible reduction (U(IV) → U(III)) and oxidation (U(IV) → U(V)), as well as two reversible reductions and one reversible oxidation (U(IV) → U(V)). The $E_{1/2}$ values for these reduction and oxidation processes lie in the ranges −1830 mV to −2790 mV and +180 mV to −480 mV, respectively [9–11].

4. Conclusions

The dialkoxo-bridged diuranyl(VI) compound described here is an addition to the family of uranium chemistry and actinide chemistry. The compound has been characterized by elemental analysis and its X-ray single crystal structure, as well as by IR, NMR and mass spectra. The participation of uranyl oxygens in the hydrogen bonding interactions and in developing a two-dimensional supramolecular structure have been enlightened in the present investigation. A cyclic voltammetric study of the title compound has been performed and compared with the electrochemical properties of previously reported uranium compounds.

Acknowledgements

Financial support from the Department of Science and Technology, Government of India (to SM; SR/S1/IC-27/2002), and CSIR, Government of India (fellowship to S. Hazra and S. Majumder) is gratefully acknowledged.

S. Mohanta thanks Mr. Supriya Dutta, Department of Chemistry, Indian Association for Cultivation of Science, for electrochemical measurements. The valuable suggestions of one reviewer are gratefully acknowledged.

Appendix A. Supplementary material

CCDC 666667 contains the supplementary crystallographic data for this paper. These data can be obtained free of charge via http://www.ccdc.cam.ac.uk/conts/retrieving.html, or from the Cambridge Crystallographic Data Centre, 12 Union Road, Cambridge CB2 1EZ, UK; fax: (+44) 1223-336-033; or e-mail: deposit@ccdc.cam.ac.uk. Supplementary data associated with this article can be found, in the online version, at doi:10.1016/j.poly.2008.01.029.

References

[1] J. Xu, K.N. Raymond, Inorg. Chem. 38 (1999) 308.
[2] A.E.V. Gorden, J. Xu, K.N. Raymond, P. Durbin, Chem. Rev. 103 (2003) 4207.
[3] M. Sawicki, J.-M. Siaugue, C. Jacopin, C. Moulin, T. Bailly, R. Burgada, S. Meunier, P. Baret, J.-L. Pierre, F. Taran, Chem. Eur. J. 11 (2005) 3689.
[4] S. Shinkai, H. Koreishi, K. Ueda, T. Arimura, O. Manabe, J. Am. Chem. Soc. 109 (1987) 6371.
[5] P.D. Beer, G.D. Brindley, D.O. Fox, A. Grieve, M.I. Ogden, F. Szemes, M.G.B. Drew, J. Chem. Soc., Dalton Trans. (2002) 3101.
[6] S.D. Conradson, D. Manara, F. Wastin, D.L. Clark, G.H. Lander, L.A. Morales, J. Rebizant, V.V. Rondinella, Inorg. Chem. 43 (2004) 6922.
[7] I.K.S. Gambarotta, L. Thompson, P.J. Hay, G.P.A. Yap, Organometallics 20 (2001) 5440.
[8] K. Mizuoka, S.-Y. Kim, M. Hasegawa, T. Hoshi, G. Uchiyama, Y. Ikeda, Inorg. Chem. 42 (2003) 1031.
[9] J.L. Kiplinger, K.D. John, D.E. Morris, B.L. Scott, C.J. Burns, Organometallics 21 (2002) 4306.
[10] E.J. Schelter, J.M. Veauthier, J.D. Thompson, B.L. Scott, K.D. John, D.E. Morris, J.L. Kiplinger, J. Am. Chem. Soc. 128 (2006) 2198.
[11] J.L. Kiplinger, D.E. Morris, B.L. Scott, C.J. Burns, Organometallics 21 (2002) 3073.
[12] K. Mizuoka, S. Tsushima, M. Hasegawa, T. Hoshi, Y. Ikeda, Inorg. Chem. 44 (2005) 6211.
[13] H. Sopo, J. Sviili, A. Valkonen, R. Sillanpää, Polyhedron 25 (2006) 1223.
[14] L. Salmon, P. Thuéry, M. Ephritikhine, Polyhedron 25 (2006) 1537.
[15] L. Salmon, P. Thuéry, M. Ephritikhine, J. Chem. Soc., Dalton Trans. (2004) 4139.
[16] L. Salmon, P. Thuéry, M. Ephritikhine, J. Chem. Soc., Dalton Trans. (2004) 1635.
[17] R. Kannappan, D.M. Tooke, A.L. Spek, J. Reedijk, Inorg. Chim. Acta 359 (2006) 334.
[18] P.V. Rao, C.P. Rao, A. Sreedhara, E.K. Wegelius, K. Rissanen, E. Kolehmainen, J. Chem. Soc., Dalton Trans. (2000) 1213.
[19] L. Cattalini, S. Degetto, M. Vidali, P.A. Vigato, Inorg. Chim. Acta 6 (1972).
[20] K. Mizuoka, Y. Ikeda, Inorg. Chem. 42 (2003) 3396.
[21] P. Gary Eller, P.J. Vergamini, Inorg. Chem. 22 (1983) 3184.
[22] C.J. Burns (INC-4), A.P. Sattelberger, Inorg. Chem. 21 (1982) 3692.
[23] Z. Szabó, I. Furó, I. Csöregh, J. Am. Chem. Soc. 127 (2005) 15236.
[24] A. Günther, G. Geipel, G. Bernhard, Polyhedron 26 (2007) 59.
[25] W.J. Evans, S.A. Kozimor, J.W. Ziller, Science 309 (2005) 1835.
[26] L. Salmon, P. Thuéry, M. Ephritikhine, Chem. Commun. (2006) 856.
[27] J. Berthet, P. Thuéry, M. Ephritikhine, Inorg. Chem. 44 (2005) 1142.
[28] Z.-T. Yu, G.-H. Li, Y.-S. Jiang, J.-J. Xu, J.-S. Chen, J. Chem. Soc., Dalton Trans. (2003) 4219.
[29] L. Salmon, P. Thuéry, M. Ephritikhine, Polyhedron 22 (2003) 2683.
[30] M.P. Wilkerson, C.J. Burns, D.E. Morris, R.T. Paine, B.L. Scott, Inorg. Chem. 41 (2002) 3110.
[31] R. Robson, in: J.L. Atwood, J.E.D. Davies, D.D. MacNicol, F. Vögtle, R.B. Toda (Eds.), Comprehensive Supramolecular Chemistry, vol. 6, Pergamon, Oxford, 1996, pp. 733–755.
[32] A.J. Blake, N.R. Champness, P. Hubberstey, M.A. Withersby, M. Schröder, Coord. Chem. Rev. 183 (1999) 117.
[33] J.-P. Sauvage (Ed.), Transition Metals in Supramolecular Chemistry (Perspectives in Supramolecular Chemistry), vol. 5, Willey, England, 1999.
[34] G.R. Desiraju (Ed.), The Crystal as a Supramolecular Entity (Perspectives in Supramolecular Chemistry), vol. 2, Willey, England, 1996.
[35] B. Moulton, M.J. Zaworotko, Chem. Rev. 101 (2001) 1629.
[36] M. Nayak, R. Koner, S. Evans, S. Mohanta, Cryst. Growth Des. 5 (2005) 1907.
[37] G.-Y. Hsu, P. Misra, S.-C. Cheng, H.-H. Wei, S. Mohanta, Polyhedron 25 (2006) 3393.
[38] M. Nayak, R. Koner, H.-H. Lin, U. Flörke, H.-H. Wei, S. Mohanta, Inorg. Chem. 45 (2006) 10764.
[39] Nonius: COLLECT, Nonius, Delft, The Netherlands, 2003.
[40] Z. Otwinowski, W. Minor, Processing of X-ray diffraction data collected in the oscillation mode, Methods Enzymol. 276 (1997) 307.
[41] G.M. Sheldrick, SHELXS-97: A Program for Crystal Structure Solution, University of Göttingen, Göttingen, Germany, 1997.
[42] G.M. Sheldrick, SHELXL-97: A Program for Crystal Structure Refinement, University of Göttingen, Göttingen, Germany, 1993.

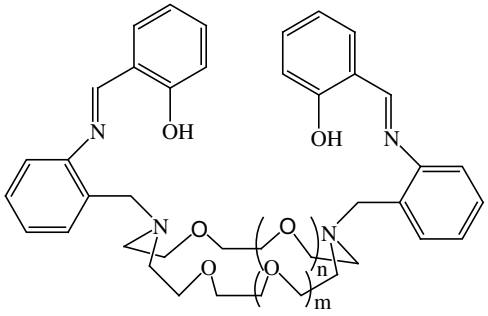
($\mathbf{L}^1$) [10], 1,10-diaza-15-crown-5 ($\mathbf{L}^2$) [11] and 4,10-diaza-12-crown-4 ($\mathbf{L}^3$) [12] (see Scheme 1).

As a continuation of our works, herein we present the corresponding synthesis and structural characterization of the lanthanide(III) complexes of the related monobracchial receptor *N*-(2-salicylaldiminatobenzyl)-1-aza-18-crown-6 ($\mathbf{L}^4$) shown in Scheme 1. The study of Ln(III) complexes of this receptor allows to evaluate the effect that the absence of one arm may have on the coordination ability of the receptor. From the structural point of view this receptor derives from $\mathbf{L}^1$ by loss of one 2-salicylaldiminato-benzyl pendant and replacement of the corresponding pivotal nitrogen atom by an oxygen donor. The complexes have been also characterized by *ab initio* calculations at the HF/3-21G* level. The crystal structures of the corresponding praseodymium and samarium compounds were determined by X-ray crystallography.

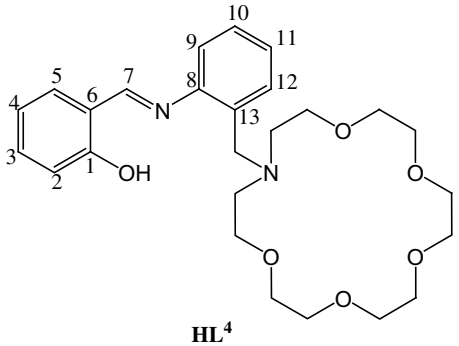
2. Experimental

2.1. Reagents

Lanthanide(III) perchlorates hydrates (La–Lu, excluding Pm) were purchased from Alfa laboratories, either as solid samples (La and Ce) or as 50% w/w aqueous solutions. All other chemicals were purchased from commercial sources and used without further purification. Solvents were of reagent grade and were purified by the usual methods. Acetonitrile-d_3 for NMR measurements (Merck, 99% D) was used as received. *Caution!* Although we have experienced no difficulties with the perchlorate salts, they are potentially explosive when combined with organic ligands and should be handled in small quantity and with the necessary precautions [13].



H_2L^1: n = 1, m = 1
H_2L^2: n = 1, m = 0
H_2L^3: n = 0, m = 0



HL^4

Scheme 1.

2.2. Synthesis

2.2.1. *N*-(2-Aminobenzyl)-1-aza-18-crown-6 ($\mathbf{pL}^4$)

2-Nitrobenzyl chloride (0.65 g, 3.79 mmol), 1-aza-18-crown-6 (1.00 g, 3.79 mmol) and Na_2CO_3 (1.20 g, 20 mmol) in acetonitrile (40 mL) were stirred and refluxed for 24 h. The mixture was filtered, the filtrate concentrated to dryness, and the yellow oily residue extracted with CH_2Cl_2/water. The organic phase was dried over anhydrous $MgSO_4$ and concentrated under reduced pressure. The resulting yellow oil was dissolved in absolute ethanol (60 mL) and Pd/C added. Hydrazine hydrate (0.7 mL) was slowly added and the reaction mixture was heated and stirred for 1 h. After filtration and evaporation of the solvent, the resulting crude product was purified by column chromatography (basic aluminium oxide, CH_2Cl_2) to afford the desired product as a pale yellow oil. ^{1}H NMR (500 MHz, CD_3Cl; δ, ppm): 7.0 (t, 1H, arH), 6.9 (d, 1H, arH), 6.6 (m, 2H, arH), 4.7 (b, 2H, –NH_2), 3.6 (m, 20 H, –CH_2–), 2.7 (m, 6H, –CH_2–). MS FAB: $m/z = 369$ ($pL^4 + H$). IR (KBr): $\nu = \nu(NH_2)$ 3432, 3353 cm^{-1}.

2.2.2. Preparation of the complexes

A stoichiometric amount (1:1) of *N*-(2-aminobenzyl)-1-aza-18-crown-6 ($\mathbf{pL}^4$) and salicylaldehyde was dissolved in 2-propanol (30 mL) and heated to reflux. After 1 h, a solution of equimolar quantity of triethylamine in 10 mL of 2-propanol was added, and the reflux was maintained for 30 min. A solution of the corresponding hydrated lanthanide(III) perchlorate (equimolar) in 25 mL of the same solvent was then added and the resultant solution was refluxed for 3 h, filtered while hot and the filtrate left to evaporate slowly at room temperature to yield yellow solids that were collected by filtration and dried under vacuum over $CaCl_2$.

$[La(L^4)(H_2O)](ClO_4)_2 \cdot 0.5C_3H_8O$ (**1**): *N*-(2-aminobenzyl)-1-aza-18-crown-6 (0.068 g, 0.160 mmol), salicylaldehyde (0.019 g, 0.160 mmol), triethylamine (0.016 g, 0.160 mmol) and $La(ClO_4)_3 \cdot 6H_2O$ (0.086 g, 0.160 mmol) (yield: 0.050 g, 36%). *Anal.* Calc. for $C_{26}H_{35}Cl_2LaN_2O_{14} \cdot H_2O \cdot 0.5C_3H_8O$ (857.42): C, 38.5; H, 4.8; N, 3.3. Found: C, 39.2; H, 4.5; N, 3.0%. MS (FAB): $m/z = 709$ $[La(L^4)(ClO_4)]^+$. IR (KBr): $\nu = \nu(C{=}N)_{imine}$ 1614, $\nu_{as}(ClO)$ 1098, $\delta_{as}(O–Cl–O)$ 623 cm^{-1}. Λ_M (acetonitrile, cm^2 Ω^{-1} mol^{-1}): 280 (2:1 electrolyte).

$[Ce(L^4)(H_2O)](ClO_4)_2$ (**2**): *N*-(2-aminobenzyl)-1-aza-18-crown-6 (0.052 g, 0.140 mmol), salicylaldehyde (0.017 g, 0.140 mmol), triethylamine (0.014 g, 0.140 mmol) and $Ce(ClO_4)_3 \cdot 6H_2O$ (0.077 g, 0.140 mmol) (yield: 0.051 g, 44%). *Anal.* Calc. for $C_{26}H_{35}CeCl_2N_2O_{14} \cdot H_2O$ (828.6): C, 37.7; H, 4.5; N, 3.4. Found: C, 37.7; H, 4.6; N, 3.1%.

MS (FAB): $m/z = 710$ $[Ce(L^4)(ClO_4)]^+$. IR (KBr): $\nu = \nu(C{=}N)_{imine}$ 1609, $\nu_{as}(ClO)$ 1084, $\delta_{as}(O–Cl–O)$ 623 cm^{-1}. Λ_M (acetonitrile, $cm^2\,\Omega^{-1}\,mol^{-1}$): 256 (2:1 electrolyte).

$[Pr(L^4)(H_2O)](ClO_4)_2$ (**3**): *N*-(2-aminobenzyl)-1-aza-18-crown-6 (0.070 g, 0.190 mmol), salicylaldehyde (0.023 g, 0.190 mmol), triethylamine (0.019 g, 0.190 mmol) and $Pr(ClO_4)_3 \cdot xH_2O$ (0.208 g, 0.190 mmol) (yield: 0.050 g, 32%). *Anal.* Calc. for $C_{26}H_{35}Cl_2N_2O_{14}Pr \cdot H_2O$ (829.39): C, 37.7; H, 4.9; N, 3.4. Found: C, 37.7; H, 5.2; N, 3.1%. MS (FAB): $m/z = 711$ $[Pr(L^4)(ClO_4)]^+$. IR (KBr): $\nu = \nu(C{=}N)_{imine}$ 1609, $\nu_{as}(ClO)$ 1083, $\delta_{as}(O–Cl–O)$ 623 cm^{-1}. Λ_M (acetonitrile, $cm^2\,\Omega^{-1}\,mol^{-1}$): 267 (2:1 electrolyte). X-ray quality crystals of formula $[Pr(L^4)(H_2O)](ClO_4)_2 \cdot H_2O \cdot C_3H_8O$ were grown by slow diffusion of diethyl ether into a solution of **3** in 2-propanol.

$[Nd(L^4)(H_2O)](ClO_4)_2$ (**4**): *N*-(2-aminobenzyl)-1-aza-18-crown-6 (0.052 g, 0.140 mmol), salicylaldehyde (0.017 g, 0.140 mmol), triethylamine (0.014 g, 0.140 mmol) and $Nd(ClO_4)_3 \cdot xH_2O$ (0.155 g, 0.140 mmol) (yield: 0.090 g, 77%). *Anal.* Calc. for $C_{26}H_{35}Cl_2N_2Nd\,O_{14} \cdot H_2O$ (832.72): C, 37.5; H, 4.9; N, 3.4. Found: C, 37.8; H, 5.2; N, 3.1%. MS (FAB): $m/z = 712$ $[Nd(L^4)(ClO_4)]^+$. IR (KBr): $\nu = \nu(C{=}N)_{imine}$ 1609, $\nu_{as}(ClO)$ 1088, $\delta_{as}(O–Cl–O)$ 623 cm^{-1}. Λ_M (acetonitrile, $cm^2\,\Omega^{-1}\,mol^{-1}$): 297 (2:1 electrolyte).

$[Sm(L^4)(H_2O)](ClO_4)_2$ (**5**): *N*-(2-aminobenzyl)-1-aza-18-crown-6 (0.048 g, 0.130 mmol), salicylaldehyde (0.016 g, 0.130 mmol), triethylamine (0.013 g, 0.130 mmol) and $Sm(ClO_4)_3 \cdot xH_2O$ (0.148 g, 0.130 mmol) (yield: 0.035 g, 32%). *Anal.* Calc. for $C_{26}H_{35}Cl_2N_2O_{14}Sm \cdot H_2O$ (838.83): C, 37.2; H, 4.5; N, 3.3. Found: C, 37.1; H, 5.0; N, 3.2%. MS (FAB): $m/z = 722$ $[Sm(L^4)(ClO_4)]^+$. IR (KBr): $\nu = \nu(C{=}N)_{imine}$ 1614, $\nu_{as}(ClO)$ 1093, $\delta_{as}(O–Cl–O)$ 623 cm^{-1}. Λ_M (acetonitrile, $cm^2\,\Omega^{-1}\,mol^{-1}$): 269 (2:1 electrolyte). X-ray quality crystals of formula $[Sm(L^4)(H_2O)](ClO_4)_2 \cdot C_3H_8O$ were grown by slow diffusion of diethyl ether into a solution of **5** in 2-propanol.

$[Eu(L^4)(H_2O)](ClO_4)_2 \cdot 3H_2O$ (**6**): *N*-(2-aminobenzyl)-1-aza-18-crown-6 (0.062 g, 0.170 mmol), salicylaldehyde (0.021 g, 0.170 mmol), triethylamine (0.017 g, 0.170 mmol) and $Eu(ClO_4)_3 \cdot xH_2O$ (0.188 g, 0.170 mmol) (yield: 0.015 g, 10%). *Anal.* Calc. for $C_{26}H_{35}Cl_2EuN_2O_{14} \cdot 4H_2O$ (894.44): C, 34.9; H, 4.8; N, 3.1. Found: C, 35.0; H, 4.8; N, 3.1%. MS (FAB): $m/z = 723$ $[Eu(L^4)(ClO_4)]^+$. IR (KBr): $\nu = \nu(C{=}N)_{imine}$ 1609, $\nu_{as}(ClO)$ 1085, $\delta_{as}(O–Cl–O)$ 623 cm^{-1}.

$[Gd(L^4)(H_2O)](ClO_4)_2 \cdot H_2O$ (**7**): *N*-(2-aminobenzyl)-1-aza-18-crown-6 (0.059 g, 0.160 mmol), salicylaldehyde (0.019 g, 0.160 mmol), triethylamine (0.016 g, 0.160 mmol) and $Gd(ClO_4)_3 \cdot xH_2O$ (0.080 g, 0.160 mmol) (yield: 0.030 g, 22%). *Anal.* Calc. for $C_{26}H_{35}Cl_2GdN_2O_{14} \cdot 2H_2O$ (863.73): C, 36.1; H, 4.6; N, 3.2. Found: C, 36.0; H, 4.5; N, 3.2%. MS (FAB): $m/z = 728$ $[Gd(L^4)(ClO_4)]^+$. IR (KBr): $\nu = \nu(C{=}N)_{imine}$ 1609, $\nu_{as}(ClO)$ 1084, $\delta_{as}(O–Cl–O)$ 623 cm^{-1}. Λ_M (acetonitrile, $cm^2\,\Omega^{-1}\,mol^{-1}$): 259 (2:1 electrolyte).

$[Tb(L^4)(H_2O)](ClO_4)_2 \cdot H_2O$ (**8**): *N*-(2-aminobenzyl)-1-aza-18-crown-6 (0.052 g, 0.140 mmol), salicylaldehyde (0.017 g, 0.140 mmol), triethylamine (0.014 g, 0.140 mmol) and $Tb(ClO_4)_3 \cdot xH_2O$ (0.163 g, 0.140 mmol) (yield: 0.022 g, 18%). *Anal.* Calc. for $C_{26}H_{35}Cl_2N_2O_{14}Tb \cdot 2H_2O$ (863.73): C, 36.1; H, 4.5; N, 3.2. Found: C, 36.0; H, 4.4; N, 3.1%. MS (FAB): $m/z = 729$ $[Tb(L^4)(ClO_4)]^+$. IR (KBr): $\nu = \nu(C{=}N)_{imine}$ 1609, $\nu_{as}(ClO)$ 1083, $\delta_{as}(O–Cl–O)$ 623 cm^{-1}. Λ_M (acetonitrile, $cm^2\,\Omega^{-1}\,mol^{-1}$): 260 (2:1 electrolyte).

2.3. Measurements

Elemental analyses were carried out on a Carlo Erba 1108 elemental analyzer. FAB-mass spectra were recorded using a FISONS QUATRO mass spectrometer with Cs ion-gun and 3-nitrobenzylalcohol as a matrix. ^1H and ^{13}C NMR spectra were run at 25 °C with Bruker AC200 F and Bruker WM-500 spectrometers. Chemical shifts are reported in parts per million with respect to TMS. Spectral assignments were based in part on two-dimensional COSY and NOESY experiments. IR-spectra were recorded, from KBr discs, using a Bruker Vector 22 spectrophotometer. Conductivity measurements were carried out at 20 °C with a Crison Micro CM 2201 conductimeter using 10^{-3} M solutions of the complexes in acetonitrile.

2.4. X-ray crystallography

Three-dimensional X-ray data were collected on a Bruker Smart 1000 CCD for compound **3** and on a Bruker X8 APEXII CCD for compound **5**. Data were corrected for Lorentz and polarization effects and for absorption by semiempirical methods [14] based on symmetry-equivalent reflections. Complex scattering factors were taken from the program SHELX97 [15] included in the WINGX program system [16] as implemented on a Pentium® computer. The structure was solved by Patterson methods (DIRDIF99) [17] and refined by full-matrix least-squares on F^2. Hydrogen atoms were included in calculated positions and refined in a riding mode, except the hydrogen atoms of the coordinated water molecule, which were first located in a difference electron-density map, fixed to the oxygen atom O(7), and then left to refine freely in the final stages of refinement in both cases. In **5** the position of the hydrogen atom of the –OH group of the 2-propanol molecule was fixed. Refinement converged with anisotropic displacement parameters for all non-hydrogen atoms. The crystal of **3** presents disorders in one perchlorate ion and in some atoms of the crown moiety. These disorders have been solved, and two atomic sites for O(20), O(22), O(23), C(17), C(18), C(19), C(20), O(3) have been observed and refined. The sites occupancy factors were 0.70(3) for O(20A), O(22A), O(23A), and 0.537(10) for C(17A), C(18A), C(19A), C(20A), O(3A). The crystal of **5** present a disordered perchlorate group and 34 least-squares restraints had to be imposed to resolve the disorder. The site occupancy factor was 0.82 for

Table 1
Crystal data and refinement details for **3** and **5**

	3	**5**
Formula	$C_{29}H_{47}Cl_2N_2O_{17}Pr$	$C_{29}H_{45}Cl_2N_2O_{16}Sm$
Mol. mass (g mol^{-1})	907.5	898.92
Crystal system	monoclinic	monoclinic
Space group	$P2_1/n$	$P2_1/c$
T (K)	120(2)	100.0(2)
a (Å)	12.193(2)	16.8602(6)
b (Å)	21.949(4)	10.0417(3)
c (Å)	14.213(2)	21.4404(7)
β (°)	106.000(3)	96.390(1)
V (Å^3)	3656.4(10)	3607.4(2)
F(000)	1856	1828
Z	4	4
λ (Mo Kα) (Å)	0.71073	0.71073
ρ_{calc} (g cm^{-3})	1.649	1.655
μ (mm^{-1})	1.555	1.849
θ Range (°)	1.76–27.16	1.22–28.3
R_{int}	0.0496	0.033
Measured reflections	32963	49 500
Unique reflections	8045	8861
Observed reflections [$I > 2\sigma(I)$]	5995	7833
Goodness-of-fit on F^2	1.07	1.137
R_1 [$I > 2\sigma(I)$][a]	0.0381	0.0265
wR_2 (all data)[b]	0.0899	0.0801
Largest differences peak and hole (e Å^{-3})	1.116 and −1.101	1.677 and −1.141

[a] $R_1 = \sum \|\|F_o\| - |F_c\|\| / \sum |F_o|$.
[b] $wR_2 = \{\sum[w(\|F_o|^2 - |F_c|^2)^2] / \sum[w(F_0^4)]\}^{1/2}$.

Cl(2BA), O(12A), O(13A), O(14A), and O(15A). Crystal data and details on data collection and refinement are summarised in Table 1.

2.5. Computational methods

Full geometry optimizations of the $[Ln(L^4)(H_2O)]^{2+}$ systems (Ln = La, Pr, Sm, Ho, Lu) were performed *in vacuo* at the RHF level. For these calculations the effective core potential (ECP) of Dolg et al. and the related [5s4p3d]-GTO valence basis set were used for the lanthanides [18], while the 3-21G* basis set was used for the ligand atoms. The X-ray structure of compound **3** was used as input geometry for each geometry optimization. The two conformations observed in the solid state for compound **3** were considered. The relative free energies of the two conformers of $[Ln(L^4)(H_2O)]^{2+}$ complexes were calculated in vacuo at the same computational level, and they include non-potential energy contributions (that is, zero point energy an thermal terms) obtained by frequency analysis. The nature of the calculated stationary points as true minima was checked by frequency analysis. All HF calculations were performed by using the GAUSSIAN 98 package (Revision A.11.3) [19].

3. Results and discussion

Reaction of HL^4 [prepared *in situ* by the condensation of *N*-2-aminobenzyl-1-aza-18-crown-6 and salicylaldehyde] with triethylamine and the corresponding hydrated lanthanide perchlorate in 2-propanol led to complexes of formula $[Ln(L^4)(H_2O)](ClO_4)_2 \cdot x$solv (Ln = La–Tb, excluding Pm). Attempts to prepare the corresponding complexes of the heaviest Ln(III) ions (Ln = Dy–Lu) under analogous conditions were unsuccessful. The IR and FAB mass spectra of the complexes confirmed the formation of the Schiff-base armed macrocycle as well as its presence in the complexes. The IR spectra (KBr discs) feature a band attributable to $\nu(C{=}N)_{imine}$ stretching mode at *ca.* 1610 cm^{-1} which, together with the absence of bands due to carbonyl and/or amine vibration modes, confirms the formation of the imine bond. Bands corresponding to the ν_{as}(Cl–O) stretching and δ_{as}(O–Cl–O) bending modes of the perchlorate groups appear at *ca.* 1090 and 623 cm^{-1}. The absorption at 623 cm^{-1} clearly shows up without splitting, as befit uncoordinated anions [20]. The FAB-mass spectrum of each complex displays a very intense peak (100% BPI) corresponding to the $[Ln(L^4)(ClO_4)]^+$ fragment. The ^{1}H NMR spectrum of the La(III) diamagnetic complex **1** recorded in acetonitrile-d_3 solution shows broad signals for the protons of the macrocyclic unit, while the signals corresponding to protons of the pendant arm are well resolved. The later signals could be assigned with the aid of the 2D COSY and NOESY spectra (see scheme 1 for labelling): δ 8.28 (s, 1H, H7), 7.57 (m, 1H, H12), 7.55 (m, 1H, H10), 7.47 (m, 2H, H5 and H3), 7.35 (ddd, 1H, H11), 7.28 (dd, 1H, H9), 7.78 (m, 2H, H2 and H4). The NOESY spectrum gives a strong cross-peak relating H7 and H5 (H7···H5 = 2.37 Å in the X-ray structure of **5**) and a weaker signal relating H7 and H9 (H7···H9 = 2.52 Å in the X-ray structure of **5**). The spectrum does not show signals attributable to the carbonyl and amine precursors, in agreement with the formation of the expected complex. The broad signals observed for the proton nuclei of the crown moiety indicate the presence of a conformational equilibrium in solution due to the flexibility of the macrocyclic unit.

The solid state structures of the praseodymium and samarium complexes have been determined by X-ray diffraction studies. Crystals consist of the $[Ln(L^4)(H_2O)]^{2+}$ cations (Ln = Pr or Sm), two well-separated perchlorate anions, and solvent molecules (2-propanol in both crystals, and also water in the praseodymium complex) hydrogen bonded to the coordinated water molecule. Fig. 1 displays a view of the structures of the cations. In the case of the $[Pr(L^4)(H_2O)]^{2+}$ complex the carbon atoms C(17), C(18), C(19) and C(20), as well as the oxygen atom of the crown moiety O(3) are disordered. It is well known that crown and aza-crown ethers may take several slightly different conformations in the solid state [21]. These different conformations are not always resolved by X-ray determinations, which often yield an average representation of the unit cell. In the Pr(III) complex two different conformations of the crown moiety are well resolved by the X-ray determination [10,11]. By contrast, only one conformation of the crown moiety is observed in the Sm(III) complex. This conformation corresponds to that observed for the Pr(III) complex taking into account the sites labeled as **A** in Fig. 1.

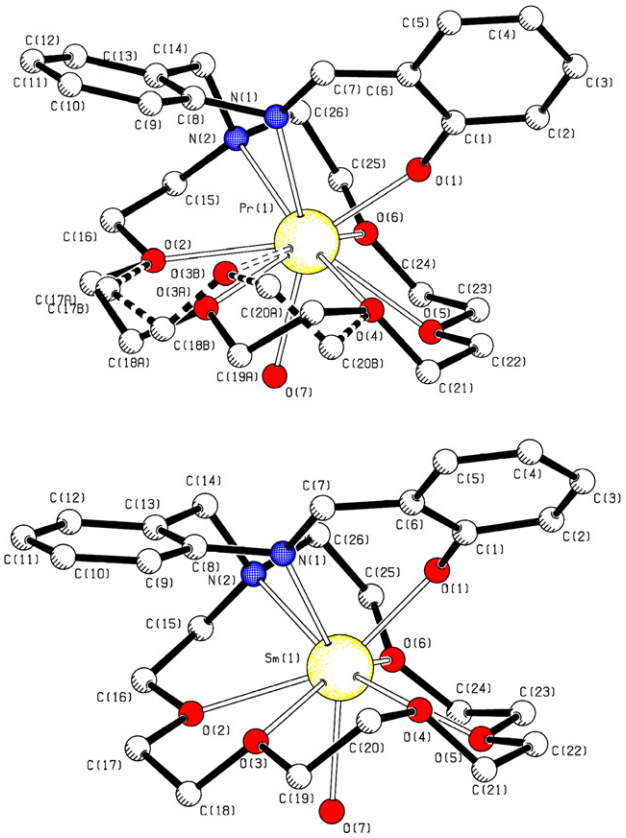


Fig. 1. X-ray crystal structures of the $[Pr(L^4)(H_2O)]^{2+}$ and $[Sm(L^4)(H_2O)]^{2+}$ cations present in **3** (top) and **5** (bottom). Hydrogen atoms are omitted for simplicity.

Bond distances of the metal coordination environment in $[Ln(L^4)(H_2O)]^{2+}$ complexes (Ln = Pr or Sm) are given in Table 2, while bond angles of the metal coordination environment are given in Table S1 (Supporting Information). The lanthanide ion is coordinated to the eight available donor atoms of the ligand and to the oxygen atom of an inner-sphere water molecule. The coordinated water molecule is located on the opposite side of the crown moiety with respect to the pendant arm. The metal ion is almost symmetrically positioned with respect to the crown cavity. The Ln-crown donors distances (Table 2) fall in the range between 2.505–2.679 (Pr) and 2.435–2.634 Å (Sm), and they are similar to the distance between the Ln(III) ion and the oxygen atom of the coordinated water molecule [2.503(5) (Pr) and 2.446(2) Å (Sm)] and Ln-imine nitrogen [2.567(3) (Pr) and 2.519(2) Å (Sm)] bond lengths. The distance to the phenolate oxygen donor atom is clearly shorter than the remaining bond distances of the Ln(III) coordination sphere [Pr(1)–O(1) 2.257(3) Å; Sm(1)–O(1) 2.2461(19) Å]. The bond distances of the metal coordination environment in $[Pr(L^4)(H_2O)]^{2+}$ are slightly shorter than those found in the related complex with the bibracchial receptor $\mathbf{L}^1$, $[Pr(L^1)]^+$ [10]. However, this is expected because the Pr(III) ion is 10-coordinate in $[Pr(L^1)]^+$, while in $[Pr(L^4)(H_2O)]^{2+}$ the metal ion is only nine-coordinate. The Sm-donor distances observed in **5** are very similar to those reported for the Sm(III) complex of $\mathbf{L}^2$ (Scheme 1), in which the metal ion is also nine-coordinate. In both $[Ln(L^4)(H_2O)]^{2+}$ complexes (Ln = Pr or Sm) the oxygen atoms O(2), O(3A), O(4) and O(6) are essentially coplanar, with a mean deviation from planarity of 0.032 (**3**) and 0.0405 Å (**5**). The pivotal nitrogen donor N(2) is located 1.664(3) (**3**) and 1.830(2) Å (**5**) above this plane, and the oxygen atom O(5) is placed 1.040(3) (**3**) and 1.098(2) Å (**5**) below it. The coordination polyhedron around the metal ion is so severely distorted that it may be viewed both as a monocapped distorted dodecahedron, where atom O(2) is capping a triangular face of the dodecahedron, or as a monocapped square antiprism comprised of two pseudoplanes defined by N(1), N(2), O(2), O(3) (lower plane) and O(1), O(4), O(6), O(7) (upper plane), with the oxygen atom O(5) capping the latter. On the other hand, the benzene and phenol rings are not coplanar, and they intersect at 56.89(11)° (**3**) and 42.42° (**5**). Thus, the coordination of the pendant arm to the Ln(III) ion provokes a loss of planarity of both aromatic rings.

In previous works, we have found that in the $[Ln(L^1)]^+$ complexes [10] the lanthanide ion is 10-coordinate and deeply buried in the receptor cavity, so that additional ligands such as water molecules are excluded from the metal coordination environment. In spite of their lower denticity, a similar situation occurs for the lanthanide complexes of the bibracchial lariat ethers *N*,*N*′-bis(2-salicylaldiminatobenzyl)-1,10-diaza-15-crown-5 ($\mathbf{L}^2$) and *N*, *N*′-bis(2-salicylaldiminato benzyl)-4,10-diaza-12-crown-4 ($\mathbf{L}^3$) [11,12], in which the metal ion is nine- or eight-coordinate. However, the X-ray crystal structures of the $[Ln(L^4)(H_2O)]^{2+}$ complexes reported here (Ln = Pr or Sm) demonstrate that the monobracchial receptor $\mathbf{L}^4$ is not able to protect the lanthanide ion from the interaction with water molecules. The inner-sphere water molecule coordinates to the Ln(III) ion in *trans* position with respect to the donor atoms of the pendant arm. As a consequence the metal ion is placed inside the crown hole, in contrast to the Ln(III) complexes of the bibracchial lariat ethers $\mathbf{L}^1$–$\mathbf{L}^3$ where the metal ion is placed over the plane of the crown moiety [10–12].

The $[Ln(L^4)(H_2O)]^{2+}$ systems (Ln = La, Pr, Sm, Ho, Lu) were investigated *in vacuo* by means of *ab initio* calculations at the HF/3-21G* level. It has been demonstrated that the use of a more extended basis sets for the ligand atoms or a higher level of theory (B3LYP, MP2) does not result in an improvement of the agreement between experimental (X-ray) and calculated structures [22,23]. As there is not a good all-electron basis set for lanthanides, the effective core potential (ECP) of Dolg et al. and the related [5s4p3d]-GTO valence basis set was applied in these calculations [18]. This ECP includes $46 + 4f^n$ electrons in the core, leaving the outermost 11 electrons to be treated explicitly, and it has been demonstrated to provide reliable results for the lanthanide aqua-ions [22], several lanthanide chelates with polyamino carboxylate ligands [24] and lanthanide dipicolinates [25]. Recently, we have proved to give excellent results also for lanthanide complexes with pendant-armed

Table 2
Experimental[a] and calculated[b] bond lengths [Å] of the metal coordination environment in $[Ln(L^4)(H_2O)]^{2+}$ complexes (Ln = La, Pr, Sm, Ho or Lu) and relative free energies [kcal mol^{-1}] of conformation **B** with respect to conformation **A**

	Ln = **La**		Ln = **Pr**			Ln = **Sm**			Ln = **Ho**		Ln = **Lu**	
	Calculated[b]		Calculated[b]		Experimental[a]	Calculated[b]		Experimental[a]	Calculated[b]		Calculated[b]	
	A	**B**	**A**	**B**	**A + B**	**A**	**B**	**A**	**A**	**B**	**A**	**B**
Ln(1)–O(1)	2.338	2.312	2.303	2.280	2.257(3)	2.260	2.238	2.246(2)	2.196	2.174	2.151	2.129
Ln(1)–O(2)	2.642	2.683	2.612	2.646	2.628(3)	2.576	2.604	2.577(2)	2.538	2.532	2.475	2.465
Ln(1)–O(3)	2.661	2.587	2.629	2.544	2.679(7) O(3A) 2.513(8) O(3B)	2.592	2.496	2.602(2)	2.542	2.430	2.501	2.375
Ln(1)–O(4)	2.577	2.676	2.544	2.641	2.614(3)	2.505	2.607	2.527(2)	2.458	2.582	2.437	2.589
Ln(1)–O(5)	2.741	2.740	2.720	2.717	2.610(2)	2.697	2.704	2.593(2)	2.712	2.771	2.801	2.935
Ln(1)–O(6)	2.562	2.589	2.529	2.550	2.505(3)	2.488	2.508	2.435(2)	2.436	2.457	2.405	2.428
Ln(1)–O(7)	2.619	2.609	2.574	2.567	2.503(3)	2.516	2.508	2.446(2)	2.430	2.420	2.362	2.351
Ln(1)–N(1)	2.605	2.627	2.569	2.595	2.567(3)	2.523	2.553	2.519(2)	2.455	2.485	2.404	2.429
Ln(1)–N(2)	2.723	2.747	2.691	2.705	2.679(3)	2.655	2.663	2.634(2)	2.608	2.606	2.570	2.552
AF_i[c]			0.022	0.019		0.019						
$\Delta G^{\circ}_{298\ K}$[d]		−0.26		0.15			0.81			1.55		1.66

[a] From single-crystal X-ray diffraction analyses.
[b] From *ab initio* calculations at the HF/3-21G* level. Two different geometries labelled as **A** and **B** were calculated.
[c] $AF_i = [\sum(\exp - \mathrm{calcd})^2 / \sum(\exp)^2]^{1/2}$, where exp and calcd denote experimental and calculated values, respectively.
[d] $\Delta G^{\circ}_{298K} = G^{\circ}_{298\ K}(\mathbf{B}) - G^{\circ}_{298\ K}(\mathbf{A})$.

crowns [12] or azacrowns [26] and chelates containing pyridine units [27]. Compared to all-electron basis sets, ECPs account to some extent for relativistic effects, which are believed to become important for the elements from the fourth row of the periodic table. Two geometries of the complexes showing the two different conformations of the crown moiety observed in the X-ray structure of the Pr(III) complex were considered. The conformation denoted as **A** corresponds to that observed for the Pr(III) complex in the solid state taking into account the sites labelled as C(17A), C(18A), C(19A), C(20A), O(3A) in Fig. 1, while the conformation denoted as **B** is generated by the occupation of sites C(17B), C(18B), C(19B), C(20B), O(3B). *In vacuo* optimized Cartesian coordinates obtained for the different $[Ln(L^4)(H_2O)]^{2+}$ systems are given in Supporting Information. The optimized geometries obtained for the $[Pr(L^4)(H_2O)]^{2+}$ system are shown in Fig. 2.

The **A** and **B** conformations calculated for the $[Pr(L^4)(H_2O)]^{2+}$ system are in good agreement with the experimental geometrical parameters obtained from the X-ray single crystal analysis of compound **3**. According to Table 2, the calculated distances between the praseodymium ion and the donor atoms are in reasonably good agreement with those observed experimentally (within 0.07 Å, except Pr–O(5) that deviates 0.11 Å), as evidenced by the excellent agreement factors obtained [$AF_i = 0.022$ (**A**) and 0.019 (**B**); $AF_i = [\sum(\exp - \mathrm{calcd})^2 / \sum(\exp)^2]^{1/2}$, where exp and calcd denote experimental and calculated values, respectively) [28]. The Sm-donor distances calculated for conformation **A** also show a good agreement with the experimental bond lengths observed in the solid state (within 0.10 Å, $AF_i = 0.019$). The calculated structures for the remaining $[Ln(L^4)(H_2O)]^{2+}$ systems investigated (Ln = La, Ho, Lu) are very similar to the experimental and calculated structures found for the Pr(III) and Sm(III) analogues, with a water molecule in the first coordination

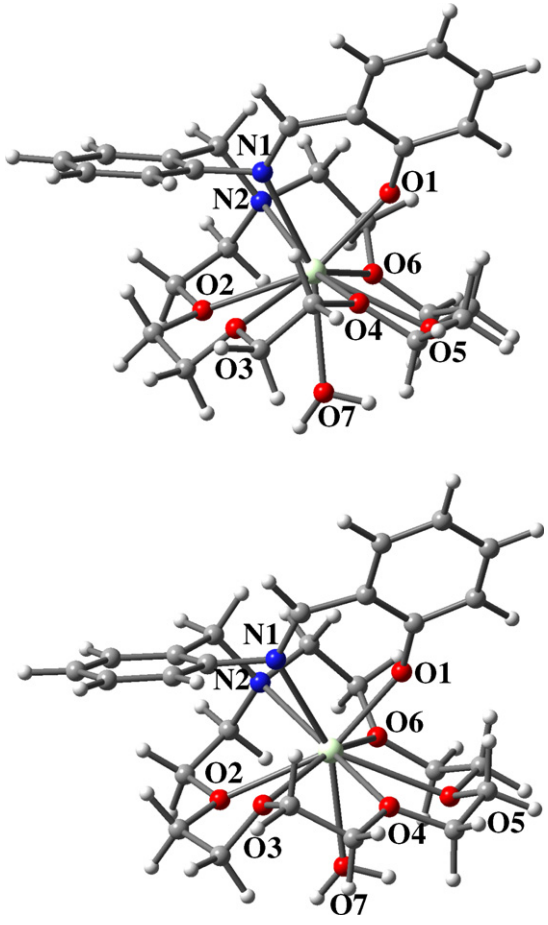


Fig. 2. Calculated structures for the $[Pr(L^4)(H_2O)]^{2+}$ system as optimised in vacuo at the HF/3-21G* level (top: conformation **A**; bottom: conformation **B**).

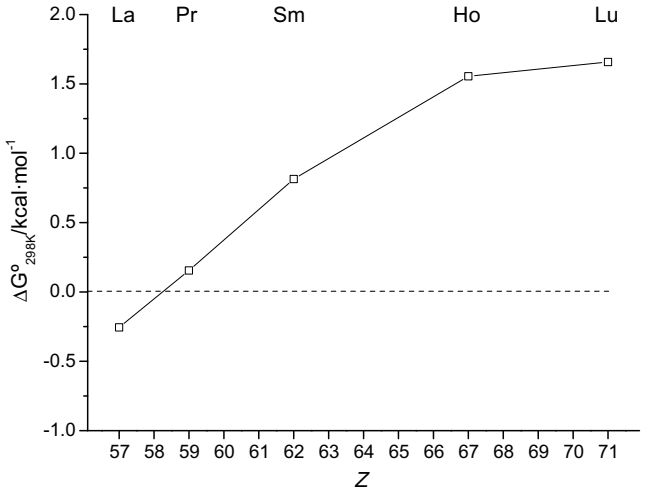


Fig. 3. In vacuo relative free energy of the **B** conformation ($\Delta G^{\circ}_{298\ K} = G^{\circ}_{\mathbf{B}} - G^{\circ}_{\mathbf{A}}$) in $[Ln(L^4)(H_2O)]^{2+}$ complexes.

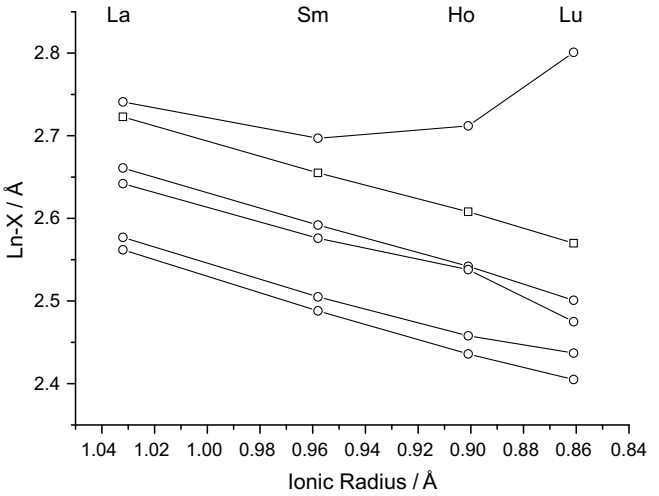


Fig. 4. Ln–O_C (-○-) and Ln–N_A (–□–) bond distances calculated at the HF/3-21G* computational level for the $[Ln(L^4)(H_2O)]^{2+}$ complexes showing conformation **A** [N_A = amine nitrogen atoms; O_C = crown ether oxygen atoms].

sphere. The calculated La-donor bond lengths (Table 2) are similar to those found experimentally in the lanthanum complex with the related receptor $\mathbf{L}^1$ [10].

The relative free energies of the **A** and **B** conformations of $[Ln(L^4)(H_2O)]^{2+}$ complexes were calculated in vacuo at the HF/3-21G* level, and the results are reported in Table 2 and Fig. 3. Relative free energies were calculated as $\Delta G^{\circ}_{298\ K} = G^{\circ}_{298\ K}(\mathbf{B}) - G^{\circ}_{298\ K}(\mathbf{A})$, and therefore a positive relative energy indicates that the **A** conformation is more stable than the **B** one. Our calculations indicate that the relative energy of conformation **B** increases along the lanthanide series. The **A** conformation is the most stable one in the case of the La(III) complex, while for the Pr(III), Sm(III), Ho(III) and Lu(III) complexes the minimum energy conformation corresponds to the **A** form. Both **A** and **B** conformations are observed in the solid state structure of the Pr(III) complex, while for Sm(III) only the **A** form is found, which suggests a stabilization of conformation **A** on decreasing the ionic radius of the Ln(III) ion, as predicted by our quantum mechanical calculations. The relative free energies reported in Table 2 for $[Pr(L^4)(H_2O)]^{2+}$ predict a small energy difference between the **A** and **B** conformations (0.15 kcal · mol^{-1}), in agreement with the fact that both conformations are observed in the solid state.

On the other hand, the calculated structures of the $[Ln(L^4)(H_2O)]^{2+}$ systems (**A** conformation) show that, with the exception of Ln–O(5), the calculated Ln-donor bond lengths decrease along the lanthanide series (Table 2, Fig. 4), as usually observed for Ln(III) complexes. However, the Ln–O(5) distance decreases from La (2.741 Å) to Sm (2.697 Å), but then increases in the Ho (2.712 Å) and Lu (2.801 Å) complexes (Fig. 4). A similar situation is found for conformation **B**, in which the Lu–O(5) distance amounts to 2.935 Å (Table 2). Although these results should be taken with care, since no geometry optimizations have been attempted for other conformations of the macrocyclic receptor in the complexes (the **A** and **B** conformations observed in the X-ray crystal structure of the Pr(III) complex were used as input geometries), the lengthening of the Ln–O(5) distance at the end of the series suggests that the macrocyclic cavity size of $\mathbf{L}^4$ provides the best fit with the lightest Ln(III) ions along the lanthanide series.

4. Concluding remarks

The mono-armed azacrown *N*-(2-salicylaldiminatobenzyl)-1-aza-18-crown-6 ($\mathbf{L}^4$) forms complexes of formula $[Ln(L^4)(H_2O)](ClO_4)_2 \cdot x$solv with lanthanides from La to Tb, excluding Pm. The solid state structures of the Pr(III) and Sm(III) complexes, as well as theoretical calculations performed at the HF level indicate that the $[Ln(L^4)(H_2O)]^{2+}$ complexes adopt at least two different conformations along the lanthanide series. Moreover, calculated relative free energies of the two isomers along the lanthanide series are in agreement with the structures observed in the solid state. These results suggest that the energetics of these complexes can be appropriately calculated at the HF level. It is well known that the conformation adopted by a macrocyclic ligand in Ln(III) complexes can affect drastically some properties such as the exchange rate of inner-sphere water molecules [29]. Thus, the prediction of the structure of lanthanide complexes by using theoretical methods is important to help on the design of systems with the desired properties.

A comparison of the coordinative properties of the monobracchial lariat ether $\mathbf{L}^4$ with those of the bibracchial receptor $\mathbf{L}^1$ shows that removing a pendant arm results in a lower encapsulating capability of the ligand, which allows additional ligands such as water molecules to enter the inner coordination sphere of the Ln(III) ion in the complexes of $\mathbf{L}^4$, a condition required for the application of Ln(III) complexes as contrast agents in MRI [1]. We are

currently investigating structural modifications in the ligand backbone to improve the solubility of the complexes in aqueous media.

Acknowledgements

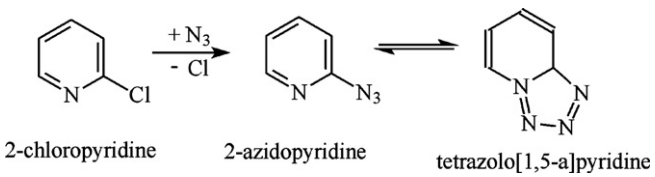
The authors thank the Ministerio de Educación y Ciencia and FEDER for financial support (Grant CTQ2006-07875), and Centro de Supercomputación of Galicia (CESGA) for providing the computer facilities.

Appendix A. Supplementary data

CCDC 666283 and 666284 contain the supplementary crystallographic data for crystal structure of **3** and **5**. These data can be obtained free of charge via http://www.ccdc.cam.ac.uk/conts/retrieving.html, or from the Cambridge Crystallographic Data Centre, 12 Union Road, Cambridge, CB2 1EZ, UK; fax: (+44) 1223-336-033 or e-mail: deposit@ccdc.cam.ac.uk. Supplementary data associated with this article can be found, in the online version, at doi:10.1016/j.poly.2008.01.004.

References

[1] (a) R.R. Edelman, M.B. Zlatkin, J.R. Hesselink (Eds.), Clinical Magnetic Resonance Imaging, 2nd ed., vol. 1, W.B. Saunders Company, Philadelphia, 1996 (Chapter 5);
(b) P. Caravan, J.J. Ellinson, T.J. McMurry, R.B. Lauffer, Chem. Rev. 99 (1999) 2293;
(c) A.E. Merbach, É. Tóth (Eds.), The Chemistry of Contrast Agents in Medical Magnetic Resonance Imaging, Wiley, New York, 2001.
[2] (a) T.C. Bruice, A. Tsubouchi, R.O. Dempcy, L.P. Olson, J. Am. Chem. Soc. 118 (1996) 9867;
(b) P. Hurst, B.K. Takasaki, J. Chin, J. Am. Chem. Soc. 118 (1996) 9982.
[3] I. Hemmilä, T. Stahlberg, P. Mottram, Bioanalytical Applications of Labelling Technologies, Wallac Oy, Turku, Finland, 1994.
[4] D. Parker, Coord. Chem. Rev. 205 (2000) 109.
[5] (a) G.L. De Nardo, G.R. Mirik, L.A. Kroger, R.T. O'Donnel, C.F. Meares, S.L. De Nardo, J. Nucl. Med. 37 (1996) 451;
(b) M.J. Heeg, S.S. Jurisson, Acc. Chem. Res. 32 (1999) 1053.
[6] (a) R. Saez-Puche, P. Caro (Eds.), Rare Earths, Editorial Complutense, Madrid, 1998;
(b) D. Parker, R.S. Dickins, H. Puschmann, C. Crossland, J.A.K. Howard, Chem. Rev. 102 (2002) 1977.
[7] Y. Liu, B.-H. Han, Y.-M. Li, R.-T. Chen, M. Ouchi, Y. Inoue, J. Chem. Phys. 100 (1996) 17361.
[8] G.W. Gokel, S.H. Korzeniowski, Macrocyclic Polyether Synthesis, Springer, Berlin, 1982.
[9] Y. Nakatsuji, T. Nakamura, M. Yometani, H. Yuya, M. Okahara, J. Am. Chem. Soc. 110 (1988) 531.
[10] C. Platas, F. Avecilla, A. de Blas, T. Rodríguez-Blas, R. Bastida, A. Macías, A. Rodríguez, H. Adams, J. Chem. Soc., Dalton Trans. (2001) 1699.
[11] M. González-Lorenzo, C. Platas-Iglesias, F. Avecilla, C.F.G.C. Geraldes, D. Imbert, J.-C.G. Bünzli, A. de Blas, T. Rodríguez-Blas, Inorg. Chem. 42 (2003) 6946.
[12] M. González-Lorenzo, C. Platas-Iglesias, F. Avecilla, S. Faulkner, S.J. Pope, A. de Blas, T. Rodríguez-Blas, Inorg. Chem. 44 (2005) 4254.
[13] W.C. Wolsey, J. Chem. Educ. 50 (1973) A335.
[14] SADABS Area-Detector Absorption Correction. Siemens Industrial Automation Inc., Madison, WI, 1996.
[15] G.M. Sheldrick, SHELX97 [Includes SHELXS97, SHELXL97, CIFTAB] – Programs for Crystal Structure Analysis (Release 97-2), Institüt für Anorganische Chemie der Universität, Tammanstrasse, Göttingen, Germany, 1998.
[16] L.J. Farrugia, WINGX MS-Windows system of programs for solving, refining and analysing single crystal X-ray diffraction data for small molecules, J. Appl. Crystallogr. 32 (1999) 837.
[17] P.T. Beurskens, G. Beurskens, R. de Gelder, S. Garcia-Granda, R.O. Gould, R. Israel, J.M.M. Smits, DIRDIF99 Program System, Crystallography Laboratory, University of Nijmegen, The Netherlands, 1999.
[18] M. Dolg, H. Stoll, A. Savin, H. Preuss, Theor. Chim. Acta 75 (1989) 173.
[19] M.J. Frisch, G.W. Trucks, H.B. Schlegel, G.E. Scuseria, M.A. Robb, J.R. Cheeseman, V.G. Zakrzewski, J.A. Montgomery Jr, R.E. Stratmann, J.C. Burant, S. Dapprich, J.M. Millam, A.D. Daniels, K.N. Kudin, M.C. Strain, O. Farkas, J. Tomasi, V. Barone, M. Cossi, R. Cammi, B. Mennucci, C. Pomelli, C. Adamo, S. Clifford, J. Ochterski, G.A. Petersson, P.Y. Ayala, K. Morokuma, Q. Cui, D.K. Malick, A.D. Rabuck, K. Raghavachari, J.B. Foresman, J. Cioslowski, J.V. Ortiz, A.G. Baboul, B.B. Stefanov, G. Liashenko, A. Liu, P. Piskorz, I. Komaromi, R. Gomperts, R.L. Martin, D.J. Fox, T. Keith, M.A. Al-Laham, C.Y. Peng, A. Nanayakkara, M. Challacombe, P.M.W. Gill, B. Johnson, W. Chen, M.W. Wong, J.L. Andres, C. Gonzalez, M. Head-Gordon, E.S. Replogle, J.A. Pople, GAUSSIAN 98, Revision A.11, Gaussian Inc., Pittsburgh, PA, 1998.
[20] K. Nakamoto, Infrared and Raman Spectra of Inorganic and Coordination Compounds, 5th ed., John Wiley, New York, Chichester, Brisbane and Toronto, 1997.
[21] F. Nicolo, D. Plancharel, G. Chapuis, J.-C.G. Bünzli, Inorg. Chem. 27 (1988) 3518.
[22] U. Cosentino, A. Villa, D. Pitea, G. Moro, V. Barone, J. Phys. Chem. B 104 (2000) 8001.
[23] R.O. Freire, G.B. Rocha, A.M. Simas, J. Mol. Model. 12 (2006) 373.
[24] U. Cosentino, A. Villa, D. Pitea, G. Moro, V. Barone, A. Maiocchi, J. Am. Chem. Soc. 124 (2002) 4901.
[25] N. Quali, B. Bocquet, S. Rigault, P.-Y. Morgantini, J. Weber, C. Piguet, Inorg. Chem. 41 (2002) 1436.
[26] M.delC. Fernández-Fernández, R. Bastida, A. Macías, P. Pérez-Lourido, C. Platas-Iglesias, L. Valencia, Inorg. Chem. 45 (2006) 4484.
[27] (a) C. Platas-Iglesias, M. Mato-Iglesias, K. Djanashvili, R.N. Muller, L. Vander Elst, J.A. Peters, A. De Blas, T. Rodríguez-Blas, Chem. Eur. J. 10 (2004) 3579;
(b) M. Mato-Iglesias, C. Platas-Iglesias, K. Djanashvili, J.A. Peters, E. Tóth, E. Balogh, R.N. Muller, L. Vander Elst, A. De Blas, T. Rodríguez-Blas, Chem. Commun. (2005) 4729;
(c) M. Mato-Iglesias, E. Balogh, C. Platas-Iglesias, E. Tóth, A. De Blas, T. Rodríguez-Blas, Dalton Trans. (2006) 5404.
[28] (a) M.R. Willcott, R.E. Lenkinski, R.E. Davis, J. Am. Chem. Soc. 94 (1972) 1742;
(b) R.E. Davis, M.R. Willcott, J. Am. Chem. Soc. 94 (1972) 1744.
[29] (a) M. Woods, S. Aime, M. Botta, J.A.K. Howard, J.M. Moloney, M. Navet, D. Parker, M. Port, O. Rousseaux, J. Am. Chem. Soc. 122 (2000) 9781;
(b) M. Woods, Z. Kovacs, S. Zhang, A.D. Sherry, Angew. Chem., Int. Ed. 42 (2003) 5889;
(c) F.A. Dunnand, S. Aime, A.E. Merbach, J. Am. Chem. Soc. 122 (2000) 1506.



Scheme 1.

we synthesized coordination polymers of Zn(II) containing these ligands. The ligand (L1) in the scheme in fact was prepared through the reaction between 2-chloropyridine and azide ion, forming tetrazolo[1,5-*a*]pyridine (abbreviated as py-tetrazole). This ligand is a potentially multi-dentate ligand, however, it acts in the synthesized complex $[Zn_2(N_3)_4(\text{py-tetrazolate})_2](\text{py-tetrazole})$ (**1**) as a monodentate and links zinc center not through the pyridinic nitrogen but through a nitrogen atom of the other three tetrazole nitrogens. This complex crystallizes with uncoordinated py-tetrazole molecule. The second ligand L2 in the scheme: 3-hydroxypyridine (3-OHpy), behaves as *O*,*O*-bridging, i.e. in the tautomeric keto-form (pyridone) in the prepared zinc(II) complex, $[Zn_2(N_3)_4(3\text{-OHpy})]\cdot 2H_2O$ (**2**) which crystallizes with two lattice water molecules. L3 is pyrimidine (pym) which is potentially bidentate and has the ability to bridge metal centers, afforded $[Zn(N_3)_2(pym)]$ (**3**). The structural motifs of these complexes are variable from ladder (1D), to rings (2D) and cubes (3D). Complexes **1** and **2** are unprecedented in all known metal azide complexes. These three new complexes are studied by spectroscopic methods and X-ray crystal diffraction. The room temperature photoluminescence of complex **2** is measured. The results of this study are reported here.

2. Experimental

2.1. Materials and instrumentation

Elemental analyses were carried out using a Perkin–Elmer analyzer and infrared spectra were recorded on a Perkin–Elmer FTIR Series 1600 spectrophotometer as KBr pellets [18]. Luminescence spectra were recorded on a Yobin Yvon SPEX Fluoromax 2 instrument. Starting ligands have been purchased from Aldrich Company, other chemicals were of analytical grade quality and used without further purification. Aqueous hydrazoic acid is obtained with a modified Kipp's generator by decomposition of NaN_3 in H_2SO_4/H_2O (1:3, v:v) and subsequent transfer of HN_3 into H_2O with aid of an inert gas stream. Stock solutions of aqueous ZnN_6 (0.89 mmol Zn/mL H_2O) are obtained in a similar manner by the reaction of HN_3 with a suspension of basic zinc carbonate (0.10 g/mL) H_2O [19].

Caution: Azide compounds and hydrazoic acid (HN_3) are potentially explosive! Only a small amount of material should be prepared and handled with care.

2.2. Synthesis

2.2.1. $\{[Zn_2(N_3)_4(\text{py-tetrazole})_2](\text{py-tetrazole})\}_n$ (1)

Complex **1** was prepared by mixing an aqueous solution of ZnN_6 saturated with hydrazoic acid (10 mL, 8.9 mmol Zn) with 2-chloropyridine (0.50 g, 4.4 mmol) in MeOH (10 mL). The mixture was heated to 95 °C for 30 min with subsequent step-wise cooling to 4 °C. Needle-shaped colorless crystals of the complex were deposited after approx.12 weeks. Yield: approx. 55%. *Anal*. Calc. for $C_{15}H_{12}N_{24}Zn_2$:

Table 1
Crystallographic data and processing parameters

Compound	1	2	3
Empirical formula	$C_{15}H_{12}N_{24}Zn_2$	$C_5H_9N_{13}O_3Zn_2$	$C_4H_4N_8Zn$
Formula mass	659.27	430.03	229.54
System	monoclinic	monoclinic	monoclinic
Space group	$P2_1/c$	$P2_1/c$	$I2/m$
a (Å)	12.909(3)	11.635(2)	7.508(2)
b (Å)	6.740(2)	10.743(2)	12.083(3)
c (Å)	28.312(9)	11.999(2)	8.500(3)
α (°)	90	90	90
β (°)	94.43(2)	104.40(3)	91.67(2)
γ (°)	90	90	90
V (Å^3)	2456.0(12)	1452.7(5)	770.8(4)
Z	4	4	4
T (K)	293(2)	100(2)	99(2)
μ (Mo Kα) (mm^{-1})	2.015	3.341	3.148
D_{calc} (Mg/m^3)	1.783	1.966	1.978
Crystal size (mm)	0.35 × 0.22 × 0.16	0.38 × 0.30 × 0.20	0.30 × 0.20 × 0.12
θ Range (°)	3.11–26.00	1.81–25.49	2.93–29.99
Reflections collected	5586	10 251	1494
Independent reflections (R_{int})	4786(0.0328)	2700(0.1071)	1178(0.0283)
Parameters	370	220	65
Goodness-of-fit on F^2	1.122	1.097	1.255
R_1/wR_2	0.0407/0.0999	0.0608/0.1433	0.0361/0.0982
Residual extrema (e Å^3)	0.509, −0.524	1.189, −1.089	0.499, −0.668

C, 27.3; H, 1.8; N, 51.0. Found: C, 27.1; H, 1.9; N, 50.8%. IR, KBr (cm^{-1}): (v, very; s, strong; m, medium; w, weak; br, broad): 3134 w, 3107 w, 3086 w, 3037 w, 2118 s, 2098 vs, 1630 m, 1492 m, 1431 w, 1302 w, 1285 m, 1266 w, 1139 m, 1093 m, 1021 w, 771 m, 749 m, 691 w, 674 w, 599 w, 556 w, 428 w.

2.2.2. $\{[Zn_2(N_3)_4(3\text{-}OHpy)] \cdot 2H_2O\}_n$ (2)

This complex was prepared by dissolving 3-hydroxypyridine (0.358 g, 3.76 mmol) in an aqueous solution of ZnN_6 saturated with hydrazoic acid (10 mL, 8.9 mmol Zn). The clear solution was stored at 4 °C to separate colorless and transparent crystals of the complex after 7 days. Yield: approx. 55%. *Anal.* Calc. for $C_5H_9N_{13}O_3Zn_2$: C, 14.0; H, 2.1; N, 42.3. Found: C, 14.2; H, 1.9; N, 42.6%. IR, KBr (cm^{-1}): 3599 mbr, 3468 br, 3115 w, 2121 vs, 2091 vs, 1603 m, 1549 m, 1471 m, 1357 m, 1305 m, 1260 m, 1179 vw, 1109 vw, 1046 vw, 1002 vw, 853 m, 805 m, 697 w, 674 m, 619 w, 580 w, 525 w.

2.2.3. $[Zn(N_3)_2(pym)]_n$ (3)

This complex was prepared by mixing an aqueous solution of ZnN_6 saturated with hydrazoic acid (15 mL, 8.9 mmol Zn) with pyrimidine (83.9 mg, 1.27 mmol). The mixture was heated to 80 °C to obtain a clear solution. Colorless crystals of the complex were deposited after 2 days at room temperature. Yield: approx. 80%. *Anal.* Calc. for $C_4H_4N_8Zn$: C, 20.9; H, 1.8; N, 48.8. Found: C, 48.5; H, 1.7; N, 20.8%. IR, KBr (cm^{-1}): 3422 w, 3393 w, 3105 w, 3087 w, 2078 vs, 1594 s, 1563 m, 1463 m, 1420 m, 1286 w, 1219 w, 1175 m, 1136 w, 1075 m, 1021w, 957 w, 819 m, 704 s, 685 m, 649 m, 656 s 616 m.

2.3. X-ray crystallography

Single crystal X-ray data for complexes **1** and **3** were measured on a modified STOE four circle diffractometer, and for **2** on a Bruker-AXS SMART APEX CCD diffractometer using graphite crystal-monochromatized Mo Kα; radiation ($\lambda = 0.7107$ Å). The intensities were corrected for Lorentz-polarisation effects and for absorption. Crystallographic data and processing parameters are given in Table 1. The structures were solved by direct methods and subsequent Fourier analyses. Anisotropic displacement parameters were applied to non-hydrogen atoms in full-matrix least-squares refinements based on F^2. The hydrogen atoms were assigned with isotropic displacement factors and included in the final refinement cycles by use of geometrical restraints. Analytical expressions of neutral-atom scattering factors were employed, and anomalous dispersion corrections were incorporated. The programs DIFABS, SADABS and SHELXTL/PC program package [20] were used for computations. Selected bond distances and bond angles are given in Tables 2, 4 and 6, for complexes **1**–**3**, respectively. Hydrogen bonds of complex **2** are summarized in Table 5.

Table 2
Selected bond lengths (Å) and angles (°) for **1**

Zn(1)–N(41)	2.047(3)	Zn(1)–N(31)	2.063(3)
Zn(1)–N(21)	2.085(3)	Zn(1)–N(11)	2.087(3)
Zn(1)–N(1)	2.252(3)	Zn(2)–N(31A)	2.038(3)
Zn(2)–N(41B)	2.050(3)	Zn(2)–N(21)	2.059(3)
Zn(2)–N(11)	2.120(3)	Zn(2)–N(5)	2.253(3)
N(11)–N(12)	1.208(4)	N(12)–N(13)	1.139(4)
N(21)–N(22)	1.206(4)	N(22)–N(23)	1.149(4)
N(31)–N(32)	1.226(4)	N(32)–N(33)	1.131(4)
N(41)–N(42)	1.224(4)	N(42)–N(43)	1.140(4)
N(1)–C(5)	1.337(5)	N(1)–N(2)	1.347(4)
N(2)–N(3)	1.297(4)	N(3)–N(4)	1.358(5)
N(4)–C(5)	1.353(5)	N(4)–C(1)	1.375(5)
N(5)–C(10)	1.337(5)	N(5)–N(6)	1.356(4)
N(6)–N(7)	1.297(5)	N(7)–N(8)	1.367(5)
N(8)–C(10)	1.345(5)	N(8)–C(6)	1.370(5)
N(18)–C(17)	1.311(6)	N(18)–N(19)	1.387(10)
C(17)–N(16)	1.337(6)	C(21)–N(16)	1.398(6)
N(16)–N(20)	1.359(7)	N(20)–N(19)	1.211(9)
Zn(1)···Zn(2)	3.2256(11)	Zn(1)···Zn(2B)	3.5929(13)
Zn(1)···Zn(2A)	3.6003(13)		
N(41)–Zn(1)–N(31)	115.20(12)	N(41)–Zn(1)–N(21)	112.70(13)
N(31)–Zn(1)–N(21)	132.04(13)	N(41)–Zn(1)–N(11)	98.67(12)
N(31)–Zn(1)–N(11)	96.60(12)	N(21)–Zn(1)–N(11)	78.30(11)
N(41)–Zn(1)–N(1)	94.60(11)	N(31)–Zn(1)–N(1)	88.04(12)
N(21)–Zn(1)–N(1)	86.00(11)	N(11)–Zn(1)–N(1)	162.43(12)
N(31A)–Zn(2)–N(41B)	117.56(12)	N(31A)–Zn(2)–N(21)	112.10(13)
N(41B)–Zn(2)–N(21)	130.34(13)	N(31A)–Zn(2)–N(11)	97.80(12)
N(41B)–Zn(2)–N(11)	94.81(12)	N(21)–Zn(2)–N(11)	78.12(12)
N(31A)–Zn(2)–N(5)	94.14(12)	N(41B)–Zn(2)–N(5)	88.47(12)
N(21)–Zn(2)–N(5)	88.14(12)	N(11)–Zn(2)–N(5)	164.42(12)
N(12)–N(11)–Zn(1)	125.2(3)	N(12)–N(11)–Zn(2)	126.4(3)
Zn(1)–N(11)–Zn(2)	100.14(12)	N(13)–N(12)–N(11)	178.8(4)
N(22)–N(21)–Zn(2)	130.1(3)	N(22)–N(21)–Zn(1)	127.4(3)
Zn(2)–N(21)–Zn(1)	102.23(12)	N(23)–N(22)–N(21)	178.5(4)
N(32)–N(31)–Zn(2B)	118.2(3)	N(32)–N(31)–Zn(1)	116.3(2)
Zn(2B)–N(31)–Zn(1)	122.34(14)	N(33)–N(32)–N(31)	179.7(4)
N(42)–N(41)–Zn(1)	118.6(2)	N(42)–N(41)–Zn(2A)	117.3(2)
Zn(1)–N(41)–Zn(2A)	122.98(14)	N(43)–N(42)–N(41)	178.3(4)
C(5)–N(1)–N(2)	106.6(3)	C(5)–N(1)–Zn(1)	133.7(3)
N(2)–N(1)–Zn(1)	114.3(2)	N(3)–N(2)–N(1)	111.9(3)
N(2)–N(3)–N(4)	105.2(3)	C(5)–N(4)–N(3)	109.6(3)
N(3)–N(4)–C(1)	126.2(4)	N(1)–C(5)–N(4)	106.6(3)
C(10)–N(5)–N(6)	106.2(3)	C(10)–N(5)–Zn(2)	128.8(3)
N(6)–N(5)–Zn(2)	117.0(3)	N(7)–N(6)–N(5)	111.8(3)
N(6)–N(7)–N(8)	105.3(3)	C(10)–N(8)–N(7)	109.3(3)
N(7)–N(8)–C(6)	126.2(4)	N(5)–C(10)–N(8)	107.5(3)
C(17)–N(18)–N(19)	104.7(6)	N(18)–C(17)–N(16)	107.5(5)
C(17)–N(16)–N(20)	108.4(5)	N(20)–N(16)–C(21)	129.7(6)
N(19)–N(20)–N(16)	106.9(7)	N(20)–N(19)–N(18)	112.5(6)

Symmetry codes: (A) $-x+1,\ y-1/2,\ -z+1/2$. (B) $-x+1,\ y+1/2,\ -z+1/2$.

3. Results and discussion

3.1. Crystal structures

3.1.1. Crystal structure of $\{[Zn_2(N_3)_4(py\text{-}tetrazole)_2](py\text{-}tetrazole)\}_n$ (1)

The X-ray structure determination for complex **1** revealed that the five coordinate Zn(II) atoms are bridged

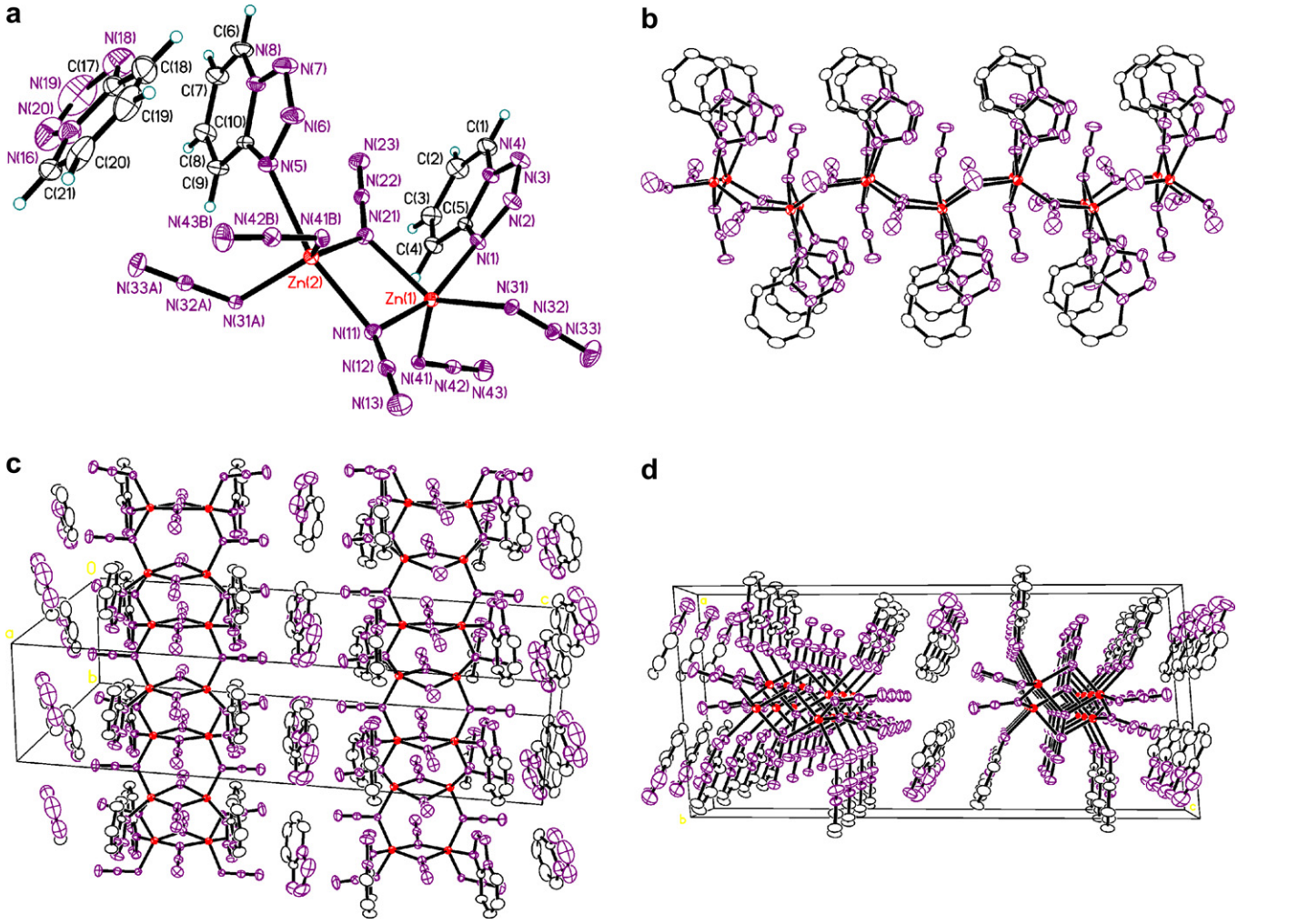


Fig. 1. (a) Perspective view with atom labeling scheme of **1**. Symmetry codes according Table 2. (b) Part of the "ladder-like" arrangement of Zn(II) azide double chains of **1**. (c) Packing view of **1** along the *a*-axis of unit cell. (d) Packing view of **1** along the *b*-axis of unit cell.

by four azido bridges in the EO fashion with a ladder-like arrangement of the 1D zinc(II) azide double chain. A drawing of the asymmetric unit with atom labeling scheme is shown in Figs. 1a–d, show the ladder-like arrangement of the double chain propagated along the crystallographic *b*-axis, and packing plots of the unit cell. Selected bond lengths and bond angles are collected in Table 2. In the coordination chain each zinc(II) ion is coordinated to di-EO azido bridges [Zn(1)–N(11) = 2.087(3), Zn(1)–N(21) = 2.085(3) Å] connecting other Zn(II) ion in the opposite chain forming four-membered Zn_2N_2 cyclic unit [maximum deviation = 0.075(3) Å] crossing the double chain, and two EO bridging azides each on one side of the Zn(II) center [Zn(1)–N(31) = 2.063(3), Zn(1)–N(41). = 2.047(3) Å]. The fifth position is occupied by the nitrogen atom N(1) [Zn(1)–N(1) = 2.252(3) Å] of the tetrazole ring, leading to the formation of a ZnN_5 chromophore. The stereochemistry around Zn(1) center is intermediate between SP and TBP (τ-value = 0.51), whereas Zn(2) is in a TBP environment (τ-value = 0.56) with N(21), N(31A) and N(41B) in the equatorial positions and N(5) and N(11) are the axial atoms. As seen from Fig. 1c and d, 4 Zn atoms are interlinked through EO bridging azides giving tetranuclear Zn(II) rings or eight-membered ring and these rings are connected successively to form a ladder of 1D double chain along the *b*-axis. The Zn···Zn distances within the four-membered Zn_2N_2 cyclic units are Zn(1)–Zn(2) = 3.2256(11) Å, whereas the Zn–Zn distances within the eight-membered rings Zn_4N_4 are Zn(1)–Zn(2A) = 3.6003(13) Å and Zn(1)–Zn(2B) = 3.5929(13) Å. In the channels between parallel ladders the py-tetrazole molecules are located Fig. 1c and d. The four bridging azido ligands are asymmetric and almost linear with N–N–N angles from 178.3(4)° to 179.7(4)°, whereas the N(1)–N(2)–N(3) and N(2)–N(3)–N(4) angles of the bonded py-tetrazolate molecule are 111.9(3)° and 105.2(3)°, respectively. The four azido groups show pronounced deviations from linearity in the connection with Zn(II) [Zn–N–N angles from 102.23(12)° to 130.1(3)°]. π–π ring–ring interactions are observed between the five- and six-membered rings of adjacent bicyclic $C_5H_{14}N_4$ molecules (Table 3).

Table 3
Possible ring interactions for **1**

Cg(A)···Cg(B)[a]	Symmetry of ring(B)	Cg(A)···Cg(B) (Å)	Angle (°)[b]
Cg(2)···Cg(4)	$x, 1/2-y, -1/2+z$	4.609(3)	14.7
Cg(2)···Cg(7)	$x, 1/2-y, -1/2+z$	3.687(3)	13.8
Cg(3)···Cg(4)		4.046(4)	32.4
Cg(3)···Cg(7)		4.531(3)	32.6
Cg(4)···Cg(5)	$x, 1/2-y, 1/2+z$	4.381(4)	15.5
Cg(4)···Cg(6)		4.127(4)	31.2
Cg(5)···Cg(7)	$x, 1/2-y, -1/2+z$	3.737(3)	14.6

[a] Cg = center of gravity of ring; ring (2): N(1)–N(4), C(5); ring (3): N(5)–N(8), C(10); ring (4): N(16)–N(19), C(17); ring (5): N(4); C(4)–C(5); ring (6): N(8), C(6)–C(10); ring (7): N(16), C(17)–C(21).
[b] Dihedral angle between planes of rings (A) and (B).

3.1.2. Crystal structure of $\{[Zn_2(N_3)_4(3\text{-}OHpy)]\cdot 2H_2O\}_n$ (**2**)

The principle structure features for complex **2** are illustrated in Fig. 2a, along with a labeling scheme, and selected bond lengths and bond angles are collected in Table 4. The X-ray structure determination of **2** revealed that the Zn(II) atoms are linked by four azido groups all behave in the μ-1,1-EO mode and an oxygen atom from the 3-OH-py ligand which means that this hydroxypyridine molecule acts in the tautomeric keto-form, i.e. as pyridone, in the present complex and bridges two Zn(II) atoms, thus behaving as an *O,O*-bidentate bridging ligand, leading to a 2D system, further carrying into a 3D supramolecular network with the help of several hydrogen bonding interactions. Fig. 2b and c, show the 2D system extented along the *b*- and *c*-axes, and a view of the 2D sheet along the *b*-axis of the unit cell. In the coordination chain each Zn(II) center links another Zn(II) center through a bridging EO azide group and O atom of an *O,O*-pyridone bridge giving rise to a four-membered Zn_2NO ring [Zn(1)–N(11) = 1.996(5) Å and Zn(1)–O(1) = 2.107(4) Å], and links a second Zn center via di-EO bridging azides [Zn(1)–N(21) = 2.054(5) Å] forming a four membered Zn_2N_2 unit [Zn(1)–Zn(2) = 3.2097(11) Å] and finally connects a third Zn(II) atom through an EO azide group. Thus, the zinc center is in a five coordinated environment with a ZnN_4O chromophore. The four-membered ring Zn_2NO deviates from planarity with a max. deviation = 0.063(6) Å for [Zn(1)/O(1)/Zn(2)/N(11)] and a maximum deviation = 0.090(6) Å for [Zn(1)/O(1)/Zn(2D)/N(11)]. The stereochemistry of both Zn centers can be best described as distorted TBP with τ-values of 0.67 and 0.61 for Zn(1) and Zn(2), respectively. Around Zn(1) and Zn(2) the equatorial atoms are N(11), N(31), N(21) and N(11), N(21B), N(41A) and the axial atoms are O(1), N(41) and O(1), N(31A), respectively. As

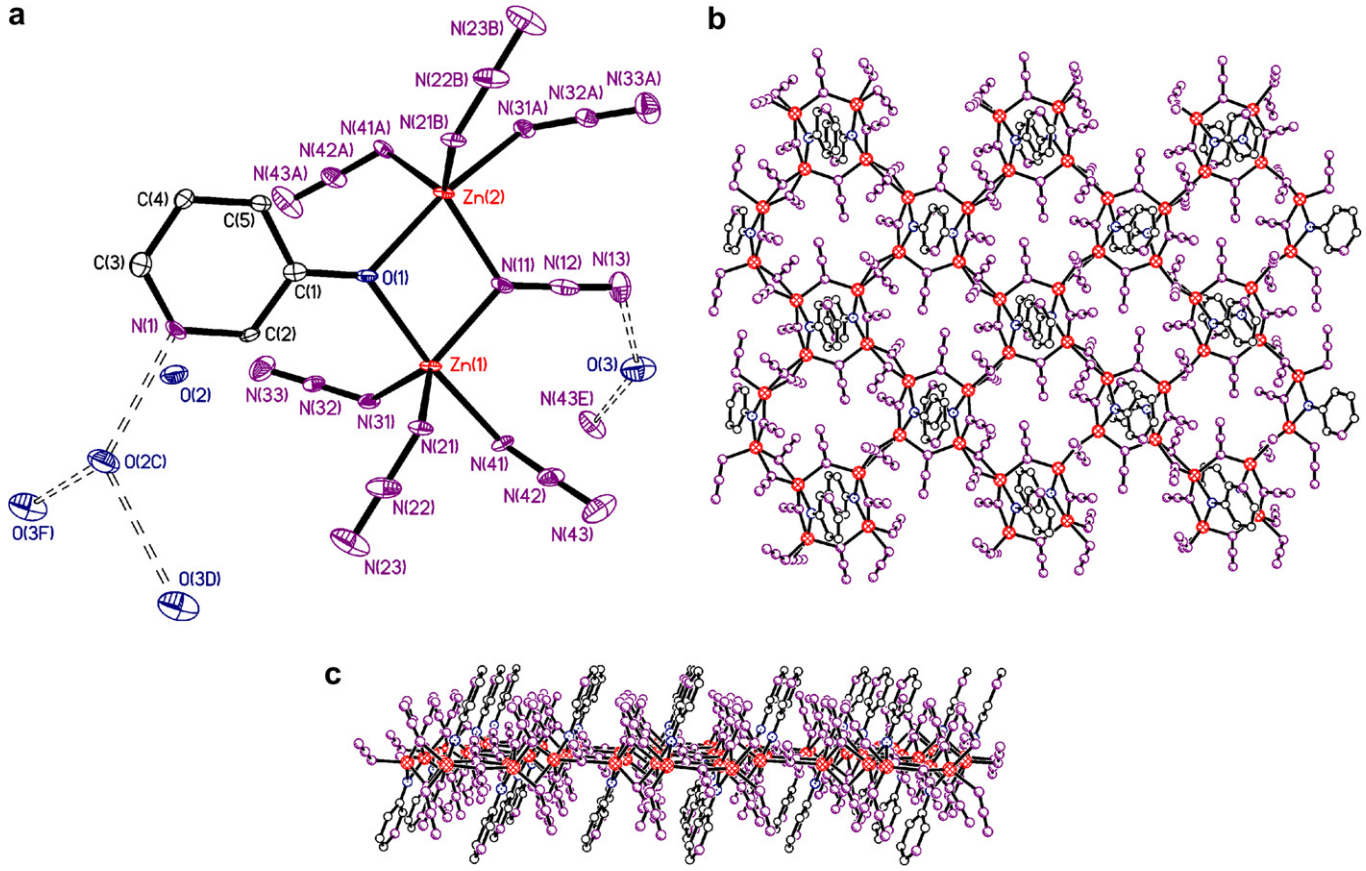


Fig. 2. (a) Perspective view with atom labeling scheme of **2**. Symmetry codes according Table 4. Hydrogen bonds are indicated by broken bonds. (b) 2D system with tetra- and octa-nuclear rings of Zn(II) centers formed by EO-bridging azido and O,O'-bridging pyridones. The 2D system is extented along the *b*- and *c*-axis of the unit cell. (c) View along the *b*-axis of unit cell into a 2D sheet of **2**.

Table 4
Selected bond lengths (Å) and angles (°) for **2**

Zn(1)–N(11)	1.996(5)	Zn(1)–N(31)	2.030(5)
Zn(1)–N(21)	2.054(5)	Zn(1)–O(1)	2.107(4)
Zn(1)–N(41)	2.234(5)	Zn(2)–N(11)	2.028(5)
Zn(2)–N(21B)	2.034(5)	Zn(2)–N(41A)	2.044(5)
Zn(2)–O(1)	2.106(4)	Zn(2)–N(31A)	2.215(5)
N(11)–N(12)	1.249(8)	N(12)–N(13)	1.150(8)
N(21)–N(22)	1.249(8)	N(22)–N(23)	1.149(8)
N(31)–N(32)	1.195(7)	N(32)–N(33)	1.142(8)
N(41)–N(42)	1.214(7)	N(42)–N(43)	1.143(8)
O(1)–C(1)	1.337(8)	N(1)···O(2C)	2.688(8)
Zn(1)···Zn(2)	3.2097(11)	Zn(1)···Zn(2D)	3.2799(11)
Zn(1)···Zn(2B)	3.6318(12)	Zn(1)···Zn(2C)	6.6202(16)
N(11)–Zn(1)–N(31)	128.6(2)	N(11)–Zn(1)–N(21)	118.1(2)
N(31)–Zn(1)–N(21)	113.2(2)	N(11)–Zn(1)–O(1)	77.3(2)
N(31)–Zn(1)–O(1)	99.5(2)	N(21)–Zn(1)–O(1)	96.7(2)
N(11)–Zn(1)–N(41)	95.1(2)	N(31)–Zn(1)–N(41)	78.5(2)
N(21)–Zn(1)–N(41)	94.3(2)	O(1)–Zn(1)–N(41)	168.7(2)
N(11)–Zn(2)–N(21B)	115.2(2)	N(11)–Zn(2)–N(41A)	125.0(2)
N(21B)–Zn(2)–N(41A)	119.8(2)	N(11)–Zn(2)–O(1)	76.7(2)
N(21B)–Zn(2)–O(1)	100.4(2)	N(41A)–Zn(2)–O(1)	94.8(2)
N(11)–Zn(2)–N(31A)	92.9(2)	N(21B)–Zn(2)–N(31A)	97.6(2)
N(41A)–Zn(2)–N(31A)	78.7(2)	O(1)–Zn(2)–N(31A)	161.7(2)
N(12)–N(11)–Zn(1)	127.3(4)	N(12)–N(11)–Zn(2)	124.8(4)
Zn(1)–N(11)–Zn(2)	105.8(2)	N(13)–N(12)–N(11)	178.1(7)
N(22)–N(21)–Zn(2B)	116.1(4)	N(22)–N(21)–Zn(1)	114.6(4)
Zn(2B)–N(21)–Zn(1)	125.4(2)	N(23)–N(22)–N(21)	179.3(7)
N(32)–N(31)–Zn(1)	131.6(4)	N(32)–N(31)–Zn(2D)	127.2(4)
Zn(1)–N(31)–Zn(2D)	101.1(2)	N(33)–N(32)–N(31)	178.9(6)
N(42)–N(41)–Zn(2D)	123.3(4)	N(42)–N(41)–Zn(1)	122.6(4)
Zn(2D)–N(41)–Zn(1)	100.0(2)	N(43)–N(42)–N(41)	178.3(7)
C(1)–O(1)–Zn(2)	130.3(4)	C(1)–O(1)–Zn(1)	130.4(4)
Zn(2)–O(1)–Zn(1)	99.3(2)		

Symmetry codes: (A) $1-x, -1/2+y, 3/2-z$. (B) $1-x, -y, 2-z$. (C) $x, 1/2-y, 1/2+z$. (D) $1-x, 1/2+y, 3/2-z$. (E) $x, 1/2-y, -1/2+z$. (F) $1+x, 1/2-y, 1/2+z$.

can be seen from Fig. 2b, four zinc(II) centers are interconnected by EO azides to afford a tetranuclear ring and eight zinc centers are interconnected to form an octanuclear ring. These two types of rings are the bases for the formation of the 2D sheet. The Zn···Zn distances within the tetranuclear zinc(II) rings are: 3.2097(11) and 3.6318(12) Å; the Zn···Zn separations between opposite pairs of metal centers within the octanuclear zinc(II) rings are in the range from 7.625(2) to 9.714(3) Å. The azide groups are asymmetric and linear [N–N–N angles are from 178.1(7)° to 179.3(7)°], and all of them deviate from linearity in connection with Zn atoms [Zn–N–N angles from 116.1(4)° to 131.6(4)°]. Hydrogen bonds of different types: [O–H···N] between O atom of a lattice water molecule and the end nitrogen atom of an EO azide, or between an oxygen atom of a lattice water and the nitrogen atom of pyridone ligand [N–H···O], and O–H···O between oxygen atoms of lattice water molecules are formed (Table 5). These hydrogen bonds consolidate the structure and lead to the formation of 3D supramolecular network.

Table 5
Hydrogen bonding system for **2**

D–H···A[a]	Symmetry of A	D···A (Å)	D–H···A (°)
N(1)–H(1)···O(2)	$x, -1/2-y, 1/2+z$	2.688(8)	171.6
O(2)–H(21)···O(3)	$1-x, -y, 1-z$	2.899(8)	156.0
O(2)–H(22)···O(3)	$1+x, y, z$	2.799(9)	175.7
O(3)–H(31)···N(43)	$x, 1/2-y, -1/2+z$	2.937(9)	140.3
O(3)–H(32)···N(13)		2.970(9)	151.9

[a] D = donor, A = acceptor.

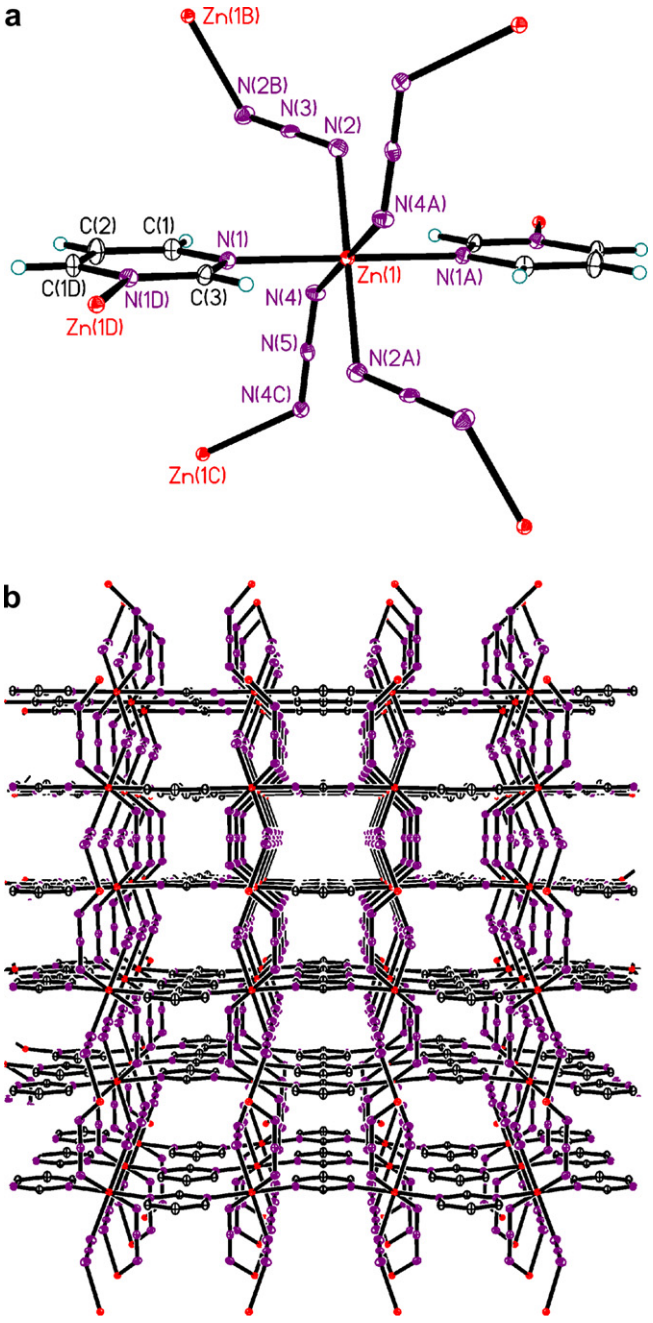


Fig. 3. (a) Perspective view with atom labeling scheme of **3**. Symmetry codes according Table 6. (b) Packing plot of **3** along the *a*-axis of the unit cell.

3.1.3. Crystal structure of $[Zn(N_3)_2(pym)]_n$ (3)

The principle structural features of complex **3** are shown in Fig. 3a, along with a labeling scheme, and selected bond lengths and bond angles are collected in Table 6. The structure features six coordinate Zn(II) atoms, EE bridging azido ligands and *N*,*N*′-bidentate bridging pym ligand forming a 3D network. In the asymmetric unit, each Zn(II) center is surrounded by four EE azide bridges [Zn(1)–N(2) = 2.151(3) Å, Zn(1)–N(4) = 2.148(3) Å], and two nitrogen atoms from bidentate *N*,*N*′-pyrimidine bridging ligands [Zn(1)–N(1) = 2.188(3) Å] to adopt ZnN_6 chromophore. The 3D system can be seen as zinc-pym chains placed in parallel planes, zinc atoms lie on inversion centers, pym ligands lie across mirror planes and azido ligands lie about 2-fold axes. The four EE azido bridges link each zinc center to two similar chains placed in the upper plane and two similar chains placed in the lower plane. The Zn–N–N bond angles lie around 122.5°. The azido ligands are symmetric [N(2)–N(3) = 1.176(2), N(3)–N(2B) = 1.176(2) Å and N(4)–N(5) = 1.179(2), N(5)–N(4C) = 1.179(2) Å] and linear [N–N–N angles = 178.1(4)° and 179.2(5)°] (Fig. 3b).

3.2. IR and luminescence spectra

The IR spectra of the title complexes in the solid state exhibit the following very strong band associated with the $\nu_{as}(N_3)$ vibration mode: 2012, 2098 cm^{-1}; 2121, 2091 cm^{-1}, and 2078 cm^{-1}, for complexes **1**, **2**, and **3**, respectively. The positions of these bands for **1** and **2** with EO azide bridges only are higher than expected [around 2090, 2070 cm^{-1}, and 2100, 2065 cm^{-1} for **1** and **2**, respectively] if the relationship $\nu_{as}(N_3)$ versus Δd [Δd the difference between the two N–N distances in an azide group] reported earlier [21,22] is valid. The existence of hydrogen bonded lattice water in complex **2** is confirmed by the appearance of broad bands in the range of 3600–2500 cm^{-1}.

Table 6
Selected bond lengths (Å) and angles (°) for **3**

Zn(1)–N(4A)	2.148(2)	Zn(1)–N(4)	2.148(2)
Zn(1)–N(2)	2.151(3)	Zn(1)–N(2A)	2.151(3)
Zn(1)–N(1A)	2.188(3)	Zn(1)–N(1)	2.188(3)
N(2)–N(3)	1.176(2)	N(3)–N(2B)	1.176(2)
N(4)–N(5)	1.179(2)	N(5)–N(4C)	1.179(2)
Zn(1)···Zn(1D)	6.042(2)	Zn(1)···Zn(1B)	5.752(2)
Zn(1)···Zn(1C)	5.588(2)		
N(4A)–Zn(1)–N(4)	180.0	N(4A)–Zn(1)–N(2)	92.16(10)
N(4)–Zn(1)–N(2)	87.84(10)	N(4A)–Zn(1)–N(2A)	87.84(10)
N(4)–Zn(1)–N(2A)	92.16(10)	N(2)–Zn(1)–N(2A)	180.0
N(4A)–Zn(1)–N(1A)	89.79(10)	N(4)–Zn(1)–N(1A)	90.21(10)
N(2)–Zn(1)–N(1A)	87.54(10)	N(2A)–Zn(1)–N(1A)	92.46(10)
N(4A)–Zn(1)–N(1)	90.21(10)	N(4)–Zn(1)–N(1)	89.79(10)
N(2)–Zn(1)–N(1)	92.46(10)	N(2A)–Zn(1)–N(1)	87.54(10)
N(1A)–Zn(1)–N(1)	180.0	N(3)–N(2)–Zn(1)	122.5(2)
N(2)–N(3)–N(2B)	179.2(5)	N(5)–N(4)–Zn(1)	123.6(2)
N(4)–N(5)–N(4C)	178.1(4)		

Symmetry codes: (A) $-x+1/2, -y+1/2, -z+3/2$. (B) $-x, y, -z+2$. (C) $-x, y, -z+1$. (D) $x, -y, z$.

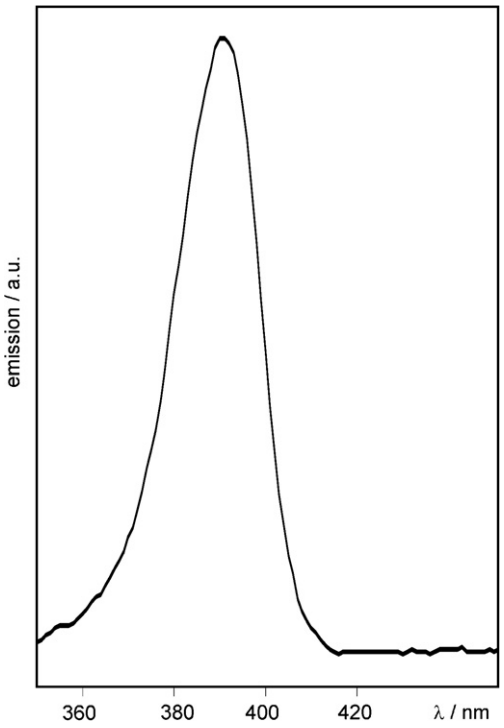


Fig. 4. Luminescence spectrum of **2**.

The photoluminescence properties of the solid zinc(II) complexes have been studied at room temperature. Complexes **1** and **3** do not flouresce, whereas complex **2** exhibits photoluminescence. 3-Hydroxypyridine shows photoluminescence at room temperature with an emission maximum at ca. 390 nm upon excitation at 300 nm. The zinc complex derived from 3-OHpy, **2** exhibits also a strong emission at 390 nm (FWHM: 22 nm) upon excitation at 300 nm (Fig. 4). As Zn(II), Cd(II) and Hg(II) are not easily oxidize or reduce due to their electronic d^{10} configuration, no emission originated from metal centers excited states are expected in case of such cations. Thus the flourescence observed in case of complex **2** is assigned to the intra-ligand flourescence [23,24]. The complexation of the ligands may also increase the rigidity and reduces the loss of energy by thermal vibrational decay. However, 3-OHpy from which complex **2** is derived, in the solid state exist in the keto and enol tautomers, and its flourescence is due to both tautomeric forms. In complex **2**, the 3-OHpy exists only in the keto form, in which the pair of electron remain as in the free ligand. This may explain why both 3-OHpy and its Zn(II) azide complex fluoresce almost at the same wavelength maximum, except that the intensity of the flouresence of the complex is more than twice the intensity of the free 3-OHpy ligand.

4. Discussion

Three zinc(II) azido complexes of three different ligands have been synthesized. In fact the ligand tetrazolo[1,5-*a*]pyridine (py-tetrazole) was prepared through the interac-

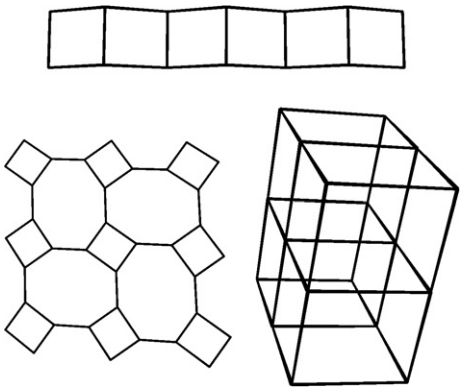


Fig. 5. Simplified representation of the structural motifs observed in complexes **1** (ladder, 1D), **2** (rings, 2D) and **3** (cubes, 3D).

tion of 2-chloropyridine with azide N_3^- ion under hydrothermal conditions, as given in Scheme 1; the py-tetrazole then interacts with zinc(II) azide affording complex **1**. In the case of complex **2**, we started with 3-hydroxypyridine, under reaction condition this ligand seems to prefer to be in the tautomeric keto-form, and we obtained a complex containing the pyridone which behaves as an *O*,*O*-bidentate bridging ligand. As we have seen the structure of complex **1** consists of a ladder-like arrangement in which four zinc centers interconnect through EO bridging azide forming tetranuclear rings and the uncoordinated py-tetrazole molecules are located in the channels between the parallel ladders. This structure is unprecedented in metal azido complexes. The structure of complex **2**, on the other hand, consists of tetranuclear zinc(II) rings fused with octanuclear zinc(II) rings forming 2D sheets, which is carrying into 3D network through the hydrogen bonding interaction. This structure too is unprecedented in known metal azido complexes (Fig. 5). In both complexes **1** and **2** with EO azide bridges only, the Zn–Zn distances within the Zn_2N_2 cyclic units fall well within the range of 3.03–3.31 Å found for other zinc(II) azido complexes containing such units [25]. All EO bridging azides in both complexes are asymmetric [the two N–N lengths within the azide group are different] and linear as reported earlier [26]. Complex **3** contains only EE bridging azido ligands which are symmetrical and linear as usual [26], and its structure resembles that of manganese(II) azide with pyrimidine [27]. In terms of network analysis [28] the topology of **2** may be described as a distorted "4.8^2" 2D net [the lengths of the edges within the tetranuclear rings are 3.210 and 3.632 Å, respectively, and additionally 3.280 Å in the octanuclear rings (Fig. 5, bottom left)]; the topology of **3** as distorted "α-Po" 3D net [the lengths of the edges of the cubes are 5.588, 5.752 and 6.042 Å, respectively (Fig. 5, bottom right)].

5. Conclusions

We isolated three zinc(II) azide complexes with some pyridines and pyrimidine by hydrothermal technique. Although we started with 2-chloropyridine which interacts with the azide ion forming py-tetrazole ligand and the isolated complex found to be $\{[Zn(N_3)_4(\text{py-tetrazole})_2](\text{py-tetrazole})\}_n$ (**1**) which links the zinc ion not through the pyridine nitrogen atom but via a nitrogen atom from the tetrazole part. The ladder-like structure of this complex contains tetranuclear zinc(II) rings. This structure is unprecedented. In complex **2**, the 3-Ohpy, starting reactant found to behave in the tautomeric keto-form and ligated zinc atoms as *O*,*O*-bidentate bridging ligand, in addition to the existence of tetranuclear zinc(II) and octanuclear zinc(II) rings fused together to generate 2D sheets which carrying into 3D supramolecular network with the help of hydrogen bonding. This complex exhibits photoluminescence at room temperature, and is unprecedented too in the metal azide complexes. Complex **3** consists of three-dimensional network. These results prompted us to explore the synthesis of zinc and other metal complexes with 2-, and 4-hydroxypyridines as well as other 2-X-pyridines in presence of azide ion and to explore the photoluminescence of the isolated complexes. Such reactions are under current investigation.

Supplementary data

CCDC 660643, 660644 and 660645 contain the supplementary crystallographic data for compounds **1**, **2** and **3**. These data can be obtained free of charge via http://www.ccdc.cam.ac.uk/const/retrieving.html or from the Cambridge Crystallographic Data Centre, 12 Union Road, Cambridge CB2 1EZ, UK; fax: (+44) 1223-336-033; or e-mail: deposit@ccdc.cam.ac.uk.

Acknowledgements

F.A.M. thanks Profs. F. Belaj and C. Kratky (Univ. Graz) and Dr. J. Baumgatrner (TU Graz) for assistance.

References

[1] (a) S.-L. Zheng, M.-L. Tong, H.-L. Zhu, Y. Fang, X.-M. Chen, J. Chem. Soc., Dalton Trans. (2001) 2049;
(b) S. Banerjee, M.G.B. Drew, A. Ghosh, Polyhedron 22 (2003) 2933;
(c) J.M. Lehn, Supramolecular Chemistry – Concepts and Perspectives, VCH, Weinheim, 1995 (Chapter 9).
[2] (a) R. Robson, B.F. Abrahams, S.R. Batten, R.W. Gable, B.F. Hoskins, J. Liu, Supramolecular Architecture, ACS, Washington, DC, 1992, p. 256.;
(b) G.R. Desiraju, Angew. Chem., Int. Ed. Engl. 34 (1995) 2311.
[3] (a) P. Lightfoot, A. Snedden, J. Chem. Soc., Dalton Trans. (1999) 3549;
(b) M.-L. Tong, X.-M. Chen, X.-L. Yu, T.C.W. Mak, J. Chem. Soc., Dalton Trans. (1998) 5.
[4] (a) L.R. MacGillivray, R.H. Groeneman, J.L. Atwood, J. Am. Chem. Soc. 120 (1998) 2676;
(b) X.-M. Chen, M.-L. Tong, Y.-J. Luo, Z.-N. Chen, Aust. J. Chem. 49 (1996) 853;
(c) M.-L. Tong, X.-M. Chen, S.W. Ng, Inorg. Chem. Commun. 3 (2000) 436.

[5] (a) M.-L. Tong, X.-M. Chen, B.-H. Ye, L.-N. Ji, Angew. Chem., Int. Ed. Engl. 38 (1999) 2237;
(b) M.-L. Tong, H.-K. Lee, X.-M. Chen, R.-B. Huang, T.C.W. Mak, J. Chem. Soc., Dalton Trans. (1999) 3657;
(c) B.D. Wagner, G.J. McManus, B. Moulton, Mu. J. Zaworotko, Chem. Commun. (2002) 2176.
[6] (a) N. Mondal, M.K. Saha, S. Mitra, V. Gramlich, J. Chem. Soc., Dalton Trans. (2000) 3218;
(b) J. Ribas, A. Escuer, M. Monfort, R. Vicente, R. Cortes, L. Lezama, T. Rojo, Coord. Chem. Rev. 193–195 (1999) 1027;
(c) G.S. Papaefstathiou, S.P. Perlepes, A. Escuer, R. Vicente, M. Font-Bardia, X. Solans, Angew. Chem., Int. Ed. Engl. 40 (2001) 884.
[7] (a) S.A. Barnett, A.J. Blake, N.R. Champness, C. Wilson, Chem. Commun. (2002) 1640;
(b) A. Escuer, J. Cano, M.A.S. Goher, Y. Journaux, F. Lloret, F.A. Mautner, R. Vicente, Inorg. Chem. 39 (2000) 4688.
[8] B. Zurowska, J. Mrozinski, M. Julve, F. Lloret, A. Maslejova, W. Sawka-Dobrowolska, Inorg. Chem. 41 (2002) 1771.
[9] (a) F. Wiesbrock, H. Schmidbaur, J. Chem. Soc., Dalton Trans. (2002) 3201;
(b) O.R. Evans, W. Lin, Inorg. Chem. 39 (2000) 1771.
[10] (a) M.A.S. Goher, T.C.W. Mak, Inorg. Chim. Acta 85 (1984) 117;
(b) M.A.S. Goher, T.C.W. Mak, Inorg. Chim. Acta 89 (1984) 119;
(c) M.A.S. Goher, F.A. Mautner, Croat. Chim. Acta 63 (1990) 559;
(d) A. Escuer, R. Vicente, M.A.S. Goher, F.A. Mautner, Inorg. Chem. 35 (1996) 6386.
[11] (a) M.A.S. Goher, N.A. Al-Salem, F.A. Mautner, J. Coord. Chem. 44 (1998) 119;
(b) M.A.S. Goher, A. Escuer, F.A. Mautner, N.A. Al-Salem, Polyhedron 20 (2001) 2971;
(c) H.-Y. Shen, D.-Z. Liau, Z.-H. Jiang, S.-P. Yan, G.-L. Wang, X.-K. Yao, H.-G. Wang, Chem. Lett. (1998) 469.
[12] (a) E.-Q. Gao, S.-Q. Bai, C.-F. Wang, Y.-F. Yue, C.-H. Yan, Inorg. Chem. 42 (2003) 8456;
(b) E.-Q. Gao, Y.-F. Yue, S.-Q. Bai, Z. He, C.-H. Yan, Chem. Mater. 16 (2004) 1590.
[13] e.g. M.A.S. Goher, R.J. Wang, T.C.W. Mak, J. Mol. Struct. 243 (1991) 179.
[14] (a) Z. Shen, J.-L. Zuo, Z. Yu, Y. Zhang, J.-F. Bai, C.-M. Che, H.-K. Fun, J.J. Vittal, X.-Z. You, Dalton Trans. (1999) 3393;
(b) A. Escuer, R. Vicente, M.A.S. Goher, F.A. Mautner, Dalton Trans. (1997) 4431;
(c) S.S. Tandon, L.K. Thompson, D.O. Miller, Chem. Commun. (1995) 1907.
[15] (a) F.A. Cotton, G. Wilkinson, C.A. Morillo, M. Bochmann, Advanced Inorganic Chemistry, 6th ed., Wiley, New York, 1999, p. 589.;
(b) K.-Y. Ho, W.-Y. Yu, K.-K. Cheung, C.-M. Che, Chem. Commun. (1998) 2101.
[16] (a) D. Bose, S.H. Rahaman, G. Mostafa, R.D.B. Walsh, M.J. Zaworotko, B.K. Ghosh, Polyhedron 23 (2004) 545;
(b) H.C. Pan, F.P. Liang, C.J. Mao, J.J. Zhu, J. Phys. Chem. B 111 (2007) 5700.
[17] (a) B. Xu, B. Yan, Spectrosc. Lett. 39 (2006) 237;
(b) L.-Y. Zhang, G.-F. Liu, S.-L. Zheng, B.-H. Ye, X.-M. Zhang, X.-M. Chen, Eur. J. Inorg. Chem. (2003) 2965.
[18] M.A.S. Goher, F.A. Mautner, K. Gatterer, M.A.M. Abu-Youssef, A.M.A. Badr, B. Sodin, C. Gspan, J. Mol. Struct., in press, doi:10.1016/j.molstruc.2007.06.020.
[19] (a) B. Bitschnau, A. Egger, A. Escuer, F.A. Mautner, B. Sodin, R. Vicente, Inorg. Chem. 45 (2006) 868;
(b) H.D. Fair, R.F. Walker (Eds.), Energetic Materials, vol. 1, Plenum Press, New York, 1977 (Chapter 1).
[20] (a) N. Walker, D. Stuart, Acta Crystallogr., Sect. A 39 (1983) 158;
(b) R.H. Blessing, Acta Crystallogr., Sect. A 51 (1995) 33, SADABS, Bruker AXS, 1998.;
(c) SHELXTL 5.03 (PC-Version) Program Library for the Solution and Molecular Graphics, Siemens Analytical Instruments Division, Madison, WI, 1995.
[21] I. Agrell, Acta Chem. Scand. 25 (1971) 2965.
[22] M.A.S. Goher, Acta Chim. Hung. 127 (1990) 213.
[23] H.F. Zhu, L. Li, T. Okamura, W. Zhao, W.Y. Skn, N. Ueyama, Bull. Chem. Soc. Jpn. 76 (2003) 761.
[24] X.H. Be, H. Liu, M. Du, K.M.C. Wong, V.W.W.W. Yam, Inorg. Chim. Acta 333 (2002) 32.
[25] e.g. F.A. Mautner, H. Krischner, Monatsh. Chem. 123 (1992) 325.
[26] (a) e.g. Z. Dori, R.F. Ziolo, Chem. Rev. 73 (1973) 248;
(b) M.A.S. Goher, F.A. Mautner, Polyhedron 18 (1999) 1805;
(c) A. Escuer, M.A.S. Goher, F.A. Mautner, R. Vicente, Inorg. Chem. 39 (2000) 2107.
[27] A. Escuer, R. Vicente, F.A. Mautner, M.A.S. Goher, M.A.M. Abu-Youssef, Chem. Commun. (2002) 64.
[28] (a) L. Öhrström, K. Larsson, Molecule-Based Materials: The Structural Network Approach, Elsevier, Amsterdam, 2005;
(b) A.F. Wells, Three-dimensional Nets and Polyhedra, Wiley, New York, 1977;
(c) M. O'Keeffe, M. Eddaoudi, H.L. Li, T. Reineke, O.M. Yaghi, J. Solid State Chem. 152 (2000) 3;
(d) O.V. Dolomanov, A.J. Blake, N.R. Champness, M. Schroder, J. Appl. Crystallogr. 36 (2003) 1283.

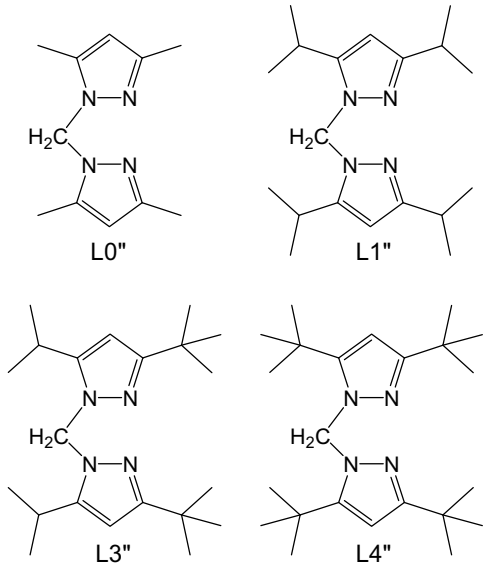


Fig. 1. Structures of N2 bidentate ligands discussed in this work: bis(3,5-dimethyl-1-pyrazolyl)methane (L0″), bis(3,5-diisopropyl-1-pyrazolyl)methane (L1″), bis(3-tertiary-butyl-5-isopropyl-1-pyrazolyl)methane (L3″), bis(3,5-ditertiary-butyl-1-pyrazolyl)methane (L4″).

and many copper(II) complexes with these ligands have been reported. For example, for $[Cu(bipy)X_2]$ ($X = NO_3$ [16], ONO [17], and Cl [18]), $[Cu(en)X'_2]$ ($X' = Cl$ [19] and $N(NO_2)CH_3$ [20]), and $[Cu(phen)(X'')_2]$ ($X'' = NO_3$ [21] and ONO [22]), and $[Cu(napy)(NO_3)_2]$ [23]. Some of the structures of these complexes were clarified by X-ray crystallography. In particular, nitrate and nitrite ions can coordinate to the central copper atom, in a unidentate or bidentate coordination mode. Differences in coordination modes of both nitrate and nitrite ions have been reported by Brill et al. for $[Cu(en)\{N(NO_2)CH_3\}_2]$ [20].

In this work, the copper(II) nitrato complexes $[Cu(L0'')_2(NO_3)]NO_3$ (**1NO$_3$**), $[Cu(L0'')(NO_3)_2]$ (**2**), $[Cu(L1'')(NO_3)_2]$ (**3**), $[Cu(L3'')(NO_3)_2]$ (**4**), and $[Cu(L4'')(NO_3)_2]$ (**5**), the chloro complexes $[Cu(L0'')_2Cl]_2(CuCl_4)$ (**6CuCl$_4$**), $[Cu(L0'')_2Cl]_2(Cu_2Cl_6)$ (**6Cu$_2$Cl$_6$**), $[Cu(L1'')Cl_2]$ (**7**), and $[Cu(L3'')Cl_2]$ (**8**), the nitrito complexes $[Cu(L0'')(ONO)_2]$ (**9**) and $[Cu(L1'')(ONO)_2]$ (**10**), and the complexes with perchlorate ions $[Cu(L0'')_2(CH_3OH)](ClO_4)_2$ (**11ClO$_4$**) and $[Cu(L1'')_2(H_2O)](ClO_4)_2$ (**12ClO$_4$**) were systematically synthesized using four different bpzm ligands that show a difference in bulkiness at the pyrazolyl rings. The complexes $[Cu(L1'')(NO_3)_2]$ (**3**), $[Cu(L1'')Cl_2]$ (**7**), and $[Cu(L1'')(ONO)_2]$ (**10**) with L1″ have been reported before [13,14]. All the complexes were characterized by X-ray crystallography and by IR, far-IR, UV–Vis absorption, and ESR spectroscopy. The influences of the second coordination sphere effects of the ligands on the complexes are examined. The structures and properties of the obtained complexes are also compared with those of the copper(II) complexes having tpzm as an N3 tridentate ligand.

2. Experimental

2.1. Materials

Preparation and handling of all of the complexes was performed under an argon atmosphere using standard Schlenk tube techniques. Dichloromethane were purified by refluxing and distilling under an argon atmosphere over phosphorous pentoxide. Diethyl ether, toluene, and heptane were purified by refluxing and distilling under an argon atmosphere over sodium benzophenone ketyl [24]. Chloroform, methanol, acetone, 2-propanol, and octane were spectroscopic grade and were used after bubbling with an argon gas. NMR solvents were obtained from Cambridge Isotope Laboratories, Inc. Silica gel for ligand purification was obtained from Merck KGaA. Other reagents are commercially available. The syntheses of ligands (L0″ [25], L1″ [13], and L4″ [26]) and complex $(Ph_4P)_2[Cu_2Cl_6]$ [27] and copper(II) complexes using L1″ ($[Cu(L1'')(NO_3)_2]$ (**3**), $[Cu(L1'')Cl_2]$ (**7**), and $[Cu(L1'')(ONO)_2]$ (**10**) [13,14]) were prepared by publish methods.

2.2. Measurements

IR and far-IR spectra were recorded on KBr pellets in the 4000–400 cm^{-1} region and Nujol mull in the 650–150 cm^{-1} region, respectively, using a JASCO FT/IR-550 spectrophotometer. ^1H NMR (600 MHz) and ^{13}C NMR (150 MHz) spectra were obtained on a Bruker AVANCE-600 NMR spectrometer in chloroform at room temperature. UV–Vis absorption spectra in dichloromethane at room temperature in the 240–1840 nm range were recorded with a JASCO V-570 spectrophotometer unless stated otherwise. ESR spectra as frozen solutions (dichloromethane/1,2-dichloroethane (1/1) or methanol/ethanol (9/1)) were recorded on a Bruker EMX-T ESR spectrometer at 140 K in quartz tubes (diameter 5 nm) with liquid nitrogen temperature controller BVT 3000. The elemental analyses (C, H, N) were performed by the Department of Chemistry at the University of Tsukuba.

2.3. Preparation of ligands

2.3.1. $H_2C(3\text{-}tBu\text{-}5\text{-}iPrpz)_2$ L3″

Dichloromethane (130 cm^3) was added to a mixture of 3-tertiary-butyl-5-isopropylpyrazole [28] (6.16 g, 37.1 mmol), potassium carbonate (7.76 g, 56.2 mmol), and tetrabutylammonium hydrogensulfate (2.00 g, 5.89 mmol). This solution was bubbled with an argon gas for 15 min. This solution was then heated and gently refluxed for 2 weeks at ~110 °C (inner temperature of autoclave). During the reaction time, the color of the solution became dark brown. The mixture was allowed to cool to room temperature, and then the insoluble material was filtered off and washed with acetone. The filtrate was evaporated under reduced pressure. The remaining dark brown solid was dissolved in toluene (50 cm^3). The solution was

refluxed for 1 day after addition of a catalytic amount of predried of *p*-toluenesulfonic acid monohydrate (0.11 g, 0.58 mmol). The mixture was allowed to cool to room temperature, and then the solvent was removed under reduced pressure. The obtained solid was dissolved in a 2:1 mixture of dichloromethane/acetone. The solution was chromatographed on a silica gel column using the 2:1 dichloromethane/acetone mixed solvent as eluent. After collection of the corresponding fractions, the solvent was removed under reduced pressure to yield a pale-yellow solid. Crystallization from heptane at −30 °C gave colorless crystals. Yield: 73% (4.70 g, 13.6 mmol). *Anal.* Calc. for $C_{21}H_{36}N_4$: C, 73.21; H, 10.53; N, 16.26. Found: C, 73.30; H, 10.72; N, 16.24%. IR (cm^{-1}): 2962vs, 2866s, 1545s, 1469s, 1384w, 1359s, 1316s, 1234s, 1094m, 1066m, 970m, 801s, 785m, 638w, 415w. ^1H NMR (δ): 1.02 (d, $J_{HH} = 6.8$ Hz, 12H, $CH(CH_3)_2$), 1.25 (s, 18H, $C(CH_3)_3$), 3.40 (sept, $J_{HH} = 6.8$ Hz, 2H, $CH(CH_3)_2$), 5.85 (s, 2H, 4-*H*(pz)), 6.23 (s, 2H, H_2C). ^{13}C NMR (δ): 23.26 ($CH(CH_3)_2$), 24.90 ($CH(CH_3)_2$), 30.50 ($C(CH_3)_3$), 31.99 ($C(CH_3)_3$), 62.29 (H_2C), 99.34 (4-*C*(pz)), 151.3 (3-*C*(pz)), 161.0 (5-*C*(pz)).

2.3.2. $H_2C(3,5\text{-}tBu_2pz)_2$ L4″

An alternative synthetic procedure of L4″ was previously reported [26]. Our synthetic procedure was carried out in the same manner as that of L3″, using 3,5-ditertiary-butylpyrazole [29] (8.00 g, 44.4 mmol), potassium carbonate (8.00 g, 58.0 mmol), and tetrabutylammonium hydrogensulfate (2.30 g, 6.77 mmol) in dichloromethane (120 cm^3). This solution was then heated and gently refluxed for 2 weeks at ~110 °C (inner temperature of autoclave). The chloroform solution was chromatographed on a silica gel column. The desired fractions were eluted using chloroform. Crystallization from heptane at −30 °C gave colorless crystals. Yield: 53% (4.36 g, 11.7 mmol). *Anal.* Calc. for $C_{23}H_{40}N_4$: C, 74.14; H, 10.82; N, 15.04. Found: C, 74.17; H, 10.86; N, 15.07%. IR (cm^{-1}): 2962vs, 1542s, 1461s, 1397m, 1362s, 1312s, 1261s, 1229s, 1093m, 795vs, 774m, 685w, 404m. ^1H NMR (δ): 1.20 (s, 18H, $C(CH_3)_3$), 1.24 (s, 18H, $C(CH_3)_3$), 5.90 (s, 2H, 4-*H*(pz)), 6.51 (s, 2H, H_2C). ^{13}C NMR (δ): 28.66 ($CH(CH_3)_3$), 29.37 ($CH(CH_3)_3$), 30.86 ($C(CH_3)_3$), 30.89 ($C(CH_3)_3$), 65.83 (H_2C), 101.0 (pz-4*C*), 151.9 (pz-3*C*), 157.9 (pz-5*C*).

2.4. Preparations of complexes

2.4.1. $[Cu\{H_2C(3,5\text{-}Me_2pz)_2\}_2(NO_3)]NO_3$, $[Cu(L0'')_2(NO_3)]NO_3$ (**1NO$_3$**)

To a solution of L0″ (0.30 g, 1.47 mmol) in dichloromethane (20 cm^3) was added a solution of $Cu(NO_3)_2 \cdot 3H_2O$ (0.20 g, 0.81 mmol) in acetone (20 cm^3). After stirring for 1 h, the solvent was removed under reduced pressure, and a light blue solid was obtained. Slow crystallization from methanol/acetone (4/1) solution at room temperature gave light blue crystals. Yield: 19% (104 mg, 0.174 mmol). *Anal.* Calc. for $C_{22}H_{32}CuN_{10}O_6$: C, 44.33; H, 5.41; N, 23.50. Found: C, 44.11; H, 5.46; N, 23.08%. IR (cm^{-1}): 3428w, 3131w, 3018w, 1557vs, 1480s, 1383s, 1285s, 1040m, 1017m, 833m, 808m, 681m. far-IR (cm^{-1}): 646w, 640w, 628w, 495m, 479m, 440w, 418w, 365m, 351m, 341m, 301vs, 269vs, 254s, 208w, 192m. UV–Vis λ/nm (ε/mol^{-1} dm^3 cm^{-1}) (CH_3OH): 696 (70). ESR (CH_3OH/CH_3CH_2OH (9/1) 140 K): $g_{\|}$, 2.30 ($A_{\|}$, 153 G); $g_{\perp}$, 2.07.

2.4.2. $[Cu\{H_2C(3,5\text{-}Me_2pz)_2\}(NO_3)_2]$, $[Cu(L0'')(NO_3)_2]$ (**2**)

The synthetic procedure was the same as **1NO$_3$**, except the ratio of the raw substrates and crystallization solvents. To a solution of L0″ (0.20 g, 0.98 mmol) in dichloromethane (20 cm^3) was added a solution of $Cu(NO_3)_2 \cdot 3H_2O$ (0.237 g, 0.98 mmol) in acetone (20 cm^3). After stirring for 2 h, the solvent was removed under reduced pressure, and a light blue solid was obtained. After extracting with dichloromethane, crystallization from dichloromethane/heptane (1/1) at −30 °C gave light blue crystals. Yield: 11% (42.5 mg, 0.108 mmol). *Anal.* Calc. for $C_{11}H_{16}CuN_6O_6 \cdot 0.25(CH_2Cl_2)$: C, 32.71; H, 4.03; N, 20.35. Found: C, 32.88; H, 4.22; N, 20.36%. IR (cm^{-1}): 3447m, 3045w, 1556m, 1517m, 1469m, 1383vs, 1273vs, 1052w, 1024w, 1006s, 806s, 795s, 678m. far-IR (cm^{-1}): 642w, 629m, 496m, 479w, 416w, 363m, 332vs, 301vs, 277vs, 245m, 175m. UV–Vis λ/nm (ε/mol^{-1} dm^3 cm^{-1}): 739 (100), 295 (2820). ESR (CH_2Cl_2/CH_2ClCH_2Cl (1/1) 140 K): $g_{\|}$, 2.29 ($A_{\|}$, 158 G); $g_{\perp}$, 2.06.

2.4.3. $[Cu\{H_2C(3\text{-}tBu\text{-}5\text{-}iPrpz)_2\}(NO_3)_2]$, $[Cu(L3'')(NO_3)_2]$ (**4**)

To a solution of L3″ (0.20 g, 0.58 mmol) in dichloromethane (15 cm^3) was added a solution of $Cu(NO_3)_2 \cdot 3H_2O$ (0.154 g, 0.64 mmol) in acetone (20 cm^3). After stirring for 1 h, the solvent was removed under reduced pressure, and a purple solid was obtained. Slow crystallization from dichloromethane/heptane (1/1) gave purple crystals. Yield: 63% (193 mg, 0.36 mmol). *Anal.* Calc. for $C_{21}H_{36}CuN_6O_6$: C, 47.40; H, 6.82; N, 15.79. Found: C, 47.24; H, 6.73; N, 15.48%. IR (cm^{-1}): 3474m, 3028m, 2969s, 2935m, 2869m, 1550s, 1502vs, 1483s, 1439s, 1384vs, 1364s, 1306s, 1267s, 1232s, 1069m, 1020s, 1004s, 990m, 807s, 768m far-IR (cm^{-1}): 633m, 543w, 505w, 475w, 433w, 409w, 392w, 373w, 348vs, 324m, 308vs, 301m, 276w, 244w, 200w, 171m. UV–Vis λ/nm (ε/mol^{-1} dm^3 cm^{-1}): 634 (90), 307 (2790). ESR (CH_2Cl_2/CH_2ClCH_2Cl (1/1) 140 K): $g_{\|}$, 2.28 ($A_{\|}$, 169 G); $g_{\perp}$, 2.06.

2.4.4. $[Cu\{H_2C(3,5\text{-}tBu_2pz)_2\}(NO_3)_2]$, $[Cu(L4'')(NO_3)_2]$ (**5**)

To a solution of L4″ (0.40 g, 1.07 mmol) in dichloromethane (20 cm^3) was added a solution of $Cu(NO_3)_2 \cdot 3H_2O$ (0.285 g, 1.18 mmol) in acetone (20 cm^3). After stirring for 1 h, the solvent was removed under reduced pressure, and a deep blue solid was obtained. Crystallization from dichloromethane/heptane (1/1) at −30 °C gave

deep blue crystals. Yield: 64% (389 mg, 0.69 mmol). *Anal.* Calc. for $C_{23}H_{40}CuN_6O_6 \cdot 0.5H_2O$: C, 48.54; H, 7.26; N, 14.77. Found: C, 48.23; H, 7.17; N, 14.68%. IR (cm^{-1}): 3463m, 2965vs, 1542m, 1500vs, 1383vs, 1283vs, 1225w, 1018m, 1001m, 805s, 755w, 419m. far-IR (cm^{-1}): 638w, 614w, 566w, 472w, 395w, 381w, 373w, 339s, 322m, 312s, 300m, 277w, 180w, 158w. UV–Vis λ/nm (ε/mol^{-1} dm^3 cm^{-1}): 589 (120), 301 (2290). ESR (CH_2Cl_2/CH_2ClCH_2Cl (1/1) 140 K): $g_{\|}$, 2.28 ($A_{\|}$, 172 G); $g_{\perp}$, 2.06.

2.4.5. *[Cu{H$_2$C(3,5-Me$_2$ pz)$_2$}$_2$Cl]$_2$(CuCl$_4$), [Cu(L0″)$_2$Cl]$_2$(CuCl$_4$) (**6CuCl$_4$**)*

To a solution of L0″ (0.30 g, 1.47 mmol) in dichloromethane (15 cm^3) was added a solution of $CuCl_2 \cdot 2H_2O$ (0.14 g, 0.81 mmol) in acetone (20 cm^3). After stirring for 1 h, the solvent was removed under reduced pressure, and a green solid was obtained. Crystallization from acetone/toluene (6/1) at −15 °C gave green crystals. Yield: 57% (260 mg, 0.21 mmol). *Anal.* Calc. for $C_{44}H_{64}Cl_6Cu_3N_{16} \cdot 3H_2O \cdot (CH_3)_2CO$: C, 42.36; H, 5.74; N, 16.82. Found: C, 42.36; H, 5.58; N, 16.92%. IR (cm^{-1}): 3504m, 3129w, 3012m, 2962w, 2922w, 1708s, 1557s, 1465m, 1419m, 1368m, 1282vs, 1219m, 1056w, 1042m, 1001w, 834w, 814w, 786w, 678m. far-IR (cm^{-1}): 627w, 528w, 495w, 476w, 434w, 391w, 349m, 296vs, 263w, 251w, 244w, 223w, 186w, 176w. UV–Vis λ/nm (ε/Cu^{-1} mol^{-1} dm^3 cm^{-1}): 908 (130), 287 (3980). ESR (CH_2Cl_2/CH_2ClCH_2Cl (1/1) 140 K): $g_{\|}$, 2.27 ($A_{\|}$, 148 G); $g_{\perp}$, 2.09.

2.4.6. *[Cu{H$_2$C(3,5-Me$_2$ pz)$_2$}$_2$Cl]$_2$(Cu$_2$Cl$_6$), [Cu(L0″)$_2$Cl]$_2$(Cu$_2$Cl$_6$) (**6Cu$_2$Cl$_6$**)*

A synthetic procedure is the same as **6CuCl$_4$**, except the ratio of the raw substrates and crystallization solvents. To a solution of L0″ (0.40 g, 1.96 mmol) in dichloromethane (15 cm^3) was added a solution of $CuCl_2 \cdot 2H_2O$ (0.37 g, 2.15 mmol) in acetone (20 cm^3). After stirring for 1 h, the solvent was removed under reduced pressure, and a deep green solid was obtained. Crystallization from dichloromethane/octane (2/1) at −15 °C gave deep green crystals. Yield: 84% (565 mg, 0.41 mmol). *Anal.* Calc. for $C_{44}H_{76}Cl_8Cu_4N_{16} \cdot 2CH_2Cl_2$: C, 36.23; H, 4.50; N, 14.70. Found: C, 36.66; H, 4.77; N, 14.39%. IR (cm^{-1}): 3467m, 3126w, 3024w, 2923w, 1626w, 1557vs, 1465s, 1388m, 1284vs, 1153w, 1043s, 824s, 677m. far-IR (cm^{-1}): 644m, 627s, 591w, 497w, 475m, 419w, 398w, 333s, 302s, 276m, 267m, 251s, 225s, 186s. UV–Vis λ/nm (ε/Cu^{-1} mol^{-1} dm^3 cm^{-1}): 893 (130), 287 (3840). ESR (CH_2Cl_2/CH_2ClCH_2Cl (1/1) 140 K): $g_{\|}$, 2.32 ($A_{\|}$, 146 G); $g_{\perp}$, 2.11.

2.4.7. *[Cu{H$_2$C(3-tBu-5-iPrpz)$_2$}Cl$_2$], [Cu(L3″)Cl$_2$] (**8**)*

To a solution of L3″ (0.40 g, 1.16 mmol) in dichloromethane (15 cm^3) was added a solution of $CuCl_2 \cdot 2H_2O$ (0.22 g, 1.29 mmol) in acetone (20 cm^3). After stirring for 1 h, the solvent was removed under reduced pressure, and a dark brown solid was obtained. Crystallization from chloroform/heptane (3/2) at −50 °C gave orange crystals. Yield: 47% (263 mg, 0.55 mmol). *Anal.* Calc. for $C_{21}H_{36}Cl_2CuN_4$: C, 52.66; H, 7.58; N, 11.70. Found: C, 52.22; H, 7.47; N, 11.52%. IR (cm^{-1}): 3445m, 2963s, 2867w, 1616w, 1545m, 1459m, 1360m, 1316m, 1234s, 1094, 801s, 409s. far-IR (cm^{-1}): 641m, 622w, 307m, 300vs, 244m, 183s. UV–Vis λ/nm (ε/mol^{-1} dm^3 cm^{-1}): 848 (150), 387 (940), 287 (3330). ESR (CH_2Cl_2/CH_2ClCH_2Cl (1/1) 140 K): $g_{\|}$, 2.27 ($A_{\|}$, 140 G); $g_{\perp}$, 2.08.

2.4.8. *[Cu{H$_2$C(3,5-Me$_2$pz)$_2$}(ONO)$_2$], [Cu(L0″)(ONO)$_2$] (**9**)*

To a solution of [Cu(L0″)$_2$Cl]$_2$(Cu$_2$Cl$_6$) **6Cu$_2$Cl$_6$** (0.56 g, 0.41 mmol) in dichloromethane (25 cm^3) was added a solution of $NaNO_2$ (0.23 g, 3.33 mmol) in methanol (15 cm^3). After stirring for 1 h, the solvent was removed under reduced pressure, and a deep green solid was obtained. Crystallization from dichloromethane/diethyl ether (2/1) at −15 °C gave green crystals. Yield: 34% (217 mg, 0.60 mmol). *Anal.* Calc. for $C_{11}H_{16}CuN_6O_4 \cdot 0.25(C_2H_5)_2O$: C, 38.09; H, 4.93; N, 22.21. Found: C, 38.77; H, 4.76; N, 22.30%. IR (cm^{-1}): 3460w, 2963m, 1556m, 1467w, 1371w, 1262s, 1199w, 1096w, 1024w, 798vs, 677w, 525w. far-IR (cm^{-1}): 635w, 615w, 604w, 590w, 494m, 478m, 374vs, 342m, 313m, 288w, 260w, 210w, 197w, 153m. UV–Vis λ/nm (ε/mol^{-1} dm^3 cm^{-1}): 693 (110), 281 (3230). ESR (CH_2Cl_2/CH_2ClCH_2Cl (1/1) 140 K): $g_{\|}$, 2.28 ($A_{\|}$, 163 G); $g_{\perp}$, 2.06.

2.4.9. *[Cu{H$_2$C(3,5-Me$_2$pz)$_2$}$_2$(CH$_3$OH)](ClO$_4$)$_2$, [Cu(L0″)$_2$(CH$_3$OH)](ClO$_4$)$_2$ (**11ClO$_4$**)*

To a solution of L0″ (0.20 g, 0.98 mmol) in methanol (20 cm^3) was added a solution of $Cu(ClO_4)_2 \cdot 6H_2O$ (0.20 g, 0.54 mmol) in methanol (10 cm^3). After stirring for 1 h, the solvent was concentrated under reduced pressure. Crystallization from methanol/2-propanol (1/1) at −30 °C gave emerald green crystals. Yield: 73% (239 mg, 0.36 mmol). *Anal.* Calc. for $C_{22}H_{31}Cl_2CuN_8O_8 \cdot H_2O$: C, 38.41; H, 4.83; N, 16.29. Found: C, 38.81; H, 4.75; N, 16.37%. IR (cm^{-1}): 3370m, 3147w, 3028w, 2964m, 1559s, 1467s, 1421w, 1390w, 1286s, 1262s, 1101vs, 1014s, 886w, 802s, 683m, 624s. far-IR (cm^{-1}): 620vs, 497w, 479m, 415w, 362m, 349s, 340m, 333m, 305s, 261s, 191s, 181m. UV–Vis λ/nm (ε/mol^{-1} dm^3 cm^{-1}): 728 (90), 370 (840), 268 (1680). ESR (CH_3OH/CH_3CH_2OH (9/1) 140 K): $g_{\|}$, 2.30 ($A_{\|}$, 146 G); $g_{\perp}$, 2.08.

2.4.10. *[Cu{H$_2$C(3,5-iPr$_2$pz)$_2$}$_2$(H$_2$O)](ClO$_4$)$_2$, [Cu(L1″)$_2$(H$_2$O)](ClO$_4$)$_2$ (**12ClO$_4$**)*

To a solution of L1″ (0.30 g, 0.95 mmol) in methanol (20 cm^3) was added a solution of $Cu(ClO_4)_2 \cdot 6H_2O$ (0.19 g, 0.52 mmol) in methanol (10 cm^3). After stirring for 1 h, the solvent was concentrated under reduced pressure. Crystallization from methanol/2-propanol (1/1) at −30 °C gave light green crystals. Yield: 72% (311 mg, 0.34 mmol). *Anal.* Calc. for $C_{38}H_{66}Cl_2CuN_8O_9 \cdot 1.5H_2O$:

Table 1
Crystallographic data of ligands L3″ and L4″ and complexes **1**, **2**, **4**, and **5**

Complex	L3″	L4″	**1**NO_3	**2** · CH_2Cl_2	**4**	**5**
CCDC number	654433	654434	654435	654436	654437	654438
Formula	$C_{21}H_{36}N_4$	$C_{23}H_{40}N_4$	$C_{22}H_{32}CuN_{10}O_6$	$C_{12}H_{18}CuN_6O_6Cl_2$	$C_{21}H_{36}CuN_6O_6$	$C_{23}H_{40}CuN_6O_6$
Formula weight	344.54	372.60	596.10	476.76	532.10	560.15
Crystal system	monoclinic	triclinic	orthorhombic	triclinic	monoclinic	monoclinic
Space group	$P2_1/c$ (#14)	$P\bar{1}$ (#2)	$Pca2_1$ (#29)	$P\bar{1}$ (#2)	$P2_1/n$ (#14)	$P2_1/n$ (#14)
a (Å)	9.4325(4)	9.5167(5)	16.0321(7)	8.22990(10)	13.0592(13)	13.0037(4)
b (Å)	9.7529(2)	11.7101(2)	8.3297(5)	8.7396(2)	10.5664(7)	11.7552(2)
c (Å)	23.5175(8)	11.91850(10)	20.3160(9)	14.5123(4)	18.8771(15)	18.8099(5)
α (°)	90	61.479(9)	90	83.191(7)	90	90
β (°)	98.0120(5)	82.159(13)	90	75.221(7)	99.4410(11)	104.5490(4)
γ (°)	90	87.438(13)	90	75.465(7)	90	90
V (Å^3)	2142.36(12)	1155.80(13)	2713.1(2)	975.32(4)	2569.5(4)	2783.10(12)
Z	4	2	4	2	4	4
D_{calc} (g cm^{-3})	1.068	1.071	1.459	1.623	1.375	1.337
μ(Mo Kα) (cm^{-1})	0.639	0.636	8.617	14.346	8.961	8.310
Temperature (°C)	−90	−80	−90	−90	−89	−80
Reflections collected	16706	9376	21200	8064	20081	21694
Unique reflections	4901	5139	5761	4387	5863	6322
R_{int}	0.025	0.022	0.035	0.019	0.025	0.049
Number of observations	3351 ($I > 3\sigma(I)$)	3982 ($I > 3\sigma(I)$)	3254 ($I > 3\sigma(I)$)	3830 ($I > 3\sigma(I)$)	4511 ($I > 3\sigma(I)$)	3125 ($I > 3\sigma(I)$)
Number of variables	262	284	384	262	343	365
Final R, Rw[a]	0.0750/0.1114	0.0532/0.0762	0.0343/0.0383	0.0397/0.0752	0.0469/0.0820	0.0480/0.0736
Goodness-of-fit	1.620	1.326	0.832	1.004	1.000	1.002
Maximum/minimum peak (e Å^{-3})	0.39/−0.34	0.26/−0.23	1.14/−0.54	0.71/−0.45	0.89/−0.52	0.47/−0.37

[a] $R = \sum||F_o| - |F_c||/\sum|F_o|$, $Rw = [\sum w(|F_o| - |F_c|)^2/\sum w\ F_o^2]^{1/2}$, $w = 1/\sigma^2(|F_o|)$.

C, 48.53; H, 7.40; N, 11.91. Found: C, 48.71; H, 7.54; N, 11.70%. IR (cm^{-1}): 3674w, 3412m, 2976s, 1621w, 1546s, 1480m, 1440w, 1384s, 1276s, 1185w, 1102vs, 1054s, 814s, 621m, 417m, 408m. far-IR (cm^{-1}): 637w, 620vs, 539w, 469m, 404m, 348m, 323w, 308w, 299m, 263m, 252w, 244w, 220m, 153m. UV–Vis λ/nm (ε/mol^{-1} dm^3 cm^{-1}):

Table 2
Crystallographic data of complexes **6**$CuCl_4$, **6**Cu_2Cl_6, **8**, **9**, **11**ClO_4, and **12**ClO_4

Complex	**6**$CuCl_4$ · 2($(CH_3)_2CO$)	**6**Cu_2Cl_6 · 3CH_2Cl_2 · H_2O	**8** · 2$CHCl_3$	**9**	**11**ClO_4 · CH_3OH	**12**ClO_4 · 2CH_3OH
CCDC number	654439	654440	654441	654442	654443	654444
Formula	$C_{50}H_{76}Cl_6Cu_3N_{16}O_2$	$C_{47}H_{72}Cl_{14}Cu_4N_{16}O$	$C_{23}H_{38}Cl_8CuN_4$	$C_{11}H_{16}CuN_6O_4$	$C_{24}H_{40}Cl_2CuN_8O_{10}$	$C_{40}H_{74}Cl_2CuN_8O_{11}$
Formula weight	1336.61	1672.72	717.75	359.83	735.08	977.52
Crystal system	monoclinic	triclinic	orthorhombic	triclinic	monoclinic	monoclinic
Space group	$P2_1/a$ (#14)	$P\bar{1}$ (#2)	$Pbca$ (#61)	$P\bar{1}$ (#2)	$P2_1/c$ (#14)	$C2/c$ (#15)
a (Å)	19.8461(11)	12.9526(9)	18.8948(4)	8.56090(10)	8.1610(4)	24.845(5)
b (Å)	15.6703(7)	15.9559(13)	16.6671(4)	9.20690(10)	21.1000(8)	10.2816(14)
c (Å)	20.6328(13)	18.2309(16)	21.1390(5)	10.65010(10)	19.5223(9)	20.493(4)
α (°)	90	108.680(3)	90	72.146(18)	90	90
β (°)	102.7530(9)	102.298(2)	90	70.781(18)	97.2340(7)	112.645(2)
γ (°)	90	93.880(2)	90	72.475(18)	90	90
V (Å^3)	6258.4(6)	3449.6(5)	6657.1(3)	735.522(14)	3334.9(3)	4831.0(15)
Z	4	2	8	2	4	4
D_{calc} (g cm^{-3})	1.418	1.567	1.432	1.625	1.464	1.344
μ(Mo Kα) (cm^{-1})	13.169	18.049	13.174	15.131	8.776	6.255
Temperature (°C)	−90	−89	−90	−90	−90	−90
Reflections collected	48269	27445	48665	5487	24204	16824
Unique reflections	14287	15373	7605	3136	7488	5472
R_{int}	0.047	0.025	0.082	0.042	0.095	0.082
Number of observations	6707 ($I > 5\sigma(I)$)	12056 ($I > 3\sigma(I)$)	2861 ($I > 3\sigma(I)$)	4923 ($I > 3\sigma(I)$)	3648 ($I > 2.5\sigma(I)$)	2951 ($I > 5\sigma(I)$)
Number of variables	770	811	363	215	446	321
Final R, Rw[a]	0.0523/0.0701	0.0676/0.1023	0.0818/0.0917	0.0789/0.1715	0.0782/0.1056	0.0961/0.1322
Goodness-of-fit	2.418	1.641	1.124	1.001	1.128	1.845
Maximum/minimum peak (e Å^{-3})	0.96/−0.71	2.32/−0.96	1.02/−0.81	3.48/−1.92	1.21/−1.20	1.25/−1.08

[a] $R = \sum||F_o| - |F_c||/\sum|F_o|$, $Rw = [\sum w(|F_o| - |F_c|)^2/\sum wF_o^2]^{1/2}$, $w = 1/\sigma^2(|F_o|)$.

712 (70), 370 (720). ESR (CH_3OH/CH_3CH_2OH (9/1) 140 K): $g_{\|}$, 2.30 ($A_{\|}$, 141 G); $g_{\perp}$, 2.08.

2.5. X-ray data collections and structural determinations

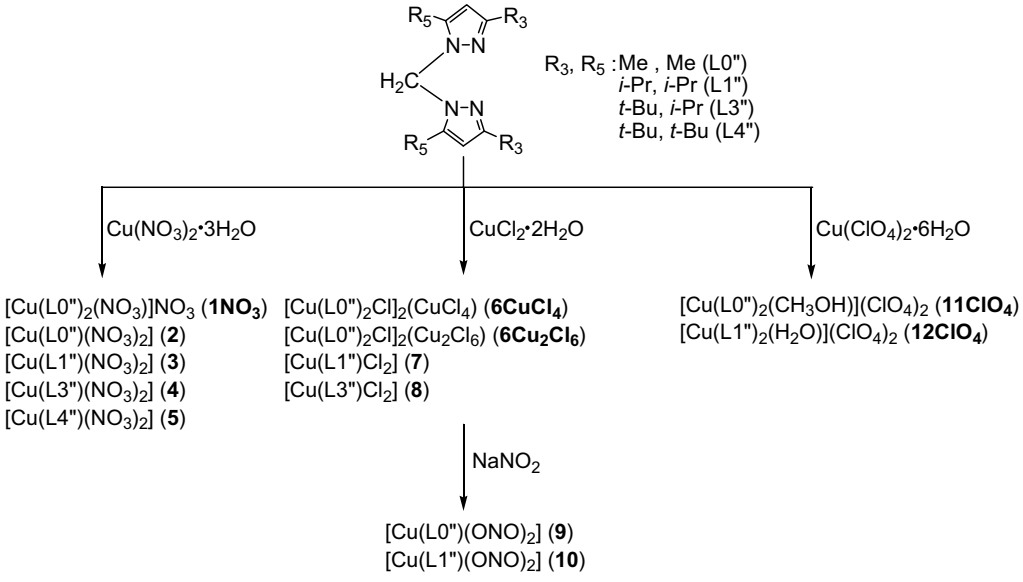
Crystal data and refinement parameters for the investigated ligands (L3″ and L4″) and the copper(II) complexes (**1NO$_3$**, **2**, **4**, **5**, **6CuCl$_4$**, **6Cu$_2$Cl$_6$**, **8**, **9**, **11ClO$_4$**, **12ClO$_4$**) are given in Tables 1, 2. The diffraction data were measured on a Rigaku/MSC Mercury CCD system with graphite monochromated Mo Kα ($\lambda = 0.71069$ Å) radiation at low temperature. Each crystal was mounted on the tip of a glass fiber by heavy-weight oil. The unit cell parameters of each crystal from six image frames were retrieved using Rigaku Daemon software and refined using CrystalClear on all observed reflection [30]. Data using 0.5° intervals in ϕ and ω for 20 s/frame (L3″ and **9**), for 40 s/frame (L4″ and **1NO$_3$**), for 45 s/frame (**2**), for 60 s/frame (**5** and **8**), for 30 s/frame (**6CuCl$_4$**, **6Cu$_2$Cl$_6$**, and **12ClO$_4$**), and for 35 s/frame (**4** and **11ClO$_4$**) were collected with a maximum two theta value of 55° (744 oscillation images). The highly redundant data sets were reduced using CrystalClear and corrected for Lorentz and polarization effects. An empirical absorption correction was applied for each complex [30–32]. Structures were solved by direct-methods (SIR92 [33] or SIR97 [34]). The position of the metal atoms and their first coordination sphere were located from the *E*-map; other non-hydrogen atoms were found in alternating difference Fourier syntheses (DIRDIF99 [35]) and least-squares refinement cycles were refined anisotropically during the final cycles (CrystalStructure) [31,32]. Hydrogen atoms were refined using the riding model. A Sheldick weighting scheme was employed except for **1NO$_3$** and **6CuCl$_4$**. Strong remaining peaks of **6Cu$_2$Cl$_6$**, and **9** are due to the disordered solvents and nitrite ions, respectively. The low qualities of crystalline of **1NO$_3$** and **6CuCl$_4$** were observed. The absolute structure of **1NO$_3$** was deduced based on Flack parameter, 0.024(18), refined using 2569 Friedel pairs [36].

3. Results and discussion

3.1. Synthesis

The synthetic methods for various bpzm ligands were reported by Trofimenko [37] and were modified by Elguero et al. [25]. Referring to the reported methods, the reaction of pyrazole with dichloromethane in an autoclave was carried out, and this way, the desired bpzm ligands could be obtained in high yield. The desired isomer of L3″ could be selectively synthesized by the reported method [38].

To avoid reactions with atmospheric moisture, all complexes were synthesized under an argon atmosphere. Schematic drawings of all complex preparations performed in this work are summarized in Scheme 1. Copper(II) nitrato complexes were synthesized with all four bpzm ligands presented here. In the case of L0″, two kinds of complexes, **1NO$_3$** and **2**, were obtained. They differ in the ligand to copper(II) ratio: Cu:L0″=1:2 in **1NO$_3$** versus Cu:L0″ = 1:1 in **2**. Both complexes **1NO$_3$** and **2** can be separated due to their different solubility in dichloromethane. Complexes **4** and **5** were synthesized by the method reported for **3** [13]. By the reaction of L0″ with $CuCl_2 \cdot 2H_2O$, two kinds of chloro complexes were obtained. The ratio of $CuCl_2$ to L0″ is different in these compounds: $CuCl_2$:L0″ = 3:4 in **6CuCl$_4$**, and $CuCl_2$:L0″ = 1:1 in **6Cu$_2$Cl$_6$**. Structures of the anions ($CuCl_4^{2-}$ in **6CuCl$_4$** and $Cu_2Cl_6^{2-}$ in **6Cu$_2$Cl$_6$**) have already been reported [27,39]. These complexes were selectively obtained by changing the ratio of the substrates



Scheme 1. Schematic drawing of each reaction for this work.

in the reaction, and the solvent used for crystallization. In the case of L1″ and L3″, the copper(II) to ligand ratio in the chloro complexes **7** [14] and **8** is 1:1. On the other hand, in the case of L4″, the chloro complex could not be synthesized, since this complex is very unstable due to the steric repulsion with the ligand. The nitrito complexes **9** and **10** were obtained from the corresponding chloro complexes $\mathbf{6Cu_2Cl_6}$ and **7**. In the case of L3″, the corresponding nitrito complex could not be obtained due to the low stability of **8** in methanol. The complexes with perchlorate ions, $\mathbf{11ClO_4}$ and $\mathbf{12ClO_4}$, contain two molecules of bpzm. Despite the preparation under the same conditions, different solvates were found in these cases (methanol in $\mathbf{11ClO_4}$ and water in $\mathbf{12ClO_4}$). Methanol cannot coordinate to the copper ion because of the bulkier pyrazolyl substituents in $\mathbf{12ClO_4}$. In the case of L3″ and L4″, the complexes with the perchlorate ions could not be isolated.

3.2. Crystal structures

The novel N2 bidentate ligand L3″ and the most hindered N2 bidentate ligand L4″ in this work were obtained as suitable crystals and their structures were determined by X-ray crystallography. ORTEP drawings of L3″ and L4″ are shown in Figs. S1 and S2, respectively. Selected bond distances and angles are listed in Tables S1 and S2, respectively. In the case of L3″, the substituent at the 3rd position of the pyrazolyl rings is the tertiary-butyl group. The increase in steric repulsion in L4″ is evident from the slightly larger C(methylene)–N bond lengths (1.462 Å in L4″ versus 1.450 Å in L3″) and more obtuse N–C(methylene)–N angles (115.5(1)° in L4″ versus 113.4(2)° in L3″). Moreover, differences in bond lengths and angles are found in the complexes derived from each of the ligands, showing the second coordination sphere effects.

Complexes $\mathbf{1NO_3}$, **2**, **4**, **5**, $\mathbf{6CuCl_4}$, $\mathbf{6Cu_2Cl_6}$, **8**, **9**, $\mathbf{11ClO_4}$, and $\mathbf{12ClO_4}$ were obtained as suitable crystals and their structures were determined by X-ray crystallography. All the complexes have a mononuclear structure. ORTEP drawings of these complexes are shown in Figs. 2, 3 and S3. Crystal structures of **3**, **7**, and **10** have been reported previously [13,14]. Selected structural parameters for the nitrato and nitrito complexes $\mathbf{1NO_3}$–**5** and **9**–**10** (Table 3), the chloro complexes **6**–**8** (Tables 4 and S3), and the solvate complexes $\mathbf{11ClO_4}$ and $\mathbf{12ClO_4}$ (Table 5) are listed as indicated.

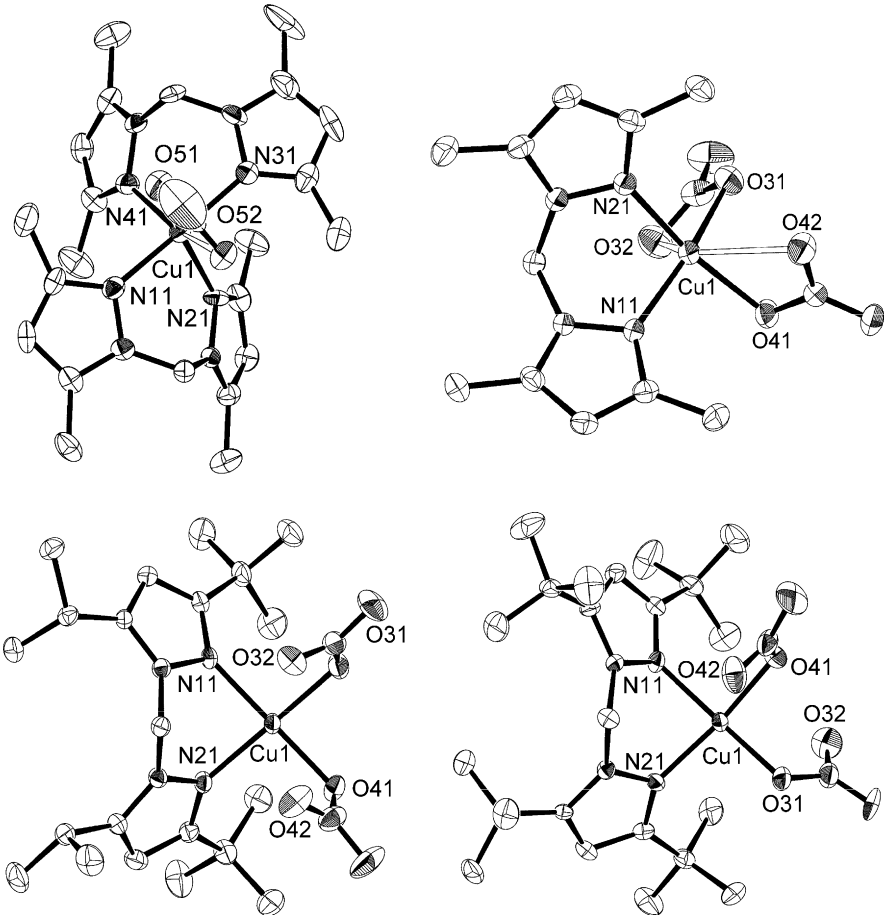


Fig. 2. Crystal structures of $[Cu(L0'')_2(NO_3)]^+$ (the cation portion of $\mathbf{1NO_3}$) (top left), $[Cu(L0'')(NO_3)_2]$ (**2**) (top right), $[Cu(L3'')(NO_3)_2]$ (**4**) (bottom left), and $[Cu(L4'')(NO_3)_2]$ (**5**) (bottom right).

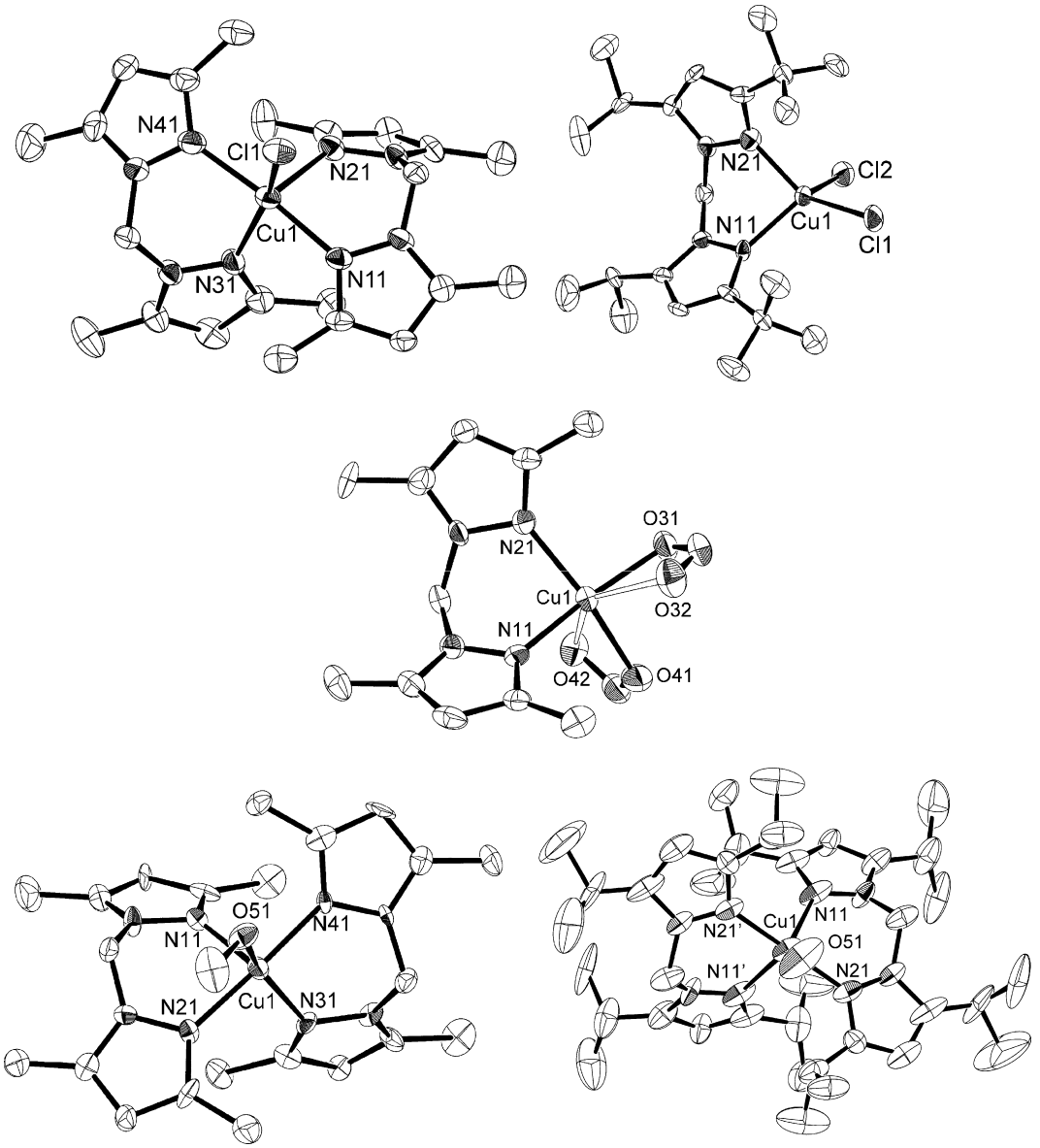


Fig. 3. Crystal structures of $[Cu(L0'')_2Cl]^+$ (the cation portion of **6CuCl$_4$**) (top left), $[Cu(L3'')Cl_2]$ (**8**) (top right), $[Cu(L0'')(ONO)_2]$ (**9**) (center), $[Cu(L0'')_2(CH_3OH)]^{2+}$ (the cation portion of **11ClO$_4$**) (bottom left), and $[Cu(L1'')_2(H_2O)]^{2+}$ (the cation portion of **12ClO$_4$**) (bottom right) (symmetry codes: $-X+2,\ Y,\ -Z+1/2$).

In this study, a distance of less than 2.25 Å between copper and an oxygen atom is identified as a Cu–O bond. In addition, Brill et al. regard an atomic distance of less than 2.50 Å as an indicator for the presence of a distinct Cu–O′ interaction [20]. All copper(II) nitrato and nitrito complexes exhibit a plane around the copper atom. The structures of these complexes are categorized as three types:

(a) Complexes where the copper atom is coordinated by two bpzm ligands and one nitrate (or nitrite) ion, showing a (close to) bidentate coordination mode of the nitrate (or nitrite) ion;
(b) Complexes where the copper atom is coordinated by one bpzm ligand and two nitrate (or nitrite) ions, showing a (close to) bidentate coordination mode of the nitrate (or nitrite) ions;
(c) Complexes that contain the same ligand to ion ratio as (b), but the coordination mode of the nitrate ion(s) is close to monodentate.

The coordination mode of the nitrate (or nitrite) ions is also judged by three additional indicators: equivalence of Cu–O and Cu–O′ bond lengths, equivalence of Cu–O–N and Cu–O′–N bond angles, and the O′–N–O bond angle. When these bond lengths and angles are equivalent, the coordination mode of the nitrate (or nitrite) ions is close to bidentate. When the O′–N–O bond angle is small, the coordination mode of these ions is almost symmetric bidentate. In Table 3, **1NO$_3$**, $[Cu(bipy)_2(ONO)]NO_3$ [40], and $[Ni(L0'')_2(NO_3)]NO_3$ [42] are included as type (a). Owing to the small bulkiness of the substituents in L0″, the steric repulsion between ligands is the smallest in **1NO$_3$**. Since

Table 3
Selected structural parameters for nitrato and nitrito complexes containing N2 bidentate and N3 tridentate ligands

	M–O (av) (Å)	M–O′ (av) (Å)	O′–N–O (av) (°)	M–O–N (av) (°)	M–O′–N (av) (°)	N–M–N (av) (°)	Reference
N2 type							
$[Cu(L0'')_2(NO_3)]NO_3$ (**1NO$_3$**)	2.120(4)	2.484(5)	116.4(4)	102.6(3)	85.9(3)	89.43	this work
$[Cu(L0'')(NO_3)_2]$ (**2**)	1.993	2.463	118.0	103.3	82.6	90.96(10)	this work
$[Cu(L1'')(NO_3)_2]$ (**3**)	1.992	2.452	117.0	102.9	82.7	90.04(6)	[13]
$[Cu(L3'')(NO_3)_2]$ (**4**)	1.963	2.687	117.9	111.0	78.0	86.41(9)	this work
$[Cu(L4'')(NO_3)_2]$ (**5**)	1.959	2.671	117.8	110.4	77.8	85.82(16)	this work
$[Cu(L0'')(ONO)_2]$ (**9**)	1.990	2.424	114.1	104.9	85.0	89.37(19)	this work
$[Cu(L1'')(ONO)_2]$ (**10**)	2.004	2.389	114.3	103.4	86.1	89.28(8)	[13]
$[Cu(bipy)(NO_3)_2]$	1.993	2.456	116.9			82.46(8)	[16]
$[Cu(phen)(NO_3)_2]$	1.978	2.839	118.8	116.2	75.8	82.8(2)	[21]
$[Cu(bipy)(ONO)_2]$	1.987	2.493	115.1	106.9	83.5	81.3(4)	[17]
$[Cu(phen)(ONO)_2]$	1.987	2.410		104.0	84.3		[22]
$[Cu(bipy)_2(ONO)]NO_3$	2.238(10)	2.329(10)	111.9(10)	99.7	95.9(7)	80.7	[40]
$[Cu(phen)_2(ONO)]BF_4$	2.072(4)	2.597(4)	113.4(5)			80.8	[41]
$[Ni(L0'')_2(NO_3)]NO_3$	2.140(3)	2.154(2)				89.28	[42]
N3 type							
$[Cu(L1')(NO_3)_2]$[a]	1.955	2.89	119.1	118.9		86.8	[10]

[a] L1′, tris(3,5-diisopropyl-1-pyrazolyl)methane.

Table 4
Selected structural parameters for copper(II) chloro complexes

	Cu–N (av) (Å)	Cu–Cl (av) (Å)	N–Cu–N (av) (°)	Cl–Cu–Cl (°)	Reference
N2 type					
$[Cu(L0'')_2Cl]_2(CuCl_4)$ (**6CuCl$_4$**)	2.075	2.287	89.7		this work
$[Cu(L0'')_2Cl]_2(Cu_2Cl_6)$ (**6Cu$_2$Cl$_6$**)	2.085	2.277	88.8		this work
$[Cu(L1'')Cl_2]$ (**7**)	1.990	2.225	90.3(2)	103.67(6)	[14]
$[Cu(L3'')Cl_2]$ (**8**)	2.026	2.227	89.0(3)	98.75(13)	this work
$[Cu(en)Cl_2]$	2.014	2.294	84.4(2)	92.84(6)	[19]
$[Cu(bipy)Cl_2]$	2.034	2.275	79.6(3)	92.31(11)	[18]
$[Cu(phen)_2Cl]Cl$	2.069	2.2745(11)	80.2		[43]
$[Cu(phen)_2Cl]ClO_4$	2.036	2.293	80.9		[44]
$[Cu(bipy)_2Cl]PF_6$	2.054	2.344(2)	79.9		[45]
$[Cu(bipy)_2Cl]BF_4$	2.053	2.285(3)	79.6		[46]
N3 type					
$[Cu(L1')Cl_2]$[a]	2.140	2.258	84.9	93.38(6)	[10]

[a] L1′, tris(3,5-diisopropyl-1-pyrazolyl)methane.

bond lengths of Cu–O and Cu–O′ are within 2.25 and 2.50 Å, respectively, the coordination mode of the nitrate ion is close to asymmetric bidentate in this case. **1NO$_3$** shows a distorted octahedral structure. These structures are clearly different from $[Ni(L0'')_2(NO_3)]NO_3$, in the case of which the coordination mode of the nitrate ion is close to symmetric bidentate [42]. Complexes **2**, **3**, **9**, **10**, $[Cu(bipy)(NO_3)_2]$ [16], $[Cu(bipy)(ONO)_2]$ [17], and $[Cu(phen)(ONO)_2]$ [22] belong to the type (b); the bond lengths of Cu–O and Cu–O′ are within 2.01 and 2.50 Å, respectively. Therefore, the coordination mode of the two ions is asymmetric bidentate. For the nitrato complexes of type (b), the Cu–O′–N angles (82.6° in **2** and 82.7° in **3**) are reduced, whereas the Cu–O–N angles (103.3° in **2** and 102.9° in **3**) are enlarged, as compared to **1NO$_3$** (Cu–O′–N angle: 85.9(3)° and Cu–O–N angle: 102.6(3)°). In addition, the O′–N–O angles (118.0° in **2** and 117.0° in **3**) are enlarged compared to the O′–N–O angle of **1NO$_3$** (116.4(4)°). Therefore, the coordination mode of the nitrate ions in **2** and **3** is close to monodentate compared to that of **1NO$_3$**. Owing to nonequivalent Cu–O and Cu–O′ bond lengths in **2**, **3**, **9**, **10**, $[Cu(bipy)(NO_3)_2]$ [16], $[Cu(bipy)(ONO)_2]$ [17], and $[Cu(phen)(ONO)_2]$ [22], these complexes show a highly distorted octahedral structure. Complexes **4**, **5**, and $[Cu(phen)(NO_3)_2]$ [21] correspond to type (c). The Cu–O and Cu–O′ bond lengths of type (c) become more nonequivalent compared to type (b), due to the increased steric repulsion related to the larger bulkiness of the pyrazolyl substituents. The Cu–O′ bond lengths of type (c) are extended to 2.6 Å. Therefore, the coordination mode of two nitrate ions is almost monodentate. As compared to type (b), the Cu–O′–N angles (78.0° in **4** and 77.8° in **5**) and the N–Cu–N angles (86.82(16)° in **4** and 89.37(19)° in **5**) of type (c) are reduced, while the Cu–O–N angles

(111.0° in **4** and 110.4° in **5**) are enlarged. On the other hand, when an N3 tridentate ligand like tris(3,5-diisopropyl-1-pyrazolyl)methane (L1′) is used, the five-coordinate complex $[Cu(L1')(NO_3)_2]$ is obtained [10]. This complex shows a square pyramidal geometry. In addition, the tris(3,5-ditertiary-butyl-1-pyrazolyl)methane (L4′) ligand could not even be synthesized. As described above, in the case of L4″, the nitrato complex **5** could be prepared. This result proves the difference in the properties of the two ligand systems (N2 bidentate versus N3 tridentate).

In the copper(II) chloro complexes, the cation $[Cu(L0'')_2Cl]^+$ (cation of **6CuCl$_4$** or **6Cu$_2$Cl$_6$**) contains the copper(II) ion and the ligand L0″ in the ratio of 1:2. This cationic complex forms an N4 plane around the copper ion. As listed in Table 4, the structures of these cation complexes are very close to $[Cu(phen)_2Cl]Cl$ [43], $[Cu(phen)_2Cl]ClO_4$ [44], $[Cu(bipy)_2Cl]PF_6$ [45], and $[Cu(bipy)_2Cl]BF_4$ [46]. The structures of the copper ions in **7** and **8** are tetrahedral due to the larger bulkiness of the pyrazolyl rings compared to L0″. The Cl–Cu–Cl angle (98.75(13)°) in **8** is more acute than that (103.67(6)°) in **7**, and the average Cu–Cl distance (2.026 Å) in **8** is longer than that (1.990 Å) in **7** because of the steric repulsion resulting from the larger bulkiness of the substituents in **8**. In our previous study, the five-coordinate chloro complex $[Cu(L1')Cl_2]$ was obtained [10]. This complex $[Cu(L1')Cl_2]$ has a square pyramidal structure with two chloride ions and three nitrogen atoms bound to copper. Therefore, the coordination number and the structure of this complex are also clearly different from those of **7** and **8**. Moreover, the average Cu–N distance (2.140 Å) in $[Cu(L1')Cl_2]$ is the largest of all complexes included in Table 4. In the case of L3′, the corresponding chloro complex could not be isolated. This result also relates to the difference in the number of donor atoms between the N2 bidentate and N3 tridentate ligands.

Two complexes with perchlorate ions show a copper atom to ligand ratio of 1:2. The two perchlorate anions exist only as counter anions due to the lower coordination ability compared to nitrate, nitrite, and chloride anions. In **11ClO$_4$**, the copper(II) ion is coordinated by two bpzm ligands and one molecule of methanol. The τ value of **11ClO$_4$** is 0.37, showing a distorted square pyramidal structure [47], where the structural parameter τ is defined as $\tau = (\alpha - \beta)/60°$, where α and β are the largest angles ($\alpha > \beta$) around a five-coordinate metal center (τ is equal to 0 for an ideal square pyramidal geometry, while for a perfect trigonal bipyramidal geometry it becomes 1). Moreover, the coordinated methanol remains bound under reduced pressure. Although two L1″ ligands coordinate to the copper(II) ion in **12ClO$_4$**, one molecule of water is coordinated instead of methanol. Despite of the same crystallization conditions, the copper(II) ion is coordinated by different solvents in **11ClO$_4$** and **12ClO$_4$**, because of the steric repulsion around the copper atom. Nevertheless, the Cu–O bond length of **11ClO$_4$** (2.039(8) Å) is almost the same as that of **12ClO$_4$** (2.044(8) Å). The τ value of **12ClO$_4$** is 0.64, showing a distorted trigonal bipyramidal structure [47]. In addition, the color of **12ClO$_4$** changed from green to red under reduced pressure. This change suggests the dissociation of water from **12ClO$_4$**, and the IR peak corresponding to the stretching vibration of ν(O–H) disappeared in the red solid. As shown in Table 5, many copper(II) aqua complexes with other N2 bidentate ligands have been reported [48–57]. However, compared to **11ClO$_4$**, there are only a few reports of complexes containing coordinated methanol [51–54].

3.3. IR spectra

In the middle-IR region, characteristic absorptions for $\nu_{as}(NO_2)$, $\nu_s(NO_2)$, ν(NO), and $\delta(NO_2)$ for the bidentate and monodentate nitrate ions are predicted [13,58–66]. Since **1NO$_3$**–**5** exhibit asymmetric bidentate or almost asymmetric bidentate or monodentate binding modes of the nitrate ions, they showed four bands; $\nu_{as}(NO_2)$: 1500–1557 cm^{-1}, $\nu_s(NO_2)$: 1267–1285 cm^{-1}, ν(NO): 1001–1020 cm^{-1}, and $\delta(NO_2)$: 805–808 cm^{-1} [58–61] (Fig. 4). Because the N–O bond lengths of the nitrate ions are almost the same in **2**–**5**, these peaks are observed at almost the same positions in the IR spectra, and no effect of the coordination mode of the nitrate ions on the IR spectroscopic property was observed. Furthermore, because the NO_3 groups do not extend themselves on the same side in **4**, one more peak at 1306 cm^{-1} is observed on the higher energy side. Moreover, **1NO$_3$** exhibits more complicated vibrational spectra compared to **2**–**5**, since **1NO$_3$** has a nitrate counter anion and an asymmetrically bidentate coordinated nitrate ion that exhibits different Cu–O bond lengths. The peaks at 833 cm^{-1} and around 1480 cm^{-1} come from the counter nitrate anion. The peak of $\nu_{as}(NO_2)$ (1557 cm^{-1}) in **1NO$_3$** is shifted to higher energy compared to **2**–**5**.

Table 5
Selected structural parameters for **11ClO$_4$**, **12ClO$_4$**, and the reported aqua complexes

	Cu–N (av) (Å)	Cu–O (av) (Å)	τ[a]	Reference
$[Cu(L0'')_2(CH_3OH)](ClO_4)_2$ (**11ClO$_4$**)	2.047	2.039(8)	0.37	this work
$[Cu(L1'')_2(H_2O)](ClO_4)_2$ (**12ClO$_4$**)	2.057	2.044(8)	0.64	this work
$[Cu(bipy)_2(H_2O)](S_2O_6)$	1.995	2.158(13)	0.84	[48]
$[Cu(bipy)_2(H_2O)](S_5O_6)$	2.026	2.054(5)	0.59	[49]
$[Cu(en)_2(H_2O)]\{C_6H_3(CH_3)_2O\}_2$	2.017	2.231(4)	0.12	[50]
$[Cu(en)_2(H_2O)](O_2CCH_2NHCO_2)$	2.017	2.591(3)	0.02	[51]
$[Cu(en)_2(H_2O)_2](O_2CCH_2NHCO_2)$[b]	2.009	2.556(3)		[51]
$[Cu(en)_2(H_2O)_2]\{C_6H_4F(CO_2)\}_2$[b]	2.020	2.579(4)		[52]
$[Cu(en)_2(H_2O)_2]\{C_{10}H_6(NH_2)(SO_3)\}_2^b$	2.022	2.437(2)		[53]
$[Cu(en)_2(H_2O)_2]\{C_5H_4N(CO_2)\}_2$[b]	2.020(2)	2.598(2)		[54]
$[Cu(phen)_2(H_2O)](CF_3SO_3)_2$	2.039	2.066(3)	0.89	[55]
$[Cu(phen)_2(H_2O)](ClO_4)_2$	2.006	2.245(4)	0.63	[55]
$[Cu(phen)_2(H_2O)](BF_4)_2$	2.013	2.238(8)	0.60	[55,56]
$[Cu(phen)_2(H_2O)](NO_3)_2$	2.009	2.180(1)	0.53	[55,57]

[a] Ref. [47].
[b] Six-coordinate complexes.

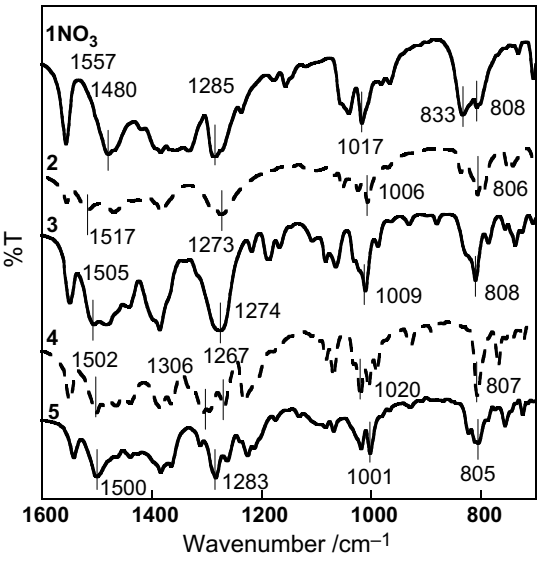


Fig. 4. IR spectra of copper(II) nitrato complexes **1NO$_3$**–**5**.

In the case of the chloro complexes, no characteristic absorptions are observed in the middle-IR region. The N–O stretching bands of the nitrito complexes **9** and **10** are indicated in the IR spectra in Fig. S4. In this case, three characteristic peaks are in observed: ν_s(N–O), ν_{as}(N–O), and δ(O–N–O) [13,58,63]. In **10**, the features at 1346, 1181, and 849 cm^{-1} have been assigned to ν_s(N–O), ν_{as}(N–O), and δ(O–N–O), respectively, by using [Cu(L1″)(O^{15}NO)$_2$] [13]. The N–O stretching bands in **9** are also assigned with respect to those of **10** as ν_s(N–O) at 1371, ν_{as}(N–O) at 1199, and δ(O–N–O) around 850 cm^{-1}. Moreover, no influence of the Cu–O′ bond on these vibrational properties was observed for the nitrito complexes. As shown in Fig. S5, two peaks resulting from the perchlorate ions are observed for **11ClO$_4$** and **12ClO$_4$**. The perchlorate ions show intense stretching vibrations at 1101 cm^{-1} and around 622 cm^{-1}. Both peaks are observed in all the complexes having perchlorate counter ions [58,61]. The ν(O–H) peak due to the coordinated methanol in **11ClO$_4$** is not observed. This lack of ν(O–H) in the IR spectrum is also observed for [Mn(L1′)Br(CH$_3$OH)$_2$]Br [12]. On the other hand, the ν(O–H) peak of the coordinated water is in fact observed at 3674 cm^{-1} in **12ClO$_4$**. After the color of **12ClO$_4$** turned from green to red under reduced pressure, this peak corresponding to ν(O–H) disappeared. This proves a dissociation of the coordinated water from **12ClO$_4$** under reduced pressure.

3.4. Far-IR spectra

In the far-IR region, the coordinated nitrate ion shows the characteristic absorptions of ν_s(Cu–O) and ν_{as}(Cu–O) in **1NO$_3$**–**5** (Fig. 5). Since the bond length of Cu–O is almost the same, the bands of ν_s(Cu–O) and ν_{as}(Cu–O) in **1NO$_3$**–**5** should be observed in 332–348 and 301–323 cm^{-1}, respectively [58,66–69]. The peaks of ν(Cu–O′) in **1NO$_3$**–**3** were observed in the lower energy side. The peak of ν(Cu–O′) depends on the coordination mode of the nitrate ions to copper atom, and this result is different from those of ν(NO$_2$) in middle-IR region. The reason of this different behavior is unclear. On the other hand, only one peak of ν(Cu–O′) was observed in 269–280 cm^{-1}, since the Cu–O′ bond is much weaker than Cu–O. The spectral shape of **4** is slightly different from the natures of other nitrato complexes due to the different geometry.

The assignments of stretching vibration bands (ν(Cu–Cl)) of the chloro complexes **6CuCl$_4$**–**8** were performed (Fig. S6) [13,66,70–72]. Complexes **6CuCl$_4$**, **6Cu$_2$Cl$_6$**, **7**, and **8** having terminal Cu–Cl bond(s) show the peaks of ν(Cu–Cl$_t$) around 300 and 280 cm^{-1} (Table 6). Because the counter anions of **6CuCl$_4$** and **6Cu$_2$Cl$_6$** also have some bridging Cu–Cl$_b$ bonds, more complicated ν(Cu–Cl) bands were observed in the 200–300 cm^{-1} region. The assignments of stretching vibration bands of these anions were referred with those of (NEt$_4$)[CuCl$_4$], (PPh$_4$)$_2$[Cu$_2$Cl$_6$], and (C$_3$N$_3$H$_2$(NH$_2$)$_3$)[Cu$_2$Cl$_6$]. Some peaks of ν(Cu–Cl$_b$) were observed in the lowest energy side from ν(Cu–Cl$_t$) region. As same as IR measurement, the stretching vibration bands in **9** have already been assigned by using

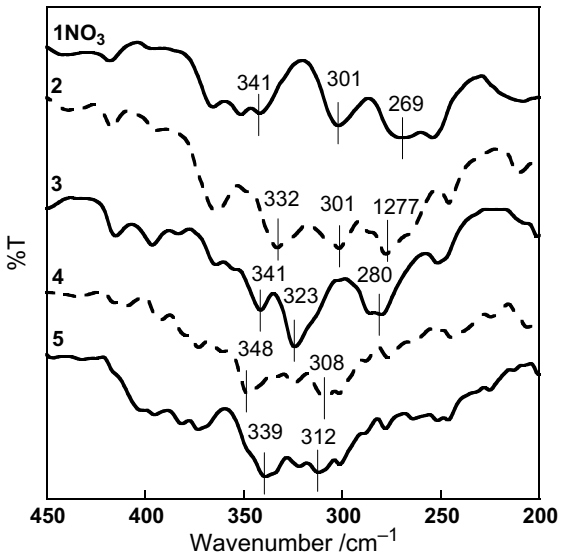


Fig. 5. Far-IR spectra of copper(II) nitrato complexes **1NO$_3$**–**5**.

Table 6
Cu–Cl stretching vibrations of copper(II) chloro complexes

ν(Cu–Cl) (cm^{-1})					Reference
[Cu(L0″)$_2$Cl]$_2$(CuCl$_4$) (**6CuCl$_4$**)	296	263	252	245	this work
[Cu(L0″)$_2$Cl]$_2$(Cu$_2$Cl$_6$) (**6Cu$_2$Cl$_6$**)	303	276	267	252	this work
[Cu(L1″)Cl$_2$] (**7**)	300	289			this work
[Cu(L3″)Cl$_2$] (**8**)	300	279			this work
(NEt$_4$)[CuCl$_4$]	267	248			[70]
(PPh$_4$)$_2$[Cu$_2$Cl$_6$]	300	277	251	244	this work
(C$_3$N$_3$H$_2$(NH$_2$)$_3$)[Cu$_2$Cl$_6$]	300	284	266	232	[71]
[Cu(bipy)Cl$_2$]	304	259			[72]
[Cu(phen)Cl$_2$]	288	281			[72]

$[Cu(L1'')(O^{15}NO)_2]$ [13]. From this assignment, the stretching vibration bands at 374 and 349 cm^{-1} in **10** are assigned to ν_s(Cu–O) and ν_{as}(Cu–O), respectively (Fig. S7). As same as **1NO$_3$–3**, the peaks of ν(Cu–O′) in **9** and **10** were observed at 319 and 330 cm^{-1}, respectively. Only the ν(Cu–O) in **11ClO$_4$** and **12ClO$_4$** due to the bond between the copper(II) ion and oxygen atom of the coordinated solvates was observed at 349 and 348 cm^{-1}, respectively (Fig. S8).

3.5. Electronic absorption spectra

The absorption maxima (λ_{max}) of all the complexes are summarized in Table 7. The d–d transition bands in **1NO$_3$–5** are almost the same as the reported nitrato complexes containing N2 bidentate ligands [63]. As shown in Fig. 6, the d–d transition bands of **4** and **5** were shifted to the higher energy side compared with those of **2** and **3**. Because of the structural distortions in **4** and **5**, the energy gap between the d orbitals should be enlarged. Additionally, in **1NO$_3$** and **2** having the same ligand, the d–d transition bands of **1NO$_3$** were shifted to the higher energy side compared with those of **2**, because of higher steric repulsion between the substituents of the ligands in **1NO$_3$**. In **2**, **3**, and **5**, the LMCT transition bands from nitrate to the copper(II) ions were observed around 300 nm. However, the CT transition bands of **4** were shifted to the lower energy sides compared with those of **2**, **3**, and **5** due to the different coordination mode. In **1NO$_3$**, only one nitrate ion coordinates to the copper(II) ion. Therefore, the CT transition absorptivity was weak as a shoulder around 300 nm.

Table 7
λ_{max} of the synthesized and the reported nitrato and chloro complexes

	λ_{max} (nm)			Reference
	d–d region	CT region		
		LMCT	π–π*	
$[Cu(L0'')(NO_3)]_2NO_3$ (**1NO$_3$**)	696			this work
$[Cu(L0'')(NO_3)_2]$ (**2**)	739	295		this work
$[Cu(L1'')(NO_3)_2]$ (**3**)	741	297		[13]
$[Cu(L3'')(NO_3)_2]$ (**4**)	634	307		this work
$[Cu(L4'')(NO_3)_2]$ (**5**)	589	301		this work
$[Cu(bipy)(NO_3)_2]$	675			[63a]
$[Cu(phen)(NO_3)_2]$	689			[63b]
$[Cu(L0'')_2Cl]_2(CuCl_4)$ (**6CuCl$_4$**)	908	287		this work
$[Cu(L0'')_2Cl]_2(Cu_2Cl_6)$ (**6Cu$_2$Cl$_6$**)	893	287		this work
$(Ph_4P)_2[Cu_2Cl_6]$	880	475, 325	276, 268, 263	this work
$(n\text{-}Bu_4N)_2[CuCl_4]$	1156	408, 340		[73]
$[Cu(L1'')Cl_2]$ (**7**)	911	375, 289		[13,14]
$[Cu(L3'')Cl_2]$ (**8**)	848	387, 287		this work
$[Cu(en)Cl_2]$	764			[63]
$[Cu(bipy)Cl_2]$	680			[63]
$[Cu(L0'')(ONO)_2]$ (**9**)	693	281		this work
$[Cu(L1'')(ONO)_2]$ (**10**)	675	280		[13]
$[Cu(bipy)(ONO)_2]$	621			[63]
$[Cu(L0'')_2(CH_3OH)](ClO_4)_2$ (**11ClO$_4$**)	728	370, 268		this work
$[Cu(L1'')_2(H_2O)](ClO_4)_2$ (**12ClO$_4$**)	712	370		this work

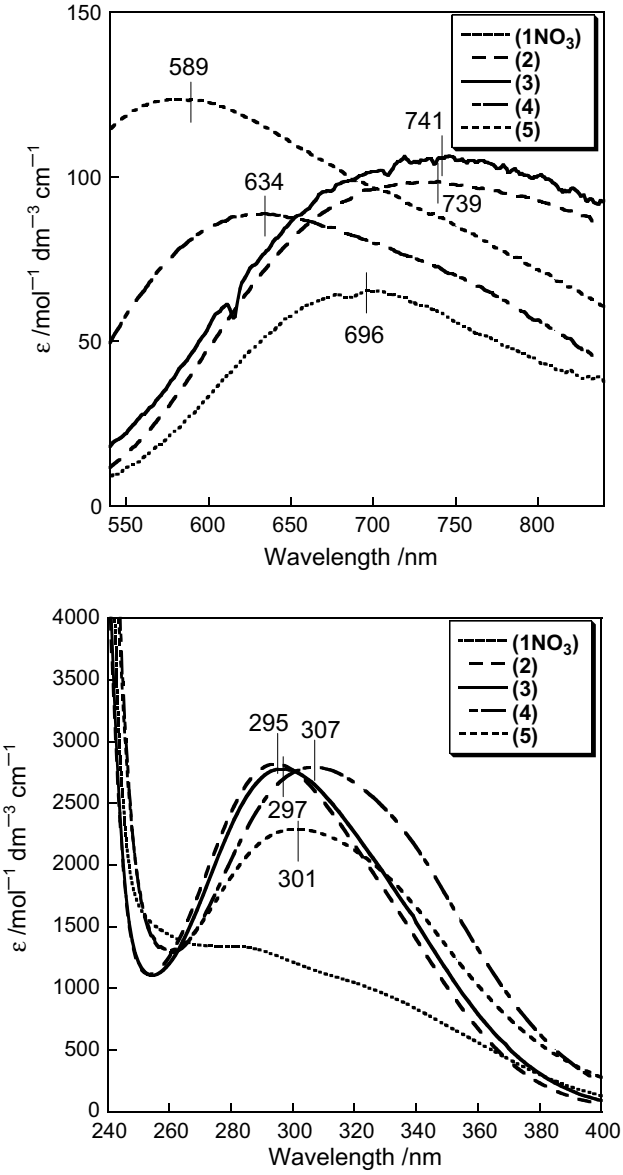


Fig. 6. Electronic absorption spectra of nitrato complexes in **1NO$_3$–5** in d–d transitions region (top) and in CT transitions region (bottom).

In **6CuCl$_4$**, **6Cu$_2$Cl$_6$**, and **7–12**, the LMCT transition bands were observed in the region of 350–450 nm (Figs. S9–S11). Complexes **6CuCl$_4$** and **6Cu$_2$Cl$_6$** containing the same cation showed almost the same absorption behavior. As listed in Table 7, these absorptions in **6CuCl$_4$** and **6Cu$_2$Cl$_6$** are very close to **7** and **8**. In $(Ph_4P)[Cu_2Cl_6]$, the LMCT transition bands were observed at 325 and 475 nm. Furthermore, the π–π* transition bands were observed around 270 nm. On the other hand, the LMCT transition bands in **6CuCl$_4$**, **6Cu$_2$Cl$_6$**, **7**, and **8** were observed around 290 nm, since the coordination modes

of the chloride ions are almost the same in these chloro complexes. As compared with **7**, the d–d transition bands in **8** were shifted to the higher energy side due to higher steric repulsion between the ligand and the chloride ions. On the other hand, the d–d transition bands in [Cu(bipy)Cl_2] and [Cu(en)Cl_2] [28] in the higher energy side than those in **8** and **9** are found [63a], since this energy gap between the d orbitals of tetrahedral type is smaller than those of square planar type. Two nitrito complexes showed almost the same absorption behavior due to almost the same coordination mode of the nitrite ions and the complex structure. The d–d transition bands in **10** were shifted to the higher energy side than those in **9** due to larger steric repulsion between the ligand and the nitrite ions. The d–d transition bands of the synthesized nitrito complexes are almost the same as those of the reported nitrito complexes containing N2 bidentate ligand [63a]. In addition, the absorption bands around 280 nm in these complexes were assigned to the LMCT transition bands from nitrite to the copper(II) ion [13]. In **11**ClO_4 and **12**ClO_4, only the LMCT transition bands was observed in the CT transitions region, since two perchlorate ions does not coordinate to copper(II) ion. The d–d transition bands in **12**ClO_4 were shifted to the higher energy side compared with those in **11**ClO_4, because of larger steric repulsion between the substituents of the ligand.

3.6. ESR spectra

The $A_{\parallel}$ and g values of the synthesized complexes are summarized in Table S4, together with the reported complexes. Two kinds of mixture solvents were used for ESR measurements. The mixture solvent α (methanol/ethanol = 9:1) was used for **1**NO_3, because **1**NO_3 was insoluble in dichloromethane. In addition, when **12**ClO_4 dissolved in the mixture solvent β (dichloromethane/1,2-dichloroethane = 1:1), the solution color turned from green to brown, accompanied by the dissociation of water. In the case of chloro complexes **6**$CuCl_4$, **6**Cu_2Cl_6, **7**, and **8** and the complexes with perchlorate ions **11**ClO_4 and **12**ClO_4, the solution colors of these complexes were changed at 140 K, since some water in solvents would coordinate to the copper atom. The spectra of **1**–**5** and **9**–**10** are shown in Figs. 7 and S12, respectively [20,63,74,75]. The order of $g_{\parallel} > g_{\perp} > 2.0023$ is satisfied in all the complexes except **8** and **9** having a tetrahedral structure, it was confirmed that the unpaired electron of the copper(II) ion exists in $d_{x^2-y^2}$ orbital. In the results of UV–Vis absorption measurements, the Δ value order is $\Delta(\mathrm{ONO}) \geqslant \Delta(\mathrm{NO_3}) > \Delta(\mathrm{Cl})$, so that the $g_{\perp}$ values are expected; $g_{\perp}(\mathrm{Cl}) > g_{\perp}(\mathrm{NO_3}) \geqslant g_{\perp}(\mathrm{ONO})$, where Δ is energy gap between the d orbitals (cm^{-1}). In general, $A_{\parallel}$ value of the complex having a tetrahedral structure is smaller than that having a square plane. However, this tendency was not observed in **7** and **8** owing to the different structures at 140 K. The ^{14}N superhyperfine coupling appeared clearly in **4** and **5**, and their $A_{\parallel}$ values were much larger than those of **1**NO_3–**3** (Fig. 7). These

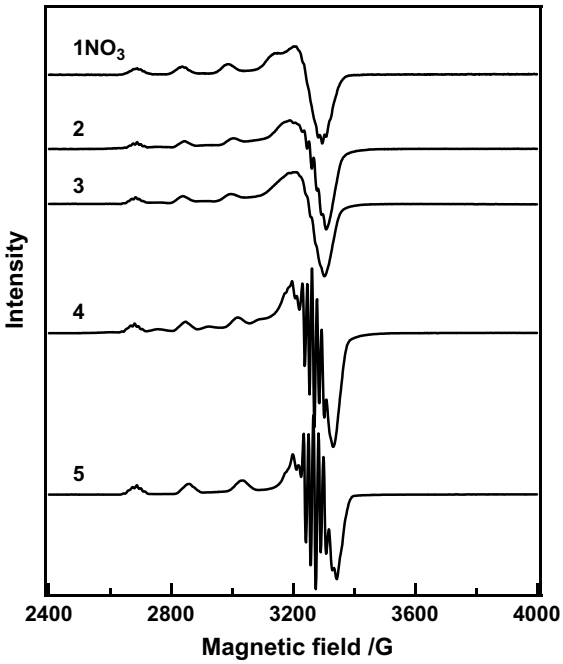


Fig. 7. ESR spectra of nitrato complexes **1**NO_3–**5**.

results prove their square planar structure [76]. On the other hand, this ^{14}N superhyperfine coupling was slightly observed in **2** and **9**, and that the ^{14}N superhyperfine coupling depends on the structures for the coordinated nitrogens. If the coordination mode of the nitrate (or nitrite) ion would be almost unidentate, the influence of the coordinated nitrogen become strong, and the ^{14}N superhyperfine coupling could appear clearly. As shown in Fig. S12, the spectra of the nitrito complexes **9** and **10** are different from those of **2** and **3**.

4. Conclusion

In this work, novel nine copper(II) complexes ligated by various bpzm ligands were systematically synthesized and characterized. As for the structures of the synthesized nitrato and nitrito complexes, the coordination mode of the nitrate or nitrite ions affected on their complex structures. In **1**NO_3, the coordination mode of the nitrate ion is almost asymmetric bidentate, taking a distorted octahedral structure. Complexes **2**, **3**, **9**, and **10** have almost asymmetric bidentate nitrate or nitrite ions, and take a highly distorted octahedral structure. On the other hand, **4** and **5** have almost unidentate nitrate ions because of the higher bulkiness of the ligands, and have a square planar structure. Further, the structural differences caused by the bulkiness of the ligands are also confirmed in the synthesized chloro complexes and the complexes with perchlorate ions. In IR measurements, three $\nu(NO_2)$ and one $\delta(NO_2)$ are observed in the nitrato complexes. However, those of **1**NO_3 and **4** were shifted because of the different coordination number and coordination mode of two nitrate ions for the copper plane. In far-IR spectra, the

peak of ν(Cu–O′) was observed when the coordination mode of the nitrate (or nitrite) ions would be bidentate. In UV–Vis spectra, the d–d transition bands were shifted to higher energy side by the distortion of the complex structure. In ESR spectra, by the effect of the nitrogen atoms of the ligand, the ^{14}N hyperfine coupling is clearly observed in **4** and **5**, and this proves their square planar structure.

From these systematic researches by using several ligands L0″, L1″, L3″, and L4″ with different steric bulkiness, we obtained many structural effects and different observations in their physicochemical properties. As for the counter anion, NO_3^-, NO_2^-, Cl^-, and ClO_4^-, different coordination ability towards copper(II) ion was observed. In particular, we can prepare all complexes with NO_3^- as $[Cu(Ln'')(NO_3)]$ ($n = 0$, 1, 3, and 4) type. However, we cannot make the following complexes even different experimental conditions; $[Cu(L0'')Cl_2]$, $[Cu(L4'')Cl_2]$, $[Cu(L3'')(NO_2)_2]$, $[Cu(L4'')(NO_2)_2]$, and $[Cu(Ln'')(ClO_4)_2]$. From this research, we also demonstrate the influences on the differences in second coordination sphere effects on the ligands and nitrogen numbers (bpzm versus tpzm). We are now underway to identify these ligand effects on their structures, reactivities, and physicochemical properties with copper(I) ion.

Acknowledgements

This research was supported by grants for Grant-in-Aid for Scientific Research (B) (14350471 and 17350043) from JSPS and for Scientific Research on Priority Areas "Advanced Molecular Transformations of Carbon Resources" (19020011) from MEXT. We appreciate the kind editing of this manuscript by Dr. Nicolai Lehnert of University of Michigan.

Appendix A. Supplementary material

CCDC 654433, 654434, 654435, 654436, 654437, 654438, 654439, 654440, 654441, 654442, 654443, and 654444 contain the supplementary crystallographic data for this paper. These data can be obtained free of charge via http://www.ccdc.cam.ac.uk/conts/retrieving.html, or from the Cambridge Crystallographic Data Centre, 12 Union Road, Cambridge CB2 1EZ, UK; fax: (+44) 1223-336-033; or e-mail: deposit@ccdc.cam.ac.uk. Supplementary data associated with this article can be found, in the online version, at doi:10.1016/j.poly.2008.01.019.

References

[1] F.A. Cotton, G. Wilkinson, C.A. Murillo, M. Bochmann, Advanced Inorganic Chemistry, 6th ed., John Wiley & Sons, Inc., New York, 1999.
[2] V. Balzani, G. Bergamini, F. Marchioni, P. Ceroni, Coord. Chem. Rev. 250 (2006) 1254.
[3] C. Kaes, A. Katz, M.W. Hosseini, Chem. Rev. 100 (2000) 3553.
[4] G. Chelucci, R.P. Thummel, Chem. Rev. 102 (2002) 3129.
[5] J. Li, Z. Chen, R. Wang, D.M. Proserpio, Coord. Chem. Rev. 190–192 (1999) 707.
[6] H. Sugihara, K. Hiratani, Coord. Chem. Rev. 148 (1996) 285.
[7] N. Kitajima, K. Fujisawa, C. Fujimoto, Y. Moro-oka, S. Hashimoto, T. Kitagawa, K. Toriumi, K. Tatsumi, A. Nakamura, J. Am. Chem. Soc. 114 (1992) 1277.
[8] Y. Matsunaga, K. Fujisawa, N. Ibi, Y. Miyashita, K. Okamoto, Inorg. Chem. 44 (2005) 325.
[9] K. Fujisawa, Y. Matsunaga, N. Ibi, N. Amir, Y. Miyashita, K. Okamoto, Bull. Chem. Soc. Jpn. 79 (2006) 1894.
[10] K. Fujisawa, T. Ono, H. Aoki, Y. Ishikawa, Y. Miyashita, K. Okamoto, H. Nakazawa, H. Higashimura, Inorg. Chem. Commun. 7 (2004) 330.
[11] K. Fujisawa, T. Ono, Y. Ishikawa, N. Amir, Y. Miyashita, K. Okamoto, N. Lehnert, Inorg. Chem. 45 (2006) 1698.
[12] M. Nabika, S. Kikuchi, T. Miyatake, K. Okamoto, K. Fujisawa, J. Mol. Catal. A. 269 (2007) 163.
[13] N. Lehnert, U. Cornelissen, F. Neese, T. Ono, Y. Noguchi, K. Okamoto, K. Fujisawa, Inorg. Chem. 46 (2007) 3916.
[14] K. Fujisawa, Y. Noguchi, Y. Miyashita, K. Okamoto, N. Lehnert, Inorg. Chem. 46 (2007) 10607.
[15] A.L. Gavrilova, B. Bosnich, Chem. Rev. 104 (2004) 349.
[16] A. Tadsanaprasittipol, H. Kraatz, G.D. Enright, Inorg. Chim. Acta 278 (1998) 143.
[17] F.S. Stephens, J. Chem. Soc. A (1969) 2081.
[18] M. Hernández-Molina, J. González-Platas, C. Ruiz-Pérez, F. Lloret, M. Julve, Inorg. Chim. Acta 284 (1999) 258.
[19] D.A. Harvey, C.J.L. Lock, Acta Crystallogr., Sect. C 42 (1986) 799.
[20] S.F. Palopoli, S.J. Geib, A.L. Rheingold, T.B. Brill, Inorg. Chem. 27 (1988) 2963.
[21] D.L. McFadden, A.T. McPhail, J. Chem. Soc., Dalton Trans. (1975) 1993.
[22] G.L. Breneman, C.W. Howald, O.J. Parker, Acta Crystallogr., Sect. E 57 (2001) m286.
[23] D.G. Hendricker, R.J. Foster, Inorg. Chem. 12 (1973) 349.
[24] W.L.F. Armarego, D.D. Perrin, Purification of Laboratory Chemicals, 4th ed., Butterworth-Heinemann, Oxford, UK, 1997.
[25] S. Juliá, P. Sala, J. del Mazo, M. Sancho, C. Ochoa, J. Elguero, J. Fayet, M. Vertut, J. Heterocycl. Chem. 19 (1982) 1141.
[26] A. Beck, B. Weibert, N. Burzlaff, Eur. J. Inorg. Chem. (2001) 521.
[27] M. Textor, E. Dubler, H.R. Oswald, Inorg. Chem. 13 (1974) 1361.
[28] S. Imai, K. Fujisawa, T. Kobayashi, N. Shirasawa, H. Fujii, T. Yoshimura, N. Kitajima, Y. Moro-oka, Inorg. Chem. 37 (1998) 3066.
[29] K. Fujisawa, Y. Ishikawa, Y. Miyashita, K. Okamoto, Chem. Lett. 33 (2004) 66.
[30] CRYSTALCLEAR 1.3: J.W. Pflugrath, Acta. Crystallogr., Sect. D 55 (1999) 1718–1725.
[31] CRYSTALSTRUCTURE 3.8: Crystal Structure Analysis Package, Rigaku and Rigaku/MSC, 2006.
[32] CRYSTAL ISSUE 10: D.J. Watkin, C.K. Prout, J.R. Carruthers, P.W. Betteridge, Crystal Issue 10, Chemical Crystallography Laboratory, Oxford, UK, 1996.
[33] SIR92: A. Altomare, G. Cascarano, C. Giacovazzo, A. Guagliardi, J. Appl. Crystallogr. 26 (1993) 343–350.
[34] SIR97: A. Altomare, M.C. Burla, M. Camalli, G.L. Cascarano, C. Giacovazzo, A. Guagliardi, A.G.G. Moliterni, G. Polidori, R. Spagna, J. Appl. Crystallogr. 32 (1999) 115–119.
[35] DIRDIF-99: P.T. Beurskens, G. Admiraal, G. Beurskens, W.P. Bosman, R. Gelder, R. Israel, J.M.M. Smits, Technical Report of the Crystallography Laboratory, University of Nijmegen, The Netherlands, 1999.
[36] H.D. Flack, Acta. Crystallogr., Sect. A 39 (1983) 876.
[37] S. Trofimenko, J. Am. Chem. Soc. 92 (1970) 5118.
[38] D.L. Reger, T.C. Crattan, K.J. Brown, C.A. Little, J.J.S. Lamba, A.L. Rheingold, R.D. Sommer, J. Organomet. Chem. 607 (2000) 120.
[39] (a) T. Kawata, T. Aoyama, S. Ohba, Acta Crystallogr., Sect. C 49 (1993) 137;
(b) A. Mahoui, J.L.J. Moret, Acta Crystallogr., Sect. C 50 (1994) 358.

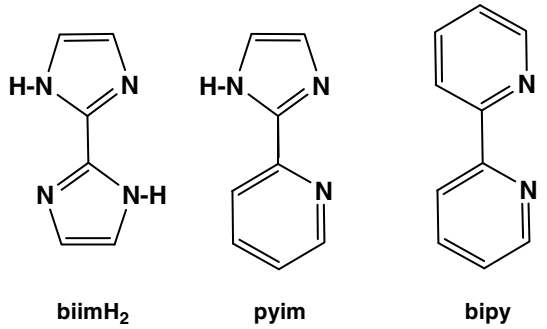
[40] I.M. Procter, F.S. Stephens, J. Chem. Soc. A (1969) 1248.
[41] C.J. Simmons, K. Seff, F. Clifford, B.J. Hathaway, Acta Crystallogr., Sect. C 39 (1983) 1360.
[42] A. Michaud, F. Fontaine, D. Zargarian, Inorg. Chim. Acta 359 (2006) 2592.
[43] E.C. O'Brien, E. Farkas, M.J. Gil, D. Fitzgerald, A. Castineras, K.B. Nolan, J. Inorg. Biochem. 79 (2000) 47.
[44] S. Tyagi, B. Hathaway, S. Kremer, H. Stratemeier, D. Reinen, J. Chem. Soc., Dalton Trans. (1984) 2087.
[45] P. Nagle, E. O'Sullivan, B.J. Hathaway, E. Muller, J. Chem. Soc., Dalton Trans. (1990) 3399.
[46] Y. Wei, P. Yang, Acta Crystallogr., Sect. E 60 (2004) m429.
[47] A.W. Addison, T.N. Rao, J. Reedijk, J. van Rijn, G.C. Verschoor, J. Chem. Soc., Dalton Trans. (1984) 1349.
[48] W.D. Harrison, B.J. Hathaway, Acta Crystallogr., Sect. B 35 (1979) 2910.
[49] W.D. Harrison, B.J. Hathaway, D. Kennedy, Acta Crystallogr., Sect. B 35 (1979) 2301.
[50] P.J. Baesjou, W.L. Driessen, J. Reedijk, A.L. Spek, Inorg. Chim. Acta 306 (2000) 237.
[51] L.A. Kovbasyuk, I.O. Fritsky, V.N. Kokozay, T.S. Iskenderov, Polyhedron 16 (1997) 1723.
[52] Z. Liu, M. Tan, H. Zhu, Acta Crystallogr., Sect. E 60 (2004) m1081.
[53] M. Li, C. Wang, Y. Wu, X. Fu, Acta Crystallogr., Sect. E 61 (2005) m1660.
[54] P. Segl'a, M. Palicová, M. Koman, D. Milkoš, M. Melník, Inorg. Chem. Commun. 3 (2000) 120.
[55] G. Murphy, C. Murphy, B. Murphy, B.J. Hathaway, J. Chem. Soc., Dalton Trans. (1997) 2653.
[56] H. Nakai, Y. Noda, Bull. Chem. Soc. Jpn. 51 (1978) 1386.
[57] H. Nakai, Y. Deguchi, Bull. Chem. Soc. Jpn. 48 (1975) 2557.
[58] K. Nakamoto, Infrared and Raman Spectra of Inorganic and Coordination Compounds, 5th ed., John Wiley & Sons, Inc., New York, 1997.
[59] C.C. Addison, L. Logan, S.C. Wallwork, C.D. Garner, Q. Rev. Chem. Soc. (1971) 289.
[60] C.C. Addison, W.B. Simpson, J. Chem. Soc. (1965) 598.
[61] M.R. Rosenthal, J. Chem. Educ. 50 (1973) 331.
[62] K. Fujisawa, T. Kobayashi, K. Fujita, N. Kitajima, Y. Moro-oka, Y. Miyashita, Y. Yamada, K. Okamoto, Bull. Chem. Soc. Jpn. 73 (2000) 1797.
[63] (a) I.M. Procter, B.J. Hathaway, P.G. Hodgson, J. Inorg. Nucl. Chem. 34 (1972) 3689;
(b) D. Rehorek, P. Thomas, Z. Anorg. Allg. Chem. 426 (1976) 309.
[64] A.B.P. Lehver, Inorg. Chem. 4 (1965) 1042.
[65] N.F. Cutris, Y.M. Curtis, Inorg. Chem. 4 (1965) 804.
[66] (a) C. Pettinari, A. Cingolani, B. Bovio, Polyhedron 15 (1996) 115;
(b) C. Pettinari, F. Marchetti, A. Cingolani, D. Leonesi, M. Colapietro, S. Margadonna, Polyhedron 17 (1998) 4145.
[67] R.H. Nuttall, D.W. Taylor, J. Chem. Soc., Chem. Commun. (1968) 1417.
[68] J.I. Bullock, F.W. Parrett, J. Chem. Soc., Chem. Commun. (1969) 157.
[69] J.R. Ferraro, A. Walker, J. Chem. Phys. 42 (1965) 1273.
[70] A. Colombo, L. Menabue, A. Motori, G.C. Pellacani, W. Porzio, F. Sandrolini, R.D. Willett, Inorg. Chem. 24 (1985) 2900.
[71] A. Sabatini, L. Sacconi, J. Am. Chem. Soc. 86 (1964) 17.
[72] R.E. Wilde, T.K.K. Srinivasan, S.N. Ghosh, J. Inorg. Nucl. Chem. 35 (1973) 1017.
[73] W. Ludwig, M. Textor, Helv. Chim. Acta 54 (1971) 1143.
[74] D.E. Billing, R. Dudley, B.J. Hathaway, P. Nicholls, I.M. Procter, J. Chem. Soc. A (1969) 312.
[75] A. Bencini, C. Benelli, D. Gatteschi, Inorg. Chem. 19 (1980) 1632.
[76] (a) P.L. Holland, W.B. Tolman, J. Am. Chem. Soc. 121 (1999) 7270;
(b) D.W. Randall, S.D. George, P.L. Holland, B. Hedman, K.O. Hodgson, W.B. Tolman, E.I. Solomon, J. Am. Chem. Soc. 122 (2000) 11632.

substitution reaction and containing the 2,2′-biimidazole ($biimH_2$), 2-(2′-pyridyl)imidazole (pyim) and 2,2′-bipyridine (bipy) chelating ligands (Scheme 1).

With rhenium and $biimH_2$, a few crystal structures involving only Re(III) and Re(V) metal ions have been reported [30–32]. Beauchamp et al. observed that the Re(V) precursors $[ReOX_3(PPh_3)_2]$ and $[ReO(OEt)X_2(PPh_3)_2]$ are reduced by PPh_3 in the presence of $biimH_2$ affording the Re(III) compounds *cis*,*trans*-$[ReX_2(PPh_3)_2(biimH_2)]X$, X being Cl^-, Br^- and I^- halide counterions [31]. Other similar Re(III) compounds of general formula $[ReX_2(PMe_3)_2(biimH_2)]X$ (X = Cl, Br and I) were further obtained [32]. In addition, the Re(V) mononuclear compound $[ReOCl_2(OPPh_3)(biimH_2)]Cl$ was prepared, by refluxing $[ReOCl_3(OPPh_3)(Me_2S)]$ and $biimH_2$ in $CHCl_3$, and characterized by X-ray diffraction. Another Re(V) mononuclear complex, $[ReOCl_3(biimH_2)]$, was also obtained by the same authors but its crystal structure was not solved [30].

As far as we know, there is only one crystal structure described with rhenium and pyim ligand, that of the Re(III) compound $[ReCl_2(PPh_3)_2(pyim)]^+$ recently reported [33]. This complex is obtained when *trans*-$[ReOCl_3(PPh_3)_2]$ is allowed to react with pyim in methanol. In the same reaction conditions but by using 2-(2′-pyridyl)-1-methylimidazole (pyimMe) instead pyim a Re(V) complex, $[ReCl_3(PPh_3)(pyimMe)]$, was also synthesized [33]. By using other derivative ligand, the 2-(2′-pyridyl)benzimidazole, one Re(III) complex and another one of Re(IV) were prepared and also characterized by X-ray diffraction [24].

Rhenium with the bipy diimine ligand present in its sphere of coordination has been much more explored with Re(I) than with other oxidation states [Re(II)–Re(V)]. Concerning rhenium(IV), in 1984 the $[ReCl_4(bipy)]$ complex was prepared, by pyrolysis reaction from $[bipyH_2][ReCl_6]$ [34]. However, its crystal structure was not solved until 1990 [18], when it was obtained unexpectedly in the reaction of $ReCl_5$ and bipy in the presence of hexamethyldisiloxane. More recently, the analogous bromo-complex, $[ReBr_4(bipy)]$, has been described [35]. It is worth noting that although two different methods of synthesis and also the X-ray structure of $[ReCl_4(bipy)]$ complex are found in the literature [18,34], to date its magnetism study has been not reported.



Scheme 1.

We report here the synthesis of two new Re(IV) solvated mononuclear complexes of formula $[ReCl_4(biimH_2)]\cdot 2DMF$ (**1**) and $[ReCl_4(pyim)]\cdot DMF$ (**2**) where $biimH_2$ = 2,2′-biimidazole, pyim = 2-(2′-pyridyl)imidazole and DMF = *N*,*N*-dimethylformamide and, moreover, an alternative method to prepare the previously reported $[ReCl_4(bipy)]$ (**3**) complex (bipy = 2,2′-bipyridine), together with the X-ray structure of **2** and the magnetic properties of all of them **1**–**3**.

2. Experimental

2.1. Materials

N,*N*-dimethylformamide (max. 0.03% water) and 2-propanol solvents, and 2,2′-bipyridine ligand employed for synthesis were purchased from commercial sources and used as received. $BiimH_2$ and pyim ligands as well as ammonium hexachlororhenate(IV), $(NH_4)_2[ReCl_6]$, were prepared by following the literature procedures of Refs. [36–38], respectively.

2.2. Synthesis of the complexes

2.2.1. $[ReCl_4(biimH_2)]\cdot 2DMF$ (1)

A mixture of $(NH_4)_2[ReCl_6]$ (0.60 g, 1.38 mmol) and 2,2′-biimidazole ($biimH_2$) (0.22 g, 1.64 mmol) in 15 mL of DMF was heated at 110 °C during 6 h leading to a dark red-orangish solution together with a white solid. After cooling at room temperature, the solid was removed by filtration and the filtrate was transferred into a flask. Then, 50 mL of 2-propanol were added very slowly by means of a Pasteur pipette, the flask was closed and left to diffuse. Red-orangish crystals of **1** were grown in a month, which were not suitable for X-ray diffraction studies and numerous attempts to grow better ones were unsuccessful. Yield: *ca.* 25–30%. *Anal.* Calc. for $C_{12}H_{20}N_6Cl_4O_2Re$ (**1**): C, 23.69; H, 3.31; N, 13.81. Found: C, 23.30; H, 3.22; N, 13.75%. IR peaks associated to $biimH_2$ ligand appear at (cm^{-1}) 3155m, 3129s, 2927m, 1906w, 1514m, 1493m, 1424s, 767s and 669m, and the peaks assigned to DMF at (cm^{-1}) 1655vs, 1380s and 705m.

2.2.2. $[ReCl_4(pyim)]\cdot DMF$ (2)

This compound was obtained by following a very similar procedure to that described above for **1**. A mixture of $(NH_4)_2[ReCl_6]$ (0.30 g, 0.69 mmol) and 2-(2′-pyridyl)imidazole (pyim) (0.30 g, 2.07 mmol) in 10 mL of DMF was heated during 3–4 h leading to a brown solution. After cooling at room temperature, any solid present was removed by filtration and discarded. **2** was separated as red-orangish crystals after slow diffusion performed in 2-propanol as in **1**. These red-orangish crystals were suitable for X-ray diffraction studies. Yield: *ca.* 35%. *Anal.* Calc. for $C_{11}H_{14}N_4Cl_4ORe$ (**1**): C, 24.19; H, 2.58; N, 10.26. Found: C, 23.98; H, 2.49; N, 10.21%. IR peaks associated to pyim ligand appear at (cm^{-1}) 3135m, 3094w, 3065m, 2926m,

1908m, 1576s, 1473s, 1256m, 790s and 674m, and those assigned to DMF at (cm^{-1}) 1639vs, 1384s and 701m.

2.2.3. [$ReCl_4$(bipy)] (3)

A mixture of ammonium hexachlororhenate(IV) (0.60 g, 1.38 mmol) and bipy (0.50 g, 3.20 mmol) in 5 mL of DMF was refluxed under argon atmosphere during 2–3 h leading to a dark green solution. After cooling at room temperature, the solution was filtered and heated at 60 °C to eliminate fully the solvent. 50 mL of acetone were added to the residue obtained stirring for 20 min. Then, the insoluble solid was removed by filtration and discarded. Finally, 4–5 drops from a 0.5 M HCl solution were added (to avoid any possible hydrolysis) and by slow evaporation at room temperature brown-yellowish needles were formed in two weeks. Yield: *ca.* 35–40%. *Anal.* Calc. for $C_{10}H_8N_2Cl_4Re$ (**1**): C, 24.81; H, 1.67; N, 5.79. Found: C, 24.56; H, 1.63; N, 5.80%. IR peaks associated to bipy ligand appear at (cm^{-1}) 3080m, 1602vs, 1563m, 1465s, 1445vs, 950m, 770s and 722m.

2.3. Physical measurements

Infrared spectra of **1**–**3** were recorded with a Nicolet 320 FTIR spectrophotometer as KBr pellets in the 4000–400 cm^{-1} region. Magnetic susceptibility measurements of **1**–**3** were carried out with a Quantum Design SQUID magnetometer in the temperature range 1.9–300 K and under an applied magnetic field of 1 T in the high-temperature range, and 250 G at low temperatures to avoid any problem of magnetic saturation. The device was calibrated with $(NH_4)_2Mn(SO_4)_2 \cdot 6H_2O$. Diamagnetic corrections of the constituent atoms were estimated from Pascal constants [39].

2.4. Crystallographic data collection and structure determination

A crystal of dimensions 0.08 × 0.18 × 0.10 mm of **2** was mounted on a Bruker-Nonius X8APEXII CCD area detector system and used for data collection. Diffraction data were collected at room temperature by using graphite-monochromated Mo K_α radiation ($\lambda = 0.71073$ Å). A total of 1938 frames of data were collected using a narrow-frame method with scan widths of 0.3° in ϕ and ω, exposure time of 5 s per frame using a crystal-to-detector distance of 50 mm. These data were processed through the SAINT [40] reduction and SADABS [41] absorption software to yield a total of 20861 reflections.

The unit cell parameters, which are listed in Table 1 together with a summary of the structure refinement data, were based upon least-squares refinement of 4467 reflections. Of the total collected reflections, 6125 were independent [$R_{int} = 0.0347$, with 4405 having $I > 2\sigma(I)$] and used to solve the structure with the SHELXTL software package [42]. The structure was solved by standard direct methods and subsequently completed by Fourier recycling. All non-hydrogen atoms were refined anisotropically. The hydrogen atoms were placed in geometrically suitable positions and were refined as riding atoms. The final full-matrix least-squares refinements on F^2, minimizing the function $\sum w(|F_o| - |F_c|)^2$, reached convergence with values of the discrepancy indices given in Table 1. The final geometrical calculations were carried out with the PARST program [43]. The graphical manipulations were performed using the XP utility of the SHELXTL system. Main interatomic bond lengths and angles for **2** are given in Table 2.

Table 1
Crystal data and structure refinement for [$ReCl_4$(pyim)] · DMF (**2**)

Compound	2
Formula	$C_{11}H_{14}Cl_4N_4ORe$
Formula weight	546.26
Temperature (K)	296(2)
Crystal system	monoclinic
Space group	$P2_1/c$
Z	4
a (Å)	8.992(1)
b (Å)	10.186(1)
c (Å)	19.311(1)
α (°)	90.0
β (°)	100.41(1)
γ (°)	90.0
V (Å^3)	1739.59(11)
D_{calc} (g cm^{-3})	2.086
$F(000)$	1036
μ (cm^{-1})	76.01
Reflection collected/observed	20861/6125
Goodness-of-fit on F^2	1.043
R_1 [$I > 2\sigma(I)$][a]	0.0394
wR_2[b,c]	0.0781

[a] $R_1 = \sum||F_o| - |F_c||/\sum|F_o|$.
[b] $wR_2 = \{\sum[w(F_o^2 - F_c^2)^2]/[w(F_o^2)^2]\}^{1/2}$.
[c] $w = 1/[\sigma^2(F_o^2) + (aP)^2 + bP]$ with $P = [F_o^2 + 2F_c^2]/3$.

Table 2
Selected bond lengths (Å) and angles (°) for **2**

Re(1)–N(1)	2.086(4)
Re(1)–N(2)	2.148(4)
Re(1)–Cl(1)	2.331(1)
Re(1)–Cl(2)	2.356(1)
Re(1)–Cl(3)	2.308(1)
Re(1)–Cl(4)	2.324(2)
N(1)–Re(1)–N(2)	76.4(2)
N(1)–Re(1)–Cl(1)	170.6(1)
N(1)–Re(1)–Cl(2)	87.4(1)
N(1)–Re(1)–Cl(3)	92.6(1)
N(1)–Re(1)–Cl(4)	88.0(1)
N(2)–Re(1)–Cl(1)	94.3(1)
N(2)–Re(1)–Cl(2)	85.7(1)
N(2)–Re(1)–Cl(3)	169.0(1)
N(2)–Re(1)–Cl(4)	88.6(1)
Cl(1)–Re(1)–Cl(2)	90.78(6)
Cl(3)–Re(1)–Cl(1)	96.67(6)
Cl(3)–Re(1)–Cl(2)	92.70(7)
Cl(3)–Re(1)–Cl(4)	92.24(7)
Cl(4)–Re(1)–Cl(1)	93.00(6)
Cl(4)–Re(1)–Cl(2)	173.40(5)

3. Results and discussion

3.1. Crystal structure of [$ReCl_4$(pyim)] · DMF (2)

The crystal structure of compound **2** is made up of discrete molecules of [$ReCl_4$(pyim)] and *N,N*-dimethylformamide (DMF) which are held together by means of van der Waals interactions and hydrogen bonds. A perspective drawing of the molecular structure of the [$ReCl_4$(pyim)] unit along with the atom numbering is depicted in Fig. 1, while selected bonds lengths and angles are listed in Table 1. Each [$ReCl_4$(pyim)] unit contains a six-coordinated rhenium atom in a distorted octahedral environment constituted by four chloride anions and one bidentate pyim molecule. The main distortion of the ideal octahedral geometry is due to the short bite angle of the bidentate pyim ligand [76.4(2)° for N(1)–Re(1)–N(2)]. The average values of Re–Cl and Re–N bond lengths [2.330 and 2.117 Å, respectively] are in agreement with those found in the literature for similar Re(IV) mononuclear complexes [15,24–28]. The N(1), N(2), Cl(1), Cl(3) set of atoms define the best equatorial plane around the Re atom, which is placed practically in this plane. The pyim rings are planar and they show C–C and C–N bonds lengths values as expected [29]. The pyrimidyl and imidazole rings form a dihedral angle of 7(1)°, while the dihedral angle between the pyim and main equatorial planes is 6.5(1)°. In the crystal packing, [$ReCl_4$(pyim)] molecules are linked through weak van der Waals forces, moreover, hydrogen bonding interactions take place between O(1) atom from carbonyl of the DMF molecule and N–H group from pyim ligand [N(3)···O(1a) distance is 2.673(6) Å, (a) = $1-x$, $1-y$, $2-z$]. On the other hand, π–π stacking interactions are also observed in the lattice of **2** with an interplanar distance of 3.45 Å and an overlap efficiency of *ca.* 50%. The shortest intermolecular Cl···Cl distance was found to be 3.621(1) Å [Cl(4)···Cl(4b), (b) = $2-x$, $2-y$, $2-z$, distances visualized as broken lines in Fig. 2] and the value of the shortest intermolecular Re···Re separation being 7.697(1) Å [Re(1)···Re(1c); (c) = $1-x$, $-0.5+y$, $1.5-z$].

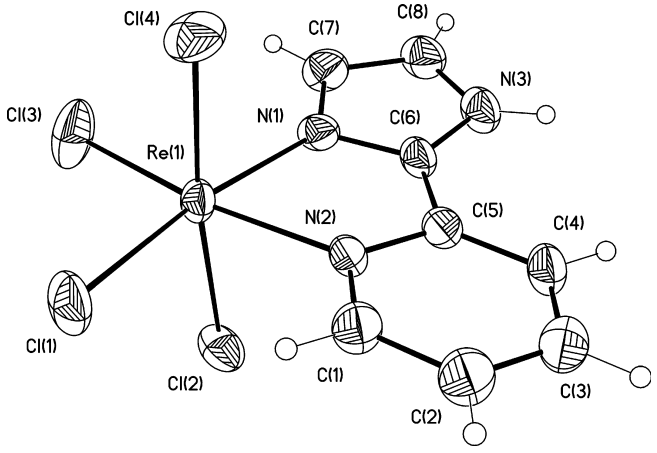


Fig. 1. Perspective drawing of the molecular structure of **2** showing the atom numbering scheme. Thermal ellipsoids are drawn at 30 % of probability level.

3.2. Magnetic properties

The magnetic properties of the compounds **1** and **2**, under the form of both $\chi_M T$ and χ_M versus T plots (χ_M being the molar magnetic susceptibility), are shown in Figs. 3 and 4, respectively. At room temperature, $\chi_M T$ values are 1.68 (**1**) and 1.60 $cm^3\ mol^{-1}$ K (**2**). These values are as expected for magnetically isolated Re(IV) ($S_{Re} = 3/2$) mononuclear complexes with $g = 1.8$–1.9 [27,29]. Upon cooling, $\chi_M T$ values for both compounds decrease very slowly until 70 (**1**) and 80 K (**2**), then they decrease quickly and vanishing practically at lower temperatures. The fact that $\chi_M T$ attains values even lower than 1 $cm^3\ mol^{-1}$ K, in low temperature range, indicates the occurrence of intermolecular antiferromagnetic interactions, as discussed in previous works [27,44]. Indeed, the susceptibility curves (χ_M versus T) exhibit small maxima at 2.8 K in both compounds (**1** and **2**), this last feature being also characteristic of antiferromagnetically coupled systems. The decrease of $\chi_M T$ values observed at higher temperatures can be attributed exclusively to the zero-field splitting ($2D$), which is very large for Re(IV) in a distorted octahedral environment, because of the high value of the spin-orbit coupling constant (λ *ca.* 1000 cm^{-1} in the free $5d^3$ ion). In fact, for six-coordinated Re(IV), the first excited term which arises from the ^4F free-ion ground term is $^4T_{2g}$ and under a tetragonal distortion, this excited state is split into $^4B_2$ and ^4E terms. Under this pattern, the interaction of these two excited terms with the quartet ground spin state, leads to two Kramers doublets, $|\pm 3/2>$ and $|\pm 1/2>$, which are separated by an energy gap of $|2D|$ (zero-field splitting resulting from the combined action of second-order spin–orbit interaction and the tetragonal crystal field). A detailed inspection of the crystal packing of **2** reveals intermolecular interactions between adjacent [$ReCl_4$(pyim)] units through space *via* Re–Cl···Cl–Re contacts. The shortest Cl···Cl separation is 3.621(1) Å and, therefore, very close to the van der Waals distance.

Taking into consideration these facts, we have used the theoretical expression for the magnetic susceptibility [Eq. (2)] derived from the Hamiltonian [Eq. (1)] to analyze the magnetic behaviour of **1** and **2**. Due to the intermolecular interactions that take place, a θ parameter was included in the expression (2) in attempt to fit the experimental data and to analyze the magnetic coupling between the mononuclear units.

$$\widehat{H} = D[(\widehat{S}_Z)^2 - S(S+1)/3] + g_{\parallel}\beta H_Z \widehat{S}_Z + g_{\perp}\beta(H_X \widehat{S}_X + H_Y \widehat{S}_Y) \quad (1)$$

$$\chi_M = \frac{\chi_{\parallel} + 2\chi_{\perp}}{3} \quad (2)$$

where

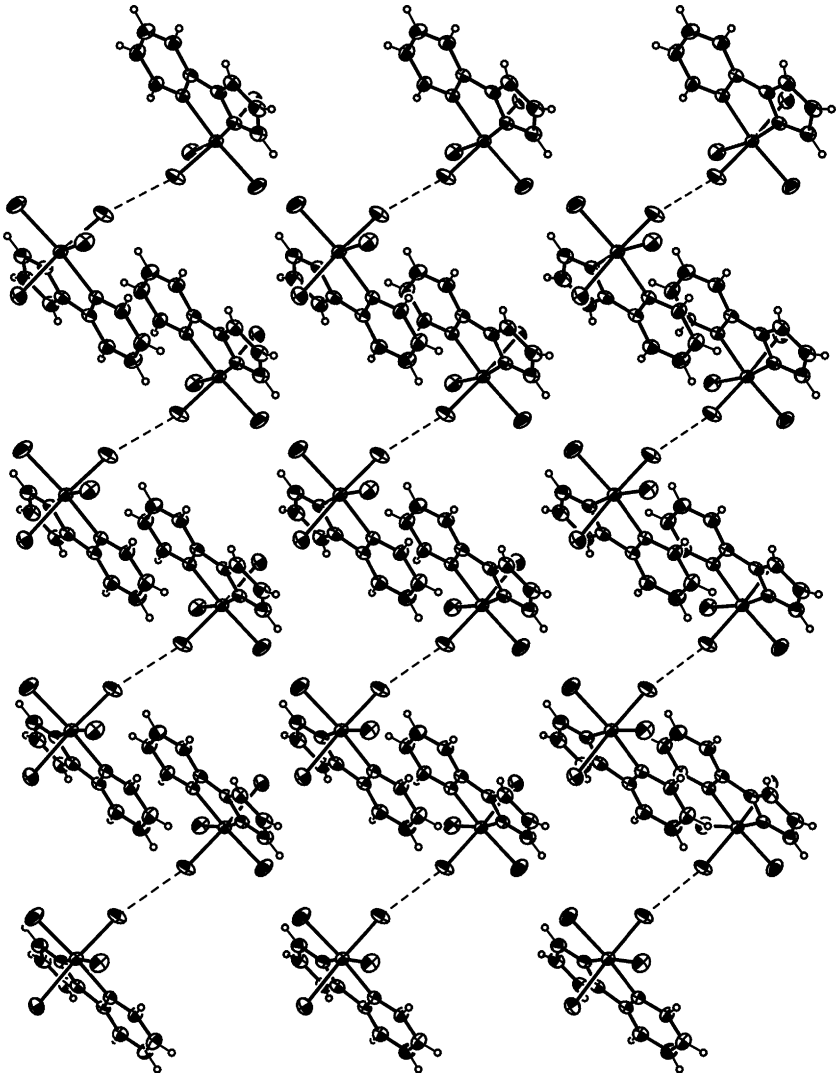


Fig. 2. View along z-axis of a crystal packing fragment in **2** showing the shortest interionic Cl···Cl contacts (broken lines) between adjacent [$ReCl_4$(pyim)] units. Solvent molecules have been omitted for clarity.

$$\chi_{\parallel} = \frac{N\beta^2 g_{\parallel}^2}{4k(T-\theta)} \frac{1+9\exp(-2D/kT)}{1+\exp(-2D/kT)}$$

$$\chi_{\perp} = \frac{N\beta^2 g_{\perp}}{k(T-\theta)} \frac{1+(3kT/4D)[1-\exp(-2D/kT)]}{1+\exp(-2D/kT)}$$

The large axial anisotropy from Re(IV) accounts for a great value of D together with different values for $g_{\parallel}$ and $g_{\perp}$. However, we have measured the magnetic susceptibility on microcrystalline powder samples of both compounds and from these measurements it is not possible to define reliable and unique values for $g_{\parallel}$ and $g_{\perp}$ or the sign of D. The fit of experimental data considering all of these parameters results in several (mathematically) possible solutions. However, in all of them the absolute value of D and the main value of g remain practically constants. Best least-squares fit parameters are: $\theta = -5.5$ K, $g = 1.90$ and $R = 2.3 \times 10^{-4}$ for **1** and $\theta = -9.6$ K, $g = 1.88$ and $R = 8.7 \times 10^{-5}$ for **2** [R being the agreement factor defined as $\sum i[(\chi_M T)_{obs}(i) - (\chi_M T)_{calc}(i)]^2/\sum i[(\chi_M T)_{obs}(i)]^2$]. As one can see, the calculated curves for **1** and **2** reproduce very well the experimental magnetic data in the whole temperature range. These results support also the formula that we propose for compound **1**, given that **1** exhibits very close magnetic curves and therefore the same magnetic behaviour that **2**. The negative θ values obtained show the occurrence of a significant antiferromagnetic coupling because of intermolecular Cl···Cl interactions, θ being for **2** almost twice the value found in compound **1**. The presence of more solvent molecules in **1**, generating a possible longer Re–Cl···Cl–Re separation and leading to a lower intensity of the magnetic coupling, would account for the larger θ value observed in **2**.

The magnetic properties of the complex **3** as $\chi_M T$ and χ_M versus T plots are shown in Fig. 5. The $\chi_M T$ value at room temperature is 1.27 $cm^3\,mol^{-1}\,K$, which is smaller than that expected for a magnetically isolated Re(IV) centre (see above), suggesting that a significant antiferromagnetic interaction occurs in this compound. Upon

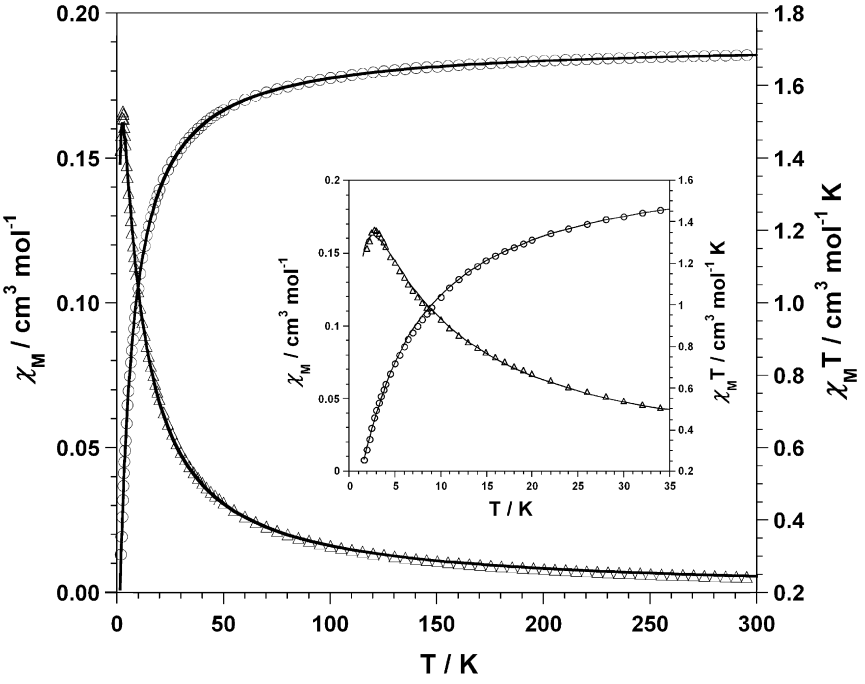


Fig. 3. Thermal variation of χ_M (Δ) and $\chi_M T$ (○) for **1**: (—) best-fit curve (see text).

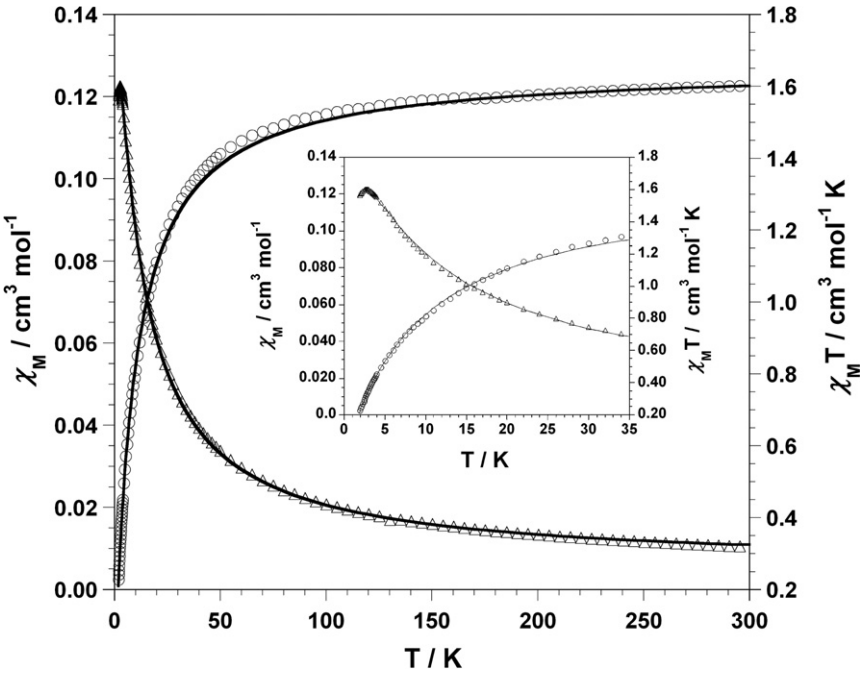


Fig. 4. Thermal variation of χ_M (Δ) and $\chi_M T$ (○) for **2**: (—) best-fit curve (see text).

cooling, $\chi_M T$ values quickly decrease to reach a value of 0.031 $cm^3\,mol^{-1}$ K at 1.9 K. The susceptibility curve (χ_M versus T) shows a maximum at 5.6 K with $\chi_{M\ (max)} = 0.052\ cm^3\,mol^{-1}$. The extrapolated value of χ_M at $T = 0$ is 0.036 $cm^3\,mol^{-1}$, that is about 2/3 its value at the temperature at which it is a maximum. This fact indicates that we are dealing with a three-dimensional antiferromagnetic ordering [45], a magnetic behaviour that also we have observed recently in a two-dimensional $Re^{IV}Ag^{I}$ species [46], however heat capacity measurements would be needed to verify this magnetic ordering.

Due to the lack of an adequate theoretical model to analyze these magnetic experimental data, the evaluation of the magnitude of the exchange coupling in **3** is precluded. Nevertheless, the $\chi_M{}^{-1}$ versus T plot in the temperature range 80–300 K exhibits a linear behaviour, and fitting the experimental data by means of a simple Curie–Weiss expression we got the following magnetic parameters:

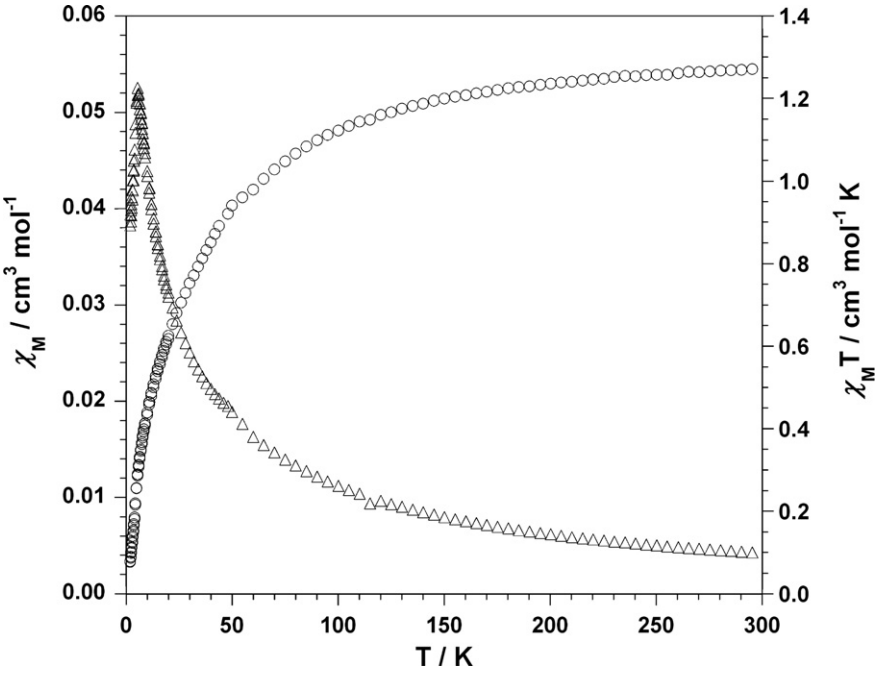


Fig. 5. Thermal variation of χ_M (Δ) and $\chi_M T$ (○) for **3**.

$C = 1.36\ \text{cm}^3\ \text{mol}^{-1}$, $\theta = -21.2$ K and $g = 1.87$. This negative θ value supports that a significant antiferromagnetic interaction takes place in **3**. As one can see, θ value in **3** is larger than those obtained for **1** and **2**. However, it deserves to be noted that in the latter fit the θ parameter includes both intermolecular interactions and the zero-field splitting and, aiming at comparing the θ parameter from **1**–**3**, it must be carefully considered. In fact, the shortest Cl···Cl distance found in **3** is somewhat longer than that of **2**, in spite of the presence of solvent molecules in **2** [3.620(1) (**2**) and 3.787(1) Å (**3**)]. So that, the magnetic coupling intensity due to intermolecular interactions between paramagnetic Re(IV) centers in **3** should not be much larger than that of **2**.

4. Conclusions

By reacting $[ReCl_6]^{2-}$ and L (L = $biimH_2$, pyim and bipy chelating ligands) in DMF we have prepared the three Re(IV) compounds namely $[ReCl_4(biimH_2)] \cdot 2DMF$ (**1**), $[ReCl_4(pyim)] \cdot DMF$ (**2**) and $[ReCl_4(bipy)]$ (**3**), and solved the crystal structure of **2** by X-ray diffraction. Magnetic susceptibility measurements reveal that **1**–**3** exhibit significant antiferromagnetic couplings, which take place by means of Re–Cl···Cl–Re type intermolecular interactions. In **3**, such interactions lead to an antiferromagnet behaviour.

Supplementary material

CCDC 669709 contains the supplementary crystallographic data for **2**. These data can be obtained free of charge via http://www.ccdc.cam.ac.uk/conts/retrieving.html, or from the Cambridge Crystallographic Data Centre, 12 Union Road, Cambridge CB2 1EZ, UK; fax: (+44) 1223-336-033; or e-mail: deposit@ccdc.cam.ac.uk.

Acknowledgements

Financial support from the Ministerio Español de Educación y Ciencia (Project No. CTQ2004-03633), and the Italian Ministero dell'Istruzione, dell'Università e della Ricerca is gratefully acknowledged. The authors thank to Dr. Francesc Lloret for SQUID magnetometer measurements.

References

[1] E.A. Deutsch, K. Libson, J.L. Vanderheyden, Technecium and Rhenium in Chemistry and Nuclear Medicine, Raven Press, New York, 1990.
[2] W. Volkert, W.F. Goeckeler, G.J. Ehrhardt, A.R. Ketring, J. Nucl. Med. 32 (1991) 174.
[3] E. John, M.L. Thakur, J. De Fulvio, M.R. McDevitt, I. Dajanov, J. Nucl. Med. 34 (1993) 260.
[4] K. Hashimoto, K. Yoshihara, Top. Curr. Chem. 176 (1995) 275.
[5] S.S. Jurisson, J.D. Lydon, Chem. Rev. 99 (1999) 2205.
[6] S. Liu, D.S. Edwards, Chem. Rev. 99 (1999) 2235.
[7] W.A. Volkert, T.J. Hoffman, Chem. Rev. 99 (1999) 2269.
[8] J. Sattigeri, A.L. Rodriguez, J.A. Katzenellenbogen, Bioorg. Med. Chem. 10 (2002) 1381.
[9] K.S. Schanze, D.B. MacQueen, T.A. Perkins, L.A. Cabana, Coord. Chem. Rev. 122 (1993) 63.
[10] K. Wang, L. Huang, L. Gao, L. Jin, Ch. Huang, Inorg. Chem. 41 (2002) 3353.
[11] E.J. Schutte, B.P. Sullivan, C.J. Chang, D.G. Nocera, Inorg. Synth. 33 (2002) 227.
[12] T.G. Gray, C.M. Rudzinski, E.E. Meyer, R.H. Holm, D.G. Nocera, J. Am. Chem. Soc. 125 (2003) 4755.
[13] C.C. Romão, F.E. Kühn, W.A. Herrmann, Chem. Rev. 97 (1997) 3197.

[14] L.E. Helberg, S.D. Orth, M. Sabat, W.D. Harman, Inorg. Chem. 35 (1996) 5584.
[15] R. Chiozzone, R. González, C. Kremer, M.F. Cerdá, D. Armentano, G. De Munno, J. Martínez-Lillo, J. Faus, Dalton Trans. (2007) 653.
[16] I.D. Brown, C.J.L. Lock, C. Wan, Can. J. Chem. 51 (1973) 2073.
[17] S. Bucknor, F.A. Cotton, L.R. Falvello, A.H. Reid, C.D. Schmulbach, Inorg. Chem. 26 (1987) 2954.
[18] W.A. Herrmann, W.R. Thiel, E. Herdtweck, Chem. Ber. 123 (1990) 271.
[19] R. Hübener, U. Abram, Inorg. Chim. Acta 211 (1993) 121.
[20] R. Rossi, A. Marchi, L. Marvelli, L. Magon, M. Peruzzini, U. Casellato, R. Graziani, Inorg. Chim. Acta 204 (1993) 63.
[21] R. Hübener, U. Abram, J. Strähle, Acta Crystallogr. Sect. C 51 (1995) 876.
[22] X. Chen, F.J. Femia, J.W. Babich, J. Zubieta, Inorg. Chim. Acta 306 (2000) 113.
[23] X. Chen, F.J. Femia, J.W. Babich, J. Zubieta, Inorg. Chim. Acta 310 (2000) 237.
[24] M.N. Sokolov, N.E. Fedorova, E.V. Peresypkina, R. Pätow, V.E. Fedorov, D. Fenske, Inorg. Chim. Acta 358 (2005) 3914.
[25] J. Martínez-Lillo, D. Armentano, G. De Munno, F. Lloret, M. Julve, J. Faus, Inorg. Chim. Acta 359 (2006) 3291.
[26] J. Martínez-Lillo, D. Armentano, G. De Munno, F. Lloret, M. Julve, J. Faus, Inorg. Chim. Acta 359 (2006) 4343.
[27] R. Chiozzone, R. González, C. Kremer, G. De Munno, J. Cano, F. Lloret, M. Julve, J. Faus, Inorg. Chem. 38 (1999) 4745.
[28] R. Chiozzone, A. Cuevas, R. González, C. Kremer, D. Armentano, G. De Munno, J. Faus, Inorg. Chim. Acta 359 (2006) 2194.
[29] J. Martínez-Lillo, D. Armentano, G. De Munno, F. Lloret, M. Julve, J. Faus, Dalton Trans. (2008) 40, and references therein.
[30] S. Fortin, A. Beauchamp, Inorg. Chem. 39 (2000) 4886.
[31] S. Fortin, A. Beauchamp, Inorg. Chem. 40 (2001) 105.
[32] S. Fortin, P.L. Fabre, M. Dartiguenave, A. Beauchamp, Dalton Trans. (2001) 3520.
[33] T.I.A. Gerber, E. Hosten, P. Mayer, Z.R. Tshentu, J. Coord. Chem. 59 (2006) 243.
[34] J.V. Caspar, B.P. Sullivan, T.J. Meyer, Inorg. Chem. 23 (1984) 2104.
[35] B. Machura, J.O. Dziegielewski, R. Kruszynksi, T.J. Bartczak, J. Kusz, Polyhedron 22 (2003) 2573.
[36] D.T. Cromer, R.R. Ryan, C.B. Storm, Acta Crystallogr. C43 (1987) 1435.
[37] K.A. Reeder, E.V. Dose, L.J. Wilson, Inorg. Chem. 17 (1978) 1071.
[38] J. Kleinberg (Ed.), Inorganic Synthesis, vol. VII, McGraw-Hill, New York, 1963, p. 189.
[39] A. Earnshaw, Introduction to Magnetochemistry, Academic Press, London, Kahn, 1968.
[40] SAINT – Version 6.45 Copyright © (2003) Bruker Analytical X-ray Systems Inc., Madison, Wisconsin, USA.
[41] Sheldrick, G.M. SADABS. Version 2.10. Bruker AXS Inc., Madison, Wisconsin, USA, 2003.
[42] SHELXTL NT – Version 5.1 Copyright©, Bruker Analytical X-ray Systems Inc., Madison, Wisconsin, USA, 1998.
[43] M. Nardelli, Comput. Chem. 7 (1983) 95.
[44] A. Cuevas, C. Kremer, M. Hummert, H. Schumann, F. Lloret, M. Julve, J. Faus, Dalton Trans. (2007) 342.
[45] R.L. Carlin, Magnetochemistry, Springer-Verlag, Berlin, 1986, p. 121.
[46] J. Martínez-Lillo, D. Armentano, G. De Munno, F. Lloret, M. Julve, J. Faus, Cryst. Growth Des. 6 (2006) 2204.

Heterocyclic bases *viz.* 2,2′-bipyridine (bipy) and 1,10-phenanthroline (phen) were used as auxiliary ligands for coordination.

2. Experimental

2.1. Materials

2-Hydroxy-4-methoxyacetophenone (Aldrich), 2-hydroxy-4-methoxybenzaldehyde (Aldrich), nicotinic acid hydrazide (Aldrich), vanadyl sulphate (Aldrich), 2,2′-bipyridine (Qualigen), 1,10-phenanthroline (Ranchem) were of analar grade and used without further purification. Solvents used were ethanol, methanol and water.

2.2. Synthesis of the ligands

The synthesis of 2-hydroxy-4-methoxybenzaldehyde nicotinic acid hydrazone (H_2L^1) has been reported by us earlier [11]. 2-Hydroxy-4-methoxyacetophenone nicotinic acid hydrazone (H_2L^2) was synthesized by the following method. An equimolar mixture of the nicotinic acid hydrazide and 2-hydroxy-4-methoxyacetophenone was refluxed in ethanol/methanol for 4 h (Scheme 1).

H_2L^2: Elemental *Anal.* Calc.: C, 63.15; H, 5.30; N, 14.73. Found: C, 62.94; H, 5.39; N, 14.46%.

2.3. Synthesis of complexes

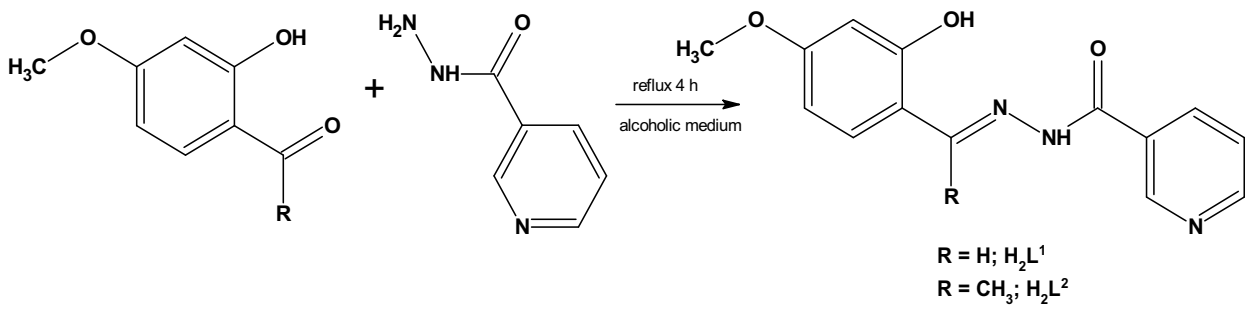
The complexes $[VOL^1]_2 \cdot H_2O$ (**1**) and $[VOL^2]_2 \cdot H_2O$ (**4**) were prepared by refluxing 1 mmol of $VOSO_4 \cdot H_2O$ in aqueous solution and 1 mmol of the corresponding ligand (H_2L^1 in ethanol or H_2L^2 in methanol) for 4 h. The complexes $[VOL^1bipy]$ (**2**), $[VOL^1phen] \cdot 1.5H_2O$ (**3**), $[VOL^2(OCH_3)]_2$(**5**) and $[VOL^2phen] \cdot 2H_2O$ (**6**) were prepared by refluxing 1 mmol each of $VOSO_4 \cdot H_2O$ in aqueous solution, heterocyclic base (bipy/ phen) in solid form and the corresponding ligand (H_2L^1 ethanol or H_2L^2 in methanol) for 4 h. In complex **5**, the base added was not incorporated and oxovanadium(IV) is oxidized to oxovanadium(V) to form a dimeric product. The structure has been determined by single crystal X-ray diffraction studies. But the yield was too low to do the remaining studies.

2.4. Physical measurements

Elemental analysis of the ligands and complexes were carried out using a Vario EL III CHNS analyzer at SAIF, Kochi, India. Infrared spectra were recorded on a JASCO FT/IR-4100 type A spectrometer in the range 4000–400 cm^{-1} using KBr pellets. Electronic spectra were recorded on a Cary 5000 version 1.09 UV–Vis–NIR spectrophotometer using DMF as the solvent. The EPR spectra of the complexes in the solid state at 298 K and in DMF at 77 K were recorded on a Varian E-112 spectrometer using TCNE as the standard, with 100 kHz modulation fre-

Table 1
Crystal data and structure refinement parameters for $[VOL^2(OCH_3)]_2$ (**5**)

Empirical formula	$C_{32}H_{32}N_6O_{10}V_2$
Formula weight	762.52
Temperature (K)	150(2)
Wavelength (Å)	0.71073
Crystal system	triclinic
Space group	$P\bar{1}$
Unit cell dimensions	
a (Å)	7.8134(8)
b (Å)	10.7745(11)
c (Å)	11.329(4)
α (°)	61.36(2)
β (°)	79.627(16)
γ (°)	70.835(9)
Volume (Å^3)	790.3(3)
Z	1
D_{calc}(Mg/m^3)	1.602
Absorption coefficient (mm^{-1})	0.662
F(000)	392
Crystal size (mm)	0.33 × 0.18 × 0.16
θ Range for data collection (°)	2.99–25.00
Index ranges	$-9 \leqslant h \leqslant 9$, $-12 \leqslant k \leqslant 12$, $-13 \leqslant l \leqslant 13$
Reflections collected	7950
Independent reflections (R_{int})	2760 (0.0152)
Refinement method	full-matrix least-squares on F^2
Data/restraints/parameters	2760/0/229
Goodness-of-fit on F^2	1.083
Final R indices [$I > 2\sigma(I)$]	$R_1 = 0.0235$, $wR_2 = 0.0655$
R indices (all data)	$R_1 = 0.0257$, $wR_2 = 0.0666$
Largest difference in peak and hole (e A^{-3})	0.269 and −0.305



Scheme 1.

quency and 9.1 GHz microwave frequency at the SAIF, IIT Bombay, India.

2.5. X-ray crystallography

A dark green crystal of the compound **5** having approximate dimensions of 0.33 × 0.18 × 0.16 mm^3 was sealed in glass capillary. The crystallographic data and structure refinement parameters for the complex **5** are given in Table 1.

The X-ray diffraction data for the compound was measured at 150(2) K, data acquisition, cell refinement and data reduction were done using the CRYSALIS CCD, Oxford Diffraction Ltd. [12]. The structure was solved by direct methods and full-matrix least-squares refinement using SHELX97 [13] package. The positions of all the non-hydrogen atoms were included in the full-matrix least-squares refinement using SHELX97 program and all the hydrogen atoms were fixed in calculated positions for compound **5**.

Table 2
Colors and partial elemental analyses data of oxovanadium(IV) complexes

Compound	Color	Found (Calc.) %		
		C	H	N
$[VOL^1]_2 \cdot H_2O$ (**1**)	Brown	48.60(48.71)	3.51(3.50)	14.08(14.22)
$[VOL^1bipy]$ (**2**)	Brown	58.26(58.54)	3.95(3.89)	13.35(12.89)
$[VOL^1phen] \cdot 1.5H_2O$ (**3**)	Brown	57.50(57.46)	4.04(4.08)	12.96(12.89)
$[VOL^2]_2 \cdot H_2O$ (**4**)	Greenish yellow	50.20(50.15)	3.70(3.93)	11.70(11.70)
$[VOL^2(OCH_3)]_2$ (**5**)	Green	50.52(50.40)	4.38(4.23)	11.01(11.02)
$[VOL^2phen] \cdot 2H_2O$ (**6**)	Brown	57.30(57.25)	4.60(4.45)	11.80(12.36)

3. Results and discussion

After double deprotonation, hydrazones coordinate as tridentate ligands in the enolate form (L^{2-}) in all the complexes. The colors and partial elemental analyses of the complexes are presented in Table 2. The elemental analyses of the complexes are in agreement with the general formula $[(VOL)_2]$ (for complexes **1** and **4**); [VOLB] (for complexes **2**, **3** and **6**) and $[VOLX]_2$ (for complex **5**). X-ray quality single crystals of the compound **5** were obtained by slow evaporation of its solution in CH_3OH/ H_2O mixture over a period of one week.

3.1. Crystal structure of the compound $[VOL^2(OCH_3)]_2$(5)

The molecular structure of the compound **5** along with atom numbering scheme is given in Fig. 1. The selected bond lengths and bond angles of the molecule is summarized in Table 3. Compound **5** crystallizes in the triclinic crystal system with a space group $P\bar{1}$. This is a centrosymmetric bis(μ-methoxy) bridged vanadium(V) dimer consists of one vanadium atom (V1), one terminal oxo group (O3), one methoxy oxygen (O5), tridentate hydrazone ligand binding to the metal center *via* phenoxy oxygen (O2), azomethine nitrogen (N1), enolic oxygen (O3) atoms. The vanadium(V) ions in the dimer exhibit distorted octahedral geometry with O3, N1, O2, O5 atoms defining the equatorial plane and O4 and O5a atoms at the apical positions;

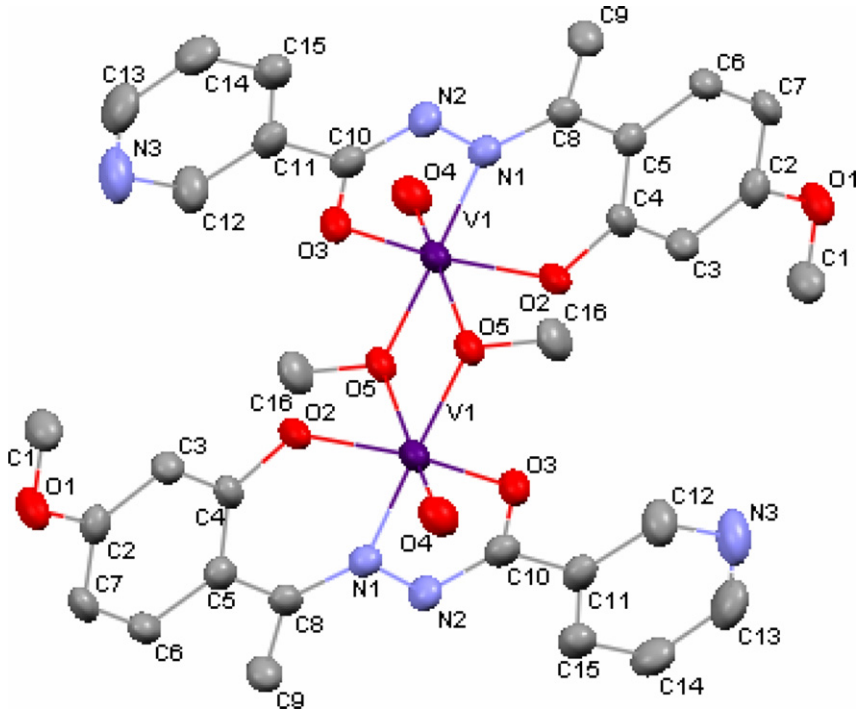


Fig. 1. Structure and labeling scheme for $[VOL^2(OCH_3)]_2$ (**5**).

Table 3
Selected bond lengths (Å) and bond angles (°) for the compound **5**

Bond lengths		Bond angles		Bond angles	
V(1)–O(4)	1.5895(12)	O(4)–V(1)–O(5)	104.33(6)	O(2)–V(1)–O(5a)	79.74(5)
V(1)–O(5)	1.8207(13)	O(4)–V(1)–O(2)	100.96(6)	O(3)–V(1)–O(5a)	80.04(4)
V(1)–O(2)	1.8215(11)	O(5)–V(1)–O(2)	104.11(5)	N(1)–V(1)–O(5a)	83.64(5)
V(1)–O(3)	1.9258(11)	O(4)–V(1)–O(3)	99.47(6)	C(4)–O(2)–V(1)	129.08(10)
V(1)–N(1)	2.1062(15)	O(5)–V(1)–O(3)	88.97(5)	C(10)–O(3)–V(1)	118.21(10)
V(1)–O(5a)	2.3656(11)	O(2)–V(1)–O(3)	152.07(5)	C(16)–O(5)–V(1)	123.43(10)
O(2)–C(4)	1.3381(19)	O(4)–V(1)–N(1)	96.92(6)	C(16)–O(5)–V(1a)	120.55(9)
O(5)–C(16)	1.4283(19)	O(5)–V(1)–N(1)	155.34(5)	V(1)–O(5)–V(1a)	105.01(5)
O(5)–V(1a)	2.3656(11)	O(2)–V(1)–N(1)	83.62(5)	C(8)–N(1)–N(2)	116.57(13)
N(1)–C(8)	1.310(2)	O(3)–V(1)–N(1)	75.16(5)	C(8)–N(1)–V(1)	127.99(11)
N(1)–N(2)	1.3999(18)	O(4)–V(1)–O(5a)	179.14(5)	N(2)–N(1)–V(1)	115.44(9)
N(2)–C(10)	1.305(2)	O(5)–V(1)–O(5a)	74.99(5)	C(10)–N(2)–N(1)	108.11(13)

the metal atom is displaced towards the axial oxo atom (O4) by 0.3548 Å from the equatorial plane.

The terminal V1–O4 (oxo) distance is 1.5896 Å, V1–O5a (bridging) is 2.3655 Å, V1–O2 (phenoxy) is 1.8215 Å and V1–O3 (ketoxy) is 1.9258 Å, these agree well with the corresponding values reported for related systems. The trans influence of the oxo (O4) ligand in one apical position of the vanadium octahedron manifests itself by elongation of the bond distance for the apically bonded bridging methoxy oxygen atom [V1–O5a = 2.3655 Å] when compared to the distance for the other methoxy oxygen atom [V1–O5 = 1.8208 Å]. The intramolecular V1–V1a distance is found to be 3.338 Å and falls within the range of known V–V distances in double bridged vanadium polynuclear systems. The centrosymmetric dimer is formed *via* the bridging oxygens connecting two vanadium atoms. Hence the vanadium atom adopts a distorted octahedral geometry [14,15].

The mean plane deviation calculations show that the atoms in the basal plane O3, N1, O2 and O5 are nearly planar with a maximum mean plane deviation of 0.007 Å and V1 is slightly deviated from planarity with a distance of 0.3548 Å. Ring puckering analyses and least-square plane

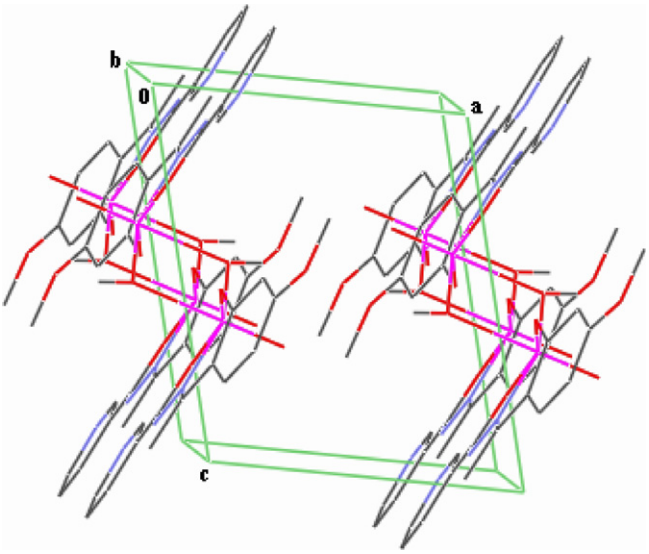


Fig. 2. Unit cell packing diagram of the compound **5** viewed along the *b* axis.

Table 4
Interaction parameters of the compound **5**

Cg(*I*)–Res(1)···Cg(*J*)	Cg–Cg (Å)	α (°)		β (°)
π–π interactions				
Cg(2)[1]→Cg(1)[a]	2.6355	79.49		55.81
XH(I)···Cg(*J*)	H···Cg (Å)	X–H···Cg (°)		X···Cg (Å)
C–H···π interactions				
C(1)–H(1C)→Cg(5)[b]	2.80	145		3.6214
D–H···A	D–H	H···A	D···A	D–H···A
H bonding				
C(12)–H(12)–O(3)	0.93	2.39	2.748(3)	102

Equivalent position codes: $a = 2 - x, 1 - y, -z$; $b = 1 - x, 1 - y, 1 - z$.
Cg(2) = V(1),O(3),C(10),N(2),N(1), Cg(1) = V(1),O(5),V(1A),O(5a), Cg(5) = C(2),C(3),C(4),C(5),C(6),C(7).
D = donor, A = acceptor, Cg = centroid, α = dihedral angles between planes *I* and *J*, β = angle Cg(1)–Cg(*J*).

Table 5
Selected IR bands (cm^{-1}) with tentative assignments of oxovanadium(IV) complexes

Compound	ν(C=O)	ν(C=N)	ν(V=O)	ν(C–O)	ν(V–O)	ν(V–N)
H_2L^1	1643	1604				
H_2L^2	1638	1602				
$[VOL^1]_2 \cdot H_2O$ (**1**)		1600	961	1255	548	427
$[VOL^1bipy]$ (**2**)		1607	953	1232	560	427
$[VOL^1phen] \cdot 1.5H_2O$ (**3**)		1596	956	1239	555	424
$[VOL^2]_2 \cdot H_2O$ (**4**)		1587	977	1246	562	422
$[VOL^2phen] \cdot 2H_2O$ (**6**)		1597	940	1246	561	428

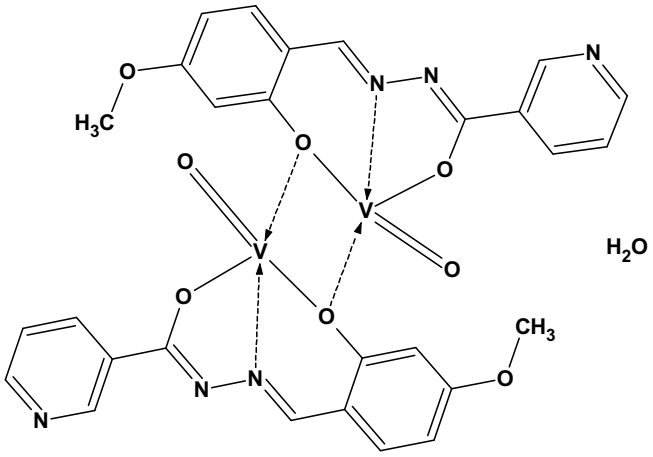


Fig. 3. Tentative structure of the complex $[VOL^1].H_2O$ (**1**).

calculations show that the ring Cg(3) comprising of atoms V1, O2, C4, C5, C8 and N1 confirms the 'screw boat' conformation ('S' configuration) [16].

Table 6
Electronic spectral assignments (cm^{-1}) of oxovanadium(IV) complexes

Compound	π–π^*	n–π^*	LMCT
H_2L^1	33557	30581	
H_2L^2	33367	30303	
$[VOL^1]_2 \cdot H_2O$ (**1**)	36764	30864	24691
$[VOL^1bipy]$ (**2**)	33222	29761	24096
$[VOL^1phen] \cdot 1.5H_2O$ (**3**)	34129	30487	24154
$[VOL^2]_2 \cdot H_2O$ (**4**)	36496	31948	25316
$[VOL^2phen] \cdot 2H_2O$ (**6**)	36232	31645	25445

Fig. 2 shows the contents of the unit cell packing. The assemblage of molecules in the respective manner in the unit cell is resulted by the π–π and C–H–π interactions as depicted in Table 4. The centroid Cg(2) is involved in π–π interaction with Cg(1) of the neighbouring unit at a distance of 2.6355 Å and C–H–π interactions C(1)–H(1C)→Cg(5) at a distance of 2.80 Å contribute stability to the unit cell packing. A weak intramolecular hydrogen bonding interaction is observed between C12–H12 and

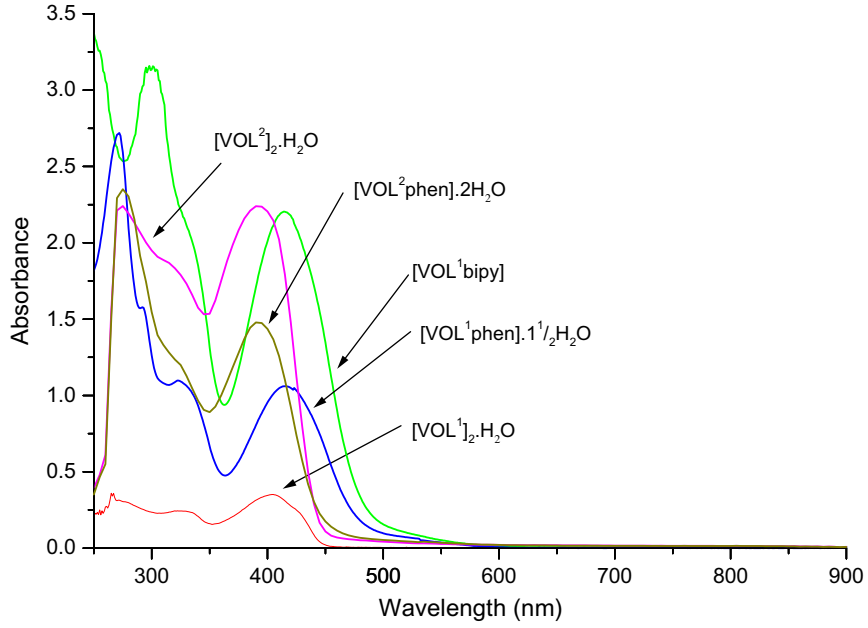


Fig. 4. Electronic spectra of the oxovanadium(IV) complexes.

Table 7
EPR spectral assignments of oxovanadium(IV) complexes in polycrystalline state at 298 K and DMF solution at 77 K

Compound	Polycrystalline state (298 K)	DMF solution (77 K)			
		$g_\parallel$	$g_\perp$	$A_\parallel^a$	$A_\perp^a$
$[VOL^1]_2 \cdot H_2O$ (**1**)	1.985/2.072 ($g_\parallel/g_\perp$)	1.950	1.984	162.6	53.4
$[VOL^1bipy]$ (**2**)	1.989 (g_{iso})	1.953	1.978	160.3	52.6
$[VOL^1phen] \cdot 1.5H_2O$ (**3**)	1.984 (g_{iso})	1.949	1.983	161.0	55.8
$[VOL^2]_2 \cdot H_2O$ (**4**)	1.991 (g_{iso})	1.951	1.981	159.9	55.6
$[VOL^2phen] \cdot 2H_2O$ (**6**)	1.990 (g_{iso})	1.948	1.977	162.7	55.5

[a] Expressed in units of cm^{-1} multiplied by a factor of 10^{-4}.

O3 with an angle of 102°. No classic hydrogen bonds were found in this compound.

3.2. Infrared and electronic spectral studies

Selected vibrational bands of the free ligands and their vanadium complexes, which are useful for determining the mode of coordination of the ligands, are given in Table 5. The ligands exhibit bands in the regions 1638–1643, 3023–3182 and 3222–3421 cm^{-1} due to C=O, N–H and O–H stretches, respectively. These bands disappear on complexation, indicating the transformation of carbonyl moiety to enolic moiety and consequent replacement of the phenolic and enolic hydrogens [7]. A new band appearing in the 1232–1255 cm^{-1} region in the metal complexes was assigned to the ν(C–O) (enolato) mode [17]. The shifting of ν(C=N)

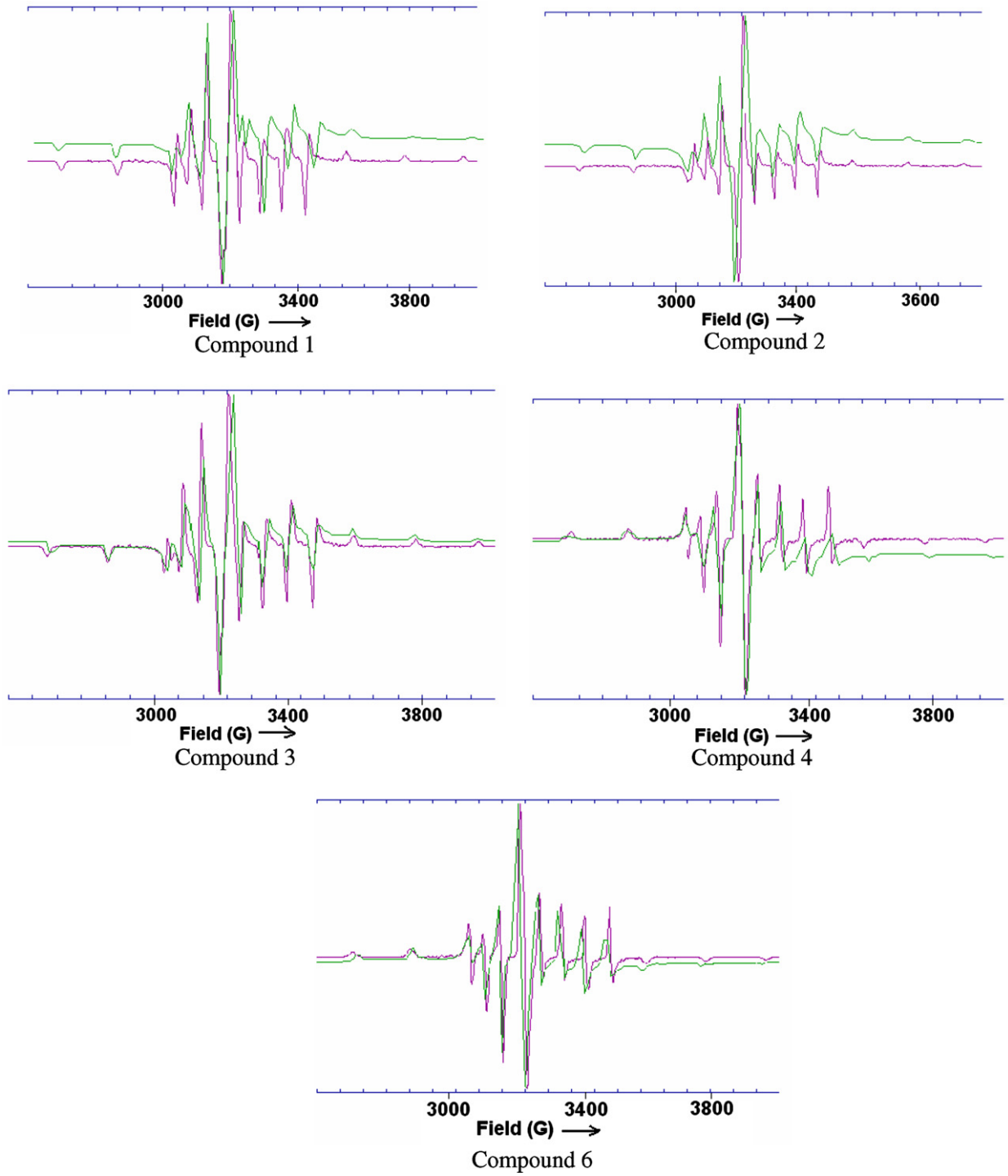


Fig. 5. Experimental (green) and simulated best fit (purple) of the EPR spectra of complexes **1**, **2**, **3**, **4** and **6** in DMF at 77 K. (For interpretation of the references to colour in this figure legend, the reader is referred to the web version of this article.)

(azomethine) of the ligands (1602–1604 cm^{-1}) to lower wavenumbers in the metal complexes (1587–1600 cm^{-1}) indicates the coordination of azomethine nitrogen to the metal. A ligand characteristic band at *ca.* 1025 cm^{-1} due to ν(N–N) stretch undergoes a shift to a higher wavenumbers upon complexation due to diminished repulsion between the lone pairs of adjacent nitrogen atoms [18]. Furthermore, the bands in the regions 548–562 and 422–428 cm^{-1} can be assigned to the stretching modes of the metal to ligand bonds, ν(V–O) and ν(V–N), respectively [19]. In addition, the compounds exhibit a strong band in the 940–977 cm^{-1} range due to the terminal V=O stretching, indicates hexacoordinated environment around the metal center. Complexes **1** and **4** have a band in the region 833–845 cm^{-1} indicating V–O–V bridge vibrations [20]. Tentative structure of compound **1** is shown in Fig. 3.

The electronic spectra of the complexes in DMF solution are presented in the Table 6. The hydrazone ligands and their vanadium(IV) complexes have bands in the range 33 000–36 000 cm^{-1} corresponding to $\pi \rightarrow \pi^*$ of the azomethine group and bands in the range 29 500–32 000 cm^{-1} due to $n \rightarrow \pi^*$ of the carbonyl group. In all the complexes an intense band at *ca.* 24 740 cm^{-1} is assignable to the phenolic oxygen$\rightarrow V_{(d\pi)}$ ligand to metal charge transfer (LMCT) band [21,22]. The d–d bands expected at higher energy regions are probably obscured by the tail of the LMCT absorption. Representative spectra of the complexes along with the simulations are presented in Fig. 4.

3.3. EPR spectra

EPR spectra of all the oxovanadium(IV) complexes (**1**–**4** and **6**) were recorded in polycrystalline state at 298 K and in DMF solution at 77 K. In polycrystalline state at 298 K, the compound **1** is axial with $g_{\parallel} = 1.985$ and $g_{\perp} = 2.072$ G and the other complexes are isotropic with $g_{iso} \sim 1.988$ G.

In frozen DMF solution at 77 K, two sets of eight line spectra showing hyperfine splitting due to the ^{51}V nucleus ($I = 7/2$) are obtained in all the complexes. The spectral parameters are given in Table 7 and the experimental and simulated best fits[1] of EPR spectra of all the complexes are given in Fig. 5. All the compounds show well-resolved axial anisotropy with two sets of eight line pattern with $g_{\parallel} < g_{\perp}$ and $A_{\parallel} \gg A_{\perp}$ relationship characteristic of an axially compressed d^1_{xy} configuration [23]. Ligand nitrogen or hydrogen superhyperfine splittings are not observed on the vanadium line. This indicates that the unpaired electron to be in b_{2g} (d_{xy}, $^2B_2$ ground state) orbital localized on metal, thus excluding the possibility of its direct interaction with the ligand [24,25]. The EPR data of Table 7 reveals that phen slightly increases $A_{\parallel}$ and decreases $g_{\parallel}$, compared to bipy for an identical primary ligand. For an identical auxiliary ligand, the complexes with $(L^2)^{2-}$ species have slightly higher $A_{\parallel}$ values compared to the complexes associated with $(L^1)^{2-}$ species. For complexes with different principal ligand and without auxiliary ligand, $(L^2)^{2-}$ species have slightly higher $A_{\parallel}$ values compared to $(L^1)^{2-}$ species.

[1] The authors thank Professor M.V. Rajasekharan, School of Chemistry, University of Hyderabad for EPR simulation package.

Acknowledgements

M.R.P. Kurup is thankful to CSIR, New Delhi, India [01(1963)/05/EMR-II] for financial assistance. The authors are thankful to the SAIF, Cochin University of Science and Technology, Kochi, Kerala, India for elemental analyses. We are thankful to the National Single Crystal X-ray diffraction studies, IIT, Bombay, India for providing single crystal XRD results.

Appendix A. Supplementary data

CCDC 669785 contains the supplementary crystallographic data for $[VOL^2 \cdot OCH_3]_2$. These data can be obtained free of charge via http://www.ccdc.cam.ac.uk/conts/retrieving.html, or from the Cambridge Crystallographic Data Centre, 12 Union Road, Cambridge CB2 1EZ, UK; fax: (+44) 1223-336-033; or e-mail: deposit@ccdc.cam.ac.uk. Supplementary data associated with this article can be found, in the online version, at doi:10.1016/j.poly.2008.01.020.

References

[1] L.F. Linday, S.E. Livingstone, Coord. Chem. Rev. 2 (1967) 173.
[2] H. Beraldo, D. Gambino, Mini. Rev. Med. Chem. 4 (2004) 159.
[3] T. Hirao, M. Mori, Y. Oshiro, J. Org. Chem. 55 (1990) 358.
[4] T. Hirao, T. Fujii, T. Tanaka, Y. Oshiro, J. Chem. Soc., Perkin Trans. 1 (1994) 3.
[5] D. Rehder, Coord. Chem. Rev. 182 (1999) 297.
[6] D.C. Crans, J. Inorg. Biochem. 80 (2000) 123.
[7] P.K. Samal, A.K. Patra, M. Nethaji, A.R. Chakravarthy, Inorg. Chem. 46 (2007) 11112.
[8] P.B. Sreeja, M.R.P. Kurup, Spectrochim. Acta, Part A 61 (2005) 331.
[9] D. Wang, M. Ebel, C. Schulzke, C. Gruning, K.S. Hazari, D. Rehder, Eur. J. Inorg. Chem. (2001) 935.
[10] S.N. Rao, D.D. Mishra, R.C. Maurya, N.N. Rao, Polyhedron 16 (1997) 1825.
[11] N. Mathew, M. Kuriakose, E.B. Seena, M.R.P. Kurup, Acta Crystallogr., Sect. E 63 (2007) o2190.
[12] CRYSALIS CCD and CRYSALIS RED Versions 1.171.29.2 (CrysAlis171.NET), Oxford Diffraction Ltd., Abingdon, Oxfordshire, England, 2006.
[13] G.M. Sheldrick, SHELXL97, SHELXS97, University of Göttingen, Germany, 1997.
[14] S. Mondal, M. Mukherjee, K. Dhara, S. Ghosh, J. Ratha, P. Banerjee, A.K. Mukherjee, Crystal Growth and Design (2007), doi:10.1021/cg060753i.
[15] A. Sreekanth, S. Sivakumar, M.R.P. Kurup, J. Mol. Struct. 655 (2003) 47.
[16] D. Cremer, J.A. Pople, J. Am. Chem. Soc. 97 (1975) 1354.
[17] S. Bhattacharya, T. Ghosh, Indian J. Chem. 38A (1999) 601.
[18] C. Tsiamis, B. Voulgaropoulos, D. Christos, G.P. Vonstas, C.A. Kavounis, Polyhedron 19 (2000) 2003.
[19] E.J. Baran, J. Coord. Chem. 54 (2001) 215.

[20] S.K. Dutta, S.B. Kumar, S. Bhattacharyya, E.R.T. Tiekink, M. Chaudhury, Inorg. Chem. 36 (1997) 4954.
[21] F.A. Walker, R.L. Carlin, P.H. Rieger, J. Chem. Phys. 45 (1966) 4181.
[22] M. Kuriakose, M.R.P. Kurup, E. Suresh, Polyhedron 26 (2007) 2713.
[23] G.R. Hausan, T.A. Kabanos, A.D. Kkeramidas, D. Mentazafos, A. Terzis, Inorg. Chem. 31 (1992) 2587.
[24] T. Ghosh, S. Bhattacharya, A. Das, G. Mukherjee, M.G.B. Drew, Inorg. Chim. Acta 358 (2005) 989.
[25] N. Raman, J.D. Raja, A. Sakthivel, J. Chem. Sci. 119 (2007) 303.

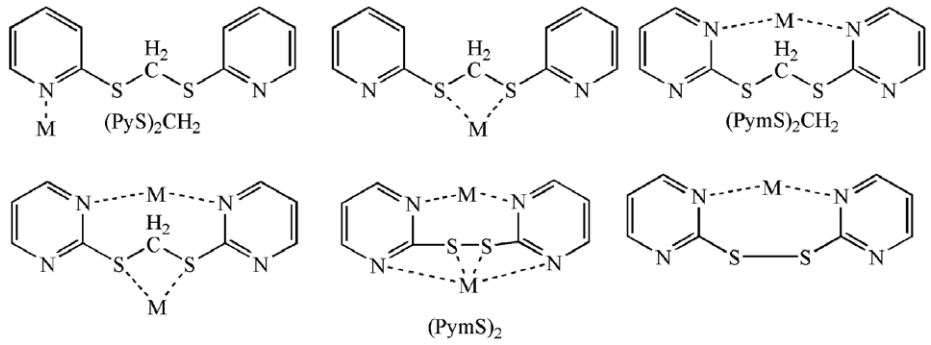


Fig. 1. Coordination modes of $(PyS)_2CH_2$, $(PymS)_2CH_2$ and $(PymS)_2$.

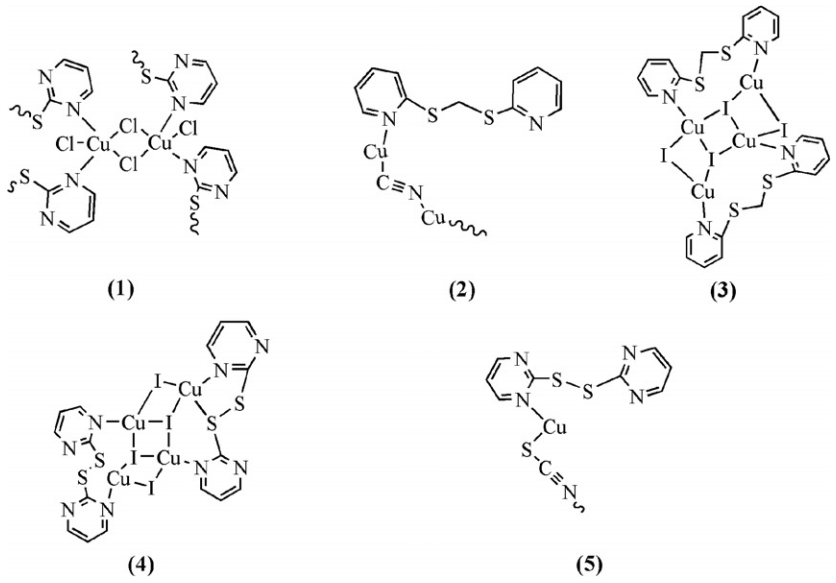


Fig. 2. Products **1**–**5** from the reactions of $(PyS)_2CH_2$, $(PymS)_2CH_2$ and $(PymS)_2$ with copper halides and pseudo halides.

advantage of these precursors is that they provide the opportunity for anion incorporation, which promotes the isolation of uncharged motifs that have accessible channels for possible small molecule adsorption. Traditionally, the synthesis of copper polymers has involved high temperature reactions as it was believed this was required to form metastable phases that would not be accessible at lower temperatures [2b,12]. For example, the reaction of CuSCN with 1,2,-bis(4pyridyl)bipyridylethane (bpa), to form the infinite polymer $[Cu(SCN)_2bpa]_\infty$, involves vacuum synthesis at 180 °C [11c]. On the other hand, slow diffusion or co-crystallization techniques have yielded polymeric chains, but usually in low yields [11a,13]. Instead of these typical methods, we wished to investigate synthetic routes that employ mild conditions and result in air stable products that can be isolated in moderate yields, thus allowing exploration of their further chemistry. Experimentally it was determined that reaction of the copper precursor and ligand in acetonitrile, followed by over night heating to 70–100 °C, afforded a series of copper complexes that vary structurally depending on the copper precursor selected. Compounds **1**–**5**, Fig. 2, were isolated at ambient conditions as thermally stable crystalline materials, in moderate to high yield. Here in we report the results of the investigation of $(PyS)_2CH_2$, $(PymS)_2CH_2$ and $(PymS)_2$ with copper halides and pseudo halides.

2. Experimental

The synthesis of $(PyS)_2CH_2$ [14] and $(PymS)_2CH_2$ [15] were performed according to the published procedure. $(PymS)_2$ was prepared through modification of the literature procedure[1].

[1] 2-Mercaptopyrimidine (1.68 g, 15 mmol) was added to a stirred solution of potassium hydroxide (0.84 g, 15 mmol) in ethanol (60 mL). The mixture was warmed to reflux and then bromoform (1.3 mL, 15 mmol) was added drop-wise. The resultant mixture was refluxed for 24 h. After adding water (90 mL), the mixture was left to stand overnight. The yellow precipitate was filtered off and washed with cold ethanol and cold water giving a brown solid that was recrystallized from hot ethanol and water (1.30 g).

Table 1
Crystal data for all complexes

Compound name	1	2	3	4	5
Chemical formula	$C_9H_8Cl_2CuN_4S_2$	$C_{12}H_{10}CuN_3S_2$	$C_{22}H_{20}Cu_4I_4N_4S_4$	$C_{16}H_{12}Cu_4I_4N_8S_4$	$C_9H_6CuN_5S_3$
Formula weight	370.75	323.89	1230.42	1206.34	343.91
Crystal system	monoclinic	orthorhombic	triclinic	monoclinic	monoclinic
Space group	$P2(1)/c$	$P2(1)2(1)2(1)$	$P\bar{1}$	$P2(1)/c$	$P2(1)/c$
T (K)	223(2)	223(2)	223(2)	213(2)	223(2)
a (Å)	10.5531(11)	8.7016(11)	8.9760(13)	10.6418(9)	8.4826(7)
b (Å)	11.7012(12)	10.3863(13)	9.2164(13)	10.8611(9)	13.9955(12)
c (Å)	12.3481(10)	14.6171(19)	10.4439(15)	13.5162(8)	11.1165(9)
α (°)	90	90	70.630(2)	90	90
β (°)	118.280(6)	90	88.535(2)	113.183(5)	110.7400(10)
γ (°)	90	90	76.640(2)	90	90
V (Å^3)	1342.8(2)	1321.1(3)	791.8(2)	1436.08(19)	1234.21(18)
Z	4	4	1	2	4
$F(000)$	740	656	572	1112	688
Reflections collected	8333	7776	4612	7375	11 855
Independent reflections (R_{int})	3184 (0.0362)	3098 (0.0291)	3498 (0.0162)	2578 (0.1782)	2226 (0.0276)
Data/restraint/parameter	3184/0/163	3098/0/164	3498/0/172	2578/0/163	2226/0/163
R indices, all data	$R_1 = 0.0519$, $wR_2 = 0.0808$	$R_1 = 0.0408$, $wR_2 = 0.0640$	$R_1 = 0.0396$, $wR_2 = 0.0917$	$R_1 = 0.0728$, $wR_2 = 0.1724$	$R_1 = 0.0302$, $wR_2 = 0.0676$
Final R indices [$I > 2\sigma(I)$]	$R_1 = 0.0328$, $wR_2 = 0.0727$	$R_1 = 0.0292$, $wR_2 = 0.0594$	$R_1 = 0.0333$, $wR_2 = 0.0868$	$R_1 = 0.0693$, $wR_2 = 0.1678$	$R_1 = 0.0242$, $wR_2 = 0.0623$
Largest difference peak and hole (e Å^{-3})	0.457 and −0.395	0.419 and −0.230	1.703 and −1.310	3.169 and −3.700	0.501 and −0.350

All chemicals were purchased from Aldrich or Acros and used as received. Melting points were preformed on a Meltemp apparatus under ambient conditions. In a typical experiment, the ligand and copper salt in a 1:1 mol ratio were dissolved in acetonitrile and heated to between 80 and 90 °C for 12 h. Grease free Teflon sealed Schlenk flasks were employed to avoid grease contamination and to allow heating of a sealed system. All crystals were obtained from slow evaporation of the solution at room temperature. Crystal data were collected with a Bruker SMART 1000 diffractometer using graphite monochromated molybdenum radiation ($\lambda = 0.7107$ Å). Crystals were attached to glass fibers using paratone oil and data were collected at −60 °C. The data were corrected for absorption. Structures were solved by direct methods using the SHELXS-97 [16,17] program and refined via full-matrix least squares [16,17]. Crystal data for all compounds are given in Table 1.

2.1. Synthesis of 1: $[(PymS)_2CH_2Cu(\mu Cl)Cl]_\infty$

In a grease free Schlenk flask, 5 mL of acetonitrile, $CuCl_2 \cdot 2H_2O$ (0.04 g, 0.23 mmol) and $(PymS)_2CH_2$ (0.05 g, 0.21 mmol) were added together. The reaction mixture was heated at ~100 °C for 14 h. After 14 h, the green colored reaction mixture was gravity filtered to remove insoluble impurities. The solution was kept at room temperature for 2 days, during which time large, teal green crystals, suitable for single crystal analysis were isolated. M.Pt. decomposes at 150–152 °C, yield: 0.045 g (51% with respect to $CuCl_2 \cdot 2H_2O$) IR (KBr pellet, υ cm^{-1}): 2956.1 (s), 2923.8 (s), 2855.3 (s), 1614.9 (m), 1578.7 (m), 1461.9 (m), 1449.8 (m), 1386.0 (m), 1181.4 (m), 817.5 (m), UV–Vis (CH_3CN): λ max (nm) = 254, 311, 462.

2.2. Synthesis of 2: $[(PyS)_2CH_2CuCN]_\infty$

In a grease free Schlenk flask, 5 mL of acetonitrile, CuCN (0.035 g, 0.391 mmol) and $(PymS)_2CH_2$ (0.1 g, 0.391 mmol) were mixed. The reaction mixture was stirred at 80–100 °C for 14 h. After cooling to room temperature the colorless solution was gravity filtered to remove insoluble particles. The solution was stored overnight at room temperature, yielding colorless single crystals of **2**. M.Pt. 72–74 °C, yield: 0.049 g (39% with respect to CuCN), IR (KBr pellet, υ cm^{-1}): 2361.0 (s), 1578.2 (s), 1554.7 (s), 1465.4 (m), 1455.1 (m), 1411.7 (m), 1337.3 (m), 1285.9 (m), 1214.1 (m), 1143.4 (m), 1123.5 (m), 1040.8 (m), 986.5 (m), 755.0 (m), 740.0 (m), 714.0 (m), ^{1}H NMR (300 MHz, CD_3CN, 25 °C): 5.01 (s, 2H), 7.13 (t, 2H), 7.26 (d, 2H), 7.62 (t, 2H), 8.49 (d, 2H). UV–Vis (CH_3CN): λ max (nm) = 250, 290.

2.3. Synthesis of 3: $[(PyS)_2CH_2Cu_2I_2]_2$

CuI (0.1 g, 0.53 mmol) and $(PyS)_2CH_2$ (0.03 g, 0.12 mmol) were dissolved in ~5 mL of acetonitrile. The solution was stirred for 14 h at 80–90 °C. Following filtration, storage of the solution at room temperature afforded pale yellow crystals of **3** suitable for X-ray diffraction. M.Pt. decomposes at 145–147 °C, yield: 0.30 g (45% with respect to CuI), IR (KBr pellet, υ cm^{-1}): 2960.0 (s), 2927.8 (s), 2854.2 (m), 1449.8 (m), 1413.5 (m), 1373.3 (m), 1260.5 (m), 797.4 (s), 765.2 (s), 749.1 (m), ^{1}H NMR

(300 MHz, CD_3CN, 25 °C): 5.02 (s, 2H), 7.14 (t, 2H), 7.28 (d, 2H), 7.63 (t, 2H), 8.49 (d, 2H). UV–Vis (CH_3CN): λ max (nm): 209, 245, 360.

2.4. Synthesis of 4: $[(PymS)_2Cu_2I_2]_2$

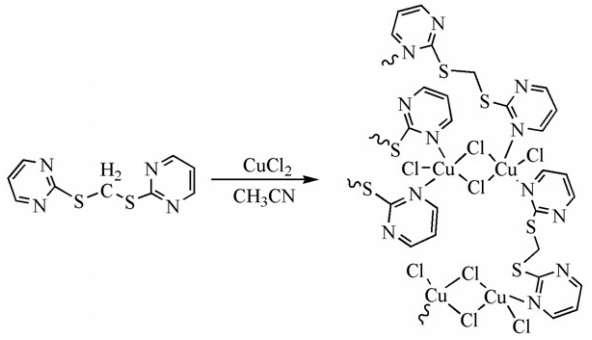
CuI (0.1 g, 0.52 mmol) and $(PymS)_2$ (0.18 g, 0.52 mmol) were dissolved in ~5 mL CH_3CN and heated to 70–80 °C for 14 h. After filtration of the yellow solution and storage at room temperature for 5 days, suitable X-ray quality yellow crystals of compound **4** were isolated. M.Pt. 175–177 °C, yield: 0.34 g (50% with respect to CuI) IR (KBr pellet, υ cm^{-1}): 2359.3 (s), 1640.2 (s), 1425.6 (m), 1376.0 (m), 1196.4 (m), 1167.2 (m), 822.6 (m), 804.9 (s), 774.1 (m), 766.9 (m), 744.4 (m), 629.0 (m), 448.5 (m), ^1H NMR (300 MHz, CD_3CN, 25 °C): 7.25 (t, 2H), 8.61 (d, 4H). UV–Vis (CH_3CN): λ max (nm) = 209, 242, 359.

2.5. Synthesis of 5: $[(PymS)_2CuSCN]_\infty$

~5 mL of acetonitrile, CuSCN (0.04 g, 0.33 mmol) and $(PymS)_2$ (0.1 g, 0.29 mmol) were added together in a grease free Schlenk flask. The reaction mixture was stirred for 14 h at 90–100 °C. The colorless solution was filtered to remove a cloudy precipitate. Slow evaporation of the colorless solution at room temperature afforded colorless crystals of **5**. M.Pt. 112–115 °C, yield: 0.037 g (30% with respect to CuSCN), IR (KBr pellet, υ cm^{-1}): 2110.1 (s), 2066.9 (s), 1550.9 (m), 1427.2 (m), 1375.6 (m), 1196.6 (m), 1169.4 (m), 817.6 (m), 767.1 (w), 743.6 (m), 629.1 (m), ^1H NMR (300 MHz, CD_3CN, 25 °C): 6.91 (t, 2H), 6.94 (t, 2H), 8.10 (d, H), 8.30 (d, 4H). UV–Vis (CH_3CN): λ max = 236 nm.

3. Results and discussion

The reaction of (bispyrimidylthio)methane with $CuCl_2$ afforded teal paramagnetic crystals of the complex $[(PymS)_2CH_2CuCl_2]_\infty$ as shown in Scheme 1. Experimentally it was determined that the choice of solvent is important. Attempts using tetrahydrofuran, benzonitrile, ethanol, water or toluene were all unsuccessful and no coordination of the ligand to the metal was observed. For all reactions acetonitrile was used as the solvent.



Scheme 1. Synthesis of $[(PymS)_2CH_2Cu(\mu Cl)Cl]_n$.

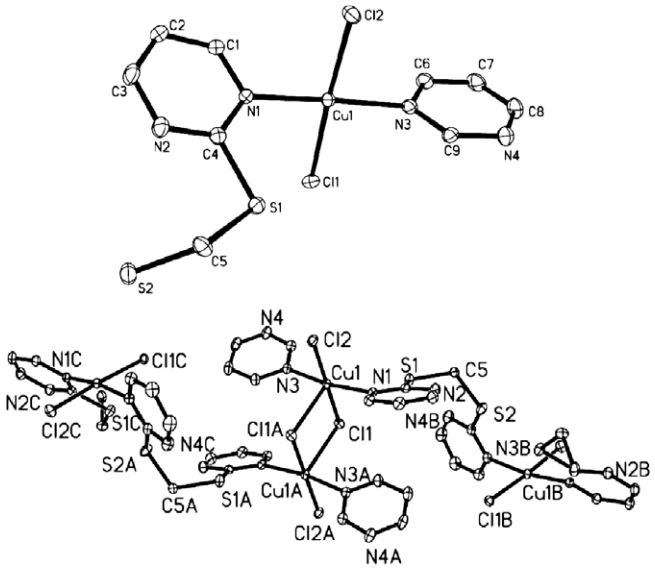


Fig. 3. Diagram of the asymmetric crystallographic unit and the polymeric structural motif. Thermal ellipsoids shown at 30% probability level, hydrogen atoms are omitted for clarity. Selected bond lengths (Å) and angles (°): Cu(1)–N(1) 2.049(2), Cl(1)–Cu(1)–N(1) 93.04(6), N(3)–Cu(1)–Cl(2) 88.11(7), Cl(1)–Cu(1)–Cl(1a) 85.97(3).

The overall structural motif can be described as two-dimensional sheet with the interchain linkage provided by the organic ligand. The X-ray crystal structure of **1** is exhibited in Fig. 3.

The geometry around each copper atom is five coordinate corresponding to distorted trigonal bypyrimidal geometry. The ligand bridges the copper centers. Every copper atom is coordinated to two nitrogen atoms, N(1) and N(3), from pyrimidine groups provided by two different ligand molecules. Making up the remaining two coordination sites on copper are chloride atoms, Cl(1) bridges two copper centers (μ2) while the other remains terminal. The bond lengths of the chlorides vary only slightly, the terminal chloride has a Cu–Cl distance of 2.2468(8) Å compared to the bridged Cu–Cl distance of 2.2822(7) Å. Compound **1** can be compared to a previously reported structure $[CuCl_2(\mu\text{-dpds})]$ (dpds = dipyridyl disulfide) (**A**) [18], Fig. 4, that was isolated from the similar reaction of bis(2pyridylthio)methane with $CuCl_2$.

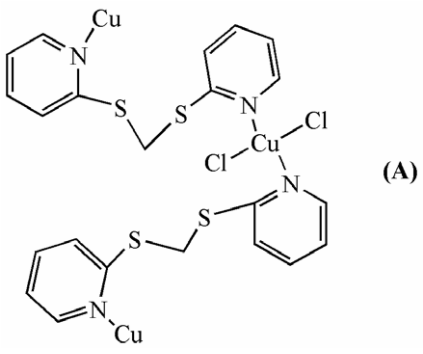


Fig. 4. Structurally similar molecule to (1), from the reaction of $CuCl_2$ with bptm [18].

Comparison of the structures of $[CuCl_2(\mu\text{-dpds})]$ with $[(PymS)_2CH_2Cu(\mu Cl)Cl]_\infty$ (**1**) reveals distinct differences that likely arise from the different experimental procedures. $[CuCl_2(\mu\text{-dpds})]$ was formed from the slow diffusion of methanol solution of copper(II) chloride and the ligand. The main difference between the two structures is that in **A** the chloride atoms do not bridge, instead they retain their trans geometry yielding an infinite helical chain. The bridging halides in complex **1** help minimize the distance between the pyridyl layers, by constraining the geometry. The Pym–Pym distance is 3.697 Å (between corresponding aromatic carbons), which is relatively short and so should allow π–π stacking, however the arrangement of the pyrimidyl rings are slightly twisted. Comparison of the bond lengths and angles between $[CuCl_2(\mu\text{-dpds})]$ and **1** show good similarity, and are detailed in Table 2.

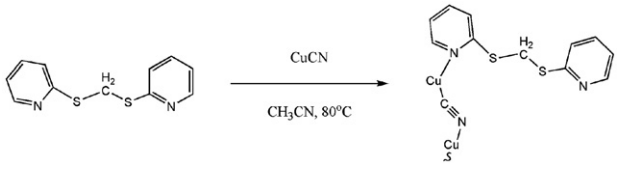
Polymer **1** is soluble in common organic solvents and is relatively thermally stable, melting to a green liquid at 150–152 °C. The UV–Vis spectrum of **1** showed broad adsorptions between 250 and 470 nm which are assigned as Cu–ligand charge transfer transitions. Luminescence measurements were attempted in acetonitrile at room temperature, but no meaningful data could be obtained.

In an attempt to further develop polymeric networks, the reaction of $(PyS)_2CH_2$ with CuCN was performed, Scheme 2. CuCN has limited solubility in acetonitrile, but the reaction proceeds as a suspension, however the lower yield of the product (39%) is due to the lower solubility of the metal salt.

Colorless crystals of **2** (Fig. 5) were isolated at room temperature and crystallize in the orthorhombic, chiral space group, $P2(1)2(1)2(1)$. Solid-state X-ray analysis revealed the ambidentate CN ligand bridges each copper center and is coordinated to a nitrogen atom of the pyridyl group from bis(bipyridylthio)methane. This results in each copper center having two cyanide groups, giving rise to distorted trigonal planar geometry. The C–N distance of

Table 2
Comparison of the bond lengths (Å) between complexes $[CuCl_2(\mu\text{-dpds})]$ [18] and (**1**)

	$[CuCl_2$ $(\mu\text{-dpds})]$ (**A**)	$[(PymS)_2CH_2$ $Cu(\mu Cl)Cl]_\infty$ (**1**)
Cu–N(1)	2.047(3)	2.049(2)
Cu–N(2) for **A**, N(3) for **1**	2.045(1)	2.038(2)
Cu–Cl(1)	2.2840(9)	2.2822(7)
Cu–Cl(2)	2.261(1)	2.2468(8)



Scheme 2. Synthesis of **2**, $[(PyS)_2CH_2CuCN]_\infty$.

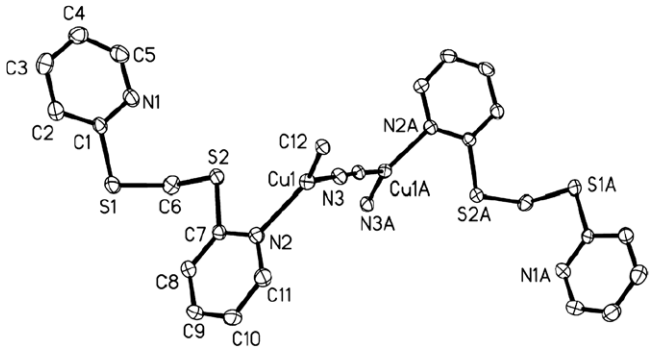


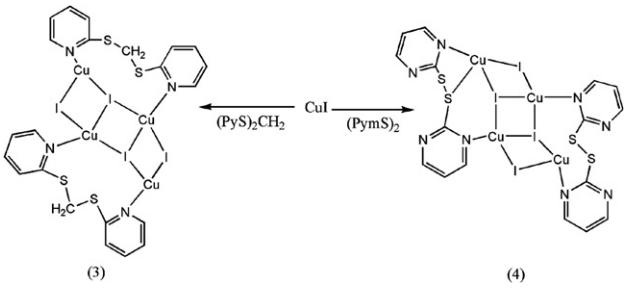
Fig. 5. Crystallographic analysis of **2** $[CuCN(PyS)_2CH_2]_\infty$. Ellipsoids are shown at 30% probability level with hydrogen atoms omitted for clarity. Selected bond lengths (Å) and angles (°) of **2**: Cu(1)–N(2) 2.034(2), Cu(1)–C(12) 1.872(3), C(12)–N(3) 1.154(3), N(2)–Cu(1)–C(12) 120.93(10), N(3)–C(12)– Cu(1) 174.9(2), Cu(1)–Cu(1a) 4.933.

1.154(3) Å is typical of the C–N bond in cyanide [11,19]. The distance between Cu centers is 4.933 Å. Each Cu(I) atom has distorted trigonal planar geometry with angles of 125.43(10)°, 113.25(9)° and 120.93(10)°. Three coordinate distorted trigonal planar geometry is a characteristic of Cu(I) cyanide structures, for example in $KCu(CN)_2$ [20]. The geometry around the Cu(1)–C(12)–N(3) ligand is close to linear, with an angle of 174.9(2). Infrared spectroscopy exhibited the distinctive CN stretch at 2361 cm^{-1} that is within the range expected for a bridged CN ligand [11f,19,20]. Proton NMR on **2** showed the proton signals shifted downfield when compared with the free ligand [10]. This was observed in the spectra of complexes **2**–**5** suggesting that the structure is retained in solution when the crystalline material is redissolved.

Bond lengths and angles of **2** show good agreement with other Py–CuCN complexes, for example $[(CuCN)_2[CuCN]_2(\mu\text{-}4\text{-}4'bipy)]$ has a Cu–CN bond length of 1.862(3) Å and a Cu–N(Py) bond length of 2.069(2) Å [21]. Within the polymeric network of **2** the distance between the aromatic layers (i.e. from C(1)–C(1a) or S(1)–S(1a)) is ~8.702 Å [22].

Having successfully isolated polymeric chains from copper(II) chloride and copper(I) cyanide, we wished to extend the series and examine if polymeric chains would be isolated using copper(I) iodide. Using similar reaction conditions as were used for the formation of **1** and **2** $(PyS)_2CH_2$ and $(PymS)_2$ were reacted with CuI (Scheme 3).

Complexes **3** and **4** show structural similarity, both feature the Cu_4I_4 core which can be described as a 'ladder type' arrangement that is well documented common for copper halides [3]. The four copper atoms and four iodine atoms form parallelograms, with Cu–Cu distances of 2.849 Å and 2.862 Å between the two copper atoms in **3** and 3.038 and 2.657 Å in **4**. This can be compared with the Cu–Cu distance in metallic copper of 2.556 Å and the Van der Waals radius of copper at 2.80 Å [23] and is a typical value for discrete Cu–I ladder structures [24]. Complex **3** is analogous to the Cu(I) bromide compound isolated by



Scheme 3. Reactions of copper(I) iodide with $(PyS)_2CH_2$ and $(PymS)_2$.

García-Martínez and co-workers [10] from the reaction of $(PyS)_2CH_2$ with Cu(I)Br, however, unlike their copper cluster, complex **3** was the major reaction product and was isolated in 67% yield.

Complex **3** crystallizes as yellow triclinic crystals (Fig. 6) space group $P\bar{1}$, while complex **4** crystallizes as yellow monoclinic crystals, space group, $P2_1/c$ (Fig. 7).

Single crystal X-ray analysis of complex **3** reveals that two different bonding arrangements occur around the copper centers, but both adopt distorted tetrahedral geometries. Cu(1) is coordinated to the pyridyl nitrogen (N1) and two bridging iodides, I(1) and I(2). The second copper center, Cu(2), has coordination to a pyridyl nitrogen atom N(2), a sulfur atom from the ligand, S(1) and two bridging iodides, I(1) and I(2). Thus, the ligand bridges two copper centers. The iodide atoms bridge the copper atoms in μ3 and μ2 modes. The two copper centers have distorted tetrahedral geometry with angles ranging from 102.43(2)° to 118.11(11)° for Cu(1) and 100.48(12)° to 116.68(4)° around Cu(2). The Cu–I bridges are found to be slightly asymmetric, Cu(1)–I(1) = 2.7257 Å, Cu(1)–Cu(I2A) = 2.6776(8) Å, but this is not uncommon for bridged halides and can be compared to $[Cu_4(L^1)_2I_4]$ (L^1 = bis(6-methyl-2 pyridyl methyl sulfide)) that has bond lengths of 2.586(1)–2.652(1) Å for the bridged iodides, a Cu–N distance of 2.031(3) Å and a Cu–S distance of 2.570(1) Å [25,26].

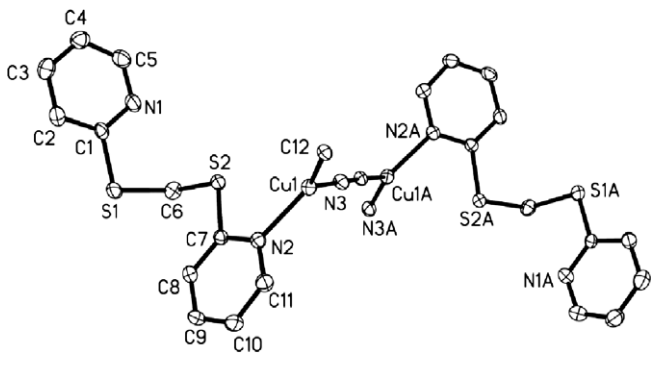


Fig. 6. Crystal structure of complex **3**, thermal ellipsoids at 30% probability level, hydrogen atoms are omitted for clarity. Key bond lengths (Å) and angles (°): Cu(1)–I(1) 2.7257(7), Cu(1)–I(2) 2.6776(8), Cu(2)–N(2) 2.079(4), Cu(2)–I(2) 2.5693(8), Cu(1)–N(1) 2.071(4), Cu(2)–S(1) 2.3010(14), N(1)–Cu(1)–I(2) 107.67(11), N(1)–Cu(1)–I(1) 104.82(11), I(1)–Cu(1)–I(2a) 106.91(2), S(1)–Cu(2)–I(2) 116.68(4), N(2)–Cu(2)–I(1a) 100.48(12).

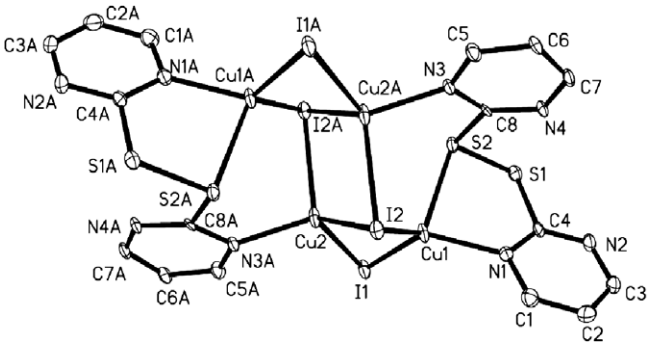


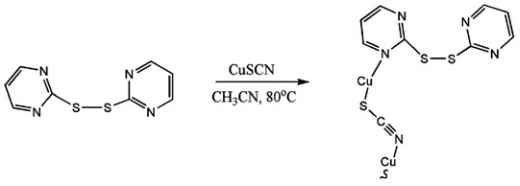
Fig. 7. X-ray crystal structure of $[(PymS)_2Cu_2I_2]_2$, complex **4**, thermal ellipsoids at 30% probability level. Hydrogen atoms are omitted for clarity. Key bond lengths (Å) and angles (°): Cu(1)–N(1) 2.053(7), Cu(2)–N(3a) 2.061(7), Cu(1)–S(2) 2.421(2), Cu(1)–I(1) 2.5612(11), N(1)–Cu(1)–I(2) 114.1(2), I(1)–Cu(1)–S(2) 106.20(6), N(1)–Cu(1)–Cu(2) 172.1(2), N(1)–Cu(1)–S(2) 85.97(19).

Unlike the analogous bromide compound, complex **3** has no hydrogen bonding existing between the CH_2 group and the iodides [10]. This is possibly due to the lower electronegativity of the iodine versus bromine, and the larger size between the atoms, therefore a polymeric chain of clusters does not form. Solution luminescent measurements in acetonitrile were performed on **3** and **4** but no luminescence was recorded, it is possible that low temperature solid-state measurements are required.

PymS–SPym was prepared serendipitously in high yield from the attempted synthesis of $(PymS)_3CH$. Despite this not being the desired product, it could be reproducibly prepared in high yield[1]. The reaction of $(PymS)_2$ with CuI (Scheme 3) afforded monoclinic yellow crystals of compound **4** in high yield, Fig. 7.

The solid-state analysis reveals a dimeric structure that features a tetrameric core of copper atoms. Each ligand chelates one copper atom through S(1) and N(1) atoms and coordinates to another Cu(2) through another nitrogen atom, thus bridging between the two. An average Cu–S bond is reported to be around 2.67 Å [26], the Cu–S distance of 2.421(2) Å is significantly shorter than this distance, and is attributed to the steric constraints of the ligand. It is noteworthy to mention that complex **4** appears to be thermally robust in the solid-state and in solution, however, attempts to use the similar system, PyS–SPy, for framework synthesis resulted in cleavage of the S–C aromatic bond and formation of elemental sulfur.

To continue the series the reaction of CuCN with $(PymS)_2$ was performed, however no crystalline product could be isolated. Exchange of copper cyanide for copper



Scheme 4. Synthesis of **5** from the reaction of $(PymS)_2$ with CuSCN.

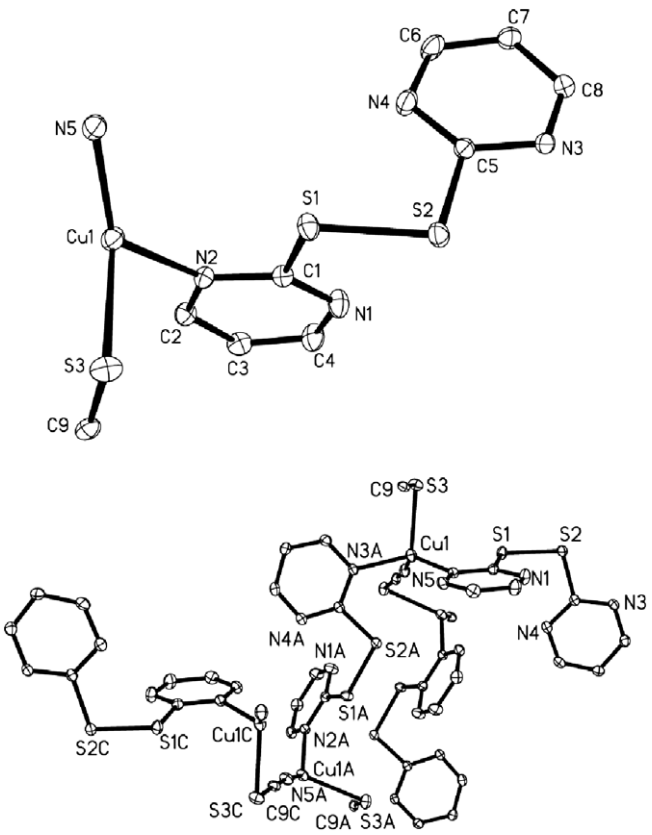


Fig. 8. Crystal structure of $[(PymS)_2CuSCN]_\infty$ (**5**) asymmetric unit and polymeric network. Thermal ellipsoids at 30% probability and hydrogen atoms are omitted for clarity. Selected bond lengths (Å) and angles (°): Cu(1)–N(3) 2.1580(19), Cu(1)–S(3) 2.3957(7), Cu(1)–N(2) 2.036(2), Cu(1)–N(5) 1.918(2), S(1)–C(1) 1.785(2), S(3)–C(9) 1.656(3), N(2)–Cu(1)–S(3) 96.95(6), N(5)–Cu(1)–S(3) 115.80(7), N(2)–Cu(1)–N(3) 105.77(8).

thiocyanate, afforded colorless crystals of an infinite two-dimensional polymeric material **5**, Scheme 4 and Fig. 8.

Use of copper(I) thiocyanate has not been well explored for use in metal organic framework construction, in part because of its limited solubility in organic solvents [11]. We were drawn to this precursor, given our success with copper cyanide, and because this copper salt exists as polymeric $[Cu(SCN)]_\infty$ [27].

Polymer **5** crystallizes in the monoclinic space group $P2_1/c$ and the X-ray analysis shows that each copper is tetrahedrally coordinated to two nitrogen atoms from two different ligands, sulfur and nitrogen atoms from the thiocyanate group. Complex **5** forms a two-dimensional network. The geometry around the thiocyanate group is nearly linear, with the S–C≡N angle of 178.3(2)°, and a Cu–Cu separation of 5.559 Å. The bond lengths and angles in **5** compare well with that of $[Cu(SCN)(pyz)]_\infty$, that has Cu–S and Cu–N bonds of 2.349(2) Å and 1.940(4) Å, respectively [11g]. Infrared spectroscopy of polymer **5** exhibited CN stretches at 2110.1 and 2066.9 cm^{-1} and at 767.1 cm^{-1}, associated with the S–C stretch and these values compare well with other reported polymeric structures [11].

4. Conclusion

We have shown that copper(II) chloride, copper(I) iodide and copper pseudo halides can be used in conjunction with flexible heteroelemental organic linkers to form polymers that can incorporate the anion into the framework. This type of preparation is a versatile useful approach for construction of neutral polymeric frameworks that offer potential for further reactions and framework growth, because of the availability of uncoordinated donor atoms present.

Future work will explore the further chemistry of these polymers and will focus on expanding the chemistry of the dipodal ligands for further polymeric materials.

Acknowledgement

The Welch Foundation (Grant Number P0176) TCU-RCAF and TCU-SERC are thanked for financial support.

Appendix A. Supplementary material

CCDC 647083, 647084, 647085, 647086 and 647087 contain the supplementary crystallographic data for this paper. These data can be obtained free of charge via http://www.ccdc.cam.ac.uk/conts/retrieving.html, or from the Cambridge Crystallographic Data Centre, 12 Union Road, Cambridge CB2 1EZ, UK; fax: (+44) 1223-336-033, or e-mail: deposit@ccdc.cam.ac.uk. Supplementary data associated with this article can be found, in the online version, at doi:10.1016/j.poly.2008.01.005.

References

[1] (a) For selected examples see: P.C. Healy, C. Pakawatchai, R.I. Papasergio, V.A. Patrick, A.H. White, Inorg. Chem. 23 (1984) 3769;
(b) S. Hong, Y. Zou, D. Moon, M.S. Lah, Chem. Commun. (2007) 1707;
(c) B. Lucchese, K.J. Humphreys, D.H. Lee, C.D. Incarnto, R.D. Sommer, A.L. Rheingold, K.D. Karlin, Inorg. Chem. 43 (2004) 5987;
(d) R. Kappoor, A. Katanna, P. Venugpalan, P. Kappor, M. Corbella, M. Rodrigues, I. Romero, A. Klobert, Inorg. Chem. 43 (2004) 6699;
(e) For the use of sulfur containing ligands see:S. Oae, Organic Sulfur Chemistry: Structure and Mechanism, CRC Press, Boca Raton, 1991;
(f) S. Oae, T. Okuyama (Eds.), Organic Sulfur Chemistry: Biological Aspects, CRC Press, Boca Raton, 1992.
[2] (a) For selected examples see: L. Hou, W.-J. Shi, Y.-G. Yin, S.W. Ng, Inorg. Chem. 44 (2005) 7825;
(b) D.J. Chesnut, A. Kusnetzow, R.R. Birge, J. Zubieta, Inorg. Chem. 38 (1999) 2663;
(c) S.L. James, Coord. Chem. Rev. 32 (2003) 276, and references therein;
(d) J.A. Cabeza, A. Llamazares, V. Riera, R. Trivedi, Organometallics 17 (1998) 550;
(e) A. Paulo, A. Domingos, I. Santos, J. Chem. Soc., Dalton Trans. (1999) 3735;
(f) L. Dahlenburg, M. Kühnlein, Eur. J. Inorg. Chem. (2000) 2117.
[3] (a) Selected Examples include: C.L. Raston, A.H. White, J. Chem. Soc., Dalton. (1976) 2153;

(b) J.J.M. Amoore, L.R. Hanton, M.D. Spicer, Dalton Trans. (2003) 1056;
(c) H.N. Peindy, F. Guyon, A. Khatyr, M. Knorr, C. Strohmann, Eur. J. Inorg. Chem. (2007) 1823;
(d) K.R. Kyle, J.A. DiBenedetto, P.C. Ford, J. Chem. Soc., Chem. Commun. (1989) 714;
(e) K.R. Kyle, P.C. Ford, J. Am. Chem. Soc. 111 (1989) 5005;
(f) G.J. Kubas, Inorg. Synth. 19 (1979) 90;
(g) M.R. Churchill, G. Davies, M.A. El-Sayed, J.P. Hutchinson, M.W. Rupich, Inorg. Chem. 21 (1982) 995.

[4] (a) P. Pyykkö, Chem. Rev. 97 (1997) 597;
(b) A.N. Khlobystov, A.J. Blake, N.R. Champness, D.A. Lemenovskii, A.G. Majouga, N.V. Zyk, M. Schröder, Coord. Chem. Rev. 222 (2001) 155;
(c) V.W.-W. Yam, K.K.-W. Lo, Chem. Soc. Rev. 28 (1999) 323.

[5] (a) P.C. Ford, E. Cariati, J. Bourassa, Chem. Rev. 99 (1999) 3625;
(b) M. Vitale, P.C. Ford, Coord. Chem. Rev. (2001) 219.

[6] M.N. Hughes, in: The Inorganic Chemistry of Biological Processes, 2nd ed., Wiley, New York, 1972, p. 125.

[7] (a) S. Kitawaga, S. Kawata, Y. Nozaka, M. Munakata, J. Chem. Soc., Dalton Trans. (1993) 1399;
(b) E. Block, M. Gernon, H. Kang, J. Zubieta, Angew. Chem., Int. Ed. 27 (1988) 1342.

[8] (a) For selected examples see: K. Umakoshi, I. Kinoshita, S. Ooi, Inorg. Chim. Acta 127 (1987) L41;
(b) K. Umakoshi, A. Ichmura, I. Kinoshita, S. Ooi, Inorg. Chem. 26 (1987) 3551.

[9] (a) Examples include: L.M. Engelhardt, C. Pakawatchai, A.H. White, P.C. Healy, J. Chem. Soc., Dalton Trans. (1985) 117;
(b) T. Kawano, J. Kuwana, I. Ueda, Bull. Chem. Soc. Japan 76 (2003) 789;
(c) S. Banthia, A. Samanta, Inorg. Chem. 43 (2004) 6890;
(d) H. Ohi, Y. Tachi, T. Kunumoto, S. Itoh, Dalton Trans. (2005) 3146;
(e) M. Munakata, M. Maekawa, S. Kitagawa, M. Adachi, H. Masuda, Inorg. Chim. Acta 167 (1990) 181;
(f) L.M. Engelhardt, G.E. Jacobsen, W.C. Patalinghug, B.W. Skelton, C.L. Raston, A.H. White, J. Chem. Soc., Dalton Trans. (1991) 2859;
(g) A. Habiyakare, E.A.C. Lucken, G. Bernardinelli, J. Chem. Soc., Dalton Trans. (1991) 2269.

[10] A.A. Portela, R. Carballo, J.S. Casas, E. García-Martínez, C. Gómez-Alonso, A. Sánchez-González, J. Sordo, E.M. Vūzques-López, Z. Anorg. Allg. Chem. 628 (2002) 939.

[11] (a) X.-M. Zhang, Z.-M. Hao, H.-S. Wu, Inorg. Chem. 44 (2005) 7301;
(b) S.A. Barnett, A.J. Blake, N.R. Champness, C. Wilson, Chem. Commun. (2002) 1640;
(c) Q.-M. Wang, G.-C. Guo, T.C.W. Mak, Chem. Commun. (1999) 1849;
(d) O. Teichert, W.S. Sheldrick, Z. Anorg. Allg. Chem. 626 (2000) 2196;
(e) J.-M. Shi, W. Xu, B. Zhao, P. Cheng, D.-Z. Liao, X.-Y. Chen, Eur. J. Inorg. Chem. (2005) 55;
(f) M. Julve, M. Verdaguer, G.D. Munno, J.A. Real, G. Bruno, Inorg. Chem. 32 (1993) 795;
(g) A.J. Blake, N.R. Brooks, N.R. Champness, M. Crew, L.R. Hanton, P. Hubbersley, S. Parsons, M. Schröder, J. Chem. Soc., Dalton Trans. (1999) 2813.

[12] (a) J.Y. Lu, Coord. Chem. Rev. 246 (2003) 327;
(b) D.J. Chesnut, J. Zubieta, Chem. Commun. 40 (1998) 81;
(c) D.J. Chesnut, J. Zubieta, A. Kusnetzow, J. Chem. Soc., Dalton Trans. (1998) 4081.

[13] (a) K.N. Power, T.C. Lennigar, M.J. Zanarotko, Chem. Commun. 48 (1998) 95;
(b) C. Hung, Y. Do, Inorg. Chem. 37 (1998) 4470.

[14] V.D. de Castro, G.M. de Lima, C.A.L. Filgueiras, M.T.P. Gambardella, J. Molec. Struct. 609 (2002) 199.

[15] Y. Zheng, M. Du, J.-R. Li, R.-H. Zhang, X.H. Bu, Dalton Trans. (2003) 1509.

[16] G.M. Sheldrick, SHELXS-97, Program for the Solution of Crystal Structures, University of Göttingen, Germany, 1997.

[17] G.M. Sheldrick, SHELXL-97, Program for the Refinement of Crystal Structures, University of Göttingen, Germany, 1997.

[18] I. Kinoshita, L.J. Wright, S. Kubo, K. Kimura, A. Sakata, T. Yano, R. Miyamoto, T. Nishioka, K. Isobe, Dalton Trans. (2003) 1993.

[19] (a) A.G. Sharpe, The Chemistry of Cyano Complexes of the Transition Metals, Academic Press, New York, 1976, p. 226;
(b) X.-M. Zhang, R.-Q. Fang, H.-S. Wu, J. Am. Chem. Soc. 127 (2005) 7670;
(c) D. Cooper, R.A. Plane, Inorg. Chem. 5 (1996) 2209.

[20] (a) D.T. Cromer, J. Phys. Chem. 61 (1957) 1388;
(b) C. Kappenstein, R.P. Hugel, Inorg. Chem. 16 (1977) 250.

[21] S. Hibble, A.M. Chippendale, Z. Anorg. Allg. Chem. 631 (2005) 542.

[22] A.J. Blake, N.R. Champness, A. Khlobystov, D.A. Lemenovskii, W.-S. Li, M. Schröder, Chem. Commun. (1997) 2813.

[23] A. Bondi, J. Phys. Chem. 68 (1964) 441.

[24] (a) B.J. Hathaway, Coordin. Chem. Rev. 52 (1983) 87;
(b) N. Kuhn, R. Fawzi, M. Grathwohl, H. Kotowski, M. Steimann, Z. Anorg. Allg. Chem. 24 (1988) 1937;
(c) J. Dai, M. Munakata, L.-P. Wu, T. Kuroda-Sowa, Y. Suenga, Inorg. Chim. Acta 258 (1997) 65;
(d) P.C. Healy, J.D. Kildea, A.H. White, Aust. J. Chem. 42 (1989) 177.

[25] P.L. Caradoc-Davies, L.R. Hanton, J.M. Hodgkiss, M.D. Spicer, J. Chem. Soc., Dalton Trans. (2002) 1581.

[26] L.R. Hanton, C. Richardson, T. Robinson, J.M. Turnbull, Chem. Commun. (2000) 2465.

[27] (a) M. Munakata, T. Kurosa-Sowa, M. Maekowa, A. Honda, S. Kitagawa, J. Chem. Soc., Dalton Trans. 1 (1994) 2771;
(b) J.M. Moreno, J. Suarez-Valera, J.C. Colacio, M.A. Avila-Rosón, D. Hildago, D. Martin-Ramos, Can. J. Chem. 73 (1995) 1591;
(c) O.M. Yaghi, G. Li, Angew Chem., Int. Ed. 34 (1995) 207;
(d) M.A.S. Goher, F.A. Mautner, Polyhedron 18 (1999) 1805.

ligand in the coordination sphere makes possible a charge transfer, LLCT type, in the form of an electronic transition directed to the diimine ligand, the origin of the excited electron depends strongly on the actual complex composition, mainly on the nature of the axial ligand. Thus, the formation of MLCT and/or LLCT excited states involves processes which may be described in terms of the redox couples Re^{I}/Re^{II}, $L_2/L_2^{\cdot -}$ and $L'/L'^{\cdot +}$.

When the axial ligand and the Re^{I} moiety are linked through a carboxylate bridge, as in the complexes $(RCO_2)Re^{I}(CO)_3(2,2'\text{-bpy})$ (R = methyl, 1-pyrenyl, 9-anthranyl, 2-naphthyl) the luminescent LLCT excited state induces photodecarboxylation [5] after the optical excitation of the Re^{I} complexes at wavelengths of the ligand-centered transitions (Eq. (1)):

$$(RCO_2)Re^{I}(CO)_3(2,2'\text{-bpy}) \xrightarrow{h\nu} \text{LLCT} \rightarrow R^{\cdot} + CO_2 + Re^{I}(CO)_3(2,2'\text{-bpy})^{\cdot} \quad (1)$$

However, this decarboxylation is inhibited [11] when R has a strong donating character as in $(RCO_2)Re^{I}(CO)_3L$ (R = 4-dimethylaminobenzyl (4-DMAB), ferrocene; L = phen, 2,2′-bpy). The photophysical and photochemical processes of (RCO_2) $Re^{I}(CO)_3L$ (R = ferrocene, 4-DMAB) are significantly different from the processes undergone by the complexes $(RCO_2)Re^{I}(CO)_3(2,2'\text{-bpy})$ (R = methyl, 1-pyrenyl, 9-anthranyl, 2-naphthyl). Differences in the quantum yields of photodecarboxylation and in the kinetics of the charge transfer excited-state relaxation are associated with the higher energies of the LLCT (RCO_2– to L) charge-transfer excited states in the latter complexes [11] and with the presence of a different excited state from the LLCT (RCO_2– to L) and MLCT (Re-to-L). This excited state was identified as having chemical properties and spectroscopic features consistent with those of a charge transfer from Re to RCO_2 [11].

The UV–Vis/IR spectroelectrochemistry of AQ-2-CO_2–$Re^{I}(CO)_3(2,2'\text{-bpy})$, (AQ = anthraquinone) was looked upon in our lab [12]. The in-situ spectra of the electrochemically reduced radical anions, $AQ^{\cdot -}$ and $2,2'\text{-bpy}^{\cdot -}$, were in excellent agreement with those obtained from the products of reductive quenching of the corresponding photochemically-excited states. In this work, the spectroelectrochemical behavior of DMAB–CO_2–$Re^{I}(CO)_3$(phen) and DMAB–COOH acid, was investigated with a view to establishing comparisons among species formed electrochemically and those arising by electron transfer quenching of excited states of the complex or its ligands. The study deals, in addition, with the nature of products and intermediates generated in the reduction and/or oxidation of DMAB–CO_2–$Re^{I}(CO)_3$(phen) and DMAB–COOH obtained through flash photolysis and pulse radiolytic techniques. A comparison is made between the nature of the radical species produced after the reduction/oxidation of DMAB–CO_2–$Re^{I}(CO)_3$(phen) and DMAB–COOH using electrochemical, flash photolytical and pulse radiolytical methods.

2. Experimental

2.1. Electrochemical procedures

The cells for voltammetry and spectroelectrochemistry experiments have been described elsewhere [13]. In addition, ac voltammograms were recorded with an exciting amplitude of 1.6 mV rms at 11 Hz with a slow sweep rate of 3 mV s^{-1}. DC voltammograms were obtained with a conventional computerized set-up. Acetonitrile, ACN, Merck "SeccoSolv", was further dried over activated alumina for several days. The procedure was found to be suitable for electrochemistry in the −2.0/+1.8 V (versus Ag/AgCl, KCl_{sat}) potential range. $(Bu_4N)PF_6$ was dried in vacuum at 60 °C for at least 24 h. Pt discs (6 mm dia) were used as working electrodes. Potentials were measured against a Ag/AgCl, KCl_{sat} reference electrode. Oxygen was removed from the solutions by bubbling purified nitrogen for at least 30 min prior to each experiment. A Pt mesh, separated from the working compartment by a porous disc, was used as a counter electrode. A fresh surface was generated before each experiment by polishing the working electrode to a mirror finish with alumina, sonicated, rinsed with Millipore-Milli-Q water and dried before being placed in the solution. The quality of the surface was tested by inspecting the response to cycling the working electrode in the supporting electrolyte. Solutions were prepared with analytical-grade reagents.

2.2. Spectroelectrochemical measurements

Potential modulated spectra were obtained in situ with a home-made, UV–Vis spectrometer [12,14,15]. In the technique, the light is focused onto the electrode at an angle of 45° while the electrode potential, and therefore the reflected light, is modulated at 11 Hz (square wave). The reflected intensity, an ac signal, ΔR, was sensed with a photomultiplier and rectified by a lock-in amplifier. The spectra are, unless stated otherwise, the normalized difference between the optical response at a given potential against that at a potential taken as reference, R_{ref}, i.e., $\Delta R/R_{ref} = (R - R_{ref})/R_{ref}$ versus wavelength (integral measurements, i.e. large modulations). Differential spectra $\delta R/R$ are taken with a small amplitude modulation as a function of potential at a set wavelength (reflectogrammes). The set-up has been described in more detail elsewhere [16–18].

2.3. Flash-photochemical procedures

Optical density changes occurring on a time scale longer than 10 ns were investigated with a flash photolysis apparatus described elsewhere [19–21]. In these experiments, 25 ns flashes of 351 nm light were generated with a Lambda Physik SLL-200 excimer laser. The energy of the laser flash was attenuated to values equal to or less than 20 mJ/pulse by absorbing some of the laser light

by solutions of $Ni(ClO_4)_2$ with appropriate optical transmittances, $T = I_t/I_0$, where I_0 and I_t are, respectively, the intensities of the light arriving to and transmitted from the photolysis cell. The transmittance, $T = 10^{-A}$, was routinely calculated by using the spectrophotometrically measured absorbance, A, of the solution. A right angle configuration was used for the pump and the probe beams. Concentrations of the complexes were adjusted to provide homogeneous profiles of photogenerated intermediates over the optical path, $l = 1$ cm, of the probe beam. To satisfy this optical condition, solutions were prepared with an absorbance equal to or less than 0.4 over the 0.2 cm optical path of the pump. Concentrations of the complexes were adjusted to give optical densities equal to or less than 0.05 for a 1 cm optical path at 350 nm. All solutions used in the photochemical work were deaerated with streams of ultrahigh-purity N_2 before and during the irradiations.

2.4. Pulse radiolysis

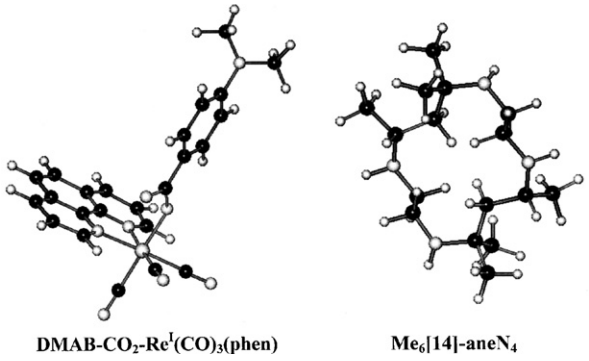
Pulse radiolysis experiments were carried out with a model TB-8/16-1S electron linear accelerator. The instrument and computerized data collection for time-resolved UV–Vis spectroscopy and reaction kinetics have been described elsewhere in the literature [22,23]. Thiocyanate dosimetry was carried out at the beginning of each experimental session. Details of the dosimetry have been reported elsewhere [22,24]. The procedure is based on the concentration of $(SCN)_2^{\bullet -}$ radicals generated by the electron pulse in a N_2O-saturated 10^{-2} M SCN^- solution. In the procedure, the calculations were made with $G = 6.13$ and an extinction coefficient $\varepsilon = 7.58 \times 10^3\ M^{-1}\ cm^{-1}$ at 472 nm [22,24] for the $(SCN)_2^{\bullet -}$ radicals In general, the experiments were carried out with doses that in N_2-saturated aqueous solutions resulted in $(2.0 \pm 0.1) \times 10^{-6}$ M to $(6.0 \pm 0.3) \times 10^{-6}$ M concentrations of e^-_{aq}. In these experiments, solutions were deaerated with streams of the O_2-free N_2 or N_2O gasses. In order to irradiate a fresh sample with each pulse, an appropriate flow of the solution through the reaction cell was maintained during the experiment.

The radiolysis of CH_3OH and CH_3OH/H_2O mixtures with ionizing radiation has been reported elsewhere in the literature [25–27]. These studies have shown that pulse radiolysis can be used as a convenient source of e^-_{sol} and $C^{\bullet}H_2OH$ radicals.

Since e^-_{sol} and $C^{\bullet}H_2OH$ have large reduction potentials, i.e., −2.8 V versus NHE for e^-_{sol} and −0.92 V versus NHE for $C^{\bullet}H_2OH$, they have been used for the reduction of coordination complexes and for the study of electron transfer reactions. The yield of e^-_{sol} in CH_3OH ($G \approx 1.1$) is about a third of the G-value in the radiolysis of H_2O ($G \approx 2.8$) [25]. In solutions where e^-_{sol} was scavenged with N_2O [27] the $C^{\bullet}H_2OH$ radical appears to be the predominant product (yield > 90%) of the reaction between CH_3OH and $O^{\bullet -}$.

2.5. Materials

4-(Dimethylamino)benzoic acid (DMAB–COOH) was obtained from Aldrich and used as received. The complex DMAB–CO_2–$Re^I(CO)_3$(phen) and the macrocycle $[Ni(Me_6[14]\text{–}aneN_4)](ClO_4)_2$ were available from previous works [11,28] (Scheme 1).



Scheme 1.

3. Results and discussion

3.1. Electrochemistry

AC voltammetry experiments conducted on DMAB–COOH (1×10^{-3} M) in Pt/ACN/Bu_4NPF_6 solutions at 11 Hz, Fig. 1, show a reversible wave at 1.00 V versus Ag/AgCl, the background being featureless. The electrochemical behavior of DMAB–COOH can be compared to that of dimethylaniline (DMA). The anodic oxidation of DMA occurs irreversibly to form $DMA^{\bullet +}$ at a potential

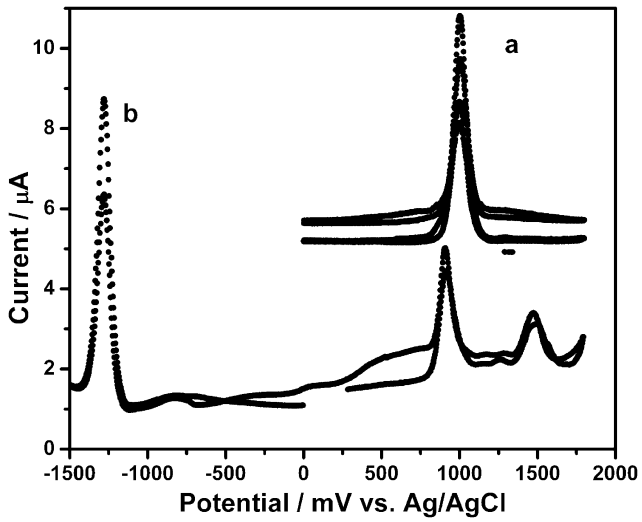


Fig. 1. (a) Alternating current voltammogram (ACV) between 0 and 1.75 V of the Pt/ACN + 0.1 M Bu_4NPF_6/1×10^{-3} M DMAB–COOH interface. (b) ACV between −1.5 and 1.75 V of the Pt/ACN + 0.1 M Bu_4NPF_6/2×10^{-4} M DMAB–CO_2–$Re^I(CO)_3$(phen). Frequency 11 Hz, amplitude 1.6 mV_{rms}, $v = 3.0\ mV\ s^{-1}$ (one cycle). Electrode area: 0.28 cm^2. Forward and back scans.

of about 0.76 V versus SCE [29]. In our case the reversible current response, corresponds to the couple of the amine in DMAB–COOH, i.e. DMAB–COOH/DMAB$^{\cdot+}$–COOH. The fact that the oxidation potential of the amine lies at more positive values in DMAB–COOH than in DMA can be rationalized in terms of the properties of the electron attracting group –CO_2 which makes the amine oxidation less facile. The electrochemical oxidation of DMA and other p-substituted dialkylanilines leads to the formation of *N*,*N*,*N*′,*N*′-tetraalkylbenzidine as the major oxidation product [29,30]. However, our electrochemical results did not show the generation of oxidation products derived from the radical cation DMAB$^{\cdot+}$–COOH. It seems that the formation of coupled compounds as products of the primary radical cation DMAB$^{\cdot+}$–COOH cannot be observed on the timescale set by the ac voltammetry modulation.

AC voltammetry experiments were conducted on DMAB–CO_2–$Re^{I}(CO)_3$(phen) (2×10^{-4} M) in Pt/ACN/Bu_4NPF_6 solutions at 11 Hz. The current response for DMAB–CO_2–$Re^{I}(CO)_3$(phen), Fig. 1, shows three reversible waves at −1.28 V, +0.91 and +1.47 V versus Ag/AgCl. Based on published reports [11,31] the reversible reduction wave at −1.28 V can be ascribed to a reduction on the phen ligand of the Re^{I} complex. The anodic wave at +0.91 V can be assigned to the amine oxidation in the Re^{I} complex. The potential (+0.91 V) lies between those corresponding to DMA and DMAB–COOH as the effect of the electron attracting group –CO_2 on the amine redox potential is less pronounced in the Re^{I} complex than in DMAB–COOH since the carboxylate group is also withdrawing electron density from the Re^{I} center and its moiety. The anodic wave at +1.47 V can be related to the Re^{I}/Re^{II} couple [11,12,31].

With a view to identifying the species electrochemically generated, associated to the waves observed on ac voltammetry, spectroelectrochemical experiments were designed to study the species generated in the redox processes of DMAB–COOH and DMAB–CO_2–$Re^{I}(CO)_3$(phen). The in situ reflectance spectrum, integral (large modulation), inset to Fig. 2, recorded in DMAB–COOH 1×10^{-3} M in Pt/ACN/Bu_4NPF_6 0.1 M solutions with a potential modulation between +0.9 and +1.5 V, shows a band peaking at 475 nm. The spectrum of the inset to Fig. 2 is in good agreement with the absorption of DMAB$^{\cdot+}$–COOH obtained in flash photolysis experiments [32] as well as with the data reported for DMA$^{\cdot+}$ ($\lambda_{max} \sim 490$ nm [33]) and *p*-bromo-*N*,*N*-dimethylaniline ($\lambda_{max} \sim 490$ nm in ACN [34]) radical cations. Therefore, the spectrum of Fig. 2 (inset) can be assigned to the amine radical cation DMAB$^{\cdot+}$–COOH detected reversibly under our experimental conditions. The detection of the spectra of the amine radical cations by spectroelectrochemistry has been considered difficult due to their high reactivity [35,36], therefore this is probably the first time the absorption of DMAB$^{\cdot+}$–COOH can be observed by using this technique.

A similar spectrum was obtained (Fig. 2) when the in situ reflectance was recorded with DMAB–CO_2–$Re^{I}(CO)_3$(phen) 2×10^{-4} M in Pt/ACN/Bu_4NPF_6 0.1 M solutions with a potential modulation between +0.9 and +1.2 V, showing the absorption spectrum ($\lambda_{max} = 475$ nm) of the amine radical cation in the Re^{I} complex.

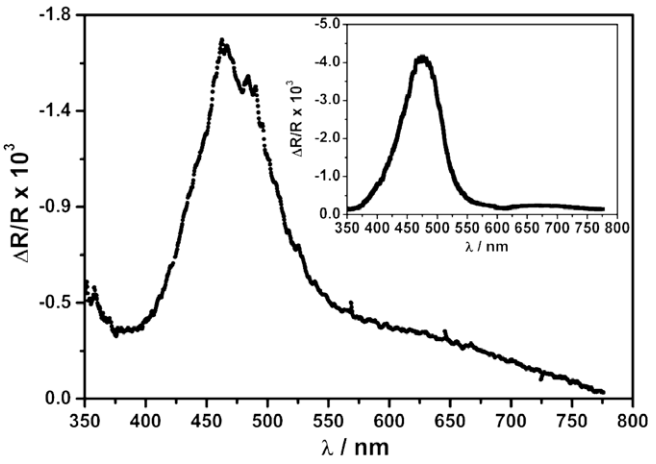


Fig. 2. Modulated reflectance spectra of the Pt/ACN + 0.1 M Bu_4NPF_6/2×10^{-4} M DMAB–CO_2–$Re^{I}(CO)_3$(phen) system between 0.9 and 1.2 V, 11 Hz. Angle of incidence $\phi = 45°$. The inset shows the modulated reflectance spectra of the Pt/ACN + 0.1 M Bu_4NPF_6/1×10^{-3} M DMAB–COOH system between 0.9 and 1.2 V.

When the in situ reflectance was recorded in DMAB–CO_2–$Re^{I}(CO)_3$(phen) with a modulation applied between −1.00 and −1.50 V under the same experimental conditions, the absorption spectrum observed is that of Fig. 3 (λ_{max} at 420 and 560 nm), which can be attributed, according to literature [11,37], as arising from the spectrum of the reduced phen radical in the Re^{I} complex.

Fig. 4 shows the spectrum observed when the potential modulation applied to the DMAB–CO_2–$Re^{I}(CO)_3$(phen) complex was set between 1.20 and 1.70 V, i.e. covering the voltammetric wave of Re^{II} in the complex. The negative lobe arises from the absorption at 1.70 V. This spectrum,

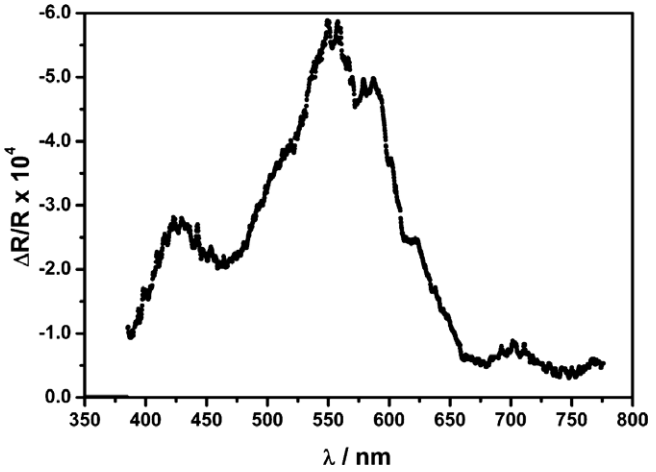


Fig. 3. Modulated reflectance spectra of the Pt/ACN + 0.1 M Bu_4NPF_6/2×10^{-4} M DMAB–CO_2–$Re^{I}(CO)_3$(phen) system between −1.00 and −1.50 V, 11 Hz.

$\lambda_{max} \sim 400$ nm (maximum is partially clipped because of the band bipolar nature), is characteristic of Re^{II} complexes [38–40] in good agreement with the spectrum of pulse radiolytically generated $(L')Re^{II}(CO)_3(L)^z$ complexes ($L' = 4,4'$-bpy; L = dipyridil [3,2-a:2′3′-c] phenazine and $z = +2$ or $L' = Cl$; L = bathocuproinedisulfonate and $z = -1$) [41]. The absorption indicated in Fig. 4 as positive, should arise from the amine oxidation, partially sensed by the modulation lower limit, at 1.20 V. In order to discard the possibility of contributions to the spectrum in Fig. 4 (to the negative lobe) from impurities generated if the amine group was oxidized at potentials higher than +1.00 V, a reflectogramme, (differential reflectance versus potential) was recorded at the absorption wavelength of Re^{II} species ($\lambda = 418$ nm) [40,42]. The comparison between the optical response ($\delta R/R$) versus potential (unfolded format), in the inset to Fig. 4, top frame, and the ac voltammogramme, bottom frame, clearly indicates the coincidence of the absorption of the Re^{II} species at the same potential of the Re^{I} oxidation.

3.2. Pulse radiolysis redox products

The spectra of the transient species produced by one-electron oxidation of DMAB–COOH was investigated by pulse radiolysis of their water solutions in the presence of NaCl 0.1 M under a N_2O atmosphere. The spectrum of the transient species, Fig. 5, corresponds to the absorptions of the oxidized amine radical cation. The absorption turned out to be in good agreement with that observed spectroelectrochemically (compare to Fig. 2). The cation radical $DMAB^{\cdot+}$–COOH is formed by the reaction of $Cl_2^{\cdot-}$ and DMAB–COOH within the first 2 μs after the radiolytic pulse and decays by first order kinetic on a 100 μs-1 ms timescale. Eqs. (2)–(5) summarize the sequence of events

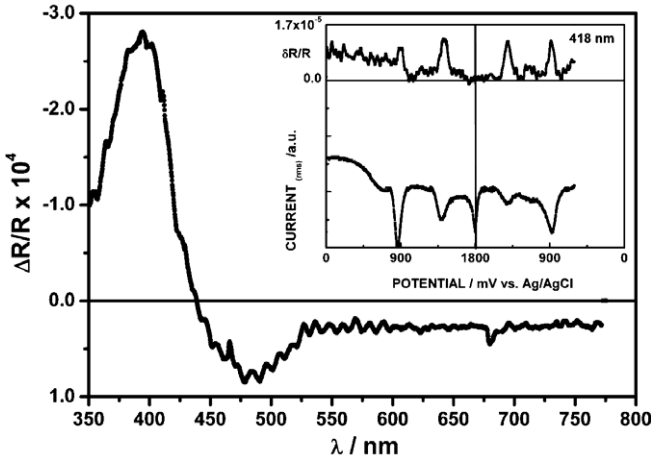


Fig. 4. Modulated reflectance spectra of the Pt/ACN + 0.1 M Bu_4NPF_6/ 2×10^{-4} M DMAB–CO_2–$Re^{I}(CO)_3$(phen) system between 1.20 and 1.70 V, 11 Hz. The inset shows in the top frame a reflectogramme (differential reflectance versus potential, unfolded format) carried out at the absorption wavelength of Re^{II} species ($\lambda = 418$ nm). The bottom frame displays the corresponding ACV.

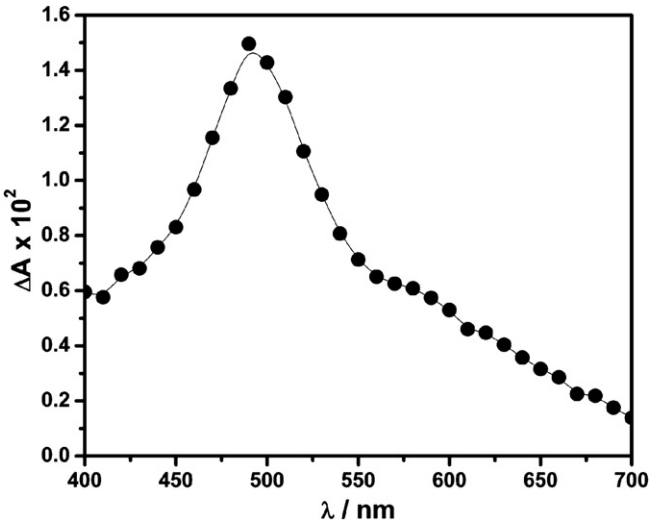


Fig. 5. Transient spectrum recorded at a delay of 7.5 μs after the radiolytic pulse in pulse radiolysis experiments conducted on DMAB–COOH 1×10^{-4} M water solutions in the presence of NaCl 0.1 M under N_2O atmosphere.

that lead to the formation of $DMAB^{\cdot+}$–COOH after the radiolytic pulse in aqueous solutions of DMAB–COOH:

$$N_2O + e^-_{sol} + H_2O \rightarrow OH^{\cdot} + OH^- + N_2 \quad (2)$$

$$OH^{\cdot} + Cl^- \rightarrow Cl^{\cdot} + OH^- \quad (3)$$

$$Cl^{\cdot} + Cl^- \rightleftarrows Cl_2^{\cdot-} \quad (4)$$

$$Cl_2^{\cdot-} + DMAB\text{–}COOH \rightarrow 2Cl^- + DMAB^{\cdot+}\text{–}COOH \quad (5)$$

The sequence of events in the radiolysis of N_2 deaereated methanolic solutions is shown in the kinetic scheme of Eqs. (6)–(8):

$$CH_3OH \rightsquigarrow CH_3OH^+, e^-_{sol} \quad (6)$$

$$CH_3OH^+ \rightarrow CH_3O^{\cdot} + H^+ \quad (7)$$

$$CH_3O^{\cdot} + CH_3OH \rightarrow CH_3OH + C^{\cdot}H_2OH \quad (8)$$

Thus, the main reducing species in pulse radiolysis of methanolic solutions under a N_2 atmosphere are e^-_{sol} and $C^{\cdot}H_2OH$.

However, when methanolic solutions are deareated with N_2O, e^-_{sol} are consumed through Eq. (9) and the main radical product of the reaction between e^-_{sol} and N_2O is $C^{\cdot}H_2OH$:

$$N_2O + e^-_{sol} + CH_3OH \rightarrow C^{\cdot}H_2OH + OH^- + N_2 \quad (9)$$

Pulse radiolytically generated e^-_{sol} reacted with 1×10^{-4} M DMAB–CO_2–$Re^{I}(CO)_3$(phen) complex in N_2-saturated methanolic solutions with a rate constant $k \sim 1.3 \times 10^{10}$ M^{-1} s^{-1}. The spectra of the transient species, Fig. 6, were recorded 29 μs after the radiolytic pulse. They correspond to Re^{I} complexes, [DMAB–CO_2–$Re^{I}(CO)_3(phen^{\cdot-})$] with coordinated $phen^{\cdot-}$ ligand radicals. The [DMAB–CO_2–$Re^{I}(CO)_3(phen^{\cdot-})$] products were stable for a time longer than 0.5 ms at the concentrations, $\sim 10^{-6}$ M, reached in the radiolysis experiments. Moreover, the spectra of the products produced by pulse radiolysis, which

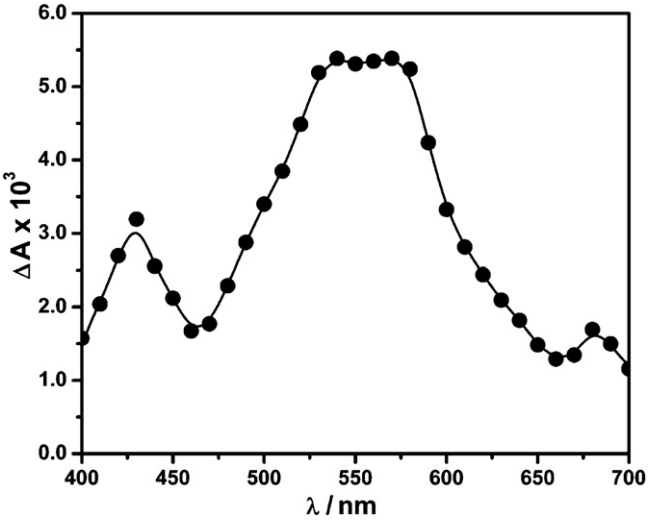


Fig. 6. Transient spectrum recorded at a delay of 29 μs after the radiolytic pulse in pulse radiolysis experiments conducted on 1×10^{-4} M DMAB–CO_2–$Re^I(CO)_3$(phen) complex in N_2-saturated methanolic solutions.

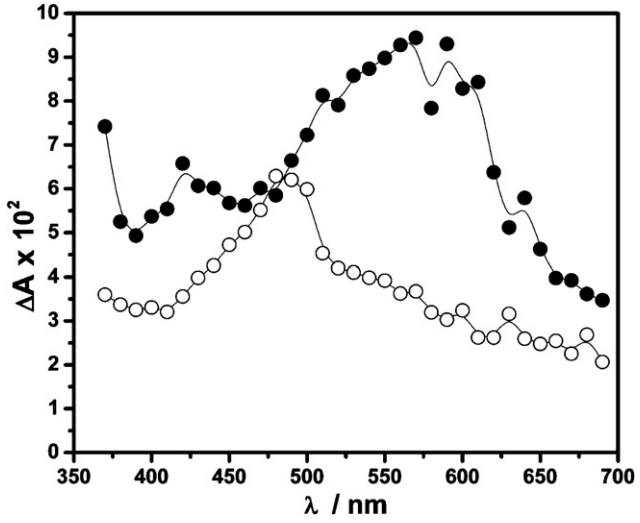


Fig. 7. Transient spectra generated after 351 nm excitation of DMAB–CO_2–$Re^I(CO)_3$(phen) in different experimental conditions: (●) DMAB–CO_2–$Re^I(CO)_3$(phen) 1×10^{-4} M in the presence of TEA 0.1 M in ACN at a time delay of 900 ns after the laser pulse and (○) DMAB–CO_2–$Re^I(CO)_3$(phen) 1×10^{-4} M in the presence of [Ni^{II}(Me_6[14]–aneN_4)] 0.1 M in ACN at a time delay of 900 ns after the laser pulse.

show the spectrum of phen$^{\bullet -}$ in the Re^I complex, are in agreement with the spectroelectrochemistry (Fig. 3).

In N_2O-saturated methanolic solutions of 1×10^{-4} M DMAB–CO_2–$Re^I(CO)_3$(phen) the reaction of $C^{\bullet}H_2OH$ radicals with the Re^I complexes did not generate detectable concentrations of [DMAB–CO_2–$Re^I(CO)_3$(phen$^{\bullet -}$)].

The standard potential of the $C^{\bullet}H_2OH$, H^+/CH_3OH couple, ~−0.92 V versus NHE, is lower than the reduction potential of the phen ligand in the Re^I complex (i.e. −1.08 V versus NHE). As a result $C^{\bullet}H_2OH$ radicals were unable to reduce the phen ligand of the DMAB–CO_2–$Re^I(CO)_3$(phen) complex.

The extinction coefficient of the transients (ε_R) were calculated using the relationship

$$\varepsilon_R = \varepsilon_P + [\Delta A_R \times (G \times \varepsilon)(SCN)_2^{\bullet -}]/[\Delta A(SCN)_2^{\bullet -} \times G_R] \quad (10)$$

where ε_P is the extinction coefficient of the parent molecule, $\Delta A(SCN)_2^{\bullet -}$ is the absorbance of the thiocyanate radical at 472 nm and G_R is the radiation chemical yield of the radical. On this basis, $\varepsilon_{560\ nm} = 3.0 \times 10^3\ M^{-1}\ cm^{-1}$ and $\varepsilon_{490\ nm} = 1.4 \times 10^3\ M^{-1}\ cm^{-1}$ were calculated for [DMAB–CO_2–$Re^I(CO)_3$(phen$^{\bullet -}$)] and DMAB$^{\bullet +}$–COOH, respectively.

3.3. Redox reactions of excited states

In order to establish a comparison between spectroelectrochemistry, pulse radiolysis and flash photolysis experiments, the reduction of the phen ligand in DMAB–CO_2–$Re^I(CO)_3$(phen) was carried out through the luminescence quenching of the complex DMAB–CO_2–$Re^I(CO)_3$(phen) with the reductant triethylamine (TEA). Fig. 7 shows the spectrum of the transient, generated after excitation with a 351 nm laser, of DMAB–CO_2–$Re^I(CO)_3$(phen) solutions in ACN in the presence of TEA at a time delay of 900 ns after the laser pulse. The spectrum observed, with λ_{max} at 420 and 560 nm, is similar to that of the phen$^{\bullet -}$ in the Re^I complex. However, a close inspection of Fig. 7 shows that the absorption peaks at 420 and 560 nm are broader and less well defined than those in the spectra of phen$^{\bullet -}$ in the Re^I complex obtained by spectroelectrochemistry and pulse radiolysis techniques. This disparate behavior can be rationalized in terms of the different quenching reactions of accessible excited states responsible of the photophysical properties of the DMAB–CO_2–$Re^I(CO)_3$(phen) complex [11] with TEA, Eqs. (11)–(16):

$$\text{DMAB–}CO_2\text{–}Re^I(CO)_3(\text{phen}) \xrightarrow{h\nu} [\text{DMAB–}CO_2\text{–}Re^{II}(CO)_3(\text{phen}^{\bullet -})]^* \quad (11)$$

$$\text{DMAB–}CO_2\text{–}Re^I(CO)_3(\text{phen}) \xrightarrow{h\nu} [(\text{DMAB}^{\bullet +} - CO_2)\text{–}Re^I(CO)_3(\text{phen}^{\bullet -})]^* \quad (12)$$

$$\text{DMAB–}CO_2\text{–}Re^I(CO)_3(\text{phen}) \xrightarrow{h\nu} [(\text{DMAB–}CO_2^{\bullet -})\text{–}Re^{II}(CO)_3(\text{phen})]^* \quad (13)$$

$$[\text{DMAB–}CO_2\text{–}Re^{II}(CO)_3(\text{phen}^{\bullet -})]^* + \text{TEA} \xrightarrow{k_{q1}} [\text{DMAB–}CO_2\text{–}Re^I(CO)_3(\text{phen}^{\bullet -})] + \text{TEA}^{\bullet +} \quad (14)$$

$$[(\text{DMAB}^{\bullet +}\text{–}CO_2)\text{–}Re^I(CO)_3(\text{phen}^{\bullet -})]^* + \text{TEA} \xrightarrow{k_{q2}} [\text{DMAB–}CO_2\text{–}Re^I(CO)_3(\text{phen}^{\bullet -})] + \text{TEA}^{\bullet +} \quad (15)$$

$$[(\text{DMAB–}CO_2^{\bullet -})\text{–}Re^{II}(CO)_3(\text{phen})]^* + \text{TEA} \xrightarrow{k_{q3}} [(\text{DMAB–}CO_2^{\bullet -})\text{–}Re^I(CO)_3(\text{phen})] + \text{TEA}^{\bullet +} \quad (16)$$

Eqs. (11)–(13) account for the formation of the excited states $MLCT_{Re\rightarrow phen}$ and $MLCT_{Re\rightarrow(DMAB–CO_2)}$ (i.e. Re^I

to phen and Re^I to $–CO_2–$DMAB in character) and the excited state $LLCT_{(DMAB–CO_2)\rightarrow phen}$ ($–CO_2–$DMAB to phen in character) after light absorption by the DMAB–CO_2–$Re^I(CO)_3$(phen) complex. The reduction of the $MLCT_{Re\rightarrow phen}$ excited state of the complex DMAB–CO_2–$Re^I(CO)_3$(phen) by TEA, represented by Eq. (14), has been previously observed with similar Re^I complexes [37,42,43], and occurs on a timescale within the excimer laser lifetime (~25 ns) to form the radical cation $TEA^{\cdot+}$ and the reduced $phen^{\cdot-}$ radical anion in the Re^I complex. The reduction of the $LLCT_{(DMAB–CO_2)\rightarrow phen}$ by TEA, Eq. (15), is a feasible process since the oxidation potentials of TEA [42] and DMAB are close together and the energy of the $LLCT_{(DMAB–CO_2)\rightarrow phen}$, as estimated from the redox potentials of DMAB/$DMAB^{\cdot+}$ and phen/$phen^{\cdot-}$ in the Re^I complex is $E_{00} \sim 2.19$ eV. As the $MLCT_{Re\rightarrow(DMAB–CO_2)}$ is higher in energy than the $MLCT_{Re\rightarrow phen}$, the reduction of $MLCT_{Re\rightarrow(DMAB–CO_2)}$ by TEA, Eq. (16), is also a possible process from a thermochemical standpoint. Therefore, [DMAB–CO_2–$Re^I(CO)_3(phen^{\cdot-})$] and [(DMAB–$CO_2^{\cdot-}$)-$Re^I(CO)_3$(phen)] species may be contributing to the spectral features of the transient generated after the reduction of the excited states of the Re^I complex by TEA. These properties may explain the spectral differences between the $phen^{\cdot-}$ spectrum obtained in flash photolysis experiments and the $phen^{\cdot-}$ spectrum obtained by spectroelectrochemical and pulse radiolysis techniques.

The oxidative quenching of the $MLCT_{Re\rightarrow phen}$ and $MLCT_{Re\rightarrow(DMAB–CO_2)}$ and $LLCT_{(DMAB–CO_2)\rightarrow phen}$ excited states of DMAB–CO_2–$Re^I(CO)_3$(phen) was carried out in laser flash photolysis experiments ($\lambda_{exc} = 351$ nm) of a 10^{-4} M solution of the Re^I complex in the presence of [Ni^{II}(Me_6[14]–$aneN_4$)]. The spectrum of the transient generated under oxidative conditions is shown in Fig. 7. This spectrum is similar to that of the oxidized amine in the Re^I complex (compare to Fig. 2), suggesting that the [Ni^{II}(Me_6[14]–$aneN_4$)] oxidant quenches the accessible excited states of the Re^I complex producing mainly [($DMAB^{\cdot+}$–CO_2)–$Re^I(CO)_3$(phen)] and Re^{II} species, according to Eqs. (17)–(19):

$$[DMAB–CO_2–Re^{II}(CO)_3(phen^{\cdot-})]^* + [Ni^{II}(Me_6[14]–aneN_4)] \xrightarrow{k_{q4}} [DMAB–CO_2–Re^{II}(CO)_3(phen)] + [Ni^{I}(Me_6[14]–aneN_4)] \quad (17)$$

$$[(DMAB^{\cdot+}–CO_2)–Re^{I}(CO)_3(phen^{\cdot-})]^* + [Ni^{II}(Me_6[14]–aneN_4)] \xrightarrow{k_{q5}} [(DMAB^{\cdot+}–CO_2)–Re^{I}(CO)_3(phen)] + [Ni^{I}(Me_6[14]–aneN_4)] \quad (18)$$

$$[(DMAB–CO_2^{\cdot-})–Re^{II}(CO)_3(phen)]^* + [Ni^{II}(Me_6[14]–aneN_4)] \xrightarrow{k_{q6}} [DMAB–CO_2–Re^{II}(CO)_3(phen)] + [Ni^{I}(Me_6[14]–aneN_4)] \quad (19)$$

A comparison of the spectra in Figs. 4 and 7 shows that the Re^{II} species formed in Eqs. (17) and (19) must contribute to the spectral features at wavelengths equal to or shorter than 400 nm. The presence of the [($DMAB^{\cdot+}$–CO_2)–$Re^I(CO)_3$(phen)] species, Eq. (18), accounts for the features between 400 and 700 nm in Fig. 7. In addition, absorptions near 380 nm can be assigned to the Ni^I macrocycle [28] produced in Eqs. (17)–(19).

In this regard, the spectrum of the excited state of DMAB–CO_2–$Re^I(CO)_3$(phen) ($\lambda_{max} \sim 475$ nm and a broad shoulder between 500 and 600 nm [11]), could be viewed as having mainly the spectral features of the $LLCT_{(DMAB–CO_2)\rightarrow phen}$ excited state [i.e. having spectral features of both $phen^{\cdot-}$ ($\lambda_{max} \sim 420$ and 550 nm) and $DMAB^{\cdot+}$–CO_2 ($\lambda_{max} \sim 475$ nm)] with smaller spectral contributions from $MLCT_{Re\rightarrow phen}$ and $MLCT_{Re\rightarrow(DMAB–CO_2)}$. However, a close comparison between the spectra of the excited states (MLCTs and LLCT) and the spectra of the species generated under pulse radiolysis/spectroelectrochemistry experiments is more dubious since in the $MLCT_{Re\rightarrow phen}$ and $MLCT_{Re\rightarrow(DMAB–CO_2)}$ excited states the $phen^{\cdot-}$ and/or $DMAB–CO_2^{\cdot-}$ ligands are coordinated to a Re^{II}, a low spin d^5, while in the latter species the reduced/oxidized ligands are coordinated to a Re^I, a low spin d^6. Therefore, differences in coulomb and exchange integrals may be making important contributions to the shapes and positions of electronic bands and the comparison may not be valid.

4. Concluding remarks

AC voltammetry experiments conducted on DMAB–COOH and DMAB–CO_2–Re(CO)$_3$(phen) in ACN solutions showed reversible anodic waves corresponding to the oxidation of DMAB in the parent compound DMAB–COOH, and the Re^I complex. The spectrum of the radical cation, $DMAB^{\cdot+}$, was detected using both spectroelectrochemistry and pulse radiolysis techniques applied to DMAB–COOH and/or DMAB–CO_2–$Re^I(CO)_3$(phen). An excellent agreement was observed between the spectrum of the radical cation $DMAB^{\cdot+}$ obtained electrochemically or radiolytically. Besides, the reduction of the phen ligand in the DMAB–CO_2–$Re^I(CO)_3$(phen) complex was also reversible as observed by ac voltammetry. The spectrum of the radical anion $phen^{\cdot-}$ in the Re^I complex was gathered by spectroelectrochemistry in good agreement with that obtained by the reaction of solvated electrons with phen ligands in the DMAB–CO_2–$Re^I(CO)_3$(phen) complex in pulse radiolysis experiments. Extinction coefficients of $\varepsilon_{560\,nm} = 3.0 \times 10^3\ M^{-1}\,cm^{-1}$ and $\varepsilon_{490\,nm} = 1.4 \times 10^3\ M^{-1}\,cm^{-1}$ were calculated for [DMAB–CO_2–$Re^I(CO)_3(phen^{\cdot-})$] and $DMAB^{\cdot+}$–COOH, respectively from pulse radiolysis experiments. The in situ UV–Vis spectra of the electrochemically reduced radical anions, $phen^{\cdot-}$, was compared with those obtained from the products of the reductive quenching of the corresponding photochemically excited states. Differences between the $phen^{\cdot-}$ spectrum obtained by spectrolectrochemistry and flash photolysis techniques were rationalized in terms of the reduction products of the excited states $MLCT_{Re\rightarrow phen}$, $MLCT_{Re\rightarrow\ (DMAB–CO_2)}$ and $LLCT_{(DMAB–CO_2)\rightarrow phen}$ of the

Re^{I} complex by TEA. The oxidative quenching of the Re^{I} complex excited states by $[Ni^{II}(Me_6[14]\text{-ane}N_4)]$ showed the formation of $[(DMAB^{\cdot+}\text{–}CO_2)\text{-}Re^{I}(CO)_3(phen)]$ as the main primary product.

Acknowledgements

Work supported in part by ANPCyT Grant No. PICT 06-12610, CONICET-PIPs 2470/00 and 6301/05, Universidad Nacional de La Plata, and CICPBA. G.F. and G.R. acknowledge support from the Office of Basic Energy Sciences of the US Department of Energy. This is contribution No. NDRL – 4710 from the Notre Dame Radiation Laboratory.

References

[1] D.J. Stufkens, Comments Inorg. Chem. 13 (1992) 359.
[2] G.J. Stor, D.J. Stufkens, A. Oskam, Inorg. Chem. 31 (1992) 1318.
[3] B.D. Rossenaar, D.J. Stufkens, A. Vlček Jr., Inorg. Chem. 35 (1996) 2902.
[4] D.J. Liard, A. Vlček Jr., Inorg. Chem. 39 (2000) 485.
[5] E. Wolcan, G. Torchia, J. Tocho, O. Piro, P. Juliarena, G. Ruiz, M.R. Féliz, J. Chem. Soc., Dalton Trans. 10 (2002) 2194.
[6] M.A. Fox, M. Chanon (Eds.), Photoinduced Electron Transfer, Elsevier, Amsterdam, 1988.
[7] V. Balzani, F. Bolleta, M.T. Gandolfi, M. Maestri, Top. Curr. Chem. 75 (1978) 1.
[8] M. Grätzel (Ed.), Energy Resources Through Photochemistry and Catalysis, Academic Press, New York, 1983.
[9] K. Kalyanasundaram, Coord. Chem. Rev. 46 (1982) 159.
[10] K. Kalyanasundaram, M. Grätzel (Eds.), Photosensitization and Photocatalysis Using Inorganic and Organometallic Compounds, Kluwer Academic Publishers, Dordrecht, 1993.
[11] M.P. Juliarena, G.T. Ruiz, E. Wolcan, R.O. Lezna, M.R. Féliz, G. Ferraudi, J. Guerrero, Organometallics 26 (2007) 272.
[12] E. Wolcan, M.R. Féliz, G.T. Ruiz, M.P. Juliarena, R.O. Lezna, J. Electroanal. Chem. 533 (2002) 101.
[13] R.O. Lezna, N.R. de Tacconi, J.A. Rapallini, A.J. Arvia, An. Asoc. Quim. Argent. 76 (1998) 25.
[14] R.O. Lezna, S. Juanto, J.H. Zagal, J. Electroanal. Chem. 389 (1995) 197.
[15] R.O. Lezna, An. Asoc. Quím. Argent. 82 (1994) 293.
[16] R.O. Lezna, N.R. de Tacconi, A.J. Arvia, J. Electroanal. Chem. Interfacial Electrochem. 283 (1990) 319.
[17] R.O. Lezna, N.R. de Tacconi, S. Centeno, A.J. Arvia, Langmuir 7 (1991) 1241.
[18] N.R. de Tacconi, R.O. Lezna, R. Konduri, F. Ongeri, K. Rajeshwar, F.M. MacDonnell, Chem. Eur. J. 11 (2005) 4327.
[19] M.R. Féliz, G. Ferraudi, J. Phys. Chem. 96 (1992) 3059.
[20] M.R. Féliz, G. Ferraudi, H. Altmiller, J. Phys. Chem. 96 (1992) 257.
[21] J. Guerrero, O.E. Piro, E. Wolcan, M.R. Féliz, G. Ferraudi, S.A. Moya, Organometallics 20 (2001) 2842.
[22] G.L. Hug, Y. Wang, C. Schöneich, P.-Y. Jiang, R.W. Fessenden, Radiat. Phys. Chem. 54 (1999) 559.
[23] G.V. Buxton, C.L. Greenstock, W.P. Helman, A.B. Ross, J. Phys. Chem. Ref. Data 17 (1988) 513.
[24] M.R. Féliz, G. Ferraudi, Inorg. Chem. 37 (1998) 2806.
[25] N. Getoff, A. Ritter, F. Schworer, Radiat. Phys. Chem. 41 (1993) 797.
[26] L.M. Dorfman, in: R.F. Gould (Ed.), The Solvated Electron in Organic Liquids, Advances in Chemistry Series 50, American Chemical Society, Washington, DC, 1965, pp. 36–44.
[27] M. Simic, P. Neta, E. Hayon, J. Phys. Chem. 73 (1969) 3794.
[28] S. Ronco, B. Van Vlierberge, G. Ferraudi, Inorg. Chem. 27 (1988) 3453.
[29] H. Yang, D.O. Wipf, A.J. Bard, J. Electroanal. Chem. 331 (1992) 913.
[30] M. Baizer, Organic Electrochemistry, Marcel Deckker Inc., 1991.
[31] L.A. Sacksteder, A.P. Zipp, E.A. Brown, J. Streich, J.N. Demas, B.A. DeGraff, Inorg. Chem. 29 (1990) 4335.
[32] J. Choi, K. Yeo, M. Yoon, S.J. Lee, K. Kim, J. Photochem. Photobiol. A: Chem. 132 (2000) 105.
[33] T. Shida, W.H. Hamill, J. Chem. Phys. 44 (1966) 2369.
[34] M. Oyama, T. Higuchi, J. Electrochem. Soc. 149 (2002) E12.
[35] A. Malinauskas, R. Holze, Electrochim. Acta 44 (1999) 2613.
[36] E.T. Seo, R.F. Nelson, J.M. Frisch, L.S. Marcoux, D.W. Leedy, R.A. Adams, J. Am. Chem. Soc. 88 (1966) 15.
[37] E. Wolcan, G. Ferraudi, J. Phys. Chem. A. 104 (2000) 9281.
[38] L.A. deLearie, C.R. Haltiwanger, C.G. Pierpont, Inorg. Chem. 28 (1989) 644.
[39] J.R. Kirchoff, M.R. Allen, B.V. Cheesman, K. Onamoto, W.R. Heineman, E. Deutsch, Inorg. Chim. Acta 262 (1997) 195.
[40] M. Féliz, G. Ferraudi, H. Altmiller, J. Phys. Chem. 96 (1992) 257.
[41] G. Ruiz, M.P. Juliarena, E. Wolcan, G. Ferraudi, Inorg. Chim. Acta (2007) 0000.
[42] G. Ruiz, E. Wolcan, M.R. Féliz, J. Photochem. Photobiol. A: Chem. 101 (1996) 119.
[43] G. Ruiz, F. Rodriguez-Nieto, E. Wolcan, M.R. Féliz, J. Photochem. Photobiol. A: Chem. 107 (1997) 47.

communities in terms of their composition and function and, in order to understand their responding strategy, we must fully characterize the complexes in hands.

This paper describes three new cadmium(II) complexes with 3-hydroxypicolinic acid which have been prepared, identified by chemical analysis, characterized by the appropriate spectroscopic methods, both in solution and in the solid state, and their crystal structures were determined by X-ray diffraction method.

2. Experimental

2.1. Materials and physical measurements

All chemicals were used as received without further purification. Cadmium(II) iodide and cadmium(II) acetate dihydrate were purchased from Aldrich, while 3-hydroxypicolinic acid was purchased from Fluka.

CHN analyses were performed in the Analytical Services Laboratories of the Ruđer Bošković Institute.

The IR spectra were obtained from KBr pellets in the range 4000–450 cm^{-1} with a Perkin–Elmer Spectrum RXI FT-spectrometer.

The one- and two-dimensional homo- and heteronuclear ^{1}H, ^{13}C, ^{15}N and ^{113}Cd NMR spectra were recorded with a Bruker AV 600 spectrometer, operating at 600.133 MHz for the ^{1}H nucleus, 150.917 MHz for the ^{13}C nucleus, 60.796 MHz for the ^{15}N nucleus and 133.096 MHz for the ^{113}Cd nucleus. Samples were measured from DMF-d_7 solutions at 25 °C (298 K) in 5 mm NMR tubes. Chemical shifts, in ppm, are referred to TMS (^{1}H and ^{13}C NMR spectra), to NH_4NO_3 (^{15}N NMR spectra) and to $Cd(NO_3)_2 \cdot 4H_2O$ (^{113}Cd NMR spectra). FID resolution in ^{1}H, ^{13}C, ^{15}N and ^{113}Cd NMR spectra was 0.29, 0.54, 0.93 and 3.05 Hz per point, respectively. The following measurement techniques were used: standard ^{1}H and ^{13}C gated proton decoupling, ^{15}N and ^{113}Cd power gated decoupling, APT, COSY, HMQC and HMBC. The 2D NMR spectra were measured in pulsed field gradient mode (z-gradient).

2.2. [CdI(3-OHpic)(3-OHpicH)(H_2O)]$_2$ (**1**)

A solution of 3-hydroxypicolinic acid (0.11 g, 0.8 mmol) in 10 mL of water was added to a solution of cadmium(II) iodide (0.14 g, 0.4 mmol) in 10 mL of water. The pH value of the resulting colourless solution was 2. The solution was left to stand at room temperature for several days. The colourless crystals were then filtered off, washed with water and dried in air. Yield: 0.08 g (40.0%). *Anal.* Calc. for $C_{24}H_{22}Cd_2I_2N_4O_{14}$: C, 26.96; H, 2.08; N, 5.24. Found: C, 27.01; H, 2.16; N, 5.12%. IR data (KBr pellet, cm^{-1}): 3245(m), 2924(m), 2853(m), 1659(s), 1617(s), 1594(m), 1570(m), 1534(s), 1526(s), 1478(s), 1447(s), 1390(m), 1356(m), 1333(m), 1314(m), 1297(s), 1264(s), 1244(s), 1225(m), 1211(m), 1149(m), 870(m), 815(m), 788(m), 678(m), 663(m).

2.3. [Cd(3-OHpic)$_2$(H_2O)$_2$] (**2**)

A solution of 3-hydroxypicolinic acid (0.20 g, 1.4 mmol) in 15 mL of water was added to a solution of cadmium(II) acetate dihydrate (0.19 g, 0.7 mmol) in 5 mL of water. The pH value of the resulting colourless solution was 4. The colourless crystals were formed immediately and filtered off the next day, washed with water and dried in a desiccator over NaOH. The crystals suitable for X-ray crystal structure analysis were obtained by slow evaporation of the mother liquor solution, remained after filtration of the product, at room temperature. Yield: 0.26 g (86.7%). *Anal.* Calc. for $C_{12}H_{12}CdN_2O_8$: C, 33.94; H, 2.85; N, 6.60%. Found: C, 34.32; H, 2.90; N, 6.93%. IR data (KBr pellet, cm^{-1}): 3317(m), 2852(m), 2359(m), 1684(m), 1653(s), 1647(s), 1635(s), 1594(m), 1576(m), 1559(m), 1482(m), 1452(s), 1392(s), 1339(s), 1303(s), 1232(s), 890(m), 855(m), 821(m), 809(m), 699(m), 688(m), 668(m).

2.4. [Cd(3-OHpic)$_2$]$_n$ (**3**)

A solution of **2** (0.15 g, 0.4 mmol) in 6 ml of *N*,*N*-dimethylformamide was left to stand at room temperature for 2 weeks to give colourless crystals. The crystals were filtered off, washed with small amount of DMF and dried in air. Yield: 0.09 g (64.3%). *Anal.* Calc. for $C_{12}H_8CdN_2O_6$: C, 37.09; H, 2.08; N, 7.21. Found: C, 37.16; H, 2.13; N, 6.98%. IR data (KBr pellet, cm^{-1}): 1634(s), 1601(s), 1578(m), 1455(s), 1407(s), 1392(s), 1328(s), 1311(s), 1261(m), 1245(s), 1226(s), 1114(m), 889(m), 824(s), 813(m), 701(m), 683(s).

2.5. X-ray crystal structure analysis

The data collection was carried out on Oxford Diffraction Xcalibur four-circle kappa geometry single-crystal diffractometer with Xcalibur Sapphire 3 CCD detector by applying the CrysAlis Software system, Version 171.31.5 at room temperature [6]. Data reduction has been applied by the same programme [6]. Seven runs containing 759 data collection frames for **1**, 9 runs containing 1196 data collection frames for **2** and 11 runs containing 1382 data collection frames for **3** were collected at the crystal-detector distance of 60 mm with the exposure time of 15, 5 and 20 s for **1**, **2** and **3**, respectively, and with ω scan type for all three structures.

The data have been corrected for Lorentz-polarization factor and scaled for absorption effects by multi-scan for all structures. The structures were solved by direct methods. Refinement procedure by full-matrix least squares methods based on F^2 values against all reflections has been performed including anisotropic displacement parameters for all non-H atoms.

In **3**, the anisotropic displacement parameters for all atoms are large and the bond precision is small due to the lower quality of crystal and the data collected. All our attempts to obtain crystals of better quality of **3** have

failed so far. Atoms N1 and C11 (having anisotropic displacement parameters non-positive defined) were refined only isotropically in order to refine well the structure of this compound. The Flack parameter for the structure of **3** could also not be refined.

The positions of hydrogen atoms belonging to the carbon atoms Csp^2 for all structures were geometrically optimized applying the riding model [Csp^2–H, 0.93 Å; $U_{iso}(H) = 1.2U_{eq}(C)$]. The positions of hydrogen atoms belonging to the hydroxyl O atoms for the structures of **1** and **3** were geometrically optimized applying the riding model [O–H, 0.82 Å; $U_{iso}(H) = 1.5U_{eq}(O)$]. The hydrogen atoms belonging to water molecule O7 atom and pyridine N2 atom in the structure of **1** have been found in the electron-density Fourier maps. The distances between N2 and H12N atoms and between O7 and H27O atoms were restrained to average value of 0.90(5) Å using SHELXL97 DFIX instruction while H17O atom was refined freely. The hydrogen atoms belonging to the water molecule O4 and hydroxyl O3 atom in the structure of **2** have been found in the electron-density Fourier maps and refined freely. The distance between O1 and O4 atoms in the structure of **3** was restrained to the average value of 2.000(5) Å using SHELXL97 DFIX instruction.

Calculations were performed with SHELXS97 [7] and SHELXL97 [8]. The molecular graphics were done with ORTEP-3 [9] and MERCURY (Version 1.4.2) [10].

3. Results and discussion

3.1. Preparation of complexes

Both cadmium(II) complexes **1** and **2** were obtained under the similar reaction conditions using different cadmium(II) salts as starting materials, while **3** was obtained by recrystallization of **2** from *N*,*N*-dimethylformamide solution. All isolated compounds are air-stable, colourless and soluble in solvents with pronounced donor properties (such as *N*,*N*-dimethylformamide, *N*,*N*-dimethylsulphoxide, pyridine and 4-picoline).

All prepared compounds were characterized by IR spectroscopy and ^1H, ^{13}C, ^{15}N and ^{113}Cd NMR spectroscopy.

3.2. Vibrational spectroscopy

Infrared spectroscopy data confirm the coordination of 3-OHpic ligand to cadmium(II) ion *via* the carboxylate group in all three compounds. In the spectra of **1** and **2** the band associated to the asymmetric stretching vibrational mode, $\nu_{asym}(-COO^-)$ is shifted for 41 cm^{-1} (**1**) and 47 cm^{-1} (**2**) to lower wave numbers, while the $\nu_{sym}(-COO^-)$ band is shifted for 11 cm^{-1} (**1**) and 17 cm^{-1} (**2**) to higher wave numbers compared with the values registered for the free ligand [3,4]. The measured values of $\Delta(\nu_{asym}(-COO^-) - \nu_{sym}(-COO^-))$ amounts 326 cm^{-1} and 314 cm^{-1} for **1** and **2**, respectively, indicating the presence of carboxylate groups coordinated to cadmium(II) ion in unidentate mode [11] which is in agreement with the crystal structure of both compounds. The typical stretching ν(C–N) vibrational mode of substituted pyridines appears for the uncoordinated ligand at 1609 cm^{-1}, but there are two bands at 1617 and 1594 cm^{-1} in the spectra of **1** corresponding to this vibrational mode. This is in a good agreement with two coordination modes of 3-OHpicH in **1**: *N*,*O*-chelation involving the endocyclic nitrogen atom of 3-OHpic ligand and monodentate binding of 3-OHpicH through carboxylic oxygen atom [4]. The typical stretching ν(C–N) vibrational mode of substituted pyridines for **2** shifts to lower wave number (for 15 cm^{-1}) in comparison with the free ligand. This is in a good agreement with *N*,*O*-chelation, involving the endocyclic nitrogen atom of 3-OHpic ligand, confirmed by the X-ray crystal structure analysis. The broad absorption band of medium intensity at 3245 cm^{-1} indicates hydrogen bonding in the structure of **1**, while the broad absorption band of medium intensity at 3317 cm^{-1} in **2** indicates hydrogen bonds involving water molecules bound to cadmium(II) ion.

Unfortunately, due to the overlapping of maxima and vibrational coupling in the spectrum of **3**, the observed shifts of absorption bands, sensitive to metal coordination relatively to those of the free ligand, could not be unambiguously assigned.

3.3. NMR spectroscopy

The assignments of NMR spectra of the ligand (3-OHpicH) and its cadmium(II) complexes were shown in Table 1. The numbering of atoms is consistent with IUPAC nomenclature and it is shown in Scheme 1.

NMR measurements were performed in DMF-d_7 solution. Cadmium induced ^1H and ^{13}C NMR shifts are defined as the difference between proton or carbon chemical shifts in the complexes and the free ligand molecule.

The ^1H and ^{13}C NMR spectra of **1** suggest that Cd(OHpic)$_2$ exists in DMF-d_7 solution, similar to previously reported spectra of [CdCl(3-OHpic)(3-OHpicH)(H_2O)]$_2$ and [CdBr(3-OHpic)(3-OHpicH)(H_2O)]$_2$ [4].

The ^1H NMR spectra of the compounds **2** and **3** revealed the largest complexation shift ($\Delta\delta$) for the H-6 proton in both complexes. Complexation with cadmium induces shielding effects for all H-atoms (−0.211 to −0.311 ppm) of the ligand molecule. The signal of the hydroxyl group of the compound **2** was not observed due to large broadening, while that of compound **3** has downfield shift. Water protons of compound **2** were not observed. This fact could be attributed to the establishing of strong hydrogen bonds between the hydroxyl and the coordinated water molecules.

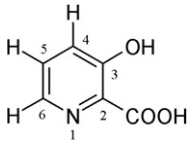
In the ^{13}C NMR spectra the greatest change upon complexation with cadmium was observed for the chemical shift of C-6. Deshielding effects were observed for C-2, C-6 and the carboxylic carbon (3.31–3.79 ppm) and shielding effects for C-3, C-4 and C-5 (−0.23 to −2.84 ppm).

In order to characterize the possible binding site for Cd^{2+} cation, ^{15}N NMR has been determined. As it can

Table 1
^{1}H[a], ^{13}C, ^{15}N[b] and ^{113}Cd[c] NMR chemical shifts (δ/ppm) and cadmium induced chemical shifts ($\Delta\delta$/ppm)[d], H–H coupling constants ($^{n}J_{HH}$/Hz)[e] and C–H coupling constants ($^{n}J_{CH}$/Hz) of 3-hydroxypicolinic acid and DMF solutions of **1**–**3**

Molecule Atom		3-OHpicH	DMF solution of **1**	DMF solution of **2**	DMF solution of **3**
H-2,3	δ	13.000 (2)	not observed	not observed	14.82 (1)
	$\Delta\delta$				+1.82
H-4	δ	7.839 (1)	7.567 (1)	7.568 (1)	7.568 (1)
	$^{3}J_{HH}$	8.56 (d)	8.27 (d)	8.44 (d)	8.35 (d)
	$\Delta\delta$		−0.272	−0.271	−0.271
H-5	δ	7.862 (1)	7.667 (1)	7.651 (1)	7.650 (1)
	$^{3}J_{HH}$	8.56; 4.52 (dd)	8.42; 4.71 (dd)	8.50; 4.68 (dd)	8.41; 4.67 (dd)
	$\Delta\delta$		−0.195	−0.211	−0.212
H-6	δ	8.332 (1)	8.124 (1)	8.026 (1)	8.021 (1)
	$^{3}J_{HH}$	4.62 (d)	4.16 (d)	4.40 (d)	4.25 (d)
	$\Delta\delta$		−0.208	−0.306	−0.311
C-2	δ	130.32	134.79	134.08	134.11
	$\Delta\delta$		4.47	3.76	3.79
C-3	δ	160.49	160.18	160.13	160.15
	$\Delta\delta$		−0.31	−0.36	−0.34
C-4	δ	130.93	128.21	128.08	128.09
	J_{CH}	168.53	167.47	165.33 (d)	165.47
	$\Delta\delta$		−1.88	−2.85	−2.84
C-5	δ	130.09	129.60	129.86	129.86
	J_{CH}	169.71	165.81 (d)	166.87 (d)	166.47
	$\Delta\delta$		−1.33	−0.23	−0.23
C-6	δ	135.36	138.06	138.68	138.67
	J_{CH}	190.86	185.94 (d)	184.62 (d)	184.63
	$\Delta\delta$		2.70	3.32	3.31
COOH	δ	167.49	170.54	171.04	171.05
	$\Delta\delta$		3.05	3.55	3.56
^{15}N	δ	103.39	103.98	104.27	104.30
	$\Delta\delta$		0.59	0.88	0.91
^{113}Cd	δ			258.99	375.39

Sign (+) denotes deshielding effect, while (−) denotes shielding effect of cadmium.
[a] Recorded in DMF-d_7 solutions. Reffered to TMS. Number of protons in brackets.
[b] Reffered to saturated aqueous NH_4NO_3 (20.8 ppm for NH_4^+).
[c] Reffered to saturated aqueous $Cd(NO_3)_2 \cdot 4H_2O$ (0 ppm).
[d] Cadmium induced chemical shifts ($\Delta\delta$/ppm) are obtained by subtracting the chemical shifts of parent compound (3-OHpicH) from the chemical shifts of Cd-complex.
[e] n denotes the number of bonds between nuclei in spin–spin coupling; (s) singlet, (d) doublet.



Scheme 1. Numbering scheme of the atoms in 3-hydroxypicolinic acid.

be seen from the Table 1, chemical shifts of the nitrogen atom for both compounds **2** (104.27) and **3** (104.30) are quite close to the corresponding chemical shift of the ligand (103.39).

Accordingly, chemical shifts and coupling constants are almost the same in both compounds **2** and **3**, so we have recorded ^{113}Cd NMR to clarify whether complexes exist in solution. ^{113}Cd chemical shifts of the compounds **2** and **3** were 258.99 ppm and 375.39 ppm, respectively. Highly coordinated cadmium(II) sphere of the compound **3** induces a subtle electron redistribution throughout the molecule, causing deshielding effect on ^{113}Cd chemical shift. Therefore, ^{113}Cd NMR opens a direct route to probe the environment of the bound cation itself [12].

3.4. Structural description of *1*

Crystal data and details of the structure determination for **1** are given in Table 2. ORTEP-3 view of the molecular structure of compound **1** is depicted in Fig. 1a and its crystal structure in Fig. 2a. Some selected interatomic bond distances and angles are listed in Table 3, as well as hydrogen bond geometry in Table 4.

Compound **1** is isostructural with [CdX(3-OHpic)(3-OHpicH)$(H_2O)]_2$ (X = Cl, Br) [4]. Its molecular structure reveals centrosymmetric dimmers containing two cadmium(II) ions with distorted octahedral coordination geometries, bridged with two iodine atoms (Cd1–I1 2.947(1) Å, Cd1–$I1^i$ 2.922(1) Å) (symmetry code (i) $1-x$, $-y$, $2-z$). The coordination environment of each cadmium(II) ion also consists of 3-hydroxypyridine-2-carboxylate ligand coordinated through *N*,*O* donor set of atoms (forming five-membered chelate ring, Cd1–N1 2.348(3) Å, Cd1–O1 2.327(2) Å), 3-hydroxypyridinium-2-carboxylate ligand coordinated monodentately through carboxylate O4 atom (Cd1–O4 2.339(2) Å) and water molecule (Cd1–O7 2.305(3) Å) (Table 3 and Fig. 1a). Monodentate 3-hydroxypyridinium-2-carboxylate ligand, bound to Cd1 as a zwitter ion with protonated N2 atom, is required to be in a neutral form by the charge balance of the molecular formula.

The bond distance Cd1–N1 is larger than the analogous one in [CdX(3-OHpic)(3-OHpicH)$(H_2O)]_2$ (X = Cl, 2.328(2) Å; X = Br, 2.334(4) Å) [4] but the bond distance Cd1–O1 is shorter (X = Cl, 2.344(2) Å; X = Br, 2.340(3) Å). The Cd1–O4 bond distance (carboxylate O4 atom from monodentate 3-hydroxypicolinate ligand) is larger than the corresponding ones in [CdX(3-OHpic)(3-OHpicH)$(H_2O)]_2$ (X = Cl, 2.314(2) Å; X = Br, 2.324(3) Å) [4] and the Cd1–O7 bond distance (water molecule O7 atom) corresponds to the ones in the latter complexes (X = Cl, 2.305(2) Å; X = Br, 2.307(4) Å) [4].

The bond angles around Cd centre are in the range of 165–175° for the formally *trans* pairs of the ligating atoms and in the range of 72–107° for the formally *cis* pairs, indicating the distortion of the octahedron. The angles indicating the largest distortion from the ideal octahedral geometry are the bite angle O1–Cd1–N1 with value equal to 71.5(1)° and angle O1–Cd1–O4 with value of 106.9(1)°.

The dihedral angle between the least squares calculated planes through the atoms of pyridine ring (N1/C1/C2/C3/C4/C5) and the corresponding five-membered chelate ring (Cd1/N1/C1/C6/O1) is 3.1(1)° while the dihedral angle

Table 2
Crystal data and details of the structure determination for [CdI(3-OHpic)(3-OHpicH)$(H_2O)]_2$ (**1**), [Cd(3-OHpic)$_2(H_2O)_2$] (**2**) and [Cd(3-OHpic)$_2]_n$ (**3**)

Compound	**1**	**2**	**3**
Formula	$C_{24}H_{22}Cd_2I_2N_4O_{14}$	$C_{12}H_{12}CdN_2O_8$	$C_{12}H_8CdN_2O_6$
M_r	1069.06	424.64	388.60
Colour and habit	colourless	colourless	colourless
Crystal system, space group	monoclinic, $P2_1/c$	monoclinic, $P2_1/n$	monoclinic, $C2$
Crystal dimensions (mm^3)	0.13 × 0.08 × 0.02	0.24 × 0.16 × 0.09	0.04 × 0.03 × 0.02
Temperature (K)	296	296	296
Unit cell parameters:			
a (Å)	9.3672(2)	5.0135(5)	18.8461(5)
b (Å)	16.2927(3)	23.356(3)	7.7183(1)
c (Å)	9.9523(3)	6.8075(6)	8.6577(2)
β (°)	95.818(2)	111.61(1)	94.498(2)
V (Å^3)	1511.07(6)	741.10(15)	1255.47(5)
Radiation, Mo Kα (Å)	0.71073	0.71073	0.71073
Z	2	2	4
D_{calc} (g cm^{-3})	2.350	1.903	2.056
μ (mm^{-1})	3.526	1.518	1.771
θ Range for data collection (°)	4-30	4-30	4-25
h, k, l range	−13:13; −22:22, −13:13	−7:7; −32:32; −9:9	−22:22; −9:9; −10:10
Diffractometer	Xcalibur κ geometry with Sapphire 3 CCD detector		
Scan type	ω	ω	ω
Number of measured reflections	19486	16022	11241
Number of independent reflections (R_{int})	4371 (0.0372)	2148 (0.0189)	2204 (0.0419)
Number of observed reflections, $I \geqslant 2\sigma(I)$	2467	1768	1953
Number of refined parameters	222	119	182
R[a], wR[b] $[I \geqslant 2\sigma(I)]$	0.0265, 0.0495	0.0215, 0.0494	0.0524, 0.1372
R, wR [all data]	0.0662, 0.0574	0.0299, 0.0511	0.0606, 0.1468
g_1, g_2 in w[c]	0.0268, 0	0.0231, 0.2007	0.0894, 13.4733
Goodness of fit on F^2, S[d]	0.872	1.122	1.087
Maximum and minimum electron-density (e Å^{-3})	1.251, −0.562	0.319, −0.234	2.017, −1.442
Maximum Δ/σ	0.002	0.001	0.002
Absorption correction type	multi-scan	multi-scan	multi-scan
Range of transmission factors minimum, maximum	0.71, 0.92	0.75, 0.87	0.94, 0.97
Extinction coefficient	none	0.0356(16)	none

[a] $R = \sum||F_o| - |F_c||/\sum|F_o|$.
[b] $wR = [\sum(F_o^2 - F_c^2)^2/\sum w(F_o^2)^2]^{1/2}$.
[c] $w = 1/[\sigma^2(F_o^2) + [(g_1P)^2 + g_2P]$ where $P = (F_o^2 + 2F_c^2)/3$.
[d] $S = \sum[w(F_o^2 - F_c^2)^2/(N_{obs} - N_{param})]^{1/2}$.

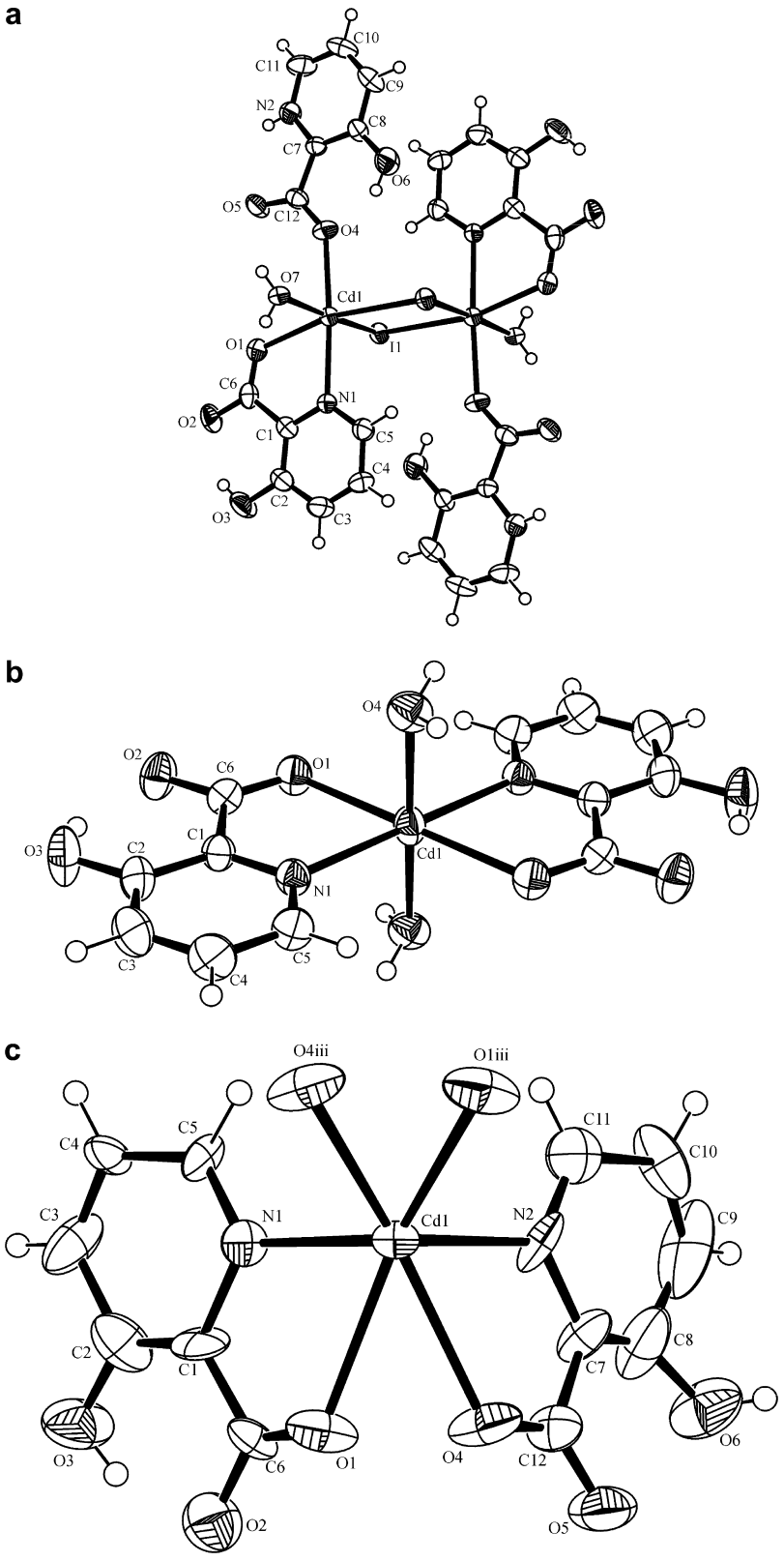


Fig. 1. ORTEP-3 drawing of $[CdI(3\text{-}OHpic)(3\text{-}OHpicH)(H_2O)]_2$ (**1**) (a), $[Cd(3\text{-}OHpic)_2(H_2O)_2]$ (**2**) (b) and $[Cd\text{-}(3\text{-}OHpic)_2]_n$ (**3**) (c) with the atomic numbering scheme of asymmetric unit. The thermal ellipsoids are drawn at the 50% probability level at 296 K.

between the plane through the atoms of five-membered chelate ring (Cd1/N1/C1/C6/O1) and the plane defined by atoms $Cd1/I1/Cd1^{i}/I1^{i}$ is 88.0(1)° (symmetry code (i) $1 - x, -y, 2 - z$).

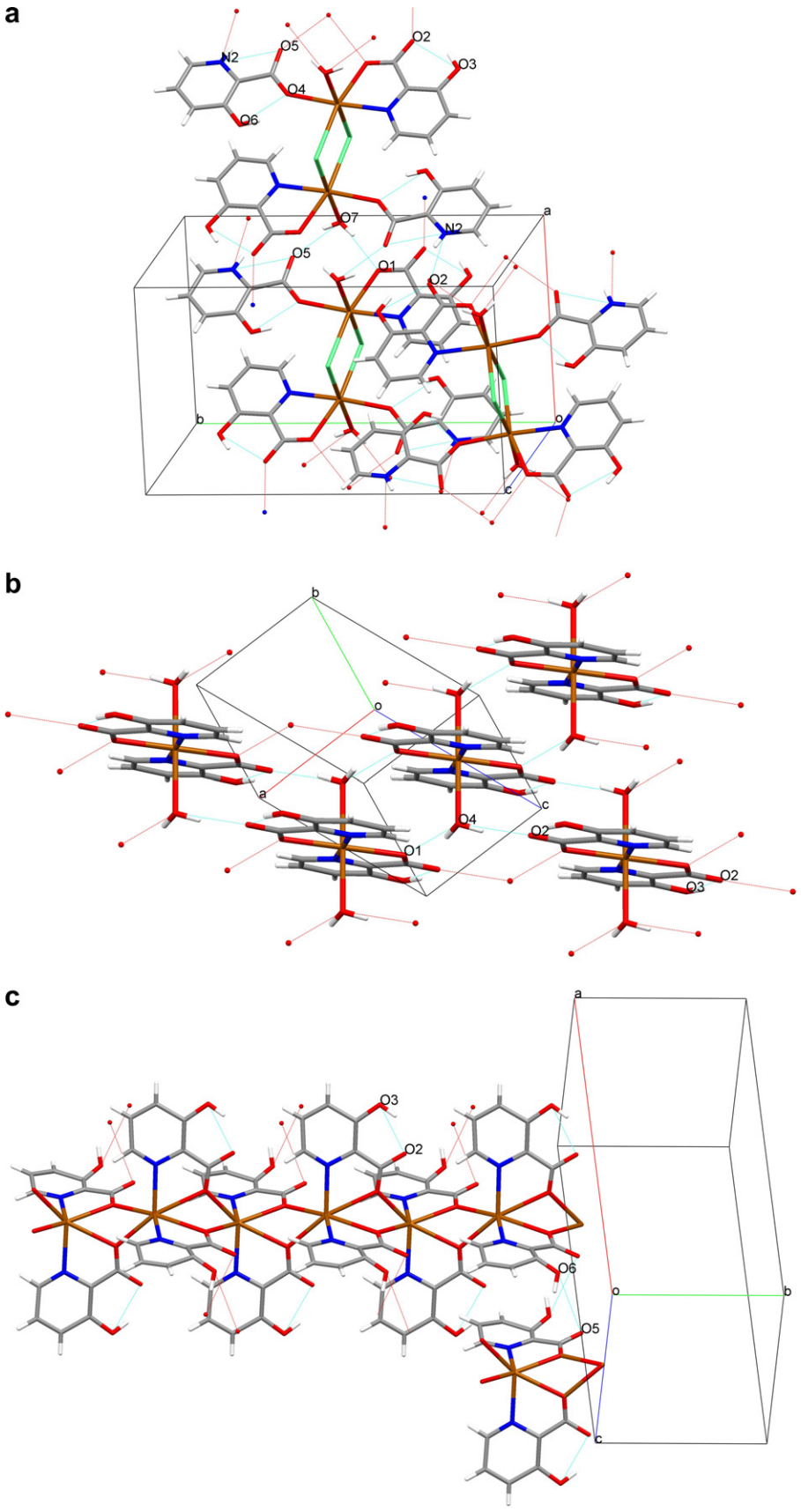


Fig. 2. MERCURY view of the packing in the crystal structures of $[CdI(3\text{-}OHpic)(3\text{-}OHpicH)(H_2O)]_2$ (**1**) (a), $[Cd(3\text{-}OHpic)_2(H_2O)_2]$ (**2**) (b) and $[Cd(3\text{-}OHpic)_2]_n$ (**3**) (c).

Table 3
Selected bond distances (Å) and angles (°) for [CdI(3-OHpic)(3-OHpicH)$(H_2O)]_2$ (**1**), [Cd(3-OHpic)$_2(H_2O)_2$] (**2**) and [Cd(3-OHpic)$_2]_n$ (**3**)

1		**2**		**3**	
Bond distances					
Cd1–N1	2.348(3)	Cd1–N1	2.299(1)	Cd1–N1	2.285(7)
Cd1–O1	2.327(2)	Cd1–O1	2.301(1)	Cd1–N2	2.290(7)
Cd1–O7	2.305(3)	Cd1–O4	2.309(1)	Cd1–O1	2.510(8)
Cd1–O4	2.339(2)			Cd1–O1	2.340(8)
Cd1–I1^{i}	2.922(1)			Cd1–O4	2.486(8)
Cd1–I1	2.947(1)			Cd1–O4^{iii}	2.344(9)
Bond angles					
O4–Cd1–N1	174.4(1)	N1–Cd1–N1^{ii}	180.0(1)	N1–Cd1–N2	105.5(3)
O1–Cd1–I1^{i}	165.4(1)	O1–Cd1–O1	180.0(1)	O1–Cd1–O1	155.3(2)
O7–Cd1–I1	172.0(1)	O4–Cd1–O4^{ii}	180.0(1)	O4–Cd1–O4^{iii}	157.0(2)
O1–Cd1–N1	71.5(1)	N1–Cd1–O1	73.3(1)	N1–Cd1–O1	65.0(6)
O1–Cd1–O4	106.9(1)	N1–Cd1–O1	106.7(1)	N2–Cd1–O4	63.0(5)
O7–Cd1–O1	85.8(1)	N1–Cd1–O4	85.6(1)	N1–Cd1–O1	132.8(6)
O7–Cd1–O4	81.9(1)	N1–Cd1–O4^{ii}	94.4(1)	N2–Cd1–O1	93.2(5)
O7–Cd1–N1	92.6(1)	O1–Cd1–O4	91.3(1)	N1–Cd1–O4^{iii}	88.8(5)
O7–Cd1–I1^{i}	93.4(1)	O1–Cd1–O4^{ii}	88.7(1)	N2–Cd1–O4^{iii}	132.8(6)
O4–Cd1–I1^{i}	87.4(1)			O1^{iii}–Cd1–O4^{iii}	49.3(2)
N1–Cd1–I1^{i}	94.0(1)			N1–Cd1–O4	103.4(5)
O1–Cd1–I1	90.0(1)			O1–Cd1–O4^{iii}	123.6(2)
O4–Cd1–I1	92.9(1)			N2–Cd1–O1	97.7(5)
N1–Cd1–I1	92.4(1)			O4–Cd1–O1	128.6(2)
I1–Cd1–I1^{i}	92.4(1)			O4–Cd1–O1	46.1(2)

Symmetry code (i) $1-x, -y, 2-z$; (ii) $-x, -y, 1-z$; (iii) $1/2-x, y-1/2, 2-z$.

Table 4
Hydrogen bond geometry (Å, °)

D–H···A	D–H	H···A	D···A	∠DHA	Symmetry code
[*CdI(3-OHpic)(3-OHpicH)*$(H_2O)]_2$ (***1***)					
O3–H3···O2	0.82	1.86	2.573(4)	145	
O6–H6···O4	0.82	1.89	2.600(4)	145	
N2–H12N···O5	0.73(4)	2.27(3)	2.683(4)	117(3)	
N2–H12N···O2	0.73(4)	2.09(4)	2.752(4)	152(3)	$-x, -1/2+y, 3/2-z$
O7–H17O···O1	0.78(3)	1.95(4)	2.708(4)	163(4)	$-x, 1-y, 1-z$
O7–H27O···O5	0.76(3)	2.01(4)	2.726(4)	158(4)	$-x, 1-y, 1-z$
C11–H11···O7	0.93	2.50	3.317(5)	147	$x, 1/2-y, 1/2+z$
[*Cd(3-OHpic)*$_2$ $(H_2O)_2$] (***2***)					
O3–H13O···O2	0.75(3)	1.86(4)	2.537(3)	150(3)	
O4–H24O···O2	0.82(3)	1.96(3)	2.727(2)	155(3)	$x, y, -1+z$
O4–H34O···O1	0.82(3)	1.92(4)	2.694(2)	156(3)	$-1-x, -y, 1-z$
C4–H4···O3	0.93	2.56	3.312(3)	138	$1/2+x, 1/2-y, -1/2+z$
C5–H5···O4	0.93	2.55	3.410(3)	154	$1+x, y, z$
[*Cd(3-OHpic)*$_2]_n$ (***3***)					
O3–H3···O2	0.82	1.91	2.54(2)	134	
O6–H6···O5	0.82	2.40	3.04(2)	135	$-x, y, 2-z$
C5–H5···O2	0.93	2.42	3.18(2)	139	$x, -1+y, z$
C9–H9···O2	0.93	2.39	3.30(2)	163	$-1/2+x, -1/2+y, z$

There are three intramolecular hydrogen bonds in the crystal structure of **1** (Table 4 and Fig. 2a), two of the type O–H···O and one of the type N–H···O. The first intramolecular O–H···O hydrogen bond (in anionic 3-OHpic ligand) is formed by the hydroxyl O3 atom and uncoordinated carboxylic O2 atom (2.573(4) Å) while the second one (in zwitterionic 3-OHpic ligand), formed by the hydroxyl O6 atom and coordinated carboxylate O4 atom, is slightly longer (2.600(4) Å) than the first one. The intramolecular N–H···O hydrogen bond is formed by endocyclic N2 atom and uncoordinated carboxylate O5 atom (2.683(4) Å) and is longer than the latter O–H···O hydrogen bonds. There are also two intermolecular hydrogen bonds of O–H···O type, the first is formed by water molecule O7 atom and coordinated carboxylate O1 atom (2.708(4) Å) and the second by the same O7 atom and uncoordinated carboxylate O5 atom (2.726(4) Å). Thus, water molecule O7 atom acts as a double proton donor (O7···O1 and O7···O5 intermolecular hydrogen bonds). Intermolecular hydrogen bond of N–H···O type is formed

by the endocyclic N2 atom and uncoordinated carboxylate O2 atom (2.752(4) Å). Endocyclic N2 atom is a double proton donor, forming both intramolecular (N2···O5) and intermolecular (N2···O2) hydrogen bonds while both carboxylate O5 and O2 atoms act as double proton acceptors, forming intramolecular (N2···O5 and O3···O2) and intermolecular (O7···O5 and N2···O2) hydrogen bonds. Intermolecular hydrogen bonds link molecules of **1** into a three-dimensional supramolecular structure. There is also one weak intermolecular hydrogen bond (3.317(5) Å) of type C–H···O in the crystal structure of **1** (Table 4).

3.5. Structural description of *2*

Crystal data and details of the structure determination for **2** are given in Table 2. ORTEP-3 view of the molecular structure of compound **2** is depicted in Fig. 1b and its crystal structure in Fig. 2b. Some selected interatomic bond distances and angles are listed in Table 3, as well as hydrogen bond geometry in Table 4.

The molecular structure of **2** consists of cadmium(II) ion with the distorted octahedral coordination geometry. Cadmium(II) ion is situated on a crystallographic inversion centre. The coordination environment contains two 3-hydroxypyridine-2-carboxylate ligands in the equatorial plane (Cd1–N1 2.299(1) Å, Cd1–O1 2.301(1) Å) and two water molecules in axial position (Cd1–O4 2.309(1) Å) (Table 3 and Fig. 1b). 3-OHpic ligands are bound to cadmium(II) ion in a bidentate *N*,*O*-chelated mode forming a five-membered chelate ring.

Complex **2** is isomorphous with zinc(II) [1,2] and manganese(II) [1] complexes with 3-hydroxypicolinic acid. The bond distance Cd1–N1 in **2** is shorter than the corresponding ones in $[Cd(pic)_2]_n$ (Cd–N1 2.35(1) Å, Cd–N2 2.34(2) Å) [13], $[Cd(6\text{-Mepic})_2]_n$ (Cd1–N1 2.374(2) Å, Cd1–N2 2.341(2) Å) [5] and in $[CdX(3\text{-OHpic})(3\text{-OHpicH})(H_2O)]_2$ (X = Cl, 2.328(2) Å; X = Br, 2.334(4) Å) [4]. The bond distance Cd1–O1 in **2** is also shorter than the analogous ones in $[Cd(pic)_2]_n$ (Cd–O2 2.35(2) Å, Cd–O4 2.36(2) Å) [13], $[Cd(6\text{-Mepic})_2]_n$ (Cd1–O1 2.332(2) Å, Cd1–O3 2.325(2) Å) [5] and in $[CdX(3\text{-OHpic})(3\text{-OHpicH})(H_2O)]_2$ (X = Cl, 2.344(2) Å; X = Br, 2.340(3) Å) [4]. However, Cd–O bond distance (carboxylate O atom from 3-OHpicH ligand bound monodentately to Cd(II) ion) in the latter compound (X = Cl, 2.314(2) Å; X = Br, 2.324(3) Å) is comparable with Cd1–O1 bond distance in **2**.

Two water molecules are bound to cadmium(II) ion in *trans* position with the angle O4–Cd1–O4^{ii} (symmetry code (ii) $-x, -y, 1-z$) of 180.0°. The bond distance Cd1–O4 (O atom from water molecule) is very similar to the ones in $[CdX(3\text{-OHpic})(3\text{-OHpicH})(H_2O)]_2$ (X = Cl, 2.304(2) Å; X = Br, 2.307(4) Å) [4].

The bond angles around Cd centre are about 180° for the formally *trans* pairs of the ligating atoms, but the distortion of the octahedron is indicated by the bond angles around Cd centre for the formally *cis* pairs lying within the range of 73–107°. The angles indicating the largest distortion from the ideal octahedral geometry are the bite angle O1–Cd1–N1 with value 73.3(1)° and angle N1–Cd1–O1^{ii} (symmetry code (ii) $-x, -y, 1-z$) with value 106.7(1)°.

The dihedral angle between the least squares calculated planes through the atoms of pyridine ring (N1/C1/C2/C3/C4/C5) and the corresponding five-membered chelate ring (Cd1/N1/C1/C6/O1) is 2.7(1)°.

There are three hydrogen bonds of the type O–H···O in the crystal structure of **2** (Table 4 and Fig. 2b). One of them is intramolecular hydrogen bond (2.537(3) Å) formed by the hydroxyl O3 atom and uncoordinated carboxylate O2 atom while the other two are intermolecular hydrogen bonds formed between water molecule O4 atom and coordinated carboxylate O1 atom (2.694(2) Å) and between water molecule O4 atom and uncoordinated carboxylate O2 atom (2.727(2) Å) (Table 4). The water molecule O4 atom acts as a double proton donor forming the latter intermolecular hydrogen bonds. On the contrary, uncoordinated O2 atom acts as double proton acceptor forming both intramolecular (O3···O2) and intermolecular (O4···O2) hydrogen bonds. Intermolecular hydrogen bonds (O4···O1 and O4···O2) link molecules of **2** into two-dimensional network in *ac* plane. There are also two weak intermolecular hydrogen bonds (3.312(3) Å and 3.410(3) Å) of type C–H···O in the crystal structure of **2** (Table 4).

3.6. Structural description of *3*

Crystal data and details of the structure determination for **3** are given in Table 2. ORTEP-3 view of the molecular structure of compound **3** is depicted in Fig. 1c and its crystal structure in Fig. 2c. Some selected interatomic bond distances and angles are listed in Table 3, as well as hydrogen bond geometry in Table 4.

In **3**, the cadmium(II) ion is octahedrally coordinated by two 3-hydroxypyridine-2-carboxylate ligands perpendicular to one another (Fig. 2c). 3-OHpic ligands are bound to cadmium(II) ion in a bidentate *N*,*O*-chelated mode forming a five-membered chelate ring (Cd1–N1 2.285(7) Å, Cd1–O1 2.510(8) Å; Cd1–N2 2.290(7) Å, Cd1–O4 2.486(8) Å) (Table 3). Two carboxylate O atoms from another two symmetry-related ligand molecules are also coordinated to the cadmium(II) ion (Cd1–O1 2.340(8) Å, Cd1–O4^{iii} 2.344(9) Å) (symmetry code (iii) $1/2-x, y-1/2, 2-z$), expanding its coordination to a distorted octahedron. Each carboxylate O atom in **3** bridges cadmium(II) ions, forming one-dimensional chain which extends in the [0 1 0] direction (Fig. 2c). The coordination mode of 3-OHpic in **3** is the same as the coordination modes of picolinic acid in $[Cd(pic)_2]_n$ [13] and 6-methypicolinic acid in $[Cd(6\text{-Mepic})_2]_n$ [5], resulting in one-dimensional polymeric chains. However, the structure of **3** is non-centrosymmetric and there are hydrogen bonds between the polymeric chains of **3** (*vide infra*), explaining good solubility of **3** in organic solvents with donor properties in comparison with $[Cd(6\text{-Mepic})_2]_n$ [5].

The bond distances Cd1–N1 and Cd1–N2 in **3** are shorter than the analogous ones in $[Cd(pic)_2]_n$ (2.35(1)

and 2.34(2) Å) [13] and in $[Cd(6\text{-Mepic})_2]_n$ (2.374(2) and 2.342(2) Å) [5]. On the contrary, the bond distances Cd1–O1 and Cd1–O4 are larger than the corresponding ones in $[Cd(pic)_2]_n$ (2.35(2) and 2.36(2) Å) [13] and in $[Cd(6\text{-Mepic})_2]_n$ (2.332(2) and 2.325(2) Å) [5], as well as the bond distances Cd1–O^{iii} and Cd1–$O4^{iii}$ (symmetry code (iii) $1/2 - x, y - 1/2, 2 - z$) are also larger than in $[Cd(pic)_2]_n$ (2.23(2) and 2.25(1) Å) [13] and in $[Cd(6\text{-Mepic})_2]_n$ (2.272(2) and 2.279(2) Å) [5].

The bond angles around Cd centre are in the range of 105–157° for the formally *trans* pairs of the ligating atoms and in the range of 46–133° for the formally *cis* pairs, indicating the large distortion of the octahedron. The angles indicating the large distortion from the ideal octahedral geometry are the bite angles N1–Cd1–O1 with value of 65.0(6)° and N2–Cd1–O4 with value equal to 63.0(5)°.

The dihedral angle between the least squares calculated planes through the atoms of pyridine ring (N1/C1/C2/C3/C4/C5) and the corresponding five-membered chelate ring (Cd1/N1/C1/C6/O1) is 1.7(7)° while the analogous angle (between planes defined by atoms N2/C7/C8/C9/C10/C11 and Cd1/N2/C7/C12/O4) is 7.3(8)°.

There are two hydrogen bonds of the type O–H···O in the crystal structure of **3** (Table 4 and Fig. 2c). One of them is intramolecular hydrogen bond (2.54(2) Å) formed by the hydroxyl O3 atom and uncoordinated carboxylate O2 atom while the other is intermolecular hydrogen bond (3.04(2) Å) formed by hydroxyl O6 atom and uncoordinated carboxylate O5 atom. The latter hydrogen bond links one-dimensional polymeric chains of **3** in [1 0 0] direction, resulting in a two-dimensional network in *ab* plane (Fig. 2c). There are also two weak intermolecular hydrogen bonds (3.18(2) Å and 3.30(2) Å) of type C–H···O in the crystal structure of **3** (Table 4). Thus, uncoordinated carboxylate O2 atom acts as triple proton acceptor, forming intramolecular (O3···O2) and two intermolecular hydrogen bonds (C5···O2 and C9···O2).

4. Conclusion

By using 3-hydroxypicolinic acid as pyridinecarboxylate ligand, we have synthesized three novel cadmium(II) complexes: diaqua-bis(3-hydroxypyridine-2-carboxylato-*N*,*O*)-bis(3-hydroxypyridinium-2-carboxylato-*O*)-diiododicadmium(II) (**1**), *trans*-diaqua-bis(3-hydroxypyridine-2-carboxylato-*N*,*O*)cadmium(II) (**2**) and *catena*-poly[bis(3-hydroxypyridine-2-carboxylato-*N*,*O*)cadmium(II)] (**3**). Synthesis of **1** and **2** were done in water solution, using different starting cadmium(II) salts, iodide and acetate, respectively. Complex **3** was obtained by recrystallization of **2** from DMF solution. All compounds were characterized by elemental analysis, IR and ^{1}H, ^{13}C, ^{15}N, ^{113}Cd NMR spectroscopy while their crystal structures were determined by X-ray single-crystal diffractometry method.

Three different coordination modes of 3-hydroxypicolinic acid in prepared complexes were established in the solid state. Bidentate *N, O*-chelated mode was found in the structure of **1** and **2**, monodentate mode through carboxylate O atom belonging to zwitterionic ligand was found only in **1**, while bidentate *N*,*O*-chelated and bridging mode were revealed in the structure of **3**. Thus, complex **1** is dimmer, **2** is monomer while **3** has polymeric structure. In all prepared complexes cadmium(II) ion has a distorted octahedral coordination.

^{15}N NMR spectroscopy confirmed that 3-OHpic ligand is not bound to cadmium(II) ion through endocyclic nitrogen atom due to the similar chemical shift of nitrogen atom in complexes in comparison with the free ligand. Thus, the ligand is apparently bound to cadmium(II) ion monodentately through carboxylate oxygen atom in DMF solution of the related complexes.

5. Supplementary data

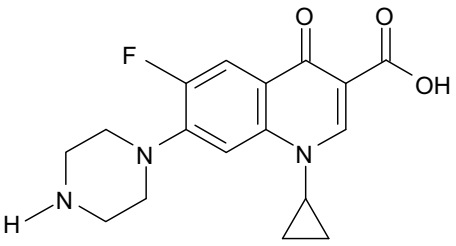
CCDC 662949, 662950 and 662951 contain the supplementary crystallographic data for this paper. These data can be obtained free of charge via http://www.ccdc.cam.ac.uk/conts/retrieving.html, or from the Cambridge Crystallographic Data Centre, 12 Union Road, Cambridge CB2 1EZ, UK; fax: (+44) 1223-336-033; or e-mail: deposit@ccdc.cam.ac.uk.

Acknowledgements

This work was supported by the Ministry of Science, Education and Sports of the Republic of Croatia within the scientific projects under the title "Chemistry of metal complexes in reactions of biological importance and new materials" (No. 119-1193079-1332) and "NMR Spectroscopy and Modeling of Bioactive Molecules" (No. 098-0982929-2917).

References

[1] C. Sun, X. Zheng, L. Jin, J. Mol. Struct. 646 (2003) 201.
[2] V.B. Di Marco, A. Tapparo, A. Dolmella, G.G. Bombi, Inorg. Chim. Acta 357 (2004) 135.
[3] Z. Popović, D. Matković-Čalogović, J. Popović, I. Vicković, M. Vinković, D. Vikić-Topić, Polyhedron 26 (2007) 1045.
[4] Z. Popović, G. Pavlović, M. Vinković, D. Vikić-Topić, M. Rajić Linarić, Polyhedron 25 (2006) 2353.
[5] B.M. Kukovec, Z. Popović, G. Pavlović, Acta Crystallogr. C 63 (2007) m389.
[6] Oxford Diffraction, Oxford Diffraction Ltd., Xcalibur CCD System, CrysAlis Software System, Version 171.31.5, 2006.
[7] G.M. Sheldrick, Acta Crystallogr. A 46 (1990) 467.
[8] G.M. Sheldrick, SHELXL97, Programme for the Refinement of Crystal Structures, 1997, University of Göttingen, Germany.
[9] L.J. Farrugia, J. Appl. Crystallogr. 30 (1997) 565.
[10] C.F. Macrae, P.R. Edgington, P. McCabe, E. Pidcock, G.P. Shields, R. Taylor, M. Towler, J. van de Streek, J. Appl. Crystallogr. 39 (2006) 453.
[11] G.B. Deacon, R.J. Phillips, Coord. Chem. Rev. 33 (1980) 227.
[12] G. Ma, A. Fischer, R. Nieuwendaal, K. Ramaswamy, S.E. Hayes, Inorg. Chim. Acta 358 (2005) 3165.
[13] J.P. Deloume, H. Loiseleur, Acta Crystallogr. B 30 (1974) 607.



Scheme 1.

Highly sensitive analytical methods for the determination of antibacterial drugs can be designed on the basis of specific luminescent properties of some lanthanide ions [8], such as Eu(III) and Tb(III). Spectra of such complexes have "linear" Stark structure that are specific [9,10].

Lanthanide–quinolone complexes could also be useful for therapeutic and diagnostic applications in medicine (fluorescence microscopy bioimaging, DNA hybridization assay, etc.) [11,12]. Labeling of DNA could be especially promising due to the fact that quinolones interact with DNA and this interaction is important for the mode of action of these drugs [13].

Luminescence spectra of Eu(III) are characterized by a narrow resonance line of $^5D_0$–$^7F_0$ transition and sufficiently informative picture of the Stark splitting. The anion charges, the distance between ligands and rare-earth metal, as well as the symmetry of the environment of the central lanthanide ion can influence the Stark splitting magnitude of the $^5D_0$–$^7F_1$ and $^5D_0$–$^7F_2$ transitions [14]. Intensification of the electrostatic interaction between a rare-earth metal and coordinated ligand and the reduction of the environmental symmetry around the central lanthanide ion result in the increase of splitting of energy levels.

There are few papers dealing with the composition, structure and spectral luminescent properties of the lanthanide complexes with fluoroquinolones [7,9,10,15,16]. Li et al. [16] described compounds with general formula $Ln(cfq)_2Cl(H_2O)_n$ (Ln–Pr, Nd, Sm, Gd, Tb, Dy, Ho, Er, Tm, Yb, $n = 7$–9) and analyzed their spectroscopic data (IR, electronic spectra). However, the crystallographic data were reported only for the cerium complex $[Ce(cf)_2(H_2O)_4]Cl \cdot (H_2O)_{3.25}(C_2H_5OH)_{0.25}$ (**2**). It was also reported that the europium(III) complex of quinolone family member ofloxacin and terbium(III) complex of ciprofloxacin could be used as fluorescent markers for histological staining [17]. This procedure is much faster than traditional hematoxylin and eosin histologic stain method but the authors have only proposed the structures of rare-earth metal–quinolone complexes whereas no crystal structures were available.

In this paper, the crystal structure and spectral luminescent properties of compound $[Eu(cfqH)(cfq)(H_2O)_4]Cl_2 \cdot 4.55H_2O$ (**1**) in the solid state have been thoroughly analyzed and its stability in aqueous and DMSO solutions evaluated by ^1H and ^{19}F NMR measurements.

2. Experimental

2.1. Synthesis of $[Eu(cfqH)(cfq)(H_2O)_4]Cl_2 \cdot 4.55H_2O$ (1)

The synthesis was carried out solvothermally in a Teflon container. Europium(III) chloride hexahydrate (0.0451 g, 0.123 mmol), ciprofloxacin hydrochloride hydrate (0.142 g, 0.369 mmol) and 1,3-bis(dimethylamino)-2-propanol ligand (bdmapH, 0.0180 g, 0.123 mmol) were added to a mixture of water (2.0 mL) and ethanol (2.0 mL). The mixture was stirred and the suspension placed in a stainless steel autoclave followed by heating at 150 °C for 48 h. Cooled orange solution was evaporated isothermally in air. After one week, a few pale yellow crystals suitable for structure determination had grown on the top of the bulk of the microcrystalline material. Yield: 0.0588 g (47.2%). $\lambda_{max}(\varepsilon)$ in water: 224 nm (9610 L mol^{-1} cm^{-1}), 272 (29 600 L mol^{-1} cm^{-1}), 321 (11 700 L mol^{-1} cm^{-1}). The results of the elemental analysis are in agreement with the formula $[Eu(cfqH)(cfq)(H_2O)_4]Cl_2 \cdot 8H_2O$ (*Anal.* Calc. for $C_{34}H_{59}Cl_2EuF_2N_6O_{18}$: C, 37.10; H, 5.40; N, 7.63. Found: C, 36.73; H, 5.16; N, 7.40%).

2.2. X-ray crystallography

The crystal data and final refinement parameters of compound **1** are presented in Table 1. Intensity data were

Table 1
Crystal data and refinement parameters of compound **1**

Formula	$C_{34}H_{52.1}Cl_2EuF_2N_6O_{14.55}$
F_r	1038.59
Crystal system	triclinic
Space group	$P\bar{1}$
a (Å)	13.5929(15)
b (Å)	13.8775(18)
c (Å)	16.205(2)
α (°)	93.966(3)
β (°)	114.372(3)
γ (°)	114.907(3)
V (Å^3)	2413.8(5)
Z	2
T (K)	150(2)
D_{calc} (g cm^{-3})	1.430
μ(Mo Kα) (mm^{-1})	1.482
Crystal size (mm)	0.15 × 0.14 × 0.12
Crystal color, shape	yellow prism
θ Range (°)	3.01–25.03
Data measured, unique (R_{int})	16 099, 8491 (0.0234)
Observed data [$I > 2\sigma(I)$]	7550
Number of parameters	543
R^a, wR_2^b [$I > 2\sigma(I)$]	0.0560, 0.1742
R, wR_2 (all data)	0.0636, 0.1654
S^c, $(\Delta/\sigma)_{max}$	1.104, 0.023
Maximum, minimum peaks (e Å^{-3})	3.970, −1.345

[a] $R = \sum||F_o| - |F_c||/\sum|F_o|$.
[b] $wR_2 = \{\sum[w(F_o^2 - F_c^2)^2]/\sum[w(F_o^2)^2]\}^{1/2}$.
[c] $S = \{\sum[(F_o^2 - F_c^2)^2]/(n/p)\}^{1/2}$, where n is the number of reflections and p is the total number of parameters refined.

collected at 150(2) K on a Nonius Kappa CCD diffractometer equipped with a cooling device (Oxford Cryosystems, Cryostream Cooler 700), a Mo Kα anode ($\lambda = 0.71073$ Å) and a graphite monochromator, and the multiscan absorption correction [18] was performed. The structure was solved by direct methods (SHELXS-97) and refined by a full-matrix, least-squares procedure based on F^2 (SHELXL-97) [19]. Hydrogen atoms attached to water oxygen atoms coordinated to europium were found from difference Fourier maps and were subjected to the constrained refinement. A check using the PLATON program [20] revealed voids of approximately 200 Å^3 in the crystal packing due to the specific shape of the coordination compound (Fig. 1). Additional solvent water molecules were found in these voids and they were taken in the refinement with the anti-bumping constraints and the atomic occupation parameters were also refined. Positions of the hydrogens of these solvent water were not located. The hydrogen atoms (apart from the terminal piperazinyl hydrogens) of the ciprofloxacin moieties were placed at calculated positions and treated using appropriate riding models.

2.3. Spectroscopy and elemental analysis

The emission spectra of the europium and gadolinium complexes were obtained on the SDL-1 (LOMO) spectrometer (the frequency measurement error is ±3 cm^{-1}) with DRSh-250 mercury lamp and "Tungsram" used as an excitation sources and monochromatic light from the xenon lamp using the KSVU monochromator. The scale of the spectrometer wavelengths was verified using lines of the helium–neon sources and mercury lines, including duplicate 5769.6–5790.6 Å. Measurements were conducted at 300 and 77 K.

A Cary Eclipse Fluorescence Spectrophotometer (Varian) was used to measure excitation spectra and fluorescence lifetimes. All measurements were performed at 300 K. Emission and excitation slit widths were 5 nm and rates of 600 nm min^{-1} were used. The metal luminescence excitation was acquired by monitoring the emission at 613 nm for Eu(III). Quoted lifetime is the average value of at least three independent measurements, each of which being obtained by monitoring the emission intensity at 613 nm after 6–8 different delay times with a gate time of 0.4 ms. Decay curves were fitted with OriginLab using built-in least-square-goodness-of-fit Levenberg–Marquardt algorithm (LMA).

NMR spectra were recorded at 9.4 T (^{1}H resonating at 400 MHz) using a Bruker Avance NMR spectrometer equipped with a 5 mm normal configuration broadband tuneable probe applying conditions previously described [21]. ^{19}F NMR spectra (resonating at 376 MHz) were acquired at 25 °C unless stated otherwise using an acquisition time of 7 s, post-acquisition delay of 2 s and a flip angle of 30°. ^{19}F NMR spectra were referenced externally to 1% CF_3CO_2H in $CDCl_3$ at 25 °C (−78.5 ppm); ^{1}H NMR spectra were referenced internally to TMS (0 ppm). Saturation transfer measurements utilized an acquisition time of 1.7 s, post-acquisition delay of 6 s for saturation, flip angle of 30° and a power level for irradiation of 57 dB relative to the full power pulse. The concentration of the NMR solutions was ca. 2 mg mL^{-1}.

UV–Vis spectrum of an aqueous solution was acquired on a Perkin–Elmer Lambda 19 spectrometer.

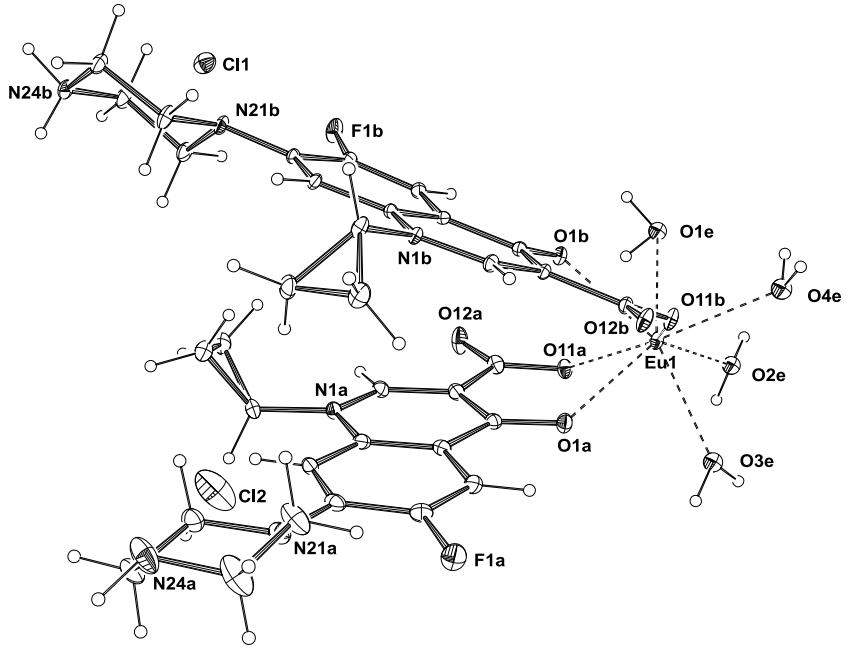


Fig. 1. ORTEP view of $[Eu(cfqH)(cfq)(H_2O)_4]Cl_2 \cdot 4.55H_2O$ showing the coordination around the europium ion.

IR spectra were recorded on a Shimadzu IRPrestige-21 infrared spectrophotometer using KBr pellets. Raman spectra were recorded on a Bruker RFS 100/s spectrophotometer.

Elemental analyzes were performed on a Perkin–Elmer 204C microanalyzer.

3. Results and discussion

3.1. Synthesis

It is interesting to note that it was necessary to use an excess of ligand in the mixture of europium salt and ciprofloxacin to obtain crystals of **1**. It was previously reported that the presence of histidine in the preparation of quinolone metal complexes could result in the isolation of new crystalline products which are different from those obtained without using this compound [22,23]. In the present case, the addition of either bdmapH or histidine provoked the formation of crystals of **1**. As reported before, we believe the additional ligand may serve to fine tune the protolytic equilibria to reach the correct species distribution for crystallization [22,23].

The crystals of the title complex are stable in solution but are not very stable in air which was already observed for other metal–quinolone complexes [24]. It was also shown before [25–27] that weakly bonded lattice water molecules could easily be lost from metal–quinolone complexes already at room temperature.

3.2. Crystal structure analysis

The crystal structure of compound **1** is shown in Fig. 1. The drawing was prepared with the aid of ORTEPII [28] program. Selected bond lengths and angles within the complex together with hydrogen bond distances around the terminal piperazinyl nitrogens are presented in Table 2.

All bond distances and angles (given in CIF Supplementary material) in **1** are in an agreement with corresponding data cited in the literature [29,30]. The asymmetric unit of **1** consists of $[Eu(cfqH)(cfq)(H_2O)_4]^{2+}$ cation, two chloride ions and six partially disordered, solvent water molecules. Both quinolone molecules are bidentately O,O-bonded to europium through the ring carbonyl (O1) and carboxylate (O11) oxygen atoms. Additionally, four water molecules are also coordinated to the metal center. The bond lengths between europium and carboxylate oxygen atoms (Eu–O11) are slightly shorter than the bond lengths between europium and ring carbonyl oxygen atoms (Eu–O1) in the same quinolone molecule (see Table 2). This is in agreement with our observation in a recent experimental charge density study where this effect was explained as a consequence of the asymmetry of C–O bond lengths of the carboxylate group [31]. One of the molecules of ciprofloxacin is in a zwitterionic form (the carboxylic hydrogen from O11 atom is bonded to a terminal nitrogen atom N24 of the piperazine ring) [6], the second one seems to appear with only one hydrogen attached to N24. This was indicated not only from the peaks in a difference electron density map, but also from the inspection of the possible hydrogen bonds around piperazinyl nitrogens (Table 2).

Table 2
Selected geometric parameters of complex **1** (Å, °) with hydrogen bonds of terminal nitrogen piperazinyl atoms (Å, °)

Europium coordination			
Eu1–O11B	2.354(4)	Eu1–O1E	2.463(4)
Eu1–O1B	2.372(4)	Eu1–O2E	2.417(4)
Eu1–O11A	2.376(4)	Eu1–O3E	2.395(4)
Eu1–O1A	2.396(4)	Eu1–O4E	2.425(7)
O11B–Eu1–O1B	72.00(19)	O11A–Eu1–O1E	78.6(2)
O1B–Eu1–O11A	79.82(19)	O11B–Eu1–O3E	88.6(2)
O11B–Eu1–O1A	75.30(18)	O11B–Eu1–O4E	69.2(2)
O1B–Eu1–O1A	77.04(16)	O2E–Eu1–O1E	72.01(19)
O11A–Eu1–O1A	70.87(19)	O3E–Eu1–O4E	86.4(2)
O1A–Eu1–O3E	71.40(18)	O3E–Eu1–O2E	72.0(2)
O1B–Eu1–O1E	69.91(18)	O4E–Eu1–O2E	73.6(2)
O11A–Eu1–O2E	80.3(2)	O4E–Eu1–O1E	78.7(2)
Hydrogen bonds			
N24a···Cl1	3.126(10)	N24a–H241···Cl1	138(6)
N24b···Cl2	3.105(6)	N24b–H243···Cl2	164(7)
N24b···O12b (x, $y-1$, z)	2.715(8)	N24b–H242···O12b	174(8)

It is interesting to compare the structure of the title complex **1** with that of compound **2** [16]. In the latter, both ciprofloxacin molecules are anionic and thus only one chloride ion is needed to compensate the charge of Ce^{3+}. Most probably the medium used in the synthesis of cerium complex was slightly more basic due to the presence of pyridine. In complex **1**, the coordination number of the metal center is 8, which is common for europium [32]. Coordination polyhedron around europium is formed by 8 oxygen atoms and could be described as a distorted square antiprism, O11b, O1b, O4e, and O1e atoms forming nearly planar quadratic arrangement (the largest deviation from the mean plane is 0.047(3) Å), whilst the opposite part of the polyhedron is closer to the dodecahedral arrangement (O3e and O11a being out of plane of the four oxygens O1a, O3e, O2e, and O11a), as depicted in Fig. 2. The Eu–O bond lengths range from 2.354(4) to 2.463(4) Å whilst the corresponding O–Eu–O angles span from 69.91(18) to 149.6(2)°. In the cerium complex **2**, the coordination number of the metal center is also 8 and the coordination polyhedron could be described as a square antiprism with the angles O–Ce–O lying in the range 68.8–140.9°.

A very complex network of hydrogen bonds involving quinolone heteroatoms, chloride ions and numerous water molecules is present in the crystal structure of **1**. However, the complete determination is not possible due to disorder of the solvent water molecules mentioned above.

3.3. IR, Raman spectroscopy studies

IR and Raman spectra have been assigned. The assignment was based on the comparison of title compound spec-

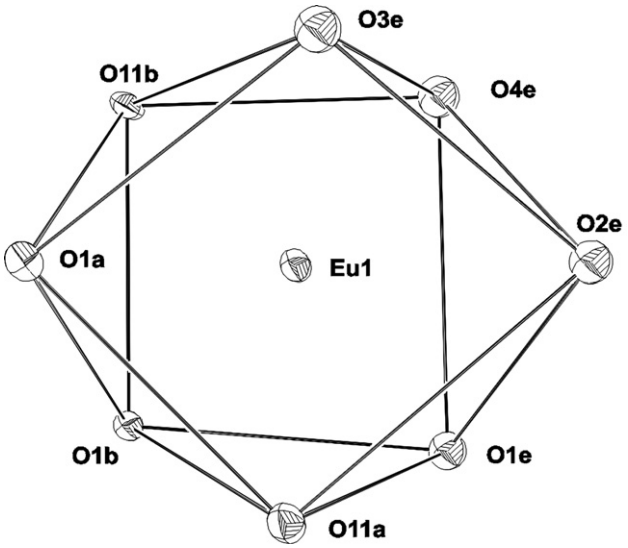


Fig. 2. Coordination polyhedron around europium atom in **1**: distorted square antiprismatic arrangement.

tra and the available literature data of quinolones and their metal complexes [33–35]. The crystallographic data, especially the interatomic distances were also taken into account (Table 2).

The most significant data from IR and Raman spectra of the complex are discussed below and selected bands are given in Table 3.

Bands in the region 3400–3200 cm^{-1} could be assigned to the symmetric and asymmetric stretching vibrations of the OH groups of the inner- and outer-sphere water molecules. The difference between vibration frequencies of $\nu_{as}(H_2O)$ and $\nu_s(H_2O)$ depends on the symmetry of the formed complexes. The shift of the characteristic bands of the IR spectra, changes of their intensity and half-width result from the increasing of bond energy of water molecules with the environment. Two types of water molecules (coordinated and crystal) are present in compound **1**. This leads to the appearance of several absorbance bands of the symmetric, asymmetric stretching vibrations and the overtone of the deformation vibrations in the region 3200–3400 cm^{-1} (Table 3).

Table 3
Selected bands of IR and Raman spectra of $[Eu(cfqH)(cfq)(H_2O)_4]Cl_2 \cdot 4.55H_2O$ with assignments

IR, cm^{-1} (I_{arb})	Raman, cm^{-1}(I_{arb})	assignment
	328(s)	ν(Eu–I)
721(m)	634(m), 702(m)	δ(C–H)
	1272(s)	ν(C–F)
1386(m)	1391(s)	ν_s(O–C–O)
1417(w)		
1456(m), 1487(sh)	1450(m), 1484(m)	ν_{as}(O–C–O)
1521, 1570	1551	ν(C–C), ν(C–N)
1616(s), 1633(s)	1627(m)	ν(C=O)
2498(m)		$\nu(NH_2^+)$
	2982(m)	ν(C=C), ν(C–H)
3396(s)		
3404(s)		$\nu_s(H_2O)$, $\nu_{as}(H_2O)$

Abbreviations: s – strong, m – medium, w – weak, sh – shoulder, I_{arb} – intensity in arbitrary units.

The absorbance band at 2498 cm^{-1} in the IR spectrum of the compound ascribed to $\nu(NH_2^+)$ results from the existence of the zwitterionic form of cfqH. There are such bands in the IR spectra of all fluoroquinolone hydrochlorides and these have been assigned to the stretching vibrations $\nu(NH_2^+)$ of the protonated secondary aliphatic nitrogen atom (2900–2300 cm^{-1}) [33].

As could be realized from the crystallographic results, both quinolone molecules are not equivalent; one ciprofloxacin molecule is zwitterionic, the other is anionic. In zwitterionic ciprofloxacin, the bond length C4B–O1B is 1.268(8) Å whereas the corresponding distance for C4A–O1A in the anionic molecule is 1.256(8) Å. Two characteristic bands observed in the IR spectrum of **1** at 1616 and 1633 cm^{-1} could be ascribed to ν(C=O) vibrations of the carbonyl group. We assume that the first corresponds to the ν(C=O) vibration in the zwitterionic molecule of quinolone, whereas the latter corresponds to the ν(C=O) vibration in the anionic molecule of quinolone.

We can assign the title compound's bands at 1487 cm^{-1} and 1386 cm^{-1} to ν_{as}(O–C–O) and ν_s(O–C–O), respectively. The corresponding bands in cfqH are found at 1451 and 1377 cm^{-1}. This shift could be explained by coordination of cfqH to Eu(III) ion. This is further supported by the Raman spectrum of the title compound where we can see that the intensity of bands assigned to ν_s(O–C–O) is twice as much as the intensity of bands ν_{as}(O–C–O) (Table 3).

3.4. Luminescence spectroscopy

It is known that the luminescence observed for aqueous solutions of Eu(III) salts is very weak as a result of a facile de-excitation pathway. Efficient luminescence requires that the lanthanide ion is well separated from any high frequency oscillators such as the overtone of the ν(OH) vibration of coordinated water molecules. Sensitized lanthanide emission can occur via energy transfer from organic ligands with excited triplet states of appropriate energy, which was first observed for lanthanide tris (β-diketonates) [36].

Under UV irradiation, the title compound **1** emits a red light, which is characteristic for Eu(III) ions. Excitation of the complex into the lowest energy ligand-centered absorption band ($\lambda_{ex} = 340$ nm according to the measured excitation spectrum) gives rise to the well-known structured emission of the Eu(III) ion.

The characteristic splitting of the bands and intensities of ^5D_j–^7F_j transitions ($j = 1$–3) of the emission spectrum of the compound **1** are typical for mononuclear compounds of Eu(III). The spectrum consists of the single line of the $^5D_0$–$^7F_0$ transition, three bands of the $^5D_0$–$^7F_1$ transition, and five components of the $^5D_0$–$^7F_2$ transition

(Fig. 3a). The spectrum is dominated by the $^5D_0$–$^7F_2$ transition; more than 50% of the total emission is centered on the 613 nm peak.

The strong deformation of the coordination sphere of the Eu(III) ion resulting from the different interatomic distances of Eu–OcfqH (2.354–2.396 Å) is reflected in the emission spectrum. The lack of the inversion centrum leads to the relieving of the prohibition so the peak intensity of the $^5D_0$–$^7F_0$ transition is almost equal to the one of the $^5D_0$–$^7F_1$ transition peaks.

The emission decay kinetics of the solid state complex **1** for the most intense emission (613 nm) is monoexponential (Fig. 4), which reveals that all Eu(III) ions lie in the same average environment. This result is in agreement with the results of the crystal structure determination. The decay curves are fitted into a single-exponential equation as $I = I_0\exp(-t/\tau)$, where I and I_0 are the luminescent intensities at times t and 0 and τ is defined as the luminescence lifetime. A value of 0.99996 for the correlation coefficient R^2 was obtained. The fitted value of τ for the complex **1** is 920 μs.

In Fig. 3b, the positional relationship of the levels of the ground and electronically excited states of the cfqH molecule and complex **1** are shown. The position of the S_1 ππ* level has been estimated according to fluorescence and absorbance spectra. The value of the energy of the Tππ* state of cfqH is 20,500 cm^{-1} and was obtained from the phosphorescence spectrum of the Gd(III) chelate of cfqH. This value is close to the value of the norfloxacin (another quinolone family member) triplet state energy (20 000 cm^{-1}) [37].

The compounds of Eu(III) with cfqH emit an intensive red luminescence under UV irradiation due to effective transfer of excitation energy from ππ and nπ – levels of cfqH to metastable $^5D_0$ level of Eu(III) which is the result of direct interatomic contacts of central ion Eu(III) with ciprofloxacin molecules linked with metal ion through oxygen heteroatoms.

3.5. NMR spectroscopy

To evaluate the stability and structure of complex **1** in aqueous solution, both ^1H and ^{19}F NMR measurements were performed on a D_2O solution of **1** whereby the complex was found to be stable without change over the course of several days. Both nuclei indicated the presence of only one species but due to the paramagnetism of the Eu^{3+} cation and dynamic exchange, all signals in both spectra were quite broad. In the ^1H NMR spectrum, only a single set of peaks appeared to be present, though disentanglement of the signals and assignment was prohibitive given the large chemical shift translations brought about by the presence of the Eu^{3+} cation. In the ^{19}F NMR spectrum, a clear single signal at −124.96 ppm, however, was present [thus also implying the equivalence of the distinct complexed cfq(H) units by rapid unit or proton exchange].

In an attempt to observe distinct ligands, e.g. by observing amine and ammonium signals in the ^1H NMR or by slowing the exchange rate of the proton transfer and thus rendering the cfq units inequivalent, complex **1** was also examined in DMSO-d_6 solution. However, this led to displacement of the cfq(H) ligand, presumably by DMSO, leading to a stable equilibrium that did not change over the course of several days and which consisted of three species: complex **1**, a complex containing only one cfq unit and

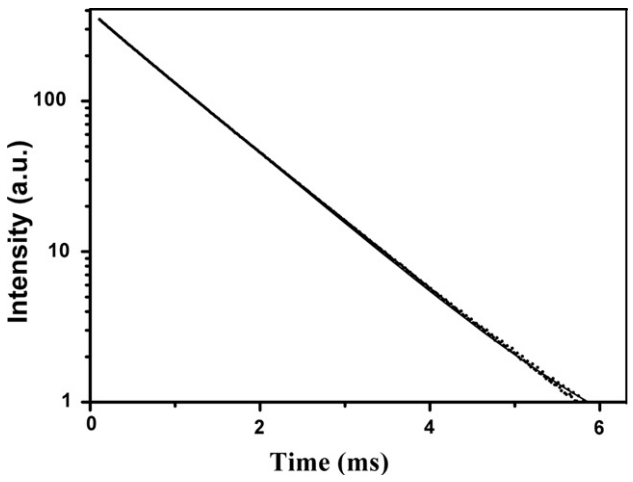


Fig. 4. The decay curve of the luminescent $^5D_0$ state for the compound **1** (···) and its fitting into a single-exponential function (—).

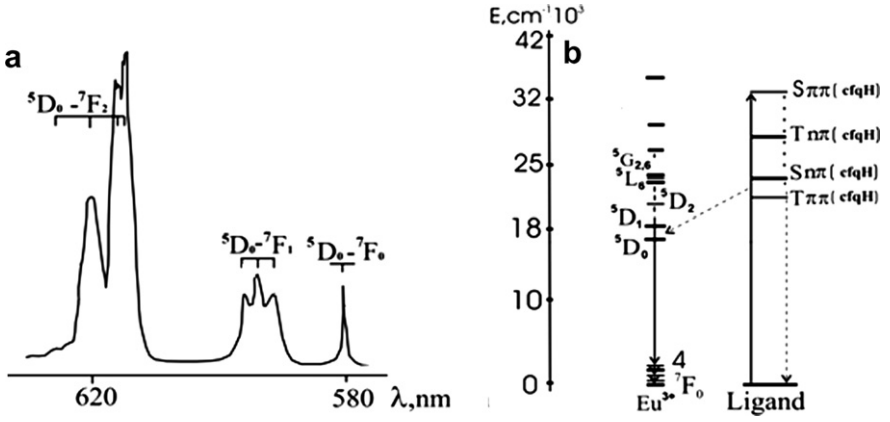


Fig. 3. Luminescence spectra of compound **1** (solid state) (a), scheme of the electronically excited states and photophysical processes of compound **1** (b). Abbreviations: S – singlet state; T – triplet state.

a complex free of any cfq moiety. This conclusion was based on the presence of three signals in the ^{19}F NMR, one of which was assigned to free cfqH due to its relatively sharp lines constituting a dd and its chemical shift which, at −124.59 ppm, was akin to a prepared sample of cfqH in DMSO-d_6 ($\delta = -124.29$ ppm). The observation of free cfqH means that at least two signals in addition are likely to be observed, one for **1** and the other for cfq-dissociated complex (thus, by default, the exchange of the distinct cfq(H) units in **1** is also rapid). The other two signals were both broad and were assigned to complex **1** ($\delta = -126.18$ ppm) and the monoligand complex ($\delta = -125.60$ ppm). The assignment of these two signals was based on ^{19}F NMR saturation transfer experiments and the relative rates of exchange between the three species as all three species readily exchanged the cfqH unit. From the integration of the ^{19}F NMR signals, the three species were present in a ratio of 11:40:49 for a complex free of any cfq moiety, a complex containing only one cfq unit and complex **1**, respectively, after consideration that the excess of free cfqH over a complex containing only one cfq unit must represent a complex free of any cfq moiety (and taking into account that this excess signal intensity must be proportioned by a factor of 2).

Interpretation of the ^{1}H NMR spectrum was complicated by the aforementioned aspects, particularly for the aliphatic region. However, sharp signals for the Hs *ortho* and *meta* ($\delta = 7.957$ ppm, d; and 7.599 ppm, d; respectively) to the F were observed and were thus assigned to free cfqH in solution. These chemical shifts are in accord with those observed for a prepared sample of cfqH in DMSO-d_6 ($\delta = 7.899$ and 7.542 ppm, respectively). By a 2D EXSY spectrum, the set of three signals comprising the exchanging spins of each species for each of these two Hs were identified and then assigned based on their integration in accordance with the ^{19}F NMR results. For complex **1**, the *ortho* and *meta* Hs resonated at 9.262 (br) and 6.544 (br d) ppm, respectively. For the complex containing only one cfq unit, the *ortho* and *meta* Hs resonated at 6.279 (br) and 5.899 (br d) ppm, respectively. That the system was a stable equilibrium was evident not only by these saturation transfer and 2D EXSY experiments, but also by ^{19}F spectra acquired at higher temperature (45 °C) which led to the perturbation of the signal intensities by a shift towards greater dissociation; upon returning to 25 °C, the original signal intensities were duly resumed. These results clearly establish the efficacy of complex **1** in solution.

4. Conclusions

In conclusion, the complex of Eu(III) ions with fluoroquinolone ciprofloxacin has unique fluorescent properties. The strong emission of complex originates from an intrachelate energy transfer from the triplet state of the ligand to the excited energy levels of the lanthanide ion, in other words, fluoroquinolone serves as an energy donor to lanthanides. Moreover, the Stark structure of the spectrum for the tested europium–ciprofloxacin complex is very specific. According to our results, we believe that the methods for the selective and sensitive determination of fluoroquinolones (in biological matrices, pharmaceutical samples, environment, etc.), can be developed on the basis of the specific luminescent properties of europium–quinolone complexes. The complex **1** was stable in aqueous solution based on ^{1}H and ^{19}F NMR measurements whilst in DMSO solution it formed a stable equilibrium with dissociated species.

Acknowledgements

This work was supported by the Ministry of Higher Education, Science and Technology (MHEST), Republic of Slovenia, Project P1-0175. We thank Dr. Timo Ala-Kleme (University of Turku), Dr. Petri Ingman (University of Turku) and Mr. Olli Martiskainen (University of Turku) for their help and suggestions.

Appendix A. Supplementary material

CCDC 646189 contains the supplementary crystallographic data for **1**. These data can be obtained free of charge via http://www.ccdc.cam.ac.uk/conts/retrieving.html, or from the Cambridge Crystallographic Data Centre, 12 Union Road, Cambridge CB2 1EZ, UK; fax: (+44) 1223-336-033; or e-mail: deposit@ccdc.cam.ac.uk. Supplementary data associated with this article can be found, in the online version, at doi:10.1016/j.poly.2008.01.014.

References

[1] L.A. Mitscher, Chem. Rev. 105 (2005) 559.
[2] K.E. Brighty, T.D. Gootz, in: V.T. Andriole (Ed.), The Quinolones, Academic Press, San Diego, 2000, p. 33.
[3] G. Sheehan, N.S.Y. Chew, in: A.R. Ronald, D.E. Low (Eds.), Fluoroquinolone Antibiotics, Birkhauser, Basel, Switzerland, 2003, p. 1.
[4] A.S. Daphne, C. Paolo, J.P. Werner, Curr. Pharm. Design 26 (2006) 3313.
[5] T.M. Wassenaar, Crit. Rev. Microbiol. 31 (3) (2005) 155.
[6] I. Turel, Coord. Chem. Rev. 232 (2002) 27.
[7] H. Sun, L. Li, X. Chen, Anal. Chem. Acta 576 (2006) 192.
[8] B.H. Bakker, M. Goes, N. Hoebe, H.J. van Ramesdonk, J.W. Verhoeven, M.H.V. Werts, J.W. Hofstraat, Coord. Chem. Rev. 208 (2000) 3.
[9] A.V. Polishchuk, E.T. Karaseva, M.A. Medkov, V.E. Karasev, Rus. J. Coord. Chem. 30 (11) (2004) 877.
[10] S. Pandya, J. Yu, D. Parker, Dalton Trans. (2006) 2752.
[11] K.H. Thompson, C. Orvig, Chem. Soc. Rev. 35 (2006) 499.
[12] T. Nishioka, J. Yuan, Y. Yamamoto, K. Sumitomo, Z. Wang, K. Hashino, C. Hosoya, K. Ikawa, G. Wang, K. Matsumoto, Inorg. Chem. 45 (2006) 4088.
[13] I.D. Vilfan, P. Drevenšek, I. Turel, N. Poklar Ulrih, Biochim. Biophys. Acta 1628 (2003) 111.
[14] M.I. Gaiduk, V.F. Zolin, L.S. Gaigerova, Luminescence Spectra of Europium, Nauka, Moscow, 1974.
[15] E.T. Karaseva, A.V. Polishchuk, M.A. Medkov, V.E. Karasev, Electronic journal "Investigated in Russia" (2004) 738. <http://zhurnal.ape.relarn.ru/articles/2004/068.pdf>.
[16] J.B. Li, P. Yang, F. Gao, G.Y. Han, K.B. Yu, Chin. J. Chem. 19 (6) (2001) 598.

[17] Y. Su, Y. Xu, L. Yang, J. Yang, S. Weng, Z. Yu, J. Wu, Anal. Biochem. 347 (2005) 89.
[18] Z. Otwinowski, W. Minor, Methods Enzymol. 276 (1997) 307.
[19] M. Sheldrick, SHELX-97, Programs for Crystal Structure Analysis, University of Göttingen, Göttingen, Germany, 1998.
[20] A.L. Spek, PLATON, University of Utrecht, The Netherlands, 1998.
[21] (a) J. Mäki, P. Tähtinen, L. Kronberg, K.D. Klika, J. Phys. Org. Chem. 18 (2005) 240;
(b) P. Virta, A. Koch, M.U. Roslund, P. Mattjus, E. Kleinpeter, L. Kronberg, R. Sjöholm, K.D. Klika, Org. Biomol. Chem. 3 (2005) 2924;
(c) E. Balentová, J. Imrich, J. Bernát, L. Suchá, M. Vilková, N. Prónayová, P. Kristian, K. Pihlaja, K.D. Klika, J. Heterocycl. Chem. 43 (2006) 645.
[22] P. Drevenšek, T. Zupančič, B. Pihlar, R. Jerala, U. Kolitsch, A. Plaper, I. Turel, J. Inorg. Biochem. 99 (2005) 432.
[23] P. Drevenšek, J. Košmrlj, G. Giester, T. Skauge, E. Sletten, K. Sepčić, I. Turel, J. Inorg. Biochem. 100 (2006) 1755.
[24] I. Turel, A. Golobič, A. Klavžar, B. Pihlar, P. Buglyó, E. Tolis, D. Rehder, K. Sepčić, J. Inorg. Biochem. 95 (2003) 199.
[25] N.C. Baenziger, C.L. Fox, S.L. Modak, Acta Crystallogr., Sect. C 42 (1986) 1505.
[26] I. Turel, I. Leban, N. Bukovec, J. Inorg. Biochem. 56 (1994) 273.
[27] I. Turel, K. Gruber, I. Leban, N. Bukovec, J. Inorg. Biochem. 61 (1996) 197.
[28] C.K. Johnson, ORTEPII, Report ORNL-5138, Oak Ridge National Laboratory, Tennessee, 1976.
[29] A.G. Orpen, L. Brammer, F.H. Allen, O. Kennard, D.G. Watson, R. Taylor, J. Chem. Soc., Dalton Trans. (1989) S1.
[30] F.H. Allen, O. Kennard, D.G. Watson, L. Brammer, A.G. Orpen, R. Taylor, J. Chem. Soc., Perkin Trans. II (1987) S1.
[31] J. Overgaard, I. Turel, D.E. Hibbs, Dalton Trans. (2007) 2171.
[32] P.C.R. Soares-Santos, H.I.S. Nogueira, J. Rocha, V. Félix, M.G.B. Drew, R.A. Sá Ferreira, L.D. Carlos, T. Trindade, Polyhedron 22 (2003) 3529.
[33] V.L. Dorofeev, Khim.-Farm. Zh. 50 (2004) 38.
[34] U. Neugebauer, A. Szeghalmi, M. Schmitt, W. Kefer, J. Popp, U. Holzgrabe, Spectrochim. Acta, Part A 61 (2005) 1505.
[35] Y. Wang, K. Yu, S. Wang, Spectrochim. Acta, Part A 65 (2006) 159.
[36] H.C. Aspinall, Chemistry of the f-block elements, Gordon and Breach Science Publishers, Amsterdam, 2001.
[37] P. Bilski, L.J. Martinez, E.B. Koker, C.F. Chignell, Photochem. Photobiol. 64 (3) (1996) 496.

1.1. Computational details

The computational geometry optimisations of the species considered in this paper were performed *in vacuo* using the hybrid DFT B3PW91 method [8] without symmetry constrains. The "restricted" formalism was applied in all calculations. The basis sets considered were CEP-121G {CEP-31G on the Pt atom} (BS1), D95V {SDD on the S, Cl and Pt atoms} (BS2), D95** {LANL2DZ on the Pt atom, D95* with diffuse sp functions on the O atoms} (BS3) [9]. Geometry convergence was accelerated using the GDIIS algorithm and a first refinement of the structures was obtained using the restricted semi-empirical PM3 method [10]. All of the resultant stationary points were characterized as true minima (i.e., no imaginary frequencies). Atomic charges derive from Mulliken population analysis [11]. After the geometry optimisations, the Onsager solvation model [12] was added (nitromethane, $\varepsilon = 39.4$) to improve B3PW91/BS1 calculations (BS1s) for the platinum-terpy-aqua-anion systems. Solute volumes were computed from the previously gas-phase optimised geometries.

PM3 calculations were carried out with computers equipped with IBM PowerPC G5 processors operating at 2.1 GHz frequency. The software used was the SPARTAN 02 Macintosh version [13]. DFT calculations were carried out at CINECA (Centro Italiano di Supercalcolo, Bologna, Italy) using IBM p5-575 computers with 64-bit IBM Power5 processors operating at 1.9 GHz frequency. The software used was the GAUSSIAN '03 [14].

2. Results and discussion

The reported X-ray structural data on $[Pt(H_2O)(terpy)](SO_3CF_3)_2$ [1] show two hydrogen-bond interactions between the coordinated water and two triflate ions, while in the optimised $[(terpy)Pt(OH_2\cdots OSO_2CF_3)]^+$ cation here reported only one triflate ion is present. This difference should not, however, greatly affect the inner Pt(II) coordination sphere, thus in Table 1 a direct comparison between experimental and computed structural data is made. Even if longer bonds are well known artefacts of pure and, to a lesser extent, hybrid DFT methods [15], the calculated Pt–L lengths and L_1–Pt–L_2 angles can be considered comparable with the experimental data: the greatest difference between DFT and X-ray data is about 1.5% for Pt–L bond lengths and less than 0.5% for L_1–Pt–L_2 angles. The computed bond length between the $[Pt(terpy)(H_2O)]$ and the $[SO_3CF_3]$ fragments can not, instead, be directly compared with the experimental data for the $[Pt(terpy)(H_2O)](SO_3CF_3)_2$, owing to the different globally positive charge of the model used, which results, as expected, in a shortening of the bond distances between cation and counter-anion.

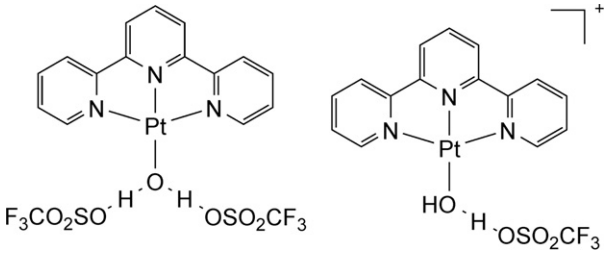
DFT calculations were mainly performed to evaluate the relative interaction energies between the $[Pt(H_2O)(terpy)]^{2+}$ cation and the triflate and perchlorate anions. The energy of the *in vacuo* interaction between the $[Pt(H_2O)(terpy)]^{2+}$ cation and the counter-anions (ΔE_X) was calculated from Eq. (1):

$$\Delta E_X = E_X + E_{Pt} - E_{PtX} \quad (1)$$

where E_X is the energy of the free counter-anion X^- {ClO_4^- or $SO_3CF_3^-$}, E_{Pt} is the energy of the $[Pt(H_2O)(terpy)]^{2+}$ cation and E_{PtX} is the energy of the adduct between one molecule of the counter-anion and the $[Pt(H_2O)(terpy)]^{2+}$ cation, as depicted in Scheme 1. The energy values E_X, E_{Pt} and E_{PtX} derive from the geometry optimisations described in the previous section and are summarized in Table 2.

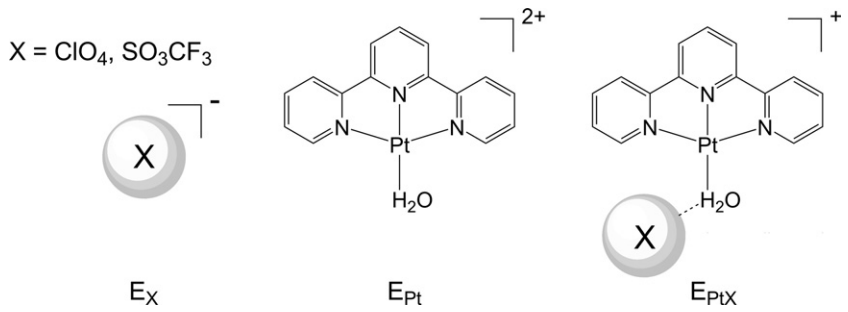
In Fig. 1 the ΔE_{ClO_4} and $\Delta E_{SO_3CF_3}$ values, expressed in kcal/mol, are compared. Absolute values of ΔE_{ClO_4} and $\Delta E_{SO_3CF_3}$ are not particularly meaningful, since they cover also the electrostatic interaction between the $[Pt(H_2O)(terpy)]^{2+}$ and the counter-anion. What is striking is that on the same basis set the $\Delta E_{SO_3CF_3}$ values is always about 5 kcal/mol higher than ΔE_{ClO_4}. This result has been confirmed also using an implicit solvation model like the Onsager one [12]: in the BS1s column of Table 2 are in fact reported the energy values obtained at the B3PW91/BS1 level of theory on considering nitromethane ($\varepsilon = 39.4$) as solvent, which is the NMR solvent of reference [1]. Data in Table 2 and Fig. 1 highlight that the interaction between the $[Pt(H_2O)(terpy)]^{2+}$ cation and the triflate anion is stronger than the one with the perchlorate anion, as expected from the previously reported NMR data [1].

Table 1
comparison between X-ray structural data of $[Pt(H_2O)(terpy)](SO_3CF_3)_2$ and computed data for $[(terpy)Pt(OH_2\cdots OSO_2CF_3)]^+$



Bond or angle[a]	X-ray	BS1	BS2	BS3
Pt–O [Å]	2.040(5)	2.056	2.045	2.060
Pt–N_{cis} [Å]	2.015(5)–2.009(4)	2.039–2.031	2.038–2.034	2.037–2.022
Pt–N_{trans}, [Å]	1.914(4)	1.944	1.942	1.934
O–Pt–N_{cis} [°]	101.5(2)–95.2(2)	100.7–95.9	100.0–96.9	102.4–94.5
O–Pt–N_{trans} [°]	176.6(6)	176.7	176.3	176.1
N_{trans}–Pt–N_{cis} [°]	81.4(2)–81.8(2)	81.6–81.7	81.4–81.5	81.2–81.5
N_{cis}–Pt–N_{cis} [°]	163.3(2)	163.2	162.7	162.6
O···H···O [Å][b]	2.650(8)–2.617(10)	2.408	2.390	2.394

[a] *cis* and *trans* positions are referred to the coordinated water molecule oxygen atom.
[b] Between coordinated H_2O and SO_3CF_3.



Scheme 1. Sketches of the species involved in the cation–counter-anion interaction energy calculations.

Table 2
Energy values from DFT B3PW91 calculations for X^- anions {X = ClO_4, SO_3CF_3}, $[Pt(H_2O)(terpy)]^{2+}$ cation and $[(terpy)Pt(OH_2\cdots X)]^+$ derivatives

Energies (a.u.)	BS1	BS1s	BS2	BS3
E_{ClO_4}	−78.3767	−78.3767	−760.4256	−760.7281
$E_{SO_3CF_3}$	−136.1020	−136.1074	−961.0599	−961.4137
E_{Pt}	−257.7724	−257.7731	−937.4763	−937.4710
E_{PtClO_4}	−336.3826	−336.3913	−1698.1432	−1698.4344
$E_{PtSO_3CF_3}$	−394.1153	−394.1310	−1898.7858	−1899.1252
E_{ClO_4}	0.2335	0.2415	0.2413	0.2333
$E_{SO_3CF_3}$	0.2409	0.2506	0.2496	0.2406
$(E_{SO_3CF_3}–E_{ClO_4})$	0.0074	0.0091	0.0083	0.0073

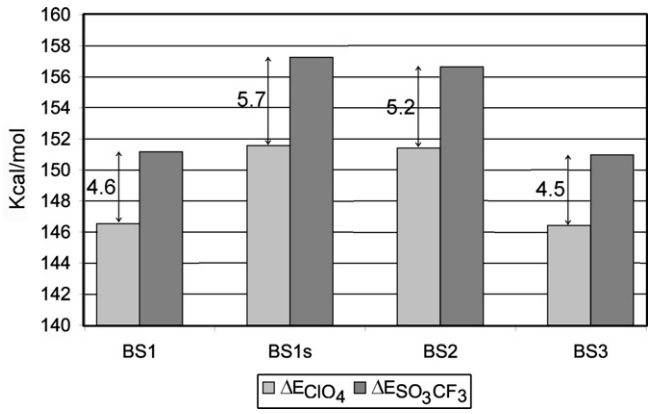


Fig. 1. Comparison between the ΔE_{ClO_4} and $\Delta E_{SO_3CF_3}$ values at different levels of theory.

The use of Eq. (1) can potentially lead to over-evaluate the molecular interactions, because of basis set superposition error (BSSE) [15]. Happily enough, for the systems described BSSE does not seem to have any important effect. In fact, we considered three different basis sets (namely BS1, BS2 and BS3) with different sizes: the number of basis functions for the Pt-terpy-aqua-triflate system is 397 with BS1, 343 with BS2 and 477 with BS3, while for the Pt-terpy-aqua-perchlorate is 361 with BS1, 313 with BS2 and 475 with BS3. The calculated interaction energy differences between perchlorate and triflate are, as already described, very similar for all the three basis sets and there does not seem to exist any meaningful correlation between energy values and the number of basis functions.

It is known that the perchlorate ion has a much less hydrogen-bond acceptor ability than triflate, therefore the $(\Delta E_{SO_3CF_3}–\Delta E_{ClO_4})$ values can be tentatively considered as an estimate of the water–triflate $[(terpy)Pt(OH_2\cdots OSO_2CF_3)]^+$ hydrogen-bond energy without the electrostatic contribution [4,16].

The greater strength of the interaction between the $[Pt(H_2O)(terpy)]^{2+}$ cation and the triflate anion, if compared to the one with the perchlorate anion, is confirmed by the $[(terpy)Pt(OH_2\cdots OClO_3)]^+$ and $[(terpy)Pt(OH_2\cdots OSO_2CF_3)]^+$ oxygen–oxygen hydrogen bond lengths, summarized in Table 3. On the same basis set the $[(terpy)Pt(OH_2\cdots OSO_2CF_3)]^+$ oxygen–oxygen bond length is always shorter (about 0.08 Å) than the $[(terpy)Pt(OH_2\cdots OClO_3)]^+$ one, in agreement with both the experimental NMR observations [1] and the computed energy values. These results confirm the relatively poor interacting ability usually attributed to the perchlorate anion [1,5,16]. The DFT B3PW91/BS3 optimised geometries of the two platinum derivatives are shown in Fig. 2.

A further confirmation of the lower hydrogen-bond character of the $[(terpy)Pt(OH_2\cdots OClO_3)]^+$ interaction, if compared to the $[(terpy)Pt(OH_2\cdots OSO_2CF_3)]^+$ one, comes from the comparison of the Mulliken charges on the H atom involved in the O···H···O bridge in the two adducts. To a lower electron density of the H atom usually corresponds a stronger hydrogen-bond [4]: as observable in Table 4, on the same basis the Mulliken charge of the H atom in the triflate derivative is always more positive than the one in the corresponding perchlorate model, this highlighting the greater hydrogen-bond character of the coordinated water–triflate interaction.

Finally, to better understand the NMR behaviour of the Pt-terpy aqua species, we considered in an explicit way also the role of the solvent (CH_3NO_2). The DFT B3PW91/BS1 energy results for the free $[Pt(H_2O)(terpy)]^{2+}$ cation, the

Table 3
Coordinated water–counter anion oxygen–oxygen bond lengths in $[(terpy)Pt(OH_2\cdots OClO_3)]^+$ and $[(terpy)Pt(OH_2\cdots OSO_2CF_3)]^+$

	BS1	BS2	BS3
$[(terpy)Pt(OH_2\cdots OClO_3)]^+$ [Å]	2.511	2.466	2.474
$[(terpy)Pt(OH_2\cdots OSO_2CF_3)]^+$ [Å]	2.408	2.390	2.394
$r_{O\cdots H\cdots O}(ClO_4)–r_{O\cdots H\cdots O}(SO_3CF_3)$ [Å]	0.103	0.076	0.080

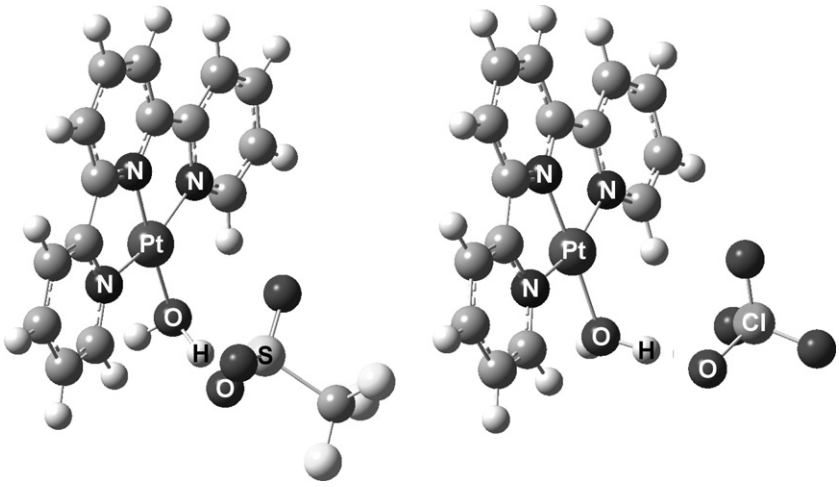


Fig. 2. DFT B3PW91/BS3 optimised geometries of the $[(terpy)Pt(OH_2\cdots OClO_3)]^+$ and $[(terpy)Pt(OH_2\cdots OSO_2CF_3)]^+$ derivatives.

Table 4
O···H···O hydrogen Mullken charges for $[(terpy)Pt(OH_2\cdots OClO_3)]^+$ and $[(terpy)Pt(OH_2\cdots OSO_2CF_3)]^+$

	$[(terpy)Pt(OH_2\cdots OClO_3)]^+$	$[(terpy)Pt(OH_2\cdots OSO_2CF_3)]^+$
BS1	0.413	0.424
BS2	0.476	0.518
BS3	0.475	0.485

free nitromethane molecule, the adduct of two nitromethane molecules and the $[(terpy)Pt(H_2O\cdots ONOCH_3)]^{2+}$ cation are reported in Table 5. The same table also reports the interaction energy between nitromethane and $[Pt(H_2O)(terpy)]^{2+}$ (ΔE_{PtS}) and between two nitromethane molecules (ΔE_{SS}), calculated on the basis of Eqs. (2) and (3):

$$\Delta E_{PtS} = E_S + E_{Pt} - E_{PtS} \quad (2)$$

$$\Delta E_{SS} = 2E_S - E_{SS} \quad (3)$$

The estimated energy of the interaction between one molecule of nitromethane and the $[Pt(H_2O)(terpy)]^{2+}$ cation is about 25.8 kcal/mol, relatively high if compared with the one existing between two solvent molecules, which is about 4.9 kcal/mol. Moreover, the computed oxygen–oxygen hydrogen-bond length in $[(terpy)Pt(OH_2\cdots ONOCH_3)]^{2+}$ is relatively short, 2.598 Å [4]. This means that the $[Pt(H_2O)(terpy)]^{2+}$ cation in solution can be better described with almost one molecule of solvent hydrogen-bonded to the aqua ligand, as in the geometry-optimised model in Fig. 3.

The ^1H NMR spectrum of the complex $[Pt(H_2O)(terpy)](SO_3CF_3)_2$ in CD_3NO_2 solution showed the presence of two species, while in the $[Pt(H_2O)(terpy)](ClO_4)_2$ ^1H NMR spectrum only one derivative was present. Moreover, both the spectra were strongly affected by the addition of salts like lithium triflate and lithium perchlorate [1]. A possible explanation to the NMR experimental results, supported by the DFT results here reported, is the presence in the case of $[Pt(H_2O)(terpy)](SO_3CF_3)_2$ of an equilibrium between a solvent-adduct like $[Pt(terpy)(OH_2\cdots ONOCD_3)](SO_3CF_3)_2$ and a hydrogen-bonded adduct of the type $[Pt(terpy)(OH_2\cdots OSO_2CF_3)](SO_3CF_3)$, as summarized in Scheme 2. The weaker interaction of perchlorate ion with coordinated water, instead, causes the

Table 5
Energy values from DFT B3PW91 calculations for $[Pt(H_2O)(terpy)]^{2+}$ cation, CH_3NO_2, $CH_3NO_2\cdots CH_3NO_2$ and the $[(terpy)Pt(OH_2\cdots ONOCH_3)]^+$ adduct

	E(B3PW91/BS1) (a.u.)
$[Pt(H_2O)(terpy)]^{2+}$	$E_{Pt} = -257.7724$
CH_3NO_2	$E_S = -49.1961$
$CH_3NO_2\cdots CH_3NO_2$	$E_{SS} = -98.4000$
$[(terpy)Pt(OH_2\cdots ONOCH_3)]^{2+}$	$E_{PtS} = -307.0096$
ΔE_{SS}	0.0078
ΔE_{PtS}	0.0411

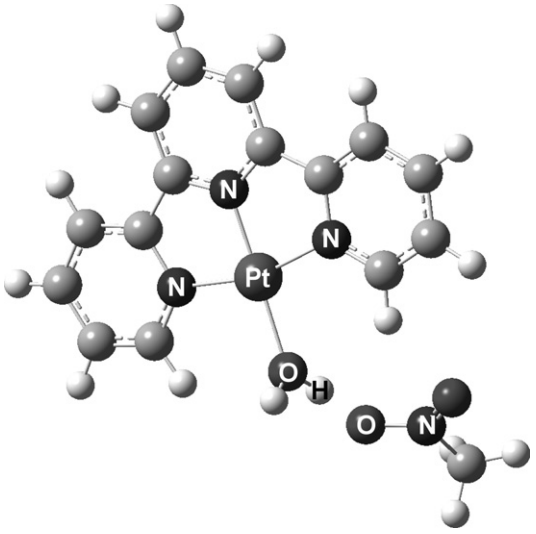
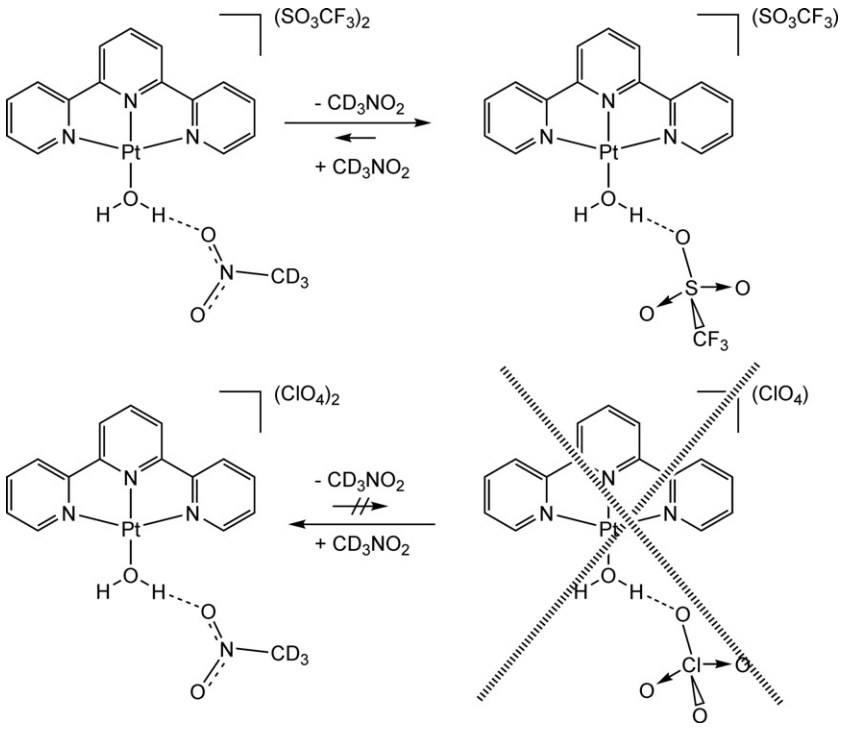


Fig. 3. DFT B3PW91/BS1 optimised geometries of the $[(terpy)Pt(OH_2\cdots ONOCH_3)]^+$ adduct.



Scheme 2. Model for the interactions between the $[Pt(H_2O)(terpy)]^{2+}$ cation and the triflate and perchlorate anions in CD_3NO_2.

presence in solution of only a solvent-adduct species of the type $[Pt(OH_2\cdots ONOCD_3)](ClO_4)_2$.

3. Conclusions

The ^1H NMR spectra of the $[Pt(H_2O)(terpy)]X_2$ $\{X = ClO_4, SO_3CF_3\}$ complexes in CD_3NO_2 showed differences which were ascribed to different hydrogen-bond interactions between the coordinated water molecule and the counter-anions [1]. Even if quite simplified, the DFT calculations described in this paper strongly confirmed the proposed explanation and allowed to estimate the energy difference between the $[(terpy)Pt(OH_2\cdots OSO_2CF_3)]^+$ and the $[(terpy)Pt(OH_2\cdots OClO_3)]^+$ hydrogen-bond adducts. The proposed model for the interaction between the Pt(II) acqua-complex and the counter-anions was also supported by the computed oxygen–oxygen hydrogen-bond lengths of the triflate and perchlorate adducts and by the Mulliken charges on the hydrogen atoms of the O···H···O bridges.

Finally, from the studies on the $[(terpy)Pt(OH_2\cdots ONOCH_3)]^{2+}$ model and from the comparison of the interaction between CH_3NO_2 and $[Pt(H_2O)$- $(terpy)]^{2+}$ and that between two solvent molecules, it was highlighted that also nitromethane is able to strongly interact with the aqua ligand of the considered complex.

4. Supplementary material

CCDC 654357 contains the supplementary crystallographic data for this paper. These data can be obtained free of charge via http://www.ccdc.cam.ac.uk/conts/retrieving.html, or from the Cambridge Crystallographic Data Centre, 12 Union Road, Cambridge CB2 1EZ, UK; fax: +44 1223 336 033; or e-mail: deposit@ccdc.cam.ac.uk.

Acknowledgements

Ca' Foscari University of Venice is gratefully acknowledged for financial support (Ateneo fund 2006).

References

[1] G. Annibale, P. Bergamini, V. Bertolasi, M. Bortoluzzi, M. Cattabriga, B. Pitteri, Eur. J. Inorg. Chem. (2007) 5743.
[2] (a) C. Klevickis, C.M. Grisham, in: H. Siegel, A. Siegel (Eds.), Metal Ions in Biological Systems, vol. 32, Dekker, New York, 1996;
(b) B. Cornils, W.A. Herrmann, Aqueous-Phase Organometallic Catalysis, VCH, Weiheim, 1998.
[3] (a) A. Macchioni, Chem. Rev. 105 (2005) 2039;
(b) M. Szwarc, Ions and Ion Pairs in Organic Reactions, Wiley Interscience, New York, 1972.
[4] (a) D. Hadži, Theoretical Treatments of Hydrogen Bonding, Wiley, Chichester, 1997;
(b) P. Schuster, G. Zundel, C. Sandorfy (Eds.), The Hydrogen Bond, Recent Developments in Theory and Experiments, North Holland, Amsterdam, 1976;
(c) M.D. Joesten, L.J. Schaad, Hydrogen Bonding, Dekker, New York, 1974;
(d) W.C. Hamilton, J.A. Ibers, Hydrogen Bonding in Solids, W.A. Benjamin Inc., New York, 1968.
[5] (a) Z. Bugarčić, G. Liehr, R. Van Eldik, Dalton Trans. (2002) 2825;
(b) Z. Bugarčić, F.W. Heinemann, R. Van Eldik, Dalton Trans. (2004) 279;

(c) Z. Bugarčić, T. Soldatović, R. Jelić, B. Aguleró, A. Grandas, Dalton Trans. (2004) 3869.
[6] (a) R. Romeo, M.R. Plutino, L. Monsù Scolaro, S. Stoccoro, G. Minghetti, Inorg. Chem. 39 (2000) 4749;
(b) D. Jaganyi, A. Hofmann, R. Van Eldik, Angew. Chem., Int. Ed. 40 (2001) 1680;
(c) A. Hofmann, D. Jaganyi, O.Q. Munro, G. Liehr, R. Van Eldik, Inorg. Chem. 42 (2003) 1688;
(d) B. Pitteri, G. Marangoni, L. Cattalini, T. Bobbo, Dalton Trans. (1995) 3853;
(e) B. Pitteri, G. Marangoni, F. Visentin, L. Cattalini, T. Bobbo, Polyhedron 17 (1998) 475, and references therein.
[7] A. Hofmann, D. Jaganyi, O. Munro, G. Liehr, R. Van Eldik, Inorg. Chem. 42 (2003) 1688.
[8] (a) R.G. Parr, W. Yang, Density-Functional Theory of Atoms and Molecules, Oxford University Press, Oxford, 1989;
(b) J.K. Labanowski, J. Andzelm, Density Functional Methods in Chemistry, Springer-Verlag, New York, 1991;
(c) P. Geerlings, F. De Proft, W. Langenaker, Chem. Rev. 103 (2003) 1793;
(d) T. Ziegler, Chem. Rev. 91 (1991) 651;
(e) A.D. Becke, J. Chem. Phys. 98 (1993) 5648;
(f) K. Burke, J.P. Perdew, Y. Wang, in: J.F. Dobson, G. Vignale, M.P. Das (Eds.), Electronic Density Functional Theory: Recent Progress and New Directions, Plenum, New York, 1998;
(g) A. Dedieu, Chem. Rev. 100 (2000) 543.
[9] (a) T.R. Cundari, W.J. Stevens, J. Chem. Phys. 98 (1993) 5555;
(b) T.H. Dunning Jr., P.J. Hay, in: H.F. Schafter (Ed.), Modern Theoretical Chemistry, vol. 3, Plenum Press, New York, 1976;
(c) E.R. Davidson, D. Feller, Chem. Rev. 86 (1986) 681;
(d) M. Dolg, Modern methods and algorithms of quantum chemistry, in: J. Grotendorst (Ed.), NIC Series, vol. 1, John Neumann Institute for Computing, Jülich, 2000, p. 479.
[10] J.J.P. Stewart, J. Comput. Chem. 10 (1989) 209.
[11] R.S. Mulliken, J. Chem. Phys. 23 (1955) 1841, 2338, 2343.
[12] (a) L. Onsager, J. Am. Chem. Soc. 58 (1936) 1486;
(b) M.W. Wong, M.J. Frish, K.B. Wiberg, J. Am. Chem. Soc. 113 (1991) 4776;
(c) M.W. Wong, K.B. Wiberg, M.J. Frish, J. Am. Chem. Soc. 114 (1992) 523;
(d) M.W. Wong, K.B. Wiberg, M.J. Frish, J. Am. Chem. Soc. 114 (1992) 1645.
[13] SPARTAN'02, Wavefunction Inc., Irvine, CA, 2002.
[14] M.J. Frish, G.W. Trucks, H.B. Schlegel, G.E. Scuseria, M.A. Robb, J.R. Cheeseman, J.A. Montgomery Jr., T. Vreven, K.N. Kudin, J.C. Burant, J.M. Millam, S.S. Ivengar, J. Tomasi, V. Barone, B. Mennucci, M. Cossi, G. Scalmani, N. Rega, G.A. Petersson, H. Nakatsuji, M. Hada, M. Ehara, K. Toyota, R. Fukuda, J. Hasegawa, M. Ishida, T. Nakajima, Y. Honda, O. Kitao, H. Nakai, M. Klene, X. Li, J.E. Knox, H.P. Hratchian, J.B. Cross, V. Bakken, C. Adamo, J. Jaramillo, R. Gomperts, R.E. Stratmann, O. Yazyev, A.J. Austin, R. Cammi, C. Pomelli, J.W. Ochterski, P.Y. Ayala, R. Morokuma, G.A. Voth, P. Salvador, J.J. Dannenberg, V.G. Zakrewski, S. Dapprich, A.D. Daniels, M.C. Strain, O. Farkas, D.K. Malick, A.D. Rabuck, K. Raghavachari, J.B. Foresman, J.V. Ortiz, Q. Cui, A.G. Baboul, S. Clifford, J. Cioslowski, B.B. Stefanov, G. Liu, A. Liashenko, P.Piskorz, I. Komaromi, R.L. Martin, D.J. Fox, T. Keith, M.A. Al-Laham, C.Y. Peng, A. Nanayakkara, M. Challacombe, P.M.W. Gill, B. Johnson, W. Chen, M.W. Wong, C. Gonzales, J.A. Pople, GAUSSIAN 03, Revision D.02, Gaussian Inc., Wallingford, CT, 2004.
[15] C.J. Cramer, Essentials of Computational Chemistry, n2d ed., Wiley, Chichester, 2004.
[16] T.G. Appleton, J.R. Hall, S.F. Ralph, C.S.M. Thompson, Inorg. Chem. 23 (1984) 3521.

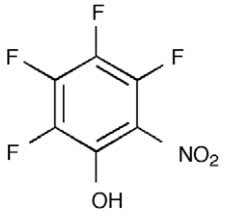
containing perfluoroaryl groups are being exploited in organic semiconductors [12]. It has been predicted that Er^{3+} complexes of fully halogenated ligands may eventually show emission quantum yields close to 100% [13]. An additional requirement for efficient photosensitization of Er^{3+} is the ability to absorb visible light. Since the existing fully halogenated ligands do not possess this feature, we are now investigating new ligand systems that combine the absence of hydrogen atoms with the provision of a chromophore.

Potassium 2-nitrophenoxide is known to combine with lanthanide ions to give a range of chains, layers and clusters [14]. We now report the synthesis, structures and luminescence properties for the first metal complexes to be prepared using the orange-coloured salts of 3,4,5,6-tetrafluoro-2-nitrophenol (**1**) (Scheme 1), a compound which is easily made by hydrolysis of commercially available pentafluoronitrobenzene, following the literature procedure [15]. We show that it is able to exclude hydrogen from the environs of lanthanide ions as well as absorbing visible light. We chose to introduce this ligand as its caesium salt, in the hope of preparing analogues of the volatile, anhydrous salts such as $Cs[Er(HFA)_4]$, where HFA = 1,1,1,5,5,5-hexafluoroacetylacetonate. However, even when the caesium salt of **1** was mixed with erbium chloride in a 4:1 molar ratio, a crystalline complex with the stoichiometry Cs_2ErL_5 (L = tetrafluoro-2-nitrophenoxide) was isolated. Our investigations have therefore focused on complexes of this type.

2. Experimental

2.1. Instrumentation and general procedures

^{19}F NMR spectra were obtained on a Bruker AMX400 and the chemical shifts were referenced to external $CFCl_3$. MALDI mass spectra were recorded using a Bruker Daltonics Autoflex. CI mass spectra were obtained by the EPSRC National Mass Spectrometry Service Centre, Swansea using a Finnigan MAT 95XP. CHN elemental analyses were performed by MEDAC Ltd., Egham, Surrey. All photoluminescence experiments were conducted using solid samples of the metal complexes. Excitation was by ~7 ns pulses from a Continuum Panther optical parametric oscillator (OPO) pumped with a Surelite I laser. The luminescence was dispersed in a Triax 550 spectrometer and detected using a Hamamatsu R5509-72 infrared photomultiplier tube.



1

Scheme 1. Chemical structure of 3,4,5,6-tetrafluoro-2-nitrophenol.

2.2. X-ray crystallography

Data for **2**, **3** and **7** were collected at 120 K using a Nonius Kappa CCD area detector diffractometer mounted at the window of a molybdenum rotating anode (50 kV, 90 mA, $\lambda = 0.71069$ Å). The crystal-to-detector distance was 30 mm and ϕ and ω scans were carried out to fill the Ewald sphere. Data collection and processing were carried out using COLLECT [16], DENZO [17] and MAXUS [18] and empirical absorption correction was applied using SORTAV [19]. Data for **5** were collected on a CAD-4 diffractometer using $\lambda = 0.71069$ Å with ω–2θ scans at 160 K. The unit cell parameters were determined by least-squares refinement on diffractometer angles for 25 automatically centred reflections [20]. Data for **5** were corrected for absorption by empirical methods (ψ scan) [21] and for Lorentz-polarization effects by XCAD4 [22].

The structures were solved by heavy-atom methods using SHELXS-97 and DIRDIF-99 programs [23,24], and were refined anisotropically (non-hydrogen atoms) by full-matrix least-squares on F^2 using SHELXL-97. The H atoms were calculated geometrically and refined using the riding model facility in the SHELXL-97 program. Solvent molecules were located in the crystal structures of **3**, **5** and **7**. All showed relatively high anisotropic thermal parameters, reflecting not only a high degree of thermal motion, but also a degree of positional disorder. In the case of **5**, two unique solvent molecules were located in the asymmetric unit. One was found to be fully occupied, however the second which lies close to the twofold axis was fixed at half occupancy as indicated by a refinement of the fractional site occupancies for the atoms in this molecule. Interatomic distances in the solvent molecules in the structure of **5** were restrained to lie within the accepted ranges. The programs ORTEP-3 [25] and PLATON [26] were used for diagrams and WINGX [27] was used to prepare material for publication.

2.3. Synthesis

2.3.1. $Cs_2Er(o\text{-}O_2N\text{–}C_6F_4\text{–}O)_5$ (**2**)

o-O_2N–C_6F_4–OH (0.422 g, 2.0 mmol) and Cs_2CO_3 (0.326 g, 1.0 mmol) were dissolved in a mixture of MeCN (10 mL) and H_2O (3 mL) with stirring at room temperature. A solution of $ErCl_3 \cdot 6H_2O$ (0.153 g, 0.40 mmol) in water (3 mL) was then added dropwise. After 2 h the solvent was evaporated to dryness under reduced pressure and the residue was extracted with Et_2O (3 × 10 mL). The Et_2O extract was filtered, concentrated and the residue recrystallized from Et_2O–hexane to give $Cs_2Er(o\text{-}O_2N\text{–}C_6F_4\text{–}O)_5$ (**2**) (0.338 g, 57%) as orange blocks. *Anal.* Calc. for $C_{30}Cs_2ErF_{20}N_5O_{15}$: C, 24.29; H, 0.00; N, 4.72. Found: C, 24.55; H, 0.10; N, 5.01%. λ_{max} (nm) (MeCN) 223 ($\varepsilon = 64000$), 266 (17700), 406 (11000); ν_{max} (cm^{-1}) (KBr)

1659 (C=C), 1541 (NO_2), 1512 (NO_2); δ_F (377 MHz, DMSO-d_6) −180 (br), −157 (br), −153.9, −149.9, *m/z* (CI–). Calc. for $C_{24}CsErF_{16}N_4O_{16}$ (M^-−O_2N–C_6F_4–OCs): 1144 (11%), 1143 (44), 1142 (14), 1141 (79), 1140 (68), 1139 (100), 1138 (1), 1137 (5). Found: 1144 (14), 1143 (48), 1142 (24), 1141 (100), 1140 (91), 1139 (94), 1138 (1), 1137 (5).

2.3.2. $Cs_2(Et_2O)Er(o\text{-}O_2N\text{–}C_6F_4\text{–}O)_5$ (3)

This was prepared as for **2** and obtained as yellow blades following recrystallization from Et_2O–pentane or Et_2O–CCl_4 by layering of solvents at room temperature. *Anal.* Calc. for $C_{34}H_{10}Cs_2ErF_{20}N_5O_{15}$: C, 26.22; H, 0.65; N, 4.50. Found: C, 26.60; H, 0.52; N, 4.27%. λ_{max} (nm) (MeCN) 222 ($\varepsilon = 67\,000$), 267 (20 800), 421 (16 100); ν_{max} (cm^{-1}) (KBr) 2982 (C–H), 2883 (C–H), 1655 (C=C), 1541 (NO_2), 1508 (NO_2).

2.3.3. $Cs_2Y(o\text{-}O_2N\text{–}C_6F_4\text{–}O)_5$ (4)

This was prepared by analogy with the Er complex **2** and was obtained in 70% yield as orange prisms. *Anal.* Calc. for $C_{30}Cs_2F_{20}N_5O_{15}Y$: C, 25.65; H, 0.00; N, 4.98. Found: C, 26.00; H, <0.10; N, 5.11%. λ_{max} (nm) (MeCN) 227 ($\varepsilon = 58\,000$), 267 (18 200), 403 (12 000); ν_{max} (cm^{-1}) (KBr) 1653 (C=C), 1541 (NO_2), 1506 (NO_2); δ_F (377 MHz, DMSO-d_6) −184 (br), −160.0, −155.4, −150.9; on heating the NMR solution to 60 °C an irreversible change occurred which caused the peaks to become sharper and to shift to the following positions −173.7 (m), −157.0 (d, $J = 23$ Hz), 151.5 (t, $J = 23$ Hz), 149.0 (dd, $J = 26$, 4 Hz); *m/z* (MALDI–) 929 {[$Y(o\text{-}O_2N\text{–}C_6F_4\text{–}O)_4]^-$, 100%}, 738 {[$Y(o\text{-}O_2N\text{–}C_6F_4\text{–}O)_3F]^-$, 3%}, 210 {$(o\text{-}O_2N\text{–}C_6F_4\text{–}O)^-$, 51%}; *m/z* (CI–). Calc. for $C_{24}CsF_{16}N_4O_{16}Y$ (M^-−*o*-O_2N–C_6F_4–OCs): 1063.7 (4), 1062.7 (26), 1061.7 (100). Found: 1063.5 (6), 1062.4 (26), 1061.4 (100).

2.3.4. $Cs_2(Et_2O)_{1.5}Y(o\text{-}O_2N\text{–}C_6F_4\text{–}O)_5$ (5)

By analogy with the preparation of **3**, recrystallization by layering ether with hexane at room temperature gave crystals of the sesqui-etherate **5** as orange blocks that were suitable for X-ray analysis, but which readily lost solvent.

2.3.5. $Cs_2(Et_2O)_{0.5}Yb(o\text{-}O_2N\text{–}C_6F_4\text{–}O)_5$ (6)

This was prepared by analogy with the Er complex **2** and was obtained in 66% yield as orange prisms. *Anal.* Calc. for $C_{30}Cs_2F_{20}N_5O_{15}Yb\cdot\ 0.5Et_2O$: C, 25.18; H, 0.33; N, 4.59. Found: C, 25.16; H, 0.15; N, 4.78%. λ_{max} (nm) (MeCN) 223 ($\varepsilon = 50\,000$), 266 (17 100), 403 (10 400) ν_{max} (cm^{-1}) (KBr) 2940 (C–H), 1659 (C=C), 1541 (NO_2) and 1512 (NO_2); δ_F (377 MHz, DMSO-d_6) −185 (br), −164 (br), −157.6, −153.0; *m/z* (MALDI–) 1014 {[^{174}Yb($o\text{-}O_2N\text{–}C_6F_4\text{–}O)_4]^-$, 87%}, 823 {[^{174}Yb($o\text{-}O_2N\text{–}C_6F_4\text{–}O)_3F]^-$, 10%}, 210 {$(o\text{-}O_2N\text{–}C_6F_4\text{–}O)^-$, 100%}; *m/z* (CI–). Calc. for $C_{24}CsF_{16}N_4O_{16}Yb$ (M^-−*o*-O_2N–C_6F_4–OCs): 1150 (10), 1149 (40), 1148 (26), 1147 (100), 1146 (50), 1145 (69), 1144 (44). Found: 1150 (8), 1149 (42), 1148 (29), 1147 (100), 1146 (59), 1145 (67), 1144 (32).

2.3.6. $Cs_2(Et_2O)_{0.5}Yb(o\text{-}O_2N\text{–}C_6F_4\text{–}O)_5$ (7)

By analogy with the preparation of **3**, recrystallization by layering ether with hexane at room temperature gave crystals of **7** as orange blocks that were suitable for X-ray analysis.

3. Results and discussion

3.1. Crystal growth and X-ray crystallography

The rare earth complexes were prepared in aqueous acetonitrile, which was then evaporated and the residue was extracted with boiling diethyl ether. Concentration of the ether extracts and the addition of pentane, hexane or carbon tetrachloride led to the formation of crystals. Samples used for X-ray diffraction were obtained by layering of solvents at room temperature and were dried only briefly, since prolonged drying under vacuum caused some of the crystals to lose their transparency. Two crystalline erbium complexes were characterized: orange blocks **2** (stoichiometry Cs_2ErL_5) and yellow blades **3** (an etherate, $Cs_2ErL_5\cdot Et_2O$). Formation of the unsolvated product **2** was favoured when solvent was allowed to evaporate from a boiling solution of the complex in Et_2O–hexane, whereas the etherate **3** crystallized following slow diffusion of CCl_4 or pentane into an ethereal solution of the complex at *ca.* 18 °C. Ether of crystallization was also present in the other two complexes that were used for X-ray diffraction [$Cs_2YL_5\cdot 1.5Et_2O$ (**5**) and $Cs_2YbL_5\cdot Et_2O$ (**7**)].

The structure of the unsolvated erbium complex **2** is shown in Fig. 1; crystallographic details, metal–ligand bond lengths and selected bond angles are provided in Tables 1–3. In the crystal structure of $Cs_2YL_5\cdot 1.5Et_2O$

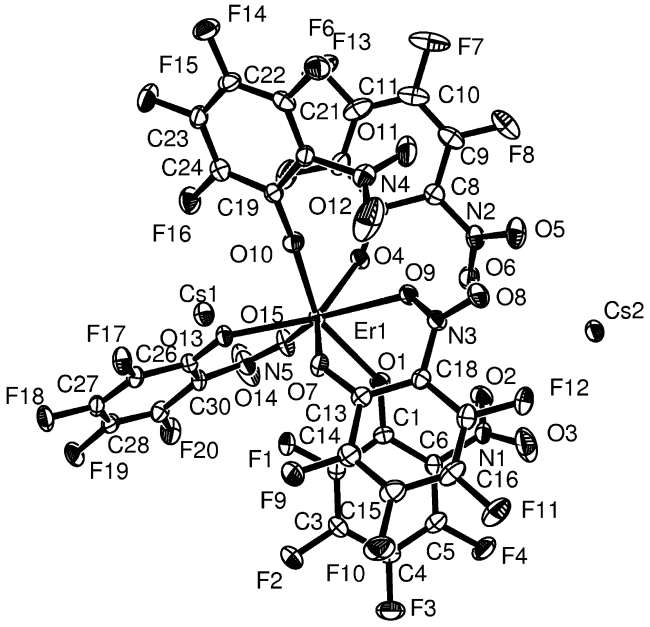


Fig. 1. Solid state structure of $Cs_2Er(o\text{-}O_2N\text{–}C_6F_4\text{–}O)_5$ (**2**) showing the coordination of Er.

Table 1
Crystallographic details of $Cs_2Er(o\text{-}O_2N\text{–}C_6F_4\text{–}O)_5$ (**2**), $Cs_2(Et_2O)Er(o\text{-}O_2N\text{–}C_6F_4\text{–}O)_5$ (**3**), $Cs_2(Et_2O)_{1.5}Y(o\text{-}O_2N\text{–}C_6F_4\text{–}O)_5$ (**5**), and $Cs_2(Et_2O)Yb(o\text{-}O_2N\text{–}C_6F_4\text{–}O)_5$ (**7**)

	2	**3**	**5**	**7**
Formula	$C_{30}Cs_2ErF_{20}N_5O_{15}$	$C_{34}H_{10}Cs_2ErF_{20}N_5O_{16}$	$C_{36}H_{15}Cs_2F_{20}N_5O_{16.5}Y$	$C_{34}H_{10}Cs_2F_{20}N_5O_{16}Yb$
Formula weight	1483.43	1557.55	1516.26	1563.33
Temperature (K)	120(2)	120(2)	160(2)	120(2)
Crystal system	triclinic	monoclinic	monoclinic	monoclinic
Space group	$P\bar{1}$	$P2_1/c$	$I2/a$	$P2_1/c$
a (Å)	8.5213(2)	13.1114(3)	23.630(9)	13.0900(3)
b (Å)	13.9433(5)	23.3692(5)	15.129(2)	23.3001(6)
c (Å)	17.5709(7)	15.0055(2)	28.778(7)	15.0004(3)
α (°)	91.266(2)°	90°	90°	90°
β	103.680(2)°	96.1220(10)°	99.09(2)°	96.1676(13)°
γ	102.206(2)	90	90	90
V (Å^3)	1976.89(12)	4571.51(16)	10159(5)	4548.61(18)
Z	2	4	8	4
D_{calc} (Mg/m^3)	2.492	2.263	1.983	2.283
Absorption coefficient (mm^{-1})	4.110	3.562	2.705	3.791
Reflections collected	39686	54306	19158	45269
Independent reflections [R_{int}]	9020 [0.0440]	10416 [0.0556]	9424 [0.1223]	10328 [0.0354]
Final R indices [$I > 2\sigma(I)$]	$R_1 = 0.0334$, $wR_2 = 0.0725$	$R_1 = 0.0340$ $wR_2 = 0.0660$	$R_1 = 0.0586$, $wR_2 = 0.1126$	$R_1 = 0.0264$, $wR_2 = 0.0644$
R indices (all data)	$R_1 = 0.0516$, $wR_2 = 0.0795$	$R_1 = 0.0499$ $wR_2 = 0.0715$	$R_1 = 0.1812$, $wR_2 = 0.1451$	$R_1 = 0.0307$, $wR_2 = 0.0669$

Table 2
Metal–ligand distances (Å) for $Cs_2Er(o\text{-}O_2N\text{–}C_6F_4\text{–}O)_5$ (**2**), $Cs_2(Et_2O)Er(o\text{-}O_2N\text{–}C_6F_4\text{–}O)_5$ (**3**), $Cs_2(Et_2O)_{1.5}Y(o\text{-}O_2N\text{–}C_6F_4\text{–}O)_5$ (**5**) and $Cs_2(Et_2O)Yb(o\text{-}O_2N\text{–}C_6F_4\text{–}O)_5$ (**7**)

	2	**3**	**5**	**7**
M–O (mondentate phenoxide)	2.186(3)	2.181(3)	2.193(6)	2.150(2)
	2.220(3)	2.235(3)	2.221(6)	2.208(2)
	2.251(3)	2.255(3)	2.249(6)	2.224(2)
M–O (bidentate phenoxide)	2.231(3)	2.220(3)	2.224(6)	2.197(2)
	2.239(3)	2.236(3)	2.232(6)	2.213(2)
M–O (nitro group)	2.370(3)	2.461(3)	2.439(7)	2.438(2)
	2.525(3)	2.464(3)	2.473(7)	2.459(2)

(**5**) the space group $I2/a$ was used as a non-standard setting of $C2/c$ in order to give a smaller β angle. The coordination of the tetrafluoronitrophenoxide ligands to the rare earth ions in the four crystal structures is very similar. Each M^{3+} ion is bound to five aryloxide ligands, of which three are monodentate; the remaining two ligands are additionally coordinated to the rare earth through one oxygen atom of the nitro group, making them bidentate and giving a coordination number of seven. Similar coordination about the rare earth has been reported for $K_2Ln(o\text{-}O_2NC_6H_4O)_5$ (Ln = Sm, Eu) [14], but the structures of these two potassium salts incorporate pentane of crystallization within the distinct channels that are present. The possibility that 2-nitrophenoxide units can be both monodentate and bidentate has also been established in the chemistry of lanthanide picrates [28]. The Et_2O molecules in our solvated complexes are somewhat disordered, particularly so in the case of the yttrium derivative **5**, but it is clear that none of this solvent coordinates to the rare earth metals. The geometry about the rare earth ions in complexes **2**, **3**, **5** and **7** is irregular. The bidentate nitrophenoxide ligands have narrow O–M–O bite angles, in the range 68–72°. The M ions are significantly closer to the phenoxide oxygen atoms than to the oxygen atoms of the coordinating nitro groups; for example the Er–O contacts range between 2.18 and 2.24 Å (phenoxide) and 2.37 and 2.53 Å (NO_2).

The two crystallographically distinct Cs^+ ions in the solvent-free form of **2** make contacts with the phenoxide and nitro groups, so that each caesium atom has eight oxygen atoms within 3.4 Å. In addition some close Cs–F contacts are present, so that Cs (1) is only 3.13 Å from F(17), which is thus its closest neighbour, and 3.34 Å from F(19). Plenio

Table 3
Bond angles at erbium for $Cs_2Er(o\text{-}O_2N\text{–}C_6F_4\text{–}O)_5$ (**2**)

Angles (°) at Er	O(1)	O(4)	O(7)	O(9)	O(10)	O(13)
O(4)	85.77(11)					
O(7)	86.14(11)	145.95(11)				
O(9)	74.56(11)	76.87(10)	69.10(10)			
O(10)	151.16(12)	86.18(11)	85.19(12)	76.66(11)		
O(13)	122.58(11)	127.12(11)	84.50(11)	148.12(10)	83.84(11)	
O(15)	76.16(12)	76.21(11)	133.15(12)	141.26(10)	128.25(12)	70.31(10)

has noted that the distribution of $CF\cdots Cs^+$ contacts in the literature shows a clear maximum in the range 3.2–3.4 Å, providing evidence for an attractive Cs–F interaction [29]. The structures of the etherates again show contact of Cs^+ with both fluorine and oxygen atoms, including those of Et_2O.

3.2. Spectroscopic and analytical characterization

Analytical samples were dried for several days at *ca.* 20 °C and 1 mm Hg, after which CHN combustion analysis indicated that materials with the compositions Cs_2ErL_5 (**2**), $Cs_2ErL_5 \cdot Et_2O$ (**3**), Cs_2YL_5 (**4**) and $Cs_2YbL_5 \cdot 0.5Et_2O$ (**6**) had been obtained. Weak IR absorptions close to 2970 cm^{-1} and small amounts of hydrogen found by combustion analysis indicate that some solvent is present at low levels (<20 mol%) in bulk samples of the 'unsolvated' materials. Removal of the remaining Et_2O from $Cs_2YbL_5 \cdot 0.5Et_2O$ (**6**) was attempted by heating under reduced pressure; significant loss in mass occurred only on heating above 120 °C and under these conditions the darkening of the sample indicated decomposition. Attempts to sublime the complexes *in vacuo* also led to decomposition.

Compounds **2**, **4** and **6** were further characterized by ^{19}F NMR, IR, UV and mass spectrometry. Despite the considerable peak broadening in the ^{19}F NMR spectra (376 MHz, DMSO-d_6, $T = 27$ °C) of the paramagnetic Er^{3+} and Yb^{3+} derivatives **2** and **6**, four fluorine environments were clearly resolved in each case. The ^{19}F NMR spectrum of the Y^{3+} salt **4** also showed some broadening, particularly in the case of the most upfield peak (assigned as F-6). This suggested that the complex might be fluxional and the spectrum was therefore recorded at a higher temperature (60 °C). The peaks became much sharper, but they then remained sharp after cooling the sample back to 27 °C, which is consistent with an irreversible ligand displacement by DMSO. Mass spectra in chemical ionization mode showed strong $[CsML_4]^-$ negative ions with the expected isotopic distribution patterns. UV–Vis spectra were recorded in acetonitrile solution and all the compounds showed similar spectra, which were dominated by three strong absorption bands of the ligand. The longest wavelength absorptions occurred at λ_{max} between 402 and 406 nm in acetonitrile solutions of concentrations of *ca.* 10^{-4} M. Fivefold dilution with acetonitrile caused the λ_{max} of the longest wavelength band to increase to 415–428 nm; this shift was accompanied by an increase in the ε value and again suggests the occurrence of solvolysis.

3.3. Photoluminescence studies

Fig. 2 shows the photoluminescence spectra for the $Cs_2(Et_2O)_{0.5}Yb(o\text{-}O_2N\text{–}C_6F_4\text{–}O)_5$ (**6**) and $Cs_2Er(o\text{-}O_2N\text{–}C_6F_4\text{–}O)_5$ (**2**) samples. Both materials show luminescence characteristic of the central ion with emission for the $^2F_{5/2} \rightarrow {}^2F_{7/2}$ transition for ytterbium and for the $^4I_{13/2} \rightarrow {}^4I_{15/2}$ transition for the erbium ion. For ytterbium an excitation wavelength of 460 nm was used. In the case of erbium an excitation wavelength of 520 nm was chosen to provide direct excitation into the $^2H_{11/2}$ level of the Er^{3+} ion, which rapidly decays to the $^4I_{13/2}$ level. The shapes of the photoluminescence spectra for both materials are independent of excitation wavelength. The rise time of the $^4I_{13/2} \rightarrow {}^4I_{15/2}$ transition gives a direct measurement of the decay time from the initially excited state into the $^4I_{13/2}$ level and was measured to be of the order of 25 ns. Photoluminescence excitation (PLE) spectroscopy of both samples (Fig. 3) was recorded by monitoring the output from the peak of the ion-related photoluminescence whilst changing the excitation wavelength over the range 410–680 nm. For the ytterbium complex **6** the PLE spectrum shows a broad feature peaking at ~520 nm and a second feature extending to shorter wavelengths (<410 nm). Also shown in Fig. 3 is the absorption spectrum of this complex which is a broad band with a peak at ~400 nm. This feature in the absorption spectra can be assumed to be the absorption into the singlet state of the ligand. The majority of the absorption that results in ytterbium emission therefore appears to come from another band at longer wavelengths than the singlet absorption. We suggest that this may be direct absorption into the triplet state, the long lifetime of which encourages transfer into the ytterbium ion. This absorption is weak, so is not seen in the visible absorption spectrum where it is masked by the tail of the singlet absorption. Also shown in Fig. 3 is the PLE spectrum of $Cs_2Er(o\text{-}O_2N\text{–}C_6F_4\text{–}O)_5$ **2**. This has the same shape as that for $Cs_2Yb(Et_2O)_{0.5}(o\text{-}O_2N\text{–}C_6F_4\text{–}O)_5$ **6** but with additional peaks due to direct absorption into the Er^{3+} ions. To illus-

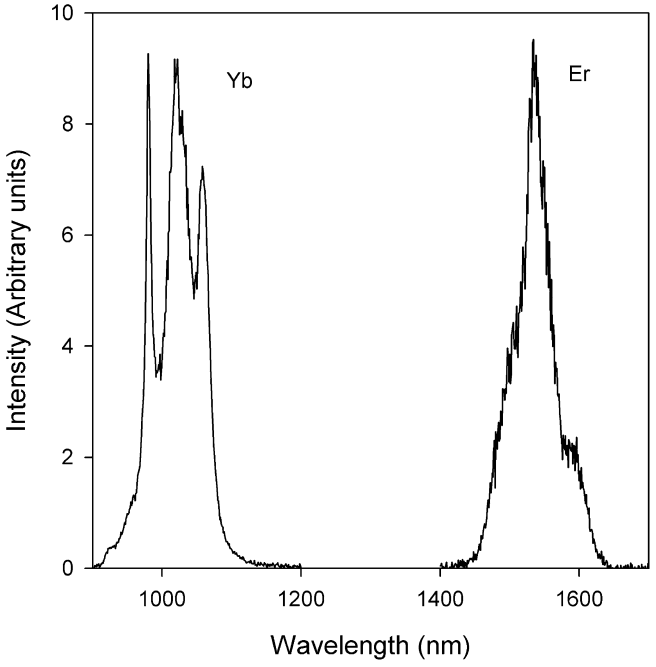


Fig. 2. Near-infrared photoluminescence spectra for $Cs_2Yb(Et_2O)_{0.5}(o\text{-}O_2N\text{–}C_6F_4\text{–}O)_5$ (**6**) and $Cs_2Er(o\text{-}O_2N\text{–}C_6F_4\text{–}O)_5$ (**2**).

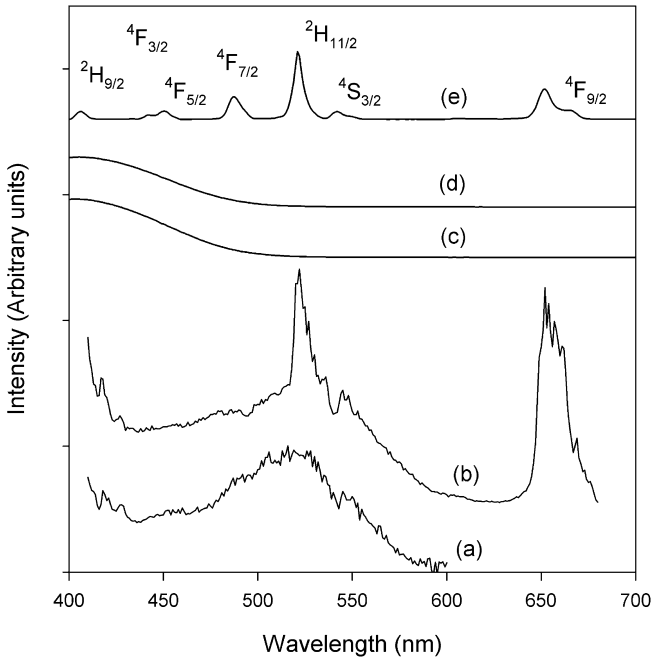


Fig. 3. Photoluminescence excitation spectrum of (a) $Cs_2Yb(Et_2O)_{0.5}(o\text{-}O_2N\text{–}C_6F_4\text{–}O)_5$ (**6**) and (b) $Cs_2Er(o\text{-}O_2N\text{–}C_6F_4\text{–}O)_5$ (**2**). Also shown for comparison are the visible absorption data for $Cs_2Yb(Et_2O)_{0.5}(o\text{-}O_2N\text{–}C_6F_4\text{–}O)_5$ (**6**) in MeCN (spectrum c: λ_{max} 403 nm, ε 10400), $Cs_2Er(o\text{-}O_2N\text{–}C_6F_4\text{–}O)_5$ (**2**) in MeCN (spectrum d: λ_{max} 406 nm, ε 11000) and for a solution of $ErCl_3 \cdot 6H_2O$ in MeOH (spectrum e: λ_{max} 520 nm, ε 3.9).

trate this the absorption spectrum of a solution of erbium chloride in methanol is also given which shows the narrow absorption into erbium ions. The fact that these lines are superimposed upon the same broad feature that was observed for the $Cs_2Yb(Et_2O)_{0.5}(o\text{-}O_2N\text{–}C_6F_4\text{–}O)_5$ **6** shows that the ligand is acting as a weak sensitizer for erbium as well as for ytterbium. The rise time for the $^4I_{13/2} \rightarrow {}^4I_{15/2}$ transition was found to be independent of the excitation wavelength used. This suggests that energy transfer from the ligand to the erbium ion is not the rate-limiting step in the energy migration. For the $Cs_2Yb(Et_2O)_{0.5}$ $(o\text{-}O_2N\text{–}C_6F_4\text{–}O)_5$ **6** the rise time was found to be identical to the laser response (~7 ns) which supports this observation.

Lifetime data were recorded at the peak of the photoluminescence spectra at a temperature of 300 K. For erbium this corresponded to the $^4I_{13/2} \rightarrow {}^4I_{15/2}$ transition (1545 nm) and for ytterbium the $^2F_{5/2} \rightarrow {}^2F_{7/2}$ transition (1032 nm). Lifetime data were fitted with either a one or two exponential decay model using a Marquardt–Levenberg algorithm to find the best fit.

The luminescence decay of the erbium complex **2** could be fitted by a single exponential function, giving a lifetime of 20.2 μs. As we have noted, it is very difficult to remove all traces of hydrogen-containing solvents from these materials. From recent work on deuterated Cs[Er(HFA)$_4$] [7], it has been demonstrated that any C–H oscillators within 20 Å of an erbium ion can quench the lifetime to <100 μs, so the low levels of solvent detected in these samples would be sufficient to limit the lifetime to the observed value of 20.2 μs. Compared with the 1.8 μs lifetime observed for Cs[Er(HFA)$_4$], where the hexafluoroacetylacetonate (HFA) ligands each contain a single C–H bond, there is a considerable extension in lifetime associated with exclusion of hydrogen from the environs of the erbium ion. The luminescence lifetime of the etherate **3** was 22.9 μs. Given that reproducibility of the lifetime measurements is of the order of ±5%, there does not appear to be a significant difference in lifetime between the two samples.

The luminescence decay of the ytterbium complex **6** was best described using two lifetimes: 142 μs (92%) and 351 μs (8%), both of which greatly exceed the value of 21.6 μs observed for Cs[Yb(HFA)$_4$]. It has been previously noted by Faulkner that the luminescence in crystalline samples does not always undergo a simple exponential decay [3d], and that this may be due to surface effects. In the case of compound **6** the relative proximity of Yb^{3+} ions to residual solvent molecules could significantly affect their lifetimes.

Photoluminescence of the yttrium complex **4** was excited using wavelengths of 355 nm and 410 nm to investigate the ligand luminescence in the absence of an optically active ion. The luminescence spectra are shown in Fig. 4. For the 355 nm excitation a peak at ~430 nm can be seen which extends towards 700 nm. At 410 nm excitation there is some evidence of the short wavelength peak being present, modified by the presence of a 435 nm high pass filter in the beam path to remove the pump laser, but the spectrum is dominated by a longer wavelength peak at *ca.* 650 nm. Both of these emission bands overlap the main absorption bands of erbium in the visible region of the spectra and this probably accounts for the fast coupling observed between the ligand and the erbium ion. It can be seen that the longer

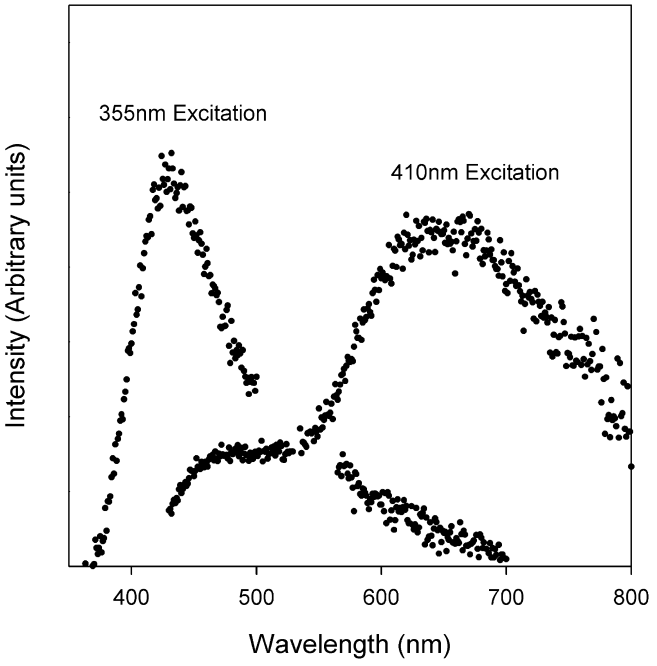


Fig. 4. Photoluminescence spectra of $Cs_2Y(o\text{-}O_2NC_6F_4O)_5$ **4** at two excitation wavelengths.

wavelength emission extends to >800 nm which just brings it within the energy of the absorption into the $^2F_{5/2}$ level for ytterbium. This may therefore account for the ability of the ligand to act as a sensitizer for ytterbium. It is possible that the longer wavelength peak observed with 410 nm excitation is radiative recombination of the triplet state. A similar change in the ligand luminescence from singlet to triplet state as the excitation wavelength is increased was observed in aluminium tris(8-hydroxyquinolinate) [30].

4. Conclusions

We have structurally characterized the first examples of rare earth pentakis(3,4,5,6-tetrafluoro-2-nitrophenoxide) complexes and have shown that this ligand can form chelates with tripositive rare earth ions in a similar way to the non-fluorinated 2-nitrophenoxide. It can completely displace water from the coordination sphere of the rare earth, thus allowing synthesis to be performed in aqueous solution. The erbium and ytterbium complexes **2** and **6** luminesce in the infrared and have luminescence lifetimes far exceeding those of typical hydrogen-containing ligands. The tetrafluoro-2-nitrophenoxide ligand absorbs blue and ultraviolet light quite strongly and shows a small antenna effect for photoexcitation of Er^{3+} and Yb^{3+} ions by visible light. Whereas the complexes are unsuitable for vacuum deposition, they are soluble in organic solvents and capable of being processed in solution.

Acknowledgements

We thank Mr. G. Coumbarides for NMR spectroscopy, the EPSRC National Mass Spectrometry Service Centre, Swansea for MS measurements, the EPSRC National Crystallography Service, Southampton for data collection, the University of London Central Research Fund (equipment grant to RHCT) and the Leverhulme Trust (visiting fellowship for Y.Z.).

Appendix A. Supplementary data

CCDC 627887, 642285, 627886 and 627885 contain the supplementary crystallographic data for **2**, **3**, **5** and **7**. These data can be obtained free of charge via http://www.ccdc.cam.ac.uk/conts/retrieving.html, or from the Cambridge Crystallographic Data Centre, 12 Union Road, Cambridge CB2 1EZ, UK; fax: (+44) 1223-336-033, or e-mail: deposit@ccdc.cam.ac.uk. Supplementary data associated with this article can be found, in the online version, at doi:10.1016/j.poly.2008.01.022.

References

[1] (a) J.-C.G. Bünzli, C. Piguet, Chem. Soc. Rev. 34 (2005) 1048;
(b) S. Comby, J.-C.G. Bünzli, in: K.A. Gschneidner, J.-C.G. Bünzli, V.K. Pecharsky (Eds.), Handbook on the Physics and Chemistry of Rare Earths, vol. 37, Elsevier, 2007 (Chapter 235).

[2] (a) A. Beeby, S. Faulkner, D. Parker, J.A.G. Williams, J. Chem. Soc., Perkin Trans. 2 (2001) 1268;
(b) S. Faulkner, M.-C. Carrié, S.J.A. Pope, J. Squire, A. Beeby, P.G. Sammes, Dalton Trans. (2004) 1405;
(c) B.P. Burton-Pye, S.L. Heath, S. Faulkner, Dalton Trans. (2005) 146;
(d) S.J.A. Pope, B.P. Burton-Pye, R. Berridge, T. Khan, P.J. Skabara, S. Faulkner, Dalton Trans. (2006) 2907;
(e) H. Wang, G. Qian, M. Wang, J. Zhang, Y. Luo, J. Phys. Chem. B 108 (2004) 8084;
(f) S. Quici, M. Cavazzini, G. Marzanni, G. Accorsi, N. Armaroli, B. Ventura, F. Barigelletti, Inorg. Chem. 44 (2005) 529;
(g) R. Van Deun, P. Fias, P. Nockemann, A. Schepers, T.N. Parac-Vogt, K. Van Hecke, L. Van Meervelt, K. Binnemans, Inorg. Chem. 43 (2004) 8461;
(h) R. Van Deun, P. Fias, P. Nockemann, K. Van Hecke, L. Van Meervelt, K. Binnemans, Inorg. Chem. 45 (2006) 10416;
(i) S. Comby, D. Imbert, C. Vandevyver, J.-C.G. Bünzli, Chem. Eur. J. 13 (2007) 936.

[3] (a) N.M. Shavaleev, L.P. Moorcraft, S.J.A. Pope, Z.R. Bell, S. Faulkner, M.D. Ward, Chem. Eur. J. 9 (2003) 5283;
(b) S.J.A. Pope, B.J. Coe, S. Faulkner, E.V. Bichenkova, X. Yu, K.T. Douglas, J. Am. Chem. Soc. 126 (2004) 9490;
(c) F. Kennedy, N.M. Shavaleev, T. Koullourou, Z.R. Bell, J.C. Jeffery, S. Faulkner, M.D. Ward, Dalton Trans. (2007) 1492;
(d) T.K. Ronson, T. Lazarides, H. Adams, S.J.A. Pope, D. Sykes, S. Faulkner, S.J. Coles, M.B. Hursthouse, W. Clegg, R.W. Harrington, M.D. Ward, Chem. Eur. J. 12 (2006) 9299.

[4] (a) Q. Zhong, H. Wang, G. Qian, Z. Wang, J. Zhang, J. Qiu, M. Wang, Inorg. Chem. 45 (2006) 4537;
(b) L. Song, Q. Wang, D. Tang, X. Liu, Z. Zhen, New J. Chem. 31 (2007) 506.

[5] Y. Hasegawa, Y. Wada, S. Yanagida, J. Photochem. Photobiol C: Photochem. Rev. 5 (2004) 183.

[6] (a) Y. Hasegawa, Y. Kimura, K. Murakoshi, Y. Wada, J.-H. Kim, N. Nakashima, T. Yamanaka, S. Yanagida, J. Phys. Chem. 100 (1996) 10201;
(b) A. Beeby, I.M. Clarkson, R.S. Dickins, S. Faulkner, D. Parker, L. Royle, A.S. de Sousa, J.A.G. Williams, M. Woods, J. Chem. Soc., Perkin Trans. 2 (1999) 493;
(c) G.A. Hebbink, D.N. Reinhoudt, F.C.J.M. van Veggel, Eur. J. Org. Chem. (2001) 4101.

[7] R.H.C. Tan, M. Motevalli, I. Abrahams, P.B. Wyatt, W.P. Gillin, J. Phys. Chem. B 110 (2006) 24476.

[8] (a) Y. Hasegawa, T. Ohkubo, K. Sogabe, Y. Kawamura, Y. Wada, N. Nakashima, S. Yanagida, Angew. Chem., Int. Ed. 39 (2000) 357;
(b) R. Van Deun, P. Nockemann, C. Görller-Walrand, K. Binnemans, Chem. Phys. Lett. 397 (2004) 447;
(c) B. Chen, Y. Yang, F. Zapata, G. Qian, Y. Luo, J. Zhang, E.B. Lobkowsky, Inorg. Chem. 45 (2006) 8882.

[9] (a) G. Mancino, A.J. Ferguson, A. Beeby, N.J. Long, T.S. Jones, J. Am. Chem. Soc. 127 (2005) 524;
(b) A.P. Bassett, R. Van Deun, P. Nockemann, P.B. Glover, B.M. Kariuki, K. Van Hecke, L. Van Meervelt, Z. Pikramenou, Inorg. Chem. 44 (2005) 6140;
(c) P.B. Glover, A.P. Bassett, P. Nockemann, B.M. Kariuki, R. Van Deun, Z. Pikramenou, Chem. Eur. J. 13 (2007) 6308.

[10] F. Auzel, D. Meichenin, A. Mendorioz, R. Balda, J. Fernandez, J. Lumin. 72–74 (1997) 152.

[11] H.V.R. Dias, S. Singh, J.A. Flores, Inorg. Chem. 45 (2006) 8859.

[12] F. Babudri, G.M. Farinola, F. Naso, R. Ragni, Chem. Commun. (2007) 1003.

[13] F. Quochi, R. Orrù, F. Cordella, A. Mura, G. Bongiovanni, F. Artizzu, P. Deplano, M.L. Mercuri, L. Pilia, A. Serpe, J. Appl. Phys. 99 (2006) 053520.

[14] M.R. Bürgstein, M.T. Gamer, P.W. Roesky, J. Am. Chem. Soc. 126 (2004) 5213.

[15] J.M. Birchall, R.N. Haszeldine, J. Nikokavouras, E.S. Wilks, J. Chem. Soc. C (1971) 562.
[16] R. Hooft, Collect: Data Collection Software, Nonius BV, Delft, The Netherlands, 1998.
[17] Z. Otwinowski, W. Minor, in: C.W. CarterJr., R.M. Sweet (Eds.), Macromolecular Crystallography, Part A, vol. 276, Academic Press, 1997, p. 307.
[18] S. Mackay, C.J. Gilmore, C. Edwards, M. Tremayne, N. Stewart, K. Shankland, MAXUS solution and refinement software suite: MAXUS: a computer program for the solution and refinement of crystal structures from diffraction data, University of Glasgow, Nonius BV, MacScience Co. Ltd., Scotland, UK, Delft, The Netherlands, Yokohama, Japan, 1998.
[19] (a) R.H. Blessing, Acta Crystrallogr., Sect. A 51 (1995) 33;
(b) R.H. Blessing, J. Appl. Cryst. 30 (1997) 421.
[20] Enraf-Nonius, CAD-4/PC Software, Version 1.5c, Enraf-Nonius, Delft, The Netherlands, 1994.
[21] A.C.T. North, D.C. Phillips, F.S. Mathews, Acta Crystallogr., Sect. A 42 (1968) 351.
[22] K. Harms, S. Wocadlo, XCAD4 – CAD4 Data Reduction, University of Marburg, Marburg, Germany, 1995.
[23] P.T. Beurskens, G. Beurskens, W.P. Bosman, R. de Gelder, S. Garcia-Granda, R.O. Gould, R. Israel, J. M.M. Smits, DIRDIF-99 Program System, Crystallography Laboratory, University of Nijmegen, The Netherlands, 1999.
[24] G.M. Sheldrick, SHELX Suite of Programs for Crystal Structure Analysis (Release 97-2), University of Göttingen, Germany, 1998.
[25] L.J. Farrugia, J. Appl. Crystallogr. 30 (1997) 565.
[26] A.L. Spek, PLATON, A Multipurpose Crystallographic Tool, Utrecht University, Utrecht, The Netherlands, 1998.
[27] L.J. Farrugia, J. Appl. Crystallogr. 32 (1999) 837.
[28] (a) J.M. Harrowfield, L. Weimin, B.W. Skelton, A.H. White, Aust. J. Chem. 47 (1994) 321;
(b) J.M. Harrowfield, L. Weimin, B.W. Skelton, A.H. White, Aust. J. Chem. 47 (1994) 339;
(c) K.-Z. Tang, J. Zhang, Y. Tang, W.-S. Liu, M.-Y. Tan, Y.-X. Sun, Inorg. Chim. Acta 359 (2006) 1207;
(d) M.I. Saleh, E. Kusrini, R. Adnan, B. Saad, B.M. Yamin, H.K. Fun, J. Mol. Struct. 837 (2007) 169.
[29] H. Plenio, Chem. Rev. 97 (1997) 3363.
[30] R.J. Curry, W.P. Gillin, J. Appl. Phys. 88 (2000) 781.

Table 1
Comparison between the CuBD sequence in APP (A) and the studied ligands (B and C)

A	^{124}SDALLVPDKCK FLHQERMDVCETHLHWHTVAKET CSEKSTNLHDYGMLLPCGIDKFRGVEFVCCPL^{189}
B	DAHQERMDVSETHLHWHT
C	Ac-DAHQERMDVSETHLHWHT-NH_2

Substitution of F → D, L → A, C → S is supposed to prevent peptide precipitation in the solution.

the three His residues and Cu-induced oxidation, or Cu(II) reduction to Cu(I) [3]. The presence of only one or zero His residues between the two cysteines (Cys144 and Cys158) does not induce Cu(II) reduction and the oxidative reactions [9].

To evaluate the binding of Cu(II) by the three histidyl region we synthesized the protected and unprotected octadecapeptide (DAHQERMDVSETHLHWHT and Ac-DAHQERMDVSETHLHWHT-NH_2) having two distinct metal-binding-domains, the albumin-like N-terminal (DAH) and APP cysteine-rich three His domain at the C-terminal. The N-terminal albumin-like motif is also present in the APP cysteine-rich region (FLH) at positions 135–137 (Table 1). This is a strongly conserved sequence in APP proteins.

2. Experimental

2.1. Chemical synthesis, purification and analysis of the synthetic peptide

Both peptides were synthesized according to published methods using standard solid phase synthesis techniques with a manual methodology [10,11].

The protected amino acids and other chemicals were purchased from Peptide International, Fluka, Sigma–Aldrich. The protected peptide was synthesized on TentaGel R RAM resin (Rapp Polymers; capacity 0.18 mmol/g, 1 g). The resin was treated with piperidine (20%) in dimethylformamide and all amino acids were linked with the use of the DIPCI/HOBt methodology. The coupling reaction time was 1 h. Piperidine (20%) in dimethylformamide was used to remove the *Fmoc* group at all steps. After deprotection of the last N^{α}-*Fmoc* group, the peptide resin was washed and treated with *N*-acetylimidazole in dimethylformamide for 24 h. After washing with methanol the protected peptide resin was dried *in vacuo*. The resin was then treated with trifluoroacetic acid/H_2O/phenol/triisopropylsilane (reagent B, 8.8/0.5/0.5/0.2) 10 ml per 1 g of the resin at room temperature for 2 h. After filtration of the exhausted resin, the solvent was concentrated in vacuo and the residue triturated with diethyl ether. The crude peptide was checked by RP-HPLC (0–100% B in 60 min ($A = 0.1\%$ TFA/H_2O, $B = 80\%$ CH_3CN/H_2O + 0.08% TFA), 1 ml/min, Kromasil C_{18} analytical column (4.6 × 250 mm, 5 μm), UV detection at 223 nm, $R_t = 21.05$ min) and MS ($M_{theoretical} = 2270.4$, $[M+H^+]_{experimental} = 2271.2$). The peptide was purified with HPLC using a Vydac C_{18} semi-preparative column (10 × 250 mm, 5 mm) with a gradient of 10–50% B in 120 min (A and B solvents as described before), flow 10 ml/min, UV detection at 223 nm. The fraction containing the pure peptide was liophylized twice and the purity assessed by analytical RP-HPLC (0–100% B in 60 min, 1 ml/min, Kromasil C_{18} analytical column (4.6 × 250 mm, 5 μm), UV detection at 223 nm, $R_t = 22.6$ min, purity 99%), and MS ($[M+H^+]_{experimental} = 2271.0$) using a Bruker Biflex III Maldi-Tof Mass Spectrometer (Bruker Daltonics).

The unprotected version of the peptide was synthesized on TentaGel PHB resin (Rapp Polymer; capacity 0.22 mmol/g, 1 g). The first amino acid was attached manually to the resin with the use of an esterification reaction of an underivatised support (6 time excess of the symmetrical anhydride in dimethylforamide, DIPCI/DMAP). The symmetrical anhydride was gently agitated with the resin for 2 h. Next the resin was washed with DMF and used for the synthesis as described above. After the peptide synthesis, the resin was washed with methanol and the free peptide resin was dried *in vacuo*. The resin was then treated with trifluoroacetic acid/H_2O/phenol/triisopropylsilane (reagent B, 8.8/0.5/0.5/0.2) 10 ml per 1 g of the resin at room temperature for 2 h. After filtration of the exhausted resin, the solvent was concentrated *in vacuo* and the residue triturated with diethyl ether. The crude peptide was checked by HPLC (0–100% B in 60 min, Kromasil C_{18} analytical column, 1 ml/min, C_{18} analytical column (4.6 × 250 mm, 5 μm), UV detection at 223 nm, $R_t = 20.05$ min) and MS ($M_{theoretical} = 2229.4$, $[M+H^+]_{experimental} = 2230.2$). The peptide was purified with RP-HPLC using a Vydac C_{18} semi-preparative column (10 × 250 mm, 5 μm), flow 10 ml/min, UV detection at 223 nm, with a gradient of 5–50% B in 120 min (A and B as described above). The fraction containing the pure peptide was lyophilized twice and the purity assessed by analytical HPLC (0–100% B in 60 min, Kromasil C_{18} analytical column, flow 1 ml/min, C_{18} analytical column (4.6 × 250 mm, 5 μm), UV detection at 223 nm, $R_t = 20.6$ min, purity 99%), and MS ($[M+H^+]_{experimental} = 2230.0$).

2.2. Potentiometric measurements

Stability constants for both the proton and Cu(II) complexes were calculated from three titrations carried out over the range pH 3–11 at 25 °C using a total volume of 1.5 cm^3. The purities and exact concentration of the solutions of the ligands were determined by the method of Gran [12]. NaOH was added from a 0.250 cm^3 micrometer syringe which was calibrated by both weight titration and titration of standard materials. The metal ion concentration was 1×10^{-3} M and the metal to ligand ratio was 1:1.1 and 0.5:1.0. The pH-metric titrations were performed at 25 °C in 0.1 M KCl on a MOLSPIN pH-meter system using a Russel CMAW 711 semi-combined electrode calibrated in hydrogen concentration using HCl [13]. The

SUPERQUAD and HYPERQUAD programs were used for stability constant calculations [14,15]. Protonation constants and stability constants were determined independently. Standard deviations were computed by SUPERQUAD and HYPERQUAD and refer to random errors only. They are, however, a good indication of the importance of a particular species in the equilibrium.

2.3. Spectroscopic measurements

Solutions for the spectroscopic measurements were of similar concentrations to those used in the potentiometric studies. Electron paramagnetic resonance (EPR) spectra were recorded on a Brucker ESP 300E spectrometer at X-band frequency (9.3 GHz) at 120 K. Circular dichroism (CD) spectra were recorded on a Jasco J-715 spectropolarimeter in the 800–235 nm range. The values of $\Delta\varepsilon$ (*i.e.* $\varepsilon_1 - \varepsilon_2$) and ε were calculated at the maximum concentration of the particular species obtained from the potentiometric data.

3. Results and discussion

3.1. Unprotected peptide

The octadecapeptide, DAHQERMDVSETHLHWHT, has 10 potential protonation sites and it behaves as a $H_{10}L$ ligand with protonation constants collected in Table 2. The protonation sites include the N-terminal amino group, four histidyl imidazoles, two glutamic and two aspartic side chain carboxylates and the carboxylate of the C-terminal Thr. The differences between the pK values of the four His are within statistical range (0.4–0.6). The same relations are observed for the pairs of Asp and Glu carboxylates, respectively, indicating no distinct interactions between the protonation sites.

The calculations based on the potentiometric titration data show formation of 9 coordination species (Table 3, Fig. 1). The coordination begins around pH 2.5 and the first clear spectroscopic evidence for metal ion binding to peptide is seen around pH 4, in which the d–d transitions centered around 620 nm indicate two nitrogen (2N) coordination [6].

The hypothetical plot calculated with use of the stability constants obtained for binary systems, showing the competition between two binding sites of the albumin N-terminal tripeptide Asp-Ala-His-NH_2 fragment [16] and the three

Table 2
Potentiometric data for the proton and Cu(II) complexes of DAHQERMDVSETHLHWHT

Species	$\log\beta$	$\log K$
DAHQERMDVSETHLHWHT		
HL	8.12(0)	$\log K_{NH_2} = 8.12$
H_2L	15.49(0)	$\log K_{im} = 7.36$
H_3L	22.39(1)	$\log K_{im} = 6.90$
H_4L	28.81(0)	$\log K_{im} = 6.42$
H_5L	34.65(0)	$\log K_{im} = 5.84$
H_6L	39.22(1)	$\log K_{coo-} = 4.56$
H_7L	43.20(1)	$\log K_{coo-} = 3.98$
H_8L	46.56(0)	$\log K_{coo-} = 3.36$
H_9L	49.45(1)	$\log K_{coo-} = 2.89$
$H_{10}L$	51.61(1)	$\log K_{coo-} = 2.16$
DAHQERMDVSETHLHWHT/Cu(II)		
CuH_6L	42.69(3)	
CuH_4L	34.90(2)	7.78 ($2H^+$)
CuH_3L	30.26(2)	4.64
CuH_2L	25.74(1)	4.52
CuHL	20.62(1)	5.12
CuL	14.69(2)	5.93
$CuH_{-1}L$	8.15(3)	6.54
$CuH_{-2}L$	0.77(3)	7.38
$CuH_{-3}L$	−10.29(4)	9.52

Metal to ligand ratio = 1:1.1; [Cu(II)] = 0.001 M.

Table 3
Spectroscopic data for the Cu(II) complexes of DAHQERMDVSETHLHWHT

pH	UV–Vis		CD		EPR	
	λ (nm)	ε (M^{-1} cm^{-1})	λ (nm)	$\Delta\varepsilon$ (M^{-1} cm^{-1})	$A_\parallel \times 10^{-4}$ (cm^{-1})	$g_\parallel$
4.5	620	48	286	−0.177	136	2.41
			264	0.231		
4.9	526	108	569	−0.212		
			491	0.392		
			364	−0.042		
			308	0.449		
			268	−1.356		
			254	−0.243		
5.5	526	128	570	−0.275		
			493	0.458		
			463	−0.040		
			308	0.572		
			275	−1.453		
			251	−0.216		
6.1	526	146	570	−0.399	200	2.18
			493	0.570		
			308	0.802		
			272	−2.194		
7.0	526	141	570	−0.402	200	2.18
			482	0.578		
			308	0.833		
			270	−2.432		
			253	−0.464		
9.0	526	146	570	−0.406	200	2.18
			492	0.593		
			376	−0.031		
			308	0.872		
			272	−2.468		
			251	−0.801		
			229	−12.868		
11.0	526	154	568	−0.616	200	2.18
			490	0.742		
			398	−0.015		
			309	0.934		
			271	−3.194		
			251	−0.493		
			230	−12.597		

Metal to ligand ratio = 1.0:1.1; [Cu(II)] = 0.001 M.

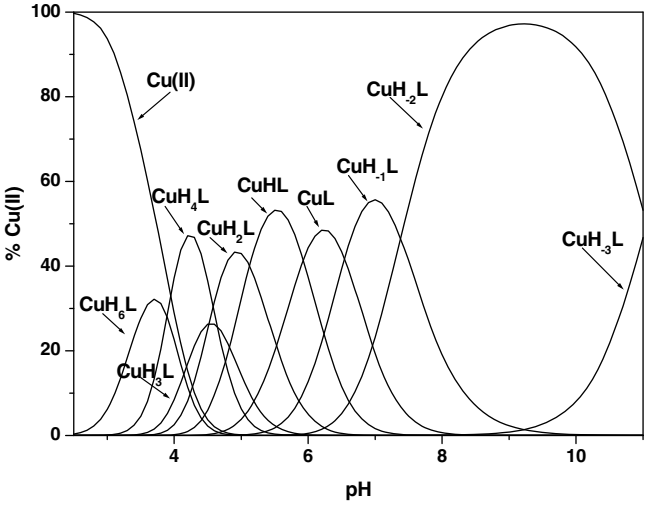


Fig. 1. Species distribution profile for the Cu(II) complexes of DAH-QERMDVSETHLHWHT. Metal to peptide molar ratio = 1:1; [Cu(II)] = 0.001 M.

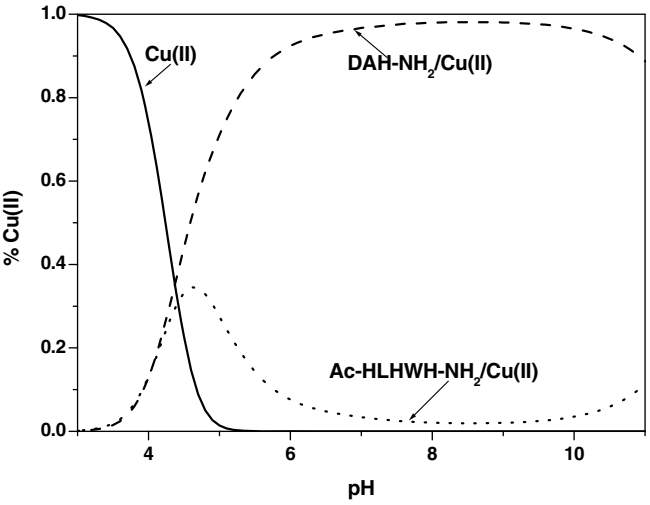


Fig. 2. Competition diagram between Ac-HLHWH-NH$_2$/Cu(II) [6] and DAH–NH$_2$/Cu(II) [16] complexes. Metal to peptide molar ratio = 1:1:1; [Cu(II)] = 0.001 M.

His region Ac-HLHWH-NH$_2$ [6] (Fig. 2) clearly indicates that the albumin-like site is more effective in coordinating the Cu(II) ion, especially above pH 6. Within the pH range 4–5 both sites are comparable in binding, but around pH 7 the "three His" APP site binds less than 5% of the copper. The CD, UV–Vis and EPR spectra for the unprotected octadecapeptide indicate that 4N {NH$_2$, 2 × N$^-$, N$_{imid}$} coordination at N-terminal begins around pH 5. This follows the formation of the CuHL species. The CuHL complex with albumin-like binding undergoes deprotonation at the three His residues within the APP-like region with a pK_a value very close to those observed for the metal-free peptide (Table 3). The spectroscopic parameters above pH 5.5 (CuHL, CuL, CuH$_{-1}$L and CuH$_{-2}$L complexes) are exactly the same, supporting the same coordination mode in all these species. The formation of CuH$_{-3}$L may result from the deprotonation of the metal-bound imidazole [16]. A comparison of the CD spectra for solutions in the physiological pH range (Fig. 4) for the considered systems, DAHQERMDVSETHLHWHT/Cu(II), Ac-HLHWH-NH$_2$/Cu(II) [6] and DAH–NH$_2$/Cu(II) [16] complexes, clearly shows that the coordination mode of DAHQERMDVSETHLHWHT/Cu(II) is similar to that found for the DAH-NH$_2$/Cu(II) system. Thus, even if the APP three His region binds Cu(II) ions in the physiological pH range very effectively *via* the five-nitrogen donor system {3 × N$_{imid}$, 2 × N$^-$} [6,7], it is poorly competitive to the

Table 4
Potentiometric data for the proton and Cu(II) complexes of Ac-DAHQERMDVSETHLHWHT-NH$_2$

Species	log β	log K
Ac-DAHQERMDVSETHLHWHT-NH$_2$		
HL	10.11(1)	log K_R = 10.11
H$_2$L	17.43(1)	log K_{im} = 7.32
H$_3$L	24.19(1)	log K_{im} = 6.76
H$_4$L	30.58(2)	log K_{im} = 6.39
H$_5$L	36.28(1)	log K_{im} = 5.70
H$_6$L	40.69(1)	log K_{coo-} = 4.41
H$_7$L	44.44(1)	log K_{coo-} = 3.75
H$_8$L	47.37(1)	log K_{coo-} = 2.95
Ac-DAHQERMDVSETHLHWHT-NH$_2$/Cu(II)		
CuH$_4$L	35.41(5)	
CuH$_3$L	30.96(4)	4.45
CuH$_2$L	26.00(3)	4.95
CuHL	19.98(3)	6.02
CuH$_{-1}$L	5.56(4)	14.42 (2H$^+$)
CuH$_{-2}$L	−4.56(5)	10.12
CuH$_{-4}$L	−26.43(5)	21.87 (2H$^+$)

Metal to ligand ratio = 0.5:1.0; [Cu(II)] = 0.001 M.

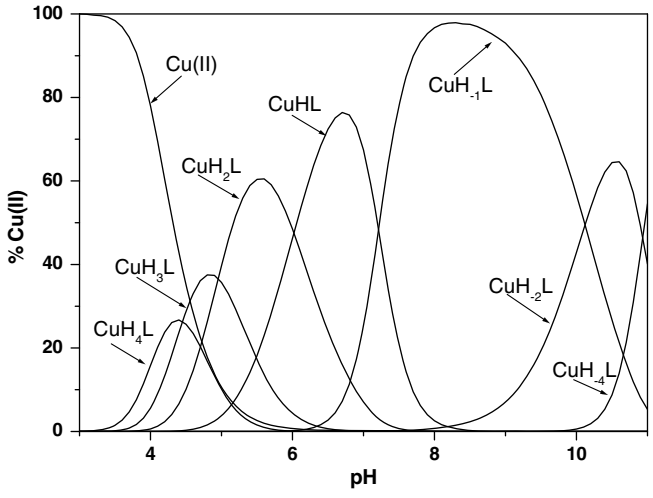


Fig. 3. Species distribution profile for the Cu(II) complexes of Ac-DAHQERMDVSETHLHWHT-NH$_2$. Metal to peptide molar ratio = 0.5:1; [Cu(II)] = 0.001 M.

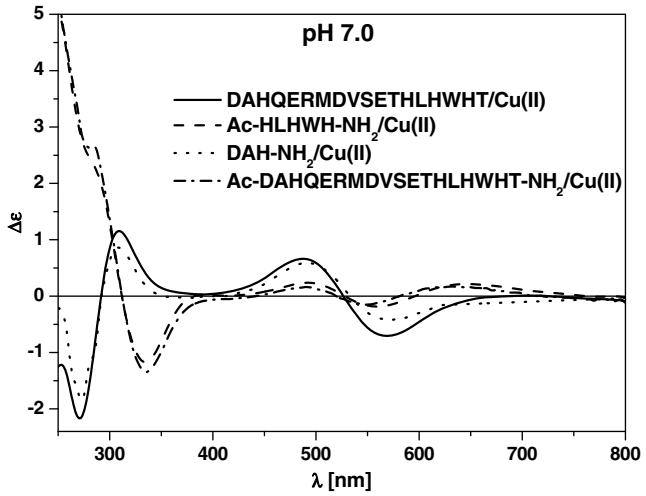


Fig. 4. Comparison of the CD spectra of DAHQERMDVSETHLHWHT/Cu(II), Ac-HLHWH-NH_2/Cu(II) [6], Ac-DAHQERMDVSETHLHWHT-NH_2/Cu(II) and DAH–NH_2/Cu(II), [16] complexes at pH 7. Metal to peptide molar ratio = 1:1:1; [Cu(II)] = 0.001 M.

albumin-like coordination (Figs. 2 and 5B). However, the presence of the second binding site, –HLHWH–, in the unprotected peptide increases the stability of the complexes formed and DAHQERMDVSETHLHWHT becomes more effective than the DAH–NH_2 ligand (Fig. 5A).

3.2. N- and C-protected peptide

The N- and C-protected peptide, Ac-DAHQERMDVSETHLHWHT-NH_2, behaves as a H_8L acid. The protonation constants corresponding to the Arg side chain (pK 10.11), 4 His imidazoles and three carboxylates are collected in Table 4. Calculations based on the potentiometric data related to titrations in the presence of Cu(II) (range pH 3–10.5) indicate the formation of six complex species; all of them are mono-complexes with different degrees of protonation. The distribution diagram reported in Fig. 3 shows that the coordination starts at a pH lower than 4. Coordination of the Cu(II) ion in CuH_4L starts at the imidazole nitrogen of the His residue, which is an anchoring site for the metal ion (a band present at 723 nm in UV–Vis and $A_{II} = 163 \times 10^{-4}\,cm^{-1}$, $g_{II} = 2.33$ in the EPR spectrum). Within the physiological pH range, the CuHL and $CuH_{-1}L$ complexes dominate. The CuHL complex at pH 7.0 involves most likely the $\{3N_{im}, N^-\}$ binding mode, supported by a d–d transition at 588 nm. Spectroscopic parameters obtained above pH 8.0 for the $CuH_{-1}L$ complex are similar to those observed for Cu(II)/APP(145–157) with the $\{3N_{im}, 2N^-\}$ coordination [7]. The potentiometric data obtained clearly show that the behavior of its binding to Cu(II) is very similar to that observed for the three histidine peptide, Ac-ETHLHWHTVAKET-NH_2 [7]. Thus, the major complexes present in the physiological pH range for protected the octadecapeptide fragment have a coordination mode as those observed earlier for the APP peptide, indicating that the basic binding site involves the three His domain when the albumin terminal is N-protected. The splitting of the d–d transitions indicates a lowering of the geometry around the metal ion in the $CuH_{-1}L$ species. Formation of $CuH_{-2}L$ results in the distinct reorganization of the coordination sphere around the Cu(II) ion, probably related to the coordination of an additional amide nitrogen. Above pH 10 two protons dissociate from $CuH_{-2}L$ to give a $CuH_{-4}L$ species derived from the deprotonation of the Arg side chain and the metal bound imidazole. CD spectra at about pH 7 (Fig. 4) for the systems Ac-DAHQERMDVSETHLHWHT-NH_2/Cu(II), Ac-HLHWH-NH_2/Cu(II) [6] and DAH–NH_2/Cu(II), [16] show that the coordination mode of

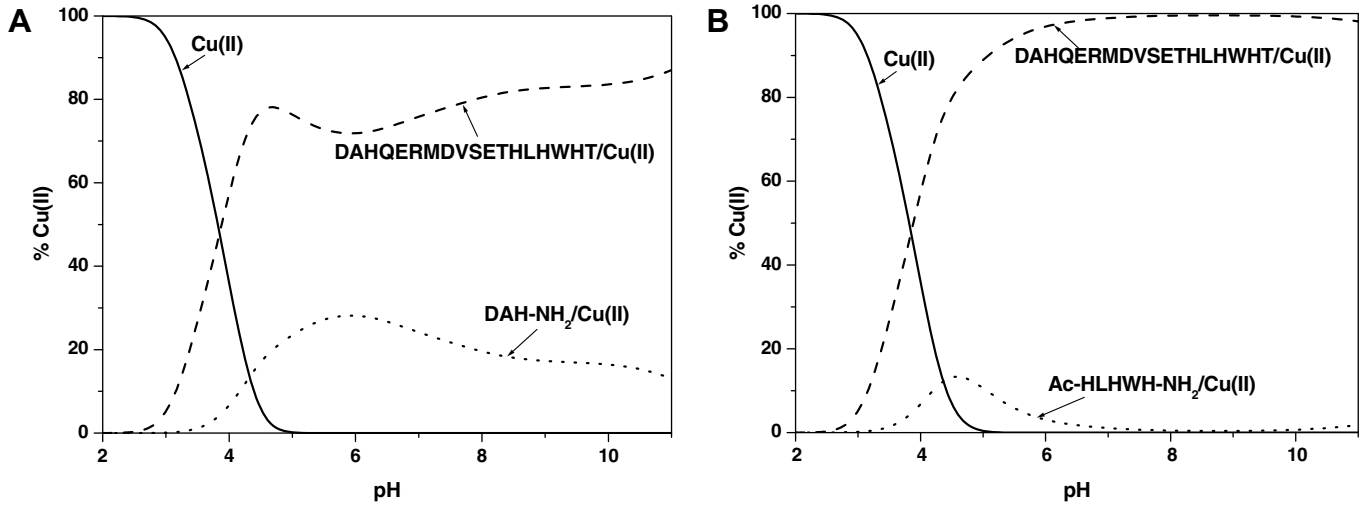


Fig. 5. Competition diagrams between the DAHQERMDVSETHLHWHT/Cu(II) and Ac-HLHWH-NH_2/Cu(II) [6] complexes, (A); DAHQERMDVSETHLHWHT/Cu(II) and DAH-NH_2/Cu(II) [16] complexes, (B). Metal to peptide molar ratio = 1:1:1; [Cu(II)] = 0.001 M.

Table 5
Spectroscopic data for the Cu(II) complexes of Ac-DAH-QERMDVSETHLHWHT-NH_2

pH	UV–Vis		CD		EPR	
	λ (nm)	ε ($M^{-1}\,cm^{-1}$)	λ (nm)	$\Delta\varepsilon$ ($M^{-1}\,cm^{-1}$)	$A_{\parallel} \times 10^{-4}$ (cm^{-1})	$g_{\parallel}$
4.0	723	41			136	2.41
4.6	662	54			175	2.30
5.5	638	90	567	0.392	197	2.26
			231	−18.122		
7.0	588	126	591	0.302	193	2.26
			333	−0.879		
			229	−19.544		
8.0	553	106	639	0.174	203	2.19
			547	−0.152		
			493	0.181		
			336	−1.586		
			251	4.652		
			227	−2.784		
10.5	533	111	651	0.352	203	2.19
			545	−0.340		
			335	−1.653		
			251	6.955		
11.0	533	119	652	0.631	203	2.19
			531	−0.767		
			339	−1.132		
			255	7.686		

Metal to ligand ratio = 0.5:1.0; [Cu(II)] = 0.001 M.

the protected peptide is similar to that found for Ac-HLHWH-NH_2/Cu(II) (see Table 5).

4. Conclusion

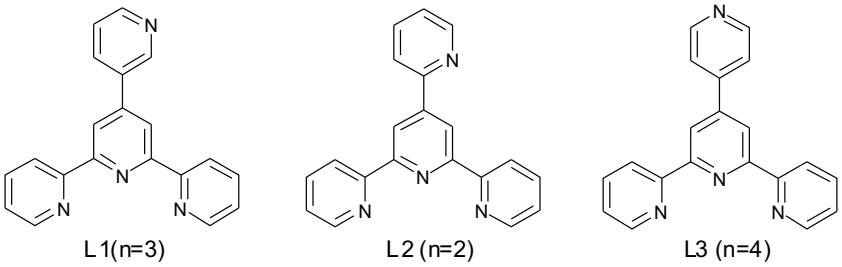
The –HXHYH– motif is very effective in binding Cu(II) although it is unable to compete with the albumin-like coordination. This could be a critical factor when both peptides are inserted into a protein sequence. This strong multi-histidine and amide binding could be responsible for the protection of Cu(II) reduction to Cu(I) reported recently for some variants of APP protein [3].

Acknowledgement

This work was supported by Project KBN 4 T09A05423.

References

[1] H. Kozłowski, D. Brown, G. Valensin, Metallochemistry of Neurodegeneration, Biological, Chemical and Genetic Aspects, RSC Publishing, Cambridge, 2006.
[2] G. Multhaup, A. Schlicksupp, L. Hesse, D. Beher, T. Ruppert, C.L. Masters, K. Beyreuther, Science 271 (1996) 1406.
[3] A. Simons, T. Ruppert, C. Schmidt, A. Schlicksupp, R. Pipkorn, J. Reed, C.L. Masters, A.R. White, R. Cappai, K. Beyreuther, T.A. Bayer, G. Multhaup, Biochemistry 41 (2002) 9310.
[4] K.J. Barnham, W.J. McKinstry, G. Multhaup, D. Galatis, C.J. Morton, C.C. Curtain, N.A. Williamson, A.R. White, M.G. Hinds, R.S. Norton, K. Beyreuther, C.L. Masters, M.W. Parker, R. Cappai, J. Biol. Chem. 278 (2003) 17401.
[5] D. Brown, H. Kozłowski, J. Chem. Soc., Dalton Trans. (2004) 1907.
[6] M. Łuczkowski, K. Wiśniewska, L. Łankiewicz, H. Kozłowski, J. Chem. Soc., Dalton Trans. (2002) 2266.
[7] D. Valensin, F.M. Mancini, M. Łuczkowski, A. Janicka, K. Wiśniewska, E. Gaggelli, G. Valensin, L. Łankiewicz, H. Kozłowski, J. Chem. Soc., Dalton Trans. (2004) 16.
[8] L. Hesse, D. Beher, C.L. Masters, G. Multhaup, FEBS Lett. 349 (1994) 109.
[9] A.R. White, G. Multhaup, D. Galatis, W.J. McKinstry, M.W. Parker, R. Pipkorn, K. Beyreuther, C.L. Masters, R. Cappai, J. Neurosci. 22 (2002) 365.
[10] E. Atherton, R.C. Sheppard, Solid Phase Peptide Synthesis, IRL Press, Oxford, 1989.
[11] G.B. Fields, R.L. Noble, Int. J. Pept. Protein Res. 35 (1990) 161.
[12] G. Gran, Acta Chem. Scand. 29 (1950) 599.
[13] H. Irving, M.G. Miles, L.D. Pettit, Anal. Chim. Acta 38 (1967) 475.
[14] P. Gans, A. Sabatini, A. Vacca, J. Chem. Soc., Dalton Trans. (1985) 1195.
[15] P. Gans, A. Sabatini, A. Vacca, Talanta 43 (1996) 1739.
[16] P. Młynarz, D. Valensin, K. Kociołek, J. Zabrodzki, J. Olejnik, H. Kozłowski, New J. Chem. 26 (2002) 264.



Scheme 1. 4′-(*n*-Pyridyl)-2,2′:6′,2″-terpyridine ($n = 2, 3, 4$).

and extend the structure into higher dimensionality [5a,7]. To our knowledge, among the three isomers, L3 is better studied than the other two. It has been found to form macrocyclic oligomers [8], 1D linear [5d,9] and grid-like [10] polymers, 3D chiral self-catenated network [11] and supramolecular motifs [12]. Studies based on the other two pytpy ligands are rare [5b,6,13]. We noticed that the angles between mono- and tridentate N-donor sites in L1 and L2 are different and we believe this subtle structural difference may affect the metal–ligand coordination environment, as well as the overall dimensionality of the architecture [6,13c].

With this understanding, one crucial aim of this work is to explore the intrinsic factors of these positional isomeric ligands for tuning the structural assembly, which may provide further insights in designing new hybrid crystalline materials, four compounds, namely, $\{[Cd_3(L1)_2(SCN)_6](THF)_2\}_n$ (**1**), $[Cd_2(L1)(CH_3OH)Cl_4]_n$ (**2**), $[Cd_2(L2)_2(N_3)_4]$ (**3**), $[Cd_2(L2)_2(SCN)_4]$ (**4**), were synthesized based on the use of L1 and L2 as ligands and Cd^{II} halides (pseudohalides) as metal salts.

2. Experimental

2.1. Materials and methods

Ligands 4′-(3-pyridyl)-2,2′:6′,2″-terpyridine (L1) and 4′-(2-pyridyl)-2,2′:6′,2″-terpyridine (L2) were prepared according to the literature method [14]. All the other chemicals were used as obtained from commercial sources without further purification. Elemental analyses (C, H and N) were performed with Elementar Vario EL III elemental analyzer. Infrared spectra were recorded on a Bruker EQUINOX55 spectrometer as KBr pellets in the range of 4000–400 cm^{-1}. Luminescent spectra were measured at room temperature on a Hitachi F4500 fluorescence spectrophotometer.

2.2. Syntheses and characterization

2.2.1. $\{[Cd_3(L1)_2(SCN)_6](THF)_2\}_n$ (*1*)

NH_4SCN (0.030 g, 0.4 mmol) was added to methanol solution (10 mL) of $Cd(NO_3)_2 \cdot 4H_2O$ (0.031 g, 0.2 mmol) with stirring. The resulting solution was carefully layered on solution of L1 (0.031 g, 0.1 mmol) in THF (10 mL). Colorless crystals formed at the methanol/THF interface and were collected by filtration to give a yield of 65% (based on Cd). *Anal.* Calc. for $C_{54}H_{44}Cd_3N_{14}O_2S_6$ (**1**): C, 44.71; H, 3.06; N, 13.52. Found: C, 44.73; H, 3.03; N, 13.53%. IR (cm^{-1}, KBr): 3422(w), 3052(w), 2967(w), 2857(w), 2113(s), 2076(s), 1597(m), 1546(m), 1472(m), 1434(w), 1394(m), 1244(w), 1056(w), 1012(w), 791(m).

2.2.2. $[Cd_2(L1)(CH_3OH)Cl_4]_n$ (*2*)

Compound **2** was obtained upon carefully layering a solution of $CdCl_2 \cdot 2.5H_2O$ (0.046 g, 0.2 mmol) in methanol (10 mL) onto the solution of L1 (0.031 g, 0.1 mmol) in THF (10 mL). The solution was left for 3 weeks at room temperature. X-ray quality transparent crystals were collected by filtration to give a yield of 52% (based on Cd). *Anal.* Calc. for $C_{21}H_{18}Cd_2Cl_4N_4O$ (**2**): C, 35.57; H, 2.56; N, 7.90. Found: C, 35.55; H, 2.57; N, 7.91%. IR (cm^{-1}, KBr): 3402(s), 3077(m), 1607(m), 1546(m), 1473(m), 1247(w), 1010(w), 797(m).

2.2.3. $[Cd_2(L2)_2(N_3)_4]$ (*3*)

Compound **3** was obtained using a procedure similar to that for **1** except that NaN_3 and L2 were used instead of NH_4SCN and L1. Colorless crystals were collected by filtration to give a yield of 73% (based on Cd). *Anal.* Calc. for $C_{40}H_{28}Cd_2N_{20}$ (**3**): C, 47.40; H, 2.78; N, 27.64. Found: C, 47.36; H, 2.80; N, 27.66%. IR (cm^{-1}, KBr): 3345(w), 2032(s), 1591(m), 1550(m), 1469(m), 1406(m), 1278(w), 1011(m), 784(m).

2.2.4. $[Cd_2(L2)_2(SCN)_4]$ (*4*)

Compound **4** was obtained using a procedure similar to that for **1** except that L2 was used instead of L1. Colorless crystals were collected by filtration to give a yield of 79% (based on Cd). *Anal.* Calc. for $C_{44}H_{28}Cd_2N_{12}S_4$ (**4**): C, 49.03; H, 2.62; N, 15.59. Found: C, 49.06; H, 2.63; N, 15.55%. IR (cm^{-1}, KBr): 3444(w), 2110(s), 2024(s), 1600(m), 1550(m), 1466(m), 1404(m), 1243(w), 1013(m), 781(m).

2.3. X-ray crystallography

Single crystal X-ray diffraction studies of complexes **1**–**4** were performed on a Bruker Smart Apex II CCD diffractometer equipped with a graphite crystal monochromator

Table 1
Crystallographic data and structure refinement parameters for **1**–**4**

Compound	**1**	**2**	**3**	**4**
Formula	$C_{54}H_{44}Cd_3N_{14}O_2S_6$	$C_{21}H_{18}Cd_2Cl_4N_4O$	$C_{40}H_{28}Cd_2N_{20}$	$C_{44}H_{28}Cd_2N_{12}S_4$
Formula mass	1450.59	708.99	1013.62	1077.82
Crystal system	triclinic	monoclinic	triclinic	triclinic
Space group	$P\bar{1}$	$P2_1/n$	$P\bar{1}$	$P\bar{1}$
a (Å)	9.033(4)	8.918(2)	8.876(1)	7.852(2)
b (Å)	11.887(6)	28.700(6)	8.969(1)	11.273(2)
c (Å)	14.214(7)	10.034(2)	13.463(1)	13.280(4)
α (°)	82.638(7)	90	93.500(2)	70.891(3)
β (°)	84.570(8)	110.96(2)	107.216(2)	87.436(4)
γ (°)	71.154(8)	90	99.691(2)	72.186(2)
V (Å^3)	1430(1)	2398.3(9)	1002.2(2)	1055.4(5)
Z	1	4	1	1
D_{calc} (g cm^{-3})	1.684	1.964	1.679	1.696
M (mm^{-1})	1.379	2.241	1.120	1.255
Total reflections	7349	19626	5150	5435
Unique reflections	5005	4247	3506	3691
R_{int}	0.0219	0.1040	0.0130	0.0247
Data/restraints/parameters	5005/1/358	4247/1/293	3506/0/280	3691/0/280
Goodness-of-fit	0.982	0.893	0.993	1.070
Final R indices[a] [$I > 2\sigma(I)$]	0.0320, 0.0700	0.0344, 0.0511	0.0231, 0.0601	0.0431, 0.1034
R indices (all data)	0.0493, 0.0732	0.0595, 0.0541	0.0279, 0.0614	0.0589, 0.1095

[a] $R_1 = \sum(|F_o| - |F_c|)/\sum|F_o|$, $wR_2 = \{\sum[w(F_o^2 - F_c^2)^2]/\sum[w(F_o^2)^2]\}^{1/2}$.

situated in the incident beam. The data collections were performed with Mo Kα radiation ($\lambda = 0.7107$ Å) by ω scan mode in the range of $1.82 < \theta < 25.10°$ (for **1**), $2.29 < \theta < 25.10°$ (for **2**), $2.32 < \theta < 25.10°$ (for **3**), $1.63 < \theta < 25.09°$ (for **4**) at 296(2) K. The crystal parameters and experimental details of the data collection are summarized in Table 1. All structures were solved by the direct methods using SHELXS program of the SHELXTL-97 package and refined with SHELXL [15]. Metal atoms in all complexes were located from the E-maps and other non-hydrogen atoms were located in successive difference Fourier syntheses. The final refinements were performed by full-matrix least-squares methods with anisotropic thermal parameters for non-hydrogen atoms on F^2. All hydrogen atoms were included in calculated positions and refined with isotropic thermal parameters riding on those of the parent atoms. Selected bond lengths and angles are given in Table 2.

3. Results and discussion

3.1. IR spectra

The IR spectra for compounds **1**–**4** contain characteristic C=N and C=C vibrational frequencies for free ligands L1 and L2 at 1600–1450 cm^{-1}. The strong ν_{as}(SCN) absorption peaks at 2113 cm^{-1} for **1** and 2110 cm^{-1} for **4** show the presence of 1,3-μ-thiocyanate ligands and that at 2076 cm^{-1} for **1** and 2024 cm^{-1} for **4** are indicative of N-terminal coordination [16]. In **2**, a broad band centered around 3402 cm^{-1} can be assignable to the O–H stretch of the coordinated MeOH molecule. In **3**, $\nu_{as}(N_3)$ appears as a very strong splitting band at 2044 cm^{-1} and 2032 cm^{-1} is assigned to the existence of both end-on bridging and terminal azide ligand [17].

3.2. Description of the structures

3.2.1. $\{[Cd_3(L1)_2(SCN)_6](THF)_2\}_n$ (**1**)

Single crystal X-ray diffraction shows that **1** consists of a 1D grid-like chain. The asymmetric unit contains one and a half crystallographically independent Cd^{II} atoms (Fig. 1). Cd1 adopts a distorted octahedral geometry in a CdN_5S fashion, in which three nitrogen atoms from the tridentate sites of one L1 and one nitrogen atom from SCN^- ligand comprise the equatorial plane, and one nitrogen atom and one sulfur atom from different SCN^- ligands occupy the axial positions. The hexa-coordinated Cd2 atom coordinates to four SCN^- ligands at the equatorial plane and two pendant pyridyl rings from two L1 at the axial positions. The Cd–N and Cd–S distances falling in the range of 2.181(3)–2.383(3) Å, and 2.720(2)–3.018(2) Å, respectively, are all within the normal range. The SCN^- groups are nearly linear with the N–C–S bond angles in the range 176.83–179.38°, C–N–Cd and C–S–Cd linkages are bent and the related bond angles are in accordance with similar types of reported complexes [16].

An interesting feature is that three cadmium atoms (Cd1, Cd2 and Cd1A) locate in a line and are bridged by four μ-1,3-SCN^- ligands with the distances of Cd1···Cd1A and Cd1···Cd2 being 11.767 Å and 5.884 Å, respectively. L1 as a bridging ligand links Cd1 and Cd2 with nitrogen atoms from tridentate and mono-dentate domains, leading to the formation of 1D chain as shown in Fig. 2. The resulting chain can be considered as a series of [2 × 2] parallelo-

Table 2
Selected bond lengths (Å) and angles (°) for **1**–**4**

Compound **1**			
Bond lengths			
Cd(1)–N(1)	2.343(3)	Cd(1)–N(2)	2.331(3)
Cd(1)–N(3)	2.343(3)	Cd(1)–N(5)	2.242(4)
Cd(1)–N(6)	2.181(3)	Cd(1)–S(3)	3.018(2)
Cd(2)–N(4)	2.383(3)	Cd(2)–N(7)	2.301(3)
Cd(2)–S(2)	2.720(2)		
Bond angles			
N(1)–Cd(1)–N(5)	93.29(1)	N(2)–Cd(1)–N(5)	103.77(1)
N(3)–Cd(1)–N(5)	92.59(1)	N(6)–Cd(1)–N(5)	98.77(1)
N(5)–Cd(1)–S(3)	176.88(9)	N(7)#1–Cd(2)–N(4)#2	87.81(1)
N(7)#1–Cd(2)–N(7)	180.0	N(7)–Cd(2)–N(4)#2	92.19(1)
N(4)#2–Cd(2)–S(2)	92.02(8)	N(4)#3–Cd(2)–S(2)	87.98(8)
N(7)–Cd(2)–S(2)	86.20(8)	N(7)#1–Cd(2)–S(2)	93.80(8)
Compound **2**			
Bond lengths			
Cd(1)–N(1)	2.339(3)	Cd(1)–N(2)	2.305(3)
Cd(1)–N(3)	2.337(3)	Cd(1)–Cl(1)	2.600(1)
Cd(1)–Cl(2)	2.931(1)	Cd(1)–Cl(3)	2.459(1)
Cd(2)–N(4)#1	2.408(3)	Cd(2)–Cl(2)	2.603(1)
Cd(2)–Cl(3)	2.691(1)	Cd(2)–Cl(4)	2.627(1)
Cd(2)–O(1)	2.367(4)		
Bond angles			
N(1)–Cd(1)–Cl(1)	93.47(9)	N(2)–Cd(1)–Cl(1)	93.43(8)
N(3)–Cd(1)–Cl(1)	92.82(9)	Cl(1)–Cd(1)–Cl(2)	173.26(3)
Cl(1)–Cd(1)–Cl(3)	100.96(4)	Cl(2)–Cd(1)–Cl(3)	83.63(4)
N(4)#1–Cd(2)-O(1)	83.88(1)	N(4)#1–Cd(2)–Cl(2)	89.88(8)
N(4)#1–Cd(2)–Cl(3)	89.01(9)	N(4)#1–Cd(2)–Cl(4)	178.76(9)
Cl(2)–Cd(2)–Cl(3)	86.00(3)	Cl(3)–Cd(2)–Cl(4)	92.02(4)
Compound **3**			
Bond lengths			
Cd(1)–N(1)	2.349(2)	Cd(1)–N(2)	2.313 (2)
Cd(1)–N(3)	2.372(2)	Cd(1)–N(5)	2.521(2)
Cd(1)–N(8)	2.270(2)		
Bond angles			
N(1)–Cd(1)–N(5)	98.45(9)	N(2)–Cd(1)–N(5)	82.42(7)
N(3)–Cd(1)–N(5)	86.69(8)	N(5)–Cd(1)–N(8)	174.37(8)
Compound **4**			
Bond lengths			
Cd(1)–N(1)	2.360(4)	Cd(1)–N(2)	2.326(4)
Cd(1)–N(3)	2.358(4)	Cd(1)–N(5)	2.366(5)
Cd(1)–N(6)	2.484(5)	Cd(1)–S(1)	2.588(2)
Bond angles			
N(1)–Cd(1)–N(6)	94.29(2)	N(2)–Cd(1)–N(6)	87.04(2)
N(3)–Cd(1)–N(6)	87.11(2)	N(5)–Cd(1)–N(6)	174.24(2)
S(1)–Cd(1)–N(6)	84.18(1)	N(5)–Cd(1)–S(1)	90.88(1)

Symmetry operation: #1: $-x+2$, $-y$, $-z$; #2: $-x+2$, $-y$, $-z+1$; #3 x, y, $z-1$; #4: x, y, $z+1$ for **1**. #1: $x+1/2$, $-y+3/2$, $z+1/2$ for **2**.

gram grids interconnected through sharing Cd2 atoms at diagonally opposite corners, which is significantly different from the reported 1D grid-type structures formed by L3 [10], in which the grids are interconnected through halide atoms.

Within the grid, the length of the long edge measured by Cd1···Cd2 distance across L1 bridge is 10.478 Å, while the long diagonal distance measured by Cd2···Cd2 distance is 14.214 Å and the angle Cd1···Cd2···Cd1B is 62.13°. The dihedral angle of 32.35° between the pendant and central pyridines of L1 is largely a consequence of the geometric requirement imposed by metal atoms and no intra-unit face-to-face π–π interactions are observed.

The chains pack together through short face–face aromatic–aromatic interactions between the terminal and central terpyridyl rings (3.904 Å centroid–centroid), giving rise to 2D sheets (Fig. 2). THF solvent molecules are located in the lattice and form short contacts with protons of pyridyl rings and nitrogen atoms from bridging SCN^- anions, respectively (C1–H1···O1^{i}, 3.408 Å, 135.4°; C25–H25B···N6^{ii}, 3.517 Å, 150.5°; symmetry code i: ($x-1$, y, z), ii: ($-x+1$, $-y+1$, $-z$)).

3.2.2. $[Cd_2(L1)(CH_3OH)Cl_4]_n$ (**2**)

Compound **2** is a 2D wave-like structure formed through L1 bridging tetranuclear cadmium building units. As shown in Fig. 3, the asymmetric unit contains one L1, two crystallographically independent cadmium atoms, four chloride anions and one methanol molecule. Cd1 atom adopts octahedral geometry with the equatorial plane defined by three nitrogen atoms [Cd1–N1 = 2.339(3), Cd1–N2 = 2.305(3) and Cd1–N3 = 2.337(3) Å] from the tridentate sites of one L1 and one bridging chloride atom. The axial positions are occupied by one terminal and one bridging chloride atoms. The Cd1–Cl distances fall in the range of 2.459(1)–2.931(1) Å similar to those found in other Cd chloride coordination polymers [18]. Cd2 atom also adopts octahedral geometry with the equatorial plane defined by one nitrogen atom from the pendant pyridine of L1, three bridging chloride atoms. The axial positions are occupied by one bridging chloride and one methanol molecule. The Cd2–N, Cd2–S and Cd2–O distances are all within the normal range.

One of the outstanding features in **2** is the tetranuclear Cd units are formed and bridged by L1 resulting in an infinite 2D non-interpenetrating architecture (Fig. 4). Four cadmium atoms locate in a zig-zag shape, bridged by three double chloride bridges into Cd1–Cl_2–Cd2–Cl_2–Cd2A–Cl_2–Cd1A subunit with the distances of Cd1···Cd2, Cd1···Cd1A and Cd2···Cd2A being 3.938, 10.068 and 3.750 Å, respectively. Within the tetranuclear unit, each Cd_2Cl_2 is nearly coplanar and adjacent Cd_2Cl_2 planes are nearly perpendicular to each other. Each Cd_4 unit is bridged by four L1 and each L1 as a mono-tridentate bridging ligand links two Cd^{II} atoms into a 2D structure with $\{Cd_{10}C_{48}Cl_6\}$ macrocycles (Fig. 4). Within the macrocycles, it is interesting that L1 selectively links metal atoms with its tri- and mono-dentate sites. The tpy domain of L1 is nearly coplanar and coordinates to Cd1 atom, while the pendant pyridine rotates 17.80° relative to the central pyridyl ring to coordinate to Cd2. Adjacent L1 ligands which, respectively, link Cd1 and Cd2 atoms in the same Cd_4 unit are approximately anti-parallel and offset. Two face-to-face interactions between the central and terminal pyridyl rings are observed with centroid–centroid distance 3.664 and 3.773 Å, respectively, which stabilized the overall structure.

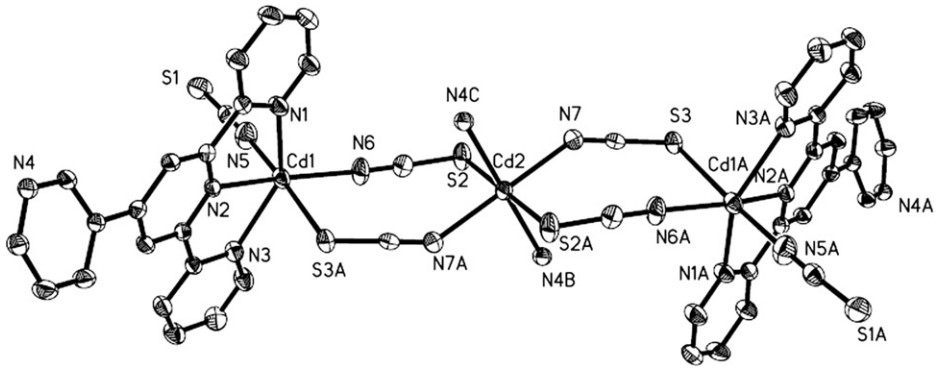


Fig. 1. ORTEP diagram of $\{[Cd_3(L1)_2(SCN)_6](THF)_2\}_n$, **1** with atom numbering scheme. Ellipsoids are drawn at 30% probability. H atoms and solvent molecules are not present for clarity.

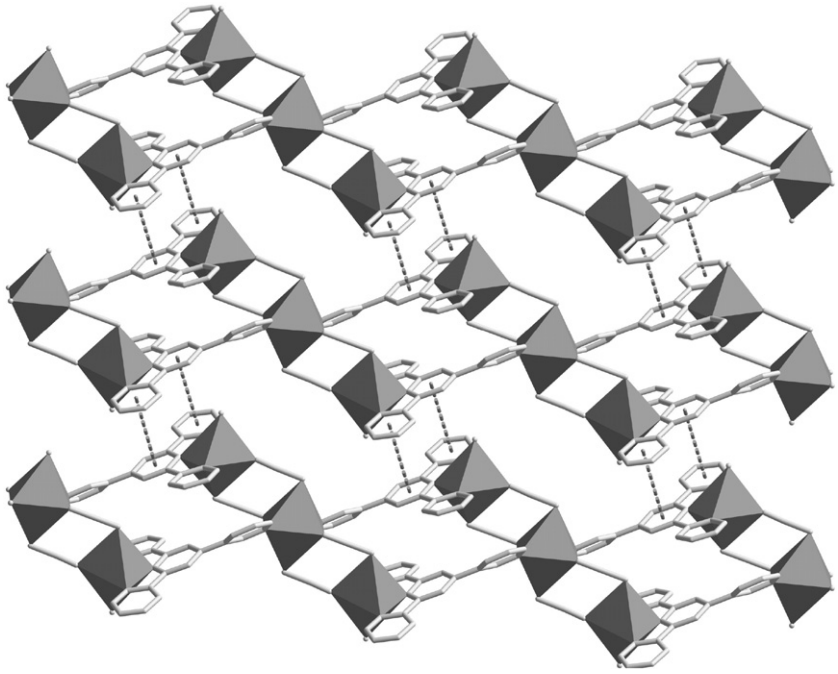


Fig. 2. View of the 1D grid-like structure of **1** packed into 2D supramolecular layer through $\pi\cdots\pi$ interactions. H atoms and solvent molecules are not present for clarity.

It should be noted that the actual structure of the 2D layer is wave-like, adjacent layers get a tightly packed structure without any guest molecules, the interlayer H-bonds *via* the interaction of terminal chloride atoms with hydrogen atoms of coordination methanol molecules [O1–H1A$\cdots$Cl1^{iii}, 3.158 Å, 162.7°, symmetry code iii: (*x*,

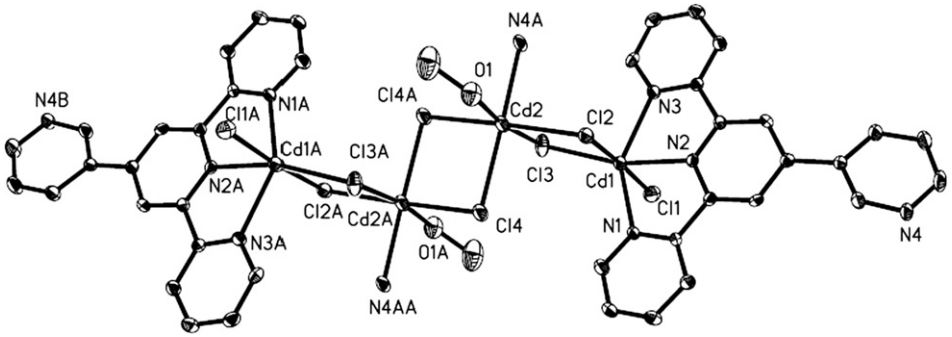


Fig. 3. ORTEP diagram of $[Cd_2(L1)(CH_3OH)Cl_4]_n$, **2** with atom numbering scheme. Ellipsoids are drawn at 30% probability.

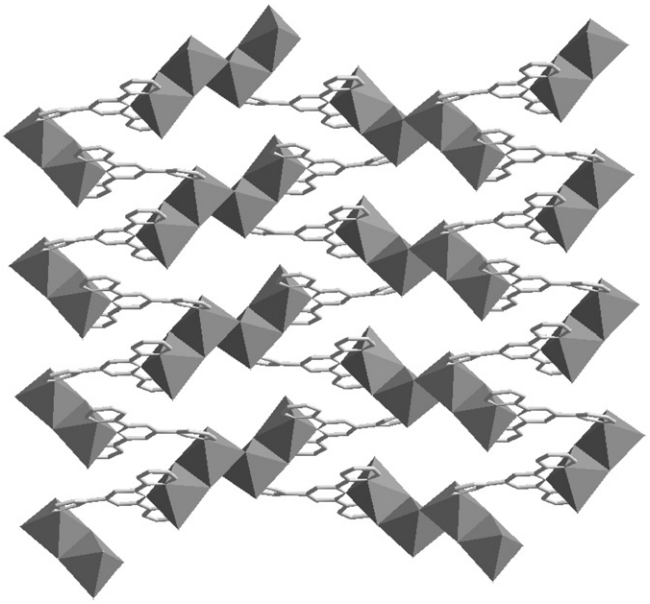


Fig. 4. View of the 2D structure of **2** with ten-metal containing macrocycles formed by Cd_4 clusters and bridging L1 along *a*-axis. H atoms are not present for clarity.

y, *z* + 1)] connect the 2D structure into 3D framework (Fig. 5).

3.2.3. $[Cd_2(L2)_2(N_3)_4]$ (**3**)

Compound **3** is a dimeric structure (Fig. 6). Each centrosymmetric dimer consists of Cd^{II} ions linked by two end-on bridging azide groups. The other two azides act as terminal ligands. The Cd_2N_2 core is planar with a Cd···Cd distance of 3.727 Å and a Cd–N–Cd bridging angle is 103.62°. The local coordination environment of each Cd^{II} ion is a distorted octahedron with the equatorial plane defined by three nitrogen atoms from the tridentate sites of one L2 and one nitrogen atom from the intra-dimer end-on azide bridge. The axial positions are occupied by two nitrogen atom from the intra-dimer end-on azide bridge and monocoordinate azide ligand, respectively. The bridging and terminal azide ligands are nearly linear and bond to Cd^{II} atoms with bent angle of Cd1–N5–N6 122.11° and Cd1–N8–N9 118.79°. Different from L1, L2 functions as a chelating ligand with the pendant uncoordinated pyridyl ring. A similar dimeric structure based on tpy and Mn-azide has been reported [19]. The pendant and central pyridines of L2 are twisted with a lower dihedral angle 4.79° than the value

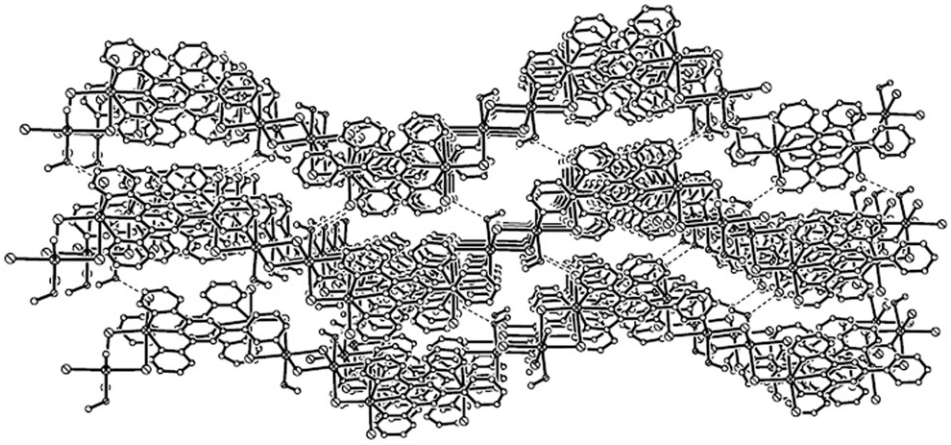


Fig. 5. Sideview of the 2D wave-like structure connected into 3D structure *via* interlayer H-bonding interactions.

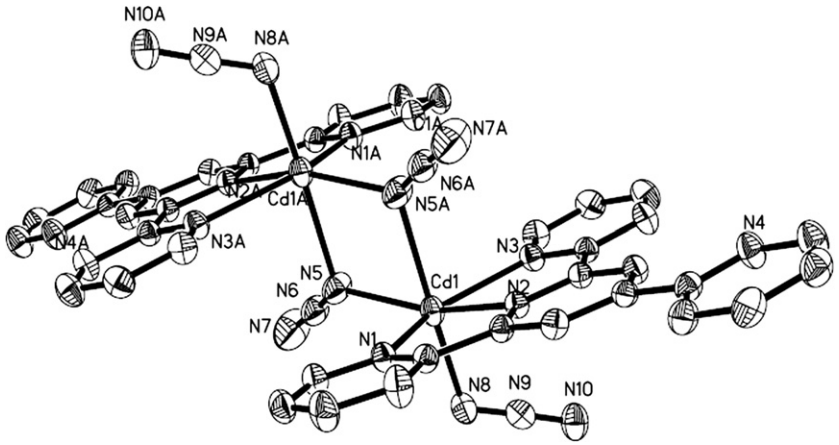


Fig. 6. ORTEP diagram of $[Cd_2(L2)_2(N_3)_4]$, **3** with atom numbering scheme. Ellipsoids are drawn at 30% probability.

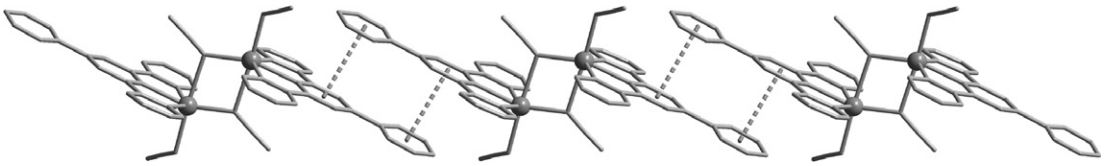


Fig. 7. Structure of the 1D chain in **3** supported by π···π interactions. All H atoms are omitted for clarity.

of L1 in compound **1**. Strikingly, the pendant rings stack with central pyridine on an adjacent molecule (3.724 Å of centroid–centroid), each pair of rings is approximately coplanar and offset. This type of intermolecular face–face aryl interactions links the dimeric units into infinite 1D chain (Fig. 7). The chains are packed together into a 2D plane, however, no short π···π interactions are observed between the chains.

3.2.4. $[Cd_2(L2)_2(SCN)_4]$ (**4**)

Compound **4** is also a dimeric structure (Fig. 8). Each centrosymmetric dimer consists of Cd^{II} ions bridged by double μ-1,3-SCN^- bridges, forming a nearly planar eight-member ring, $Cd(SCN)_2Cd$, with a Cd···Cd separation of 5.898 Å. The coordination environment of each Cd^{II} ion is a distorted octahedron with the equatorial plane defined by three nitrogen atoms from the tridentate sites of one L2 and one S atom from the intra-dimer SCN^- bridge. The axial positions are occupied by two nitrogen atoms from the intra-dimer SCN^- bridges and monocoordinate SCN^- ligand, respectively. The bridging SCN^- ligands are nearly linear with angle of S–C–N 178.92° and bond to Cd^{II} atoms with bent angle of Cd1–N5–C21 152.35° and Cd1–S1–C21 162.09°. The terminal SCN^- ligands themselves bent with angle of S–C–N 174.71° bond to Cd^{II} atoms with bent angle of Cd1–N6–C22 119.34°. Similar to compound **3**, the nitrogen atom at the 2-position from the pendant pyridyl ring does not participant in the coordination. The pendant and central pyridines of L2 are twisted with a dihedral angle 10.03°, two terminal pyridyl rings are twisted with dihedral angles 8.26°, 9.77° respect to the central pyridyl ring. The intermolecular face–face aryl interactions between the terminal terpyridyl rings and the pendant pyridyl rings from adjacent molecules link the dimeric structures into 1D chain (Fig. 9). This kind of stacking way is significantly different from above mentioned structure **3** and no short aryl–aryl interactions are observed between chains.

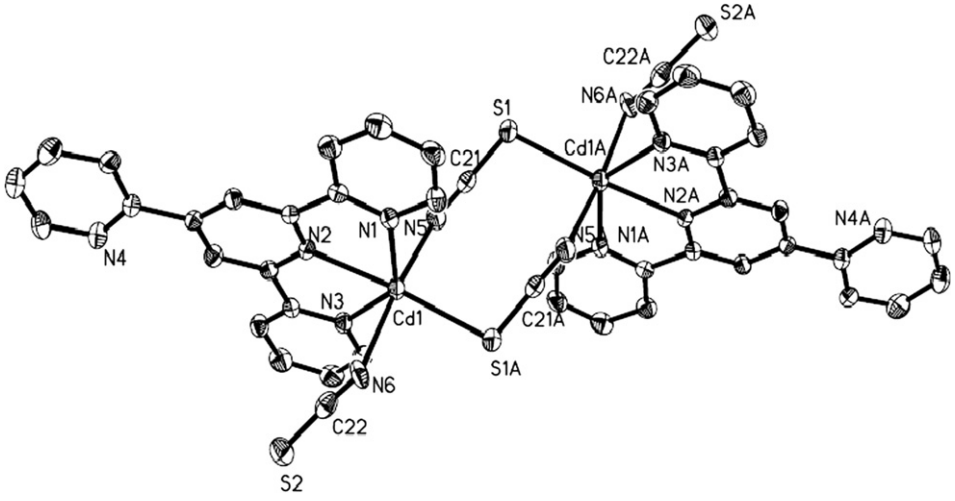


Fig. 8. ORTEP diagram of $[Cd_2(L2)_2(SCN)_4]$, **4** with atom numbering scheme. Ellipsoids are drawn at 30% probability.

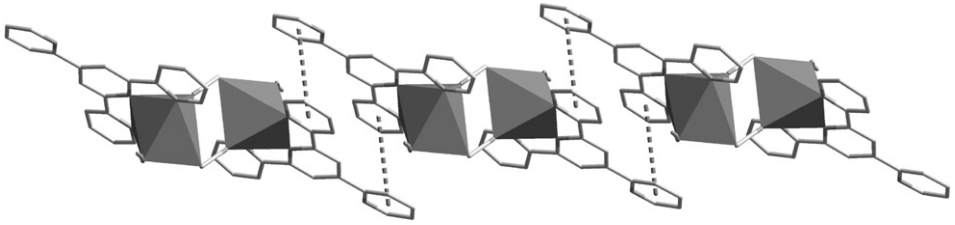


Fig. 9. Structure of the 1D chain in complex **4** supported by π···π interactions. H atoms are omitted for clarity.

3.3. Structural comparison

L1 and L2 are pyridyl substituted terpyridine isomers which are only differ in the position of nitrogen atom at substituted pyridyl ring. However, subtle structural difference may influence the overall metal–organic frameworks. L1 has a bite angle of 120° between mono-dentate and tridentate motifs while L2 has a bite angle of 60°. L1 itself rotates a larger angle between tpy domain and pendant pyridyl ring than L2 because of the repulsion force arising from the central and pendant pyridyl β-hydrogen atoms and thus enjoy less space-crowding than L2. As a result, it is easier for L1 to coordinate a second metal with covalent bond. The pendant pyridyl ring of L2 prefers to be involved in the non-covalent bond unless a serious rotation [20]. Consistent to the above analysis, in compounds **1** and **2**, L1 as mono-tridentate bridging ligand with the corresponding twist angles of 32.35° and 17.80° between central and pendant pyridines, respectively, and links metal atoms into 1D and 2D structures. While in compounds **3** and **4**, L2 as chelating ligand forms the dimeric structures with the corresponding twist angles of 4.79° and 10.03° between central and pendant pyridines, respectively.

Unsubstituted tpy as an excellent chelating ligand has been widely used, which can easily form mononuclear complexes $[M(tpy)_2]^{n+}$[21]. Dance et al. have reported the packing modes of the unsubstituted terpyridyl complexes [22]. Compared to unsubstituted tpy, more types of short $\pi\cdots\pi$ contacts could be observed. Constable and others have discussed the role of aromatic stacking of substituents in the crystal engineering of tpy complexes [5a,5f,7,9,23]. The aromatic stacking interactions were observed in the four compounds (Scheme 2). In compound **1** and **2**, type A interactions exist, in which two adjacent ligands anti-orientation arranged and the central pyridyl ring packs on the adjacent terminal pyridyl ring form tpy unit with centroid–centroid distance 3.904 Å and 3.664 Å, respectively. In compound **3**, dimmers packed together though the pendant rings stack with central pyridine on an adjacent molecule with centroid–centroid distance 3.724 Å as shown in type B. Type C can be found in compound **4**, in which the terminal pyridine contact with pendant pyridyl rings from adjacent molecules with centroid–centroid distance 3.774 Å.

3.4. UV–Vis and luminescent spectra

The UV–Vis absorption of ligands L1, L2 and compounds **1**, **3** and **4** were examined. Compound **2** is insoluble in common organic solvent, so, its UV–Vis spectrum could not be carried out. The UV–Vis absorption bands for L1 in DMF are at ca. 278 and 308 nm while that for L2 at ca. 280 and 318 nm, these two bands are assigned to intraligand π–π^* or n–π^* transition [24]. The absorption bands for compounds **1**, **3** and **4** shift to 284 and 325 nm for **1**, 284 and 327 for **3**, 286 and 328 for **4**, respectively. This kind of shift in the energy may be related to the π orbital being perturbed by the coordination effect of Cd^{II} ion.

Metal–organic polymeric compounds with d^{10} configuration have been found to exhibit photoluminescent properties [25]. The photoluminescent spectra of L1, L2 and complexes **1**–**4** in the solid state at room temperature were examined. The fluorescence emission band for L1 is at ca. 368 nm in the solid state upon excitation at 255 nm, while that for L2 is at ca. 373 nm, which correspond to π–π^* transition [26]. Compounds **1** and **2** exhibit emission peaks at 391 and 402 nm upon excitation at 255 nm, respectively. The emission bands are compared to that of the free L1

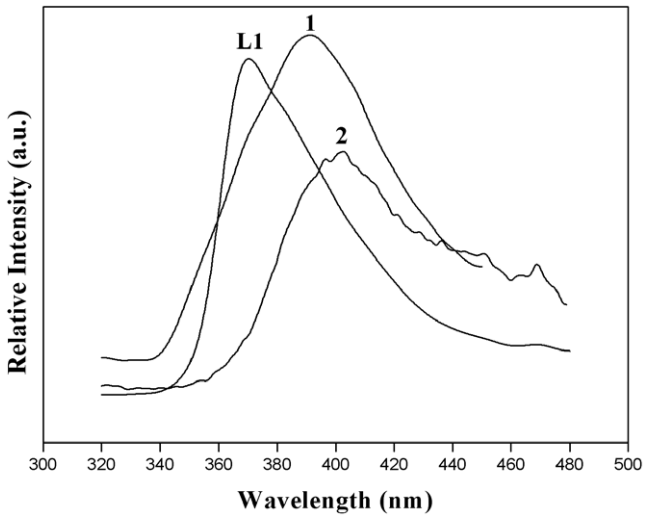
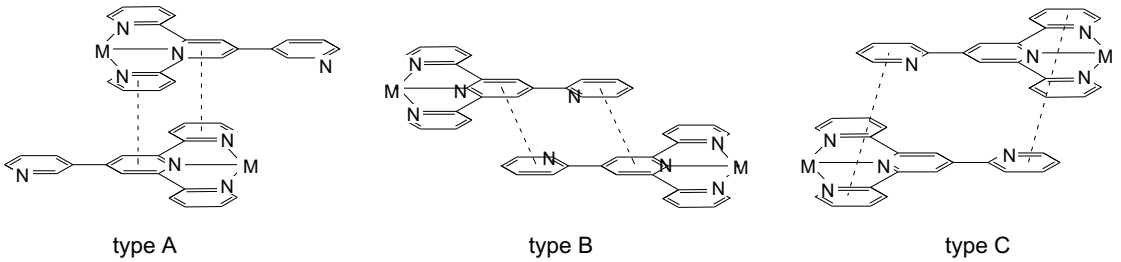


Fig. 10. Emission spectra of L1, **1** and **2** in the solid state at room temperature.



Scheme 2. Stacking motifs observed in the four compounds.

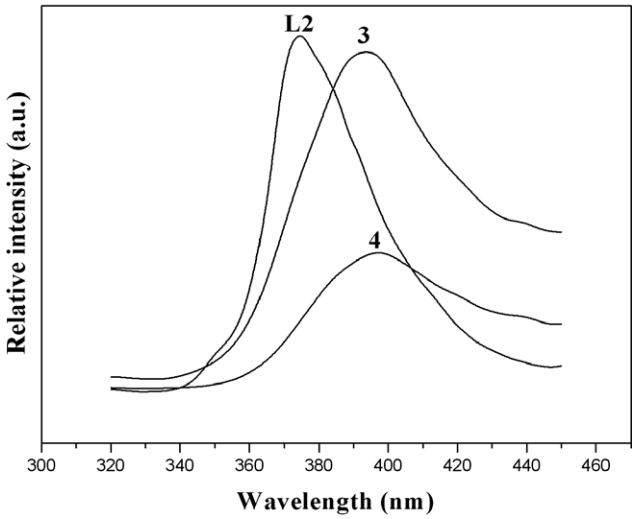


Fig. 11. Emission spectra of L2, **3** and **4** in the solid state at room temperature.

and exhibit red-shift of ca. 23 and 34 nm, suggesting that the emissions of **1** and **2** originated from the intraligand transition (Fig. 10) [27]. Similarly, compounds **3** and **4** exhibit emission peaks at 393 and 397 nm, respectively, which are ca. 20 and 24 nm red-shift to L2. These emissions may also be attributed to the intraligand transition (Fig. 11).

4. Conclusion

In summary, the reaction of Cd^{II} halide or pseudohalide with two terpyridine derived isomers resulted in four novel Cd^{II} coordination compounds. Compound **1** shows a 1D grid-like structure constructed from Cd_3 units with L1 bridges. Compound **2** is a 2D wave-like structure consisting of Cd_4 unit bridged by L1. Compound **3** and **4** are dimeric structures and extends into 1D chains by different types of $\pi\cdots\pi$ stacking interactions. Compared the four structures, we found that two isomers exhibit different coordination behavior under the same reaction conditions and extend structures into diverse dimensionalities. This result undoubtedly indicates that the isomers with different disposition of the coordination atoms do play a dominating role in the construction of crystalline materials. The successful synthesis of these compounds may provide some new information on the selection of suitable organic building blocks for controllable synthesis of desired species with predictable structures and properties.

Acknowledgements

This work was supported by National Natural Science Foundation of China (Grant No. 20573083) and the Natural Science Foundation of the Educational Bureau of Shaanxi Province (Grant No. 07JK385).

Appendix A. Supplementary data

CCDC 626583, 626584, 626585 and 626586 contain the supplementary crystallographic data for **1**, **2**, **3** and **4**. These data can be obtained free of charge via http://www.ccdc.cam.ac.uk/conts/retrieving.html, or from the Cambridge Crystallographic Data Centre, 12 Union Road, Cambridge CB2 1EZ, UK; fax: (+44) 1223-336-033; or e-mail: deposit@ccdc.cam.ac.uk. Supplementary data associated with this article can be found, in the online version, at doi:10.1016/j.poly.2008.01.024.

References

[1] (a) G.F. Swiegers, T.J. Malefetse, Chem. Rev. 100 (2000) 3483;
(b) B. Moulton, M.J. Zaworotko, Chem. Rev. 101 (2001) 1629;
(c) M. Eddaoudi, D.B. Moler, H. Li, B. Chen, T.M. Reineke, M. O'Keeffe, O.M. Yaghi, Acc. Chem. Res. 34 (2001) 319;
(d) S. Leininger, B. Olenyuk, P.J. Stang, Chem. Rev. 100 (2000) 853;
(e) H.K. Chae, D.Y. Siberio-Pérez, J. Kim, Y.B. Go, M. Eddaoudl, A.J. Matzger, M. O'Keeffe, O.M. Yaghi, Nature 427 (2004) 523;
(f) N.L. Rosi, J. Eckert, M. Eddaoudi, D.T. Vodak, J. Kim, M. O'Keeffe, O.M. Yaghi, Science 300 (2003) 1127.
[2] (a) G.-H. Cui, J.-R. Li, J.-L. Tian, X.-H. Bu, S.R. Batten, Cryst. Growth Des. 5 (2005) 1775;
(b) H.-F. Zhu, J. Fan, T. Okamura, W.-Y. Sun, N. Ueyama, Cryst. Growth Des. 5 (2005) 289;
(c) X.-H. Bu, Y.-B. Xie, J.-R. Li, R.-H. Zhang, Inorg. Chem. 42 (2003) 7422;
(d) D.M. Shin, I.S. Lee, D. Cho, Y.K. Chung, Inorg. Chem. 42 (2003) 7722.
[3] (a) R. Vilar, Angew. Chem., Int. Ed. 42 (2003) 1460;
(b) B. Chen, F.R. Fronczek, A.W. Maverick, Chem. Commun. (2003) 2166;
(c) M. Yoshizawa, M. Nagao, K. Umemoto, K. Biradha, M. Fujita, S. Sakamoto, K. Yamaguchi, Chem. Commun. (2003) 1808;
(d) S. Banfi, L. Carlucci, E. Caruso, G. Ciani, D.M. Proserpio, J. Chem. Soc., Dalton Trans. (2002) 2714.
[4] (a) E.C. Constable, Pure Appl. Chem. 68 (1996) 253;
(b) E.C. Constable, R.W. Handel, C.E. Housecroft, A.F. Morales, L. Flamigni, F. Barigelletti, Dalton Trans. (2003) 1220;
(c) O. Johansson, M. Borgström, R. Lomoth, M. Palmblad, J. Bergquist, L. Hammarström, L.C. Sun, B. Åkermark, Inorg. Chem. 42 (2003) 2908;
(d) H. Hofmeier, U.S. Schubert, Chem. Soc. Rev. 33 (2004) 373;
(e) U.S. Schubert, C. Eschbaumer, Angew. Chem., Int. Ed. 41 (2002) 2892;
(f) E.C. Constable, B.A. Hermann, C.E. Housecroft, M. Neuburger, S. Schaffner, L.J. Scherer, New J. Chem. 29 (2005) 1475;
(g) H.S. Chow, E.C. Constable, C.E. Housecroft, M. Neuburger, S. Schaffner, Dalton Trans. (2006) 2881;
(h) J.E. Beves, E.C. Constable, C.E. Housecroft, M. Neuburger, S. Schaffner, E.J. Shardlow, Dalton Trans. (2007) 1593;
(i) S. Encinas, L. Flamigni, F. Barigelletti, E.C. Constable, C.E. Housecroft, E.R. Schofield, E. Figgemeier, D. Fenske, M. Neuburger, J.G. Vos, M. Zehnder, Chem. Eur. J. 8 (2002) 137;
(j) E.C. Constable, C.E. Housecroft, M. Neuburger, S. Schaffner, E.J. Shardlow, Polyhedron 27 (2008) 65;
(k) E.C. Constable, C.E. Housecroft, M. Neuburger, S. Schaffner, E.J. Shardlow, Inorg. Chim. Acta 360 (2007) 4069;
(l) E.C. Constable, Chem. Soc. Rev. 36 (2007) 246.
[5] (a) J. Granifo, M.T. Garland, R. Baggio, Inorg. Chem. Commun. 7 (2004) 77;
(b) H. Feng, X.-P. Zhou, T. Wu, D. Li, Y.-G. Yin, S.W. Ng, Inorg. Chim. Acta 359 (2006) 4027;

(c) J. Paul, S. Spey, H. Adams, J.A. Thomas, Inorg. Chim. Acta 357 (2004) 2827;
(d) S. Hayami, K. Hashiguchi, G. Juhasz, M. Ohba, H. Okawa, Y. Maeda, K. Kato, K. Osaka, M. Takata, K. Inoue, Inorg. Chem. 43 (2004) 4124;
(e) N. Noshiranzadeh, A. Ramazani, A. Morsali, A.D. Hunter, M. Zeller, Inorg. Chim. Acta 360 (2007) 3603;
(f) J.E. Beves, E.C. Constable, C.E. Housecroft, M. Neuburger, S. Schaffner, Inorg. Chem. Commun. 10 (2007) 1185.
[6] W.-J. Shi, L. Hou, D. Li, Y.-G. Yin, Inorg. Chim. Acta 360 (2007) 588.
[7] J.P. López, W. Kraus, G. Reck, A. Thünemann, D.G. Kurth, Inorg. Chem. Commun. 8 (2005) 281.
[8] (a) S.-S. Sun, A.J. Lees, Inorg. Chem. 40 (2001) 3154;
(b) S.-S. Sun, A.S. Silva, I.M. Brinn, A.J. Lees, Inorg. Chem. 39 (2000) 1344.
[9] J.E. Beves, E.C. Constable, C.E. Housecroft, C.J. Kepert, D.J. Price, CrystEngComm 9 (2007) 456.
[10] L. Hou, D. Li, W.-J. Shi, Y.-G. Yin, S.W. Ng, Inorg. Chem. 44 (2005) 7825.
[11] S.-S. Zhang, S.-Z. Zhan, M. Li, R. Peng, D. Li, Inorg. Chem. 46 (2007) 4365.
[12] E.C. Constable, C.E. Housecroft, M. Neuburger, S. Schaffner, F. Schaper, Inorg. Chem. Commun. 9 (2006) 616.
[13] (a) K.J. Arm, W. Leslie, J.A.G. Williams, Inorg. Chim. Acta 359 (2006) 1222;
(b) W. Goodall, J.A.G. Williams, J. Chem. Soc., Dalton Trans. (2000) 2893;
(c) E.C. Constable, C.E. Housecroft, M. Neuburger, S. Schaffner, F. Schaper, Inorg. Chem. Commun. 9 (2006) 433.
[14] F. Kröhnke, Synthesis (1976) 1.
[15] G.M. Sheldrick, SHELXS, Program for the Refinement of Crystal Structures, University of Göttingen, Germany, 1997.
[16] L. Shen, Y.Z. Xu, J. Chem. Soc., Dalton Trans. (2001) 3413.
[17] R. Cortés, J.L. Pizarro, L. Lezama, M.I. Arriortua, T. Rojo, Inorg. Chem. 33 (1994) 2697.
[18] (a) L. Yi, B. Ding, B. Zhao, P. Cheng, D.-Z. Liao, S.-P. Yan, Z.-H. Jiang, Inorg. Chem. 43 (2004) 33;
(b) N.A. Bell, T.D. Dee, M. Goldstein, I.W. Nowell, Inorg. Chim. Acta 65 (1982) L87.
[19] L.-Y. Wang, B. Zhao, C.-X. Zhang, D.-Z. Liao, Z.-H. Jiang, S.-P. Yan, Inorg. Chem. 42 (2003) 5804.
[20] L. Hou, D. Li, S.W. Ng, Acta Crystallogr., Sect. E 61 (2005) M21.
[21] (a) R. Allmann, W. Henke, D. Reinen, Inorg. Chem. 17 (1978) 378;
(b) J.V. Folgado, W. Henke, R. Allmann, H. Stratemeier, D. Beltrán-Porter, T. Rojo, D. Reinen, Inorg. Chem. 29 (1990) 2035;
(c) J.-P. Collin, I.M. Dixon, J.-P. Souvage, J.A.G. Williams, F. Barigelletti, L. Flamigni, J. Am. Chem. Soc. 121 (1999) 5009.
[22] M.L. Scudder, H.A. Godwin, I.G. Dance, New J. Chem. 23 (1999) 695.
[23] N.W. Alcock, P.R. Barker, J.M. Haider, M.J. Hannon, C.L. Painting, Z. Pikramenou, E.A. Plummer, K. Rissanen, P. Saarenketo, J. Chem. Soc., Dalton Trans. (2000) 1447.
[24] (a) X. Shi, G. Zhu, X. Wang, G. Li, Q. Fang, X. Zhao, G. Wu, G. Tian, M. Xue, R. Wang, S. Qiu, Cryst. Growth Des. 5 (2005) 341;
(b) X.-J. Liu, Q.-R. Fang, G.-S. Zhu, M. Xue, X. Shi, G. Wu, G. Tian, S.-L. Qiu, L. Fang, Inorg. Chem. Commun. 7 (2004) 31.
[25] H. Zhu, M. Ströbele, Z. Yu, Z. Wang, H.-J. Meyer, X.Z. You, Inorg. Chem. Commun. 4 (2001) 577.
[26] J.-R. He, Y.-L. Wang, W.-H. Bi, Y.-Q. Wang, R. Cao, Polyhedron 25 (2006) 1239.
[27] (a) L.Y. Zhang, G.F. Liu, S.L. Zheng, B.H. Ye, X.M. Zhang, X.M. Chen, Eur. J. Inorg. Chem. (2003) 2965;
(b) W. Goodall, K. Wild, K.J. Arm, J.A.G. Williams, J. Chem. Soc., Perkin Trans. 2 (2002) 1669;
(c) R.X. Yuan, R.G. Xiong, Y.L. Xie, X.Z. You, S.M. Peng, G.H. Lee, Inorg. Chem. Commun. 4 (2001) 384.

2. Experimental

2.1. General procedures

Melting points were determined using an Electrothermal melting point apparatus and are uncorrected. Elemental analyses were performed by the Campbell microanalytical laboratory at the University of Otago. Ligands **1**–**3** were prepared by literature procedures [7,9b]. Solvents were purified according to standard procedures. Other reagents were obtained from commercial sources and used as supplied.

2.2. Complexes of 2,2′-biquinazoline (*1*)

2.2.1. Preparation of silver(I) nitrate complex *4*

Reaction of **1** (12.6 mg, 0.049 mmol) in methanol with silver nitrate (17.0 mg, 0.10 mmol) in methanol gave a yellow precipitate. Yield 15.1 mg (48%), m.p. >250 °C (dec.). *Anal.* Calc. for $C_{16}H_{10}N_4Ag_2(NO_3)_2 \cdot H_2O \cdot MeOH$ C, 31.51; H, 2.49; N, 12.97. Found: C, 31.39; H, 2.47; N, 13.08%.

2.2.2. Preparation of palladium(II) chloride complex *5*

Reaction of **1** (13.0 mg, 0.05 mmol) dissolved in hot acetone and a methanolic solution of 0.151 M Li_2PdCl_4 (0.7 ml, 0.10 mmol) gave a yellow crystalline solid. Yield 19.0 mg (95%), m.p. > 300 °C (dec.). *Anal.* Calc. for $C_{16}H_{10}N_4PdCl_2 \cdot 1/2MeOH$: C, 43.88; H, 2.68; N, 12.41. Found: C, 43.69; H, 2.40; N, 12.17%. ^1H NMR (500 MHz, DMSO): δ 10.30 (2H, s, H4), 8.73 (2H, d), 8.51 (4H, m), 8.16 (2H, t, H). Single crystals were grown by immersion of a Li_2PdCl_4 solution in a solution of **1**.

2.2.3. Preparation of copper(II) chloride complex *6*

Reaction of **1** (12.8 mg, 0.05 mmol) in methanol with copper(II) chloride (17.1 mg, 0.10 mmol) in methanol gave a green precipitate. Crystals suitable for X-ray structure analysis were grown from diffusion of acetonitrile into a DMF solution of the complex. Yield 20.7 mg (95%), m.p. 279 °C. *Anal.* Calc. for $C_{16}H_{10}N_4CuCl_2 \cdot 2/3DMF$: C, 48.98; H, 3.35; N, 14.81. Found: C, 48.67; H, 3.13; N, 15.18%.

2.2.4. Preparation of copper(I) iodide complex *7*

Reaction of **1** (12.9 mg, 0.05 mmol) in methanol with copper(I) iodide (19.7 mg, 0.10 mmol) in acetonitrile gave a black precipitate. Yield 21.0 mg (66%), m.p. >280 °C. *Anal.* Calc. for $C_{16}H_{10}N_4Cu_2I_2 \cdot 1/2MeOH$ C, 30.26 H, 1.45; N, 8.55. Found: C, 30.54; H, 1.45; N, 8.26%.

2.2.5. Preparation of cadmium(II) nitrate complex *8*

Reaction of **1** (12.8 mg, 0.05 mmol) dissolved in dichloromethane with cadmium nitrate (31.4 mg, 0.10 mmol) dissolved in hot methanol gave a colourless solution. A colourless crystalline solid appeared on cooling. Yield 24.1 mg (71%). *Anal.* Calc. for $C_{16}H_{10}N_8O_{12}Cd_2 \cdot H_2O$: C, 25.55; H, 1.67; N, 14.96. Found: C, 25.50; H, 1.67; N, 14.87%. Crystals suitable for X-ray diffraction were obtained by recrystallisation from 1:1 $MeOH/H_2O$.

2.3. Complexes of 4,4′-biquinazoline (*2*)

2.3.1. Preparation of silver(I) nitrate complex *9*

Reaction of **2** (12.8 mg, 0.05 mmol) in acetone with silver(I) nitrate (17.2 mg, 0.10 mmol) in methanol gave a white precipitate. Yield 8.1 mg (34%), m.p. >250 °C (dec.). *Anal.* Calc. for $C_{32}H_{20}N_{11}O_9Ag_3 \cdot 1/2(CH_3)_2CO$: C, 38.13; H, 2.20; N, 14.60. Found: C, 38.03; H, 2.27; N, 14.61%.

2.3.2. Preparation of palladium(II) chloride complex *10*

Reaction of **2** (12.8 mg, 0.050 mmol) in acetonitrile with a methanolic solution of 0.151 M Li_2PdCl_4 (0.7 ml, 0.10 mmol) gave a yellow solid. Yield 17.4 mg (72%), m.p. >330 °C. *Anal.* Calc. for $C_{16}H_{10}N_4PdCl_2 \cdot MeOH$: C, 43.66; H, 3.02; N, 11.98. Found: C, 43.31; H, 3.31; N, 12.25%.

2.3.3. Preparation of copper(II) chloride complex *11*

Reaction of **2** (12.8 mg, 0.05 mmol) in acetone with copper(II) chloride (17.4 mg, 0.10 mmol) in acetonitrile gave a green solution. Small green crystals appeared on standing overnight. Yield 11.1 mg (53%), m.p. >200 °C (dec.). *Anal.* Calc. for $C_{16}H_{10}N_4CuCl_2 \cdot 1/2CH_3CN \cdot 1/3(CH_3)_2CO$: C, 49.95; H, 3.22; N, 14.56. Found: C, 49.91; H, 2.90; N, 14.68%.

2.4. Complexes of 2,2′-biquinoxaline (*3*)

2.4.1. Preparation of silver(I) nitrate complex *12*

Reaction of **3** (13.3 mg, 0.051 mmol) in dichloromethane (10 ml) with silver(I) nitrate (17.4 mg, 0.10 mmol) in methanol (10 ml) gave an orange solution. Orange crystals suitable for X-ray structure analysis were obtained from this solution on standing. Yield 16.2 mg (74%), m.p. 199–201 °C. *Anal.* Calc for $C_{16}H_{10}N_5O_3Ag$: C, 44.88; H, 2.39; N, 16.36. Found: C, 44.75; H, 2.47; N, 15.99%.

2.4.2. Preparation of copper(II) chloride complex *13*

Reaction of **3** (13.3 mg, 0.052 mmol) with copper(II) chloride (18.5 mg, 0.107 mmol) in methanol gave a dark green crystalline solid. Yield 18.5 mg (84.6%), m.p. >350 °C. *Anal.* Calc. for $C_{16}H_{10}N_4CuCl_2 \cdot MeOH \cdot 1/2H_2O$: C, 47.08; H, 3.59; N, 12.92. Found: C, 46.94; H, 3.27; N, 12.65%. Crystals suitable for X-ray crystal structure analysis were obtained by layering a methanol solution of copper(II) chloride onto a dichloromethane solution of **3**.

2.4.3. Preparation of copper(I) iodide complex *14*

Reaction of **3** (12.9 mg, 0.05 mmol) in acetone with copper(I) iodide (19.7 mg, 0.10 mmol) in acetonitrile gave a black precipitate. Yield 19.4 mg (65%), m.p. >300 °C. *Anal.*

Table 1
Crystal data and X-ray experimental details for **5**, **6**, **8**, **12**, **13**, **14**, **15**

Compound	**5**	**6**	**8**	**12**	**13**	**14**	**15**
Empirical formula	$C_{16}H_{10}N_4Cl_2Pd$	$C_{37}H_{31}N_{10}O_2Cl_4Cu_2$	$C_{17}H_{16}N_6O_8Cd$	$C_{16}H_{10}N_5O_3Ag$	$C_{17}H_{14}N_4OCl_2Cu$	$C_{32}H_{20}N_8Cu_2I_2$	$C_{53}H_{44}N_5O_5P_2Cu$
Formula weight	435.58	916.60	544.76	428.16	424.76	897.44	956.41
T (K)	163(2)	168(2)	163(2)	163(2)	163(2)	163(2)	153(2)
Crystal system	orthorhombic	monoclinic	monoclinic	monoclinic	monoclinic	triclinic	triclinic
Space group	*Pbcn*	*C2/c*	$P2_1/n$	$P2_1/n$	$P2_1/c$	$P\bar{1}$	$P\bar{1}$
Unit cell dimensions							
a (Å)	10.253(3)	17.248(8)	7.313(2)	5.204(2)	6.422(3)	8.803(3)	12.753(7)
b (Å)	20.818(7)	11.026(5)	19.961(7)	18.144(8)	17.547(9)	9.075(3)	14.889(8)
c (Å)	7.096(2)	21.533(10)	13.306(4)	16.841(7)	15.140(8)	10.273(3)	15.340(8)
α (°)	90	90	90	90	90	88.022(4)	69.043(7)
β (°)	90	112.869(6)	97.533(5)	98.400(5)	100.063(7)	65.351(4)	88.944(7)
γ (°)	90	90	90	90	90	79.028(4)	65.952(8)
V (Å^3)	1514.6(8)	3773(3)	1925.6(11)	1573.0(12)	1679.8(15)	731.4(4)	2456(2)
Z	4	4	4	4	4	1	2
D_{calc} (Mg/m^3)	1.910	1.614	1.879	1.808	1.680	2.038	1.293
Absorption coefficient (mm^{-1})	1.581	1.461	1.197	1.309	1.631	3.604	0.562
F(000)	856	1860	1088	848	860	432	992
Crystal size (mm)	0.52 × 0.24 × 0.01	0.34 × 0.19 × 0.02	0.47 × 0.15 × 0.08	0.50 × 0.14 × 0.10	0.27 × 0.10 × 0.03	0.35 × 0.20 × 0.03	0.39 × 0.17 × 0.11
θ Range for data collection (°)	2.21–26.37	2.05–26.37	1.85–26.41	2.24–26.41	2.32–26.40	2.18–26.00	1.77–25.00
Reflections collected	13 169	23 865	24 163	19 251	21 107	8962	28 694
Independent reflections (R_{int})	1535 (0.0399)	3843 (0.0679)	3926 (0.0304)	3179 (0.0385)	3411 (0.0676)	2812 (0.0165)	8543 (0.0822)
Observed reflections [$I > 2\sigma(I)$]	1106	2549	3436	2433	2039	2550	4213
Data/restraints/parameters	1535/0/105	3843/31/274	3926/0/298	3179/0/226	3411/0/229	2812/0/199	8543/91/642
Goodness-of-fit on F^2	1.017	1.030	1.081	0.959	0.922	1.029	0.966
R_1 [$I > 2\sigma(I)$]	0.0228	0.0492	0.0211	0.0298	0.0367	0.0237	0.0758
wR_2 (all data)	0.0603	0.0812	0.0260	0.0742	0.0966	0.0635	0.2456

Calc. for $C_{32}H_{20}N_8Cu_5I_5 \cdot 1/2(CH_3)_2CO$: C, 26.87; H, 1.55; N, 7.57. Found: C, 27.14; H, 1.34; N, 7.57%. Recrystallisation of this black solid from DMSO gave deep red square plates.

2.4.4. Preparation of bistriphenylphosphinecopper(I) nitrate complex *15*

Reaction of **3** (12.7 mg, 0.049 mmol) in methanol (10 ml) with bis(triphenylphosphine)copper(I) nitrate (65.0 mg, 0.10 mmol) in methanol (10 ml) gave a red solution, which on slow evaporation furnished large red crystals. Yield 32.6 mg (73%), m.p. 210–212 °C. *Anal.* Calc. for $C_{52}H_{40}N_5O_3P_2Cu \cdot 1/2MeOH$: C, 68.22; H, 4.58; N, 7.58. Found: C, 68.19; H, 4.61; N, 7.46%.

2.4.5. Preparation of cadmium(II) chloride complex *16*

Reaction of **3** (13.3 mg, 0.05 mmol) dissolved in hot dichloromethane with cadmium chloride (17.4 mg, 0.10 mmol) dissolved in hot methanol gave a white precipitate immediately. The precipitate was filtered off and washed (2 × 2 ml MeOH). Yield 15.3 mg (69%), m.p. 278–280 °C. *Anal.* Calc. for $C_{16}H_{10}N_4CdCl_2$: C, 43.52; H, 2.28; N, 12.69. Found: C, 43.59; H, 2.51; N, 12.61%.

2.5. X-ray crystallography

The crystal data and details of the data collections and refinements for the X-ray structures are listed in Table 1. Measurements were made with a SMART CCD area detector using graphite-monochromatized Mo Kα ($\lambda =$ 0.71073 Å) radiation. The structures were solved by direct methods using SHELXS [13] and refined on F^2 using all data by full-matrix least-squares procedures with SHELXL-97 [14]. Non-hydrogen atoms were refined with anisotropic displacement parameters. Hydrogen atoms were included in calculated positions with isotropic displacement parameters 1.2 times the isotropic equivalent of their carrier atoms. The functions minimised were $\sum w(F_o^2 - F_c^2)$, with $w = [\sigma_2(F_o^2) + aP_2 + bP]^{-1}$, where $P = [\max(F_o)^2 + 2F_c^2]/3$.

3. Results and discussion

We decided to explore the coordination chemistry of ligands **1**–**3** by examining their reactions with a selection of late transition metals. For this purpose we chose silver(I), palladium(II), copper(II), copper(I) and cadmium(II) reagents, since we have previously found that these metals lead to a diverse array of interesting metallosupramolecular assemblies [4]. In each case, the ligand was reacted with 2 equiv. of the metal reactant, in an attempt to induce the highest nuclearity of the resulting assemblies.

2,2′-Biquinazoline (**1**) is structurally related to 2,2′-bipyrimidine, which is well known to form binuclear complexes in which two metals are held together with a separation of *ca* 5.5 Å [15]. However, ligand **1** differs in that not all the nitrogens are symmetrically equivalent, there being two more hindered nitrogens adjacent to the fused benzo rings. As a consequence of this reduced symmetry there are three possible chelating modes of coordination in a mononuclear complex (Fig. 1) depending on which nitrogens are coordinated. Similarly, there are two possible coordination modes for a homobinuclear complex. Such unsymmetrical derivatives of 2,2′-bipyrimidine have been surprisingly ignored by coordination chemists [16].

Reaction of **1** with silver nitrate led to a complex **4** in moderate yield that was shown by elemental analysis to have a 2:1 M:L ratio. Despite numerous attempts to grow

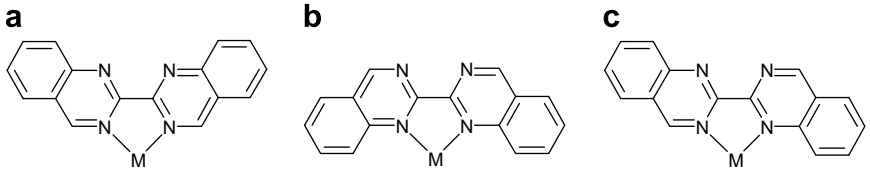


Fig. 1. The three possible modes of chelation by **1**.

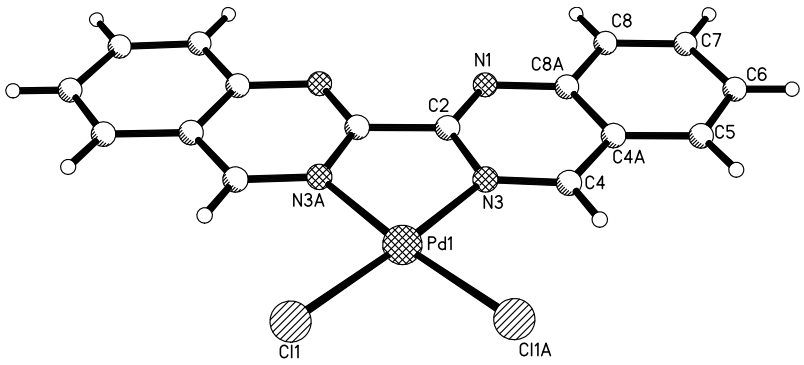


Fig. 2. Perspective view of **5**. Selected bond lengths (Å) and angles (°): Pd1–N3 2.027(2), Pd1–Cl1 2.2925(9), N3–Pd1–N3A 80.72(13), N3–Pd1–Cl1A 94.34(7), N3–Pd1–Cl1 174.85(7), Cl1–Pd1–Cl1A 90.63(5).

crystals of this complex, none were formed and the complex was shown by NMR to dissociate in donating solvents, such as acetonitrile. Reaction of **1** with lithium tetrachloropalladate gave, in high yield, a palladium complex **5** that was soluble in DMSO and showed a significant downfield shift of the H4 singlet in the ^{1}H NMR spectrum, relative to the free ligand. This suggested that this proton lies close to the chlorine atoms and hence that the ligand chelates in mode (a) of Fig. 1. In order to confirm this, a single crystal X-ray structure determination was carried out.

The palladium complex **5** crystallises in the orthorhombic space group *Pbcn*, with half a molecule in the asymmetric unit, the other half being generated by a twofold rotation axis. A perspective view of the structure is shown in Fig. 2, which reveals that the ligand binds to the metal

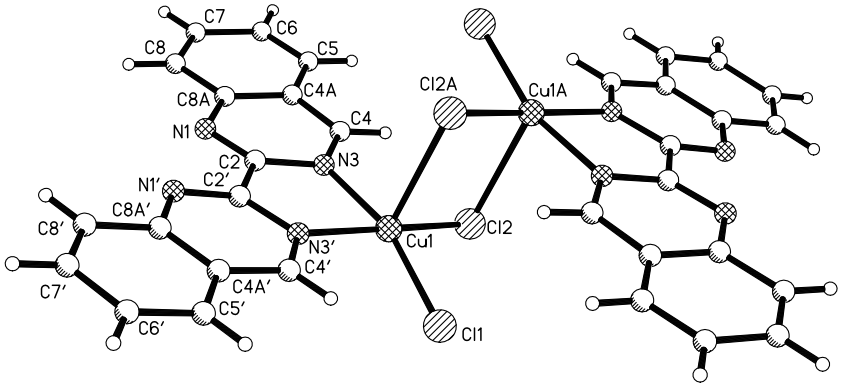


Fig. 3. Perspective view of **6**, with the molecular labelling shown; solvate molecules have been removed for clarity. Selected bond lengths (Å) and bond angles (°): Cu1–N3′ 2.024(4), Cu1–N3 2.033(4), Cu1–Cl1 2.258(2), Cu1–Cl2 2.270(2), Cu1–Cl2A 2.694(2), N3′–Cu1–N3 79.7(2), N3′–Cu1–Cl1 92.84(13), N3–Cu1–Cl1 163.85(13), N3′–Cu1–Cl2 169.60(13), Cl1–Cu1–Cl2 93.51(6), N3′–Cu1–Cl2A 96.38(13), Cl1–Cu1–Cl2A 104.49(6), Cu1–Cl2–Cu1A 90.01(5).

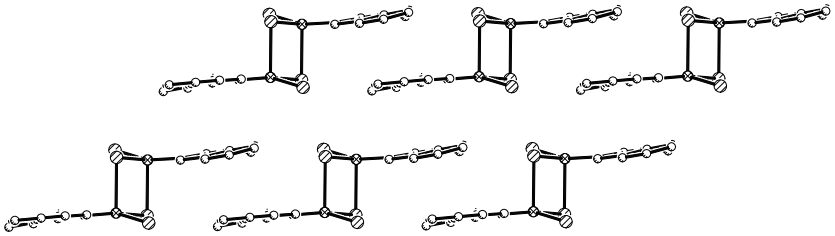


Fig. 4. View of the packing of **6**; DMF, water solvate molecules and hydrogen atoms have been removed for clarity.

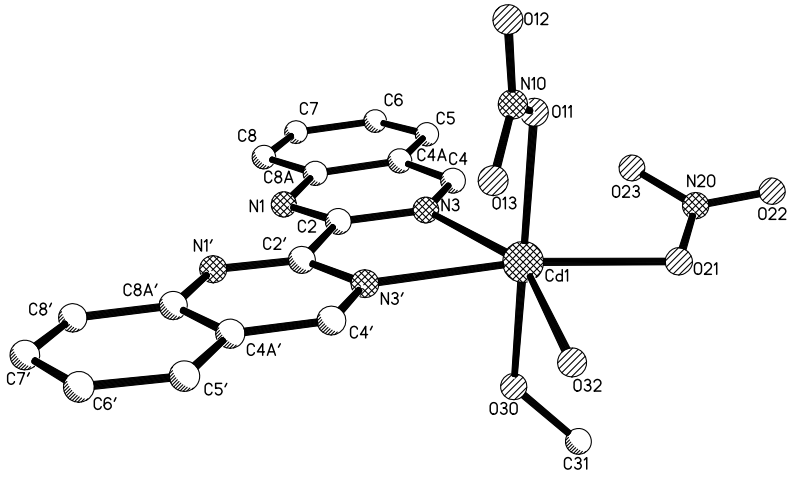


Fig. 5. Perspective view of the asymmetric unit of **8**; hydrogen atoms have been removed for clarity. Selected bond lengths (Å) and angles (°): Cd1–N3′ 2.394 (2), Cd1–N3 2.398(2), Cd1–O30 2.306(2), Cd1–O21 2.309(2), Cd1–O11 2.311(2), Cd1–O32 2.328(2), N3′–Cd1–N3 69.54(6), O30–Cd1–O21 89.64(6), O30–Cd1–O11 168.30(7), O30–Cd1–O32 87.12(8), O30–Cd1–N3′ 89.73(6), O30–Cd1–N3 80.89(7).

through the least hindered nitrogens, as suggested by the NMR results. The bond lengths to the palladium atom are similar to those in the palladium chloride complex of 2,2′-bipyridine [17]. The molecules of **1** are planar (mean deviation from plane: 0.018(5) Å), and the molecules pack in alternating columns.

A 1:1 copper(II) chloride complex **6** was obtained by reaction of **1** with $CuCl_2$ in methanol. Recrystallisation by diffusion of acetonitrile into a DMF solution of this compound furnished crystals suitable for X-ray structure determination. Fig. 3 shows the structure of **6**, which crystallises in the monoclinic space group $C2/c$. The asymmetric unit contains one molecule of **1**, one $CuCl_2$, one-third of a water molecule, and disordered DMF molecules with occupancies of one-half and two-thirds. The complex has a 1:1 M:L ratio but is binuclear, with two chlorine atoms bridging two copper atoms, having a Cu···Cu separation of 3.521(2) Å. The two halves of the complex are related by a crystallographic centre of inversion. Again ligand **1** chelates the metal using the least hindered nitrogens. The copper atom has square-pyramidal geometry with two nitrogens, monodentate and bridging chlorides in the basal plane, and a bridging chloride at the apex. The copper atom is positioned 0.263(6) Å out of the basal plane towards the apical chlorine. The Cu–Cl bond lengths for the bridging and non-bridging chlorines are both within the normal range for structures of this type [18].

The binuclear copper units pack in strips, shown in Fig. 4, with the edges of the coplanar aromatic rings adjacent and 3.269(4) Å apart. A partially occupied DMF solvate molecule shares the space between the binuclear units of the strips with a water molecule, the DMF occurring two-thirds of the time. The strips organize in layers with the centroid of one of the fused pyrimidine rings of the ligand lying 3.471(4) Å above the midpoint of the C4A–C8A bond of another, indicating a weaker π–π interaction than occurs within the strips. Another DMF molecule lies on a mirror plane in the space between the strips.

Reaction of **1** with copper(I) iodide gave a product **7** with a 2:1 M:L ratio, which was extremely insoluble and probably polymeric. Reaction with cadmium(II) nitrate gave a product that was also shown to have a 2:1 M:L ratio. However, recrystallisation of this from a methanol/water mixture furnished crystals with a 1:1 ratio, the structure of which is shown in Fig. 5.

This mononuclear complex **8** crystallises in the monoclinic space group $P2_1/n$. Once again the ligand chelates the metal through the least hindered nitrogens. The cadmium is hexacoordinate with the remaining sites occupied by oxygen atoms of two monodentate nitrates and coordinated water and methanol molecules. Compared to the two previous structures the bite angle subtended by the ligand is considerably reduced, due to the much longer M–N bond lengths.

In the solid state, the mononuclear cadmium units assemble into hydrogen bonded dimers about a centre of inversion, as shown in Fig. 6. The non-coordinated nitrogens of **1** interact with the hydroxyl hydrogen of the coordinated methanol of the adjacent unit. The bifurcated hydrogen is slightly closer to one of the two nitrogens, with H30A lying 2.30(3) Å from N1 and 2.55(3) Å from N1′. These hydrogen bonds distort the coordination geometry of the cadmium by pulling the methanol towards the hindered nitrogens of the adjacent molecule, which results in an O30–Cd1–O11 angle of 168.28(7)°. The dimers are also held together by π–π stacking between the coplanar rings of **1**, which are separated by 3.369(6) Å. Within the crystal further intermolecular aggregation occurs through more conventional [19,20] hydrogen bonds from each of the coordinated water hydrogen atoms to nitrate oxygens of adjacent units.

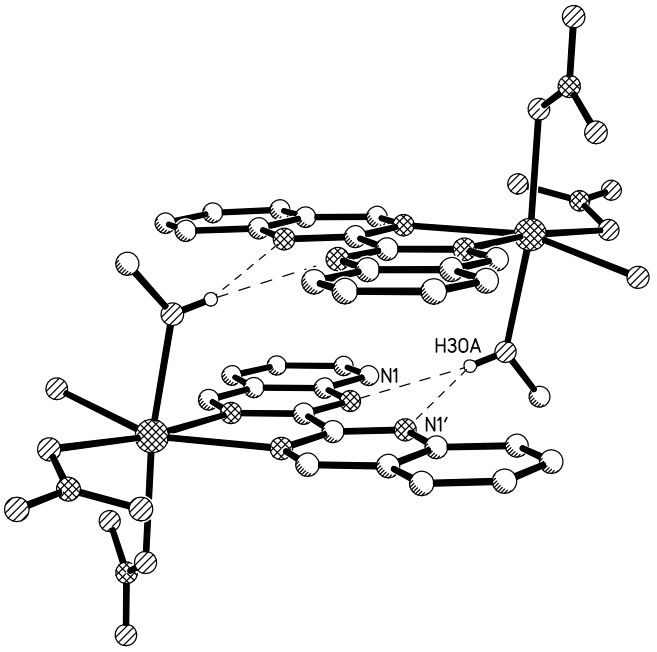


Fig. 6. Perspective view of a dimer of **8**, with the hydrogen bonding of H30A shown.

Having established that 2,2′-biquinazoline (**1**) prefers to form mononuclear complexes through chelation using the less hindered nitrogens, we next turned our attention to the coordination chemistry of the regioisomer 4,4′-biquinazoline (**2**). As shown in Fig. 7, this ambivergent ligand can be viewed as having the combined features of the divergent ligand 4,4′-biquinoline (**a**) and the convergent ligand 1,1′-biisoquinoline (**b**). 4,4′-Biquinoline is a linear bridging ligand, similar to the well studied 4,4′-bipyridine [15]. 1,1′-Biisoquinoline exists in a non-planar form due to the steric

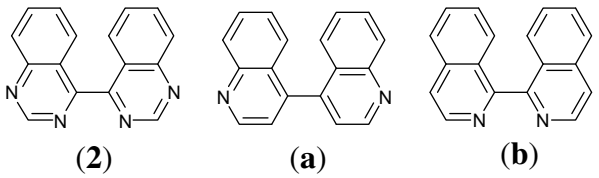


Fig. 7. Relationship of **2** to 4,4′-biquinoline (**a**) and 1,1′-biisoquinoline (**b**).

interaction between H8 and H8′, which leads to the formation of an atropisomeric mixture. The coordination chemistry of 1,1′-biisoquinoline is dominated by this non-planarity, which also distorts the chelate ring of the complexes formed [21] and allows 1,1′-biisoquinoline to bridge two metals [22]. The crystal structure of **2** has shown that

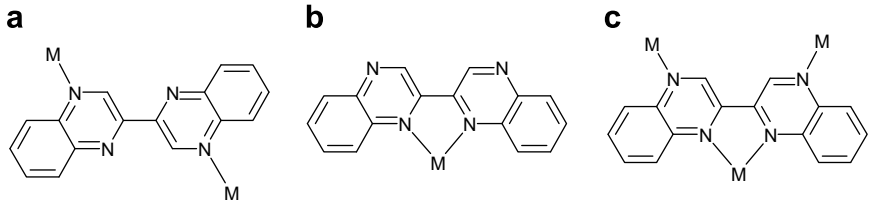


Fig. 8. Potential modes of coordination available to **3**.

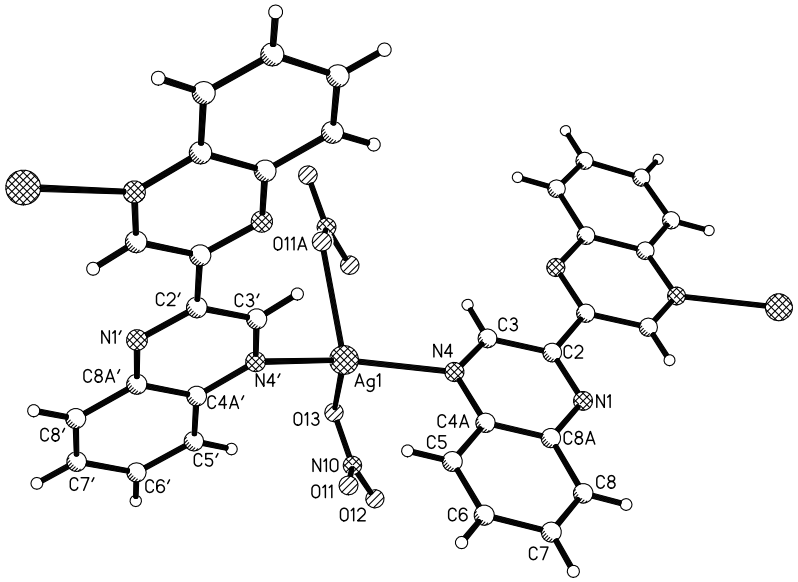


Fig. 9. Perspective view and atom labelling of **12**. Selected bond lengths (Å) and bond angles (°): Ag1–N4′ 2.303(2), Ag1–N4 2.308(2), Ag1–O11A 2.501(3), Ag1–O13 2.590(2), N4′–Ag1–N4 140.85(8), N4′–Ag1–O11 81.77(9), N4–Ag1–O11 106.86(9), N4′–Ag1–O13 119.92(8), N4–Ag1–O13 91.08(8), O11A–Ag1–O13 116.16(8).

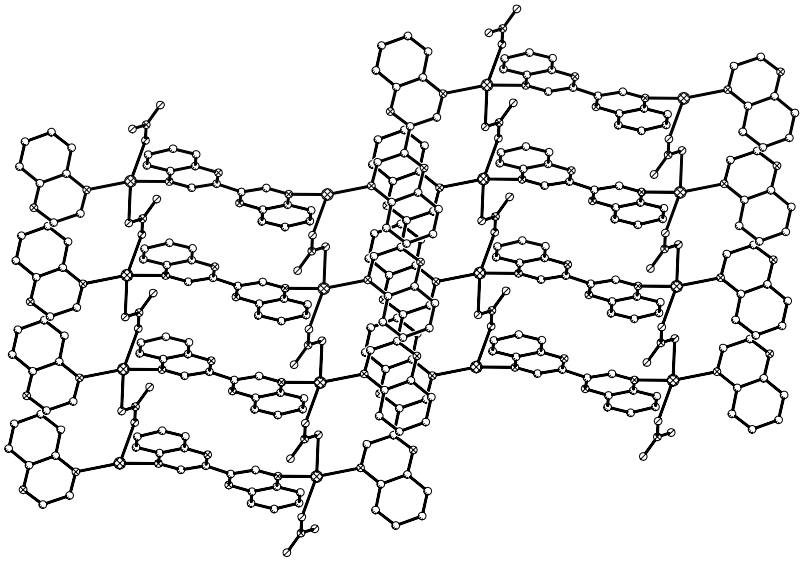


Fig. 10. View of the two-dimensional polymeric nature of **12**, showing the bridging nitrates and the π–π stacking between the aromatic ligands.

the molecule is twisted in this way, and formation of complexes from this non-planar ligand could allow interesting structures to form.

The coordination chemistry of **2** was investigated by the formation of complexes with $AgNO_3$, $PdCl_2$ and $CuCl_2$. Reaction with silver nitrate produced a complex **9** that analysed with an intriguing 2:3 ligand–metal stoichiometry. Such a ligand–metal ratio was observed in three silver complexes of 2,2′-dimethyl-4,4′-bipyrimidine, a molecule similar to **2** [23]. These complexes were polymeric, with the ligands being tetradentate with both the chelating and bridging sites occupied. Unfortunately, no crystals of **9** were obtained from attempted recrystallisations. Reaction with Li_2PdCl_4 produced a 1:1 complex **10** that was highly insoluble and not further investigated. Reaction with copper(II) chloride produced a crystalline 1:1 complex **11** but, alas, the crystals were too small for X-ray structure determination. Thus, in the absence of crystallographic evidence we are unable to confirm the structure of any complex of **2**.

2,2′-Biquinoxaline (**3**) is also an ambivergent ligand. The free ligand itself exists in a *transoid* conformation [12] in which case it would be expected to act as a divergent, "stepped-linear" bridging ligand, with coordination by the less hindered nitrogens [24], as shown in Fig. 8a. Unlike **1** and **2**, in order to chelate to a metal it must use the more hindered nitrogens and convert to the *cisoid* conformation (Fig. 8b). Finally, it could use all four available nitrogens and act in an ambivergent manner (Fig. 8c).

The coordination chemistry of **3** was investigated *via* the synthesis of complexes using $AgNO_3$, $CuCl_2$, CuI, $Cd(NO_3)_2$ and $Cu(PPh_3)_2NO_3$. The silver nitrate complex **12** was isolated as orange crystals in good yield. It has a two-dimensional polymeric structure, and crystallises in the monoclinic space group $P2_1/n$. The asymmetric unit contains two independent half molecules of ligand **3** and one silver nitrate unit (Fig. 9). The organic ligands both lie with centres of inversion at the midpoint of the interring bond and are consequently planar and in *transoid* conformations. The coordination mode is that shown in Fig. 8a, wherein the organic ligand acts as a "stepped-linear" bridge between two silver atoms separated by 10.088(1) Å.

The geometry of the silver atom can best be described as distorted tetrahedral, with the largest deviation from ideal geometry being an angle of 140.85(8)° subtended by the two coordinated nitrogens. The silver atoms are also bridged by nitrate anions, which separate them by a distance of 5.204(2) Å. This results in a two-dimensional network (Fig. 10), within which the coplanar rings of both the

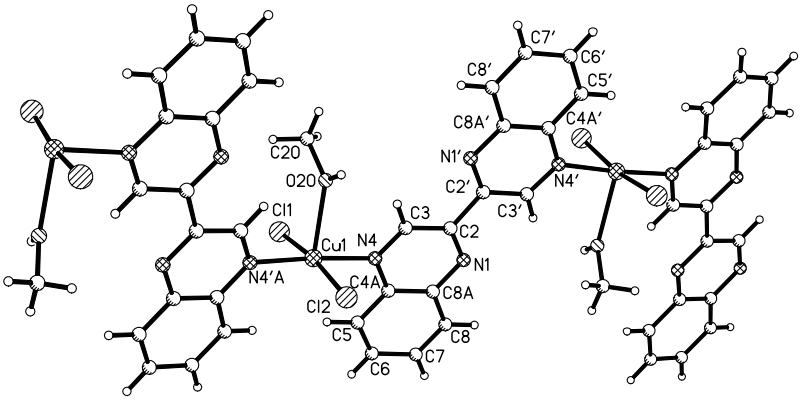


Fig. 11. Perspective view of **13**, with the atomic labelling shown. Selected bond lengths (Å) and bond angles (°): Cu1–N4 2.030(3), Cu1–N4′A 2.038(3), Cu1–Cl2 2.259(1), Cu1–Cl1 2.276(1), Cu1–O20 2.390(3), N4–Cu1–N4′A 176.1(1), N4–Cu1–Cl2 89.1(1), N4′A–Cu1–Cl2 88.12(9), N4–Cu1–Cl1 91.02(9), N4′A–Cu1–Cl1 91.26(9), Cl2–Cu1–Cl1 170.96(4), N4–Cu1–O20 91.5(1), N4′A–Cu1–O20 91.6(1), Cl2–Cu1–O20 97.92(8), Cl1–Cu1–O20 91.11(8).

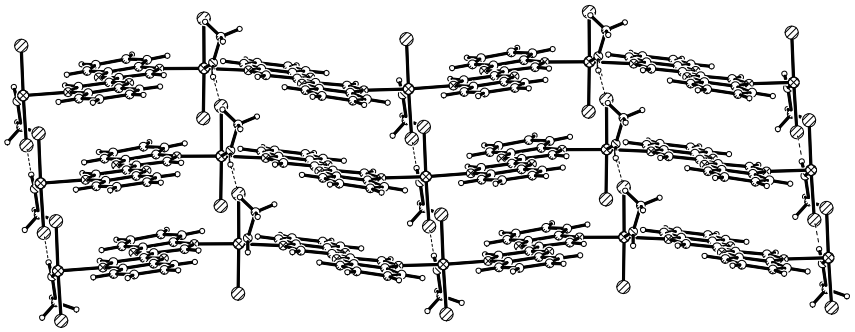


Fig. 12. Perspective view of the polymeric chains of **13**, showing the hydrogen bonds.

independent ligands stack in different directions, with the rings lying 3.585(4) and 3.462(4) Å apart, indicating weak π–π stacking interactions.

Reaction of **3** with copper(II) chloride produced a crystalline complex **13** which was suitable for X-ray crystallography. It is a one-dimensional coordination polymer that crystallises in the monoclinic space group $P2_1/c$, with one molecule of **3**, one copper(II) chloride and one coordinated methanol in the asymmetric unit (Fig. 11). The ligand **3** has a planar *transoid* conformation (mean deviation from plane: 0.026(5) Å) and bridges two copper atoms using the least hindered nitrogens, with a Cu···Cu separation of 9.549(1) Å. The geometry around the copper atom is slightly distorted square pyramidal, with *trans*-chlorine atoms and *trans*-nitrogens of **3** in the basal plane and the copper atom positioned 0.391(3) Å above the basal plane.

The polymer propagates along the *b*-axis of the unit cell in an undulating fashion with adjacent polymer chains arranged with the molecules of **3** π–π stacked and coplanar, the edge of each quinoxaline ring lying above another at a distance of 3.281(5) Å. There is also a hydrogen bond between the hydroxyl hydrogen of the methanol and a chlorine atom of an adjacent chain, as shown in Fig. 12, with a O–Cl distance of 3.091(3) Å and an O–H···Cl angle of 161(4)°. Thus, in both **12** and **13** the ligand acts in a divergent mode (Fig. 8a).

A copper(I) iodide complex with an intriguing 5:2 metal:ligand ratio was obtained as a black precipitate from reaction of CuI with **3**. However, recrystallisation of this from DMSO furnished red plates of a complex **14** with a 1:1 ratio. This crystallises in the triclinic space group $P\bar{1}$, with one molecule of **3** and one copper(I) iodide in the asymmetric unit (Fig. 13). The complex is binuclear, with two copper atoms bridged by iodine atoms, giving a Cu···Cu separation of 2.712(1) Å, about a crystallographic centre of inversion. The ligand **3** chelates the copper using the most hindered nitrogen atoms (mode (b) of Fig. 8), and this restricts **3** to planarity, with a mean deviation of

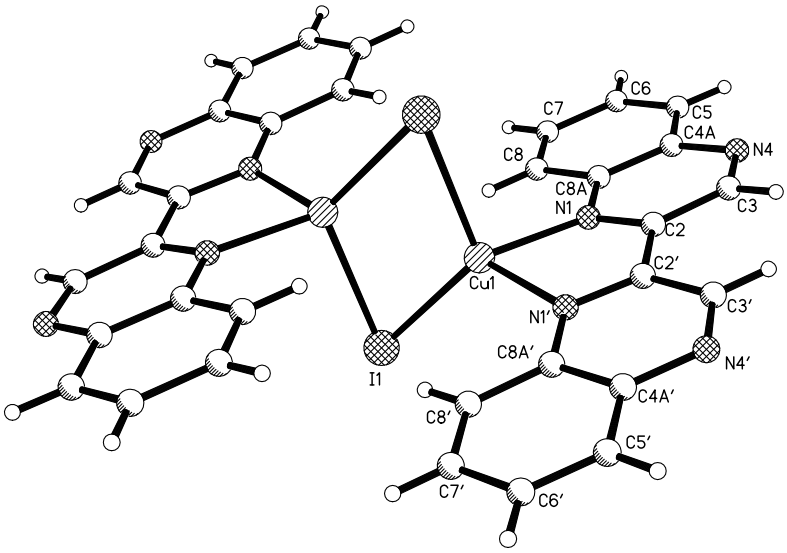


Fig. 13. Perspective view of **14**, with the asymmetric unit labelled. Selected bond lengths (Å) and bond angles (°): Cu1–N1 2.099(2), Cu1–N1′ 2.114(2), Cu1–I1 2.5742(9), Cu1–I1′ 2.6815(9), N1–Cu1–N1′ 78.66(9), N1–Cu1–I1 125.95(7), N1′–Cu1–I1 120.66(6), N1–Cu1–I1′ 99.66(6), N1′–Cu1–I1′ 106.43(6), I1–Cu1–I1′ 117.90(2).

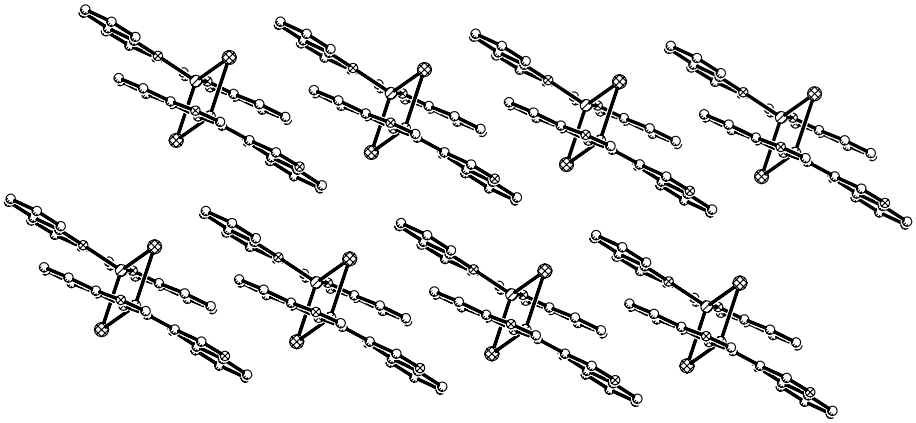


Fig. 14. View of the packing of **14**, with hydrogen atoms removed for clarity.

0.062(5) Å from the plane. The copper has a distorted tetrahedral geometry. The two molecules of **3** are coplanar, but are stepped with respect to one another, there being a distance of 2.338(5) Å between the planes. This stepping pulls the copper out of the coordination plane of **3** by 0.497(5) Å.

In the crystal packing the binuclear units stack with the C4A–C8A ring of one molecule coplanar and 3.389(5) Å above the C4A′–C8A′ ring of an adjacent ligand, and vice versa (Fig. 14). The rings of adjacent stacks also lie coplanar, with C6 of one ligand lying 3.275(5) Å above the centroid of the C4A–C8A ring of another. The structure of **14** is similar to the copper(I) iodide complex of 2,9-dimethyl-1,10-phenanthralene, which has similar bond lengths and geometry, although the Cu···Cu distance of 3.024(2) Å is slightly longer [25].

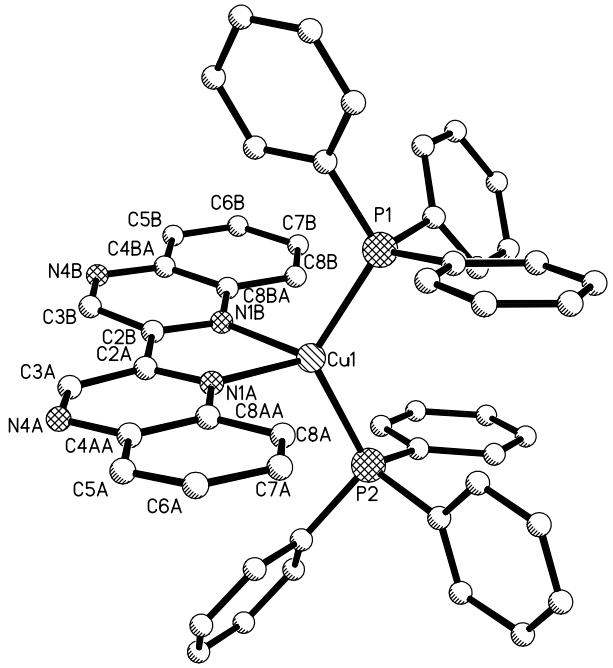


Fig. 15. Perspective view of **15**, with the labelling of **3** shown. Disordered nitrate, solvate molecules and hydrogen atoms have been omitted for clarity. Selected bond lengths (Å) and bond angles (°): Cu1–N1A 2.101(6), Cu1–N1B 2.109(4), Cu1–P1 2.283(2), Cu1–P2 2.293(2), N1A–Cu1–N1B 78.6(2), N1A–Cu1–P1 114.6(2), N1B–Cu1–P1 107.8(2), N1A–Cu1–P2 112.3(2), P1–Cu1–P2 122.23(7).

Finally, a second copper(I) complex **15** was prepared by reaction of **3** with bis(triphenylphosphine)copper(I) nitrate. It crystallises in $P\bar{1}$ with the bis(triphenylphosphine)copper chelated to **3** and a highly disordered nitrate counterion, as well as methanol and water solvate molecules in the asymmetric unit (Fig. 15). The ligand **3** is coordinated to the copper atom through the most hindered nitrogens, and is in a planar *cisoid* conformation (mean deviation from planarity 0.16(1) Å). One of the phenyl groups of a triphenylphosphine points towards the plane of **3**, with the closest approach made by C6, 3.270(8) Å above the ring.

One of the triphenylphosphine groups of **15** is involved in a 'hexa-aryl embrace' type interaction [26], as shown in Fig. 16. The PPh_3 groups, related by a centre of symmetry, are close, with a P···P distance of 6.422(6) Å, and are approximately colinear [170.4(2)°]. The closest interactions of the 'hexa-aryl embrace' occur between H6 of the aryl groups of the triphenylphosphine and the C1–C6 bond, with distances within the range 2.708(8)–2.791(8) Å. The second PPh_3 group of **15**, while not involved in a 'hexa-aryl embrace', is interacting with another PPh_3 group via an edge-to-face interaction. The closest approach involves H5F which lies 2.64(1) Å away from the centre of the C5H–C6H bond. The bulky triphenylphosphine groups of **15** preclude the face-to-face stacking of the heterocyclic ligand molecules that were seen in the previous compounds. The molecules pack into columns along the *c*-axis of the unit cell, leaving large voids that are occupied by disordered solvent molecules and nitrate counterions.

A 1:1 complex **16** of **3** with cadmium(II) nitrate was also prepared but proved to be curiously insoluble in all common solvents and was not investigated further.

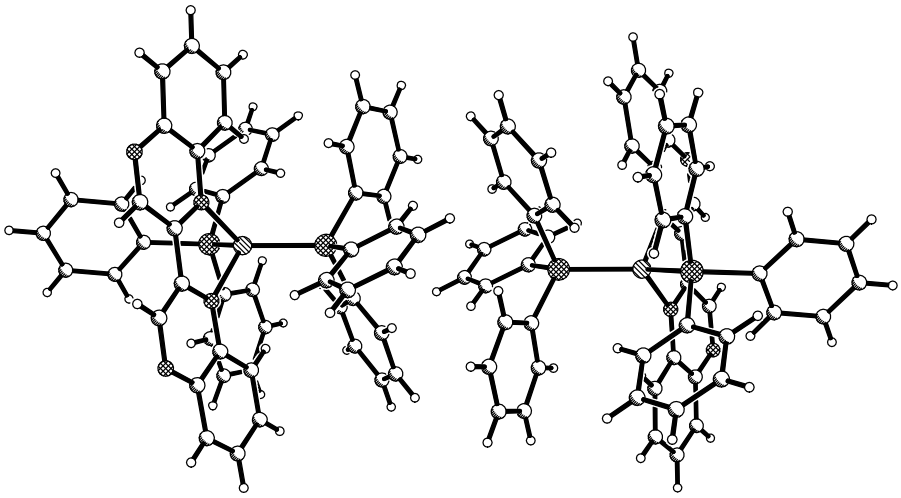


Fig. 16. Perspective view of the 'hexa-phenyl embrace' between the PPh_3 groups in the structure of **15**.

4. Conclusion

It has been shown that 2,2′-biquinazoline (**1**) prefers to form mononuclear complexes with chelation by the less hindered nitrogen donors. Complexes of 4,4′-biquinazoline (**2**) failed to provide suitable crystals for X-ray structure determination. 2,2′-Biquinoxaline (**3**) has been shown to offer two modes of coordination; in the first it acts as a "stepped-linear" bridging ligand using the two less hindered nitrogens. In the second mode it chelates to copper(I) centres using its more hindered nitrogens. Compared to the related ligands 2,2′-bipyrimidine and 2,2′-bipyrazine, the presence of the fused benzo rings leads to a higher propensity for π–π stacking of the heterocyclic ligands within the complexes, a phenomenon we have recently identified in other systems [24,27].

Acknowledgement

We thank the Royal Society of New Zealand for funding through the Marsden Fund a James Cook Research Fellowship.

Appendix A. Supplementary data

CCDC 665084, 665085, 665086, 665087, 665088, 665089 and 665089 contain the supplementary crystallographic data for this paper. These data can be obtained free of charge via http://www.ccdc.cam.ac.uk/conts/retrieving.html, or from the Cambridge Crystallographic Data Centre, 12 Union Road, Cambridge CB2 1EZ, UK; fax: (+44) 1223-336-033; or e-mail: deposit@ccdc.cam.ac.uk. Supplementary data associated with this article can be found, in the online version, at doi:10.1016/j.poly.2008.01.026.

References

[1] (a) S. Leininger, B. Olenyuk, P.J. Stang, Chem. Rev. 100 (2000) 853;
(b) G.F. Swiegers, T.J. Malefetse, Chem. Rev. 100 (2000) 3483;
(c) B. Moulton, M.J. Zaworotko, Chem. Rev. 101 (2001) 1629;
(d) M. Fujita, K. Umemoto, M. Yoshizawa, N. Fujita, T. Kusukawa, K. Biradha, Chem. Commun. (2001) 509;
(e) D.W. Johnson, K.N. Raymond, Supramol. Chem. 13 (2001) 639;
(f) B.J. Holliday, C.A. Mirkin, Angew. Chem., Int. Ed. 40 (2001) 2022;
(g) G.F. Swiegers, T.J. Malefetse, Coord. Chem. Rev. 225 (2002) 91;
(h) L. James, Chem. Soc. Rev. 32 (2003) 276;
(i) M.J. Hannon, L.J. Childs, Supramol. Chem. 16 (2004) 7;
(j) F. Würthner, C.-C. You, C.R. Saha-Möller, Chem. Soc. Rev. 33 (2004) 133;
(k) H. Hofmeier, U.S. Schubert, Chem. Soc. Rev. 33 (2004) 373;
(l) A.L. Gavrilova, B. Bosnich, Chem. Rev. 104 (2004) 349;
(m) P. Thanasekaran, R.-T. Liao, Y.-H. Liu, T. Rajendran, S. Rajagopal, K.-L. Lu, Coord. Chem. Rev. 249 (2005) 1085;
(n) M.W. Hosseini, Acc. Chem. Res. 38 (2005) 313.
[2] E.C. Constable, D. Morris, S. Carr, New J. Chem. (1998) 287.
[3] C.M. Fitchett, P.J. Steel, Polyhedron 26 (2007) 400.
[4] P.J. Steel, Acc. Chem. Res. 38 (2005) 243, and references therein.
[5] P.J. Steel, Adv. Heterocycl. Chem. 67 (1997) 1.
[6] C. Richardson, P.J. Steel, Inorg. Chem. Commun. 10 (2007) 884, and references therein.
[7] W.L.F. Armarego, R.E. Willette, J. Chem. Soc. (1965) 1258.
[8] T. Higashino, Chem. Pharm. Bull. 10 (1943) 1043.
[9] (a) K. Maurere, B. Boettger, Chem. Ber. 71B (1938) 2092;
(b) O.N. Chupakhin, E.O. Sidorov, S.M. Shein, I.I. Bil'kis, Zh. Org. Khim. 12 (1976) 2464.
[10] (a) A.L. Gershuns, A.N. Brizitskaya, Ukr. Khim. Zh. 36 (1970) 652;
(b) A.L. Gershuns, A.N. Brizitskaya, Izvest. Vysshikh Uchebnykh Zavedenii 17 (1974) 1626.
[11] L. Ademi, E.C. Constable, C.E. Housecroft, M. Neuburger, S. Schaffner, Dalton Trans. (2003) 4565.
[12] C.M. Fitchett, C. Richardson, P.J. Steel, Org. Biomol. Chem. 3 (2005) 498.
[13] G.M. Sheldrick, Acta Crystallogr., Sect. A 46 (1990) 467.
[14] G.M. Sheldrick, SHELXL-97, University of Göttingen, 1997.
[15] P.J. Steel, Coord. Chem. Rev. 106 (1990) 227.
[16] A.J. Downard, I.G. Phillips, P.J. Steel, Aust. J. Chem. 57 (2004) 865, and references therein.
[17] A.J. Canty, B.W. Skelton, P.R. Traill, A.H. White, Aust. J. Chem. 45 (1992) 417.
[18] M. Melnik, M. Kabesova, M. Koman, L.U. Macaskova, J. Garaj, C.E. Holloway, A. Valent, J. Coord. Chem. 45 (1998) 147.
[19] G.R. Desiraju, J. Chem. Soc., Dalton Trans. (2000) 3745.
[20] A.M. Beatty, CrystEngComm 3 (2001) 243.
[21] L.K. Cheng, K.S. Yeung, C.M. Che, M.C. Cheng, Y. Wang, Polyhedron 12 (1993) 1201.
[22] L. Dai, Z. Zhou, Y. Zhang, C. Ni, Z. Zhang, Y. Zhou, J. Chem. Soc., Chem. Commun. (1987) 1760.
[23] C. Janiak, L. Uehlin, H.-P. Wu, P. Klufers, H. Piotrowski, T.G. Scharmann, J. Chem. Soc., Dalton Trans. (1999) 3121.
[24] P.J. Steel, C.M. Fitchett, Coord. Chem. Rev., in press, doi:10.1016/j.ccr.2007.07.018.
[25] P.C. Healy, C. Pakawatchai, A.H. White, J. Chem. Soc., Dalton Trans. (1985) 2531.
[26] I. Dance, M. Scudder, Chem. Commun. (1995) 1039.
[27] B.J. O'Keefe, P.J. Steel, Inorg. Chem. Commun. 10 (2007) 247.

Peptides possess many unusual features to be specific ligands for a variety of metal ions. They contain a lot of potential donor atoms like amino and amide nitrogens and oxygens from carboxyl or carbonyl groups. The side chains of some amino acids have very efficient donor atoms, i.e. the imidazole moiety in the histidine residue. The cooperativity of all three donor groups of the histidine residue in the metal binding properties is made by the formation of two fused chelate rings. First is a five-membered $\{NH_2, COO^-\}$ amino acid-like ring, and the second one a six-membered $\{NH_2, N_{im}\}$ histamine-like ring [4].

The metal ion coordination to the histidine residue generally takes place via the N(1) or N(3) atoms of the imidazole, as is found in copper, zinc and iron proteins including myoglobin and other heme proteins, carbonic anhydrase and blue copper proteins [5].

The multi-histidine sequence is characteristic for Cu^{2+} binding motifs in proteins like prions [2], amyloid precursor protein (APP) [6–8] or secreted protein acidic and rich in cysteine (SPARC) [9] and also some groups of enzymes, i.e. copper containing oxidases (-His-His-Gly-His-) in the catecholase catalytic centre [10].

A number of in vivo studies have shown that metal ions such as copper, iron and zinc can cause oxidative damage to neuronal cells [11–13]. These observations are significant due to the fact that, for example, the plaques in Alzheimer disease contain elevated concentration of copper, zinc and iron. Surprisingly, although Cu^{2+}-amyloid β is more toxic to cultured neurons than amyloid β alone, these complexes are less toxic than copper alone. It is suggested that the complex with the three histidines of amyloid β peptide control the redox activity of the copper and iron [14].

Thus, peptides containing histidine residues are *per se* interesting for studies of Cu^{2+} complexation. The presence of a multi-histidine sequence in the peptide determines the high structural variety in the complex formation with Cu^{2+} in addition to the general coordination modes of peptides in formation of macrochelates or bent structures. Although the macrochelation by the histidine residues is crucial in acidic pH, especially for N-terminally protected peptides, it cannot protect against the deprotonation of the amide nitrogen and its coordination to the metal ion in the physiological pH range.

Very efficient coordination abilities of histidine residues towards transition metal ions and the stabilizing role in the complex formation reactions caused that previous studies were focused on oligopeptides having potentially favorable Cu^{2+} ions binding features. In the previous papers, the role of one histidine residue in a specific position in the peptide sequence was investigated [15]. Furthermore, cyclic peptides with two histidine residues were analyzed with basic and acidic side-chains added to the sequence [16,17]. Surprisingly, for the cyclic peptides the 3N coordination mode with two amide nitrogens and imidazole was determined, while for linear N,C-terminally protected peptides the 4N binding mode with three amide nitrogens and imidazole was found.

The effect of further increasing of the number of histidine residues in the peptide sequence has been studied below. It has induced us to perform a detailed analysis of a group of linear hexapeptides with three histidine residues located in different positions in the peptide sequence. The studies were focused on the influence of the histidine residue position on the binding possibilities towards Cu^{2+} ions.

The investigated group consist four N-protected peptides Ac-His-Arg-His-Gly-His-Gly, Ac-His-Gly-His-Arg-His-Gly, Ac-Gly-His-His-Arg-His-Gly and Ac-His-His-Gly-His-Arg-Gly, and four analogs with an unprotected amino group His-Arg-His-Gly-His-Gly, His-Gly-His-Arg-His-Gly, Gly-His-His-Arg-His-Gly and His-His-Gly-His-Arg-Gly. Spectroscopic and potentiometric methods were used to analyze the species formed. Binding properties and the coordination modes in the formed Cu^{2+}-peptide complexes have been proposed. For each system only the mononuclear species have been found, as was described by Kállay et al. for similar systems [18].

2. Experimental

2.1. Synthesis and purification of the peptides

All peptides were synthesized by a manual solid phase peptide synthesis method. Syntheses were performed in 5 ml disposable reaction columns (Intavis) starting from Fmoc-Gly-Wang resin (0.86 mmol/g from Iris or 1 mmol/g from Novabiochem). Fmoc-Gly-OH, Fmoc-His(Trt)-OH and Fmoc-Arg(Pbf)-OH were used as amino acid derivatives. Deprotection of the Fmoc groups was performed with 25% piperidine in DMF. The coupling reactions were performed by using an excess of the amino acids, HOBt and HBTU (3 eq.) and of DIEA (6 eq.) in DMF, under mixing for 2 h. Coupling reactions were controlled by the Kaiser test and repeated if the test was positive. The final acetylation of the hexapeptides was performed directly on the solid phase by adding a solution of 50% acetic anhydride in 0.4 M *N*-ethylmorpholine in DMF, with mixing for 1 h. The resin was then washed with DMF, DCM and methanol, and dried under vacuum.

Crude peptides were cleaved from the resin, simultaneously with the removal of the side-chain protecting groups, by treatment with the Reagent K (trifluoroacetic acid/water/phenol/tioanisole/triisopropylsilane, 82.5/5/5/5/2.5 v/v/m/v/v) for 3 h. The TFA solutions were filtered into cold *t*-butylmethyl ether, precipitated, filtered, washed few times with ether, dissolved in water and lyophilized.

Peptides were purified by semi-preparative HPLC using a Varian ProStar HPLC apparatus equipped with a TOSOH Bioscience C18 column (300 × 21.5 mm, 10 μm beads) and 220 nm UV/Vis detector. Water–acetonitrile gradients containing 0.1% TFA at a flow rate of 7 ml/min. were used for the purifications. The final purity of

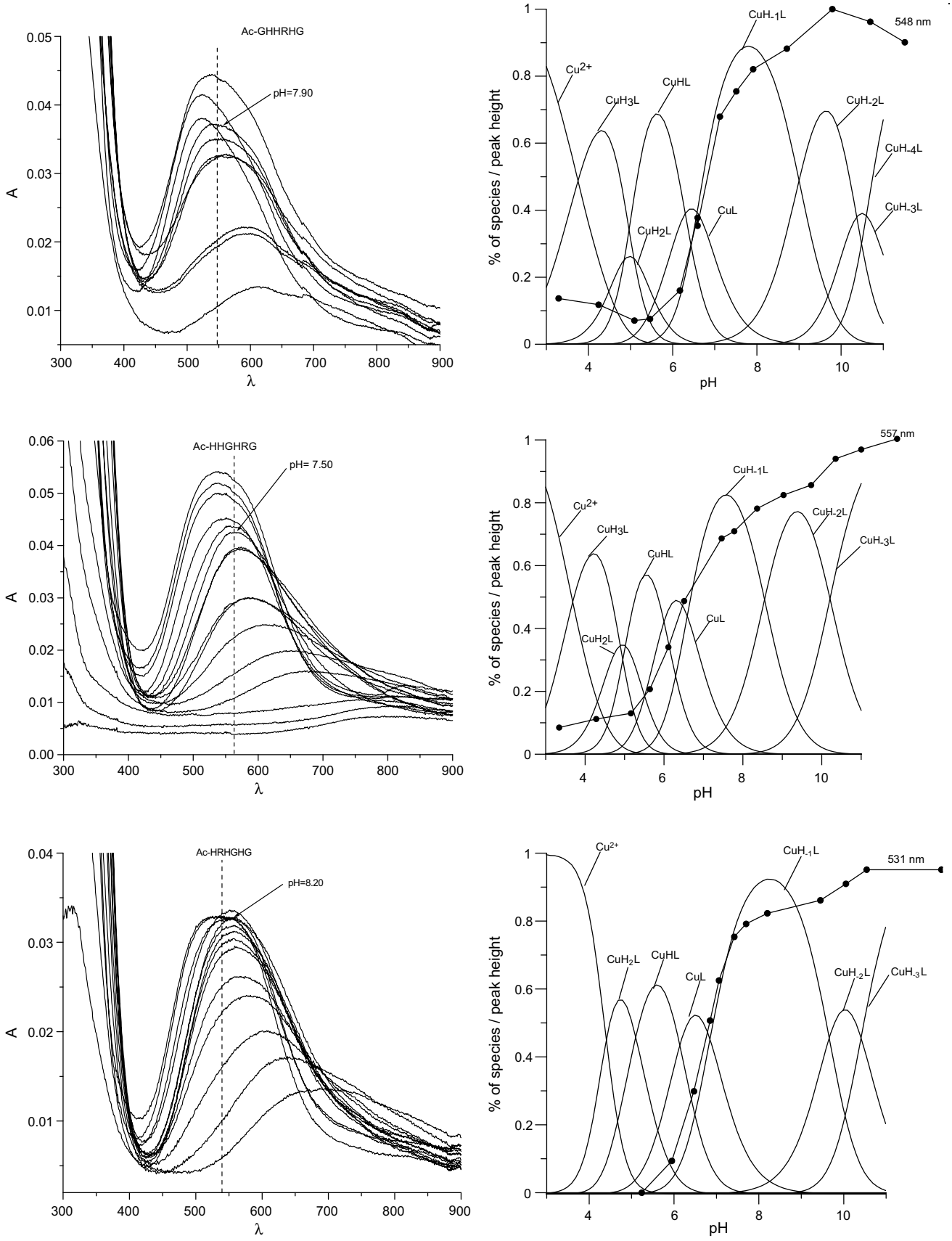


Fig. 1. Contribution of each distributed species to the UV/Vis spectra and corresponding peak heights in a single spectrum decomposed in the SPECPEAK program.

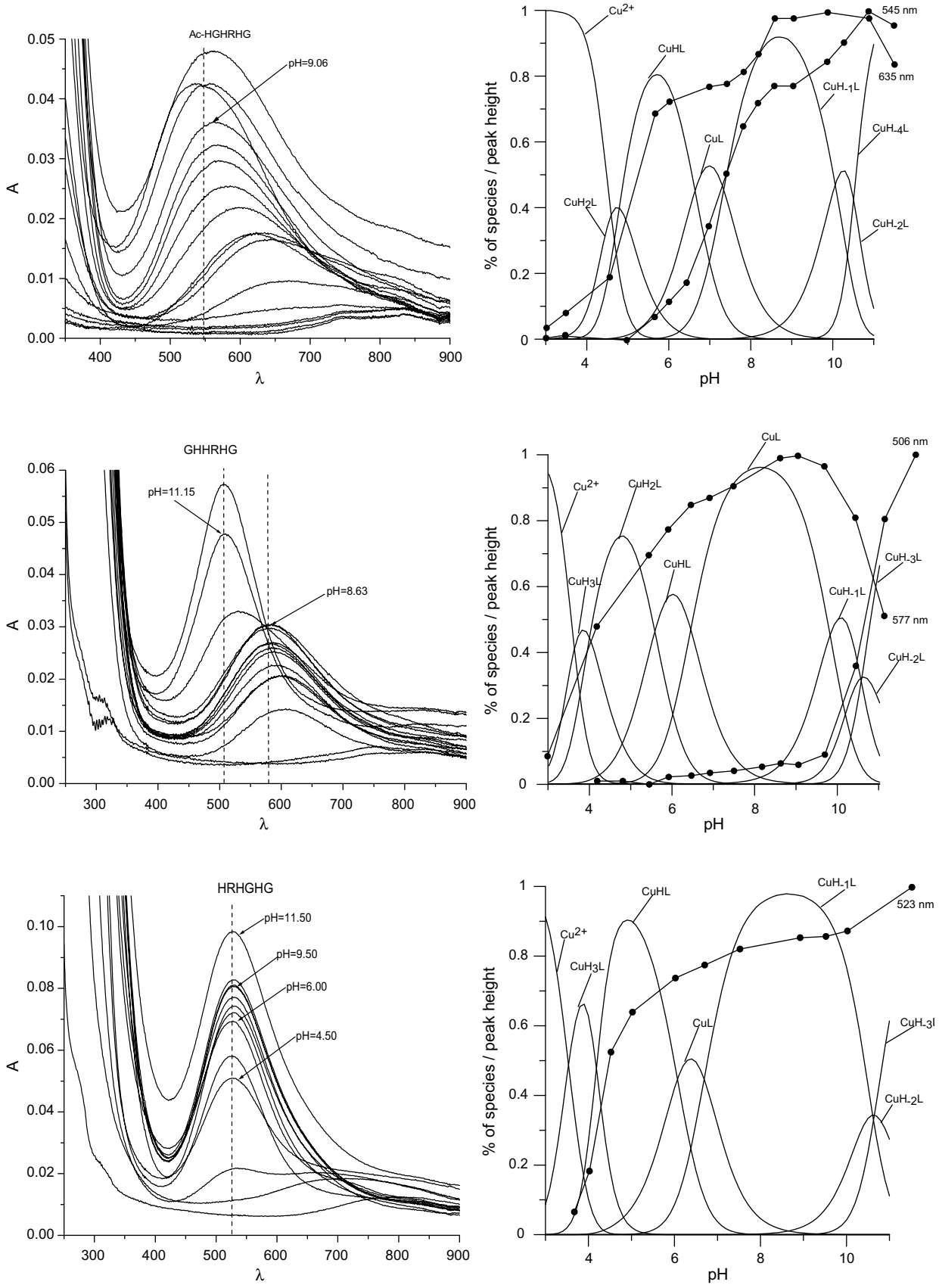


Fig. 1 (*continued*)

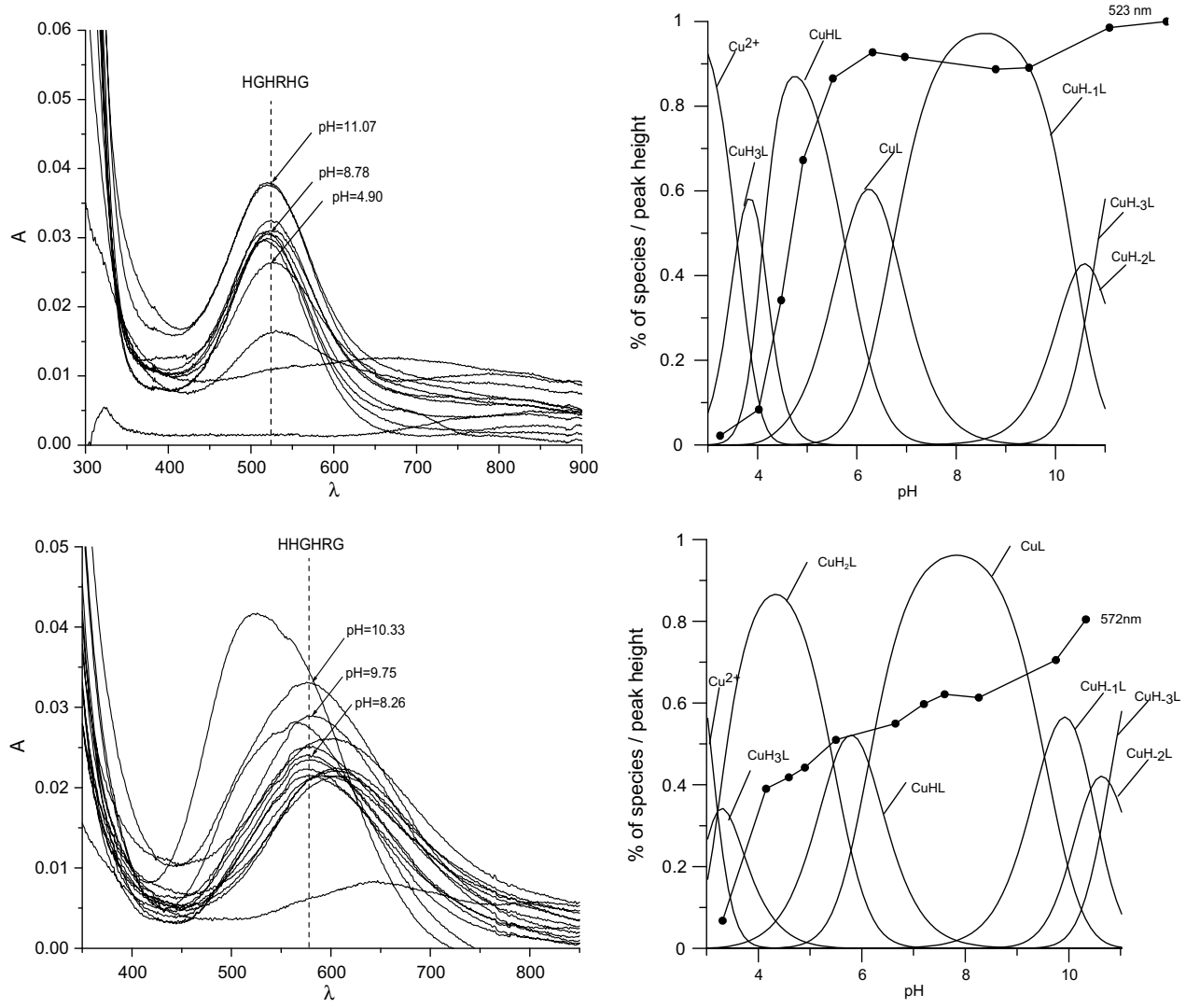


Fig. 1 (*continued*)

the lyophilized peptides was better than 98% by analytical HPLC. The chemical identity of the ligands was confirmed by ESI-MS on a Finnigan MAT TQS 700. Ms measurements were also made on a micrOTOF-Q Bruker Daltonics in the Laboratory of Spectrometry in the Faculty of Chemistry, University of Wroclaw.

2.2. Potentiometric measurements

Stability constants were calculated from the potentiometric titrations, carried out at 25 °C, using sample volumes of 1.5 ml. The ligand concentration was 1×10^{-3} M, and the metal-to-ligand ratio was 1:2 apart from the ligand Ac-His-His-Gly-His-Arg-Gly, where the metal-to-ligand ratio was 1:3. The pH-metric titrations were performed in 0.1 M KNO_3 on a MOLSPIN pH-meter system using a Mettler Toledo InLab 422 semi-micro combined electrode calibrated in hydrogen ion concentration using HNO_3. Stability constants $\beta_{pqr} = [M_pH_qL_r]/[M]^p[H]^q[L]^r$ and the stoichiometry of complexes were calculated with the SUPERQUAD [19] program. The standard deviations quoted were also computed by SUPERQUAD and referred to random errors only. The range of pH for each titration for the free ligand and metal–ligand system was 3–11. In the manuscript the charge for each forming species is omitted.

2.3. Spectroscopic measurements

Absorption spectra were recorded on a Perkin–Elmer Lambda Bio 20 spectrophotometer, circular dichroism (CD) spectra on a JASCO J 715 spectropolarimeter in the 850–200 nm range and electron paramagnetic resonance (EPR) spectra on a Bruker ESP 300E spectrometer at the X-band frequency (9.4 GHz) at 120 K. The ligand concentration was 1×10^{-3} M and the metal-to-ligand ratio was 1:2. For the ligand Ac-His-His-Gly-His-Arg-Gly the metal-to-ligand ratio was 1:3.

Table 1
Potentiometric data for the Cu^{2+} complexes with the ligands Ac-His-Arg-His-Gly-His-Gly, Ac-His-Gly-His-Arg-His-Gly and Ac-Gly-His-His-Arg-His-Gly, Ac-His-His-Gly-His-Arg-Gly

	Ac-Gly-His-His-Arg-His-Gly	Ac-His-Arg-His-Gly-His-Gly	Ac-His-Gly-His-Arg-His-Gly	Ac-His-His-Gly-His-Arg-Gly
HL	10.42	10.28	10.21	10.81
H_2L	17.72	17.23	17.21	17.79
H_3L	23.65	23.53	23.54	23.99
H_4L	29.16	29.05	29.12	29.47
H_5L	31.12	31.42	31.41	32.18
$\log K$ (Arg)	10.42	10.28	10.21	10.81
$\log K$ (Im)	7.3	6.95	7	6.58
$\log K$ (Im)	5.93	6.3	6.33	6.2
$\log K$ (Im)	5.51	5.52	5.58	5.48
$\log K$ (COO^-)	1.96	2.37	2.29	2.71
$\log \beta$				
CuH_3L	28.55			28.74
CuH_2L	23.47	23.39	23.14	23.85
CuHL	18.62	18.28	18.35	18.83
CuL	12.32	12.13	11.71	12.83
$CuH_{-1}L$	5.74	5.27	4.37	6.24
$CuH_{-2}L$	−3.26	−4.40	−5.69	−2.31
$CuH_{-3}L$	−13.63	−14.82	-	−12.52
$CuH_{-4}L$	−24.03		−26.71	
$\log \beta_{CuH_3L} - \log \beta_{CuH_2L}$	4.85			4.89
$\log \beta_{CuH_2L} - \log \beta_{CuHL}$	5.08	5.11	4.79	5.02
$\log \beta_{CuHL} - \log \beta_{CuL}$	6.30	6.15	6.64	6.00
$\log \beta_{CuL} - \log \beta_{CuH-1L}$	6.58	6.86	7.34	6.59
$\log \beta_{CuH_{-1}L} - \log \beta_{CuH_{-2}L}$	9.00	9.67	10.06	8.55
$\log \beta_{CuH_{-2}L} - \log \beta_{CuH_{-3}L}$	10.37	10.42		10.21
$\log \beta_{CuH_{-3}L} - \log \beta_{CuH_{-4}L}$	10.40			
$\log K_{CuH_3L} - \log K_{H_3L}$	4.90			4.75
$\log K_{CuH_2L} - \log K_{H_2L}$	5.75	6.16	5.93	6.06
$\log K_{CuHL} - \log K_{HL}$	8.20	8.00	8.14	8.02

2.4. Deconvolution of the spectra into the constituent Gaussian peaks

The obtained UV/Vis spectra were deconvoluted into their constituent Gaussian peaks by the SPECPEAK computer program according to the procedure which has been described elsewhere [20,21]. It allows for optimisation of the wavelengths of the maxima and the half-band-widths of all the spectra while the heights of each peak are optimized in each single spectrum [21]. It makes it possible to evaluate the spectroscopic parameters for each separate species and to follow a trend for the concentration of each single absorbing component as a function of the reagent concentrations [22]. The results are shown in Fig. 1.

The overlay of the trend of the height for the principal deconvoluted band and a specific form of complex, obtained from potentiometric calculations, determines the convergence of the corresponding spectroscopic parameters to a detailed forming species (i.e. for the Ac-GHHRHG–Cu^{2+} system the band at 548 nm, which was calculated from SPECPEAK program, corresponds to the formation of the $CuH_{-1}L$ species with the maximum of the form at pH 7.90, Fig. 1; the error of the calculated and experimentally obtained wavelength is 5 nm and can be neglected).

3. Results

3.1. Protonation constants of the free ligands

The acid-base properties of the metal-free peptides were investigated by potentiometric titrations. For each ligand at least five titrations were done to determine the pK values.

All the peptides with a protected N-terminal amino group are characterized by five protonation constants which could be assigned to the same set of functions (Table 1). The highest pK value corresponds to the arginine side chain, the following three lower pKs could be attributed to the imidazole histidine residues and the lowest pK value to the carboxyl group of the C-terminal amino acid.

The unprotected peptides are characterized by six protonation constants (Table 2). The additional sixth pK value, ranged from 7.29 to 7.95, can be assigned to the N-terminal amino group.

3.2. Coordination abilities of the N-protected peptides towards Cu^{2+} ions

According to the calculations based on potentiometric titrations, the investigated peptides form a different number of mononuclear complexes.

Table 2
Potentiometric data for the Cu^{2+} complexes with the ligands His-Arg-His-Gly-His-Gly, His-Gly-His-Arg-His-Gly, Gly-His-His-Arg-His-Gly and His-His-Gly-His-Arg-Gly

	Gly-His-His-Arg-His-Gly	His-Arg-His-Gly-His-Gly	His-Gly-His-Arg-His-Gly	His-His-Gly-His-Arg-Gly
HL	10.60	10.59	10.44	10.67
H_2L	18.55	18.02	17.94	17.96
H_3L	25.38	24.55	24.50	24.36
H_4L	31.64	30.53	30.47	30.11
H_5L	37.01	35.42	35.50	34.88
H_6L	39.79	38.08	37.91	36.86
$\log K$ (Arg)	10.60	10.59	10.44	10.67
$\log K$ (NH_2)	7.95	7.43	7.50	7.29
$\log K$ (Im)	6.83	6.53	6.56	6.4
$\log K$ (Im)	6.26	5.98	5.97	5.75
$\log K$ (Im)	5.37	4.89	5.03	4.77
$\log K$ (COO^-)	2.78	2.66	2.41	1.98
$\log \beta$				
CuH_3L	33.00	31.60	31.59	31.71
CuH_2L	29.02			28.51
CuHL	23.46	23.21	23.36	23.08
CuL	17.03	17.17	17.72	16.97
$CuH_{-1}L$	7.23	10.45	11.09	7.46
$CuH_{-2}L$	−3.31	0.19	0.83	−2.94
$CuH_{-3}L$	−13.88	−10.49	−9.92	−13.70
$\log \beta_{CuH_3L} - \log \beta_{CuH_2L}$	3.98			3.2
$\log \beta_{CuH_2L} - \log \beta_{CuHL}$	5.56	8.39	8.23	5.43
$\log \beta_{CuHL} - \log \beta_{CuL}$	6.43	6.04	5.64	6.11
$\log \beta_{CuL} - \log \beta_{CuH_{-1}L}$	9.80	6.72	6.63	9.51
$\log \beta_{CuH_{-1}L} - \log \beta_{CuH_{-2}L}$	10.54	10.26	10.26	10.40
$\log \beta_{CuH_{-2}L} - \log \beta_{CuH_{-3}L}$	10.57	10.68	10.75	10.76
$\log K_{CuH_3L} - \log K_{H_3L}$	7.62	7.05	7.09	7.35

Ac-GHHRHG with Cu^{2+} ions forms eight distinct species: CuH_3L, CuH_2L, CuHL, CuL, $CuH_{-1}L$, $CuH_{-2}L$, $CuH_{-3}L$ and $CuH_{-4}L$ (Table 1). The coordination begins around pH 3 with the loss of two protons from the ligand molecule and the formation of CuH_3L. At pH 4 the maximum of this species is observed (Fig. 1). The absorption spectra with a d–d band at 740 nm may suggest the coordination of one nitrogen donor (Table 3). It is supposed that one imidazole from the histidine residue is involved in the Cu^{2+} binding centre. CuH_2L, present around pH 5, is a minor species and its spectroscopic data are not available. Nevertheless, $\log K = \log K_{CuH_2L} - \log K_{H_2L} = 5.75$ suggests the involvement of two imidazole rings in the complex formation as was proposed in previous papers [23–25]. As the pH increases, the CuHL species is formed, which is a dominant form in the pH range 5–6.5. The d–d transitions at 688 nm in the UV/Vis spectrum and the EPR parameters ($A_{II} = 196$ and $g_{II} = 2.24$) suggest the involvement of the third nitrogen donor. The $\log K = \log K_{CuHL} - \log K_{HL} = 8.2$ value can be assigned to the species involving three imidazoles in the metal ion binding [23]. The successive species dominating in the pH range 7–9 is $CuH_{-1}L$, with the d–d transitions at 562 nm and the EPR parameters $A_{II} = 203$ and $g_{II} = 2.20$, is most likely the 4N complex. The CD spectra with d–d bands at 553 and 476 nm suggest involvement of at least two amide donors. It involves two or three imidazole nitrogens, as was proved in the case of a similar three-His ligand using NMR studies [7]. The coordination is suggested to occur via His^3 and His^5 imidazole nitrogens and the amide nitrogens of Arg and His^5 in the plane, while His^2 is thought to be bound in the apical position. Above pH 9.5 the dominant species is $CuH_{-2}L$. The shift of the band by 14 nm may suggest the involvement of a third amide nitrogen in the coordination sphere. The presence of a new band in the CD spectrum at 633 nm supports this assumption. The coordination could involve the $\{N^-, N^-, N^-, N_{im}, N_{im}\}$ donor system [7]. Above pH 10.5, where $CuH_{-3}L$ is formed, there is another shift of the d–d transition energy to 523 nm, suggesting the increase of electron density around the metal ion derived from the proton dissociation from the metal bound imidazole [26]. The final proton dissociation ($CuH_{-4}L$), with $pK = 10.40$, occurs most probably on the arginine residue ($pK = 10.42$ of the free ligand).

For Ac-HHGHRG-Cu^{2+} seven distinct species are formed according to the potentiometric data calculations: CuH_3L, CuH_2L, CuHL, CuL, $CuH_{-1}L$, $CuH_{-2}L$ and $CuH_{-3}L$ (Table 1 and Fig. 1). The CuH_3L, CuH_2L and CuHL complexes involve one, two and three imidazole nitrogens respectively, similar to the Ac-GHHRHG-

Table 3
UV/Vis, CD and EPR parameters for the Cu^{2+} complexes with the ligands Ac-His-Arg-His-Gly-His-Gly, Ac-His-Gly-His-Arg-His-Gly, Ac-Gly-His-His-Arg-His-Gly and Ac-His-His-Gly-His-Arg-Gly

Species	Ac-GHHRHG						Ac-HRHGHG						Ac-HGHRHG						Ac-HHGHRG					
	UV/Vis		CD		EPR		UV/Vis		CD		EPR		UV/Vis		CD		EPR		UV/Vis		CD		EPR	
	λ	ε	λ	$\Delta\varepsilon$	A_{II}	g_{II}	λ	ε	λ	$\Delta\varepsilon$	A_{II}	g_{II}	λ	ε	λ	$\Delta\varepsilon$	A_{II}	g_{II}	λ	ε	λ	$\Delta\varepsilon$	A_{II}	g_{II}
CuH_3L	740	42																	755	38			170	2.30
CuH_2L							687	56			166	2.31	670	39	251	0.55	170	2.30						
CuHL	688	49	338	−0.26	196	2.24	638	70	344	−0.3			620	70	576	−0.33	173	2.28	651	70	256	0.6	199	2.24
CuL							607	82	338	−1.1	200	2.23	598	88			187	2.25	586	105	304	−0.6	199	2.23
									490	0.38											347	0.67		
$CuH_{-1}L$	553	131	338	−1.79	203	2.20	557	128	336	−1.2	197	2.18	564	155	323	−0.85	180	2.20	574	139	300	−1.1	197	2.20
			479	0.33					490	0.52					371	0.33					347	1.3		
			545	−0.51											480	0.21					596	0.46		
$CuH_{-2}L$	539	177	326	0.64	194	2.20	551	131	336	−1.2	197	2.18	564	155	324	−0.34			551	157	282	−1.5	205	2.19
			512	−0.85					603	0.38					368	0.28					321	2.43		
			633	0.69											519	−0.2					492	−0.7		
															612	0.38					594	1.4		
$CuH_{-3}L$	523	165	296	−0.55	203	2.20	525	134	322	1.99	197	2.18							534	181	282	−1.6	205	2.19
			326	0.77					477	−0.9											321	2.8		
			519	−0.9					595	1.39											492	−0.8		
			655	0.72																	600	1.5		
$CuH_{-4}L$	523	152	296	−0.55	203	2.20							539	185	288	−0.48	193	2.19						
			326	0.77											322	1.23								
			519	−0.9											491	−0.87								
			655	0.72											609	0.97								

Cu^{2+} system. Both the spectroscopic parameters and pK values of the single deprotonation steps are similar to each other (Tables 1 and 3). As the pH increases, the CuL species is formed (Fig. 1). The significant shift of the absorption band by 65 nm indicates binding of the consecutive nitrogen donor atom. The $CuH_{-1}L$ and $CuH_{-2}L$ species exhibit a similar coordination pattern as that found for the Ac-GHHRHG-Cu^{2+} system (Table 3). The last complex, $CuH_{-3}L$, is formed as a result of proton dissociation from the arginine side chain. Lack of any distinct changes in the spectroscopic parameters and the pK value of 10.21 confirm the above assumptions.

Ac-HRHGHG with Cu^{2+} ions forms six distinct species in the pH range 3–11: CuH_2L, CuHL, CuL, $CuH_{-1}L$, $CuH_{-2}L$ and $CuH_{-3}L$ (Table 1). The coordination begins near pH 4, when the CuH_2L species is formed (Fig. 1). The d–d transitions at 687 nm in the absorption spectra indicate the 2N binding mode (Table 3). The $\log K = \log K_{CuH_2L} - \log K_{H_2L} = 6.16$ value (Table 1) suggests coordination of two imidazole nitrogens [23]. Further deprotonation and formation of CuHL, CuL and $CuH_{-1}L$ can be assigned to the coordination modes determined for the previous peptide-Cu^{2+} systems. The reaction $[CuH_{-1}L] \leftrightarrow [CuH_{-2}L]+H^+$ at p$K = 9.67$ and a minor modification seen in CD and UV/Vis spectra suggests that the deprotonation occurs at the arginine residue side chain (p$K = 10.28$ in the free ligand). Further deprotonation and formation of $CuH_{-3}L$ at p$K = 10.42$ derives from the binding of the third amide nitrogen. This is strongly supported by the d–d band shift from 557 to 525 nm and the distinct changes in the CD spectra at the CT range (at 322 nm) and formation of the bands at 595 and 476 nm (Table 3).

Ac-HGHRHG with Cu^{2+} forms six distinct species in the pH range 3-11: CuH_2L, CuHL, CuL, $CuH_{-1}L$, $CuH_{-2}L$ and $CuH_{-4}L$ (Table 1 and Fig. 1). The only differences in the coordination modes between Ac-HRHGHG and Ac-HGHRHG are seen where the $CuH_{-4}L$ species is formed (Fig. 1) The latter species results most likely from proton dissociation from the metal bound imidazole [26].

3.3. Coordination abilities of the group of unprotected peptides towards Cu^{2+} ions

According to the results which have been obtained from potentiometric and spectroscopic measurements, each ligand–Cu^{2+} system forms mononuclear complexes in the pH range 3–11. The coordination mode is dependent on the position of the histidine residue in the peptide sequence.

GHHRHG is representative of a peptide with histidine residues at the second and third positions in the peptide chain with an unprotected N-terminal amino group. Seven distinct species have been found in the Cu^{2+}-GHHRHG system (Fig. 1 and Table 2). The first complex, CuH_3L, is the result of dissociation of three protons from the ligand molecule. The band at 259 nm in the CD spectrum suggests involvement of the amino nitrogen in the coordination binding centre. The EPR parameters ($A_{II} = 185$, $g_{II} = 2.23$) clearly indicate a 2N complex (Table 4). Moreover, $\log K = \log K_{CuH_3L} - \log K_{H_3L} = 7.62$ suggests that the amino and imidazole nitrogen donors are bound to the metal ion centre [4,5]. The third proton dissociation could be assigned to a carboxyl group from the C-terminal amino acid.

The pK value of 3.98 for the reaction $[CuH_3L] \leftrightarrow [CuH_2L]+H^+$ may suggest the deprotonation of the amide nitrogen and formation of the $\{NH_2, N^-, N_{im}\}$ donor set, characteristic for peptides with Xaa-His units, where the first amide deprotonation occurs near pH 4 [4,5]. This binding mode is confirmed by the spectroscopic data (Table 4). Further deprotonations to CuHL and CuL species occurring below pH 10 do not affect distinctly the spectroscopic parameters, suggesting that both proton releases are from non-coordinating imidazole moieties (Fig. 1). Above pH 10 the $CuH_{-1}L$ complex is formed. The presence of a new band at 500 nm in the CD spectra may suggest the involvement of an additional nitrogen donor atom in the metal ion coordination sphere. It is derived from the second amide nitrogen binding and the albumin-like coordination mode formation (Table 4) [4,5]. Further deprotonations, resulting in $CuH_{-2}L$ and $CuH_{-3}L$ formation, have no impact on the metal ion coordination mode. It is suggested that it derives most likely from the arginine side chain. The second deprotonation can be assigned to the metal bound imidazole [26].

HRHGHG and HGHRHG form six distinct species: CuH_3L, CuHL, CuL, $CuH_{-1}L$, $CuH_{-2}L$ and $CuH_{-3}L$ (Table 3 and Fig. 1). The presence of the histidine residue in the N-terminal position implies differences in the binding ability and coordination mode when compared to the protected ligands discussed above [4,5]. The CuH_3L species is formed by coordination of the imidazole and amino nitrogen, resulting in a 2N complex with a histamine-like $\{NH_2, N_{im}\}$ binding mode, specific for His^1 peptides [19]. UV/Vis spectroscopy and EPR parameters confirm the 2N coordination mode (Table 4). The CuHL species, which is a dominant form in the pH range 4–6, results from two consecutive deprotonations. The large shift in the absorption spectrum from 662 to 526 nm (in the case of the HRHGHG-Cu^{2+} system) and the presence of the distinct bands in the CD spectrum (562, 487, 311 and 272 nm) strongly suggest coordination of the amidic donors to the metal ion and formation of the albumin-like 4N complex, typical for His^3 motif peptides [26] (Fig. 1 and Table 4). The $\{NH_2, 2N^-, N_{im}\}$ binding mode seems to be the final mode of coordination to the Cu^{2+} ions. Further deprotonations to CuL and $CuH_{-1}L$ are concerned with the loss of protons from the imidazole moieties, without taking part in a binding process. The last forming species, $CuH_{-2}L$ and $CuH_{-3}L$, are the

Table 4
UV/Vis, CD and EPR parameters for the Cu^{2+} complexes with the ligands His-Arg-His-Gly-His-Gly, His-Gly-His-Arg-His-Gly, Gly-His-His-Arg-His-Gly and His-His-Gly-His-Arg-Gly

Species	GHHRHG						HRHGHG						HGHRHG						HHGHRG					
	UV/Vis		CD		EPR		UV/Vis		CD		EPR		UV/Vis		CD		EPR		UV/Vis		CD		EPR	
	λ	ε	λ	$\Delta\varepsilon$	A_{II}	g_{II}	λ	ε	λ	$\Delta\varepsilon$	A_{II}	g_{II}	λ	ε	λ	$\Delta\varepsilon$	A_{II}	g_{II}	λ	ε	λ	$\Delta\varepsilon$	A_{II}	g_{II}
CuH_3L			259	1.8	185	2.23	662	31			165	2.30	667	54			167	2.27						
			300	−0.2																				
CuH_2L	600	92	263	1.8	197	2.21													605	109	267	1.7	192	2.23
			597	0.3																				
CuHL	597	102	263	2.2			526	87	272	−3.1	199	2.18	524	134	308	0.6	193	2.19	591	106	267	1.7		
			599	0.3					311	1.3					503	1.3					344	0.2		
									487	0.5														
									562	−0.8														
CuL	587	121	264	2.5	199	2.21	526	108	270	−3.4			524	132	304	0.7	195	2.19	578	116	265	2.9	205	2.21
			624	0.3					311	1.4					504	1.3					628	0.5		
									485	0.6														
									561	−0.8														
$CuH_{-1}L$			260	2.3	193	2.20	526	120	272	−2.9	204	2.17	519	129	297	0.7	203	2.18	578	116	265	2.9	205	2.21
			500	−0.23					310	1.4					502	1.4					628	0.5		
			595	−0.2					486	0.6														
			624	0.3					562	−0.8														
$CuH_{-2}L$													519	164	297	0.7								
															503	1.3								
$CuH_{-3}L$	506	257	275	−2.7	204	2.20	526	147	271	−2.9	200	2.18	519	164	316	0.6	203	2.18	526	206	277	−1.9	207	2.17
			311	1.3					309	1.4					502	1.8					317	2.0		
			507	−1.6					491	0.7											493	−0.5		
									563	−0.8														

result of the loss of a proton from the arginine side chain and metal bound imidazole [21].

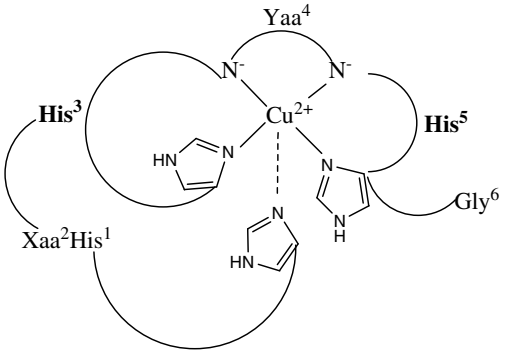
According to the potentiometric data, HHGHRG forms seven distinct species: CuH_3L, CuH_2L, CuHL, CuL, $CuH_{-1}L$, $CuH_{-2}L$ and $CuH_{-3}L$ (Fig. 1 and Table 2). The CuH_3L species is formed with the 2N coordination mode. $\log K = \log K_{CuH_3L} - \log K_{H_3L} = 7.35$ suggests an amino and an imidazole nitrogen involved in the binding of Cu^{2+}, as was suggested for the ligands discussed above. CuH_2L, with the d–d band at 605 nm and $A_{II} = 193$, is the 3N complex with the $\{NH_2, N^-, N_{im}\}$ binding pattern (Table 4). The proton dissociation $[CuH_2L] \leftrightarrow [CuHL] + H^+$ with $pK = 5.43$ could be assigned to the imidazole moiety as well as the further deprotonation with $pK = 6.11$, resulting in the formation of CuL, dominating in the pH range 6–9.5 (Fig. 1). Any relevant spectroscopic changes suggest the same coordination mode $\{NH_2, N^-, N_{im}\}$, only the deprotonations of imidazole moieties take place without taking part in metal ion coordination [26]. The $CuH_{-1}L$ species is characterized by the same spectroscopic parameters as CuL, indicating proton loss from the arginine side chain ($pK = 9.51$) (Table 4). The formation of $CuH_{-3}L$ corresponds to distinct changes in the d–d transitions, shifting from 578 to 526 nm (628 to 493 nm in the CD spectrum). This strongly suggests that $CuH_{-3}L$ is the 4N complex with a $\{NH_2, 3N^-\}$ binding mode (Table 4 and Fig. 1).

4. Discussion

The histidine residue is well known for its critical impact on complex stability and its structure [2,4–7]. According to data obtained for N-terminally protected peptides, the impact of histidine residues in the multi-histidine peptides on the binding mode is critical and it has a crucial contribution to the Cu^{2+} binding affinity of protein fragments [2,6–9].

A comparison of binding abilities of N-terminally protected peptides towards Cu^{2+} ions determine some differences. For peptides with the His-His motif (Ac-GHHRHG and Ac-HHGHRG) the coordination begins with 1N species involving the imidazole nitrogen, while for ligands with His-Xaa-His (Ac-HRHGHG, Ac-HGHRHG), the first species formed is the 2N complex (Fig. 2).

However, a peptide with the His-Xaa-His motif in the presence of the copper ion undergoes two strongly overlap-



Scheme 1. Hypothesized structure of the complexes with Cu^{2+} ions at physiological pH and Ac-His-Arg-His-Gly-His-Gly or Ac-His-Gly-His-Arg-His-Gly.

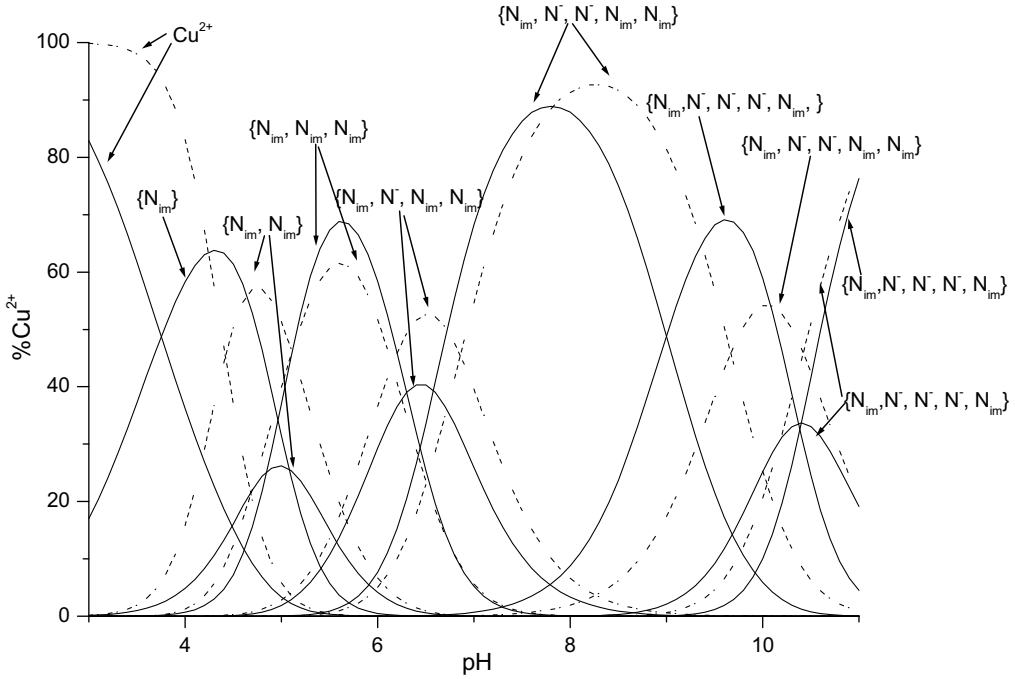
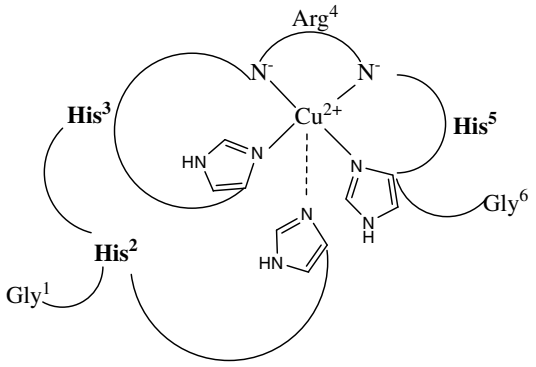


Fig. 2. Distribution diagram of complexed species formed as a function of pH in the Ac-Gly-His-His-Arg-His-Gly-Cu^{2+} (solid line) and Ac-His-Arg-His-Gly-His-Gly-Cu^{2+} (dashed line) systems.

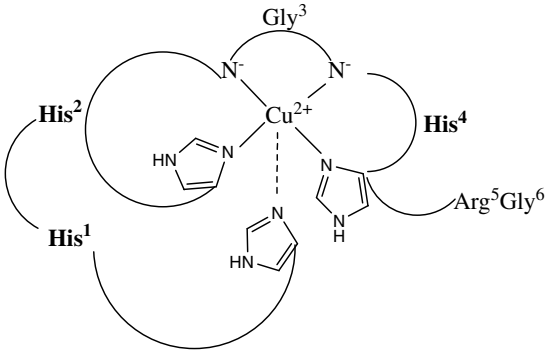


Scheme 2. Hypothesized structure of the complex with Cu^{2+} and Ac-Gly-His-His-Arg-His-Gly.

ping amide deprotonations ($\Delta pK = pK_{CuH_{-1}L} - pK_{CuL} = 0.19$ for Ac-HLHWH-NH_2 [27]) due to the favored formation of the $\{N_{im}, N^-, N^-, N_{im}, N_{im}\}$ binding mode (Scheme 1). According to the investigated N-terminally protected systems, strongly cooperative amide deprotonations are observed for each system, but for Ac-GHHRHG (Scheme 2) the value of $\Delta pK = 0.28$ is much lower than for the other systems ($\Delta pK_{Ac\text{-}HHGHRG} = 0.59$, $\Delta pK_{Ac\text{-}HGHRHG} = 0.70$, $\Delta pK_{Ac\text{-}HRHGHG} = 0.71$). Moreover, the final mode of binding with three amide nitrogens occurs for each N-terminally protected ligand–Cu^{2+} systems, but deprotonation of the third amide nitrogen seems to be easier for His-His peptides; the pK of reaction is 9.00, around 1.5 units lower than that for His-Xaa-His peptides.

Comparison of Ac-HHGHRG with Ac-HHGH-NH_2 [10] may suggest some involvement the in coordination mode of the arginine residue or C-terminal carboxyl group, which may contribute to the stabilization of the forming species. Although the binding modes are the same for both systems, the stability constants of the forming species are about 10 units higher for Ac-HHGHRG-Cu^{2+} (Fig. 3).

Despite the fact that $pK_{Ac\text{-}HHGHRG}$ of the second imidazole nitrogen coordination to the metal ion binding centre is about 0.5 units higher, the deprotonation of consecutive donors has occurred with lower pK values. The binding of the amidic donors begins at pH 5 with strong perturbations seen in the CD spectra, while for Ac-HHGH-NH_2 the coordination of the amide nitrogen occurs in distinctly more basic pH. In the physiological pH range, the second amide coordination is observed for Ac-HHGHRG



Scheme 3. Hypothesized structure of the complex with Cu^{2+} and Ac-His-His-Gly-His-Arg-Gly.

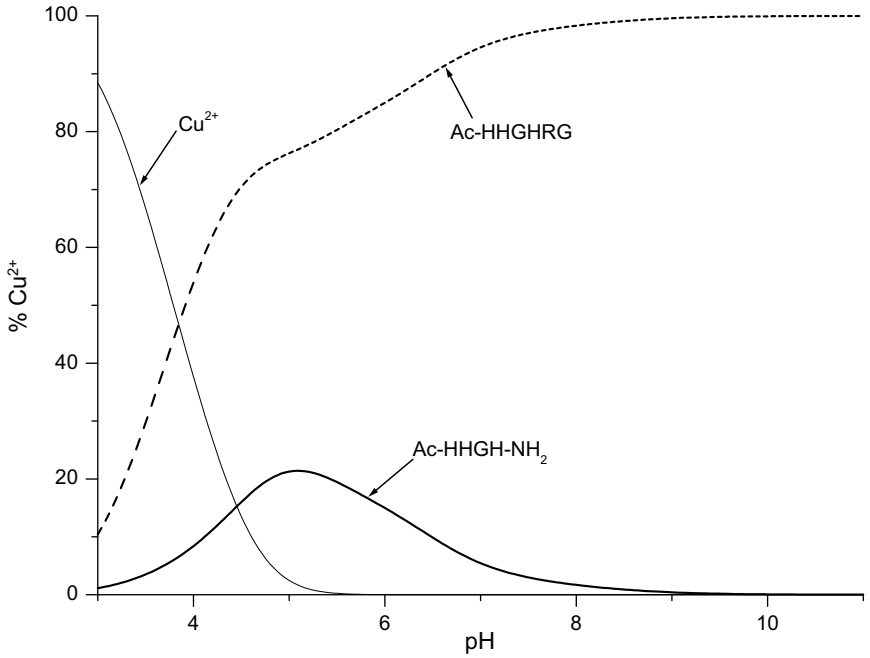


Fig. 3. Distribution profiles of free and complexed fractions of Cu^{2+} ions in the presence of both His-Ac-His-His-Gly-His-NH_2 (solid line) and Ac-His-His-Gly-His-Arg-Gly (dashed line).

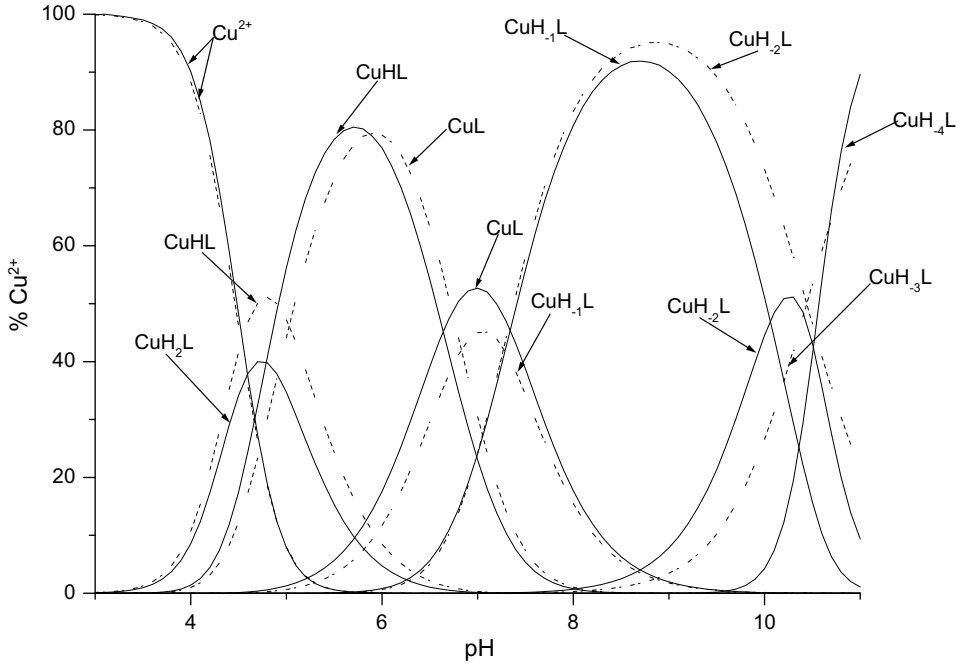


Fig. 4. Distribution diagram of complexed species formed as a function of pH in the Ac-His-Gly-His-Arg-His-Gly-Cu^{2+} (solid line) and Ac-His-Gly-His-Val-His-NH_2-Cu^{2+} [18] (dashed line) systems.

(Scheme 3), while for Ac-HHGH-NH_2 the imidazole macrochelate ring dominates [10].

According to the peptides with the His-Xaa-His motif in the sequence, the coordination modes which have been obtained for the investigated peptide-Cu^{2+} systems (Ac-HGHRHG, Ac-HRHGHG) are similar to that seen in the fragment (145–155) of the amyloid precursor protein [7] and Ac-HGHVH-NH_2 [18] with metal to ligand ratios of 1:1 and 1:2, respectively.

At acidic pH, the macrochelates including imidazole donors are present, while in physiological pH second amide coordination to the metal ion binding centre occurs. The p*K* values of donor deprotonations and distribution profiles are strictly similar with Ac-HGHVH-NH_2, which can suggest that in the ion case of Ac-HGHRHG and Ac-HRHGHG the involvement of arginine or carboxyl residues do not occur as was supposed in the Ac-HHGHRG-Cu^{2+} system (Fig. 4).

According to the study on the unprotected peptides, the increase of the thermodynamic stability of the complex species is caused by the presence of both anchoring sites: the terminal amino group and the histidine residue [4,5]. The position of the histidine residues within the peptide sequence strongly influences the binding properties in the unprotected ligands (see Fig. 5).

Peptides which contain His at the first position in the peptide sequence have specific coordination towards metal ions unlike ordinary peptides. The first major species involves a histamine-like donor set $\{NH_2, N_{im}\}$ [4]. Thus, for HRHGHG, HGHRHG and HHGHRG the first defined species is a histamine-like 2N chelate $\{NH_2, N_{im}\}$ ring [4]. Deprotonation and coordination of amide nitrogens takes place above pH 5, as it is found for oligoglicynes [28,29].

Nevertheless, the presence of multi-histidine sequences (His-Xaa-His) implies a crucial difference in the complex formation. As far as the histamine-like donor set was determined for peptides with the His^1 motif, a second characteristic albumin-like binding mode for His^3 is also observed [4,5,26]. It occurs not only for HRHGHG and HGHRHG peptides (Scheme 4), but also for GHHRHG. Moreover, the $\{NH_2, N^-, N^-, N_{im}\}$ binding mode takes place much easier for HRHGHG and HGHRHG than for GHHRHG, because of the fact that for peptides with a histidine residue in the second position in the peptide chain the most stable form is the 3N species with very high thermodynamic stability. It is caused by the simultaneous participation of $\{NH_2, N_{im}$ and $N^-\}$ donor atoms and formation of two fused chelate rings: five membered $\{NH_2, N^-\}$ and six-membered $\{N^-, N_{im}\}^-$. For ligands with His^2 the 3N complex with the $\{NH_2, N^-, N_{im}\}$ binding mode is the dominant species in the physiological pH range (Scheme 5).

For ligands with the His-His motif the final $\{N_{im}, 3N^-\}$ coordination mode occurs, e.g. for HHGHRG-Cu^{2+}. The formation of this binding mode is rather unusual for GHHRHG-Cu^{2+}, where albumin-like binding is more stable.

A comparison of the species distribution curves for unprotected ligands with the His-Xaa-His and His-His motif clearly shows that at low pH the coordination process is more effective for HHGHRG (Fig. 6) than for HGHRHG. At pH 3 around 50% of the Cu^{2+} ions are bound with HHGHRG, while only 10% of the Cu^{2+} ions are coordinated by HGHRHG. The formation of $\{NH_2,$

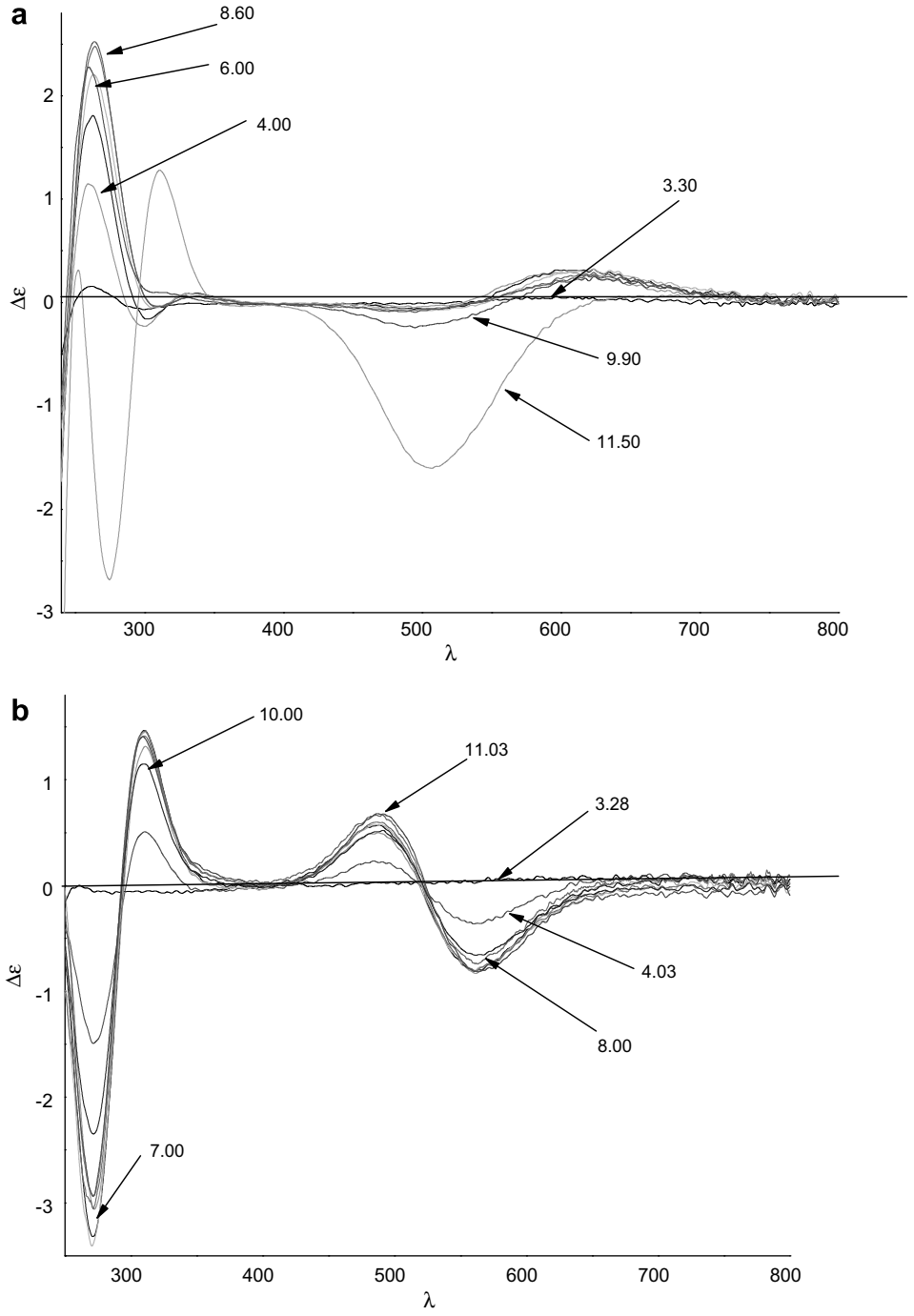


Fig. 5. CD spectra for (A) Gly-His-His-Arg-His-Gly-Cu^{2+}, (B) His-Arg-His-Gly-His-Gly-Cu^{2+}, (C) His-Gly-His-Arg-His-Gly-Cu^{2+} and (D) His-His-Gly-His-Arg-Gly-Cu^{2+}.

N^-, N_{im}} in the case of HHGHRG determines the dominance of this ligand at acidic pH. Above pH 5.5 the albumin-like coordination possible in the latter peptide causes HGHRHG to become a more effective ligand for Cu^{2+} ions (Fig. 7).

The obtained results have shown clear trends in the formation of complexes of Cu^{2+} ions with N-protected peptides. Metal ion coordination begins at the imidazole nitrogens which act as the anchoring groups [30,31]. The formation of CuL species involves the amide nitrogen. At physiological pH the dominant species is $CuH_{-1}L$ with the {$3N_{im}$, $2N^-$} binding mode. At high pH three amide nitrogens could be involved in Cu^{2+} ion binding [24].

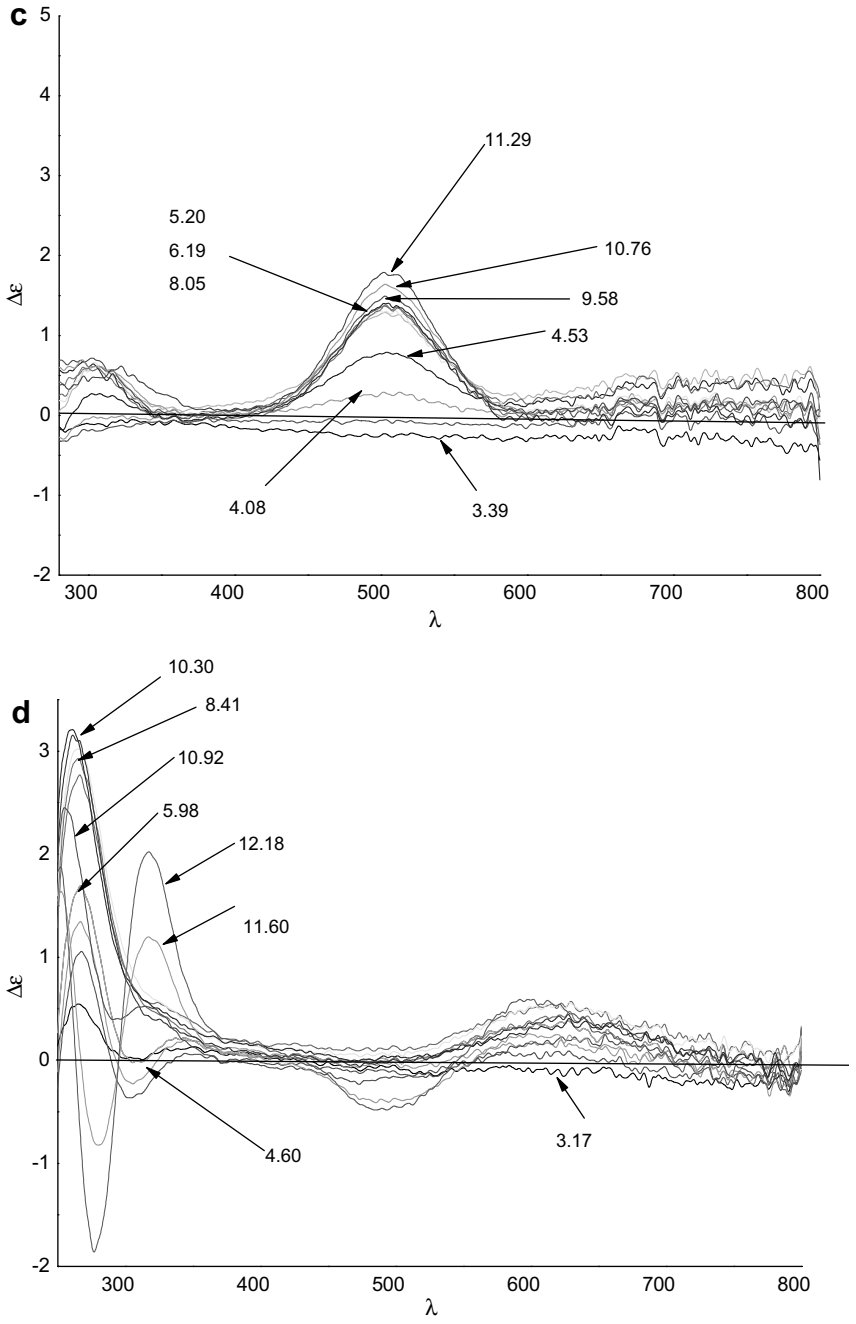
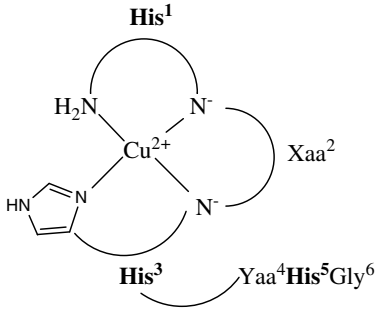
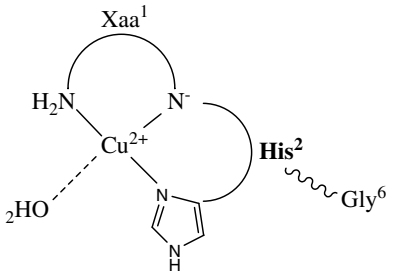


Fig. 5 (*continued*)



Scheme 4. Hypothesized structure of the complex with Cu^{2+} and His-Gly-His-Arg-His-Gly or His-Arg-His-Gly-His-Gly.



Scheme 5. Hypothesized structure of Cu^{2+} and Gly-His-His-Arg-His-Gly or His-His-Gly-His-Arg-Gly.

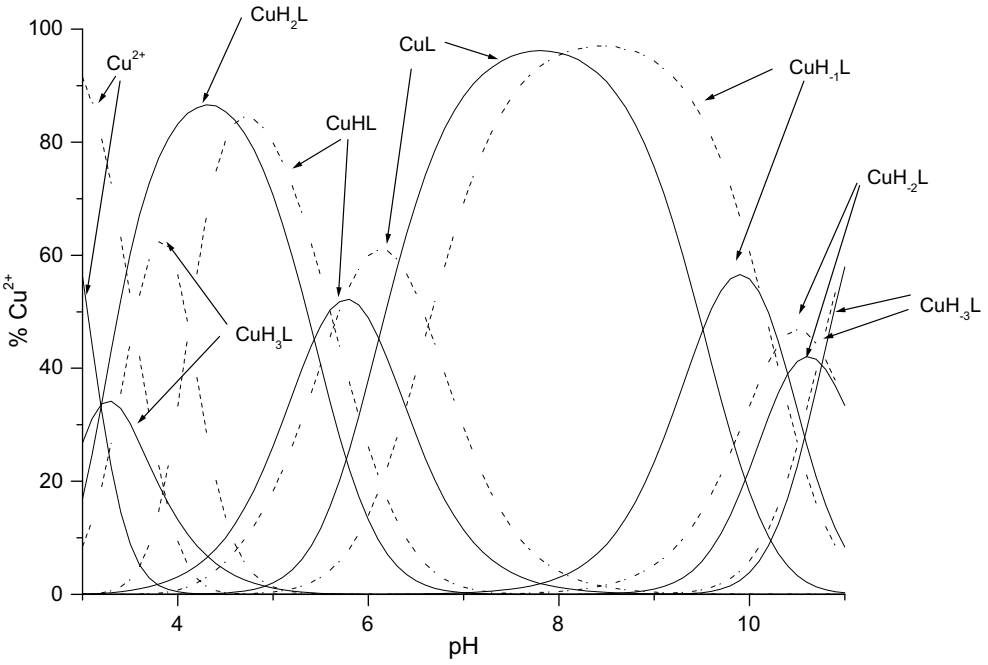


Fig. 6. Distribution diagram of complexed species formed as a function of pH in the His-His-Gly-His-Arg-Gly-Cu^{2+} (solid line) and His-Gly-His-Arg-His-Gly-Cu^{2+} (dashed line) systems.

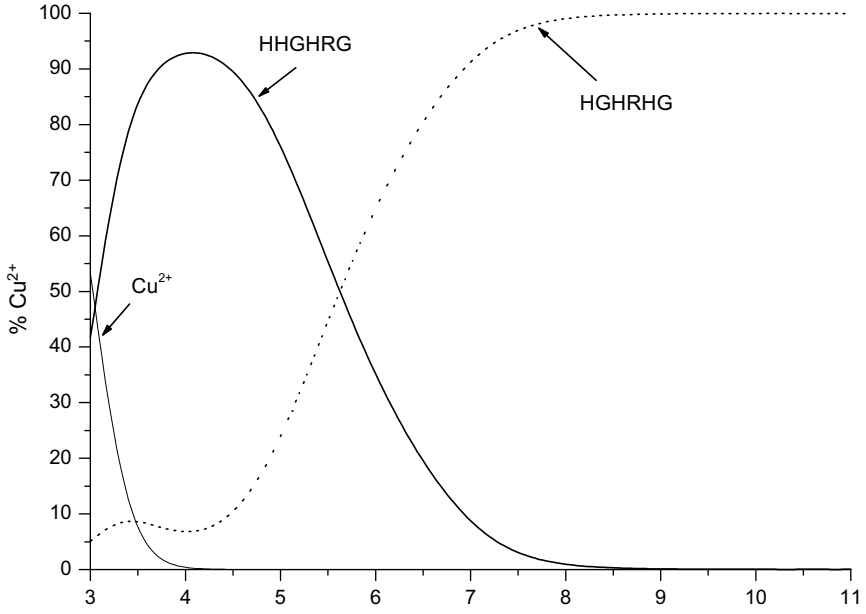


Fig. 7. Distribution profiles of free and complexed fractions of Cu^{2+} ions in the presence of both His-His-Gly-Arg-His-Gly (solid line) and His-Gly-His-Arg-His-Gly (dashed line).

The protection of the N-terminal amino group has a great impact on the binding affinity of the peptide. As seen in Fig. 8, a competition diagram obtained for Ac-HRHGHG and HRHGHG clearly shows that around pH 4 almost 100% of the Cu^{2+} ions are bound by an unprotected ligand, while the protected analog coordinates less than 5% of Cu^{2+}. The main reason derives from the involvement of the amino group in the coordination of Cu^{2+}.

Acknowledgement

This work is supported by the Ministry of Science and Higher Education (No. 405 038 32/2687).

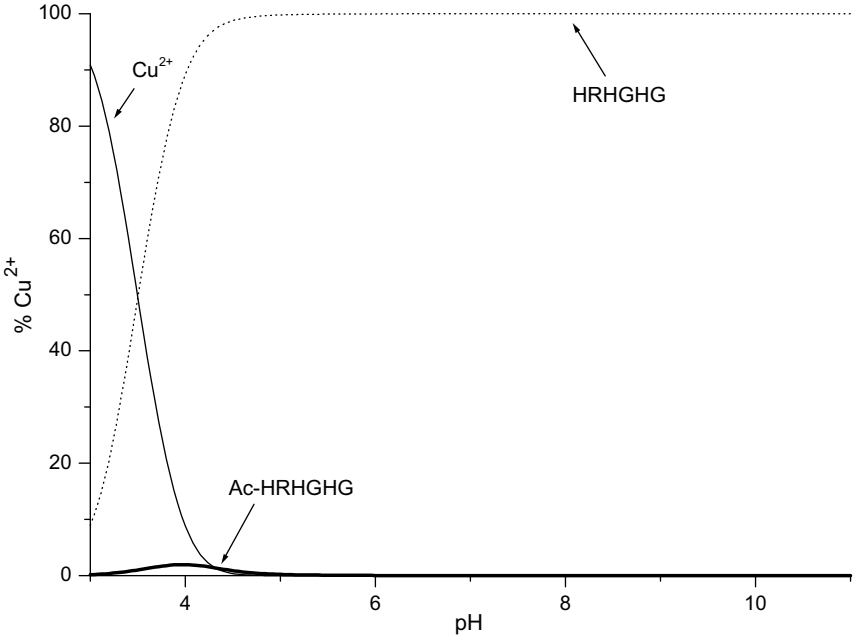


Fig. 8. Distribution profiles of free and complexed fractions of Cu^{2+} ions in the presence of both His-Arg-His-Gly-His-Gly (dashed line) and Ac-His-Arg-His-Gly-His-Gly (solid line).

References

[1] J.J.R.F.D. Silva, R.J.P. Williams, The Biological Chemistry of the Elements, Clarendon Press, Oxford, 1991.
[2] E. Gagelli, H. Kozłowski, D. Valensin, G. Valensin, Chem. Rev. 106 (2006) 1995.
[3] P.W. Jones, D.M. Taylor, D.R. Williams, J. Inorg. Biochem. 81 (2000) 1.
[4] H. Kozłowski, W. Bal, M. Dyba, T. Kowalik-Jankowska, Coord. Chem. Rev. 184 (1999) 319.
[5] H. Kozłowski, T. Kowalik-Jankowska, M. Jeżowska-Bojczuk, Coord. Chem. Rev. 249 (2005) 2323.
[6] M. Łuczkowski, K. Wiśniewska, L. Łankiewicz, H. Kozłowski, J. Chem. Soc., Dalton Trans. (2002) 2266.
[7] D. Valensin, F.M. Mancini, M. Łuczkowski, A. Janicka, K. Wiśniewska, E. Gaggelli, G. Valensin, L. Łankiewicz, H. Kozłowski, J. Chem. Soc., Dalton Trans. (2004) 16.
[8] G. Multhaup, A. Schlicksupp, L. Hesse, D. Beher, Th. Ruppert, C.L. Masters, K. Beyreuter, Science 271 (1996) 1406.
[9] M. Remelli, M. Łuczkowski, A.M. Bonna, Z. Mickiewicz, C. Conato, H. Kozłowski, New J. Chem. 27 (2003) 245.
[10] A. Janscó, Z. Paksi, N. Jakab, B. Gyurcsik, A. Rockenbauer, T. Gajda, J. Chem. Soc., Dalton Trans. (2005) 3187.
[11] M.A. Smith, P.L.R. Harris, L.M. Sayre, G. Perry, Proc. Natl. Acad. Sci. USA 94 (1997) 9866.
[12] M.A. Lovell, J.D. Robertson, W.J. Teesdale, J.L. Cambell, W.R. Markesbery, J. Neurol. Sci. 158 (1998) 47.
[13] G. Perry, M.A. Taddeo, R.B. Petersen, R.J. Castellani, P.L.R. Harris, S.L. Siedlak, A.D. Cash, Q. Liu, A. Nunomura, C.S. Atwood, M.A. Smith, Biometals 16 (2003) 77.
[14] M. Nakamura, N. Shishido, A. Nunomura, M.A. Smith, G. Perry, Y. Hayashi, K. Nakayama, T. Hayashi, Biochemistry 46 (2007) 12737.
[15] M. Orfei, M.C. Alcaro, G. Marcon, M. Chelli, M. Ginnaneschi, H. Kozłowski, J. Brasuń, L. Messori, J. Inorg. Biochem. 97 (2003) 299.
[16] J. Brasuń, C. Gabbiani, M. Ginnaneschi, L. Messori, M. Orfei, J. Świątek-Kozłowska, J. Inorg. Biochem. 98 (2004) 2016.
[17] J. Brasuń, A. Matera, S. Ołdziej, J. Świątek-Kozłowska, L. Messori, C. Gabbiani, M. Orfei, M. Ginnaneschi, J. Inorg. Biochem. 101 (2007) 452.
[18] C. Kállay, K. Várnagy, G. Malandrinos, N. Hadjiliadis, D. Sanna, I. Sóvágó, J. Chem. Soc., Dalton Trans. (2006) 4545.
[19] P. Gans, A. Sabatini, A. Vacca, J. Chem. Soc., Dalton Trans. (1985) 1195.
[20] G. Crisponi, F. Cristiani, V.M. Nurchi, Anal. Chim. Acta 281 (1993) 197.
[21] M.C. Aragoni, M. Arca, G. Crisponi, V.M. Nurchi, Anal. Chim. Acta 316 (1995) 195.
[22] G. Crisponi, F. Cristiani, V.M. Nurchi, R. Silvagni, Polyhedron 14 (1995) 1517.
[23] P. Stańczak, M. Łuczkowski, P. Juszczyk, Z. Grzonka, H. Kozłowski, J. Chem. Soc., Dalton Trans. (2004) 2102.
[24] D. Valensin, M. Łuczkowski, F.M. Mancini, A. Legowska, E. Gaggelli, G. Valensin, K. Rolka, H. Kozłowski, J. Chem. Soc., Dalton Trans. (2004) 1284.
[25] M. Łuczkowski, H. Kozłowski, M. Stawikowski, K. Rolka, E. Gaggelli, D. Valensin, G. Valensin, J. Chem. Soc., Dalton Trans. (2002) 2269.
[26] P. Młynarz, D. Valensin, K. Kociołek, J. Zabrocki, J. Olejnik, H. Kozłowski, New J. Chem. 26 (2002) 264.
[27] R.P. Bonomo, L. Casella, L. De Gioia, H. Molinari, G. Impellizzeri, T. Jordan, G. Pappalardo, R. Purello, E. Rizzarelli, J. Chem. Soc., Dalton Trans. (1997) 2387.
[28] A. Maryi, G. Malandrinos, J.C. Plakatouras, N. Hadjiliadis, I. Sóvágó, Bioinorg. Chem. Appl. 1 (2003) 99.
[29] C.E. Livera, L.D. Petit, M. Bataille, B. Perly, H. Kozłowski, B. Radomska, J. Chem. Soc., Dalton Trans. (1987) 661.
[30] M. Casolaro, M. Chelli, M. Ginnaneschi, F. Laschi, L. Messori, M. Muniz-Miranda, A.M. Papini, T. Kowalik-Jankowska, H. Kozłowski, J. Inorg. Biochem. 89 (2002) 181.
[31] H. Sigel, R.B. Martin, Chem. Rev. 82 (1982) 385.

heterogeneous catalysts. Studies on oxidation reactions catalyzed by such hybrid materials have received intense attention in the last few decades [18–21]. Copper(II) Schiff-base complexes, upon immobilization into microporous or mesoporous aluminosilicates, are capable of catalyzing olefin epoxidations and/or oxidations [20,21]. However, the activity of Schiff-base copper(II) complexes towards catalytic oxidation in a homogeneous medium is not well documented in the literature. So far only a few copper(II) Schiff-base complexes are reported to be catalytically active towards olefin oxidation [22].

There are some reports of molecular oxygen catalyzed oxidation, and 30% hydrogen peroxide is usually considered an environmental friendly oxidant, nevertheless, due to the explosive nature of hydrogen peroxide, industrial processes still mainly rely on *tert*-butyl-hydroperoxide (*tert*-BuOOH) [23]. Alkyl-hydroperoxides are used on a large scale in industrial epoxidation, for example in the Halcon-Arco and Sumitomo processes [24,25]. The recycling of the end-product of the oxidant, *viz.* *tert*-BuOH, has been realized in the Sumitomo process. Notably, *tert*-BuOOH has seldom been used as an oxidant in the investigations of the catalytic efficiency of copper(II) complexes towards epoxidation/oxidation reactions in a homogeneous medium.

We report here the synthesis, characterization and catalytic efficacy of three copper(II) Schiff-base complexes towards olefin oxidation of a variety of alkenes in different solvent media using *tert*-butyl-hydroperoxide as an oxidant. The molecular structure of complex **1** is determined by single crystal X-ray analysis.

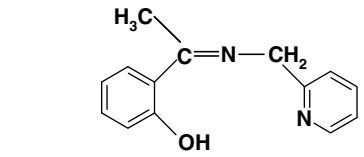
2. Experimental

2.1. General

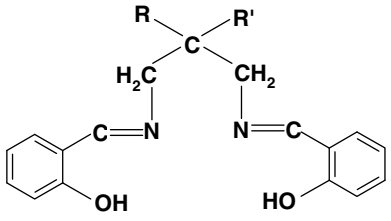
All solvents used were of AR grade and were distilled and dried before use. Salicyaldehyde, *ortho*-hydroxyacetophenone, copper(II) nitrate trihydrate and copper(II) perchlorate hexahydrate were purchased from Merck (India) and were used as received. Styrene, norbornene, cyclooctene, cyclohexene, *tert*-BuOOH (70% aq.), 2,2-dimethyl-1,3-diamino-propane, 1,3-diamino-2-propanol and 2-aminomethyl-pyridine were purchased form Aldrich and were used as received. Elemental analyses (CHN) were performed using a Perkin–Elmer 240 elemental analyzer. IR spectra were recorded on a Nicolate Magna IR 750 Series II FT-IR spectrometer and UV/Vis spectra were recorded on a Perkin–Elmer LAMBDA EZ-301 spectrophotometer. The ligands HL^1, H_2L^2 and H_2L^3 (Scheme 1) were synthesized following the reported procedures [26].

2.1.1. Synthesis of the complexes $[Cu(L^1)(H_2O)](ClO_4)$ (1), $[Cu(L^2)]$ (2) and $[Cu(L^3)]$ (3)

To prepare complex **1**, a methanolic solution of HL^1 (1 mmol, 0.226 g) was added to a methanolic solution of copper (II) perchlorate hexahydrate (1 mmol, 0.371 g)



HL^1



H_2L^2; R = H, R' = OH

H_2L^3; R = R' = Me

Scheme 1.

and stirred for 45 min. The resulting solution, upon slow evaporation, affords violet prismatic crystals (yield: 60%). *Anal.* Calc. for $C_{14}H_{15}ClCuN_2O_6$: C, 41.4; H, 3.7; N, 6.9. Found: C, 41.89; H, 4.0; N, 7.3%. IR (KBr): υ(C=N), 1597 cm^{-1}; $\upsilon(ClO_4)$, 1145, 1118, 1084 cm^{-1}. λ_{max}/nm (methanol), 620, 370, 297. Complexes **2** and **3** were synthesized by following the reported procedures [27]. Analysis of complex **2**. *Anal.* Calc. for $C_{17}H_{16}CuN_2O_3$: C, 56.6; H, 4.4; N, 7.7. Found: C, 56.8; H, 4.7; N, 7.6%. IR (KBr): υ(C=N), 1597 cm^{-1}. λ_{max}/nm (methanol), 594; 350. Analysis of complex **3**. *Anal.* Calc. for $C_{19}H_{20}CuN_2O_2$: C, 61.3; H, 5.3; N, 7.5. Found: C, 61.6; H, 5.9; N, 8.0%. IR (KBr): υ(C=N), 1630 cm^{-1}. λ_{max}/nm (methanol), 594.

2.2. X-ray crystallography

2.2.1. Crystal data for complex 1

$C_{14}H_{15}ClCuN_2O_6$, $M = 406.27$, monoclinic, space group $P2_1/c$, $a = 15.148(3)$, $b = 14.491(3)$, $c = 15.364(3)$ Å, $\gamma = 112.02(2)°$, $V = 3126.5(11)$ Å^3, $Z = 8$, $R_{int} = 0.0711$, $D_{calc} = 1.726$ g cm^{-3}, $F_{000} = 1656$, $\mu = 1.602$ mm^{-1}, dimensions = 0.05 × 0.07 × 0.09 mm, $T = 293$ K.

2.2.2. X-ray single crystal structure determination of 1

Cell dimensions and intensity data for complex **1** were measured at 293 K with graphite-monochromated Mo Kα radiation, on a Bruker AXS Smart single crystal diffractometer with a CCD area detector. The data were corrected for Lorentz, polarisation and absorption effects. The structure was solved by direct methods using SHELXS [28] and refined by the full-matrix least-squares method based on $|F_{obs}|^2$ using SHELXL [28]. The non-hydrogen atoms were refined anisotropically, while the hydrogen atoms, generated using idealized geometry, were made to 'ride' on their parent atoms and used in the structure factor calculations. Neutral atom scattering factors were taken from Cromer

and Weber [29a] and anomalous dispersion effects were included in F_{calc} [29b].

2.3. Catalytic reactions

The catalytic reactions were carried out in a glass batch reactor according to the following procedure. The olefin (9–12 mmol) and catalyst (0.005 mmol) were added to 8 ml of acetonitrile in a round-bottom flask. The mixture was then equilibrated to 70 °C in an oil bath. After addition of *tert*-BuOOH (20 mmol) the mixture was stirred continuously. The products of the catalytic reactions were collected at different time intervals and were identified and quantified with a VARIAN CP-3800 gas chromatograph equipped with an FID detector. A CP-Sil 8 CB capillary column was used for analysis of the products.

3. Results and discussion

3.1. Description of the structure of complex *1*

Fig. 1 shows the ORTEP diagram of complex **1** with thermal ellipsoids drawn at 50% probability. Selected bond distances and angles of complex **1** are collated in Table 1. The crystal structure of complex **1** consists of two independent molecules, labelled A and B, in the crystallographic asymmetric unit. In both the molecules, the copper(II) ion assumes a distorted square planar geometry. The coordination plane is composed of NNO donor atoms (nitrogen atoms of the azomethine and pyridine ring and the phenoxo oxygen atom, respectively) of the tridentate Schiff-base ligand and an oxygen atom of the water molecule. The deviation of the four basal donor atoms, O(1A), O(2A), N(2A) and N(1A), in molecule A from the least-squares plane through them were −0.134(3), 0.210(3), −0.206(3) and 0.170(3) Å, respectively. Similarly the deviation of the four basal donor atoms, O(1B), O(2B), N(2B) and N(1B), in molecule B from the least-squares mean plane through them were 0.107(3), −0.157(3), 0.194(3) and −0.176(3) Å, respectively. In both the molecules, the perchlorate ions are coordinated to the copper center distally via oxygen atoms [O(3C) and O(3D) for molecule A and molecule B, respectively]. In this complex, the coordinated water molecules, the phenoxo oxygen atoms and the perchlorate oxygen atoms are involved in the formation of multiple bifurcated and trifurcated hydrogen bonds.

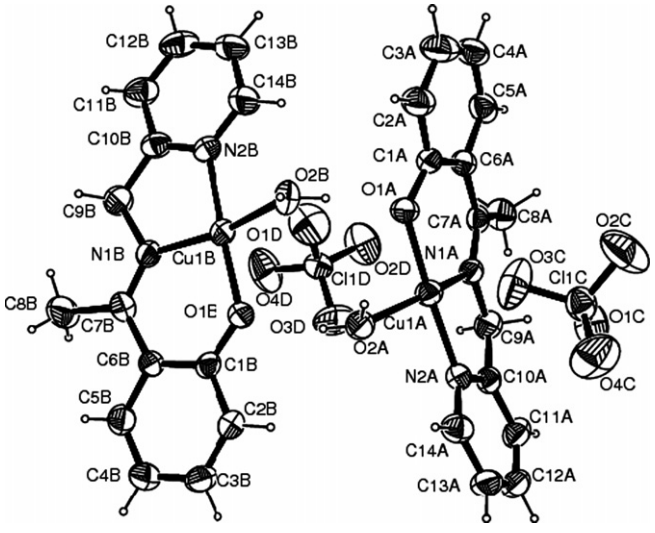


Fig. 1. ORTEP diagram of complex $[Cu(L^1)(H_2O)](ClO_4)$ (**1**) with the atom numbering scheme.

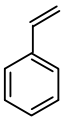
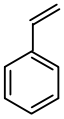
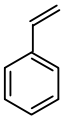
Table 1
Selected bond lengths (Å) and angles (°) for $[Cu(L^1)(H_2O)](ClO_4)$ (**1**)

Molecule A		Molecule B	
Cu(1A)–O(1A)	1.866(2)	Cu(1B)–O(1B)	1.874(2)
Cu(1A)–N(1A)	1.937(3)	Cu(1B)–N(1B)	1.937(3)
Cu(1A)–N(2A)	1.949(3)	Cu(1B)–N(2B)	1.967(3)
Cu(1A)–O(2A)	2.035(3)	Cu(1B)–O(2B)	1.983(3)
N(1A)–Cu(1A)–O(1A)	93.85(12)	N(1B)–Cu(1B)–O(1B)	94.51(12)
N(1A)–Cu(1A)–N(2A)	85.33(13)	N(1B)–Cu(1B)–N(2B)	84.81(13)
N(1A)–Cu(1A)–O(2A)	161.90(13)	N(1B)–Cu(1B)–O(2B)	165.70(12)
O(1A)–Cu(1A)–O(2A)	89.58(11)	O(1B)–Cu(1B)–O(2B)	91.73(11)
O(1A)–Cu(1A)–N(2A)	176.63(12)	O(1B)–Cu(1B)–N(2B)	174.20(12)
N(2A)–Cu(1A)–O(2A)	92.20(13)	N(2B)–Cu(1B)–O(2B)	90.25(13)

3.2. Catalytic activities

Aromatic and aliphatic alkenes react with *tert*-BuOOH to produce the corresponding oxides and/or epoxides in good yield, with moderate selectivity, in acetonitrile when catalyzed by the Cu Schiff-base complexes (Fig. 2). The results of the catalytic oxidation of different substrates are given in Table 2. The oxidation of styrene with *tert*-BuOOH gives styrene epoxide in 54–39% yield (selectivity 72–39%) (Table 2) under the homogeneous conditions, and along with this a moderate amount (60–21%) of benzaldehyde is also detected. A turnover frequency of 79–60 has been attained in the styrene oxidation reaction. While complex **3** shows the lowest selectivity in the production of styrene epoxide, complex **2** shows the highest selectivity. Consequently the benzaldehyde production was highest in the case of complex **3** whereas it was lowest in the case of complex **2**. Even though copper(II) Schiff-base complexes have been well known for some time, they have scarcely been used as homogeneous catalysts in olefin oxidation reactions. Epoxidation of styrene with different oxidizing agents over copper(II) Schiff-base catalysts under homogeneous conditions have been studied in the recent past [22]. Das et al. have obtained a moderate yield of olefin epoxide using a copper(II) Schiff-base complex as a catalyst in the presence of 2-methylpropanal and molecular oxygen under homogeneous conditions [22a], while a maximum yield of ca. 15% of styrene epoxide has been achieved with iodosylbenzene using Schiff-base copper complexes [22c]. It is noteworthy that complex **2** has been studied as a possible galactose oxidase model in an earlier study and showed remarkable catalytic activity in the oxidation of *n*-propanol or hydroxyacetone in the presence of KOH under O_2 [27c].

Table 2
Homogeneous alkene oxidation catalyzed by complexes $[Cu(L^1)(H_2O)](ClO_4)$ (**1**), $[Cu(L^2)]$ (**2**) and $[Cu(L^3)]$ (**3**) at 70 °C[a]

Catalyst	Substrate	Reaction time (h)	Conversion (wt%)	% Yield of products		TOF[b] (h^{-1})
				Epoxide	Others	
$[Cu(L^1)(H_2O)](ClO_4)$ (**1**)		10	98	100[c]		208
		24	86	42	44[d]	69
		24	93	44	49[e]	94
		24	75	60	15[f]	57
$[Cu(L^2)]$ (**2**)		24	99	99[c]		88
		24	75	54	21[d]	60
		24	84	30	54[e]	85
		24	75	56	19[f]	57
$[Cu(L^3)]$ (**3**)		24	97	97[c]		86
		24	99	39	60[d]	79
		24	100	26	74[e]	102
		24	76	63	13[f]	58

[a] Reaction conditions: alkenes (9–12 mmol); catalysts (0.005 mmol); *tert*-BuOOH (20 mmol); acetonitrile (8 ml).
[b] Turn over frequency = mol converted/mol of active site/time.
[c] *exo*-Epoxynorbornane.
[d] Benzaldehyde and benzoic acid.
[e] Cyclohex-2-en-1-ol and cyclohex-2-en-1-one.
[f] Cyclooctane-1,2-diol.

The oxidation of cyclohexene (Table 2) proceeds smoothly catalyzed by complexes **1**–**3**, showing excellent conversion of 100–84%, but cyclohexene oxide was not the major product in this reaction. The desired product, cyclohexene oxide, was produced with only poor to moderate selectivity (47–26%). Apart from cyclohexene-oxide, cyclohex-2-en-1-ol and cyclohex-2-en-1-one were also generated (74-49%) owing to allylic C–H oxidation. Salavati-

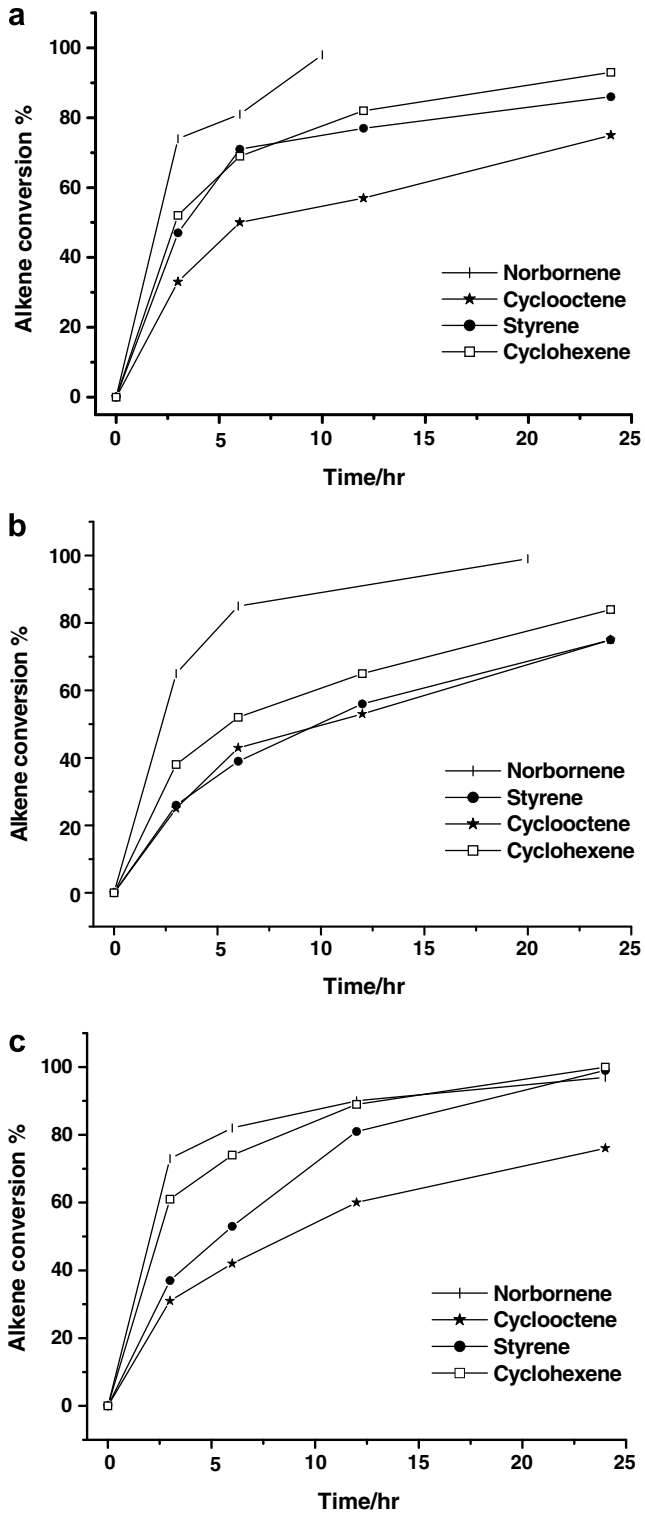


Fig. 2. Reaction profile for the oxidation of olefins with *tert*-BuOOH in the presence of complexes $[Cu(L^1)(H_2O)](ClO_4)$ (**1**) (a); $[Cu(L^2)]$ (**2**) (b); $[Cu(L^3)]$ (**3**) (c).

Niasari et al. have reported that oxidation of cyclohexene with *tert*-BuOOH catalyzed by alumina supported copper(II) Schiff-base complexes afforded cyclohex-2-en-1-ol, cyclohex-2-en-1-one and 1-(*tert*-butylperoxy)-2-cyclohexene [21g,21h]. Clearly, this alumina based catalyst activates

Table 3
Comparison of the catalytic efficacy of complexes $[Cu(L^1)(H_2O)](ClO_4)$ (**1**), $[Cu(L^2)]$ (**2**) and $[Cu(L^3)]$ (**3**) with other reported copper(II) catalysts for the oxidation of cyclohexene with *tert*-BuOOH in different solvent media

Complexes	CH_3CN	$CHCl_3$	CH_2Cl_2	CH_3OH	Reference
$[Cu(Me_2salpnMe_2)]$–Al_2O_3	42	57	60	55	[21h]
$[Cu(Me_2salpnMe_2)]$			37		[21h]
$[Cu(salpnMe_2)]$–Al_2O_3	36	54	57	52	[21g]
$[Cu(L^1)(H_2O)](ClO_4)$ (**1**)	93	51	69	39	this work
$[Cu(L^2)]$ (**2**)	84	94	75	33	this work
$[Cu(L^3)]$ (**3**)	100	75	68	30	this work

$H_2Me_2salpnMe_2$ = *N*,*N*′-bis(α-methylsalicylidene)-2,2-dimethylpropane-1,3-diamine. $salpnMe_2$ = *N*,*N*′-bis(salicylidene)-2,2-dimethylpropane-1,3-diamine.

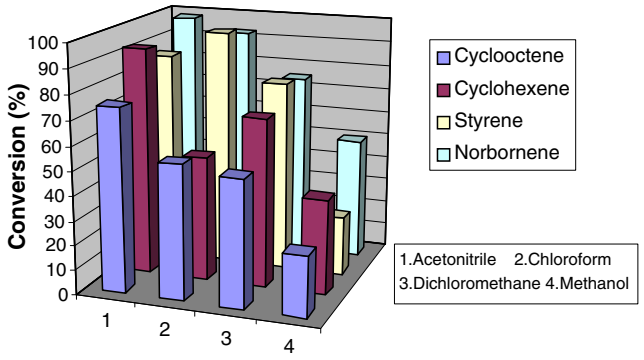


Fig. 3. Effect of solvent on the conversion in olefin oxidation reactions catalyzed by complex $[Cu(L^1)(H_2O)](ClO_4)$ (**1**).

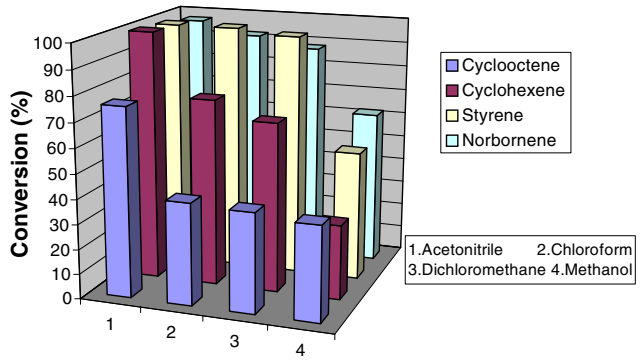


Fig. 4. Effect of solvent on the conversion in olefin oxidation reactions catalyzed by complex $[Cu(L^3)]$ (**3**).

preferentially the C–H bond over the C=C bond. Moreover the presence of 1-(*tert*-butylperoxy)-2-cyclohexene among the products indicates the possibility of the occurrence of a radical mechanism in the allylic C–H oxidation in this case. Salavati-Niasari et al. have proposed that alumina supported transition metal catalysts with *tert*-BuOOH as an oxidant promotes the allylic oxidation pathway while epoxidation attains the least preference due to the highly acidic properties of the alumina support [21h]. In contrast, epoxidation of cyclohexene with *tert*-BuOOH catalyzed by complexes **1**–**3** afforded a considerable

amount of cyclohexene-oxide while CH_3CN was found to be the preferred solvent for this reaction in our study (Table 3).

Among the bulkier cycloalkenes, such as norbornene and cyclooctene, norbornene has been effectively converted selectively to *exo*-epoxynorbornane (conversion 98–97%, selectivity 100%). On the other hand in the case of cyclooctene, its epoxide was not the sole product, along with the desired epoxide, cyclooctane-1,2-diol (19–13%) was also generated (Table 2).

The effect of various reaction media on the oxidation of cyclohexene catalyzed by complexes **1**–**3** has been studied. The results of this study have been collated in Table 3. The variation of catalytic efficacies of complexes **1**–**3** in different solvents has been compared with the other similar kinds of catalytic systems reported earlier [21g,21h]. A graphical representation of the relative efficacies of the catalysts in different solvents has been given in Figs. 3 and 4 for complexes **1** and **3**, respectively. Even from a cursory look at Table 3 it is apparent that the efficiency of the catalysts [Cu(salpnMe_2)]–Al_2O_3 and [Cu(Me_2salpnMe_2)]–Al_2O_3 for the oxidation of cyclohexene in different solvents decreases in the order: dichloromethane > chloroform > methanol > acetonitrile [21g,21h]. However, our results showed a completely different trend. The efficiency of the catalysts, in general, followed the order: acetonitrile > chloroform > dichloromethane > methanol.

4. Conclusions

In summary, we have synthesized and characterized three Schiff-base copper(II) complexes, and have used them as catalysts in olefin oxidation. All of them are found to be catalytically active in industrially important epoxidation reactions in different solvent media under homogeneous conditions. At a variance with the earlier reports, complexes **1**–**3** have shown the highest catalytic efficacy in CH_3CN. *tert*-BuOOH was used as the oxidant in these reactions. It is known that copper(II) can bind the peroxo-group on treatment with peroxides [30] and the precatalyst species containing L_xCu–OOR (where L = ligand) type moieties seem to be capable of transferring the oxo functionality to the organic substrates to give the corresponding oxidized products [31]. We speculate that, in our case, a similar kind of mechanism is operative. X-ray crystal structure analysis of complexes **1**–**3** shows that the coordination environment around the copper(II) ion in these complexes is easily accessible for an external ligand, as a result alkyl-hydroperoxide gets enough space to bind copper in the intermediate stages of the catalytic cycle.

Acknowledgements

The work is financially supported by the Department of Science and Technology, Government of India, by a Grant (SR/S1/IC-12/2003) (to S.K.). Financial support from the University Grants Commission, New Delhi, by a Grant (F. No. 32-235/2006 (SR)) is also gratefully acknowledged. R.B. thanks the CSIR (India) for a JRF award. We are grateful to CDRI, Lucknow for elemental analyses (on a chargeable basis).

Appendix A. Supplementary data

CCDC 638942 contains the supplementary crystallographic data for **1**. These data can be obtained free of charge via http://www.ccdc.cam.ac.uk/conts/retrieving.html, or from the Cambridge Crystallographic Data Centre, 12 Union Road, Cambridge CB2 1EZ, UK; fax: (+44) 1223-336-033; or e-mail: deposit@ccdc.cam.ac.uk. Supplementary data associated with this article can be found, in the online version, at doi:10.1016/j.poly.2008.01.030.

References

[1] (a) J.B. Longenecker, E.E. Snell, J. Am. Chem. Soc. 79 (1957) 142;
(b) E.E. Snell, A.E. Braunstein, E.S. Severin, Yu.M. Torchinsky, Pyridoxal Catalysis: Enzymes and Model Systems, Interscience, New York, 1968;
(c) E.E. Snell, P.M. Fassella, A. Braunstein, A. Ross-Fanelli, Chemical and Biological Aspects of Pyridoxal Catalysis, MacMillan, New York, 1963;
(d) V.M. Doctor, J. Oro, J. Biochem. 112 (1969) 691.

[2] (a) G. Plesch, C. Friebel, O. Svajlenova, J. Krätsmar-Smogrovic, D. Mlynarcik, Inorg. Chim. Acta 139 (1988) 151;
(b) M. Blahova, J. Sokolik, S. Sedlácková, E. Burianova, D. Mlynarcik, Czech. Farm. 42 (1993) 137 (Chem. Abstr. 120, 293910t);
(c) J. Krätsmar-Smogrovic, V. Svajlenová, V. Seressova, Czech. Pat., 1991, 271991 (cl.co7FI/08) (Chem. Abstr. 199, P84669m).

[3] (a) M.C. Apella, R. Totaro, E.J. Baran, Biol. Trace Elem. Res. 37 (1993) 293;
(b) R.M. Totaro, M.C. Apella, M.H. Torre, E. Friet, I. Viera, E. Kremer, E.J. Baran, Acta Farm. Bonaerense. 12 (1993) 73 (Chem. Abstr. 121, 271279n);
(c) J. Casanova, G. Alzuet, J. Borr'as, O. Carugo, J. Chem. Soc., Dalton Trans. (1996) 2239.

[4] (a) G.A. Morris, H. Zhou, C.L. Stern, S.T. Nguyen, Inorg. Chem. 40 (2001) 3222;
(b) E.N. Jacobsen, M.H. Wu, in: E.N. Jacobsen, A. Pfaltz, H. Yamamoto (Eds.), Comprehensive Asymmetric Catalysis, vol. 2, Springer-Verlag, Berlin, 1999, p. 649;
(c) T. Katsuki, Coord. Chem. Rev. 140 (1995) 189.

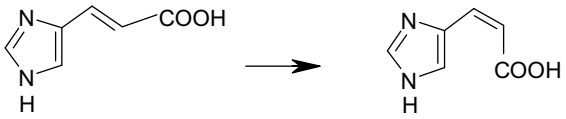
[5] (a) P. Chaudhuri, C. Stockheim, K. Wieghardt, W. Deck, R. Gregorzik, H. Vahrenkamp, B. Nuber, J. Weiss, Inorg. Chem. 31 (1992) 1451;
(b) S. Uhlenbrock, B. Krebs, Angew. Chem. Int., Ed. Engl. 31 (1992) 1647;
(c) N.N. Murthy, K.D. Karlin, J. Chem. Soc., Chem. Commun. (1993) 1236;
(d) X.-M. Chen, Y.-X. Tong, T.C.W. Mak, Inorg. Chem. 33 (1994) 4586;
(e) C. Bazzicalupi, A. Bencini, A. Bianchi, V. Fusi, P. Paoletti, B. Valtancoli, J. Chem. Soc., Chem. Commun. (1994) 881;
(f) C. Bazzicalupi, A. Bencini, A. Bianchi, V. Fusi, L. Mazzanti, P. Paoletti, B. Valtancoli, Inorg. Chem. 34 (1995) 3003;
(g) C. Bazzicalupi, A. Bencini, A. Bianchi, V. Fusi, P. Paoletti, G. Piccardi, B. Valtancoli, Inorg. Chem. 34 (1995) 5622;
(h) J.W. Yun, T. Tanase, S.J. Lippard, Inorg. Chem. 35 (1996) 7590;
(i) M. Yamami, M. Tanaka, H. Sakiyama, T. Koga, K. Kobayashi, H. Miyasaka, M. Ohba, H. Okawa, J. Chem. Soc., Dalton. Trans. (1997) 4595;

(j) F. Meyer, P. Rutsch, Chem. Commun. (1998) 1037;
(k) E.I. Solomon, U.M. Sundaram, T.E. Machonkin, Chem. Rev. 96 (1996) 2563.
[6] A. Berkessel, M. Frauenkon, T. Schwenkreis, A. Steinmetz, J. Mol. Catal. A: Chem. 117 (1997) 339.
[7] L.A. Kovbasyuk, I.O. Fritzky, V.N. Kokozay, T.S. Iskenderov, Tetrahedron 16 (1997) 1723.
[8] C.-W. Ho, W.-C. Cheng, M.-C. Cheng, S.-M. Peng, K.-F. Cheng, C.-M. Che, J. Chem. Soc., Dalton Trans. (1996) 405.
[9] S.S. Tandon, L.K. Thompson, J.N. Bridson, V. Mckee, A.J. Downard, Inorg. Chem. 31 (1992) 4635.
[10] J. Topich, J.O. Bachert, Inorg. Chem. 31 (1992) 511.
[11] (a) S. Ulmann, Encyclopedia of Industrial Chemistry, 6th ed., Wiley/VCH, New York/Weinheim, 1998;
(b) K.A. Jørgenson, Chem. Rev. 89 (1989) 431.
[12] (a) W. Zhang, J.L. Loebach, S.R. Wilson, E.N. Jacobsen, J. Am. Chem. Soc. 112 (1990) 2801;
(b) K.I. Kureshy, N.H. Khan, S.H.R. Abdi, P. Iyer, A.K. Bhatt, J. Mol. Catal. A: Chem. 120 (1997) 101;
(c) M. Palucki, G.J. McCormick, E.N. Jacobsen, Tetrahedron Lett. 36 (1995) 5457;
(d) R. Krishan, S. Vancheesan, J. Mol. Catal. A: Chem. 157 (2000) 15.
[13] (a) C. Bousquet, D.G. Gilheany, Tetrahedron Lett. 36 (1995) 7739;
(b) H. Imanishi, T. Katsuki, Tetrahedron Lett. 38 (1997) 251.
[14] R.I. Kureshy, N.H. Khan, S.H.R. Abdi, S.T. Patel, P. Iyer, J. Mol. Catal. A: Chem. 150 (1999) 175.
[15] E.G. Samsel, K. Srinivasan, J.K. Kochi, J. Am. Chem. Soc. 107 (1985) 7606.
[16] P.S. Dixit, K. Srinivasan, Inorg. Chem. 27 (1988) 4507.
[17] E.M. McGarrigle, D.G. Gilheany, Chem. Rev. 105 (2005) 1563, and references therein.
[18] J.M. Thomas, Angew. Chem., Int. Ed. Engl. 38 (1999) 3588.
[19] D.E. De Vos, M. Dams, B.F. Sels, P.A. Jacobs, Chem. Rev. 102 (2002) 3615.
[20] P. Karandikar, M. Agashe, K. Vijayamohanan, A.J. Chandwadkar, Appl. Catal. A 257 (2004) 133.
[21] (a) S. Koner, Chem. Commun. (1998) 593;
(b) S. Jana, B. Dutta, R. Bera, S. Koner, Langmuir 23 (2007) 2492;
(c) M. Salavati-Niasari, S.N. Mirsattari, J. Mol. Catal. A: Chem. 268 (2007) 50;
(d) C. Jin, W. Fan, Y. Jia, B. Fan, J. Ma, R. Li, J. Mol. Catal. A: Chem. 249 (2006) 23;
(e) M.R. Maurya, A.K. Chandrakar, S. Chand, J. Mol. Catal. A: Chem. 263 (2007) 227;
(f) A. Sakthivel, W. Sun, G. Raudaschl-Sieber, A.S.T. Chiang, M. Hanzlik, F.E. Kühn, Catal. Commun. 7 (2006) 302;
(g) M. Salavati-Niasari, M. Hassani-Kabutarkhani, F. Davar, Catal. Commun. 7 (2006) 955, and refereces therein;
(h) M. Salavati-Niasari, P. Salemi, F. Davar, J. Mol. Catal. A: Chem. 238 (2005) 215.
[22] (a) G. Das, R. Shukla, S. Mandal, R. Singh, P.K. Bharadwaj, Inorg. Chem. 36 (1997) 323;
(b) S. Bunce, R.J. Cross, L.J. Farrugia, S. Kunchandy, L.L. Meason, K.W. Muir, M. O Donnell, R.D. Peacock, D. Stirling, S.J. Teat, Polyhedron 17 (1998) 4179;
(c) S. Zolezzi, E. Spodine, A. Decinti, Polyhedron 22 (2003) 1653;
(d) X.-H. Lu, Q.-H. Xia, H.-J. Zhan, H.-X. Yuan, C.-P. Ye, K.-X. Su, G. Xu, J. Mol. Catal. A: Chem. 250 (2006) 62.
[23] L.F. Veiros, A. Prazeres, P.J. Costa, C.C. Romão, F.E. Kühn, M.J. Calhorda, J. Chem. Soc., Dalton Trans. (2006) 1383.
[24] J.-M. Brégeault, J. Chem. Soc., Dalton Trans. (2003) 3289.
[25] (a) M.N. Sheng, G.J. Zajaczek, ARCO, Br. Pat., 1.136.923, 1968.;
(b) J. Halcon Kollar, US Pat., 3.350.422, 1967;
(c) J Halcon Kollar, US Pat., 3.351.635, 1967.
[26] (a) R.H. Bailes, M.J. Caovin, J. Am. Chem. Soc. 69 (1947) 1886;
(b) Y. Nishida, S. Kida, J. Chem. Soc., Dalton Trans. (1986) 2633.
[27] (a) B.H. Chen, H.H. Yao, W.T. Huang, P. Chattopadhyay, J.M. Lo, T.H. Lu, Solid State Sci. 1 (1999) 119;
(b) C. Arici, F. Ercan, R. Kurtaran, O. Atakol, Acta Crystallogr.: Cryst. Struct. Commun. 57C (2001) 812;
(c) N. Kitajima, K. Whang, Y. Morooka, A. Uchida, Y. Sasada, J. Chem. Soc., Chem. Commun. (1986) 1504.
[28] G.M. Sheldrick, SHELX 97, Program for the Refinement of Crystal Structure, University of Göttingen, Germany, 1997.
[29] (a) D.T. Cromer, J.T. Weber, International Tables for X-ray Crystallography, Table 2.2A., vol. IV, The Keynoch Press, Birmingham, UK, 1994;
(b) J.A. Ibers, W.C. Hamilton, Acta Crystallogr. 17 (1964) 781.
[30] T. Osako, S. Nagatomo, Y. Tachi, T. Kitagawa, S. Itoh, Angew. Chem. Int., Ed. Eng. 41 (2002) 4325.
[31] (a) S.T. Prigge, B.A. Eipper, R.E. Mains, L.M. Amzel, Science 304 (2004) 864;
(b) R.A. Ghiladi, K.R. Hatwell, K.D. Karlin, H.-W. Huang, P. Moënne-Loccoz, C. Krebs, B.H. Huynh, L.A. Marzilli, R.J. Cotter, S. Kaderli, A.D. Zuberbühler, J. Am. Chem. Soc. 123 (2001) 6183.

in aqueous solution [15,20]. The aromatic nitrogen of L-histidine significantly enhances the stability of the metal complexes. For histidine complexes, in the oxo-dimer each V(III) center is coordinated tridentately (N_{im}, N_{am}, O) with one imidazole ring of histidine and bidentately (N_{im}, N_{am}) with another one [17–19]. Such a complex predominantly exists in aqueous solution in the pH 6–8.5 range [20].

In the present work we have investigated the interaction of vanadium(III) with L-histidine derivatives: urocanic acid (UA), imidazole carboxylic acid (Im(COOH)) and imidazole-4,5-dicarboxylic acid ($Im(COOH)_2$).

Urocanic acid (2-propenoic acid, 3-[1H-imidazol-4(5)-yl]) is a metabolic product of histidine. It is present (in quite high concentration) in the skin epidermis as a *trans* isomer. Absorption of UV radiation is responsible for the conversion of *trans* urocanic acid to its *cis* form [21,22].



Detailed studies of the electronic structure, absorption and emission spectra and possible mechanisms of photoisomerization of urocanic acid are the subject of numerous papers in the last decade [22–27]. It has been proposed that the *cis* isomer is immunosuppressive and is also connected to skin cancer [28,29]. Both UA and DNA are present in the skin of animals most exposed to sunlight, so it is very important to recognize all environmental factors which allow penetration of more sun UVB radiation to living organisms and create damage in nucleic acids [30,31].

The interaction of such an interesting molecule with different metals ions is almost unknown. We have only found the X-ray structure and catalytic activity of the manganese complex $[Mn(E\text{-}UA)_2(H_2O)_4]$, isolated from aqueous solutions [32].

Imidazole-4-carboxylic acid is one of the natural oxidation products of urocanic acid [33]. This compound is present also in UV-B-exposed human stratum corneum and may play some role in UV-B-induced immunosuppression [33]. To the best of our knowledge, complexes of imidazole-4-carboxylic acid with metal ions are almost unknown. In the solid phase only the complex $[^{99}Tc(OH)_2(imc)(CO)_3]$ has been isolated and coordination of the metal ion by the oxygen atom of the carboxylic group and one nitrogen atom of the imidazole ring was proved by X-ray data. This complex has importance in a clinical application [34].

Complex compounds of another derivative of urocanic acid – imidazole-4-acetic acid with different metal ions [Ni^{2+}, Cu^{2+}, Cd^{2+}, Zn^{2+}, Co^{2+}, Mn^{2+}, and VO^{2+}] were, on the other hand, extensively investigated [35–39]. The chelating character of imidazole-4-acetic acid has been demonstrated in the solid phase [35] and in aqueous solution [36–39]. As was studied by Sanna and coworkers [39], the oxovanadium(IV) ion forms monomeric and/or mixed hydroxo-bridged dimeric species in which both the oxygen of the carboxylate group and the nitrogen of the imidazole ring atoms are coordinated to metal ions.

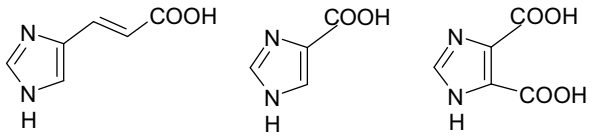
Some results of the coordination properties of imidazole-4,5-dicarboxylic acid are also available in the literature. Solid state complexes were isolated with Rh and Ir [40,41], where this ligand acts as a dinucleating ligand. For VO^{2+}, the formation of dimeric and cyclic tetrameric species is strongly favored in aqueous solution [39].

The aim of the present study is to determine the complex equilibria of the V^{3+} ion with urocanic acid (UA), imidazole-4-carboxylic acid (ImCOOH) and imidazole-4,5-dicarboxylic acid ($Im(COOH)_2$). Potentiometry was used to determine the stoichiometries and stability constants of the complexes formed in aqueous solution. Spectroscopic methods have been used to confirm of these models of complexation and to understand the structures of the species formed in aqueous solution. We also have isolated a complex of vanadium(III) with urocanic acid in the solid phase.

2. Experimental

2.1. Reagents

VCl_3 p.a (Riedel-de-Ha,n), $VCl_3(THF)_3$ (Sigma–Aldrich), tetrahydrofuran (Sigma–Aldrich), NaOH (Merck), $NaClO_4$ (Merck), the *trans* isomer of urocanic acid (Sigma–Aldrich), imidazole-4-carboxylic acid (Sigma–Aldrich), imidazole-4,5-dicarboxylic acid (Sigma–Aldrich).



The bottle of VCl_3 was kept in a nitrogen filled box.

2.2. Preparation of solutions

All manipulations were performed in a nitrogen filled box. The vanadium(III) solutions were prepared just before each measurement by direct dissolution of accurately weighed amounts of VCl_3 salt (in deoxygenated water or $HClO_4$ solution). The molar percentage of VO^{2+} in each investigated solution did not exceed 1% (the concentration of VO^{2+} was determined potentiometrically by titration with an oxygen free $KMnO_4$ standard solution and spectrophotometrically). We checked the total vanadium concentration by the ICP method. Hydrogen ion concentrations in VCl_3 solutions were determined by the

Gran method according to the procedure described by Pajdowski and Krzewska [42]. The titration of V(III) solution was carried with an acid solution ($HClO_4$) of relatively high concentration in order to minimize the hydrolysis of the vanadium(III) ion.

The ligands solutions were prepared just before each measurement and their purity and concentrations were checked by NaOH potentiometric titrations (by the Gran method) [43]. The NaOH solution was standardized against potassium hydrogen phthalate.

All solutions were prepared in an inert atmosphere and using doubly distilled water.

The total metal concentrations varied from 0.1 to 10 mM. The ligand to metal ratios varied from L/M = 1–10.

2.3. Measurements

Both potentiometric and spectroscopic measurements were performed at 25 °C at constant ionic strength (0.5 M $NaClO_4$). An EMU/0 (electrochemical universal meter) produced by the Technical University of Wrocław was applied to the potentiometric measurements. This instrument was combined with an automatic burette and an appropriate computer set. The pH measurements were also taken with a precise digital pH-meter PHM-84 "Radiometer".

The potentiometric measurements were taken by means of the cell SCE‖S|GE, where SCE = $Hg|Hg_2Cl_2|$ saturated NaCl solution; S-equilibrium solution and GE the glass electrode ("pHG 211-8 Radiometer"). The calibration procedure was described in Ref. [9]. Anaerobic conditions were maintained both in the titration vessel and in the titrant solutions by circulating argon.

Protonation constants of the ligands and concentration stability constants of the vanadium(III) complexes, $\beta_{pqr} = [M_p\ L_q H_r]/[M]^p[L]^q\ [H]^r$, were calculated by the HYPERQUAD program [44]. Formation constants of V(III)-hydroxo complexes were taken into account in these calculations. The applied constants were recalculated to the ionic strength 0.5 M $NaClO_4$, from Pajdowski data [45]. The following set of hydrolytic species were assumed: $[V(OH)]^{2+}$, $\log\beta_{1-1} = -3.1$; $[V_2O]^{4+}$ $\log\beta_{2-2} = -4.28$; and $[V(OH)_2]^{+}$, $\log\beta_{1-2} = -7.24$.

Cary 50 and Cary 5 – Varian spectrophotometers were used to perform the measurements of UV–VIS absorption spectra. IR spectra were measured in KBr pellets with a Bruker IFS 113 v IR spectrophotometer in the 4000–200 cm^{-1} range. For measurements of fluorescence spectra a SLM Aminco APF-500 spectrophotometer was applied, using a Xenon arc lamp as the excitation source with 7.5 and 2.5 mm excitation and emission slits.

All operations were performed in a nitrogen filled box. The cuvettes used for absorption and fluorescence measurements were closed in these conditions.

The magnetic moment was measured at room temperature with a Bruker BM-4 system.

2.4. Syntheses of the solid compound of vanadium(III) with urocanic acid

0.327 g $VCl_3(THF)_3$ (1 mmol) was dissolved in 20 cm^3 hot tetrahydrofuran (THF) (under a stream of N_2). 0.2428 g (2 mmol) of urocanic acid was added to this solution. The mixture was kept at 60 °C for 0.5 h and stirred. After some time, dark green microcrystals precipitated. This product was filtered off, washed with dry diethylether and dried in a dessicator (yield: 49.5%) in N_2 atmosphere.

The solid compound was characterized by thermogravimetric, elemental and IR analysis. The vanadium concentration was determined by the ICP method. Chloride ions were determined potentiometrically using an ion-selective electrode.

Anal. Calc.: V, 11.0; N, 12.1; C, 41.4; Cl, 7.7.

Found: V, 10.8; N, 12.2; C, 40.8, Cl: 8.1%.

The results of the thermogravimetric analysis indicate that in this compound vanadium is coordinated to the urocanic ligand, a chloride ion and tetrahydrofuran molecules. It is consistent with the elemental formula: $V^{III}(THF)(UA)_2Cl$.

3. Results and discussion

3.1. Solid compound: $V^{III}(THF)(UA)_2Cl$

IR spectra confirmed the coordination of urocanic ligand molecules by the V(III) ion (Table 1).

A significant shift of OCO and NH stretching frequencies of the imidazole ring suggests that the ligand molecule coordinates by the carboxylic group and the nitrogen atom of the imidazole ring. On the other hand, the difference $[\nu(COO^-)_{as} - \nu(COO^-)_{sym}] = 171.9\ cm^{-1}$ can indicate bridging character of a carboxylic group [46]. The complex of vanadium(III) with urocanic acid is probably dimeric or a polymeric compound bridging through COO^- groups.

The magnetic moment of the complex is 2.72 B.M. at room temperature, confirming the +3 state of vanadium (d^2 electronic structure). The diffuse reflectance spectrum (Fig. 1a, curve 1) and the absorption spectrum of this compound dissolved in water (Fig. 1a, curve 2) unequivocally proved that both in the solid phase and in aqueous solution the V^{3+} ion was the coordination center. The wide unstructured band with a maximum about 600 nm can be identified as d–d transitions of the V^{3+} ion, which corresponds to splitting in the low symmetry ligand field states.

It should be pointed out that in the solid phase the complex $V^{III}(THF)(UA)_2Cl$ exhibits quite intense luminescence even at 25 °C. The emission spectrum of the complex

Table 1
IR spectral characteristics for the vanadium(III)–urocanic acid complex

Compound	ν (NH)	ν (NH) + ν (CH)	ν_{as} (OCO)	ν_{sym} (OCO)
Urocanic acid	2590	3162.2, 3087.48	1664.6, 1589	1343, 1470
V(III)–UA	2614.98	3123.47	1580.9	1409

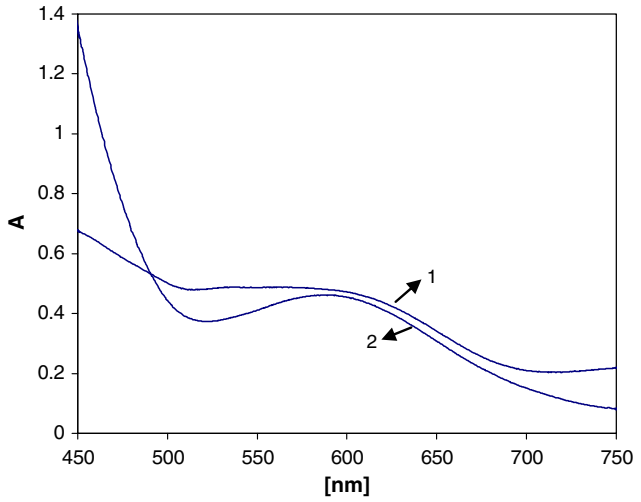


Fig. 1a. Diffuse reflectance spectrum of the solid complex $V^{III}(THF)(UA)_2Cl$ (curve 1) and absorption spectrum of this compound diluted in water (curve 2, pH 5).

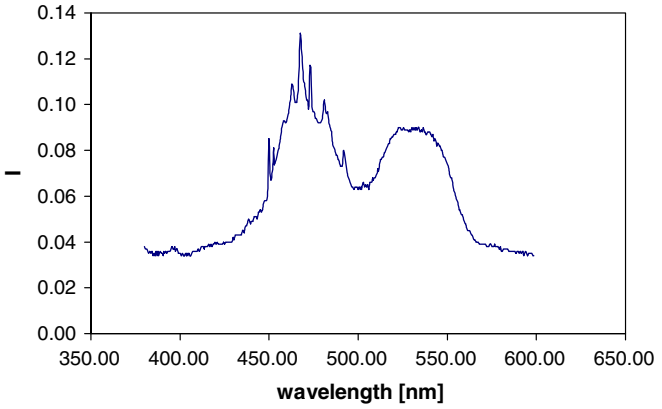


Fig. 1b. The emission spectrum of $V^{III}(THF)(UA)_2Cl$ in the solid state. $\lambda_{exc} = 330$ nm.

$V^{III}(THF)(UA)_2Cl$ is presented in Fig. 1b. It means that quite an effective conversion processes from the excited ligand state (presumably $^1\pi^* \rightarrow {}^1\pi$) through a lower lying triplet state of the ligand occurs to the split d–d states of V^{3+}. All these results well confirm the mode of the urocanate ligand coordination to V(III).

3.2. Complexation studies in aqueous solution

3.2.1. Protonation constants

Protonation constants of the ligands were calculated from titrations curves of the H^+-ligand systems in the pH range 1.8–12. In the case of imidazole-4,5-dicarboxylic acid, back titrations ($HClO_4$ as the titrant) were also performed because of the low solubility of the neutral ligand form. The values of the evaluated protonation constants are presented in Table 2, together with the vanadium(III) complex formation constants. All the ligands exhibit two protonation processes in the measurable pH region. The proton related to the N pyrrole site does not dissociate in this pH range. The protonation constant of the imidazole site is equal to $\log K_1 = 5.78$ for urocanic acid, 6.28 for imidazole-4-carboxylic acid and 7.84 for imidazole-4,5-dicarboxylic acid. The protonation constant of the carboxylic group is $\log K_2 = 3.48$ for UA, 2.3 for ImCOOH and 3.17 for $Im(COOH)_2$. Because a strong internal hydrogen bond exists between the carboxylic groups in $Im(COOH)_2$, the second proton of the carboxylic group of the ligand dissociates in a more acidic pH range ($\log K_3$ is about 1.5).

The log K values for urocanic acid and imidazole-4,5-dicarboxylic acid are in good agreement with earlier published data [21,39], considering the differences in ionic strength and ionic medium.

3.2.2. Vanadium(III) complexes

3.2.2.1. Vanadium(III)–urocanic acid system.

3.2.2.1.1. Potentiometric results. Only a weak interaction between the metal ions and the ligand in aqueous solution was stated, considering the potentiometric titration data. Hydrolysis of vanadium(III) competes with the complexation processes. This is a reason that in aqueous solutions only 1:1 species are formed. The competition between ML and MLH complex species with hydrolysis products is observed in the pH 2.5–4.5 range for the considered metal ion and ligand concentrations (Fig. 2). The slightly

Table 2
Protonation constants of the ligands and stability constants of the complexes of vanadium(III) evaluated from potentiometric data

Species	V(III)–UA		V(III)–ImCOOH		V(III)–Im(COOH)$_2$	
	$\log \beta_{pqr}$	$\log K_a$	$\log \beta_{pqr}$	$\log K_a$	$\log \beta_{pqr}$	$\log K_a$
H_3L						~1.5
H_2L	9.26 (0.01)	3.48	8.58 (0.04)	2.3	11.01 (0.2)	3.17
HL	5.78 (0.015)	5.78	6.28 (0.03)	6.28	7.84 (0.1)	7.84
MLH	8.51 (0.1)					
ML	5.92 (0.05)		6.95 (0.06)		8.55 (0.1)	
ML_2			12.61 (0.04)			
ML_2H_{-1}			9.04 (0.06)			
ML_2H_{-2}			1.07 (0.12)			
$M_2L_2H_{-2}$			11.47 (0.02)		15.17 (0.1)	
$M_2L_4H_{-2}$			19.76 (0.01)			

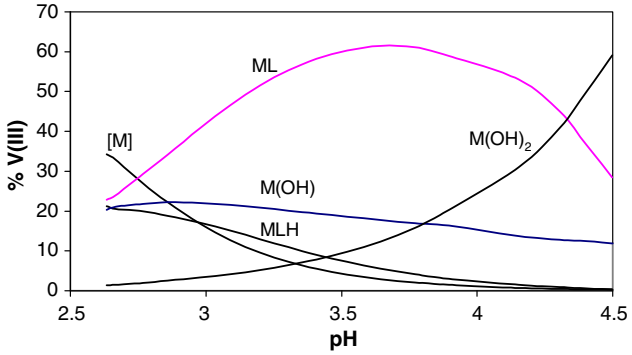


Fig. 2. Concentration distribution of the complexes formed in the V(III)–urocanic acid system in aqueous solution in the pH range 2.5–4.5 using β_{pqr} of the equilibrium model of Table 2 ($C_V = 3.75$ mM, $C_{UA} = 9.89$ mM).

soluble vanadium(III) mixed hydroxo urocanate species are probably formed above pH 4.5.

3.2.2.1.2. Spectroscopic results. Urocanic acid exhibits fluorescence even in aqueous solutions. Absorption and fluorescence spectra of urocanic acid in aqueous solutions at different pH values are presented in Figs. 3a and 3b respectively.

The absorption spectra of urocanic acid in aqueous solutions exhibit a distinct difference between the protonated and unprotonated form of this ligand (Fig. 3a). For the more stable *trans* isomer of this compound two electronic transitions $^1\pi \rightarrow {}^1\pi^*$ and $n \rightarrow \pi^*$ should be observed in this spectral range, however this last one is significantly less intense.

The most efficient excitation of fluorescence was found in the range 300-350 nm [22]. In agreement with recent studies [27] this excitation occurs via the n state which is hidden in the tail of the absorption resulting from the $^1\pi \rightarrow {}^1\pi^*$ transition. It should be pointed out that such an excitation result is wave dependent fluorescence which is very characteristic for the emission spectra of urocanic acid [23–27].

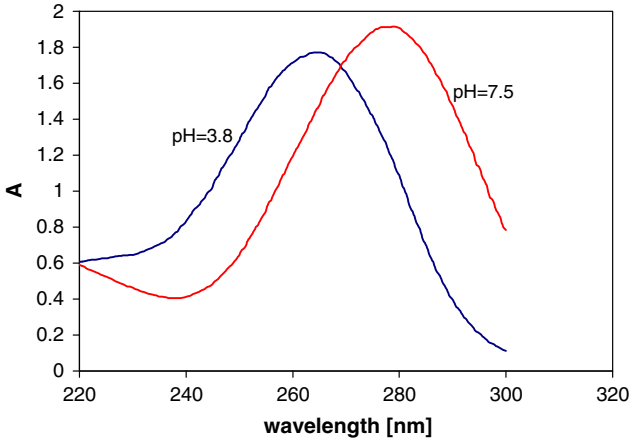


Fig. 3a. Absorption spectra of urocanic acid in aqueous solution. [UA] = 0.1 mM.

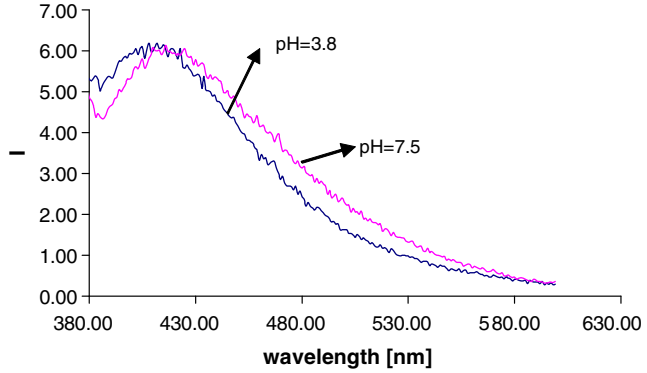


Fig. 3b. Fluorescence spectra of urocanic acid at different pH values. [UA] = 2 mM. $\lambda_{exc} = 330$ nm.

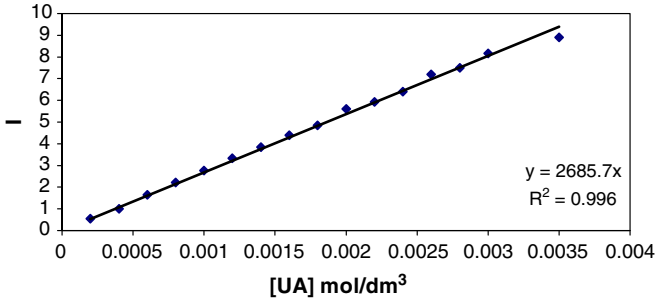


Fig. 4. Concentration dependence of the fluorescence intensity of urocanic acid at 410 nm. $\lambda_{exc} = 330$ nm, pH 3.

We have measured fluorescence of this ligand excited in such a spectral region in which the quantum efficiency of emission was the highest. The fluorescence spectra of urocanic acid in aqueous solutions of its protonated and deprotonated forms are presented in Fig. 3b. Fig. 4 presents the relationship between fluorescence intensity and concentration of urocanic acid at a constant pH value. The relationship is linear in the concentration range 0.2-3 mM UA.

We have also measured the influence of vanadium(III) concentration on the emission intensity of the $^1\pi \leftarrow {}^1\pi^*$ transition of urocanic acid. For the solutions with constant pH value and constant ligand concentration, distinct fluorescence quenching of urocanate by the vanadium(III) ion was observed (Fig. 5). These results enabled us to determine the stability constant of the V(III)–urocanate complex. The fluorescence titration technique was used to determine 1:1 conditional stability constants of fluorescing ligands with metal ions by several authors [47,48]. The results of the potentiometric measurements (Table 2 and Fig. 2) show that urocanic acid forms only 1:1 species with vanadium(III). As can be seen in Fig. 2, the complex ML is the prevailing form existing in aqueous solution. We decided to use the fluorescence quenching method for determination of stability constant of the ML species. The formation of the protonated species MHL was neglected because its concentration in the pH range 3–4

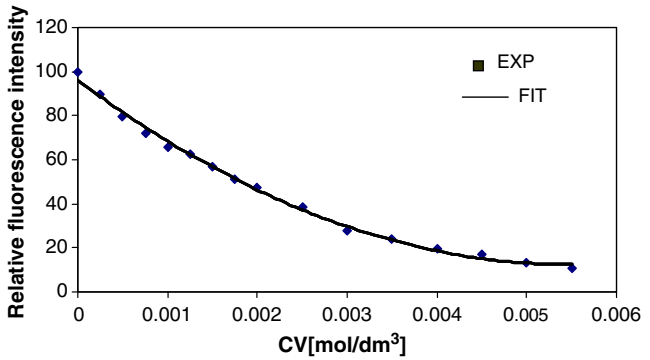


Fig. 5. Fluorescence quenching curve for 2 mM of urocanic acid in 0.5 M $NaClO_4$ at pH 3.0. $\lambda_{exc} = 330$ nm, $\lambda_{em} = 410$ nm.

Table 3
Stability constants of the complexes of vanadium(III) with urocanic acid (ML) evaluated from fluorescence data

pH	C_L [M]	I_{RES}	R	$\log K_{ML}$	$\log \beta_{ML}$
3.0	0.00091	1.2	0.996	2.17	6.22
3.0	0.002	1.8	0.997	2.20	6.25
3.5	0.0011	2.1	0.998	2.27	6.23
3.5	0.002	2.4	0.996	2.16	6.22

Where K_{ML} is the conditional stability constant at a constant pH value.
β_{ML} is the stability constant of the ML complex.
$\log \beta_{ML} = \log K_{ML} + \log \alpha_{L(H)} + \log \alpha_{M(H)}$.
Where $\alpha_{L(H)} = 1 + [H^+]\,K_1 + [H^+]^2\,K_1\,K_2$.
K_1, K_2 is the protonation constants of urocanic acid.
$\alpha_{M(H)} = 1 + K_{1h}/[H]^+ + K_{2h}/[H+]^2$.
Where K_{1h}, K_{2h} is the hydrolysis constants of vanadium(III).

is low (see Fig. 2). The experimental fluorescence data for the titrations of urocanic acid with V^{3+} at constant pH value have been fit to the non-linear fluorescence data treatment model of Ryan and Weber [47]. This method is based on the relationship linking fluorescence quenching of a ligand L by complexation with the metal ion M.

$$[ML]/C_L = (I_0 - I)/(I_0 - I_{RES})$$

where [ML] is the concentration of the metal–ligand complex, C_L is the concentration of the ligand, I_0 is the initial intensity value (before any metal ions have been added to the sample of the ligand), and I_{RES} is the residual intensity, when all the ligand is bound to the complex.

The simple 1:1 equilibrium between a metal ion and ligand can be written as follows:

$$K = [ML]/[M][L]$$

where K is a conditional stability constant at a given pH value.

Ryan and Weber [47] derived a final non-linear expression:

$$I = [(I_{RES} - I_0)/2KC_L]\{[KC_L + KC_M + 1] - [(KC_L + KC_M + 1)^2 - 4KC_LC_M]^{0.5}\} + I_0$$

In this equation K, C_L and I_{RES} are parameters to be fit by the program NLREG [49].

The results of fluorescence quenching are presented in Fig. 5 and the values K, C_L and I_{RES} as well as the correlation coefficients are presented in Table 3.

When conditional stability constants were recalculated, taking into account the protonation constants of urocanic acid and the hydrolysis constant of vanadium(III) ions (for a comparison with potentiometric results), quite a good agreement between both sets of values was found (Table 3).

The weak interaction between the vanadium(III) ion and the ligand in the aqueous solution can be confirmed by the measurements of absorption spectra. These spectra in the pH range 1–4 are presented in Fig. 6.

The spectra of the metal ion in aqueous solution ($I = 0.5$ M $NaClO_4$) are also included for comparison, in the same figure (curves 1 and 7). At low pH values, the

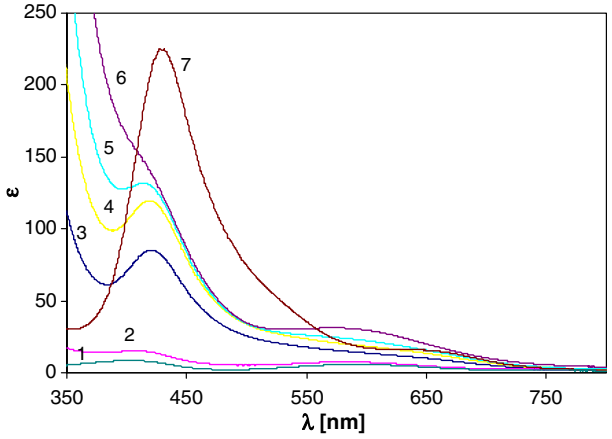


Fig. 6. Absorption spectra of VCl_3 aqueous solutions (curves 1 and 7) and absorption spectra of the vanadium(III)–urocanic acid system (curves 2–6) at different pH values ([V] = [UA] = 10 mM) (1) VCl_3 pH 0.864, (2) V(III) + UA pH 1.53, (3) V(III) + UA pH 2.36, (4) V(III) + UA pH 2.62, (5) V(III) + UA pH 2.88, (6) V(III) + UA pH 3.34, (7) VCl_3 pH 2.45.

spectra of vanadium(III) and vanadium(III) with ligand added do not differ significantly between each other (curves 1 and 2). These spectra are typical for vanadium(III) where two weak bands corresponding to the d–d transitions of the d^2 configuration of vanadium(III) are observed. This spectral picture distinctly changes for solutions with higher pH values (curves 3–7, Fig. 6). For the spectrum of an aqueous solution of V(III) alone at pH 2.45, a distinct intensity increase and a small red-shift of the band at 400–450 nm is observed (curve 7). As it was proved earlier [45,50], a small amount of hydrolytic vanadium(III) μ-oxo dinuclear species ($[V–O–V]^{4+}$) exists under such conditions and the CT band origin from the bridge bounded oxygen to vanadium(III) of this species overlaps with the weak d–d transition. Curves 3–6 (Fig. 6) present the spectra of vanadium(III) solutions with urocanic acid at different pH values. A distinct intensity increase of the 400–450 nm band is observed, however, in all the measured solutions their intensity is lower than in the spectrum of V(III) alone at pH 2.45 (curve 7). It means that urocanic acid reverses, to some degree, the hydrolysis process of

the vanadium(III) ion. This process obviously lowers the concentration of hydrolytic dimeric vanadium(III) μ-oxo species in the presence of the ligand. Such behaviors of absorption spectra were observed earlier for different V(III) complexes with amino acids as well [9,20,51].

3.2.2.2. Vanadium(III) complexes with imidazole-4-carboxylic and imidazole-4,5-dicarboxylic acids. Imidazole-4-carboxylic acid and imidazole-4,5-dicarboxylic acid are more efficient ligands than urocanic acid. Both ligands can form stable [N,O] chelates with V(III) and suppress the hydrolysis process. For the vanadium(III)–imidazole-4,5-dicarboxylic acid system, however, a precipitate was observed above pH 5.

The results of potentiometric titration prove that both ligands form mono and dinuclear species with vanadium(III). The average ligand number depends both on the total concentration of the metal ion and on the concentration of the free ligand (see Figs. 1 and 2 in the Supplementary Material). The stability constants of the complexes formed are presented in Table 2.

Comparison of the stability constants for the complexes of vanadium(III) with these ligands to the stability constants of complexes of VO^{2+} with imidazole-4,5-dicarboxylic acid and imidazole-4-acetic acid [39] indicates higher thermodynamic stability of the vanadium(III) complexes.

A relatively simple model of the complexation was observed in the vanadium(III)–imidazole-4,5-dicarboxylic acid system (Fig. 7).

As is shown in Fig. 7, in the prevailing pH range, the complex $M_2L_2H_{-2}$ exists in solution. This complex formation was also monitored by UV–Vis spectroscopy. The absorption spectra in this system (Fig. 8) are dominated by the strong CT band in the range 400–550 nm.

The presence of this intense absorption CT band in the visible region (400–550 nm) indicates that the complex $M_2L_2H_{-2}$ contains a μ-oxo $[V–O–V]^{4+}$ core [10,11,16–20]. As can be seen in Fig. 8 and Tables 1 and 2 in the Supplementary Material, both the energy and intensity of this band strongly depend on the pH value, the ligand concentration and the metal concentration. High average molar absorbance coefficients indicate that in this case dinuclear μ-oxo species are formed (see Tables 1 and 2 in the Supplementary Material). Such a spectral feature becomes clear when we assume a composed nature of this band. The $[V–O–V]^{4+}$ unit in the hydrolytic vanadium complex has an intense charge-transfer band at 428 nm (Fig. 6, curve 7). Significant changes of both energy and intensity of this band with changing pH and L/M ratios (Tables 1 and 2 in the Supplementary Material) clearly indicate that in the V(III)–imidazole-4,5-dicarboxylic acid system in aqueous solution at pH > 2, coordination of this dimeric species with the ligand occurs. Above pH 3.5 the energy of this CT band does not change (Fig. 8, Table 2 in the Supplementary Material) and its intensity increase depends on the vanadium(III) concentration. These results are in good agreement with recent data for μ-oxo-bridged species of vanadium(III) for which a chelate bond with a N aromatic atom exists (e.g. 2,2′bipyridine, 1,10-phenanthroline, L-histidine) [52,53,16–20]. The second absorption band at $\lambda_{max} = 650$ nm ($\varepsilon \sim 300\ M^{-1}\ cm^{-1}$ in Fig. 8) corresponds probably to a V^{3+} d–d transition, which is presumably intensified by the neighboring strong CT band, by a splitting of the d^2 states in a low symmetry field (by the coordination of the N-heterocyclic atom). This coordination is confirmed as well by the shift of this band towards lower energies in comparison with the aqua ion ($\lambda_{max} = 590$ nm for the aqua ion and $\lambda_{max} = 650$ nm for the complexes with imidazole-4,5-dicarboxylate). At a pH above 4.3, the intensity of the two transitions decreases (Fig. 8). It is in good agreement with the potentiometric data (Fig. 7). Above pH 5 in the solution of vanadium(III) with imidazole-4,5-dicarboxylic acid, a precipitate was observed even for low concentrations of the metal ion and ligand. The V_2OL_2 species formed in aqueous solution has a neutral charge. The $[V–O–V]^{4+}$ core in this species is complexed with two bidentate ligands (five-membered chelate rings are formed by the N_{im}, COO^- donor set). The remaining carboxylic groups may form hydrogen bonds with water molecules or bind to the next vanadium ions forming insoluble polymeric complexes.

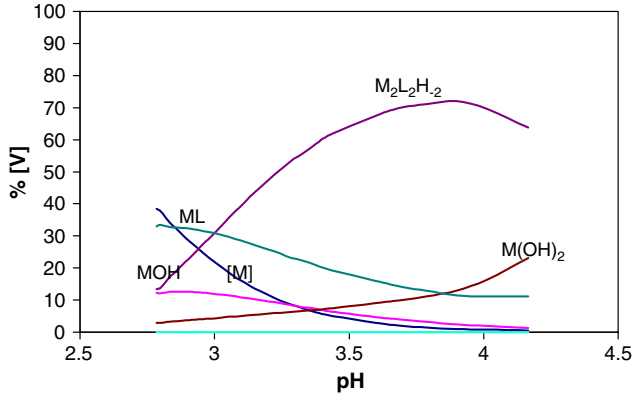


Fig. 7. Species distribution diagram as a function of pH for the V(III)–imidazole-4,5-dicarboxylic acid system. [V] = 2.7 mM, [Im(COOH)$_2$] = 5.8 mM.

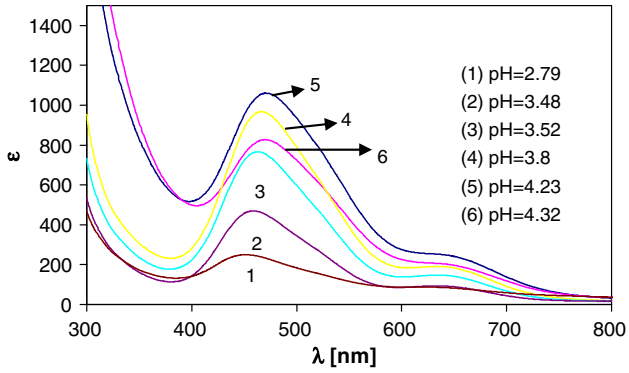


Fig. 8. Absorption spectra in the V(III)–Im(COOH)$_2$ system [V] = 2 mM, [Im(COOH)$_2$] = 10 mM.

In the V(III)–imidazole-4-carboxylic acid system we obtained clear solutions in the pH range of about 2–9 with L/M > 5. The rather limited ligand excess needed for complete metal complex formation prove the chelate nature of the species formed by imidazole-4-carboxylic acid. A typical species distribution diagram is presented in Fig. 9.

Complex formation starts with ML species at pH < 2. The "basicity adjusted" stability constant for the reaction: $V^{3+} + HL = VL + H^{+}$ is 0.67, which is greater by about two orders of magnitude than V(III)-complexes of simple amino acids (−1.41 for alanine [51]) and is comparable with V(III) – picolinic and 6-methylpicolinic acid ($\log K = 1.12$ and 0.12, respectively [5]). This is a further proof for the chelating nature of the species formed by imidazole-4-carboxylic acid. As can be seen in Fig. 9, in the pH range ~2–4, two main species, ML_2 and $M_2L_2H_{-2}$, are present in the equilibrium. In the pH range 4–7, new species, ML_2H_{-1} and $M_2L_4H_{-2}$ exist in solution. Above pH 7, ML_2H_{-2} starts to appear.

In Figs. 10a and 10b the spectra of the V(III)–imidazole-4-carboxylic acid system are presented in the pH range 1.52–8.89.

In the absorption spectra of all the solutions investigated two bands in the visible region were observed. In acidic solutions (Fig. 10a) the weak band at about 600 nm obviously corresponds to the V^{3+} ion d–d transitions ($^3T_{2g}(F) \leftarrow {}^3T_{1g}(F)$ in O_h symmetry). This band is very wide, because lower than O_h symmetry of both species ML and ML_2 exist in solution. The absorption spectra at higher pH values for this system are very similar to those obtained in the V(III)–$Im(COOH)_2$ system. As can be seen in Fig. 10b, a strong absorption band, CT in origin, appears in the range 400–550 nm. This is in good agreement with the potentiometric data (Fig. 9) which indicate that the formation of the $M_2L_2H_{-2}$ species begins at pH > 2. When the formation of this complex starts, the solution turns a red–brown color, typical for μ-oxo V(III)-complexes. $M_2L_2H_{-2}$ (V_2OL_2) has a CT band at $\lambda = 450$ nm (average ε ~200 $M^{-1}\,cm^{-1}$). In the pH range ~4–8 two main species, ML_2H_{-1} and $M_2L_4H_{-2}$ (V_2OL_4), exist in solution. As can be seen in Fig. 9, the amount of

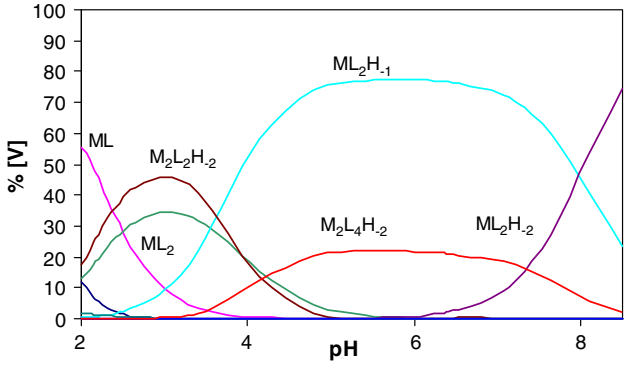


Fig. 9. Species distribution diagram as a function of pH for the V(III)–imidazole-carboxylic acid system. [V] = 4.71 mM, [L] = 25.88.

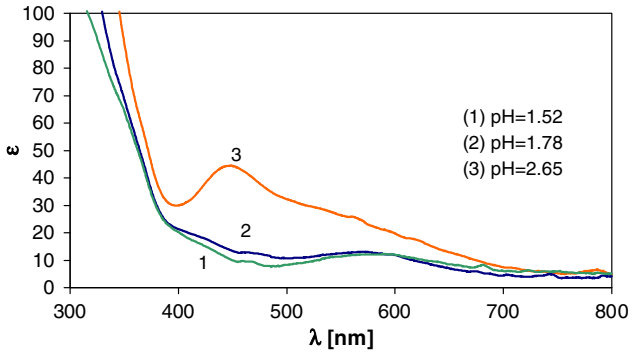


Fig. 10a. Absorption spectra for the V(III)–ImCOOH system in the pH range 1.52–2.65.

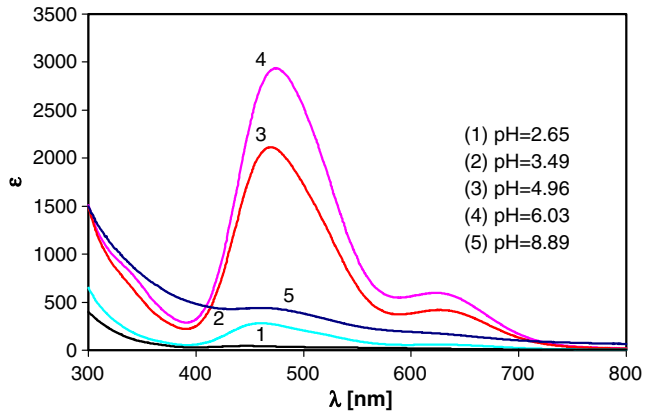


Fig. 10b. Absorption spectra for the V(III)–ImCOOH system in the pH range 2.65–8.89 [V] = 4.71 mM, [Im(COOH)] = 26.1 mM.

$[V_2OL_4]$ species is relatively small, but its presence determines the character of the spectral picture. The $[V_2OL_4]$ complex shows a CT band at $\lambda_{max} = 480$ nm (average ε ~3000 $M^{-1}\,cm^{-1}$) and a d–d transition at $\lambda_{max} = 630$ nm (average ε~800 $M^{-1}\,cm^{-1}$1), which is presumably intensified by the neighboring strong CT band. At the highest pH values, the intensity of these transitions decreases (Fig. 10b – spectrum at pH 8.89). This is related to the progress of hydrolysis. As can be seen in Fig. 9 at pH > 8, the $ML_2(OH)_2$ complex exists in solution.

4. Conclusions

The presented results clearly indicate that urocanic acid is a weak V(III) binder. Imidazole mono and di-carboxylate are relatively stronger ligands and are able to prevent the hydrolysis processes to some degree. Similarly, as for other ligands in quite a large pH range of investigated systems, the existence of several di-nuclear complex species with a $[V–O–V]^{4+}$core has been stated [11,14–20,52,53].

Imidazole-4-carboxylic and imidazole-4,5-dicarboxylic complexes of vanadium(III) in solution, however, have behaved differently. The main complex species in the V(III)–imidazole-4,5-dicarboxylic acid system that exists in the 3–4.5 pH range is $M_2L_2H_{-2}$ (V_2OL_2) (Fig. 7). In

the absorption spectra of the investigated solutions in this pH range the spectrum of this species is dominant (Fig. 8).

These results are in good agreement with the coordination mode of the V^{3+} ion [11,14–20,52,53]. Each V^{3+}ion is coordinated by the oxygen of one carboxylate group and the imidazole nitrogen atom. The coordination sphere of vanadium(III) is fulfilled by the bridge-oxygen and water molecule. However, the V_2OL_2 species can very easy form oligomers by polymerization through the carboxylic bridges. Such oligomers have low solubility, so it is difficult to keep them in solutions at higher pH values. The formation of cyclic oligomeric species has been observed in aqueous solutions of vanadium(IV) and imidazole-4,5-dicarboxylic acid at pH > 4, however, they are more soluble in this case [39].

For the vanadium(III) complexation with the imidazole-4-carboxylate ligand, formation of several mononuclear and dinuclear complex species in equilibrium is very characteristic. It is worth noticing that no such equilibrium has been observed in the solution of V(III) and imidazole-4,5-dicarboxylic acid so far. This can be explained by the differences in the coordination mode between both ligands. In imidazole monocarboxylate complex species both donor groups of the ligand (O, N_{im}) are involved in the complexation process. On the other hand in imidazole-4,5-dicarboxylate complex species a free carboxylic group, which is not involved in the complexation process, can form relatively strong hydrogen bonds with water molecules. This tendency is limited in solutions at higher pH values, in which there are significantly more negatively charged OH^- groups. It also confirms the formation of low soluble oligomers by the imidazole-4,5-dicarboxylate ligand.

As one can expect, the weakest ligand among those investigated is the urocanate ligand. With the vanadium(III) ion only two mononuclear complex species (MLH, ML) exist in aqueous solution. The steric hindrance is responsible for such behavior. Nevertheless, we should assume that whereas in MLH species vanadium(III) is bound with the ligand through an oxygen of carboxylate group, in the ML species presumably a weak chelate ring through the O and imidazole N atoms can be also expected. We cannot exclude also some equilibrium with the mixed hydroxo M(HL)(OH) species. Unfortunately potentiometric and spectroscopic results cannot explain this question unequivocally. The ''basicity adjusted'' stability constants ($\log K$) for the ML complexes are: 0.14 for V(III)–UA species, 0.67 for V(III)–ImCOOH species and 0.71 for V(III)–$Im(COOH)_2$ species. These values indicate that urocanic acid is the weakest ligand, however a weak chelation bond is possible. The chelating bond in the V(III)–UA species is too weak to prevent the hydrolysis. So far, in this system we have not observed either formation of ML_2 species or dinuclear complexes.

In contrast to the unsuccessful efforts of the syntheses of a vanadium(III) complex with the urocanate ligand in aqueous solutions, we have been able to get a solid compound in the microcrystalline form from a non-aqueous solvent (tetrahydrofuran). This compound, contrary to the species in aqueous solution, consists of two ligand molecules in the first coordination sphere of the vanadium(III) ion. The elemental formula is $[V^{III}(THF)(UA)_2Cl]$. We assume that the formation of oligomers through the carboxylic group is possible in the solid phase. This compound has very interesting luminescent properties, which result in an effective energy transfer from the ligand molecule to the d electronic vanadium(III) states. The unusual photophysical properties of the urocanate ligand [21–31] (among others the *trans–cis* isomerization) are presumably responsible for this phenomenon. It seems that further investigation of such phenomena may be quite interesting – both for the better knowledge of the energy transfer mechanism and for possible applications.

We have applied the photophysical properties of this ligand to the determination of the conditional stability constant of the V(III) complex species in aqueous solution by the fluorescence quenching method. It should be noted that other analytical applications of this system to quantitative determination of urocanic acid is possible.

Acknowledgement

The author is indebted to Prof. Krystyna Bukietyńska for very helpful suggestions and discussion during the preparation of this paper.

Appendix A. Supplementary data

Supplementary data associated with this article can be found, in the online version, at doi:10.1016/j.poly.2008.01.035.

References

[1] M. Melchior, S.J. Rettig, B.D. Liboiron, K.H. Thompson, V.G. Yuen, J.H. McNeill, Ch. Orvig, Inorg. Chem. 40 (2001) 4686.
[2] K. Saatchi, K.H. Thompson, B.O. Patrick, M. Pink, V.G. Yuen, J.H. McNeill, Ch. Orvig, Inorg. Chem. 44 (2005) 2689.
[3] Y. Zhang, X.D. Yang, K. Wang, D.C. Crans, J. Inorg. Biochem. 100 (2006) 80.
[4] P. Buglyo, D.C. Crans, E.M. Nagy, R.L. Lindo, L. Yang, J.J. Smee, W. Jin, L.H. Chi, M.E. Godzala, G.R. Willsky, Inorg. Chem. 44 (2005) 5416.
[5] J. Gätjens, B. Meier, Y. Adachi, H. Sakurai, D. Rehder, Eur. J. Inorg. Chem. (2006) 3575.
[6] A. Evangelou, S. Karkabounas, G. Kalpouzos, M. Malamas, R. Liasko, D. Stefanou, A.T. Vlahos, T.A. Kabanos, Cancer Lett. 119 (1997) 221.
[7] R. Liasko, T.A. Kabanos, S. Karkabounas, M. Malamas, A.T. Tasiopoulos, D. Stefanou, P. Collery, Anticancer Res. 18 (1998) 3609.
[8] A. Papaioannou, M. Mahos, S. Karkabounas, R. Liasko, A.M. Evangelou, J. Correia, V. Kalfakakou, J. Costa Pessoa, T. Kabanos, J. Inorg. Biochem. 98 (2004) 959.
[9] I. Osińska-Królicka, H. Podsiadły, K. Bukietyńska, M. Zemanek-Zboch, D. Nowak, K. Suchoszek-Łukaniuk, M. Malicka-Błaszkiewicz, J. Inorg. Biochem. 98 (2004) 2087.
[10] J. Piątkowski, H. Podsiadły, K. Bukietyńska, J. Biochem. 141 (4) (2007) 545.

[11] Kan Kanamori, Coord. Chem. Rev. 237 (2003) 147.
[12] M. Chatterje, S. Ghosh, A.K. Nandi, Polyhedron 16 (7) (1997) 2917.
[13] M. Chatterje, M. Maji, S. Ghosh, T.C.W. Mak, J. Chem. Soc., Dalton Trans. (1998) 3641.
[14] V. Lubes, J. Sol. Chem. 34 (8) (2005) 899.
[15] P. Buglyo, E.M. Nagy, I. Sovago, Pure Appl. Chem. 77 (9) (2005) 1583.
[16] M. Kumagai, S. Kitagawa, M. Maekawa, S. Kawata, H. Kiso, M. Munakata, J. Chem. Soc., Dalton Trans. (2002) 2390.
[17] K. Kanamori, M. Teraoka, H. Maeda, K. Okamoto, Chem. Lett. (1993) 1731.
[18] R.S. Czernuszewicz, Q. Yan, M.R. Bond, C.J. Carrano, Inorg. Chem. 33 (1994) 6116.
[19] F.H. Herbstein, R.E. Marsh, Acta Crystallogr. B 54 (1998) 677.
[20] K. Bukietynska, Z. Karwecka, H. Podsiadły, Polyhedron 16 (1997) 2613.
[21] T. Mohammad, H. Morrison, H. Hogen Esch, Photochem. Photobiol. 69 (1999) 115.
[22] T. Mohammad, Tetrahedron Lett. 43 (2002) 8897.
[23] M.K. Shukla, P.C. Mishra, Spectrochim. Acta 51A (1995) 831.
[24] K.M. Hanson, B. Li, J.D. Simon, J. Am. Chem. Soc. 119 (1997) 2715.
[25] A. Lahti, M. Hotokka, K. Neuvonen, G. Karlström, Int. J. Quant. Chem. 72 (1999) 25.
[26] Ch.S. Page, M. Merchan, L. Serrano-Andres, M. Olivucci, J. Phys. Chem. A 103 (1999) 9864.
[27] W.L. Ryan, D.H. Levy, J. Am. Chem. Soc. 123 (2001) 961.
[28] H. Morrison, C. Bernasconi, G. Pandey, Photochem. Photobiol. 40 (1984) 549.
[29] D.H. Hug, J.K. Hunter, D.D. Dunkerson, J. Photochem. Photobiol. B: Biol. 44 (1998) 117.
[30] R.M. Deibel, H.A. Morrison, W.M. Baird, Photochem. Photobiol. 45 (1987) 421.
[31] H. Morrison, B. Manclair, R.M. Deibel, G. Pandey, W.M. Baird, Photochem. Photobiol. 41 (1985) 254.
[32] M. McCann, R.M.T. Casey, M. Devereux, M. Curran, V. Mckee, Polyhedron 15 (14) (1996) 2321.
[33] A. Kammeyer, J. Garssen, A. Sleijffers, H. van Loveren, Photochem. Photobiol. (2004) 1.
[34] S. Mundwiler, M. Kündig, K. Ortner, R. Alberto, J. Chem. Soc., Dalton Trans. (2004) 1320.
[35] K. Kurdziel, T. Głowiak, S. Materazzi, J. Jezierska, Polyhedron 22 (2003) 3123.
[36] I. Torok, P. Surdy, A. Rockenbauer, L. Korecz, G.J. Anthony, A. Koolhaas, T. Gajda, J. Inorg. Biochem. 71 (1998) 7.
[37] P. Surdy, P. Rubini, N. Buzas, B. Henry, L. Pellerito, T. Gajda, Inorg. Chem. 38 (1999) 346.
[38] H. Sigel, A. Saha, P. Carloni, L.E. Kapinos, R. Griesser, J. Inorg. Biochem. 78 (2000) 129.
[39] D. Sanna, G. Micera, P. Buglyo, T. Kiss, T. Gajda, P. Surdy, Inorg. Chim. Acta (1998) 297.
[40] J.C. Bayon, G. Net, P.G. Rasmussen, J.B. Kolowich, J. Chem. Soc., Dalton Trans. (1987) 3003.
[41] G. Net, J.C. Bayon, W.M. Butler, P.G. Rasmussen, J. Chem. Soc., Chem. Commun. (1989) 1022.
[42] L. Pajdowski, S. Krzewska, Chem. Anal. 15 (1970) 377.
[43] G. Gran, Acta Chem. Scand. 4 (1950) 599.
[44] A. Sabatini, A. Vacca, P. Gans, Coord. Chem. Rev. 120 (1992) 389.
[45] L. Pajdowski, J. Nucl. Chem. 28 (1966) 433.
[46] G.B. Deacon, R.J. Philips, Coord. Chem. Rev. 33 (1980) 227.
[47] D.K. Ryan, J.H. Weber, Anal. Chem. 54 (1982) 986.
[48] K.M. Elkins, D.J. Nelson, J. Inorg. Biochem. 87 (2001) 81.
[49] http//www.nlreg.com.
[50] R. Meier, M. Boddin, S. Mitzenheim, K. Kanamori, Metal Ions in Biological Systems, vol. 31, Sigel and Sigel, New York, 1995, p. 45.
[51] K. Bukietyńska, H. Podsiadły, Z. Karwecka, J. Inorg. Biochem. 94 (2003) 317.
[52] S.J. Heater, M.W. Carrano, D. Rains, R.B. Walter, D. Ji, Q. Yan, R.S. Czernuszewicz, C.J. Carrano, Inorg. Chem. 39 (2000) 3881.
[53] C.M. Grant, B.J. Stamper, M.J. Knapp, K. Folting, J.C. Hoffman, D.N. Hendricksom, G. Christou, J. Chem. Soc., Dalton Trans. (1999) 3399.

with both electron rich and electron poor metals [20–22]. The mode of bonding depends on the nature of the ligand, the metal ion and the solvent used [23,24]. As the substituents present in the hydrazone strongly influence the reactivity of proximal C–H bonds, a CNO mode of bonding of aryl hydrazones may be expected, provided suitable substituents are located on the aryl ring. With this background, the present work was carried out to study the role of nitro groups towards metal assisted C–H activation of 2,4-dinitrophenyl hydrazone derivatives [25] (Chart 1) using $[RuHCl(CO)(PPh_3)_3]$ [26] and $[RuHCl(CO)(AsPh_3)_3]$ [27] as the metal complex precursors.

2. Experimental

2.1. Materials and methods

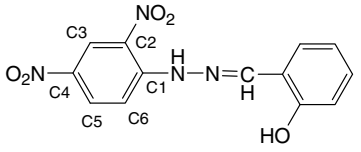
All chemicals were of reagent grade and were used without further purification. Solvents were purified and dried according to standard procedures [25]. Commercially available TBAP (tetra butyl ammonium phosphate) was properly dried and used as a supporting electrolyte for recording cyclic voltammograms of the complexes. FT-IR spectra (4000–400 cm^{-1}) of the complexes and the free ligand were recorded from KBr pellets with a Nicolet Avatar Model FT-IR spectrophotometer. UV–Vis spectra (800–250 nm) of the complexes were obtained on a Systronics 119 UV–Vis spectrophotometer. ^1H NMR spectra of the complexes were recorded using a Varian-Australia AMX-400 spectrometer. Micro analyses (C, H and N) were performed on a Vario EL III Elementary analyzer. Cyclic voltammograms were recorded on a CHI 1120A electrochemical analyzer with a three electrode compartment consisting of a platinum disc working electrode, platinum wire counter electrode and Ag/Ag^+ reference electrode.

2.2. X-ray crystallography

Crystal parameters and details of the collection and refinement are given in Table 1. X-ray diffraction measurements for **1** and **2** were performed on a Bruker AXS SMART APEX CCD diffractometer with graphite mono-

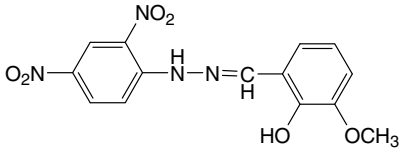
Table 1
Crystal data for **1** and **2**

	1	**2**
Empirical formula	$C_{53}H_{45}N_5O_7P_2Ru_1 \cdot C_3H_7NO$	$C_{54}H_{48}N_5O_8P_2Ru_1$
Formula weight	1026.95	1057.98
Crystal color, habit	red, rod	red, plate
Crystal dimensions (mm)	0.54 × 0.25 × 0.25	0.50 × 0.40 × 0.10
Crystal system	monoclinic	monoclinic
Lattice type	primitive	primitive
Space group	$P2_1/n$	$P2/n$
a (Å)	11.7502 (10)	14.0407(8)
b (Å)	26.274 (2)	8.8981(5)
c (Å)	16.1387 (14)	19.0602(11)
α (°)	90	90
β (°)	98.847 (2)	90.2010(10)
γ (°)	90	90
V (Å^3)	4923.1 (7)	2381.3(2)
Z	4	2
Reflections collected	50007	23735
Unique reflections	12232	5909
Reflections $[I > 2\sigma(I)]$	9995	5678
R $[F^2 > 2\sigma(F^2)]$	0.0482	0.0541
wR $[F^2]$	0.1128	0.1251
D_{calc} (Mg m^{-3})	1.386	1.478
F_{000}	2112	1092
μ (Mo Kα) (mm^{-1})	0.441	0.460
R_{int}	0.0367	0.0313
Goodness-of-fit (S)	1.119	1.225
θ_{max} (°)	30.55	28.28



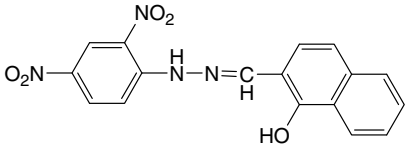
2-[(2,4-Dinitro-phenyl)-hydrazonomethyl]-phenol

H_2php



2-[(2,4-Dinitro-phenyl)-hydrazonomethyl]-6-methoxy-phenol

H_2phm



2-[(2,4-Dinitro-phenyl)-hydrazonomethyl]-naphthalen-1-ol

H_2phn

Chart 1. Structural drawings of the hydrazone derivatives.

chromatized Mo Kα radiation. The unit cells were determined using SMART [28] and SAINT+ [29], and the data were corrected for absorption using SADABS [30]. The structures were solved by direct methods and refinements were carried out by full-matrix least-square techniques. The hydrogen atoms were treated by a mixture of independent and constrained refinement. The computer program SHELXTL 6.14 [31] was used for structure solution, refinement and molecular graphics.

The structure of **2** is heavily disordered with both the solvate DMF molecule as well as the complex molecule disordered as a whole. Only the central Ru atom and the phosphine P atom show no disorder. The DMF solvate molecule is disordered around the twofold axis. The two methyl nitrogen distances within the DMF molecule were restrained to be identical within a standard deviation of 0.02 Å, and all DMF atoms were restrained to be isotropic within a standard deviation of 0.1 Å^2. The different types of disorder within the complex molecule are all related to each other. They are caused by the molecule being located on a crystallographic twofold axis (perpendicular to the Ru–P axis) that is not resembled by the symmetry of the complex molecule. Attempts to solve the structure in the space group Pn (without the twofold axis) resulted in less satisfactory results. The disorder consists in detail of the following. The azo-ligand, which has no twofold symmetry, is rotated by the twofold axis through the Ru atom, resulting in two alternative positions for the ligand with a 1:1 occupancy ratio. The two positions are taking up nearly the same space around the Ru atom. The slight differences for the two orientations are causing disorder for the phenyl rings of the triphenylphosphine ligand, and for the carbon monoxide ligand, which thus also show a 1:1 disorder. For the refinement the following restraints were applied to the complex molecule. All anisotropic displacement parameters of the azo ligand were restraint to have the same U_{ij} components (within a standard deviation of 0.04 for *s* and 0.08 for *st*) using a SIMU command in SHELXTL [31]. The carbonyl carbon atoms C51 and C43 and nitrogen atoms N3 and N7 (which are all nearly superimposed with symmetry generated counterparts) were restrained to be isotropic within standard deviations of 0.01 (C51, C43, N7) or 0.001 Å^2 (N3). All the aromatic rings of the azo ligand and the triphenylphosphine were restrained to be ideal six membered rings (AFIX 66 command) with C–C distances of 1.39 Å. No further positional restraints were applied. All hydrogen atoms were placed in calculated positions and were isotropically refined with a displacement parameter of 1.5 (methyl) or 1.2 times (all others) that of the adjacent carbon atom. With the beta angle in the structure of **2** being very close to 90°, we tested for the possibility of pseudo-merohedral twinning. Refinement using the usual twinning laws (twin instructions 1000 −1000 −1 and 1000 −10001) however, did not result in a significant improvement of the structure quality, and the BASF values refined to values less than one percent. It was thus assumed that the structure was not twinned and the twin instruction was omitted from the refinement instructions.

2.3. Synthesis

2.3.1. Synthesis of [Ru(CO)(PPh$_3$)$_2$(php)] (1)

[RuHCl(CO)(PPh$_3$)$_3$] (0.1 g, 0.105 mmol) and the ligand H$_2$php (0.0317 g) were mixed and heated to reflux in dry ethanol (30 mL) for 9 h. The resulting brown crystalline product was collected and washed with cold ethanol and diethyl ether. Subsequent recrystallization by slow diffusion of $CHCl_3$ vapour into a concentrated DMF solution of the complex yielded brown crystals. Yield: 71 mg (71%). *Anal.* Calc. for $C_{50}H_{38}N_4O_6P_2Ru$: C, 62.99; H, 4.01; N, 5.87. Found: C, 62.96; H, 4.04; N, 5.84%. IR (KBr) ν/cm^{-1}: 1595 (νC=N)imine, 1264 (νC–O). UV/Vis ($CHCl_3$) λ_{max}/nm (ε/dm^3 mol^{-1} cm^{-1}): 264 (11 870), 336 (3400), 454 (3820), 504 (3300). ^{1}H NMR (400 MHz, $CDCl_3$) δ/ppm: 6.60 (1H, s, CH), 6.90 (1H, s, CH) 7.18–7.85 (multiplet, aromatic protons), 8.4 (1H, s, –CH=N), 11.0 (1H, s, NH).

2.3.2. Synthesis of [Ru(CO)(PPh$_3$)$_2$(phm)] (2)

This was prepared by the same procedure as **1** with [RuHCl(CO)(PPh$_3$)$_3$] (0.1 g, 0.105 mmol) and H$_2$phm (0.0349 g). Yield: 89 mg (86%). *Anal.* Calc. for $C_{51}H_{40}N_4O_7P_2Ru$: C, 62.35; H, 4.10; N, 5.70. Found: C, 62.36; H, 4.08; N, 5.74%. IR (KBr) ν/cm^{-1}: 1600 (νC=N)imine, 1264 (νC–O). UV/Vis ($CHCl_3$) λ_{max}/nm (ε/dm^3 mol^{-1} cm^{-1}): 263 (21 580), 313 (7550), 384 (1710), 515 (345). ^{1}H NMR (400 MHz, $CDCl_3$) δ/ppm: 3.90 (3H, s, –OCH$_3$), 6.47 (1H, s, CH), 6.67 (1H, s, CH) 7.14–7.82 (multiplet, aromatic protons), 8.4 (1H, s, –CH=N), 11.01 (1H, s, NH).

2.3.3. Synthesis of [Ru(CO)(PPh$_3$)$_2$(phn)] (3)

This was prepared by the same procedure as **1** with [RuHCl(CO)(PPh$_3$)$_3$] (0.1 g, 0.105 mmol) and H$_2$phn (0.0369 g). Yield: 61 mg (58%). *Anal.* Calc. for $C_{54}H_{42}N_4O_6P_2Ru$: C, 64.50; H, 4.21; N, 5.57. Found: C, 64.56; H, 4.20; N, 5.51%. IR (KBr) ν/cm^{-1}: 1610 (νC=N)imine, 1254 (νC–O). UV/Vis ($CHCl_3$) λ_{max}/nm (ε/dm^3 mol^{-1} cm^{-1}): 272 (12 650), 359 (5800), 431 (2260). ^{1}H NMR (400 MHz, $CDCl_3$) δ/ppm: 6.52 (1H, s, CH), 6.85 (1H, s, CH) 7.12–7.90 (multiplet, aromatic protons), 8.35 (1H, s, –CH=N), 11.0 (1H, s, NH).

2.3.4. Synthesis of [Ru(CO)(AsPh$_3$)$_2$(php)] (4)

This was prepared by the same procedure as **1** with [RuHCl(CO)(AsPh$_3$)$_3$] (0.1 g, 0.107 mmol) and H$_2$php (0.0323 g). Yield: 77 mg (69%). *Anal.* Calc. for $C_{50}H_{38}N_4O_6As_2Ru$: C, 57.67; H, 3.67; N, 5.38. Found: C, 57.61; H, 3.68; N, 5.35%. IR (KBr) ν/cm^{-1}: 1607 (νC=N)imine, 1268 (νC–O). UV/Vis ($CHCl_3$) λ_{max}/nm (ε/dm^3 mol^{-1} cm^{-1}): 266 (13 820), 340 (4450). ^{1}H NMR (400 MHz, $CDCl_3$) δ/ppm: 6.58 (1H, s, CH), 6.90 (1H, s, CH) 7.20–7.88 (multiplet, aromatic protons), 8.4 (1H, s, –CH=N), 11.0 (1H, s, NH).

*2.3.5. Synthesis of [Ru(CO)(AsPh$_3$)$_2$(phm)] (**5**)*

This was prepared by the same procedure as **1** with [RuHCl(CO)(AsPh$_3$)$_3$] (0.1 g, 0.107 mmol) and H$_2$phm (0.0356 g). Yield: 87 mg (76%). *Anal.* Calc. for $C_{51}H_{40}N_4O_7As_2Ru$: C, 57.23; H, 3.76; N, 5.23. Found: C, 57.26; H, 3.78; N, 5.27%. IR (KBr) ν/cm^{-1}: 1602 (νC=N)imine, 1472, 1263 (νC–O). UV/Vis ($CHCl_3$) λ_{max}/nm (ε/dm^3 mol^{-1} cm^{-1}): 268 (3720), 360 (4230). ^{1}H NMR (400 MHz, $CDCl_3$) δ/ppm: 3.90 (3H, s, –OCH$_3$), 6.58 (1H, s, CH), 6.78 (1H, s, CH) 7.0-7.82 (multiplet, aromatic protons), 8.3 (1H, s, –CH=N), 11.01 (1H, s, NH).

*2.3.6. Synthesis of [Ru(CO)(AsPh$_3$)$_2$(phn)] (**6**)*

This was prepared by the same procedure as **1** with [RuHCl(CO)(AsPh$_3$)$_3$] (0.1 g, 0.107 mmol) and H$_2$phn (0.0376 g). Yield: 76 mg (65%). *Anal.* Calc. for $C_{54}H_{42}N_4O_6As_2Ru$: C, 59.32; H, 3.87; N, 5.12. Found: C, 59.36; H, 3.88; N, 5.16%. IR (KBr) ν/cm^{-1}: 1610 (νC=N)imine, 1258 (νC–O). UV/Vis ($CHCl_3$) λ_{max}/nm (ε/dm^3 mol^{-1} cm^{-1}): 268 (24 550), 340 (5930), 444 (2560). ^{1}H NMR (400 MHz, $CDCl_3$) δ/ppm: 6.48 (1H, s, CH), 6.75 (1H, s, CH) 7.10–7.86 (multiplet, aromatic protons), 8.38 (1H, s, –CH=N), 11.0 (1H, s, NH).

3. Results and discussion

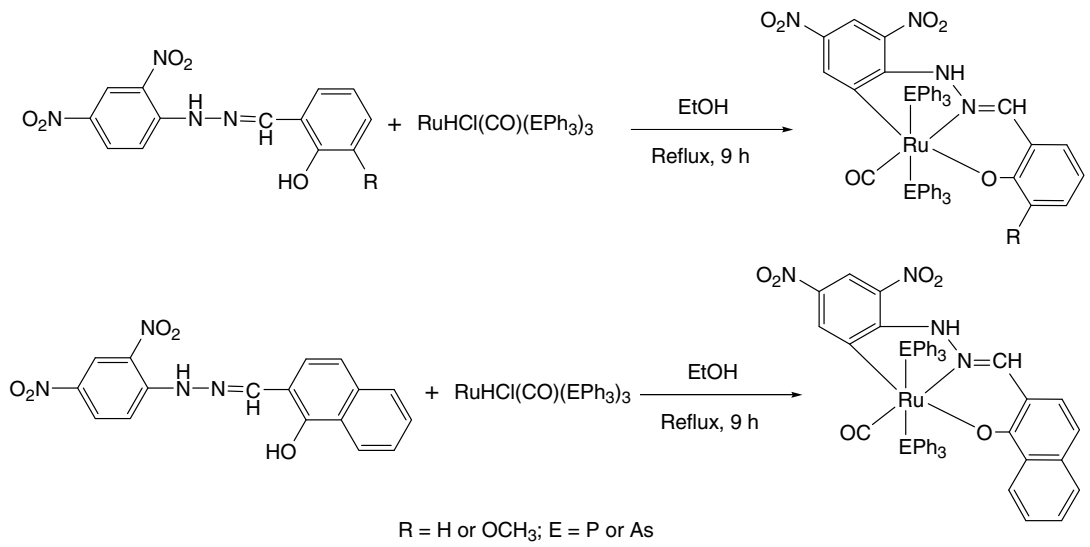
The reaction of 2,4-dinitrophenyl hydrazone ligands with [RuHCl(CO)(EPh$_3$)$_3$] (E = P or As) in a 1:1 molar ratio proceeds smoothly in refluxing ethanol, yielding the cycloruthenated complexes through the carbon atom, which is *meta* to both the NO$_2$ groups, the azomethine nitrogen atom and the phenolate oxygen atom by substitution of one chloride, one of the triphenylphosphines or arsines and one hydride from the Ru(II) precursor. All the complexes are non-hygroscopic, brown in color and found to be air stable at room temperature. Most of the cyclometallation reactions carried out earlier were thought to be favored when the reaction medium contained added bases [32–34] (like NaOH, NaOAc, N(Et)$_3$, etc.), and the presence of electron releasing substituents such as CH$_3$, OCH$_3$ and NH$_2$ in the aryl ring that is to be cyclometallated seemed to be essential [35,36]. The presence of electron withdrawing substituents such as a NO$_2$ group on the aryl ring was regarded to inhibit cyclometallation by rendering the aryl ring as an electrophile, which in turn would have made it unavailable for the attack of an electron deficient metal center [37]. In contrast to these two criteria, cyclometallation has been achieved in the present case without any added base in the reaction medium and with the presence of two electron withdrawing NO$_2$ groups in the hydrazine moiety. A possible explanation could be given the nature of the metal center and that of the electron withdrawing group. The two most likely mechanisms proposed for metal complex promoted C-H activation reactions are oxidative addition and electrophilic substitution. These two alternatives have different requirements for electron density at the metal center. The metal center may behave as an electrophile or as a nucleophile in its attack on the aromatic ring. In general, electrophilic attack is favored by electron poor metal centers whilst oxidative addition is favored by electron rich metal centers. There are many instances of cyclometallation where the oxidative addition and electrophilic mechanism cannot be easily distinguished [38,39]. In the present case the C–H activation seems to proceed via an eletrophilic attack of the electron deficient metal center on the C–H bond present in the aryl ring which is *meta* to both the nitro substituents. The primary ligands (CO and PPh$_3$/AsPh$_3$) present in the precursor complexes are π-acidic in nature and are capable of acquiring electron density from the metal through back bonding, thereby making the metal center electron deficient (an electrophile). At the same time, the *meta*-directing NO$_2$ groups, which are *meta* to each other, withdraw electron density only from the C3 (*ortho* to both NO$_2$ groups) and C5 (*ortho* to the 4-NO$_2$ group and *para* to the 2-NO$_2$ group) atoms and makes the C6 atom (*meta* to both NO$_2$ groups) relatively electron rich (a nucleophile). These two key steps, i.e. the formation of an electrophile and a nucleophile initiate cyclometallation, which is propagated through a series of steps as detailed below Scheme 1.

3.1. Mechanism for C–H activation

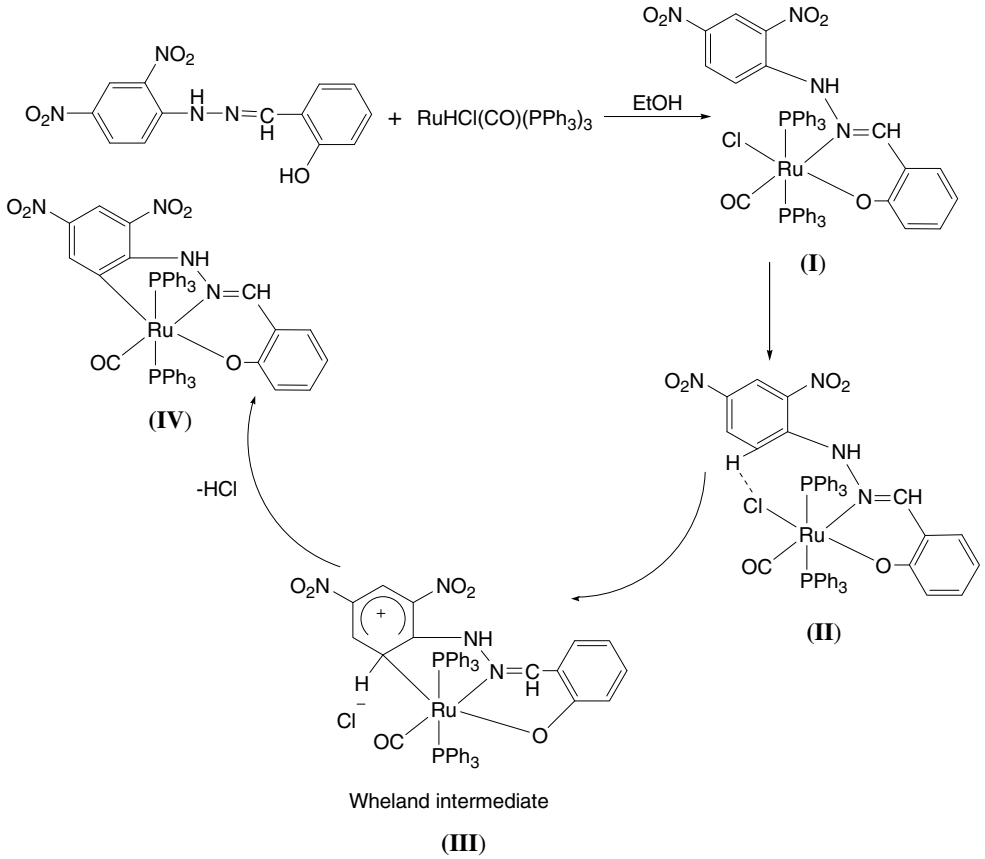
On the basis of the above points, the mechanism of the C–H activation has been deduced and depicted in Scheme 2. In the first step, the weakly coordinated hydrido ligand and a neutrally coordinated PPh$_3$/AsPh$_3$ are substituted by the phenolate oxygen and azomethine nitrogen of the hydrazone ligand. In the second step, the metal center is located in close proximity to the C6 atom of the aryl ring to be cyclometallated, which has become a nucleophile due to the meta-directing effect of the NO$_2$ groups. Then, the C6–H bond is considerably weakened by the interaction of the proton with the metal bound chloride and may be envisaged as an activated bond. In the next step, the electrophilicity of the ruthenium center is further increased due to the reduced σ-donation of the chloride to the metal center. The electrophilic attack at the C6–H bond is instigated by **II** affording the Wheland intermediate **III** and deprotonation occurs subsequently to expel HCl. The proposed electrophilic substitution is supported by the elimination of HCl during the cyclometallation, which is a unique feature of the electrophilic pathway [5,40,41].

3.2. IR spectra

The important IR frequencies of the complexes are given in the experimental section. The band due to NH stretching in the free ligands occurs in the 3400–3290 cm^{-1} region and remains unaffected after complexation. This precludes the possibility of coordination through the hydrazinic nitrogen atom. In the IR spectra of the complexes a considerable negative shift in ν(C=N) is observed, indicating coordina-



Scheme 1. Synthesis of complexes **1**–**6**.



Scheme 2. Proposed mechanism for C–H activation.

tion through the azomethine nitrogen atom. The hypsochromic shift of the N–N vibration also supports the above coordination. A peak at around 3100 cm^{-1} due to ν(O–H) stretching is absent in the spectra of the complexes, suggesting the deprotonation of the –OH group of the ligands prior to coordination to the metal. The ν(C–O) phenolic modes of the ligands appearing in the region 1218–1222 cm^{-1} are shifted to 1254–1268 cm^{-1} in the complexes, indicating complex formation via deprotonation of the phenolic OH. The presence of the nitro group in the complexes are characterized by the two bands observed at around 1518–1534 cm^{-1} and 1322–1340 cm^{-1} which arise due to symmetric and asymmetric stretching modes of NO_2.

3.3. Electronic spectra

The UV–Vis spectral bands of all the complexes were measured in dichloromethane. All the complexes exhibited two to four bands in the region 264–504 nm. The two absorption bands appearing in the range 264–272 nm and 336–360 nm may be assigned to a $\pi \rightarrow \pi^*$ transition of the aromatic ring and a $n \rightarrow \pi^*$ transition of the –C=N group, respectively. In addition, the low energy absorption peaks in the wavelength range 431–504 nm are associated with a charge transfer transition. The spectra of the complexes do not show any d–d transitions [42,43].

3.4. ^1H NMR spectra

^{1}H NMR spectra of the complexes show all the expected signals. In all the spectra, a singlet corresponding to a single proton is observed in the range δ 8.0–8.4 ppm, which is attributed to the azomethine proton (–HC=N). The singlet due to the NH proton appears at δ 11.0 ppm. Two singlets observed around δ 6.40–6.60 and 6.70–6.90 ppm are due to the protons of the metallated ring. The triphenylphosphine/triphenylarsine and other ring protons are observed as overlapping signals around δ 7.1–7.9 ppm. A sharp singlet at δ 3.9 ppm is assigned to the methoxy protons of complexes **2** and **5**.

3.5. X-ray crystallography

The molecular structures of complexes **1** and **2** have been determined by single crystal X-ray diffraction. The molecular structures of **1** and **2** are shown in Figs. 1 and 2. Selected bond distances and bond angles are given in Table 2. The $RuNOC_2P_2$ coordination sphere is distorted octahedral, as can be seen from the angles subtended at the ruthenium center. The basal plane is made up from C, N and O atoms of the dibasic tridentate hydrazone ligand and one carbonyl carbon, while the two PPh_3 groups occupy the apical positions. The structure shows that the hydrazone ligand is coordinated to Ru through the imine

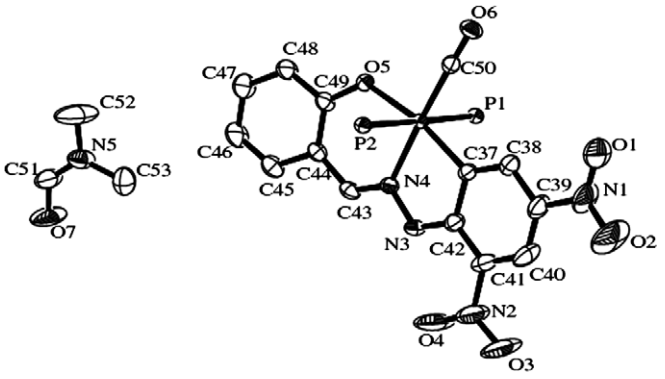


Fig. 1. Labelled ORTEP diagram of **1** with the thermal ellipsoids at 50% probability. Hydrogen atoms and phenyl rings of PPh_3 are omitted for clarity.

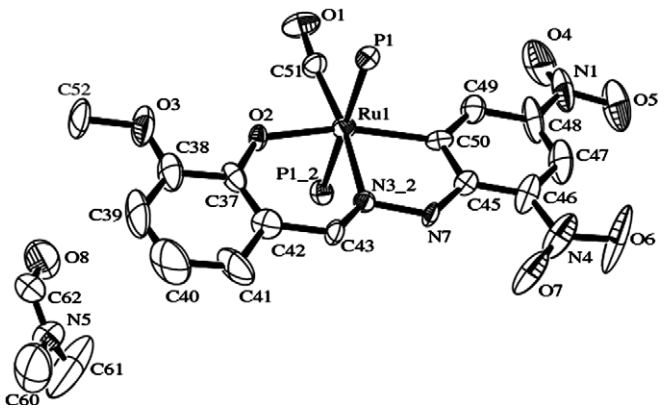


Fig. 2. Labelled ORTEP diagram of **2** with the thermal ellipsoids at 50% probability. Hydrogen atoms and phenyl rings of PPh_3 are omitted for clarity.

nitrogen, phenolic oxygen and aryl carbon, forming a six membered ring by O, N chelation and a five member ring by C, N chelation with bite angles O5–Ru1–N4 (87.75°) and N4–Ru1–C37 (80.15°). From the covalent radii values, the Ru(II)–C(sp^2) length is estimated to be 2.06 Å [44] and the observed values span the range 1.96–2.16 Å [45]. In our complex the Ru1–C37 distance is 2.040 Å, which is identical to that of the other structurally characterized cyclometallated Ru(II) complexes [46,33]. The Ru1–C50 bond distance (1.860 Å) is in accordance with those found in another Ru(II) complex [47]. The Ru–C37(sp^2) bond is 0.18 Å longer than the Ru1–C50(sp) distance, due to Ru–CO back bonding. The two Ru–P bond lengths are similar and are comparable to those reported for other PPh_3 coordinated Ru(II) complexes [48,49]. The Ru1–O5(phenolato) distance of 2.139 Å is slightly longer than those reported previously for similar Ru(II) complexes [50–53]. This lengthening of the Ru–O bond distance can be explained by the trans influence of the soft aryl carbon atom which is present trans to the phenolic oxygen. The trans weakening effect of CO is evident in the Ru1–N4 bond distance (2.065 Å), which is significantly longer than those that found for $[Ru(pabh)_2]$ [54] (pabh = *N*-(aryl)-*N*′-(picolinylidene)hydrazine) (1.960(3) and 1.958(3) Å), *trans*-$[Ru(pamh)(PPh_3)_2Cl]$ [55] (pamh = *N*-(aryl)-*N*′-(picolinylidene)hydrazine) (1.933(3) Å), $[Ru(HL)(PPh_3)Cl]Cl$ (1.984(5) Å) and $[Ru(HL)(PPh_3)(mpi)]Cl_2$ (1.991(5) Å) (HL = methyl 2-pyridylketone 4-(4-tolyl)thiosemicarbazones), (mpi = methyl (2-pyridylmethyleneimine)) [56].

3.6. Electrochemistry

Dichloromethane solutions of the complexes have been used to study the electrochemical properties, with the help of cyclic voltammetry. The potential data are listed in Table 3 and a representative voltammogram of **2** is illustrated in Fig. 3. The potentials of both the metal centered oxidation and reduction reflect the influence of the electronic nature of the substitutions present in the ligands.

Table 2
Selected bond lengths (Å) and bond angles (°) for **1** and **2**

1		**2**	
Ru1–C50	1.860(3)	Ru1–C51	1.840(5)
Ru1–C37	2.040(3)	Ru1–C50	2.202(4)
Ru1–N4	2.065(2)	Ru1–N3	2.065(3)
Ru1–O5	2.1391(18)	Ru1–O2	2.023(5)
Ru1–P1	2.3792(7)	Ru1–P1	2.3914(7)
Ru1–P2	2.3837(7)	Ru1–P2	2.3914(7)
C50–Ru1–C37	95.99(11)	C51–Ru1–C50	95.2(2)
C50–Ru1–N4	176.08(10)	C51–Ru1–N3	170.9(4)
C50–Ru1–O5	96.11(9)	C51–Ru1–O2	100.7(3)
C50–Ru1–P1	88.59(8)	C51–Ru1–P1	92.4(4)
C50–Ru1–P2	89.93(8)	C51–Ru1–P2	87.5(4)
C37–Ru1–N4	80.16(10)	C50–Ru1–N3	78.1(4)
C37–Ru1–O5	167.88(9)	C50–Ru1–O2	163.8(2)
C37–Ru1–P1	89.82(7)	C50–Ru1–P1	90.98(18)
C37–Ru1–P2	90.21(7)	C50–Ru1–P2	89.1(7)
N4–Ru1–O5	87.75(8)	N3–Ru1–O2	85.8(4)
N4–Ru1–P1	92.11(6)	N3–Ru1–P1	87.8(4)
N4–Ru1–P2	89.36(6)	N3–Ru1–P2	92.4(4)
O5–Ru1–P1	89.90(5)	O2–Ru1–P1	91.28(18)
O5–Ru1–P2	90.39(5)	O2–Ru1–P2	88.73(18)
P1–Ru1–P2	178.51(2)	P1–Ru–P2	179.81(4)

Hydrogen bonding geometry for **2**

D–H···A	D–H (Å)	H···A (Å)	D···A (Å)	D–H–A (°)
N7– H7A···O1	0.88	2.61	3.395(10)	149(5)
N7– H7A···O7	0.88	1.93	2.563(11)	127(8)

Table 3
Cyclic voltammetric data for the Ru(II) complexes

Complex	Ru(III)/Ru(II)[a] $E_{1/2}$/V(ΔEp/mV)	Ru(II)/Ru(I)[b] $E_{1/2}$/V(ΔEp/mV)	Ligand based reduction[d]
1	0.84[c]	−0.42(210)	−1.28
2	0.92 (1080)	−0.55(460)	−1.18
3	0.82[c]	−0.40(250)	−1.30
4	0.83[c]	−0.50(400)	−1.24
5	0.84[c]	−0.60(520)	−1.28
6	0.83[c]	−0.48(680)	−1.34

[a] Oxidation couple.
[b] Reduction couple.
[c] Irreversible, Ep_a value.
[d] Irreversible, Ep_c value.

Each complex displays a reductive response on the negative side and an oxidative response on the positive side of the Ag/AgCl electrode. The oxidation couple observed for complex **2** is assigned to the Ru(III)–Ru(II) oxidation. In all the other complexes, the Ru(III)–Ru(II) oxidation process takes place irreversibly in the range 0.82–0.84 V. Thus, as the σ-bonding ability of the O-atom of the deprotonated phenol functionality decreases with the increasing electron withdrawing ability of the substituents, the Ru(III)–Ru(II) oxidation becomes more difficult. The reductive response, observed in the range −0.40 to −0.60 V is quasireversible with a peak-to-peak separation (ΔEp) of 210–680 mV, and it is attributed to the Ru(II)–Ru(I) couple. The electron withdrawing substituents on the ligands have a significant effect on the observed reduction peak potentials. Electron withdrawing groups lower the electron density on the metal center even further and lead to less negative

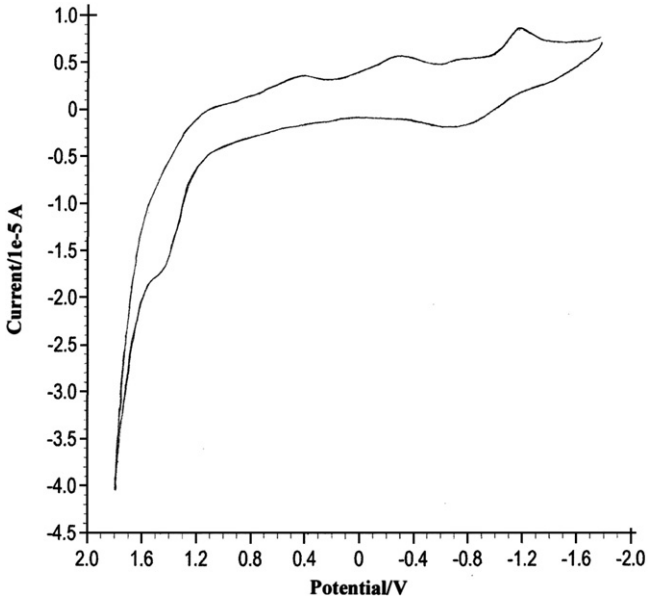


Fig. 3. Cyclic voltammogram of complex **2**.

potentials than for complexes with electro releasing groups. In addition, the M–C bond largely lowers the redox potentials of Ru(II) complexes [3]. Generally, the presence of an electron withdrawing group stabilizes the lower oxidation state and an electron donating group favors the higher oxidation state of the metal. The cyclic voltammograms of all the complexes were unfailing with one irreversible ligand based reduction due to the reduction of the HC=N group. These reduction peaks were shifted to more negative potentials with respect to the free ligands, which was consistent with the complex formation. It is interesting to note that a substituent which is somewhat away from the electroactive metal center can influence the metal centered redox potentials in a predictable manner.

4. Conclusion

A new family of cyclometallated Ru(II) complexes has been prepared and characterized. This C–H activation process is believed to proceed via an electrophilic substitution mechanism. What is more interesting is that the cyclometallation reaction presented here takes place under neutral conditions and without auxiliaries. Voltammetric results obtained in this study showed that the hydrazone ligands stabilize a lower oxidation state of the metal complexes. The substituents on the hydrazone ligands were found to have a significant effect on the redox potential. All the new complexes seem of interest for general synthetic and theoretical chemical research and may have some potential for catalytic applications.

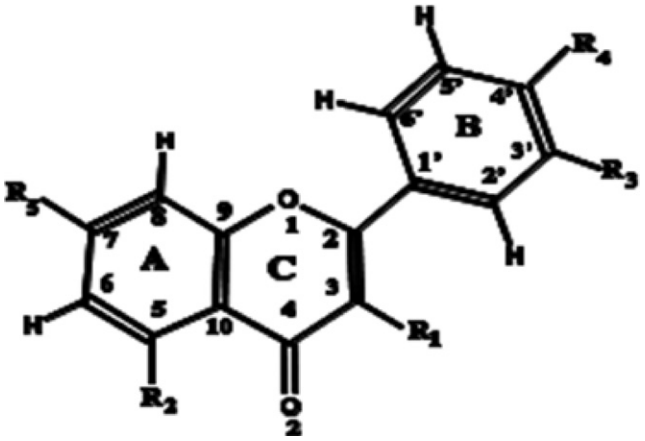
Appendix A. Supplementary data

CCDC 663252 and 613459 contain the supplementary crystallographic data for **1** and **2**. These data can be

obtained free of charge via http://www.ccdc.cam.ac.uk/conts/retrieving.html, or from the Cambridge Crystallographic Data Centre, 12 Union Road, Cambridge CB2 1EZ, UK; fax: (+44) 1223-336-033; or e-mail: deposit@ccdc.cam.ac.uk. Supplementary data associated with this article can be found, in the online version, at doi:10.1016/j.poly.2008.01.032.

References

[1] Y. Guari, S. Sabo-Etienne, B. Chaudret, Eur. J. Inorg. Chem. (1999) 1047.
[2] S. Niu, M.B. Hall, J. Am. Chem. Soc. 120 (1998) 6169.
[3] A.D. Ryabov, V.S. Sukharev, L. Alexandrova, R.L. Lagadec, M. Pfeffer, Inorg. Chem. 40 (2001) 6529.
[4] T. Matsubara, N. Koga, D.G. Musaev, K. Morokuma, J. Am. Chem. Soc. 120 (1998) 12692.
[5] A.E. Shilov, G.B. Shulpin, Chem. Rev. 97 (1997) 2879.
[6] D.J. de Geest, B.J. O'keefe, P.J. Stell, J. Organomet. Chem. 97 (1999) 579.
[7] V. Ritling, C. Sirlin, M. Pfeffer, Chem. Rev. 102 (2002) 1713.
[8] J. Halpern, Acc. Chem. Res. 15 (1982) 238.
[9] I.C.M. Wehman-Ooyevaar, I.F. Luitwieler, K. Vatter, D.M. Grove, W.J.J. Smeets, E. Horn, A.L. Spek, G. van Koten, Inorg. Chim. Acta 252 (1996) 55.
[10] H.L.L. Abbenhuis, M. Pfeffer, J.-P. Sutter, A. de Cian, J. Fischer, Organometallics 12 (1993) 4464.
[11] P.L. Alsters, P.F. Engel, M.P. Hogerheide, M. Copijn, A.L. Spek, G. van Koten, Organometallics 12 (1993) 1831.
[12] C. Cativaela, L.R. Falvello, J.C. Gines, R. Navarro, E.P. Urriolabeitia, New J. Chem. 25 (2001) 344.
[13] G. Zhao, Q.G. Wang, T.C.W. Mak, J. Organomet. Chem. 311 (1999) 574.
[14] P. Espinet, M.A. Esteruelas, L.A. Oro, J.L. Serrano, E. Sola, Coord. Chem. Rev. 17 (1992) 215.
[15] A. Von zelewsky, P. Belser, P. Hayoz, R. Dux, X. Hua, A. Suckling, H. Stoeckli-Evans, Coord. Chem. Rev. 75 (1994) 132.
[16] J. Dupont, M. Pfeffer, J. Spencer, Eur. J. Inorg. Chem. (2001) 1917.
[17] D.J. Saccomando, C. Black, G.W.V. Cave, D.P. Lydon, J.R. Rourke, J. Organomet. Chem. 305 (2001) 601.
[18] E.P. Urriolabeitia, M.D. Diaz-de-villegas, J. Chem. Edu. 77 (1999) 76.
[19] J.D. Higgius, J. Inorg. Biochem. 49 (1993) 149.
[20] M. Wang, E.W. Volkert, P.R. Singh, K.K. Katti, P. Lusiak, K.V. Katti, C.L. Barnes, Inorg. Chem. 33 (1994) 1184.
[21] K.V. Katti, V.S. Reddy, P.R. Singh, Chem. Soc. Rev. 24 (1995) 97.
[22] K.V. Katti, P.R. Singh, C.L. Barnes, Inorg. Chem. 31 (1992) 4588.
[23] R.M. Issa, H. El-Baradie, M. Gaber, Egypt J. Chem. 31 (1988) 251.
[24] M.F. Iskander, L. El-Sayed, N.M. Salem, R. Werner, W. Haase, J. Coord. Chem. 56 (2003) 1075.
[25] A.I. Vogel, Text Book of Practical Organic Chemistry, 5th ed., Longman, London, 1989.
[26] N. Ahmed, J.J. Lewison, S.D. Robinson, M.F. Uttley, Inorg. Synth. 15 (1974) 48.
[27] R.A.S. Pelgado, W.Y. Lee, S.R. Choi, Y. Cho, M.J. Jun, Trans. Met. Chem. 16 (1991) 241.
[28] Bruker Advanced X-ray Solutions SMART for WNT/2000 (Version 5.628), Bruker AXS Inc., Madison, WI, USA, 1997–2002.
[29] Bruker Advanced X-ray Solutions SAINT (Version 6.45), Bruker AXS Inc., Madison, WI, USA, 1997–2003.
[30] Bruker Advanced X-ray Solutions SADABS in SAINT (Version 6.45), Bruker AXS Inc., Madison, Wisconsin, USA, 1997–2003.
[31] G.M. Sheldrick, SHELXTL v.6.14, Bruker AXS Inc., Madison, WI, 2003.
[32] S. Fernandez, M. Pfeffer, V. Ritleng, C. Sirlin, Organometallics 18 (1999) 2390.
[33] V. Perez, A. Riera, A. Rodriguez, D. Miguel, Organometallics 21 (2002) 5437.
[34] D.L. Davies, O. Al-Duaij, J. Fawcett, M. Giardiello, S.T. Hilton, D.R. Russell, J. Chem. Soc., Dalton Trans. (2003) 4132.
[35] H. Takahashi, J. Tsuji, J. Organomet. Chem. 10 (1967) 511.
[36] J. Vicente, I. Saura-Llamas, P.G. Jones, J. Chem. Soc., Dalton Trans. (1993) 3619.
[37] A.C. Cope, E.C. Friedrich, J. Am. Chem. Soc. 90 (1968) 909.
[38] R.L. Brainard, W.R. Nutt, T.R. Lee, G.M. Whitesides, Organometallics 7 (1988) 2379.
[39] R. Cordone, W.D. Harman, H. Taube, J. Am. Chem. Soc. 111 (1989) 2896.
[40] G.B. Shulpin, G.V. Nizova, A.T. Nikitaev, J. Organomet. Chem. 276 (1984) 115.
[41] C. Crocker, R.J. Errington, R. Markham, C.J. Moulton, B.L. Shaw, J. Chem. Soc., Dalton Trans. (1982) 387.
[42] A.R. Salib, S.L. Stefun, S.M.A. El-Wafa, H.F. El-Shafiy, Synth. React. Inorg. Met.-Org. Chem. 31 (5) (2001) 895.
[43] M.A. Greaney, C.L. Coyle, M.A. Harmer, A. Jordan, E.I. Stifel, Inorg. Chem. 28 (1989) 912.
[44] A.K. Rappe, C.J. Casewit, K.S. Colwell, W.A. Goddard, W.M. Skiff, J. Am. Chem. Soc. 114 (1992) 10024.
[45] M.D. Fryzuk, C.D. Montgomery, S.J. Rettig, Organometallics 10 (1991) 467.
[46] H. Aneetha, C.R.K. Rao, K.M. Rao, P.S. Zacharias, X. Feng, T.C.W. Mak, B. Srinivas, M.Y. Chiang, J. Chem. Soc., Dalton Trans. (1997) 1697.
[47] A. Hijazi, J-P. Djukic, M. Pfeffer, L. Ricard, N.K. Gruber, J. Raya, P. Bertani, A. deCian, Inorg. Chem. Commun. 45 (2006) 4586.
[48] K. Nareshkumar, R. Ramesh, Yu Liu, J. Inorg. Biochem. 100 (2006) 18.
[49] P. Ghosh, A. Pramanik, A. Chakravorty, Organometallics 15 (1996) 4147.
[50] S. Chakraborty, M.G. Walawalkar, G.K. Lahiri, J. Chem. Soc., Dalton Trans. (2000) 2875.
[51] V.R.L. Constantino, H.E. Toma, L.F.C. de Oliveira, F.N. Rein, R.C. Rocha, D.O. Silva, J. Chem. Soc., Dalton Trans. (1999) 1735.
[52] P. Bhattacharyya, M.L. Loza, J. Parr, A.M.Z. Slawin, J. Chem. Soc., Dalton Trans. (1999) 2917.
[53] S.A. Serron, C.M. Haar, S.P. Nolan, Organometallics 16 (1997) 5120.
[54] S. Pal, S. Pal, J. Chem. Soc., Dalton Trans. (2002) 2102.
[55] R. Raveendran, S. Pal, Polyhedron 24 (2005) 57.
[56] M. Maji, M. Chatterjee, S. Ghosh, S.K. Chattopadhyay, B-M. Wu, T.C.W. Mak, J. Chem. Soc., Dalton Trans. (1999) 135.



Compound	abbreviation	R1	R2	R3	R4	R5
3-hydroxyflavone	3HF	OH	H	H	H	H
5-hydroxyflavone	5HF	H	OH	H	H	H
3',4'-dihydroxyflavone	3'4'diHF	H	H	OH	OH	H
quercetin	Q	OH	OH	OH	OH	OH

Fig. 1. Atomic numbering (IUPAC nomenclature) and substitution pattern of the studied flavonoids.

second step, the quercetin ligand was studied under the same conditions with the same methodology. Quercetin (Q) is a flavonol that is ubiquitous in edible plant material, and has been the subject of detailed examination for its antioxidant, complexing and other biological properties [22–26]. This ligand simultaneously presents within its structure the three potential sites previously studied. The goal of this second part is to determine which of these sites presents the greatest affinity for Al(III) and to check if the classification obtained by means of the study of the mono-site compounds is preserved for this multi-site ligand. Density functional theory (DFT) and time-dependent density functional theory (TD-DFT) were used to calculate the theoretical electronic spectra of quercetin complexes, the results of which were compared with the experimental spectrum to identify the preferential chelating site of Al(III).

2. Experimental and theoretical methods

2.1. Reagents and chemicals

The hydroxyflavones were obtained from Extrasynthèse (France). Aluminium chloride and spectroscopic grade methanol were used without purification. Water was delivered by a Milli-Q-water purification system. The stoichiometries of the complexes were determined by the molar ratio method from the UV–Vis data set. For this method, solutions containing a constant concentration (4×10^{-5} M) of hydroxyflavone in methanol/water and variable concentrations of $AlCl_3$ (from 4×10^{-7} to 1×10^{-4} M) were used. A broad range of metal-to-ligand molar ratios was used in the equilibrium studies. The stoichiometries of the complexes were also verified by the method of continuous variation (Job's method). The ionic strength was fixed to 0.1 M with NaCl.

2.2. Instrumentation

The UV–Vis spectra were recorded on a Cary-l (Varian) spectrophotometer with cells of 1 cm path length, at 25 °C. A flow cell was used to allow successive additions of small amounts of aluminium chloride directly to the flavonoid solution.

2.3. Chemometric methods

The absorption spectra collected during the course of the metal-binding experiment were analyzed with the fitting program SPECFIT (version 3.0) [27]. This software allows the determination of the number of species that contribute to the absorption spectra using a factor analysis procedure (EFA) [28–30], and the electronic spectrum of each pure complex. The SPECFIT software has also been used to estimate the apparent stability constants (β) of the different complexed forms. In order to obtain the best fit between the complexation model and the experimental data, several models of complexes have been envisaged for the refinement of the stability constants. The stability constant:

$$\beta = \frac{[Al_aF_b]}{[Al]^a \cdot [F]^b}$$

results from the equilibrium between the flavonoid F and the complex Al_aF_b (without taking into account the protonation state of the ligand):

$$aAl(III) + bF \leftrightarrow Al_aF_b$$

2.4. Quantum chemical calculations

All calculations were performed at the density functional level of theory with the B3LYP hybrid functional

[31,32], using the GAUSSIAN (G03) program package [33]. Geometry optimizations were carried out, without any symmetry constraints, using the 6-31+G(d,p) basis set [34], including polarization functions to correctly take into account intramolecular H-bonding in the ligand. Vibrational frequency calculations have been performed to ensure that all the optimized structures of the free and complexed quercetin correspond to energy minima. The low-lying excited states were treated within the adiabatic approximation of time-dependent density functional theory (DFT-RPA) [35] with the B3LYP hybrid functional. Vertical excitation energies were computed for the first 60 singlet excited states, in order to reproduce the UV–Vis spectra of the free and complexed ligands. As it is well known that UV–Vis absorption spectra are very sensitive to solvent effects, these were introduced by the SCRF method, via the polarized continuum model (IEF-PCM) [36,37] implemented in the GAUSSIAN program, with the default parameters. In the results, only transitions presenting high oscillator strengths (>0.05) have been considered.

3. Results

3.1. 3-Hydroxyflavone

The absorption spectrum of 3HF in a methanol/water 1:1 mixture is characterized by a double band at 343 and 308 nm (band I) and another one at 241 nm (band II). By successive additions of Al(III) to the solution, the intensity of band I of free 3HF decreases gradually, being stabilized

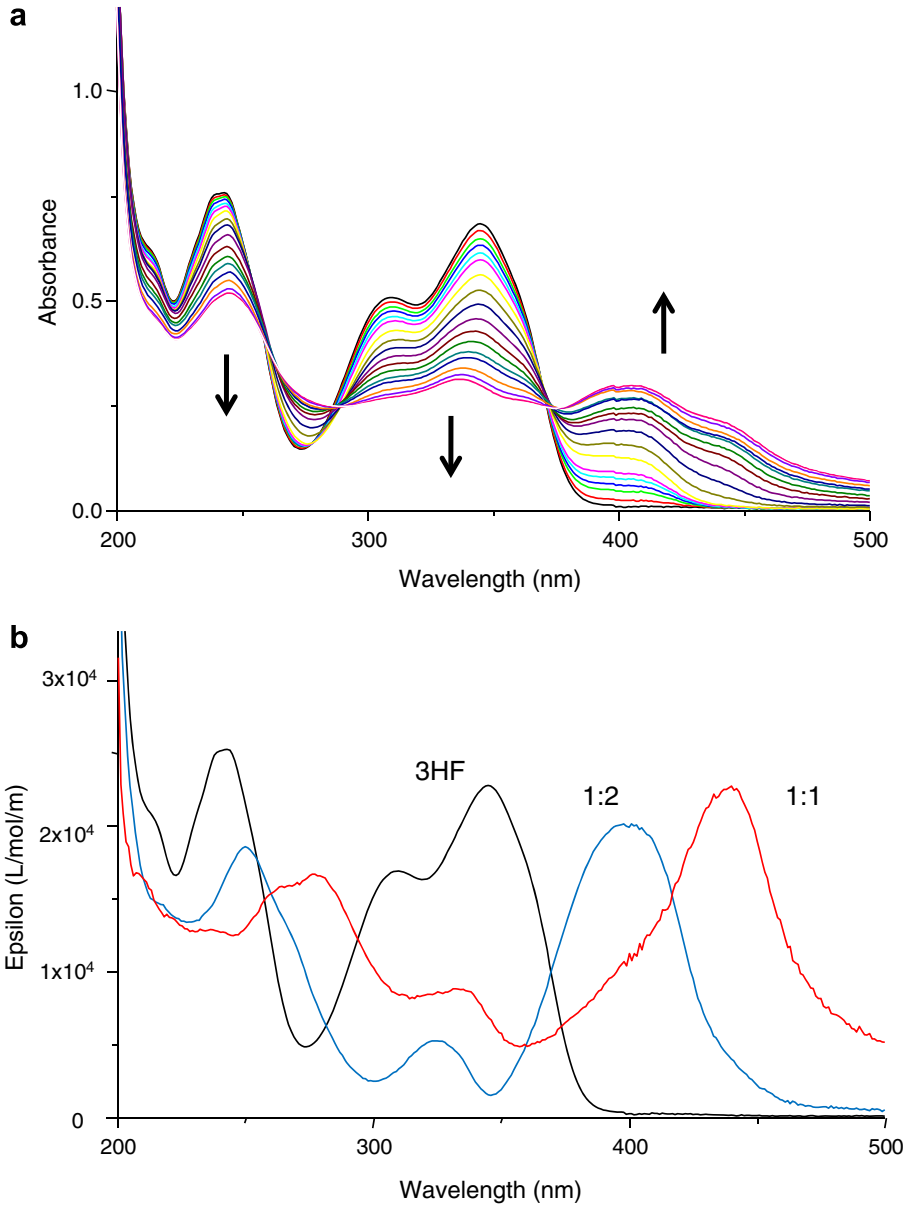


Fig. 2. UV–Vis spectra of 3HF in the absence and in the presence of Al(III). [Al(III)]/[3HF] molar ratios vary from 0 to 2.5 (a) and pure absorption spectra of 3HF, 1:2 and 1:1 complexes in methanol/water mixture (b).

towards a molar ratio of 1.5. At the same time, two new bands appear with wavelengths ranging between 400 and 470 nm (404 and 440 nm), reflecting the formation of at least two complexes (Fig. 2a).

For a relatively significant amount of Al(III) added, the appearance of a continuous background is observed for wavelengths higher than 450 nm, which is due to a scattering phenomenon caused by the beginning of precipitation. The presence of an aluminium hydroxide precipitate can be excluded because the concentrations of Al(III) used in the dosage are too low, but, due to the presence of water, it can be assumed that the solubility of the complexed forms in methanol/water mixture is lower than that of the free ligand, and the precipitation of the second complex is possible when it reaches significant concentrations. Only the spectra that did not present a background were taken into account in the numerical treatment.

The molar ratio method applied to the spectra set shows the formation of three complexes of stoichiometry (metal:-ligand) 1:3, 1:2 and 1:1. The analysis by numerical treatment of the spectra set allows the extraction of only three spectra, corresponding to majority pure species (the free and two complexed forms). The model which allows the best fit with the experimental data shows the predominant presence of the complexes 1:2 and 1:1. The spectra of these species are presented in Fig. 2b. The 1:2 complex spectrum is very similar to that obtained in neat methanol ($\lambda_{max} = 402$ nm), apart from the solvent effects [38], whereas the 1:1 complex spectrum has never been reported in the literature. The values of the formation constants are $\log\beta_{1:2} = 9.91 \pm 0.15$ and $\log\beta_{1:1} = 5.17 \pm 0.12$ for the $[Al(3HF)_2]^+$ and $[Al(3HF)]^{2+}$ complexes, respectively. The complex $[Al(3HF)_3]^0$ must be a minority species, present at a very weak concentration at the beginning of the dosage and it is not highlighted by the numerical treatment.

Fig. 3 presents the variation of the concentrations of the various species during the dosage. For small added quantities of Al(III) ($R < 0.4$) the 1:2 complex is in the majority. From a molar ratio of 0.5, the concentration of the 1:2 complex decreases in favour of 1:1 complex formation. For a molar ratio of 2.5, only 7% of the free ligand remains in solution.

In pure methanol, 3HF also forms a complex of 1:2 stoichiometry on the addition of Al(III), and the 1:3 complex was not detected in this medium [38]. A comparison of the chelating power of 3HF in the two different media shows that Al(III) is more easily complexed in neat methanol than in the presence of water at pH 6. Indeed, for a molar ratio of 1:1, the complexation reaction is complete and less than 10% of free ligand remains in the methanol

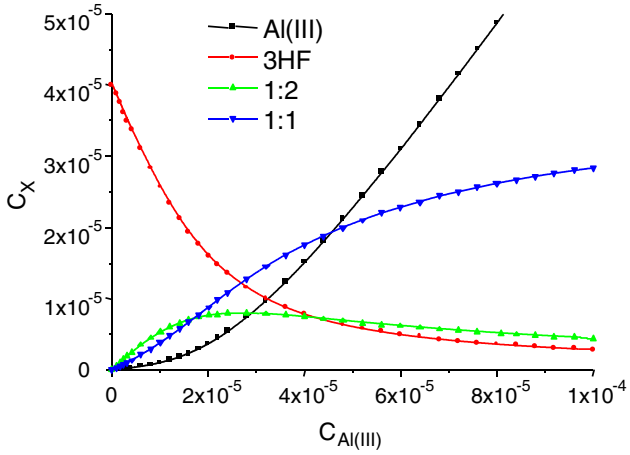


Fig. 3. Distribution curves of the concentration of the aluminium complexes of 3HF as a function of Al(III) concentration.

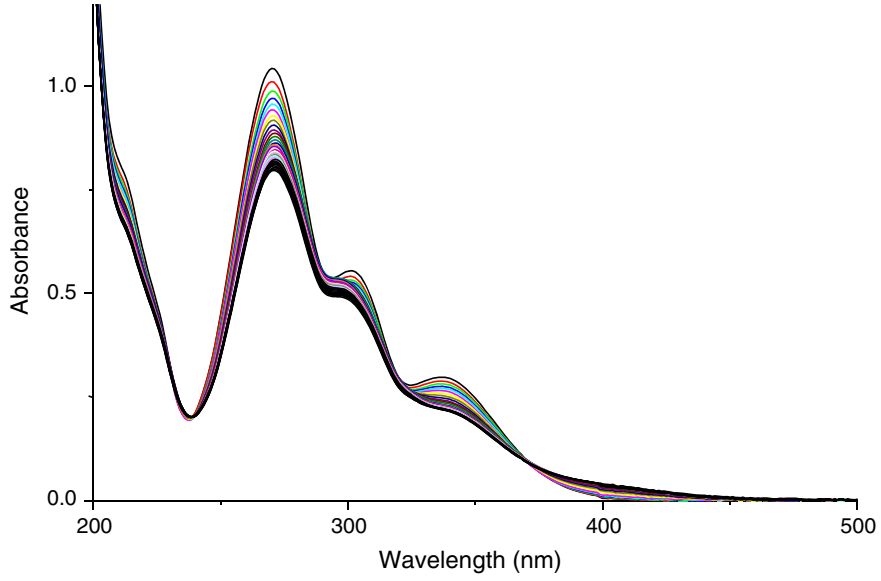


Fig. 4. UV–Vis spectra of 5HF in the absence and in the presence of Al(III). [Al(III)]/[5HF] molar ratios vary from 0 to 2.5.

solution, whereas 20% of free 3HF is still present in the mixed medium at pH 6 for this same ratio.

3.2. 5-Hydroxyflavone

Free 5HF presents an intramolecular hydrogen bond stronger than 3HF, and consequently the complexing power of 5HF is generally weaker than that of 3HF [39].

The spectra set resulting from the complexation of Al(III) by 5HF shows weak variations of the intensity of bands I (339 nm) and II (270 nm) of the free ligand (Fig. 4). A new band of low intensity appears towards 400 nm with the addition of Al(III) and a light hypsochromic effect (4 nm) is observed on the band of 5HF at 300 nm. The presence of an isosbestic point at 370 nm indicates the presence of an equilibrium between the free ligand and one complexed species.

The molar ratio method clearly shows the formation of a species with a 1:2 stoichiometry. The hydroxyl group of the ligand is deprotonated and the formula of the complex is $[Al(5HF)_2]^+$. The computed value of the formation constant of the complex is $\log \beta_{1:2} = 8.37 \pm 0.03$.

In neat methanol, 5HF forms a 1:1 complex with Al(III), with a red shift of 61 and 23 nm for bands I and II, respectively [40]. In $50\%_{aq}$ MeOH, the complex stoichiometry is different, and consequently the absorption spectrum of the 1:2 complex formed in methanol/water differs from the spectrum of the 1:1 complex in pure methanol (a shift of 65 nm of band I and only a few nanometers for band II).

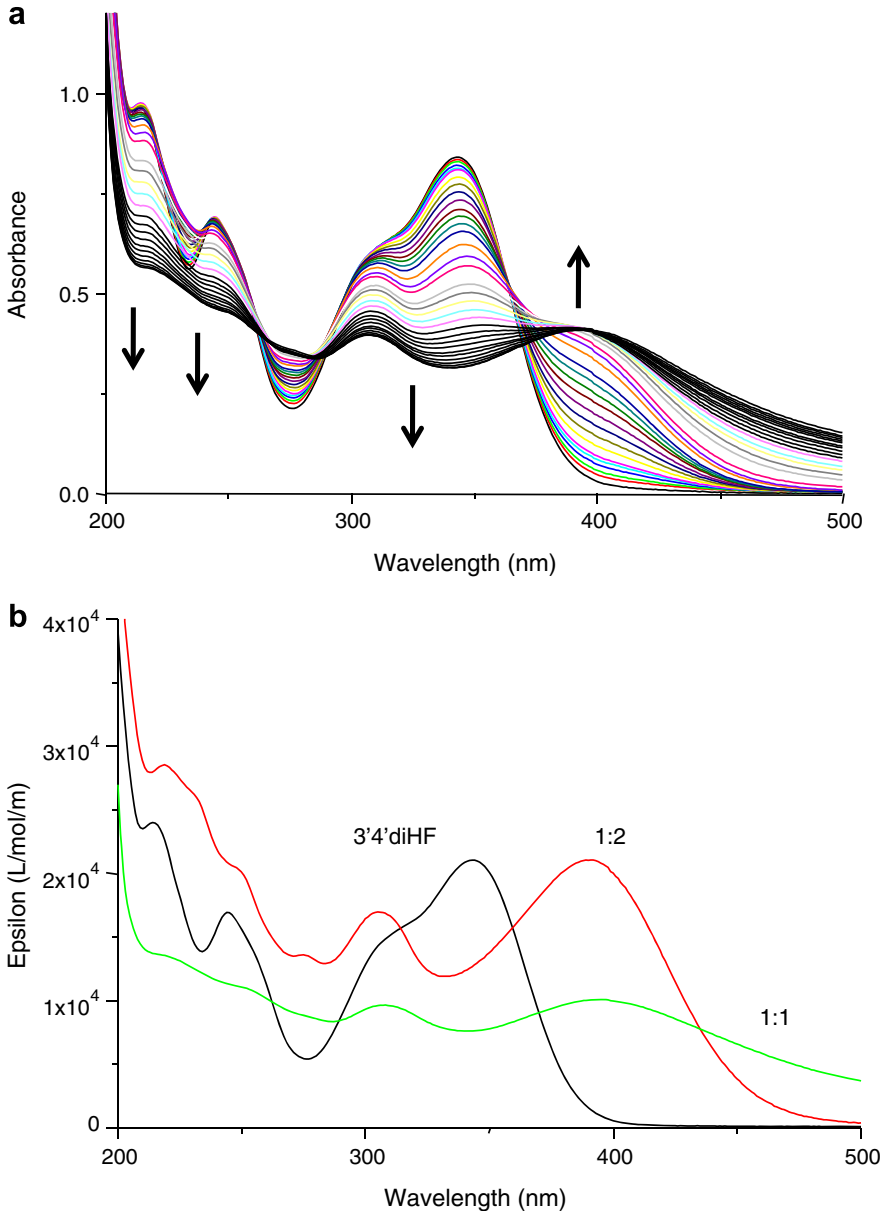


Fig. 5. UV–Vis spectra of 3′4′diHF in the absence and in the presence of Al(III). [Al(III)]/[3′4′diHF] molar ratios vary from 0 to 2.5 (a) and pure absorption spectra of 3′4′diHF, 1:2 and 1:1 complexes in methanol/water mixture (b).

Even if the complex stoichiometry obtained in mixed solvent is higher than that observed in neat methanol, complexation in this last medium is favoured. For instance, for a molar ratio of 2.5, all the ligand is implicated in the formation of the complex in methanol whereas 44% of the free ligand remains in solution in the mixed medium. Al(III) is less complexed by 5HF than by 3HF in the methanol/water mixture, since the quantity of complex measured at the end of the dosage is much smaller. It should be noted that no background appeared on the 5HF data set, which can be explained by the weakest concentration of complex, confirming the assumption of a lower solubility of the complex than that of the ligand in the presence of water.

3.3. 3′,4′-Dihydroxyflavone

The spectrum of 3′4′diHF in methanol/water solution at pH 6 presents a double absorption band at 341–308 nm (band I), a band centred at 243 nm (band II) and a shoulder at 212 nm. The increasing addition of Al(III) metal ions causes the appearance of new bands (Fig. 5a). No isosbestic point is observed throughout the dosage, which indicates the simultaneous formation of several complexes. However, it is difficult to distinguish, in the spectra obtained, the maxima corresponding to distinct complexes. The molar ratio method applied to the experimental data highlights two complexes of stoichiometry 1:2 and 1:1. Numerical analyses made it possible to extract the spectra of the two pure complexes and to obtain the formation constants of $[Al(3'4'diHF)_2]^-$ and $[Al(3'4'diHF)]^+$: $\log\beta_{1:2} = 9.24 \pm 0.07$ and $\log\beta_{1:1} = 4.85 \pm 0.04$.

The spectra of the $[Al(3'4'diHF)_2]^-$ and $[Al(3'4'diHF)]^+$ complexes are very similar, only a slight shift of 4 nm between the absorption band located at high wavelengths for $[Al(3'4'diHF)_2]^-$ (387 nm) and $[Al(3'4'diHF)]^+$ (391 nm) is observed (Fig. 5b). The curves of Fig. 6 illustrate the evolution of the concentration of the different species in solution. Until a molar ratio of 0.3, the $[Al(3'4'diHF)_2]^-$ and $[Al(3'4'diHF)]^+$ complexes are formed simultaneously in the same proportions, for a ratio higher than 0.3 the 1:1 complex becomes predominant. For a molar ratio of 1, 25% of the free ligand remains in the mixed solution. It should be noted that a background towards high wavelengths is observed in the spectra when significant concentrations of Al(III) are added. Once more, this is in agreement with the formation of a complex to a considerable extent, and consequently the beginning of precipitation.

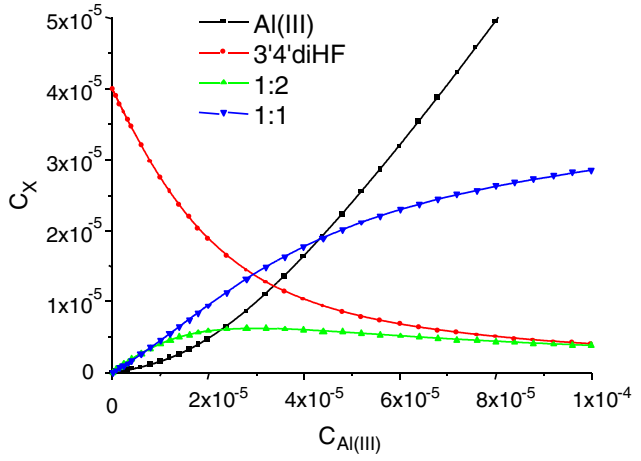


Fig. 6. Distribution curves of the concentration of the aluminium complexes of 3′4′diHF as a function of Al(III) concentration.

In pure MeOH, the formation of a 1:1 complex has been reported [40], and it has been shown that a twofold excess of Al(III) was necessary to obtain a full complexation of 3′4′diHF. Porter and Markham [41] reported the formation of a 1:2 and 1:3 complex in methanol in the presence of potassium acetate and sodium methoxide, respectively. This result shows that an increase in pH, facilitating the deprotonation of the catechol function leads to complexes of a high stoichiometry.

3.4. Comparison of the hydroxyflavones complexation

The principal results obtained previously for the complexation of aluminium(III) by flavonoids in methanol [39], like those obtained at pH 6 in a methanol/water mixed solvent, are joined together in Table 1.

Whatever the ligand, the stoichiometry of the complex formed in pure methanol is lower than that obtained in the methanol/water mixture at pH 6. The complexation of Al(III) is accompanied by the deprotonation of the hydroxyl functions of the ligand, and consequently an increase of pH facilitates this deprotonation and leads to the formation of complexes of higher stoichiometry. This observation was reported on several occasions for similar ligands, which present, in particular, a catechol group [42–44]. In our case, the apparent pH of the pure methanol solution must be lower than 6, and the pure methanol solution must be more "acidic" than the mixed solution of pH 6, which explains the difference in the stoichiometry of the complexes formed in these two media.

Whatever the ligand, for a given quantity of Al(III) added, the percentage of free ligand in the mixed solvent

Table 1
Comparison of the Al(III) complexation by hydroxyflavones in methanol and methanol/water medium

	Methanol			Methanol/water pH 6		
	Al:L	$\Delta\lambda$ (nm)	Logβ	Al:L	$\Delta\lambda$ (nm)	Logβ
3HF				1:3		
	1:2	58	12.3	1:2	61	9.91
				1:1	97	5.17
5HF				1:2	65	8.37
	1:1	61	6.5			
3′4′diHF				1:2	46	9.24
	1:1	43	6.7	1:1	50	4.85

$\Delta\lambda$ is the shift of band I upon complexation.

is always higher than in pure methanol. The complexation of Al(III) is thus more important in neat methanol than in the mixed solvent at pH 6. That has been checked for complexes having identical stoichiometries in the two media, the formation constant of the complex in pure methanol is always higher than that calculated in the mixed solvent. The presence of water inhibits partially the metal cation complexation. The hydration of the cation and/or the free ligand decreases the chelating capacity of the studied functions. Moreover complementary experiments, with constant pH and constant molar ratio, showed that an increase in the percentage of water (from 0% to 50%) in the solution decreased in a significant way the quantity of the formed complexes.

In a given medium, the complexation capacity of the studied chelating sites with respect to the Al(III) ion can be compared. The greater the stoichiometry of the obtained complexes, the more the function is chelating. If two hydroxyflavone complexes have the same stoichiometry, the complex which has the highest formation constant presents the chelating site having the greatest affinity towards the metal cation. Thus for Al(III), one can classify the sites according to their capacity of complexation in the following way:

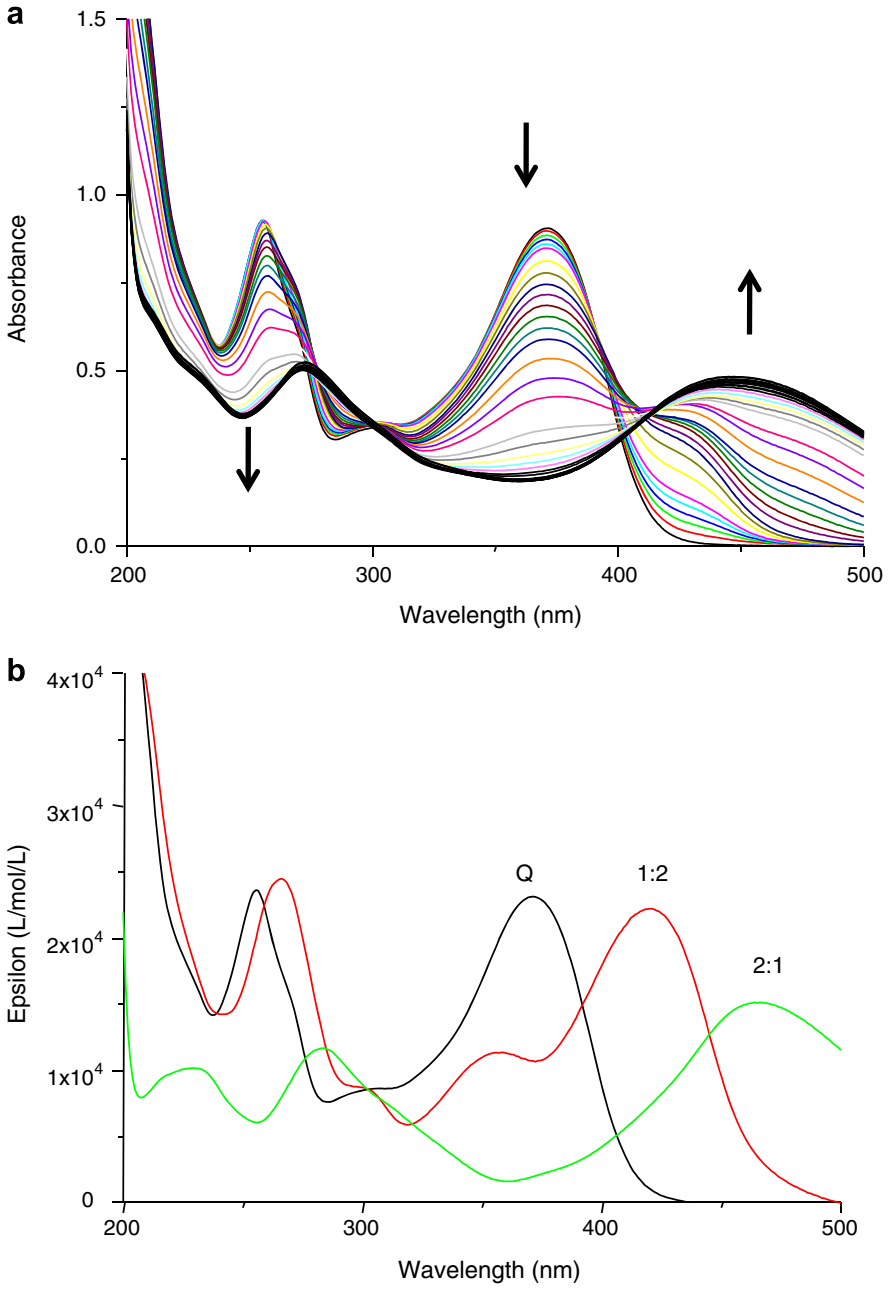


Fig. 7. UV–Vis spectra of Q in the absence and in the presence of Al(III). [Al(III)]/[Q] molar ratios vary from 0 to 2.5 (a) and pure absorption spectra of Q, 1:2 and 2:1 complexes in methanol/water mixture (b).

α-hydroxy − carbonyl > catechol > β-hydroxy − carbonyl

This order is the same in a mixed solvent as in neat methanol. Thus, if the presence of water decreases the chelating power of the hydroxyflavone site, it does not modify the order of the studied functions in their complexing capacity towards Al(III).

3.5. Complexation of Al(III) by a multi-binding site flavonoid

Q presents the three complexing sites (α-hydroxy-carbonyl, β-hydroxy-carbonyl and catechol) in competition towards the Al(III) fixation.

The electronic spectrum of free quercetin in methanol/water solution exhibits two major absorption bands: the band I lies at 370 nm and the second one is located at 253 nm (band II) with a shoulder at 265 nm (Fig. 7a). Upon addition of Al(III) to the quercetin solution, significant changes are observed in the electronic spectra. The intensity of band I decreases and a new band appears around 420 nm. From a molar ration higher than 0.3, the maximum of this band shifts towards longer wavelengths and a broad absorption band is observed around 450 nm. The set of obtained spectra does not clearly show an isosbestic point, which would mean that several complexes are simultaneously formed. The molar ratio method was used to determine the stoichiometry of the different complexed forms of quercetin with Al(III). The molar ratio plots at different wavelengths clearly indicate the formation of complexes of stoichiometry 1:3, 1:2 and 2:1.

From the UV–Vis absorption spectra, a finer determination of the number of different absorbing species was estimated by evolving factor analysis. Only three distinct components were found, corresponding to free quercetin and two complexes with 1:2 and 2:1 stoichiometries, and temporarily noted AlQ_2 and Al_2Q, respectively. To estimate the stability constants, a numerical treatment of the electronic spectra has been carried out with a model implicating the two complexes. The best fitting model to the experimental data gives the following stability constants: $\log\beta_{1:2} = 9.55 \pm 0.11$, and $\log\beta_{2:1} = 10.22 \pm 0.16$ for the AlQ_2 and Al_2Q complexes, respectively. Once more, the numerical analysis could not highlight the presence of the 1:3 complex. This complex must exist in a very weak concentration at the beginning of the dosage.

The pure electronic spectra of AlQ_2 and Al_2Q (Fig. 7b) present an absorption maximum at 420 and 464 nm, respectively. The 1:2 complex, where only one preferential site is implied, is formed in a great quantity at the beginning of the dosage, and its concentration reaches a maximum for a molar ratio of 0.5 (Fig. 8). Even if the 2:1 complex appears relatively rapidly in solution on metal cation addition (for a molar ratio of ~0.1), this one is formed in a lesser proportion. The fact that the second complexation site is involved also quickly shows that

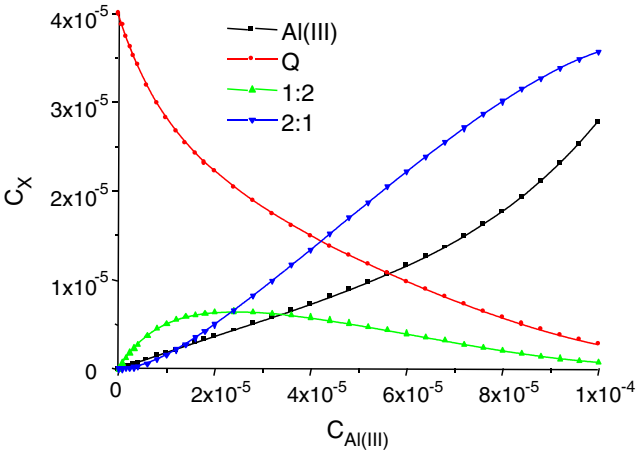


Fig. 8. Distribution curves of the concentration of the aluminium complexes of Q as a function of Al(III) concentration.

the two chelating functions, in competition within Q, have relatively close capacities of Al(III) fixing. However, for weak metal concentrations, compared to the number of potential complexation sites within the ligand, only one site is implied in AlQ_2 and one can reasonably think, on the basis of the results obtained previously with the mono-site flavonoids, that only the catechol and 3-hydroxy-carbonyl functions are in competition in the complex formation.

To determine which of these sites is involved in Al(III) fixation, the theoretical absorption spectra of the various possible complexed forms have been calculated. Firstly, the structures of $[Al(H_2O)(OH)Q_2]^0_\alpha$ and $[Al(H_2O)(OH)Q_2]^{2-}_{cat}$, corresponding, respectively, to complexation with the α-hydroxy-carbonyl and catechol function, were optimized at the B3LYP/6-31+G(d,p)/IEF-PCM level of theory. A water molecule and a hydroxyl ion have been added to the Al atom to complete its valence. The presence of the hydroxyl ion makes it possible to take into account the pH of the medium, since under the experimental conditions the $[Al(H_2O)_5(OH)]^{2+}$ species is predominant in aqueous solution. It should be noted that the two complexes do not have the same charge insofar as the number of deprotonations occurring with Al(III) chelation is different according to the site. Then, from these optimized structures, the electronic transitions were calculated by TD-DFT. For each complex, several stable conformers exist, their structures depending on the respective orientation of the ligands. These conformers present very similar theoretical electronic spectra, and this makes it impossible to differentiate them. In Fig. 9, the calculated absorption spectra of $[Al(H_2O)(OH)Q_2]^0_\alpha$ and $[Al(H_2O)(OH)Q_2]^{2-}_{cat}$, represented in the form of a vertical line corresponding to the absorption wavelength, can be compared with the spectrum of AlQ_2, obtained by fitting the experimental data. The theoretical spectra of $[Al(H_2O)(OH)Q_2]^0_\alpha$ and $[Al(H_2O)(OH)Q_2]^{2-}_{cat}$ present a very great number of calculated transitions, and both are likely to reproduce the absorption bands observed in the

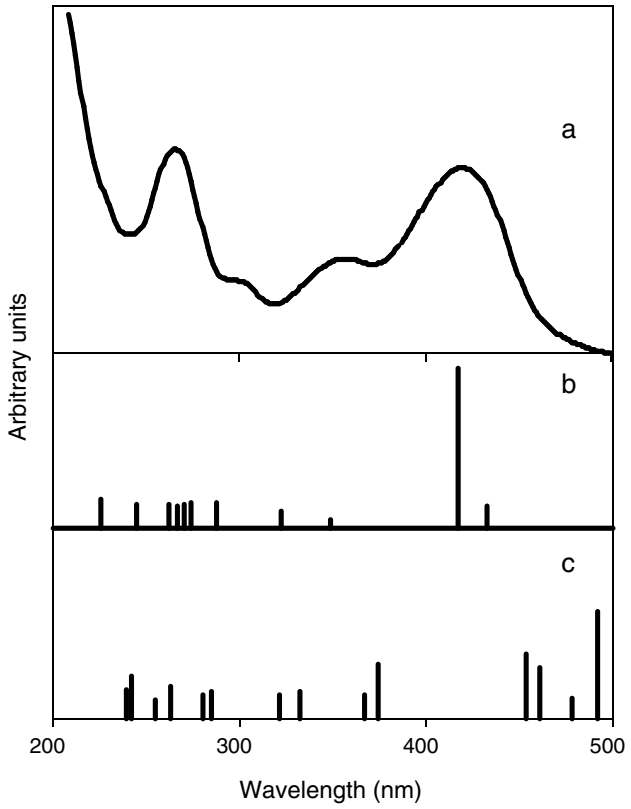


Fig. 9. Experimental spectrum of the 1:2 complex of Q (obtained by the EFA method) (a) and theoretical spectra of $[Al(H_2O)(OH)Q_2]^0_\alpha$ (b) and $[Al(H_2O)(OH)Q_2]^{2-}_{cat}$ (c).

UV range. The band observed at 420 nm in the experimental spectrum is reproduced perfectly in the theoretical spectrum of $[Al(H_2O)(OH)Q_2]^0_\alpha$ (417 nm), while no transition calculated for the complex $[Al(H_2O)(OH)Q_2]^{2-}_{cat}$ makes it possible to explain this absorption. The good agreement between the experimental features and theoretical spectrum of $[Al(H_2O)(OH)Q_2]^0_\alpha$ ensures that the fixing of Al(III) with Q is done via the α-hydroxy-carbonyl function. This function was that which presented the most important complexing capacity with respect to Al(III) in the study of the mono-site flavonoids. This result obtained with Q shows that the classification obtained for the mono-site ligands is preserved when these different sites are in competition within the same structure.

For reasons of steric hindrance, after the first site involving the carbonyl function in the formation of the AlQ_2 complex, it could be envisaged that the catechol group is the second fixing site in Al_2Q, whose formula would be $[Al_2(H_2O)_6(OH)_2Q]^+$. A comparison of these results with those obtained for the system Al(III)–quercetin in neat methanol shows that the same mechanism is observed whatever the solvent [12,14,45]. But once more, the presence of water in solution reduces the quantity of the formed complexes. The α-hydroxy-carbonyl group of Q also presents the highest affinity for the Zn(II) cation in the hydro-organic solvent [46].

4. Conclusion

This study made it possible to establish a classification of three chelating sites of flavonoid compounds towards Al(III) in a methanol/water medium, at pH 6. This classification is the same as that obtained in pure methanol, namely the α-hydroxy-carbonyl group presents the greatest affinity with respect to Al(III). Nevertheless the presence of water in the medium decreases the chelating power of all the studied sites. Combined spectroscopic and theoretical approaches have been used to determine the preferential complexing site of quercetin that presents the three investigated sites in competition. The results show that the α-hydroxy-carbonyl site remains the most powerful for Al(III) fixation.

If it is not possible to obtain structural information on the studied system using electronic absorption spectroscopy alone, the last part of this paper shows that when it is associated to the techniques of quantum chemistry, it is possible to elucidate a complexation mechanism.

Acknowledgements

"Institut du Développement et des Ressources en Informatique Scientifique" (IDRIS – Orsay, France) is thankfully acknowledged for the CPU time allocation. The authors also thank the Lille University Computational Center (C.R.I.).

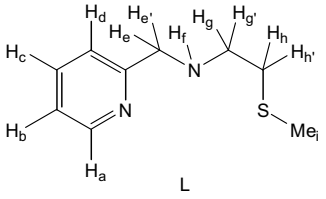
References

[1] J.B. Harborne, Biochemistry of Phenolic Compounds, Academic Press, New York, 1964.
[2] S. Teixeira, C. Siquet, C. Alves, I. Boal, M.P. Marques, F. Borges, J.L.F.C. Lima, S. Reis, Free Radical Biol. Med. 39 (2005) 1099.
[3] L. Mira, M.T. Fernandez, M. Santos, R. Rocha, M.H. Florêncio, K.R. Jennings, Free Radical Res. 36 (2002) 1199.
[4] C. Rice-Evans, Curr. Med. Chem. 8 (2001) 797.
[5] C.A. Rice-Evans, N.J. Miller, Biochem. Soc. Trans. 24 (1996) 790.
[6] C.A. Rice-Evans, N.J. Miller, G. Paganga, Free Radical Biol. Med. 20 (1996) 933.
[7] F.V. Botelho, J.I. Alvarez-Leite, V.S. Lemos, A.M.C. Pimenta, H.D.R. Calado, T. Matencio, C.T. Miranda, E.C. Pereira-Maia, J. Inorg. Biochem. 101 (2007) 935.
[8] L.J. Porter, K.R. Markham, Phytochemistry 11 (1972) 1477.
[9] J.P. Cornard, J.C. Merlin, Polyhedron 21 (2002) 2801.
[10] T. Jun, W. Bochu, Z. Liancai, Colloids Surf. B 55 (2007) 149.
[11] M. Leopoldini, N. Russo, S. Chiodo, M. Toscano, J. Agric. Food Chem. 54 (2006) 6343.
[12] T.L. Lin, B.Z. Yan, G.F. Hu, M. Wang, Chin. Chem. Lett. 17 (2006) 937.
[13] G.J. Smith, S.J. Thomsen, K.R. Markham, C. Andary, D. Cardon, J. Photochem. Photobiol. A 136 (2000) 87.
[14] R.F.V. De Souza, W.F. De Giovani, Spectrochim. Acta, Part A 61 (2005) 1985.
[15] M. Guo, C. Perez, Y. Wei, E. Rapoza, G. Su, F. Bou-Abdallah, N.D. Chasteen, J. Chem. Soc., Dalton Trans. 43 (2007) 4951.
[16] N. Binbuga, W.P. Henry, T.P. Schultz, Polyhedron 26 (2007) 6.
[17] F.L. Urbach, A. Timnick, Anal. Chem. 40 (1968) 1269.
[18] S. Sathish, G. Narayan, N. Rao, C. Janardhana, J. Fluoresc. 17 (2007) 1.
[19] G.T. Castro, S.E. Blanco, Spectrochim. Acta, Part A 60 (2004) 2235.

[20] S. Yumoto, H. Nagai, H. Matsuzaki, H. Matsumura, W. Tada, E. Nagatsuma, K. Kobayashi, Brain Res. Bull. 55 (2001) 229.
[21] J.M. Cranmer, J.D. Wilkins, D.J. Cannon, L. Smith, Neurotoxicology 7 (1986) 601.
[22] A. Gülsen, B. Turan, D.P. Makris, P. Kefalas, Eur. Food Res. Technol. 225 (2007) 435.
[23] J. Zhou, L. Wang, J. Wang, N. Tang, Transition Met. Chem. 26 (2001) 57.
[24] G. Erdogan, R. Karadag, Rev. Anal. Chem. 24 (2005) 9.
[25] M.T. Fernandez, M.L. Mira, M.H. Florencio, K.R. Jennings, J. Inorg. Biochem. 92 (2002) 105.
[26] B. Alluis, O. Dangles, Helv. Chim. Acta 84 (2001) 1133.
[27] S.S.A. Specfit Global Analysis System, Marlborough, MA, USA.
[28] H. Gampp, M. Maeder, C.J. Meyer, A. Zuberbühler, Talanta 33 (1986) 943.
[29] H. Gampp, M. Maeder, A.D. Zuberbühler, Trends Anal. Chem. 7 (1988) 111.
[30] M. Maeder, A.D. Zuberbühler, Anal. Chem. 62 (1990) 2220.
[31] A.D. Becke, J. Chem. Phys. 98 (1993) 5648.
[32] C. Lee, W. Yang, R.G. Parr, Phys. Rev. B 37 (1988) 785.
[33] M.J. Frisch, G.W. Trucks, H.B. Schlegel, G.E. Scuseria, M.A. Robb, J.R. Cheeseman, J.A. Montgomery Jr., T. Vreven, K.N. Kudin, J.C. Burant, J.M. Millam, S.S. Iyengar, J. Tomasi, V. Barone, B. Mennucci, M. Cossi, G. Scalmani, N. Rega, G.A. Petersson, H. Nakatsuji, M. Hada, M. Ehara, K. Toyota, R. Fukuda, J. Hasegawa, M. Ishida, T. Nakajima, Y. Honda, O. Kitao, H. Nakai, M. Klene, X. Li, J.E. Knox, H.P. Hratchian, J.B. Cross, V. Bakken, C. Adamo, J. Jaramillo, R. Gomperts, R.E. Stratmann, O. Yazyev, A.J. Austin, R. Cammi, C. Pomelli, J.W. Ochterski, P.Y. Ayala, K. Morokuma, G.A. Voth, P. Salvador, J.J. Dannenberg, V.G. Zakrzewski, S. Dapprich, A.D. Daniels, M.C. Strain, O. Farkas, D.K. Malick, A.D. Rabuck, K. Raghavachari, J.B. Foresman, J.V. Ortiz, Q. Cui, A.G. Baboul, S. Clifford, J. Cioslowski, B.B. Stefanov, G. Liu, A. Liashenko, P. Piskorz, I. Komaromi, R.L. Martin, D.J. Fox, T. Keith, M.A. Al-Laham, C.Y. Peng, A. Nanayakkara, M. Challacombe, P.M.W. Gill, B. Johnson, W. Chen, M.W. Wong, C. Gonzalez, J.A. Pople, GAUSSIAN 03, Revision B.04 ed., Gaussian Inc., Pittsburgh, PA, 2003.
[34] R. Ditchfield, W.L. Hehre, J.A. Pople, J. Chem. Phys. 54 (1971) 724.
[35] R. Bauernschmitt, R. Ahlrichs, Chem. Phys. 256 (1996) 454.
[36] M. Cossi, G. Scalmani, N. Rega, V. Barone, J. Chem. Phys. 117 (2002) 43.
[37] J. Tomasi, R. Cammi, B. Mennucci, C. Cappelli, S. Corni, P.C.C.P. 4 (2002) 5697.
[38] A.-C. Boudet, J.-P. Cornard, J.-C. Merlin, Spectrochim. Acta, Part A 56 (2000) 829.
[39] J.P. Cornard, J.C. Merlin, J. Mol. Struct. 651–653 (2003) 381.
[40] J.P. Cornard, J.C. Merlin, J. Mol. Struct. 569 (2001) 129.
[41] L.J. Porter, K.R. Markham, J. Chem. Soc. (C) (1970) 344.
[42] P.A.M. Williams, A.C. Gonzalez Baro, E.G. Ferrer, Polyhedron 21 (2002) 1979.
[43] M.I. Sancho, A.H. Jubert, S.E. Blanco, F.H. Ferretti, E.A. Castro, Spectrochim. Acta, Part A 68 (2007) 387.
[44] C.-H. Wang, J.-W. Lu, H.-H. Wei, M. Takeda, Inorg. Chim. Acta 360 (2007) 2944.
[45] J.P. Cornard, J.C. Merlin, J. Inorg. Biochem. 92 (2002) 19.
[46] G. Le Nest, O. Caille, M. Woudstra, S. Roche, F. Guerlesquin, D. Lexa, Inorg. Chim. Acta 357 (2004) 775.

scales, respectively, may be observed [4–11]. In addition, ^{113}Cd and ^{199}Hg NMR have been used as metallobioprobes for characterization of a variety of metal-substituted proteins [12–16].

Previously, we have reported solid- and solution-state characterization of group 12 metal ion bis-tridentate chelate complexes with symmetric pyridine-containing ligands bis(2-methylpyridyl)amine ($\mathbf{L}^1$) [8,9], bis(2-methylpyridyl)sulfide ($\mathbf{L}^2$) [5] and 2,6-bis(methylthiomethyl)pyridine ($\mathbf{L}^3$) [4]. Conditions for slow intermolecular change were found for dilute solutions of these complexes in acetonitrile-d_3. In this paper, the synthesis and characterization of $M(ClO_4)_2$ (M = Zn(II), Cd(II), Hg(II)) complexes of the non-C_2 symmetric ligand *N*-(2-pyridylmethyl)-*N*-(2-(methylthio)ethyl)amine (**L**) are reported. X-ray crystallography revealed homologous *trans* facial octahedral $[M(\mathbf{L})_2](ClO_4)_2$ complex structures. In dilute acetonitrile-d_3 solutions, each complex was in slow intermolecular exchange even at elevated temperatures. Furthermore, $[M(\mathbf{L})_2]^{2+}$ are the first group 12 bis-tridentate chelates for which conditions favoring slow intramolecular isomerization have been accessible in acetonitrile-d_3. These results are discussed in the context of the nine regular polyhedral forms of bis-tridentate chelate complexes.



L

2. Experimental

2.1. Methods and materials

Solvents and reagents were of commercial grade and used as received unless otherwise stated. Elemental analyses were carried out by Atlantic Microlab Inc., Norcross, Georgia. *J* values are given in Hz. *Caution!* All the perchlorate salts of metal complexes included in this work were stable for routine synthesis and purification procedures. However, organic perchlorates are potentially explosive and should be handled with care [17].

2.2. Solution-state NMR spectroscopy

Proton NMR spectra were collected in 5 mm o.d. NMR tubes on a Varian Mercury 400VX NMR spectrometer operating in the pulse Fourier transform mode. Calibrated autopipets were used to prepare nominally 2 mM solutions for variable temperature NMR measurements by dissolution of elementally analyzed complexes. The sample temperature was maintained by blowing chilled nitrogen over the NMR tube in the probe. Proton chemical shifts were measured relative to internal solvent but are reported relative to tetramethylsilane (TMS).

2.3. X-ray crystallography

Selected crystallographic data are given in Tables 1 and 2. Data were collected on a Siemens P4 four-circle diffractometer using a graphite-monochromated Mo Kα X-radia-

Table 1
Crystallographic data for complexes **1a**–**c**

Complex	$Zn(\mathbf{L})_2(ClO_4)_2 \cdot H_2O$ (**1a**)	$Cd(\mathbf{L})_2(ClO_4)_2 \cdot H_2O$ (**1b**)	$Hg(\mathbf{L})_2(ClO_4)_2$ (**1c**)
Empirical formula	$C_{18}H_{30}Cl_2N_4O_9S_2Zn$	$C_{18}H_{30}CdCl_2N_4O_9S_2$	$C_{18}H_{28}Cl_2HgN_4O_8S_2$
Formula weight	646.85	693.88	764.05
Crystal system	monoclinic	monoclinic	monoclinic
Space group	*C2/c*	*C2/c*	*P2(1)/c*
Crystal size (mm^3)	0.72 × 0.40 × 0.30	0.95 × 0.85 × 0.55	0.60 × 0.40 × 0.25
a (Å)	21.472(16)	20.807(8)	8.116(5)
b (Å)	10.014(6)	10.357(4)	13.048(8)
c (Å)	13.625(12)	13.487(5)	12.213(7)
β (°)	119.36(2)	115.659(6)	107.596(10)
V ($Å^3$)	2553(3)	2619.8(17)	1232.7(12)
Z	4	4	2
ρ_{calcd} ($Mg\,m^{-3}$)	1.683	1.759	2.058
μ (Mo Kα)(mm^{-1})	1.391	1.251	6.682
T (K)	93(2)	93(2)	93(2)
Total data	10202	8869	9910
Unique data	2845	2968	2758
Refined parameters	170	170	161
R_1,[a] wR_2[b] [$I > 2\sigma(I)$]	0.0267, 0.0669	0.0257, 0.0633	0.0224, 0.0571
R_1,[a] wR_2[b] (all data)	0.0304, 0.0690	0.0278, 0.0647	0.0251, 0.0587
Goodness-of-fit	1.035	1.088	1.056

[a] $R_1 = \sum||F_o| - |F_c|\,|/\sum|F_o|$.
[b] $wR_2 = [\sum[w(F_o^2 - F_c^2)^2]/\sum[w(F_o^2)^2]^{1/2}$ GOF (goodness-of-fit) is defined as $[w(F_o - F_c)/(n_o - n_v)]^{1/2}$, where n_o and n_v denote the number of data and variables, respectively.

Table 2
Selected bond distances (Å) and bond angles (°) for complexes **1a**–**c**

	$Zn(\mathbf{L})_2(ClO_4)_2 \cdot H_2O$ (**1a**)[a]	$Cd(\mathbf{L})_2(ClO_4)_2 \cdot H_2O$ (**1b**)[b]	$Hg(\mathbf{L})_2(ClO_4)_2$ (**1c**)[c]
M–N(1)	2.1059(19)	2.3133(17)	2.424(2)
M–N(2)	2.1773(17)	2.3826(17)	2.305(2)
M–S	2.5978(13)	2.7115(7)	2.7989(13)
N(2)–M–N(2)#1	180.0	180.0	180.0
N(2)–M–N(1)	79.80(5)	74.38(5)	73.26(8)
N(2)–M–N(1)#1	100.20(5)	105.62(5)	106.75(8)
N(2)–M–S#1	95.85(5)	99.76(4)	99.59(7)
N(2)–M–S	84.15(5)	80.24(4)	80.41(7)
N(1)–M–S	88.13(7)	87.84(5)	95.51(6)
N(1)–M–N(1)#1	179.999(1)	180.0	180.0
N(1)–M–S#1	91.87(7)	92.16(5)	84.49(6)
S–M–S#1	180.0	180.0	180.0

[a] Symmetry transformations used to generate equivalent atoms: $-x, -y+2, -z-1$.
[b] Symmetry transformations used to generate equivalent atoms: $-x, -y+2, -z+2$.
[c] Symmetry transformations used to generate equivalent atoms: $-x, -y+2, -z$.

tion ($\lambda = 0.71073$ Å). During data collection three standard reflections were measured after every 97 reflections. The structures were solved by direct methods and refined on F^2 by full-matrix least squares using the SHELXTL 97 program package [18,19]. All non-hydrogen atoms were refined with anisotropic displacement parameters; hydrogen atoms were refined as riding atoms with relative displacement parameters.

2.4. Synthesis of N-(2-pyridylmethyl)-N-(2-(methylthio)ethyl)-amine (*L*)

The ligand was prepared by adaptation of procedures for related ligands [20]. A solution of 2-chloroethyl methyl sulfide (2.4 mL, 24 mmol) in 20 mL deionized water was cooled to 0 °C in an ice bath. To this solution was added slowly with stirring a solution of 2-(aminomethyl)pyridine (2.1 mL, 20 mmol) in 35 mL methylene chloride. The mixture was then allowed to warm to room temperature. Over a 48 h period, 12 mL of 2 M NaOH was added by syringe pump. The crude mixture was washed with 40 mL of 4 M NaOH. The organic phase was dried with sodium sulfate and filtered. Removal of methylene chloride yielded a brown liquid. Fractional vacuum distillation yielded **L** as a colorless oil (94 °C/0.05 mmHg, 1.8 g, 49%). (*Anal.* Calc. for $C_9H_{14}N_2S$ requires: C, 59.3; H, 7.7; N, 15.4. Found: C, 58.0; H, 7.8; N, 15.0%) ^{1}H NMR (CD_3CN, −40 °C): δ 2.02 (3H, s, H_i), 2.62 (2H, t, J_{HH} 7, H_h), 2.73 (2H, t,J_{HH} 7, H_g), 3.83 (2H, s, H_f), 7.23 (1H, dd, J_{HH} 5,7, H_b), 7.37 (1H, d, J_{HH} 8, H_d), 7.72 (1H, dt, J_{HH} 2,8, H_c), 8.51 (1H, d, J_{HH} 5, H_a).

2.5. Preparation of $Zn(L)_2(ClO_4)_2 \cdot H_2O$ (*1a*)

A solution of $Zn(ClO_4)_2 \cdot 6\,H_2O$ (190 mg, 0.50 mmol) in 3 mL acetonitrile was added to a solution of **L** (190 mg, 1.0 mmol) in 3 mL methanol with stirring. Pale pink crystals of **1a** (105 mg, 32.5%) suitable for X-ray crystallography were obtained in 5 mm glass tubes after a week by slow diffusion of the mixture into benzene. M.p.: 188–189 °C. (*Anal.* Calc. for $C_{18}H_{30}Cl_2N_4O_9S_2Zn$ requires: C, 33.4; H, 4.7; N, 8.7. Found: C, 33.4; H, 4.7; N, 8.8%) ^{1}H NMR (2 mM, CD_3CN, 60 °C): δ 1.92 (3H, s, H_i), 2.74 (2H, bs, H_h), 2.96 (2H, bs, H_g), 4.05 (1H, bs, H_f), 4.22 (2H, bs, H_e), 7.60 (1H, dd, J_{HH} 5, 8, H_b), 7.65 (1H, d, J_{HH} 8 Hz, H_d), 8.14 (1H, dt, J_{HH} 1, 8, H_c), 8.21 (1H, bs, H_a).

2.6. Preparation of $Cd(L)_2(ClO_4)_2 \cdot H_2O$ (*1b*)

A solution of $Cd(ClO_4)_2 \cdot 6H_2O$ (210 mg, 0.50 mmol) in 3 mL acetonitrile was added to a solution of **L** (190 mg, 1.0 mmol) in 3 mL methanol with stirring. Small, colorless crystals of **1b** (70 mg, 20 %) suitable for X-ray crystallography were obtained in 5 mm glass tubes after a week of slow diffusion into toluene. M.p.: 163–165 °C. (*Anal.* Calc. for $C_{18}H_{30}CdCl_2N_4O_9S_2$ requires: C, 31.15; H, 4.4; N, 8.1%. Found: C, 31.3; H, 4.3; N, 8.1.) ^{1}H NMR (2 mM, CD_3CN, 20 °C): δ 1.98 (3H, s, H_i), 2.55 (1H, bs, H_g), 2.79 (2H, bs, H_h), 3.26 (1H, bs, $H_{g'}$), 3.66 (1H, bs, H_f), 4.06 (1H, bs, H_e), 4.27 (1H, bs, $H_{e'}$), 7.54 (1H, dd, J_{HH} 5,8, H_b), 7.60 (1H, d, J_{HH} 8, H_d), 8.08 (1H, dt, J_{HH} 1, 8, H_c), 8.15 (1H, bs, H_a).

2.7. Preparation of the complex $Hg(L)_2(ClO_4)_2$ (*1c*)

A solution of $Hg(ClO_4)_2 \cdot 3H_2O$ (230 mg, 0.50 mmol) in 3 mL acetonitrile was added to a solution of **L** (190 mg, 1.0 mmol) in 3 mL methanol with stirring. Colorless small crystals of **1** (48 mg, 13%) suitable for X-ray crystallography were obtained in 5 mm glass tubes after 6 days of slow diffusion into benzene. M.p.: 101–102 °C. (*Anal.* Calc. for $C_{18}H_{28}Cl_2HgN_4O_8S_2$ requires C, 28.3; H, 3.7; N, 7.3. Found: C, 28.2; H, 3.6; N, 7.3%.) ^{1}H NMR (2 mM, CD_3CN, 60 °C): δ 2.10 (3H, s, H_i), 2.92 (2H, bt, H_h), 3.07 (2H, bs, H_g), 4.03 (1H, bs, H_f), 4.26 (2 H, s, J_{HgH} 70, H_e), 7.53 (1H, dd, J_{HH} 4, 8, H_b), 7.56 (1H, d, J_{HH} 8, H_d), 8.04 (1H, dt, J_{HH} 2,7, H_c), 8.27 (1H, d, $J = 4$, H_a).

3. Results

3.1. Crystal structures of $M(L)_2(ClO_4)_2$ complexes

Complexes $[Zn(\mathbf{L})_2](ClO_4)_2 \cdot H_2O$ (**1a**), $[Cd(\mathbf{L})_2](ClO_4)_2 \cdot H_2O$ (**1b**) and $[Hg(\mathbf{L})_2](ClO_4)_2$ (**1c**) contain $[M(\mathbf{L})_2]^{2+}$ dications (Figs. 2–4) and well-separated perchlorate anions. These are the first structurally characterized complexes of divalent zinc triad metal ions with an $N_4(SR)_2$ coordination sphere involving a non-C_2 symmetric ligand. Selected crystallographic data for complexes **1a**–**1c** are given in Table 2. All three $[M(\mathbf{L})_2]^{2+}$ cations have *trans* facial octahedral geometry with the metal ion as an inversion center within a rectangular basal plane formed by the four nitrogen donor groups. Each pair of ligand nitrogens forms a pseudo-envelope chelate ring with the alkyl amino nitrogen on the flap (Fig. 1a). Complexes **1a** and **1b** are isostructural and isomorphous, containing twisted conformation *N*,*S* chelate rings with the ethylene carbons out of the plane formed by the other atoms (Fig. 1b). In contrast, these chelate rings have a pseudo-envelope conformation in **1c** with the ethylene carbons closest to S on the flaps (Fig. 1c).

3.2. Crystal structure of $Zn(L)_2(ClO_4)_2H_2O$ (**1a**)

Seven structurally characterized complexes of Zn(II) with a $N_4(SR)_2$ coordination sphere have been reported [5,21–25]. Complex **1a** contains a $[Zn(\mathbf{L})_2]^{2+}$ cation (Fig. 2), two perchlorate anions and a non-coordinated water molecule. The ligands have $N_{pyridyl}$–N_{alkyl}–S angles of 66.4°. The planes formed by the coordinating atoms from each of the individual ligand are 2.88 Å apart. The methyl groups are oriented toward the opposing ligand in the crystal structure.

The intraligand S–M–N_{alkyl} and N_{alkyl}–M–$N_{pyridyl}$ bond angles of 84.15(5)° and 79.80(5)° are closer to 90° than those observed for **1b** and **1c** in which the metal ions are larger. Shorter M–N and M–S distances are observed in complex **1a** than **1b** and **1c** as expected for the smaller zinc ion. The Zn–$N_{pyridyl}$ distance of 2.1059(19) Å is normal for six coordinate Zn(II) complexes [5,26–29]. The Zn–N_{alkyl} distance of 2.1773(17) Å is within the range (2.07–2.229 Å) reported for $N_4(SR)_2$ Zn(II) complexes. The Zn–S bond distance of 2.5978(13) Å is in the known range for six-coordinate thioether-containing complexes of Zn(II) [5,23,25,30].

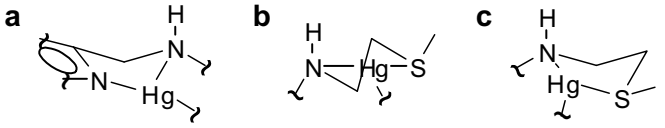


Fig. 1. Schematic diagrams of chelate ring conformations in complexes **1a**–**c**. (a) Psuedo-envelope *N*,*N* chelate ring in all three complexes with N_{alkyl} out of plane formed by other atoms. (b) Twisted *N*,*S* chelate ring in **1a** and **1b**. (c) Psuedo-envelope *N*,*S* chelate ring in **1c** with C8 out of plane formed by other atoms.

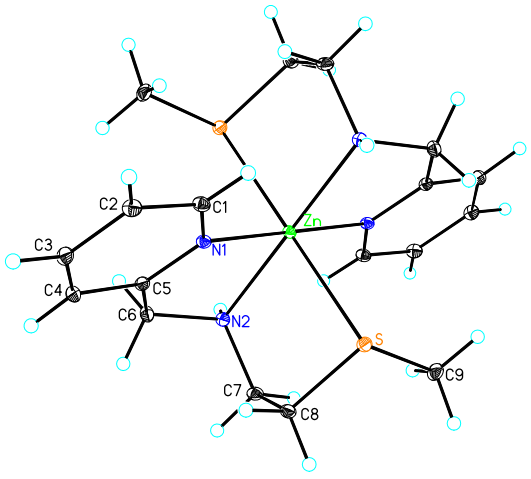


Fig. 2. Structure of $Zn(\mathbf{L})_2^{2+}$ in **1a**. Thermal ellipsoids shown at 50% level.

3.3. Crystal structure of $Cd(L)_2(ClO_4)_2 \cdot H_2O$ (**1b**)

Similar to complex **1a**, complex **1b** consists of a $[Cd(\mathbf{L})_2]^{2+}$ cation (Fig. 3), two perchlorate anions and a non-coordinated water molecule. Distorted octahedral $[Cd(\mathbf{L}^3)_2](ClO_4)_2$ is the only other structurally characterized Cd(II) complex with a $N_4(SR)_2$ coordination sphere [4]. The ligands in **1b** have $N_{pyridyl}$–N_{alkyl}–S angles of 69.1° forming coordinating atom planes that are 3.25 Å apart. The methyl groups are oriented toward the opposing ligand in the crystal structure as observed in **1a**.

The intraligand S–M–N_{alkyl} and N_{alkyl}–M–$N_{pyridyl}$ bond angles of 80.24(4)° and 74.38(5)° are somewhat smaller in complex **1b** than in complex **1a**. The Cd–$N_{pyridyl}$ distance of 2.3132(17) Å is comparable to those (2.266–2.442 Å) found in pyridine-containing six-coordinate Cd(II) complexes [5]. The Cd–N_{alkyl} distance of 2.3826(17) Å resembles those found in the six coordinate complex $[Cd(TAT)](ClO_4) \cdot 0.5H_2O$ (TAT = 1,4,7-tris(*o*-aminobenzyl)-1,4,7-triazacyclononane) [31]. The Cd–S distance of 2.7115(7) Å is similar to other six coordinate thioether Cd(II) complexes [5,30,32].

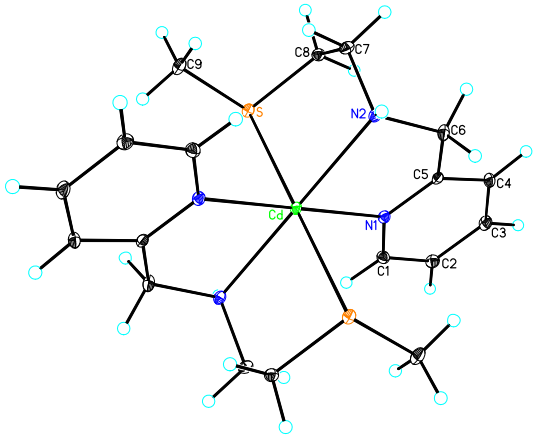


Fig. 3. Structure of $Cd(\mathbf{L})_2^{2+}$ in **1b**. Thermal ellipsoids shown at 50% level.

3.4. Crystal structure of $Hg(L)_2(ClO_4)_2$ (1c)

Complex **1c** (Fig. 4) is the third structurally characterized complex of Hg(II) with a $N_4(SR)_2$ coordination sphere [4,33]. The other two complexes have significantly more trigonal prismatic coordination geometry, however in solution bis-tridentate chelates of divalent zinc triad metal ions typically exhibit exchange between as many as nine geometric isomers [9]. The ligands have $N_{pyridyl}$–N_{alkyl}–S angles of 77.8°, significantly larger than both **1a** and **1b**. The coordinated ligand atoms form planes that are 3.19 Å apart, further apart than **1a** but closer than **1b**. Unlike the complexes of the smaller metal ions, the methyl groups are oriented away from the opposing ligand in the crystal structure of **1c**.

Complex **1c** has intraligand S–Hg–N_{alkyl} and N_{alkyl}–Hg–$N_{pyridyl}$ bond angles of 80.41(7)° and 73.26(8)°, respectively, which are very close to the bond angles observed for **1b**. The 2.424(2) Å Hg–$N_{pyridyl}$ distance is comparable to those observed in other six coordinate Hg(II) complexes including $[Hg(\mathbf{L}^1)_2](ClO_4)_2$, [9] $[Hg(\mathbf{L}^3)_2](ClO_4)_2$ [4] and $[Hg(pyridine)_6](CF_3SO_3)_2$ [34]. The 2.305(2) Å Hg–N_{alkyl} distance is slightly shorter than the range of 2.37(2)–2.473(11) Å observed in the six coordinate complexes $[Hg(TAT)](ClO_4)_2 \cdot 0.5H_2O$ [31] $[Hg(TDO)](PF_6)_2$ (TDO = 1,4,10, 13-tetrathia-7,16-diazacyclooctadecane) [35] and $[Hg([9]aneN_2S)_2](HgBr_4)$ ([9]aneN$_2$S = 1-thia-4,7-diazacyclononane) [33]. In contrast, the Hg–S bond distance of 2.7989(13) Å is slightly longer than the previously reported range of 2.458–2.751 Å for six coordinate Hg(II) complexes involving thioether donors [5,33].

3.5. Solution state investigation of L coordination to divalent zinc triad metal ions

The solution state coordination chemistry of bis-tridentate chelates of **L** with divalent zinc triad perchlorates was studied in acetonitrile-d_3 using variable temperature ^{1}H NMR spectroscopy. The NMR samples were prepared from elementally analyzed, X-ray quality crystalline materials, creating samples with well defined metal-to-ligand mole ratios. The labeling scheme for the protons of **L** is provided in the introduction.

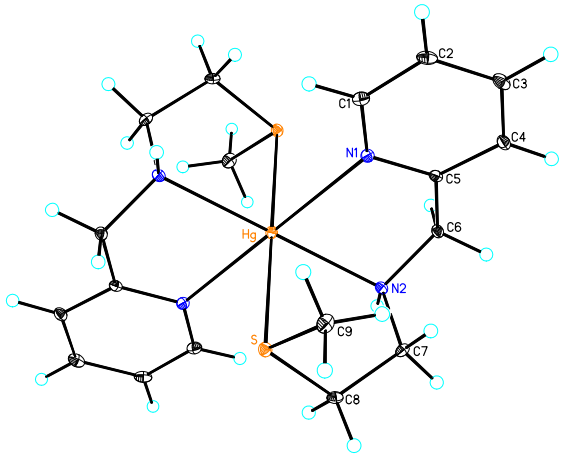


Fig. 4. Structure of $Hg(\mathbf{L})_2^{2+}$ in **1c**. Thermal ellipsoids shown at 50% level.

The proton NMR spectra of **1a**–**c** were qualitatively similar with severely broadened resonances for H_a, H_e, H_g and H_h at 20 °C (Fig. 5). Cooling to −40 °C had previously generated slow intermolecular exchange conditions on the J_{HH}, J_{CdH} and J_{HgH} time scales for related complexes [4,5,8,9]. Although the proton NMR spectra of **1a**–**c** lacked evidence for J_{CdH} or J_{HgH} interactions at −40 °C, they were surprisingly complex. Resonances for H_b, H_c and H_d changed little upon cooling. In contrast, extensive geminal coupling of the methylene and ethylene protons appeared for all three complexes indicating the ligands remained tridentate on the J_{HH} time scale [8,9]. Furthermore, major and minor environments were evident for some ligand protons. For example, the doublet with J_{HH} 5 Hz for H_a appeared at approximately 8.4 and 8.0 ppm in the minor and major environments, respectively, placing an upper limit of approximately 15 ms on their rate of exchange. Neither H_a environment grew in relative intensity following addition of excess ligand or metal salt to the samples (data not shown). As will be elaborated in the discussion, the simplest explanation for these observations is slow intramolecular exchange between isomeric bis-tridentate chelate forms.

Further proton spectra for these samples were collected at 20 °C intervals up to 80 °C (Fig. 5). Resonances were generally observed to broaden and coalesce as the temperature was raised until there were only nine ligand proton resonances. The coalescence temperature for the various peaks increased in the order Zn(II) > Cd(II) > Hg(II). Interestingly, the major H_a resonance for **1a** originally got sharper as the temperature was raised. To determine whether additional exchange processes could be frozen out at lower temperature, a 2 mM solution of **1a** in acetone-d_6 was prepared. The proton NMR of **1a** was qualitatively similar at −40 °C in the two solvents (data not shown). Unfortunately, further cooling of the acetone-d_6 solution to −90 °C resulted in broadening to extinction, foiling efforts to better characterize the species contributing to the major environment (data not shown). Further analysis of the H_a chemical shifts of $[M(\mathbf{L})_2]^{2+}$ as a function of temperature indicated near temperature independence for the minor resonance observed at low temperature, as expected for a single species. In contrast, the major resonance shifted significantly with temperature, consistent with an exchange equilibrium occurring on a submillisecond time scale. As a result, detailed quantitative analysis of the spectra for calculation of activation energies or accurate exchange rates is precluded.

Significantly, J_{HgH} 70 Hz involving H_e was observed for dilute solutions of **1c**, but only at elevated temperatures between 40 and 80 °C. Comparable magnitude coupling interactions between H_g and ^{199}Hg were also evident but

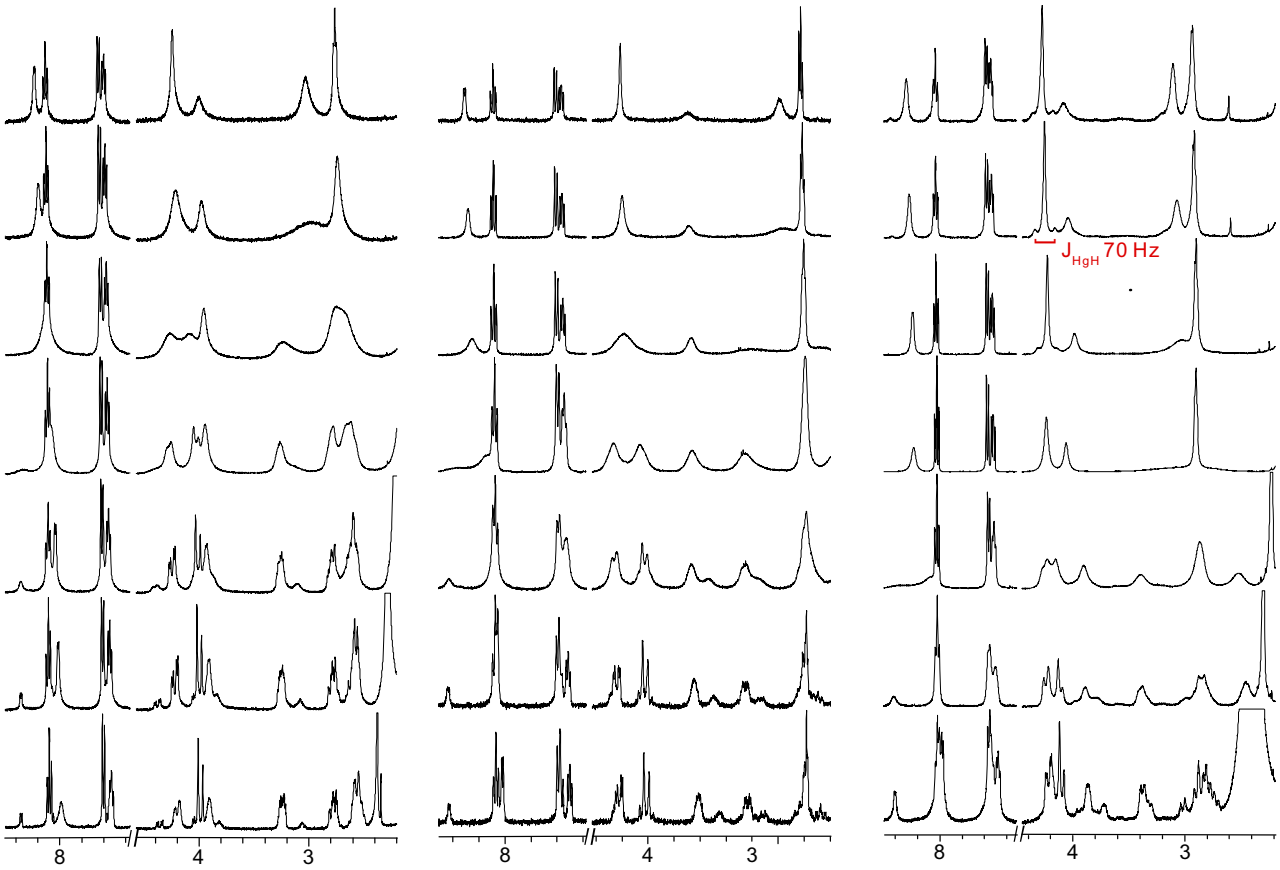


Fig. 5. Variable temperature proton NMR spectra highlights: nominally 2 mM CD_3CN solutions of **1a** (left), **1b** (center) and **1c** (right) at (from top) 80, 60, 40, 20, 0, −20 and −40 °C.

poorly resolved. Notoriously rapid intermolecular exchange processes are commonly associated with coordination complexes of Hg(II). Heteronuclear coupling between ^{199}Hg and ligand protons provides definitive evidence for slow intermolecular exchange. These coupling interactions indirectly suggest the ligands remain tridentate on the coupling constant time scale, since J_{HgH} have not been reported between ^{199}Hg and bidentate nitrogen or N,S donor ligands. Furthermore, this interaction was not observed in a more concentrated solution of **1c** (data not shown), likely because intermolecular exchange processes became more rapid. Significant broadening of resonances was observed for **1c** in dilute solution at 80 °C, suggesting intermolecular exchange at an appreciable rate. In contrast, resonances for **1a** and **1b** were still getting progressively sharper as the upper temperature limit for studies in acetonitrile-d_3 was approached.

4. Discussion

Detailed investigation of the coordination chemistry of divalent zinc triad metal ions is generally hampered by plasticity in coordination number and geometry, which leads to rapid intramolecular isomerization and intermolecular exchange rates. A variety of multidentate ligands have been used to create complexes with slow intermolecular exchange behavior on the NMR chemical shift and coupling constant time scales. Multidentate ligands have also provided group 12 coordination complexes in which different types of intramolecular exchange behavior was amenable to detailed characterization. Published studies have documented ligand-centered isomerization processes with no metal coordination changes [36] and slow intramolecular isomerization involving either changes in coordination number or identity of ligating atoms [10,37–39]. In addition, exclusion of specific geometric isomers from solution equilibria has been observed [8,9]. However, to the best of our knowledge only the novel $N_4(SR_2)_2$ coordination sphere divalent zinc triad metal ion complexes investigated here have enabled any characterization of individual geometric isomerization processes without cleavage of metal–ligand bonds.

Bis-tridentate chelates have nine regular polyhedral isomeric forms [9]. A mechanism for concerted isomer interconversion without bond cleavage is depicted in Fig. 6, patterned after the mechanism for racemization of tris-bidentate complexes described by Rodger and Johnson [40]. In this model, the terminal ligating atoms form 60° or 90° angles, respectively, around the central ligating atom in **1**–**4** and **5**–**6**. Polyhedra **1**–**4** can be interconverted, ostensibly without ligand reorganization, by rotation about a single pseudo-C_3 axis perpendicular to the planes formed

by the ligating atoms of the individual ligands. Polyhedra **3**–**6** can be interconverted by rotation about an orthogonal pseudo-C_3, but both ligand reorganization and changes in the relative orientation of the ligating atom planes occur. Repulsion-energy calculations have predicted octahedral isomers **1**, **3**, and **6** to be associated with potential energy minima [41]. Calculations with updated methodologies have not been identified.

Another hurdle to detailed characterization of the coordination chemistry of divalent zinc triad metal ions is the limited number of applicable instrumental methods. X-ray crystallography provides detailed bond lengths and bond angles, but these solid state measurements cannot be assumed to provide a complete description of solution species. Both kinetic and thermodynamic factors determine what crystallizes and crystallizes first from a mixture in solution and can favor isolation of minor solution species. All three divalent zinc triad metal ion complexes of type $M(\mathbf{L})_2(ClO_4)_2$ were isolated in bis-tridentate chelate form **1**. In contrast, bis-tridentate chelates of other pyridyl ligands have crystallized in different forms, and not necessarily the same form for all three metals (Table 3).

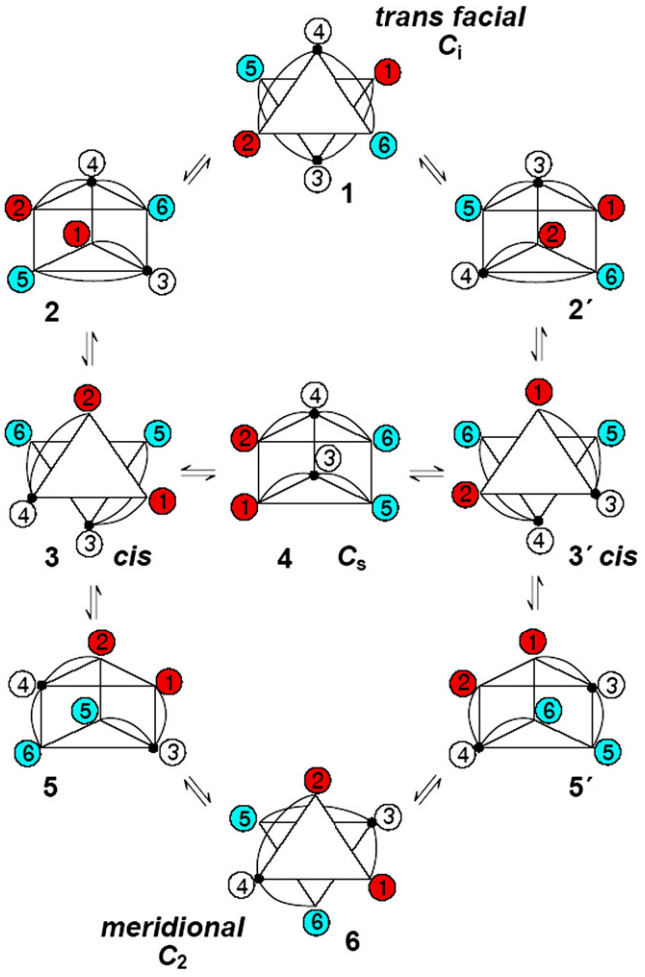
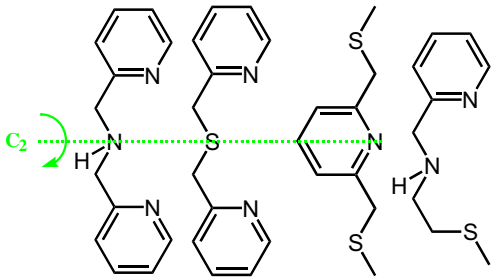


Fig. 6. Model of concerted isomerization for asymmetric bis-tridentate chelates involving regular polyhedral forms.

Crystallization documents the presence of a complex with a particular structure in solution, but not its relative abundance. Furthermore, correlations between crystallographic and solution state methods have to be made especially carefully with divalent zinc triad metal ions in the context of the facility with which they normally undergo intramolecular isomerization and intermolecular exchange.

NMR is one of the most valuable solution methods for characterization of divalent zinc triad metal ion complexes of organic ligands because chemical shift, coupling constant and exchange time information can be collected simultaneously for selected nuclei. Furthermore, both cadmium and mercury have high natural abundance spin $I = 1/2$ isotopes. In the absence of coincidental chemical shifts and exchange processes faster than the chemical shift time scale in solution, the symmetry of complexes of form **1** and **4** would lead to a singlet methyl proton resonance and one discrete resonance for every other ligand proton. Similarly, asymmetric complexes of form **2**, **3** and **5** would have two singlet methyl proton resonances and discrete resonances for every other proton of both ligands. In contrast, complex **6** is a higher symmetry form with four pyridyl proton resonances, three methylene proton resonances and one methyl resonance expected. Either coincident chemical

Table 3
Overview of crystallographic and solution state proton NMR properties[a] for bis-tridentate chelates of divalent zinc triad metal ions



Properties		L^1	L^2	L^3	L
Crystal form[b]					
	Zn^{2+}	**5**, **5′**	**1**	**6**	**1**
	Cd^{2+}	**5**, **5′**	**3**, **3′**	**6**	**1**
	Hg^{2+}	**5**, **5′**	**2**, **2′**	**6**	**1**
	$J(M^1H)$	^{113}Cd, ^{199}Hg	^{199}Hg	^{199}Hg	NA
Low T NMR					
	inversion	slow	fast	na	slow
	Py ^1H sets	one	one	one	>one[c]
	CH_2 ^1H sets	two	one	one	>six[d]
Reference		[8,9]	[5]	[4]	this work

[a] 2 mM, CD_3CN, −40 °C.
[b] Refer to Fig. 6; with C_2 symmetric ligands, groups 1, 3, 4 and 6 are identical, which increases the symmetry of all the complexes.
[c] Major and minor resonances were resolved for H_a only.
[d] More than three major and three minor methylene proton resonances were observed.

shifts or exchange rates faster than the chemical shift time scale can reduce the number of discrete proton resonances observed.

The proton NMR spectra of **1a**–**c** were strongly temperature dependent. At low temperature, extensive geminal coupling of methylene proton resonances provided definitive evidence for slow intermolecular exchange and preservation of all metal-ligand bonds. Even more significant were protons giving rise to two resonances in slow exchange on the chemical shift time scale of inequivalent intensity for all three metals. Detection of independent sets of ligand resonances for $[M(\mathbf{L})_2]^{2+}$ supports slow intramolecular geometric isomerization between bis-tridentate chelate forms on the NMR chemical shift time scale.

Structural and chemical shift considerations can be used to generate initial form assignments for the major and minor ligand environments observed in low temperature NMR experiments. Interligand steric interactions are anticipated to be greater in trigonal prismatic forms **2**, **4** and **5** than the octahedral complexes. However, in previous studies of bis-tridentate chelates the differences were not great enough to observe slow exchange between individual octahedral and trigonal prismatic forms [4,5,8,9]. Strong geminal coupling of the methylene protons of $\mathbf{L}^1$ provided evidence that form **6** was excluded from the solution equilibria between all or most of the other $[M(\mathbf{L}^1)_2]^{2+}$ forms at low temperature [8,9]. Similarly, geminal coupling is evident for both minor and major $[M(\mathbf{L})_2]^{2+}$ ligand environments observed at low temperature, leaving forms **1** and **3** as their most likely assignments.

Although some ligand protons only had one well-resolved resonance at −40 °C, for H_a there were two resonances with an approximate 0.4 ppm chemical shift differences. A difference of this magnitude is often induced by interactions with the ring current of opposing ligands in bis-chelates [8,9,11,42]. Significantly, the enantiomeric **3** and **3′** forms have the pyridyl rings in close proximity where interactions could occur between them while form **1** does not. Based on this analysis, the minor low temperature species with H_a resonance only slightly upfield of free ligand at ~8.4 ppm is assigned to form **1**, which has C_i symmetry and one environment for each proton type. Assignment of the major ligand environment at ~8.0 ppm to chiral enantiomeric forms **3** and **3′** then follows, but requires either widespread unresolved chemical shift differences or a rapid exchange process on the chemical shift time scale for the two ligands.

Significantly, for $Zn(\mathbf{L})_2^{2+}$ the fairly sharp major ~8.0 ppm H_a resonance observed below 0 °C began to broaden as the temperature approached −40 °C, suggesting an exchange process was approaching the slow exchange limit. Unfortunately, while the proton spectra of $[Zn(\mathbf{L})_2]^{2+}$ were qualitatively similar in acetone-d_6 and CD_3CN solutions at −40 °C, further cooling of the acetone-d_6 sample resulted in broadening to extinction (data not shown). A suitable NMR solvent with lower freezing point could not be found. Since the slow exchange limit could not be reached for these H_a environments, neither the number of exchanged average species nor their NMR parameters could be readily determined experimentally. Given evidence for an exchange process, interconversion of complexes with forms **3** and **3′** through form **4** becomes an attractive hypothesis. Significantly, the interconversion of **3** and **3′** became rapid on the chemical shift time scale at a higher temperature for $Zn(\mathbf{L})_2^{2+}$ than for the complexes involving larger metal ions and larger interligand separations.

Proposing involvement of a complex with trigonal pyramidal form **4** in low temperature equilibria, but not complexes with forms **2**, **2′**, **5** and **5′**, requires further comment. Examination of space filling crystal structure diagrams for **1a**–**1c** suggested that the *trans* facial orientation permitted the smallest interligand separation (Figs. S1–3). In structures **1a** and **1b**, for example, the thioether methyls extended more than halfway across the space between the donor atom planes associated with the two ligands. The opposing ligand had H_b of the pyridyl rings in distant opposition with the thioether methyl and aliphatic amine hydrogen blocking rotation in either direction. As a result, rotating through trigonal planar forms **2** and **2′** would require energetically demanding lengthening of many metal–ligand bonds. In contrast, form **4** has equivalent donor groups eclipsed and therefore has the potential to alter the angle between the planes formed by the donor atom. The energetic cost of lengthening a pair of M–L bonds can then be offset by shortening another pair without ligand reorganization. This model can also explain why the exchange rate between forms **3** and **3′** approaches the chemical shift time scale for Zn(II) but not its larger congeners. The distance separating the parallel donor atom planes of the two ligands is smaller for Zn(II) and interligand steric constraints would become significant with lesser deviations from parallel. As mentioned earlier, forms **5** and **5′** formally require increasing the N(1)–N(2)–S angle from 60° to 90°. The necessary ligand reorganization and requisite M–L bond stretches likely create an energy barrier that cannot be overcome on the chemical shift time scale at low temperature.

Thus, the simplest explanation for the low temperature proton NMR spectra of **1a**–**1c** is slow exchange on the chemical shift time scale between a complex of form **1** and an equilibrated form involving **3**, **3′** and **4** (or a variant with non-parallel donor atom planes). Assuming the concentration of the form most resembling **4** is modest compared to octahedral forms **3** and **3′**, the relative size of the two H_a peaks in the low temperature spectra suggests the stabilities of the three octahedral forms are comparable but form **1** is slightly less thermodynamically stable with all three metal ions. This is consistent with the conclusions of repulsion-energy calculations for bis-tridentate chelates of asymmetric ligands [41]. As the temperature is increased, exchange with the other complexes becomes possible,

particularly **6**, which allows exchange of methylene protons and collapses geminal coupling.

This model is fully consistent with the observed zinc triad metal ion coordination behavior of symmetric tridentate ligands $\mathbf{L}^1$, $\mathbf{L}^2$ and $\mathbf{L}^3$ (Table 3). Differences in the nature of the central donor atom of these ligands typically impact speciation equilibria at temperatures approaching −40 °C. Slow inversion at the secondary aliphatic amine excludes form **6** from low temperature equilibria for $M(\mathbf{L}^1)_2^{2+}$[8,9]. In contrast, thioethers have a much lower barrier to inversion and $M(\mathbf{L}^3)_2^{2+}$ had no detectable geometric preferences [5]. For $M(\mathbf{L}^3)_2^{2+}$, ligand geometry suggests form **6** is preferred, although rapid exchange between multiple forms including form **6** could not be distinguished [4].

Interestingly, the bis-tridentate chelates of symmetric ligands had readily detected J_{HgH} and smaller J_{CdH} at low temperature for pyridyl and methylene protons (Table 3). These complexes were either in rapid intramolecular exchange on the chemical shift time scale or non-exchanging. Rapid intramolecular isomerization with preservation of bonding interactions leads to exchange averaged coupling constants. On the other hand, slow exchange on the chemical shift time scale for major and minor forms of $M(\mathbf{L})_2^{2+}$ led to chemical shift differences of 0.4 ppm for H_a. Isomer interconversion at a rate which is slow relative to the chemical shift time scale but intermediate on the J_{MH} time scale for $Hg(\mathbf{L})_2^{2+}$ and $Cd(\mathbf{L})_2^{2+}$ would explain the absence of metal coupling satellites in low temperature proton NMR spectra.

In this study, samples that had exchange broadened NMR spectra at room temperature were also examined at higher temperature, resulting in coalescence and significant sharpening of some resonances. For $Hg(\mathbf{L})_2^{2+}$, J_{HgH} 70 Hz with H_e was measurable at 40 °C and notably broadened at 80 °C. In addition, less distinct J_{HgH} with H_g was evident between 60 and 80 °C. At these temperatures, the intramolecular isomerization between bis-tridentate forms **1**–**6** has become rapid enough for exchange averaged chemical shifts and coupling constants to be observed. Increasing the sample concentration increased the rate of intermolecular exchange and obscured the J_{HgH} interactions. Although comparable J_{CdH} interactions were not observed for $Cd(\mathbf{L})_2^{2+}$, their typically smaller magnitude and the comparable chemical shift behavior for all three zinc triad bis-tridentate chelates suggests that intermolecular exchange was slow even at elevated temperatures. Interestingly, exchange broadening of resonances has been observed for other bis-tridentate chelates at ambient temperature [9]. Spectra were never taken at higher temperature to possibly distinguish between intramolecular and intermolecular exchange processes as the source of broadening.

5. Conclusions

An asymmetric tridentate ligand permitted more detailed comparisons of the coordination chemistry of divalent group 12 metal ions to be made than related symmetric ligands. Fortuitous crystallization of isostructural bis-tridentate zinc triad complexes allowed for detailed structural comparisons. Unfortunately, the properties of the crystallized complexes were incompatible with assignment to the predominant solution species at −40 °C and prospects for crystallizing additional species associated with the complex solution equilibria are limited.

These studies suggest the resilience of high coordination number divalent zinc triad metal ion complexes to intermolecular exchange may be obscured by intramolecular exchange processes. These findings need to be thoughtfully considered when designing experiments to probe the bioactivity differences of Zn(II), Cd(II) and Hg(II).

Acknowledgements

This work was supported in part by the Petroleum Research Fund under Grant 40151-B3, the US National Science Foundation Division of Chemistry under Grant 0315934, the National Institutes of Health Academic Research Enhancement Aware 1 R15 GM59043-01 and the Jeffress Memorial Trust under J-627. Any opinions, findings, and conclusions or recommendations expressed in this material are those of the author(s) and do not necessarily reflect the views of the National Science Foundation. We also thank the Camille and Henry Dreyfus Foundation for a Scholar/Fellow award to D.C.B. for support of S.M.B. and the research, as well as a Jean Boissevain Dreyfus Undergraduate Scholarship for S.MS. R.J.B. acknowledges the DoD-ONR instrumentation program for funds to upgrade the diffractometer and the NIH-MBRS program for funds to maintain the diffractometer. The authors are also thankful for the help of Louise Menges in preparing Fig. 6 and for many helpful discussions with Christopher Abelt.

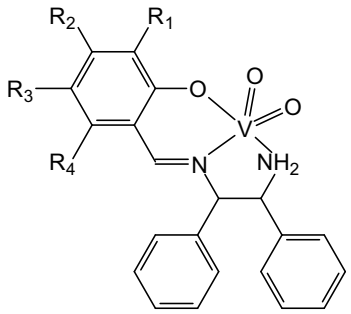
Appendix A. Supplementary data

CCDC 653864, 653865 and 653866 contain the supplementary crystallographic data for **1a**, **1b** and **1c**, respectively. These data can be obtained free of charge via http://www.ccdc.cam.ac.uk/conts/retrieving.html, or from the Cambridge Crystallographic Data Centre, 12 Union Road, Cambridge CB2 1EZ, UK; fax:(+44) 1223-336-033; or e-mail: deposit@ccdc.cam.ac.uk. Supplementary data associated with this article can be found, in the online version, at doi:10.1016/j.poly.2008.01.018.

References

[1] C.J. Matthews, W. Clegg, S.L. Heath, N.C. Martin, M.N.S. Hill, J.C. Lockhart, Inorg. Chem. 37 (1998) 199.
[2] H.M. Alvarez, T.B. Tran, M.A. Richter, D.M. Alyounes, D. Rabinovich, J.M. Tanski, M. Krawiec, Inorg. Chem. 42 (2003) 2149.
[3] E. Lopez-Torres, M.A. Mendiola, J. Rodriguez-Procopio, M.T. Sevilla, E. Colacio, J. Ma Moreno, I. Sobrados, Inorg. Chim. Acta 323 (2001) 130.

[4] W. Lai, S.M. Berry, D.C. Bebout, R.J. Butcher, Inorg. Chem. 45 (2006) 571.
[5] S.M. Berry, D.C. Bebout, R.J. Butcher, Inorg. Chem. 44 (2005) 27.
[6] D.C. Bebout, M.M. Garland, G.S. Murphy, E.V. Bowers, C.J. Abelt, R.J. Butcher, J. Chem. Soc., Dalton Trans. (2003) 2578.
[7] D.C. Bebout, J.F. Bush II, K.K. Crahan, E.V. Bowers, R.J. Butcher, Inorg. Chem. 41 (2002) 2529.
[8] D.C. Bebout, S.W. Stokes, R.J. Butcher, Inorg. Chem. 38 (1999) 1126.
[9] D.C. Bebout, A.E. DeLanoy, D.E. Ehmann, M.E. Kastner, D.A. Parrish, R.J. Butcher, Inorg. Chem. 37 (1998) 2952.
[10] D.C. Bebout, J.F. Bush II, K.K. Crahan, M.E. Kastner, D.A. Parrish, Inorg. Chem. 37 (1998) 4641.
[11] D.C. Bebout, D.E. Ehmann, J.C. Trinidad, K.K. Crahan, M.E. Kastner, D. Parrish, Inorg. Chem. 36 (1997) 4257.
[12] L.M. Utschig, T. Baynard, C. Strong, T.V. O'Halloran, Inorg. Chem. 36 (1997) 2926.
[13] L.M. Utschig, J.G. Wright, T.V. O'Halloran, Methods Enzymol. 226 (1993) 71.
[14] L.M. Utschig, J.G. Wright, G. Dieckmann, V. Pecoraro, T.V. O'Halloran, Inorg. Chem. 34 (1995) 2497.
[15] P.R. Blake, B. Lee, M.F. Summers, J.B. Park, Z.H. Zhou, M.W.W. Adams, New J. Chem. 18 (1994) 387.
[16] M.F. Summers, Coord. Chem. Rev. 86 (1988) 43.
[17] K.N. Raymond, Chem. Eng. News 61 (1983) 4.
[18] G.M. Sheldrick, SHELXL 97: Program for Crystal Structure Refinement, University of Göttingen (1997).
[19] G.M. Sheldrick, SHELXS 97: Program for Crystal Structure Solution, University of Göttingen (1997).
[20] Z. Tyeklar, R.R. Jacobson, N. Wei, N.N. Murthy, J. Zubieta, K.D. Karlin, J. Am. Chem. Soc. 115 (1993) 2677.
[21] F.E. Hahn, C. Jocher, H. Schroeder, Z. Naturforsch., B: Chem. Sci. 58 (2003) 1027.
[22] B.S. Hammes, C.J. Carrano, Inorg. Chem. 40 (2001) 919.
[23] C. Jubert, A. Mohamadou, J. Marrot, J.-P. Barbier, J. Chem. Soc., Dalton Trans. (2001) 1230.
[24] U. Heinzel, A. Henke, R. Mattes, J. Chem. Soc., Dalton Trans. (1997) 501.
[25] J.I. Bruce, T.M. Donlevy, L.R. Gahan, C.H. Kennard, K.A. Byriel, Polyhedron 15 (1996) 49.
[26] K. Matsuda, K. Takayama, M. Irie, Inorg. Chem. 43 (2004) 482.
[27] M. Parra-Hake, M.L. Larter, P. Gantzel, G. Aguirre, F. Ortega, R. Somanathan, P.J. Walsh, Inorg. Chem. 39 (2000) 5400.
[28] A. Neels, H. Stoeckli-Evans, Inorg. Chem. 38 (1999) 6164.
[29] U. Brand, H. Vahrenkamp, Inorg. Chem. 34 (1995) 3285.
[30] M.L. Helm, C.M. Combs, D.G. VanDerveer, G.J. Grant, Inorg. Chim. Acta 338 (2002) 182.
[31] O. Schlager, K. Wieghardt, H. Grondey, A. Rufinska, B. Nuber, Inorg. Chem. 34 (1995) 6440.
[32] R.A. Allred, A.M. Arif, L.M. Berreau, J. Chem. Soc., Dalton Trans. (2002) 300.
[33] U. Heinzel, R. Mattes, Polyhedron 11 (1992) 597.
[34] R. Aakesson, M. Sandstroem, C. Staalhandske, I. Persson, Acta Chem. Scand. 45 (1991) 165.
[35] A.J. Blake, G. Reid, M. Schroeder, Polyhedron 9 (1990) 2931.
[36] P.A.W. Dean, V. Manivannan, Inorg. Chem. 29 (1990) 2997.
[37] M.C. Copsey, T. Chivers, J. Chem. Soc., Dalton Trans. (2006) 4114.
[38] W. Yang, H. Schmider, Q. Wu, Y.-s. Zhang, S. Wang, Inorg. Chem. 39 (2000) 2397.
[39] V.I. Minkin, M.S. Korobov, L.E. Nivorozhkin, O.E. Kompan, G.S. Borodkin, Olekhnovich, R. Ya, Russ. J. Coord. Chem. 24 (1998) 152.
[40] A. Rodger, B.F.G. Johnson, Inorg. Chem. 27 (1988) 3061.
[41] M.C. Favas, D.L. Kepert, J. Chem. Soc., Dalton Trans. (1978) 793.
[42] H. Toftlund, S. Ishiguro, Inorg. Chem. 28 (1989) 2236.



	R_1	R_2	R_3	R_4
1	H	H	H	H
2, 2r	OMe	H	H	H
3, 3r	H	H	OMe	H
4	H	OMe	H	OMe
5	H	H	Me	H
6	H	H	Br	H
7	H	H	NO_2	H
8	H	H	$-(CH)_4-$	

Fig. 1. Structural formulae of dioxovanadium(V) complexes with deprotonated 1:1 condensation products of (*S*,*S*)-(−)-1,2-diphenyl-1,2-diaminoethane and of (*R*,*R*)-(+)-1,2-diphenyl-1,2-diaminoethane with salicylaldehyde and its derivatives. The numbers without the alphabetical symbol denote complexes with ligands derived from (*S*,*S*)-(−) configurated diamine, but those which are "r" signed denote complexes with ligands derived from (*R*,*R*)-(+) configurated diamine.

between chiral β-aminoalcohols and salicylaldehydes [10], hydroxybinaphtylcarbaldehydes [11] and hydroxybiphenylcarbaldehydes [12]. Vanadium complexes bearing tridentate Schiff base ligands derived from amino acid and amino acid esters [13] and the reported by us very recently dioxovanadium(V) complexes with the monobasic tridentate Schiff base ligands that were synthesized by 1:1 condensation of chiral 1,2-diaminocyclohexane with aromatic *o*-hydroxycarbonyl compounds [14] are catalysts in mediated oxidation of prochiral sulfides to enantiometrically enriched sulfoxides. To our best knowledge, the vanadium complexes with 1:1 condensation products between hydroxycarbonyl compounds and chiral diamines that possess primary amino groups bound to asymmetric carbon atoms were reported to date only in one paper [14]. To continue exploring structural and electronic effects of chiral dioxovanadium(V) complexes applied in asymmetric catalysis we report here the synthesis, spectroscopic characterization, efficiency in mediated asymmetric sulfide oxidation of a series of dioxovanadium(V) complexes comprising coordinated single condensation products of (*S*,*S*)-(−)-1,2-diphenyl-1,2-diaminoethane and (*R*,*R*)-(+)-1,2-diphenyl-1,2-diaminoethane with aromatic *o*-hydroxyaldehydes along with the X-ray structure analysis carried out on one representative complex. Structural formulae of the synthesized compounds with omitted solvated water molecules are displayed in Fig. 1.

2. Experimental

2.1. Abbreviations

To avoid in the discussion part lengthy systematic names of ligands, the abbreviation HpnSal was used for the referred single condensation product of salicylaldehyde with 1,2-diaminopropane [15] and HMepnSalXY, HchxnSalXY for single condensation products of the XY-substituted salicylaldehydes with 1,2-diamino-2-methylpropane [16] and 1,2-diaminocyclohexane [14], respectively. HchxnNaph denotes the single condensation product of 1-hydroxy-2-acetonaphthone.

2.2. Measurements

Carbon, hydrogen and nitrogen contents were determined on a Carlo Erba MOD 1106 elemental analyzer. FTIR spectra of solid samples (KBr pellets) were run on a Brucker IFS 66, and electronic spectra on the Perkin–Elmer LAMBDA 18 spectrophotometer. ^1H and ^{51}V NMR spectra were obtained in DMSO-d_6 solutions with a Varian Mercury-400BB (400 MHz) spectrometer using TMS (^1H) and $VOCl_3$ (^{51}V) as reference compounds. Chro-

Table 1
Crystal data and structure refinement for $(\mathbf{4}\cdot H_2O)_2$

Empirical formula	$(C_{23}H_{23}N_2O_5V\cdot H_2O)_2$
Formula weight	952.78
Temperature (K)	120(2)
Wavelength (Å)	1.5418
Crystal system	monoclinic
Space group	*C*2
Unit cell dimensions	
a (Å)	23.303(7)
b (Å)	7.062(3)
c (Å)	27.457(9)
β (°)	104.80(3)
Volume (Å^3)	4369(3)
Z	4
D_{calc} (g cm^{-3})	1.449
Absorption coefficient (mm^{-1})	4.167
F(000)	1984
Crystal size (mm)	0.55 × 0.13 × 0.04
T(min), T(max)	0.283, 0.826
Limiting indices	$-26 \leqslant h \leqslant 26$, $-8 \leqslant k \leqslant 7$, $-34 \leqslant l \leqslant 22$
Reflections collected/unique [R_{int}]	17 591/7361 [0.0447]
Completeness to $\theta = 67.5$ (%)	98.0
Refinement method	full-matrix least-squares on F^2
Data/restraints/parameters	7361/5/593
Goodness-of-fit on F^2	1.008
Final *R* indices [$I > 2\sigma(I)$]	$R_1 = 0.0385$, $wR_2 = 0.0950$
R indices (all data)	$R_1 = 0.0447$, $wR_2 = 0.0968$
Absolute structure (Flack) parameter	0.002(5)
Largest difference peak and hole (e Å^{-3})	0.49 and −0.45

matography was carried out with a Hewlett–Packard 1050 chromatograph.

2.3. X-ray investigations

Diffraction measurements were made on an Xcalibur PX kappa-geometry diffractometer with CCD Onyx camera (graphite monochromatized Cu Kα radiation $\lambda = 1.5418$ Å) and determination of unit cell parameters was performed according to established procedures. Intensities were recorded at 120(2) K. Data collection and processing parameters are summarized in Table 1. The structure of $(\mathbf{4} \cdot H_2O)_2$ was solved by direct methods using SHELXS-97 [17]. All non-hydrogen atoms in the molecule were subjected to anisotropic refinement [18]. The hydrogen atoms of Schiff base ligand were generated geometrically (C_{ar}–H, C_{en}–H and N–H fixed at 0.95, 1.00 and 0.92 Å, respectively) and were allowed to ride on their parent atoms. They were included along with hydrogen atoms of water molecules in structure factor calculations with assigned isotropic thermal parameters. Analysis utilizes the 2003 version of the program PLATON [19].

2.4. Catalytic oxidation of sulfides

A DMSO solution containing a dioxovanadium(V) Schiff base complex (4×10^{-5} mol) and cumene hydroperoxide (4×10^{-3} mol) was stirred for 5 h at 20 °C. To the resulting yellow solution thermostated to 20 °C methyl phenyl sulfide (4×10^{-4} mol) was added. The kinetics of the oxidation reaction was investigated by high performance chromatography. Samples of the reaction mixture were withdrawn at intervals and then analyzed with a Hewlett–Packard 1050 chromatograph equipped with a Shimadzu C-R4A Chromatopack area peak calculator and with a Kromasil-100 C-8 column (Knauer GmBH, Germany) using acetonitrile–water (4:6 v/v) as eluent. Chromatography was carried out with a flow rate of 1 ml min^{-1} and the components were detected with a UV Detector ($\lambda = 254$ nm). The enantiomeric excesses (ee) were determined either from the specific rotation at 589 nm of the sulfoxide isolated by chromatographic elution or by measurement of intensities of ^{1}H NMR signals of sulfoxide in the presence of chiral shift reagent Eu(hfc)$_3$. In order to perform the latter procedure the sample (10 ml) withdrawn from of the reaction mixture was poured in the 40% aqueous solution (30 ml) of sodium bisulfite and the resulting suspension was extracted several times with methylene chloride. The collected extracts were dried over sodium sulfate, filtered and evaporated to dryness under diminished pressure. The solid product dissolved in $CDCl_3$ was analyzed by ^{1}H NMR in the presence of chiral shift reagent.

2.5. Complexes

Ten dioxovanadium(V) complexes incorporating 1:1 condensation products of chiral 1,2-diphenyl-1,2-diaminoethane and aromatic *o*-hydroxyaldehydes were prepared according to the following synthetic procedure. A solution of 10 mmol of (*S*,*S*)-(−)-1,2-diphenyl-1,2-diaminoethane or (*R*,*R*)-(+)-1,2-diphenyl-1,2-diaminoethane in absolute ethanol was added under stirring to a freshly filtered solution of triethyl vanadate (10 mmol) in 250 ml of absolute EtOH [15] producing a dark suspension of the intermediate. An aromatic *o*-hydroxyaldehyde (salicylaldehyde, 3-methoxysalicylaldehyde, 5-methoxysalicylaldehyde, 4,6-dimethoxysalicylaldehyde, 5-methylsalicylaldehyde, 5-bromosalicylaldehyde, 5-nitrosalicylaldehyde, 2-hydroxy-1-naphthaldehyde) dissolved in absolute EtOH was added to the aforementioned suspension. After refluxing of the resulting mixture for 2 h and its cooling to room temperature the separated solids were filtered off, washed several times with EtOH, recrystallized from DMSO–EtOH mixtures and dried over molecular sieves.

2.5.1. {*S,S*(−)-1-amino-2-*N*-[(2′-oxido-κ*O*-phenyl)methylene]amino-1,2-diphenylethane-$\kappa^2 N$}dioxovanadium(V) (**1**)

Yield 81%. *Anal.* Calc. for $C_{21}H_{19}N_2O_3V$: C, 63.3; H, 4.8; N, 7.0. Found: C, 63.0; H, 4.7; N, 6.9%. IR (KBr, cm^{-1}): 3197 (ν_{N-H}); 1617 ($\nu_{C=N}$); 927, 862 ($\nu_{V=O}$). UV–Vis spectrum in DMSO [λ_{max} (nm), ε (M^{-1} cm^{-1})]: 263 (18 800), 379 (4200). CD spectrum in DMSO [λ_{max} (nm), $\Delta\varepsilon$ (M^{-1} cm^{-1})]: 265 (6.46), 323 (1.87), 378 (−5.00). ^{1}H NMR DMSO-d_6 (ppm): 7.449 (1H, t, $J = 8$ Hz), 7.27–7.33 (6H, m), 7.17–7.23 (5H, m), 6.827 (1H, d, $^3J = 9$ Hz), 6.725 (1H, t, $J = 7$ Hz) (aromatic); 8.353 (1H, s) (azomethine); 6.092 (1H, d, $^2J = 9$ Hz), 5.772 (1H, t, $J = 11$ Hz) (NH_2); 5.086 (1H, d, $^3J = 11$ Hz), 4.273 (1H, t, $J = 11$ Hz) (methine). ^{51}V NMR DMSO-d_6 (ppm): −550.4.

2.5.2. {*S,S*(−)-1-amino-2-*N*-[(2′-oxido-κ*O*-3′-methoxyphenyl)methylene]amino-1,2-diphenylethane-$\kappa^2 N$}dioxovanadium(V) monohydrate (**2** · H_2O)

Yield 80%. *Anal.* Calc. for $C_{22}H_{23}N_2O_5V$: C, 59.2; H, 5.2; N, 6.3. Found: C, 59.5; H, 5.1; N, 6.3%. IR (KBr, cm^{-1}): 3221 (ν_{N-H}); 2832 (ν_{C-H} of OMe), 1634 ($\nu_{C=N}$); 936, 857 ($\nu_{V=O}$). UV–Vis spectrum in DMSO [λ_{max} (nm), ε (M^{-1} cm^{-1})]: 281 (14 500), 397 (4300). CD spectrum in DMSO [λ_{max} (nm), $\Delta\varepsilon$ (M^{-1} cm^{-1})]: 263 (5.57), 300 (1.71), 338 (0.24), 390 (−2.90). ^{1}H NMR DMSO-d_6 (ppm): 7.27–7.34 (5H, m), 7.16–7.23 (5H, m), 7.069 (1H, dd, $^3J = 8$ Hz, $^4J = 2$ Hz), 6.872 (1H, dd, $^3J = 8$ Hz, $^4J = 2$ Hz), 6.653 (1H, t, $^3J = 8$ Hz) (aromatic); 8.334 (1H, s) (azomethine); 6.083 (1H, d, $^2J = 9$ Hz), 5.767 (1H, t, $J = 11$ Hz) (NH_2); 5.088 (1H, d, $^3J = 11$ Hz), 4.271 (1H, t, $J = 11$ Hz) (methine); 3.762 (3H, s) (methoxy). ^{51}V NMR DMSO-d_6 (ppm): −547.7.

2.5.3. {*R,R*(+)-1-amino-2-*N*-[(2′-oxido-κ*O*-3′-methoxyphenyl)methylene]amino-1,2-diphenylethane-$\kappa^2 N$}dioxovanadium(V) monohydrate (**2r** · H_2O)

Yield 83%. *Anal.* Calc. for $C_{22}H_{23}N_2O_5V$: C, 59.2; H, 5.2; N, 6.3. Found: C, 59.5; H, 5.0; N, 6.3%. IR (KBr,

cm^{-1}): 3219 (ν_{N-H}); 2832 (ν_{C-H} of OMe), 1634 ($\nu_{C=N}$); 935, 856 ($\nu_{V=O}$). UV–Vis spectrum in DMSO [λ_{max} (nm), ε ($M^{-1}\,cm^{-1}$)]: 281 (14600), 395 (4400). CD spectrum in DMSO [λ_{max} (nm), $\Delta\varepsilon$ ($M^{-1}\,cm^{-1}$)]: 263 (−5.75), 301 (−1.89), 338 (−0.28), 390 (−2.96).

2.5.4. {S,S (−)-1-amino-2-N-[(2′-oxido-κO-5′-methoxyphenyl)methylene]amino-1,2-diphenylethane-κ^2N}dioxovanadium(V) (3)

Yield 85%. *Anal.* Calc. for $C_{22}H_{21}N_2O_4V$: C, 61.7; H, 4.9; N, 6.5. Found: C, 61.5; H, 5.0; N, 6.4%. IR (KBr, cm^{-1}): 3231 (ν_{N-H}); 2831 (ν_{C-H} of OMe), 1630 ($\nu_{C=N}$); 927, 858 ($\nu_{V=O}$). UV–Vis spectrum in DMSO [λ_{max} (nm), ε ($M^{-1}\,cm^{-1}$)]: 267 (16800), 413 (4400). CD spectrum in DMSO [λ_{max} (nm), $\Delta\varepsilon$ ($M^{-1}\,cm^{-1}$)]: 270 (8.33), 335 (1.07), 403 (−3.01). ^{1}H NMR DMSO-d_6 (ppm): 7.26–7.34 (5H, m), 7.16–7.24 (5H, m), 7.108 (1H, dd, $^3J = 9$ Hz, $^4J = 3$ Hz), 6.882 (1H, d, $J = 3$ Hz), 6.778 (1H, d, $^3J = 9$ Hz) (aromatic); 8.353 (1H, s) (azomethine); 6.058 (1H, d, $^2J = 9$ Hz), 5.716 (1H, t, $J = 11$ Hz) (NH_2); 5.061 (1H, d, $^3J = 11$ Hz), 4.249 (1H, t, $J = 11$ Hz) (methine); 3.645 (3H, s) (methoxy). ^{51}V NMR DMSO-d_6 (ppm): −548.2.

2.5.5. {R,R(+)-1-amino-2-N-[(2′-oxido-κO-5′-methoxyphenyl)methylene]amino-1,2-diphenylethane-κ^2N}dioxovanadium(V) (3r)

Yield 87%. *Anal.* Calc. for $C_{22}H_{21}N_2O_4V$: C, 61.7; H, 4.9; N, 6.5. Found: C, 61.4; H, 5.0; N, 6.4%. IR (KBr, cm^{-1}): 3217 (ν_{N-H}); 2831 (ν_{C-H} of OMe), 1634 ($\nu_{C=N}$); 926, 865 ($\nu_{V=O}$). UV–Vis spectrum in DMSO [λ_{max} (nm), ε ($M^{-1}\,cm^{-1}$)]: 263 (16800), 410 (4500). CD spectrum in DMSO [λ_{max} (nm), $\Delta\varepsilon$ ($M^{-1}\,cm^{-1}$)]: 272 (−8.31), 332 (−1.06), 404 (2.92).

2.5.6. {S,S(−)-1-amino-2-N-[(2′-oxido-κO-4′,6′-dimethoxyphenyl)methylene]amino-1,2-diphenylethane-κ^2N}dioxovanadium(V) monohydrate (4 · H_2O)

Yield 80%. *Anal.* Calc. for $C_{23}H_{25}N_2O_6V$: C, 58.0; H, 5.3; N, 5.9. Found: C, 58.2; H, 5.2; N, 6.0%. IR (KBr, cm^{-1}): 3227 (ν_{N-H}); 2832 (ν_{C-H} of OMe), 1601 ($\nu_{C=N} + \nu_{C=C}$); 928, 854 ($\nu_{V=O}$). UV–Vis spectrum in DMSO [λ_{max} (nm), ε ($M^{-1}\,cm^{-1}$)]: 325 (18000). CD spectrum in DMSO [λ_{max} (nm), $\Delta\varepsilon$ ($M^{-1}\,cm^{-1}$)]: 257 (6.66), 282 (−1.10), 313 (6.97), 365 (−7.11). ^{1}H NMR DMSO-d_6 (ppm): 7.24–7.31 (5H, m), 7.15–7.21 (5H, m), 5.985 (1H, d, $^4J = 3$ Hz), 5.888 (1H, d, $^4J = 3$ Hz) (aromatic); 8.511 (1H, s) (azomethine); 5.943 (1H, d, $^2J = 9$ Hz), 5.734 (1H, t, $J = 11$ Hz) (NH_2); 5.063 (1H, d, $^3J = 11$ Hz), 4.232 (1H, t, $J = 11$ Hz) (methine); 3.775 (3H, s), 3.643 (3H, s) (methoxy). ^{51}V NMR DMSO-d_6 (ppm): −550.4.

2.5.7. {S,S(−)-1-amino-2-N-[(2′-oxido-κO-5′-methylphenyl)methylene]amino-1,2-diphenylethane-κ^2N}dioxovanadium(V) monohydrate (5 · H_2O)

Yield 88%. *Anal.* Calc. for $C_{22}H_{23}N_2O_4V$: C, 61.4; H, 5.3; N, 6.5. Found: C, 61.4; H, 5.3; N, 6.5%. IR (KBr, cm^{-1}): 3202 (ν_{N-H}); 1627 ($\nu_{C=N}$); 924, 855 ($\nu_{V=O}$). UV–Vis spectrum in DMSO [λ_{max} (nm), ε ($M^{-1}\,cm^{-1}$)]: 266 (16200), 391 (4300). CD spectrum in DMSO [λ_{max} (nm), $\Delta\varepsilon$ ($M^{-1}\,cm^{-1}$)]: 268 (6.57), 329 (1.23), 388 (−3.63). ^{1}H NMR DMSO-d_6 (ppm): 7.26–7.32 (6H, m), 7.17–7.23 (5H, m), 7.083 (1H, d, $^4J = 3$ Hz), 6.741 (1H, d, $^3J = 9$ Hz) (aromatic); 8.270 (1H, s) (azomethine); 6.068 (1H, d, $^2J = 9$ Hz), 5.738 (1H, t, $J = 11$ Hz) (NH_2); 5.066 (1H, d, $^3J = 11$ Hz), 4.255 (1H, t, $J = 11$ Hz) (methine); 2.163 (3H, s) (methyl). ^{51}V NMR DMSO-d_6 (ppm): −549.4.

2.5.8. {S,S(−)-1-amino-2-N-[(2′-oxido-κO-5′-bromophenyl)methylene]amino-1,2-diphenylethane-κ^2N}dioxovanadium(V) monohydrate (6 · H_2O)

Yield 89%. *Anal.* Calc. for $BrC_{21}H_{18}N_2O_3V$: C, 51.0; H, 4.0; N, 5.7. Found: C, 51.4; H, 3.8; N, 5.7%. IR (KBr, cm^{-1}): 3236 (ν_{N-H}); 1629 ($\nu_{C=N}$); 929, 861 ($\nu_{V=O}$). UV–Vis spectrum in DMSO [λ_{max} (nm), ε ($M^{-1}\,cm^{-1}$)]: 262 (18500), 387 (4200). CD spectrum in DMSO [λ_{max} (nm), $\Delta\varepsilon$ ($M^{-1}\,cm^{-1}$)]: 271 (5.23), 320 (1.98), 385 (−3.79). ^{1}H NMR DMSO-d_6 (ppm): 7.608 (1H, d, $^4J = 3$ Hz), 7.539 (1H, dd, $^3J = 9$ Hz, $^4J = 3$ Hz), 7.27–7.32 (5H, m), 7.15–7.22 (5H, m), 6.802 (1H, d, $^3J = 9$ Hz) (aromatic); 8.381 (1H, s) (azomethine); 6.138 (1H, d, $^2J = 9$ Hz), 5.764 (1H, t, $J = 11$ Hz) (NH_2); 5.081 (1H, d, $^3J = 11$ Hz), 4.282 (1H, t, $J = 11$ Hz) (methine). ^{51}V NMR DMSO-d_6 (ppm): −551.3.

2.5.9. {S,S(−)-1-amino-2-N-[(2′-oxido-κO-5′-nitrophenyl)methylene]amino-1,2-diphenylethane-κ^2N}dioxovanadium(V) (7)

Yield 86%. *Anal.* Calc. for $C_{21}H_{18}N_3O_5V$: C, 56.9; H, 4.1; N, 9.5. Found: C, 56.8; H, 4.0; N, 9.3%. IR (KBr, cm^{-1}): 3255 (ν_{N-H}); 1648 ($\nu_{C=N}$); 917, 904 ($\nu_{V=O}$). UV–Vis spectrum in DMSO [λ_{max} (nm), ε ($M^{-1}\,cm^{-1}$)]: 354 (17500). CD spectrum in DMSO [λ_{max} (nm), $\Delta\varepsilon$ ($M^{-1}\,cm^{-1}$)]: 273 (6.62), 332 (2.32), 373 (−2.36). ^{1}H NMR DMSO-d_6 (ppm): 8.505 (1H, d, $^4J = 3$ Hz), 8.237 (1H, dd, $^3J = 9$ Hz, $^4J = 3$ Hz), 7.27–7.33 (5H, m), 7.19–7.24 (5H, m), 6.952 (1H, d, $^3J = 9$ Hz) (aromatic); 8.611 (1H, s) (azomethine); 6.246 (1H, d, $^2J = 9$ Hz), 5.802 (1H, t, $J = 11$ Hz) (NH_2); 5.118 (1H, d, $^3J = 11$ Hz), 4.356 (1H, t, $J = 11$ Hz) (methine). ^{51}V NMR DMSO-d_6 (ppm): −549.2.

2.5.10. {S,S(−)-1-amino-2-N-[(2′-oxido-κO-1′-naphthyl)methylene]amino-1,2-diphenylethane-κ^2N}dioxovanadium(V) monohydrate (8 · H_2O)

Yield 83%. *Anal.* Calc. for $C_{25}H_{21}N_2O_3V$: C, 64.4; H, 5.0; N, 6.0. Found: C, 64.2; H, 4.8; N, 5.7%. IR (KBr, cm^{-1}): 3116 (ν_{N-H}); 1620 ($\nu_{C=N}$); 924, 861 ($\nu_{V=O}$). UV–Vis spectrum in DMSO [λ_{max} (nm), ε ($M^{-1}\,cm^{-1}$)]: 320 (20700), 399 (7000). CD spectrum in DMSO [λ_{max} (nm), $\Delta\varepsilon$ ($M^{-1}\,cm^{-1}$)]: 263 (10.85), 319 (6.89), 406 (−5.52). ^{1}H NMR DMSO-d_6 (ppm): 8.014 (1H, d, $^3J = 7$ Hz), 7.806 (2H, t, $J = 7$ Hz), 7.452 (1H, t, $J = 8$ Hz), 7.21–7.36

(11H, m), 7.079 (1H, d, $^3J = 9$ Hz) (aromatic); 9.211 (1H, s) (azomethine); 6.114 (1H, d, $^2J = 9$ Hz), 5.994 (1H, t, $J = 11$ Hz) (NH_2); 5.337 (1H, d, $^3J = 11$ Hz), 4.385 (1H, t, $J = 11$ Hz) (methine). ^{51}V NMR DMSO-d_6 (ppm): −548.3.

3. Results and discussion

A series of dioxovanadium(V) complexes with singly condensed chiral 1,2-diphenyl-1,2-diaminoethane and aromatic *o*-hydroxycarbonyl compounds were prepared by the same procedure that was used to prepare V(V) complexes with other singly condensed diamines following the strategy of Root et al. [15]. The complexes were obtained in high yields. Their analytical data summarized in Section 2 are consistent with their Fig. 1 formulation. Complex **4** crystallizes from ethanol after one month at room temperature yielding crystals of $(\mathbf{4} \cdot H_2O)_2$ suitable for X-ray diffraction studies.

3.1. Crystal and molecular structure of $(\mathbf{4} \cdot H_2O)_2$

An ORTEP diagram of **4** is shown in Fig. 2 and important bond lengths and angles are collected in Table 2. The structure indicates that each vanadium atom is six-coordinated, while both V29–O31A and V29–O31 distances of 2.370(2) Å and 2.415(2) Å, respectively, are considered as V–O bond lengths like the 2.427 Å V–O distance in $[VO_2(pnSal)]_2$ [15]. It may be noted that the PLATON program [19] does not handle the longest V–O approach (2.415 Å) as a coordination since it describes V29A as five-coordinate. The vanadium atoms V29 and V29A are joined together through two oxygen bridges, O31 and O31A being the bridging atoms coordinated to vanadium atoms at short and long distances [V29–O31 = 1.675(2) Å; V29A–O31 = 2.413(3) Å; V29–O31A = 2.370 (2) Å; V29A–O31A = 1.678(2) Å]. The coordination sphere around each vanadium atom is composed of phenolate oxygen atoms (O7 or O7A) and of primary amine nitrogen atom (N16 or N16A) occupying axial positions and of imine nitrogen atom (N13 or N13A), two strongly coordinated terminal oxo (O30, O31 or O30A, O31A) and one weakly associated oxo group (O31A or O31) derived from the neighbouring VO_2 unit defining the equatorial plane; symbols in parentheses written before the conjuction "or" refer to the coordination sphere of V29, those behind it to that around V29A. The polyhedron that describes the quadrilateral core consisting of the non-centrosymmetric V_2O_2 unit and the spatial arrangement of remaining coordinated atoms resembles two edge shared octahedrons that are significantly distorted. The V29═O30 and V29A═O30A bond lengths of 1.622(2) and 1.619(3) Å, respectively, compare well with the distances between vanadium and the doubly bonded oxygen atoms, which do not participate in bridging, reported for $[VO_2(pnSal)]_2$ [15] and VO_2(MepnSalXY) (X = 4-OMe, Y = 6-OMe) [16] complexes. The V29–O31 and V29A–O31A bonds (average 1.677 Å) are longer than V29–O30 and V29A–O30A bonds (average 1.621 Å) by 0.056(4) Å due to involvement of O31 and O31A atoms in V29–V29A bridging and hydrogen

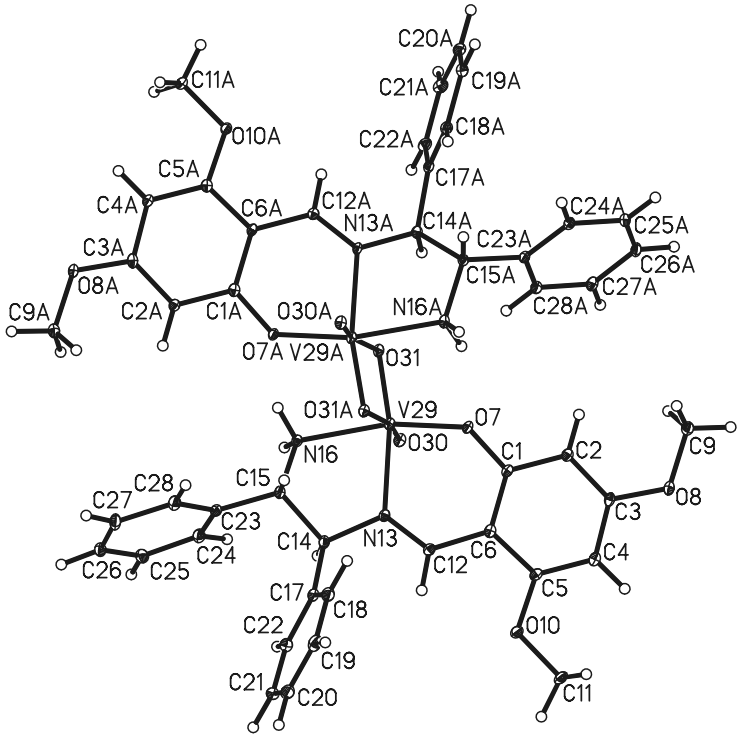


Fig. 2. An ORTEP drawing of the dimeric **4** molecule without water molecules showing atom labelling system. The displacement ellipsoids are drawn at the 30% probability level.

Table 2
Selected bond lengths (Å) and angles (°) and hydrogen bonding parameters (Å, °) for $(\mathbf{4}\cdot H_2O)_2$

V29–O30	1.622(2)	O7–V29–N16	153.85(10)
V29–O31	1.675(2)	O30–V29–N13	94.66(11)
V29–O7	1.904(2)	O31–V29–N13	156.73(11)
V29–N16	2.126(3)	O7–V29–N13	84.19(10)
V29–N13	2.170(3)	N16–V29–N13	76.78(10)
V29–O31A	2.370(2)	O30–V29–O31A	171.80(10)
O30–V29–O31	106.85(12)	O31–V29–O31A	78.11(10)
O30–V29–O7	102.92(11)	O7–V29–O31A	82.39(9)
O31–V29–O7	99.14(10)	N16–V29–O31A	76.69(10)
O30–V29–N16	96.42(12)	N13–V29–O31A	79.54(9)
O31–V29–N16	91.79(11)	V29–O31–V29A	101.72(10)
V29A–O30A	1.619(3)	O7A–V29A–N16A	154.76(10)
V29A–O31A	1.678(2)	O30A–V29A–N13A	98.48(11)
V29A–O7A	1.907(2)	O31A–V29A–N13A	152.38(11)
V29A–N16A	2.123(3)	O7A–V29A–N13A	83.69(10)
V29A–N13A	2.151(3)	N16A–V29A–N13A	77.12(10)
V29A–O31	2.413(3)	O30A–V29A–O31	172.17(10)
O30A–V29A–O31A	107.37(12)	O31A–V29A–O31	76.81(10)
O30A–V29A–O7A	102.50(12)	O7A–V29A–O31	83.01(9)
O31A–V29A–O7A	99.71(10)	N16A–V29A–O31	76.71(10)
O30A–V29A–N16A	96.46(12)	N13A–V29A–O31	76.43(9)
O31A–V29A–N16A	90.22(11)	V29A–O31A–V29	103.35(10)

DH···A	D–H	H···A	D···A	DH···A
O1W–H1W1···O8^{i}	0.86	2.16	2.923(3)	147
O1W–H2W1···O31	0.86	1.95	2.768(4)	158
O2W–H1W2···O8A^{ii}	0.86	2.08	2.856(3)	150
O2W–H2W2···O31A	0.86	1.88	2.723(4)	168
N16–H16A···O7A	0.92	2.13	2.966(4)	150
N16–H16B···O30A^{iii}	0.92	2.21	2.978(4)	140
N16A–H16C···O30^{iv}	0.92	2.04	2.955(4)	173
N16A–H16D···O7	0.92	2.12	2.965(4)	153
N16A–H16D···O31	0.92	2.52	2.824(4)	100
C14–H14···O2W^{iii}	1.00	2.24	3.199(5)	161
C15–H15···O31A	1.00	2.43	2.998(4)	115
C14A–H14A···O31	1.00	2.43	3.010(4)	117
C15A–H15A···O1W^{iv}	1.00	2.43	3.375(5)	157
C22–H22···O2W	0.95	2.40	3.326(5)	165
C18A–H18A···O1W^{iv}	0.95	2.46	3.373(4)	162
C12–H12A···O10	0.95	2.35	2.715(4)	102
C12–H12A···O10A	0.95	2.42	2.753(4)	100

Symmetry code: (i) $1/2+x$, $-1/2+y$, z; (ii) $-1/2+x$, $1/2+y$, z; (iii) x, $y-1$, z; and (iv) x, $1+y$, z.

bonding interactions with water molecules (*vide infra*). The V29–V29A distance of 3.204(2) Å is somewhat shorter than the V(V)–V(V) distance of 3.222 Å found in $[VO_2(pnSal)]_2$ [15]. The O30–V29–O31 and O30A–V29A–O31A angles of 106.85(12)° and 107.37(12)°, respectively, indicate significant double bond character of these bonds [20] and are close to other *cis*-VO_2 units [21]. Both six-membered chelate rings assume a non-typical conformation since two atoms of each ring (vanadium and imine nitrogen) are out the plane defined by remaining four non-hydrogen atoms, their displacements in Å from the respective C_3O planes being: 0.791(7) for V29; 0.196(7) for N13; −0.967(6) for V29A and −0.283(6) for N13A. The two five-membered chelate rings adopt envelope conformations which are differently puckered. The ring defined by V29, N13, C14, C15, N16 chooses an envelope conformation on C15, the asymmetric carbon atom attached to the amino nitrogen while the other, formed by V29A, N13A, C14A, C15A, N16A takes the envelope conformation on C14A, the asymmetric carbon atom linked to the imine nitrogen. Fig. 3 shows that the crystal structure of $(\mathbf{4}\cdot H_2O)_2$ is stabilized by intermolecular hydrogen bonds linking dimeric molecules both directly by N–H···O interactions and indirectly through water molecules giving rise to O···H–O–H···O chain formation. The remaining hydrogen atoms of NH_2 groups are involved in intramolecular interactions linking the N16 atom to the phenolate oxygen O7A and the N16A atom to both O7 and O31 forming a tricenter hydrogen bond. In addition, there are relatively close intramolecular contacts between O10, O10A, the oxygen atoms of the 6-OMe phenyl ring substituents, and the methine hydrogens bonded to C12 and C12A, respectively. These distances are collected in Table 2. In contrast to $(\mathbf{4}\cdot H_2O)_2$ the solid VO_2(MepnSalXY) (X = 4-OMe, Y = 6-OMe) [16] and VO_2(chxnNaph) [14], which bear similar ligands and contain mononuclear species, have no hydrogen bonds linking the NH_2 nitrogen of one species with the phenolate oxygen of the other species. This may imply that hydrogen bonds stabilize the dimeric species in solid $(\mathbf{4}\cdot H_2O)_2$ essentially.

3.2. Spectroscopic properties of complexes

The electronic, circular dichroism, NMR spectral data and selected solid-state infrared spectral data are listed in Section 2. Strong C=N stretch (around 1630 cm^{-1}) indicates the C=N group of the coordinated Schiff base ligands [22,23]. The *cis*-dioxo nature of **1**–**6**, **8** complexes is evidenced by two V=O stretching vibrations one in the 924–935 cm^{-1} and the other in the 855–865 cm^{-1}

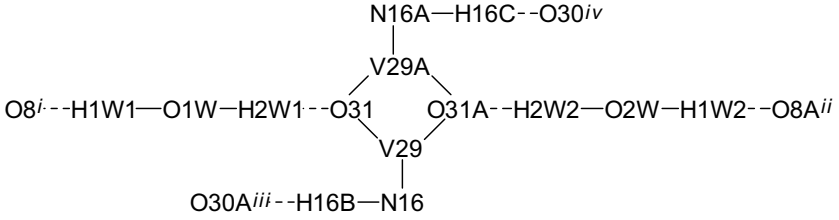


Fig. 3. Schematic representation of intermolecular hydrogen bonds in $(\mathbf{4}\cdot H_2O)_2$.

ranges which are close to V=O vibrations reported for related VO_2–Schiff base complexes [24]. Infrared spectrum of anhydrous **7** reveals two V=O stretching bands above 900 cm^{-1} (at 904 and 917 cm^{-1}) as the reported spectra of VO_2(bispyridineimine ligand) complexes (at 926 and 949 cm^{-1} and also at 918 and 953 cm^{-1}), which in the solid state do not show intermolecular interaction *via* O-bridges [25]. Since the variation of V=O stretching frequencies indicates differing strengths and/or different lengths of V=O bonds [24] its value of 13 cm^{-1} (917–904 cm^{-1}) for **7** compared with 74.5 cm^{-1} (928.3–853.8 cm^{-1}) for **4** suggests for the former compound a considerably smaller difference between V=O bond lengths within the VO_2 unit than that of 0.053(4) Å known from X-ray diffraction studies of $(\mathbf{4}\cdot H_2O)_2$. Moreover, the IR spectrum of **7** reveals two sharp bands at 3307.6 and 3254.8 cm^{-1} arising from the ν_{as} and ν_sN–H modes of the NH_2 group, respectively, and a very strong absorption band at 1318.8 cm^{-1}, corresponding to the presence of the nitro group. The stretching vibrations of OH groups in **1**–**6**, **8** complexes giving rise to medium bands in the range 3417–3108 cm^{-1} are in agreement with the microanalysis data as they support the presence of water molecules in composition of complexes. The appearance of weak/medium band near 2830 cm^{-1} separate from other C–H stretching vibrations in **2**, **2r**, **3**, **3r**, **4** complexes indicates the presence of the methoxy substituents [26].

The electronic absorption spectra recorded for **1**–**3**, **5**, **6**, **8** complexes dissolved in DMSO exhibit two absorption bands one in the 260–281 nm range ($\log\varepsilon_{max} = 4.4 - 4.3$) assigned to π–π* transition of an aromatic ring and the other in the 379–413 nm range ($\log\varepsilon_{max} = 3.6$) attributed to ligand-to-metal charge transfer band overlapped by π–π* transition encompassing the azomethine chromophore. The spectra of **4**, **7**, **8** complexes examined in the same spectral region display single bands in the 320–354 nm region ($\log\varepsilon = 4.4 - 4.3$) having in the case of **8** and **4** shoulders at around 310 nm ($\log\varepsilon_{max} = 4.0$) and at 370 nm ($\log\varepsilon_{max} = 3.7$), respectively. Circular dichroism spectra of **2**, **2r** and **4** complexes revealed an additional band at 280–300 nm which was not resolved in ordinary absorption spectrum. In contrast to the CD spectra of **1**, **3**–**8** the CD spectra of **2** and **2r** complexes reveal small bisignated couplets centered at about 330 nm (Fig. 4), arising probably due to weak exciton coupling between chromophores undergoing electronic transition near 330 nm. Bosnich [27] assigned the positive-negative couplet at 28 700 cm^{-1} (348 nm) in the CD spectrum of *N*,*N*′-bis(salicylidene)-(−)-propylenediaminozinc(II) to π–π* transitions encompassing the two azomethine chromophores. An evidence of a similar couplet in the same spectral region was given for oxovanadium(IV) complexes with tetradentate Schiff bases derived from (*S*)-(+)-propane-1,2-diamine and (*S*,*S*)-(+)-cyclohexane-1,2-diamine [28]. Positions of couplets in the CD spectra of **2** and **2r** near the wavelength value reported for π–π* transitions assigned to azomethine

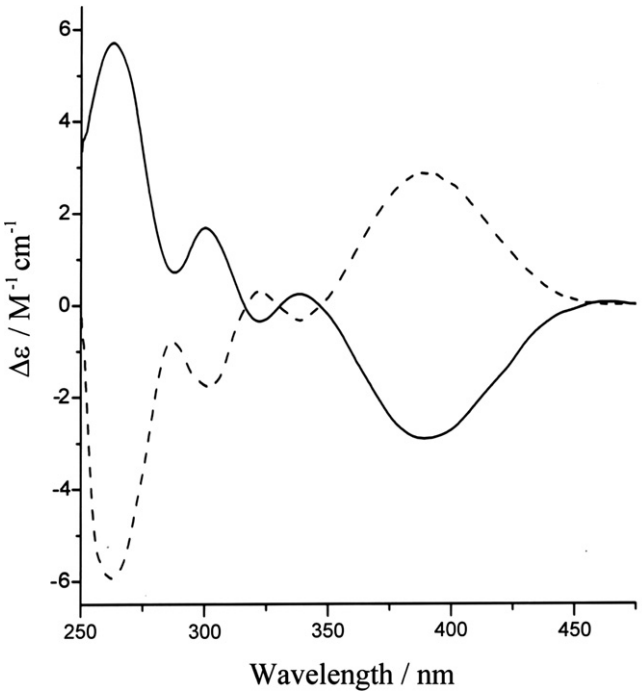


Fig. 4. CD spectra of **2** and **2r** complexes containing singly condensed (*S*,*S*)-(−)-1,2-diphenyl-1,2-diaminoethane and singly condensed (*R*,*R*)-(+)-1,2-diphenyl-1,2-diaminoethane with 3-methoxysalicylaldehyde (*o*-vanillin), respectively, in DMSO solution.

chromophore suggest that the single azomethine group in monomeric forms of **2** and **2r** complexes may interact with the other chromophores positioned in their close proximity to produce an exciton splitting. The sign of the low energy component of the couplet in the spectrum of **2** and the sign of the Cotton effect of transitions around 330 nm in other complexes derived from diamine of *S*,*S* configuration are positive, in contrast to the negative sign of **2r** couplet and of the Cotton effect for the corresponding transition in **3r** compound, derived from diamine of *R*,*R* configuration.

The ^1H and ^{51}V NMR spectral data were recorded in DMSO-d_6. Signals are assigned on the basis of intensity, spin–spin coupling pattern, chemical shift and deuteration experiment. Since the ^1H NMR spectra derived from (*R*,*R*)-(+) and (*S*,*S*)-(−)-1,2-diphenyl-1,2-diaminoethane are superimposable, Section 2 lists NMR data only for the latter complexes. Single condensation of the 1,2-diphenyl-1,2-diaminoethane is confirmed by the presence of amine and azomethine proton signals in the spectra of all complexes. The two NH_2 protons are magnetically inequivalent and produce a doublet in the 5.94–6.25 ppm range and a triplet in the 5.72–5.99 ppm range the multiciplity of the latter is due to geminal and vicinal coupling with the proton attached to the nearest asymmetric carbon atom. Signals originating from the methine protons attached to asymmetric carbon atoms are by *ca.* 1.5 ppm downfield with respect to those, which have been found in the spectra of the VO_2(chxnSalXY) complexes [14], due to their increased deshielding, as a result of the mag-

Table 3
Asymmetric oxidation of methyl phenyl sulfide with cumene hydroperoxide catalyzed by **2**, **2r**, **3**, **3r** complexes which had favourable influence upon enantioselection and the degree of conversion

Entry	Complex	X	Diamine conf.	Temp/ °C	Yield[a] %	ee% (conf.)
1	2	3-OMe	*S*,*S*	20	87	34 (*S*)
2	2r	3-OMe	*R*,*R*	20	90	38 (*R*)
3	3	5-OMe	*S*,*S*	20	93	39 (*S*)
4	3r	5-OMe	*R*,*R*	20	91	36 (*R*)

[a] The percentage of the conversion of methyl phenyl sulfide into the corresponding sulfoxide after the 36 h course of the reaction.

netic anisotropy (ring current effect) of phenyl substituents. The aromatic protons of the salicylidene moiety, which in the **2**, **2r**, **3**, **4**, **6** and **7** complexes are not overlapped by signals of the phenyl substituents and the signals of all complexes, which originate from the methine protons, show first order splitting pattern and could be assigned straightforward. Protons of phenyl substituents in **2**, **2r**, **3**, **4**, **6** and **7** complexes give rise to two separate 5-H multiplets one in 7.27–7.34 ppm and the other one in 7.16–7.24 ppm ranges.

All the complexes exhibit single ^{51}V resonances in the narrower range −547.8 to −551.3 ppm than that of −547.8 to −556 ppm found for dimeric $[VO_2(pnSal)]_2$, monomeric VO_2(MepnSalXY) and VO_2(chxnSalXY) complexes. Single ^{51}V resonances indicate that the complexes occur in single (presumably monomeric) form in DMSO solution, since the weakly associated $(\mathbf{4}\cdot H_2O)_2$ dimer as well as the remaining (**1**–**3**, **5**–**8**) compounds, supposed to be also weakly associated in the solid state can be considered as dissociated into monomers in this solvent by analogy to $[VO_2(pnSal)]_2$.

3.3. Catalytic oxidation of methyl phenyl sulfide (thioanisole)

Yields and enantiomeric excesses in oxidation catalysis of methyl phenyl sulfide at 20 °C and the configurations of the formed sulfoxide are given in Table 3. It is evident that **2**, **2r**, **3** and **3r** complexes attained in high yields and in higher enantiomeric excesses (34–39%) than the reported earlier VO_2(chxnSalXY) complexes with ligands bearing X = 3-OMe and X = 5-OMe phenyl ring substituents (19–23%) [14].

4. Supplementary data

CCDC 669707 contains the supplementary crystallographic data for this paper. These data can be obtained free of charge via http://www.ccdc.cam.ac.uk/conts/retrieving.html, or from the Cambridge Crystallographic Data Centre, 12 Union Road, Cambridge CB2 1EZ, UK; fax: (+44) 1223-336-033, or e-mail: deposit@ccdc.cam.ac.uk.

Acknowledgement

This scientific work has been supported from funds for science in years 2007–2009 as a research project (N N204 0355 33, BW/8000-5-0388-7, DS/8210-4-0086-7 and DS/8210-4-0086-8).

References

[1] R.L. Robinson, R.R. Eady, T.H. Richardson, R.W. Miller, M. Hawkins, J.R. Postgate, Nature 322 (1986) 388.
[2] (a) H. Vilter, Phytochemistry 23 (1984) 1387;
(b) J.M. Arbor, M. de Boer, C.D. Garner, S.S. Hasnain, R. Wever, Biochemistry 28 (1989) 7968.
[3] (a) M. Casny, D. Rehder, Chem. Commun. (2001) 921;
(b) C. Gruning, D. Rehder, J. Inorg. Biochem. 80 (2000) 185.
[4] C. Kimblin, X. Bu, A. Butler, Inorg. Chem. 41 (2002) 161.
[5] (a) M.A. Anderson, A.S.G. Willets, G. Allenmark, J. Org. Chem. 62 (1997) 8455;
(b) H.L. Dekker, W. Hemrika, T. Izumi, T. Oshiro, H.E. Schoemaker, R. Wever, Inorg. Chem. 37 (1998) 6780;
(c) H.B. ten Brink, H.L. Holland, H.E. Schoemaker, H. van Lingen, R. Wever, Tetrahedron Asymm. 10 (1999) 4563;
(d) H.B. ten Brink, H.E. Schoemaker, R. Wever, Eur. J. Biochem. 268 (2001) 132.
[6] F. van de Velde, I.W.C.E. Arends, R.A. Sheldon, J. Inorg. Biochem. 80 (2000) 81.
[7] (a) D.A. Cogan, G. Liu, K. Kim, B.J. Backes, J. Ellman, J. Am. Chem. Soc. 120 (1998) 8011;
(b) C. Bolm, F. Bienewald, Synlett (1998) 1327;
(c) A.G.J. Ligtenbarg, R. Hage, B.L. Feringa, Coord. Chem. Rev. 237 (2003) 84.
[8] M.C. Carreno, Chem. Rev. 95 (1995) 1717.
[9] (a) K. Nakajima, M. Kojima, J. Fujita, Chem. Lett. (1986) 1483;
(b) K. Nakajima, K. Kojima, M. Kojima, J. Fujita, Bull. Chem. Soc. Jpn. 63 (1990) 2620.
[10] (a) C. Bolm, F. Bienewald, Angew. Chem., Int. Ed. Engl. 14 (1995) 2460;
(b) H. Schmidt, M. Bashirpoor, D. Rehder, J. Chem. Soc., Dalton Trans. (1996) 3865;
(c) J. Skarżewski, R. Ostrycharz, R. Siedlecka, Tetrahedron Asymm. 10 (1999) 3457;
(d) D. Rehder, Coord. Chem. Rev. 188 (1999) 297;
(e) N.N. Karpyshev, O.D. Yakovleva, E.P. Talsi, K.P. Bryliakov, O.V. Tolstikova, A.G. Tolstokov, J. Mol. Catal. 157 (2000) 91;
(f) S. Blum, R.G. Bergman, J.A. Ellman, J. Org. Chem. 68 (2003) 150;
(g) D. Balcells, F. Maseras, A. Lledos, J. Org. Chem. 68 (2003) 4265;
(h) C. Bolm, Coord. Chem. Rev. 237 (2003) 245.
[11] (a) A.H. Vetter, A. Berkessel, Tetrahedron Lett. 39 (1998) 1741;
(b) Y.-C. Jeong, S. Choi, Y.D. Hwang, K.-H. Ahn, Tetrahedron Lett. 45 (2004) 9249.
[12] (a) C. Ohta, H. Shimizu, A. Kondo, T. Katsuki, Synlett (2002) 161;
(b) P. Plitt, H. Pritzkow, R. Kramer, J. Chem. Soc., Dalton Trans. (2004) 2314.
[13] (a) R. Ando, H. Inden, M. Sugino, H. Ono, D. Sakaeda, T. Yagyu, M. Maeda, Inorg. Chim. Acta 357 (2004) 1337;
(b) S.-H. Hsieh, Y.-P. Kuo, H.-M. Gau, J. Chem. Soc., Dalton Trans. (2007) 97.
[14] E. Kwiatkowski, G. Romanowski, W. Nowicki, M. Kwiatkowski, K. Suwińska, Polyhedron 26 (2007) 2559.
[15] C.A. Root, J.D. Hoeschele, C.R. Cornman, J.W. Kampf, V.L. Pecoraro, Inorg. Chem. 32 (1993) 3855.
[16] E. Kwiatkowski, G. Romanowski, W. Nowicki, M. Kwiatkowski, K. Suwińska, Polyhedron 22 (2003) 1009.
[17] G.M. Sheldrick, SHELXS-97, Program for Crystal Structure Solution, University of Gottingen, Germany, 1997.

[18] G.M. Sheldrick, SHELXL-97, Program for Structure Refinement, University of Gottingen, Germany, 1997.
[19] A.L. Spek, J. Appl. Crystallogr. 36 (2003) 7.
[20] G.J. Colpas, B.J. Hamstra, J.W. Kampf, V.L. Pecoraro, Inorg. Chem. 33 (1994) 4669.
[21] X. Li, M.S. Lah, V.L. Pecoraro, Inorg. Chem. 27 (1988) 4657.
[22] G.C. Percy, D.A. Thornton, J. Inorg. Nucl. Chem. 34 (1972) 3369.
[23] G. Kolawole, K.S. Patel, J. Chem. Soc., Dalton Trans. (1981) 1241.
[24] G. Asgedom, A. Sreedhara, J. Kivikoski, J. Valkonen, C.P. Rao, J. Chem. Soc., Dalton Trans (1995) 2459.
[25] A.G.J. Ligtenbarg, A.L. Spek, R. Hage, B.L. Feringa, J. Chem. Soc., Dalton Trans. (1999) 659.
[26] J.B. Lambert, H.E. Shurvell, D.A. Lighter, R.G. Cooks, Organic Structural Spectroscopy, Prentice Hall Inc., New Jersey, 1998, p. 208.
[27] B. Bosnich, J. Am. Chem. Soc. 90 (1968) 627.
[28] R.L. Farmer, F.L. Urbach, Inorg. Chem. 9 (1970) 2562.

(diphenylphoshino) ethyl amine ($\mathbf{L}^4$) and *N*-(1′-methyl)-1′-(2-hydroxyphenyl)-2-(diphenylphosphino) ethyl amine ($\mathbf{L}^5$) are potentially of the (N,O,S) or (N,O,P) type (Fig. 1) and their complexation reactions have not been investigated so far. It was therefore was thought worthwhile to investigate them. Additionally, the catalytic activity of metal complexes [22–29] of 'Salen' type of ligands is a motivating factor for exploring $\mathbf{L}^1$–$\mathbf{L}^5$, as the introduction of one soft donor site in a framework of a tridentate ligand may tune the activity towards a new direction. In this paper their syntheses and complexation with Pd(II) and Ni(II) are described. Single crystal structures of $\mathbf{L}^1$, $\mathbf{L}^2$, [PdCl ($\mathbf{L}^1$–H)] (**1**), [PdCl($\mathbf{L}^3$–H)] (**3**) and [NiCl($\mathbf{L}^4$–H)] (**6**) have been reported. The Pd(II) complex of $\mathbf{L}^2$ was immobilized on silica gel via a $-CH_2CH_2CH_2Si$ linker and the resulting matrix was found suitable for the Suzuki–Miyaura reaction. These results are also part of the present paper.

2. Experimental

The C and H analyses were carried out with a Perkin–Elmer elemental analyzer 240 C. The ^1H, $^{13}C\{^1H\}$ and $^{31}P\{^1H\}$ NMR spectra were recorded on a Bruker Spectrospin DPX-300 NMR spectrometer at 300.13, 75.47 and 121.49 MHz, respectively.

The ^{13}C CPMAS NMR spectrum was recorded on a Bruker FT-NMR Spectrometer (DSX 300) at 75.46 MHz. IR spectra in the range 4000–250 cm^{-1} were recorded on a Nicolet Protége 460 FT-IR spectrometer as KBr pellets. The melting points were determined in open capillary, and are reported as such. The conductivity measurements were carried out in CH_3CN (concentration ca. 1 mM) using an ORION conductivity meter model 162.

$PhSCH_2CH_2NH_2$ was synthesized by the literature method [30,31]. To prepare $Ph_2PCH_2CH_2NH_2$ the literature method [30,31] was modified as detailed below. 2-Chloroethylamine hydrochloride (0.58 g, 5 mmol) dissolved in 20 ml of freshly distilled THF was taken in a Schlenk flask and stirred for 10 min under nitrogen atmosphere at −78 °C. A freshly prepared solution of $LiPPh_2$ (5 mmol) in THF (50 ml) was added to it dropwise with stirring. After complete addition, the temperature of the flask was slowly increased to room temperature and then its contents were refluxed for 10 h under nitrogen atmosphere. During this period the deep red solution became colourless. The reaction mixture was cooled to room temperature and the solvent was removed on a rotary evaporator. The resulting semi-solid was treated with 10% HCl solution and the solution was washed with benzene (3 × 15 ml) and made alkaline with 10% NaOH solution. The phosphinated amine from this solution was extracted into benzene, washed with brine (2 × 25 ml) and dried with anhydrous Na_2SO_4. After evaporation of the solvent on a rotary evaporator, a colourless highly viscous liquid was obtained. It was further purified by dissolving in 20 ml of benzene and washing with brine (20 ml). The benzene layer was dried with Na_2SO_4 and filtered through celite before evaporating off the solvent again on a rotary evaporator to get the viscous liquid. Yield: 60%; ^1H NMR: 2.23–2.28 (t, 2H, CH_2N), 2.82–2.89 (m, 2H, CH_2P), 7.32–7.46 (m, 10H, ArH).

2.1. Synthesis of $\mathbf{L}^1$

o-Hydroxyacetophenone (0.71 g, 5.26 mmol) dissolved in 20 ml of dry methanol was stirred for 30 min and mixed with a solution of $PhSCH_2CH_2NH_2$ (0.81 g, 5.26 mmol) made in 10 ml of dry methanol, which was added dropwise with stirring. The mixture, which became yellow instantaneously, was stirred further for ~5–6 h at room tempera-

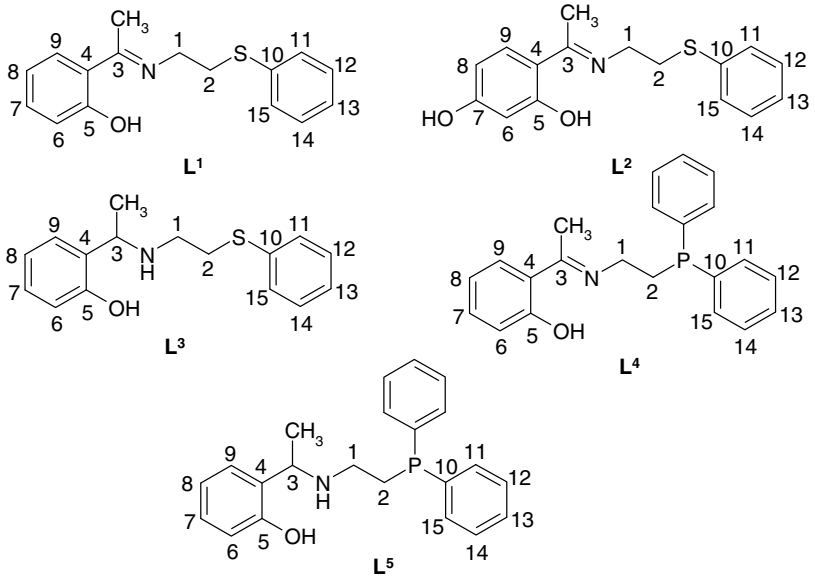


Fig. 1. Structures of $\mathbf{L}^1$ to $\mathbf{L}^5$.

ture. The solvent was evaporated off on a rotary evaporator to yield a yellow solid. The single crystals of $\mathbf{L}^1$ were grown from its solution in a chloroform–hexane (1:2) mixture at low temperature (0–5 °C). Yield: 1.36 g; 95% m.p. 55 °C. *Anal.* Calc. for $C_{16}H_{17}NOS$: C, 70.82; H, 6.31; N, 5.16. Found C, 70.52; H, 6.26; N, 5.31%. NMR: (^{1}H, 25 °C, $CDCl_3$) δ: 2.27 (s, 3H, CH_3), 3.29 (t, $J = 7.0$ Hz, 2H, H_2), 3.76 (t, $J = 6.9$ Hz, 2H, H_1), 6.79 (t, $J = 7.3$ Hz, 2H, H_{13}), 6.92–6.95 (d, d, $J = 8.3$ Hz, 1H, H_6), 7.17–7.41, (m, 6H, H_{11} to H_{15} and H_7), 7.48–7.51 (d, $J = 8.0$ Hz, 1H, H_9), 15.82 (bs, 1H, OH); (^{13}C{^{1}H}, 25 °C, $CDCl_3$) δ: 14.3 (CH_3), 34.1 (C_2), 48.3 (C_1), 117.0 (C_6), 118.2 (C_8), 121.7 (C_4), 126.1 (C_{13}), 127.9 ($C_{12,14}$), 129.4 ($C_{11,15}$), 129.9 (C_9), 132.1 (C_7), 135.2 (C_{10}), 163.0 (C_5), 172.1 (C_3).

2.2. Synthesis of $\mathbf{L}^2$

2,4-Dihydroxyacetophenone (0.61 g, 4.0 mmol) was dissolved in 20 ml of dry methanol and stirred for 30 min. $PhSCH_2CH_2NH_2$ (0.81 g, 5.26 mmol) dissolved in 10 ml of methanol was added and the mixture was heated over a water bath at 50 °C for 3 h. The solvent was evaporated off on a rotary evaporator to give a light yellow solid $\mathbf{L}^2$. Yellow single crystals of $\mathbf{L}^2$ were obtained by slow evaporation of its solution made in a chloroform–hexane (2:1) mixture. Yield: 1.04 g; 90%; m.p. 113 °C. *Anal.* Calc. for $C_{16}H_{17}NO_2S$: C, 66.87; H, 5.96; N, 4.87. Found: C, 66.52; H, 6.12; N, 4.71%. NMR: (^{1}H, 25 °C, DMSO-d_6) δ: 2.23 (s, 3H, CH_3), 3.31 (t, $J = 6.2$ Hz, 2H, H_2), 3.71 (t, $J = 6.2$ Hz, 2H, H_1), 6.11 (s, 1H, H_6), 6.17–6.19 (d, $J = 10.5$ Hz, 1H, H_8), 7.20–7.30 (d, $J = 9.0$ Hz, 1H, H_9), 7.36–7.48 (m, 5H, H_{11-15}), 9.82 (bs, 1H, OH *p* to C=N), 16.43 (s, 1H, OH *o* to C=N); (^{13}C{^{1}H}, 25 °C, DMSO-d_6) δ: 14.3 (CH_3), 33.1 (C_2), 46.5 (C_1), 103.5 (C_6), 105.7 (C_8), 111.5 (C_4), 125.9 (C_{13}), 128.4 ($C_{12,14}$), 129.1 ($C_{11,15}$), 129.1 (C_9), 135.6 (C_{10}), 161.7 (C_5), 167.4 (C_7), 172.1 (C_3).

2.3. Synthesis of $\mathbf{L}^3$

$\mathbf{L}^1$ (0.2714 g, 1 mmol) and $NaBH_4$ (0.2 g, 5 mmol) were taken in 50 ml of dry ethanol and refluxed for 24 h. The reaction mixture was cooled and its solvent evaporated off on a rotary evaporator to result in a semi-solid product. $\mathbf{L}^3$ was leached out from this product with dry dichloromethane (5×25 ml). The combined dichloromethane extract was filtered through celite, washed with distilled water (4×25 ml) and dried with anhydrous sodium sulfate. The solvent from the extract was removed on a rotary evaporator and $\mathbf{L}^3$ was obtained as a highly viscous colorless oil. Yield: 0.23 g; 85%. NMR: (^{1}H, 25 °C, $CDCl_3$) δ: 1.37–1.40 (d, $J = 6.7$ Hz, 3H, CH_3), 2.75–2.45 (m, 2H, H_2), 2.92–3.00 (m, 1H, H_1), 3.06–3.15 (m, 1H, H_1), 3.80–3.87 (q, $J = 6.5$ Hz, 1H, CH), 6.71–6.90 (m, 3H, H_6, H_7, H_8), 7.01–7.27 (m, 5H, H_{11} to H_{15}), 7.23–7.32 (d, $J = 6.3$ Hz, 1H, H_9); (^{13}C{^{1}H}, 25 °C, $CDCl_3$) δ: 22.12 (CH_3), 33.41 (C_2), 45.22 (C_1), 58.31 (C_3), 116.6 (C_6), 119.0 (C_8), 126.4 (C_{13}), 127.9 (C_7), 127.3 (C_4), 128.3 (C_9), 128.9 ($C_{12,14}$), 129.7 ($C_{11,15}$), 135.0 (C_{10}), 157.0 (C_5).

2.4. Synthesis of $\mathbf{L}^4$

(2-Aminoethyl)diphenylphosphine (1.2 g, 5.0 mmol) was stirred for 0.5 h in 5 ml dry ethanol at room temperature. *o*-Hydroxyacetophenone (0.13 g, 1.0 mmol) dissolved in 5 ml of dry ethanol was added to the above solution dropwise with stirring under a N_2 atmosphere. The mixture was stirred further for 6 h at room temperature. Its solvent was evaporated off on a rotary evaporator resulting in $\mathbf{L}^4$ as a viscous yellow liquid, which on recrystallization from a chloroform–hexane mixture (1:10) gave $\mathbf{L}^4$ as a yellow solid. Single crystals of $\mathbf{L}^4$ were grown by slow evaporation of its solution made in a mixture of chloroform and hexane (1:10). Yield 1.36 g; 78%; m.p. 82-83 °C *Anal.* Calc. for $C_{22}H_{22}NOP$: C, 76.06; H, 6.38; N, 4.03. Found: C, 75.20; H, 6.52; N, 4.25%. NMR: (^{1}H, 25 °C, $CDCl_3$) δ: 2.21 (s, 3H, CH_3), 2.51 (t, $J = 8.0$ Hz, 2H, H_2), 3.59–3.67 (q, $J = 7.7$ Hz, 2H, H_1), 6.75 (t, $J = 7.4$ Hz, 2H, $H_{13,19}$), 6.90–6.93 (d, $J = 8.2$ Hz, 1H, H_6), 7.24–7.46, (m, 11H, ArH), 16.27 (bs, 1H, OH); (^{13}C{^{1}H}, 25 °C, $CDCl_3$) δ: 14.3 (CH_3), 29.4–29.6 (d, $J_{P-C} = 12$ Hz, C_2), 46.0–46.3 (d, $J_{P-C} = 22.5$ Hz, C_1), 116.9 (C_6), 118.7 (C_8), 119.2 (C_4), 127.9 (C_{13}), 128.5–128.8 ($C_{12,14}$), 132.4–132.5 (d, $C_{11,15}$), 132.8 (C_7), 137.8 (C_{10}), 163.8 (C_5), 171.4 (C_3); (^{31}P{1H}, 25 °C, $CDCl_3$): δ −20.4.

2.5. Synthesis of $\mathbf{L}^5$

$\mathbf{L}^4$ (0.3474, 1 mmol) and $NaBH_4$ (0.2 g, 5 mmol) were refluxed together in 50 ml dry ethanol under a N_2 atmosphere for 12 h. The mixture was cooled and the solvent was evaporated off on a rotary evaporator. $\mathbf{L}^5$ was extracted from the residue into dry dichloromethane (4×20 ml) and the extract was filtered through celite. The filtrate was washed with distilled water (4×25 ml) and dried with anhydrous sodium sulfate. $\mathbf{L}^5$ was obtained from the dried extract as a viscous colourless oil by evaporation of the solvent on a rotary evaporator. Yield 0.26 g; 75%. NMR: (^{1}H, 25 °C, $CDCl_3$) δ: 1.34–1.37 (d, $J = 11.63$ Hz, 3H, CH_3), 2.16–2.35 (m, 2H, H_1), 2.69–2.77 (m, 2H, H_2), 3.80–3.86 (q, $J = 7.4$ Hz, 1H, H_3), 6.86–6.88 (d, $J = 6.00$ Hz, 2H, $H_{11,15}$), 6.78–6.80 (d, $J = 6.00$ Hz, 1H, H_6), 7.09 (t, $J = 7.7$ Hz, 1H, H_7), 7.28–7.69 (m, 10H, ArH); (^{13}C{^{1}H}, 25 °C, $CDCl_3$) δ: 22.0 (CH_3), 28.2–28.3 (d, $J_{P-C} = 12$ Hz, C_2), 46.0–46.3 (d, $J_{P-C} = 21.9$ Hz, C_1), 61.4 (C_3), 116.9 (C_6), 118.7 (C_8), 126.3 (C_4), 127.8 (C_7), 128.0 (C_9), 128.3 ($C_{12,14}$), 132.4 (C_{13}), 137.4–137.6 ($C_{11,15}$), 138.8 (C_{10}), 157.0 (C_5); (^{31}P{^{1}H}, 25 °C, $CDCl_3$): δ −21.4.

2.6. Synthesis of [PdCl($\mathbf{L}^1$–H)] (1)

To a stirred solution of $Na_2[PdCl_4]$ (0.294 g, 1 mmol) made in 5 ml of distilled water was added a solution of

$\mathbf{L}^1$ (0.2714 g, 1 mmol) made in 10 ml of acetone. The mixture was stirred for 30 min and thereafter it was poured into 50 ml of distilled water. The complex was extracted with 100 ml of chloroform. The chloroform extract was washed with distilled water (3×20 ml) and dried with anhydrous sodium sulfate. The solvent was evaporated off on a rotary evaporator and the residue was dried under vacuum to obtain an orange powder of **1**. On recrystallization of the powder from a mixture (1:1) of chloroform and hexane, single crystals of **1** were obtained. Yield: 0.32 g; 78%; m.p. 140 °C. *Anal.* Calc. for $C_{16}H_{16}NOSPdCl$: C, 46.62; H, 3.91; N, 3.40. Found: C, 46.71; H, 3.92; N, 3.61%. NMR: (^1H, 25 °C, $CDCl_3$) δ: 2.47 (s, 3H, CH_3), 2.75–2.81 (td, $J = 13.5$ Hz, 1H, H_1), 3.32–3.42 (dt, $J = 4.5$ Hz, $J = 13.4$ Hz, 1H, H_2), 3.72–3.82 (dt, $J = 3.5$ Hz, $J = 14.0$ Hz, 1H, H_2), 4.03–4.11 (td, $J = 13.4$ Hz, 1H, H_1), 6.64 (t, $J = 7.7$ Hz, 1H, H_6), 7.14–7.24 (m, 3H, $H_{8,12-14}$), 7.29–7.33 (m, $H_{11,15,7}$), 8.17–8.21 (m, 1H, H_9); ($^{13}C\{^1H\}$, 25 °C, $CDCl_3$) δ: 18.6 (CH_3), 39.7 (C_2), 58.3 (C_1), 114.7 (C_6), 120.3 (C_8), 121.7 (C_4), 127.5 (C_{10}), 128.8 ($C_{12,14}$), 129.6 (C_{13}), 129.9 (C_9), 131.8 ($C_{11,15}$), 132.5 (C_7), 163.0 (C_5), 167.2 (C_3).

2.7. Synthesis of [PdCl($\mathbf{L}^2$–H)] (2)

$Na_2[PdCl_4]$ (0.294 g, 1 mmol) dissolved in 5 ml of water was treated with $\mathbf{L}^2$ (0.2874 g, 1 mmol) dissolved in 10 ml of acetone as described above for **1**, except that the complex was extracted into 50 ml of chloroform. The extract was dried with anhydrous sodium sulfate. Its solvent was evaporated off on a rotary evaporator resulting in an orange coloured powder of **2**. The orange coloured crystals of **2** were grown by slow evaporation of its solution made in a mixture of chloroform and methanol (10:1). Yield: 0.30 g; 70%; m.p. 170–172 °C. *Anal.* Calc. for $C_{16}H_{16}NO_2SPdCl$: C, 44.88; H, 3.77; N, 3.27. Found: C, 44.75; H, 3.76; N, 3.27%. NMR: (^1H, 25 °C, DMSO-d_6) δ: 2.23 (s, 3H, CH_3), 2.70–2.74 (td, $J = 13.3$ Hz, 1H, H_1), 3.30–3.46 (dt, $J = 4.4$ Hz, $J = 13.2$ Hz, 1H, H_2), 3.55–3.62 (dt, $J = 11.0$ Hz, 1H, H_2), 3.87–3.92 (td, $J = 12.9$ Hz, 1H, H_1), 7.15–7.19 (d, $J = 9.2$ Hz, 1H, H_8), 7.4–7.44 (m, 4H, $H_{11,12,14,15}$), 6.13–6.17 (m, 1H, H_{13}), 6.44–6.45 (d, $J = 3.0$ Hz, 1H, H_6), 8.08–8.11 (m, 1H, H_9), 9.32 (bs, 1H, OH); ($^{13}C\{^1H\}$, 25 °C, DMSO-d_6) δ: 17.6 (CH_3), 39.3 (C_2), 57.5 (C_1), 103.0 (C_6), 105.9 (C_8), 114.5 (C_4), 127.4 (C_{10}), 129.1 ($C_{9,13}$), 128.4 ($C_{12,14}$), 131.3 ($C_{11,15}$), 161.3 (C_5), 164.1 (C_7), 165.4 (C_3).

2.8. Synthesis of [PdCl($\mathbf{L}^3$–H)] (3)

A solution of $Na_2[PdCl_4]$ (0.294 g, 1 mmol) made in 5 ml of water was added to a solution of $\mathbf{L}^3$ (0.2734 g, 1 mmol) prepared in 10 ml of acetone with vigorous stirring. The mixture was stirred further for 2 h. It was then poured into 50 ml of distilled water. Complex **3** was extracted into 100 ml of chloroform. The chloroform extract was washed with distilled water (2×25 ml) and dried with anhydrous sodium sulfate. Slow evaporation of solvent from the dried extract at room temperature gave orange-red single crystals of **3**. Yield 0.32 g; 78%; m.p. 185 °C. *Anal.* Calc. for $C_{16}H_{18}NOSPdCl$: C, 46.39; H, 4.38; N, 3.38. Found: C, 46.52; H, 4.26; N, 3.43%. NMR: (^1H, 25 °C, $CDCl_3$) δ: 1.60 (bs, 3H, CH_3), 2.86 (bs, 1H, NH), 3.14–3.26 (two bs, 2H, H_2), 3.63 (bs, 2H, H_1), 6.95 (bs, 2H, $H_{12,14}$), 7.58 (bs, $H_{11,13,15}$), 8.00 (bs, 1H, H_7), 8.30 (bs, 1H, H_9); ($^{13}C\{^1H\}$, 25 °C, $CDCl_3$) δ: 18.7 (CH_3), 41.6 (C_2), 51.8 (C_1), 57.4 (C_3), 114.2 (C_6), 118.6 (C_8), 127.3 (C_4), 128.7 (C_{13}), 129.4 (C_7), 130.5 (C_9), 129.9 ($C_{12,14}$), 132.4 ($C_{11,15}$), 135.0 (C_{10}), 162.2 (C_5).

2.9. Synthesis of [PdCl($\mathbf{L}^4$–H)] (4)

$Na_2[PdCl_4]$ (0.294 g, 1 mmol) was dissolved in 5 ml of water. A solution of $\mathbf{L}^4$ (0.3474 g, 1 mmol) made in 10 ml of acetone was added to it with stirring. The mixture was stirred for a further 30 min which resulted in a yellow coloured solution. The complex was extracted into 50 ml of chloroform. The chloroform layer was washed with 20 ml of distilled water, dried with anhydrous sodium sulfate and reduced in volume to 10 ml by evaporating off the solvent on a rotary evaporator. The resulting precipitate was filtered, washed with hexane and dried under vacuum to give **4** as a yellow solid. Yield: 0.39 g; 80%; m.p. 158 °C. *Anal.* Calc. for $C_{22}H_{21}NOPPdCl$: C, 54.12; H, 4.34; N, 2.87. Found: C, 54.01; H, 4.32; N, 2.81%. NMR: (^1H, 25 °C, $CDCl_3$) δ: 2.17 (s, 3H, CH_3), 2.38–2.45 (two t, $J = 6.5$ Hz, 2H, H_2), 3.81 (t, $J = 6.2$ Hz, 2H, H_1), 3.92 (t, $J = 6.2$ Hz, 1H, H_1), 6.57 (t, $J = 7.9$ Hz, 1H, H_{13}), 7.14–7.17 (d, $J = 8.5$ Hz, 1H, H_6), 7.26 (t, merged with $CHCl_3$ signal, 2H, H_8), 7.44–7.53 (m, 8H, ArH *o* and *m* to P), 7.91–7.97 (m, 2H, $H_{7,9}$); ($^{13}C\{^1H\}$, 25 °C, $CDCl_3$) δ: 21.2 (CH_3), 30.1–30.5 (d, $J_{P-C} = 12$ Hz C_2), 56.6 (C_1), 114.8 (C_6), 119.2 (C_4), 123.3 (C_8), 128.0 (C_9), 129.0–129.1 ($C_{12,14}$), 130.4 (C_{13}), 133.3–133.5 ($C_{11,15}$), 132.4 (C_7), 144.6 (C_{10}), 158.0 (C_5), 170.7 (C_3); ($^{31}P\{^1H\}$, 25 °C, $CDCl_3$): δ 35.1.

2.10. Synthesis of [PdCl($\mathbf{L}^5$–H)] (5)

$Na_2[PdCl_4]$ (0.294 g, 1 mmol) dissolved in 5 ml of water and a solution of $\mathbf{L}^5$ (0.35 g, 1 mmol) made in 10 ml of acetone were mixed with vigorous stirring. The stirring was continued further for 1 h. The complex was extracted into 40 ml of chloroform. The organic layer was washed with distilled water (2×20 ml), dried with anhydrous sodium sulfate and evaporated on a rotary evaporator. The resulting residue was recrystallized with a chloroform–hexane mixture (1:10) to obtain **5** as a yellow solid, which was separated and dried under vacuo. Yield: 0.32 g; 65%; m.p. 169 °C. *Anal.* Calc. for $C_{22}H_{23}NO$ PPdCl: C, 53.79; H, 4.92; N, 2.85. Found: C, 53.81; H, 4.86; N, 2.94%.

2.11. Synthesis of [NiCl($\mathbf{L}^4$–H)] (6)

$NiCl_2 \cdot 6H_2O$ (0.284 g, 1 mmol) was dissolved in 2 ml of dry methanol. A solution of $\mathbf{L}^4$ (0.3474 g, 1 mmol) made in

10 ml of chloroform was added to it with vigorous stirring. The mixture was stirred for a further 0.5 h. The resulting red coloured solution was poured into 50 ml of distilled water. The complex was extracted into 50 ml of chloroform. The chloroform layer was washed with 25 ml of distilled water and dried with anhydrous sodium sulfate. The solvent of the extract was evaporated off on a rotary evaporator to get **6** as a red solid. Its single crystals were grown in a chloroform and hexane mixture (2:1). Yield: 0.39 g; 88%; m.p. 140 °C. *Anal.* Calc. for $C_{22}H_{21}NO$ PNiCl: C, 59.98; H, 4.80; N, 3.18. Found: C, 60.01; H, 4.92; N, 3.21%. NMR: (^{1}H, 25 °C, $CDCl_3$) δ: 2.48 (s, 3H, CH_3), 2.02–2.10 (two t, $J = 6.78$ Hz, 2H, H_2), 3.50 (t, $J = 6.53$ Hz, 1H, H_1), 3.59 (t, $J = 6.5$ Hz, 1H, H_1), 6.56, (t, $J = 7.3$ Hz, 1H, H_{13}), 7.08–7.11 (d, $J = 8.4$ Hz, 1H, H_6), 7.21 (t, $J = 7.5$ Hz, 1H, H_8), 7.41–7.57 (m, 8H, ArH *o* and *m* to P), 8.04–8.10 (m, 2H, $H_{7,9}$); (^{13}C{^{1}H}, 25 °C, $CDCl_3$) δ: 20.4 (CH_3), 28.9–29.3 (d, $J_{P-C} =$ Hz C_2), 55.0 (C_1), 114.8 (C_6), 121.7 (C_8), 127.4 (C_4), 128.9–129.2 ($C_{12,14}$), 130.4 (C_{13}), 131.5 (C_9), 133.0 (C_7), 133.1–133.4 (d, $C_{11,15}$), 144.6 (C_{10}), 158.0 (C_5), 170.7 (C_3); (^{31}P{^{1}H}, 25 °C, $CDCl_3$): δ 37.0.

2.12. Synthesis of [NiCl(L^5–H)] (7)

$NiCl_2 \cdot 6H_2O$ (0.284 g, 1 mmol) was dissolved in 5 ml of dry methanol. A solution of L^5 (0.35 g, 1 mmol) made in 10 ml of methanol was added to it with vigorous stirring. The mixture was stirred for a further 0.5 h. Complex **7** was extracted and treated further as given above in Section 2.11, to get it as a red solid. Yield: 0.35 g; 80%; m.p. 140 °C. *Anal.* Calc. for $C_{22}H_{23}NO$ PNiCl: C, 59.57; H, 5.45; N, 3.16. Found: C, 59.54; H, 5.42; N, 3.25%. NMR: (^{1}H, 25 °C, $CDCl_3$) δ: 1.58–1.60 (d, $J = 5.13$ Hz, 3H, CH_3), 2.50 (bs, 1H, NH), 2.90 (bs, 2H, H_2), 3.13 (bs, 2H, H_1), 4.46 (q, 1H, CH), 6.76 (t, $J = 7.2$ Hz, 2H, H_{13}), 7.03 (d, 1H, H_6), 7.12 (t, $J = 6.91$ Hz, 1H, H_8), 7.60–7.90 (bs, 1H, $H_{7,9}$), 7.24–7.48 (m, 8H, ArH *o* and *m* to P).

2.13. [PdCl(L^2–H)] (2) anchored silica gel (Catalyst 1)

Activated silica gel [32] (30 g), suspended in 100 ml solution of (3-chloropropyl)triethoxysilane in dry xylene (15% v/v), was refluxed with stirring for 72 h under a nitrogen atmosphere. The solid 3-chloropropyl silica gel (CPSG), separated by filtration, was washed (4 × 25 ml) successively with xylene, ethanol and diethylether. It was dried and degassed at 373 K under vacuum for 6 h, under anhydrous conditions. The CPSG (1 g) was added to a mixture made by stirring for about 15 min, 1 mmol (0.024 g) of sodium hydride (60% in mineral oil), 10 ml of a DMF–THF mixture (1:1) and an orange-red solution of complex **2** (1 mmol, 0.429 g) made in 2 ml of DMF (the solution of **2** was added dropwise with stirring with a magnetic bead at room temperature to the other contents taken in a 100 ml round bottom flask). The mixture was stirred further for 12 h. The silica gel became orange in colour. It was filtered, washed with DMF (3 × 5 ml) and THF (3 × 5 ml), dried in vacuo, to give a slippery orange-yellow solid (**Catalyst 1**). The palladium content was found to be 0.08 mmol/g in **Catalyst 1** by flame AAS after decomposing 0.1 g of it with 20 ml of concentrated $HNO_3 + HCl$ (1:3) and 70% $HClO_4$ (5 ml).

2.14. Coupling of aryl bromides with benzeneboronic acid

A mixture of bromobenzene or its derivative (1 mmol), benzeneboronic acid (0.183 g, 1.5 mmol), Na_2CO_3 (0.212 g, 2 mmol), distilled water (0.5 ml), isopropanol (10 ml) and **Catalyst 1** (0.1 g, ~0.008 mmol of Pd) was stirred under reflux over an oil bath for 8–10 h under ambient conditions. The reaction mixture was cooled to room temperature. The solid was filtered off and the filtrate was extracted with hexane/diethyl ether (25–50 ml). The solvent from the extract was evaporated off to give a white crystalline solid product, which was authenticated by NMR. Further details and results are given in Table 8.

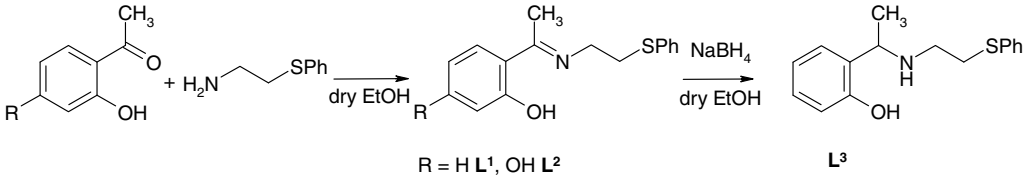
2.15. X-ray diffraction analysis

Single crystal X-ray diffraction studies of L^1, L^2, **3** and **6** were carried out with a Bruker SMART CCD diffractometer (at IIT Delhi) using Mo Kα ($\lambda = 0.71073$ Å) radiation at 298(2) °C. The software SADABS was used for absorption corrections and SHELXTL for space group, structure determination and refinements [33]. All non-hydrogen atoms were located from a difference Fourier map using geometrical constraints and were refined anisotropically. Hydrogen atoms were included in idealized positions with isotropic thermal parameters set at 1.2 times that of the carbon atom to which they were attached. The least-squares refinement cycles on F^2 were performed until the model converged. Data for **1** was collected (at the Instituto de Quimica, UNAM, Mexico) on a Bruker Smart APEX CCD diffractometer, using graphite monochromatized Mo Kα radiation ($\lambda = 0.71073$ Å) at 293(2) K. An analytical face indexed absorption correction was applied. The structure was solved by direct methods. Refinement was carried out by full-matrix least-squares analysis with anisotropic thermal parameters for all non-hydrogen atoms. Hydrogen atoms were placed into calculated positions and refined using a riding model with fixed isotropic thermal parameters. Calculations were carried out with SMART software for data collection and reduction, and SHELXTL for solution and refinement [34].

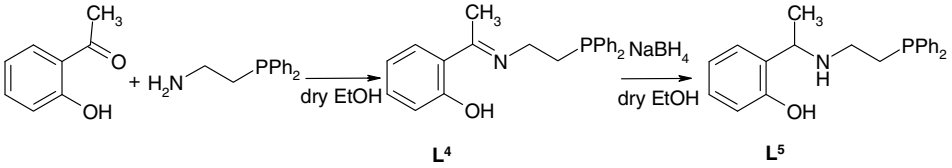
3. Results and discussion

The ligands L^1 to L^5 were synthesized by the reactions given in Eqs. (1) and (2). They are soluble in common organic solvents, except L^2 which is sparingly soluble in chloroform, dichloromethane and methanol and insoluble in hexane and diethyl ether. L^4 and L^5 are highly viscous oily liquids and consequently could not be subjected to

elemental analyses. The Pd(II) and Ni(II) complexes (**1**–**7**) of $\mathbf{L}^1$–$\mathbf{L}^5$ were synthesized according to Eqs. (3) and (4).



(1)



(2)

$$\mathbf{L^1}\text{ to }\mathbf{L^5} \quad + \quad Na_2PdCl_4 \xrightarrow[H_2O]{\text{Acetone}} [PdCl(\mathbf{L}\text{-H})]\ (\mathbf{1\text{-}5}) \quad + 2\,NaCl + HCl \tag{3}$$

$$\mathbf{L^4}\text{ to }\mathbf{L^5} \quad + \quad NiCl_2{\cdot}6\,H_2O \xrightarrow{\text{Methanol}} [NiCl(\mathbf{L}\text{-H})]\ (\mathbf{6\text{-}7}) \quad + HCl \tag{4}$$

All the complexes were soluble in common organic solvents such as chloroform, dichloromethane, acetonitrile, methanol, ethanol, DMF and DMSO, except **5**. In hexane and diethyl ether all the complexes were sparingly soluble. However, the solubility of **7** in common organic solvents was to be found relatively low. The molar conductance (Λ_M) of the ligands and the complexes was measured in acetonitrile at a concentration of about 1 mM at room temperature. The values of 0.5–10 Omega^{-1} cm^2 mol^{-1} suggest that they are non-electrolytic in nature.

In the IR spectra of $\mathbf{L}^1$, $\mathbf{L}^2$ and $\mathbf{L}^4$ the >C=N stretching vibration appears at 1612, 1618 and 1605 cm^{-1} respectively, while the C–S stretching band in the case of $\mathbf{L}^1$ to $\mathbf{L}^3$ appears between 782 and 797 cm^{-1}. The N–H bending absorption appears at 1595 cm^{-1} in the IR spectrum of $\mathbf{L}^3$. In the IR spectra of **1**, **2** and **6**, the >C=N stretching band shows a red shift with respect to those of the corresponding free ligands by ~15 cm^{-1}. In the IR spectra of the complexes of $\mathbf{L}^1$–$\mathbf{L}^3$, the C–S stretching bands appear at around 745 cm^{-1} (red shifted in comparison to those of the corresponding free ligands). In the IR spectra of **3**, **5** and **7** the N–H stretching and bending absorptions also show a red shift of the order of 10–15 cm^{-1} with respect to those of the corresponding ligands.

3.1. NMR spectra

The ^{1}H NMR spectra of the ligands $\mathbf{L}^1$ to $\mathbf{L}^5$ were found to be characteristic. The OH (*ortho* to azomethine) proton appears as a singlet at 15.82 ppm in the spectrum of $\mathbf{L}^1$ and at 16.43 ppm in that of $\mathbf{L}^2$. They are highly deshielded due to OH···N intra-molecular hydrogen bonding (supported by their single crystal structures). In the ^{1}H NMR spectrum of $\mathbf{L}^2$, the OH (*para* to azomethine) proton appears as a broad singlet at 9.82 ppm. The OH proton appears as a singlet at 16.27 ppm in the spectrum of $\mathbf{L}^4$, which is also highly deshielded due to OH···N intra-molecular hydrogen bonding. The OH signal could not be observed in the spectra of $\mathbf{L}^3$ and $\mathbf{L}^5$, which have reduced >C–NH rather than >C=N groups. Most probably the OH proton is not stabilized by intra-molecular hydrogen bonding in $\mathbf{L}^3$ and $\mathbf{L}^5$ and consequently intermolecular exchange between the phenolic protons broadens the OH signal so that it is not identifiable. In the ^{1}H NMR spectra of **1** and **2** the CH_3 protons were deshielded by ~0.2 ppm relative to those of the corresponding free ligand protons. The two protons of each CH_2 in the S–CH_2–CH_2–N system i.e. H_2 and H_1

are diastereotopic and magnetically non-equivalent, thus producing a group of four signals, each one corresponding to a single proton. The H_2 protons give two doublets of a triplet in which one signal is deshielded by 0.2–0.3 ppm and the other one by 0.3–0.4 ppm with respect to those of the free ligand. The H_1 protons give two triplets of a doublet in which one signal is deshielded by ~0.3–0.4 ppm and the other is shielded by ~1 ppm (relative to those of free $\mathbf{L}^1/\mathbf{L}^2$). The signals of the H_6 proton appear shielded (~0.3 ppm) compared to those of free ligands. In the ^1H NMR spectrum of **3** the signals were somewhat broad. The CH_3 protons were deshielded (~0.3 ppm) with respect to the corresponding protons of $\mathbf{L}^3$. The H_2 and H_1 protons also appear deshielded (~0.2 and 0.5 ppm, respectively) relative to the corresponding protons of the ligand $\mathbf{L}^3$. Additionally, the NH proton signal has been observed at 2.86 ppm. The signal of the H_6 proton was shielded (~0.3 ppm) whereas the signals of the other aromatic protons were deshielded (0.2–1.0 ppm) in comparison to the corresponding protons of $\mathbf{L}^3$. In the proton NMR spectrum of **4** the H_2 protons were shielded (~0.1 ppm). The H_1 protons give two characteristic triplets which were deshielded by ~0.4 and 0.5 ppm compared to the corresponding $\mathbf{L}^4$ protons. The OH signal present in the spectra of ligands $\mathbf{L}^1$, $\mathbf{L}^2$ and $\mathbf{L}^4$ was found to be absent in the spectra of complexes **1**, **2**, **4** and **6**. In the ^1H NMR spectra of **6** and **7**, the CH_3 protons were deshielded by ~0.3 ppm compared to those of the ligands. The H_2 protons in the spectrum of **6** give two triplets (due to P–H coupling) merged with each other, but these signals are shielded by 0.5 ppm with respect to the signals of the corresponding ligand protons. The H_1 protons also gave characteristic triplets (due to coupling with P) at 3.50 and 3.59 ppm. The signals of the H_2 and H_1 protons were also deshielded by ~0.7 ppm in the spectrum of **7** with respect to the signals of the corresponding ligand protons. The solubility of **5** was inadequate even for proton NMR.

The carbon-13 NMR spectra of $\mathbf{L}^1$–$\mathbf{L}^5$ and their metal complexes are characteristic. In the spectrum of $\mathbf{L}^3$, the signal of the C_3 carbon atom appears shielded by about 113.8 ppm relative to that of $\mathbf{L}^1$. The methyl carbon peak was also deshielded by 7.8 ppm with respect to that of $\mathbf{L}^1$. In the carbon-13 NMR spectrum of $\mathbf{L}^4$, the signals of the C_2 and C_1 carbon atoms appear as doublets at 29.4–29.6 and 46.0–46.3 ppm, respectively. The splitting of these peaks into doublets is due to coupling with phosphorous. The signal of the azomethine carbon atom has been observed at 171.4 ppm. On reduction of $\mathbf{L}^4$ to $\mathbf{L}^5$ the signal of the azomethine carbon was replaced with a signal of a CH carbon atom, shielded by 110 ppm with respect to the signal of the corresponding carbon of $\mathbf{L}^4$. In the $^{13}C\{^1H\}$ NMR spectra of **1** and **2** the signals of C_1 and C_2 carbon atoms were deshielded by ~10 and 5–6 ppm, respectively, relative to the signals of the corresponding carbon atoms of the ligands. The signals of the CH_3 carbon atoms were also deshielded by ~4 ppm on complexation, with respect to those of $\mathbf{L}^1$ and $\mathbf{L}^2$. The signal of the azomethine carbon atom was shielded by ~5 and 7 ppm, respectively, (relative to the ligands) in the spectra of **1** and **2**. The signals of C_{10} show a deshielding of ~7–8 ppm in comparison to those of the ligands. In the carbon-13 spectrum of **3** the signals of the C_1 and C_2 carbon atoms were deshielded by ~5 and 7 ppm respectively. The $^{13}C\{^1H\}$ NMR spectra of **4** and **6** exhibit signals for C_1, C_2 and CH_3 which are deshielded by ~6–7 ppm with respect to those of the ligands. Thus the above mentioned deshielding of the signals in the $^{13}C\{^1H\}$ and ^1H NMR spectra suggests that ligands $\mathbf{L}^1$ to $\mathbf{L}^5$ behave as $(N, O^-, S/P)$ donors in all the complexes. This is corroborated by the single crystal structures of **1**, **3** and **6**, indicating similarity in the solid state and solution structures. The $^{13}C\{^1H\}$ NMR spectrum of **7** could not be recorded due to its inadequate solubility.

In the $^{31}P\{^1H\}$ NMR spectra of $\mathbf{L}^4$ and $\mathbf{L}^5$ a sharp singlet was observed at −20.2 and −21.4 ppm, respectively, indicating the presence of only one type of phosphorus

Table 1
Crystal data and structure refinement parameters of $\mathbf{L}^1$ and $\mathbf{L}^2$

	$\mathbf{L}^1$	$\mathbf{L}^2$
Empirical formula	$C_{16}H_{17}NOS$	$C_{16}H_{17}NO_2S \cdot 1/6C_6H_6$
Formula weight	271.38	1808.5
Colour	yellow	yellow
Crystal size (mm)	0.312 × 0.109 × 0.098	0.312 × 0.192 × 0.056
Crystal system	monoclinic	rhombohedral
Space group	$P21/c$	$R\bar{3}$
Unit cell dimensions		
a (Å)	14.938(3)	15.1642(10)
b (Å)	5.4453(10)	15.1642(10)
c (Å)	18.138(3)	15.1642(10)
α (°)	90	112.35
β (°)	104.619(4)	112.35
γ (°)	90	112.35
V (Å^3)	1427.7(5)	2355.0(3)
Z	4	1
ρ_{calc} (Mg/m^3)	1.263	1.275
μ (mm^{-1})	0.218	0.210
$F(000)$	576	960
θ Range (°)	1.41–25.50	1.62–25.50
Index ranges	$-18 \leqslant h \leqslant 18$, $-6 \leqslant k \leqslant 6$, $-21 \leqslant l \leqslant 21$	$-17 \leqslant h \leqslant 17$, $-17 \leqslant k \leqslant 17$, $-17 \leqslant l \leqslant 17$
Reflections collected	8719	15893
Independent reflections [R_{int}]	1836 [0.0535]	2937 [0.0493]
Maximum and minimum transmission	0.971–0.981	none
Completeness to maximum θ (%)	100	98.6
Data/restraints/parameters	2467/0/150	2343/0/193
Goodness-of-fit on F^2	1.238	1.298
Final R indices [$I > 2\sigma(I)$]	$R_1 = 0.0710$, $wR_2 = 0.1686$	$R_1 = 0.0904$, $wR_2 = 0.2255$
R indices (all data)	$R_1 = 0.0796$, $wR_2 = 0.1840$	$R_1 = 0.1018$, $wR_2 = 0.2447$
Largest difference in peak and hole (e Å^{-3})	0.200 and −0.178	0.423 and −0.371

containing species. In the $^{31}P\{^{1}H\}$ NMR spectra of complexes **4** and **6** sharp signals at 35 and 37 ppm were observed, deshielded by ~55–57 ppm in comparison to those of the corresponding ligands. This supports the ligation of L^4 and L^5 through phosphorus in solution as well.

3.2. Single crystal structures

The crystal structures of L^1, L^2, **1**, **3** and **6** have been determined by X-ray diffraction on their single crystals. The twinning in crystals of **2** restricted us from solving its structure. The crystal data and structure refinement details

Table 2
Crystal data and structure refinement parameters of **1**, **3** and **6**

	1	**3**	**6**
Empirical formula	$C_{16}H_{16}ClNOPdS$	$C_{16}H_{18}ClNOPdS$	$C_{22}H_{21}ClNNiOP$
Formula weight	412.21	414.22	440.53
Colour	orange	red	red
Crystal size (mm)	0.446 × 0.072 × 0.048	0.219 × 0.138 × 0.089	0.319 × .102 × 0.089
Crystal system	monoclinic	triclinic	monoclinic
Space group	*P21/n*	$P\bar{1}$	*P21/c*
Unit cell dimensions			
a (Å)	12.6507(8)	10.6388(12)	10.7188(12)
b (Å)	8.7952(6)	11.6769(14)	12.0840(13)
c (Å)	15.566(1)	14.9603(17)	16.4529(18)
α (°)	90	76.857(2)	90.00
β (°)	112.904(1)	64.884(2)	100.520(2)
γ (°)	90	71.233(2)	90
V (Å^3)	1595.2(2)	1584.3(3)	2095.3(4)
Z	4	4	4
D_{calc} (Mg/m^3)	1.716	1.737	1.397
μ (mm^{-1})	1.458	1.469	1.141
F(000)	824	832	912
θ Range (°)	1.77–25.03	1.45–25.11	0.997–25.27
Index ranges	$-15 \leqslant h \leqslant 15$, $-10 \leqslant k \leqslant 10$, $-18 \leqslant l \leqslant 18$	$-12 \leqslant h \leqslant 12$, $-13 \leqslant k \leqslant 13$, $-17 \leqslant l \leqslant 17$	$-11 \leqslant h \leqslant 11$, $-13 \leqslant k \leqslant 13$, $-18 \leqslant l \leqslant 18$
Reflections collected	12699	14715	12711
Independent reflections [R_{int}]	2819 [0.0510]	4755 [0.0515]	3811 [0.0284]
Maximum and minimum transmission	0.9397 and 0.6681	0.782 and 0.879	0.868 and 0.905
Completeness to maximum θ (%)	99.9	98.3	99.7
Data/restraints/parameters	2891/0/191	5554/0/393	3000/0/245
Goodness-of-fit on F^2	0.957	1.312	1.024
Final *R* indices [$I > 2\sigma(I)$]	$R_1 = 0.0326$, $wR_2 = 0.736$	$R_1 = 0.0810$, $wR_2 = 0.1674$	$R_1 = 0.0315$, $wR_2 = 0.0809$
R indices (all data)	$R_1 = 0.0429$, $wR_2 = 0.0759$	$R_1 = 0.1034$, $wR_2 = 0.1846$	$R_1 = 0.0365$ $wR_2 = 0.0842$
Largest difference in peak and hole (e Å^{-3})	1.048 and −0.295	1.132 and −2.068	0.208 and −0.195

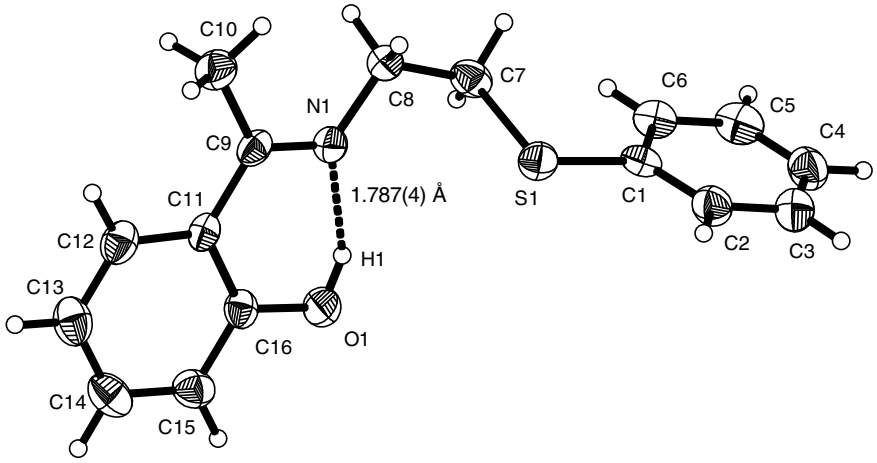


Fig. 2. ORTEP diagram of L^1 (thermal ellipsoids are drawn with 30% probability).

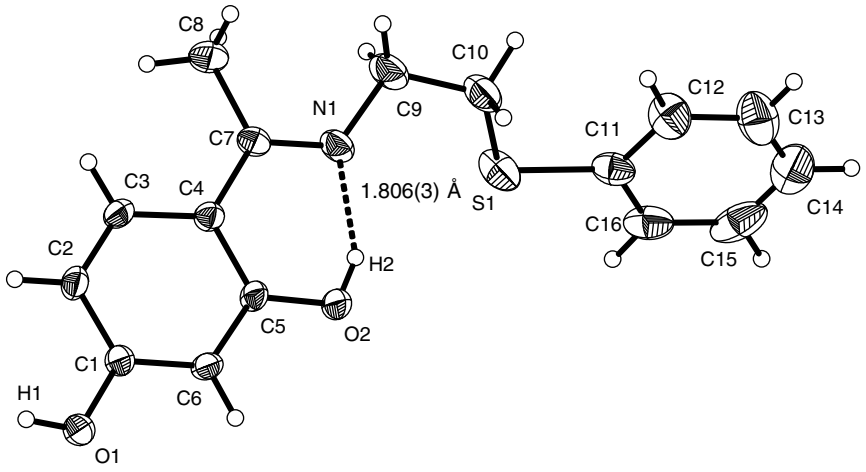


Fig. 3. ORTEP diagram of $\mathbf{L}^2$ (thermal ellipsoids are drawn with 30% probability).

are given in Tables 1 and 2. The molecular structures of $\mathbf{L}^1$ and $\mathbf{L}^2$ are shown in Figs. 2 and 3. Selected bond lengths and bond angles are given in Tables 3 and 4. The S–C (alkyl) bond length is longer than the S–C (aryl) bond, as expected. The geometry around the sulfur is V-shaped. The C–S–C bond angle is almost normal. The bond lengths and angles in the benzene ring and alkyl chain were also found to be normal. There exists a strong O–H···N intramolecular H-bond in $\mathbf{L}^1$ and $\mathbf{L}^2$.

The molecular structure of **1** is shown in Fig. 4. Selected bond lengths and bond angles are given in Table 5. The Pd centre has a square planar geometry in **1**. The ligand is coordinated with Pd in a monoanionic tridentate (O, N, S) mode, forming a six membered chelate ring with O^- and N (azomethine) and a five membered ring with S and N (azomethine). The Pd–N, Pd–O, Pd–S and Pd–Cl bond lengths 2.005(3), 1.971(2), 2.2644(11) and 2.3091(11) Å are in agreement with the reported values [35] for [PdCl{EtNHC(=S)NH–N=CH–C_6H_4-2-O^-}] [Pd–N = 1.965(2) Å, Pd–O = 2.019(2) Å, Pd–S = 2.2456 (9) Å and Pd–Cl = 2.3078(8) Å]. The Pd–S and Pd–Cl bond length of **1** are

Table 3
Selected bond lengths (Å) and bond angles (°) of $\mathbf{L}^1$

Bond lengths (Å)			
S(1)–C(1)	1.771(6)	S(1)–C(7)	1.794(6)
N(1)–C(9)	1.279(6)	N(1)–C(8)	1.461(6)
O–H(1)···N(1)	1.787(4)		
Bond angles (°)			
C(9)–N(1)–C(8)	121.4(5)	C(2)–C(1)–C(6)	118.4(5)
C(2)–C(1)–S(1)	117.3(4)	C(6)–C(1)–S(1)	124.3(5)
C(1)–C(2)–C(3)	120.8(6)	C(8)–C(7)–S(1)	109.4(4)
C(1)–S(1)–C(7)	104.1(3)		

Table 4
Selected bond lengths (Å) and bond angles (°) of $\mathbf{L}^2$

Bond lengths (Å)			
S(1)–C(1)	1.763(7)	S(1)–C(7)	1.818(5)
O(2)–C(14)	1.341(8)	N(1)–C(9)	1.304(8)
N(1)–C(8)	1.466(10)	O(2)–H(2)···N(1)	1.806(3)
Bond angles (°)			
C(1)–S(1)–C(7)	102.55(28)	C(9)–N(1)–C(8)	124.72(50)
C(2)–C(1)–S(1)	124.91(55)	C(1)–C(2)–C(3)	120.35(76)

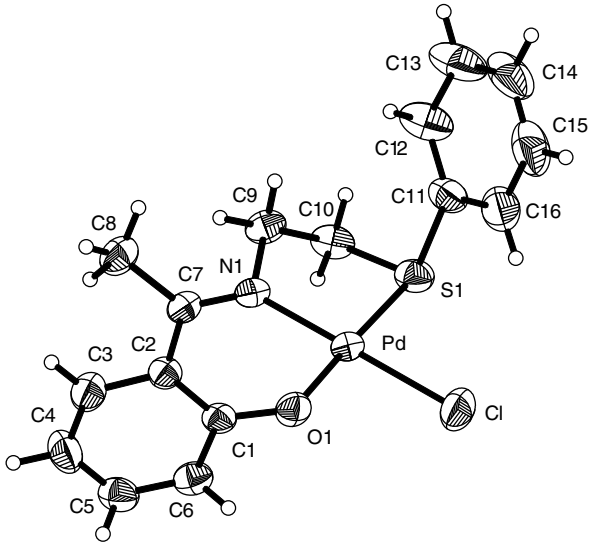


Fig. 4. ORTEP diagram of **1** (thermal ellipsoids are drawn with 30% probability).

Table 5
Selected bond lengths (Å) and bond angles (°) of **1**

Bond lengths (Å)			
Pd(1)–O(1)	1.971(2)	Pd(1)–N(1)	2.005(3)
Pd(1)–S(1)	2.2644(11)	Pd(1)–Cl(1)	2.3091(11)
S(1)–C(10)	1.788(4)	S(1)–C(11)	1.793(4)
N(1)–C(7)	1.289(4)	N(1)–C(9)	1.484(4)
O(1)–C(1)	1.311(4)		
Bond angles (°)			
O(1)–Pd(1)–N(1)	93.00(11)	O(1)–Pd(1)–S(1)	177.70(8)
N(1)–Pd(1)–S(1)	89.27(9)	O(1)–Pd(1)–Cl(1)	87.74(8)
N(1)–Pd(1)–Cl(1)	178.60(9)	S(1)–Pd(1)–Cl(1)	89.99(4)
C(10)–S(1)–C(11)	104.8(2)		

consistent with the values (2.268(4) and 2.316(4) Å) reported for [$PdCl_2${4-$MeOC_6H_4TeCH_2CH_2SEt$}] [36]. Surprisingly, the Pd–S bond distance in *cis*-Pd(SNNMe$_2$-S)($AsPh_3$)Cl_2 (2.249(1) Å) is some what shorter [37] than that of **1**. In *trans*-[Pd(SCN)$_2$[P(OPh)$_3$]$_2$] the Pd–S bond length is 2.352 Å [38], longer than that of **1**, probably due to the *trans* influence of S. The four bond lengths of **1** involving Pd are also consistent with the sum of the covalent radii for Pd–Cl, Pd–N, Pd–O and Pd–S (2.27, 1.98, 2.01 and 2.32 Å respectively).

The molecular structure of **3** is shown in the Fig. 5. Selected bond lengths and bond angles are given in Table 6. The crystal of **3** contains two types of molecules, consequently there are two types of N–H···Cl intermolecular hydrogen bonds (2.407(3) and 2.502(5) Å) (Fig. 5a and 5b). The Pd–N, Pd–O, Pd–S and Pd–Cl bond lengths 2.042(7)/2.035(7), 1.996(6), 2.257(2)/2.263(2) and 2.321(2)/2.329(2) Å are in agreement with the reported values [35] for [PdCl{EtNHC(=S)NH–N=CH–C_6H_4-2-O^-}] mentioned above as well as with those of **1**. The Pd–S and Pd–Cl bond lengths of **3** are also consistent with those of [$PdCl_2${4-$MeOC_6H_4TeCH_2CH_2SEt$}] [36], mentioned above. They are also consistent with the sum of covalent radii mentioned above. The Pd in **3** also has a square planar geometry. Generally the Pd–N bond distance [39–42] is close to 2.0 Å, however the values 1.857(4) [43] and 2.461(3) Å [44] have also been reported. Thus the Pd–N bond distance values in the present complexes **1** and **3** (2.005(3)–2.042(7) Å) fall in the common range. Pd–S bond lengths are commonly between 2.25 and 2.30 Å [45–47]. Our values (2.257(2)–2.2644(11) Å) are closer to the lower end as the uninegative ligands coordinate with Pd strongly due to the formation of two chelate rings. Pd–O bond distances are generally observed between 2.0 and 2.1 Å [48–50]. These distances in the case of the present complexes

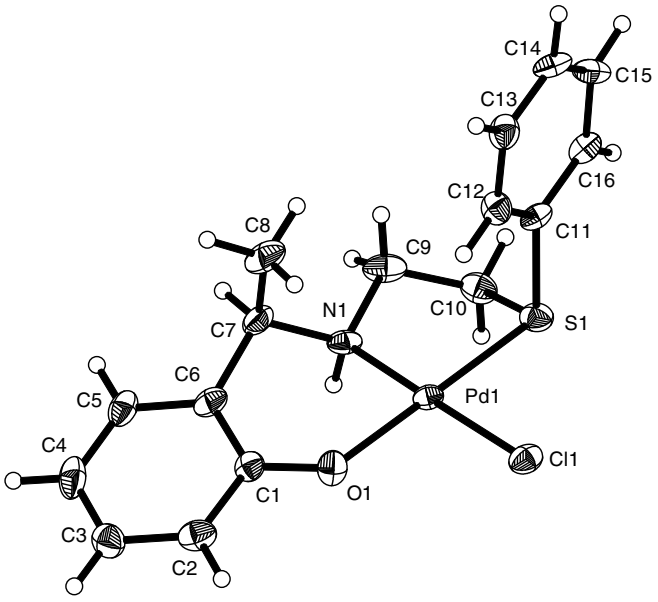


Fig. 5. ORTEP diagram of **3** (thermal ellipsoids are drawn with 30% probability).

Table 6
Selected bond lengths (Å) and bond angles (°) of **3**

Bond lengths (Å)			
Pd(1)–O(1)	1.996(6)	Pd(2)–O(2)	1.996(6)
Pd(1)–S(1)	2.257(2)	Pd(2)–S(2)	2.263(2)
Pd(1)–N(1)	2.042(7)	Pd(2)–N(2)	2.035(7)
Pd(1)–Cl(1)	2.321(2)	Pd(2)–Cl(2)	2.329(2)
O(1)–C(1)	1.322(11)	O(2)–C(17)	1.317(11)
S(1)–C(10)	1.807(10)	S(2)–C(26)	1.832(9)
S(1)–C(11)	1.780(9)	S(2)–C(27)	1.797(9)
N(1)–C(7)	1.487(12)	N(2)–C(23)	1.477(12)
N(1)–C(9)	1.500(12)	N(2)–C(25)	1.490(11)
N(1)–H(1)···Cl(1)	2.407(3)	N(2)–H(2)···Cl(2)	2.502(5)
Bond angles (°)			
O(1)–Pd(1)–N(1)	91.7(3)	O(2)–Pd(2)–N(2)	91.0(3)
N(1)–Pd(1)–S(1)	88.1(2)	N(2)–Pd(2)–S(2)	88.0(2)
N(1)–Pd(1)–Cl(1)	178.8(2)	N(2)–Pd(2)–Cl(2)	179.2(2)
O(1)–Pd(1)–S(1)	179.7(2)	O(2)–Pd(2)–S(2)	176.5(2)
O(1)–Pd(1)–Cl(1)	89.45(18)	O(2)–Pd(2)–Cl(2)	88.97(19)
S(1)–Pd(1)–Cl(1)	90.78(9)	S(2)–Pd(2)–Cl(2)	92.03(9)
C(11)–S(1)–C(10)	101.8(4)	C(27)–S(2)–C(26)	101.3(4)

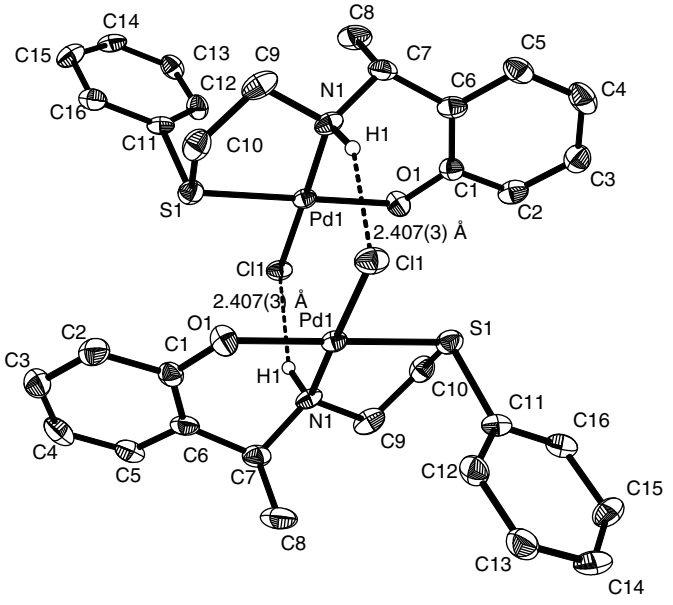


Fig. 5a. NH···Cl weak interactions in **3** (H atoms have been omitted for clarity).

1 and **3** (1.971(2)–1.999(6) Å) are somewhat on the lower side, suggesting strong chelation by the uninegative tridentate ligand.

The molecular structure of **6** is shown in Fig. 6. Selected bond lengths and bond angles are given in Table 7. The geometry around Ni is square planar. The ligand is coordinated with Ni in a monoanionic tridentate mode, forming a six membered chelate ring with O^- and N (azomethine) and a five membered ring with P and N (azomethine). The Ni–P, Ni–N, Ni–O and Ni–Cl bond lengths 2.1324(8), 1.896(2) 1.8428(19) and 2.1940(7) Å are consistent with the earlier reported values, Ni–P = 2.142(2) Å, Ni–N = 1.900(7) Å, Ni–O = 1.875(5) Å and Ni–Cl =

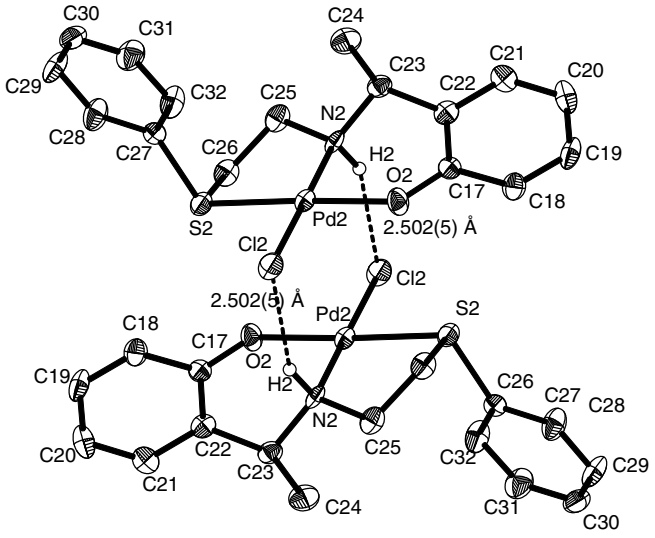
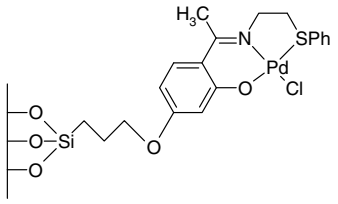


Fig. 5b. NH···Cl weak interactions in **3** (H atoms have been omitted for clarity).

2.148(3) Å for [NiCl(2-$PPh_2C_6H_4$–CH=N–C_6H_4-2-O^-)] [19]. The Ni–P bond distance of **6** is shorter than that of bis[1,2-bis(diphenylphosphino)ethene]nickel(II) diperchlorate (2.2374(7) Å) [51] but longer than that of tetrakis-(2-thienyldifluorophosphine)nickel (2.092(3) Å) [52]. The sum of the covalent radii for Ni–P, Ni–O, Ni–N and Ni–Cl are 2.21, 1.88, 1.90 and 2.14 Å, respectively. The values of the bond lengths of **6** are consistent with the sum of the radii, except Ni–P which is somewhat shorter. Generally the Ni–O bond distance is around 2.0 or 2.1 Å [53–55]. Values around 1.82 Å have also been reported for this bond length [56,57]. The Ni–O distance in **6** (1.8428(19) Å) is closer to the later value, which is interesting and indicates strong chelation of Ni by the (P, N, O^-) ligand. The Ni–N bond length of **6** (1.896(2) Å) is also shorter than the commonly observed value of around 2.05/2.10 Å [58,59], indicating its strong nature. On the contrary the commonly found value of around 2.15 Å for the Ni–P bond [60,61] is similar to that of **6** (2.1324(8) Å).

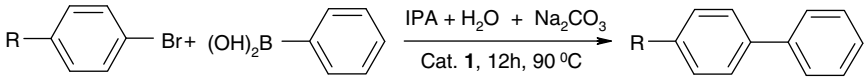
3.3. Catalytic coupling reaction

'**Catalyst 1**' is stable under ambient conditions. Its IR spectrum has bands at 2943 (ν_{C-H}), 1600 (b, $\nu_{C=N}$), 1219 (ν_{C-O}) and 799 (ν_{C-S}) cm^{-1}. There are similarities between the ^{13}C CPMAS NMR spectrum of '**Catalyst 1**′ and the solution $^{13}C\{^1H\}$ NMR spectrum of **2**. Additional signals for the propyl group (-Si-$CH_2CH_2CH_2$–O–) have been observed in the case of the ^{13}C CPMAS NMR spectrum. The $SiCH_2$, middle CH_2 and OCH_2 carbon atom signals appear at 10.5, 26.4 and 47.0 ppm respectively. The methyl carbon signal appears at 18.6 ppm. The signals for the C_2 and C_1 atoms appear at 38.8 and 60.5 ppm, respectively. The signals of C_{10}, C_9, C_{13}, C_{12} and C_{14} merge and appear as a broad peak at 130.5 ppm. The signals for C_{11} and C_{15} appear at 132.0 ppm, for C_3 and C_7 at 164.1 ppm and for C_5, C_6/C_8 and C_4 at 158.8, 106.6 and 119.8 ppm, respectively (see Fig. 1 for the numbering of the carbon atoms).



Catalyst 1.

'**Catalyst 1**' was used in the Suzuki–Miyaura C–C coupling reactions of benzeneboronic acid with bromobenzene and substituted bromobenzenes (Eq. (5)) in an isopropanol and water mixture using Na_2CO_3 as a base at 90 °C.



where R = CH_3O, CH_3, H, NO_2, CO_2H
IPA = isopropanol

(5)

The yields were maximal when 0.001 mol% of catalyst (Pd) was taken. The catalytic activity was dependent on

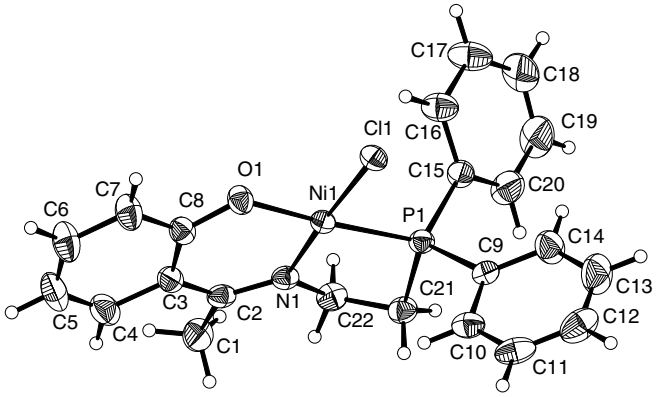
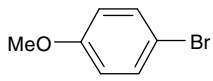
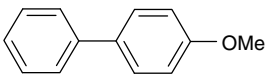
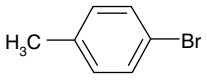
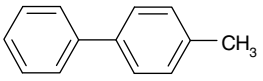
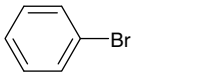
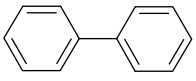
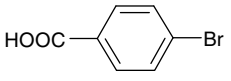
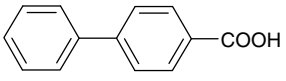
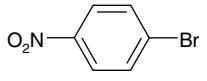
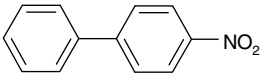


Fig. 6. ORTEP diagram of **3** (thermal ellipsoids are drawn with 30% probability).

Table 7
Selected bond lengths (Å) and bond angles (°) of **6**

Bond lengths (Å)			
Ni(1)–O(1)	1.8428(19)	Ni(1)–N(1)	1.896(2)
Ni(1)–P(1)	2.1324(8)	Ni(1)–Cl(1)	2.1940(7)
P(1)–C(9)	1.809(3)	P(1)–C(21)	1.810(3)
P(1)–C(15)	1.815(3)	O(1)–C(8)	1.308(3)
N(1)–C(2)	1.310(3)	N(1)–C(22)	1.493(4)
Bond angles (°)			
O(1)–Ni(1)–N(1)	95.10(9)	O(1)–Ni(1)–P(1)	175.72(6)
N(1)–Ni(1)–P(1)	89.15(7)	O(1)–Ni(1)–Cl(1)	89.07(6)
N(1)–Ni(1)–Cl(1)	175.81(7)	P(1)–Ni(1)–Cl(1)	86.68(3)
C(9)–P(1)–C(21)	106.88(13)	C(9)–P(1)–C(15)	106.87(13)
C(21)–P(1)–C(15)	107.32(14)	C(9)–P(1)–Ni(1)	117.53(9)
C(21)–P(1)–Ni(1)	100.60(10)	C(15)–P(1)–Ni(1)	116.62(10)
C(8)–O(1)–Ni(1)	126.79(19)	C(2)–N(1)–C(22)	117.9(2)
C(2)–N(1)–Ni(1)	125.9(2)	C(22)–N(1)–Ni(1)	116.02(17)
N(1)–C(2)–C(3)	123.1(2)	N(1)–C(2)–C(1)	119.2(3)
C(20)–C(15)–P(1)	121.0(2)	C(16)–C(15)–P(1)	120.4(2)
N(1)–C(22)–H(22A)	109.6	C(22)–C(21)–P(1)	106.4(2)
N(1)–C(22)–H(22B)	109.6	P(1)–C(21)–H(21A)	110.5
C(10)–C(9)–P(1)	118.2(2)	P(1)–C(21)–H(21B)	110.5
C(14)–C(9)–P(1)	123.4(2)	N(1)–C(22)–C(21)	110.3(2)

Table 8
Suzuki–Miyaura coupling reaction with **Catalyst 1**

Aryl bromide	Product	% Yield of biphenyl
		75
		78
		89
		80
		90

the nature of the halide. The presence of electron withdrawing groups on the aryl ring increased the yield of the product biphenyl. The results are given in Table 8. The turnover number was between 75 000 and 90 000.

4. Conclusion

New (N, O, S) and (N, O, P) types of ligands $\mathbf{L}^1$ to $\mathbf{L}^5$ have been synthesized and explored for ligation with Pd(II) and Ni(II). They all behave as uni-negative tridenate donor ligands as evidenced in the case of [PdCl($\mathbf{L}^1$–H)] (**1**), [PdCl($\mathbf{L}^3$–H)] (**3**) and [NiCl($\mathbf{L}^4$–H)] (**6**) by their single crystal structures. The palladium complex of $\mathbf{L}^2$ has been grafted on silica gel to prepare '**Catalyst 1**', which was used for Suzuki–Miyaura C–C coupling reactions with good yields.

Acknowledgements

A.K.S. is grateful to Professor John E. Drake, University of Windsor, Canada for his valuable help in solving the single crystal structures of the compounds synthesized in the research group of AKS at IIT Delhi, for more than one and a half decades. To acknowledge it further, this paper is dedicated to John. He thanks Department of Science and Technology (India) for research project SR/S1/IC-23/06. The authors also thank the Department of Science and Technology (India) for partial financial assistance given to establish the single crystal X-ray diffraction facility under its FIST program at IIT Delhi. R.K.P. thanks the University Grants Commission (India) for a Senior Research Fellowship.

Appendix A. Supplementary data

CCDC numbers 639950, 639951, 639952, 639953 and 639954 contain the supplementary crystallographic data for $\mathbf{L}^1$, $\mathbf{L}^2$, **1**, **3** and **6**, respectively. These data can be obtained free of charge at www.ccdc.cam.ac.uk/conts/retrieving.html [or from the Cambridge Crystallographic Data Centre, 12, Union Road, Cambridge CB2 1EZ, UK; fax: (internat.) +44-1223/336-033; E-mail: deposit@ccdc.cam.ac.uk]. Supplementary data associated with this article can be found, in the online version, at doi:10.1016/j.poly.2008.01.027.

References

[1] I.D. Kostas, F.J. Andreadaki, D.K. Demertzi, C. Prentjas, M.A. Demerpzas, Tetrahedran Lett. 46 (2005) 1967.
[2] R.B. Bedford, C.S.J. Cazin, M.B. Hursthouse, M.E. Light, K.J.P.S. Wimperis, J. Organomet. Chem. 633 (2001) 173.
[3] M.A. Ali, M. Nazimuddin, R. Shaha, R.J. Butcher, J.C. Bryand, Polyhedron 6 (1998) 2844.
[4] R.P. John, A. Sreekanth, M.R.P. Kurup, A. Usman, A.R. Ibrahim, H.K. Fun, Spectrochim. Acta. A 59 (2003) 1349.
[5] H. Adams, S. Clunas, D.E. Fenton, T.J. Gregson, P.E. McHugh, S.E. Spey, Inorg. Chim. Acta 346 (2003) 239.
[6] H. Adams, S. Clunas, D.E. Fenton, G. Handley, P.E. McHugh, Inorg. Chem. Commun. 5 (2002) 1044.
[7] H. Adams, S. Clunas, L.R. Cummings, D.E. Fenton, P.E. McHugh, Inorg. Chem. Commun. 6 (2003) 837.
[8] A. Rana, R. Dinda, S. Ghosh, A.J. Blake, Polyhedron 22 (2003) 3075.
[9] N.R. Pramanik, S. Ghosh, T.K. Raychaudhuri, S. Ray, R.J. Butcher, S.S. Mandal, Polyhedron 23 (2004) 1595.
[10] S. Dhar, M. Nethaji, A.R. Chakravarty, Inorg. Chim. Acta. 358 (2005) 2437.
[11] G.M. Gray, J.M. George, M. Jan, Inorg. Chim. Acta. 314 (2001) 133.

[12] K. Nakajima, S. Ishibashi, M. Inamo, M. Kojima, Inorg. Chim. Acta. 325 (2001) 36.
[13] K. Nakajima, S. Ishibashi, M. Kojima, Chem. Lett. (1998) 997.
[14] H. Dai, X. Hu, H. Chen, C. Bai, Z. Zheng, Tetrahedron: Asymmetry 14 (2003) 1467.
[15] H.L. Kwong, W.S. Lee, T.S. Lai, W.T. Wong, Inorg Chem. Commun. 2 (1999) 66.
[16] T. Kniess, J.D.G. Correia, A. Domingos, E. Palma, I. Santos, Inorg. Chem. 42 (2003) 6131.
[17] J.W. Faller, G. Mason, J. Parr, J. Organomet. Chem. 626 (2001) 181.
[18] J. Parr, A.M.Z. Slawin, Inorg. Chim. Acta. 303 (2000) 116.
[19] O.M. Ni Dhubhghaill, J. Lennon, M.G.B. Drew, J. Chem Soc., Dalton Trans. (2005) 3213.
[20] S.R. Korupoju, R.Y. Lai, Y.H. Liu, S.M. Peng, S.T. Liu, Inorg. Chim. Acta 358 (2005) 3003.
[21] A. Bacchi, M. Carcelli, M. Costa, A. Fochi, C. Monici, P. Pelagatti, C. Pelizzi, G. Pelizzi, L. Maria, S. Roca, J. Organomet. Chem. 593 (2000) 180.
[22] E.M. McGarrigle, D.G. Gilheany, Chem. Rev. 105 (2005) 1563.
[23] D. Wang, M. Wang, X. Wang, Y. Chen, A. Gao, L. Sun, J. Catal. 237 (2006) 248.
[24] R. Ferreira, H. Garcia, B. de Castro, C. Freire, Eur. J. Inorg. Chem. (2005) 4272.
[25] A. Martinez, C. Hemmert, C. Loup, G. Barre, B. Meunier, J. Org. Chem. 71 (2006) 1449.
[26] H. Zhang, S. Xiang, C. Li, Chem. Commun. (2005) 1209.
[27] C.P. Chow, K.J. Shea, J. Am. Chem. Soc. 127 (2005) 3678.
[28] M.S. Taylor, D.N. Zalatan, A.M. Lerchner, E.N. Jacobsen, J. Am. Chem. Soc. 127 (2005) 1313.
[29] D.J. Darensbourg, P. Ganguly, D. Billodeaux, Macromolecules 39 (2006) 2722.
[30] A.R. Katritzky, Y.J. Xu, H.Y. He, S. Mehta, J. Org. Chem. 66 (2001) 5590.
[31] A. Habtemariam, B. Watchman, B.S. Potter, R. Palmer, S. Parsons, A. Parkin, P.J. Sadler, J. Chem. Soc., Dalton Trans. (2001) 1306.
[32] G. Singh, S. Bali, A.K. Singh, Polyhedron 26 (2007) 897.
[33] G.M. Sheldrick, SHELXL-NT Version 6.12, University of Gottingen, Germany, 2000.
[34] Bruker, SMART (Version 5.624) and SAINT (Version 6.04) programs using the Windows NT system, Bruker AXS Inc., Madison, WI, USA, 2001.
[35] K.D. Dimitra, P.N. Yadav, M.A. Demertzis, J.P. Jasiski, F.J. Andreadakic, I.D. Kostasc, Tetrahedron Lett. 45 (2004) 2923.
[36] A.K. Singh, C.V. Amburose, M. Mishra, R.J. Butcher, J. Chem. Res. (S) (1999) 716.
[37] G. Tresoldi, G. Bruno, P. Piraino, G. Faraone, G. Bombieri, J. Organomet. Chem. 265 (1984) 311.
[38] A.J. Carty, P.C. Chieh, N.J. Taylor, W.T. Wong, S. Yau, J. Chem. Soc., Dalton Trans. (1976) 572.
[39] K. Polborn, Ch-. Missling, W. Beck, Z. Kristall. New Cryst. Struct. 216 (2001) 233.
[40] K. Noguchi, H. Yuge, T.K. Miyamoto, Acta Cryst. C56 (2000) e40.
[41] J.L. Sessler, J.W. Sibert, V. Lynch, Inorg. Chim. Acta 206 (1993) 63.
[42] Y.-J. Kim, J.-C. Choi, K. Osakada, J. Organomet. Chem. 491 (1995) 97.
[43] Y. Li, Y.-H. Lai, K.F. Mok, M.G.B. Drew, Inorg. Chim. Acta 279 (1998) 221.
[44] T.J. Hubin, N.W. Alcock, D.H. Busch, Acta Cryst. C55 (1999) 1404.
[45] K.S. Bousman, P.J. Toscano, J.T. Welch, Inorg. Chim. Acta 357 (2004) 3871.
[46] G.-H. Lee, B.-C. Tzeng, Acta Cryst. C52 (1996) 879.
[47] S. Liu, C.R. Lucas, M.J. Newlands, J.P. Charland, Inorg. Chem. 29 (1990) 4380.
[48] H. Weissmann, L.J.W. Shimon, D. Milstane, Organometallics 23 (2004) 3931.
[49] T. Motoyama, Y. Shimazaki, T. Yajima, Y. Nakabayashi, Y. Naruta, O. Yamauchi, J. Am. Chem. Soc. 126 (2004) 7379.
[50] F. Pointillart, C. Train, F. Villain, C. Cartier dit Moulin, P. Gredin, L.-M. Chamoreau, M. Gruselle, G. Aullon, S. Alvarez, M. Verdaguer, J. Am. Chem. Soc. 129 (2007) 1327.
[51] Y.Z. Li, J.C. Liu, J.Q. Qu, L.F. Wang, C.G. Xia, J.Z. Niu, Acta Cryst., Sect. E E58 (2002) m237.
[52] W.S. Sheldrick, Acta Cryst., Sect. B B31 (1975) 305.
[53] L.R. Favello, R. Garde, M. Tomas, Inorg. Chem. 41 (2002) 4599.
[54] O. Kristiansson, I. Persson, D. Bobicz, D. Xu, Inorg. Chim. Acta 344 (2003) 15.
[55] P. Romain, C.G. Miralles, A. Luque, J.I. Beitia, J. Cano, F. Lloret, M. Julve, S. Alvarez, Inorg. Chem. 35 (1996) 3741.
[56] H. Ohtsu, K. Tanaka, Inorg. Chem. 43 (2004) 3024.
[57] Y. Abe, H. Akao, Y. Yoshida, H. Takashima, T. Tanase, H. Mukai, K. Ohta, Inorg. Chim. Acta 359 (2006) 3147.
[58] X.-H. Li, M.-L. Hu, Z. Kristall. 218 (2003) 494.
[59] R.K. Hocking, T.W. Hambley, Inorg. Chem. 41 (2002) 2660.
[60] K. Herbst, B. Rink, L. Dahlenburg, M. Brorson, Organmetallics 20 (2001) 3655.
[61] J. Münchenberg, A.K. Fisher, H. Thönnesson, R. Schmutzler, J. Organomet. Chem. 529 (1997) 361.

interactions of some copper(II) salts with 2-pmpe and 2-qmpe ligands lead to the formation of several copper-picolinate or quinaldinate species [10,11] in an oxidative P-dealcylation/dephosphorylation reaction. These products are interesting from a structural and magnetic point of view. The studies of these reactions clearly demonstrate that copper(II) ions promote/enhance the decomposition of $R–CH_2P(O)(OEt)_2$ *N*-heterocyclic ligands (R = pyridine or quinoline) and catalyze the oxidation process by atmospheric oxygen.

It is worth mentioning that the continuing interest in metal-assisted transformations of organic functionalities is primary due to the quest for convenient synthetic methods and region- and stereoselective processes [12–17].

In this paper, we present the synthetic studies, spectral and magnetic properties, and the X-ray single-crystal analysis of a cobalt(II) compound of the formula $[Co(2\text{-qca})_2(EtOH)_2]$. This compound was formed in an interesting reaction in which diethyl(quinolin-2-ylmethyl) phosphonate (2-qmpe) was transformed to the quinoline-2-carboxylate (2-qca) ligand.

2. Experimental

2.1. Reagents and physical measurements

The starting materials and solvents for the synthesis were obtained commercially and were used as received. The metal content was determined using a Carl–Zeiss–Jena atomic absorption spectrophotometer. Elemental analyses were carried out using a Perkin–Elmer elemental analyzer 2400CHN.

Infrared spectra (100–4000 cm^{-1}) were recorded on a Bruker IFS 113v spectrophotometer using KBr pellets, and solid-state electronic spectra (28 000–4000 cm^{-1}) were recorded on a Cary 500 spectrophotometer.

The EPR spectra of a powder sample were recorded (at 295 and 77 K) on a Bruker ESP 300E spectrometer operating at the X-band frequency and equipped with a Bruker NMR. The spectrum at 4.5 K was measured with an X-band radiopan SE/X 2543 spectrometer.

Magnetic measurements of a polycrystalline sample were carried out with a Quantum Design SQUID magnetometer (MPMSXL-5 type). The measurements were recorded at a magnetic field of 0.5 T over the temperature range 1.8–300 K. The correction for diamagnetism of the experimental susceptibility was based on subtracting the sample-holder signal and estimating the contribution χ_D from Pascal constants [18]. The effective magnetic moments were calculated from $\mu_{eff} = 2.83(\chi_M T)^{1/2}$, using a temperature-independent paramagnetism of 150×10^{-6} cm^3 mol^{-1} for Co(II) [18,19].

2.2. Crystal structure determination of $[Co(2\text{-qca})_2(EtOH)_2]$

The X-ray data were collected at low temperature using an Oxford Cryosystem device on a Kuma KM4CCD κ-axis diffractometer with graphite-monochromated Mo Kα radiation. Data were corrected for Lorentz polarization effects and a correction absorption was also applied. The crystal structure was solved by direct methods (program SHELXS97 [20]) and refined by the full-matrix least-squares method on all F^2 data using the SHELXL97 [21] programs. Non-hydrogen atoms were refined with anisotropic displacement parameters; hydrogen atoms were included from the geometry of the molecules and $\Delta\rho$ maps, and were refined isotropically. Crystal data are given in Table 1, together with refinement details.

2.3. Synthesis of the ligand (2-qmpe) and the $[Co(2\text{-qca})_2(EtOH)_2]$ compound

The diethyl(quinolin-2-ylmethyl)phosphonate (2-qmpe) ligand was prepared according to the procedure described in detail elsewhere [7].

The coordination compound was prepared by dissolving $CoCl_2 \cdot 2H_2O$ (1 mmol) in ethanol (10 cm^3) and dropwise adding this to a stirred solution of the ligand (2 mmol) in ethanol (15 cm^3), according to the procedure described earlier [9]. The dark green product of $[Co(2\text{-qmpe})_2Cl_2]$ slowly precipitated from the dark green reaction mixture after evaporation of the solvent [9]. This compound was then dissolved in ethanol. The yellow single crystals of $[Co(2\text{-qca})_2(EtOH)_2]$, suitable for X-ray analysis, were slowly grown after evaporation of the solvent. The yellow product was filtered off and washed carefully with ethanol and ether.

Table 1
Crystal data and structure refinement for $[Co(2\text{-qca})_2(EtOH)_2]$

Empirical formula	$C_{24}H_{24}CoN_2O_6$
Formula weight	495.38
Temperature (K)	100(2)
Wavelength (Å)	0.71073
Crystal system	monoclinic
Space group	$P2_1/n$
a (Å)	5.839(4)
b (Å)	9.560(6)
c (Å)	19.6750(10)
β (°)	91.10(5)
V (Å^3)	1098.1(10)
Z	2
D_{calc} (Mg m^{-3})	1.498
Absorption coefficient (mm^{-1})	0.826
$F(000)$	514
Crystal size (mm)	0.25 × 0.15 × 0.15
θ Range for data collection (°)	3.62–27.50
Index ranges	$-7 \leqslant h \leqslant 7$, $-12 \leqslant k \leqslant 12$, $-25 \leqslant l \leqslant 25$
Reflections collected	8981
Independent reflections (R_{int})	2504 (0.0298)
Data/parameters	2504/155
Goodness-of-fit (F^2)	1.120
Final R_1/wR_2 indices ($I > 2sI$)	0.0373/0.0741
Largest difference in peak/hole (e Å^{-3})	0.340/−0.210

Anal. Calc. for $C_{24}H_{24}CoN_2O_6$: C, 58.18; H, 4.89; N, 5.66; Co, 12.98. Found: C, 58.05; H, 4.81; N, 5.44; Co, 12.13%.

3. Results and discussion

A compound of the formula $[Co(2\text{-qmpe})_2Cl_2]$ is formed in the reaction of $CoCl_2 \cdot 2H_2O$ with the diethyl(quinolin-2-ylmethyl)phosphonate ligand, (2-qmpe). The physicochemical properties of this compound were presented earlier [9]. In solution this compound undergoes a slowly transformation to $[Co(2\text{-qca})_2(EtOH)_2]$. Thus, an oxidative decomposition process of the starting 2-qmpe ligand through the cleavage of the C–P bond occurs, according to the scheme presented in Fig. 1.

Aspects of this reaction are presented in Section 3.4.

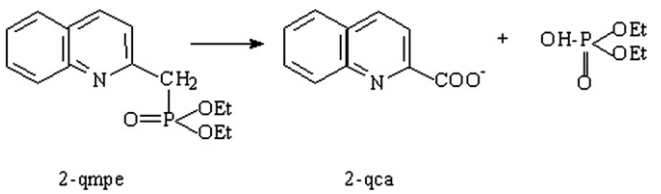


Fig. 1. A schematic drawing showing the transformation of the starting 2-qmpe ligand to 2-qca.

3.1. Description of the structure of $[Co(2\text{-qca})_2(EtOH)_2]$

The crystallographic parameters are summarized in Table 1. The most important bond lengths and angles are listed in Table 2.

Table 2
Selected bond lengths (Å) and angles (°) for $[Co(2\text{-qca})_2(EtOH)_2]$

Co(1)–O(2)	2.0179(17)	O(2)–Co(1)–N(1)	79.04(6)
Co(1)–O(3)	2.0998(16)	$O(2)^i$–Co(1)–N(1)	100.96(6)
Co(1)–N(1)	2.2003(15)	O(3)–Co(1)–N(1)	86.22(6)
O(2)–Co(1)–O(3)	88.33(7)	O(3)–Co(1)–$N(1)^i$	93.78(6)
$O(2)$–Co(1)–$O(3)^i$	91.67(7)		

Symmetry transformations used to generate equivalent atoms: (i) $1-x+1$, $-y$, $-z$.

Fig. 2 shows the structure and labelling scheme of the Co(II) complex. Its crystal structure consists of mononuclear units in which the cobalt atom lies at the centre of symmetry. The quinoline-2-carboxylate (2-qic) anion acts as a chelating ligand coordinating through a quinoline nitrogen and carboxylate oxygen, forming a five-membered ring. The other remaining carboxylate oxygen atoms are not involved in coordination to the metal ion. Two strongly N,O-bonded picolinate ligands lie on the equatorial plane. In other words, the monomeric unit $Co(2\text{-qca})_2$, treated as a whole molecule, is planar. The cobalt atom is octahedrally surrounded by two quinoline nitrogens at a distance of 2.203(15) Å and two oxygen atoms of the carboxylate groups from two 2-qca ligands at a distance of 2.0179(17) Å. Two ethanol molecules occupy the fifth and the sixth coordination sites, with Co–O bond distances of

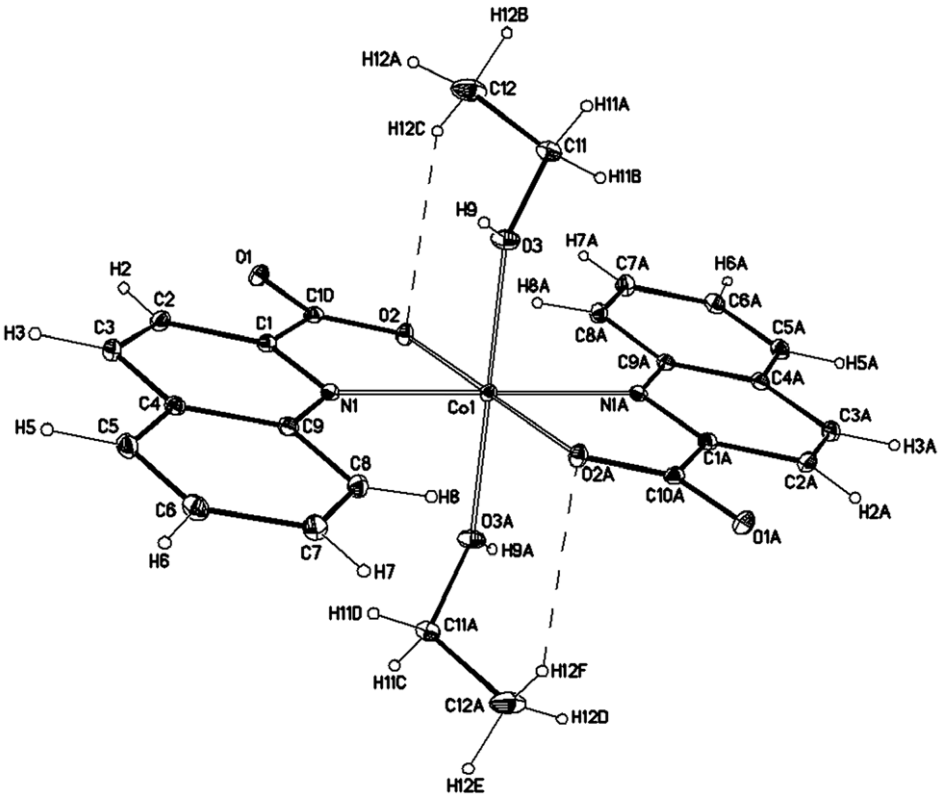


Fig. 2. Molecular structure of $[Co(2\text{-qca})_2(EtOH)_2]$ showing the atomic numbering. Intramolecular hydrogen bonds are indicated by a dotted line.

2.0998(16) Å. As shown in Table 2, the Co–N bonds are significantly longer compared to the Co–O bonds, causing a distortion of the coordination polyhedron around the metal ion. In fact, the polyhedron can be described as an elongated octahedron, elongated symmetrically along the Co–N direction.

The values observed for the Co–N and Co–O distances are characteristic of high-spin cobalt(II) [6,7,22]. The average C–C and C–N lengths in the quinoline ring of 1.398 and 1.353 Å, respectively, are typical [23]. The crystal packing is depicted in Fig. 3. There are three types of intermolecular hydrogen bonds linking the molecules in different directions.

In the first of these interactions, weak C–H···O contacts are formed between aromatic C–H groups of the quinoline rings and the coordinated [C(8)–H(8)···O(2)^{i}] and uncoordinated carboxylic oxygens [C(3)–H(3)···O(1)^{i} and C(5)–H(5)···O(1)^{iii}] (symmetry codes are given in Table 3) with the values of the hydrogen donor···acceptor distance, D···A bond distance and D–H···A angle suggested for C–H···O hydrogen bonds [24]. Another, the strong O–H···O type of interactions, are formed between the O–H group of the ethanol molecule and the coordinated and uncoordinated carboxylic oxygens of an adjacent molecule [O(3)–H(9)···O(1)^{ii} and O(3)–H(9)···O(2)^{ii}]. The shortest O···O length for the O–H···O bond systems is found between the ethanol O(3) atom and the coordinated carboxylate oxygen O(1)^{ii}. This bond O(3)–H(9)···O(1)^{ii} is short, $d_{D-A} = 2.664(2)$ Å, and approaches linearity, with an angle of 174(3)°. The last type of intermolecular contacts in this structure is a weak C–H···π interaction formed between the C(12)–H(12B) group of an ethanol molecule and the quinoline ring from the neighboring molecule [H···centroid 2.88 Å, C(12)···centroid 3.659(4) Å, C–H···centroid angle 134(2)°].

Additionally, the crystal packing is due to π–π stacking interactions involving quinoline rings of adjacent molecules. This stacking results in a Co···Co distance of 4.156 Å. The corresponding plane distances are 3.392 and 3.444 Å, with offsets of 0.874 and 0.844 Å, respectively, and these are slightly longer than those for typical aromatic–aromatic π-stacking interactions [25]. These H-bonds and π–π interactions result in the formation of a three-dimensional (3D) network (Fig. 3). The shortest metal–metal separation (Co···Co^{i}, i = $x + 1$, y, z and $x - 1$, y, z) is 5.839 Å. Further examination of the structure reveals weak intramolecular hydrogen bond contacts (Table 3).

3.2. Spectroscopic properties

The title compound shows in the IR spectrum strong carboxylate stretching frequencies ν_{as}(COO) and ν_{s}(COO) at 1626 and 1397 cm^{-1}, respectively, in the range character-

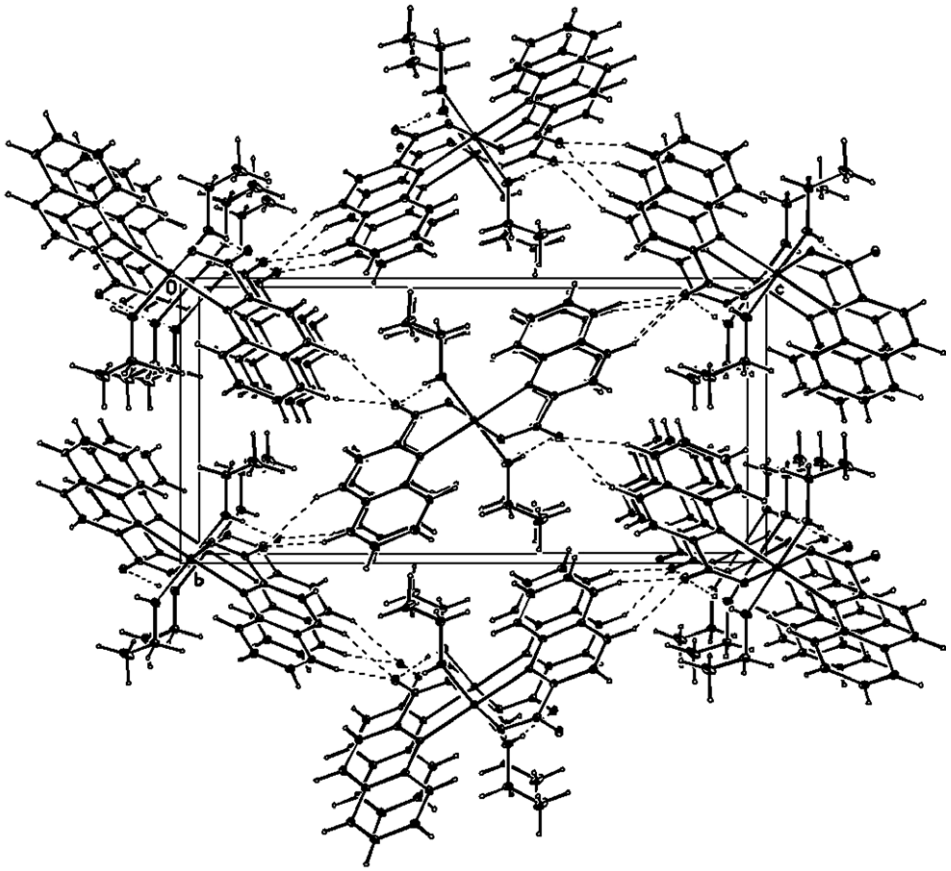


Fig. 3. Crystal packing of [Co(2-qic)$_2$(EtOH)$_2$] showing the 3D intermolecular H-bonding.

Table 3
Hydrogen-bonds and contacts for $[Co(2\text{-qca})_2(EtOH)_2]$ (Å, °)

D–H···A	d(D–H)	d(H···A)	d(D···A)	∠(DHA)
C(8)–H(8)···O(2)^{i}	0.95	2.23	3.097(2)	150.7
O(3)–H(9)···O(1)^{ii}	0.82(3)	1.85(3)	2.664(2)	174(3)
O(3)–H(9)···O(2)^{ii}	0.82(3)	2.70(3)	3.225(3)	124(2)
C(3)–H(3)···O(1)^{iii}	0.95	2.50	3.356(2)	149.8
C(5)–H(5)···O(1)^{iii}	0.95	2.59	3.420(3)	146.8
C(12)–H(12C)···O(2)	0.98	2.72	3.452(3)	131.5
C(12)–H(12A)···O(2)^{vi}	0.98	2.93	3.660	132.2

Symmetry transformations used to generate equivalent atoms: (i) $-x+1$, $-y$, $-z$; (ii) $x-1$, y, z; (iii) $-x+3/2$, $y+1/2$, $-z+1/2$; (iv) x, $y-1$, z.

istic of the carboxylate compounds. The observed $\Delta\nu$ separation value of 229 cm^{-1} is in the range expected for a monodentate carboxylate group [26,27].

The d–d spectrum shows bands (21 620, 18 700 and 8730 cm^{-1}) typical for an octahedral environment of a high-spin cobalt(II) ion, corresponding to the $^4T_{1g}(F) \rightarrow {}^4T_{2g}(F)$, $^4T_{1g}(F) \rightarrow {}^4A_{2g}$ and $^4T_{1g}(F) \rightarrow {}^4T_{1g}(P)$ transitions [28,29]. Asymmetric bands in the near-IR region show that the Co(II) ion is in an octahedral tetragonally distorted N_2O_4 environment. The calculated spectrochemical parameters D_q and B (940 and 950 cm^{-1}, respectively) were calculated by a well-known method [29]. The relatively high value of the ligand-field Racah parameter B might reflect the deviation from an octahedral geometry [28,29].

The EPR spectrum of a polycrystalline powder of the studied complex shows no lines at room temperature but does display a broad isotropic signal with $g = 4.08$ at 77 K, as expected for a high-spin Co(II) complex for which the electron spin-lattice relaxation time is very fast.

3.3. Magnetic properties

The magnetic behavior of the complex is depicted in Fig. 4 in the form $\chi_M T$ versus T (χ_M is the molar magnetic susceptibility of the cobalt(II) ion). The value of $\chi_M T$ at room temperature is 2.90 $cm^3\,mol^{-1}\,K$ ($\mu_{eff} = 4.82\ \mu_B$), which is larger than that calculated for a spin quartet ($\chi_M T = 1.87\ cm^3\,mol^{-1}\,K$, 3.87 μ_B, for $S = 3/2$ with $g = 2.0$), but it agrees with the values observed for octahedral cobalt(II) complexes with a significant first-order orbital contribution to the magnetic moment [30,31], typical of the $^4T_{1g}$ ground state.

The $\chi_M T$ plot (Fig. 4) gradually decreases with temperature and reaches a minimum value of 1.78 $cm^3\,K\,mol^{-1}$ ($\mu_{eff} = 3.77\ \mu_B$) at 1.8 K; therefore cobalt(II) remains totally in the high-spin state down to 1.8 K. The $\chi_M T$ values follow the Curie–Weiss law $\chi_M(T) = C/(T-\theta)$ from room temperature to 130 K with $C = 3.04\ cm^3\,K/mol$ and $\theta = -15.13$ K, where C and θ are the Curie and Weiss constants, respectively. The calculated [32] effective magnetic moment μ_{eff} per cobalt is 4.91 μ_B. This is close to the experimental value and to the values of 4.7 and 5.1 μ_B calculated for the medium and weak octahedral crystal fields, respectively [33].

The decrease of the $\chi_M T$ value is mainly due to zero-field splitting [34,35], but a steeper decreases is observed at lower temperatures. This is probably due to weak antiferromagnetic intermolecular interactions between the Co(II) ions.

With the assumption that the non-axial zero-field parameter E is negligible, the magnetic data for $[Co(2\text{-qic})_2(EtOH)_2]$ could be fitted very well to the appropriate axial spin Hamiltonian, where $S = 3/2$ [34,35]: $\widehat{H} = g\beta H \cdot S + D[S_z^2 - 1/3S(S+1)]$, and D is the axial ZFS parameter and g is a factor for the 3/2 quartet. The fitting results provide a typical parameter set of $|D| = 65.1\ cm^{-1}$, $g_{\parallel} = 2.14$ and $g_{\perp} = 2.58$ [36,37]. The plot of the best fit is shown in Fig. 4 as a solid line. The good fit ($R = 2.52 \times 10^{-4}$) does not reflect the need to include a rhombic (E) zero-field splitting term in the Hamiltonian.

The molar magnetization M of a powder sample of the studied complex was measured as a function of the applied magnetic field H at 2 K (Fig. 5). No differences were

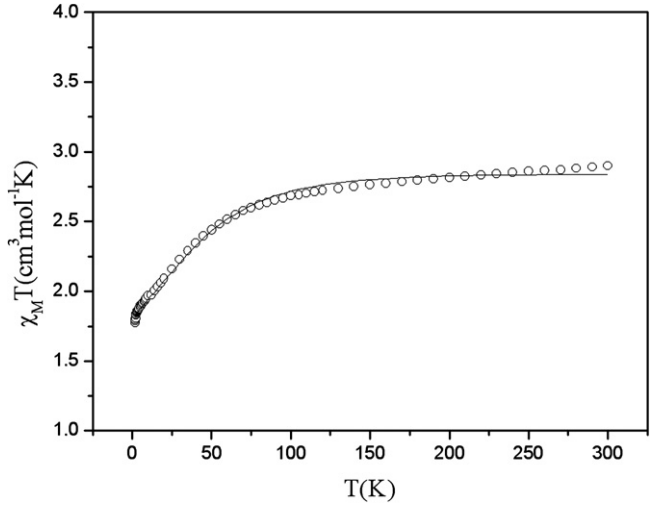


Fig. 4. Plot of $\chi_M T$ (○) vs. temperature for $[Co(2\text{-qic})_2(EtOH)_2]$. The solid line is calculated with the use of the spin Hamiltonian analysis described in the text.

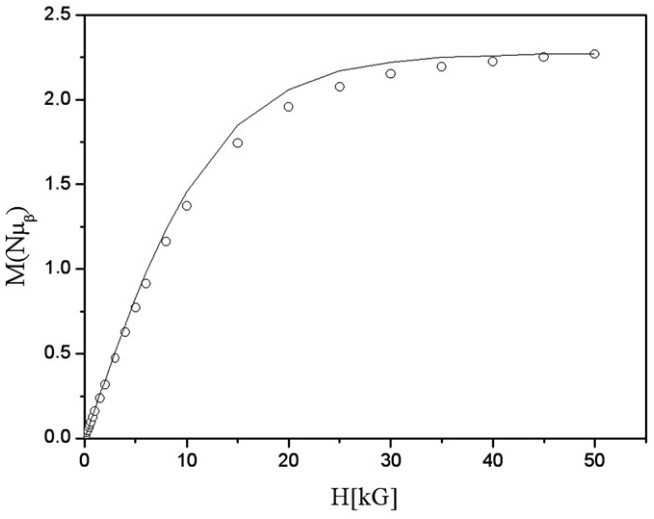


Fig. 5. Molar magnetization in $N\mu_\beta$ units of $[Co(2\text{-qic})_2(EtOH)_2]$ measured in 2 K as a function of magnetic field.

observed between the $M(H)$ curves measured with increasing or decreasing magnetic field strength.

Upon applying a magnetic field, the magnetization increases gradually. The value of $M_{sat} = 2.27\ N\mu_B$ was reached at 50 kG. The solid line (Fig. 5) represent the theoretical magnetization curves for a system in a ground state with an effective spin $S' = 1/2$ and effective g value equal to 4.58. The shape of the experimental points do not exactly follow the Brillouin formula for isolated Co(II) ions. At intermediate fields the experimental points are below the theoretical curve, indicating a weak antiferromagnetic interaction.

The intermolecular exchange does not affect the magnetic moment in the Curie–Weiss region, but it influences the very low-temperature magnetic behavior. Parameters C of 1.95 cm^3 K/mol and θ of −0.17 K were obtained from a fit to the Curie–Weiss law in the 1.8–7 K temperature region (Fig. 6) where $1/\chi_M = f(T)$ is linear (inset of Fig. 6). At low temperatures this small negative value of θ may suggest the existence of a very weak intermolecular antiferromagnetic exchange between the cobalt ions (within the crystal lattice) via the hydrogen bond system and stacking interactions in the crystal lattice.

In general, the effect of weak spin interactions on the magnetic susceptibility may be treated by the molecular field approximation. Therefore, in order to evaluate the interaction of the magnetic center of the three-dimensional network of the $[Co(2\text{-qca})_2(EtOH)_2]$ compound, a molecular exchange field model was used, Eqs. (1) and (2) [38]:

$$\chi_M = \frac{N\beta^2 g^2}{3kT} S(S+1) \tag{1}$$

$$\chi_M^{corr} = \frac{\chi_M}{1 - \frac{2zJ'}{N\beta^2 g^2}\chi_M} \tag{2}$$

where χ_M is the molar susceptibility of a paramagnetic center, χ_M^{corr} is the measured experimental susceptibility,

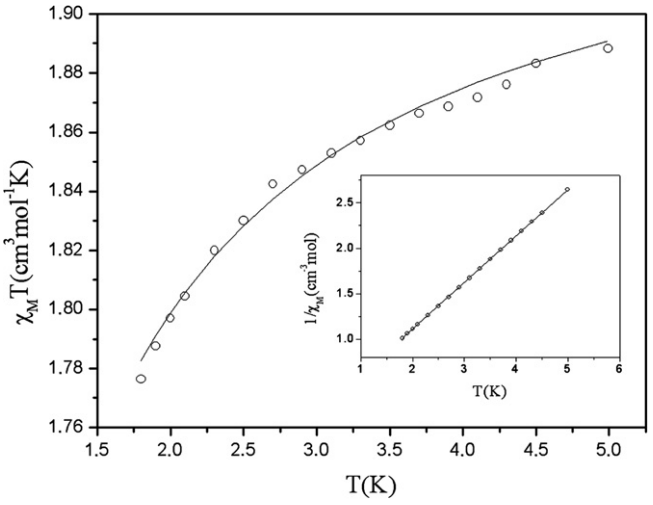


Fig. 6. Plot of $\chi_M T$ (o) vs. temperature in the $T < 5$ K. temperature region for $[Co(2\text{-qic})_2(EtOH)_2]$. The solid line is calculated with the use of the model described in the text using an effective spin $S' = 1/2$. The inset shows the fit to the Curie–Weiss law.

zJ' is the exchange between magnetic ions belonging to different molecules, z is the number of nearest neighbors and the other symbols have their usual meanings. Since the EPR transition occurs only within the ground Kramers doublet, the cobalt(II) system may be characterized by an effective spin of 1/2. Therefore, an attempt to describe the intermolecular exchange has been made in Eq. (2), using the effective $S' = 1/2$. The fitting procedure provides the following parameters: $zJ' = -0.25\ cm^{-1}$, $g = 4.57$ and $R = 1.33 \times 10^{-4}$. R is the agreement factor defined as $R = \sum_{i=1}^{n}(\chi_i^{exp} - \chi_i^{calc})^2/(\chi_i^{exp})^2$. The result is shown in Fig. 6. The effective g value is consistent with the value of 4.58 obtained with the theoretical magnetization. The small value of zJ obtained in the above approximations is compatible with the expected limit $|J| < 0.5\ cm^{-1}$ for an exchange interaction between the cobalt(II) ions with a Co···Co distance of 5.84 Å, transmitted through weak intermolecular non-covalent interactions [39].

3.4. Aspects of the synthesis

As mentioned earlier, the reaction of the (quinolin-2-ylmethyl)phosphonate ligand (2-qmpe) with $CoCl_2 \cdot 2H_2O$ performed in air in ethanol solution primarily leads to the formation of the green compound of the formula $[Co(2\text{-qmpe})_2Cl_2]$, containing the O-bonded 2-qmpe ligand as previously observed [9]. This compound is unstable in solution and slowly undergoes decomposition to a compound of the formula $[Co(2\text{-qca})_2(EtOH)_2]$, (2-qca = quinoline-2-carboxylate). The starting compound is stable in solution under an inert atmosphere (N_2). In a recent paper [10] we demonstrated that copper(II) ions promote and catalyze oxidative decomposition of the phosphonate ligands 2-pmpe and 2-qmpe according to the scheme:

$$R\text{–}CH_2\text{–}P(O)(OEt)_2 \rightarrow R\text{–}COOH + OH\text{–}P(OEt)_2.$$

Additionally, we showed that the other divalent transition metal ions do not exhibit this activity under comparable experimental conditions. The process of decomposition of the primary formed compounds of Cu(II) strongly depends on the bonding properties of the ligands. The copper(II) coordination compounds with monodentate coordinating phosphonate ligands undergo decomposition. However, with the N,O-bonded ligands 2-pmpe and 4-pmpe, chelating and bridging, respectively, these compounds are stable in solution in air. These complexes are probably stabilized by the didentate coordination of the ligands to the copper(II) ion.

The present results also indicate that the Co(II) ion, with participation of dioxygen, promotes conversion of the 2-qmpe ligand into quinoline-2-carboxylate (2-qca) according to the scheme presented in Fig. 1. All the remaining phosphonate Co(II) complexes studied by us so far [6–9], in which the ligands are N,O-bonded to the Co(II) ion, are stable in solution in air, supporting our earlier suppositions for Cu(II) compounds. Namely, the didentate coordination of the phosphonate ligands to Co(II) ions stabilized

these complexes, preventing oxidative cleavage of the starting organophosphonate ligands and the formation of the carboxylate ligands.

Our experiments do not provide us with clear information of the mechanism of these reactions with the participation of the Cu(II) and Co(II) ions. Oxidation reactions that involve copper-ion promoted activation of dioxygen are well known and have numerous catalytic and synthetic applications [40–43], although the mechanism is still poorly understood. The Co(II) complexes are also known as being active toward O_2 [44–46]. However, to the best of our knowledge, there is no example of a reaction between O_2 and cobalt(II) complexes in which ligand degradation occurs.

Within any mechanistic implication we suggest that the formation of the carboxylate compounds under strictly aerobic conditions involves cobalt ion promoted activation of dioxygen.

4. Conclusions

We have synthesized and characterized the Co(II) complex with quinoline-2-carboxylate (2-qca), which has been obtained in the decomposition reaction of the Co(II) compound with diethyl(quinolin-2-ylmethyl)phosphonate (2-qmpe). In this reaction oxidative cleavage of the starting ligand occurs. The final product of this process was the Co(II) compound with 2-qca. Detailed characterization of $[Co(2\text{-qca})_2(EtOH)_2]$ includes structural, spectroscopic and magnetic studies.

In our recent paper [10] we have reported on an oxidative reaction with the aid of the copper(II) ion in which oxidative cleavage of the C–P bond occurs. In this paper we have presented this reaction with the participation of the cobalt(II) ion. This reaction is an important issue in contemporary research of the interaction of molecular oxygen with copper(II) and cobalt(II) species and will be the subject of further studies.

Finally, it is worth highlighting that the chemical degradation of organic phosphonates is of fundamental importance. This is due to their role played in the environment as pesticides, herbicides and other products of economic activity, which are an ecological problem. The importance of the chemistry exploited during the chemical degradation is difficult to understate given its direct relevance to detoxification of herbicides, pesticides, insecticides and other agents containing the organophosphonate moiety.

Acknowledgement

This work was supported by the Polish Ministry of Science and Higher Education (Grant No. 1T09A 12430).

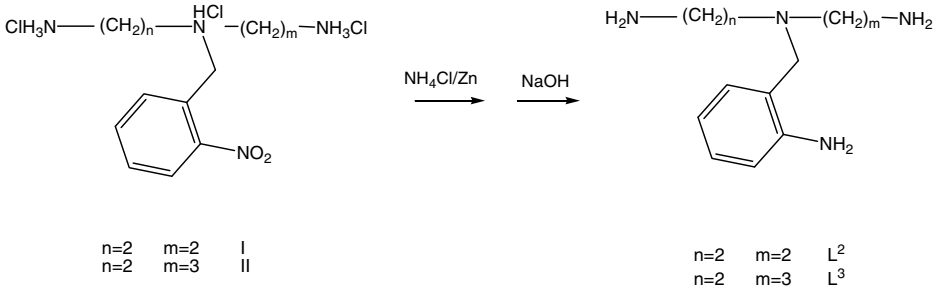
Appendix A. Supplementary material

CCDC 668270 contains the supplementary crystallographic data for this paper. These data can be obtained free of charge via http://www.ccdc.cam.ac.uk/conts/retrieving.html, or from the Cambridge Crystallographic Data Centre, 12 Union Road, Cambridge CB2 1EZ, UK; fax: (+44) 1223-336-033; or e-mail: deposit@ccdc.cam.ac.uk. Supplementary data associated with this article can be found, in the online version, at doi:10.1016/j.poly.2008.01.028.

References

[1] S.V. Kononova, M.A. Nesmeyanova, Biochemistry (Moscov) 67 (2002) 184.
[2] L.D. Freedman, G.O. Doak, Chem. Rev. 57 (1957) 479.
[3] T. Murai, C. Tomizawa, J. Environ. Sci. Health B 11 (1976) 185.
[4] L. Tušek-Božić, I. Matijašić, G. Bocelli, G. Calestani, A. Furlani, V. Starcia, A. Papaioannou, J. Chem. Soc., Dalton Trans. (1991) 195.
[5] L. Chęcińska, M. Małecka, K. Aranowska, J. Ochocki, Acta Crystallogr. C61 (2005) o4.
[6] J. Ochocki, K. Kostka, B. Żurowska, J. Mroziński, E. Gałdecka, Z. Gałdecki, J. Reedijk, J. Chem. Soc., Dalton Trans. (1992) 2955.
[7] J. Ochocki, B. Żurowska, J. Mroziński, H. Kooijman, A.L. Spek, J. Reedijk, Eur. J. Inorg. Chem. (1998) 169.
[8] B. Żurowska, J. Mroziński, Z. Ciunik, J. Ochocki, J. Mol. Struct. 791 (2006) 98.
[9] B. Żurowska, J. Mroziński, J. Ochocki, Mater. Sci. 25 (2007) 1063.
[10] B. Żurowska, J. Ochocki, Z. Ciunik, J. Mroziński, J. Reedijk, Inorg. Chim. Acta 357 (2004) 755.
[11] B. Żurowska, K. Ślepokura, J. Mroziński, Polyhedron 26 (2007) 3379.
[12] T. Katsuki, Coord. Chem. Rev. 140 (1995) 189.
[13] M. Schuster, S. Blechert, Angev. Chem., Int. Ed. Engl. 36 (1997) 2036.
[14] R.A. Gossage, L.A. van de Kuil, G. van Koten, Acc. Chem. Res. 31 (1998) 423.
[15] A.V. Yamamoto, J. Chem. Soc., Dalton Trans. (1999) 1027.
[16] S. Kobayashi, H. Ishitani, Chem. Rev. 99 (1999) 1069.
[17] B.A. Bovikin, A.M. Omel'Chenko, R.N. Sharonina, I.A. Zanina, Abstracts of Proceedings of 15th All-Union Chugaevskii Conference on the Chemistry of Complex Compounds, vol. 1, Ukraine, 1985, p. 229.
[18] E. König, Magnetic Properties of Coordination and Organometallic Transition Metal Compounds, Springer, Berlin, 1966.
[19] R.L. Carlin, Magnetochemistry, Springer, Heidelberg, 1986.
[20] G.M. Sheldrick, Acta Crystallogr. A46 (1990) 467.
[21] G.M. Sheldrick, SHELXL97, Program for Crystal Structure Refinement, University of Göttingen, 1997.
[22] A. Maslejova, S. Uhrinova, J. Mroziński, B. Żurowska, M.C. Munoz, M. Julve, Inorg. Chim. Acta 255 (1997) 343.
[23] H.M. Handler, Acta Crystallogr., Sect. C 42 (1986) 147.
[24] G.R. Desiraju, ACC. Chem. Res. 29 (1996) 441.
[25] Ch. Janiak, J. Chem. Soc., Dalton Trans. (2000) 3885.
[26] G.B. Deacon, R.J. Phillips, Coord. Chem. Rev. 33 (1980) 227.
[27] K. Nakamoto, Infrared in Raman Spectra of Inorganic and Coordination Compounds, 4th ed., Wiley, New York, 1986.
[28] A.B.P. Lever, Inorganic Electronic Spectroscopy, 2nd ed., Elsevier, Amsterdam, 1984.
[29] J. Reedijk, W.L. Driessen, W.L. Groeneveld, Recl. Trav. Chim. Pays Bas 88 (1969) 1095.
[30] F.E. Mabbs, D.J. Machin, Magnetism of Transition Metal Complexes, Chapman and Hall, London, 1973.
[31] B.N. Figgis, J. Lewis, Prog. Inorg. Chem. 6 (1964) 37.
[32] J.S. Smart, in: G.T. Rado, H. Shul (Eds.), Magnetism, vol. 3, Academic Press, New York, 1963, p. 63.
[33] B.N. Figgis, Nature 182 (1958) 1568.
[34] O. Kahn, Molecular Magnetism, VCH Publishers., New York, 1993.
[35] O. Kahn, J. Larionova, J.V. Yakhim, Chem. Eur. J. 5 (1999) 3443.

[36] H. Jancovics, M. Daskalakis, C.P. Raptopoulou, A. Terzis, V. Tanggoulis, J. Giapintzakis, T. Kiss, A. Salifoglou, Inorg. Chem. 41 (2002) 3366.
[37] M. Matzapetakis, M. Dakanali, C.P. Raptopoulou, V. Tangoulis, A. Terzis, N. Moon, J. Giapintzakis, J. Salifoglou, J. Biol. Inorg. Chem. 5 (2000) 469.
[38] J.S. Smart, Effective Field Theories of Magnetism, Saunders W.B. Comp., Philadelphia and London, 1966.
[39] A.C. Rizzi, C.D. Brondino, R. Calvo, R. Baggio, M.T. Garland, R.E. Rapp, Inorg. Chem. 42 (2003) 4409.
[40] P. Gamez, P.G. Aubel, W.L. Driessen, J. Reedijk, Chem. Soc. Rev. 30 (2001) 376.
[41] J.E. Bol, W.L. Driessen, R.Y.N. Ho, B. Maase, L. Que Jr., J. Reedijk, J. Angew. Chem., Int. Ed. Eng. (1997) 998.
[42] P.G. Aubel, S.S. Khokhar, W.L. Driessen, G. Challa, J. Reedijk, J. Inorg. Biochem. 86 (2001) 229.
[43] N. Kitajima, Y. Moro-oka, Chem. Rev. 94 (1994) 737.
[44] P.D.W. Boyd, M. Gerloch, G.M. Sheldrick, J. Chem. Soc., Dalton Trans. (1974) 1097.
[45] Z. Xu, L.K. Thompson, D.O. Miller, H.J. Clase, J.A.K. Howard, A.E. Goeta, Inorg. Chem. 37 (1998) 3620.
[46] W.J. Stratton, D.H. Busch, J. Am. Chem. Soc. 80 (1958) 1286.



Scheme 1.

2-[2-(2-formylphenoxy)ethoxy]benzaldehyde in the presence of Mn(II) and/or Cd(II) ions.

2. Experimental

2.1. Starting materials

All solvents were of reagent grade quality and were purchased commercially. *N*1-(2-Nitrobenzyl)-*N*1-(2-aminoethyl)-ethane-1,2-diaminetrishydrochloride (I), *N*1-(2-nitrobenzyl)-*N*1-(2-aminoethyl)propane-1,3-diaminetrishydrochloride (II) and 2-[2-(2-formylphenoxy)ethoxy]benzaldehyde were synthesized according to the literature method [14,15].

2.2. Instrumentation

NMR spectra were obtained using a Bruker A V 300 MHz spectrometer. Infrared spectra were recorded in KBr pellets using a BIO-RAD FTS-40A spectrophotometer (4000–400 cm^{-1}).

2.3. X-ray crystal structure determination

Vapor diffusion of diethyl ether into a solution of $[MnL^4(CH_3OH)](ClO_4)_2$ and $[CdL^5(H_2O)](NO_3)_2$ in MeOH afforded pale yellow crystalline needles. X-ray data for $[MnL^4(CH_3OH)](ClO_4)_2$ were measured on a STOE IPDS-II two circle diffractometer at 293 °C, using graphite monochromated Mo Kα X-ray radiation ($\lambda = 0.7107$ nm) for $[MnL^4(CH_3OH)](ClO_4)_2$. X-ray data for $[CdL^5(H_2O)](NO_3)_2$ were also measured on a Bruker SMART-1000 diffractometer. Other crystallographic data are summarized in Table 1.

A full minimization of the structure for each macrocyclic complex was performed at the ab initio HF level of theory using gradient techniques with the GAUSSIAN-98 set of programs [16], on a Pentium-PC computer with a 3000 MHz processor. The effective core potential (ECP) standard basis set LanL2DZ [17] was utilized for the cadmium and manganese metal ions. The full-electron standard basis set 3-21G* or 6-31G* [18] were used for all other atoms. A starting semi-empirical structure for the ab initio 3-21G* calculations was obtained using the HYPERCHEM 5.02 program [19]. The resulting structures of the 3-21G* calculations were then used for the 6-31G* basis set.

2.4. Synthesis

2.4.1. Ligand synthesis

2.4.1.1. 2-((Bis(2-aminoethyl)amino)methyl)benzenamine (L^2). A mixture of *N*1-(2-nitrobenzyl)-*N*1-(2-aminoethyl)ethane-1,2-diaminetrishydrochloride (I) (3.47 g, 10 mmol), ammonium chloride (4 g) and water (2 ml) in 100 ml of ethanol was heated to boiling and 3 g of zinc dust was added. When the solution was pale green it was filtered. The volume was then reduced to 20 ml by rotary evaporation. Excess water was added to the mixture and the pH was adjusted to 12 with potassium hydroxide. The solution was extracted with chloroform (×3). The chloroform extracts were combined and dried over anhydrous sodium sulfate. The dried extracts were then reduced to a small volume on a rotary evaporator. The product was obtained as an oil. Yield (1.3 g, 62%). *Anal.* Calc. for ($C_{11}H_{20}N_4 + 1/10CHCl_3$): C, 60.53; H, 9.20; N, 25.44. Found: C, 60.61; H, 9.23; N, 25.31%. IR (Nujol, cm^{-1}) 3360, 3380 $\nu(NH_2)$, 3082 $\nu(CH)$; ^1H NMR δ_H ($CDCl_3$, ppm) 2.59 (t, 4H), 2.75 (t, 4H), 3.08 (NH_2, 6H, b), 3.56 (s, 2H), 6.62 (m, Ph, 2H), 6.91 (m, Ph, 2H); ^{13}C NMR δ_C ($CDCl_3$, ppm) 39.95, 58.81, 59.87,115.11, 116.30, 123.41, 129.90, 131.27, 147.47.

2.4.1.2. 2-(((2-Aminoethyl)(3-aminopropyl)amino)methyl) benzenamine (L^3). The ligand (L^3) can be readily prepared by the above procedure except using *N*1-(2-nitrobenzyl)-*N*1-(2-aminoethyl)propane-1,3-diaminetrishydrochloride (II) (3.61 g, 10 mmol) instead of (I). Yield (1.4 g, 63%) *Anal.* Calc. for ($C_{12}H_{22}N_4 + 1/11CHCl_3$): C, 62.28; H, 9.55; N, 24.03. Found: C, 62.22; H, 9.39; N, 24.13%. IR (KBr, cm^{-1}) 3361 and 3385 (NH_2), 3070 (CH); ^1H NMR δ_H ($CDCl_3$, ppm) 1.52 (m, 2H), 2.19, 2.40, 2.60 (m, 14H), 3.79 (s, 2H), 7.25–7.88 (b, 4H); ^{13}C NMR δ_C ($CDCl_3$, ppm) 29.49, 38.97, 39.52, 51.10, 56.22, 58.16, 114.84, 116.82, 122.35, 127.78, 130.04, 146.32.

2.5. Preparation of the complexes

2.5.1. General procedure

All the complexes were readily prepared by template condensation. The required amine (0.5 mmol) in methanol (10 ml) was added dropwise to a mixture of the appropriate manganese (II) or cadmium (II) salts (0.5 mmol) in methanol

Table 1
Crystal data and structure refinement for $[MnL^4(CH_3OH)](ClO_4)_2$ (**1**) and $[CdL^5(H_2O)](NO_3)_2$ (**4**)

Compound	$[CdL^5(H_2O)](NO_3)_2$ (**4**)	$[MnL^4(CH_3OH)](ClO_4)_2$ (**1**)
Empirical formula	$C_{28}H_{34}CdN_6O_9$	$C_{28}H_{34}Cl_2Mn_1N_4O_{11}$
Formula weight	711.01	728.43
Temperature (K)	150(2)	293(2)
Wavelength (Å)	0.71073	0.71073
Crystal system	monoclinic	monoclinic
Space group	$P2_1/c$	$P21/n$
Unit cell dimensions		
a (Å)	18.182(3)	10.029(2)
b (Å)	8.8905(12)	10.216(2)
c (Å)	19.373(3)	31.391(6)
α (°)	90	90
β (°)	114.009(2)	94.19(3)
γ (°)	90	90
Volume (Å^3)	2860.8(7)	3207.6(11)
Z	4	4
D_{calc} (Mg/m^{-3})	1.651	1.508
Absorption coefficient (mm^{-1})	0.830	0.643
$F(000)$	1456	1508
Crystal size (mm)	0.23 × 0.16 × 0.12	0.25 × 0.15 × 0.06
θ Range for data collection (°)	1.23–25.00	2.09–26.91
Limiting indices	$-21 \leqslant h \leqslant 21$, $-10 \leqslant k \leqslant 10$, $-23 \leqslant l \leqslant 23$	$-12 \leqslant h \leqslant 12$, $-12 \leqslant k \leqslant 12$, $-39 \leqslant l \leqslant 39$
Reflections collected/ unique (R_{int})	26722/5040 (0.1159)	29648/6835 (0.1068)
Completeness to $\theta = 26.91$ (%)	100.0	98.7
Absorption correction	semi-empirical from equivalents	numerical
Maximum and minimum transmission	0.9070 and 0.8321	0.970 and 0.880
Refinement method	full-matrix least-squares on F^2	full-matrix least-squares on F^2
Data/restraints/parameters	5040/238/416	6835/0/428
Goodness-of-fit on F^2	1.053	1.165
Final R indices [$I > 2\sigma(I)$]	$R_1 = 0.0629$, $wR_2 = 0.1375$	$R_1 = 0.0836$, $wR_2 = 0.2071$
R indices (all data)	$R_1 = 0.0964$, $wR_2 = 0.1569$	$R_1 = 0.1120$, $wR_2 = 0.2232$
Largest difference in peak and hole (e Å^{-3})	1.574 and −1.509	1.209 and −0.453

and 2-[2-(2-formylphenoxy)ethoxy]benzaldehyde (0.135 g, 0.5 mmol) in methanol (60 ml), with stirring. The reaction was carried out for 12 h at reflux (Scheme 2). The solution volume was then reduced to 10 ml by rotory evaporation and a yellow precipitate formed on addition of a small amount of diethyl ether. This was filtered off, washed with ether and dried in vacuo.

2.5.2. $[MnL^4(CH_3OH)](ClO_4)_2$ (**1**)

Yield (0.24 g, 65%). *Anal.* Calc. for $C_{28}H_{34}Cl_2MnN_4O_{11}$: C, 46.17; H, 4.70; N, 7.63. Found: C, 46.21; H, 4.71; N, 7.59%. IR (KBr, cm^{-1}) 3420 (OH, CH_3OH), 3262 and 3306 (NH_2), 1644 (C=N), 1095 and 622 (ClO_4^-). UV–Vis [λ (nm), ε (M^{-1} cm^{-1}), (acetonitrile)]: 257(149360), 303(35980).

2.5.3. $[MnL^5(CH_3OH)](ClO_4)_2$ (**2**)

Yield (0.21 g, 56%). *Anal.* Calc. for $C_{29}H_{36}Cl_2MnN_4O_{11}$: C, 46.91; H, 4.83; N, 7.55. Found: C, 46.89; H, 4.90; N, 7.51%. IR (KBr, cm^{-1}) 3430 (OH, CH_3OH), 3264 and 3312 (NH_2), 1644 (C=N), 1096 and 622 (ClO_4^-). UV–Vis [λ (nm), ε (M^{-1} cm^{-1}), (acetonitrile)]: 257(156260), 302(42420).

2.5.4. $[CdL^4(H_2O)](NO_3)_2$ (**3**)

Yield (0.19 g, 56%). *Anal.* Calc. for $C_{27}H_{32}CdN_6O_9$: C, 46.53; H, 4.63; N, 12.06. Found: C, 46.46; H, 4.51; N, 12.15%. IR (KBr, cm^{-1}) 3267 and 3317 (NH_2), 3422 and 3473 (H_2O), 1645 (C=N), 1601. UV–Vis [λ (nm), ε (M^{-1} cm^{-1}), (acetonitrile)]: 257(120320), 307(2772).

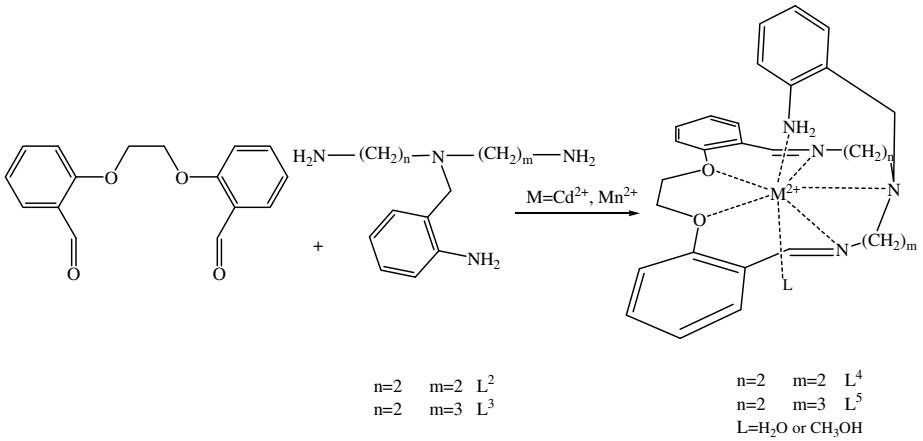
2.5.5. $[CdL^5(H_2O)](NO_3)_2$ (**4**)

Yield (0.2 g, 56%). *Anal.* Calc. for $C_{28}H_{34}CdN_6O_9$: C, 47.30; H, 4.82; N, 11.82. Found: C, 47.76; H, 4.91; N, 11.85%. IR (KBr, cm^{-1}) 3148 and 3226 (NH), 3430 and 3479 (H_2O), 1641 (C=N), 1603. UV–Vis [λ (nm), ε (M^{-1} cm^{-1}), (acetonitrile)]: 257(156260), 302(42420).

3. Results and discussion

3.1. Synthesis and characterization

Template condensation of 2-[2-(2-formylphenoxy)ethoxy]benzaldehyde with (L^2) and (L^3) in the presence of a Mn(II) or Cd(II) template in refluxing methanol cleanly yields the target macrocyclic Schiff base complexes



Scheme 2.

$[MnL^4(CH_3OH)](ClO_4)_2$, $[MnL^5(CH_3OH)](ClO_4)_2$, $[CdL^4(H_2O)](NO_3)_2$ and $[CdL^5(H_2O)](NO_3)_2$ (Scheme 1). All the complexes are air-stable solids, moderately soluble in CH_3CN and DMSO and have similar IR spectra, and the data are consistent with the presence of imine bonds. Each complex exhibits the (C=N) mode at *ca.* 1642–1644 cm^{-1} and the (NH_2) mode at *ca.* 3228–3317 cm^{-1}, while no bands attributable to C=O are detected. All the manganese complexes exhibit a broad medium-intensity band at 3428–3445 cm^{-1} assigned to the (OH) group of MeOH, a very strong band at ≈1100 cm^{-1} and a medium band at ≈625 cm^{-1} due to the uncoordinated perchlorate ion.

The cadmium complexes exhibit a broad medium-intensity doublet band at ≈3422 and 3577 cm^{-1} assigned to the H_2O group. The NMR studies of the Cd(II) complexes also provide strong evidence for the formation of the macrocyclic complexes.

3.2. X-ray crystal structures

The molecular structures of $[MnL^4(CH_3OH)](ClO_4)_2$ and $[CdL^5(H_2O)](NO_3)_2$ are shown in Fig. 1, together with the atomic numbering scheme. Selected bond lengths and angles are given in Table 2. The ligands are 17-membered and 18-membered [1+1] Schiff base macrocycles with a 2-aminobenzyl pendant-arm. The coordination sphere around the Mn(II) and Cd(II) ions can be described as slightly distorted pentagonal bipyramidal with the metal ion, three nitrogen and two oxygen atoms lying in an approximately pentagonal plane and a 2-aminobenzyl nitrogen atom situated in the axial position. The coordinated solvent oxygen atom is situated in the axial position in both $[MnL^4(CH_3OH)](ClO_4)_2$ and $[CdL^5(H_2O)](NO_3)_2$, with the *trans* angles O(3)–Mn(1)–N(1) [172.08(19)°] and O(3)–Cd(1)–N(4) [168.3(2)°] close to linearity. The X-ray crystal structure of **1** shows that the macrocyclic ring is not strictly planar and the Mn–N(3) and Mn–O(2) bond lengths are significantly longer than their related Mn–N(4) and Mn–O(1) bond lengths. This suggests that the binding cavity presented by the 17-membered macrocycle, L^4, is slightly larger than the optimum amount for Mn(II).

The sum of the angles subtended by the donor atoms at Mn is 364.89°, the plane containing N(3), N(2), N(4), O(2) and O(1) has a r.m.s. value of 0.2839 Å and the metal atom

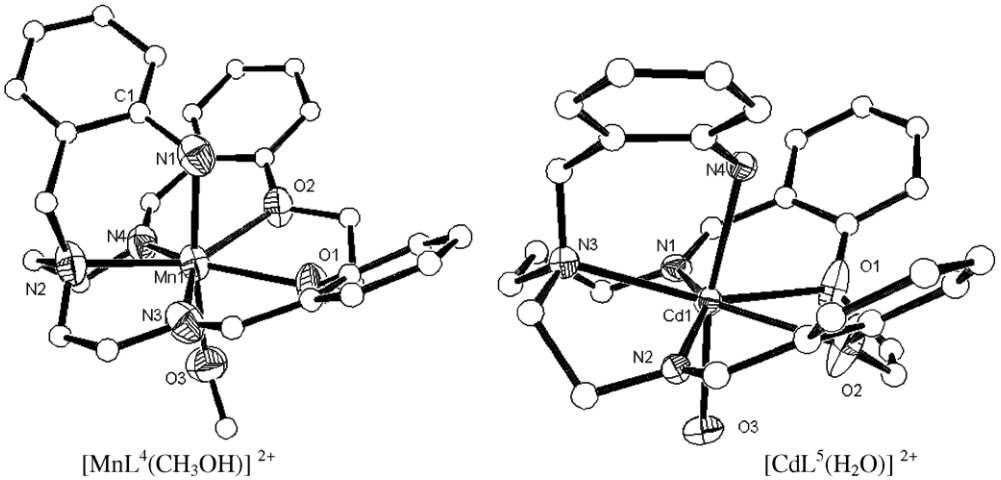


Fig. 1. Structures of the cations $[MnL^4(CH_3OH)]^{2+}$ and $[CdL^5(H_2O)]^{2+}$.

Table 2
Selected bond lengths (Å) and angles (°) for $[MnL^4(CH_3OH)]^{2+}$ (**1**), $[MnL^5(CH_3OH)]^{2+}$ (**2**), $[CdL^4(H_2O)]^{2+}$ (**3**) and $[CdL^5(H_2O)]^{2+}$ (**4**)

$[MnL_5(CH_3OH)]^{2+}$ (**1**) (experimental)		**1** HF/3-21G*	**1** HF/6-31G*	**2** HF/3-21G*	**2** HF/6-31G*
Bond length (Å)					
Mn(1)–N(1)	2.239(5)	2.299	2.347	2.289	2.272
Mn(1)–N(2)	2.365(4)	2.362	2.409	2.424	2.468
Mn(1)–N(3)	2.261(5)	2.34	2.328	2.341	2.336
Mn(1)–N(4)	2.230(4)	2.273	2.287	2.294	2.286
Mn(1)–O(1)	2.345(4)	2.299	2.365	2.31	2.393
Mn(1)–O(2)	2.528(4)	2.461	2.573	2.705	2.696
Mn(1)–O(3)	2.197(5)	2.237	2.364	2.224	2.277
Bond angle (°)					
O(3)–Mn(1)–N(1)	172.08(19)	172.06	172.91	164.1	165.66
O(3)–Mn(1)–N(2)	101.17(17)	100.39	102.00	108.66	108.93
O(3)–Mn(1)–N(3)	87.33(19)	87.73	86.51	87.85	86.91
O(3)–Mn(1)–N(4)	81.00(18)	80.83	79.45	78.77	79.52
O(3)–Mn(1)–O(1)	80.87(16)	83.07	82.63	86.76	81.86
O(3)–Mn(1)–O(2)	93.80(16)	92.89	88.98	85.45	85.45
N(1)–Mn(1)–N(3)	90.2(2)	90.37	91.60	99.05	94.26
N(1)–Mn(1)–O(1)	91.22(17)	88.99	90.28	81.48	84.82
N(4)–Mn(1)–N(1)	105.23(19)	105.16	106.06	101.48	105.98
N(1)–Mn(1)–N(2)	85.39(18)	86.37	83.93	86.59	85.38
N(1)–Mn(1)–O(2)	83.57(17)	83.93	88.35	79.79	84.05
O(1)–Mn(1)–O(2)	67.82(12)	68.42	67.02	63.77	64.52
N(4)–Mn(1)–O(2)	73.03(14)	74.09	73.72	70.31	70.51
N(4)–Mn(1)–N(2)	74.45(16)	74.81	74.92	75.65	74.73
N(3)–Mn(1)–N(2)	74.61(17)	72.42	72.93	82.28	82.64
N(3)–Mn(1)–O(1)	75.02(15)	74.39	75.35	73.61	73.01
$[CdL_6(H_2O)]^{2+}$ (**5**) (experimental)		**3** HF/3-21G*	**3** HF/6-31G*	**4** HF/3-21G*	**4** HF/6-31G*
Bond length (Å)					
Cd(1)–N(4)	2.333(6)	2.381	2.404	2.373	2.389
Cd(1)–N(3)	2.465(6)	2.399	2.474	2.451	2.571
Cd(1)–N(2)	2.310(6)	2.316	2.349	2.338	2.362
Cd(1)–N(1)	2.329(6)	2.407	2.446	2.417	2.474
Cd(1)–O(2)	2.574(6)	2.476	2.397	2.645	2.509
Cd(1)–O(1)	2.577(6)	2.359	2.325	2.374	2.338
Cd(1)–O(3)	2.311(5)	2.371	2.348	2.355	2.329
Bond angle (°)					
O(3)–Cd(1)–N(4)	168.3(2)	169.3	165.93	166.58	166.42
O(3)–Cd(1)–N(3)	106.5(2)	98.07	98.02	106.47	105.05
N(2)–Cd(1)–O(3)	82.22(19)	82.56	82.28	79.41	80.81
O(3)–Cd(1)–N(1)	85.2(2)	81.64	80.72	83.17	81.74
O(3)–Cd(1)–O(2)	86.0(2)	93.73	94.37	87.17	90.33
O(3)–Cd(1)–O(1)	86.2(2)	79.49	79.9	84.28	83.29
N(2)–Cd(1)–N(4)	103.6(2)	108.02	111.2	106.02	112.24
N(4)–Cd(1)–O(2)	86.4(2)	87.83	93.11	83.17	90.93
N(1)–Cd(1)–N(4)	93.8(2)	90.63	86.29	97.38	89.29
N(4)–Cd(1)–N(3)	85.1(2)	85.51	82.77	86.87	82.37
N(4)–Cd(1)–O(1)	82.4(2)	91.24	91.3	83.21	84.23
O(2)–Cd(1)–O(1)	64.17(18)	68.99	71.1	65.04	68.41
N(1)–Cd(1)–O(1)	71.2(2)	73.27	73.65	71.47	71.69
N(1)–Cd(1)–N(3)	85.7(2)	72.32	71.25	82.08	80.87
N(2)–Cd(1)–N(3)	73.4(2)	75.07	72.95	75.44	72.39
N(2)–Cd(1)–O(2)	69.79(19)	74.09	75.14	71.05	73.16

is close to co-planarity, being only 0.034 Å out of this plane. The r.m.s. value of the plane of the aromatic carbon ring of the pendant arm is 0.0162 Å and among them the C_1 carbon atom has the maximum displacement. The angle between the plane containing the aromatic ring of the pendant arm and that of the macrocyclic ring containing N(3), N(2), N(4), O(2) and O(1) is 143.92°. The r.m.s. values of the aromatic rings within the macrocyclic framework are 0.0145 and 0.0067 Å and the angle between these rings is 137.58°.

The structure **4** also shows that the macrocyclic ring is not strictly planar and the Cd–N(1) and Cd–O(1) bond lengths are significantly longer than the Cd–N(2) and Cd–O(2) bond lengths, respectively. This suggests that

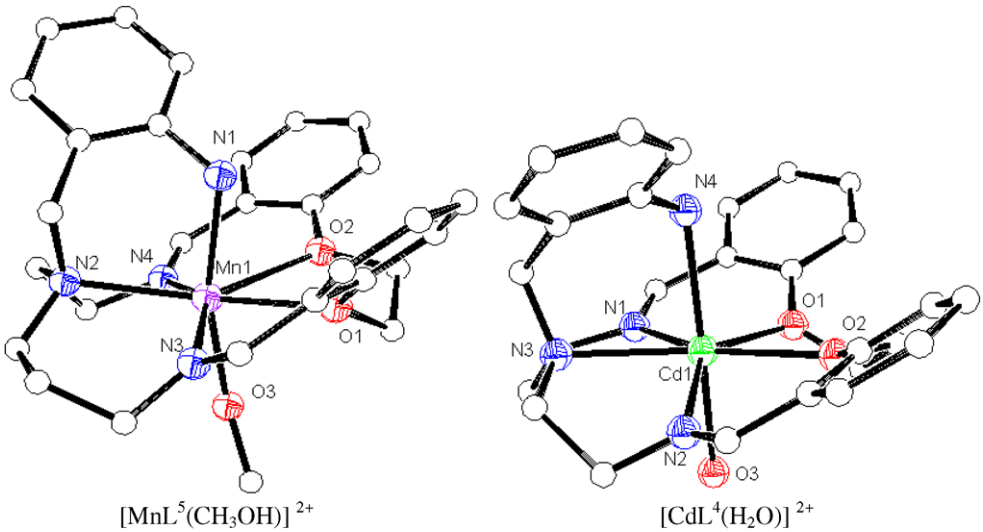


Fig. 2. The ab initio optimized structures of the cations $[MnL^5(CH_3OH)]^{2+}$ and $[CdL^4(H_2O)]^{2+}$.

Table 3
^1H NMR and ^{13}C NMR{^1H} spectral assignments for $[CdL^4]^{2+}$ and $[CdL^5]^{2+}$ recorded in DMSO-d_6

Hydrogen atom	δ_H (ppm)	Carbon atom	δ_C (ppm)
$[CdL^5]^{2+}$			
Haα, Haβ (4H)	4.44	Ca (2C)	67.52
Hcα, Hcβ (2H)	6.00–7.86	Cj (2C)	54.69
Hdα, Hdβ (2H)		Ci (2C)	60.27
Heα, Heβ (2H)		Ck (1C)	69.09
Hfα, Hfβ (2H)		Ch	157.35
Hn (1H)		Cb(2C), Cg(2C)	125.01,157.35, 130.33, 134.62
Ho (1H)		Cl(1C), Cm(1C)	
Hp (1H)		Cc(2C), Cd(2C)	114.23, 115.00, 120.23, 123.17, 126.90, 132.54, 137.37, 148.22
Hq (1H)		Ce(2C), Cf(2C)	
Hiα, Hiβ (4H)	3.54	Cn(1C), Co(1C)	
Hjα, Hjβ (4H)	2.65	Cp(1C), Cq(1C)	
Hkα, Hkβ (2H)	4.70, 5.22		
H_2O	5.05		
NH_2	3.54		
$[CdL^6]^{2+}$			
Ha, Ha	4.42	Ci(1C)	59.52
Hj (2H)	1.69	Cj(1C)	28.21
Hk (2H)	2.34	Ck(1C)	51.13
Hi (2H)	3.4	Cs(1C)	55.21
hs (2H)	2.67	Ct(1C)	58.58
Ht (2H)	3.47	Cl(1C)	69.86
Hlα, Hlβ (2H)	4.41, 5.02	Chα, hβ(2C)	156.8
Hv, h (2H)	8.69	Cv(1C)	157.95
Hc, d, e, f (4H)	6.58–7.79	Ca (1C)	67.31
Ho, p, q, r (4H)		Ca (1C)	67.55
Hw, x, y, z (4H)			113.90, 114.31, 115.21, 116.47, 121.63, 123,96, 124.89, 125.12, 126.92, 12710, 128.23, 130.43, 132.49,
NH_2	3.51	Cb,b*, g, u (4C)	147.97,
H_20	5.02	Cm, n (2C)	
		Cc, d, e, f (4C)	
		Co, p, q, r (4C)	
		Cw, x, y, z (4C)	

the binding cavity presented by the 18-membered macrcocyle, L^5, is slightly larger than the optimum amount for Cd(II).

The sum of the angles subtended by the donor atoms at Cd is 364.24° and the plane containing N(2), N(3), N(1), O(1) and O(2) atoms has a r.m.s. value of 0.2761 Å. The 2-aminobenzyl pendant arm in both complexes is orientated on the same side of the macrocyclic plane so that steric hindrance is small. While the L^4 and L^5 macrocycles in the Mn(II) and Cd(II) complexes are 17- and 18-membered

rings, respectively, their r.m.s. values are almost the same due to the larger size of Cd(II).

3.3. Ab initio modelling studies

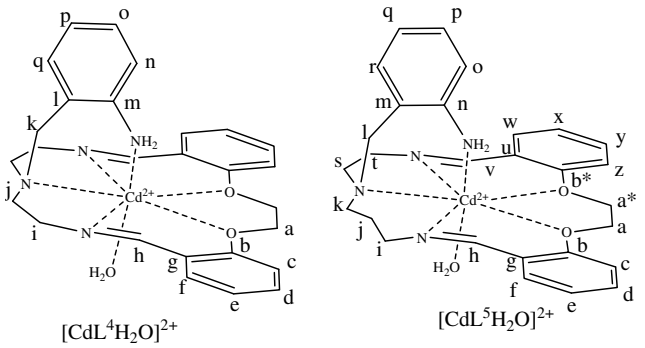
We assumed that the same mode of [1+1] cyclization as found for $[CdL^5(H_2O)]^{2+}$ had occurred with other cadmium complexes, due to the similarity of their IR, NMR spectra and microanalyses, and so undertook a full geometry optimization at the HF/3-21G* and HF/6-31G* levels of theory, using the LanL2DZ basis set for cadmium. We applied such an assumption for the manganese complexes. The resulting structural diagrams are shown in Fig. 2 and corresponding selected calculated bond distances and angles are shown in Table 2 along with the corresponding values obtained for $[CdL^5(H_2O)]^{2+}$ and $[MnL^4(CH_3OH)]^{2+}$. As can be seen, the results of the 3-21G* calculations for both the $[CdL^5(H_2O)]^{2+}$ and $[MnL^4(CH_3OH)]^{2+}$ complexes are slightly closer to the experimental data than those of the 6-31G* calculations. There are good agreements between the calculated and observed distances. It is thus the results of these calculations that are considered further.

The 3-21G* calculated r.m.s. values of the planes containing N(3), N(2), N(4), O(2) and O(1) in complexes **1** and **2** are 0.2616 and 0.3149 Å, respectively. The similar r.m.s. values of the planes containing N(1), N(2), N(3), O(1) and O(2) in complexes **4** and **5** are 0.2670 and 0.3273 Å, respectively. The sum of the bond lengths subtended by the donor atoms at Mn in **1** and **2** are 16.268 and 16.59 Å, respectively, and those at Cd in **3** and **4** are 16.609 and 16.953, respectively, and these show that the L^4 macrocycle has a suitable cavity in comparison with the other macrocycle, and on the other hand the cadmium ion is more appropriate than the manganese ion for the L^4 macrocycle.

3.4. NMR studies

The ^1H as well as $^{13}C\{1H\}$ NMR data for $[CdL^n]^{2+}$ ($n = 4$ and 5) dissolved in DMSO-d_6 are shown in Table 3, which uses the lettering scheme shown in Scheme 3. The ^1H and ^{13}C signals were assigned using one- and two-dimensional ^1H–^1H COSY, ^1H–^{13}C HMQC and DEPT spectra. The ^{13}C NMR spectrum of $[CdL^4]^{2+}$ shows seventeen carbons as expected. The $[CdL^5]^{2+}$ complex, in the region corresponding to the signals of aliphatic carbons (28.21–67.55 ppm) shows eight peaks, indicating all aliphatic methylene carbons are inequivalent. In the region corresponding to the signals of the aromatic ring carbons (113.90–1147.97 ppm) fourteen peaks instead of eighteen expected peaks are observed, due to the high similarity of the head unit and low resolution of the instrument.

In each complex, two signals corresponding to the methylene protons of 2-aminobenzyl are observed and these show that the protons are inequivalent, due to the bend orientation of the 2-aminobenzyl group in the complexes. The ^1H NMR spectra of the complexes show a signal at *ca.* 5.02 ppm, corresponding to coordinated H_2O. Unfortunately, since the protons do not show scalar-coupling, we were not able to assign explicitly the coupling constants.



Scheme 3.

4. Conclusions

Cd(II) and Mn(II) ions are effective as templates for the Schiff base condensation of 2-[2-(2-formylphenoxy)ethoxy]benzaldehyde and two tetraamine tripodal ligands (L^2 and L^3), resulting in the formation of macrocyclic complexes having a pendant arm (2-aminobenzyl) based on the X-membered N_3O_2 rings (X = 17 and 18).

Acknowledgements

We are grateful to the Faculty of chemistry of Bu-Ali Sina Universities, Arak University, Shahid Beheshti University and the Ministry of Science Research and Technology for financial support. The authors thank Prof. Michael D. Ward (Department of Chemistry, University of Sheffield, Sheffield S3 7HF, UK) for his invaluable support in one of the X-ray experiments.

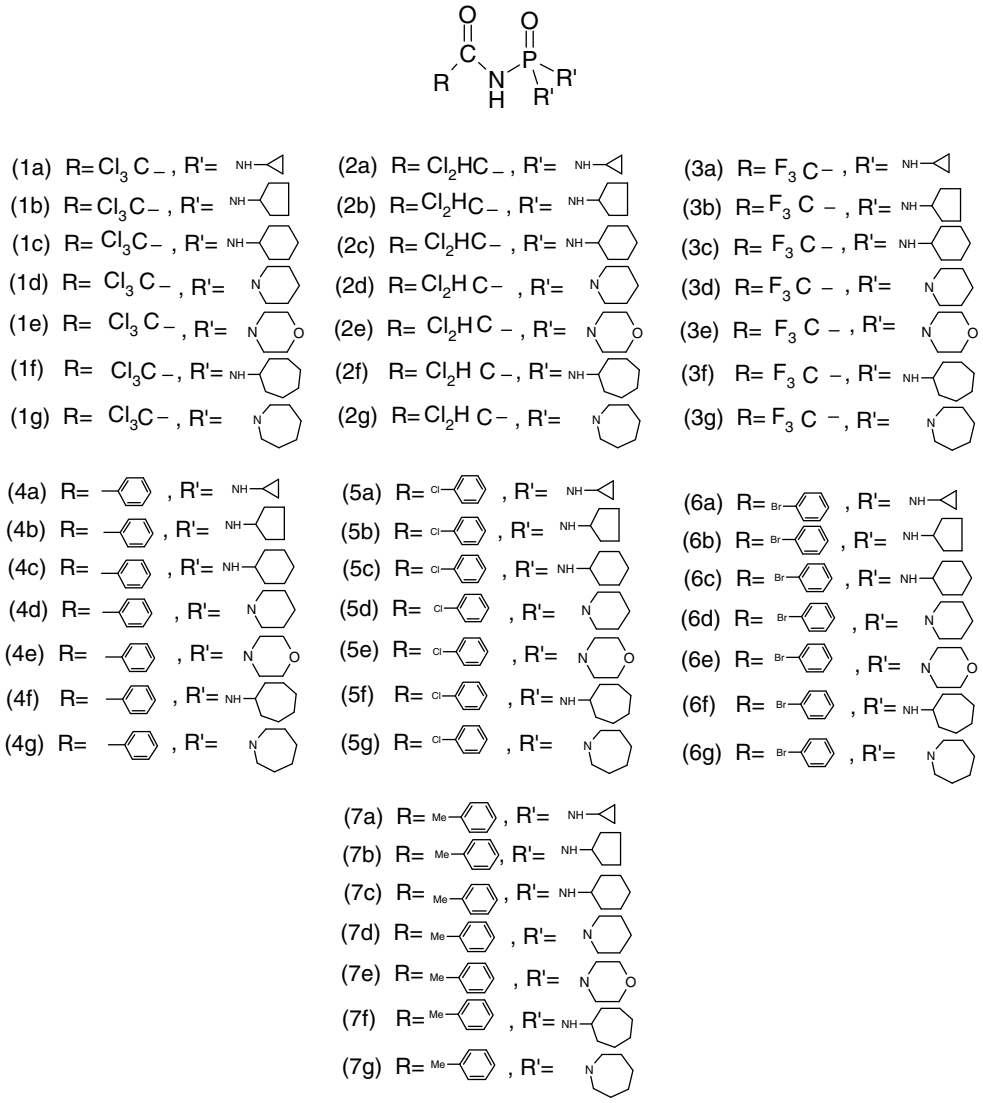
Appendix A. Supplementary data

CCDC 649841 and 663127 contain the supplementary crystallographic data for this paper. These data can be obtained free of charge via http://www.ccdc.cam.ac.uk/conts/retrieving.html, or from the Cambridge Crystallographic Data Centre, 12 Union Road, Cambridge CB2 1EZ, UK; fax: (+44) 1223-336-033; or e-mail: deposit@ccdc.cam.ac.uk. Supplementary data associated with this article can be found, in the online version, at doi:10.1016/j.poly.2008.01.036.

References

[1] P.V. Bernhardt, G.A. Lawrence, Coord. Chem. Rev. 104 (1990) 297.
[2] T.A. Kaden, Pure Appl. Chem. 65 (1993) 1477.
[3] K.P. Wainwright, Coord. Chem. Rev. 166 (1997) 35.

[4] T. Koike, T. Watanabe, S. Aoke, E. Kimura, M. Shiro, J. Am. Chem. Soc. 118 (1996) 12696.
[5] A.S. Craig, A.M. Helps, K.J. Jankowski, D. Parker, N.R.A. Beeley, B.A. Boyce, M.A.W. Eaton, A.T. Millican, K. Millar, A. Phipps, S.K. Rhind, A. Harrison, C. Walker, J. Chem. Soc., Chem. Commun. (1989) 794.
[6] M.K. Moi, C.F. Meares, M.J. McCall, W.C. Cole, S. DeNardo, J. Anal. Biochem. 148 (1985) 249.
[7] J. Costamagna, G. Ferraudi, B. Matsuhiro, M. Campos-Vallette, J. Canales, M. Villagra'n, J. Vargas, M.J. Aguirre, Chem. Rev. 196 (2000) 125.
[8] R.I. Haines, Rev. Inorg. Chem. 21 (2002) 165.
[9] H. Keypour, D.A. Stotter, Inorg. Chim. Acta 33 (1979) 149.
[10] H. Keypour, S. Salehzadeh, R.G. Pritchard, R.V. Parish, Inorg. Chem. 39 (2000) 5787.
[11] H. Keypour, S. Salehzadeh, Transition Met. Chem. 25 (2000) 205.
[12] E.V. Rybak-Akimova, A.Y. Nazarenko, S.S. Silchenko, Inorg. Chem. 38 (1999) 2974.
[13] A.M. Herrera, R.J. Staples, S. Kryatov, A. Nazarenko, E.V. Rybak-Akimova, J. Chem. Soc., Dalton Trans. (2003) 846.
[14] H. Keypour, R. Azadbakht, H. Khavasi, Polyhedron 27 (2008) 648.
[15] Ian M. Atkinson, Karl A. Byriel, Peter S.K. Chia, Colin H.L. Kennard, Anthony J. Leong, Leonard F. Lindoy, Mark P. Lowe, Sumathi Mahendran, Graham Smith, Gang Wei, Aust. J. Chem. 51 (1998) 985.
[16] M.J. Frisch, G.W. Trucks, H.B. Schlegel, G.E. Scuseria, M.A. Robb, J.R. Cheeseman, V.G. Zakrazewski, J.A. Montgomery Jr., R.E. Startmann, J.C. Burant, S. Dapprich, J.M. Millam, A.D. Daniels, K.N. Kudin, M.C. Strain, O. Farkas, J. Tomasi, V. Barone, M. Cossi, R. Cammi, B. Mennucci, C. Adamo, S. Clifford, J. Ochterski, G.A. Petersson, P.Y. Ayala, Q. Cui, K. Morokuma, D.K. Malik, A.D. Rabuck, K. Raghavachar, J.B. Foresman, J. Cioslowski, J.V. Ortiz, B.B. Stefanov, G. Liu, A. Liashenko, P. Piskorz, I. Komaromi, R. Gomperts, R.L. Martin, D.J. Fox, T. Keith, M.A. Al-Laham, C.Y. Peng, A. Nanyakkara, C. Gonzalez, M. Challacombe, P.M.W. Gill, B. Johnson, W. Chen, M.W. Wong, J.L. Andres, M. Head-Gordon, E.S. Replogle, J.A. Pople, GAUSSIAN 98 (Revision A.3), Gaussian Inc., Pittsburgh, PA, 1998.
[17] P.J. Hay, W.R. Wadt, J. Chem. Phys. 82 (1985) 299.
[18] K.D. Dobbs, W.J. Hehre, J. Comp. Chem. 8 (1987) 880.
[19] HYPERCHEM, Release 5.02, Hypercube Inc., Gainesville, 1997.



Scheme 1. Chemical structures of the synthesized compounds.

characterization and crystal structure study of $CCl_3C(O)NHP(O)[N(C_5H_{10})]_2$ (**1d**), $CHCl_2C(O)NHP(O)[N(C_5H_{10})]_2$ (**2d**), $Cl–C_6H_4C(O)NHP(O)[NH(C_5H_9)]_2$ (**5b**) and $Cl–C_6H_4C(O)NHP(O)[N(C_4H_8)O]_2$ (**5e**), we also recorded their mass spectra together with 29 of our previously synthesized compounds [15–18]. Also, the observed fragmentation behaviors are compared with those reported in the literature [7].

2. Experimental

2.1. Materials

2,2,2-Trichloroacetamide, 2,2-dichloroacetamide, 2-chloroacetamide, 2,2,2-trifluoroacetamide, phosphorus pentachloride (⩾98%), formic acid (⩾98%), cyclohexylamine (⩾98%), cyclopropylamine (⩾98%) (Merck) and cycloheptylamine (⩾98%), 4-bromobenzamide (⩾98%), 4-methylbenzamide (⩾98%) (Fluka) were used as supplied. In all reactions low temperatures were used.

2.2. Spectroscopic measurements

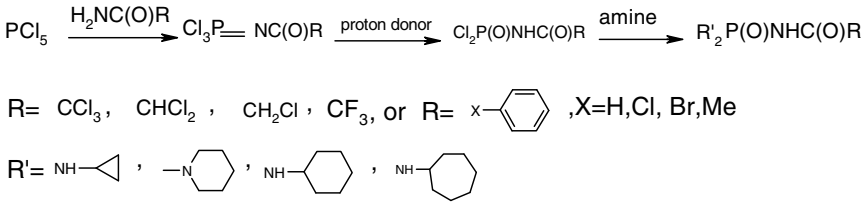
All reactions were performed under an argon atmosphere and in dry solvents. ^1H, ^{13}C and ^{31}P NMR spectra were recorded on a Bruker Avance DRS 500 spectrometer. ^1H and ^{13}C chemical shifts were determined relative to internal TMS and ^{31}P chemical shifts relative to 85% H_3PO_4 as an external standard. Infrared (IR) spectra were recorded on a Shimadzu model IR-60 spectrometer. Elemental analysis was performed using a Heraeus CHN-O-RAPID apparatus. Mass spectra were obtained with a Finnigan-mat gaschromatograph/mass spectrometer (Bremen, Germany), magnetic sector, high resolution, double focusing, model 8430. It was operated in the 70 ev positive ionization mode. Instrument calibration was performed

routinely using the calibration compound, perfluorokerosene (PFK) through the reference inlet system. All samples were introduced to the ion source through the introduction solid probe system. The scanning rate of the mass spectrometer was set as 1 s/decade at a mass range of 33–600 a.m.u. All mass spectra were taken by the manufacturer's software SS300.

3. Results and discussion

3.1. Synthesis procedure

A series of new carbacylamidophosphates with various substituents based on phosphorus pentachloride as a starting material, shown in the scheme below, were synthesized



2.3. X-ray measurements

X-ray data of compounds **1d**, **2d**, **5b** and **5e** were collected on a Bruker SMART 1000CCD [19] with graphite monochromated Mo Kα radiation ($\lambda = 0.71073$ Å). The structures were solved by the direct method using the SHELX-97 program package [20]. The non-hydrogen atoms were refined anisotropically and all located from subsequent difference Fourier maps and refer to final *R* values of 0.0471, 0.0322, 0.0518 and 0.0412 for **1d**, **2d**, **5b** and **5e**, respectively.

2.4. Synthesis

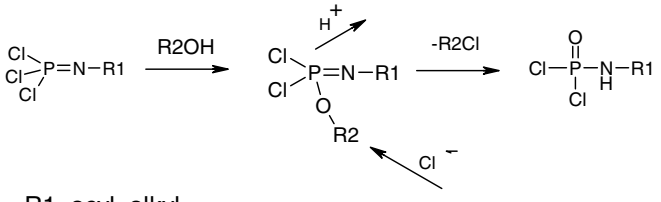
2.4.1. General procedure for the synthesis of compounds as starting materials

2,2,2-Trichloroacetyl phosphoramidic dichloride, 2,2-dichloroacetyl phosphoramidic dichloride, 2-chloroacetyl phosphoramidic dichloride, 2,2,2-trifluroacetyl phosphoramidic dichloride, benzoyl phosphoramidic dichloride, 4-chlorobenzoyl phosphoramidic dichloride, 4-bromobenzoyl phosphoramidic dichloride and 4-methylbenzoyl phosphoramidic dichloride were prepared according to the literature methods [21,22].

2.4.2. General procedure for the synthesis of compounds *(1–7)a, (1–3)d, (1–3)d, (1–3)c and (1–7)f*

The above mentioned compounds were prepared by the reaction of 15 mmol of the phosphoric dichloride derivatives (described in Section 2.4.1) with 60 mmol of the corresponding amines in dry chloroform or acetonitrile. The amines were added dropwise to a solution with stirring. The temperature was controlled in range −5 to −8 °C. After stirring for 6–8 h, the products were filtered off and then washed with H_2O. The compounds were recrystallized from chloroform and *n*-heptane. Colorless crystals of compounds **1d**, **2d**, **5b** and **5e** were obtained by slow evaporation of *n*-heptane–chloroform (1:5) as rod shaped crystals which were air stable. The crystallographic data for these compounds are listed in Table 3.

The method for the preparation of compounds with a –C(O)NHP(O)- core unit was presented first by Kirsanov and coworkers [22]. The protonation of trichlorophosphazene, formed from the reaction of PCl_5 with a proper amide, has been strictly followed when the proton donor is a weak acid like a carboxylic acid. Considering the much reduced basicity of the N atom in trichlorophosphazene, the acidolysis with weak proton donors, especially formic acid, starts with the initially nucleophilic P atom, and this is followed by protonation on the N atom:



Irrespective of the protic agent used, no changes are observed in the structure of the protonated product.

3.1.1. Spectral study

As shown in Table 1, the C=O vibrational frequencies of compounds **1a**, **2a**, **3a**, **1c**, **2c**, **3c**, **1d**, **2d**, **3d**, **1f**, **2f** and **3f** with the $CH_xCl_yC(O)NH$– moiety (haloacetamide derivatives) appear in the range 1637–1714 cm^{-1} and those of compounds **4a**, **5a**, **6a**, **7a**, **4f**, **5f** and **6f** containing the $XC_6H_4C(O)NH$– moiety (halo and alkyl benzoyl amide derivatives) are at 1627–1654 cm^{-1}, due to greater electronegativity of the halo-acetamide than the halo or methyl-benzoyl amide groups. These results are confirmed by crystallographic data by comparing the C=O bond lengths, which will be discussed in the X-ray structural investigation (Section 3.1.3). In all the synthesized compounds, the $P–N_{amine}$ stretching vibrations (1015–1161 cm^{-1}) appear at higher frequencies than the $P–N_{amide}$

Table 1
IR vibration frequencies (cm^{-1}) in the synthesized compounds

Compound	ν (P=O)	ν (C=O)	ν (P–N)[a]	ν (P–N)[b]	ν (N–H)[a]	ν (N–H)[b]
1a	1192	1712	872	1025	3082	3261
2a	1211	1684	897	1023	3095	3265
3a	1195	1707	888	1161	3095	3265
4a	1202	1635	886	1022	2960	3250
5a	1205	1642	888	1015	3090	3250
6a	1205	1643	897	1016	3090	3255
7a	1195	1649	886	1029	3180	3300
1c	1246	1673	847	1083	3075	3330
2c	1210	1684	840	1068	2915	3265
3c	1201	1637	879	1091	2920	3270
1d	1193	1714	864	1067	2970	3410
2d	1194	1701	852	1060	2925	3088
3d	1204	1698	835	1068	2920	3080
1f	1218	1685	861	1061	3030	3375
2f	1232	1672	871	1062	3024	3422
3f	1185	1696	857	1054	2915	3080
4f	1215	1627	891	1058	2890	3105
5f	1214	1637	941	1056	2920	3100
6f	1194	1642	948	1054	2882	3115
7f	1179	1654	834	1054	2915	3090

[a] Amide.
[b] Amine.

Table 2
^{31}P chemical shifts (ppm) and coupling constants (Hz), of the synthesized compounds

Compound	$^2J_{(P,Caliphatic)}$	$^2J_{(P,C(O))}$	$^3J_{(P,Caliphatic)}$	$\delta(^{31}P)$
1a			6.98(CH_2), 5.4(CH_2), 8.8(CCl_3)	8.21
2a			5.9(CH_2), 5.3(CH_2), 9.8($CHCl_2$)	8.45
3a		3.8	5.8(CH_2), 5.5(CH_2), 12.1(CF_3)	7.52
4a			5.9(CH_2), 4.9(CH_2)	8.8
5a			5.8(CH_2), 5.1(CH_2)	10.5
6a			6.1(CH_2), 4.9(CH_2)	10.6
7a			6.0(CH_2), 5.2(CH_2)	10.7
1c			6.2(CH_2), 3.8(CH_2), 13.7(CCl_3)	5.1
2c			5.5(CH_2), 4.4(CH_2), 4.3($CHCl_2$)	4.2
3c		3.5	6.3(CH_2), 3.9(CH_2), 11.7(CF_3)	4.7
1d	2.6		4.6(CH_2), 5.5(CCl_3)	10.1
2d	2.4		4.5(CH_2), 9.8($CHCl_2$)	10.6
3d	2.7	2.9	4.8(CH_2), 11.4(CFl_3)	10.3
1f			6.0(CH_2), 4.1(CH_2), 5.1(CCl_3)	4.7
2f			6.1(CH_2), 4.3(CH_2), 10.2($CHCl_2$)	5.4
3f		2.6	4.1(CH_2), 4.1(CH_2), 10.9(CF_3)	13.8
4f			6.1(CH_2), 3.9(CH_2)	7.6
5f			6.2(CH_2), 4.3(CH_2)	7.5
6f			5.8(CH_2), 4.4(CH_2)	7.3
7f			4.3(CH_2), 4.1(CH_2)	14.6

vibrational bands (834–948 cm^{-1}). The NMR data, summarized in Table 2, show that in compounds **1c**, **2c** and **3c**, with cyclohexylamine substituents, the ^{31}P chemical shifts (5.1–4.2 ppm) appear more upfield relative to the other synthesized molecules. Also, the ^{31}P chemical shifts in structurally similar compounds are very close to each other. ^{13}C NMR spectral studies show that $^2J_{(P,Caliphatic)}$ is only observed in **1d**, **2d** and **3d**, and this coupling is absent in the other synthesized compounds (Table 2). Also, in these compounds (**1d**, **2d** and **3d**) with a tertiary amine, $^3J_{(P,Calphatic)} > {}^2J_{(P,Caliphatic)}$ is in agreement with our previous studies [23,24]. It is observed from Table 2 that the carbons with two bond distances from the N atom in **1d**, **2d** and **3d** are equivalent and $^3J_{(P,Caliphatic)}$ values are between 4.5 and 4.8 Hz, but in compounds **1a**–**7a**, **1c**–**3c** and **1f**–**7f** non-equivalent β-carbon atoms are indicated. However, two different $^3J_{(P,Caliphatic)}$ values are observed which are between 3.8–5.5 Hz and 4.1–6.98 Hz. As shown in Table 2, on increasing the ring size of the amine groups, the $^3J_{(P,Caliphatic)}$ value becomes smaller and the results are similar to our previous work [12]. The $^2J_{(P,C(O))}$ couplings are only observed in **3a**, **3c**, **3d** and **3f**, with the CF_3 amide derivatives. The ^{13}C NMR spectra of those compounds show quartets for CF_3 and C(O) carbon atoms which are due to the three fluorine atoms with coupling constants ranging from 290.3–304.2 Hz for $^1J_{CF}$ and 38.5–45.7 Hz for $^2J_{CF}$, respectively. The quartets are further split into doublets, arising from coupling to the phosphorus atom with coupling constants in the range 10.9–12.1 Hz ($^3J_{PC}$) for CF_3 and 2.6–3.8 Hz ($^2J_{PC}$) for C(O) carbon atoms. Since the former involves three bonds and the later only two, it must be concluded that through space coupling is significant in those four molecules. Furthermore, three bond distance coupling between the phosphorous atom and haloalkyl carbon atom in **1a**, **1c**, **1d** and **1f** are observed and vary between 5.1 and 13.7 Hz. No coupling between the phosphorous atom and the hydrogen atom of the NH amide group in the ^1H NMR spectral data for all the synthesized compounds could be observed.

3.1.2. X-ray structural investigation

The results of the single crystal X-ray structure analysis for compounds **1d**, **2d**, **5b** and **5e** are shown in Figs. 1, 3, 5 and 7, respectively, along with their numbering schemes. Crystallographic data are summarized in Table 3 and selected bond lengths and bond angles are given in Tables 4 and 5. Details of the hydrogen bonding interactions for all four structures are summarized in Table 6. Unit cell packing diagrams for compounds **1d**, **2d**, **5b** and **5e** are shown in Figs. 2, 4, 6 and 8. The four reported crystals contain one amidic hydrogen atom and form dimers via intermolecular –P=O...H–N– hydrogen bonds, that in **1d** is a dimeric aggregate (Fig. 2). Similarly, the intermolecular hydrogen bonds formed via the haloalkyl hydrogen atom and the phosphoryl oxygen, in addition to the amidic hydrogen, lead to the formation of dimeric aggregates in the unit cell of **2d** (Fig. 4). As shown in Fig. 6, the carbonyl oxygen atom, O(1), makes an intermolecular hydrogen

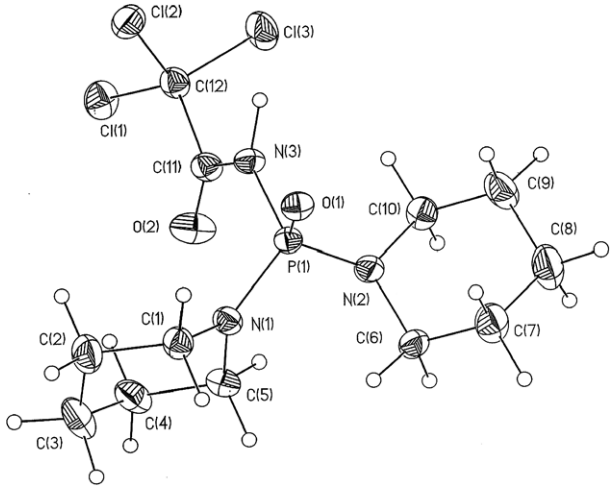


Fig. 1. Molecular structure for **1d** with the atomic numbering (50% probability ellipsoids).

Table 4
Selected interatomic distances and angles between interatomic vectors for **1d** and **2d** with standard uncertainties in parentheses

Bond distances (Å) (***1d***)			
P(1)–O(1)	1.4847(14)	Cl(1)–C(12)	1.760(2)
P(1)–N(1)	1.6293(17)	Cl(2)–C(12)	1.769(2)
P(1)–N(2)	1.6266(17)	Cl(3)–Cl(12)	1.766(2)
P(1)–N(3)	1.7046(16)	O(2)–C(11)	1.202(3)
Bond angles (°) (***1d***)			
C(11)–N(3)–P(1)	126.59(14)	N(2)–P(1)–N(3)	103.90(8)
O(2)–C(11)–N(3)	126.45(19)	O(1)–P(1)–N(1)	105.10(6)
N(2)–P(1)–N(1)	104.86(9)	O(1)–P(1)–N(2)	120.28(9)
N(1)–P(1)–N(3)	112.56(9)	O(1)–P(1)–N(3)	104.28(8)
Bond distances (Å) (***2d***)			
P(1)–O(1)	1.4818(11)	C(2)–Cl(2)	1.776(18)
P(1)–N(1)	1.6980(13)	Cl(1)–C(2)	1.7541(17)
P(1)–N(2)	1.6260(14)	O(2)–C (1)	1.2065(19)
P(1)–N(3)	1.6280(14)		
Bond angles (°) (***2d***)			
C(1)–N(1)–P(1)	130.04(10)	N(2)–P(1)–N(3)	104.91(7)
O(2)–C(1)–N(1)	126.53(14)	O(1)–P(1)–N(1)	105.101(6)
N(2)–P(1)–N(1)	111.50(7)	O(1)–P(1)–N(2)	110.75(7)
N(3)–P(1)–N(1)	104.64(7)	O(1)–P(1)–N(3)	119.83(7)

bond with the proton which is connected to N(2) (aminic hydrogen) and the other aminic hydrogen, bonded to N(1) makes a hydrogen bond with the terminal chlorine atom of the benzoyl amide derivative. Also, the formation of hydrogen bonds between the amidic hydrogen and the phosphoryl oxygen in **5b** leads to a centrosymmetric dimer, similar to the dimer in the unit cell of **5e** (Fig. 8). In all four crystal structures, the phosphoryl and the carbonyl groups are in anti positions to each other, which is in accordance with other carbacylamidophosphates with a –C(O)NHP(O)– core unit [23–25]. As shown in Table 7, the P=O bond lengths in molecules **1d**, **2d**, **5b** and **5e** are longer than the normal P=O bond length (1.45 Å) [26] and they in accord with another similar compounds previously synthesized (listed in Table 7). Also, the C=O bond length is the longest (1.23(3) Å) in **5b** relative to the other reported structures in Table 7. Structural studies of those crystals show that the P–N_{amine} bond lengths are shorter than the P–N_{amide} bond lengths. It is electrostatic

Table 3
Crystal data and structure refinement parameters for **1d**, **2d**, **5b** and **5e**

Structure parameter	**1d**	**2d**	**5b**	**5e**
Empirical formula	$C_{12}H_{21}Cl_3N_3O_2P$	$C_{12}H_{22}Cl_2N_3O_2P$	$C_{17}H_{25}ClN_3O_2P$	$C_{15}H_{21}ClN_3O_4P$
Temperature (K)	120(292)	200(2)	120(2)	120(2)
Formula weight (g/mol)	376.64	342.20	369.82	373.77
Wavelength (Å)	0.71073	0.71073	0.71073	0.71073
Crystal system	monoclinic	monoclinic	triclinic	monoclinic
Space Group	*C*2/*c*	$P2_1/n$	$P\bar{1}$	$P2_1/n$
a (Å)	17.464(2)	9.7216(19)	9.9255(14)	10.4739(10)
b (Å)	9.8130(11)	10.906(2)	10.1545(14)	9.3400(9)
c (Å)	19.959(2)	15.558(3)	10.7348(15)	18.0110(17)
V (Å^3)	3345.5	1611.6(6)	935.0(2)	1736.7(3)
Z	8	4	2	4
D_{calc} (Mg/m^3)	1.496	1.410	1.314	1.429
Absorption coefficient (mm^{-1})	0.650	0.507	0.304	0.337
F(000)	1568	720	392	784
Crystal size (mm)	0.25 × 0.2 × 0.1	0.35 × 0.20 × 0.20	0.45 × 0.25 × 0.15	0.30 × 0.30 × 0.20
Reflections collected	16352	3330	7872	17261
Data/restraints/parameters	4400/0/190	3143/0/182	3476/22/300	4185/0/217
Goodness-of-fit on F^2	1.038	1.022	0.992	1.010
Final R_1 and wR_2 [$I > 2\sigma(I)$]	0.0471, 0.1143	0.0322, 0.0876	0.0518, 0.1259	0.0412, 0.1053
R_1 and wR_2 indices (all data)	0.0576, 0.1196	0.0376, 0.0890	0.0785, 0.1557	0.0481, 0.1116
Largest difference in peak and hole (e/Å^3)	0.781 and −0.294	0.488 and −0.473	0.487 and −0.17	0.383 and −0.391
Index ranges	$-23 \leqslant h \leqslant 23$, $-13 \leqslant k \leqslant 13$, $-27 \leqslant l \leqslant 27$	$0 \leqslant h \leqslant 11$, $0 \leqslant k \leqslant 13$, $-19 \leqslant l \leqslant 18$	$-12 \leqslant h \leqslant 12$, $-12 \leqslant k \leqslant 12$, $-13 \leqslant l \leqslant 13$	$-13 \leqslant h \leqslant 13$, $-12 \leqslant k \leqslant 12$, $-23 \leqslant l \leqslant 23$

Table 5
Selected interatomic distances and angles between interatomic vectors for **5b** and **5e** with standard uncertainties in parentheses

Bond distances (Å) (**5b**)			
P(1)–O(2)	1.4770(16)	C(1)–O(1)	1.231(3)
P(1)–N(1)	1.687(2)	C(8)–N(2)	1.449(3)
P(1)–N(2)	1.621(2)	C(13)–N(3)	1.475(10)
P(1)–N(3)	1.620(2)	N(1)–C(1)	1.357(3)
Bond angles (°) (**5b**)			
C(1)–N(1)–P(1)	124.46(16)	N(1)–P(1)–N(3)	104.33(11)
O(1)–C(1)–N(1)	120.8(2)	O(2)–P(1)–N(1)	107.76(9)
N(2)–P(1)–N(3)	106.96(10)	O(2)–P(1)–N(2)	110.20(10)
N(2)–P(1)–N(1)	110.97(10)	O(2)–P(1)–N(3)	116.48(11)
Bond distances (Å) (**5e**)			
P(1)–O(1)	1.4850(11)	Cl(1)–C (5)	1.7424(16)
P(1)–N(1)	1.6792(13)	C (1)–C(2)	1.497(2)
P(1)–N(2)	1.6351(13)	O(2)–C (1)	1.2236(18)
P(1)–N(3)	1.6307(14)	C(1)–N(1)	1.3721(19)
Bond angles (°) (**5e**)			
C(1)–N(1)–P(1)	125.22(10)	N(2)–P(1)–N(3)	106.92(7)
O(2)–C(1)–N(1)	122.73(14)	O(1)–P(1)–N(1)	107.36(6)
N(2)–P(1)–N(1)	109.84(7)	O(1)–P(1)–N(2)	110.22(7)
N(3)–P(1)–N(1)	107.78(7)	O(1)–P(1)–N(3)	114.66(7)

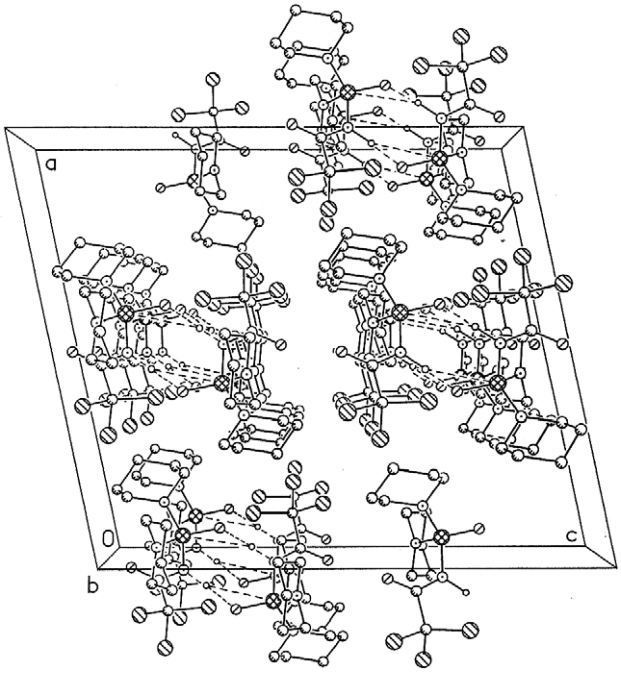


Fig. 2. Unit cell for **1d**, showing the hydrogen bonds.

interactions in the –C(O)–NH–P(O)–N– moiety that cause shortening of the C–N_{amide} bond lengths and the longer C–N_{amine} bond lengths [27]. A comparison to the P–N bond lengths in the literature [27] shows that the P–N_{amine} bond lengths are shorter than typical P–N single bonds (1.77 Å) and longer than P=N double bond lengths (1.57 Å). The coordination environment around the phosphorus atoms of these compounds is approximately tetrahedral, since the average of the six angles involving P atoms for **1d**, **2d**, **5b** and **5e** are 108.49°, 109.45°, 109.45° and 109.46°, respectively. The configurations around the phosphorus atoms, due to their substituents, are slightly disordered tetrahedral and the distortion is much greater in **1d** relative to the other compounds. It is of interest to note that the low values of some OPN angles in the –C(O)NHP(O)– moieties can be explained by the influence of hydrogen bonds formed in the unit cell packing of the compounds. The environments of the nitrogen atoms are nearly planar. The average of the angles around the amine nitrogens in the four crystal structures are 118.58 and 119.07° for **1d**, 118.01 and 119.45° for **2d**, 117.5 and 119.05° for **5b**, 119.98 and 119.59° for **5e**. Also, the sums of the surrounding angles for each aminic nitrogen atom are 355.76 and

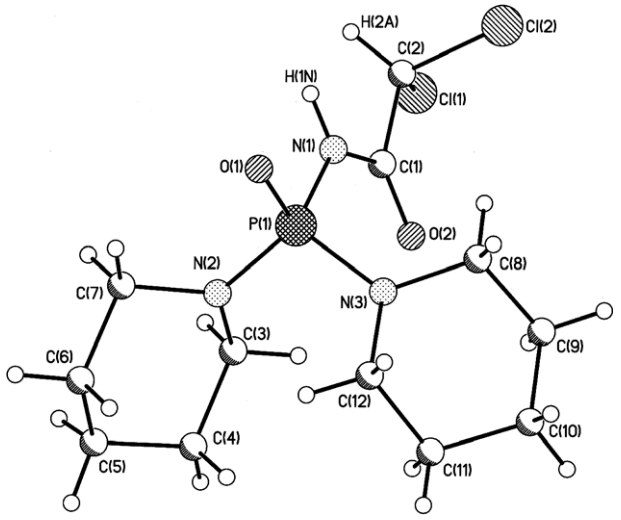


Fig. 3. Molecular structure for **2d** with the atomic numbering (50% probability ellipsoids).

359.63° (**1d**), 354.03 and 358.35° (**2d**), 352.5 and 357.05° (**5b**) and 359.95 and 358.77° (**5e**). The trigonal–planar bond

Table 6
Hydrogen bonds D–H...A in compounds **1d**, **2d**, **5b** and **5e**

Compound	D–H...A (Å)	*d*(D–H) (Å)	*d*(H...A) (Å)	*d*(D...A) (Å)	∠DHA(°)
1d	N3–H3A...O1[$-x$, y, $-z+1/2$]	0.880	1.969	2.763(2)	149.32
2d	N1–H1N...O1[$-x+1$, $-y+1$, $-z$]	0.89	1.90	2.780(2)	172
	C2–H2A...O1[$-x+1$, $-y+1$, $-z$]	0.89	2.38	3.157(2)	167
5b	N1–H1N...O2[$-x+1$, $-y+1$, $-z+1$]	0.870	1.921	2.781(2)	169.33
	N2–H2N...O1[$-x+1$, $-y+2$, $-z+1$]	0.870	2.130	2.993(2)	171.54
	N3–H3N...Cl1[$-x$, $-y+1$, $-z+1$]	0.870	2.905	3.553(2)	132.70
5e	N1–H1N...O1[$-x$, $-y+1$, $-z$]	0.86	1.92	2.777(2)	173

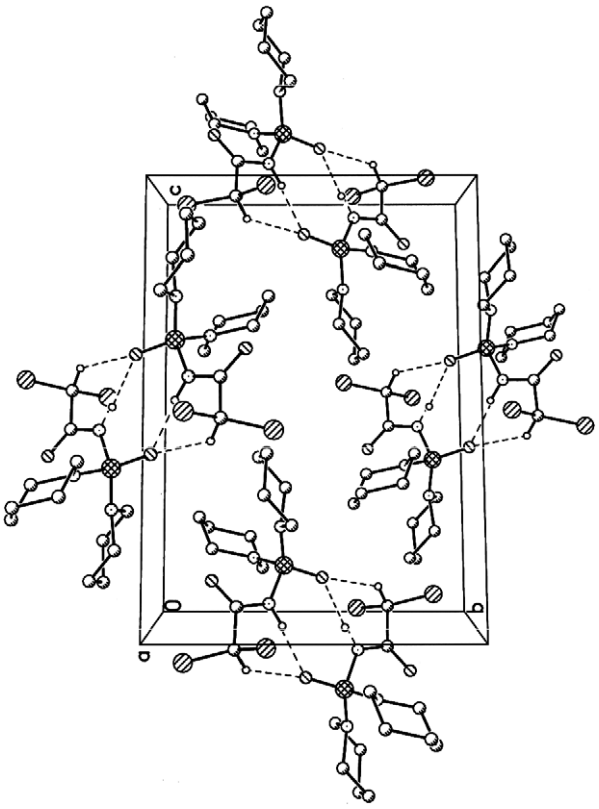


Fig. 4. Unit cell for **2d**, showing the hydrogen bonds.

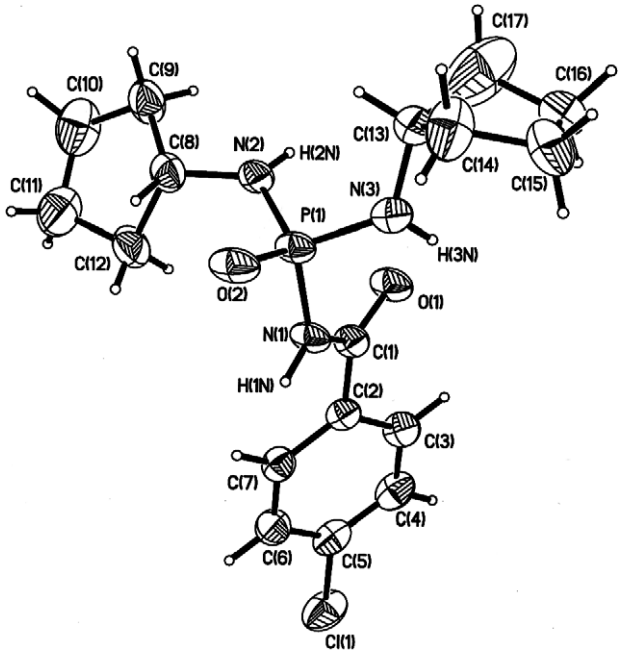


Fig. 5. Molecular structure for **5b** with the atomic numbering (50% probability ellipsoids).

angles observed in these compounds suggested that π delocalization exist in the O–P–N_{amine} moiety, leading to a change in the nitrogen amines hybridization from sp^3 to sp^2. Furthermore, the repulsion and steric hindrances in

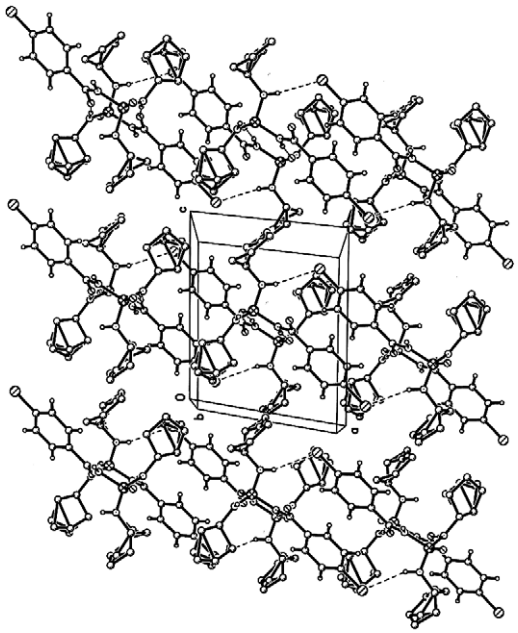


Fig. 6. Unit cell for **5b**, showing the hydrogen bonds.

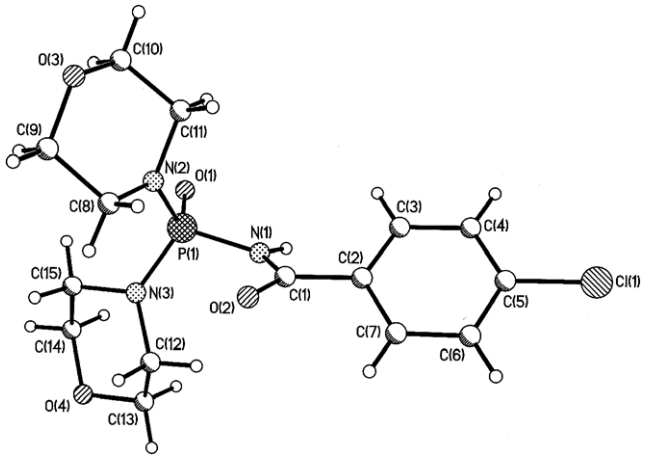


Fig. 7. Molecular structure for **5e** with the atomic numbering (50% probability ellipsoids).

the above mentioned compounds cause some deviation from planarity in the angles around the aminic nitrogen atoms.

3.1.3. Mass spectral study

The mass spectra of the 20 newly synthesized carbacylamidophosphates and the 29 compounds which were synthesized in our previous works were recorded. Fragmentation data are listed in Tables S1 and S2. Molecular ions derived from all the substrates are relatively stable since they were observed for all compounds except for **5f** and **6c**, and varied in intensity from 2% to 42%. As the carbacylamidophosphates with the general formula $R'_2P(O)NHC(O)R$ are derived from both carboxylic and phosphoric amides, the interpretation of their mass spectra

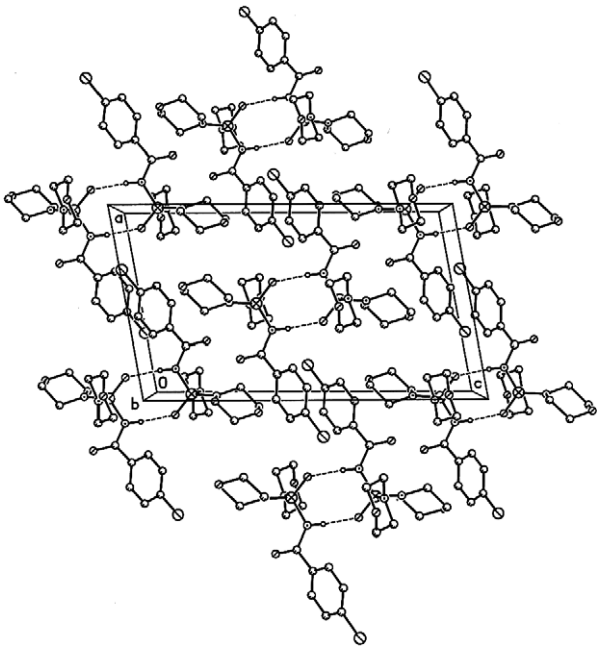


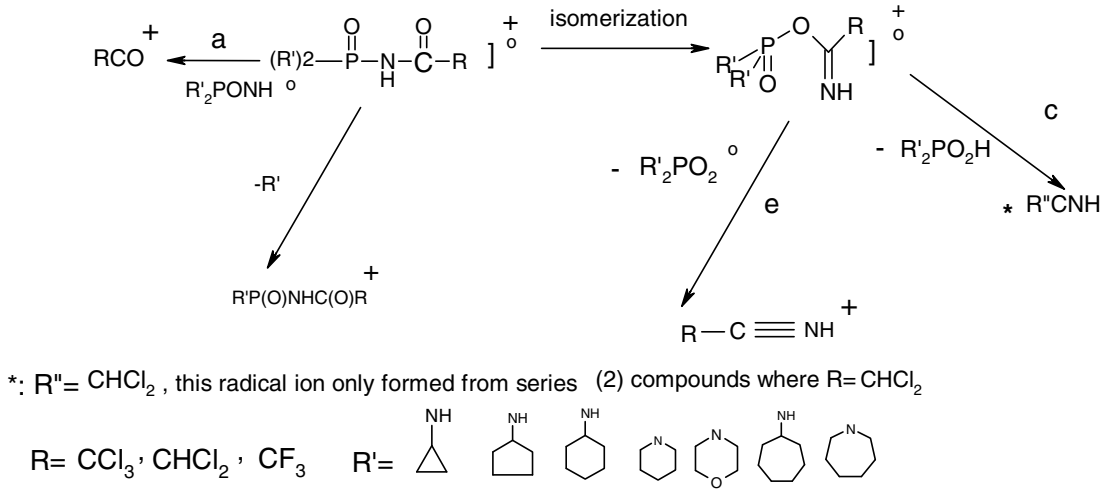
Fig. 8. Unit cell for **5e**, showing the hydrogen bonds.

is related to the behavior of the parent system. Also, the detailed electron distribution in these compounds should of course modify the ionization potential of the oxygen and nitrogen atoms of the (O)PNC(O) linkage and thus determine the predominant structures of the radical ions derived from the above mentioned structures upon electron impact [7]. Besides the structural studies, the fragmentation pattern under the conditions of electron impact seems to be a useful probe for investigation of the bonding characteristics of these phosphoramidic derivatives. Mass spectral studies of carbacylamidophosphates are scarce in the literature and only the fragmentation pattern for some secondary (R = H) and tertiary (R = alkyl) derivatives of phosphoric amides, $X_2P(O)NRC(O)R'$, have been recorded by Modro and coworkers [7] where X = MeO, EtO, Et, R′= Me, Ph and R = H, Me. Since we are interested in determining the degree of the fragmentation pattern characteristics of carbacylamidophosphates with many kinds of cyclic amines connected to a P(O) group, as well as finding new pathways, the mass spectra of those types of phosphoric amides were recorded and the available information derived from the spectra. In this respect, we considered two categories of carbacylamidophosphate, groups, ones with acetamide derivatives and the others with benzamide derivatives. As was studied before, the characteristic features of the mass spectra of aromatic amides are the presence of an M-1 peak (loss of H° from the aromatic ring) and a benzoylium ion peak, resulting from acyl-nitrogen bond cleavage [28]. The typical mass spectral behavior of acetamides, most relevant to our discussion, is the loss of ketene from the parent ion [29]. However, the fragmentation behaviors of the mixed phosphoric carboxylic amides are derived with respect to the behavior of the two phosphoryl and carbonyl groups, but at the same time some new features are also observed. Lapidot and Samuel reported on the pyrolysis of *N*-benzoyl phosphoramidates during a mass spectral process that led to the formation of PhCN+ and the related amidophosphoric acids [30]. In our previous work, during the study of the mass spectra of some new phosphoramidate derivatives [31], we considered the formation of PhCN+ and related amidophosphoric acid derivatives. It was assumed that the fragmentation pathway contains P–N cleavage and P–O formation and then the rearranged molecule is cleaved in a pseudo MacLafferty mechanism to PhCN+ and the related amidophosphoric acid cations [31]. Later, Modro and coworkers [7] suggested new fragmentation pathways for benzoyl and acetyl amide derivatives of some *N*-acyl phosphoramidates. According to those pathways, we studied the fragmentation of our synthesized products, resulting in two different patterns which are presented in Schemes 2 and 3. Also, the most important fragmentation products and their intensities observed for *N*-acetyl and *N*-benzoyl derivatives of 49 synthesized com-

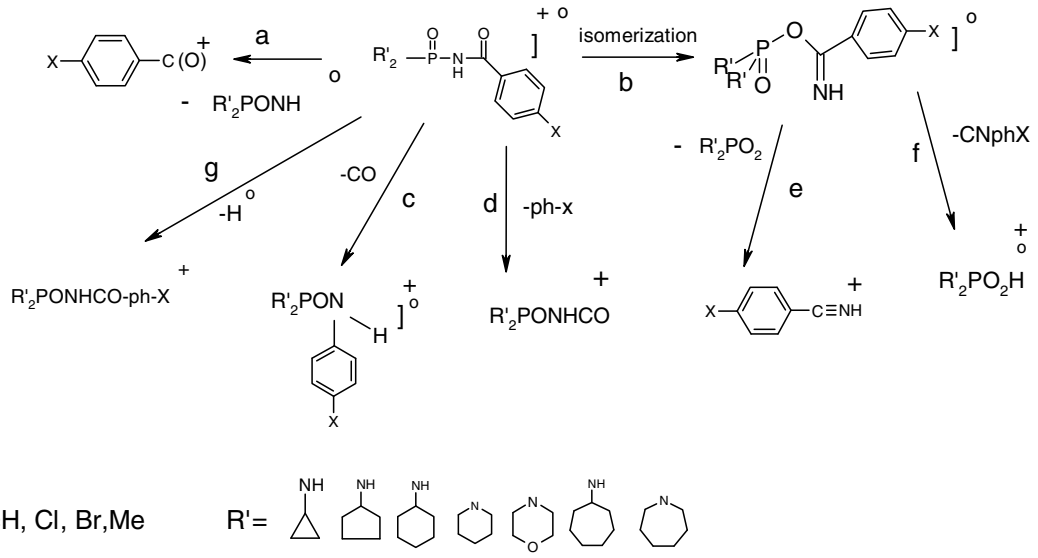
Table 7
Selected bond lengths (Å) and IR frequencies (cm^{-1}) for some synthesized compounds

Compound	P–N_{amide}	C–N_{amide}	P=O	C=O	$\nu_{P=O}$	$\nu_{C=O}$	Ref.
ph-C(O)NHP(O)[$N(C_5H_{10})$]$_2$	1.671(13)	1.368(18)	1.463(11)	1.223(17)	1203	1667	[10]
p-Cl-ph-C(O)NHP(O)[$N(C_5H_{10})$]$_2$	1.689(2)	1.364(3)	1.479(2)	1.223(2)	1207	1667	[15]
p-Br-ph-C(O)NHP(O)[$N(C_5H_{10})$]$_2$	1.682(8)	1.366(12)	1.476(6)	1.238(10)	1206	1666	[15]
p-Cl-ph-C(O)NHP(O)[$NH(C_5H_9)$]$_2$ (**5b**)	1.687(2)	1.357(3)	1.477(16)	1.231(3)	1218	1621	[a]
p-Me-ph-C(O)NHP(O)[$NH(C_5H_9)$]$_2$	1.701(13)	1.364(19)	1.475(12)	1.232(19)	1218	1631	[15]
p-Cl-ph-C(O)NHP(O)[$N(C_4H_8)O$]$_2$ (**5e**)	1.679(13)	1.372(19)	1.485(11)	1.224(18)	1193	1666	[a]
p-Br-ph-C(O)NHP(O)[$N(C_4H_8)O$]$_2$	1.683(11)	1.367(2)	1.483(10)	1.223(16)	1191	1667	[16]
Ph-C(O)NHP(O)[$N(C_6H_{12})$]$_2$	1.692(16)	1.377(2)	1.488(1)	1.227(2)	1218	1660	[24]
p-Cl-Ph-C(O)NHP(O)[$N(C_6H_{12})$]$_2$	1.696(10)	1.374(14)	1.487(9)	1.228(14)	1176	1660	[17]
p-Br-Ph-C(O)NHP(O)[$N(C_6H_{12})$]$_2$	1.697(3)	1.363(4)	1.484(3)	1.229(4)	1184	1656	[17]
CCl_3C(O)NHP(O)[$NH(C_5H_9)$]$_2$	1.729(2)	1.338(3)	1.471(18)	1.221(3)	1243	1671	[18]
CCl_3C(O)NHP(O)[$N(C_5H_{10})$]$_2$ (**1d**)	1.704(16)	1.352(2)	1.485(14)	1.202(3)	1193	1714	[a]
$CHCl_2$C(O)NHP(O)[$N(C_5H_{10})$]$_2$ (**2d**)	1.698(13)	1.356(19)	1.481(11)	1.206(19)	1194	1701	[a]
CF_3C(O)NHP(O)[$N(C_4H_8)O$]$_2$	1.702(13)	1.348(18)	1.484(11)	1.208(18)	1193	1733	[16]
CF_3C(O)NHP(O)[$N(C_6H_{12})$]$_2$	1.697(15)	1.340(2)	1.461(12)	1.206(2)	1200	1716	[17]

[a] This work.



Scheme 2. Fragmentation pathway for the synthesized *N*-acetyl phosphoramidate derivatives in the mass spectra.



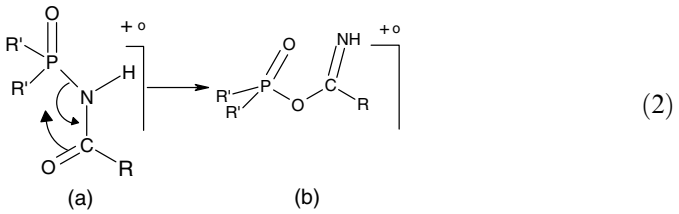
Scheme 3. Fragmentation pathway for the synthesized *N*-benzoyl phosphoramidate derivatives in the mass spectra.

pounds are listed in Tables S1 and S2. For the *N*-benzoyl derivatives, only **6b** and **6g** show the loss of H° from the parent ion (pathway g, Scheme 3) but all 28 compounds undergo carbonyl–nitrogen bond cleavage producing the benzoylium derivative ions (pathway a, Scheme 3). Similar carboxylic–nitrogen fission yielding acetylium derivative ions are found for all 21 *N*-acetyl derivative compounds (pathway a, Scheme 2). The analogous cleavage of the P-N bond in the parent ion should produce the corresponding phosphorylium ion and the carboxylic amide radical (Eq. (1)):

$$R'_2P(O)NHC(O)R]^{+\cdot} \rightarrow R'_2PO^+ + R - C(O)NH^{\cdot} \qquad (1)$$

Although we observed the formation of R'_2PO^+ in the mass spectra of some of our synthesized compounds, we did not report those ion formations due to lesser relative intensities in comparison with $RC(O)^+$ or $X\text{-}C_6H_4C(O)^+$ ions. Such a difference in the N–P(O) versus N–C(O) bond cleavage can be produced by two different reasons. Firstly, the acylium ions $RC(O)^+$ or $X\text{-}C_6H_4C(O)^+$ are much more stable species than the phosphorylium ions R'_2PO^+ [7]. Acylium ions can easily be generated in solution from a variety of precursors [32], whereas there is no evidence for the participation of phosphorylium ions in the reactions of phosphoryl compounds [33]. Secondly, the observed fragmentation preference can indicate that in the parent ions derived from the parent compounds the radical ion character is localized at the N–C(O) function rather than at the N–P(O) function [7]. In all of the 28 benzoyl derivatives, the benzoylium derivative ions have large intensities and in some of them they can be observed as the base peak (Table S2), which is indicative of the high stability of the ions. Loss of ketene which was reported by Modro and coworkers [7] to give radical ions such as $[(R')_2P(O)NH_2]^{+\cdot}$

in *N*-acetyl amide derivatives was not observed. Another feature of the mass spectra of carbacylamidophosphates with *N*-benzoyl derivatives is the loss of C(O), which can be observed in Scheme 3 (pathway c). The *m/e* and intensities of the driven radical ions with the formula $[(R')_2P(O)NH(C_6H_4\text{-}X)]^{+\cdot}$ are reported in Table S2. The common property of all the *N*-benzoyl and *N*-acetyl phosphoramidates (a) is that they rearrange to the corresponding *O*-phosphorylated benz- or acetamides (b) (Eq. (2)):



(2)

The rearranged products (b) give rise to new fragmentation patterns, also included in Scheme 2 and scheme IV (pathway e). The compounds (b) readily lose the $(R')_2PO_2^{\cdot}$ radical and yield the N-protonated nitrilium ions R–C≡NH^+ and X-C_6H_4–C≡NH^+. As shown in Tables S1and S2, the X-C_6H_4–C≡NH^+ ions have much greater intensity relative to R–C≡NH^+ which indicates higher stability of the X-C_6H_4–C≡NH^+ ions relative to the R–C≡NH^+ ions. The crystal structures of some of synthesized compounds in our previous works and the four new synthesized compounds **1d**, **2d**, **5b** and **5e** are summarized in Table 7. Comparing the P–N_{amide}, C–N_{amide}, P=O and C=O bond lengths for the *N*-benzoyl and *N*-acetyl phosphoramidate derivatives shows that the C=O bond lengths are shorter in the *N*-acetyl derivatives, which may be due to the greater electrostatic interactions between the oxygen lone pair of the C=O bond with the σ^* orbital of the C–N_{amide} bond and the lone pair of the amidic nitrogen atom with the π^* orbital of the C=O double bond [34]. It can be suggested that halogen atoms (chlorine and fluorine) may increase these electrostatic interactions. Also, as shown in Table 7, the C–N_{amide} bond lengths in the *N*-acetyl derivatives are shorter than the C–N_{amide} bond lengths in the*N*-benzoyl derivatives. This can be emphasise our above mentioned suggestion. On the other hand, comparing the P=O and P–N_{amide} bond lengths in the *N*-acetyl and *N*-benzoyl derivatives (Table 7) shows that these bonds are longer in *N*-acetyl than *N*-benzoyl derivatives (in accordance with $\nu_{P=O}$ and $\nu_{C=O}$). In spite of the fact that the P–N_{amide} and P=O bond lengths are longer in the *N*-acetyl derivatives, it can be considered that the low intensities for R–C≡NH^+ relative to X-C_6H_4–C≡NH^+ (Tables S1 and S2) may be due to length shortening in the C–N_{amide} and C=O bonds in *N*-acetyl rather than *N*-benzoyl derivatives, which hardens the rearrangement according to Eq. (2). Furthermore, as indicated in Scheme 3, the rearranged products (b) via pathway f can produce $(R')_2PO_2H^{+\cdot}$ radical ions. Hydrogen transfer to the phosphoryl group accompanied by C–O bond fission takes place and the above mentioned radical ions are formed. Although the formation of these radical ions has been mentioned in the literature [7], we did not observe them in the *N*-acetyl derivatives of our synthesized carbacylamidophosphates (Table S1).

4. Conclusion

This investigation establishes that carbacylamidophosphates with a –P(O)C(O)NH– core with different amide structures have different NMR splitting patterns. Their X-ray structural studies show that the *N*-acetyl derivatives have shorter C=O and C–N_{amide} bond lengths relative to the *N*-benzoyl derivatives. This may be due to greater electrostatic interactions between the lone pairs of the oxygen atom in the C=O bond and the amidic nitrogen atom with σ^* and π^* orbitals of C–N_{amide} and C=O bonds, respectively. These different interactions in the *N*-acetyl and *N*-benzoyl derivatives cause different pathways in the mass spectral studies and it can affect the intensities of R–C≡NH^+ relative to X-C_6H_4–C≡NH^+, which are the most important ions in the phosphoramidates fragmentation.

Appendix A. Supplementary data

CCDC 240148, 286222, 601418 and 292753 contain the supplementary crystallographic data for **1d**, **2d**, **5b** and **5e**. These data can be obtained free of charge via http://www.ccdc.cam.ac.uk/conts/retrieving.html, or from the Cambridge Crystallographic Data Centre, 12 Union Road, Cambridge CB2 1EZ, UK; fax: (+44) 1223-336-033; or e-mail: deposit@ccdc.cam.ac.uk. Supplementary data associated with this article can be found, in the online version, at doi:10.1016/j.poly.2008.01.023.

References

[1] E.A. Trush, V.A. Ovchyunikov, K.V. Domasevitch, J.S. Wiatekkozlowska, V.Y. Zub, V.M. Amirkhanov, Z. Naturforsch. 57b (2002) 746.
[2] V.V. Skopenko, V.M. Amirkhanov, T.Yu. Sliva, I.S. Vasilchenko, E.L. Anpilova, A.D. Garnovski, Russ. Chem. Rev. 73 (2004) 737.
[3] D. Barak, A. Ordentlich, D. Kaplan, R. Barak, D. Mizrahi, C. Kronman, Y. Segall, B. Velan, A. Shafferman, Biochemistry 39 (2000) 1156.
[4] W.D. Mallender, T. Szegletes, T.L. Rosenberry, Biochemistry 39 (2000) 7753.
[5] K. Jaroslav, F. Swerdloff, U.S. Patent 4, 517, 003 (1985).
[6] V. Mizrahi, L.D. Quin, J. Verkade (Eds.), Phosphorus Chemistry, No. 171, 128, ACS Sump. Ser. Washington.
[7] V. Mizrahi, T.A. Modro, J. Org. Chem. 47 (1982) 3533.
[8] K. Gholivand, M. Pourayoubi, Z. Anorg. Allg. Chem. 630 (2004) 1330.
[9] K. Gholivand, M. Pourayoubi, Z. Shariatinia, H. Mostaanzadeh, Polyhedron 24 (2005) 655.
[10] K. Gholivand, C.O. Vedova, A. Anaraki Firooz, A. Madani Alizadehgan, M.C. Michelini, R. Pis Diez, J. Mol. Struct. 750 (2005) 64.
[11] K. Gholivand, A. Madani Alizadehgan, S. Arshadi, A. Anaraki Firooz, J. Mol. Struct. 791 (2006) 193.
[12] K. Gholivand, Z. Shariatinia, M. Pourayoubi, Polyhedron 25 (2005) 11.

[13] K. Gholivand, Z. Shariatinia, K. Khajeh, H. Naderimanesh, J. Enzym. Inhib. Med. Chem. 21 (2006) 31.
[14] K. Gholivand, A. Madani Alizadehgan, A. Anaraki Firooz, K. Khajeh, H. Naderi-Manesh, H. Bijanzadeh, J. Enzym. Inhibit. Med. Chem. 21 (2006) 105.
[15] K. Gholivand, F. Mojahed, A. Madani Alizadehgan, H.R. Bijanzadeh, Z. Anorg. Allg. Chem. 632 (2006) 1570.
[16] K. Gholivand, F. Mojahed, A. Madani Alizadehgan, Polish J. Chem. 81 (2007) 393.
[17] K. Gholivand, F. Mojahed, A. Madani Alizadehgan, Polish J. Chem. 81 (2007) 1829.
[18] K. Gholivand, A. Madani Alizadehgan, F. Mojahed, A. Anaraki Firooz, S. Afr. J. Chem. 60 (2007) 91.
[19] Bruker, SMART. Bruker Molecular Analysis Research Tool, V. 5. 059. Bruker AXS, Madison, WI, USA, 1998.
[20] G.M.Sheldrick, SHELX TL V.5.10, Structure Determination Software Suite, Bruker AXS, Madison, WI, USA, 1998.
[21] L.D. Protsanko, I.A. Avrutskaya, T.N. Dneprova, E. YU. Sologub, Khim. Farm. Zh. (Kiev. NII. Farmakol. Toksikol. Kiev, USSR) 7 (1998) 803.
[22] I.N. Zhmurova, A.V. Kirsanov, Zh. Obshch. Khim. 30 (1960) 4048.
[23] k. Gholivand, Z. Shariatinia, M. Pourayoubi, Z. Anorg. Allg. Chem. 631 (2005) 961.
[24] K. Gholivand, Z. Hosseini, M. Pourayoubi, Z. Shariatinia, Z. Anorg. Allg. Chem. 631 (2005) 3074.
[25] K.E. Gubina, V.M. Amirkhanov, Z. Naturforsch. 55b (2000) 1015.
[26] D.E.C. Corbridge, Phosphorus an Outline of its Chemistry, Biochemistry and Technology, 5th ed., Elsevier, Amsterdam, 1995.
[27] D.G. Gilheany, Chem. Rev. 94 (1994) 1339.
[28] A.M. Duffield, G. de Martino, C. Djerassi, Org. Mass. Spectrosc. 9 (1974) 137.
[29] Z. Pelah, M.A. Kielczewski, J.M. Wilson, M. Ohashi, H. Budzikiewicz, C. Djerassi, J. Am. Chem. Soc. 85 (1963) 2470.
[30] A. Lapidot, D. Samuel, J. Chem. Soc. (1962) 2110.
[31] K. Gholivand, M. Pourayoubi, Z. Shariatinia, Polyhedron 26 (2007) 837.
[32] M. Liler, Reaction Mechanism in Sulfuric Acid, 4.3.1.3, Academic Press, London, 1971.
[33] P. Haake, P.S. Ossip, J. Am. Chem. Soc. 93 (1971) 6919.
[34] A.G. Iriarte, M.F. Erben, K. Gholivand, J.L. Jios, S.E. Ulic, C.O Della Vedova, J. Mol. Struct. (in press).

prepared according to the literature. All reagents and solvents were of reagent grade quality and were obtained from commercial suppliers. All solvents were dried and purified as described by Perrin and Armarego [25]. The IR spectra were recorded on a Perkin–Elmer 1600 FT-IR spectrophotometer, using KBr pellets or NaCl discs. ^{1}H and ^{13}C NMR spectra were recorded on a Varian Mercury 200 MHz spectrometer in $CDCl_3$, and chemical shifts were reported (δ) relative to Me_4Si as an internal standard. Mass spectra were measured on a Micromass Quatro LC/ULTIMA LC–MS/MS spectrometer. The elemental analyses were performed on a Costech ECS 4010 instrument. Melting points were measured on an electrothermal apparatus and are uncorrected. Optical spectra in the UV–Vis region were recorded with a Unicam UV2-100 spectrophotometer, using 1 cm pathlength cuvettes at room temperature. Domestic ovens were used in all syntheses of the phthalocyanines.

2.2. Synthesis

2.2.1. *N,N*-Bis{2-[2-(3,4-dicyanophenoxy)ethoxy]ethyl}-4-methylbenzenesulfonamide (**3**)

N,N-Bis[2-(2-hydroxyethoxy)ethyl]-4-methylbenzenesulfonamide (**1**) (2.5 g, 7.20 mmol) was dissolved in dry DMF (25 ml) under N_2 atmosphere and 4-nitrophthalonitrile (**2**) (2.49 g, 14.40 mmol) was added to the solution. After stirring for 10 min, finely ground anhydrous K_2CO_3 (2.98 g, 21.60 mmol) was added portion-wise over 2 h, with efficient stirring. The reaction mixture was stirred under N_2 at 50 °C for 4 days. Then the solution was poured into ice-water (100 ml) and the aqueous phase was extracted with chloroform (3 × 60 ml). The combined extracts were dried over anhydrous sodium sulfate. Purification of the product was accomplished by column chromatography with silica gel (chloroform). Yield: 2.67 g (62%), *Anal.* Calc. for $C_{31}H_{29}N_5O_6S$: C, 62.09; H, 4.87; N, 11.68; S, 5.35. Found: C, 62.19; H, 4.97; N, 11.60; S, 5.46%. IR (KBr tablet) ν_{max}/cm^{-1}: 3076 (Ar-H), 2924–28,681 (Aliph. C–H), 2230 (C≡N), 1598, 1562, 1492, 1453, 1322–1158 (SO_2), 1255, 1126, 1089, 965, 816, 653 (C–S). ^{1}H NMR ($CDCl_3$) (δ: ppm): 7.71 (d, 2H, Ar-H), 7.66 (d, 2H, Ar-H), 7.30 (s, 2H, Ar-H), 7.25 (d, 2H, Ar-H), 7.20 (d, 2H, Ar-H), 4.18 (t, 4H, CH_2–O), 3.82 (t, 4H, CH_2–O), 3.65 (m, 4H, CH_2–O), 3.36 (t, 4H, CH_2–N), 2.41 (s, 3H, CH_3). ^{13}C NMR ($CDCl_3$) (δ: ppm): 162.13, 143.85, 136.37, 135.52, 129.99, 127.38, 120.08, 119.78, 117.50, 115.92, 115.55, 107.82, 72.58, 68.68, 61.82, 49.42, 21.76. MS (EI) (*m*/*z*): 617 $[M+H_2O]^+$.

2.2.2. Metal-free polymeric phthalocyanine (**4**)

A mixture of *N,N*-bis{2-[2-(3,4-dicyanophenoxy)ethoxy]ethyl}-4-methylbenzenesul-fonamide (**3**) (0.4 g, 0.66 mmol) and 2-(dimethylamino)ethanol (DMAE) (3 ml) was irradiated in a microwave oven at 175 °C, 350 W for 10 min. After cooling to room temperature the reaction mixture refluxed with ethanol to precipitate the product, which was filtered off. The green solid product was washed with hot ethanol and diethyl ether. The product was purified by preparative thin layer chromatography (TLC) using a $CHCl_3$ solvent system. Yield: 158 mg (20%), m.p. > 300 °C. Elemental *Anal.* (for CN end groups) Calc. $(C_{124}H_{118}N_{20}O_{24}S_4)_n$ $(2400.64)_n$: C, 62.04; H, 4.95; N, 11.67; S, 5.34. Found: C, 62.40; H, 5.13; N, 11.30; S, 5.42%. IR (KBr tablet) ν_{max}/cm^{-1}: 3285 (N–H), 3082 (Ar-H), 2925–2868 (Aliph. C–H), 2230 (C≡N), 1598, 1563, 1490, 1454, 1322–1156 (SO_2), 1255 (Ar-O–C), 1125, 1089, 816, 732, 653. ^{1}H NMR ($CDCl_3$) (δ: ppm): 7.66–7.64 (d, 8H, Ar-H), 7.62 (s, 8H, Ar-H), 7.48 (m, 8H, Ar-H), 7.20 (m, 8H, Ar-H), 7.17 (m, 8H, Ar-H), 4.12 (m, 16H, CH_2–O), 3.66 (m, 16H, CH_2–O), 3.61 (m, 16H, CH_2–O), 3.28 (m, 16H, CH_2–N), 2.34 (s, 12H, CH_3). UV–Vis (chloroform): λ_{max}/nm (10^{-5} ε dm^3 mol^{-1} cm^{-1}): 285 (5.13), 326 (5.10), 644 (4.68), 674 (5.13), 704 (5.14). MS (FAB) (*m*/*z*): 2400 $[M]^+$.

2.2.3. Ni(II)-containing polymer (**5**)

A mixture of *N,N*-bis{2-[2-(3,4-dicyanophenoxy)ethoxy]ethyl}-4-methylbenzenesul-fonamide (**3**) (0.4 g, 0.66 mmol), anhydrous $NiCl_2$ (42.7 mg, 0.33 mmol) and 2-(dimethylamino)ethanol (DMAE) (3 ml) was irradiated in a microwave oven at 175 °C, 350 W for 10 min. After cooling to room temperature the reaction mixture was refluxed with ethanol to precipitate the product, which was filtered off. The green solid product was washed with hot ethanol and diethyl ether. The product was purified by preparative thin layer chromatography (TLC) using a $CHCl_3$ solvent system. Yield: 268 mg (32%), m.p. > 300 °C. Elemental *Anal.* (for imide end groups) Calc. $(C_{124}H_{120}N_{16}O_{32}S_4Ni)_n$ $(2533.32)_n$: C, 58.79; H, 4.77; N, 8.85; S, 5.06, Ni, 2.32. Found: C, 58.87; H, 4.89; N, 8.98; S, 4.97; Ni, 2.38%. IR (KBr tablet) ν_{max}/cm^{-1}: 3390 (imide N–H), 3054 (Ar-H), 2923–2857 (Aliph. C–H), 1714 (C=O), 1608, 1456, 1331–1119 (SO_2), 1237 (Ar-O–C), 1089, 1061, 952, 814, 732, 651. UV–Vis (chloroform): λ_{max}/nm (10^{-5} ε dm^3 mol^{-1} cm^{-1}): 292 (5.09), 317 (5.07), 629 (4.50), 680 (5.16). MS (FAB) (*m*/*z*): 2532 $[M-H]^+$.

2.2.4. Zn(II)-containing polymer (**6**)

A mixture of *N,N*-bis{2-[2-(3,4-dicyanophenoxy)ethoxy]ethyl}-4-methylbenzenesul-fonamide (**3**) (0.4 g, 0.66 mmol), anhydrous $Zn(CH_3COO)_2$ (60.5 mg, 0.33 mmol) and 2-(dimethylamino)ethanol (DMAE) (3 ml) was irradiated in a microwave oven at 175 °C, 350 W for 10 min. After cooling to room temperature the reaction mixture refluxed with ethanol to precipitate the product, which was filtered off. The green solid product was washed with hot ethanol and diethyl ether. The product was purified by preparative thin layer chromatography (TLC) using a $CHCl_3$ solvent system. Yield: 309 mg (37%), m.p. > 300 °C. Elemental *Anal.* (for imide end groups) Calc. $(C_{124}H_{120}N_{16}O_{32}S_4Zn)_n$ $(2540.02)_n$: C, 58.63; H, 4.76; N, 8.82; S, 5.05; Zn, 2.57. Found: C, 58.73; H, 4.88; N, 8.90; S, 5.02; Zn, 2.65%. IR (KBr tablet) ν_{max}/cm^{-1}:

3307 (imide N–H), 3054 (Ar-H), 2924–2873 (Aliph. C–H), 1711 (C=O), 1599, 1487, 1448, 1334–1124 (SO_2), 1286 (Ar-O–C), 1089, 952, 746, 549. UV–Vis (chloroform): λ_{max}/nm (10^{-5} ε dm^3 mol^{-1} cm^{-1}): 295 (5.13), 345 (5.09), 629 (4.57), 689 (5.22).

2.2.5. Co(II)-containing polymer (7)

A mixture of *N*,*N*-bis{2-[2-(3,4-dicyanophenoxy)ethoxy]ethyl}-4-methylbenzenesul-fonamide (**3**) (0.4 g, 0.66 mmol), anhydrous $CoCl_2$ (42.8 mg, 0.33 mmol) and 2-(dimethylamino)ethanol (DMAE) (3 ml) was irradiated in a microwave oven at 175 °C, 350 W for 10 min. After cooling to room temperature the reaction mixture refluxed with ethanol to precipitate the product, which was filtered off. The green solid product was washed with hot ethanol and diethyl ether. The product was purified by preparative thin layer chromatography (TLC) using a $CHCl_3$ solvent system. Yield: 250 mg (30%), m.p. > 300 °C. Elemental *Anal*. (for imide end groups) Calc. $(C_{124}H_{120}N_{16}O_{32}S_4Co)_n$ $(2533.58)_n$: C, 58.78; H, 4.77; N, 8.85; S, 5.06; Co, 2.33. Found: C, 58.96; H, 4.80; N, 8.80; S, 5.01; Co, 2.42%. IR (KBr tablet) ν_{max}/cm^{-1}: 3296 (imide N–H), 3054 (Ar-H), 2923–2865 (Aliph. C–H), 1708 (C=O), 1607, 1481, 1451, 1404, 1332–1121 (SO_2), 1238 (Ar-O–C), 1090, 815, 732, 652, 548. UV–Vis (chloroform): λ_{max}/nm (10^{-5} ε dm^3 mol^{-1} cm^{-1}): 280 (5.08), 341 (5.06), 623 (4.49), 680 (5.16).

2.2.6. Cu(II)-containing polymer (8)

A mixture of *N*,*N*-bis{2-[2-(3,4-dicyanophenoxy) ethoxy]ethyl}-4-methylbenzenesul-fonamide (**3**) (0.4 g, 0.66 mmol), anhydrous $CuCl_2$ (44.3 mg, 0.33 mmol) and 2-(dimethylamino)ethanol (DMAE) (3 ml) was irradiated in a microwave oven at 175 °C, 350 W for 10 min. After cooling to room temperature the reaction mixture refluxed with ethanol to precipitate the product, which was filtered off. The green solid product was washed with hot ethanol and diethyl ether. The product was purified by preparative thin layer chromatography (TLC) using a $CHCl_3$ solvent system. Yield: 326 mg (39%), m.p. > 300 °C. Elemental *Anal*. (for imide end groups) Calc. $(C_{124}H_{120}N_{16}O_{32}S_4Cu)_n$ $(2538.19)_n$: C, 58.68; H, 4.77; N, 8.83; S, 5.05; Cu, 2.50. Found: C, 58.60; H, 4.90; N, 8.72; S, 5.16; Cu, 2.62%. IR (KBr tablet) ν_{max}/cm^{-1}: 3253 (imide N–H), 3060 (Ar-H), 2917–2869 (Aliph. C–H), 1703 (C=O), 1595, 1486, 1454, 1331–1150 (SO_2), 1287 (Ar-O–C), 1088, 956, 815, 734, 652, 549. UV–Vis (chloroform): λ_{max}/nm (10^{-5} ε dm^3 mol^{-1} cm^{-1}): 275 (5.07), 377 (5.08), 635 (4.54), 692 (5.20). MS (FAB) (*m*/*z*): 2555 $[M+H_2O-H]^+$.

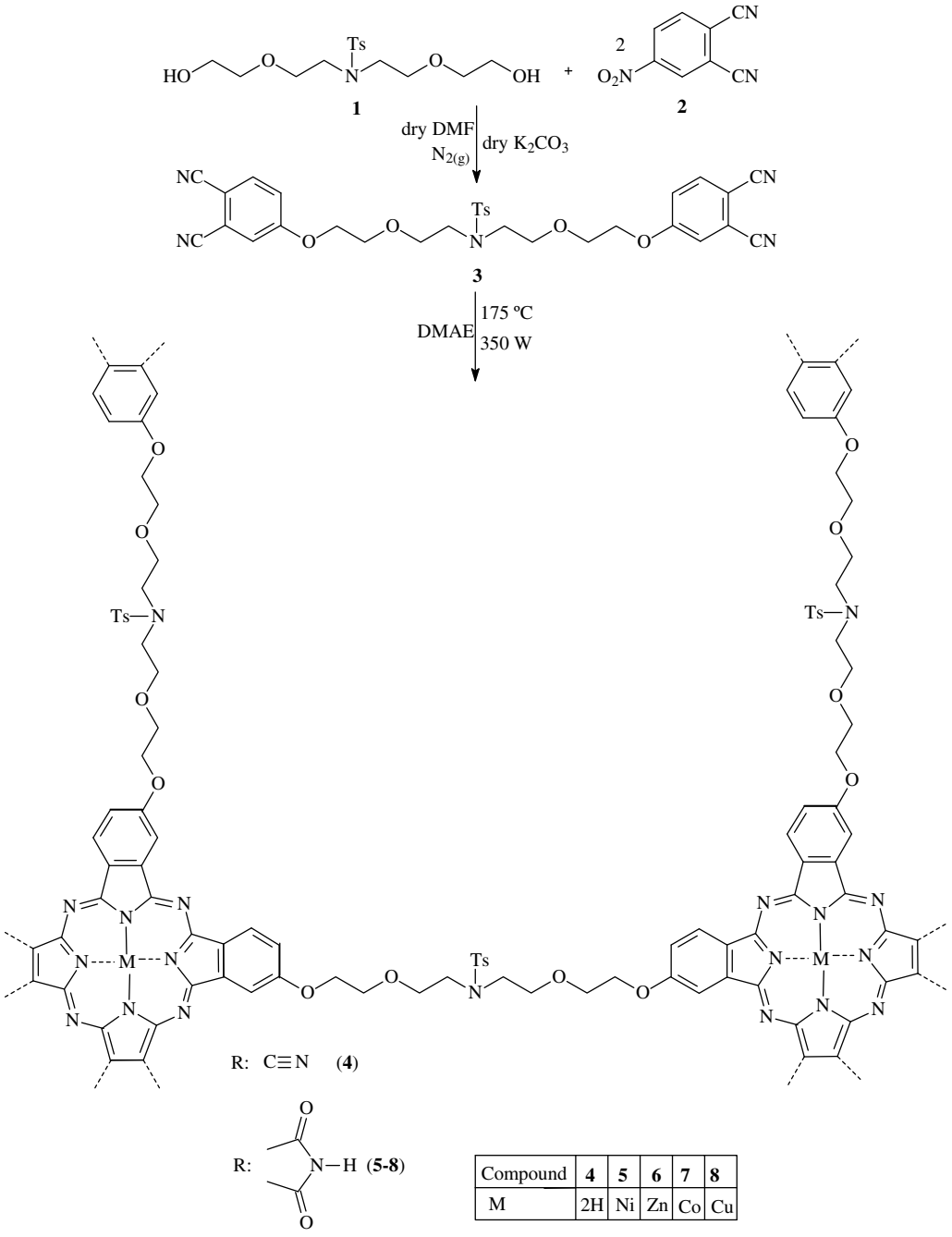
3. Results and discussion

Metal-free **4** and metallophthalocyanine polymers **5**–**8** were synthesized by a polymeric tetramerization reaction of bisphthalonitrile monomer with the appropriate materials (Scheme 1). At the beginning, the base-catalyzed nucleophilic aromatic nitro displacement [26,27] of 4-nitrophthalonitrile (**2**) with **1** afforded the bisphthalonitrile monomer **2**. After that, metal-free and metallophthalocyanine polymers were synthesized. The yields of all the synthesized polymers were between 20% and 39% conversion. The metal-free phthalocyanine (**4**) was synthesized by microwave irridation of the corresponding dicyano compound **3** in 2-(dimethylamino)ethanol for 8 min. The metallophthalocyanines **5**–**8** were obtained from the tetracyano derivative **3** and the corresponding anhydrous metal salt, $NiCl_2$, $Zn(CH_3COO)_2$, $CoCl_2$ and CuCl, respectively, by microwave irradiation [15–19] in 2-(dimethylamino)ethanol for 8 min.

In the IR spectra, the formation of compound **3** was clearly confirmed by the disappearance of the OH and NO_2 bands at 3400 and 1538–1355 cm^{-1} and the appearance of the C≡N band at 2230 cm^{-1}. In the ^{1}H NMR spectrum of **3**, the OH group of compound **1** disappeared, as expected. The ^{1}H NMR spectrum of **3** showed new signals at $\delta = 7.71$ (d, 2H, Ar-H), 7.66 (d, 2H, Ar-H), 7.30 (s, 2H, Ar-H) and 4.18 (t, 4H, CH_2–O). The ^{13}C NMR spectrum of **3** indicated the presence of nitrile carbon atoms at $\delta = 115.92$ and 115.55 ppm. Elemental analysis and EI mass spectral data were satisfactory: 617 $[M+H_2O]^+$.

In the IR spectrum of **4** characteristic peaks for the metal-free phthalocyanine were observed. The peak at 3285 cm^{-1} is the characteristic metal-free phthalocyanine N–H stretching band. The end groups of the metal-free phthalocyanine polymer were cyano groups, with a peak at 2230 cm^{-1}. In the ^{1}H NMR spectrum of **4**, the typical shielding of the inner core protons could not be observed due to the probable strong aggregation of the molecules [28]. The signals related to aromatic protons 7.66–7.64 (d, 8H, Ar-H), 7.62 (s, 8H, Ar-H) and 7.48 (m, 8H, Ar-H) and aliphatic protons in compound **3** and the phthalocyanine skeleton gave significant absorbances characteristic of the proposed structure. The MS mass spectrum of compound **4** displayed the $[M]^+$ parent ion peak at $m/z = 2400$, which confirms the same structure. The results of the elemental analysis confirmed the proposed structure of compound **4**.

The IR spectra of the metallophthalocyanine polymers **5**–**8** are very similar, and they differ from the metal-free phthalocyanine polymer (**4**) which showed an N–H stretching band at 3281 cm^{-1}. This band disappears in the spectra of the metallophthalocyanine polymers. The end groups of the metallophthalocyanine polymers are imido groups (~1703–1714 cm^{-1}) [20–22]. ^{1}H NMR measurements of the cobalt and copper metallophthalocyanine polymers were precluded due to their paramagnetic nature. Also, the ^{1}H NMR spectra of the soluble part of the nickel and zinc metallophthalocyanine polymers in $CDCl_3$ displayed broad signals, and the protons of the phthalocyanine core were invisible. This effect was attributed to strong aggregation of the molecules [21]. In the mass spectra of the Ni and Cu polymers, the presence of molecular ion peaks at $m/z = 2532$ $[M-H]^+$ and 2555 $[M+H_2O-H]^+$, respectively, confirmed the proposed structures. Elemental analysis data were satisfactory.



Compound	4	5	6	7	8
M	2H	Ni	Zn	Co	Cu

Scheme 1. Synthesis of the polymeric metal-free phthalocyanine and metallophthalocyanines (Ts = *p*-toluenesulphonyl).

The end groups of the metal-free phthalocyanine polymer were cyano groups while the end groups of the metallophthalocyanine polymers were imido groups [20–22]. The existence of imido groups in the case of the metallophthalocyanine polymers was attributed to the presence of moisture during work-up [29,30]. Because the phthalocyanines were polymeric, one monomer molecule was calculated to determine the molecular mass of the phthalocyanines. On the other hand, according to the FAB mass spectra analysis of **4**, **5** and **8**, we can say they are monomer molecules [21].

The UV–Vis absorption spectra of these polymers exhibit Q and B bands, which are the characteristic bands for phthalocyanine polymers. The experimental UV–Vis bands of the phthalocyanine polymers were slightly different from the theoretical values [31]. The metal-free phthalocyanine polymer (**4**) showed a typical electronic spectrum with two absorption regions, one of them in the UV region at 285 and 326 nm (B band) and the other in the visible region at 644, 674 and 704 nm (Q band) in chloroform (Fig. 1).

The UV–Vis absorption spectra of metallophthalocyanine polymers **5**–**8** in chloroform show an intense Q absorption at $\lambda_{max} = 680$, 689, 680 and 692 nm, with a weaker absorption at 629, 629, 623 and 635 nm, respectively

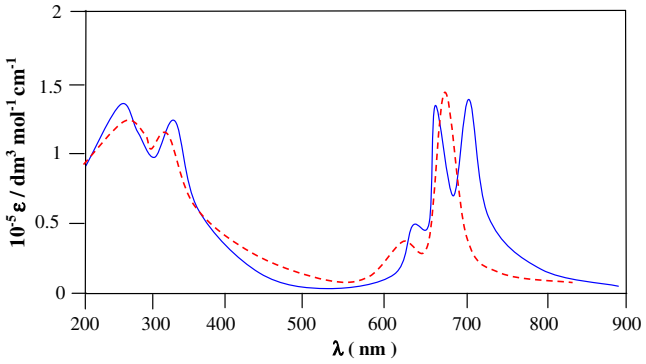


Fig. 1. UV–Vis spectra of compounds **4** (—) and **5** (---) in chloroform.

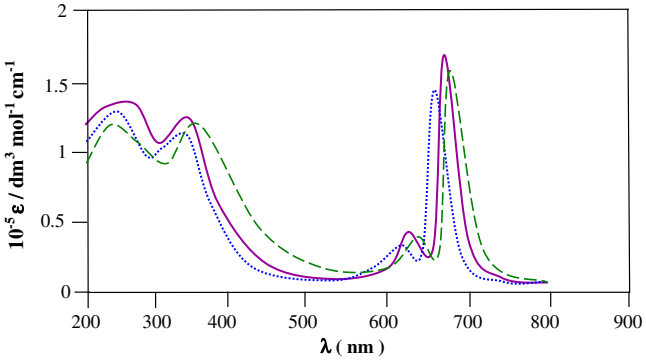


Fig. 2. UV–Vis spectra of compounds **6** (—), **7** (···) and 8 (---) in chloroform.

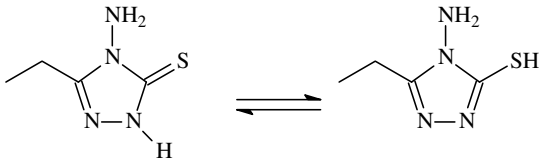
(Figs. 1 and 2). The single Q bands in the metallo derivatives **5**–**8** are characteristic. This result is typical of metal complexes of substituted and unsubstituted metallophthalocyanines with D_{4h} symmetry [32]. B band absorptions of compound **5**–**8** were observed at $\lambda_{max} =$ (292, 317), (295, 345), (280, 341) and (275, 377) nm as expected, respectively.

Acknowledgement

This study was supported by the Research Fund of Karadeniz Technical University, Project No. 2006.111.002.1 (Trabzon, Turkey).

References

[1] J. Simon, P. Bassoul, Supramolecular Engineering, VCH, Weinheim, 2000.
[2] M. Hanack, M. Lang, Adv. Mater. 6 (1994) 819.
[3] M.J. Cook, N.B. McKeown, J.M. Simmons, A.J. Thomson, M.F. Daniel, K.J. Harrison, R.M. Richardson, S.J. Roser, J. Mater. Chem. 1 (1991) 121.
[4] D. Schlettwein, D. Wöhrle, N.I. Jaeger, J. Electrochem. Soc. 136 (1989) 2882.
[5] T. Basova, C. Tasaltin, A.G. Gürek, M.A. Ebeoğlu, Z.Z. Öztürk, V. Ahsen, Sens. Actuator B 96 (2003) 70.
[6] T. Basova, E. Kol'tsov, A.K. Ray, A.K. Hassan, A.G. Gürek, V. Ahsen, Sens. Actuator B 113 (2006) 127.
[7] G. De la Torre, P. Vazquez, F. Agullo-Lopez, T. Torres, J. Mater. Chem. 8 (1998) 1671.
[8] A.B.P. Lever, M.R. Hempstead, C.C. Leznoff, W. Liu, M. Melnik, W.A. Nevin, P. Seymour, Pure Appl. Chem. 58 (1986) 1467.
[9] N. Bhardwaj, J. Andraos, C.C. Leznoff, Can. J. Chem. 80 (2002) 141.
[10] M. Hanack, S. Knecht, R. Polley, Chem. Ber. 128 (1995) 929.
[11] S. Foley, G. Jones, R. Liuzzi, D.J. McGarvey, M.H. Perry, T.G. Truscott, J. Chem. Soc., Perkin Trans. 2 (1997) 1725.
[12] M. Koçak, A. Cihan, A.I. Okur, Ö. Bekaroğlu, J. Chem. Soc. Chem. Commun. (1991) 577.
[13] V. Csokai, G. Parlagh, A. Grofcsik, M. Kubinyi, I. Bitter, Synth. Commun. 33 (2003) 1615.
[14] A. Burczyk, A. Loupy, D. Bogdal, A. Petit, Tetrahedron 61 (2005) 179.
[15] Z. Bıyıklıoğlu, H. Kantekin, M. Özil, J. Organomet. Chem. 692 (2007) 2436.
[16] Z. Bıyıklıoğlu, H. Kantekin, Transition Met. Chem. 32 (2007) 851.
[17] H. Kantekin, Z. Bıyıklıoğlu, Dyes Pigments 77 (2008) 98.
[18] H. Kantekin, Z. Bıyıklıoğlu, Dyes Pigments 77 (2008) 432.
[19] Z. Bıyıklıoğlu, H. Kantekin, J. Organomet. Chem. 693 (2008) 505.
[20] H. Kantekin, G. Dilber, Z. Býyýklýoðlu, J. Organomet. Chem. 693 (2008) 1038.
[21] A. Bilgin, Ç. Yağcı, A. Mendi, U. Yıldız, Polyhedron 26 (2007) 617.
[22] A. Bilgin, A. Mendi, U. Yıldız, Polymer 47 (2006) 8462.
[23] P.L. Anelli, F. Montanari, S. Quici, J. Org. Chem. 53 (1988) 5292.
[24] G.J. Young, W. Onyebuagu, J. Org. Chem. 55 (1990) 2155.
[25] D.D. Perrin, W.L.F. Armarego, D.R. Perrin, Purification of Laboratory Chemicals, 2nd ed., Pergamon Press, New York, 1985.
[26] M.J. Sumner, R.Y. Weyers, A.C. Rosario, J.S. Riffle, U. Sorathia, Polymer 45 (2004) 5199.
[27] T.M. Keller, T.R. Price, J.R. Griffith, Synthesis 8 (1980) 613.
[28] C.F. van Nostrum, S.J. Picken, A.J. Schouten, R.J.M. Nolte, J. Am. Chem. Soc. 117 (1995) 9957.
[29] D. Wöhrle, U. Marose, R. Knoop, Makromol. Chem. 186 (1985) 2209.
[30] D. Wöhrle, E. Preubner, Makromol. Chem. 186 (1985) 2189.
[31] E. Orti, J.L. Breads, C. Clarisse, J. Chem. Phys. 92 (1990) 1228.
[32] A. Riesen, M. Zehnder, T.A. Kaden, Helv. Chim. Acta 69 (1986) 2067.



I II

Scheme 1. Tautomeric forms in AETT.

of this compound with silver(I), copper(I), palladium(II) and platinum(II) ions, including their molecular structures [6b,6c]. According to the molecular structures, ATT acts in presence of sodium acetate as a ionic bidentate ligand with palladium(II) and platinum(II) ions to give the dimeric tetranuclear Pd(II) complex $[\{(L_4Pd_2)NaCl\}_2]\cdot 8MeOH$ and the air-stable dinuclear Pt(III) complex $[L_4Pt_2Cl_2]\cdot 6MeOH\cdot H_2O$ [6c]. Similar complexes could be obtained by the reaction of several Schiff-bases based on 1,2,4-triazines and 1,2,4-trizoles with silver(I) and copper(I) ions [6b,7].

In this communication, we wish to report on the synthesis and characterization of a new Ag(I) complex of AETT with an interesting "mosaic" pattern, and furthermore on a Schiff-base based on AETT and its mixed-ligand Ag(I) and Pd(II) complexes.

2. Experimental

2.1. Materials

AETT (**L1**) was prepared according to the literature procedures [8]. All chemicals were purchased from Merck and Fluka and were used without further purification.

2.2. Physical measurements

IR spectra were recorded on a Shimadzu spectrometer 470 (KBr pellets 4000–400 cm^{-1}). ^1H NMR and ^{31}P NMR spectra were recorded on a Bruker-AQS advance 300 MHz and a Bruker AVANCE 400 MHz using TMS ($\delta = 0.0$ ppm) as an internal standard and 85% aqueous H_3PO_4 as an external standard. Mass spectra were recorded on a Fisons Instruments Trio 1000 spectrometer. Elemental analyses were performed by the following methods: C, H, N analyses; combustion method; sulfur analyses: combustion and titration with $Ba(ClO_4)_2$.

2.3. Synthesis

2.3.1. Synthesis of *HL1a*

A solution of AETT (0.14 g, 1 mmol) in methanol (40 mL) was treated with thiophene-2-carboxaldehyde (0.16 g, 1.5 mmol) and was refluxed for 6 hrs. The progress of the reaction was monitored by TLC using ethyl acetate:petroleum ether (1:2) as the eluent. After completion of the reaction, the solvent was evaporated to 20 mL, the solid crude was filtered and washed with cold methanol (2×5 mL). The clear filtrate was kept at 4 °C to give colorless single crystals of the corresponding Schiff base **LH1a**. Yield: 0.19 g, 80%, m.p.: 185 °C, *Anal.* Calc. for $C_9H_{10}N_4S_2$ (238.03): C, 45.36; H, 4.23; N, 23.51; S, 26.91. Found: C, 45.30; H, 4.25; N, 23.49; S, 26.88%. IR (KBr) [ν/cm^{-1}] 3043w, 2872s, 1583vs, 1500s, 1427s, 1280s, 714s. MS (70 eV) m/z (%) 238 (24, M^+), 129 (100), 109 (20), 96 (8), 70 (28), 55 (8), 41 (16), 39 (26), ^1H NMR δ ($CDCl_3$) 1.36 (t, 3H, Me), 2.81 (q, 2H, CH_2), 7.02–7.47 (d+q, 4H, thiophene + N = C**H**), 10.53 (s, 1H, imine NH).

2.3.2. Synthesis of complex *1*

To a solution of **L1** (0.14 g, 1 mmol) in methanol (20 mL) was added silver nitrate (0.17 g, 1 mmol) and the reaction mixture was stirred for 5 h at room temperature. After completion of the reaction, which was monitored by TLC using ethyl acetate/petroleum ether (1/2), a white precipitate was filtered off and washed with cold methanol (5 mL). The filtrate was stored at room temperature for 1 week to yield colorless crystals suitable for X-ray diffraction measurements. Yield: 0.26 g, 84%. *Anal.* Calc. for $C_4H_8AgN_5O_3S$ (314.07): C, 15.30; H, 2.57; N, 22.30; S, 10.21. Found: C, 15.29; H, 2.40; N, 21.90; S, 10.03%. IR (KBr) [ν/cm^{-1}]: 3448w, 3263m, 3124s, 2974s, 2935s, 2796w, 2700w, 2418w, 2360w, 1624m, 1527w, 1373s, 1211w, 1029m, 979m, 736w, 671w, 590m, 532w. EI-MS (70 eV): m/z (%) 146 (4.5), 145 (5), 144 (100) $(\mathbf{L1})^+$, 142 (2), 129 (29), 128 (42), 113 (40), 111 (14), 98 (25), 96 (13), 71 (18), 69 (38), 60 (70), 56 (65), 54 (35), 45 (10), 43 (25), 41 (31), 29 (17), 28 (69).

2.3.3. Synthesis of complex *2*

A solution of **HL1a** (0.48 g, 2 mmol) in methanol/acetonitrile (1/1, 30 mL) was treated with silver nitrate (0.17 g, 1 mmol) and stirred for 3 h, then a solution of triphenylphosphine (0.52 g, 2 mmol) in the same solvent (15 mL) was added. The reaction mixture was stirred for a further 3 h and the completion of the reaction was monitored by TLC using ethyl acetate/petroleum ether (1/2 v/v) as the eluent. After completion, the reaction mixture was filtered off and washed with cold methanol. The filtrate was kept at 4 °C to give colorless single crystals after a few weeks. Yield: 0.93 g, 80%. *Anal.* Calc. for $C_{54}H_{50}AgN_9O_3P_2S_4$ (1171.11): C, 55.38; H, 4.30; N, 10.76; S, 10.95. Found: C, 55.02; H, 4.18; N, 10.68; S, 10.80%. IR (KBr) [ν/cm^{-1}]: 3048m, 2925–2840w, br, 2910s, 1718s, 1606s, 1543s, 1460s, 1429s, 1379s, 1287m, 1245w, 1094s, 1014s, 966s, 937m, 856m, 821m, 745s, 694s, 540s, 530s, 501s, 430m. EI-MS (70 eV): m/z (%) 238 (100) $(\mathbf{HL1a})^+$, 145 (5), 146 (4), 129 (29), 128 (42), 113 (40), 111 (14), 98 (25), 96 (13), 71 (18), 69 (38), 60 (70), 56 (65), 54 (35), 45 (10), 43 (25), 41 (31), 29 (17), 28 (69); ^1H NMR δ ($CDCl_3$) 1.25 (t, 3H, Me), 2.74 (q, 2H, CH_2), 7.00–7.80 (m, 4H, thiophene), 10.01 (s, 1H N=C**H**), 12.71 (s, 1H, imine NH); ^{31}P NMR δ ($CDCl_3$) 29.39s.

*2.3.4. Synthesis of complex **3***

A solution of **HL1a** (0.48 g, 2 mmol) in methanol/acetonitrile (1/1, 30 mL) was treated with sodium acetate (0.16 g, 2 mmol) and stirred for 3 h. To this solution was added $[(PPh_3)_2PdCl_2]$ (0.70 g, 1 mmol) in methanol (15 mL) (prepared *in situ* from palladium chloride (0.18 g, 1 mmol) and triphenylphosphine (0.52 g, 2 mmol)) under stirring. After 3 h and the completion of the reaction, which was monitored by TLC using ethyl acetate/petroleum ether (1/2 v/v) as eluent, the reaction mixture was filtered off, washed with water (5 mL) and cold methanol (2 × 5 mL). The filtrate was kept at 4 °C to give yellow single crystals after a few days. Yield: 0.91 g, 83%. *Anal.* Calc. for $C_{54}H_{48}N_8P_2PdS_4$ (1105.65): C, 58.66; H, 4.38; N, 10.13; S, 11.60. Found: C, 58.59; H, 4.32; N, 10.21; S, 11.71%. IR (KBr) [ν/cm^{-1}]: 3398s, 3285m, 2974m, 2931m, 2875w, 2359w, 2332w, 1591m, 1531m, 1477w, 1433s, 1375m, 1265s, 1178m, 1091m, 1035w, 945w, 744s, 698s, 514s, 460w. EI-MS (70 eV): *m/z* (%) 262 (32) PPh_3, 237 (5) $(\mathbf{L1a})^+$, 183 (85), 152 (25), 139 (14), 129 (18), 128 (20), 127 (32), 115 (8), 110 (25), 108 (35), 107 (49), 97 (60), 95 (100), 77 (60), 51 (49); ^{1}H NMR δ ($CDCl_3$) 1.20 (t, 3H, Me), 2.70 (q, 2H, CH_2), 6.95–7.75 (m, 4H, thiophene), 9.97 (s, 1H N=C**H**); ^{31}P NMR δ ($CDCl_3$) 29.76 (s).

*2.4. Crystal structure analyses of HL1a, **1**, **2** and **3***

Table 1 shows the crystallographic data of **HL1a**, **1**, **2** and **3**. The crystals of **HL1a**, **1**, **2** and **3** were covered with perfluorinated oil and mounted on the top of a glass capillary under a flow of cold gaseous nitrogen. The orientation matrix and unit cell dimensions were determined from *ca.* 3000 (**HL1a**; Stoe IPDS II), *ca.* 4500 (**1**, Stoe IPDS I), *ca.* 8000 (**2**; Stoe IPDS I) and *ca.* 8000 (**3**; Stoe IPDS I) reflections (graphite-monochromated Mo Kα radiation, $\lambda = 71.073$ pm). The intensities were corrected for Lorentz and polarization effects. In addition, absorption corrections were applied for **1**, **2** and **3** (numerical). The structures were solved by the direct methods for **HL1a** (SHELXS-97) and **3** (SIR-92) and by the Patterson method for **1** and **2** (SHELXTL-PLUS) and refined against F^2 by full-matrix least-squares using the program SHELXL-97 (see Section 5). The positions of the carbon bonded hydrogen atoms (except H1 for **HL1a** and **3**) in all the compounds

Table 1
Crystallographic data for **HL1a**, **1**, **2** and **3**

Compound	**HL1a**	**1**	**2**	**3**
Empirical formula	$C_9H_{10}N_4S_2$	$C_8H_{16}Ag_2N_{10}O_6S_2$	$C_{56}H_{53}AgN_{10}O_3P_2S_4$	$C_{58}H_{64}N_8O_4P_2PdS_4$
Formula mass	238.33	628.13	1212.16	1233.80
Crystal size (mm)	0.26 × 0.22 × 0.13	0.17 × 0.08 × 0.08	0.17 × 0.11 × 0.1	0.15 × 0.13 × 0.07
Crystal system	triclinic	triclinic	monoclinic	orthorhombic
Space group	$P\bar{1}$	$P\bar{1}$	$C2/c$	$Pbca$
a (pm)	801.6(1)	1033.2(3)	3075.4(3)	1462.0(1)
b (pm)	887.2(2)	699.0(1)	1468.0(1)	1826.2(1)
c (pm)	900.8(2)	2576.0(5)	2850.5(3)	2130.8(1)
α (°)	80.74(1)	90	90	90
β (°)	74.68(1)	98.61(3)	116.96(2)	90
γ (°)	63.52(1)	90	90	90
Volume (pm^3 × 10^6)	552.4(2)	1839.4(7)	11471(2)	5689.0(6)
Z	2	4	8	4
D_{calcd} (g cm^{-3})	1.433	2.268	1.404	1.44
Absorption correction		numerical	numerical	numerical
μ (cm^{-1})	4.5 (Mo Kα)	24.1(Mo Kα)	6.1 (Mo Kα)	5.8 (Mo Kα)
Temperature (K)	193	193	193	173
$2\theta_{max}$ (°)	51.87	52.23	51.89	52.09
Index range (h,k,l)	−9 → 9, −10 → 10, −11 → 11	−12 → 12, −8 → 8, −31 → 31	−37 → 37, −18 → 18, −34 → 34	−17 → 17, −22 → 22, −26 → 26
Reflections collected	7797	17545	53801	53791
Unique reflections (R_{int})	2132 (0.0662)	3616 (0.1322)	11115 (0.1772)	5482 (0.1211)
Reflections with $F_o > 4\ \sigma(F_o)$	1728	1635	3683	2469
Parameters	173	256	692	359
R_1	0.0411	0.0718	0.0415	0.0411
wR_2 (all data)	0.1317[a]	0.1707[b]	0.0634[c]	0.0736[d]
Maximum residual electron density [(e pm^{-3}) × 10^{-6}]	0.60	1.98	0.53	0.63

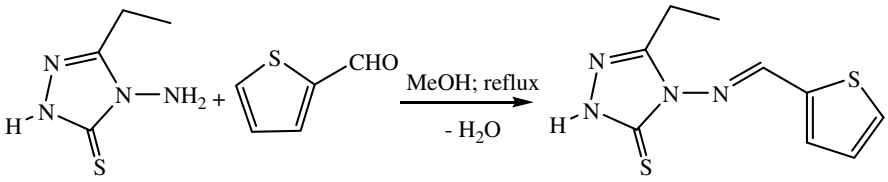
[a] $w = 1/[\sigma^2(F_o)^2 + (0.0899 \cdot P)^2]$; $P = [\max(F_o^2, 0) + 2\ F_c^2]/3$.
[b] $w = 1/[\sigma^2(F_o)^2 + (0.0921 \cdot P)^2]$.
[c] $w = 1/[\sigma^2(F_o)^2]$.
[d] $w = 1/[\sigma^2(F_o)^2 + (0.0276 \cdot P)^2]$.

were calculated for ideal positions and refined with a common displacement parameter. H1 atoms in **HL1a** and **3** were included with a free refinement. The programs used were SHELXS-97 [9], SIR-92 [10], SHELXL-97 [11], SHELXTL-Plus [12] and PLATON [13].

3. Results and discussion

3.1. Syntheses and characterization of *HL1a, 1, 2 and 3*

Treatment of **L1** with 2-thiophene carbaldehyde in methanol under reflux conditions led to the corresponding imine compound **HL1a** in high yield



L1 **HL1a** (1)

Compound **1** can be obtained by the reaction of **L1** with $AgNO_3$ in methanol according to the following equation:

$$2\mathbf{L1} + 2AgNO_3 \xrightarrow{MeOH} \underset{\mathbf{1}}{[\{(\mathbf{L1})_2Ag_2\}NO_3]_n} \quad (2)$$

Compound **2** can be prepared by the reaction of **HL1a**, $AgNO_3$ and PPh_3 in a 2:1:2 molar ratio in ethanol and acetonitrile, and compound **3** can be obtained by the treatment of the same ligand with $PdCl_2$ and PPh_3 in methanol in the presence of sodium acetate in a 2:1:2:2 molar ratio, according to the following equations:

$$2\mathbf{HL1a} + AgNO_3 + 2PPh_3 \xrightarrow{EtOH/CH_3CN} \underset{\mathbf{2}}{[(PPh_3)_2Ag(\mathbf{HL1a})_2]NO_3 \cdot CH_3CN} \quad (3)$$

$$2\mathbf{HL1a} + PdCl_2 + 2PPh_3 \xrightarrow[-2NaCl;\ -2\ AcOH]{2NaOAc;\ MeOH} \underset{\mathbf{3}}{[(PPh_3)_2Pd(\mathbf{L1a})_2] \cdot 4MeOH} \quad (4)$$

The synthesized compounds **HL1a** and both silver complexes are colorless, while **3** is a yellow solid material and all of them are air-stable. The absorptions at about 3043 cm^{-1} **HL1a**, 3124 cm^{-1} **1** and 3048 cm^{-1} **2** can be assigned to N–H stretching vibrations, which disappeared in the IR spectrum of **3**. The $C{=}N_{ring}$ causes vibrations at 1583 cm^{-1} in the free ligand, and these vibrations were observed at 1527 cm^{-1} in **1**, 1543 cm^{-1} in **2** and 1591 cm^{-1} in **3**. Broad weak absorptions due to O–H stretching vibrations could be found at 3398 cm^{-1} for **3**. Strong absorptions at about 2910–2935 cm^{-1} are ascribed to the vibrations of the $–CH_2$-groups in the free ligand and the complexes. The P–C vibrations of the PPh_3 moiety are found in the range 744–691 cm^{-1} for both complexes **2** and **3** [14]. The NO_3^- anion in **1** presents its N–O asymmetric stretching mode at 1373 cm^{-1}, and at 1379 cm^{-1} for **2**.

The mass spectra of the complexes show only the main peak of the corresponding ligand [$m/z = 144$ (**1**), $m/z = 238$ (**2**) and $m/z = 237$ (**3**)].

Consistent with the structures of **2** and **3**, the solution ^{31}P NMR in $CDCl_3$ of **2** and **3** showed only one ^{31}P resonance at δ 29.39 ppm and 29.76 ppm, respectively. On the other hand, the ^1H NMR assignments for complex **2** were similar to those for the ligand, while in the ^1H NMR spectrum of **3** no NH signal was observed, in accordance with the deprotonated ligand in the complex.

3.2. Crystal structure of *HL1a, 1, 2 and 3*

3.2.1. Compound *HL1a*

Selected bond distances and angles of all the synthesized compounds are given in Table 2. Compound **HL1a** crystallizes in the triclinic space group $P\bar{1}$. The basic five-membered ring skeleton in this compound is planar and the dihedral angle between the best planes through the triazole ring and the aldehyde fragment is 12° (Fig. 1). The bond distances in the triazole five-membered heterocycles are in good agreement with those observed in iminic derivatives of 1,2,4-triazole, such as 4-(4-methoxybenzylidene-amino)-5-methyl-2H-1,2,4-triazole-3(4H)-thione and 4-(3-methoxybenzylideneamino)-5-methyl-2H-1,2,4-triazole-3(4H)-thione [7b].

In **HL1a**, the S1–C1 mean bond length of 168.5(2) pm shows significantly high double bond character, such as observed in AMTT [15]. The iminic C–N mean bond distance of 127.2(3) pm lies in the range observed in similar compounds, such as 2-acetylthiophene thiosemicarbazone (129.2(3) pm) and 2-acetyl thiophene 4-phenyl thiosemicarbazone (128.2(3) pm) [16].

In **LH1a**, intermolecular weak hydrogen bonding links the thiocarbonyl sulfur atom of one molecule to the NH-group of the adjacent one (N4–H1···S1a: 330.5(3) pm) and is responsible for the centrosymmetric geometry of the compound.

Table 2
Selected bond lengths (pm) and bond angles (°)

HL1a		**1**			
S1–C1	168.5(2)	Ag1–S1	264.7(3)	N3–N4	139(1)
C1–N4	133.1(3)	Ag1–N8	231.8(8)	N3–C2	129(1)
N4–N3	137.6(4)	Ag1–S1a	258.7(3)	N4–C1	133(1)
N3–C2	130.1(3)	Ag1–N2a	241.7(8)	N5–N6	139(1)
C2–C3	148.8(4)	Ag2–S1	245.1(3)	N5–C5	138(1)
C3–C4	152.8(4)	Ag2–S2	289.9(4)	N7–C6	132(1)
C2–N1	138.1(3)	Ag2–S2d	247.4(3)	N7–N8	137(1)
N1–N2	139.5(2)	Ag2–N6d	244.1(8)	O1–N9	122(1)
N2–C5	127.2(3)	S1–C1	171(1)	O2–N9	128(1)
C5–C6	144.4(3)	S2–C5	169(1)	O3–N9	118(1)
C6–S2	170.4(3)	N1–N2	139(1)	O4–N10	118(1)
		N1–C1	135(1)	O5–N10	123(1)
		N1–C2	141(1)	O6–N10	123(1)
S1–C1–N4	126.6(2)	S1–Ag1–N8	96.2(2)	C1–S1–Ag1c	96.6(3)
C1–N4–N3	114.8(2)	S1–Ag1–S1a	131.0(1)	Ag2–S2–C5	93.1(4)
N4–N3–C2	103.7(2)	S1–Ag1–N2a	112.4(3)	Ag2–S2–Ag2b	106.9(1)
N3–C2–N1	110.9(2)	N8–ag1–S1a	124.2(2)	C5–S2–Ag2b	97.6(4)
C2–N1–C1	108.2(2)	N8–Ag1–N2a	114.4(3)	N2–N1–C1	123.9(8)
C1–N1–N2	132.6(2)	S1a–Ag1–N2a	77.6(2)	N1–N2–Ag1c	111.2(6)
N1–N2–C5	118.7(2)	S1–Ag2–S2	103.1(1)	N6–N5–C5	123.9(8)
N2–C5–C6	119.4(2)	S1–Ag2–S2d	147.3(1)	N6–N5–C6	126.5(8)
C5–C6–S2	122.5(2)	S1–Ag2–N6d	121.9(2)	N5–N6–Ag2b	108.8(5)
N1–C2–C3	123.7(2)	S2–Ag2–S2d	101.6(1)	Ag1–N8–N7	132.9(6)
C2–C3–C4	112.5(2)	S2–Ag2–N6d	86.5(3)	Ag1–N8–C5	116.3(7)
		S2d–Ag2–N6d	80.5(2)	O1–N9–O2	117(1)
		Ag1–S1–Ag2	95.9(1)	O2–N9–O3	120(1)
		Ag1–S1–C1	95.5(4)	O1–N9–O3	123(1)
		Ag1–S1–Ag1c	93.96(9)	O4–N10–O5	120(1)
		Ag2–S1–C1	110.9(3)	O5–N10–O6	116(1)
		Ag2–S1–Ag1c	149.7(1)	O4–N10–O6	124(1)
2				**3**	
Ag1–S1	260.6(1)	N1–C1	137.8(6)	Pd1–S1	232.7(1)
Ag1–S3	259.0(1)	N2–C5	128.2(6)	Pd1–P1	232.4(1)
Ag1–P1	248.3(1)	N3–N4	135.8(6)	S1–C1	171.7(4)
Ag1–P2	248.3(1)	N5–N6	139.8(5)	S2–C6	170.9(4)
S1–C1	169.0(5)	N5–C10	135.8(6)	S2–C9	169.9(4)
S2–C6	172.0(5)	N6–C14	128.1(6)	N1–N2	139.4(4)
S2–C9	169.9(5)	N7–N8	136.8(6)	N1–C1	138.6(4)
S3–C10	170.4(5)			N2–C5	126.9(5)
S4–C15	170.9(5)	O1–N9	125.9(5)	N3–C2	130.9(5)
S4–C18	169.9(5)	O2–N9	122.1(5)	N4–C1	131.4(4)
N1–N2	140.0(6)	O3–N9	123.8(5)	N3–N4	139.8(4)
S1–Ag1–S3	109.18(5)			S1–Pd1–P1	84.88(4)
S1–Ag1–P1	104.54(5)			S1–Pd1–S1a	180
S1–Ag1–P2	111.46(5)			S1–Pd1–P1a	95.12(4)
S3–Ag1–P1	113.72(5)			P1–Pd1–S1a	95.12(4)
S3–Ag1–P2	103.84(5)			P1–Pd1–P1a	180
P1–Ag1–P2	114.20(5)			S1a–Pd1–P1a	84.88(4)
Ag1–S1–C1	111.2(2)			Pd1–S1–C1	105.8(1)
Ag1–S3–C10	104.8(2)			N1–N2–C5	117.5(3)
N1–N2–C5	115.1(4)			S1–C1–N1	124.1(3)
N5–N6–C14	116.4(4)			S1–C1–N4	127.3(3)
O1–N9–O2	118.4(5)			C2–N3–N4	108.2(3)
O1–N9–O3	117.2(5)			C1–N4–N3	107.9(3)
O2–N9–O3	124.4(5)			N2–C5–C6	119.7(3)

3.2.2. Complex *1*

As mentioned above, 4-amino-5-ethyl-2H-1,2,4-triazole-3(4H)-thione (AETT, **L1**) shows thione-thiol tautomerism (Scheme 1). It is also reported that such ligands can act as a neutral thione (**I**), a bidentate chelating one through the sulfur and the amine nitrogen atoms, as a deprotonated thiol (**II**) ligand or as a tridentate chelating *N*,*S* agent with an additional bridge through the endocyclic nitrogen atom with the metal atoms as shown in Scheme 2 [17].

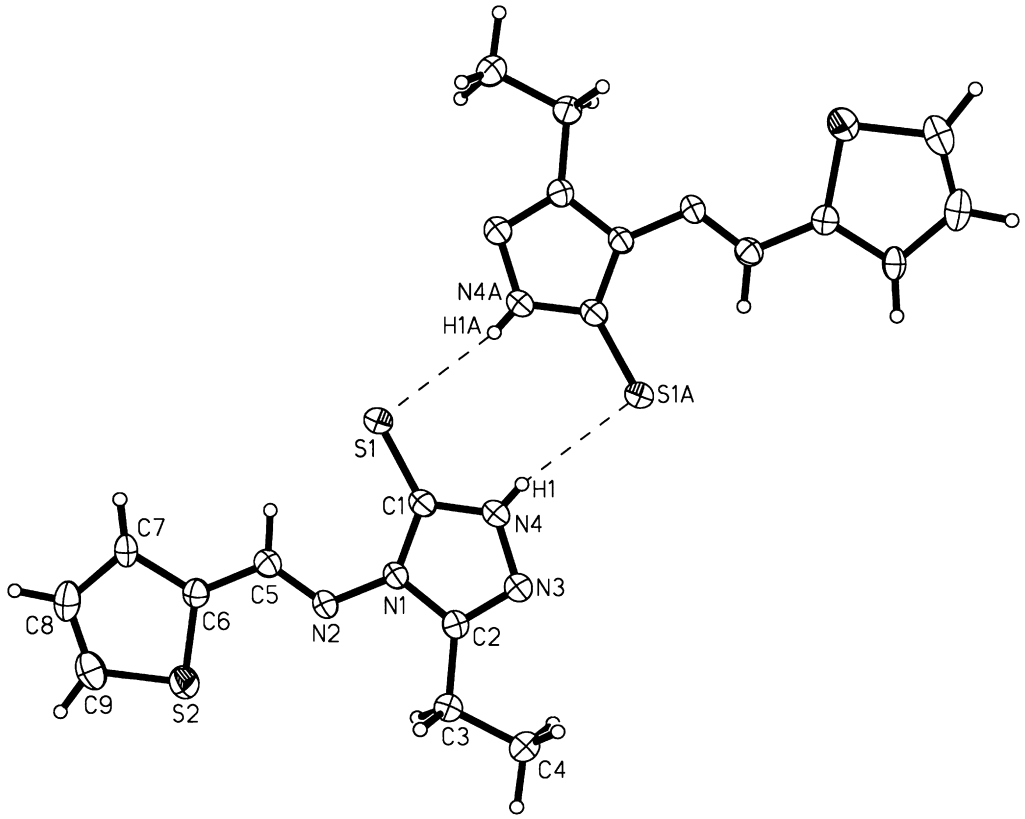
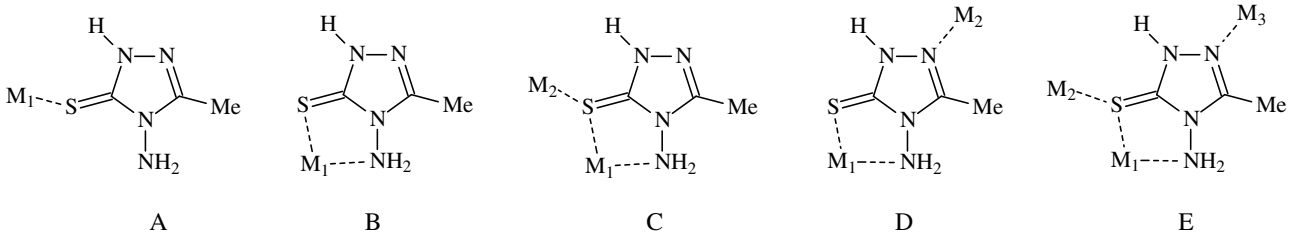
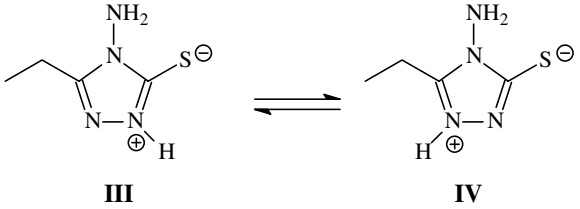


Fig. 1. Molecular structure of **HL1a** dimerized by H bridges (thermal ellipsoids are at the 40% probability level).



Scheme 2.



Scheme 3.

They can also act as ionic ligands in the form of **III** or **IV**, which have a *Hückel* aromaticity, with the metal atoms (Scheme 3).

Complex **1** consists of two dimensional polymers of $\{(\mathbf{L1})_2Ag_2\}^{2+}$ cations and NO_3^- anions (Fig. 2). In the cation of **1**, both ligands exist in two tautomeric forms **III** and **IV**, as shown in Scheme 4.

The coordination mode of the ligands to the metal centers can be described as a combination of form E and the modified form of C (with an additional coordination of a sulfur atom to a third metal center, form F) as shown in Scheme 5.

The Ag1 atom links the sulfur atom of one ligand to the endocyclic nitrogen atom of another one and the completion of the distorted tetrahedral geometry around Ag1 occurs by the coordination of the sulfur atom and the NH_2-group of the adjacent ligand. The Ag2 atom acts also as a bridging agent and links the sulfur atoms of two ligands of different layers. The linear geometry around Ag2 is also distorted by the coordination of the sulfur atom and one hydrazine nitrogen atom of two adjacent ligands. So, in the cation of **1**, each metal atom is coordinated to three different adjacent triazole ligands. This coordination mode of silver atoms and sulfur atoms lead to the forma-

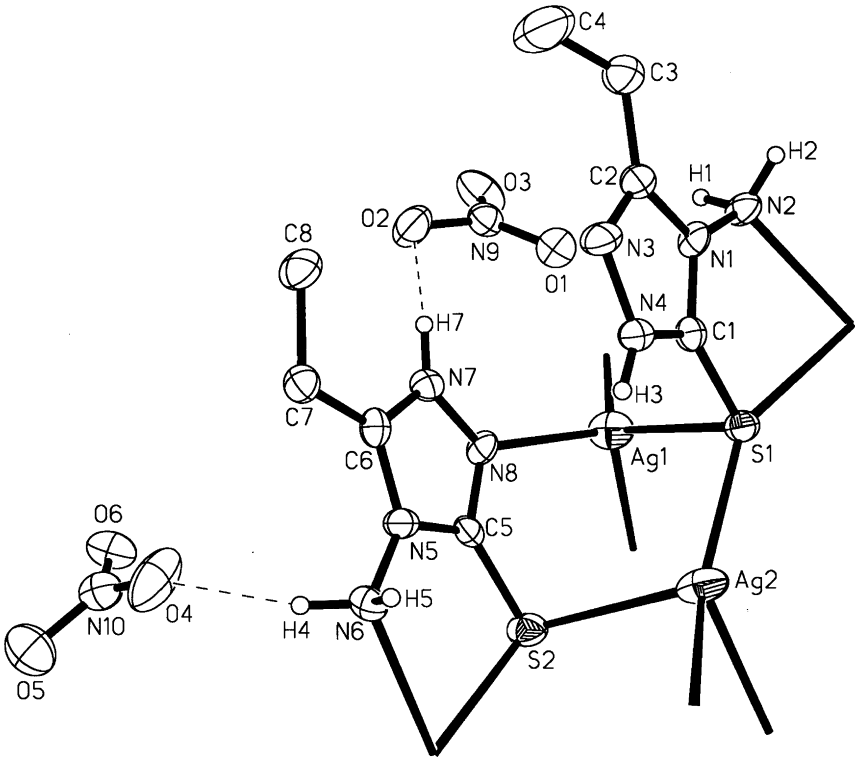
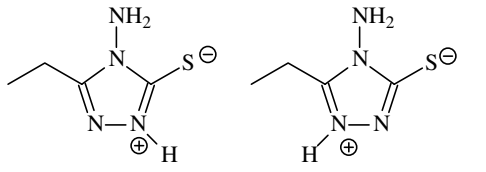
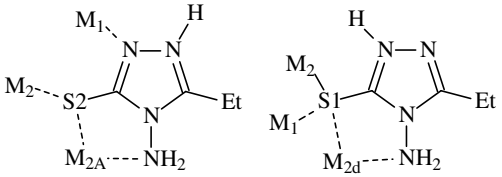


Fig. 2. Graphical representation of a part of the coordination polymer **1** (thermal ellipsoids at the 30% probability level).



Ring around S1 Ring around S2

Scheme 4.



E F

Scheme 5.

tion of a 10-membered Ag–S "mosaic" pattern as shown in Fig. 3. This coordination mode caused a two dimensional endless framework and is responsible for the formation of layers parallel to (0 0 1).

The C–N bond distances in the triazole ligands, C1–N1: 133(1) pm, C2–N3: 129(1) pm, C5–N8: 131(1) pm and C6–N7: 132(1) pm, show that both ligands exist in forms **III** and **IV** and show *Hückel* aromaticity.

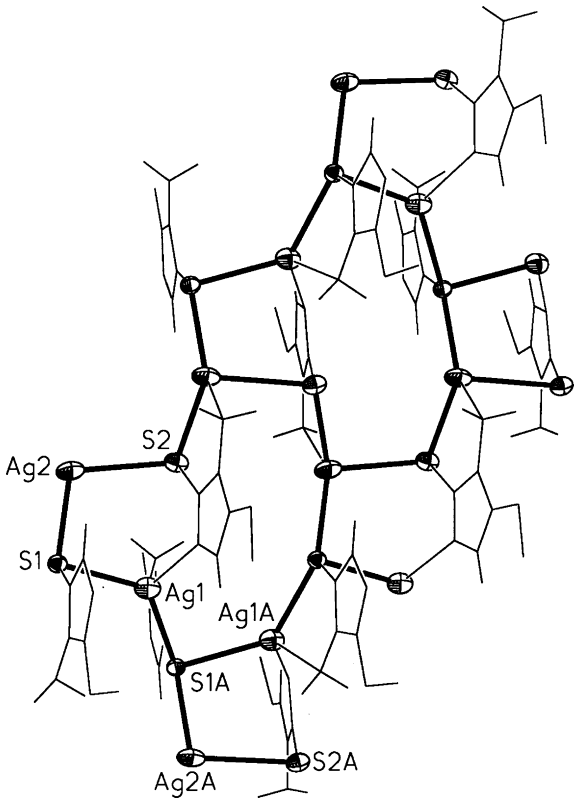


Fig. 3. Graphical representation of the Ag–S "mosaic" pattern in **1**. Only the cations are shown.

The Ag1–S1 and Ag1–S1a bond distances in **1** of 264.7(3) and 258.7(3) pm lie within the ranges observed

for silver complexes containing a sulfur atom with a coordination number (c.n.) of four (256.8–272.1 pm) [18]. While the Ag1–N8 bond length of 231.8(8) pm is near in the generally accepted Ag–N distance of 234 pm [19], the Ag1–N2a bond length of 241.7(8) pm is clearly longer than 234 pm but is significantly shorter than the 250.4(3) pm observed in $[(AMTTO)_2Ag]NO_3$ [4]. It is also shorter than the sum of the van der Waals radii of silver and nitrogen (155 + 170 = 325 pm) [20]. In addition, the AgS2 axis in **1** with a S1–Ag–S1a angle of 131.0(1)° is clearly smaller than the observed angle in $[(AMTTO)_2Ag]NO_3$ (S–Ag–S: 160.77(3)° [4]) caused by stronger Ag–N bonds. Therefore, the coordination sphere around Ag1 can be described as distorted tetrahedral or as a 3+1 coordination.

The Ag2–S1 and Ag2–S2d bond distances in **1** of 245.1(3) and 247.4(3) pm lie within the range observed for silver complexes containing a sulfur atom with a c.n. of two (236.2–241.8 pm) [18,21] and c.n. of three (246.4–253.7 pm) [22], while the Ag2–S2 bond length of 289.9(4) pm is clearly longer than the distances observed for silver complexes containing sulfur atom with a c.n. of four (256.8–272.1 pm) [18]. The Ag2–N6d bond distance in **1** of 244.1(8) pm is longer than the Ag–N distance of 234 pm [19] but it is clearly shorter than the sum of the van der Waals radii of silver and nitrogen [20]. In addition, the S1–Ag2–S2d angle of 147.3(1)° is somewhat smaller than the observed angle in $[(AMTTO)_2Ag]NO_3$ [4], caused by stronger Ag–N bonds. They are characteristic for a distorted linear coordination sphere, caused by additional Ag–S and Ag–N contacts. The coordination sphere around the Ag2-center can be described as 2+2.

Table 3
Hydrogen bonding distances (pm) in **1**

	X···Y
N2–H1···O1	283(1)
N2–H1···O5a	326(1)
N2–H2···O3b	289(1)
N4–H3···O6b	266(1)
N6–H4···O4	293(1)
N6–H5···O5b	302(1)
N6–H6···O6b	300(1)
N7–H7···O1	311(1)
N7–H7···O2	263(1)

The two nitrate anions are linked to cations *via* hydrogen bonding, using their oxygen atoms, and link the NH_2 and NH groups in the same cations. The hydrogen bonds observed in this molecule are listed in Table 3. These hydrogen bridges cause slightly different N–O bond lengths and O–N–O bond angles within the standard deviations of nitrate ions (Table 3).

The dihedral angles formed by the "best" planes through the five-membered triazole heterocycles (A: N1 N3 N4 C1 C2 and B: N5 N7 N8 C5 C6) is 4°.

3.2.3. Complex 2

The ionic complex **2** crystallizes in the monoclinic space group $C2/c$. In the cation of **2**, $[(PPh_3)_2Ag(\mathbf{HL1a})_2]^+$, the silver atom displays a distorted tetrahedral environment (Fig. 4). The coordination spheres around the metal centre are occupied with two P atoms of the phosphane molecules

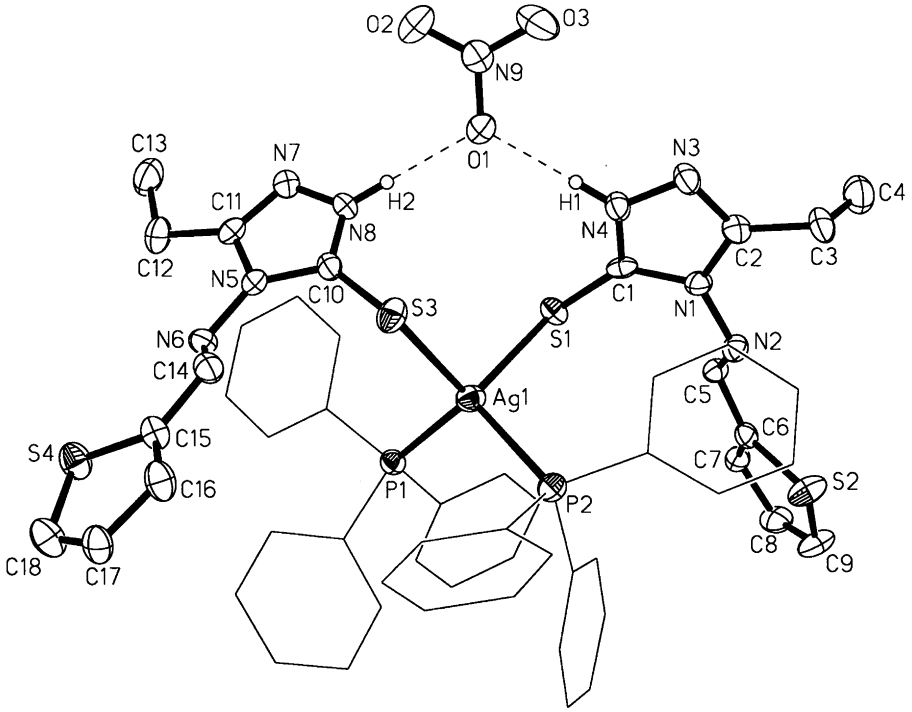


Fig. 4. Molecular structure of **2** (thermal ellipsoids at the 40% probability level).

and two thione S atoms of two **LH1a** Schiff-bases. This arrangement is slightly distorted since, except the S angle at the metal site of 109.18(5)° (S1–Ag1–S3), the other three selected angles in the AgP_2S_2 group, P1–Ag1–P2, S1–Ag1–P2 and S3–Ag1–P1 with 114.20(5)°, 111.46(5)° and 113.72(5)°, are greater than those of a regular tetrahedron. The tetrahedral distortion is due to steric hindrance of the bulky phosphane ligands and was observed in a series of analogous complexes [23]. The Ag–P bond distances, mean 248.3(1) pm, are within the range of the corresponding distances reported for other silver(I) complexes (227.7–230.7 pm) [7a,18b]. The Ag1–S1 and Ag1–S3 bond distances of 260.6(1) pm and 259.0(1) pm lie in the range observed for complexes with tetrahedral Ag(I) centers [24]. The nitrate ion acts as a bridging agent between two NH groups of the Schiff-bases of the cation through one of its oxygen atoms *via* hydrogen bonds (N4–H1···O1: 274.3(5) pm and N8–H2···O1: 275.6(6) pm). This coordination mode causes a slightly lengthening of the N9–O1 bond distance (125.9(5) pm) compared to the other N–O distances in the nitrate ion (N9–O2: 122.1(5) and N9–O3: 123.8(5) pm).

3.2.4. Complex *3*

The Pd atom in **3** has the usual ideal square planar coordination arrangement with P–Pd–P and S–Pd–S axes of 180° (Fig. 5). The metal atom is located on the point of intersection of the mirror plane (center) and sits on the twofold axis. Each ligand in **3** is singly deprotonated, and therefore can be assigned as a compound with *Hückel* aromaticity. They occupy the positions *trans* to each other and

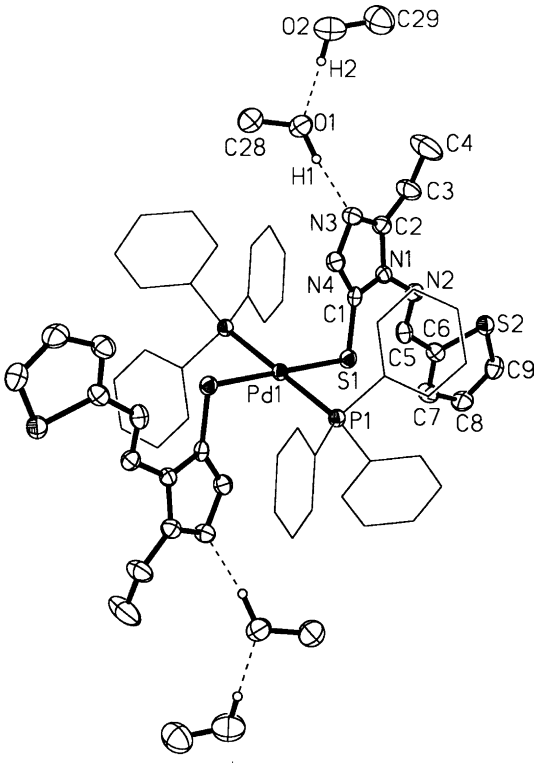


Fig. 5. Molecular structure of **3** (thermal ellipsoids at the 40% probability level).

are coordinated to the metal center as monodentate ligands using their thione sulfur atoms.

The Pd–P bond length of 232.4(1) pm is shorter than the sum of the single bond radii for palladium and phosphorus, i.e. 241 pm [25], is slightly longer than the Pd^{II}–PPh_3 bond reference value (320.2 pm) encountered in 248 entries [26], and falls in the middle of the wide range of values (221–246 pm).

The Pd–S bond distance of 232.7(1) pm is in the range observed in the complexes $[(HL)_4Pd]Cl_2 \cdot 8MeOH$ (mean Pd–S: 231.97 pm) [6c], $[(HL)_2PdI_2] \cdot 2MeOH$ (Pd–S: 232.1(1) pm) [6c] and $[\{(L_4Pd_2)NaCl\}_2] \cdot 8MeOH$ (mean Pd–S: 231.95 pm) [6c]. In **3**, one methanol molecule acts as a bridging agent using its oxygen atom between each heterocycle and another solvate molecule, and links the endocyclic nitrogen atom of the heterocycle to the oxygen atom of the solvate molecule *via* medium to strong hydrogen bonds (N3···O1–H1: 286.2(5) pm, O2–H2···O1: 273.3(6) pm). The dihedral angle between the "best" planes of the complex (A: Pd1 S1 S1a P1 P1a, B: N1 N2 N3 N4 C1 C2, C: S2 C5 C6 C7 C8 C9) are 116° (A, B), 93° (A, C) and 29° (B, C).

4. Conclusion

Two new complexes containing silver(I) atoms and a new complex with a palladium(II) core have been synthesized and characterized. All the complexes contain 1,2,4-triazoles derivatives as ligands. The molecular structure of complex **1** shows a new coordination mode between the metal atom and the sulfur atoms of the triazole moieties, which has not been observed previously to the best of our knowledge. This coordination mode leads to the formation of a 10-membered Ag–S "mosaic" pattern, causing a two dimensional endless framework and is responsible for the formation of layers parallel to (0 0 1). The two other complexes, **2** and **3**, can be assigned as the first examples with the coordination of two Schiff-bases based on 1,2,4-triazole to metal-bis(triphenylphosphine) moieties. The silver(I) complex (**2**) is an ionic one, while the palladium complex contains two singly deprotonated Schiff-bases and is therefore a neutral complex.

5. Supplementary data

CCDC 661633, 661634, 661635, 661636 contain the supplementary crystallographic data for **HL1a**, **1**, **2**, **3**. These data can be obtained free of charge via http://www.ccdc.cam.ac.uk/conts/retrieving.html, or from the Cambridge Crystallographic Data Centre, 12 Union Road, Cambridge CB2 1EZ, UK; fax: (+44) 1223-336-033; or e-mail: deposit@ccdc.cam.ac.uk.

Acknowledgement

This work has been supported by the Presidential Office of Iran for Research (No. 84186). We are grateful for this partial financial research.

References

[1] (a) H. Beraldo, D. Gambino, Mini Rev. Med. Chem. 4 (2004) 31;
(b) A. Gómez Quiroga, C. Navarro Ranninger, Coord. Chem. Rev. 248 (2004) 119.

[2] (a) I. Kucukguzel, S.G. Kucukguzel, S. Rollas, M. Kiraz, Bioorg. Chem. Lett. 11 (2001) 1703;
(b) S. Bala, R.P. Gupta, M.L. Sachedeva, M. Lal, A.K. Singh, H.K. Pujari, Ind. J. Chem. 16B (1978) 481;
(c) S. Jantova, G. Greif, R. Pavlovicova, L. Cipak, Folia Microbiol. 43 (1998) 75;
(d) Y.S. Sadadudam, M.M. Shetty, P.V. Dlawan, Eur. J. Med. Chem. 27 (1992) 87.

[3] (a) M. Akbar Ali, S.E. Livingstone, Coord. Chem. Rev. 13 (1974) 101;
(b) K. Severin, R. Bergs, W. Beck, Angew. Chem., Int. Ed. 37 (1998) 1722.

[4] F. Adhami, M. Ghassemzadeh, M.M. Heravi, A. Taeb, B. Neumüller, Z. Anorg. Allg. Chem. 625 (1999) 1411.

[5] M. Yazdanbakhsh, M. Hakimi, M.M. Heravi, M. Ghassemzadeh, B. Neumüller, Z. Anorg. Allg. Chem. 631 (2005) 924.

[6] (a) M. Ghassemzadeh, F. Adhami, M.M. Heravi, A. Taeb, S. Chitsaz, B. Neumüller, Z. Anorg. Allg. Chem. 628 (2002) 2887;
(b) M. Ghassemzadeh, M.M. Pooramini, M. Tabatabaee, M.M. Heravi, B. Neumüller, Z. Anorg. Allg. Chem. 630 (2004) 403;
(c) M. Ghassemzadeh, M.M. Heravi, B. Neumüller, Z. Anorg. Allg. Chem. 631 (2005) 2401.

[7] (a) M. Ghassemzadeh, A. Sharifi, J. Malakootikhah, B. Neumüller, E. Iravani, Inorg. Chim. Acta 357 (2004) 2245;
(b) M. Ghassemzadeh, M. Tabatabaee, S. Soleimani, B. Neumüller, Z. Anorg. Allg. Chem. 631 (2005) 1871;
(c) M. Ghassemzadeh, M. Tabatabaee, M.M. Pooramini, M.M. Heravi, A. Eslami, B. Neumüller, Z. Anorg. Allg. Chem. 632 (2006) 786;
(d) F. Heshmatpour, M. Ghassemzadeh, M. Semsarha, B. Neumüller, Z. Anorg. Allg. Chem. 633 (2007) 465.

[8] H. Beyer, C.-F. Kröger, Anal. Chem. 637 (1960) 135.

[9] G.M. Sheldrick, SHELXS-97, Universität Göttingen 1997.

[10] G.M. Sheldrick, SHELXL-97, Göttingen 1997.

[11] A. Altmore, G. Cascarano, C. Giacovazzo, A. Guagliardi, M.C. Burla, G. Polidori, M. Camalli, SIR-92, Bari, Perugia, Rome, 1992.

[12] G.M. Sheldrick, SHELXTL-Plus, Release 5.05/VMS for Siemens R3 Crystallographic Research Systems, Siemens Analytical X-ray Instruments Inc., Madison (WI), 1996.

[13] A.L. Spek, PLATON-98, Utrecht, 1998.

[14] J. Weidlein, U. Müller, K. Dehnicke, Schwingungsspektroskopie, 2. Aufl., G. Thieme Verlag, Stuttgart, 1988.

[15] J.L. Escobar-Valderrama, J.H. Garcia-Tapia, J. Ramirez-Ortiz, M.J. Rosales, R.A. Toscano, J. Valdes-Martinez, Can. J. Chem. 67 (1989) 198.

[16] G.M. de Lima, J.L. Neto, H. Beraldo, H.G.L. Siebald, D.J. Duncalf, J. Mol. Struct. 604 (2002) 287.

[17] (a) M. Cingi Biagini, F. Bigoli, M. Lanfranchi, E. Leporati, M.A. Pellinghelli, C. Foglia, Inorg. Chim. Acta 235 (1995) 37;
(b) F. Bigoli, M. Lanfranchi, M.A. Pellinghelli, J. Chem. Res. (1990) 1712;
(c) M. Cingi Biagini, F. Bigoli, M. Lanfranchi, M.A. Pellinghelli, A. Vera, E. Buluggiu, J. Chem. Soc., Dalton Trans. (1992) 3145;
(d) M.C. Biagini, M. Lanfranchi, L. Marchio, M.A. Pallinghelli, Inorg. Chim. Acta 305 (2000) 95.

[18] (a) I.G. Dance, L.J. Fitzpatrick, M.L. Scudder, Inorg. Chem. 23 (1984) 2276;
(b) D.D. Heinrich, J.P. Fackler Jr., P. Lahuerta, Inorg. Chim. Acta 116 (1986) 15.

[19] International Tables for X-ray Crystallography, vol. IV, Kynoch Press, Birmingham (UK), 1974: covalent radii (pm): Ag 159, S 102 and N 75.

[20] A. Bondi, J. Phys. Chem. 68 (1964) 441.

[21] (a) E. Block, M. Gernon, H. Kang, J. Zubieta, Angew. Chem. 100 (1988) 1389. Angew. Chem. Int. Ed. Engl. 27 (1988) 1342;
(b) E. Block, D. Macherone, S.N. Shaikh, J. Zubita, Polyhedron 9 (1990) 1429;
(c) P.A. Perez-Lourido, J.A. Garcia-Vazquez, J. Romero, M.S. Louro, A. Sousa, Q. Chen, Y. Chang, J. Zubieta, J. Chem. Soc., Dalton Trans. (1996) 2047.

[22] (a) S. Kawata, S.S. Kitagawa, M. Kondo, I. Furuchi, M. Munakata, Angew. Chem. 106 (1994) 1851–1854. Angew. Chem., Int. Ed. Engl. 33 (1994) 1759;
(b) T. Kuroda-Sowa, M. Munakata, H. Matsuda, S. Akiyama, M. Maekawa, J. Chem. Soc., Dalton Trans. (1995) 2201–2208;
(c) K. Tang, X. Jin, Q. Xiao, Y. Tang, Jiegou Huaxue [J. Struct. Chem.] 7 (1988) 159.

[23] S. Skoulika, A. Aubru, P. Karagiannidis, P. Aslanadis, P. Papastefanou, Inorg. Chim. Acta 183 (1991) 207–211.

[24] (a) D. Coucouvanis, N.C. Baenzinger, S.M. Johnson, Inorg. Chem. 13 (1974) 1191;
(b) F.J. Hollander, D. Coucouvanis, Inorg. Chem. 13 (1974) 2381;
(c) R. Alessio, D. Belli Dell'amico, F. Calderazzo, U. Englert, Gazz. Chim. Ital. 123 (1993) 719.

[25] L. Pauling, The Nature of the Chemical Bond, 3rd ed., Cornell University Press, New York, 1960.

[26] Established by a search of the Cambridge Structural Database: see F.A. Allen, O. Kennard, R. Taylor, Acc. Chem. Res. 16 (1983) 146.

the heterometal alkoxide clusters of lanthanide and sodium $[Ln_2Na_8(OCH_2CH_2NMe_2)_{12}(OH)_2]$ (Ln = Nd, Pr, Sm, Y, Ho) are very active single-component catalysts for the polymerization of ε-CL and TMC. The reactivity is as high as 1.03×10^5 kg/mol h for the polymerization of ε-CL and 4.61×10^4 kg/mol h for TMC at room temperature [12]. These results promote us to further understanding the relationship between the structures and reactivity of heterometal alkoxides clusters and their cooperative bimetallic mechanism in the polymerization of cyclic esters.

With this goal in mind we have synthesized and structurally characterized the new heterometal alkoxide clusters of lanthanide and sodium $Ln_2Na_8(OCH_2CF_3)_{14}(THF)_6$ (Ln = Sm **1**, Y **2**, Yb **3**), and further tested their catalytic activities for the ring-opening polymerization of ε-CL as well as TMC. It was found that these clusters can initiate the polymerizations of both monomers in high activity as single-component initiators, and the activities are much higher than those found for the related monometallic lanthanide alkoxides complexes reported, such as $Ln(OAr)_3$, $Ln_5O(O^iPr)_{13}$ and LLn(OR) (L = bridged biphenolate, OR = OMe, O^{i}Pr and OCH_2Ph) [2–5] as well as anionic phenoxide complex $[Ln(OAr)_4][Na(DME)_3]$ [11]. Here we would like to report these results.

2. Experimental

2.1. Materials

All the manipulations are conducted under pure Ar atmosphere with rigorous exclusion of air and moisture using Schlenk tube and vacuum-line technique. ε-CL was purchased from Acros, dried over CaH_2 and distilled at reduced pressure. TMC was prepared by the reaction of 1,3-propandeidol with diethyl carbonate according to published method [13], and further dried over CaH_2 and purified by recrystallization before use. Anhydrous lanthanides $LnCl_3$ were prepared according to the literature [14]. Toluene, dimethoxy-ethane (DME) and tetrahydrofuran (THF) were distilled from sodium/benzophenone ketyl.

2.2. Synthesis of the clusters

2.2.1. $Sm_2Na_8(OCH_2CF_3)_{14}(THF)_6$ (*1*)

To a suspension of $SmCl_3$ (0.51 g, 2.0 mmol) in 40 ml THF was slowly added a solution of $NaOCH_2CF_3$ (11.2 ml, 14.0 mmol) in THF at r.t. The solution changed gradually from light gray to pale yellow. The resulting solution was stirred for another 24 h, and then evaporated to dry *via* vacuum. The residue was extracted with toluene and NaCl was removed by centrifugation. After the solution was concentrated, the product was obtained as colorless powder. Yield: 1.57 g (68%). Crystallization from THF–toluene gave colorless crystals at r.t.. Decomposition point: 162–164 °C. *Anal.* Calc. for $C_{52}H_{76}F_{42}Na_8O_{20}Sm_2$ (2303.75): C, 27.10; H, 3.33; Sm, 13.05. Found: C, 27.09; H, 3.29; Sm, 13.02%. IR (KBr pellets cm^{-1}): 3442 (s), 2863 (m), 1643 (w), 1443 (s), 1273 (m), 1158 (s), 957 (w), 880 (m), 826 (w), 671 (m), 556 (w), 509 (w).

2.2.2. $Y_2Na_8(OCH_2CF_3)_{14}(THF)_6$ (*2*)

By the same procedure as that for **1**, **2** was prepared from the reaction of YCl_3 (0.39 g, 2.0 mmol) with $NaOCH_2CF_3$ (11.2 ml, 14.0 mmol) in THF as colorless powder. Yield: 1.64 g (75%). Crystallization from THF–toluene gave colorless crystals at r.t.. Decomposition point: 149–151 °C. *Anal.* Calc. for $C_{52}H_{76}F_{42}Na_8O_{20}Y_2$ (2180.87): C, 28.64; H, 3.51; Y, 8.15. Found: C, 28.56; H, 3.44; Y, 8.14%. ^{1}H NMR (400 MHz, THF-d_8 25 °C): $\delta = 4.15$ (s, 28H, OCH_2CF_3), 3.60 (m, 24H, THF), 1.76 (m, 24H, THF) ppm. ^{13}C NMR (400 MHz, THF-d_8 25 °C): $\delta = 65.44$ (s, OCH_2CF_3), 130.16 (m, OCH_2CF_3), 67.40 (m, THF), 25.30 (m, THF) ppm. IR (KBr pellets cm^{-1}): 3454 (s), 2988 (w), 2860 (m), 1686 (m), 1455 (w), 1267 (s), 1158 (s), 894 (w), 820 (m), 672 (m), 552 (w), 477 (m).

2.2.3. $Yb_2Na_8(OCH_2CF_3)_{14}(THF)_6$ (*3*)

By the same procedure as that for **1**, **3** was prepared from the reaction of $YbCl_3$ (0.56 g, 2.0 mmol) with $NaOCH_2CF_3$ (11.2 ml, 14.0 mmol) as colorless powder. Yield: 1.69 g (72%). Crystallization from THF–toluene gave colorless crystals at r.t.. Decomposition point: 171–174 °C. *Anal.* Calc. for $C_{52}H_{76}F_{42}Na_8O_{20}Yb_2$ (2349.13): C, 26.59; H, 3.26; Yb, 14.73. Found: C, 26.57; H, 3.24; Yb, 14.70%. IR (KBr pellets cm^{-1}): 3419 (s), 2862 (m), 1528 (m), 1389 (m), 1219 (s), 1158 (s), 864 (w), 632 (m), 556 (w), 509 (s).

2.3. Polymerization

2.3.1. General procedure

To a stirred solution of TMC or ε-CL in toluene, a toluene solution of initiator was added with a syringe. The polymerization mixture was stirred for a definite time at the desired temperature and then quenched with an ethanol solution containing a small amount of hydrochloric acid. The polymer was precipitated from ethanol and washed with ethanol three times and dried under vacuum.

2.3.2. Oligomer for end group analysis

The oligomerization of ε-CL was carried out with **1** in toluene at 25 °C under the condition of [ε-CL]/[**1**](mole ratio) of 30. The reaction was terminated by adding 1 ml of 5% HCl/^{i}PrOH after 30 min. The oligomer was precipitated from ethanol. The product was dissolved in THF, followed by precipitation in ethanol. The procedure was repeated two times. The white product was dried in vacuum.

2.4. Analysis and characterization

Metal analyses were carried out by complexometric titration. Carbon, hydrogen, and nitrogen analyses were

performed by direct combustion on a Carlo-Erba EA = 1110 instrument. Melting points were determined on a Yanaco MP-500 melting point apparatus and were uncorrected. The IR spectra were recorded on a Nicolet Magna-IR 550 spectrometer. The ^{1}H NMR spectrums were recorded on a Unity Inova-400 spectrometer. The number-average (M_n) and weight-average (M_w) molecular weights and molecular weight distributions (M_w/M_n) were determined by gel permeation chromatography (GPC) with THF as an eluent and polystyrene as a standard on a Waters 1515 apparatus equipped with three HR columns (HR-1, HR-2, and HR-4) and an ultraviolet visible detector.

The suitable single crystals of clusters **1**–**3** were sealed in thin-walled glass capillaries for single-crystal structure determination. Intensity data were collected at a low temperature on a Rigaku Mercury CCD. The crystal structure was solved by a direct method and expanded by Fourier techniques. Atomic coordinates and thermal parameters were refined anisotropically.

3. Results and discussion

3.1. Synthesis of 1–3

As reported in our previous work, the metathesis reaction of anhydrous $LnCl_3$ with 3 equiv. of $NaOCH_2CF_3$ in THF gave the cluster $[Y_6(\mu_6\text{-}O)(OCH_2CF_3)_{18}][Na(THF)_3]_2 \cdot PhMe$ in low yield [15]. In our effort to prepare heterometal alkoxide clusters of lanthanide and sodium, a new cluster $Sm_2Na_8(OCH_2CF_3)_{14}(THF)_6$ **1** was synthesized by treatment of anhydrous $SmCl_3$ with a large excess of $NaOCH_2CF_3$ (7 equiv.) in 68% yield (yield based on samarium) (Eq. (1)). The synthesis can be reproduced.

$$2LnCl_3 + 14NaOCH_2CF_3 \xrightarrow{THF} Ln_2Na_8(OCH_2CF_3)_{14}(THF)_6 + 6NaCl \quad (Ln = Sm\ \mathbf{1}, Y\ \mathbf{2}, Yb\ \mathbf{3}) \quad (1)$$

The outcome of the metathesis reaction of $LnCl_3$ with alkali metal alkoxide was reported to depend on the metals used. For example, the reaction of YCl_3 with $NaOCMe_3$ in the molar ratio of 1:3 afforded the complex $Y_3(OCMe_3)_8Cl(THF)_2$, while the same reaction with $LaCl_3$ produced the complex $La_3(OCMe_3)_9(THF)_2$ [16]. Therefore, the syntheses of clusters of Y and Yb were also tried to evaluate the validity of this approach. The same reaction with YCl_3 and $YbCl_3$, respectively, went smoothly and gave the corresponding clusters $Y_2Na_8(OCH_2CF_3)_{14}(THF)_6$ (**2**) and $Yb_2Na_8(OCH_2CF_3)_{14}(THF)_6$ (**3**) in 75% and 72% yields, respectively. Clusters **1**–**3** are all soluble in THF and toluene but not in hexane. The results of elemental analysis for **1**–**3** were all identical to the formula; and indicated the molar ratio of Ln and Na to be 1:4. The ^{1}H NMR spectra for paramagnetic clusters **1** and **3** showed a very broad shift range, while the ^{1}H NMR spectrum of **2** in THF-d_8 showed the chemical shifts of CH_2CF_3 at 4.15 ppm. To understand the structure of cluster in THF solution the ^{1}H NMR spectrum of $NaOCH_2CF_3$ in THF-d_8 was measured and the chemical shift of CH_2CF_3 was appeared at 4.11 ppm. The result demonstrates that a dynamic of ligand going on and off might be existed.

Clusters **1**–**3** were further characterized by X-ray crystallography. The determination of crystal structures revealed **1**–**3** have the same solid-state structure. The molecular structures diagram with all the CH_2CF_3 groups omitted for clarity are shown in Fig. 1. The details of the crystallographic data are listed in Table 1, and the selected bond lengths and bond angles are provided in Tables 2 and 3, respectively.

The clusters are centrosymmetric and the overall structure in each case is composed of two cubanes and a double open cubane, with one face of an $Ln_1Na_2O_4$ open cubane cluster capped by an additional Ln_1O_2 layer. The double open cubane locates as a core capped by two cubanes in opposite side via two lanthanide atoms. The synthesis of such an extended series of structurally identical heterometal alkoxide clusters indicated that the structure framework here is particularly stable.

Each lanthanide atom is coordinated by four triple-bridged oxygen atoms [O(2), O(4), O(5), O(6)] and two double-bridged oxygen atoms [O(3), O(1)] from OCH_2CF_3 groups. The coordination geometry around the lanthanide atom can be best described as a distorted octahedron geometry, in which O(1), O(3), O(4) and O(6) can be considered to occupy equatorial positions with the angles sum about the lanthanide center of $\sum$O–Ln–O = 360.3° for **1**; 360.2° for **2**, and 360.2° for **3**; O(2) and O(5) occupy axial positions with the O(2)–Ln–O(5) angle of 167.7° for **1**, 171.7° for **2** and 171.8° for **3**, which is slightly distorted away from the idealized value of 180°. Each Na atoms coordinated to four oxygen atoms forming a distorted tetrahedral geometry. There is different coordinated environment around Na atoms between the Na atoms [Na(1), Na(1A)] in a double open cubane and the Na atoms [Na(2), Na(2A); Na(3), Na(3A); Na(4), Na(4A)] in cubane; in the former the four oxygen atoms all come from OCH_2CF_3 groups in two μ_2-O and two μ_3-O fashion, respectively, in the later case three μ_3-O from OCH_2CF_3 groups and one terminal-O from THF molecule.

The Ln–O(OCH_2CF_3) bond are of two types: Ln-μ_2-O and Ln-μ_3-O. The average bond length of Ln–O(μ_2-OCH_2CF_3) is 2.266(4), 2.213(3) and 2.187(4) Å for **1**, **2** and **3**, respectively, and the average bond length of Ln–O(μ_3-OCH_2CF_3) is 2.333(3), 2.260(3) and 2.234(3) Å for **1**, **2** and **3**, respectively. The 0.06 Å larger for Ln–O(μ_3-OCH_2CF_3) in comparison with Ln–O(μ_2-OCH_2CF_3) is reasonable, and it is also observed in other alkoxides complexes [7,16,17]. These bond parameters are comparable with each other when the difference in the ionic radii among Sm, Y and Yb is considered. Therefore, the comparison of the data for **2** with those found in other yttrium clusters is made as an example. The range of Y–O(μ_3-OCH_2CF_3) bond distances from 2.232(3) to 2.278(3) Å

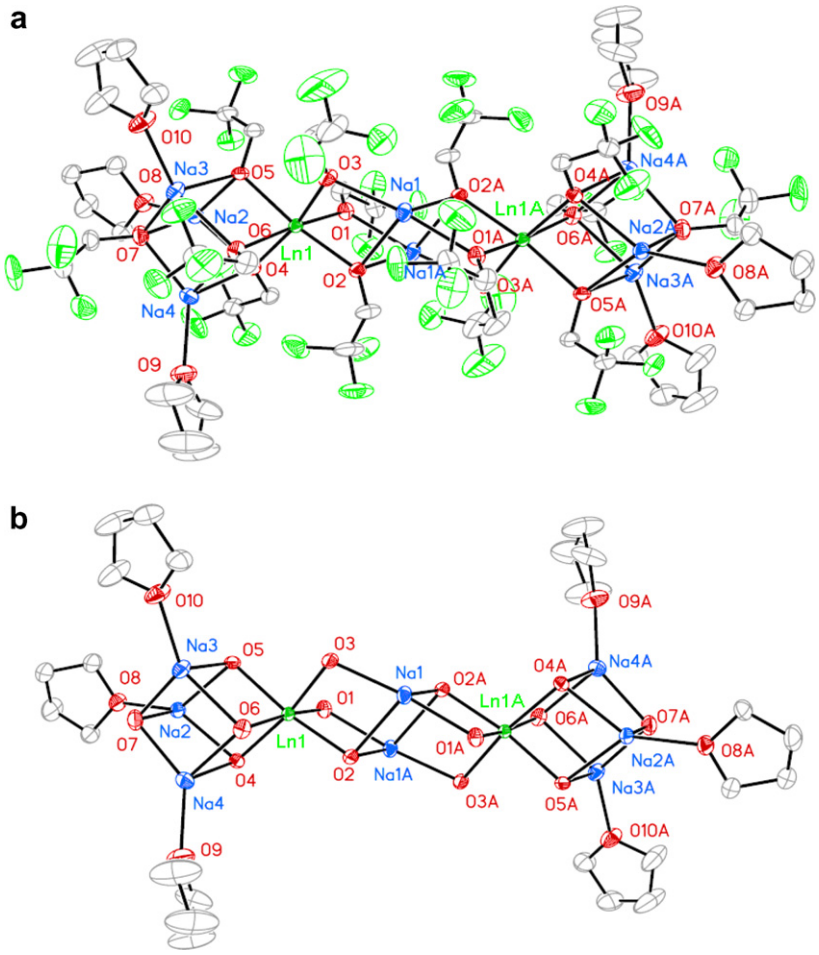


Fig. 1. (a) Molecular structures of **1**–**3**; (b) ORTEP diagram of **1**–**3** all the CH_2CF_3 groups deleted for clarity (atomic displacement parameters set at the 30% level).

are consistent with the values of Y–O(μ_3-OR) previously observed: 2.275(6)–2.287(6) Å for $YNa_8(OCMe_3)_{10}Cl$ and 2.263(13)–2.291(14) Å for $YNa_8(OCMe_3)_{10}(OH)$ [8b]. The range of 2.209(3)–2.217(3) Å for Y–O(μ_2-OCH_2CF_3) distances lie in the low end of the range of analogous distances for clusters in which only yttrium atoms are contained in the bonding: 2.25(2)–2.32(2) Å for $Y_7Cl_5(OCMe_3)_{14}$-$(THF)_2O$; 2.241(10)–2.358(10) Å for $Y_3Cl(OCMe_3)_8$-$(THF)_2$ and 2.26(2)–2.34(2) Å for $Y_4Cl_2(OCMe_3)_{10}O$ [17].

The Na–O bonds are of three types. The average bond length of the terminate Na–O(THF) for **1**, **2** and **3** is 2.306(5), 2.312(4) and 2.312(5) Å, respectively, which are almost equal. The average bond lengths of Na–O(μ_2-OCH_2CF_3) and Na–O(μ_3-OCH_2CF_3) for **1**, **2** and **3** are also normal, and comparable each other.

3.2. Polymerization of ε-CL and TMC with clusters *1*–*3*

Clusters **1**–**3** were found to be able to initiate the ring-opening polymerization of ε-CL in toluene at room temperature with high activity. In contrast, no polymer was obtained under the same reaction conditions when $Na(OCH_2CF_3)$ was used as initiator (Table 4, entry 13). The dependence of activity on lanthanide metals was observed. For example, when the mole ratio of [M]/[I] was 4000 at 25 °C within 30 min, the conversion was as high as 96% for **1**, while only trace for **2** and 12% for **3** (Table 4, entries 3, 9 and 12). The active sequence of Yb ≈ Y < Sm observed here is almost consistent with the increase in ionic radius (Yb < Y < Sm), which is similar to those found in the polymerization systems based lanthanide complexes [3a,18]. The conversion can still reach to 81% even the mole ratio of [M]/[I] as high as 7000 for the system with cluster **1** (Table 4, entry 4). Such high reactivity has not been found for the systems with monometallic lanthanide alkoxides (phenoxides) complexes published previously (Table 4, entries 15–19), indicating that the extremely high reactivity shown by **1**–**3** may result from the activation of monomer via coordination to both lanthanide metal and alkali metal and the rapid ligand exchange existed in solution. It was noticed that the reactivity of **1**–**3** is lower than that of the heterobimetallic alkoxide clusters $[Ln_2Na_8(OCH_2CH_2NMe_2)_{12}(OH)_2]$ (Table 4, entry 14) published recently [12]. The lower reactivity of **1**–**3** in comparison with clusters $[Ln_2Na_8(OCH_2CH_2NMe_2)_{12}(OH)_2]$ demonstrates that the reactivity of heterometal alkoxides

Table 1
Details of the crystallographic data of clusters **1**–**3**

	1	**2**	**3**
Empirical formula	$C_{52}H_{76}F_{42}Na_8O_{20}Sm_2$	$C_{52}H_{76}F_{42}Na_8O_{20}Y_2$	$C_{52}H_{76}F_{42}Na_8O_{20}Yb_2$
Formula weight	2303.75	2180.87	2349.13
Crystal color	colorless	colorless	colorless
Temperature (K)	193(2)	193(2)	193(2)
Wavelength (Å)	0.71070	0.71070	0.71070
Size (mm)	0.60 × 0.50 × 0.40	0.70 × 0.67 × 0.60	0.50 × 0.40 × 039
Crystal system	monoclinic	monoclinic	monoclinic
Space group	$P2_1/n$	$P2_1/n$	$P2_1/n$
a (Å)	12.8370(15)	12.9435(15)	12.7674(10)
b (Å)	24.460(3)	24.405(3)	24.4353(18)
c (Å)	14.2972(16)	14.1479(17)	14.1360(11)
α (°)	90	90	90
β (°)	91.962(3)	92.653(4)	93.338(2)
γ (°)	90	90	90
V (Å^3)	4486.6(9)	4464.4(9)	4402.6(6)
Z	2	2	2
D_{calc} (mg m^{-3})	1.705	1.622	1.772
Absorption coefficient (mm^{-1})	1.479	1.478	2.298
$F(000)$	2276	2184	2308
θ (°)	3.18–25.35	3.15–25.35	3.00–25.35
Reflection collected	42652	42543	37270
Independent reflections [R_{int}]	8195 [0.0337]	8145 [0.0428]	7964 [0.0303]
Variables	396	396	396
R [$I > 3\sigma(I)$]	0.0541	0.0689	0.0474
Rw	0.1421	0.1653	0.1065
Goodness-of-fit on F^2	1.119	1.122	1.128

Table 2
Selected bond distances (Å) for clusters **1**–**3**

	1	**2**	**3**
Ln–O(μ$_2$-OCH$_2$CF$_3$)			
Ln(1)–O(1)	2.254(4)	2.209(3)	2.186(4)
Ln(1)–O(3)	2.277(4)	2.217(3)	2.188(4)
Ln–O(μ$_3$-OCH$_2$CF$_3$)			
Ln(1)–O(2)	2.310(3)	2.232(3)	2.204(3)
Ln(1)–O(4)	2.346(4)	2.268(3)	2.237(4)
Ln(1)–O(5)	2.347(3)	2.278(3)	2.252(3)
Ln(1)–O(6)	2.330(4)	2.260(3)	2.243(4)
Na–O(THF)			
Na(2)–O(8)	2.320(5)	2.332(4)	2.329(4)
Na(3)–O(10)	2.290(5)	2.301(4)	2.298(5)
Na(4)–O(9)	2.309(6)	2.303(5)	2.309(5)
Na–O(μ$_2$-OCH$_2$CF$_3$)			
Na(1)–O(3)	2.300(5)	2.281(4)	2.273(4)
Na(1)–O(1A)	2.308(5)	2.301(3)	2.297(4)
Na–O(μ$_3$-OCH$_2$CF$_3$)			
Na(1)–O(2A)	2.400(4)	2.382(4)	2.374(4)
Na(1)–O(2)	2.379(4)	2.438(3)	2.439(4)
Na(2)–O(4)	2.384(4)	2.390(3)	2.379(4)
Na(2)–O(5)	2.405(4)	2.404(3)	2.388(4)
Na(2)–O(7)	2.242(6)	2.240(4)	2.242(5)
Na(3)–O(5)	2.356(5)	2.370(4)	2.366(4)
Na(3)–O(6)	2.399(4)	2.399(4)	2.398(4)
Na(3)–O(7)	2.222(6)	2.245(4)	2.240(5)
Na(4)–O(4)	2.379(6)	2.374(4)	2.375(5)
Na(4)–O(6)	2.356(6)	2.361(4)	2.346(5)
Na(4)–O(7)	2.308(5)	2.299(4)	2.306(5)

Table 3
Selected bond angles (°) for clusters **1**–**3**

	1	**2**	**3**
O(1)–Ln(1)–O(4)	88.3(2)	89.3(2)	89.2(2)
O(4)–Ln(1)–O(6)	80.6(2)	81.9(2)	81.9(2)
O(6)–Ln(1)–O(3)	92.7(2)	92.3(2)	91.8(2)
O(3)–Ln(1)–O(1)	98.7(2)	96.8(2)	97.3(2)
O(2)–Ln(1)–O(5)	167.7(2)	171.7(2)	171.8(2)
O(3)–Na(1)–O(1A)	176.6(2)	174.4(2)	172.9(2)
O(3)–Na(1)–O(2A)	103.7(2)	106.2(2)	108.0(2)
O(1A)–Na(1)–O(2A)	79.7(2)	78.1(2)	77.3(2)
O(2A)–Na(1)–O(2)	91.6(2)	93.8(2)	94.6(2)
O(4)–Na(2)–O(7)	91.5(2)	90.8(2)	90.9(2)
O(7)–Na(2)–O(8)	101.4(2)	100.8(2)	99.9(2)
O(7)–Na(3)–O(10)	123.7(2)	126.2(2)	126.5(2)
O(7)–Na(3)–O(5)	90.9(2)	90.9(2)	90.5(2)
O(7)–Na(4)–O(6)	90.4(2)	90.7(2)	90.4(2)
O(9)–Na(4)–O(6)	117.3(3)	119.9(2)	119.9(2)

clusters depends profoundly on the alkoxide groups and/or on the skeleton of clusters.

The polymers resulted by **1**–**3** show a unimodal molecular weight distribution with moderate polydispersities ($M_w/M_n < 1.70$), indicating **1**–**3** are really used as single-component catalysts in the ring-opening polymerization of ε-CL. However, the molecular weights of the resulting polymers are always lower than those expected from the monomer-to-initiator ratio. This may be caused from the multi-active species existed in cluster, which come from the distinct

Table 4
Polymerization of ε-CL initiated by clusters **1**–**3**[a]

Entry	Initiator	[M]/[I]	T (°C)	t (min)	Conv. (%)[b]	M_n($\times10^{-4}$)[c]	PDI[c]	Reference
1	**1**	4000	25	3	35	3.41	1.44	
2	**1**	4000	25	15	72	3.89	1.55	
3	**1**	4000	25	30	96	4.69	1.69	
4	**1**	7000	25	30	81	5.19	1.68	
5	**1**	8000	25	30	45	3.45	1.50	
6[d]	**1**	4000	25	30	38	2.05	1.36	
7	**2**	1500	25	30	95	4.03	1.58	
8	**2**	2000	25	30	78	3.28	1.67	
9	**2**	4000	25	30	trace			
10	**3**	1500	25	30	100	8.38	1.61	
11	**3**	2000	25	30	80	10.6	1.63	
12	**3**	4000	25	30	12			
13	$NaOCH_2CF_3$	1000	25	180	0			
14	$Sm_2Na_8(OCH_2CH_2NMe_2)_{12}(OH)_2$	8000	25	1	77	3.1	1.56	[11]
15[e]	$[Sm(OAr')_4][Na(DME)_3]$	2000	25	3	18	7.54	1.52	[10]
16[f]	$Sm(OAr)_3(THF)_2$	1000	25	30	37			[4f]
17[g]	$[(mbmp)Yb(O^iPr)]_2$	400	50	240	51	1.76	1.23	[3a]
18[g]	$[(mbmp)Yb(OMe)]_2$	400	50	240	53	1.89	1.17	[3a]
19[g]	$[(mbmp)Yb(OCH_2Ph)]_2$	400	50	240	49	1.71	1.18	[3a]

[a] Conditions: [cat] = 0.01 mol/L, toluene as solvent, $V_{sol.}/V_{mon.}$ = 5:1.
[b] Conv. %: weight of polymer obtained/weight of monomer used.
[c] Measured by GPC calibrated with standard polystyrene samples.
[d] THF as solvent.
[e] OAr′ = 2,6-*tert*-butyl-phenoxo.
[f] OAr = 2,6-*tert*-butyl-4-methylphenoxo.
[g] mbmp = 2,2′-methylenebis(6-*tert*-butyl-4-methylphenoxo).

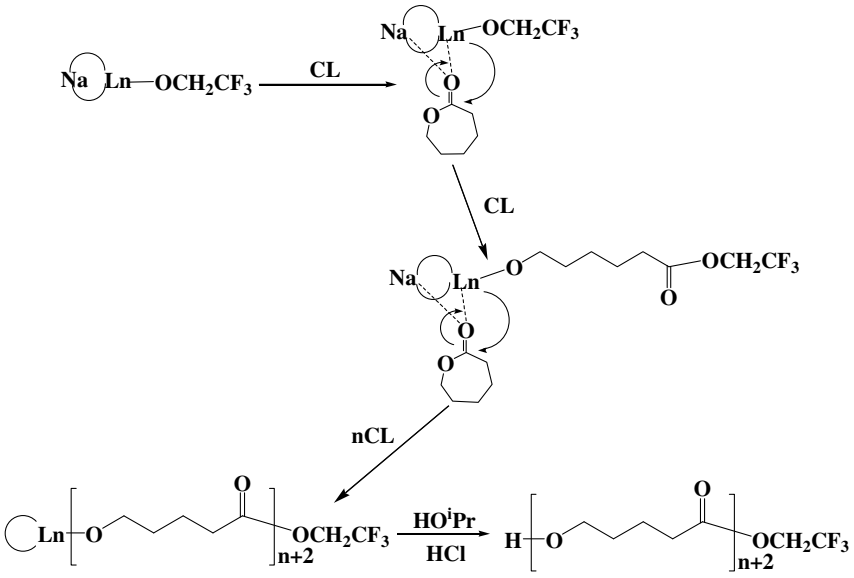
types of Ln–O bond, both in terms of connectivity count and length, or from the possible transesterification. Moreover, the polymerization in toluene yielded much higher conversion and the polymers with higher molecular weight than that in THF (Table 4, entries 3 and 6). The result indicates the present polymerization may belong to a coordinate/insertion mechanism. That is way the polymerization in protic solvent gives the worse result.

In order to understand the catalytic behavior of clusters **1**–**3** further, the ring-opening polymerizations of TMC catalyzed by them were tested. The representative results are listed in Table 5. Clusters **1**–**3** are all very active catalysts for the ring-opening polymerizations of TMC at 25 °C in toluene while the complex $Na(OCH_2CF_3)$ shows no activity under the same conditions (Table 5, entry 14). The catalytic behavior of clusters **1**–**3** for TMC is similar to that for ε-CL. For example, The activities of clusters **1**–**3** are much higher than those of the related lanthanide complexes published [19], the similar dependence of reactivity on lanthanide metals, Yb < Y < Sm, and the same solvent dependence of the polymerization (the polymerization in toluene yields higher conversion and the polymers with higher molecular weight than that in THF) were observed (Table 5, entries 2, 8–13). All the resulting polymers show unimodal molecular weight distributions with moderate polydispersities (M_w/M_n around 1.50), although the molecular weights of the resulting polymers are lower than those expected from the monomer-to-cluster ratio. It is unexpected that the difference in polymerization rate between the two polymerizations was observed. Polymerization of TMC is much faster than that of the ε-CL. For example, complete conversion of TMC into PTMC is achieved within 1 min for monomer to initiator ratios of up to 4000 with cluster **1** as initiator (Table 5, entry 2), while only 72% conversion is obtained within 15 min for the polymerization of ε-CL under the same conditions (Table 4, entry 2).

Table 5
Polymerization of TMC initiated by clusters **1**–**3**[a]

Entry	Initiator	[M]/[I]	T (°C)	t (min)	Conv. (%)[b]	M_n ($\times10^{-4}$)[c]	PDI[c]
1	**1**	1000	25	1	100	2.86	1.41
2	**1**	4000	25	1	100	7.97	1.44
3	**1**	4000	25	30	100	7.20	1.53
4	**1**	6000	25	1	79	8.22	1.52
5	**1**	8000	25	1	62	8.48	1.38
6	**1**	4000	0	1	90	3.13	1.61
7	**1**	4000	−15	1	21	1.35	1.82
8[d]	**1**	2000	25	1	61	2.17	1.70
9[d]	**1**	4000	25	1	trace		
10	**2**	2000	25	1	92	4.20	1.60
11	**2**	4000	25	1	83	8.44	1.45
12	**3**	2000	25	1	70	3.19	1.66
13	**3**	4000	25	1	49	4.81	1.36
14	$NaOCH_2CF_3$	1000	25	180	0		

[a] Conditions: [cat] = 0.01 mol/L, toluene as solvent, (TMC) = 1 mol/L.
[b] Conv. %: weight of polymer obtained/weight of monomer used.
[c] Measured by GPC calibrated with standard polystyrene samples.
[d] THF as solvent.



Scheme 1. Postulated cooperation mechanism for the ring-opening polymerization of ε-CL.

3.3. Polymerization mechanism

The dependence of activity on lanthanide metals for polymerization of both monomers demonstrates the active species here is the intermediate containing Ln–O bond. Much better results obtained in toluene than in THF indicates the present polymerization system may be conducted by the coordination–insertion mechanism.

In addition, the ring-opening polymerization of cyclolactones is known to conduct by either acyl–oxygen bond cleavage or alkyl–oxygen bond cleavage depending on the initiator used. To understand further the polymerization mechanism, the end-group of the oligomer was analyzed by ^{1}H NMR and ^{9}F NMR. An oligomer of ε-CL was produced from the oligomerization of ε-CL with a [ε-CL]/[**1**] of 30 and terminated by isopropyl alcohol. The ^{1}H NMR spectroscopy showed the signal at 4.48 ppm assigned to OCH_2CF_3 group and the ^{9}F NMR spectroscopy indicated the existence of an OCH_2CF_3 end group. These results obviously demonstrate the polymerization conducted by an acyl–oxygen bond cleavage. To explain the very high reactivity shown by clusters **1**–**3**, a cooperation mechanism of bimetals is supposed as shown in Scheme 1. First, ε-CL could coordinate to both Ln and Na metals concomitantly and then activated ε-CL inserts into one of Ln–OCH_2CF_3 bonds. The process repeats to yield the polymer.

4. Conclusion

New heterometal alkoxide clusters of lanthanide and sodium **1**–**3** were synthesized by the reaction of anhydrous $LnCl_3$ with $NaOCH_2CF_3$ at the mole ratio of 1:7 and structurally characterized. The clusters are found to be the highly active single-component initiators for the ring-opening polymerization of ε-CL and TMC. The activities are much higher than related monometallic alkoxides lanthanide complexes published previously. The polymerization reactions yield the polymers with moderate molecular weight distributions ranging from 1.4 to 1.7 for both PCL and PTMC. The cooperation of Ln and Na metals and the coordination–insertion mechanism were supposed. The further study on the catalytic behavior of the heterometal clusters of lanthanide and alkali with diverse alkoxide groups and structural motifies in polymerization reactions of polar monomers are preceeding in our laboratory.

Acknowledgements

We are indebted to the Chinese National Natural Science Foundation Grant No. 20632040 for financial support.

Appendix A. Supplementary data

CCDC 640783, 640784 and 640785 contain the supplementary crystallographic data for this paper. These data can be obtained free of charge via http://www.ccdc.cam.ac.uk/conts/retrieving.html, or from the Cambridge Crystallographic Data Centre, 12 Union Road, Cambridge CB2 1EZ, UK; fax: (+44) 1223-336-033; or e-mail: deposit@ccdc.cam.ac.uk. Supplementary data associated with this article can be found, in the online version.

References

[1] (a) A.C. Albertsson, I.K. Varma, Adv. Polym. Sci. 157 (2002) 1;
(b) K.M. Stridsberg, M. Ryner, A.C. Albertsson, Adv. Polym. Sci. 157 (2002) 42;
(c) M. Vert, Biomacromolecules 6 (2005) 538;
(d) A.C. Albertsson, I.K. Varma, Biomacromolecules 4 (2003) 1466.
[2] (a) Y.Q. Shen, Z.Q. Shen, F.Y. Zhang, Y.F. Zhang, Polym. J. 27 (1995) 59;

(b) Y.Q. Shen, Z.Q. Shen, F.Y. Zhang, J.Q. Sun, Y.F. Zhang, Chin. Sci. Bull. 39 (1994) 1096;
(c) W.M. Stevels, M.J.K. Ankone, P.J. Dijkstra, J. Feijen, Macromolecules 29 (1996) 8296;
(d) W.M. Stevels, M.J.K. Ankone, P.J. Dijkstra, J. Feijen, Polym. Prepr. 37 (1996) 190;
(e) M. Schappacher, T. Fabre, A.F. Mingotaud, A. Soum, Biomaterials 22 (2001) 2849.

[3] (a) Y.M. Yao, X.P. Xu, B. Liu, Q. Shen, Inorg. Chem. 44 (2005) 5133;
(b) X.P. Xu, Y.M. Yao, Q. Shen, J. Polym. Sci.: Part A: Polym. Chem. 44 (2006) 4409.

[4] (a) J. Ling, Z.Q. Shen, Q.H. Huang, Macromolecules 34 (2001) 7613;
(b) C.P. Yu, L.F. Zhang, Z.Q. Shen, J. Mol. Catal. A 212 (2004) 365;
(c) J. Ling, Z.Q. Shen, Macromol. Chem. Phys. 203 (2002) 735;
(d) E. Martin, P. Dubois, J. Robert, Macromolecules 33 (2000) 1530;
(e) J. Ling, W. Chen, Z.Q. Shen, J. Polym. Sci. Part A: Polym. Chem. 43 (2005) 1787;
(f) H.T. Sheng, H. Zhou, Y. Zhang, Y.M. Yao, Q. Shen, J. Organomet. Chem. 692 (2006) 1118.

[5] (a) M. Nishiura, Z.M. Hou, T.A. Koizumi, T. Imamoto, Y. Wakatsuki, Macromolecules 32 (1999) 8245;
(b) B. Zhao, C.R. Lu, Q. Shen, J. Appl. Polym. Sci. 106 (2007) 1383.

[6] (a) S. Singh, H.W. Roesky, Dalton Trans. (2007) 1360;
(b) R.E. Mulvey, Organometallics 25 (2006) 1060;
(c) G.B. Nikiforov, H.W. Roesky, P.G. Jones, R.B. Oswald, M. Noltemeyer, Dalton Trans. (2007) 4149;
(d) P.M. Gurubasavaraj, H.W. Roesky, P.M.V. Sharma, R.B. Oswald, V. Dolle, R.H. Irmer, Organometallics 26 (2007) 3346;
(e) E. Colacio, J.P. Costes, J.M. Dominguez-Vera, J.B. Maimoun, J. Suarez-Varela, Chem. Commun. (2005) 534;
(f) A. Mishra, W. Wernsdorfer, K.A. Abboud, G. Christou, J. Am. Chem. Soc. 126 (2004) 15648.

[7] S. Habaue, M. Yoshikawa, Y. Okamoto, Polym. J. 27 (1995) 986.

[8] (a) W.J. Evans, M.S. Sollberger, T.P. Hanusa, J. Am. Chem. Soc. 110 (1988) 1841;
(b) W.J. Evans, M.S. Sollberger, J.W. Ziller, J. Am. Chem. Soc. 115 (1993) 4120;
(c) W.J. Evans, T.J. Deming, J.M. Olofson, J.W. Ziller, Inorg. Chem. 28 (1989) 4027.

[9] J. Gromada, A. Mortreux, T. Chenal, J.W. Ziller, F. Leising, J.F. Carpentier, Chem. Eur. J. 8 (2002) 3773.

[10] (a) H. Schumann, G. Kociok-köhn, J. Loebl, Z. Anorg. Allg. Chem. 581 (1990) 69;
(b) H. Schumann et al., Z. Naturforsch. B: Chem. Sci. 46 (1991) 896.

[11] H.T. Sheng, L.Y. Zhou, Y. Zhang, Y.M. Yao, Q. Shen, J. Polym. Sci.: Part A: Polym. Chem. 45 (2007) 1210.

[12] H.T. Sheng, F. Xu, Y.M. Yao, Y. Zhang, Q. Shen, Inorg. Chem. 46 (2007) 7722.

[13] S. Sarel, L.A. Pohoryles, J. Am. Chem. Soc. 80 (1958) 4596.

[14] M.D. Taylor, C.P. Carter, J. Inorg. Nucl. Chem. 24 (1962) 387.

[15] H.M. Peng, Y.M. Yao, M.Y. Deng, Y. Zhang, Q. Shen, J. Rare Earths 24 (2006) 509.

[16] W.J. Evans, J.M. Olofson, J.W. Ziller, J. Am. Chem. Soc. 112 (1990) 2308.

[17] W.J. Evans, M.S. Sollberger, Inorg. Chem. 27 (1988) 4417.

[18] M. Yamashita, Y. Takemoto, E. Ihara, H. Yasuda, Macromolecules 29 (1996) 1798.

[19] (a) H. Li, Y. Yao, C. Yao, H. Sheng, Q. Shen, J. Polym. Sci.: Part A: Polym. Chem. 43 (2005) 1312;
(b) L. Zhou, H. Sun, J. Chen, Y. Yao, Q. Shen, J. Polym. Sci.: Part A: Polym. Chem. 43 (2005) 1778;
(c) L. Zhou, Y. Yao, Y. Zhang, M. Xue, J. Chen, Q. Shen, Eur. J. Inorg. Chem. (2004) 2167;
(d) A.P. Pêgo, Z. Zhong, P.J. Dijkstra, D.W. Grijpma, J. Feijen, Macromol. Chem. Phys. 204 (2003) 747;
(e) J. Ling, Z. Shen, Macromol. Chem. Phys. 203 (2002) 735;
(f) J. Ling, Z. Shen, Q. Huang, Macromolecules 34 (2001) 7613.

Co(III), Ni(II), Cu(II), Zn(II), Zr(IV), Pd(II), Ag(I), Cd(II), Hg(II), Sn(II), Sn(IV), Pb(II), P(III), As(III), Sb(III), Bi(III), Se(II), Te(II), Th(IV) and U(VI). Other studies include the synthesis of a few series of compounds of the type, $M[O(S)P(OR)_2]_3$ (M = As, Sb and Bi) [12], $R_2As[O(S)P(OR)_2]$ [13] and mixed ligand complexes of arsenic(III), $[OCMe_2CH_2CHMeOAsO(S)P(OR)_2]$ [14], $R_2Sb[O(S)P(OR)_2]$ [15] and $[Sb(S_2CNR_2)_2\{O(S)P(OR)_2\}]$ [12]. Limited information about a cobalt(II) diisopropyl monothiophosphate complex has been presented in the literature [11,16].

Variation in the mode of coordination to the central atom and in the core geometry is common; the central Sn_2O_2 core in $[(Me_2Sn\{O(S)P(OEt)_2\})_2O]_2$ [9], connected via an oxygen atom of the thiophosphate ligand, is coordinated through oxygen to give a distorted trigonal bipyramid arrangement around tin; $[Ph_2Sn(\mu\text{-}OH)\{O(S)P(OPh)_2\}]_2$ [10] has a similar structure except that the tin atoms are connected by hydroxo bridges; $[Zn_4\{O(S)P(OPh)_2\}_6O]$ [17] and $[Zn_4\{O(S)P(OMe)_2\}_6O]$ [17] possess a central tetrahedral Zn_4O core and the monothiophosphates ligands bridge the three basal zinc atoms through sulfur and oxygen atoms (bridging chelation); and $[Cd_2\{O(S)P(OPr^i)_2\}_3]$ [16] comprises pairs of tetrahedral coordinated cadmium atoms linked via three monothiophosphates ligands to give Cd_2L_3 units. The ligands bridge through sulfur and oxygen atoms to two cadmium atoms, giving rise to a polymeric chain.

This background led us to work on the synthesis and characterization of a series of bis(*O*,*O*-dialkylmonothiophosphato)cobalt(II) complexes and to determine the variations in the electronic environment, bonding modes and geometrical configuration. Nitrogen base donors such as pyridine or 2,2-bipyridyl were added to the tetrahedral cobalt(II) complexes to yield adducts of the type $[Co\{O(S)P(OPr^i)_2\}_2(C_5H_5N)_4]$, $[Co\{O(S)P(OPr^n)_2\}_2(C_{10}H_8N_2)_2]$ and $[Co\{O(S)P(OBu^n)_2\}_2(C_{10}H_8N_2)_2]$. Single crystal X-ray studies of $[Co\{O(S)P(OPr^i)_2\}_2(C_5H_5N)_4]$ and $[Co\{O(S)P(OPr^n)_2\}_2(C_{10}H_8N_2)_2]$ are the first examples of structurally characterized nitrogen base adducts of monothiophosphate complexes of cobalt(II).

2. Results and discussion

The reactions of cobalt(II) chloride hexahydrate with sodium salts of *O*,*O*-dialkylmonothiophosphoric acids in a 1:2 molar ratio in benzene yield bis(*O*,*O*-dialkylmonothiophosphato)cobalt(II) complexes of the type $[Co\{O(S)P(OR)_2\}_2]$.

$$CoCl_2\cdot 6H_2O + 2NaO(S)P(OR)_2 \xrightarrow{3\text{ h, stirring}} [Co\{O(S)P(OR)_2\}_2] + 2NaCl \quad (R = Pr^n, Pr^i, Bu^n)$$

Further reaction of these cobalt(II) complexes with neutral nitrogen donor bases such as pyridine and 2,2-bipyridyl results in the formation of adducts of the type, $[Co\{O(S)P(OR)_2\}_2L_n]$.

$$[Co\{O(S)P(OR)_2\}_2] + nL \xrightarrow{C_6H_6} [Co\{O(S)P(OR)_2\}_2L_n] \quad (R = Pr^i, n = 4, L = \text{pyridine}; R = Pr^n, Bu^n, n = 2, L = 2,2'\text{-bipyridyl})$$

These reactions are quite facile, but to ensure completion the reaction solutions were stirred for 3 h. All of the bis(*O*,*O*-dialkylmonothiophosphato)cobalt(II) complexes are blue solids and their adducts are pink or orange solids. The cobalt(II) complexes as well as their adducts are soluble in common organic solvents such as benzene, chloroform and dichloromethane. The products were characterized by elemental analysis, IR and UV–Vis spectroscopy and magnetic susceptibility measurements.

Despite extensive efforts at crystallization by various methods, it was not possible to obtain single crystals of good enough quality to obtain a crystal structure for complexes **1**–**3**. It has been claimed that the structure of these complexes is polymeric with cobalt having tetrahedral coordination and they are isostructural to $[Cd_2\{O(S)P(OPr^i)_2\}_3]$ [16]. X-ray quality crystals of adducts **4** and **5** were obtained, however, on re-crystallization from benzene: hexane (1:1 ratio).

2.1. IR spectra

The IR spectra of the bis(*O*,*O*-dialkylmonothiophosphato)cobalt(II) complexes and their adducts are summarized in Table 1. The effect of coordination is most evident in the shifts of the peaks attributable to the P–S and P–O stretching vibrations. In the cobalt(II) complexes **1**–**3**, a single broad strong band or two close bands are seen in the region 613–629 cm^{-1} that are shifted to higher frequencies by ca. 20–30 cm^{-1} compared to their corresponding sodium salts, suggesting that the P–S bond is involved in the coordination sphere of these tetrahedral complexes, as was proposed for $[Co\{O(S)P(OPr^i)_2\}_2]$ [16]. By contrast, in adducts **4**–**6**, two close bands are seen at almost the same frequencies as in the sodium salts, suggesting that cobalt is not coordinated through the P=S bond in these adducts. The medium to very strong intensity bands observed in the regions 1140–1149 and 1091–1110 cm^{-1} are assigned to the P–O stretching vibrations in complexes **1**–**6**, consistent with coordination of the oxygen atom to the metal centre. The vibrations for (P)–O–C and P–O–(C) bonds are observed in the region 958–994 and 753–764 cm^{-1}, respectively. In complexes **1**–**3**, new bands of medium to weak intensity in the region 341–358 cm^{-1} can be assigned to the Co–S stretching vibration, resulting from coordination of the metal to the ligand. In adducts **4**–**6**, strong bands due to the C–N bond are seen in the region 1570–1602 cm^{-1} which are shifted to higher frequency in comparison to free pyridine (1580, 1600 cm^{-1}) and bipyridyl (1579, 1595 cm^{-1}).

Table 1
IR spectral data (cm^{-1}) for the bis(*O*,*O*′-dialkylmonothiophosphato)cobalt(II) complexes and their nitrogen base adducts[a]

No.	Compound	*ν*(C–N)	*ν*(P–O)	*ν*[(P)–O–C]	*ν*[P–O–(C)]	*ν*(P–S)	*ν*(Co–S)
1	$[Co\{O(S)P(OPr^n)_2\}_2]$		1174m, 1149s	990s	757s	613s	341w
2	$[Co\{O(S)P(OPr^i)_2\}_2]$		1173m, 1144s	988s	760s	616s	358w
3	$[Co\{O(S)P(OBu^n)_2\}_2]$		1172m	994m	756s	629m	350w
4	$[Co\{O(S)P(OPr^i)_2\}_2(C_5H_5N)_4]$	1599m, 1570m	1174m, 1140s	973s	753s	615s	
5	$[Co\{O(S)P(OPr^n)_2\}_2(C_{10}H_8N_2)_2]$	1602s, 1582m	1172m, 1140s	970s	755s	619s	
6	$[Co\{O(S)P(OBu^n)_2\}_2(C_{10}H_8N_2)_2]$	1602s, 1583s	1173m, 1144s	978m	759m	625s	

[a] Key: s = strong, m = medium, w = weak.

2.2. Magnetic measurements

The magnetic susceptibilities of these paramagnetic compounds were determined using the Evans NMR method [18]. The values are in the range 4.5–5.3 and 5.0–5.3 BM and are in the range expected for the tetrahedral (**1**–**3**) and the octahedral (**4**–**6**) cobalt(II) complexes [19], respectively.

2.3. Crystal structures of $[Co\{O(S)P(OPr^i)_2\}_2(C_5H_5N)_4]$ and $[Co\{O(S)P(OPr^n)_2\}_2(C_{10}H_8N_2)_2]$

$[Co\{O(S)P(OPr^i)_2\}_2(C_5H_5N)_4]$, **4** and $[Co\{O(S)P(OPr^n)_2\}_2(C_{10}H_8N_2)_2]$, **5**, crystallize as triclinic in the space group $P\bar{1}$ and monoclinic in the space group $C2/c$, respectively. In both **4** and **5** the geometry around cobalt(II) is distorted octahedral with the CoO_2N_4 chromophore arising because the unidentate monothiophosphate ligands are linked through oxygen, as is evident from the molecular structures shown in Figs. 1 and 2. Bond distances and bond angles for **4** and **5** are given in Tables 3 and 4, respectively. The outstanding difference between the two structures is that in **4** the two monothiophosphate ligands are *trans* with a O–Co–O bond angle of 180°, as required by symmetry. By contrast, in **5** these ligands are *cis* with a O–Co–O bond angle of 97.19(7)°. In general, the distortion, not surprisingly, is more obvious in **5** with the constraints on the bidentate nitrogen base resulting in N–Co–N bite angles of 76.05(6)° compared with the N–Co–N bite angles in **4** of 87.67(3)°. The remaining *cis* angles in **4** are all close to 90°, ranging from 88.34(3)° to 92.33(3)°, whereas those in **5** range from 76.05(6)° to 97.29(6)°. Also, whereas all of the *trans* angles in **4** are 180.00 those in **5** range from 164.95(5)° to 171.04(8)°.

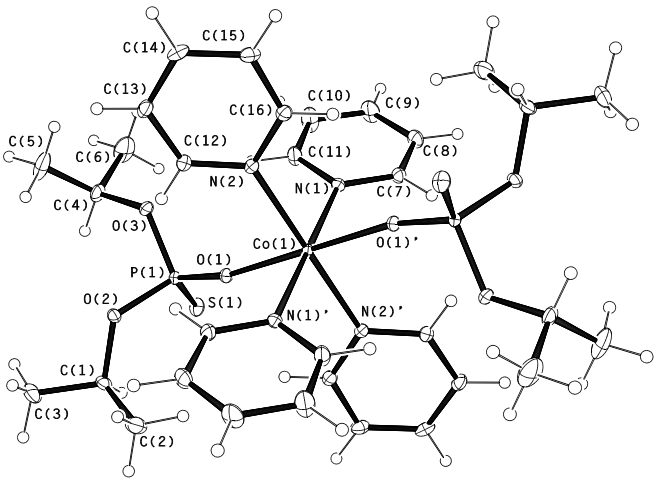


Fig. 1. ORTEP plot of the molecule $[Co\{O(S)P(OPr^i)_2\}_2(C_5H_5N)_4]$. The non-hydrogen atoms are drawn with 50% probability ellipsoids.

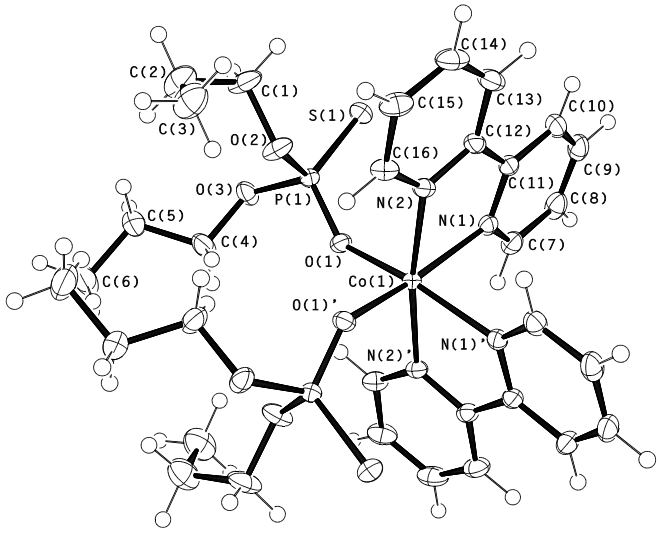


Fig. 2. ORTEP plot of the molecule $[Co\{O(S)P(OPr^n)_2\}_2(C_{10}H_8N_2)_2]$. The non-hydrogen atoms are drawn with 50% probability ellipsoids.

The Co–O bond distance (2.0757(8) Å) is slightly longer in **4** than in **5** (2.045(1) Å), as might be expected from the *trans* influence of O relative to N. The values are close to that obtained for $Co_5(OH_2)_4(HPO_4)_2(PO_4)_2$ (~2.05 Å) [20]. The average Co–N bond distances (2.1800(9) Å in **4**) and (2.146(2) Å in **5**) are comparable to those obtained for $[Co\{S_2P(OC_6H_5Me\text{-}p)_2\}_2(C_5H_5N)_2]$ [21] (2.162(2) Å) and $[Co\{S_2P(OEt)_2\}_2(C_5H_5N)_2]$ (2.164(3) Å) [22]. The cobalt to sulfur distances of 4.740(1) and 4.397(1) Å in **4** and **5**, respectively, emphasize that there is no Co–S intramolecular interaction in these adducts. A similar coordination pattern is seen in $Me_2Sn\{O(S)PPh_2\}_2$ [23] where the ligand is attached through oxygen and no appreciable Sn–S interaction is observed, with Sn–S distances of 3.901(3) and 3.530(4) Å. The average P–S bond length is 1.9565(4) Å in **4** and 1.9568(7) Å in **5**. A slightly shorter P–S bond (1.944(1) Å) was found in $[HOPh_2SnO(S)P(OPh)_2]_2$ [10], where the monothiophosphate ligand is

monodentate, and a longer P–S bonds were found in $[Cd_2\{O(S)P(OPr^i)_2\}_3]$ (ave. 1.971(9) Å) and $[Zn_4O\{O(S)P(OPh)_2\}_6]$ (ave. 1.980(3) Å), where the ligand is bridging bidentate. The closest Co–S intermolecular distances are 8.786(1) in **4** and 7.742(1) Å in **5**. The S–P–O bond angles are 117.94(7)° and 119.58(6)° in **4** and **5**, respectively; slightly higher than reported for $Me_2Sn\{S(O)PPh_2\}_2$ [23] (113.7(3)° and 115.0(3)°).

3. Experimental

Solvents (benzene, dichloromethane, *n*-hexane and diethyl ether) were dried by standard methods before use. All reactions were carried out in pre-dried glassware under anhydrous conditions. Sodium salts of *O*,*O*-dialkylmonothiophosphoric acids were prepared according to the literature procedure [24]. Sulfur was estimated gravimetrically as barium sulfate (Messengers Method) and cobalt by the pyridine method [25]. IR spectra were recorded on a Perkin–Elmer PE 983G spectrophotometer as Nujol mulls in the range 4000–200 cm^{-1}.

3.1. Preparations

3.1.1. $[Co\{O(S)P(OPr^n)_2\}_2]$ (**1**)

Typically, $CoCl_2 \cdot 6H_2O$ (0.078 g, 0.328 mmol) was added to a solution of $NaO(S)P(OPr^n)_2$ (0.145 g, 0.658 mmol) in benzene (10 mL) with constant stirring. The solution turned blue, was filtered and concentrated in vacuo before hexane (10 mL) was added to precipitate the blue solid. This was then filtered, washed with *n*-hexane and dried in vacuo. Yield: 0.216 g (72.3%). *Anal.* Calc. for $C_{12}H_{28}S_2P_2O_6Co$ (453.36): Co, 13.00; S, 14.15. Found: Co, 12.67; S, 13.84%. μ_{eff} 4.5 BM.

3.1.2. $[Co\{O(S)P(OPr^i)_2\}_2]$ (**2**)

Same as for $[Co\{O(S)P(OPr^n)_2\}_2]$. Yield: 0.179 g (68%). *Anal.* Cacl. for $C_{12}H_{28}S_2P_2O_6Co$ (453.36): Co, 13.01; S, 14.13. Found: Co, 13.17; S, 14.29%. μ_{eff} 4.7 BM.

3.1.3. $[Co\{O(S)P(OBu^n)_2\}_2]$ (**3**)

Same as for $[Co\{O(S)P(OPr^n)_2\}_2]$. Yield: 0.241 g (63%). *Anal.* Cacl. for $C_{16}H_{36}S_2P_2O_6Co$ (504.47): Co, 11.57; S, 12.59. Found: Co, 11.38; S, 12.25%. μ_{eff} 4.6 BM.

3.1.4. $[Co\{O(S)P(OPr^i)_2\}_2(C_5H_5N)_4]$ (**4**)

Typically, pyridine (0.134 g, 1.696 mmol) in benzene (5 mL) was added dropwise, with constant stirring, to a solution of $[Co\{O(S)P(OPr^i)_2\}_2]$ (0.192 g, 0.423 mmol) in benzene (10 mL). The colour of solution turned from blue to pink. The solution was concentrated in vacuo before hexane (10 mL) was added to precipitate a pink solid, which was then filtered, washed with hexane and dried in vacuo. Yield: 0.293 g (89.9%). *Anal.* Calc. for $C_{32}H_{48}S_2P_2O_6N_4Co$ (769.76): Co, 7.66; S, 8.33. Found: Co, 6.95; S, 8.46%. μ_{eff} 5.0 BM.

3.1.5. $[Co\{O(S)P(OPr^n)_2\}_2(C_{10}H_8N_2)_2]$ (**5**)

Same as $[Co\{O(S)P(OPr^i)_2\}_2(C_5H_5N)_4]$. Yield: 0.252 g (88%). *Anal.* Calc. for $C_{32}H_{44}S_2P_2O_6N_4Co$ (765.73): Co, 7.70; S, 8.38. Found: Co, 7.88; S, 8.51%. μ_{eff} 5.3 BM.

3.1.6. $[Co\{O(S)P(OBu^n)_2\}_2(C_{10}H_8N_2)_2]$ (**6**)

Same as $[Co\{O(S)P(OPr^i)_2\}_2(C_5H_5N)_4]$. Yield: 0.176 g (89%). *Anal.* Cacl. for $C_{36}H_{52}S_2P_2O_6N_4Co$ (821.83): Co, 7.17; S, 7.80. Found: Co, 6.79; S, 7.56%. μ_{eff} 5.2 BM.

3.2. Crystallography

A pink block crystal of $[Co\{O(S)P(OPr^i)_2\}_2(C_5H_5N)_4]$, **4**, and an orange block crystal of $[Co\{O(S)P(OPr^n)_2\}_2(C_{10}H_8N_2)_2]$, **5**, were mounted on glass fibres. Data were collected on a Bruker-Nonius Kappa CCD area detector diffractometer, with ϕ and ω scans chosen to give a complete asymmetric unit. Cell refinement [26] gave cell constants corresponding to triclinic and monoclinic cells for **4** and **5**, respectively, whose dimensions are given in

Table 2
Crystal data and structure refinements for $[Co\{O(S)P(OPr^i)_2\}_2(C_5H_5N)_4]$ and $[Co\{O(S)P(OPr^n)_2\}_2(C_{10}H_8N_2)_2]$

Empirical formula	$C_{32}H_{48}O_6N_4P_2S_2Co$	$C_{32}H_{44}O_6N_4P_2S_2Co$
Formula weight	769.73	765.70
Temperature (K)	120(2)	120(2)
Wavelength (Å)	0.71073	0.71073
Crystal system	triclinic	monoclinic
Space group	$P\bar{1}$	$C2/c$
a (Å)	9.0515(4)	8.404(2)
b (Å)	10.1629(5)	22.855(5)
c (Å)	11.8468(5)	18.913(4)
α (°)	88.389(3)	
β, °	71.984(4)	97.56(3)
γ (°)	69.181(3)	
Volume (Å^3)	964.57(8)	3601(1)
Z	1	4
D_{calc} (g/cm^3)	1.325	1.412
Absorption coefficient (mm^{-1})	0.681	0.729
$F(000)$	405	1604
Crystal size (mm)	0.20 × 0.20 × 0.20	0.10 × 0.10 × 0.10
θ Range for data collection (°)	2.94–27.52	2.94–27.46
Index ranges	$-11 \leqslant h \leqslant 11$, $-13 \leqslant k \leqslant 13$, $-15 \leqslant l \leqslant 15$	$-10 \leqslant h \leqslant 10$, $-29 \leqslant k \leqslant 28$, $-20 \leqslant l \leqslant 24$
Reflections collected	21075	21701
Independent reflections [R_{int}]	4417 [0.0270]	4107 [0.0430]
Ratio of minimum to maximum apparent transmission	0.9235	0.7561
Refinement method	full-matrix least-squares on F^2	full-matrix least-squares on F^2
Data/restraints/parameters	4417/0/219	4107/0/216
Goodness-of-fit on F^2	1.040	1.041
Final R indices [$F^2 > 4\sigma(F^2)$]	$R_1 = 0.0238$, $wR_2 = 0.0610$	$R_1 = 0.0331$, $wR_2 = 0.0798$
R indices (all data)	$R_1 = 0.0260$, $wR_2 = 0.0620$	$R_1 = 0.0395$, $wR_2 = 0.0834$
Extinction coefficient	0.017(2)	0.001(2)
Largest difference peak and hole (e Å^{-3})	0.278 and −0.367	1.015 and −0.403

Table 2, along with other experimental parameters. An absorption correction was applied [27]. The structures were solved by the direct method [28] and were refined using the WINGX version [29] of SHELX-97 [30]. All of the non-hydrogen atoms were treated anisotropically. Hydrogen atoms were included in idealized positions with isotropic thermal parameters set at 1.2 times that of the carbon atom to which they were attached. The final cycle of full-matrix least-squares refinement was based on 4417 observed reflections (4121 for $F^2 > 4\sigma(F^2)$) for **4** and 4107 observed reflections (3629 for $F^2 > 4\sigma(F^2)$) for **5**, and 219 variable parameters for **4** and 216 variable parameters for **5**, and converged (the largest parameter shift was 0.001 times its esd). Selected distances and bond angles are given in Tables 3 and 4 and the molecules are displayed as ORTEP diagrams in Figs. 1 and 2.

Table 3
Bond distances (Å) and angles (°) for $[Co\{O(S)P(OPr^i)_2\}_2(C_5H_5N)_4]$[a]

Co(1)–O(1)	2.0757(8)	Co(1)–O(1)′	2.0757(8)
Co(1)–N(1)	2.1701(9)	Co(1)–N(2)	2.1899(9)
Co(1)–N(1)′	2.1701(9)	Co(1)–N(2)′	2.1899(9)
S(1)–P(1)	1.9565(4)	P(1)–O(1)	1.4965(8)
P(1)–O(2)	1.6016(8)	P(1)–O(3)	1.5938(8)
O(2)–C(1)	1.451(1)	O(3)–C(4)	1.459(1)
N(1)–C(7)	1.337(2)	N(2)–C(12)	1.341(2)
N(1)–C(11)	1.337(2)	N(2)–C(16)	1.341(2)
O(1)–Co(1)–N(1)	91.66(3)	O(1)′–Co(1)–N(1)′	91.66(3)
O(1)–Co(1)–N(2)	89.36(3)	O(1)′–Co(1)–N(2)′	89.36(3)
N(1)–Co(1)–N(2)	87.67(3)	N(1)′–Co(1)–N(2)′	87.67(3)
O(1)–Co(1)–N(1)′	88.34(3)	O(1)′Co(1)–N(1)	88.34(3)
O(1)–Co(1)–N(2)′	90.64(3)	O(1)′–Co(1)–N(2)	90.64(3)
N(1)–Co(1)–N(2)′	92.33(3)	N(1)′–Co(1)–N(2)	92.33(3)
N(1)–Co(1)–N(1)′	180.00	N(2)–Co(1)–N(2)′	180.00
O(1)–Co(1)–O(1)′	180.00	Co(1)–O(1)–P(1)	165.27(5)
S(1)–P(1)–O(1)	117.97(4)	O(2)–P(1)–O(3)	99.53(4)
S(1)–P(1)–O(2)	111.43(3)	S(1)–P(1)–O(3)	112.56(4)
O(1)–P(1)–O(2)	108.90(5)	O(1)–P(1)–O(3)	104.70(5)
P(1)–O(2)–C(1)	123.34(7)	P(1)–O(3)–C(4)	121.42(8)
Co(1)–N(1)–C(7)	123.25(8)	Co(1)–N(2)–C(12)	122.52(8)
Co(1)–N(1)–C(11)	119.36(8)	Co(1)–N(2)–C(16)	120.39(8)

[a] Symmetry equivalent position $(-x, -y, -z)$ given by a prime.

Table 4
Bond distances (Å) and angles (°) for $[Co\{O(S)P(OPr^n)_2\}_2(C_{10}H_8N_2)_2]$[a]

Co(1)–O(1)	2.045(1)	Co(1)–O(1)′	2.045(1)
Co(1)–N(1)	2.162(2)	Co(1)–N(1)′	2.162(2)
Co(1)–N(2)	2.129(2)	Co(1)–N(2)′	2.129(2)
S(1)–P(1)	1.9568(7)	P(1)–O(1)	1.505(1)
P(1)–O(2)	1.598(1)	P(1)–O(3)	1.605(1)
O(2)–C(1)	1.454(2)	O(3)–C(4)	1.450(2)
N(1)–C(7)	1.339(2)	N(2)–C(12)	1.354(2)
N(1)–C(11)	1.351(2)	N(2)–C(16)	1.343(2)
O(1)–Co(1)–N(1)	90.07(5)	O(1)′–Co(1)–N(1)′	90.07(5)
O(1)–Co(1)–N(2)	95.87(5)	O(1)′–Co(1)–N(2)′	95.87(5)
N(1)–Co(1)–N(2)	76.05(6)	N(1)′–Co(1)–N(2)′	76.05(6)
O(1)–Co(1)–N(1)′	164.95(5)	O(1)′–Co(1)–N(1)	164.95(5)
O(1)–Co(1)–N(2)′	90.06(5)	O(1)′–Co(1)–N(2)	90.06(5)
N(1)–Co(1)–N(2)′	97.29(6)	N(1)′–Co(1)–N(2)	97.29(6)
N(1)–Co(1)–N(1)′	86.06(8)	N(2)–Co(1)–N(2)′	171.04(8)
O(1)–Co(1)–O(1)′	97.19(7)	Co(1)–O(1)–P(1)	138.30(8)
S(1)–P(1)–O(1)	119.58(6)	O(2)–P(1)–O(3)	103.83(8)
S(1)–P(1)–O(2)	112.75(6)	S(1)–P(1)–O(3)	107.05(5)
O(1)–P(1)–O(2)	104.67(7)	O(1)–P(1)–O(3)	107.79(7)
P(1)–O(2)–C(1)	119.9(1)	P(1)–O(3)–C(4)	117.8(1)
Co(1)–N(1)–C(7)	125.3(1)	Co(1)–N(2)–C(16)	124.3(1)
Co(1)–N(1)–C(11)	116.0(1)	Co(1)–N(2)–C(12)	117.2(1)
C(7)–N(1)–C(11)	118.7(2)	C(16)–N(2)–C(12)	118.5(2)

[a] Symmetry equivalent position $(-x, y, -z + 1/2)$ given by a prime.

4. Concluding comments

We have successfully prepared and characterized the following complexes: $[Co\{O(S)P(OPr^n)_2\}_2]$, $[Co\{O(S)P(OPr^i)_2\}_2]$, $[Co\{O(S)P(OBu^n)_2\}_2]$, $[Co\{O(S)P(OPr^i)_2\}_2(C_5H_5N)_4]$, $[Co\{O(S)P(OPr^n)_2\}_2(C_{10}H_8N_2)_2]$ and $[Co\{O(S)P(OBu^n)_2\}_2(C_{10}H_8N_2)_2]$. The IR spectra and magnetic measurements of all of these cobalt complexes are consistent with the proposed structures. The molecular structures of $[Co\{O(S)P(OPr^i)_2\}_2(C_5H_5N)_4]$ and $[Co\{O(S)P(OPr^n)_2\}_2(C_{10}H_8N_2)_2]$ were determined to have distorted octahedral environments around cobalt with *trans* and *cis* arrangements of the monothiophosphate ligands, respectively.

Acknowledgements

One of us (M.N.) is grateful to CSIR, New Delhi for financial support. M.E.L. thanks the UK Engineering and Physical Sciences Council for support of the X-ray facilities and IR and magnetic measurement facilities at the Department of Chemistry, University of Southampton. J.E.D. wishes to thank the University of Windsor for financial support.

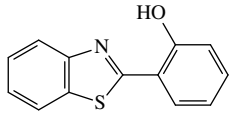
Appendix A. Supplementary data

CCDC 660401 and 660402 contain the supplementary crystallographic data for $[Co\{O(S)P(OPr^i)_2\}_2(C_5H_5N)_4]$ and $[Co\{O(S)P(OPr^n)_2\}_2(C_{10}H_8N_2)_2]$. These data can be obtained free of charge via http://www.ccdc.cam.ac.uk/conts/retrieving.html, or from the Cambridge Crystallographic Data Centre, 12 Union Road, Cambridge CB2 1EZ, UK; fax: (+44) 1223-336-033, or e-mail: deposit@ccdc.cam.ac.uk. Supplementary data associated with this article can be found, in the online version, at doi:10.1016/j.poly.2008.01.037.

References

[1] (a) R. Micu-Semeniuc, L. Dumitrescu-Silaghi, I. Haiduc, Inorg. Chim. Acta 33 (1979) 281;
(b) V.V. Ovchinnikov, V.I. Galkin, A.R. Garifzyanov, V.F. Toropova, R.A. Cherkasov, Zh. Obsh. Khim. 55 (2) (1985) 357;
(c) M. Shimoi, A. Quchi, T. Uehiro, Y. Yoshino, S. Sato, Y. Saito, Bull. Chem. Soc. Jpn. 55 (1982) 2371;
(d) Y. Yamada, M. Shimoi, A. Ouchi, Chem. Lett. (1978) 867.
[2] (a) J.L. Sabot, D. Bauer, Bull. Soc. Chim. France (1979) 150;
(b) C.K. Salmanova, K.G. Gasanov, A.P. Mamedov, N.F. Dzhanibekov, M.Kh. Mamedov, Azarbaycan Neft Tasarrufati (4) (1989) 39.

[3] (a) H. Zinke, R. Schumacher, Phosphorous Sulfur Silicon Relat. Elem. 63 (3–4) (1991) 315;
(b) A. Kulczycki, S. Sarna, A. Wachal, Tribologia 20 (6) (1989) 12.
[4] (a) T. Yamaguchi, T. Yamamoto, K. Umamura, Nippon Chem. Co. Ltd., 1960, JP 35009767 19600725.;
(b) J. Metivier, Societe des Usines Chimiques Rhone-Poulenc, 1957, US 2811476 19571029.
[5] E.G. Wallace, L.W. Fancher, Stauffer Chemical Co., 1958, US 2854469 19580930.
[6] (a) K. Forrest, D. Yan, R. Dunne, Miner. Eng. 14 (2) (2001) 227;
(b) D.R. Nagaraj, Trans. Ind. Inst. Met. 50 (5) (1997) 355.
[7] (a) K. Issleib, B. Walther, J. Organomet. Chem. 22 (1970) 375;
(b) I.A. Duncan, C. Glidwell, J. Organomet. Chem. 97 (1975) 51;
(c) G. Avar, W.P. Neumann, J. Organomet. Chem. 131 (1977) 215;
(d) F.A.K. Nasser, J.J. Zuckerman, J. Organomet. Chem. 244 (1983) 17;
(e) A.A.S. Khaldy, Synth. React. Inorg. Met. Org. Chem. 29 (4) (1999) 643;
(f) P.N. Nagar, Phosphorous Sulfur Silicon Relat. Elem. 40 (1988) 177;
(g) J.G. Masters, F.A.K. Nasser, M.B. Hossain, A.P. Hagen, D. van der Helm, J.J. Zuckerman, J. Organomet. Chem. 385 (1990) 39;
(h) A.A.S. Khaldy, Synth. React. Inorg. Met. Org. Chem. 33 (2) (2003) 183.
[8] V.K. Jain, Coord. Chem. Rev. 135/136 (1994) 809.
[9] V.B. Mokal, V.K. Jain, E.R.T. Tiekink, J. Organomet. Chem. 471 (1994) 53.
[10] F.A.K. Nasser, M.B. Hossain, D. Van der Helm, J.J. Zuckerman, Inorg. Chem. 22 (1983) 3107.
[11] C. Glidwell, Inorg. Chim. Acta 24 (1977) 255.
[12] (a) J.N. Pandey, Ph.D. Thesis, University of Rajasthan, Jaipur, 1986, p. 147;
(b) V.K. Jain, J. Indian Chem. Soc. 78 (2001) 224.
[13] S.S. Garje, V.K. Jain, Main Group Met. Chem. 20 (1997) 217.
[14] R. Poptani, Ph.D. Thesis, M.D.S. University, Ajmer, 2007, p. 74.
[15] S.S. Garje, V.K. Jain, Main Group Met. Chem. 18 (1995) 387.
[16] J.R. Phillips, J.C. Poat, A.M.Z. Slawin, D.J. Williams, P.T. Wood, J.D. Woollins, J. Chem. Soc., Dalton Trans. (1995) 2369.
[17] S. Menzer, J.R. Phillips, A.M.Z. Slawin, D.J. Williams, J.D. Woollins, J. Chem. Soc., Dalton Trans. (19) (2000) 3269.
[18] D.F. Evans, J. Chem. Soc. (1959) 2003.
[19] U.N. Tripathi, M.S. Singh, J. Indian Chem. Soc. 76 (1999) 360.
[20] Z. Han, A. Tian, J. Peng, X. Zhai, J. Solid State Chem. 179 (10) (2006) 3209.
[21] M. Nirwan, Ph.D. Thesis, M.D.S. University, Ajmer, 2007, p. 106.
[22] Z. Xu, J.H. Lin, Y.P. Yu, J. Xu, X.Z. You, S.X. Liu, C.C. Lin, Huaxue Xuebao 7 (47) (1989) 623.
[23] C. Silvestru, I. Haiduc, F. Caruso, M. Rossi, B. Mahieu, M. Gielen, J. Organomet. Chem. 448 (1993) 75.
[24] O. Foss, Acta Chem. Scand. 1 (1947) 8.
[25] A.I. Vogel, Quantitative Inorganic Analysis, 2nd ed., ELBS and Longmans, Green & Co. Ltd., London, 1951, p. 461.
[26] A.J.M. Duisenberg, J. Appl. Crystallogr. 25 (1992) 92.
[27] G.M. Sheldrick, SADABS V2.10, University of Gottingen, Germany, 2003.
[28] G.M. Sheldrick, Acta. Crystallogr., Sect. A 46 (1990) 467.
[29] L.J. Farrugia, J. Appl. Crystallogr. 32 (1999) 837.
[30] G.M. Sheldrick, SHELXL97, Structure Determination Software, University of Gottingen, Germany, 1997.



Scheme 1. Structure of hbtH ligand.

Continuing our researchers we focus on the synthesis and characterization of oxorhenium(V) chelates $[ReOX_2(O–N)(PPh_3)]$ and $[ReOX_2(O–N)(AsPh_3)]$ with 2-(2′-hydroxyphenyl)-2-benzothiazolinato ligand (hbtH, Scheme 1). Some other mono- and bis(2-(2′-hydroxyphenyl)-2-benzothiazolinato) complexes of Re(V) have been reported previously [9,10].

The $[ReOX_2(hbt)(EPh_3)]$ (X = Cl, Br; E = As, P) chelates have been prepared in the reactions of $[ReOX_3(EPh_3)_2]$ complexes (X = Cl, Br; E = P, As) with 2-(2′-hydroxyphenyl)-2-benzothiazole in acetone. From the reactions of $[ReOX_3(PPh_3)_2]$ with 2-(2′-hydroxyphenyl)-2-benzothiazole (hbtH) two kind of crystals $[ReOX_2(hbt)(PPh_3)] \cdot MeCN$ and $[ReOX_2(hbt)(PPh_3)]$ with different arrangement of halide ions (*cis* and *trans*, respectively) were isolated, whereas the $[ReOX_3(AsPh_3)_2]$ oxocompounds react with hbtH to give only *cis*-halide isomers $[ReOX_2(hbt)(AsPh_3)] \cdot MeCN$. The *cis* and *trans* geometry of the halide ligands in the oxorhenium complexes of the $[ReOX_2(O–N)(PPh_3)]$ and $[ReOX_2(O–P)(py)]$ type has been confirmed previously [11,12]. The number of the structurally characterized $[ReOX_2(O–N)(AsPh_3)]$ complexes is relatively small and all they are *cis* stereoisomers [13–15].

Here, we presents results of our studies on the structural and spectral properties of $[ReOX_2(hbt)(EPh_3)] \cdot MeCN$ (**1a**, **2a**, **3** and **4**) and $[ReOX_2(hbt)(EPh_3)]$ (**1b** and **2b**).

The electronic structures of **1a** and **1b** have been calculated with the density functional theory (DFT), and TDDFT/PCM calculations have been employed to produce a hundred of singlet excited-states starting from the ground-state geometries optimized in the gas phase.

Currently, density functional theory (DFT) is commonly used to examine the electronic structure of transition metal complexes. It meets with the requirements of being accurate, easy to use and fast enough to allow the study of relatively large molecules of transition metal complexes, including rhenium compounds [16,17].

2. Experimental

2.1. General procedure

All the reagents used to the synthesis were commercially available and were used without further purification. The $[ReOX_3(PPh_3)_2]$ and $[ReOX_3(AsPh_3)_2]$ complexes were prepared according to the literature methods [18].

IR spectra were recorded on a Nicolet Magna 560 spectrophotometer in the spectral range 4000–400 cm^{-1} with the samples in the form of KBr pellets. Electronic spectra were measured on a spectrophotometer Lab Alliance UV–VIS 8500 in the range 1100–180 nm in acetonitrile solution. Elemental analyses (C, H, N) were performed on a Perkin–Elmer CHN-2400 analyzer.

2.2. Preparation of $[ReOBr_2(hbt)(PPh_3)] \cdot MeCN$ and $[ReOBr_2(hbt)(PPh_3)]$ (*1a* and *1b*)

A mixture of $[ReOBr_3(PPh_3)_2]$ (0.50 g, 0.52 mmol), hbtH (0.125 g, 0.55 mmol) and acetone (70 ml) was stirred for 3 h. 50 ml of acetone was distilled off and 100 ml of diethyl ether was added. $[ReOBr_2(hbt)(PPh_3)]$ was filtered off, washed with ethanol, diethyl ether, dried and recrystallized from acetonitrile. Green crystals of $[ReOBr_2(hbt)(PPh_3)] \cdot MeCN$ (**1a**) and red crystals of $[ReOBr_2(hbt)(PPh_3)]$ (**1b**) were collected in 70% and 10% yield, respectively. Crystals of **1a** and **1b** were separated using microscope.

IR of **1a** (KBr; ν/cm^{-1}): 1596 (m) and 1561 (m) ν_{CN} and $\nu_{C=C}$; 961 (s) $\nu_{Re=O}$.

IR of **1b** (KBr; ν/cm^{-1}): 1595 (m) and 1561(m) ν_{CN} and $\nu_{C=C}$; 960 (s) $\nu_{Re=O}$.

Anal. Calc. for $C_{33}H_{26}Br_2N_2O_2PSRe$: C, 44.45; H, 2.94; N, 3.14. Found: C, 44.80; H, 3.05; N, 3.35%.

Anal. Calc. for $C_{31}H_{23}Br_2NO_2PSRe$: C, 43.78; H, 2.73; N, 1.65. Found: C, 44.10; H, 2.96; N, 1.84%.

2.3. Preparation of $[ReOCl_2(hbt)(PPh_3)] \cdot MeCN$ and $[ReOCl_2(hbt)(PPh_3)]$ (*2a* and *2b*)

A procedure similar to that for **1a** and **1b** was used with $[ReOCl_3(PPh_3)_2]$ (0.50 g, 0.60 mmol) and hbtH (0.145 g, 0.64 mmol). Green crystals of $[ReOBr_2(hbt)(PPh_3)] \cdot MeCN$ (**2a**) and red crystals of $[ReOBr_2(hbt)(PPh_3)]$ (**2b**) were collected in 68% and 8% yield, respectively. Crystals of **2a** and **2b** were separated using microscope.

IR of **2a** (KBr; ν/cm^{-1}): 1597 (m) and 1566 (m) ν_{CN} and $\nu_{C=C}$; 965 (s) $\nu_{Re=O}$.

IR of **2b** (KBr; ν/cm^{-1}): 1597 (m) and 1567 (m) ν_{CN} and $\nu_{C=C}$; 966 (s) $\nu_{Re=O}$.

UV–Vis of **2a** (CH_3CN; λ_{max} [nm] (ε; [$dm^3\ mol^{-1}\ cm^{-1}$])): 647.0 (50), 454.0 (400), 370.0 (2500), 323.0 (4680), 256.0 (6740) and 207.5 (25 900).

UV–Vis of **2b** (CH_3CN; λ_{max} [nm] (ε; [$dm^3\ mol^{-1}\ cm^{-1}$])): 638.5 (60), 453.0 (560), 365.5 (3100), 318.0 (4450), 259.0 (9960) and 207.5 (28 950).

Anal. Calc. for $C_{33}H_{26}Cl_2N_2O_2PSRe$: C, 49.38; H, 3.26; N, 3.49. Found: C, 49.82; H, 3.06; N, 3.30%.

Anal. Calc. for $C_{31}H_{23}Cl_2NO_2PSRe$: C, 48.88; H, 3.04; N, 1.84. Found: C, 48.15; H, 2.87; N, 1.92%.

2.4. $[ReOCl_2(hbt)(AsPh_3)] \cdot MeCN$ (*3*)

A procedure similar to that for phosphine analogues was used with $[ReOCl_3(AsPh_3)_2]$ (0.50 g, 0.54 mmol) and hbtH (0.13 g, 0.57 mmol). Crystalline green precipitate of $[ReOCl_2(hbt)(AsPh_3)] \cdot MeCN$ was collected in 85% yield.

IR (KBr; ν/cm^{-1}): 1598 (m) and 1566 (m) ν_{CN} and $\nu_{C=C}$; 965 (s) $\nu_{Re=O}$.

UV–Vis (CH_3CN; λ_{max} [nm] (ε; [$dm^3\,mol^{-1}\,cm^{-1}$])): 688.0 (95), 443.5 (640), 359.5 (6500), 313.0 (10,500), 242,5 (16 150) and 203.5 (47 500).

Anal. Calc. for $C_{33}H_{26}Cl_2N_2O_2AsSRe$: C, 46.81; H, 3.10; N, 3.31. Found: C, 46.52; H, 3.16; N, 3.42%.

2.5. Preparation of $[ReOBr_2(hbt)(AsPh_3)] \cdot MeCN$ (4)

A procedure similar to that for phosphine analogues was used with $[ReOBr_3(AsPh_3)_2]$ (0.50 g, 0.47 mmol) and hbtH (0.115 g, 0.50 mmol). Crystalline green precipitate of $[ReOBr_2(hbt)(AsPh_3)] \cdot MeCN$ was collected in 80% yield.

IR (KBr; ν/cm^{-1}): 1597 (m) and 1566 (m) ν_{CN} and $\nu_{C=C}$; 966 (s) $\nu_{Re=O}$.

UV–Vis (CH_3CN; λ_{max} [nm] (ε; [$dm^3\,mol^{-1}\,cm^{-1}$])): 672.0 (70), 439.5 (900), 358.5 (6700), 315.0 (12 400), 245,5 (18 100) and 210.5 (52 500).

Anal. Calc. for $C_{33}H_{26}Br_2N_2O_2AsSRe$: C, 42.37; H, 2.80; N, 2.99. Found: C, 42.92; H, 3.13; N, 3.22%.

2.6. Crystal structures determination and refinement

The X-ray intensity data of **1a**, **1b**, **2a**, **2b**, **3** and **4** were collected on a KM-4-CCD automatic diffractometer equipped with CCD detector and graphite monochromated Mo Kα radiation ($\lambda = 0.71073$ Å) at room temperature. Details concerning crystal data and refinement are given in Table 1. Lorentz, polarization and absorption correction [19] were applied. The structures were solved by the Patterson method and subsequently completed by the difference Fourier recycling. All the non-hydrogen atoms were refined anisotropically using full-matrix, least-squares technique. The hydrogen atoms were treated as "riding" on their parent carbon atoms and assigned isotropic temperature factors equal 1.2 (non-methyl) and 1.5 (methyl) times the value of equivalent temperature factor of the parent atom. The methyl groups were allowed to rotate about their local threefold axis. In containing solvent compounds the MeCN molecules show symptoms of disorder, what exhibits in relatively large displacement parameters and residual density

Table 1
Crystal data and structure refinement for $[ReOX_2(hbt)(EPh_3)] \cdot MeCN$ and $[ReOX_2(O–N)(PPh_3)]$ (X = Cl, Br; E = P, As) complexes

	1a	2a	3	4	1b	2b
Empirical formula	$C_{33}H_{26}Br_2N_2O_2PSRe$	$C_{33}H_{26}Cl_2N_2O_2PSRe$	$C_{33}H_{26}AsCl_2N_2O_2SRe$	$C_{33}H_{26}AsBr_2N_2O_2SRe$	$C_{31}H_{23}Br_2NO_2PSRe$	$C_{31}H_{23}Cl_2NO_2PSRe$
Formula weight	891.61	802.69	846.64	935.56	850.55	761.63
Temperature (K)	293(1)	293(1)	291.0(3)	291.0(3)	291.0(3)	291.0(3)
Wavelength (Å)	0.71073	0.71073	0.71073	0.71073	0.71073	0.71073
Crystal system	triclinic	triclinic	triclinic	triclinic	monoclinic	monoclinic
Space group	$P\bar{1}$	$P\bar{1}$	$P\bar{1}$	$P\bar{1}$	$P2_1/n$	$P2_1/n$
Unit cell dimensions						
a (Å)	11.197(2)	11.1730(3)	11.4176(7)	11.5857(5)	18.6496(5)	18.3899(5)
α (°)	87.71(3)	88.030(2)	87.937(6)	86.558(3)		
b (Å)	11.532(2)	11.4490(3)	11.5447(8)	11.6384(4)	9.1939(2)	9.1125(2)
β (°)	85.39(3)	85.780(2)	86.158(6)	87.335(4)	113.959(3)	113.743(3)
c (Å)	13.221(3)	13.1280(2)	13.1933(10)	13.2846(6)	19.0220(4)	18.7215(5)
γ (°)	65.59(3)	65.700(2)	65.521(7)	64.872(4)		
Volume (Å^3)	1549.4(5)	1526.38(6)	1579.11(19)	1618.40(12)	2980.53(12)	2871.77(13)
Z	2	2	2	2	4	4
D_{calc} (Mg/m^3)	1.911	1.746	1.781	1.920	1.895	1.762
Absorption coefficient (mm^{-1})	6.653	4.311	5.156	7.335	6.911	4.576
F(000)	860	788	824	896	1632	1488
Crystal size (mm)	0.02 × 0.10 × 0.20	0.07 × 0.10 × 0.13	0.379 × 0.158 × 0.132	0.271, 0.009, 0.007	0.04 × 0.19 × 0.20	0.007 × 0.009 × 0.197
θ Range for data collection (°)	3.09–25.00	3.11–25.00	3.28–25.10	1.54–25.02	1.98–25.00	2.01–25.05
Index ranges	$-9 \leqslant h \leqslant 13$, $-13 \leqslant k \leqslant 13$, $-14 \leqslant l \leqslant 15$	$-12 \leqslant h \leqslant 13$, $-10 \leqslant k \leqslant 13$, $-15 \leqslant l \leqslant 14$	$-13 \leqslant h \leqslant 13$, $-13 \leqslant k \leqslant 13$, $-12 \leqslant l \leqslant 15$	$-13 \leqslant h \leqslant 12$, $-13 \leqslant k \leqslant 13$, $-12 \leqslant l \leqslant 14$	$-22 \leqslant h \leqslant 22$ $-10 \leqslant k \leqslant 10$ $-22 \leqslant l \leqslant 22$	$-21 \leqslant h \leqslant 21$ $-10 \leqslant k \leqslant 10$ $-21 \leqslant l \leqslant 22$
Reflections collected	9884	9474	15,624	16,504	28,699	28,280
Independent reflections	5322 ($R_{int} = 0.0257$)	5198 ($R_{int} = 0.0890$)	5598 ($R_{int} = 0.0343$)	5717 ($R_{int} = 0.0237$)	5236 ($R_{int} = 0.0456$)	5091 ($R_{int} = 0.0262$)
Completeness to $2\theta = 50°$	98.6%	96.6%	99.6%	100%	100.0%	100.0%
Minimum and maximum transmission	0.442 and 0.878	0.599 and 0.765	0.599 and 0.181	0.920 and 0.963	0.286 and 0.751	0.955 and 0.972
Data/restraints/parameters	5322/0/380	5198/0/380	5598/0/380	5717/0/380	5236/0/352	5091/0/352
Goodness-of-fit on F^2	1.087	0.964	1.052	1.114	1.073	0.972
Final R indices [$I > 2\sigma(I)$]	$R_1 = 0.0622$ $wR_2 = 0.1945$	$R_1 = 0.0751$ $wR_2 = 0.1649$	$R_1 = 0.0274$ $wR_2 = 0.0626$	$R_1 = 0.0479$ $wR_2 = 0.1654$	$R_1 = 0.0206$ $wR_2 = 0.0475$	$R_1 = 0.0154$ $wR_2 = 0.0333$
R indices (all data)	$R_1 = 0.0744$ $wR_2 = 0.2020$	$R_1 = 0.1262$ $wR_2 = 0.1724$	$R_1 = 0.0310$ $wR_2 = 0.0643$	$R_1 = 0.0587$ $wR_2 = 0.1780$	$R_1 = 0.0308$ $wR_2 = 0.0628$	$R_1 = 0.0235$ $wR_2 = 0.0353$
Largest diffraction peak and hole (e Å^{-3})	1.844 and −2.366	3.827 and −2.483	0.988 and −1.177	1.330 and −1.218	0.674 and −0.861	0.641 and −0.542

around acetonitrile atoms. This is probably caused by absence of strong intermolecular interactions, which could stabilise the solvent in the crystal net. SHELXS97 [20], SHELXL97 [21] and SHELXTL [22] programs were used for all the calculations. Atomic scattering factors were those incorporated in the computer programs.

3. Computational details

The gas phase geometries of **1a** and **1b** were optimized without any symmetry restrictions in the singlet ground-state with the DFT method using the hybrid B3LYP functional of GAUSSIAN-03 [23–25]. The calculations were performed by using ECP basis set on the rhenium atom,

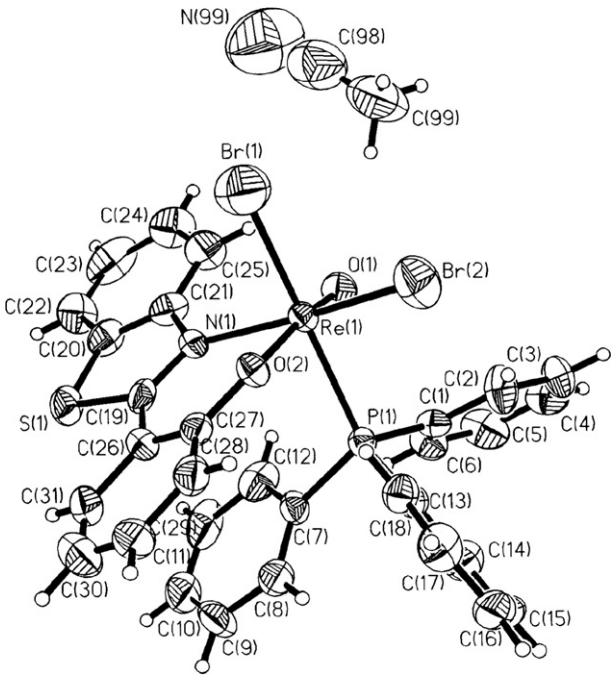


Fig. 1. The molecular structure of **1a**. Displacement ellipsoids are drawn at 50% probability.

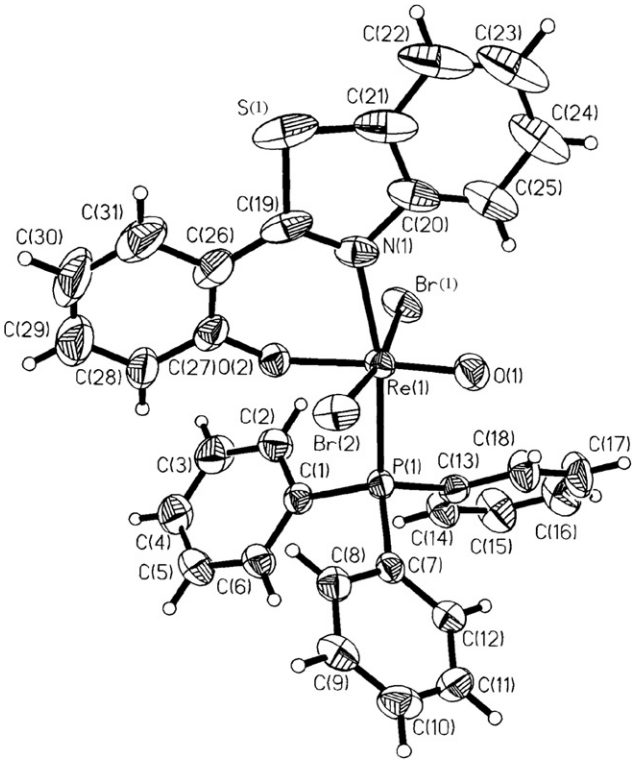


Fig. 2. The molecular structure of **1b**. Displacement ellipsoids are drawn at 50% probability.

Table 2
The selected experimental and optimized bond lengths (Å) and angles (°) for **1a**

Bond lengths	Experimental	Optimized
Re(1)–O(1)	1.698(9)	1.682
Re(1)–O(2)	1.932(8)	1.987
Re(1)–N(1)	2.176(10)	2.218
Re(1)–Br(1)	2.472(3)	2.581
Re(1)–Br(2)	2.437(2)	2.572
Re(1)–P(1)	2.491(3)	2.602
O(1)–Re(1)–O(2)	167.6(4)	163.80
O(1)–Re(1)–N(1)	90.6(4)	90.22
O(2)–Re(1)–N(1)	82.1(4)	81.13
O(1)–Re(1)–Br(2)	98.8(3)	99.50
O(2)–Re(1)–Br(2)	89.4(2)	90.57
N(1)–Re(1)–Br(2)	169.9(3)	169.03
O(1)–Re(1)–Br(1)	99.1(3)	102.07
O(2)–Re(1)–Br(1)	90.5(3)	90.87
N(1)–Re(1)–Br(1)	87.2(3)	85.11
Br(2)–Re(1)–Br(1)	87.47(8)	87.88
O(1)–Re(1)–P(1)	84.1(3)	82.62
O(2)–Re(1)–P(1)	86.5(3)	84.66
N(1)–Re(1)–P(1)	94.4(3)	95.81
Br(2)–Re(1)–P(1)	90.50(9)	90.51
Br(1)–Re(1)–P(1)	176.44(9)	175.24

Table 3
The experimental and optimized bond lengths (Å) and angles (°) for **1b**

Bond lengths	Experimental	Optimized
Re(1)–O(1)	1.690(3)	1.684
Re(1)–O(2)	1.933(3)	1.977
Re(1)–N(1)	2.158(4)	2.179
Re(1)–Br(1)	2.5371(5)	2.622
Re(1)–Br(2)	2.5479(5)	2.647
Re(1)–P(1)	2.4701(11)	2.540
O(1)–Re(1)–O(2)	174.16(13)	173.97
O(1)–Re(1)–N(1)	99.02(15)	100.12
O(2)–Re(1)–N(1)	81.86(14)	81.61
O(1)–Re(1)–Br(2)	89.72(11)	90.13
O(2)–Re(1)–Br(2)	84.61(8)	84.25
N(1)–Re(1)–Br(2)	84.52(9)	85.00
O(1)–Re(1)–Br(1)	97.30(11)	97.36
O(2)–Re(1)–Br(1)	88.50(8)	88.48
N(1)–Re(1)–Br(1)	88.00(9)	87.11
Br(2)–Re(1)–Br(1)	170.476(17)	169.07
O(1)–Re(1)–P(1)	91.96(11)	90.93
O(2)–Re(1)–P(1)	87.23(9)	87.49
N(1)–Re(1)–P(1)	169.01(11)	168.91
Br(2)–Re(1)–P(1)	95.80(3)	96.00
Br(1)–Re(1)–P(1)	90.41(3)	90.57

the standard 6-31+G** basis for bromine, phosphorous, oxygen and nitrogen, 6-31G* for carbon and 6-31G for hydrogen atoms [26,27]. The Xe core electrons of Re were replaced by an effective core potential and DZ quality Hay and Wadt Los Alamos ECP basis set (LANL2DZ) [28] was used for the valence electrons. Additional d function with exponent $\alpha = 0.3811$ and f function with exponent $\alpha = 2.033$ on the rhenium atom were added [29]. All vibrations in the calculated vibrational spectrum of **1a** and **1b** were real thus the both geometries correspond to true energy minimum.

The electronic spectrum of **1a** and **1b** were calculated with the TDDFT method, and the solvent effect was simulated using the polarizable continuum model with the integral equation formalism (IEF-PCM) [30].

Natural bond orbital (NBO) calculations were performed with the NBO code [31] included in GAUSSIAN03.

4. Results and discussion

4.1. Preparation and infrared data

The $[ReOX_2(hbt)(EPh_3)]$ (X = Cl, Br; E = As, P) complexes were prepared in good yield by ligand exchange reactions starting from $[ReOX_3(EPh_3)_2]$ complexes and 2-(2′-hydroxyphenyl)-2-benzothiazole (hbtH) in acetone:

$$[ReOX_3(EPh_3)_2] + hbtH \rightarrow [ReOX_2(hbt)(EPh_3)] + HX + EPh_3 \quad X = Cl, Br;\ E = As, P$$

From the reactions of $[ReOX_3(PPh_3)_2]$ with 2-(2′-hydroxyphenyl)-2-benzothiazole two kind of crystals $[ReOX_2(hbt)(PPh_3)] \cdot MeCN$ and $[ReOX_2(hbt)(PPh_3)]$ with different arrangement of halide ions (*cis* and *trans*, respectively) were isolated, whereas the arsine starting oxocompounds react with hbtH to give only $[ReOX_2(hbt)(AsPh_3)] \cdot MeCN$ with halide ligands in *cis* arrangement. The examined previously reactions of $[ReOX_3(EPh_3)_2]$ (E = P, As) with 2-(2′-hydroxyphenyl)-2-benzoxazole, 8-hydroxyquinoline and quinoline-2-carboxylic acid resulted in the isolation only $[ReOX_2(N–O)(EPh_3)]$ with *cis* halide arrangement [13–15].

All the isolated complexes are air stable and slightly soluble in acetonitrile, dichloromethane, chloroform, sparingly soluble in benzene and toluene. The solubility of the *trans* stereoisomers are somewhat better than the *cis* ones. All the crystals suitable for X-ray investigation were obtained by recrystallization from acetonitrile.

The IR spectroscopic measurements outlined in the Section 2 are not distinctive for molecular structure determination. The IR spectra of the *cis* and *trans* stereoisomers are very similar in terms of the position, intensity and shape of the bands in the whole region 4000–400 cm^{-1}. The strong ν(Re=O) stretching bands of both *cis* and *trans* stereoisomers of $[ReOX_2(hbt)(EPh_3)]$ are found in the narrow range 960–966 cm^{-1}, similar to those observed for the other $[ReOX_2(O–N)(PPh_3)]$ chelates [13–15]. Relatively high wavenumbers of the ν(Re=O) absorption bands suggest that the Re–hydroxy bond *trans* to the oxo ligand does not compete effectively for the Re_d orbitals and indicate the presence of very stable {O≡Re–O} structural moiety in the examined structures.

The calculated (non-scaled) vibrational spectra of the *cis* and *trans* stereoisomers are in a reasonable agreement with the experimental data. Similar to the experimental, the calculated IR spectra of both isomers are very similar in terms of the position, intensity and shape of the bands. The calculated ν(Re=O) values (1019 cm^{-1} for of **1a** and 1024 cm^{-1} for **1b**) are higher than the experimental ones by ~7%, what is usual for this approach.

Table 4
Electron population of the valence core for **1a** and **1b**

Complex	Re(1)		O(1)		O(2)		Br(1)		Br(2)		N(1)		P(1)	
	6s	5d	2s	2p	2s	2p	4s	4p	4s	4p	2s	2p	3s	3p
1a	0.43	5.58	1.83	4.62	1.63	5.02	1.93	5.41	1.92	5.40	1.30	4.16	1.15	2.42
1b	0.43	5.57	1.83	4.60	1.63	5.02	1.93	5.46	1.94	5.47	1.29	4.18	1.12	2.40

Table 5
The occupancy and composition of the calculated natural bond orbitals (NBOs) between the rhenium and the oxo ligand for **1a** and **1b**

BD	Occupancy	Composition of NBO	BD[a]	Occupancy
1a				
Re–O_t	1.992	$0.566(d)_{Re} + 0.825(p)_O$	$0.825(d)_{Re} - 0.566(p)_O$	0.257
Re–O_t	1.986	$0.569(d)_{Re} + 0.822(p)_O$	$0.822\ (d)_{Re} - 0.569(p)_O$	0.313
1b				
Re–O_t	1.990	$0.557(d)_{Re} + 0.831(p)_O$	$0.831(d)_{Re} - 0.557(p)_O$	0.322
Re–O_t	1.984	$0.579(d)_{Re} + 0.816(p)_O$	$0.816(d)_{Re} - 0.579(p)_O$	0.200

BD denotes 2-center bond.
[a] Denotes antibond NBO.

4.2. Crystal structures

The crystallographic data of $[ReOX_2(hbt)(EPh_3)]\cdot MeCN$ and $[ReOX_2(O–N)(PPh_3)]$ (X = Cl, Br; E = P, As) complexes are summarized in Table 1. The *cis*-halide complexes are isostructural and crystallise as acetonitrile solvates in the triclinic $P\bar{1}$ space group. The *trans* stereoisomers are also isostructural but consist of discrete and well-separated $[ReOX_2(O–N)(PPh_3)]$ monomers and crystallise in the monoclinic $P2_1/n$ space group.

The perspective drawing of $[ReOBr_2(hbt)(PPh_3)]\cdot MeCN$ (**1a**) is presented in Fig. 1, and the selected bond distances and angles of **1a** are collected in Table 2. Fig. 2 presents the molecular structure of $[ReOBr_2(hbt)(PPh_3)]$ (**1b**), and its selected bond distances and angles are gathered in Table 3.

All the complexes show octahedral geometry about the central rhenium atom defined by the terminal oxo-group, two halide ions, the phosphorus or arsine atom of EPh_3 molecule, and the bidentate *N*,*O* donors of the hbt ligand. The halide ions of $[ReOX_2(hbt)(PPh_3)]\cdot MeCN$ (**1a**, **2a**, **3** and **4**) are arranged in *cis* geometry, whereas the halide ligands of $[ReOX_2(hbt)(PPh_3)]$ occupy *trans* positions to each other. In all the complexes triphenylphosphine or triphenylarsine molecule with their π-acidity adopts *cis* position with respect to the linear O≡Re–O unit. Consequently, the O≡Re–O core with multiply bonded oxo ligand is stabilized to some extent due to accessible π-donation from rhenium to phosphine or arsine molecule. The multiple bonding ligand (terminal oxo) and narrow bite angle of the chelating ligand contribute to clear distortions of the pseudooctahedral environment of Re center in both *cis*- and *trans*-halide complexes.

In complexes **1a**, **2a**, **3** and **4** the rhenium atom is displaced, respectively, 0.121(3), 0.128(3), 0.1289(10), 0.133(2) Å from the plane formed by the two halogen, one nitrogen and one phosphorous (or arsine) atoms (plane A), 0.043(3), 0.033(4), 0.0396(10), 0.037(2) Å from the plane formed by the two oxygen, one halogen and one phosphorous (or arsine) atoms (plane B) and 0.029(4), 0.049(8), 0.0667(14), 0.061(3) Å from the plane formed by two oxygen, one halogen and one nitrogen atoms (plane C). Least squares plane A is inclined at 89.78(23)°, 89.3(2)°, 89.75(7)°, 89.77(18)° to plane B and at 87.38(24)°, 86.5(3)°, 87.38(8)°, 87.15(18)° to plane C; planes B and C are inclined at 89.53(13)°, 89.08(14)°, 89.42(4)°, 89.92(9)°, respectively as above.

In complexes **1b** and **2b** the rhenium atom is displaced, respectively, 0.1834(10), 0.1855(7) Å from the plane formed by the two halogen, one nitrogen and one phosphorous atoms (plane A), 0.0636(11), 0.0480(7) Å from the plane formed by the two oxygen and two halogen ions (plane B) and 0.0379(14), 0.0380(9) Å from the plane formed by two oxygen, one nitrogen and one phosphorous atoms (plane C). Least squares plane A is inclined at 87.33(7)°, 87.21(4)° to plane B and at 89.07(6)°, 89.39(4)° to plane C; planes B and C are inclined at 87.66(7)°, 87.90(4)°, respectively as above.

The 2-hydroxyphenyl moiety is inclined to the benzothiazolie moiety at 11.2(9)°, 10.3(9)°, 11.0(3)°, 12.9(6)°, 12.2(3)°, 12.62(15)°, respectively, for compound **1a**, **2a**, **3**, **4**, **1b**, **2b**.

No extraordinary features in terms of bond lengths and angles can be noticed between *cis*- and *trans*-halide $[ReOX_2(hbt)(PPh_3)]$ complexes. The Re–O_t (O_t = terminal

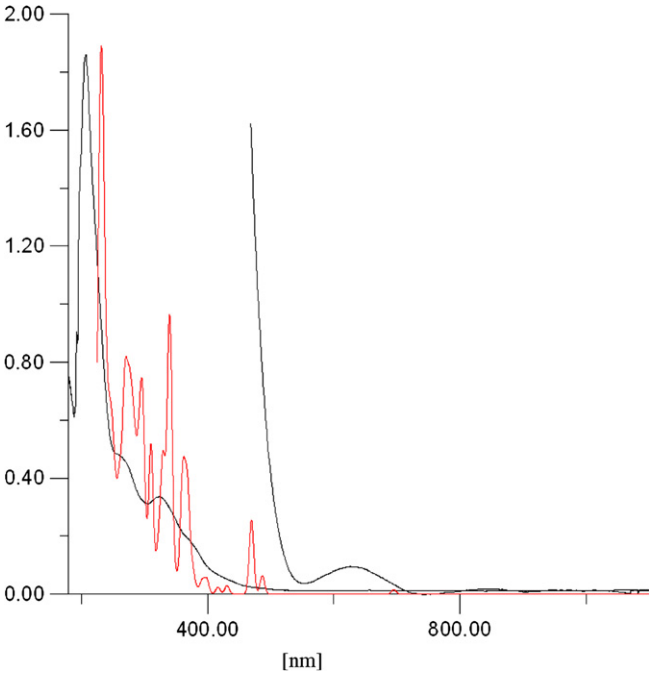


Fig. 3. The experimental (black) and calculated (red) electronic absorption spectra of **1a**. (For interpretation of the references to colour in this figure legend, the reader is referred to the web version of this article.)

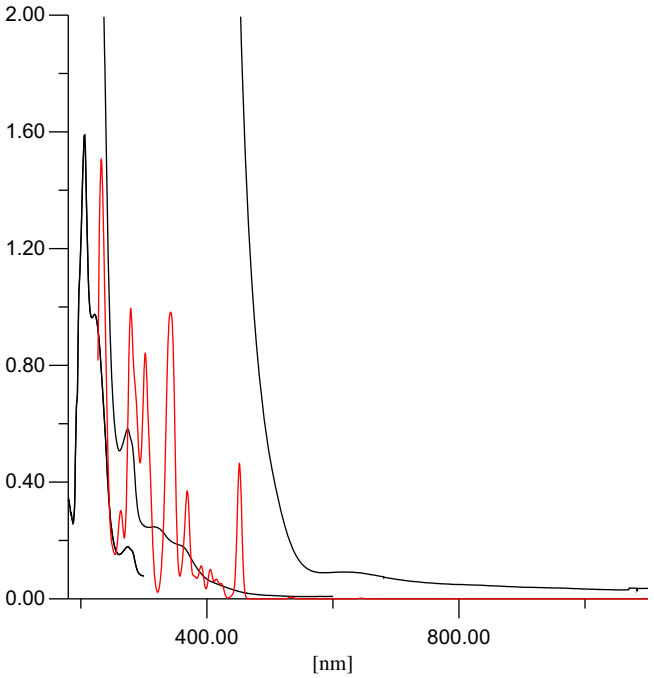


Fig. 4. The experimental (black) and calculated (red) electronic absorption spectra of **1b**. (For interpretation of the references to colour in this figure legend, the reader is referred to the web version of this article.)

oxygen) bond lengths fall in the range 1.639–1.76 Å, typical of mononuclear complexes of rhenium(V) having $[ReO]^{3+}$ core, and indicate the presence of a triple bond Re≡O [32].

The interatomic distances between the rhenium atom and the oxygen atom of 2-(2′-hydroxyphenyl)-2-benzothiazolinato ligand are somewhat shorter than an ideal single Re–O bond length (*ca.* 2.04 Å) [33], indicating only small delocalization in the O(2)–Re(1)–O(1) moiety.

For *cis*-halide $[ReOX_2(hbt)(PPh_3)]$ complexes clear difference between Re(1)–X(1) and Re(1)–X(2) bond lengths can be noticed. The Re(1)–X(1) distances *trans* to the phosphorus or arsine atom of EPh_3 molecule are slightly longer than the Re(1)–X(2) bonds *trans* to the nitrogen atom of the hbt^- ligand. It indicates *structural trans* effect of the EPh_3 ligands. A similar trend was observed in the other $[ReOCl_2(O–N)(PPh_3)]$ chelates [13–15].

4.3. Geometry optimisation, charge distribution, electronic structure and NBO analysis

The geometries of **1a** and **1b** were optimized in a singlet state by the DFT method with the B3LYP functional. The optimized geometric parameters of **1a** and **1b** are gathered in Tables 2 and 3, respectively. In general, the predicted bond lengths and angles are in agreement with the values based upon the X-ray crystal structure data, and the general trends observed in the experimental data are well reproduced in the calculations.

Table 4 presents electron population of the valence core of metal and donor atoms for **1a** and **1b**. The population at Re center and oxygen O(1) and O(2) atoms of both isomers remains almost constant. The calculated charges on the rhenium atoms in **1a** and **1b** are considerably lower than the formal charge +5, which results from significant charge donation from the oxygen atoms, bromine ions and triphenylphosphine molecule. The considerable differences in values of charges are observed for the terminal oxo ligand and the oxygen atom of hbt ligand – less negative are the terminal oxo ligands, which indicate the higher electron density delocalization from the terminal ligands towards the rhenium centers and correspond to differences in the Re–O_t and Re–O_{hbt} bonds lengths. The higher charge donation from the bromide ions can be noticed for the *cis*-halide $[ReOBr_2(hbt)(PPh_3)]$ complex, whereas the population at

Table 6
The energy and molar absorption coefficients of experimental absorption bands and the electronic transitions calculated with the TDDFT method for **1a**

The most important orbital excitations	Character	λ [nm]	E [eV]	f	Experimental		
					Λ [nm]	(E [eV])	ε
H → L	d/π(Br)/π(hbt) → d	695.0	1.78	0.0024	649.5	(1.91)	50
H → L + 1	d/π(Br)/π(hbt) → d	644.0	1.93	0.0002			
H-1 → L	d/π(Br)/π(hbt) → d	486.3	2.55	0.0106	446.0	(2.78)	450
H-1 → L + 1							
H-1 → L	d/π(Br)/π(hbt) → d	469.4	2.64	0.0425			
H-1 → L + 1							
H → L + 2	d/π(Br)/π(hbt) → π*(hbt)	368.0	3.37	0.0561	361.2	(3.43)	2700
H-5 → L + 1	π(Br)/π(PPh_3) → d						
H-5 → L + 1	π(Br)/π(PPh_3) → d	362.4	3.42	0.0308			
H-6 → L	π(PPh_3) → d	359.7	3.45	0.0401			
H-1 → L + 2	d/π(Br)/π(hbt) → π*(hbt)	341.0	3.64	0.0926	324.5	(3.82)	4080
H-8 → L	π(PPh_3) → d						
H-1 → L + 2	d/π(Br)/π(hbt) → π*(hbt)	338.2	3.67	0.0757			
H-8 → L	π(PPh_3) → d						
H-1 → L + 3	d/π(Br)/π(hbt) → d	329.9	3.76	0.0565			
H-2 → L + 2	π(hbt)/π(Br)/*n*(P) → π*(hbt)	310.4	3.99	0.0730			
H-3 → L + 2	π(hbt)/π(Br)/π(PPh_3) → π*(hbt)	296.9	4.18	0.0639			
H-2 → L + 3	π(hbt)/π(Br)/*n*(P) → d	288.6	4.30	0.0303			
H-3 → L + 3	π(hbt)/π(Br)/π(PPh_3) → d	282.4	4.39	0.0447			
H-5 → L + 3	π(Br)/π(PPh_3) → d	276.2	4.49	0.0766			
H-4 → L + 3	π(Br)/π(hbt)/π(PPh_3) → d						
H-15 → L + 1	π (hbt)/*n*(P)/σ(Br) → d	271.2	4.57	0.0339			
H-6 → L + 3	π(PPh_3) → d	269.0	4.61	0.0491			
H-1 → L + 5	d/π(Br)/π(hbt) → π*(PPh_3)	260.6	4.76	0.0345	269.5	(4.60)	5640
H-5 → L + 4	π(Br)/π(PPh_3) → π*(PPh_3)	235.9	5.26	0.0304			
H-16 → L + 1	d/π(Br)/π(hbt) → π*(hbt)/π*(PPh_3)	233.8	5.30	0.0348			
H-1 → L + 9	π(Br)/π(PPh_3) → d						
H-14 → L + 3	π(Br)/π(bthoz)/*n*(P) → d	233.0	5.32	0.0454			
H → L + 11	d/π(Br)/π(hbt) → π*(hbt)/π*(PPh_3)	228.4	5.43	0.0367			
H-5 → L + 5	π(Br)/π(PPh_3) → π*(PPh_3)	228.4	5.43	0.0798			
H-14 → L + 3	π(Br)/π(hbt)/*n*(P) → d	226.6	5.47	0.0319			
H-2 → L + 7	π(hbt)/π(Br)/*n*(P) → π*(hbt)/π*(PPh_3)						
					209.0	(5.93)	23 000

ε – molar absorption coefficient [$dm^3\ mol^{-1}\ cm^{-1}$]; f – oscillator strength; H – highest occupied molecular orbital; L – lowest unoccupied molecular orbital.

the p-orbitals of the phosphorous atom of *trans*-halide is smaller.

The nature of rhenium–terminal oxygen (O_t) interaction in **1a** and **1b** has been studied by NBO analysis. The occupancy and composition of the calculated Re–O_t natural bond orbitals (NBOs) are given in Table 5. The Re–O_{hbt} bond orbital were not detected indicating a conceivable predominant Coulomb-type Re–ligand interaction in both isomers.

Each natural bond orbital (NBO) σ_{AB} can be written in terms of two directed valence hybrids (NHOs) h_A and h_B on atoms A and B:

$$\sigma_{AB} = c_A h_A + c_B h_B$$

where c_A and c_B are polarization coefficients. Each valence bonding NBO must in turn be paired with a corresponding valence *anti*-bonding NBO:

$$\sigma^*_{AB} = c_B h_A - c_A h_B$$

to complete the span of the valence space. The Lewis-type (donor) NBOs are thereby complemented by the non-Lewis-type (acceptor) NBOs that are formally empty in an idealized Lewis picture. The interactions between 'filled' Lewis-type NBOs and 'empty' non-Lewis NBOs lead to loss of occupancy from the localized NBOs of the idealized Lewis structure into the empty non-Lewis orbitals, and they are referred to as 'delocalization' corrections to the zeroth-order natural Lewis structure [31].

Similar to the previous described [$ReOX_2$(O–N)(PPh_3)] chelates [13–15], two strongly polarized to the oxygen atom natural Re–O_t bond orbitals were detected for **1a** and **1b**, whereas the NBO analysis of [$ReOX_3$(N–N)] oxocompounds [34,35] confirms three natural bond orbitals between metal and oxygen. As the results for the last ones are very clear (one σ-bond and two π bonds), the interpretation of NBO analysis for **1a** and **1b** is not straightforward. The both detected natural Re–O_t bond orbitals of **1a** and **1b** are similar in energy and they are composed of the p oxygen and d rhenium orbitals. The terminal oxo ligand of **1a** and **1b** has two lone pair orbitals, and electron density from one of them is strongly delocalized into non-Lewis rhenium orbital. It can be assumed that the detected natural Re–O_t bond orbitals are of π character and not detected σ_{Re-Ot} bond has ionic character, similar as Re–N bond orbital in [$ReCl_4(MeCN)_2$] [17]. However, another interpretation may be also concluded from the NBO analysis for the examined isomers. Instead of the mentioned triple bond, the double Re–O_t bond with relevant negative hyperconjugation may be proposed for **1a** and **1b**.

4.4. Electronic spectra

The experimental electronic spectra of **1a** and **1b** are presented in Figs. 3 and 4, respectively. The positions of absorption bands for the other [$ReOX_2$(hbo)(EPh_3)] complexes are given in the experimental part. As can be seen from Figs. 3 and 4 the UV–Vis spectra of the *cis* and *trans* stereoisomers are very similar in terms of the position, intensity and shape of the bands in the whole region 1100–180 nm. Similar to the IR measurements they are

Table 7
The energy and molar absorption coefficients of experimental absorption bands and the electronic transitions calculated with the TDDFT method for **1b**

The most important orbital excitations	Character	λ [nm]	E [eV]	f	Experimental		
					Λ [nm]	E [eV]	ε
H → L + 1	d/π(hbt)/π(Br) → d	644.9	1.92	0.0003	638.5	(1.94)	80
H-1 → L	π(hbt)/π(Br)/d → d	533.7	2.32	0.0010			
H-1 → L + 1	π(hbt)/π(Br)/d → d	451.6	2.74	0.0772	445.0	(2.79)	550
H-2 → L	π(hbt) → d	414.9	2.99	*0.0104*			
H-4 → L	π(PPh_3)/*n*(P) → d	405.2	3.06	0.0165			
H-5 → L	π(PPh_3) → d	391.5	3.17	0.0130	359.0	(3.45)	3450
H → L + 2	d → π*(hbt)	369.3	3.36	0.0530			
H-9 → L + 1	π(Br)/π(O_t) → d	361.5	3.43	0.0130			
H-8 → L	π(PPh_3)/π(Br) → d						
H-10 → L	π (PPh_3)/π(Br) → d	346.2	3.58	0.1086	317.0	(3.91)	4650
H-1 → L + 2	π(hbt)/π(Br)/d → π*(hbt)						
H-2 → L + 3	π(hbt)/π(Br)/d → d	340.4	3.64	0.0392			
H-8 → L + 1	π (PPh_3)/π(Br) → d						
H-8 → L + 1	π (PPh_3)/π(Br) → d	339.0	3.66	0.0701			
H-12 → L	π(Cl)/π(O_t)/π (PPh_3) → d	335.0	3.70	0.0439			
H-2 → L + 2	π(hbt) → π*(hbt)	309.1	4.01	0.0597	274.0	(4.52)	10950
H-3 → L + 2	π(hbt)/π(Br)/π(PPh_3) → π*(hbt)	302.4	4.10	0.1055			
H-4 → L + 3	π(PPh_3)/*n*(P) → d	278.9	4.31	0.0645			
H-16 → L + 1	π(Br)/π(hbt)/π(O_t)/*n*(P) → d	277.8	4.46	0.0960			
H-7 → L + 4	π(PPh_3)/π(Br) → π*(PPh_3)	238.2	5.21	0.0236	222.0	(5.58)	18400
H-4 → L + 4	π(PPh_3)/*n*(P) → π*(PPh_3)						
H-4 → L + 4	π(PPh_3)/*n*(P) → π*(PPh_3)	236.3	5.25	0.0342			
H-4 → L + 5	π(PPh_3)/*n*(P) → π*(PPh_3)	232.2	5.34	0.0276			
H-13 → L + 3	π(hbt)/π(Br) → d						
H-13 → L + 3	π(hbt)/π(Br) → d	232.2	5.34	0.0442			
					206.0	(6.02)	29980

indistinctive for molecular structure determination. In order to discussion this observation in more detail, the time-dependent density functional calculations (TDDFT) were employed to produce a hundred of singlet excited-states starting from the ground-state geometries of **1a** and **1b** optimized in the gas phase. The calculated electronic spectra of **1a** and **1b** are presented in Figs. 3 and 4, respectively. Each calculated transition is represented by a gaussian function $y = ce^{-bx^2}$ with the height (c) equal to the oscillator strength and b equal to 0.04 nm^{-2}.

Tables 6 and 7 present the most important electronic transitions calculated with the TDDFT method assigned to the observed absorption bands of **1a** and **1b**. The assignment of the calculated orbital excitations to the experimental bands was based on an overview of the contour plots and relative energy to the orbitals HOMO and LUMO involved in the electronic transitions. The simplified molecular orbital diagrams of **1a** and **1b** with several contours of occupied and unoccupied MOs (active in the electronic transitions) are presented in Figs. 5 and 6, respectively.

The TDDFT/PCM calculations show that the longest wavelength experimental bands of **1a** and **1b** (at 649.5 for *cis* and 638.5 nm for *trans*) originate in the HOMO → LUMO and HOMO → LUMO + 1 transitions. The HOMO, LUMO and LUMO + 1 orbitals are delocalized among rhenium ion, bromide, oxo and hbt ligands, so a delocalized *MLLCT* (metal-ligand-to-ligand CT) description also can be used. However, considering that these molecular orbitals comprise mainly rhenium 5d atomic orbitals (Figs. 5 and 6), the HOMO → LUMO and

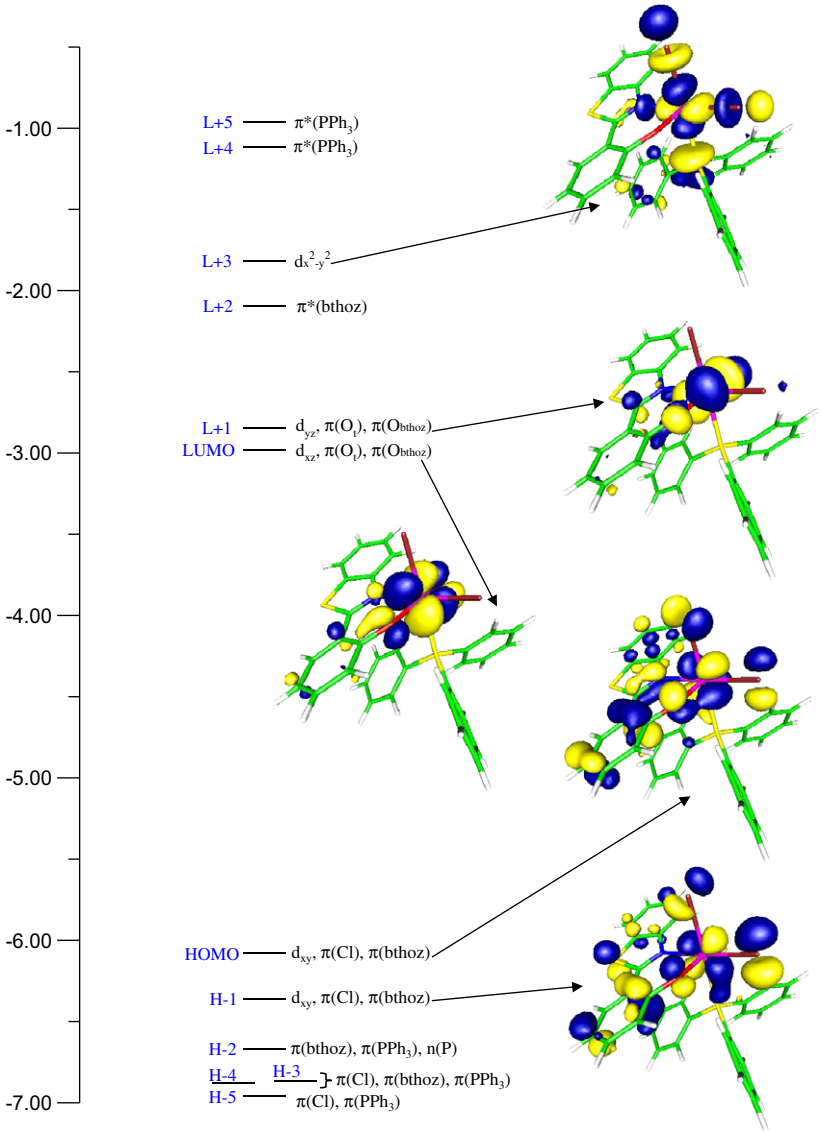


Fig. 5. The energy (eV), character and some contours of the unoccupied molecular orbitals of **1a**. Positive values of the orbital contour are represented in blue (0.04 a.u.) and negative values – in yellow (−0.04 a.u.). (For interpretation of the references to colour in this figure legend, the reader is referred to the web version of this article.)

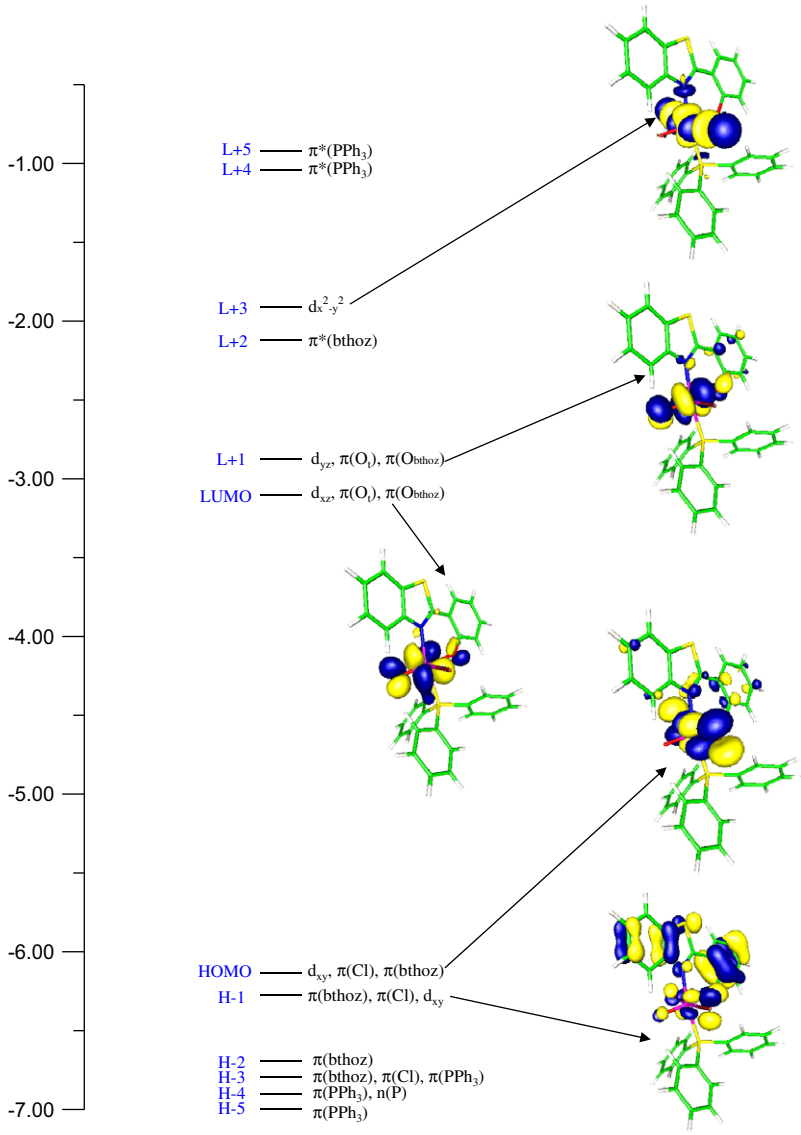


Fig. 6. The energy (eV), character and some contours of the unoccupied molecular orbitals of **1b**. Positive values of the orbital contour are represented in blue (0.04 a.u.) and negative values – in yellow (−0.04 a.u.). (For interpretation of the references to colour in this figure legend, the reader is referred to the web version of this article.)

HOMO → LUMO+1 transitions may be ascribed as transitions of d → d character.

The observed absorptions at 446.0 nm (*cis*-Br) and 445.0 nm (*trans*-Br) can be assigned to *Ligand-Metal Charge Transfer* transitions occurring from the bromide and hbt^- ligand for *cis* and bromide, hbt^- and phosphine ligand for *trans* halide complex.

The absorption band at 361.2 nm (*cis*-Br) and 359.0 nm (*trans*-Br) can be related to HOMO → LUMO + 2 excitation of d/π(Br)/π(bthoz) → π*(bthoz) character with a certain contribution of *Ligand-Metal Charge Transfer* transitions.

For both stereoisomers the experimental bands below 300 nm result mainly from *Ligand–Ligand Charge Transfer* and interligand (IL) transitions.

Acknowledgement

The Gaussian03 calculations were carried out in the Wrocł aw Centre for Networking and Supercomputing, WCSS, Wrocław, Poland.

Appendix A. Supplementary data

CCDC 673361, 673362, 673363, 673364, 673365, and 673366 contain the supplementary crystallographic data for this paper. These data can be obtained free of charge via http://www.ccdc.cam.ac.uk/conts/retrieving.html, or from the Cambridge Crystallographic Data Centre, 12 Union Road, Cambridge CB2 1EZ, UK; fax: (+44) 1223-336-033; or e-mail:deposit@ccdc.cam.ac.uk. Supplemen-

tary data associated with this article can be found, in the online version, at doi:10.1016/j.poly.2008.02.018.

References

[1] C.C. Romão, F.E. Kühn, W.A. Hermann, Chem. Rev. 97 (1997) 3197.
[2] A.A. Shteinman, Russ. Chem., Bull. Int. Ed. 50 (2001) 1795.
[3] F.E. Kühn, A. Scherbaum, W.A. Herrmann, J. Organomet. Chem. 689 (2004) 4149.
[4] G.S. Owens, J. Arias, M.M. Abu-Omar, Catal. Today 55 (2000) 317.
[5] A.M. Kirillov, M. Haukka, M.V. Kirillova, A.J.L. Pombeiro, Adv. Synth. Catal. 347 (2005) 1435.
[6] A. Deloffre, S. Halut, L. Salles, J.-M. Brégeault, J.R. Gregorio, B. Denise, H. Rudler, J. Chem. Soc., Dalton Trans. (1999) 2897.
[7] J.R. Dilworth, S.J. Parrott, Chem. Soc. Rev. 27 (1998) 43.
[8] P. Blower, Dalton Trans. (2006) 1705.
[9] A. Duatti, A. Marchi, R. Rossi, L. Magon, E. Deutsch, V. Bertolasi, F. Bellucci, Inorg. Chem. 27 (1988) 4208.
[10] X. Chen, F.J. Femia, J.W. Babich, J. Zubieta, Inorg. Chim. Acta 307 (2000) 149.
[11] F.H. Allen, Acta Crystallogr., Sect. B 58 (2002) 380.
[12] W.K. Rybak, A. Skarżyńska, L. Szterenberg, Z. Ciunik, T. Głowiak, Eur. J. Inorg. Chem. (2005) 4964.
[13] B. Machura, R. Kruszynski, Polyhedron 26 (2007) 3686.
[14] B. Machura, R. Kruszynski, J. Kusz, Polyhedron 26 (2007) 3455.
[15] B. Machura, S. Michalik, R. Kruszynski, J. Kusz, Polyhedron 26 (2007) 2837.
[16] J. Gancheff, C. Kremer, E. Kremer, O.N. Ventura, J. Mol. Struct. (Theochem) 580 (2002) 107.
[17] M.L. Kuznestov, E.A. Klestova-Nadeeva, A.I. Dement'ev, J. Mol. Struct. (Theochem) 671 (2004) 229.
[18] G. Rouschias, G. Wilkinson, J. Chem. Soc. A (1966) 465.
[19] (a) STOE and Cie (1999). X-RED. Version 1.18. STOE & Cie GmbH, Darmstadt, Germany;
(b) CrysAlis RED, Oxford Diffraction Ltd., Version 1.171.29.2.G.M. Sheldrick Acta Crystallogr., Sect A, 46 (1990) 467.
[20] G.M. Sheldrick, Acta Crystallogr., Sect. A A46 (1990) 467.
[21] G.M. Sheldrick, SHELXL97. Program for the Refinement of Crystal Structures, University of Göottingen, Germany, 1997.
[22] G.M. Sheldrick, SHELXTL: release 4.1 for Siemens Crystallographic Research Systems (1990).
[23] Gaussian 03, Revision B.03, M.J. Frisch, G.W. Trucks, H.B. Schlegel, G.E. Scuseria, M.A. Robb, J.R. Cheeseman, J.A. Montgomery, Jr., T. Vreven, K.N. Kudin, J.C. Burant, J.M. Millam, S.S. Iyengar, J. Tomasi, V. Barone, B. Mennucci, M. Cossi, G. Scalmani, N. Rega, G.A. Petersson, H. Nakatsuji, M. Hada, M. Ehara, K. Toyota, R. Fukuda, J. Hasegawa, M. Ishida, T. Nakajima, Y. Honda, O. Kitao, H. Nakai, M. Klene, X. Li, J.E. Knox, H.P. Hratchian, J.B. Cross, C. Adamo, J. Jaramillo, R. Gomperts, R.E. Stratmann, O. Yazyev, A.J. Austin, R. Cammi, C. Pomelli, J.W. Ochterski, P.Y. Ayala, K. Morokuma, G.A. Voth, P. Salvador, J.J. Dannenberg, V.G. Zakrzewski, S. Dapprich, A.D. Daniels, M.C. Strain, O. Farkas, D.K. Malick, A.D. Rabuck, K. Raghavachari, J.B. Foresman, J.V. Ortiz, Q. Cui, A.G. Baboul, S. Clifford, J. Cioslowski, B.B. Stefanov, G. Liu, A. Liashenko, P. Piskorz, I. Komaromi, R.L. Martin, D.J. Fox, T. Keith, M.A. Al-Laham, C.Y. Peng, A. Nanayakkara, M. Challacombe, P.M.W. Gill, B. Johnson, W. Chen, M.W. Wong, C. Gonzalez, J.A. Pople, Gaussian Inc., Pittsburgh PA, 2003.
[24] A.D. Becke, J. Chem. Phys. 98 (1993) 5648.
[25] C. Lee, W. Yang, R.G. Parr, Phys. Rev. B 37 (1988) 785.
[26] P.C. Hariharan, J.A. Pople, Theor. Chim. Acta 28 (1973) 213.
[27] V.A. Rassolov, M.A. Ratner, J.A. Pople, P.C. Redfern, L.A. Curtiss, J. Comp. Chem. 22 (2001) 976.
[28] P.J. Hay, W.R. Wadt, J. Chem. Phys. 82 (1985) 299.
[29] K. Eichkorn, F. Weigend, O. Treutler, R. Ahlrichs, Theor. Chem. Acc. 97 (1997) 119.
[30] M.E. Casida, in: J.M. Seminario (Ed.), Recent developments and applications in modern density functional theory, Theoretical and Computational Chemistry, vol. 4, Elsevier, Amsterdam, 1996.
[31] E. Reed, L.A. Curtiss, F. Weinhold, Chem. Rev. 88 (1988) 899.
[32] J.M. Mayer, Inorg. Chem. 27 (1988) 3899.
[33] S.R. Flechter, A.C. Skapski, J. Chem. Soc., Dalton Trans. (1972) 1073.
[34] B. Machura, R. Kruszynski, M. Jaworska, J. Kłak, J. Mroziński, Polyhedron 25 (2006) 2537.
[35] B. Machura, R. Penczek, R. Kruszynski, J. Kusz, Polyhedron 26 (2007) 2581.

occurring. For example, CD can coordinate a number of metals in alkaline media. On deprotonation, the anionic hydroxyls on the CD primary face become effective ligands [5]. If these metals have appropriate redox properties, they may participate in photoinduced redox reactions, with appended luminophores and provide a means of interrogating the ability of the CD to support electron transfer through the CD framework as opposed to through inclusion.

Our group reported previously on the synthesis and characterization of a novel donor–acceptor complex comprised of an OH bridged manganese(III) dimer covalently linked to a ruthenium polypyridyl sensitizer via a β-cyclodextrin moiety [6]. We observed photoinduced intramolecular transfer in this species, the k_{et} was modest, estimated to be $2 \times 10^6\ s^{-1}$, but suggested that the CD framework can support electron transfer.

In addition to manganese(III), copper(II) can coordinate effectively to CD. Cyclodextrin is known to bind copper(II) under neutral and particularly under alkaline conditions [7–11]. It has been demonstrated to form a hydroxyo-bridged dimer, this copper dimer is considerably more stable than the analogous manganese system, and is also expected, on the basis of thermodynamic arguments to quench the excited state of a pendant ruthenium polypyridyl complex. Copper is of particular interest because it is both an essential trace element whereby it acts as a cofactor for a number of metalloenzymes, and it is an important environmental pollutant.

We report here on a donor–acceptor system incorporating a ruthenium polypyridyl functionalized β-cyclodextrin moiety with an hydroxo bridged Cu(II) dimer and provide evidence for photoinduced electron transfer between the copper centre and the ruthenium. We illustrate the effects of solution phase binding of Cu^{2+} and Zn^{2+} ions to the ruthenium modified CD on the photophysics of the ruthenium luminophore. This work demonstrates that ruthenium polypyridyl functionalized β-cyclodextrin moiety binds copper(II) with concomitant transduction of this binding through modulation of luminescence intensity and lifetime. Such materials may have potential in analytical applications for metal ion sensing. Ultimately, because of the synthetic versatility of the metal luminophore, selectivity in sensing applications may be exerted by modifying the ligands in this complex, thereby altering the redox chemistry and thermodynamics of a given excited-state reaction.

2. Experimental

2.1. Chemicals and materials

β-Cyclodextrin, 5-nitro-1,10-phenanthroline, 2,2′-bipyridine, $RuCl_3 \cdot 3H_2O$, Cu(II)acetate monohydrate, zinc acetate dihydrate, DMF and NMP were all obtained from Sigma Aldrich and used as received.

6^A-Deoxy-6^A-*p*-toluenesulphonyl-β-cyclodextrin, *cis*-$Ru(bpy)_2Cl_2$, 6^A-(5-amino-1,10-phenanthroline)-6^A-deoxy-β-cycoldextrin, and Cu_2CD were synthesized and purified according to published procedures [8,12,6,13].

Ruthenium(II)(bisbipyridine)(6^A-(5-amino-1,10-phenanthroline)-6^A-deoxy-β-cyclodextrin: CDRu was synthesized as described previously,[6] and purified using size-exclusion chromatography on Sephadex G-75, with water as eluent. {$m/z = 878.8$, $[M-2PF6]^{+2}$, 1637, $[M-PF6]^{+1}$, structure was confirmed from 2D ^1H NMR which conformed with previously reported values [6].

Synthesis of dicopper-dihydroxo-ruthenium (II)(bisbipyridine) (6^A-deoxy-5-amino-1,10-phenanthroline)-6^A-deoxy-β-cyclodextrin: Cu_2CDRu: (0.10 g, 0.05 mmol) CDRu was dissolved in 0.5 M NaOH, (0.03 g, 0.1 mmol) $Cu(CH_3CHOO)_2$ (cupric acetate) was added, the mixture was stirred for 2 h under N_2. Ethanol was added to precipitate the product. The dark red product was recrystallized from 0.2 M NaOH [14]. ($m/z = 2022$, $[Cu_2CDRu][PF_6]$).

2.2. Physical measurements

Electronic absorption spectroscopy was conducted on a Shimadzu 3500 UV–Vis/NIR spectrophotometer.

Cyclic voltammetry was carried out using a CH instrument Model 660 electrochemical work station. A conventional three-electrode cell arrangement was used. This comprised a platinum microelectrode (50 μm ϕ) polished and electrochemically cleaned as described previously, an Ag/AgCl reference electrode and platinum wire counter electrode [15]. The complexes were dissolved in DMF with 0.1 M tetrabutylammonium hexaflourophosphate as supporting electrolyte. The working electrode was polished using 0.05 mm alumina. The solution was degassed for 30 minutes with N_2 and a gas blanket was maintained over the solution surface during all experiments. The solution was sonicated between each experiment.

Fourier transform Infrared experiments (FT-IR) were recorded in a KBr Discs using a Perkin Elmer FT-IR spectrometer.

Magnetic moments were determined via the Evans method on a Sherwood Scientific, magnetic susceptibility balance, spin only values were calculated according to $\mu_{Cu} = 2[S_{Cu}(S_{Cu}+1)]^{1/2}$ [16].

^1H NMR spectra were recorded on a Bruker Avance series 400 MHz NMR spectrometer; chemical shifts are reported relative to the solvent reference [D_6] DMSO 2.49 ppm.

Mass spectra were obtained by Electrospray Ionization in positive ion mode using a Bruker LC/MS Esquire series. Steady-state emission spectra were recorded on a Varian Cary Eclipse luminescence spectrophotometer. Luminescence lifetimes were measured using the third harmonic (355 nm, 30 mJ/pulse) of a continuum surelite Q-switched ND:YAG laser for excitation, emission was detected in a right-angled configuration to the laser using Andor Model M20 gated intensified CCD coupled to an Oriel Model MS125 spectrograph. This configuration allows a complete emission spectrum (spectral width 250 nm) to be obtained

within times as short as 10 ns. The gate width, i.e. the exposure time of the CCD was never more than 5% of the excited-state lifetime. The step size, i.e., the time between the acquisition of discrete spectra was typically 5% of the excited half-life. Time-resolved absorption spectra were collected using the instrumentation in absorption mode with an Applied Photophysics 300 W pulsed Xe arc lamp as a monitoring source. In this instance, spectra were typically recorded using the average of 25 laser shots. The gate width was never more than 10% of the excited-state lifetime.

Luminescence titration of CDRu with $M(CH_3COO)_2 \cdot H_2O$ ($M = Cu^{2+}$, Zn^{2+}) was conducted using stock solutions of 2.7×10^{-4} M CDRu and 0.01 M $M(CH_3COO)_2 \cdot H_2O$ in aqueous solution at pH 12. Eighteen solutions were prepared by combining 40 μL of CDRu solution with increasing aliquots of $M(CH_3COO)_2 \cdot H_2O$ titrant up to 2 mM. The final volume was made up in order that CDRu concentration remains constant in all experiments at 2.1×10^{-6} M.

Raman spectroscopy was conducted on a Dilor.Jobinyvon.Spex HR Labram. The exciting Argon ion laser, Coherant Innova 300c (514.5, 488, 457.9 nm) was focused on the sample using a 10× objective lens. Focusing was confirmed by using an imaging video camera. A spectral resolution of 0.5 cm^{-1} per pixel was achieved using an 1800 lines mm^{-1} grating and the *x*-axis was calibrated against the phonon mode of silicon and the Rayleigh line.

Quantum yields were measured using the comparative method of Williams et al. [17].

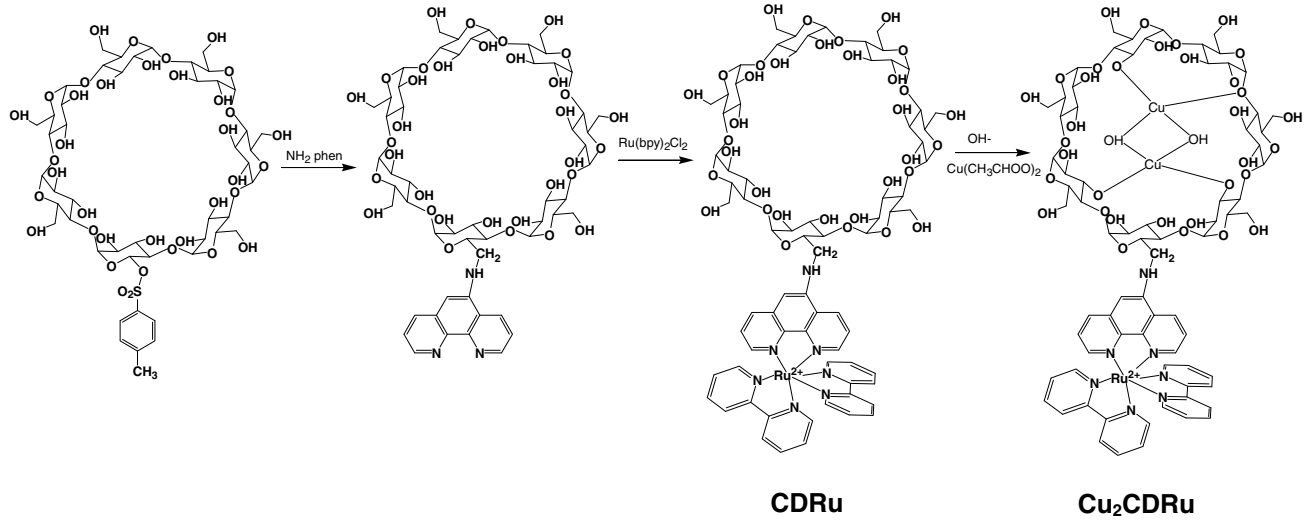
3. Results and discussion

3.1. Synthesis

The synthetic steps leading to production of Cu_2CDRu are shown in Scheme 1. The synthesis of the phenanthroline substituted β-CD and ruthenium polypyridyl complex, CDRu, were reported previously and the mass spectral, NMR and elemental analysis conformed to those reported [6,18]. The ability of β-CD to coordinate Cu(II) is well established. Under alkaline conditions a combination of cupric acetate and β-CD yields a 2:1 hydroxy-bridged Cu(II) dimer coordinated to the deprotonated hydroxyls on the secondary face of β-CD [19,7–9]. This complex is quite stable in alkaline solution [20,10,21]. An analogous procedure to that reported for β-CD was followed here, except that CDRu complex was employed instead of β-CD, this was treated with cupric acetate in 0.5 M NaOH. The resulting paramagnetic complex was studied using mass spectrometry, magnetochemistry, vibrational spectroscopy and elemental analysis which all confirmed that the Cu had coordinated in 2:1 ratio. The coordination mode to the CD is expected to be the same as that described for free β-CD and this is consistent with our vibrational spectral and magnetic results. The complex was stable in the solid state, in the absence of air for months and in aqueous alkaline media for at least a week. It was stable for several hours in DMF, however, the copper centre was very labile in neutral aqueous media.

3.2. Magnetic susceptibility studies

The effective magnetic moment for Cu_2CDRu was found to be $1.075\mu_B$ per Cu at 294 K which is lower than the anticipated value of $1.79\mu_B$ for the spin only value of the d^9 electronic configuration of Cu(II), calculated on the basis that no magnetic interactions are occurring between the metal ions. These values are in good agreement with those reported for the parent unfunctionalised Cu_2(II,II)-CD complex [21,22]. Detailed temperature dependent magnetic studies for this analogous complex indicated a weak antiferromagnetic exchange between the two high spin Cu(II) metal ions acting through the hydroxyl bridged system [19].



Scheme 1. Schematic showing the synthetic route to Cu_2CDRu.

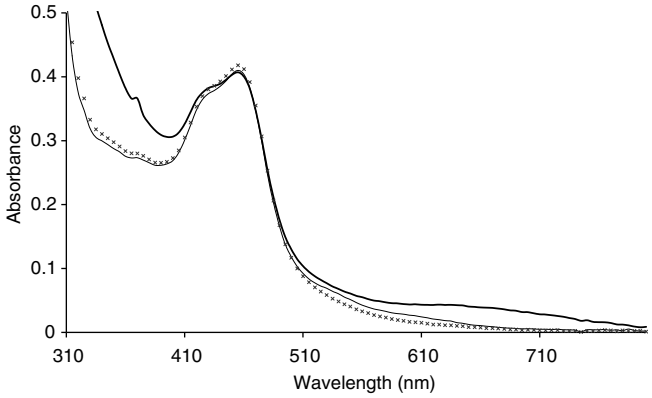


Fig. 1. Electronic absorption spectroscopy of Cu_2CDRu (heavy line), CDRu at pH 7 (dotted line), and CDRu at pH 12 (light line) in DMF.

3.3. FTIR spectroscopy

The FTIR spectra of the CDRu complexes before and after coordination to Cu were compared.[1] The region between 1200 and 1000 cm^{-1} are dominated by exocyclic OH modes, which are shifted to higher frequency on coordination of the Cu site. These changes conformed to those reported previously for Cu_2CD and are attributed to perturbations of CH_2 and OH bending modes induced by coordination of metal to the secondary side of CD [21]. There is also significant broadening to the OH stretch band with the appearance of a shoulder at approximately 3250 cm^{-1} not apparent in CDRu. This is attributed to the copper bridged OH stretching mode [24,21].

3.4. Electronic spectroscopy

Fig. 1 shows the UV–vis spectra of CDRu under neutral aqueous conditions and pH 12 respectively. In the latter case this corresponds to the pH at which the copper is coordinated. The spectra exhibit maxima around 455 nm attributed to Ru (dπ) to L (π*) MLCT transitions and ligand centred (LC) features below 300 nm. The spectra are essentially identical, indicating any new transitions on coordination of the copper do not arise from deprotonation of the CD. The absorbance spectrum of Cu_2CDRu is also shown in Fig. 1. Coordination of the dinuclear copper centre to the CDRu complex results in a slight red shift of the MLCT and the appearance of a feature centred around 620 nm, this feature is weak and very broad extending to approximately 700 nm. It is attributed to the Cu(II) d–d transition from comparison with the Cu_2CD complex [8,10]. In addition, there are changes in the UV spectral region, a new feature appears (from spectral fitting) centred around 320 nm, a similar feature appears in the spectrum of the Cu_2CD complex and is also associated with the copper coordination, possibly attributed to a Cu → OH charge transfer transition [21,25]. There is no evidence for any new optical transitions arising from interaction between the Ru and Cu centres in the trinuclear complex, as the electronic spectrum of Cu_2CDRu appears to be largely a composite of the two separate complexes.

To gain insight into the origin of the optical transitions resonance Raman spectroscopy was conducted for both CDRu and Cu_2CDRu, Fig. 2. In resonance Raman spectroscopy, the exciting laser line is resonant with an optical transition and this yields enhancements in vibrational modes associated with the chromophores of up to 7 orders of magnitude. This provides a relatively unambiguous means of characterizing optical transitions. The results are shown in Fig. 3, for optical excitation at 488, and 514.5 nm. The Raman spectra exciting at 514 nm are similar for Cu_2CDRu and CDRu. The spectra contain signature bipyridyl modes and an Ru–N stretch vibration (~372 cm^{-1}) typical of resonance with a Ru (dπ) to bpy (π*) MLCT transition. Exciting at 488 nm, however there are significant differences between the complexes in which the copper is present and absent. Both Cu_2CDRu and CDRu share common features attributed to bpy or phen and Ru-modes, but in addition, the Cu_2CDRu complex contains additional modes, most notably an intense feature at 565 cm^{-1} and a second feature at 635 cm^{-1}. The identity

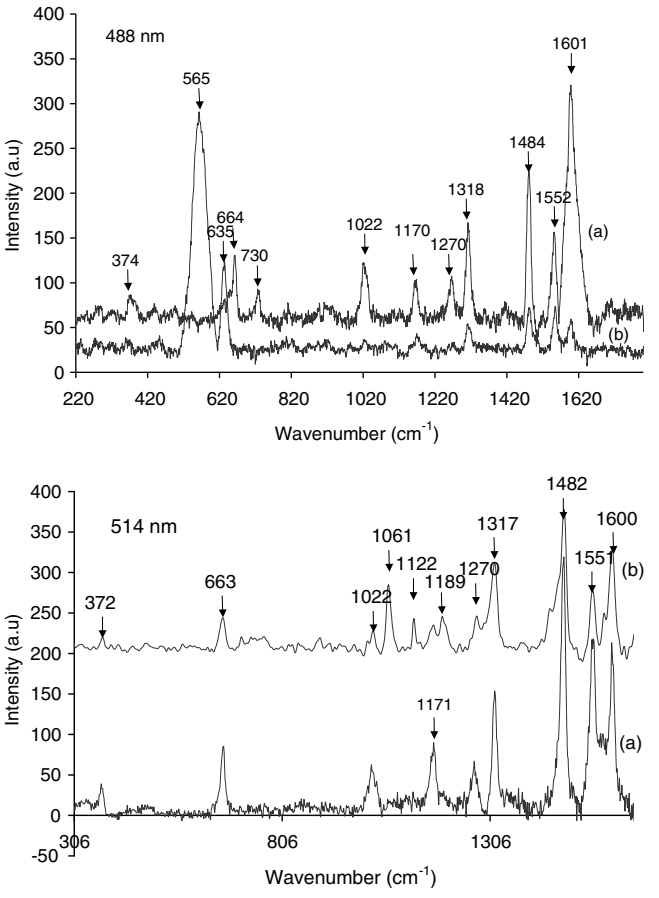


Fig. 2. Resonance Raman spectroscopy of (a) CDRu and (b) Cu_2CDRu excited at 488 nm (top) and (a) CDRu and (b) Cu_2CDRu 514.5 nm (bottom).

[1] See Supplementary material.

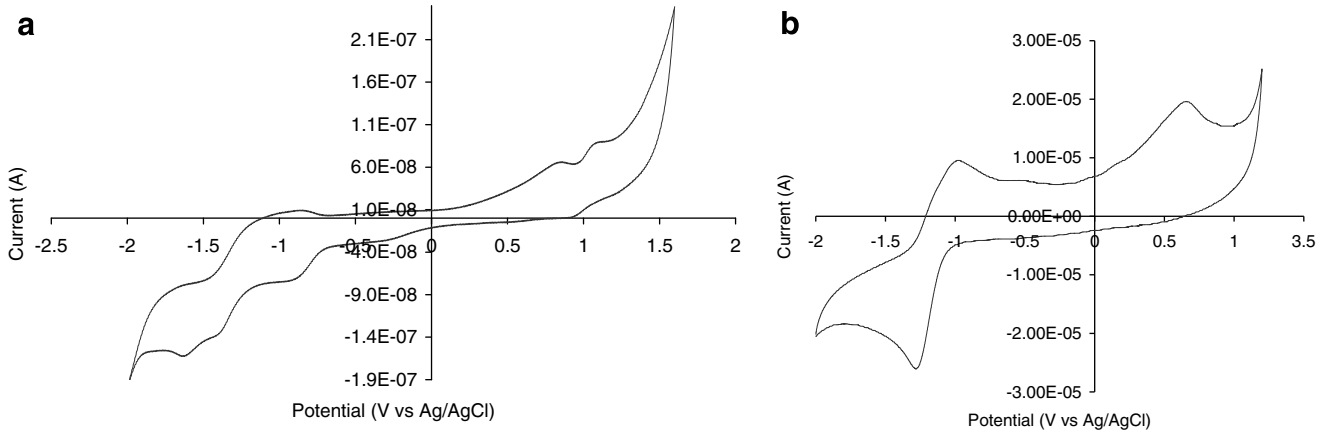


Fig. 3. Cyclic voltammetry of (a) Cu_2CDRu, on a platinum microelectrode (∅ 50 μm) working electrode, at $v = 500$ mV/s (b) Cu_2CD at (∅ 3 mm) diameter glassy carbon working electrode at $v = 100$ mV/s, potentials quoted vs. Ag/AgCl reference electrode, solvent was dry DMF with tetrabutylammoniumperclorate as a supporting electrolyte.

Table 1
Spectroscopic and photophysical data of CDRu, Cu_2CDRu and $[Ru(bpy)_3]^{+2}$ as a reference in spectroscopic grade DMF

Complex	Absolute λ_{max} (nm)	E_m λ_{max} (nm)	$\tau_{deaerated}$ (ns)	$\tau_{aerated}$ (ns)	$\Phi_{aerated}$	ε (M^{-1} cm^{-1})
CDRu	450	618	900	249	0.013	7500
Cu_2CDRu	455	618	336	159	0.006	6750
$[Ru(bpy)_3]^{+2}$	450	605	935	247	0.028	12500

of the latter is not clear, but may be associated with the CD, the former feature is attributed to a Cu–O stretch mode, which is enhanced from resonance with the underlying copper based electronic transition [24]. This provides useful evidence for the presence of the copper dimer. Similarly this mode is present when exciting at 458 nm in addition to a new feature at 1095 cm^{-1}, which is likely to originate from the CD backbone. The dominance of these new features at 488 and 458 nm excitation is likely to arise from post-resonance with the new feature at 320 nm, which, as described, may arise from a Cu(II) ← O^- ligand to metal charge transfer (LMCT) transition, possibly associated with deprotonated hydroxyl on cyclodextrin [26,21,27]. Resonance Raman spectroscopy of the low energy d–d optical transition at 620 nm was probed with 633 excitation, unfortunately luminescence interference from the ruthenium centre at this wavelength prevented the collection of meaningful Raman data.

3.5. Electrochemistry

Voltammetric data for CDRu, Cu_2CD and Cu_2CDRu in dry DMF is provided in Table 2. The electrochemistry of CDRu was reported previously, a reversible ruthenium based oxidation is observed at 0.95 V which conforms well to this reported value [6]. In the cathodic region, three irreversible one electron reductions are observed corresponding to reduction of the bpy and phen moieties.

The cyclic voltammetry for Cu_2CDRu in dry DMF using a carbon macroelectrode is shown in Fig. 3. Cu_2CDRu voltammetry displays a reversible oxidative process at 0.97 V versus Ag/AgCl, attributed to the $Ru^{(II/III)}$ couple and ligand-based reductions at −1.53 V and −1.71 V versus Ag/AgCl. In addition, new irreversible waves at 0.703 V and −0.96 V versus Ag/AgCl, appear which are not observed in the parent complex, CDRu appear.[2]

Table 2
Electrochemical data for Cu_2CD, Cu_2CDRu and CDRu in dry DMF $E_{1/2}$ values determined by cyclic voltammetry and differential pulse voltammetry

Complex	Ru(II)/Ru(III)	(bpy/bpy^{-1})	M(II)/M(III)	M(II)/M(I)
CDRu[a]	0.95	−1.21, −1.40	–	–
Cu_2CDRu	0.97	−1.53, −1.71	0.703 irr.	−0.96
Cu_2CD	–	–	0.592 irr.	−1.229

Potentials (V) vs. Ag/AgCl. The processes are reversible except when indicated (irr).
[a] From Ref. [6].

For comparison, Fig. 3b shows the CV for Cu_2CD in dry DMF, which exhibits an irreversible anodic wave at 0.59 V versus Ag/AgCl and a cathodic, quasi-reversible wave at $E_{1/2} = -1.23$ V ($\Delta E_p = 0.23$ V). The electrochemistry of this species has not, to our knowledge been reported previously. The latter process is assigned to the Cu(II)/Cu(I) redox couple and the former to the Cu(III)/Cu(II) couple. These data are consistent with reported values for other hydroxy-bridged Cu(II) dimers and are similar to those obtained for Cu(II,II) complexes with ligands other

[2] These potentials were also confirmed from differential pulse voltammetry.

than cyclodextrin [29–33]. The irreversibility of the oxidation response probably indicates that the oxidized copper undergoes bond cleavage within the timescale of the electrochemical experiment.

The changes to the electrochemistry of the copper centres on coordination to CDRu by comparison with Cu_2CD were surprisingly large. The ruthenium oxidation shifts anodically by approximately 20 mV on coordination of the copper centers, which small enough to originate from the influence of electrostatics. However, the new oxidation process for Cu_2CDRu at 0.703 V attributed to Cu(III)/Cu(II) is shifted by 111 mV by comparison with Cu_2CD. The identity of the new reduction process in Cu_2CDRu is not entirely clear, but if attributed to the copper centre, it has shifted by 270 mV. Overall, this suggests that derivatisation of the CD with the ruthenium centre exerts a surprisingly significant influence over the copper centre. The ligand-based reductions are also cathodically shifted and become irreversible in the copper complex, the reason for this is unclear but may arise from adsorption at the electrode.

3.6. Photophysical properties

As reported previously, CDRu exhibits an intense luminescence attributed to the ^{3}MLCT state with λ_{max} of 618 nm, Fig. 4, a quantum yield of 0.013 and a lifetime of 900 ns [6]. The luminescence lifetimes and emission quantum yields values are significantly reduced upon coordination of copper to the secondary rim of CDRu in both aerated and deaerated media, Table 1.

The quantum yield is reduced by over 50% compared with the free CDRu in DMF and the lifetime is reduced from 900 ns to 336 ns in deaerated DMF.

The association of copper with the CD was investigated using steady state and time resolved luminescence, whereby increasing aliquots of Cu(II) acetate were combined with aqueous solution of CDRu (2×10^{-6} M) at pH 12. Fig. 5a and b shows a comparison of the effects of addition of Cu(II) and Zn(II) on a solution of CDRu at high pH. Zn^{2+} is expected to bind to the CD centre in an analogous way to Cu, however, with its d^{10} electronic configuration it is unlikely to be involved in either energy or electron transfer with the ruthenium centre [34,34]. As anticipated, on the basis of the isolated Cu_2CDRu complex, binding of Cu to CD results in a decrease to the luminescence intensity by up to approximately 50%, whereas Zn^{2+} had negligible impact on luminescence intensity. Correspondingly, for Zn^{2+}, within experimental error, no change to the luminescent lifetime of CDRu was observed, whereas for Cu^{2+}, the luminescence quenching was confirmed to be static. Addition of this metal ion to a solution of CDRu caused a biexponential luminescent decay, whose components matched the lifetime of CDRu and Cu_2CDRu. Increasing concentrations of copper did not change the lifetimes, but merely changed the ratio of the short and long components in the luminescent decay.

3.7. Nature of the excited state process

The reduction in lifetime and luminescent quantum yield in the CDRu observed on coordination of the copper dimer suggests that a photoinduced process is occurring in Cu_2CDRu. Introduction of new non-radiative pathways as a consequence of structural changes on formation of the metallocyclodextrin can be excluded on the basis that no photophysical changes were observed on binding of Zn^{2+}. In a related study Balzani et al. [35] reported on a Cu(I)–catenate moiety covalently linked to $[Ru(tpy)_2]^{2+}$. The oxidation potential of Ru(III)/(II) occurred at +1.2 V and that of Cu II/I at +0.58 V versus SCE at a Pt working electrode. They observed quenching of ruthenium based emission at 77 K and 298 K. They suggested energy transfer from $Ru(II)^*$ to Cu(I) at 77 K with a rate constant of $3 \times 10^8\ s^{-1}$ and a thermodynamically allowed photoinduced electron transfer from Cu(I) to Ru(II) at 298 K with a rate constant of $1 \times 10^{10}\ s^{-1}$. Energy transfer is a possibility in

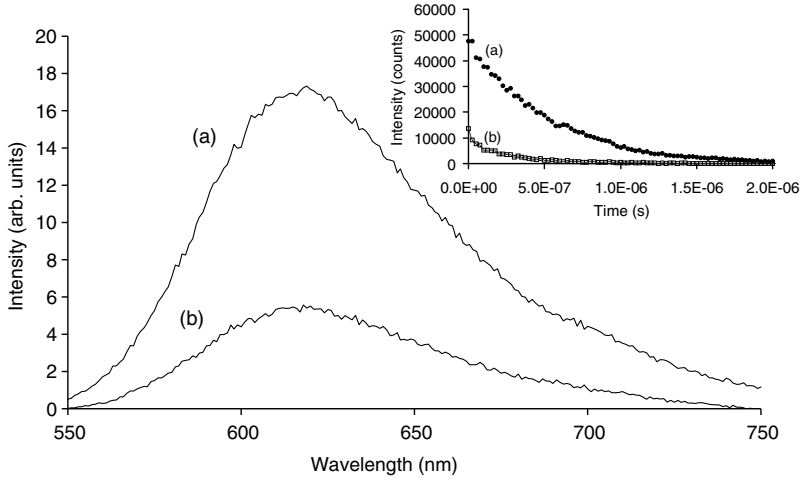


Fig. 4. Luminescence spectroscopy excited at 450 nm and emission decays, excited at 355 nm (inset) of (a) CDRu and (b) Cu_2CDRu in DMF, emission decays were monitored at 618 nm.

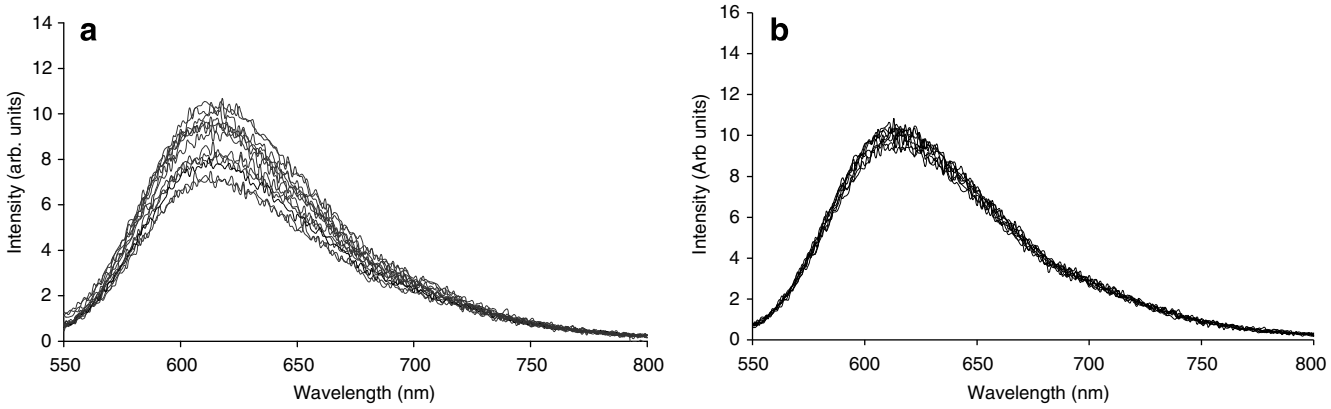


Fig. 5. Emission spectra of CDRu, 2.1×10^{-6} mol dm^{-3}, at pH 12 on addition of increasing aliquots (up to 1000 μl) of aqueous (a) 0.01 M $[Cu(CH_3COO)_2] \cdot 2H_2O$ and (b) 0.01 M $[Zn(CH_3COO)_2] \cdot 2H_2O$.

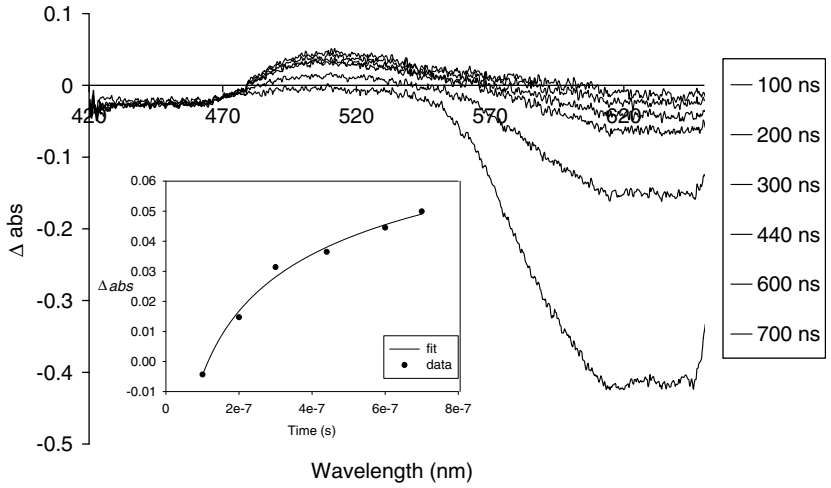


Fig. 6. Transient absorption of Cu_2CDRu (b) in spectroscopic grade DMF, 100, 200, 300, 440, 600, and 700 ns after the excitation at 355 nm. Inset, shows grow in of the absorbance at 510 nm.

the present case as the d–d transition at 620 nm for Cu_2CDRu overlaps effectively with the ruthenium emission. However, as the 620 nm absorbance is forbidden, it is very weak, ($\varepsilon = 33$ M cm^{-1}) and unlikely, on the basis of Laporte and spin selection rules to facilitate efficient energy transfer. On the other hand, photoinduced electron transfer is thermodynamically feasible. ΔG for a process in which the copper centre is reduced by excited-state ruthenium, calculated from electrochemical and photophysical data is estimated to be exoergonic at −0.16 eV. Reduction of the copper by photoexcited ruthenium is anticipated to be very modestly exoergonic at approximately −0.05 eV. [3]

To confirm that electron transfer is the origin of the luminescence quenching in Cu_2CDRu transient absorption studies were conducted on this complex and on CDRu for comparison. Firstly, following 355 nm excitation of a deoxygenated aqueous alkaline solution of CDRu, the depletion of the MLCT band is observed at 450 nm and negative amplitude signal ($-\Delta A$) in the region 600–700 nm arises from stimulated emission from the triplet MLCT state [37]. Unsurprisingly, the kinetics for both grow in of the depletion and emission are the same and match the luminescent lifetime.

Fig. 6 shows the transient absorption spectra of Cu_2CDRu in aqueous alkaline media. On excitation at 355 nm depletion of the MLCT occurs around 450 nm, however, in addition, a new absorption feature around 510 nm grows in. The luminescence, seen as a depletion centered around 610 nm is lost at a rate that matches the luminescence decay rate of Cu_2CDRu. However, the MLCT depletion remains relatively unchanged during the decay of the luminescence, while the 510 feature grows in. Over the time

[3] The driving force for an excited-state electron transfer can be evaluated from the approximation : $\Delta G^\circ \cong [E(B/B^+) - E(A/A^-)] - \Delta E^{\circ\circ}$, where $E(B/B^+)$, $E(A/A^-)$ are the energies (eV) of one-electron reduction processes and $E^{\circ\circ}$ is the spectroscopic energy, taken as the energy of the maximum of the emission spectrum at 77 K. $\Delta E^{\circ\circ}_{CDRu} = 2.069$ eV, $\Delta E^{\circ\circ}_{Cu2CDRu} = 2.085$ eV.

scale of the experiment, the MLCT is not recovered and the 510 feature remains. Absence of recovery of the MLCT confirms that the ruthenium is photooxidised and is consistent with the process predicted on thermodynamic grounds [38]. The identity of the 510 nm absorbance is unclear but may be due to Cu(I). The kinetics for grow in of this band are complex and appear be second order, inset, however as described below, the primary electron transfer process is intramolecular. The complex kinetics of the 510 nm grow in may be due to chemical reaction following reduction of the copper centre. The details of this mechanism and studies of the charge separated state are currently under more detailed study.

The rate constant for the photoinduced electron transfer was calculated according to Eq. (1).

$$k_{et} = 1/\tau_{complex} - 1/\tau_{model} \quad (1)$$

where $\tau_{complex}$ represents the luminescent lifetime of Cu_2CDRu, and τ_{model} represents lifetime of the model complex, CDRu in absence of any photoinduced process.

For Cu_2CDRu k_{et} was found to be $1.86 \times 10^6\ s^{-1}$ which is similar to the rate measure for electron transfer from an Mn(III) centre, the driving force for this process is also similar [39]. Importantly, in both cases, the photoinduced electron transfer rate is modest, while this is not surprising, given the likely poor conductivity of the CD bridge. It suggests that for such cyclodextrin complexes to be useful in sensing applications the luminophore must be relatively long lived to facilitate the electron transfer process.

Finally, the rate of electron transfer was measured over range of concentrations of Cu_2CDRu and laser powers (supplementary material), since a bimolecular reaction would be expected to be dependent on both these factors. However k_{et} was found, within experimental error, to be independent of these parameters confirming that the electron transfer is an intramolecular process.

Currently, detailed mechanistic studies on charge separation in this and analogous complexes with different metals is underway.

4. Conclusions

A new supramolecular donor–acceptor complex comprised of a ruthenium polypyridyl unit covalently linked to the secondary face of β-cyclodextrin which has a hydroxo bridged dinuclear copper(II) moiety at its primary face was synthesized. IR and magnetochemistry confirm that the structure of hydroxo bridged Cu(II) dimer is conserved from the parent Cu_2CD complex. Efficient photoinduced electron transfer from the copper centre to the pendant ruthenium polypyridyl centre is evident, with a rate constant of $1.86 \times 10^6\ s^{-1}$. The electron transfer process from transient absorption spectroscopy is attributed to a photooxidation of the excited ruthenium center by the copper dimer and this mechanism is consistent with thermodynamic predictions. The luminescence intensity of the ruthenium appended CD is correspondingly statically quenched on exposure to aqueous $Cu(CH_3COOH)_2$. This works suggests that luminescently labeled CDs may have value in metal sensing provided the luminophore is sufficiently long lived. The synthetic versatility of the ruthenium polypyridyl unit may mean that in the future the redox properties of this centre can be modified to tune selectivity for different metal ion.

Acknowledgements

The authors gratefully acknowledge DIT scholarship fund and enterprise Ireland (Grant IF/2001/365) for funding. Mr. Damien McGuirk, DCU is gratefully acknowledged for NMR spectroscopy.

Appendix A. Supplementary data

Supplementary data associated with this article can be found, in the online version, at doi:10.1016/j.poly.2008.02.002.

References

[1] A.R. Hedges, Chem. Rev. 98 (1998) 2035.
[2] S. Flink, F.C.J.M. Van Veggel, D.N. Reinhoudt, Sensors Update 8 (2001) 3.
[3] J.M. Haider, Z. Pikramenou, Chem. Soc. Rev. 34 (2005) 120, and references therein.
[4] A. McNally, N.R. Russell, R.J. Forster, T.E. Keyes, Dalton Trans. (2006) 1729.
[5] S.E. Brown, J.H. Coates, C.J. Easton, S.F. Lincoln, J. Chem. Soc., Faraday Trans. 90 (1994) 739.
[6] N. Van Hoof, T.E. Keyes, A. McNally, N.R. Russell, Chem. Commun. 13 (2001) 1156.
[7] G. Kurokawa, M. Sekii, T. Ishida, T. Nogami, Supramol. Chem. 16 (2004) 381.
[8] N.R. Russell, M. McNamara, J. Incl. Phenom. Mol. Recogn. Chem. 7 (1989) 455.
[9] E. Harris, N.R. Russell, J. Incl. Phenom. Mol. Recogn. Chem. 16 (1993) 355.
[10] E. Norkus, G. Grinciene, T. Vuorinen, E. Butkus, R. Vaitkus, Supramol. Chem. 15 (2003) 425.
[11] M. Darj, E.R. Malinowski, Appl. Spectrosc. 56 (2002) 257.
[12] B. Brady, N. Lynam, T. O'Sullivan, C. Ahern, R. Darcy, Organic Synth. 10 (2004) 686.
[13] B.P. Sullivan, D.J. Salmo, T.J. Meyer, Inorg. Chem. 17 (1978) 3334.
[14] E. Norkus, G. Grinciene, T. Vuorinen, E. Butkus, R. Vatkus, Supramol. Chem. 15 (2003) 425.
[15] R.J. Forster, L.K. Faulkner, J. Am. Chem. Soc. 116 (1994) 5444.
[16] D.F. Evans, J. Chem. Soc. (1959) 2003.
[17] A.T.R. Williams, S.A. Winfield, J.N. Miller, Analyst 108 (1983) 1067.
[18] M. Atmeh, N.R. Russell, T.E. Keyes, J. Incl. Phenom. Mol. Recog. Chem. 57 (2006) 607.
[19] M. McNamara, N.R. Russell, J. Incl. Phen. Molec. Recogn. Chem. 13 (1992) 145.
[20] Y. Matsui, T. Kurita, M. Yagi, T. Okyama, K. Mochida, Y. Date, Bull Chem. Soc. Jpn. 48 (1975) 2187.
[21] M. McNamara, N.R. Russell, J. Incl. Phen. Mol. Recogn. Chem. 10 (1991) 485.
[22] B.U. Nair, G.C. Dismukes, J. Am. Chem. Soc. 105 (1983) 124.
[24] J.R. Ferraro, W.R. Walker, Inorg. Chem. 4 (1965) 1382.
[25] A. Gergely, I. Sovago, Inorg. Chim. Acta 20 (1976) 19.

[26] J. Ling, L.P. Nestor, R.S. Czernuszewicz, T.G. Spiro, R. Fraczkiewicz, K.D. Sharma, T.M. Loehr, J.J. Sanders-Loehr, J. Am. Chem. Soc. 116 (1994) 7682.
[27] P.J. Carroll, L.E. Brus, J. Am. Chem. Soc. 109 (1987) 7613.
[29] J. Hanss, A. Beckmann, H.-J. Kruger, Eur. J. Inorg. Chem. 38 (1999) 163.
[30] R. Sarangi, N. Aboelella, K. Fujisawa, W.B. Tolman, B. Hedman, K.O. Hodgson, E.I. Solomon, J. Am. Chem. Soc. 128 (2006) 8286.
[31] S. Jain, J. Crayston, D. Richens, J. Woollins, Inorg. Chem. Commun. 5 (2002) 853.
[32] V. Kasumov, F. Koksal, Spectrochim. Acta Part A 61 (2005) 225.
[33] S. Brooker, T. Davidson, S.T. Hay, R.J. Kelley, D. Kennepohl, Paul G. Plieger, B. Moubaraki, K.S. Murray, E. Bill, E. Bothe, Coord. Chem. Rev. 3 (2001) 216.
[34] M. McNamara, N.R. Russell, J. Incl. Phen. Molec. Recogn. 7 (1989) 455.
[35] D.J. Cárdenas, J. Collin, P. Gaviña, J. Sauvage, A. De Cian, J. Fischer, N. Armaroli, L. Flamigni, V. Vicinelli, V. Balzani, J. Am. Chem. Soc. 121 (1999) 481.
[37] D. Burdinski, K. Weighardt, S. Steenken, J. Am. Chem. Soc. 121 (1999) 10781.
[38] R. Lomoth, T. Haupl, O. Johansson, L. Hammarstrom, Chem. Eur. J. 8 (2002) 102.
[39] E. Yonemoto, G. Saupe, R. Schmehl, S. Hubig, R. Riley, B. Iverson, T. Mallouk, J. Am. Chem. Soc. 116 (1994) 4786.

–NCO– bridging ligands and their use as precursors of mononuclear N-bonded imidate derivatives [15,16]. Those dinuclear and mononuclear derivatives, containing an azobenzene, 2-phenylpyridine or benzoquinoline backbone, have shown to be active catalysts/precatalysts for the Suzuki–Miyaura cross-coupling reactions of aryl bromides with aryl boronic acids, and the Sonogashira reactions of aryl halides (in the presence and absence of Cu(I) salts) [17]. The conversions are dependent, to some extent, on the cyclometallated backbone and the imidate ligand, suggesting a role for these pseudohalides in the catalytic cycle in both cross-coupling processes and encouraging us to expand the range of systems under study.

On the other hand, the synthetic value of palladium(II) and platinum(II) di-μ-hydroxo-complexes is a subject of continuous study [18–22]. During the last few years we have also been developing the usefulness of binuclear hydroxo complexes of palladium, some of them with a cyclometallated backbone [23], in the preparation of an extensive selection of new compounds, by means of a simple acid–base reaction [24].

We report here the use of the hydroxo-complex [{Pd(μ-OH)(Phox)}$_2$] (Phox = 2-(2-oxazolinyl)phenyl) in the preparation of new dinuclear palladium(II) derivatives of simple and sterically not hindered 2-phenyl-2-oxazoline with bridging succinimide, phtalimide, maleimide, 2,3-dibromomaleimide and glutarimide ligands acting in the coordination mode mentioned above. We also describe the synthesis of mononuclear N-bonded imidate derivatives, by the reaction of the corresponding dinuclear precursor with neutral phosphine ligands. X-ray diffraction analyses of both mononuclear (**4a**, **5a**) and binuclear (**4**) derivatives are also given. To date, just three complexes containing an orthopalladated 2-phenyl-2-oxazoline ligand have been crystallographically characterised (searched at the Cambridge Structural Database (CSD) v. 5.28 updated till August 2007) [23a,25].

2. Experimental

2.1. Materials and methods

C, H, and N analyses were carried out with a Carlo Erba instrument. IR spectra were recorded on a Perkin–Elmer spectrophotometer 16F PC FT-IR, using Nujol mulls between polyethylene sheets. NMR data (^{1}H, ^{31}P) were recorded on Bruker Avance 300 spectrometer. Conductance measurements were performed with a Crison 525 conductimeter (in acetone, 5×10^{-4} M). Mass spectrometric analyses were performed on a Fisons VG Autospec double-focusing spectrometer, operated in the negative mode. Ions were produced by fast atom bombardment (FAB) with a beam of 25-keV Cs atoms. The mass spectrometer was operated with an accelerating voltage of 8 kV and a resolution of at least 1000.

The cyclometallated precursors [{Pd(μ-OOCMe)(Phox)}$_2$] [25] and [{Pd(μ-OH)(Phox)}$_2$] [23a] were prepared as described in the literature. The commercially available chemicals were purchased from Aldrich Chemical Co. and were used without further purification, and all the solvents were dried by standard methods before use.

2.2. Synthesis

2.2.1. Preparation of complexes [{Pd(μ-NCO)(Phox)}$_2$] (–NCO– = suc (**1**); R = phtal (**2**); R = mal (**3**); R = 2,3-diBrmal (**4**); R = glut (**5**))

The new complexes were obtained by treating [{Pd(μ-OH)(Phox)}$_2$] with the corresponding imidate ligand in molar ratio 1:2, using $(CH_3)_2CO$ as the solvent and according to the following general method. To an acetone suspension (20 mL) of the precursor (250 mg; 0.464 mmol) was added the stoichiometric amount of the corresponding imidate ligand. The resulting suspension was stirred for 60 min at reflux temperature and then concentrated to a quarter of volume under reduced pressure. Addition of $(CH_3CH_2)_2O$ caused precipitation of the new complexes, which were filtered off, air dried and recrystallised from CH_2Cl_2/C_6H_{14}.

*[{Pd(μ-suc)(Phox)}$_2$] (**1**):* (85% yield). *Anal.* Calc. for $C_{26}H_{24}N_4O_6Pd_2$: C, 44.5; H, 3.5; N, 8.0. Found: C, 44.3; H, 3.6; N, 8.3%. FT-IR (nujol mull cm^{-1}): *ν*(CN–Phox) 1640(vs); *ν*(CO) 1720(vs); 1592(vs). ^{1}H NMR (300 MHz, $CDCl_3$): *δ* ($SiMe_4$) (ppm): 2.17 (m, 4H, suc), 2.79 (m, 6H, 4Hsuc + 2H NCH_2), 3.56 (m, 4H, $2NCH_2 + 2OCH_2$), 4.29 (m, 2H, OCH_2), 6.75 (m, 2H, arom.), 7.04 (m, 6H, arom.). FAB-MS (positive mode) *m/z*: 702 (M^+), 604 (M^+-suc).

*[{Pd(μ-phtal)(Phox)}$_2$] (**2**):* (82% yield). *Anal.* Calc. for $C_{34}H_{24}N_4O_6Pd_2$: C, 51.2; H, 3.0; N, 7.0. Found: C, 51.0; H, 3.3; N, 7.3%. FT-IR (nujol mull cm^{-1}): *ν*(CN–Phox) 1630(vs); *ν*(CO) 1730(vs); 1598(vs). ^{1}H NMR (300 MHz, $CDCl_3$): *δ* ($SiMe_4$) (ppm): 2.90 (m, 2H, NCH_2), 3.58 (m, 4H, $2NCH_2 + 2OCH_2$), 4.33 (m, 2H, OCH_2), 6.84 (m, 2H, phtal), 7.08 (m, 4H, arom.), 7.11 (m, 2H, phtal), 7.53 (m, 4H, arom.), 7.62 (m, 2H, phtal), 7.75 (m, 2H, phtal). FAB-MS (positive mode) *m/z*: 798 (M^+), 652 (M^+-phtal).

*[{Pd(μ-mal)(Phox)}$_2$] (**3**)*: (75% yield). *Anal.* Calc. for $C_{26}H_{20}N_4O_6Pd_2$: C, 44.8; H, 2.9; N, 8.0. Found: C, 45.0; H, 3.0; N, 8.2%. FT-IR (nujol mull cm^{-1}): *ν*(CN–Phox) 1620(vs); *ν*(CO) 1720(vs); 1584(vs). ^{1}H NMR (300 MHz, $CDCl_3$): *δ* ($SiMe_4$) (ppm): 2.86 (m, 2H, NCH_2), 3.58 (m, 4H, $2NCH_2 + 2OCH_2$), 4.34 (m, 2H, OCH_2), 6.65 (d, 2H, mal), 7.00 (m, 4H, 2mal + 2H, arom.), 7.08 (m, 6H, arom.). FAB-MS (positive mode) *m/z*: 698 (M^+), 600 (M^+-mal).

*[{Pd(μ-2,3-diBrmal)(Phox)}$_2$] (**4**)*: (62% yield). *Anal.* Calc. for $C_{26}H_{16}Br_4N_4O_6Pd_2$: C, 30.8; H, 1.6; N, 5.5. Found: C, 30.9; H, 1.7; N, 5.5%. FT-IR (nujol mull cm^{-1}): *ν*(CN-2,3-dibrmal) 1640(vs); *ν*(CO) 1738(s); 1574(s). ^{1}H NMR (300 MHz, $CDCl_3$): *δ* ($SiMe_4$) (ppm): 2.88 (m, 2H, NCH_2), 3.61 (m, 4H, $2NCH_2 + 2OCH_2$), 4.32 (m, 2H, OCH_2), 6.71 (m, 2H, arom.), 7.08 (m, 6H, arom.). FAB-MS (positive mode) *m/z*: 1012 (M^+), 760 (M^+-2,3-diBrmal).

*[{Pd(μ-glut)(Phox)}$_2$] (**5**):* (52% yield). *Anal.* Calc. for $C_{28}H_{28}N_4O_6Pd_2$: C, 44.5; H, 3.5; N, 8.0. Found: C, 44.3; H, 3.6; N, 8.3%. FT-IR (nujol mull cm^{-1}): *ν*(CN–Phox) 1646–1634(vs); *ν*(CO) 1560–1538(vs). ^{1}H NMR (300 MHz, $CDCl_3$): *δ* ($SiMe_4$) (ppm): 1.92 (m, 4H, glut), 2.70–2.44 (m, 10H, 8 glut + 2H NCH_2), 3.52 (m, 4H, $2NCH_2 + 2OCH_2$), 4.27 (m, 2H, OCH_2), 6.66 (m, 2H, arom.), 7.00 (m, 4H, arom.), 7.10 (m, 2H, arom.). FAB-MS (positive mode) *m*/*z*: 729 (M^+), 618 (M^+-glut).

2.2.2. Preparation of complexes

*[Pd(imidate)(Phox)(PR$_3$)] (imidate = suc (**1**); phtal (**2**); mal (**3**); 2,3-diBrmal (**4**); glut (**5**); R = Ph (**a**); 4-F–C_6H_4 (**b**); CH_2CH_2CN(**c**))*

The new complexes were obtained by treating the former bridging imidate complexes [{Pd(μ–NCO–)(Phox)}$_2$] with the corresponding phosphine in molar ratio 1:2, using CH_2Cl_2 as the solvent and according to the following general method. To a CH_2Cl_2 suspension (20 mL) of the precursor (0.142 mmol) was added the stoichiometric amount of the corresponding phosphine ligand. The resulting suspension was stirred for 90 min at reflux temperature and then concentrated to a quarter of the volume under reduced pressure. Addition of C_6H_{14} caused the precipitation of the new complexes, which were filtered off, air-dried and recrystallised from CH_2Cl_2/C_6H_{14}.

*[Pd(suc)(Phox)(PPh$_3$)] (**1a**):* (84% yield). *Anal.* Calc. for $C_{31}H_{27}N_2O_3PPd$: C, 60.7; H,4.4; N, 4.6. Found: C, 60.8; H, 4.5; N, 4.6%. FT-IR (nujol mull cm^{-1}): *ν*(CN–Phox) 1625(vs); *ν*(CO) 1618(vs); *ν*(PPh_3) 534(m). ^{1}H NMR (300 MHz, $CDCl_3$): *δ* ($SiMe_4$) (ppm): 1.7–1.87 (m, 2H, suc), 2.2–2.3 (m, 2H, suc), 3.97 (m, 2H, NCH_2), 4.75 (m, 2H, OCH_2), 6.51 (1H, arom.), 6.60 (1H, arom.), 6.96 (1H, arom.), 7.43 (m, 10H, 9PPh_3 + 1H arom.), 7.82 (m, 6H, PPh_3). ^{31}P NMR (300 MHz, $CDCl_3$): *δ* (ppm): 41.9 (s). FAB-MS (positive mode) *m*/*z*: 514 (M^+-suc).

*[Pd(suc)(Phox){P(4-F–C_6H_4)$_3$}] (**1b**):* (77% yield). *Anal.* Calc. for $C_{31}H_{24}F_3N_2O_3PPd$: C, 55.8; H, 3.6; N, 4.2. Found: C, 55.9; H, 3.7; N, 4.2%. FT-IR (nujol mull cm^{-1}): *ν*(CN–Phox) 1642(vs); *ν*(CO) 1620(vs); *ν*(P(C_6H_4F)$_3$) 536(m). ^{1}H NMR (300 MHz, $CDCl_3$): d ($SiMe_4$) (ppm): 1.83 (m, 2H, suc), 2.29 (m, 2H, suc), 3.94 (m, 2H, NCH_2), 4.72 (m, 2H, OCH_2), 6.41 (1H, arom.), 6.70 (1H, arom.), 6.92 (1H, arom.), 7.08 (m, 6H, phosphine), 7.30 (1H, arom.), 7.76 (m, 6H, phosphine). ^{31}P NMR (300 MHz, $CDCl_3$): *δ* (ppm): 39.6 (s). FAB-MS (positive mode) *m*/*z*: 568 (M^+-suc).

*[Pd(suc)(Phox){P(CH_2CH_2CN)$_3$}] (**1c**):* (76% yield). *Anal.* Calc. for $C_{22}H_{24}N_5O_3PPd$: C, 48.6; H,4.5; N, 12.9. Found: C, 48.7; H, 4.5; N, 12.9%. FT-IR (nujol mull cm^{-1}): *ν*(CN–Phox) 1625(vs); *ν*(CO) 1614(vs); *ν*(C≡N) 2240(s). ^{1}H NMR (300 MHz, $CDCl_3$): *δ* ($SiMe_4$) (ppm): 1.99 (m, 2H, suc), 2.39 (m, 6H, phosphine), 2.75 (m, 8H, 6H phosphine + 2H suc), 3.84 (m, 2H, NCH_2), 4.71 (m, 2H, OCH_2), 6.95–7.41 (m, 4H, arom.). ^{31}P NMR (300 MHz, $CDCl_3$): *δ* (ppm): 32.3 (s). FAB-MS (positive mode) *m*/*z*: 442 (M^+-suc).

*[Pd(phtal)(Phox)(PPh$_3$)] (**2a**):* (72% yield). *Anal.* Calc. for $C_{35}H_{27}N_2O_3PPd$: C, 63.6; H, 4.1; N, 4.2. Found: C, 63.8; H, 4.2; N, 4.2%. FT-IR (nujol mull cm^{-1}): *ν*(CN–Phox) 1622(vs); *ν*(CO) 1644(vs); *ν*(PPh_3) 534(m). ^{1}H NMR (300 MHz, $CDCl_3$): *δ* ($SiMe_4$) (ppm): 3.92 (m, 2H, NCH_2); 4.66 (m, 2H, OCH_2); 6.55 (1H, arom.), 6.68 (1H, arom.), 6.98 (1H, arom.), 7.43 (m, 14H, 4H phtal + 9H PPh_3 + 1H arom.); 7.76 (m, 6H, PPh_3). ^{31}P NMR (300 MHz, $CDCl_3$): *δ* (ppm): 41.9(s). FAB-MS (positive mode) *m*/*z*: 514 (M^+-phtal).

*[Pd(phtal)(Phox){P(4-F–C_6H_4)$_3$}] (**2b**):* (84% yield). *Anal.* Calc. for $C_{35}H_{24}F_3N_2O_3PPd$: C, 58.8; H, 3.4; N, 3.9. Found: C, 58.9; H, 3.6; N, 3.9%. FT-IR (nujol mull cm^{-1}): *ν*(CN–Phox) 1620(vs); *ν*(CO) 1644(vs); *ν*(P(C_6H_4F)$_3$) 536(m). ^{1}H NMR (300 MHz, $CDCl_3$): *δ* ($SiMe_4$) (ppm): 3.93 (m, 2H, NCH_2); 4.69 (m, 2H, OCH_2); 6.44 (1H, arom.); 6.71 (1H, arom.); 6.92–6.97 (m, 7H, 1H, arom. + 6H phosphine); 7.26 (1H, arom., Phox); 7.37 (s, 4H, phtal); 7.72 (m, 6H, phosphine). ^{31}P NMR (300 MHz, $CDCl_3$): *δ* (ppm): 39.8(s). FAB-MS (positive mode) *m*/*z*: 715 (M^+); 568 (M^+-phtal).

*[Pd(phtal)(Phox){P(CH_2CH_2CN)$_3$}] (**2c**):* (78% yield). *Anal.* Calc. for $C_{26}H_{24}N_5O_3PPd$: C, 52.8; H, 4.1; N, 11.8. Found: C, 52.9; H, 4.2; N, 11.9%. FT-IR (nujol mull cm^{-1}): *ν*(CN–Phox) 1620(vs); *ν*(CO) 1650(vs); *ν*(C≡N) 2242(s). ^{1}H NMR (300 MHz, $CDCl_3$): *δ* ($SiMe_4$) (ppm): 2.45 (m, 6H, phosphine), 2.89 (m, 6H, phosphine), 3.72 (m, 2H, NCH_2), 4.64 (m, 2H, OCH_2), 6.97–7.42 (m, 4H, arom.); 7.49–7.69 (m, 4H, phtal). ^{31}P NMR (300 MHz, $CDCl_3$): *δ* (ppm): 32.4 (s). FAB-MS (positive mode) *m*/*z*: 591 (M^+); 444 (M^+-phtal).

*[Pd(mal)(Phox)(PPh$_3$)] (**3a**):* (64% yield). *Anal.* Calc. for $C_{31}H_{25}N_2O_3PPd$: C, 60.9; H, 4.1; N, 4.6. Found:C, 70.0; H, 4.2; N, 4.6%. FT-IR (nujol mull cm^{-1}): *ν*(CN–Phox) 1620(vs); *ν*(CO) 1634(vs); *ν*(PPh_3) 534(m). ^{1}H NMR (300 MHz, $CDCl_3$): *δ* ($SiMe_4$) (ppm): 3.89 (m, 2H, NCH_2); 4.68 (m, 2H, OCH_2); 6.05 (s, 2H, mal); 6.49 (m, 1H, arom.); 6.64 (m, 1H, arom.); 6.89 (m, 1H, arom.); 7.25 (m, 1H, arom.); 7.34 (m, 9H, PPh_3); 7.74 (m, 6H, PPh_3). ^{31}P NMR (300 MHz, $CDCl_3$): *δ* (ppm): 41.8 (s). FAB-MS (positive mode) *m*/*z*: 514 (M^+-mal).

*[Pd(mal)(Phox){P(4-F–C_6H_4)$_3$}] (**3b**):* (68% yield). *Anal.* Calc. for $C_{31}H_{22}F_3N_2O_3PPd$: C, 56.0; H, 3.3; N, 4.2. Found: C, 56.1; H, 3.5, N, 4.2%. FT-IR (nujol mull cm^{-1}): *ν*(CN–Phox) 1600(vs); *ν*(CO) 1642(vs); *ν*(P(C_6H_4F)$_3$) 536(m). ^{1}H NMR (300 MHz, $CDCl_3$): *δ* ($SiMe_4$) (ppm): 3.88 (m, 2H, NCH_2); 4.70 (m, 2H, OCH_2); 6.12 (s, 2H, mal); 6.41 (1H, arom.); 6.69 (1H, arom.); 6.94 (1H, arom.); 7.04 (m, 6H, phosphine); 7.29 (1H, arom.); 7.70 (m, 6H, phosphine). ^{31}P NMR (300 MHz, $CDCl_3$): *δ* (ppm): 39.6(s). FAB-MS (positive mode) *m*/*z*: 568 (M^+-mal).

*[Pd(mal)(Phox){P(CH_2CH_2CN)$_3$}] (**3c**):* (69% yield). *Anal.* Calc. for $C_{22}H_{22}N_5O_3PPd$: C, 48.8; H, 4.1; N, 12.9. Found: C, 48.9; H, 4.2; N, 13.0%. FT-IR (nujol mull cm^{-1}): *ν*(CN–Phox) 1620(vs); *ν*(CO) 1644(vs); *ν*(C≡N) 2242(s). ^{1}H NMR (300 MHz, $CDCl_3$): *δ* ($SiMe_4$)

(ppm): 2.40 (m, 6H, phosphine); 2.83 (m, 6H, phosphine); 3.78 (m, 2H, NCH_2); 4.69 (m, 2H, OCH_2); 6.60 (s, 2H, mal); 6.70 (m, 1H, arom.); 7.0 (m, 1H, arom.); 7.18 (m, 1H, arom.); 7.39 (m, 1H, arom.). ^{31}P NMR (300 MHz, $CDCl_3$): δ (ppm): 32.3(s). FAB-MS (positive mode) *m/z*: 444 (M^+-mal).

[Pd(2,3-diBrmal)(Phox)(PPh$_3$)] (**4a**): (68% yield). *Anal.* Calc. for $C_{31}H_{23}Br_2N_2O_3PPd$: C, 48.4; H, 3.0; N, 3.6. Found: C, 48.5; H, 3.1; N, 3.6%. FT-IR (nujol mull cm^{-1}): ν(CN–Phox) 1640(vs); ν(CO) 1654(vs); ν(PPh_3) 534(m). ^1H NMR (300 MHz, $CDCl_3$): δ ($SiMe_4$) (ppm): 3.92 (m, 2H, NCH_2); 4.66 (m, 2H, OCH_2); 6.40 (m, 1H, arom.); 6.65 (m, 1H, arom.); 6.92 (m, 1H, arom.); 7.25–7.50 (m, 10H, 9PPh_3 + 1H arom.); 7.76 (m, 6H, PPh_3). ^{31}P NMR (300 MHz, $CDCl_3$): δ (ppm): 41.9(s). FAB-MS (positive mode) *m/z*: 768 (M^+), 514 (M^+-2,3-diBrmal).

[Pd(2,3-diBrmal)(Phox){P(4-F–C$_6$H$_4$)$_3$}] (**4b**): (82% yield). *Anal.* Calc. for $C_{31}H_{20}Br_2F_3N_2O_3PPd$: C, 45.3; H, 2.5; N, 3.4. Found: C, 45.4; H, 2.5, N, 3.4%. FT-IR (nujol mull cm^{-1}): ν(CN–Phox) 1642(vs); ν(CO) 1658(vs); ν(P(*p*-$C_6H_4F)_3$) 540(m). ^1H NMR (300 MHz, $CDCl_3$): δ ($SiMe_4$) (ppm): 3.91 (m, 2H, NCH_2); 4.71 (m, 2H, OCH_2); 6.37 (m, 1H, arom.); 6.69 (m, 1H, arom.); 7.06 (m, 7H, 6H phosphine + 1H, arom. Phox); 7.29 (1H, arom.); 7.69 (m, 6H, phosphine). ^{31}P NMR (300 MHz, $CDCl_3$): δ (ppm): 39.6(s). FAB-MS (positive mode) *m/z*: 822 (M^+), 568 (M^+-2,3-diBrmal).

[Pd(2,3-diBrmal)(Phox){P(CH$_2$CH$_2$CN)$_3$}] (**4c**): (72% yield). *Anal.* Calc. for $C_{22}H_{20}Br_2N_5O_3PPd$: C, 37.8; H, 2.9; N, 10.0. Found: C, 37.9; H, 3.0; N, 10.1%. FT-IR (nujol mull cm^{-1}): ν(CN–Phox) 1642(vs); ν(CO) 1656(vs); ν(C≡N) 2244(s). ^1H NMR (300 MHz, $CDCl_3$): δ ($SiMe_4$) (ppm): 2.27 (m, 6H, phosphine); 2.83 (m, 6H, phosphine); 3.95 (m, 2H, NCH_2); 4.63 (m, 2H, OCH_2); 7.18–7.31 (m, 2H, arom.), 7.40–7.52 (m, 2H, arom.). ^{31}P NMR (300 MHz, $CDCl_3$): δ (ppm): 42.06(s). FAB-MS (positive mode) *m/z*: 445 (M^+-2,3-diBrmal).

[Pd(glut)(Phox)(PPh$_3$)] (**5a**): (53% yield). *Anal.* Calc. for $C_{32}H_{29}N_2O_3PPd$: C, 61.3; H, 4.7; N, 4.5. Found: C, 61.6; H, 4.8; N, 4.7%. FT-IR (nujol mull cm^{-1}): ν(CN–Phox) 1644(vs); ν(CO) 1574(vs); ν(PPh_3) 534(m). ^1H NMR (300 MHz, $CDCl_3$): δ ($SiMe_4$) (ppm): 1.24 (m, 2H, glut); 1.63 (m, 2H, glut); 2.16 (m, 2H, glut); 3.86 (m, 2H, NCH_2); 4.68 (m, 2H, OCH_2); 6.47 (m, 1H, arom.); 6.62 (m, 1H, arom.); 6.86 (m, 1H, arom.); 7.23 (m, 1H, arom.); 7.36 (m, 9H, phosphine); 7.82 (m, 6H, phosphine). ^{31}P NMR (300 MHz, $CDCl_3$): δ (ppm): 42.4(s). FAB-MS (positive mode) *m/z*: 626 (M^+), 514 (M^+-glut).

[Pd(glut)(Phox){P(4-F–C$_6$H$_4$)$_3$}] (**5b**): (60% yield). *Anal.* Calc. for $C_{32}H_{26}F_3N_2O_3PPd$: C, 56.4; H, 3.9; N, 4.1. Found: C, 56.5; H, 4.0; N, 4.3%. FT-IR (nujol mull cm^{-1}): ν(CN–Phox) 1644(vs); ν(CO) 1588(vs); ν(P(*p*-$C_6H_4F)_3$) 536(m). ^1H NMR (300 MHz, $CDCl_3$): δ ($SiMe_4$) (ppm): 1.32 (m, 2H, glut); 1.57 (m, 2H, glut); 2.21 (m, 2H, glut); 3.84 (m, 2H, NCH_2); 4.69 (m, 2H, OCH_2); 6.36 (m, 1H, arom.); 6.65 (m, 1H, arom.); 6.90 (m, 1H, arom.); 7.05 (m, 6H, phosphine); 7.28 (m, 1H, arom.); 7.05 (m, 6H, phosphine). ^{31}P NMR (300 MHz, $CDCl_3$): δ (ppm): 40.3(s). FAB-MS (positive mode) *m/z*: 679 (M^+), 568 (M^+-glut).

[Pd(glut)(Phox){P(CH$_2$CH$_2$CN)$_3$}] (**5c**): (49% yield). *Anal.* Calc. for $C_{23}H_{26}N_5O_3PPd$: C, 49.5; H, 4.7; N, 8.6. Found: C, 49.7; H, 4.6; N, 8.7%. FT-IR (nujol mull cm^{-1}): ν(CN–Phox) 1646(vs); ν(CO) 1578(vs); ν(C≡N) 2245(s). ^1H NMR (300 MHz, $CDCl_3$): δ ($SiMe_4$) (ppm): 1.95 (m, 2H glut); 2.26–2.40 (m, 6H, phosphine) 2.48–2.61 (m, 4H, glut); 2.75–2.93 (m, 6H, phosphine); 3.76 (m, 2H, NCH_2); 4.70 (m, 2H, OCH_2); 7.00 (m, 1H, arom.); 7.10–7.25 (m, 2H, arom); 7.38 (m, 1H, arom). ^{31}P NMR (300 MHz, $CDCl_3$): δ (ppm): 31.4(s). FAB-MS (positive mode) *m/z*: 445.1 (M^+-glut).

2.3. Crystal structure determination of [{Pd(μ-2,3-diBrmal)(Phox)}$_2$] (4), [Pd(2,3-diBrmal)(Phox)(PPh$_3$)] (4a) and [Pd(glut)(Phox)(PPh$_3$)] (5a)

Crystals suitable for a diffraction study were prepared by a slow diffusion of hexane into their CH_2Cl_2 solutions. Crystallographic data are summarized in Table 1. Data collection for **4** and **4a** was performed at −173 °C on a Bruker Smart CCD diffractometer with a nominal crystal to detector distance of 4.5 cm. Diffraction data were collected based on a ω scan run. A total of 2524 frames were collected at 0.3° intervals and 10 s per frame. The diffraction frames were integrated using the SAINT package [26] and corrected for absorption with SADABS [27]. For **5a** data collection was performed at 293 K on a Nonius Kappa-CCD single crystal diffractometer. Crystal-detector distance was fixed at 35 mm, and a total of 122 images were collected using the oscillation method, with scan angle per frame, 2° oscillation and 20 s exposure time per image. Data collection strategy was calculated with the program COLLECT [28]. Data reduction and cell refinement were performed with the programs HKL DENZO and SCALEPACK [29].

The structures were solved by direct methods [30] and refined by full-matrix least-squares techniques using anisotropic thermal parameters for non-H atoms [30] (Table 1). Hydrogen atoms were introduced in the calculated positions and refined during the last stages of the refinement.

3. Results and discussion

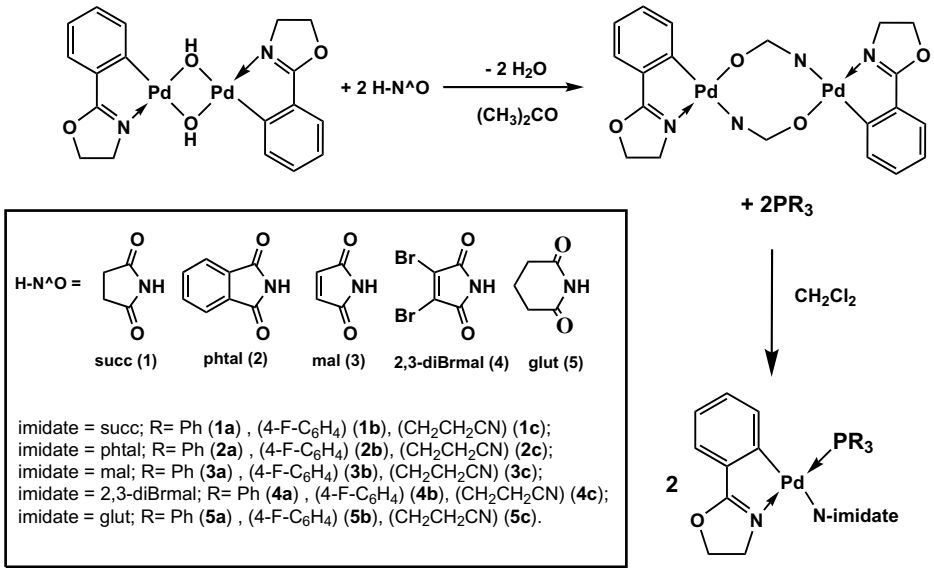
Under the conditions described in Section 2, [{Pd(μ-OH)(Phox)}$_2$] reacts with several imidate-type ligands to give dinuclear complexes **1**–**5** in which the imidate ligands replace the bridging hydroxo group as presented in Scheme 1.

Both the precursor and the new complexes are quite insoluble in the reaction media, so that just a change in the suspension colour is observed. The new 2-(2-oxazolinyl)phenyl) derivatives are air-stable yellow solids and their infrared spectra show only one absorption around 730 cm^{-1}, as expected for the region of out-of-plane C–H bending in disubstituted arenes. Also the characteristic

Table 1
Crystal data and structure refinement for compounds **4**, **4a** and **5a**

	4 · CH_2Cl_2	**4a**	**5a** · $1/2CH_2Cl_2$
Empirical formula	$C_{27}H_{18}Br_4Cl_2N_4O_6Pd_2$	$C_{31}H_{23}Br_2N_2O_3PPd$	$C_{32.5}H_{30}ClN_2O_3PPd$
Formula weight	1097.79	768.70	653.90
Temperature (K)	100(2)	100(2)	293(2)
Wavelength (Å)	0.71073	0.71073	0.71073
Crystal system	monoclinic	monoclinic	monoclinic
Space group	*P*21/*n*	*C*2/*c*	*C*2/*c*
Unit cell dimensions			
a (Å)	8.5336(3)	23.3725(11)	26.6920(5)
b (Å)	22.9656(9)	11.7735(6)	16.6670(4)
c (Å)	16.5248(7)	20.2239(10)	15.8240(3)
β (°)	102.0920(10)	95.2240(10)	119.8430(10)
V (Å^3)	3166.7(2)	5542.0(5)	6106.2(2)
Z	4	8	8
D_{calc} (Mg m^{-3})	2.303	1.843	1.423
Absorption coefficient (mm^{-1})	6.401	3.649	0.702
F(000)	2088	3024	2648
Crystal size (mm^3)	0.08 × 0.07 × 0.04	0.27 × 0.25 × 0.15	0.60 × 0.02 × 0.02
θ Range for data collection (°)	1.54–28.19	1.75–28.18	1.51–27.52
Index ranges	$-11 \leqslant h \leqslant 11$	$-30 \leqslant h \leqslant 30$	$-34 \leqslant h \leqslant 34$
	$-29 \leqslant k \leqslant 29$	$-15 \leqslant k \leqslant 15$	$-19 \leqslant k \leqslant 21$
	$-20 \leqslant l \leqslant 20$	$-26 \leqslant l \leqslant 26$	$-20 \leqslant l \leqslant 20$
Reflections collected	36697	31927	12355
Independent reflections [R_{int}]	7367 [0.0394]	6468 [0.0353]	6994 [0.0554]
Refinement method	full-matrix least-squares on F^2	full-matrix least-squares on F^2	full-matrix least-squares on F^2
Data/parameters	7367/425	6468/361	6994/362
R^a, Rw^b [$I > 2\sigma(I)$]	$R_1 = 0.0315$, $wR_2 = 0.0696$	$R_1 = 0.0375$, $wR_2 = 0.0793$	$R_1 = 0.1056$, $wR_2 = 0.3249$
R^a, Rw^b [all data]	$R_1 = 0.0430$, $wR_2 = 0.0816$	$R_1 = 0.0397$, $wR_2 = 0.0804$	$R_1 = 0.1575$, $wR_2 = 0.3495$
S^c	0.794	1.202	2.103
Maximum, minimum $\Delta\rho$ (e Å^{-3})	2.518, −2.082	0.953, −0.386	2.691, −5.682

[a] $R = \sum \|F_o| - |F_C\| / \sum |F_o|$.
[b] $Rw = \{\sum[w(F_o^2 - F_c^2)^2] / \sum[w(F_o^2)^2]\}^{1/2}$; $w = 1/\sigma^2(|F_o^2|)$.
[c] $S = [\sum[w(F_o^2 - F_c^2)^2] / (N_{obs} - N_{param})]^{1/2}$.



Scheme 1.

C=N absorption of the cyclometallated ligand around 1630 cm^{-1} is observed, shifted to lower frequencies compared to the free ligand (1649 cm^{-1}) and partially overlapped with those two strong bands attributed to imidato-carbonyl stretching in the range 1738–1720 and 1598–1562 cm^{-1}, respectively. According to the previously reported data [10] the appearance of two bands in this region suggests the coordination of one carbonyl group

to the metal as a part of an –NCO– bridging unit. Support for the proposed dinuclearity of complexes **1**–**5** comes from the FAB mass spectrometry, as can be implied by the *m*/*z* values for the observed fragments. Spectra of the new bridged compounds show a similar fragmentation pattern which includes the peaks corresponding to $[M]^+$, $[M^+$-imidate$]^+$ and $[Pd(Phox)]^+$. The abundances of the signals around the pattern ion are consistent with the natural isotopic ones.

Despite the low solubility in common solvents of some of the new derivatives, further evidence of the proposed coordination comes from the ^{1}H NMR spectroscopy. It has been reported for the related complex $[\{Pd(\mu\text{-OOCMe})(Phox)\}_2]$ that, as a consequence of its open-book structure, each of the two methylene protons of the oxazoline ring is non-equivalent, displaying a set of three unresolved multiplets (ratio 1:2:1) [25]. In $CDCl_3$ the new binuclear complexes showed this behaviour for the oxazoline protons, which appeared in the spectra together with the expected resonances of the imidate ligands (see Section 2). The preparation of single crystals of complex **4** suitable for X-ray diffraction was also possible and unambiguously confirmed the molecular structure. This is presented in Fig. 1 together with selected bond distances and angles.

The unit cell of complex **4** contains two molecules. In accordance with the geometries displayed by the previously

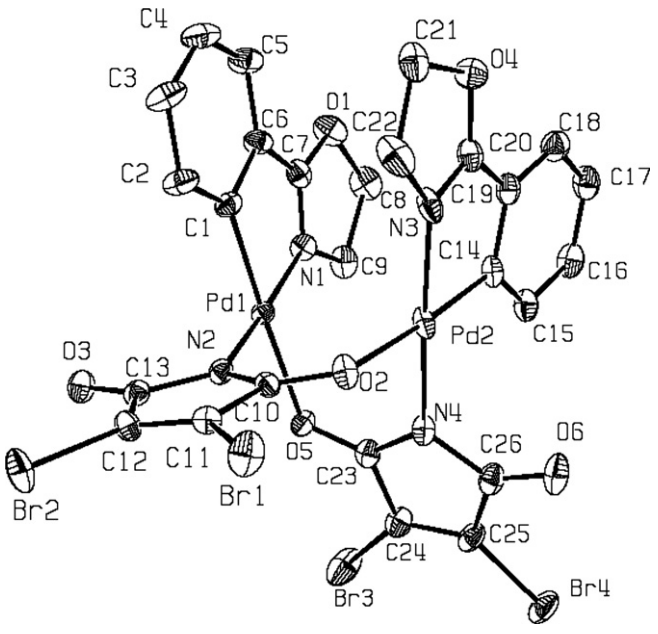


Fig. 1. ORTEP diagram of complex **4** with the atom numbering scheme; thermal ellipsoids are drawn at the 50% propability level. Hydrogen atoms are omitted for clarity. Selected distances (Å): Pd(1)–C(1) 1.976(4); Pd(1)–N(1) 2.017(3); Pd(1)–N(2) 2.024(3); Pd(1)–O(5) 2.175(3); Pd(1)–Pd(2) 2.9279(4); Pd(2)–C(14) 1.980(4); Pd(2)–N(3) 2.024(4); Pd(2)–N(4) 2.030(4); Pd(2)–O(2) 2.189(3). Selected angles (°): C(1)–Pd(1)–N(1) 81.08(6); C(1)–Pd(1)–N(2) 92.68(15); N(1)–Pd(1)–N(2) 172.91(14); C(1)–Pd(1)–O(5) 175.64(14); N(1)–Pd(1)–O(5) 94.56(13); N(2)–Pd(1)–O(5) 91.66(12); C(14)–Pd(2)–N(3) 81.42(16); C(14)–Pd(2)–N(4) 92.53(16); N(3)–Pd(2)–N(4) 173.82(14); C(14)–Pd(2)–O(2) 173.71(15); N(3)–Pd(2)–O(2) 92.47(13); N(4)–Pd(2)–O(2) 93.61(13).

reported oxazoline-derived μ-chloro [31] and μ-acetate dimers [32], an *anti*-arrangement of identical donor atoms is found, supporting the pseudohalide character of imidate ligands. Also in common with the mentioned compounds and our previously described structure $[\{Pd(\mu\text{-suc})(Phpy)\}_2]$ [15] is the so-called open-book geometry accompanied by a rather short Pd(1)–Pd(2) distance of 2.9279(4) Å, within the generally accepted value for a Pd–Pd intramolecular interaction (<3.00 Å). An interesting structural aspect is that two hydrogens bonded to C22 ad C8, respectively, point towards the centre of the phenyl rings: distance H22B-centroid (C1–C6) = 3.106 Å; distance H8A-centroid (C14–C19) = 3.199 Å, suggesting an interaction between the rings of the two cyclometallated ligands. We have recently developed methods for the conformational classification of eight-membered rings [33]. From this perspective the Pd1–N2–C10–O2–Pd2–N4–C23–O5 ring displays a chair-chair conformation (CC = 0.9985; TCC = 0.0015 for $\sigma = 10$). Using the same Classification method, the five-membered palladacycles Pd1–C1–C6–C7–N1 and Pd2–C14–C19–C20–N3 exhibit almost planar conformations for $\sigma = 10$ (HC = 0.5095; E = 0.4905 and HC = 0.5138; E = 0.4862, respectively).

The structure around the two palladium atoms may be described as nearly planar, and their deviation from the planar coordination has been quantified by measures of improper torsion angles: 2.38° and −0.00° for Pd1 (square pyramidal); −0.96° and −1.01° for Pd2 (tetrahedral) [16]. In the 2,3-dibromomaleimide ligand the C=O distance, 1.228(5) and 1.232(5) Å, is elongated in the bridged group with respect to the non-coordinated C=O, 1.208(5) Å, in both Pd atoms.

As expected, the reactions of the imidate-bridged compounds against tertiary phosphines take place *via* bridge-splitting to yield the mononuclear N-bonded imidate derivatives $[Pd(imidate)(Phox)(PR_3)]$ presented in Scheme 1.

The yellow to orange air-stable solids display negligible molar conductivity values, and their IR spectra show the expected bands for the 2-(2-oxazolinyl)phenyl backbone, together with those attributed to the incoming phosphine ligand and just one strong carbonyl band around 1630 cm^{-1}, typical of N-bonded imidate ligands. The characterisation in solid state was completed with the FAB mass spectrometry, that shows fragments at $[M^+$-imidate] in all cases, being also possible to detect $[M^+]$ and $[Pd(Phox)]^+$ for several compounds. The ^{1}H and ^{31}P NMR data of the mononuclear complexes are collected in Section 2, the latter consisting of singlets with chemical shifts in the usual range of Pd(II) complexes. With regard to the ^{1}H NMR spectra, they show the expected resonances of the cyclometallated 2-phenyl-2-oxazoline, now with just two triplets for the NCH_2 and OCH_2 protons in the 3.70–4.80 ppm region, together with those signals attributed to the corresponding imidate ligand and coordinated phosphine.

The structures of $[Pd(2,3\text{-diBrmal})(Phox)(PPh_3)]$ (**4a**) and $[Pd(glut)(Phox)(PPh_3)]$ (**5a**) have been confirmed by X-ray diffraction study and are presented together with

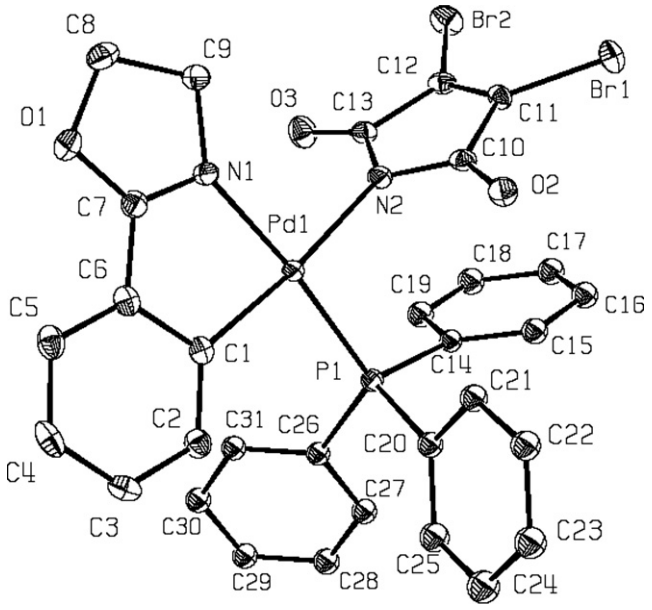


Fig. 2. ORTEP diagram of complex **4a**. Thermal ellipsoids are drawn at the 50% probability level. Hydrogen atoms are omitted for clarity. Selected distances (Å): Pd(1)–C(1) 2.027(3); Pd(1)–N(1) 2.068(3); Pd(1)–N(2) 2.113(3); Pd(1)–P(1) 2.2438(9). Selected angles (°): C(1)–Pd(1)–N(1) 81.04(12); C(1)–Pd(1)–N(2) 171.23(12); N(1)–Pd(1)–N(2) 91.43(11); C(1)–Pd(1)–P(1) 94.19(10); N(1)–Pd(1)–P(1) 174.12(8); N(2)–Pd(1)–P(1) 93.58(8).

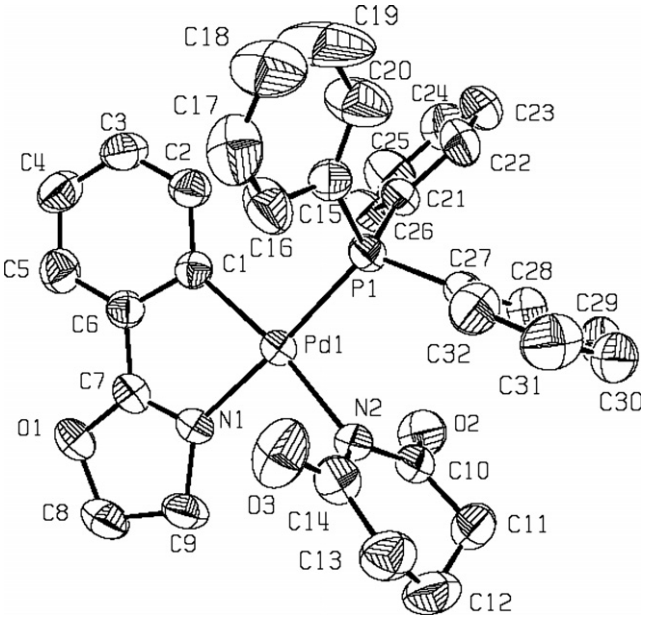


Fig. 3. ORTEP diagram of complex **5a**. Thermal ellipsoids are drawn at 50% probability. Hydrogen atoms are omitted for clarity. Selected distances (Å): Pd(1)–C(1) 2.046(12); Pd(1)–N(1) 2.062(10); Pd(1)–N(2) 2.091(10); Pd(1)–P(1) 2.246(3). Selected angles (°): C(1)–Pd(1)–N(1) 81.0(4); C(1)–Pd(1)–N(2) 171.4(4); N(1)–Pd(1)–N(2) 91.4(4); C(1)–Pd(1)–P(1) 94.8(4); N(1)–Pd(1)–P(1) 175.5(3); N(2)–Pd(1)–P(1) 92.9(3).

the selected bond distances and angles in Figs. 2 and 3, respectively. The coordination around the Pd atoms based on measures of torsion angles is approximately planar with slight tetrahedral distortion [16] (N1–C1–P1–Pd1 is 2.67° and −1.14°; N2–P1–C1–Pd1 2.72° and −2.42°, respectively). The displacement of the Pd atom from the mean coordination plane is 0.0524(57) and 0.1586(92) Å (rms = 0.0139 and 0.0017, respectively).

The N–Pd–C angle in the orthometallated moiety, around 81.0° in the three complexes, is similar to that found in complexes containing the same ligand [25,31,32]. The structural analysis of complexes **4a** and **5a** confirms the relative *cis*-position of the phosphine ligand and the metallated carbon atom suggested by the NMR data. This is the typical arrangement of the phosphine group in cyclopalladated complexes of the type [Pd(C^N)(phosphine)(X)] (X = anionic monodentate ligand) due to the so-called *transphobia* effect [34,35]. Following the classification of Dance and Scudder [36] for PPh_3 based on measures of torsion angles M–P–C_{ipso}–C, the conformation of Pd–PPh_3 groups is described as *no rotor* for the new complexes, presenting values $T_3 - T_2 = 38.55°$; $T_2 - T_1 = 31.28°$ for **4a** and $T_3 - T_2 = 22.17°$; $T_2 - T_1 = 88.30°$ for **5a**, that differ to those which would have the ideal *rotor* ($T_1 = T_2 = T_3 = 44°$).

As found for complexes **4**, **4a** and **5a** also display almost planar conformations in the five-membered palladacycles Pd1–C1–C6–C7–N1 (HC = 0.5138; E = 0.4862 and HC = 0.5114; E = 0.4886).

In complex **4a**, the C10–O2 and C13–O3 distances of 2,3-dibromomaleimide ligand are 1.204(4) and 1.209(4) Å, very close to the non-coordinated C=O distances in dinuclear complex **4** (1.208(5) Å). In complex **5a** those distances are slightly higher: 1.216(16) and 1.227(16) Å.

4. Conclusions

Twenty new imidate-palladium(II) complexes with 2-phenyl-2-oxazoline acting as cyclometallated backbone have been prepared and characterized by spectroscopic techniques and single crystal X-ray diffraction analysis. Imidate ligands exhibit two different coordination modes: –NCO– bridging two Pd atoms or N-bonded. We enlarge in this paper the range of imidate and phosphine systems under study in comparison with our previous results, and we present the first X-ray crystal structures of complexes containing 2,3 dibromomaleimide (bonded as –NCO– bridging group (**4**) and as N-bonded (**4a**)), as searched at the Cambridge Structural Database (CSD) v. 5.28 updated till August 2007. Preliminary results show that the new complexes are active catalysts/precatalysts in Suzuki–Miyaura cross-coupling reactions of aryl bromides with aryl boronic acids. A comprehensive study will be reported in due course.

5. Supplementary data

CCDC 671662, 671663 and 671664 contain the supplementary crystallographic data for **4**, **4a** and **5a**. These data

can be obtained free of charge via http://www.ccdc.cam.ac.uk/conts/retrieving.html, or from the Cambridge Crystallographic Data Centre, 12 Union Road, Cambridge CB2 1EZ, UK; fax: (+44) 1223-336-033; or e-mail: deposit@ccdc.cam.ac.uk.

Acknowledgements

Financial support of this work by Dirección General de Investigación (project-CTQ2005-09231-C02-01/02) and Fundación Séneca de la Región de Murcia (00484/PI/04) is gratefully acknowledged. We are grateful to the EPSRC for funding (EP/DO78776/1) and the Royal Society (I.J.S.F.).

References

[1] I. Omae, Coord. Chem. Rev. 83 (1988) 137.
[2] A.C. Cope, R.W. Siekman, J. Am. Chem. Soc. 87 (1965) 3273.
[3] A. Kasahara, Bull. Chem. Soc. Jpn. 41 (1968) 1272.
[4] E.C. Constable, A.M.W. Cargill Thompson, T.A. Leese, D.G.F. Reese, D.A. Tocher, Inorg. Chim. Acta 182 (1991) 93.
[5] D.L. Weaver, Inorg. Chem. 9 (1970) 2250.
[6] M.A. Gutiérrez, G.R. Newkome, J. Selbin, J. Organomet. Chem., 202 (1980) 341.
[7] J.M. Vila, M. Gayoso, M. Pereira, A. Romar, J.J. Fernández, M. Thornton-Pett, J. Organomet. Chem. 401 (1991) 385.
[8] M.M. Mdleleni, J.S. Bridgewater, R.J. Watts, P.C. Ford, Inorg. Chem. 34 (1995) 2334.
[9] C.A. Craig, R.J. Watts, Inorg. Chem. 28 (1989) 309.
[10] H. Adams, N.A. Bailey, T.N. Briggs, J.A. McCleverty, H.M. Colquhoun, D.J. Williams, Dalton Trans. (1986) 813.
[11] G. Sánchez, J.L. Serrano, M.A. Moral, J. Pérez, E. Molins, G. López, Polyhedron 18 (1999) 3057.
[12] I. Aiello, A. Crispini, M. Ghedini, M. La Deda, F. Barigelletti, Inorg. Chim. Acta 308 (2000) 121.
[13] (a) I. Omae, J. Organomet. Chem. 692 (2007) 2608;
(b) K. Gogula, D. Sames, Science 312 (2006) 67;
(c) J. Dupont, C.S. Consorte, J. Spencer, Chem. Rev. 105 (2005) 2527, and references therein.
[14] I.J.S. Fairlamb, R.J.K. Taylor, J.L. Serrano, G. Sanchez, New J. Chem. 30 (2006) 1695, and references therein.
[15] J.L. Serrano, L. García, J. Pérez, E. Pérez, J. Vives, G. Sánchez, G. López, E. Molins, A.G. Orpen, Polyhedron 21 (2002) 1589.
[16] J. Pérez, L. García, E. Pérez, J.L. Serrano, J.F. Martínez, G. Sánchez, G. López, A. Espinosa, M. Liu, F. Sanz, New J. Chem. 27 (2003) 1490.
[17] I.J.S. Fairlamb, A.R. Kapdi, A.F. Lee, G. Sánchez, G. López, J.L. Serrano, L. García, J. Pérez, E. Pérez, Dalton Trans. (2004) 3970.
[18] (a) S. Kannan, A.J. James, P.R. Sharp, Inorg. Chim. Acta 345 (2003) 8;
(b) S. Kannan, A.J. James, P.R. Sharp, Polyhedron 19 (2000) 155, and references therein.
[19] R.A. Adrian, S. Zhu, D.R. Powell, G.A. Broker, E.R.T. Tiekink, J.A. Walmsley, Dalton Trans. (2007) 4399.
[20] (a) U. Anandhi, T. Holbert, D. Lueng, P.R. Sharp, Inorg. Chem. 42 (2003) 1282;
(b) P.R. Sharp, Dalton Trans. (2000) 2647.
[21] B. Longato, G. Bandoli, A. Dolmella, Eur. J. Inorg. Chem. (2004) 1092.
[22] (a) L. Díez, P. Espinet, J.A. Miguel, Dalton Trans. (2001) 1189;
(b) P. Espinet, C. Hernández, J.M. Martín-Álvarez, J.A. Miguel, Inorg. Chem. 43 (2004) 843.
[23] (a) G. Sánchez, J. García, D. Meseguer, J.L. Serrano, L. García, J. Pérez, G. López, Dalton Trans. (2003) 4709;
(b) G. Sánchez, J. Vives, G. López, J.L. Serrano, L. García, J. Pérez, Eur. J. Inorg. Chem. (2005) 2360;
(c) J. Pérez, J.L. Serrano, J.M. Galiana, F.L. Cumbrera, A.L. Ortiz, G. Sánchez, J. García, Acta Cryst. B63 (2007) 75.
[24] (a) J.L. Serrano, I.J.S. Fairlamb, G. Sánchez, L. García, J. Pérez, J. Vives, G. López, C.M. Crawforth, R.J.K. Taylor, Eur. J. Inorg. Chem. (2004) 2706;
(b) J. Ruiz, V. Rodríguez, G. López, J. Casabó, E. Molins, C. Miravitlles, Organometallics 18 (1999) 1177, and references therein;
(c) J. Ruiz, N. Cutillas, V. Rodríguez, J. Sampedro, G. López, P.A. Chalonner, P.B. Hitchcock, Dalton Trans. (1999) 2939;
(d) G. Sánchez, J.L. Serrano, J. García, G. López, J. Pérez, E. Molins, Inorg. Chim. Acta 287 (1999) 37;
(e) G. Sánchez, J.L. Serrano, J. Pérez, M.C. Ramírez de Arellano, G. López, E. Molins, Inorg. Chim. Acta 295 (1999) 136.
[25] I.P. Smoliakova, K.J. Keuseman, D.C. Haagenson, D.M. Wellmann, P.B. Colligan, N.A. Kataeva, A.V. Churakov, L.G. Kuz'mina, V.V. Dunina, J. Organomet. Chem. 603 (2000) 86.
[26] SAINT, Version 6.22, Bruker AXS Inc.
[27] G.M. Sheldrick, SADABS, University of Göttingen, 1996.
[28] COLLECT, Nonius BV, 1997–2000.
[29] DENZO-SCALEPACK: Z. Otwinowski, W. Minor, in: C.W. CarterJr., R.M. Sweet (Eds.), Methods in Enzymology, Macromolecular Crystallography, Part A, vol. 276, Academic Press, 1997, pp. 307–326.
[30] G. M Sheldrick, SHELX-97 Programs for Crystal Structure Analysis (Release 97-2), University of Göttingen, 1998.
[31] D.L. Peterson, K.J. Keuseman, N.A. Kataeva, L.G. Kuz'mina, J.A.K. Howard, V.V. Dunina, I.P. Smoliakova, J. Organomet. Chem. 654 (2002) 66.
[32] (a) O.N. Gorunova, K.J. Keuseman, B.M. Goebel, N.A. Kataeva, A.V. Churakov, L.G. Kuz'mina, V.V. Dunina, I.P. Smoliakova, J. Organomet. Chem. 689 (2004) 2382;
(b) R.Y. Mawo, D.M. Johnson, J.L. Wood, I.P. Smoliakova, J. Organomet. Chem. 693 (2008) 33.
[33] J. Pérez, K. Nolsøe, M. Kessler, L. García, E. Pérez, J.L. Serrano, Acta Cryst. B61 (2005) 585.
[34] J. Vicente, A. Arcas, D. Bautista, P.G. Jones, Organometallics 16 (1997) 2127.
[35] J. Vicente, J.A. Abad, A.D. Frankland, M.C. Ramírez de Arellano, Chem. Eur. J. 5 (1999) 3066.
[36] I. Dance, M. Scudder, Dalton Trans. (2000) 1579.

We have previously synthesized phthalocyanines containing tetraaza [18], dithiadiaza [19] macrocyclic moieties, pyridyl groups [20] and polymeric [21,22]. In this paper, we describe the synthesis and characterization of metal-free **4** and metallophthalocyanine **5**–**8**. Cyclic voltammetry of these compounds is also presented.

2. Experimental

2-(Phenylthio)ethanol **1** [23] and 4-nitrophthalonitrile [24]**2** was prepared according to the literature. All reagents and solvents were of reagent grade quality and were obtained from commercial suppliers. All solvents were dried and purified as described by Perrin and Armarego [25]. The IR spectra were recorded on a Perkin Elmer 1600 FT-IR Spectrophotometer, using KBr pellets or NaCl disc. ^{1}H and ^{13}C NMR spectra were recorded on a Varian Mercury 200 MHz spectrometer in $CDCl_3$, and chemical shifts were reported (δ) relative to Me_4Si as internal standard. Mass spectra were measured on a Micromass Quatro LC/ULTIMA LC–MS/MS spectrometer. The elemental analyses were performed on a Costech ECS 4010 instrument. Melting points were measured on an electrothermal apparatus and are uncorrected. Optical spectra in the UV–Vis region were recorded with a Unicam UV2-100 spectrophotometer, using 1 cm pathlength cuvettes at room temperature.

The cyclic voltammetry (CV), differential pulse voltammetry (DPV) measurements were carried out with a Princeton Applied Research Model 2273 potentiostat/Galvanostat controlled by an external PC at 25 °C. A three electrode system was used: a platinum wire counter electrode, an Ag/AgCl reference electrode and a 2 mm sized glassy carbon disc electrode as working electrode. The surface of the working electrode was polished with a H_2O suspension of Al_2O_3 before each run. High purity N_2 was used for deoxygenating the solution for at least 15 min prior to each run and maintain a nitrogen blanked during the measurements.

2.1. 4-[2-(Phenylthio)ethoxy]phthalonitrile (3)

2-(Phenylthio)ethanol **1** (2 g, 12.96 mmol, 1.76 ml) was dissolved in dry DMF (20 ml) under N_2 atmosphere and 4-nitrophthalonitrile **2** (2.24 g, 12.96 mmol) was added to the solution. After stirring 10 min, finely ground anhydrous K_2CO_3 (5.36 g, 38.88 mmol) was added portionwise within 2 h with efficient stirring. The reaction mixture was stirred under N_2 at 50 °C for 3 days. Then the solution was poured into ice-water (200 ml). The precipitate formed was filtered off, washed first with water until the filtrate was neutral and then diethyl ether and dried in vacuo over P_2O_5. The crude product was crystallized from ethanol. Yield: 1.88 g (52%), mp: 78–80 °C. *Anal.* Calc. for $C_{16}H_{12}N_2SO$: C, 68.57; H, 4.28; N, 10.0; S, 11.43. Found: C, 68.77; H, 4.43; N, 10.22; S, 11.56%. IR (KBr tablet) ν_{max}/cm^{-1}: 3077 (Ar-H), 2933, 2851 (Aliph. C–H), 2229 (C≡N), 1598, 1562, 1489, 1319, 1253, 1090, 1012, 741, 691. ^{1}H NMR. ($CDCl_3$), (δ: ppm): 7.64 (d, 1H, ArH), 7.39 (d, 1H, ArH), 7.38 (s, 1H, ArH), 7.32 (d, 2H, ArH), 7.28 (t, 1H, ArH), 7.15 (d, 2H, ArH), 4.20 (t, 2H, CH_2–O), 3.31 (t, 2H, CH_2–S). ^{13}C NMR. ($CDCl_3$), (δ: ppm): 161.39, 135.20, 134.37, 130.38, 129.22, 127.13, 119.53, 119.29, 117.31, 115.61, 115.15, 115.42, 67.67, 32.63. MS (EI), (*m*/*z*): 319 $[M+K]^+$.

2.2. Metal-free phthalocyanine (4)

A mixture of 4-[2-(phenylthio)ethoxy]phthalonitrile **3** (250 mg, 0.89 mmol) and 2-(dimethylamino)ethanol (DMAE) (3 ml) was placed in Schlenk tube at 130 °C for 24 h. After cooling to room temperature the reaction mixture refluxed with ethanol (45 ml) to precipitate the product which was filtered off. The green solid product was washed with hot ethanol, diethyl ether and dried in vacuo. This product is soluble in $CHCl_3$, CH_2Cl_2, THF, DMF, DMSO. After that the green solid product is purified from the column in which is placed silicagel using only chloroform as solvent system. At the end of this purification step, the suitable fractions are put together and solvent of these is evaporated under low pressure until the dryness. Yield: 103 mg (41%), mp 145–147 °C. Elemental *Anal.* Calc. for $C_{64}H_{50}N_8O_4S_4$: C, 68.36; H, 4.45; N, 9.96; S, 11.39. Found: C, 67.90; H, 4.60; N, 9.60; S, 12.02%. IR (KBr tablet) ν_{max}/cm^{-1}: 3296 (N–H), 3060 (Ar-H), 2926–2857 (Aliph. C–H), 1602 (N–H bending), 1591, 1517, 1463, 1283 (Ar-O–C), 1121, 1070, 1017, 825, 743, 691. ^{1}H NMR ($CDCl_3$), (δ: ppm) 7.64 (d, 1H, ArH), 7.39 (d, 1H, ArH), 7.38 (s, 1H, ArH), 7.32 (d, 2H, ArH), 7.28 (t, 1H, ArH), 7.15 (d, 2H, ArH), 4.20 (t, 2H, CH_2–O), 3.31 (t, 2H, CH_2–S). ^{1}H NMR ($CDCl_3$), (δ: ppm) 7.66 (d, 4H, ArH), 7.61 (d, 4H, ArH), 7.48 (s, 4H, ArH), 7.43 (d, 8H, ArH), 7.28 (t, 4H, ArH), 7.19 (d, 8H, ArH), 4.25 (m, 8H, CH_2–O), 4.13 (m, 8H, CH_2–S). ^{13}C NMR ($CDCl_3$), (δ: ppm) 167.96, 139.12, 132.70, 131.09, 129.02, 124.68, 124.18, 119.92, 119.86, 113.26, 104.38, 99.55, 68.38, 38.96. UV–Vis (chloroform): λ_{max}/nm: [(10^{-5} ε dm^3 mol^{-1} cm^{-1})]: 287 (5.21), 335 (5.20), 392 (4.82), 644 (4.93), 671 (5.10), 707 (5.11). MS (FAB), (*m*/*z*): 1122 $[M-H]^+$.

2.3. Ni(II)-containing phthalocyanine (5)

A mixture of 4-[2-(phenylthio)ethoxy]phthalonitrile **3** (220 mg, 0.78 mmol), anhydrous $NiCl_2$ (25.34 mg, 0.196 mmol) and 2-(dimethylamino)ethanol (DMAE) (2 ml) placed in Schlenk tube at 130 °C for 24 h. After cooling to room temperature the reaction mixture refluxed with ethanol (40 ml) to precipitate the product which was filtered off. The green solid product was washed with hot ethanol, diethyl ether and dried in vacuo. This product is soluble in $CHCl_3$, CH_2Cl_2, THF, DMF, DMSO. After that the green solid product is purified from the column in which is placed silicagel using chloroform:methanol (9.9:0.1) as solvent system. At the end of this purification step, the suitable fractions are put together and solvent

of these is evaporated under low pressure until the dryness. Yield: 37 mg (37%), mp > 300 °C. Elemental *Anal*. Calc. for $C_{64}H_{48}N_8O_4S_4Ni$: C, 65.08; H, 4.06; N, 9.49; S, 10.84. Found: C, 65.10; H, 4.40; N, 9.90; S, 10.90%. IR (KBr tablet) ν_{max}/cm^{-1}: 3043 (Ar-H), 2923, 2862 (Aliph. C–H), 1606 (C=N), 1529, 1479, 1415, 1329 1271, 1230 (Ar-O–C), 1120, 1090, 1012, 820, 737, 689. ^1H NMR ($CDCl_3$), (δ: ppm) 7.64 (d, 4H, ArH), 7.47 (d, 4H, ArH), 7.45 (s, 4H, ArH), 7.43 (d, 8H, ArH), 7.28 (t, 4H, ArH), 7.18 (d, 8H, ArH), 4.21 (t, 8H, CH_2–O), 3.53 (t, 8H, CH_2–S). ^{13}C NMR ($CDCl_3$), (δ: ppm) 167.74, 142.45, 132.52, 130.90, 129.23, 128.84, 125.88, 124.53, 123.68, 119.12, 102.24, 68.21, 38.80. UV–Vis (pyridine): λ_{max}/nm: [(10^{-5} ε dm^3 mol^{-1} cm^{-1})]: 295 (5.17), 329 (5.18), 389 (4.83), 620 (4.60), 677 (5.17). MS (FAB), (*m*/*z*): 1182 $[M+2H]^+$.

2.4. Zn(II)-containing phthalocyanine (6)

A mixture of 4-[2-(phenylthio)ethoxy]phthalonitrile **3** (230 mg, 0.82 mmol), anhydrous $Zn(CH_3COO)_2$ (44.97 mg, 0.205 mmol) and 2-(dimethylamino)ethanol (DMAE) (2 ml) was placed in Schlenk tube at 130 °C for 24 h. After cooling to room temperature the reaction mixture refluxed with ethanol (40 ml) to precipitate the product which was filtered off. The green solid product was washed with hot ethanol, diethyl ether and dried in vacuo. This product is soluble in $CHCl_3$, CH_2Cl_2, THF, DMF, DMSO. After that the green solid product is purified from the column in which is placed silicagel using only chloroform as solvent system. At the end of this purification step, the suitable fractions are put together and solvent of these is evaporated under low pressure until the dryness. Yield: 121 mg (%50), mp > 300 °C. Elemental *Anal*. Calc. for $C_{64}H_{48}N_8O_4S_4Zn$: C, 67.71; H, 4.04; N, 9.44; S, 10.79. Found: C, 66.60; H, 4.20; N, 10.0; S, 11.0%. IR (KBr tablet) ν_{max}/cm^{-1}: 3049 (Ar-H), 2924, 2857 (Aliph. C–H), 1606 (C=N), 1481, 1379, 1337, 1230 (Ar-O–C), 1092, 1045, 946, 823, 743, 690. ^1H NMR ($CDCl_3$), (δ: ppm) 7.69 (d, 4H, ArH), 7.55 (d, 4H, ArH), 7.53 (s, 4H, ArH), 7.50 (d, 8H, ArH), 7.26 (t, 4H, ArH), 7.16 (d, 8H, ArH), 4.28 (m, 8H, CH_2–O), 4.21 (m, 8H, CH_2–S). UV–Vis (chloroform): λ_{max}/nm: [(10^{-5} ε dm^3 mol^{-1} cm^{-1})]: 270 (5.22), 353 (5.19), 617 (4.64), 686 (5.23). MS (FAB), (*m*/*z*): 1186 $[M]^+$.

2.5. Co(II)-containing phthalocyanine (7)

A mixture of 4-[2-(phenylthio)ethoxy]phthalonitrile **3** (220 mg, 0.78 mmol), anhydrous $CoCl_2$ (25.53 mg, 0.196 mmol) and 2-(dimethylamino)ethanol (DMAE) (2 ml) was placed in Schlenk tube at 130 °C for 24 h. After cooling to room temperature the reaction mixture refluxed with ethanol (45 ml) to precipitate the product which was filtered off. The green solid product was washed with hot ethanol, diethyl ether and dried in vacuo. This product is soluble in $CHCl_3$, CH_2Cl_2, THF, DMF, DMSO. After that the green solid product is purified from the column in which is placed silicagel using chloroform:methanol (9.5:0.5) as solvent system. At the end of this purification step, the suitable fractions are put together and solvent of these is evaporated under low pressure until the dryness. Yield: 92 mg (40%), mp 171–173 °C. Elemental *Anal*. Calc. for $C_{64}H_{48}N_8O_4S_4Co$: C, 65.07; H, 4.07; N, 9.49; S, 10. Found: C, 65.10; H, 4.40; N, 9.90; S, 10.80%. IR (KBr tablet) ν_{max}/cm^{-1}: 3056 (Ar-H), 2926, 2868 (Aliph. C–H), 1603, 1481, 1382, 1279, 1228 (Ar-O–C), 1072, 1014, 829, 739, 690. ^1H NMR ($CDCl_3$), (δ: ppm) 7.71 (d, 4H, ArH), 7.69 (d, 4H, ArH), 7.54 (s, 4H, ArH), 7.50 (d, 8H, ArH), 7.27 (t, 4H, ArH), 7.23 (d, 8H, ArH), 4.29 (m, 8H, CH_2–O), 4.20 (m, 8H, CH_2–S). UV–Vis (pyridine): λ_{max}/nm: [(10^{-5} ε dm^3 mol^{-1} cm^{-1})]: 275 (5.14), 345 (5.16), 611 (4.59), 677 (5.18). MS (FAB), (*m*/*z*): 1181 $[M]^+$.

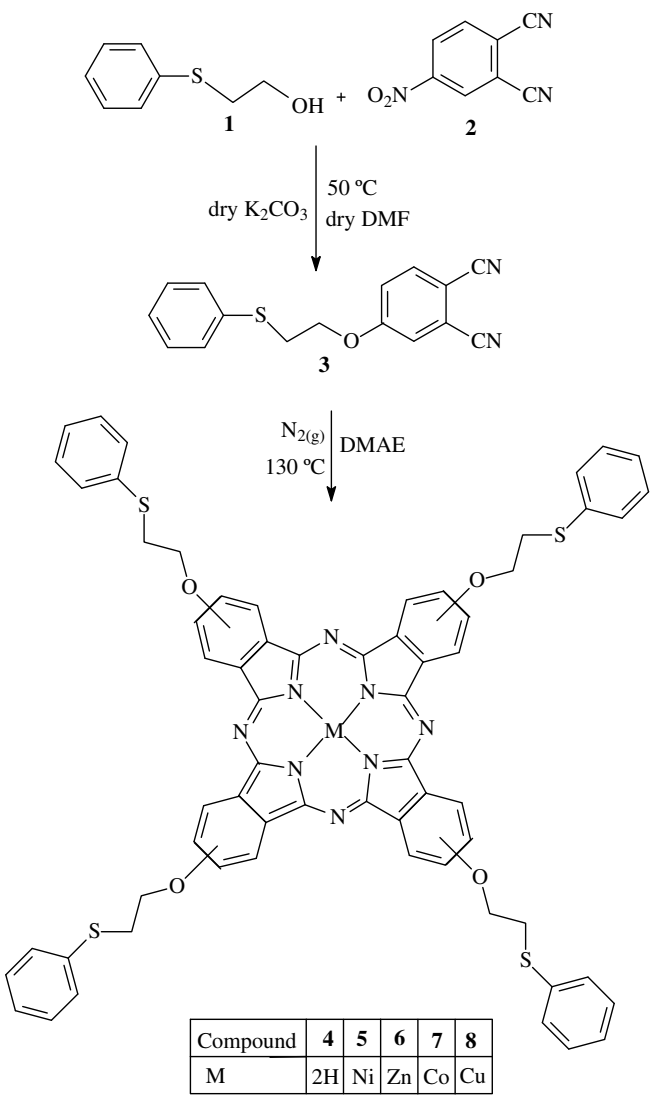
2.6. Cu(I)-containing phthalocyanine (8)

A mixture of 4-[2-(phenylthio)ethoxy]phthalonitrile **3** (240 mg, 0.857 mmol), anhydrous CuCl (21.21 mg, 0.214 mmol) and 2-(dimethylamino)ethanol (DMAE) (2 ml) was placed in Schlenk tube at 130 °C for 24 h. After cooling to room temperature the reaction mixture refluxed with ethanol (45 ml) to precipitate the product which was filtered off. The green solid product was washed with hot ethanol, diethyl ether and dried in vacuo. This product is soluble in $CHCl_3$, CH_2Cl_2, THF, DMF, DMSO. After that the green solid product is purified from the column in which is placed silicagel using only chloroform as solvent system. At the end of this purification step, the suitable fractions are put together and solvent of these is evaporated under low pressure until the dryness. Yield: 109 mg (43%), mp > 300 °C. Elemental *Anal*. Calc. for $C_{64}H_{48}N_8O_4S_4Cu$: C, 64.81; H, 4.05; N, 9.45; S, 10.80. Found: C, 64.90; H, 4.30; N, 9.90; S, 10%. IR (KBr tablet) ν_{max}/cm^{-1}: 3049 (Ar-H), 2923, 2851 (Aliph. C–H), 1592, 1484, 1382, 1327, 1224 (Ar-O–C), 1188, 1147, 1076, 1014, 897, 787, 737, 690. UV–Vis (pyridine): λ_{max}/nm: [(10^{-5} ε dm^3 mol^{-1} cm^{-1})]: 265 (5.15), 334 (5.17), 617 (4.52), 686 (5.20). MS (FAB), (*m*/*z*): 1184 $[M]^+$.

3. Results and discussion

3.1. Synthesis and characterization

Metal-free **4** and metallophthalocyanines **5**, **6**, **7** and **8** were synthesized in two steps (Scheme 1). In the first step, the base-catalyzed nucleophilic aromatic nitro displacement of 4-nitrophthalonitrile **2** with 2-(phenylthio)ethanol **1** afforded the dinitrile monomer **3**. In the second step, metal-free and metallophthalocyanine molecules were synthesized. The metal-free phthalocyanine **4** was synthesized with adding 2-(dimethylamino)ethanol in Schlenk tube at 130 °C for 24 h. The metallophthalocyanines **5**, **6**, **7** and **8** were obtained from tetracyano derivative **3** and corresponding anhydrous metal salts $NiCl_2$, $Zn(CH_3COO)_2$, $CoCl_2$ and CuCl, respectively, with adding 2-(dimethylamino)ethanol in Schlenk tube for at reflux temperature.



Compound	4	5	6	7	8
M	2H	Ni	Zn	Co	Cu

Scheme 1. The synthesis of the metal-free phthalocyanine and metallophthalocyanines.

In the IR spectrum of **3** the disappearance of NO_2 and OH groups stretching vibrations belong to compounds **1**, **2**, along with the appearance of new bands at 2229 and 1253 cm^{-1} arising from C≡N and Ar-O–C groups, respectively, are in agreement with the proposed structure. In the ^1H NMR spectrum of **3**, OH group of compound **1** disappeared as expected. ^1H NMR spectrum of **3** showed new signals at $\delta = 7.64$ (d, 1H, ArH), 7.39 (d, 1H, ArH), 7.38 (s, 1H, ArH), 7.32 (d, 2H, ArH), 7.28 (t, 1H, ArH), 7.15 (d, 2H, ArH), 4.20 (t, 2H, CH_2–O), 3.31 (t, 2H, CH_2–S). In the ^{13}C NMR spectrum of **3** indicated the presence of nitrile carbon atoms in **3** at $\delta = 115.61$ and 115.15 ppm. Elemental analysis and EI mass spectral data were satisfactory: 319 $[M+K]^+$.

In the IR spectrum of **4** characteristic peaks for phthalocyanines were observed. The peak at 3296 cm^{-1} is the characteristic metal-free phthalocyanine N–H stretching bands. Also, 3060 (Ar-H), 2926-2857 (Aliph. C–H), 1602 (N–H bending) bands were present in the spectrum. The disappearance of the C≡N stretching vibration on the IR spectra of **3** suggested the formation of compound **4**. In the ^1H NMR spectrum of **4**, the typical shielding of inner core protons could not be observed due to the probable strong aggregation of the molecules [26]. The MS mass spectrum of compound **4** displayed the $[M-2H]^+$ parent ion peak at $m/z = 1122$ which confirms the same structure. The results of the elemental analysis confirmed the proposed structure of compound **4**.

The IR spectra of metallophthalocyanines **5**, **6**, **7** and **8** the disappearance of strong C≡N stretching vibration of **3** is an evidence for the formation of metallophthalocyanines **5**, **6**, **7** and **8**. The rest of the IR spectra of metallophthalocyanines are very similar to those of the metal-free phthalocyanine **4**. In the ^1H NMR spectra of these compounds are almost identical to those of metal-free phthalocyanine **4**. In the mass spectrum of compounds **5**, **6**, **7** and **8**, the presence of molecular ion peaks at $m/z = 1182$ $[M+2H]^+$, 1186 $[M]^+$, 1181 $[M]^+$ and 1184 $[M]^+$, respectively, confirmed the proposed structures.

The electronic spectra of phthalocyanines **4**, **5**, **6**, **7** and **8** show the typical B and Q bands of symmetrical Pc. The energy level location corresponding to those bands is illustrated in Figs. 1 and 2. There are the split Q-band as expected and there are two strong bands in the visible

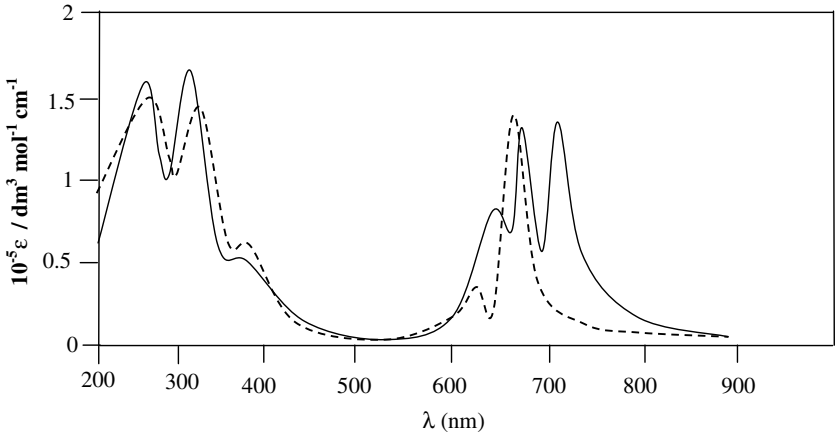


Fig. 1. UV–Vis spectra of compounds **4** (—) and **5** (---) and in chloroform.

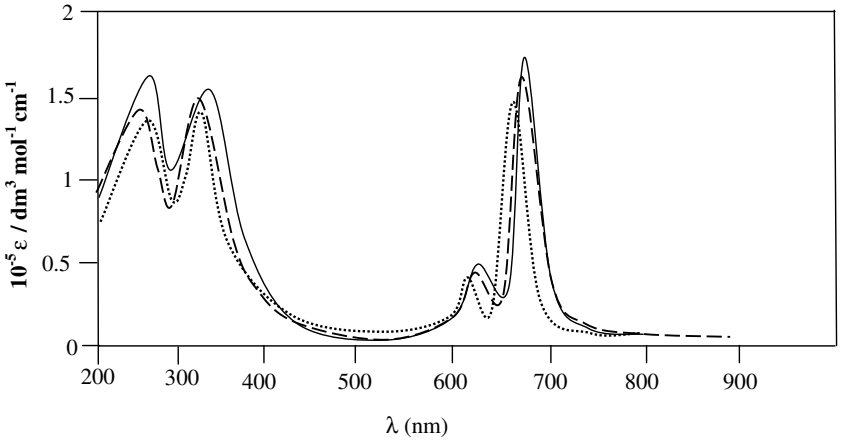


Fig. 2. UV–Vis spectra of compounds **6** (—), **7** (···) and **8** (---) in chloroform.

region [27]. The split Q-band which is characteristic for metal-free phthalocyanines **4** observed at $\lambda_{max} = 707$ and 671 nm with a shoulder at 644 nm, indicating the monomeric species with D_{2h} symmetry shows two intense absorptions at around 700 nm [28,29]. On the other hand, such split Q-band absorptions in chloroform are due to π–π* transition of this fully conjugated 18π electron systems [30].

The UV–Vis absorption spectra of metallophthalocyanines **5**, **6**, **7** and **8** in chloroform show intense Q absorption at $\lambda_{max} = 677$, 686, 677 and 686 nm, with a weaker absorptions at 620, 617, 611 and 617 nm, respectively. The single Q bands in metallo derivatives **5**, **6**, **7** and **8** are characteristic. This result is typical of metal complexes of substituted and unsubstituted metallophthalocyanines with D_{4h} symmetry [31]. B band absorptions of compound **5**, **6**, **7** and **8** were observed at $\lambda_{max} = (295, 329, 389)$, (270, 353), (275, 345), (265, 334) nm as expected.

3.2. Electrochemical measurements

Redox properties of the free base phthalocyanine (H_2Pc) and ZnPc, CoPc complexes were studied using cyclic voltammetry and differential pulse voltammetry in dichloromethane (DCM) containing 0.1 M tetra(*n*-butyl)ammonium tetrafluoroborate (TBATFB). Voltammetric data and the assignment of the redox couples recorded for the ligand and its complexes are listed in Table 1. The potentials are given versus Ag/AgCl reference electrode.

Fig. 3 shows the CV and DPV of the metal-free phthalocyanine. It gives three one-electron reduction processes labelled as R_1 at −0.820 V, R_2 at −1.058 V and R_3 −1.408 V and ill defined two oxidation processes labelled O_1 and O_2 at 0.1 V s^{-1} scan rate. The peak currents increased linearly with the square root of the scan rate at a range of 10–500 mV s^{-1} indicating the purely diffusion-controlled behaviours of the reduction couples. The values of $I_{p,a}/I_{p,c}$ for reduction couples of (H_2Pc) are close to unity, suggesting reversible redox processes. The anodic to cathodic peak separation (ΔE_p) changed from 58 to

Table 1
The electrochemical data of phthalocyanines

Compound	Redox process	E_p (V)	ΔE_p (mV)	$I_{p,a}/I_{p,c}$	$\Delta E^{1/2}$ (V)
FPc	R_1	−0.820 (−0.750)	70	0.70	1.530
	R_2	−1.058 (−1.010)	48	1.15	
	R_3	−1.408 (−1.284)	124	0.40	
	O_1	0.710[a]			
	O_2	0.850[a]			
CoPc	R_1	−0.406 (–)	70	–	1.228
	R_2	−1.204 (–)			
	R_3	−1.528 (−1.428)	100		
	O_1	0.822 (0.704)	118	0.96	
ZnPc	R_1	−1.072 (−1.004)	68	0.70	1.570
	R_2	−1.288 (−1.180)	108	1.12	
	O_1	0.498 (0.440)	58	0.75	

[a] From DPV measurements.

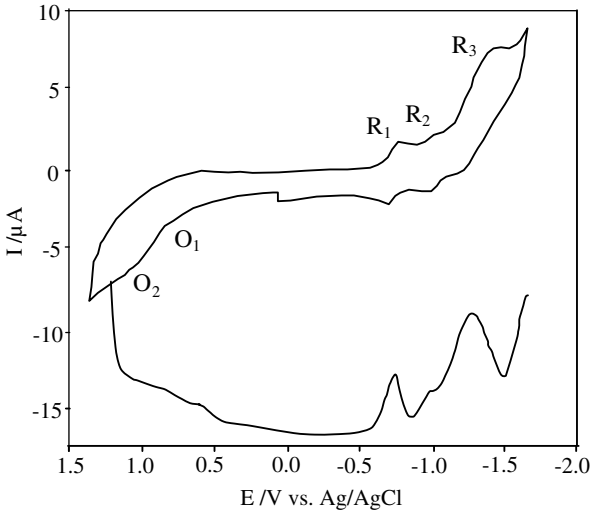


Fig. 3. Cyclic and differential pulse voltammograms of H_2Pc at 0.100 V s^{-1} scan rate on GCE in DCM/TBATFB. Inset: DPV of H_2Pc (1.10^{-3} mol dm^{-3}). Pulse width = 50 ms, pulse height = 100 mV, step height = 5 mV, step time = 100 mS.

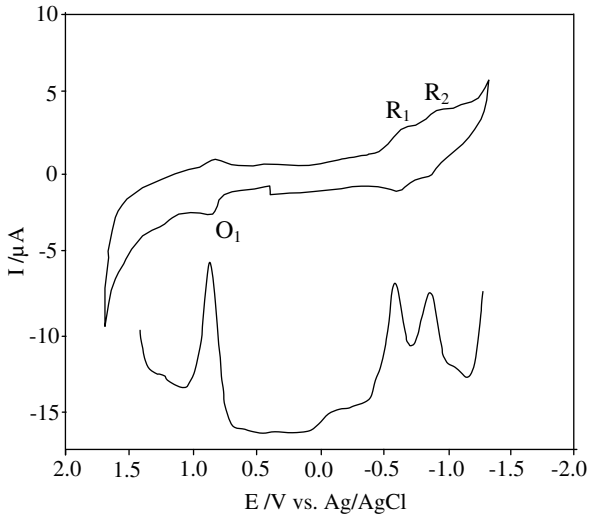


Fig. 4. Cyclic and differential pulse voltammograms of ZnPc at 0.100 V s^{-1} scan rate on GCE in DCM/TBATFB. Inset: DPV of ZnPc (1.10^{-3} mol dm^{-3}). Pulse width = 50 ms, pulse height = 100 mV, step height = 5 mV, step time = 100 mS.

124 mV with scan rate suggesting the reversible or a quasi-reversible electron transfer.

The ZnPc complex exhibited three redox couples in the +1.50 to −1.80 V range. Scanning the potential to positive side, a reversible oxidation process of the complex at +0.498 V was seen, and upon scanning cathodically, two reduction peaks with the corresponding anodic waves on the reverse step were recorded at −1.044 V and −1.380 V (Fig. 4). Fig. 5. shows the CV and DPV of the cobalt complex gives three reduction and two oxidation couples.

The reduction and oxidation behaviour of metallophthalocyanine derivatives is due to the interaction between the phthalocyanine ring and the central metal. The redox

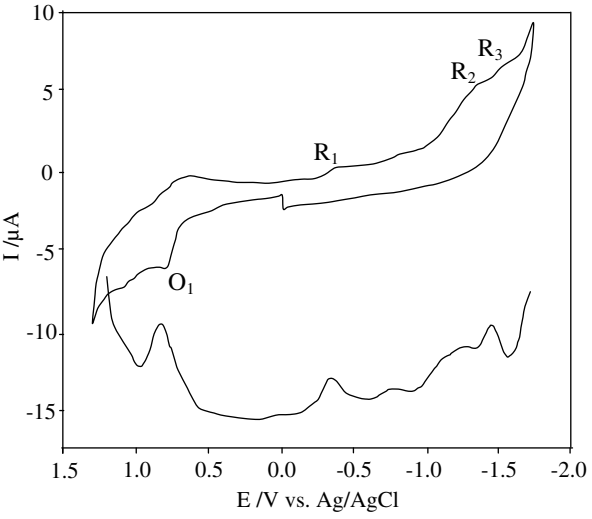


Fig. 5. Cyclic and differential pulse voltammograms of CoPc at 0.100 V s^{-1} scan rate on GCE in DCM/TBATFB. Inset: DPV of CoPc (1.10^{-3} mol dm^{-3}). Pulse width = 50 ms, pulse height = 100 mV, step height = 5 mV, step time = 100 mS.

properties of the of metallophthalocyanines have been studied by many authors [32–34]. According to these studies for the CoPc complexes, the first oxidation and first reduction processes occurs on the metal centre in polar solvent such as DMF and DMSO, however, the first oxidation processes occur on the Pc ring in apolar solvent such as DCM and THF. This study indicates that the first reduction at −0.406 V could be assigned easily to the [Co(II)Pc(-2)]/[Co(I)Pc(-2)]$^{-}$ redox couple and the remaining processes to the phthalocyanine ring. Since the difference between the first oxidation and reduction potentials ($\Delta E_{1/2}$) reflects the HOMO–LUMO gap in related molecule the $\Delta E_{1/2}$ value of CoPc are comparable to those given in corresponding papers and smaller than the (H_2Pc) [35]. In contrast to CoPc all redox processes of the ZnPc complex take place on the phthalocyanine ring system.

Acknowledgment

This study was supported by the Research Fund of Karadeniz Technical University, Project No. 2006.111. 002.1 (Trabzon, Turkey).

References

[1] J.J. Simon, H.J. Andre, Molecular Semiconductors, Springer, Berlin, 1985.
[2] M.J. Crossley, P.L. Burn, S.J. Langford, J.K. Prashar, J. Chem. Soc., Chem. Commun. (1995) 1991.
[3] H. Eichhorn, D. Wöhrle, D. Presner, Liquid Cryst. 22 (1997) 643.
[4] D. Lelievre, M.A. Petit, J. Simon, Liquid Cryst. 4 (1989) 707.
[5] M.A. Diaz Garcia, I. Ledoux, J.A. Duro, T. Tores, F. Agullolopez, J. Zyss, J. Phys. Chem. 98 (1994) 8761.
[6] I. Rosenthal, in: C.C. Leznoff, A.B.P. Lewer (Eds.), Phthalocyanines: Properties and Applications, vol. 4, VCH, New York, 1996, p. 485.
[7] G.E. Collins, N.R. Armstrong, J.W. Pankow, C. Oden, R. Brina, C. Anbour, J.-P. Dodelet, J. Vac. Sci. Technol. A 11 (1993) 1383.
[8] K.K. Dailey, G.P.A. Yap, A.L. Rheingold, T.B. Rauchfuss, Angew. Chem., Int. Ed. Engl. 35 (1996) 1833.
[9] D. Wöhrle, J. Gitzel, G. Krawczyk, E. Tsuchida, H. Ohno, T. Nishisaka, J. Macromol. Sci. Chem. A 25 (1998) 1227.
[10] D. Wöhrle, D. Meissner, Adv. Mater. 3 (1991) 129.
[11] C.S. Frampton, J.M. O'Conner, J. Silver, Display (1998) 174.
[12] A. Gürek, V. Ahsen, A. Gül, Ö. Bekaroğlu, J. Chem. Soc., Dalton Trans. (1991) 3367.
[13] C.C. Leznoff, A.B.P. Lever (Eds.), Phthalocyanines, Properties, and Applications, vols. 1–4, VCH, New York, 1989.
[14] M. Hanack, M. Lang, Adv. Mater. 6 (1994) 819.
[15] A. Koca, H.A. Dinçer, H. Çerlek, A. Gül, M.B. Koçak, Electrochim. Acta 52 (2006) 1199.
[16] N.B. McKeown, Phthalocyanine Materials: Synthesis Structure and Function, Cambridge University Press, Cambridge, 1998.
[17] A. Beck, K.M. Mangold, M. Hanack, Chem. Ber. 124 (1991) 2315.
[18] Z. Bıyıklıoğlu, H. Kantekin, M. Özil, J. Organomet. Chem. 692 (2007) 2436.
[19] H. Kantekin, Z. Bıyıklıoğlu, Dyes Pigments 77 (2008) 98.
[20] Z. Bıyıklıoğlu, H. Kantekin, Transition Met. Chem. 32 (2007) 851.
[21] H. Kantekin, Z. Bıyıklıoğlu, Dyes Pigments 77 (2008) 432.
[22] Z. Bıyıklıoğlu, H. Kantekin, J. Organomet. Chem. 693 (2008) 505.
[23] D.A. Alonso, C. Najera, M. Varea, Synthesis 2 (2003) 277.
[24] G.J. Young, W. Onyebuagu, J. Org. Chem. 55 (1990) 2155.

[25] D.D. Perrin, W.L.F. Armarego, D.R. Perrin, Purification of Laboratory Chemicals, 2nd ed., Pergamon Press, New York, 1985.
[26] van C.F. Nostrum, S.J. Picken, A.-J. Schouten, R.J.M. Nolte, J. Am. Chem. Soc. 117 (1995) 9957.
[27] I. Yılmaz, Ö. Bekaroğlu, Chem. Ber. 129 (1996) 967.
[28] O.E. Sielcken, M.M. van Tilborg, R. Hendricks, W. Drenth, R.J.M. Nolte, J. Am. Chem. Soc. 109 (1987) 4261.
[29] E.A. Cuellar, T.J. Marks, Inorg. Chem. 20 (1981) 3766.
[30] Y. Gök, H. Kantekin, A. Bilgin, D. Mendil, İ. Değirmencioğlu, J. Chem. Soc., Chem. Commun. 3 (2001) 285.
[31] A. Riesen, M. Zehnder, T.A. Kaden, Helv. Chim. Acta 69 (1986) 2074.
[32] M. Kandaz, M.N. Yaraşir, A. Koca, Ö. Bekaroğlu, Polyhedron 21 (2002) 255.
[33] A. Koca, H.A. Dinçer, H. Çerlek, A. Gül, M.B. Koçak, Electrochim. Acta 52 (2006) 1199.
[34] M. Kandaz, A.R. Özkaya, Ö. Bekaroğlu, Monatsh. Chem. 132 (2001) 1013.
[35] A.R. Özkaya, A.İ. Okur, A. Gül, Ö. Bekaroğlu, J. Porphyrin. Phthalocyan. 4 (2000) 689.

2. Experimental

2.1. Instrumentation and materials

A Perkin–Elmer Spectrum One spectrometer was used for recording FT–IR spectrum in the range 4000–250 cm^{-1} and Cary Eclipse EL05033882 for fluorescence. UV–Vis spectra were recorded in a Perkin–Elmer Lambda 25 spectrometer. The EPR spectra were recorded on a JEOL JES FA-200 X-band EPR spectrometer. The epr spectra were simulated using EPR-NMR programme package (version 6.08) developed by professor John Weil's group [8] and it was kindly supplied by Dr. P. Sambasiva Rao, Pondicherry University. The spin Hamiltonian parameters were determined by trial and error method and the exact diagonalization of the spin Hamiltonian was used in this programme. Isotropic *g*-values, *D* and *E* parameters were used as inputs in the simulation programme. The room temperature VSM data were recorded on a Lakshore VSM Setup.

X-ray crystallographic data were collected using Bruker SMART APEX-CCD diffractometer with Mo Kα radiation ($\lambda = 0.71073$ Å). The intensity data were corrected for Lorentz and polarization effects and empirical absorption corrections was applied using SAINT programme [9,10]. All the structures were solved by direct methods using SHELXS-97 [11]. Non-hydrogen atoms located from the difference Fourier maps were refined anisotropically by full-matrix least-squares on F^2, using SHELXL-97 [11]. The hydrogen atoms were included in the calculated positions and refined isotropically using a riding model.

2-Acetylpyridine, 2-picolylamine (Aldrich, USA), $CrCl_3 \cdot 6H_2O$ (Fluka, USA), Zn powder, Na_2EDTA, KSCN, NaN_3 (Merck India Ltd.), and other reagent grade chemicals were used as received without further purification. 4′-(2-pyridyl)-2,2′:6′,2″-terpyridine, **L**, was prepared using the procedure reported by us [7].

2.2. Synthesis of the complexes

2.2.1. $[Cr\mathbf{L}Cl_3] \cdot DMF$ (**1**)

To a hot ethanolic solution (20 mL) containing $CrCl_3 \cdot 6H_2O$ (65 mg, 0.24 mmol) and **L** (76 mg, 0.24 mmol), was added zinc powder (2 mg) and heated at reflux for 1 h. The green solid which precipitated was filtered, washed successively with water and ethanol. The solid was dissolved in minimum amount of DMF and kept undisturbed for about a week. The crystals deposited were collected and used for further characterizations. Yield: 36 mg, 31%. *Anal.* Calc. for $[Cr\mathbf{L}Cl_3] \cdot DMF = C_{23}H_{21}N_5OCl_3Cr$: C, 50.94; H, 3.87; N, 12.92. Found: C, 50.79; H, 3.91; N, 12.83%.

2.2.2. $[Cr\mathbf{L}(N_3)_3] \cdot CH_3CN$ (**2**)

To a hot methanolic solution (20 ml) containing $CrCl_3 \cdot 6H_2O$ (32 mg, 0.12 mmol), **L** (37 mg, 0.12 mmol) and NaN_3 (24 mg 0.38 mmol), zinc powder (1 mg) was added and heated at reflux for 0.5 h. The resulting greenish brown solution was filtered and left undisturbed. The brown crystals deposited after a week were separated and washed with ice-cold methanol. Yield: 15 mg (26%). Crystals suitable for X-ray crystallography were obtained by slow evaporation of acetonitrile solution of **2**. *Anal.* Calc. for $[Cr\mathbf{L}(N_3)_3] \cdot CH_3CN = C_{22}H_{17}N_{14}Cr$: C, 49.90; H, 3.21; N, 37.05. Found: C, 49.75; H, 3.14; N, 36.91%.

2.2.3. $Cr\mathbf{L}(NCS)_3] \cdot DMF$ (**3**)

An ethanolic solution (30 ml) containing $CrCl_3 \cdot 6H_2O$ (60 mg, 0.22 mmol) zinc powder (2 mg) and KSCN (67 mg, 0.68 mmol) were heated at reflux for few minutes. Then solid **L** (68 mg, 0.22 mmol) was added and refluxed for 0.5 h. The precipitated brown crystalline solid was filtered and washed with ethanol. Yield: 90 mg (74%). Crystals suitable for X-ray crystallography were obtained by slow evaporation of DMF solution of **3**. *Anal.* Calc. for $[Cr\mathbf{L}(NCS)_3] \cdot DMF = C_{26}H_{21}N_8OS_3Cr$: C, 51.17; H, 3.44; N, 18.37. Found: C, 51.29; H, 3.48; N, 18.26%.

3. Results and discussion

3.1. Syntheses

The common coordination number for chromium(III) is six and has a $t_{2g}^3e_g^0$ electronic configuration in an octahedral ligand field. Therefore, Cr^{3+} is a substitutionally inert metal ion. However, in the presence of trace quantities of reducing agent, catalytic amounts of Cr^{2+} are generated. Since Cr^{2+} in a weak field environment has $t_{2g}^3e_g^1$ electronic configuration, is substitutionally labile and readily undergo substitution reactions [12]. Using this principle, we could synthesize $[Cr\mathbf{L}(N_3)_3] \cdot DMF$ by heating equimolar quantities of $CrCl_3 \cdot 6H_2O$ and **L** in ethanol in the presence of catalytic amount of zinc powder. Similarly, in the presence of N_3^- and NCS^- ions, $[Cr\mathbf{L}(N_3)_3] \cdot CH_3CN$ and $[Cr\mathbf{L}(NCS)_3] \cdot DMF$ were obtained, respectively.

3.2. Optical spectra

The presence of **L** in **1**, **2**, and **3** can be inferred from the presence of ν(C=N) at 1605 cm^{-1}. In **1**, ν(Cr–Cl) at 400 cm^{-1} can be assigned to the equatorial bond and the IR active asymmetric ν(Cr–Cl) for the axial bonds occur at 350 cm^{-1}. In case of **2**, the bands at 2072 and 2036 cm^{-1} are due to ν(azide, axial) and ν(azide, equatorial), respectively. The ν(N≡C) occurs at 2074 and 2054 cm^{-1} in **3** [13]. The trends, ν(Cr–Cl, equatorial) > ν(Cr–Cl, axial) and $\nu(N_3$, axial) > $\nu(N_3$, equatorial) are in agreement with the bond distances determined through X-ray crystallography. Complexes **1** and **3** show characteristic amide band for DMF, the solvent of crystallization, at 1650 cm^{-1}.

All the three complexes **1**, **2**, and **3** have distorted octahedral geometry (*vide infra*) having one meridionally coordinating tridentate **L** and three anions. In DMF solution,

they exhibit some of d–d transitions in the visible region and intra-ligand transitions in the UV region. The λ_{max} and their molar extinction coefficient values are listed in Table 1. Chromium(III) is a d^3 ion in a perfect octahedral geometry has $^4A_{2g}$ as its electronic ground state along with the $^4T_{2g}$, $^4T_{1g}(F)$, and $^4T_{1g}(P)$ excited states. Usually, the d–d bands originating from $^4A_{2g} \rightarrow {}^4T_{2g}$, $^4A_{2g} \rightarrow {}^4T_{1g}(F)$ fall in the visible region and $^4A_2 \rightarrow {}^4T_1(P)$ in the UV region [14]. Since these complexes has a pseudo octahedral geometry and hence lower symmetry, the splitting of the orbitally degenerate terms should be possible. Observation of three bands in the visible region is reasonable with the lower symmetry. The lowest energy band is originating from the $^4A_{2g} \rightarrow {}^4T_{2g}$ (from O_h symmetry) transition, which directly corresponds to 10Dq, follow the trend $[CrLCl_3] < [CrL(N_3)_3] < [CrL(NCS)_3]$ consistent with the spectrochemical series, $Cl^- < N_3^- < NCS^-$. The energy trends of the other transitions also follow the same order, but with a small difference.

The emission spectra of **1**, **2**, and **3** were recorded in DMF and exhibit $\pi \rightarrow \pi^*$ character; which indicates an emission from the significant intra-ligand $\pi \rightarrow \pi^*$ state at higher energy [15]. In case of **1** an excitation band with vibronic components 504 and 517 nm observed for $\lambda_{ex} =$ 450 nm. For **2**, an excitation consists of a structured band with vibronic components 350 and 360 nm observed for $\lambda_{ex} = 285$ nm. But in case of **3** there is a single emission peak at 375 nm for $\lambda_{ex} = 290$ nm.

3.3. EPR and magnetism

The EPR spectra (9.49 GHz) of **1**, **2**, and **3**, recorded at 77 K in DMF, indicate deviation from the cubic symmetry along with the zero-field splitting. The Cr^{3+}, a d^3 ion ($S = 3/2$) with a $^4A_2$ ground state, in an octahedral field has an orbitally non-degenerate ground state. The spin–orbit coupling or a low symmetry ligand field may mix the ground state with the excited states, thus giving rise to zero-field splitting. Compounds **1** and **3** appear to have larger zero-field splitting compared to **2** [16].

The spectra were investigated in terms of the conventional spin Hamiltonian operator,

$$\mathscr{H} = g|\beta|S_z B_o + D[S_z^2 - (1/3)S(S+1)] + E(S_x^2 - S_y^2)$$

where β is the Bohr magneton, B_o is the static external magnetic field, D is the axial zero-field splitting parameter, and E is the rhombic component. Fig. 1 displays the computer simulated as well as experimental EPR spectra for complexes **1**–**3**. The spin Hamiltonian parameters were determined by trial and error method and isotropic g-values were used in the simulation. Exact diagonalization of the spin Hamiltonian was used for the computer-simulation of the spectrum, from which the following parameters were extracted: for **1**: $g = 1.990$; $D = 0.034\ cm^{-1}$; $E/D = 0.30$, **2**: $g = 1.983$; $D = 0.017\ cm^{-1}$; $E/D = 0.31$, **3**: $g = 2.010$; $D = 0.031\ cm^{-1}$; $E/D = 0.23$. From these parameters it is evident that **1** and **3** have greater distortions from cubic nature as compared **2**, which is more cubic. Overall, the deviation from cubic symmetry is only marginal since $D \ll hv$, where hv is the microwave energy and these results are consistent with their molecular structures (*vide infra*). A list of zero-field splitting parameters for Cr(III) complexes based primarily on pyridine ligand are provided in Supporting information Table S1.

Table 1
UV–Vis data

Complex	λ_{max}, nm (ε, $M^{-1}\ cm^{-1}$)	
	d–d transition	ILCT
1	600(120), 450(145)[a], 425(180)[a]	340(9160), 330(9615)[a], 290(20775)
2	560(235), 445(290)[a], 420(770)[a]	350(5380)[a], 330(6570)[a], 290(17010)
3	525(155), 443(310)[a], 417(1235)[a]	350(17475), 340(18310), 290(23830)

[a] Shoulder.

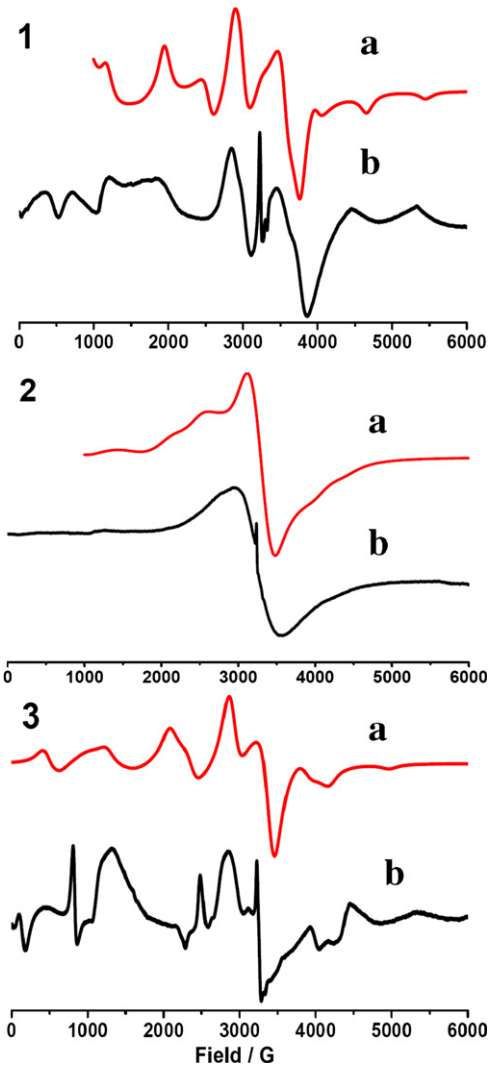


Fig. 1. EPR spectrum of **1**–**3** in DMF solution at 77 K (**a** is simulated and **b** is experimental).

The μ_{eff} values of **1**, **2**, and **3** are, respectively, 3.90, 3.72, and 3.73 B.M. and these values were calculated from the least square fitting of the initial magnetization curve ($\chi = M/H$). Only in case of **1** μ_{eff} is nearly closer to $\mu_{s.o.}$ value, where as in **2** and **3**, μ_{eff}, is slightly less than $\mu_{s.o.}$ value. In all the cases there is an increase in magnetic moment with respect to the applied magnetic field, which is a general behavior of paramagnetic substances. Only the complex **3** exhibits a distinct hysteresis loop and the coercivity loss is 570 G (Fig. 2) and the hysteresis exhibited by mononuclear complexes are reported [16e,16f].

3.4. Molecular structures

The molecular structures of $[CrLCl_3]\cdot DMF$ (**1**), $[CrL(N_3)_3]\cdot CH_3CN$ (**2**), and $[CrL(NCS)_3]\cdot DMF$ (**3**) were determined by X-ray crystallography. The crystallographic data and refinement parameters are summarized in Table 2 and selected bond parameters are listed in Tables 3 and 4. In all the three cases, Cr(III) is coordinated by three N atoms of **L** in a meridional fashion. The anions occupy the other three coordination sites completing the *mer*-N_3Cl_3 (in **1**) and *mer*-N_3N_3 (in **2** and **3**), distorted octahedral geometry.

A perspective view of **1** along with the packing diagram viewing down the a^*-axis, is shown in Fig. 3. The Cr1–N2 distance is shorter than that of Cr1–N1 and Cr1–N3 distances. This distortion, observed in 4′-(2-pyridyl)-2,2′:6′,2″-terpyridine complexes of first-row transition metals is attributed to a more efficient overlap of metal t_{2g} orbitals with the π^* orbitals of the central pyridyl group compared to the other two pyridyl rings. The apical Cr–Cl distances are on average, 0.035(1) Å longer than the equatorial Cr1–Cl1 contact. This is due to stronger π back-bonding of **L** in the equatorial N_3Cl plane, which reduces the repulsive interaction between the lone-pair of electrons on the chlorine atom (Cl1) and the metal t_{2g} electrons. The basal plane containing N1, N2, N3, and Cl1 atoms is nearly planar as inferred from the following torsional angles

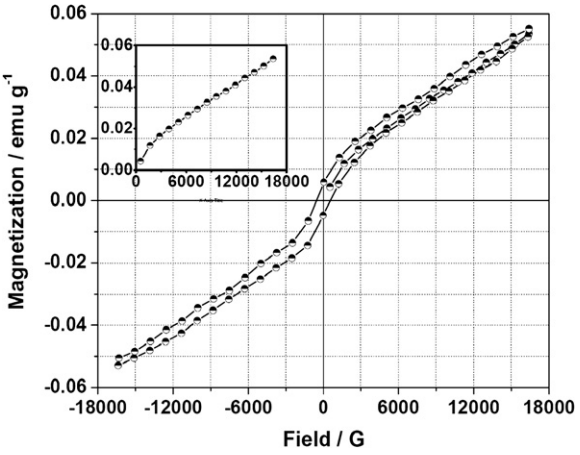


Fig. 2. Hysteresis loop and initial magnetization (inset) plot for **3**.

Table 2
Crystallographic data and refinement parameters

	1	2	3
Empirical formula	$C_{23}H_{21}N_5OCl_3Cr$	$C_{22}H_{17}N_{14}Cr$	$C_{26}H_{21}N_8OS_3Cr$
Formula weight	541.80	529.05	609.69
Temperature (K)	296(2)	296(2)	296(2)
Wavelength (Å)	0.71073	0.71073	0.71073
Crystal system	monoclinic	triclinic	triclinic
Space group	*P2(1)/c*	$P\bar{1}$	$P\bar{1}$
a (Å)	10.120(1)	10.751(1)	8.742(3)
b (Å)	12.821(1)	10.875 (1)	12.992(5)
c (Å)	18.201(1)	11.599(1)	13.244(6)
α (°)		86.864(1)	111.05(2)
β (°)	93.25(1)	64.34(1)	92.52(3)
γ (°)		75.41(1)	91.41(3)
V (Å^3)	2357.7(2)	1180.65(4)	1401.1(10)
Z	4	2	2
D_{calc} (g cm^{-3})	1.526	1.489	1.445
μ (mm^{-1})	0.852	0.528	0.668
Goodness-of-fit[a] on F^2	1.085	1.036	1.084
Mean $[I/\sigma]$	8.80	20.93	2.22
R $[I > 2\sigma(I)]$	$R_1^b = 0.0113$, $wR_2^c = 0.0361$	$R_1^b = 0.0124$, $wR_2^c = 0.0264$	$R_1^b = 0.0811$, $wR_2^c = 0.1469$
R indices (all data)	$R_1^b = 0.0116$, $wR_2^c = 0.0364$	$R_1^b = 0.0124$, $wR_2^c = 0.0264$	$R_1^b = 0.0811$, $wR_2^c = 0.1470$

[a] Goodness − of − fit $= [\sum[w(F_o^2 - F_c^2)^2]/M - N]^{1/2}$ (M = number of reflections, N = number of parameters refined).
[b] $R_1 = \sum||F_o| - |F_c||/\sum|F_o|$.
[c] $wR_2 = [\sum[w(F_o^2 - F_c^2)^2]/\sum[w(F_o^2)^2]]$.

Table 3
Selected bond distances (Å)

1		2		3	
Cr1–N1	2.0670(4)	Cr1–N1	2.0648(5)	Cr1–N1	2.085(3)
Cr1–N2	1.9899(4)	Cr1–N2	2.0003(5)	Cr1–N2	1.990(3)
Cr1–N3	2.0684(4)	Cr1–N3	2.0859(5)	Cr1–N3	2.075(3)
Cr1–Cl1	2.2982(2)	Cr1–N5	1.9940(6)	Cr1–N5	1.978(4)
Cr1–Cl2	2.3376(2)	Cr1–N8	2.0033(6)	Cr1–N6	1.979(3)
Cr1–Cl3	2.3274(2)	Cr1–N11	2.0279(6)	Cr1–N7	1.998(4)

N2–Cr1–N1–C5, −2.54(1)°; N2–Cr1–N3–C11, −4.09(1)°; C15–N3–Cr1–Cl1, −2.61(1)°; and C1–N1–Cr1–Cl1, 6.94(1)°. The bond parameters are very much comparable to that of $[Cr(tpy)Cl_3]\cdot DMSO$ [4d]. The molecular packing shows the presence of: (a) π–π stacking having shortest contact of C2···C9 3.833(1) Å along $-x, +y + 1/2, -z + 1/2$ (b) an intermolecular contact of 3.315(1) Å between C12 with O1 of DMF along $-x, -y + 1, -z + 1$ and (c) D–H···A interactions between C22···O1 of 2.767(1) Å. All these interactions generate a channel of approximate rectangular cavity (8.849 × 11.205 Å) along a^*-axis and is occupied by the DMF molecules.

A perspective view of **2** along with the packing diagram viewing down the *c*-axis is shown in Fig. 4. The N_3^- anions bind in a monodentate end-on bent fashion. The basal plane formed by N1, N2, N3, and N5 is near-planar as the torsional angles N2–Cr1–N1–C5, N2–Cr1–N3–C11, C1–N1–Cr1–N5, and C15–N3–Cr1–N5 are 2.65(1)°, 0.99(1)°, 0.53(1)°, and 0.97(1)°, respectively. The apical

Table 4
Selected bond angles (°)

1		2		3	
N2–Cr1–N1	78.23(2)	N2–Cr1–N1	78.04(2)	N2–Cr1–N1	77.74(13)
N2–Cr1–N3	78.25(2)	N2–Cr1–N3	77.81(2)	N2–Cr1–N3	78.19(13)
N1–Cr1–N3	156.44(2)	N1–Cr1–N3	155.78(2)	N1–Cr1–N3	155.83(13)
N2–Cr1–Cl1	179.03(2)	N1–Cr1–N5	178.7(2)	N1–Cr1–N5	104.22(15)
N2–Cr1–Cl2	85.60(2)	N1–Cr1–N8	178.58(3)	N1–Cr1–N6	89.27(15)
N2–Cr1–Cl3	88.08(2)	N1–Cr1–N11	89.76(2)	N1–Cr1–N7	90.51(14)
N1–Cr1–Cl1	101.37(2)	N2–Cr1–N5	178.76(3)	N2–Cr1–N5	176.06(14)
N1–Cr1–Cl2	91.63(2)	N2–Cr1–N8	89.06(2)	N2–Cr1–N6	92.29(15)
N1–Cr1–Cl3	86.62(2)	N2–Cr1–N11	89.63(2)	N2–Cr1–N7	87.44(14)
N3–Cr1–Cl1	102.17(1)	N3–Cr1–N5	101.77(3)	N3–Cr1–N5	99.94(14)
N3–Cr1–Cl2	87.85(1)	N3–Cr1–N8	88.35(2)	N3–Cr1–N6	89.52(14)
N3–Cr1–Cl3	91.32(1)	N3–Cr1–N11	91.90(2)	N3–Cr1–N7	90.59(14)
Cl1–Cr1–Cl2	93.53(1)	N5–Cr1–N11	91.56(3)	N5–Cr1–N6	91.15(15)
Cl1–Cr1–Cl3	92.78(1)	N5–Cr1–N8	89.76(3)	N5–Cr1–N7	89.13(15)
Cl2–Cr1–Cl3	173.66(1)	N8–Cr1–N11	178.58(3)	N6–Cr1–N7	179.68(15)

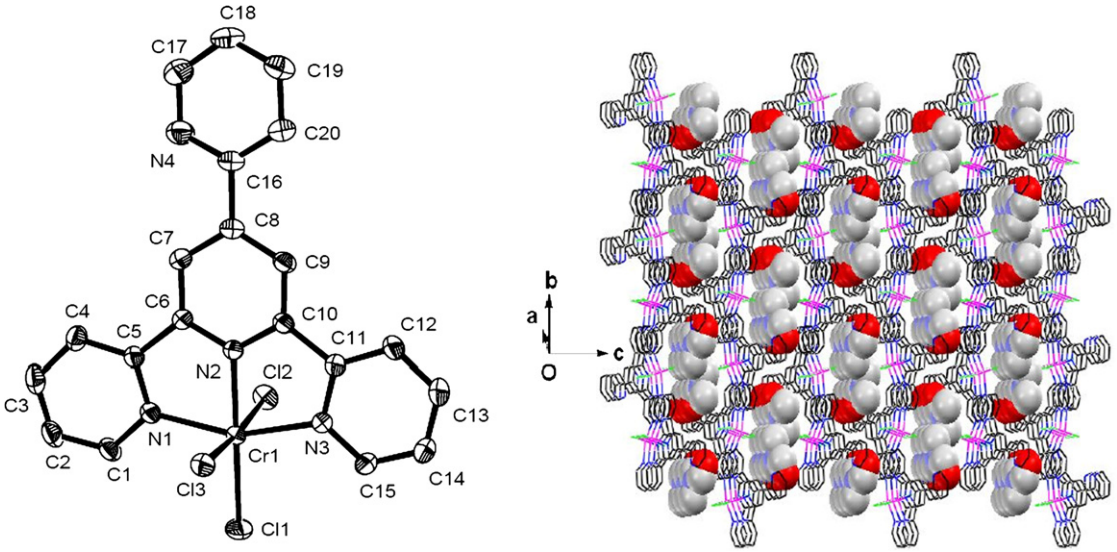


Fig. 3. ORTEP (30% probability) and packing diagrams of **1**.

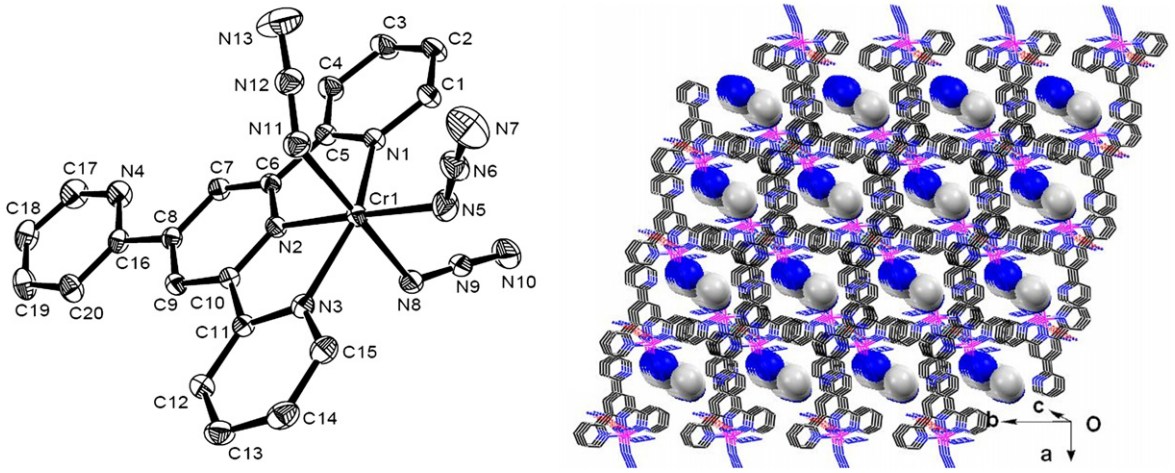


Fig. 4. ORTEP (30% probability) and packing diagram of **2**.

positions are occupied by N8 and N11. The trans-spanning Cr1–N1 and Cr1–N3 distances are longer by an average distance of 0.0755(5) Å as compared to Cr1–N2. The Cr–N(azido) apical distances are about 0.0215(5) Å longer than the equatorial one. In the crystal lattice, the molecule exists as a dimer (Fig. 5) with a non-bonded Cr···Cr distance of 6.974(1) Å. This dimeric form is generated as a result of an intermolecular interaction between the coordinated azide ligand having the non-bonded contact N8···N9 (3.086(1) Å). The molecular packing also shows the presence of π–π interaction of shortest C2···C13 contact of 3.372(1) Å along x, $+y+1$, $+z$. A channel of approximate dimension 7.818 × 8.632 Å is present along the c-axis and is occupied by the acetonitrile molecules and the equatorially coordinated azide groups. Within the azide moiety, N–N(terminal) bond is shorter by 0.048(1) Å than N–N(coordinated) and deviate from the linearity by an average of 3.29(8)°.

A perspective view of **3** along with the packing diagram viewing down the b-axis is shown in Fig. 6. The NCS^- anions bind in a monodentate end-on linear fashion. Cr^{3+} is a hard acid and NCS^- is an ambidentate base having hard-N and soft-S donor atoms. Coordination of NCS^- through N-atom is as per the HSAB principle. The basal plane is generated by N1, N2, N3, N5 and deviation from planarity is as shown by the torsional angles N2–Cr1–N1–C5, 0.40(5)°; N2–Cr1–N3–C11, 1.56(5)°; C1–N1–Cr1–N5, −8.35(7)°; C15–N3–Cr1–N5, 7.14(6)°. Cr1–N2 has a shorter distance than the trans-occupying Cr1–N1 and Cr1–N3 by an average of 0.09(3) Å. The molecular packing shows the presence of: (a) π–π interaction having shortest contact of N4···C15 of 3.247(1) Å along $-x$, $-y$, $-z$. (b) intermolecular hydrogen bonding between S3···O1 of 3.301(2) Å (c) D–H···A interaction C26–H26C···O1, 2.751(1) Å. These interactions create a channel of approximate rectangular cavity 7.913 × 20.269 Å, within which the DMF molecules are present. The central angle at NCS moiety deviates from linearity by about 3.96(4)°. The C–N(amide) length of DMF in **3** is shorter by 0.020(6) Å when compared to that in **1**. The O–C–N–C torsional angle is −0.35(10)° and 2.75(11)°, respectively, in **3** and **1**.

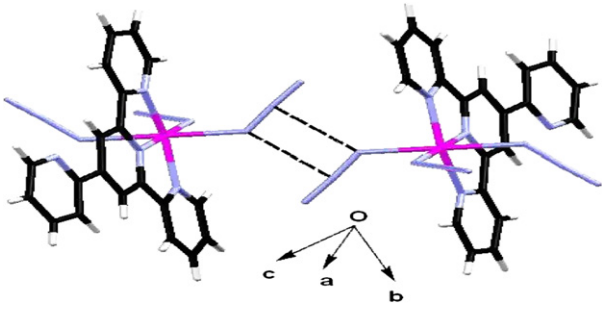


Fig. 5. Intermolecular interaction between the coordinated azide ligand in **2**.

4. Conclusion

Three complexes viz., $[CrLCl_3]\cdot DMF$ (**1**), $[CrL(N_3)_3]\cdot CH_3CN$ (**2**) and $[CrL(NCS)_3]\cdot DMF$ (**3**) were synthesized. Structural studies reveal that the Cr(III) ion is coordinated by three N atoms of **L** in a meridional fashion. The three anions occupy the other three coordination sites completing the *mer*-N_3Cl_3 (**1**) and *mer*-N_3N_3 (**2** and **3**), distorted octahedral geometry. Cr–N2 has a shorter length than the Cr–N1 and Cr–N3 distances and the order $Cr–N(NCS^-) < Cr–N(N_3^-) < Cr–Cl$ is observed. These complexes crystallize as solvate DMF (**1**, **3**) and CH_3CN (**2**) and the solvent molecules are present in the channel created by weak intermolecular forces. The complexes exhibit some of the d–d transitions in the visible and intra-ligand transitions in the UV regions. The lowest energy d–d transition follows the trend $[CrLCl_3] < [CrL(N_3)_3] < [CrL(NCS)_3]$ consistent with the spectrochemical series, $Cl^- < N_3^- < NCS^-$. In DMF, they exhibit fluorescence having $\pi \rightarrow \pi^*$ character. All the complexes show deviation from cubic symmetry as well as zero-field splitting (zfs) in X-band EPR spectra at 77 K.

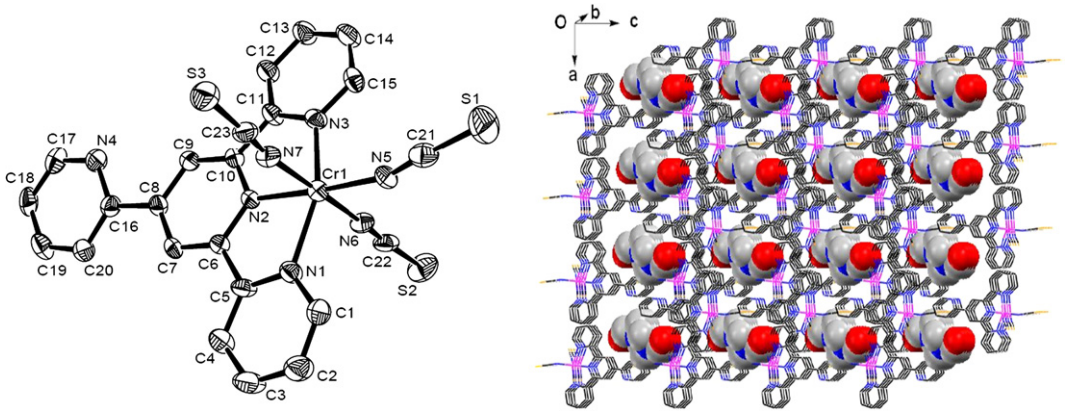


Fig. 6. ORTEP (30% probability) and packing diagram of **3**.

Acknowledgements

We are grateful to the Department of Science and Technology, New Delhi, for establishing single crystal X-ray diffractometer facility under FIST scheme and to Council of Scientific and Industrial Research, New Delhi, for financial grant. The authors are thankful to CIF, IIT Guwhati, for the EPR and VSM data and Babulal Das for X-ray data.

Appendix A. Supplementary data

CCDC 645461, 645461 and 645463 contain the supplementary crystallographic data for this paper. These data can be obtained free of charge via http://www.ccdc.ac.uk/conts/retrieving.html or from the Cambridge Crystallographic Data Centre, 12 Union Road, Cambridge CB2 1EZ, UK; fax: (+44) 1223-336-033; or e-mail: deposit@ccdc.cam.ac.uk. Supplementary data associated with this article can be found, in the online version, at doi:10.1016/j.poly.2008.02.011.

References

[1] (a) V. Balzani, F. Scandola, in: J.S. Connolly (Ed.), Photochemical Conversion and Storage of Solar Energy, Academic Press, New York, 1981, p. 97;
(b) C. Klein, M.K. Nazeeruddin, P. Liska, D. Di Censo, N. Hirata, E. Palomares, J.R. Durrant, M. Gratzel, Inorg. Chem. 44 (2005) 178;
(c) J.H. Alstrum-Acevedo, M.K. Brennaman, T.J. Meyer, Inorg. Chem. 44 (2005) 6802;
(d) G.J. Meyer, Inorg. Chem. 44 (2005) 6852;
(e) S. Chakraborty, T.J. Wadas, H. Hester, R. Schmehl, R. Eisenberg, Inorg. Chem. 44 (2005) 6865;
(f) M.D. Ward, Chem. Soc. Rev. 24 (1995) 121;
(g) J.-P. Sauvage, J.-P. Collin, J.-C. Chambron, S. Guillerez, C. Coudret, V. Balzani, F. Barigelletti, L. De Cola, L. Flamigni, Chem. Rev. 94 (1994) 993.

[2] (a) K. Jennette, S.J. Lippard, G. Vassiliades, W. Bauer, Proc. Natl. Acad. Sci. USA 71 (1974) 3839;
(b) S. Bonse, J.M. Richards, S.A. Ross, G. Lowe, R.L. Krauth-Siegel, J. Med. Chem. 43 (2000) 4812;
(c) Z. Long-Xuan, Y.-S. Moon, A. Basnet, E.-k. Kim, Y. Jahng, J.G. Park, T.C. Jeong, W.-J. Cho, S.-U. Choi, C.O. Lee, S.-Y. Lee, C.-S. Lee, E.-S. Lee, Bioorg. Med. Chem. Lett. 14 (2004) 1333.

[3] (a) G.F. Swiegers, T.J. Malefetse, Chem. Rev. 100 (2000) 3483;
(b) H. Hofmeier, U.S. Schubert, Chem. Soc. Rev. 33 (2004) 373.

[4] (a) K. Shiren, K. Tanaka, Inorg. Chem. 41 (2002) 5912;
(b) J.A. Broomhead, J. Evans, W.D. Grumley, M. Sterns, Dalton Trans. (1977) 173;
(c) C.S. Lee, E.M. Gorton, H.M. Neumann, H.R. Hunt, Inorg. Chem. 5 (1966) 1397;
(d) N. Cloete, H.G. Visser, A. Roodt, Acta Crystallogr. E63 (2007) m45;
(e) A.L. Balch, J.R.B.H. Hope, M.M. Olmstead, J. Am. Chem. Soc. 98 (1976) 7432;
(f) M. Maestri, F. Bolletta, L. Moggi, V. Balzani, M.S. Henry, M.Z. Hoffman, J. Am. Chem. Soc. 100 (1978) 2694;
(g) J. Lilie, W.L. Waltz, S.H. Lee, L.L. Gregor, Inorg. Chem. 25 (1986) 4487;
(h) B.R. Baker, B.D. Mehta, Inorg. Chem. 4 (1965) 848.

[5] (a) F. Kröhnke, Synthesis (1976) 1;
(b) V. Hegde, Y. Jahng, R.P. Thummel, Tetrahedron Lett. 28 (1987) 4023;
(c) E.C. Constable, A.M.W.C. Thompson, J. Chem. Soc., Dalton Trans. (1992) 2947;
(d) C.B. Smith, C.L. Raston, A.N. Sobolev, Green Chem. 7 (2005) 650.

[6] (a) L. Zhao, Y. Moon, A. Basnet, E. Kim, Y. Jahng, J.G. Park, T.C. Jeong, W.-j. Cho, S. Choi, C.O. Lee, S. Lee, C. Lee, E. Lee, Bioorg. Med. Chem. Lett. 14 (2004) 1333;
(b) L. Hou, D. Li, Y. Yin, S.W. Ng, Acta Crystallogr. E61 (2005) m21;
(c) L. Hou, D. Li, W. Shi, Y. Yin, S.W. Ng, Inorg. Chem. 44 (2005) 7825;
(d) H. Feng, X. Zhou, T. Wu, D. Li, Y. Yin, S.W. Ng, Inorg. Chim. Acta 359 (2006) 4027;
(e) W. Shi, L. Hou, D. Li, Y. Yin, Inorg. Chim. Acta 360 (2007) 588;
(f) L. Hou, D. Li, S.W. Ng, Acta Crystallogr. E61 (2005) m404;
(g) K.J. Arm, W. Leslie, J.A.G. Williams, Inorg. Chim. Acta 359 (2006) 1222.

[7] S.K. Padhi, V. Manivannan, Inorg. Chem. 45 (2006) 7994.

[8] F. Clark, R.S. Dickson, D.B. Fulton, J. Isoya, A. Lent, D.G. McGavin, M.J. Mombourquette, R.H.D. Nuttall, P.S. Rao, H. Rinneberg, W.C. Tennant, J.A. Weil, University of Saskatchewan, Saskatoon, Canada, 1996.

[9] G.M. Sheldrick, SADABS, University of Göttingen, Göttingen, Germany, 1996.

[10] SMART and SAINT, Siemens Analytical X-ray Instruments Inc., Madison, WI, 1996.

[11] G.M. Sheldrick, SHELXS-97 and SHELXL-97, University of Göttingen, Göttingen, Germany, 1997.

[12] J.E. Huheey, E.A. Keiter, R.L. Keiter, Inorganic Chemistry: Principles of Structure and Reactivity, 4th ed., Harper Collins, 1993, p. 549.

[13] K. Nakamoto, Infrared and Raman Spectra of Inorganic and Coordination Compounds. Part B, 5th ed., Wiley, New York, 1997.

[14] A.B.P. Lever, Inorganic Electronic Spectroscopy, Elsevier, Amsterdam, 1986.

[15] (a) J.S. Field, R.J. Haines, L.P. Ledwaba Jr., R. McGuire, O.Q. Murno, M.R. Low, D.R. McMillin, Dalton Trans. (2007) 192;
(b) J.J. Moore, J.J. Nash, P.E. Fanwick, D.R. McMillin, Inorg. Chem. 41 (2001) 6387;
(c) H. Yersin, D. Donges, Top. Curr. Chem. (2001) 81;
(d) M.K. DeArmond, J.E. Hills, J. Chem. Phys. 54 (1971) 2247.

[16] (a) R.S. Drago, Physical Methods for Chemists, 2nd ed., Saunders College Publishers, New York, 1992;
(b) E. Pedersen, H. Toftlund, Inorg. Chem. 13 (1974) 1603;
(c) A. Vlachos, V. Psycharis, C.P. Raptopoulou, N. Lalioti, Y. Sanakis, G. Diamantopoulos, M. Fardis, M. Karayanni, G. Papavassiliou, A. Terzis, Inorg. Chim. Acta 357 (2004) 3162;
(d) C.J. O'Connor, Prog. Inorg. Chem. 29 (1982) 203;
(e) O. Kahn, Molecular Magnetism, Wiley–VCH, 1993;
(f) M.A. Halcrow, Polyhedron 26 (2007) 3523;
(g) D.K. Prassides Arcon, π-Electron magnetism, in: J. Veciana (Ed.), Structure and Bonding, vol. 100, Springer, Berlin, 2001, p. 129.

complexes containing multidentate bridging ligand (e.g. COO, XCN, X = O, S, Se), the copper(II) compounds with OPO bridge for which also the magnetic interactions are reported are still rare [18–24].

It is worth emphasized that the structural and magnetic studies of binuclear and polynuclear complexes containing multidentate bridging ligands, in which such metal–metal interactions as magnetic coupling, energy or electron transfer, and intervalence transfer [25–27] may occur, are of considerable interest from the standpoint of inorganic and bio-inorganic chemistry [28–30]. Among these complexes the copper(II) compounds are of particular interest from a theoretical point of view, since they provide examples of the simplest case of magnetic interaction involving only two unpaired electrons [31–33].

In this work, we present a synthesis, the spectral and magnetic properties, and the X-ray crystal analysis of copper(II) compound with 2-mpmpe ligand of the formula $Cu_2(2\text{-mpmpe})_2(H_2O)_2(NO_3)_2$. The object of our particular interest was investigation of magnetic properties of this compound and estimation of the magnitude of the exchange interactions between copper(II) ions. It is, to the best of our knowledge, the first example structurally and magnetically characterized dinuclear copper(II) compound of phosphonate monoester bearing a heterocyclic nitrogen with phosphonate bridge. A detailed structural description as well as the magnetic behavior of the compound is presented.

2. Experimental

2.1. Reagents and physical measurements

Starting materials and solvents for the synthesis were obtained commercially and used as received. Metal content was determined using a Carl-Zeiss-Jena atomic absorption spectrophotometer. Elemental analyses were carried out using a Perkin–Elmer elemental analyzer 2400CHN.

Infrared spectra (100–4000 cm^{-1}) were recorded on a Bruker IFS 113v spectrophotometer using KBr pellets, and solid-state electronic spectra (28 000–4000 cm^{-1}) were performed on a Cary 500 spectrophotometer. Solid-state EPR spectra were recorded at room temperature and at 77 K on a Bruker ESP 300E spectrometer operating at X-band, equipped with a Bruker NMR gaussmeter ER 0.35 M and a Hewlett Packard microwave frequency counter HP 5350B. Magnetic measurements of a polycrystalline sample were carried out with a Quantum Design SQUID magnetometer (MPMSXL-5 type). The measurements were recorded at magnetic field of 0.5 T over the temperature range 1.8–300 K. The correction for diamagnetism of the experimental susceptibility was based on subtracting the sample-holder signal and estimating the contribution χ_D from Pascal constants [34]. The effective magnetic moments were calculated from $\mu_{eff} = 2.83(\chi_M T)^{1/2}$, using temperature-independent paramagnetism of 60×10^{-6} cm^3 mol^{-1} for Cu(II).

2.2. Crystal structure determination of $Cu_2(2\text{-mpmpe})_2(H_2O)_2(NO_3)_2$

X-ray data were collected at low temperature using an Oxford Cryosystem device on a Kuma KM4CCD κ-axis diffractometer with graphite-monochromated Mo Kα radiation ($\lambda = 0.71073$ Å). The crystal was positioned at 65 mm from the CCD camera. Frames (612) were measured at 0.75° intervals with a counting time of 33 s. Accurate cell parameters were determined and refined by least-squares fit of 6000 the strongest reflections. Data were corrected for Lorentz and polarization effects. Analytical absorption correction was also applied. Data reduction and analysis were carried out with the Oxford Diffraction (Poland) programs. The structure was solved by direct methods (program SHELXS 97 [35]) and refined by the full-matrix least-squares method on all F^2 data using the SHELXL 97 [36] programs. Non-hydrogen atoms were refined with anisotropic displacement parameters; hydrogen atoms were included from geometry of molecules and $\Delta\rho$ maps and were refined isotropically. Crystal data are given in Table 1, together with refinement details.

2.3. Synthesis of the ligand (2-pmpe) and $Cu_2(2\text{-mpmpe})_2(H_2O)_2(NO_3)_2$ compound

The diethyl (pyridyn-2-ylmethyl)phosphonate (2-pmpe) ligand was prepared according to the procedure described in detail elsewhere [14]. The copper compound with monoethyl (pyridyn-2-ylmethyl)phosphonate of formula $Cu_2(2\text{-mpmpe})_2(H_2O)_2(NO_3)_2$ was prepared by dissolving $Cu(NO_3)_2 \cdot 6H_2O$ (1 mmol) in warm ethanol (10 cm^3) and adding to a solution of the 2-pmpe ligand (2 mmol) in

Table 1
Crystal data and structure refinement for $Cu_2(2\text{-mpmpe})_2(H_2O)_2(NO_3)_2$

Empirical formula	$C_{16}H_{26}Cu_2N_4O_{14}P_2$
Formula weight	687.43
Temperature (K)	100(2)
Wavelength/Å	0.71073
Crystal system	monoclinic
Space group	$P2_1/n$
a (Å)	7.523(2)
b (Å)	12.174(4)
c (Å)	14.079(4)
β (°)	93.42(3)
V (Å^3)	1287.1(7)
Z	2
D_c (Mg m^{-3})	1.774
Absorption coefficient (mm^{-1})	1.851
F (000)	700
Crystal size (mm)	0.3 × 0.15 × 0.1
Θ Range for data collection (°)	2.90–27.50
Ranges of h, k, l	$-8 \geqslant 9$, $-15 \geqslant 15$, $-18 \geqslant 17$
Reflections collected	8864
Independent reflections (R_{int})	2940 (0.0502)
Data/parameters	2940/200
Goodness-of-fit (F^2)	0.964
Final R_1/wR_2 indices ($I > 2sI$)	0.0342/0.0808
Largest difference in peak/hole (e Å^{-3})	0.639/−0.421

warm ethanol (20 cm^3). The reaction mixture was refluxed by 8 h in ethanol and then left to evaporate at room temperature. Blue monocrystals of the compound suitable for X-ray determination were precipitated during slow evaporation of the solvent.

Anal. Calc. for $C_{16}H_{26}N_4O_{14}P_2Cu_2$: C, 38.29; H, 1.43; N, 4.27; Cu, 20.43. Found: C, 38.05; H, 1.92; N, 4.44; Cu, 20.13%.

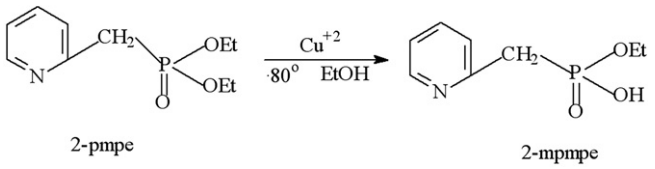
3. Results and discussion

The title compound of formula Cu_2(2-mpmpe)$_2(H_2O)_2(NO_3)_2$ was obtained by a solvothermal reaction between $Cu(NO_3)_2 \cdot 6H_2O$ and diethyl (pyridyn-2-ylmethyl)phosphonate ligand (2-pmpe) at 80 °C. Thus, the process of a partial solvothermal hydrolysis of starting 2-pmpe ligand occurs according to the scheme (Fig. 1).

3.1. Description of the structure of Cu_2(2-mpmpe)$_2(H_2O)_2(NO_3)_2$

Crystallographic parameters of title compound are summarized in Table 1. Selected bond distances and angles are listed in Table 2.

Fig. 2 shows the structure and the labeling scheme of Cu(II) compound. As it can be seen from Fig. 2, the two Cu(II) ions, Cu(1) and Cu(1A) are connected by two OPO bridge groups creating a centrosymmetric dinuclear structure. Monoethyl (pyridyn-2-ylmethyl)phosphonate (2-mpmpe) acts as multidentate bonded ligand, chelates to the Cu(1) atom through its pyridyl nitrogen N(1), and



2-pmpe 2-mpmpe

Fig. 1. Scheme of the starting ligand (2-pmpe) and 2-mpmpe ligand.

Table 2
Selected bond lengths (Å) and angles (°) for Cu_2(2-mpmpe)$_2(H_2O)_2(NO_3)_2$

Cu(1)–O(3)^i	1.9560(18)	P(1)–O(3)	1.5004(18)
Cu(1)–O(1)	1.9665(18)	P(1)–O(1)	1.5114(18)
Cu(1)–O(5)	1.9979(18)	P(1)–O(2)	1.6010(19)
Cu(1)–N(1)	2.018(2)	P(1)–C(6)	1.806(3)
Cu(1)–O(4)	2.184(2)		
O(3)^i–Cu(1)–O(1)	92.06(7)	N(1)–Cu(1)–O(4)	99.01(9)
O(3)^i–Cu(1)–O(5)	89.44(7)	Cu(1)–O(1)–P(1)	121.10(10)
O(1)–Cu(1)–O(5)	178.50(7)	Cu(1)^i–O(3)–P(1)	125.41(10)
O(3)^i–Cu(1)–N(1)	161.80(8)	O(3)–P(1)–O(1)	117.60(10)
O(1)–Cu(1)–N(1)	90.54(8)	O(3)–P(1)–O(2)	106.85(10)
O(5)–Cu(1)–N(1)	88.03(8)	O(1)–P(1)–O(2)	109.00(10)
O(3)^i–Cu(1)–O(4)	98.94(9)	O(3)–P(1)–C(6)	110.50(12)
O(1)–Cu(1)–O(4)	91.32(8)	O(1)–P(1)–C(6)	108.07(11)
O(5)–Cu(1)–O(4)	88.49(8)	O(2)–P(1)–C(6)	103.96(11)

Symmetry transformations used to generate equivalent atoms: (i) $-x$, $-y$, $-z+1$.

phosphoryl oxygen O(1) from the P=O group, forming six-membered ring. The terminal oxygen atom O(3) from the phosphonate group bridges to Cu(1A) atom. The coordination about the copper atoms is five-coordinate. The equatorial plane is composed of the N(1), O(1) from 2-mpmpe ligand and bridging O(3A) from 2-mpmpe ligand, and O(5) from a coordinating nitrate anion with distance to Cu(1): 2.018(2), 1.9665(18), 1.9560(18), and 1.9979(18) Å, respectively, while the O(4) atom from water molecule occupy apical position with significantly longer Cu(1)–O(4) distance of 2.184(2) Å. The O(1)–Cu(1)–O(5) and O(3A)–Cu(1)–N(1) angles of the basal plane are 178.50(7)° and 161.80(8)°, respectively resulting in a τ value of 0.28 (parameter describing the degree of trigonal distortion τ is defined as $(\beta - \alpha)/60$, where β and α are the largest coordination angles). A regular trigonal-bipyramid (TBP) and square-based pyramid (SP) have τ values of 1 and 0, respectively [37]. Therefore, the geometry around Cu atoms can be better described as quite distorted square-pyramidal ($CuNO_4$ chromophore). The copper(II) centres are slightly deviated (0.154 Å) from the least-squares plane toward the axially coordinated water molecule. The least-squares planes corresponding to two nearest neighbours copper centers are parallel (dihedral angle of 0°). The nitrate anion has its expected planar trigonal geometry.

As previously noted, the two OPO phosphonate groups bridge two copper(II) ions through the O(1) and O(3) and O(1A) and O(3A) oxygen atoms of the pseudo-equatorial position on the copper(II) coordination polyhedron. The distortion of the coordination polyhedron gives rise to the formation of a chair-like eight-membered ring Cu(1)–O(1)–P(1)–O(3)–Cu(1A)–O(1A)–P(1A)–O(3A)–Cu(1) with the Cu(1)···Cu(1A) distance of 4.69 Å. This distance is near the range of reported values of ca. 5 Å observed for polyatomic bridges [38] and, hence, interesting magnetic exchange properties are anticipated (vide infra).

The most important features of the structure result from the fact that the copper(II) ions are a doubly bridged by OPO groups in μ_2-fashion to form a dinuclear structure. The O(1)–P(1)–O(3) angle is 117.60(10)° near value of 118.8(1)° observed in monoethyl (pyridyn-2-ylmethyl)phosphonate [39]. It is interesting that the bridging pathway Cu–O–P–O–Cu is asymmetric in its conformation with respect to the Cu–O–P angle and Cu–O bond length. The Cu(1)–O(1)–P(1) and Cu(1A)–O(3)–P(1) angles are 121.10(10)° and 125.41(10)°, respectively, and bond length Cu(1)–O(1) and Cu(1A)–O(3) bonds are 1.9665(18) and 1.9560(18) Å, respectively. The average C–C and C–N lengths in the pyridine ring of 1.380 Å and 1.345 Å, respectively, are typical. The lattice structure is stabilized by a complicated hydrogen-bonding 3D network (Table 3). The crystal packing is depicted in Fig. 3.

As mentioned above, two oxygen atoms of the phosphonate group are involved in the bridging as shown in Fig. 2 forming $Cu_2(–OPO–)_2$ dimeric unit. These units are further connected by two groups of H-bond: O(4) oxygen atom of the coordinated water molecule and phosphoryl oxygen

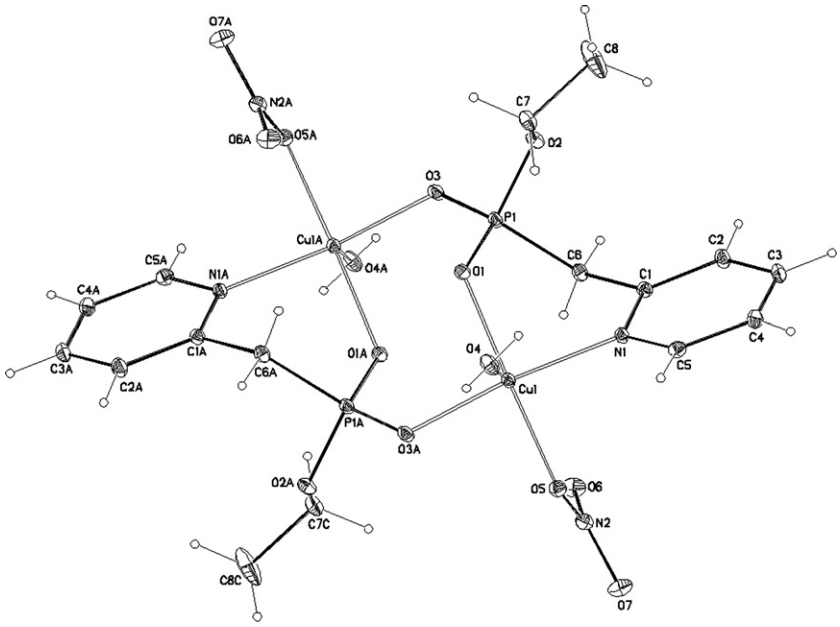


Fig. 2. Molecular structure of $Cu_2(2\text{-mpmpe})_2(H_2O)_2(NO_3)_2$ showing the atomic numbering.

Table 3
Hydrogen-bonds for $Cu_2(2\text{-mpmpe})_2(H_2O)_2(NO_3)_2$ (Å, °)

D–H···A	*d*(D–H)	*d*(H···A)	*d*(D···A)	∠(DHA)
O(4)–H(4A)···O(7)^{ii}	0.81(4)	2.02(4)	2.815(3)	170(3)
O(4)–H(4A)···O(6)^{ii}	0.81(4)	2.63(3)	3.225(3)	132(3)
O(4)–H(4A)···N(2)^{ii}	0.81(4)	2.65(4)	3.409(3)	158(3)
O(4)–H(4B)···O(2)^{iii}	0.71(4)	2.18(4)	2.884(3)	176(4)
C(2)–H(2)···O(5)^{iv}	0.95(3)	2.61(3)	3.458(3)	149(4)
C(6)–H(6B)···O(5)^{iv}	0.99	2.47	3.420(3)	161(7)
C(3)–H(3)···O(1)^{v}	0.95	2.43	3.371(3)	170(1)
C(7)–H(7A)···O(1)	0.99	2.53	2.874(7)	100(4)
C(7A)–H(7A2)···O(1)	0.99	2.55	2.994(11)	107.3
C(7B)–H(7B1)···O(1)	0.99	2.48	3.01(4)	113.1
C(5)–H(5)···O(5)	0.95	2.73	3.055(3)	100.9
C(6)–H(6A)···O(6)	0.99	2.82	3.568(3)	132.5

Symmetry transformations used to generate equivalent atoms:
(ii) $-x+1/2, y+1/2, -z+1/2$; (iii) $x+1, y, z$; (iv) $x-1, y, z$; (v) $x-1/2, -y+1/2, z-1/2$.

atom O(2)^{iii} of ester group OC_2H_5 and oxygens O(7)^{ii}, O(6)^{ii}, and N(2)^{ii} nitrogen atoms of nitrate group. These hydrogen bonds and additional hydrogen bonding between the aromatic C–H group of the pyridine ring and nitrate oxygen, C(2)–H(2)···O(5)^{iv}, form 2D layer network along *a* axis. The interlayer H-bond between C(6) atom of aliphatic CH_2 group and O(5)^{iv} atom of the nitrate group leads to 3D polymeric arrangement (symmetry codes are given in Table 3).

Additionally, interesting feature of the crystal structure results from the fact that the four dinuclear $Cu_2(\mu_2\text{-O})_2$ moiety are interconnected by hydrogen bonds between the aromatic C–H groups of the pyridine rings and phosphoryl oxygen of the P=O groups from adjacent dimeric unit results in the formation of $[Cu_2(\mu_2\text{-O})]_4$ hydrogen bonded ring. The regarding to observed weak C–H···O hydrogen bonds, the D···A bond distances and D–H···A angles are well within the range suggested for similar C–H···O hydrogen bonds [40]. Further examination of the structure reveals intramolecular hydrogen bonds and contacts. Details of the hydrogen bond network are given in Table 3. The shortest interdinuclear Cu···Cu separations are: Cu(1)···Cu(1)^{vi} 6.34 Å, vi $= -x+1, -y, -z+1$; Cu(1)···Cu(1)^{vii} 7.23 Å, vii $= -x+1/2, y-1/2, -z+1/2$; Cu(1)···Cu(1)^{ii} 7.52 Å, ii $= -x+1/2, y+1/2, -z+1/2$.

3.2. Spectroscopic properties

The very strong band at about 1250 cm^{-1}, which corresponds to the P=O stretching frequencies of the free ligand, in the spectrum of a studied compound is shifted by ca. 70 cm^{-1} towards lower frequency, suggesting the coordination of the phosphoryl oxygen to the metal ion. The infrared spectrum shows a very strong bands at 1314 and 1451 cm^{-1} typical for monodentate coordination of the nitrate ion ($\Delta\nu = 137\ cm^{-1}$), which is confirmed by the structure determination [41–43]. The δ(HOH) bending vibration and the O–H stretching band of coordinated water are observed at 1636 cm^{-1} and 3409 and 3539 cm^{-1}, respectively [42]. A split observed in the stretching O–H region is probably caused of the water molecule included in the strong hydrogen bond.

Ligand field spectrum shows a very broad absorption band in the visible region with two maxima centered at 14 100 and 11 100 cm^{-1}, corresponding to the d(xy), d(yz), d(zx) → d(x^2-y^2) and the d(z^2) → d(x^2-y^2) transitions, suggesting distorted square-pyramidal geometry for the copper ion [44,45], which is confirmed by the structure determination.

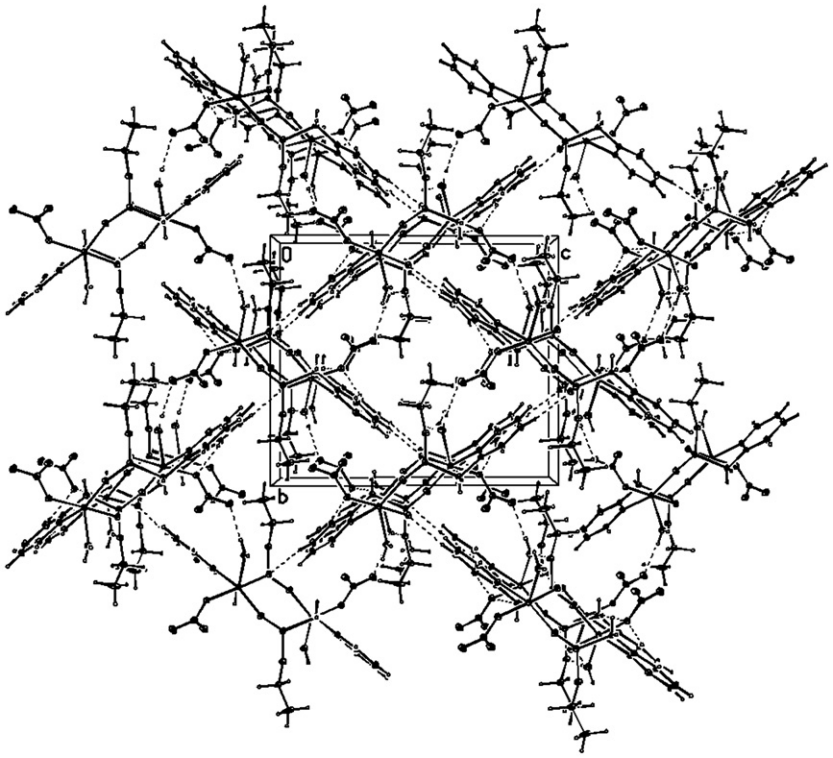


Fig. 3. Crystal packing of $Cu_2(2\text{-mpmpe})_2(H_2O)_2(NO_3)_2$ showing the 3D interdinuclear H-bonding.

The EPR X-band powder spectrum of the copper compound is of the rhombic type with g values of $g_1 = 2.27_2$, $g_2 = 2.18_8$, and $g_3 = 2.05_4$ at room temperature. The spectrum is independent of temperature.

3.3. Magnetic properties

The magnetic properties of the compound in the form of $\chi_{Cu}T$ versus temperature plots in the 1.8–300 K temperature range is shown in Fig. 4 (χ_{Cu} is the magnetic susceptibility per Cu(II) ions).

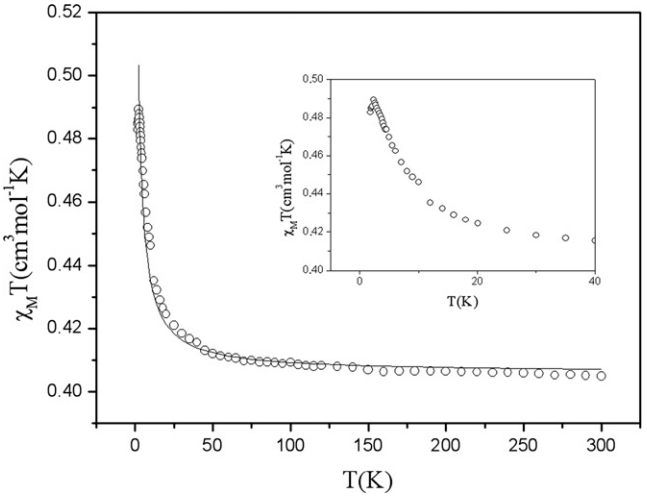


Fig. 4. Plot of $\chi_{Cu}T$ vs. temperature for $Cu_2(2\text{-mpmpe})_2(H_2O)_2(NO_3)_2$. Solid lines correspond to the best theoretical fit (see text).

The values of $\chi_{Cu}T$ at room temperature (0.405 cm^3 mol^{-1} K, $\mu_{eff} = 1.80\ \mu_B$) corresponds to one isolated copper(II) ion. However, upon cooling down, the $\chi_{Cu}T$ value increases, reaches a maximum at 2.3 K (0.489 cm^3 mol^{-1} K) and then decreases to a value of 0.483 cm^3 mol^{-1} K at 1.8 K (inset Fig. 4).

The shape of the curve is typical of intramolecular ferromagnetic coupling with the presence of intermolecular a weak antiferromagnetic interaction (J') and/or zero field splitting (D parameter) [46].

On the basis of the structural data, the magnetic experimental data were fitted using the Bleaney–Bowers equation (1) [47] to account for the ferromagnetic interaction within a dinuclear unit. The weaker interdimer antiferromagnetic exchange was introduced using the molecular field approximation (2) [48,49]:

$$\chi_{Cu} = \frac{Ng^2\beta^2}{3kT}[1 + 1/3\exp(-2J/kT)]^{-1} \quad (1)$$

$$\chi^{exp} = \frac{\chi_{Cu}}{1 - (2zJ'/Ng^2\mu_B^2)\chi_{Cu}} \quad (2)$$

where χ^{exp} is the measured magnetic susceptibility, zJ' is the interdimer exchange parameter, and z is the number of nearest neighbours. Within the frame of this approximation, with the interaction Hamiltonian $H = -J\hat{S}_1 \cdot \hat{S}_2$, the best-fit parameters obtained by least-squares fit through Eq. (2) are as follows: $J = 1.86\ cm^{-1}$, $zJ' = -0.17\ cm^{-1}$, $g = 2.075$ with R value of 6.70×10^{-6}, where R is the agreement factor defined as

$$R = \sqrt{\sum \frac{1}{(\chi_i^{exp})^2}(\chi_i^{exp} - \chi_i^{calc})^2 \Big/ \sum \frac{1}{(\chi_i^{exp})^2}}$$

The shape of the magnetization curve at 2 K does not exactly follow the Brillouin function (Fig. 5). At intermediate fields, the experimental points are above the theoretical curve, indicating weak ferromagnetic coupling. At 5 T the $M/N\beta$ value tends to 2.0, which corresponds to an $S = 1$ ground state (close saturation) [50].

3.4. Magneto-structural correlations

Inspection of the structure shows that the two exchange pathways are possible: one through Cu(1)–N(1)–C(1)–C(6)–P(1)–O(3)–Cu(1A) and the other through Cu(1)–O(1)–P(1)–O(3)–Cu(1A) phosphonate bridges with the Cu···Cu distance of 4.69 Å (path length 10.14 Å and 6.93 Å, respectively). The observed Cu···Cu distance suggests that both pathways may be operative but in former, only weak antiferromagnetic interaction is possible due to extended five-atom bridge (path length 10.14 Å). On the other hand, the O–P–O bridge is known to be efficient in transmitting weak to moderately strong antiferromagnetic and ferromagnetic exchange interaction [18–24] between two copper(II) ions. It is worth to mention here that these compounds presented in Refs. [18–24] are interesting structurally and magnetically organic–inorganic hybrid materials including inorganic phosphate, hydrogenophosphate, and pyrophosphate as bridging ligands in which magnetic interactions occur through the Cu–O–P–O–Cu pathway [18–24]. For the phosphate group (μ-OPO_3) coordination through a single oxygen atom (Cu–O–Cu) has been also obtained [18].

Among above complexes some magneto-structural correlations have been presented [18–24]. However, there is no obvious relationship between the structural parameter of the OPO bridge and the observed magnitude of the magnetic coupling exchange, often due to the complicated structures of these compounds and observed different conformation modes and structural parameters of the O–P–O triatomic bridge. It is worth to note, that within these compounds, the phosphate with the O–P–O bridge in *syn–syn* conformation has been obtained [18]. In the compound presented here, the O–P–O bridge is in *syn–anti* conformation, has not been described in literature. Because the exact bridging mode, the structural parameters of the bridge, and orbitals involved, all are responsible for the strength of magnetic exchange coupling in three atomic bridges (i.e. OCO carboxylate bridge) [50], magneto-structural correlations for phosphate bridging complexes [18–24] including of the title compound are not possible.

The influence of stereochemical and electronic features of the phosphonate bridge on the magnetic properties in our compounds is discussed below.

The OPO bridge in our compound indicates certain structural similarity to a *syn–anti* carboxylate group OCO, substituting the carbon atom from the carboxylate by phosphorous atom, because both indicate delocalized character (Fig. 6). Examination of the magneto-structural data of well-characterized copper(II) complexes in which the carboxylate adopts the *syn–anti* conformation [51,52] indicates that weak ferromagnetic or antiferromagnetic coupling depends on the structural features of the Cu–O–C–O–Cu bridge, the coordination geometry of the exchange-coupled copper ions, and the relative position of the carboxylate bridge with respect to the copper(II) ions: equatorial–equatorial (weak antiferromagnetic interaction), equatorial–apical (weak ferromagnetic interaction) and apical–apical (negligible interaction). These features decide of overlap of magnetic orbitals, thus of sign and magnitude of exchange interactions according to the concept of the overlap of magnetic orbitals developed by Kahn [53] and Alvarez [54]. On the other hand, some structural features of the bridging network would reduce the antiferromagnetic contribution according to Khan's model in which the exchange coupling constant J, is sum of both ferromagnetic (J_F) and antiferromagnetic (J_{AF}) contributions $J = J_F + J_{AF}$ and J_{AF} is sensitive on structural features of the bridging network.

As recently indicated [51,52], ferromagnetic coupling in the *syn–anti* carboxylato-bridged copper(II) compounds has been observed in the light of the following electronic and structural features: conformation of the carboxylate group, asymmetry with respect to the Cu–O bond, non-pla-

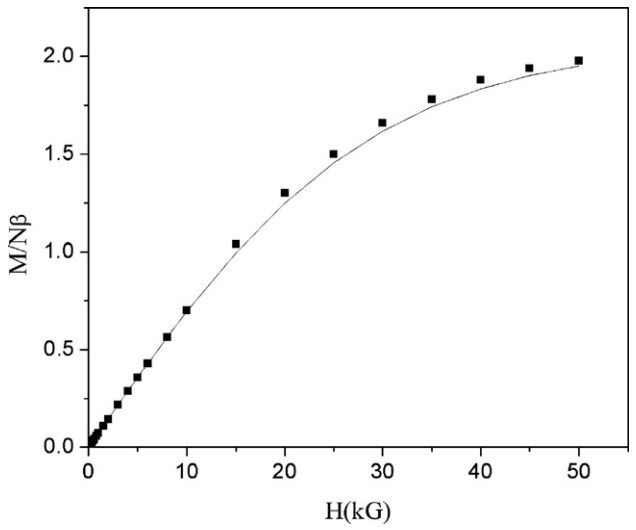


Fig. 5. Molar magnetization in $N\mu_\beta$ units of Cu_2(2-mpmpe)$_2$(-$H_2O)_2(NO_3)_2$ measured at 2 K as a function of magnetic field. The solid line represents the Brillouin function assuming $g = 2.075$ (the value of the fit).

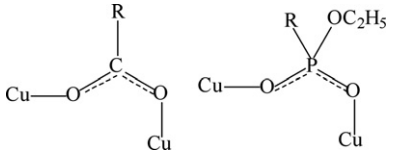


Fig. 6. Scheme of the carboxylate (OCO) and the phosphonate (OPO) bridges.

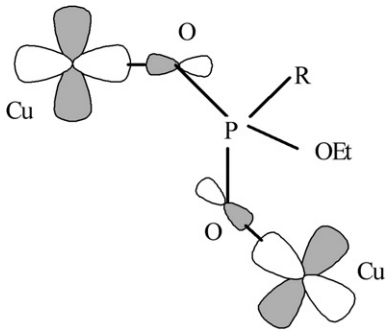


Fig. 7. Relative orientation of the copper(II) magnetic orbitals and their interaction through the phosphonate bridge with *syn–anti* conformation.

narity of the Cu–O–C–O–Cu bridging network and low symmetry of the chromophore.

As it was mentioned previously, the geometry around Cu atom in the studied compound is a distorted square-pyramidal ($\tau = 0.28$). The magnetic orbital on each copper atom is predominantly of the $d(x^2 - y^2)$ with some admixture of dz^2. Thus, both magnetic orbitals on Cu(1) and Cu(1A) are delocalized toward the 2p oxygen orbitals of the OPO bridge (Fig. 7) and, then, the exchange coupling through the phosphonate groups might be operative suggests the weak antiferromagnetic exchange coupling in contrary to the observed ferromagnetic interaction.

However, the overlap between the two non-coplanar copper centered magnetic orbital through the pseudo-equatorial O(1)–P(1)–O(3) and O(1A)–P(1A)–O(3A) bridging network cause that the exchange coupling through the phosphonate group to be less operative in comparison with the square-planar geometry, with the phosphonate group bridging two strictly equatorial positions at copper ions. In this case, the conformation is not planar reducing the antiferromagnetic coupling.

In the light of the above consideration, we can expect a weak ferromagnetic coupling through the O–P–O bridge in our compound, similar to that created by the *syn–anti* carboxylate bridge in the light of the following electronic and structural features: (i) conformation of the phosphonate group; (ii) non-planarity of the Cu–O–P–O–Cu bridging network (out-of-phase exchange pathway), thus reducing the antiferromagnetic contribution (iii) asymmetry with respect to the Cu–O bond (see Section 3.1). Additionally, the higher electronegativity of the phosphorous atom in comparison to the carbon atom and presence of the oxygen atom of OEt group could reduce of the antiferromagnetic contribution to such extent that the ferromagnetic one would become predominant as it is observed in our compound.

4. Conclusions

In this paper, we have discussed the synthesis, crystal structure, and magnetic behavior of the Cu(II) compound with monoethyl (pyridyn-2-ylmethyl)phosphonate ligand of the formula $Cu_2(2\text{-mpmpe})_2(H_2O)_2(NO_3)_2$. This complex is the first example of ferromagnetically coupled dinuclear copper(II) organophosphonate compound in which copper ions are double bridged by the OPO from phosphonate groups. To the best of our knowledge, the OPO bridging group in *syn–anti* conformation, has not reported in literature yet. The structure is extended to supramolecular 3D network. Interesting feature of the crystal structure results from the fact that the four dinuclear $Cu_2(\mu_2\text{-O})_2$ moiety are interconnected by hydrogen bonds between the aromatic C–H groups of the pyridine rings and phosphoryl oxygen of the P=O groups from adjacent dimeric unit results in the formation of $[Cu_2(\mu_2\text{-O})]_4$ hydrogen bonded ring. This cyclic motif is novel in supramolecular chemistry.

Variable temperature magnetic study shows the existence of dominant ferromagnetic interaction in the compound. The magnetic data were fitted using both intradinuclear and interdinuclear ($J = 1.86\ cm^{-1}$, $zJ' = -0.17\ cm^{-1}$) interactions. Another possible very weak antiferromagnetic contribution to J (pathway Cu–N–C–C–P–O–Cu) has been negligible due to the lack of a model including this interaction.

Acknowledgements

The work was supported by the by the Polish Ministry of Science and Higher Education – Grant No. 1T09A 12430 (J.M.). The study was also supported by Medical University of Lodz (Statute fund. No. 503-30-16-2) (J.O.).

Appendix A. Supplementary data

CCDC 668271 contains the supplementary crystallographic data for this paper. These data can be obtained free of charge via http://www.ccdc.cam.ac.uk/conts/retrieving.html, or from the Cambridge Crystallographic Data Centre, 12 Union Road, Cambridge CB2 1EZ, UK; fax:(+44) 1223-336-033; or e-mail: deposit@ccdc.cam.ac.uk. Supplementary data associated with this article can be found, in the online version, at doi:10.1016/j.poly.2008.02.003.

References

[1] G. Alberti, F. Marmottini, S. Murcia-Mascaros, R. Vivani, P. Zappelli, Angew. Chem., Int. Ed. Engl. 32 (1993) 1357.
[2] G. Alberti, F. Marmottini, S. Murcia-Mascaros, R. Vivani, P. Zappelli, Angew. Chem., Int. Ed. Engl. 33 (1994) 1594.
[3] V.V. Krishnan, A.G. Dokoutchaev, M.E. Thomson, J. Catal. 196 (2000) 366.
[4] G. Alberti, U. Costantino, C. Dionigi, S. Murcia-Mascaros, R. Vivani, Supramol. Chem. 6 (1995) 29.
[5] B. Zang, A. Clearfield, J. Am. Chem. Soc. 119 (1997) 2751.
[6] H.E. Katz, G. Scheller, T.M. Putvinski, M.L. Schilling, W.L. Wilson, C.E.D. Chidsey, Science 254 (1991) 1484.
[7] G.A. Neff, T.M. Mahon, T.A. Abshere, C.J. Page, Mater. Res. Soc. Symp. Proc. 435 (1996) 661.
[8] A.K. Cheetham, G. Férey, T. Loiseau, Angew. Chem., Int. Ed. 38 (1999) 3268.
[9] P. Ayyappan, O.R. Evans, B.M. Foxman, A. Kraig, K.A. Wheeler, T.H. Warren, W. Lin, Inorg. Chem. 40 (2001) 5954.

[10] B. Żurowska, J. Mroziński, Z. Ciunik, J. Ochocki, J. Mol. Struct. 834 (2007) 26.
[11] B. Żurowska, J. Mroziński, J. Ochocki, Mater. Sci. 25 (4) (2007) 1063.
[12] J. Ochocki, B. Żurowska, J. Mroziński, J. Reedijk, in: IIIrd Symposium on Inorganic Biochemistry and Molecular Biophysics, VIth International Scientific School on Biological Macromolecules, 1991, Proceedings, p. 212.
[13] B. Żurowska, J. Mroziński, Z. Ciunik, J. Ochocki, J. Mol. Struct. 79 (2006) 98.
[14] J. Ochocki, K. Kostka, B. Żurowska, J. Mroziński, E. Gałdecka, Z. Gałdecki, J. Reedijk, J. Chem. Soc., Dalton Trans. (1992) 2955.
[15] J. Ochocki, B. Żurowska, J. Mroziński, H. Kooijman, A.L. Spek, J. Reedijk, Eur. J. Inorg. Chem. (1998) 169.
[16] B. Żurowska, J. Ochocki, J. Mroziński, Z. Ciunik, J. Reedijk, Inorg. Chim. Acta 357 (2004) 755.
[17] B. Żurowska, K. Ślepokura, T.Lis, J. Ochocki, B. Lippert, Inorg. Chim. Acta (2008, Special issue).
[18] R.P. Doyle, T. Bauer, M. Julve, F. Lloret, J. Cano, M. Nieuwenhuyzen, P.E. Kruger, Dalton Trans. (2007) 5140, and references therein.
[19] R.P. Doyle, P.E. Kruger, B. Moubaraki, K.S. Murray, M. Nieuwenhuyzen, Dalton Trans. (2003) 4230, and references therein.
[20] S. Youngme, P. Phuengphai, N. Chaichit, G.A. van Albada, O. Roubeau, J. Reedijk, Inorg. Chim. Acta 358 (2005) 849.
[21] S. Youngme, P. Phuengphai, C. Pakawatchai, G.A. van Albada, J. Reedijk, Inorg. Chim. Acta 358 (2005) 2125.
[22] S. Youngme, P. Phuengphai, N. Chaichit, G.A. van Albada, O. Roubeau, J. Reedijk, Inorg. Chim. Acta 358 (2005) 2262.
[23] Y. Moreno, A. Vega, S. Suhak, R. Baggio, O. Peña, E. Le Fur, J.-Y. Pivan, E. Spodine, J. Mater. Chem. 13 (2003) 2381.
[24] P.E. Kruger, R.P. Doyle, M. Julie, F. Floret, M. Nieuwenhuyzen, Inorg. Chem. 40 (2001) 1726.
[25] J.D. Peterson, W.R. Murphy, R. Sahai, K.J. Brewer, R.R. Ruminski, Coord. Chem. Rev. 64 (1985) 261.
[26] P.J. Steel, Coord. Chem. Rev. 106 (1990) 227.
[27] C.T. Chen, K.S. Suslick, Coord. Chem. Rev. 128 (1993) 293.
[28] O. Kahn, Angev. Chem., Int. Ed. Engl. 24 (1985) 834.
[29] O. Kahn, Struct. Bonding (Berlin) 68 (1987) 89.
[30] D. Gatteschi, O. Kahn, J.S. Miller, F. Palacio (Eds.), Magnetic Molecular Materials, NATO ASI Series E198, Kluwer, Dordrecht, 1991.
[31] R.D. Willet, d. Gattesdhi, O. Kahn (Eds.), Magneto-Structural Correlation in Exchange Coupled Systems, Reidel, Dordrecht, 1985.
[32] R.L. Carlin, A.J. van Duyneveldt, Magnetic Properties of Transition Metal Compounds, Springer, Berlin, 1997.
[33] F.E. Mabbs, D.J. Machin, Magnetism and Transition Metal Complexes, Chapman & Hall, London, 1973.
[34] E. König, Magnetic Properties of Coordination and Organometallic Transition Metal Compounds, Springer, Berlin, 1966.
[35] G.M. Sheldrick, Acta Crystallogr., Sect. A 46 (1990) 467.
[36] G.M. Sheldrick, SHELXL 97, Program for Crystal Structure Refinement, University of Göttingen, 1997.
[37] A.W. Addison, T.N. Rao, J. Reedijk, J. van Rijn, G.C. Verschoor, J. Chem. Soc., Dalton Trans. (1984) 1349.
[38] E. Colacio, J.P. Costes, R. Kivekäs, J.P. Laurent, J. Ruiz, M. Sundberg, Inorg. Chem. 30 (1991) 1475.
[39] L. Chęcińska, M. Małecka, K. Aranowska, J. Ochocki, Acta Crystallogr., Sect. C 61 (2005) 04.
[40] G.R. Desiraju, ACC. Chem. Res. 29 (1996) 441.
[41] G.J. Kleywegt, W.G.R. Wiesmeijer, G.J. van Driel, W.L. Driessen, J. Reedijk, J.H. Nordik, J. Chem. Soc., Dalton Trans. (1985) 2177.
[42] K. Nakamoto, Infrared and Raman Spectra of Inorganic and Coordination Compounds, 4th ed., Wiley, New York, 1986.
[43] N.F. Curtis, Y.M. Curtis, Inorg. Chem. 4 (1965) 804.
[44] B.J. Hathaway, Struct. Bond. (Berlin) 57 (1984) 55.
[45] B.J. Hathaway, in: G. Wilkinson, R.D. Gillard, J.A. McCleverty (Eds.), Comprehensive Coordination Chemistry, vol. 5, Pergamon Press, Oxfort, 1987, p. 605.
[46] M.L. Boillot, Y. Journaux, A. Bencini, D. Gatteschi, O. Kahn, Inorg. Chem. 24 (1985) 263.
[47] B. Bleaney, K.D. Bowers, Proc. Roy. Soc., London, A 214 (1952) 451.
[48] J.W. Stout, R.C. Chisholm, J. Chem. Phys. 36 (1962) 979.
[49] D.K. Towle, S.K. Hoffmann, W.E. Hatfield, P. Singh, P. Chaudhuri, K. Weighardt, Inorg. Chem. 24 (1985) 4393.
[50] M. Du, Y.-M. Guo, X.-H. Bu, J. Ribas, M. Monfort, New. J. Chem. 26 (2002) 939.
[51] B. Żurowska, J. Mroziński, Inorg. Chim. Acta 342 (2003) 23, and references therein.
[52] B. Żurowska, J. Mroziński, Z. Ciunik, Polyhedron 26 (2007) 3085, and references therein.
[53] O. Kahn, Molecular Magnetism, Wiley–VCH, New York, 1993.
[54] E. Ruiz, P. Alemany, S. Alvarez, J. Cano, J. Am. Chem. Soc. 119 (1997) 1297.

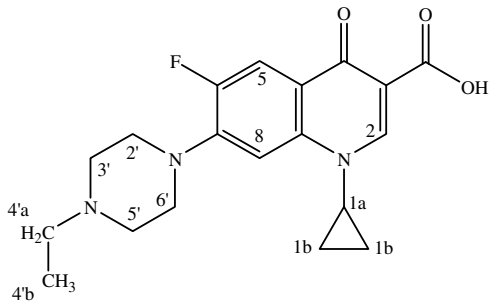


Fig. 1. Enrofloxacin (Herx = 1-cyclopropyl-7-(4-ethyl-piperazin-1-yl)-6-fluoro-4-oxo-1,4-dihydro-quinoline-3-carboxylic acid) and H atom labeling.

ation quinolone enrofloxacin in order to study the mode of coordination and the biological properties of the resultant complexes. More specifically, the binary complexes of enrofloxacin with Mn^{2+}, Fe^{3+}, Co^{2+}, Ni^{2+}, Zn^{2+}, Cd^{2+} and UO_2^{2+} have been synthesized and characterized with elemental analysis and infrared (IR), UV–Visible (UV–Vis) and nuclear magnetic resonance (NMR) spectroscopies. Molecular modeling techniques have been employed to assess the lowest energy model structure of the Mn^{2+}, Fe^{3+} and UO_2^{2+} complexes. The interaction of the complexes with calf-thymus (CT) DNA has been investigated with UV and circular dichroism (CD) spectroscopy. The biological activity of the complexes has been evaluated by determining the minimum inhibitory concentration (MIC) against three microorganisms.

2. Experimental

2.1. Materials

Enrofloxacin and CT DNA were purchased from Sigma, NaCl was purchased from Merck, trisodium citrate was purchased from Riedel-de Haen, $MnCl_2 \cdot 4H_2O$, $FeCl_3 \cdot 3H_2O$, $CoCl_2 \cdot 6H_2O$, $NiCl_2 \cdot 6H_2O$, $ZnCl_2$, $CdCl_2 \cdot 2.5H_2O$, $UO_2(NO_3)_2 \cdot 6H_2O$, KOH and all the solvents were purchased from Aldrich Co. Tryptone and yeast extract were purchased from Oxoid (Unipath, Hampshire, UK). All the chemicals and solvents were reagent grade and were used as purchased.

DNA stock solutions (5 mM) were prepared by dilution of CT DNA to buffer (containing 150 mM NaCl and 15 mM trisodium citrate at pH 7.0) followed by exhaustive stirring at 4 °C for three days [29], and kept at 4 °C for no longer than a week. The nucleotide concentrations were determined by their absorption at 260 nm using $\varepsilon = 6600$ $M^{-1}\,cm^{-1}$ (expressed as phosphate) [30].

2.2. Synthesis of the complexes

2.2.1. $Mn(erx)_2(H_2O)_2$ (**1**)

A methanolic solution (10 mL) of enrofloxacin (0.6 mmol, 216 mg), deprotonated with KOH (0.6 mmol, 34 mg), was added to a methanolic solution (10 mL) of $MnCl_2 \cdot 4H_2O$ (0.3 mmol, 60 mg) and the reaction mixture was refluxed for 2 h. The solution was filtered and left for slow evaporation. After a few days a light yellow microcrystalline product was deposited, collected with filtration, washed with methanol and dried. Yield: 180 mg, 75%. *Anal.* Calc. for $Mn(erx)_2(H_2O)_2$ ($C_{38}H_{46}N_6O_8F_2Mn$) ($M_W = 807.75$): C, 56.51; H, 5.74; N, 10.40. Found: C, 56.19; H, 5.57; N, 10.47%. The complex is soluble in dmso, dmf and H_2O and is non-electrolyte.

In a similar way, complexes **2**–**7** were prepared with the use of the corresponding metal salt. All the resultant complexes are non-electrolytes.

2.2.2. $Fe(erx)_3$ (**2**)

$FeCl_3 \cdot 3H_2O$ (0.2 mmol, 44 mg) was used. A yellow microcrystalline product was collected. Yield: 147 mg, 65%. *Anal.* Calc. for $Fe(erx)_3$ ($C_{57}H_{63}N_9O_9F_3Fe$) ($M_W = 1131.01$): C, 60.53; H, 5.61; N, 11.15. Found: C, 60.41; H, 5.78; N, 11.29%. The complex is soluble in dmso, dmf and H_2O.

2.2.3. $Co(erx)_2(H_2O)_2$ (**3**)

$CoCl_2 \cdot 6H_2O$ (0.3 mmol, 72 mg) was used. A yellow microcrystalline product was collected. Yield: 170 mg, 70%. *Anal.* Calc. for $Co(erx)_2(H_2O)_2$ ($C_{38}H_{46}N_6O_8F_2Co$) ($M_W = 811.75$): C, 56.23; H, 5.71; N, 10.35. Found: C, 56.05; H, 5.61; N, 10.32%. The complex is soluble in dmso, dmf and H_2O.

2.2.4. $Ni(erx)_2(H_2O)_2$ (**4**)

$NiCl_2 \cdot 6H_2O$ (0.3 mmol, 72 mg) was used. A pale green microcrystalline product was collected. Yield: 145 mg, 60%. *Anal.* Calc. for $Ni(erx)_2(H_2O)_2$ ($C_{38}H_{46}N_6O_8F_2Ni$) ($M_W = 811.53$): C, 56.24; H, 5.71; N, 10.35. Found: C, 55.89; H, 5.52; N, 10.17%. The complex is soluble in dmso, dmf and H_2O.

2.2.5. $Zn(erx)_2(H_2O)_2$ (**5**)

$ZnCl_2$ (0.3 mmol, 42 mg) was used. A pale yellow microcrystalline product was collected. Yield: 160 mg, 65%. *Anal.* Calc. for $Zn(erx)_2(H_2O)_2$ ($C_{38}H_{46}N_6O_8F_2Zn$) ($M_W = 818.20$): C, 55.78; H, 5.67; N, 10.27. Found: C, 55.92; H, 5.47; N, 10.08%. The complex is soluble in dmso and dmf.

2.2.6. $Cd(erx)_2(H_2O)_2$ (**6**)

$CdCl_2 \cdot 2.5H_2O$ (0.3 mmol, 69 mg) was used. A white microcrystalline product was collected. Yield: 155 mg, 60%. *Anal.* Calc. for $Cd(erx)_2(H_2O)_2$ ($C_{38}H_{46}N_6O_8F_2Cd$) ($M_W = 865.23$): C, 52.75; H, 5.36; N, 9.71. Found: C, 52.39; H, 5.27; N, 9.45%. The complex is soluble in dmso and dmf.

2.2.7. $UO_2(erx)_2$ (**7**)

$UO_2(NO_3)_2 \cdot 6H_2O$ (0.3 mmol, 150 mg) was used. A yellow microcrystalline product was collected. Yield: 180 mg, 60%. *Anal.* Calc. for $UO_2(erx)_2$ ($C_{38}H_{42}N_6O_8F_2U$)

($M_W = 986.80$): C, 46.25; H, 4.29; N, 8.52. Found: C, 45.87; H, 4.10; N, 8.37%. The complex is soluble in dmso and dmf.

2.3. Instrumentation

IR spectra (400–4000 cm^{-1}) were recorded on a Nicolet Magna-IR 550 with samples prepared as KBr pellets. UV–Vis spectra were recorded as nujol mulls and in solution at concentrations in the range 10^{-5}–2×10^{-3} M on a Thermo Electron Corporation Helios α dual beam spectrophotometer. C, H and N elemental analysis were performed on a Perkin–Elmer 240B elemental analyzer. Electric conductance measurements were carried out with a WTW model LF 530 conductivity outfit and a type C cell, which had a cell constant of 0.996. NMR spectra were recorded with a Bruker Avance 500 MHz instrument and were processed by X-WIN NMR 2.6 (Bruker Analytik GmbH).

The interaction of the complexes with CT DNA has been investigated with UV and CD spectroscopies. In both techniques, the spectra of CT DNA in the presence of each complex have been recorded for a constant CT DNA concentration (3.125×10^{-4} M) in diverse [complex]/[CT DNA] mixing ratios (r). All the UV and CD spectra were recorded after incubation of the sample with CT DNA for 24 h at 37 °C.

The CD spectra were recorded on a Jasco J-700 spectropolarimeter using a 1.0 cm path quartz cell and the following acquisition parameters: $\lambda = 190$–400 nm, scan speed 50 nm min^{-1}, resolution step 0.2 nm, sensitivity 50 mdeg, response 1 s, bandwidth 1.0 nm, accumulations 10. In some cases, the spectra were averaged over an appropriate number of scans.

2.4. Molecular modeling

Although diverse crystallization techniques were employed, we did not manage to obtain a crystal suitable for the structure determination with X-ray crystallography.

With the aim to present a molecular model for each new complex that is unbiased by the starting structure, we have used Langevin dynamics with a simulated annealing protocol. Using this method, the mean total energy of an ensemble of structures guides the selection of the most favorable configuration for each complex. Starting structures were constructed using the program HYPERCHEM and the MM+ force field that is based on the Allinger's MM2 force field [31]. For all the metal ions, we used a default parameter set with $R^* = 2.20$ Å and $e^* = 0.02$ kcal mol^{-1}, since the van der Waals interactions are not expected to play a major role in such bonded representations as in octahedral complexes. Metal–ligand bond lengths were corrected in the final models using harmonic restraints with equilibrium values that were extracted from crystallographic data of similar compounds [32–45] (Tables S1, S3 and S5). Non-bonded interactions were calculated in vacuo with no cutoff and the electrostatic energy term was treated using bond dipoles. Initial energy minimizations were carried out by a conjugate gradient method with rms gradient <0.01 as convergence criterion.

Each model (Schemes S1–S3) was subjected to 20 individual rounds of simulated annealing setting different value to the seed for the assignment of the starting velocities. To integrate the Langevin equation [46] the step size was set to 1 fs and the collision frequency to 1 ps^{-1}. The annealing calculation comprised three phases: (i) raising the temperature of the system from 10 to 1000 K over 2 ps, (ii) keeping the system at 1000 K for 3 ps and (iii) cooling the system down to 0 K over 15 ps. A tight coupling of the system with temperature (0.1 ps) was used for the heating and equilibration phases. During the cooling phase the bath relaxation time was gradually decreased from 5.0 ps (7000 steps), 2.0 ps (3000 steps), 1.0 ps (2000 steps), 0.5 ps (2000 steps) to 0.05 ps (1000 steps). At the final step all structures had rms gradient <0.01 and their total energy was recorded (Tables S2, S4 and S6). The models presented herein were selected among the lowest energy structures generated for each starting geometry. A final minimization of their energy was performed as above after applying the metal–ligand distance restraints.

2.5. Antibacterial activity – minimum inhibitory concentration

The antibacterial activity of the compounds (ligand and complexes) was studied against *Staphylococcus aureus* (*S. aureus*), *Escherichia coli* (*E. coli*) and *Pseudomonas aeruginosa* (*P. aeruginosa*). The microorganisms were generously supplied from the laboratory of Dr. I. Eskioglou, Department of Medical Laboratories, Technological and Educational Institution of Larissa, Greece and were maintained in the laboratory of "Chemical Biology" of NCSR "Demokritos". Screening was performed by determining the MIC. Two different media [Luria broth medium (=LB, containing 1% w/v tryptone, 0.5% w/v NaCl and 0.5% w/v yeast extract) and minimal medium salts broth (=MMS, containing 1.5% w/v glucose, 0.5% w/v NH_4Cl, 0.5% w/v K_2HPO_4, 0.1% w/v NaCl, 0.01% w/v $MgSO_4 \cdot 7H_2O$ and 0.1% w/v yeast extract)] were used. The compounds were dissolved in distilled water with twofold serial dilutions from 8 to 0.125 μg mL^{-1}. All cultures were incubated at 37 °C. Control tests with no active ingredients were also performed.

MIC was determined using twofold serial dilutions in liquid media containing 0.125–8 μg mL^{-1} of the compound being tested. A preculture of bacteria was grown in LB overnight at the optimal temperature of each species. Two mL of MMS were inoculated with 20 mL of this preculture. This culture was used as a control to examine if the growth of the bacteria tested is normal. In a similar second culture, 20 μL of the bacteria as well as the tested compound at the desired concentration were added. A third sample containing 2 mL MMS supplemented with the same compound concentration was used as a second control to

check the effect of the compound on MMS. All samples were measured in duplicate. We monitored bacterial growth by measuring the turbidity of the culture after 12 and 24 h. If a certain concentration of a compound inhibited bacterial growth, half the concentration of the compound was tested. This procedure was carried on to a concentration where bacteria grow normally. The lowest concentration that inhibited bacterial growth was determined as the MIC value. All the equipment and culture media were sterile.

3. Results and discussion

3.1. Synthesis and spectroscopic study of the complexes

All the complexes have been prepared in high yield (60–75%) via the addition of methanolic solution of deprotonated enrofloxacin to a methanolic solution of the metal ion at a 3:1 ratio for Fe^{3+} and 2:1 for the divalent metal ions.

In Table 1, the characteristic absorptions of the IR spectra of the complexes are listed. In the IR spectra of complexes **1**–**7**, the absorption at 1733 cm^{-1} in the spectrum of Herx attributed to the absorption of the $\nu(C{=}O)_{carb}$ has disappeared. Two very strong characteristic bands are present in the range 1595–1605 cm^{-1} and 1380–1395 cm^{-1} that could be assigned as ν(O–C–O) asymmetric and symmetric stretching vibrations, respectively, whereas $\nu(C{=}O)_p$ is shifted from 1622 cm^{-1} up to 1633 cm^{-1} upon bonding. The Δ values ($\Delta = \nu_{asym}(CO_2) - \nu_{sym}(CO_2)$, a useful characteristic for determining the coordination mode of the ligands) fall in the range 208–224 cm^{-1} indicating a monodentate coordination mode of the carboxylato group [47] of the enrofloxacinato ligands. These changes in the IR spectra suggest that enrofloxacin is coordinated to the metal via the pyridone (O_p) and one carboxylate (O_c) oxygen atoms [1,15].

Additionally, the band in the range 3405–3420 cm^{-1} in the IR spectra of complexes **1** and **3**–**6** can be attributed to ν(O–H) vibration of the coordinated water molecules [20,47].

The UV–Vis spectra of the complexes have been recorded as nujol mulls and in dmso solution. Practically, the spectra in dmso solution are identical with those in nujol, with the exception of a few nm shifts in some cases, suggesting that the complexes retain their structure in solution. The UV–Vis spectral data for the complexes in dmso solution are given in Table 2.

The UV spectra of the complexes are practically identical with those of enrofloxacin but slightly shifted, indicative of coordination through the O_p and one O_c atoms.

In the visible spectra, characteristic bands attributed to d–d transitions are observed only for the Fe^{3+}, Co^{2+} and Ni^{2+} complexes.

The spectrum of $Fe(erx)_3$ exhibits two bands that can be attributed to d–d transitions: one weak band (as a shoulder) at 610 nm ($\varepsilon = 40\ M^{-1}\ cm^{-1}$) which can be assigned as a $^6A_{1g} \rightarrow {}^5T_{1g}$ transition and an intense one at $\lambda = 505$ nm ($\varepsilon = 75\ M^{-1}\ cm^{-1}$) assigned as a $^6A_{1g} \rightarrow T_{2g}$ (G) transition. These bands are typical for distorted octahedral Fe^{3+} [39–42] complexes.

In the spectra of $Co(erx)_2(H_2O)_2$ and $Ni(erx)_2(H_2O)_2$ one band at 555 nm ($\varepsilon = 35\ M^{-1}\ cm^{-1}$) for **3** and 640 nm ($\varepsilon = 45\ M^{-1}\ cm^{-1}$) for **4** attributed to d–d transition has been observed, as it is expected for octahedral high-spin Co^{2+} [48,49] and Ni^{2+} [50,51] complexes. Similar behavior

Table 1
Characteristic absorptions (in cm^{-1}) of the IR spectra of the complexes

	$\nu(C{=}O)_p$	$\nu(CO_2)_{asym}$	$\nu(CO_2)_{sym}$	Δ[a]
Herx	1622	1733[b]		
$Mn(erx)_2(H_2O)_2$	1629	1600	1392	208
$Fe(erx)_3$	1633	1605	1381	224
$Co(erx)_2(H_2O)_2$	1629	1599	1383	216
$Ni(erx)_2(H_2O)_2$	1625	1602	1388	214
$Zn(erx)_2(H_2O)_2$	1628	1598	1387	211
$Cd(erx)_2(H_2O)_2$	1628	1601	1383	218
$UO_2(erx)_2$	1629	1598	1389	209
$VO(erx)_2(H_2O)$ [21]	1629	1602	1395	207
$Cu(erx)_2(H_2O)$ [15]	1630	1611	1381	230
$MoO_2(erx)_2$ [26]	1628	1606	1388	218

[a] $\Delta = \nu(CO_2)_{asym} - \nu(CO_2)_{sym}$.
[b] As ν(COOH).

Table 2
Characteristic bands (λ_{max}, in nm (ε, in M cm^{-1})) in the UV–Vis spectra of the complexes in dmso solution

	IL[a] bands			Band CT[b]	d–d bands	
Herx	280 (11200)	310 (sh)[c] (6100)	335 (2800)			
$Mn(erx)_2(H_2O)_2$	285 (8200)	313 (5200)	340 (2300)	431 (sh)[c] (155)		
$Fe(erx)_3$	287 (7850)	317 (5300)	343 (2550)	434 (sh) (160)	505 (75)	610 (sh) (40)
$Co(erx)_2(H_2O)_2$	285 (7400)	315 (4850)	342 (2400)	432 (sh) (170)	555 (40)	
$Ni(erx)_2(H_2O)_2$	284 (7250)	316 (4600)	345 (2600)	433 (sh) (160)		640 (45)
$Zn(erx)_2(H_2O)_2$	284 (7500)	314 (4500)	340 (2300)	432 (sh) (190)		
$Cd(erx)_2(H_2O)_2$	287 (8100)	318 (5400)	345 (2100)	430 (sh) (175)		
$UO_2(erx)_2$	285 (7800)	315 (5200)	344 (2350)	432 (sh) (190)		

[a] IL = Intraligand.
[b] CT = Charge transfer.
[c] sh = shoulder.

Table 3
Chemical shifts (δ, in ppm) in ^{1}H NMR spectra of Herx, $Zn(erx)_2(H_2O)_2$, $Cd(erx)_2(H_2O)_2$ and $UO_2(erx)_2$ in d_6-dmso

Atom[a]	Herx	$Zn(erx)_2(H_2O)_2$	$Cd(erx)_2(H_2O)_2$	$UO_2(erx)_2$
H1a	1.49 (1H)	1.50 (1H)	1.47 (1H)	1.49 (1H)
H1b and H4′b	1.20 (7H)	1.18 (7H)	1.20 (7H)	1.21 (7H)
H2	8.85 (1H)	9.15 (1H)	9.12 (1H)	9.08 (1H)
H5	7.80 (1H)	8.20 (1H)	8.15 (1H)	8.16 (1H)
H8	7.40 (1H)	7.45 (1H)	7.48 (1H)	7.50 (1H)
H2′, H6′ or H3′, H5′	3.20–3.30 (4H), 3.65–3.70 (4H)	3.15–3.25 (4H), 3.70 (4H)	3.20–3.25 (4H), 3.65–3.75 (4H)	3.15–3.20 (4H), 3.70 (4H)
H4′a	3.35 (2H)	3.40 (2H)	3.38 (2H)	3.40 (2H)

[a] Numbering of protons according to Fig. 1.

has been also observed for the octahedral high-spin Co^{2+} [52] and Ni^{2+} [53] cinoxacin complexes.

Additionally, all complexes also exhibit an absorption band (as a shoulder) at 430–435 nm ($\varepsilon = 155$–$190\ M^{-1}\ cm^{-1}$) which can be assigned to the ligand-to-metal charge-transfer transition for the quinolone ligand, as observed in a series of quinolone binary complexes [15–28].

^{1}H NMR spectra of Herx, $Zn(erx)_2(H_2O)_2$, $Cd(erx)_2(H_2O)_2$ and $UO_2(erx)_2$ were recorded in d_6-dmso. Full assignment of every signal in the ^{1}H NMR spectrum of complexes **5**–**7** was achieved by comparing the spectrum of each complex with the spectrum of the ligand and the spectra reported in the literature [20–23,26]. The results are shown in Table 3.

Comparison of the ^{1}H NMR spectra of $Zn(erx)_2(H_2O)_2$, $Cd(erx)_2(H_2O)_2$ and $UO_2(erx)_2$ with that of Herx shows a significant perturbation of the chemical shifts of the aromatic protons H2 (up to 0.3 ppm) and H5 (up to 0.4 ppm) indicating that H2 and H5 are adjacent to the coordination sites of the ligand. The signals for the aliphatic protons H1a and H1b as well as those of H8 and the piperazine ring protons (perturbations of the chemical shifts up to 0.1 ppm) are practically unchanged since they lie further than H2 and H5 from the binding site. The overall changes of the NMR spectra of the complexes are indicative of coordination of the enrofloxacinato ligands to the metal via the pyridone oxygen and one carboxylate oxygen [20–23,26].

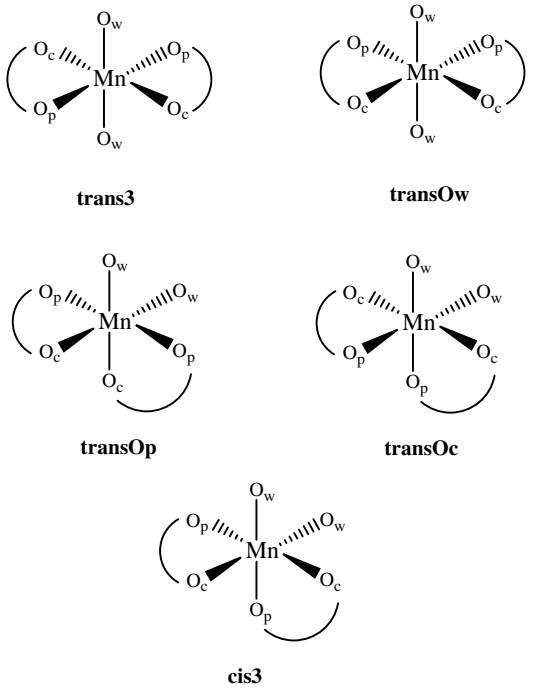
3.2. Molecular dynamics

Diverse crystallization techniques were employed in order to obtain a crystal suitable for the structure determination with X-ray crystallography. Nevertheless, all the complexes were collected as microcrystalline products. In order to propose a possible structure for the complexes, the lowest energy model structures of $Mn(erx)_2(H_2O)_2$, $Fe(erx)_3$ and $UO_2(erx)_2$ have been determined with molecular modeling calculations.

3.2.1. $Mn(erx)_2(H_2O)_2$

We have constructed 10 diastereoisomers as starting models of $Mn(erx)_2(H_2O)_2$ (Scheme S1). The total number of all the possible diastereoisomers could not be limited since, according to similar Mn(II) complexes reported in the literature, the two Ow atoms can lie either at *trans* [33–35] or at *cis* [36–38] positions. After the Langevin dynamics simulated annealing calculations, we obtained the total energy results of 20 different conformations for each starting model (Table S2). The average energy of each set of enantiomers is almost equal, as it is expected from such molecular mechanics calculations [54]. However, the final structures of the *transOc* isomers (Scheme1) exhibit lower average energies by more than 1.0 kcal mol^{-1} than the other four isomers (*cis3*, *trans3*, *transOp* and *transOw*).

Applying the distance restraints (Table S1) to M–L bonds [32–38] for the *transOc* model with the lowest energy and making corrections of the geometry by minimizing the energy of the complex once again, the structure of the predicted most stable isomer (a *transOc* isomer) has been obtained (Fig. 2). However, we cannot exclude the formation of any of the other isomers.



Scheme 1. The isomers of $Mn(erx)_2(H_2O)_2$ employed in the simulated annealing calculations. Oc and Op are the carboxylate and the pyridone oxygen atoms, respectively, of enrofloxacin.

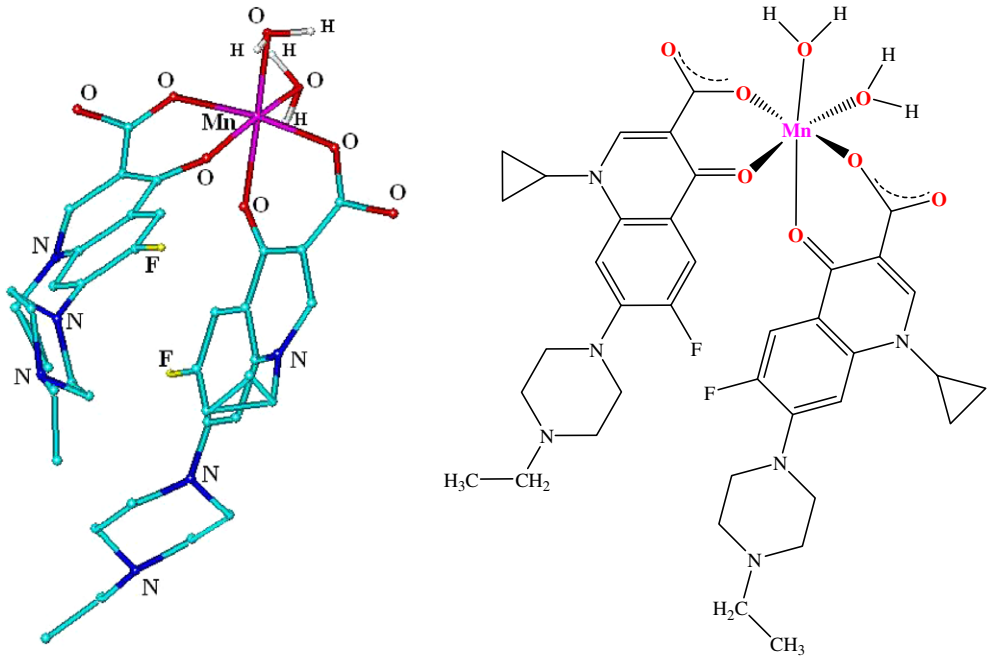
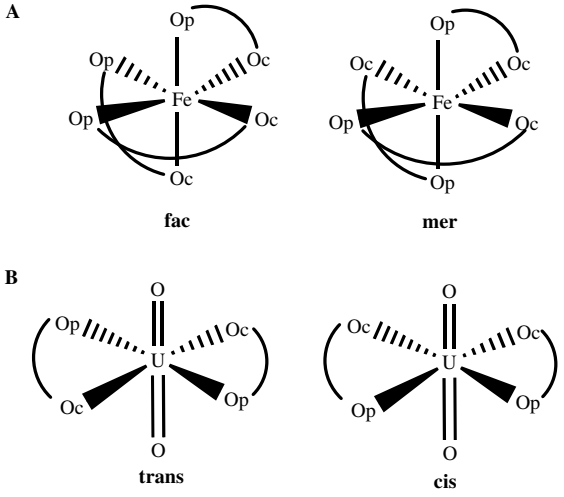


Fig. 2. Lowest model structure for $Mn(erx)_2(H_2O)_2$.



Scheme 2. The isomers of (A) $Fe(erx)_3$ and (B) $UO_2(erx)_2$ employed in the simulated annealing calculations. Oc and Op are the carboxylate and the pyridone oxygen atoms, respectively, of enrofloxacin.

3.2.2. $Fe(erx)_3$

In order to present a model for the complex, we have constructed the two *fac*- and the two *mer*-$Fe(erx)_3$ enantiomers (Scheme S2). The average energy of each set of enantiomers is almost equal (Table S4), as it is expected from such molecular mechanics calculations [54]. However, the final structures of *mer*-$Fe(erx)_3$ (Scheme2A) exhibit lower energies by more than 1 kcal mol^{-1} in comparison to the energies of the *fac* isomers.

For the *mer* models we have applied a set of harmonic restraints at the metal–ligand bonds [39–42] during an additional minimization phase (Table S3). Based on these results, we present the lowest energy model of one *mer*-$Fe(erx)_3$ enantiomer as the favorable configuration of the complex (Fig. 3). However, we can neither exclude the formation of any of the other isomers, nor unambiguously distinguish between the favorable enantiomers.

3.2.3. $UO_2(erx)_2$

Using the same approach as above, only the enantiomers having the two uranyl oxygen atoms at *trans* position were constructed as starting models of $UO_2(erx)_2$ (Scheme S3). This is in accordance with the structure of all the uranyl(VI) complexes reported in the literature [43–45]. After the Langevin dynamics simulated annealing calculations, we obtained the total energy results of 20 different conformations for each starting model (Table S6). The average energy of the isomers is almost equal, as expected [54]. Nevertheless, the *trans* isomers exhibit lower energy than the *cis* ones by more than 0.5 kcal mol^{-1}, which guide us to select the *trans* isomers (Scheme2B) as the most favorable.

Applying the distance restraints (Table S5) to M–L bonds [43–45] for the *trans* model with the lowest energy and making corrections of the geometry by minimizing the energy of the complex once again, the structure of the predicted most stable isomer (a *trans* isomer) has been obtained (Fig. 4). However, we cannot exclude the formation of the *cis* isomers, or distinguish unambiguously between the favorable enantiomers.

3.3. Antibacterial activity

The efficiencies of the ligand and the complexes have been tested against two Gram(−), *E. coli* and *P. aeruginosa*,

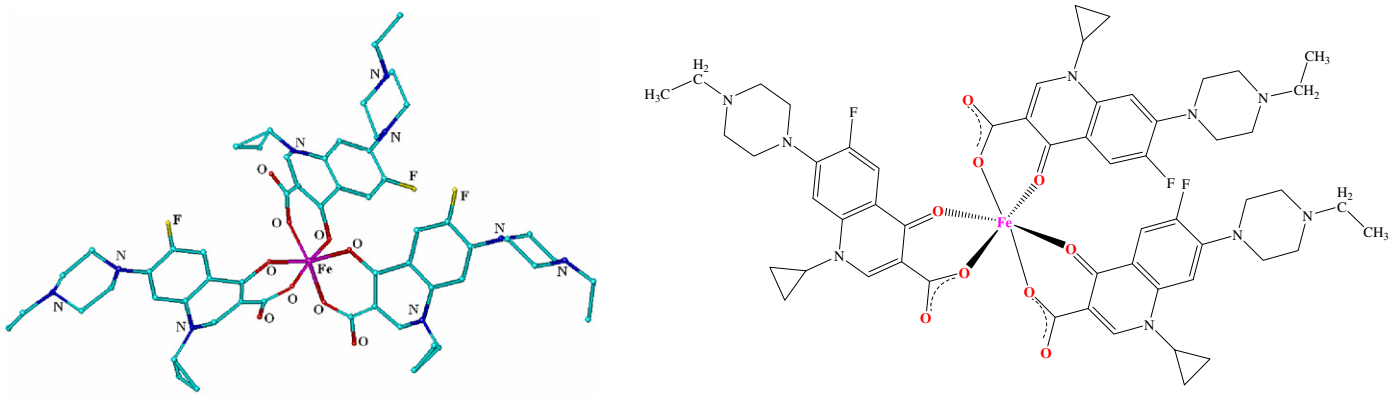


Fig. 3. Lowest model structure for $Fe(erx)_3$.

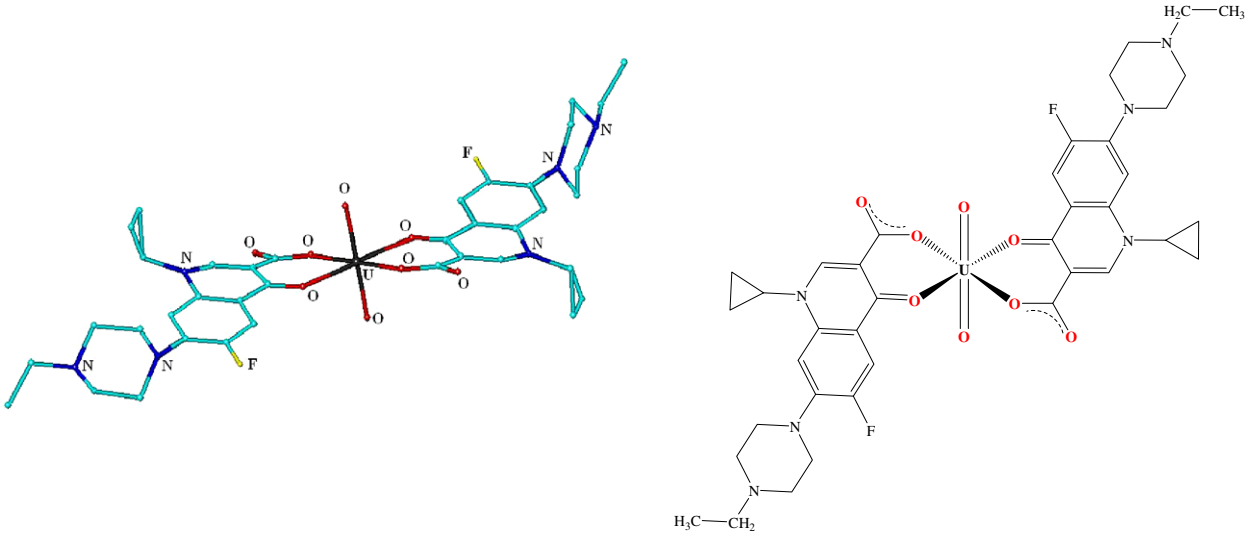


Fig. 4. Lowest model structure for $UO_2(erx)_2$.

and one Gram(+), *S. aureus*, microorganisms. The results are presented in Table 4.

The ligand and the complexes present inhibitory action against all the microorganisms tested (Table 4) and the coordination of enrofloxacin (MIC = 1–8 μg mL^{-1}) with transition metal ions results to an enhanced biological activity (MIC for the complexes = 0.25–4 μg mL^{-1}). The antimicrobial activity of the metal salts has also been investigated. It has been found that the metal salts do not exhibit antimicrobial activity, at the concentration range used to assay the activity of the complexes in this work. The MIC values found for the complexes are low and can be mainly attributed to the existence of the enrofloxacinato ligands in the molecule.

When the antimicrobial activity of metal complexes is investigated, the following principal factors [55–58] should be considered: (i) the chelate effect of the ligands; (ii) the nature of the N-donor ligands; (iii) the total charge of the complex; (iv) the existence and the nature of the ion neutralizing the ionic complex and (v) the nuclearity of the metal center in the complex. For complexes **1**–**7**, only the first factor is present, i.e. the chelate effect of the ligand. This is probably one of the reasons for the diverse antibacterial activity shown by the complexes while the nature of the metal ion coordinated to enrofloxacinato ligand may have a significant role to this diversity.

In general, all the complexes exhibit better inhibition than free enrofloxacin against *S. aureus* and equal or better

Table 4
MIC in μg mL^{-1}

	E. coli	*P. aeruginosa*	*S. aureus*
Herx	1.0	1.0	8.0
$Mn(erx)_2(H_2O)_2$	1.0	1.0	8.0
$Fe(erx)_3$	0.25	0.25	2.0
$Co(erx)_2(H_2O)_2$	1.0	1.0	2.0
$Ni(erx)_2(H_2O)_2$	1.0	1.0	8.0
$Zn(erx)_2(H_2O)_2$	1.0	1.0	2.0
$Cd(erx)_2(H_2O)_2$	1.0	1.0	8.0
$UO_2(erx)_2$	1.0	1.0	8.0
$VO(erx)_2(H_2O)$ [21]	4.0	4.0	8.0
$Cu(erx)_2(H_2O)$ [15]	0.125	0.125	4.0
$MoO_2(erx)_2$ [26]	1.0	1.0	4.0

inhibition against *E. coli* and *P. aeruginosa* (Table 4). More specifically, $Fe(erx)_3$ shows the best inhibition among all the complexes in this study and it is four times more active than enrofloxacin against all the microorganisms used, indicating that the coordination of the enrofloxacinato ligand to Fe^{3+} has enhanced its antimicrobial activity. On the other hand, the rest complexes present equal antimicrobial activity to enrofloxacin against the two Gram(−) microorganisms while they are two to four times more active than enrofloxacin against *S. aureus*. Nevertheless, the best inhibition among all the enrofloxacinato complexes reported has been provided by $Cu(erx)_2(H_2O)$ ($MIC = 0.125\ \mu g\ mL^{-1}$) [15,28] against the two Gram(−) microorganisms (Table 4).

3.4. Interaction of the complexes with DNA

DNA can provide three distinctive binding sites for quinolone metal complexes; namely, groove binding, binding to phosphate group and intercalation [59,60]. This behavior is of great importance with regard to the relevant biological role of quinolone antibiotics in the body [61,62].

3.4.1. UV spectroscopy

The absorption spectra of the interaction of complexes **1**–**7** with CT DNA have been recorded for a constant CT DNA concentration (3.125×10^{-4} M) in different [complex]/[CT DNA] mixing ratios (r). Representative spectra are shown in Fig. 5. The changes observed (either the increase of the intensity at $\lambda_{max} = 258$ nm or the shift of the λ_{max} up to 265 nm) in the UV spectra of the complexes after mixing with CT DNA indicate that complexes **1**–**7** can bind to CT DNA [63,64] and the interaction of each complex with CT DNA takes place by a direct formation of a new complex with double-helical CT DNA [62].

3.4.2. CD spectroscopy

CD spectroscopy is a useful tool to diagnose changes in DNA morphology during drug–DNA interactions, since the positive band due to base stacking (273 nm) and the negative one due to right-handed helicity (246 nm) are quite sensitive to the interaction mode of DNA with small molecules [65]. The changes in CD signals of DNA observed on interaction with drugs may often be assigned to the corresponding changes in DNA structure [66]. Thus, simple groove binding and electrostatic interaction of small molecules show less or no perturbation on the base stacking and helicity bands, while intercalation enhances the intensities of both the bands stabilizing the right-handed B conformation of CT DNA, as observed for the classical intercalator methylene blue [67].

The CD spectra of the complexes with double-stranded CT DNA for different r values can provide us with useful information concerning the complex-nucleotide interaction. The CD spectrum of free CT DNA is conservative and consists of a negative band at 246 nm and a positive one at 273 nm, characteristic of the B-form of DNA [68].

The CD spectra of CT DNA in the presence of complex $Mn(erx)_2(H_2O)_2$ (**1**) are shown in Fig. 6. They consist of a strong negative band I at 246 nm and two discrete positive bands II at 273 nm and III at 282 nm. More specifically, for r values up to 1:300, each CD spectrum consists of one negative band I at 246 nm and two positive bands II at 273 nm and III at 282 nm. Upon increase of the r value, the λ_{max} of these three bands remain, in general, unchanged while the intensity of helicity band I is increased and the intensity of bands II and III is decreased. Nevertheless, the exact mode of binding cannot be safely concluded. When r increases further (up to 1:50), the two positive bands II and III cannot be distinguished resulting to a unique broad band at $\lambda_{max} = 275$ nm while the intensity increases marginally. On the other hand, the negative band I at $\lambda_{max} = 246$ nm remains unchanged in all the spectra,

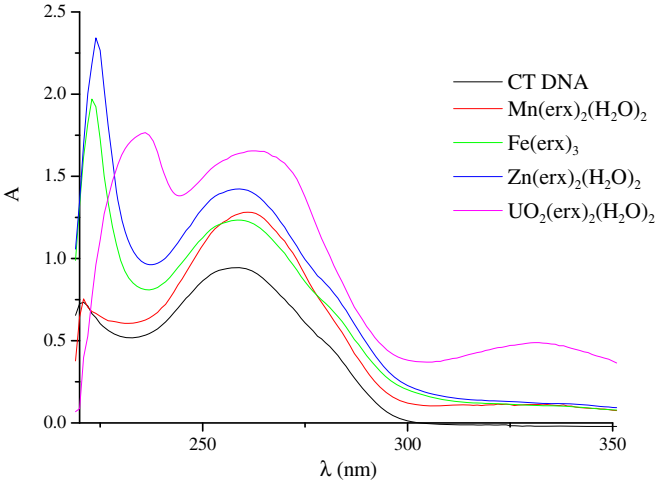


Fig. 5. Absorption spectra of complexes **1**, **2**, **5** and **7** in the presence of CT DNA ($[CT\ DNA] = 3.125 \times 10^{-4}$ M). The r value is 1:200 (r = [complex]/[CT DNA] mixing ratio). The spectra were recorded at 25 °C after incubation of the complexes with CT DNA for 24 h at 37 °C.

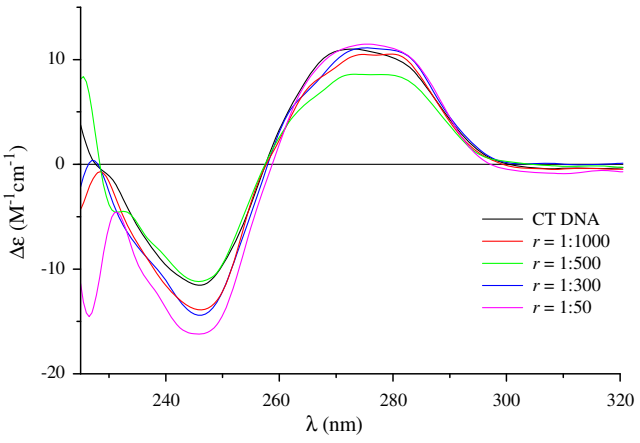


Fig. 6. CD spectra of CT DNA ($[CT\ DNA] = 3.125 \times 10^{-4}$ M) in 5 mM buffer (containing 150 mM NaCl and 15 mM trisodium citrate at pH 7.0) in the presence of complex **1** $Mn(erx)_2(H_2O)$ in different r values (r = [complex]/[CT DNA] mixing ratio). The spectra were recorded at 25 °C after incubation of the complex with CT DNA for 24 h at 37 °C.

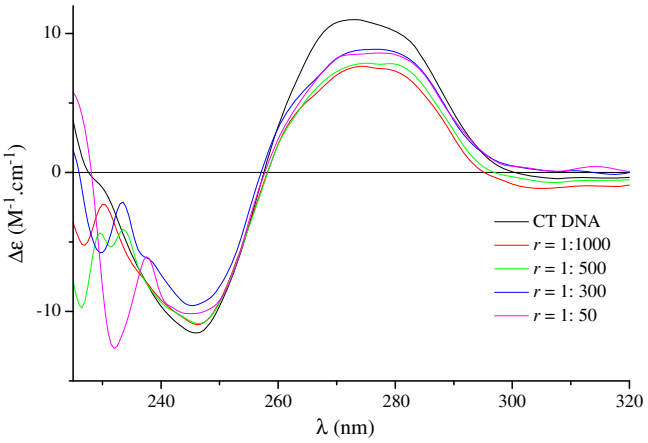


Fig. 7. CD spectra of CT DNA ([CT DNA] = 3.125×10^{-4} M) in 5 mM buffer (containing 150 mM NaCl and 15 mM trisodium citrate at pH 7.0) in the presence of complex **5** $Zn(erx)_2(H_2O)_2$ in different r values (r = [complex]/[CT DNA] mixing ratio). The spectra were recorded at 25 °C after incubation of the complex with CT DNA for 24 h at 37 °C.

although a slight increase of the intensity is observed. The dominating spectral feature for this series of spectra is the slight increase of the intensities of both the bands of CT DNA. Taking into account all the changes observed, the exact mode of binding of **1** to CT DNA cannot be safely concluded [67]. Similar behavior is observed in the CD spectra of CT DNA in the presence of complexes **2**–**4**.

The CD spectra of CT DNA in the presence of complex $Zn(erx)_2(H_2O)_2$ (**5**) are shown in Fig. 7. They consist of a strong negative band I at 246 nm and two discrete positive bands II at 273 nm and III at 281 nm. More specifically, for r values up to 1:300, each spectrum consists of one negative band I at 246 nm and two positive bands II at 273 nm and III at 281 nm. Upon increase of the r value, the λ_{max} of these three bands remain practically unchanged while the intensities of all the bands are marginally decreased. In these spectra, the exact mode of binding cannot be safely concluded. For further increase of r (up to 1:50), the two positive bands II and III are consolidated and cannot be distinguished resulting to a unique broad band at $\lambda_{max} = 276$ nm while the intensity remains practically unchanged. On the other hand, the λ_{max} of the negative band I at 246 nm remains unchanged in all the spectra. The dominating spectral feature for this series of spectra is the lack of any perturbation on both bands of CT DNA and shows the possible existence of simple groove binding or electrostatic interaction [67]. Quite similar behavior is observed in the CD spectra of CT DNA in the presence of complexes $Cd(erx)_2(H_2O)_2$ and $UO_2(erx)_2$.

In conclusion, the behavior of CT DNA in the presence of complexes **1**–**7** is interesting. All the complexes can bind to CT DNA and, at low r values, the exact mode of binding cannot be safely concluded. At high r values, the dominating spectral feature in the spectra of complexes **1**–**4** is the slight increase of the intensities of both the bands of CT DNA, while for complexes **5**–**7** the dominating spectral feature is the lack of any perturbation showing the possibility of simple groove binding or electrostatic interactions.

4. Conclusions

The synthesis and characterization of seven novel mononuclear complexes of the second-generation quinolone antibacterial drug enrofloxacin with the ions Mn^{2+}, Fe^{3+}, Co^{2+}, Ni^{2+}, Zn^{2+}, Cd^{2+} and UO_2^{2+} has been realized with physicochemical and spectroscopic methods. In the complexes, enrofloxacin is bound to the metal via the pyridone and one carboxylate oxygen atoms. Each metal is six-coordinate and the environment around could be described as a distorted octahedron. With the use of molecular modeling calculations, we have proposed a low energy model for the structures of $Mn(erx)_2(H_2O)_2$, $Fe(erx)_3$ and $UO_2(erx)_2$. The antimicrobial activity of the complexes has been tested on three different microorganisms. In general, the complexes present equal or better inhibition than the free enrofloxacin against the three microorganisms tested. The best inhibition among the complexes studied is provided by $Fe(erx)_3$ (MIC = 0.25 μg mL^{-1}) against *E. coli* and *P. aeruginosa*. The interaction of complexes **1**–**7** with CT DNA has been investigated with UV and CD spectroscopies and has shown that the complexes can bind to CT DNA, but the exact binding mode cannot be safely concluded. Nevertheless, at high r values, the simple groove binding or electrostatic interactions for complexes **5**–**7** cannot be ruled out.

Acknowledgements

We thank Dr. I. Eskioglou, Department of Medical Laboratories, Technological and Educational Institution of Larissa, Larissa, Greece for the supply of the microorganisms and Dr. A. Papakyriakou, Institute of Physical Chemistry, NCSR "Demokritos", Greece, for the supply of the molecular modeling routine.

Appendix A. Supplementary data

Supplementary data associated with this article can be found, in the online version, at doi:10.1016/j.poly.2008.02.006.

References

[1] I. Turel, Coord. Chem. Rev. 232 (2002) 27, and references cited therein.
[2] D.C. Hooper, E. Rubinstein (Eds.), Quinolone Antimicrobial Agents, 3rd ed., ASM Press, Washington, DC, 2003.
[3] V.T. Andriole (Ed.), The Quinolones, 3rd ed., Academic Press, San Diego, 2000.
[4] D.T.W. Chu, P.B. Fernandes, in: B. Testa (Ed.), Advances in Drug Research, vol. 21, Academic Press, London, 1991, p. 39.
[5] J.E.F. Reynolds (Ed.), Martindale, The Extra Pharmacopeia, 30th ed., The Pharmaceutical Press, London, 1993, p. 145.
[6] R.E. Polk, Am. J. Med. 87 (1989) S76.
[7] M.J. e Souza, C.F. Bittencourt, L.M. Morsch, J. Pharm. Biomed. Anal. 28 (2002) 1197.

[8] M. Scheer, Vet. Med. Rev. 2 (1987) 90.
[9] D.M. Boothe, Vet. Med. 89 (1994) 744.
[10] R. Bauditz, Vet. Med. Rev. 2 (1987) 122.
[11] J.-Y. Fan, D. Sun, H. Yu, S.M. Kerwin, L.H. Hurley, J. Med. Chem. 38 (1995) 408.
[12] S. Dessus-Babus, C.M. Bebear, A. Charron, C. Bebear, B. De Barbeyrac, Antimicr. Agent Chemother. 42 (1998) 2474.
[13] S. Ameyama, Y. Shinmura, M. Takahata, Antimicr. Agent Chemother. 47 (2003) 2327.
[14] D.E. King, R. Malone, S.H. Lilley, Am. Fam. Phys. 61 (2000) 2741.
[15] E.K. Efthimiadou, M. Katsarou, Y. Sanakis, C.P. Raptopoulou, A. Karaliota, N. Katsaros, G. Psomas, J. Inorg. Biochem. 100 (2006) 1378.
[16] E.K. Efthimiadou, Y. Sanakis, C.P. Raptopoulou, A. Karaliota, N. Katsaros, G. Psomas, Bioorg. Med. Chem. Lett. 16 (2006) 3864.
[17] G. Psomas, A. Tarushi, E.K. Efthimiadou, Y. Sanakis, C.P. Raptopoulou, N. Katsaros, J. Inorg. Biochem. 100 (2006) 1764.
[18] E.K. Efthimiadou, H. Thomadaki, Y. Sanakis, C.P. Raptopoulou, N. Katsaros, A. Scorilas, A. Karaliota, G. Psomas, J. Inorg. Biochem. 101 (2007) 64.
[19] E.K. Efthimiadou, G. Psomas, Y. Sanakis, N. Katsaros, A. Karaliota, J. Inorg. Biochem. 101 (2007) 525.
[20] E.K. Efthimiadou, Y. Sanakis, N. Katsaros, A. Karaliota, G. Psomas, Polyhedron 26 (2007) 1148.
[21] E.K. Efthimiadou, N. Katsaros, A. Karaliota, G. Psomas, Bioorg. Med. Chem. Lett. 17 (2007) 1238.
[22] A. Tarushi, P. Christofis, G. Psomas, Polyhedron 26 (2007) 3963.
[23] A. Tarushi, E.K. Efthimiadou, P. Christofis, G. Psomas, Inorg. Chim. Acta 360 (2007) 3978.
[24] E.K. Efthimiadou, N. Katsaros, A. Karaliota, G. Psomas, Inorg. Chim. Acta 360 (2007) 4093.
[25] G. Psomas, A. Tarushi, E.K. Efthimiadou, Polyhedron 27 (2008) 133.
[26] E.K. Efthimiadou, A. Karaliota, G. Psomas, Polyhedron 27 (2008) 349.
[27] M.E. Katsarou, E.K. Efthimiadou, G. Psomas, A. Karaliota, D. Vourloumis, J. Med. Chem. 51 (2008) 470.
[28] E.K. Efthimiadou, M.E. Katsarou, A. Karaliota, G. Psomas, J. Inorg. Biochem. 102 (2008) 910.
[29] E. Tselepi-Kalouli, N. Katsaros, J. Inorg. Biochem. 37 (1989) 271.
[30] M.E. Reichman, S.A. Rice, C.A. Thomas, P. Doty, J. Am. Chem. Soc. 76 (1954) 3047.
[31] N.L. Allinger, J. Am. Chem. Soc. 99 (1977) 8127.
[32] D.C. Weatherburn, S. Mandal, S. Mukhopadhyay, S. Bhaduri, L.F. Lindoy, in: J.A. McCleverty, T.J. Meyer (Eds.), Comprehensive Coordination Chemistry II, vol. 5, Elsevier, 2003, p. 1, and references cited therein.
[33] V. Tangoulis, G. Psomas, C. Dendrinou-Samara, C.P. Raptopoulou, A. Terzis, D.P. Kessissoglou, Inorg. Chem. 35 (1996) 7655, and references cited therein.
[34] D. Huang, W. Wang, X. Zhang, C. Chen, F. Chen, Q. Liu, D. Liao, L. Li, L. Sun, Eur. J. Inorg. Chem. (2004) 1454.
[35] T. Lis, Acta Crystallogr., Sect. B 33 (1977) 2964.
[36] D. Armentano, G. de Munno, F. Guerra, J. Faus, F. Lloret, M. Julve, Dalton Trans. (2003) 4626.
[37] M. McCann, M.T. Casey, M. Devereux, M. Curran, V. McKee, Polyhedron 16 (1997) 2741, and references cited therein.
[38] A. Karipides, A.T. Reed, Inorg. Chem. 15 (1976) 44.
[39] M.V. Twigg, J. Burgess, in: J.A. McCleverty, T.J. Meyer (Eds.), Comprehensive Coordination Chemistry II, vol. 5, Elsevier, 2003, p. 403, and references cited therein.
[40] M. Scarpellini, A. Neves, A.J. Bortoluzzi, I. Vencato, V. Drago, W.A. Ortiz, C. Zucco, J. Chem. Soc., Dalton Trans. (2001) 2616.
[41] L. Westerheide, F.K. Muller, R. Than, B. Krebs, J. Dietrich, S. Schindler, Inorg. Chem. 40 (2001) 1951.
[42] J.M. Rowland, M. Olmstead, P.K. Mascharak, Inorg. Chem. 40 (2001) 2810.
[43] C.J. Burns, M.P. Neu, H. Boukhalfa, K.E. Gutowski, N.J. Bridges, R.D. Rogers, in: J.A. McCleverty, T.J. Meyer (Eds.), Comprehensive Coordination Chemistry II, vol. 3, Elsevier, 2003, p. 189, and references cited therein.
[44] P. Thuery, C. Villiers, J. Jaud, M. Ephritikhine, B. Masci, J. Am. Chem. Soc. 126 (2004) 6838.
[45] A.D. Sutton, G.H. John, M.J. Sarsfield, J.C. Renshaw, I. May, L.R. Martin, A.J. Selvage, D. Collison, M. Helliwell, Inorg. Chem. 43 (2004) 5480.
[46] M.P. Allen, D.J. Tildesley (Eds.), Computer Simulation of Liquids, Oxford University Press, 1989.
[47] K. Nakamoto, Infrared and Raman Spectra of Inorganic and Coordination Compounds, 4th ed., Wiley, New York, 1986.
[48] D.A. Buckingham, C.R. Clark, in: G. Wilkinson (Ed.), Comprehensive Coordination Chemistry, vol. 4, Pergamon Press, Oxford, 1989, p. 635.
[49] P.V. Bernhardt, G.A. Lawrance, in: J.A. McCleverty, T.J. Meyer (Eds.), Comprehensive Coordination Chemistry II, vol. 6, Elsevier, 2003, p. 1, and references cited therein.
[50] L. Sacconi, F. Mani, A. Bencini, in: G. Wilkinson (Ed.), Comprehensive Coordination Chemistry, vol. 5, Pergamon Press, Oxford, 1989, p. 1.
[51] F. Meyer, H. Kozlowski, in: J.A. McCleverty, T.J. Meyer (Eds.), Comprehensive Coordination Chemistry II, vol. 6, Elsevier, 2003, p. 247, and references cited therein.
[52] M. Ruiz, R. Ortiz, L. Perello, J. Latorre, J. Server-Carrio, J. Inorg. Biochem. 65 (1997) 87.
[53] M. Ruiz, R. Ortiz, L. Perello, A. Castineiras, M. Quiros, Inorg. Chim. Acta 211 (1993) 133.
[54] P. Christofis, M. Katsarou, A. Papakyriakou, Y. Sanakis, N. Katsaros, G. Psomas, J. Inorg. Biochem. 99 (2005) 2197, and references cited therein.
[55] A.D. Russell, in: S.S. Block (Ed.), Disinfection, Sterilization and Preservation, 4th ed., Lea and Febinger, Philadelphia, 1991, p. 27.
[56] H.W. Rossmore, in: S.S. Block (Ed.), Disinfection, Sterilization and Preservation, 4th ed., Lea and Febinger, Philadelphia, 1991, p. 290.
[57] C. Dendrinou-Samara, G. Psomas, C.P. Raptopoulou, D.P. Kessissoglou, J. Inorg. Biochem. 83 (2001) 7.
[58] G. Psomas, C. Dendrinou-Samara, P. Philippakopoulos, V. Tangoulis, C.P. Raptopoulou, E. Samaras, D.P. Kessissoglou, Inorg. Chim. Acta 272 (1998) 24.
[59] A. Rodger, B. Norden (Eds.), Circular Dichroism and Linear Dichroism, Oxford University Press, Oxford, New York, Tokyo, 1997.
[60] B.M. Zeglis, V.C. Pierre, J.K. Barton, Chem. Commun. (2007) 4565.
[61] T.C. Jenkins, in: K.R. Fox (Ed.), Drug–DNA Interaction Protocols, Humana Press Inc., Totowa, New Jersey, 1997, p. 195.
[62] G.S. Son, J.-A. Yeo, M.-S. Kim, S.K. Kim, A. Holmen, B. Akerman, B. Norden, J. Am. Chem. Soc. 120 (1998) 6451.
[63] J.K. Barton, A.L. Raphael, J. Am. Chem. Soc. 106 (1984) 2172.
[64] A.M. Pyle, J.P. Rehmann, R. Meshoyrer, C.V. Kumar, N.J. Turro, J.K. Barton, J. Am. Chem. Soc. 111 (1989) 3053.
[65] P. Uma Maheswari, M. Palaniandavar, J. Inorg. Biochem. 98 (2004) 219.
[66] P. Lincoln, E. Tuite, B. Norden, J. Am. Chem. Soc. 119 (1997) 1454.
[67] B. Norden, F. Tjerneld, Biopolymers 21 (1982) 1713.
[68] W. Curtis-Johnson, in: K. Nakanishi, N. Berova, R.W. Woody (Eds.), CD of Nucleic Acids in Circular Dichroism, Principles and Applications, VHS, New York, 1994, p. 523.

central ion occurs through the N–O chelating site. This coordination produces a five-membered ring containing an unsaturated α-iminoketo function which can act as a π acceptor towards a bound π electron-rich metal center such as rhenium(III). The α-iminoketo chelation plays an important role in the biosynthesis of the pterins, lumazines, flavins coenzymes [9,10]. Accordingly, complex **1** may be viewed as a simple model for such metalloenzymes. Furthermore, to our knowledge, *fac*-[$ReCl_3$(N–O)(PPh_3)] is the first structurally characterised complex with 1-isoquinolinyl phenyl ketone.

The electronic structure of **1** has been determined with the density functional theory (DFT) method, and time-dependent DFT (TD-DFT) calculations have been employed in order to discussion of its spectroscopic properties in more detail. Currently, density functional theory (DFT) is commonly used to examine the electronic structure of transition metal complexes. It meets with the requirements of being accurate, easy to use and fast enough to allow the study of relatively large molecules of transition metal complexes [11]. Recent studies have also supported the TD-DFT method to be applicable for open- and closed-shell of 5d-metal complexes giving good assignment of experimental spectra [12,13].

2. Experimental

2.1. General procedure

All the reagents used to the syntheses were commercially available and were used without further purification. The [$ReCl_3$(MeCN)(PPh_3)$_2$] complex was prepared according to the literature method [7].

IR spectrum was recorded on a Nicolet Magna 560 spectrophotometer in the spectral range 4000–400 cm^{-1} with the samples in the form of KBr pellets. Electronic spectrum was measured on a spectrophotometer Lab Alliance UV–VIS 8500 in the range 1000–200 nm in acetonitrile solution. Elemental analyses (C, H, N) were performed on a Perkin–Elmer CHN-2400 analyzer.

2.2. Preparation of [$ReCl_3$(N–O)(PPh_3)] (1)

[Re(MeCN)Cl_3(PPh_3)$_2$] (0.5 g, 0.58 mmol) and 1-isoquinolinyl phenyl ketone (0.15 g, 0.64 mmol) in dichloromethane (40 cm^3) were refluxed for 4 h. The starting material gradually dissolved and the colour of the reaction solution became brown. The volume was condensed to 10 cm^3, diethyl ether (50 cm^3) was added and brown microcrystalline solid was filtered. The product was washed with EtOH and cold ether, and dried *in vacuo* (Yield 80%). The crystals suitable for X-ray investigation were obtained by recrystallization from a mixture dichloromethane/methanol.

IR (KBr; ν/cm^{-1}): ν_{CO} = 1677 cm^{-1}; ν_{CN} and $\nu_{C=C}$ = 1586(m), 1572(w) and 1539(m) ν_{CN} and $\nu_{C=C}$. *Anal*. Calc. for $C_{34}H_{26}Cl_3NOPRe$: C, 51.82; H, 3.33; N, 1.78. Found: C, 52.15; H, 3.24; N, 1.63%.

2.3. X-ray diffraction studies

A dark red crystal of **1** was mounted on a KM-4-CCD automatic diffractometer equipped with a CCD detector, and used for data collection. X-ray intensity data were collected with graphite monochromated Mo Kα radiation (λ = 0.71073 Å) at 295(1) K. Details concerning crystal data and refinement are given in Table 1. Lorentz, polarization and empirical absorption correction using spherical harmonics implemented in SCALE3 ABSPACK scaling algorithm [14] were applied. The structure was solved by the Patterson method and subsequently completed by the difference Fourier recycling. All the non-hydrogen atoms were refined anisotropically using full-matrix, least-squares technique. The hydrogen atoms were treated as "riding" on their parent carbon atoms and assigned isotropic temperature factors equal 1.2 times the value of equivalent temperature factor of the parent atom. SHELXS97 [15], SHELXL97 [16] and SHELXTL [17] programs were used for all the calculations. Atomic scattering factors were those incorporated in the computer programs.

2.4. Magnetic measurement

Magnetization measurements of polycrystalline samples were carried out with a Quantum Design SQUID

Table 1
Crystal data and structure refinement for **1**

Empirical formula	$C_{34}H_{26}Cl_3NOPRe$
Formula weight	788.08
Temperature (K)	293(2)
Wavelength (Å)	0.71073
Crystal system	orthorhombic
Space group	$P2_12_12_1$
Unit cell dimensions	
	a (Å) = 13.706(3)
	b (Å) = 14.172(3)
	c Å = 15.150(3)
V (Å^3)	2942.7(10)
Z	4
D_{calc} (Mg/m^3)	1.779
Absorption coefficient (mm^{-1})	4.486
F(000)	1544
Crystal size (mm)	0.12 × 0.10 × 0.07
θ Range for data collection (°)	2.87–25.04
Index ranges	$-14 \leqslant h \leqslant 16$
	$-16 \leqslant k \leqslant 16$
	$-18 \leqslant l \leqslant 16$
Reflections collected	18 558
Independent reflections (R_{int})	5206 (0.0448)
Completeness to 2θ	99.8%
Maximum and minimum transmission	0.586 and 0.260
Data/restraints/parameters	5206/0/370
Goodness-of-fit on F^2	0.988
Final R indices [$I > 2\sigma(I)$]	R_1 = 0.0269
	wR_2 = 0.0438
R indices (all data)	R_1 = 0.0395
	wR_2 = 0.0451
Absolute structure parameter	−0.004(6)
Largest difference in peak and hole (e Å^{-3})	0.641 and −0.684

magnetometer (MPMSXL-5-type) at a magnetic field of 0.5 T over the temperature range 1.8–300 K. Magnetization measurements versus magnetic field (0–5 T) were made at 2 K.

Corrections are based on subtracting the sample–holder signal and contribution χ_D estimated from the Pascal constants [18] and equal -411×10^{-6} for complex Re(III). The effective magnetic moment was calculated from the equation, $\mu_{eff} = 2.83\chi_M^{corr} \times T^{1/2}$ B.M.

2.5. Computational details

GAUSSIAN03 program [19] was used in the calculations. The geometry optimizations of **1** in triplet and singlet states were carried out with the DFT method with the use of B3LYP functional [20,21]. The energy of the singlet state is of 12.8 kcal higher. All vibrations in the calculated vibrational spectrum of triplet state were real thus the geometry corresponds to true energy minimum.

The electronic spectrum of **1** was calculated with the TDDFT method [22]. The calculations were performed by using ECP basis set on the rhenium atom, the standard 6-31 + g** basis for chlorine, phosphorus, and nitrogen, 6-31g* basis for carbon and 6-31G basis for hydrogen atoms. The Xe core electrons of Re were replaced by an effective core potential and DZ quality Hay and Wadt Los Alamos ECP basis set (LANL2DZ) [23] was used for the valence electrons. Additional *d* function with exponent $\alpha = 0.3811$ and *f* function with exponent $\alpha = 2.033$ on the rhenium atom were added.

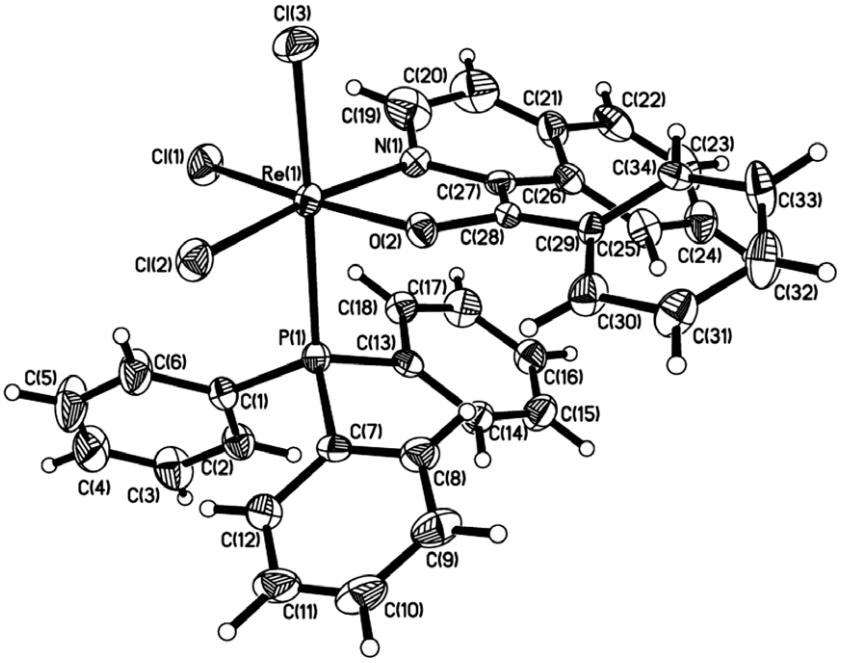


Fig. 1. The molecular structure of **1**. Displacement ellipsoids are drawn at 30% probability.

Table 2
The experimental and optimized bond lengths (Å) and angles (°) for **1**

Bond lengths	Experimental	Optimized	Bond angles	Experimental	Optimized
Re(1)–O(1)	1.990(3)	1.992	O(1)–Re(1)–N(1)	74.75(15)	75.20
Re(1)–N(1)	2.026(3)	2.074	O(1)–Re(1)–P(1)	87.92(9)	93.48
Re(1)–P(1)	2.5005(14)	2.565	N(1)–Re(1)–P(1)	92.34(13)	96.33
Re(1)–Cl(1)	2.3352(15)	2.416	O(1)–Re(1)–Cl(1)	169.07(12)	171.60
Re(1)–Cl(2)	2.3519(13)	2.402	O(1)–Re(1)–Cl(2)	95.10(12)	90.87
Re(1)–Cl(3)	2.3694(15)	2.422	O(1)–Re(1)–Cl(3)	91.96(9)	89.15
			N(1)–Re(1)–Cl(1)	94.63(11)	96.40
			N(1)–Re(1)–Cl(2)	169.78(11)	166.07
			N(1)–Re(1)–Cl(3)	90.46(13)	87.36
			Cl(1)–Re(1)–P(1)	89.94(5)	87.24
			Cl(2)–Re(1)–P(1)	85.97(6)	84.58
			Cl(3)–Re(1)–P(1)	177.06(6)	175.92
			Cl(1)–Re(1)–Cl(2)	95.44(5)	97.53
			Cl(1)–Re(1)–Cl(3)	90.72(6)	90.61
			Cl(2)–Re(1)–Cl(3)	91.12(7)	92.27

3. Results and discussion

The $[ReCl_3(N–O)(PPh_3)]$ (**1**) complex was prepared in good yield by ligand exchange reaction starting from $[ReCl_3(MeCN)(PPh_3)]$ and 1-isoquinolinyl phenyl ketone (N–O):

$$[ReCl_3(MeCN)(PPh_3)] + \text{1-isoquinolinyl phenyl ketone} \rightarrow [ReCl_3(N–O)(PPh_3)] + PPh_3$$

It was isolated as brown microcrystalline solid, soluble in common organic solvents. The elemental analysis of the complex is in good agreement with its formulation. A band due to the ν(C=O) vibration of 1-isoquinolinyl phenyl ketone appears at 1677 cm^{-1}, and characteristic bands of the C=C and C=N stretching modes are observed in the range 1600–1500 cm^{-1} [24].

3.1. Crystal structure

The molecular structure of **1** is given in Fig. 1, and the selected bond distances and angles are collected in Table 2.

The overall structure of **1** can be considered as a distorted octahedral with the largest deviations from the expected 90° bond angles coming from the bite angle of 1-isoquinolinyl phenyl ketone. It equals to 74.75(15)°, and it is similar to that reported for the related $[Re(CO)_3(6\text{-ATML})Cl] \cdot 3C_6H_6$ (6-ATML = 6-acetyl-1,3,7-trimethyllumazine) [75.2(1)°] [10]. The bite angles O–M–N in the structures with α-iminoketo chelate ligands bounded to transition metals depend mainly on the size of the metal center, the smallest values (down to 67°) were found for Ag^I complexes and the largest angles (up to 85°) were observed for compounds with Cu^{II} [9].

The central ion of **1** shows slightly larger affinity towards the less basic but strongly π accepting carbonyl oxo atom, and the Re–O(1) is shorter than the Re–N(1) bond (Table 2). The value $\Delta = d(M–N) - d(M–O)$, which reflects the symmetry of the chelate arrangement in such structures, is equal to 0.036 Å for **1**, indicating that the Re center is situated symmetrically between N(1) and O(1) donor atoms.

The chloride ions of **1** are arranged in a *facial* fashion, and the phosphorous atom of the phosphine ligand occupies the *trans* position to the Cl(3) ion. Geometrical preferences of the $ReCl_3$ unit in the $[ReCl_3(L–L)(PPh_3)]$ complexes can be rationalized in terms of the electronic nature of the L–L ligand. Triphenylphosphine is a π-accepting ligand, and trivalent rhenium is prone to

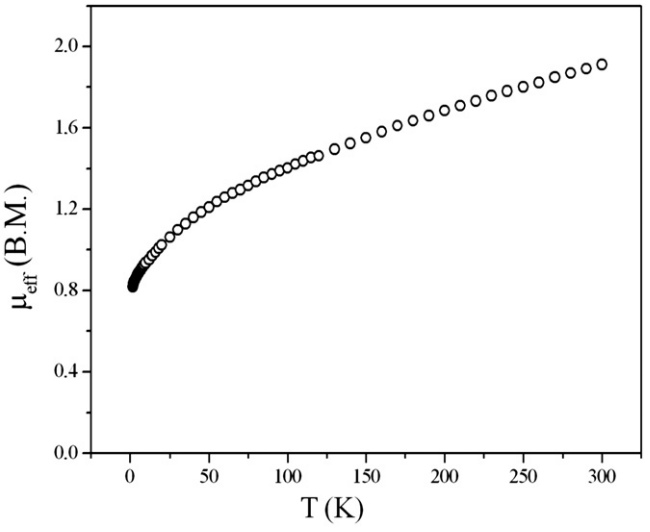


Fig. 2. The effective magnetic moment (μ_{eff}) vs temperature for complex **1**.

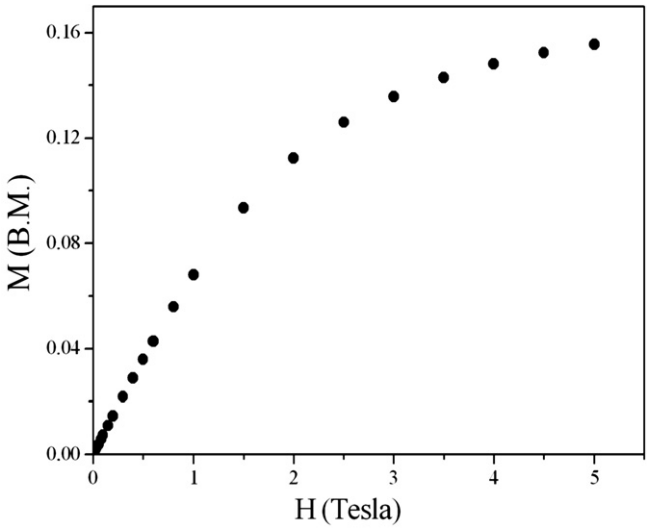


Fig. 3. The variation of the magnetization (M) vs the magnetic field (H) at 2 K for complex **1**.

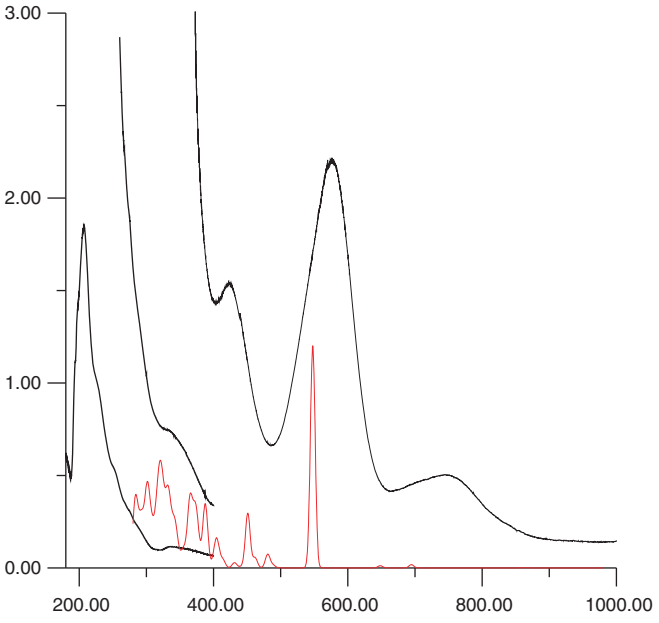


Fig. 4. The experimental (black) and calculated (red) electronic absorption spectrum of **1**. (For interpretation of the references to colour in this figure legend, the reader is referred to the web version of this article.)

back-bonding. When the L–L ligand is a strong π-acid, the *facial* geometry is preferred as it maximizes the back-bonding effect. Assuming idealized octahedral geometry the back-bonding has $t_{2g}(Re) \rightarrow \sigma^*(P–C)$ and $t_{2g}(Re) \rightarrow \pi^*(L–L)$ components. This bonding is maximized when the competition between ligands for identical metal orbitals is minimal – what requires facially disposed π acceptor ligands [25–31].

It is significant that the Re–N distance in **1** (2.026(3) Å) is shorter than comparable distances for saturated amine complexes, where metal-to-ligand π-back-bonding is not possible [32]. Similarly, the interatomic distance between the rhenium atom and the oxygen atom of 1-isoquinolinyl phenyl ketone is shorter than an ideal single Re–O bond length (*ca.* 2.04 Å) [33].

The Re–X(3) bond length is longer in comparison with the corresponding Re–X(1) and Re–X(2) distances. Furthermore, the Re–X(2) bond lengths in *trans* position to the N atom of the bidentate ligand are longer in comparison with the Re–Cl(1) bonds opposite the O atom of the 1-isoquinolinyl phenyl ketone. This is consistent with the presence of $t_{2g}(Re) \rightarrow \sigma^*(P–C)$ and $t_{2g}(Re) \rightarrow \pi^*(N–O)$ back-bonding discussed above.

3.2. Magnetic properties

The magnetic properties of complex under the form μ_{eff} versus temperature (μ_{eff} – the effective magnetic moment) is shown in Fig. 2.

The complex of rhenium(III) shows room temperature magnetic moment 1.91 B.M. (0.456 cm^3 mol^{-1} K). In the whole temperature range lowering magnetic moment is observed from 1.91 B.M. at 300 K up to 0.82 B.M. at 1.8 K.

Table 3
The spin-allowed triplet–triplet electronic transitions calculated with the TDDFT method and the assignments of the calculated transitions to the experimental absorption bands for **1**

The most important orbital excitations	Character	λ (nm)	*E* (eV)	*f*	Experimental Λ (nm) (*E* [eV]) ε
H(β) → L + 2(β)	d/π(N–O)/π(Cl) → d	862.3	1.44	*0.0001*	777.1 (1.60) 760
H(α) → L(α)	d/π(Cl) → π*(N–O)	694.7	1.78	*0.0022*	
H − 1(α) → L(α)	d/π(Cl) → π*(N–O)	648.4	1.91	*0.0015*	
H − 2(α) → L(α)					
H − 1(α) → L(α)	d/π(Cl) → π*(N–O)	547.7	2.26	*0.1501*	570.0 (2.18) 3800
H − 2(α) → L(α)					
H − 2(β) → L(β)	π(Cl) → d	461.8	2.68	*0.0068*	432.4 (2.87) 2520
H(β) → L + 3(β)	d/π(N–O)/π(Cl) → π*(N–O)	450.9	2.75	*0.0369*	
H(β) → L + 4(β)	d/π(N–O)/π(Cl) → π*(N–O)	414.0	3.00	*0.0051*	
H − 2(β) → L + 2(β)	π(Cl) → d	406.1	3.05	*0.0101*	
H − 2(β) → L + 2(β)	π(Cl) → d	403.8	3.07	*0.0051*	
H − 7(α) → L(α)	π(Cl) → π*(N–O)	402.2	3.08	*0.0071*	
H − 3(β) → L + 1(β)	π(N–O)/π(Cl) → d/π* (N–O)	387.2	3.20	*0.0376*	347.0 (3.57) 5960
H(α) → L + 2(α)	d/π(Cl) → d/π* (PPh_3)/π*(N–O)	374.5	3.31	*0.0193*	
H(β) → L + 5(β)	d/π(N–O)/π(Cl) → d/π*(PPh_3)				
H − 7(α) → L(α)	π(Cl) → π*(N–O)	372.4	3.33	*0.0126*	
H(β) → L + 5(β)	d/π(N–O)/π(Cl) → d/π*(PPh_3)				
H − 5(β) → L + 1(β)	π(Cl)/π(N–O)/π(PPh_3) → d/π*(π*(N–O))	365.2	3.40	*0.0138*	
H − 5(β) → L + 2(β)	π(Cl)/π(N–O)/π(PPh_3) → d	364.5	3.40	*0.0229*	
H − 3(β) → L + 2(β)	π(N–O)/π(Cl) → d				
H − 13(α) → L(α)	π(Cl)/π(PPh_3) → π*(N–O)	332.7	3.73	*0.0203*	
H − 12(α) → L(α)	π(N–O)/π(Cl)/π(PPh_3) → π*(N–O)	330.2	3.75	*0.0135*	
H − 7(β) → L + 1(β)	π(N–O)/π(PPh_3) → d/π*(N–O)				
H − 11(β) → L(β)	π(N–O)/π(Cl)/π(PPh_3) → d	325.7	3.80	*0.0123*	
H − 4(β) → L + 2(β)	π(PPh_3)/π(Cl) → d	322.5	3.84	*0.0150*	
H − 8(β) → L(β)	π(Cl)/π(PPh_3) → d	320.3	3.87	*0.0165*	
H − 14(β) → L + 2(β)	π(Cl) → d				
H − 2(α) → L + 1(α)	d/π(Cl) → π*(N–O)	319.1	3.88	*0.0126*	
H − 14(β) → L(β)	π(Cl) → d	318.0	3.90	*0.0105*	
H(α) → L + 3(α)	d/π(Cl) → d/π*(N–O)	315.6	3.92	*0.0158*	
H − 14(β) → L + 1(β)	π(Cl) → d/π*(N–O)	301.0	4.12	*0.0139*	285.6 (4.34) 9980
H − 7(β) → L + 2(β)	π(N–O)/π(PPh_3) → d	300.3	4.13	*0.0168*	
H − 9(β) → L + 2(β)	π(PPh_3)/π(Cl)/π(N–O) → d	294.6	4.21	*0.0110*	
H(β) → L + 11(β)	d/π(N–O)/π(Cl) → π* (N–O)	292.0	4.25	*0.0187*	
H − 2(α) → L + 4(α)	d/π(Cl) → π*(PPh_3)	283.1	4.38	*0.0101*	
H − 18(β) → L + (β)	π(Cl) → d	282.9	4.38	*0.0112*	
					266.0 (4.66) 15670
					231.2 (5.36) 39500
					208.0 (5.96) 79100

This behavior is characteristic of mononuclear Re(III)complexes ($^3T_{1g}$ ground state) with d^4 low-spin octahedral [34–42] and arises from the large spin–orbit coupling ($\zeta = 2500\ cm^{-1}$ [43]), which gives diamagnetic ground state. It seems that in room temperature, in accordance Boltzmann's distribution, it is populated higher magnetic state, which is depopulated with temperature lowering and decreasing of the magnetic moment is observed.

The variation of the magnetization M versus the magnetic field H for complex at 2 K is shown in Fig. 3.

The magnetization versus magnetic field curve for complex very slowly increases and indicates value of the magnetization near zero (0.16 B.M) at 5 T. Magnetization of the sample confirms that the ground state is diamagnetic.

3.3. Geometry optimization

The optimized geometric parameters of the triplet state are gathered in Table 2. In general, the predicted bond lengths and angles are in agreement with the values based upon the X-ray crystal structure data. However, some differences may be noticed between the experimental and optimized structures. The experimental Re(1)–Cl(2) is longer than the Re(1)–Cl(1), whereas the other relation is observed for the optimized structure. It may come from the basis sets which are approximated to a certain extent or may indicate the influence of the crystal packing on the values of the experimental bond lengths. The theoretical calculations do not consider the effects of chemical environment.

3.4. Electronic spectrum

The experimental and calculated electronic spectra of **1** are presented in Fig. 4. Each calculated transition is represented by a gaussian function $y = c\,e^{-bx2}$ with the height (c) equal to the oscillator strength and b equal to $0.04\ nm^{-2}$. The electronic absorption spectrum of **1** is similar to those

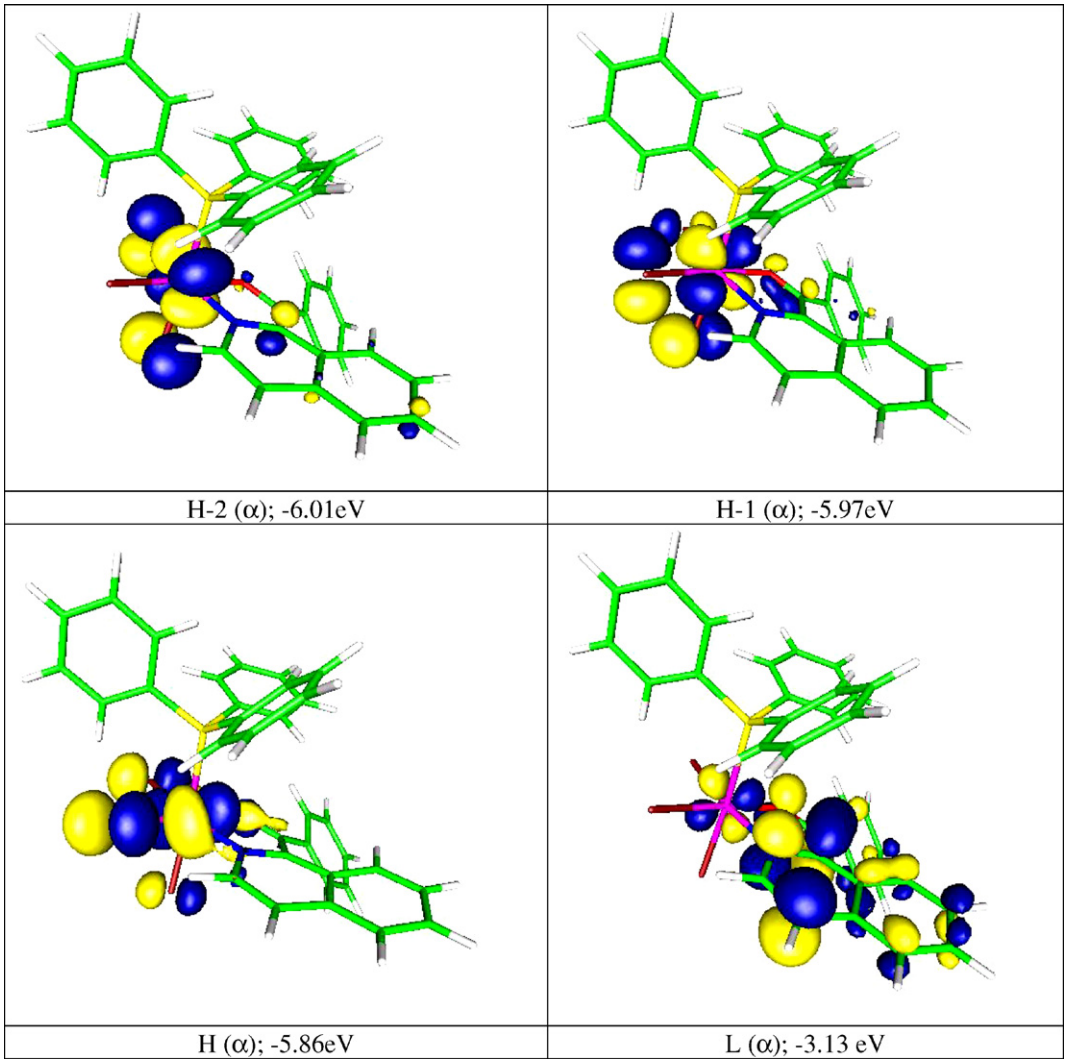


Fig. 5. Energy and contour plots of the selected occupied and unoccupied molecular orbitals with α spin active in the electronic transitions for complex **1**. Positive values of the orbital contour are represented in blue (0.04 au) and negative values – in yellow (−0.04 au). (For interpretation of the references to colour in this figure legend, the reader is referred to the web version of this article.)

observed for *fac*-[$ReCl_3$(L–L)(PPh_3)] with bipy-like ligands. It displays transitions of moderate intensity in the form of peaks and shoulders in the visible region (400–1000 nm).

Table 3 presents the most important spin-allowed triplet–triplet electronic transitions calculated with the TDDFT method assigned to the observed absorption bands of **1**. The assignment of the calculated orbital excitations to the experimental bands was based on an overview of the contour plots and relative energy to the orbitals HOMO and LUMO involved in the electronic transitions. The selected HOMO and LUMO orbitals of **1** with α and β spins active in the electronic transitions are presented in Figs. 5 and 6.

The investigated complex is of large size, the number of basis functions is equal 686. A hundred electron transitions calculated by the TDDFT method do not comprise all the experimental absorption bands. The UV–Vis spectrum of **1** was calculated only to 280 nm, so the shortest wavelength experimental bands can not be assigned to the calculated transitions. Some additional intraligand and interligand transitions are expected to be found at higher energies in the calculation for **1**.

The TDDFT calculations show that two longest wavelength experimental bands of **1** at 777.1 and 570.0 nm originate in the HOMO−2(α) → LUMO(α), HUMO−1(α) → LUMO(α) and HOMO(α) → LUMO(α) transitions. The HOMO−2, HOMO−1 and HOMO orbitals with α-spin can be considered as π_{Re-Cl} orbitals – in all these MOs the rhenium d_{xz}, d_{yz} and d_{xy} orbitals bear antibonding character towards the p_π orbitals of the chloride ligands. The lowest unoccupied molecular orbital with α-spin is centered on the π-antibonding orbitals of the N–O ligand. Consequently, the HOMO−2(α) → LUMO(α), HUMO−1(α) → LUMO(α) and HOMO(α) → LUMO(α) excitations can be seen as mixed Re → N–O (MLCT) and Cl → N–O (LLCT) or a delocalized MLLCT (metal–ligand-to-ligand CT) description can be used.

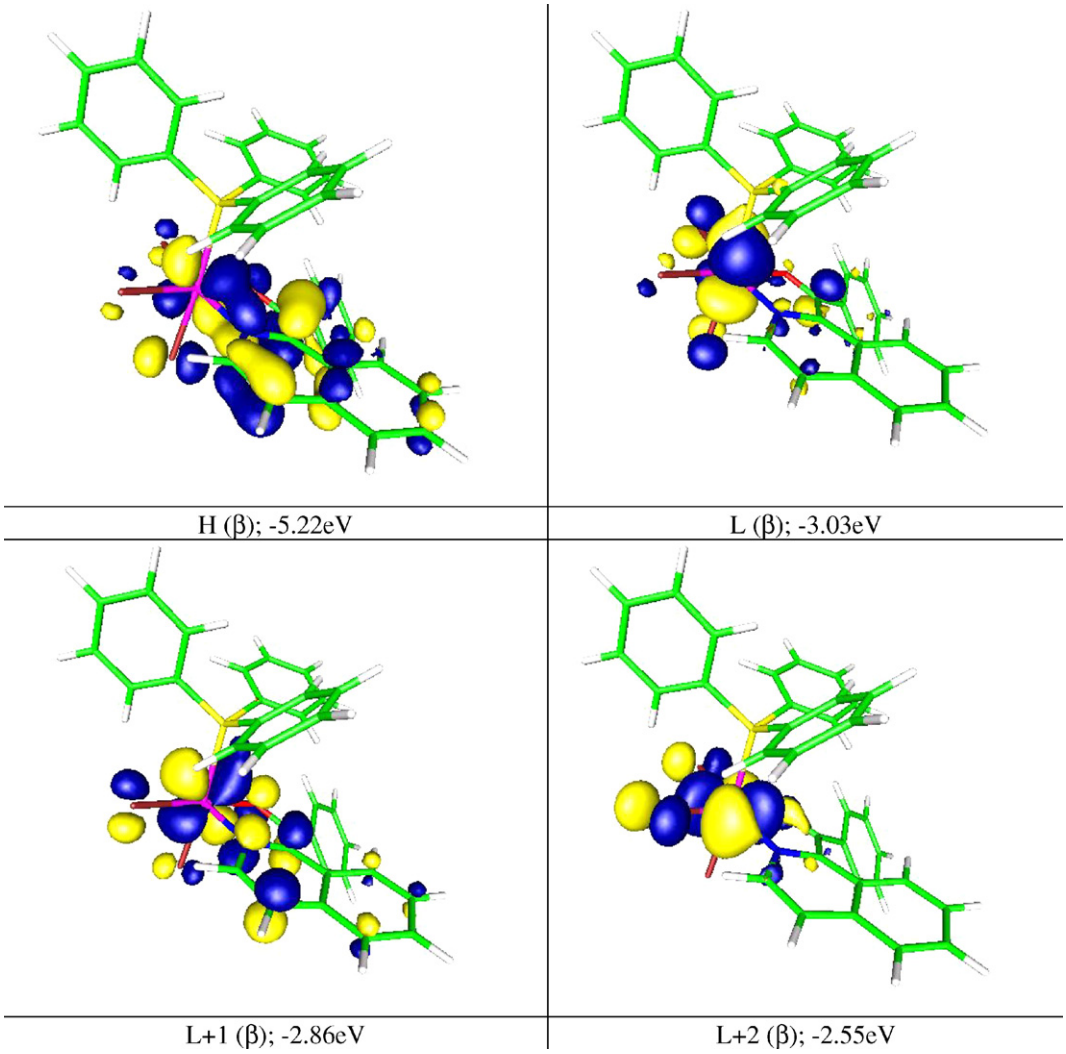


Fig. 6. Energy and contour plots of the selected occupied and unoccupied molecular orbitals with β spin active in the electronic transitions for complex **1**. Positive values of the orbital contour are represented in blue (0.04 au) and negative values – in yellow (−0.04 au). (For interpretation of the references to colour in this figure legend, the reader is referred to the web version of this article.)

The absorption band at 432.4 nm originates mainly from the HOMO(β) → LUMO+3(β) transition of d/π (N–O)/π(Cl) → π*(N–O) character. The highest occupied molecular orbital with β-spin is delocalized among rhenium ion, chloride and N–O ligand, and the LUMO-3 orbital with β-spin is centered on the 1-isoquinolinyl phenyl ketone. To the absorption band at 432.4 nm have been also assigned *Ligand–Metal Charge Transfer* excitations calculated in 460–400 nm region.

Similarly, the absorption at 347.0 nm is attributed to *Ligand–Metal Charge Transfer* and *Ligand–Ligand Charge Transfer* excitations.

4. Supplementary data

CCDC 674873 contains the supplementary crystallographic data for $C_{26}H_{25}Cl_5N_4PRe$. These data can be obtained free of charge via http://www.ccdc.cam.ac.uk/conts/retrieving.html, or from the Cambridge Crystallographic Data Centre, 12 Union Road, Cambridge CB2 1EZ, UK; fax: (+44) 1223-336-033; or e-mail: deposit@ccdc.cam.ac.uk.

Acknowledgement

The GAUSSIAN03 calculations were carried out in the Wrocław Centre for Networking and Supercomputing, WCSS, Wrocław, Poland, under calculational Grant No. 51/96.

References

[1] D.S. Urch, M.J. Welch, Annu. Rep. Prog. Chem., Sect. A 101 (2005) 585.
[2] P. Blower, Dalton Trans. (2006) 1705.
[3] F. Tisato, M. Porchia, C. Bolzati, F. Refosco, A. Vittadini, Coord. Chem. Rev. 250 (2006) 2034.
[4] Jonathan R. Dilworth, Suzanne J. Parrott, Chem. Soc. Rev. 27 (1998) 43.
[5] R.C. Elder, J. Yuan, B. Helmer, D. Pipes, K. Deutsch, E. Deutsch, Inorg. Chem. 36 (1997) 3055.
[6] U. Abram, R. Alberto, J. Braz. Chem. Soc. 17 (2006) 1486.
[7] G. Rouschias, G. Wilkinson, J. Chem. Soc. A (1967) 993.
[8] P. Ghosh, A. Pramanik, N. Bag, A. Chakravorty, J. Chem. Soc., Dalton Trans. (1992) 1883.
[9] W. Kaim, B. Schwederski, O. Heilmann, F.M. Hornung, Coord. Chem. Rev. 182 (1999) 323.
[10] S.B. Jiménez-Pulido, M. Sieger, A. Knödler, O. Heilmann, M. Wanner, B. Schwederski, J. Fiedler, M.N. Moreno-Carretero, W. Kaim, Inorg. Chim. Acta 325 (2001) 65.
[11] H. Chermette, Coord. Chem. Rev. 178–180 (1998) 699.
[12] M.C. Aragoni, M. Arca, T. Cassano, C. Denotti, F.A. Devillanova, F. Isaia, V. Lippolis, D. Natali, L. Niti, M. Sampietro, R. Tommasi, G. Verani, Inorg. Chem. Commun. 5 (2002) 869.
[13] P. Romaniello, F. Lelj, Chem. Phys. Lett. 372 (2003) 51.
[14] CRYSALIS RED, Oxford Diffraction Ltd., Version 1.171.29.2.
[15] G.M. Sheldrick, Acta Crystallogr. A64 (2008) 112.
[16] G.M. Sheldrick, SHELXL97. Program for the Refinement of Crystal Structures, University of Göttingen, Germany, 1997.
[17] G.M. Sheldrick, SHELXTL: Release 4.1 for Siemens Crystallographic Research Systems, Simens Analytical X-ray Instruments Inc., Madison, Wisconsin, USA, 1990.
[18] E. König, Magnetic Properties of Coordination and Organometallic Transition Metal Compounds, Springer, Berlin, 1966.
[19] M.J. Frisch, G.W. Trucks, H.B. Schlegel, G.E. Scuseria, M.A. Robb, J.R. Cheeseman, J.A. Montgomery Jr., T. Vreven, K.N. Kudin, J.C. Burant, J.M. Millam, S.S. Iyengar, J. Tomasi, V. Barone, B. Mennucci, M. Cossi, G. Scalmani, N. Rega, G.A. Petersson, H. Nakatsuji, M. Hada, M. Ehara, K. Toyota, R. Fukuda, J. Hasegawa, M. Ishida, T. Nakajima, Y. Honda, O. Kitao, H. Nakai, M. Klene, X. Li, J.E. Knox, H.P. Hratchian, J.B. Cross, C. Adamo, J. Jaramillo, R. Gomperts, R.E. Stratmann, O. Yazyev, A.J. Austin, R. Cammi, C. Pomelli, J.W. Ochterski, P.Y. Ayala, K. Morokuma, G.A. Voth, P. Salvador, J.J. Dannenberg, V.G. Zakrzewski, S. Dapprich, A.D. Daniels, M.C. Strain, O. Farkas, D.K. Malick, A.D. Rabuck, K. Raghavachari, J.B. Foresman, J.V. Ortiz, Q. Cui, A.G. Baboul, S. Clifford, J. Cioslowski, B.B. Stefanov, G. Liu, A. Liashenko, P. Piskorz, I. Komaromi, R.L. Martin, D.J. Fox, T. Keith, M.A. Al-Laham, C.Y. Peng, A. Nanayakkara, M. Challacombe, P.M.W. Gill, B. Johnson, W. Chen, M.W. Wong, C. Gonzalez, J.A. Pople, GAUSSIAN 03, Revision B.03, Gaussian Inc., Pittsburgh, PA, 2003.
[20] A.D. Becke, J. Chem. Phys. 98 (1993) 5648.
[21] C. Lee, W. Yang, R.G. Parr, Phys. Rev. B 37 (1988) 785.
[22] M.E. Casida, in: J.M. Seminario (Ed.), Recent Developments and Applications in Modern Density Functional Theory, Theoretical and Computational Chemistry, vol. 4, Elsevier, Amsterdam, 1996.
[23] P.J. Hay, W.R. Wadt, J. Chem. Phys. 82 (1985) 299.
[24] K. Nakamoto, Infrared and Raman Spectra of Inorganic and Coordination Compounds, 4th ed., Wiley-Interscience, New York, 1986.
[25] S. Bhattacharyya, S. Banerjee, B.K. Dirghangi, M. Menon, A. Chakravorty, J. Chem. Soc., Dalton Trans. (1999) 155.
[26] I. Chakraborty, S. Bhattacharyya, S. Banerjee, B.K. Dirghangi, A. Chakravorty, J. Chem. Soc., Dalton Trans. (1999) 3747.
[27] S. Bhattacharyya, I. Chakraborty, B.K. Dirghangi, A. Chakravorty, Inorg. Chem. 40 (2001) 286.
[28] Y. Miyashita, N. Mahboob, S. Tsuboi, Y. Yamada, K. Fujisawa, K. Okamoto, Acta Crystallogr. C57 (2001) 558.
[29] F. Tisato, F. Refosco, C. Bolzati, A. Cagnolini, S. Gatto, G. Bandoli, J. Chem. Soc., Dalton Trans. (1997) 1421.
[30] C. Pearson, A.L. Beauchamp, Inorg. Chem. 37 (1998) 1242.
[31] A. Vogler, H. Kunkely, Coord. Chem. Rev. 230 (2002) 243.
[32] D. Orth, J. Barrerra, M. Sabat, W.D. Harman, Inorg. Chem. 33 (1994) 3026.
[33] S.R. Fletcher, A.C. Skapski, J. Chem. Soc., Dalton Trans. (1972) 1073.
[34] J.E. Fergusson, Coord. Chem. Rev. 1 (1966) 459.
[35] B.N. Figgis, J. Lewis, Prog. Inorg. Chem. 6 (1964) 37.
[36] B.N. Figgis, Introduction to Ligand Field, Wiley-Interscience, New York, 1966, p. 248.
[37] J. Chatt, G.J. Leigh, D.M.P. Mingos, E.W. Randall, D. Shaw, J. Chem. Soc., Chem. Commun. (1968) 419.
[38] H.P. Gunz, G.J. Leigh, J. Chem. Soc. (1971) 2229.
[39] B. Coutinho, J.R. Dilworth, P. Jobanputra, R.M. Thompson, S. Schmidt, J. Strähle, C.M. Archer, J. Chem. Soc., Dalton Trans. (1995) 1663.
[40] M. Hirsch-Kuchma, T. Nicholson, A. Davison, W.M. Davis, A.G. Jones, Inorg. Chem. 36 (1997) 3237.
[41] C.A. McConnachie, E.I. Stiefel, Inorg. Chem. 36 (1997) 6144.
[42] C. Pearson, A.L. Beauchamp, Can. J. Chem. 75 (1997) 220.
[43] A. Earnshaw, B.N. Figgis, J. Lewis, R.D. Peacok, J. Chem. Soc. (1961) 3132.

monoclinic system (space group $P2_1/m$) [8]. The phase transition between the hexagonal system and monoclinic system occurs through shifts of O(3) atom position in the crystal structure of mimetite [9,10]. The study of lead calcium arsenate apatites from Franklin, New Jersey and Langban, Sweden infers additional studies are necessary. In this study, hedyphane was redefined as $Ca_2Pb_3(AsO_4)_3Cl$. The space group is $P6_3/m$ with $a = 1.0140$ nm and $c = 0.7185$ nm and cation ordering in hedyphane is attributed to a preference by atoms with sterically active electron lone pairs, example, Pb(II), for the asymmetrically coordinated 6h site. The silent features drawn from tabulation of chemical composition indicate both the ions of phosphate and arsenate are involved [11]. Ca-bearing phosphatian mimetite (honey yellow colour) is composed of Pb (major), in addition, Ca, Cd, Mn, Sb, Fe, As and P in minor amounts. The unit cell parameters are $a = 1.0087$ nm and $c = 0.7335$ nm (space group, $P6_3/m$). X-ray and IR data have shown that it represents a transitional phase in the ternary system mimetite–pyromorphite–turneaureite [12]. Phosphohedyphane, $Ca_2Pb_3(PO_4)_3Cl$, the phosphate analog of hedyphane has been described recently shows the mineral has hexagonal structure (space group, $P6_3/m$, $a = 0.9857$ nm and $c = 0.7130$ nm) and chemical variability [13].

Minerals containing phosphate, arsenate and vanadinate anions have the general formulae $A_m[XO_4]_pZ_{q\cdot x}H_2O$ and $A_mB_m[XO_4]_pZ_{q\cdot x}H_2O$ where $[XO_4]$ is $[PO_4]$, $[AsO_4]$ and $[VO_4]$; Z is OH, F, Cl, O; A and B-metals. Mineral species are formed by the interaction of cations with phosphate, arsenate and vanadinate. Indeed minerals may contain mixed anionic species. Also many of these minerals may contain mixed cationic species. Many of these minerals contain Fe and also other metals like Ca, Al, Mn, Cu, etc. [14]. Farmer reported infrared bands for pyromorphite at 1030 and 970 cm^{-1} assigned to phosphate mode, ν_3, antisymmetric stretching vibrations and at 572 and 542 cm^{-1} for ν_4, bending modes [15]. The infrared spectrum of mimetite is different form pyromorphite, displacing bands at 815, 803 and 783 cm^{-1} attributed to arsenate ν_3, antisymmetric stretching vibrations and at 415 and 383 cm^{-1} assigned to arsenate ν_4 bending modes [15]. The free ion, AsO_4^{3-} has four vibrational modes and are observed by IR and Raman at 810 cm^{-1} (ν_1); ν_2 at 342 cm^{-1}; ν_3 at 810 cm^{-1} and ν_4 at 398 cm^{-1}[16]. For vanadinites, Ross reported ν_3-bands at 800 and 736 cm^{-1}, and the ν_4 modes at 419, 380 and 322 cm^{-1} [16]. Gadsen also investigated the infrared spectrum of the mimetite [17]. The ν_3 mode is reported to occur in the range, 700–900 cm^{-1} and the ν_4 mode between 300 and 410 cm^{-1}. Griffith reported the Raman spectrum of mimetite [18]. Levitt and Condrate reported the infrared and Raman spectra of lead apatite powdered minerals [6].

Earlier papers were limited to the mid-infrared absorption data on apatite, pyromorphite, mimetite and vanadinite [19,20]. Some other studies of Raman and IR spectra of calcium and lead apatites including mimetite show no detailed analysis [6,21,22]. The Raman and IR spectra of single crystals of pyromorphite, vanadinite, and mimetite were recorded and focused mainly on coordinate analysis and force constants of the three minerals that include the assignments of the vibrational frequencies [23]. For mimetite, this paper shows the ν_1 mode observed at 816 cm^{-1}, the ν_3 vibrations at 809 and 787 cm^{-1}, the ν_2 at 414, 390 and 335 cm^{-1} and ν_4 at 424, 373 and 314 cm^{-1}. None of these reports include NIR spectroscopy. There has been almost no research carried out on NIR spectroscopy of the mimetite and pyromorphite series.

In the present work, we analysed spectroscopically selected mimetite minerals, arsenian pyromorphite and hedyphane minerals and the spectra are related to the structure of the minerals.

2. Experimental

2.1. Minerals

The minerals used in this work, their formula and origin are listed in Table 1. The phase purity of the minerals was checked by X-ray diffraction and the chemical composition by EDX measurements.

2.2. Near-infrared (NIR) spectroscopy

NIR spectra were collected on a Nicolet Nexus FT-IR spectrometer with a Nicolet Near-IR Fibreport accessory (Madison, WI). A white light source was used, with a quartz beam splitter and TEC NIR InGaAs detector. Spectra were obtained from 13 000 to 4000 cm^{-1} (0.77–2.50 μm) by the co-addition of 64 scans at a spectral resolution of 8 cm^{-1}. A mirror velocity of 1.266 m s^{-1} was used. The spectra were transformed using the Kubelka-Munk algorithm to provide spectra for comparison with published absorption spectra. Spectral manipulations, such as baseline correction, smoothing and normalisation, were performed using the software package GRAMS (Galactic Industries Corporation, NH, USA).

2.3. Mid-IR spectroscopy

Infrared spectra were obtained using a Nicolet Nexus 870 FTIR spectrometer with a smart endurance single bounce diamond ATR cell. Spectra over the 4000–525 cm^{-1} range were obtained by the co-addition of 64 scans with a resolution of 4 cm^{-1} and a mirror velocity of 0.6329 cm/s. Spectra were co-added to improve the signal to noise ratio.

Band component analysis was undertaken using the Jandel 'Peakfit' (Erkrath, Germany) software package which enabled the type of fitting function to be selected and allows specific parameters to be fixed or varied accordingly. Band fitting was done using a Lorentz–Gauss cross-product function with the minimum number of component

Table 1
Table of the minerals, their origin and formula

Code	Mineral	Colour	Formula	Origin
Mime-1	mimetite	yellow	$Pb_5(AsO_4)_3Cl$	Tsumeb, Namibia, South Africa
Mime-2	mimetite	orange	$Pb_5(AsO_4)_3Cl$	Geronimo Mine, Yuma Co., AZ, USA
Mime-3	mimetite	black	$Pb_5(AsO_4)_3Cl$	Mount Bonnie Mine, Northern Territory, Australia
Pyro-8	arsenian pyromorphite	light brown	$Pb_5(PO_4,AsO_4)_3Cl$	Bunker Hill Mine, Kellogg, ID, USA
Hedy-1	hedyphane	grey white	$Pb_3Ca_2(AsO_4)_3Cl$	Puttapa Mine, Beltana, South Australia

bands used for the fitting process. The Lorentz–Gauss ratio was maintained at values greater than 0.7 and fitting was undertaken until reproducible results were obtained with squared correlations (r^2) greater than 0.995. Band fitting of the spectra is quite reliable providing there is some band separation or changes in the spectral profile.

3. Results and discussion

3.1. Near-infrared (NIR) spectroscopy

Spectral studies have not been made to examine the effect of cation substitution and its symmetry in any of these minerals. The most common electronic process in minerals results from transition metals and iron is usually suspected in minerals either as a major or minor impurity. The electronic spectra of complex ferrous silicates have been interpreted by crystal field theory and attributed peaks in the 11 000–9000 cm^{-1} (0.91–1.11 μm) region to Fe^{2+} ion [24]. Results are given from electronic and vibrational spectra and are explained in terms of the structure of cations and anions in the minerals of mimetite, arsenian pyromorphite and hedyphane.

The spectra of the samples are presented in three parts: The spectra of electronic part in the high wavenumber region, 12 000–8000 cm^{-1} (0.83–1.25 μm) are depicted in Fig. 1. A unique spectral feature with variable band position and intensity observed at ~10 000 cm^{-1} (1.00 μm) (Fig. 1) results from the Fe^{2+} ion. This band is a common feature in all the spectra. This broad feature is resolved into two less intense bands in mimetite-1 and mimetite-2 and an additional intense band on high energy side at ~11 145 cm^{-1} (0.90 μm). Vibrational spectra in the wavenumber region from 8000 to 6500 cm^{-1} (1.25–1.54 μm) are shown in Fig. 2. A broad band observed in the region, 7500–7000 cm^{-1} (1.33–1.43 μm) is due to overtones of the first fundamental hydroxyl stretching modes observed in the mid-infrared spectra around 3600 cm^{-1} (2.78 μm). The spectra in the low wavenumber region, 6500–4000 cm^{-1} (1.54–2.50 μm) are shown in Fig. 3. The strong feature centred at ~5000 cm^{-1} (2.00 μm) is the result of overtones of OH-stretching bands observed in the lower range of IR spectrum at 3400 cm^{-1} (2.94 μm) The vibrational spectra, in the lower wavenumber region, a complex profile contains a series of multiple sharp bands at wavenumbers <4600 cm^{-1} (2.17 μm). These sharp series of bands are produced by the combination of vibrational modes of phosphate and or arsenate ions.

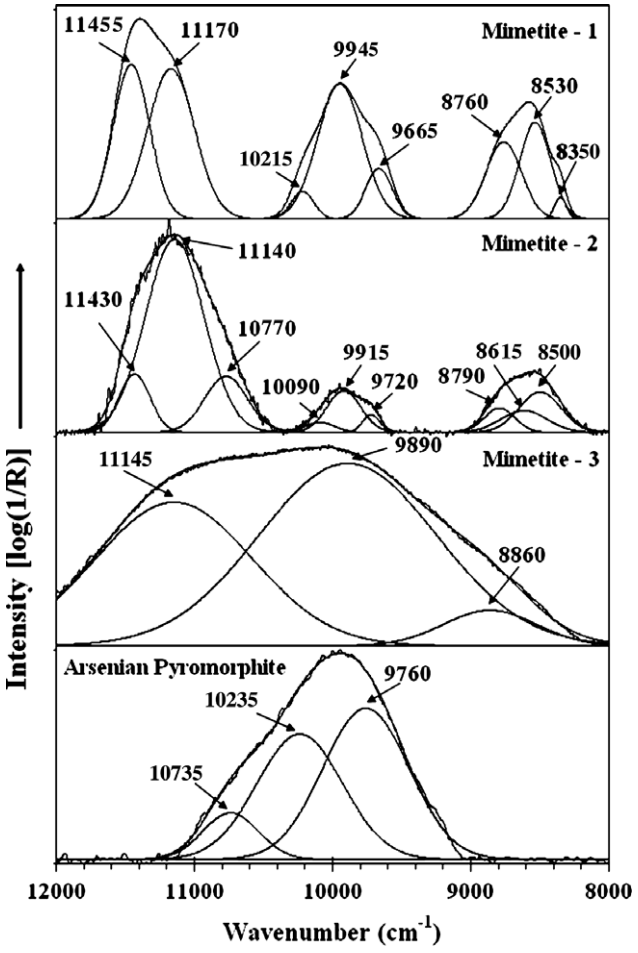


Fig. 1. Near-IR spectra of mimetite (samples 1–3) and arsenian pyromorphite in the 8000–12 000 cm^{-1} region.

3.1.1. Electronic spectra: 12 000–8000 cm^{-1} (0.83–1.25 μm) region

Divalent cations like Ca^{2+}, Cd^{2+}, Mn^{2+}, Fe^{2+} and Cu^{2+} in a complex influence the band positions in the electronic spectrum. The cations also cause shifts for the OH-stretching units, carbonate and arsenate bands both in the near-infrared and IR spectra of the minerals. Spectral properties are related to the structure of minerals. Distinctive band positions are shown in the spectra as depicted in Fig. 1. Mimetite (yellow-orange) and pyromorphite (brown) minerals are differentiated from their electronic spectral features. A vertical line may be drawn across the central portion of the spectral pattern to see an unique spectral feature with variable band position and intensity at

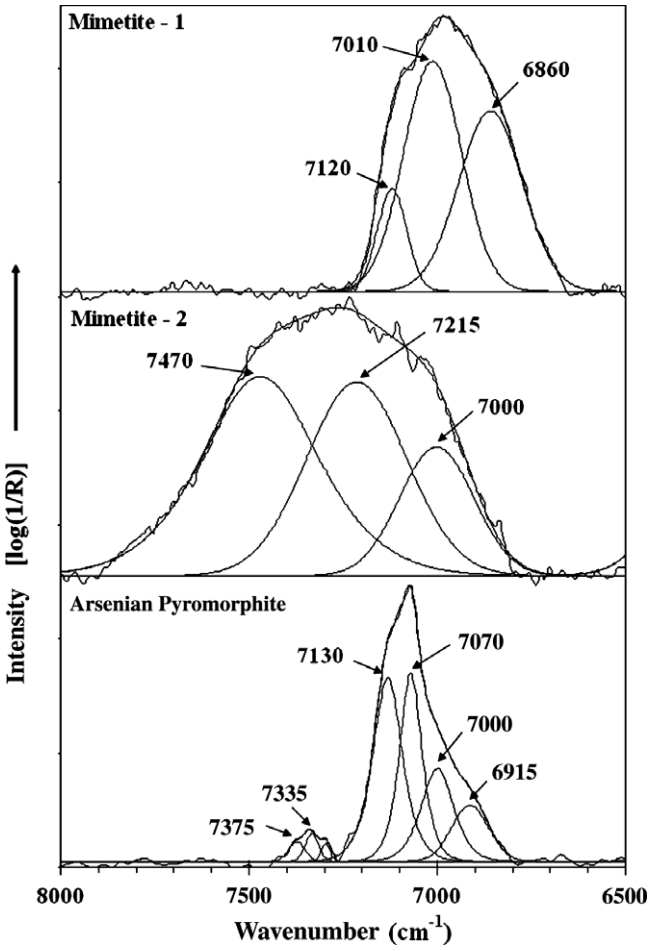


Fig. 2. Near-IR spectra of mimetite (samples 1 and 2) and arsenian pyromorphite in the 6500–8000 cm^{-1} region.

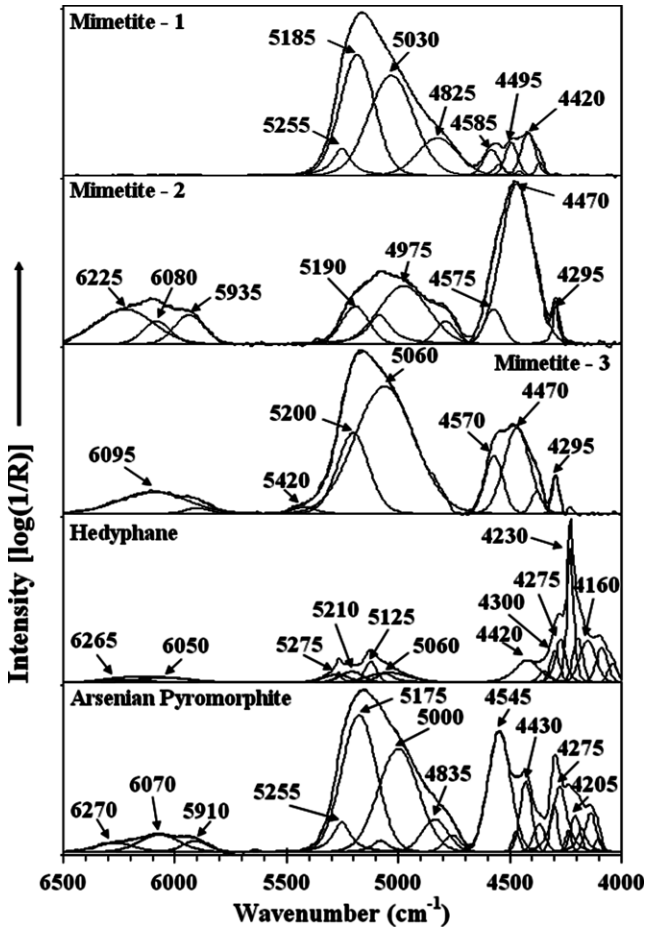


Fig. 3. Near-IR spectra of mimetite (samples 1–3), hedyphane and arsenian pyromorphite in the 4000–6500 cm^{-1} region.

~10000 cm^{-1} (1.00 μm) (Fig. 1) resulting from Fe^{2+} ion substitution. This band is a common feature in all the spectra. Burns [24] attributed peaks in cummintonite–grunerites and actinolite in the 11000–9000 cm^{-1} (0.91–1.11 μm) region to Fe^{2+}, while Goldman and Rossman [25] interpreted many of the amphibole spectra claiming that only iron in the M4 site causes the band at 10000 cm^{-1} (1.00 μm). Later it was confirmed the Fe^{2+} band at 10000 cm^{-1} (1.00 μm) for M4 site for the calcic amphibole [26]. The dependence of Fe(II) band with pressure shifts in ferromagnesian olivine has also been analysed [27]. A prominent feature reported for an iron-rich humite is a complex band system in the NIR and is assigned to dd-transitions of Fe^{2+} bands at 10800 and 7600 cm^{-1} (0.93 and1.32 μm) [28].

A broad profile shown (Fig. 1) by mimetite-3 is characterised by a single band at 9890 cm^{-1} (1.01 μm) attributable to Fe(II) ion. This band appears at ~10000 cm^{-1} (1.00 μm) in arsenian pyromorphite splits into two components and are displaced to 10235 and 9760 cm^{-1} (0.98 and 1.02 μm). For mimetite-1 and mimetite-2 samples, the Fe(II) band split into two with a separation of 1415 cm^{-1}. The two bands in mimetite-1 are shown at 9945 and 8530 cm^{-1} (1.00 and 1.17 μm) while they are weak in mimetite-2 at 9915 and 8615 cm^{-1} (1.01 and 1.16 μm). A similar situation was observed from the study of electronic absorption spectra of the orthorhombic olivine-type phosphate minerals of the triphylite–lithiophilite series. All triphylite–lithiophilite spectra showed an intense band system in the NIR around 9400–9100 cm^{-1} (1.06–1.10 μm) is a typical of spin allowed dd-transition in octahedral Fe(II) [29]. Electronic spectrum of Chevreul's salt $[Cu_2^{I}(SO_3)_2(SO_3)_2]^{6-}$ consists of two ligand field transitions for Cu(II) at 785 and 1000 nm (12740 and 10000 cm^{-1}) and the isomorphic species present distinct colours. The intense red colour of the Chevreul's salt changes to yellowish-brown, after the substitution of Cu(II) by Fe(II) and the observation of band at 865 nm (11560 cm^{-1}) supports the Fe(II) derivative [30]. Mimetite and pyromorphite minerals are distinguished by means of electronic spectra. An additional weak band in arsenian pyromorphite at 10735 cm^{-1} (0.93 μm) may be assigned to Cu(II) dd-transition. The intensity of this band is enhanced at the cost of Fe(II) in mimetite-1 and mimetite-2 and appeared at ~11140 cm^{-1} (0.90 μm). There is an exception in mimetite-3 in which more iron impurity

causes a complex broad band profile. The change of brown colour to orange-yellow relates to the amount of Cu and or Fe impurities in the mimetite minerals. Colour of the minerals may be related to the compositional variations in the minerals.

3.1.2. Vibrational spectra: 8000–6500 cm^{-1} (1.25–1.54 μm) region

The vibrational absorption characteristics of mimetite and arsenian pyromorphite minerals are shown in Fig. 2. Spectral variations support mineralogical variations especially in composition. Selected absorption bands were studied at high resolution. The minerals show fine structure particularly in the OH-stretching overtone region near 7000 cm^{-1} (1.43 μm) region [31]. The multi-component bands derived for each profile in spectra enhance the ability to discriminate between the minerals. Arsenian pyromorphite, $Pb_5(PO_4,AsO_4)_3Cl$ exhibits a sharp band at 7070 cm^{-1} (1.41 μm) with four components due to OH-stretching overtones. The observation of OH-stretching overtones implies substitution for Cl by OH. Mimetite samples show variable band positions with more intensity at 7010 and 7215 cm^{-1} (1.43–1.39 μm). The cause for the shifts of bands may be attributed to the presence of Fe and Cu in mimetites and Ca(II) perhaps substitution by Fe(II) and or Cu(II). Vibrational bands for several minerals like turquoise, rosasite, smithsonite, rhodochrosite, alunite, rectorite and jarosite reported in 7200–7000 region (1.39–1.43 μm) [31–34].

3.1.3. Near-IR spectra: 6500–4000 cm^{-1} (1.54–2.5 μm) region

The overtones of water are observed in the spectra of H_2O-bearing minerals near 5200 cm^{-1} (1.92 μm) [35,36]. Vibrational spectra of the minerals shown in Fig. 3 contain many significant absorption features. A strong feature at ~5000 cm^{-1} (2.00 μm) accompanied by a weak feature at 6100 cm^{-1} (1.64 μm) suggests incorporation of H_2O into the mineral structure. Arsenian pyromorphite band is strong at 5175 cm^{-1} (1.93 μm). For mimetites this band is almost equally strong but displaced differently at 5185, 5190 and 5200 cm^{-1} (1.93, 193 and 1.92 μm) respectively, because, the functional ions and cations are compositionally variant in the isomorphic series. The liquid water band was observed in sedimentary rocks at 1.90 μm (5260 cm^{-1}) [37]. A series of sharp bands are observed in the spectra of the lower wavenumbers. Despite the complexity of the overlapping bands a sequence of bands in each of the spectra can be observed. The sequence for mimetites is observed at ~4500, 4400 and 4300 cm^{-1} (2.22, 2.27 and 2.33 μm) in which a single anion (AsO_4) is involved. The sequence of bands in arsenian phosphate and hedyphane becomes much more complicated. The modified features result from the substitution of Pb(II) by Ca(II) and $(AsO_4)^{3-}$ by $(PO_4)^{3-}$ are reflected by the number of overlapping bands which are shifted to lower wavenumbers.

3.2. Mid-IR spectroscopy

In the mid-IR spectral region bands attributable to phosphate and arsenate anions can be observed. These features in the vibrational stretching region of 1300–500 cm^{-1} is shown in Fig. 4. The spectra of the minerals are complex with the spectral profile in the 900–500 cm^{-1} region. For three mineral samples mimetite-3, arsenian pyromorphite and hedyphane additional bands produced by the phosphate anion are included in the 900–1100 cm^{-1} region. Infrared spectra were poorly defined in the 3600–1500 cm^{-1} region and they are not included here. Bands are strong in Raman for mimetites and pyromorphites in high wavenumber region, 4000–3000 cm^{-1} as reported by Frost et al. [38,39] and the assignments of these bands are correlated with NIR data in the present work.

The observation of isomorphic substitution for $(PO_4)^{3-}$ by $(AsO_4)^{3-}$ in mimetites could easily be distinguished on the basis of their spectral properties from the mixed spectra of phosphate and arsenate ions in arsenian pyromorphite. As shown in Fig. 4, the spectrum of mimetite-3 is a simple system where arsenate bands are moderately resolved at 887 and 788 cm^{-1} and are identified as ν_1 and ν_3 modes of $(AsO_4)^{3-}$ ion. On either side of this low intensity profiles

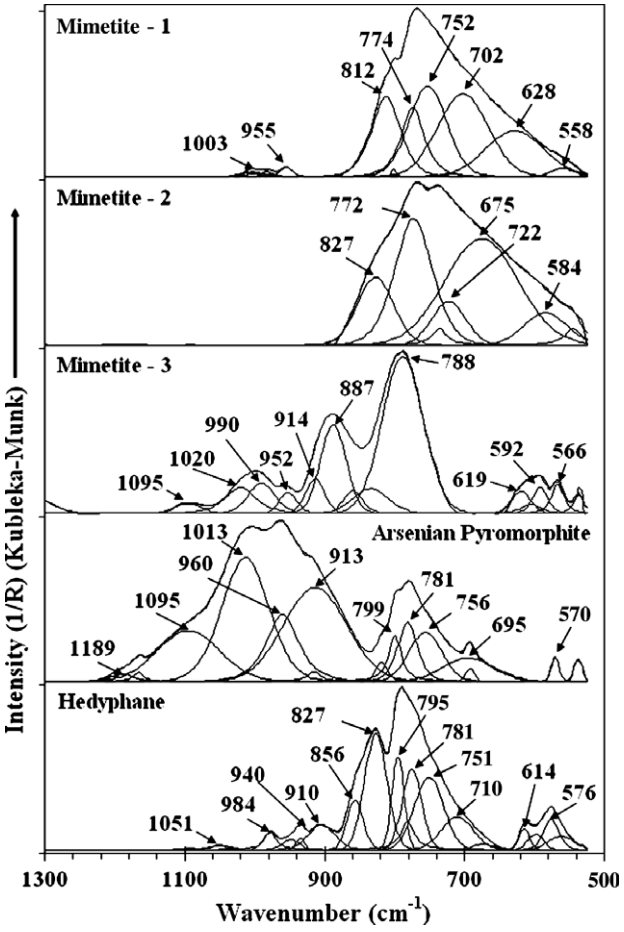


Fig. 4. Mid-IR spectra of mimetite (samples 1–3), hedyphane and arsenian pyromorphite in the 500–1300 cm^{-1} region.

that contain multiple bands are the cause of partial substitution for $(PO_4)^{3-}$. A series of bands observed on high wavenumbers side of the spectrum at 1095, 1020, 990 and 914 cm^{-1}. The first three bands are assigned to ν_3, antisymmetric mode, and last one at 914 cm^{-1} is attributed to ν_1, the symmetric mode of phosphate ion. Farmer reported infrared bands for pyromorphite at 1030 and 970 cm^{-1} assigned to phosphate mode, ν_3, and antisymmetric stretching vibrations [15]. The range of bands observed for phosphate in other samples are not found in mimetite-1 and mimetite-2 spectra but appeared with single broad profile having four component bands near 800 cm^{-1}. In this case $(PO_4)^{3-}$ is almost completely substituted by $(AsO_4)^{3-}$. Mimetite-1 bands are located at 812, 774, 752 and 702 cm^{-1}. Band at 812 cm^{-1} is attributed to ν_1 mode and the last three bands are due to ν_3 mode of AsO_4^{3-} ion. In mimetite-2, these bands are shifted to lower wavenumbers. A similar set of bands with variable band positions and intensity are seen in arsenian pyromorphite and hedyphane. The spectrum of hedyphane is significant with arsenate bands at 900–700 cm^{-1} and weak bands appear on either side of this due to the phosphate ion. Arsenian pyromorphite spectrum is also a mixed profile dominated by PO stretching vibrations at 1100–900 cm^{-1}. The effect of anion substitution is noticed in the spectra of mimetites and hedyphane. The substitution of $(PO_4)^{3-}$ for $(AsO_4)^{3-}$ characteristically decreases the vibrational frequencies of ν_3 and ν_1 modes of the $(PO_4)^{3-}$ slightly to lower wavenumbers with respect to arsenian pyromorphite. Investigations of anion substitutions in lead apatites reveal the effect of substitution of Ca^{2+} by Pb^{2+} and $(PO_4)^{3-}$ by $(AsO_4)^{3-}$ and $(VO_4)^{3-}$ in apatites cause a shift of the ν_3 (1082 cm^{-1}) and ν_1 (980 cm^{-1}) [40]. Raman studies show a complexity of band systems for phosphate and arsenate ions in mimetites, pyromorphite and hedyphane in three ranges at ~500–400 cm^{-1}, 400–300 cm^{-1} and 200–100 cm^{-1} assigned to $(PO_4)^{3-}$ and/or $(AsO_4)^3$ bending modes [38,39]. The low wavenumber region of the mid-IR spectrum (Fig. 4) are very weak from 650 to 500 cm^{-1} may be attributed to ν_4 bending modes of $(PO_4)^{3-}$. In the spectra in Fig. 4, the spectra for mimetites 1 and 2 are due to the $(AsO_4)^{3-}$ ion only. Whereas in Fig. 4, the spectra of the other three samples show bands attributable to both $(PO_4)^{3-}$ and $(AsO_4)^{3-}$ anions. Thus the fundamental bands of $(PO_4)^{3-}$ and $(AsO_4)^{3-}$ can be interpreted to identify the minerals. The spectra for mimetites 1 and 2 can be considered as standard. Mimetite 3 is strictly a phosphated mimetite.

4. Conclusions

The minerals of mimetite, arsenian pyromorphite and hedyphane have been analysed using NIR spectroscopy and the spectra related to the mineral structure.

(1) The minerals of mimetite and pyromorphite can be distinguished by means of the electronic spectra.
(2 In NIR spectra of the mimetite minerals, a prominent spectral feature observed for ferrous ion is a complex band system at ~10 000 cm^{-1} (1.00 μm).
(3) For arsenian pyromorphite, an additional feature observed at 10 735 cm^{-1} (0.93 μm) is assigned to the Cu(II) dd-transition. The intensity of this band is enhanced at the expense of Fe(II) in mimetite-1 and mimetite-2 and appeared at higher wavenumbers at ~11 140 cm^{-1} (0.90 μm).
(4) The cause of colour in mimetites (brown through to orange to yellow) depends on the impurities of Fe and/or Cu.
(5) The variation of spectral properties is related to the compositional variation of the minerals.
(6) The minerals show fine structure particularly in OH-stretching fundamental overtone region and the PO_4/AsO_4 stretching region. The multi-component bands derived for each profile in vibrational spectra enhance the ability to discriminate between the minerals. The presence of OH-stretching overtones at 7000 cm^{-1} (1.43 μm) is the effect of Cl substitution by OH.
(7) The observation of isomorphic substitution of $(AsO_4)^{3-}$ by $(PO_4)^{3-}$ in mimetites could easily be distinguished on the basis of their spectral properties from the mixed spectra of phosphate and arsenate ions in arsenian pyromorphite.
(8) The range of bands observed for phosphate in other samples are not observed in the spectra of mimetite-1 and mimetite-2 but appeared with a single broad profile having four component bands near 800 cm^{-1} attributed to the presence of the arsenate ion.
(9) The observation of single profile in the mid-IR with four component bands due to $(AsO_4)^{3-}$ ion near 800 cm^{-1} in mimetite-1 and mimetite-2 is evidence for isomorphic substitution of $(PO_4)^{3-}$ by $(AsO_4)^{3-}$.
(10) The substitution of $(PO_4)^{3-}$ for $(AsO_4)^{3-}$ characteristically decreases the vibrational wavenumbers of ν_3 and ν_1 modes of the $(PO_4)^{3-}$ slightly to lower wavenumbers when compared with the spectra of arsenian pyromorphite.

Acknowledgements

The financial and infra-structure support of the Queensland University of Technology, Inorganic Materials Research Program is gratefully acknowledged. The Australian Research Council (ARC) is thanked for funding the instrumentation. One of the authors, B. Jagannadha Reddy is grateful to the Queensland University of Technology for the award of a Visiting Fellowship.

References

[1] C.C. McDonnell, C.M. Smith, Am. J. Sci. 42 (1916) 139.
[2] R.B. Fischer, C.E. Ring, Anal. Chem. 29 (1957) 431.
[3] W.E. Baker, Am. Mineral. 51 (1966) 1712.
[4] A.G. Cockbain, Mineral. Mag. 36 (1968) 171.

[5] S.R. Levitt, K.C. Blakeslee, R.A. Condrate, Memoires de la Societe Royale des Sciences de Liege, Collection in 8 Deg 20 (1970) 121.
[6] S.R. Levitt, R.A. Condrate, Am. Mineral. 55 (1970) 1562.
[7] N.J. Calos, C.H.L. Kennard, R.L. Davis, Z. Kristallogr. 191 (1990) 125.
[8] J.W. Anthony, R.A. Bideaux, K.W. Bladh, M.C. Nichols, Handbook of mineralogy, Arsenates, Phosphates, Vanadates, vol. IV, Mineral Data Publishing, Tucson, AZ, 2000.
[9] Y. Dai, J.M. Hughes, P.B. Moore, Can. Mineral. 29 (1991) 369.
[10] Y. Dai, Miner. Record 24 (1993) 307.
[11] R.C. Rouse, P.J. Dunn, D.R. Peacor, Am. Mineral. 69 (1984) 920.
[12] B. Golebiowska, A. Pieczka, W. Franus, N. Jb. Miner. Mh. 1 (2002) 31.
[13] A.R. Kampf, I.M. Steele, R.A. Jenkins, Am. Mineral. 91 (2006) 1909.
[14] A.V. Kunov, Dokladi Bulgarskata Akademiya Naukite 58 (2005) 679.
[15] V.C. Farmer, Mineralogical Society Monograph 4: The Infrared Spectra of Minerals, 1974.
[16] S.D. Ross, Inorganic Infrared and Raman Spectra, McGraw-Hill Book Company Ltd., London, 1972.
[17] J. Gadsen, Infrared Spectra of Minerals and Related Inorganic Compounds, Butterworth & Co. (Publishers) Ltd., London, England, 1975.
[18] W.P. Griffith, J. Chem. Soc. Sect. A Inorg. Phys. Theor. (1970) 286.
[19] H.H. Adler, Am. Mineral. 49 (1964) 1002.
[20] H.H. Adler, Am. Mineral. 53 (1964) 1740.
[21] L.C. Kravitz, J.D. Kingsley, E.L. Elkin, J. Chem. Phys. 49 (1968) 4600.
[22] I.B. Petrov, Soptrajanov, N. Fuson, J.R. Lawson, Spectrochim. Acta Part A 23 (1967) 2637.
[23] G. Bartholomai, W.E. Klee, Spectrochim. Acta Part A 34 (1978) 831.
[24] R.G. Burns, Mineralogical Applications of Crystal Field Theory, Cambridge University Press, 1970.
[25] D.S. Goldman, G.R. Rossman, Am. Mineral. 67 (1977) 05.
[26] L.P. Aldridge, J.S. Tse, G.M. Bancroft, Am. Mineral. 67 (1982) 335.
[27] F. Ke, Z.Y. Yang, J. Phys. C: Solid State Phys. 21 (1988) 861.
[28] A.N. Platonov, K. Langer, M. Wildner, E.V. Polshin, S.S. Matsyuk, Z. Kristallogr. 216 (2001) 154.
[29] K. Langer, M.N. Taran, A.M. Fransolet, Eur. J. Mineral. 18 (2006) 337.
[30] L.A. Silva, J.B. Andrade, H.E. Toma, Braz. Chem. Soc. 13 (2002) 624.
[31] R.N. Clark, T.V.V. King, M. Klejwa, G.A. Swayze, N. Vergo, J. Geophys. Res. 95 (1990) 12653.
[32] B. Jagannadha Reddy, R.L. Frost, M.L. Weir, W.N. Martens, J. Near Infrared Spectrosc. 14 (2006) 41.
[33] R.L. Frost, B. Jagannadha Reddy, D.L. Wain, W.N. Martens, Spectrochim. Acta Part A 66 (2007) 1075.
[34] R.L. Frost, B. Jagannadha Reddy, D.L. Wain, M.C. Hales, J. Near Infrared Spectrosc. 14 (2006) 17.
[35] R.D. Aines, G.R. Rossman, J. Geophys. Res. 89 (1984) 4059.
[36] G.R. Hunt, R.P. Ashley, Econ. Geol. 74 (1979) 613.
[37] G.R. Hunt, J.W. Salisbury, Mod. Geol. 5 (1976) 211.
[38] R.L. Frost, J.M. Bouzaid, S.J. Palmer, Polyhedron 26 (2007) 2964.
[39] R.L. Frost, S.J. Palmer, Polyhedron 26 (2007) 4533.
[40] V.M. Bhatnagar, Z. Anorg. Allg. Chem. 367 (1969) 289.

exclusively the cis complex [15,16]. The pronounced dependence of stereochemistry of the complex formed on the nature of the substituents on the phosphorus atom of the ligand prompted us to investigate the structure of tin complexes with other type of phosphoryl ligands.

In the present paper, we extend our studies to the complexation of the two fluoroalkyl phosphoramidates $(R_2N)_2P(O)OCH_2CF_3$ (R = Me and Et) with $SnCl_4$. The results are compared with those of related HMPA and $(Me_2N)_2P(O)F$ complexes [12,16].

2. Experimental

2.1. General experimental procedures

All preparations were carried out under a nitrogen atmosphere in solvents dried by standard techniques [17] and stored over molecular sieves. NMR spectra were recorded on a Bruker AC-300 spectrometer in CD_2Cl_2 solutions; ^{31}P at 121 MHz (85% H_3PO_4) and ^{119}Sn at 111.8 MHz ($SnCl_4$). ^{119}Sn NMR spectra were recorded in 10 mm NMR tubes containing 15–20% deuterated solvent. IR spectra: Perkin–Elmer Paragon 1000 PC.

Tin tetrachloride was distilled under vacuum before use. The ligands, 2,2,2-trifluoroethyl N,N,N′,N′-tetraalkylphosphorodiamidates $(R_2N)_2P(O)OCH_2CF_3$, were prepared as previously described in the literature [18].

2.2. Preparation of complexes

In a typical reaction $(R_2N)_2P(O)OCH_2CF_3$ (8 mmol) in dry $CHCl_3$ (10 cm^3) was slowly added to $SnCl_4$ (1.04 g, 4 mmol) in $CHCl_3$ (20 cm^3) and the mixture stirred at room temperature for 2 h. The complex $SnCl_4 \cdot 2(O)P(NR_2)_2OCH_2CF_3$ precipitated as a white powder which was filtered off, recrystallised from hot CH_2Cl_2 and dried in vacuo. Yields R = Me (**1**): 2.42 g, 83 % R = Et (**2**): 2.62 g, 78%. *Anal.* Calc. for $C_{12}H_{28}Cl_4F_6N_4O_4P_2Sn$ (**1**): C, 19.78; H, 3.87; N, 7.69. Found: C, 20.06; H, 3.95; N, 7.52%. *Anal.* Calc. for $C_{20}H_{44}Cl_4F_6N_4O_4P_2Sn$ (**2**): C, 28.56; H, 5.27; N, 6.66. Found: C, 28.22; H, 5.40; N, 6.70%. IR (KBr): $\nu_{P=O}$ (1150–1170 cm^{-1}); ν_{Sn-O} (470–480 cm^{-1}).

2.3. X-ray experimental

Details of the crystallographic data collection and refinement parameters are presented in Table 1. Crystals of **1** were obtained from a CH_2Cl_2 solution layered with hexane. Single crystal X-ray collection used an Enraf-Nonius CAD-4 automatic four-circle diffractometer operating at 298 K, using graphite-monochromated Mo Kα X-radiation ($\lambda = 0.71069$ Å). Structure solution and refinement were carried out using SHELX-97 computer programs [19,20] included in the WINGX software package [21]. Several attempts were made to grow good quality crystals of **2**, but these were unsuccessful.

Table 1
Crystal data, data collection and refinement parameters of **1**

Compound	$SnCl_4 \cdot 2(O)P(NMe_2)_2OCH_2CF_3$
Empirical formula	$C_{12}H_{28}Cl_4F_6N_4O_4P_2Sn$
Formula weight (g/mol)	728.81
Crystal system	monoclinic
Space group	$P2_1/c$
a (Å)	7.9425(15)
b (Å)	20.427(3)
c (Å)	8.882(2)
β (°)	103.69(2)
V (Å^3)	1400.0(5)
Z	2
Crystal shape, color	parallelepiped, white
Crystal size (mm)	0.43 × 0.29 × 0.22
D_{calc} (Mg/m^3)	1.729
Absorption coefficient (mm^{-1})	1.47
F (000)	724
θRange for data collection (°)	$2.62 \leqslant \theta \leqslant 7.0$
Limiting indices	$0 \leqslant h \leqslant 20$, $-1 \leqslant k \leqslant 26$, $-11 \leqslant l \leqslant 11$
Standards, frequency (min), decay (%)	2, 120, 2
Reflections collected	3441
Independent reflections	3043
Observed reflections [$I > 2\sigma(I)$]	2579
Data, parameters	3043, 176
Goodness-of-fit on F^2	1.15
Residual peaks (e Å^{-3})	−0.33, 0.40
Final R indices ($I > 2\sigma(I)$)	$R = 0.028$, $wR = 0.085$
R indices (all data)	$R = 0.036$, $wR = 0.089$

2.4. Computational details

Density functional theory (DFT) calculations were carried out on the cis and trans isomers of complex **1** and its ligand using the GAUSSIAN 98 suite of programs [22], with the hybrid functional B3LYP [23]. Basis sets used were LanL2DZ [24] for Sn and 6-31G* [25] for the other atoms. The geometries of both the cis and trans isomers of complex **1** and its ligand were optimised using analytical gradient. The harmonic vibrational frequencies of the different stationary points of the potential energy surfaces (PES) have been calculated at the same level of theory in order to identify the local minima as well as to estimate the corresponding zero-point vibrational energy (ZPE).

3. Results and discussion

3.1. Synthesis

The reaction of $SnCl_4$ with $(R_2N)_2P(O)OCH_2CF_3$ (R = Me or Et) in anhydrous chloroform resulted in the formation of white solids with the composition $SnCl_4 \cdot 2L$ ($L = (R_2N)_2P(O)OCH_2CF_3$). The solids are partially soluble in dichloromethane and chloroform, with **2** being more soluble. The complexes could be recrystallised from a large volume of anhydrous dichloromethane. They were characterised by elemental analysis and particularly by their NMR data and comparison with the corresponding data for the free ligands (see Table 2).

Table 2
NMR data (δ/ppm and J/Hz) for complexes **1** and **2** and their ligands in CD_2Cl_2 at 208 K

Compound	$\delta_{^{31}P}$		$\delta_{^{119}Sn}$ [a]	($^2J_{P-Sn}$)
$(Me_2N)_2P(O)OCH_2CF_3$		20.80		
$(Et_2N)_2P(O)OCH_2CF_3$		18.83		
$SnCl_4 \cdot 2(O)P(NMe_2)_2$-$OCH_2CF_3$ (**1**)	14.93[b]	14.84	−555(t, 107)	−574(t, 172) [b]
$SnCl_4 \cdot 2(O)P(NEt_2)_2$-$OCH_2CF_3$ (**2**)	13.56[b]		−557(t, 115)	−576(t, 197) [b]

[a] In a CD_2Cl_2/CH_2Cl_2 mixture.
[b] Major peaks observed in the spectra.

3.2. Spectroscopic studies

The infrared spectra show strong bands within the range 1150–1170 cm^{-1} attributed to $\nu_{P=O}$. The P=O stretching vibration is shifted towards lower wave numbers on coordination to the tin atom compared with its value for the free ligands. The coordination shift is about 130 cm^{-1} and is consistent with phosphoryl coordination to the tin atom. This shift is 128 cm^{-1} for $(Me_2N)_2P(O)OCH_2CF_3$ against 138 and 30 cm^{-1} for HMPA and $(Me_2N)_2P(O)F$, respectively [8,15] reflecting the relative similarity in the basicity strength with HMPA and the striking difference from $(Me_2N)_2P(O)F$. This is most probably due to the nature of the substituents on the phosphorus atom in these ligands (i.e. due to difference in the electronegativities of nitrogen, oxygen and fluorine atoms linked directly to the phosphorus atom of the ligand). The absorption band at 470–480 cm^{-1} corresponds to a stretching vibration of the Sn–O group.

The NMR spectra of the two complexes prepared are quite similar and the data obtained from these spectra are summarised in Table 2.

The ^{31}P NMR spectra of each of the complexes prepared showed at room temperature one signal flanked with Sn satellites. This signal is shifted to lower frequency compared with that of the free ligand. Such a behaviour is interpreted in terms of inductive effects resulting from a decrease in the electron density at phosphorus owing to the coordination of the phosphoryl oxygen of the ligand.

At low temperature (228 K), while the ^{31}P NMR spectrum of complex **2** remained practically unchanged, two signals displaying Sn satellites were observed in the spectrum of **1** (Fig. 1).

The corresponding ^{119}Sn NMR spectra of each complex displayed at room temperature a minor broad signal and a major lower frequency triplet in the region of hexacoordinated species [26]. The minor broad signal was converted at low temperature into the expected triplet. At 208 K, the spectrum showed therefore two triplet signals due to ^{119}Sn–^{31}P coupling (ratio of signals = ~1/1.3 for **1** and ~1/5 for **2**) (Fig. 2). Clearly, two species (isomers) with different proportions were present at this temperature and in each species the tin atom is coupled to two phosphorus

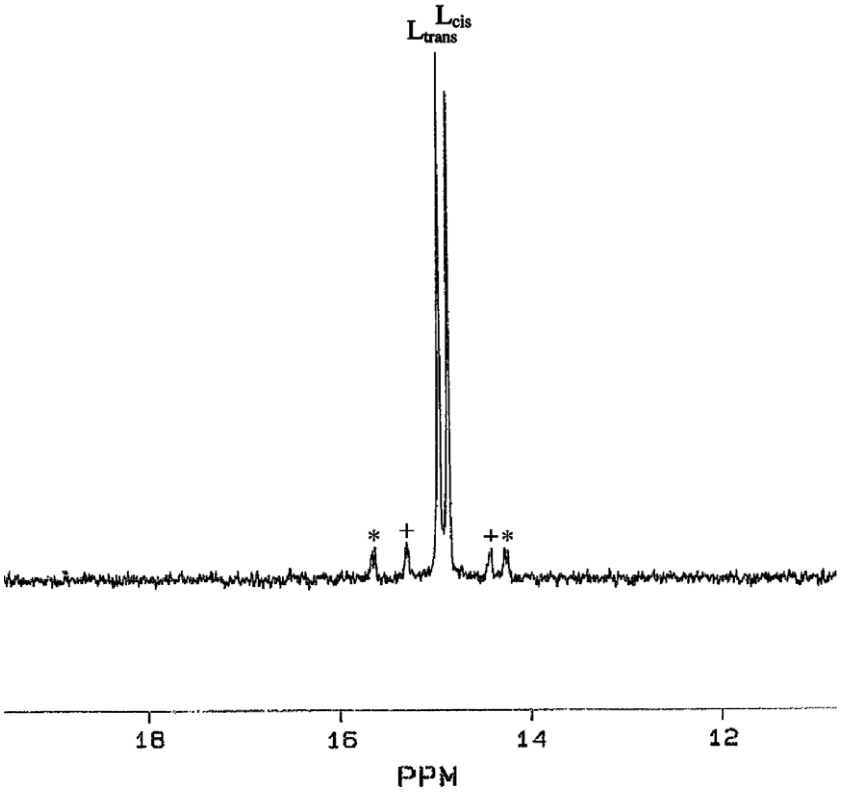


Fig. 1. ^{31}P–{^1H} NMR spectrum of complex **1** in CD_2Cl_2 at 228 K (* and + are Sn satellites of the ligand signal in trans (L_{trans}) and cis (L_{cis}) forms, respectively).

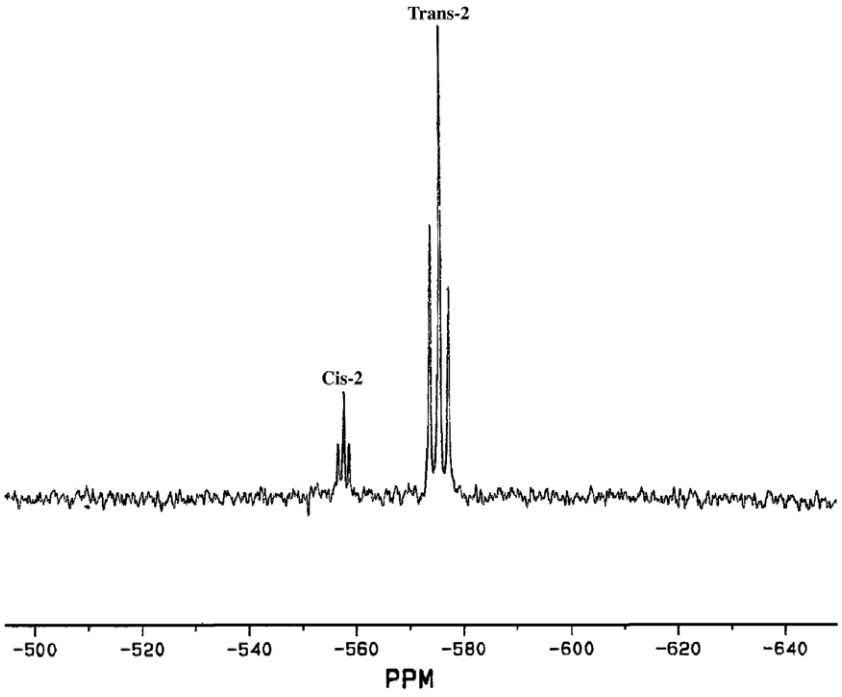


Fig. 2. ^{119}Sn NMR spectrum of complex **2** in CD_2Cl_2/CH_2Cl_2 at 208 K.

atoms, showing a stoichiometry of $SnCl_4 \cdot 2L$. This is in agreement with the ^{31}P NMR spectra where signals displaying Sn satellites with the corresponding coupling constants were observed.

It has been previously shown that the formation of hexacoordinate, 2:1, cis or trans-complexes of phosphoryl ligands with $SnCl_4$ is supported in solution by the appearance of a triplet pattern in the ^{119}Sn NMR spectrum [3,12]. In addition, the chemical shift and coupling constant of the ^{119}Sn signal provided valuable information on the geometry of the two phosphoramides in the hexacoordinate tin complex [11,12]. The trans hexacoordinate complexes have generally higher coupling constants than the corresponding cis complexes. For example, in the ^{119}Sn spectrum of $SnCl_4 \cdot 2$(HMPA), the trans complex has a $^2J(^{31}P–^{119}Sn)$ of 167 Hz at −727 ppm, whereas the cis-complex shows a $^2J(^{31}P–^{119}Sn)$ of 102 Hz at −719 ppm [12]. With this information, the isomers of the complexes in Table 2 could be assigned by analogy, i.e., all of the complexes which have higher $^2J(^{31}P–^{119}Sn)$ coupling constants could be assigned to the trans isomers and those with smaller $^2J(^{31}P–^{119}Sn)$ could be assigned to the cis ones.

It is therefore possible to assign the major species observed in the ^{31}P and ^{119}Sn NMR spectra of $SnCl_4 \cdot 2(O)P(NR_2)_2OCH_2CF_3$ (see Table 2) as the trans isomers. This is in contrast with the complex of $(Me_2N)_2P(O)F$ which forms predominantly the cis isomer, but in fair agreement with the HMPA complex that we have re-examined in the same conditions (see Table 3).

The ^{119}Sn NMR spectra also showed that the percentage of the trans isomer is, as expected, more important in **2** than in **1**. This difference between the methyl (**1**) and the ethyl (**2**) derivatives could be interpreted as due to steric effects, consistent with the ^{31}P NMR spectrum of **2** which showed only one signal (the trans isomer) even at low temperature.

Table 3
^{119}Sn NMR data[a] of the complexes $SnCl_4 \cdot 2L$ in dichloromethane

Ligand (L)	$\delta_{^{119}Sn}$		$^2J_{P–Sn}$		% trans[e]
	cis	trans	cis	trans	
$(Me_2N)_3P(O)$[b]	−569	−580	120	191	50
$(Me_2N)_2P(O)F$[c]	−548	−567	126	192	20
$(Me_2N)_2P(O)OCH_2CF_3$[d]	−555	−574	115	172	60

[a] Measured at slow exchange where both triplets are observed.
[b] 25 °C.
[c] −5 °C.
[d] −65 °C and e is the approximate percentage of the trans isomer measured from ^{119}Sn NMR signals.

3.3. X-ray crystallography

To elucidate the constitution of the complexes formed, as well as to provide a clear understanding of the effect of ligand structure on the stereochemistry of these complexes, we examined the solid state structure of complex **1**.

From a CH_2Cl_2 solution containing complex **1**, single crystals suitable for X-ray analysis were obtained through slow diffusion of hexane and found to contain 1:2 complex of the stoichiometry $SnCl_4 \cdot 2(O)P(NMe_2)_2OCH_2CF_3$. Selected bond lengths and angles are given in Table 4. The tin atom adopts an octahedral geometry with the two phosphoramide ligands trans to each other (Fig. 3) in agreement with $SnCl_4 \cdot 2$HMPA [10]. The molecule is

Table 4
Selected bond lengths (Å) and angles (°) for **1**[a]

Sn–Cl1	2.3955(9)	P1–N2	1.620(3)
Sn–Cl2	2.4002(10)	O2–C5	1.437(4)
Sn–O1	2.094(2)	C5–C6	1.493(5)
O1–P1	1.507(2)	C6–F1	1.333(5)
P1–O2	1.584(2)	C6–F2	1.321(5)
P1–N1	1.621(3)	C6–F3	1.324(5)
Cl1–Sn–Cl2	90.08(4)	O1–P1–O2	109.30(13)
Cl2–Sn–Cl3	89.92(4)	O1–P1–N1	107.18(14)
Cl1–Sn–O1	89.21(7)	N1–P1–O2	111.29(15)
Sn–O1–P1	151.24(16)	N1–P1–N2	108.73(16)
O1–Sn–O3	180.000(1)	O2–C5–C6	106.8(3)

[a] See Fig. 3 for labeling of the atoms, the tin atom is on a centre of symmetry.

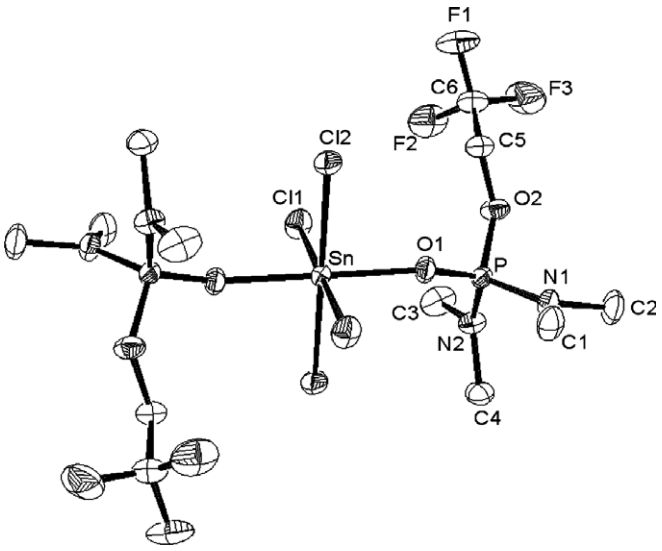


Fig. 3. ORTEP view of the crystal structure of complex **1** showing the atom numbering scheme. Atomic displacement ellipsoids are drawn at the 30% probability level and H atoms omitted for clarity. There is a centre of symmetry at the Sn atom.

centrosymmetric with Sn–Cl = 2.395(9), 2.400(10) Å. The Sn–O bond (2.094(2) Å) is slightly shorter than that in $SnCl_4 \cdot 2HMPA$ (2.130 Å) while the P=O bond is longer (1.507(2) versus 1.49 Å in $SnCl_4 \cdot 2HMPA$). These bond length changes presumably reflect the effect of the substitution of one dimethylamino group in HMPA by a fluoroalkoxy group. As a consequence, the P–N bonds in complex **1** are shorter (1.621(3) versus ~166 Å in $SnCl_4 \cdot 2HMPA$) due to increased hyperconjugation of the nitrogen lone pairs to the phosphorus atom [27]. This is also consistent with the sharper Sn–O–P bond angle (151° versus 165° in the HMPA complex) observed in **1** as compared to the HMPA complex.

3.4. Theoretical calculations

To shed more insight into the structures of the two complexes prepared, the geometries of the cis and trans isomers of **1** were optimised by means of the DFT/B3LYP method. The fully optimised structure of the trans isomer shown in Fig. 4 is very similar to the X-ray structure. The cis and trans isomers of complex **1** and its ligand have been identified as local minima on the singlet potential energy surfaces (PES). Optimised values of selected geometrical parameters are listed in Table 5. The potential energy difference between the two isomers of **1** was 4.2 kcal/mol, indicating the stability of the trans over the cis isomer (see Fig. 4). This difference is in good agreement with both the experimental NMR and X-ray data. For comparison purposes, we have also carried out DFT/B3LYP calculations at the same level of theory on the complex $SnCl_4 \cdot 2(O)PF(NMe_2)_2$ and found that, in contrast to complex **1**, the trans isomer was 2.1 kcal/mol less stable than the cis form which further confirms the interpretation of our NMR data.

The value of the Sn–O distance, 2.094 Å, as well as the other bond distances and angles are in good agreement with the values obtained in the crystal structure. Interestingly, complex **1** shows a lengthening of the Sn–O bond and a shortening of the Sn–Cl bond on going from the trans to the cis isomer (see Table 5), consistent with X-ray analysis reported for similar molecules [10,12,28].

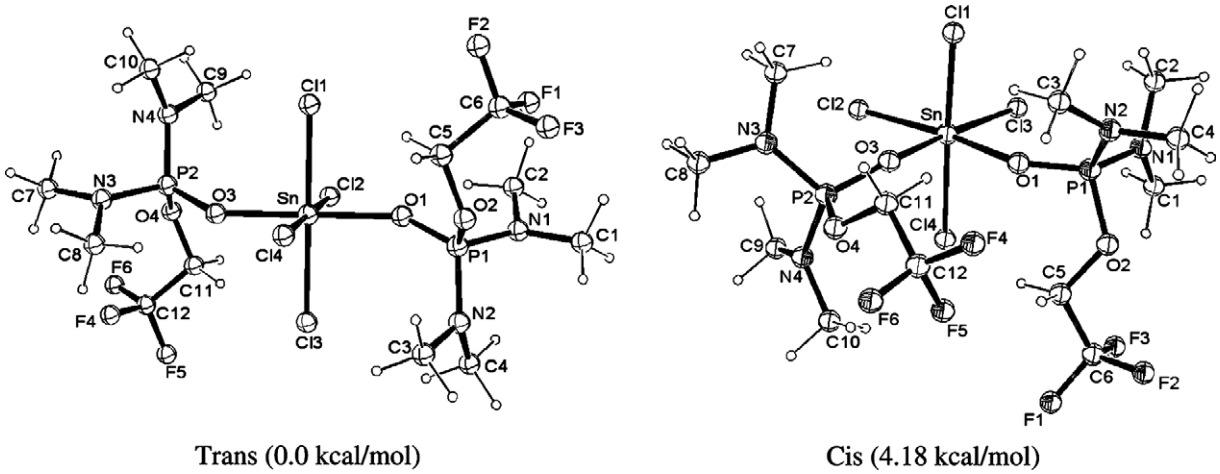


Fig. 4. ORTEP view of the DFT/B3LYP optimised structures and relative energies of cis and trans isomers of complex **1**.

Table 5
Selected DFT/B3LYP optimised geometrical parameters[a] for complex **1** and its ligand

Parameter	Ligand	cis	trans
Sn–Cl1		2.426	2.438
Sn–Cl2		2.408	2.429
Sn–Cl3		2.404	2.438
Sn–Cl4		2.443	2.429
Sn–O1		2.130	2.085
Sn–O3		2.129	2.085
O1–P1	1.490	1.529	1.531
O3–P2		1.529	1.531
P1–O2	1.650	1.618	1.619
P2–O4		1.633	1.619
P1–N1	1.677	1.644	1.649
P1–N2	1.672	1.652	1.645
P2–N3		1.644	1.649
P2–N4		1.643	1.645
O2–C5	1.421	1.431	1.432
O4–C11		1.423	1.432
C5–C6	1.518	1.517	1.518
C11–C12		1.517	1.518
C6–F1	1.346	1.348	1.355
C6–F2	1.350	1.346	1.345
C6–F3	1.350	1.347	1.345
C12–F4		1.352	1.355
C12–F5		1.353	1.345
C12–F6		1.340	1.345
Cl1–Sn–Cl2		95.0	90.2
Cl2–Sn–Cl3		97.7	89.8
Cl3–Sn–Cl4		93.3	90.2
Cl1–Sn–O1		85.2	88.1
Sn–O1–P1		148.9	146.7
Sn–O3–P2		145.1	146.7
O1–Sn–O3		80.2	180.0
O1–P1–O2	112.2	108.9	109.8
O1–P1–N1	121.4	122.3	106.6
N1–P1–O2	98.5	100.5	112.6
N1–P1–N2	103.3	106.2	106.7
O2–C5–C6	108.9	106.8	109.3

[a] See Fig. 4 for labeling of the atoms. Distances are in Å and angles in °.

In complex **1**, the coordination mode is confirmed by a lengthening of the P═O bond compared to that of the free ligand (1.490 Å) calculated at the same level of theory. This lengthening is consistent with the low stretching frequency observed in the IR spectra and may also explain the differences observed in the ^{31}P NMR chemical shifts between the free and bound ligands in solution. On forming complex **1**, the ligand also shows a shortening of both the P–O and P–N bond distances by about 0.03 Å. This is accompanied by an increase in the bond angles at the phosphorus atom, i.e., the O–P–N and N–P–N angles are increased by ~2° and 3°, respectively, compared to those of the free ligand (see Table 5). Comparable changes in geometry, i.e., shortened bonds and increased angles at the phosphorus atom have been observed in related complexes [29,30].

It is worthnoting that, as shown in Tables 4 and 5, the overall agreement between theoretical and experimental X-ray structures leads further support to the structural characterisation discussed above. Differences in the details may be due in part to crystal packing influences. For example, in *trans*-**1**, the P–O–Sn angle is predicted to be more acute (see Table 5) than actually observed. Similarly, the predicted structure of *trans*-**1** is much more symmetrical than observed in the crystal (see Fig. 4).

4. Conclusion

New complexes of phosphoramidates with $SnCl_4$ have been synthesised and studied by a combination of NMR spectroscopy, X-ray analysis and DFT/B3LYP calculations. It was shown that, unlike the analogous $(R_2N)_2$-P(O)F, the phosphoramidates examined prefer to form a trans complex with $SnCl_4$. This preferential complexation is likely due to steric hindrance from the fluoroalkoxy group on the phosphorus atom of the phosphoramidate ligand. We have also shown that the insights provided by combining experimental and theoretical studies can offer new concepts for a better understanding of the stereochemistry of such complexes.

Acknowledgements

We are grateful to the Tunisian Ministry of High Education and Scientific Research and Technology for financial support (LR99ES14) of this research and to Professor Emeritus A. Baklouti of the Department of Chemistry, Faculty of Sciences of Tunis, University of Tunis El Manar, for his valuable help and continuous support.

Appendix A. Supplementary data

CCDC 671245 contains the supplementary crystallographic data for **1**. These data can be obtained free of charge via http://www.ccdc.cam.ac.uk/conts/retrieving.html, or from the Cambridge Crystallographic Data Centre, 12 Union Road, Cambridge CB2 1EZ, UK; fax: (+44) 1223-336-033; or e-mail: deposit@ccdc.cam.ac.uk.. Supplementary data associated with this article can be found, in the online version, at doi:10.1016/j.poly.2008.02.009.

References

[1] A.G. Davies, in: E.W. Abel, F.G.A. Stone, G. Wilkinson (Eds.), Comprehensive Organometallic Chemistry II, vol. 2, Elsevier Science Inc., Tarrytown, NY, 1995.
[2] (a) P.G. Harrison, Compounds of tin: general trends, in: P.G. Harrison (Ed.), Chemistry of Tin, Chapman and Hall, New York, 1989;
(b) T. Munguia, M. Lopez-Cardoso, F. Cervantes-Lee, K.H. Pannell, Inorg. Chem. 46 (2007) 1305.
[3] S.E. Denmark, J. Fu, J. Am. Chem. Soc. 125 (2003) 2208.
[4] D. Fàrsaiu, R. Leu, P.J. Ream, J. Chem. Soc., Perkin Trans. 2 (2001) 427.
[5] S.E. Dann, A.R.J. Genge, W. Levason, G. Reid, J. Chem. Soc., Dalton Trans. (1997) 2207.
[6] C.H. Yoder, L.A. Margolis, J.M. Horne, J. Organomet. Chem. 633 (2001) 33, and refs. therein.

[7] See for example: A.R.J. Genge, W. Levason, G. Reid, J. Chem. Soc., Dalton Trans. (1997) 4549, and refs. therein.
[8] E. Le Coz, J.E. Guerchais, Bull. Soc. Chim. Fr. 1 (1971) 80.
[9] S.J. Ruzicka, A.E. Merbach, Inorg. Chim. Acta 20 (1976) 221.
[10] L.A. Aslanov, V.M. Ionov, V.M. Attiya, A.B. Permin, V.S. Petrosyan, Zh. Strukt. Khim. 18 (1977) 1103.
[11] S.J. Ruzicka, A.E. Merbach, Inorg. Chim. Acta 22 (1977) 191.
[12] S.E. Denmark, X. Su, Tetrahedron 55 (1999) 8727.
[13] D. Tudela, V. Fernàndez, J.D. Tornero, J. Chem. Soc., Dalton Trans. (1985) 1281.
[14] J. Rupp-Bensadon, E.A.C. Lucken, J. Chem. Soc., Dalton Trans. (1983) 495.
[15] M.A.M. Khouna, M.T. Ben Dhia, M.R. Khaddar, Phosphorus Sulfur Silicon 180 (2005) 1673.
[16] M.A.M. Khouna Sanhoury, M.T. Ben Dhia, K. Essalah, M.R. Khaddar, Polyhedron 25 (2006) 3299.
[17] D.D. Perrin, W.L.F. Armarego, D.R. Perrin, Purification of Laboratory Chemicals, Pergamon Press, Oxford, 1966.
[18] C.M. Timperley, M. Bird, J.F. Broderick, I. Holden, I.J. Morton, M.J. Waters, J. Fluorine Chem. 104 (2000) 215.
[19] G.M. Sheldrick, SHELXS-97 A Program for Crystal Structure Determination, University of Gottingen, Germany, 1997.
[20] G.M. Sheldrick, SHELXL-97 A Program for the Refinement of Crystal Structures, University of Gottingen, Germany, 1997.
[21] L.J. Farrugia, J. Appl. Crystallogr. 32 (1999) 837.
[22] M.J. Frisch, G.W. Trucks, H.B. Schlegel, G.E. Scuseria, M.A. Robb, J.R. Cheeseman, V.G. Zakrzewski, J.R.E. Montgomery, J.C. Stratmann, J.C. Burant, S. Dapprich, J.M. Millam, A.D. Daniels, K.N. Kudin, M.C. Strain, O. Farkas, J. Tomasi, V. Barone, M. Cossi, R. Cammi, B. Menucci, C. Pomelli, C. Adamo, S. Clifford, J. Ochterski, G.A. Petersson, P.Y. Ayala, Q. Cui, K. Morokuma, D.K. Malick, A.D. Rabuck, K. Raghavachari, J.B. Foresman, J. Cioslowski, J.V. Ortiz, B.B.J. Stefanov, G. Liu, A. Liashenko, P. Piskorz, I. Koaromi, R. Gomperts, R.L. Martin, D.J. Fox, T. Keith, M.A. Al-Laham, C.Y. Peng, A. Nanayakkara, C. Gonzalez, M. Challcombe, P.M.W. Gill, B.G. Johnson, W. Chen, M.W. Wong, J.L. Andres, M. Head-Gordon, E.S. Replogle, J.A. Pople, GAUSSIAN 98 Revision A.7, Gaussian Inc., Pittsburgh PA, 1998.
[23] (a) A.D. Becke, J. Chem. Phys. 98 (1993) 5648;
(b) C. Lee, W. Yang, R.G. Parr, Phys. Rev. B 37 (1988) 785.
[24] (a) P.J. Hay, W.R. Wadt, J. Chem. Phys. 82 (1985) 270;
(b) W.R. Wadt, P.J. Hay, J. Chem. Phys. 82 (1985) 284;
(c) P.J. Hay, W.R. Wadt, J. Chem. Phys. 82 (1985) 299.
[25] (a) W.J. Hehre, R. Ditchfield, J.A. Pople, J. Chem. Phys. 56 (1972) 2257;
(b) G.A. Petersson, A. Bennett, T.G. Tensfeldt, M.A. Al-Laham, W.A. Shirley, J. Mantzaris, J. Chem. Phys. 89 (1988) 2193;
(c) G.A. Petersson, M.A. Al-Laham, J. Chem. Phys. 94 (1991) 6081;
(d) P.C. Hariharan, J.A. Pople, Theor. Chim. Acta 28 (1973) 213;
(e) V.A. Rassolov, M.A. Ratner, J.A. Pople, P.C. Redfern, L.A. Curtiss, J. Comp. Chem. 22 (2001) 976.
[26] M.S. Holt, W.L. Wilson, J.H. Nelson, Chem. Rev. 89 (1989) 11.
[27] (a) For a discussion of bond lengths and angles in phosphoramides see: M. Kranz, S.E. Denmark, J. Org. Chem. 60 (1995) 5867;
(b) M. Kranz, S.E. Denmark, K.A. Swiss, S.R. Wilson, J. Org. Chem. 61 (1996) 8551;
(c) For a discussion of hybridisation see: D.G. Gilheany, Chem. Rev. 94 (1994) 1339;
(d) J.A. Dobado, G. Marinez-García, J.M. Molina, M.R. Sundberg, J. Am. Chem. Soc. 120 (1998) 8461.
[28] C.I. Bränden, Acta Chem. Scand. 17 (1963) 759.
[29] M.D. La Prade, C.E. Nordman, Inorg. Chem. 8 (1969) 1669.
[30] L.E. Sutton (Ed.), Tables of Interatomic Distances and Configuration in Molecules and Ions, The Chemical Society, London, 1958 (Supplement, 1965).

polymers of sac with mercury(II) [20], lead(II) [21–23], silver(I) [24–29] and copper(II) [30]. In the present study, we utilized the sac ligand together with piperazine (ppz) and *N*,*N*′-bis(2-hydroxyethyl)piperazine (bheppz). In this paper, we report synthesis and single-crystal structures of two new coordination polymers, $[Ag(\mu\text{-sac})(\mu\text{-ppz})]_n$, **1** and $[Ag(\mu\text{-sac})(\mu\text{-bheppz})]_n$, **2**, constructed from assembly of silver(I) with the corresponding ligands. Both complexes consist of single linear chains, and hydrogen bonding and π–π stacking interactions between these chains led to the generation of two-dimensional networks.

2. Experimental

2.1. Materials and measurements

All reagents were purchased from commercial sources and used without further purification. The elemental analyses (C, H and N) were performed on a Vario EL Elemental Analyser. IR spectra were recorded on a MATTSON 1000 FT/IR spectrophotometer as KBr pellets in the frequency range 4000–400 cm^{-1}. Thermal analysis curves (TG and DTA) were obtained from a Rigaku TG8110 thermal analyzer in a static air atmosphere using a sample size of 5–10 mg with a heating rate of 10 °C min^{-1}.

2.2. Synthesis of the silver(I) complexes

Complex **1** was prepared by the following method: $Na(sac) \cdot 2H_2O$ (1 mmol, 0.24 g) was added to the solution (20 ml) of $AgNO_3$ (1 mmol, 0.17 g) dissolved in the mixture of water and isopropanol (1:3, v:v) with stirring. Then, a suspension with a white precipitate formed and the drop-wise addition of the aqueous solution (10 ml) of ppz (1 mmol, 0.09 g) to the suspension resulted in a clear solution, which was kept in darkness at room temperature and pale yellow prisms were obtained after two months. $[Ag(\mu\text{-sac})(\mu\text{-ppz})]_n$ (**1**): Yield 83%. *Anal.* Calc. for $C_{11}H_{14}N_3O_3SAg$: C, 35.12; H, 3.75; N, 11.17. Found: C, 35.35; H, 3.84; N, 11.42%. IR data (KBr): *v* (cm^{-1}) 3538–3268 sb, 3062 w, 2937 vw, 2864 vw, 1651 vs, 1584 s, 1450 m, 1327 m, 1265 vs, 1141 vs, 966 s, 874 m, 750 m, 688 w, 616 m, 544 m.

Complex **2** was prepared using the same method as for **1**. The initial ligand was *N*,*N*′-bis(2-hydroxyethyl)piperazine (bheppz). Colorless prism-shaped crystals of **2** were obtained at room temperature after four days. $[Ag(\mu\text{-sac})(\mu\text{-bheppz})]_n$ (**2**): Yield 86%. *Anal.* Calc. for $C_{15}H_{22}N_3O_5SAg$: C, 35.03; H, 3.47; N, 7.43. Found: C, 35.25; H, 3.65; N, 7.66%. IR data (KBr): *v* (cm^{-1}) 3400–3147 sb, 3062 vw, 2981 vw, 1651 vs, 1630 vs, 1585 s, 1456 m, 1331 m, 1284 vs, 1250 vs, 1153 vs, 968 s, 928 s, 772 s, 705 m, 675 vs, 636 m, 609 s, 543 s, 509 m.

2.3. X-ray crystallography

Intensity data for the title complexes were collected using a Stoe-IPDS-2 diffractometer equipped with a graphite monochromated (Mo Kα radiation, $\lambda = 0.71073$ Å) at 100 K. The structure was solved by direct methods using SHELXS-97 [31] and refined by a full-matrix least-squares procedure using the program SHELXL-97 [31]. All non-hydrogen atoms were easily found from the difference Fourier map and refined anisotropically. All hydrogen atoms were included using a riding model. Details of crystal data, data collection, structure solution and refinement are given in Table 1.

Table 1
Crystallographic data for **1** and **2**

	1	**2**
Empirical formula	$C_9H_9N_2O_3SAg$	$C_{11}H_{13}N_3O_4SAg$
Formula weight	333.11	377.16
Temperature (K)	100(2)	100(2)
Wavelength (Å)	0.71073	0.71073
Crystal system	triclinic	triclinic
Space group	$P\bar{1}$	$P\bar{1}$
a (Å)	7.0373(9)	8.0255(7)
b (Å)	8.2418(10)	8.4925(8)
c (Å)	9.2150(10)	9.8866(9)
α (°)	70.812(9)	68.130(7)
β (°)	83.801(10)	85.256(7)
γ (°)	80.635(10)	85.432(7)
V (Å^3)	497.20(10)	622.33(10)
Z	2	2
D_c (g/cm^3)	2.225	2.013
μ (mm^{-1})	2.228	1.798
F(000)	328	376
Crystal size (mm)	0.44 × 0.32 × 0.25	0.27 × 0.20 × 0.17
θ Range (°)	2.34–26.00	3.29–26.00
Index range (*h*,*k*,*l*)	−8/8, −10/10, −11/11	−9/9, −10/10, −12/12
Reflections collected/unique	5264/1949	11 803/2441
Absorption correction	integration	integration
T_{max} and T_{min}	0.670 and 0.495	0.9108 and 0.6719
Data/parameters	1949/145	2441/167
Goodness-of-fit on F^2	1.096	1.139
R_1 [$I > 2\sigma(I)$]	0.0298	0.0175
wR_2	0.0887	0.0424
Residuals (e Å^{-3})	1.013/−1.618	0.428/−0.772

3. Results and discussion

3.1. Synthesis and FT-IR characterization

Complexes **1** and **2** were readily prepared by the direct reaction of $AgNO_3$ and $Na(sac) \cdot 2H_2O$ in the presence of corresponding co-ligands ppz and bheppz in dark at room temperature and obtained in high yields of over 80%. The analytical data (C, H, and N) and X-ray crystal structure analysis confirmed the chemical formulation of these complexes. The title complexes are non-hygroscopic and stable in air at ambient temperatures, but somewhat light sensitive after a long exposure to light. Complex **1** is insoluble in water and common organic solvents, but complex **2** shows moderate solubility in the mixtures of isopropanol and water.

The FT-IR spectra of both complexes exhibit the characteristic bands of the sac and secondary ligands. The strong and broad absorption bands occurred above 3150 cm^{-1} are assigned to the ν(OH) or ν(NH) vibrations of co-ligands involved in hydrogen bonding, while the relatively weak bands in the frequency range 2900–31 000 cm^{-1} are due to the absorption of the CH groups. The ν(C=O) vibrations of sac in the title complexes are observed as a very sharp band centered at *ca.* 1650 cm^{-1}. In complex **2**, the carbonyl O atom of the sac ligand does not participate in metal bonding and appears as two sharp bands at 1651 and 1630 cm^{-1}. However, complex **1** contains bridging sac ligands *via* the carbonyl O atom, and in this case, a significant shift to lower frequencies should be occurred due to a weakening of the carbon–oxygen bond. The spectral analysis shows that the band of the carbonyl group in **1** appears at 1651 cm^{-1} and no significant shift in the carbonyl band of **1** is observed compared to that of complex **2**. It is an unexpected observation and similar findings in the carbonyl band of sac were also observed in the IR spectra of $[Ag(sac)(nia)]_n$ [29]. It may be concluded that in the presence of intra- and intermolecular interactions such as hydrogen bonds, the ν(C=O) frequency does often not correlate to the coordination mode of the sac ligand. The asymmetric and symmetric stretchings of the SO_2 group in the spectra of **1** and **2** are observed as two strong IR bands at *ca.* 1260 and 1150 cm^{-1}, respectively. Among these complexes, the coordination of the sulfonyl group occurs only in **2**, but no significant changes were observed in the frequency of this group compared to those found in the spectra of **1**. In conclusion, the sulfonyl stretching modes in metal complexes are not easily assigned as that of the carbonyl stretching.

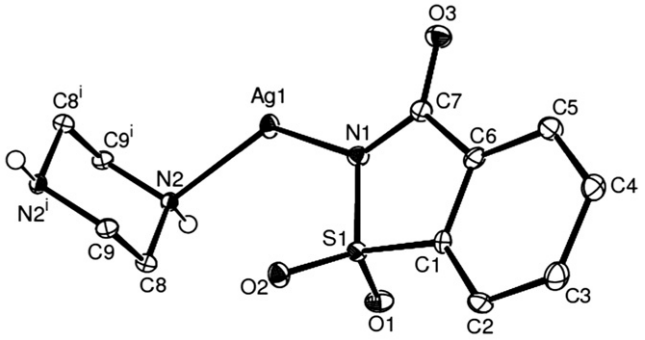


Fig. 1. The building-block unit of **1** with the atom labeling scheme. CH hydrogen atoms are omitted for clarity. Symmetry code (i) $-x, -y, 1-z$.

3.2. Description of crystal structures

The structure of the building-block unit of **1** is shown in Fig. 1, together with the atom labeling scheme. The selected bond lengths and angles are given in Table 2. Each sac anion adopts a μ_2-bridging mode to connect with two silver ions through the imino N and carbonyl O atoms, forming binuclear $[Ag_2(sac)_2]$ units. Thus, a planar eight-membered bimetallic ring is formed by two silver(I) ions linked by two N–C–O bridges. These dimeric units are further bridged by neutral ppz ligands, leading to an infinite linear chain propagating along *c* (Fig. 2). The Ag–Ag separation within the metallocycle is 3.673 Å, and slightly larger than the upper limit value of 3.30 Å for an Ag···Ag contact in coordination compounds [32]. The Ag–Ag distance separated by the ppz ligands is 6.063 Å. In the crystal structure of **1**, the silver(I) ions are coordinated by one nitrogen atom from ppz, one N atom from sac and one O atom from another sac. The coordination geometry is considered T-shaped rather than trigonal, because of the significant deviation from the ideal trigonal geometry (120°), N1–Ag1–N2 127.47(9)°, N1–Ag1–O3^{i} 143.95(9)°, N1–Ag1–O3^{i} 88.20(9)°.

Table 2
Selected bond lengths (Å) and bond angles (°) for **1** and **2**

[Ag(sac)(ppz)]$_n$ (**1**)			
Ag1–N1	2.172(3)	N1–Ag1–N2	127.47(9)
Ag1–N2	2.325(3)	N1–Ag1–O3^{i}	143.95(9)
Ag1–O3^{i}	2.297(2)	N1–Ag1–O3^{i}	88.20(9)
[Ag(sac)(bheppz)]$_n$ (**2**)			
Ag1–N1	2.1467(15)	N1–Ag1– O2^{ii}	108.91(5)
Ag1–N2	2.2884(15)	N2–Ag1–O2^{ii}	88.08(5)
Ag1–O2^{ii}	2.5787(13)	N1–Ag1–O6	127.91(4)
Ag1–O6	2.4590(13)	N2–Ag1–O6	73.77(4)
N1–Ag1–N2	151.91(5)	O2^{ii}–Ag1–O6	86.43(3)

Symmetry operations: (i) $-x, -y, 2-z$ and (ii) $1-x, 1-y, 1-z$.

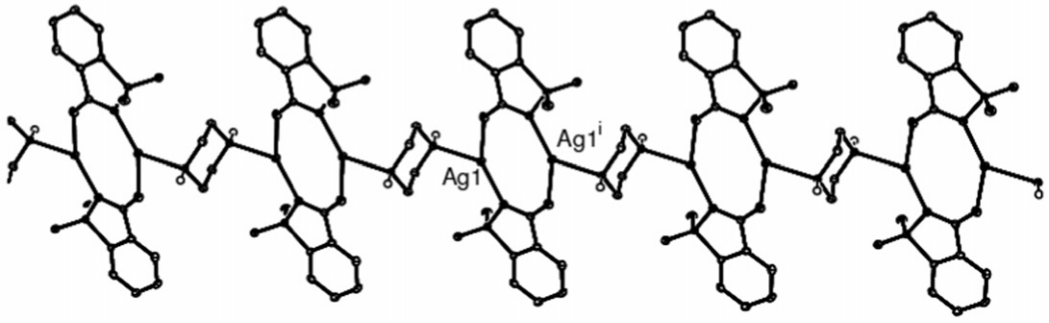


Fig. 2. A fragment of a one-dimensional chain in **1**. Symmetry code (i) $-x, -y, 2-z$.

Three coordination polymers, $[Ag_2(\mu\text{-sac})_2(\mu\text{-hep})_2]_n$ [25], $[Ag_2(sac)_2(en)(H_2O)]_n$ [27] and $[Ag(sac)(nia)]_n$ [29], containing N, $O_{carbonyl}$ bridging sac ligands have been reported so far. The Ag–N_{sac} bond distance of 2.172(3) Å in **1** is similar to those found in the reported complexes, while the Ag–$O_{carbonyl}$ bond distance of 2.297(2) Å is considerably shorter than that of $[Ag_2(\mu\text{-sac})_2(\mu\text{-hep})_2]_n$ [25].

The sac ligand is essentially planar and the puckering parameters of the ppz ring system in **1** are $q = 0.605(2)$ Å and $\theta = 0°$, suggesting that the ppz ring exhibits an essentially "undistorted" (cyclohexane like) chair conformation. The individual chains interact with each other *via* N–H···O hydrogen bonds (see Table 3), leading to a two-dimensional layer parallel to the *bc*-crystallographic plane as shown in Fig. 3a. The nearest Ag–Ag separation between the polymeric chains is 7.037 Å. These hydrogen bonded layers stack by way of face to face aromatic π(sac)···π(sac) interactions [$C_g \cdots C_g^i$ 3.605(2) Å; C_g = centroid of atoms C1–C6; (i): $1-x$, $1-y$, $2-z$], resulting in the formation of extended three-dimensional supramolecular network (Fig. 3).

The fundamental building unit of the crystal structure of **2** is shown in Fig. 4, together the atom labeling scheme. The selected bond lengths and angles are listed in Table 2. Each silver(I) ion in the building block of **2** is doubly bridged by two sac ligands forming non-planar eight-membered metallo-chelate rings as shown in Fig. 5. These dimeric units are further bridged by bheppz ligands leading to a one-dimensional polymeric chain running along the crystallographic axis *a* (Fig. 5). The coordination geometry around the silver(I) ions is a highly distorted tetrahedron with an AgN_2O_2 chromophore with two N, O bonds from sac, and two N, O bonds from bheppz. The large distortion in the coordination geometry is evident from the angles around the silver(I) ion (see Table 2). The Ag–Ag distances separated by bridging sac and bhep ligands are 4.462 Å and 5.935 Å, respectively, indicating that there is no metallophilic interaction between the two adjacent Ag atoms.

The bhep ligand has four donor sites and each end having a N atom and a O atom behaves as a bidentate donor, forming a five-membered chelate ring around silver(I). In contrast to $[Ag_2(sac)_2(heppz)]_n$ [30], containing a similar ligand with the same moiety of bheppz, all the silver atoms are equivalent in **2**. The most interesting aspect of complex **2** is the coordination of the sulfonyl O atom of the sac ligand, since the sulfonyl group is less basic and only occasionally involves in coordination and the only known examples are [Ag(sac)] [33], Na[$Ag(sac)_2$] [24] and $[Ag(sac)(dmpy)]_n$ [26], where dmpy is 2,6-pyridinedimethanol. The Ag–$O_{sulfonyl}$ bond distance of 2.5787(13) Å is similar to those of [Ag(sac)] [2.45 Å] [33] and Na[$Ag(sac)_2$] [2.6390(10) Å] [24], but much shorter than those found in $[Ag(sac)(dmpy)]_n$ [2.8218(13) and 2.9379(14) Å] [26]. A tetranuclear silver(I)-sac complex, $[Ag_4(sac)_4(pypr)_2]$, is an

Table 3
Hydrogen bond data for complexes **1** and **2**

D–H···A	D–H (Å)	H···A (Å)	D···A (Å)	D–H···A (°)
[Ag(sac)(ppz)]$_n$ (**1**)				
N2–H2A···O1^{i}	0.91	2.33	3.058(4)	137.0
N2–H2A···O1^{ii}	0.91	2.55	3.186(3)	127.3
[Ag(sac)(bheppz)]$_n$ (**2**)				
O6–H6···O1^{iii}	0.82	1.92	2.7432(13)	177
C2–H2···O2^{iv}	0.93	2.39	3.288(2)	161
C3–H3···O1^{v}	0.93	2.58	3.437(2)	154
C11–H11···O3^{vi}	0.97	2.51	3.437(2)	159

Symmetry operations: (i) $-x$, $1-y$, $1-z$; (ii) $x-1$, y, z; (iii) $1-x$, $1-y$, $-z$; (iv) $1-x$, $-y$, $1-z$; (v) x, $-1+y$, z and (vi) $-1+x$, y, z.

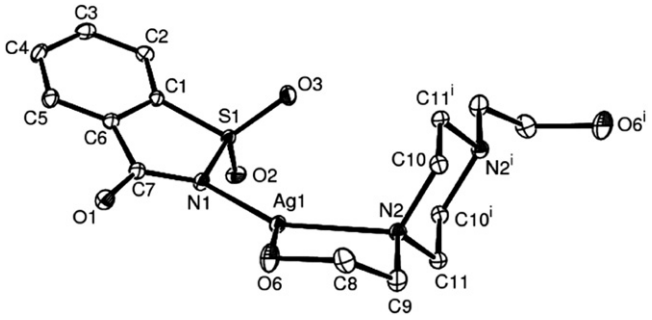


Fig. 4. The building-block unit of **2** with the atom labeling scheme. CH hydrogen atoms are omitted for clarity. Symmetry code (i) $-x$, $1-y$, $1-z$.

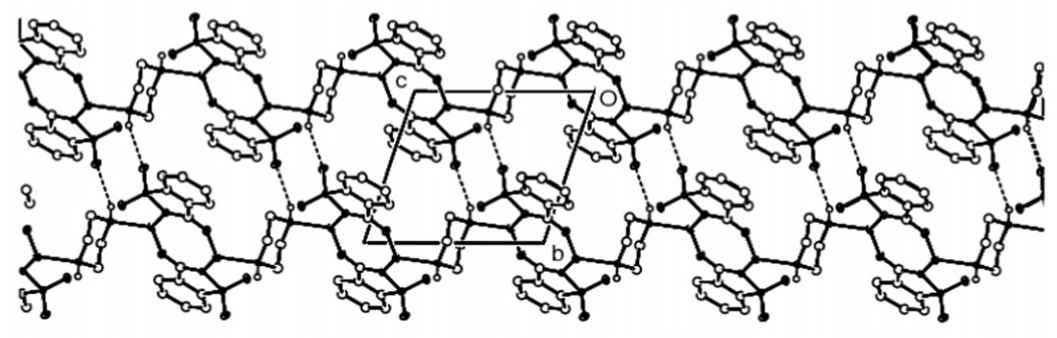


Fig. 3. The assembly of polymeric chains of **1** into a two-dimensional layer by N–H···O hydrogen bonds.

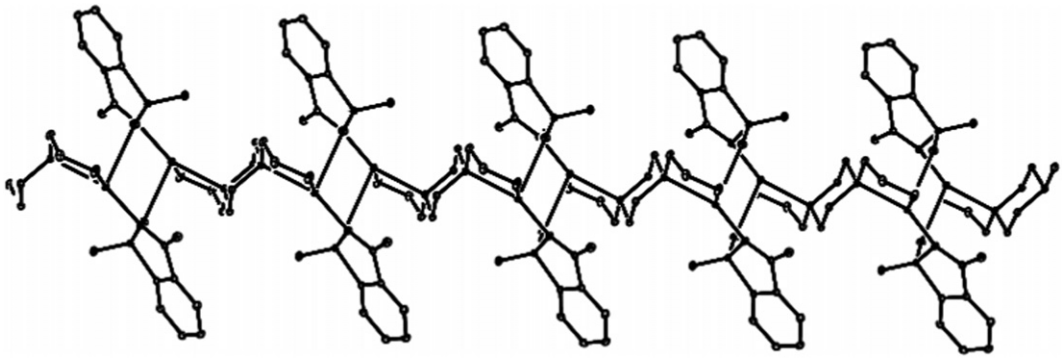


Fig. 5. View of one-dimensional chain of **2**.

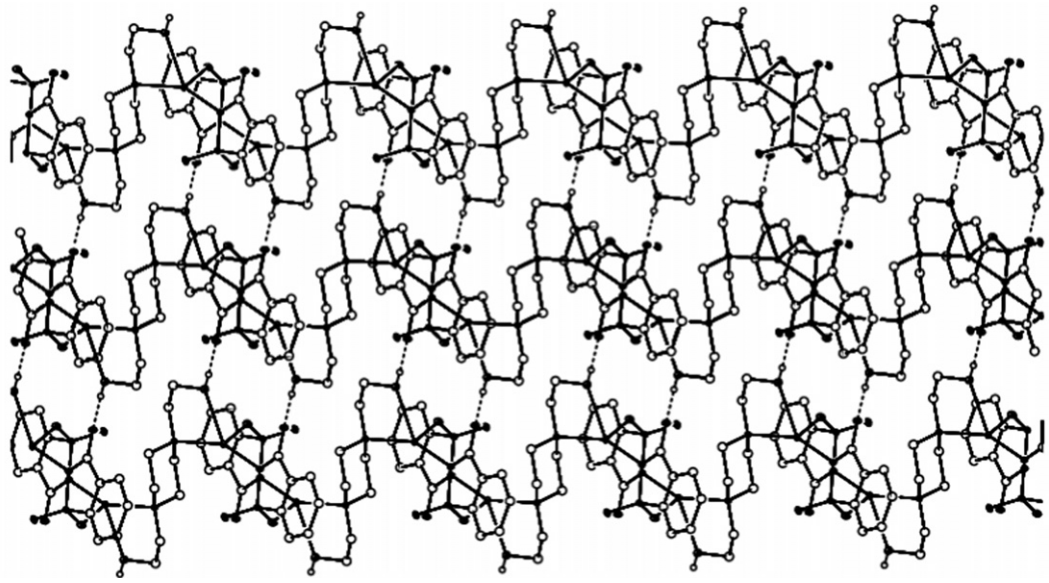


Fig. 6. Perspective view of the two-dimensional framework of **2** along *b* formed by O–H···O hydrogen bonds.

interesting example, exhibiting both N, $O_{carbonyl}$ and N, $O_{sulfonyl}$ bridges of sac [34].

The sac ligand in **2** is essentially planar, whereas the puckering parameters of the piperazine ring system of bheppz are $q = 0.600(2)$ Å and $\theta = 179.55°$, suggesting that the piperazine ring exhibits a typical chair conformation as in ppz in **1**. As shown in Fig. 6, individual polymeric chains are cross linked by the strong O–H···O and weak C–H···O intermolecular hydrogen bonds, leading to a hydrogen bonded two-dimensional layer parallel to the *ac* plane.

3.3. Thermal analysis

The thermal behaviors of complexes **1** and **2** were examined by DTA and TGA under the atmosphere of air. The DTA and TGA curves in Fig. 7a show that **1** does not decompose up to 215 °C. The total weight loss of 48.87% between 215 and 300 °C is consistent with the mass loss of one mole of ppz and 0.5 moles of sac ligands. The removal of ppz is indicated by an endothermic peak at 252 °C. The decomposition of the rest of sac is observed as a highly endothermic peak at 461 °C and completed at 498 °C. The remaining mass of 28.58% is metallic silver that is in agreement with the calculated value of 28.68%.

Thermal curves of **2** are illustrated in Fig. 7b. The DTA and TGA results indicate that the thermal stability of complex **2** is somewhat lower than that of complex **1**, and it begins to decompose at 188 °C displaying two stages of mass loss (Fig. 3b). The first mass loss of 37.02% from 188 to 331 °C is due to the loss of the bheppz ligand (calculated value 37.54%). An endothermic at 225 °C and an exothermic peak 273 °C are mainly attributed to the decomposition of the bhep ligand. Upon increasing temperature, the degradation of the sac anion occurs in the second step in the temperature range 332–619 °C with a violently exothermic reaction which is characteristic for the decomposition of the sac moiety in metal sac complexes [35]. The remaining mass of 22.90% is presumably metallic

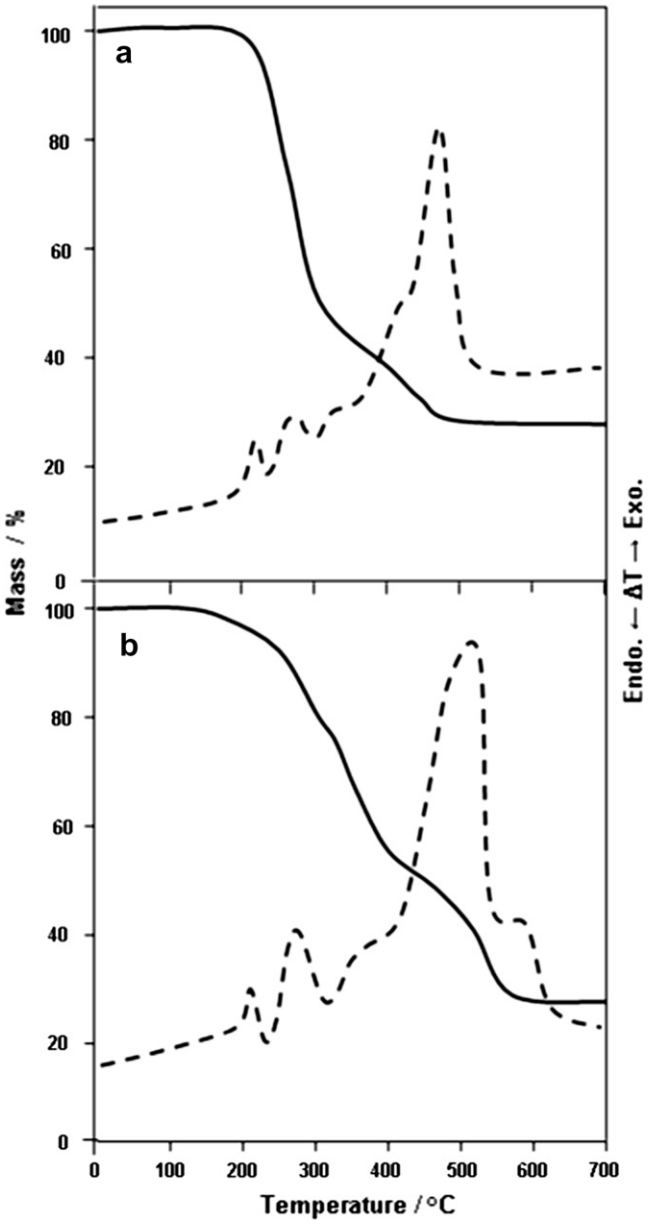


Fig. 7. Thermal analysis (TG and DTA) curves of **1** (a) and **2** (b).

silver that is in agreement with the calculated value of 23.25%.

Appendix A. Supplementary data

CCDC 281719 and 658776 contain the supplementary crystallographic data for **1** and **2**. These data can be obtained free of charge via http://www.ccdc.cam.ac.uk/conts/retrieving.html, or from the Cambridge Crystallographic Data Centre, 12 Union Road, Cambridge CB2 1EZ, UK; fax: (+44) 1223-336-033, or e-mail: deposit@ccdc.cam.ac.uk.

References

[1] S.R. Batten, B.F. Hoskins, R. Robson, Angew. Chem., Int. Ed. 34 (1995) 820.
[2] S. Leininger, B. Olenyuk, P.J. Stang, Chem. Rev. 100 (2000) 853.
[3] M.J. Zaworotko, Angew. Chem., Int. Ed. 39 (2000) 3052.
[4] S.R. Batten, Cryst. Eng. Commun. 3 (2001) 67.
[5] S.A. Barnett, A.J. Blake, N.R. Champness, J.E.B. Nicolson, C. Wilson, J. Chem. Soc., Dalton Trans. (2001) 567.
[6] S. Dalai, P.S. Mukherjee, E. Zangrando, F. Lloret, N.R. Chaudhuri, J. Chem. Soc., Dalton Trans. (2002) 822.
[7] S.L. James, Chem. Soc. Rev. 32 (2003) 276.
[8] M. Fujita, Y.J. Kwon, S. Washizu, K. Ogura, J. Am. Chem. Soc. 116 (1994) 1151.
[9] O.M. Yaghi, H. Li, C. Davis, D. Richardson, T.L. Groy, Acc. Chem. Res. 31 (1998) 474.
[10] H. Gudbjartson, K. Biradha, K.M. Poirier, M.J. Zaworotko, J. Am. Chem. Soc. 121 (1999) 2599.
[11] J. Tao, M.L. Tong, X.M. Chen, J. Chem. Soc., Dalton Trans. 20 (2000) 3669.
[12] S.M. Humphrey, R.A. Mole, J.M. Rawson, P.T. Wood, J. Chem. Soc., Dalton Trans. 11 (2004) 1670.
[13] J.M. Li, H.Q. Zeng, J.H. Chen, Q.M. Wang, X.T. Wu, Chem. Commun. 13 (1997) 1213.
[14] L.J. Zhang, J.Q. Xu, Z. Shi, X.L. Zhao, T.G. Wang, J. Solid State Chem. 32 (2003) 32.
[15] D.F. Sun, R. Cao, Y.C. Liang, Q. Shi, W.P. Su, M.C. Hong, J. Chem. Soc., Dalton Trans. 16 (2001) 2335.
[16] D. Venkataraman, Y.H. Du, S.R. Wilson, K.A. Hirsch, P. Zhang, J.S. Moore, J. Chem. Edu. 74 (1997) 915.
[17] A.N. Khlobystov, A.J. Blake, N.R. Champness, D.A. Lemenovskii, A.G. Majouga, N.V. Zyk, M. Schroder, Coord. Chem. Rev. 222 (2001) 155.
[18] A.Y. Robin, K.M. Fromm, Coord. Chem. Rev. 250 (2006) 2127.
[19] E.J. Baran, V.T. Yilmaz, Coord. Chem. Rev. 250 (2006) 1980.
[20] V.T. Yilmaz, S. Guney, O. Andac, W.T.A. Harrison, Polyhedron 21 (2002) 2393.
[21] V.T. Yilmaz, S. Guney, C. Thone, Z. Anorg. Allg. Chem. 628 (2002) 1406.
[22] V.T. Yilmaz, S. Hamamci, O. Andac, K. Guven, Z. Anorg. Allg. Chem. 629 (2003) 172.
[23] V.T. Yilmaz, S. Caglar, W.T.A. Harrison, Z. Anorg. Allg. Chem. 630 (2004) 948.
[24] V.T. Yilmaz, S. Hamamci, C. Thone, Z. Anorg. Allg. Chem. 630 (2004) 1641.
[25] S. Hamamci, V.T. Yilmaz, W.T.A. Harrison, J. Mol. Struct. 734 (2004) 191.
[26] S. Hamamci, V.T. Yilmaz, W.T.A. Harrison, C. Thone, Solid State Sci. 7 (2005) 423.
[27] V.T. Yilmaz, S. Hamamci, C. Kazak, Z. Anorg. Allg. Chem. 631 (2005) 1961.
[28] S. Hamamci, V.T. Yilmaz, W.T.A. Harrison, Struct. Chem. 16 (2005) 379.
[29] S. Hamamci, V.T. Yilmaz, C. Kazak, Struct. Chem. 17 (2006) 57.
[30] V.T. Yilmaz, V. Kars, C. Kazak, Z. Anorg. Allg. Chem. 632 (2006) 505.
[31] G.M. Sheldrick, SHELX-97. Programs for Crystal Structure Analysis, University of Göttingen, Germany, 1997.
[32] M. Jansen, Angew. Chem., Int. Ed. Engl. 26 (1987) 1098.
[33] R. Weber, M. Gilles, G. Bergerhoff, Z. Kristallogr. 206 (1993) 273.
[34] S. Hamamci, V.T. Yilmaz, W.T.A. Harrison, C. Thone, Polyhedron 24 (2005) 693.
[35] H. Icbudak, V.T. Yilmaz, H. Olmez, J. Therm. Anal. 53 (1998) 843.

The spectroscopic and redox behaviour of the Re(I) complexes are ligand dependent and can be tuned by varying the identity of their chelate ligands, so there is a clear need to synthesize and investigate novel species of this type.

Bis(pyrazol-1-yl)alkanes constitute a family of stable and flexible bidentate ligands, isoelectronic and isosteric with the well-known bis(pyrazolyl)borates. The coordination properties of bis(pyrazol-1-yl)alkanes may be varied in a rather wide range by introducing substituents into the pyrazole rings. Hence, the donor ability of the ligands is determined by the presence of electron-withdrawing or electron-donating functional groups, and steric factors are altered by the introduction of bulky alkyl groups into the rings and the alkane bridge between them [13].

These molecules form a variety of coordination compounds with main group and transition metals [14–19], but rhenium complexes with bis(pyrazol-1-yl)alkane ligands have been studied relatively little [20,21].

Here, we present the synthesis, spectroscopic characterization, crystal and molecular structures of two novel rhenium tricarbonyl complexes $[Re(CO)_3(bdmpzm)Cl]$ (**1**) and $[Re(CO)_3(bpzm)Cl]$ (**2**), where bdmpzm stands for bis(3,5-dimethylpyrazol-1-yl)methane and bpzm is bis(pyrazol-1-yl)methane.

The geometry of **1** has been optimized with density functional theory (DFT) calculations. Currently, the DFT method is commonly used to examine the electronic structure of transition metal complexes. It meets with the requirements of being accurate, easy to use and fast enough to allow the study of relatively large molecules of transition metal complexes [22,23]. The spin-allowed singlet–singlet electronic transitions of **1** have been calculated with the time-dependent DFT method (TDDFT method), and a good assignment with the experimental spectrum has been observed. The lowest excited singlet and triplet sates were optimized for complex **1** and its photophysics was investigated.

2. Experimental

2.1. General procedure

The reactions were performed under an argon atmosphere. The solvents were dried before use, using the appropriate drying reagents. $Re(CO)_5Cl$ was purchased from Aldrich and used as received. The bis(3,5-dimethylpyrazol-1-yl)methane and bis(pyrazol-1-yl)methane were synthesized according to the literature methods [24].

The IR spectra were recorded on a Nicolet Magna 560 spectrophotometer in the spectral range 4000–400 cm^{-1} with the samples in the form of KBr pellets. The electronic spectra were measured on a spectrophotometer Lab Alliance UV–Vis 8500 in the range 1000–200 nm in chloroform solution. The ^1H NMR spectrum was recorded with a Bruker AM 400 spectrometer at room temperature using $CDCl_3$ as a solvent. Elemental analyses (C H N) were performed on a Perkin–Elmer CHN-2400 analyzer.

2.2. Preparation of $[Re(CO)_3(bdmpzm)Cl]$ (**1**)

$Re(CO)_5Cl$ (0.2 g, 0.55 mmol) and bdmpzm (0.13 g, 0.64 mmol) in toluene (80 cm^3) were refluxed for 6 h. The resulting reaction mixture was allowed to cool to room temperature and reduced in volume to ~10 ml. A white solid was filtered off, washed with hexane, then diethyl ether, and dried; yield 85%. Single crystals of complex **1**were grown by the slow diffusion of diethyl ether into a solution of the complex dissolved in dichloromethane.

IR (KBr, cm^{-1}): $\nu_{CO} = 2025$, 1923 and 1868; ν_{CN} and $\nu_{C=C} = 1574$ and 1560.

Anal. Calc. for $C_{14}H_{16}N_4O_3ClRe$: C, 31.97; H, 3.07; N, 10.65. Found: C, 31.76; H, 3.20; N, 10.76%.

^1H NMR (400 MHz, $CDCl_3$): $\delta = 2.40$ (s, 6H, $-CH_3$), 2.60 (s, 6H, $-CH_3$), 6.04 (s, 2H, $-CH_2-$), 7.56 (s, 2H, HC).

Table 1
Crystal data and structure refinement for **1** and **2**

	1	**2**
Empirical formula	$C_{14}H_{16}N_4O_3ClRe$	$C_{10}H_8N_4O_3ClRe$
Formula weight	509.96	453.85
Temperature (K)	291.0(3)	293(2)
Wavelength (Å)	0.71073	0.71073
Crystal system	triclinic	triclinic
Space group	$P\bar{1}$	$P\bar{1}$
Unit cell dimensions		
a (Å)	8.0235(6)	7.7551(6)
b (Å)	8.9825(6)	8.8398(6)
c (Å)	12.2672(10)	10.657(6)
α (°)	98.770(6)	97.410(5)
β (°)	90.060(6)	94.328(5)
γ (°)	95.173(6)	109.942(6)
Volume (Å^3)	870.12(11)	675.4(4)
Z	2	2
D_{calc} (Mg/m^3)	1.946	2.232
Absorption coefficient (mm^{-1})	7.154	9.201
$F(000)$	488	424
Crystal size (mm)	0.096 × 0.023 × 0.021	0.04 × 0.12 × 0.36
θ Range for data collection (°)	1.68 to 25.00	3.02 to 25.05
Index ranges	$-9 \leqslant h \leqslant 9$, $-10 \leqslant k \leqslant 10$, $-14 \leqslant l \leqslant 14$	$-9 \leqslant h \leqslant 7$, $-8 \leqslant k \leqslant 10$, $-12 \leqslant l \leqslant 11$
Reflections collected	8549	4291
Independent reflections [R_{int}]	3071 [0.0327]	2331 [0.0154]
Completeness to $2\theta = 50°$ (%)	100.0	97.3
Maximum and minimum transmission	0.858 and 0.819	0.836 and 0.717
Data/restraints/parameters	3071/0/212	2331/0/172
Goodness-of-fit on F^2	1.048	1.132
Final R indices [$I > 2\sigma(I)$]	$R_1 = 0.0380$ $wR_2 = 0.0930$	$R_1 = 0.0151$ $wR_2 = 0.0418$
R indices (all data)	$R_1 = 0.0537$ $wR_2 = 0.1024$	$R_1 = 0.0162$ $wR_2 = 0.0421$
Largest difference in peak and hole (e Å^{-3})	1.133 and −0.782	0.951 and −0.634

2.3. Preparation of $[Re(CO)_3(bpzm)Cl]$ (2)

A procedure similar to that for **1** was used with $Re(CO)_5Cl$ (0.2 g, 0.55 mmol) and bpzm (0.1 g, 0.67 mmol). A white precipitate of **2** was collected in 90% yield. Single crystals of complex **2** were grown by slow diffusion of diethyl ether into a solution of the complex dissolved in dichloromethane.

IR (KBr, cm^{-1}): $\nu_{CO} = 2028$, 1920 and 1895; ν_{CN} and $\nu_{C=C} = 1520$ and 1510.

Anal. Calc. for $C_{10}H_8N_4O_3ClRe$: C, 26.46; H, 1.78; N, 12.34. Found: C, 26.56; H, 1.70; N, 12.49%.

2.4. Crystal structure determination and refinement

The X-ray intensity data of **1** and **2** were collected on a KM-4-CCD automatic diffractometer equipped with a CCD detector and graphite-monochromated Mo Kα radiation ($\lambda = 0.71073$ Å) at room temperature. Details concerning crystal data and refinement are given in Table 1. Lorentz, polarization and absorption corrections [25] were applied. The structures were solved by the Patterson method and subsequently completed by difference Fourier recycling. All the non-hydrogen atoms were refined anisotropically using the full-matrix, least-squares technique. All the hydrogen atoms were found from difference Fourier synthesis after four cycles of anisotropic refinement, and refined as "riding" on the adjacent carbon atom with an individual isotropic temperature factor equal to 1.2 times the value of the equivalent temperature factor of the aromatic parent atom and equal to 1.5 times the value of the equivalent temperature factor of the methyl parent carbon atom. During refinement the methyl groups were allowed to rotate about their local threefold axis. SHELXS97 [26], SHELXL97 [27] and SHELXTL [28] programs were used for all the calculations. Atomic scattering factors were those incorporated in the computer programs. In compound **1**,

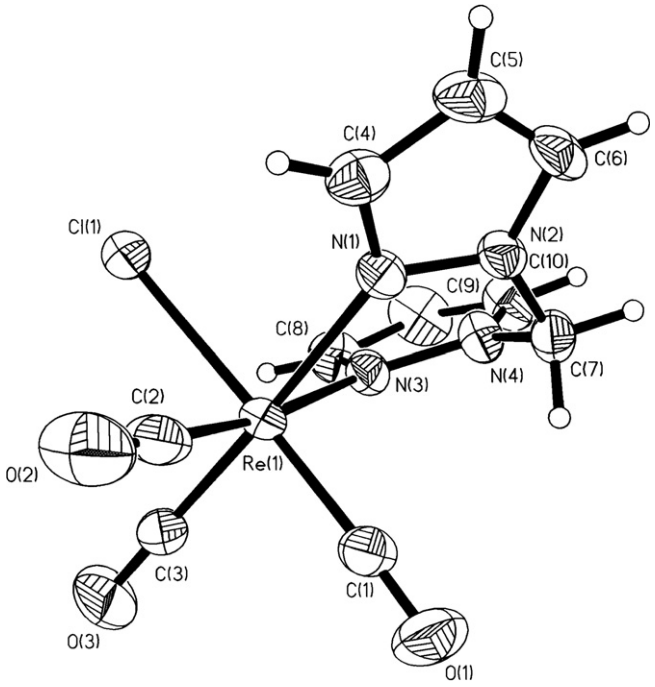


Fig. 2. Molecular structure of **2**.

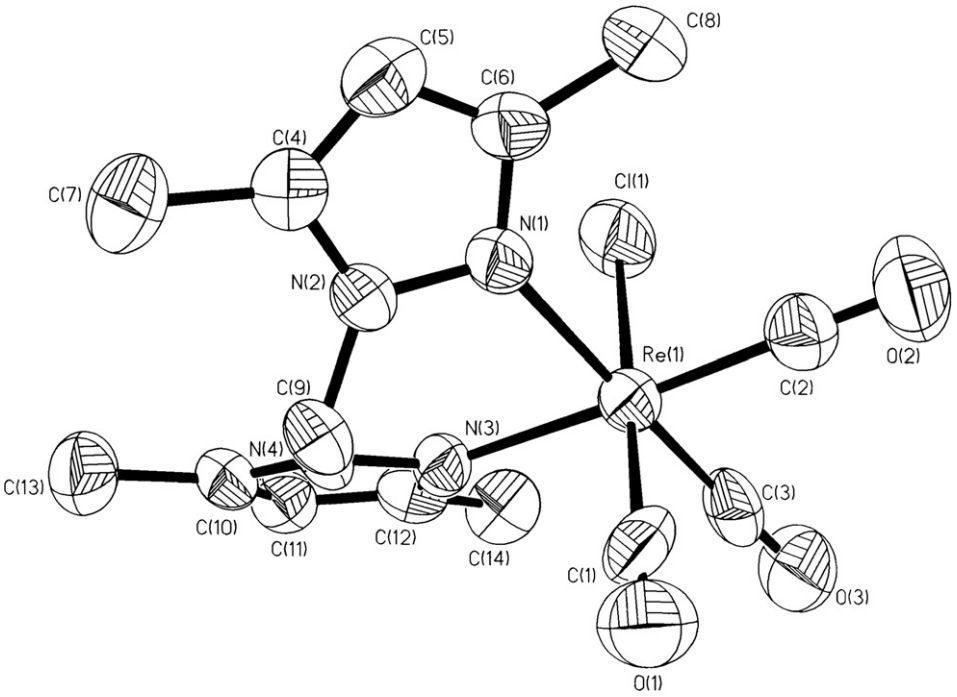


Fig. 1. Molecular structure of **1** (50% probability ellipsoids). The hydrogen atoms are omitted for clarity.

Table 2
The experimental and optimized bond lengths (Å) and angles (°) for **1**

Experimental		Optimized		
		B3LYP/ LANL2DZ	B3LYP/ MBW60	BP86/ MBW60
Bond lengths				
Re(1)–C(1)	1.971(12) 1.904(12)[a]	1.908	1.916	1.916
Re(1)–C(2)	1.903(10)	1.923	1.931	1.927
Re(1)–C(3)	1.907(10)	1.923	1.931	1.927
Re(1)–Cl(1)	2.487(3)	2.540	2.513	2.496
Re(1)–N(1)	2.213(7)	2.262	2.263	2.244
Re(1)–N(3)	2.221(6)	2.262	2.263	2.244
C(1)–O(1)	0.976(11) 1.152(11)[a]	1.170	1.172	1.186
C(2)–O(2)	1.169(12)	1.161	1.162	1.176
C(3)–O(3)	1.154(11)	1.161	1.162	1.176
Bond angles				
C(2)–Re(1)–C(1)	89.1(4)	89.66	89.01	88.68
C(3)–Re(1)–C(1)	88.5(4)	89.65	89.02	88.69
C(2)–Re(1)–C(3)	84.1(4)	88.01	87.70	87.50
C(1)–Re(1)–N(1)	93.2(3)	94.08	93.88	93.95
C(2)–Re(1)–N(1)	95.9(3)	94.45	94.69	94.58
C(3)–Re(1)–N(1)	178.3(3)	175.54	176.26	176.67
C(1)–Re(1)–N(3)	94.8(3)	94.07	93.88	93.95
C(2)–Re(1)–N(3)	176.1(3)	175.54	176.27	176.68
C(3)–Re(1)–N(3)	96.0(3)	94.46	94.69	94.58
C(1)–Re(1)–Cl(1)	179.2(3)	177.51	177.60	177.67
C(2)–Re(1)–Cl(1)	91.1(3)	92.14	92.72	92.99
C(3)–Re(1)–Cl(1)	92.3(3)	92.14	92.72	92.99
N(1)–Re(1)–Cl(1)	86.08(18)	84.07	84.32	84.31
N(3)–Re(1)–Cl(1)	84.99(17)	84.06	84.32	84.31
N(1)–Re(1)–N(3)	83.9(2)	82.85	82.78	83.23
O(1)–C(1)–Re(1)	178.2(11)	179.92	179.80	179.42
O(2)–C(2)–Re(1)	175.6(9)	178.91	179.76	178.42
O(3)–C(3)–Re(1)	175.6(9)	179.92	178.76	178.43

[a] Value corrected for libration.

Table 3
The experimental bond lengths (Å) and angles (°) for **2**

Bond lengths		Bond angles	
Re(1)–C(1)	1.905(4)	C(2)–Re(1)–C(1)	89.43(17)
Re(1)–C(2)	1.924(4)	C(2)–Re(1)–C(3)	89.78(17)
Re(1)–C(3)	1.933(4)	C(3)–Re(1)–C(1)	89.14(16)
Re(1)–Cl(1)	2.5183(14)	C(1)–Re(1)–N(1)	93.72(13)
Re(1)–N(1)	2.185(3)	C(2)–Re(1)–N(1)	92.94(14)
Re(1)–N(3)	2.213(3)	C(3)–Re(1)–N(1)	176.07(12)
C(1)–O(1)	1.158(5)	C(1)–Re(1)–N(3)	95.67(14)
C(2)–O(2)	1.161(5)	C(2)–Re(1)–N(3)	172.09(13)
C(3)–O(3)	1.159(5)	C(3)–Re(1)–N(3)	96.33(14)
		C(1)–Re(1)–Cl(1)	178.76(11)
		C(2)–Re(1)–Cl(1)	89.78(13)
		C(3)–Re(1)–Cl(1)	89.90(12)
		N(1)–Re(1)–Cl(1)	87.28(8)
		N(3)–Re(1)–Cl(1)	85.22(8)
		N(1)–Re(1)–N(3)	80.72(10)
		O(1)–C(1)–Re(1)	177.6(3)
		O(2)–C(2)–Re(1)	177.6(4)
		O(3)–C(3)–Re(1)	179.2(4)

along the Re(1)–C(1)–O(1) bonds some peaks and holes are found on difference Fourier synthesis and the largest U values of the C(1) and O(1) atoms displacement parameters are directed along the bonds, so libration analysis was performed and corrected values of the lengthened Re(1)–C(1) bond and shortened C(1)–O(1) bond are given in Table 1.

3. Computational details

The gas phase geometry of the neutral complex **1** was optimized without any symmetry restrictions in the singlet ground-state using the hybrid B3LYP [29,30] and pure BP86 [31] functionals of GAUSSIAN-03 [32]. LANL2DZ with an additional *d* function with the exponent $\alpha = 0.3811$ and *f* function with the exponent $\alpha = 2.033$ or MWB60 with an additional *f* function with the exponent $\alpha = 0.48989$ basis sets were [33–35] chosen for the rhenium atom and the standard 6-31G basis set was used for all other atoms. For chloride, oxygen, carbon and nitrogen atoms, diffuse and polarization functions were added [36,37]. The optimized ground-state geometry of **1** was verified by performing a frequency calculation. All vibrations were real, thus the optimized geometry corresponds to a true energy minimum.

TDDFT and TDDFT/PCM [38] calculations were employed to produce a number (90) of singlet excited-states starting from the ground-state geometry optimized in the gas phase. The ground-state gas phase structure of **1** was not re-optimized in solvent using the PCM calculation.

The geometry of the singlet excited states was optimized in the gas phase with the use of the TURBOMOLE [39,40] program. The photophysical property calculations were performed with the use of the B3LYP functional and MBW60 basis set for the rhenium atom.

4. Results and discussion

4.1. Preparation and infrared data

The title complexes were prepared by refluxing $[Re(CO)_5Cl]$ with a small excess of the appropriate N–N ligand (bdmpzm or bpzm) in toluene. They were isolated as air-stable, microcrystalline solids, soluble in common organic solvents. The infrared spectra of **1** and **2** display three bands in the carbonyl stretching region: a sharp intense band at ~2025 cm^{-1} and two lower-energy bands. This pattern corresponds to three CO units in a *fac* isomer arrangement [41].

4.2. Crystal structures

The crystallographic data for the title complexes are given in Table 1, and the molecular structures of **1** and **2** are shown in Figs. 1 and 2. The two crystal structures belong to the centrosymmetric $P\bar{1}$ triclinic space group and the ligand arrangement around the rhenium atom is the same for both structures.

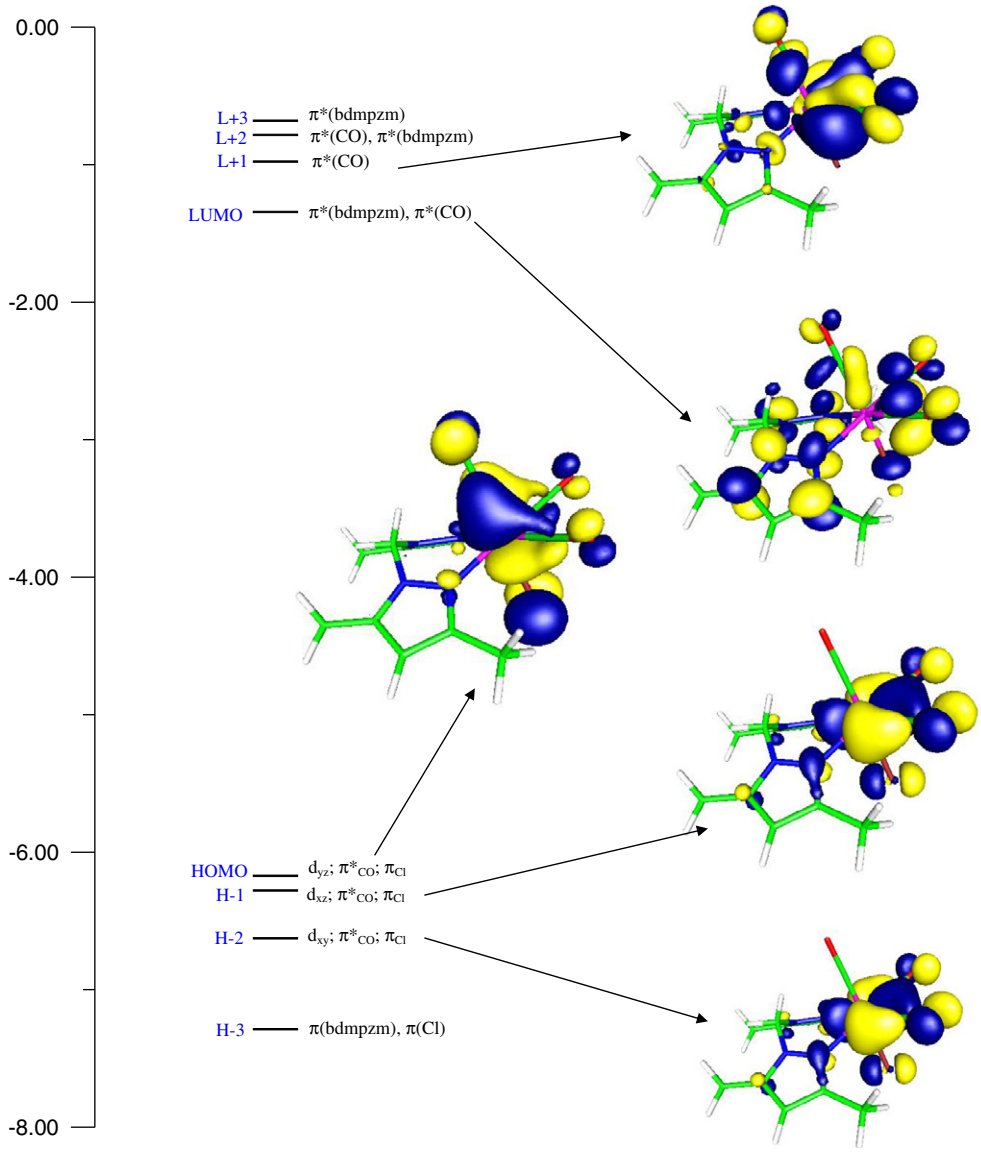


Fig. 3. The energy (eV), character and some contours of the occupied and unoccupied molecular orbitals of **1**.

Upon coordination of bis(3,5-dimethylpyrazol-1-yl)methane and bis(pyrazol-1-yl)methane to rhenium, a six-membered cycle (made by the four nitrogen atoms, the rhenium atom and the carbon atom) is formed, and the formed ring shows a *boat* conformation with the rhenium and the carbon atoms off the plane defined by the four nitrogen atoms (the deviations from the least-squares plane are equal to 0.728(11) and 0.660(11) Å for **1** and 0.772(5) and 0.627(5) Å for **2**). The planar pyrazole rings, in the range of experimental error, are inclined at 54.90(35)° and 60.81(13)°, respectively, for **1** and **2**. The major difference between **1** and **2** is caused by the presence of the additional methyl groups, which leads to overcrowding in the equatorial plane and interactions between the chloride and methyl groups in **1** (C(8)–H(8C)···Cl(1) with a D···A distance of 3.611(12) Å and a D–H···A angle of 141.5°) [42,43]. This manifests itself in bond length extensions and bond angle changes to overcome overcrowding. Thus, the Re–N distances in **1** are longer than the Re–N distances in **2** (Tables 2 and 3). Concomitant with the Re–N bond length extension, on going from **1** to **2**, there is a 3.18° increase in the N–Re–N angle.

4.3. Optimized geometry

The gas phase geometry of **1** was optimized in a singlet state by the DFT method with the hybrid B3LYP and pure BP86 functionals using two different basis sets (see Section 3). Selected calculated bond lengths and valence angles of **1** are gathered in Table 2.

For both functionals the predicted bond lengths and angles are in agreement with the values based upon the X-ray crystal structure data, and the general trends observed in the experimental data are well reproduced in

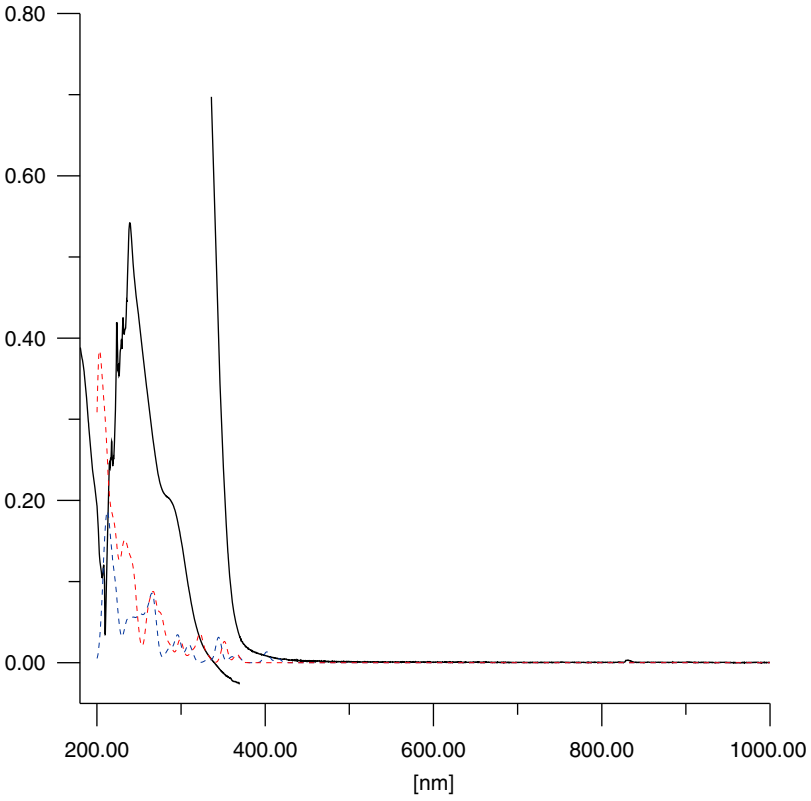


Fig. 3a. The experimental (——) and calculated (– – – –) electronic absorption spectra of **1**. Calculations: TD-DFT method with BP86 functional and MBW60 basis set for the rhenium atom. Blue dashed line: spectrum calculated in vacuum. Red dashed line: spectrum calculated in chloroform. (For interpretation of the references in colour in this figure legend, the reader is referred to the web version of this article.)

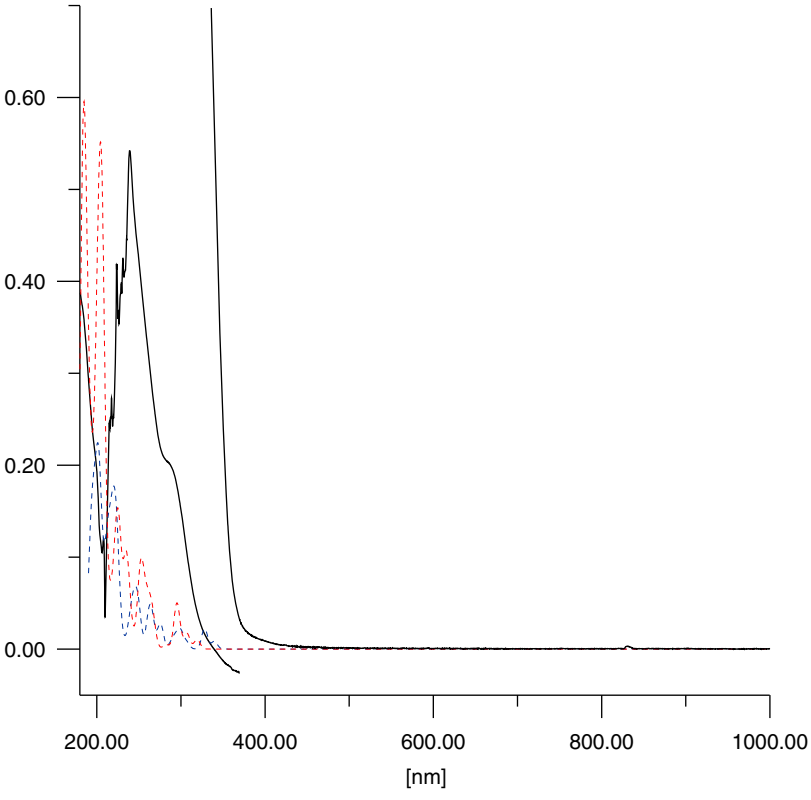


Fig. 3b. The experimental (——) and calculated (– – – –) electronic absorption spectra of **1**. Calculations: TD-DFT method with B3LYP functional and MBW60 basis set for the rhenium atom. Blue dashed line: spectrum calculated in vacuum. Red dashed line: spectrum calculated in chloroform. (For interpretation of the references in colour in this figure legend, the reader is referred to the web version of this article.)

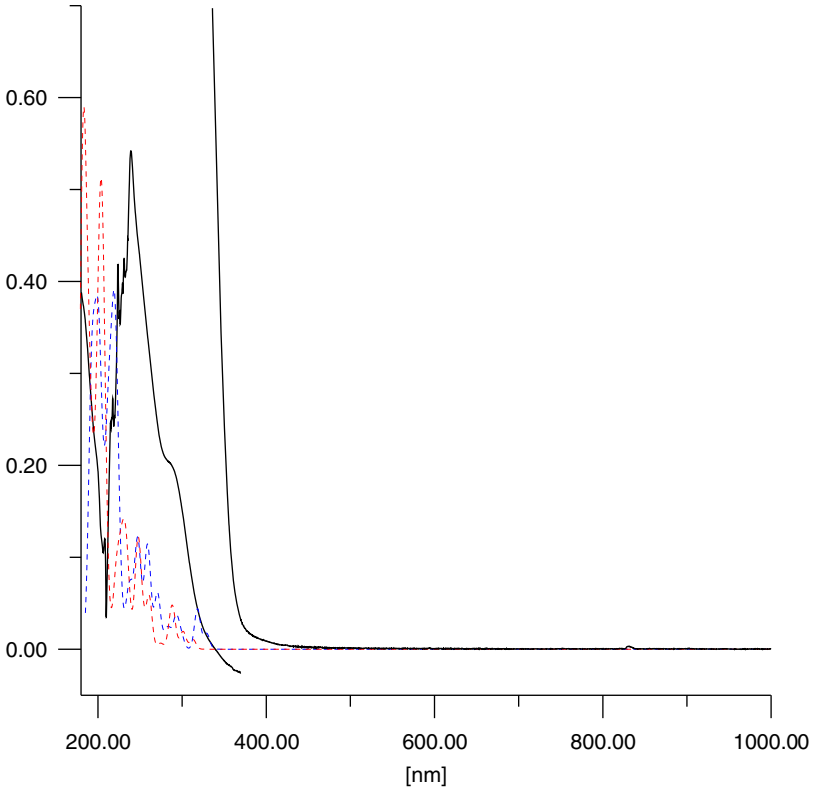


Fig. 3c. The experimental (——) and calculated (– – – –) electronic absorption spectra of **1**. Calculations: TD-DFT method with B3LYP functional and LANL2DZ basis set for the rhenium atom. Blue dashed line: spectrum calculated in vacuum. Red dashed line: spectrum calculated in chloroform. (For interpretation of the references in colour in this figure legend, the reader is referred to the web version of this article.)

Table 4
The energy and molar absorption coefficients of the experimental absorption bands and the electronic transitions calculated with the TDDFT/B3LYP method for **1**

The most important orbital excitations	Character	λ (nm)	E (eV)	f	Experimental λ (nm) (E (eV)) ε
H → L	d/π(Cl) → π*/π*(CO)	319.1	3.89	*0.0104*	307.2 (4.04) 8560
H−1 → L	d/π(Cl) → π*/π*(CO)	307.0	4.04	*0.0171*	
H−1 → L + 1	d/π(Cl) → π*(CO)	297.5	4.17	*0.0044*	
H → L + 1	d/π(Cl) → π*(CO)	295.0	4.20	*0.0465*	
H−1 → L	d/π(Cl) → π*/π*(CO)				
H−1 → L + 2	d/π(Cl) → π*/π*(CO)	267.9	4.63	*0.0134*	239.5 (5.18) 22 240
H−2 → L + 1	d/π(Cl) → π*(CO)	264.5	4.69	*0.0312*	
H → L + 3	d/π(Cl) → π*	259.8	4.77	*0.0344*	
H−1 → L + 3	d/π(Cl) → π*	256.1	4.84	*0.0232*	
H−2 → L + 2	d/π(Cl) → π*/π*(CO)	252.0	4.92	*0.0788*	
H → L + 5	d/π(Cl) → π*(CO)	239.4	5.18	*0.0212*	
H−4 → L	π(Cl)/π/d → π*/π*(CO)	234.7	5.28	*0.0848*	
H−5 → L	π(Cl)/π → π*/π*(CO)	225.5	5.50	*0.1125*	
H−6 → L	π → π*/π*(CO)	220.9	5.61	*0.0263*	
H−3 → L + 1	π(Cl)/π → π*(CO)				
H−3 → L + 3	π(Cl)/π → π*	207.2	5.98	*0.0904*	
H−5 → L + 2	π(Cl)/π → π*/π*(CO)	206.9	5.99	*0.0265*	
H−8 → L	π(Cl)/π/d → π*/π*(CO)	205.7	6.03	*0.2323*	
H−3 → L + 3	π(Cl)/π → π*				
H−4 → L + 3	π(Cl)/π/d → π*	204.0	6.08	*0.0658*	
H−6 → L + 2	π → π*/π*(CO)	201.7	6.15	*0.1072*	
H−2 → L + 8	d/π(Cl) → d/π*(CO)	200.9	6.17	*0.0359*	
H−2 → L + 8	d/π(Cl) → d/π*(CO)	199.9	6.20	*0.0512*	
H−5 → L + 3	π(Cl)/π → π*	199.2	6.22	*0.0228*	

ε – Molar absorption coefficient [$dm^3\ mol^{-1}\ cm^{-1}$].
f – Oscillator strength.
π,π* – Denote orbitals of the bdmpzm ligand.

Table 5
DFT/B3LYP optimized bond lengths (Å) and angles (°) for the S_1, S_2 and T_1 states of **1**

ΔE[a]	S_1 3.75	T_1 2.72	S_2 3.17
Bond lengths			
Re(1)–C(1)	1.973	2.101	2.192
Re(1)–C(2)	1.978	1.937	1.917
Re(1)–C(3)	1.947	1.943	1.936
Re(1)–Cl(1)	2.396	2.542	2.466
Re(1)–N(1)	2.216	2.253	2.270
Re(1)–N(3)	2.206	2.225	2.248
C(1)–O(1)	1.156	1.197	1.186
C(2)–O(2)	1.152	1.163	1.166
C(3)–O(3)	1.161	1.162	1.164
Bond angles			
C(2)–Re(1)–C(1)	86.1	87.6	87.3
C(3)–Re(1)–C(1)	91.8	95.9	99.4
C(3)–Re(1)–C(2)	83.4	81.6	82.6
C(1)–Re(1)–N(1)	90.1	85.9	81.5
C(2)–Re(1)–N(1)	97.4	97.2	96.9
C(3)–Re(1)–N(1)	177.9	177.8	178.9
C(1)–Re(1)–N(3)	90.5	92.6	92.0
C(2)–Re(1)–N(3)	175.6	178.5	178.9
C(3)–Re(1)–N(3)	93.8	96.9	96.7
C(1)–Re(1)–Cl(1)	174.1	169.8	164.5
C(2)–Re(1)–Cl(1)	89.8	93.0	94.7
C(3)–Re(1)–Cl(1)	92.0	94.2	96.1
N(1)–Re(1)–Cl(1)	86.1	84.0	83.0
N(3)–Re(1)–Cl(1)	93.7	87.2	86.2
N(1)–Re(1)–N(3)	85.5	84.3	83.8
O(1)–C(1)–Re(1)	178.1	131.2	121.6
O(2)–C(2)–Re(1)	175.3	177.0	178.0
O(3)–C(3)–Re(1)	177.0	176.3	177.5

[a] ΔE – Energy difference between the excited states and ground state minimum (S_0) from the PCM solvent model in DCM.

the calculations. The Re–Cl bond length is considerably better reproduced by the pure BP86 functional. In the case of the calculations with the hybrid functional, the Re–Cl bond is overestimated. However, the choice of the basis set has only a small effect on the geometric parameters of the optimized molecule.

4.4. Electronic structure

The simplified molecular orbital diagram of **1** with several contours of occupied and unoccupied MOs is presented in Fig. 3. The energy and compositions of the molecular orbitals were calculated by the DFT method with the hybrid B3LYP functional and MBW60 basis set for the rhenium atom, including a solvent effect. The HOMO–LUMO gap equals 4.83 eV. The low-lying virtual orbitals correspond mainly to π^*_{bdmpzm} and π^*_{CO}. The higher virtual orbitals are delocalized amongst the Re and carbonyls.

The three highest occupied molecular orbitals are predominately localized on the rhenium atom, corresponding to a $(5d_{xy})^2(5d_{xz})^2(5d_{yz})^2$ occupation of the central ion. However, ligand contributions are also important. All these orbitals have a considerable CO and Cl character.

4.5. Electronic spectra

The electronic absorption spectra of the prepared complexes were measured at room temperature in chloroform solution. The experimental and calculated electronic spectra of **1** are compared in Figs. 3a–3c. Each calculated transition is represented by the gaussian function $y = ce^{-bx^2}$ with the height (c) equal to the oscillator strength and b equal to 0.04 nm^{-2}. The shape of the UV–Vis spectrum of **2** is the same as for **1**; the absorption bands of complex **2** were recorded at 289.0 ($\varepsilon = 8460\ dm^3\ mol^{-1}\ cm^{-1}$) and 227.2 nm ($\varepsilon = 22{,}320\ dm^3\ mol^{-1}\ cm^{-1}$).

Figs. 3a–3c present the effect of the functional, basis set and solvent on the TD-DFT simulation of the UV–Vis spectrum of **1**. As seen in Figs. 3a–3c, the use of the pure functional BP86 and neglecting the solvent strongly underestimate the energies of the low-lying electronic transitions. Changing the functional from BP86 to B3LYP shifts the

Table 6
Four calculated singlet states for **1** in S_0, S_1, T_1 and S_2 optimized geometries with the TDDFT/B3LYP method

	E (eV)	λ (nm)	Weight	Character of the most important excitations	
S_0 geometry					
1	3.89	319.1	83	H(92) → L(93)	d/π(Cl) → π*/π*(CO)
2	4.04	307.0	66	H−1(91) → L(93)	d/π(Cl) → π*/π*(CO)
3	4.17	297.5	85	H−1(91) → L + 1(94)	d/π(Cl) → π*(CO)
4	4.20	295.0	61	H(92) → L + 1(94)	d/π(Cl) → π*(CO)
			22	H−1(91) → L(93)	d/π(Cl) → π*/π*(CO)
S_1 geometry					
1	2.87	432.6	98	H(92) → L(93)	d/π(Cl) → π*
2	3.21	386.3	95	H−1(91) → L(93)	d/π(Cl) → π*
3	3.65	339.9	97	H−2(90) → L(93)	d/π(CO) → π*
4	3.73	332.3	36	H(92) → L + 1(94)	d/π(Cl) → π*/π*(CO)
			54	H(92) → L + 2(95)	d/π(Cl) → π*(CO)
T_1 geometry					
1	1.56	793.7	81	H(92) → L(93)	d/π(Cl) → d/π*(CO)
2	1.99	623.7	86	H−1(91) → L(93)	d/π(Cl) → d/π*(CO)
3	2.43	511.0	94	H−2(90) → L(93)	d/π (CO) → d/π*(CO)
4	3.12	396.9	75	H(92) → L + 1(94)	d/π(Cl) → π*(CO)
			11	H(92) → L + 2(95)	d/π(Cl) → π*/π*(CO)
S_2 geometry					
1	0.88	1403.7	86	H(92) → L(93)	d/π(Cl) → d/π*(CO)
2	1.40	882.9	91	H−1(91) → L(93)	d/π(Cl) → d/π*(CO)
3	1.94	639.2	95	H−2(90) → L(93)	d/π (CO) → d/π*(CO)
4	2.64	469.0	90	H(92) → L + 1(94)	d/π(Cl) → π*(CO)

π* – Denote orbitals of the bdmpzm ligand.

Table 7
Four calculated triplet states for **1** in S_0, S_1, T_1 and S_2 optimized geometries with the TDDFT/B3LYP method

	E (eV)	λ (nm)	Weight	Character of the most important excitations	
S_0 geometry					
1	3.55	349.1	42	H(92) → L(93)	d/π(Cl) → π*/π*(CO)
			6	H(92) → L + 2(95)	d/π(Cl) → π*(CO)/π*
2	3.59	345.0	38	H−1(91) → L(93)	d/π(Cl) → π*/π*(CO)
			6	H−1(91) → L + 2(95)	d/π(Cl) → π*(CO)/π*
			6	H(92) → L + 1(94)	d/π(Cl) → π*(CO)
3	3.78	328.0	37	H(92) → L + 1(94)	d/π(Cl) → π*(CO)
4	3.87	320.2	23	H−2(90) → L(93)	d/π (CO) → π*/π*(CO)
			12	H−1(91) → L + 2(95)	d/π(Cl) → π*(CO)/π*
S_1 geometry					
1	2.63	470.6	17	H−3(89) → L(93)	π/p(Cl) → π*
			27	H−1(91) → L(93)	d/π(Cl) → π*
			11	H(92) → L(93)	d/π(Cl) → π*
2	2.86	433.5	9	H−1(91) → L(93)	d/π (Cl) → π*
			38	H(92) → L(93)	d/π(Cl) → π*
3	3.37	367.5	16	H−3(89) → L(93)	π/p(Cl) → π*
			7	H−2(90) → L(93)	d/π (CO) → π*
			12	H−1(91) → L(93)	d/π (Cl) → π*
4	3.42	362.1	25	H(92) → L + 1(94)	d/π(Cl) → π*/π*(CO)
			10	H(92) → L + 2(95)	d/π(Cl) → π*(CO)
T_1 geometry					
1	1.01	1223.8	65	H(92) → L(93)	d/π(Cl) → d/π*(CO)
2	1.62	767.6	54	H−1(91) → L(93)	d/π(Cl) → d/π*(CO)
3	2.24	553.0	49	H−2(90) → L(93)	d/π (CO) → d/π*(CO)
4	2.76	449.4	44	H(92) → L + 1(94)	d/π(Cl) → π*(CO)
S_2 geometry					
1	0.52	2386.9	72	H(92) → L(93)	d/π(Cl) → d/π*(CO)
2	1.12	1111.7	56	H−1(91) → L(93)	d/π(Cl) → d/π*(CO)
3	1.80	690.2	50	H−2(90) → L(93)	d/π (CO) → d/π*(CO)
4	2.35	527.3	49	H(92) → L + 1(94)	d/π(Cl) → π*(CO)

π,π* – Denote orbitals of the bdmpzm ligand.

low-lying CT transitions to higher energies. Including the solvent in the calculations has a similar effect – low-lying CT transitions are shifted to higher energies. The choice of the basis set has only a small effect on the transition energies. Thus, a very good agreement with the experimental spectrum is obtained when the hybrid B3LYP functional is used together with the PCM model for $CHCl_3$ solvent.

Table 4 shows the spin-allowed singlet–singlet electronic transitions of **1** calculated with the TDDFT method using the hybrid B3LYP functional and MBW60 basis set for the rhenium atom. The assignments of the transition states are based on the major contributing excitation. For the high energy part of the spectrum, only transitions with oscillator strengths larger than 0.02 are listed in Table 4.

The TDDFT/PCM calculations show that the low-energy absorption band of **1** originates predominately in the transitions between the HOMO/HOMO−1 and LUMO/LUMO+1 orbitals. As can be seen from Fig. 3, the HOMO−1 and HOMO are delocalized on the whole $Re(CO)_3Cl$ unit, and the LUMO and LUMO+1 are centered on the bdmpzm and CO ligands. Accordingly, these transitions can be seen as mixed Re → bdmpzm/CO (*MLCT*) and Cl → bdmpzm/CO (*LLCT*), or a delocalized *MLLCT* (metal–ligand-to-ligand CT) description can be used.

The experimental absorption band at 239.5 nm is attributed to metal-to-ligand charge transfer (occurring from the rhenium ion to the π-antibonding orbitals of the bdmpzm ligand or π-antibonding orbitals of the carbonyl group), ligand–ligand charge transfer and intraligand (IL) transitions (Table 4).

Complex **1** does not exhibit any luminescence properties. To explain this fact we optimized the first excited singlet and triplet states of **1**. The triplet state was optimized by independent DFT calculations. In Table 5 the geometry parameters of the optimized lowest triplet (T_1) and singlet (S_1) states are gathered. It can be seen from Table 5 that the Re–Cl bond is shortened and Re–CO(1) is elongated in S_1, on comparison to the geometry of the ground state. The Re–CO(1) bond is even more elongated in the T_1 state. In T_1 the Re–C(1)–O(1) angle of the axial carbonyl is equal to 131°, which significantly differs from the almost linear arrangement in S_0 and S_1. The triplet state geometry of the Re–CO(1) fragment and the small energy difference between this state and the ground state (that is the first triplet state excitation energy, which is 1.01 eV, see Table 7) is an indication that a facile detachment of a carbonyl from this state could occur under the influence of light. One may expect that in coordinating solvents $[Re(CO)_3(bdmpzm)Cl]$ will undergo a photochemical axial carbonyl exchange reaction.

In Table 5 the energies of the S_1 and T_1 excited states, relative to the ground state (S_0) minimum, are given. The T_1 state has significantly lower energy than S_1 and, as stated above, there are considerable differences in the geometric parameters. We again performed an optimization of the singlet state geometry starting from T_1 geometry. We obtained another singlet state, denoted S_2. The relative energy and geometry of this state are also given in Table 5. It can be seen from Table 5 that the geometry of S_2 is very similar to that of T_1, with an even somewhat longer

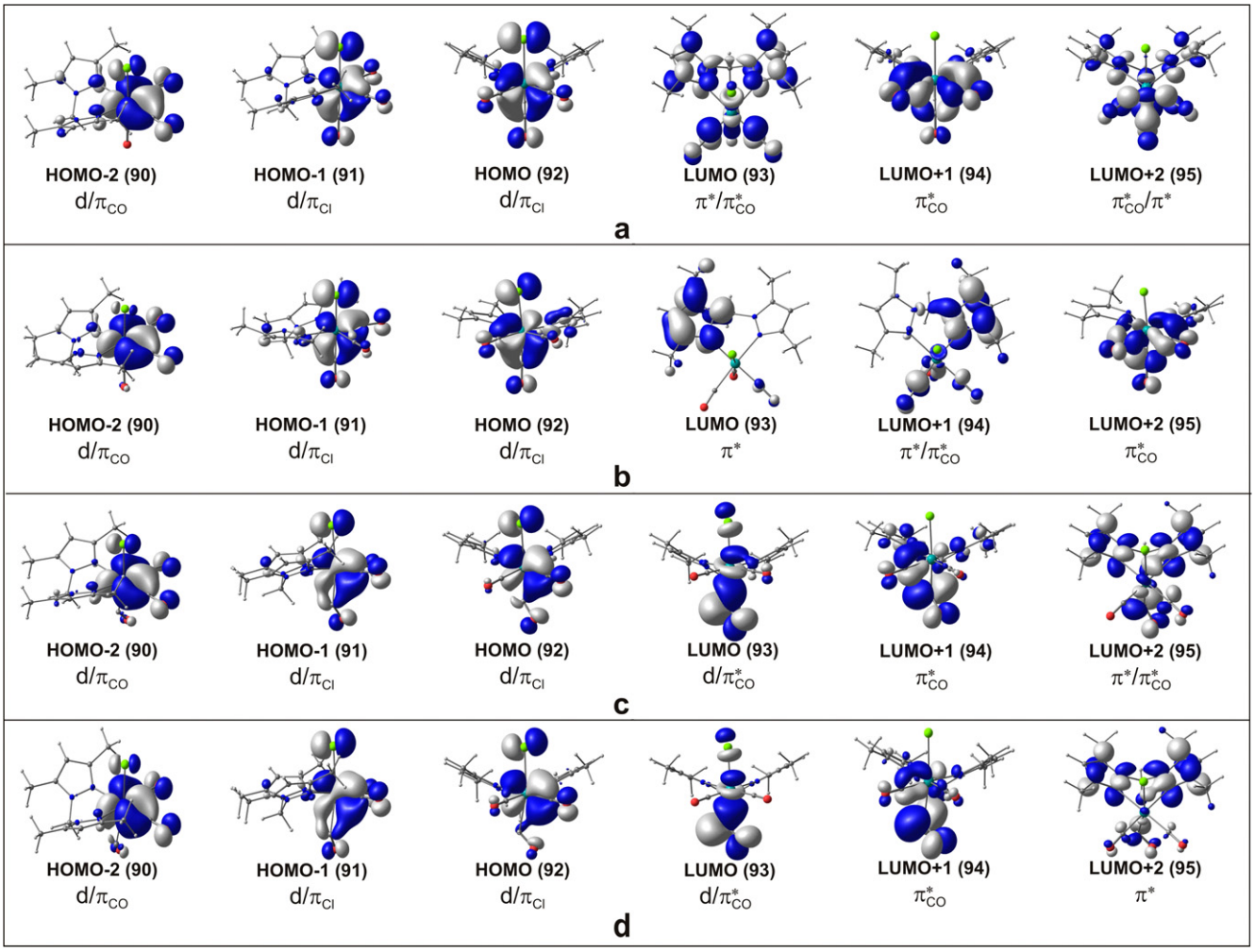


Fig. 4. Molecular orbitals in the ground state (a), S_1 state (b), T_1 state (c) and S_2 state (d) geometry of **1**.

Re-CO(1) bond and a more bent Re–C(1)–O(1) angle. The energy of S_2 is lower than that of S_1.

To characterize the photophysics of **1**, we calculated several singlet and triplet states in the geometries of the S_1, T_1 and S_2 excited states. Four calculated singlet excited states for each geometry are given in Table 6 (with the respective excited states in the ground state geometry for comparison). The relevant triplet states are given in Table 7. In Fig. 4 three HOMO and three LUMO orbitals of [Re(CO)$_3$(bdmpzm)Cl] are given for these geometries. In all cases the HOMO orbitals are rhenium d orbitals with an admixture of carbonyl and chlorine orbitals. The LUMO orbitals in the ground state and S_1 state geometries are bdmpzm ligand and carbonyl π orbitals. In the T_1 and S_2 state geometries, however, the LUMO orbital is basically the d_{z2} orbital of rhenium mixed with a π orbital of the axial carbonyl group. This is reflected in the electronic transitions character in these four geometries. The lowest singlet transitions at the ground state and S_1 state geometries are of the MLCT, $d \rightarrow \pi^*_{bdmpzm}$ type, while in the T_1 and S_2 geometries the lowest transitions are of $d \rightarrow d/\pi^*_{CO}$ character. The large participation of the d_{z2} orbital in the LUMO orbital makes this transition of partly LF type. The different character of the LUMO orbitals in T_1 and S_2 compared to the S_0 and S_1 states, and resulting from it the differences in the lowest excited states character, explain why S_2, although lower in energy than S_1, was not found in the optimization starting from the ground state geometry. The relevant state of $d \rightarrow d/\pi^*_{CO}$ is of very high energy in this geometry and is not accessible in the determination of the character of the excited state wave function.

In Fig. 5 a schematic depiction of the electronic excited states of the [Re(CO)$_3$(bdmpzm)Cl] complex is presented, which is based on the calculations described above. After the absorption at 307 nm (calculated at 319 nm) to the $d \rightarrow \pi^*_{bdmpzm}$ (^{1}MLCT, S_1) state (or absorption to a higher energy state and then internal conversion to S_1) a prompt intersystem crossing to the T_1 state can occur followed by radiationless conversion from T_1 to the ground state. The minimum of the T_1 state is only 1.01 eV higher than the ground state (Table 7), implying an even smaller energy barrier for the $T_1 \rightarrow S_0$ intersystem crossing which should make this process very fast.

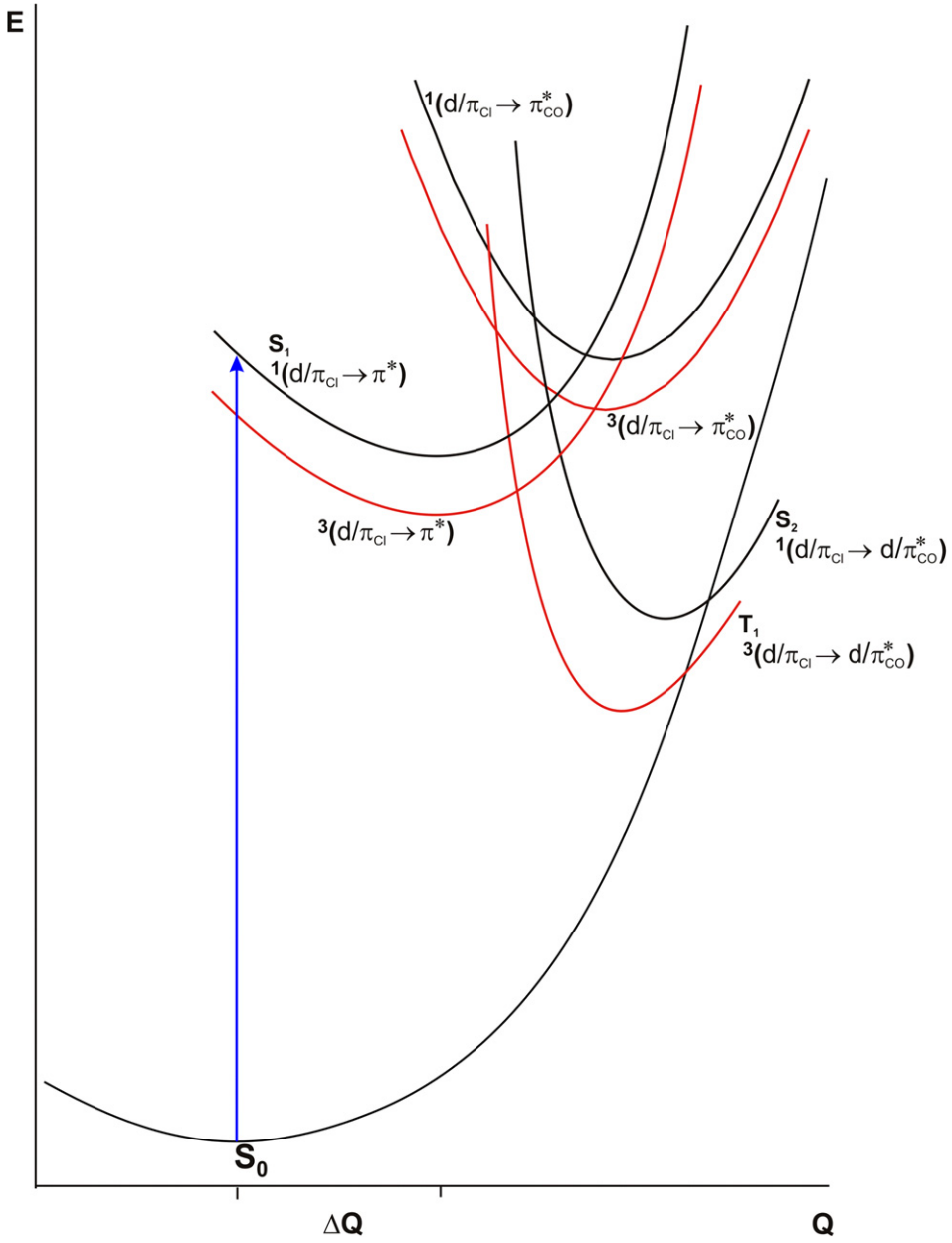


Fig. 5. Schematic representation of the ground and excited states of **1**.

5. Supplementary data

CCDC 674970 and 674971 contain the supplementary crystallographic data for $C_{14}H_{16}N_4O_3ClRe$ and $C_{10}H_8N_4O_3ClRe$. These data can be obtained free of charge via http://www.ccdc.cam.ac.uk/conts/retrieving.html, or from the Cambridge Crystallographic Data Centre, 12 Union Road, Cambridge CB2 1EZ, UK; fax: (+44) 1223-336-033; or e-mail: deposit@ccdc.cam.ac.uk.

Acknowledgements

The crystallographic part was financed by funds allocated by the Ministry Science and Higher Education to the Institute of General and Ecological Chemistry, Technical University of Łódź. The GAUSSIAN-03 calculations were carried out in the Wrocław Centre for Networking and Supercomputing, WCSS, Wrocław, Poland, under calculational Grant No. 51/96. The TURBOMOLE calculations were carried out in the Academic Computer Centre CYFRONET of the University of Science and Technology in Cracow, ACC CYFRONET AGH, Kraków, Poland, http://www.cyfronet.pl, under Grant No. MNiSW/SGI3700/UŚląski/111/2007 and MNiSW/IBM_BC_HS21/UŚląski/111/2007.

References

[1] V. Balzani, A. Juris, M. Venturi, S. Campagna, S. Serroni, Chem. Rev. 96 (1996) 759.
[2] D.J. Stufkens, A. Vlček Jr., Coord. Chem. Rev. 177 (1998) 127.

[3] I.R. Farrell, A. Vlček Jr., Coord. Chem. Rev. 208 (2000) 87.
[4] A. Vogler, H. Kunkely, Coord. Chem. Rev. 200-202 (2000) 991.
[5] D.R. Striplin, G.A. Crosby, Coord. Chem. Rev. 211 (2001) 163.
[6] A. Vlček Jr., M. Busby, Coord. Chem. Rev. 250 (2006) 1755.
[7] S. Ranjan, S.-Y. Li, K.-C. Hwang, W.-L. Ching, C.-S. Liu, Y.-T. Tao, C.-H. Chien, S.-M. Peng, G.-H. Lee, Inorg. Chem. 42 (2003) 1248.
[8] F. Li, G. Cheng, Y. Zhao, J. Feng, S. Liu, M. Zhang, Y. Ma, J. Shen, Appl. Phys. Lett. 83 (2003) 4716.
[9] P. Christensen, A. Hamnett, A.V.G. Muir, J.A. Timney, J. Chem. Soc., Dalton Trans. (1992) 1455.
[10] H. Hori, F.P.A. Johnson, K. Koike, K. Takeuchi, T. Ibusuki, O. Ishitani, J. Chem. Soc., Dalton Trans. (1997) 1019.
[11] S.S. Jurisson, J.D. Lydon, Chem. Rev. 99 (1999) 2205.
[12] W.A. Volkert, T.J. Hoffman, Chem. Rev. 99 (1999) 2269.
[13] C. Pettinari, R. Pettinari, Coord. Chem. Rev. 249 (2005) 663.
[14] L.-F. Tang, Z.-H. Wang, W.-L. Jia, Y.-M. Xu, J.T. Wang, Polyhedron 19 (2000) 381.
[15] E. Teuma, M. Loy, C. Le Berre, M. Etienne, J.C. Daran, P. Kalck, Organometallics 22 (2003) 5261.
[16] K.A. Van Langenberg, B. Moubaraki, K.S. Murray, E.R.T. Tiekink, Z. Kristallogr. – New Cryst. Struct. 218 (2003) 345.
[17] J. Ruiz, V. Rodriguez, C. De Haro, J. Perez, G. Lopez, Inorg. Chim. Acta 357 (2004) 2331.
[18] J. Ruiz, N. Cutillas, C. Vincente, M.D. Villa, G. Lopez, J. Lorenzo, F.X. Aviles, V. Moreno, D. Bautista, Inorg. Chem. 44 (2005) 7365.
[19] A.S. Potapov, A.I. Khlebnikov, Polyhedron 25 (2006) 2683.
[20] D.L. Reger, J.R. Gardinier, P.J. Pellechia, M.D. Smith, K.J. Brown, Inorg. Chem. 42 (2003) 7635.
[21] M. Porchia, G. Papini, C. Santini, G.G. Lobia, M. Pellei, F. Tisato, G. Bandoli, A. Dolmella, Inorg. Chem. 44 (2005) 4045.
[22] H. Chermette, Coord. Chem. Rev. 178–180 (1998) 699.
[23] A. Vlček Jr., S. Záliš, Chem. Rev. 208 (2000) 87.
[24] S. Julia, P. Sala, J. del Mazo, M. Sancho, C. Ochoa, J. Elguero, J.P. Fayet, M.C. Vertut, J. Heterocyclic Chem. 19 (1982) 1141.
[25] (a) STOE & Cie, X-RED. Version 1.18. STOE & Cie GmbH, Darmstadt, Germany, 1999;
(b) CrysAlis RED, Oxford Diffraction Ltd., Version 1.171.29.2.
[26] G.M. Sheldrick, Acta Crystallogr. A46 (1990) 467.
[27] G.M. Sheldrick, SHELXL97. Program for the Solution and Refinement of Crystal Structures, University of Göottingen, Germany, 1997.
[28] G.M. Sheldrick, SHELXTL: Release 4.1 for Siemens Crystallographic Research Systems, 1990.
[29] A.D. Becke, J. Chem. Phys. 98 (1993) 5648.
[30] C. Lee, W. Yang, R.G. Parr, Phys. Rev. B 37 (1988) 785.
[31] A.D. Becke, Phys. Rev. A 38 (1988) 3098.
[32] GAUSSIAN 03, Revision B.03: M.J. Frisch, G.W. Trucks, H.B. Schlegel, G.E. Scuseria, M.A. Robb, J.R. Cheeseman, J.A. Montgomery, Jr., T. Vreven, K.N. Kudin, J.C. Burant, J.M. Millam, S.S. Iyengar, J. Tomasi, V. Barone, B. Mennucci, M. Cossi, G. Scalmani, N. Rega, G.A. Petersson, H. Nakatsuji, M. Hada, M. Ehara, K. Toyota, R. Fukuda, J. Hasegawa, M. Ishida, T. Nakajima, Y. Honda, O. Kitao, H. Nakai, M. Klene, X. Li, J.E. Knox, H.P. Hratchian, J.B. Cross, C. Adamo, J. Jaramillo, R. Gomperts, R.E. Stratmann, O. Yazyev, A.J. Austin, R. Cammi, C. Pomelli, J.W. Ochterski, P.Y. Ayala, K. Morokuma, G.A. Voth, P. Salvador, J.J. Dannenberg, V.G. Zakrzewski, S. Dapprich, A.D. Daniels, M.C. Strain, O. Farkas, D.K. Malick, A.D. Rabuck, K. Raghavachari, J.B. Foresman, J.V. Ortiz, Q. Cui, A.G. Baboul, S. Clifford, J. Cioslowski, B.B. Stefanov, G. Liu, A. Liashenko, P. Piskorz, I. Komaromi, R.L. Martin, D.J. Fox, T. Keith, M.A. Al-Laham, C.Y. Peng, A. Nanayakkara, M. Challacombe, P.M.W. Gill, B. Johnson, W. Chen, M.W. Wong, C. Gonzalez, J.A. Pople, Gaussian Inc., Pittsburgh, PA, 2003.
[33] P.J. Hay, W.R. Wadt, J. Chem. Phys. 82 (1985) 299.
[34] K. Eichkorn, F. Weigend, O. Treutler, R. Ahlrichs, Theor. Chem. Acc. 97 (1997) 119.
[35] D. Andrae, U. Haussermann, M. Dolg, H. Stoll, H. Preuss, Theor. Chim. Acta 77 (1990) 123.
[36] P.C. Hariharan, J.A. Pople, Theor. Chim. Acta 28 (1973) 213.
[37] V.A. Rassolov, M.A. Ratner, J.A. Pople, P.C. Redfern, L.A. Curtiss, J. Comp. Chem. 22 (2001) 976.
[38] M.E. Casida, in: J.M. Seminario (Ed.), Recent Developments and Applications in Modern Density Functional Theory, Theoretical and Computational Chemistry, vol. 4, Elsevier, Amsterdam, 1996.
[39] R. Ahlrichs, M. Bär, M. Häser, H. Horn, C. Kölmel, Chem. Phys. Lett. 162 (3) (1989) 165.
[40] TURBOMOLE has been designed by the Quantum Chemistry Group, University of Karlsruhe, Germany, since 1988. The following members of the group have made contributions: Reinhart Ahlrichs, Michael Bär, Hans-Peter Baron, Rüdiger Bauernschmitt, Stephan Böcker, Nathan Crawford, Peter Deglmann, Michael Ehrig, Karin Eichkorn, Simon Elliott, Filipp Furche, Frank Haase, Marco Häser, Christof Hättig, Arnim Hellweg, Hans Horn, Christian Huber, Uwe Huniar, Marco Kattannek, Andreas Köhn, Christoph Kölmel, Markus Kollwitz, Klaus May, Paola Nava, Christian Ochsenfeld, Holger Öhm, Holger Patzelt, Dmitrij Rappoport, Oliver Rubner, Ansgar Schäfer, Uwe Schneider, Marek Sierka, Oliver Treutler, Barbara Unterreiner, Malte von Arnim, Florian Weigend, Patrick Weis, Horst Weiss, http://www.turbomole.com.
[41] P.J. Giordano, M.S. Wrighton, J. Am. Chem. Soc. 101 (1979) 2888.
[42] G.A. Jeffrey, W. Saenger, Hydrogen Bonding in Biological Structures, Springer-Verlag, 1994.
[43] G.R. Desiraju, T. Steiner, The Weak Hydrogen Bond in Structural Chemistry and Biology, Oxford University Press, 1999.

cussed by Maeda et al. [8] and Seymour [9] – the process in which macromolecules accumulate within tumour tissue due to poor lymphatic clearance, *inter alia*. Zeevaart et al. [10] took this into consideration and proposed a novel water-soluble phosphonate polymer: *N*,*N*′,*N*′-trimethylenephosphonate-polyethyleneimine (PEI-MP) to be combined with a radioactive tin isotope. The radionuclide of interest was ^{117m}Sn, which reduces the risk of radiotoxicity to the marrow due to its favourable radiation characteristics: ^{117m}Sn has a half-life of 13.6 days and emits electrons with energies of 126–158 keV, and a range of 0.2–0.3 mm in bone tissue [13]. It also emits a photon (~160 keV, 88.5%) enabling visualisation of radio-treatment localization. In addition to these favourable radiation characteristics, tin-ions exhibit an inherent affinity for bone as observed in biodistribution experiments with rats [11] and adsorption studies of hydroxyapatite [12].

A fundamental aspect of the biological activity of the tin-based radiopharmaceutical could be the oxidation state of tin. The results may vary with different ligands. As Srivastava [13] found, the *in vivo* bone uptake of $[Sn(II)–HEDP]^0$ in rodents exceeded that of the Sn^{4+} analogue, whereas for methylenediphosphonate (MDP or medronate) and diethylenetriaminepentaacetate (DTPA) the inverse was observed. Notwithstanding the stability of tin-based radiopharmaceuticals [10], the fate of the drug-complex may also depend on the valence stability of the metal-ion *in vivo*. Oxidation of the Sn^{2+} *in vivo* could influence the biodistribution of the complex due to its overall charge. In a study towards determining the possible toxicological effects of tin in rats – in the exclusive divalent and tetravalent forms [11], Hiles reports that no interconversion of the oxidation states occurred. However, this was not based on any physicochemical measurement, but rationalized in terms of the relative biodistributions of the respective Sn-salts. Furthermore, Hiles highlighted the dependence of the biological fate of tin – in the respective oxidation state – on the "anion complement", i.e. counter ion or ligand. In an attempt to elucidate Sn^{2+} complexation by HEDP, combining ^{31}P NMR and ^{119}Sn NMR with ^{119m}Sn Mossbauer spectroscopy, Alberola [14] found that the $[Sn(II)–HEDP]^0$ indeed undergoes oxidation within 3 h of preparation. Whether this is complete, is unclear. Furthermore, with the exception of the free-ligand signal, the only visible ^{31}P peaks were those of $[Sn(IV)–HEDP]^{2+}$. The $[Sn(II)–HEDP]^0$ signal was not observed. The ^{119}Sn NMR spectrum (quintuplet, $J \sim 30$ Hz) revealed the possible existence of a symmetrical spiro-structure, with stoichiometry $[Sn(IV)–(HEDP)_2]^0$.

In the study presented here, we have addressed the question of the valence stability of prospective Sn-based radiopharmaceuticals with HEDP and PEI-MP as ligands (Fig. 1). The objective was to establish the extent of oxidation of Sn^{2+}, if any, in solution; with the intention of evaluating the complexes for eventual application *in vivo*.

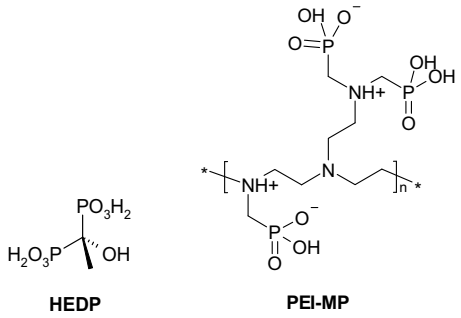


Fig. 1. Molecular structures of 1-hydroxyethylene-diphosphonate (HEDP), and *N*,*N*′,*N*′-trimethylenephosphonate-polyethyleneimine (PEI-MP). Both ligands are represented in arbitrary protonation states.

2. Experimental

2.1. Reagents

Analytical grade HEDP, $SnCl_2 \cdot 2H_2O$ and $SnCl_4 \cdot 5H_2O$ were obtained from Merck. PEI-MP was synthesized according to the method outlined by Jarvis et al. [15], with the final product – in form of the sodium salt – obtained as various size-fractions after ultra-filtration. Using appropriate membrane filters, the polymer was fractionated according to the following molecular sizes. The fraction of 10–30 kDa was used in the NMR study. All other reagents used were of analytical grade.

2.2. Preparation of the NMR samples

The NMR samples of the metal complexes were prepared by mixing appropriate amounts of a deuterated (D_2O) stock solution containing about 1 mol dm^{-3} of the metal chloride ($SnCl_2$, acidified $SnCl_4$, $CaCl_2$, or $CdCl_2$) and a stock solution of HEDP (1 mol dm^{-3}) or PEI-MP (0.0592 mol dm^{-3}, based on monomeric units). The tin–PEI-MP samples were prepared by firstly adjusting the stock solution of PEI-MP to pH 12 prior to the addition of the respective tin solutions. All solutions were allowed to equilibrate overnight at room temperature before measurements.

2.3. Solutions for oxidation and reduction experiments: hydrogen-peroxide and glutathione, respectively

Glutathione (GSH) was dissolved in 0.5 ml water to produce a 1.191 mol dm^{-3} solution. Three dilutions of hydrogen-peroxide were prepared from 30% H_2O_2: 0.500 mol dm^{-3}; 0.050 mol dm^{-3} and 0.010 mol dm^{-3}.

The H_2O_2 and GSH solutions were added directly to the NMR tubes for the respective studies, in increments of 30 μl – unless otherwise specified.

2.4. NMR spectroscopy

All NMR measurements were performed on Varian Unity Inova-300 spectrometer, in 5 mm tubes, operating

at 25 °C. Chemical shifts (δ) are reported in ppm. The proton-decoupled ^{31}P NMR spectra of these solutions were measured operating at 121.504 MHz. The acquisitions were performed using a relatively long delay (10 s) and short pulse (30°). Furthermore, gated-decoupling was applied to avoid nuclear Overhauser effect. In so doing it was possible to compare the intensities of signals that may have had different relaxation times. Changes in the chemical shifts of the phosphorous signals of the free and complexed ligand were observed by performing pH-titrations, within the NMR tubes, over the range pH 0–10. The pH was manipulated with a freshly prepared NaOH solution. An inner-tube with 30% H_3PO_4 was used for referencing the ^{31}P chemical shifts. All ^{13}C (proton-decoupled) measurements were referenced with an internal standard of tertiary-butanol with the methyl resonance calibrated at 31.2 ppm. ^{113}Cd spectra were obtained at a frequency of 66.557 MHz, using $CdCl_2$ (1 mol dm^{-3}) in D_2O as external reference.

3. Results and discussion

Extreme line broadening due to exchange between Sn-nuclei in various species made it difficult to obtain reasonable and reproducible ^{119}Sn NMR spectra, therefore ^{31}P NMR was applied to study the complexation phenomena.

3.1. Sn^{4+}–HEDP system

Upon addition of a small amount of Sn^{4+} to a sample with HEDP at pH 9, a new very complex cluster of resonances at about 17.16 ppm showed up next to the resonance for free HEDP at 19.52 ppm in the ^{31}P NMR spectrum, which may be attributed to Sn(IV)–HEDP complexes formed (Figs. 2 and 3). Upon increase of the molar ratio $[Sn^{4+}]_{tot}/[HEDP]_{tot}$, the intensity of the resonances at 17.16 ppm increased at the expense of those for the free ligand. Therefore, it can be concluded that the exchange between free and Sn^{4+} bound HEDP is slow on the NMR time scale.

From the integrals of the resonances at 17.16 ppm and 19.52 ppm, the mol% bound HEDP was calculated. The latter is displayed versus the molar ratio $[Sn^{4+}]_{tot}/[HEDP]_{tot}$ in Fig. 4.

The flattening of the curve in Fig. 4 at $[Sn^{4+}]_{tot}/[HEDP]_{tot} \approx 0.33$ suggests that the major species has 1:3 metal:ligand stoichiometry, although it cannot be excluded on the basis of the ^{31}P NMR spectra that dinuclear complexes play a role as well. Most likely the HEDP ligands in the major complex are bound to Sn^{4+} in a bidentate fashion through an oxygen atom of each of the phosphonate moieties. Such structures have a chiral Sn(IV) atom (Δ and Λ isomers). Furthermore, the C-atoms of the HEDP ligand become chiral upon binding to the Sn^{4+} ion and, consequently a large number of diastereomers are possible for this complex. Since the phosphorus nuclei in the bound ligand are chemically inequivalent, a large number of ^{31}P resonances may be observed for these complexes, which is in agreement with the observed spectrum. The situation becomes even more complex as result of couplings among the various P-nuclei in the complexes.

An NMR chemical shift pH titration with a sample with $[Sn^{4+}]_{tot}/[HEDP]_{tot} = 1/3$ shows inflections at about pH 2 and 6 for both the free ligand and the Sn(IV)-complexes (Fig. 7). Most likely, these inflections may be attributed to the pK_{a1} and pK_{a2} of the bisphosphonate functional groups, which means that these groups are deprotonated at physiological pH. This is in agreement with the generally observed trends in pK_as of bisphosphonates [20]. In the pH range 0–10, the ligand remained fully complexed. Similar experiments at higher $[Sn^{4+}]_{tot}/[HEDP]_{tot}$ ratios gave rise to precipitation at pH values higher than 3, which may be ascribed to hydrolysis of the Sn^{4+} present.

Sn(IV)–HEDP complexes are present as a cocktail of a variety of species, from the spiro-type structures as suggested by Alberola [14] to the multinuclear structures found by potentiometric data [16]. ^{13}C and ^{1}H spectra reveal a change in chemical shift of new resonances for the C-PO_3H_2 and CH_3 groups, respectively, as observed by the appearance of additional triplets at 51.40 ppm and 51.68 ppm ($^2J_{CP} = 133.94$ Hz and $^3J_{HP} = 14.34$ Hz, respectively) – other than that of the free ligand at 52.47 ppm – upon coordination of HEDP with tin. The appearance of additional peaks is consistent with the ^{31}P spectra. ^{119}Sn NMR spectrum by Alberola [14] reveals a quintuplet ($J \sim 30.00$ Hz), confirming the existence of a symmetrical spiro-structure.

3.2. Sn^{2+}–HEDP system

^{31}P NMR samples of Sn^{2+} and HEDP in molar ratios 1:1 to 1:3 species showed a major resonance in the same region as that of the uncomplexed ligand, 19.24 ppm, regardless of pH-conditions (see Fig. 2). The free ligand was therefore indistinguishable from the [Sn(II)–HEDP]^0 complex(es). In the absence of organic ligands, Sn(II) precipitates under the conditions applied, which suggests that a substantial part of the Sn(II) is coordinated to HEDP. At molar ratios of Sn^{2+} and HEDP higher than 1, precipitation of oxides occurs. Therefore most likely the stoichiometry of the dominant species at lower molar ratios has a Sn(II):ligand ratio of 1:1.

In this respect Sn^{2+} appears to behave much like other familiar divalent metal-ions such as Ca^{2+} and Cd^{2+}, which with the possibility a single symmetrical species predominating, results also in a ^{31}P NMR spectrum with a singlet in the same region as the free HEDP. For Cd^{2+} the binding by HEDP is demonstrated by ^{113}Cd NMR spectra, which display a single peak at approximately 34.00 ppm up-field from the reference $CdCl_2$. No free metal was observed, which indicates that all Cd-ions were successfully complexed. However, contrary to Sn^{2+} the Cd^{2+} complexation is rather complex, and produces ^{31}P NMR spectra that appear to be a result of many overlapping signals.

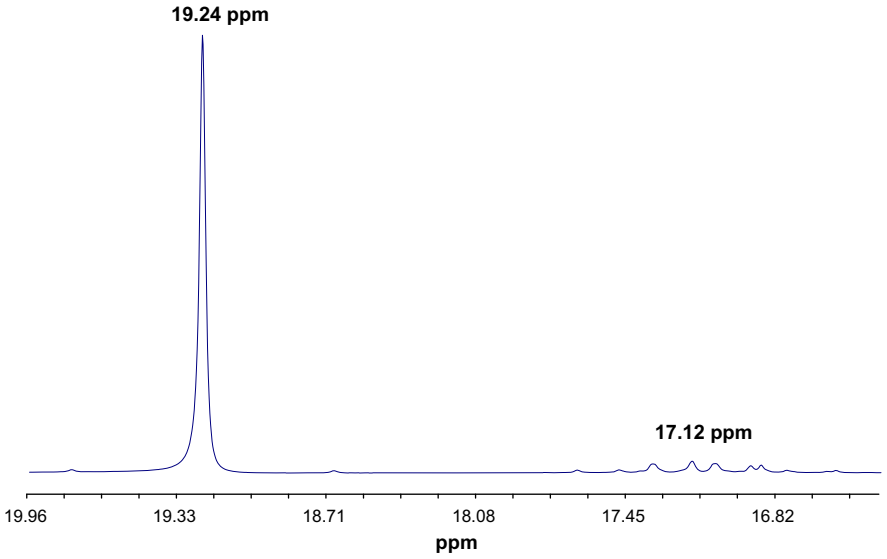


Fig. 2. ^{31}P NMR spectrum of Sn(II)–HEDP solution (M:L = 1:3) at pH 7.4; showing the free ligand and [Sn(II)–HEDP]^{0} complex(es) as a singlet at 19.24 ppm ($I = 87\%$) and the [Sn(IV)–HEDP]$^{2+}$ complex(es) as a multiplet centred at 17.12 ppm ($I = 13\%$).

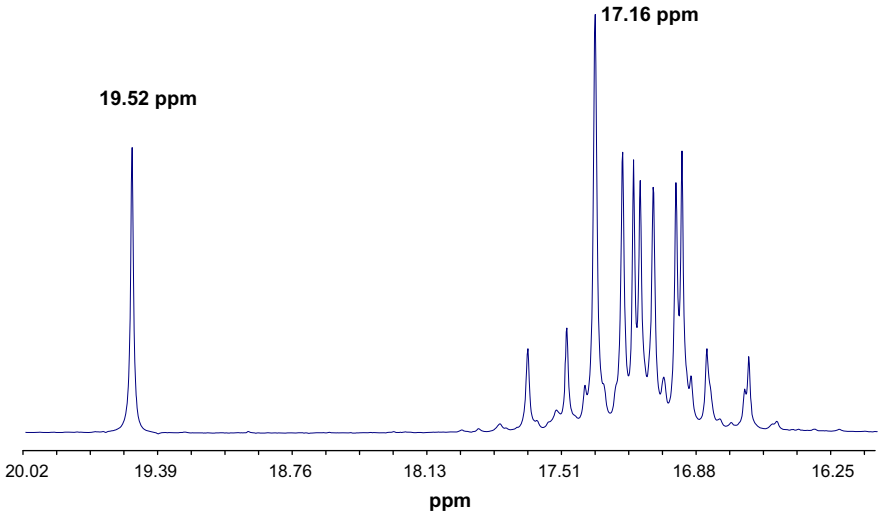


Fig. 3. ^{31}P NMR spectrum of Sn(IV)–HEDP solution (M:L = 1:3) at pH 7.4; showing the free ligand as a singlet at 19.52 ppm ($I = 9$) and the complex(es) [Sn(IV)–HEDP]$^{2+}$ as a multiplet centred at 17.16 ppm ($I = 91$).

This difference in complexation between Sn^{2+} and Sn^{4+} can be attributed to the charge, i.e. the greater the charge, the greater the affinity per ligand and hence more possibility for coordination.

It should be noted that in all ^{31}P NMR spectra of samples with Sn^{2+} and HEDP, an additional characteristic set of signals occurred in the 17.00 ppm region throughout the pH range studied (pH 0–10), which is evident to the presence of Sn^{4+} (Figs. 2 and 3). The intensity of these signals was about 15% of that of the resonance at about 19.00 ppm. The presence of resonances for Sn(IV) complexes is not surprising, since no special care was taken to eliminate/prevent its occurrence. However, the presence of Sn^{4+} did prove useful for the evaluation of the extent of oxidation of Sn^{2+} under normal working conditions. The same phenomenon was observed for [Cd(II)–HEDP]^{0} and [Ca(II)–HEDP]^{0}, with no other ^{31}P signals.

Probably due to rapid exchange within the Sn^{2+}-complex we do not see the ^{31}P signal due Sn^{2+} complexation, which is consistent with findings by Alberola [14]. The same was found to be true for [Ca(II)–HEDP]^{0} and [Cd(II)–HEDP]^{0}. Although unusual, the complex formation might occur within the same chemical shift region as the free ligand (19.71 ppm), therefore it is practically impossible to distinguish between [Sn(II)–HEDP]^{0} complexes and free ligand by merely considering the chemical shift. This is supported by potentiometric data of divalent metal-ions when complexed to HEDP [16], in which binuclear (M_2L) species occurred (Fig. 5). From the thermody-

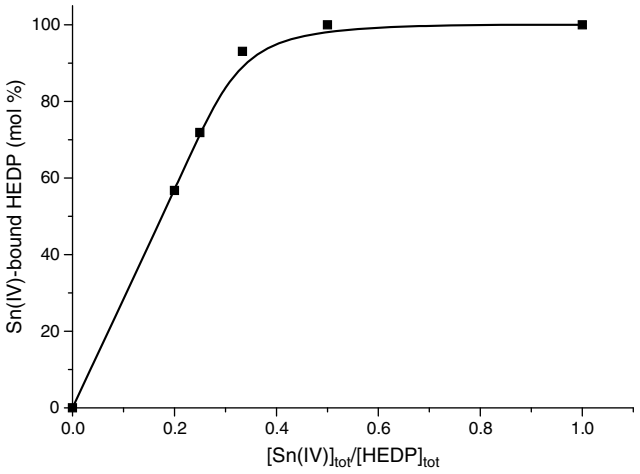


Fig. 4. Graph showing the change in the mole percentage of HEDP bound by Sn^{4+} vs. the molar ratio $[Sn^{4+}]_{tot}/[HEDP]_{tot}$.

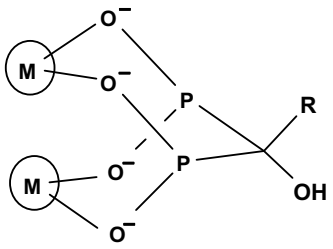


Fig. 5. Proposed binuclear diphosphonate complex according to potentiometric data.

namic data species such as ML and M_2L or M_2LH_{-2} could account for this phenomenon. For example, Ca^{2+}: $\log\beta_{110} = 5.34$ and $\log\beta_{210} = 9.53$, Cd^{2+}: $\log\beta_{110} = 7.26$ and $\log\beta_{210} = 12.67$ [16], and Sn^{2+}: $\log\beta_{21-2} = 11.85$ [10]. We would therefore expect a singlet since all phosphorous nuclei are equivalent. Furthermore, according to extensive crystallographic research of diphosphonates by Matczak-Jon et al. [17,18] and Zapf et al. [19], certain bridged-binuclear diphosphonate complexes were reported, particularly with Zn^{2+} and Mg^{2+}. Although unsymmetrical, the complexes yielded representative ^{31}P spectra.

The important information obtained from the ^{31}P spectra of HEDP when complexed with Sn^{2+} and Sn^{4+}, is the relative extent of complexation of the Sn^{4+} in each.

3.3. Sn(II)–Sn(IV)–PEI-MP system

The complexes of Sn^{2+} and Sn^{4+} with PEI-MP are also distinguishable by their ^{31}P chemical shifts, and especially when present in the same solution (Fig. 6). The Sn^{4+}–PEI-MP complexes appeared as a broad peak at about 16.63 ppm whilst the Sn^{2+}–PEI-MP species occurred at slightly lower chemical shift (16.26 ppm), with the free ligand at 15.68 ppm.

3.4. Elucidating the possible oxidation of Sn^{2+} within Sn–HEDP and Sn–PEI-MP complexes

There were no changes in the ^{31}P NMR spectra of samples of Sn(II) with HEDP or PEI-MP overnight, hence we can assume that no oxidation of Sn^{2+} occurred. Should this have been the case we would expect an increase in the ratio of intensities of the corresponding peaks, which would eventually approach the spectrum of the concerning Sn(IV)-complex at the respective pH.

In a study to understand the conditions needed for the oxidation of Sn^{2+} in the presence of HEDP, the complex was titrated with hydrogen-peroxide (30% H_2O_2). The metal to ligand ratio of 1:3 (pH 7.3) was chosen so as to limit any free/uncomplexed tin which would hydrolyze and precipitate out during the titrations. Throughout the investigation no precipitation was observed within the 1:3 mixtures, even over prolonged periods, which indicates that all tin was successfully complexed in solution and

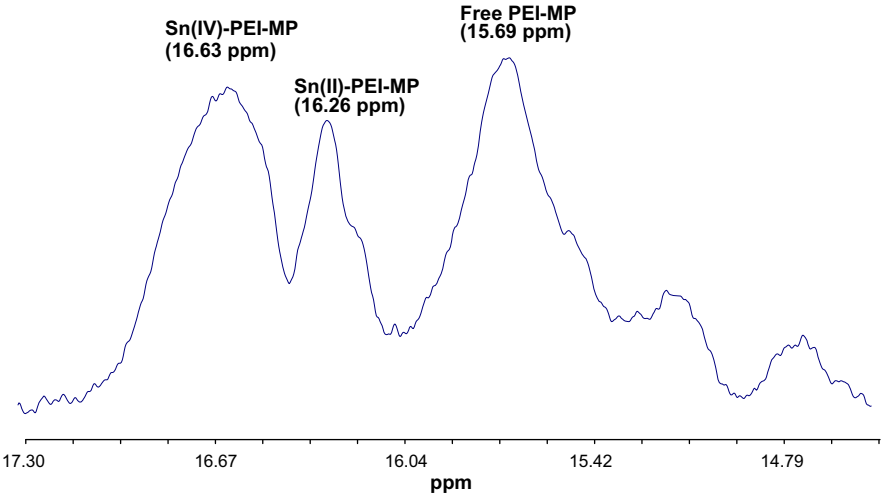


Fig. 6. ^{31}P spectrum of tin(II)–tin(IV)–PEI-MP system (1:1:8) at pH 12; where 15.69 ppm is free ligand, 16.26 ppm is the Sn^{2+}-complex(es) and 16.63 ppm represents the Sn^{4+}-complex(es).

variations in the pH did not influence the Sn-ions directly – the [Sn–HEDP] complexes are stable enough to withstand fluctuations in pH. Mixtures in which the metal-ion concentration was in excess, i.e. M:L > 1:1, exhibited immediate precipitation upon addition of NaOH. Precipitation eventually occurred in these solutions, even without any pH manipulation after a few hours – for both Sn^{2+} and Sn^{4+}.

Oxidation of the tin in the $[Sn(II)–HEDP]^0$ and the $[Sn(II)–Sn(IV)–PEI\text{-}MP]^{4+}$ systems was induced by the addition of 30 μl of H_2O_2, 0.05 mol dm^{-3} (Fig. 9) and 0.010 mol dm^{-3} (Fig. 8) respectively. As expected, an increase in intensity of the resonances of the Sn(IV) complexes was observed in the case of HEDP, with a steady decrease in the intensity of the resonance at about 19 ppm, and for PEI-MP we observed the disappearance of the signal for the Sn(II) chelate, although only realizing some increase (~35–45%) in intensity of the resonances for the Sn^{4+} complex. There is a increase in the free-ligand concentration (~40–~55%), which could be due to the liberation of ligand that had been previously bound to Sn^{2+}. The simultaneous increase in both amounts of [Sn(IV)–

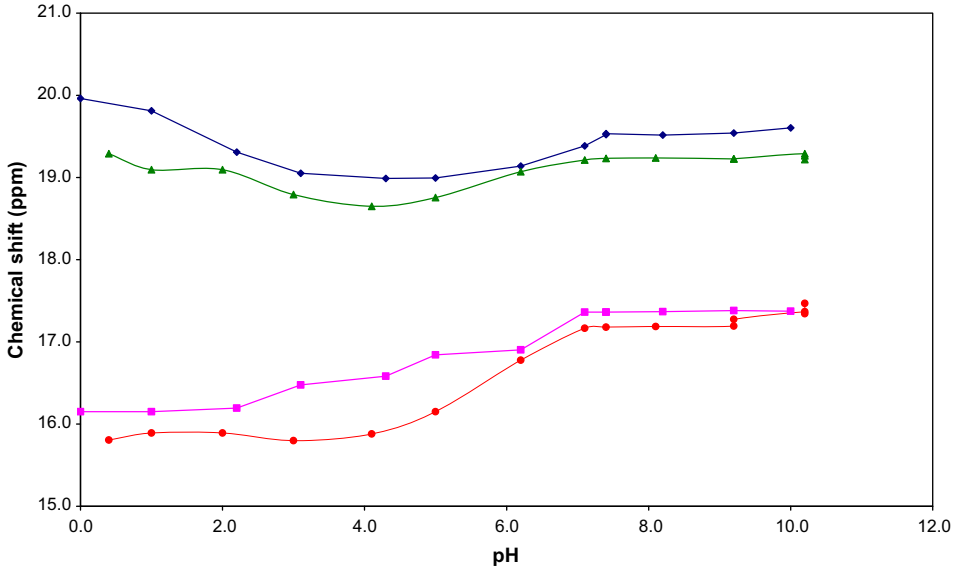


Fig. 7. Changes in the chemical shift of the ^{31}P signal for the free and complexed HEDP for the respective systems: Sn^{2+} and Sn^{4+}, at varying pH. (i) Sn^{4+} system: (■) complexed $[Sn(IV)–HEDP]^{2+}$; (◇) free HEDP; (ii) Sn^{2+} system; (●) complexed $[Sn(IV)–HEDP]^{2+}$; (▲) free HEDP + $[Sn(II)–HEDP]^0$.

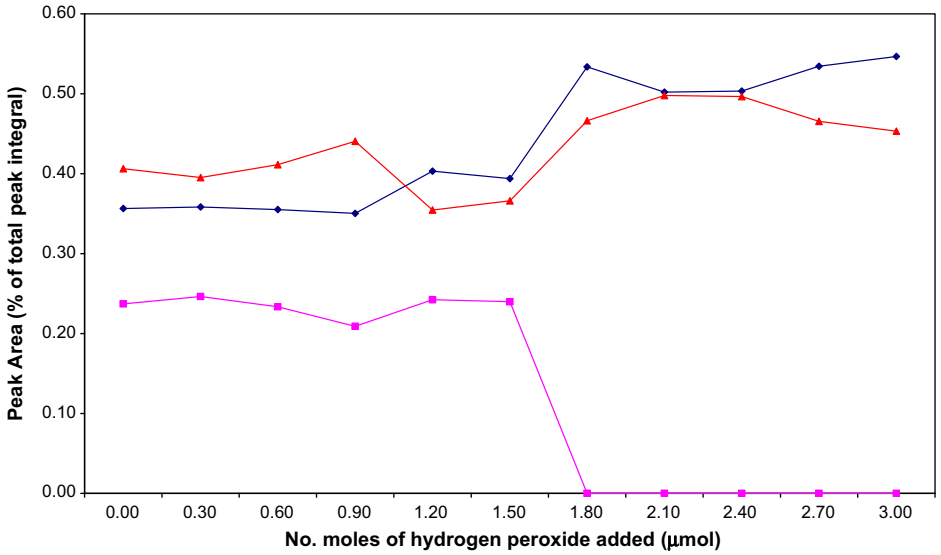


Fig. 8. Determination of the amount of hydrogen-peroxide needed to completely oxidize the Sn^{2+} in the PEI-MP complex in a sample containing Sn^{2+}:Sn^{4+}:ligand = 1:1:8 at pH 12. H_2O_2 concentration = 0.010 mol dm^{-3}, and ^{31}P spectra were recorded 30 min after each addition (i.e. total acquisition time = 30 min). (◇) Free PEI-MP, (■) $[Sn(II)–PEI\text{-}MP]^0$, and (▲) $[Sn(IV)–PEI\text{-}MP]^{2+}$.

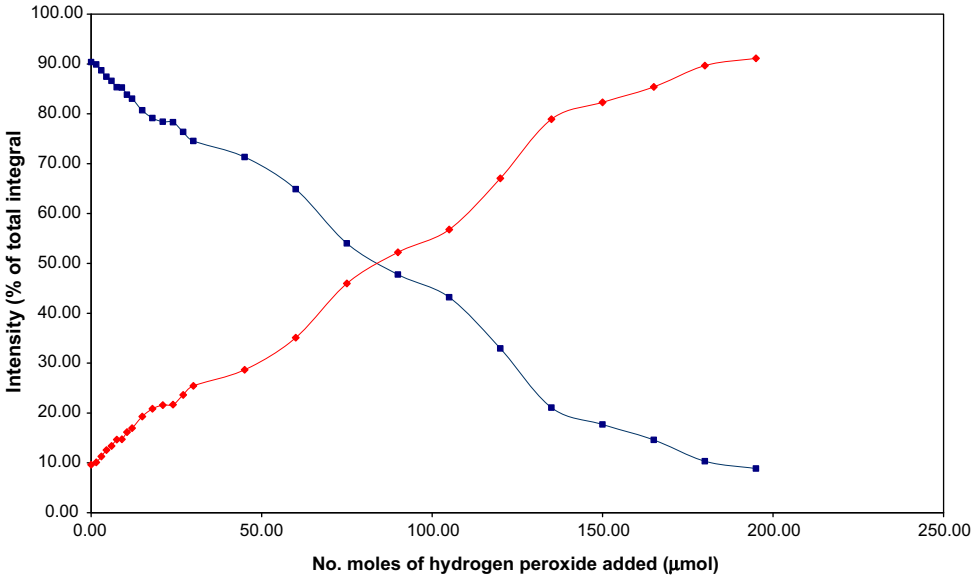


Fig. 9. Determination of the amount of hydrogen-peroxide needed to oxidize the Sn^{2+} in the HEDP complex in a sample containing metal-to-ligand = 1:3 at pH 7.3. H_2O_2 concentration = 0.050 mol dm^{-3}, and ^{31}P spectra were recorded 30 min after each addition (i.e. total acquisition time = 30 min). (■) Free + $[Sn(II)–HEDP]^0$ and (◇) $[Sn(IV)–HEDP]^{2+}$.

$PEI-MP]^{2+}$ and free ligand after oxidation implies that the PEI-MP that had formerly been bound to Sn^{2+} is evenly distributed between Sn^{4+}-bound and free ligand in solution. Furthermore, this would mean an increase in the free metal-ion concentration (i.e. at least half the tin-ions being released as reflected by the increase in free-ligand concentration). This is confirmed by the occurrence of slight precipitation upon completion of the oxidation driven by the reaction of $Sn(IV) + 4OH^- \leftrightharpoons Sn(OH)_{4(s)}$. Approximately 1.6 μmol of H_2O_2 per μmol of Sn^{2+} within the HEDP system, was needed to oxidize it in order to reach the equivalent complexation of Sn^{4+} at the same pH (Fig. 9). For the $[Sn(II)–PEI-MP]^0$ system 1.4 μmol H_2O_2 per μmol Sn(II)–PEI-MP is needed.

The rate at which the oxidation (induced) occurs was tested on a sample of 125 μmol $[Sn(II)–HEDP]^0$ (M:L = 1:3), by adding 30 μl of 0.5 mol dm^{-3} H_2O_2 and monitoring the change over the required period of time to reach saturation. The oxidation reaches a maximum at about 28% conversion within 40 min.

The oxidation was reversible to a certain extent. A sample containing $[Sn(II)–HEDP]^0$ that had previously been completely oxidized using ca. 70 μl of H_2O_2 (30%), and exhibiting 92% complexation due to Sn^{4+}, was treated with ca. 300 μl of 1 mol dm^{-3} glutathione (GSH). This resulted in decrease of the intensity of the Sn(IV) complexes with 50% and a corresponding increase of the resonance for free and complexed Sn(II). The results were reproduced with a fresh sample prepared exclusively with Sn^{4+}, using the same specifications as the previous. This experiment could not be performed with PEI-MP as it appeared that the glutathione possibly reduced the ligand, and as a result no meaningful ^{31}P spectra were obtainable – this was confirmed with a sample comprising of only free ligand.

4. Conclusion

We found that Sn^{2+} and Sn^{4+} diphosphonate complexes can co-exist in solution without any interconversion over prolonged periods. This serves to confirm a study conducted by Hiles [11] who found this to be true for the respective ions when introduced into the blood stream (in rats). However, upon complexation with bisphosphonates, immediate oxidation of Sn^{2+} did occur (to a limited extent and not continuing with time) with Sn(II)–HEDP. This could also have been attributed to the likelihood that the Sn(II) salt contained some Sn(IV). This can be regarded as acceptable since the experiments were conducted without extensive measures to avoid this (such as inert atmosphere or de-aerated solutions). In practice this can be avoided in preparing the complexes (and eventual radiopharmaceuticals) with de-aerated solutions under Ar. Oxidation was induced by addition of H_2O_2, in which a slight excess of the molar amount of Sn^{2+} was required to achieve equivalent Sn^{4+} complexation. This reaction reaches completion after about 40 min. The oxidation is reversible, by addition of reducing agent, such as glutathione (GSH). Although this was proven to a limited extent for HEDP, it does not hold true for PEI-MP – which itself appears to be reduced in the presence of excess GSH, given that $SnCl_2$ too is a reducing agent.

Considering the findings by Hiles [11], and the extreme oxidizing conditions employed in our experiments, the likelihood of oxidation of the Sn^{2+}-complex is minimal under mild physiological conditions. Should the complex dissociate *in vivo*, the Sn^{2+}-ion should still survive, and possibly be complexed by other blood plasma ligands, if not hydrolysed. This brings to question the stability of the Sn^{2+}-based radiopharmaceutical within blood plasma, where it would

be susceptible to dissociation due to competition by physiological ligands and metal-ions. This has been already been addressed by Zeevaart et al. [10] with the aid of a computational blood plasma model of Sn^{2+}. This model predicts whether the complex is strong enough to prevent dissociation and formation of $Sn(OH)_2$. Only ligands that pass this evaluation should be considered for bone-seeking radiopharmaceuticals.

Acknowledgement

This research was supported by a grant from WOTRO Science for Global Development of the Netherlands Organization for Scientific Research (w 01.83.2004.031).

References

[1] A. Schoutens, Calsif. Tiss. Int. 42 (1988) 136.
[2] B. Thürlimann, R. Morant, W.F. Jungi, A. Radziwill, Support Care Cancer 2 (1994) 61.
[3] J. Simon, D.A. Wilson, J.R. Garlich, D.E. Troutner, Patent 899734, Dow Chemical Company, 1989.
[4] F. Hosain, R.P. Spencer, Sem. Nucl. Med. 22 (1992) 11.
[5] J.M.H. de Klerk, PhD thesis, University of Utrecht, Ponsen & Vlooijen, Wageningen, 1995.
[6] H.R. Mascon, M. Verhas, N. Dourov, P. Bergmann, F. Caulin, A. Verschaeren, M. Mone, A. Heilporn, Sem. Nucl. Med. 22 (1992) 33.
[7] M. Eisenhut, Int. J. Appl. Rad. Iso. 33 (1982) 99.
[8] H. Maeda, K. Greish, J. Fang, Adv. Polym. Sci. 193 (2006) 103.
[9] L.W. Seymour, CRC Crit. Rev. Ther. Drug Carrier Syst. 9 (1992) 249.
[10] J.R. Zeevaart, W.K.A. Louw, Z.I. Kolar, J.M. Wagener, N.V. Jarvis, R.A.M.J. Claessens, J. Radioanal. Nucl. Chem. 257 (2003) 83.
[11] R.A. Hiles, Toxicol. Appl. Pharmacol. 27 (1974) 366.
[12] R.A.M.J. Claessens, Z.I. Kolar, Langmuir 16 (2000) 1360.
[13] S.C. Srivastava, G.E. Meinken, P. Richards, P. Som, Z.H. Oster, H.L. Atkins, A.B. Brill, F.F. Knapp, T.A. Butler, Int. J. Nucl. Med. Biol. 12 (1985) 167.
[14] N. Alberola, Polyhedron 4 (11) (1985) 1853.
[15] N.V. Jarvis, J.R. Zeevaart, J.M. Wagener, W.K.A. Louw, I.C. Dormehl, R.J. Milner, E. Killian, Radiochim. Acta 90 (2002) 1.
[16] J.R. Zeevaart, N.V. Jarvis, I. Cukrowski, G.E. Jackson, South Afr. J. Chem. 50 (1997) 189.
[17] E. Matczak-Jon, V. Videnova-Adrabinska, Coord. Chem. Rev. 249 (2005) 2458.
[18] E. Matczak-Jon, B. Kurzak, P. Kafarski, A. Wozna, J. Inorg. Biochem. 100 (2006) 1155.
[19] P.J. Zapf, D.J. Rose, R.C. Haushalter, J. Zubieta, J. Solid State Chem. 125 (1996) 182.
[20] V. Kubíček, J. Kotek, P. Hermann, I. Lukeš, Eur. J. Inorg. Chem. (2007) 333.

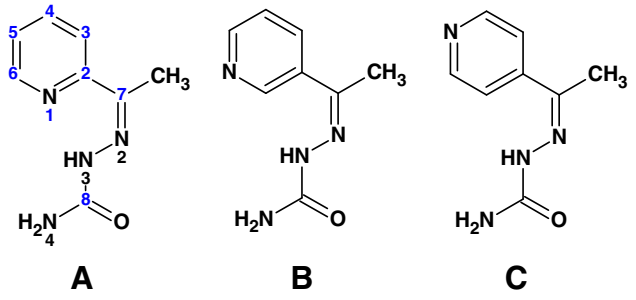


Fig. 1. Structural representation of 2-acetylpyridine semicarbazone (H2APS = A), 3-acetylpiridine semicarbazone (H3APS = B), and 4-acetylpyridine semicarbazone (H4APS = C).

2. Experimental

2.1. Materials and measurements

All common chemicals were purchased from Aldrich and used without further purification. The semicarbazones were prepared according to standard procedures [6].

Partial elemental analyses were performed on a Perkin–Elmer CHN 2400 analyzer. An YSI model 31 conductivity bridge was employed for molar conductivity measurements. Thermogravimetric curves were obtained with a Mettler TA-4000 equipment. Magnetic susceptibility measurements were carried out on a Johnson Matthey MSB/AUTO balance. UV spectra in solid-state were obtained with an UV-2401PC – (P/N 206-82201) – Shimadzu equipment using $BaSO_4$ as support; infrared spectra were recorded on a Perkin–Elmer FT-IR Spectrum GX spectrometer using nujol mulls between CsI plates; NMR spectra were obtained with a Bruker DRX-400 Avance (400 MHz) spectrometer using d_6-DMSO as the solvent and TMS as internal reference.

2.2. Preparation of [VO(H2APS)(acac)$_2$] (1), [VO(H3APS)(acac)$_2$] (2), [VO(4APS)(acac)(H$_2$O)] · 1/2H$_2$O (3) and [VO$_2$(2APS)] (4)

Complexes **1**–**3** were obtained by reacting the desired ligand with [VO(acac)$_2$] (acac = acetylacetonate), in 1:1 ligand-to-metal molar ratio (0.005 mol), in methanol under reflux and nitrogen atmosphere for 4 h. The solids were washed with ethanol followed by diethylether and then dried *in vacuo*. Upon reaction of [VO(acac)$_2$] with H2APS in acetonitrile in 1:1 ligand-to-metal molar ratio (0.005 mol) for 72 hours [VO$_2$(2APS)] (**4**) precipitates. Similar procedure using H3APS and H4APS did not lead to oxidation but gave the same oxovanadium(IV) complexes which had been obtained before in methanol.

2.3. Oxovanadium(IV) complex of 2-acetylpyridine semicarbazone [VO(H2APS)(acac)$_2$] (1)

Light green solid. *Anal.* Calc. for $VC_{18}H_{24}N_4O_6$: C, 48.8; H, 5.5; N, 12.6. Found: C, 48.6; H, 5.4; N, 12.5%. FW: 443.35 g mol^{-1}. UV$_{solid}$: λ_{max} (cm^{-1}): 37 453, 30 580, 23 640, 17 544, 13 227. IR (CsI/nujol, cm^{-1}): ν(C=N) 1584, ν(C=O) 1699, ν(V=O) 969, ρ(py) 624. $\Lambda_M = 2.92\ \Omega^{-1}\ cm^2\ mol^{-1}$ in DMF. Magnetic moment = 1.87 BM. Yield 74%.

2.4. Oxovanadium(IV) complex of 3-acetylpyridine semicarbazone [VO(H3APS)(acac)$_2$] (2)

Light green solid. *Anal.* Calc. for $VC_{18}H_{24}N_4O_6$: C, 48.8; H, 5.5; N, 12.6. Found: C, 48.6; H, 5.5; N, 12.6%. FW: 443.35 g mol^{-1}. UV$_{solid}$: λ_{max} (cm^{-1}): 34 247, 30 581, 24 450, 17 544, 12 903. IR (CsI/nujol, cm^{-1}): ν(C=N) 1579, ν(C=O) 1687, ν(V=O) 965, ρ(py) 631. $\Lambda_M = 8.69\ \Omega^{-1}\ cm^2\ mol^{-1}$ in DMF. Magnetic moment = 2.13 BM. Yield 72%.

2.5. Oxovanadium(IV) complex of 4-acetylpyridine semicarbazone [VO(4APS)(acac)(H$_2$O)] · 1/2H$_2$O (3)

Light green solid. *Anal.* Calc. for $VC_{13}H_{19}N_4O_{5.5}$: C, 42.2; H, 5.2; N, 15.1. Found: C, 42.3; H, 5.2; N, 15.0%. FW: 370.26 g mol^{-1}. UV$_{solid}$: λ_{max} (cm^{-1}): 36 364, 28 011, 23 838, 17 746, 12 903. IR (CsI/nujol, cm^{-1}): δ (H$_2$O) 1638, ν(C=N) 1603, ν(C=O) 1687, ν(V=O) 959, ρ(py) 591, ν(V–N) 504, ν(V–O) 416. $\Lambda_M = 18.88\ \Omega^{-1}\ cm^2\ mol^{-1}$ in DMF. Magnetic moment = 1.89 BM. Yield 81%.

2.6. Oxovanadium(V) complex of 2-acetylpyridine semicarbazone [VO$_2$(2APS)] (4)

Yellow solid. *Anal.* Calc. $VC_8H_9N_4O_3$: C, 36.9; H, 3.5; N, 21.5. Found: C, 36.8; H, 3.5; N, 21.4%. FW: 260.13 g mol^{-1}. UV$_{solid}$: λ_{max} (cm^{-1}): 34 014, 27 310, 22 321. IR (CsI/nujol, cm^{-1}): ν(C=N) 1562, ν(C=O) 1656, ν(V=O) 959, 941, ρ(py) 609, ν(V–N) 495, ν(V–O) 426. $\Lambda_M = 2.47\ \Omega^{-1}\ cm^2\ mol^{-1}$ in DMF. ^{1}H NMR (400 MHz, d_6-DMSO, 25 °C): δ (ppm) = 8.64 (d, 1H, H(6)), 8.27 (td, 1H, H(4)), 7.91 (d, 1H, H(3)), 7.65 (t, 1H, H(2)), 7.18 (s, 2H, N(4)H), 2.46 (s, 3H, CH_3). ^{13}C NMR (400 MHz, d_6-DMSO, 25 °C): δ (ppm) = 172.52 (1C, C(8)=O), 155.53 (1C, C(2)), 152.46 (1C, C(7)=N), 142.82 (1C, C(4)), 124.30 (1C, C(5)), 122.87 (1C, C(3)), 12.33 (1C, CH_3). ^{51}V NMR (400 MHz, d_6-DMSO, 25 °C): δ (ppm) = −528.44. Yield 77%.

2.7. Crystal structure determination

Single crystals of [VO(H2APS)(acac)$_2$] (**1**) and [VO$_2$(2APS)] (**4**) suitable for X-ray diffraction were obtained from CH_3CN solutions. Data collection were performed with Cu Kα radiation (λ = 154.184 pm) on an Enraf-Nonius CAD-4 diffractometer applying standard procedures.

The structures were solved by direct methods with SIR-92 [7] and refined with SHELXL-97 [8]. The hydrogen atoms of the methyl groups in **1** were fixed at idealized positions with

Table 1
Crystal data and refinement results for [VO(H2APS)(acac)$_2$] (**1**) and [VO$_2$(2APS)] (**4**)

Complex	**1**	**4**
Empirical formula	$C_{18}H_{24}N_4O_6V$	$C_8H_9N_4O_3V$
Formula weight	443.35	260.13
T (K)	213(2)	293(2)
Crystal system	monoclinic	triclinic
Space group	$P2_1/a$	$P\bar{1}$
a (pm)	1027.04(5)	767.74(9)
b (pm)	1567.46(9)	862.86(11)
c (pm)	1406.61(9)	872.89(6)
α (°)	90	65.429(7)
β (°)	104.402(5)	79.754(6)
γ (°)	90	69.391(6)
V (pm^3)	$2.1933(2) \times 10^6$	$4.9189(9) \times 10^6$
Z	4	2
Absorption coefficient (mm^{-1})	4.131	8.469
Absorption correction	ψ-scan [17]	ψ-scan [17]
T_{max}/T_{min}	0.8201/0.2319	0.6768/0.2260
Crystal size (mm)	$0.50 \times 0.05 \times 0.05$	$0.25 \times 0.10 \times 0.05$
Crystal shape and color	green needle	yellow plate
θ Range for data collection (°)	5.27–64.87	5.58–65.01
Index ranges (h,k,l)	$-1 \rightarrow h \rightarrow 10$, $0 \rightarrow k \rightarrow 18$, $-16 \rightarrow l \rightarrow 16$	$-1 \rightarrow h \rightarrow 9$, $-9 \rightarrow k \rightarrow 10$, $-9 \rightarrow l \rightarrow 10$
Collected reflections	4261	2018
Unique reflections/R_{int}	3587/0.0509	1636/0.0201
Observed data [$I > 2\sigma(I)$]	2100	1498
Refined parameters	267	146
Structure factors [$I > 2\sigma(I)$]	$R_1 = 0.0505$, $wR_2 = 0.0982$	$R_1 = 0.0364$, $wR_2 = 0.0938$
Goodness-of-fit, S	1.005	1.045
Largest diffraction peak and hole (e Å^{-3})	0.228 and −0.309	0.388 and −0.501

torsion angle from electron density, using the riding model of SHELXL-97 [8]. All other hydrogen atoms' positions were located in a difference Fourier map and were refined using SHELXL-97 with isotropic displacement parameters [8]. Additional crystal data and more information about the X-ray structural analyses are shown in Table 1.

2.8. In vitro insulin-mimetic studies

2.8.1. Adipocyte isolation

Adipocytes were isolated from epididymal fat pads of Wistar male rats, by the method of Rodbell [9]. Digestion was carried out at 37 °C with constant shaking for 45 min. Cells were filtered through nylon mesh and washed three times with buffer containing (mM): 137 NaCl, 5 KCl, 4.2 $NaHCO_3$, 1.3 $CaCl_2$, 0.5 $MgCl_2$, 0.5 $MgSO_4$, 0.5 KH_2PO_4, 20 HEPES (pH 7.4), plus 1% BSA.

2.8.2. Glucose transport assay

After isolation, adipocytes were incubated for 45 min and 2-deoxy-[^{3}H]glucose uptake was used as an assay to determine the effect of the compounds (10^{-3} M) or insulin (50 ng/mL) on the rate of glucose transport, as previously described [10]. Glucose uptake was initiated by the addition of 2-deoxy-[^{3}H]glucose (0.2 μCi/tube) for 3 min. Thereafter, cells were separated by centrifugation through silicone oil and the cell associated radioactivity determined by scintillation counting. Nonspecific association of 2-deoxy-[^{3}H]glucose was determined by performing parallel incubations in the presence of phloretin (15 mM), and this value was subtracted from glucose transport activity at each condition.

2.8.3. Lipolysis assay

Lipolysis was measured by following the rate of glycerol release, as previously described [11]. After washing, adipocytes were preincubated at 37 °C in a water bath for 30 min, in basal conditions or in the presence of the vanadium compounds (10^{-3} M) [12] dissolved in DMSO (20% v/v). Then, isoproterenol (0.1 μM) was added in the tubes containing the compounds, and the cells were incubated for additional 30 min. At the end of the incubation period, an aliquot of the infranatant was removed for enzymatic determination of glycerol released into the incubation medium.

2.9. Statistical analysis

All experiments were performed in at least three replicates per compound and the results shown are the average of at least four independent experiments. Data, represented as the means ± SEM, were analyzed by one-way analysis of variance (ANOVA) followed by Newman–Keuls post hoc test to establish differences between the groups. A $P < 0.05$ was considered significant. All data and statistical analyses were performed using GraphPad Prism version 4.0 for Windows, GraphPad Software, San Diego, CA, USA.

3. Results and discussion

Microanalyses suggest the formation of [VO(H2APS)(acac)$_2$] (**1**), [VO(H3APS)(acac)$_2$] (**2**) and of [VO(4APS)(acac)(H_2O)] · 1/2H_2O (**3**). In complexes **1** and **2** the semicarbazone acts as a neutral ligand while in **3** the semicarbazone is attached to the metal centre in the anionic (4APS) form. A second product was isolated in the reaction with H2APS, [VO$_2$(2APS)] (**4**), containing vanadium(V) and an anionic semicarbazone. Complex **4** was also obtained by reacting [VO(acac)$_2$] with H2APS in acetonitrile during 72 h. The TG curve of [VO(4APS)(acac)(H_2O)] · 1/2H_2O (**3**) shows a weight loss of 2.7% (Calc. 2.4%) in the 33–70 °C range corresponding to the release of 1/2H_2O, followed by a second weight loss of 33.3% (Calc. 31.6%), corresponding to the release of the acac ligand along with the coordination water. Interestingly, the TG curves of **1**, **2** and **4** do not show weight losses attributable to the release of water molecules.

3.1. Spectroscopic characterization

Absorptions at 1550–1500 cm^{-1}, characteristic of coordinated acac [13] were observed in the infrared spectra of

complexes **1**–**3** but were not observed in the spectrum of **4**. In the spectra of H2APS and H3APS a broad absorption at 1700 and 1683 cm^{-1}, respectively, was attributed to ν(C=O) [6]. This absorption is observed as a narrow band at 1699 and 1687 cm^{-1} in the spectra of complexes **1** and **2**, respectively, suggesting coordination through the carbonyl oxygen. The absorptions assigned to ν(C=N) at 1583 and 1582 cm^{-1} and those at 626 and 627 cm^{-1} assigned to the in-plane deformation mode of pyridine in the spectra of H2APS and H3APS, respectively [6] do not change in the spectra of **1** and **2**, indicating that the semicarbazones are attached to the metal as monodentate ligands, as confirmed by the crystal structure determination of complex **1** (see Section 3.2).

The absorptions attributed to ν(C=O) at 1684 and 1700 cm^{-1} in the spectra of H4APS and H2APS [6], respectively, shift to 1687 and 1656 cm^{-1} in the spectra of complexes **3** and **4** respectively, indicating coordination through the oxygen. The bands associated to ν(C=N) at 1594 and 1583 cm^{-1} in the spectra of H4APS and H2APS, respectively, shift to 1603 and 1562 cm^{-1} in the spectra of **3** and **4**, respectively, suggesting coordination through the azomethine nitrogen [6,14]. The absorptions assigned to the in-plane deformation mode of pyridine observed at 629 and 626 cm^{-1} in the spectra of H4APS and H2APS, respectively, shift to 591 and 609 cm^{-1} in the spectra of **3** and **4**, respectively. However, since in H4APS the semicarbazone chain is located in γ-position in relation to the heteroaromatic nitrogen, coordination through the imine nitrogen and the oxygen is suggested for complex **3**. Hence the large shift of the pyridine deformation mode upon coordination is probably due to extensive conjugation involving the semicarbazone skeleton and the heteroaromatic ring. In complex **4** coordination through the N_{py}–N–O chelating system occurs, as confirmed by crystal structure determination (Section 3.2).

The ν(V=O) vibration of [VO(acac)$_2$] is found at ca. 999 cm^{-1} [13]. This absorption is shifted to 941–969 cm^{-1} in the spectra of complexes **1**–**4**, in accordance with the presence of a ligand in *trans* position to the V=O bond. For complex **4** the presence of two absorptions attributed to $\nu_{sym.}$ (O=V=O) and $\nu_{asym.}$ (O=V=O) at 959 and 941 cm^{-1} corroborates the formation of [VO_2(2APS)] [15].

The electronic spectrum of [VO(acac)$_2$] shows absorptions at 30 530–36 900 cm^{-1} associated to acac and at 25 000 cm^{-1} assigned to a ligand-to-metal charge transfer transition. Bands at 14 430 and 17 000 cm^{-1} were attributed to ligand field transitions. In the electronic spectra (solid) of the free semicarbazones the $\pi \rightarrow \pi^*$ transitions of the pyridine ring were found at 45 660–47 160 cm^{-1}. The $n \rightarrow \pi^*$ transitions of the carbonyl and the azomethine functions were observed at 34 250–39 680 cm^{-1} and 26 810–30 960 cm^{-1}, respectively [6,14].

In the spectra of complexes **1**–**3** absorptions at 26 800–36 760 cm^{-1} were assigned to the $n \rightarrow \pi^*$ transitions of the semicarbazones and to transitions of acac overlapped under the same envelope. Bands in the 23 810–26 320 cm^{-1} range were attributed to ligand-to-metal charge transfer transitions of the complexes and of acac $\rightarrow$ VO^{2+}. Ligand field transitions of **1**–**3** were observed at 13 120–17 760 cm^{-1}.

In the spectrum of **4** a large absorption at 25 500–39 000 cm^{-1} was assigned to the $n \rightarrow \pi^*$ transitions of the semicarbazone along with a ligand-to-metal charge transfer transition. In this case no absorptions attributable to ligand field transitions were observed, according to the presence of V(V).

The NMR spectra of H2APS and complex **4** were recorded in d_6-DMSO because this is the only solvent which dissolves both compounds. The ^{1}H resonances were assigned on the basis of chemical shifts, multiplicities and coupling constants. The carbon type (C, CH) was determined by using DEPT135 experiments. The assignments of the protonated carbons were made by 2D heteronuclear-correlated experiments (HMQC) using delay values which correspond to ^1J(C, H).

In the ^{1}H NMR spectrum of H2APS the signal of N(3)–H appears at 9.45 δ. This signal is not observed in the spectrum of complex **4**, indicating deprotonation upon coordination to the metal centre. On coordination the signals of the pyridine hydrogens as well as the signal of N(4)–H_2 undergo significant shifts, suggesting coordination through the heteroaromatic nitrogen and through the oxygen. In the ^{13}C NMR spectrum large shifts occur for C=O, C=N and the pyridine carbons, in accordance with coordination of the semicarbazone through the N_{py}–N–O tridentate chelating system. One signal was observed at −528.44 δ in the ^{51}V NMR spectrum, consistent with the presence of vanadium(V) [16].

3.2. X-ray crystallography

Crystal data and refinement results for [VO(H2APS)(acac)$_2$] (**1**) and [VO_2(2APS)] (**4**) are shown in Table 1. Selected intra-molecular bond distances and angles around the metal are given in Table 2. Figs. 2 and 3 show ellipsoid representations of **1** and **4**.

Complex **1** shows a quite distorted octahedral coordination sphere, with the semicarbazone attached to the vanadium centre as a neutral ligand, through the carbonyl oxygen atom O(1), which occupies the axial *trans* position to the oxo ligand O(2). The four acetylacetone oxygens O(3), O(4), O(5) and O(6) show a mean deviation of 1.37 pm from planarity. The vanadium center is displaced by 31.5(2) pm from the equatorial base toward the apical oxo ligand O(2). The rather long V–O(1) bond distance, 233.3(3) pm, is caused by the strong *trans* influence of the oxo ligand, with V–O(2) distance = 159.4(3) pm, which corresponds to a double bond. The interatomic distances within the [VO(acac)$_2$] entity of **1** are comparable with the values found in [VO(acac)$_2$] itself [18]. Furthermore, the average value of 99.4° observed for the O_{oxo}–V–O_{acac} angles in **1** is 6.6° smaller than the corresponding value for [VO(acac)$_2$] (106.2°) [18], due to coordination of the

Table 2
Selected bond distances (pm) and angles (°) in the molecular structures of $[VO(acac)_2(H2APS)]$ (**1**) and $[VO_2(2APS)]$ (**4**)

1		**4**	
Bond lengths		Bond lengths	
V–O(2)	159.4(2)	V–O(2) V–O(3)	161.7(2) 160.7(2)
V–O(1)	233.3(3)	V–O(1)	194.3(2)
V–O(3) V–O(4)	198.8(3) 198.4(3)	V–N(1)	209.8(2)
V–O(5) V–O(6)	198.6(3) 198.6(3)	V–N(2)	210.6(2)
N(1)–C(1)	134.4(5)	N(1)–C(1)	134.1(4)
N(1)–C(5)	134.1(5)	N(1)–C(5)	136.1(3)
C(6)–N(2)	128.1(5)	C(6)–N(2)	129.8(3)
N(2)–N(3)	137.2(4)	N(2)–N(3)	137.6(3)
N(3)–C(8)	136.4(5)	N(3)–C(8)	134.6(4)
C(8)–O(1)	124.0(4)	C(8)–O(1)	129.1(3)
C(8)–N(4)	132.9(5)	C(8)–N(4)	132.7(4)
Bond angles		*Bond angles*	
O(2)–V–O(3)	98.4(1)	O(1)–V–O(2)	100.5(1)
O(2)–V–O(4)	100.5(1)	O(2)–V–O(3)	110.2(1)
O(2)–V–O(5)	98.6(1)	O(1)–V–N(1)	146.45(9)
O(2)–V–O(6)	99.1(1)	O(3)–V–N(1)	97.8(1)
O(3)–V–O(4)	90.3(1)	O(2)–V–N(1)	94.7(1)
O(3)–V–O(5)	88.7(1)	O(2)–V–N(2)	132.6(1)
O(3)–V–O(6)	162.5(1)	N(1)–V–N(2)	73.63(9)
O(4)–V–O(5)	160.8(1)	O(3)–V–O(1)	104.5(1)
O(5)–V–O(6)	89.7(1)	O(3)–V–N(2)	116.9(1)
O(4)–V–O(6)	85.6(1)	N(2)–V–O(1)	74.04(8)
O(1)–V–O(2)	175.2(1)		

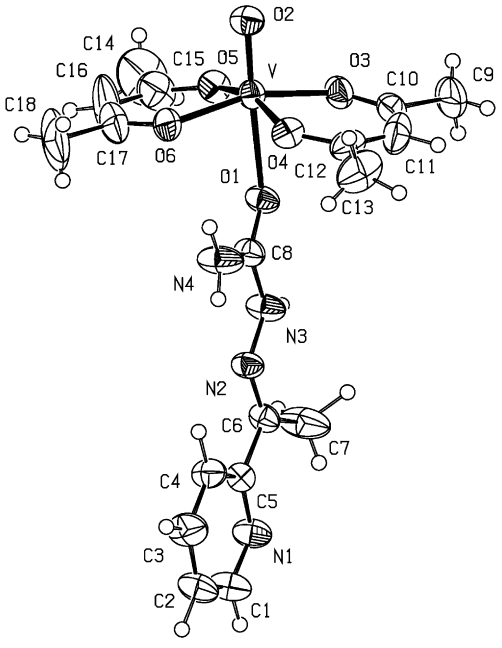


Fig. 2. Ellipsoid representation of the molecule of $[VO(H2APS)(acac)_2]$ (**1**) with the thermal ellipsoids representing 50% probability level.

oxygen from the semicarbazone in *trans* position to the oxo ligand.

The coordination sphere of the dioxocomplex **4** adopts a relatively distorted square pyramidal geometry, with the parameter $\tau = 0.23$ (for an ideal square pyramid $\tau = 0$ while for an ideal trigonal bipyramid $\tau = 1$) [19]. The oxo atom O(3) is considered to be in the apical position, with the basal positions being occupied by the remaining oxo atom O(2) and the N(1), N(2) and O(1) donor atoms from 2APS, which coordinates through the N–N–O-tridentate system. The vanadium centre is placed 54.1(1) pm above the basal atoms, which show a mean deviation from planarity of 19.58 pm.

The atoms of the semicarbazone remain almost planar in **1** and **4**, presenting mean deviations from planarity of 6.50 pm and 9.78 pm, respectively. The N(3)–C(8) bond distance is 1.8 pm shorter in **4** due to deprotonation at N(3) and formation of a predominantly double N–C bond. In addition, the C(8)–O(1) bond is 5.1 pm larger in **4** compared to **1** due to the formation of a predominantly single C–O bond upon deprotonation at N(3).

Supramolecular assemblies in the crystal structures of **1** and **4** are built up by diverse intermolecular hydrogen bonds, shown in Figs. 4 and 5, whose distances and angles are given in Table 3. In **1** the molecules of the complex are interconnected forming layers perpendicular to the [0 0 1] direction. In **4** the molecules linked in a zigzag outline form chains parallel to the [0 1 0] direction. In **4** N–H···N and N–H···O hydrogen bonds were observed. Besides these types of bonding, the structure of **1** also shows C–H···N, and C–H···O interactions (see Fig. 4).

*3.3. Insulin-mimic activity: effect of complexes **1–4** on glucose uptake and glycerol release from isolated adipocytes*

The insulin-mimetic activity was evaluated by means of *in vitro* measurements of the glucose transport in adipocytes incubated in the presence of insulin (50 ng/mL) as positive control, or in the presence of the vanadium complexes (10^{-3} M). As shown in Fig. 6, the presence of the complexes in the incubation medium stimulated glucose uptake, except for complex **4**, that did not have any influence on glucose transport. The results demonstrate that

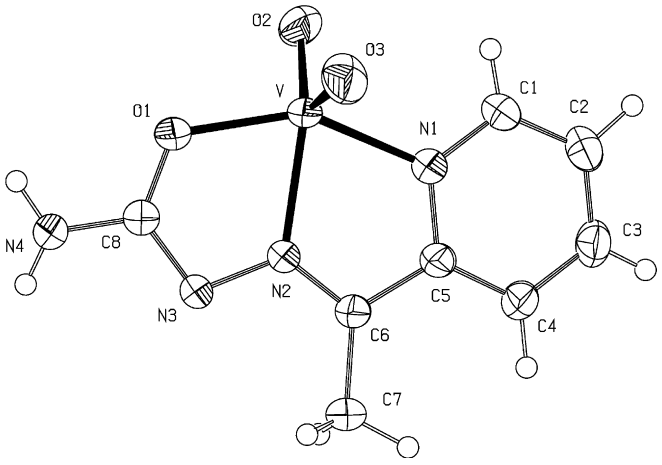


Fig. 3. Ellipsoid representation of the molecule of $[VO_2(2APS)]$ (**4**) with the thermal ellipsoids representing 50% probability level.

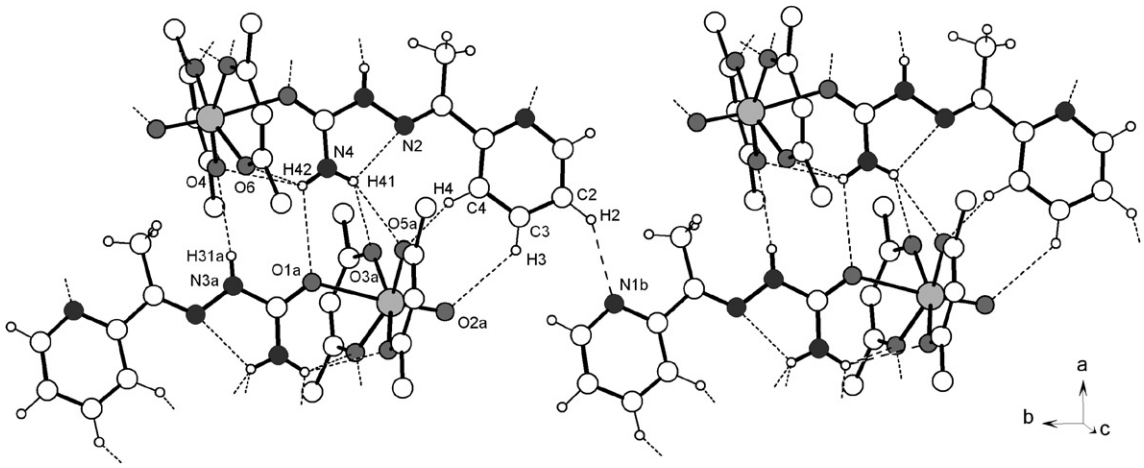


Fig. 4. View of the crystal structure of [VO(H2APS)(acac)$_2$] (**1**) showing the hydrogen bonds as dashed lines. The H-atoms of the acac ligands, which do not participate in H-bonds, were omitted for clarity.

Table 3
Selected hydrogen bonds distances (pm) and angles (°) observed in the crystal structures of [VO(H2APS)(acac)$_2$] (**1**) and [VO$_2$(2APS)] (**4**) (D = H-donor, A = H-acceptor)

D–H···A	*d*(H···A)	∠(D–H···A)	*d*(D···A)
Complex **1**			
N(4)–H(B)···N(2)	222	105.4	259.2(5)
N(4)–H(A)···O(4)	256	120.2	308.7(5)
N(4)–H(A)···O(6)	239	130.9	303.1(5)
C(4)–H(4)···N(2)	243	97.9	272.0(5)
C(4)–H(4)···O(5)[a]	254	149.0	338.5(5)
C(3)–H(3)···O(2)[a]	261	134.4	334.1(6)
C(2)–H(2)···N(1)[b]	258	141.2	336.5(6)
N(4)–H(B)···O(3)[a]	262	132.9	327.8(5)
N(4)–H(B)···O(5)[a]	246	136.2	314.7(4)
N(3)–H(A)···O(4)[c]	263	165.1	347.8(4)
Complex **4**			
N(4)–H(B)···N(3)[a]	219	160.7	301.3(3)
N(4)–H(A)···O(2)[b]	214	151.2	291.9(3)

Symmetry operators used for **1** [[a]$x-1/2, -y+1/2, z$; [b]$x-1/2, -y+3/2, z$, [c]$x+1/2, -y+1/2, z$] and **4** [[a]$-x+1, -y+1, -z$; [b]$-x+1, -y+2, -z$].

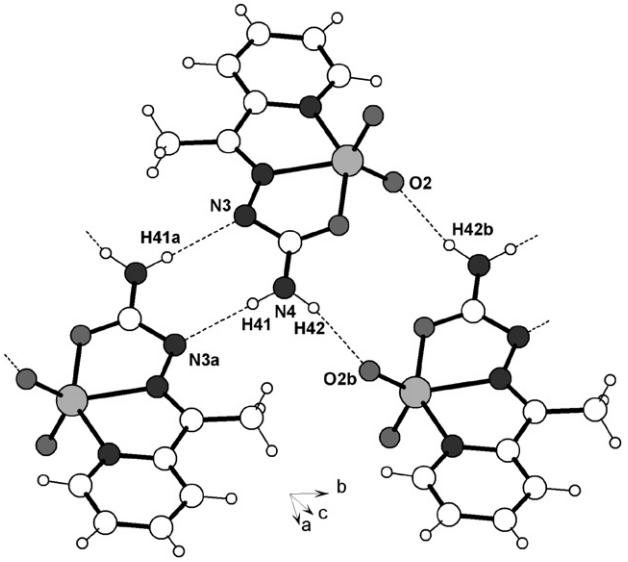


Fig. 5. View of the crystal structure of [VO$_2$(2APS)] (**4**) showing the hydrogen bonds as dashed lines.

[VO(acac)$_2$] is more effective than all its derivatives in enhancing glucose uptake by adipocytes (Fig. 6).

The effect of the vanadium complexes on lipolysis in adipocytes is illustrated in Fig. 7. As can be seen, all complexes inhibited glycerol release by adipocytes in a similar way to that observed with insulin.

Although several vanadium complexes have shown significant biological potential, new complexes are presently under investigation in an attempt to reduce the dose and increase safety and efficacy. Our experimental findings have shown that the studied vanadyl complexes alone enhance glucose uptake and inhibit glycerol release from adipocytes. The ability of these compounds to stimulate glucose uptake as well as to inhibit lipolysis in fat cells indicates potential mechanisms of their anti-diabetic insulin-like effects.

At the cellular level, it was demonstrated that vanadium activates several key elements of the insulin signal transduction pathway, such as the tyrosine phosphorylation of insulin receptor substrate 1, and extracellular signal-regulated kinase 1 and 2, phosphatidylinositol 3-kinase B activation [20]. These pathways are believed to mediate the metabolic actions of insulin, e.g. GLUT4 translocation [21], glucose uptake in muscle [12] and in adipocytes [22]. Because protein tyrosine phosphatases (PTPases) are considered to be negative regulators of the insulin-signaling pathway, it is suggested that the studied compounds could enhance insulin signaling and act by virtue of their capacity to inhibit protein tyrosine phosphatase activity and to increase phosphorylation of substrate proteins [23].

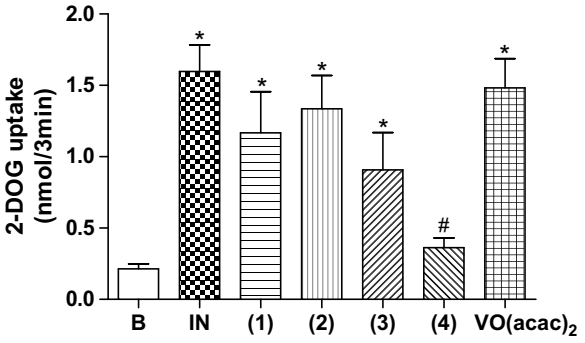


Fig. 6. Stimulation of glucose transport by the vanadium complexes in adipocytes. Freshly prepared rat adipocytes were preincubated with vanadyl complexes (10^{-3} M) or insulin (50 ng/mL) for 45 min. The cells were then supplemented with 2-deoxy-[^{3}H]glucose (0,2 μCi/tube) and after 3 min, deoxy-glucose uptake was evaluated. Cell associated radioactivity was determined by scintillation counting. Data are means ± SE. $^{*}P < 0.05$ vs Basal (B); $^{\#}P < 0.05$ vs insulin (In).

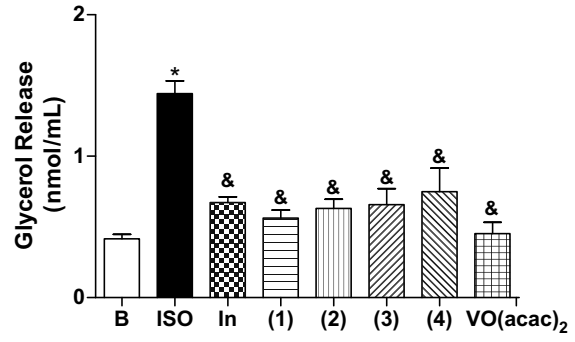


Fig. 7. Antilipolytic effects of the vanadium complexes (10^{-3} M) and insulin (50 ng/mL) on isoproterenol-stimulated lipolysis. Adipocytes were incubated for 30 min with the complexes, then 0,1 μM isoproterenol was added to incubation medium and lipolysis was measured by following the rate of glycerol release. Data are means ± SE. $^{*}P < 0.05$ vs Basal (B); $^{\&}P < 0.05$ vs isoproterenol (ISO).

For vanadyl complexes it has been suggested that *in situ* formation of peroxovanadates leads to inhibition of PTPases, as shown in the case of vanadium(IV) oxo bis(maltolato) (BMOV) [24]. Complexes **1**–**3** exhibited insulin mimic effect by enhancing glucose uptake, while complex **4** did not show such behavior. In the cases of complexes **1** and **2** the APS ligands coordinate as monodentate species, being probably easily released from the metal centre in biological media, with formation of [VO(acac)$_2$]. In the case of **3** the semicarbazone acts as a bidentate ligand, probably being equally well removed from the metal coordination sphere. Therefore in the cases of **1**–**3** uncomplexed vanadium is probably the species which undergoes oxidation after the release of all ligands. By contrast in **4**, the APS ligand is attached to the metal as a tridentate species, which possibly makes the metal centre less available for interaction in biological media.

In addition to their action on glucose metabolism, vanadium compounds can modulate lipolytic rates in adipose tissue, as shown in the present paper. An alternative hypothesis to account for the insulin-like actions of vanadium involves attenuation of signaling by 3′,5′-cyclic adenosine monophosphate (cAMP) through activation of cyclic nucleotide phosphodiesterase isoforms [25]. In other studies, however, the antilipolytic effects of vanadium were shown to be independent of phosphatidylinositol 3-kinase B and phosphodiesterase [26], or involve inhibition cAMP-dependent protein kinase [25]. Therefore, although insulin itself does enhance cAMP degradation, it is not clear if the antilipolytic effect of the vanadium complexes depends entirely on this mechanism.

4. Conclusions

The oxovanadium(IV) complexes with 2-, 3- and 4-acetylpyridine semicarbazones were able to enhance glucose uptake and inhibit glycerol release from adipocytes. In complex **4** the ability to promote glucose uptake was lost. Although the vanadyl complexes showed insulin-mimic properties, this effect is not better than that of the starting salt. Further investigation is underway with vanadium complexes of a variety of semicarbazones.

Acknowledgements

This work was supported by Capes, CNPq, Instituto do Milênio – Inovação e Desenvolvimento de Novos Fármacos e Medicamentos (IM-INOFAR) (Proc. CNPq 420015/05-1), and FAPESP of Brazil.

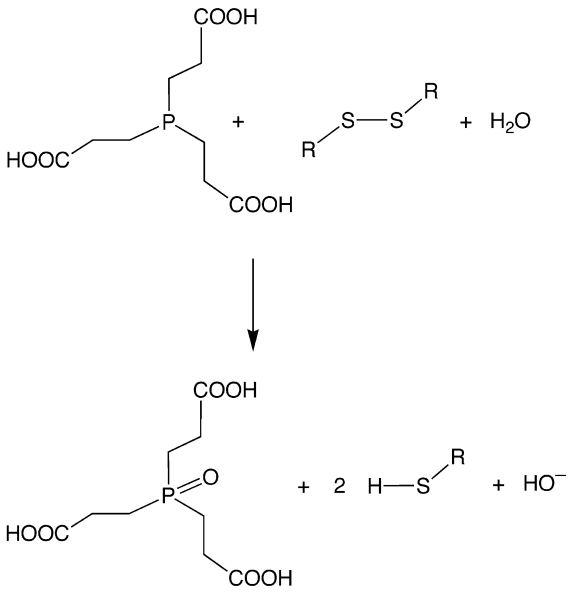
Appendix A. Supplementary data

CCDC 65936 and 65937 contain the supplementary crystallographic data for [VO(H2APS)(acac)$_2$] (**1**) and [VO$_2$(2APS)] (**4**). These data can be obtained free of charge via http://www.ccdc.cam.ac.uk/conts/retrieving.html, or from the Cambridge Crystallographic Data Centre, 12 Union Road, Cambridge CB2 1EZ, UK; fax: (+44) 1223-336-033, or e-mail: deposit@ccdc.cam.ac.uk. Supplementary data associated with this article can be found, in the online version, at doi:10.1016/j.poly.2008.02.014.

References

[1] P. Noblía, M. Vieites, B.S. Parajón-Costa, E.J. Baran, H. Cerecetto, P. Draper, M. González, O.E. Piro, E.E. Castellano, A. Azqueta, A.L. Ceráin, A. Monge-Vega, D. Gambino, J. Inorg. Biochem. 99 (2005) 443.
[2] K.H. Thompson, C. Orvig, J. Inorg. Biochem. 100 (2006) 1925.
[3] P. Noblía, E.J. Baran, L. Otero, P. Draper, H. Cerecetto, M. González, O.E. Piro, E.E. Castellano, T. Inohara, Y. Adachi, H. Sakurai, D. Gambino, Eur. J. Inorg. Chem. 2 (2004) 322.
[4] H. Beraldo, D. Gambino, Mini Rev. Med. Chem. 4 (2004) 159.
[5] K.H. Thompson, J.H. McNeill, C. Orvig, Chem. Rev. 99 (1999) 2561.
[6] H. Beraldo, W.F. Nacif, D.X. West, Spectrochim. Acta 57 (2001) 1847.

[7] A. Altomare, G. Cascarano, C. Giacovazzo, A. Gualardi, J. Appl. Crystallogr. 26 (1993) 343.
[8] G.M. Sheldrick, SHELXL-97, Program for Refinement of Crystal Structures, University of Göttingen, Germany, 1997.
[9] M. Rodbell, J. Biol. Chem. 239 (1964) 375.
[10] L.M. Botion, A. Green, Diabetes 48 (1999) 1691.
[11] S. Gasic, A. Green, Biochem. Pharm. 49 (1995) 785.
[12] H. Sakurai, H. Watanabe, H. Tamura, H. Yasui, R. Matsushita, J. Takada, Inorg. Chim. Acta 283 (1998) 175.
[13] K. Nakamoto, in: Infrared and Raman Spectra of Inorganic and Coordination Compounds, 4th ed., John Wiley and Sons, New York, 1986.
[14] A. Perez-Rebolledo, O.E. Piro, E.E. Castellano, L.R. Teixeira, A.A. Batista, H. Beraldo, J. Mol. Struct. 794 (2006) 18.
[15] M.R. Maurya, Coord. Chem. Rev. 237 (2003) 163.
[16] M.R. Maurya, A. Kumar, M. Abid, A. Azam, Inorg. Chim. Acta 359 (2006) 2439.
[17] A.L. Spek, PLATON – A Multipurpose Crystallographic Tool, University of Utrecht, The Netherlands, 2004.
[18] R.P. Dodge, D.H. Templeton, A. Zelkin, J. Chem. Phys. 35 (1961) 55.
[19] M.R. Maurya, A. Kumar, M. Ebel, D. Rehder, Inorg. Chem. 45 (2006) 5924.
[20] M.Z. Mehdi, A.K. Srivastava, Arch. Biochem. Biophys. 440 (2005) 158.
[21] W. Basuki, M. Hiromura, Y. Adachi, K. Tayama, M. Hattori, H. Sakurai, Biochem. Biophys. Res. Commun. 349 (2006) 1163.
[22] B. Lu, D. Ennis, R. Lai, E. Bogdanovic, R. Nikolov, L. Salamon, C. Fantus, H. Le-Tien, I.G. Fantus, J. Biol. Chem. 276 (2001) 35589.
[23] G. Swarup, S. Cohen, D.L. Garbers, Biochem. Biophys. Res. Commun. 107 (1982) 1104.
[24] K.G. Peters, M.G. Davis, B.W. Howard, M. Pokross, V. Rastogi, C. Diven, K.D. Greis, E. Eby-Wilkens, M. Maier, A. Evdokimov, S. Soper, F. Genbauffe, J. Inorg. Biochem. 96 (2003) 321.
[25] K.A. Jelveh, R. Zhande, R.W. Brownsey, J. Biol. Inorg. Chem. 11 (2006) 379.
[26] I. Castan, J. Wijkander, V. Manganiello, E. Degerman, J. Biochem. 339 (1999) 281.



Scheme 1. TCEP mediated reduction of disulfide to thiol.

reported [8] and all crystal structures published to date describe only a metal–metal bridging mode for the TCEP ligand. Surprisingly, no reports of TCEP binding in a chelating, non-metal–metal bridging mode to a single ion have been described. An additional interest in hard–soft donor ligands such as TCEP is their ability to stabilize both high and low oxidation states in mixed-valence metal coordination complexes. One of us has recently described the synthesis and catalytic properties of a mixed-valence Co(I)(II) complex stabilized with the phosphine–phosphonic acid, triphenylphosphine triphosphonic acid (TPPTP) [9]. Finally, polydentate ligands are of interest as potential sequestering agents for radioactive heavy metals. Herein, we describe the reaction of TCEP with cobalt(II) chloride in aqueous solution to give a trimetallic mixed-valence Co(II)/Co(III) complex in which the ligand displays a previously unseen coordination mode involving non-metal–metal bonding of the TCEP ligand in a tridentate chelating fashion to Co(III). The spectral properties of this new complex are also described.

2. Experimental

2.1. General data

All reactions and manipulations were conducted in air. IR spectra were recorded on a Bruker Tensor 27 FT-IR spectrometer in the range of 4000–400 cm^{-1}. UV–Vis absorption spectra in aqueous solutions were recorded on a Hewlett–Packard 8453 diode array spectrometer at 23 °C over the spectral range 200–800 nm, in 1 cm quartz cuvettes. Measurements were made using the concentration range 6.470×10^{-5}–8.360×10^{-5} mol dm^{-3}. ESI-MS were recorded in methanol on an MDS Sciex API QStar Pulsar Quadrupole-TOF hybrid. Microanalyses were performed by Atlantic Microlab. Reagents and solvents were obtained as follows: cobalt chloride hexahydrate, sodium hydroxide, 95% ethanol (Sigma–Aldrich), and tris(2-carboxyethyl)phosphine hydrochloride (Pierce) used as received.

2.2. Synthesis of $[Co\{P(CH_2CH_2COO)_2(CH_2CH_2COOH)\}_2]_2[Co(H_2O)_4][Na_2(H_2O)_4]Cl_2 \cdot 6H_2O$ (1)

A round-bottomed flask was charged with $CoCl_2 \cdot 6H_2O$ (1.26 g, 5.30 mmol), tris(2-carboxyethyl)phosphine hydrochloride (1.72 g, 6.00 mmol), DI water (5 mL), and a stir bar. Then, 2 mL of 4 M NaOH was added drop-wise to the flask with stirring. The resulting deep-red solution was heated at 50 °C for 12 h. The solution was allowed to cool to room temperature, ethanol was added and the resulting solution cooled to 4 °C. After 4 days, the resulting purple crystals were collected by filtration and dried in air to give **1** (0.506 g, 22%). *Anal.* Calc. for $C_{36}H_{80}Cl_2Co_3Na_2O_{38}P_4$: C, 28.10; H, 5.24. Found: C, 28.18; H, 5.23%. IR (KBr pellet, cm^{-1}): ν(OH) 3383 (s, br), ν(C=O) 1721 (s), ν(C–O) 1602 (s, sh) 1564 (s). Electronic absorption spectra, λ_{max}, nm (ε, $dm^3\ mol^{-1}\ cm^{-1}$): H_2O, 208 (5.128×10^4), 276 (4.215×10^4), 446 (938), 578 (1022).

2.3. X-ray analysis

Single-crystal X-ray diffraction data on compound **1** were collected at 103 K using Mo Kα radiation and a Bruker APEX 2 CCD area detector. A $0.46 \times 0.16 \times 0.02$ mm^3 purple blade was prepared for data collection coating with high viscosity microscope oil (Paratone-N, Hampton Research). The oil-coated crystal was mounted on a glass rod and transferred immediately to the cold stream (−170 °C) on the diffractometer. The crystal was triclinic in space group $P\bar{1}$ with unit cell dimensions $a = 8.1927(12)$ Å, $b = 10.4031(15)$ Å, $c = 18.875(3)$ Å, $\alpha = 104.418(2)°$, $\beta = 93.904(2)°$, and $\gamma = 97.089(2)°$. Corrections were applied for Lorentz, polarization, and absorption effects. Data were 96.5% complete to 25.00° θ (approximately 0.72 Å) with an average redundancy of 1.9. The structure was solved by direct methods and refined by full-matrix least squares on F^2 values using the programs found in the SHELXTL suite [10]. Parameters refined included atomic coordinates and anisotropic thermal parameters for all non-hydrogen atoms. Hydrogen atoms on carbons were included using a riding model (coordinate shifts of C applied to H atoms) with C–H distance set at 0.96 Å.

3. Results and discussion

3.1. Synthesis

The synthesis of complex **1** was carried out by reaction of a slight molar excess of tris(2-carboxyethyl)phosphine hydrochloride (TCEP) with aqueous cobalt chloride in air as shown in Scheme 2.

The pH of the resulting solution was slowly adjusted to 4.0 using 4 M sodium hydroxide solution and a deep-red

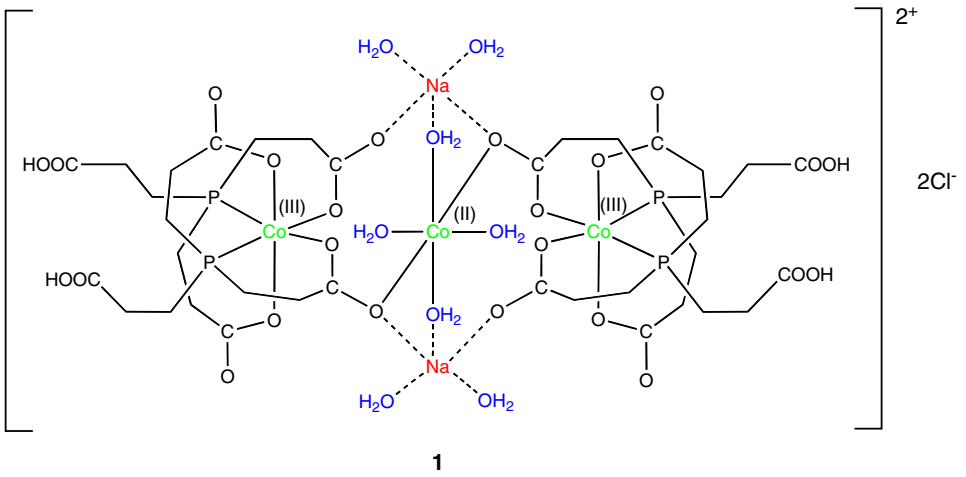
$$CoCl_2{\cdot}6H_2O + P(CH_2CH_2CH_2COOH)_3 \xrightarrow[H_2O,\ 50\ ^\circ]{NaOH,\ pH\ 4.0} \mathbf{1}$$

Scheme 2. Synthesis of TCEP cobalt complex **1**.

solution resulted from which **1** was isolated as purple crystals after cooling the reaction mixture to 4 °C for 4 days. The molecular structure of **1** is shown in Fig. 1. No other discreet cobalt containing complexes could be isolated from the filtrate. Compound **1** is air stable as a solid for at least 6 months and is stable and very soluble in water giving dark green solutions. It is insoluble in most common organic solvents such as ether, acetone and dichloromethane.

3.2. Structure

Crystals of **1** obtained directly from the reaction described above were of sufficient quality to be used directly for X-ray crystal structure analysis. The ORTEP representation of **1** is shown in Fig. 2 and crystal structure data and refinement details are given in Table 1. Compound **1** crystallized in the space group $P\bar{1}$ with the unit cell containing one molecule. The unit cell contains three cobalt ions, one unique Co(II) ion and two identical Co(III) ions each with a distorted octahedral geometry. Presumably, partial oxidation of the aqua Co(II) ion takes place in the presence of air [11] and interestingly the phosphine does not reduce Co(III) to Co(II) in spite of being an excellent reducing agent. A symmetry plane passes through the central Co(II) ion and one sodium ion and two-coordinated TCEP ligands lie on each side of the symmetry plane. Co1 lies in a general position and Co2 lies on a crystallographic symmetric center. The complex is trinuclear with repeating units lying along the *c* axis. Six non-coordinated water molecules are also present along with two chloride anions which are located between the carboxy groups, again one on either side of the symmetry plane. The Co(III) ions are each coordinated to



1

Fig. 1. Structure of **1** (solvate water molecules omitted for clarity).

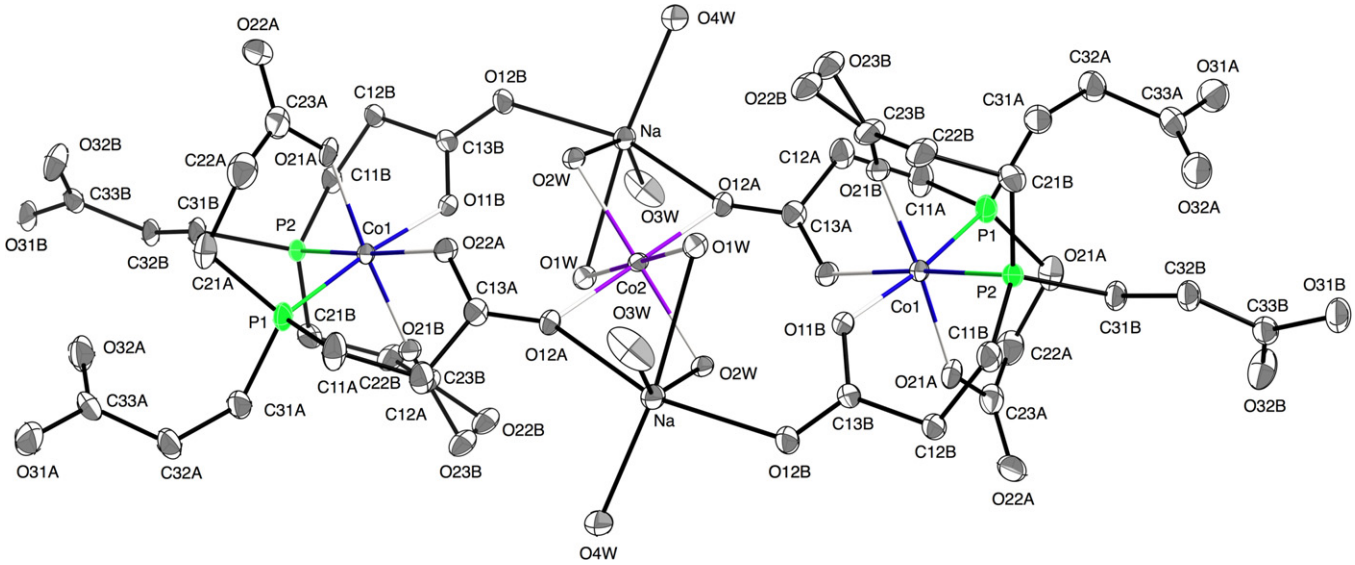


Fig. 2. ORTEP representation of **1** with ellipsoids at 50% probability. Solvate water molecules, hydrogen atoms, and chloride anions omitted for clarity.

Table 1
Crystal data and structure refinement details for **1**

Empirical formula	$C_{36}H_{80}Cl_2Co_3Na_2O_{38}P_4$
Formula weight	1538.55
Temperature (K)	103(2)
Wavelength (Å)	0.71073
Crystal system	triclinic
Space group	$P\bar{1}$
Unit cell parameters	
a (Å)	8.1927(12)
b (Å)	10.4031(15)
c (Å)	18.875(3)
α (°)	104.418(2)
β (°)	93.904(2)
γ (°)	97.089(2)
Volume (Å^3)	1537.9(4)
Z	1
D_{calc} (Mg/m^{-3})	1.661
Absorption coefficient (mm^{-1})	1.103
$F(000)$	797.0
Crystal size (mm)	0.46 × 0.16 × 0.02
θ Range for data collection (°)	2.52–28.85
Reflections collected	17011
Independent reflections	8378
Absorption correction	multi-scan
Maximum and minimum transmission	1.000 and 0.732
Refinement method	full-matrix least-squares on F^2
Data/restraints/parameters	8378/12/473
Goodness-of-fit on F^2	1.030
$R[F^2 > 2\sigma(F^2)]$	0.047
$wR(F^2)$[a]	0.125
Largest difference peak and hole (e Å^{-3})	0.946 and −0.937

[a] $w = 1/[\sigma^2(F_o^2) + (0.0601P)2 + 0.508P]$ where $P = (F_o^2 + 2F_c^2)/3$.

two TCEP ligands in a tridentate chelating mode with two arms of the ligands binding through deprotonated carboxy groups, with the third arm containing an uncoordinated carboxylic acid moiety. All previous metal complexes of TCEP contain the ligand in the trianionic form, however the dianionic form is found in complex **1**. The Co(II) ion Co2 is coordinated by the carboxylate group from two different TCEP ligands. The carboxylate oxygen atoms are *trans* to each other around Co2 and the remaining axial and equatorial sites are occupied by coordinated water molecules. The phosphorus donor atoms have the *cis*-orientation and the P–Co–O bite angles for TCEP to Co1 fall in the range 87.22(6)–94.99(7)°, similar to those found in other cobalt(III) complexes containing P–O chelates [12]. The P–Co bond lengths 2.1735(8) and 2.1803(9) are shorter than those found in the complexes *cis*-$[Co(acac)_2(PMe_3)_2]PF_6$ and $[Co(acac)_2(dmpf)]B(C_6H_5)_4$ (bmpf = 1,1′bis(dimethylphosphino)ferrocene), Co–P = 2.226(2)–2.257(2) [13] but are similar to that found in the chelating ligand complex $[Co(acac)_2(edmp)]ClO_4$ (edmp = (2-aminoethyl)(dimethylphosphine)), Co–P = 2.192(2) [14,15]. Both TCEP and edmp are both less sterically demanding than either PMe_3 or bmpf resulting in shorter Co–P bond lengths than complexes with bulkier ligands.

A comparison of the Co–O(carboxylate) bond lengths of **1** with other cobalt(II) and cobalt(III) carboxylate complexes indicates that all Co–O bonds are within the normal range for this type of coordination [8,16–18]. The geometry

Table 2
Bond lengths (Å) and angles (°) for **1**

Co(1)–O(11A)	2.013(2)	P(1)–C(21A)	1.813(3)
Co(1)–O(11B)	2.003(2)	P(1)–C(31A)	1.822(3)
Co(1)–O(21A)	1.916(2)	P(2)–C(11B)	1.822(3)
Co(1)–O(21B)	1.891(2)	P(2)–C(21B)	1.816(3)
Co(1)–P(1)	2.1803(9)	P(2)–C(31B)	1.809(3)
Co(1)–P(2)	2.1735(8)	Na–O(1W)	2.600(3)
Co(2)–O(12A)	2.081(2)	Na–O(2W)	2.420(3)
Co(2)–O(1W)	2.097(2)	Na–O(3W)	2.316(3)
Co(2)–O(2W)	2.083(2)	Na–O(4W)	2.337(3)
O(11A)–C(13A)	1.280(3)	Na–O(12A)	2.413(2)
O(11B)–C(13B)	1.289(3)	Na–O(12B)	2.331(2)
O(12A)–C(13A)	1.250(4)	C(11A)–C(12A)	1.515(5)
O(12B)–C(13B)	1.239(4)	C(11B)–C(12B)	1.522(4)
O(21A)–C(23A)	1.277(4)	C(12A)–C(13A)	1.508(4)
O(21B)–C(23B)	1.276(4)	C(12B)–C(13B)	1.510(4)
O(22A)–C(23A)	1.237(4)	C(21A)–C(22A)	1.534(5)
O(22B)–C(23B)	1.291(6)	C(21B)–C(22B)	1.526(5)
O(23B)–C(23B)	1.287(7)	C(22A)–C(23A)	1.519(5)
O(31A)–C(33A)	1.318(4)	C(22B)–C(23B)	1.498(5)
O(31B)–C(33B)	1.326(4)	C(31A)–C(32A)	1.536(5)
O(32A)–C(33A)	1.208(4)	C(31B)–C(32B)	1.526(4)
O(32B)–C(33B)	1.212(4)	C(32A)–C(33A)	1.511(5)
O(12A)–Na	2.413(2)	C(32B)–C(33B)	1.496(4)
P(1)–C(11A)	1.818(3)		
O(11A)–Co(1)–P(1)	90.02(7)	O(12A)–Co(2)–O(2W)	92.93(9)
O(11B)–Co(1)–P(1)	173.28(6)	O(12A)–Co(2)–O(2W)	92.93(9)
O(11A)–Co(1)–P(2)	171.58(7)	O(12A)–Co(2)–O(2W)	87.07(9)
O(11B)–Co(1)–P(2)	87.22(6)	O(2W)–Co(2)–O(2W)	180.0(11)

Table 2 (*continued*)

O(11B)–Co(1)–O(11A)	84.36(8)	O(12A)–Co(2)–O(1W)	85.76(9)
O(21A)–Co(1)–O(11A)	90.96(8)	O(12A)–Co(2)–O(1W)	94.24(9)
O(21A)–Co(1)–O(11B)	88.79(8)	O(2W)–Co(2)–O(1W)	81.43(9)
O(21A)–Co(1)–P(1)	94.99(7)	O(2W)–Co(2)–O(1W)	98.57(9)
O(21A)–Co(1)–P(2)	89.07(7)	O(12A)–Co(2)–O(1W)	94.24(9)
O(21B)–Co(1)–O(11A)	85.28(9)	O(12A)–Co(2)–O(1W)	85.76(9)
O(21B)–Co(1)–O(11B)	88.40(9)	O(2W)–Co(2)–O(1W)	98.57(9)
O(21B)–Co(1)–O(21A)	175.51(9)	O(2W)–Co(2)–O(1W)	81.43(9)
O(21B)–Co(1)–P(1)	87.46(7)	O(1W)–Co(2)–O(1W)	180.00(13)
O(21B)–Co(1)–P(2)	94.29(7)	O(12A)–Co(2)–Na	49.50(6)
P(2)–Co(1)–P(1)	98.37(3)	O(12A)–Co(2)–Na	130.50(6)
O(12A)–Co(2)–O(12A)	180.00(11)	O(2W)–Co(2)–Na	49.68(7)
O(12A)–Co(2)–O(2W)	87.07(9)	O(2W)–Co(2)–Na	130.32(7)
O(1W)–Co(2)–Na	54.62(7)	C(13B)–O(12B)–Na	124.36(19)
O(1W)–Co(2)–Na	125.38(7)	C(23B)–O(21B)–Co(1)	133.8(2)
O(12A)–Co(2)–Na	130.50(6)	Co(2)–O(1W)–Na	84.28(8)
O(12A)–Co(2)–Na	49.50(6)	Co(2)–O(2W)–Na	89.30(9)
O(2W)–Co(2)–Na	130.32(7)	C(12A)–C(11A)–P(1)	115.9(2)
O(2W)–Co(2)–Na	49.68(7)	C(13A)–C(12A)–C(11A)	114.5(3)
O(1W)–Co(2)–Na	125.38(7)	O(12A)–C(13A)–O(11A)	123.0(3)
O(1W)–Co(2)–Na	54.62(7)	O(12A)–C(13A)–C(12A)	117.1(3)
C(21A)–P(1)–C(11A)	102.87(16)	O(11A)–C(13A)–C(12A)	119.9(3)
C(21A)–P(1)–C(31A)	110.62(16)	C(22A)–C(21A)–P(1)	110.3(2)
C(11A)–P(1)–C(31A)	104.85(16)	C(23A)–C(22A)–C(21A)	113.4(3)
C(21A)–P(1)–Co(1)	111.59(12)	O(22A)–C(23A)–O(21A)	119.1(3)
C(11A)–P(1)–Co(1)	109.05(11)	O(22A)–C(23A)–C(22A)	119.3(3)
C(31A)–P(1)–Co(1)	116.70(12)	O(21A)–C(23A)–C(22A)	121.6(3)
C(31B)–P(2)–C(21B)	109.86(15)	C(32A)–C(31A)–P(1)	115.8(3)
C(31B)–P(2)–C(11B)	106.05(14)	C(33A)–C(32A)–C(31A)	113.4(3)
C(21B)–P(2)–C(11B)	104.21(15)	O(32A)–C(33A)–O(31A)	124.7(3)
C(31B)–P(2)–Co(1)	116.28(10)	O(32A)–C(33A)–C(32A)	124.3(3)
C(21B)–P(2)–Co(1)	109.37(10)	O(31A)–C(33A)–C(32A)	111.1(3)
C(11B)–P(2)–Co(1)	110.37(10)	C(12B)–C(11B)–P(2)	115.8(2)
O(3W)–Na–(O12B)	92.89(12)	C(13B)–C(12B)–C(11B)	112.2(2)
O(3W)–Na–O(4W)	117.60(11)	O(12B)–C(13B)–O(11B)	121.8(3)
O(12B)–Na–O(4W)	98.08(10)	O(12B)–C(13B)–C(12B)	119.8(3)
O(3W)–Na–(O12A)	99.74(11)	O(11B)–C(13B)–C(12B)	118.4(3)
O(12B)–Na–(O12A)	156.26(9)	C(22B)–C(21B)–P(2)	111.2(2)
O(4W)–Na–O(12A)	93.78(9)	C(23B)–C(22B)–C(21B)	115.0(3)
O(3W)–Na–O(2W)	146.68(11)	O(21B)–C(23B)–O(23B)	110.2(4)
O(12B)–Na–O(2W)	85.59(9)	O(21B)–C(23B)–O(22B)	125.0(4)
O(4W)–Na–O(2W)	95.51(9)	O(23B)–C(23B)–O(22B)	31.6(3)
O(12A)–Na–O(2W)	72.81(8)	O(21B)–C(23B)–C(22B)	121.6(3)
O(3W)–Na–O(1W)	81.24(10)	O(23B)–C(23B)–C(22B)	126.1(4)
O(12B)–Na–O(1W)	93.48(9)	O(22B)–C(23B)–C(22B)	111.6(4)
O(4W)–Na–O(1W)	157.12(10)	C(32B)–C(31B)–P(2)	117.2(2)
O(12A)–Na–O(1W)	68.97(8)	C(33B)–C(32B)–C(31B)	110.3(2)
O(2W)–Na–O(1W)	65.68(8)	O(32B)–C(33B)–O(31B)	123.2(3)
O(3W)–Na–Co(2)	113.35(9)	O(32B)–C(33B)–C(32B)	123.7(3)
O(12B)–Na–Co(2)	115.39(7)	O(31B)–C(33B)–C(32B)	113.1(3)
O(4W)–Na–Co(2)	116.09(8)		
O(12A)–Na–Co(2)	40.97(5)		
O(2W)–Na–Co(2)	41.02(5)		
O(1W)–Na–Co(2)	41.10(5)		
C(13A)–O(11A)–Co(1)	124.21(19)		
C(13A)–O(12A)–Co(2)	127.74(19)		
C(13A)–O(12A)–Na	142.55(19)		
Co(2)–O(12A)–Na	89.53(8)		
C(23A)–O(21A)–Co(1)	135.3(2)		
C(13B)–O(11B)–Co(1)	128.16(19)		

of the six-coordinate Na ion in **1** is distorted octahedral with coordination by four water oxygen and two carboxylate oxygen atoms. A list of bond lengths and angles for **1** is given in Table 2.

3.3. Spectroscopy

The UV–Vis spectrum of **1** recorded in H_2O at neutral pH contains two high energy bands at 208 nm ($5.128 \times$

10^4 dm^3 mol^{-1} cm^{-1}) and 276 nm (4.215×10^4 dm^3 mol^{-1} cm^{-1}). These absorptions can be assigned to charge transfer bands of bound TCEP and are consistent with those reported for other metal complexes in which the ligand is present in the deprotonated form [10]. Two lower intensity visible absorptions at 446 and 578 nm have been assigned to $^1A_{1g} \rightarrow {}^1T_{1g}$ and $^1A_{1g} \rightarrow {}^1T_{2g}$ transitions for a diamagnetic ground state Co^{3+} ion [11] although a weak absorption at 578 nm could correspond to a transition for octahedral Co^{2+} ion [19]. The UV–Vis spectrum of **1** is shown in Fig. 3. Precipitation of metal hydroxide precluded the spectrophotometric analysis of **1** at higher pH values.

The FT-IR spectrum of **1** recorded as a KBr disc, shows the presence of both free COOH and bound carboxylate functionalities. An intense broad absorption at 3383 cm^{-1} is typical of a carboxylic acid–OH stretching frequency and/or the presence of cobalt bound water and waters of crystallization. No –OH absorptions were seen at lower wave-numbers which would be attributed to strongly hydrogen bonded O–H groups. The intense carbonyl C=O stretching frequency of the free COOH is located at 1721 cm^{-1} and the asymmetric stretching vibrations of coordinated COO^- appear at 1602 and 1554 cm^{-1}.

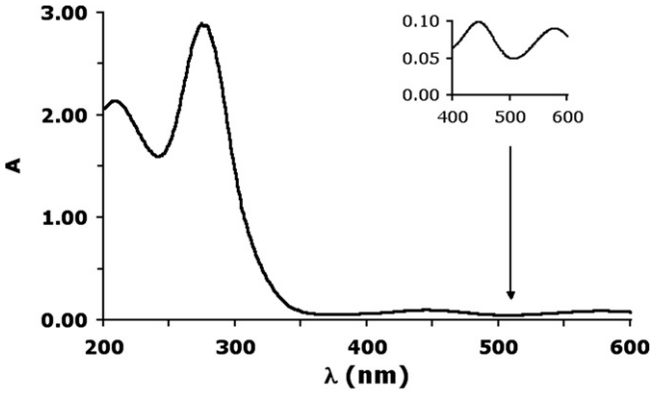


Fig. 3. UV–Vis spectrum of **1**.

3.4. Electrospray mass spectrometry

The ESI-MS spectrum of **1** was recorded in positive ion mode in methanol and shows a dominant doubly charged ion (100%) at 614 a.m.u. and has been tentatively assigned to species **2** in which the trimetalllic cobalt core found in **1** remains intact and two Na^+ ions and five water molecules have been lost giving rise to a seven-coordinate Co^{2+} ion (Fig. 4) [20]. A smaller doubly charged ion peak (20%) at 607 a.m.u. has been assigned to structure **3** (formed via loss of two Na^+ ions and six water molecules). Singly charged ions at 646 (15%) and 601 (23%) a.m.u. presumably arise from dissociation of the trimetallic cobalt core (see Supplementary Material).

4. Conclusions

The water-soluble phosphine ligand TCEP reacted with Co(II) in aqueous solution to give an unusual trimetallic mixed-valence Co(III)/Co(II)/Co(III) complex [21]. Single-crystal X-ray analysis reveals that the ligand is bound in a tridentate mode to Co(III) and additionally bridges a Co(II) and Na ion. Compound **1** represents the first mixed-valence complex of the ligand TCEP.

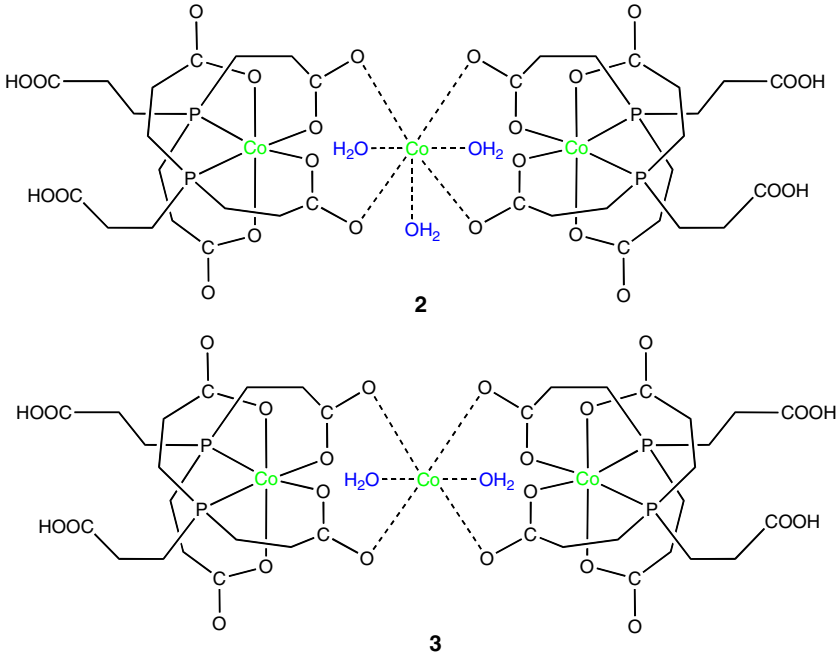


Fig. 4. Trimetallic species identified in ESI-MS analysis of **1**.

Acknowledgements

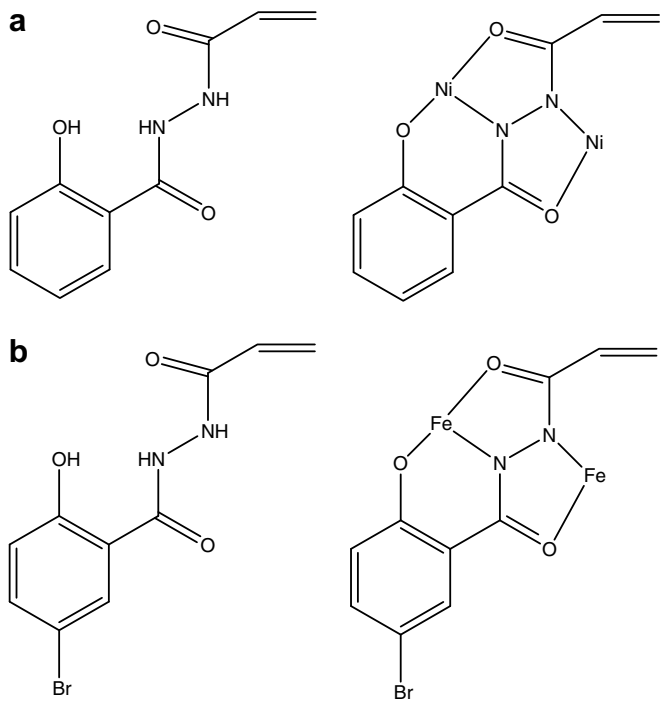
This work was supported by the Defense Threat Reduction Agency Grant No. 4.10004.05.NRL.B to ELC. D.A.K. was supported in part by the Summer Research Faculty at NRL Program. The Naval Research Laboratory and Office of Naval Research are acknowledged for support of the crystallographic studies.

Appendix A. Supplementary data

CCDC 657979 contains the supplementary crystallographic data for **1**. These data can be obtained free of charge via http://www.ccdc.cam.ac.uk/conts/retrieving.html, or from the Cambridge Crystallographic Data Centre, 12 Union Road, Cambridge CB2 1EZ, UK; fax: (+44) 1223-336-033, or e-mail: deposit@ccdc.cam.ac.uk. Supplementary data associated with this article can be found, in the online version, at doi:10.1016/j.poly.2008.02.013.

References

[1] (a) See for example J.P. Tam, Y.A. Lu, C.F. Liu, J. Shao, Proc. Natl. Acad. Sci. USA 92 (1995) 12485;
(b) P. Blauenstein, J.T. Locker, K. Seybold, H. Koprivova, G.A. Janoki, H.R. Macke, P. Hasler, A. Ammann, I. Novakhofer, A. Smith, P.A. Schubiger, Eur. J. Nucl. Med. 22 (1995) 690;
(c) J.J. Gorman, B.L. Ferguson, T.B. Ngyuyen, Rapid Commun. Mass Spectrom. 10 (1996) 529;
(d) T. Kirsch, M. Boehm, O. Schuckert, A.U. Metzger, D. Willbold, R.W. Frank, P. Rosch, Protein Express. Purif. 8 (1996) 75;
(e) J. Wu, J.T. Watson, Protein Sci. 6 (1997) 391;
(f) C.L. Bernard, J.C. Hirsch, R. Khazipov, Y. Ben Ari, H. Gozlan, Exp. Brain Res. 113 (1997) 343;
(g) K. Huh, R.J. Wenthold, J. Biol. Chem. 274 (1999) 151;
(h) Y. Oda, T. Nagasu, B.T. Chait, Nature Biotechnol. 19 (2001) 379.
[2] (a) G.M. Schratt, F. Tuebing, E.A. Nigh, C.G. Kane, M.E. Sabatini, M. Kiebler, M.E. Greenberg, Nature 439 (2006) 283;
(b) C.B. Swearingen, D.P. Wernette, D.M. Cropek, Y. Liu, J.V. Sweedler, P.W. Bohn, Anal. Chem. 77 (2005) 442;
(c) C. Yoshina-Ishii, S.G. Boxer, J. Am. Chem. Soc. 125 (2003) 3696.
[3] F. Ferreira, F. Morvan, Nucleos. Nucleot. Nucl. Acid 24 (2005) 1009.
[4] (a) G. Aldrian-Herrada, A. Rabie, R. Wintersteiger, J. Brugidou, J. Peptide Sci. 4 (1998) 266;
(b) F.J. Dieguez-Acuna, J.S. Woods, Toxicol. In Vitro 14 (2000) 7.
[5] J.B. Delehanty, T.C. Stuart, D.A. Knight, E.R. Goldman, E.L. Chang, RNA 11 (2005) 831.
[6] A. Krezel, R. Latajka, G.D. Bujacz, W. Bal, Inorg. Chem. 42 (2003) 1994.
[7] J. Podlahova, B. Kratochvil, J. Podlaha, J. Hasek, J. Chem. Soc., Dalton Trans. (1985) 2393.
[8] J. Podlaha, J. Podlahova, P. Stepnicka, M. Rieder, Polyhedron 13 (1994) 2847.
[9] T.L. Schull, L. Henley, J.R. Deschamps, R.J. Butcher, D.P. Maher, C.A. Klug, K. Swider-Lyons, W.J. Dressick, B. Bujoli, A.E. Greenwood, L.K. Byington Congiardo, D.A. Knight, Organometallics 26 (2007) 2272.
[10] Bruker, SHELXTL v6.14, Bruker AXS Inc., Madison, WI, 2000.
[11] F.A. Cotton, G. Wilkinson, C.A. Murillo, M. Bochmann, Advanced Inorganic Chemistry, 6th ed., John Wiley and Sons Inc., New York, 1999.
[12] M. Ciampolini, P. Dapporto, N. Nicoletta, F. Zanobini, Inorg. Chem. 22 (1983) 13.
[13] T. Suzuki, K. Kashiwabara, M. Kita, J. Fujita, S. Kaizaki, Inorg. Chim. Acta 281 (1998) 77.
[14] M. Kita, K. Kashiwabara, J. Fujita, H. Tanaka, S. Ohba, Bull. Chem. Soc. Jpn. 67 (1994) 2457.
[15] M. Adachi, M. Kita, K. Kashiwabara, J. Fujita, N. Iitaka, S. Kurachi, S. Ohba, D. Jin, Bull. Chem. Soc. Jpn. 65 (1992) 2037.
[16] J.H. Liao, S.H. Cheng, C.T. Su, Inorg. Chem. Commun. 5 (2002) 761.
[17] Y.F. Deng, Z.H. Zhou, Z.X. Cao, J. Inorg. Biochem. 98 (2004) 1110.
[18] L. Kryger, S.E. Rasmussen, Acta Chem. Scand. 26 (1972) 2349.
[19] C. Sudfeldt, A. Schäffer, J.H.R. Kägi, R. Bogumil, H.-P. Schultz, S. Wulff, H. Witzel, Eur. J. Biochem. 193 (1990) 863.
[20] (a) Seven-coordinate Co(II) ions have been previously reported. See for example: J.L. Atwood, P.C. Junk, Polyhedron 19 (2000) 85;
(b) G. Smith, E.J. O'Reilly, C.H.L. Kennard, Polyhedron 6 (1987) 871.
[21] Structurally characterized Co(III)/Co(II)Co(III) clusters containing other supporting ligands have been previously reported. See for example: T.C. Stamatatos, A. Bell, P. Cooper, A. Terzis, C.P. Raptopoulou, S.L. Heath, R.E.P. Winpenny, S.P. Perlepes, Inorg. Chem. Commun. 8 (2005) 533, and references therein.



Scheme 1. Ligand H_3acshz (a), H_3acbshz (b) and the basic bonding sites of them in the compounds.

complex, $[Ni_3(H_2O)_2(DMA)_2(acshz)_2]\cdot 2DMF$ (**1**); use H_3acbshz and trivalent iron ion to form a new iron(III) 18-metallacrown-6 compound, $[Fe_6(acbshz)_6(DMF)(H_2O)_5]\cdot 5DMF$ (**2**). Minimum inhibitory concentrations (MIC) against four different bacteria species of the two compounds were also measured.

2. Experiment

2.1. General

All reagents for the syntheses were obtained commercially with analytical grade and were used without further purification. ^1H and ^{13}C NMR spectra were recorded on a Varian Inova 600 MHz NMR spectrometer at 25 °C. Chemical shifts were referenced to the residual solvent peak. IR spectra were recorded on AVATAR 360 FT-IR spectrophotometer in the range 4000–400 cm^{-1} (KBr pellets). Element analyses were performed on a Perkin–Elmer 2400 CHN elemental analytical instrument. TG analysis was performed on a Pekin–Elmer DF40 instrument in flowing N_2 with a heating rate of 10 °C min^{-1}. UV–Vis spectra were recorded on a Shimadzu-UV-2501 spectrophotometer. Positive and negative electrospray ionization mass spectra (ESI-MS) were performed on API-2000 LC/MS/MS system for the metallacrown dissolved in DMF.

2.2. Synthesis of the ligands and metal complexes

2.2.1. N-Acryloyl-5-bromosalicylhydrazide (H_3acbshz)

Acryloyl chloride (1.6 ml, 19.7 mmol) was added to a solution of chloroform (100 ml) containing water (0.36 ml, 20.0 mmol) and triethylamine (5.7 ml, 40.0 mmol) at 0 °C. The reaction mixture was slowly warmed to ambient temperature. Then a further amount of acryloyl chloride (1.6 ml, 19.7 mmol) was added to the mixture and stirred for a further 1 h. After the completion of the above reaction, 5-bromosalicylhydrazide (3.7 g, 16.4 mmol) was added to the reaction mixture. The resulting reaction mixture was stirred at ambient temperature for 1 day. The solution was diluted with hexane (90 ml), kept under refrigeration overnight, filtered, and washed with ether, and rinsed with water (30 ml × 3) followed by ether. It was then dried in vacuo over P_2O_5. Yield: 3.85 g, 82.5%. *Anal.* Calc. for $C_{10}H_9N_2O_3Br$: C, 42.10; H, 3.15; N, 9.82. Found: C, 42.04; H, 3.25; N, 9.92%. IR (KBr pellet, cm^{-1}): 3310 (s), 3190 (s, broad), 2900 (s, broad), 2690 (m), 2620 (m), 1640 (s), 1600 (s), 1480 (s), 1400 (m), 1290 (s). ^1H NMR (DMSO-d_6), δ ppm: 12.01 (s, 1H, Ar-OH); 10.83 (s, 1H, Ar-CO–NH–); 10.78 (s, 1H, C_2H_3–CO–NH–); 8.04 (dd, 1H, *o*-ArH); 7.60 (m, 1H, *p*-ArH); 7.11 (m, 1H, *m*-ArH); 7.02 (dd, 1H, *m*-ArH); 6.41 (dd, 1H, –CO–CH=); 6.24 (dd, 1H, –CO–C=CH–); 5.77 (dd, 1H, –CO–C=CH–). ^{13}C NMR (DMSO-d_6), δ ppm: 169.10; 167.96; 162.63; 141.80; 137.35; 136.70; 134.31; 124.95; 115.76.

2.2.2. N-Acryloyl-salicylhydrazide (H_3acshz)

The ligand *N*-acryloyl-salicylhydrazide (H_3acshz) was prepared in an analogous manner to that used for *N*-acryloyl-5-bromosalicylhydrazide (H_3acbshz). Salicylhydrazide (2.5 g, 16.4 mmol) was used. 85% yield. *Anal.* Calc. for $C_{10}H_{10}N_2O_3$: C, 58.25; H, 4.85; N, 13.59. Found: C, 58.19; H, 4.92; N, 13.65%. IR (KBr pellet, cm^{-1}): 3440 (vs, broad), 3150 (vs, broad), 2780 (m), 2680 (m), 2490 (m), 1720 (m), 1630 (s), 1400 (s). ^1H NMR (DMSO-d_6), δ ppm: 11.91 (s, 1H, Ar-OH); 10.75 (s, 1H, Ar-CO–NH–); 10.25 (b, 1H, C_2H_3–CO–NH–); 7.93 (d, 1H, *m*-ArH); 7.44 (t, 1H, *m*-ArH); 7.03 (d, 1H, *o*-ArH); 6.95 (t, 1H, *p*-ArH); 6.42 (q, 1H, –CO–CH=); 6.22 (d, 1H, –CO–C=CH–); 5.75 (d, 1H, –CO–C=CH–). ^{13}C NMR (DMSO-d_6), δ ppm: 166.40; 163.52; 159.19; 134.66; 129.67; 127.79; 119.84; 117.92; 115.65.

2.2.3. $[Ni_3(H_2O)_2(DMA)_2(acshz)_2]\cdot 2DMF$ (**1**)

H_3acshz (20.6 mg, 0.1 mmol) was dissolved in 30 ml of 2:1 methanol + DMF with sodium hydroxide (12 mg, 0.3 mmol), then nickel chloride hexahydrate (23.7 mg, 0.1 mmol) was added. The mixture was stirred for 1 h, the resulting solution was filtered. After standing for several days, red block crystals were obtained from the filtrate. *Anal.* Calc. for $[Ni_3(H_2O)_2(DMA)_2(acshz)_2]\cdot 2DMF$: C, 42.11; H, 5.38; N, 13.10. Found: C, 42.16; H, 5.30, N, 13.17. IR (KBr pellet, cm^{-1}): 1720 (m), 1630 (m), 1520 (m), 1400 (s), 753 (m), 558 (m).

2.2.4. $[Fe_6(acbshz)_6(DMF)(H_2O)_5]\cdot 5DMF$ (**2**)

H_3acbshz (28.5 mg, 0.1 mmol) was dissolved in 30 ml of 2:1 methanol + DMF, and iron(III) nitrate nonahydrate

(40.4 mg, 0.1 mmol) was added to it, stirred for 2 h with the color of the solution changing to dark brown, then the mixture was filtered. After slow evaporation of the mother liquor over several weeks, dark brown block crystals suitable for X-ray diffraction were obtained. Yield: 75.4%. IR (KBr pellet, cm^{-1}): 1650 (s), 1590 (s), 1480 (s), 1410 (s), 632 (m), 534 (m).

2.3. Crystallographic data collection and refinement of the structures

X-ray single-crystal diffraction data for compounds **1** and **2** were collected on a Bruker Smart APEX diffractometer at 292(2) K with Mo Kα radiation ($\lambda = 0.71073$ Å). There was no evidence of crystal decay during data collection of compound **1**. In the data collection of compound **2**, suitable crystal was mounted in glass capillaries with the mother liquor to prevent the loss of the structural solvent molecules. In the compound **2**, the crystals diffracted poorly, with a relatively low percentage of observed intensities above the threshold of $2\sigma(I)$ within the 0.94–26.00° θ range. The non-coordinated solvent molecules are severely disordered which could not be modeled by discrete atoms in the compound. Correspondingly, the contribution of the solvent to the diffraction pattern was subtracted using SQUEEZE procedure of the PLATON. These voids consist of about 24.4% of the crystal volume (1533.7 Å per unit cell). Conventional least-squares refinement of the same solvent-exclude structural model against the original data set converged only at $R_1 = 0.15$. Refinement calculations with the modified data converged at $R_1 = 0.0893$ for 5471 reflections with intensities above the threshold of $2\sigma(I)$. In both compounds, the structures were solved by direct methods and all non-hydrogen atoms were refined with anisotropic thermal parameters. All hydrogen atoms were located in calculated positions and/or in the positions from difference Fourier map. The positions and anisotropy from difference of non-hydrogen atoms were refined on F^2 by full-matrix least-squares techniques with the SHELXTL program package [21,22]. Crystallographic data are summarized in Table 1. Selected bond lengths and angles for complex **1** are listed in Table 2.

2.4. Antimicrobial activities of the complexes

The antimicrobial activity of the complexes were assessed by their ability to inhibit the growth of *Staphylococcus aureus*, *Escherichia coli*, *Bacillus subtilis* and *Proteus vulgaris* in Mueller–Hinton broth medium. The minimum inhibitory concentration in μg/ml against the four bacteria species was measured. The bacteria concentration was $5 \times (10^5$–$10^6)$ cfu/ml and concentrations of 1600, 800, 400, 200, 100, 50 and 25 μg/ml of the complexes in DMF were tested. The solvent showed no antimicrobial action.

Table 1
The crystallographic data for compounds **1** and **2**

	1	**2**
Empirical formula	$C_{30}H_{46}N_8Ni_3O_{10}$	$C_{78}H_{88}Br_6Fe_6N_{18}O_{29}$
F_w (amu)	854.88	2556.22
T (K)	292(2)	292(2)
Crystal system, space group	monoclinic, $P2(1)/c$	triclinic, $P\bar{1}$
a (Å)	10.6902(5)	18.195(3)
b (Å)	16.1234(8)	18.334(3)
c (Å)	11.0535(5)	23.348(4)
α (°)	90	94.294(3)
β (°)	92.652(1)	106.238(3)
γ (°)	90	119.530(3)
V (Å^3)	1903.2(2)	6292.1(2)
Z, D_{calc} (g cm^{-3})	2, 1.492	2, 1.349
μ (mm^{-1})	1.531	2.644
$F(000)$	892	2560
Crystal size (mm)	0.30 × 0.20 × 0.16	0.30 × 0.06 × 0.04
Number of data/restraints/parameters	4113/0/293	24439/18/1246
R_{int}	0.0272	0.1674
Goodness-of-fit on F^2	1.087	0.704
Final R indices [$I > 2\sigma(I)$]	$R_1 = 0.0417$	$R_1 = 0.0893$
R indices (all data)	$wR_2 = 0.1071$	$wR_2 = 0.2516$

Table 2
Selected bond lengths (Å) and angles (°) for compound **1**

Ni(1)–O(2)	2.021(2)	Ni(2)–N(1)	1.823(2)
Ni(1)–N(2)	2.076(2)	Ni(2)–O(1)	1.823(2)
Ni(1)–O(4)	2.097(2)	Ni(2)–O(3)	1.850(2)
		Ni(2)–N(3)	1.942(2)
O(2)–Ni(1)–N(2)	78.44(8)	O(2)#1–Ni(1)–N(2)	101.56(8)
O(2)–Ni(1)–N(2)#1	101.56(8)	O(2)#1–Ni(1)–N(2)#1	78.44(8)
O(2)#1–Ni(1)–O(4)	88.34(8)	O(2)–Ni(1)–O(4)	91.66(8)
N(2)–Ni(1)–O(4)	89.8(1)	N(2)#1–Ni(1)–O(4)	90.2(1)
O(2)#1–Ni(1)–O(4)#1	91.66(8)	O(2)–Ni(1)–O(4)#1	88.34(8)
N(2)–Ni(1)–O(4)#1	90.2(1)	N(2)#1–Ni(1)–O(4)#1	89.8(1)
N(1)–Ni(2)–O(3)	84.24(9)	N(1)–Ni(2)–O(1)	95.32(9)
N(1)–Ni(2)–N(3)	175.8(1)	O(1)–Ni(2)–O(3)	178.7(1)
O(3)–Ni(2)–N(3)	92.1(1)	O(1)–Ni(2)–N(3)	88.3(1)

Symmetry codes: #1: $-x+2$, $-y$, $-z+2$.

3. Results and discussion

3.1. Spectral characterization

In the IR spectra, the ligands H_3acbshz and H_3acshz show stretching bands attributed to C=O, PhO–H (phenolic, including intramolecular and intermolecular hydrogen bond) and N–H at 1600, 1640, 2620–3190, 3310 cm^{-1} and 1720, 1630, 2490–3150, 3440 cm^{-1}, respectively [23]. The infrared stretching bands for compounds **1** and **2** are quite similar. The absence of the N–H band and the weakness of the C=O stretching bands are consistent with the deprotonation of the CONH groups and coordination to the Fe(III) and Ni(II) ions, which indicate the same chelating modes of the ligands to metal ions. The deprotonation and coordination are also confirmed by the bands at 632 and 753 cm^{-1}, attributed to M–O linkages, and the bands

at 534 and 558 cm^{-1} assigned to M–N linkage [24]. The C=N–C=N framework bands are found at 1480 and 1400 cm^{-1}, respectively [25].

3.2. Integrity and stability of metallacrown

Solution stability of the metallacrowns is a fundamental property for the proposed applications of metallacrowns [26]. Electrospray ionization (ESI) mass spectroscopy, a soft ionization technique, has been proved useful in providing solution molecular weights of formally neutral metallacrown salt complexes [27]. The DMF solution of the compound **2** gave some peaks at *m/z* 1905.4 and 1018.1 in ESI(+)-MS, corresponding to the hexanuclear cluster ion, $[Fe_6(acbshz)_6(DMF)(H_2O)_5+2H]^{2+}$ and $[Fe_6(acbshz)_6+2H]^{2+}$, respectively. To explore the solution stability of the metallacrown in DMF solution, the concentration-dependent absorbance was measures at 319 nm for compound **2**. The concentration variation result to a linear change in absorbance across the range of 3.1 and 100 μM of concentrations (Fig. 1). No change was observed for the absorption of the solution after 2 weeks. The result indicates that the compound **2** retains the integrity of the ring and is stable at least in these concentration ranges in DMF.

UV–Vis titrations were undertaken both to determine the extent of solution integrity and gain insight into the formation of the compound **2**. Titration of the DMF solution of H_3acbshz with $Fe(NO_3)_3$ in steps of 0.1 equiv. causes obvious increase in the intensity of the broader at 319 nm, and also slight increase of d–d transition band at 470 nm. The plot of the ratio of concentrations of $Fe(NO_3)_3$ to H_3acbshz versus the molar absorptivity at 319 nm is shown in Fig. 2. We can see that an increase in the absorbance at 319 nm was observed with a metal ligand endpoint ratio of 1:1, which is consistent with the formation of the compound **2** in DMF solution. Addition of excess metal does not alter the field band. These observations are consistent with the stability of the compound **2** in DMF solution even in the presence of excess metal.

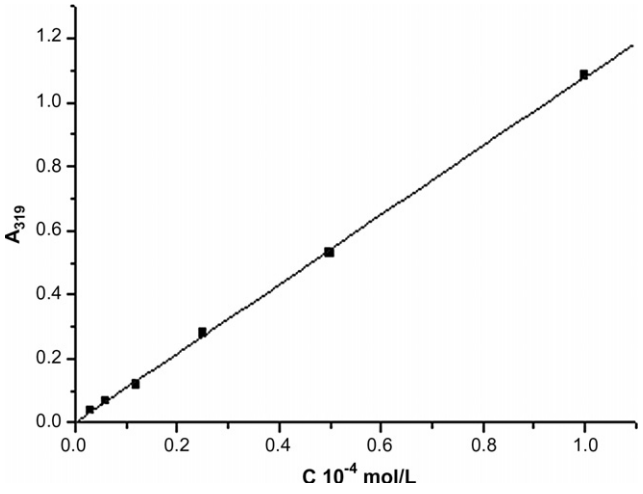


Fig. 1. The concentration-dependent absorbance of compound **2** in DMF was measured at 319 nm.

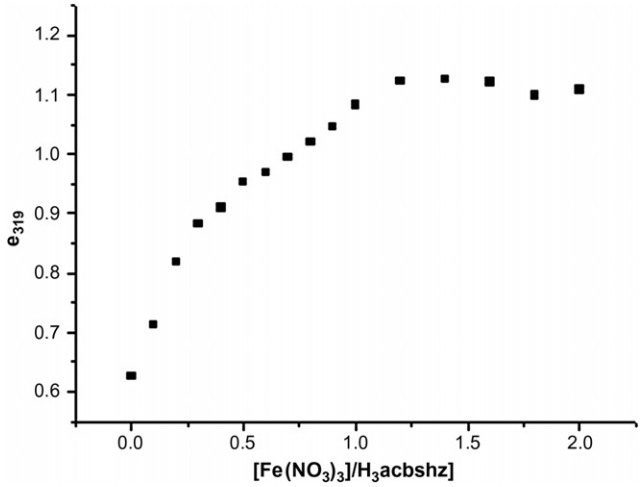


Fig. 2. UV–Vis titration curve of the addition of 0.0–2.0 equiv. of $Fe(NO_3)_3$ into 1 mM H_3acbshz in DMF.

3.3. Description of the structures of *1* and *2*

The structure of the linear trinuclear nickel compound **1** is provided in Fig. 3. The deprotonated ligand $acshz^{3-}$ acts as a trianionic pentadentate ligand, one phenolate oxygen, one carbonyl oxygen and one hydrazide nitrogen in one ligand are bound to the terminal nickel ions and the other carbonyl oxygen plus the other hydrazide nitrogen in the two ligands are chelated to the central nickel ion. Central nickel ion (Ni1) is octahedral while the other two terminal nickel ions are square-planar. They are connected by two bridging deprotonated $acshz^{3-}$ ligands, forming a linear trinuclear nickel structure unit with a Ni–N–N–Ni–N–N–Ni core with the neighboring Ni···Ni distance is 4.615 Å. The trinuclear nickel complex molecule is strictly linear by symmetry, because of that central nickel atom (Ni1) is on a crystallographic symmetry center. The equatorial plane of the octahedron is perfectly planar and the nickel ion (Ni1) lies in this plane. The axial coordination sites are occupied by two water molecules. The terminal nickel ions have a perfect square-planar surrounding with the rest site coordinated by dimethylamine molecules (DMA), which are believed to be the result of the decomposition of the DMF solvent under basic conditions. This phenomenon has been commonly observed in the literature [28,29]. The terminal Ni–O and Ni–N bond lengths for Ni–O(phenolate), Ni–O(carbonyl), Ni–N(diazine) and Ni–N(DMA) are 1.823, 1.850, 1.823 and 1.942 Å, respectively. They are slight shorter than the central Ni–O and Ni–N bond lengths for Ni–O(carbonyl), Ni–O(H_2O), Ni–N(diazine) which are 2.021, 2.097 and 2.076 Å, respectively. Adjacent molecules are linked by intermolecular H bonds to form a 2D infinite wave-like structure (Fig. 4).

A perspective view of the complete Fe_6 cluster molecule of $[Fe_6(acbshz)_6(DMF)(H_2O)_5]\cdot 5DMF$ is provided in

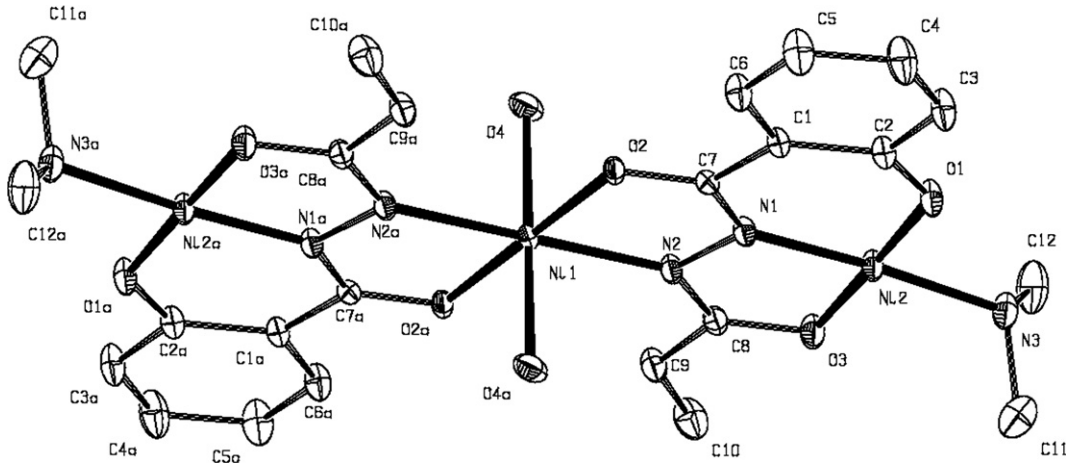


Fig. 3. Perspective view of compound **1**, solvent molecules and all hydrogen atoms have been omitted for clarity.

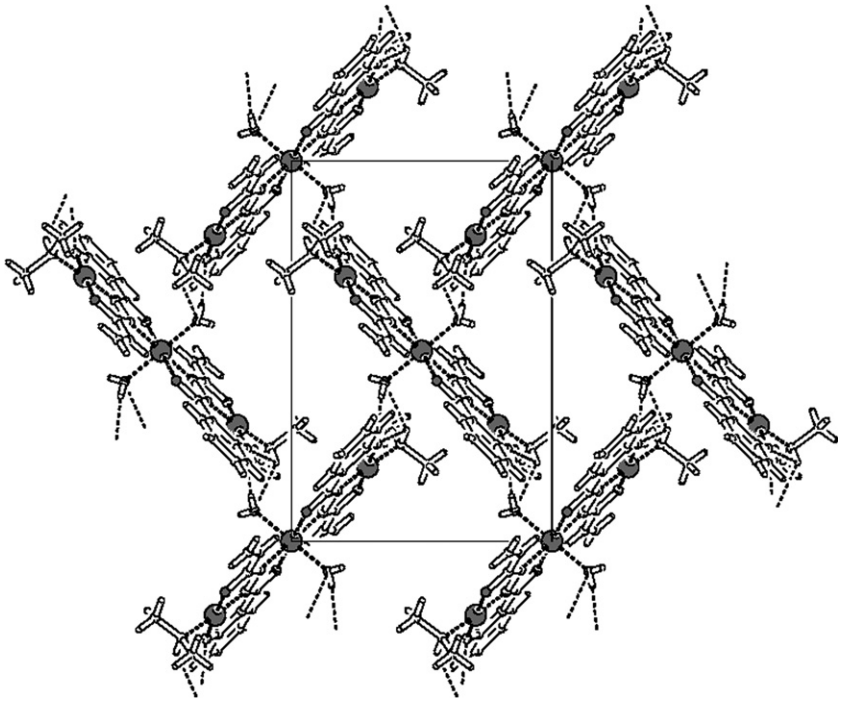


Fig. 4. The 2D structure formed by intermolecular H bond with the use of the trinuclear complex as a building block.

Fig. 5. The chelating modes of the ligands H_3acbshz and H_3acshz to metal ions are the same, the whole atoms in the ligand are almost in co-plane. All iron ions are in an octahedral FeN_2O_4 environment with one phenolate oxygen, one carbonyl oxygen and one hydrazine nitrogen in one ligand, one carbonyl oxygen and one hydrazine nitrogen in the other ligand. The rest site of five iron ions was occupied by oxygen atom from H_2O molecules while it was fitted by oxygen atom from DMF molecules in the other iron ion (Fe4). It is the first metallacrown that the coordination environments of metal ions in the cycle ring are different. The Jahn–Teller distortion is not observed because of the high-spin d^5 iron(III) ion configuration compared with some Mn(III) ion metallacrown compounds [10,14,30]. Meanwhile, the ligand forces all iron(III) cations into a propeller configuration with alternating Λ/Δ stereochemistry as ΛΔΛ forms. The specific connectivity of the atoms forming the ring is Fe1–N4–N3–Fe2–N5–N6–Fe3–N8–N7–Fe4–N10–N9–Fe5–N12–N11–Fe6–N2–N1–. This organization leads to the 18-numbered hexanuclear core ring system with [Fe–N–N] repeated unit. Three water groups coordinated at the metal centers with Λ configuration are found on one face of the metallacrown, and two water and one DMF groups coordinated to the other metal centers with Δ configuration are found on the other face of the metallacrown. Due to the difference coordination environments of the central metal ions, the two faces of the disc-shaped hexanuclear ring do not have opposite chiralities. But to our knowledge, the opposite chiratilies can be found in the all existent metallacrowns. The average

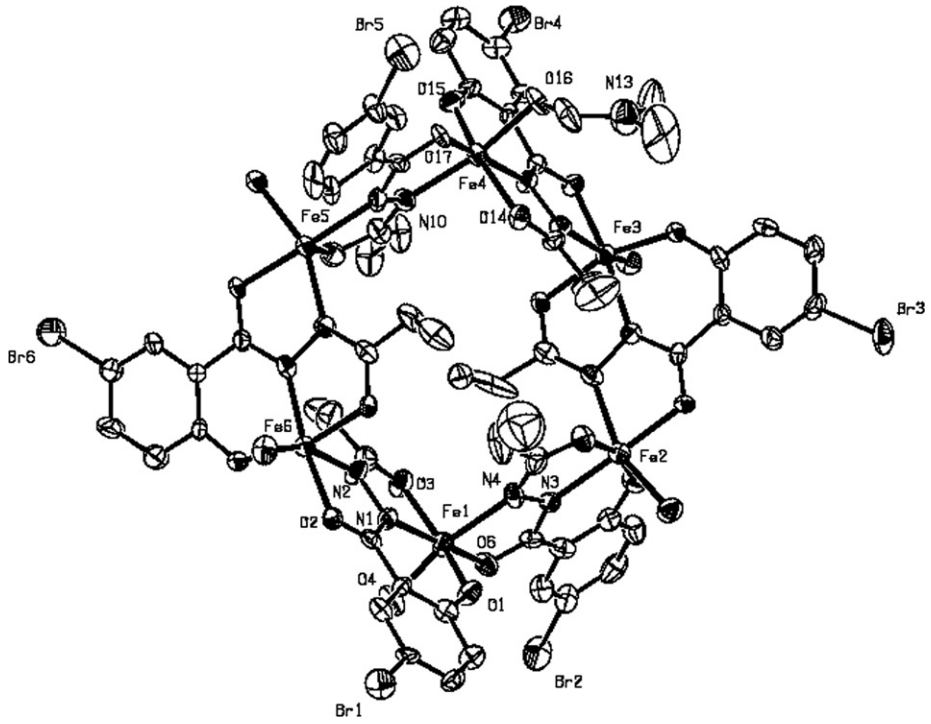


Fig. 5. Perspective view of compound **2**, solvent molecules and all hydrogen atoms have been omitted for clarity. Selected bond lengths (Å) and angles (°): Fe(1)–O(1) 1.923(7), Fe(1)–O(6) 1.985 (7), Fe(1)–O(4) 2.042(7), Fe(1)–O(3) 2.048(8), Fe(1)–N(1) 2.077(9), Fe(1)–N(4) 2.113(9); O(1)–Fe(1)–O(6) 104.3(3), O(1)–Fe(1)–O(4) 93.5(3), O(4)–Fe(1)–O(3) 89.0(3), O(1)–Fe(1)–N(1) 84.9(3), O(6)–Fe(1)–N(1) 170.0(3), O(4)–Fe(1)–N(1) 95.6(3), O(3)–Fe(1)–N(1) 77.5(3), O(1)–Fe(1)–N(4) 91.5(3), O(6)–Fe(1)–N(4) 75.8(4), O(4)–Fe(1)–N(4) 155.6(4), O(3)–Fe(1)–N(3) 91.9(3), N(1)–Fe(1)–N(4) 108.4(4).

neighboring Fe···Fe separation is 4.924 Å. There are no solvent molecules in the 'host' cavity of the metallacrown.

3.4. TG analysis of compound *1*

The TG curve of compound **1** exhibits three steps of weight losses. The first weight loss is about 21.5% (Calc. value 21.3%) in the range of 30–170 °C, corresponds to the loss of two DMF molecules and two coordinated water molecules. The second weight loss is about 10.1% (Calc. value 10.3%) in the range of 170–272 °C, corresponds to the loss of two coordinated DMA molecules. The third weight loss is about 73.1% (Calc. value 73.6%), which can be attributed to the complete decomposition of the complex to form NiO as a final product.

3.5. Antimicrobial activities

Minimum inhibitory concentration of two ligands and compounds **1** and **2** against *S. aureus*, *E. coli*, *B. subtilis* and *P. vulgaris* are listed in Table 3. As can be clearly seen from the table, none of the ligands show strong antimicrobial activity against the tested microorganism while the compounds **1** and **2** all have strong antimicrobial activities. Moreover, in this study, the result do not indicate specificity against Gram-positive or Gram-negative bacterial in spite of it is generally expected that a much greater number would be active against Gram-positive than Gram-negative bacteria [31]. Antibacterial screening data indicated that the metallacrown **2** is more active than the trinuclear compound **1**.

Table 3
Minimum inhibitory concentration (MIC) of ligands (*N*-acryloyl-salicylhydrazide and *N*-acryloyl-5-bromosalicylhydrazide) and compounds (**1** and **2**) in μg/ml

Microorganisms	Ligands		Compounds	
	H_3acshz	H_3acbshz	**1**	**2**
Staphylococcus aureus (Gram$^+$)	800	800	200	50
Escherichia coli (Gram$^-$)	800	800	100	50
Bacillus subtilis (Gram$^+$)	800	400	100	25
P. vulgaris (Gram$^-$)	400	400	200	25

MIC showed that among all the compounds tested, metallacrowns are more active than the simple metal complexes. For the same type of salicylhydrazide derivatives, the best inhibition is given by $[Fe_6(acshz)_6(CH_3OH)_6]\cdot 6CH_3OH\cdot 6H_2O$ (MIC = 25–200 μg/ml against all microorganisms) [13]. But in this study, the compound **2** are more active than $[Fe_6(acshz)_6(CH_3OH)_6]\cdot 6CH_3OH\cdot 6H_2O$. Although it is risky to correlate the bioactivity of these compounds to the structural features, we can stress that the different bonding modes of iron(III) ions in compound **2** and $[Fe_6(acshz)_6(CH_3OH)_6]\cdot 6CH_3OH\cdot 6H_2O$ are important. Compared to the tetranuclear nickel(II) complex ($[12\text{-}MC_{Ni(II)N(Hshi)2(pko)2}\text{-}4](NNN)_2(DMF)(CH_3OH)$) with the low MIC value (12–25 μg/ml) [32], the MIC value in this trinuclear nickel(II) compound **1** is much

higher, but it is risky to correlate the nuclearity and antibacterial activity just based on these limited present complexes. The work to prepare more polynuclear nickel compounds and correlate the relationship between the nuclearity and antibacterial activity is in progress in our laboratory.

4. Conclusion

In this paper, we synthesize two trianionic pentadentate *N*-acylsalicylhydrazide ligands, *N*-acryloyl-salicylhydrazide (H_3acshz) and *N*-acryloyl-5-bromosalicylhydrazide (H_3acbshz), and use different metal ions with these ligands to form a new Fe(III) 18-metallacrown-6 and a new linear trinuclear Ni(II) complexes. The chelating modes of the two ligands to metal ions are the same. The three nickel ions in compound **1** arrange in a strictly linear structure, exhibit alternating square-planar and octahedral coordination environments. The six iron(III) ions in compound **2** are connected through hydrazide N–N groups to form a 18-membered ring. The ligand enforces the stereochemistry of the Fe^{3+} ions as a propeller configuration with alternating Λ/Δ forms. The coordination environments of iron ions in the cycle ring are different, and these differences make the two faces of the disc-shaped hexanuclear ring do not have opposite chiralities, which is different from all the existent metallacrowns. Antibacterial screening data showed that the metallacrown **2** has stronger antimicrobial activity than the trinuclear compound **1** against all tested microorganisms.

Acknowledgement

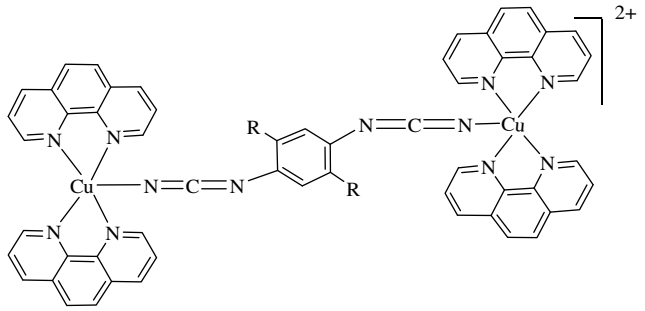
This work was supported by the National Natural Science Foundation of China (Grant No. 20171035).

Appendix A. Supplementary data

CCDC 661929 and 661930 contain the supplementary crystallographic data for **1** and **2**. These data can be obtained free of charge via http://www.ccdc.cam.ac.uk/conts/retrieving.html, or from the Cambridge Crystallographic Data Centre, 12 Union Road, Cambridge CB2 1EZ, UK; fax: (+44) 1223-336-033; or e-mail: deposit@ccdc.cam.ac.uk. Supplementary data associated with this article can be found, in the online version, at doi:10.1016/j.poly.2008.02.016.

References

[1] D. Gatteschi, Adv. Mater. 6 (1994) 635.
[2] S. Leininger, B. Olenyuk, P.J. Stang, Chem. Rev. 100 (2000) 853.
[3] E.I. Solomon, R.K. Szilagyi, S.D. George, L. Basumallick, Chem. Rev. 104 (2004) 419.
[4] M. Du, X.-J. Zhao, J.-H. Guo, X.-H. Bu, J. Ribas, Eur. J. Inorg. Chem. (2005) 294.
[5] D.C. Smith, C.H. Lake, G.M. Gray, Chem. Commun. (1998) 2771.
[6] V. Tangoulis, C.P. Raptopoulou, S. Paschalidou, E.G. Bakalbassis, S.P. Perlepes, A. Terzis, Angew. Chem., Int. Ed. 36 (1997) 1083.
[7] A. Mukherjee, M. Nethaji, A.R. Chakravarty, Angew. Chem., Int. Ed. 43 (2004) 87.
[8] T.C. Higgs, K. Spartalian, C.J. O'Connor, B.F. Matzanke, C.J. Carrano, Inorg. Chem. 37 (1998) 2263.
[9] Y.-F. Song, G.A. van Albada, J.-K. Tang, I. Mutikainen, U. Turpeinen, C. Massera, O. Roubeau, J.S. Costa, P. Gamez, J. Reedijk, Inorg. Chem. 46 (2007) 4944.
[10] B. Kwak, H. Rhee, S. Park, M.S. Lah, Inorg. Chem. 37 (1998) 3599.
[11] B. Kwak, H. Rhee, M.S. Lah, Polyhedron 19 (2000) 1985.
[12] S. Lin, S.-X. Liu, B.-Z. Lin, Inorg. Chim. Acta 328 (2002) 69.
[13] F.-P. Xiao, L.-F. Jin, G.-Z. Cheng, Z.-P. Ji, Polyhedron 26 (2007) 2695.
[14] F.-P. Xiao, L.-F. Jin, W. Luo, G.-Z. Cheng, Z.-P. Ji, Inorg. Chim. Acta 360 (2007) 3341.
[15] S. Lin, S.-X. Liu, Z. Chen, B.-Z. Lin, S. Gao, Inorg. Chem. 43 (2004) 2222.
[16] S.-X. Liu, S. Lin, B.-Z. Lin, C.-C. Lin, J.-Q. Huang, Angew. Chem., Int. Ed. 40 (2001) 1084.
[17] R.P. John, K. Lee, M.S. Lah, Chem. Commun. (2004) 2660.
[18] M.-X. Yang, S. Lin, L.-J. Chen, S.-X. Liu, Chin. J. Inorg. Chem. 19 (2003) 433.
[19] S. Lin, M.-X. Yang, S.-X. Liu, Polyhedron 26 (2007) 4793.
[20] W. Luo, X.-G. Meng, X.-Z. Sun, F.-P. Xiao, J.-F. Shen, Y. Zhou, G.-Z. Cheng, Z.-P. Ji, Inorg. Chem. Commun. 10 (2007) 1351.
[21] G.M. Sheldrick, Acta Crystallogr., Sect. A 46 (1990) 467.
[22] G.M. Sheldrick, SHELXL-97, Program for Crystal Structure Refinement, University of Göttingen, 1997.
[23] S.N. Rao, K.N. Munshi, N.N. Rao, M.M. Bhadbadc, E. Syresh, Polyhedron 18 (1999) 2491.
[24] G.R. Angel, J.F. Juan, B. Ferran, Polyhedron 15 (1996) 4407.
[25] M.A. Ali, A.H. Mirza, R.J. Butcher, M.T.H. Tarafder, Inorg. Chim. Acta 320 (2001) 1.
[26] B.R. Gibney, D.P. Kessissglou, J.W. Kampf, V.L. Pecoraro, Inorg. Chem. 33 (1994) 4840.
[27] A.J. Stemmler, J.W. Kampf, M.L. Kirk, B.H. Atasi, V.L. Pecoraro, Inorg. Chem. 38 (1999) 2807.
[28] L.-H. Xie, S.-X. Liu, B. Gao, C.-D. Zhang, C.-Y. Sun, D.-H. Li, Z.-M. Su, Chem. Commun. (2005) 2402.
[29] A.D. Burrows, K. Cassar, R.M.W. Friend, M.F. Mahon, S.P. Rigby, J.E. Warren, Cryst. Eng. Commun. 7 (2005) 548.
[30] J.-M. Dou, M.-L. Liu, D.-C. Li, D.-Q. Wang, Eur. J. Inorg. Chem. (2006) 4866.
[31] A.R. McCutheon, S.M. Ellis, R.E.W. Hancock, G.H.N. Towers, J. Ethnopharmacol. 37 (1992) 213.
[32] M. Alexiou, I. Tsivikas, C. Dendrinou-Samara, A.A. Pantazaki, P. Trikalitis, N. Lalitoti, D.A. Kyriakidis, D.P. Kessissoglou, J. Inorg. Biochem. 93 (2003) 256.



1) R = H
2) R = CH_3
3) R = Cl

Scheme 1.

rich metal center. Previous studies in binuclear transition metal complexes were shown that, the bridging ligand can behave as an innocent or not during the superexchange process [26–33]. In the dicyanamidobenzene-bridge diruthenium complex, the dicyd bridging ligand was shown a non-innocent behavior [19].

Work on dinuclear and polynuclear systems derived from cyanamide or dicyanamide anions acting as bridging ligands is a fast-growing research field due to the large variety of topologies, dimensionalities, and magnetic properties that can be obtained [34].

We now report the preparation, crystal structure, spectroscopic characterization and electrochemical behavior of $[\{Cu(phen)_2\}_2(\mu\text{-dicyd})](PF_6)_2$, $[\{Cu(phen)_2\}_2(\mu\text{-Me}_2\text{dicyd})](PF_6)_2$, $[\{Cu(phen)_2\}_2(\mu\text{-Cl}_2\text{dicyd})](PF_6)_2$ (Scheme 1), and $[\{Cu(phen)_2\}_2(\mu\text{-apc})](PF_6)_3$.

2. Experimental

2.1. Materials and measurements

All chemicals and solvents were reagent grade, obtained from either Merck or Aldrich and used without further purification. 1,4-dicyanamidobenzene, 1,4-dicyanamido-2,5-dimethylbenzene, 1,4-dicyanamido-2,5-dichlorobenzene, and 4-azo(phenylcyanamido)benzene were synthesized according to published procedures [23,35]. $[Cu(phen)_2Cl]PF_6$ was prepared according to the literature [36]. Elemental analyses were performed on a Perkin–Elmer 2400 CHNS/O elemental analyzer. IR spectra (4000–400 cm^{-1}) were measured on a FT-IR JASCO 460 spectrophotometer with KBr pellets and electronic spectra on a JASCO 7850 spectrophotometer. Cyclic voltammograms were recorded by using a Metrohm 694 apparatus. Three electrodes were utilized in this system, a platinum disk working electrode (RDE), a platinum wire auxiliary electrode and Ag/AgCl reference electrode. The platinum disk working electrode was manually cleaned with 1-μm diamond polish prior to each scan. The supporting electrolyte, tetrabutylammonium hexafluorophosphate (TBAH), was twice recrystallized from 1:1 ethanol/water and vacuum-dried at 110 °C. Acetonitrile was dried over P_2O_5 and vacuum distilled. The solutions were deoxygenated by bubbling with argon (Ar) for 15 min. Ferrocene ($E^\circ = 0.665$ V) was used as an internal reference [37].

2.2. Synthesis of $[\{Cu(phen)_2\}_2(\mu\text{-dicyd})](PF_6)_2$

A mixture of 1,10-phenanthroline (0.793 g, 4 mmol) and $Cu(NO_3)_2 \cdot 6H_2O$ (0.483 g, 2 mmol) was placed in 50 mL of water/ethanol (1:1 v/v) and stirred at room temperature for 24 h. To the reaction mixture was then added excess NH_4PF_6 (0.82 g, 5 mmol). The resulting light blue-green precipitate, $[Cu(phen)_2(H_2O)](PF_6)_2$, was collected by filtration, washed with cold water and diethyl ether, and then air dried. A solution of $[Cu(phen)_2(H_2O)](PF_6)_2$ (0.551 g, 1 mmol) in 100 mL acetone was degassed and under argon atmosphere, the neutral $dicydH_2$ (0.282 g, 0.5 mmol) was added. The solution was then stirred with slight heating (30°C) under Ar overnight. To this was added triethylamine (1.5 mL, 0.5 mmol), and the solution was stirred for 1 h. The dark brown precipitate, $[\{Cu(phen)_2\}_2(\mu\text{-dicyd})](PF_6)_2$, was collected by suction filtration, washed with diethyl ether, and then air dried. For further purification, the complex was recrystallized by diffusing diethyl ether into a saturated solution of the complex in DMF. After 3 days, green ultrafine crystals of the dinuclear complex, $[\{Cu(phen)_2\}_2(\mu\text{-dicyd})](PF_6)_2$, were collected and washed with diethyl ether and vacuum dried. Yield: 0.29 g (45%). *Anal.* Calc. for $Cu_2C_{56}H_{36}N_{12}P_2F_{12}$: C, 51.97; H, 2.80; N, 12.99. Found: C, 51.83; H, 2.75; N, 12.87%.

2.3. Synthesis of $[\{Cu(phen)_2\}_2(\mu\text{-Me}_2\text{dicyd})](PF_6)_2$

This complex was prepared by the same procedure, except that $dicydH_2$ was replaced by $Me_2dicydH_2$. Yield was 0.22 g (33%). *Anal.* Calc. for $Cu_2C_{58}H_{40}N_{12}P_2F_{12}$: C, 52.68; H, 3.05; N, 12.72. Found: C, 52.46; H, 2.99; N, 12.91%.

2.4. Synthesis of $[\{Cu(phen)_2\}_2(\mu\text{-Cl}_2\text{dicyd})](PF_6)_2$

Due to the poor solubility of $Cl_2dicydH_2$ in common organic solvents, the tetraphenylarsonium salt of Cl_2dicyd^{2-}, $[AsPh_4]_2[Cl_2dicyd]$ was used. $[AsPh_4]_2[Cl_2dicyd]$ was synthesized according to published procedure [23]. A solution of $[Cu(phen)_2(H_2O)](PF_6)_2$(0.551 g, 1 mmol) in 100 mL acetone was degassed and under argon atmosphere, $[AsPh_4]_2[Cl_2dicyd]$ (0.475 g, 0.5 mmol) was added. The solution was then stirred with slight heating (30 °C) under Ar overnight. The precipitated $[AsPh_4][PF_6]$ was then filtered off and the filtrate was evaporated to dryness by rotary evaporator. For further purification, the dark green precipitate, $[\{Cu(phen)_2\}_2(\mu\text{-Cl}_2\text{dicyd})](PF_6)_2$, was recrystallized by diffusing diethyl ether into a saturated solution of the complex in DMF. After 2 days, dark green ultrafine crystals of the dinuclear complex, $[\{Cu(phen)_2\}_2(\mu\text{-Cl}_2\text{dicyd})](PF_6)_2$, were collected, washed with diethyl ether and vacuum dried.

Yield: 0.28 g (41%). *Anal.* Calc. for $Cu_2C_{56}H_{34}N_{12}Cl_2P_2F_{12}$: C, 49.35; H, 2.51; N, 12.34. Found: C, 49.59; H, 2.48; N, 12.40%.

2.5. Synthesis of $[\{Cu(phen)_2\}_2(\mu\text{-apc})](PF_6)_3 \cdot 2CH_3COCH_3$

$[Cu(phen)_2Cl]PF_6$ (1.212 g, 2 mmol) was dissolved in 150 mL of acetonitrile in a 250 mL round-bottom flask. To this was added thallium salt of 4-azo(phenylcyanamido)benzene (Tlapc) (0.426 g, 1 mmol). The reaction mixture was stirred at room temperature for 24 h. The reaction mixture was then chilled to −10 °C and filtrate to remove a fine white TlCl precipitate. The filtrate was then evaporated to dryness and the brown product was recrystallized by the diffusion of diethyl ether into an acetone solution of the complex. After 6 days, dark green crystals of $[\{Cu(phen)_2\}_2(\mu\text{-apc})](PF_6)_3 \cdot 2CH_3COCH_3$ formed. Yield: 0.62 g (38%). *Anal.* Calc. for $Cu_2C_{67}H_{53}N_{12}O_2F_{18}P_3$: C, 49.67; H, 3.29; N, 10.37. Found: C, 49.93; H, 3.31; N, 10.44%.

2.6. X-ray crystallographic study of $[\{Cu(phen)_2\}_2(\mu\text{-apc})](PF_6)_3 \cdot 2CH_3COCH_3$

Dark green crystals of $[\{Cu(phen)_2\}_2(\mu\text{-apc})](PF_6)_3 \cdot 2CH_3COCH_3$ were grown by ether diffusion into an acetone solution of the complex. Single-crystal X-ray diffraction measurements were carried out on a Bruker Apex II, using graphite-monochromated Mo Kα radiation ($\lambda = 0.71073$ Å, $2\theta < 56°$) at 100(2) K. Unit cell parameters were determined by the least-squares calculation with θ angle ranging from 1.62° to 28.00°. Intensities of 38 055 reflections were measured using Bruker Apex II CCD Area detector giving 16 038 unique reflections. The structures were solved by direct method and refined by the full-matrix least-squares against F^2 in anisotropic (for non-hydrogen atoms) approximation. All hydrogen atoms were located from the difference Fourier syntheses and placed in geometrically calculated positions. All hydrogen atom positions were refined in isotropic approximation in riding model with the U_{iso}(H) parameters equal to $1.5U_{eq}$(Ci) for methyl groups and $1.2U_{eq}$(Ci) for other carbon atoms, where U(Ci) are the equivalent thermal parameters of the atoms to which corresponding H atoms are bonded. All calculations were performed on an IBM PC/AT using the SHELXTL version 5.1 software [38] giving a final $R_1 = 0.0541$, $wR_2 = 0.0833$ (for 9656 reflections with $I > 2\sigma(I)$). The largest diffraction peak and hole on the final difference-Fourier map were 0.633 and −0.551 e A^{-3}.

Further details of the structural analyses are given in Table 1. Selected bond lengths and bond angles are listed in Table 2.

3. Results and discussion

The dinuclear complexes, $[\{Cu(phen)_2\}_2(\mu\text{-dicyd})](PF_6)_2$ and $[\{Cu(phen)_2\}_2(\mu\text{-Me}_2\text{dicyd})](PF_6)_2$ were synthesized by the reaction of $[Cu(phen)_2(H_2O)](PF_6)_2$ with the neutral dicydH_2 or Me_2dicyd in the presence of triethylamine. As is shown in Scheme 2, the amine protons of neutral dicyanamidobenzene ligands are acidic, the anion is resonance stabilized and this increases the amine proton acidity [22,39]. The poor solubility of Cl_2dicydH_2 in acetone required $[AsPh_4]_2[Cl_2dicyd]$ to be used instead [40]. $[\{Cu(phen)_2\}_2(\mu\text{-}Cl_2dicyd)](PF_6)_2$ was synthesized by the reaction of $[Cu(phen)_2(H_2O)](PF_6)_2$ with the tetraphenylarsonium salt of Cl_2dicyd^{2-} in acetone. $[\{Cu(phen)_2\}_2(\mu\text{-apc})](PF_6)_3$ was prepared by the metathesis reaction of $[Cu(phen)_2Cl]PF_6$ with the thallium salts of apc^- in acetonitrile. Elemental analysis of the complexes was entirely consistent with their formulation. The complexes were further characterized by IR and UV–Vis spectroscopies and cyclic voltammetry.

Dark green crystals of the dinuclear Cu(II) complex, $[\{Cu(phen)_2\}_2(\mu\text{-apc})](PF_6)_3 \cdot 2CH_3COCH_3$, that were suitable for crystallography were grown by diffusion of diethyl ether into a solution of the complex in acetone. An ORTEP drawing of the complex cation with the atomic labeling scheme is shown in Fig. 1, and selected bond lengths and bond angles are listed in Table 2. Anionic phenylcyanamides (Ph–NCN) have three non-bonding pairs of electrons that can be involved in coordination chemistry. There are many crystal structures of monodentate phenylcyanamide ligands showing coordination through the cyano-nitrogen but there are no examples of amido-nitrogen coordination [22,41–45]. The neutral or anionic phenylcyanamides can function as bridging ligands although this has only been observed for the anionic cyanamide [22,34,46]. As is shown in Fig. 1, both five-coordinate Cu(II) ions in the dinuclear unit are linked through a bridging 4-azo(phenylcyanamido)benzene (apc) ligand. The cyanamide group (N=C=N) of the bridging ligand is coordinated to Cu(II) ions through the cyano-N(5) and amido-N(6) nitrogen atoms. The bond length between Cu(1) and cyano-N(5) nitrogen (Cu(1)–N(5) = 2.025(3) Å) is slightly larger than that formed by Cu(2) and amido-N(6) nitrogen (Cu(2)–N(6) = 2.016(3) Å). The Cu(1)–cyanamide bond angle (Cu(1)–NCN) is approximately linear, having an angle of 163.1(3)°. In Ni(II), Pd(II), Co(III) and Rh(III) complexes, the metal–cyanamide bond is bent [22,41,42]. The Cu–N(phen) bond distances are consistent with values in previously reported structures [47–52]. The copper–cyanamide distances, Cu(1)–N(5) and Cu(2)–N(6) [2.025(3) and 2.016(3) Å, respectively], have no significant difference with the Cu–N(phen) distances (mean 2.04 Å). The molecular structures of five-coordinate copper(II) complexes show an extensive range from a regular trigonal bipyramidal (RTBP) to regular square-based pyramidal (RSBP) [53–57]. The structure index parameter, $\tau = (\beta - \alpha/60)$, was evaluated by the two large angles ($\alpha < \beta$) in the five-coordinated geometry indicative of $\tau = 1.0$ for a RTBP geometry and $\tau = 0.0$ for a RSBP [55]. The coordination geometry of the Cu(1) ($\tau = 0.9$) is best described as a trigonal bipyramidal with the equatorial

Table 1
Crystallographic and data collection parameters for $[\{Cu(phen)_2\}_2(\mu\text{-apc})](PF_6)_3 \cdot 2CH_3COCH_3$.

Chemical formula	$C_{67}H_{53}Cu_2F_{18}N_{12}O_2\ P_3$
Formula weight	1620.20
Crystal size (mm)	$0.45 \times 0.38 \times 0.15$
Crystal system	triclinic
Space group	$P\bar{1}$
Z	2
a (Å)	12.7700(19)
b (Å)	13.1230(16)
c (Å)	20.855(3)
α (°)	74.893(3)
β (°)	84.568(4)
γ (°)	82.277(4)
Collection ranges	$-16 \leqslant h \leqslant 16$; $-17 \leqslant k \leqslant 17$; $-27 \leqslant l \leqslant 27$
Temperature (K)	100(2)
Volume (Å^3)	3337.0(8)
D_{calc} (Mg m^{-3})	1.612
Radiation	Mo Kα ($\lambda = 0.71073$ Å)
Absorption coefficient (μ) (mm^{-1})	0.816
Absorption correction	multi-scan
$F(000)$	1640
θ Range for data collection (°)	1.62–28.00
Observed reflections	38055
Independent reflections (R_{int})	16038 (0.0685)
Data/restraints/parameters	16038/9/979
Goodness-of-fit on F^2	1.014
Final R indices [$I > 2\sigma(I)$]	$R_1 = 0.0541$, $wR_2 = 0.0833$
R indices (all data)	$R_1 = 0.1110$, $wR_2 = 0.0992$
Largest difference peak and hole (e Å^{-3})	0.633 and −0.551

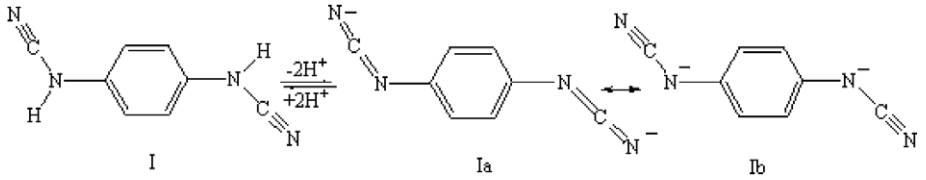
Table 2
Selected bond lengths (Å) and bond angles (°) for $[\{Cu(phen)_2\}_2(\mu\text{-apc})](PF_6)_3 \cdot 2CH_3COCH_3$

Bond lengths			
Cu(1)–N(4)	1.993(3)	Cu(2)–N(8)	1.983(3)
Cu(1)–N(2)	2.007(3)	Cu(2)–N(10)	2.000(3)
Cu(1)–N(5)	2.025(3)	Cu(2)–N(6)	2.016(3)
Cu(1)–N(3)	2.060(3)	Cu(2)–N(9)	2.060(3)
Cu(1)–N(1)	2.093(3)	Cu(2)–N(7)	2.163(3)
Bond angles			
N(4)–Cu(1)–N(2)	178.14(11)	N(8)–Cu(2)–N(10)	174.36(11)
N(4)–Cu(1)–N(5)	91.18(11)	N(8)–Cu(2)–N(6)	92.55(11)
N(2)–Cu(1)–N(5)	90.66(11)	N(10)–Cu(2)–N(6)	92.88(11)
N(4)–Cu(1)–N(3)	81.87(11)	N(8)–Cu(2)–N(9)	93.20(11)
N(2)–Cu(1)–N(3)	97.29(11)	N(10)–Cu(2)–N(9)	81.48(11)
N(5)–Cu(1)–N(3)	123.61(11)	N(6)–Cu(2)–N(9)	144.29(11)
N(4)–Cu(1)–N(1)	98.13(11)	N(8)–Cu(2)–N(7)	80.40(11)
N(2)–Cu(1)–N(1)	80.89(10)	N(10)–Cu(2)–N(7)	98.58(11)
N(5)–Cu(1)–N(1)	114.16(11)	N(6)–Cu(2)–N(7)	115.83(11)
N(3)–Cu(1)–N(1)	122.23(11)	N(9)–Cu(2)–N(7)	99.88(10)

plane comprised of N(1), N(3), Cu(1) and N(5) (see Fig. 1). There is a small difference in axial and equatorial Cu–N bond lengths. The coordination geometry around the Cu(2) is approximately trigonal bipyramidal with a N_5 donor set (see Fig. 1). This coordination geometry is distorted from regular trigonal bipyramidal, as ascertained by the observed τ value of 0.5. Two nitrogen atoms of the phen ligands are in the axial positions and amido-N(6) nitrogen of cyanamide group and two nitrogens of phen ligands constitute the basal plane of the TBP. In the crystal of this dinuclear complex (Fig. 2), the distances between copper(II) ions and the fluorine of PF_6^- are too great to suggest coordination. The Cu(1)···Cu(2) distance is fairly large (5.156(1) Å). There is no strong hydrogen bond in the crystal of the complex. The counter ions (PF_6^- anions) are not close enough to interact with hydrogens of phen or apc ligands. As is shown in Fig. 2, there are some very weak π–π aromatic interactions between phenanthroline rings (including N(1), N(2), N(9), and N(10) atoms) and the angle between rings is 15.1°. The shortest distance between carbon atoms of two phen ligands (C(55)–C(4)) is 3.525 Å. The shortest distance between C(54) and plane of neighboring phen ligand is 3.202 Å.

The IR spectra of the neutral ligands ($dicydH_2$ and $Me_2dicydH_2$) show a strong band around 2250 cm^{-1} that is assigned to ν(C≡N) of the cyanamide groups. The IR spectrum of the tetraphenylarsonium salt of the anion ligand, $[AsPh_4]_2[Cl_2dicyd]$, shows a very strong band at 2050 cm^{-1} that is assigned to ν(N=C=N). The strong band at 2059 cm^{-1} in IR spectrum of Tlapc is assigned to ν(N=C=N).

Coordination of neutral and anionic dicyanamidobenzene ligands to metal cations can occur via amine or nitrile nitrogens and there are examples in the literature of both types of coordination [22]. Transition metal complexes appear to prefer coordination to the nitrile nitrogen. This may be due to the π-back-bonding and donor properties of the nitrile groups and the steric hindrance that would be experienced upon coordination to the amine of N-alkyl- or N-phenyl-substituted cyanamides. The neutral cyanamide ligands have π-donor properties that are due to the delocalization of the amine electron lone pair into a nitrile π-bond of the correct symmetry [22,58,59]. The anionic cyanamide ligand is expected to be a strong π-donor ligand because two lone pairs can delocalize into the nitrile π system. It is suggested that the resonance structure Ia (Scheme 2) will dominate when the anion ligand is coordinated to Cu (II) or Cu(I).



Scheme 2.

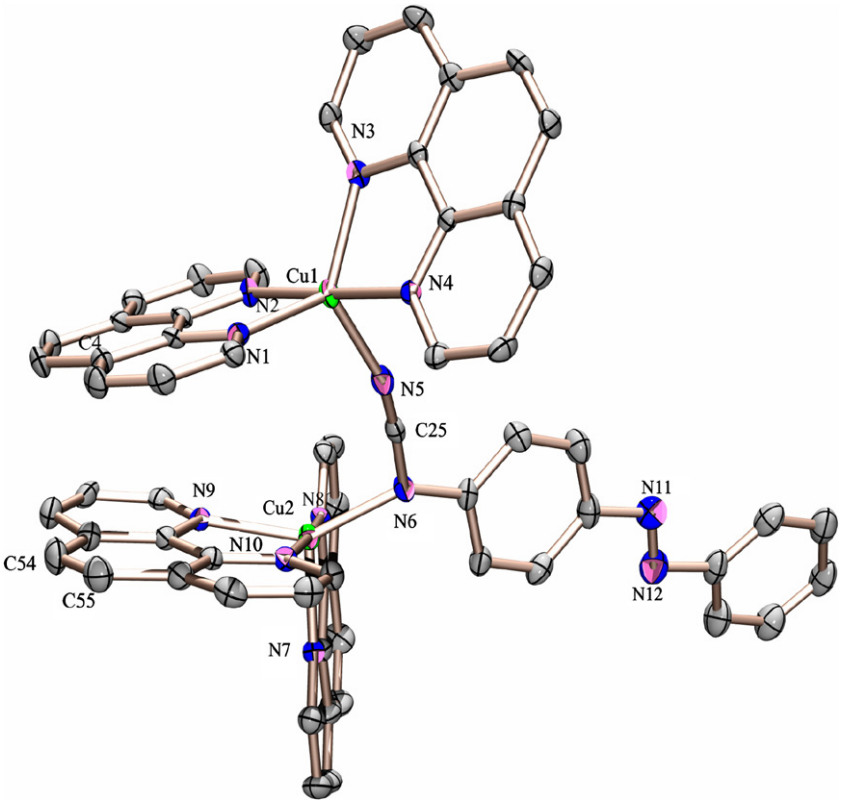


Fig. 1. ORTEP drawing of the $[\{Cu(phen)_2\}_2(\mu\text{-apc})]^{3+}$. The counterions, hydrogen atoms, and solvents of crystallization (two acetone) have been omitted for clarity.

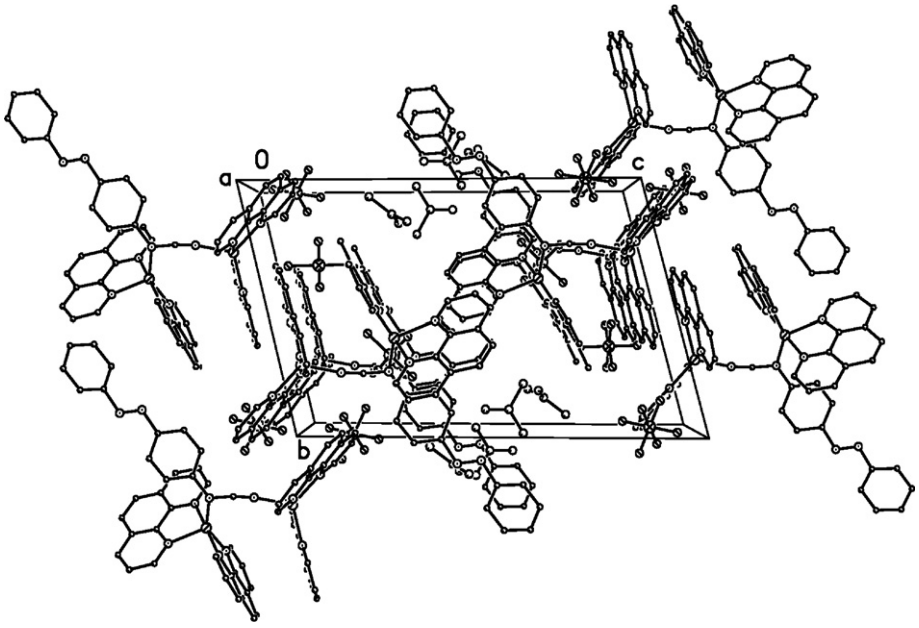


Fig. 2. Packing diagram of $[\{Cu(phen)_2\}_2(\mu\text{-apc})](PF_6)_3 \cdot 2CH_3COCH_3$.

The IR spectra of the complexes exhibit a strong absorption band around 2100 cm^{-1} which can assigned to the ν(N=C=N) band. In these complexes, the ν(N=C=N) was shifted 100–150 cm^{-1} to the lower wave number in contrast of the neutral ligand. The presence of only one sharp and intense absorption band for the cyanamide stretching frequency in the dinuclear complexes, $[\{Cu(phen)_2\}_2(\mu\text{-dicyd})](PF_6)_2$, $[\{Cu(phen)_2\}_2(\mu\text{-Me}_2\text{dicyd})](PF_6)_2$ and $[\{Cu(phen)_2\}_2(\mu\text{-Cl}_2\text{dicyd})](PF_6)_2$ provides evidence that both cyanamide moieties on the phenyl ring of

the bridging ligands, dicyd, Me_2dicyd and Cl_2dicyd are equivalent in the solid state [22,35,60]. When the cyanamide moieties are inequivalent, multiple ν(N=C=N) bands are observed [61]. The presence of a strong absorption band at 840 cm^{-1} in the complexes, which is assigned to ν(P–F), demonstrates the existence of PF_6^- as a counter ion [62]. The IR spectral data of the complexes are given in Table 3.

Electronic spectral data for the dinuclear complexes in DMF are given in Table 4, and the representative spectrum of $[\{Cu(phen)_2\}_2(\mu\text{-}Me_2dicyd)](PF_6)_2$ is shown in Fig. 3. The absorption band seen in the UV region ($\lambda < 352$ nm) is assigned to ligand-centered transition ($\pi \rightarrow \pi^*$) [63]. Spectroelectrochemical study of the free $dicyd^{-2}$ ligand was shown the radical anion absorption spectrum. Solutions of 1,4-dicyanamidobenzene dianion and its substituted derivatives are very air sensitive and upon oxidation to the radical anion give blue solutions which show a characteristic three-band pattern in the visible region [64]. In the visible region for $[\{Cu(phen)_2\}_2(\mu\text{-dicyd})](PF_6)_2$, $[\{Cu(phen)_2\}_2(\mu\text{-}Me_2dicyd)](PF_6)_2$ and $[\{Cu(phen)_2\}_2(\mu\text{-}Cl_2dicyd)](PF_6)_2$ complexes, the three bands at $\lambda > 550$ nm are suggested to originate from radical anion absorption. Spectroscopic analyses of Cu(II)–NCN chromophore have shown one ligand-to-metal charge transfer (LMCT) transition [61,65]. In these complexes, the band at $\lambda < 400$ nm shifts to higher energy as the numbers of electron-withdrawing substituents increase on the phenyl ring or as the donor number of the solvent is increased [66]. This behavior is consistent with a LMCT transition, which can be assigned to cyanamide anion to Cu(II) [61,65]. In $[\{Cu(phen)_2\}_2(\mu\text{-apc})](PF_6)_3$, the band at 712 nm is assigned to d-d transition. Two ligand field transitions for five-coordinated Cu(II) with distorted trigonal-bipyramidal geometry ($d_{xz} \approx d_{yz} \rightarrow d_{z^2}$ and $d_{x^2-y^2}$) are expected [36,56]. This complex showed only one broad transition at 712 nm. The transition with the higher wavelength ($\lambda > 900$ nm) cannot be detected by ordinary UV–Vis spectrophotometer.

Cyclic voltammetry data for the complexes in acetonitrile solution have been placed in Table 5, and a representative cyclic voltammogram of $[\{Cu(phen)_2\}_2(\mu\text{-}Me_2dicyd)](PF_6)_2$ complex is shown in Fig. 4. In these dinuclear complexes, the two quasi-reversible reduction couples at negative potential are assigned to the sequential reductions of phenanthroline ligands. Anionic phenylcyanamides do not have well-behaved cyclic voltammetry and generally give an irreversible oxidation wave [22,45]. However, 1,4-dicyanamidobenzene dianion ligands do give reversible oxidation waves with electrochemistry analogous to that of the quinone/hydroquinone system [67]. Cyclic voltammetry of the free $dicyd^{2-}$ and its derivatives (Cl_2dicyd^{2-} and Me_2dicyd^{2-}) in acetonitrile showed two redox couples corresponding to L(1−/2−) and L(0/1−), for example: $dicyd^{-/2-} = -0.200$ and $dicyd^{0/-} = 0.475$ V versus NHE [22,23]. These couples shift anodically when coordinated to Cu(II) (see Table 5). The L(1−/2−) and L(0/1−) couples also shift to more positive potentials as the electron-withdrawing ability of the substituents on the phenyl ring increase from CH_3 to Cl. This is consistent with the expected decrease in the basicity of 1,4-dicyanamidobenzene ligands [22,68]. Cyclic voltammetry of the thallium salt of apc^- in DMF showed one redox couple corresponding to apc(0/1−) = 0.86 V versus NHE [35]. For the complex $[\{Cu(phen)_2\}_2(\mu\text{-apc})]^{3+}$, the apc(0/1−) couple shifts to more positive potential (see Table 5). No reduction couple observed for the azo group (–N=N–) of the apc^- ligand.

According to the electronic spectral data for $[\{Cu(phen)_2\}_2(\mu\text{-dicyd})](PF_6)_2$, $[\{Cu(phen)_2\}_2(\mu\text{-}Me_2dicyd)](PF_6)_2$ and $[\{Cu(phen)_2\}_2(\mu\text{-}Cl_2dicyd)](PF_6)_2$, all of these complexes show radical anion absorption and to be consistent with the elemental analyses requires that a radical anion ($dicyd^{\cdot-}$) bridges Cu(I) and Cu(II). Therefore, the two couples seen between 0 and 0.5 V versus NHE (Fig. 4) are likely Cu(II/I) and dicyd(0/1−) and so their difference is not representative of the comproportionation constant (K_c). It is important to note that the dicyd-bridge dicopper complex is not really a mixed-valance system in the classical sense. The most positive couple in Fig. 4 is probably Cu(III/II).

The dinuclear copper(II) complex, $[\{Cu(phen)_2\}_2(\mu\text{-apc})](PF_6)_3$, can not show a radical anion absorption because the apc bridging ligand has one cyanamide group. The copper redox couples in this dinuclear complex occur in approximately the same region as the Cu(II/I) of mononuclear Cu(II) complexes with phen ligands. However, these reduction couples are split into two one-electron waves at 0.787 and 0.341 V which correspond to Cu(II,II/II,I) and Cu(II,I/I,I), respectively, and is indicative of significant metal–metal coupling. These redox couples seem to be quasi-reversible with an average separation between the cathodic and anodic waves of 100 mV, which is independent of the scan rate between 100–600 mV/s. The stability of a mixed-valance form can be quantified by the comproportionation equilibrium constant (K_c). The larger K_c is, the greater the electronic coupling. K_c is usually deduced from the difference in potential between metal center reduction couples, $\log K_c = 16.9(\Delta E)$. From the difference in Cu(II/I) couples of the dinuclear complexes (ΔE), the comproportionation constant (K_c) for the formation of the Cu(II/I) mixed-valence complex,

$$\text{Cu(II)–Cu(II)} + \text{Cu(I)–Cu(I)} \overset{K_c}{\rightleftharpoons} 2\text{Cu(II)–Cu(I)}$$

Table 3
IR[a] data for dinuclear copper complexes

Complex	ν(NCN)	ν(P–F)
$[\{Cu(phen)_2\}_2(\mu\text{-dicyd})](PF_6)_2$	2111	849
$[\{Cu(phen)_2\}_2(\mu\text{-}Me_2dicyd)](PF_6)_2$	2108	842
$[\{Cu(phen)_2\}_2(\mu\text{-}Cl_2dicyd)](PF_6)_2$	2122	846
$[\{Cu(phen)_2\}_2(\mu\text{-apc})](PF_6)_3$	2193	840

[a] IR data (KBr pellets) in cm^{-1}; strong absorptions.

Table 4
UV–Vis data[a] for dinuclear copper complexes

Complex	$\pi \rightarrow \pi^*$	Radical anion absorption	LMCT
$[\{Cu(phen)_2\}_2(\mu\text{-dicyd})](PF_6)_2$	267 (4.62)	573 (3.20), 618 (3.42), 687 (3.17)	361 (3.60)
$[\{Cu(phen)_2\}_2(\mu\text{-Me}_2\text{dicyd})](PF_6)_2$	269 (4.60)	577 (3.22), 621 (3.49), 689 (3.21)	363 (3.65)
$[\{Cu(phen)_2\}_2(\mu\text{-Cl}_2\text{dicyd})](PF_6)_2$	265 (4.68)	565 (3.16), 611 (3.37), 683 (3.05)	357 (3.53)
$[\{Cu(phen)_2\}_2(\mu\text{-apc})](PF_6)_3$	287 (4.73), 352 (3.49)		400 (3.25)

[a] λ in the nm with $\log\varepsilon$(ε in $M^{-1}\,cm^{-1}$) in parentheses; in DMF solution.

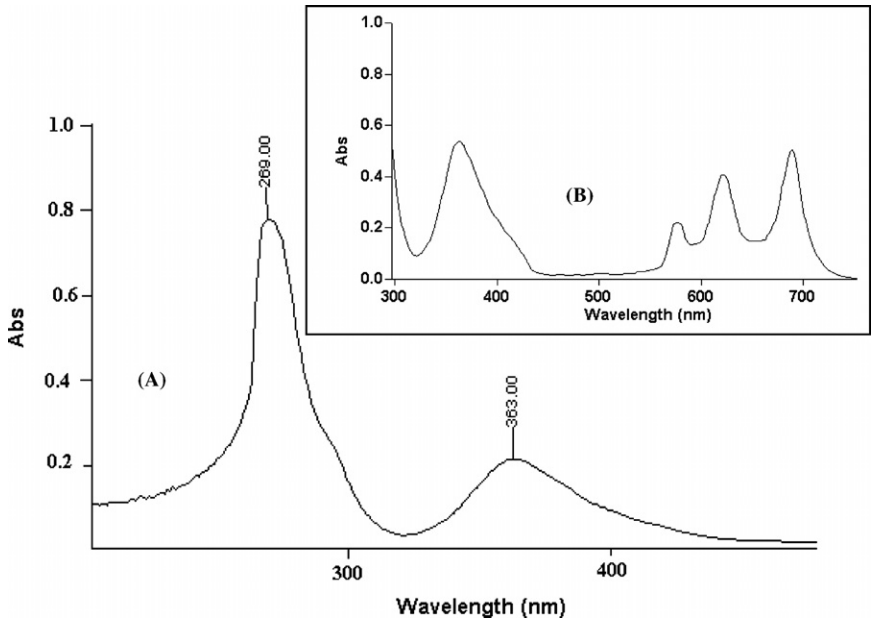


Fig. 3. Electronic spectra of $[\{Cu(phen)_2\}_2(\mu\text{-Me}_2\text{dicyd})](PF_6)_2$ in DMF, (A) 1×10^{-4} M; (B) 1×10^{-5} M.

Table 5
Cyclic votammetry data[a] for dinuclear copper complexes

Complex	L(0/1−)	Cu(III/II)	Cu(II/I)	Cu(II/I)
$[\{Cu(phen)_2\}_2(\mu\text{-dicyd})](PF_6)_2$	0.536	1.309	0.235	
$[\{Cu(phen)_2\}_2(\mu\text{-Me}_2\text{dicyd})](PF_6)_2$	0.482	1.262	0.173	
$[\{Cu(phen)_2\}_2(\mu\text{-Cl}_2\text{dicyd})](PF_6)_2$	0.560	1.340	0.324	
$[\{Cu(phen)_2\}_2(\mu\text{-apc})](PF_6)_3$	1.066		0.787	0.341

[a] Volts vs. NHE at scan rate 100 mV/s; in 0.1 M TBAH acetonitrile.



Fig. 4. Cyclic voltammogram of $[\{Cu(phen)_2\}_2(\mu\text{-Me}_2\text{dicyd})](PF_6)_2$ in acetonitrile, 0.1 M TBAH, at 100 mV/s.

was determined to be 3.45×10^7. This value is on the borderline between Classes II and III behavior in the Robin and Day classification [22,35,40,57,69–72] and requires further study before an absolute assignment can be given. In particular, the difference in solid state coordination environments may significantly perturb the Cu(II/I) couples and hence make a contribution to the comproportionation equilibrium. Whether this difference exists in solution is at the present unknown.

4. Conclusion

Several dinuclear copper complexes with cyanamide ligands have been synthesized and characterized. The dicyd-bridge dicopper complexes, $[\{Cu(phen)_2\}_2(\mu\text{-dicyd})](PF_6)_2$, $[\{Cu(phen)_2\}_2(\mu\text{-Me}_2\text{dicyd})](PF_6)_2$ and

[{Cu(phen)$_2$}$_2$(μ-Cl$_2$dicyd)](PF$_6$)$_2$, show radical anion absorption. [{Cu(phen)$_2$}$_2$(μ-apc)](PF$_6$)$_3$. 2CH$_3$COCH$_3$ has been characterized by X-ray crystallography. The phenycyanamides are ambidentate ligands whether neutral or in anionic form and so the possibility of linkage isomerism must be recognized. In this complex, the cyanamide group (NCN) of the bridging ligand is coordinated to Cu(II) ions through the nitrile and the amine nitrogen atoms. In contrast, a crystal structure of the complex [Cu(bpy)(2,3-Cl$_2$pcyd)$_2$], where bpy = 2,2′-bipyridine, showed only monodentate phenylcyanamide ligand coordinated through the cyano-nitrogen and Cu(II) in a distorted square plane of nitrogen donor atoms [22,61]. It was suggested that the reason dimerization does not occur for this complex, may be the greater steric crowding of the Cl atoms and/or the inductive effect of chlorine which makes the cyanamide group less basic and therefore a poorer bridging ligand.

It is interesting to speculate about the magnitude of comproportionation constant that would be consist with full delocalization and class III properties. The Creutz-Taube ion, [{(NH$_3$)$_5$Ru}$_2$(μ-pyrazine)]$^{5+}$, has been studied extensively, with the majority of evidence supporting a class III assignment for this ion. Its comproportionation constant has been found to be 1.9×10^7 in acetonitrile [69]. This value is close to K_c for complex [{Cu(phen)$_2$}$_2$-(μ-apc)](PF$_6$)$_3$ and suggests a considerable degree of delocalization in this complex.

The coordination chemistry of phenylcyanamide ligands still requires much effort to complete. The ability of the dicyd^{2-} bridging ligands to mediate metal–metal coupling suggests that phenylcyanamide derivatives may find their way into molecular materials possessing useful electronic and/or magnetic properties.

Acknowledgements

We are grateful to the Isfahan University of Technology (IUT) and University of Sistan and Baluchestan (USB) for financial support.

Appendix A. Supplementary data

CCDC 661573 contains the supplementary crystallographic data for [{Cu(phen)$_2$}$_2$(μ-apc)](PF$_6$)$_3$. 2CH$_3$COCH$_3$. These data can be obtained free of charge via http://www.ccdc.cam.ac.uk/conts/retrieving.html, or from the Cambridge Crystallographic Data Centre, 12 Union Road, Cambridge CB2 1EZ, UK; fax: (+44) 1223-336-033, or e-mail: deposit@ccdc.cam.ac.uk.

References

[1] S. Youngme, J. Phatchimkun, N. Wannarit, N. Chaichit, S. Meejoo, G.A. van Albada, J. Reedijk, Polyhedron 27 (2008) 304.
[2] K.S. Min, A.G. Dipasquale, J.A. Golen, A.L. Rheingold, A.M. Arif, J.S. Miller, J. Am. Chem. Soc. 129 (2007) 6056.
[3] V. Balzani, A. Juris, M. Venturi, S. Campagna, S. Serroni, Chem. Rev. 96 (1996) 759.
[4] T. Cauchy, E. Ruiz, S. Alvarez, J. Am. Chem. Soc. 128 (2006) 15722.
[5] S.S. Isied, M.Y. Ogawa, F.J. Wishart, Chem. Rev. 92 (1992) 381.
[6] G. Simonneaux, A. Bondon, Chem. Rev. 105 (2005) 2672.
[7] R. Abdel Malak, Z. Gao, J.F. Wishart, S.S. Isied, J. Am. Chem. Soc. 126 (2004) 13888.
[8] C.Y. Duan, Z.L. Lu, X.Z. You, Z.Y. Zhou, T.C.W. Mak, Q. Luo, J.Y. Zhou, Polyhedron 17 (1998) 4131.
[9] C. Herrmann, J. Neugebauer, J.A. Gladysz, M. Reiher, Inorg. Chem. 44 (2005) 6174.
[10] L. De Cola, Topics in Current Chemistry, vol. 257, Springer, New York, 2005.
[11] A.S. Blum, T. Ren, D.A. Parish, S.A. Trammell, M.H. Moore, J.G. Kushmerick, G.L. Xu, J.R. Deschamps, S.K. Pollack, R. Shashidhar, J. Am. Chem. Soc. 127 (2005) 10010.
[12] J.A. Thomas, C.J. Jones, J.A. McCleverty, M.G. Hutchings, Polyhedron 15 (1996) 1409.
[13] J.W. Steed, J.L. Atwood, Supramolecular Chemistry, John Wiley & Sons Ltd., Chichester, 2000.
[14] S. Arounaguiri, B.G. Maiya, Inorg. Chem. 38 (1999) 842.
[15] J.K. Barton, J. Am. Chem. Soc. 112 (1990) 4960.
[16] M.J. Han, Z.M. Duan, Q. Hao, S.Z. Zheng, K.Z. Wang, J. Phys. Chem. C 111 (2007) 16577.
[17] M. Querol, B. bozic, N. Salluce, P. Belser, Polyhedron 22 (2003) 655.
[18] J.-P. Launay, Chem. Soc. Rev. 30 (2001) 386.
[19] M. Fabre, J. Jaud, M. Hliwa, J.-P. Launay, J. Bonvoisin, Inorg. Chem. 45 (2006) 9332.
[20] J.A. McCleverty, M.D. Ward, Acc. Chem. Res. 31 (1998) 842.
[21] W. Kaim, A. Klein, M. Gloeckle, Acc. Chem. Res. 33 (2000) 755.
[22] R.J. Crutchley, Coord. Chem. Rev. 219–221 (2001) 125.
[23] M.A.S. Aquino, F.L. Lee, E.J. Gabe, C. Bensimon, J.E. Greedan, R.J. Crutchley, J. Am. Chem. Soc. 114 (1992) 5130.
[24] R.J. Crutchley, Adv. Inorg. Chem. 41 (1994) 273.
[25] R.J. Crutchley, Compr. Coord. Chem. II 2 (2004) 785.
[26] M.D. Ward, J.A. McCleverty, J. Chem. Soc., Dalton Trans. (2002) 275.
[27] V. Kasack, W. Kaim, H. Binder, J. Jordanov, E. Roth, Inorg. Chem. 34 (1995) 1924.
[28] B. Sarkar, S. patra, J. Fiedler, R.B. Sunoj, D. Janardanan, S.M. Mobin, M. Niemeyer, G.K. Lahiri, W. Kaim, Angew. Chem., Int. Ed. 44 (2005) 5655.
[29] A. Klein, O. Lavastre, J. Fiedler, Organometallics 25 (2006) 635.
[30] M. Heilmann, S. Frantz, W. Kaim, J. Fiedler, C. Duboc, Inorg. Chim. Acta 359 (2006) 821.
[31] S. Bayly, J.A. McCleverty, M.D. Ward, D. Gatteschi, F. Totti, Inorg. Chem. 39 (2000) 1288.
[32] A.P. Meacham, K.L. Druce, Z.R. Bell, M.D. Ward, J.B. Keister, A.B.P. Lever, Inorg. Chem. 42 (2003) 7887.
[33] S. Patra, B. Sarkar, S. Ghumaan, J. Fiedler, W. Kaim, G.K. Lahiri, Inorg. Chem. 43 (2004) 6108.
[34] A. Escuer, F.A. Mautner, N. Sanz, R. Vicente, Polyhedron 23 (2004) 1409.
[35] P.J. Mosher, G.P.A. Yap, R.J. Crutchley, Inorg. Chem. 40 (2001) 1189.
[36] G. Murphy, P. Nagle, B. Murphy, B. Hathaway, J. Chem. Soc., Dalton Trans. (1997) 2645.
[37] T. Gennett, D.F. Milner, M.J. Wearer, J. Phys. Chem. 89 (1985) 2787.
[38] G.M. Sheldrick, SHELXS v. 5.1, Structure Determination Software Suite, Bruker AXS, Madison, WI, USA, 1998.
[39] A.C. Hopkinson, M.H. Line, Int. J. Quant. Chem. 13 (1978) 349.
[40] A.R. Rezvani, C. Bensimon, B. Cromp, C. Reber, J.E. Greedan, V.V. Kondratiev, R.J. Crutchley, Inorg. Chem. 36 (1997) 3322.
[41] H. Hadadzadeh, A.R. Rezvani, F. Belangar-Gariepy, J. Mol. Struct. 740 (2005) 165.
[42] A.R. Rezvani, H. Hadadzadeh, B. Patrick, Inorg. Chim. Acta 336 (2002) 125.

[43] H. Chiniforoshan, N. Safari, J. Mohammad Nezhad, H. Hadadzadeh, A.H. Mahmoudkhani, Inorg. Chim. Acta 359 (2006) 2101.
[44] N. Safari, B. Notash, J. Mohammad Nezhad, H. Chiniforoshan, H. Hadadzadeh, A.R. Rezvani, Inorg. Chim. Acta 358 (2005) 2967.
[45] R.J. Crutchley, M.L. Naklicki, Inorg. Chem. 28 (1989) 1955.
[46] A. Escuer, N. Sanz, R. Vicente, F. Mautner, Inorg. Chem. 42 (2003) 541.
[47] J. Zhou, C.Y. Sun, L.P. Jin, Polyhedron 26 (2007) 4025.
[48] C. Gkioni, A.K. Boudalis, Y. Sanakis, C.P. Raptopoulou, Polyhedron 26 (2007) 2536.
[49] S. Youngme, N. Wannarit, C. Pakawatchai, N. Chaichit, E. Somsook, U. Turpeinen, I. Mutikainen, Polyhedron 26 (2007) 1459.
[50] F.P. Pruchnik, U. Dawid, A. Kochel, Polyhedron 25 (2006) 3647.
[51] P. Phuengphai, S. Youngme, N. Chaichit, C. Pakawatchai, G.A. van Albada, M. Quesada, J. Reedijk, Polyhedron 25 (2006) 2198.
[52] M. Devereux, M. McCann, J.F. Cronin, G. Ferguson, V. McKee, Polyhedron 18 (1999) 2141.
[53] M. Brophy, G. Murphy, C. O'Sullivan, B. Hathaway, B. Murphy, Polyhedron 18 (1999) 611.
[54] B. Murphy, B. Hathaway, Coord. Chem. Rev. 243 (2003) 237.
[55] A.W. Addison, T.N. Rao, J. Reedijk, J. VanRijn, G.C. Verschoor, J. Chem. Soc., Dalton Trans. (1984) 1349.
[56] H. Saravani, A.R. Rezvani, G. Mansouri, A.R. Salehi Rad, H.R. Khavasi, H. Hadadzadeh, Inorg. Chim. Acta 360 (2007) 2829.
[57] H. Hadadzadeh, S.J.A. Fatemi, S.R. Hosseinian, H.R. Khavasi, R. Pöttgen, Polyhedron 27 (2008) 249.
[58] H.F. Hanneike, R.S. Drago, J. Am. Chem. Soc. 90 (1968) 5112.
[59] H. Stafast, H. Bock, Chem. Ber. 107 (1974) 1882.
[60] A.R. Rezvani, H. Hadadzadeh, L. Mazi Esfahani, J. Chem. Res. (S) (3) (2002) 139.
[61] R.J. Crutchley, R. Hynes, E.J. Gabe, Inorg. Chem. 29 (1990) 4921.
[62] K. Nakamato, Infrared and Ramgan Spectra of Inorganic and Coordination Compounds Part II: Application in Coordination Organometallic and Bioinorganic Chemistry, 5th ed., Wiley-Interscience, New York, 1997.
[63] A.B.P. Lever, Inorganic Electronic Spectroscopy, 2nd ed., Elsevier, Amsterdam, 1984.
[64] A.R. Rezvani, C.E.B. Evans, R.J. Crutchley, Inorg. Chem. 34 (1995) 4600.
[65] M.K. Brader, E.W. Ainscough, E.N. Baker, A.M. Brodie, S.L. Ingham, J. Chem. Soc., Dalton Trans. (1990) 2785.
[66] V. Gutmann, The Donor–Acceptor Approach to Molecular Interactions, Plenum Press, New York, 1978.
[67] C.K. Mann, K.K. Barnes, Electrochemical Reactions in Nonaqueous Systems, Marcel Dekker, New York, 1970.
[68] C.E.B. Evans, G.P.A. Yap, R.J. Crutchley, Inorg. Chem. 37 (1998) 6161.
[69] C. Creutz, M.H. Chou, Inorg. Chem. 26 (1987) 2995.
[70] M.L. Naklicki, R.J. Crutchley, J. Am. Chem. Soc. 116 (1994) 6045.
[71] M.L. Naklicki, R.J. Crutchley, Inorg. Chim. Acta 225 (1994) 123.
[72] M.B. Robin, P. Day, Adv. Inorg. Chem. Radiochem. 10 (1967) 247.

surprisingly the corresponding selenium analogues, namely, diselenophosph(in)ato metal compounds are only observed for Ni(II) [7]. The reaction of Pd(II) and Pt(II) salts with diselenophosphonates $[(RO)RPSe_2]^-$ was proved unsuccessful by Woolins and co-workers [8] due to the immediate precipitation of black amorphous solids. Thus, this report provides not only non-covalent Se···Se secondary interactions revealed in adjacent, square-planar $M[Se_2P(OR)_2]_2$ units but also a valuable addition to the coordination chemistry of group 10 metals, incorporating a PSe_2 motif.

2. Experimental

2.1. General procedures and instrumentation

Commercial CH_2Cl_2 and alcohol were distilled from P_4O_{10} and Mg, respectively. Hexane was distilled from Na/K. All chemicals were purchased from commercial sources, and used as received. All reactions were performed in oven-dried Schlenk glassware by using standard inert-atmosphere techniques. $Pt(CH_3CH_2CN)_2Cl_2$ [9] and $NH_4[Se_2P(OR)_2]$ (R = Et, ^{n}Pr, ^{i}Pr) [10] were prepared according to the literature methods. $Pd(CH_3CN)_2Cl_2$ was obtained from Aldrich. The elemental analyses were done using a Perkin–Elmer 2400 CHN analyzer. ^{1}H, ^{31}P and ^{77}Se NMR spectra were recorded on an Advance-300 Fourier transform spectrometer. The $^{31}P\{^1H\}$ and $^{77}Se\{^1H\}$ are referenced externally against 85% H_3PO_4 ($\delta = 0$ ppm) and PhSeSePh ($\delta = 463$ ppm), respectively. Melting points were measured by using a Fargo melting point apparatus, MP-2D.

2.2. Preparation of $Pd[Se_2P(OR)_2]_2$ (R = Et, **1a**; ^{i}Pr, **1b**; ^{n}Pr, **1c**)

$Pd(CH_3CN)_2Cl_2$ (0.10 g, 0.38 mmol) and the diselenophosphate ligands $NH_4[Se_2P(OR)_2]$ (R = Et, 0.23 g; ^{i}Pr, 0.25 g; ^{n}Pr, 0.25 g, 0.77 mmol) were dissolved in 30 mL of dichloromethane in a 100 mL Schlenk flask. The solution was stirred for 12 h at room temperature under a nitrogen atmosphere. After filtration, the filtrate was evaporated under vacuum, re-dissolved in dichloromethane and layered with hexane which afforded the red brown crystalline material of $Pd[Se_2P(OR)_2]_2$.

Compound **1a**: Yield, 62% (0.20 g). Elemental *Anal.* Calc. for $PdSe_4P_2O_4C_8H_{20}$: C, 14.46; H, 3.03. Found: C, 14.50; H, 2.98%. ^{1}H NMR ($CDCl_3$): δ 1.37 (t, $^3J_{HH} = 7.2$ Hz, 12H, OCH_2CH_3), 4.17 (dq, $^3J_{PH} = 2.5$ Hz, $^3J_{HH} = 7.2$ Hz, 8H, OCH_2CH_3); m.p., 167 °C.

Compound **1b**: Yield, 82% (0.30 g). Elemental *Anal.* Calc. for $PdSe_4P_2O_4C_{12}H_{28}$: C, 20.00; H, 3.92. Found: C, 20.15; H, 4.03%. ^{1}H NMR ($CDCl_3$): δ 1.37 (d, $^3J_{HH} = 6.2$ Hz, 24H, $OCH(CH_3)_2$), 4.80 (m, 4H, $OCH(CH_3)_2$); m.p., 171 °C.

Compound **1c**: Yield, 65% (0.24 g). Elemental *Anal.* Calc. for $PdSe_4P_2O_4C_{12}H_{28}$: C, 20.00; H, 3.92. Found: C, 20.05; H, 4.06%. ^{1}H NMR ($CDCl_3$): δ 0.96 (t, $^3J_{HH} = 7.2$ Hz, 12H, $OCH_2CH_2CH_3$), 1.77 (sextet, $^3J_{HH} = 7.2$ Hz, 8H, $OCH_2CH_2CH_3$), 4.08 (td, $^3J_{PH} = 2.9$ Hz, $^3J_{HH} = 7.0$ Hz, 8H, $OCH_2CH_2CH_3$); m.p., 172 °C.

2.3. Preparation of $Pt[Se_2P(OR)_2]_2$ (R = Et, **2a**; ^{i}Pr, **2b**; ^{n}Pr, **2c**)

$Pt(CH_3CH_2CN)_2Cl_2$ (0.10 g, 0.26 mmol) and $NH_4[Se_2P(OR)_2]$ (R = Et, 0.16 g; ^{i}Pr, 0.17 g; ^{n}Pr, 0.17 g, 0.53 mmol) were dissolved in 30 mL of dichloromethane in a 100 mL Schlenk flask. The solution was stirred for 12 h at room temperature under a nitrogen atmosphere. After filtration, the filtrate was evaporated under vacuum, then re-dissolved in dichloromethane and layered with hexane, which afforded the red brown crystalline material of $Pt[Se_2P(OR)_2]_2$.

Compound **2a**: Yield, 62% (0.12 g). Elemental *Anal.* Calc. for $PtSe_4P_2O_4C_8H_{20}$: C, 12.76; H, 2.68. Found: C, 12.68; H, 2.59%. ^{1}H NMR ($CDCl_3$): δ 1.38 (t, $^3J_{HH} = 7.0$ Hz, 12H, OCH_2CH_3), 4.24 (dq, $^3J_{PH} = 3.0$ Hz, $^3J_{HH} = 7.0$ Hz, 8H, OCH_2CH_3); m.p., 165 °C.

Compound **2b**: Yield, 71% (0.14 g). Elemental *Anal.* Calc. for $PtSe_4P_2O_4C_{12}H_{28}$: C, 17.81; H, 3.49. Found: C, 17.95; H, 3.62%. ^{1}H NMR ($CDCl_3$): δ 1.40 (d, $^3J_{HH} = 6.2$ Hz, 24H, $OCH(CH_3)_2$), 4.96 (m, 4H, $OCH(CH_3)_2$); m.p., 168 °C.

Compound **2c**: Yield, 64% (0.13 g). Elemental *Anal.* Calc. for $PtSe_4P_2O_4C_{12}H_{28}$: C, 17.81; H, 3.49. Found: C, 17.75; H, 3.46%. ^{1}H NMR ($CDCl_3$): δ 0.96 (bs, 12H, $OCH_2CH_2CH_3$), 1.63 (m, 8H, $OCH_2CH_2CH_3$), 4.13 (m, 8H, $OCH_2CH_2CH_3$); m.p., 169 °C.

2.4. Crystallography

The structures of **1b** and **2b** were obtained by single crystal X-ray diffraction. Crystals were grown from CH_2Cl_2 layered with hexane and were mounted on the tips of glass fibers with epoxy resin. For compound **1b**, data were collected at 293 K on a Siemens P4, and were corrected for Lorentzian, polarization and ψ-scan absorption effects. Data were collected on a Siemens SMART CCD diffractometer for compound **2b**. Cell parameters were retrieved with SMART software [11] and refined with SAINT software [12] on all observed reflections ($I > 10\sigma(I)$). Data reduction was performed with SAINT, which corrects for Lorentzian, polarization and ψ-scan absorption effects. The structures of **1b** and **2b** were solved by the use of direct methods, and refinement was performed by the least-squares method on F^2 with the SHELXL-97 package [13], incorporated in SHELXTL/PC V5.10 [14]. Hydrogen atoms were added. Selected crystal data for compounds **1b** and **2b** are summarized in Table 1 and selected bond distances and angles are given in Table 2.

Table 1
Crystallographic data of complexes **1b** and **2b**

	1b	**2b**
Formula	$C_{12}H_{28}PdO_4P_2Se_4$	$C_{12}H_{28}PtO_4P_2Se_4$
Fw	720.52	809.21
Crystal system	triclinic	triclinic
Space group	$P\bar{1}$	$P\bar{1}$
a (Å)	6.546(3)	6.510(1)
b (Å)	8.507(2)	8.555(1)
c (Å)	11.205(3)	11.174(1)
α (°)	101.70(2)	102.24(1)
β (°)	96.85(2)	96.57(1)
γ (°)	98.83(3)	98.31(1)
V (Å^3)	596.4(3)	595.0(1)
Z	1	1
Crystal size (mm)	0.40 × 0.30 × 0.20	0.30 × 0.10 × 0.10
ρ_{calc} (g cm^{-3})	2.006	2.259
λ (Mo Kα) (Å)	0.71073	0.71073
μ (mm^{-1})	7.026	12.160
T (K)	293(2)	298(2)
Reflections collected	3251	2994
Independent reflections (R_{int})	2581 (0.0300)	2053 (0.0357)
Data/parameters	2153/107	1972/106
R_1^a	0.0434	0.0325
wR_2^b	0.1133	0.0850
Goodness-of-fit	1.083	1.111
Largest difference peak and hole (e/Å^3)	0.936 and −1.212	1.000 and −1.540

[a] $R_1 = |F_o| - |F_c||/|F_o|$.
[b] $wR_2 = [w(F_o^2 - F_c^2)^2]/[w(F_o^2)^2]^{1/2}$.

Table 2
Selected bond distances (Å) and angles (°) for $M[Se_2P(O^iPr)_2]_2$

Compound ***1b***			
Pd(1)–Se(2)	2.440(1)	Se(1)–P(1)	2.157(2)
Pd(1)–Se(1)	2.456(1)	Se(2)–P(1)	2.152(2)
Se(2)–Pd(1)–Se(2A)	180.0	P(1)–Se(1)–Pd(1)	85.52(4)
Se(2)–Pd(1)–Se(1A)	93.77(3)	P(1)–Se(2)–Pd(1)	86.02(5)
Se(2)–Pd(1)–Se(1)	86.23(3)	Se(1)–P(1)–Se(2)	101.93(6)
Compound ***2b***			
Pt(1)–Se(1)	2.439(1)	Se(1)–P(1)	2.165(2)
Pt(1)–Se(2)	2.451(1)	Se(2)–P(1)	2.165(2)
Se(1)–Pt(1)–Se(1A)	180.0	P(1)–Se(1)–Pt(1)	86.65(5)
Se(1)–Pt(1)–Se(2A)	85.85(2)	P(1)–Se(2A)–Pt(1)	86.36(5)
Se(1)–Pt(1)–Se(2)	94.15(2)	Se(1)–P(1)–Se(2A)	100.55(7)

Symmetry transformations used to generate equivalent atoms – A: $-x+1$, $-y+1$, $-z$.

3. Results and discussion

3.1. Synthesis and multinuclear NMR spectroscopy

The reactions of dsep with $Pd(CH_3CN)_2Cl_2$ or $Pt(C_2H_5CN)_2Cl_2$ afford complexes which can be formulated as $M[Se_2P(OR)_2]_2$ (M = Pd, Pt). Two representative molecular structures, determined by single-crystal X-ray analysis, contain metal ions in a square-planar environment (vide infra). These complexes can be dissolved in any organic solvent but are insoluble in water. A summary of the $^{31}P\{^1H\}$ and $^{77}Se\{^1H\}$ NMR data for all of the compounds is shown in Table 3.

Table 3
^{31}P and ^{77}Se NMR data for compounds **1** and **2**

Complex	^{31}P δ (ppm) $J_{(P-Se)}$ or $^2J_{(P-Pt)}$ (Hz)	^{77}Se δ (ppm) $J_{(Se-P)}$ or $J_{(Se-Pt)}$ (Hz)
1a	65.3 $^1J_{(P-Se)} = 594.5, 618.0$ $^3J_{(P-Se)} = 22.4$	−12.0 (Se_A–P); −12.0 (Se_B–P) $J_{(SeA-P)} = 617.3$; $J_{(SeB-P)} = 595.6$
1b	60.2 $^1J_{(P-Se)} = 586.7, 610.9$ $^3J_{(P-Se)} = 22.4$	16.877 (Se_A–P); 16.875 (Se_B–P) $J_{(SeA-P)} = 609.4$; $J_{(SeB-P)} = 588.2$
1c	66.5 $^1J_{(P-Se)} = 594.4, 617.7$ $^3J_{(P-Se)} = 22.4$	−13.0 (Se_A–P); −13.0(Se_B–P) $J_{(SeA-P)} = 616.9$; $J_{(SeB-P)} = 595.2$
2a	56.2 $^1J_{(P-Se)} = 547, 576$ $^3J_{(P-Se)} = 15$ $^2J_{(P-Pt)} = 505$	80.1 $J_{(Se-Pt)} = 87$ $J_{(Se-P)} = 561$
2b	50.1 $^1J_{(P-Se)} = 540, 571$ $^3J_{(P-Se)} = 15$ $^2J_{(P-Pt)} = 498$	104.8 $J_{(Se-Pt)} = 85$ $J_{(Se-P)} = 556$
2c	57.5 $^1J_{(P-Se)} = 548, 577$ $^3J_{(P-Se)} = 14$ $^2J_{(P-Pt)} = 506$	75.0 $J_{(Se-Pt)} = 88$ $J_{(Se-P)} = 563$

Both ^{31}P and ^{77}Se NMR spectra display interesting structural characteristics. Three sets of selenium satellite peaks are identified in compounds **1** in the ^{31}P NMR spectra (Fig. 1). Two sets of satellite peaks are due to the one-bond coupling ($^1J_{P-Se} = 586$–618 Hz) between the phosphorus and selenium nuclei, a reflection of unequal Pd–Se bond lengths (vide infra). The third pair originates from the three-bond coupling ($^3J_{P-Se} = 22.4$ Hz) to the selenium nuclei on the opposite side. The $^{77}Se\{^1H\}$ NMR spectrum of **1b** (the inset of Fig. 1) displays two doublets with $^1J_{Se-P}$ values of 588 and 618 Hz, apparently arising from the phosphorus nuclei coupled to two different selenium nuclei (Se_A and Se_B), and these values are in good agreement with those obtained from the ^{31}P NMR spectrum. Presumably the Se_A and Se_B nuclei in **1b** have almost identical chemical shifts.

Thus, both chemically and magnetically inequivalent selenium nuclei within the PSe_2 moiety were identified in the square-planar palladium(II) complexes of **1**. Although a diselenoimidodiphosphinato compound of palladium, $Pd[(SePPh_2)_2N]_2$ [15], has been characterized, its ^{31}P NMR spectrum, which exhibited a singlet with selenium satellites ($^1J_{Se-P} = 543$ Hz), apparently did not display a coupling pattern as complicated as those in compounds **1a**–**1c**.

The ^{31}P NMR spectrum of compound **2b** (Fig. 2) exhibited a single resonance at 50.1 ppm (56.2 and 57.5 ppm for **2a** and **2c**). This peak was further flanked by four sets of satellites: one due to phosphorus–platinum coupling ($^2J_{P-Pt} = 505$ Hz), the other three attributable to phosphorus–selenium coupling ($^1J_{P-Se} = 571$, 540 Hz, and $^3J_{P-Se} =$ 15 Hz). Therefore, two non-equivalent selenium nuclei

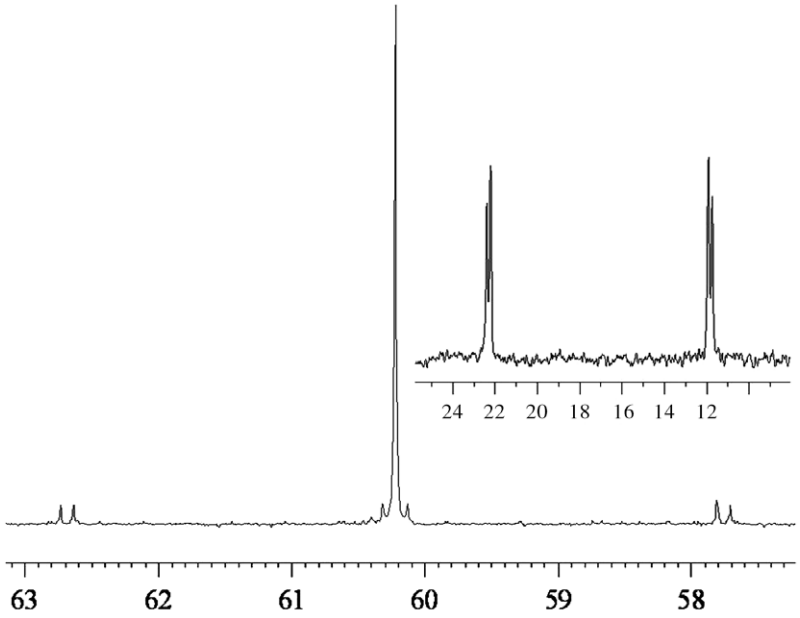


Fig. 1. The $^{31}P\{^{1}H\}$ and $^{77}Se\{^{1}H\}$ (inset) NMR spectra of $Pd[Se_2P(O^iPr)_2]_2$ (**1b**) in $CDCl_3$ solution.

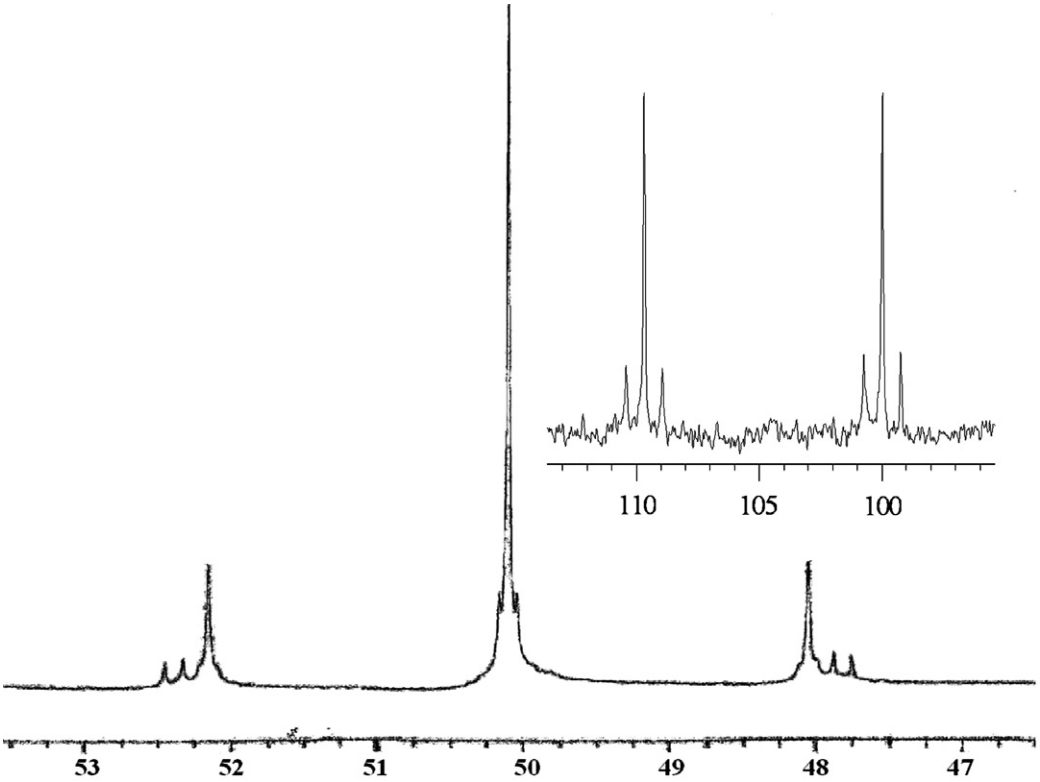


Fig. 2. The $^{31}P\{^{1}H\}$ and $^{77}Se\{^{1}H\}$ (inset) NMR spectra of $Pt[Se_2P(O^iPr)_2]_2$ (**2b**) in $CDCl_3$ solution.

within the PSe_2 moiety of the platinum complex were resolved, which was reminiscent of unequal Pt–Se bond distances (vide infra). Although the phosphorus–selenium coupling constant (539 Hz) in $Pt[(SePPh_2)_2N]_2$ [15] was similar to those in **2**; surprisingly the phosphorus–platinum coupling constant (105 Hz) was much smaller than those in **2**.

The $^{77}Se\{^{1}H\}$ NMR spectrum of **2** displayed a central doublet arising from selenium–phosphorous coupling ($^{1}J_{Se-P} = 561$, 556, 563 Hz, **2a**–**2c**) and two smaller doublets flanking the central doublet arising from selenium coupled to ^{195}Pt ($I = 1/2$, natural abundance 33.6%). The separation of these two doublets was $^{1}J_{Se-Pt} = 87$ Hz (85 and 88 Hz for **2b** and **2c**, respectively) and this is similar

to the reported values for $Pt(Se_2CNEt_2)PR_3Cl$ [16] and $Pt(dppe)(SePh)_2$ [17]. Presently, it is not known exactly why only one doublet due to coupling to the phosphorus nuclei is observed in the ^{77}Se NMR spectrum. Additionally, the $^1J_{Se-P}$ value revealed in the ^{77}Se NMR spectrum is approximately the average value of those from the ^{31}P NMR measurements (Table 3).

The ethyl and propyl derivatives of both compounds **1** and **2** always display a chemical shift in close proximity in both the ^{31}P and ^{77}Se NMR spectra, while the isopropyl derivatives are much further off. This is not unusual since a similar trend appears to be general to copper(I) and silver(I) cluster compounds incorporating diselenophosphate ligands [4]. Presumably, the chemical shift difference is due to the different steric effect of the isopropyl group.

3.2. Structure of $Pd[Se_2P(O^iPr)_2]_2$ (**1b**)

Compound **1b** crystallizes in the triclinic space group $P\bar{1}$ with a molecule per unit cell. A perspective view of complex **1** is shown in Fig. 3a. The Pd(II) ion is located on a center of symmetry and is linked by four selenium atoms of two dsep ligands in a square-planar arrangement. The Se–Pd bond distances are unequal, 2.440(1) and 2.456(1) Å, which are comparable to those observed in $Pd[(SePPh_2)_2N]_2$ (2.4368(6) and 2.4594(6) Å) [15]. The Se–Pd–Se angle within the chelated ring is 86.23(3)°. The average torsion angle of Se–P–Se–Pd is 4.32(6)°. A similar structural motif was revealed in $Pd[Se_2CN^iBu_2]_2$ [18] and $Pd[Se_2CC(CN)_2]_2^{2-}$ [19]. The average P–Se bond length, 2.154(2) Å, is intermediate between those expected for P–Se single (2.26 Å) and double (2.09 Å) bonds. Weak intermolecular interactions exist between the Se atoms of adjacent molecules, which lead to the formation of a polymeric chain in the solid state. A packing diagram along the *a* axis showing the Se···Se interactions is displayed in Fig. 3b. The Se···Se distances, depicted by broken lines, are 3.545 and 3.303 Å, which is much shorter than the sum of the van der Waals radii of selenium, 4.0 Å, and can be considered as weak secondary interactions.

3.3. Structure of $Pt[Se_2P(O^iPr)_2]_2$ (**2b**)

Compound **2b** crystallizes in the triclinic space group $P\bar{1}$ with one molecule per unit cell. The crystal structure of compound **2b** is shown in Fig. 4a. The Pt atom lies on a crystallographic inversion center and is tetragonally coordinated by four Se atoms from two dsep ligands. Thus, a four-membered chelate ring is formed. The average torsion

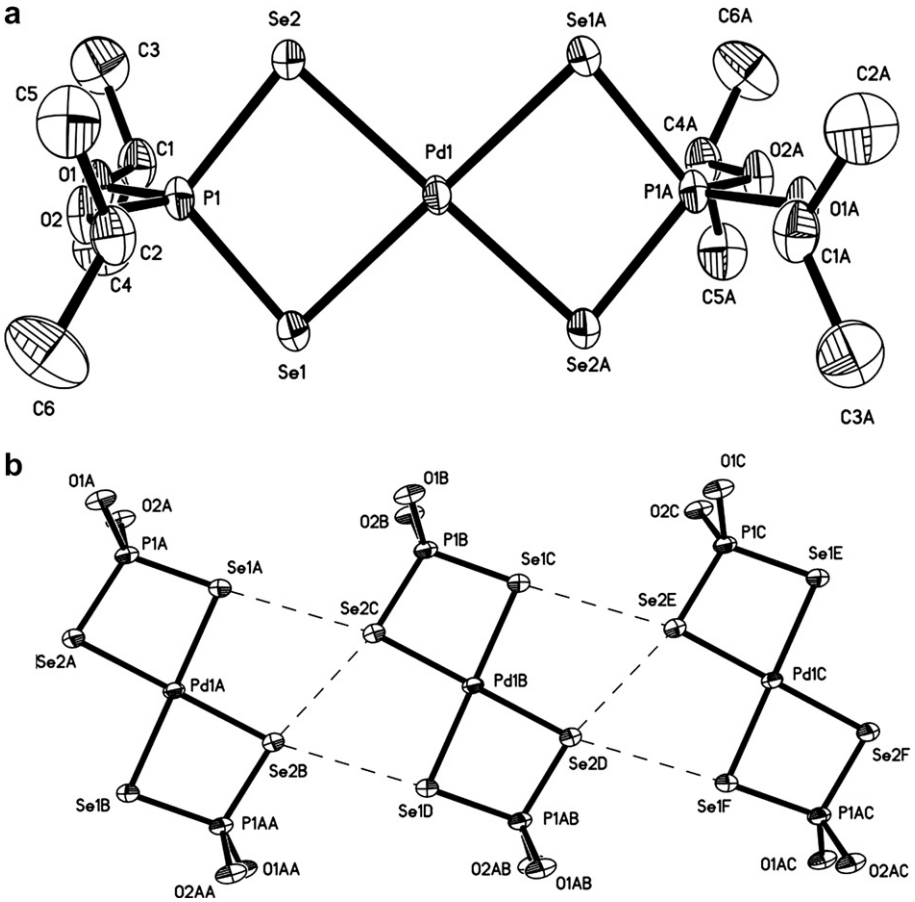


Fig. 3. (a) The structure of $[Pd\{Se_2P(O^iPr)_2\}_2]$ (**1b**) (thermal ellipsoids at the 30% probability level). (b) The packing diagram of $[Pd\{Se_2P(O^iPr)_2\}_2]$ (**1b**) along the *a* axis.

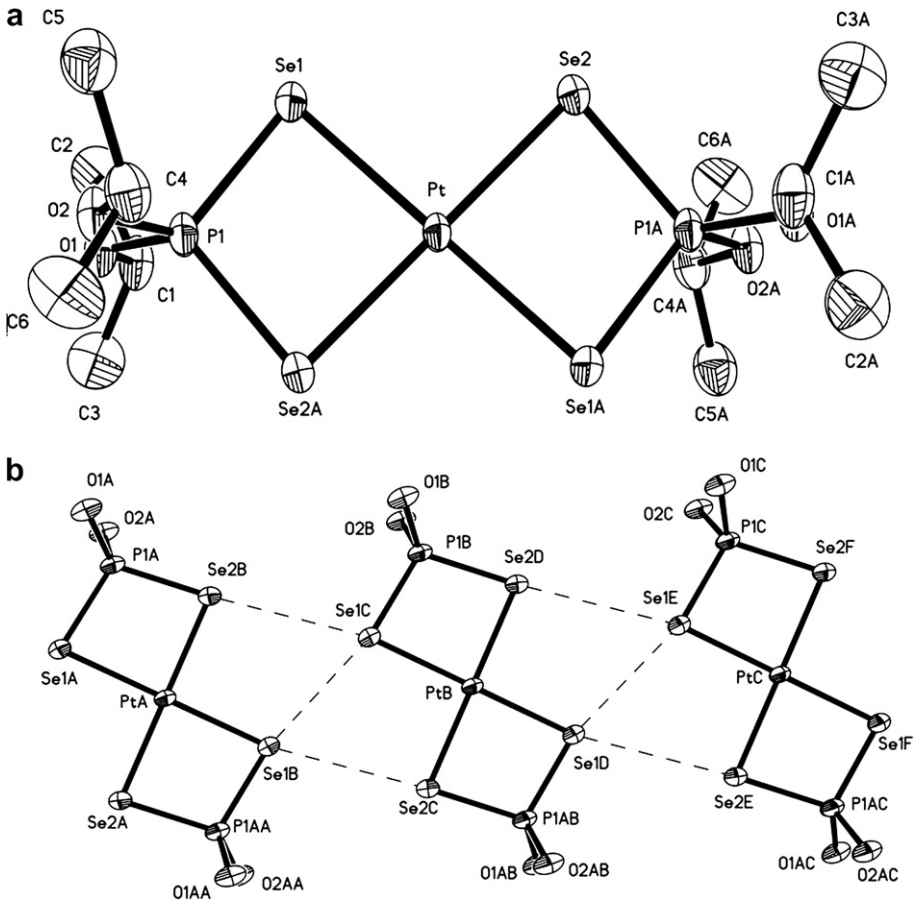


Fig. 4. (a) The structure of $[Pt\{Se_2P(O^iPr)_2\}_2]$ (**2b**) (thermal ellipsoids at the 30% probability level). (b) The packing diagram viewed down the *a* axis of $[Pt\{Se_2P(O^iPr)_2\}_2]$ (**2b**).

angle of Se–P–Se–Pt is 5.83(5)°. The geometry at the platinum center is square-planar as a consequence of the restricted bite, 100.55(7)°, of the chelating dsep ligand and the Se–Pt–Se bond angles are in the range 85.85(2)–94.15(2)°. Unequal Pt–Se bond distances, 2.439(1) and 2.451(1) Å, are also observed. These distances are comparable with those in $Pt[Se_2CC(CN)_2]_2^{2-}$, $Pt[(SePPh_2)_2N]_2$ and $Pt[(SeP^iPr_2)_2N]_2$ [20]. The P–Se bond distances, 2.165(2) Å, are almost identical and are indicative of delocalization of the negative charge across the PSe_2 unit. The packing diagram (Fig. 4b) displays a polymeric chain which is formed via Se···Se interactions with distances of 3.698 and 3.386 Å.

It is of interest to know that the observed M–Se bond distances for platinum(II) are almost identical to those for palladium(II). This is significant since the non-polar covalent radius of Pt (1.30 Å) is longer than that of Pd (1.28 Å) [21].

4. Conclusions

Square-planar complexes of palladium(II) and platinum(II) incorporating dialkyl diselenophsphato ligands have been successfully prepared. Weak intermolecular Se···Se interactions from adjacent dsep ligands yield a one-dimensional chain structure. Solution ^{31}P NMR studies reveal that the two selenium atoms within the four-membered chelate rings are both chemically and magnetically inequivalent. This observation is largely due to the existence of unequal M–Se bond lengths.

Acknowledgement

This research was supported by the National Science Council of Taiwan (NSC 96-2113-M-259–004).

Appendix A. Supplementary data

CCDC 667558 and 667559 contain the supplementary crystallographic data for **1b** and **2b**. These data can be obtained free of charge via http://www.ccdc.cam.ac.uk/conts/retrieving.html, or from the Cambridge Crystallographic Data Centre, 12 Union Road, Cambridge CB2 1EZ, UK; fax: (+44) 1223-336-033; or e-mail: deposit@ccdc.cam.ac.uk. Supplementary data associated with this article can be found, in the online version, at doi:10.1016/j.poly.2008.02.021.

References

[1] (a) I. Haiduc, F.T. Edelmann, Supramolecular Organometallic Chemistry, Wiley, Weinheim, New York, 1999;
(b) R. Gleiter, D.B. Werz, B.J. Rausch, Chem. Eur. J. 9 (2003) 2676.

[2] (a) J.M. Chen, B.K. Santra, C.W. Liu, Inorg. Chem. Commun. 7 (2004) 1103;
(b) H.W. Chang, B. Sarker, C.W. Liu, Cryst. Growth Des. 7 (2007) 2691;
(c) Y.F. Lin, H.W. Chang, S.Y. Lu, C.W. Liu, J. Phys. Chem. C 111 (2007) 18538.

[3] C.W. Liu, C.S. Fang, C.W. Chuang, T.S. Lobana, B.J. Liaw, J.C. Wang, J. Organomet. Chem. 692 (2007) 1726.

[4] (a) C.W. Liu, H.C. Chen, J.C. Wang, T.C. Keng, Chem. Commun. (1998) 1831;
(b) C.W. Liu, I.J. Shang, J.C. Wang, T.C. Keng, Chem. Commun. (1999) 995;
(c) C.W. Liu, C.M. Hung, H.C. Chen, J.C. Wang, T.C. Keng, K.M. Guo, Chem. Commun. (2000) 1897;
(d) C.W. Liu, H.C. Chen, J.C. Wang, T.C. Keng, Angew. Chem., Int. Ed. 40 (2001) 2342;
(e) C.W. Liu, C.M. Hung, J.C. Wang, T.C. Keng, J. Chem. Soc., Dalton Trans. (2002) 3482;
(f) C.W. Liu, C.M. Hung, B.K. Santra, H.C. Chen, H.H. Hsueh, Inorg. Chem. 42 (2003) 3216;
(g) C.W. Liu, C.M. Hung, H.C. Haia, B.J. Liaw, L.S. Liou, Y.F. Tsai, J.C. Wang, Chem. Commun. (2003) 976;
(h) C.W. Liu, C.M. Hung, B.K. Santra, Y.H. Chu, Z. Lin, Inorg. Chem. 43 (2004) 4306;
(i) C.W. Liu, H.C. Haia, C.M. Hung, B.K. Santra, B.J. Liaw, Z. Lin, J.C. Wang, Inorg. Chem. 43 (2004) 4464;
(j) C.W. Liu, I.J. Shang, R.J. Fu, B.J. Liaw, J.C. Wang, I.J. Chang, Inorg. Chem. 45 (2006) 2335;
(k) C.M. Hung, Y.H. Chu, B.K. Santra, B.J. Liaw, J.C. Wang, C.W. Liu, J. Chin. Chem. Soc. 53 (2006) 825;
(l) Y.J. Hsu, C.M. Hung, Y.F. Lin, B.J. Liaw, T.S. Lobana, S.Y. Lu, C.W. Liu, Chem. Mater. 18 (2006) 3323;
(m) T.S. Lobana, J.C. Wang, C.W. Liu, Coord. Chem. Rev. 251 (2007) 91.

[5] I. Haiduc, D.B. Sowerby, S.F. Lu, Polyhedron 14 (1995) 3389.

[6] I. Haiduc, D.B. Sowerby, S.F. Lu, Polyhedron 15 (1996) 2469.

[7] (a) L. Gastaldi, P. Porta, Cryst. Struct. Commun. 6 (1977) 175;
(b) P.J.H.A.M. Leemput, T.W. Hummelink, J.H. Noordik, P.J. Beurskens, Cryst. Struct. Commun. 4 (1975) 167.

[8] I.P. Gray, A.M.Z. Slawin, J.D. Woollins, J. Chem. Soc., Dalton Trans. (2005) 2188.

[9] V.Y. Kukushkin, Å. Oskarsson, L.I. Elding, Inorg. Synth. 31 (1997) 279.

[10] (a) M.V. Kudchadker, R.A. Zingaro, K.J. Irgolic, Can. J. Chem. 46 (1968) 1415;
(b) C.W. Liu, I.J. Shang, C.M. Hung, J.C. Wang, T.C. Keng, J. Chem. Soc., Dalton Trans. (2002) 1974.

[11] SAINT V4.043: Software for the CCD Detector System, Bruker Analytical X-ray System, Madison, WI, 1995.

[12] SMART V4.043: Software for the CCD Detector System, Bruker Analytical X-ray System, Madison, WI, 1995.

[13] G.M. Sheldrick, SHELXL-97: Program for the Refinement of Crystal Structure, University of Göttingen, Göttingen, Germany, 1997.

[14] SHELXL 5.10 (PC Version): Program Library for Structure Solution and Molecular Graphics, Bruker Analytical X-ray System, Madison, WI, 1998.

[15] C. Papadimitriou, P. Veltsistas, J. Novosad, R. Cea-Olivares, A. Toscano, P. Garcia y Garcia, M. Lopez-Cardosa, A.M.Z. Slawin, J.D. Woollins, Polyhedron 16 (1997) 2727.

[16] W.H. Pan, J.P. Fackler Jr., J. Am. Chem. Soc. 110 (1978) 5783.

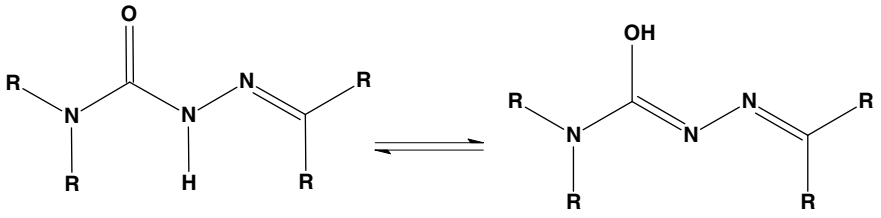
[17] A. Singhal, V.K. Jain, B. Varghese, E.R.T. Tiekink, Inorg. Chim. Acta 285 (1999) 190.

[18] J.C. Wang, J.P. Fackler Jr., Acta Crystallogr., Sect. C 45 (1989) 951.

[19] C.C. McLauchlan, S.D. Robowski, J.A. Ibers, Inorg. Chem. 40 (2001) 1372.

[20] D. Cupertino, D.J. Birdsall, A.M.Z. Slawin, J.D. Woollins, Inorg. Chim. Acta 290 (1999) 1.

[21] E.C.M. Chen, W.E. Wentworth, J. Phys. Chem. A 101 (1997) 3088.



Keto (A) Enol (B)

Scheme 1.

structural reports on cadmium(II) complexes of a semicarbazone according to the best of our knowledge [5].

2. Experimental

2.1. Materials

Di-2-pyridyl ketone (Aldrich) was used as received. $CdBr_2 \cdot 4H_2O$, $(CH_3COO)_2Cd \cdot 2H_2O$ and NaN_3 were commercial products of higher grade (Aldrich) and solvents were purified according to standard procedures. Elemental analyses were carried out using a vario EL III CHNS analyzer at SAIF, Kochi, India. Infrared spectra were recorded on a JASCO FT-IR-5300 spectrometer in the range 4000–400 cm^{-1} using KBr pellets. Electronic spectra were recorded on a Cary 5000 version 1.09 UV–Vis–NIR spectrophotometer using solutions in DMF. The ^1H and ^{13}C NMR spectra were recorded using Bruker DRX 500, with $CDCl_3$ as solvent and TMS as standard at the Sophisticated Instruments Facility, Indian Institute of Science, Bangalore, India.

2.2. Synthesis of di-2-pyridyl ketone-N^4-phenyl semicarbazone (HL)

The semicarbazone was synthesized by the following method. A methanolic solution of di-2-pyridyl ketone (0.184 g, 1 mmol) was mixed with N^4-phenylsemicarbazide (0.151 g, 1 mmol) in methanol and three drops of glacial acetic acid. The reaction mixture was refluxed for 2 h. On slow evaporation, colorless crystalline compound formed was filtered, washed with ether and recrystallized from ethanol and dried over P_4O_{10} *in vacuo*. Melting point = 160 °C. ^1H NMR ($CDCl_3$, 400 MHz, δ from TMS): 13.37 (s, N^4H, 1H), 8.78 (d, C^1H, 1H, $J = 6.4$ Hz), 8.66 (d, $C^{11}H$, 1H, $J = 7.2$ Hz), 8.37 (s, N^5H, 1H), 7.87 (t, C^3H, 1H, $J = 7$), 7.79 (t, C^9H, 1H, $J = 6$), 7.56 (d, C^4H, 1H, J = 8), 7.51 (d, C^8H, 1H, $J = 8$), 7.34 (m, $C^{2,10,14,15,17,18}$, 6H), 7.07 (t, $C^{16}H$, 1H, $J = 7$). ^{13}C NMR ($CDCl_3$, δ from TMS): C(1), 148.68, C(2), 123.87, C(3), 136.81, C(4), 126.24, C(5), 151.96, C(6), 152.95, C(7), 148.0; C(8), 128.89, C(9), 137.98, C(10), 123.87, C(11), 140.28, C(12), 156.20, C(13), 137.98, C(14), 123.75, C(15), 123.38, C(16), 119.60, C(17), 123.38, C(18), 123.75 (see Fig. 1).

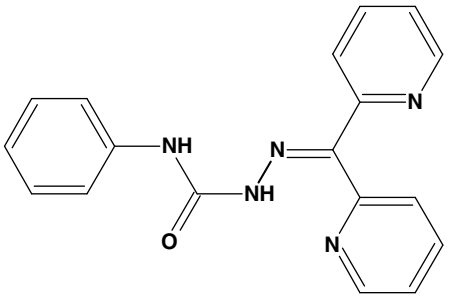


Fig. 1. Molecular structure of HL.

2.3. Synthesis of $[CdL(CH_3COO)]_2 \cdot 2CH_3OH$ (**1**)

A methanolic solution of HL (0.317 g, 1 mmol) and $Cd(CH_3COO)_2 \cdot 2H_2O$ (0.266 g, 1 mmol) were mixed and heated under reflux for 5 h. On slow evaporation, yellow crystals were obtained, which were separated, washed with ether and dried over P_4O_{10} *in vacuo.*

2.4. Synthesis of $Cd(HL)Br_2$ (**2**)

A methanolic solution of HL (0.317 g, 1 mmol) and $CdBr_2 \cdot 4H_2O$ (0.344 g, 1 mmol) were mixed and heated under reflux for 5 h. On slow evaporation, yellow coloured solid was resulted which were separated, washed with ether and dried over P_4O_{10} *in vacuo*.

2.5. Synthesis of $Cd_2L_2(N_3)_2 \cdot H_2O$ (**3**)

A methanolic solution of HL (0.317 g, 1 mmol) and $Cd(CH_3COO)_2 \cdot 2H_2O$ (0.266 g, 1 mmol) were mixed and heated under reflux for 2 h and then added methanolic solution of NaN_3 (0.065 g, 1 mmol). The resulting mixture was refluxed for 4 h. On slow evaporation yellow colored solid formed was separated, washed with ether and dried over P_4O_{10} *in vacuo*.

2.6. X-ray crystallography

Single crystals of compound **1** suitable for X-ray analysis were obtained from its methanolic solution and were found to be orthorhombic with a space group '*pbca*'. X-ray diffraction measurements were carried out on CrysAlis CCD diffractometer with graphite-monochromated

Mo Kα ($\lambda = 0.71073$ Å) radiation. The program CRYSALIS RED was used for data reduction and cell refinement [8]. The structure was solved by direct methods using SHELXS [9] and refined by full-matrix least-squares refinement on F^2 using SHELXL [10]. The N–H hydrogen atoms were located from difference Fourier maps and refined isotropically. The remainder of the H-atoms were included in calculated positions and refined as riding atoms using default SHELXL parameters. The structure of the compound **1** was plotted using the program DIAMOND Version 3.1d [11] and PLATON [12]. The final refinement cycle was based on all 3610 independent reflections and 290 variables with $R_1 = 0.0301$, $wR_2 = 0.0665$. The crystallographic data along with the structural refinements are given in Table 1.

Table 1
Crystal data and structure refinement parameters for $[CdL(CH_3COO)]_2 \cdot 2CH_3OH$

Empirical formula	$C_{42}H_{42}Cd_2N_{10}O_8$
Formula weight	1039.68
Temperature (K)	120(2)
Wavelength (Å)	0.71073
Crystal system	orthorhombic
Space group	'*pbca*'
Unit cell dimensions	
a (Å)	13.8648(3)
b (Å)	15.3588(5)
c (Å)	19.2468(4)
α (°)	90
β (°)	90
γ (°)	90
Volume (Å^3)	4098.54(18)
Z	4
D_{calc} (g/cm^3)	1.685
Absorption coefficient	1.105 mm^{-1}
F(000)	2096
Crystal size (mm)	0.23 × 0.18 × 0.13
θ Range for data collection (°)	2.86–25
Index ranges	$-13 \leqslant h \leqslant 16$, $-18 \leqslant k \leqslant 15$, $-22 \leqslant l \leqslant 22$
Reflections collected	3610
Independent reflections [*R*(int)]	290 [0.0361]
Refinement method	full-matrix least-squares on F^2
Data/restraints/parameters	5041/0/313
Goodness-of-fit on F^2	1.065
Final *R* indices [$I > 2\sigma(I)$]	$R_1 = 0.0301$, $wR_2 = 0.0665$
R indices (all data)	$R_1 = 0.0440$, $wR_2 = 0.0725$

3. Results and discussion

3.1. Synthesis of complexes

Compounds **1** and **2** were prepared by direct reaction between the ligand and the corresponding salts, while compound **3** was prepared by the replacement of the acetate in $Cd(CH_3COO)_2 \cdot 2H_2O$ by the azide ion. Elemental analyses data (Table 2) of complexes **1** and **3** reveal that metal–ligand are in the ratio 1:1 and in complex **2**, di-2-pyridyl ketone-N^4-phenyl semicarbazone (HL) interacts with Cd(II) ions in the presence of anion Br^- in the ratio 1:1.

3.2. Crystal structure of $[CdL(CH_3COO)]_2 \cdot 2CH_3OH$

Fig. 2 shows the molecular structure of the binuclear centrosymmetric Cd(II) complex with the atom numbering scheme. Both Cd centers being hexacoordinated and the coordination around the Cd(II) ion can be best described as a distorted octahedron with a CdO_3N_3 chromophore. Each Cd atom is coordinated by azomethine nitrogen, oxygen atom from the principal ligand, two pyridyl nitrogens and two oxygen atoms from the acetate group. The acetate groups serve as bidentate ligands and the semicarbazones as tetradentate ligands. The two pyridyl nitrogens from the principal ligand are coordinated to two different Cd centers forming a cyclic type architecture (Fig. 3). The coordination of oxygen from the semicarbazone ligand occurs through deprotonation after enolization, confirmed by the partial single and double bond nature of C7–O1 [1.350(4)] Å and N3–C7 [1.368(4) Å] bond lengths [13,14]. The C6–N2 and N2–N3 bond distances are 1.257(4) Å and 1.338(3) Å respectively, which reveal extensive delocalization over the entire binuclear coordination framework. Table 3 shows the selected bond lengths and bond angles of compound **1**.

In the case of this Cd-semicarbazone complex, Cd–O bond distances are Cd1–O1, 2.249(2) Å; Cd1–O2, 2.7666 Å; Cd1–O3, 2.434(2) Å and Cd–N bond distances are Cd1–N1, 2.168(3) Å; Cd1–N2, 2.515(3) Å and Cd1–N5, 2.155(3) Å respectively. The Cd1–O1 bond distance is slightly less than the other Cd–O bond distances reported for other octahedral Cd(II) complexes [15,16]. The Cd1–O2 and Cd1–O3 bond distances lie within the range of $Cd–O_{carboxylate}$ bond distances [2.209(2)–2.879(2) Å]

Table 2
Elemental analyses and color of Cd(II) complexes

Compound	Color	Calc. (found) (%)		
		C	H	N
HL	yellow	68.13 (67.44)	4.76 (4.80)	22.07 (22.14)
$[CdL(CH_3COO)]_2 \cdot 2CH_3OH$ (**1**)	yellow	48.16 (48.52)	3.97 (4.07)	13.20 (13.47)
$[Cd(HL)Br_2]$ (**2**)	yellow	36.69 (36.67)	2.64 (2.56)	12.45 (11.80)
$[CdLN_3]_2$ (**3**)	yellow	44.46 (45.06)	3.05 (3.15)	24.15 (23.36)

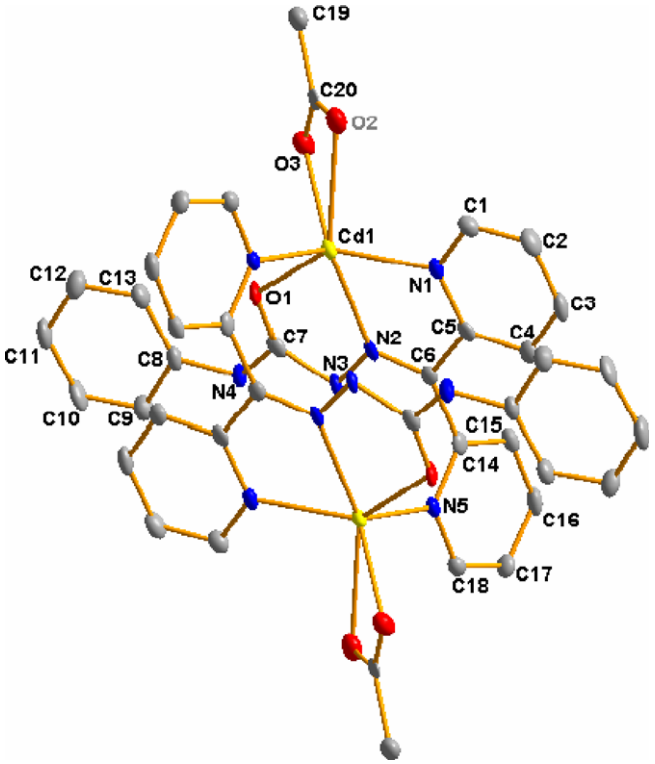


Fig. 2. Structure and labeling diagram for compound 1 (hydrogen atoms and methanol molecules are omitted for clarity).

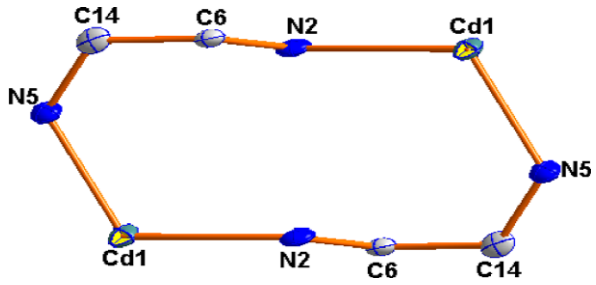


Fig. 3. Cyclic formation through cadmium centers.

Table 3
Selected bond lengths (Å) and bond angles (°) for $[CdL(CH_3COO)]_2 \cdot 2CH_3OH$

Bond lengths	Bond angles
Cd(1)–N(5) 2.155(3)	N(5)–Cd(1)–N(1) 116.23(9)
Cd(1)–N(1) 2.168(3)	N(5)–Cd(1)–O(1) 92.67(9)
Cd(1)–O(1) 2.249(2)	N(1)–Cd(1)–O(1) 132.65(9)
Cd(1)–O(3) 2.434(2)	N(5)–Cd(1)–O(3) 107.15(9)
Cd(1)–N(2) 2.515(3)	N(1)–Cd(1)–O(3) 116.82(9)
O(1)–C(7) 1.350(4)	N(5)–Cd(1)–N(2) 119.45(9)
N(1)–C(1) 1.349(4)	O(3)–Cd(1)–N(2) 123.35(8)
N(1)–C(5) 1.479(4)	C(7)–O(1)–Cd(1) 119.56(18)
N(2)–C(6) 1.257(4)	C(1)–N(1)–C(5) 125.7(3)
N(2)–N(3) 1.338(3)	C(6)–N(2)–N(3) 113.1(3)
N(3)–C(7) 1.368(4)	C(6)–N(2)–Cd(1) 120.7(2)
N(4)–C(8) 1.326(4)	N(3)–N(2)–Cd(1) 126.16(19)
N(4)–C(7) 1.354(4)	N(2)–N(3)–C(7) 100.2(3)
N(4)–H(4N) 0.85(3)	O(1)–C(7)–N(3) 130.7(3)

reported for Cd(II)–$O_{carboxylate}$ coordination polymers [17]. The Cd1–N2 bond distance is slightly larger than the other Cd–N bond distances, which supports the lack of significant out-of-plane π-bonding. The trans angle, O2–Cd1–N2 is 155.84(8)° indicating that the compound **1** has large distortion from octahedral geometry [18]. Other indication of distorted octahedral geometry is the bond angle of O1–Cd1–O3, 85.51(8)°.

The unit cell packing diagram of the complex viewed along the *b* axis is given in Fig. 4. It can be observed that the molecules are packed in a zig-zag manner. The molecules in the unit cell are connected through intermolecular hydrogen bonding interactions involving the oxygen atom of the methanol molecule [O(4)–H(104)–O(3); O(4)–H(104), 0.81(4) Å; O(4)···O(3), 2.726(4) Å; H(104)···O(3), 1.92(4) Å; O(4)–H(104)···O3, 174(3)° and N4–H4N···$O4^{i}$ [i = $-x$, $-1/2 + y$, $3/2 - z$]; N4–H4N, 0.85(3) Å; N4···O4, 3.132(4) Å; H4N···O4, 2.30(3) Å; N4–H4N···O4, 166(3)°] (Fig. 5).

Ring puckering analysis show that the ring Cg(3) consisting of atoms Cd1–N1–C5–C6–N2 adopts an envelope on Cd1 [$Q_T = 0.1086$ (22) Å] [19]. The diverse π–π stacking and C–H–π interactions give rise to polymeric chains in the unit cell. The shortest π–π interactions are perceived at 3.1992 Å for Cg(2)–$Cg(3)^{ii}$ [Cg(2) = Cd1–O1–C7–N3–N2; ii = $-x$, $-y$, $2 - z$]. Two C–H–π interactions are present in the unit cell. They are C(11)–H(11)–$Cg(2)^{iii}$ [d_{H-Cg} = 2.94 Å; iii = $-1/2 + x$, y, $3/2 - z$] and C(21)–H(21)–$Cg(5)^{iii}$ [$d_{H-Cg} = 2.93$ Å; iii = x, $1/2 - y$, $-1/2 + z$]. The π–π, C–H–π and hydrogen bonding interactions contribute stability to the unit cell packing.

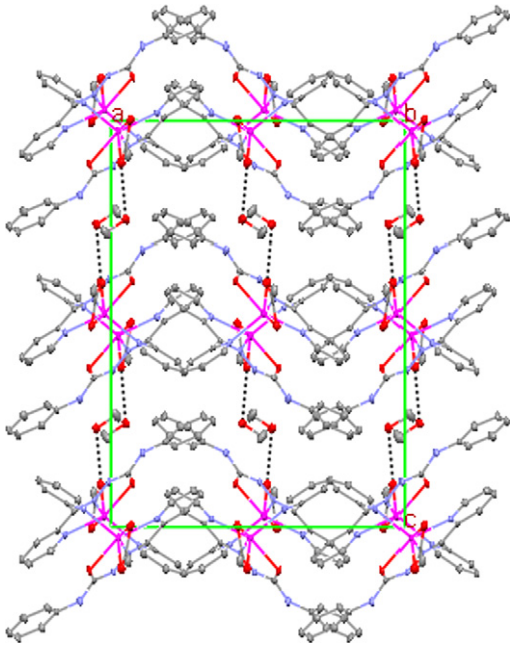


Fig. 4. Unit cell packing diagram viewed along b axis.

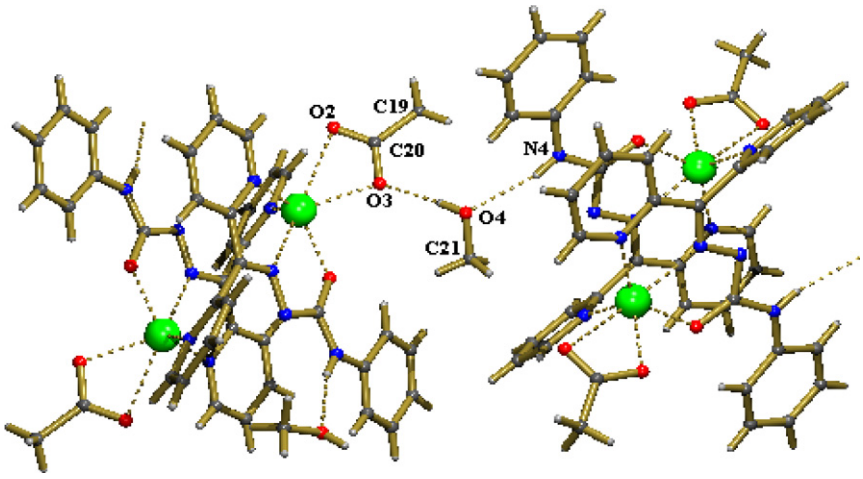


Fig. 5. Intermolecular hydrogen bonding interactions through methanol molecule.

3.3. Spectroscopic studies

The tentative assignments of the selected IR bands are listed in the Table 4. The spectrum of the ligand exhibits a medium band at 3369 cm^{-1} which is assigned to ν(NH) vibration. The absence of ν(NH) in the spectra of complexes **1** and **3** suggests that the ligand loses this proton on complexation, thus acting as uninegative ligand [20]. In complex **2**, the presence of a band at 3251 cm^{-1} corresponding to ν(NH) vibration indicates that the semicarbazone is coordinated in the neutral form. A band at 1718 cm^{-1} in the ligand has significant contribution from C=O stretching vibration and absence of such band in complexes **1** and **3** confirming the coordination through enolate oxygen. The presence of a band at 1656 cm^{-1} for complex **2** supports the keto form of the ligand in this complex.

On coordination of the azomethine nitrogen, the IR stretching frequency ν(C=N) at 1591 cm^{-1} shifts to 1605, 1597 and 1596 cm^{-1} for complexes **1**, **2** and **3**, respectively [21–23]. The spectra of the complexes exhibit a systematic shift in the position of ν(N–N) bands in the region 1148–1141 cm^{-1} and confirms the coordination of the azomethine nitrogen. The bands appearing at 457, 451 and 463 cm^{-1} which correspond to ν(Cd–N) for complexes **1**–**3** again confirm the coordination of the azomethine nitrogen [24]. Coordination of pyridyl nitrogen causes the out-of-plane bending vibrational band to shift from 601 cm^{-1} to higher frequencies 622, 621 and 627 cm^{-1} for complexes **1**–**3** [25]. Presence of a band at 1515 and 1521 cm^{-1} for complexes **1** and **3** are assigned to the newly formed ν(N=C) after enolization [26]. The asymmetric and symmetric stretching vibrations of the acetate group appear at 1568 and 1437 cm^{-1}, respectively, for complex **1** having the separation value $\Delta\nu = 131$ cm^{-1} suggests the presence of chelating acetate group linked with the metal center for the complex [27,28]. The azido complex **3** exhibits a strong band at 2052 cm^{-1} corresponding to ν_a(NNN) stretching vibration of the coordinating azido group.

Electronic spectrum of the ligand shows an absorption maximum at 40000 cm^{-1} attributed to intra-ligand $\pi \rightarrow \pi^*$ transitions of the pyridyl ring and imine function of the semicarbazone moiety. The peak at 30770 cm^{-1} indicate $n \rightarrow \pi^*$ transition of the amide function, which is shifted to higher energy values upon complexation [23] (Table 5).

The ^{1}H NMR spectrum of the compound HL along with the assignments is given in Fig. 6. A sharp singlet, which integrate as one hydrogen at $\delta = 13.37$ ppm is assigned to the proton attached to the nitrogen atom N(4). The downfield shift of this proton is assigned to its

Table 5
Electronic spectral assignments for the ligand and its Cd(II) complexes

Compound	π–π^*	n–π^*	MLCT
HL	40000	30770	
$[CdL(CH_3COO)]_2 \cdot 2CH_3OH$ (**1**)	37590	31640	24810
$[Cd(HL)Br_2]$ (**2**)	36360	31250	23530
$[CdLN_3]_2$(**3**)	37310	31850	24690

Table 4
IR spectral assignments for ligand and its Cd(II) complexes

Compound	ν(NH)	ν(C=N)	ν(CO)	ν(N=C)	ν(N–N)
HL	3369	1591	1718		1129
$[CdL(CH_3COO)]_2 \cdot 2CH_3OH$ (**1**)		1605		1515	1148
$[Cd(HL)Br_2]$ (**2**)	3257	1597	1656		1147
$[CdLN_3]_2$ (**3**)		1596		1521	1141

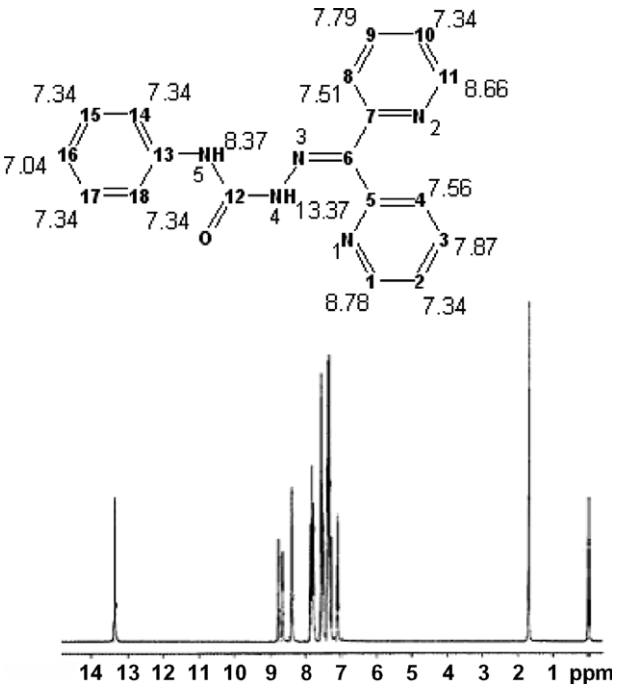


Fig. 6. ^{1}H NMR spectrum of HL.

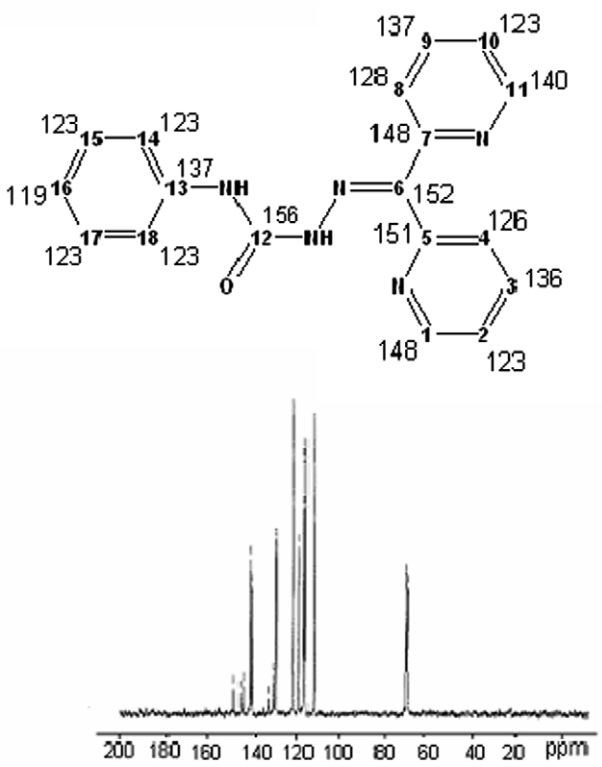


Fig. 7. ^{13}C NMR spectrum of HL.

hydrogen bonding interaction with adjacent nitrogen atom N(1). Another singlet at $\delta = 8.37$ ppm is assigned to the N(5) proton. This downfield also explained with the hydrogen bonding interaction with nitrogen atom N(3). Hydrogen bonding decreases the electron density around the proton and thus moves the proton absorption to a lower field. Absence of any coupling interactions by N(4) H and N(5) H protons due to the lack of availability of protons on neighboring atoms render singlet peaks for the imine protons.

Two doublets at $\delta = 8.78$ and 8.66 ppm are assigned to the C(1)H and C(11)H protons respectively. These signals are shifted to lower field due to electronic effect of the adjacent electronegative pyridyl nitrogens and the more downfield shift of C(1)H can be attributed to the increased charge density on N(1) resulted by its hydrogen bonding to N(4)H. The proton resonance of the two pyridyl rings also appear separately in the NMR spectrum, due to the intramolecular hydrogen bonding. There are two triplets at $\delta = 7.87$ and 7.79 ppm corresponding to similar protons on C(3) and C(9) of the two pyridyl rings, while the C(2) and C(10) protons resonances appear overlapped in the multiplet 7.345 ppm. Another two doublets at $\delta = 7.56$ and 7.51 ppm are assigned to C(4) and C(8) protons. The resonances for the C_6H_5-group appear as triplet at 7.04 ppm for para proton and as multiplets at 7.34 ppm for *ortho* and *meta* phenyl protons [29].

The ^{13}C NMR spectrum provides direct information about the carbon skeleton of the compound HL. Assignment of different resonant peaks to respective carbon atoms is presented in Fig. 7. Considering the two pyridyl rings non-equivalent, resulting from the hydrogen-bonding interaction, there are 15 unique carbon atoms in the molecule, which give a total of 15 different peaks in the ^{13}C NMR spectrum. In both the pyridyl rings, the C(1) and C(11) carbon atoms adjacent to the more electronegative nitrogen atoms N(1) and N(2) are shifted farther downfield when compared to the neighboring carbon atoms. Also the carbon atoms at para position to the hetero atoms viz. C(3) and C(9) resonate at lower field values when compared to the *meta* positioned carbons C(2), C(4), C(8) and C(10). The ^{13}C peaks are assigned as follows: C(1), 148.68 ppm; C(2), 123.87 ppm; C(3), 136.81 ppm; C(4), 126.24 ppm; C(5), 151.96; C(6), 152.95 ppm; C(7), 148.0 ppm C(8), 128.89 ppm; C(9), 137.01 ppm; C(10), 123.87 ppm; C(11), 140.28 ppm; C(12), 156.20 ppm; C(13), 137.98 ppm; C(14), 123.75 ppm; C(15), 123.38 ppm; C(16), 119.60 ppm; C(17), 123.38 ppm; C(18), 123,75 ppm. The non-protonated carbon atom at C(6) is found downfield in the spectrum ($\delta = 152.95$ ppm), effected by the magnetic interaction of two bulky pyridyl rings and π electron delocalization on the C(6)=N(3) bond. Similarly, the C(12) carbon atom resonance is also observed farthest downfield of 156.20 ppm resultant of the conjugative effect of the –N(3)–N(4)–C(O)–N(5)– semicarbazone skeleton. The NMR data for the complexes are not available because of poor solubility.

Acknowledgements

M.R.P. Kurup is thankful to the Council of Scientific & Industrial Research (CSIR), New Delhi, India for the financial assistance. The authors are thankful to the

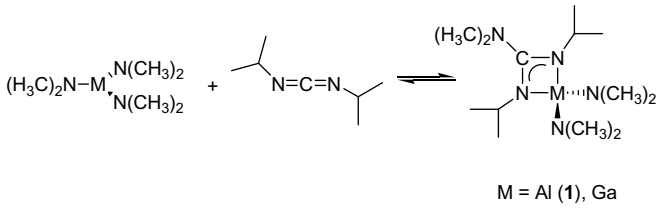
National Single Crystal X-ray diffraction Facility, IIT, Bombay, India for providing single crystal XRD data.

Appendix A. Supplementary data

CCDC 645825 contain the supplementary crystallographic data for **1**. These data can be obtained free of charge via http://www.ccdc.cam.ac.uk/conts/retrieving.html, or from the Cambridge Crystallographic Data Centre, 12 Union Road, Cambridge CB2 1EZ, UK; fax: (+44) 1223-336-033, or e-mail: deposit@ccdc.cam.ac.uk. Supplementary data associated with this article can be found, in the online version, at doi:10.1016/j.poly.2008.02.020.

References

[1] D.X. West, S.B. Padhye, P.S. Sonawane, Struct. Bond. 76 (1991) 1.
[2] S.N. Pandeya, J.P. Dimmock, Pharmazie 48 (1993) 659.
[3] Q. Li, H. Tang, Y. Li, M. Wang, L. Wang, C. Xia, J. Inorg. Biochem. 78 (2000) 167.
[4] J. Dimmock, K. Sidhu, S. Tumber, S. Basran, M. Chen, J. Quail, I. Rozas, D. Weaver, Eur. J. Med. Chem. 30 (1995) 303.
[5] J.S. Casas, M.S. Garcia-Tasende, J. Sordo, Coord. Chem. Rev. 209 (2000) 197.
[6] M.L. Post, J. Trotter, J. Chem. Soc., Dalton Trans. (1974) 674.
[7] P.A. Prasad, S. Neeraj, S. Natarajan, C.N.R. Rao, J. Chem. Soc., Chem. Commun. (2000) 1251.
[8] CRYSALIS CCD and CRYSALIS RED Versions 1.171.29.2 (CrysAlis171. NET), Oxford Diffraction Ltd., Abingdon, Oxfordshire, England, 2006.
[9] G.M. Sheldrick, Acta Crystallogr., Sect. A 46 (1990) 467.
[10] G.M. Sheldrick, SHELXS-97 Program for X-ray Crystal Structure Refinement, University of Göttingen, Germany, 1997.
[11] K. Brandenburg, DIAMOND Version 3.1d, Crystal Impact GbR, Bonn, Germany, 2006.
[12] A.L. Spek, J. Appl. Crystallogr. 36 (2003) 7.
[13] U.L. Kala, S. Suma, M.R.P. Kurup, S. Krishnan, R.P. John, Polyhedron 26 (2007) 1427.
[14] V.M. Kolb, W.S. Joseph, T.E. Janota, W.L. Duax, J. Org. Chem. 54 (1989) 2341.
[15] S. Sen, M.K. Saha, P. Kundu, S. Mitra, C. Kruger, J. Bruckmann, Inorg. Chim. Acta 288 (1999) 118.
[16] A.F. Cameron, R.H. Nuttall, D.W. Taylor, J. Chem. Soc., Chem. Commun. (1971) 129.
[17] W. Clegg, J.T. Cressey, A. McCamley, B.P. Straughan, Acta Crystallogr., Sect. C 51 (1995) 234.
[18] A.F. Cameron, R.H. Nuttall, D.W. Taylor, J. Chem. Soc., Dalton Trans. (1972) 1608.
[19] D. Cremer, J.A. Pople, J. Am. Chem. Soc. 97 (1975) 1354.
[20] M.T.H. Tarafder, A. Kasbollah, K.A. Crouse, A.M. Ali, B.M. Yamin, H.-K. Fun, Polyhedron 20 (2001) 2363.
[21] A. Sreekanth, H.-K. Fun, M.R.P. Kurup, Inorg. Chem. Commun. 7 (2004) 324.
[22] V. Philip, V. Suni, M.R.P. Kurup, M. Nethaji, Polyhedron 25 (2006) 1931.
[23] V. Philip, V. Suni, M.R.P. Kurup, M. Nethaji, Polyhedron 24 (2005) 1133.
[24] A. Majumder, G.M. Rosair, A. Mallick, N. Chattopadhyay, S. Mitra, Polyhedron 25 (2006) 1753.
[25] V. Philip, V. Suni, M.R.P. Kurup, M. Nethaji, Spectrochim. Acta A 64 (2006) 171.
[26] K. Nakamoto, Infrared and Raman spectra of Inorganic and Coordination compounds, 5th ed., Wiley, New York, 1997.
[27] R. Kruszynski, A. Turek, J. Coord. Chem. 57 (2004) 1089.
[28] A. Sreekanth, U.L. Kala, C.R. Nayar, M.R.P. Kurup, Polyhedron 23 (2004) 41.
[29] S.R. Breeze, S. Wang, J.E. Greedan, N.P. Raju, Inorg. Chem. 35 (1996) 6945.



Scheme 1. Carbodimide insertion and deinsertion.

In this article, we report on the results of the thermolysis experiments with the aluminum guanidinate compound $[Me_2NC(N^iPr_2)]Al(NMe_2)_2$ (**1**) (Scheme 1), as well as the carbodiimide $[(CH_3)_2CHN{=}C{=}NCH(CH_3)_2]$ (**2**) and aluminum amide $[Al(NMe_2)_3]_2$ (**3d**). The results of MI FTIR spectroscopy and TOF MS will be discussed.

2. Experimental

2.1. General remarks

Complex **1** [3] and **3d** [8] were synthesized via known procedures and purified by sublimation prior to use (**1**: 50–55 °C, 10^{-2}–10^{-3} mbar; **3d**: 55–60 °C, 10^{-2}–10^{-3} mbar). Compound **2** was purchased from Aldrich Chemical Co. and purified via flask-to-flask condensation at ambient temperatures (approx. 10^{-2}–10^{-3} mbar).

The matrix-isolation and the time-of-flight MS apparatus were separate instruments. Each instrument was equipped with its own thermolysis oven, both identical in construction. Both instruments were in close proximity, so that the heatable container, loaded with the compound of interest, could be detached from one instrument and attached to the other instrument without exposing the sample to air. In addition to the sample container, both instruments used the same carrier gas supply and the same thermolysis oven temperature controller. The facility was constructed in this way so that a series of experiments with one sample batch could be performed using one method, e.g. MI FTIR spectroscopy, followed by a series of experiments using the other method, e.g. TOF MS, and still being able to keep the experimental conditions similar in both consecutive series of experiments.

A thermolysis oven was equipped with an Al_2O_3 tube (OD = 4 mm) with two parallel, inner canals (ID = 1 mm). The overall length of the tube was 35 mm with the last 10 mm heated with a tungsten wire, coiled around the outside and coated with ZrO_2 cement. One of the inner canals was equipped with a thermocouple (Thermocoax: NiCrSi/NiSi), while the second canal was used to let a carrier gas/sample mixture pass trough. With this set-up, reliable thermolysis temperatures at the inside of the thermolysis tube could be measured without exposing the thermocouple to the gaseous sample. A schematic drawing of the thermolysis oven can be found in Ref. [9].

Thermolysis series with compounds **1** and **3d**, respectively, were done in the temperature range between 300 and 600 °C (MI FTIR: 50 °C increments; TOF MS: 25 °C increments). The thermolysis of compound **2** was investigated exclusively at the temperatures 300, 500 and 700 °C for both MI FTIR and TOF MS. As compound **2** was thermally stable in this temperature range, a more detailed series of thermolysis experiments was not necessary.

2.2. Matrix-isolation FTIR spectroscopy

The matrix apparatus consisted of a vacuum line (Varian TV 551 Navigator; Varian DS 402) and a Sumitomo CSW-71 cryogenic closed cycle system (Sumitomo Heavy Industries, Ltd.) including a Sumitomo RDK-415D 4 K cold head fitted with CsI windows (vacuum shroud design and fabrication by Janis Research Company, Inc.). The sample was loaded into a heatable container connected to the thermolysis oven [9]. In a typical experiment, the evacuated container, loaded with the compound of interest, was kept at constant temperature (**1**: 45–50 °C; **2**: −20 °C; **3d**: 55–60 °C) while a flow of argon (1.250 sccm; Praxair 6.0) was conducted over the sample (mass flow controller: MKS Type 1179A). The resulting gaseous mixture was passed through a thermolysis oven for 30–90 min and deposited onto a CsI window cooled to 20 K. The distance between the end of the heated oven tube to the CsI window was 54 mm. The so-prepared matrices were cooled to 4 K for FTIR measurements (Bruker Tensor 27 FTIR; 200–5000 cm^{-1}; resolution of 1 cm^{-1}).

Compound **4** ($H_2C{=}NMe$) have been identified by its typical IR bands at 2953.7, 2900.9, 2854.8, 2849.4, 1658.6, 1469.7, 1440.3, 1221.0, 1026.5 and 949.5 cm^{-1}.

2.3. Time-of-flight mass spectrometry

The apparatus consisted of a custom designed vacuum chamber (designed by Stefan Kaesdorf, Geräte für Forschung und Industrie; built by Johnsen Ultravac Inc.), equipped with one roughing vacuum pump (Varian DS 602) and three turbo vacuum pumps, and a reflectron time-of-flight spectrometer with electron impact ionization (Stefan Kaesdorf, Geräte für Forschung und Industrie; time resolution under favorable conditions $T/\Delta T = 10\,000$). The apparatus was composed of three connected vacuum chambers, with the third chamber being the TOF MS itself (Figs. S1 and S2, Supplementary data). A fraction of the gaseous molecules that enter chamber 1 (Varian TV 1001 Navigator) through the thermolysis oven is sampled by a skimmer (model 2 from Beam Dynamics, Inc.; orifice 1.5 mm) so that a molecular beam enters chamber 2 (Varian TV 551 Navigator) where the electron impact ionization takes place. Produced ions are accelerated perpendicular to the molecular beam into the TOF MS (chamber 3; Varian TV 551 Navigator). The distance between the end of the heated oven tube to the orifice of the skimmer was 12 mm. During thermolysis experiments (argon flow of 1.250 sscm) the pressures in chambers 1, 2 and 3 were measured to be around 5.0×10^{-4}, 3.0×10^{-8}, 5.0×10^{-9} mbar, respectively. As described before,

in a typical experiment, the sample container was kept at constant temperature (**1**: 50–55 °C; **2**: 0 °C; **3d**: 60–65 °C) while a flow of argon was conducted over the sample. To get acceptable signal to noise ratios, the temperatures needed for the TOF MS measurements were slightly higher than those for MI FTIR spectroscopy (see above). For all measurements electron impact of 70 eV and 10 million sweeps per oven temperature were applied. The signal of the carrier gas argon at 40 u was reduced in intensity by using a mass filter at 4.35 kV (delay: 3.1000 μs; duration: 0.9000 μs). This prevented the MCP detector from exceeding its detection limit. Calibration of the flight time was done within every new series of measurements using Xe 132 (131.90415 u), Xe 129 (128.90478 u), Ar 40 (39.96230 u) and H_2O (18.01050 u) as internal standards.

Calculated masses of selected fragments (u): $\mathbf{1}^+$: 285.25; $\mathbf{2}^+$: 126.12; $\mathbf{2}^+$–$NCH(CH_3)_2$: 69.06; $\mathbf{3d}^+$: 318.26; $\mathbf{3m}^+$: 159.13; $\mathbf{3m}^+$–$N(CH_3)_2$: 115.08; $AlNH(CH_3)_2^+$: 72.04; $AlN(CH_3)_2^+$: 71.03; $AlNHCH_3^+$: 57.02, $HN(CH_3)_2^+$: 45.06; $N(CH_3)_2^+$: 44.05; $\mathbf{4}^+$: 43.04; $NC_2H_4^+$: 42.03.

2.4. DFT Calculations

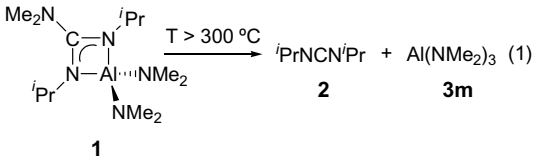
All *ab initio* calculations were carried out using the GAUSSIAN 03 suite [10]. Geometry optimization and calculations of harmonic frequencies were done on the B3LYP/6-31G(d) level of theory using the Western Canada Research Grid (WESTGRID). First, compound **3m** was optimized in *z*-matrix coordinates to enforce a D_3 point group symmetry ($E_h = -646.226377$ hartree). Secondly, all symmetry constrains were removed and a full optimization followed by a frequency calculation have shown that the D_3 symmetrical species indeed refers to a local minimum at the potential energy surface ($E_h = -646.226397$ hartree; zero-point vibrational energy = 653.2 kJ/mol).

3. Results and discussion

In order to illuminate the fragmentation of the aluminum guanidinate precursor **1**, its gas-phase thermolysis in the range of 300–600 °C has been investigated with MI FTIR spectroscopy and TOF MS. We designed a facility that combines both methods. A series of experiments can be performed initially using one method, which can then be followed by a similar series of experiments, with the same precursor sample and carrier gas supply, using the second method (see Section 2). Even though MI FTIR and TOF MS data are collected consecutively and not simultaneously, conditions in both series of experiments can be kept similar that both methods independently illuminate the same chemical events, hence, providing data that complement one another.

3.1. MI FTIR spectroscopy

Between oven temperatures of 25 and 300 °C the matrix IR spectra did not change and indicated that precursor **1** is thermally stable in this range. At 350 °C a weak IR band with a maximum at 2118.8 cm^{-1} appeared, signaling the start of thermolysis of **1**. While the intensity of the band at 2118.8 cm^{-1} kept growing with increasing temperature, the typical IR bands of **1** could no longer be detected at oven temperatures above 450 °C. The IR band at 2118.8 cm^{-1}, which is in a typical area of asymmetric NCN stretching modes of carbodiimides, prompted us to propose that precursor **1** fragments according to Eq. (1), which is the reverse reaction of its preparative synthesis shown in Scheme 1.



However, for both the carbodiimide **2** and the aluminum amide **3m**, complete sets of matrix IR data were not available in the literature. In the context of studying astrophysical chemistry, compound **2** together with nitriles and isonitriles had been investigated in solid argon matrices, but only the IR range of 2050–2320 cm^{-1} was reported [11]. According to this paper, compound **2** showed a broad, structured IR band with a maximum at 2123.7 cm^{-1} (complete set: 2144.3, 2137.5, 2128.5, 2123.7, 2118.6 and 2112.7 cm^{-1}). In thermolysis experiments of precursor **1**, the IR band with the maximum at 2118.8 cm^{-1} also showed a structure with a second maximum at 2123.1 cm^{-1} and a shoulder at 2128.2 cm^{-1}. We measured compound **2**, matrix-isolated in argon, and based on these data an unequivocal identification of **2** as a thermolysis product was achieved (Fig. S3, Supplementary data). Fig. 1 illustrates the results with an IR spectrum obtained from a thermolysis at 450 °C. Under these conditions, small amounts of precursor **1** could still be trapped in solid argon.

As one can see from Fig. 1, the aluminum amide **3m** was also identified as a thermolysis product (indicated with ∅). Compound **3m** is unstable at ambient temperature, but can be synthesized as a dimer $[Al(NMe_2)_3]_2$ (**3d**) under ambient conditions, exhibiting the expected diborane(6) structure [8,12]. A series of experiments with **3d** as a precursor with oven temperatures of up to 600 °C was carried out. Between ambient temperatures and 300 °C the matrix IR spectra did not change, indicating that they were caused by matrix-isolated **3d**. At oven temperatures of 350 °C, new IR bands appeared while the intensity of precursor **3d** decreased. Fig. 2 shows a typical spectrum of matrix-isolated **3d** and spectra obtained from a thermolysis of **3d** at 450 °C.

Under these conditions a mixture of **3d** and **3m** was obtained in matrices. We could not find thermolysis conditions to trap the monomer **3m** without the starting dimer

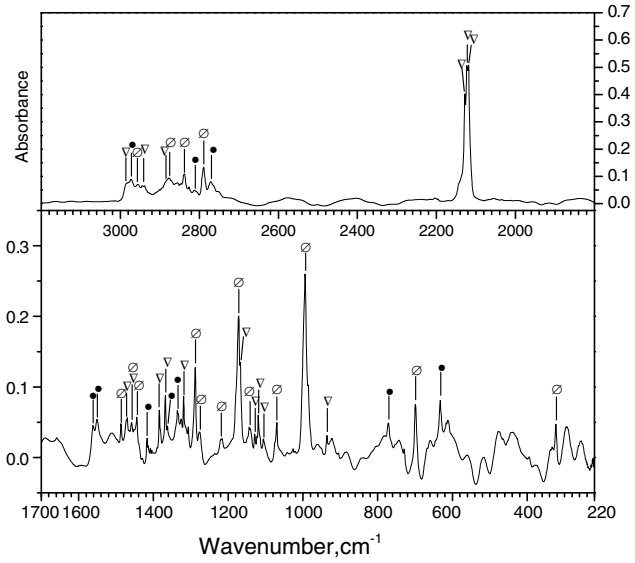


Fig. 1. IR spectrum of matrix-isolated products from a thermolysis at 400 °C of **1** (*x* axis, 1800–3200 cm^{-1} (top), 220–1700 cm^{-1} (bottom); *y* axis, absorbance). Compound **1**: ● (2969.7, 2944.4, 2870.4, 2863.8, 2825.8, 2812.5, 2769.9, 2753.9, 1561.6, 1551.1, 1496.2, 1486.2, 1470.8, 1465.2, 1445.3, 1429.9, 1417.1, 1412.2, 1408.5, 1380.9, 1362.8, 1335.0, 1325.9, 1294.9, 1279.0, 1216.7, 1179.9, 1173.6, 1148.3, 1128.2, 1075.4, 996.8, 991.5, 950.6, 845.5, 771.6, 753.6, 742.6, 668.5, 632.7, 464.3, 445.3 and 326.0 cm^{-1}); compound **2**: ∇ (2984.7, 2938.9, 2883.1, 2128.2, 2123.1, 2118.8, 1470.6, 1457.8, 1384.4, 1368.7, 1335.9, 1319.4, 1307.0, 1168.8, 1129.4, 1123.1, 1119.6, 1105.7, 936.4, 633.2 617.6, 609.6 and 425.5 cm^{-1}); compound **3m**: ∅ (see Table 2).

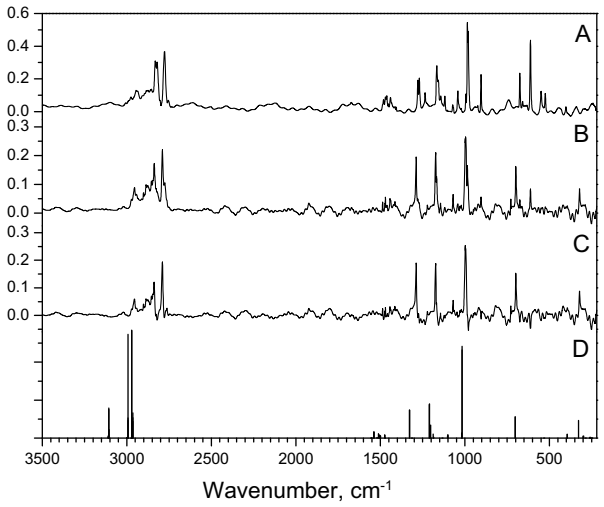


Fig. 2. Measured and calculated IR spectra of aluminum amides **3d** and **3m** (*x* axis, 220–3500 cm^{-1}; *y* axis, absorbance). Spectrum A: **3d** in solid argon (oven at ambient temperature). Spectrum B: results of a thermolysis of complex **3d** at 450 °C. Spectrum C: spectrum B from which the absorptions from **3d** (spectrum A) have been electronically eliminated. Spectrum D: calculated IR spectrum of **3m** (B3LYP/6-31G(d); see Tables 1 and 2).

3d. Fig. 2C shows a thermolysis IR spectrum from which the spectrum of the dimer **3d** has been electronically eliminated. The excellent match of spectrum C with the calculated spectrum of **3m** (B3LYP/6-31G(d) level) proves that

Table 1
Calculated harmonic frequencies (cm^{-1}),[a] intensities (km/mol), and approximate descriptions[b,c] of normal vibrations of $Al[N(CH_3)_2]_3$ (**3m**)

		Frequency	Intensity
A$_1$			
ν_1	ν(CH)	3110.3	0.0
ν_2	$\nu_{as}(CH_2)$	3000.6	0.0
ν_3	$\nu_s(CH_3)$	2976.8	0.0
ν_4	$\delta(CH_2)_{scis}$	1556.6	0.0
ν_5	$\delta_{as}(CH_3)$	1514.4	0.0
ν_6	$\delta_s(CH_3)$	1501.8	0.0
ν_7	$\delta(CH_3)_{wagg}$	1315.7	0.0
ν_8	$\delta(CH_3)_{rock}$	1136.0	0.0
ν_9	ν_s(NC)	1019.4	0.0
ν_{10}	ν_s(AlN)	533.8	0.0
ν_{11}	$\delta(NC_2)$	289.1	0.0
ν_{12}	$\delta(CH_3)_{tors}$	262.0	0.0
ν_{13}	$\delta(NMe_2)_{tors}$	99.3	0.0
A$_2$			
ν_{14}	ν(CH)	3104.9	21.8
ν_{15}	$\nu_{as}(CH_2)$	2993.6	282.3
ν_{16}	$\nu_s(CH_3)$	2963.6	31.1
ν_{17}	$\delta(CH_2)_{scis}$	1538.9	15.7
ν_{18}	$\delta_{as}(CH_3)$	1511.1	11.8
ν_{19}	$\delta_s(CH_3)$	1469.9	0.5
ν_{20}	ν_{as}(CN)	1202.3	34.2
ν_{21}	$\delta(CH_3)_{rock}$	1187.1	11.2
ν_{22}	$\delta(CH_3)_{wagg}$	1101.6	5.2
ν_{23}	$\delta_s(NAlC_2)$[d]	327.6	46.0
ν_{24}	$\delta(CH_3)_{tors}$	264.0	0.0
ν_{25}	$\delta(NMe_2)_{rock}$	174.5	5.8
ν_{26}	$\delta(AlN_3)$	101.4	0.2
E			
ν_{27}	ν(CH)	3110.0	6.9
ν_{28}	ν(CH)	3106.1	157.3
ν_{29}	$\nu_{as}(CH_2)_{ip}$	3000.3	2.3
ν_{30}	$\nu_{as}(CH_2)_{oop}$	2993.3	90.9
ν_{31}	$\nu_s(CH_3)_{ip}$	2971.3	566.3
ν_{32}	$\nu_s(CH_3)_{oop}$	2963.9	132.8
ν_{33}	$\delta_{ip}(CH_2)_{scis}$	1556.5	0.0
ν_{34}	$\delta_{oop}(CH_2)_{scis}$	1538.1	31.5
ν_{35}	$\delta_{as}(CH_3)_{oop}$	1520.5	2.2
ν_{36}	$\delta_{as}(CH_3)_{ip}$	1504.8	13.7
ν_{37}	$\delta_s(CH_3)_{ip}$	1499.8	14.2
ν_{38}	$\delta_s(CH_3)_{oop}$	1474.2	15.6
ν_{39}	$\delta_{ip}(CH_3)_{wagg}$	1327.3	147.4
ν_{40}	ν_{as}(CN)	1210.4	178.7
ν_{41}	$\delta_{oop}(CH_3)_{rock}$	1185.7	3.7
ν_{42}	$\delta_{ip}(CH_3)_{rock}$	1135.3	0.2
ν_{43}	$\delta_{oop}(CH_3)_{wagg}$	1100.5	16.0
ν_{44}	ν_s(NC)	1016.2	485.4
ν_{45}	ν_{as}(AlN)	702.2	111.8
ν_{46}	$\delta(NC_2)$	394.1	19.5
ν_{47}	$\delta_s(NAlC_2)$[d]	302.1	9.9
ν_{48}	$\delta_{oop}(CH_3)_{tors}$	259.8	5.6
ν_{49}	$\delta_{ip}(CH_3)_{tors}$	256.6	0.3
ν_{50}	$\delta(NMe_2)_{rock}$	184.6	6.3
ν_{51}	$\delta(AlN_3)$	101.6	0.3
ν_{52}	$\delta(NMe_2)_{tors}$	59.7	0.2

[a] Intensities of the E modes are the sum of the two degenerated vibrations.
[b] ip and oop: symmetrical equivalent atoms of within one NMe_2 moiety move in phase and out of phase, respectively.
[c] Wagging and rocking modes of the CH_3 groups are very similar: wagging modes are approximately in the molecular planes, whereas rocking modes are approximately perpendicular to the molecular plane.
[d] Appears like a motion of a trampoline: involves pyramidalizations at Al and N.

indeed **3d** monomerises to **3m**. Table 1 compiles the calculated harmonic vibrational modes and Table 2 shows the measured IR frequencies and their assignments. The D_3 symmetrical alane **3m** (Fig. 3) is expected to show 78 normal modes that transform to the irreducible representations A_1 (13), A_2 (13) and E (26). If one takes into account that A_1 symmetrical modes are IR inactive, the A_2 and E modes could result in 39 IR bands. Typically, a molecule of this size shows many CH stretching modes in a narrow range, and, as expected, an assignment of measured to calculated frequencies of CH stretching modes for **3m** was impossible. If one subtracts the CH stretches (3 A1 and 6 E modes) from the expected 39 IR bands, the modes below the detection limit of 200 cm^{-1} (ν_{25}, ν_{26}, ν_{50}, ν_{51}, ν_{52}), and all modes with calculated intensities below 10 km/mol (ν_{19}, ν_{22}, ν_{24}, ν_{33}, ν_{35}, ν_{41}, ν_{42}, ν_{47}, ν_{48}, ν_{49}), 15 IR bands remain to be expected in the range of 1500–200 cm^{-1}. All expected IR bands were found in these experiments; Table 2 illustrates the assignment and the match between experiment and theory by observed-to-calculated frequency ratios that vary between 0.95910 and 1.001. These are typical ratios for the B3LYP/6-31G(d) level and show the expected trend: the lower the frequency is the better the fit [13,14]. However, the assignment of IR bands in the range of 1400–1500 cm^{-1} is not straightforward. According to the calculation, 6 modes are expected with low intensities (11.8–31.5 km/mol) and 6 IR bands were detected. We assigned the IR bands to calculated modes taking the calculated frequencies and intensities into account. However, this resulted in an assignment of one IR band at 1487.0 to two calculated modes (ν_{17} at 1538.9 and ν_{34} at 1538.1), leaving the IR band at 1473.8 cm^{-1} unassigned. Even though the calculated frequencies for ν_{17} and ν_{34} are nearly identical, it is feasible that both modes do not result in overlapping IR bands in the experiment and one of the two modes causes the measured IR band at 1473.8 cm^{-1}. Without matrix-isolation experiments with isotopomers of **3m**, an assignment in this IR range will remain tentative. However, the remaining IR bands are spread over a larger IR range and most of them show high intensities and thus could be assigned with certainty (see Table 2 for details). Based on these data, the monomer **3m** could be identified as a thermolysis product of precursor **1** (Fig. 1). Furthermore, and very importantly, the formation of the dimer **3d** as a product of the fragmentation of **1** could be excluded.

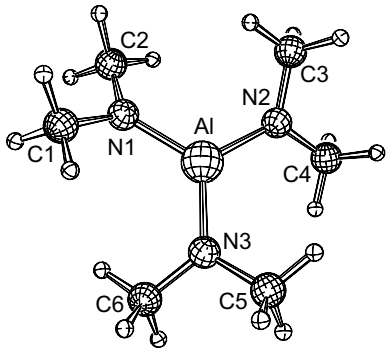


Fig. 3. D_3 symmetrical geometry of $Al(NMe_2)_3$ (**3m**) (B3LYP/6-31G(d) level). Selected bond lengths (Å), angles and torsion angles (°): Al–N = 1.7958, N–C = 1.4536, Al–N–C = 123.96, C–N–C = 112.08 and C1–N1–Al–N2 = −150.72.

While the intensities of the IR bands of the carbodiimide **2** were unaffected at higher thermolysis temperatures

Table 2
Experimental IR frequencies (cm^{-1}), assignments and observed-to-calculated frequency ratios of $Al(NMe_2)_3$ (**3m**)

Experimental frequencies	Assignment	Calculated frequency (int)	Observed: calculated ratio
2972.4, 2955.3, 2854.8, 2838.3, 2837.6, 2826.7, 2789.7, 2773.7, 2763.2, 2748.3[a]	CH stretches		
1487.0	ν_{17}: $\delta(CH_2)_{scis}$ and ν_{34}: $\delta_{oop}(CH_2)_{scis}$	1538.9 (15.7) and 1538.1 (31.5)	0.96627 and 0.96678
1473.8	[b]		
1458.6	ν_{18}: $\delta_{as}(CH_3)$	1511.1 (11.8)	0.96526
1443.9	ν_{36}: $\delta_{as}(CH_3)_{ip}$	1504.8 (13.7)	0.95953
1438.5	ν_{37}: $\delta_{s}(CH_3)_{ip}$	1499.8 (14.2)	0.95913
1413.9	ν_{38}: $\delta_{s}(CH_3)_{oop}$	1474.2 (15.6)	0.95910
1288.4	ν_{39}: $\delta_{ip}(CH_3)_{wagg}$	1327.3 (147.4)	0.97069
1171.8	ν_{40}: $\nu_{as}(CN)$	1210.4 (178.7)	0.96811
1167.8	ν_{20}: $\nu_{as}(CN)$	1202.3 (34.2)	0.97130
1143.8	ν_{21}: $\delta(CH_3)_{rock}$	1187.1 (11.2)	0.96352
1069.6	ν_{43}: $\delta_{oop}(CH_3)_{wagg}$	1100.5 (16.0)	0.97192
994.4[c] and 986.0[d]	ν_{44}: $\nu_{s}(NC)$	1016.2 (485.4)	0.9785 and 0.97028
699.4	ν_{45}: $\nu_{as}(AlN)$	702.2 (111.8)	0.9960
394.6	ν_{46}: $\delta(NC_2)$	394.1 (19.5)	1.001
323.9	ν_{23}: $\delta_{s}(NAlC_2)$	327.6 (46.0)	0.9887

[a] Most intense IR bands at 2955.3, 2837.6 and 2789.7 cm^{-1}.
[b] Could not be assigned; see text for discussion.
[c] Shoulder at 998.1 cm^{-1}.
[d] Less intense IR band at 986.0 cm^{-1} presumably caused by matrix effects.

(450–600 °C), those of the monomer **3m** were strongly temperature dependent. As the thermolysis temperature for precursor **1** was increased from 400 to 600 °C, the amount of the monomer **3m** decreased and it could no longer be detected at thermolysis temperatures above 500 °C. While the intensities of the IR bands of **3m** decreased, a new set of IR frequencies grew in, which were clearly identified as being due to methyl(methylene)amine, $H_2C{=}NCH_3$ (**4**). This product was previously identified by matrix-isolation thermolysis experiments with other dimethylamino-containing precursors [6]. Under our thermolysis conditions the first IR bands of **4** were detected at oven temperatures of 500 °C (see Section 2). Similar to the thermolysis of compound **1**, the thermolysis of the aluminum amide **3d** also gave product **4** at higher oven temperatures, with the IR bands of **4** being detectable starting at 450 °C. In addition to the IR bands of **4**, a very weak band at 729.0 cm^{-1} was detected in the temperature range between 400 and 600 °C. This IR band could be caused by small amounts of Me_2NH, which shows its most intense IR absorption at this frequency [15]. In the thermolysis series with precursor **1**, a weak IR band at 729.0 cm^{-1} was also detected. However, the identification of Me_2NH by only one frequency can only be tentative.

3.2. TOF mass spectrometry

As mentioned above, a series of thermolyses of compounds **1**, **2** and **3d** with similar conditions as for the MI FTIR spectroscopy have been performed using a TOF MS apparatus. The main disadvantage of MS with respect to MI FTIR spectroscopy stems from the fact that a detection of a species requires modification of the species: it needs to be ionized. We used electron impact ionization, and 70 eV were applied in order to have an optimum ion yield. However, through this method a species is provided with an excess of energy that leads to further fragmentation. Depending on the case, instead of the molecular ion M^+ of the species of interest, which results in the most informative signal, only signals of molecular fragments can be detected.

The TOF MS measurements of **1**, **2** and **3d** supported and complemented the conclusions drawn from the MI FTIR experiments. Fig. 4 compares mass-spectra of precursor **1** obtained at oven temperatures of 25 and 425 °C. The signals indicative of the precursor **1** were not detected at 425 °C. Instead, two ions at 126.14 and 69.07 u dominated the spectrum. Both masses belong to the carbodiimide **2**; the higher mass due to $\mathbf{2}^+$ and the more intense peak at 69.06 u due to a loss of $NCH(CH_3)_2$ from $\mathbf{2}^+$. Independent measurements of **2** alone supported this interpretation (Fig. S4, Supplementary data).

Fig. 5 shows a plot of intensities of selected ions with respect to oven temperatures. Above 225 °C the amount of precursor **1** (285.30 u) started to decrease while the amount of the carbodiimide **2** (126.14 and 69.06 u) increased. The most intense signals for **2** have been measured at 400 °C, above which their intensities decreased again.

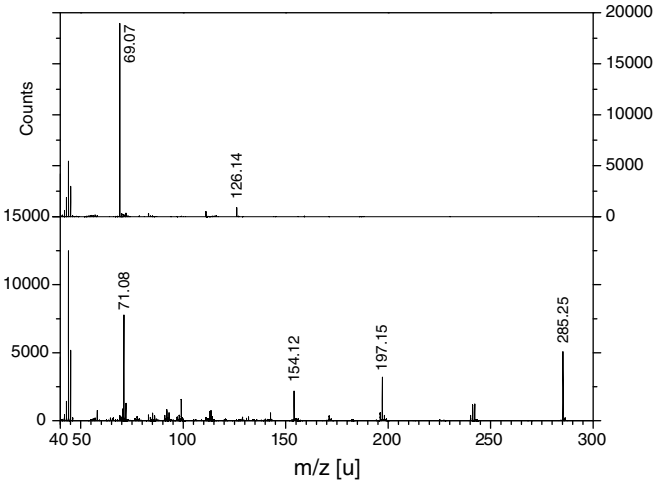


Fig. 4. Mass-spectra of complex **1** measured at oven temperatures of 25 °C (bottom) and 425 °C (top).

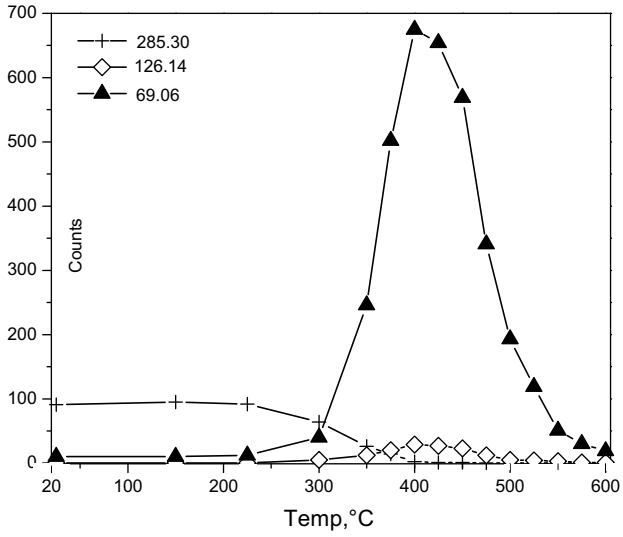


Fig. 5. Temperature dependence of selected ions of the thermolysis of **1** [m/z = 285.30 ($\mathbf{1}^+$), 126.14 ($\mathbf{2}^+$) and 69.06 ($\mathbf{2}^+$–NC_3H_7)].

For the same series of thermolysis experiments, Fig. 6 shows a similar plot as that of Fig. 5, with a focus on fragments that could be interpreted as being due to the formation of the aluminum amide **3m**. The signal at 159.14 u clearly indicates the presence of $\mathbf{3m}^+$, whereas the mass at 115.10 u can be interpreted as $Al[N(CH_3)_2]_2^+$ resulting from $\mathbf{3m}^+$ losing a $N(CH_3)_2$ group. In addition, the ion of mass 43.06 u indicates the presence of $H_2C{=}NCH_3$ (**4**). Fig. 6 shows that the presence of the monomeric aluminum amide **3m** (159.14 and 115.10 u) is restricted to the narrow temperature range of approximately 350–450 °C, whereas the signal for compound **4** (43.06 u) persisted over a broader temperature range. The fact that the signal of **4** at 43.06 u and the signals indicative of **3m** follow a different temperature profile indicates that **4** cannot result from the

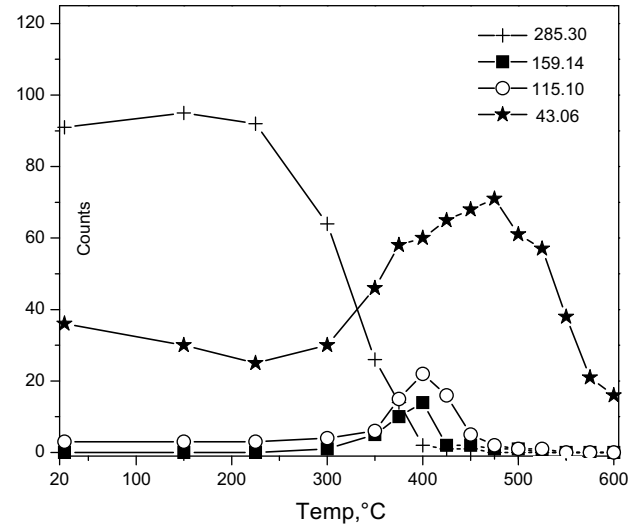


Fig. 6. Temperature dependence of selected ions of the thermolysis of **1** [m/z = 285.30 (**1**$^+$), 159.14 (**3m**$^+$), 115.10 (**3m**$^+$–N(CH$_3$)$_2$) and 43.06 (**4**$^+$)].

fragmentation of **3m**$^+$ in the MS. Combined with the fact that product **4** could be trapped in matrices in thermolysis experiments of precursor **1**, it seems likely to interpret the signal at 43.06 u as the molecular ion of the thermolysis product **4**. It is worth noting that the peaks caused by **3m** are very weak in intensity (Fig. 6); with a maximum count of 22 for 115.10 u at 400 °C, these signals are just above the threshold of being detectable with our set-up.

Similar to the matrix-isolation investigation, the thermolysis of the dimer **3d** has been investigated. Fig. 7 shows a comparison between the mass-spectrum of compound **3d** at room temperature and that at 450 °C. All signals corresponding to **3d** were no longer present at 450 °C, revealing a completed thermolysis of **3d** under these conditions. The most intense peaks at 450 °C were found at 45.06, 44.05, 43.04 and 42.03 u indicating the presence of HN(CH$_3$)$_2$$^+$, N(CH$_3$)$_2$$^+$, H$_2$C=NCH$_3$$^+$ (**4**$^+$), and N(CH$_2$)$_2$$^+$, respectively. The signals at 72.04 and 57.03 u can be interpreted as being caused by AlNH(CH$_3$)$_2$$^+$ and AlNH(CH$_3$)$^+$, respectively.

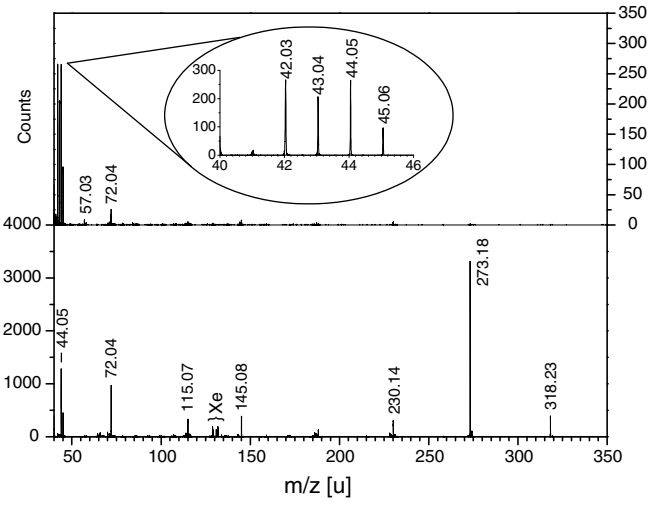


Fig. 7. Mass-spectra of complex **3d** measured at 25 °C (bottom) and 450 °C (top). Mass region 40–46 u expanded (top) for clarity.

Figs. 8 and 9 show temperature dependences of selected ions. The ions at 318.23, 159.12. 115.07, 72.04, 45.06 and 44.05 u show a decrease of intensity with increasing thermolysis temperature (Fig. 8), whereas those at 71.04 and 57.03 u (Fig. 8) and those at 43.04 and 42.03 u (Fig. 9) show an increase of intensity at elevated temperatures. In the case of the thermolysis of precursor **1**, the two peaks at 159.12 and 115.07 u were weak in intensity but indicative

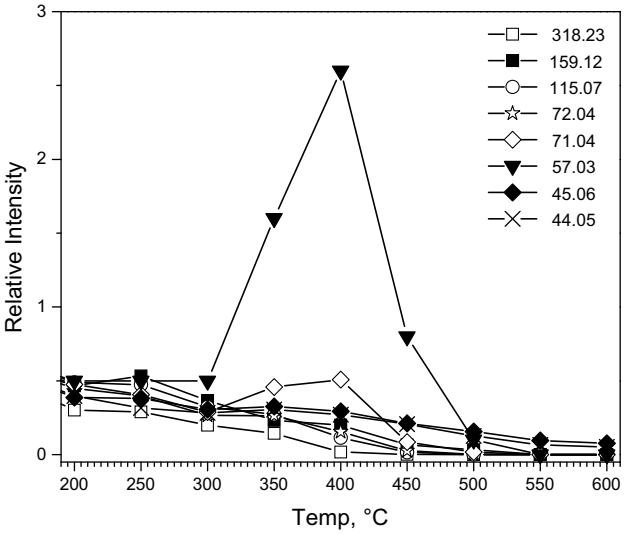


Fig. 8. Temperature dependence of selected ions of the thermolysis of **3d** [m/z = 318.23 (**3d**$^+$), 159.12 (**3m**$^+$), 115.07 (**3m**$^+$–N(CH$_3$)$_2$), 72.04 (AlNH(CH$_3$)$_2$$^+$), 71.04 (AlN(CH$_3$)$_2$$^+$), 57.03 (AlNHCH$_3$$^+$), 45.06 (HN(CH$_3$)$_2$$^+$) and 44.05 (N(CH$_3$)$_2$$^+$)]. Relative intensity normalized to data points at ambient temperature.

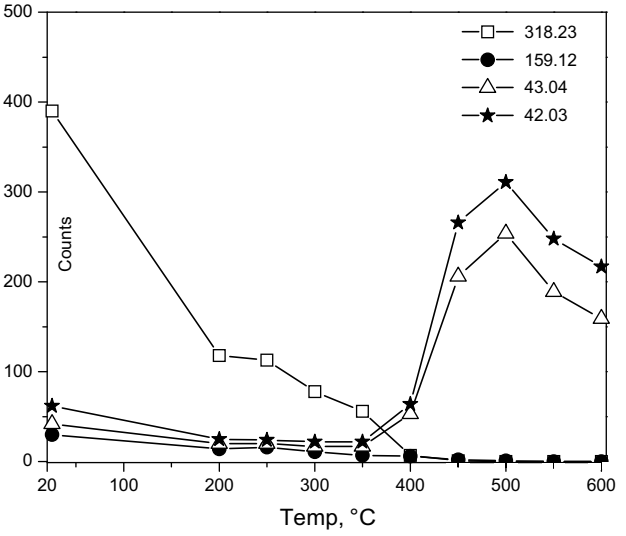


Fig. 9. Temperature dependence of selected mass fragments showing the formation of thermolysis product **4** [m/z = 318.23 (**3d**$^+$), 159.12 (**3m**$^+$), 43.04 (**4**$^+$) and 42.03 (N(CH$_2$)$_2$$^+$)].

of the production of monomer **3m** (Fig. 6). However, in the case of the thermolysis of **3d**, both signals at 159.12 and 115.07 u did not gain in intensities (Fig. 8), and, consequently, could not prove that **3d** monomerises to **3m** upon heating. Both signals are already present in the room temperature spectrum of **3d** and their intensities decrease with increasing thermolysis temperature. It seems that this decrease overcompensates the small increase in intensity caused by the formation of **3m**. However, from the matrix-isolation experiments discussed above, there is no doubt that **3m** is formed from **3d**. As it can be seen in Fig. 8, only the two masses at 71.04 and 57.03 u increase significantly in the thermolysis range of approx. 300–450 °C. The mass at 71.04 u can be interpreted as being caused by $AlN(CH_3)_2^+$, whereas that at 57.03 u fits to $AlNHCH_3^+$ and it is feasible that both ions stem from $\mathbf{3m}^+$. Fig. 9 clearly indicates that the two signals at 43.04 and 42.03 u start to increase in intensity above 350 °C and their temperature profiles are very similar. The peak at 43.04 u is caused by thermolysis product **4** that losses a H atom in the mass spectrometer to also cause the peak at 42.03 u [$N(CH_2)_2^+$].

4. Conclusion

With series of thermolysis experiments of aluminum guanidinate precursor **1** using matrix-isolation FTIR spectroscopy and time-of-flight mass spectrometry we demonstrated that **1** fragments above 300 °C to form the diisopropylcarbodimide **2** and monomeric tris(dimethylamino)alane **3m** (Eq. (1)). Independent thermolysis series with **2** and the aluminum amide dimer **3d** were conducted and had been used to interpret the results of the fragmentation of precursor **1**. Under our experimental conditions, monomer **3m** was present in the thermolysis range of 350–450 °C. Already at 500 °C signals indicative for methyl(methylene)amine (**4**) were found, showing that **3m** fragments further at higher temperature. The thermolysis product **2** (*i*PrCNC*i*Pr) withstands the higher thermolysis temperatures. With respect to material deposition processes we could show that precursor **1** cleanly delivers the monomeric aluminum alane **3m**, which then acts as the reactive material forming species.

Within this study, the monomeric aluminum amide **3m** has been characterized for the first time. Based on DFT calculations, all expected IR bands were found experimentally and could be assigned to normal modes. Species **3m** is one of the very few monomeric aminoalanes that could be characterized to date. The sterically crowded aminoalane $Al[N(SiMe_3)_2]_3$ was the first aminoalanes shown to be monomeric in the crystalline state [16]. The first sterically crowded monomeric aminoalane equipped with only one amino group had been described by Power et al. [17]. The first non-crowded monomeric aminoalane $Me_2Al{=}NH_2$ had been formed photolytically from $Me_3Al{-}NH_3$ in argon matrices and characterized by FTIR spectroscopy [18]. The parent compound H_2AlNH_2 was obtained from co-depositions of Al atoms with ammonia in argon matrices and was characterized by matrix-isolation FTIR spectroscopy [19].

Acknowledgements

We thank the Natural Sciences and Engineering Research Council of Canada (NSERC Discovery Grant, JM), the Department of Chemistry, the Saskatchewan Structural Sciences Centre, and the University of Saskatchewan for their generous support. We thank the Canada Foundation for Innovation (CFI) and the government of Saskatchewan for funding of the MI FTIR spectrometer and the TOF MS facility. We thank WESTGRID for CPU time.

Appendix A. Supplementary data

Supplementary data associated with this article can be found, in the online version, at doi:10.1016/j.poly.2008.02.024.

References

[1] S. Dagorne, I.A. Guzei, M.P. Coles, R.F. Jordan, J. Am. Chem. Soc. 122 (2000) 274.
[2] J. Barker, N.C. Blacker, P.R. Phillips, N.W. Alcock, W. Errington, M.G.H. Wallbridge, J. Chem. Soc., Dalton Trans. (1996) 431.
[3] A.P. Kenney, G.P.A. Yap, D.S. Richeson, S.T. Barry, Inorg. Chem. 44 (2005) 2926.
[4] R. Duchateau, A. Meetsma, J.H. Teuben, Chem. Commun. (1996) 223.
[5] A.L. Brazeau, Z. Wang, C.N. Rowley, S.T. Barry, Inorg. Chem. 45 (2006) 2276.
[6] E. Gemel, J. Müller, Inorg. Chem. 43 (2004) 3955 and references therein.
[7] Selected articles: (a) S.S. Lin, J. Electrochem. Soc. 122 (1975) 1405; (b) T. Morimoto, S.G. Ansari, K. Yoneyama, T. Nakajima, A. Masuda, H. Matsumura, M. Nakamura, H. Umemoto, Jpn. J. Appl. Phys. Part 1 45 (2006) 961; (c) X.M. Li, B.D. Eustergerling, Y.J. Shi, Int. J. Mass Spectrom. 263 (2007) 233.
[8] K.M. Waggoner, M.M. Olmstead, P.P. Power, Polyhedron 9 (1990) 257.
[9] J. Müller, B. Wittig, H. Sternkicker, S. Bendix, J. Phys. IV 11 (2001) 17.
[10] M.J. Frisch, G.W. Trucks, H.B. Schlegel, G.E. Scuseria, M.A. Robb, J.R. Cheeseman, J.J.A. Montgomery, T. Vreven, K.N. Kudin, J.C. Burant, J.M. Millam, S.S. Iyengar, J. Tomasi, V. Barone, B. Mennucci, M. Cossi, G. Scalmani, N. Rega, G.A. Petersson, H. Nakatsuji, M. Hada, M. Ehara, K. Toyota, R. Fukuda, J. Hasegawa, M. Ishida, T. Nakajima, Y. Honda, O. Kitao, H. Nakai, M. Klene, X. Li, J.E. Knox, H.P. Hratchian, J.B. Cross, V. Bakken, C. Adamo, J. Jaramillo, R. Gomperts, R.E. Stratmann, O. Yazyev, A.J. Austin, R. Cammi, C. Pomelli, J.W. Ochterski, P.Y. Ayala, K. Morokuma, G.A. Voth, P. Salvador, J.J. Dannenberg, V.G. Zakrzewski, S. Dapprich, A.D. Daniels, M.C. Strain, O. Farkas, D.K. Malick, A.D. Rabuck, K. Raghavachari, J.B. Foresman, J.V. Ortiz, Q. Cui, A.G. Baboul, S. Clifford, J. Cioslowski, B.B. Stefanov, G. Liu, A. Liashenko, P. Piskorz, I. Komaromi, R.L. Martin, D.J. Fox, T. Keith, M.A. Al-Laham, C.Y. Peng, A. Nanayakkara, M. Challacombe, P.M.W. Gill, B. Johnson, W. Chen, M.W. Wong, C. Gonzalez, J.A. Pople, Gaussian 03, Revision D.02, Gaussian, Inc., Wallingford, CT, 2004.

[11] M.P. Bernstein, S.A. Sandford, L.J. Allamandola, Astrophys. J. 476 (1997) 932.
[12] K. Ouzounis, H. Riffel, H. Hess, U. Kohler, J. Weidlein, Z. Anorg. Allg. Chem. 504 (1983) 67.
[13] G. Rauhut, P. Pulay, J. Phys. Chem. 99 (1995) 3093.
[14] A.P. Scott, L. Radom, J. Phys. Chem. 100 (1996) 16502.
[15] B. Wittig, J. Müller, unpublished results.
[16] G.M. Sheldrick, W.S. Sheldrick, J. Chem. Soc. (A) (1969) 2279.
[17] M.A. Petrie, K. Ruhlandt-Senge, P.P. Power, Inorg. Chem. 32 (1993) 1135.
[18] J. Müller, J. Am. Chem. Soc. 118 (1996) 6370.
[19] H.-J. Himmel, A.J. Downs, T.M. Green, J. Am. Chem. Soc. 122 (2000) 9793.

2. Results and discussion

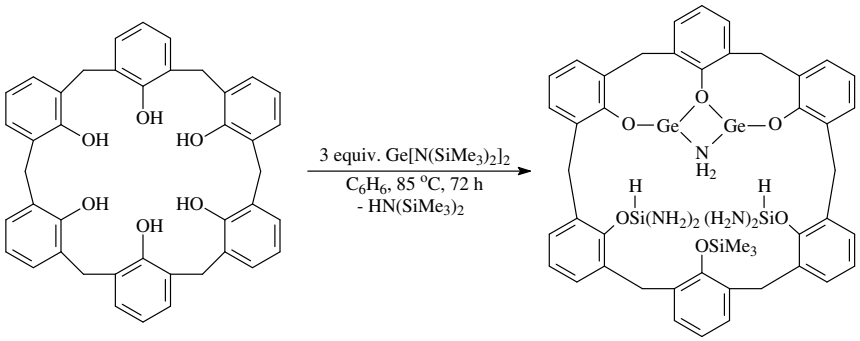
2.1. Synthesis and structure of compound 1

Treatment of calix[6]arene with three equivalents of Ge[N(SiMe$_3$)$_2$]$_2$ yielded complex **1** in 41% yield as shown in Eq. (1). The identity of **1** was ascertained by obtaining its X-ray crystal structure, and an ORTEP diagram of **1** is shown in Fig. 1 while selected bond distances and angles are collected in Table 1. Of the six phenolic oxygen atoms present in **1**, three are bound to the two Ge atoms in either a terminal or bridging fashion while the remaining three oxygen atoms have been incorporated into to either –OSiMe$_3$ or –OSi(H)(NH$_2$)$_2$ groups. We have previously observed the transformation of hydroxyl groups to trimethylsiloxy groups in the reactions of 3,3′-disubstituted binaphthols with metal(II) amides M[N(SiMe$_3$)$_2$]$_2$ (M = Be, Zn, Ge, Sn) [48]; however, the conversion of –OH groups to silylamides has not been previously described.

Table 1
Selected bond distances (Å) and angles (°) for compound **1** · 0.5 (C_6H_6)

Ge(1)–O(1)	1.860(3)	O(1)–Ge(1)–O(3)	91.4(1)
Ge(1)–O(3)	1.992(3)	O(1)–Ge(1)–N(5)	89.7(1)
Ge(1)–N(5)	2.011(4)	O(2)–Ge(2)–O(3)	91.6(1)
Ge(2)–O(2)	1.835(3)	O(2)–Ge(2)–N(5)	91.4(1)
Ge(2)–O(3)	1.993(3)	O(3)–Ge(1)–N(5)	77.1(1)
Ge(2)–N(5)	1.995(4)	O(3)–Ge(2)–N(5)	77.4(1)
Si(1)–O(6)	1.664(3)	Ge(1)–O(3)–Ge(2)	103.0(1)
Si(2)–O(5)[a]	1.696(5)	Ge(1)–N(5)–Ge(2)	102.3(2)
Si(2)–N(3)[a]	1.816(8)	O(5)–Si(2)–N(3)[a]	111.6(3)
Si(2)–N(4)[a]	1.715(8)	O(5)–Si(2)–N(4)[a]	108.2(3)
Si(3)–O(4)[a]	1.712(4)	N(3)–Si(2)–N(4)[a]	122.8(5)
Si(3)–N(1)[a]	1.700(8)	O(4)–Si(3)–N(1)[a]	112.4(4)
Si(3)–N(2)[a]	1.806(9)	O(4)–Si(3)–N(2)[a]	108.8(4)
		N(1)–Si(3)–N(2)[a]	119.6(4)

[a] The atoms Si(2) and Si(3) are disordered over two positions. The tabulated values are for the average of the two positions.



(1)

Compound **1** contains an unusual bridging –NH$_2$– group between the two germanium centers, and the structure of **1** can be compared to the two related calixarene complexes {calix[4]}Ge$_2$ (**2**) and {calix[8]}Ge$_4$ (**3**) [47] as well as the dimeric species [(C$_6$H$_3${C$_6$H$_3$Pr$^i_2$-2,6}$_2$-2,6)GeNH$_2$]$_2$ (**4**) which also contains bridging –NH$_2$– moieties [49]. Similar to the Ge$_2$O$_2$ rhombus in compound **2** the Ge$_2$NO rhombus adopts a planar geometry. The Ge(1)–O(3)–Ge(2) angle of 103.0(1)° is significantly more acute than the Ge–O$_{br}$–Ge angles in **2** and **3** which range from 106.1(1) to 107.89(6)° [47]. Furthermore, the Ge(1)–N(5)–Ge(2) angle measures 102.3(2)° which is more obtuse than the average Ge–N$_{br}$–Ge angles in **4** (100.0(1)°) [49]. The O(3)–Ge(1)–N(5) and O(3)–Ge(2)–N(5) angles average 77.3(1)° which are wider than the O$_{br}$–Ge–O$_{br}$ angles in **2** and **3** but more acute than the N$_{br}$–Ge–N$_{br}$ ligands angles in **4**. These structural differences can be attributed to the presence of two different types of bridging atoms in **1** and the internal angles in the Ge$_2$NO rhombus can be regarded as being intermediate between the Ge$_2$O$_2$ rhombi of **2** and **3** and the Ge$_2$N$_2$ rhombus of **4**.

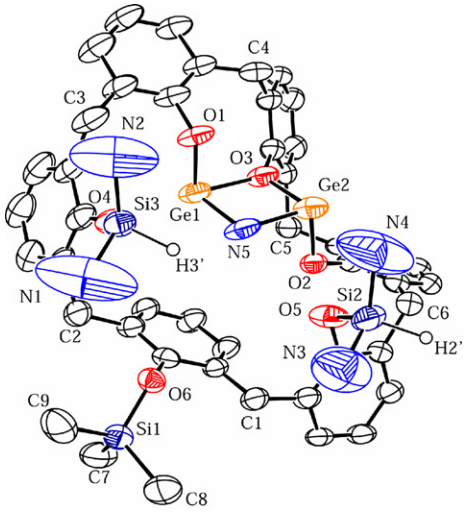


Fig. 1. ORTEP diagram of compound **1**. Thermal ellipsoids are drawn at 50% probability.

The terminal Ge(1)–O(1) and Ge(2)–O(2) bond lengths in **1** are typical for germanium(II)–oxygen distances and are comparable to those in compounds **2** and **3** [47] as well as in other Ge(II) aryloxides [50–54]. The bridging Ge(1)–O(3) and Ge(2)–O(3) bond lengths in **1** are 1.992(3) and 1.993(3) Å (respectively) which fall between the average Ge–O$_{br}$ bond distances in **2** (1.988 Å) and **3** (2.000 Å) [47]. The bridging N atom is not symmetrically disposed between the two germanium atoms in **1** as indicated by the two Ge–N bond lengths measuring 2.011(4) and 1.995(4) Å. These distances are shorter than those found in the structure of **4** which has an average Ge–N distance of 2.013(3) Å [49]. The Ge–N distances in **1** are longer than those in germanium(II) compounds bearing ligands with terminal Ge–N bonds, including the well-known bulky bisamide Ge[N(SiMe$_3$)$_2$]$_2$ which has Ge–N bond lengths of 1.873(5) and 1.878(5) Å [55] and the bis(piperidinato) complex Ge[NC$_5$H$_6$Me$_4$-2,2,6,6]$_2$ which has distances of 1.87(1) and 1.90(1) Å [56]. However, the Ge–N distances in **1** are considerably shorter than those in divalent germanium compounds having dative N → Ge bonds including those in [Ge(2-{(Me$_3$Si)$_2$C}-C$_5$H$_4$N)R] which measure 2.082(4) or 2.089(7) Å (R = Cl or CH(PPh$_2$)$_2$, respectively) [57]. These distances are also shorter than those in the divalent binhapthoxide complex

(*R*)-[Ge{$O_2C_{20}H_{10}(SiMe_2Ph)_2$-3, 3′}{$NH_3$}] (*d* Ge–N = 2.093(4) Å) which contains a coordinated NH_3 molecule [51] and also in [Ge{$OCH(CF_3)_2$}$_2${NH_2Ph}] (*d* Ge–N = 2.092(3) Å) which contains a coordinated aniline molecule [58].

The three remaining oxygen atoms in **1** are each attached to a silicon atom. One of these is incorporated into a –$OSiMe_3$ silyl ether group which arises from the transfer of the –$SiMe_3$ moiety from a –$N(SiMe_3)_2$ ligand in $Ge[N(SiMe_3)_2]_2$ to the phenolic oxygen atom [48]. The geometry of the silyl ether moiety is normal with an approximate tetrahedral environment at silicon and a typical Si–O bond distance of 1.664(3) Å. The Si–O–C_{ipso} angle is 123.7(2)° and the –$SiMe_3$ group is directed outward from the central cavity of the molecule. The other two oxygen atoms have been incorporated into unusual –$OSi(H)(NH_2)_2$ groups. The silicon atoms in both groups are disordered over two positions (50% occupancy) which also results in each of the nitrogen atoms of the four attached –NH_2 groups also being disordered over two positions. The four nitrogen atoms were also disordered with very small positional differences over the two individual positions, and these were refined with a broad thermal parameter which resulted in the large ellipsoids present in the ORTEP plot of **1** (Fig. 1).

The Si–N bond distances (when taking into consideration the distortion of the silicon atoms) are 1.816(8), 1.715(8), 1.700(8), and 1.806(9) Å while, the N–Si–N angles are 122.8(5) and 119.6(4)° at Si(2) and Si(3), respectively. Diaminosilyl ether groups similar to those attached to O(4) and O(5) in **1** have not been described previously and thus a direct comparison to other structurally characterized species is not possible. However, a few small molecules containing –NH_2 groups bound to silicon and having –NH_2 and –OH groups attached to the same silicon atom have been reported [59,60]. The structure of $Mes_2Si(NH_2)_2$ has Si–N distances of 1.713(2) and 1.717(2) Å and a N–Si–N angle of 106.89(5)° [59] while that of $Bu^t_2Si(OH)NH_2$ exhibits a Si–N distance of 1.746(4) Å [60].

The average of the four Si–N distances is 1.759(8) Å in **1** which is longer than the corresponding bond distance in $Bu^t_2Si(OH)NH_2$ [60] and can be attributed to the attachment of the –$Si(H)(NH_2)_2$ moieties in **1** to a phenolic oxygen atom. The two N–Si–N angles in **1** average 121.2(5)° which is significantly more obtuse than the N–Si–N angle in $Mes_2Si(NH_2)_2$ [59]. This structural difference is expected since the latter compound contains two sterically encumbering mesityl groups, while compound **1** instead has a proton and an oxygen atom bound to silicon.

2.2. NMR spectra of compound *1*

Spectroscopic (^{1}H, ^{13}C and ^{29}Si NMR) data in benzene-d_6 are consistent with the solid-state structure of **1**. Similar to compounds **2** and **3**, the conformational flexibility of **1** is restricted versus the calix[6]arene starting material due to the presence of the Ge_2NO rhombus and the relatively large –$OSiMe_3$ and –$OSi(H)(NH_2)_2$ groups. This renders the individual protons of the six methylene units in **1** magnetically non-equivalent, resulting in twelve distinct doublets in the ^{1}H NMR spectrum in the chemical shift range δ 3.1–4.8 ppm which are divided into two sets of six features. The downfield grouping of resonances correspond to the methylene protons directed inward toward the Ge_2NO rhombus while the upfield features are attributed to those directed away.

In the downfield grouping of resonances, the doublet at δ 4.74 (J = 13.2 Hz) ppm is assigned to the proton attached to C(5) which has two close contacts with O(2) and O(3) measuring 2.498 and 2.549 Å (respectively). The two sets of closely grouped doublets at δ 4.66 (J = 14.7 Hz) and 4.64 (J = 12.6 Hz) ppm correspond to the protons bound to C(4) and C(3) (respectively) due to their relative proximity to O(3) and O(1), and the features at δ 4.53 (J = 16.2 Hz) and 4.51 (J = 11.7 Hz) ppm are assigned to the protons attached to C(6) and C(2) (respectively) due to their proximity to the silylated oxygen atoms O(4) and O(5). The remaining doublet at δ 4.34 (J = 13.5 Hz) ppm arises from the proton attached to C(1) which only has long (>2.6 Å) contacts with the neighboring oxygen atoms.

Assignments for the upfield group of six resonances are based on a COSY NMR experiment. The doublet at δ 3.53 (J = 16.2 Hz) ppm corresponds to the second proton bound to C(6), while the four closely spaced features at δ 3.32 (J = 13.2 Hz), 3.30 (J = 14.7 Hz), 3.24 (J = 13.5 Hz), 3.23 (J = 12.6 Hz) ppm arise from the remaining protons attached to C(5), C(4), C(1) and C(3) (respectively). The resonance at δ 3.19 (J = 11.7 Hz) ppm results from the second proton bound to C(2). Due to the rigidity in the Ge_2NO rhombus, the protons in the bridging –NH_2 group also are magnetically non-equivalent, appearing as two broad but clearly resolved doublets at δ 1.66 (J = 9.6 Hz) and 1.04 (J = 9.6 Hz) ppm. The two Si–*H* protons are also non-equivalent and appear as two singlets in the ^{1}H NMR spectrum at δ 6.34 and 6.32 ppm. The –$Si(NH_2)_2$ protons appear as two upfield singlets at δ 0.27 and 0.24 ppm while the protons of the –$OSiMe_3$ moiety appear as a singlet at δ 0.42 ppm. The ^{13}C NMR spectrum of **1** also is consistent with its solid-state structure and exhibits six distinct lines for the each of non-equivalent *ipso*- and *para*-carbon atoms as well as twelve lines for both the *ortho*- and *meta*-carbons. The six methylene groups result in six features between δ 31–35 ppm and there is only one resonance in the –SiR_3 region of the spectrum at δ 1.6 ppm corresponding to the carbon atoms of the –$OSi(CH_3)_3$ group.

The ^{29}Si{^{1}H} NMR spectrum of **1** contains three singlets at δ 21.63, 21.17, and 21.07 ppm, where the downfield resonance arises from the silicon atom in the –$OSiMe_3$ group and the two upfield resonances correspond to the silicon atoms in the two –$Si(H)(NH_2)_2$ groups. The chemical shift for the silyl ether feature is similar to that of $C_6H_5OSiMe_3$ which appears at δ 19.43 ppm [61]. The proton-coupled ^{29}Si NMR spectrum of **1** was also recorded, and the singlet at δ 21.63 in the ^{1}H-decoupled spectrum splits into a multiplet with eight of the ten expected lines being clearly discernable. This arises from the two-bond coupling between the silicon atom and the protons of the methyl groups, with a coupling constant of 6.43 Hz. The two features for the –$Si(H)(NH_2)_2$ groups are more complex due to the presence of both one-bond Si–*H* and three bond Si–NH_2 coupling. Each of these features are expected to appear as a doublet of quintets but their proximity resulted in overlap with one another such that the expected one-bond Si–H coupling could not be clearly observed.

2.3. Analysis of compound *1* using mass spectrometry

The mass spectrum of compound **1** acquired using electrospray mass spectrometry (positive ion mode) exhibited a clear fragmentation pattern having nine well-defined peaks which are listed in Table 2. The proposed fragmentation pattern is illustrated in

Table 2
Electrospray mass spectrometry data for compound **1**

Ion	*m*/*z*	Formula	Relative intensity (%)
1a	988.5	$[(C_6H_3)_6(CH_2)_6O_3Ge_2(NH_2)\{OSi(H)(NH_2)_2\}_2OSiMe_3]H^+$	n/a
1b	927.5	$[(C_6H_3)_6(CH_2)_6O_3Ge_2(NH_2)OSi(H)(NH_2)_2OSiMe_3O]H^+$	2
1c	898.5	$[(C_6H_3)_6(CH_2)_6O_3Ge_2(NH_2)OSiH_3OSiMe_3OH]H^+$	29
1d	826.4	$[(C_6H_3)_6(CH_2)_6O_3Ge_2(NH_2)OSiH_3(OH)_2]H^+$	72
1e	798.4	$[(C_6H_3)_6(CH_2)_6O_2Ge_2(NH_3)(OH)_4]H^+$	100
1f	754.4	$[(C_6H_3)_6(CH_2)_6O_2Ge(NH_2)OSiH_3(OH)_3]H^+$	8
1g	726.4	$[(C_6H_3)_6(CH_2)_6OGe(NH_3)(OH)_5]H^+$	12
1h	682.4	$[(C_6H_3)_6(CH_2)_6O(NH_2)OSiH_3(OH)_4]H^+$	16
1i	654.4	$[(C_6H_3)_6(CH_2)_6(NH_3)(OH)_6]H^+$	28
1j	637.3	$[(C_6H_3)_6(CH_2)_6(OH)_6]H^+$	4

Scheme 1. Although the parent molecular ion at m/z = 988.5 was not observed a feature at m/z = 927.5 corresponding to the loss of one –SiH$(NH_2)_2$ fragment and monoprotonation of the remaining molecule was present in the spectrum. Subsequent fragmentations involve the loss of the –$SiMe_3$ group, the two germanium atoms, the oxygen atoms, and the bridging –NH_2– group. The –O and –NH_2 groups to which these fragments were bound appear to be protonated during the course of this process to yield –OH or NH_3 groups (respectively). Ultimately, all of the substituents in compound **1** undergo fragmentation to produce the parent calix[6]arene in protonated form.

2.4. Pathway for the formation of compound *1*

The pathway for the formation of **1** is likely complex, but two key aspects for the generation of this species are evident. First, compound **1** contains twelve protons distributed among the single bridging –NH_2– and the two –Si(H)$(NH_2)_2$ groups. Since calix[6]arene is the only proton source present in the reaction, all of these must originate from this starting material. Furthermore, 2 equiv. of calix[6]arene must be consumed for every one equiv. of **1** generated in the reaction since calix[6]arene contains only six phenolic protons. This dictates a maximum theoretical yield of 50% for **1** with the concomitant formation of one or more other products, and this postulate is further supported by the complete consumption of calix[6]arene in the reaction. Compound **1** has been isolated in a maximum of 41% during the course of these studies.

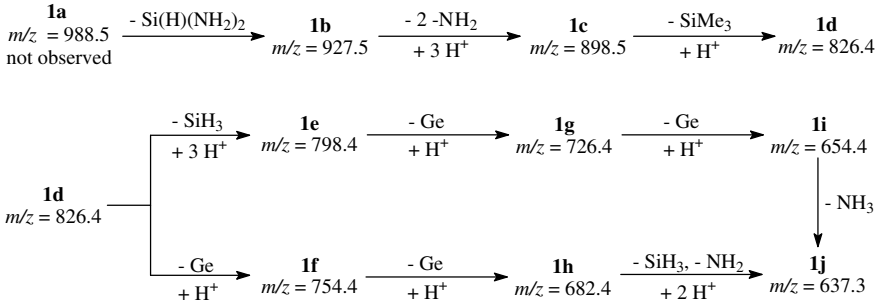
Second, the –N$(SiMe_3)_2$ ligands of Ge[N$(SiMe_3)_2]_2$ are the source of both the bridging –NH_2– group and the –Si(H)$(NH_2)_2$ groups in **1**. We have recently demonstrated that Ge[N$(SiMe_3)_2]_2$ reacts with binaphthols via formation of an intermediate bearing a –OGe[N$(SiMe_3)_2$] moiety which subsequently transfers a –$SiMe_3$ fragment to the oxygen atom of one –OH substituent of the binaphthol [48]. This results in generation of a –OGe[NH$(SiMe_3)$] group and this process can occur a second time to yield a –OGe[NH_2] moiety which could then serve as the source of the bridging amide in **1**. The –Si(H)$(NH_2)_2$ groups, however, must ultimately result from the demethylation of a –$SiMe_3$ group during the course of the reaction. The transfer of a methyl group to gallium in the reaction of $GaCl_3$ with Li[N$(SiMe_3)_2$] has been reported [62], and similar methyl group migrations have been found upon treatment of $GaCl_3$ with N$(SiMe_3)_3$ [63] or $SiMe_4$ [64]. The germanium atoms present in **1** clearly are not methylated, but the generation of Me_4Ge or CH_4 might be expected to occur during the course of this reaction.

In order to probe the pathway for the formation of **1**, the progress of the reaction of one, two and three equivalents of Ge[N$(SiMe_3)_2]_2$ with calix[6]arene was monitored over time using ^{1}H NMR spectroscopy in benzene-d_6 in three separate experiments. The methylene (δ 5.2–3.0 ppm) and alkylsilyl (δ 0.4–0.0 ppm) regions of these spectra contained diagnostic features which were compared over a reaction period of 120 h in each case. Upon treatment of calix[6]arene with 3 equiv. of Ge[N$(SiMe_3)_2]_2$, a resonance for the formation of free HN$(SiMe_3)_2$ at δ 0.09 ppm was observed after 10 min at room temperature and Ge[N$(SiMe_3)_2]_2$ and a trace amount of calix[6]arene were still present in solution. After heating the sample at 85 °C for 1 h, the aromatic and methylene regions of the spectrum were complex but the appearance of peaks at δ 0.42, 0.29 and 0.25 ppm indicated that compound **1** was already present in solution. The absence of a resonance at δ 10.50 ppm attributable to the six phenolic protons also indicated all of the calix[6]arene had been consumed at this time.

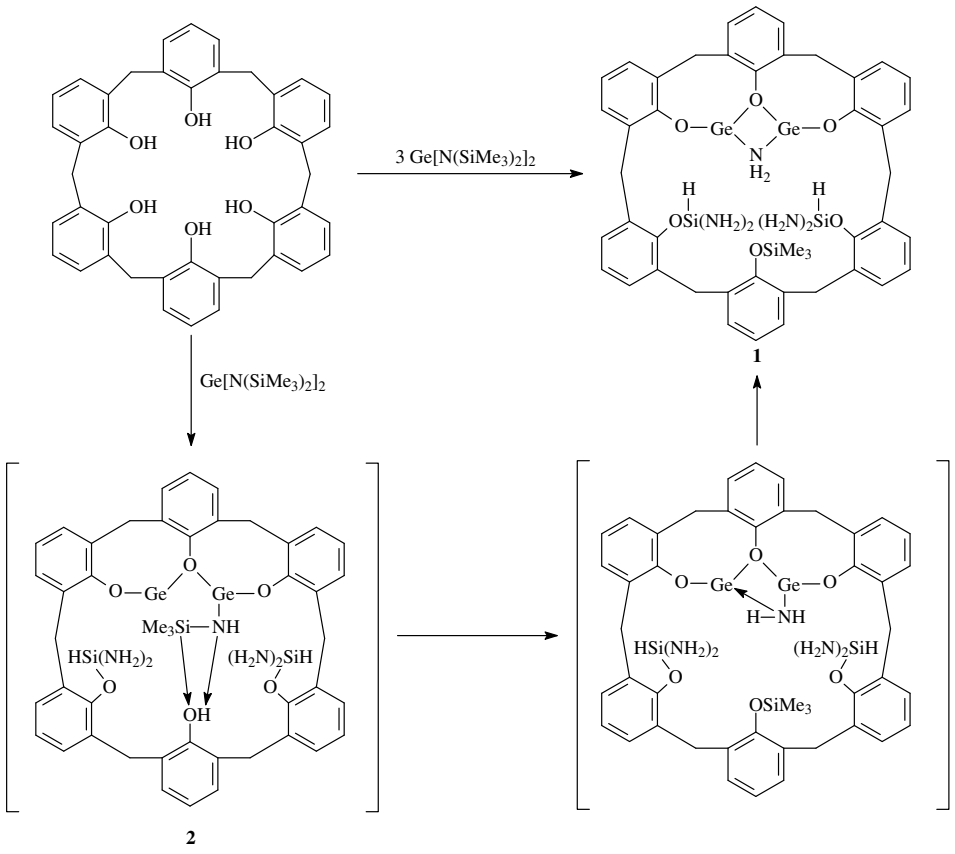
After heating the sample at 85 °C for a total of 6 h, the overall appearance of the spectrum had simplified and suggested that compound **1** was present in solution along with a second intermediate species. The methylene region of the spectrum contained 24 doublets divided into an upfield and downfield grouping of 12 features. Some overlap of these resonances was observed but four distinct peaks at δ 5.08 (J = 15.0 Hz), 4.43 (J = 13.5 Hz), 3.15 (J = 12.3 Hz), and 3.13 (J = 12.9 Hz) ppm were visible, which clearly are not attributable to **1** but arise from a second compound present in solution. Similarly, two additional peaks at δ 0.36 and 0.30 ppm in the alkylsilyl region were observed at this time as were two additional downfield singlets at δ 6.32 and 6.30 ppm arising from Si–*H* protons.

The presence of the four features at δ 6.32, 6.30, 0.36 and 0.30 ppm along with the structural rigidity apparent in the intermediate species suggest that all or part of the Ge_2NO rhombus and the two –Si(H)$(NH_2)_2$ groups are generated prior to silylation of the remaining hydroxyl group to generate the silyl ether moiety. Further evidence for this results from the presence of a broad singlet at δ 5.92 ppm which suggests the presence of a single hydroxyl group in the intermediate species. Similar ^{1}H NMR –OH features were observed for the main group calixarenes {(OH)(calix[4]arene)P} (δ 5.4 ppm) [20], {(OH)(*p*-*tert*-butylcalix[4]arene)Si} (δ 4.59 ppm) [21], {(OH)(calix[4]arene)As} (δ 4.90 ppm) [19], and {(OH)(*p*-*tert*-butylcalix[4]arene)As} (δ 4.74 ppm) [19], all of which have a single unbound –OH group and three oxygen atoms bound to the main group element. The resonance at δ 5.92 ppm had significantly reduced in intensity after heating the sample for a total of 48 h, as had the two features at δ 6.32 and 6.30 ppm and the upfield peaks at δ 0.36 and 0.30 ppm. We therefore postulate that the structure of the intermediate detected by ^{1}H NMR spectroscopy is that of **2** illustrated in Scheme 2, which undergoes an exchange of the –$SiMe_3$ group attached to the nitrogen with the remaining hydroxyl proton followed by closure of the Ge_2NO rhombus.

After heating the sample for an additional 12 h resonances corresponding only to **1**, free HN$(SiMe_3)_2$, and unreacted Ge[N$(SiMe_3)_2]_2$ remained. The appearance of the spectrum remained unchanged with up to 120 h of heating at 85 °C. Nearly identical results were obtained when calix[6]arene was treated with 2 equiv. of Ge[N$(SiMe_3)_2]_2$ under the same reaction conditions except that Ge[N$(SiMe_3)_2]_2$ was absent after the reaction had gone



Scheme 1.



Scheme 2.

to completion. The outcome of this process is consistent with the overall reaction stoichiometry since two germanium atoms are present in the framework of **1**. The ^{1}H NMR spectra of the reaction of calix[6]arene with 1 equiv. of Ge[N(SiMe$_3$)$_2$]$_2$ in benzene-d_6 indicated the formation of a complex mixture of species which included **1** and the intermediate **2** which remained present in solution even after heating the reaction mixture for 120 h.

In the course of these studies, no conclusive evidence for the formation of Me_4Ge or CH_4 was found which exhibit similar ^{1}H NMR resonances at δ 0.14 and 0.15 ppm in benzene-d_6. However, identification of calix[6]arene as the source of all of the protons in the two –Si(H)(NH$_2$)$_2$ groups and in the bridging –NH$_2$– group was confirmed by the reaction of three equiv. of Ge[N(SiMe$_3$)$_2$]$_2$ with calix[6]arene-d_6 which contained six deuterated hydroxyl groups. The ^{1}H NMR spectrum of the resulting product contained only a single line at δ 0.42 ppm arising from the –OSiMe$_3$ moiety as well as a feature corresponding to unreacted germanium amide.

3. Conclusions

In conclusion, the reactivity of calix[6]arene with Ge[N(SiMe$_3$)$_2$]$_2$ differs considerably from that found in reactions involving calix[4]arene and calix[8]arene. Instead of forming complexes containing Ge_2O_2 rhombi, the germanium calix[6]arene complex **1** contains a central Ge_2NO rhombus incorporating three of the six oxygen atoms of the macrocycle. The remaining three oxygen atoms have been converted to two –OSi(H)(NH$_2$)$_2$ moieties and one –OSiMe$_3$ group. The pathway for the formation of **1** is likely complex, but involves the consumption of two equivalents of calix[6]arene for each equivalent of **1** produced in the reaction.

4. Experimental

All manipulations were carried out using standard Schlenk, syringe, and glovebox techniques [65]. Calix[6]arene was purchased from Alfa Aesar and Ge[N(SiMe$_3$)$_2$]$_2$ was synthesized according to the published procedure [66–68]. Solvents were dried using a Glass Contour Solvent Purification System. One and two-dimensional ^{1}H NMR spectra were recorded at 400 MHz on a Varian Unity INOVA 400 spectrometer and referenced to residual protio solvent. For the ^{1}H NMR assignments in **1**, the numbering scheme of the carbon atoms corresponds to the crystal structure of **1**, *i.e.* –C(5)H_2– refers to a proton bound to C(5). ^{13}C NMR spectra were recorded at a frequency of 100.6 MHz on a Varian Unity INOVA 400 and referenced to the solvent while ^{29}Si NMR were acquired using a Varian Unity INOVA 600 operating at 119.2 MHz and were referenced to external $SiMe_4$. Mass spectra were acquired using a Bruker Agilent 1100 LC/MSD System in acetonitrile solvent. Elemental analysis was performed by Midwest Microlab, LLC (Indianapolis, IN).

4.1. Synthesis of compound *1*

To a solution of calix[6]arene (0.458 g, 0.719 mmol) in benzene (10 mL) was added a solution of Ge[N(SiMe$_3$)$_2$]$_2$ (0.852 g, 2.17 mmol) in benzene (4 mL). The mixture was sealed in a Schlenk tube and heated at 85 °C for 72 h. The solvent was removed *in vacuo* to yield a white solid which was recrystallized from hot benzene (5 mL) to yield **1** as colorless crystals which were washed with hexane (3 × 5 mL) and dried *in vacuo*. Yield: 0.292 g (41%). ^{1}H NMR (C_6D_6, 25 °C): δ 7.29–6.75 (m, 18H, aromatics), 6.34 (s, 1H, –Si(*H*)(NH$_2$)$_2$), 6.32 (s, 1H, –Si(*H*)(NH$_2$)$_2$), 4.74 (d, J = 13.2 Hz, 1H –C(5)H_2–), 4.66 (d, J = 14.7 Hz, 1H, –C(4)H_2–), 4.64 (d, J = 12.6 Hz, 1H, –C(3)H_2-), 4.53 (d, J = 16.2 Hz, 1H, –C(6)H_2–), 4.51

(d, J = 11.7 Hz, 1H, –C(2)H_2–), 4.34 (d, J = 13.5 Hz, 1H, –C(1)H_2–), 3.53 (d, J = 16.2 Hz, 1H, –C(6)H_2-), 3.32 (d, J = 13.2 Hz, 1H, –C(5)H_2–), 3.30 (d, J = 14.7 Hz, 1H, –C(4)H_2–), 3.24 (d, J = 13.5 Hz, 1H, –C(1)H_2-), 3.23 (d, J = 12.6 Hz, 1H, –C(3)H_2–), 3.19 (d, J = 11.7 Hz, 1H, -C(2)H_2–), 1.66 (br d, J = 9.6 Hz, 1H, –NH_2–), 1.04 (br d, J = 9.6 Hz, 1H, –NH_2–), 0.42 (s, 9H, –OSi(CH_3)$_3$), 0.27 (s, 4H, –Si(H)(NH_2)$_2$), 0.24 (s, 4H, –Si(H)(NH_2)$_2$) ppm. ^{13}C NMR (C_6D_6, 25 °C) δ 156.1, 154.4, 152.0, 151.6, 151.1, 150.8 (*ipso*-C), 136.8, 136.6, 136.4, 136.1, 135.9, 135.2, 134.5, 133.3, 132.8, 132.6, 132.1, 132.0 (*meta*-C), 131.0, 130.8, 130.7, 130.5, 130.4, 130.3, 129.8, 129.7, 129.4, 129.3, 129.1, 128.8 (*ortho*-C), 123.6, 122.7, 122.3, 122.2, 120.9, 120.8 (*para*-C), 34.2, 34.0, 33.9, 33.4, 33.1, 31.1 (–CH_2–), 1.6 (-OSi(CH_3)$_3$) ppm. ^{29}Si{^{1}H} NMR (C_6D_6, 25 °C): δ 21.63, 21.17, and 21.07 ppm. IR (Nujol): 3348, 3266, 3255, 2720, 2664, 2288, 1916, 1859, 1807, 1713, 1661, 1589 cm^{-1}. *Anal.* Calc. for $C_{45}H_{51}Ge_2N_5O_6Si_3$: C, 54.74; H, 5.21. Found: 54.15; H, 5.41%.

4.2. NMR scale reaction of calix[6]arene with 3 equiv. Ge[N(SiMe$_3$)$_2$]$_2$

A solution of calix[6]arene (0.050 g, 0.078 mmol) in benzene-d_6 (0.25 mL) was treated with a solution of Ge[N(SiMe$_3$)$_2$]$_2$ (0.093 g, 0.24 mmol) in benzene-d_6 (0.25 mL) in a screw-cap NMR tube.

4.3. NMR scale reaction of calix[6]arene with 2 equiv. Ge[N(SiMe$_3$)$_2$]$_2$

A solution of calix[6]arene (0.050 g, 0.078 mmol) in benzene-d_6 (0.25 mL) was treated with a solution of Ge[N(SiMe$_3$)$_2$]$_2$ (0.062 g, 0.16 mmol) in benzene-d_6 (0.25 mL) in a screw-cap NMR tube.

4.4. NMR scale reaction of calix[6]arene with 1 equiv. Ge[N(SiMe$_3$)$_2$]$_2$

A solution of calix[6]arene (0.050 g, 0.078 mmol) in benzene-d_6 (0.25 mL) was treated with a solution of Ge[N(SiMe$_3$)$_2$]$_2$ (0.031 g, 0.079 mmol) in benzene-d_6 (0.25 mL) in a screw-cap NMR tube.

4.5. Synthesis of calix[6]arene-d_6

To a solution of calix[6]arene (0.300 g, 0.471 mmol) in diethyl ether (30 mL) was added a solution of 2.5 M Bu^{n}Li in hexanes (1.51 mL, 3.78 mmol) at −78 °C. The reaction mixture was allowed to come to room temperature and was stirred for 4 h. The reaction mixture was quenched with D_2O (5 mL) at −78 °C via cannula from a sure-seal bottle. The organic layer was separated and dried over anhydrous $MgSO_4$ and the solvent was removed *in vacuo* to yield calix[6]arene-d_6 (0.221 g, 72%). The ^{1}H NMR spectrum of the product recorded in benzene-d_6 did not exhibit an –OH resonance.

4.6. NMR scale reaction of calix[6]arene-d_6 with 3 equiv. Ge[N(SiMe$_3$)$_2$]$_2$

To a solution of calix[6]arene-d_6 (0.057 g, 0.088 mmol) in benzene-d_6 (0.35 mL) was added a solution of Ge[N(SiMe$_3$)$_2$]$_2$ (0.107 g, 0.272 mmol) in benzene-d_6 (0.30 mL). The reaction mixture was heated in an oil bath for 48 h and the ^{1}H NMR spectrum was recorded.

4.7. X-ray crystal structure of 1 · 0.5(C_6H_6)

Diffraction intensity data were collected with a Siemens P4/CCD diffractometer. Absorption corrections were applied for all data by SADABS. The structures were solved using direct methods, completed by Fourier syntheses, and refined by full-matrix least squares procedures on F^2. All non-hydrogen atoms were refined with anisotropic displacement coefficients, and hydrogen atoms were treated as idealized contributions. Contributions from the benzene solvent molecule were removed using SQUEEZE. All software and sources of scattering factors are contained in the SHEXTL (5.10) program package (G. Sheldrick, Bruker XRD, Madison, WI). ORTEP diagrams were drawn using the ORTEP3 program (L.J. Farrugia, Glasgow).

Crystallographic data for **1 · 0.5(C_6H_6)**: Crystal size: 0 × 0.22 × 0.17 mm. Crystal color and habit: colorless block. Empirical formula: $C_{48}H_{54}Ge_2N_5O_6Si_3$. Formula weight: 1026.42. Wavlength: 0.71073 Å. Temperature: 100(2) K. Crystal system: triclinic. Space group: $P\bar{1}$. Unit cell dimensions: a = 13.199(2) Å, b = 14.774(2) Å; c = 16.569(4) Å; α = 105.373(4)°; β = 102.641(4)°; γ = 115.225(3)°. Volume = 2606.5(9) Å^3. Z = 2. D_{calc} = 1.309 g/cm^3. Absorption coefficient = 1.274 mm^{-1}. F(000) = 1064. θ-Range for data collection = 1.67–25.00°. Index ranges: $-14 \leqslant h \leqslant -15$; $-15 \leqslant k \leqslant 17$; $-19 \leqslant l \leqslant 19$. Reflections collected = 15 228. Independent reflections = 9124 (R_{int} = 0.0295). Completeness to θ = 99.2% (θ = 25.00°). Absorption correction = multi-scan. Refinement method = full-matrix least-squares on F^2. Data/restraints/parameters = 9124/0/584. Goodness-of-fit on F^2 = 1.014. Final R indices [$I > 2\sigma(I)$]: R_1 = 0.0581; wR_2 = 0.1414. R indices (all data): R_1 = 0.0884; wR_2 = 0.1580. Largest difference in peak and hole = 0.512 and −0.547 e Å^{-3}.

Acknowledgement

Funding for this project was provided by the Department of Chemistry at Oklahoma State University.

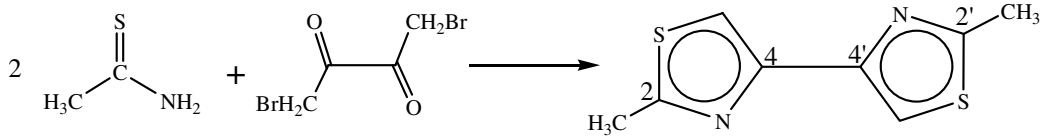
Appendix A. Supplementary data

CCDC 669869 contains the supplementary crystallographic data for **1**. These data can be obtained free of charge via http://www.ccdc.cam.ac.uk/conts/retrieving.html or from the Cambridge Crystallographic Data Centre, 12 Union Road, Cambridge CB2 1EZ, UK; fax: (+44) 1223-336-033; or deposit@ccdc.cam.ac.uk. Supplementary data associated with this article can be found, in the online version, at doi:10.1016/j.poly.2008.02.027.

References

[1] F. Hof, S.L. Craig, C. Nuckolls, J. Rebek Jr., Angew. Chem., Int. Ed. Engl. 41 (2002) 1488.
[2] Z. Asfari, V. Böhmer, J. Harrowfield, J. Vincens, Calixarenes 2001, Kluwer Academic Publishers, Dordrecht, The Netherlands, 2001.
[3] A.F.D. de Namor, R.M. Cleverley, M.L. Zapata-Ormachea, Chem. Rev. 98 (1998) 2495.
[4] J. Vincens, V. Böhmer, Calixarenes, A Versatile Class of Macrocyclic Compounds, Kluwer Academic Publishers, Dordrecht, The Netherlands, 1991.
[5] A. Pochini, R. Ungaro, in: F. Vögtle (Ed.), Comprehensive Supramolecular Chemistry, Pergamon Press, New York, 1996.
[6] V. Böhmer, Angew. Chem., Int. Ed. Engl. 34 (1995) 713.
[7] C.D. Gutsche, Calixarenes Revisited, Royal Society of Chemistry, Cambridge, 1998.
[8] D.M. Redkevich, Angew. Chem., Int. Ed. Engl. 43 (2004) 558.
[9] M. Lattman, in: R.A. Kemp (Ed.), Modern Aspects of Main Group Chemistry, ACS Symposium Series, 2006, pp. 237–251.
[10] M. Fan, H. Zhang, M. Lattman, Inorg. Chem. 45 (2006) 6490.
[11] P. Sood, M. Koutha, M. Fan, Y. Klichko, H. Zhang, M. Lattman, Inorg. Chem. 43 (2004) 2975.
[12] M. Fan, H. Zhang, M. Lattman, Phosphorus, Sulfur, Silicon Relat. Elem. 177 (2002) 1549.
[13] M. Fan, I.V. Shevchenko, R.H. Voorhies, S.F. Eckert, H. Zhang, M. Lattman, Inorg. Chem. 39 (2000) 4704.
[14] M. Fan, H. Zhang, M. Lattman, Phosphorus, Sulfur, Silicon Relat. Elem. 144–146 (1999) 257.
[15] M. Fan, H. Zhang, M. Lattman, Chem. Commun. (1998) 99.
[16] M. Fan, H. Zhang, M. Lattman, Organometallics 15 (1996) 5216.
[17] P. Sood, H. Zhang, M. Lattman, Organometallics 21 (2002) 4442.
[18] I.V. Shevchenko, H. Zhang, M. Lattman, Inorg. Chem. 34 (1995) 5405.
[19] S. Shang, D.V. Khasnis, H. Zhang, A.C. Small, M. Fan, M. Lattman, Inorg. Chem. 34 (1995) 3610.
[20] D.V. Khasnis, J.M. Burton, J.D. McNeil, C.J. Santini, H. Zhang, M. Lattman, Inorg. Chem. 33 (1994) 2657.
[21] S. Shang, D.V. Khasnis, J.M. Burton, C.J. Santini, M. Fan, A.C. Small, M. Lattman, Organometallics 13 (1994) 5157.

[22] D.V. Khasnis, J.M. Burton, J.D. McNeil, H. Zhang, M. Lattman, Phosphorus, Sulfur, Silicon Relat. Elem. 75 (1993) 253.
[23] D.V. Khasnis, J.M. Burton, M. Lattman, H. Zhang, J. Chem. Soc., Chem. Commun. (1991) 562.
[24] D.V. Khasnis, M. Lattman, C.D. Gutsche, J. Am. Chem. Soc. 112 (1990) 9422.
[25] J.O. Magrans, A.M. Rincón, F. Cuevas, J. López-Prados, P.M. Nieto, M. Pons, P. Prados, J. de Mendoza, J. Org. Chem. 63 (1998) 1079.
[26] S. Kanamathareddy, C.D. Gutsche, J. Org. Chem. 57 (1992) 3160.
[27] S. Shinkai, Tetrahedron 49 (1993) 8933.
[28] C.D. Gutsche, L.J. Bauer, J. Am. Chem. Soc. 107 (1985) 6052.
[29] J.C. Iglesias-Sánchez, B. Souto, C.J. Pastor, J. de Mendoza, P. Prados, J. Org. Chem. 70 (2005) 10400.
[30] G. Izzet, M.-N. Rager, O. Reinaud, Dalton Trans. (2007) 771.
[31] U. Darbost, O. Sénèque, Y. Li, G. Bertho, J. Marrot, M.-N. Rager, O. Reinaud, I. Jabin, Chem. Eur. J. 13 (2007) 2078.
[32] B. Boulet, C. Bouvier-Capely, C. Cossonnet, G. Cote, Solvent Extr. Ion Exc. 24 (2006) 319.
[33] J.P.W. Eggert, J.M. Harrowfield, U. Lüning, B.W. Skelton, A.H. White, Polyhedron 25 (2006) 910.
[34] Y. Obora, Y.K. Liu, S. Kubouchi, M. Tokunaga, Y. Tsuji, Eur. J. Inorg. Chem. (2006) 222.
[35] G. Izzet, H. Akdas, N. Hucher, M. Giorgi, T. Prange, O. Reinaud, Inorg. Chem. 45 (2006) 1069.
[36] O. Sénèque, M.-N. Rager, M. Giorgi, T. Prange, A. Tomas, O. Reinaud, J. Am. Chem. Soc. 127 (2005) 14833.
[37] Y. Obora, Y.K. Liu, L.H. Jiang, K. Takenaka, M. Tokunaga, Y. Tsuji, Organometallics 24 (2005) 4.
[38] K. Belhamel, T.K.D. Nguyen, M. Benamor, R. Ludwig, Eur. J. Inorg. Chem. (2003) 4110.
[39] R. Souane, V. Hubscher, Z. Asfari, F. Arnaud, J. Vicens, Tetrahedron Lett. 44 (2003) 9061.
[40] O. Sénèque, Y. Rondelez, L. Le Clainche, C. Inisan, M.-N. Rager, M. Giorgi, O. Reinaud, Eur. J. Inorg. Chem. (2001) 2597.
[41] F. Loffler, U. Luning, G. Gohar, New J. Chem. 24 (2000) 935.
[42] Y. Rondelez, O. Sénèque, M.-N. Rager, A.F. Duprat, O. Reinaud, Chem. Eur. J. 6 (2000) 4218.
[43] O. Sénèque, M.-N. Rager, M. Giorgi, O. Reinaud, J. Am. Chem. Soc. 122 (2000) 6183.
[44] A.J. Petrella, N.K. Roberts, D.C. Craig, C.L. Raston, R.N. Lamb, Chem. Commun. (2003) 2288.
[45] A.J. Petrella, D.C. Craig, R.N. Lamb, C.L. Raston, N.K. Roberts, Dalton Trans. (2004) 327.
[46] A.J. Petrella, N.K. Roberts, D.C. Craig, C.L. Raston, R.N. Lamb, Chem. Commun. (2003) 1014.
[47] A.E. Wetherby Jr., L.R. Goeller, A.G. DiPasquale, A.L. Rheingold, C.S. Weinert, Inorg. Chem. 46 (2007) 7579.
[48] A.E. Wetherby Jr., L.R. Goeller, A.G. DiPasquale, A.L. Rheingold, C.S. Weinert, Inorg. Chem. 47 (2008) 2162.
[49] C. Stanciu, S.S. Hino, M. Stender, A.F. Richards, M.M. Olmstead, P.P. Power, Inorg. Chem. 44 (2005) 2774.
[50] C.S. Weinert, A.E. Fenwick, P.E. Fanwick, I.P. Rothwell, J. Chem. Soc., Dalton Trans. (2003) 1795.
[51] C.S. Weinert, P.E. Fanwick, I.P. Rothwell, J. Chem. Soc., Dalton Trans. (2002) 2948.
[52] T. Hascall, A.L. Rheingold, I. Guzei, G. Parkin, Chem. Commun. (1998) 101.
[53] B.G. McBurnett, A.H. Cowley, Chem. Commun. (1999) 17.
[54] B. Çetinkaya, I. Gümrükçü, M.F. Lappert, J.L. Atwood, R.D. Rogers, M.J. Zaworotko, J. Am. Chem. Soc. 102 (1980) 2088.
[55] R.W. Chorley, P.B. Hitchcock, M.F. Lappert, W.P. Leung, P.P. Power, M.M. Olmstead, Inorg. Chim. Acta 198–200 (1992) 203.
[56] M.F. Lappert, M.J. Slade, J.L. Atwood, M.J. Zaworotko, J. Chem. Soc., Chem. Commun. (1980) 621.
[57] S. Benet, C.J. Cardin, D.J. Cardin, S.P. Constantine, P. Heath, H. Rashid, S. Teixeira, J.H. Thorpe, A.K. Todd, Organometallics 18 (1999) 389.
[58] S. Suh, D.M. Hoffman, Inorg. Chem. 35 (1996) 6164.
[59] K. Ruhland-Senge, R.A. Bartlett, M.M. Olmstead, P.P. Power, Angew. Chem., Int. Ed. Engl. 32 (1993) 425.
[60] C. Reiche, S. Kliem, U. Klingebiel, M. Noltemeyer, C. Voit, R. Herbst-Immer, S. Schmatz, J. Organomet. Chem. 667 (2003) 24.
[61] J. Schraml, M. Kvicalova, V. Blechta, J. Cermak, Mag. Res. Chem. 35 (1997) 659.
[62] B. Luo, V.G. Young Jr., W.L. Gladfelter, J. Organomet. Chem. 649 (2002) 268.
[63] C.J. Carmalt, J.D. Mileham, A.J.P. White, D.J. Williams, J.W. Steed, Inorg. Chem. 40 (2001) 6035.
[64] H. Schmidbaur, W. Findeiss, Angew. Chem., Int. Ed. Engl. 3 (1964) 696.
[65] D.F. Shriver, M.A. Drezdzon, The Manipulation of Air Sensitive Comounds, John Wiley and Sons, New York, 1986.
[66] D.H. Harris, M.F. Lappert, J. Chem. Soc., Chem. Commun. (1974) 895.
[67] M.J.S. Gynane, D.H. Harris, M.F. Lappert, P.P. Power, P. Rivière, M. Rivière-Baudet, J. Chem. Soc., Dalton Trans. (1977) 2004.
[68] Q. Zhu, K.L. Ford, E.J. Roskamp, Heteroatom Chem. 3 (1992) 647.



Scheme 1. The synthetic route and numbering scheme of 2,2′-dimethyl 4,4′-bithiazole (dm4bt) (**1**).

($CDCl_3$): 7.61 (s, 2H, Ar) and 2.78 (s, 6H, CH_3). ^{13}C NMR δ_C ($CDCl_3$): 166.46, 150.08, 114.52 (Ar) and 19.45(CH_3). IR (KBr, cm^{-1}): 879 (νS–C), 1184 (νC–N), 1419 (νC–C), 1496 (νC=N), 1558 (νC=C), 3103 (νC–H, Me) and 3434 (νC–H, cycle). UV–Vis (CH_3OH): λ_{max}: 3.76×10^4 cm^{-1}. *Anal.* Calc. for **1**: C, 48.90; H, 4.07; N, 14.26. Found: C, 48.71; H, 3.96; N, 14.12%.

2.3. Synthesis of [Zn(dm4bt)Cl_2] (**2**)

$ZnCl_2$ (0.040 g, 0.285 mmol) was dissolved in water (10 ml), mixed with methanol (50 ml) and reacted with 2,2′-dimethyl-4,4′-bithiazole (0.056 g, 0.285 mmol) dissolved in 10 ml of methanol. The mixture was stirred at 40 °C for 2 h, then the resulting solution was filtered and left at room temperature. After a week, it began to produce colorless crystals of **2** (yield 0.073 g, 76%). ^1H NMR δ_H (DMSO): 7.74 (s, 2H, Ar) and 2.70 (s, 6H, CH_3). IR (KBr, cm^{-1}): 600, 856, 981 (νnew), 884 (νS–C), 1219 (νC–N), 1442 (νC–C), 1532 (νC=N), 1563 (νC=C), 3097 (νC–H, Me), 3429 (νC–H, cycle). UV–Vis (DMSO): λ_{max}: 3.21×10^4 cm^{-1}. *Anal.* Calc. for **2**: C, 28.86; H, 2.40; N, 8.42. Found: C, 28.71; H, 2.34; N, 8.26%.

2.4. Synthesis of [Hg(dm4bt)Cl_2] (**3**)

$HgCl_2$ (0.070 g, 0.255 mmol) and 2,2′-dimethyl-4,4′-bithiazole (0.050 g, 0.255 mmol) were separately dissolved in methanol (10 ml) and added together slowly (without stirring). The mixture was filtered and the solution was left at room temperature. After a week, complex **3** was obtained as colorless crystals (yield 0.10 g, 84%). ^1H NMR δ_H (DMSO): 7.86 (s, 2H, Ar) and 2.73 (s, 6H, CH_3). IR (KBr, cm^{-1}): 635, 863, 967 (νnew), 883 (νS–C), 1207 (νC–N), 1426 (νC–C), 1514 (νC=N), 1634 (νC=C), 3074 (νC–H, Me), 3440 (νC–H, cycle). UV–Vis (DMSO): λ_{max}: 3.62×10^4 cm^{-1}.*Anal.* Calc. for **3**: C, 20.52; H, 1.71; N, 5.98. Found: C, 20.41; H, 1.62; N, 5.83%.

2.5. Computational details

All calculations have been carried out by using GAUSSIAN-03 software [19]. In order to obtain local minima geometries in the ground states, two different ab initio methods, HF and B3LYP [20–22] have been employed with the 6-31G* set [23]. Atom hybridisation was obtained and partitioned using the natural bond orbital (NBO) method incorporated in GAUSSIAN-03 [19]. Also this method gives aromatic interaction energies both by deletion of the off-diagonal Fock matrix elements between the interacting orbitals and from the second-order perturbation approach.

2.6. Crystal structure determination and refinement

The X-ray diffraction measurements were made on a STOE IPDS-II diffractometer with graphite monochromated Mo Kα radiation. For 2,2′-dimethyl-4,4′-bithiazole (dm4bt) (**1**), [Zn(dm4bt)Cl_2] (**2**) and [Hg(dm4bt)Cl_2] (**3**), colorless prismatic crystals with dimensions of $0.50 \times 0.20 \times 0.15$ mm, $0.40 \times 0.35 \times 0.30$ mm and $0.40 \times 0.20 \times 0.17$ mm, were, respectively, chosen and mounted on a glass fiber and used for data collection. Cell constants and an orientation matrix for data collection were obtained by least-squares refinement of diffraction data from 1060 unique reflections for **1**, 2866 for **2** and 2908 for **3**. Data were collected at a temperature of 293(2) K to a maximum 2θ value of 56.00° for **1** and 55.88° for **3** and at a temperature of 120(2) K to a maximum 2θ value of 55.86° for **2**, in a series of ω scans in 1° oscillations, and integrated using the Stoe X-AREA [24] software package. The numerical absorption coefficient, μ, for Mo Kα radiation is 0.528 mm^{-1} for **1**, 2.685 mm^{-1} for **2** and 13.220 mm^{-1} for **3**. A numerical absorption correction was applied using X-RED [25] and X-SHAPE [26] software. The data were corrected for Lorentz and Polarizing effects. The structures were solved by direct methods [27] and subsequent difference Fourier maps and then refined on F^2 by a full-matrix least-squares procedure using anisotropic displacement parameters [28]. All of the hydrogen atoms were located in a difference Fourier map and then refined isotropically. Subsequent refinement then converged with R factors and parameters errors significantly better than for all attempts to model the solvent disorder. Atomic factors are from the International Tables for X-ray Crystallography [29]. All refinements were performed using the X-STEP32 crystallographic software package [30]. A summary of the crystal data, experimental details and refinement results is given in Table 1.

Table 1
Crystallographic and structure refinement data for compounds **1–3**

	1	**2**	**3**
Formula	$C_8H_8N_2S_2$	$C_8H_8Cl_2N_2S_2Zn$	$C_8H_8Cl_2HgN_2S_2$
Formula weight	196.30	332.59	467.79
T (K)	293(2)	120(2)	293(2)
λ (Å)	0.71073	0.71073	0.71073
Crystal system	monoclinic	monoclinic	monoclinic
Space group	$P2_1/a$	$P2_1/n$	$P2_1/c$
Crystal size (mm)	$0.50 \times 0.20 \times 0.15$	$0.40 \times 0.35 \times 0.30$	$0.40 \times 0.20 \times 0.17$
a (Å)	6.217(3)	8.7980(17)	8.6020(14)
b (Å)	10.651(3)	12.165(4)	13.083(3)
c (Å)	7.292(3)	12.139(2)	11.2737(19)
β (°)	109.68(3)	105.169(14)	103.602(12)
V (Å^3)	454.6(3)	1253.9(5)	1233.2(4)
Z	2	4	4
D_{calc} (g cm^{-3})	1.434	1.762	2.520
θ Range for data collection	3.53–28.00	2.41–27.93	2.42–27.94
F(000)	204	664	864
Absorption coefficient	0.528	2.685	13.220
Index ranges	$-8 \leqslant h \leqslant 8$, $-14 \leqslant k \leqslant 14$, $-8 \leqslant l \leqslant 9$	$-11 \leqslant h \leqslant 11$, $-15 \leqslant k \leqslant 12$, $-15 \leqslant l \leqslant 15$	$-9 \leqslant h \leqslant 11$, $-17 \leqslant k \leqslant 15$, $-14 \leqslant l \leqslant 14$
Data collected	3089	6685	8121
Unique data (R_{int})	1060 (0.0666)	2866 (0.0220)	2908 (0.0624)
Parameters, restrains	55, 0	137, 0	137, 0
Final R_1, wR_2[a] (observed data)	0.0548, 0.1546	0.0318, 0.0968	0.0340, 0.0696
Final R_1, wR_2[a] (all data)	0.0581, 0.1594	0.0363, 0.0999	0.0403, 0.0723
Goodness-of-fit on F^2 (S)	1.107	1.154	1.156
Extinction coefficient		0.007(2)	0.0041(2)
Largest difference in peak and hole (e Å^{-3})	0.278, −0.420	0.448, −0.391	1.748, −1.455

[a] $R_1 = \sum||F_o| - |F_c||/\sum|F_o|$, $wR_2 = [\sum(w(F_o^2 - F_c^2)^2)/\sum w(F_o^2)^2]^{1/2}$.

3. Results and discussion

3.1. Synthesis of compounds 1–3

2,2′-Dimethyl-4,4′-bithiazole (**1**) was synthesized according to the reported procedure [18]. Suitable crystals of **1** for X-ray diffraction study were grown by slow evaporation of a 2:1 ratio of methanol:water solution at ambient temperature over 4 weeks.

To obtain details of the electronic nature of the ligand and coordinative ability of it relative to other bithiazole and bipyridine derivatives, a DFT calculation was performed on them by using HF and B3LYP with the 6-31G* basis set. The optimized geometry and thermal ellipsoid plot of **1**, with the atomic numbering, are shown in Fig. 1. As can be seen from this figure, the considered conformation of the ligand is anti. The calculated bond distances and angels are in good agreement with the experimental values. Calculated and experimental structural parameters (distances and angles) were compared and mean differences between the experimental and calculated data obtained by the SPSS program are about 0.007 Å for bond distances and about 0.15° for bond angles, confirming the fairness of the minimal consumed time and acceptable error. An electrostatic potential calculation was performed by the HF/6-31G* method/basis set on the optimized structure obtained at the B3LYP/6-31G* method/basis set to calculate the Mulliken and ESP filling charge for 4,4′-bithiazole (4bt), 2,2′-dimethyl-4,4′-bithiazole (dm4bt) and for their bipyridine analogues, 2,2′-bipyridine (bipy) and 6,6′-dimethyl-2,2′-bipyridine (dm2bipy). Table 2 summarizes the charges of the nitrogen and sulfur atoms in bithiazole and similar compounds. As can be seen from this table, the sulfur atoms in the bithiazole ligands have a positive or very slightly negative charge and cannot act as a donor atom in coordination to metals. Nevertheless the nitrogens have a considerable negative charge and play the role of coordination as expected.

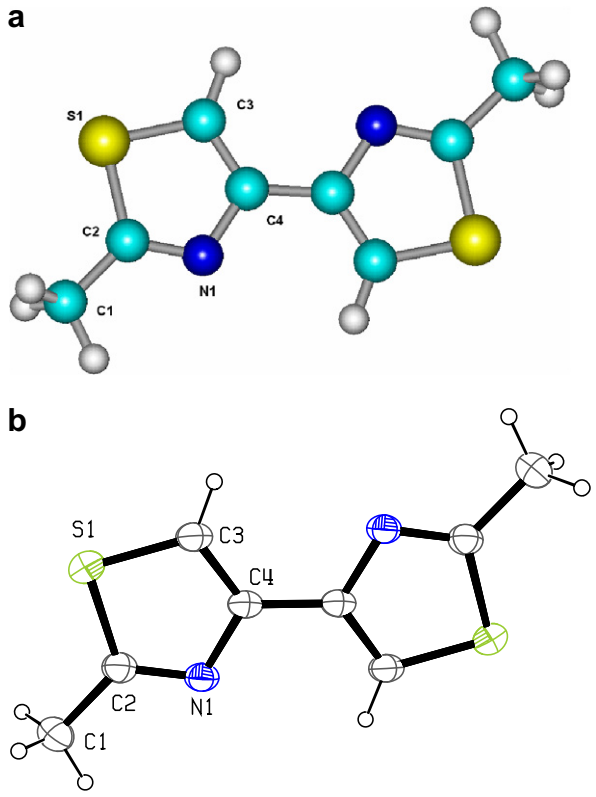


Fig. 1. (a) Optimized geometry and (b) thermal ellipsoid plot of 2,2′-dimethyl-4,4′-bithiazole (**1**) (30% probability level) showing the numbering scheme.

Table 2
Charge of nitrogen and sulfur atoms in bithiazole and similar compounds at B3LYP/6-31G*//HF/6-31G*

Compound	Nitrogen		Sulfur	
	MUL.	ESP	MUL.	ESP
dm4bt (**1**)	−0.491	−0.502	0.272	−0.081
4bt[a]	−0.441	−0.492	0.285	0.051
dm2bip[b]	−0.576	−0.695		
bipy[c]	−0.531	−0.661		

[a] 4bt is bithiazole.
[b] dm2bip is 6,6′-dimethyl-2,2′-bipyridine.
[c] bipy is 2,2′-bipyridine.

According to these calculations, the coordination ability of 4,4′-bithiazole is less than that of bipyridine, since the charge on the nitrogen is less. However, the negative charge on the nitrogens of dm4bt is a little larger than that of 4bt and is less than the charge for bipy, so we expect that dm4bt has a coordination ability close to that of bipy.

The addition of **1** in an equimolar ratio to a methanolic solution of $ZnCl_2$ after a few days, accompanied with slow evaporation of the solvent at room temperature, results in colorless crystals of **2**, Eq. (1). When $HgCl_2$ was used instead of $ZnCl_2$, the same reaction gives **3**. All efforts to prepare a 2:1 ratio of the ligand to the metals were not successful.

$$MCl_2 + \text{dm4bt} \rightarrow [M(\text{dm4bt})Cl_2] \quad \begin{matrix} M = Zn, \text{ compound } \mathbf{2} \\ M = Hg, \text{ compound } \mathbf{3} \end{matrix} \qquad (1)$$

3.2. Spectroscopic characterization

The infrared spectra for compounds **1**–**3** are presented in Table 3. They contain several bands in the region 800–3400 cm^{-1}, which are related to the hetero aromatic ring modes related to C–H, C=C, C=N, C–C, C–N and S-C [31,32]. For instance, bands observed at 1496, 1419, 1184 and 879 cm^{-1} for the free ligand are shifted to higher frequencies upon coordination and are observed at 1532, 1442, 1219 and 884 cm^{-1} in **2**. This shift to higher frequencies upon coordination to metal has been observed for bipyridine and other ligands coordinated to metals as well [33–37], and can be explained by changing the geometry of the free ligand from a syn to anti orientation in the coordinated case. The same trend was observed for compound **3**, Table 3. The IR spectra of **2** and **3** are distinguished from that of **1** mainly by the metal to ligand bands. Strong peaks at 266 and 240 cm^{-1} were assigned to the M–Cl frequencies for **2** and **3**, respectively [38,39]. The bands at 589 and 578 cm^{-1}, which are absent in **1**, can be assigned to the M–N frequencies, consistent with the other reported frequencies for similar compounds [40].

When a NBO calculation was performed on the non-coordinated dm4bt ligand, a bond order of 2 was only found for the C3–C4 and N–C2 bonds (Scheme 1). Furthermore, the C2 and C3 hybridization toward S is near to sp^3, showing a single C–S bond, Table 4.

The UV–Vis spectra of the colorless compounds lack any d–d transitions in the visible region, as expected, but a signal around 3.7×10^4 cm^{-1} is assigned to the π–π^* transition in the aromatic ligand. Furthermore, compounds **1**–**3** show the same ^1H NMR spectra, consisting of a singlet in the aromatic C–H region, around 7.7 ppm and another singlet at 2.7 ppm for the methyls groups. The similarity of the NMR pattern in **2** and **3** confirms the similarity of their structures in solution.

3.3. Description of the molecular structures

Compounds **1**, **2** and **3** crystallize in the space groups $P2_1/a$, $P2_1/n$ and $P2_1/c$, respectively, which belong to the monoclinic system.

Table 3
Selected IR frequencies of compounds **1**–**3** (cm^{-1})

Compound	ν(C–H) cycle	ν(C–H) Me	ν(c=c)	ν(C2=N)	ν(C4–C5)	ν(C4–N)	ν(S–C)	ν(M–N)	ν(M–Cl)
dm4bt(**1**)	3434	3103	1558	1496	1419	1184	879		
Zn-complex(**2**)	3430	3097	1563	1532	1442	1219	884	589	266
Hg-complex(**3**)	3440	3074	1634	1514	1426	1207	883	578	240

Table 4
The calculated hybridization of atoms of optimized dm4bt at B3LYP/cc-pVTZ (NBO) method

$N \rightarrow C_2$	$C_2 \rightarrow N$	$N \rightarrow C_4$	$C_4 \rightarrow N$	$C_2 \rightarrow S$	$C_3 \rightarrow S$	$C_4 \rightarrow C_3$	$C_3 \rightarrow C_4$	$C_2 \rightarrow C_1$	$C_1 \rightarrow C_2$
$sp^{1.62}$	$sp^{1.87}$	$sp^{2.10}$	$sp^{2.53}$	$sp^{2.69}$	$sp^{2.89}$	$sp^{1.71}$	$sp^{1.58}$	$sp^{1.63}$	$sp^{2.63}$

ORTEP diagrams of the ligand, zinc and mercury complexes with the atom numbering scheme are presented in Figs. 1–3, respectively. Table 5 summarizes the selected structural parameters for compounds **1**–**3**.

3.3.1. Structure of 2,2′-dimethyl-4,4′-bithiazole (dm4bt) (*1*)

The asymmetric unit of **1** contains one-half of a bithiazole molecule. As it is clear from Fig. 1, the ligand, **1** has an anti configuration, while its orientation has changed to the syn configuration to chelate to the metal centers in **2** and **3**. The DFT calculation shows there is about a 32.01 kJ/mol barrier energy for the syn to anti rotation, as is shown in the diagram of energy versus the torsion angle for (dm4bt), Fig. 4. The conversion of the anti orientation to the syn orientation is endothermic (22.83 kJ/mol), and this is compensated by the M–N bond formation in the complexes.

In compound **1**, the thiazole rings (N1/S1/C2–C4) are, of course, planar and according to the inversion point between C4 and C4′ for production of the molecule from the asymmetric unit, that it is a half of the molecule, the dihedral angle between them is 0°. The bond lengths and angles are within the normal ranges. As it is shown in Fig. 5, in compound **1** the bithiazole rings form π bonding stacks in which each thiazole ring of bithiazole lies between two thiazole rings of an adjacent molecule. The close contact distance between adjacent aromatic rings is 3.63(3) Å and it seems that this π–π stacking is effective in the packing formation.

3.3.2. Structure of [Zn(dm4bt)Cl_2] (*2*)

The Zn environment in complex **2** consists of two chloride ions and a bithiazole ligand which is coordinated to the Zn in a bidentate fashion via the nitrogen atoms. The geometry around the Zn atom is distorted tetrahedral. The different bond distances of Zn–N and Zn–Cl, accompanied with the small bite angle of 4,4′-dimethyl-2,2′-bithiazole (80.8° for N1–Zn–N2) and the compensated large angles of N1–Zn–Cl2 and N2–Zn–Cl2, which are 119.5° and 115.7° respectively, are the main factors accounting for this distortion. Most of the bithiazole derivative complexes with Zn found in the literature have six coordinate octahedral environments [41–43], although some tetrahedral complexes were found [32,44]. The Zn–N and Zn–Cl average bond distances are 2.07 and 2.20 Å. These bond distances are 0.5–1 Å smaller than the distances found in the analogous six-coordinated complexes, and are in the range of [Zn(bipy)Cl_2] bond distances [45]. This observation confirms that the donor ability of the 2,2′-dimethyl-4,4′-bithiazole ligand

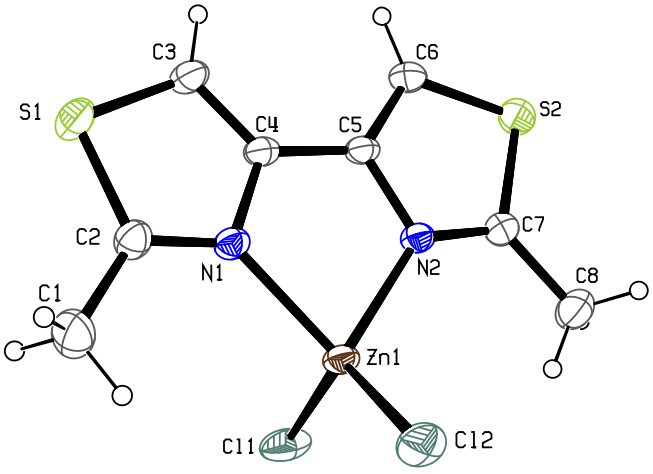


Fig. 2. The labelled diagram of [Zn(dm4bt)Cl_2] (**2**). Thermal ellipsoids are at the 30% probability level.

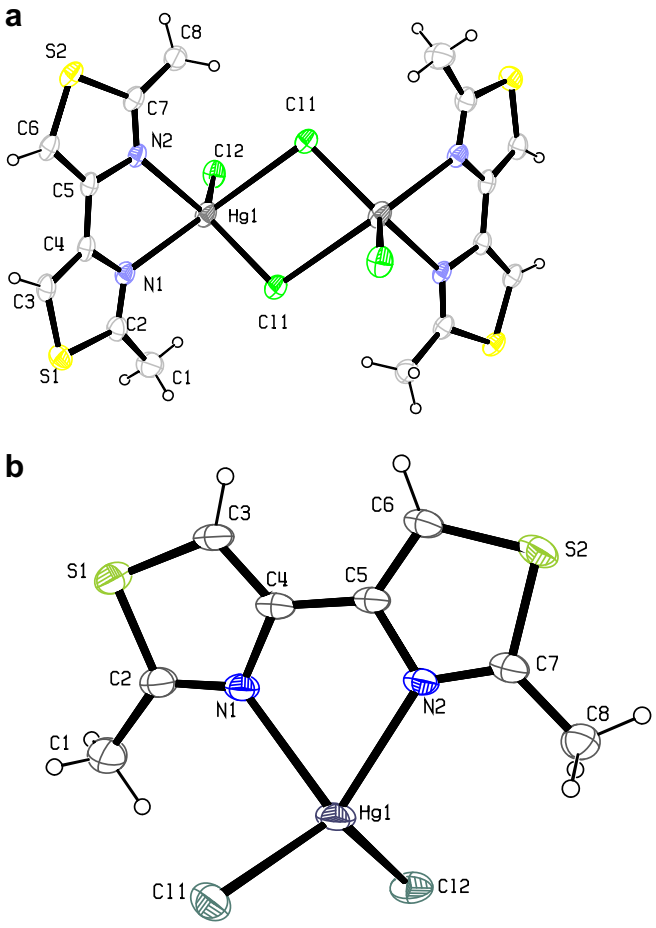


Fig. 3. The labelled diagram of the (a) dimeric and (b) monomeric asymmetric unit of [Hg(dm4bt)Cl_2] (**3**). Thermal ellipsoids are at the 30% probability level.

Table 5
Selected bond distances (Å), bond angles and dihedral (°) for compounds **1–3**

	1 (calc.)[a]	**1**	**2**	**3**
Bond distances				
S1–C2	1.768	1.731(2)	1.719(3)	1.720(5)
S1–C3	1.732	1.712(2)	1.713(3)	1.709(7)
N1–C2	1.299	1.301(3)	1.313(4)	1.298(8)
N1–C4	1.386	1.386(3)	1.388(3)	1.381(6)
C4–C3	1.369	1.366(3)	1.357(4)	1.364(8)
C4–C5	1.462	1.462(4)	1.457(4)	1.454(8)
C2–C1	1.498	1.502(3)	1.486(4)	1.490(9)
M–N1			2.074(2)	2.421(4)
M–N2			2.064(2)	2.374(4)
M–Cl1			2.213(1)	2.457(2)
M–Cl2			2.179(1)	2.394(2)
M–Cl1′				3.098(6)
Bond angles				
N1–C2– C1	124.35	124.6(2)	123.7(3)	125.0(5)
S1–C2–N1	114.33	114.3(2)	113.0(2)	113.6(4)
S1–C2– C1	121.12	121.1(2)	123.3(2)	121.4(5)
C2–N1–C4	111.02	111.1(2)	111.8(2)	112.4(5)
N1–C4–C1	119.15	119.2(2)	116.3(2)	118.6(4)
N1–C4–C3	115.04	115.0(2)	114.7(2)	113.8(5)
C3–C4–C5	125.12	125.8(2)	129.0(2)	127.5(5)
C4–C3–S1	109.84	109.9(2)	109.6(2)	110.2(4)
C2–S1–C3	89.77	89.8(1)	90.8(2)	90.1(3)
C2–N1–M			134.7(2)	130.9(3)
C4–N1–M			113.1(2)	114.1(4)
N1–M–N2			80.8(1)	70.8(2)
Cl1–M–Cl2			119.8(3)	119.7(6)
N1–M–Cl1			106.8(7)	92.2(2)
N1–M–Cl2			119.5(6)	124.1(1)
N2–M–Cl2			115.7(6)	105.3(1)
N2–M–Cl1			107.4(7)	133.4(1)
N2–M–Cl1′				89.9(3)
N1–M–Cl1′				141.0(3)
Cl1–M–Cl1′				76.6(4)
Cl2–M–Cl1′				93.1(4)
Dihedral angles				
C4–N1–C2–C1	179.97	178.92(5)	178.8(3)	178.9(7)
C2–N1–C4–C5	179.97	−179.8(3)	−178.6(2)	−179.5(5)
C2–N1–C4–C3	0.00	−0.11(1)	0.4(3)	−1.1(3)
N1–C4–C5–N2	179.96	180.0(2)	1.2(3)	−9.2(7)
N1–C4–C5–C6	0.10	−0.32(2)	−179.2(3)	168.5(6)
N1–C4–C3–S1	−0.01	0.18(3)	−0.2(3)	1.1(6)
C4–C3–S1–C2	0.01	−0.15(3)	−0.1(2)	−0.7(5)
C3–S–C2–N1	−0.01	0.10(1)	0.3(2)	0.1(5)
C3–C4–N1–M			174.0(2)	164.7(4)
C2–N1–M–N2			176.8(3)	−173.2(6)
C4-N1-M-Cl1			−100.4(2)	122.3(4)
C4–N1–M–Cl2			119.6(2)	−109.0(3)
C12–M–Cl1–M′				85.9(3)
C12–M–Cl1′–M′				−119.8(3)

[a] Structural amount for optimized dm4bt (**1**) at the B3LYP/6–31G* method/basis set.

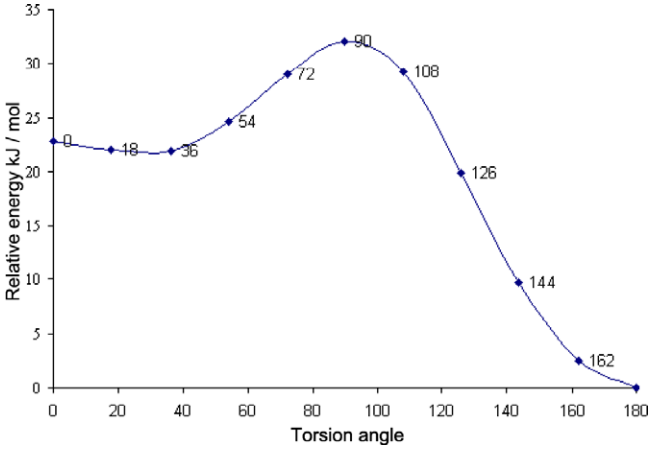


Fig. 4. Comparison of the relative torsion energies for dm4bt (**1**) at the B3LYP/6-31G* level.

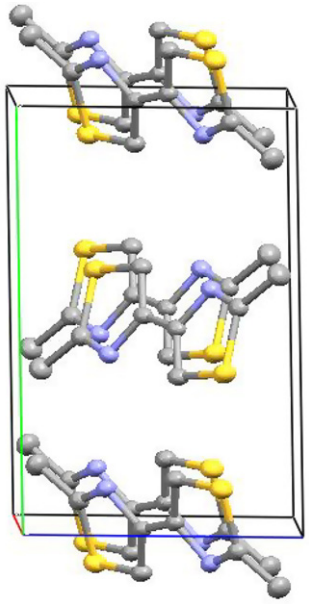


Fig. 5. Crystal packing diagram for compound **1**. Hydrogen atoms are omitted for clarity.

is the same as bipyridine, as is obvious from the charge calculation by the DFT method, Table 2.

No considerable change was observed in the ligand bond distances before and after coordination to the metal in **2**. The two thiazole rings are in the same plane in **1** with a dihedral angle of 0°, and this changes to 1.87° in the Zn complex. The dihedral angles vary from 2° to 14° in the literature for other reported Zn bithiazole derivatives. This small dihedral angle of 1.87° in **2** is in accord with the angle found in the six-coordinated 2,2′-diamine-4,4′-bithiazole complexes of Zn [41–43].

As can be seen from the packing diagram of complex **2**, Fig. 6, the closest distance between two adjacent bithiazole ring planes is 3.60(4) Å, which shows π–π stacking. There are also some C–H···Cl [H3···Cl1^{i} = 2.841(1), C3···Cl^{i} = 3.360(4) Å and C3–H3···Cl1^{i} = 115.9(2)°; H6···Cl2^{ii} = 2.919(1), C6···Cl2^{ii} = 3.663(3) Å and C6–H6···Cl2^{ii} = 137.9(2)°] short contacts [symmetry codes: (i) $x-1/2$, $-y+1/2+1$, $+z+1/2$ and (ii) $x-1$,$+y$,$+z$]. These π–π stacking and short contacts seem to be effective factors in the stabilization of the crystal structure.

3.3.3. Structure of [Hg(dm4bt)Cl$_2$] (**3**)

Fig. 3 illustrates the crystal structure of compound **3**. This compound has a highly distorted tetrahedral structure with four different bond distances and bond angles. The variations in bond angles are significant, from 71° to 133°, as is evident from Table 5. The bite angle for N1–Hg–N2 is 70.8(2)° and it is 10° smaller than the bite angle in the Zn complex **2**, 80.8(1)°. The smaller bite angle is dictated by the larger metal to ligand bond distances with Hg relative to Zn (2.40 Å relative to 2.06 Å).

The Hg–N and Hg–Cl distances are in the range 2.374(4)–2.457(2) Å, with almost the same range for Hg–N as Hg–Cl. This is in contrast to the Zn complex in which Zn–Cl is around 0.23 Å larger than Zn–N. However, the bond distances observed are in the ranges reported for analogous structures [31,45–47]. Many structures of four coordinated Hg have been found in which chloride acts as a bridging ligand [46–49]. In these structures the terminal Hg–Cl bond distances are in the range 2.29 (in $HgCl_2$) to

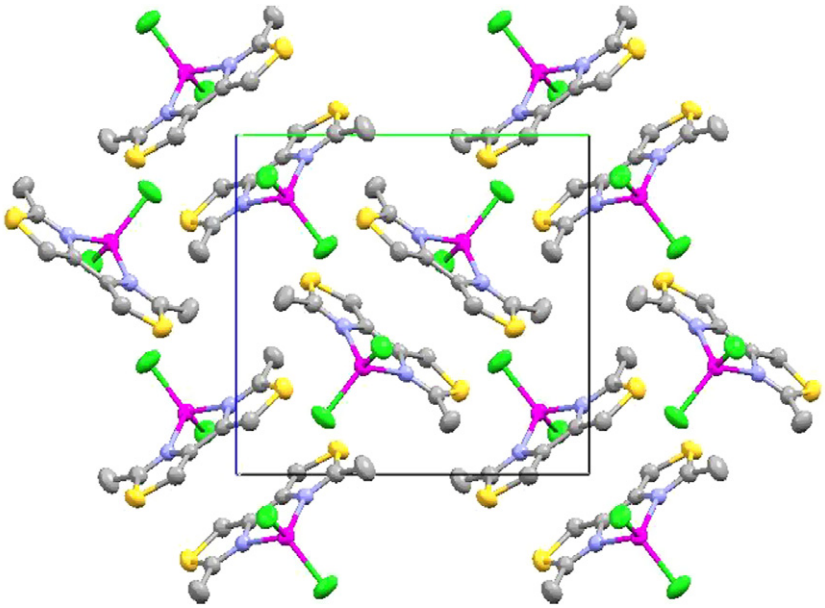


Fig. 6. Crystal packing diagram for complex **2** in the *a*-direction. Hydrogen atoms are omitted for clarity.

2.43 Å and bridge chloride ligands are in the range 2.42–2.96 Å. The bond distances of 2.394(2) and 2.457(2) Å in **3** are in accord with terminal bond coordination. A crystal packing diagram image for compound **3** is presented in Fig. 7. It is evident from this packing diagram that one of the chloride ligands is positioned towards the Hg from another neighboring molecule, and the distance of Hg–Cl'_1 is 3.098(6) Å. This distance is a little larger than the bond distance observed for bridging Hg···Cl–Hg. Therefore, we conclude that there is a semi-bridging interaction between this chloride and the neighboring Hg atom. This kind of interaction has shown itself in the difference of the Hg–Cl bond lengths which are 2.394(2) and 2.457(2) Å. The chloride which is towards Hg has a longer bond distance due to transfer of electron density to Hg. So there is a tendency to form a five coordinated structure, as shown in Fig. 4a. Other scientists observed the same interaction between Hg and chloride and they interpreted it as bridged five coordinated Hg complexes, although there is a significant difference between the two bridge bonds (around 0.65 Å) and one of the bridge bonds has a bond distance that is closer to terminal. So we believe that a better explanation is to look at this bond as a semi-bridging bond instead of as a bridging one. However, the Hg–Cl bond of the length 3.42 Å was reported as a bridging one [50] despite this length being longer than the sum of the Hg and Cl atomic distances, and a semi-bridging expression may be more suitable.

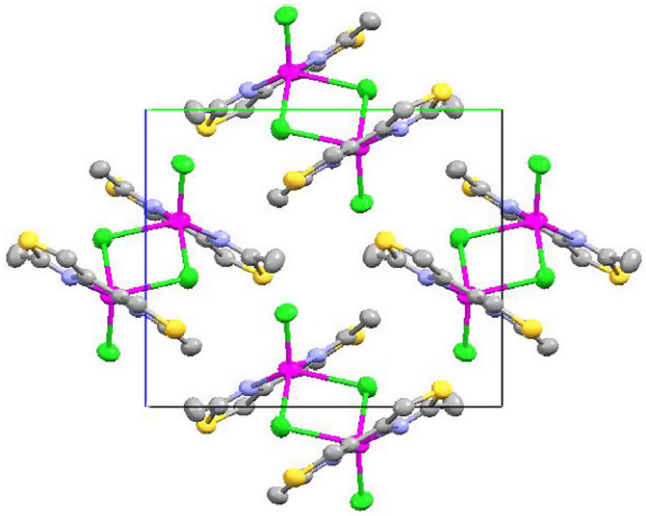


Fig. 7. Crystal packing diagram for complex **3** in the *a*-direction. Hydrogen atoms are omitted for clarity.

The spectroscopic data obtained for the Zn and Hg complexes **2** and **3** are very similar and show that in solution both complexes are monomers.

In complex **3** there are no π–π aromatic interactions between the thiazole rings, Fig. 7, but there are many kinds of C–H···N [H1b···N2 = 2.953(4), C1···N2 = 3.811(10) Å and C1–H1b···N2 = 149.5(5)°, symmetry code: $x,-y+1/2,+z+1/2$], C–H···Cl [H1a···$Cl2^{i}$ = 2.952(2), C1···$Cl2^{i}$ = 3.852(8) Å and C1–H1a···$Cl2^{i}$ = 156.7(5)°, H1b···$Cl2^{ii}$ = 2.991(2), C1···$Cl2^{ii}$ = 3.589(9) Å and C1–H1b···$Cl2^{ii}$ = 121.6(5)°, H3···$Cl1^{iii}$ = 2.839(2), C3···$Cl1^{iii}$ = 3.754(5) Å and C3–H3···$Cl1^{iii}$ = 168.2(3)° and H8b···$Cl1^{iv}$ = 2.748(2), C8···$Cl1^{iv}$ = 3.612(7) Å and C8–H8b···$Cl1^{iv}$ = 150.0(4)°, symmetry codes: (i) $-x+1,+y+1/2,-z+1/2$, (ii) $x,-y+1/2,+z+1/2$, (iii) $x+1,+y,+z$ and (iv) $-x+1,-y,-z+1$] and C–H···S [H8c···S2 = 2.790(2), C8···S2 = 2.819(6) Å and C8–H8c···S2 = 81.9(4)°, symmetry code: x,y,z] short contacts that are effective in stabilizing the lattice.

Acknowledgement

We would like to thank the Graduate Study Councils of Shahid Beheshti University for financial support.

Appendix A. Supplementary data

CCDC 662124, 662123 and 662122 contain the supplementary crystallographic data for **1**, **2** and **3**. These data can be obtained free of charge via http://www.ccdc.cam.ac.uk/conts/retrieving.html, or from the Cambridge Crystallographic Data Centre, 12 Union Road, Cambridge CB2 1EZ, UK; fax: (+44) 1223-336-033; or e-mail: deposit@ccdc.cam.ac.uk. Supplementary data associated with this article can be found, in the online version, at doi:10.1016/j.poly.2008.02.029.

References

[1] H. Umezawa, Fed. Proc. 33 (1974) 2296.
[2] R. Kuroda, S. Neidlet, J.M. Riordan, T.T. Sakai, Nucleic Acids Res. 10 (1982) 4753.
[3] M. Sugiyama, T. Kumagai, J. Biosci. Bioeng. 93 (2002) 105.
[4] J.P. Henichart, J.L. Bernier, N. Helbecque, R. Houssin, Nucleic Acids Res. 13 (1985) 6703.
[5] W. Wu, D.E. Vanderwall, C.J. Turner, J.W. Kozarich, J. Stubbe, J. Am. Chem. Soc. 118 (1996) 1281.
[6] J. Stubbe, J.W. Kozarich, Chem. Rev. 87 (1987) 1107.
[7] M. Ohno, Pure Appl. Chem. 61 (1989) 581.
[8] W.E. Antholine, D.H. Petering, L.A. Saryan, C.E. Browns, Proc. Nat. Acad. Sci. USA 78 (1981) 7517.
[9] Y. Tian, P. Yang, Q. Li, S. Liu, J. Coord. Chem. 41 (1997) 223.
[10] Y. Tian, P. Yang, H.F. Wang, Y.L. Feng, S.X. Liu, J.L. Huang, Polyhedron 15 (1996) 2771.
[11] W. Sun, X. Gao, F. Lu, J. Appl. Polym. Sci. 64 (1997) 2309.
[12] J. Weng, W. Sun, L. Jiang, Z. Shen, Macromol. Rapid Commun. 21 (2000) 1099.
[13] L. Jiang, W. Sun, Polym. Adv. Technol. 16 (2005) 646.
[14] H.C. Lukaski, Am. J. Clin. Nutr. 72 (2000) 585S.
[15] M. Jonsson, S. Linse, B. Frohm, A. Lundwall, J. Malm, Biochem. J. 387 (2005) 447.
[16] Y. Iwatani, H. Takeuchi, K. Strebel, J.G. Levin, J. Urol. (2006) 5992.
[17] Y.-H. Shen, J.-G. Liu, D.-J. Xu, W.-L. Sun, J. Coord. Chem. 59 (2006) 1983.
[18] C. Janiak, L. Uhelin, H. Wu, P. Klufers, H.G. Piotrowski, T. Scharmann, J. Chem. Soc., Dalton Trans. (1999) 3121.
[19] M.J. Frisch, G.W. Trucks, H.B. Schlegel, G.E. Scuseria, M.A. Robb, J.R. Cheeseman, V.G. Zakrzewski, J.A. Montgomery, R.E. Stratmann, J.C. Burant, S. Dapprich, J.M. Millam, A.D. Daniels, K.N. Kudin, M.C. Strain, O. Farkas, J. Tomasi, V. Barone, M. Cossi, R. Cammi, B. Mennucci, C. Pomelli, C. Adamo, S. Clifford, J. Ochterski, G.A. Petersson, P.Y. Ayala, Q. Cui, K. Morokuma, D.K. Malick, A.D. Rabuck, K. Raghavachari, J.B. Foresman, J. Cioslowski, J.V. Ortiz, B.B. Stefanov, G. Liu, A. Liashenko, P. Piskorz, I. Komaromi, R. Gomperts, R.L. Martin, D.J. Fox, T. Keith, M.A. Al-Laham, C.Y. Peng, A. Nanayakkara, C. Gonzalez, M. Challacombe, P.M.W. Gill, B.G. Johnson, W. Chen, M.W. Wong, J.L. Andres, M. Head-Gordon, E. Replogle, J.A. Pople, GAUSSIAN 03, Revision A.1, Gaussian Inc., Pittsburgh, PA, 2003.
[20] A.D. Becke, Phys. Rev. A 38 (1988) 3098.
[21] A.D. Becke, J. Chem. Phys. 98 (1993) 1372.
[22] C. Lee, W. Yang, R.G. Parr, Phys. Rev. B 37 (1988) 785.
[23] G.A. Peterson, M.A. Al-Laham, J. Chem. Phys. 94 (1991) 6081.
[24] STOE & CIE, X-AREA, Version 1.30: Program for the Acquisition and Analysis of Data, Stoe & Cie GmbH, Darmatadt, Germany, 2005.
[25] STOE & CIE, X-RED, version 1.28b: Program for Data Reduction and Absorption Correction, Stoe & Cie GmbH, Darmatadt, Germany, 2005.
[26] STOE & CIE, X-SHAPE, version 2.05: Program for Crystal Optimization for Numerical Absorption Correction, Stoe & Cie GmbH, Darmatadt, Germany, 2004.
[27] G.M. Sheldrick, SHELX97, Program for Crystal Structure Solution, University of Göttingen, Germany, 1997.
[28] G.M. Sheldrick, SHELX97, Program for Crystal Structure Refinement, University of Göttingen, Germany, 1997.
[29] International Tables For X-ray Crystallography, vol. C, Kluwer Academic Publisher, Doordrecht, The Netherlands, 1995.
[30] STOE & CIE, X-STEP32, Version 1.07b: Crystallographic Package, Stoe & Cie GmbH, Darmstadt, Germany, 2000.
[31] M.G. Drew, T.R. Pearson, B.P. Murphy, S.M. Nelson, Polyhedron 2 (1983) 269.
[32] A. Morsali, M. Payheghader, M.R. Poorheravi, F. Jamali, Z. Anorg. Allg. Chem. 629 (2003) 1627.
[33] A. Neels, H.S. Evans, Inorg. Chem. 38 (1999) 6164.
[34] K. Nakamoto, Infrared and Raman Spectra of Inorganic and Coordination Compound. Part B: Application in Coordination, Organometallic and Bioinorganic Chemistry, John Wiley and Sons Inc., New York, 1997.
[35] L. Jiang, W. Sun, J. Weng, Z. Shen, Polymer 43 (2002) 1563.
[36] A.K. Boudalis, C.P. Raptopoulou, A. Terzis, S.P. Perlepes, Polyhedron 23 (2004) 1271.
[37] V. Amani, N. Safari, H.R. Khavasi, Polyhedron 26 (2007) 4257.
[38] O.A. Deolivera, A. Chagas, C. Airoldi, Inorg. Chem. 22 (1983) 136.
[39] N.A. Bell, S.J. Coles, M.B. Hursthouse, M.E. Light, K.A. Malik, R. Mansor, Polyhedron 19 (2000) 1719.
[40] A. Hosseinian, A.R. Mahjoub, Z. Anorg. Allg. Chem. 632 (2006) 2505.
[41] H. Li, Y. Luo, D.J. Xu, J.Y. Wu, M.Y. Chiang, Acta Crystallogr. E 59 (2003) m622.
[42] B.X. Liu, H.G. Yan, D.J. Xu, Acta Crystallogr. E 62 (2006) m1969.
[43] H. Ahankar, S. Taheri, A. Morsali, A. Ramazai, L.G. Zhu, J. Coord. Chem. 59 (2006) 2039.
[44] J. Mathieu, N. Ghermani, N. Bouhmaida, B. Fenet, A. Marsura, Eur. J. Inorg. Chem. (2004) 3172.
[45] H.L. Kwong, K.M. Lau, W.S. Lee, W.T. Wong, New J. Chem. 23 (1999) 629.
[46] B. Chand, U. Ray, P.K. Santra, G. Mostafa, T.H. Lu, C. Sinha, Polyhedron 22 (2003) 1205.
[47] T.S.B. Baul, A. Lycka, R. Butcher, F.E. Smith, Polyhedron 23 (2004) 2323.
[48] L.Y. Wang, C.X. Zhang, D.Z. Liao, Z.H. Jiang, S.P. Yan, J. Coord. Chem. 58 (2005) 969.
[49] G. Meyer, P. Nockemann, Z. Anorg. Allg. Chem. 629 (2003) 1447.
[50] P. Nockemann, G. Meyer, Z. Anorg. Allg. Chem. 629 (2003) 123.

sodium silicate solution ($d = 1.35$) instead of Na_2SiO_3. Infrared spectra were recorded in KBr plates on a Thermo Nicolet FT-IR model Nexus-670 and NMR spectra were recorded on a BRX-500 AVANCE spectrometer. The resonance frequency is 125.75 and 99.36 MHz for ^{13}C and ^{29}Si, respectively. The chemical shifts are given with respect to chloroform for ^{13}C NMR spectra and TMS for ^{29}Si NMR spectra as an external standard.

Thermogravimetric Analysis (TGA) and Differential Scanning Calorimetric were carried out using a PL-1500 TGA and NETZSCH DSC 200 F3 apparatus, respectively. The electronic spectra were recorded on a Varian, CARY 1E UV–Vis spectrophotometer. ICP was used for the elemental analysis of yttrium, ytterbium, tungsten and silicon, whereas flame photometry was used for the elemental analysis of sodium and potassium. TGA was used for the analysis of carbon.

Strongly acidic (Dowex HCR-W2 H^+ form) and basic (Amberjet 4200 Cl^- form) resins packed into a column (20 cm length; 1 cm diameter) were used for ion exchange chromatography studies. For acidification, solutions of the complexes were eluted through the acidic form of the cationic resin column. For cation exchange, first 1 M NaOH or KOH was eluted through the acidic form of the cationic resin followed by distilled water and then the solutions of the complexes were eluted through it. For anion exchange, solutions of the complexes were eluted through the anion exchange resin column. The eluants were collected and studied by IR spectroscopy after solvent evaporation.

2.2. Preparation of complexes

2.2.1. $Na_{13}[(A\text{-}\beta\text{-}SiW_9O_{34})_2(YOH_2)_3CO_3] \cdot 27H_2O$ (**1**)

A 0.45 g (1.5 mmol) sample of $YCl_3 \cdot 6H_2O$ was dissolved in 20 mL of twice distilled water, and 2 mL of 1 M Na_2CO_3 was slowly added to the solution with stirring. Solid $Na_9H[A\text{-}\beta\text{-}SiW_9O_{34}] \cdot xH_2O$ (3.00 g, 1.0 mmol) was quickly added with vigorous stirring. The solution was maintained at room temperature (30 °C) for 60 min and then centrifuged for the removal of insoluble material. Solid NaCl (1.5 g) was added and the solution was cooled in an ice water bath and then filtered off. The crude product was recrystallized at least twice in hot water. Colorless crystals were obtained by slow evaporation. Yield: 1.5 g, (51%). *Anal.* Calc. for $Na_{13}[(A\text{-}\beta\text{-}SiW_9O_{34})_2(YOH_2)_3CO_3] \cdot 27H_2O$ (**1**): C, 0.21; Na, 5.32; Si, 1.00; W, 58.89; Y, 4.75; H_2O, 9.60. Found: C, 0.19; Na, 5.28; Si, 0.95; W, 58.00; Y, 4.84; H_2O, 9.66%.

2.2.2. $K_{11}Na_2[(A\text{-}\beta\text{-}SiW_9O_{34})_2(YOH_2)_3CO_3] \cdot 18H_2O$ (**2**)

The procedure for **1** was repeated, but using KCl (0.57 g) instead of NaCl. Yield: 2.0 g (66.6%). Single crystals suitable for X-ray crystallography were obtained from the second recrystallization at 5 °C by slow evaporation.

Anal. Calc. for $K_{11}Na_2[(A\text{-}\beta\text{-}SiW_9O_{34})_2(YOH_2)_3CO_3] \cdot 18H_2O$ (**2**): C, 0.21; K, 7.56; Na, 0.81; Si, 0.98; W, 58.18; Y, 4.69; H_2O, 6.64. Found: C, 0.19; K, 6.64; Na, 0.75; Si, 0.95; W, 57.51; Y, 4.70; H_2O, 6.46%.

2.2.3. $Na_{13}[(A\text{-}\beta\text{-}SiW_9O_{34})_2(YbOH_2)_3CO_3] \cdot 32H_2O$ (**3**)

The procedure for **1** was repeated, but using $YbCl_3 \cdot 6H_2O$ (0.57 g) instead of $YCl_3 \cdot 6H_2O$. Yield: 1.5 g (48%). *Anal.* Calc. for $Na_{13}[(A\text{-}\beta\text{-}SiW_9O_{34})_2(YbOH_2)_3CO_3] \cdot 32H_2O$: C, 0.20; Na, 5.02; Si, 0.94; W, 55.51; Yb, 8.71; H_2O, 10.50. Found: C, 0.17; Na, 4.85; Si, 0.95; W, 55.10; Yb, 8.85; H_2O, 10.6%.

2.2.4. $K_{11}Na_2[(A\text{-}\beta\text{-}SiW_9O_{34})_2(YbOH_2)_3CO_3] \cdot 20H_2O$ (**4**)

The procedure for **3** was repeated, but using KCl (0.57 g) instead of NaCl. Yield: 1.9 g (59%). *Anal.* Calc. for $K_{11}Na_2[(A\text{-}\beta\text{-}SiW_9O_{34})_2(YbOH_2)_3CO_3] \cdot 20H_2O$: C, 0.20; K, 7.26; Na, 0.78; Si, 0.95; W, 55.88; Yb, 8.77; H_2O, 7.00. Found: C, 0.17; K, 7.04; Na, 0.70; Si, 0.90; W, 55.91; Yb, 8.97; H_2O, 6.94%.

Single crystals suitable for X-ray crystallography were obtained from the second recrystallization at 5 °C by slow evaporation.

2.3. X-ray crystallographic structure determination

Crystal data collection and refinement parameters for **4** are given in Table 1. The data were collected at 100 K on a Bruker APEX 1000 CCD area detector single crystal diffractometer with graphite-monochromated Mo Kα radiation ($\lambda = 0.71073$ Å). Data collection, indexing and initial cell refinements were all handled using APEX2 software [19]. The final cell parameters were determined from least-squares refinement on 7336 reflections. The multi-scan method was used to carry out absorption corrections. The structure was solved using direct methods and difference maps techniques (SHELXTL, V5.1) [20]. All metal atoms were refined anisotropically. Scattering factors and anomalous dispersion corrections were taken from the International Tables for X-ray Crystallography [21]. Structure solution, refinement and generation of publication materials were performed by using SHELXTL, V5.1 software. Selected bond lengths and bonds angles of **4** are given in Table 2.

3. Result and discussion

3.1. Syntheses and stabilities

A-β-$SiW_9O_{34}^{10-}$ at room temperature reacts with MCl_3 (M = Y^{3+} and Yb^{3+}) in aqueous Na_2CO_3 solution (~0.1 M) to form **1** and **3** in medium yields, respectively. Monitoring of the reaction progress by the pH of the solution shows a decrease with addition of MCl_3 (5.5) and increase with addition of A-β-$SiW_9O_{34}^{10-}$ (8.9). The trivalent metals react with the carbonate ion to form the corresponding insoluble metal carbonate (the solution become turbid) and then A-β-$SiW_9O_{34}^{10-}$ reacts with the metal carbonate (the solution become clearer). The syntheses of the complexes require the presence of CO_3^{2-}. In order to establish the compositions of the complexes in solution, turbidity variations of the solution as a function of addition of A-β-$SiW_9O_{34}^{10-}$ were recorded. The titration

Table 1
Crystal data and structure refinement for **4**

Chemical formula	$CH_{64}K_9Na_4O_{103}Si_2W_{18}Yb_3$
Formula weight	6052.98
Crystal system	monoclinic
Space group	*C*2/*c*
Unit cell dimensions	
a (Å)	33.230(8)
b (Å)	16.303(4)
c (Å)	17.146(4)
β (°)	99.724(6)
V (Å^3)	9155(4)
Z	4
D_{calc} (Mg/m^3)	4.363
Absorption coefficient (mm^{-1})	26.082
F(000)	10640
$2\theta_{max}$ (°)	60.00
Reflections collected	46623
Crystal size (mm)	0.13 × 0.10 × 0.09
Crystal description	prism
Independent reflections [R_{int}]	13241 [0.1388]
Absorption correction	semi-empirical from equivalents
Refinement method	full-matrix least-squares on F^2
Data/restraints/parameters	13241/12/540
Goodness-of-fit on F^2	0.998
Final *R* indices with $I > 2\sigma(I)$]	$R_1 = 0.0588$, $wR_2 = 0.1212$ [for 7336 rfls.]
R indices (all data)	$R_1 = 0.1289$, $wR_2 = 0.1515$
Largest difference in peak and hole (e Å^{-3})	4.498 and −5.661

Table 2
Selected bond lengths and angles for **4**

		VBV
Bond lengths (Å)		
Yb1–O30	2.202(14)	0.527
Yb1–O26	2.211(15)	0.514
Yb1–O35	2.336(14)	0.367
Yb1–O(2W)	2.443(19)	0.274
Yb2–O33A	2.198(14)	0.533
Yb2–O19	2.203(13)	0.525
Yb2–O14A	2.212(13)	0.513
Yb2–O23	2.252(13)	0.460
Yb2–O35A	2.409(14)	0.301
Yb2–O36	2.4363(12)	0.280
Yb2–O(1W)	2.333(13)	0.37
C1–O35	1.238(18)	1.506
C1–O36	1.27(3)	1.380
W7–O26(Yb1)	1.791(15)	1.404
W8–O30(Yb1)	1.805(15)	1.352
W4–O14A(Yb2)	1.801(13)	1.367
W5–O19(Yb2)	1.785(13)	1.427
W6–O23(Yb2)	1.790(12)	1.409
W9–O33A(Yb2)	1.803(15)	1.360
W–Od (All)	1.735(2)	1.635
W–Ob (All)	1.940(10)	0.94
W–Oc (All)	1.943(2)	0.93
W–Oa (Si, W)(All)	2.290(3)	0.17
Si–Oa (All)	1.629(1)	0.988
Bond angles (°)		
O(30)A–Yb(1)–O(30)	153.9(7)	
O(30)A–Yb(1)–O(26)A	90.8(5)	
O(30)–Yb(1)–O(26)A	83.3(5)	
O(30)–Yb(1)–O(26)	90.8(5)	
O(26)A–Yb(1)–O(26)	153.6(7)	
O(30)–Yb(1)–O(35)A	121.7(5)	
O(26)A–Yb(1)–O(35)A	121.8(5)	
O(26)–Yb(1)–O(35)A	83.1(5)	
O(30)–Yb(1)–O(35)	82.9(5)	
O(26)–Yb(1)–O(35)	121.8(5)	
O(35)A–Yb(1)–O(35)	54.1(7)	
O(30)–Yb(1)–O(2W)	76.9(4)	
O(26)–Yb(1)–O(2W)	76.8(4)	
O(35)–Yb(1)–O(2W)	152.9(3)	
O(30)–Yb(1)–C(1)	103.1(4)	
O(26)–Yb(1)–C(1)	103.2(4)	
O(35)–Yb(1)–C(1)	27.1(3)	
O(2W)–Yb(1)–C(1)	180.0(4)	

Symmetry transformations used to generate equivalent atoms: A: $-x+2, y, -z+3/2$.

results show a breakpoint at a 2:3 L:M^{3+} (L = A-β-$SiW_9O_{34}^{10-}$) ratio (see the Electronic Supplementary material). Unlike MCl_3 salt solution behavior, when solutions of the complexes are eluted through the cation exchange resin column (K^+ or Na^+ form) no retention of the complexes is observed. The IR spectrum of each individual eluant is the same as that of the eluted parent complex. On the other hand, when solutions of the complexes are loaded onto an anion-exchange column (Cl^- form) the anionic complexes are retained on the column [22]. These observations provide good evidence for inner-sphere bonding of the M^{3+} cations to A-β-$SiW_9O_{34}^{10-}$. When the complex solutions are eluted through the strongly acidic ion exchange the product is the Keggin anion, β-$SiW_{12}O_{40}^{4-}$, which is isolated as β-$H_4SiW_{12}O_{40}$ and confirmed with its IR spectrum and cyclic voltamogram (CV). This observation confirms retention of the isomeric form of lacunary A-β-$SiW_9O_{34}^{10-}$ upon complexation with these M^{3+} ions. In a second series of experiments, we repeated the above synthetic procedure with A-α-$SiW_9O_{34}^{10-}$ [17,18] instead of A-β-$SiW_9O_{34}^{10-}$. The results show that the sandwich type complexes $[(A\text{-}\alpha\text{-}SiW_9O_{34})_2(MOH_2)_3CO_3]^{13-}$ are formed. IR spectra of the isolated complexes are almost the same as those of the A-β-$SiW_9O_{34}^{10-}$ complexes. However, the α-$H_4SiW_{12}O_{40}$ is a product of strongly acidic ion exchange treatment, which suggests that the $SiW_9O_{34}^{10-}$ units in these later complexes are α-isomers. The complexes are stable under reflux in unbuffered water for a long time. Decomposition of the complexes takes place by dissolving them in 10^{-2} M HCl and NaOH. Experimental results show that the complexes are stable from pH 3 (10^{-3} M HCl) to pH 11 (10^{-3} M NaOH). These observations are unlike the A-type sandwiches based on divalent d-block metals [8–10]. Preliminary studies suggest that the divalent first-row transition-metal and early-group lanthanide, such as La^{3+}, Ce^{3+} and Pr^{3+}, A-type sandwiches do not complex carbonate. However, A-β-$SiW_9O_{34}^{10-}$ and some of the lanthanides, such as Sm^{3+}, Gd^{3+} and Eu^{3+}, do appear to form carbonate encapsulated complexes. We repeated the above synthetic procedures with NO_3^- instead of CO_3^{2-} but we could not isolation any product containing the nitrate anion. It seems that products isostructural with the carbonate containing complexes are not formed.

3.2. Structures

Single crystal analysis was carried out on **4**, which is isostructural with **2**. The complex crystallizes in the monoclinic space group *C*2/*c*, with a total number of 51 atoms in the anionic part containing 9W (W1–W9), 1Si (Si1), 2Yb (Yb1–Yb2), 36O (O1–O36), 1C (C1) and $2H_2O$ (O1W–O2W) atoms in the asymmetric unit. The structure of **4** consists of two lacunary $SiW_9O_{34}^{10-}$ Keggin moieties which are linked by an equatorial $(H_2OYbO)_3C$ belt (Fig. 1). The W–Ob–W angle and W···W separation in the W–Ob–W linkage between the rotated group (the W_3O_{13} cap) and the rest of the anion are 143.20° and 3.63 Å, respectively, which are comparable with those of the A-β-$[SiW_{12}O_{40}]^{4-}$ Keggin anion, 145° and 3.65 Å, respectively. The corresponding data for α-$[SiW_{12}O_{40}]^{4-}$ are 155° and 3.72 Å, respectively. These results show that the $SiW_9O_{34}^{10-}$ units have the same A-β structure as the precursor trilacunary anion. Two A-β-$SiW_9O_{34}^{10-}$ units in the complex are slightly distorted toward Yb1 (Si1–C1–Si1A 177.8°). As a result of this distortion: (a) the symmetry of the anion is reduced from D_{3h} [12] to a virtual C_2 symmetry, (b) the average Yb1–O bond length is slightly shorter then that of Yb2–O, while Yb2–O(1W) is somewhat shorter than Yb1–O(2W) (Table 2). The C_2 axis of the anion passes through the Yb1 atom and between the Yb2 and Yb2A atoms. The metal ions form an isosceles triangle and are fixed together by oxygen atoms of a carbonate anion lying in the center and being coplanar to the metal ions. The oxygen atoms of the carbonate anion lie on the midpoint of the side of the isosceles triangle (Fig. 2). On the basis of valance bond sum (VBS) calculations, derived by Brown and Altermatt [22,23], the oxygen atoms of the belt act as an oxide (VBS = 2.11). This is opposite to the isostructural complex $[(A\text{-}\beta\text{-}SiW_9O_{34})_2(HOZr)_3]^{11-}$ in which the Zr^{4+} ions are linked by hydroxide groups [12]. The overall coordination geometry of the Yb atoms is close to mono capped trigonal prismatic, the local 3-fold axis of the YbO_7 group lying in the equatorial plane. The trigonal prismatic geometry is achieved by the two terminal oxygens of an edge shared pair of WO_6 octahedra to each A-β-$SiW_9O_{34}^{10-}$ moiety and two oxygens from the belt. Coordination of the A-β-$[SiW_9O_{34}]^{10-}$ moiety to the Yb atom has reduced the average O···O distance between the O atoms, now bridged by a Yb atom, to 3.125 Å compared with 3.38 Å for the same unshared atoms in the free ligand. This change results largely from the bond angle change [12]. The cap is achieved by one external water ligand (OnW). The Yb–O bond lengths in the YbO_6 group and Yb–O(nW) are in the range 2.198(14)–2.436(12) Å, average 2.273(9) Å, and 2.333(13)–2.443(19) Å, average 2.370(6) Å, respectively (Table 2). The VBS values for the ytterbium, tungsten, silicon and carbon atoms are 3.02(6), 6.18(5), 3.95 and 4.40, respectively.

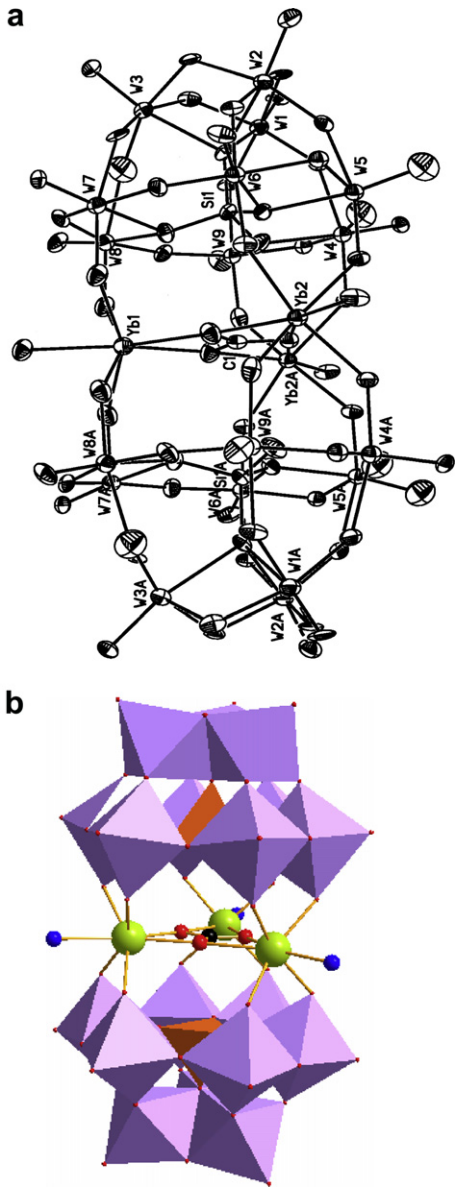


Fig. 1. (a) Structure of $[(A\text{-}\beta\text{-}SiW_9O_{34})_2(YbOH_2)_3CO_3]^{13-}$ (**4**) showing 50% probability thermal ellipsoids (b) Combination ball-and-stick/polyhedral representation of **4**. The W, Si, Yb, C, O atoms and water molecule are shown in lavender, orange, lime, black, red and blue, respectively. (For interpretation of the references in colour in this figure legend, the reader is referred to the web version of this article.)

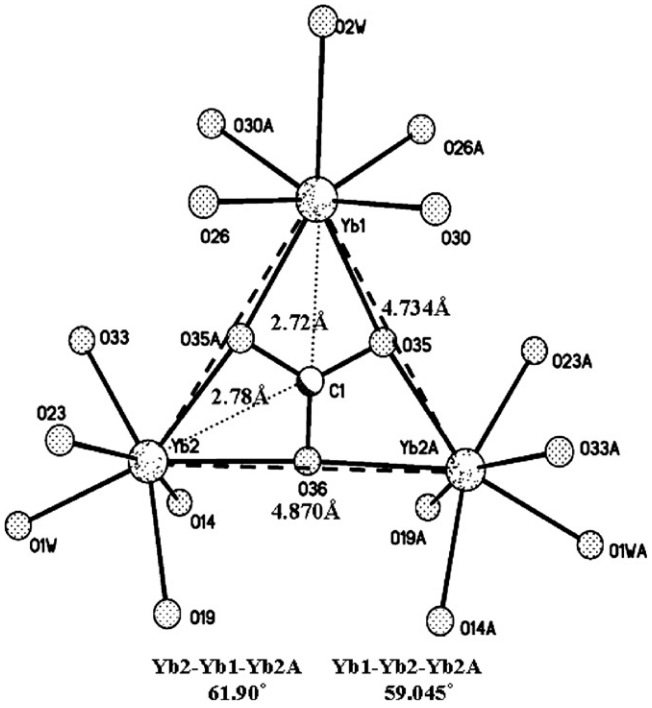


Fig. 2. SHELXP representation of the coordination spheres of the Yb atoms in **4**.

3.3. IR and NMR spectroscopy

IR spectra of **1** and **3** are similar to **2** and **4**, respectively. When comparing the IR spectra of the complexes with that of the trivacant lacunary $A\text{-}\beta\text{-}SiW_9O_{34}{}^{10}$, a shift of the stretching vibrations appearing in the 1200–700 cm^{-1} range towards higher frequencies is observed (Fig. 3). This is consistent with a decrease of the negative charge per $A\text{-}\beta\text{-}SiW_9O_{34}{}^{10-}$ moiety in the complexes. In the range 1000–700 cm^{-1}, characteristic bands were assigned to the asymmetric stretching vibrations of the bridges W–Oc–W (715–785 cm^{-1}), W–Ob–W (823 cm^{-1} and Si–Oa (885 cm^{-1}), and of the terminal bonds W–Od (950–1000 cm^{-1}) [24,25]. The IR spectra of the complexes show bands in the region 1492–1482 cm^{-1}, which were assigned to the doubly degenerate v_3 vibrational mode of $CO_3{}^{2-}$ with a small splitting of 10 cm^{-1}. This splitting is attributed to distortion of the $CO_3{}^{2-}$ group. This splitting is commonly observed in carbonate complexes [26]. The other two infrared active modes, v_2 and v_4, overlap with the W–O stretching bands.

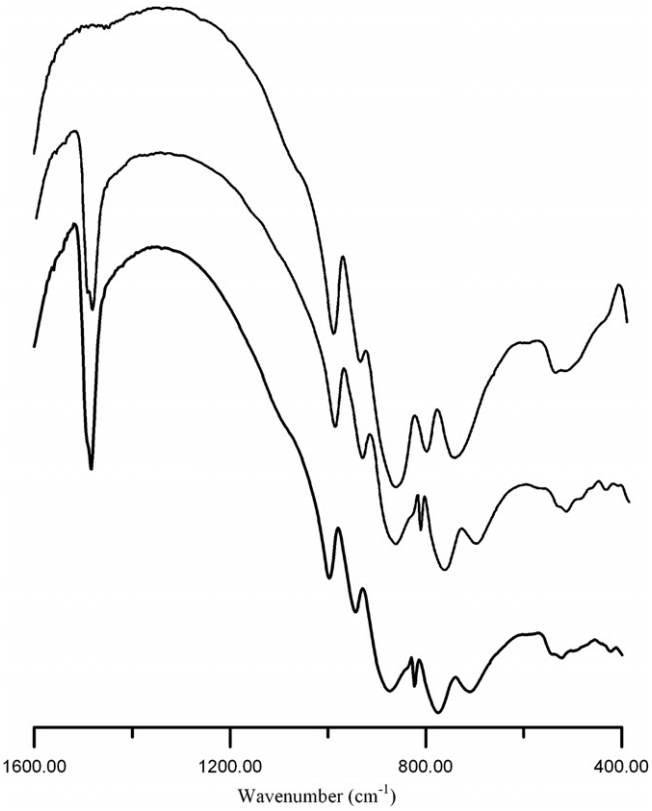


Fig. 3. IR spectra of **2** (inner), **4** (lower) and $Na_{10}[A\text{-}\beta\text{-}SiW_9O_{34}] \cdot xH_2O$ (upper) in KBr plates.

The ^{29}Si NMR spectrum of **2** shows one peak at −84.895 ppm corresponding to the two symmetry-equivalent Si atoms in each

A-β-$SiW_9O_{34}^{10-}$ unit and it is consistent with the solid-state C_2 structure. The values for the chemical shifts are similar to the values observed for other 3:2 sandwich complexes of $SiW_9O_{34}^{10-}$, $[(A\text{-}\alpha\text{-}SiW_9O_{34})_2Sn_3]^{14-}$, −85.2 ppm; $[(A\text{-}\beta\text{-}SiW_9O_{34})_2Sn_3]^{14-}$, −85.0 ppm [27] and $[(A\text{-}\beta\text{-}SiW_9O_{34})_2(HOZr)_3]^{11-}$, −84.2 ppm [12]. The ^{13}C NMR spectrum of **2** (0.1 mM) shows one peak at 170.297 ppm which is attributed to the encapsulated CO_3^{2-} anion In order to obtain a solution of **2** that was concentrated enough for ^{13}C NMR spectroscopy it was necessary to convert the potassium salt to the lithium salt by addition of $LiCLO_4$. The lithium salt of **2** is stable for several months and its solution is stable for at least the duration of the NMR scanning (see NMR spectra in the Electronic Supplementary material).

3.4. Thermal properties TGA and DSC

Thermogravimetric analysis (TGA) curves of **1**, **2**, **3** and **4** show two mass loss regions below 500 °C. First, 30–300 °C with 9.66%, 6.46%, 10.60% and 6.94% weight loss, which are assigned to lattice and coordinated (bond to Yb or Y atoms) water loss equal to 30, 21, 35 and 23 molecules for **1**, **2**, **3** and **4**, respectively. Second, 430–500 °C with approximately 0.68%, 0.68%, 0.63% and 0.63% weight loss for **1**, **2**, **3** and **4**, respectively, which are assigned to loss of one CO_2 molecule from the decomposition of CO_3^{2-} (Fig. 6). Differential Scanning Calorimetry (DSC) curves of **4** show two endothermal and some exothermal processes. The endothermal processes at 80–120 °C and 491 °C are attributed to exit of lattice and coordinated water and CO_2, respectively, and the exothermal process at 510 °C to decomposition of the structure. Another exothermal process possibility is attributed to SiO_2 formation. On the basis of the TGA and DSC studies it can be thus concluded that the complexes are thermally stable up to 430 °C (see TGA and DSC plots in the Electronic Supplementary material).

3.5. Electronic spectroscopy

The UV-electronic spectra of **2** and **4** exhibit two characteristic bands at ∼200 and ∼250 nm ($\varepsilon = 67\,500\ cm^{-1}\ M^{-1}$), assigned to W–Od and W–Ob–W transitions, respectively (Od is a terminal oxygen and Ob is a bridging oxygen) [1]. These bands are shifted to lower frequencies on comparison with the A-β-$SiW_9O_{34}^{10-}$ ligand, due to the coordination of the Y^{3+} and Yb^{3+} cations (see UV spectra in the Electronic Supplementary material).

4. Conclusion

Two (four salts) new sandwich-type polyoxometallate complexes $[(A\text{-}\beta\text{-}SiW_9O_{34})_2(MOH_2)_3CO_3]^{13-}$ (M = Y^{3+} and Yb^{3+}) were synthesized by the reaction of M^{3+} ions with A-β-$SiW_9O_{34}^{10}$ in carbonate solution. The experimental data show that the synthesis of the complexes requires the presence of the carbonate anion. The crystal structure of the complexes consist of two lacunary A-β-$SiW_9O_{34}^{10-}$ Keggin moieties which are linked by a $(H_2OMO)_3C$ belt into an assembly of virtual C_2 symmetry. The results prove the retention of the isomeric form of the starting lacunary anion A-β-$SiW_9O_{34}^{10-}$ upon the preparation of the complexes. The results suggest that the complexes are stable over a large range of pH, 3–11, and up to ∼430 °C, and decomposition of the complexes is followed by loss of the carbonate anion. Other tools such as IR, ^{13}C NMR, ^{29}Si NMR, UV spectroscopy, TGA and DSC confirm the structures.

Appendix A. Supplementary data

Crystallographic data (CIF file) for the structural analysis have been deposited with the Fachinformationszentium Karlsruhe (FIZ), CSD-number 418797. These data can be obtained free of charge via E-mail: crysdata@FIZ-Karsruhe.de. Tel.: +49 7247 808 310; fax: +49 7247 808 136. Supplementary data associated with this article can be found, in the online version, at doi:10.1016/j.poly.2008.02.035.

References

[1] De-L. Long, E. Burkholder, L. Cronin, Chem. Soc. Rev. 36 (2007) 105.
[2] L. Cronin, J.A. McCleverty, T.J. Meyer (Eds.), Comprehensive Coordination Chemistry II, vol. 7, Elsevier, Amsterdam, 2004, pp. 1–57.
[3] M.T. Pope, in: G. Wilkinson, R.D. Gillard, J.A. McCleverty (Eds.), Comprehensive Coordination Chemistry, vol. 3, Pergamon Press, 1987, pp. 1023–1058.
[4] M.T. Pope, in: A.G. Wedd (Ed.), Comprehensive Coordination Chemistry II: Transition Metal Groups 3–6, vol. 4, Elsevier Science, New York, 2004, p. 635.
[5] M.T. Pope, A. Müller (Eds.), Polyoxometallates. From Platonic Solids to Anti-Retroviral Activity, Kluwer Academic Publishers, Dordrecht, The Netherlands, 1994.
[6] M.T. Pope, A. Müller (Eds.), Polyoxometallate Chemistry: from Topology via Self-assembly to Applications, Kluwer Academic Publishers, Dordrecht, 2001.
[8] W.H. Knoth, P.J. Domaille, R.L. Harlow, Inorg. Chem. 25 (1986) 1577.
[9] W.H. Knoth, P.J. Domaille, R.D. Farlee, Organometallics 4 (1985) 62–68.
[10] N. Laronze, J. Marrot, G. Herve', Inorg. Chem. 42 (2003) 5857.
[11] M.H. Alizadeh, H. Eshtiagh-Hosseini, R. Khoshnavazi, J. Mol. Struct. 688 (2004) 33.
[12] R.G. Finke, B. Rapko, T.J.R. Weakley, Inorg. Chem. 28 (1989) 1573.
[13] X. Fang, T.M. Anderson, W.A. Neiwert, C.L. Hill, Inorg. Chem. 42 (26) (2003) 8600.
[14] R. Khoshnavazi, A. Salimi, A. Ghiasi Moaser, Polyhedron 27 (2008) 1303.
[15] R. Khoshnaavazi, H. Estiagh-hossieni, M.H. Alizadeh, M.T. Pope, Polyhedron 25 (2006) 1921.
[16] R. Khoshnavazi, H. Eshtiagh-hossieni, M.H. Alizadeh, M.T. Pope, Inorg. Chim. Acta 360 (2) (2007) 686.
[17] G. Hervé, A. Tézé, Inorg. Chem. 16 (1977) 2115.
[18] F. Robert, A. Tézé, Acta Crystallogr., Sect. B. 37 (1981) 1318.
[19] Bruker, APEX2 Software Package, Bruker AXS Inc., 5465, East Cheryl Parkway, Madison, WI 5317, 2005.
[20] G.M. Sheldrick, SHELXTL v. 5.10, Structure Determination Software Suite, Bruker AXS, Madison, WI, USA, 1998.
[21] A.J.C. Wilson (Ed.), International Tables for X-ray Crystallography, vol. C, Kluwer Academic, Dordrecht, 1992, Tables 4.2.6.8 (pp. 219–222) and 6.1.1.4 (pp. 500–502).
[22] A.R. Tomsa, L. Muresan, A. Koutsodimou, P. Falaras, M. Rusu, Polyhedron 22 (2003) 2901.
[22] I.D. Brown, D. Altermatt, Acta Crystallogr., Sect. B. 41 (1985) 244.
[23] http://www.ccp14.ac.uk/ccp/web-mirrors/i_d_brown/bond_valence_param/.
[24] R. Contant, R. Thouvenot, Can. J. Chem. 69 (1991) 1498.
[25] M. Rocchiccioli-Deltcheff, Fournier, R. Franck, Inorg. Chem. 22 (1983) 207.
[26] K. Nakamoto (Ed.), Infrared and Raman Spectra of Inorganic and Coordination Compounds, Part B, fourth ed., Wiley-Interscience, New York, 1986; planar XY_3 molecules, pp. 121–125; carbonate complexes, pp. 252–254.

$[Fe(C_{42}H_{32}N_8)](PF_6)$ (M chelate) = 993.8 g mol^{-1}. Calc. C, 50.72; H, 3.24; N, 11.26. Found: C, 50.55; H, 3.24; N, 11.26%. Tetraethylammonium perchlorate, TEAP (Fluka), was dried in an oven at 60 °C prior to use. All other reagents and solvents were of the highest purity grade available from Merck, Mallinckrodt and Sigma Chemical Co. Ltd., and were used as received.

2.2. Characterization

The elemental analysis was performed on a Carlo Erba Elemental Analyzer model EA1110. ^{1}H NMR spectra were obtained in CD_3CN and $CDCl_3$ solutions in a Bruker 300 MHz spectrometer model DPX 300. Electrochemical experiments were conducted using a PAR model 273 Potentiostat/Galvanostat. Cyclic voltammetric and chronoamperometric experiments were carried out in conventional three-compartment glass cells under argon atmosphere using a glassy-carbon disc working electrode (0.08 cm^2 area), a platinum wire auxiliary electrode and a Ag/AgCl reference electrode. The glassy-carbon electrode was polished to a mirror finish with different grades of alumina as low as 0.05 μm and ultrasonically cleaned before the experiments. Cyclic voltammetric, chronoamperometric and spectroelectrochemical experiments were performed in acetonitrile/TEAP solutions. UV–Vis spectra were obtained in quartz cells by using an 8452A Hewlett–Packard spectrophotometer. Polymer film electropolymerized on ITO was kept in a quartz cell equipped with a counter and reference electrode, and the electronic spectra were measured under controlled potential using a BAS CV27 Potentiostat. The spectra were recorded with an interval of 1 s during a potential sweep of 50 mV s^{-1}.

Apparent surface coverages (Γ_{app}, mol cm^{-2}) were calculated using the equation $\Gamma_{app} = Q/nFA$, where n is the number of transferred electrons, F is the Faraday's constant, A is the electrode area in cm^2, and Q is the charge (area) under the cyclic voltammetric oxidation $Fe^{III/II}$ wave at 50 mV s^{-1}.

3. Results and discussion

The ^{1}H NMR spectrum of a CD_3CN solution of $[Fe(tpy\text{-}NH_2)_2](PF_6)_2$ is shown in Fig. 1. The spectrum is relatively sharp and well resolved, and illustrates the high symmetry of the iron(II) complex in the ^{1}H NMR time-scale. The spectrum can be unambiguously assigned by comparison with the spectrum of $[Fe(tpy)_2](PF_6)_2$ [9]. The ^{1}H NMR spectra of the complex $[Fe(tpy\text{-}NH_2)_2](PF_6)_2$ exhibit characteristic coordination shifts $\Delta\delta$ ($\Delta\delta = \delta$ (complex, CD_3CN – δ (ligand, $CDCl_3$)), indicative of the conformational changes from a transoid arrangement about the interannular C–C bonds in the free ligand to a cisoid arrangement in the complex [10]. The use of coordination shifts is more reliable than the direct comparison of chemical shift in comparisons of this type of complex.

^{1}H NMR data are presented in Table 1. The protons of the amino groups in the complex can be observed as a broad singlet at $\delta = 4.58$. The remarkably constant coordination shifts observed for the iron complex of tpy[1] and terpy-NH_2 confirm that the structures of these complexes are similar. The consistency in the $\Delta\delta$ values for $H^{3'}$ suggests that the interplanar angles between the aryl substituent and the central pyridine ring are also similar in the tpy and tpy-NH_2 complex.

The cyclic voltammogram between 0 and +1.6 V (versus Ag/AgCl) in an acetonitrile solution containing 1.0 mM of the iron complex and 0.1 M of TEAP displays two overlapped waves with peak potential values of 0.88 and 1.12 V, which can be ascribed to irreversible aniline oxidation and reversible Fe(III)/Fe(II) oxidation/reduction, respectively. Repeatedly scanning the potential of a glassy-carbon electrode over the range 0–1.6 V versus Ag/AgCl results in a continuous increase in the size of the cyclic voltammetric wave for the $Fe^{III/II}$couple, as shown in Fig. 2. If after a scanning period the electrode is transferred (with thoroughly rinsing in acetonitrile) to a fresh electrolyte (containing no monomeric complex), the observed $Fe^{III/II}$ couple persists. The cyclic voltammogram response is quickly dominated by the polymer. Visual inspection of the electrode also gives evidence of deposition of a purple film.

The behavior shown in Fig. 2 suggests that an electroactive and presumably polymeric film of the complex is formed on the electrode as a consequence of oxidation. The current observed in Fig. 2 for the $Fe^{III/II}$ wave arises from the $Fe^{III/II}$ couple within the growing film and from the mediated oxidation of the monomeric complex in the external solution, part of which becomes incorporated into the film as it grows. The same results can also be obtained with Pt or highly doped SnO_2 electrodes. This modified electrode is also stable under repeated scanning (for at least 30 cycles) in the potential range 0 and 1.6 V in a clean electrolyte solution. In contrast, we should note that these films are unstable toward cycling through the potential where ligand reductions occur (0 and −1.8 V range). Scanning over this region destroys the electroactive behavior of the film.

The modified electrode obtained by electropolymerization exhibits reversible electrochromism, changing from purple to pale yellow due to Fe(II) to Fe(III) oxidation.

By scanning the potential from 0 to 1.6 V, a single reversible peak can be observed at 1.12 V, which leads to the complete decay

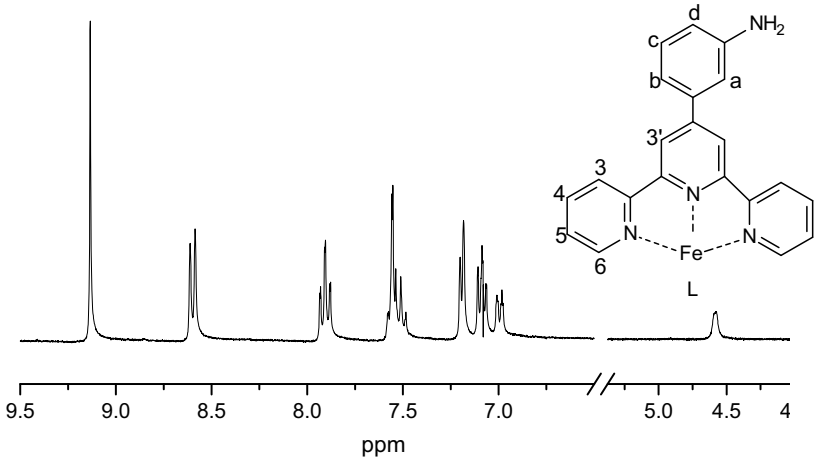


Fig. 1. 300 MHz ^{1}H NMR spectrum of a $[Fe(tpy\text{-}NH_2)_2]^{2+}$ CD_3CN solution.

Table 1
^{1}H NMR data and coordination shifts of the ligands tpy and terpy-NH_2 and its iron complexes

Ligand or complex	Proton chemical shift ($\Delta\delta^e$)									
	H^6	H^5	H^4	H^3	$H^{3'}$	$H^{4'}$	H^a	H^b	H^a	H^d
tpy[f]	8.69	7.42	7.95	8.66	8.46	8.02				
$[Fe(tpy)_2]^{2+}$[g]	7.06	7.06	7.87	8.47	8.91	8.68				
[e]	−1.63	−0.36	−0.08	−0.19	0.45	0.66				
tpy-NH_2[f]	8.67	7.51	8.03	8.75	8.67		7.05	7.20	7.20	6.71
$[Fe(tpy\text{-}NH_2)_2]^{2+}$[g]	7.19	7.08	7.97	8.59	9.13		7.53	7.53	7.53	6.99
[e]	−1.48	−0.43	−0.06	−0.16	0.46		0.48	0.33	0.33	0.28

[e] $\Delta\delta = \delta$ (complex, CD_3CN – δ (ligand, $CDCl_3$).
[f] $CDCl_3$ solution.
[g] CD_3CN solution.

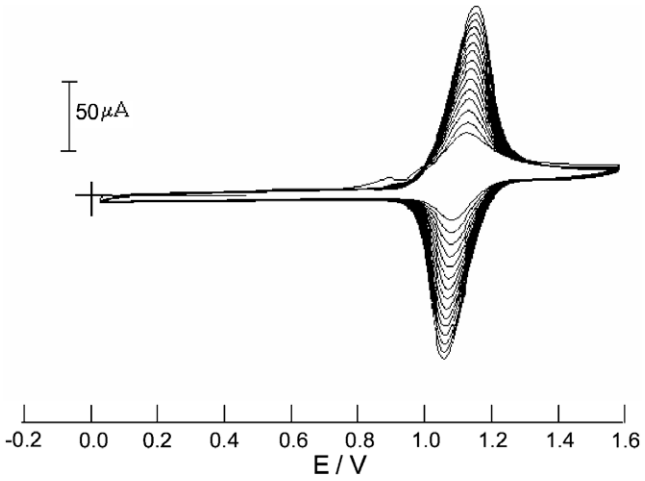


Fig. 2. Cyclic voltammogram showing deposition of poly-$[[Fe(tpy\text{-}NH_2)_2]^{2+}]_n$ onto a glassy-carbon electrode by repeated potential scans between 0 and +1.6 V vs Ag/AgCl in acetonitrile 0.1 M in TEAP, scan rate = 100 mV s^{-1}.

of the characteristic MLCT bands in the visible region, as shown in the spectroelectrochemical results in Fig. 3. This electrochemical peak can be ascribed to the oxidation of Fe(II), by analogy with related iron–terpyridine complexes from the literature [11]. In the reverse sweep, the spectrum changed rapidly, to recover the original absorbance.

Polymeric films of different thicknesses were prepared by controlling the time of electropolymerization in a 1.0 mM $[Fe(tpy\text{-}NH_2)_2]^{2+}$ solution. The polymer coverage can be readily and reproducibly adjusted by varying the number of cyclic potential scans and sweep rate. Essentially identical plots of coverage versus number of scans were obtained in a series of experiments using several electrodes sequentially electropolymerized in the same monomer solution.

Fig. 4 shows how the charge under the $Fe^{III/II}$ surface wave increases with an increasing number of electropolymerizing potential scans for $[Fe(tpy\text{-}NH_2)_2]^{2+}$. The apparent surface coverage by the film increases linearly over the first three potential scans, and less rapidly thereafter. The extent of surface coverage is dependent on the scan rate, showing that the origin of the nonlinearity in Fig. 4 is due to the onset of charge transport limitations in the thickening film, where not all the $Fe^{III/II}$ sites are oxidized during an oxidative potential scan.

Two different types of behavior are observed for peak potential and peak current as a function of the scan rate. For the thin film (i.e. $\Gamma_{app} < 6 \times 10^{-9}$ mol cm^{-2}), the waves are symmetrically shaped irrespective of υ, and a linear dependence of the anodic peak current is observed. Thin layer/surface-type behavior is thus exhibited by thinner films. Such behavior is expected for a surface-immobilized electroactive film sufficiently thin for all of the redox sites within the film to undergo oxidation and reduction during one potential cycle [12].

For slow scan rates the thicker films display voltammetric waves with characteristics similar to those described for the thin film. With increasing υ, the voltammograms start to qualitatively resemble those of solution reactants diffusing to the electrode (current–potential responses show tailing), for which semi-infinitive diffusion predicts a linear relationship between i_p and $\upsilon^{1/2}$ (Fig. 5). This transition between the two regimes, due to the onset

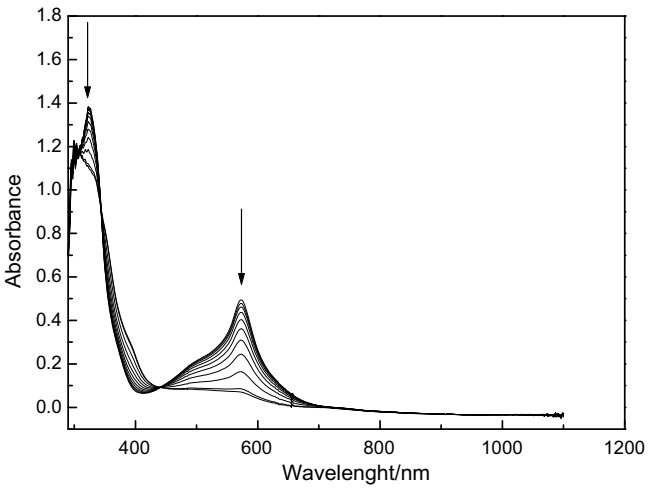


Fig. 3. Visible absorption spectra for ITO modified electrode during the potential sweep from 0 to 1.6 V at 50 mV interval.

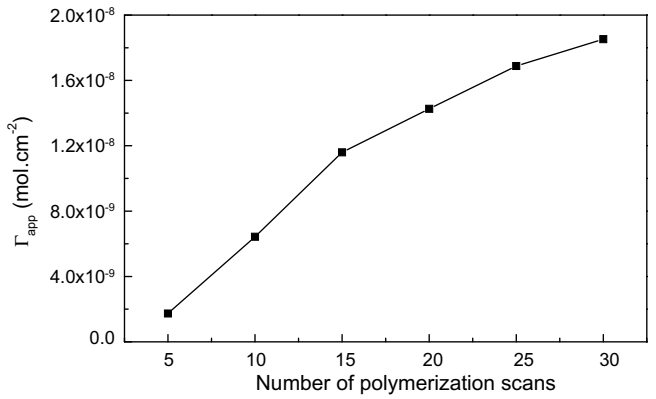


Fig. 4. Plot of the apparent surface coverage, Γ_{app}, with the number of scans employed in the polymerization. The modified electrodes were prepared as in Fig. 2. Note that the apparent surface coverages were determined after each scan in a fresh electrolyte solution.

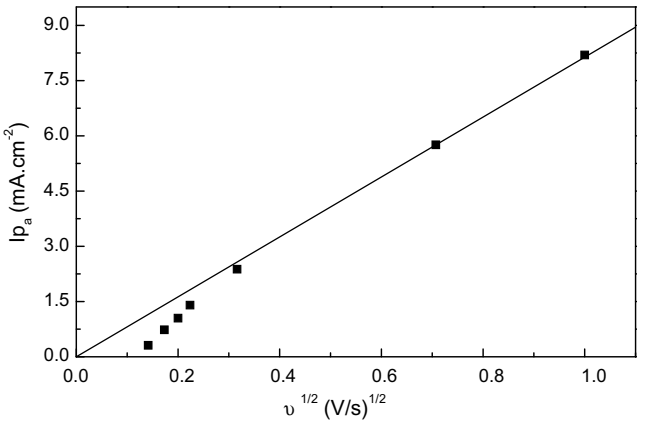


Fig. 5. Anodic peak current (Ip_a) vs $\upsilon^{1/2}$ (υ = scan rate) for a thick film, (i.e. $\Gamma_{app} = 1.8 \times 10^{-8}$ mol cm^{-2}) of poly-$[[Fe(tpy\text{-}NH_2)_2]^{2+}]_n$ in a fresh electrolyte solution, acetonitrile 0.1 M in TEAP.

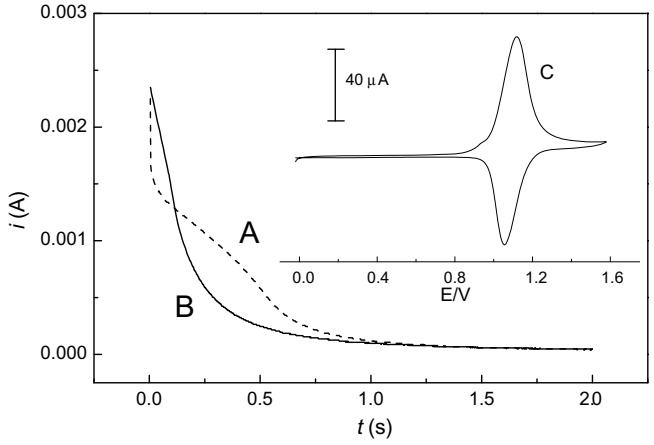


Fig. 6. (A, B) Potential step chronoamperometry of $\Gamma_{app} = 7.3 \times 10^{-8}$ mol cm^{-2} film of poly-$[[Fe(tpy\text{-}NH_2)_2]^{2+}]_n$ in a fresh electrolyte solution, acetonitrile 0.1 M in TEAP; (A) 0–1.35 V potential step; (B) 0–1.6 V vs Ag/AgCl; (C) cyclic voltammetry of the same electrode at 20 mV s^{-1}.

of rate-limiting charge transport through film as thickness film increases, has been observed for other polymer-modified electrodes [11,13]. The peak splitting and the anodic peak FWHM (full width at half-maximum) increase with the sweep rate and the film thickness.

Potential-step chronoamperometry was employed in the study of the charge transport process close to the electrode surface.

The current response of redox polymer films depends upon the relative sizes of the diffusion layer δ (the layer adjacent to the electrode surface where the concentrations differ from those in the bulk polymer), the film thickness d, the diffusion coefficient (D_{ct}), and the experimental time-scale (t_e). In redox polymer films, D_{ct} is related to charge transfer through the polymer. There are two limiting cases to consider – semi-infinitive diffusion and thin layer behavior, finite diffusion. Many redox polymers exhibit behavior that is intermediate between these two limiting cases [14].

When the film thickness is much larger than the diffusion layer ($d \gg \delta$), the system will exhibit semi-infinite behavior. When the film thickness is the same as that of the diffusion layer ($d \approx \delta$), then thin layer behavior will be observed, where the electroactive material immobilized on the electrode surface is electrolyzed very rapidly when the applied potential is changed.

Potential step chronoamperometric experiments with films of several thicknesses were performed to assess the charge diffusion behavior of these polymers. In these experiments, a large-amplitude potential step was used to avoid any complication from ohmic resistance of the polymer film. Murray and Daum [15] showed that if the polymer film exhibits an ohmic resistance to charge flow, this can cause loss of potential control in the electrochemical experiment.

The consequence of an oxidative potential step from 0 to 1.35 V, insufficiently positive to overcome the film resistance, is shown in Fig. 6A. The slow potential scan cyclic voltammetry of Fig. 6C would suggest that 1.35 V is thermodynamically sufficient for rapid film oxidation. Yet the current–time curve exhibiting an abnormal maximum is seen. On the other hand, if the potential step is repeated on the same electrode, but now from 0 to 1.6 V versus Ag/AgCl a smoothly decaying current–time curve is seen (Fig. 6B). The current maximum for the 1.35 V step is recognized as an artefact resulting from the film's ohmic resistance. However, interpretation of the results in figure requires consideration of the film's ohmic resistance only and no association of ion migration rates in the film with the overall charge transport kinetics need or should be made from such data.

Kaufman et al. [16] proposed a charge transport model through polymer films where charge propagation takes place via electron-self-exchange reaction between oxidized and reduced neighbors within the film. Since the electron transport accomplishes an overall oxidation state change during the film's electrochemical reaction, charge neutrality within the polymer film requires uptake of counterions into the polymer matrix, or expulsion of co-ions initially in the film as an ion-pair, to coincide with charge propagation. Moreover, segmental motion of the polymer chain, and motion of the solvent, may also be important in dictating the overall charge transport rate. Murray refers to the overall process as charge transport [14]. This process is mathematically equivalent to diffusion of such localized states (whether electron hopping, or an associated event such as charge compensating counterion hopping, or polymer lattice motion governing either process, is the rate-determining step). If charge transport follows Fick's law, the potential step current–time response will be described by the Cottrell equation (1) [17]:

$$i = nFAD_{ct}^{1/2}C/\pi^{1/2}t^{1/2} \quad (1)$$

The current transient shown in Fig. 6B is plotted in this form in Fig. 7. It can clearly be seen that the experimental data do not yield a linear i versus $t^{-1/2}$ plot. Deviation from the predicted straight line, based on the Cottrell equation for a semi-infinitive diffusion system, is observed.

Two factors are responsible for this curvature. At short times, the current intensity is significantly smaller than the one expected

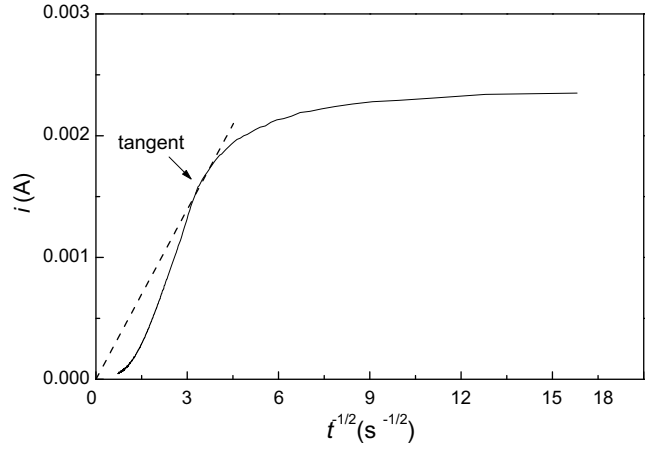


Fig. 7. i vs $t^{-1/2}$ plot for a 0–1.6 V potential step, $\Gamma_{app} = 7.3 \times 10^{-8}$ mol cm^{-2} film of poly-$[[Fe(tpy\text{-}NH_2)_2]^{2+}]_n$ in a fresh electrolyte solution, acetonitrile 0.1 M in TEAP.

theoretically; this has been attributed to uncompensated solution resistance effects [13]. At long times, the fall-off of the current indicates that the volume of the polymer cannot be taken as infinite and a finite diffusion boundary condition must be invoked. Pause and Pickup [18] assume that the Cottrell equation (semi-infinitive diffusion system) pertains to the central portion of the i versus $t^{-1/2}$ plot, and the most reasonable slope to adopt for data analysis is the tangent to the curve from the origin. In this way, we can extract values for $D_{ct}{}^{1/2}C$, where D_{ct} is the diffusion coefficient and C is the concentration of the electroactive species.

At longer times, where the semi-infinitive boundary condition of Eq. 1 becomes violated, we were also interested to confirm the idea that deviations from the predicted values for semi-infinite Cottrell behavior were due to the finite boundary condition. For a potential step experiment with a reactant solution of thickness d, the finite diffusion current–time dependence is described by the following equation [14,15]:

$$i = \frac{nFAD^{1/2}C}{\pi^{1/2}t^{1/2}}\left[\sum_{K=0}^{\infty}(-1)^K\left\{\exp\left(\frac{-K^2d^2}{Dt}\right) - \exp\left(\frac{-(K+1)^2d^2}{Dt}\right)\right\}\right] \quad (2)$$

where A is the area of the electrode, D is taken to be D_{ct} (charge transport diffusion coefficient determined by chronoamperometry), C is the concentration of the redox species, d is the thickness of the film, and n, F, and t have their usual meanings. For a comparison of Eq. 2 with the experiment, D and d are required, or more precisely, the ratio d^2/D is needed. From $C = (\Gamma/d)$ it follows that $d^2/D = (\Gamma/D^{1/2}C)^2$, and using for $D^{1/2}C$ the $D_{ct}{}^{1/2}C$ values obtained from the slope of the tangent to the i versus $t^{-1/2}$ curve from the origin, and the apparent surface coverage, $\Gamma_{app} = Q/nFA$, it is possible to estimate d^2/D. Experimental i versus $t^{-1/2}$ curves and chronoamperometric current–time responses predicted by the Cottrell equation and by Eq. 2, for $\Gamma_{app} = 7.3 \times 10^{-8}$ mol cm^{-2}, are shown in Fig. 8.

The theoretical prediction (open cycles) reasonably agrees with the experimental points, except for very short times, where the current intensity is controlled by the solution resistance. This agreement clearly indicates that in these experiments a changeover occurs, from a semi-infinite diffusion condition described by the Cottrell equation to a finite diffusion regime, with time following the potential step. In the context of the above discussion, it is predicted that the changeover between the two regimes occurs at different times for polymers of different thickness. At longer times, the diffusion layer approaches the film thickness and a transition to thin layer behavior occurs: for thicker films, the transition between "diffusional" behavior to "monolayer" behavior will be observed at longer times. This means that as film thickness increases, the larger is its diffusional character behavior; the current response is that for a species in solution.

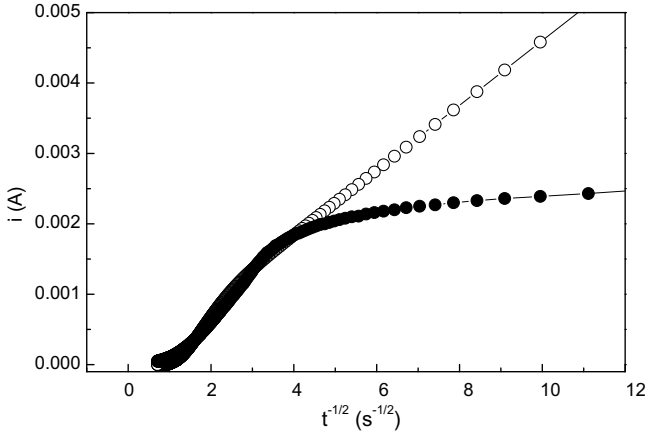


Fig. 8. i vs $t^{-1/2}$ plot for a 0–1.6 V potential step, $\Gamma_{app} = 7.3 \times 10^{-8}$ mol cm^{-2} film of poly-[[Fe(tpy-NH$_2$)$_2$]$^{2+}$]$_n$. Solid cycles, experimental data; open cycles are values calculated from finite-diffusion theory, $D_{ct}{}^{1/2}C = 1.0 \times 10^{-7}$ A s$^{-1/2}$, $A = 0.082$ cm^2.

Table 2 shows the $D_{ct}{}^{1/2}C$ values for poly-[[Fe(tpy-NH$_2$)$_2$]$^{2+}$]$_n$ with different thicknesses.

When the electron-exchange mechanism of Kaufman and Engler [16] is followed, electrons are removed from sites that are far from the electrode by successive electron transfers between neighboring sites in the film. The rate at which these electron transfers occur and the rate at which counterions enter the film for charge compensation influences D_{ct}. However, similar diffusion coefficients were observed when the film thickness was varied. A diffusion coefficient that is insensitive to the film thickness suggests that movement of charge compensating counterions through the polymeric matrix is relatively facile and does not limit the overall charge transport rate [19].

Studies where the electrolyte concentration was varied, using electrodes with the same film thickness, demonstrated that the cell resistance of the coated electrode is dominated by the solution resistance rather than the film resistance. At high electrolyte concentration, the solution resistance is reduced, as expected. This fact is evidenced by large increase in the current intensity in short times in the case of chronoamperometric experiments. The reverse occurs when we keep the electrolyte concentration constant and alter the film thickness; however, the chronoamperometric experiments give evidence of a smooth decrease in the current intensity.

With regard to the electrolyte concentration, other effects must be considered. In the chronoamperometric experiments, the changeover between the two regimes (from a semi-infinite diffusion condition to a finite diffusion regime) occurs at different times for polymers of the same thickness as a function of the TEAP concentration. The transition to a finite diffusion regime takes place in shorter times as the electrolyte concentration is changed from 0.05 to 0.5 M (Fig. 9). The cyclic voltammogram shows that there is a decrease in the peak currents as the electrolyte concentration is increased. Obviously, a good deal of electroactive Fe^{II} sites are not oxidized as the salt concentration is increased. This decrease in the maximum peak currents likely reflects swelling of the layer at higher electrolyte concentrations, which is related to changes in polymer structure, leading to increased redox site separation. In this way, the electron hopping of the redox sites within the polymeric matrix requires cooperative motion of the polymer backbone to which they are attached. Furthermore, transport of the companion counterion (and solvent) requires expansion of the polymer lattice, reducing the mobility of polymer segments. These facts suggest that polymer chain motion is the rate-limiting step in the case of poly-[[Fe(tpy-NH$_2$)$_2$]$^{2+}$]$_n$ films.

The ability of the polymer film to act as a mediator between the electrode and the external solution was evaluated. Electrodes coated with [[Fe(tpy-NH$_2$)$_2$]$^{2+}$]$_n$ film were examined by cyclic voltammetry in the presence of ferrocene, which undergoes one-electron oxidation at less positive potentials than the Fe(III)/Fe(II) couple inside the film ($E_{sol} = 0.40$ V and $E_{pol} = 1.12$ V, respectively). These experiments were carried out with an electrode covered with increasingly thicker films of [[Fe(tpy-NH$_2$)$_2$]$^{2+}$]$_n$, prepared by cycling the potential (0–1.6 V, 50 mV s^{-1}) in a 10^{-3} M solution of

Table 2
$D_{ct}{}^{1/2}C$ values obtained from chronoamperometry using Cottrell equation, for polymers with different thickness

Γ_{app} (mol cm^{-2})	$D_{ct}{}^{1/2}C$ (A s$^{-1/2}$)
1.4×10^{-8}	0.6×10^{-7}
7.3×10^{-8}	1.0×10^{-7}
1.2×10^{-7}	1.0×10^{-7}
1.6×10^{-7}	1.1×10^{-7}

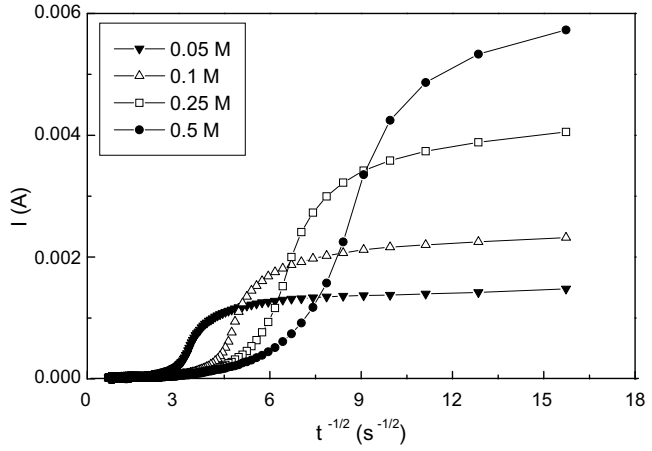


Fig. 9. Effect of electrolyte concentration (TEAP) on i vs $t^{-1/2}$ plot for poly-$[[Fe(tpy\text{-}NH_2)_2]^{2+}]_n$ films of the same thickness. The potential was stepped from 0 to 1.6 V.

$[Fe(tpy\text{-}NH_2)_2]^{+2}$ in CH_3CN/0.1 M TEAP. They were washed with acetonitrile and transferred to a of ferrocene 4×10^{-3} M solution in clean supporting electrolyte. It is known that ferrocene may be oxidized at the electrode/polymer interface after diffusion through a continuous polymer film. Alternatively, it may be oxidized at a polymer film/solution interface, a process that requires either redox conduction through the film or an electronically conducting film. In the case of redox-conductivity-mediated electron transfer, irreversible oxidation of the solution species will occur at or near E_{pol}. For electron transfer mediated by an electronically conducting film, reversible oxidation will occur at or near E_{sol}. Electron transfer involving solution species at a redox-polymer-coated electrode at both E_{pol} and E_{sol} have been reported previously [20,21].

A cyclic voltammogram for a of 4×10^{-3} M ferrocene solution at an electrode freshly coated with 2.1×10^{-8} mol cm^{-2} $[[Fe(tpy\text{-}NH_2)_2]^{2+}]_n$ is shown in Fig. 10. Almost all of the ferrocene oxidation occurs at E_{sol}, although some oxidation also occurs at E_{pol},. However, as the surface coverage is increased, the peak currents for the solution species decrease (E_{sol}) and may be interpreted as the onset of membrane-controlled diffusion [22], since the solution species must diffuse through hole channels in the film to get to the electrode. At thick films, oxidation of the external couple occurs by charge transfer through the films rather than mass transfer (diffusion).

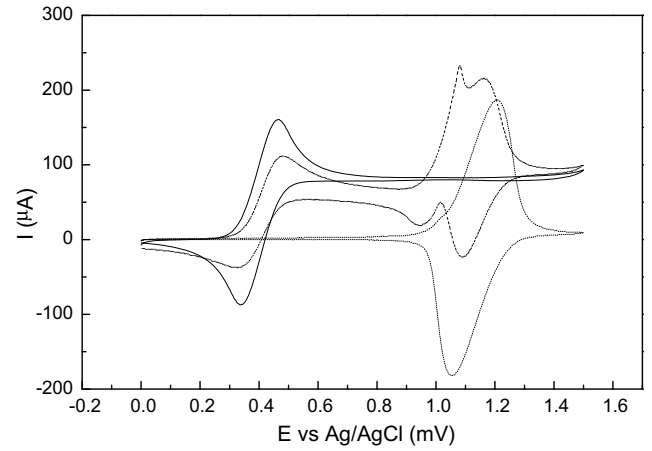


Fig. 10. Cyclic voltammogram of 4×10^{-3} ferrocene in acetonitrile 0.1 M TEAP (scan rate = 100 mVs^{-1}); (—) bare glassy-carbon electrode; (...) glassy-carbon coated with 2.1×10^{-8} mol cm^{-2} $[[Fe(tpy\text{-}NH_2)_2]^{2+}]_n$; (- - -) glassy-carbon/poly-$[[Fe(tpy\text{-}NH_2)_2]^{2+}]_n$ without ferrocene.

Table 3
Roughness and thickness of poly-$[[Fe(tpy\text{-}NH_2)_2]^{2+}]_n$ films as a function of deposition time

	20 cycles	50 cycles
Thickness (nm)	106	380
Roughness (nm)	9	19

The experiments demonstrate the existence of two discrete pathways for net charge transfer – a diffusional or mass-transfer pathway, which is a slow process at thick films (at least on the time-scale of cyclic voltammetry), and a charge-transfer pathway, which is dictated by the redox properties of the film.

Atomic force microscopy was used to obtain information concerning polymer morphology. Roughness and film thickness values are listed in Table 3. The table shows the thickness and roughness increase with the increasing number of electropolymerizing potential scans for poly-$[[Fe(tpy\text{-}NH_2)_2]^{2+}]_n$. The AFM image of a poly-$[[Fe(tpy\text{-}NH_2)_2]^{2+}]_n$ film deposited onto an ITO electrode shows that the polymer looks compact and displays continuous morphology over the entire film. The image reveals that the polymer completely covers the electrode surface without pore or channel defects, indicating that there is a 2-D layer-by-layer growth mechanism, where the nuclei grow more quickly in the parallel direction than in the perpendicular direction until they meet and overlap. Conducting polymers deposited layer-by-layer via the lateral growth of 2-D nuclei may be expected to have a more uniform and compact arrangement [23] of polymer chains.

4. Conclusion

The characterization of the complex $[Fe(tpy\text{-}NH_2)_2](PF_6)_2$ by elemental analysis, and ^{1}H NMR spectra confirmed the composition of the monomer. By using the monomer, it was possible to electrogenerate polymer films having high conductivity, stability, permeability, and uniform and controllable thickness by oxidative polymerisation. Electrochemical measurements were reproducible over the potential range 0–1.6 V. The film completely loses its electroactivity when the potential is scanned from 0 to −1.6 V. We determined charge transport parameters as a function of time-scale and thickness of the modified electrode. The results showed that poly-$[[Fe(tpy\text{-}NH_2)_2]^{2+}]_n$ can be made to exhibit the three regimes of charge transport behavior by manipulation of the film thickness and the experimental time-scale. Morphological characterization of the film was provided by atomic force microscopy. The polymer looks compact and displays continuous morphology over the entire film. The image reveals that the polymer completely covers the electrode surface without pore or channel defects. The results indicate that this system may be adequate for electrocatalytic purposes or application in electrochromic display devices.

Note: The table of the variation of peak splitting and anodic FWHM with sweep rate and film thickness, and an AFM image of the complex deposited onto an ITO electrode are available on request.

Acknowledgements

We gratefully acknowledge Luciana Simionatto Guinesi and the financial support from FAPESP and CAPES.

References

[1] X. Cui, L. Hong, X. Lin, J. Electroanal. Chem. 526 (2002) 115.
[2] A. Deronzier, J.C. Moutet, Acc. Chem. Res. 22 (1989) 249.
[3] A. Malinauskas, Synth. Met. 107 (1999) 75.

[4] J. Stejskal, I. Sapurina, J. Prokes, J. Zemek, Synth. Met. 105 (1999) 195.
[5] L.M. Abrantes, J.P. Correia, M. Savic, G. Jin, Electrochim. Acta 46 (2001) 3181.
[6] C. Barbero, M.C. Miras, E.J. Calvo, R. Kotz, O. Hass, Langmuir 18 (2002) 2756.
[7] L.M. Abrantes, C.M. Cordas, E. Vieil, Electrochim. Acta 47 (2002) 1481.
[8] K. Hanabusa, A. Nakamura, T. Koyama, H. Shirai, Polym. Int. 35 (1994) 231.
[9] E.C. Constable, A.M.W. Cargill Thompson, J. Chem. Soc., Dalton Trans. (1992) 2947.
[10] E.C. Constable, M. Neuburger, D.R. Smith, M. Zehnder, Inorg. Chim. Acta 275–276 (1998) 359.
[11] P. Braterman, J.-I. Song, R. Peacock, Inorg. Chem. 31 (1992) 555.
[12] H.D. Abruña, Coord. Chem. Rev. 86 (1988) 135.
[13] P.K. Ghosh, A.J. Bard, J. Electroanal. Chem. 169 (1984) 113.
[14] M. Vilas-Boas, C. Freire, B. Castro, A.R. Hillman, J. Phys. Chem. B 102 (1998) 8533.
[15] P. Daum, R. Murray, J. Phys. Chem. 85 (1981) 389.
[16] F.B. Kaufman, A.H. Schroeder, E.M. Engler, S.R. Kramer, J.Q. Chambers, J. Am. Chem. Soc. 102 (1980) 483.
[17] A.J. Bard, L.R. Faulkner, Electrochemical Methods Fundamentals and Applications, John Wiley & Sons, New York, 1980. p. 142.
[18] C.D. Pause, P.G. Pickup, J. Phys. Chem. 92 (1988) 7002.
[19] A.J. Heller, J. Phys. Chem. 96 (1992) 3579.
[20] J.G. Eaves, H.S. Munro, D. Parker, Inorg. Chem. 26 (1987) 644.
[21] G. Chiericato Júnior, A.P.S. Silva, L.S. Guinesi, Polyhedron 23 (2004) 1953.
[22] C.D. Ellis, W.R. Murphy, T.J. Meyer, J. Am. Chem. Soc. 103 (1981) 7480.
[23] F. Li, W.J. Albery, Electrochim. Acta 37 (1992) 393.

binuclear metalloproteins [14], their interesting catalytic properties [15] and their ability to stabilize unusual oxidation states and mixed-valance compounds. In particular, phenol based macrocyclic binucleating ligands containing two different compartments have particularly received great attention due to their capability to bind two metal centers in close proximity [16–21]. The influence of the donor atoms and their relative position, the number and size of the chelate ring formed, shape of the coordination moiety play important role in the biological and catalytic activity of the complexes formed [22–29]. Hence, synthesis of model compounds that mimic the physical and chemical properties of the active sites present in metalloenzymes is very essential and the studies on such compounds is becoming increasingly important in understanding biological functions of the bimetallic cores [30]. Various types of compartmental ligands and their complexes have been prepared, and their structures and reactivities were investigated by Bosnich [31–33] and Busch [34]. Such ligands contain two compartments: one includes six coordination atoms (N_4O_2) and the other with tetradentate N_2O_2 donor set.

Our research focuses on the synthesis of cyclam based dissimilar dicompartmental binuclear nickel(II) complexes containing hexa (amine compartment) and tetra (imine compartment) coordination sites. The amine compartment consists of two secondary nitrogens, two tertiary nitrogens and two phenolic oxygens (N_4O_2), whilst the imine compartment comprises of two imine nitrogens and two phenolic oxygens (N_2O_2). In these systems, one metal is in six-coordinate site and the other is in four-coordinate site, if a ligand like ClO_4^- is coordinated, this site can be made five-coordinate [34]. Spectral, electrochemical, catalytic and hydrolysis of 4-nitrophenyl phosphate of the complexes were discussed. Antifungal and antibacterial activities of the complexes were also discussed.

2. Experimental

2.1. Analytical and physical measurements

Elemental analysis of the complexes was obtained using Haereus CHN rapid analyzer. ^{1}H NMR spectra were recorded using JEOL GSX 400 MHz NMR spectrometer. Electronic spectral studies were carried out on a Hitachi 320 spectrophotometer in the range 200–1100 nm. IR spectra were recorded on a Shimadzu FTIR 8300 series spectrophotometer on KBr disks in the range 4000–400 cm^{-1}. Molar conductivity was measured by using an Elico digital conductivity bridge model CM-88 using freshly prepared solution of the complex in dimethylformamide. The atomic absorption spectral data were recorded using Varian spectra AA-200 model atomic absorption spectrophotometer. Mass spectra were obtained on a JEOL SX-102 (FAB) mass spectrometer. Cyclic voltammograms were obtained on CHI-600A electrochemical analyzer. The measurements were carried out under oxygen free condition using a three-electrode cell in which a glassy carbon electrode was the working electrode, a saturated Ag/AgCl electrode was the reference electrode and platinum wire was used as the auxiliary electrode. A ferrocene/ferrocenium (1+) couple was used as an internal standard and $E_{1/2}$ of the ferrocene/ferrocenium (Fc/Fc^+) couple under the experimental condition is 470 mV. Tetra(*n*-butyl)ammonium perchlorate (TBAP) was used as the supporting electrolyte. Room temperature magnetic moment was measured on a PAR vibrating sample magnetometer Model-155. The hydrolysis of 4-nitrophenylphosphate by the nickel(II) complexes were studied in a 10^{-3} M dimethylformamide solution. The reaction was followed spectrophotometrically and the hydrolysis of *p*-nitrophenylphosphate was monitored by following the UV absorbance change at 420 nm (assigned to the 4-nitrophenolate anion) as a function of time. A plot of $\log(A\alpha/A\alpha - A_t)$ versus time was made for each complex and the rate constant for the hydrolysis of 4-nitrophenylphosphate was calculated.

2.1.1. Chemicals and reagents

5-Methyl salicylaldehyde [35], 3-chloromethyl-5-methyl salicylaldehyde [36], 1,4,8,11-tetraazatricyclo[9.3.1.1[4,8]]-hexadecane [37] and 1,8-[bis(3-formyl-2-hydroxy-5-methyl)-benzyl]-4,11-diazaniatricyclo[9.3.1.1[4,8]]hexadecane dichloride [38] were prepared by following the literature methods. Analytical grade methanol, acetonitrile and dimethylformamide were purchased from Qualigens and used as such. TBAP used as supporting electrolyte in electrochemical measurement was purchased from Fluka and recrystallised from hot methanol. (*Caution!* TBAP is potentially explosive; hence care should be taken in handling the compound). All other chemicals and solvents were of analytical grade and were used as received without any further purification.

2.2. Synthesis of ligand (L)

2.2.1. Synthesis of 1,8-[bis(3-formyl-2-hydroxy-5-methyl)-benzyl]-l,4,8,11-tetraazacyclotetradecane (L)

The compound 1,8-[bis(3-formyl-2-hydroxy-5-methyl)-benzyl]-4,11-diazaniatricyclo[9.3.1.1[4,8]]hexadecane dichloride (1 g, 0.0017 mol) was dissolved in 200 ml of an aqueous NaOH solution (0.3 M) with stirring. After stirring for 4 h, the solution was extracted with $CHCl_3$ (5 × 30 ml). The combined $CHCl_3$ extracts were dried with anhydrous $MgSO_4$, and concentrated under vacuum to give the expected compound 1,8-[bis(3-formyl-2-hydroxy-5-methyl)benzyl]-l,4,8,-11-tetraazacyclotetradecane. Yield: 72%. m.p.: 282 °C (dec). *Anal.* Calc. for $C_{28}H_{40}N_4O_4$: C, 67.72; H, 8.12; N, 11.28. Found: C, 67.64; H, 8.02; N, 11.17%. IR data (KBr disc): 3389 cm^{-1}, 3285 cm^{-1}, 1680 cm^{-1}; ^{1}H NMR: δ (ppm in $CDCl_3$), 1.5 (q, 4H, β-CH_2), 2.32 (t, 16H, α-CH_2), 4.1 (s, 4H, N–CH_2–Ar), 7.26 (d, 4H, Ar–H), 9.92 (s, 2H, Ar–CHO), 12.5 4 (br, s, Ar–OH). ^{13}C NMR: δ (ppm in $CDCl_3$), 28.3, 49.4, 54.8, 55.2, 55.7, 60.5, 122.4, 126.2, 126.8, 131.0, 136.8, 157.6, 196.0.

2.3. Synthesis of the macrobicyclic binuclear nickel(II) complexes

2.3.1. $[Ni_2L[1a](ClO_4)](ClO_4)$

A methanolic solution of nickel(II) perchlorate hexahydrate (0.74 g, 0.002 mol) was added to a hot solution of ligand L (1.00 g, 0.002 mol) in methanol, followed by the addition of 1,2-diaminoethane (0.12 g, 0.002 mol) and triethylamine (0.41 g, 0.004 mol) in methanol. After an hour, another 1 equiv. of nickel(II) perchlorate (0.74 g, 0.002 mol) was added and the solution was refluxed in a water bath for 24 h. The resulting solution was filtered whilst hot and allowed to stand at room temperature. After slow evaporation of the solvent at 25 °C, dark green compound was collected by filtration, which was recrystallised in acetonitrile, and dried in vacuum.

Yield: 0.96 g (58%). *Anal*. Calc. for $C_{30}H_{42}N_6O_{10}Cl_2Ni_2$: C, 43.15; H, 5.07; N, 10.07; Ni, 14.06. Found: C, 43.09; H, 4.97; N, 10.01; Ni, 14.00%. FAB mass (*m*/*z* (%)): $[Ni_2L[1a](ClO_4)–ClO_4]^+$ 736. Conductance (Λ_m, S cm^2 mol^{-1}) in DMF: 73. Selected IR data (KBr) (ν, cm^{-1}): 3385, 1630, 1100, 1104, 1093, 626.

The complexes $[Ni_2L[1b](ClO_4)](ClO_4)$, $[Ni_2L[1c](ClO_4)](ClO_4)$, $[Ni_2L[1d](ClO_4)](ClO_4)$, and $[Ni_2L[1e](ClO_4)](ClO_4)$ were synthesized by following the above procedure using 1,3-diaminopropane (0.15 g, 0.002 mol), 1,4-diaminobutane (0.18 g, 0.002 mol), 1,2-diaminobenzene (0.22 g, 0.002 mol) and 1,8-diaminonaphthalene (0.32 g, 0.002 mol) respectively, instead of using 1,2-diaminoethane.

2.3.2. $[Ni_2L[1b](ClO_4)](ClO_4)$

Dark green compound. Yield: 1.07 g (63%). *Anal*. Calc. for $C_{31}H_{44}N_6O_{10}Cl_2Ni_2$: C, 43.86; H, 5.22; N, 9.89; Ni, 13.83. Found: C, 43.80; H, 5.19; N, 9.81; Ni, 13.78%. FAB mass (*m*/*z* (%)): $[Ni_2L[1b]–2ClO_4]^+$ 650. Conductance (Λ_m, S cm^2 mol^{-1}) in DMF: 78. Selected IR data (KBr) (ν, cm^{-1}): 3389, 1634, 1105, 1095, 1089, 626.

2.3.3. $[Ni_2L[1c](ClO_4)](ClO_4)$

Dark green compound. Yield: 0.89 g (52%). *Anal*. Calc. for $C_{32}H_{46}N_6O_{10}Cl_2Ni_2$: C, 44.51; H, 5.37; N, 9.74; Ni, 13.61. Found: C, 44.47; H, 5.33; N, 9.69; Ni, 13.58%. FAB mass (*m*/*z* (%)): $[Ni_2L[1c]–2ClO_4]^+$ 664. Conductance (Λ_m, S cm^2 mol^{-1}) in DMF: 85. Selected IR data (KBr) (ν, cm^{-1}): 3385, 1637, 1103, 1093, 1087, 624.

2.3.4. $[Ni_2L[1d](ClO_4)](ClO_4)$

Dark green compound. Yield: 1.0 g (57%). *Anal*. Calc. for $C_{34}H_{42}N_6O_{10}Cl_2Ni_2$: C, 46.25; H, 4.97; N, 9.52; Ni, 13.29. Found: C, 46.21; H, 4.93; N, 9.48; Ni, 13.26%. FAB mass (*m*/*z* (%)): $[Ni_2L[1d]ClO_4–ClO_4]^+$ 783. Conductance (Λ_m, S cm^2 mol^{-1}) in DMF: 91. Selected IR data (KBr) (ν, cm^{-1}): 3392, 1643, 1107, 1090, 1083, 626.

2.3.5. $[Ni_2L[1e](ClO_4)](ClO_4)$

Dark green compound. Yield: 1.1 g (59%). *Anal*. Calc. for $C_{38}H_{44}N_6O_{10}Cl_2Ni_2$: C, 48.91; H, 4.75; N, 9.01; Ni, 12.58. Found: C, 48.89; H, 4.73; N, 8.97; Ni, 12.54%. FAB mass (*m*/*z* (%)): $[Ni_2L[1e]ClO_4–ClO_4]^+$ 843. Conductance (Λ_m, S cm^2 mol^{-1}) in DMF: 97. Selected IR data (KBr) (ν, cm^{-1}): 3395, 1650, 1102, 1094, 1085, 626.

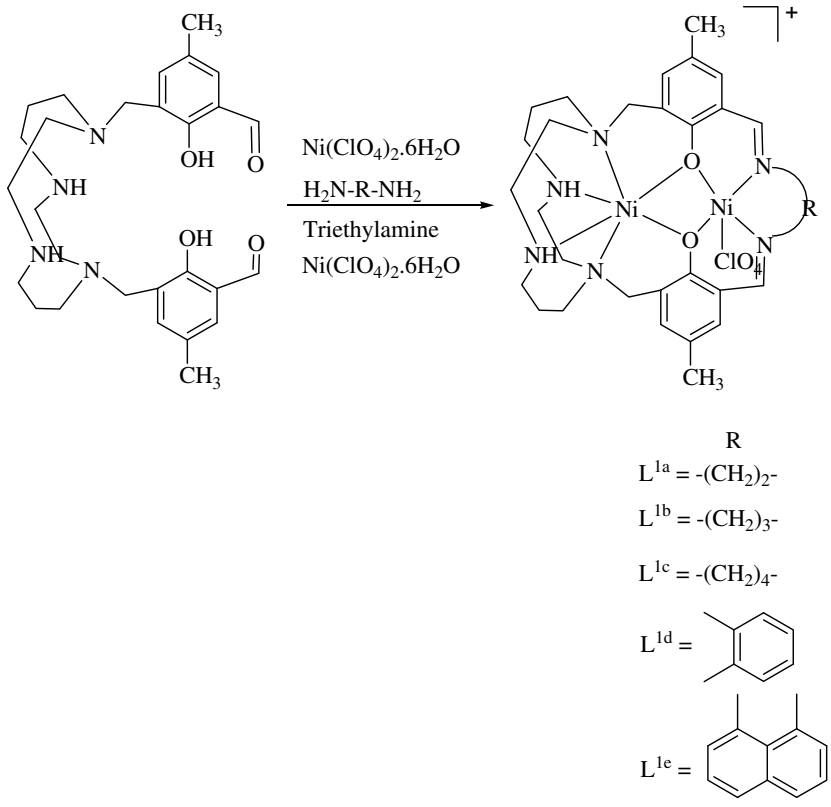
3. Results and discussion

A series of macrobicyclic binuclear nickel(II) complexes were synthesized by Schiff's base condensation of the precursor compounds with diamines in presence of metal ion. The synthetic pathway of binuclear complexes is shown in Scheme 1. In all the prepared nickel(II) complexes, one of the nickel(II) ion in the amine compartment is six coordinated, and the other in the imine compartment is five coordinated. Conductivity measurements of (Λ_m, 73–97 S cm^2 mol^{-1}) all the complexes show that they are 1:1 conductors in DMF solution [39]. The effective magnetic moments per mole of nickel for the nickel(II) complexes fall in the range of 2.94–3.05 μ_B at room temperature. This may be caused by a strong nickel–nickel interaction. The magnetic moment value for the nickel(II) complex fall in the range usually observed for octahedral nickel(II) complexes. All attempts to grow single crystals of the complexes (e.g. by the diffusion of diethyl ether vapor into DMF solutions or recrystallization of the complexes from acetonitrile) have failed and only green powder or micro crystals were obtained. Spectral, electrochemical, catalytic and antimicrobial studies of the complexes were carried out.

3.1. Spectral studies

The IR spectra of all the binuclear nickel(II) complexes show bands in the region 3245–3320 cm^{-1}, indicating the presence of NH groups in the complexes. The IR spectra of ligand L shows a band at 1680 cm^{-1} due to the presence of C=O (–CHO) group. All the complexes show a sharp band in the region of 1630–1650 cm^{-1} due to the presence of C=N in the complexes. This shows that the aldehyde groups had been completely converted into imine groups, by the disappearance of the aldehyde C=O stretching band at around 1680 cm^{-1} and the appearance of a strong band at around 1630–1650 cm^{-1} assigned to C=N stretching vibration mode (Schiff base condensation) [40,41,33]. All the binuclear nickel(II) complexes showed two sharp peaks at near 1100 cm^{-1} and 620 cm^{-1}, which are assigned to perchlorate ions [42]. The peak around 1100 cm^{-1} is split, which clearly explains the presence of a coordinated perchlorate ion [43], while the other peak does not show any splitting, indicating the presence of an uncoordinated perchlorate ion. The IR spectral data of the complexes, clearly shows that the presence of two different types of perchlorate ions. Further, the appearance of new bands in the 1530–1560 cm^{-1} region in all the complexes suggests phenoxide bridging with the metal ions [44].

Electronic spectra of all the complexes were obtained in DMF medium. The electronic spectra of all the complexes



Scheme 1.

exhibit three main features. One or two peaks in the range of 250–300 nm is assigned to the intra ligand charge transfer transition (π–π^*). An intense peak in the range of 380–420 nm is due to ligand-to-metal charge transfer transition, and the d–d transition for the nickel(II) complexes show three main bands in the range of 550–1040 nm, which is characteristic of Ni^{2+} in the 5/6 coordination environment [45]. Although the appearance of the spectra bear similarities with those for octahedrally coordinated Ni(II) ions, the assignment of the three most intense bands to the spin allowed transitions from the $^3A_{2g}$ ground state of an octahedrally coordinated d^8 ion to the next higher excited triplet states ($^3T_{1g}(P)$, $^3T_{1g}(F)$ and $^3T_{2g}(F)$) would be a misinterpretation. Furthermore, the molar extinction coefficients of the absorption band maxima of are unusually high. The spectra in fact indicate a square pyramidal or trigonal bipyramidal coordination environment of at least one of the Nickel(II) ions [45]. The electronic spectral studies inferred that an increase in λ_{max} (red shift) of the d–d transition of nickel(II) ion in the ligand L[1a] to L[1c] and L[1d] to L[1e]. This is due to the flexibility of the macrocyclic ring that is imparted by the distortion of the geometry of the complexes due to the increase in macrocyclic ring size, which causes more distortion of the geometry [46,47]. The electronic spectral data of the binuclear nickel(II) complexes are given in Table 1.

3.2. Electrochemical properties of the complexes

The electrochemical properties of all the binuclear nickel(II) complexes were studied by Cyclic voltammetry in dimethylformamide containing 10^{-1} M tetra(*n*-butyl)-ammonium perchlorate. The electrochemical data are summarized in Table 2. Cyclic voltammograms for the nickel(II) complexes are shown in Fig. 1.

Table 1
Electronic spectral data of binuclear nickel(II) complexes

No.	Complexes	λ_{max}, nm (ε, $M^{-1}\,cm^{-1}$)	
		d–d	Charge transfer
1	$[Ni_2L[1a](ClO_4)](ClO_4)$	987 (48), 705 (85), 552 (367)	357 (10800), 269 (14400)
2	$[Ni_2L[1b](ClO_4)](ClO_4)$	997 (78), 717 (96), 564 (347)	363 (11400), 271 (14840)
3	$[Ni_2L[1c](ClO_4)](ClO_4)$	1017 (53), 723 (94), 581 (318)	370 (12100), 273 (15000)
4	$[Ni_2L[1d](ClO_4)](ClO_4)$	1030 (67), 742 (98), 605 (180)	375 (12800), 277 (17000)
5	$[Ni_2L[1e](ClO_4)](ClO_4)$	1037 (43), 754 (69), 613 (247)	383 (13600), 277 (17800)

Table 2
Electrochemical[a] and hydrolysis of 4-nitrophenylphosphate[b] data for the complexes

No.	Complexes	Reduction (at cathodic)		Oxidation (at anodic)		Rate constant (k) ($\times 10^{-3}$) min^{-1}
		E^1_{pc} (V)	E^2_{pc} (V)	E^1_{pc} (V)	E^1_{pc} (V)	
1	$[Ni_2L[1a](ClO_4)](ClO_4)$	−1.00	−1.43	0.72	1.23	10.36
2	$[Ni_2L[1b](ClO_4)](ClO_4)$	−0.91	−1.31	0.80	1.32	13.13
3	$[Ni_2L[1c](ClO_4)](ClO_4)$	−0.79	−1.28	0.98	1.39	16.81
4	$[Ni_2L[1d](ClO_4)](ClO_4)$	−1.27	−1.37	1.10	1.43	9.20
5	$[Ni_2L[1e](ClO_4)](ClO_4)$	−1.21	−1.31	1.18	1.52	9.87

Concentration of the complexes: 1×10^{-3} M. Concentration of 4-nitrophenylphosphate: 1×10^{-1} M. The rate constant values the are average of three experiments.

[a] Measured by CV at 50 mV/s. E vs. Ag/AgCl conditions: GC working and Ag/AgCl reference electrodes; supporting electrolyte TBAP; concentration of complex 1×10^{-3} M, concentration of TBAP 1×10^{-1} M.

[b] Measured spectrophotometrically in DMF. Concentration of the complexes: 1×10^{-3} M. Concentration of 4-nitrophenylphosphate: 1×10^{-1} M. The rate constant values are average of three experiments.

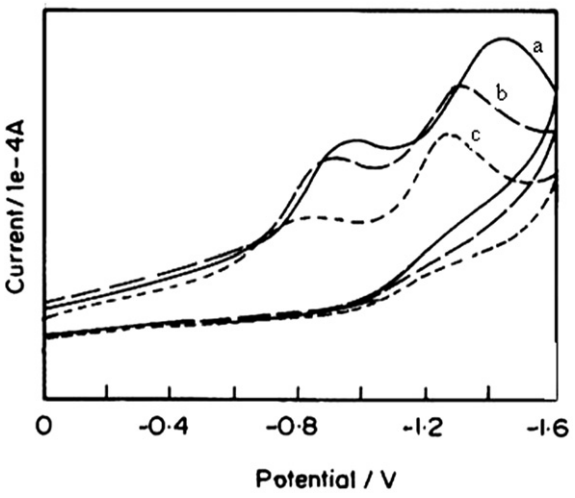


Fig. 1. Cyclic voltammogram of the binuclear nickel(II) complexes: (a) $[Ni_2L[1a](ClO_4)](ClO_4)$, (b) $[Ni_2L[1b](ClO_4)](ClO_4)$ and (c) $[Ni_2L[1c]-(ClO_4)](ClO_4)$ (reduction process).

3.3. Reduction process at negative potential

The cyclic voltammograms of the nickel(II) complexes were recorded in the potential range 0 to −1.6 V in DMF. Cyclic voltammogram for nickel(II) complexes are shown in Fig. 1. The electrochemical data are summarized in Table 2. The macrocyclic doubly phenoxo-bridged dinickel complexes typically undergo two well-separated one electron reductions [48,49a]. It is observed that all the binuclear complexes show two irreversible reduction waves in the cathodic potential region. The first reduction potential ranges from −0.79 to −1.27 V and the second reduction potential lies in the range of −1.19 to −1.43 V. Controlled potential electrolysis was also carried out and the experiment reports that each couple corresponds to one-electron transfer process. The two reduction processes are assigned as follows:

$$Ni^{II}Ni^{II} \rightarrow Ni^{II}Ni^{I} \rightarrow Ni^{I}Ni^{I}$$

The first reduction potential of the Ni^{2+}/Ni^{+} couple of $[NiL[1a–c](ClO_4)]ClO_4$ complexes in the range of −0.79 to −1.27 (Table 2) is similar to that observed for $[Ni(salen)]^{2+}$ complexes, and may suggest that the reduction wave observed for these bimetallic complexes refer to reduction of the nickel(II) in the four-coordinate site. Similarly, the second reduction wave observed for $[NiL[1a–c](ClO_4)]ClO_4$ in the range −1.28 to −1.43 V, is attributed reduction of nickel(II) ion in the amine compartment (N_4O_2). Hence the second reduction potential suggests that the reduction wave observed for these bimetallic complexes refers to the reduction of the nickel(II) in the six-coordinate site [49b,49c].

It seems, interesting to compare the reduction potential of the nickel(II) complexes. It is apparent to say that in the binuclear nickel(II) complexes, both first and second reduction potentials shift towards anodically, from −0.79 to −1.27 V and from −1.28 to −1.43 V, respectively, as the number of methylene groups is increased [50–53]. For example, the complex $[Ni_2L[1c](ClO_4)](ClO_4)$ (E^1_{pc} −0.79 V and E^2_{pc} −1.28 V), which are less negative in comparison to those of the complex $[Ni_2L[1b](ClO_4)]-(ClO_4)$ (E^1_{pc} −0.91 V and E^2_{pc} −1.31 V), which, in turn, are less negative in comparison to those of the complex $[Ni_2L[1a](ClO_4)](ClO_4)$ has the values of (E^1_{pc} −1.00 V and E^2_{pc} −1.43 V). This shows that as the number of methylene groups between the imine nitrogen (chain length) increases, the entire macrocyclic ring becomes more flexible, which causes easy reduction. Thus, the large size of the cavity easily holds the reduced cation and stabilizes the formation of Ni(I) in both compartments. The observed reduction potential for $[Ni_2L[1d](ClO_4)](ClO_4)$ (E^1_{pc} −1.06 V and E^2_{pc} −1.28 V) and $[Ni_2L[1e](ClO_4)](ClO_4)$ (E^1_{pc} −1.31 V and E^2_{pc} −1.47 V), shows that the reduction of complexes of the ligands L[1d] and L[1e] is rather difficult when compared to the reduction of the complexes of the ligands L[1a–1c] due to the planarity induced by the aromatic ring, which makes the system more rigid.

3.4. Oxidation process at anodic potential

All the nickel complexes show two oxidation processes in the range 0.72–1.52 V. The cyclic voltammogram of the complexes is shown in Fig. 2 and the data are

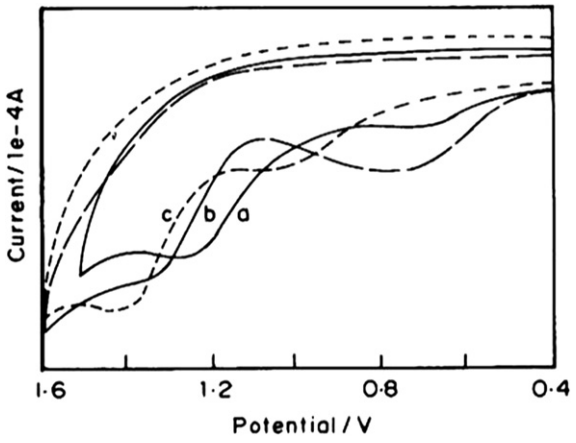


Fig. 2. Cyclic voltammogram of the binuclear nickel(II) complexes: (a) $[Ni_2L[1a](ClO_4)](ClO_4)$, (b) $[Ni_2L[1b](ClO_4)](ClO_4)$ and (c) $[Ni_2L[1c](ClO_4)](ClO_4)$ (oxidation process).

summarized in Table 2. The oxidation process is irreversible in nature. Controlled potential electrolysis experiment indicates that the two oxidation peaks are associated with stepwise oxidation process at nickel(II) center

$$Ni^{II}Ni^{II} \rightarrow Ni^{II}Ni^{III} \rightarrow Ni^{III}Ni^{III}$$

The first and second oxidation potential of the complexes $[Ni_2L[1a–c](ClO_4)](ClO_4)]$ shifts towards more positive value [53] (from E^1_{pc} 0.72 to 0.98 V and E^2_{pc} 1.23 to 1.39 V) as the number of methylene groups (chain length) increases in the imine compartment. This is because as the ring size increases due to flexibility, the planarity of the complex decreases and the electrochemical oxidation process occurs with difficult. For example the first oxidation potential of the complex $[NiL[1c](ClO_4)]ClO_4$ is 0.91 V (E^1_{pc}) and the second oxidation potential is 1.39 V (E^2_{pc}) which are more positive when compared $[NiL[1b](ClO_4)]ClO_4$ (E^1_{pc} 0.80 V and E^2_{pc} 1.32 V) which is more positive than $[NiL[1a](ClO_4)]ClO_4$ (E^1_{pc} 0.72 V and E^2_{pc} 1.23 V). Similar trend has been observed for complexes $[NiL[1d–e](ClO_4)]ClO_4$. This is because for complexes with aromatic diimines, an increase in unsaturation will decrease the electron on the metal through delocalization, on to the ligand and this increases the difficulty to oxidize the metal ion.

3.5. Kinetic studies of hydrolysis of 4-nitrophenylphosphate

The catalytic activity of the nickel(II) complexes on the hydrolysis of 4-nitrophenylphosphate was determined spectrophotometrically by monitoring the increase in the characteristic absorbance of the 4-nitrophenolate anion at 420 nm over the time in dimethylformamide at 25 °C. For this purpose, 10^{-3} mol dm^{-3} solutions of complexes in dimethylformamide were treated with 100 equivalents of 4-nitrophenyl phosphate in the presence of air.

The course of the reaction was followed at 420 nm for nearly 45 min at regular time intervals. The slope was determined by the method of initial rates by monitoring the growth of the 420 nm band of the product 4-nitrophenolate anion. A linear relationship for all the complexes shows a first-order dependence on the complex concentration for the systems. Plots of $\log(A_\infty/A_\alpha - A_t)$ versus time for hydrolysis of 4-nitrophenylphosphate activity of the complexes are obtained and shown in Fig. 2. The inset in Fig. 3 shows the time dependent growth of *p*-nitrophenolate chromophore in the presence of $[Ni_2L[1a](ClO_4)](ClO_4)$. The observed initial rate constant values for all the nickel(II) complexes are given in Table 2.

The catalytic activities of the binuclear complexes are found to increase as the macrocyclic ring size increases due to the intrinsic flexibility, i.e. increase in the chelate ring size enhances the rate constant of hydrolysis fairly well by producing distortion in the geometry around the metal ion that enhances the accessibility of the metal ion for the bonding of phosphate and OH groups. The catalytic activity of the complexes containing aromatic diimines $[Ni_2L[1d](ClO_4)](ClO_4)$ and $[Ni_2L[1e](ClO_4)](ClO_4)$ is found to be less than that of the complexes containing aliphatic diimines. This may be due to the planarity, which is associated with aromatic ring, imparts less catalytic efficiency due to the rigidity of the systems as observed in the case of previous literature reports [54–56].

3.6. Antifungal and antimicrobial activities

Antifungal and antimicrobial activities of the complexes were tested by the cup plate method using nutrient agar. The radial growth of the colony was recorded on completion of the incubation and the mean diameter for each complex at a concentration of 100 μg/ml was recorded. The average percentage inhibition of the bactericidal growth medium was compared using the Vincent (Vincent, 1947) equation: $I = 100(C - T)/C$, where I = percentage inhibition, T = average diameter of the bacterial growth on the tested plates and C = average diameter of the growth on the control plates.

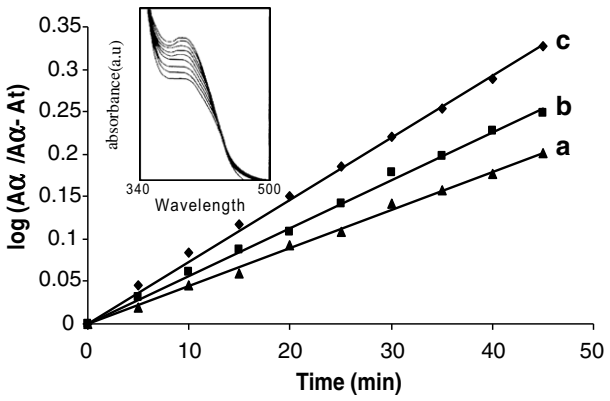


Fig. 3. Hydrolysis of 4-nitrophenylphosphate by binuclear nickel(II) complexes: (a) $[Ni_2L[1a](ClO_4)](ClO_4)$, (b) $[Ni_2L[1b](ClO_4)](ClO_4)$ and (c) $[Ni_2L[1c](ClO_4)](ClO_4)$ The inset is the time dependent growth of *p*-nitrophenolate chromophore in the presence of $[Ni_2L[1a](ClO_4)](ClO_4)$.

Table 3
Antibacterial and antifungal screening data of complexes

No.	Complexes	Representation zone of inhibition (100 μg/ml)					
		Antibacterial					Antifungal
		Staphylococcus aureus	*Bacillus cearus*	*Klebsiella pneumonia*	*pseudomonas aureginosa*	*Escherichia coli*	*Candida albicans*
1	$[Ni_2L[1a](ClO_4)](ClO_4)$	16	15	14	15		14
2	$[Ni_2L[1b](ClO_4)](ClO_4)$	14	14	15	14		14
3	$[Ni_2L[1c](ClO_4)](ClO_4)$	16	20	15	16		16
4	$[Ni_2L[1d](ClO_4)](ClO_4)$	18	24	25	20		18
5	$[Ni_2L[1e](ClO_4)](ClO_4)$	19	26	25	19		21

3.6.1. Antifungal activity

Studies on the antifungal activity of tetraazamacrocyclic ligands and their complexes are limited in the literature [57–60]. We have evaluated the antifungal activity of all the nickel(II) complexes against the phytopathogenic fungus *Candida albicans*. The screening data were reported in Table 3. It is observed from the results that all tested complexes show some antifungal activity. The activity reported by the present complexes was comparable with the *N*-substituted tetraazamacrocycles [58,61]. Generally nickel(II) complexes of *N*-substituted tetraazamacrocycles shows higher activity than their corresponding cobalt(III) complexes [62]. Another interesting result observed here is that the complexes of L[1d] and L[1e] shows higher activity than the complexes of the ligand L[1a] to L[1c], which contain aliphatic diimines. It seems from the results that the nature of the ligand and the coordinated metal ion plays a significant role in the inhibition activity.

3.6.2. Antibacterial activity

All the prepared binuclear nickel(II) complexes have been subjected to antibacterial activity against selected five bacteria's such as *Pseudomonas aeroginosa* (ATCC 2036), *Staphylococcus aureus* (ATCC 2079), *Escherichia coli* (ATCC 2567), *Bacillus cereus* (ATCC 11778), and *Klebsiella pneumonia* (ATCC 29665), respectively. The screening results are shown in Table 3. From the results it is observed that all the complexes shows higher activities against *S. aureus*, *P. aeroginosa*, *K. pneumonia* and *B. cearus*, but all the complexes were in-active against *E. coli*. The higher activity of the complexes may be ascribed to Tweedy's theory, according to which chelation reduces the polarity of the central metal atom because of partial sharing of its positive charge with the ligand, which favors the permeation of the complexes through the lipid layer of the membrane [63]. However, further more studies are needed to understand the functions, which are responsible for antifungal and antibacterial activities of the tested complexes.

4. Conclusion

In conclusion, it has been observed that the small variation in the chain length of the imine compartment, (i) cause red shift in the electronic spectra. (ii) Shift the reduction potential anodically on increasing chain length. (iii) Shift the oxidation potential to more positive potential as the chain length increases. (iv) Shows higher catalytic activity on increasing chain length. All these studies of the complexes which agree well with the established trend.

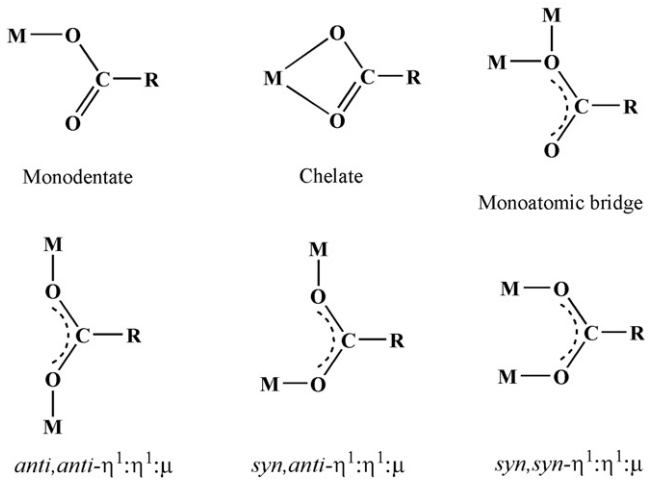
Acknowledgements

Financial support from University Grants Commission (RGNF), New Delhi, is gratefully acknowledged. We are thankful to CDRI-Lucknow for providing FAB mass spectral analysis.

References

[1] A. Binachi, L. Calabi, F. Corana, S. Fontana, P. Losi, A. Maiocchi, L. Paleari, B. Valtancoli, Coord. Chem. Rev. 204 (2000) 309.
[2] O. Reany, T. Gunnlaugsson, D. Parker, Chem. Commun. (2000) 473.
[3] T.A. Kaden, Top. Curr. Chem. 121 (1984) 157.
[4] R.W. Hay, in: E. Kimura (Ed.), Current Topics in Macrocyclic Chemistry in Japan, Hiroshima University, 1987, p. 56.
[5] N.W. Alcock, K.P. Balakrishnan, P. Moore, G.A. Pike, J. Chem. Soc., Dalton Trans. (1987) 889.
[6] K.A. Arnold, L. Echegoyen, F.R. Fronczek, R.D. Gandour, V.J. Gatto, D. White, G.W. Gokel, J. Am. Chem. Soc. 109 (1987) 3716.
[7] D.E. Fenton, G. Rossi, Inorg. Chim. Acta 98 (1985) L29.
[8] V.J. Gatto, G.W. Gokel, J. Am. Chem. Soc. 106 (1984) 8240.
[9] H. Adams, N.A. Bailey, W.D. Carlisle, D.E. Fenton, G. Rossi, J. Chem. Soc., Dalton Trans. (1990) 1271.
[10] T. Koga, H. Furutachi, T. Nakamura, N. Fukita, M. Ohba, K. Takahashi, H. Okawa, Inorg. Chem. 37 (1998) 989.
[11] S. Uozumi, H. Furutachi, M. Ohba, H. Okawa, D.E. Fenton, K. Shindo, S. Murata, D.J. Kitko, Inorg. Chem. 37 (1998) 6281.
[12] D.E. Fenton, Inorg. Chem. Commun. 5 (2002) 537.
[13] P.A. Vigato, S. Tamburini, Coord. Chem. Rev. 248 (2004) 1717.
[14] S.A. Duclos, H. Stoeckli-Evans, T.R. Ward, Helv. Chim. Acta 84 (2001) 3148.
[15] H. Golchoubian, A. Nemati Kharat, Polish J. Chem. 79 (2005) 825.
[16] A. Niazi Rahnama, H. Golchoubian, R. Pritchard, Bull. Chem. Soc. Jpn. 78 (2005) 1047.
[17] H. Golchoubian, W.L. Waltz, J.W. Quail, Can. J. Chem. 37 (1999) 77.
[18] A. Ghaffarinia, H. Golchoubian, R. Hosseinzadeh, J. Chin. Chem. Soc. 52 (2005) 531.
[19] H. Okawa, H. Furutachi, D.E. Fenton, Coord. Chem. Rev. 51 (1998) 174.
[20] D.E. Fenton, in: A.G. Sykes (Ed.), Advances in Inorganic and Bioinorganic Mechanisms, vol. 2, Academic Press, London, 1983, p. 187.

[21] (a) D.E. Fenton, U. Casellato, P.A. Vigato, M. Vidali, Inorg. Chim. Acta 95 (1984) 187;
(b) D.E. Fenton, U. Casellato, P.A. Vigato, M. Vidali, Inorg. Chim. Acta 62 (1982) 57.
[22] P. Guerriero, P.A. Vigato, D.E. Fenton, P.C. Hellier, Acta Chem. Scand. 46 (1992) 1025.
[23] U. Casellato, P.A. Vigato, D.E. Fenton, M. Vidali, Chem. Soc. Rev. 8 (1979) 199.
[24] P. Zanello, S. Tamburini, P.A. Vigato, S.A. Mazzocchin, Coord. Chem. Rev. 77 (1987) 165.
[25] (a) P.A. Vigato, S. Tamburini, D.E. Fenton, Coord. Chem. Rev. 106 (1990) 25;
(b) D.E. Fenton, P.A. Vigato, Chem. Sot. Rev. 17 (1988) 69.
[26] (a) T.M. Sorrell, Tetrahedron 45 (1989) 3;
(b) J.-M. Lehn, Pure Appl. Chem. 50 (1978) 871.
[27] J.-M. Lehn, Angew. Chem., Int. Ed. Engl. 27 (1988) 89.
[28] J.-M. Lehn, Angew. Chem., Int. Ed. Engl. 30 (1990) 1304.
[29] J.-M. Lehn, Science 227 (1985) 849.
[30] D.E. Fenton, H. Okawa, Perspectives on Bioinorganic Chemistry, JAI Press, London, 1993, p. 8.
[31] D.G. McCollum, C. Fraser, R. Ostrander, A.L. Rheingold, B. Bosnich, Inorg. Chem. 33 (1994) 2383.
[32] D.G. McCollum, L. Hall, C. White, R. Ostrander, A.L. Rheingold, J. Whelan, B. Bosnich, Inorg. Chem. 33 (1994) 924.
[33] C. Fraser, R. Ostrander, A.L. Rheingold, C. White, B. Bosnich, Inorg. Chem. 33 (1994) 324.
[34] (a) E.V. Rybak-Akimova, N.W. Alcock, D.H. Busch, Inorg. Chem. 37 (1998) 1563;
(b) C. Fraser, L. Johnston, A.L. Rheingold, B.S. Haggerty, C.K. Williams, J. Whelan, B. Bosnich, Inorg. Chem. 31 (1992) 1835;
(c) C. Fraser, R. Ostrander, A.L. Rheingold, C. White, B. Bosnich, Inorg. Chem. 33 (1994) 324;
(d) C. Fraser, B. Bosnich, Inorg. Chem. 33 (1994) 338;
(e) D.G. McCollum, G.P.A. Yap, L. Liable-Sands, A.L. Rheingold, B. Bosnich, Inorg. Chem. 36 (1997) 2230.
[35] J.C. Duff, J. Chem. Soc. (1941) 547.
[36] J.D. Gane, D.E. Fenton, J.M. Latour, A.J. Smith, J. Chem. Soc., Dalton Trans. (1991) 2279.
[37] G. Royal, V.D. Gindrey, S. Dahaowi, A. Tabard, R. Guilard, P. Pullumbi, C. Lecomte, Eur. J. Org. Chem. (1998) 1971.
[38] D. Gayathri, D. Velmurugan, K. Ravikumar, S. Sreedaran, V. Narayanan, Acta. Cystallogr., Sect. E 62 (2006) o3714.
[39] J. Geary, Coord. Chem. Rev. 7 (1971) 81.
[40] G. Das, R. shukala, S. Mandal, R. Singh, P.K. Bharadwaj, J.V. Singh, K.H. Whitemine, Inorg. Chem. 36 (1997) 323.
[41] R.M. Silverstein, G.C. Bassler, Spectrometric Identification of Organic Compounds, John Wiley & Sons, New York, 1991.
[42] M. Lachkar, R. Guilard, A. Attamani, A. De. Clan, J. Fisher, R. Weiss, Inorg. Chem. 37 (1997) 1575.
[43] S.S. Tandon, L.K. Thompson, J.N. Bridson, V. Mekee, A.J. Downard, Inorg. Chem. 31 (1992) 4635.
[44] B. Srinivas, N. Arulsamy, P.S. Zacharias, Polyhedron 10 (1991) 731.
[45] (a) D. Volkmer, B. Hommerich, K. Griesar, W. Haase, B. Krebs, Inorg. Chem. 35 (1996) 3792;
(b) M. Ciampolini, Inorg. Chem. 5 (1966) 35;
(c) L. Sacconi, M. Ciampolini, G.P. Speroni, J. Am. Chem. Soc. 87 (1965) 3102;
(d) M. Ciampolini, N. Nardi, Inorg. Chem. 5 (1966) 41.
[46] H. Okawa, S. Kida, Bull. Chem. Soc. Jpn. 45 (1972) 1759.
[47] H. Wada, T. Aono, K. Moodo, M. Ohba, N. Makstumoto, H. Okawa, Inorg. Chem. Acta 246 (1996) 13.
[48] A. Benzekeri, P. Dubourdeax, J.M. Latour, P. Rey, J. Laugier, J. Chem. Soc., Dalton Trans. (1991) 3359.
[49] (a) R.R. Gagne, L.M. Henling, T.J. Kistenmacher, Inorg. Chem. 19 (1980) 1226;
(b) C. Fraser, B. Bosnich, Inorg. Chem. 41 (2002) 1788;
(c) K.R. Krishnapriya, M. Kandaswamy, Polyhedron 24 (2005) 113.
[50] F. Abba, G.D. Santis, L. Fabbrizzi, M. Licchelli, A.M.M. Lanfredi, P. Pallavicini, A. Poggi, F. Ugozzoli, Inorg. Chem. 33 (1994) 1366.
[51] F.V. Lovecchino, E.S. Gore, D.H. Bush, J. Am. Chem. Soc. 96 (1974) 3104.
[52] G.K. Bareford, G.M. Freeman, D.G. Erver, Inorg. Chem. 86 (1986) 552.
[53] (a) G.A. Bowmaker, J.P. Williams, J. Chem. Soc., Dalton. Trans. (1993) 3593;
(b) G.K. Bareford, G.M. Freeman, D.G. Erver, Inorg. Chem. 86 (1986) 552;
(c) E. Gao, W. Bu, G. Yang, D. Liao, Z. Jiang, S. Yan, G. Wang, J. Chem. Soc., Dalton Trans. (2000) 1431.
[54] J. Reim, B. Kreks, J. Chem. Soc., Dalton. Trans. (1997) 3793.
[55] M. Thirumavalavan, P. Akilan, M. Kandaswamy, K. Chinnakali, G. Senthil Kumar, H.K. Fun, Inorg. Chem. 42 (2003) 3308.
[56] P. Akilan, M. Thirumavalan, M. Kandaswamy, Polyhedron 22 (2003) 3483.
[57] T.G. Roy, S.K.S. Hazari, B.K. Dey, S. Chakraborty, E.R.T. Tiekink, Met. Based Drugs 6 (1999) 345.
[58] S.K.S. Hazari, T.G. Roy, B.K. Dey, S.C. Das, E.R.T. Tiekink, Met. Based Drugs 4 (1997) 255.
[59] M.A. Ali, A.H. Mirza, A. Monsur, S. Hossain, M. Nazimuddin, Polyhedron 20 (2001) 1045.
[60] M.E. Hossain, M.N. Alam, J. Begum, M.A. Ali, M. Nazimuddin, E.E. Smith, R.C. Haynes, Inorg. Chim. Acta 249 (1996) 207.
[61] T.G. Roy, S.K.S. Hazari, B.K. Dey, H.A. Miah, C. Bader, D. Rehder, Eur. J. Inorg. Chem. (2004) 4115.
[62] T.G. Roy, S.K.S. Hazari, B.K. Dey, R. Sutradhar, L. Dey, N. Anowar, E.R.T. Tiekink, J. Coord. Chem. Rev. 59 (2006) 351.
[63] BG. Tweedy, Phytopathology 55 (1964) 910.



Scheme 1.

magnetic exchange interaction which occurs between two Cu(II) ions of a paddle-wheel moiety [10–29].

In the present paper, we report the synthesis, crystal structure, spectroscopic and magnetic properties of three copper(II) compounds, i.e. a polynuclear $\{[Cu_4(phen)_2(\mu\text{-}O_2CC_2H_5)_8]\cdot(H_2O)\}_n$ (**1**) and two dinuclear compounds, $[Cu_2(\mu\text{-}O_2CC_6H_4OH)_4(C_7H_7NO)_2]\cdot 6H_2O$ (**2**) and $[Cu_2(\mu\text{-}O_2CCH_3)_4(C_7H_7NO)_2]$ (**3**). The magnetism of the polynuclear compound can be understood on the basis of two species, *i.e.* 50% paddle-wheel (strongly coupled) and 50% dinuclear-propionato bridged (weakly coupled).

2. Experimental

2.1. Materials and measurements

The ligands 1,10-phenanthroline, propionic acid, 3-hydroxybenzoic acid and 4-acetylpyridine were purchased as commercial chemicals from Aldrich. All other reagents are commercial grade materials and were used without further purification. Elemental analyses (C, H, N) were determined on a Perkin–Elmer PE 2400 CHNS/O Analyzer.

IR spectra were recorded on a Perkin–Elmer Spectrum One FT-IR spectrophotometer as KBr disc in the 4000–450 cm^{-1} spectral range. Solid-state (diffuse reflectance) electronic spectra were measured as polycrystalline samples on a Perkin–Elmer Lambda2S spectrophotometer. X-band powder EPR spectra were obtained on a Bruker-EMX*plus* electron spin resonance spectrometer (Field calibrated with DPPH ($g = 2.0036$)). Magnetic susceptibility measurements (2–320 K for **1** and 5–350 K for **2** and **3**) were carried out using a Quantum design MPMS-5 S SQUID magnetometer (measurements carried out at 0.1 mT). Data were corrected for magnetization of the sample holder and for diamagnetic contributions, which were estimated from the Pascal constants.

2.2. Syntheses

2.2.1. $\{[Cu_4(phen)_2(\mu\text{-}O_2CC_2H_5)_8]\cdot(H_2O)\}_n$ (*1*)

A hot aqueous solution (10 ml) of $Cu(CO_3)\cdot Cu(OH)_2$ (0.22 g, 1.0 mmol) was stirred and a blue precipitate formed within a few minutes. The resulting suspension became clear and light blue in color by slow addition of the concentrate propionic acid (2 ml) and stirred for 1 h. A solution of phen (0.20 g, 1.0 mmol) in acetonitrile: ethanol (20:10 ml) was added to the mixture, followed by addition of an aqueous solution of $NaO_2CCH_2CH_3$ (0.10 g, 1.0 mmol) with continuous stirring. After a month, blue polygon-shaped crystals of compound **1** were obtained which were filtered off, washed with the mother liquid and air-dried. Yield, ca. 70%. IR (KBr, cm^{-1}) ν: 3435 s, 1632 s, 1588 s, 1567 s,1465 m, 1426 s, 1372 m, 1301 m, 1262 m, 1078 m, 848 m, 811 w, 723 m. The electronic diffuse reflectance spectrum of **1** exhibits a broad band centered at 13 510 cm^{-1}. These features are consistent with the square-pyramidal based geometry and all d_{xy}, d_{yz}, d_{xz}, $d_{z^2} \rightarrow d_{x^2-y^2}$ transitions are assigned to this broad band. *Anal.* Calc. for $C_{48}H_{56}Cu_4N_4O_{17}$: C, 47.4; H, 4.7; N, 4.6. Found: C, 47.3; H, 4.7; N, 4.6%.

2.2.2. $[Cu_2(\mu\text{-}O_2CC_6H_4OH)_4(C_7H_7NO)_2]\cdot 6H_2O$ (*2*)

A warm solution of 3-hydroxybenzoic acid (0.14 g, 1.0 mmol) in methanol (20 ml) was added to a hot aqueous solution (10 ml) of $Cu(BF_4)_2$ (0.24 g, 1.0 mmol). An aqueous solution (10 ml) of 4-Acetylpyridine (0.12 g, 1.0 mmol) was then added. The light blue solution was slowly evaporated at room temperature. After several days, green rod crystals of **2** were formed. The crystals were filtered off, washed with mother liquid and air-dried. Yield, ca. 80%. IR (KBr, cm^{-1}) ν: 3292 s, 1698 m, 1578 s, 1451 m, 1400 s, 1360 m, 1258 m, 1215 w, 1051 w, 938 w, 822 w, 802 m, 767 m. The electronic diffuse reflectance spectrum of **2** exhibits a broad band centered at 13 460 cm^{-1}. These features are consistent with the square-pyramidal based geometry and all d_{xy}, d_{yz}, d_{xz}, $d_{z^2} \rightarrow d_{x^2-y^2}$ transitions are assigned to this broad band. *Anal.* Calc. for $C_{42}H_{46}Cu_2N_2O_{20}$: C, 49.2; H, 4.5; N, 2.7. Found: C, 51.0; H, 4.2; N, 2.8%.

2.2.3. $[Cu_2(\mu\text{-}O_2CCH_3)_4(C_7H_7NO)_2]$ (*3*)

The ligand 4-acetylpyridine (0.12 g, 1.0 mmol), dissolved in acetonitrile (10 ml) and a warm solution of $Cu(CH_3COO)_2$ (0.18 g, 1.0 mmol) were mixed together. The blue solution was slowly evaporated at room temperature until dark blue crystals of **3** separated. Yield ca. 70%. IR (KBr, cm^{-1}) ν: 1697 s, 1625 s, 1433 s, 1366 m, 1261 s, 1060 w, 834 w, 684 w. The electronic diffuse reflectance spectrum of **3** exhibits a broad band centered at 14 470 cm^{-1}. These features are consistent with the square-pyramidal based geometry and all d_{xy}, d_{yz}, d_{xz}, $d_{z^2} \rightarrow d_{x^2-y^2}$ transitions are assigned to this broad band. *Anal.* Calc. for $C_{22}H_{26}Cu_2N_2O_{10}$: C, 43.6; H, 4.3; N, 4.6. Found: C, 43.4; H, 4.1; N, 4.6%.

2.3. Crystallography

The X-ray single-crystal data for the three compounds were collected at 273 K for compounds **1** and at 293 K for **2**, **3**, respectively, on a 1 K Bruker SMART CCD area-detector diffractometer using graphite monochromated Mo Kα radiation ($\lambda = 0.71073$ Å) at a detector distance of 4.5 cm and swing angle of −30°. A hemisphere of the reciprocal space was covered by combination of three sets of exposures; each set had a different ϕ angle (0°, 88°, 180°) and each exposure of 40 s covered 0.3° in ω. Data reduction and cell refinements were performed using the program SAINT [30]. An empirical absorption correction by using the SADABS [31] program was applied, which resulted in transmission coefficients ranging from 0.624 to 1.000 for compound **1**, 0.845 to 1.000 for compound **2** and 0.695 to 1.000 for compound **3**. The structures were solved by direct methods and refined by full matrix least-squares method on $(F_{obs})^2$ with anisotropic thermal parameters for all non-hydrogen atoms using the SHELXTL-PC V 6.12 software package [32]. All hydrogen atoms were located in a difference Fourier map and refined isotropically, except the H atoms of the propionate groups in **1**, which were fixed geometrically with the HFIX utility and the hydrogen atoms of one water molecule in **1** and four water molecules in **2**, which we were unable to locate and also could not be located at fixed positions. The terminal C atom in three propionate groups of **1** showed disorder; the occupancies of the

Table 1
Crystal and refinement data for complexes **1**, **2** and **3**

Complex	**1**	**2**	**3**
Molecular formula	$C_{48}H_{54}Cu_4N_4O_{17}$	$C_{42}H_{41}Cu_2N_2O_{20}$	$C_{22}H_{26}Cu_2N_2O_{10}$
Molecular weight	1213.11	1020.85	605.53
T (K)	273(2)	293(2)	293(2)
Crystal system	triclinic	monoclinic	monoclinic
Space group	$P\bar{1}$	$P2_1/n$	$P2_1/c$
a (Å)	10.2456(3)	9.1164(6)	11.7573(6)
b (Å)	12.0032(3)	22.2155(14)	12.9823(6)
c (Å)	13.0657(3)	10.9944(7)	8.6637(4)
α (°)	100.4180(10)	90.00	90.00
β (°)	106.09	93.921(2)	105.6180(10)
γ (°)	114.5540(10)	90.00	90.00
V (Å^3)	1321.29(6)	2221.4(2)	1273.57(11)
Z	1	2	2
D_c (g cm^{-3})	1.525	1.536	1.579
μ (mm^{-1})	1.660	1.041	1.726
F(000)	622	1050	620
Crystal size (mm)	0.18 × 0.38 × 0.88	0.17 × 0.08 × 0.03	0.30 × 0.27 × 0.09
Number of reflection collected	9503	2435	12607
Number of unique reflections [R_{int}]	6926 [0.0238]	4064 [0.0514]	3078 [0.0291]
Data/restraints/parameter	6926/0/416	4064/0/391	3078/0/182
Goodness-of-fit	1.012	1.089	1.046
Final R indices [$I > 2\sigma(I)$]	R_1 = 0.0497, wR_2 = 0.1285	R_1 = 0.0399, wR_2 = 0.0898	R_1 = 0.0255, wR_2 = 0.0744
R indices (all data)	R_1 = 0.0849, wR_2 = 0.1544	R_1 = 0.0526, wR_2 = 0.0952	R_1 = 0.0285, wR_2 = 0.0761
Largest difference in peak and hole (e Å^3)	0.53 and −0.65	0.36 and −0.23	0.30 and −0.24

$R = \sum ||F_o| - |F_c|| / \sum |F_o|, R_w = \left[\sum w\{|F_o| - |F_c|\}^2 / \sum w|F_o^2|^2\right]^{1/2}$.

disordered positions were initially refined and later fixed at 0.5. The molecular graphics were created by using SHELXTL-PC [32] package. The crystal and refinement details for the three compounds are listed in Table 1.

3. Results and discussion

3.1. Crystal structure of $\{[Cu_4(phen)_2(\mu\text{-}O_2CC_2H_5)_8]\cdot(H_2O)\}_n$ (**1**)

The structure of compound **1** involves a one-dimensional overall structure constructed from tetranuclear units and consists of chains of dinuclear $Cu_2(\mu\text{-}OCOC_2H_5)_2(\mu\text{-}O_2CC_2H_5)_2(phen)_2$ repeating units which are connected to each other along the unit cell diagonal by $Cu_2(\mu\text{-}O_2CC_2H_5)_4$ paddle-wheel dinuclear units. This structure is depicted in Fig. 1 together with the numbering scheme. Selected distances and angles are listed in Table 2. The two dinuclear units are linked by the *syn,anti*-triatomic propionato bridge in an axial-equatorial configuration. The polynuclear copper(II) carboxylates are known to exhibit three classes of local paddle-wheel structure. Compound **1** has a structure derived from *class B*, with a dinuclear molecule bridging two dinuclear units [9].

The paddle-wheel dinuclear $Cu_2(\mu\text{-}O_2CC_2H_5)_4$ unit in the chain contains four bridging propionates in the *syn,syn*-$\eta^1:\eta^1:\mu$ coordination mode, as known for the compound $[Cu_2(\mu\text{-}O_2CC_2H_5)_4(H_2O)_2]$ [33]. The geometry around the Cu(2) and Cu(2)A atoms can be considered as square-pyramidal with a τ value of 0.005 (in which the structural parameter τ describes the relative amount of trigonality; $\tau = 0$ for square pyramid and $\tau = 1$ for trigonal bipyramidal [34]) arising from five oxygen atoms of five different propionate groups. The corresponding Cu–O distances in the basal plane are in the range 1.952(3)–1.962(3)(2) Å. An O atom of a bridging propionate molecule occupies the axial position at a distance of 2.120(2) Å.

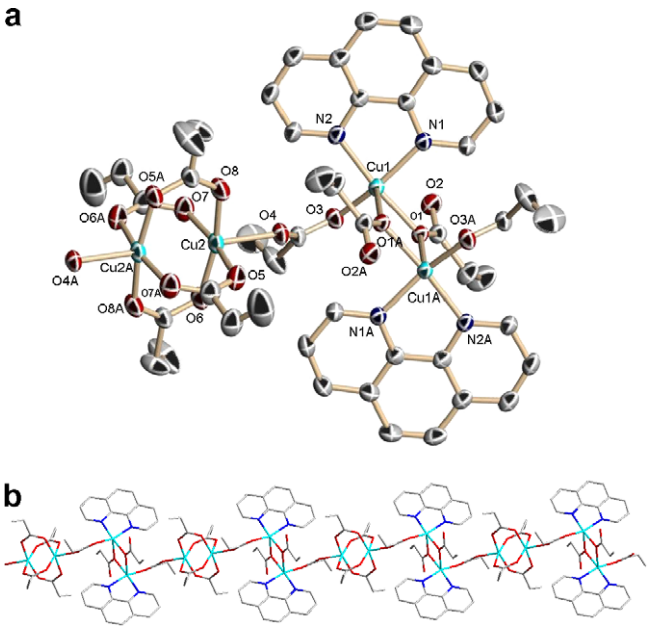


Fig. 1. (a) Thermal ellipsoid (30% probability) plot of $\{[Cu_4(phen)_2(\mu\text{-}O_2CC_2H_5)_8]\cdot(H_2O)\}_n$ (**1**). Hydrogen atoms and water molecules are omitted for clarity. (b) View of the 1-D polymeric chain.

Table 2
Selected bond lengths (Å) and angles (°) of $\{[Cu_4(phen)_2(\mu\text{-}O_2CC_2H_5)_8]\cdot(H_2O)\}_n$ (**1**)

Cu(1)–N(1)	2.031(3)	Cu(2)–O(4)	2.120(2)
Cu(1)–N(2)	2.044(3)	Cu(2)–O(5)	1.952(3)
Cu(1)–O(1)	1.960(2)	Cu(2)–O(6)	1.962(3)
Cu(1)–O(1)A	2.354(2)	Cu(2)–O(7)	1.960(3)
Cu(1)–O(3)	1.931(3)	Cu(2)–O(8)	1.962(3)
Cu(1)–Cu(1)A	3.408(1)	Cu(2)–Cu(2)A	2.623(8)
N(1)–Cu(1)–N(2)	80.4(1)	O(4)–Cu(2)–O(5)	94.5(1)
N(1)–Cu(1)–O(1)	94.5(1)	O(4)–Cu(2)–O(6)	99.5(1)
N(2)–Cu(1)–O(1)	101.8(1)	O(4)–Cu(2)–O(7)	97.2(1)
O(1)–Cu(1)–N(1)	93.5(1)	O(4)–Cu(2)–O(8)	92.5(1)
O(1)–Cu(1)–N(2)	173.4(1)	O(5)–Cu(2)–O(6)	89.1(1)
O(1)–Cu(1)–O(1)A	76.0(1)	O(5)–Cu(2)–O(8)	89.3(1)
O(1)–Cu(1)–O(3)	90.2(1)	O(6)–Cu(2)–O(7)	90.2(1)
O(3)–Cu(1)–N(1)	155.9(1)	O(7)–Cu(2)–O(5)	168.3(1)
O(3)–Cu(1)–N(2)	96.5(1)	O(7)–Cu(2)–O(8)	88.9(1)
O(3)–Cu(1)–O(1)A	109.5(1)	O(8)–Cu(2)–O(6)	167.9(1)
Cu(1)–O(1)–Cu(1)A	103.9(1)		

The basal planes have a slight tetrahedral twist of 16.72(1)°. The Cu atoms are displaced from the basal planes at distances of 0.003 Å. The Cu(2)–Cu(2)A distance is 2.623(1) Å and is slightly longer than the Cu···Cu distance in $[Cu_2(\mu\text{-}O_2CC_2H_5)_4(H_2O)_2]$ (2.611(2) Å) [33].

The dinuclear $[Cu_2(\mu\text{-}OCOC_2H_5)_2(\mu\text{-}O_2CC_2H_5)_2(phen)_2]$ unit has a CuN_2O_2O' chromophore and the geometry around the Cu(II) ions (Cu(1) and Cu(1)A) is distorted square pyramidal with a τ value of 0.290. The basal plane of CuN_2O_2O' chromophore consists of two N atoms from the phen ligand and two O atoms from two different propionato bridging molecules and is non-planar with a slight tetrahedral twist of 24.05(1)°. An O atom of a propionato bridging ligand occupies the axial position with a distance of 2.354(2) Å. The Cu atom is situated above the basal planes, 0.215 Å toward the axial sites. Both Cu(1) and Cu(1)A are linked by doubly bridged monoatomic propionato molecules in an axial-equatorial configuration with a Cu···Cu distance of 3.408(1) Å. The structural parameters of compound **1** are compared with some related compounds in Table 5.

The interplanar distances between the phen rings of two adjacent chains are 3.488–3.494 Å, indicating suggests π-stacking interactions. The π–π interaction between parallel phen rings of different chains are shown in Fig. 2. The 2D layer resulting form stacks in the crystal is presented in Fig. 2.

3.2. Crystal structure of $[Cu_2(\mu\text{-}O_2CC_6H_4OH)_4(C_7H_7NO)_2] \cdot 6H_2O$ (**2**)

The structure of compound **2** consists of centrosymmetric dinuclear paddle-wheel unit. The structure is depicted in Fig. 3 together with the numbering scheme. Selected distances and angles are listed in Table 3. Both Cu(II) ions are linked by four carboxylato groups of the 3-hydroxybenzoate ligand in a *syn,syn*-$\eta^1:\eta^1:\mu$ disposition. The pyridyl nitrogen atom of 4-acetylpyridine is axially coordinated, completing the square-pyramidal coordination geometry with a τ value of 0.002. The Cu–O distances are ranging from 1.958 to 1.970 Å and the Cu–N distance is 2.181(2) Å. The Cu···Cu distance is 2.654(1) Å. The basal plane is non-planar with a slight tetrahedral twist of 17.2(1)° and the Cu atoms lie 0.001 Å above the basal plane toward the axial sites. The structural parameters of compound **2** are in the normal range found for other paddle-wheel copper(II) dinuclear units [35], as shown in Table 5.

The crystal lattice is stabilized by hydrogen bonding between the O atom of uncoordinated water and an O atom of neighbouring carboxylato group; between the O atom of uncoordinated water and O atom of neighbouring hydroxy group of 3-hydroxybenzoate ligand (O···O distances vary from 2.591(1) to 3.257(1) Å) leading to the formation of a one-dimensional chain in the lattice. Details of the hydrogen bonding are listed in Table 3.

Table 3
Selected bond lengths (Å) and angles (°) of $[Cu_2(\mu\text{-}O_2CC_6H_4OH)_4(C_7H_7NO)_2] \cdot 6H_2O$ (**2**)

Cu(1)–N(1)	2.181(2)	Cu(1)–O(3)	1.969(2)
Cu(1)–O(1)	1.970(2)	Cu(1)–O(4)	1.958(2)
Cu(1)–O(2)	1.962(2)	Cu(1)–Cu(1)A	2.654(6)
O(1)–Cu(1)–N(1)	95.2(1)	O(4)–Cu(1)–N(1)	97.9(1)
O(2)–Cu(1)–N(1)	95.0(1)	O(3)–Cu(1)–O(1)	167.2(1)
O(2)–Cu(1)–O(1)	89.8(1)	O(4)–Cu(1)–O(1)	89.2(1)
O(2)–Cu(1)–O(3)	89.0(1)	O(4)–Cu(1)–O(2)	167.0(1)
O(3)–Cu(1)–N(1)	97.6(1)	O(4)–Cu(1)–O(3)	89.1(1)

Hydrogen bonds	D–H	H···A	D···A	D–H···A
O(6)–H(19)···O(5)[i]	0.564	2.313	2.874	173.94
O(8)–H(21)···O(1)[ii]	0.739	2.549	3.257	161.09
O(8)–H(21)···O(4)[ii]	0.739	2.631	3.191	134.23
O(10)–H(11)···O(7)[iii]	0.738	1.860	2.591	170.49
O(9)–H(16)···O(10)[iv]	0.752	2.025	2.774	173.46
O(7)–H(18)A···O(8)	0.664	2.109	2.769	172.63
O(8)–H(20)···O(9)[v]	0.631	2.211	2.835	170.75

[i] $[x+1, y, z]$,
[ii] $[x+1/2, -y+3/2, z-1/2]$,
[iii] $[-x+3/2, y-1/2, -z+1/2]$,
[iv] $[x, y, z+1]$,
[v] $[-x+1, -y+1, -z+2]$.

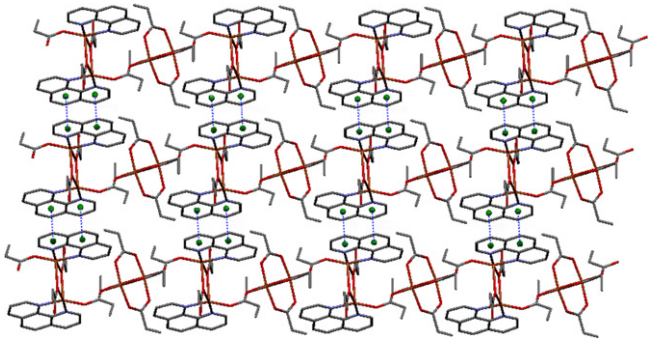


Fig. 2. 2D structure of compound **1** connected by face-to-face π–π interaction between pyridine rings of phen ligand. Hydrogen atoms and non-coordinating H_2O are omitted for clarity.

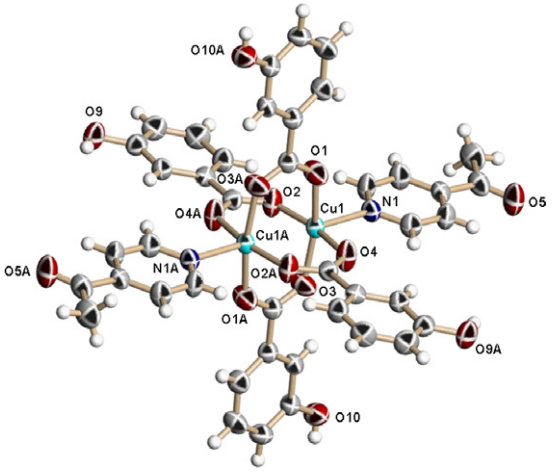


Fig. 3. Thermal ellipsoid (50% probability) plot of $[Cu_2(\mu\text{-}O_2CC_6H_4OH)_4(C_7H_7NO)_2] \cdot 6H_2O$ (**2**). The water molecules are omitted for clarity.

3.3. Crystal structure of $[Cu_2(\mu\text{-}O_2CCH_3)_4(C_7H_7NO)_2]$ (**3**)

Compound **3** consists of centrosymmetric dinuclear units, similar to other copper acetate derivates, in which four acetate groups are bridging two Cu atoms and 4-acetylpyridine as a ligand occupies the axial position, giving a CuO_4N chromophore. This structure is depicted in Fig. 4 together with the numbering scheme. Selected distances and angles are listed in Table 4. Each copper atom has a square-pyramidal geometry, with four oxygen atoms in a basal plane (Cu–O distances vary from 1.965(1) to 1.972(1) Å); the fifth coordination position is occupied by the nitrogen of a 4-acetylpyridine ligand with a distance of 2.198(1) Å. The CuO_4N chromophore

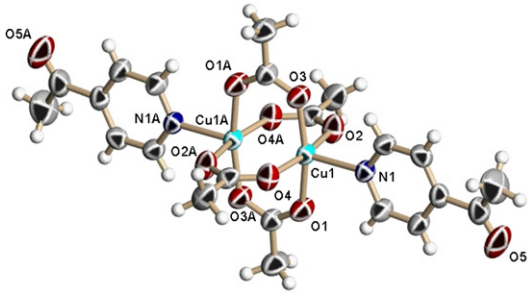


Fig. 4. Thermal ellipsoid (50% probability) plot of $[Cu_2(\mu\text{-}O_2CCH_3)_4(C_7H_7NO)_2]$ (**3**).

Table 4
Selected bond lengths (Å) and angles (°) of $[Cu_2(\mu\text{-}O_2CCH_3)_4(C_7H_7NO)_2]$ (**3**)

Cu(1)–N(1)	2.198(13)	Cu(1)–O(4)	1.968(12)
Cu(1)–O(1)	1.972(12)	Cu(1)–O(3)	1.965(12)
Cu(1)–O(2)	1.968 (12)	Cu(1)–Cu(1)A	2.631(4)
O(1)–Cu(1)–N(1)	94.3(1)	O(3)–Cu(1)–O(2)	89.2(1)
O(2)–Cu(1)–N(1)	97.1(1)	O(3)–Cu(1)–O(4)	89.5(1)
O(2)–Cu(1)–O(1)	89.5(1)	O(4)–Cu(1)–N(1)	94.7(1)
O(3)–Cu(1)–N(1)	97.6(1)	O(4)–Cu(1)–O(1)	89.5(1)
O(3)–Cu(1)–O(1)	168.1(1)	O(4)–Cu(1)–O(2)	168.2(1)

is non-planar with tetrahedral twist of 18.15(1)°. The copper atoms are displaced by 0.001 Å from the basal planes toward the apical positions. The value of τ is 0.002, corresponds to a square-pyramidal coordination [34]. Four acetate anions bridge two copper ions in a *syn*,*syn*-η^1:η^1:μ showing a paddle-wheel unit with a Cu···Cu distance of 2.631(4) Å. The structural parameters of compound **3** compare well with some related compounds, as shown in Table 5.

3.4. EPR and magnetic properties

The EPR spectra of the compounds were recorded as a polycrystalline powder at RT and at 70 K (compound **2** also 120 K) from 0 to 800 mT at X-band frequency ($h\nu$ = 0.325 cm^{-1}). The EPR spectrum of compound **1** is rather complicated and consists at RT of a very broad and strong signal centered around 290 mT and a shoulder at 249 mT (see Fig. 5A). Furthermore weak signals are observed at about 15, 369, 469 and 532 mT, which can be assigned to S = 1 triplet signals [36,37]. The signal at 159 mT can be assigned to the forbidden half-field signal (ΔM_s = ±2). At 70 K the signal decreases in intensity (see Fig. 5B), due to the depopulation of the triplet state and in this case at 325 mT the S = 1/2 resonance from a mononuclear impurity, which usually is present in dinuclear Cu(II) compounds, becomes visible. At RT this band is hidden under the strong resonance at 290 mT. The g values calculated from the EPR spectrum (considering the fact that the lines are broad and not resolved) is estimated as g_{xy} = 2.06 and g_z = 2.25, values considered normal for a Cu(II) signal.

As compounds **2** and **3** are almost isostructural, also the EPR spectra of both compounds are very similar as expected. The EPR spectrum of compound **2** is shown in Fig. 6 at RT, 120 and 70 K (the EPR spectrum of compound **3** is given as Supplementary material). The spectrum at RT (Fig. 6A) shows three bands at 23, 470 and 600 mT (that last band is only partly visible due to the limitations of the EPR magnetic field). These bands are typical for a triplet state of a copper(II) acetate hydrate type [11,24–27,36–39] with three resonance lines (H_{z1}, $H_{\perp}$, H_{z2}). At 120 K (Fig. 6B) the H_{z1} signal splits, due to hyperfine interaction of the unpaired electron within the dinuclear unit (A = 6.2 mT). The small feature at around 320 mT is from a monomeric impurity, which is in most cases always present in dinuclear bulk material. At 70 K the triplet signal becomes very weak (Fig. 6C), and therefore the monomeric impurity at 320 mT appears as relatively very strong. This behaviour is consistent with the magnetic susceptibility of these compounds (see magnetism below). The same type of signals was observed for compound **3** (see Supplementary material). Similar spectra with the same type of bands are observed for the compounds [Cu_2(OOC-C_5H_{11})$_4$(urea)$_2$] [11] and {[Cu_2(β-alanine)$_4$(H_2O)$_2$](NO_3)$_4$(H_2O)$_4$} [26]. For these compounds the zero-field splitting parameter D was calculated as being 0.34 cm^{-1}, so we can estimate that the value of D is also around 0.34 cm^{-1} for compound **2** and **3**.

The magnetic susceptibility of a powdered sample of compound **1** was measured from 2 to 320 K under a constant magnetic field of 0.1 T. The magnetic properties are depicted in Fig. 7 in the form of $\chi_M T$ *versus* T for four Cu(II) ions. At 320 K the $\chi_M T$ product has a value of 1.60 cm^3 · K · mol^{-1}, which is just a little higher than the value expected for four uncorrelated Cu(II) ions (1.40 cm^3 · K · mol^{-1} for g = 2) showing at best a very weak interaction between the metallic centers at 320 K. Upon cooling the $\chi_M T$ product gradually decreased as the temperature was lowered and reached a value of 1.05 cm^3 mol^{-1} K at 75 K, stays constant till about 20 K, where it decreases till it reached a value of 0.98 cm^3 mol^{-1} K at 2 K. This magnetic behaviour agrees with a overall strong antiferromagnetic interaction, at least for part of the Cu(II) ions.

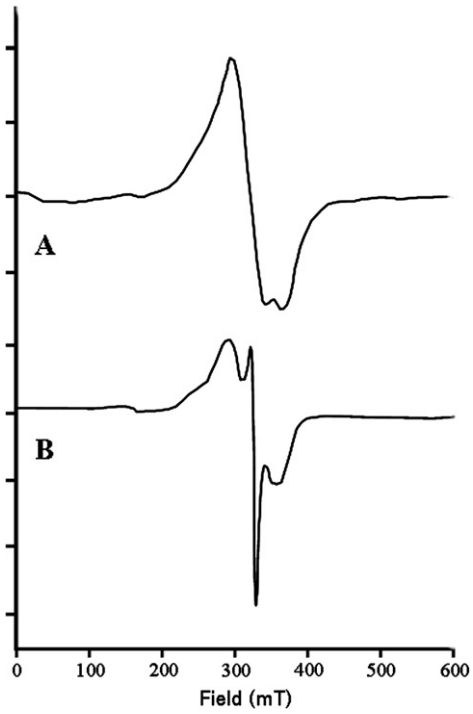


Fig. 5. X-band powder EPR spectrum of compound **1** at RT (A) and at 70 K (B).

Table 5
Structural data and magnetic properties for some relevant paddle-wheel copper(II) complexes[a]

Complex[b]	Structure type	Chromophore	τ[c]	Cu···Cu (Å)	J (cm^{-1})	Refs.
{[Cu_4(phen)$_2$(μ-$O_2CC_2H_5$)$_8$] · (H_2O)}$_n$ (**1**)	1D	CuO_5	0.005	2.623	−299.5	this work
[Cu_2(μ-$O_2CC_6H_4OH$)$_4$(C_7H_7NO)$_2$] · 6H_2O (**2**)	dinuclear	CuO_4N	0.002	2.654	−278.5	this work
[Cu_2(μ-O_2CCH_3)$_4$(C_7H_7NO)$_2$] (**3**)	dinuclear	CuO_4N	0.002	2.631	−287.0	this work
[Cu_2(μ-O_2CH)$_4$(DMF)$_2$] (**4**)	dinuclear	CuO_4O'	0	2.651	−470	[37e]
[Cu_2(μ-O_2CCH_3)$_4$(H_2O)$_2$] (**5**)	dinuclear	CuO_4O'		2.620	−299	[24]
[Cu_2(μ-O_2CCH_3)$_4$(NH_3)$_2$] (**6**)	dinuclear	CuO_4N		2.620	−284	[24]
[Cu_2(μ-O_2CCH_3)$_4$(MeNHpy)$_2$] (**7**)	dinuclear	CuO_4N	0.004	2.272	−285	[37d]
[Cu_2(μ-O_2CCH_3)$_4$(NITpPy)$_2$] (**8**)	dinuclear	CuO_4N		2.622	−172	[12]
[Cu_2(μ-$O_2CC(CH_3)_3$)$_4$(NITpPy)$_2$](C_6H_6) (**9**)	dinuclear	CuO_4N		2.614	−192	[12]
[Cu_2(μ-$O_2CC_2H_5$)$_4$(H_2O)$_2$] (**10**)	dinuclear	CuO_4O'		2.575	−311	[33]
[Cu_2(μ-DMB)$_4$(H_2O)$_2$] (**11**)	dinuclear	CuO_4O'		2.619	−325	[25]
[Cu_2(μ-DMB)$_2$(μ-O_2CCH_3)$_2$(H_2O)$_2$] (**12**)	dinuclear	CuO_4O'		2.597	−250	[25]

[a] All with square-pyramidal geometry and an equatorial–equatorial configuration.
[b] Abbreviation: MeNHpy, 2-methylaminopyridine; NITpPy, 4,4,5,5-tetramethyl-2-(4-pyridyl)-2-imidazoline-N^1-oxyl N^3-oxide and DMB, 2,6-dimethoxybenzoate.
[c] τ: calculated from structural data.

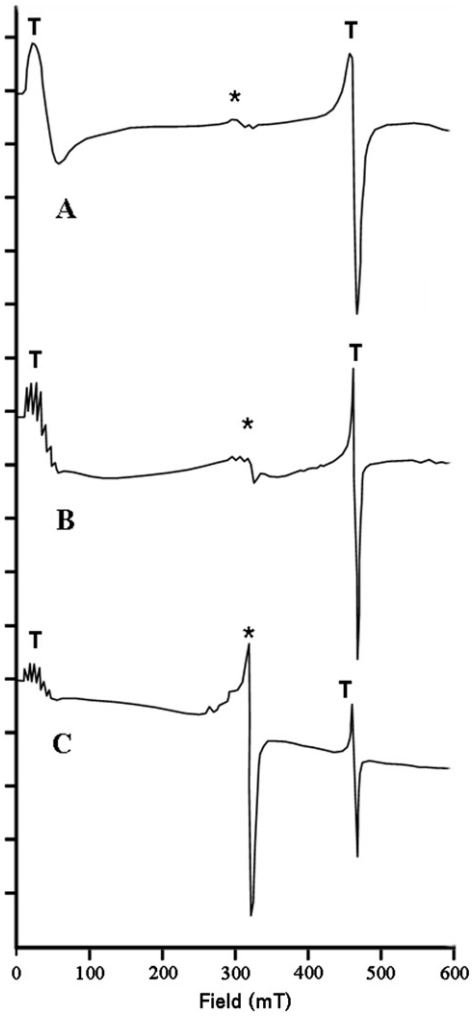


Fig. 6. X-band powder EPR spectrum of compound **2** at RT (A), at 120 K (B) and at 70 K (C). (* = signal of the mononuclear signal; T = triplet signal).

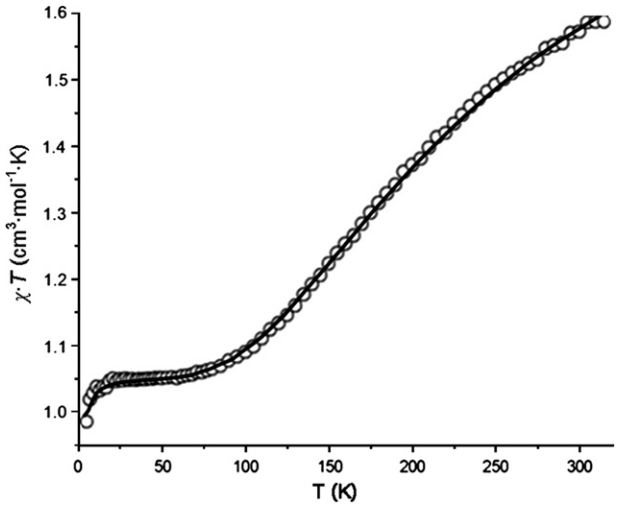


Fig. 7. A plot of the temperature dependence of $\chi_M T$ *vs. T* for compound **1** in the range 2–320 K.

To explain the magnetic interaction of compound **1** the general Heisenberg Hamiltonian [40] $H_{ex} = -JS_1S_2$, in which the exchange parameter J, is negative for antiferromagnetic and positive for ferromagnetic interaction.

To simplify the expression for the susceptibility it was decided to use a combination of a two term contribution, i.e. $\chi = \chi Cu(1) + \chi Cu(2)$, in which

$$\chi Cu(1) = 2Ng_1^2\beta^2[kT(3 + \exp(-J_1/kT))]^{-1} \quad \text{and}$$
$$\chi Cu(2) = 2Ng_2^2\beta^2[kT(3 + \exp(-J_2/kT))]^{-1}$$

In these expressions J_1 and J_2 corresponds to the singlet–triplet energy gap for the two dinuclear sub-units in compound **1** (J_1 for the Cu(1)–Cu(1)A unit; J_2 for the Cu(2)–Cu(2)A unit), and N, g, β, k and T have their usual meanings [40]. The best-fit parameters, depicted in Fig. 7 as a solid line, were: $g_1 = 2.35$, $g_2 = 2.22$, $J_1 = -0.75$ cm^{-1}, $J_2 = -299.5$ cm^{-1}, with $R = 5 \times 10^{-5}$, the agreement factor defined as $\sum_i(\chi_{calcd} - \chi_{obs})^2/\sum_i(\chi_{obs})^2$. In a first approximation the g values obtained by EPR have been used to properly fit the magnetic behavior, however, a poor result was achieved likely due to the fact that the formula of the magnetic susceptibility is of course based on a number of approximations.

The magnetic susceptibility of powdered samples of compounds **2** and **3** were measured from 5 to 350 K. As the two compounds are structural similar, also the magnetic properties are similar. The magnetic properties of the compounds are depicted in Fig. 8 for compound **2** and in Fig. S3 for compound **3** in the form of $\chi_M T$ *versus* T for two Cu(II) ions. At 350 K the $\chi_M T$ product of **2** has a value of 0.575 cm^3 mol^{-1} K (0.554 cm^3 mol^{-1} K for **3**), which is below the spin-only value for two non-interacting Cu(II) ions (0.75 cm^3 mol^{-1}K at RT). From 350 K the $\chi_M T$ product decreases gradually to a value of 0.014 cm^3 mol^{-1} K for compound **2** at 50 K (0.006 cm^3 mol^{-1} K for **3**) and stays constant till 5 K. This magnetic behaviour agrees with a strong antiferromagnetic interaction.

The theoretical expression for the magnetic susceptibility for two interacting $S = 1/2$ centres, which is based on the general Hamiltonian [40] is: $H_{ex} = -JS_1S_2$, in which the exchange parameter J, is negative for antiferromagnetic and positive for ferromagnetic interaction. The magnetic data were fitted to the equation given in the literature [40] for dinuclear copper compounds:

$$\chi_M = (2Ng^2\beta^2)[kT - (2zJ'/(3 + \exp(-J/kT)))]^{-1} \times [3 + \exp(-J/kT)]^{-1}(1 - p) + \chi_p p,$$

in which N, g, β, k and T have their usual meanings [40]. The parameter p denotes the fraction of paramagnetic impurity in the sample and zJ' the interaction between neighbouring dinuclear identities. The fit was accomplished by minimisation of $R = (\chi_M T_{calc} - \chi_M$-

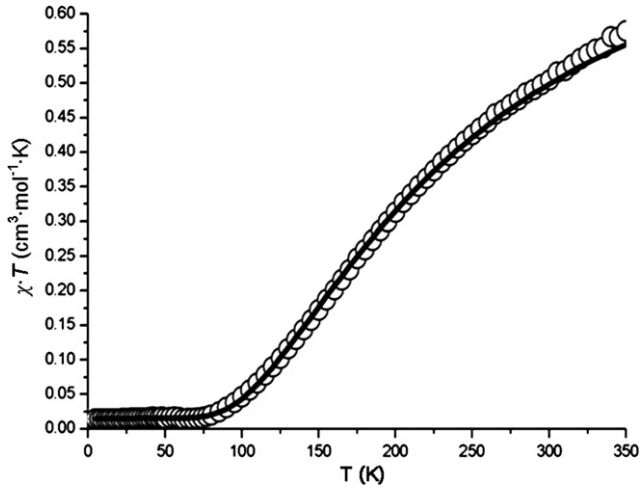


Fig. 8. A plot of the temperature dependence of $\chi_M T$ *vs. T* for compound **2**.

$T_{obs})^2/(\chi_M T_{obs})^2$ by a least-squares procedure. The best fit for compound **2**, depicted in Fig. 8 as a solid line, was obtained for $J = -278.5\ cm^{-1}$, $g = 2.15$, $zJ' = -26.3\ cm^{-1}$, $p = 0.02$, with a final R of 1.5×10^{-2}. The best fit for compound **3**, depicted in Fig. S3 as a solid line, was obtained for $J = -287.0\ cm^{-1}$, $g = 2.15$, $zJ' = -24.7\ cm^{-1}$, $p = 0.01$, with a final R of 1.5×10^{-2}. The R values appear a bit high, but can be ascribed to the fact that susceptibility measurements above 300 K are less accurate due to a reduced accuracy in temperature, in fact when only the temperature range of 5–280 K is considered the R-value is much better, *i.e.* 3×10^{-3}.

Recently, Rodr˘guez-Fortea et al.[24] have reported a density functional study of the exchange coupling in carboxylato-bridged dinuclear copper(II) compounds. They compared the J values for several substituents in $[Cu_2(\mu\text{-}RCOO)_4L_2]$ and concluded that the electron-withdrawing groups reduce the strength of the exchange coupling. Another factor is the Cu–O bridging bond in copper(II) carboxylate dinuclear units, which is considered to be quite important in the super-exchange mechanism; it is the basis for the super-exchange pathway of the Cu–O–C(R)–O–Cu fragments. When R is strongly σ-bonded to the carboxylato carbon, the strong coordination of the Cu–O bonds in the CuO_4 basal plane will become stronger, in order to maintain the electron neutrality over the whole molecule. Thus, the J value increases when the Cu–O bond length decreases. In addition the coupling constant is weakly dependent on the Cu···Cu distance. If the Cu···Cu distance increases, the overlap of the δ-bonding between the two Cu atoms decreases and the J value would be slightly lower.

The structure of compound **1** is compared with the most related carboxylato-bridged compound $[Cu_2(\mu\text{-}O_2CC_2H_5)_4(H_2O)_2]$ **10** ($J = -311\ cm^{-1}$) in Table 5. When water molecules in axial positions of compound **10** are replaced by propionate bridges (compound **1**), the average Cu–O distance is 1.959 Å and the Cu···Cu distance is 2.623 Å, which both are longer than those of the corresponding compound **10** (1.948 and 2.575 Å, respectively). Thus, the strong Cu–O bonds in the CuO_4 basal plane of **1** will become weaker than those of compound **10**; this may result in a decreased $-J$ value. In addition, a longer Cu···Cu distance would lead to a smaller $-J$ value (in this case $-299\ cm^{-1}$). Nevertheless, it should be mentioned that the approximation used to obtain the Hamiltonian to calculate the J value is somewhat simplified, which can explain that the g values are somewhat higher then expected for Cu(1) and Cu(2). Indeed, it was observed that below 50 K the magnetism of compound **1** can be depicted as a unidimensional assembly of antiferromagnetically coupled $S = 1/2$ spins. Confirmation of this magnetic chain behaviour is seen from the linear $\ln \chi_M T$ *versus* T^{-1} curve in this temperature range (Fig. S4) [41]. In addition, the value of the dinuclear coupling via Cu(1)···Cu(1)A for compound **1** is expected to be small, as predicted by the theoretical calculation. The Cu(1)–O(1)–Cu(1)A pathway involve the d_{z^2} and $d_{x^2-y^2}$ orbital for Cu(1) and for Cu(1)A, therefore and because of the copper symmetry, the unpaired electron around copper(II) are described mainly by a magnetic orbital built from the $d_{x^2-y^2}$, confirming the theoretical result.

Complexes with the $Cu_2(\mu\text{-}O_2CCH_3)_4$ basic unit all have relatively high negative magnetic exchange coupling constants. For $[Cu_2(\mu\text{-}O_2CCH_3)_4(H_2O)_2]$ **5** with a coupling constant J of $-299\ cm^{-1}$, water molecules in axial positions are replaced by NH_3 for compound **6** [24], or MeNHpy for compound **7** [37] the coupling constant is slightly less negative of −284 and −285 cm^{-1}, respectively. It is indicating that the change of the axial ligand induces smaller variations in the coupling constant. Consequently, compound **3** with the axial 4-acetylpyridine ligands, the slightly decreased $-J$ value is expected. When the acetate groups in compound **3** are replaced by 3-hydroxybenzoate groups (compound **2**), which is a stronger electron-donating group, the increased $-J$ value is expected. According to that, it is reasonable to imply that the 3-hydroxybenzoate bridge in **2** should provide a somewhat larger exchange coupling than the acetato bridge in compound **3**. However, the experimental results are almost the same ($J = -278.5$ and $-287.0\ cm^{-1}$ for complexes **2** and **3**, respectively) and lie almost in the experimental deviation for such large values.

4. Conclusion

We have presented the synthesis and magnetic study of three new polynuclear tetracarboxylato-bridged copper(II) complexes. Four carboxylate ligands bridge two copper ions in a *syn*,*syn*-η^1:η^1:μ showing the paddle-wheel unit. Compound **1** exhibits an one-dimensional chain structure build from two different dinuclear units. The adjacent chains are connected to form a 2D structure through the π–π interaction. Both compounds **2** and **3** are dinuclear with a paddle-wheel structure with 4-acetylpyridine at the apical position. The coordination geometry around each copper(II) ion is (distorted) square-pyramidal for all three compounds. All compounds show a strong antiferromagnetic interaction between the Cu(II) magnetic centres of the dinuclear units, with different magnitude of J values mainly depending on substituents of the carboxylate groups. The observed J values correspond nicely with values found in the literature for other carboxylato-bridged dinuclear units (see Table 5).

Acknowledgements

The authors gratefully acknowledge the Thailand Research Fund (Agreement Numbers RTA 4880008 and BRG 4980007), Khon Kaen University and the Center for Innovation in Chemistry: Postgraduate Education and Research Program in Chemistry, Thailand, for financial support. The work described in the present paper has also been supported by the Leiden University Study group WFMO (Werkgroep Fundamenteel MaterialenOnderzoek). Support of the NRSC Catalysis (Research School Combination of HRSMC and NIOK) is kindly acknowledged. Financial support and coordination by the FP6 Network of Excellence "MAGMANet" (contract number 515767) is kindly acknowledged.

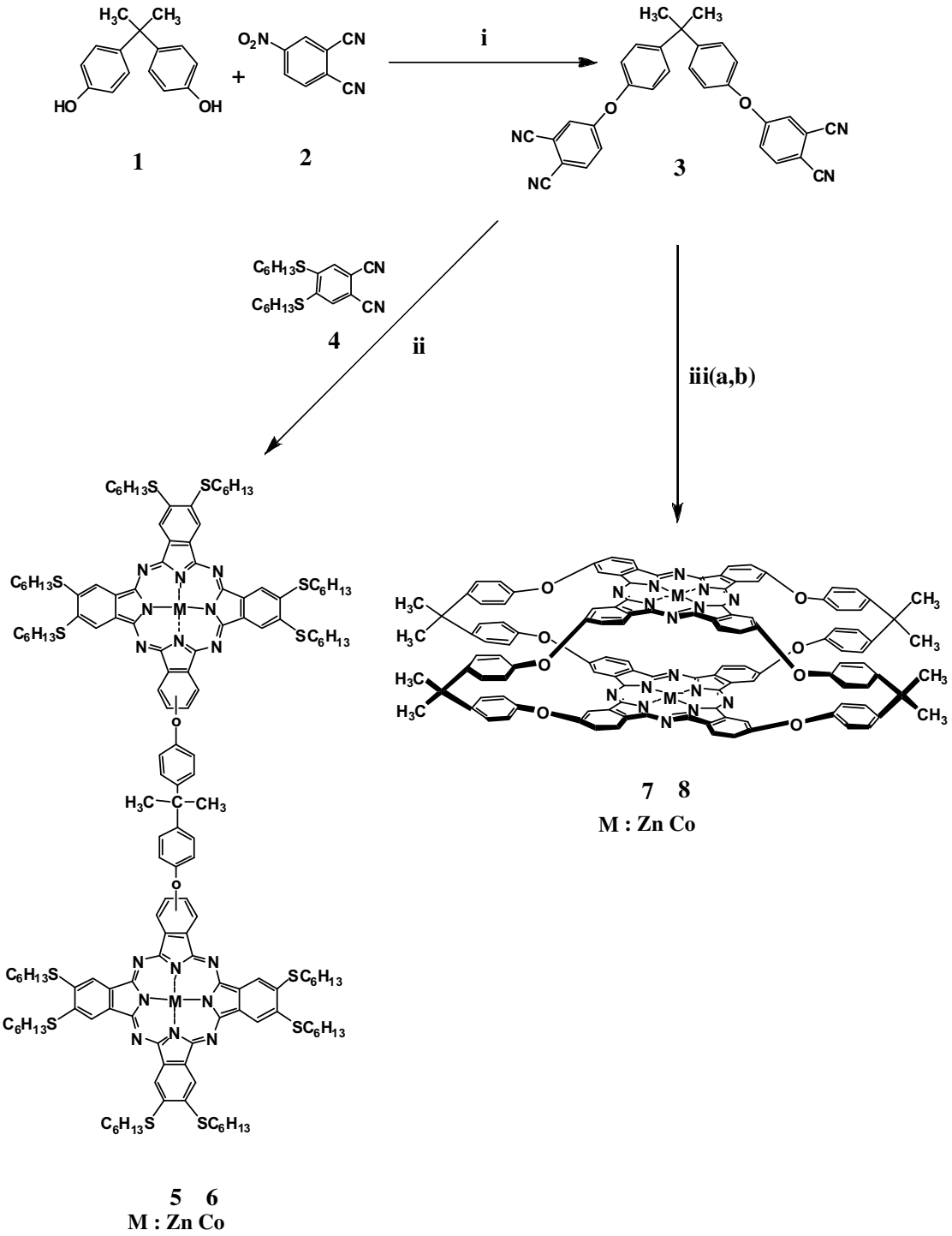
Appendix A. Supplementary data

CCDC 674731, 674732 and 674733 contain the supplementary crystallographic data for **1**, **2** and **3**. These data can be obtained free of charge via http://www.ccdc.cam.ac.uk/conts/retrieving.html, or from the Cambridge Crystallographic Data Centre, 12 Union Road, Cambridge CB2 1EZ, UK; fax: (+44) 1223 336 033; or e-mail: deposit@ccdc.cam.ac.uk. Supplementary data associated with this article can be found, in the online version, at doi:10.1016/j.poly.2008.02.023.

References

[1] I. Chadjistamatis, A. Terzis, C.P. Raptopoulou, S.P. Perlepes, Inorg. Chem. Commun. 6 (2003) 1365.
[2] B.P. Baranwal, S.S. Das, P. Singh, Synth. React. Inorg. Met.-Org. Chem. 28 (1998) 1689.
[3] E.J. Baran, S.B. Etcheverry, M.H. Torre, E. Kremer, Polyhedron 13 (1994) 1859.
[4] G.C. Campbell, J.F. Haw, Inorg. Chem. 27 (1988) 3706.
[5] G.C. Campbell, J.H. Reibenspies, J.F. Haw, Inorg. Chem. 30 (1991) 171 .
[6] R.D. Harcourt, F.L. Skrezenek, R.G.A.R. Maclagan, J. Am. Chem. Soc. 108 (1986) 5403.
[7] R.D. Harcourt, G.E. Martin, J. Chem. Soc., Faraday Trans. II 73 (1977) 114.
[8] M. Kato, Y. Muto, Coord. Chem. Rev. 92 (1988) 45.
[9] F.P.W. Agterberg, H.A.J. Provó Kluit, W.L. Driessen, H. Oevering, W. Buijs, M.T. Lakin, A.L. Spek, J. Reedijk, Inorg. Chem. 36 (1997) 4321.

[10] M.V. Marinho, M.I. Yoshida, K.J. Guedes, K. Krambrock, A.J. Bortoluzzi, M. Hörner, F.C. Machado, W.M. Teles, Inorg. Chem. 43 (2004) 1539.
[11] B. Kozlevčar, I. Leban, M. Petrič, S. Petriček, O. Roubeau, J. Reedijk, P. Šegedin, Inorg. Chim. Acta 357 (2004) 4220.
[12] Y.-H. Chung, H.-H. Wei, G.-H. Lee, Y. Wang, Inorg. Chim. Acta 293 (1999) 30.
[13] (a) A.V. Ablov, T.N. Tarkhova, Y.A. Simonov, Acta Crystallogr. A 21 (1966) 134; (b) M.J. Bird, T.R. Lomer, Acta Crystallogr. B 28 (1972) 242; (c) T.R. Lomer, K. Perera, Acta Crystallogr. B 30 (1974) 2912.
[14] W.-H. Chan, T.C.W. Mak, W.-H. Yip, G. Smith, E.J. O'Reilly, C.H.L. Kennard, Polyhedron 6 (1987) 881.
[15] G. Smith, E.J. O'Reilly, C.H.L. Kennard, A.H.J. White, J. Chem. Soc., Dalton Trans. (1985) 243.
[16] J.M. Seco, M.J. González Garmendia, E. Pinilla, M.R. Torres, Polyhedron 21 (2002) 457.
[17] A. Doyle, J. Felcman, M.T.D.P. Gambardella, C.N. Verani, M.L.B. Tristão, Polyhedron 19 (2000) 2621.
[18] M. Barquín, M.J. González Garmendia, L. Larrínaga, E. Pinilla, M.R. Torres, Inorg. Chim. Acta 359 (2006) 2424.
[19] B. Chiari, O. Piovesana, T. Tarantelli, P.F. Zanazzi, Inorg. Chem. 32 (1993) 4834.
[20] J.S. Valentine, A.J. Silverstein, Z.G. Soos, J. Am. Chem. Soc. 96 (1974) 97.
[21] (a) B. Morosin, R.C. Hughes, Z.G. Soos, Acta Crystallogr. B 31 (1975) 762; (b) J. Pickardt, Acta Crystallogr. B 37 (1981) 1753; (c) M.M. Borel, A. Leclaire, Acta Crystallogr. B 32 (1976) 1275; (d) M. Yamanaka, H. Ueska, S. Ohba, Y. Saito, S. Iwata, M. Kato, T. Tokii, Y. Muto, O.W. Steward, Acta Crystallogr. B 47 (1991) 344.
[22] Y.-H. Wen, J.-K. Cheng, J. Zhang, Z.-J. Li, Y. Kang, Y.-G. Yao, Inorg. Chem. Commun. 7 (2004) 1120.
[23] V.M. Rao, D.N. Sathyanarayana, H.J. Manohar, J. Chem. Soc., Dalton Trans. (1983) 2167.
[24] A. Rodríguez-Fortea, P. Alemany, S. Alvarez, E. Ruiz, Chem. Eur. J. 7 (2001) 627.
[25] L.S. Erre, G. Micera, P. Piu, F. Cariati, G. Ciani, Inorg. Chem. 24 (1985) 2297.
[26] J. Jezierska, T. Glowiak, A. Oźarowski, Y.V. Yablokov, Z. Rzaczyńska, Inorg. Chim. Acta 2750276 (1998) 28.
[27] B. Kozlevčar, D. Odlazek, A. Golobič, A. Pevec, P. Strauch, P. Šegedin, Polyhedron 25 (2006) 1161.
[28] B. Kozlevčar, M. Radišek, Z. Jagličič, F. Merzel, L. Glažar, A. Golobič, P. Šegedin, Polyhedron 26 (2007) 5414.
[29] L. Gutiérrez, G. Alzuet, J. Borrás, A. Castiñeiras, A. Rodríguez-Fortea, E. Ruiz, Inorg. Chem. 40 (2001) 3089.
[30] Siemens SAINT 1996, Version4 Software Reference Manual, Siemens Analytical X-ray Systems Inc., Madison, WI, USA.
[31] G.M. Sheldrick, SADABS, Program for Empirical Absorption Correction of Area Detector Data, University of Göttingen, Goöttingen, Germany, 1996.
[32] Bruker XSHELL 1999, Version 6.12 Reference Manual, Bruker AXS Inc., Madison, WI, USA.
[33] L.P. Battaglia, A.B. Corradi, L. Menabue, J. Chem. Soc., Dalton Trans. (1986) 1653.
[34] A.W. Addison, T.N. Rao, J. Reedijk, J. van Rijn, G.C. Verschoor, J. Chem. Soc., Dalton Trans. (1984) 1349.
[35] M.R. Sundberga, R. Uggla, M. Melnik, Polyhedron 15 (1996) 1157.
[36] G. Christou, S.P. Perlepes, E. Libby, K. Folting, J.C. Huffman, R.J. Webb, D.N. Hendrickson, Inorg. Chem. 29 (1990) 3657.
[37] (a) K. Skorda, G.S. Papaefstathiou, A. Vafiadis, A. Lithoxoidou, C.P. Raptopoulou, A. Terzis, V. Psycharis, E. Bakalbassis, V. Tangoulis, S.P. Perlepes, Inorg. Chim. Acta 326 (2001) 53; (b) Y.-H. Chung, H.-H. Wei, Inorg. Chem. Commun. 2 (1999) 269; (c) G. Smith, C.H.L. Kennard, K.A. Byriel, Polyhedron 10 (1991) 873; (d) M. Barquín, M.J. González Garmendia, S. Pacheco, E. Pinilla, S. Quintela, J.M. Seco, M.R. Torres, Inorg. Chim. Acta 357 (2004) 3230; (e) R. Cejudo, G. Alzuet, J. Borrás, M. Liu-González, F. Sanz-Ruiz, Polyhedron 21 (2002) 1057.
[38] S.P. Harish, J. Sobhanadri, Inorg. Chim. Acta 108 (1985) 147.
[39] M. Valko, M. Mazúr, H. Morris, R. Klement, C.J. Williams, M. Melník, J. Coord. Chem. 52 (2000) 129.
[40] O. Kahn, Molecular Magnetism, VCH Publ., NY, 1993.
[41] L. Lecren, O. Roubeau, C. Coulon, Y.-G. Li, X.F. Le Goff, W. Wernsdorfer, H. Miyasaka, R. Clerac, J. Am. Chem. Soc. 127 (2005) 17353.



Scheme 1. (i) K_2CO_3, DMF; (ii) **4** and $Zn(CH_3COO)_2 \cdot 2H_2O$ or $Co(CH_3COO)_2 \cdot 4H_2O$ in DMF; (iii) **a**: $Zn(CH_3COO)_2 \cdot 2H_2O$, **b**: $Co(CH_3COO)_2 \cdot 4H_2O$.

novel 4,4′-isopropylidendioxydiphenyl bridged bis-metallophthalocyanines Zn(II) and Co(II) (Scheme 1).

2. Experimental

2.1. Synthesis and characterization

The starting materials **2** and **4** were synthesized by the methods described previously in the literature [21]. Compound **1** was used as supplied commercially. IR Spectra were recorded on a Mattson 1000 FTIR spectrophotometer using KBr pellets. Electronic spectra were recorded on a Unicam UV/Vis spectrophotometer and elemental analyses were performed by the Instrumental Analysis Laboratory of Chemistry Department, Yildiz Technical University. ^{1}H NMR spectra were recorded in *d*-chloroform with an instrument Mercury-Vx 500 MHz. Mass spectra were acquired in linear and reflectron modes with average of 50 and 100 shots on a Voyager-DE™ PRO MALDI-TOF mass spectrometer (Applied Biosystems, USA) equipped with a nitrogen UV-Laser operating at 337 nm.

Dithranol (1,8-dihydroxy-10H-anthracene-9-one) (20 mg/mL in tetrahydrofuran) matrix for **5**, **6**, **8** and α-cyano-4-hydroxycinnamic acid (ACCA) (15 mg/mL 1:1 water–acetonitrile) MALDI matrix for **7** were prepared. MALDI samples were prepared by mixing complex (2 mg/mL in chloroform) with the matrix solution (1:10 v/v) in a 0.5 mL eppendorf® micro tube. Finally 1 μL of this mixture was deposited on the sample plate, dried at room temperature and then analyzed.

*2.1.1. 4,4′-Isopropyliden-bis-dioxydiphthalonitrile (**3**)*

Compound **1** (1.979 g, 8.67 mmol) and compound **2** (3 g, 17.34 mmol) were dissolved in dry DMF under argon. After stirring for 15 min, finely ground anhydrous K_2CO_3 (2.39 g, 0.017 mmol) was added portion wise in 15 min with efficient stirring. The reaction mixture was heated and stirred at 90 °C for 24 h under argon. After cooling to room temperature it was treated with water and the product filtered off and washed with water and ethanol. The product was purified on a silica gel column with chloroform as a eluent. Yield: 2.5 g, (60.08%). This compound is soluble in $CHCl_3$, DCM, and MeOH. Mp: 160 °C. *Anal.* Calc. for $C_{31}H_{20}N_4O_2$: C, 77.45; H, 4.58; N, 11.66. Found: C, 77.52; H, 4.68; N, 11.46%. IR (KBr pellet) ν, cm^{-1}: 3074 (Ar–H), 2231 (C≡N), 1566–1587 (C=C), 1245–1282 (Ar–O–Ar); ^1H NMR ($CDCl_3$) δ 8.32 (d, J = 8.19 Hz, 2H), 7.92 (d, J = 8.58 Hz, 2H), 7.82 (d, J = 2.34 Hz, 2H), 7.70 (d, J = 8.58 Hz, 2H), 7.56 (m, 4H), 7.10 (brs, 2H), 6.92 (d, J = 2.34 Hz, 2H), 6.86 (dd, J = 8.78 Hz, J = 2.34 Hz, 2H), 4.95 (s, 2H) ppm.

*2.1.2. 14′[4,4′-Isopropylidendiphenoxy]bis- 3′,4′,7′,8′,11′, 12′(hexahexylthiophthalocyaninato) dizinc(II)(**5**)*

A mixture of compound **3** (0.449 g, 1.248 mmol), compound **4** (0,100 g, 0.208 mmol), and $Zn(OAc)_2 \cdot 2H_2O$ (0.035 g, 0.212 mmol) in 5 mL of DMF was refluxed in a sealed tube under Ar for 24 h. After cooling to room temperature the reaction mixture was treated with water to precipitate the product and then filtered. The crude product was washed with common organic solvents. The product was separated by column chromatography on silica gel with chloroform and a gradient of chloroform–MeOH up to 100% MeOH as eluent. Yield: 0.053 g (9.18%). This compound was soluble in $CHCl_3$, DCM and THF. Mp: > 300 °C. *Anal.* Calc. for $C_{151}H_{188}N_{16}O_2S_{12}Zn_2$: C, 65.42; H, 6.71; N, 8.09; S, 13.86. Found: C, 66.01; H, 6.86; N, 7.89; S, 13.76%. MS (MALDI-TOF): m/z 2772 $[M+H]^+$, IR (KBr pellet) ν, cm^{-1}: 3060 (arom. –CH), 2953–2853 (aliph. $-CH_2$), 1592 (C=C), 1229 (Ar–O–Ar); UV–Vis ($CHCl_3$) λ, nm ($\log\varepsilon$): 701 (4.88), 630 (4.34), 361 (4.88); ^1H NMR ($CDCl_3$): δ, ppm 7.51–6.97 (m, 30H, arom.), 1.62 (m, 6H, $-CH_3$), 1.33–1.19 (m, 120H, aliph. $-CH_2$), 0.95–0.93 (m, 36H, $-CH_3$).

*2.1.3. 14′[4,4′-Isopropylidendiphenoxy]bis- 3′,4′,7′,8′,11′,12′(hexahexylthiophthalocyaninato) dicobalt(II) (**6**)*

A mixture of compound **3** (0.449 g, 1.248 mmol), compound **4** (0,100 g, 0.208 mmol), and $Co(OAc)_2 \cdot 4H_2O$ (0.053 g, 0.212 mmol) in 5 mL of DMF was refluxed in a sealed tube under Ar for 24 h. After cooling to room temperature, the blue-green reaction product was obtained, isolated and purified with using the same procedure explained above for **5**. Yield: 0.078 g (13.56%). This compound was soluble in $CHCl_3$, THF, DMF. Mp: >300 °C. *Anal.* Calc. for $C_{151}H_{188}N_{16}O_2S_{12}Co_2$: C, 65.69; H, 6.74; N, 8.12; S, 13.92. Found: C, 64.88; H, 6.64; N, 7.88; S, 13.76%. MS (MALDI-TOF): m/z 2759 $[M+H]^+$, IR (KBr pellet) ν, cm^{-1}: 3060 (arom. –CH), 2953–2853 (aliph. $-CH_2$), 1592 (C=C), 1229 (Ar–O–Ar); UV–Vis ($CHCl_3$), λ, nm ($\log\varepsilon$): 682 (4.95), 624 (4.64), 325 (5.02).

*2.1.4. 2′,10′,16′,24′-[Tetrakis(4,4′-isopropylidenedioxydiphenyl)]bis-phthalocyaninatodizinc(II) (**7**)*

The mixture of compound **3** (0.100 g, 0.208 mmol) and $Zn(OAc)_2 \cdot 2H_2O$ (0.052 g, 0.312 mmol) was powdered in quartz crucible and heated in a sealed glass tube for 10 min under dry N_2 atmosphere at 250 °C. After cooling to room temperature, 5 mL of DMF was added to the residue to solve the product. The reaction mixture was precipitated by adding water. The precipitate was filtered, at first several times washed with hot water and then with hot ethanol in order to eliminate the unreacted starting materials and dried *in vacuo*. Then, the crude product was washed with methanol, ethanol, acetonitrile and acetone for 36 h, respectively in the Soxhlet apparatus. The product was separated by column chromatography on silica gel with chloroform as eluent. Yield: 0.040 g (9.39%). This compound is soluble in $CHCl_3$ and DCM. Mp >350 °C. *Anal.* Calc. for $C_{124}H_{72}N_{16}O_8Zn_2$: C, 72.84; H, 3.55; N, 10.96. Found: C, 72.94; H, 3.64; N, 10.77%. MS (MALDI-TOF): m/z 2044 $[M+H]^+$, IR (KBr pellet) ν, cm^{-1}: 3060 (arom. –CH), 1591 (C=C), 1231 (Ar–O–Ar); UV–Vis ($CHCl_3$), λ, nm ($\log\varepsilon$): 682 (4.56), 613 (3.88), 337 (4.33), 307 (4.49); ^1H NMR ($CDCl_3$): δ, ppm 7.75–6.92 (m, 72H, arom.), 1.68 (m, 24H, $-CH_3$).

*2.1.5. 2′,10′,16′,24′-[Tetrakis(4,4′-isopropylidenedioxydiphenyl)]bis-phthalocyaninatodicobalt(II) (**8**)*

The mixture of compound **3** (0.100 g, 0.208 mmol) and $Co(OAc)_2 \cdot 4H_2O$ (0.078 g, 0.313 mmol) was powdered in quartz crucible and heated in a sealed glass tube for 10 min under dry N_2 atmosphere at 250 °C. After cooling to room temperature, the blue-green reaction product was obtained, isolated and purified with using the same procedure explained above for **7**. Yield: 0.035 g (8.27%). This compound is soluble in $CHCl_3$, DCM and THF. Mp >350 °C. *Anal.* Calc. for $C_{124}H_{72}N_{16}O_8Co_2$: C, 73.30; H, 3.57; N, 11.03. Found: C, 73.45; H, 4.01; N, 11.12%. MS (MALDI-TOF): m/z 2031 $[M+H]^+$, IR (KBr pellet) ν, cm^{-1}: 3063 (arom. –CH), 1591 (C=C), 1231 (Ar–O–Ar); UV–Vis ($CHCl_3$), λ, nm ($\log\varepsilon$): 675 (4.70), 613 (4.32), 330 (4.67).

2.2. Electrochemical measurements

Electrochemical measurements were carried out with a PAR Model VersoStat II potentiostat/galvanostat controlled by an external PC, and utilizing a three electrode configuration at 25 °C. Tetrabutylammonium perchlorate (TBAP) (Electrochemical grade, Fluka Chemical Co.) was used as the supporting electrolyte in extra pure DCM. A saturated calomel electrode (SCE) was employed as the reference electrode and separated from the bulk of the solution by a fritted glass bridge filled with the solvent/supporting electrolyte mixture. The ferrocene/ferrocenium couple (Fc/Fc^+) was used as an internal standard, but potentials were reported with respect to SCE. The working electrode was platinum in the measurements. The surface of the platinum working electrode was polished with a H_2O suspension of Al_2O_3 before each run. The last polishing was done with a particle size of 50 nm. A platinum spiral wire was used as the auxillary electrode. Solutions containing the complexes were deoxygenated by a stream of high-purity nitrogen for at least 20 min prior to running the experiment, and the solution was protected from air by a blanket of nitrogen during the experiment. For the controlled-potential coulometry (CPC) studies, a platinum gauze working electrode, a platinum wire counter electrode separated with a bridge and a SCE as reference electrode were used.

2.3. Electrical measurements

The measurement electrodes used in the dc and ac conductivity measurements consist of an interdigital array of metal electrodes photolitographically patterned on pre-cleaned glass substrate. Glass substrates were throughly cleaned by ultrasonically and then coated with 100 Å of chromium followed by 1200 Å of gold in a Leybold Univex 450 coater system. The film patterned photolitographically and etched to provide 10 fingers pairs of electrodes

having a width of 100 μm, spaced 100 μm from the adjacent electrodes. Gold was selected as the electrode material, since it is well-known that it forms ohmic contact to the phthalocyanine. Thin film of compounds was prepared by spin coating method on ohmic gold interdigital electrodes (IDT). For the spin coating, coating solutions were prepared by dissolving of the Pcs in extra pure grade chloroform at concentrations of 6.4×10^{-3} M for all compounds. Twenty micro liters of such solutions were added with a glass pipette onto the IDT structure held onto spinner (Speciality Coatings Systems Inc., Model P6700 Series). The substrate spun at 2000 rpm for 15 s and the solvent had evaporated during this period, producing a homogeneous film of phthalocyanine derivatives. The substrate temperature was kept constant at 300 K during deposition of the materials over the electrodes. Dc conductivity measurements were performed between 300 K and 470 K by using a Keithley 617 electrometer. Impedance spectroscopy and ac conductivity measurements were carried out with a Keithley 3330 LCZ meter in the frequency range, 40–10^5 Hz, and in the temperature range from 300 K to 470 K. All the measurements were performed under 10^{-3} mbar in the dark. Both dc and ac conductivity data were recorded using an IEEE 488 data acquisition system incorporated to a personnel computer.

3. Results and discussion

3.1. Synthesis and characterization

The synthesis of bisphthalodinitriles is based on the reaction of diols with excess of compound **2** (DMF or DMSO in the presence of K_2CO_3 as a base, at 20°C, for 60–96 h) [22,23]. Our key starting material is compound **3** which can be obtained via a reaction of compound **1** and **2**, in dry DMF in the presence of K_2CO_3 in a yield 60.08%. Bis-Pcs **5** and **6** were also obtained by the reaction of compound **3** with **4** using statistically mixed condensation method in dry DMF and in the presence of Zn(II)acetate and Co(II)acetate, respectively (Scheme 1).

In this work, for the synthesis of the new cofacial bis-Pcs, we have developed a solid phase method in the absence of catalysts. The preparation of phthalocyanine derivatives **7** and **8** were achieved by heating the homogenized mixture of **3** with Zn(II)acetate and Co(II)acetate in the ratio 1:1.5 through the cyclotetramerization reaction in a sealed tube at 250 °C in 10 min, respectively (Scheme 1).

Elemental analysis, IR, ^{1}H NMR, MASS and UV/Vis spectra confirmed the proposed structures of the compounds. A diagnostic feature of Pc formation from compound **3** was the disappearance of the sharp intense CN vibration band 2231 cm^{-1} in IR spectrum. The spectra of compounds **5**–**8** showed Ar–O–Ar peaks at 1246–1288 cm^{-1}, C=C (in phenyl) peaks at 1560–1689 cm^{-1}, aromatic CH peaks at 3060–3070 cm^{-1} and aliphatic CH_2 and CH_3 peaks at 2860–2945 cm^{-1}.

The UV–Vis spectra of **5**–**8** in $CHCl_3$ showed characteristic absorptions between 613 and 701 nm in the Q-band region (Table 1). The Q-band observed for the compounds was attributed to the $\pi \rightarrow \pi^*$ transition from the highest occupied molecular orbital (HOMO) to the lowest unoccupied molecular orbital (LUMO) of the Pc ring. The other bands (B) in the UV region at 307–361 nm were observed due to the transitions from the deeper π levels to LUMO. When aggregation occurs, a band ca. 630 nm arises in the electronic spectrum as a result of the intramolecular interactions between the Pc units [28,35]. Thus, the band at around 620 nm can be attributed to intramolecular interactions, although the Q-band is not split.

^{1}H NMR spectra were also in good correlation with the structure of the synthesized compounds. In the ^{1}H NMR spectrum of compound **3** which was taken in *d*-chloroform, phenyl protons appeared at 7.73 ppm(d), 7.34 ppm (dd), 7.28 ppm (dd), and 7.01 ppm (dd), and C–CH_3 protons at 1.75 ppm (s). In the ^{1}H NMR spectra of **5** and **7** which were taken in *d*-chloroform, the aromatic protons appeared at 7.75–6.92 ppm (m) and C–CH_3 peaks at 1.62 and 1.68 ppm (m). In addition, in the ^{1}H NMR spectrum of **5**, the –CH_3 protons at the end of the chain appeared at 0.95–0.87 ppm and aliphatic –CH_2– protons at 1.33–1.26 ppm.

Table 1
UV–Vis data in $CHCl_3$ for phthalocyanine complexes, **5**–**8**

Compound	λ/nm ($\log \varepsilon$/dm^3 mol^{-1} cm^{-1})
5	701 (4.88), 630 (4.34), 361 (4.88)
6	682 (4.95), 624 (4.64), 325 (5.02)
7	682 (4.56), 613 (3.88), 337 (4.33), 307 (4.49)
8	675 (4.70), 613 (4.32), 330 (4.67)

3.2. Electrochemistry

The voltammetric measurements were carried out on platinum in DCM for **5**–**8**. The relevant data are given in Table 2. Compound **5** displayed two reductions at $E_{1/2} = -0.78$ V and $E_{1/2} = -1.14$ V versus SCE, and a single oxidation at $E_{1/2} = 0.71$ V versus SCE. The electrochemical data for **6** is shown in Table 2. The CPC studies showed that each redox process of **5** and **6** involves the transfer of two electrons. Typical steady state cyclic voltammograms (CV) recorded after several scans for these complexes at 0.100 V s^{-1} are shown in Figs. 1 and 2. The redox behaviours of **5** and **6** are similar to mononuclear phthalocyanines, in terms of the half-wave potentials, suggesting that there is not any considerable interaction between two Pc rings and/or two metal centers in these complexes, and that two rings and/or two metal centers react electrochemically at the same potentials. The overall splitting of the molecular orbitals with a high degree on going from the monomeric to dimeric, trimeric or oligomeric Pcs depending on the intermolecular interactions between the rings are expected to occur only in the case that the rings are positioned in face to face orientation as in the sandwich-type Pcs. Thus, it can be concluded that two Pc rings in **5** and **6** are approximately planar in nature. The half-peak potential difference between the first oxidation and the first reduction, $\Delta E_{1/2}$, for **5** and **6** also provides an additional support for the absence of or very weak interactions between two Pc rings and/or two metal centers. $\Delta E_{1/2}$ values ranging from 1.36 to 1.70 V and 0.97 to 1.10 V have been reported for mononuclear and polynuclear no interacting Pc compounds involving redox inactive metal center such as Cu(II), Ni(II) and Zn(II), and involving redox active Co(II) center, respectively [36–40]. The separation between the first oxidation and the first reduction for **5** and **6** was found to be 1.49 and 1.23 V, respectively. In the case that there is strong interaction between two Pcs in a dimer, this separation is expected to decrease as a result of the splitting of molecular orbitals [8,41].

The voltammetric behaviour of cofacial bis-Pcs, **7** and **8**, are considerably different from those of **5** and **6**. These compounds show one-electron redox processes. Typical voltammograms for these compounds are presented in Figs. 3 and 4. The transfer of one electron in each step indicates that the splitting of the molecular orbitals occurs as a result of the strong interaction between the two Pc rings and/or two metal centers in each cofacial bis-Pcs, **7** and **8**, and thus the redox process of each Pc ring and/or metal center in coafacial complexes occurs at different potentials. The strong interaction between the molecular orbitals of two Pcs and/or two metal centers, in a dimer cause remarkable changes in redox potentials, compared with corresponding mono Pcs and non-interacting planar dimers. Generally, the oxidation potentials shift to less positive potentials while the reduction

Table 2
The electrochemical data for **5**–**8** in DCM[a]

Complex	Redox processes		$E_{1/2}$ (V)	ΔE_p (V)	$\Delta E_{1/2}$ (V)	ΔE_s (V)
5	$[Zn(II)Pc(-1)]^{2+}{}_2/[Zn(II)Pc(-2)]_2$	(I)	0.71	0.06	1.49	
	$[Zn(II)Pc(-2)]_2/[Zn(II)Pc(-3)]^{2-}{}_2$	(II)	−0.78	0.06		
	$[Zn(II)Pc(-3)]^{2-}{}_2/[Zn(II)Pc(-4)]^{4-}{}_2$	(III)	−1.14	0.06		
6	$[Co(II)Pc(-1)]^{2+}{}_2/[Co(II)Pc(-2)]_2$	(I)	0.91	0.10	1.23	
	$[Co(II)Pc(-2)]_2/[Co(I)Pc(-2)]^{2-}{}_2$	(II)	−0.32	0.16		
	$[Co(II)Pc(-2)]^{2-}{}_2/[Co(I)Pc(-3)]^{4-}{}_2$	(III)	−1.35	0.10		
	$[Co(I)Pc(-3)]^{4-}{}_2/[Co(I)Pc(-4)]^{6-}{}_2$	(IV)	−1.64	0.20		
7	$[Zn(II)Pc(-2)\cdot Zn(II)Pc(-1)]^{+}/[Zn(II)Pc(-2)]_2$	(I)	0.60	0.10	1.32	
	$[Zn(II)Pc(-2)]_2/[Zn(II)Pc(-2)\cdot Zn(II)Pc(-3)]^{-}$	(II)	−0.72	0.12		0.21
	$[Zn(II)Pc(-2)\cdot Zn(II)Pc(-3)]^{-}/[Zn(II)Pc(-3)]^{2-}{}_2$	(III)	−0.93	0.30		
	$[Zn(II)Pc(-3)]^{2-}{}_2/[Zn(II)Pc(-3)\cdot Pc(-4)]^{3-}$	(IV)	−1.47	0.14		0.23
	$[Zn(II)Pc(-3)\cdot Zn(II)Pc(-4)]^{3-}/[Zn(II)Pc(-4)]^{4-}{}_2$	(V)	−1.70	0.16		
8	$[Co(II)Pc(-1)]^{2+}{}_2/[Co(II)Pc(-2)\cdot Co(II)Pc(-1)]^{+}$	(I)	0.91	0.06		0.28
	$[Co(II)Pc(-2)\cdot Co(II)Pc(-1)]^{+}/[Co(II)Pc(-2)]_2$	(II)	0.63	0.10	0.91	
	$[Co(II)Pc(-2)]_2/[Co(II)Pc(-2)\cdot Co(I)Pc(-2)]^{-}$	(III)	−0.28	0.12		0.30
	$[Co(II)Pc(-2)\cdot Co(I)Pc(-2)]^{-}/[Co(I)Pc(-2)]^{2-}{}_2$	(IV)	−0.58	0.08		
	$[Co(I)Pc(-2)]^{2-}{}_2/[Co(I)Pc(-2)\cdot Co(I)Pc(-3)]^{3-}$	(V)	−1.29	0.10		0.32
	$[Co(I)Pc(-2)\cdot Co(I)Pc(-3)]^{3-}/[Co(I)Pc(-3)]^{4-}{}_2$	(VI)	−1.61	0.22		

[a] Potentials are reported with respect to the SCE. Half-wave potentials in DCM vs. Fc/Fc^+ couple correspond approximately with the above **5**–**8** data minus 0.45 V. $E_{1/2}$ values were measured by cyclic voltammetry [$E_{1/2} = (E_{pa} + E_{pc})/2$] and/or differential pulse voltammetry. The peak separation values ($\Delta E_p = E_{pa} - E_{pc}$) are reported at 0.100 V s^{-1}. $\Delta E_{1/2}$ is the potential difference between the first oxidation and first reduction potentials. It represents the HOMO–LUMO gap for **5** and **7**, but the charge transfer transition for **6** and **8** involving redox-active metal centers. ΔE_s indicates mixed-valence splitting energy for the relevant split redox couple.

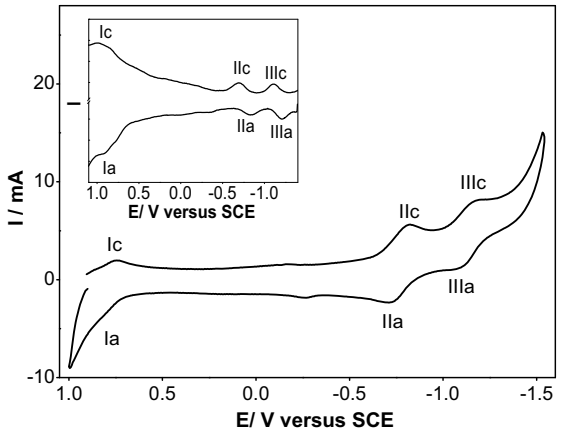


Fig. 1. Cyclic and differential pulse (inner) voltammograms of **5** at 0.100 V s^{-1} on Pt in DCM/TBAP.

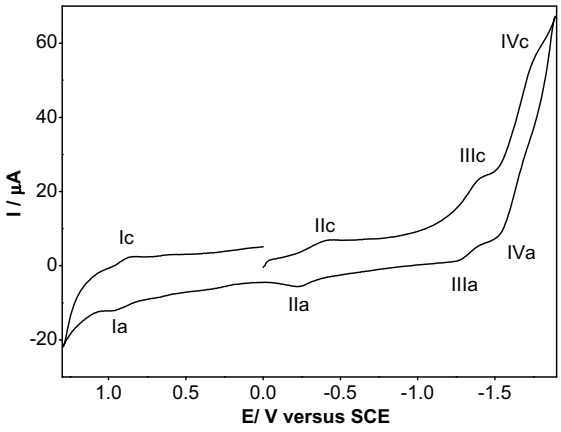


Fig. 2. Cyclic voltammograms of **6** at 0.100 V s^{-1} on Pt in DCM/TBAP.

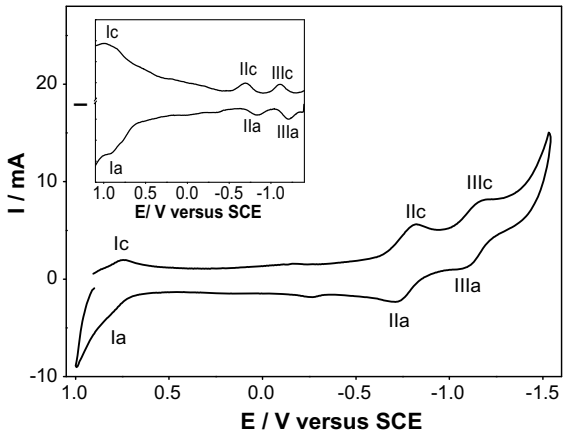


Fig. 3. Cyclic voltammograms of **7** at 0.100 V s^{-1} on Pt in DCM/TBAP.

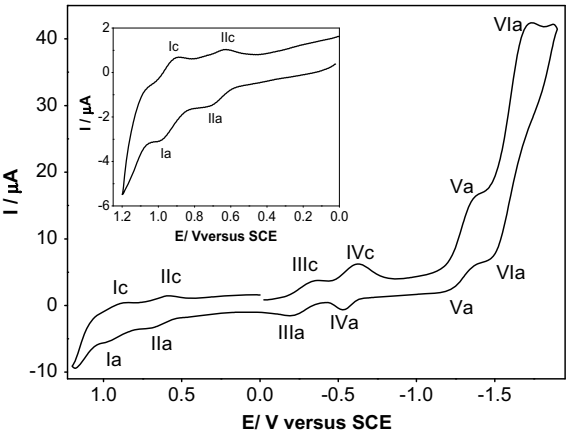


Fig. 4. Cyclic voltammograms of **8** at 0.100 V s^{-1} on Pt in DCM/TBAP.

potentials shift to less negative potentials, the shift in oxidation potentials being more remarkable. Taking this observed behaviour into consideration, it can be concluded from the comparison of voltammetric behaviour of **7** and **8** with the behaviour of **5** and **6** that the high splitting of the redox processes, i.e., mixed-valence behaviour is observed, and thus each redox process of **7** and **8**

occurs at remarkably different potentials as a result of the expected strong interactions between the cofacial Pc rings and/or metal centers. The electrode reactions are schematically illustrated in Chart 1 for **7** and in Chart 2 for **8**.

The mixed-valence splitting, ΔE_s, values in V for the redox processes of **7** and **8** are presented in Table 2. These values give evidence of the delocalization of charge among the cofacial Pc rings and/or metal centers in each cofacial bis-Psc, **7** and **8**, and thus the formation of electrochemically stable oxidized and reduced mixed-valence species.

Some binuclear and tetranuclear Pcs [14,17,35,42–44] showed metal-centered type or ring-centered type mixed-valence behaviour, but some of them did not. The difference was attributed mainly to the presence or absence of axial ligands, respectively inhibiting or facilitating the close approach of the rings, and to the other steric factors. The least strongly coupled systems include some zinc complexes of binuclear Pcs with flexible bridging links [14,17,35]. Moreover, mixed-valence ring reduction, Pc (-2) · Pc (-3), was observed previously only in strongly coupled silicon species [44], but was not unequivocally observed with the other bridged binuclear species. The presence of an extra π-electron repels the π-electron density in the other ring and therefore inhibits formation of these species unless they are constrained to lie close together. The large splitting values for the silicon species was attributed to the shorter Pc ·· Pc contacts than in the bridged systems. The splitting of the redox processes of the Pc ring for **7** and Pc ring and/or metal center for **8** are consistent with those observed previously in literature for a series of mixed-valence Pc complexes [14,17,35,42–44] and with the rigid structure of these cofacial complexes.

3.3. Electrical measurements

Dc electrical properties of thin film of compounds were investigated by means of current–voltage (*I–V*), measurements. The measurements were carried out at different temperatures between 300 K and 470 K. It was observed that the *I–V* curves are straight lines without hysteresis effect for the temperature below 380 K. This indicates that the material has an ohmic resistance, which can be calculated from the slope of the *I–V* curve at each temperature. Above this temperature, the measured *I–V* characteristics show considerable hysteresis between increasing and decreasing voltage sweeps. Fig. 5 shows the dependence of *I–V* characteristics on sweep direction at 300 K and 470 K for compound **5**. In this measurements the voltage has been incremented in steps of 50 mV from −1 to 1 V and back again. It can be seen from Fig. 5 that during the negative to positive voltage sweep, the magnitude of the current at zero applied voltage was higher than positive to negative sweep. It is also observed that the area within the loop increased with an increase in temperature. This effect is likely due to the presence of deep traps, which require a large time constant for charging and discharging in response to a change of the external voltage. Same type of hysteresis behaviour was observed in many other phthalocyanines [45,46]. The interpretation of appearance of the hysteresis effect at high temperature requires to take into account many elementary physical processes such as, density of mobile ions or deep trap level, delay time between two successive measurements separated by a potential step, bulk conductivity of the materials and temperature. High temperature hysteresis behavior suggests that this is due to the formation of space charge polarization in the phthalocyanine thin film. Hysteresis effect was observed for other compounds. The temperature at which the hysteresis effect observed is nearly the same for all compounds. The dc conductivity values of the films were calculated from the slope of the measured *I–V* characteristics by using,

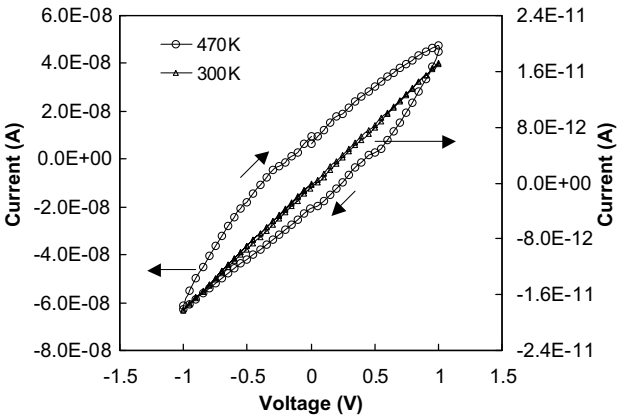


Fig. 5. *I–V* characteristics of the compound **5** at two different temperatures.

$$\sigma_{dc} = \frac{I}{V}\frac{d}{(2n-1)l \cdot h} \quad (1)$$

where I is the measured current, V is the applied voltage, d is the distance between the finger pair, n is the number of the finger pair, l is the overlap length and h is the thickness of the electrode. It was observed that the measured conductivity for the film of compound depend exponentially on temperature such that the conductivity exhibits a variation of the form,

$$\sigma_{dc} = \sigma_0 \exp(-E_A/kT) \quad (2)$$

where E_A is the activation energy, T is the temperature, k is the Boltzmann's constant and σ_0 is the constant of proportionality. The relationship between the conductivity and temperature which

$$[MPc(-1)MPc(-2)]^{+} \overset{e^-}{\rightleftarrows} [MPc(-2)]_2 \overset{e^-}{\rightleftarrows} [MPc(-3)MPc(-2)]^{-} \overset{e^-}{\rightleftarrows} [MPc(-3)]_2^{2-} \overset{e^-}{\rightleftarrows} [MPc(-3)MPc(-4)]^{3-} \overset{e^-}{\rightleftarrows} [MPc(-4)]_2^{4-}$$
$$\text{I} \qquad\qquad \text{II} \qquad\qquad \text{III} \qquad\qquad \text{IV} \qquad\qquad \text{V}$$

Chart 1. Electrode reactions for **7**. M: Zn(II).

$$[M(II)Pc(-1)]_2^{2+} \overset{e^-}{\rightleftarrows} [M(II)Pc(-1).M(II)Pc(-2)]^{+} \overset{e^-}{\rightleftarrows} [M(II)Pc(-2)]_2 \overset{e^-}{\rightleftarrows} [M(II)Pc(-2)M(I)Pc(-2)]^{-} \overset{e^-}{\rightleftarrows} [M(I)Pc(-2)]_2^{2-}$$
$$\text{I} \qquad\qquad\qquad\qquad \text{II} \qquad\qquad \text{III} \qquad\qquad\qquad\qquad \text{IV}$$

$$[M(I)Pc(-2)]_2^{2-} \overset{e^-}{\rightleftarrows} [M(I)Pc(-2).M(I)Pc(-3)]^{3-} \overset{e^-}{\rightleftarrows} [M(I)Pc(-3)]_2^{4-}$$
$$\text{V} \qquad\qquad\qquad\qquad \text{VI}$$

Chart 2. Electrode reactions for **8**. M: Co.

is given by Eq. (2) shows that the materials behave as an intrinsic semiconductor in the measured temperature range (300–470 K).

The activation energies for the samples were evaluated from the slopes of the $\ln\sigma_{dc}$ versus $1/T$ graphs. The obtained conductivity values for two different temperature (300 K and 470 K), and the calculated activation energies are given in Table 3.

The ac electrical conductivity, σ_{ac}, as a function of temperature has also been investigated for all film of compounds at several frequencies. Fig. 6 shows semi logarithmic plot of ac conductivity versus reciprocal temperature at indicated frequencies for compound **5**. At least two temperature ranges, $300 < T < \sim 400$ K and $410 < T < 470$ K can be identified from Fig. 6 for the film of **5**. The same type temperature dependence with different temperature range was observed for other films. This indicates that the temperature dependence of the ac conductivity is not uniform process and results in activation energies corresponding to the different temperature range. The values of ac activation energies associated with this two temperatures region were calculated from the slope of $\log\sigma_{ac}$–$1/T$ graph for different frequencies and collected in Table 4.

Ac conductivity measurements as function of frequency on the film of compounds were also investigated at different temperatures. It was observed that ac conductivity follows power law as

$$\sigma_{ac} = A\omega^n \quad (3)$$

where ω is the angular frequency, A is the material dependent constant, and the frequency exponent n which normally takes the value of less than unity. The value of exponent n and its behavior with temperature determines the dominant conduction mechanism in phthalocyanine film.

In the models which are used to investigate the power law of ac conductivity, the frequency exponent n is found to have two different trends with temperature and frequency [47]. The value of frequency exponent is obtained from the measured conductivity data. It was observed that n strongly temperature dependent and decreases with increasing temperature for all films. This dependence of n on temperature is in agreement with the prediction of the correlated barrier-hoping model. The same type of temperature dependence for n were observed in our earlier report in different phthalocyanine films [48,49].

The effect of temperature on the capacitance of the films are investigated in the frequency range of 40–10^5 Hz. Variations of capacitance of the film of **5** with frequency for different temperatures is shown in Fig. 7. From Fig. 7, it becomes clear that there is a monotonic decrease in the capacitance for the film of **5** at low frequencies. At higher frequency the value of capacitance merges irrespective of temperature. It can also be seen from Fig. 7 that the effect of temperature on capacitance is more significant at lower frequencies. The increase in capacitance with increasing temperature can be explained in terms of ionization of acceptors, which causes an increase in carrier concentrations and hence an increase in the capacitance. The frequency dependence of the capacitance can qualitatively be explained employing equivalent circuit model developed by Goswami and Goswami [50]. Equivalent circuit model assumes that the measured capacitance C depends on a frequency a resistive element representing the resistance of the film. The value of resistive element decreases with

Table 3
Measured conductivity values of the compounds at room temperature ($\sigma_{300\,K}$), 470 K ($\sigma_{470\,K}$) and calculated activation energies

Sample	$\sigma_{300\,K}$ (S/cm)	$\sigma_{470\,K}$ (S/cm)	E_A (eV)
5	3.05×10^{-12}	4.80×10^{-8}	0.73
6	3.21×10^{-12}	1.07×10^{-7}	0.80
7	1.79×10^{-12}	5.50×10^{-8}	0.76
8	5.13×10^{-12}	5.00×10^{-8}	0.67

Table 4
Activation energy values for the ac conductivity calculated at two different temperature region and at different frequencies

Sample	Frequency (Hz)	Activation energy (eV)	
		$300 < T < \sim 400$ K	$400 < T < 470$ K
5	2×10^3	0.31	0.60
	1×10^4	0.26	0.51
	5×10^4	0.18	0.40
	7×10^4	0.18	0.39
		$300 < T < \sim 405$ K	$405 < T < 470$ K
6	2×10^3	0.27	0.58
	1×10^4	0.22	0.47
	5×10^4	0.33	0.82
	7×10^4	0.25	0.73
		$300 < T < 390$ K	$390 < T < 470$ K
7	2×10^3	0.30	0.66
	1×10^4	0.21	0.53
	5×10^4	0.34	0.70
	7×10^4	0.15	0.43
		$300 < T < 430$ K	$430 < T < 470$ K
8	2×10^3	0.22	0.58
	1×10^4	0.30	0.80
	5×10^4	0.14	0.76
	7×10^4	0.17	0.64

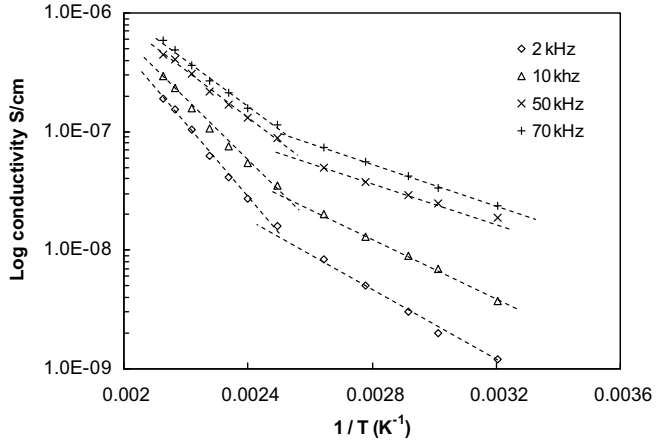


Fig. 6. Temperature dependence of ac conductivity for the compound **5** at indicated frequencies.

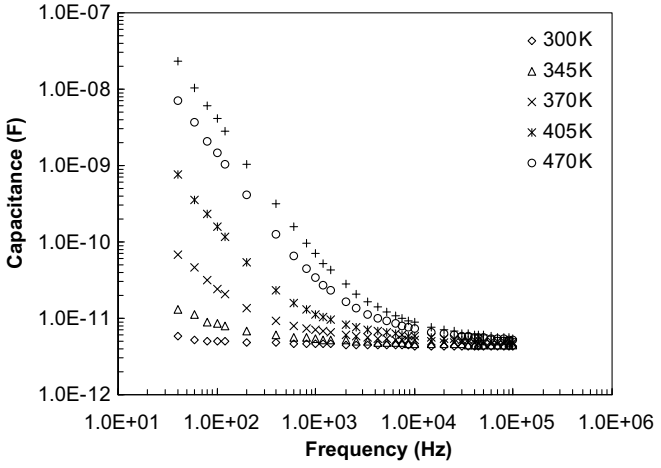


Fig. 7. Variation of capacitance with frequency at indicated temperature for **5**.

increase in the temperature results in a decrease in the value capacitance. It was observed that the temperature and frequency dependence of the measured capacitance for compounds **6**, **7** and **8** are the same.

Acknowledgements

This work is supported by the Research Fund of the Yildiz Technical University (Project No.: 24-01-02-12), TUBITAK (Project No: TBAG-106T326) and The Turkish Academy of Sciences (TUBA).

Appendix A. Supplementary data

Supplementary data associated with this article can be found, in the online version, at doi:10.1016/j.poly.2008.02.031.

References

[1] C.C. Leznoff, A.B.P. Lever (Eds.), Phthalocyanines – Properties and Applications, vols. 1–4, New York, (1989, 1992, 1993 and 1996).
[2] N.B. McKeown, Phthalocyanines Materials – Synthesis, Structure and Functions, Cambridge University Press, Cambridge, 1998.
[3] N. Kobayashi, P. Janda, A.B.P. Lever, Inorg. Chem. 31 (1994) 5172.
[4] J. Simon, T. Toupance, in: D.N. Reinhoudt (Ed.), Supramolecular Technology, vol. 10, Pergamon, Exeter, 1996.
[5] G. de la Torre, T. Torres, F. Aqullo-Lopez, Adv. Mater. 9 (1997) 265.
[6] N. Toshima, T. Tominaga, S. Kawamura, Bull. Chem. Soc. Jpn. 69 (1996) 245.
[7] B. Lukas, J. Silver, D. Lovett, M.J. Cook, Chem. Phys. Lett. 241 (1995) 351.
[8] Ş. Abdurrahmanoğlu, A.R. Özkaya, M. Bulut, Ö. Bekaroğlu, Dalton Trans. (2004) 4022.
[9] H. Eichhorn, D. Wöhrle, D. Pressner, Liq. Cryst. 22 (1997) 643.
[10] D. Lelievre, M.A. Petit, J. Simon, Liq. Cryst. 4 (1989) 707.
[11] Ş. Merey, Ö. Bekaroğlu, J. Chem. Soc. (1999) 4503.
[12] N. Koike, H. Uekusa, Y. Ohashi, C. Harnoode, F. Kitamura, T. Ohsaka, K. Tokuda, Inorg. Chem. 35 (1996) 5798.
[13] J. Jiang, D.P. Arnold, H. Yu, Polyhedron 18 (1999) 2129.
[14] C.C. Leznoff, H. Lam, W.A. Nevin, N. Kobayashi, P. Janda, A.B.P. Lever, Angew. Chem., Int. Engl. 26 (1987) 1021.
[15] H. Lam, S.M. Marcuccio, P.I. Svirskaya, S. Greenberg, C.C. Leznoff, R.L. Cerny, Can. J. Chem. 67 (1989) 1087.
[16] N. Kobayashi, Y. Yanagisawa, T. Osa, H. Lam, C.C. Leznoff, Anal. Chem. 6 (1990) 813.
[17] N. Kobayashi, H. Lam, W.A. Nevin, P. Janda, C.C. Leznoff, A.B.P. Lever, Inorg. Chem. 29 (1990) 3415.
[18] N. Kobayashi, H. Lam, W.A. Nevin, P. Janda, C.C. Leznoff, T. Koyama, A. Monden, H. Shirai, J. Am. Chem. Soc. 116 (1994) 879.
[19] N. Kobayashi, M. Numao, R. Kondo, S. Nakajima, T. Osa, Inorg. Chem. 30 (1991) 2241.
[20] N. Kobayashi, J. Chem. Soc., Chem. Commun. (1991) 1203.
[21] N. Kobayashi, Y. Higashi, T. Osa, Chem. Lett. (1994) 1813.
[22] E.M. Garcia-Frutos, F. Fernandez-Lazaro, E.M. Maya, P. Vazquez, T. Torres, J. Org. Chem. 65 (2000) 6841.
[23] S. Vigh, H. Lam, P. Janda, A.B.P. Lever, C.C. Leznoff, R.L. Cerny, Can. J. Chem. 69 (1991) 1457.
[24] E.M. Maya, P. Vazquez, T. Torres, Chem. Eur. J. 5 (1999) 2004.
[25] K.H. Schweikart, M. Hanack, Eur. J. Org. Chem. (2000) 2551.
[26] E.M. Maya, P. Vazquez, T. Torres, L. Gobbi, F. Diedrich, S. Pyo, L. Echegoyen, J. Org. Chem. 65 (2000) 823.
[27] N. Kobayashi, Coord. Chem. Rev. 227 (2002) 29.
[28] Z. Odabaş, A. Altındal, A.R. Özkaya, M. Bulut, B. Salih, Ö. Bekaroğlu, Polyhedron 26 (2007) 695.
[29] Z. Odabaş, A. Altındal, A.R. Özkaya, M. Bulut, B. Salih, Ö. Bekaroğlu, Polyhedron 26 (2007) 3505.
[30] T. Ceyhan, A. Altındal, A.R. Özkaya, M.K. Erbil, B. Salih, Ö. Bekaroğlu, Chem. Commun. (2006) 320.
[31] T. Ceyhan, A. Altındal, A.R. Özkaya, Ö. Çelikbıçak, B. Salih, M.K. Erbil, Ö. Bekaroğlu, Polyhedron 26 (2007) 4239.
[32] M. Özer, A. Altındal, A.R. Özkaya, B. Salih, M. Bulut, Ö. Bekaroğlu, Eur. J. Inorg. Chem. 22 (2007) 3519.
[33] A.Y. Tolbin, A.V. Ivanov, L.G. Tomilova, N.S. Zefirov, Mendeleev Commun. 7 (2002) 96.
[34] A.Y. Tolbin, A.V. Ivanov, L. G Tomilova, N.S. Zefirov, J. Porphyr. Phthalocya. 7 (2003) 162.
[35] V. Manivannan, W.A. Nevin, C.C. Leznoff, A.B.P. Lever, J. Coord. Chem. 19 (1988) 139.
[36] A.B.P. Lever, E.R. Milaeva, G. Speier, in: C.C. Leznoff, A.B.P. Lever (Eds.), Phthalocyanines: Properties and Applications, vol. 3, VCH, Weinheim, 1993, p. 1.
[37] A.R. Özkaya, A.G. Gürek, A. Gül, O. Bekaroğlu, Polyhedron 16 (1997) 1877.
[38] A.R. Özkaya, I. Yılmaz, O. Bekaroğlu, J. Porphyr. Phthalocya. 2 (1998) 483.
[39] A.R. Özkaya, E. Hamuryudan, Z.A. Bayır, O. Bekaroğlu, J. Porphyr. Phthalocya. 4 (2000) 689.
[40] M. Kandaz, A.R. Özkaya, O. Bekaroğlu, Monats. Chem. 132 (2001) 1013.
[41] S. Abdurrahmanoglu, A. Altındal, A.R. Özkaya, M. Bulut, Ö. Bekaroglu, Chem. Commun. (2004) 2096.
[42] W.A. Nevin, W. Liu, S. Greenberg, M.R. Hempstead, S.M. Marcuccio, M. Melnik, C.C. Leznoff, A.B.P. Lever, Inorg. Chem. 26 (1987) 891.
[43] C.C. Leznoff, H. Lam, S.M. Marcuccio, W.A. Nevin, P. Janda, N. Kobayashi, A.B.P. Lever, J. Chem. Soc., Chem. Commun. (1987) 699.
[44] D.W. DeWulf, J.K. Lelend, B.L. Wheeler, A.J. Bard, D.A. Batzel, D.R. Dininny, M.E. Kenney, Inorg. Chem. 26 (1987) 266.
[45] I. Thurzo, G. Pham, D.R.T. Zahn, Chem. Phys. 287 (2003) 43.
[46] P.D. Hooper, M.I. Newton, G. McHale, M.R. Willist, Semicond. Sci. Technol. 12 (1997) 455.
[47] S.R. Elliot, Adv. Phys. 36 (1987) 135.
[48] A. Altındal, S. Abdurrahmanoğlu, M. Bulut, Ö. Bekaroğlu, Syn. Metals 150 (2005) 181.
[49] T. Ceyhan, A. Altındal, M.K. Erbil, Ö. Bekaroğlu, Polyhedron 25 (2006) 737.
[50] A. Goswami, A.P. Goswami, Thin Solid Films 16 (1973) 175.

2. Experimental

2.1. Materials and methods

Solvents (dichloromethane, dimethylformamide, ethanol and methanol) were purchased from Merck and were used as supplied. 4-Fluorobenzenesulfonamide, 4-iodobenzenesulfonyl chloride, potassium tetrachloroplatinate(II) and tetrabutylammonium bromide were purchased from Aldrich. KOH and CS_2 were purchased from Vetec. The 4-iodobenzenesulfonamide was prepared from 4-iodobenzenesulfonyl chloride in reaction with concentrated ammonia solution, according to the methodology applied for the syntheses of similar compounds [13] and potassium *N*-4-iodophenylsulfonyldithiocarbimate was prepared from the parent sulfonamide as described in the literature [12]. This salt, which is soluble in H_2O and insoluble in most organic solvents, was recrystallized from a hot mixture of ethanol and water. IR spectra were recorded with a Perkin–Elmer 1000 FT-IR spectrophotometer using CsI pellets. The NMR spectra were recorded with a Bruker DPX-200-AVANCE or a VARIAN-300 spectrophotometers in D_2O (**1**, **2**), DMSO-D_6 (**3**) and $CDCl_3$ (**4**) with TMS as internal standard. Microanalyses for C, H and N were obtained from a Perkin–Elmer 2400 CHN elemental analyzer. Platinum was analyzed by atomic absorption on a Hitachi Z-8200 atomic absorption spectrophotometer. Uncorrected melting points were measured with a Mettler FP5 melting point apparatus. The molar conductances (Λ_M) were measured in acetonitrile solutions at 25 °C with a Conductivity Meter Jenway 4010.

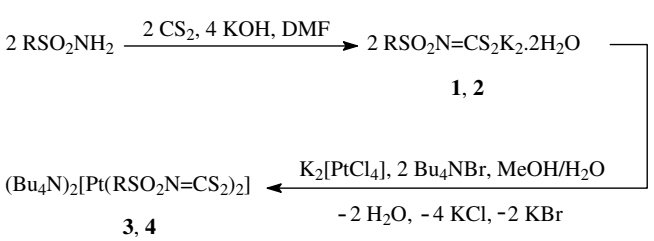
2.2. Syntheses of the dithiocarbimate potassium salts

Compound **1** was prepared as described in the literature [12]. Compound **2** was prepared as described, see Scheme 1.

Carbon disulfide (0.02 mol) and potassium hydroxide (0.01 mol) were added to a solution of 4-fluorobenzenesulfonamide (0.02 mol) in DMF (20 mL). The mixture was stirred at room temperature for 2 h previous to the addition of a second portion of potassium hydroxide (0.01 mol). After stirring for further 1 h, the yellow solid formed was filtered, washed with DMF, ethanol and ethyl acetate and dried under reduced pressure yielding the potassium *N*-4-fluorophenylsulfonyldithiocarbimate (80% based on the sulfonamide). Suitable crystals for X-ray structure analysis were obtained after recrystallization in ethanol:water 1:1 mixture.

2.2.1. Potassium N-4-fluorophenylsulfonyldithiocarbimate dihydrate (**2**)

Elemental *Anal.* Calc. for $C_7H_8FNO_4S_3K_2$: C, 23.13; H, 2.22; N, 3.85. Found: C, 23.10; H, 2.02; N, 3.85%. IR (most important bands) (cm^{-1}): 3340 (water), 1259 (νCN) + (νSO_{2asym}), 1135 (νSO_{2sym}), 977 (νCS_{2asym}). ^{1}H NMR (300 MHz, D_2O), (δ): 7.72–7.65 (m, 4H, H2 and H6), 7.15–7.07 (m, 4H, H3 and H5). ^{13}C NMR (δ), *J* (Hz): 225.29 (N=CS_2), 164.35 (d, $^1J_{C,F}$ = 248.4, C4), 137.96 (C1), 129,31 (d, $^3J_{C,F}$ = 9.8, C2 and C6), 115.90 (d, $^2J_{C,F}$ = 22.9, C3 and C5).



1, 3 (R = 4-IC_6H_4) **2, 4** (R = 4-FC_6H_4)

Scheme 1. Syntheses of **1**–**4**.

2.3. Syntheses of the platinum complexes

The syntheses of the platinum complexes were performed according to Scheme 1. Potassium tetrachloroplatinate(II) (0.001 mol) and tetrabutylammonium bromide (0.002 mol) were added to a solution of potassium *N*-R-sulfonyldithiocarbimate dihydrate (**1** or **2**, 0.002 mol) in methanol/water 1:1 (10 mL). The reaction mixture was stirred for 3 h at room temperature. The yellow solid obtained was filtered, washed with distilled water and dried under reduced pressure for one day, yielding $(Bu_4N)_2$[Pt(*N*-$RSO_2N{=}CS_2)_2$] (*ca.* 70% based on the $K_2[PtCl_2]$). Suitable crystals for X-ray structure analyses were obtained after slow evaporation of the solutions of compounds **3** and **4** (R = 4-IC_6H_4 and 4-FC_6H_4, respectively) in methanol/water 4:1.

2.3.1. Tetrabutylammonium bis(N-4-iodophenylsulfonyldithiocarbimato)platinate(II) (**3**)

Elemental *Anal.* Calc. for $(C_{16}H_{36}N)_2C_{14}H_8I_2N_2O_4S_6Pt$: C, 39.62; H, 5.78; N, 4.02; Pt, 13.99. Found: C, 39.68; H, 5.63; N, 3.96; Pt, 13.72%. M.p. (°C): 168.3–169.7. Molar conductance [Λ_M (Ω^{-1} cm^2 mol^{-1})]: 220. IR (most important bands) (cm^{-1}): 1384 (νCN), 1287 (νSO_{2asym}), 1143 (νSO_{2sym}), 936 (νCS_{2asym}), 334 (νPtS). ^{1}H NMR (200 MHz, DMSO-D_6, complex anion signals) (δ), *J* (Hz): 7.86 (d, 4H, *J* = 8.4, H3 and H5), 7.52(d, 4H, *J* = 8.4, H2 and H6). ^{13}C NMR (50 MHz, DMSO-D_6, complex anion signals) (δ): 212.37 (N=CS_2), 142.82 (C1), 137.03 (C3 and C5), 128.76 (C2 and C6), 98.96 (C4).

2.3.2. Tetrabutylammonium bis(N-4-fluorophenylsulfonyldithiocarbimato)platinate(II) (**4**)

Elemental *Anal.* Calc. for $(C_{16}H_{36}N)_2C_{14}H_8I_2N_2O_4S_6Pt$: C, 46.88; H, 6.84; N, 4.75; Pt, 16.55%. Found: C, 46.93; H, 6.79; N, 4.75; Pt, 16.52%. M.p. (°C): 163.8–165.0. Molar conductances [Λ_M (Ω^{-1} cm^2 mol^{-1})]: 249. IR (most important bands) (cm^{-1}): 1376 (νCN), 1283 (νSO_{2asym}), 1145 (νSO_{2sym}), 934 (νCS_{2asym}), 330 (νPtS). ^{1}H NMR (200 MHz, $CDCl_3$, complex anion signals) (δ), *J* (Hz): 8.05–7.95 (m, 4H, H2 and H6), 7.04 (br, t, 4H, $J \approx 8$, H3 and H5). ^{13}C NMR (50 MHz, $CDCl_3$, complex anion signals) (δ), *J* (Hz): 212.96 (N=CS_2), 164.27 (d, $^1J_{C,F}$ = 249.7, C4), 139.79 (C1), 130.32 (d, $^3J_{C,F}$ = 8.9, C2 and C6), 114.77 (d, $^2J_{C,F}$ = 22.0, C3 and C5).

2.4. X-ray diffraction experiments

X-ray intensity data for single crystals were collected using graphite monochromatic Mo Kα radiation on a four-circle κ-geometry KUMA KM-4 diffractometer with a two-dimensional area CCD detector. The ω-scan technique with $\Delta\omega = 0.80°$ for each image was used for data collection. The 880 images for six different runs covered about 98% of the Ewald sphere were collected using the CRYSALIS CCD program [14]. The lattice parameters were refined by least-squares methods based on all the reflections with $I > 2\sigma(F^2)$. One image was used as a standard for monitoring of the stability of the crystals as well as for monitoring the data collection after every 50 images, and no correction on the relative intensity variation was necessary. Integration of the intensities, correction for Lorenz and polarization effects and the numerical absorption correction were performed using a CRYSALIS RED program [14]. The structures were solved by direct methods using SHELXS97 [15]. The calculated E map revealed the metals, S, O, N and most of the C atoms. The remaining C atoms were located from the difference Fourier synthesis. The structures were refined with the anisotropic thermal parameters for all non-hydrogen atoms using SHELXL97 [15]. Difference Fourier maps gave electron density concentrations

approximately located for all hydrogen atoms positions; these positions were idealised (HFIX 43 for all H atoms of the phenyl rings with isotropic thermal parameters of 1.2 U_{eq} of the carbon atoms joined directly to the hydrogen atoms, and HFIX 137 for the CH_3 and HFIX 23 for the CH_{2l} with isotropic thermal parameters of 1.5 U_{eq} of the carbon atom). Final difference Fourier maps showed no peaks of chemical significance. Details of the data collection parameters and final agreement factors are collected in Table 1. Selected bond lengths and angles and torsion angles are listed in Table 2.

2.5. Theoretical calculations

Ab initio molecular orbital calculations full geometry optimizations were performed with the GAUSSIAN98 program package [16]. The calculations were performed for the isolated 4-fluorophenylsulfonyldithiocarbimate(2-) ligand by the density functional three-parameters hybrid (B3LYP) methods [17,18] with the 6-31+G(d) basis set starting from the X-ray geometry. As convergence criterion the threshold limits of 0.00025 and 0.0012 a.u. were applied for the maximum force and the displacement, respectively.

3. Results and discussion

Compounds **1** and **2** are yellow solids. They are insoluble in organic solvents and soluble in water. They are not very stable and a white solid is obtained from their aqueous solutions after some days at room temperature. At ambient temperature, the yellow solids are also converted into white solids after several months. Both, **3** and **4**, are yellow crystalline solids insoluble in water and very stable at room temperature. Compound **4** is soluble in polar organic solvents such as DMF, DMSO, ethanol, methanol, dichloromethane and chloroform. Compound **3** is soluble in DMF, DMSO, and differently from compound **4** and the analogues with R = C_6H_5 and 4-BrC_6H_4 [10], only slightly soluble in the other organic solvents mentioned above. The molar conductances of **3** and **4** at 10^{-3} mol L^{-1} in acetonitrile are in the range of 220–300 Ω^{-1} cm^2 mol^{-1}, commonly attributed to 1:2 electrolytes [19].

The spectroscopic properties of compounds **3** and **4** are similar to those presented by other platinum(II) complexes of dithiocarbimate from sulfonamides described in the literature [10] (Tables 3 and 4). In the IR spectra of the potassium dithiocarbimates **1** and **2**, there are no strong bands in the 1450–1550 cm^{-1} spectral region, the νCN band being observed at 1280 and 1259 cm^{-1}, respectively. A strong band observed at 1384 cm^{-1} in the spectrum of compound **3** and at 1376 cm^{-1} in the spectrum of compound **4** was assigned to the νCN. The CN bond is formally a double bond. However, because of the SO_2 neighbour group, the canonical forms (a) and (b) (Scheme 2) contribute appreciably to the resonance hybrid. This fact explains the low values observed for the νCN band wavenumbers. The νCS_{2asym} were observed at higher wavenumbers in the spectra of the potassium salts of dithiocarbimates (971 and 977 cm^{-1} for **1** and **2**, respectively) than in the spectra of compounds **3** and **4** (936 and 934 cm^{-1}, respectively). The shifts observed in the νCS_{2asym} and νCN bands in the vibrational spectra of the complexes when compared to the spectra of the free ligands, are consistent with the increased importance of the canonical form (c) after complexation (Scheme 2). The spectra of compounds **3** and **4** also show the expected medium/strong band in the 300–400 cm^{-1} range assigned to the νPtS.

The NMR spectra were typical for diamagnetic species and were consistent with the proposed structures. The integration curves on the ^{1}H NMR spectra of **3** and **4** were consistent with a 2:1 proportion between the tetrabutylammonium cation and the Pt-bis(dithiocarbimato) complex anion. In the ^{13}C NMR spectra of compounds **3** and **4** the signal of the quaternary carbon of the dithiocarbimate

Table 1
Crystallographic data and structure refinement parameters

	2	3	4
Crystal data			
Formula	$C_7H_8FNO_4S_3K_2$	$C_{46}H_{80}I_2N_4O_4S_6Pt$	$C_{46}H_{80}F_2N_4O_4S_6Pt$
Molecular weight (g mol^{-1})	363.52	1394.39	1178.59
Crystal system	monoclinic	monoclinic	triclinic
Space group	$P2_1/c$ (No. 14)	$P2_1/c$ (No. 14)	$P\bar{1}$ (No. 2)
a (Å)	6.251(1)	9.099(2)	9.837(2)
b (Å)	7.178(1)	12.6451(3)	9.969(2)
c (Å)	30.105(5)	24.716(4)	15.435(3)
α (°)			89.79(2)
β (°)	90.34(2)	94.23(2)	74.50(2)
γ (°)			69.55(2)
Volume, V (Å^3)	1350.8(4)	2837.3(11)	1359.9(5)
Z	4	2	1
$D_{calc.}$; $D_{obs.}$ (flotation) (g cm^{-3})	1.788; 1.78	1.632;1.63	1.439; 1.43
Radiation, λ (Å)		Mo Kα (0.71073)	
Absorption coefficient μ (mm^{-1})	1.18	3.82	2.86
Transmission factor, T_{max}; T_{min}	0.855; 0.736	0.681; 0.362	0.588; 0.350
Data collection			
$2\theta_{max}$ (°)	59.2	59.4	58.2
Collected/unique reflections	16650/3501	36868/7392	17388/6619
Observed reflections ($I > 2\sigma(I)$)	3029	4698	4722
R_{int}	0.019	0.045	0.041
Refinement			
$R(F_o^2 > 2\sigma(F_o^2))$	0.033	0.037	0.039
$wR(F_o^2$, all reflections)	0.070	0.081	0.081
$\Delta\rho_{min}$; $\Delta\rho_{max}$ (e Å^{-3})	−0.309; +0.401	−1.139; +1.769	−1.119; +0.668
Goodness-of-fit	1.001	1.010	1.010

Table 2
Selected bond lengths (Å) and angles (°)

Compound **2**					
K1–O3	2.822(2)	K2–O1^{iv}	2.680(2)	S1–C1	1.731(2)
K1–O3^{i}	2.902(2)	K2–O2	2.725(2)	S2–C1	1.706(2)
K1–O4^{i}	2.759(2)	K2–O3	3.130(2)	C1–N1	1.351(2)
K1–O4^{ii}	3.056(2)	K2–O4^{i}	2.947(2)	N1–S3	1.610(2)
K1–N1	3.051(2)	K2–S2^{iv}	3.206(2)	S3–O1	1.443(2)
K1–O2	3.051(2)	K2–F1^{v}	2.785(2)	S3–O2	1.445(2)
K1–S1^{iii}	3.371(2)	K2–S1^{vi}	3.375(2)	S3–C2	1.768(2)
K1–K2	3.974(2)	K2–S2^{vi}	3.195(2)	C5–F1	1.362(2)
	Compound **3**	Compound **4**		Compound **3**	Compound **4**
Pt–S1	2.325(2)	2.325(2)	S3–O1	1.432(3)	1.435(3)
Pt–S2	2.314(1)	2.316(3)	S3–O2	1.436(3)	1.434(3)
S1–C1	1.735(4)	1.732(4)	S3–C2	1.770(4)	1.764(4)
S2–C1	1.732(4)	1.739(4)	C5–I1	2.094(4)	
C1–N1	1.302(4)	1.299(4)	C5–F1		1.364(5)
N1–S3	1.619(3)	1.615(3)			
S1–Pt–S2	74.39(4)	73.88(5)	S1–Pt–S2^{i}	105.61(4)	106.12(5)

Torsion angles	**3**	4-BrC_6H_4-derivative[a]	**4**	Ph-derivative[a]
Bu_4N^+				
C11–C12–C13–C14	−179.6(1)	−178.3(1)	172.3(1)	175.3(1)
C21–C22–C23–C24	175.9(1)	174.8(1)	174.5(1)	174.4(1)
C31–C32–C33–C34	176.1(1)	178.6(1)	−177.3(1)	−178.3(1)
C41–C42–C43–C44	164.2(1)	160.8(1)	−92.9(1)	−173.2(1)

Symmetry code compound **2**: (i) $-x+1, -y+1, -z$; (ii) $x-1, y, z$; (iii) $-x, -y, -z$; (iv) $x, y+1, z$; (v) $-x, y+0.5, -z+0.5$; (vi) $x+1, y+1, z$.
Symmetry code compounds **3** and **4**: (i) $-x, -y, -z$.
[a] Data from Ref. [10].

Table 3
Comparison between the νCS_2 and the CS_2 bond lengths and angles in dithiocarbimate potassium salts and complexes

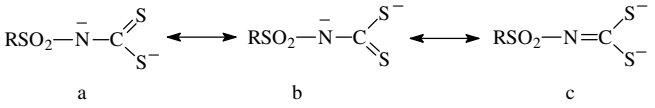
Substances	νCS_2 (cm^{-1})	C(1)–S(1) (Å)	C(1)–S(2) (Å)	S(1)–C(1)–S(2) (°)
$K_2(C_6H_5SO_2C{=}NS_2)$[a]	971			
$K_2(4\text{-}BrC_6H_5SO_2C{=}NS_2)$[a]	973			
$K_2(4\text{-}IC_6H_5SO_2C{=}NS_2)$ (**1**)	971			
$K_2(4\text{-}FC_6H_5SO_2C{=}NS_2)$ (**2**)	977	1.731(2)	1.706(2)	119.5(1)
$[Pt(C_6H_5SO_2C{=}NS_2)_2]^{2-}$[a]	934	1.733(2)	1.750(2)	107.87(11)
$[Pt(4\text{-}BrC_6H_4SO_2C{=}NS_2)_2]^{2-}$[a]	930	1.732(4)	1.737(4)	108.5(2)
$[Pt(4\text{-}IC_6H_4SO_2C{=}NS_2)_2]^{2-}$ (**3**)	936	1.735(2)	1.732(2)	108.0(2)
$[Pt(4\text{-}FC_6H_4SO_2C{=}NS_2)_2]^{2-}$ (**4**)	934	1.732(4)	1.739(4)	106.9(2)

[a] Data from Ref. [10].

Table 4
Comparison between the crystallographic and spectroscopic data for the CN bond in the NCS_2 moiety of the dithiocarbimate anions

Substances	νCN (cm^{-1})	^{13}C NMR (NCS_2) (ppm)	CN length (Å)
$K_2(C_6H_5SO_2C{=}NS_2)$[a]	1267	223.19	
$K_2(4\text{-}BrC_6H_5SO_2C{=}NS_2)$[a]	1258	225.74	
$K_2(4\text{-}IC_6H_5SO_2C{=}NS_2)$ (**1**)	1280	225.62	
$K_2(4\text{-}FC_6H_5SO_2C{=}NS_2)$ (**2**)	1259	225. 29	1.351(2)
$[Pt(C_6H_5SO_2C{=}NS_2)_2]^{2-}$[a]	1395	212.74	1.293(3)
$[Pt(4\text{-}BrC_6H_4SO_2C{=}NS_2)_2]^{2-}$[a]	1380	213.29	1.313(4)
$[Pt(4\text{-}IC_6H_4SO_2C{=}NS_2)_2]^{2-}$ (**3**)	1384	212.37	1.302(4)
$[Pt(4\text{-}FC_6H_4SO_2C{=}NS_2)_2]^{2-}$ (**4**)	1376	212.96	1.299(4)

[a] Data from Ref. [10].



Scheme 2. Three canonical forms for *N*-R-sulfonyldithiocarbimate anion.

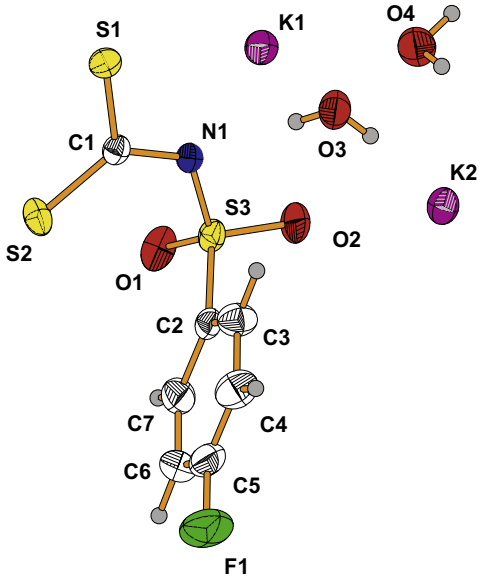


Fig. 1. The atomic numbering scheme of $K_2(4\text{-}FC_6H_4SO_2N{=}CS_2)\cdot 2(H_2O)$. Displacement ellipsoids are drawn at the 50% probability level.

moiety is shifted upfield when compared to the corresponding signal in the potassium dithiocarbimates spectra. This fact is also consistent with the increase in the contribution of canonical form (c) after the complexation (Scheme 2). The coupling constants between the fluorine and the carbon atoms in the spectra of compounds **2** and **4** were observed in the normal range for other fluorinated aromatic compounds ($^1J_{C4,F} \approx 249$ Hz and $^2J_{C3,F} \approx 22.5$ Hz), and it was also possible to observe the coupling with C-2 ($^3J_{C2,F} \approx 9$ Hz).

The asymmetric unit of compound **2** is illustrated in Fig. 1. The dithiocarbimate(2-) group together with the sulfur atom of sulfonyl group of the 4-fluorophenyl-sulfonyldithiocarbimate(2-) anion (the S1S2C1N1S3 fragment) is planar and almost perpendicular to the phenyl ring. The dihedral angle between the planes defined by the S1S2C1N1S3 atoms and by the C atoms of the phenyl ring is equal to 98.9(1)°. The potassium cations, K1 and K2, have different coordination envinronments. The K1 cation is surrounded by two 4-fluorophenylsulfonyldithiocarbimate(2-) anions and three water molecules (Fig. 2a). One of the 4-fluorophenylsulfonyldithiocarbimate(2-) ligands is joined to K1 by the S1 atom of dithiocarbimate group, while the other ligand by O2 of sulfonyl group and by the N1 atom. The K2 cation interacts with four neighbouring 4-fluorophenylsulfonyldithiocarbimate(2-) ligands and with two water molecules (Fig. 2b). Each of these 4-fluorophenylsulfonyldithiocarbimate(2-) ligands interacts differently with the K2 cation. One of them inteacts by both S atoms of CS_2 group, the other by the O atom of sulfonyl group and by one S atom of CS_2 group. The third 4-fluorophenylsulfonyldithiocarbimate(2-) ligand is directed towards the K2 cation by the F atom (K2–F1, 2.785(2) Å), and the fourth ligand is oriented to the K2 cation by the O atom of sulfonyl group (K2–O2, 2.725(2) Å). Thus the potassium cations, K1 and K2, have not only different environments, but also different coordination numbers. Ab initio molecular orbital calculations performed for an isolated 4-fluorophenylsulfonyldithiocarbimate(2-) ligand have shown a quite similar conformation of the anion as found in the crystal of the potassium salt (Table 5). Thus the interaction between the potassium cations and the 4-fluorophenylsulfonyldithiocarbimate(2-) anions is mainly ionic which does not disturb significantly the geometric conformation of the ligand. The bond lengths and angles, as well as the orientation of the almost planar dithiocarbimate group (CS_2), together with the sulfur atom of the sulfonyl group (S1S2C1N1S3 fragment) in relation to the phenyl ring in the potassium salt preserve almost the same values as in the gas-phase which describes the most stable conformation of the ligand. The arrangement of the molecules in the crystal **2** (Fig. 2c) is mainly determined by the ionic interaction of the oppositely charged moieties, i.e. the 4-fluorophenylsulfonyldithiocarbimate(2-) ligand and the potassium cations surrounded by the water molecules. The water molecules interact with the potassium cations forming infinite 2D-layers parallel to the (001) plane at $z = 0$ and $z = 1/2$, while the 4-fluorophenylsulfonyldithiocarbimate(2-) ligands are alternatively oriented and located almost per-

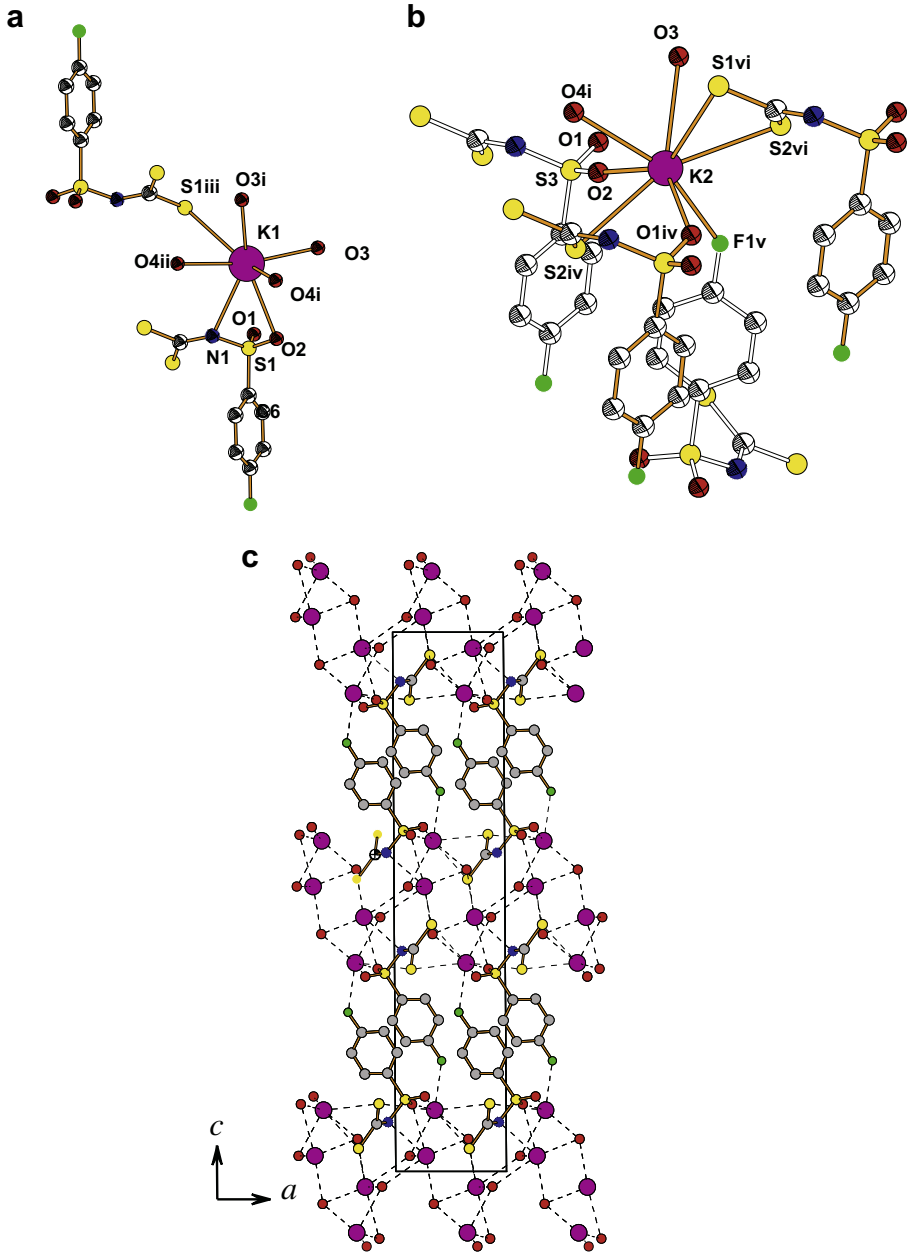


Fig. 2. Coordination environment of K1 (a) and K2 (b) and the molecular arrangement of compound **2** in the unit cell showing the 2D-layers of K1 and K2 surrounded by water at $z = 0$ and 1/2 and the layers of 4-fluorophenylsulfonyldithiocarbimate(2-) anions at $z = 1/4$ and 3/4 (c). H atoms are omitted for clarity. Symmetry code: (i) $-x + 1, -y + 1, -z$; (ii) $x - 1, y, z$; (iii) $-x, -y, -z$; (iv) $x, y + 1, z$; (v) $-x, y + 0.5, -z + 0.5$; (vi) $x + 1, y + 1, z$.

pendicularly to the (0 0 1) plane by their phenyl ring, and also form layers parallel to the (0 0 1) plane at $z = 1/4$ and $z = 3/4$. Besides, due to the ionic attraction between the oppositely charged layers, the hydrogen bond between the water molecule (O3) as a donor and the nitrogen atom (N1) as an acceptor is formed (O3–H31 ⋯ N1, the distance between donor and acceptor and the D–H⋯A angle are 2.970(3) Å, and 171.5°). This hydrogen bond slightly diminishes the steric effect of the lone pair of electrons at the N atom and leads to a decreased C1–N1–S3 angle by about 3° compared to the gas-phase structure.

The molecular structures of compounds **3** and **4** are shown in Fig. 3a and b, respectively. The crystals are built up from the $[Pt(R\text{-}SO_2N{=}CS_2)_2]^{2-}$ anions (R = 4-IC_6H_4 (**3**) and 4-FC_6H_4 (**4**)) and two univalent Bu_4N^+ cations related by the inversion centre at the Pt atom. In both complexes the Pt cation is coordinated by two symmetrically equivalent dithiocarbimate(2-) ligands into a distorted square-planar configuration. However, in compound **3**, due to mutual orientation of the $[Pt(4\text{-}IC_6H_4SO_2N{=}CS_2)_2]^{2-}$ anions, the iodine atoms of two neighbouring complex anions interact with the central Pt cation forming chains along the *b*-axis (Fig. 4a) with the elongated square bipyramid around the Pt cations (average Pt–S distance is 2.319(3) Å, Pt–I, 4.253(1) Å). For a comparison the axial Pt⋯Br distance in the isostructural 4-BrC_6H_4-derivative with a value of 4.249(3) Å [10] indicates significantly weaker interaction between the neighbouring complex anions than in the 4-IC_6H_5-derivative due to their ionic radii ($r_I = 2.20$ Å and $r_{Br} = 1.81$ Å) [20]. The bidentate chelation by two sulfur atoms of the dithiocarbimate(2-) ligands to Pt in both complexes makes the S1–C1–S2 angle significantly smaller (∼108°) than those found in the parent dipotassium salt (119.5(1)°) in

Table 5
Comparison of the X-ray and gas-phase geometry of the 4-fluorophenylsulfonyldithiocarbimate(2-) anion (in Å, °)

Bonds	X-ray (in **2**)	X-ray (in **4**)	Ab initio
C1–S1	1.731(2)	1.732(4)	1.747
C1–S2	1.706(2)	1.739(4)	1.743
C1–N1	1.351(2)	1.299(4)	1.368
N1–S3	1.610(2)	1.615(3)	1.613
S3–O1	1.443(2)	1.435(3)	1.491
S3–O2	1.445(2)	1.434(3)	1.494
S3–C2	1.768(2)	1.764(4)	1.839
C5–F1	1.362(3)	1.364(5)	1.385
S1–C1–S2	119.5(1)	106.9(2)	121.8
S1–C1–N1	114.9(1)	121.6(3)	114.3
S2–C1–N1	125.6(2)	131.5(3)	123.9
C1–N1–S3	122.0(1)	123.2(3)	125.0
N1–S3–O1	114.7(1)	114.4(2)	117.7
N1–S3–O2	104.1(1)	106.2(2)	106.6
N1–S3–C2	108.1(1)	104.9(2)	110.2
O1–S3–O2	114.4(1)	117.5(2)	114.2
O2–S3–C2	107.1(1)	106.4(2)	102.0
S1–C1–N1–S3	178.5(1)	177.7(2)	175.2
Dihedral angle between the S3N1=C1S1S2	98.9(1)	103.2(2)	98.3

which the interaction between the K^+ cations and the dithiocarbimate(2-) ligands is mainly ionic (Table 5). The arrangement of the molecules in the crystal of compound **4** is shown in Fig. 4b, as a packing diagram of the unit cell on the *bc* plane. The square plane of the Pt coordination in the $[Pt(4\text{-}FC_6H_4SO_2N{=}CS_2)_2]^{2-}$ entities is perpendicular to the (1 0 0) plane and the Bu_4N^+ cations are located on both sides of the anions.

In compounds **3** and **4**, the CS bond lengths are nearly equal and are slightly shorter than typical C–S single bond lengths (*ca.* 1.815 Å) but longer than typical C=S double bonds (*ca.* 1.671 Å) [21] due to the partial π-delocalization in the S–C–S group (Scheme 2). Quite similar behaviour is observed in the square-planar palladium(II) and nickel(II) complexes of dithiocarbimates [10,12,22,23]. However, in compound **2** they are slightly different [C1–S1 is 1.731(2) Å and C1–S2 is 1.706(2) Å] (Table 3). This difference can be explained by a balance between the repulsive interactions of the lone-pair of electrons on the nitrogen atom and the S2, as well as between the S1 and the RSO_2 group. When the complexation occurs two factors must be considered. First, the S1–C1–S2 angle decreases, weakening the interactions mentioned above, and diminishing the difference between the C1–S1 and the C1–S2 bond lengths. Another factor is the increasing importance of the canonical form (c) upon complexation, explaining not only a shorter CN bond length in **3** and **4** than in **2**, but also the lower wavenumbers for the νCS_2 in the spectra of the complexes when compared with the spectra of the ligands, the higher wavenumbers for the νCN in the spectra of the complexes, and the variation on the chemical shift of the dithiocarbimate group carbon atom signal in the ^{13}C NMR spectra after the complexation (Tables 3 and 4).

The bond lengths and angles of the tetrabuthylamonium cations are in agreement with the expected values (Table 2). However, the torsion angle C41–C42–C43–C44 in the compound **4** is deviated significantly from 180° due to repulsive interaction between the hydrogen atoms of the symmetrically equivalent Bu_4N^+ cations, which are oriented by the terminal methyl group of C44 atom, as well as due to attractive interaction of the H atom of the methyl group with the phenyl ring (C44–H44A···π(phenyl ring) ~3.2). The conformation of the tetrabuthylamonium cation is different from that found in the isostructural Pt-phenyl-derivative dithiocarbimate complex [10] in which all torsion angles of the carbonic chains of the tetrabuthylamonium cation are only slightly distorted from the expected value of 180° (Table 2).

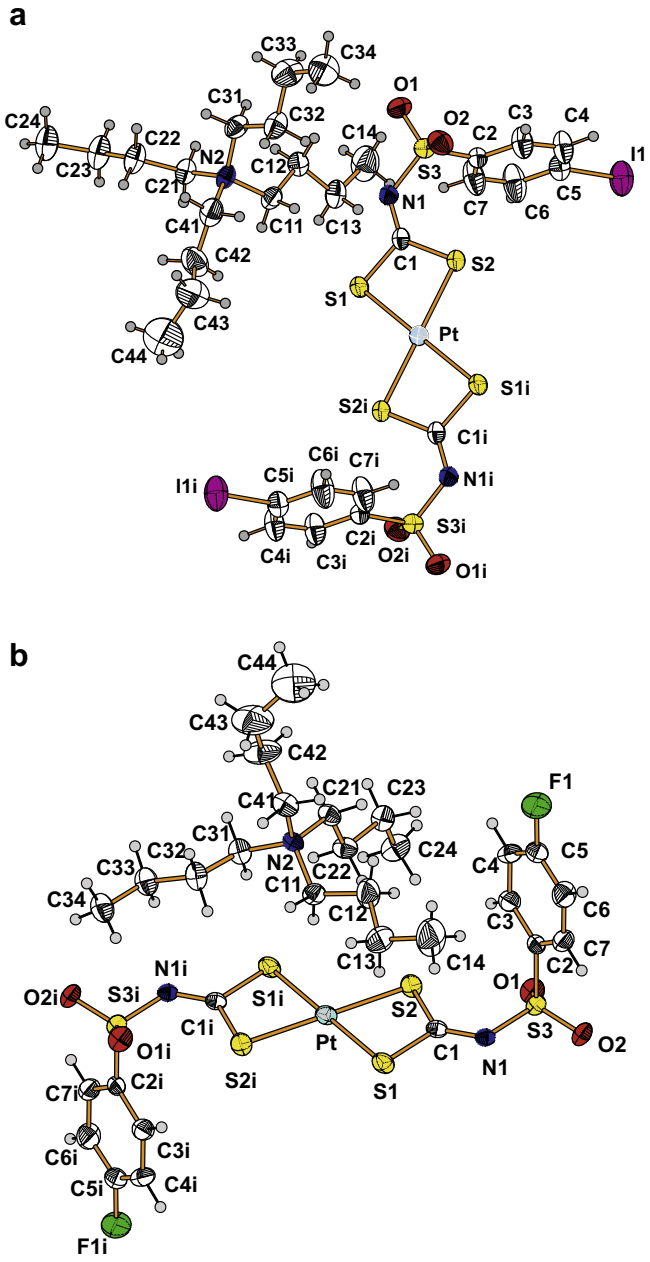


Fig. 3. View of the molecular structure of compounds **3** (a) and **4** (b) with the labelling scheme. Displacement ellipsoids are drawn at the 50% probability level.

4. Conclusion

A new dithiocarbimate anion (4-fluorophenylsulfonyldithiocarbimate) was obtained and its potassium salt was characterized by X-ray diffraction techniques. Besides, two new platinum(II)-bis(dithiocarbimato) complexes were obtained as tetrabutylammonium salts in the crystalline form and their structures were characterized by single crystal X-ray diffraction. The Pt^{2+} in both complexes is located at the inversion centre and the PtS_4 moiety has a square-planar configuration. Spectroscopic data are consistent with the X-ray experimental results and point to an increase of the contribution of the canonical form (c) to the resonance hybrid upon complexation with a consequent increase of the CN double bond character. Thus, in the IR spectra the wavenumbers of the νCN are smaller for the ligands than for the complexes, and the ^{13}C NMR spectra show that the carbon atom of the dithiocarbimate

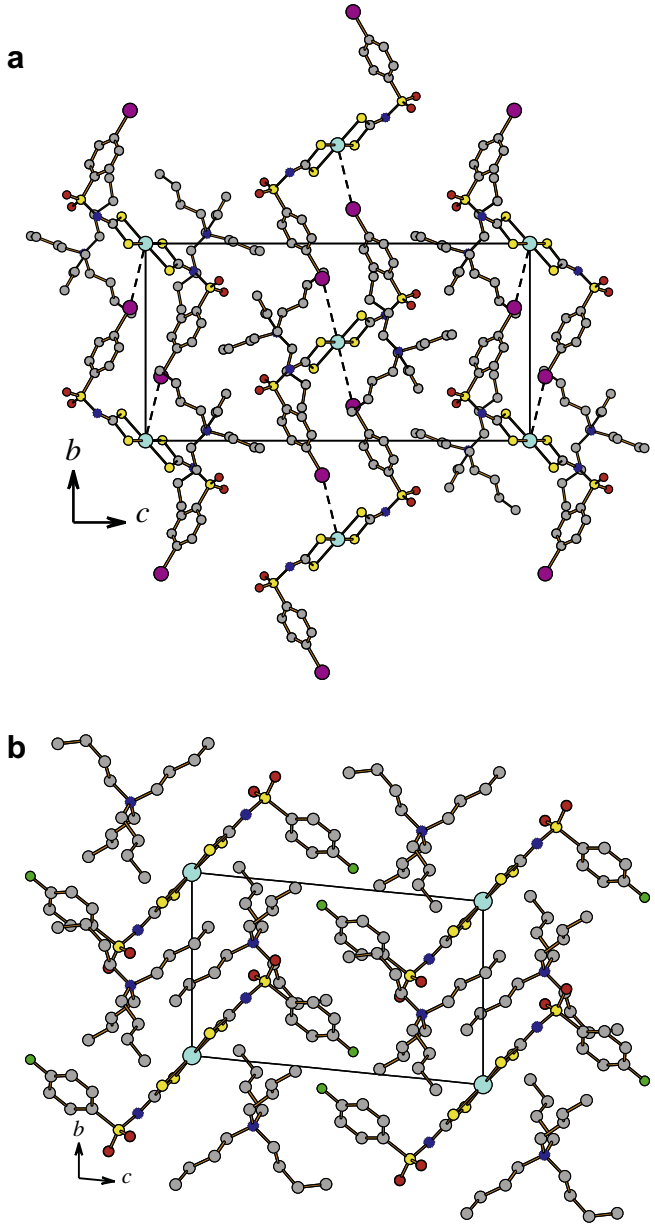


Fig. 4. Molecular arrangement of the complexes **3** (a) and **4** (b) in the unit cell. H atoms are omitted for clarity.

moiety is more shielded in the complexes than in free ligands. The ionic interaction between the potassium cations and the 4-fluorophenylsulfonyldithiocarbimate dianions does not disturb significantly the conformation of the anionic ligand, while the bidentate chelation by two S atoms of dithiocarbimate group to Pt cation is more covalent and leads to a decrease on the S1–C1–S2 angle in the ligand.

Acknowledgement

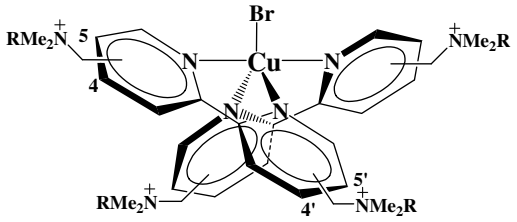
This work has been supported by FAPEMIG (Brazil).

Appendix A. Supplementary data

CCDC 671481, 671482 and 671483 contain the supplementary crystallographic data for **2**, **3** and **4**. These data can be obtained free of charge via http://www.ccdc.cam.ac.uk/conts/retrieving.html, or from the Cambridge Crystallographic Data Centre, 12 Union Road, Cambridge CB2 1EZ, UK; fax: (+44) 1223-336-033, or e-mail: deposit@ccdc.cam.ac.uk. Supplementary data associated with this article can be found, in the online version, at doi:10.1016/j.poly.2008.02.030.

References

[1] D. Hogarth, Prog. Inorg. Chem. 53 (2005) 71.
[2] P.J. Nieuwenhuizen, A.W. Ehlers, J.G. Haasnoot, S.R. Janse, J. Reedijk, E.J. Baerends, J. Am. Chem. Soc. 121 (1999) 163.
[3] D. Coucouvanis, Prog. Inorg. Chem. 11 (1969) 233.
[4] G. Faraglia, D. Fregona, S. Sitran, L. Giovagnini, C. Marzano, F. Baccichetti, U. Casellato, R. Graziani, J. Inorg. Biochem. 83 (2001) 31.
[5] G. Gattow, Sulfur Reports 14 (1993) 1.
[6] J.P. Fackler, D. Coucouvanis, Chem. Commun. (1965) 556.
[7] F.A. Cotton, J.A. McCleverty, Inorg. Chem. 6 (1967) 229.
[8] C.C. Hadjikostas, G.A. Katsoulos, S.K. Shakhatreh, Inorg. Chim. Acta 133 (1987) 129.
[9] Y. Tian, C. Duan, Z. Lu, X. You, Polyhedron 15 (1996) 1495.
[10] M.R.L. Oliveira, M.M.M. Rubinger, S. Guilardi, E.F. Franca, J. Ellena, V.M. De Bellis, Polyhedron 23 (2004) 1153.
[11] H.U. Hummel, U.Z. Korn, Z. Naturforsch 44B (1989) 24.
[12] E.F. Franca, M.R.L. Oliveira, S. Guilardi, R.P. Andrade, R.H. Lindemann, J. Amim Jr., J. Ellena, V.M. De Bellis, M.M.M. Rubinger, Polyhedron 25 (2006) 2119.
[13] A.I. Vogel, A Textbook of Practical Organic Chemistry Including Qualitative Organic Analysis, Logmans, Green and Co. LTDA., London, 1996.
[14] CRYSALIS CCD and CRYSALIS RED program, Ver. 171.31.8, Oxford Diffraction Poland, Wrocław, Poland, 2005.
[15] G.M. Sheldrick, SHELXS97, SHELXL97, Programs for Crystal Structure Solution and Refinement, University of Göttingen, Göttingen, Germany, 1997.
[16] J.M. Frisch, G.W. Trucks, H.B. Schlegel, P.M.W. Gill, B.G. Johnson, M.A. Robb, J. Cheeseman, T. Keith, G.A. Petersson, J.A. Montgomery, K. Raghavachari, M.A. Al-Laham, V.G. Zakrzewski, J.V. Ortiz, J.B. Foresman, J. Cislowski, B.B. Stefanov, A. Nanayakkara, M. Challacombe, C.Y. Peng, P.Y. Ayala, W. Chen, M.W. Wong, J.L. Andres, E.S. Replogle, R. Gomperts, R.L. Martin, D.J. Fox, J.S. Binkley, D.J. Defrees, J. Baker, J.P. Stewart, M. Head-Gordon, C. Gonzales, J.A. Pople, GAUSSIAN98, Revision A.3, Gaussian Inc., Pittsburgh, PA, 1998.
[17] A.D. Becke, J. Chem. Phys. 104 (1996) 1040.
[18] C. Lee, W. Yang, R.G. Parr, Phys. Rev. B 37 (1988) 785.
[19] W.J. Geary, Coord. Chem. Rev. 7 (1971) 81.
[20] L. Pauling, The Nature of the Chemical Bond, 3rd ed., Coronell University Press, Ithaca, 1960.
[21] F.H. Allen, O. Kennard, D.G. Watson, L. Brammer, A.G. Orpen, J. Chem. Soc., Perkin Trans. 2 (1987) S1–S19.
[22] Y.P. Tian, C.Y. Duan, Z.L. Lu, X.Z. You, H.K. Fun, B.C. Yip, Polyhedron 15 (1996) 1495.
[23] M.R.L. Oliveira, H.P. Vieira, G.J. Perpétuo, J. Janczak, V.M. De Bellis, Polyhedron 21 (2002) 2243.



5,5': R = H, **1** Me, **2** 4,4': R = H, **3** Me, **4**

Scheme 1. Schematic illustration for all Cu(II) complexes (cation moiety).

2. Experimental

2.1. Materials and general information

5,5′-Dimethyl-2,2′-bipyridine was purchased from Sigma–Aldrich Chemical Co., 4,4′-dimethyl-2,2′-bipyridine was purchased from Alfa Aesar Co. Ltd. pBR322 DNA was purchased from MBI, catalase and Tris were purchased from BBI, CT-DNA and ethidium bromide were purchased from Sino-American Biotechnology. Other reagents of analytical grades were obtained from domestic chemical corporations and used without further purification. Milli-Q water was used in all physical measurement experiments.

Microanalyses (C, H and N) were carried out on an Elementar Vario EL elemental analyzer. ESI-Mass spectra were recorded using a LCMS-2010A Liquid Chromatograph Mass Spectrometer. ^{1}H NMR spectra were collected on a Varian Mercury-plus 300 NMR spectrometer.

2.2. Synthesis

2.2.1. 4,4′-Dibromomethyl-2,2′-bipyridine

To a stirred mixture of 4,4′-dihydroxymethyl-2,2′-bipyridine [56–59] (1.797 g, 8.310 mmol), 40% hydrobromic acid (50 mL) and sodium bromide (16.800 g, 0.163 mol), 16.8 mL concentrated sulfuric acid was added dropwise. The mixture was then refluxed for 24 h, followed by being cooled to 0 °C in ice-water bath and addition of 100 mL ice water. The pH was adjusted to 8–9 with saturated aqueous solution of sodium hydroxide. The produced precipitate was filtered, washed with cold water and dried to offer 2.026 g grey powder (71.3%).

All the ligands were prepared similarly, and the preparation of L^1Br_2 was presented as general procedure.

2.2.2. 5,5′-Bis(dimethylaminomethyl)-2,2′-bipyridine dihydrobromide (L^1Br_2)

5,5′-Dibromomethyl-2,2′-bipyridine [47] (0.300 g, 0.877 mmol) was suspended in 10 mL ethanol and stirred at room temperature, to which 33% aqueous dimethylamine (1.0 mL, 6.6 mmol) was added dropwise and the reaction mixture was stirred at room temperature until the reaction mixture became clear (about 30 min). The solvent was evaporated, then the solid was washed with 5 mL ethanol for three times and dried *in vacuum* to give white powder (0.312 g, 81.3%). *Anal.* Calc. for $C_{16}H_{22}N_4 \cdot 2HBr \cdot 0.3\,H_2O$ (437.61): C, 43.92; H, 5.67; N, 12.80. Found: C, 43.93; H, 5.56; N, 12.73%. ESI-MS, *m*/*z* (%): 136.25 (100), $[L^1]^{2+}$; 271.65 (43), $[L^1-H]^+$. ^{1}H NMR (D_2O, 300 MHz): δ 8.576 (d, J = 2.1 Hz, 2H, bpy-H); 8.051 (d, J = 8.1 Hz, 2H, bpy-H); 7.970 (dd, J_1 = 8.1 Hz, J_2 = 2.1 Hz, 2H, bpy-H); 4.303 (s, 4H, CH_2); 2.746 (s, 12H, CH_3).

2.2.3. 5,5′-Bis(trimethylaminomethyl)-2,2′-bipyridine dibromide (L^2Br_2)

Addition of 1.0 mL (5.0 mmol) trimethylamine to the solution of 5,5′-dibromomethyl-2,2′-bipyridine (0.200 g, 0.585 mmol) in ethanol gave 0.252 g L^2Br_2 as white powder (86.8%). *Anal.* Calc. for $C_{18}H_{28}N_4Br_2 \cdot 2H_2O$ (496.29): C, 43.56; H, 6.50; N, 11.29. Found: C, 43.91; H, 6.29; N, 11.28%. ESI-MS, *m*/*z* (%): 150.25 (100), $[L^2]^{2+}$. ^{1}H NMR (D_2O, 300 MHz): δ 8.729 (d, 2H, J = 2.1 Hz, bpy-H); 8.204 (d, 2H, J = 8.1 Hz, bpy-H); 8.130 (dd, 2H, J_1 = 8.1, J_2 = 2.1, bpy-H); 4.584 (s, 4H, CH_2); 3.094 (s, 18H, CH_3).

2.2.4. 4,4′-Bis(dimethylaminomethyl)-2,2′-bipyridine dihydrobromide (L^3Br_2)

The reaction of 1.0 mL dimethylamine and 0.310 g (0.906 mmol) 4,4′-dibromomethyl-2,2′-bipyridine produced 0.305 g L^3Br_2 as pale pink powder (77.9%). *Anal.* Calc. for $C_{16}H_{22}N_4 \cdot 2HBr$ (432.20): C, 44.46; H, 5.60; N, 12.96. Found: C, 44.33; H, 5.55; N, 12.78%. ESI-MS, *m*/*z* (%): 271.40 (100), $[L^3-H]^+$. ^{1}H NMR (D_2O, 300 MHz): δ: 8.526 (s, 2H, bpy-H); 7.930 (s, 2H, bpy-H); 7.406 (s, 2H, bpy-H); 3.950 (s, 4H, CH_2); 2.493 (s, 12H, CH_3).

2.2.5. 4,4′-Bis(trimethylaminomethyl)-2,2′-bipyridine dibromide (L^4Br_2)

0.200 g (0.585 mmol) 4,4′-dibromomethyl-2,2′-bipyridine and 1.0 mL trimethylamine offered 0.235 g L^4Br_2 as pale pink powder (87.2%). *Anal.* Calc. for $C_{18}H_{28}N_4Br_2$ (460.26): C, 46.97; H, 6.13; N, 12.17. Found: C, 46.88; H, 6.25; N, 12.18%. ESI-MS, *m*/*z* (%): 150.30 (100), $[L^4]^{2+}$. ^{1}H NMR (D_2O, 300 MHz): δ 8.723 (d, 2H, J = 5.1 Hz, bpy-H); 8.218 (s, 2H, bpy-H); 7.621 (dd, 2H, J_1 = 5.1, J_2 = 1.5, bpy-H); 4.572 (s, 4H, CH_2); 3.110 (s, 18H, CH_3).

All the Cu(II) complexes were prepared in a similar way, the preparation of **1** was described here as general procedure.

2.2.6. $[Cu(L^1)_2Br](ClO_4)_2Br_3 \cdot 3H_2O$ (**1**)

0.150 g $L^1Br_2 \cdot 0.3H2O$ (0.343 mmol) was suspended in 10 mL ethanol, followed by addition of 3 mL ethanol solution of $Cu(ClO_4)_2 \cdot 6H_2O$ (0.300 g, 0.810 mmol). Brown precipitate appeared immediately, which was filtrated and washed with ethanol for several times. The precipitate was recrystallized from 1:4 H_2O–MeOH (~1 mL) at 4 °C overnight, then was filtrated and dried, 0.143 g green powder was obtained (70.6%). Elemental *Anal.* (EA) Calc. for $[Cu(C_{16}H_{24}N_4)_2Br](ClO_4)_2Br_3 \cdot 3H_2O$ (1180.90): C, 32.55; H, 4.61; N, 9.49. Found: C, 32.60; H, 4.38; N, 9.40%.

Green single crystals suitable for X-ray analysis were prepared by slow diffusion of methanol into aqueous solution of **1**.

2.2.7. $[Cu(L^2)_2Br](ClO_4)_5 \cdot 4H_2O$ (**2**)

0.200 g (0.402 mmol) L^2Br_2 gave 0.171 g **2** as green powder (64.7%). *Anal.* Calc. for $[Cu(C_{18}H_{28}N_4)_2Br](ClO_4)_5 \cdot 4H_2O$ (1313.66): C, 32.92; H, 4.91; N, 8.53. Found: C, 32.83; H, 4.49; N, 8.45%.

2.2.8. $[Cu(L^3)_2Br](ClO_4)_5 \cdot 2H_2O$ (**3**)

0.150 g (0.347 mmol) L^3Br_2 offered 0.135 g of **3** as green powder (63.9%). *Anal.* Calc. for $[Cu(C_{16}H_{24}N_4)_2Br](ClO_4)_5 \cdot 2H_2O$ (1217.01): C, 31.55; H, 4.31; N, 9.20. Found: C, 31.48; H, 4.48; N, 9.14%.

2.2.9. $[Cu(L^4)_2Br](ClO_4)_{4.5}(OH)_{0.5} \cdot 6H_2O$ (**4**)

0.195 g (0.424 mmol) L^4Br_2 produced 0.167 g **4** as green powder (60.2%). *Anal.* Calc. for $[Cu(C_{18}H_{28}N_4)_2Br](ClO_4)_{4.5}(OH)_{0.5} \cdot 6H_2O$ (1308.47): C, 33.05; H, 5.28; N, 8.56. Found: C, 33.55; H, 5.67; N, 8.09%.

Green single crystals suitable for X-ray analysis were prepared by slow evaporation of solution of **4** in 3:1 EtOH–H_2O solution.

2.3. X-ray crystallography

Single crystals sized 0.20 × 0.08 × 0.08 mm and 0.48 × 0.35 × 0.31 mm for **1** and **4**, respectively, were used for X-ray diffraction analyses. Data collections of **1** and **4** were performed with Cu Kα

(λ = 1.54178 Å) and Mo Kα (λ = 0.71073 Å) radiation, respectively, on an Oxford Germini S Ultra CCDC diffractometer at 293(2) K. An absorption correction by multi-scan was applied to the intensity data. The structure was solved by direct method and the heavy atoms were located from E-map. The remaining non-hydrogen atoms were determined from the successive difference Fourier syntheses. The non-hydrogen atoms were refined anisotropically, whereas the hydrogen atoms were generated geometrically with isotropic thermal parameters. The structure was refined on F^2 by full-matrix least-squares methods using the SHELXTL-97 program package [60].

2.4. Thermal-denaturation experiments

Thermal-denaturation experiments were carried out on a Varian Cary 300 UV/Vis spectrophotometer. UV absorbance of CT-DNA was recorded in 5 mM Tris–50 mM NaCl buffer solution (pH 7.5). The concentration of DNA was determined according to the literatures [28,61], and 100 μM DNA was used. The melting curves were recorded at different concentration ratio of complexes to DNA (r = 0, 0.1 and 0.2, r = [complex]/[DNA]) by plotting the absorption at 260 nm as function of temperature in the range of 55–95 °C. The melting temperature (T_m) was determined from the maximum of the first derivative or tangentially from the graph at midpoint of the transition curves. ΔT_m was defined as the difference between the T_m of free DNA and the T_m of DNA in the presence of complexes.

2.5. CD spectroscopy

CD spectra of CT-DNA were recorded on a Jasco J-810 spectropolarimeter at room temperature in the absence or presence of 45 μM complex. The concentration of DNA was 150 μM and the buffer solution was the same as thermal-denaturation experiments. Each test solution was scanned at a speed of 50 nm min^{-1} for five repetitions, and the average spectra were used. The buffer background was subtracted automatically.

2.6. DNA cleavage

The cleavage of plasmid DNA (pBR322, 38 μM bp) was performed in 20 mM Tris buffer (pH 7.5) by treating DNA with a certain concentration of complex. The total volume of 10 μL sample solution was incubated in a sealed plastic vessel and the cleavage was carried out at 37 °C for a defined time, then 4 μL loading buffer (bromophenol blue, 50% glycerol and 2 mM EDTA) was added. The sample was stored at −20 °C for preservation, then was loaded onto a 0.9% agarose gel and electrophoresed at a constant voltage of 120 V for 100 min in TBE buffer (100 mM Tris–2 mM EDTA–HBO_3, pH 8.3). DNA bands were visualized in an electrophoresis documentation and analysis system 120. Densitometeric calculations were made using analysis method in Image Tools 3.00. A correction factor of 1.47 was used for supercoiled DNA taking into account its weaker staining capacity by ethidium bromide compared to nicked and linear DNA. The apparent rate constant (k_{obs}) at a certain complex concentration, k_{cat} and K_M values were calculated according to the literature [23].

3. Results and discussion

3.1. Preparation of Cu(II) complexes

The synthesis route for these Cu(II) complexes is shown in Scheme 2. 5,5′-Dibromomethyl-2,2′-bipyridine was prepared according to the literature [55], it was allowed to react with dimethylamine or trimethylamine to give 5,5′-bis(dimethylaminomethyl)-2,2′-bipyridine dihydro-bromide (L^1Br_2) and 5,5′-bis(trimethylaminomethyl)-2,2′-bipyridine dibromide (L^2Br_2), respectively. The reaction of L^1Br_2 or L^2Br_2 with $Cu(ClO_4)_2$ gave complexes **1** and **2**, respectively.

4,4′-Dibromomethyl-2,2′-bipyridine cannot be successfully prepared by the direct bromization of 4,4′-dimethyl-2,2′-bipyridine using *N*-bromosuccinimide, and a four-step synthesis route was adopted. Firstly, 4,4′-dicarboxyl-2,2′-bipyridine was prepared according to the literature [56]. The following esterification similar to the literature procedure offered 4,4′-diethoxyacyl-2,2′-bipyridine [57]. The reduction of this diester using sodium borohydride in ethanol yielded 4,4′-dihydroxymethyl-2,2′-bipyridine [57,58]. 4,4′-Dibromomethyl-2,2′-bipyridine can be prepared according to the general bromization procedure for alkyl alcohols [58,59], and a modified method is described in experimental section. Then the dibromide was allowed to react with dimethylamine or trimethylamine to offer 4,4-bis(dimethylaminomethyl)-2,2′-bipyridine dihydrobromide (L^3Br_2) and 4,4′-bis(trimethylaminomethyl)-2,2′-bipyridine dibromide (L^4Br_2), respectively. The reaction of L^3Br_2 or L^4Br_2 with $Cu(ClO_4)_2$ gave Cu(II) complexes **3** and **4**, respectively.

The MS and ^1H NMR spectra of all ligands are presented in supplementary material (Figures S1 and S2, respectively). However the ESI-MS spectra of all Cu(II) complexes were not included since only m/z peaks of the ligands are found due to these Cu(II) complexes are degraded into ligands under strong electric field conditions of MS.

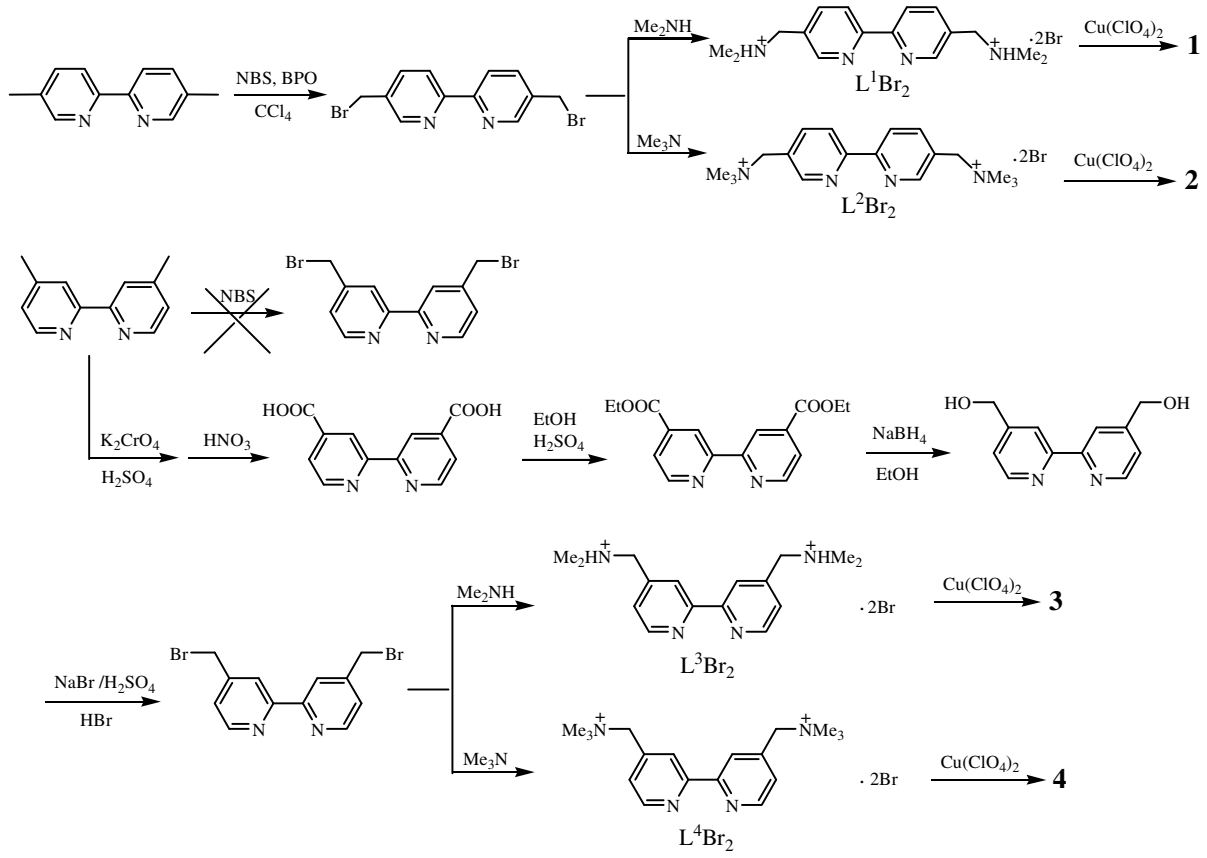
3.2. Crystal structure of complex *1* and *4*

A summary of the crystallographic data is given in Table 1. The molecular structure of **1** is very similar to those reported Cu(II) complexes of 2,2′-bipyridine or its derivatives [55,62]. It consists of a $[Cu(L^1)_2(Br)]^{5+}$ cation, two ClO_4^-, three Br^- anions and three water molecules. Each structural motif contains two independent symmetric molecules (A and B), and the other halve of the complex was generated by the twofold diad present in the space group $P2/c$. Both molecules display very similar coordination geometries. Selected bond lengths and angels for the coordination of Cu(II) are shown in Table 2, and the ORTEP drawing of the cationic moiety in molecule A is shown in Fig. 1 as an example. The coordination configuration of the divalent Cu(1) can be described as a distorted trigonal bipyramid, in which atoms N(1), N(1A) and Br(1) define the equatorial plane and atoms N(3) and N(3A) occupy the apical sites. The degree of trigonality (τ) of this molecule is calculated as 0.79 according to the literature [63]. The distances between the N atoms in ammonium groups and the Br^- anion defined by N(4)···Br(1) or N(4A)···Br(1) is 6.201 Å.

As shown in Fig. 2, the molecular structure of complex **4** is quite similar to that of **1**, and the configuration of five-coordinated Cu(1) ion can also be described as a distorted trigonal bipyramidal. Atoms N(2), N(5) and Br(1) define the equatorial plane while N(1) and N(6) occupy vertical sites. The calculated τ value is 0.53. The distances between tetraalkylammonium groups and Br^- anion defined by N(3)···Br(1) and N(8)···Br(1) are 7.835(1) Å and 8.117(1) Å, respectively (Table 3).

3.3. Interaction with CT-DNA

T_m of CT-DNA was measured in the presence of different molar ratio of complexes to DNA. ΔT_m values are listed in Table 4, and thermal melting curves are presented in the supporting information (Fig. S3). The result shows that with the addition of complexes to DNA, the melting temperature decreases slightly in each case, indicating the slight destabilization of the DNA duplex induced by all the complexes. Although ΔT_m values are quite low, they follows the order of **1** > **2** > **3** > **4**, which basically display the binding abilities of these complexes towards CT-DNA.



Scheme 2. Synthesis route for Cu(II) complexes.

Table 1
Crystallographic data for complexes **1** and **4**

Complex	**1**	**4**
Empirical formula	$C_{33}H_{53}Br_4Cl_2CuN_8O_{9.5}$	$C_{36}H_{56.5}BrCl_{4.5}CuN_8O_{18.5}$
Formula weight	1167.92	1200.37
Temperature (K)	293(2)	293(2)
Wavelength (Å)	1.54178	0.71073
Crystal system, space group	monoclinic, *P*2/*c*	monoclinic, *C*2/*c*
a (Å)	15.7940(2)	28.537(5)
b (Å)	19.8156(3)	27.955(4)
c (Å)	14.6777(2)	13.657(2)
β (°)	90.9230(10)	103.494(3)
Volume (Å^3)	4593.05(11)	10594(3)
Z	2	8
D_{calc} (g cm^{-3})	1.689	1.515
μ (mm^{-1})	6.307	1.469
F(000)	2344	4968
Crystal size (mm)	0.20 × 0.08 × 0.08	0.48 × 0.35 × 0.31
θ Range for data collection (°)	2.23–61.72	2.12–25.0
Limiting indices	$-18 \leqslant h \leqslant 17$, $-22 \leqslant k \leqslant 22$, $-12 \leqslant l \leqslant 16$	$-14 \leqslant h \leqslant 33$, $-33 \leqslant k \leqslant 30$, $-16 \leqslant l \leqslant 15$
Reflections collected	25895	21971
Independent reflections (R_{int})	6957 (0.0411)	9150 (0.0503)
Goodness-of-fit on F^2	1.033	1.016
R_1/wR_2 [$I > 2\sigma(I)$][a]	0.0796/0.2054	0.0848/0.2221
R_1/wR_2 (all data)	0.1080/0.2192	0.1594/0.2780
Largest difference peak (e A^{-3})	2.299/−1.656	1.559/−0.923

[a] $R_1 = \sum ||F_o| - |F_c|| / \sum |F_o|$, $wR_2 = \left[\sum w(F_o^2 - F_c^2)^2 / \sum w(F_o^2)^2\right]^{1/2}$.

Table 2
Selected bond lengths (Å) and angles (°) for metal environments of complex **1**

Molecule A		Molecule B	
Cu(1)–N(1)	2.071(8)	Cu(2)–N(5)	2.072(7)
Cu(1)–N(3)	1.995(7)	Cu(2)–N(7)	1.994(7)
Cu(1)–Br(1)	2.430(2)	Cu(2)–Br(2)	2.472(2)
N(4)···Br(1)	6.201(6)	N(8)···Br(2)	6.473(6)
N(1)–Cu(1)–N(1′)	102.3(4)	N(5)–Cu(2)–N(5′)	113.3(4)
N(1)–Cu(1)–N(3)	80.8(3)	N(5)–Cu(2)–N(7)	79.8(3)
N(1)–Cu(1)–N(3′)	96.8(3)	N(5)–Cu(2)–N(7′)	99.6(3)
N(3)–Cu(1)–N(3′)	176.1(4)	N(7)–Cu(2)–N(7′)	178.9(4)
N(1)–Cu(1)–Br(1)	128.9(2)	N(5)–Cu(2)–Br(2)	123.3(2)
N(3)–Cu(1)–Br(1)	91.9(2)	N(7)–Cu(2)–Br(2)	90.6(2)

The interaction between these complexes and CT-DNA was further investigated by CD spectroscopy (Fig. 3). The CD spectra consist of a positive band at 275 nm due to base stacking and a negative band at 245 nm due to the right-handed helicity. Both bands are quite sensitive to the intercalation mode with small molecules [64]. Addition of each complex into CT-DNA induced slight decrease in ellipticity of both positive and negative bands. The calculated percent of decrease in ellipticity are 13.4%, 9.4%, 3.1%, 2.4% at 275 nm and 15.0%, 9.5%, 4.1%, 3.4% at 245 nm for **1**, **2**, **3**, **4**, respectively, from which it can be concluded that the interaction of all complexes towards CT-DNA follows the same order as the thermal melting curves experiment. No evident red shift or blue shift was observed, indicating all complexes induced only slight loss of characteristic B-type DNA conformation, however did not resulted in the formation of other types of DNA.

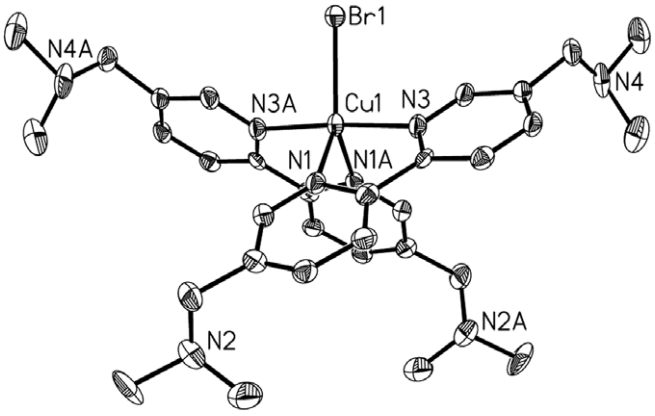


Fig. 1. The ORTEP drawing (30% probability) of cation moiety of one out of two symmetrically independent molecules in complex **1**.

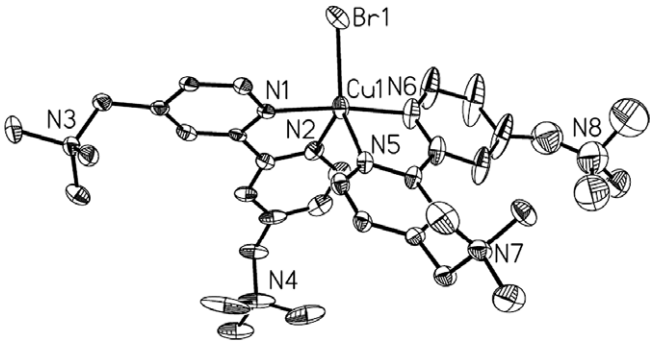


Fig. 2. The ORTEP drawing (30% probability) of cation moiety in complex **4**.

Table 3
Selected bond lengths (Å) and angles (°) for metal environments of complex **4**

Cu(1)–N(1)	2.009(6)	Cu(1)–Br(1)	2.406(2)
Cu(1)–N(2)	2.147(7)	N(3)···Br(1)	7.835(1)
Cu(1)–N(5)	2.053(7)	N(8)···Br(1)	8.117(1)
Cu(1)–N(6)	2.014(7)		
N(1)–Cu(1)–N(2)	78.7(3)	N(5)–Cu(1)–N(6)	80.1(3)
N(1)–Cu(1)–N(5)	97.4(2)	N(1)–Cu(1)–Br(1)	92.1(2)
N(1)–Cu(1)–N(6)	171.6(3)	N(2)–Cu(1)–Br(1)	117.9(2)
N(2)–Cu(1)–N(5)	102.5(2)	N(5)–Cu(1)–Br(1)	139.5(2)
N(2)–Cu(1)–N(6)	93.9(3)	N(6)–Cu(1)–Br(1)	95.0(3)

Table 4
Thermal melting temperature of CT-DNA[a]

r[b]	$-\Delta T_m$ (°C)[c]			
	1	**2**	**3**	**4**
0.1	1.92	0.84	0.51	0.43
0.2	3.09	2.36	1.79	1.12

[a] Experimental conditions: 5 mM Tris–50 mM NaCl buffer, pH 7.5, [DNA] = 100 μM.
[b] r = [complex]/[DNA].
[c] ΔT_m (°C) = the melting temperature of DNA in the presence of complex – the melting temperature of free DNA. Errors of T_m = ±0.1 °C.

It has been widely accepted that there are three non-covalent interaction modes between metal complexes and DNA: outside binding, groove binding and intercalation binding. In general, intercalation binding causes evident increase (5–8 °C) in T_m of DNA [65] and obvious decrease in both positive and negative bands

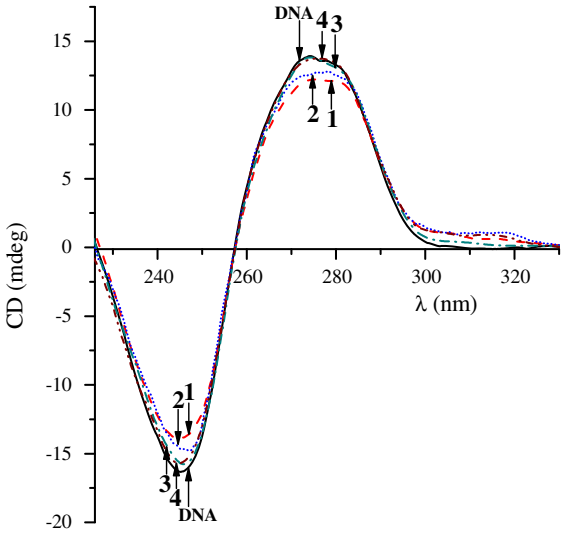


Fig. 3. CD spectra of 150 μM CT-DNA in the absence and presence of 45 μM complexes **1**–**4**: DNA (——), **1** (– – –), **2** (· · ·), 3 (–·–·–), 4 (–··–··). Experimental conditions: 5 mM Tris–50 mM NaCl buffer, pH 7.5, room temperature.

of CD spectra of DNA [66]. The quite low and negative ΔT_m values indicate that the interaction mode between these complexes and CT-DNA does not belong to intercalation. It also can be easily concluded from the structures of these complexes. In each complex, there are four ammonium groups in the side chains. According to Lewis theory, these positively-charged N atoms of ammonium groups belong to hard acid, and they are mostly bound to negatively-charged phosphate groups rather than bases pairs of DNA [67]. Therefore, outside electrostatic interaction is the most possible binding mode between theses complexes and CT-DNA.

3.4. Mechanism of DNA cleavage

The cleavage of supercoiled double-strand DNA by these complexes was studied in the absence of any reducing agents. In order to investigate the possible cleavage mechanism, DNA cleavage by complex **2** was examined as an example in the presence of hydroxyl radical scavengers (DMSO and *t*-BuOH) [68], peroxide scavenger (catalase), superoxide scavenger (SOD) [69] and chelating agent (EDTA). As shown in Fig. 4, all the scavengers threw little effect on DNA cleavage. This result basically rules out the possibility of DNA cleavage by hydroxyl radicals, superoxide anion and peroxide. EDTA can efficiently inhibit DNA cleavage, indicating Cu(II) complexes play the key role in the cleavage. Therefore, in the absence of any reducing agents, DNA cleavage by these Cu(II) complexes preferably undergoes a hydrolytic degradation pathway.

3.5. The identification of the hydrolytically active species

Bipyridine and its derivatives may form 1:1 or 1:2 copper complexes (CuL or CuL_2). The identification of the hydrolytically active species was investigated by the cleavage of DNA in the presence of ligands alone, the mixture of ligands and free copper with different molar ratio. Ligands L^1 and L^4 were chosen as examples to illustrate this question, and the results are shown in Fig. 5. For both ligands, with the increase of molar ratio (r = [L]/[Cu(II)]), the percent of nicked DNA (form II) increased and arrived at the maximum when r = 2, then stay on the maximum around. As the case stands, the brown CuL species has been prepared in dry organic solvent by us. It's extremely readily to become green CuL_2 in aqueous solution. The results indicate

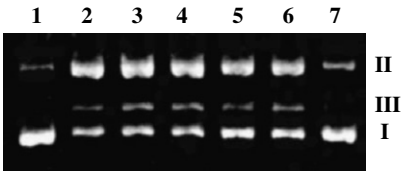


Fig. 4. The cleavage of pBR322 DNA after incubated with **2** (150 μM) for 0.5 h in the absence and presence of radical scavengers. Reaction conditions: [DNA] = 38 μM bp, 20 mM Tris–0.1 M $NaClO_4$ buffer, pH 7.5, 37 °C. Lane 1: DNA control; lane 2: DNA + 2; lanes 3–6: DNA + 2 + 1 M DMSO, 1 M *t*-BuOH, 1000 U/mL catalase, 1000 U/mL SOD, 0.1 M EDTA, respectively.

that CuL_2 species rather than CuL species are the hydrolytically active species in the cleavage of DNA.

3.6. Pseudo-Michaelis–Menten kinetics of DNA cleavage

Under hydrolytic conditions, DNA can be cleaved from supercoiled (form I) into nicked (form II) or linear form (form III) by each complex of varied concentrations. A series of DNA cleavage experiments have been performed, and time-dependent and concentration-dependent cleavages were observed. The time-dependent decrease of form I and increase of form II follow *pseudo*-first-order kinetic profiles and fit in well with single exponential function (supporting information, Fig. S4). A typical agarose gel electrophoresis pattern and the corresponding time course plot for DNA cleavage by **2** (120 μM) are shown in Fig. 6. The hydrolysis kinetics of DNA cleavage was studied with increased concentration of each complex (60–300 μM). The plots of k_{obs} values versus concentrations of all complexes are shown in Fig. S5. The *pseudo*-Michaelis–Menten kinetic parameter k_{cat}, affinity constant (K_M) and specificity constant k_{cat}/K_M are listed in Table 5. As is well known, the first-order hydrolysis rate constant for a phosphodiester bond of double-stranded DNA is estimated to be 3.6×10^{-8} h^{-1} [70]. Rate enhancements of reported Cu(II) complexes are in the range

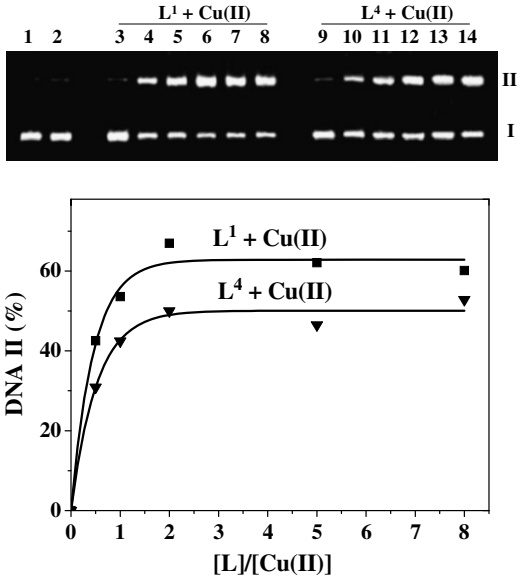


Fig. 5. The cleavage of pBR322 DNA in the presence of ligands alone and the mixture of ligands and $Cu(ClO_4)_2$ with different molar ratio. Reaction conditions: [DNA] = 38 μM bp, 20 mM Tris–0.1 M $NaClO_4$ buffer, pH 7.5, 37 °C. Lane 1: DNA control, 2 h; lane 2: DNA + 300 μM $Cu(ClO_4)_2$, 2 h; lane 3: DNA + 300 μM L^1, 0.5 h; lanes 4–8: DNA + 150 μ M $Cu(ClO_4)_2$ + L^1 (r = 0.5, 1, 2, 5 and 8, respectively, r = [L]/[Cu]), 0.5 h; lane 9: DNA + 600 μM L^4, 2 h; lanes 10–14: DNA + 300 μM $Cu(ClO_4)_2$ + L^4 (r = 0.5, 1, 2, 5 and 8, respectively), 2 h.

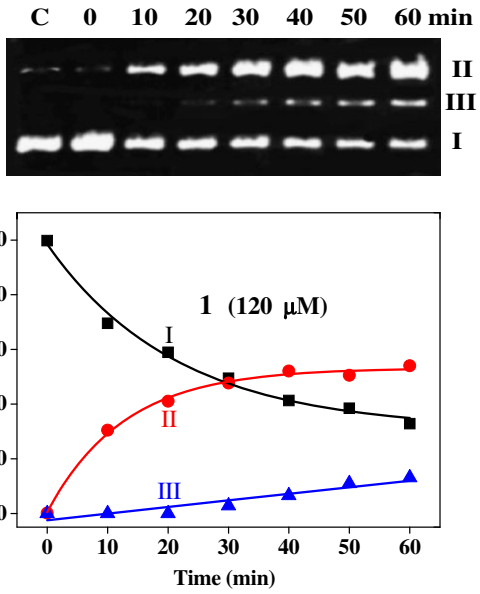


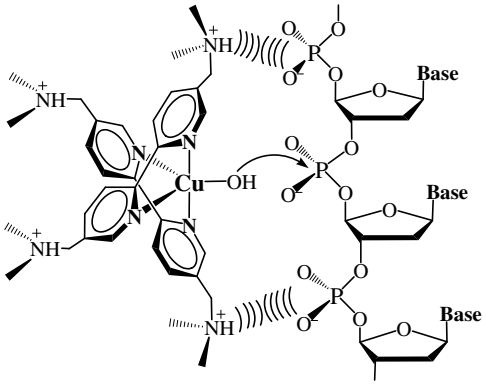
Fig. 6. Electrophoresis pattern and time course plot for the cleavage of pBR322 DNA by **2** (120 μM).

of 1.1×10^6–2.3×10^8 fold [27]. As shown in Table 5, the obtained k_{cat} values of 15.0, 13.7, 2.0 and 1.7 h^{-1} for **1**, **2**, **3** and **4**, respectively (37 °C, pH 7.5), indicate that these Cu(II) complexes exhibit very high hydrolytic cleavage reactivity, giving 4.7×10^7–4.2×10^8 fold rate enhancement.

Interestingly, the cleavage reactivity of **1** and **2** with 5,5′-ammonium groups is much higher than that of **3** and **4** with 4,4′-ammonium groups. The high cleavage reactivity may be attributed to the cooperativity between ammonium groups and the active Cu(II) center when these complexes are bound to DNA *via* electrostatic interactions (for all complexes) and hydrogen bonding (for **1** and **3**) (Scheme 3). Crystal data of **1** show that each distance between positively-charged N atoms in ammonium groups and the coordinated Br is 6.201 Å, which is in the range of the distance between the two adjacent phosphate groups in B-DNA (6–7 Å) [55,71]. However, distances between positively-charged N atoms and the coordinated Br atom in **4** are in the range of 7.835–8.117 Å (Table 3), which deviates from 6 to 7 Å. Although the crystal structures of **2** and **3** have not been obtained, one can conclude that their structures should be similar to **1** and **4** respectively. As a result, complexes **1** and **2** can more effectively match the phosphate groups of nucleic acid at space intervals than **3** and **4** do. The conclusion has also been supported by DNA binding experiments. The different position of the functional groups in **1**, **2** and **3**, **4**, results in the evident difference on their cleavage reactivity. On the other hand, the cleavage reactivity of **1** and **2** with 5,5′-dimethylamino/trimethylamino groups is also much higher than that of reported complex analogues with 5,5′-triethylamino/tributylamino groups [55]. It indicates that the steric hindrance of organic functional groups in mimics is also a significant factor to DNA cleavage activity of metal moiety in mimics.

Table 5
The kinetic parameters for hydrolytic cleavage of DNA by all complexes

Parameters	1	2	3	4
k_{cat} (h^{-1})	15.0 ± 0.4	13.7 ± 0.3	2.1 ± 0.2	1.7 ± 0.2
K_M (10^{-4} M)	4.5 ± 0.2	4.7 ± 0.3	2.8 ± 0.2	2.3 ± 0.1
k_{cat}/K_M (10^4 h^{-1} M^{-1})	3.37	2.94	0.75	0.75



Scheme 3. Proposed cooperativity between ammonium groups and cooper-coordinated hydroxyl in **1** when interact with DNA.

4. Conclusion

A series of Cu(II) complexes of disubstituted 2,2′-bipyridine bearing dimethylamino and trimethylamino groups at 5,5′- and 4,4′-positions were synthesized. The Cu(II) complexes with ammonium groups at 5,5′-positions exhibit very high DNA cleavage reactivity under hydrolytic conditions. The positively-charged functional groups of these complexes facilitate their binding to DNA and accelerate the cleavage of DNA especially when they match phosphodiester groups of nucleic acid better at space intervals.

Acknowledgements

This work was supported by the National Natural Science Foundation of China (Nos. 20529101, 20671098, 20725103 and 20770494), the Guangdong Provincial Natural Science Foundation (No. 07117637) and National Basic Research Program of China (973 Program No. 2007CB815306).

Appendix A. Supplementary data

CCDC 664062 and 664063 contain the supplementary crystallographic data for **1** and **4**. These data can be obtained free of charge via http://www.ccdc.cam.ac.uk/conts/retrieving.html, or from the Cambridge Crystallographic Data Centre, 12 Union Road, Cambridge CB2 1EZ, UK; fax: (+44) 1223-336-033, or e-mail: deposit@ccdc.cam.ac.uk.

References

[1] A. Radzicka, R. Wolfenden, Science 267 (1995) 90.
[2] M.S. Deshpande, A.A. Kumbhar, A.S. Kumbhar, Inorg. Chem. 46 (2007) 5450.
[3] P.U. Maheswari, S. Roy, H.den. Dulk, S. Barends, G.V. Wezel, B. Kozlevcčar, P. Gamez, J. Reedijk, J. Am. Chem. Soc. 128 (2006) 710.
[4] I. Boll, E. Jentzsch, R. Krämer, A. Mokhir, Chem. Commun. (2006) 3447.
[5] F. Mancin, P. Scrimin, P. Tecilla, U. Tonellato, Chem. Commun. (2005) 2540.
[6] J. Suh, Acc. Chem. Res. 36 (2003) 562.
[7] A. Sreedhara, J.A. Cowan, J. Biol. Inorg. Chem. 6 (2001) 337.
[8] J.A. Cowan, Chem. Rev. 98 (1998) 1067.
[9] N.H. Williams, B. Takasaki, M. Wall, J. Chin, Acc. Chem. Res. 32 (1999) 485.
[10] E.L. Hegg, J.N. Burstyn, Coord. Chem. Rev. 173 (1998) 133.
[11] C.J. Burrows, J.G. Muller, Chem. Rev. 98 (1998) 1109.
[12] W.K. Pogozelski, T.D. Tullius, Chem. Rev. 98 (1998) 1089.
[13] R.R. Breaker, Chem. Rev. 97 (1997) 371.
[14] D.E. Wilcox, Chem. Rev. 96 (1996) 2435.
[15] D.S. Sigman, A. Mazumder, D.M. Perrin, Chem. Rev. 93 (1993) 2295.
[16] D.S. Sigman, Acc. Chem. Res. 19 (1986) 180.
[17] S. Dhar, P.A.N. Reddy, A.R. Chakravarty, Dalton Trans. (2004) 697.
[18] P.A.N. Reddy, M. Nethaji, A.R. Chakravarty, Eur. J. Inorg. Chem. (2004) 1440.
[19] X.M. Xu, J.H. Yao, Z.W. Mao, K.B. Yu, L.N. Ji, Inorg. Chem. Commun. 7 (2004) 803.
[20] L.P. Lu, M.L. Zhu, P. Yang, J. Inorg. Biochem. 95 (2003) 31.
[21] R. Ren, P. Yang, W.J. Zheng, Z.C. Hua, Inorg. Chem. 39 (2000) 5454.
[22] A.M. Thomas, M. Nethaji, S. Mahadevan, A.R. Chakravarty, J. Inorg. Biochem. 94 (2003) 171.
[23] M. Kathryn, T. Deck, A. Tseng, J.N. Burstyn, Inorg. Chem. 41 (2002) 669.
[24] E.L. Hegg, J.N. Burstyn, Inorg. Chem. 35 (1996) 7474.
[25] J. Gao, A.E. Martell, J. Reibenspies 329 (2002) 122.
[26] M. Jezowska-Bojczuk, W. Lesniak, W. Szczepanik, K. Gatner, A. Jezierski, M. Smoluch, W. Bal, J. Inorg. Biochem. 84 (2001) 189.
[27] A. Sreedhara, J.D. Freed, J.A. Cowan, J. Am. Chem. Soc. 122 (2000) 8814.
[28] D.K. Chand, H.J. Schneider, A. Bencini, A. Bianchi, C. Giorgi, S. Ciattini, B. Valtancoli, Chem.-Eur. J. 6 (2000) 4001.
[29] D.K. Chand, H.J. Schneider, J.A. Aguilar, F. Escarti, E. Garcia-Espan, S.V. Luis, Inorg. Chim. Acta 316 (2000) 71.
[30] M.S. Melvin, J.T. Tomlinson, G.R. Saluta, G.L. Kucera, N. Lindquist, R.A. Manderville, J. Am. Chem. Soc. 122 (2000) 6333.
[31] S. Borah, M.S. Melvin, N. Lindquist, R.A. Manderville, J. Am. Chem. Soc. 120 (1998) 4557.
[32] U. Itoh, H. Hisada, T. Sumiya, M. Hosono, Y. Usui, Y. Fujii, Chem. Commun. (1997) 677.
[33] F.V. Pamatong, C.A. Detmer III, J.R. Bocarsly, J. Am. Chem. Soc. 118 (1996) 5339.
[34] C.A. Detmer III, F.V. Pamatong, J.R. Bocarsly, Inorg. Chem. 35 (1996) 6292.
[35] C. Sissi, F. Mancin, M. Gatos, M. Palumbo, P. Tecilla, U. Tonellato, Inorg. Chem. 44 (2005) 2310.
[36] S.C. Zhang, Y. Shao, C. Tu, C.H. Dai, Z.J. Guo, Chinese J. Inorg. Chem. 20 (2004) 1159.
[37] M. Gonzalez-Alvarez, G. Alzuet, J. Borras, M. Pitie, B. Meunier, J. Biol. Inorg. Chem. 8 (2003) 644.
[38] D.Y. Kong, J. Reibenspies, J.G. Mao, A. Clearfield, A.E. Martell, Inorg. Chim. Acta 342 (2003) 158.
[39] L. Zhu, O. dos Santos, C.W. Koo, M. Rybstein, L. Pape, J.W. Canary, Inorg. Chem. 42 (2003) 7912.
[40] L.M. Rossi, A. Neves, R. Horner, H. Terenzi, B. Szpoganicz, J. Sugai, Inorg. Chim. Acta 337 (2002) 366.
[41] A.M. Thomas, G. Neelakanta, S. Mahadevan, M. Nethaji, A.R. Chakravarty, Eur. J. Inorg. Chem. (2002) 2720.
[42] K.J. Humphreys, K.D. Karlin, S.E. Rokita, J. Am. Chem. Soc. 124 (2002) 6009.
[43] K.J. Humphreys, A.E. Johnson, K.D. Karlin, S.E. Rokita, J. Biol. Inorg. Chem. 7 (2002) 835.
[44] G.N. De Iuliis, G.A. Lawrance, S. Fieuw-Makaroff, Inorg. Chem. Commun. 3 (2000) 307.
[45] C. Tu, Y. Shao, N. Gan, D. Xu, Z.J. Guo, Inorg. Chem. 43 (2004) 4761.
[46] A. Bencini, E. Berni, A. Bianchi, C. Giorgi, B. Valtancoli, D.K. Chand, H.J. Schneider, Dalton Trans. (2003) 793.
[47] K.J. Humphreys, K.D. Karlin, S.E. Rokita, J. Am. Chem. Soc. 124 (2002) 8055.
[48] I.O. Fritsky, R. Ott, H. Pritzkow, R. Krämer, Chem.-Eur. J. 7 (2001) 1221.
[49] P. Molenveld, J.F.J. Engbersen, D.N. Reinhoudt, Angew. Chem., Int. Ed. Engl. 38 (1999) 3189.
[50] S.G. Srivatsan, S. Verma, Chem.-Eur. J. 7 (2001) 828.
[51] J. Suh, S.J. Moon, Inorg. Chem. 40 (2001) 4890.
[52] B.B. Jang, K.P. Lee, D.H. Min, J. Suh, J. Am. Chem. Soc. 120 (1998) 12008.
[53] E. Kövári, R. Krämer, J. Am. Chem. Soc. 118 (1996) 12704.
[54] R. Hettich, H.J. Schneider, J. Am. Chem. Soc. 119 (1997) 5638.
[55] Y. An, M.L. Tong, L.N. Ji, Z.W. Mao, Dalton Trans. (2006) 2066.
[56] R.O. Adremi, J.M. Robert, Synth. Commun. 25 (1995) 4093.
[57] D.C. Leopoldo, J.D. Walter, A.V. Zelewsky, J. Heterocyclic Chem. 27 (1990) 163.
[58] W. Geoffrey, B. Gerrit, S.R. Nagaraja, F. Donald, J. Phys. Chem. B 103 (1999) 8067.
[59] S.W. Robert, B. Denis, A.D. Rosemary, C.P. Martyn, Heterocycles 56 (2002) 157.
[60] G.M. Sheldrick, SHELXL-97, Program for the Refinement of Crystal Structures, University of Göttingen, Göttingen, 1997.
[61] L.E. Gunther, A.S. Yong, J. Am. Chem. Soc. 90 (1968) 7323.
[62] C. O'Sullivan, G. Murphy, B. Murphy, B. Hathaway, Dalton Trans. (1999) 1835.
[63] A.W. Addison, T. Nageswara Rao, Dalton Trans. (1984) 1349.
[64] V.I. Ivanov, L.E. Minchenkova, A.K. Schyolkina, A.I. Poletayev, Biopolymers 12 (1973) 89.
[65] C.V. Kumar, R.S. Turner, E.H. Asuncion, J. Photochem. Photobiol. A: Chem. 74 (1993) 231.
[66] D.R. McMillin, K.M. McNett, Chem. Rev. 98 (1998) 1201.
[67] R.F. Pasternack, P.G. Collings, Science 269 (1995) 935.
[68] O.I. Aruoma, B. Halliwell, M. Dizdaroglu, J. Biol. Chem. 264 (1989) 13024.
[69] K. Yamamoto, S. Kawanishi, J. Biol. Chem. 264 (1989) 15435.
[70] J. Eigner, H. Boedtker, G. Michaels, Biochim. Biophys. Acta 51 (1961) 165.
[71] C. Sissi, P. Rosso, F. Felluga, F. Formaggio, M. Palumbo, P. Tecilla, C. Tonilo, P. Scrimin, J. Am. Chem. Soc. 123 (2001) 3169.

prepared every day and standardized against standard potassium dichromate solution iodometrically [21]. The ammonium salt of Mn^{IV} complex, $(NH_4)_6[Mn^{IV}Mo_9O_{32}]$ was prepared by reported method [32] as follows: 50 g of ammonium molybdate was dissolved in 200 ml of water and excess of hydrogen peroxide as oxidant was added to it and the resultant solution was heated to 95 °C. To this hot solution, 5 g of $MnSO_4 \cdot H_2O$ in 50 ml of water was added slowly with constant stirring. The resultant orange-red colored solution was boiled for 10 min and quickly filtered and cooled. The orange-red colored crystals were recrystallized thrice from hot (70 °C) water. The solution of $(NH_4)_6[Mn^{IV}Mo_9O_{32}]$ was standardised by treating known amount of complex solution with excess of As^{III}, and back titrating As^{III}. The oxidation state of hetero-atom was also confirmed to be four, by iodometric method.

2.2. Kinetic study

The reaction between $[Mn^{IV}Mo_9O_{32}]^{6-}$ and P^I was carried out under pseudo-first-order conditions at a constant temperature of 27.0 ± 0.1 °C. The reaction was initiated by mixing the previously thermostated solutions of P^I and $[Mn^{IV}Mo_9O_{32}]^{6-}$, which also contained the required amount of perchloric acid, and doubly distilled water. The reaction was followed by determining the concentration of remaining $[Mn^{IV}Mo_9O_{32}]^{6-}$ iodometrically. The rate constants were determined from the linear pseudo-first-order plots of $\log[Mn^{IV}Mo_9O_{32}]^{6-}$ against time and the rate constants were reproducible within ±6%.

2.3. Stoichiometry and product analysis

The stoichiometry was studied by keeping concentration of $[Mn^{IV}Mo_9O_{32}]^{6-}$ constant at 8×10^{-3} mol dm^{-3} and varying concentration of P^I from 0.5×10^{-3} to 6.0×10^{-3} mol dm^{-3}. Different reaction mixtures containing varying concentration of P^I were prepared, which also contained required amount of perchloric acid. The concentration of unreacted $[Mn^{IV}Mo_9O_{32}]^{6-}$ was determined after 24 h iodometrically. The stoichiometry was found to be one mole of $[Mn^{IV}Mo_9O_{32}]^{6-}$ per mole of P^I. When the reaction mixture containing excess of hypophosphite was kept undisturbed up to 48 h a blue color was developed. The blue product was isolated from the reaction mixture by crystallization and recrystallized form alcohol. The UV–Vis spectra of the resulting blue product was recorded, which shows a peak at 840 nm corresponding to the molybdenum blue [20]. Further, when a strong reductant like ascorbic acid or hydrazine sulfate was added to the reaction mixture containing excess of hypophosphite there was rapid formation of molybdenum blue just after 24 h.

2.4. Atomic absorption analysis

The complex $(NH_4)_6[Mn^{IV}Mo_9O_{32}] \cdot 3H_2O$ was analyzed by AAS. The solution for AAS analysis was prepared by dissolving 100 mg of recrystallized sample in double distilled water and 5 ml of this stock solution was diluted to 100 ml. The diluted solution was used for AAS analysis of Mn and Mo using Perkin–Elmer AAnalyst-300 instrument. The complex $(NH_4)_6[Mn^{IV}Mo_9O_{32}] \cdot 3H_2O$ shows (theoretical): Mn – 3.501% (3.4493%) and Mo – 54.217% (54.2125%). The results of the AAS analysis of the blue products are Mn – 0%, Mo – 26.7% and P – 1.5%.

2.5. Spectrophotometric measurements

The visible spectra of $(NH_4)_6[Mn^{IV}Mo_9O_{32}]$ complex, the blue product and the reaction mixture were recorded by using Elico SL-177 spectrophotometer between the wavelength region 400 and 900 nm. The spectra of the $(NH_4)_6[Mn^{IV}Mo_9O_{32}]$ complex in water, in presence of 0.1 mol dm^{-3} perchloric acid and the reaction mixture soon after the mixing of reactants is given in Fig. 1. The spectrum of the blue product obtained is shown in Fig. 2.

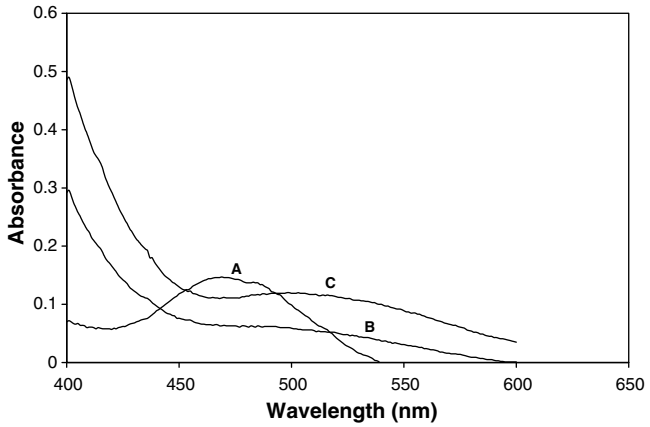


Fig. 1. UV–Vis spectra of $[Mn^{IV}Mo_9O_{32}]^{6-}$: (A) in water, (B) in 0.1 mol dm^{-3} $HClO_4$ and (C) reaction mixture. $10^3[Mn^{IV}Mo_9O_{32}]^{6-}$ = 1.0 mol dm^{-3}, 10^2[Hypophosphite] = 6.0 mol dm^{-3}.

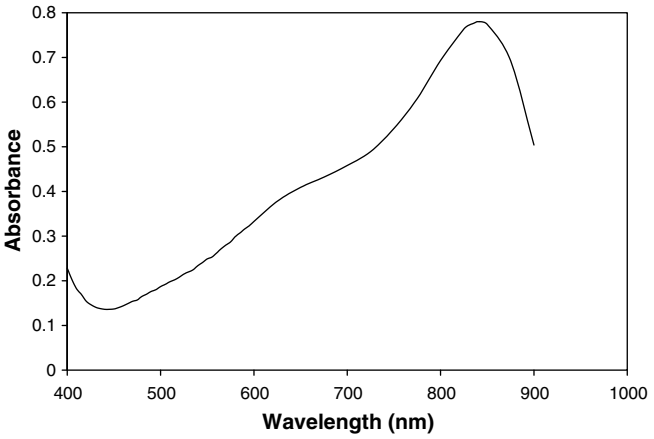


Fig. 2. UV–Vis spectrum of the blue product. $10^3[H_{10}(HP)Mo_6O_{26}]^{2-}$ = 1.4 mol dm^{-3}.

2.6. FTIR-spectral study

The FTIR-Spectra of $(NH_4)_6[Mn^{IV}Mo_9O_{32}]$ complex and the blue product were taken in KBr by using Perkin–Elmer Spectrumone spectrophotometer. The complex $(NH_4)_6[Mn^{IV}Mo_9O_{32}]$ contains Mn^{IV} as a hetero-atom surrounded by octahedral groups of MoO_6^{2-}. In the IR-spectrum of Mn^{IV} complex, the peaks obtained at 3521 cm^{-1}, 933 cm^{-1}, 918 cm^{-1} and 900 cm^{-1} corresponds to lattice water molecules [33], Mo–O stretching [34], Mn^{IV}–O stretching and tetrahedral MoO_4^{2-} groups [33], respectively. The FTIR spectra of the blue product shows the peaks at 3400, 2405, 1120, 1043, 941, 905, 804 and 626 cm^{-1} corresponding to lattice water [33], PH stretching [35], PO_3 groups [35], PH deformation, Mo–O stretching, MoO_4^{2-} groups, MoO_4^{3-} groups and Mo–O–P [34] stretching, respectively.

2.7. Test for free radicals

The reaction was also studied in presence of added acrylonitrile to understand the intervention of free radicals [36,37] in the reaction. There was no effect of added acrylonitrile on the reaction and

also no precipitate due to the polymerization of the added acrylonitrile was observed thus confirming the absence of any free radical formation in the reaction.

3. Results and discussion

3.1. Reaction order

The reaction was carried out under pseudo-first-order conditions, keeping the concentration of perchloric acid constant at 0.5 mol dm^{-3} and varying either [P^{I}] from 2.5×10^{-2} to 2.5×10^{-1} mol dm^{-3} at constant $[Mn^{IV}Mo_9O_{32}]^{6-}$ (2.0×10^{-3} mol dm^{-3}) or $[Mn^{IV}Mo_9O_{32}]^{6-}$ from 0.4×10^{-3} to 4.0×10^{-3} mol dm^{-3} at constant [P^{I}] (1.0×10^{-1} mol dm^{-3}). The pseudo-first-order rate constants were found to be increased with increase in the concentration of the reductant (Table 1) and the order was found to be fractional as determined by $\log(k_{obs})$ against log[P^{I}] plot. The Michaelis–Menten plot of $1/k_{obs}$ against 1/[Hypophosphite] was also found to be linear with an intercept (Fig. 3) indicating the formation of a complex between the two reactants. Therefore, the effect of hypophosphite was studied at four different temperatures and from the slope and intercept of Fig. 3, the formation constants of the complex and rate constants for its decomposition were determined at all the temperatures studied (Table 2). The pseudo-first-order plots were found to be linear and the pseudo-first-order rate constants were fairly constant as the concentration of oxidant is varied (Table 3), indicating the order in oxidant to be unity. There was no effect of added product, P^{III} whereas the added molybdate ion over the concentration range of 0.1×10^{-2} to 1.0×10^{-2} mol dm^{-3} decreases the values of k_{obs} considerably (Table 3). Free radical intervention during the reaction was tested by studying the reaction in presence of added acrylonitrile, a free radical scavenger. There was no precipitation due to polymerization of added acrylonitrile and the rate also remains unaffected which indicates no formation of free radicals in the reaction.

Table 1
Effect of concentration of hypophosphite on the reaction between hypophosphite and enneamolybdomanganate(IV) at different temperatures

10[Hypophosphite] (mol dm^{-3})	$10^3 k_{obs}$ (s^{-1})			
	288 K	293 K	300 K	308 K
0.25	0.35	0.46	0.61	1.3
0.5	0.69	0.89	1.19	2.7
1.0	1.3	1.6	2.0	4.7
2.0	2.0	2.7	3.7	7.6
2.5	2.5	3.3	4.8	10.4

$10^3[Mn^{IV}Mo_9O_{32}]^{6-}$ = 2.0 mol dm^{-3}, $[HClO_4]$ = 0.5 mol dm^{-3}, I = 0.6 mol dm^{-3}.

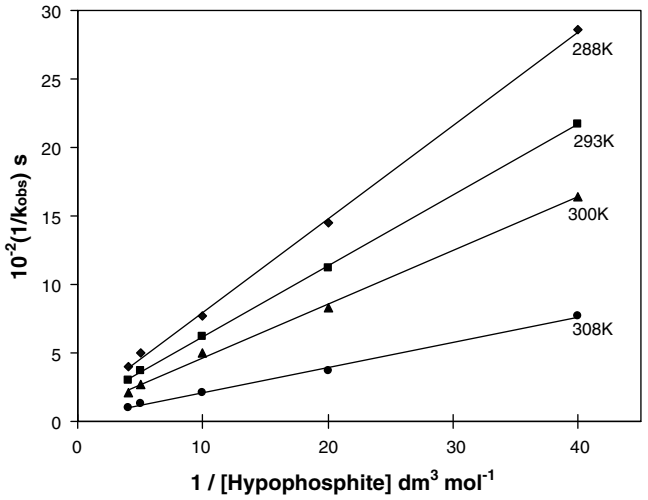


Fig. 3. Michaelis–Menten plot of $1/k_{obs}$ against 1/[Hypophosphite] at different temperatures (conditions as in Table 1).

Table 2
The formation constant and decomposition rate constants of the complex and the thermodynamic parameters with respect to slow step[a]

T (°C)	K_2 (dm^3 mol^{-1})	$10^3 k_1$ (s^{-1})
15	1.8	8.2
20	2.0	9.7
27	1.9	14.0
35	1.4	38.6

$\Delta H^{\#}$ = 54.5 ± 6 kJ mol^{-1}, $\Delta G^{\#}$ = 83.0 ± 6 kJ mol^{-1}, $\Delta S^{\#}$ = −95.30 ± 5 J K^{-1} mol^{-1}

[a] Conditions as in Table 1.

Table 3
Effect of concentration of enneamolybdomanganate(IV) ion, perchloric acid and molybdate ion on the reaction between hypophosphite and enneamolybdomanganate(IV) at 27 °C

$10^3[Mn^{IV}Mo_9O_{32}]^{6-}$ (mol dm^{-3})	$[HClO_4]$ (mol dm^{-3})	$10^2[MoO_4]$ (mol dm^{-3})	$10^3 k_{obs}$ (s^{-1})
0.4	0.5	0.0	2.0
1.0	0.5	0.0	2.0
2.0	0.5	0.0	2.0
3.0	0.5	0.0	2.0
4.0	0.5	0.0	2.0
2.0	0.1	0.0	0.59
2.0	0.2	0.0	1.2
2.0	0.5	0.0	2.0
2.0	1.0	0.0	4.1
2.0	1.5	0.0	6.2
2.0	2.0	0.0	7.8
2.0	0.5	0.1	1.5
2.0	0.5	0.25	1.0
2.0	0.5	0.50	0.76
2.0	0.5	0.75	0.51
2.0	0.5	1.0	0.38

10[Hypophosphite] = 1.0 mol dm^{-3}, I = 0.6 mol dm^{-3}.

3.2. Effect of hydrogen ion concentration

The effect of hydrogen ion concentration on the reaction was studied in order to understand the nature of reactant species present in the solution. The concentration of H^+ ion was varied from 0.1 to 1.0 mol dm^{-3} keeping all other concentrations constant. It was found that the reaction rate increases with the concentration of H^+ ions (Table 3) and the graph of k_{obs} against $[H^+]$ was found to be linear without intercept. The order in hydrogen ion concentration was found to be 0.87 as found from $\log k_{obs}$ against $\log[H^+]$ plot.

3.3. Effect of solvent polarity, ionic strength and temperature

The effects of ionic strength, solvent polarity and temperature were studied keeping concentration of $[Mn^{IV}Mo_9O_{32}]^{6-}$, P^{I} and perchloric acid constant at 2.0×10^{-3} mol dm^{-3}, 0.1 mol dm^{-3} and 0.5 mol dm^{-3}, respectively, at 27 °C. Sodium perchlorate and acetonitrile were used to vary the ionic strength and solvent polarity, respectively. The rate of the reaction was unaffected by increase in ionic strength from 0.5 to 1.0 mol dm^{-3} and as the percentage of acetonitrile increases from 0% to 40% v/v. The effect of temperature was studied at 15, 20, 27 and 35 °C and the activation parameters were determined with respect to the slow step of the reaction are given in Table 2.

Enneamolybdomanganate(IV) is one of the stable heteropolymolybdate containing Mn^{IV} as a hetero atom and is noncentrosymmetric. It also shows a characteristic charge transfer band at 468 nm which has been assigned to $^4A_{2g} \rightarrow {}^4T_{2g}$ transition of Mn^{IV}. This band is sensitive [38] to the changes in the electronic state of the Mn^{IV} ion and any perturbations due to interaction of MnO_6 groups with neighboring ions will result in the shift of band. The arrangements of oxygen atoms [38] around $[MnMo_9O_{32}]^{6-}$ are of two different types A and B as shown in Fig. 4. From the spectrophotometric investigation on interaction [38] of various cations with the anion, it was concluded that metal cations will bind to site A due to their larger negative charge in comparison with that of site B. Such type of cation interaction at site A perturbs the electronic state of the central hetero atom, manganese, resulting in change of absorption spectra of the anion. In aqueous solution the UV–Vis spectrum of the anion, $[MnMo_9O_{32}]^{6-}$, shows a peak at 468 nm and in presence of acid two isosbestic points are obtained at 435 and 520 nm due to its protonation (Fig. 1A and B, respectively). At high metal ion concentrations the peak at 468 nm is reappeared [38] as a result of metal ion substitution on the anion at oxygen atoms of A type. In order to understand the interaction between the hypophosphite and $[MnMo_9O_{32}]^{6-}$ UV–Vis spectra of the reaction mixture was examined. The anion shows a characteristic peak at 468 nm in aqueous solution as in Fig. 1A and addition of 0.1 mol dm^{-3} perchloric acid the spectrum of protonated anion is obtained (Fig. 1B) with two isosbestic points are obtained at 435 and 520 nm due to its protonation. To an acidic solution of the anion when hypophosphite is added the reappearance of peak at 468 nm was not observed instead there was considerable increase in the intensity of absorption about 504 nm (Fig. 1C). The reappearance of peak at 468 nm in presence of hypophosphite is expected if the interaction of added hypophosphite would have been through oxygen atoms of site A. Therefore, the hypophosphite is interacting with the anion, $[MnMo_9O_{32}]^{6-}$, through the oxygen atoms of site B without perturbing the electronic state of MnO_6 octahedra. An increase in the intensity of peak at 504 nm in presence of hypophosphite is also an indication of formation of complex between the two. Such complex formation was also supported kinetically from the fractional order in [Hypophosphite] and Michaelis–Menten plot of $1/k_{obs}$ against 1/[Hypophosphite] as shown in Fig. 3.

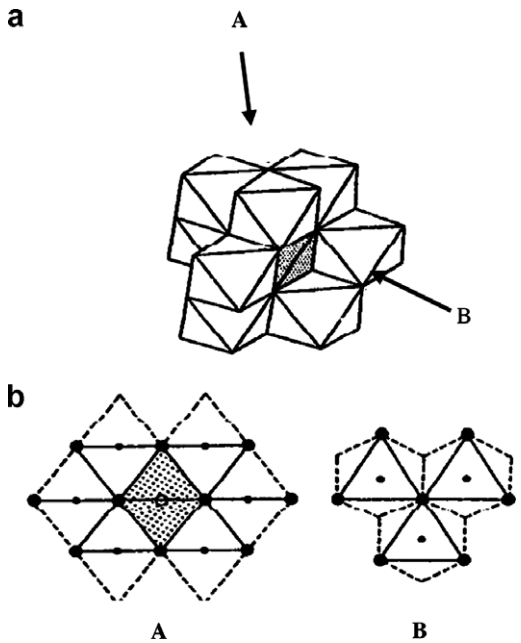


Fig. 4. Arrangements of oxygen atoms in $[MnMo_9O_{32}]^{6-}$ (from Ref. [36]): (a) structure of the $[MnMo_9O_{32}]^{6-}$ anion (shaded octahedron in (a) is MnO_6 and (b) two arrays of oxygen atoms as the potential metal binding sites. (large solid circles in (b) are oxygen atoms, small solid circles are Mo atoms and an open circle is a Mn atom.)

In aqueous solution hypophosphorous acid acts as a monobasic acid [19] and its dissociation constant is 5.9×10^{-2} mol dm^{-3} and in acidic solutions it exists in the undissociated form. The pK_a of hexaprotonated anion, $[MnMo_9O_{32}]^{6-}$, is reported [38] to be around 3.0 and at pH 2 approximately 90% of the anion is totally protonated and it is completely deprotonated at pH 4. Therefore, at a pH bellow 2 the protonation equilibria of the anion, $[MnMo_9O_{32}]^{6-}$, can be represented by Eq. (1). The dependence of rate of the reaction on hydrogen ion concentration is shown in Table 3 and the order in its concentration was found to be 0.87(R^2 = 0.996) as found from

$$[H_6Mn^{IV}Mo_9O_{32}] \overset{K_1}{\rightleftharpoons} [H_5Mn^{IV}Mo_9O_{32}] + H^+ \quad (1)$$

the plot of $\log k_{obs}$ against $\log[H^+]$ plot. The plot of k_{obs} against $[H^+]$ was also found to be linear (R^2 = 0.997) without any intercept indicating that only protonated form of the oxidant is the active species. Therefore, under the reaction conditions employed in the present study the hexaprotonated anion, $[MnMo_9O_{32}]^{6-}$, and the undissociated hypophosporous acid are the reactive species.

The rate of oxidation of phosphite ion under the experimental conditions was also examined in order to know its simultaneous oxidation by the oxidant, $[MnMo_9O_{32}]^{6-}$. The rate constant for the phosphite ion oxidation was found to be 1.2×10^{-4} s^{-1} which is approximately six times slower than that for the hypophosphite. Since the reaction was carried out under pseudo-first-order conditions keeping large excess of hypophosphite it was assumed that the contribution of the phosphite oxidation to the total rate constant is negligible. The color of the reaction mixture after 24 h during stoichiometric studies was light yellow and a blue color appears after 48 h. This appearance of blue color is due to the further reaction of the yellow product obtained after 24 h with excess reductant, hypophosphite. The blue color was not obtained when the reaction was carried out under second-order conditions which indicates that the excess hypophosphite during first-order conditions acts as a reductant. If another strong reductant like ascorbic acid or hydrazine sulfate was added to the light yellow reaction mixture the blue color appears immediately. This confirms that the light yellow product obtained undergo slow reduction with excess of hypophosphite or rapid reduction in presence of strong reductants. Spectrophotometric determination of phosphorous content is generally carried out by molybdenum blue method [21–23]. The basis for the analysis of phosphorous by this method involves initial formation of a yellow complex, phosphomolybdic acid, between phosphate and molybdate ions which then will be reduced by various reductants. This polyoxometalate is capable of undergoing reversible multivalent reduction forming reduced mixed-valence (Mo^V–Mo^{VI}) heteropolyblues. In the present investigation there was appearance of blue color in the reaction mixture containing excess of hypophosphite after 48 h. But, the stoichiometry of the reaction was found to be 1:1 in presence of excess of enneamolybdomanganate (IV) when analyzed after 24 h. Therefore, the hypophosphite ion is oxidized to phosphite ion with formation of a yellow phosphitomolybdate ion which then undergoes redox reaction with the available reductant to generate molybdenum blue. The mechanism up to the formation of yellow reaction product with the observed stoichiometry 1:1 can be represented as in Scheme 1 in terms of the active species of the reactants. The corresponding rate law according to Scheme 1 also considering protonation equilibria 1 of the oxidant is given by Eq. (6).

$$[H_6Mn^{IV}Mo_9O_{32}] + H_3PO_2 \overset{K_2}{\rightleftharpoons} \text{Complex} \quad (2)$$

$$\text{Complex} + 5H_2O \xrightarrow{k_1} [Mn^{II}Mo_6O_{24}]^{10-} + 3HMoO_4^- + H_3PO_3 + 13H^+ \quad (3)$$

$$[Mn^{II}Mo_6O_{24}]^{10-} \xrightarrow{\text{fast}} Mn^{2+} + 6MoO_4^{2-} \quad (4)$$

$$H_3PO_3 + 6MoO_4^{2-} + 10H^+ \xrightarrow{\text{fast}} [H_{10}(HP)Mo_6O_{26}]^{2-} + H_2O \quad (5)$$

Scheme 1.

The corresponding expression for observed pseudo-first-order rate constant can be represented by Eq. (7). According to Eq. (7) the plot of $1/k_{obs}$ against

$$\text{Rate} = \frac{k_1K_2[H_+][\ H_3PO_2][H_6Mn^{IV}Mo_9O_{32}]}{([H^+]+K_1)(1+K_2[H_3PO_2])} \quad (6)$$

$$k_{obs} = \frac{k_1K_2[H^+][\ H_3PO_2]}{([H^+]+K_1)(1+K_2[H_3PO_2])} \quad (7)$$

$1/[H_3PO_2]$ at four different temperatures were found to be linear with intercept (Fig. 3) and the formation constants of the complex as well as rate constant for its decomposition were calculated form such plots (Table 2). The plot of $1/k_{obs}$ against $1/[H^+]$ was also found to be linear with intercept (Fig. 5) and from the slope and intercept the dissociation constant of equilibria 1 was calculated as 1.71 mol dm^{-3}. Linearity of both Figs. 3 and 5 verify the rate law derived. The activation parameters for the slow step of the reaction were also determined and are given in Table 2. The inhibiting effect of added molybdate ion is due to the formation of a molybdate complex of hypophosphite thus decreasing the free hypophosphite ion concentration in the solution. The involvement of molybdate ion in reversible equilibria of the mechanism was ruled out as the pseudo-first-order plots were linear up to 80% of the reaction without any deviation.

The mechanism according to Scheme 1 proceeds with the formation of a complex between the hypophosphite and $[H_6Mn^{IV}Mo_9O_{32}]$ in a prior equilibria which then decomposes to give phosphite and $[Mn^{II}Mo_6O_{24}]^{10-}$ in a rate determining step. The interaction between hypophosphite and $[H_6MnMo_9O_{32}]$ during complex formation occurs through the oxygen atoms of the site B as evidenced by the increase in the absorbance of the peak at 504 nm (Fig. 1). The reduced polyoxometalate, $[Mn^{II}Mo_6O_{24}]^{10-}$, undergo fast decomposition to generate aqueous Mn^{2+} ion and molybdate ions. In an earlier ESR study the interaction between aqueous Mn^{2+} and molybdate ions was examined and the alteration of linewidth of the Mn^{2+} signal in presence of molybdate [39] was found to be comparable with that in presence of acetate ions. From this result it has been concluded that the interaction between molybdate ions and Mn^{2+} ions in aqueous solutions is weak one. Therefore, the dissociation of the $[Mn^{II}Mo_6O_{24}]^{10-}$ under the present reaction conditions is considered to be fast. In the next step the molybdate ions combine with phosphite ion to form a phosphitomolybdate ion again in a fast step. An equilibrium analysis of phosphite and molybdate ions in acidic solutions by potentiometry and ^{31}PNMR studies has been recently reported [40]. According to the study between pH 1 and 2 formation of $[H_{10}(HP)Mo_6O_{26}]^{2-}$ is most probable with a high formation constant ($\log\beta = 68.99$) therefore, in the present study Eq. (5) of Scheme 1 is also considered as a fast step. The blue product of the reaction after 48 h was also analysed by AAS and the molar ratio of P:Mo was found to be 1:6 without any Mn^{2+} further confirming the $[H_{10}(HP)Mo_6O_{26}]^{2-}$ ion formation under the reaction conditions. The FTIR spectra of the $(NH_4)_6[MnMo_9O_{32}]$, phosphite ion and the blue product were also examined to know the structure of the product formed and the assignment of various vibrational frequencies are given Table 4. The data of Table 4 for $(NH_4)_6[MnMo_9O_{32}]$ shows characteristic peaks for the lattice water, NH_3 groups and corresponding peaks due to Mo–O stretching, Mn^{IV}–O stretching and MoO_4^{2-} groups, respectively. The peak due to Mn^{IV}–O stretching is absent in the blue product obtained where as the peaks corresponding to Mo–O stretching and MoO_4^{2-} groups have been shifted slightly due to the change in their electronic environment. A new peak at 804 cm^{-1} in the blue product might be ascribed to $Mo^VO_4^{3-}$ groups generated due to the reduction of the yellow product after long standing. The reported frequencies [35] of aqueous phosphite ion

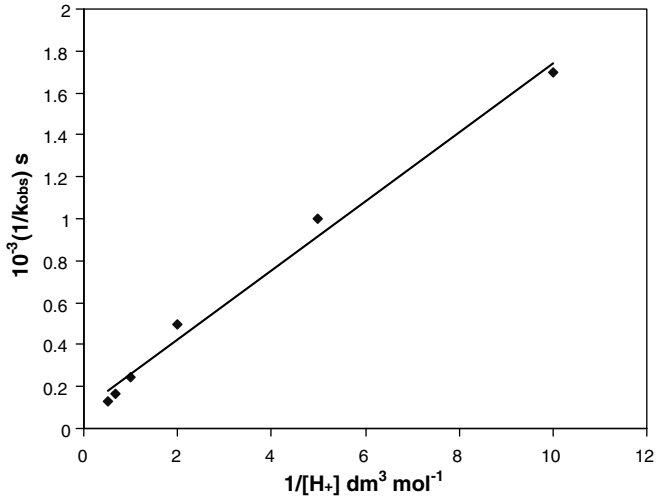


Fig. 5. Plot of $1/k_{obs}$ against $1/[H^+]$(Conditions as in Table 3).

Table 4
Vibrational frequencies and IR band assignments (cm^{-1}) of the reaction product and phosphite

Reaction product	Phosphite[a]	$[Mn^{IV}Mo_9O_{32}]^{6-}$	Assignments	Shift
3400		3521	lattice water	
		1400	NH_3 group	
2405	2315		PH stretching	90
1120	1085		PO_3 deg def	35
1043	1027		PH Def	16
941		933	Mo–O stretching	08
		918	Mn^{IV}–O stretching	
905		900	MoO_4^{2-} groups	05
804			MoO_4^{3-} groups	
626			Mo–O–P	

[a] From Ref. [35].

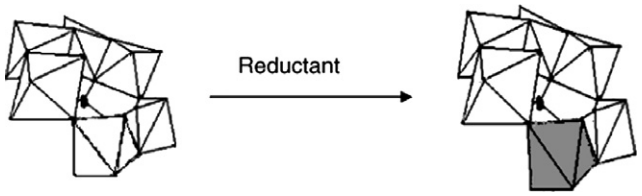


Fig. 6. Conversion of yellow product (from Ref. [39]) into blue product. (The shaded part in the figure represents the reduced Mo^{V}.)

due to PH stretching, PO_3 degenerate deformation and PH deformation are shifted in the blue product considerably as a result of its interaction with the molybdate ion to form phosphitomolybdate. The AAS analysis of the blue product also did not show the presence of Mn^{2+} and the molar ratio of P:Mo was found to be 1:6. On the basis of the FTIR and AAS results obtained the structure of the yellow product can be as that proposed earlier [40] which in presence of a reducing agent will be converted in to the blue product. The conversion of yellow product into the blue product can be shown as in Fig. 6. Acrylonitrile, free radical scavenger, did not affect the reaction rate indicate direct two-electron transfer from P^{I} to $[Mn^{IV}Mo_9O_{32}]^{6-}$. The effect of ionic strength and the solvent polarity on the rate qualitatively explains the reaction involves an uncharged species, as shown in Eq. (2) of Scheme 1. The moderate values of $\Delta H^{\#}$ and $\Delta S^{\#}$ were both favourable [41] for electron transfer processes. The negative value of $\Delta S^{\#}$, can be ascribed to the nature of electron pairing and unpairing processes and to the loss of degrees of freedom formerly available to the reactants upon the formation of transition state.

4. Conclusions

The reaction between hypophosphite and enneamolybdomanganate (IV) in perchloric acid was carried out under pseudo-first-order conditions keeping large excess of hypophosphite. The hexaprotonated oxidant and undissociated hypophosphite were found to be reactive species under the reaction conditions. The reaction proceeds with formation of complex between the active forms of the reactants supported by both kinetically and spectrophotometrically. The enneamolybdomanganate (IV) ion dissociates completely after its reduction to $[Mn^{II}Mo_6O_{24}]^{10-}$ in presence of phosphite ions forming $[H_{10}(HP)Mo_6O_{26}]^{2-}$. Comparatively higher stability of $[H_{10}(HP)Mo_6O_{26}]^{2-}$ than that of $[Mn^{II}Mo_6O_{24}]^{10-}$ ion under the reaction conditions makes the product formation feasible. The free radical intervention was not detected in the reaction as the added acrylonitrile did not affect the rate of the reaction. A mechanism involving complex formation and its decomposition in a rate determining two-electron transfer step is proposed. The effect of ionic strength, solvent polarity and the activation parameters were in support of the mechanism proposed.

References

[1] M. Sadakane, E. Steckhan, Chem. Rev. 98 (1998) 219.
[2] D.E. Katsoulis, Chem. Rev. 98 (1998) 359.
[3] I.A. Weinstock, Chem. Rev. 98 (1998) 113.
[4] G.A. Ayoko, Transit. Met. Chem. 15 (1990) 421.
[5] A.M. Hasure, G.S. Gokavi, React. Kinet. Catal. Lett. 80 (2003) 59.
[6] S.K. Saha, M.C. Ghosh, P. Banerjee, Int. J. Chem. Kinet. 20 (2004) 699.
[7] M. Mehrotra, R.N. Mehrotra, J. Chem. Soc., Dalton Trans. (2003) 3606.
[8] P.K. Satpathy, G.C. Dash, S. Acharya, P. Mohanty, J. Indian Chem. Soc. 83 (2006) 891.
[9] B.D. Bhosale, G.S. Gokavi, Indian J. Chem. A 43 (2004) 799.
[10] B.D. Bhosale, G.S. Gokavi, Inorg. React. Mech. 5 (2) (2004) 79.
[11] B.D. Bhosale, G.S. Gokavi, Int. J. Chem. Kinet. 35 (2003) 9.
[12] E. Baciocchi, M. Bietti, S. Steenken, J. Chem. Soc., Perkin Trans. 2 (1996) 1261.
[13] E. Baciocchi, M. Putignani, S. Steenken, J. Am. Chem. Soc. 118 (1996) 595.
[14] R. Shah, A. Prakash, R.N. Mehrotra, Indian J. Chem. A 38 (1999) 541.
[15] B. Goyal, A. Prakash, R.N. Mehrotra, Indian J. Chem. A 37 (1998) 973.
[16] S. Dholia, A. Prakash, R.N. Mehrotra, Indian J. Chem. A 36 (1997) 857.
[17] B.D. Bhosale, G.S. Gokavi, Indian J. Chem. A 45 (2006) 398.
[18] S.J. Dunne, R.C. Burns, T.W. Hambey, G.A. Lawrance, Aust. J. Chem. 45 (1992) 685.
[19] F.A. Cotton, J. Wilkinson, C.A. Murillo, M. Bochmann, Advanced Inorganic Chemistry, 6th ed., Wiley Interscience, Singapore, 1999. p. 411, 932.
[20] R.P. Mihojlvic, N.R. Ignjatovic, J. Serb. Chem. Soc. 68 (2003) 65.
[21] A.I. Vogel, Textbook of Quantitative Inorganic Analysis including Elementary Instrumental Analysis, 3rd ed., Longman, 1961. p. 350, 411, 810.
[22] A.P. Scanzillo, Anal. Chem. 26 (1954) 411.
[23] S.R. Crouch, H.V. Malmstadt, Anal. Chem. 9 (1967) 1084.
[24] P.M. Beckwith, A. Scheeline, S.R. Crouch, Anal. Chem. 47 (1975) 1930.
[25] R.L. Carroll, L.B. Thomas, J. Am. Chem. Soc. 88 (1986) 1376.
[26] K.K. Sen Gupta, S. Maity, S. Ghosh, Indian J. Chem. A 19 (1980) 869.
[27] K.K. Sen Gupta, J.K. Chakladar, J. Chem. Soc., Perkin Trans. II (1973) 929.
[28] K.S. Gupta, Y.K. Gupta, J. Chem. Soc. A (1971) 1180.
[29] K. Chandra, E. Gelerinter, E.S. Gould, Inorg. Chem. 34 (1995) 4057.
[30] D.D. Virkar, G.S. Gokavi, Oxidation Commun. 25 (2002) 111.
[31] M.S. Prasad Rao, R. Kalavathi, T. Siva Rao, P. Sunita, Oxidation Commun. 20 (1997) 552.
[32] L.C.W. Baker, T.J.R. Weakly, J. Inorg. Nucl. Chem. 28 (1966) 447.
[33] K. Nakamoto, Infrared and Raman spectra of Inorganic Compounds, Third ed., John Wiley and Sons, New York, 1977. p. 115, 226, 143.
[34] C. Martin, C. Lamonier, M. Fournier, O. Mentre, V. Harle, D. Guillaume, E. Payen, Inorg. Chem. 43 (2004) 4636.
[35] M. Tsuboi, J. Am. Chem. Soc. 79 (1957) 1351.
[36] R.T. Mahesh, M.B. Bellakki, S.T. Nandibewoor, Catal. Lett. 97 (2004) 91.
[37] I.M. Kolthoff, E.J. Meehan, E.M. Carr, J. Am. Chem. Soc. 75 (1953) 1439.
[38] A. Saito, H. Tomari, G.R. Choppin, Inorg. Chim. Acta 258 (1997) 145.
[39] S.J. Dunne, J.A. Irwin, R.C. Burns, G.A. Lawrance, J. Chem. Soc., Dalton Trans. (1993) 2717.
[40] M. Hashimoto, I. Andersson, L. Pettersson, J. Chem. Soc., Dalton Trans. (2007) 124.
[41] R.G. Panari, R.B. Chougale, S.T. Nandibewoor, J. Phys. Org. Chem. 11 (1998) 44.

2.4. GC–MS analysis

GC analyses were carried out using a Varian 3900 gas chromatograph equipped with an FID and a 30 m × 0.32 mm CP-Wax 52 CB column (0.25 μm film thickness). The carrier gas was helium at 5.0 psi. The oven was programmed to hold at 32 °C for 4 min and then to ramp to 200 °C at 10°/min and hold 5 min. GC–MS analyses for peak identification were performed using an Agilent 5973 gas chromatograph equipped with MSD and a 60 m × 0.25 mm Rtx-1 column (0.5 μm film thickness). The carrier gas was helium at 0.9 ml/min. The oven was programmed to hold at 50 °C for 2 min and then ramp to 250 °C at 10°/min and hold for 8 min.

2.5. Infrared spectroscopy

Infrared spectra were recorded on a Perkin–Elmer Spectrum One FT-IR spectrometer.

2.6. Materials

$Ru_3(CO)_{12}$ (**1**), $Os_3(CO)_{12}$, $Re_2(CO)_{10}$, $Co_2(CO)_8$, $Mo(CO)_6$, and $W(CO)_6$ were purchased from Aldrich and used without further purification. $PPh_2CH_2CH_2CH_2CH{=}CH_2$ [17] was prepared as previously described. The solvents were commercially available and distilled from dark purple solutions of sodium/benzophenone ketyl. ^1H and ^{31}P NMR spectra were recorded on a Bruker DMX-400 spectrometer and all ^1H chemical shifts are reported relative to the residual proton resonance in the deuterated solvents. The compounds **3**–**6** were prepared by the reported literature procedures [18,19].

2.6.1. $Ru_3(CO)_{11}[PPh_2(CH_2CH_2CH{=}CHCH_3)]$ (**2**)

In a Schlenk flask, $PPh_2CH_2CH_2CH_2CH{=}CH_2$ (248 mg, 0.975 mmol) was added to $Ru_3(CO)_{12}$ (750 mg, 1.173 mmol) in 50 ml acetonitrile. Slowly, the colour of the solution changed to intense red. The solution was heated 80 °C for 72 h under constant stirring to yield **2** as a product and the reaction was monitored by ^{31}P NMR. The product was isolated by using preparative TLC using dichloromethane as eluent. The major red band was extracted using dichloromethane. After removing the solvent, the product was dried under high vacuum for 6 h to give red crystals of **2**; m.p. 156–158 °C (with decomposition); yield 47%; ^1H NMR δ 7.28–7.46 (m, 10H, Ph); 5.34–5.39 (m, 2H, =CH); 2.41–2.54 (m, 2H, P–CH_2); 1.81–1.99 (m, 2H, CH_2); 2.17 (s, 3H, CH_3); $^{31}P\{^1H\}$ 26.70 (s) and 27.36 (s); *Anal.* Calc. for $C_{28}H_{19}O_{11}PRu_3$: C, 38.85; H, 2.21. Found: C, 38.69; H, 2.32%. IR data in CH_2Cl_2: ν (cm^{-1}) 2060 (s), 2045 (s), 2028 (broad), 2012 (broad), 1966 (broad). $Ru_3(CO)_9[PPh_2CH_2\text{-}CH_2CH{=}CHCH_3]_3$ was also isolated as a secondary product (12%) from the orange yellow band on preparative TLC. *Anal.* Calc. for $C_{60}H_{57}O_9P_3Ru_3$: C, 54.67; H, 4.36. Found: C, 55.04; H, 4.21%.

Table 1
Various substrates tested for the isomerization with $Ru_3(CO)_{12}$

Substrate	Experimental conditions	Product	% Conversion (a mixture of *cis* and *trans* isomers)[a]
1-Pentene	3 h, 80 °C	2-pentene	100
1-Hexene	3 h, 80 °C	2-hexene	100
1-Heptene	3 h, 80 °C	2-heptene	100
1-Octene	3 h, 80 °C	2-octene	100
1-Decene	3 h, 80 °C	2-decene	100
5-Bromo-1-pentene	10 d, 80 °C	5-bromo-2-pentene	84
6-Chloro-1-hexene	16 d, 80 °C	6-chloro-2-hexene	93
1,5-Hexadiene	3 h, 80 °C	2,4-hexadiene	100
5-Hexen-1-ol	6 h, 80 °C	4-hexene-1-ol	100
7-Hexene-1,2-diol	6 h, 80 °C	6-hexene-1,2-diol	100

[a] Analyzed by GC–MS.

Table 2
Various catalysts tested for the isomerization of 1-pentene to 2-pentene

Catalyst used	Experimental conditions: 80 °C, toluene	% Conversion (a mixture of *cis* and *trans* isomers)
1	3 h	100
2	8 h	100[a]
3	10 d	66
4	5 d	100
5	10 d	35
6	10 d	0
$Os_3(CO)_{12}$	10 d	100
$Re_2(CO)_{10}$	10 d	4
$Co_2(CO)_8$	3 d	100[a]
$W(CO)_6$	10 d	0
$Mo(CO)_6$	10 d	80[a]

[a] Catalyst decomposed under these experimental conditions.

2.6.2. General procedure for 1-alkene isomerization reactions

All the isomerization reactions were carried out in sealed John-Young NMR tubes (Aldrich). The reaction mixture containing solvent, catalyst and olefin was cooled, evacuated and heated in an oil bath thermostated at the prescribed temperature (±1 °C). The reaction progress was monitored by ^1H NMR and then the products analyzed by GC and GC–MS to identify and quantify the final organic products. The results of these catalytic experiments are reported in Tables 1 and 2.

3. Results and discussion

$Ru_3(CO)_{12}$ (**1**), $Ru_3(CO)_{11}L$ [L = (2-pentenyl)diphenylphosphine] (**2**), $[Ru(CO)_2(MeCO_2)_2]_n$ (**3**), $[Ru_2(CO)_4(\mu\text{-}MeCO_2)_2(CH_3CN)_2]$ (**4**), $[Ru_2(CO)_4(\mu\text{-}MeCO_2)(\mu\text{-dppm})_2][PF_6]$ (**5**) [where dppm = bis(diphenylphosphino)methane], $[Os_2(CO)_6(\mu\text{-}MeCO_2)_2]$ (**6**), $Os_3(CO)_{12}$, $Re_2(CO)_{10}$, $Co_2(CO)_8$, $Mo(CO)_6$, and $W(CO)_6$ were all tested as homogeneous catalysts for the 1-alkene isomerization reactions (see Tables 1 and 2). Complexes **1** and **2** are catalytically active for olefin isomerization in a broad range of solvents (see below) and at temperatures above 60 °C. Our attempts to carry out the isomerization reaction of (1-pentenyl)diphenylphosphine with **1** on heating in order to examine the effect of the bulky phosphine group on the alkenyl chain, yielded **2** ($Ru_3(CO)_{11}L$) (Chart 1). Compound **2** was obtained as an intense red solid in good yield after the reaction of $Ru_3(CO)_{12}$with (1-pentenyl)diphenylphosphine [17] [L] as ligand in a molar ratio of 1:1. It was recrystallized from CH_2Cl_2/diethylether and was characterized spectroscopically and analytically. The studies with the phosphine derivative $Ru_3(CO)_{11}L$ (**2**) were carried out in order to explore the influence of this functionalized phosphine ligand on the catalytic activity in the isomerization reactions. The other compounds (**3**–**5**) were synthesized from $Ru_3(CO)_{12}$ (**1**) using literature procedures [19] to explore the catalytic activity towards 1-alkene isomerization reactions. In a similar way, compound **6** was obtained from the reaction of acetic acid with $Os_3(CO)_{12}$ [20]. Various 1-alkenes were tested for the isomerization reactions to give their corresponding 2-alkenes as shown in Eq. (1). In a similar way, the isomerization of 1,5-hexadiene yielded 2,4-hexadiene quantitatively (Eq. (2)).

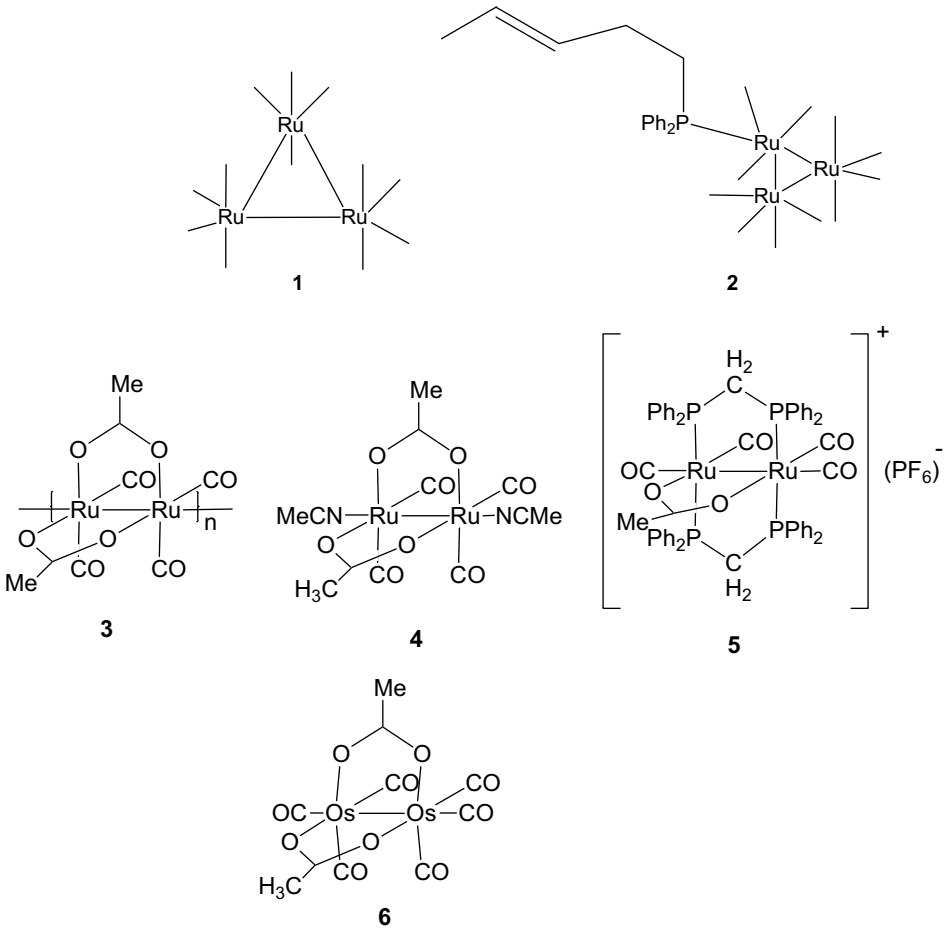
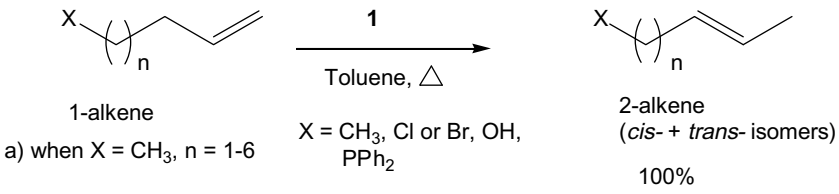
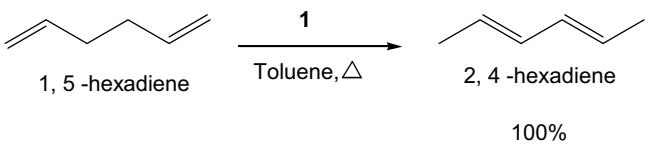


Chart 1. Catalysts used in olefin isomerization reactions.

polymeric compound **3** is decreased considerably relative to **4**, which might be due to the insoluble nature of the compound in



(1)



(2)

Although we find that many mononuclear, binuclear and trinuclear metal carbonyl compounds can, in fact, isomerize olefins, significant differences in the activity of the various complexes are formed (see Table 2): $W(CO)_6$ and **6** are mainly inactive in isomerization reactions of aliphatic alkenes and dienes. In case of $Re_2(CO)_{10}$, the catalytic activity was extremely low. The activity of **5** was decreased relative to **4** due to the steric as well as chelating nature of diphosphine ligands. The catalytic activity of the aromatic solvents. In contrast, the compound **4**, which was derived from **3** by reaction with acetonitrile, catalyzes the isomerization of 1-pentene to 2-pentene quantitatively. The other metal carbonyl compounds such as $Os_3(CO)_{12}$, $Mo(CO)_6$ and $Co_2(CO)_8$ showed significant activity under similar experimental conditions. $Ru_3(CO)_{12}$ however showed the best results (the turnover number for $Ru_3(CO)_{12}$ was found to be 10000 h^{-1}) among the other catalysts, while the activity is quite dependent on the nature of the metal at 80 °C. The rate of the isomerization reaction decreases along the series: $Ru_3(CO)_{12} > Os_3(CO)_{12} > Mo(CO)_6 > Re_2(CO)_{10} > W(CO)_6$ (see Table 2). It was also found that the di-ruthenium compounds $L_2PtRu_2(CO)_8$ [20] and $[Cp^*Ru(CO)_2]_2$ were inactive towards the olefin isomerization reactions, which could be due to the steric, and electronic properties of these compounds. At high temperatures, the isomerization of 1-alkenes to their internal alkenes is

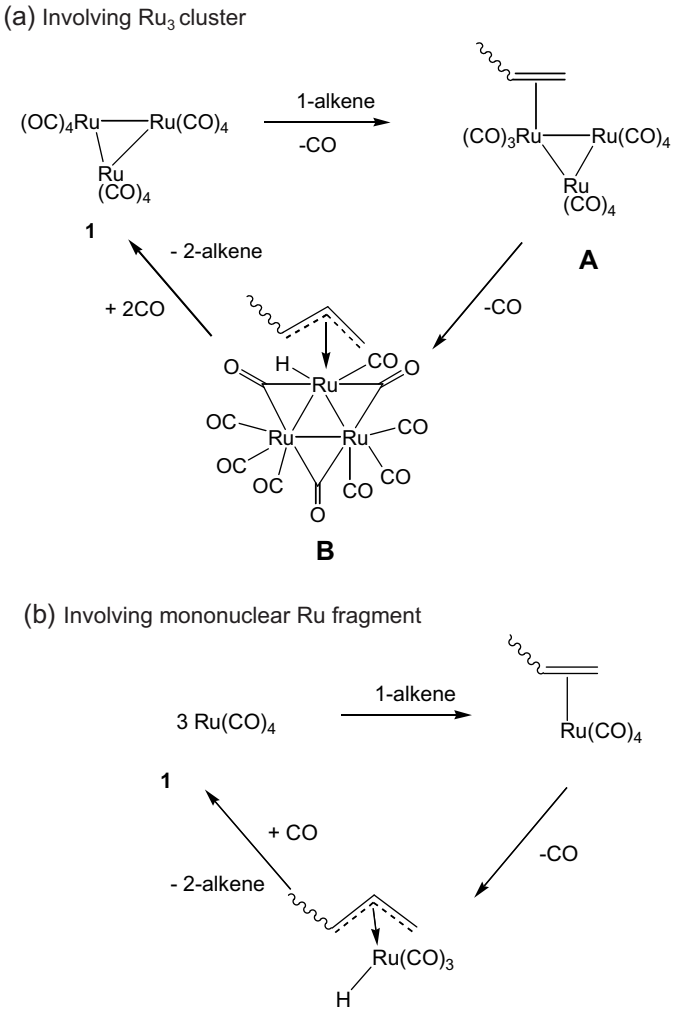
feasible with the other metal carbonyl compounds but the catalyst recovery is difficult. In all of these isomerizations of 1-olefins, the *trans*-2-olefin is the major product. Tables 1 and 2 summarize the results of the isomerization of aliphatic olefins. We find that the order of activity of the various catalysts we tested is as follows: $Ru_3(CO)_{12} > Ru_3(CO)_{11}L > Co_2(CO)_8 > Os_3(CO)_{12} > Mo(CO)_6 \gg Re_2(CO)_{10} \gg W(CO)_6$.

3.1. Mechanistic pathways

We have carried out a number of experiments to try and shed light on the mechanism of these isomerization reactions. Thus, we have carried out IR and NMR spectral studies of the reaction of $Ru_3(CO)_{12}$ with 1-octene in $CDCl_3$. We have made attempts using ^1H NMR to observe an η^3-allyl ruthenium hydride intermediate **B** in Scheme 1a, which is an established mechanism for other metal complexes [10,16]. However, these attempts were unsuccessful. We also used IR to obtain new information thus after heating the reaction mixture for 20 min at 80 °C, the reaction mixture was cooled and the IR spectrum was recorded [bands were now seen at 2100 (vw), 2061 (vs), 2028 (vs), 1985 (vw), 1825 (m), 1795 (m), 1652 (vs) cm^{-1}] (Fig. 1). Thus, new bands are seen which are not present in $Ru_3(CO)_{12}$ [the bands of $Ru_3(CO)_{12}$ are: ν(CO) 2061 (vs), 2028 (vs) and 1985 (vw) cm^{-1}]. Most striking bands are at 1825 (m) and 1795 (m) which could be due to bridging carbonyls of a ruthenium intermediate such as **B** in Scheme 1a.

A key step in the alkene isomerization reaction could be the dissociation of a CO ligand and olefin coordination to give the intermediate species **A**. That CO dissociation occurs during the isomerization reaction was supported by the observation that 1-alkene isomerization is inhibited when the reaction was carried out under a CO atmosphere. The oxidative addition of a C–H bond to the metal centre could lead to the formation of η^3-allyl metal hydride complex **B** which then decomposes to give the 2-alkene product and **1** as shown in Scheme 1. An alternative mechanism could involve mononuclear ruthenium species as shown in Scheme 1b. Both the mechanisms could be expected to be inhibited by CO, as is found.

We could not detect any ruthenium hydride species in the ^1H NMR spectra of the reaction mixtures even at temperatures up to 90 °C in $CD_3C_6D_5$. After heating at 80 °C for 3 h, the reaction was complete as the IR showed the disappearance of the new bands of the intermediate and indicated that the trinuclear ruthenium catalyst is restored (see Fig. 1). The GC analyses of the solution at the end of reaction showed mainly, the presence of *cis*-oct-2-ene (14%) and *trans*-oct-2-ene (86%). As the isomerization activity is high at high temperatures (>120 °C), there is a significant increase in the formation of oct-3-ene (>5%). The reactions of olefins in the presence of other catalysts showed similar trends in the isomerization reactions and analogous behaviour was noticed with **2**, which could go via a similar mechanism. These suggestions are also in agreement with previous studies reported where $Fe_3(CO)_{12}$ was used as catalyst [12].



Scheme 1. Two possible reaction mechanisms for the catalytic 1-alkene isomerization. (a) Involving Ru_3 cluster. (b) Involving mononuclear Ru fragment.

4. Factors affecting the isomerization reaction

4.1. Solvent effects

The factors influencing the rate of the alkene isomerization reactions are the solvent system, temperature, remote substituent on the alkene, and nature of catalyst used. The polarity of the solvent using either methanol or hexane did not affect the isomerization reaction. However, catalyst recovery was not possible when halogenated solvents were used as these solvents make the catalyst inactive. In the other solvent systems, the catalyst recovery was more than 60% in case of $Ru_3(CO)_{12}$. The absence of solvent increased the rate of reaction significantly, for example the isomerization of 1-octene to 2-octene occurred quantitatively within 60 s at 80 °C, in the presence of $Ru_3(CO)_{12}$. It was also found that these reactions do not involve heterogeneous catalysts as the dilute solutions (where catalytic amount of catalysts used) also perform the isomerization reaction in a similar way to concentrated solutions.

4.2. Effect of temperature

A series of experiments on the alkene isomerization reactions, using $Ru_3(CO)_{12}$, as a function of temperature were carried out. The ideal temperature range was found to be 80–100 °C. When the temperature was >120 °C, the catalyst recovery was not possible even though the rate of reaction was increased dramatically. With compound **2**, the recovery of the catalyst was not successful. It was observed however that this monosubstituted phosphine derivative at high temperatures was converted to the stable tris(phosphine) derivative, i.e. $Ru_3(CO)_9(PPh_2R)_3$. Also at high temperatures (>150 °C), the formation of traces of 3-alkenes is observed with the longer alkenyl chain, i.e. $\geqslant C_7$.

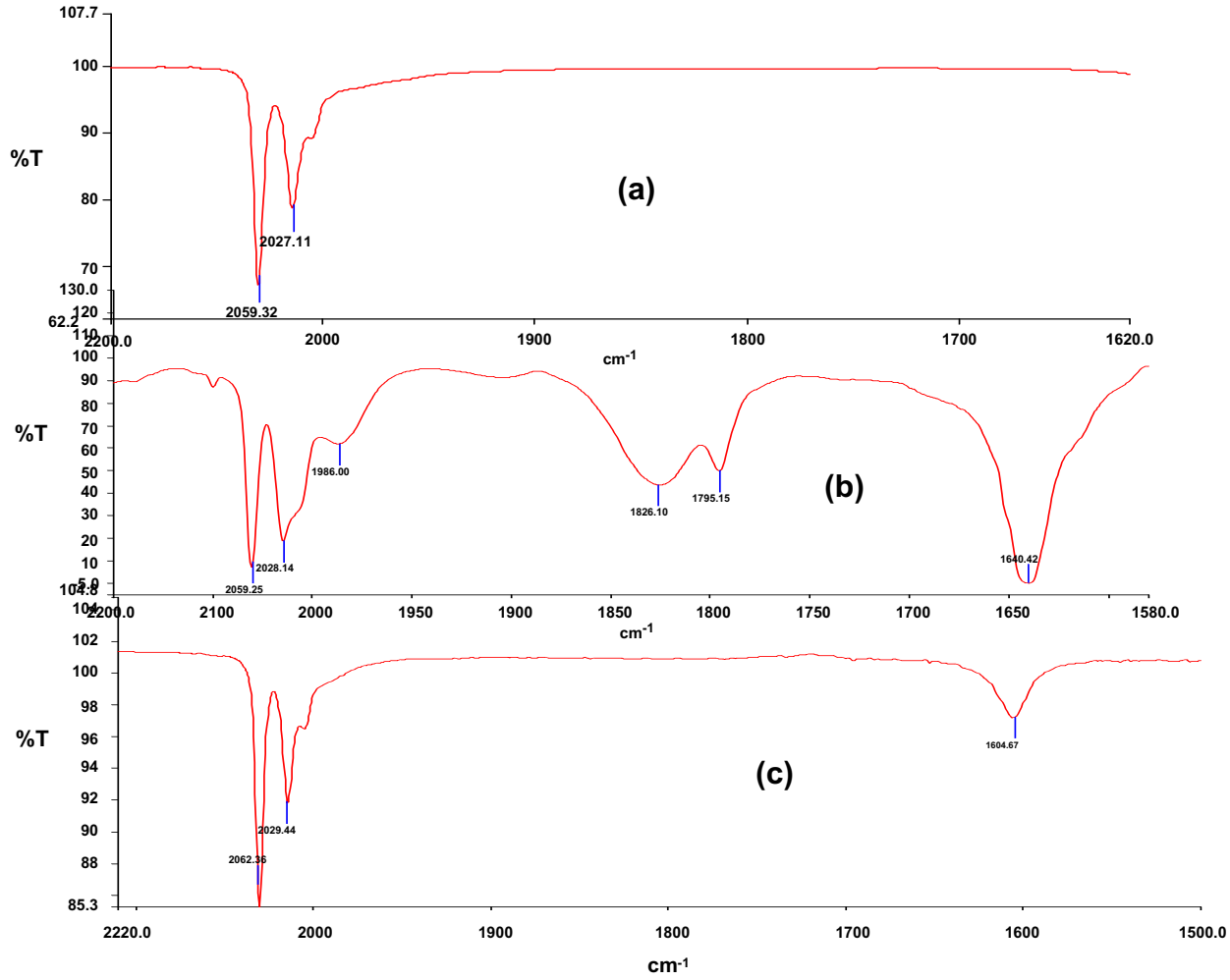


Fig. 1. IR spectra showing the intermediate formed during the olefin isomerization (spectra recorded in $CHCl_3$). (a) $Ru_3(CO)_{12}$. (b) The reaction mixture; after heating with 1-pentene for 20 min at 80 °C. (c) After the complete isomerization reaction after 3 h at 80 °C.

4.3. Substituent effect

Substituents on the alkenyl chains show a significant effect on the isomerization reaction (see Table 1). When X = Cl, Br, the rate of reaction decreases drastically and the formation of different isomeric species was also observed. This could be due to the electron withdrawing effect of the halogens in the alkenyl chain and competing reactions of catalysts with the haloalkenes. Mass spectral studies of the reaction of **1** with 6-chloro-1-hexene indicated the formation of $[Ru(CO)_3Cl]_2$ as one of the products. The presence of hydroxyl groups (X = OH or $(OH)_2$) did not have any significant effect on the isomerization (Eq. (1)). When X = PPh_2, the rate of reaction decreased sharply, which may be due to the steric bulk of the phosphine as well as the phosphine coordinating to the metal and positioning the alkenyl chain away from the cluster. However, on long heating at 80 °C, in acetonitrile for 72 h the corresponding complex **2** was formed. The ^{31}P NMR spectrum showed two singlets close together at δ 26.70 and 27.36 for this compound which could be due to the presence of possible alkene isomers of the compound.

4.4. Effect of catalyst

While $Ru_3(CO)_{12}$ was found to be the most active catalyst (see Table 2), some mononuclear carbonyls, notably $Mo(CO)_6$, were also found to be active. This may suggest that the first step in the mechanistic pathway can be CO loss (as for $Mo(CO)_6$ or $Ru_3(CO)_{12}$). It is also possible that both pathways involving either CO loss or metal–metal bond cleavage could operate for the cluster compounds (see Scheme 1a and b).

4.5. Addition of excess ligands

As expected, the addition of excess ligands such as (diphenylphosphino)methane (dppm) or acetonitrile to the reaction mixture ($Ru_3(CO)_{12}$ and 1-pentene in toulene) resulted in a dramatic decrease in isomerization activity. There was no isomerization observed in the presence of excess of dppm ligand even after the long heating at 80 °C. This is probably due to the phosphine ligand blocking the coordinating sites at ruthenium. Similarly, the isomerization was also retarded when the experiment was carried out under an atmosphere of CO. This suggests that the dissociation of CO from the metal carbonyls is a key step in these catalytic reactions.

5. Conclusions

Some ruthenium carbonyl cluster complexes are efficient and selective catalysts for the isomerization of 1-alkenes to their corresponding 2-alkenes under the mild conditions. The turnover number for the $Ru_3(CO)_{12}$ was found to be 10000 h^{-1} and possible mechanistic pathways for these isomerization reactions are discussed. Other metal carbonyl compounds also show some activity for this reaction.

Acknowledgements

We thank Johnson Matthey (London), Anglo Platinum Corporation, C* Change, NRF, UCT for the financial support.

References

[1] (a) W.A. Herman, M. Prinz, A Text Book on Homogeneous Catalysis, 2002, p. 1119 (and the references therin).;
(b) W.A. Herman, Kontakte (Darmstadt), No. 1, 1991.;
(c) N.R. Davis, Rev. Pure Appl. Chem. 17 (1967) 83.
[2] R.A. van Santen, P.W.N.M. van Leeuwen, J.A. Moulijn, B.A. Averill, Catalysis: An Integrated Approach, 2nd ed., Elsevier Science, Amsterdam, 1999. pp. 209–288.
[3] (a) C.A. Tolman, J. Am. Chem. Soc. 94 (1972) 2994;
(b) M. Mirza-Aghayan, R. Boukherroub, M. Bolourtchian, M. Hoseini, K. Tabar-Hydar, J. Organomet. Chem. 678 (2003) 1.
[4] (a) M. Beller, C. Bolm, Transition Metals for Organic Synthesis, Wiley–VCH, Weinheim, 1998. p. 147;
(b) D.B. Grotjahn, C.R. Larsen, J.L. Gustafson, R. Nair, A. Sharma, J. Am. Chem. Soc. 129 (2007) 9592.
[5] L.J. Gazzard, W.B. Motherwell, D.A. Sandham, J. Chem. Soc., Perkin Trans. 1 (1999) 979.
[6] G.V. Strate, Encycl. Polym. Sci. 6 (1986) 522.
[7] T. Faitg, J. Soulie, J-.Y. Lallemand, F. Mercier, F. Mathey, Tetrahedron 56 (2000) 101.
[8] D.E. Bergbreiter, G.L. Parsons, J. Organomet. Chem. 208 (1981) 47.
[9] (a) N.S. Sampson, I.J. Kass, J. Am. Chem. Soc. 119 (1997) 855;
(b) A. Ohff, V.V. Burlakov, U. Rosenthal, J. Mol. Catal. A: Chem. 105 (1996) 103.
[10] (a) M. Bianchi, F. Piacenti, P. Frediani, U. Matteoli, J. Organomet. Chem. 135 (1977) 387;
(b) B. Fontal, M. Reyes, T. Suarez, F. Bellandi, N. Ruiz, J. Mol. Catal. A: Chem. 149 (1999) 87.
[11] (a) A. Salvini, P. Frediani, F. Piacenti, J. Mol. Catal. A: Chem. 159 (2000) 185;
(b) K. Dallmann, R. Buffon, J. Mol. Catal. A: Chem. 172 (2001) 81 (and the references therein).
[12] (a) C.P. Casey, C.R. Cyr, J. Am. Chem. Soc. 95 (1973) 2248;
(b) D. Bingham, B. Hudson, D.E. Webster, P.B. Wells, J. Chem. Soc., Dalton Trans. Inorg. Chem. (1972–1999) (1974) 1521.
[13] (a) O. Gambino, M. Valle, S. Aime, G.A. Vaglio, Inorg. Chim. Acta 8 (1974) 71;
(b) J.L. Graff, R.D. Sanner, M.S. Wrighton, J. Am. Chem. Soc. 101 (1979) 273.
[14] F. Porta, S. Cenini, S. Giordano, M. Pizzotti, J. Organomet. Chem. 150 (1978) 261.
[15] F.C. Courchay, J.C. Sworen, K.B. Wagener, Macromolecules 36 (2003) 8231 (and the references therein).
[16] (a) F. Piacenti, M. Bianchi, P. Frediani, G. Menchi, U. Matteoli, J. Organomet. Chem. 417 (1991) 77;
(b) J.P. Collman, L.S. Hegedus, J.R. Norton, R.G. Finke, Principles and Applications of Organotransition Metal Chemistry, University Science Books, Mill Valley, CA, 1987. p. 527.
[17] P.H. Wermer, C.B. Dobson, G.R. Dobson, J. Organomet. Chem. 311 (1986) C47.
[18] G.B.R. Crooks, B.F.G. Johnson, J. Lewis, I.G. Williams, G. Gamlen, J. Chem. Soc. A (1969) 2761.
[19] S.J. Sherlock, M. Cowie, E. Singleton, M.M.V. Steyn, Organometallics 7 (1988) 2761.
[20] M.I. Bruce, G. Shaw, F.G.A. Stone, J. Chem. Soc., Dalton Trans. (1972) 1781.

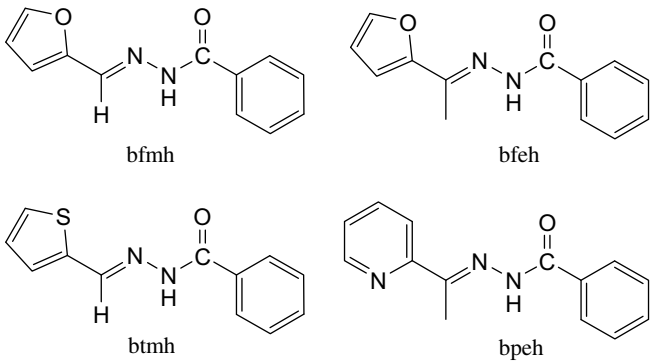


Chart 1. Structure of the hydrazone ligands.

double-distilled water and its pH was adjusted to 7.1 using 0.1 M NaOH solution. DNA stock solutions were freshly prepared before use with this buffer solution. Ethanol was purified following standard procedures for the preparation of the ligands and complexes. Distilled dmso was used for the preparation of the starting complex and for the preparation of solutions of complexes for DNA-binding studies. Purified dry methanol was used to record the electronic spectra of the complexes. Commercially available TBAP was properly dried and used as a supporting electrolyte for recording cyclic voltammograms of the complexes (except for DNA-binding studies). The starting complexes [9], *cis*-[$RuCl_2(dmso)_4$] (**Ru1**), *trans*(Cl)–[$RuCl_2(dmso)_2(bpy)$] (**Ru2**) and the ligands [10] were prepared according to the literature procedures.

2.2. Physical measurements

FT-IR spectra (4000–400 cm^{-1}) of the complexes and the free ligands were recorded as KBr pellets with a Nicolet Avatar Model FT-IR spectrophotometer. Electronic spectra (800–250 nm) of the complexes were obtained on a Systronics 119 UV–Vis spectrophotometer. ^1H NMR spectra were recorded on a Varian-Australia AMX-400. The absorption titrations were carried out with a JASCO spectrophotometer. Micro analyses (C, H, N and S) were performed on a Vario EL III Elementar analyzer. Cyclic voltammograms were recorded on a CHI 1120A electrochemical analyzer with a three electrode compartment consisting of a platinum disc working electrode, a platinum wire counter electrode and an Ag/Ag^+ reference electrode.

2.3. Synthesis

2.3.1. [$RuCl_2(dmso)_2(bfmh)$] (**1**)

Cis-[$RuCl_2(dmso)_4$] (0.21 mmol) and the ligand bfmh (0.21 mmol) were heated under reflux in ethanol for 6–8 h. Slow evaporation of the solvent after reduction to 50% gave crystals suitable for single crystal XRD studies. Yield, 70 mg, 61%. Elemental *Anal.* Calc. for $C_{16}H_{22}N_2S_2O_4Cl_2Ru$ (542.464): C, 35.42; H, 4.08; N, 5.16; S, 11.82. Found: C, 35.26; H, 4.12; N, 5.24; S, 11.37%. IR (KBr, cm^{-1}): ν(NH), 3112(w); ν(C=O), 1639(s); (νC=N), 1598(m) (s, strong; m, medium; w, weak). UV–Vis (dmso) λ, nm (ε, $mol^{-1}\,cm^{-1}\,L$): 308 (14900), 359 (3950). ^1H NMR (dmso-d_6, δ ppm): 3.2–3.5 (group of peaks, dmso protons, 12H), 8.1 (s, H–C=N, 1H), 7.5–8.1 (multiplet, aromatic protons, 8H), 9.2 (s, –NH, 1H).

2.3.2. [$RuCl_2(dmso)_2(bfmh)] \cdot 0.5C_2H_5OH$ (**1a**)

trans(Cl)–[$RuCl_2(dmso)_2(bpy)$] (0.21 mmol) and the ligand bfmh (0.21 mmol) were heated under reflux in ethanol for 6–8 h. Slow evaporation of the solvent after reduction to 50% gave crystals suitable for single crystal XRD studies. Yield, 69 mg, 58%. Elemental *Anal.* Calc. for $C_{17}H_{25}N_2S_2O_{4.5}Cl_2Ru$ (565.494): C, 36.10; H, 4.45; N, 4.95; S, 11.34. Found: C, 35.92; H, 4.33; N, 4.71; S, 11.27%. IR (KBr, cm^{-1}): ν(NH), 3110(w); ν(C=O), 1639(s); (νC=N), 1598(m).

2.3.3. [$RuCl_2(dmso)_2(btmh)$] (**2**)

Cis-[$RuCl_2(dmso)_4$] (0.21 mmol) and the ligand btmh (0.21 mmol) were heated under reflux in ethanol for 6–8 h. Slow evaporation of the solvent after reduction to 50% gave orange crystals suitable for single crystal XRD studies. Yield, 75 mg, 64%. Elemental *Anal.* Calc. for $C_{16}H_{22}N_2S_3O_3Cl_2Ru$ (558.531): C, 34.40; H, 3.97; N, 5.01; S, 17.22. Found: C, 34.28; H, 3.87; N, 5.32; S, 17.37%. IR (KBr, cm^{-1}): ν(NH), 3080(w); ν(C=O), 1620(s); ν(C=N), 1592(m). UV–Vis (dmso) λ, nm (ε, $mol^{-1}\,cm^{-1}\,L$): 254 (25320), 313 (19320), 392 (5480). ^1H NMR (dmso-d_6, δ ppm): 3.2–3.5 (group of peaks, dmso, 12H), 7.9 (s, H–C=N, 1H), 7.4–8.5 (multiplet, aromatic protons, 8H), 9.4 (s, –NH, 1H). The same reaction when carried out with *trans*(Cl)–[$RuCl_2(dmso)_2(bpy)$] yielded a crystalline product (**2a**) which conformed to the analytical and IR data of **2** but was not structurally characterized.

2.3.4. [$RuCl_2(dmso)_2(bfeh)$] (**3**)

Cis-[$RuCl_2(dmso)_4$] (0.21 mmol) and the ligand bfeh (0.21 mmol) were heated under reflux in ethanol for 6–8 h. Slow evaporation of the solvent gave only an amorphous powder which was recrystallised from hot dmso. Yield, 69 mg, 59%. Elemental *Anal.* Calc. for $C_{17}H_{24}N_2S_2O_4Cl_2Ru$ (556.491): C, 36.69; H, 4.34; N, 5.03; S, 11.52. Found: C, 36.28; H, 4.02; N, 5.39; S, 11.11%. IR (KBr, cm^{-1}): ν(NH), 3073(w); ν(C=O), 1650(s); ν(C=N), 1593(m). UV–Vis (dmso) λ, nm (ε, $mol^{-1}\,cm^{-1}\,L$): 288 (9780), 354 (2620). ^1H NMR (dmso-d_6, δ ppm): 3.1–3.4 (group of peaks, dmso, 12H), 2.2 (s, $-CH_3$, 3H), 7.2–8.2 (multiplet, aromatic protons, 8H), 9.4 (s, –NH, 1H). The same reaction when carried out with *trans*(Cl)–[$RuCl_2(dmso)_2(bpy)$] yielded an amorphous product (**3a**) which conformed to the analytical and IR data of **3**.

2.3.5. [$RuCl_2(dmso)_2(bpeh)$] (**4**)

Cis-[$RuCl_2(dmso)_4$] (0.21 mmol) and the ligand bpeh (0.21 mmol) were heated under reflux in ethanol for 6–8 h. Slow evaporation of the solvent gave only an amorphous powder which was recrystallised from hot dmso. Yield, 82 mg, 69%. Elemental *Anal.* Calc. for $C_{18}H_{25}N_3S_2O_3Cl_2Ru$ (567.518): C, 38.09; H, 4.40; N, 7.40; S, 11.30. Found: C, 38.44; H, 4.32; N, 7.12; S, 11.47%. IR (KBr, cm^{-1}): ν(NH), 3056(w); ν(C=O), 1689(s); ν(C=N), 1598(m). UV–Vis (dmso) λ, nm (ε, $mol^{-1}\,cm^{-1}\,L$): 275 (7540), 304 (5700). ^1H NMR (dmso-d_6, δ ppm): 3.1–3.4 (group of peaks, dmso, 12H), 2.2 (s, $-CH_3$, 3H), 7.3–8.3 (multiplet, aromatic protons, 9H), 9.4 (s, –NH, 1H). The same reaction when carried out with *trans*(Cl)–[$RuCl_2(dmso)_2(bpy)$] yielded an amorphous product (**4a**) which conformed to the analytical and IR data of **4**.

2.4. Crystallographic structure determination

Single crystal X-ray diffraction measurements were performed on a Nonius Kappa CCD (with Oxford Cryostream) diffractometer with graphite monochromatized Mo Kα radiation. The structures of **1** and **2** were solved by direct methods and refinements were carried out by full-matrix least-square techniques. The hydrogen atoms were treated by a mixture of independent and constrained refinement. The following computer programs were used: structure solution SIR-97 [11], refinement SHELXL-97 [12], molecular diagrams ORTEP-3 [13] for windows.

2.5. Anti-microbial screening

The bacterial strains, *Escherichia coli* NCIM 2831, *Staphylococcus aureus* NCIM 2492, *Staphylococcus epidermidis* NCIM 2493,

Klebsiella pneumoniae NCIM 5082 and *Shigella sonnei* MTCC 2957 were used in the study. The agar-well diffusion method [14] was employed for the determination of anti-microbial activities. MICs (minimum inhibitory concentration) of the compounds against test organisms were determined by the broth micro dilution method. All the tests were performed in duplicate and repeated twice. Modal values were selected.

2.5.1. Agar-well diffusion method

The compounds were weighed and dissolved in dimethyl sulfoxide (dmso), then the solutions were filter sterilized using a 0.45 μm membrane filter. Each microorganism was suspended in sterile saline and diluted at *ca.* 106 colony forming units (cfu/ml). They were flood inoculated onto the surface of Mueller–Hinton Agar (MHA). The wells (8 mm in diameter) were cut from the agar and 0.1 mL of solution was delivered into them. After incubation for 24 h at 37 °C, all the plates were examined for any zones of growth inhibition, and the diameter of these zones were measured in millimeters.

2.5.2. Determination of minimum inhibitory concentration (MIC)

A broth microdilution susceptibility assay was used as recommended [15] by NCCLS for determination of the MIC. All the tests were performed in Mueller–Hinton Broth (MHB) supplemented with Tween 80 detergent (final concentration 0.5% (v/v)). Bacterial strains were cultured overnight at 37 °C in MHA. Test strains were suspended in MHB to give a final density of 5×105 cfu/ml and these were confirmed by viable counts. Geometric dilutions of the compounds were prepared in a 96-well microtiter plate, including one growth control (MHB + Tween 80) and one sterility control (MHB + Tween 80 + compound). The plates were incubated under normal atmospheric conditions at 37 °C for 24 h. The MIC of kanamycin and oxytetracycline were individually determined in parallel experiments in order to control the sensitivity of the test organisms. The bacterial growth was indicated by the presence of a white "pellet" on the well bottom.

3. Results and discussion

The reactions of either **Ru1** or **Ru2** with the hydrazone ligands in a 1:1 mol ratio in ethanol has yielded complexes of the type $[RuCl_2(dmso)_2(L)]$ (L = hydrazone ligand), as illustrated in Scheme 1. All the complexes are stable to air and light, and are soluble in organic solvents such as dmso, dmf and dichloromethane. The hydrazone ligands act as neutral bidentate donors replacing two dmso ligands from **Ru1**. In the precursor **Ru2**, there is a bipyridine chelate and two S-bonded dmso ligands in the equatorial plane. Although the chelate effect should hinder the replacement of the bpy ligand from **Ru2**, the two mutually *cis* S-bonded dmso ligands that are capable of accepting π-back donated electrons from the metal, along with the larger trans influence, weakens the metal-N bonds, facilitating the replacement of the chelate [16].

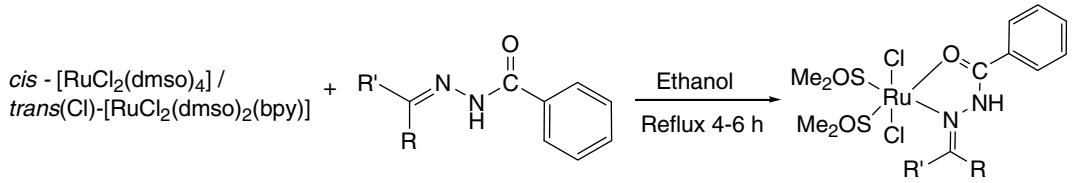
3.1. IR and electronic spectra

The IR spectra of the free ligands and the new Ru(II) complexes were compared in order to ascertain the probable mode of coordination of the ligands. Vibration bands of primary importance of the free ligands were observed around 3250, 1650, 1600–1620 and 1080 cm^{-1} for ν(NH), ν(CO), ν(CN) and ν(NN) respectively. The presence of the ν(NH) band confirms that the free ligands are in the keto form. The IR spectra of the complex pairs **1** and **1a**, **2** and **2a**, **3** and **3a**, and **4** and **4a** were identical, suggesting the formation of the same complexes when the ligands are treated with either **Ru1** or **Ru2**. None of the complexes obtained from **Ru2** displayed a pyridine ring breathing band around 995 cm^{-1}, which implies the replacement of bpy from **Ru2** by the ligands. This directed us to formulate the complexes in general as $[RuCl_2(dmso)_2(L)]$(L = bfmh, bfeh, btmh or bpeh). In all of the complexes, the observed significant decrement of ν(CO) and ν(CN) does evidence the neutral bidentate nature of the ligands. Being so, the ligands have two possibilities for chelation with the metal, either replacing two S-bonded dmso ligands or one S-bonded and one O-bonded dmso ligand when treated with **Ru1**. Scrutinizing the IR spectra of the precursor *cis*-$[RuCl_2(dmso)_4]$ and that of the new complexes was useful in determining the elimination of one of the above possibilities. In the IR spectrum of *cis*-$[RuCl_2(dmso)_4]$, the S=O stretch of the S-bonded dmso appears at a higher frequency (1090 cm^{-1}) in comparison with that of the O-bonded dmso (915 cm^{-1}) due to the increase in the S=O bond order in the former case. The desertion and retention of the bands at 915 cm^{-1} and around 1090 cm^{-1} respectively in the new complexes indicate the replacement of one O-bonded and one S-bonded dmso ligand from the precursor by the Schiff base chelate. This is consistent with the previous observation that chelating ligands will replace first the weakly held O-bonded dmso and then the S-bonded dmso *cis* to it [9].

The absorption spectra of the diamagnetic Ru(II) complexes were recorded as 10^{-4} M dmso solutions in the range 800–250 nm using a quartz cuvette of 1 cm path length. All the new ruthenium(II) complexes, except **4**, exhibit bands in both UV and visible regions. Based on the position and nature of the peaks, all the bands are assigned to either $n \rightarrow \pi^*$ or $\pi \rightarrow \pi^*$ intraligand transitions (data given in experimental section).

3.2. X-ray crystallography

Though slow evaporation of the respective reaction mixtures yielded X-ray quality single crystals of **1**, **1a**, **2** and **2a**, only structures of the first three complexes were solved. Structure determination of **1** and **1a** showed that the two compounds are one and the same, as the unit cell parameters of the two complexes were very close and other structural features and geometric parameters were similar. The crystal data and data collection procedure are supplied in Table 1. Selected geometrical parameters are listed in Table 2. Figs. 1 and 2 show the ORTEP diagrams of **1** and **2** respectively. In both of the complexes, there are two independent



Scheme 1. Synthesis of the new Cl–Ru(II)–dmso complexes

Table 1
Crystal structure data of the complexes **1** and **2**

Crystal data	**1**	**2**
Formula	$C_{16}H_{22}Cl_2N_2O_4RuS_2 \cdot 0.5(C_2H_6O)$	$C_{16}H_{22}Cl_2N_2O_3RuS_3 \cdot 0.5(C_2H_6O)$
Formula weight	565.48	581.54
Color, habit	colorless, fragment	orange, parallelepiped
Dimensions	0.23 × 0.20 × 0.12 mm	0.25 × 0.10 × 0.05 mm
Space group	$P\bar{1}$	$P\bar{1}$
a (Å)	11.2248(11)	11.0411(15)
b (Å)	14.1644(15)	14.2763(16)
c (Å)	14.663(2)	15.1254(16)
α (°)	92.762(4)	92.617(7)
β (°)	98.201(3)	100.003(7)
γ (°)	103.233(8)	104.928(5)
V (Å^3)	2238.3(4)	2258.4(5)
Z	4	4
D_{calc} (Mg m^{-3})	1.678	1.710
T (K)	110	115
F_{000}	1148	1180
μ(Mo Kα) (mm^{-1})	1.154	1.232
R_{int}	0.075	0.035
Goodness of fit (S)	1.077	1.024
θ_{max} (°)	32.5	30.6

complexes (**A** and **B**) in the asymmetric units and a disordered solvent molecule. Refinement of the disordered regions of both **1** and **2** has been carried out, but the fit to the data did not really improved in either case, nor were there any significant changes in the interesting parts of the structure.

In complex **1**, the ruthenium(II) ion is in a distorted octahedral environment equatorially coordinated by an ON chelate of the hydrazone ligand and two sulfur atoms of the dmso ligands at *cis* positions. A pair of chlorine atoms at the axial positions completes the octahedral coordination. The Ru–N (Ru1a–N1a = 2.107(2) and Ru1b–N1b = 2.098(3) Å) and Ru–O (Ru1a–O1a = 2.123(2) and Ru1b–O1b = 2.101(2) Å) bond lengths observed in the two independent complexes are comparable to literature values [17–23]. The two Ru–S bond lengths observed in the independent complexes **A** and **B** are comparable with that of similar Ru(II) complexes [17] and with that of the precursor, *cis*-[$RuCl_2(dmso)_4$] [24]. As expected and previously observed [24,25] there is a change in the S–O bond length of dmso after coordination in comparison with the free ligand.

The substitution of one O-bonded dmso and one S-bonded dmso in the precursor *cis*-[$RuCl_2(dmso)_4$] by the ON chelating ligand has yielded **1** in which the two chloro ligands take mutual *trans* positions, which is in accordance with a previous study [17]. The two Cl ligands in the axial positions are faintly bent to-

Table 2
Selected geometrical parameters for **1** and **2**

Bond distances (Å)			Bond angles (°)		
	1	**2**		**1**	**2**
Ru1a–N1a	2.107(2)	2.107(2)	Cl1a–Ru1a–Cl2a	174.30(3)	173.95(3)
Ru1a–O1a	2.123(2)	2.115(2)	S1a–Ru1a–S2a	94.50(3)	94.69(3)
Ru1a–S1a	2.2242(9)	2.2304(8)	N1a–Ru1a–O1a	77.31(9)	77.12(8)
Ru1a–S2a	2.2584(8)	2.2487(7)	Cl1b–Ru1b–Cl2b	172.28(3)	172.06(3)
Ru1a–Cl1a	2.4174(8)	2.4054(8)	S1b–Ru1b–S2b	94.14(3)	94.52(3)
Ru1a–Cl2a	2.3959(8)	2.3964(8)	N1b–Ru1b–O1b	77.86(9)	77.54(9)
Ru1b–N1b	2.098(3)	2.083(2)	C13a–S1a–C14a	100.09(16)	99.55(16)
Ru1b–O1b	2.101(2)	2.088(2)	C15a–S2a–C16a	99.1(2)	98.67(18)
Ru1b–S1b	2.2297(9)	2.2264(8)	C13b–S1b–C14b	99.17(17)	99.54(15)
Ru1b–S2b	2.2453(9)	2.2547(8)	C15b–S2b–C16b	98.7(2)	99.71(17)
Ru1b–Cl1b	2.3934(8)	2.4037(7)	C13a–S1a–O3a	104.07(15)	104.78(16)
Ru1b–Cl2b	2.4091(8)	2.4095(8)	C14a–S1a–O3a	106.34(16)	106.63(16)
S1a–O3a	1.489(2)	1.485(2)	C15a–S2a–O4a	106.28(16)	106.03(15)
S2a–O4a	1.486(2)	1.490(2)	C16a–S2a–O4a	106.75(17)	106.43(16)
S1b–O3b	1.493(3)	1.497(2)	C13b–S1b–O3b	107.37(17)	106.71(14)
S2b–O4b	1.487(3)	1.490(2)	C14b–S1b–O3b	105.56(17)	104.90(14)
			C15b–S2b–O4b	107.18(17)	106.73(16)
			C16b–S2b–O4b	106.3(2)	104.91(13)

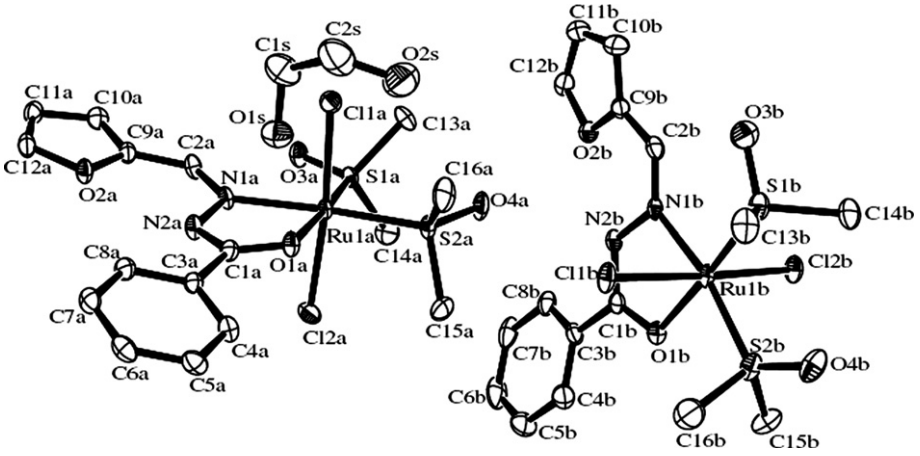


Fig. 1. Asymmetric unit of **1** with anisotropic displacement ellipsoids at 50% probability. Hydrogen atoms are omitted for clarity.

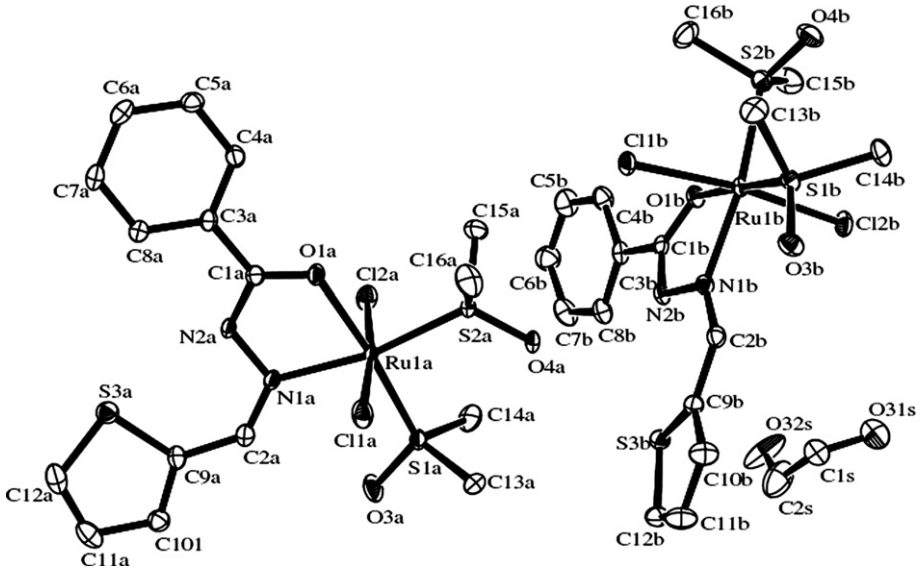


Fig. 2. Asymmetric unit of **2** with anisotropic displacement ellipsoids at 50% probability. Hydrogen atoms and disorder in thiophene ring are omitted for clarity.

wards the chelate (the angle Cl2a–Ru1a–Cl1a is 174.30(3)° and Cl2b–Ru1b–Cl1b is 172.28(3)°) due to the pushing by the somewhat bulky *cis* dmso ligands. The Ru–Cl distances in **1** (Ru1a–Cl1a = 2.4174(8), Ru1a–Cl2a = 2.3959(8) Å; Ru1b–Cl1b = 2.3934(8), Ru1b–Cl2b = 2.4091(8) Å) are shorter than that of **Ru1** (mean Ru–Cl distance of the different forms is 2.425 Å) and fairly comparable with that of **Ru2** (2.402 Å). This is in agreement with the greater trans influence of dmso [24].

The angles O–S–C and C–S–C in **A** and **B** of **1** are comparable with that of the S-bonded dmso ligands in *cis*- and *trans*-$[RuCl_2(dmso)_4]$. But these angles of O-bonded dmso in one of the precursors, **Ru1**, is relatively narrow when compared with that of S-bonded dmso ligands. This is due to the different electronic situation of the two types of sulfur atom and can be attributed to the compression effect of the bulkier lone pair of the pyramidal sulfur atoms on the bonding pairs [25]. The bite angles of the ON chelate in **A** and **B** are 77.31(9) and 77.86(9)° respectively, and these are comparable with that of a similar chelate [17].

The structure of **2** shares similar properties and the same discussion goes well with that for **1** except in a few aspects. The heterocyclic ring in **1** is furan whereas in **2** it is thiophene and there is a slight distortion in the thiophene moiety in one of the two independent complexes. Further refinement, using a number of restraints, of the disordered thiophene led to a slight improvement, most notably in the reduction of residual electron densities. However, full anisotropic refinement did not lead to realistic displacement parameters. The independent complexes in the asymmetric units of **1** are stabilized by intramolecular N(amide)–H···O(furan) bonds and intermolecular N(amide)–H···O(dmso) bonds in addition to bifurcated weak interactions, O(disordered ethanol)–H···Cl and O(disordered ethanol)–H···O(furan). In contrast to **1**, intermolecular hydrogen-bonding, N(amide)–H···O(dmso) appears to be predominant in complex **2**. The geometric parameters pertaining to hydrogen-bonding are provided in Table 3.

With the single crystal X-ray structures of **1** and **1a**, it is clear that the chelating ligands replace the coordinated ligands that are *trans* to the two S-bonded dmso from either of the precursors **Ru1** and **Ru2**. This is due to the strong *trans* influence of the S-bonded dmso ligands. Also, in **Ru2**, the chelating bpy ligands are replaced by the ON hydrazone chelate relatively easily compared to the two S-bonded dmso ligands because of the strong π-acceptor character of the two sulfur atoms. Hence, the complex pairs **2** and **2a**, **3** and **3a**, and **4** and **4a** will be mentioned henceforth as **2**, **3** and **4** respectively assuming that they have same chemical composition (based on the microanalyses) although no structural evidence is currently available for the other complexes.

Table 3
Hydrogen-bonding distances (Å) and angles (°)

Complex	D–H···A	D–H	H···A	D···A	D–H···A
1	N2a–H2Na···O2a	0.77(4)	2.28(4)	2.750(3)	120(3)
	N2b–H2Nb···O4a	0.87(4)	2.14(4)	2.917(3)	149(3)
	N2b–H2Nb···O2b	0.87(4)	2.21(4)	2.682(3)	114(3)
2	N2a–H2Na···O3b[i]	0.85(4)	2.18(4)	2.988(3)	159(3)
	N2b–H2Nb···O4a	0.85(3)	1.96(3)	2.803(3)	167(3)

[i] Symmetry codes used to generate identical atoms: x, y − 1, z.

3.3. ^1H NMR spectra

The ^1H NMR spectra of the complexes recorded in dmso showed narrow signals typical for diamagnetic Ru(II) complexes. A comparison of the ^1H NMR data [9] of the precursor *cis*-$[RuCl_2(dmso)_4]$ with that of the new complexes seems indispensable in order to ascertain the bonding mode of the two dmso ligands, as evidenced by the single crystal X-ray diffraction studies (for **1** and **2**), and to predict the same in **3** and **4**. The resonance for methyl protons of free dmso is ~δ 2.5 ppm. The complex *cis*-$[RuCl_2(dmso)_4]$ (contains three S-bonded dmso and one O-bonded dmso) displayed six singlets at δ 3.50, 3.48, 3.43, 3.32, 2.72 and 2.66 ppm due to six sets of chemically different protons. The peak at δ 2.66 ppm has been assigned to free dmso which resulted from the 10% dissociation of O-bonded dmso. Similarly the peak at δ 2.72 ppm has been attributed to the O-bonded dmso since the methyl resonance is close to that of free dmso. The other peaks appearing in a group have been assigned to S-bonded dmso but the integration of these peaks had not been possible owing to their proximity and their sharing of the same broad base line. The three S-bonded dmso ligands in the complex are *trans* to either O-bonded dmso, S-bonded dmso or Cl ligands. This, along with some degree of methyl inequivalency, has been thought of as responsible for the complexity of the spectra. Keeping all these in mind, the group of peaks appearing in the new complexes around ~δ 3.2–3.4 ppm is attributed to S-bonded dmso resonances. Here no resonance was observed at δ

2.7 ppm for any of the complexes, suggesting that there is no O-bonded dmso in the complexes which is consistent with the single crystal X-ray diffraction results obtained for **1** and **2**, and predicts the same for **3** and **4**. Thus the inequivalency in the methyl groups is due to the chelating ligand. The resonance around δ 2.5 ppm in all the complexes is due to the solvent. The azomethine proton in **1** and **2** appears as a singlet at δ 8.1 and 7.9 ppm respectively. The protons of the methyl group in **3** and **4** gave a resonance at δ 2.2 ppm. The multiplet around δ 7.2–8.5 ppm is due to aromatic and heterocyclic ring protons. The appearance of a singlet in all the complexes around δ 9.2–9.4 ppm is due to the NH proton and this suggests that the chelating ligand coordinates in its keto form to the metal and supports a neutral bidentate coordination of the hydrazone ligands.

3.4. Cyclic voltammetric studies

The electrochemical behavior of the complexes was studied with the help of cyclic voltammetry using dmso solutions of the complexes and TBAP as a supporting electrolyte. All the potentials were referenced to the Ag/AgCl electrode and scanned at a rate of 0.1 V/s. The complexes show different redox behavior in the chosen potential window. Complexes **1** and **4** show only a Ru^{III}/Ru^{II} oxidation couple with the formal potentials 0.63 and 0.50 V respectively. Complex **2** shows only an irreversible oxidation wave with E_{pa} = 0.49 V. This irreversibility may be anticipated due to the transient lifetime of the reduced state. The peak-to-peak separation value ΔE_p for **1** and **4** is 240 and 80 mV suggesting a quasireversible and reversible one electron transfer process respectively. A reversible reduction (Ru^{II}/Ru^{I}) is observed for **3** with a formal potential of −0.39 V (ΔE_p = 80 mV). These different conducts of the complexes can be accredited to the different electronic nature of the substituents present in the hydrazone ligands. When the E_f values for the oxidation couple for **1** and **4** are compared, a negative shift in the potential is observed. This shift is due to the presence of an electron releasing CH_3 group and pyridine moiety in **4** which favor easier oxidation of the central metal ion. The more electron withdrawing furan ring of **3** renders the molecule prone to reduction of the ruthenium centre [26]. In summary it can be drawn that electron releasing substituents stabilize the +3 oxidation state whereas electron withdrawing substituents stabilize the +2 oxidation state of ruthenium.

3.5. DNA-binding studies

Most ruthenium complexes bind to DNA by non-covalent interactions such as electrostatic binding, groove binding, intercalative binding and partial intercalative binding [27]. A quantitative understanding of the factors that determine the recognition of DNA sites would be valuable in the rational drug design of new DNA targeted molecules for application in chemotherapy. The binding of the new ruthenium complexes to the Herring sperm ds DNA has been monitored through absorption titration and cyclic voltammetry.

3.5.1. Absorption titration

The experiments were carried out in Tris–HCl buffer (50 mM,pH 7.2) using a solution of Herring sperm DNA which gave a ratio of UV absorbance at 260 and 280 nm in the ratio 1.8:1, indicating that the DNA is sufficiently free from protein. So no further effort was made to purify the commercially obtained DNA. The concentration of DNA was determined by absorption spectroscopy using the ε value of 6600 M^{-1} cm^{-1} at 260 nm. Absorption titrations were performed using a fixed ruthenium concentration to which increments of the DNA stock solutions were added in different ratios ranging from 0 to 3 [DNA]/[Ru]. Complex–DNA solutions were allowed to stand for 5 min before recording their absorption. The titration process was repeated until no further change was observed in the spectra.

The binding of the ruthenium complexes to the DNA helix was characterized by following the changes in the absorbance and shift in wavelength upon each addition of DNA solution to the complex. Representative absorption spectra are given in Figs. 3 and 4. The ruthenium(II) complexes in dmso-buffer mixture exhibit an intense intraligand transition in the region around 315–330 nm. On the titration of Herring sperm DNA with the complexes, a considerable increase or decrease in the absorption along with a small red or blue shift was observed. The initial increase in absorption for complexes **2** and **3** is due to the electrostatic interaction of DNA and the complexes [28]. In complexes **2** and **4** remarkable hypochromicity is noted after the ratio [DNA]:[Ru] becomes 1. In complex **1** the absorption decreases and increases at random with a small red shift (2–4 nm) on titration with the DNA solution. These trends show that the complexes bind to the DNA double-helix in different modes to different extents [29]. As can be perceived from Figs. 3 and 4, the shift in absorption and λ_{max} are random and this tendency frustrated the calculation of intrinsic binding constants of the complexes using the equation valid for perfect intercalators.

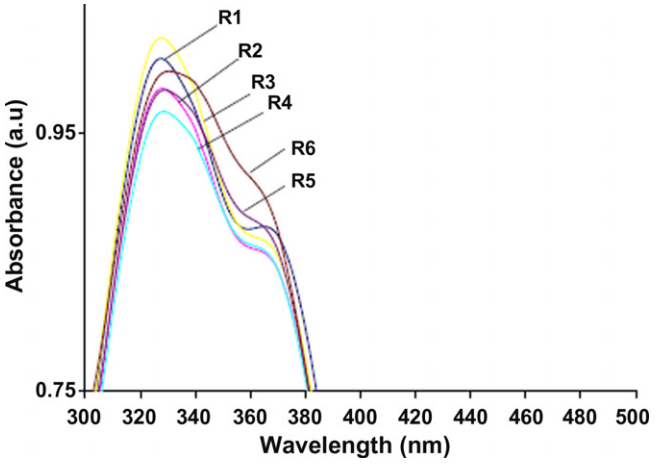


Fig. 3. Absorption bands of **1** on titration with DNA at different [DNA]/[Ru] ratios (*R*). *R*1 = 0, *R*2 = 0.25, *R*3 = 0.50, *R*4 = 0.75, *R*5 = 1 and *R*6 = 1.5.

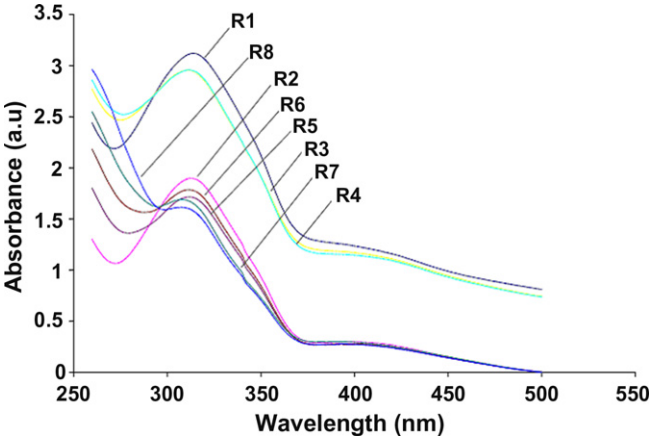


Fig. 4. Absorption bands of **4** on titration with DNA at different [DNA]/[Ru] ratios (*R*). *R*1 = 0, *R*2 = 0.25, *R*3 = 0.50, *R*4 = 0.75, *R*5 = 1, *R*6 = 1.5, *R*7 = 2 and *R*8 = 3.

Table 4
Antibacterial activity data for the ligands and complexes

Compound	*Escherichia coli*		*Shigella sonnei*		*Staphylococcus aureus*		*Staphylococcus epidermidis*		*Klebsiella pneumoniae*	
	WD[a]	MIC[b]	WD	MIC	WD	MIC	WD	MIC	WD	MIC
2	NA	136	17	74	12	31	14	46	NA	144
4	NA	121	NA	82	16	153	15	32	NA	140
bfmh	15	25	20	28	16	18	12	26	15	47
btmh	NA	85	16	97	NA	44	14	87	NA	124
bfeh	30	24	33	26	26	21	20	23	30	28
bpeh	20	23	25	34	NA	137	14	92	20	52
Oxytetracycline	30	15	37	8	32	7	44	8	30	8
Kanamycin	32	18	48	9	40	10	60	11	35	10

NA – not active.
[a] WD, disc diffusion method as recommended by NCCLS. Diameter of zone of inhibition (mm) including well diameter 8 mm. 100 μg of both compound and antibiotics were used.
[b] MIC, minimum inhibitory concentration.Values given as μg/ml for both compounds and antibiotics.

3.5.2. Cyclic voltammetry

Since all the new complexes are electroactive, electrochemical methods such as cyclic voltammetry can be used effectively to monitor their binding to DNA as a complement to the absorption spectral technique. In a typical cyclic voltammetric titration, a fixed concentration of the complex was taken and DNA solution in buffer was added in different ratios as done in the absorption titration, and the voltammetric response was recorded. As observed in the UV experiments, an increase or decrease of the peak current was observed for all the complexes. The peak current increased initially and then decreased. The initial increase in the peak current is due to the absorption of the DNA bound complex onto the electrode surface [30]. The decrease in peak current on the addition of DNA to the complex is suggestive of an interaction between the complex and DNA [31]. Except for complex **1**, a decrease in the peak-to-peak separation was observed, which is consistent with non-coordinating intercalative binding of the complexes through the planar aromatic rings between the DNA base pairs [32]. The formal potential E_f shifts slightly towards the positive side and is attributed to characteristic behavior of intercalation of the complexes into the DNA double-helix [33], and suggests that Ru(II) and Ru(I) forms bind to DNA at different rates [34,35].

3.6. Antibacterial activity

All the ligands and their ruthenium complexes were screened *in vitro* for their growth inhibitory activity against the pathogenic bacteria *E. coli*, *S. aureus*, *S. epidermidis*, *K. pneumoniae* and *S. sonnei*. The inhibition zone (in mm) and MIC of the ligands and their ruthenium complexes are given in Table 4. From the figures it is perceived that the ligands bfmh and btmh inhibit the growth of all the test organisms to a moderately comparable extent to that of standard antibiotics and they can be said to be resistive to the organisms. The ligand btmh is resistive only to *S. sonnei* and *S. epidermidis* since no inhibition zone is found for the other organisms. Except for *S. aureus*, the ligand bpeh is resistive to all other pathogenic bacteria. All the complexes except **3** are resistive to at least one of the organisms under study. Complex **2** shows considerable resistivity to *S. aureus*, *S. epidermidis* and *S. sonnei*. Similarly **4** is active against *S. aureus* and *S. epidermidis* and **1** is active against only *S. sonnei*. None of the complexes are active against the other two organisms. Thus all the ligands and complexes **2** and **4** alone have been studied further to evaluate the MIC because only these two complexes demonstrate activity against at least two of the five organisms. A low value of MIC implies high resistivity against the particular organism. No serious attempts were made to correlate the activity to the structures of the compounds since too many chemical and biochemical factors are responsible for the process of inhibition of the growth of the bacteria.

4. Conclusions

The present study demonstrates a simplistic synthesis of a family of new Cl–dmso–Ru(II) complexes. The greater *trans* influence of mutually *cis* S-bonded dmso ligands in comparison to the bipyridine ligand has been proved by the observed replacement of bipyridine from **Ru2** by the hydrazone ligands, with crystallographic evidence. The electrochemical properties of the complexes are very sensitive to the electronic nature of the substituents present in the hydrazone ligands. The new complexes have been shown to possess DNA-binding abilities. The *in vitro* antineoplastic activity of the complexes against human breast cancer cell lines is under investigation and the results will be published shortly.

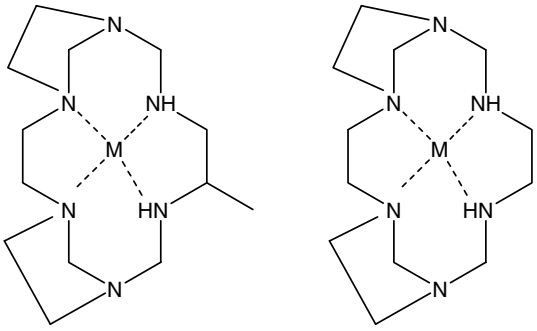
Appendix A. Supplementary data

CCDC 613460 and 632085 contain the supplementary crystallographic data for **1** and **2**. These data can be obtained free of charge via http://www.ccdc.cam.ac.uk/conts/retrieving.html, or from the Cambridge Crystallographic Data Centre, 12 Union Road, Cambridge CB2 1EZ, UK; fax: (+44) 1223-336-033; or e-mail: deposit@ccdc.cam.ac.uk. Supplementary data associated with this article can be found, in the online version, at doi:10.1016/j.poly.2008.02.036.

References

[1] G. Sava, S. Pacer, A. Bergamo, M. Cocchettio, G. Mestroni, E. Alessio, Chem.-Biol. Interact. 95 (1995) 109.
[2] E. Wong, C.M. Giandomenico, Chem. Rev. 99 (1999) 2451.
[3] D.P. Riley, Inorg. Chem. 22 (1983) 1965.
[4] D.P. Riley, R. Shumate, J. Am. Chem. Soc. 106 (1984) 3179.
[5] D.P. Riley, J.D. Oliver, Inorg. Chem. 25 (1986) 1814.
[6] A. Bergamo, G. Stocco, C. Casarsa, M. Cocchettio, E. Alessio, B. Serli, S. Zorzet, G. Sava, Int. J. Oncol. 24 (2004) 373.
[7] G. Sava, S. Zorzet, T. Giraldi, G. Mestroni, G. Zessinovich, Eur. J. Cancer Clin. Oncol. 20 (1984) 841.
[8] S. Zorzet, A. Bergamo, M. Cocchettio, A. Sore, B. Gava, E. Alessio, E. Iengo, G. Sava, J. Pharmacol. Expl. Ther. 295 (2000) 927.
[9] I.P. Evans, A. Spencer, G. Wilkinson, J. Chem. Soc., Dalton Trans. (1973) 204.
[10] M.F. Iskander, L. Labib, M.M.Z. Nour El-Din, M. Tawfik, Polyhedron 8 (1989) 2755.
[11] A. Altomare, M.C. Burla, M. Camalli, G. Cascarano, C. Giacovazzo, A. Guagliardi, A.G.G. Moliterni, G. Polidori, R. Spagna, J. Appl. Crystallogr. 32 (1999) 115.
[12] G.M. Sheldrick, SHELXL-97. A Program for Structure Refinement, University of Göttingen, Göttingen, Germany, 1997.

[13] L.J. Farrugia, J. Appl. Crystallogr. 30 (1997) 565.
[14] NCCLS (National Committee for Clinical Laboratory Standards), Performance standards for antimicrobial disk susceptibility test, 6th ed., Approved standard, Wayne Pa., M2-A6, 1997.
[15] NCCLS (National Committee for Clinical Laboratory Standards), Performance standards for antimicrobial susceptibility testing, Ninth International Supplement, Wayne Pa. M100-S9, 1999.
[16] M. Ghassemzadeh, M. Bolourtchian, S. Chitsaz, B. Neumüller, M.M. Heravi, Eur. J. Inorg. Chem. 8 (2000) 1877.
[17] L. Otero, P. Nobilia, D. Gambino, H. Cerecetto, M. González, J.A. Ellena, O.E. Piro, Inorg. Chim. Acta 344 (2003) 85.
[18] R. Cini, G. Tamasi, S. Defazio, M. Corsini, P. Zanello, L. Messori, G. Marcon, F. Piccioli, R. Orioli, Inorg. Chem. 42 (2003) 8038.
[19] Q.A. de Paula, A.A. Batista, O.R. Nascimento, A.J. da Costa-Filho, M.S. Schultz, M.R. Bonfadini, G. Oliva, J. Braz. Chem. Soc. 11 (5) (2000) 530.
[20] R.E. Morris, R.E. Arid, P.D.S. Murdoch, H. Chen, J. Cummings, N.D. Hughes, S. Parson, A. Parkin, G. Boyd, D.I. Jodrell, P.J. Sadler, J. Med. Chem. 44 (2001) 3616.
[21] P. Braunstein, C. Graiff, F. Naud, A. Pfaltz, T. Tiripicchio, Inorg. Chem. 39 (2000) 4468.
[22] S.A. Serron, C.M. Haar, S.P. Nolan, Organometallics 16 (1997) 5120.
[23] R.C. van der Drift, E. Bouwman, E. Drent, H. Kooijman, A.L. Spek, A.B. van Oort, W.P. Mul, Organometallics 21 (2002) 3401.
[24] E. Alessio, G. Mestroni, G. Nardin, W.M. Attia, M. Calligaris, G. Sava, S. Zorzet, Inorg. Chem. 27 (1998) 4099.
[25] E. Alessio, G. Balducci, M. Calligaris, G. Costa, W.M. Attia, G. Mestroni, Inorg. Chem. 30 (1991) 609.
[26] A.R. Cowley, J.R. Dilworth, P.S. Donnelly, J.M. White, Inorg. Chem. 45 (2006) 496.
[27] J.K. Barton, Science 233 (1986) 727.
[28] P.R. Reddy, V. Radhika, K.S.J. Rao, Chem. Sci. 116 (4) (2004) 221.
[29] S. Ramakrishnan, M. Palaniandavar, J. Chem. Sci. 117 (2) (2005) 179.
[30] X.M. Li, H.Q. Ju, C.F. Ding, S.S. Zhang, Anal. Chim. Acta 582 (1) (2007) 158.
[31] Z.S. Yang, Y.L. Wang, G.C. Zhao, Anal. Sci. 20 (2004) 1127.
[32] J. Annaraj, S. Srinivasan, K.M. Ponvel, K.P.R. Athappan, J. Inorg. Biochem. 99 (2005) 669.
[33] X. Lu, M. Zhang, J. Kang, X. Wang, L. Zhuo, H. Liu, J. Inorg. Biochem. 98 (2004) 582.
[34] S. Srinivasan, J. Annaraj, P.R. Athappan, J. Inorg. Biochem. 99 (2005) 876.
[35] V.G. Vaidyanathan, B.U. Nair, J. Chem Soc., Dalton Trans. (2005) 2842.



2. Experimental

2.1. Materials

The reagents and solvents were purified and dried according to the standard literature methods [20]. The distilled water was further purified by passing through a purification train (MILLI-Q), Millipore water was used for the preparation of solutions.

Caution: Although no problems were encountered during this work with perchlorate salt, it should be regarded as potentially explosive.

2.2. Physical measurements

Electronic spectra were recorded on a HITACHI 320 UV–Vis double beam spectrophotometer. Infrared spectra were recorded on a Perkin–Elmer infrared spectrophotometer using KBr disks. Conductance measurements were performed on a ELICO CMI85 conductivity bridge and a DEEP VISION conductivity cell. ^{1}H and ^{13}C NMR spectra were recorded on a JEOL GSX 400 MHz NMR spectrometer. EPR measurement of copper complex was made using E-112 VARIAN EPR spectrometer. Mass spectra of both the complexes were recorded on a JEOL SX 102/DA-600 Mass spectrometer.

Equilibrium constants were calculated from UV–Vis spectra. For variable temperature measurements, the temperature variation was controlled with in ±0.2 °C using a thermostated cell holder, connected to a ULTRA CRYOSTAT, supplied by Inlab Equipments Pvt. Ltd. The concentration of the complex was maintained at 1×10^{-3} M in 0.1 M $NaClO_4$ aqueous solution and each spectrum has taken at 5 min interval with in a temperature range of 283–313 K. Cyclic voltammetry was performed using a CHI600A electrochemical analyzer. The measurements were conducted under oxygen free conditions, using a three-electrode cell in which a glassy carbon electrode was the working electrode, a saturated calomel electrode was the reference electrode, and platinum wire was used as the auxiliary electrode. The electrochemical data were obtained in aqueous medium containing 0.1 M $NaClO_4$ as a supporting electrolyte.

2.3. X-ray crystallography

A crystal of size $0.27 \times 0.48 \times 0.53$ mm was used for intensity data collection on a Bruker SMART APEX CCD area-detector diffractometer with Mo Kα radiation ($\lambda = 0.7107$ Å) at 100 K. Empirical absorption correction was applied by using the SADABS program. The structure was solved by direct methods and refined by full-matrix least-square technique on F^2 by using SHELXTL with 4932 reflections ($2.14° \leqslant \theta \leqslant 33.25°$) and 308 parameters. All non-hydrogen atoms were refined anisotropically, and C and N-bound hydrogen atoms were positioned geometrically and refined using a riding model. The final cycle of the refinement converged with $R = 0.061$. The crystal and refinement data are listed in Table 1.

2.4. Synthesis of the complexes

2.4.1. [Ni(PCHA)](ClO$_4$)$_2$(PCHA = $C_{13}H_{28}N_6$)

To a stirred methanolic solution (70 mL) of $Ni(OAc)_2 \cdot 4H_2O$ (0.95 g, 3.8 mmol) were added triethylenetetraamine (0.56 mL, 4.1 mmol), 36% formaldehyde (1.2 mL, 15.2 mmol) and 1,2-diaminopropane (0.33 mL, 3.8 mmol). The mixture was heated at reflux for 24 h. The solution was filtered to remove insoluble material. A saturated solution of excess $NaClO_4$ was added to the filtrate and the solution was allowed to stand at room temperature until orange crystals formed. The crystals were filtered out, washed with methanol, diethyl ether and recrystallized from hot water yield ~60%, (1.20 g).

2.4.2. [Cu(PCHA)](ClO$_4$)$_2$

The red crystals of $[Cu(PCHA)](ClO_4)_2$ was synthesized by a procedure similar to that of $[Ni(PCHA)]^{2+}$ using $Cu(OAc)_2 \cdot H_2O$ in place of $Ni(OAc)_2$. Yield ~80% (1.60 g).

3. Results and discussion

3.1. Synthesis of macrocyclic complexes

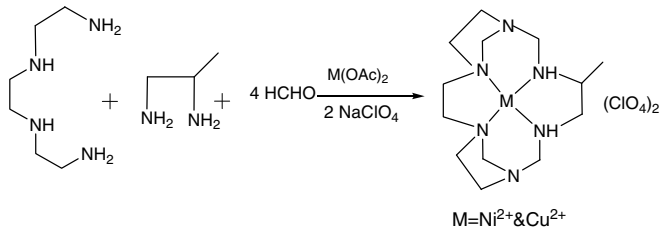
The hexaaza macrocyclic complexes $[M(PCHA)](ClO_4)_2$ ($M = Ni^{2+}$ and Cu^{2+}) have been synthesized in high yield (60–80%) by the simple template condensation of triethylenetetramine, 1,2-propanediamine and formaldehyde in the presence of divalent metal ion. Both Ni(II) and Cu(II) complexes are soluble in water, acetone, MeCN and Me_2SO but insoluble in alcohol. All efforts to obtain the free ligand from the complexes by treating the complexes with excess NaCN or strong acid were unsuccessful. Free ligand must be unstable because they contain methylene diamine moiety with secondary nitrogens. A possible route for the formation of hexaaza macrotricyclic complexes $[Ni(PCHA)](ClO_4)_2$ and $[Cu(PCHA)](ClO_4)_2$ is presented in Scheme 1.

3.2. Spectral studies

The spectral and conductance data of the complexes are summarized in Table 2. The molar conductance of the complexes mea-

Table 1
Crystal data for $[Ni(PCHA)](ClO_4)_2$

Empirical formula	$C_{13}H_{28}N_6Cl_2O_8Ni$
Formula weight	526.02
Temperature	100 K
Wavelength (Å)	0.71073
Crystal system	orthorhombic
Space group	P212121
a (Å)	11.2531(4)
b (Å)	12.7903(4)
c (Å)	14.2098(4)
Volume (Å^3)	2045.22(11)
Z	4
D_{calc} (g^{-3})	1.708
Absorption coefficient (mm^{-1})	1.265
$F(000)$	1096
Crystal size	$0.27 \times 0.48 \times 0.53$
θ Range for data collection (°)	2.3–28.0
Reflections collected/unique [R_{int}]	26718/4932 [0.033]
Refinement method	full-matrix least-squares on F^2
Reflections with $I > 2\sigma(I)$	4662
R indices	$R = 0.0611$ $wR_2 = 0.1661$ $S = 1.11$
Largest differents peak and hole (Å^{-3})	1.29 and −0.81e



Scheme 1.

Table 2
Spectral and conductance data for hexaazamacrocylic nickel(II) and copper(II) complexes

Complex	Electronic spectral data[a], λ_{max} (ε, $M^{-1}\,cm^{-1}$)	IR frequency, ν_{NH} (cm^{-1})	Conductance[a] Λ_M ($\Omega^{-1}\,cm^{-2}\,M^{-1}$)
$[Ni(PCHA)](ClO_4)_2$	452(102) 226(20336)	3143	239
$[Cu(PCHA)](ClO_4)_2$	507(143) 268(5877)	3237	220

[a] Measured in water.

sured in aqueous solutions was 239 and 220 $\Omega^{-1}\,cm^{-2}\,M^{-1}$ for $[M(PCHA)]^{2+}$ corresponding to a 2:1 electrolyte [21]. The electronic spectrum of the aqueous solution of $[Ni(PCHA)]^{2+}$ complex exhibits a strong intense peak at 452 nm which may correspond to $^1A_{2g} \leftarrow {}^1A_{1g}$ transition in a d^8 system of D_{4h} symmetry. The copper complex shows a single peak at 507 nm, which may assigned to the $^2B_{1g} \leftarrow {}^2E_g$ which is also consistent with a square-planar geometry [22].

The charge transfer bands of Ni(II) and Cu(II) complexes appear at 226 and 268 nm, respectively (Table 2). The infrared spectra (Table 2) of the complexes show ν(NH) bands for the secondary amines of the ligands in the region 3143–3237 cm^{-1} and $\nu(ClO_4)$ 1045–1091 and 620–629 cm^{-1} [23]. The mass spectra of both nickel(II) and copper(II) complexes show (M–ClO_4) and (M–2ClO_4) peaks with m/e values 426, 326 and 431, 330, respectively.

The ^{1}H NMR spectrum of Ni(II) complex shows a doublet at 0.94 ppm which is attributed to methyl group present in the macrocycle. The N–CH_2–N signals appear as singlet at 4.56, 4.64 and 4.67 ppm. The N–CH– and N–CH_2–CH_2–N signals have been observed in the region 2.37–3.3 ppm, which is consistent with the ligand structure. The –NH protons are not observed in the spectrum owing to exchange with D_2O. Due to the introduction of methyl group in the macrocyle, the symmetry of the molecule is such that the ^{13}C NMR spectrum of the complex shows 13 signals (12.72, 47.9, 48.1, 53.9, 54.9, 55.1, 55.6, 58.0, 63.0, 68.5, 70.0, 74.4 and 75.0 ppm) which confirms the presence of 13 different types of aliphatic carbons in the complex. But in the case of unmethylated complex $[Ni(CHA)]^{2+}$, only six signals (47.8, 48.8, 55.8, 55.9, 70.7 and 76.1) are observed due to the symmetric nature of the molecule [19].

The ESR spectra of $[Cu(PCHA)]^{2+}$ and the corresponding unsubstituted complex $[Cu(CHA)]^{2+}$ were recorded as polycrystalline sample and in CH_3CN solution at liquid nitrogen temperature. The polycrystalline sample at LNT shows one intense absorption band in the high field region, which is isotropic due to the tumbling motion of the molecule. However in the CH_3CN solution at LNT both the complexes show hyperfine splitting, which indicates that there is an interaction with four nitrogen nuclei adjacent to the copper ions. The spectrum of $[Cu(PCHA)]^{2+}$ is similar to that of $[Cu(CHA)]^{2+}$ and so too are their electronic spectra, indicating that the geometries of the two chromophore in solution are essentially the same. The g tensor values of the Cu^{2+} complexes can be used to derive the ground state. In tetragonal and square-planar geometry the unpaired electron lies in the $d_{x^2-y^2}$ orbital with $^2B_{1g}$ as the ground state and also $g_\parallel > g_\perp$ [24]. The observed g values are summarized in Table 3.

According to Hathaway [25] $G = (g_\parallel - 2)/(g_\perp - 2)$ and if $G > 4$, the exchange interaction is negligible, whereas when $G < 4$, a considerable interaction is indicated in the solid complex. The calculated G values are less than four, suggesting that there is exchange interaction between adjacent copper centers. The spectral parameters indicate approximately square-planar co-ordination around the copper(II) ion [26]. The ESR parameters of the $[Cu(PCHA)]^{2+}$ in CH_3CN solution (LNT) are: $g_\parallel = 2.09$, $g_\perp = 1.93$ and $A_\parallel = 236 \times 10^{-4}\,cm^{-1}$ (Table 3) and the spectral trace is reproduced in Fig. 1.

3.3. The crystal structure of $[Ni(PCHA)](ClO_4)_2$

The ORTEP view of the complex with the atomic numbering scheme is presented in Fig. 2. The bond lengths and bond angles are listed in Table 4. A stereoscopic crystal packing diagram is shown in Fig. 3. There are two coordinated tertiary nitrogens N4 and N5, two coordinated secondary nitrogens N1 and N2 and two uncoordinated tertiary nitrogens N3 and N6 present in the ligand.

The structure of the complex consists of discrete mononuclear $[Ni(PCHA)]^{2+}$ cation and two perchlorate anions. The cation possess one methyl group in the five-membered chelate ring and two 1,3-diaza cyclopentane subunits in the six-membered chelate rings. The Ni–N bond distances range from 1.908(4) to 1.931(5) Å and the average of the four distances is 1.922 Å. The values are comparable to those of the square-planar nickel(II) complexes of various other related polyaza macrocycles [27,28] The N–Ni–N angles (93.8(2)° and 93.0(2)°) of six-membered chelate rings are larger than those of five-membered chelate rings. Interestingly, among the two five-membered chelate rings, the bond angle of

Table 3
EPR spectral data of Cu(II) complexes as polycrystalline solid and in acetonitrile at LNT

Complex	Poly crystalline			CH_3CN solution		
	$g_\parallel$	$g_\perp$	G	$g_\parallel$	$g_\perp$	$A_\parallel$ ($10^{-4}\,cm^{-1}$)
$[Cu(PCHA)]^{2+}$	2.10	2.06	1.59	2.13	1.93	208
$[Cu(CHA)]^{2+}$	2.11	2.06	1.70	2.07	1.91	231

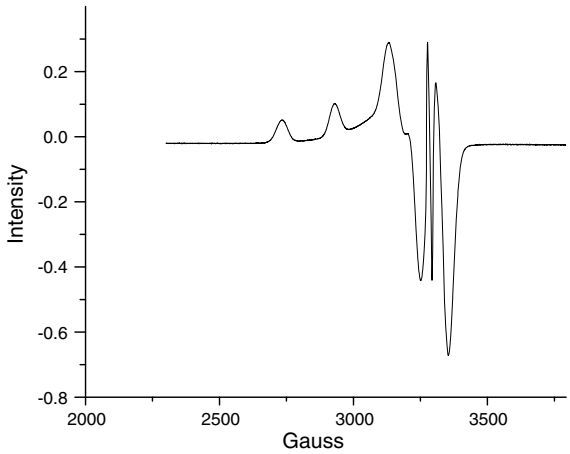


Fig. 1. ESR spectrum of $[Cu(PCHA)](ClO_4)_2$ in CH_3CN at LNT.

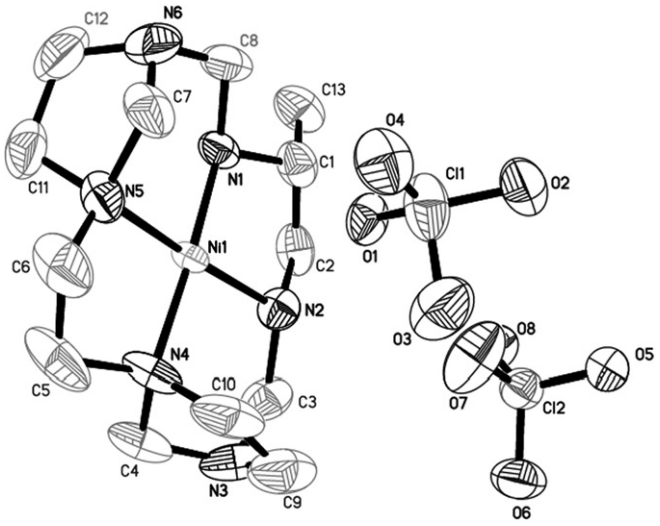


Fig. 2. ORTEP plot of Nickel complex $[Ni(PCHA)](ClO_4)_2$.

Table 4
Bond distances (Å) and angles (°) for [Ni (PCHA)]$(ClO_4)_2$

(a) Bond distances			
Ni1–N1	1.920(4)	N5–C11	1.529(11)
Ni1–N2	1.931(5)	N1–H1	0.9300
Ni1–N4	1.908(4))	Cl1–O2A	1.417(13)
Ni1–N5	1.929(5)	N2–H2	0.9300
N1–C1	1.516(9)	Cl1–O1A	1.407(14)
N2–C2	1.502(8)	C4–H4A	0.9900
N3–C3	1.401(10)	N4–C5	1.511(10)
(b) Bond angles			
N1–Ni1–N2	86.3(2)	Ni1–N2–C3	119.4(4)
Ni1–N1–C1	110.2(4)	Ni1–N2–H2	105.00
N1–Ni–N4	175.17(19)	C2–N2–C3	112.0(5)
N1–Ni1–N5	93.0(2)	C3–N3–C4	111.8(6)
N2–Ni1–N4	93.8(2)	C3–N3–C9	115.3(6)
N2–Ni1–N5	174.9(2)	C4–N3–C9	102.4(7)
N4–Ni1–N5	87.3(2)	Ni–N4–C5	107.4(4)
Ni1–N1–C8	119.6(4)	N1–C1–C2	107.7(5)
Ni1–N2–C2	108.8(4)	N1–C1–C13	114.2(6)
O5–Cl2–O7	106.4(4)	C8–N6–C12	112.6(7)

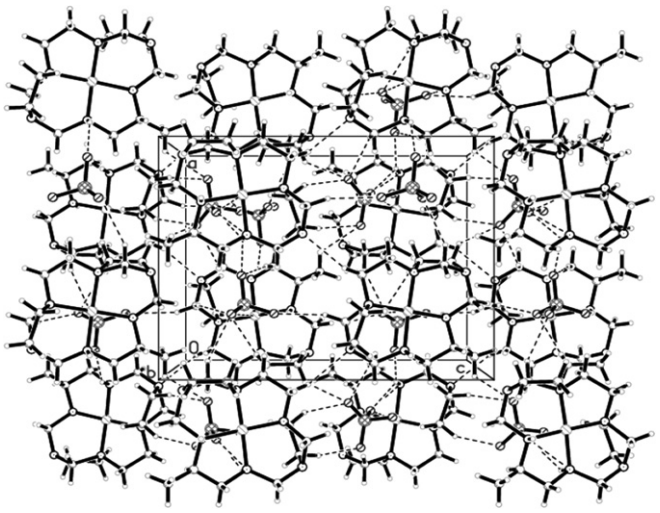


Fig. 3. Packing diagram of $[Ni(PCHA)](ClO_4)_2$.

one which contains the methyl group (N1–Ni–N2) is small compared to the other ring (N4–Ni–N5). The N4–C5–C6–N5 torsion angle in the ethylene moiety is 49.8(9)°. The tetra co-ordination of nickel(II) ions cause the four macrocyclic donor atoms to lie in one plane. The axial sites on nickel are not sterically protected and are accessible to additional ligands so that planar ⇌ octahedral equilibrium is observed. The perchlorate ions form hydrogen bond with the secondary amine of the macrocycle (Fig. 3).

3.4. Electrochemical studies

The nickel(II) and copper(II) complexes exhibit an one electron irreversible oxidation and reduction process in aqueous medium. Both nickel(II) and copper(II) complexes show a chemically irreversible oxidation process ($Ni^{2+} \rightarrow Ni^{3+}$) with a peak potential of +1.20 and +1.13 V, respectively, at a scan rate of 100 mV s^{-1}. The irreversible reduction process ($Ni^{2+} \rightarrow Ni^{+}$) occurs at −1.22 V for nickel and −1.03 V for copper complex. The increase in scan rate shows a small change in the reduction peak position towards more negative potential (Fig. 4).

It has been reported [29] that *N*-alkylation of tetraaza macrocyclic ligands exhibits an anodic shift for both oxidation and reduction of the Ni(II) complexes. The average change in $E_{1/2}$ for the oxidation and reduction process due to the introduction of a methyl group is ∼0.14 and 0.1 V, respectively, for the $[Ni(cyclam)]^{2+}$ complexes. The cyclic voltammetric data (Table 5) show that the potentials for the *C*-alkylated hexaaza macrotricyclic complexes $[M(PCHA)]^{2+}$ (M = Ni, Cu) are more cathodic than the corresponding unsubstituted complexes with the difference in oxidation potential of 0.1 and 0.22 V, respectively, for nickel(II) and copper(II) complexes. The complexes $[M(PCHA)]^{2+}$ and $[M(CHA)]^{2+}$ exhibit an anodic shift for both oxidation and reduction potentials when compared to that of macromonocyclic complex [18] $[NiMe_2[14]aneN_6](ClO_4)_2$. This behaviour is attributed to the presence of tertiary amine donors present in the former ligands. The absence of reversible $M^{II} \rightarrow M^{I}$ reduction suggests [30] that the ligand assembly is not sufficiently flexible to support the increase in ionic radius. The more negative value observed in the case of the reduc-

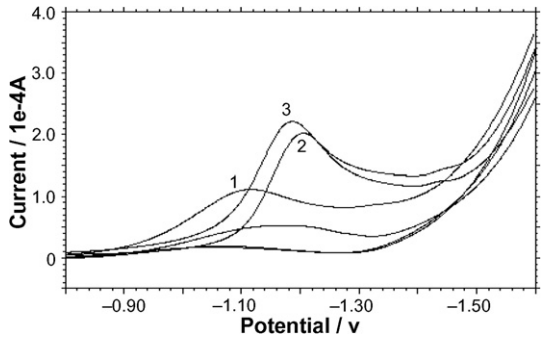


Fig. 4. Cyclic voltammogram of $[Ni(PCHA)]^{2+}$ (reduction process) at different scan rates (mV s^{-1}): (1) 50 (2) 75 and (3) 100.

Table 5
Electro chemical data for hexaaza macrocylic nickel(II) and copper(II) complexes

Complex	E_1 (V)	E_2 (V)
$[Ni(PCHA)](ClO_4)_2$	+1.20	−1.22
$[Ni(CHA)](ClO_4)_2$	+1.30	−1.26
$[Cu(PCHA)](ClO_4)_2$	+1.13	−1.03
$[Cu(CHA)](ClO_4)_2$	+1.35	−1.12
$[NiMe_2[14]aneN_6](ClO_4)^a{}_2$	+0.93	−1.55

Scan rate = 100 mV s^{-1}; [a] Measured in acetronitrile solution.

tion process indicates the stability of the metal complexes in the divalent oxidation state.

3.5. Equilibrium between square-planar and octahedral species of $[Ni(PCHA)]^{2+}$

Ni(II) complexes exist in aqueous solution as an equilibrium mixture of a blue, octahedral, high-spin species and a yellow, planar, low-spin species [31–33] as described by the following equation:

$$[Ni(L)(H_2O)_2]^{2+} \rightleftharpoons [Ni(L)]^{2+} + 2(H_2O)$$

The equilibrium has been reported [34] to be dependant on temperature, ionic strength, and the nature of the added electrolyte. The electronic spectrum of $[Ni(PCHA)]^{2+}$ shows λ_{max} at 459 nm (ε = 107 M^{-1} cm^{-1}) in CH_3NO_2 medium at room temperature. The molar extinction coefficient measured in water is smaller (102 M^{-1} cm^{-1}) than that of in CH_3NO_2, indicating that some of the square-planar species are converted into octahedral species in water. Similar behaviour is observed in unmethylated complex $[Ni(CHA)]^{2+}$ in which the ε value is 89 and 84 M^{-1} cm^{-1}, respectively, in CH_3NO_2 and aqueous medium. The electronic spectrum of $[Ni(PCHA)]^{2+}$ which has λ_{max} at 454 nm (ε = 102 M^{-1} cm^{-1}) in aqueous solution is temperature dependant. The intensity of the band increases with increase in temperature, and it restores to the original value while reversing the temperature, which is a characteristic behaviour observed in many hexaaza Ni(II) macrocycles [18,19,35]. In CH_3NO_2 medium the complex is expected to be 100% planar and the equilibrium constant is obtained from the ratio $K=(\varepsilon_{lim} - \varepsilon)/\varepsilon$ where ε_{lim} and ε represent limiting values of molar extinction coefficient for the square-planar and the apparent molar extinction coefficient in 0.1 M $NaClO_4$, respectively. The ΔH° and ΔS° values were calculated as described in the literature [36]. A plot of $\ln K$ versus $1/T$ is linear, and the ΔH° and ΔS° values were found to be -10.83 ± 0.03 kJ mol^{-1} and $\Delta S = -46.59 \pm 0.04$ J K^{-1} mol^{-1}, respectively. In aqueous solution at 30 °C, 79.1% of the complex is planar and 20.9% is octahedral, and the equilibrium constant (K) value is 0.26 ± 0.05. Thermodynamic data for the equilibrium process are listed in Table 6. The values obtained for $[Ni(PCHA)]^{2+}$ is comparable to those previously obtained for the unmethylated hexaazamacrocylic complexes [18,19,35]. The formation constant of octahedral species viz. $[Ni(PCHA)]^{2+}$, $[Ni(CHA)]^{2+}$ and $[Ni(THA)]^{2+}$ are very small when compared to those of $[Ni(cyclam)]^{2+}$ and $[Ni(isocyclam)]^{2+}$ (Table 6). The Ni–N bond distances in octahedral species are longer than those in square-planar species (~1.9 Å for square-planar and ~2.1 Å for octahedral). The ligands cyclam and isocyclam have larger macrocyclic hole and are capable of accommodating the larger Ni(II) ion while the ligands PCHA, CHA and THA have rigid hole size and hardly accept it.

Noticeably both the ΔH° and ΔS° values in the case of C°-alkyl substituted macrocyles are smaller than those for the unsubstituted ligands (CHA and THA). It has been reported [37] that positive values of ΔS°, observed for the blue to yellow conversion of nickel complexes of cyclam and isocyclam are due to the increase in translational entropy. The presence of methyl group on the macrocyclic backbone may exert a steric repulsion and, hence the equilibrium constant for $[Ni(PCHA)]^{2+}$ is smaller when compared to those of $[Ni(CHA)]^{2+}$ and $[Ni(THA)]^{2+}$.

Table 6
Thermodynamic data for the equilibrium $[Ni(L)(H_2O)_2]^{2+} [Ni(L)]^{2+} + 2(H_2O)$

L	K_{25} (°C)	ΔH° (kJ mol^{-1})	ΔS° (J K^{-1} mol^{-1})	Ref.
PCHA	0.26 ± 0.05[a]	−10.83 ± 0.03	−46.59 ± 0.04	This work
CHA	0.07	−12.9	−65.4	[19]
THA	0.05	−21.4	−96.2	[19]
Cyclam	2.5	5.4	16.3	[36]
Isocylam	1.6	5.3	16.9	[36]

[a] Measured at 30 °C.

The negative ΔH° value for $[Ni(PCHA)]^{2+}$ indicates the endothermic effect resulting from the formation of the two axial Ni–OH_2 bonds. The Ni—N bond distances in octahedral species are longer than those in square-planar species. The high-spin to low-spin conversion of Ni(II) complexes can occur either by the release of apical water molecules or through elongation of the axial Ni–OH_2 bonds. However, the present results indicate that the value of ΔS° nearly corresponds to those expected for the loss of two water molecules in the octahedral species.

Acknowledgements

We thank the University Grants Commission, New Delhi and the University of Madras (Project No. HS-49) for the financial support.

Appendix A. Supplementary data

CCDC 656554 contains the supplementary crystallographic data for $[Ni(PCHA)]^{2+}$. These data can be obtained free of charge via http://www.ccdc.cam.ac.uk/conts/retrieving.html, or from the Cambridge Crystallographic Data Centre, 12 Union Road, Cambridge CB2 1EZ,UK; fax: (+44) 1223-336-033; or e-mail: deposit@ccdc.cam.ac.uk.

References

[1] H. Elias, Coord. Chem. Rev. 187 (1999) 37.
[2] G.A. Melson, Coordination Chemistry of Macrocyclic Compounds, Plenum, New York, 1979.
[3] O. Labudova, J. Labuda, L. Feenikova, M. Kollarova, Z. Durackova, J. Inorg. Biochem. 61 (1996) 227.
[4] R.I. Haines, D.R. Hutchings, T.M. McCormack, J. Inorg. Biochem. 85 (2001) 1.
[5] W. Li, S.E. Fraser, T.J. Meade, J. Am. Chem. Soc. 121 (1999) 1413.
[6] A. Chaudhary, N. Bansal, A. Gajraj, R.V. Singh, J. Inorg. Biochem. 96 (2003) 393.
[7] J.W. Sibert, A.H. Cory, J.G. Cory, J. Chem. Soc. Chem. Commun. (2002) 154.
[8] M. Botta, Eur. J. Inorg. Chem. (2000) 399.
[9] X. Liang, P.J. Sadler, Chem. Soc. Rev. 33 (2004) 246.
[10] N.M. Di Bartolo, A.M. Sargeson, T.M. Donlevy, S.V. Smith, J. Chem. Soc., Dalton Trans. (2001) 2303.
[11] J.J.R. Fransto da Silva, R.J.P. Williams, The Biological Chemistry of the Elements, Clarendon Press, Oxford, 1991.
[12] K.R. Adam, M. Antolovich, D.S. Baldwin, P.A. Duckworth, A.J. Ceong, L.F. Lindoy, M. McPartlin, P.A. Taskar, J. Chem. Soc., Dalton Trans. (1993) 1013.
[13] J.P.L. Cox, K.J. Jankowski, R. Kataky, D. Pasker, M.A. Eaton, M.R. Belley, A.T. Millican, A. Harrison, C. Walker, J. Chem. Soc. Chem. Commun. (1989) 797.
[14] R.B. Lauffer, Chem. Rev. 87 (1987) 901.
[15] M.P. Suh, W. Shin, S.G. Kang, M. Lah, T. Chang, Inorg. Chem. 28 (1989) 1602.
[16] T. Lu, S. Lin, H. Aneetha, K. Paneerselvam, C. Chuny, J. Chem. Soc., Dalton Trans. (1999) 3385.
[17] K.P. Wainwright, Coord. Chem. Rev. 166 (1997) 35.
[18] M.P. Suh, W. Shin, H. Kim, C.H. Koo, S.G. Kang, Inorg. Chem. 27 (1988) 2544.
[19] M.P. Suh, S.G. Kang, V.L. Goedken, H. Park, Inorg. Chem. 30 (1991) 365.
[20] D.D. Perrin, W.L.F. Armarego, D.R. Perrin, Purification of Laboratory Chemicals, 2nd ed., Pergamon, Oxford, England, 1980.
[21] W.J. Geary, Coord. Chem. Rev. 7 (1971) 81.
[22] A.B.P. Lever, Inorganic Electronic Spectroscopy, Elsevier, Amsterdam, The Netherlands, 1984.
[23] K. Nakamoto, Infrared and Raman Spectra of Inorganic and Coordination Compounds, 3rd ed., Wiley Interscience, New York, 1977.
[24] D. Kivelson, R. Neiman, J. Chem. Phys. 35 (1961) 149.
[25] B.J. Hathaway, D.E. Billing, Coord. Chem. Rev. 5 (1970) 143.
[26] R.C. Agarwal, N.K. Singh, R.P. Singh, Inorg. Chem. 20 (1981) 2794.
[27] S.G. Kang, K. Ryu, S.K. Jung, J. Kim, Inorg. Chim. Acta 293 (1999) 140.
[28] D. Lee, M.P. Suh, J.W. Lee, J. Chem. Soc., Dalton Trans. (1997) 577.
[29] E.K. Barefield, G.M. Freeman, D.G. Van Derveer, Inorg. Chem. 25 (1986) 552.
[30] P. Barbaro, C. Bianchini, G. Capannesi, L. Di Luca, F. Laschi, D. Petroni, P.A. Salvadori, A. Vacca, F. Vizza, J. Chem. Soc., Dalton Trans. (2000) 2393.
[31] L. Sabatini, L. Fabbrizzi, Inorg. Chem. 18 (1979) 438.
[32] C.K. Jorgenson, Acta. Chem. Scand. 11 (1957) 399.
[33] A. Anichini, L. Fabbrizzi, P. Paoletti, R.M. Clay, Inorg. Chim. Acta 24 (1977) L21.
[34] L. Fabbrizzi, J. Chem. Soc., Dalton Trans. (1979) 1857.
[35] R.W. Hay, A. Danby, P. Lightfoot, Transition Met. Chem. 22 (1997) 395.
[36] K. Mochizuki, M. Fujimoto, H. Ito, T. Ito, Bull. Chem. Soc. Jpn. 53 (1980) 2535.
[37] M. Ciampolini, L. Fabbrizzi, M. Licchelli, A. Perotti, F. Pezzini, A. Poggi, Inorg. Chem. 25 (1986) 4131.

and deoxygenated by standard methods [13]. $ReOCl_3(OPPh_3)(SMe_2)$ was prepared according to the literature procedure [3]. IR and FIR measurements were performed in KBr pellets, either with a Nicolet FTIR Impact 400 instrument or in Nujol with a Brucker IFS 113V instrument. ^1H, $^{31}P\{^1H\}$ NMR spectra were obtained on a Bruker AMX and Avance III (300 MHz for ^1H NMR) device at room temperature. The chemical shifts δ, are given in ppm relative to TMS (^1H) and H_3PO_4 (^{31}P) using deuterated solvents as lock and reference (^1H), respectively. UV–Vis spectra in CH_2Cl_2 solution were obtained on a Carry 500 spectrophotometer. Elemental analyses were performed on a Vario EL III apparatus.

2.2. Synthesis of the complexes

2.2.1. *mer*-$ReOCl_3(OPPh_3)(pym)$ (**1** · CH_3CN)

Pyrimidine (0.02 cm^3, 0.25 mmol) was added to a stirred suspension of the complex $ReOCl_3(OPPh_3)(SMe_2)$ (0.15 g, 0.23 mmol) in acetonitrile (25 cm^3). The mixture was heated to reflux within 3 h generating a green solution. Upon slow cooling to room temperature, green crystals suitable for X-ray analysis were afforded. The product was filtered, washed with diethyl ether and dried in vacuo (0.1 g, 66%). (*Anal.* Calc. for $C_{22}H_{19}Cl_3N_2O_2PRe \cdot C_2H_3N$: C, 40.71; H, 3.13; N, 5.94; Cl, 15.02. Found: C, 40.69; H, 3.10; N, 5.77; Cl, 15.05%); ν_{max}(KBr)/cm^{-1} 540s, 1123vs (P═O), 990vs (Re═O), 1557w, 1592w (C═N); ν_{max}(nujol)/cm^{-1} 256m, 317vs, 332s, 341s (Re–N), (Re–Cl); $\lambda_{max}(CH_2Cl_2)$/nm 355 (ε/dm^3 mol^{-1} cm^{-1} 1520), 380 (1499), 745 (115).

2.2.2. *mer*-$ReOCl_3(OPPh_3)(pyz)$ (**2**)

Pyrazine (0.054 g, 0.675 mmol) was added to a stirred suspension of the complex $ReOCl_3(OPPh_3)(SMe_2)$ (0.27 g, 0.42 mmol) in acetonitrile (30 cm^3). The mixture was heated to reflux within 2 h, generating greenish-brown solution. The solution was concentrated to ~7 cm^3 and stored in a refrigerator. Green crystals of **2** suitable for X-ray analysis were formed overnight.[1] The product was filtered, washed with diethyl ether and dried in vacuo (0.18 g, 65%). (*Anal.* Calc for $C_{22}H_{19}Cl_3N_2O_2PRe$: C, 39.62; H, 2.87; N, 4.20; Cl, 15.95. Found: C, 39.61; H, 2.77; N, 4.21; Cl, 15.70%.); ν_{max}(KBr)/cm^{-1} 540s, 1122vs (P═O), 990vs (Re═O), 1557w, 1592w (C═N); ν_{max}(nujol)/cm^{-1} 253m, 317vs, 336s, 339vs (Re–N), (Re–Cl).

2.2.3. $[ReOCl_3(OPPh_3)]_2(\mu$-pym) (**3**)

Pyrimidine (0.015 cm^3, 0.19 mmol) was added to a stirred suspension of the complex $ReOCl_3(OPPh_3)(SMe_2)$ (0.24 g, 0.38 mmol) in acetonitrile (25 cm^3). The mixture was heated to reflux for 8 h, generating a yellow greenish solution. Upon slow cooling, a greenish crystalline precipitate was afforded. The product was filtered, washed with absolute ethanol, diethyl ether and dried in vacuo (0.14 g, 60%). The monomeric complex *mer*-$ReOCl_3(OPPh_3)$-(pym)**1** · CH_3CN was obtained from the mother liquor as a by-product. Single crystals suitable for X-ray analysis were obtained by re-crystallization from acetonitrile solution as yellow-green compound. (*Anal.* Calc for $C_{40}H_{34}O_4Cl_6N_2P_2Re_2$: C, 38.32; H, 2.73; N, 2.23; Cl, 16.97. Found: C, 38.62; H, 2.68; N, 2.65; Cl, 17.01%.) ν_{max}(KBr)/cm^{-1} 540s, 1123vs (P═O), 989vs (Re═O), 1603w C═N; ν_{max}(nujol)/cm^{-1} 259m, 306s, 329vs, 346vs (Re–N), (Re-Cl); $\lambda_{max}(CH_2Cl_2)$/nm 393 (ε/dm^3 mol^{-1} cm^{-1} 120) 450 (132), 752 (16).

2.2.4. $[ReOCl_3(OPPh_3)]_2(\mu$-pyz) (**4**)

A suspension of the light-green complex $ReOCl_3(OPPh_3)(SMe_2)$ (0.3 g, 0.46 mmol) and pyrazine (0.018 g, 0.22 mmol) in acetonitrile (10 cm^3) was stirred and boiled for 2 h until the starting rhenium compound reacted and a red-brown crystalline solid was afforded. The product was filtered, washed with absolute ethanol, diethyl ether and dried in vacuo (0.25 g, 86%). If the mother liquor was allowed to cool to room temperature, single crystals of a red-brown compound suitable for X-ray analysis were obtained. (*Anal.* Calc for $C_{40}H_{34}O_4Cl_6N_2P_2Re_2$: C, 38.32; H, 2.73; N, 2.23; Cl, 16.97. Found: C, 38.22; H, 2.66; N, 2.26; Cl, 16.74%.) ν_{max}(KBr)/cm^{-1} 538s, 1122vs (P═O), 990vs (Re═O), 1591w C═N; ν_{max}(nujol)/cm^{-1} 260s, 324s, 334s, 343vs, (Re–N), (Re–Cl); $\lambda_{max}(CH_2Cl_2)$/nm 485sh (ε/dm^3 mol^{-1} cm^{-1} 4727) 520 (8000), 780 (1160).

2.3. Crystal structure determination

The data collected on KM4CCD diffractometer were corrected for Lorentz and polarization effects. Data reduction were carried out using the Oxford Diffraction (Poland) programs. The structure was solved by Patterson method using SHELXS-97 and refined by the full-matrix least-squares method on F^2 using SHELXL-97 software [14]. Non-hydrogen atoms were refined with anisotropic thermal parameters. The hydrogen atoms were set in calculated positions and refined using the riding model with a common fixed isotropically thermal parameter.

3. Results and discussion

3.1. Synthesis of the complexes

Starting with $ReOCl_3(OPPh_3)(SMe_2)$, the reactions at a 1:1 metal-to-diaza ligand ratio gave the mononuclear oxo-rhenium(V) complexes $ReOCl_3(OPPh_3)$(pym) (**1**), and $ReOCl_3(OPPh_3)$(pyz) (**2**), whereas those performed at 2:1 ratio yielded dinuclear compounds $[ReOCl_3(OPPh_3)]_2(\mu$-pym) (**3**), and $[ReOCl_3(OPPh_3)]_2(\mu$-pyz) (**4**) (see Chart 1). All one-pot reactions were performed in boiling acetonitrile, whereas the analogous monosubstituted complexes $ReOCl_3(OPPh_3)$(py) or $ReOCl_3(OPPh_3)(Me_3Bzm)$ obtained by Marzilli et al. [15] had been obtained under mild reaction condition, at ambient temperature over several hours in the presence of a stoichiometric amount of the aza ligand. Similar gentle reaction conditions were used for the synthesis of even the disubstituted pyridine complex $ReOCl_3(py)_2$ obtained by Choi and Muetterties [16]. Apart from the sluggish synthesis of **3** which took 8 h, the preparation of **1**, **2**, and **4** was completed in 2–3 h.

Compounds **1** and **2** were achieved in ligand substitution reaction of the N ~ N heterocycle for the most labile dimethyl sulphide. Replacement of the second labile triphenylphosphine oxide ligand was not observed. Complexes **1** and **2** containing one bridging

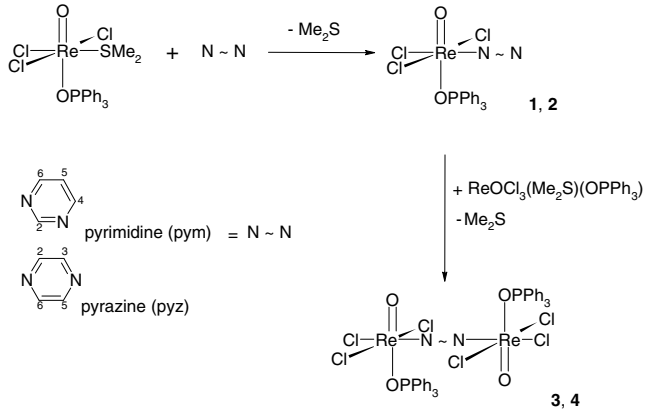


Chart 1.

[1] *mer*-$ReOCl_3(OPPh_3)$(pyz) 2 was characterized by X-ray crystallography, but the X-ray diffraction data were not of sufficient quality to publish because of additional high peaks on Fourier map. The preliminary results allowed us to estimate rugged geometry of the complex.

Table 1
^{1}H NMR, ^{31}P NMR spectroscopic data for mono $ReOCl_3(OPPh_3)(N\sim N)$ **1**, **2** and dinuclear $[ReOCl_3(OPPh_3)]_2(\mu\text{-}N\sim N)$ **3**, **4** complexes in CD_2Cl_2 solution at room temperature

Complex	^{1}H NMR δ/ppm (int., mult., J/Hz)		^{31}P{^{1}H} NMR δ/ppm
	Triphenylphosphine oxide	N ∼ N ligand	
$ReOCl_3(OPPh_3)$(pym) (**1**)	7.46, 7.63 (15H, m′s)	7.38 (1H, t, 5 Hz), 8.50 (1H, m′s) 8.95 (1H, m′d), 9.45 (1H, s)	49.10
$ReOCl_3(OPPh_3)$(pyz) (**2**)	7.46, 7.64[a] (15H, m′s)	8.62 (2H, m′d), 8.64 (2H, m′d)	49.48
$[ReOCl_3(OPPh_3)]_2(\mu$-pym) (**3**)	7.46, 7.60 (30H, m′s)	7.34 (1H, t $^3J_{HH}$ = 6), 8.99 (2H, d, $^3J_{HH}$ = 6) 10.24 (1H, s)	50.53
$[ReOCl_3(OPPh_3)]_2(\mu$-pyz) (**4**)	7.44, 7.62 (15H, m′s)	8.42 (2H, s)	50.37

[a] Signals overlapped with the resonances due to the phenyl groups of corresponding dimer **4**.

diaza ligand were still able to react further yielding the dimers **3** and **4**.

In contrast to **1**, complex **2** is unstable: when dissolved in acetonitrile it immediately reacts further, yielding a thermodynamically more stable product, dimer **4**. On this account, no UV–Vis spectrum was recorded for **2**, and NMR spectra consist of additional, partially overlapped signals attributed to phenyl protons belonging to **4**. The high yield and short reaction time of **4** also corroborate the lability of **2**. The lower stability of **2** in contrast to **1** can be cautiously explained as a less steric effect of pyrazine compared with pyrimidine as well as the effect of the increase in pyrazine basicity on complexation already announced in the literature for pentaaminaruthenium(II) complexes $(NH_3)_5Ru^{II}L^{2+}$ (where L = pyz or pym) [17].

Unlike the monomers **1** and **2**, the dimers **3** and **4** are slightly soluble in dichloromethane and poorly soluble in chloroform. They are stable on air both in solid state and in solution. Both compounds are inert to substitution reaction. Even prolonged heating with an excess of pyrazine or pyrimidine as a ligands in acetonitrile does not substitute triphenylphoshine oxide under applied reaction conditions. However, traces of water in the system generate a stable $Re_2O_3Cl_4(N\sim N)_4$, already known from the literature [8,18], which contains the (O═Re–O–Re═O) arrangement, due to hydrolysis.

3.2. Spectroscopic characterization

For all the complexes, monomeric as well as dimeric, strong IR band at around 990 cm^{-1} is relevant. The invariable position of the band corresponds to the stretching vibration ν(Re═O) and exists in the upper range observed for the *trans*-arrangement of the oxygen donors O═Re–O– [19]. The stretching vibrations of triphenylphosphine oxide ν(P═O) at 1193 cm^{-1} are shifted at ca. 70 cm^{-1} to a lower frequency when it coordinates to rhenium.

Based on our previous work on experimental and theoretical FIR spectra of oxo-rhenium(V) complexes [20], we identified the position of the stretching vibrations ν(Re–N) of medium and strong intensity at 250–260 cm^{-1}. FIR spectra permitted us to elucidate the geometry of the chloride ligands. Three ν(Re–Cl) absorptions occur in the 300–350 cm^{-1}. These data lead to a local C_{2v} symmetry and a meridional arrangement of halogen ligands around the metal.

The NMR spectra of all the compounds show sharp peaks in the 7–11 ppm range (summarized in Table 1, signals due to CH_3CN solvate were not presented). ^{1}H NMR spectroscopic studies revealed two sets of signals relevant to triphenylphosphine oxide and N-heterocycle. Moreover, they make it possible to distinguish between monomers or dimers. It is noteworthy that all the complexes at room temperature exhibit C_s symmetry around the metal centre. The spectra for **1**, **2** are simple: two multiplets at 7.46 and 7.63 ppm indicate phenyl protons of phosphine oxide (in a case of **2**, partly overlapped with the multiplets attributed to dimer **4**). Four signals relevant to H2, H4, H5 and H6 for **1** and two multiplets H2,6 and H3,5, for **2** correspond to one mono-coordinated pyrimidine and pyrazine molecule, respectively. For the mononuclear complexes **1** and **2**, coordination of diaza congeners to the $ReOCl_3(OPPh_3)$ unit lowers the symmetry of the ligand and shifts resonances slightly downfield ($\Delta\delta$ value) compared with the *trans*-$ReOCl_2(OEt)(N\sim N)_2$ complexes (ESI Table S1). The symmetry of the heterocycles in the dinuclear compounds **3** and **4** corresponds to the unsubstituted complexes and the resonances are moved slightly downfield for **3** ($\Delta\delta$ = 0.03–0.27). The highest downfield shift [(1.02) for H2, dimer **3**)] is exhibited by the H2 protons most sensitive to metallation. Thus, the spectrum of

Table 2
Crystallographic data for $ReOCl_3(OPPh_3)$pym (**1**), $[ReOCl_3(OPPh_3)]_2(\mu$-pym) (**3**) and $[ReOCl_3(OPPh_3)]_2(\mu$-pyz) (**4**)

	$ReOCl_3(OPPh_3)$pym (**1** · CH_3CN)	$[ReOCl_3(OPPh_3)]_2$-(μ-pym) (**3** · CH_3CN)	$[ReOCl_3(OPPh_3)]_2$-(μ-pyz) (**4** · CH_3CN)
Empirical formula	$C_{22}H_{19}Cl_3N_2O_2$-PRe · C_2H_3N	$C_{40}H_{34}Cl_6N_2O_4$-P_2Re_2 · C_2H_3N	$C_{40}H_{34}Cl_6N_2O_4P_2$ Re_2 · C_2H_3N
Formula weight	707.97	1294.79	1294.79
Temperature (K)	100(2)	100(2)	100(2)
λ (Å)	0.71073	0.71073	0.71073
Crystal system	triclinic	orthorhombic	monoclinic
Space group	$P\bar{1}$	$P2_12_12_1$	Cc
Unit cell dimensions			
a (Å)	8.906(3)	15.110(4)	26.261(9)
b (Å)	12.095(4)	16.436(5)	9.826(3)
c (Å)	13.110(4)	18.288(6)	17.679(6)
α (°)	69.58(4)		
β (°)	77.14(3)		101.84 (4)
γ (°)	83.33(3)		
Volume (Å^3)	1289.1 (8)	4542 (2)	4465 (3)
Z	2	4	4
D_{calc} (Mg m^{-3})	1.824	1.894	1.926
Absorption coefficient (mm^{-1})	5.11	5.79	5.89
F(000)	688	2496	2496
Crystal size (mm)	0.39 × 0.24 × 0.06	0.37 × 0.15 × 0.08	0.25 × 0.17 × 0.06
θ Range (°)	2.8–36.5	4.6–35.4	2.6–36.6
Number of collected reflection	15265	46618	36815
Independent reflection (R_{int})	7668 (0.040)	17820 (0.042)	16034 (0.080)
Completeness to 2θ = 50°	100%	100%	100%
S	1.00	1.00	1.00
R_1/ wR_2 indices	0.027/0.069	0.039/0.050	0.046/0.084
Flack parameter		−0.030(3)	

$R_1 = \sum||F_o| - |F_c||/\sum|F_o|$.
$wR_2 = \{\Sigma[w(F_o^2 - F_c^2)^2]/[w(F_o^2))^2]\}^{1/2}$.
$w = 1/[\sigma^2(F_o^2) + (aP)^2]$, where $P = (F_o^2 + 2F_c^2)/3$, a = 0.0436 (**1**), 0.001 (**2**), 0.0199 (**3**).

Table 3
Relevant bond distances (Å) and angles (°) for $ReOCl_3(OPPh_3)$pym (**1**), $[ReOCl_3(OPPh_3)]_2$(μ-pym) (**3**) and $[ReOCl_3(OPPh_3)]_2$(μ-pyz) (**4**)

	$ReOCl_3(OPPh_3)$-pym (**1** · CH_3CN)	$[ReOCl_3(OPPh_3)]_2$-(μ-pym) (**3** · CH_3CN)	$[ReOCl_3(OPPh_3)]_2$-(μ-pyz) (**4** · CH_3CN)
Bond lengths			
Re(1)–O(1)	1.660(2)	1.668(2)	1.644(5)
Re(2)–O(3)		1.670(2)	1.664(6)
Re(1)–O(2)	2.079(2)	2.062(2)	2.097(5)
Re(2)–O(4)		2.069(2)	2.047(5)
Re(1)–N(1)	2.150(3)	2.198(3)	2.167(6)
Re(2)–N(*)		2.189(3)	2.189(5)
Re(1)–Cl(1)	2.376(1)	2.388(1)	2.392(2)
Re(2)–Cl(4)		2.330(1)	2.363(2)
Re(1)–Cl(2)	2.351(1)	2.330(1)	2.345(2)
Re(2)–Cl(5)		2.397(1)	2.315(2)
Re(1)–Cl(3)	2.372(1)	2.374(1)	2.354(2)
Re(2)–Cl(6)		2.362(1)	2.381(2)
Bond angles			
O(1)–Re(1)–O(2)	171.7(1)	169.8(1)	170.1(2)
O(3)–Re(2)–O(4)		167.1(1)	166.4(2)
O(1)–Re(1)–N(1)	89.7(1)	88.3(1)	89.5(2)
O(3)–Re(2)–N(*)		88.2(1)	86.0(3)
O(1)–Re(1)–Cl(2)	99.57(9)	100.00(9)	102.6(2)
O(3)–Re(2)–Cl(4)		101.67(9)	94.1(2)
O(2)–Re(1)–N(1)	82.01(9)	81.5(1)	80.8(2)
O(4)–Re(2)–N(*)		79.2(1)	80.5(2)
O(2)–Re(1)–Cl(2)	88.72(7)	90.23(8)	87.2(2)
O(4)–Re(2)–Cl(5)		84.07(7)	91.4(2)
N(1)–Re(1)–Cl(1)	89.71(8)	89.95(8)	90.9(2)
N(*)–Re(2)–Cl(4)		170.14(8)	90.7(2)
N(1)–Re(1)–Cl(2)	170.71(6)	171.68(8)	167.8(2)
N(4)–Re(2)–Cl(5)		90.98(9)	171.8(2)
N(1)–Re(1)– Cl(3)	88.64(8)	90.59(8)	89.2(2)
N(*)–Re(2)–Cl(6)		90.00(9)	90.9(2)
Torsion angles			
N(1)–Re(1)–O(2)–P(1)	−75.3(3)	55.8(6)	−65(1)
N(*)–Re(2)–O(4)–P(2)		68.5(4)	−69.8(9)
Cl(1)–Re(1)–O(2)–P(1)	15.1(3)	−35.0(6)	27(1)
Cl(4)–Re(2)–O(4)–P(2)		−112.5(4)	21.4(9)
Cl(2)–Re(1)–O(2)–P(1)	105.2(3)	−124.6(6)	117(1)
Cl(5)–Re(2)–O(4)–P(2)		−23.6(4)	110.8(9)
Cl(3)–Re(1)–O(2)–P(1)	−164.9(3)	147.2(6)	−154(1)
Cl(6)–Re(2)–O(4)–P(2)		159.6(4)	−161.7(9)

N(*) corresponds to N(3) for $[ReOCl_3(OPPh_3)]_2$(μ-pym) (**3** · CH_3CN) or N(4) for $[ReOCl_3(OPPh_3)]_2$(μ-pyz) (**4** · CH_3CN).

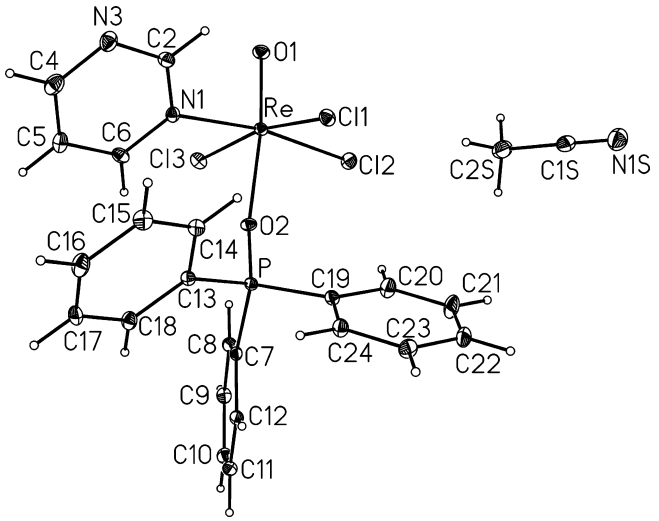


Fig. 1. Molecular structure of $ReOCl_3(OPPh_3)$(pym) (**1** · CH_3CN), the thermal displacement ellipsoids are drawn with 30% probability level.

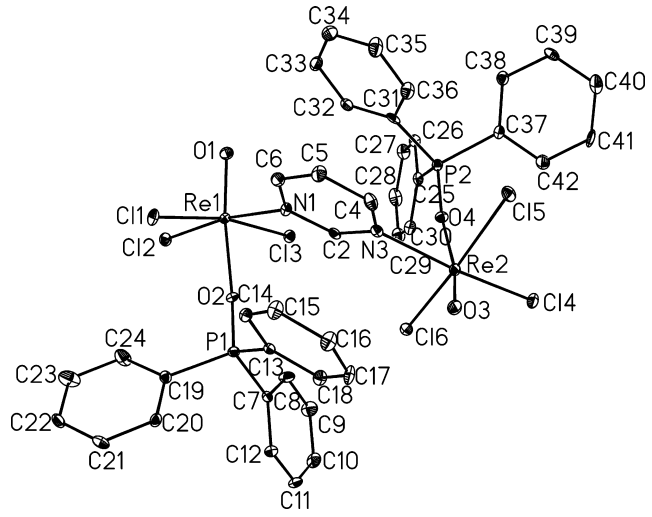


Fig. 2. Molecular structure of $[ReOCl_3(OPPh_3)]_2$(μ–pym) (**3**), the thermal displacement ellipsoids are drawn with 30% probability level. The hydrogen atoms have been omitted for clarity.

$[ReOCl_3(OPPh_3)]_2$(μ-pym) (**3**) consists of five group of signals. Two of them are characteristic for triphenylphosphine oxide, three others for bridging pyrimidine. Protons H4 and H6 are magnetically equivalent, in contrast to H2 and H5. Based on signals integration, two molecules of phosphine oxide and one molecule of the N-heterocyclic ligand form a dimeric molecule. Yet, the ^1H NMR spectrum of $[ReOCl_3(OPPh_3)]_2$(μ-pyz) (**4**) besides the resonances assigned to coordinated phosphine oxide contains a singlet, which is attributed to the equivalent protons of bridging pyrazine. The electrophilic nature of rhenium(V) shifts the proton signal of coordinated pyrazine, δ = 8.42 ppm, towards the high field region (free pyrazine δ 8.61 ppm).

$^{31}P\{^1H\}$ NMR spectra show singlets at δ 49 ppm or 50 ppm due to coordinated triphenylphosphine oxide for monomers and dimers, respectively.

The electronic absorption bands for **1**, **3** and **4** are given in Section 2. The differences for both dinuclear complexes are striking. Although **1** and **3** exhibit in solution a yellow green colour, complex **4** is dark pink. The visible spectrum of **4** consists of two bands at 780 nm and 520 nm with large absorption coefficient, ($1160\ M^{-1}\ cm^{-1}$) and ($8000\ M^{-1}\ cm^{-1}$) respectively, probably caused by a significant contribution of CT transitions. In contrast, **3** is characterized by a very weak absorption band at 752 (16) and 450 (132). High values of absorption coefficients are not unusual and have also been reported in the literature for other oxorhenium(V) complexes with N-heterocyclic ligands [8,21]. The lower energy bands observed in the spectra of $5d^2$ rhenium complexes are usually described as nd–σ^*d and nd–π^*d transitions [1]. Bands with large extinction exhibit CT character. The d–d transitions are forbidden, so they overlap with neighbouring transitions lowering these bands.

Unfortunately, we observed that neither of the complexes **3** and **4** is luminescent in aprotic solvent.[2]

4. X-ray structure analysis of complexes 1, 3 and 4

The crystal and molecular structure of complexes **1**, **3** and **4** determined by X-ray diffractometry confirms that the stereochem-

[2] Attempted measurement of the high-resolution luminescence excitation spectra was performed at 293, 77 K in dichloromethane, using a Spectra Pro 0.75-m monochromator equipped with Hamamatsu R928 photomultiplier tube as a detector.

istry of the molecules is the same in solution and in the solid state. The crystallographic data for **1** · CH_3CN, **3** · CH_3CN and **4** · CH_3CN, selected bond lengths and bond angles and the molecular structures with atomic labelling schemes, are shown in Tables 2, 3 and Figs. 1–3, respectively. The rugged geometries of the distorted octahedral $ReOCl_3NO$ coordination spheres are very similar for all complexes. The coordination geometry about rhenium is established by tree chlorides and one nitrogen atom in equatorial plane.

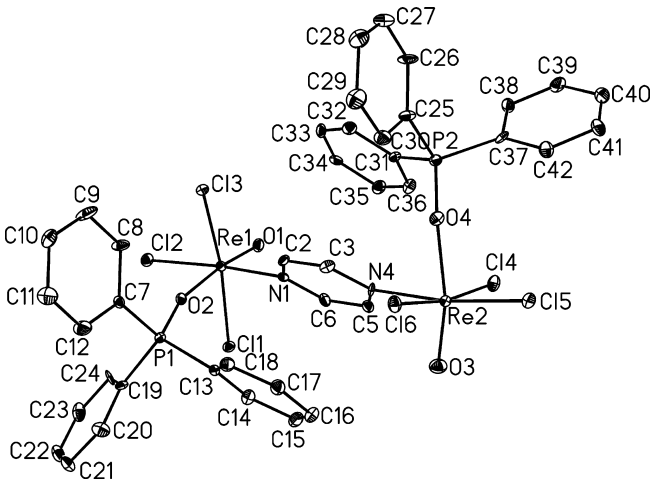


Fig. 3. Molecular structure of $[ReOCl_3(OPPh_3)]_2(\mu\text{-pyz})$ (**4**), the thermal displacement ellipsoids are drawn with 30% probability level. The hydrogen atoms have been omitted for clarity.

Two apical positions are occupied by two donor atoms: terminal oxygen and oxygen of triphenylphosphine oxide. The molecules of **3** and **4** consist of two units connected *via* pyrimidine or pyrazine rings which effect coordination of two metal centres at 120° and 180°, respectively. In all the complexes, the rhenium atoms deviate from the equatorial planes (Cl–Cl–Cl–N) towards the oxo atoms by 0.179–0.228 Å. The short Re(1)–O(1) and Re(2)–O(3) bonds lengths, 1.660–1.670 Å found for **1**, **3** and **4** are typical for rhenium (V) monooxo complexes and indicate formally triple bonds (Re≡O) [1,22]. The Re–$OPPh_3$ distances also lie within the usual range [15,23]. The other coordination bonds and distances fit well with the values found in the literature [24,25]. It is interesting to note that in complex **1** and **2**,[1] the pyrimidine or pyrazine ring is involved in stacking interaction with one phenyl ring belonging to phosphine oxide (3.87(2) Å centroid to centroid, c_t–c_t for **1**, ~3.6 Å for **2**). The same structural features are found for compounds **3** and **4**. The rhenium units are twisted almost perpendicular with respect diaza ligand, the pseudo torsion angles O(1)Re(1)···Re(2)O(3) being 125.6(1)° (**3**) and 105.2(3)° (**4**), respectively. Thus, one phenyl ring of each triphenylphosphine oxide is stacked with bridging diaza ring forming a π–π interactions (3.64(3) Å and 3.78(3) Å c_t–c_t (**3**)) and (3.62(2) and 3.62(2) Å c_t–c_t (**4**)). For all of the complexes **1**, **3** and **4**, the rings are displayed parallel and the angles formed by the ring normal and the vector between the diaza and phenyl ring centroid are approximately 20°. Hence, according to Janiak [26], such a parallel-displaced structures exhibit not only π–π interaction but also contribution from π–σ attraction. It is thought that π–π interactions may play a crucial role in the assembly process of complexes. In contrast to intermolecular π–π interaction, intramolecular ones are rare within ligands coordinated to transition metals [27–29]. Noncovalent

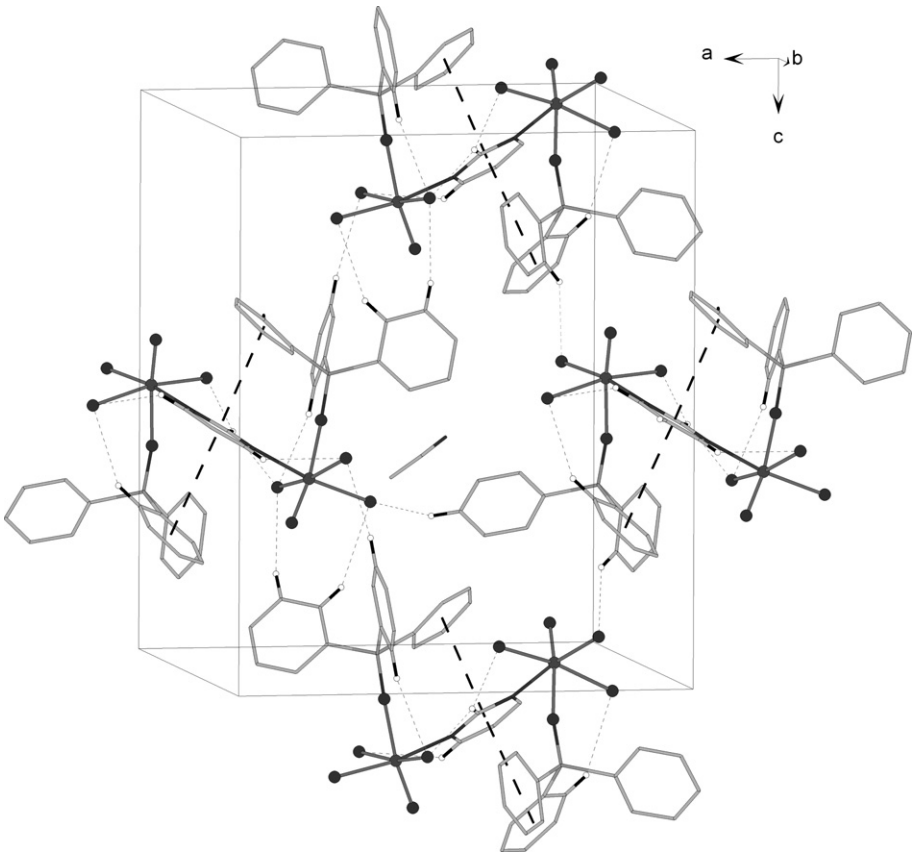


Fig. 4. Packing diagram for **3** showing intramolecular π–π stacking interactions (dashed line) and hydrogen bonding interactions (dotted line), hydrogens not involved in any interaction have been omitted for clarity.

π–π interactions between phenyl ring and the aza ligand are exhibited by the rhenium complex *fac*-$(CO)_3$(dmbpy)Re(I)Ph_3Sn(I) [30] (dmbpy = 4,4′-dimethyl-2,2′-bipyridine). Along with intermolecular ones, unusual intramolecular forces stabilise the coordination geometry of such organometallic complex. The stacking intramolecular interactions reported for complex $ReOCl_3(OPPh_3)(Me_3Bzm)$ [15] (3.58(2) Å c_t–c_t) between the imidazole ring of Me_3Bzm and the aromatic ring of $OPPh_3$ appeared to be responsible for the stability of the complex, too.

The extensive intramolecular π–π interactions observed for all complexes **1**–**4** may contribute to the lack of triphenylphosphine oxide substitution reaction. Another feature of interest is that beside π–π stacking, intra- and intermolecular hydrogen bonding (Figs. 4 and 5) could be responsible for the poor solubility of dimers **3** and **4** as well (see supporting materials).

5. Conclusions

Our endeavours to obtain mononuclear oxo-rhenium(V) complexes with diaza congeners resulted in the mono substituted $ReOCl_3(OPPh_3)$(pym) (**1**) and $ReOCl_3(OPPh_3)$(pyz) (**2**) complexes. Attempts to incorporate a second equivalent of the diaza ligand did not lead to any observable changes, although the pyridine analogue $ReOCl_3(OPPh_3)$(py) reacted further, generating $ReOCl_3(py)_2$. The higher basicity of pyridine compared with pyrimidine or pyrazine (pK_a values of 5.23 for py, 1.30 pym, 0.6 pyz [17]) makes it more favourable to obtain mono or disubstituted complexes as well. The coordination abilities of the monomers **1** and **2** were examined, as a result of which dinuclear complexes $[ReOCl_3(OPPh_3)]_2$(μ-pym) (**3**) and $[ReOCl_3(OPPh_3)]_2$(μ-pym) (**4**) with the diaza linkers were obtained. These are the first oxo-rhenium(V)

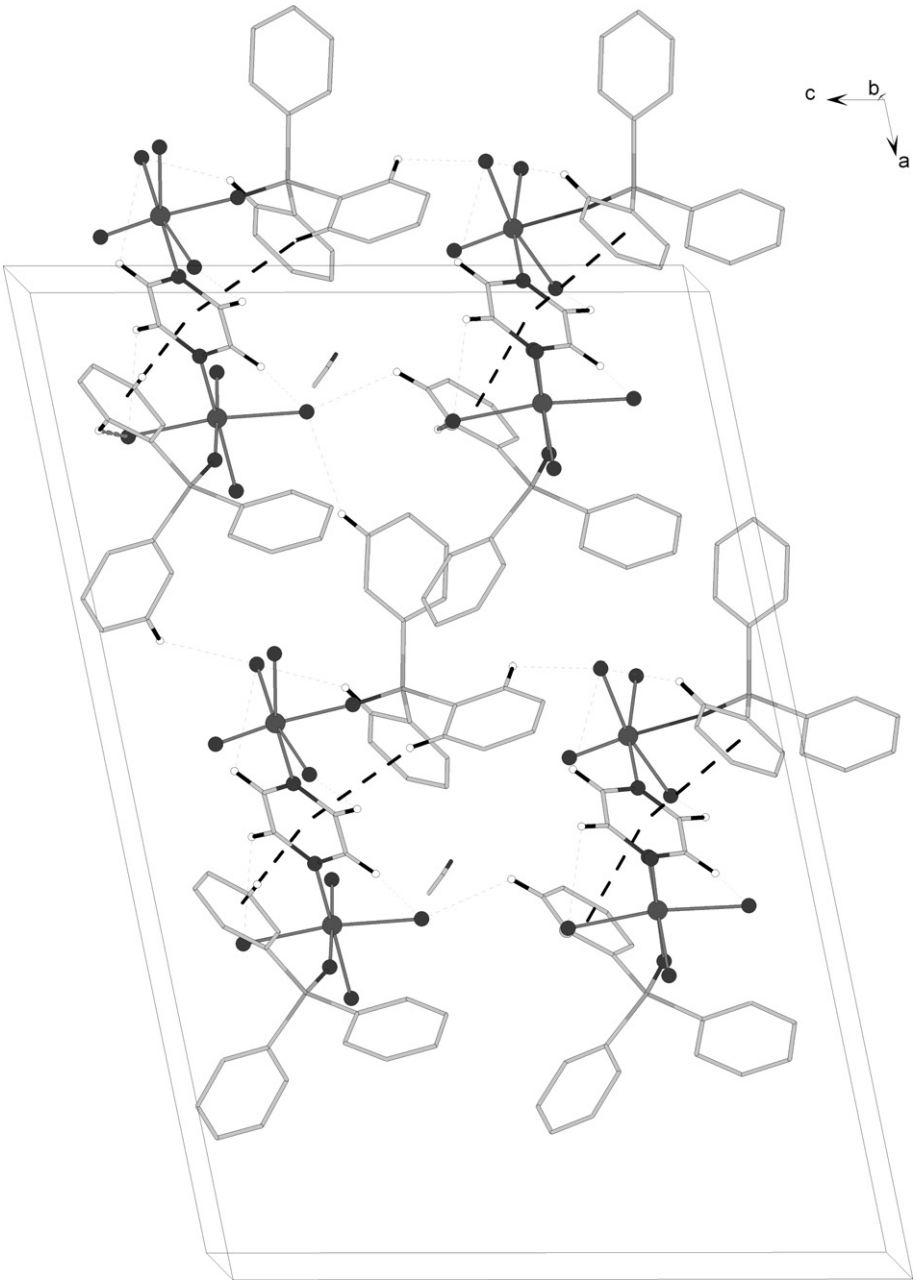


Fig. 5. Packing diagram for **4** showing intramolecular π–π stacking interactions (dashed line) and hydrogen bonding interactions (dotted line), hydrogens not involved in any interaction have been omitted for clarity.

complexes with bridging diaza ligands. All complexes were characterized in solution, three of them **1**, **3** and **4** in a solid state as well. The crystallographic analysis of mono **1** and dinuclear complexes **3**, **4** reveal uncommon examples of one or two intramolecular π–π interactions. The π–π stacking forces impose the geometric constrains on the two rhenium units in **3** and **4** as well. Furthermore, X-ray diffraction studies on **3** and **4** showed that the two units are twisted about Re–(N ∼ N)–Re linkage. The nitrogen ligands are stacked with two phenyl rings corresponding to two molecules of triphenylphospine oxide. ^{1}H NMR studies reveal that $ReOCl_3(OPPh_3)$ moiety induces insignificant coordination shifts in the hydrogens of the diaza ring. The resonances attributed to heterocycle ligands experience either slightly downfield or even upfield ($\Delta\delta = -0.19$ for **4**) chemical shifts. The NMR behaviour of the diaza rings manifests unique π–π stacking interactions that are considered to enhance stability of the structure and contribute significantly to inertness to further substitution reaction.

Acknowledgement

We would like to thank Dr Jerzy Sokolnicki from our Department for attempts to record luminescence excitation spectra.

Appendix A. Supplementary data

CCDC 657244, 657245 and 657246 contains the supplementary crystallographic data for **1**, **3** and **4**. These data can be obtained free of charge via http://www.ccdc.cam.ac.uk/conts/retrieving.html, or from the Cambridge Crystallographic Data Centre, 12 Union Road, Cambridge CB2 1EZ, UK; fax: (+44) 1223-336-033; or e-mail: deposit@ccdc.cam.ac.uk. Supplementary data associated with this article can be found, in the online version, at doi:10.1016/j.poly.2008.02.033.

References

[1] W.A. Nugent, J.M. Mayer, Metal–Ligand Multiple Bonds, Wiley, New York, 1988.
[2] R.H. Holmes, Chem. Rev. 87 (1987) 1401.
[3] D.E. Grove, G. Wilkinson, J. Chem. Soc. A (1966) 1224.
[4] J.C. Bryan, R.E. Stenkamp, T.H. Tulip, J.M. Mayer, Inorg. Chem. 26 (1987) 2283.
[5] K.A. Conner, R.A. Walton, in: G. Wilkinson, R.D. Gillard, J.A. McCleverty (Eds.), Comprehensive Coordination Compounds, The Synthesis, Reactions, Properties and Applications of Coordination Compounds, vol. 4, Pergamon Press, Oxford, UK, 1987, p. 125.
[6] M. M Abu-Omar, S.I. Kahn, Inorg. Chem. 37 (1998) 4979.
[7] B.D. Sherry, R.N. Loy, F. Toste, J. Am. Chem. Soc. 126 (2004) 4510.
[8] E. Iengo, E. Zangrando, S. Mestroni, G. Fronzoni, M. Stener, E. Alessio, J. Chem. Soc., Dalton Trans. (2001) 1338.
[9] R.V. Slone, J. Hupp, C.L. Stern, T.E. Albrecht-Schmitt, Inorg. Chem. 35 (1996) 4096.
[10] B. Manimaran, T. Rajendran, Yi.-L. Lu, G.-H. Lee, S.-M. Peng, K.-L. Lu, J. Chem. Soc., Dalton Trans. (2001) 515.
[11] T. Rajendran, B. Manimaran, R.-T. Liao, R.-J. Lin, P. Thanasekaran, G.-H. Lee, S.-M. Peng, Y.-H. Liu, I.-J. Cjhang, S. Rajagopal, K.-L. Lu, Inorg. Chem. 42 (2003) 6388.
[12] F.E. Kuhn, A.M. Santos, P.W. Roesky, E. Herdtweck, W. Scherer, P. Gisdakis, C.Di. Valentin, I.V. Yudanov, N. Rosch, Chem. Eur. J. 5 (1999) 3603.
[13] D.D. Perrin, W.L.F. Armarego, Purification of Laboratory Chemicals, 3rd ed., Pergamon Press, Oxford, 1998.
[14] G.M. Sheldrick, SHELXL 97, Program for Crystal Structure Refinement, University of Götingen, 1997.
[15] L. Hansen, E. Alessio, M. Iwamoto, P.A. Marzilli, L.G. Marzilli, Inorg. Chim. Acta 240 (1995) 413.
[16] H.W. Choi, E.L. Muetterties, J. Am. Chem. Soc. 104 (1982) 153.
[17] D.K. Lavallee, E.B. Fleischer, J. Am. Chem. Soc. 94 (1972) 2583.
[18] E. Alesio, E. Zangrando, E. Iengo, M. Macchi, P.A. Marzilli, L.G. Marzilli, Inorg. Chem. 39 (2000) 294.
[19] U. Abram, in J.A. McCleverty, T.J. Mayer (Eds.), Comprehensive Coordination Chemistry II – From Biology to Nanotechnology, vol. 5, Elsevier Ltd., Oxford, UK, 2004, p. 271.
[20] W.K. Rybak, A. Skarżyńska, L. Szternberg, Z. Ciunik, T. Głowiak, Eur. J. Inorg. Chem. (2005) 4964.
[21] M.S. Ram, L.M. Skeens-Jones, C.S. Johson, X.L. Zhang, C. Stern, D.I. Yoon, D. Selmarten, J.T. Hupp, J. Am. Chem. Soc. 117 (1995) 1411.
[22] J.M. Mayer, Inorg. Chem. 27 (1988) 3899.
[23] I. Chakraborty, S. Bhattacharyya, S. Banerjee, B.K. Dirghandi, A. Chakravorty, J. Chem. Soc., Dalton Trans. (1999) 3747.
[24] S. Fortin, A.L. Beauchamp, Inorg. Chim. Acta 279 (1988) 159.
[25] S. Das, A. Chakravorty, Eur. J. Inorg. Chem. (2006) 2285.
[26] C.J. Janiak, Chem. Soc. Dalton Trans. (2000) 3885.
[27] A. Magistrato, P.S. Pregosin, A. Albinati, U. Rothlisberger, Organometallics 20 (2001) 4178.
[28] F. Yang, P.E. Fanwick, C.P. Kubiak, Organometallics 18 (1999) 4222.
[29] K. Selvakumar, M. Valentini, P.S. Pregosin, A. Albinati, F. Eisentrager, Organometallics 19 (2000) 1299.
[30] D.H. Gibson, M.S. Mashuta, X. Yin, Acta Crystallogr., Sect. C 60 (2004) 366.

recrystallized from a solution of absolute ethanol/chloroform (v/v, 1/1) and dried at room temperature; yield: 12.11 g (75%) as a white solid; m.p. 220 °C. ^{1}H NMR (300 MHz; DMSO-d^6; J (Hz), Me_4Si at 25 °C, ppm) δ = 0.887 (t, $^3J_{H-H}$ = 7.2, 3H, –CH_3), 1.313–1.773 (m, 8H, –CH_2), 4.092 (t, $^3J_{H-H}$ = 6.6, 2H, –OCH_2), 6.864 (1H, d, $^3J_{H-H}$ = 6.9, –C_5H), 6.874 (1H, s, –C_3H), 7.117 (2H, d, $^3J_{H-H}$ = 9.0, —$C_{3'}$H), 7.710 (d, $^3J_{H-H}$ = 9.0, 1H, –C_6H), 7.855 (d, $^3J_{H-H}$ = 5.4, 2H, —$C_{3''}$H), 8.064 (d, $^3J_{H-H}$ = 8.7, 2H, —$C_{2'}$H), 8.704 (s, 1H, –NCH), 8.800 (d, $^3J_{H-H}$ = 8.1, 2H, —$C_{2''}$H), 11.400 (br s, 1H, –NH), and 12.311 (br s, 1H, Ph–OH); ^{13}C{^{1}H} NMR (75.45 MHz; DMSO-d^6; Me_4Si at 25 °C, ppm) δ = 163.841 (–COO), 163.306 (py-CO), 161.353 (—$C_{4'}$), 158.344 (–NCH), 153.136 (–C_2), 150.399 (–C_4), 148.001 (—$C_{2''}$), 139.990 (—$C_{4''}$), 132.095 (–C_6), 129.812 (—$C_{2'}$), 121.512 (—$C_{3''}$), 120.556 (—$C_{1'}$), 116.798 (–C_1), 114.713 (–C_5), 113.436 (—$C_{3'}$) and 109.974 (–C_3). m/z (EI): 121 (py-CONH$^+$, 100), 205 (C_6H_{13}-Ph-CO$^+$, 88), IR (KBr)/cm^{-1}: 3435br ν(O–H)$_{phenol}$, 3279 ν_s(N–H)$_{amide}$, 1726vs ν(>C=O), 1626w ν(C=N), 1253s ν_{as}(C–O)$_{esteric}$, 1153s ν(C–O)$_{phenol}$. *Anal.* Calc. for $C_{26}H_{27}N_3O_5$ (461.51): C, 67.66; H, 5.90; N, 9.10. Found C, 67.58; H, 5.88; N, 9.07%.

2.2.2. Synthesis of [Ni(HL)$_2$]

The micro-crystalline product was recrystallized from a solution of absolute ethanol/chloroform (v/v, 1/1) and dried at room temperature; yield: 0.67 g (68%) as an orange coloured solid; m.p. 310 °C (decompose). ^{1}H NMR (300 MHz; $CDCl_3$; J(Hz), Me_4Si) δ = 0.922 (t, $^3J_{H-H}$ = 6.0, 3H, –CH_3), 1.255–1.852 (m, 8H, –CH_2), 4.053 (t, $^3J_{H-H}$ = 6.6, 2H, –OCH_2), 6.787 (d, $^3J_{H-H}$ = 6.9, 1H, –C_5H), 6.850 (s, 1H, –C_3H), 6.972 (d, $^3J_{H-H}$ = 8.4, 2H, —$C_{3'}$H), 7.129 (d, $^3J_{H-H}$ = 8.5, 1H, –C_6H), 8.103 (d, $^3J_{H-H}$ = 7.8, 2H, —$C_{3''}$H), 8.164 (d, $^3J_{H-H}$ = 8.0, 2H, —$C_{2'}$H), 8.770 (s, 1H, –NCH), 8.805 (d, $^3J_{H-H}$ = 7.9, 2H, —$C_{2''}$H), 11.399 (br s, 1H, –NH), and (Ph–OH) absent; ^{13}C{^{1}H} NMR (75.45 MHz; $CDCl_3$; Me_4Si at 25 °C, ppm) δ = 163.933 (–COO), 163.504 (py-CO), 164.132 (–NCH), 150.713 (–C_4), 132.433 (–C_6), 132.054 (—$C_{2'}$), 120.936 (—$C_{1'}$), 114.549 (—$C_{3'}$) and 110.791 (–C_3). m/z (FAB): 121 (py-CONH$^+$, 100), IR (KBr)/cm^{-1}: 3280br ν_s(N–H)$_{amide}$, 1722vs ν(>C=O), 1612w ν(C=N), 1255s ν_{as}(C–O)$_{esteric}$, 1150s ν(C–O)$_{phenol,}$ 485s ν(Ni–N), 450s ν(Ni–O). *Anal.* Calc. for $C_{52}H_{52}N_6O_{10}Ni$ (979.70): C, 63.75; N, 8.58; N_2H_4, 6.53; Ni, 5.99. Found: C, 63.72; N 8.51; N_2H_4, 6.50; Ni, 5.96%.

2.2.3. Synthesis of [Zn(HL)$_2$]

Yield: 0.71 g (72%) as a yellow solid; m.p. 230 °C (decompose); ^{1}H NMR (300 MHz; C_5D_5N; J (Hz), Me_4Si) δ = 0.847 (t, $^3J_{H-H}$ = 6.2, 3H, –CH_3), 1.235–1.718 (m, 8H, –CH_2), 3.981 (t, $^3J_{H-H}$ = 6.5, 2H, –OCH_2), 6.774 (d, $^3J_{H-H}$ = 6.0, 1H, –C_5H), 6.850 (s, 1H, –C_3H), 7.196 (d, $^3J_{H-H}$ = 8.0, 2H, —$C_{3'}$H), 7.438 (d, $^3J_{H-H}$ = 8.1, 1H, –C_6H), 7.387 (d, $^3J_{H-H}$ = 8.0, 2H, —$C_{3''}$H), 7.583 (d, ^3J_H–H = 8.0, 2H, —$C_{2'}$H), 8.750 (s, 1H, –NCH), 8.791 (d, $^3J_{H-H}$ = 7.9, 2H, —$C_{2''}$H), 11.394 (br s, 1H, –NH), and (Ph–OH) absent; ^{13}C{^{1}H} NMR (75.45 MHz; C_5D_5N; Me_4Si at 25 °C, ppm) δ = 163.930 (–COO), 172.415 (py-CO), 168.517 (–NCH), 150.369 (–C_4), 132.624 (–C_6), 114.979 (—$C_{3'}$) and 108.213 (–C_3). m/z (FAB): 121 (py-CONH$^+$, 100), IR (KBr)/cm^{-1}: 3280 ν_s(N–H)$_{amide}$, 1724vs ν(>C=O), 1608w ν(C=N), 1253s ν_{as}(C–O)$_{esteric}$, 1148s ν(C–O)$_{phenol,}$ 482s ν(Zn–N), 448s ν(Zn–O); the IR data for [M(HL)$_2$] (M = Mn, Co and Cu) are similar. *Anal.* Calc. for $C_{52}H_{52}N_6O_{10}Zn$(984.30): C, 63.32; N, 8.52; N_2H_4, 6.50; Zn, 6.63. Found: C, 63.29; N 8.50; N_2H_4, 6.47; Zn, 6.60%.

2.2.4. Synthesis of [ZnL · 2py]

Light-yellow coloured crystalline solid; ^{1}H NMR (300 MHz; C_5D_5N; J (Hz), Me_4Si) δ = 0.845 (t, $^3J_{H-H}$ = 6.1, 3H, –CH_3), 1.230–1.711 (m, 8H, –CH_2), 3.979 (t, $^3J_{H-H}$ = 6.3, 2H, –OCH_2), 6.769 (d, $^3J_{H-H}$ = 6.1, 1H, –C_5H), 6.852 (s, 1H, –C_3H), 7.211 (d, $^3J_{H-H}$ = 8.3, 2H, —$C_{3'}$H), 7.430 (d, $^3J_{H-H}$ = 8.0, 1H, –C_6H), 7.390 (d, $^3J_{H-H}$ = 8.3, 2H, —$C_{3''}$H), 7.580 (d, $^3J_{H-H}$ = 7.9, 2H, —$C_{2'}$H), 8.755 (s, 1H, –NCH), 8.788 (d, $^3J_{H-H}$ = 8.2, 2H, —$C_{2''}$H); ^{13}C{^{1}H} NMR (75.45 MHz; C_5D_5N; Me_4Si at 25 °C, ppm) δ = 164.330 (–COO), 170.517 (–NCH), 151.468 (–C_4), 131.689 (–C_6), 114.980 (—$C_{3'}$) and 108.218 (–C_3), IR (KBr)/cm^{-1}: 1725vs ν(>C=O), 1605s ν(C=N), 1256s ν_{as}(C–O)$_{esteric}$, 1140s ν(C–O)$_{phenol}$, 478s ν(Zn–N), 455s ν(Zn–O). *Anal.* Calc. for $C_{36}H_{35}N_5O_5Zn$ (683.08): C, 63.30; N, 10.25; N_2H_4, 4.68; Zn, 9.57. Found: C, 63.29; N 10.21; N_2H_4, 4.65; Zn, 9.55%.

2.3. Physical measurements

The ^{1}H and ^{13}C NMR spectra were recorded on a JEOL AL-300 MHz FTNMR multinuclear spectrometer; C, H, and N contents were micro analyzed on Elemental Vario EL III Carlo Erba 1108 analyzer. Infrared spectra were recorded on JASCO FT/IR (model-5300) spectrophotometer in the 4000–400 cm^{-1} region. The mass spectra were recorded on JEOL SX-102 (EI/FAB) mass spectrometers. The UV–Vis spectra were recorded on Shimadzu spectrophotometer, model, Pharmaspec, UV 1700. Magnetic susceptibility measurements were made at room temperature on a Cahn-Faraday balance.

2.4. X-ray crystallographic data collection and refinement of the structure

X-ray data for compounds **H_2L** [***ab83m***] and [**ZnL** · 2**py**] [***ab64m***] were collected at room temperature using a Bruker Smart Apex CCD diffractometer with graphite monochromated Mo Kα radiation (λ = 0.71073 Å) with ω-scan method. Preliminary lattice parameters and orientation matrices were obtained from four sets of frames. Unit cell dimensions were determined from the setting angles of 9745/8981 reflections in the range of 2.69° < θ < 27.85°/ 2.25° < θ < 27.37°. Integration and scaling of intensity data was accomplished using SAINT program [8]. The structure was solved by direct methods using SHELXS97 [9] and refinement was carried out by full-matrix least-squares technique using SHELXL97 [9]. Anisotropic displacement parameters were included for all non-hydrogen atoms. In [ZnL · 2py], the atoms C22, C23 and C24 are disordered over two positions and their site-occupation factors were refined to 0.737(6) and 0.263(6). The distance of the disordered side chain atoms were restraint with DFIX command. In H_2L, all N-bound H atoms, O-bound H atoms and H atoms of the water molecules were located in a difference Fourier map and their positions and isotropic parameters were refined. All other hydrogen atoms were positioned geometrically and treated as riding atoms, with C–H distances in the range of 0.93–0.97 Å and with U_{iso}(H) values of 1.5U_{eq}(C) for methyl hydrogen and 1.2U_{eq}(C) for other hydrogen atoms.

Table 1
Magnetic and electronic spectral data[a] of complexes of H_2L

Complex	Colour	μ_{eff} (BM)	d–d transitions (cm^{-1})	Transition		Assignment
				Ground state(s)	Excited state(s)	
[Mn(HL)$_2$]	yellow	5.14	30120, 24038	$^6A_{1g}$	^4E_g(D); $^4A_{1g}$	octahedral
[Co(HL)$_2$]	reddish brown	diamag.	13333, 23310	$^2B_2$; ^2E	$^2A_1$; $^2A_1$	square pyramidal[b] (l.s.) (M–M bonding)
[Ni(HL)$_2$]	yellow	diamag.	23474, 25773	$^1A_{1g}$	$^1A_{2g}$; $^1B_{1g}$	square planar
[Cu(HL)$_2$]	yellowish green	3.67	15798	xy	x^2–y^2	octahedral

[a] Spectra recorded in solutions of DMSO/chloroform (1:1 v/v).
[b] The ground state configuration with increasing energy: (xy, $(b_2)^2$); (xz, yz, (e))^4; (z^2, (a_1)).

Table 2
Crystal data and structure refinement parameters of ligand H_2L [***ab83m***] and [ZnL · 2py] [***ab64m***]

Empirical formula	$C_{26}H_{29}N_3O_6$	$C_{36}H_{35}N_5O_5Zn$
Formula weight	479.52	683.06
Cell axes (Å)		
a	11.1888(6)	10.2286(8)
b	13.1068(7)	11.6022(9)
c	18.2186(10)	17.0491(13)
Cell angles (°)		
α	80.904(1)	108.619(1)
β	74.771(1)	90.103(1)
γ	73.494(1)	115.916(1)
Cell volume *V* (Å)^3	2461.6(2)	1700.7(2)
Crystal system	triclinic	triclinic
Crystal size (mm)	0.19 × 0.14 × 0.09	16 × 10 × 0.06
Temperature (K)	273(2)	293(2)
Wavelength (Å)	0.71073	0.71073
Space group	$P\bar{1}$	$P\bar{1}$
F(000)	1016	712
Density (Mg/m^3)	1.294	1.334
No form. Unit Z	4	2
Absorption coefficient (mm^{-1})	0.093	0.771
Reflections collected/unique [*R*(int)]	23929/8669 [0.0229]	16496/5968 [0.0204]
Completeness to θ = 25.00 (%)	99.7	99.7
Absorption correction	none	none
Refinement method	full-matrix least-squares on F^2	full-matrix least-squares on F^2
Data/restraints/parameters	8669/0/665	5968/79/452
H min, max	−13, 13	−12, 12
K min, max	−15, 15	−13, 13
L min, max	−21, 21	−20, 20
θ min, max	1.16, 25.0	2.02, 25.0
Goodness-of-fit on F^2	1.029	1.044
Final *R* indices [$I > 2\sigma(I)$]	R_1 = 0.0403, wR_2 = 0.1020	R_1 = 0.0353, wR_2 = 0.0948
R indices (all data)	R_1 = 0.0502, wR_2 = 0.1107	R_1 = 0.0387, wR_2 = 0.0975
Largest difference peak and hole (e Å^{-3})	0.202 and −0.195	0.289 and −0.194

3. Results and discussion

3.1. Physical properties and spectral investigation

The white-coloured Schiff-base ligand (H_2L) is soluble in hot chloroform, DMSO, DMF and pyridine but insoluble in water, methanol, ethanol, and acetonitrile; the orange-coloured Ni(II) complex, $[Ni(HL)_2]$, is soluble in chloroform, and hot DMSO and DMF; $[Zn(HL)_2]$/[ZnL · 2py] is only soluble in hot/cold pyridine; all other complexes are soluble in DMSO, DMF and pyridine. The Schiff-base showed a nematic meso-phase at 168 °C under a polarizing microscope while none of the corresponding metal complexes were found to show any mesogenic behaviour. The structures and purity of the parent ligand and of the complexes were checked and confirmed by elemental analyses and IR, ^{1}H NMR and EI/FAB mass spectra.

The room temperature magnetic moments and electronic spectral data of the present complexes are included in Table 1. The overall geometry around the metal ion has been assigned (Table 1) not only on the basis of μ_{eff} values and the nature of the electronic spectra, but also on the basis of denticity of the ligand (vide IR and NMR) and the number of the ligands coordinated to the metal ion (vide elemental analyses). The μ_{eff} values imply anti-ferromagnetic/ferromagnetic type interactions in the Mn(II) and Cu(II) complexes respectively. The Mn^{II} complex provides with extremely weak bands in the electronic spectrum in an octahedral environment of the metal ion [10]. The diamagnetic reddish brown complex, $[Co(HL)_2]$, may be understood to have a low-spin square-pyramidal geometry with M–M bonding [11]. The yellow-coloured complex, $[Ni(HL)_2]$, implies square-planar [12] type geometry; it is fairly common practice to assign the first band to the $^1A_{2g} \leftarrow {}^1A_{1g}$ transition and the second major band to the $^1B_{1g} \leftarrow {}^1A_{1g}$ transition assuming a square-planar geometry [13].

In the IR spectrum of H_2L the broad absorptions centered at 3435 and 3279 cm^{-1} may be assigned to the $\nu(O–H)_{phenol}$ and $\nu_s(N–H)_{amide}$ vibration [14]; further, the strong bands occurring at 1726 and 1253 cm^{-1} may be assigned [14] to $\nu(>C=O)$ and $\nu(C–O)$ modes of aromatic ester; the band occurring at 1626 cm^{-1} may be assigned to $\nu(C=N)$ absorption of the azomethine moiety; these bands are shifted to lower frequencies in the complexes, indicating that the nitrogen atom of the azomethine group is coordinated to the metal ion [15]. Coordination through a nitrogen atom of the ligand is also implied by the appearance of a new band in the complexes in the region, 468–485 cm^{-1}, assignable to $\nu(M–N)$ [16,17]. Coordination through phenolate oxygen to the metal ion is implied by the shifts of the $\nu(C–O)$ band in the complexes [18] and by the appearance of new bands, assignable to $\nu(M–O)$, in the 443–455 cm^{-1} region in the spectra of the complexes.

A comparison of the ^{1}H and $^{13}C\{^1H\}$ NMR spectral data of the ligand with those of the Ni(II) and Zn(II) complexes shows the absence of the phenolic-OH signal (12.311 ppm) and a significant shift in the peak position of the –N=CH signal [from 8.704 ppm of the ligand to 8.770, 8.750, and 8.755 ppm in $[Ni(HL)_2]$, $[Zn(HL)_2]$ and [ZnL · 2py], respectively] and the absence of the –N–H signal at 11.400 ppm exclusively in [ZnL · 2py], a complex of the di-deprotonated ligand, imply bonding through the phenolate oxygen and azomethine nitrogen atoms. Similar shifts observed in the $^{13}C\{^1H\}$ NMR spectra were of considerable magnitude in the case of the carbon atoms directly attached to the bonding atoms and

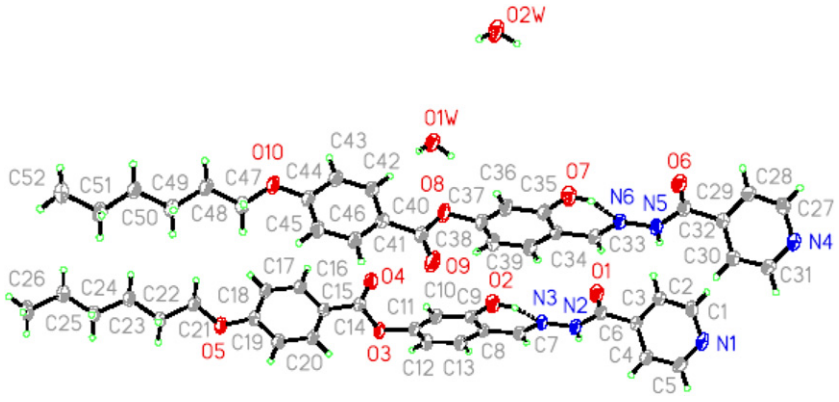


Fig. 1. Molecular structure and atomic labeling scheme of the H_2L [***ab83m***] of 30% ellipsoid probability.

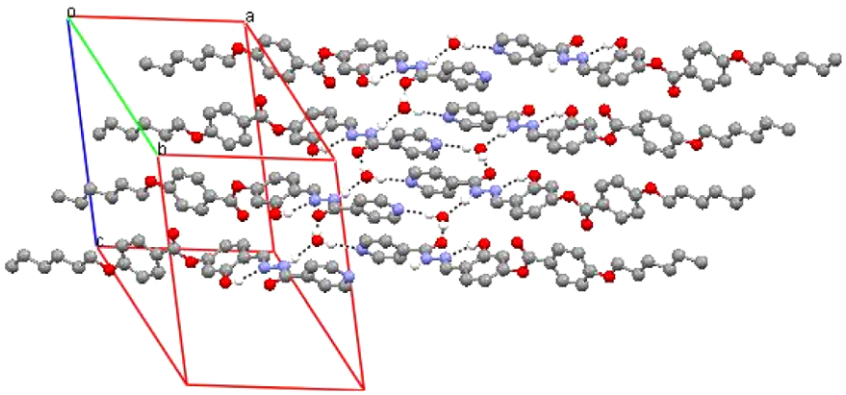


Fig. 2. Packing of molecules in the unit cell of H_2L [***ab83m***] showing intermolecular and intramolecular H-bonding.

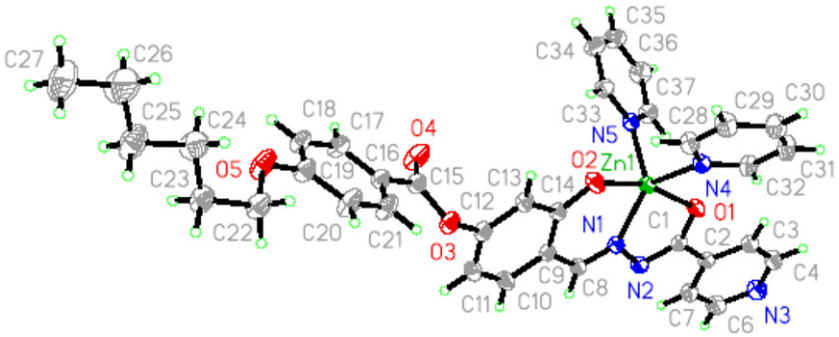


Fig. 3. Molecular structure and atomic labeling scheme of [ZnL · 2py] [***ab64m***] of 30% ellipsoid probability.

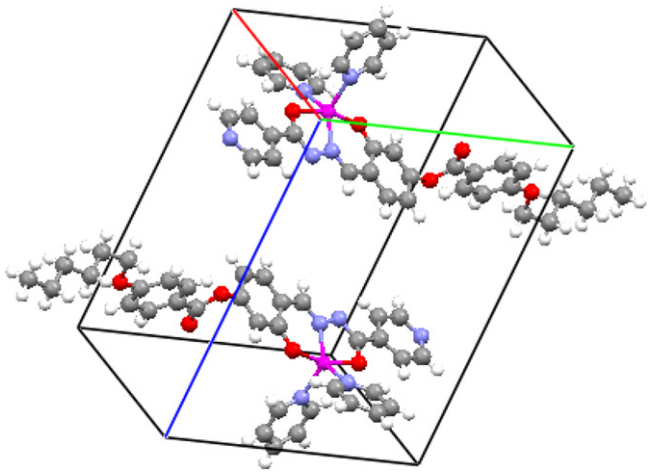


Fig. 4. Packing diagram of molecules [ZnL · 2py] [***ab64m***] along *a*-axis in the unit cell.

amidic carbon. Thus, the NMR spectral data imply bi-dentate bonding (>C=N, and phenolate oxygen) of HL^- in [$Ni(HL)_2$] and tri-dentate bonding (>C=N, phenolate oxygen and amidic oxygen) of HL^- and L^{2-}, respectively in [Zn(HL)2] and [ZnL · 2py].

3.2. Crystal structure and molecular association

Both ligands [H_2L] [***ab83m***] and [ZnL · 2py] [***ab64m***] are crystallized in triclinic space group, *viz.*, $P\bar{1}$ with $Z = 4$ and $Z = 2$,respectively. The crystal data and structure refinement details for [H_2L] [***ab83m***] and [ZnL · 2py] [***ab64m***] are given in Table 2. The asymmetric unit of H_2L contains two crystallographically independent molecules and two water molecules, while [ZnL · 2py] comprises one ligand molecule and two pyridine solvent molecules in the asymmetric unit. The molecular structure and atomic labeling scheme of the ligand and the Zn(II) complex are as shown in Figs. 1 and 3 and the packing diagrams of the ligand and the complex are as shown in Figs. 2 and 4.

The bond distances and angles for the [ZnL · 2py] complex are shown in Table 3. As per the crystal structure of the complex, the ligand coordinates to the Zn(II) ion through phenolate oxygen (O(2)), amidic oxygen (O(1))and azomethine nitrogens (N(1)); further, two pyridine molecules act as solvent molecules, thus, rendering the overall geometry around Zn(II) to distorted square pyramid. The details of the hydrogen-bonded geometry of H_2L are tabulated in Table 4. The crystal structure of H_2L is stabilized by both intra- and intermolecular N–H...O, O–H...N and O–H...O hydrogen bond interactions. The two water molecules bridge

Table 3
Bond lengths (Å) and angles (°) involved in the square pyramidal unit of the complex [ZnL · 2py] [***ab64m***]

N(1)–Zn(1)	2.0370(16)	N(1)–Zn(1)–N(5)	115.83(6)	O(1)–Zn(1)–N(4)	93.71(6)
N(4)–Zn(1)	2.0793(17)	N(1)–Zn(1)–N(4)	140.04(7)	O(2)–Zn(1)–N(1)	88.80(6)
N(5)–Zn(1)	2.0737(17)	N(5)–Zn(1)–N(4)	103.60(7)	O(2)–Zn(1)–N(4)	91.50(7)
O(1)–Zn(1)	2.0764(14)	N(1)–Zn(1)–O(1)	76.96(6)	O(2)–Zn(1)–N(5)	98.83(7)
O(2)–Zn(1)	1.9840(14)	N(5)–Zn(1)–O(1)	95.51(6)	O(2)–Zn(1)–O(1)	163.15(7)

Table 4
Hydrogen bonds geometry (Å,°) for the ligand H_2L [***ab83m***]

D–H...A	d(D–H)	d(H...A)	d(D...A)	d(D...A)	Symmetry
N(2)–H(2N)...O(1W)#1	0.92(2)	1.87(2)	2.793(2)	178(2)	$x+1, y, z$
N(5)–H(5N)...O(2W)#1	0.90(2)	1.91(2)	2.804(2)	173(2)	$x+1, y, z$
O(2)–H(2O)...N(3)	0.91(2)	1.80(2)	2.613(2)	146(2)	x, y, z
O(7)–H(7O)...N(6)	0.86(2)	1.82(2)	2.587(2)	148(2)	x, y, z
O(1W)–H(1W)...N(4)#2	0.89(2)	1.94(2)	2.828(2)	174(2)	$-x+2, -y+2, -z$
O(1W)–H(2W)...O(6)#3	0.86(2)	1.99(2)	2.846(2)	174(2)	$x, y-1, z$
O(2W)–H(3W)...O(1)#4	0.82(2)	2.17(2)	2.986(2)	171(2)	$x-1, y, z$
O(2W)–H(4W)...N(1)#2	0.88(2)	1.97(3)	2.846(2)	173(2)	$-x+2, -y+2, -z$

the two ligand molecules through O–H...N and O–H...O hydrogen bonds, thereby forming an infinite hydrogen bonded network chain along the crystallographic *a* axes. Only the non-conventional interactions, *viz*., C–H...O and C–H...N, are observed in the crystal structure of the [ZnL · 2py] complex.

4. Conclusion

The mesogenic (nematic) Schiff-base, *N*-(4″-pyridylcarboxamido)-4-(4′-hexyloxy-benzoato)salicylaldimine (H_2L) coordinates to M(II) (M = Mn, Co, Ni, Cu, Zn) as a uninegative tri-dentate species to yield non-mesogenic complexes of the type, $[M(HL)_2]$, which are believed to involve M–M bonding. The complex $[Zn(HL)_2]$ gives rise, from a solution of pyridine, to single crystals of the non-mesogenic square-pyramidal complex, [ZnL · 2py]; as per the crystal structure, the complex involves di-negative tridentate species of the ligand, L^{2-}, which coordinates to the metal ion through phenolate oxygen, amidic oxygen and azomethine nitrogen atoms.

5. Supplementary data

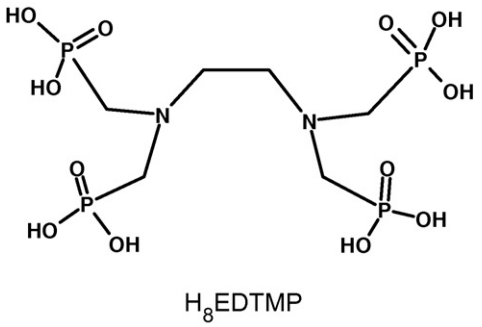
CCDC 672486 and 672487 contain the supplementary crystallographic data for this paper. These data can be obtained free of charge via http://www.ccdc.cam.ac.uk/conts/retrieving.html, or from the Cambridge Crystallographic Data Centre, 12 Union Road, Cambridge CB2 1EZ, UK; fax: (+44) 1223-336-033, or e-mail: deposit@ccdc.cam.ac.uk.

Acknowledgements

We wish to acknowledge recording of FAB Mass spectra and elemental analyses at the Central Drug Research Institute, Lucknow. One of the authors, Prof. T.R. Rao, gratefully acknowledges the financial grant received from the Council of Scientific and Industrial Research, New Delhi [Vide Grant No. 01(1834)/03/EMR-II], the University Grants Commission [Vide Grant No. F.12-26/2003 (S.R.)] and the Department of Science and Technology, New Delhi [Vide Grant No. SR/S1/IC-26/2004].

References

[1] M.B. Hursthouse, S.A.A. Jayaweera, A. Quick, J. Chem. Soc., Dalton Trans. (1979) 279.
[2] A. Haran, J. Gairin, G. Commenges, Inorg. Chim. Acta 46 (1980) 62.
[3] M. Gallego, M. Gareia-Varges, M. Valcaral, Analyst 104 (1979) 613.
[4] Angad Kumar Singh, Sanyucta Kumari, K. Ravi Kumar, B. Sridhar, T.R. Rao, Polyhedron 27 (2008) 181.
[5] N.V.S. Rao, M.K. Paul, T.R. Rao, Archana Prasad, Liquid Cryst. 29 (2002) 1243.
[6] T.R. Rao, Archana Prasad, Synth. React. Inorg. Met-Org. Nano-Metal Chem. 35 (2005) 299.
[7] A. Weisberger, F.S. Praskver, Organic Solvents, International Publishers Inc., New York, 1956. p. 1263.
[8] SMART & SAINT, Software Reference manuals, Versions 6.28a & 5.625, Bruker Analytical X-ray Systems Inc., Madisom, WI, USA, 2001.
[9] G.M. Sheldrick, SHELXS97 and SHELXL97 Programs for Crystal Structure Solution and Refinement, University of Gottingen, Germany, 1997.
[10] L. Banci, A. Bencini, C. Benelli, D. Gatteschi, C. Zanchin, Struct. Bond. 5 (1982) 38.
[11] G. Singh, P.S.S.J. Shastry, R.K. Lonibala, T.R. Rao, Synth. Inorg. Met. Org. Chem. 22 (1992) 1041.
[12] B.N. Figgis, J. Lewis, S.J. Lippard, Progress in Inorganic Chemistry, vol. 6, John Wiley & Sons, New York, 1964, p. 197.
[13] D. Nicholls, Comprehensive Inorganic Chemistry, vol. 3, Pergamon Press, Oxford, 1983, p. 1109 (Chapter 42).
[14] R.M. Silverstein, F.X. Webster, Spectroscopic Identification of Organic Compounds, 6th ed., John-Wiley & Sons. Inc., New York, 2002.
[15] P. Sousa, J.A.G. Vazquez, J.A. Masaquer, Trans. Met. Chem. 9 (1984) 318.
[16] S.K. Agrawal, D.R. Tuflani, R. Gupta, S.K. Hajela, Inorg. Chim. Acta 129 (1987) 257.
[17] N. Saha, S. Sinha, Ind. J. Chem. 29 (1990) 292.
[18] K. Nakamoto, Infrared and Raman Spectra of Inorganic and Coordination Compounds, Wiley, New York, 1978.



Scheme 1.

absorption, the last being calculated from the crystal habit captured from photoscans. The positions of Eu atoms were found from Patterson maps, the rest of the non-H atoms were found from difference Fourier maps. The positions of the C-bonded hydrogen atoms were calculated geometrically. The refinement was full-matrix with all ordered non-H atoms being anisotropic. All computations were performed using SHELXS 97 and SHELXL 97 programs [7]. The molecular graphics was prepared with DIAMOND.[1] The crystal data and structure refinement for **I** are as follows: empirical formula $C_{24}H_{146}Eu_4K_{12}N_8O_{93}P_{16}$, $M = 3608.04$, $T = 100$ K, λ/Å = 0.71073, tetragonal $I\bar{4}c2$, $Z = 8$, $a = 27.43(2)$ Å, $c = 33.17(3)$ Å, $V = 24960(30)$ Å^3, $\mu = 2.702$ mm^{-1}, $\rho_{calc} = 1.920$ g cm^{-3}, $F(000) = 14640$, crystal size = 0.4 × 0.3 × 0.2 mm, $\theta = 3$–28.5°, index ranges = $-36 \leqslant h \leqslant 28$, $-36 \leqslant k \leqslant 35$, $-43 \leqslant l \leqslant 43$, reflections collected/unique = 85266/14973 ($R_{int} = 0.0943$). Final R indices [$I > 2\sigma(I)$] $R(F) = 0.0562$, $R_w(F^2) = 0.1264$ and $R(F) = 0.0793$, $R_w(F^2) = 0.1341$ (all data). Data completeness to $2\theta = 28.6°$, 95.6%. Largest difference in peak and hole 1.024 and −0.819 e Å^{-3}.

2.3. Spectroscopy

The luminescence spectra ($\lambda_{exc} = 394$ nm), corrected for the lamp characteristics, were measured on a SLM Aminco 500 spectrofluorometer at 298 and 77 K. The luminescence decay curves were detected on a device equipped with a Hamamatsu photomultiplier and a Tektronix TDS-3052 digital oscilloscope. The sample was excited with a N_2-pumped dye laser with the monitored emission at 612 nm.

The IR spectra of the complexes in KBr pellets and nujol suspensions were recorded in the range 50–4000 cm^{-1} with a Bruker IF S66 spectrometer.

Electronic absorption spectra were recorded on a Cary 500 UV–Vis–NIR spectrophotometer at 298 K. The oscillator strengths (P) were determined using the equation:

$$P = 4.32 \times 10^{-9}(cd)^{-1} \int A(\sigma)\mathrm{d}\sigma \qquad (1)$$

where c is the concentration of the Eu^{3+} ion in M, d is the length of the optical way in cm and $A(\sigma)$ is the absorbance as the function of the wavenumber in cm^{-1}.

3. Results and discussion

3.1. Structure

Compound **I** crystallizes in the tetragonal system in the $I\bar{4}c2$ space group. There are two symmetry independent Eu^{3+} cations,

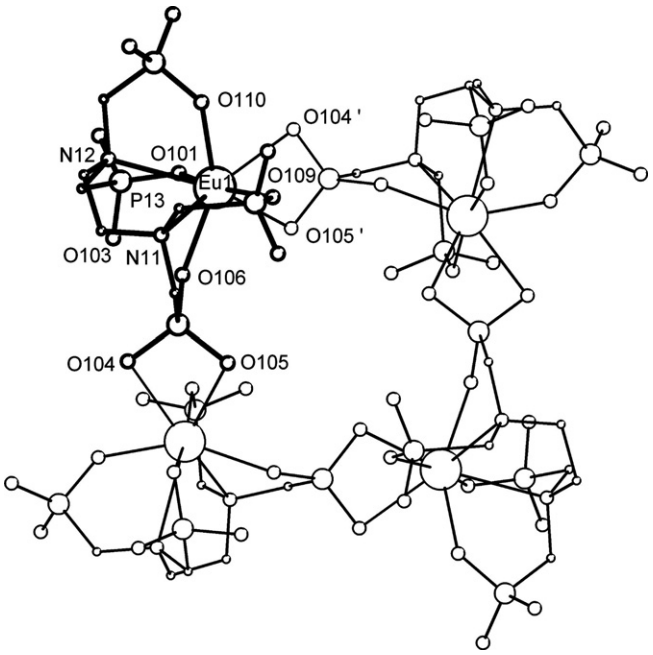


Fig. 1. A view of the tetrameric complex anions in **I**.

Table 1
Selected bond lengths (Å) for **I**

Eu(1)–EDTMP		Eu(2)–EDTMP	
Eu1–O110	2.349(6)	Eu2–O201	2.345(6)
Eu1–O109	2.339(6)	Eu2–O207	2.376(6)
Eu1–O106	2.348(6)	Eu2–O210	2.301(6)
Eu1–O101	2.394(6)	Eu2–O204	2.378(7)
Eu–O_{av}	2.36(3)	Eu–O_{av}	2.35(4)
Eu1–O104′	2.526(6)	Eu2–O202′	2.397(6)
Eu1–O105′	2.408(6)	Eu2–O203′	2.534(6)
Eu–O_{av}	2.47(8)	Eu–O_{av}	2.47(10)
Eu1–N11	2.640(7)	Eu2–N22	2.681(8)
Eu1–N12	2.683(8)	Eu2–N21	2.654(7)
Eu–N_{av}	2.66(3)	Eu–N_{av}	2.67(2)
Eu–Eu	6.301(8)	Eu–Eu	6.327(8)

both are octacoordinate and have an identical composition of the first coordination spheres. Each Eu^{3+} ion is surrounded by two nitrogen atoms and six oxygen atoms from phosphonic groups. The coordination sphere of the Eu^{3+} ions may be described as a distorted square antiprism. The EDTMP anion is involved in bonds with two neighbouring Eu^{3+} cations. Three of the ligand phosphonic groups are monodendate, whereas the fourth one is three-coordinate, *i.e.* one oxygen atom coordinates to Eu1 and the two others (hereinafter called 'bridging') coordinate to a Eu cation generated by symmetry from Eu1. In this way four Eu(EDTMP) entities are bonded together to create a cyclic tetramer with S_4 symmetry (Fig. 1). In a similar fashion, Eu2 generates another tetramer with the same symmetry. The conformations of the tetramers are very similar, the difference being only minute variations of bond lengths and angles. Inside each tetramer a hole is formed and its diameter is 5.2 Å in both cases. The cavities host in part potassium cations and water molecules. The whole structure is held together by a network of complicated hydrogen bonds and electrostatic interactions.

Selected bond lengths are presented in Table 1. In the present structure the average Eu–O bond length equals 2.35(4) Å (where the O atoms belong to the EDTMP molecule wrapped around the respective Eu cation) which is shorter than the average length of

[1] DIAMOND – Visual Crystal Structure Information System, CRYSTAL IMPACT, Postfach 1251, D-53002 Bonn, Germany.

the Eu–O bonds, 2.47(9) Å, formed by the bridging O atoms belonging to the neighbouring EDTMP anions. All Eu–O distances involving non-bridging O atoms are similar to those observed in **II** [6]. The average distance of the remaining four bridging Eu–O bonds is 0.03 Å longer as compared to the Eu–O (bidentate carbonate anion) observed in **II**, probably due to the greater bulkiness of the tetrahedral phosphonate group in comparison with a planar carbonate anion. In **I** the Eu–N average distance is 0.05 Å shorter than that in **II**. The shortest Eu–Eu distances are 6.301(8) Å for Eu(1) and 6.327(8) Å for Eu(2), and are smaller than that in **II** (9.998(3) Å). On average two of the phosphonic groups *per* EDTMP molecule are protonated. The longest P13–O103 distance, 1.582(7) Å, may indicate that the O103 oxygen atom is protonated. The three other protons seem to be disordered. Some of the potassium ions and water molecules are disordered too.

3.2. Spectroscopic results

The low symmetry of the Eu^{3+} ion surroundings has been reflected by the luminescence and absorption spectra of the crystal. The corrected luminescence spectra of **I**, presented in Fig. 2, were measured at 298 and 77 K. The large half-width (23 cm^{-1} at 77 K) of the symmetrical, unsplit $^5D_0 \rightarrow {}^7F_0$ band confirms the results obtained from the X-ray analysis, namely the Eu^{3+} ions are located in very similar coordination environments of a low symmetry.

It is worth stressing that in the present crystal, luminescence from the $^5D_1$ state could also be recorded. This emission, which is not common in Eu^{3+} compounds with organic ligands (it has been observed for example in Eu^{3+} chelates with β-diketones [8–10] and in 1:3 Eu^{3+}:oxydiacetate single crystals of D_3 symmetry at low temperatures [11] as well as in a macrocyclic carboxylate complex incorporated into sol–gel glass [12]), is probably brought about by the saturation of the europium coordination sphere with the phosphonate groups.

Although the $^5D_1$ emission for this compound is significantly less intense than the emission from the $^5D_0$ state, it is observed both at 77 K and at room temperature. The emission intensities of the $^5D_{0,1} \rightarrow {}^7F_J$ transitions determined from the spectra recorded under the same measurement conditions (excitation and emission slits, intensity of the light beam) as well as the ratios of intensities of the $^5D_1 \rightarrow {}^7F_J$ transitions relative to the $^5D_0 \rightarrow {}^7F_J$ ones are presented in Table 2. Since the distances between the $^5D_1$ and $^5D_0$ levels are comparable for both Eu^{3+}–EDTMP compounds and amount to 1744 and 1747 cm^{-1} for **I** and **II**, respectively, one may assume that the luminescence quenching from the $^5D_1$ state in the latter crystal is brought about by one or two high energy phonons which do not occur in **I**. Therefore, comparison between the IR spectra and the $^7F_0 \rightarrow {}^5D_2$ excitation spectra recorded at 77 K (the electron–phonon coupling is the strongest for the hypersensitive transition) of both compounds may be helpful in adjudicating which of the phonons is responsible for the luminescence quenching (Fig. 3). The intense bands observed in the IR spectrum of **I** at 1057 and 1653 cm^{-1} may be attributed to the ν_{P-O} vibration and an overtone or combination bands of the ν_{C-PO_3H} vibrations [13,14], whereas the bands at 1036, 1369 and 1663 cm^{-1} in the spectrum of **II** correspond to ν_{P-O}, ν_{C-O} and δ_{NH_2} vibrations.

As it may be seen in Fig. 3, the vibronics originating from the ν_{P-O} oscillations are observed in the excitation spectra of both compounds. Apart from that, in the spectrum of **II** the ν_{C-O} vibronic component at 22813 cm^{-1} (1369 cm^{-1} off the zero-phonon line) is also detected. Thus, the ν_{C-O} oscillation (with the C–O oscillators

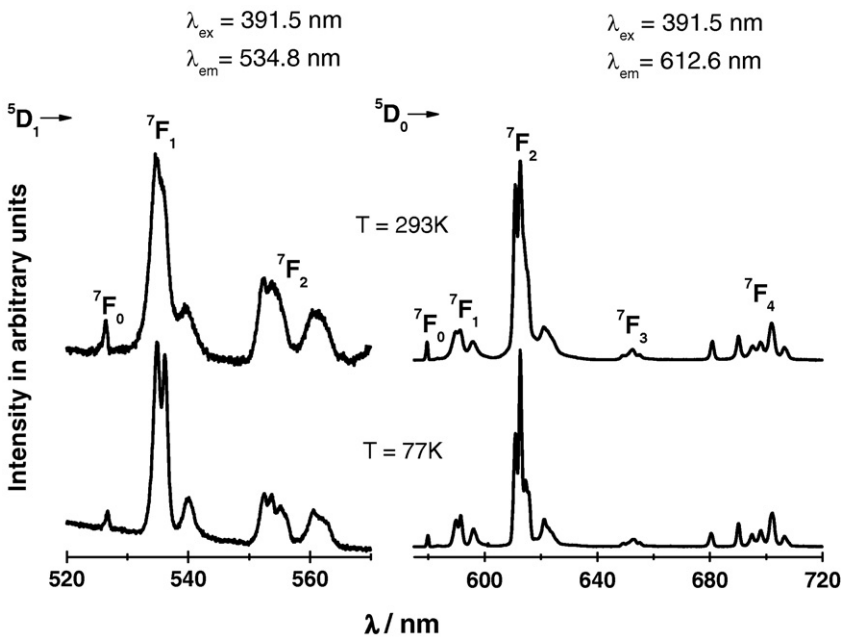


Fig. 2. Emission spectra of **I** at room and liquid nitrogen temperatures.

Table 2
Intensity of emission bands determined for **I**

	$^5D_1 \rightarrow {}^7F_0$	$^5D_1 \rightarrow {}^7F_1$	$^5D_1 \rightarrow {}^7F_2$	$^5D_0 \rightarrow {}^7F_0$	$^5D_0 \rightarrow {}^7F_1$	$^5D_0 \rightarrow {}^7F_2$	$\frac{^5D_1 \rightarrow {}^7F_0}{^5D_0 \rightarrow {}^7F_0}$	$\frac{^5D_1 \rightarrow {}^7F_1}{^5D_0 \rightarrow {}^7F_1}$	$\frac{^5D_1 \rightarrow {}^7F_2}{^5D_0 \rightarrow {}^7F_2}$
T = 298 K	0.0092	0.40	0.26	2.4	28.8	154	0.0038	0.014	0.0016
T = 77 K	0.0083	0.39	0.17	1.5	21.0	96.7	0.0055	0.018	0.0018

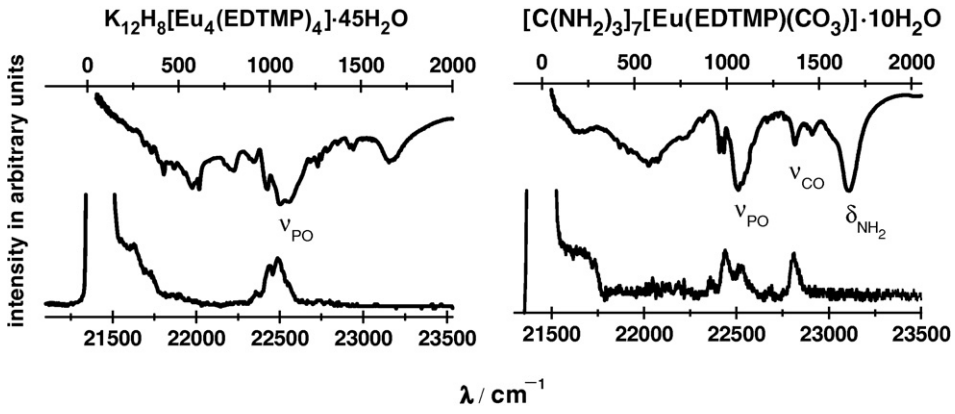


Fig. 3. IR spectra (upper trace) and excitation $^7F_0 \rightarrow {}^5D_2$ spectra obtained at 77 K (lower trace) of **I** and **II**.

located nearest to the Eu^{3+} cation) fits well in the $^5D_1$–$^5D_0$ gap and is probably responsible for the radiationless decay path of the $^5D_1$ state in the latter compound. Absence of this phonon in **I** may be one of the reasons of a longer luminescence lifetime in this compound than in **II**. The decay lifetimes with estimated error of measurements ±10%, obtained by fitting the curves to a single exponential function, were found as 1340 μs for the present crystal and 1036 μs for the previously studied one [6].

The absorption spectra of **I**, at different orientations of the crystal with respect to the incident light beam, were also measured at room temperature (Fig. 4). The crystal is anisotropic; the intensities of the bands, especially those of the hypersensitive $^7F_0 \rightarrow {}^5D_2$ transition, depend on the orientation of the crystal, whereas the energies of all the crystal field components do not change. The orientation averaged oscillator strength values of the f–f transitions of the complex are given in Table 3. One may notice that the average oscillator strength value of the $^7F_0 \rightarrow {}^5D_2$ transition for **I** is similar to that observed in **II**, which may result from the analogous arrangement of the first coordination sphere of the Eu^{3+} ion. The splitting of the f–f levels is also similar, although the $^7F_0 \rightarrow {}^5D_{0,1,2}$ bands in the present complex are slightly (a few cm^{-1}) red-shifted in comparison to those observed in **II** (Fig. 4). The high value of the oscillator strength of the $^7F_0 \rightarrow {}^5D_0$ transition as well as the large half-width of this band at 298 K (15 cm^{-1}) may be connected to the low symmetry of the surroundings of the Eu^{3+} ions.

Table 3
Oscillator strength values (P) of **I** determined at different orientations of the crystal (I–III)

Transitions	I, $P \times 10^8$	II, $P \times 10^8$	III, $P \times 10^8$	$P_{av} \times 10^8$
$^7F_0 \rightarrow {}^5D_0$	0.44	0.69	0.63	0.59
$^7F_0 \rightarrow {}^5D_1$	1.55	1.72	1.63	1.63
$^7F_0 \rightarrow {}^5D_2$	14.23	21.62	24.70	20.18
$^7F_0 \rightarrow {}^5L_6$	132.25	144.62	157.42	144.76

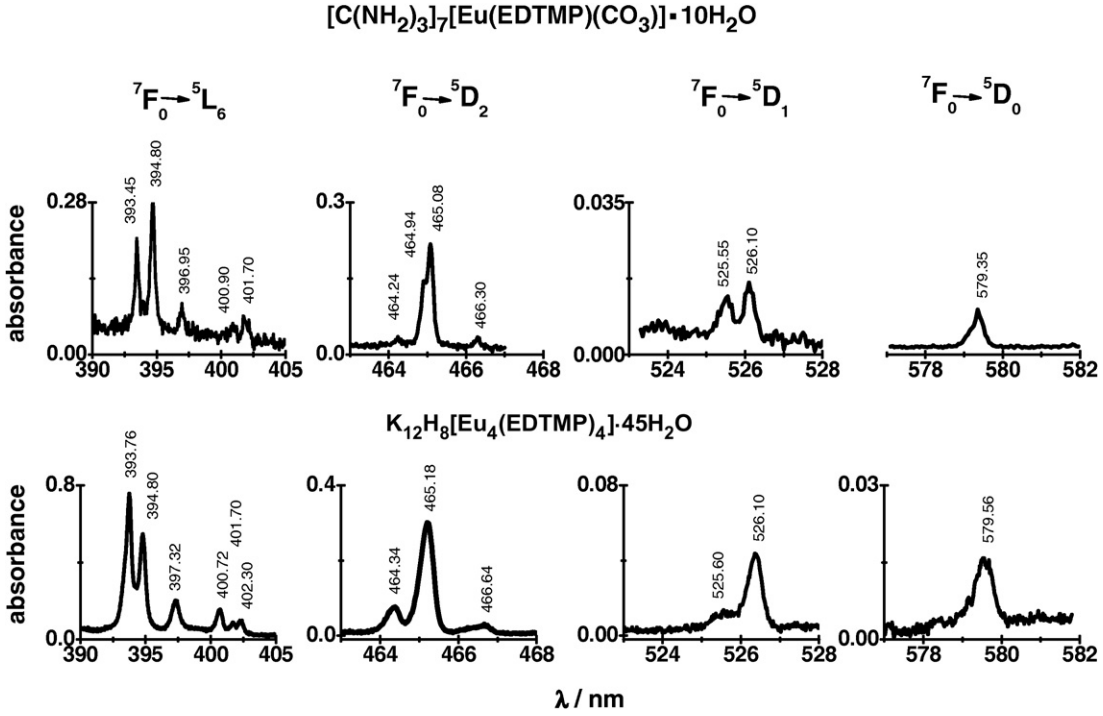


Fig. 4. Absorption spectra of the f–f transitions of **I** and **II** [6] at 298 K. For **II** instead of the the $^7F_0 \rightarrow {}^5D_0$ absorption spectrum, which could not be recorded due its low intensity, the luminescence excitation spectrum of this transition is displayed.

4. Conclusions

The coordination sphere of the Eu^{3+} ion in the studied crystal consists of the same donor atoms (six oxygen atoms, two nitrogen atoms) as in the previously reported structure of **II** [6]. However, it should be noted that two of the coordinated oxygen atoms are of different origin for the two crystals. In the present crystal they belong to a tridentate phosphonate group, giving thus rise to formation of cyclic tetrameric complex anions, whereas in the former monomeric complex anion they come from the bidentate carbonate anion.

Although such differences of the Eu^{3+}–EDTMP complex structure do not influence the oscillator strengths of the f–f transitions significantly, they affect the luminescence lifetimes of the excited states of the Eu^{3+} ion. The more rigid structure of **I** is a reason for a longer (approximately 300 μs) europium $^5D_0$ level lifetime, as compared to that found for **II**. The present crystal, contrary to the former one, also displays luminescence from both $^5D_0$ and $^5D_1$ states.

The structural and spectroscopic results presented here, show that the acyclic polyaminopolyphosphonate ligands, upon interacting with Ln^{3+} cations, may form non-trivial complexes with interesting properties.

Acknowledgements

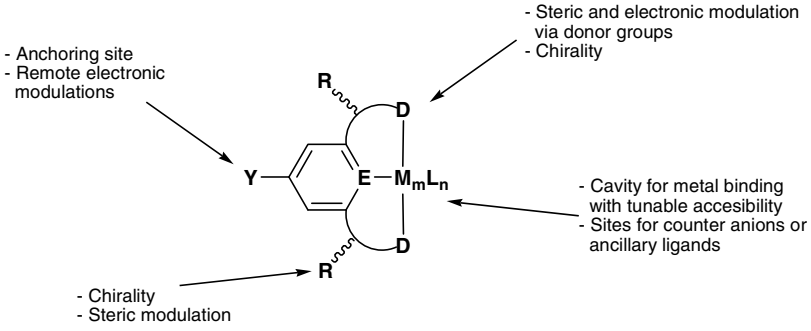
We thank Dr. P. Starynowicz for the X-ray measurements and for assistance during the structure solution. This work was supported by MNiSW N204 135 31/3127.

Appendix A. Supplementary data

CCDC 632399 contains the supplementary crystallographic data for compound **I**. These data can be obtained free of charge via http://www.ccdc.cam.ac.uk/conts/retrieving.html, or from the Cambridge Crystallographic Data Centre, 12 Union Road, Cambridge CB2 1EZ, UK; fax: (+44) 1223-336-033; or e-mail: deposit@ccdc.cam.ac.uk. Supplementary data associated with this article can be found, in the online version, at doi:10.1016/j.poly.2008.03.002.

References

[1] W.A. Volkert, T.J. Hoffman, Chem. Rev. 99 (1999) 2269.
[2] H.T. Gasiglia, H. Okada, J. Radioanal. Nucl. Chem. Lett. 199 (1995) 295.
[3] W.K.A. Louw, I.C. Dormehl, A.J. van Rensburg, N. Hugo, A.S. Alberts, O.E. Forsyth, G. Beverley, M.A. Sweetlove, J. Marais, M.G. Lötter, A. van Aswegen, Nucl. Med. Biol. 23 (1996) 935.
[4] I.G. Finlay, M.D. Mason, M. Shelley, Lancet Oncol. 6 (2005) 392.
[5] J. Gałęzowska, R. Janicki, A. Mondry, R. Burgada, T. Bailly, M. Lecouvey, H. Kozłowski, Dalton Trans. (2006) 4384.
[6] A. Mondry, R. Janicki, Dalton Trans. (2006) 4702.
[7] (a) G.M. Sheldrick, SHELXS-97, Program for Structure Solution, University of Göttingen, 1997;
(b) G.M. Sheldrick, SHELXL-97, Program for Structure Refinement, University of Göttingen, 1997.
[8] A.F. Kirby, F.S. Richardson, J. Phys. Chem. 87 (1983) 2544.
[9] R. Brennetot, J. Georges, Spectrochim. Acta, Part A 56 (2000) 703.
[10] Y. An, G.E. Schramm, M.T. Berry, J. Lumin. 97 (2002) 7.
[11] A.F. Kirby, F.S. Richardson, J. Phys. Chem. 87 (1983) 2557.
[12] M. Zaitoun, Appl. Spectrosc. 60 (2006) 418.
[13] A. Cabeza, M.A.G. Aranda, S. Bruque, J. Mater. Chem. 9 (1999) 571.
[14] A. Cabeza, X. Ouyang, C.V.K. Sharma, M.A.G. Aranda, S. Bruque, A. Clearfield, Inorg. Chem. 41 (2002) 2325.



Scheme 1. Versatility of the pincer framework.

and requires a series of steps to introduce different groups or donors. Moreover, complexes bearing asymmetric pincer ligands have shown enhanced and in many cases markedly different reactivities, such as hemilability [11].

From the above discussion, it clearly results that the design of ligands is one of the most important aspects in the chemistry of this kind of compounds, this being specially important in homogeneous catalysis. The ability to simply and independently vary the steric and electronic properties of a given ligand may provide a wealth of opportunities to influence reactivity, stability, catalysis and other important properties at the metal center. Hence, following our continuous interest in the development on pincer chemistry [12], herein we would like to report a simple protocol for the high yield synthesis of the asymmetric ligand [C_6H_4-1-(CH_2PPh_2)-3-($CH(CH_3)PPh_2$)] (**4**) and its Pd(II) derivative [PdCl{C_6H_3-2-(CH_2PPh_2)-6-($CH(CH_3)PPh_2$)}] (**5**).

2. Experimental

2.1. Materials and methods

Unless otherwise stated, all reactions were carried out under an atmosphere of purified argon using conventional Schlenk glassware and glovebox techniques; solvents were dried using the established procedures and distilled under dinitrogen and freeze–pump–thaw degassed immediately prior to use. The ^1H, $^{13}C\{1H\}$, $^{31}P\{^1H\}$ NMR spectra were recorded at 300, 75.4 and 121.4 MHz, respectively at 295 K, using a Bruker Avance DRX 300 MHz NMR spectrometer. ^1H NMR and $^{13}C\{^1H\}$ NMR chemical shifts are reported in ppm downfield from TMS. ^1H NMR chemical shifts are referenced to the residual hydrogen signal of the deuterated solvents and in $^{13}C\{^1H\}$ NMR the ^{13}C signal of the deuterated solvents was used as a reference. $^{31}P\{^1H\}$ NMR chemical shifts are reported in ppm downfield from H_3PO_4 and referenced to high frequency of 85% H_3PO_4. Elemental analyses were determined on a Heraeus CHN-O-RAPID elemental analyzer. The starting materials α,α′-dibromo-*m*-xylene, chlorodiphenylphosphine, $PdCl_2$, $CDCl_3$ were purchased from Aldrich Chemical Co. and used without further purification. The complex [$PdCl_2$-(COD)] was synthesized according to the published procedure [13].

2.2. Synthesis of {C_6H_4-1-(CH_2Br)-3-(CH_2PPh_3Br)} (**1**)

To a stirred solution of α,α′-dibromo-*m*-xylene (3.70 g, 14 mmol) in THF (100 ml) was added a solution of triphenylphosphine (4.3 g, 16 mmol) in THF (20 ml) at room temperature and the solution allowed to reach 60 °C slowly. The resulting white suspension was stirred overnight. The reaction mixture was allowed to reach room temperature, the mixture was filtered off and the remaining solid was washed with THF (3 × 10 ml) and dried under vacuum to give a pure white powder of **1** (6.3 g, 12 mmol, 85%). ^1H NMR (300 MHz, $CDCl_3$): δ 4.17 (s, 2H, CH_2Br); 5.32 (d, $J = 14.39$ Hz, CH_2P); 6.97–7.27 (m, 4H, Ph); 7.53–7.73 (m, 15H, PPh_3). $^{13}C\{^1H\}$ NMR (75.40 MHz, $CDCl_3$): δ 30.37 (d, $J_{CP} = 47.66$ Hz, CH_2P); 32.64 (CH_2Br); 116.62, 117.76, 127.64, 128.83, 129.09, 130.01 (d, $J = 12.1$ Hz), 131.29, 131.90, 134.09 (d, $J = 9.80$ Hz) 134.84, 138.08. $^{31}P\{^1H\}$ NMR (121 MHz, $CDCl_3$): δ 24.22. *Anal.* Calc. for $C_{26}H_{23}Br_2P$ ($M_r = 526.24$): C, 59.34; H, 4.41. Found: C, 59.38; H, 4.45%.

2.3. Synthesis of {C_6H_4-1-(CH_2Br)-3-($CH{=}CH_2$)} (**2**)

To a stirred solution of **1** (2.63 g, 5 mmol) in dichloromethane (40 ml) was added *para*-formaldehyde (0.27 g, 9 mmol) and KOH solution (6 ml, 50%) at room temperature, respectively and stirred for 1 h. The organic layer was separated and the aqueous layer extracted with ether. The combined organic extracts were washed and dried over $MgSO_4$. After filtration, the solution was passed through a short plug of celite and the solvent evaporated under vacuum to afford a white solid. The remaining solid was extracted with *n*-hexane and then the solvent evaporated under vacuum to afford **2** as a pure colorless oil (0.79 g, 4 mmol, 80%). ^1H NMR (300 MHz, $CDCl_3$): δ 4.37 (s, 2H, CH_2Br), 5.18 (d, $J_{HH} = 11.1$ Hz, 1H, CH_2), 5.67 (d, $J_{HH} = 17.4$ Hz, 1H, $CH{=}CH_2$), 6.60 (dd, $J_{HH} = 17.70$ HZ, $J_{HH} = 10.8$ Hz, $CH{=}CH_2$), 7.15–7.314 (m, 4H, Ar). $^{13}C\{^1H\}$ NMR (75.40 MHz, $CDCl_3$): δ 33.39 (CH_2Br), 114.54 ($CH{=}CH_2$), 126.17, 126.78, 128.32, 128.93, 136.13

(CH=CH_2), 137.93, 138.02. *Anal.* Calc. for C_9H_9Br ($M_r = 197.07$): C, 54.85; H, 4.60. Found: C, 54.90; H, 4.57%.

2.4. Synthesis of {C_6H_4-1-(CH_2Br)-3-($CH(CH_3)Br$)} (3)

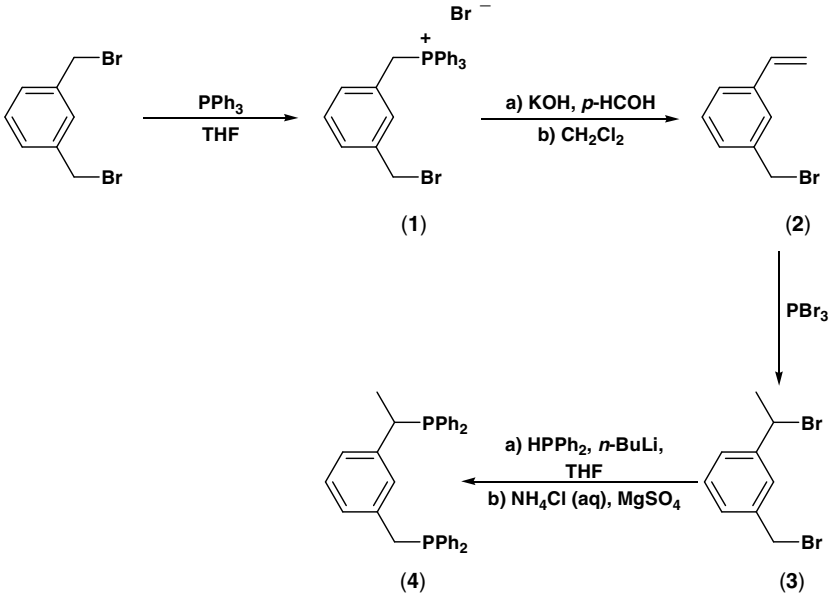
To a stirred solution of **2** (0.62 g, 3.1 mmol) in dichloromethane (15 ml), PBr_3 (0.123 ml, 1.3 mmol) was added at room temperature and stirred for 3 h. After this time, the solution is then washed with aqueous $NaHCO_3$ and then with water, the organic phase is separated and the aqueous layer extracted twice with CH_2Cl_2 (2 × 10 ml). The organic phase is dried over $MgSO_4$ and the solvent removed by rotary evaporation to afford **3** as a colorless oil (0.86 g, 3.1 mmol, 98%). ^{1}H NMR (300 MHz, $CDCl_3$): δ 1.95 (d, $J = 6.90$ Hz, 3H, CH_3); 4.39 (s, 2H, CH_2Br); 5.10 (q, $J = 6.90$ Hz, 1H, CH), 7.15–7.36 (m, 4h, Ar). $^{13}C\{^1H\}$ NMR (75.40 MHz, $CDCl_3$): δ 26.65 (CH_3), 33.01 (CH_2Br), 48.76 (CHBr), 126.83, 127.35, 128.94, 129.13, 138.13, 143.74. *Anal.* Calc. for $C_9H_{10}Br_2$ ($M_r = 277.98$): C, 38.89; H, 3.63. Found: C, 38.85; H, 3.65%.

2.5. Synthesis of {C_6H_4-1-(CH_2PPh_2)-3-($CH(CH_3)PPh_2$)} (4)

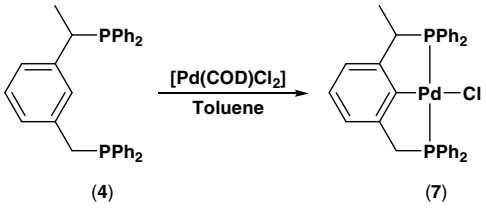
To a solution of Ph_2PH (1.17 g, 6 mmol) in THF (35 ml) was added dropwise a solution of *n*-BuLi in hexane (3.75 ml of 1.6 M/l hexane solution, 6 mmol) at −78 °C, over a period of 30 min with stirring. After this time, the reaction mixture was allowed to reach room temperature. The resulting orange suspension was cooled to −78 °C and a THF solution (20 ml) of **3** (0.834 g, 3 mmol) was added dropwise with a syringe over 30 min. The resulting mixture is allowed to reach room temperature and the stirring continued for an additional 1 h to give a clear mixture. After this time, the resulting reaction mixture is placed into a salt-ice bath (0 °C) and a solution of NH_4Cl in water (10 wt%, 45 ml) is carefully added to afford a colorless mixture. The THF layer was separated and the aqueous layer extracted twice with ether (2 × 15 ml). The combined extracts were dried over $MgSO_4$ and passed through a short column of alumina. Finally, the solvent was removed under vacuum to afford **4** as a colorless oil (1.39 g, 2.85 mmol, 95%). ^{1}H NMR (300 MHZ, $CDCl_3$): δ 1.02 (dd, $^3J_{HP} = 14.7$ Hz, $^3J_{HH} = 7.35$ Hz, 3H, CH_3), 2.94 (d, $^2J_{HP} = 18$ Hz, 2H, CH_2P), 3.10 (m, 1H, CHP), 6.52–6.91 (m, 20H, PPh_2), 7.04–7.30 (m, 4H, Ar). $^{13}C\{^1H\}$ NMR (75.40 MHz, $CDCl_3$): δ 20.17 (d, $J_{CP} = 21.2$ Hz, $CHPPh_2$), 36.26 (d, $J_{CP} = 16.1$ Hz, CH_2PPh_2); 39.47 (d, $J_{CP} = 13.2$ Hz, CH_3), 126.60 (d, $J = 5.3$ Hz), 127.67, 128.00, 128.15, 128.33, 128.52, 128..60, 128.69, 129.23, 129.90, 130.76, 131.34, 133.08, 133.28, 133.33, 133.39, 133.53, 133.62, 134.36, 134.64, 137.80, 137.91, 138.02, 138.49, 139.12 (d, $J = 4.8$ Hz), 143.96 (d, $J = 8.60$ Hz), Ar. $^{31}P\{^1H\}$ NMR (121 MHz, $CDCl_3$): δ −9.157 (CH_2PPh_2), 2.69 ($CHPPh_2$). *Anal.* Calc. for $C_{33}H_{30}P_2$ ($M_r = 488.54$): C, 81.13; H, 6.19. Found: C, 81.20; H, 6.25% (see Scheme 2).

2.6. Synthesis of [PdCl{C_6H_3-2-(CH_2PPh_2)-6-($CH(CH_3)PPh_2$)}] (7)

To a stirred suspension of [Pd(COD)Cl_2] (0.777 g, 2.72 mmol) in toluene (25 ml), a solution of ligand **4** (1.329 g, 2.72 mmol) in toluene (20 ml) was slowly added. The resulting solution was set to reflux for 5 h. After this time, the solution was filtered over cotton pad and pumped



Scheme 2. Synthesis of the asymmetric PCP pincer ligand (**4**).



Scheme 3. Synthesis of the asymmetric Pd(II)-PCP pincer complex (**7**).

off under vacuum to dryness. The crude solid was purified by recrystallization from $CHCl_3$/MeOH to afford complex **7** as a white microcrystalline powder (1.46 g, 2.31 mmol, 85%): ^{1}H NMR (300 MHZ, $CDCl_3$): δ 1.02 (dd, $^3J_{HP} = 16.04$ Hz, $^3J_{HH} = 7.1$ Hz, 3H, CH_3), 3.82 (d, $J = 6$ Hz, 2H, CH_2PPh_2), 4.00 (m, 1H, $CHPPh_2$), 6.95–7.04 (m, 3H, Ar), 7.26–7.82 (m, 20H, Ar). $^{13}C\{^1H\}$ NMR (75.40 MHz, $CDCl_3$): δ 21.46 (s, CH_3), 49.37 (d, $J =$ 31.0 Hz, CH_2PPh_2), 46.31 (d, $J = 30.4$ Hz, $CH(CH_3)PPh_2$), 122.56 (d, $J = 20.7$ Hz), 123.54 (d, $J = 22.4$ Hz), 126.21, 128.52 (d, $J = 24.1$ Hz), 128.55, 129.98, 130.42, 130.86, 132.13 (d, $J = 9.7$ Hz), 132.97 (d, $J = 17.3$ Hz), 132.99, 134.92 (d, $J = 10.86$ Hz), 147.67 (d, $J = 21.2$ Hz), 153.87(d, $J = 22.3$ Hz). $^{31}P\{^1H\}$ NMR (121 MHz, $CDCl_3$): δ 34.32 (d, $J_{PP} = 418$ Hz, CH_2PPh_2), 48.57 (d, $J_{PP} =$ 418 Hz, $CH(CH_3)PPh_2$). *Anal.* Calc. for $C_{33}H_{29}ClP_2Pd$ ($M_r = 629.40$): C, 62.97; H, 4.64. Found: C, 63.00; H, 4.60% (see Scheme 3).

3. Results and discussion

The initial step for the formation of PCP pincer ligand (**4**) very much resembles the initial step employed by Shaw on his seminal report in the 1970s [14]. Thus, α,α′-dibromo-*m*-xylene was treated with one equivalent of triphenylphosphine in THF to afford the single substituted triphenyphosphonium salt {C_6H_4-1-(CH_2Br)-3-(CH_2PPh_3Br)} (**1**). Analysis of the solid product (**1**) by ^{1}H reveals that the α,α′-dibromo-*m*-xylene has been substituted in only one arm. Thus, signals corresponding to two different CH_2 groups in the molecule can be observed, a singlet corresponding to the CH_2Br located at δ 4.17 ppm and a doublet due to the presence of the CH_2PPh_3Br found at δ 5.32 ppm. Similar assignation can be done from the results obtained from the analysis of the same sample by $^{13}C\{^1H\}$ NMR, where besides the signals observed for the aromatic carbons in the usual region (δ 116–138 ppm) signals corresponding to the two different CH_2 can be observed at δ 32.64 and δ 30.37 ppm for the CH_2Br and CH_2PPh_3Br moieties, respectively. Furthermore, the presence of the phosphonium group was detected by $^{31}P\{^1H\}$ NMR, this analysis showing a single signal at δ 22.24 ppm due to the PPh_3Br group. Elemental analysis is also consistent with the proposed formulation.

In contrast to the procedure employed by Shaw [14], where the phosphonium salt was treated with a mild base to afford the corresponding phosphine, compound (**1**) was treated with a strong base (KOH) in the presence of an excess of *para*-formaldehyde to afford the Witting [15] product {C_6H_4-1-(CH_2Br)-3-($CH{=}CH_2$)} (**2**). Analysis of this compound by ^{1}H NMR shows a typical pattern for a single substituted ethylene type olefin, exhibiting two sets of doublets for the terminal protons of the alkene at δ 5.18 and δ 5.67 ppm and a doublet of doublets for the methyne group at δ 6.60 ppm. A further singlet at δ 4.37 ppm and signals due to the aromatic protons between δ 7.15 and 7.31 ppm are also observed in the spectrum.

Bromination of the olefin compound (**2**) with PBr_3 gives place to the formation of the asymmetric dibromo starting material {C_6H_4-1-(CH_2Br)-3-($CH(CH_3)Br$)} (**3**). This compound afforded a ^{1}H NMR spectrum where the most notorious signal is a doublet located at δ 1.95 ppm corresponding to the newly formed CH_3 group in one of the arms. Complementary to this signal is a quartet at δ 5.10 ppm due to the methyne group of the same arm. While the signal corresponding to the un-substituted arm and those due to the aromatic protons can be observed at δ 4.39 and 7.15–7.36 ppm, respectively. Signals concurrent with the previous analysis can be observed at δ 26.65, 33.01 and 48.76 ppm in the $^{13}C\{^1H\}$ NMR spectrum, these signals being assigned to the methyl, methylene and methyne groups in (**3**), respectively. Results obtained from elemental analysis are also in agreement with the proposed formulation.

The final step leading to the synthesis of the PCP pincer ligand involved the reaction of the lithium salt of the diphenylphosphine with the dibromo compound (**3**), at a low temperature to afford compound {C_6H_4-1-(CH_2PPh_2)-3-($CH(CH_3)PPh_2$)} (**4**) as an air sensitive colorless oil in excellent yield (95%). Once again signals corresponding to the CH_3, CH_2 and CH groups can be observed in the corresponding ^{1}H NMR spectrum at δ 1.02 (dd), 2.94 (d) and 3.10 (m) ppm, respectively. The substitution of the bromides for the phosphine groups can be inferred for the multiplicity observed in these signals due to the coupling with the *P* nuclei and for the shift of these signals to higher field due to the inductive effect of the phosphine moieties. As is the case for the previous intermediates, a similar behavior is observed in the $^{13}C\{^1H\}$ NMR. More illustrative are the results of the analysis by $^{31}P\{^1H\}$ NMR, where two different signals, due to two inequivalent phosphorus nuclei are observed; one due to the substituted arm at a lower field (δ 2.69 ppm) and the other centered at δ −9.16 ppm. It is very interesting to note that these chemical shifts agree well when compared to the bis-disubstituted ligand {C_6H_4-1,3-($CH(CH_3)PPh_2$)} (**5**) reported by Venanzi [16] and Zhang [17] and the simple PCP pincer ligand {C_6H_4-1,3-(CH_2PPh_2)} (**6**) reported earlier by Venanzi [18] with only very slight variations (Fig. 1).

As for most of the cases, metallation of ligand (**4**) proceeds in a very facile manner via the C–H activation of the aromatic ring by $[Pd(COD)Cl_2]$ under reflux using toluene as solvent. The white product of [PdCl{C_6H_3-2-(CH_2PPh_2)-6-($CH(CH_3)PPh_2$)}] (**7**) thus obtained was

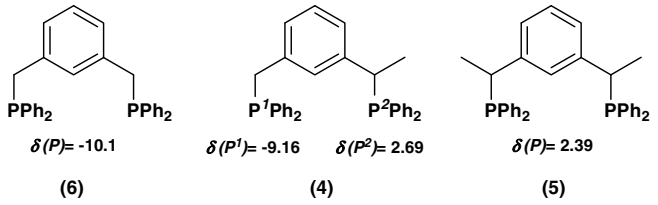


Fig. 1. Chemical shift (δ) Comparison between symmetric PCP pincer ligands and compound (**4**).

analyzed by ^{1}H NMR, showing signals similar to those of the free ligand but slightly shifted to lower field, a fact that agrees well with the metal being coordinated to the ligand. This argument is also supported for the more notorious shift to the lower field of the signals in the $^{31}P\{^{1}H\}$ NMR spectra, passing from δ −9.16 and δ 2.69 ppm in the free ligand (**4**) to δ 34.32 and δ 48.57 ppm in the metallated complex (**7**) for the CH_2PPh_2 and $CH(CH_3)PPh_2$, respectively. Moreover, the signals of the phosphorus nuclei of compound (**7**) are shown as doublets, which also accounts for the ligand to be coordinated to the metal in a κ^2-P,P form. Besides the J^2_{pp} value of 418 Hz, it is consistent with a *trans* arrangement of the two phosphorus nuclei. Once again, the chemical shifts observed for (**7**) agree well when compared to their symmetric analogous [PdCl{C_6H_3-2,6-($CH(CH_3)PPh_2$)$_2$}] (**8**) [16,17b] and [PdCl{C_6H_3-2,6-(CH_2PPh_2)$_2$}] (**9**) [18] (Fig. 2).

Results obtained from elemental analysis are also in agreement with the proposed formulation. Unfortunately, multiple attempts to obtain suitable crystals of complex (**7**) for their analysis by single crystals X-ray diffraction techniques afforded in amorphous powder or very low quality crystals all cases.

In summary, the present method represents an attractive and easy to perform methodology for the synthesis of asymmetric PCP pincer ligands and their palladium derivatives. It is important to note that the method may not be limited to the synthesis of ligand (**4**) but by careful selection of the aldehyde and reaction conditions, the methyl group in the substituted arm can be changed for various other substituents or even lead to the elongation of the arm thus affording another group of potentially interesting PCP pincer ligands having 5 and 6 membered rings. Moreover, exploitation of the different reactivities of the two different arms in compound (**3**) may offer the opportunity to attain PCP pincer ligands with different donor groups, since it is expected that the more substituted arm would react slowly when compared to the un-substituted arm. Experiments aimed to confirm these theories and the synthesis of other group 10 transition metal derivatives of ligand (**4**) and the study of the potential activity of complex (**7**) are currently underway in our laboratories.

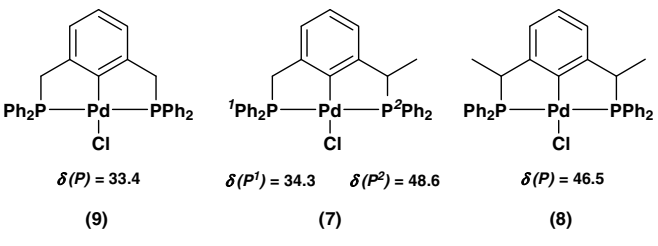


Fig. 2. Chemical shift (δ) Comparison between symmetric Pd(II)-PCP pincer complexes and compound (**7**).

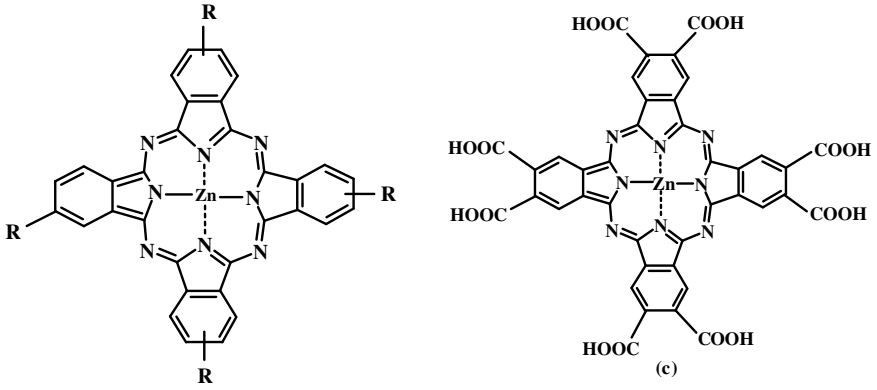
Acknowledgements

We are grateful to the ILAM University and the Ministry of Science, Research & Technology of Iran, for financial support. J.M. S.-B. would like to thank CONACYT for financial support. D. M.-M. would like to thank CONACYT (Grant F58692) and PAPIIT (Grant IN227008) for financial support.

References

[1] (a) M. Albrecht, G. van Koten, Angew. Chem., Int. Ed. 40 (2001) 3750;
(b) M.E. van der Boom, D. Milstein, Chem. Rev. 103 (2003) 1759;
(c) J.T. Singleton, Tetrahedron 59 (2003) 1837;
(d) D. Morales-Morales, Rev. Soc. Quim. Mex. 48 (2004) 338;
(e) K.J. Szabo, Synlett (2006) 811;
(f) D. Morales-Morales, C.M. Jensen (Eds.), The Chemistry of Pincer Compounds, Elsevier, Amsterdam, The Netherlands, 2007.
[2] (a) See for instance J.A. Mata, M. Poyatos, E. Peris, Coord. Chem. Rev. 251 (2007) 841, and references therein;
(b) D. Pugh, A.A. Danopoulos, Coord. Chem. Rev. 251 (2007) 610, and references therein.
[3] (a) See for instance D. Morales-Morales, C. Grause, K. Kasaoka, R. Redón, R.E. Cramer, C.M. Jensen, Inorg. Chim. Acta 300–302 (2000) 958;
(b) R.B. Bedford, S.M. Draper, P.N. Scully, S.L. Welch, New J. Chem. 24 (2000) 745;
(c) D. Morales-Morales, R. Redón, C. Yung, C.M. Jensen, Chem. Commun. (2000) 1619;
(d) O.A. Wallner, K.J. Szabó, Org. Lett. 6 (2004) 1829;
(e) D. Olsson, P. Nilsson, M. El Masnaouy, O.F. Wendt, Dalton Trans. 11 (2005) 1924;
(f) P.A. Chase, M. Gagliardo, M. Lutz, A.L. Spek, G.P.M. van Klink, G. van Koten, Organometallics 24 (2005) 2016;
(g) D. Benito-Garagorri, V. Bocokic, K. Mereiter, K. Kirchner, Organometallics 25 (2006) 3817;
(h) R.A. Baber, R.B. Bedford, M.B. Betham, M.E. Blake, S.J. Coles, M.F. Haddow, M.B. Hursthouse, A.G. Orpen, L.T. Pilarski, P.G. Pringle, R.L. Wingad, Chem. Commun. (2006) 3880;
(i) T. Kimura, Y. Uozumi, Organometallics 25 (2006) 4883;
(j) F. Churruca, R. SanMartin, I. Tellitu, E. Domínguez, Tetrahedron Lett. 47 (2006) 3233;
(k) D. Morales-Morales, R. Redón, C. Yung, C.M. Jensen, Inorg. Chim. Acta 357 (2004) 2953;
(l) D. Morales-Morales, R. Redón, Z. Wang, D.W. Lee, C. Yung, K. Magnuson, C.M. Jensen, Can. J. Chem. 79 (2001) 823, and references cited therein.
[4] (a) See for instance T. Kanbara, T. Yamamoto, J. Organomet. Chem. 688 (2003) 15;
(b) M.D. Meijer, B. Mulder, G.P.M. van Klink, G. van Koten, Inorg. Chim. Acta 352 (2003) 247;
(c) K. Yu, W. Sommer, M. Weck, C.W.S. Jones, J. Catal. 226 (2004) 101;
(d) M. Akaiwa, T. Kanbara, H. Fukumoto, T. Yamamoto, J. Organomet. Chem. 690 (2005) 4192;
(e) D.E. Bergbreiter, P.L. Osburn, J.D. Frels, Adv. Synth. Catal. 347 (2005) 172;

(f) M. Arroyo, R. Cervantes, V. Gómez-Benítez, P. López, D. Morales-Morales, H. Torrens, R.A. Toscano, Synthesis (2003) 1565.
[5] See for instance H. Nishiyama, Chem. Soc. Rev. 36 (2007) 1133, and references therein.
[6] (a) See for instance D. Morales-Morales, in: D. Morales-Morales, C. Jensen (Eds.), The Chemistry of Pincer Compounds, Elsevier, Amsterdam, 2007, p. 151;
(b) D. Morales-Morales, Mini-Rev. Org. Chem. 5 (2008) 141.
[7] (a) See for instance I.G. Jung, S.U. Son, K.H. Park, K. Chung, J.W. Lee, Y.K. Chung, Organometallics 22 (2003) 4715;
(b) M.Q. Slagt, G. Rodríguez, M.M.P. Grutters, R.J.M.K. Gebbink, W. Klopper, L.W. Jenneskens, M. Lutz, A.L. Spek, G. van Koten, Chem. Eur. J. 10 (2004) 1331;
(c) J. Kjellgren, H. Sundén, K.J. Szabó, J. Am. Chem. Soc. 126 (2004) 474;
(d) K. Takenaka, Y. Uozumi, Adv. Synth. Catal. 346 (2004) 1693;
(e) K. Takenaka, M. Minakawa, Y. Uozumi, J. Am. Chem. Soc. 127 (2005) 12273;
(f) B. Soro, S. Stoccoro, G. Minghetti, A. Zucca, M.A. Cinellu, S. Gladiali, M. Manassero, M. Sansoni, Organometallics 24 (2005) 53;
(g) O. Baldovino-Pantaleón, S. Hernández-Ortega, D. Morales-Morales, Adv. Synth. Catal. 348 (2006) 236;
(h) M.S. Yoon, R. Ramesh, J. Kim, D. Ryu, K.H. Ahn, J. Organomet. Chem. 691 (2006) 5927;
(i) O. Baldovino-Pantaleón, S. Hernandez-Ortega, D. Morales-Morales, Inorg. Chem. Commun. 8 (2005) 955.
[8] (a) See for instance M. Weck, Polym. Int. 56 (2007) 453;
(b) C.R. South, C. Burd, M. Weck, Acc. Chem. Res. 40 (2007) 63, and references therein.
[9] (a) See for instance R. Kreiter, A.W. Kleij, R.J.M. Klein Gebbink, G. van Koten, Top. Curr. Chem. 217 (2001) 164;
(b) P.A. Chase, R.J.M. Klein Gebbink, G. van Koten, J. Organomet. Chem. 689 (2004) 4016;
(c) H.P. Dijkstra, G.P.M. van Klink, G. van Koten, Acc. Chem. Res. 35 (2002) 798;
(d) P.A. Chase, G. van Koten, in: D. Morales-Morales, C. Jensen (Eds.), The Chemistry of Pincer Compounds, Elsevier, Amsterdam, 2007, p. 399, and references therein.
[10] See J. Dupont, C.S. Consorti, J. Spencer, Chem. Rev. 105 (2005) 2527, and references therein.
[11] See for instance Ch. Gunanathan, Y. Ben-david, D. Milstein, Science 317 (2007) 790, and references therein.
[12] (a) F.E. Hahn, M.C. Jahnke, V. Gómez-Benítez, D. Morales-Morales, T. Pape, Organometallics 24 (2005) 6458;
(b) Z. Wang, S. Sugiarti, C.M. Morales, C.M. Jensen, D. Morales-Morales, Inorg. Chim. Acta 359 (2006) 1923;
(c) V. Gómez-Benítez, O. Baldovino-Pantaleón, C. Herrera-Álvarez, R.A. Toscano, D. Morales-Morales, Tetrahedron Lett. 47 (2006) 5059;
(d) V. Gómez-Benítez, R.A. Toscano, D. Morales-Morales, Inorg. Chem. Commun. 10 (2007) 1;
(e) A. Naghipour, S.J. Sabounchei, D. Morales-Morales, S. Hernández-Ortega, C.M. Jensen, J. Organomet. Chem. 689 (2004) 2494;
(f) A. Naghipour, S.J. Sabounchei, D. Morales-Morales, D. Canseco-González, C.M. Jensen, Polyhedron 26 (2007) 1445;
(g) D. Morales-Morales, in: L. Kollár (Ed.), Modern Carbonylation Methods, Wiley–VCH Verlag GmbH, Weinheim, Germany, 2008, p. 27 (Chapter 2).
[13] D. Drew, J.R. Doyle, Inorg. Synth. 28 (1990) 348.
[14] C.J. Moulton, B.L. Shaw, J. Chem. Soc., Dalton. (1976) 1020.
[15] J. March, Advanced Organic Chemistry. Reactions, Mechanisms and Structure, 3rd ed., John Wiley & Sons, USA, 1985, p. 845.
[16] F. Gorla, L.M. Venanzi, Organometallics 13 (1994) 43.
[17] (a) J.M. Longmire, X. Zhang, Tetrahedron Lett. 38 (1997) 1725;
(b) J.M. Longmire, X. Zhang, Organometallics 17 (1998) 4374.
[18] H. Rimml, L.M. Venanzi, J. Organomet. Chem. 259 (1983) C6.



(a) R = SO_3Na; (b) R = COOH

Fig. 1. Molecular Structures of (a) zinc tetrasulfo phthalocyanine (ZnTSPc), (b) zinc tetracarboxy phthalocyanine (ZnTCPc) and (c) zinc octacarboxyphthalocyanine (ZnOCPc).

monohydrate, sodium borohydride, ammonium chloride, ammonium molybdate, urea, sodium hydroxide, and sulphuric acid were obtained from Saarchem. 1,8-Diazabicyclo[5,4,0]undec-7-ene (DBU) was obtained from Fluka. Ultra pure water was obtained from a Milli-Q Water System (Millipore Corp., Bedford, MA, USA). Solvent mixture: (1:1, 0.1 M NaOH, ethanol) was employed.

2.2. Synthesis of ZnPc derivatives and quantum dots

Zinc tetracarboxy (ZnTCPc), octacarboxy (ZnOCPc) and tetrasulphonated (ZnTSPc) phthalocyanines were synthesized and characterized according to reported methods [27–30]. CdTe quantum dots were synthesized using wet chemical routes with thioglycolic acid and 2-mercaptoethanol cappings, using reported methods [4]. Briefly, $CdCl_2$ 0.22 g (1.18 mmol) was dissolved in 65 mL of deionized water and 0.26 g (2.86 mmol) TGA or 2-ME was added to the $CdCl_2$ solution. The pH of this precursor solution was adjusted to 11.5 with 1 M NaOH and left under a flow of nitrogen gas for half an hour. The solution of NaHTe was prepared by modified literature method [4] as follows: 0.05 M NaOH was reacted with H_2Te gas (the latter generated by reaction of $NaBH_4$ with Te powder in the presence of 0.5 M H_2SO_4 under a flow of nitrogen gas). Then the freshly prepared NaHTe 0.18 g (1.2 mmol) was added to the precursor solution. The solution was then refluxed under air at 100 °C for different times to control the size of the CdTe QDs. Precipitation of the QDs from the aqueous colloidal solution was achieved by using propan-2-ol yielding a yellow–green and orange–maroon colour of CdTe quantum dots powder for 2-ME and TGA cappings, respectively.

The quantum dots sizes were estimated using a polynomial fitting function (Eq. (1)) derived in the literature [36]

$$D = (9.8127 \times 10 - 7)\lambda^3 - (1.7147 \times 10 - 3)\lambda^2 + (1.0064)\lambda - (194.84) \quad (1)$$

where λ is the absorption maxima of the QDs. The fitting function is not valid for sizes of quantum dots outside the size range of 1–9 nm [36]. It is valid in this work since as reported before [32] the quantum dots sizes are within this range.

2.3. Photophysical studies

Fluorescence quantum yields (Φ_F) were determined by comparative method [37] using the following equation:

$$\Phi_F = \Phi_{F(Std)} \frac{F \cdot A_{Std} \cdot n^2}{F_{Std} \cdot A \cdot n_{Std}^2} \quad (2)$$

where F and F_{Std} are the areas under the fluorescence curves of the MPc derivatives and the reference, respectively. A and A_{Std} are the absorbances of the sample and reference at the excitation wavelength, and n and n_{Std} are the refractive indices of solvents used for the sample and standard, respectively. ZnPc in DMSO was used as a standard, $\Phi_F = 0.20$ [38] for the determination of fluorescence quantum yields of the ZnPc derivatives in the 0.1 M NaOH:ethanol solvent mixture. Rhodamine 6G in ethanol with $\Phi_F = 0.94$ was employed as the standard for the quantum dots [39,40]. Both the sample and the standard were excited at the same relevant wavelength. The fluorescence quantum yields of the QDs are represented as $\Phi_{F(QD)}$, where QD represents either 2-ME or TGA capped QDs. And for ZnPc complexes the Φ_F are represented as $\Phi_{F(ZnPc)}$ (where ZnPc represents ZnTSPc, ZnOCPc, ZnTCPc). The determined fluorescence quantum yield values of the QDs were employed in determining their fluorescence quantum yields in the mixture with ZnPc derivatives ($\Phi_{F(QD)}^{Mix}$) using a modified form of Eq. (2) as shown by

$$\Phi_{F(QD)}^{Mix} = \Phi_{F(QD)} \frac{F_{QD}^{Mix}}{F_{QD}} \quad (3)$$

where $\Phi_{F(QD)}$ is the fluorescence quantum yield of the QDs alone, and was used as standard, $F_{QD}{}^{Mix}$ is the fluorescence intensity of QDs in the mixture (with ZnPc derivatives) when excited at the excitation wavelength of the QDs (500 nm) and F_{QD} is the fluorescence intensity of the QD alone at the same excitation wavelength.

Triplet quantum yields were determined using a comparative method based on triplet decay, using the following equation:

$$\Phi_T^{Sample} = \Phi_T^{Std} \frac{\Delta A_T^{Sample} \cdot \varepsilon_T^{Std}}{\Delta A_T^{Std} \cdot \varepsilon_T^{Sample}} \quad (4)$$

where ΔA_T^{Sample} and ΔA_T^{Std} are the changes in the triplet state absorbance of the MPc derivatives and the standard, respectively. ε_T^{Sample} and ε_T^{Std} are the triplet state extinction coefficients for the ZnPc derivative and standard, respectively, and were determined as previously reported [41]. Φ_T^{Std} is the triplet state quantum yield for the standard, ZnTSPc in aqueous solution, $\Phi_T^{Std} = 0.56$ [42]. Φ_T was also determined for the mixture of QDs and ZnPc derivatives and is represented as $\Phi_{T(ZnPc)}^{Mix}$ and the corresponding triplet lifetime as $\tau_{T(ZnPc)}^{Mix}$. The error in the determination of triplet yield was ±10%.

2.4. Determination of FRET parameters

Fluorescence resonance energy transfer (FRET) involves energy transfer from a photoexcited donor fluorophore to an acceptor fluorophore of a different species which is in close proximity. FRET is dependent on the center-to-center separation distance between

donor and acceptor (r), the degree of spectral overlap of the donor's fluorescence emission spectrum and the acceptor's absorption spectrum [33,40]. There is a decrease of the donor photoemission and an increase in the acceptor's fluorescence when FRET has occurred. FRET efficiency (Eff) is determined experimentally from the fluorescence quantum yields of the donor in the absence ($\Phi_{F(QD)}$) and presence ($\Phi^{Mix}_{F(QD)}$) of the acceptor using Eq. (5) [33,40]

$$\text{Eff} = 1 - \frac{\Phi^{Mix}_{F(QD)}}{\Phi_{F(QD)}} \quad (5)$$

FRET efficiency (Eff) is related to r (Å) by Eq. (6) [40]

$$\text{Eff} = \frac{R_0^6}{R_0^6 + r^6} \quad (6)$$

where R_0 (The Förster distance, Å) is the critical distance between the donor and the acceptor molecules for which efficiency of energy transfer is 50% and depends on the quantum yield of the donor, Eq. (7) [40]

$$R_0^6 = 8.8 \times 10^{23} \kappa^2 n^{-4} \Phi_{F(QD)} J \quad (7)$$

where κ^2 is the dipole orientation factor; n, the refractive index of the medium; Φ_F, the fluorescence quantum yield of the donor in the absence of the acceptor; and J (cm^6) is the Förster overlap integral, defined by

$$J = \int f_{QD}(\lambda)\varepsilon_{ZnPc}(\lambda)\lambda^4 d\lambda \quad (8)$$

where f_{QD} is the normalized QD emission spectrum and ε_{ZnPc}, is the molar extinction coefficient of ZnPc derivatives. In this case, it is assumed that κ^2 is 2/3; such assumption is often made for donor–acceptor pairs in a liquid medium, which are considered to be isotropically oriented during their fluorescence lifetimes. λ is the wavelength of the acceptor, the Q band. FRET parameters were computed using the programme PhotochemCAD [43]. The overlap integral (J) has been defined in several ways with different units [40]. The program PhotochemCAD gives the units as cm^6 using ε in $M^{-1}\,cm^{-1}$ and the wavelength in nm.

2.5. Equipment

Fluorescence excitation and emission spectra were recorded on a Varian Eclipse spectrofluoremeter. UV–Vis spectra were recorded on a Varian 500 UV–Vis/NIR spectrophotometer.

Laser flash photolysis experiments were performed with light pulses produced by a Quanta-Ray Nd: YAG laser providing 400 mJ, 90 ns pulses of laser light at 10 Hz, pumping a Lambda-Physik FL3002 dye (Pyridin 1 dye in methanol). Single pulse energy ranged from 2 to 7 mJ. The analyzing beam source was from a Thermo Oriel xenon arc lamp, and a photomultiplier tube was used as a detector. Signals were recorded with a digital real-time oscilloscope (Tektronix TDS 360). The triplet life times were determined by exponential fitting of the kinetic curves using the program Origin Pro 7.5.

3. Results and discussion

3.1. Absorption and emission spectra

The synthesis of the ZnPc complexes (ZnTCPc, ZnOCPc and ZnTSPc) is well established, and in this work literature methods of synthesis and characterization were employed and gave expected results [27–30]. The quantum dots (QDs) were also synthesized using literature methods [4]. QDs are characterized by their absorption and photoluminescence spectra which are also related to their size. The CdTe QDs synthesized in this work according to literature methods, gave characteristic spectral behavior [4]. As heating is prolonged during the formation of QDs, both the absorption and the emission spectra continue to get red shifted as the quantum dots grow [44]. The 2-ME capped CdTe QDs had their first emission peak at 524 nm after 15 min of heating under reflux, and their growth ceased when they reached 555 nm (Fig. 2a) after heating for 64 h. The first emission peak was observed around 525 nm after 15 min of heating for TGA capped CdTe quantum dots and the peak shifted to 645 nm (Fig. 2b) after 56 h of reflux, at which time they stopped growing. It was observed that the 2-ME capped CdTe nanoparticles grow at a much slower rate than those that were capped with TGA as was mentioned in literature [44]. The estimated full width at half maximum (FWHM) was 60 nm for the 2-ME capped CdTe nanoparticles (at 555 nm) and 83 nm for the TGA capped counterparts (at 645 nm). The sizes (diameter) of QDs were used for this study are 3.3 and 4.2 nm for 2-ME and TGA capped QDs, respectively.

Absorbance and fluorescence emission spectra of the MPc complexes are shown in Fig. 3 (for ZnTSPc and ZnOCPc) in a mixture of 0.1 M NaOH and ethanol (50:50). In this solvent mixture, the ZnPc derivatives are monomeric. Aggregation in MPc complexes is due to a coplanar association of rings, resulting in splitting and broadening of spectra, with a blue shifted peak at ~630 nm being due to the aggregate. Addition of organic solvents normally breaks the aggregates, resulting in monomeric species, hence the NaOH:ethanol solvent mixture was employed in this work. The ZnPc derivatives obeyed Beer's law for concentrations less than 1×10^{-5} mol dm^{-3} in this solvent mixture. For all the ZnPc complexes (Fig. 3), the fluorescence emission spectra were mirror images of the absorption spectra which in turn were similar to excitation spectra. At the high pH employed for the synthesis of the QDs and also used for the photophysical studies, the 2-ME and TGA capping will be ionized. It is known that the thiol moiety donates electrons to the surface of QDs, hence reducing the so called "blinking" [26]. The MPcs were not chemically linked to the ligands on the QDs surface, and thus the MPcs are most likely to adsorb onto the surface of the QDs.

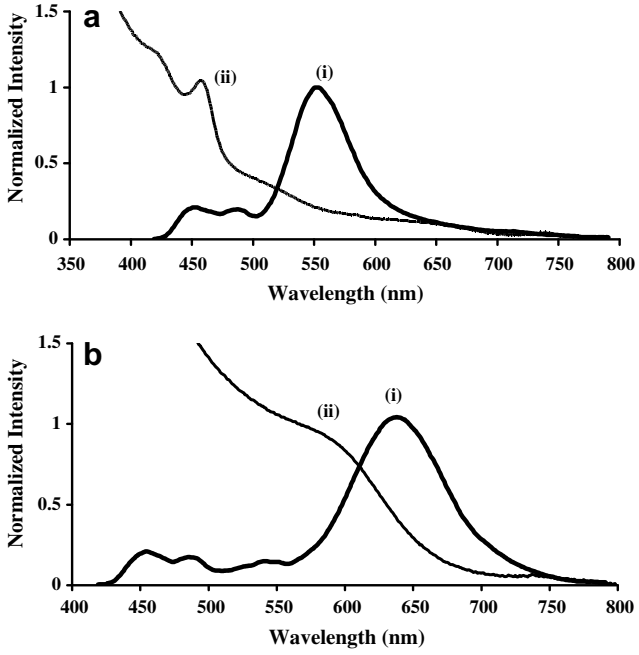


Fig. 2. (i) Emission and (ii) absorbance spectra of (a) CdTe–2-ME and (b) CdTe-TGA and in 50:50, NaOH:EtOH solution.

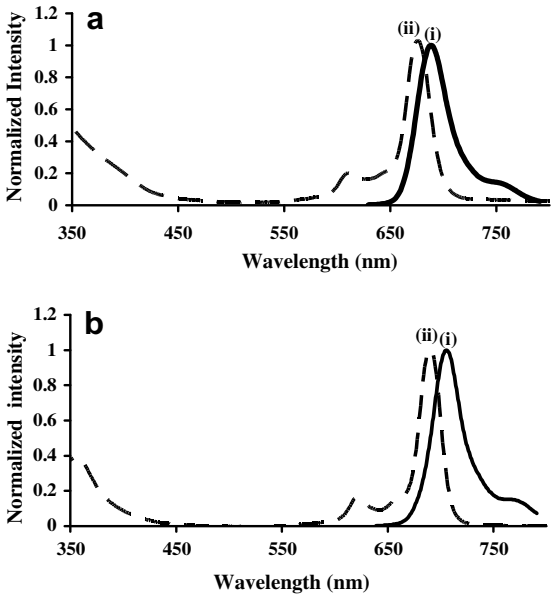


Fig. 3. Fluorescence (i) and absorbance (ii) spectra of (a) ZnTSPc (excitation = 610 nm) and (b) ZnOCPc (excitation = 620 nm) in 50:50, NaOH:EtOH solution.

3.2. Fluorescence quantum yields and energy transfer studies

Fluorescence quantum yield (Φ_F) values of the ZnPc derivatives (in the absence of QDs) are shown in Table 1 for excitation at 630 nm. ZnTSPc and ZnOCPc gave Φ_F values of 0.21 and a very low value for ZnTCPc (Φ_F values <0.01) was obtained. The Φ_F values for the CdTe QDs were calculated in 0.1 M NaOH:ethanol solvent mixture using Eq. (2) and are listed in Table 1. The fluorescence quantum yields (Φ_F) of the QDs were observed to be fairly low (0.037 for 2-ME capped and 0.11 for TGA capped) and they decreased further in the presence of Pc's. The lower fluorescence quantum yields of QDs was expected because as the QD (donor) particles fluoresce there is a transfer of energy to the MPc molecules (acceptor) and this reduces the fluorescence intensity of the QDs in the QD–MPc mixture through FRET (discussed below), hence the reduced quantum yields of the QDs in the QD–MPc mixture.

As stated above the efficiency of energy transfer depends upon the amount of spectral overlap between the emission spectrum of the donor and the absorption spectrum of the acceptor. A poor overlap was obtained for 2-ME capped QDs (Fig. 4). CdTe-TGA QDs had a good overlap with all the MPcs (Fig. 5), hence FRET parameters were calculated only for the mixture of CdTe-TGA capped QDs and ZnPc derivatives.

Excitation of the QDs at 500 nm in the presence of ZnPc derivatives, where Pcs do not absorb, resulted in significant fluorescence of the ZnPc derivatives as observed in Fig. 6. The 2-ME-QDs have been left out from Fig. 6 due to weak overlap between the emission spectra of 2-ME-QDs and absorption spectra of ZnPc derivatives. There was clear transfer of energy (FRET) from the TGA QDs to ZnPc derivatives (for ZnTSPc and ZnOCPc), Fig. 6a and b. This is judged by the increase in the emission spectra of ZnPc derivatives in the presence of QDs. There was insignificant emission by these two complexes (in the absence of QDs) on excitation at 500 nm, Fig. 6a–c (curves ii). For ZnTCPc there was no increase in the emission spectra of ZnTCPc probably due to a small fraction of fluorescing molecules of the Pc (Fig. 6c). This complex has a very low Φ_F (<0.01, Table 1), hence no fluorescence peak is observed, but there was a decrease in the fluorescence intensity of the QDs.

The overlap integral (J) values were computed using PhotochemCAD [43]. The J values are usually of the order 10^{-14} cm^6 for porphyrin based molecules and the values obtained in this work were of the order 10^{-13} cm^6 for the overlap between the ZnPc derivatives and CdTe QDs, Table 2. The overlap integral was largest for ZnTSPc in the presence of CdTe-TGA QDs and decreasing as follows: ZnTSPc > ZnOCPc > ZnTCPc. It would be reasonable to assume that the QD–Pc mixture having the highest J value would also have the highest efficiency of energy transfer (Eff, calculated using Eq. (5)) from the QD to the Pc, and this was observed in Table 2 for ZnTSPc.

The values of the Förster distance, R_0 (Å) which is the critical distance between the donor and the acceptor molecules for which efficiency of energy transfer is 50% [43,44], were computed with PhotochemCAD and the values are shown in Table 2. The center-to-center separation distance (r, Å) between donor and acceptor chromophores, were calculated using Eq. (6) and the values are shown in Table 2, ZnOCPc–CdTe-TGA QDs mixture showed the lowest value of r compared to the others. This indicates that the ZnOCPc is in close proximity to the donor (QDs) and thus there should be an ease of energy transfer (Eff) between the excited TGA capped QDs and the ZnOCPc. The center to center distance (r) increased with MPc in the order ZnTSPc > ZnTCPc > ZnOCPc for TGA capped QDs–MPc mixture. However it is ZnTSPc with the largest r (Å) and J (cm^6), which had the largest FRET efficiency and not ZnOCPc.

3.2.1. Triplet quantum yields (Φ_T) and lifetime (τ_T) studies

The transient absorption spectra were recorded in argon degassed solutions by exciting the ZnPc photosensitizer (in NaOH:EtOH mixture) in the Q band region and recording the transient absorption spectra point by point from 400 to 820 nm (Fig. 7), showing a triplet absorption near 530 nm. A representative decay profile is shown in Fig. 8. The triplet decay curves for ZnPc derivatives alone and in the presence of QDs were similar. The triplet

Table 1
Fluorescence quantum yields of QDs and photophysical parameters of ZnPc derivatives in the presence of QD's in 0.1 M NaOH/ethanol (1:1)

ZnPc derivative[b]	$\Phi^{Mix}_{F(QD)}$ λ_{exc} = 500 nm[a]	$\Phi_{F(ZnPc)}$ λ_{exc} = 630 nm	$\Phi^{Mix}_{T(ZnPc)}$ [b]	$\tau^{Mix}_{T(ZnPc)}$ (μs)[b]
ZnTSPc				
ZnTSPc + CdTe-QD (TGA)	0.014	0.21	0.25 (0.56)	230 (170)
ZnTSPc + CdTe-QD (2-ME)	0.011	0.21	0.44 (0.56)	160 (170)
ZnTCPc				
ZnTCPc + CdTe-QD (TGA)	0.06	<0.01	0.53 (0.50)	1300 (600)
ZnTCPc + CdTe-QD (2-ME)	0.017	<0.01	0.34 (0.50)	730 (600)
ZnOCPc				
ZnOCPc + CdTe-QD (TGA)	0.018	0.21	0.63 (0.75)	190 (140)
ZnOCPc + CdTe-QD (2-ME)	0.012	0.21	0.72 (0.75)	130 (140)

[a] QDs size: 2-ME = 3.3 nm and TGA = 4.2 nm. TGA = thioglycolic acid, 2ME = 2-mercaptoethanol. Φ_F values for quantum dots alone are: CdTe-2ME = 0.037; CdTe-TGA = 0.11.
[b] Values in brackets are for ZnPc derivatives in the absence of QDs.

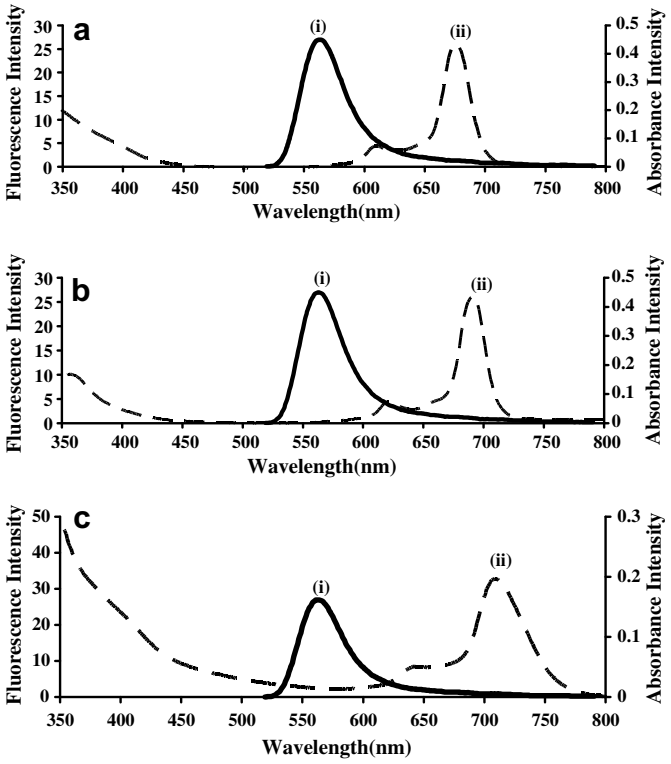


Fig. 4. Emission of CdTe (2-ME) (i) and absorbance (ii) of (a) ZnTSPc, (b) ZnOCPc and (c) ZnTCPc in 50:50, NaOH:EtOH solution. $\lambda_{excitation}$ = 500 nm.

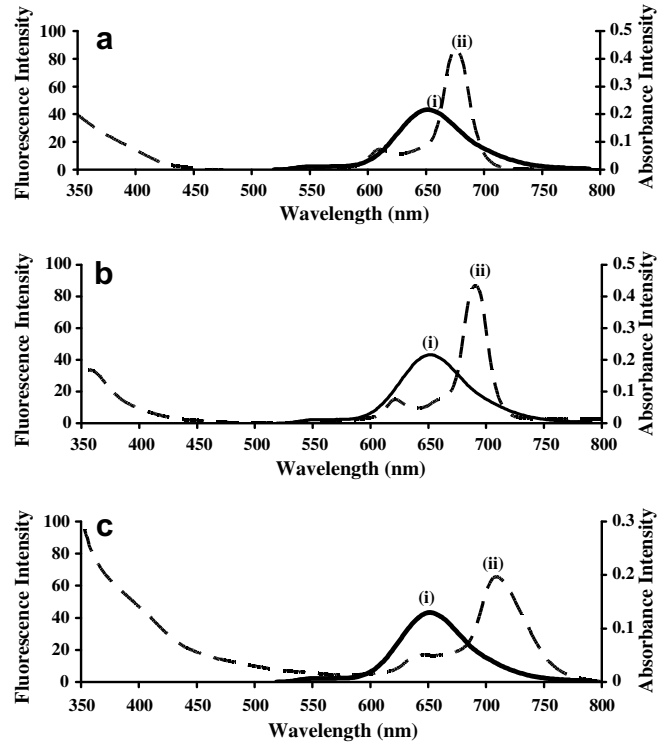


Fig. 5. Emission of CdTe (TGA) (i) and absorbance (ii) of (a) ZnTSPc, (b) ZnOCPc and (c) ZnTCPc in 50:50, NaOH:EtOH solution. $\lambda_{excitation}$ = 500 nm.

curve in Fig. 8 obeyed second order kinetics. This is typical of MPc complexes at high concentrations (>1×10^4 M) [45] due to the triplet–triplet recombination. The concentrations employed in this

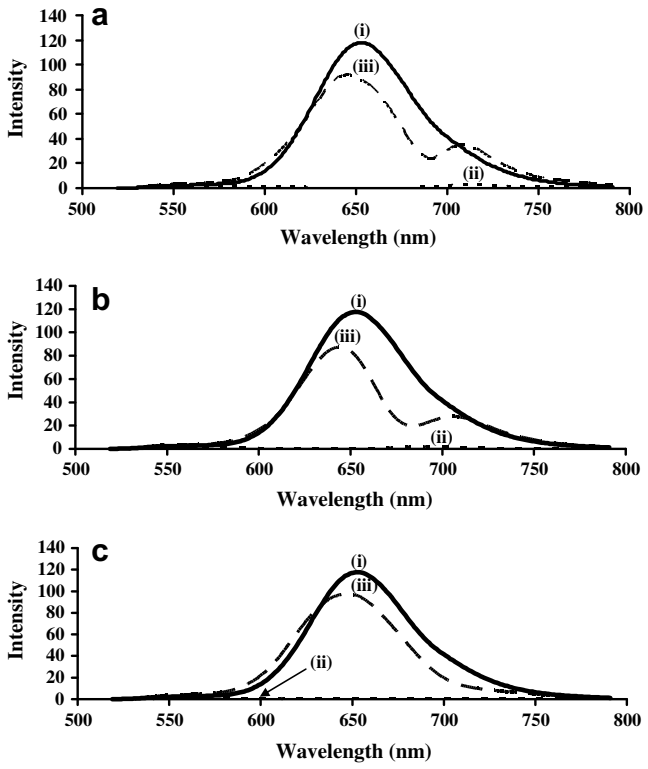


Fig. 6. Emission of (i) CdTe (TGA) alone, (ii) ZnPc derivative alone and (iii) a mixture of ZnPc derivative and QDs. (a) ZnOCPc, (b) ZnTSPc and (c) ZnTCPc in 50:50, NaOH:EtOH solution. $\lambda_{excitation}$ = 500 nm.

Table 2
Energy transfer parameters for ZnPc–CdTe-TGA QDs interactions in 0.1 M NaOH:ethanol (1:1)

Capping thiol	J (10^{13} cm^6)	R_0 (Å)	r (Å)	Eff
ZnTSPc + CdTe-QD (TGA)	18	57	67	0.3
ZnTCPc + CdTe-QD (TGA)	7.2	49	63	0.2
ZnOCPc + CdTe-QD (TGA)	7.9	50	60	0.2

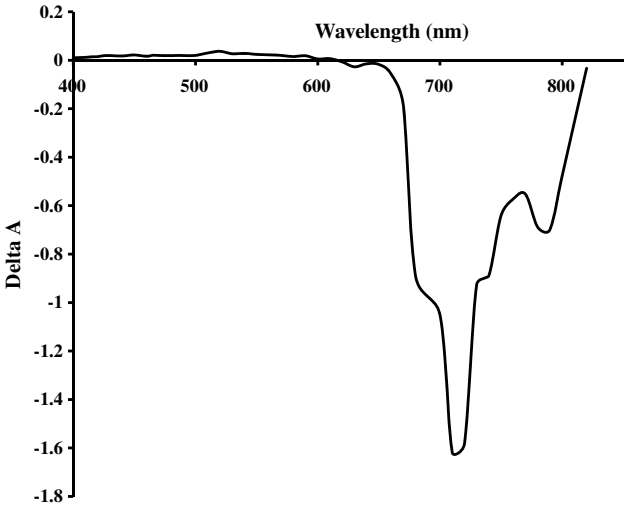


Fig. 7. Transient differential spectrum of complex ZnOCPc (excitation wavelength = 690 nm), in 50:50, NaOH:EtOH solution.

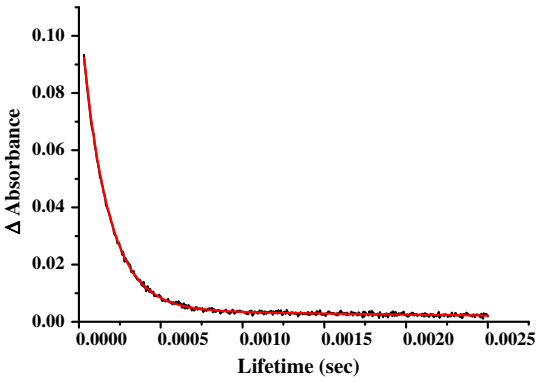


Fig. 8. A representative (for ZnOCPc) triplet decay curve in 50:50, NaOH:EtOH solution.

work were in this range hence triplet–triplet recombination is expected. Fig. 7 shows that the Q band is split upon laser excitation, thus suggesting change in symmetry.

Φ_T values provide a measure of the fraction of absorbing molecules that undergo intersystem crossing (ISC) to the triplet state (Φ_T). The variation of Φ_T values of ZnPc derivatives in 0.1 M NaOH:ethanol and in the presence of the QDs are shown in Table 1. The Φ_T of the ZnOCPc complex both in the presence and the absence of QDs was much larger than those of the ZnTSPc and ZnTCPc derivatives. This indicates that a greater portion of the ZnOCPc molecules undergoes ISC. Although it could be expected that the Φ_T would increase in the presence of the quantum dots because they contain Cd and Te atoms which are heavy and thus would encourage ISC, it was observed that the Φ_T of the MPcs decreased (except for ZnTCPc–CdTe-TGA and ZnOCPc–CdTe-2-ME which remained unchanged considering the experimental error) in the presence of the QDs. A slight increase in the Φ_T values was reported by us [32] for AlTSPc in the presence of CdTe QDs capped with thioglycolic acid or 3-mercaptopropionic acid and for cysteine capped QDs. Thus the QDs do not seem to induce an increase in Φ_T values as expected on the basis of the heavy atom effect.

The triplet lifetimes (τ_T) of the ZnPc derivatives were higher in the presence of QDs (except for ZnOCPc in the presence of 2-ME capped QDs, where τ_T values were slightly lower in the presence of QDs). The higher τ_T values of the MPc derivatives in the presence of QDs, corresponds well with the lowering of the Φ_T values of the ZnPc derivatives in the presence of QDs. The higher τ_T values in the presence of QDs then shows that the MPc molecules will spend more time in the triplet state thereby allowing for increased photosensitizing abilities.

4. Conclusions

The interaction of CdTe quantum dots with ZnPc derivatives shows that a strong overlap occurs between the emission of the TGA capped QDs and the absorption spectra of the ZnPc derivatives (ZnTSPc, ZnOCPc, and ZnTCPc). The largest fluorescence energy transfer (FRET) was observed for ZnTSPc followed by ZnOCPc and then ZnTCPc. The triplet quantum yields of the ZnPc derivatives decreased in the presence of QDs but the lifetimes increased, hence making the combination of ZnPc derivatives and QDs potential candidates for applications as photosensitisers in PDT.

Acknowledgements

This work has been supported by the National Research Foundation (NRF GUN 2053657) of South Africa as well as Rhodes University. SM thanks DAAD foundation for a scholarship.

References

[1] M. Gao, S. Kirstein, H. Möhwald, J. Phys. Chem. B 102 (1998) 8360.
[2] A. Eychmuller, A.L. Rogach, Pure Appl. Chem. 72 (2000) 179.
[3] J. Aldana, Y.A. Wang, X. Peng, J. Am. Chem. Soc. 123 (2001) 8844.
[4] A.L. Rogach, L. Katsikas, A. Kornowski, D. Su, A. Eychmüller, H. Weller, Ber. Bunsenges. Phys. Chem. 100 (1996) 1772.
[5] H. Zhang, Z. Zhou, B. Yang, J. Phys. Chem. B 107 (2003) 8.
[6] M. Zhou, I. Ghosh, Peptide Sci. 88 (2006) 325.
[7] A.G. Kanaras, C. Sönnichsen, H. Liu, A.P. Alivisatos, Nano Lett. 5 (2005) 2164.
[8] L. Manna, D.J. Milliron, A. Meisel, E.C. Scher, A.P. Alivisatos, Nat. Mater. 2 (2003) 382.
[9] D.J. Milliron, S.M. Hughes, Y. Cui, L. Manna, J. Li, L.-W. Wang, A.P. Alivisatos, Nature 430 (2004) 190.
[10] H. Liu, A.P. Alivisatos, Nano Lett. 4 (2004) 2397.
[11] A.M. Smith, S. Nie, Analyst 129 (2004) 673.
[12] S. Sapra, D.D. Sarma, Pramana 65 (2005) 565.
[13] R.E. Bailey, A.M. Smith, S. Nie, Physica E 25 (2004) 1.
[14] X. Gao, S. Nie, Trends Biotechnol. 21 (2003) 371.
[15] R.E. Bailey, S. Nie, J. Am. Chem. Soc. 125 (2003) 7100.
[16] R. Bakalova, H. Ohba, Z. Zhelev, T. Nagase, R. Jose, M. Ishikawa, Y. Baba, Nano Lett. 4 (2004) 1567.
[17] Z. Lin, S. Cui, H. Zhang, Q. Chen, B. Yang, X. Su, J. Zhang, Q. Jin, Anal. Biochem. 319 (2003) 239.
[18] A.C.S. Samia, X. Chen, C. Burda, J. Am. Chem. Soc. 125 (2003) 15736.
[19] A.C.S. Samia, S. Dayal, C. Burda, Photochem. Photobiol. 82 (2006) 617.
[20] J. Guo, W. Yang, C. Wang, J. Phys. Chem. B 109 (2005) 17467.
[21] L. Shi, B. Hernandez, M. Selke, J. Am. Chem. Soc. 128 (2006) 6278.
[22] N. Kaji, M. Tokeshi, Y. Baba, Anal. Sci. 23 (2007) 21.
[23] E.R. Goldman, I.L. Medintz, H. Mattoussi, Anal. Bioanal. Chem. 384 (2006) 560.
[24] I.L. Medintz, H.T. Uyeda, E.R. Goldman, H. Mattoussi, Nat. Mater. 4 (2005) 435.
[25] Y. Wang, N. Herron, J. Phys. Chem. 95 (1991) 525.
[26] S. Hohng, T. Ha, J. Am. Chem. Soc. 126 (2004) 1324.
[27] H. Shirai, A. Maruyama, K. Kobayashi, N. Hojo, Makromol. Chem. 181 (1980) 575.
[28] K. Sakamoto, E. Ohno, Prog. Org. Coat. 31 (1997) 139.
[29] M.O. Liu, C. Tai, M. Sain, A.T. Hu, F. Chou, Photochem. Photobiol. 165 (2004) 131.
[30] J.H. Weber, D.H. Busch, Inorg. Chem. 4 (1965) 469.
[31] S. Dayal, Y. Lou, A.C.S. Samia, J.C. Berlin, M.E. Kenney, C. Burda, J. Am. Chem. Soc. 128 (2006) 13974.
[32] M. Idowu, J.-Y. Chen, T. Nyokong, New J. Chem. 32 (2008) 290.
[33] L. Stryer, Annu. Rev. Biochem. 47 (1978) 819.
[34] L. Lankiewicz, J. Malicka, W. Wiczk, Acta Biochim. Pol. 44 (1997) 477.
[35] D. Sokol, X. Zhang, P. Lu, A. Gewirtz, Proc. Natl. Acad. Sci. USA 35 (1998) 11538.
[36] W.W. Yu, L. Qu, W. Guo, X. Peng, Chem. Mater. 15 (2003) 2854.
[37] S. Fery-Forgues, D. Lavabre, J. Chem. Ed. 76 (1999) 1260.
[38] A. Ogunsipe, J.-Y. Chen, T. Nyokong, New J. Chem. 28 (2004) 822.
[39] R.F. Kubin, A.N. Fletcher, J. Lumin. 27 (1982) 455.
[40] J.R. Lakowicz, Principles of Fluorescence Spectroscopy, second ed., Kluwer Academic/Plenum Publishers, New York, 1999.
[41] V. Chauke, A. Ogunsipe, M. Durmus, T. Nyokong, Polyhedron 26 (2007) 2663.
[42] A. Harriman, M.C. Richoux, J. Chem. Soc., Faraday Trans. 76 (1980) 1618.
[43] H. Du, R.A. Fuh, J. Li, L.A. Cockan, J.S. Lindsey, Photochem. Photobiol. 68 (1998) 141.
[44] N. Gaponik, V.D. Talapin, K. Hoppe, E.V. Shevchenko, A. Kornowski, A. Eychmuller, H. Weller, J. Phys. Chem. B 106 (2002) 7177.
[45] M.G. Debacker, O. Deleplanque, B. Van Vlieberge, F.X. Sauvage, Laser Chem. 8 (1988) 1.

Table 1
Crystal data and structure refinement for **1**, **2**, and **3**

	$[Ir_2(\mu\text{-}SC_6F_5)_2(cod)_2]$ (**1**)	$[Ir(SC_6F_5)(H)(SiPh_3)(XNC)_3](C_6H_6)$ (**2**)	$[Ir_3(\mu\text{-}SC_6F_5)_2(SC_6F_5)(\mu\mu'\text{-}XNC)(XNC)_4(cod)]$-(*n*-hexane) (**3**)
Empirical formula	$C_{28}H_{24}F_{10}Ir_2S_2$	$C_{54}H_{46}F_5IrN_3SSi$	$C_{77}H_{71}F_{15}Ir_3N_5S_3$
Formula weight	998.99	1084.29	2024.17
Temperature (*K*)	173(2)	173(2)	173(2)
Wavelength (Å)	0.71073	0.71073	0.71073
Crystal system	triclinic	monoclinic	monoclinic
Space group	$P\bar{1}$	$P2_1/n$	$P2_1/n$
Unit cell dimensions			
a (Å)	9.9103(2)	11.6883(2)	14.1753(2)
b(Å)	11.4053(2)	24.0283(5)	20.2895(3)
c(Å)	13.0978(2)	16.9430(3)	25.6554(4)
α (°)	76.705(1)	90	90
β (°)	79.999(1)	98.102(1)	95.804(1)
γ (°)	75.487(1)	90	90
Volume (Å^3)	1384.17(4)	4710.95(15)	7340.92(19)
Z	2	4	4
D_{calc} (Mg/m^3)	2.397	1.529	1.831
Goodness-of-fit on F^2	1.001	0.978	1.055
R indices [$I > 2\sigma(I)$]	$R_1 = 0.0265$, $wR_2 = 0.0603$	$R_1 = 0.0341$, $wR_2 = 0.0824$	$R_1 = 0.0305$, $wR_2 = 0.0642$
Minimum and maximum residual densities (e Å^{-3})	2.523 and −1.375	1.655 and −1.587	2.402 and −0.653

for X-ray diffraction were grown by evaporation of a chloroform solution.

2.3. Preparation of $[Ir(SC_6F_5)(H)(SiPh_3)(XNC)_3](C_6H_6)$ (**2**)

A stirred mixture of $[Ir_2(\mu\text{-}SC_6F_5)_2(cod)_2]$ (0.015 g, 0.030 mmol) and Ph_3SiH (0.009 g, 0.035 mmol) in benzene (~1 ml) was treated with xylyl isocyanide (0.012 g, 0.091 mmol) to give (within seconds) a pale yellow solution. The solution was concentrated and hexane was added. After 3 days at −20 °C colourless crystals were obtained which were washed with hexane. Yield: 0.018 g (53%). ^{1}H NMR (C_6D_6, 300 K) δ 7.90–6.57 (mults, aromatic H), 2.13 (S, 6H, CH_3), 2.10 (S, 12H, CH_3), −8.55 (S, 1H, IrH). Elemental analysis showed the percentage of carbon to be lower than that calculated for **2**, possibly as a result of loss of co-crystallised benzene.

2.4. Preparation of $[Ir_3(\mu\text{-}SC_6F_5)_2(SC_6F_5)(\mu,\mu'\text{-}XNC)(XNC)_4(cod)]$ (**3**)

A mixture of **1** (0.085 g, 0.017 mmol) and xylyl isocyanide (0.0025 g, 0.019 mmol) was dissolved in CH_2Cl_2 (~1 ml) to give a dark red solution. The solution was treated with hexane, concentrated and allowed to stand at −20 °C for 6 days to give an orange powder (2.3 mg) and a few small orange crystals/crystalline lumps. Yield of crystalline material ~0.5 mg (~4% based on Ir). ^{1}H NMR of the powder indicated a mixture of products. Attempts to repeat the result failed to yield crystals.

2.5. NMR spectroscopy

^{1}H spectra were recorded on a Bruker DRX 400 spectrometer and referenced to TMS (internal standard).

2.6. X-ray structure determination

Intensity data were collected on a Bruker APEX II CCD area detector diffractometer with graphite monochromated Mo Kα radiation (50 kV, 30 mA) using the APEX2 [17] data collection software. The collection method involved ω-scans of width 0.5° and 512 × 512 bit data frames. Data reduction was carried out using the program SAINT+ [18]. Face indexed absorption corrections were carried out for **1** and **2** using XPREP [18] while multiscan absorption corrections were carried out for **3** using SADABS. The crystal structures were solved by direct methods using SHELXTL [19]. Non-hydrogen atoms were first refined isotropically followed by anisotropic refinement by full matrix least-squares calculations based on F^2 using SHELXTL. With the exception of the hydride (structure **2**) all hydrogen atoms were first located in the difference map, then positioned geometrically and allowed to ride on their respective parent atoms. The hydride of **2** was placed geometrically, equidistant from the adjacent C, S and Si atoms and 1.60 Å from the iridium atom.

The structure of **2** contains disorder. One of the phenyl groups of the triphenylsilane was found to be disordered and was refined with isotropic atoms over three positions using rigid body restraints. Final occupancies were 0.36(1), 0.30(1) and 0.34(1) for the three respective positions. One of the neighbouring isocyanide ligands was also found to be disordered and was refined over two positions using rigid body, SIMU, SADI and FLAT restraints with the final occupancies being 0.48(1) and 0.52(1), respectively. The structure also contains a benzene solvent molecule which was found to be disordered over a centre of inversion. This was refined isotropically as a rigid body with a site occupancy of 0.5. Crystal and refinement data are given in Table 1.

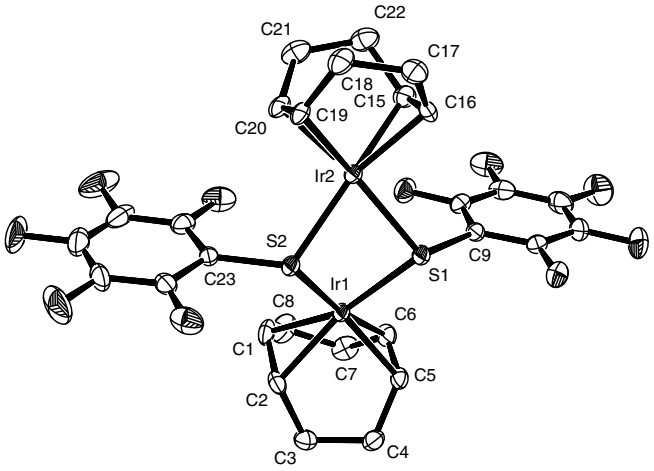


Fig. 1. Thermal ellipsoid plot of $[Ir_2(\mu\text{-}SC_6F_5)_2(cod)_2]$ (**1**) with ellipsoids drawn at the 30% probability level.

Table 2
Selected bond lengths (Å) and angles (°)

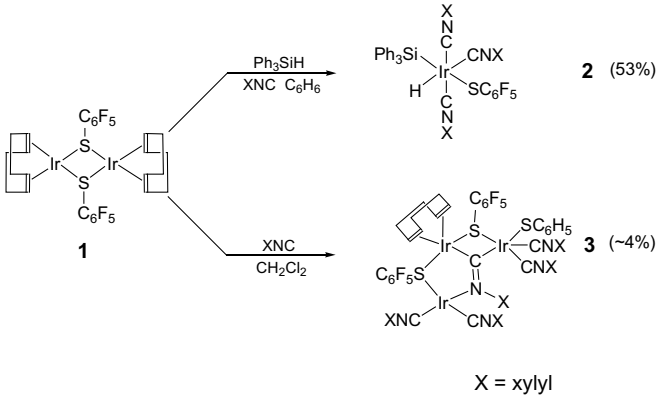
(a) $[Ir_2(\mu\text{-}SC_6F_5)_2(cod)_2]$ (**1**)					
Bond lengths					
Ir(1)–C(1)	2.124(4)	Ir(1)–S(2)	2.3466(10)	Ir(2)–S(1)	2.3622(10)
Ir(1)–C(2)	2.140(4)	Ir(2)–C(15)	2.125(4)	Ir(2)–S(2)	2.3598(9)
Ir(1)–C(5)	2.116(4)	Ir(2)–C(16)	2.130(4)	S(1)–C(9)	1.771(4)
Ir(1)–C(6)	2.143(4)	Ir(2)–C(19)	2.129(4)	S(2)–C(23)	1.765(4)
Ir(1)–S(1)	2.3629(9)	Ir(2)–C(20)	2.123(4)		
Bond angles					
S(1)–Ir(1)–C(1)	160.17(13)	S(2)–Ir(1)–C(1)	99.82(12)	Ir(1)–S(1)–C(9)	112.59(13)
S(1)–Ir(1)–C(2)	159.94(12)	S(2)–Ir(1)–C(2)	97.63(11)	Ir(1)–S(2)–C(23)	116.36(13)
S(1)–Ir(1)–C(5)	94.95(11)	S(2)–Ir(1)–C(5)	150.10(12)	Ir(2)–S(1)–C(9)	114.51(14)
S(1)–Ir(1)–C(6)	98.85(11)	S(2)–Ir(1)–C(6)	169.25(12)	Ir(2)–S(2)–C(23)	117.16(13)
S(1)–Ir(1)–S(2)	76.38(3)	Ir(1)–S(1)–Ir(2)	93.62(3)		
S(1)–Ir(2)–S(2)	76.14(3)	Ir(1)–S(2)–Ir(2)	94.10(3)		
(b) $[Ir(SC_6F_5)(H)(SiPh_3)(XNC)_3](C_6H_6)$ (**2**)					
Bond lengths					
Ir–S	2.4919(10)	Ir–C(21)	1.941(3)	Ir–C(41)	1.972(4)
Ir–Si	2.3963(10)	Ir–C(31)	1.994(4)		
Bond angles					
S–Ir–Si	172.91(4)	Si–Ir–C(21)	87.83(9)	C(21)–Ir–C(41)	168.15(15)
S–Ir–C(21)	90.05(9)	Si–Ir–C(31)	92.22(10)	C(31)–Ir–C(41)	92.98(14)
S–Ir–C(31)	94.80(10)	Si–Ir–C(41)	91.73(9)		
S–Ir–C(41)	88.95(9)	C(21)–Ir–C(31)	98.87(14)		
(c) $[Ir_3(\mu\text{-}SC_6F_5)_2(SC_6F_5)(\mu\mu'\text{-}XNC)(XNC)_4(cod)](n\text{-hexane})$ (**3**)					
Bond lengths					
Ir(1)–C(1)	2.203(5)	Ir(1)–S(3)	2.4624(13)	Ir(3)–C(71)	1.879(5)
Ir(1)–C(2)	2.201(5)	Ir(2)–C(41)	1.928(5)	Ir(3)–C(81)	1.872(6)
Ir(1)–C(5)	2.146(5)	Ir(2)–C(51)	1.920(6)	Ir(3)–N(60)	2.112(4)
Ir(1)–C(6)	2.148(5)	Ir(2)–C(61)	1.990(5)	Ir(3)–S(3)	2.3716(13)
Ir(1)–C(61)	2.011(5)	Ir(2)–S(1)	2.4726(13)	C(61)–N(60)	1.281(6)
Ir(1)–S(2)	2.4698(13)	Ir(2)–S(2)	2.3852(13)	Ir(1)–Ir(2)	2.6882(3)
Bond angles					
Ir(1)–C(61)–Ir(2)	84.41(18)	S(2)–Ir(2)–C(41)	168.80(15)	C(41)–Ir(2)–C(51)	94.7(2)
Ir(1)–S(2)–Ir(2)	67.22(3)	S(2)–Ir(2)–C(51)	95.22(15)	C(41)–Ir(2)–C(61)	95.80(19)
Ir(1)–S(3)–Ir(3)	103.97(5)	S(2)–Ir(2)–C(61)	76.27(14)	C(51)–Ir(2)–C(61)	107.4(2)
S(1)–Ir(2)–S(2)	95.53(4)	S(3)–Ir(1)–C(61)	78.73(14)	C(61)–N(60)–C(62)	117.7(4)
S(1)–Ir(2)–C(41)	87.54(15)	S(3)–Ir(3)–C(71)	170.83(16)	C(71)–Ir(3)–C(81)	90.7(2)
S(1)–Ir(2)–C(51)	101.53(15)	S(3)–Ir(3)–C(81)	96.58(16)	Ir(3)–N(60)–C(61)	122.0(3)
S(1)–Ir(2)–C(61)	150.42(14)	N(60)–Ir(3)–S(3)	81.64(11)	Ir(3)–N(60)–C(62)	120.0(3)
S(2)–Ir(1)–S(3)	87.32(4)	N(60)–Ir(3)–C(71)	91.16(18)		
S(2)–Ir(1)–C(61)	73.93(14)	N(60)–Ir(3)–C(81)	178.04(19)		

3. Results and discussion

The complex $[Ir_2(\mu\text{-}SC_6F_5)_2(cod)_2]$ (**1**) was reported a number of years ago by Terreros and co-workers [8] who prepared it from $[Ir_2(\mu\text{-}Cl)_2(cod)_2]$ using a mixture of C_6F_5SH and NEt_3. Our method, starting from $[Ir_2(\mu\text{-}OMe)_2(cod)_2]$, offers a slightly improved yield (75%). The structure of **1** (Fig. 1) has a geometry at Ir that can be described as square planar distorted towards square pyramidal, with the alkene groups each occupying a single coordination site. Selected bond lengths and angles are given in Table 2. The sharply angled Ir–S–Ir bonds cause the molecule to adopt a pyramidal structure with the dienes and C_6F_5 groups forming the base and the two sulphurs a truncated apex. Although the two iridiums bear identical substituents and bridging groups which closely approach a symmetrical arrangement, they are not related by any crystallographic symmetry element.

In dichloromethane at room temperature **1** is unreactive towards triphenylsilane, but upon addition of xylyl isocyanide (XNC) a product $[Ir(SC_6F_5)(H)(SiPh_3)(XNC)_3]$ (**2**) is rapidly formed regardless of whether one or three equivalents of XNC is used (Scheme 1). The geometry of **2** (Fig. 2) is distorted octahedral, with ligands showing displacement towards the hydride. The hydride (the presence of which was confirmed by a ^1H NMR signal at δ −8.55 ppm) was not located in the electron density map but instead geometrically inserted. One of the phenyl groups of the silane is disordered and was refined over three positions.

When complex **1** in dichloromethane is treated with one equivalent of XNC an immediate colour change from red to orange is observed. Attempts to isolate a product yielded small quantities of **3** (Scheme 1 and Fig. 3), a trinuclear complex containing two bridging thiolates and a triply bridging isocyanide. Complex **3** exists in two mirror image forms related, in the unit cell, by an inversion centre. Selected bond lengths and angles are given in Table 2. The N(60)–C(61) distance of 1.28 Å indicates a double bond consis-



Scheme 1.

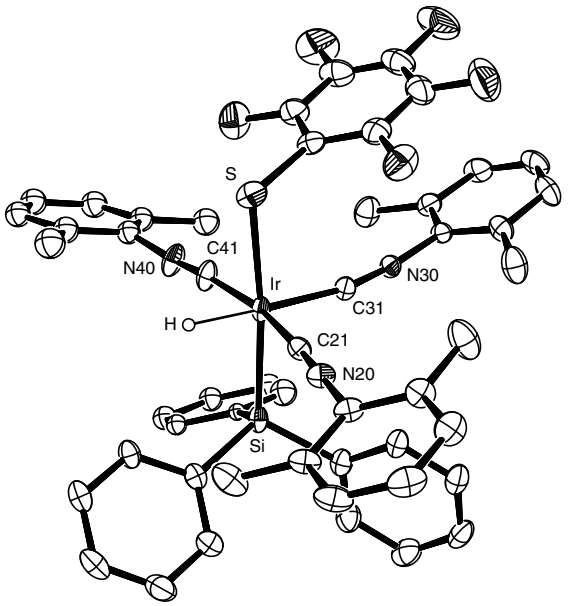


Fig. 2. Thermal ellipsoid plot of $[Ir(SC_6F_5)(H)(SiPh_3)(XNC)_3]$ (**2**) with ellipsoids drawn at the 30% probability level. A co-crystallised benzene is omitted. Hydride inserted geometrically.

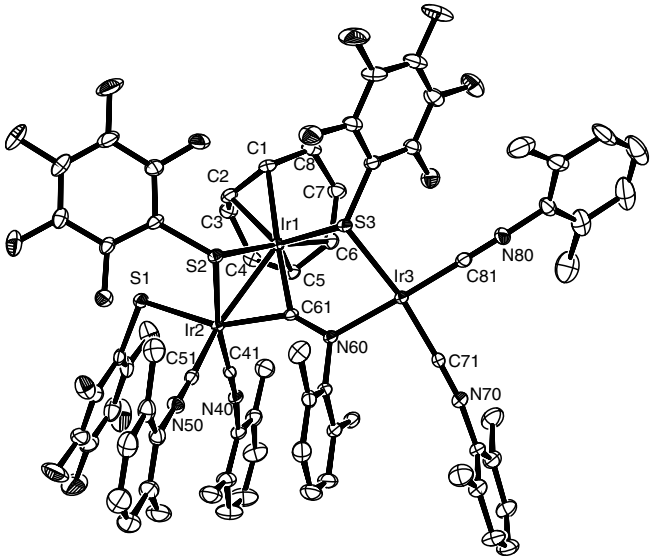


Fig. 3. Thermal ellipsoid plot of $[Ir_3(\mu\text{-}SC_6F_5)_2(SC_6F_5)(\mu\mu'\text{-}XNC)(XNC)_4(cod)]$ (**3**) with ellipsoids drawn at the 30% probability level. A co-crystallised *n*-hexane is omitted.

tent with an imino group, i.e. the bridging isocyanide might more accurately be regarded as an iminocarbene. In this formulation a lone pair of electrons becomes available on the nitrogen to partake in further bonding to give a triply bridged structure in which all three iridiums are nominally in the +1 oxidation state. Dinuclear iridium complexes having bridging (via carbon) isocyanides are known [20,21] as are trinuclear rhodium [22] and osmium [23–27] complexes having triply bridging isocyanides, bonded in the manner of complex **3**. To our knowledge **3** is the first example of an iridium complex exhibiting such bonding. Whilst it is possible to speculate that the initial stages of formation of **3** might involve nucleophilic attack of an electron-rich derivative of **1**, possibly $[Ir(SC_6F_5)(XNC)(cod)]$, on the α carbon of a coordinated isocyanide, further work is required to establish the identity of this reactive intermediate.

4. Supplementary data

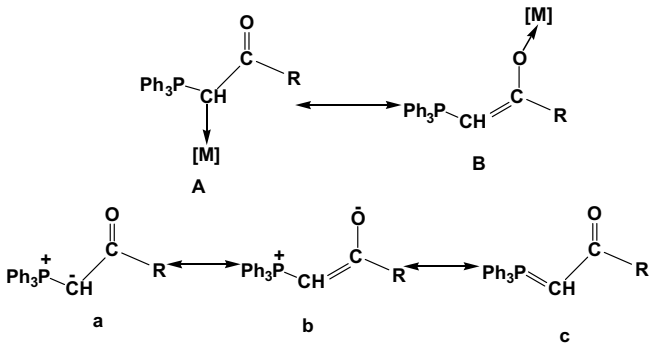
CCDC 668581, 668582 and 668583 contain the supplementary crystallographic data for **1**, **2** and **3**. These data can be obtained free of charge via http://www.ccdc.cam.ac.uk/conts/retrieving.html, or from the Cambridge Crystallographic Data Centre, 12 Union Road, Cambridge CB2 1EZ, UK; fax: (+44) 1223-336-033; or e-mail: deposit@ccdc.cam.ac.uk.

Acknowledgement

We thank the University of the Witwatersrand for financial support.

References

[1] I.G. Dance, Polyhedron 5 (1986) 1037.
[2] P. Kalck, Polyhedron 7 (1988) 2441.
[3] F. Monteil, R. Queau, P. Kalck, J. Organomet. Chem. 480 (1994) 177.
[4] H. Torrens, Coord. Chem. Rev. 196 (2000) 331.
[5] J. Cooke, M. Green, F.G.A. Stone, J. Chem. Soc. A (1968) 170.
[6] E.S. Bolton, R. Havlin, G.R. Knox, J. Organomet. Chem. 18 (1969) 153.
[7] P. Kalck, F. Senocq, M. Siani, A. Thorez, J. Organomet. Chem. 350 (1988) 77.
[8] I. Fonseca, E. Hernández, J. Sanz-Aparicio, P. Terreros, H. Torrens, J. Chem. Soc., Dalton Trans. (1994) 781.
[9] R. Salcedo, H. Torrens, Transition Met. Chem. 5 (1980) 247.
[10] D. Cruz-Garritz, R. Rodríguez, J. Leal, H. Torrens, Transition Met. Chem. 9 (1984) 284.
[11] L. Carlton, J. Organomet. Chem. 431 (1992) 103.
[12] V. Cîrcu, M.A. Fernándes, L. Carlton, Polyhedron 21 (2002) 1775.
[13] L. Carlton, L.V. Mokoena, M.A. Fernandes, Inorg. Chem. (submitted for publication).
[14] L. Carlton, J.J. Molapisi, J. Organomet. Chem. 609 (2000) 60.
[15] M.A. Bennett, D.L. Milner, J. Am. Chem. Soc. 91 (1969) 6983.
[16] S.D. Robinson, B.L. Shaw, J. Chem. Soc. (1965) 4997.
[17] APEX2 Version 2.0-1, Bruker AXS Inc., Madison, WI, USA, 2005.
[18] SAINT-NT Version 6.0 (includes XPREP and SADABS), Bruker AXS Inc., Madison, WI, USA, 2005.
[19] SHELXTL Version 5.1, Bruker AXS Inc., Madison, WI, USA, 1999.
[20] J. Wu, P.E. Fanwick, C.P. Kubiak, J. Am. Chem. Soc. 110 (1988) 1319.
[21] J. Wu, P.E. Fanwick, C.P. Kubiak, J. Am. Chem. Soc. 111 (1989) 7812.
[22] A.L. Balch, L.A. Fossett, M.M. Olmstead, Organometallics 6 (1987) 1827.
[23] A.V. Rivera, G.M. Sheldrick, M.B. Hursthouse, Acta Crystallogr. B34 (1978) 1985.
[24] H. Song, K. Lee, C.H. Lee, J.T. Park, H.Y. Chang, M.-G. Choi, Angew Chem., Int. Ed. 40 (2001) 1500.
[25] H. Song, K. Lee, M.-G. Choi, J.T. Park, Organometallics 21 (2002) 1756.
[26] H. Song, C.H. Lee, K. Lee, J.T. Park, Organometallics 21 (2002) 2514.
[27] H. Song, J.I. Choi, K. Lee, M.-G. Choi, J.T. Park, Organometallics 21 (2002) 5221.



Scheme 1.

series analyzer. Fourier transform IR spectra were recorded on a Shimadzu 435-U-04 spectrophotometer and samples were prepared as KBr pellets. ^{1}H, ^{13}C and ^{31}P spectra were recorded on a 90 MHz Jeol spectrometer. X-ray analysis was performed on a STOE IPDS-II diffractometer.

2.3. Synthesis of the ligand and the metal complexes

2.3.1. Synthesis of BAPPY

A solution of triphenylphosphine (0.52 g, 2 mmol) and bromobenzylacetate (0.42 g, 2 mmol) in dry chloroform (15 mL) was stirred at room temperature for 10 h. The resulting white precipitate was filtered off, washed with diethyl ether and dried. Further treatment with an aqueous solution of NaOH (0.5 M, 50 mL) led to elimination of HBr, giving the free ligand. Yield: 0.66 g (89.3%), m.p. 118–120 °C. *Anal.* Calc. for for $C_{27}H_{20}O_2P$: C, 79.00; H, 5.64. Found: C, 78.44; H, 5.43%.

2.3.2. Synthesis of $[(BAPPY)\cdot HgCl_2]_2$ (**1**)

General procedure: To a magnetically stirred solution of $HgCl_2$ (0.135 g, 0.5 mmol) in methanol (10 mL), was added a methanolic solution (5 mL) of the ylide BAPPY (0.205 g 0.5 mmol). After 8 h the solvent was removed under reduced pressure to 3 mL. After addition of diethyl ether (30 mL) a white solid product was separated by filtration. Yield: 0.28 g (82.7%), m.p. 173–176 °C. *Anal.* Calc. for $C_{54}H_{40}Cl_4Hg_2O_4P_2$: C, 47.55; H, 3.39. Found: C, 46.26; H, 3.17%.

2.3.3. Synthesis of $[(BAPPY)\cdot HgBr_2]_2$ (**2**)

Yield: 0.35 g (85.2%), m.p. 177–179 °C. *Anal.* Calc. for $C_{54}H_{40}Br_4Hg_2O_4P_2$: C, 42.07; H, 3.00. C, 41.18; H, 2.83%.

2.3.4. Synthesis of $[(BAPPY)\cdot HgI_2]_2$ (**3**)

Yield: 0.36 g (81.8%), m.p. 167–170 °C. *Anal.* Calc. for $C_{54}H_{40}I_4Hg_2O_4P_2$: C, 37.49; H, 2.67. C, 37.10; H, 2.55%.

2.4. X-ray crystallography

Crystals were obtained from a dichloromethane/diethyl ether solution by solvent diffusion. A block colorless crystal of **3** having approximate dimensions of 0.25 × 0.15 × 0.12 mm was mounted on a glass fiber. All measurements were made on a STOE IPDS-II diffractometer with graphite monochoromated Mo Kα radiation (λ = 0.7107 nm).

The data were collected at 298 K to a maximum θ value of 26.78 ° and in a series of ω scans in 1 ° oscillations with 60 s exposures. Of the 33 902 reflections that were collected, 11 871 were unique (R_{int} = 0.0442), equivalent reflections were merged. Data were collected and integrated using the STOE X-AREA software package [8]. The refinement was performed using the X-STEP32 crystallographic software package [9]. The numerical absorption coefficient, μ, for Mo Kα radiation is 7.748 mm^{-1}. A numerical absorption correction was applied using X-RED [10] and X-SHAPE [11] software packages which resulted in transmission factors ranging from 0.212 and 0.083. The data were corrected for Lorentz and polarizing effects. The structure was solved by direct methods [12]. All of the non-hydrogen atoms were refined anisotropically. All of the hydrogen atoms were located in ideal positions. Anomalous dispersion effects were included in F_{calc} [13], the values for $\Delta f'$ and $\Delta f''$ were those of Creagh and McAuley [14]. The values for the mass attenuation coefficient are those of Creagh and Hubbell [15].

2.5. Computational methods

The quantum chemical calculations were performed with GAUSSIAN03 [16]. The geometries were fully optimized using DFT at the B3LYP/LanL2MB level of theory [17]. This basis set includes effective core potentials (ECP) for both the mercury and phosphorus as well as halide (Cl, Br, and I) ions. The stability energy values for the complex and the energies of the highest occupied molecular orbital (HOMO) and lowest unoccupied molecular orbital (LUMO) of complex were calculated. Moreover, the HOMO–LUMO (H–L) energy gap, partial charges calculated from NBO analysis (natural bond orbital), structural parameters (such as bond lengths, bond angles), dipole and quadrupole moment were evaluated by DFT calculations. Atomic coordinates for the DFT calculations were obtained from the data of the X-ray crystal structure analyses for **3**.

3. Results and discussion

3.1. Synthesis

Reactions of HgX_2 (X = Cl, Br and I) with ylides in a 1:1 stoichiometry afforded halide-bridged dimeric structures **1–3** (Scheme 2) containing C-coordinated ylide ligands.

3.2. Infra-red spectra

The ν(CO) band, which is sensitive to complexation, occurs at 1610 cm^{-1} for the parent ylide, as in the case of other resonance stabilized ylides [18]. Coordination of the ylide through carbon causes an increase in ν(CO), while for O-coordination a lowering of ν(CO) is expected (Table 1).

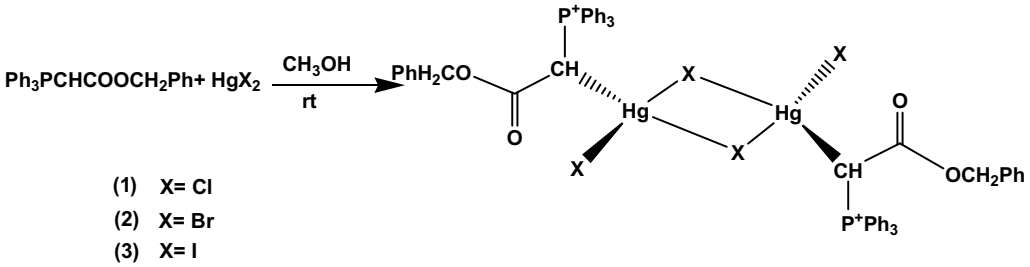
The infrared absorption bands observed for the three complexes at 1707, 1702 and 1688 cm^{-1} indicate coordination of the ylide through carbon. The $\nu(P^+–C^-)$ value, which is also diagnostic for the coordination, occurs at 958 cm^{-1} in $Ph_3P^+–^-CH_2$ and at 887 cm^{-1} in BAPPY. In the present study, the ν $(P^+–C^-)$ values for all three complexes were shifted to lower frequencies and were observed at 839, 831 and 827 cm^{-1} for **1**, **2** and **3**, respectively, suggesting some removal of electron density from the P–C bond [19].

3.3. NMR spectral data

The ^{1}H NMR data for the mercury(II) complexes, along with those of the parent ylide, are listed in Table 2.

The signals due to the methine protons, when recorded in $CDCl_3$, were either broad or unobserved, probably due to the very low solubility of all the complexes in $CDCl_3$. Similar behavior was observed earlier in the case of ylide complexes of mercury(II) halides [20,21].

The expected downfield shifts of ^{31}P and ^{1}H signals for the PCH group upon complexation were observed in their corresponding



Scheme 2.

Table 1
ν(CO) of selected phosphoranes and their metal complexes

Compound	ν(CO) cm^{-1}	Ref.
$Ph_3PCHCON(CH_3)_2$	1530	[24]
$Ph_3PCHCOCH_3$ (APPY)	1530	[25]
$Ph_3PCHCOPh$ (BPPY)	1525	[26]
$(C_6H_4CH_3)_3PCHCOOCH_2C_6H_5$ (BAPPY)	1610	This work
C-coordination		
BAPPY · $HgCl_2$ (**1**)	1707	This work
BAPPY · $HgBr_2$ (**2**)	1702	This work
BAPPY · HgI_2 (**3**)	1688	This work
BPPY · $HgCl_2$	1635	[12]
BPPY · $HgBr_2$	1630	[12]
Au [$CH(PPh_3)CON(CH_3)_2$]	1605	[24]
O-coordination		
[$(Sn(CH_3)_3$ · BPPY]Cl	1480	[27]
[$(SnPh_3)$.BPPY]Cl	1470	[27]
[$Pd\{C_6F_5\}(PPh_3\}_2$(APPY)]ClO_4	1513	[9]

APPY = acetylmethylenetriphenylphosphorane;
BPPY = benzoylmethylenephenylphosphorane.

Table 2
^{1}H and ^{31}P NMR data of BAPPY and its complexes with Hg(II) halides

Compound	δ (CH)	$^2J_{PH}$	δ (PPh_3)	δ (^{31}P)
BAPPY	2.93 (br)	–	7.16–7.88 (m)	15.04 (s)
BAPPY · $HgCl_2$	4.31 (br)	–	7.25–7.85 (m)	23.22 (s)
BAPPY · $HgBr_2$	4.17 (br)	–	7.26–7.95 (m)	21.85 (s)
BAPPY · HgI_2	4.19 (br)	–	7.35–8.05 (m)	20.24 (s)

(T = 298 K; J in Hz; TMS δ = 0.00 ppm). Recorded in $CDCl_3$, values (ppm) relative to internal TMS and external 85% phosphoric acid. s, singlet; m, multiplet; br, broad.

Table 3
^{13}C NMR data of BAPPY and its complexes with mercury (II) halides

Possible assignments	BAPPY[a]	BAPPY · $HgCl_2$[b]	BAPPY · $HgBr_2$[b]	BAPPY · HgI_2[b]
CH	30.03 (d)	br	br	br
$^1J_{PC}$	124.89	–	–	–
CH_2	63.58 (s)	66.35 (s)	67.09 (s)	65.56 (s)
(CH_2Ph) (*i*)	138.32 (s)	135.50 (s)	135.50 (s)	135.78 (s)
(CH_2Ph) (*o*)	127.68 (s)	127.97 (s)	127.91 (s)	127.95 (s)
(CH_2Ph) (*m*)	127.36 (s)	127.79 (s)	127.74 (s)	128.75 (s)
(CH_2Ph) (*p*)	126.66 (s)	127.97 (s)	127.91 (s)	127.95 (s)
PPh_3 (*i*)	125.93 (d)	121.84 (d)	122.54 (d)	119.74 (d)
$^1J_{PC}$	63.19	88.69	89.32	92.72
PPh_3 (*o*)	132.55 (d)	132.54 (d)	132.97 (d)	133.04 (d)
$^2J_{PC}$	9.88	10.00	10.15	10.48
PPh_3 (*m*)	128.34 (d)	129.41 (d)	129.25 (d)	130.00 (d)
$^3J_{PC}$	12.25	12.34	12.29	11.78
PPh_3 (*p*)	131.64 (s)	133.86 (s)	133.63 (s)	133.20 (s)
CO	170.46 (s)	168.69 (s)	168.35 (s)	168.90 (s)

s, singlet; d, doublet; (*o*), ortho; (*m*), meta; (*p*), para; (*i*), ipso; br, broad.
[a] Recorded in $CDCl_3$.
[b] Recorded in DMSO-d_6.

spectra. The appearance of single signals for the PCH group in both the ^{31}P and ^{1}H NMR spectra at ambient temperature indicates the presence of only one molecule for all the three complexes, as expected for C-coordination. It must be noted that O-coordination of the ylide leads to the formation of *cis* and *trans* isomers which would give rise to two different signals in the ^{31}P and ^{1}H NMR spectra [6b]. The resonances in the ^{31}P NMR spectra of complexes **1**, **2** and **3** were observed to occur at a lower field with respect to the free ylide (Table 2). A comparison of the ^{31}P chemical shift of the three complexes at ambient temperature indicates a decrease in the order **1** > **2** > **3**. The ^{13}C NMR data of the complexes and the title ylide, along with possible assignments, are listed in Table 3.

The ^{13}C shifts of the CO group in the complexes are around 168 ppm, which is higher field than the 170 ppm noted for the same carbon in the parent ylide, indicating much higher shielding of the carbon atom of the CO group in the complexes [21]. No coupling to Hg was observed at room temperature in the ^{1}H, ^{13}C and ^{31}P NMR spectra. Failure to observe satellites in the above spectra was previously noted in the ylide complexes of Hg(II) [22] and Ag(I) [23], which had been explained by fast exchange of the ylide with the metal.

3.4. Crystal structures analysis

Table 4 provides the crystallographic results and refinement information for complex **3**. The molecular structure of **3** is shown in Fig. 1. Fractional atomic coordinates and equivalent isotropic displacement coefficients (U_{eq}) for the non-hydrogen atoms of complex **3** and a view of the crystal packing are shown in Fig. S1. Table 5 lists key bond lengths and angles for complex **3**.

The dimeric structure adopted by complexes **1**, **2** and **3** is in contrast to the O-coordinated trinuclear mercury(II) complex of the phosphorus ylide $Ph_3PCHCOPh$ [24], but is similar to the structure of the C-coordinated dinuclear mercury(II) halide complexes of $Ph_3PCHCOOEt$ (EPPY) [25a] and $Ph_3PCHCOPh$ (BPPY) [25b]. The C-coordination of BAPPY is in stark contrast to the O-coordination of the phosphorus ylide $Ph_3PC(COCH_3)(COC_6H_5)$ (ABPPY) to the Hg(II) center [26]. The difference in coordination mode between ABPPY and BAPPY to Hg(II) can be rationalized in terms of the electronic properties and steric requirements of the ylides. The nucleophilicity of the carbanion in ABPPY is less than for BAPPY; this is due to the additional delocalization of the ylide electron density in ABPPY which is facilitated by the second carbonyl group. This will reduce the ability of ABPPY to bind via the ylidic carbon. Belluco et al. have studied steric influences on the coordination modes of ylide molecules to Pt(II) systems [27]. These authors concluded that the preferred coordination mode is via the ylidic carbon, but that steric hindrance around the metal center or the ylidic carbon will necessitate O-coordination. Indeed, this trend is reflected here, both BPPY and BAPPY are slightly less sterically demanding than

ABPPY and are both C-coordinated to Hg(II). The Hg(II) in **3** is sp^3 hybridized and has a tetrahedral coordination environment with one short Hg–I bond, one Hg–C bond and two asymmetric bridging Hg–I bonds at distances of 2.841(9) and 3.129(8) Å. The significance of the Hg–C bond of length, 2.263(6) Å, compared to analogous distances in $[BPPY \cdot HgI_2]_2$ [25] and $[(C_6H_5)_3PC_5H_4 \cdot HgI_2]_2$ [22] (2.312(13) and 2.292(8) Å, respectively) must be attributed to the use of Hg(II) orbitals with high s character for bonding to the ylidic carbon. The use of non-equivalent hybrid orbitals with high s character to bond to low electronegative atoms was proposed by Bent in the concept of isovalent hybridization to account for the variation in bond lengths and bond angles around a central

Table 4
Crystal data and refinement parameter for **3**

Empirical formula	$C_{54}H_{46}I_4Hg_2O_4P_2$
Formula weight	1729.63
Temperature (K)	293(2)
Wavelength (Å)	0.71073
Crystal system, space group	monoclinic, $P2_1/c$
Unit cell dimensions	
a (Å)	20.493(4)
b (Å)	12.496(3)
c (Å)	23.293(5)
β (°)	109.52(3)
Volume (A^3)	5623(2)
Z, D_{calc} (Mg/m^3)	4, 2.043
Absorption coefficient (mm^{-1})	7.748
F(000)	32.16
Crystal size (mm)	0.35 × 0.30 × 0.20
Theta Range for data collection (°)	1.62–26.81
Limiting indices	$-25 \leqslant h \leqslant 23$, $-15 \leqslant k \leqslant 15$, $-29 \leqslant l \leqslant 29$
Reflections collected/unique	33 902/11 871 [R(int) = 0.0442]
Completeness to Theta = 23.78° (%)	98.60
Absorption correction	numerical
Maximum and minimum transmission	0.212 and 0.083
Refinement method	full-matrix least-squares on F^2
Data/restraints/parameters	11 871/0/595
Goodness-of-fit on F^2	1.139
Final R_1, wR_2[a] (observation data)	0.0514, 0.0854
Final R_1, wR_2[a] (All data)	0.0755, 0.0928
Largest diffraction peak and hole ($e\,A^{-3}$)	0.920 and −1.004

[a] $R_1 = \Sigma||F_o| - |F_c||/\Sigma|F_o|, wR_2 = [\Sigma(w(F_o^2 - F_c^2)^2)/\Sigma w(F_o^2)^2]^{1/2}$.

Table 5
A comparison between the selected calculated bond lengths (Å) and bond angles (°) for compound **3** with X-ray data

	X-ray	B3LYP/Lanl2mb
Bond lengths		
Hg(1)–C(1)	2.263(6)	2.341
Hg(1)–I(1)	2.6719(9)	3.042
Hg(1)–I(2)	2.8410(9)	3.197
Hg(1)–I(2)#1	3.1296(8)	3.316
P(1)–C(1)	1.783(6)	1.969
P(1)–C(10)	1.792(6)	1.949
P(1)–C(16)	1.808(7)	1.940
P(1)–C(22)	1.806(7)	1.961
Bond angles		
C(1)–Hg(1)–I(1)	129.12(15)	135.91
C(1)–Hg(1)–I(2)	113.42(16)	105.293
I(1)–Hg(1)–I(2)	111.88(3)	103.448
C(1)–Hg(1)–I(2)#1	96.84(15)	99.912
I(1)–Hg(1)–I(2)#1	102.57(3)	111.639
I(2)–Hg(1)–I(2)#1	93.22(3)	92.252
C(1)–P(1)–C(10)	115.4(3)	109.17
C(1)–P(1)–C(16)	108.4(3)	109.74
C(10)–P(1)–C(22)	106.8(3)	106.81
C(22)–P(1)–C(16)	107.4(3)	107.10
C(10)–P(1)–C(16)	108.3(3)	109.84
O(1)–C(2)–O(2)	123.4(6)	123.62
O(1)–C(2)–C(1)	126.4(6)	131.18
O(2)–C(3)–C(4)	114.0(6)	111.41
P(1)–C(1)–Hg(1)	113.1(3)	118.45

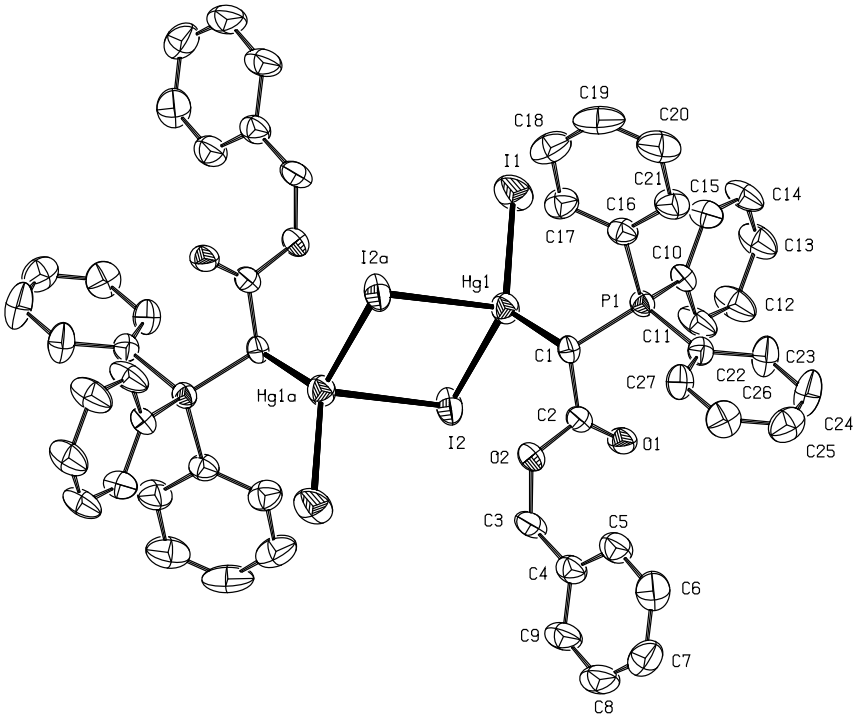


Fig. 1. Molecular structure of the complex $[(BAPPY) \cdot HgI_2]_2$. H atoms are omitted for clarity.

atom. The internuclear distances between mercury atoms were found to be 4.090(5), 4.014(1) and 3.810(2) Å in the structures **3**, $[BPPY \cdot HgI_2]_2$ and $[BPPY \cdot HgCl_2]_2$, respectively. These distances are much longer than the sum of the Van der Waals radii (1.5 Å) of the two mercury atoms [28] indicating the absence of significant bonding interactions between the mercury atoms in the molecular structures. The adaptation of dimeric structures in the Hg(II) ylide complexes may be explained by both the preference of Hg(II) for four coordination and the stability of the 18 electron configuration around Hg(II).

3.5. Theoretical studies

The optimized structure of this compound is shown in Fig. 2 and selected bond lengths and bond angles are given in Table 5.

As can be seen, the calculated bond lengths are slightly longer than the measured bond lengths but the similarity of calculated and measured bond angles reflects the similar geometrical structures for this compound in both the solid state and gas-phase. It is clear that the dimeric structure with the general formula $[BAPPY \cdot HgX_2]_2$ can be considered as both the observed *trans*-like or possible *cis*-like isomers. Table 5 shows the complete data collections for the X-ray results and theoretical calculation. In the *trans*-like structure of the compound, the internuclear distances between the mercury atoms were calculated to be 4.514 Å, indicating the absence of significant bonding interactions between the mercury atoms in the molecular structure. The Hg–C bond length in the trans structure is calculated to be 2.341 Å. A comparison of the bond lengths and bond angles from both methods (X-ray crystallography and quantum calculation) shows that the results of the calculation are the same as the X-ray crystallography results. For example the distances: P(1)–C(1), P(1)–C(10), P(1)–C(16), P(1)–C(22) have approximately equal values. These data show that the phenyl rings attached to phosphorus have little effect on the bond lengths between the phosphorus and carbon atoms. The stability energy values for this complex are reported in Table 6.

Furthermore, the energies of the HOMO and LUMO for the complex are summarized in Table 6. In this case, partial charge transfer will occur by a contribution from the mixing of the filled orbital of one component molecule with the vacant orbital of another. The most important terms in this kind of interaction are contributed from the partial charge transfer between the HOMO of one component and the LUMO of another. The HOMO–LUMO (H–L) energy gap is large in magnitude for this complex and corresponds to 4.161 eV. As listed in Table 6, the dipole moment of the trans complex in the *x*, *y* and *z* planes was only 0.0 De. This result shows that the complex has no polarity in the three planes. The structure of the HOMO and LUMO are shown in Figs. 3a and 3b.

Table 6
Energies, partial charges, dipole moment (De), quadrupole moment (De) and HOMO and LUMO energy of the B3LYP/lanl2mb optimized trans structure at the DFT/LanL2MB level of theory

Species		Values
E (eV)		−68048.41
HOMO (eV)		−4.403
LUMO (eV)		−0.242
H–L (eV)		4.161
Charge *s* (esu)		
Hg(1)		0.202
C(1)		−0.150
C(2)		0.228
C(3)		−0.043
C(4)		−0.008
P(1)		0.201
O(1)		−0.198
O(2)		−0.114
Dipole moment (De)		
X	*Y*	*Z*
0.00	0.00	0.00
Quadrupole moment (De)		
XX	*YY*	*ZZ*
−392.29	−399.01	−379.54
XY	*XZ*	*YZ*
−45.0531	104.66	−43.59

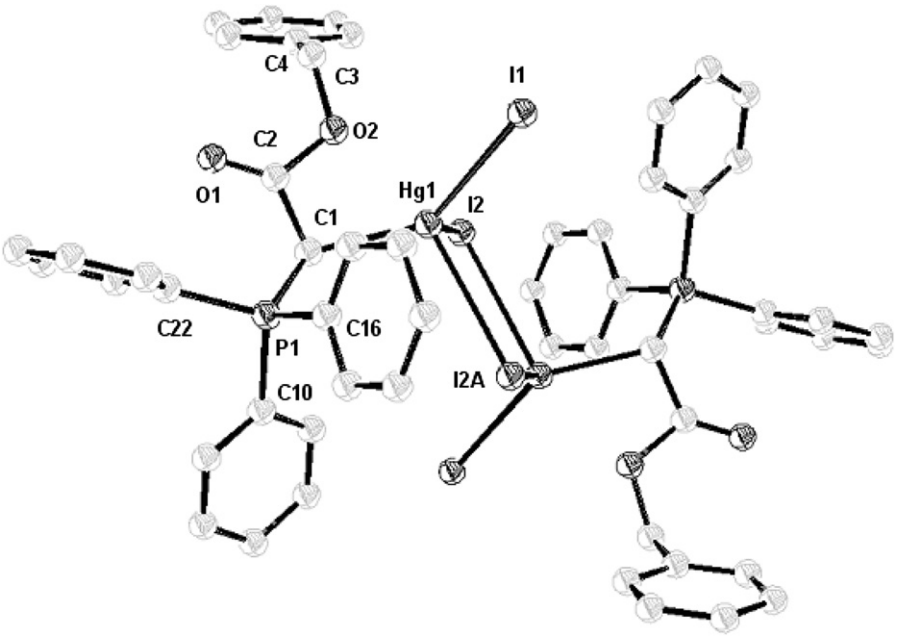


Fig. 2. Optimized structure of the complex $[(BAPPY) \cdot HgI_2]_2$.

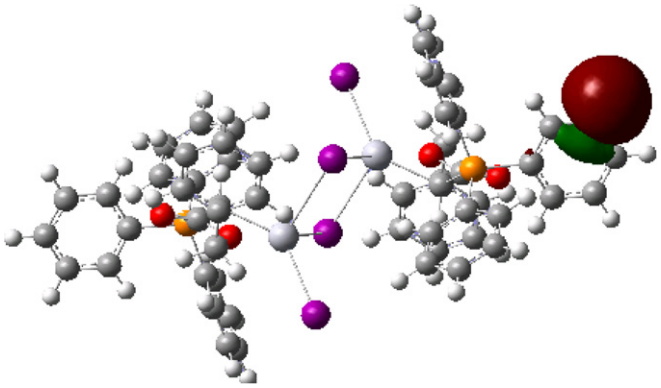


Fig. 3a. Structure of the HOMO of the complex $[(BAPPY)\cdot HgI_2]_2$.

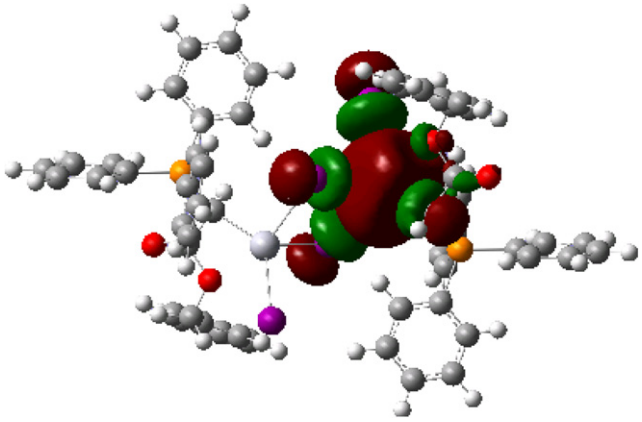


Fig. 3b. Structure of the LUMO of the complex $[(BAPPY)\cdot HgI_2]_2$.

4. Conclusions

The present study describes the synthesis and characterization of a new ylide (BAPPY) and its mercury(II) complexes of the general formula $[BAPPY.HgX_2]_2$ (X = Cl, Br, I). On the basis of the physicochemical and spectroscopic data we propose that BAPPY herein exhibits monodentate C-coordination to the metal center. In addition theoretical studies on the gas phase structure of **3** confirms the *trans*-like dimeric structure for this compound, as obtained by X-ray crystal structure analyses.

Acknowledgement

We are highly grateful to the University of Bu-AliSina for a Grant and Mr. Zebarjadian for recording the NMR spectra.

Appendix A. Supplementary data

CCDC 648218 contains the supplementary crystallographic data for **3**. These data can be obtained free of charge via http://www.ccdc.cam.ac.uk/conts/retrieving.html, or from the Cambridge Crystallographic Data Centre, 12 Union Road, Cambridge CB2 1EZ, UK; fax: (+44) 1223-336-033; or e-mail: deposit@ccdc.cam.ac.uk. Supplementary data associated with this article can be found, in the online version, at doi:10.1016/j.poly.2008.03.010.

References

[1] J. Vicente, M.T. Chicote, I. Saura-Llamas, J. Chem. Soc., Dalton Trans. (1990) 1941.
[2] R. Uson, J. Fornies, R. Navarro, P. Espinet, C. Mendivil, J. Organomet. Chem. 290 (1985) 125.
[3] (a) Y. Shen, Acc. Chem. Res. 31 (1998) 584;
(b) C. Puke, G. Erker, N.C. Aust, E.U. Wurthweine, R. Frohich, J. Am. Chem. Soc. 120 (1998) 4863;
(c) O.I. Kolodiazhnyi, Russ. Chem. Rev. 66 (1997) 225;
(d) D.E.C. Cobridge, Phosphorus an Outline of Chemistry, Biochemistry and Uses, fifth ed., Elsevier, Amsterdam, 1995.
[4] (a) O.I. Kolodiazhnyi, Tetrahedron 52 (1996) 1855;
(b) M. Taillefer, H.J. Cristau, Top. Curr. Chem. 229 (2003) 41.
[5] (a) H. Nishiyama, K. Itoh, Y. Ishii, J. Organomet. Chem. 87 (1975) 129;
(b) J. Vicent, M.T. Chicote, M.C. Lagunas, P.G. Jones, J. Chem. Soc., Dalton Trans. (1991) 2579;
(c) M. Onishi, Y. Ohama, K. Hiraki, H. Shintani, Polyhedron 1 (1982) 539.
[6] (a) J. Buckle, P.G. Harrison, J. Organomet. Chem. 49 (1973) C17;
(b) J.A. Albanese, D.L. Staley, A.L. Rheingold, J.L. Burmeister, Inorg. Chem. 29 (1990) 2209;
(c) I. Kawafune, G. Matsubayashi, Inorg. Chim. Acta 70 (1983) 1.
[7] (a) J.L. Burmeister, J.L. Silver, E.T. Weleski, E.E. Schweizer, C.M. Kopay, Synth. Inorg. Met. Org. Chem. 3 (1973) 339;
(b) M.L. Illingsworth, J.A. Teagle, J.L. Burmeister, W.C. Fultz, A.L. Rheingold, Organometallics 2 (1983) 1364.
[8] Stoe & Cie, X-AREA, version 1.30: Program for the Acquisition and Analysis of Data, Stoe & Cie GmbH, Darmstadt, Germany, 2005.
[9] Stoe & Cie, X-STEP32, version 1.07b: Crystallographic package; Stoe & Cie GmbH: Darmstadt, Gemany, 2000.
[10] Stoe & Cie, X-RED, version 1.28b: Program for Data Reduction and Absorption Correction, Stoe & Cie GmbH, Darmstadt, Germany, 2005.
[11] Stoe & Cie, X-SHAP, version 2.05: Program for Crystal Optimization for Numerical Absorption Correction, Stoe & Cie GmbH, Darmstadt, Germany, 2004.
[12] G.M. Sheldrik, SHELX97. Program for Crystal Structure Solution and Refinement, University of Gottingen, Germany, 1997.
[13] J.A. Ibers, W.C. Hamilton, Acta Crystallogr. (1964) 17781.
[14] D.C. Creagh, W.J. McAuley, in: A.J.C. Wilson (Ed.), International Tables for Crystallography, vol. C, Kluwer Academic Publishers, Boston, 1992, p. 219. Table 4.2.6.8.
[15] D.C. Creagh, J.H. Habbell, in: A.J.C. Wilson (Ed.), International Tables for Crystallography, vol. C, Kluwer Academic Publishers, Boston, 1992, p. 200. Table 4.2.6.8.
[16] M.J. Frisch, G.W. Trucks, H.B. Schlegel, G.E. Scuseria, M.A. Robb, J.R. Cheeseman, J.A. Montgomery, Jr., T. Vreven, K.N. Kudin, J.C. Burant, J.M. Millam, S.S. Iyengar, J. Tomasi, V. Barone, B. Mennucci, M. Cossi, G. Scalmani, N. Rega, G.A. Petersson, H. Nakatsuji, M. Hada, M. Ehara, K. Toyota, R. Fukuda, J. Hasegawa, M. Ishida, T. Nakajima, Y. Honda, O. Kitao, H. Nakai, M. Klene, X. Li, J.E. Knox, H.P. Hratchian, J.B. Cross, C. Adamo, J. Jaramillo, R. Gomperts, R.E. Stratmann, O. Yazyev, A.J. Austin, R. Cammi, C. Pomelli, J.W. Ochterski, P.Y. Ayala, K. Morokuma, G.A. Voth, P. Salvador, J.J. Dannenberg, V.G. Zakrzewski, S. Dapprich, A.D. Daniels, M.C. Strain, O. Farkas, D.K. Malick, A.D. Rabuck, K. Raghavachari, J.B. Foresman, J.V. Ortiz, Q. Cui, A.G. Baboul, S. Clifford, J. Cioslowski, B.B. Stefanov, G. Liu, A. Liashenko, P. Piskorz, I. Komaromi, R.L. Martin, D.J. Fox, T. Keith, M.A. Al-Laham, C.Y. Peng, A. Nanayakkara, M. Challacombe, P.M.W. Gill, B. Johnson, W. Chen, M.W. Wong, C. Gonzalez, J.A. Pople, Gaussian, Inc. Pittsburg, PA, 2003.
[17] J.B. Collins, P.V.R. Schleyer, J.S. Binkley, J.A. Pople, J. Chem. Phys. 64 (1967) 5142.
[18] J. Vicente, M.T. Chicote, J.A. Cayuelas, J. Fernandez-Baeza, P.G. Jones, G.M. Sheldrick, P. Espinet, J. Chem. Soc., Dalton Trans. (1991) 2579.
[19] W. Luttke, K. Wilhelm, Angew. Chem., Int. Ed. Engl. 4 (1965) 875.
[20] S.J. Sabounchei, V. Jodaian, H.R. Khavasi, Polyhedron 26 (2007) 2845.
[21] S.J. Sabounchei, A.R. Dadrass, M. Jafarzadeh, S. Salehzadeh, H.R. Khavasi, J. Organomet. Chem. 692 (2007) 2500.
[22] N.L. Holy, N.C. Baenziger, R.M. Flynn, D.C. Swenson, J. Am. Chem. Soc. 98 (1976) 7823.
[23] J. Vicente, M.T. Chicote, J. Fernandez-Baeza, J. Martin, I. Saura-Llamas, J. Turpin, P.G. Jones, J. Organomet. Chem. 331 (1987) 409.
[24] M. Kalyanasundari, K. Panchanatheswaran, W.T. Robinson, Bull. Chem. Soc. Jpn. 72 (1999) 33.
[25] (a) E.C. Spencer, M.B. Mariyatra, J.A.K. Howard, A.M. Kenwright, K. Panchanatheswaran, J. Organomet. Chem. 692 (2007) 1081;
(b) M. Kalyanasundari, K. Panchanatheswaran, W.T. Robinson, H. Wen, J. Organomet. Chem. 491 (1995) 103.
[26] P. Laavanya, U. Venkatasubramanian, K. Panchanatheswaran, J.A.K. Bauer, Chem. Commun. (2001) 1660.
[27] U. Belluco, R.A. Michelin, R. Bertani, G. Facchin, G. Pace, L. Zanotto, M. Mozzon, M. Furlan, E. Zangrando, Inorg. Chim. Acta (1996) 355.
[28] J.E. Huheey, Inorganic Chemistry – Principles of Structure and Reactivity, second ed., Harper Int. Ed., New York, 1978. pp. 233.

The products, **2a**–**c**, have been purified by crystallization, and have been fully characterized by means of IR and NMR spectroscopies, and elemental analysis. Moreover, the molecular structure of **2b** has been ascertained by X-ray diffraction (Fig. 1 and Table 1).

The molecular structure of **2b** resembles those previously reported for $Ta_2Cl_8[\mu\text{-}OOC(p\text{-}ClC_6H_4)]_2$ and $Nb_2Cl_8(\mu\text{-}OOCC_6F_5)_2$ [4]. Compound **2b** possesses C_i symmetry and only half of the molecule is present in the asymmetric unit. The distorted octahedrally coordinated Ta(V) centres display a *cis* arrangement of the ligands and the Ta–Cl bond distances [range 2.2857(11)–2.3393(11) Å; average 2.303(2) Å] are comparable to those present in the dinuclear $Ta_2Cl_8[\mu\text{-}OOC(p\text{-}ClC_6H_4)]_2$ [range 2.282(4)–2.308(4) Å; average 2.296(10) Å] [4] and the tetranuclear $Ta_4Cl_8(\mu\text{-}O)_4[\mu\text{-}OOC(p\text{-}MeC_6H_4)]_4$ [range 2.263(7)–2.322(4) Å; average 2.292(8) Å] [6]. Conversely, the Ta–O interactions [2.104(3) and 2.008(3) Å] display some asymmetry, whereas they are almost identical in $Ta_2Cl_8[\mu\text{-}OOC(p\text{-}ClC_6H_4)]_2$ [2.001(8) and 2.006(9) Å]. The C(1)–O(1) [1.260(5) Å] and C(1)–O(2)#1 [1.282(5) Å] distances are in agreement with a delocalised π-interaction and C(1) displays an almost perfect sp^2 hybridisation [sum angles 360.0(7)°]. The tantalum–tantalum distance (4.913(8) Å) indicates that no direct interaction between the two metal atoms occurs.

The spectroscopic data collected for **2a**–**c** are coherent with the X-ray features of **2b**. The ^{1}H NMR spectra (in CD_2Cl_2 solutions) exhibit one singlet due to the methyl groups, occurring at *ca.* 2.7 ppm. The ^{13}C NMR resonances are seen at *ca.* 185 (*C*OO) and 24 (*C*H$_3$) ppm. Furthermore, the IR spectra (recorded in the solid state) display the absorptions typical of bridging carboxylate moieties [8], *e.g.* for **2a** at 1545 [ν_{as}(COO)] and 1489 [ν_s(COO)] cm^{-1}.

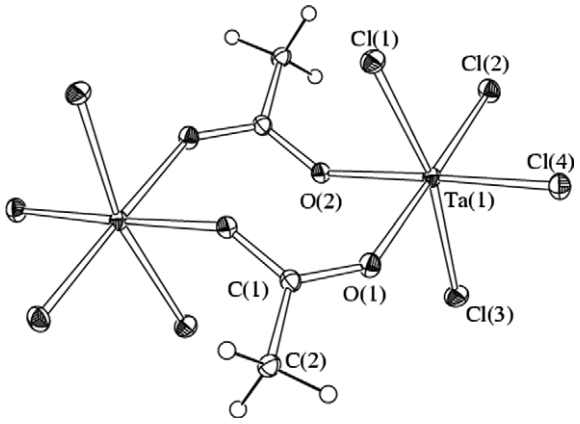


Fig. 1. Molecular structure of $[TaCl_4(\mu\text{-}OOCMe)]_2$, **2b**. Thermal ellipsoids are drawn at 30% probability level. Only independent atoms are labelled.

Table 1
Selected bond distances (Å) and angles (°) of $[TaCl_4(\mu\text{-}OOCMe)]_2$, **2b**

Ta(1)–Cl(1)	2.3393(11)	Ta(1)–O(2)	2.008(3)
Ta(1)–Cl(2)	2.2857(11)	C(1)–O(1)	1.260(5)
Ta(1)–Cl(3)	2.2977(11)	C(1)–O(2)#1	1.282(5)
Ta(1)–Cl(4)	2.2908(11)	C(1)–C(2)	1.485(6)
Ta(1)–O(1)	2.104(3)		
O(2)–Ta(1)–O(1)	86.15(12)	Cl(2)–Ta(1)–Cl(3)	95.38(4)
O(2)–Ta(1)–Cl(2)	91.83(9)	Cl(4)–Ta(1)–Cl(3)	95.81(4)
O(1)–Ta(1)–Cl(2)	177.94(8)	O(2)–Ta(1)–Cl(1)	84.07(9)
O(2)–Ta(1)–Cl(4)	172.86(9)	O(1)–Ta(1)–Cl(1)	86.06(9)
O(1)–Ta(1)–Cl(4)	87.54(9)	Cl(2)–Ta(1)–Cl(1)	94.14(4)
Cl(2)–Ta(1)–Cl(4)	94.50(4)	Cl(4)–Ta(1)–Cl(1)	92.16(4)
O(2)–Ta(1)–Cl(3)	86.87(9)	Cl(3)–Ta(1)–Cl(1)	167.05(4)
O(1)–Ta(1)–Cl(3)	84.11(9)	O(1)–C(1)–O(2)#1	120.5(4)
C(1)–O(1)–Ta(1)	138.2(3)	O(1)–C(1)–C(2)	120.1(4)
C(1)#1–O(2)–Ta(1)	143.3(3)	O(2)#1–C(1)–C(2)	119.4(4)

Symmetry transformations used to generate equivalent atoms: #1 $-x$, $-y+1$, $-z+1$.

Since the chemistry of **1** with carboxylic anhydrides has been explored in less detail than that with the corresponding acids, we decided to study the reactions of MX_5 with the stoichiometric amount of acetic anhydride. Particular care was taken in order to have an anhydrous reaction system, so to eliminate the presence of adventitious water and/or of acetic acid. The complete absence of acetic acid was verified before each reaction by ^{1}H NMR spectroscopy.

Thus, the reactions of **1** (M = Nb, X = Cl, M = Ta, X = Cl, Br) with a slight excess of $(MeCO)_2O$ resulted in the formation of the dimeric species **2a**–**c**, Eq. (2). Coherently to what reported above, when compound TaI_5, in $CDCl_3$, was mixed with one equivalent of $(MeCO)_2O$, the ^{1}H NMR spectrum of the solution exhibited the resonances due to the free anhydride only.

$$2MX_5 + 2(\mathrm{Me\ CO})_2O \rightarrow \underset{\mathbf{2a-c}}{[MX_4(\mu - OOCMe)]_2} + 2\mathrm{MeCOX} \qquad (2)$$

When the reaction of MX_5 with a slight excess of acetic anhydride was performed in a NMR tube, the ^{1}H NMR spectrum of the solution showed resonances due to **2**, MeCOX (X = Cl, Br) and to an additional compound characterized by a single resonance at *ca.* 2.8 ppm ($CDCl_3$, X = Cl). Although μ-oxo derivatives of niobium(V) and tantalum(V) have been obtained by reacting MCl_5 with acetic anhydride [3a,3c], our present result suggests that a different compound is formed in our system.

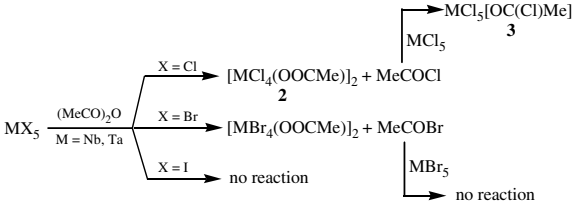
As a matter of fact, according to Eq. (2), see also [3c], the anhydride C–O bond activation produces MeCOX, a potentially good ligand for a strong Lewis acid such as MX_5 [7a,7c]. In order to investigate the hypothesis that the compounds formed in admixture with **2** are adducts of acetyl chloride, MeCOCl was added in 1:1 ratio to dichloromethane suspension of MCl_5: the soluble adducts $MCl_5[OC(Cl)Me]$ [M = Nb, **3a**; M = Ta, **3b**] formed rapidly, Eq. (3). It has to be noticed that $TaBr_5$ resulted unreactive towards MeCOBr.

$$MCl_5 + \mathrm{Me\ COCl} \rightarrow \underset{\mathbf{3a,b}}{MCl_5[OC(Cl)Me]} \qquad (3)$$

The complexes **3a**–**b** have been isolated as microcrystalline solids upon removal of the volatile materials, and characterized by means of IR and NMR spectroscopies, and elemental analysis. The infrared carbonyl stretching vibration has been found at 1560 cm^{-1}, *i.e.* at significantly lower frequencies with respect to the uncoordinated acetyl chloride (1806 cm^{-1} [9]). The ^{1}H and ^{13}C NMR resonances appear downfield shifted (2.81 ppm in **3a**) with respect to uncoordinated MeCOCl (2.66 ppm [10]).

At variance to what observed in the reactions of **1** with other C=O containing species [7a], the addition of a fivefold excess of acetyl chloride to $NbCl_5$ did not result in the formation of by-products. This evidence strongly suggests that only compounds **3** can result from combination of MCl_5 with *in situ* generated MeCOCl.

On the basis of these results, it has to be concluded that the reactivity of MX_5 with acetic anhydride depends on the nature of X, and it can be summarized as in Scheme 1. Indeed, when $NbCl_5$



Scheme 1. The reactivity of MX_5 with acetic anhydride.

was treated with $(MeCO)_2O$ in CD_2Cl_2 inside a NMR tube, some solid formed and the ^1H NMR spectrum of the solution revealed the presence of **2a**, MeCOCl and **3a** in 1:3:7 molar ratio, which changed to 1:2:3 on increasing the $(MeCO)_2O/NbCl_5$ molar ratio from 1 to 2. The formation of **3a** was almost suppressed by using a $(MeCO)_2O/NbCl_5$ molar ratio of 5. These evidences point out that acetyl chloride, formed as result of the anhydride fragmentation, competes with the uncoordinated anhydride in the coordination to the unreacted inorganic substrate to give **3a**, thus decreasing the yield of **2a**. The usage of an excess of anhydride limits the formation of **3a**. Under these conditions, we did not collect any evidence for the occurrence of *O*-abstraction reactions which appear instead to be the main process when the system is heated [3a].

Considerations similar to what reported above are valid for the reaction of $TaCl_5$ with MeCOCl (see Section 4). Furthermore, the reaction of $TaBr_5$ with acetic anhydride, followed by ^1H NMR spectroscopy, resulted in formation of **2c** and MeCOBr in 1:3 ratio: no traces of coordination adducts of MeCOBr with $TaBr_5$ were recognized, in accordance with the reactivity of MX_5 with acetyl halides discussed above.

2.2. Reactivity of MCl_5 (M = Nb, Ta) with halo-substituted acetic acids and acetic anhydrides

The results presented in the previous section have pointed out that **1** (M = Nb, Ta, X = Cl, Br) exhibit analogous reactivity towards acetic acid or acetic anhydride. Nevertheless, the dinuclear acetato complexes are obtained in high yields by using acetic acid as reactant, the use of the anhydride leading to lower yields.

In order to see if this chemistry could be extended to other acids/anhydrides, we studied the reactions of MCl_5 (M = Nb, Ta) with halo-substituted acetic acids and with the corresponding anhydrides. The reactions with halo acetic acids led to the isolation and identification of the complexes $[MCl_4(\mu\text{-}OOCR)]_2$ [M = Nb, R = CH_2Cl, **4a**; M = Ta, R = CH_2Cl, **4b**; M = Nb, R = $CHCl_2$, **4c**; M = Ta, R = $CHCl_2$, **4d**; M = Nb, R = CCl_3, **4e**; M = Ta, R = CCl_3, **4f**; M = Nb, R = CF_3, **4g**; M = Ta, R = CF_3, **4h**; M = Nb, R = $CHBr_2$, **4i**; M = Nb, R = CH_2I, **4j**] in good yields. In agreement with what reported in Section 1, most of compounds **4** could be prepared alternatively by reacting **1** with the appropriate anhydride (Scheme 2). These latter reactions are accompanied by production of RCOCl, which has been detected by ^1H NMR in the reaction medium in the majority of the cases (see Section 4). The ^1H NMR spectra of the mixtures suggest that $CH_2ClCOCl$ and $CHCl_2COCl$ give coordination adducts with unreacted **1** as discussed above about the reaction of MeCOCl and MCl_5.

Compounds **4** have been characterized by IR and NMR spectroscopies, and elemental analyses. Moreover, the X-ray molecular structure of **4e** has been determined (Fig. 2 and Table 2).

The molecular structure of **4e** is closely related to the one of **2b**, being the replacement of Ta(V) with Nb(V) and $-CH_3$ with $-CCl_3$ the major differences. Also in this case, each metal centre is coordinated to four chloride ligands and two bridging carboxylates with a relative *cis* geometry of the ligands and a distorted octahedral coordination. Despite the fact that the two halves of **4e** are crystallographically independent, their bonding parameters are almost identical (see Table 2) and comparable to the ones reported for the analogous Nb(V) dinuclear derivative $Nb_2Cl_8(\mu\text{-}OOCC_6F_5)_2$ [4]. Finally, it is noteworthy that the dimeric nature of both **2b** and **4e** originates an octa-membered ring, which is puckered in **2b** [mean deviation from the Ta(1)O(2)C(1)#1 O(1)#1 Ta(1)#1 O(2)#1 O(1) least squares plane 0.1882 Å] but almost planar in **4e** [mean deviation from the Nb(1)O(1)C(1)O(2)Nb(2)O(3)C(3)O(4) least squares plane 0.0850 Å].

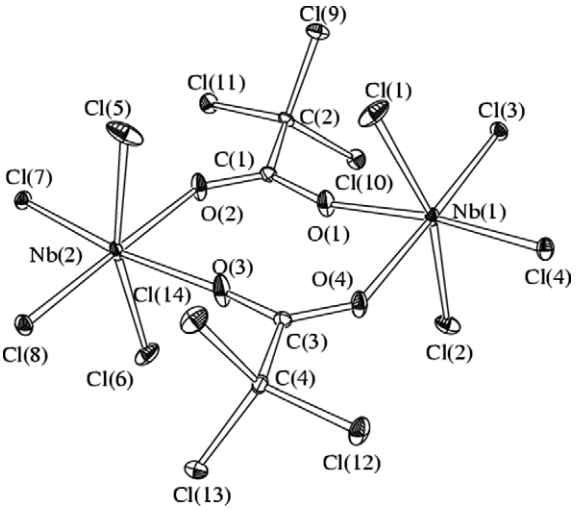
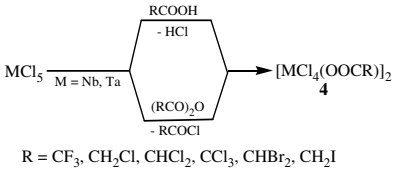


Fig. 2. Molecular structure of $[NbCl_4(\mu\text{-}OOCCl_3)]_2$, **4e**. Thermal ellipsoids are drawn at 30% probability level.

Table 2
Selected bond distances (Å) and angles (°) of $[NbCl_4(\mu\text{-}OOCCl_3)]_2$, **4e**

Nb(1)–Cl(1)	2.3005(7)	Nb(2)–Cl(5)	2.3023(8)
Nb(1)–Cl(2)	2.2931(7)	Nb(2)–Cl(6)	2.3006(8)
Nb(1)–Cl(3)	2.2574(5)	Nb(2)–Cl(7)	2.2600(6)
Nb(1)–Cl(4)	2.2550(6)	Nb(2)–Cl(8)	2.2626(5)
Nb(1)–O(1)	2.0828(17)	Nb(2)–O(2)	2.1534(17)
Nb(1)–O(4)	2.1676(16)	Nb(2)–O(3)	2.0635(18)
O(1)–C(1)	1.244(3)	O(3)–C(3)	1.236(3)
O(2)–C(1)	1.231(3)	O(4)–C(3)	1.238(3)
C(1)–C(2)	1.553(3)	C(3)–C(4)	1.550(3)
O(1)–Nb(1)–O(4)	84.72(6)	O(3)–Nb(2)–O(2)	84.89(7)
O(1)–Nb(1)–Cl(4)	170.39(5)	O(3)–Nb(2)–Cl(7)	170.37(5)
O(4)–Nb(1)–Cl(4)	85.66(5)	O(2)–Nb(2)–Cl(7)	85.48(5)
O(1)–Nb(1)–Cl(3)	93.49(5)	O(3)–Nb(2)–Cl(8)	93.65(5)
O(4)–Nb(1)–Cl(3)	178.10(5)	O(2)–Nb(2)–Cl(8)	178.41(5)
Cl(4)–Nb(1)–Cl(3)	96.12(2)	Cl(7)–Nb(2)–Cl(8)	95.98(2)
O(1)–Nb(1)–Cl(2)	83.40(6)	O(3)–Nb(2)–Cl(6)	83.54(7)
O(4)–Nb(1)–Cl(2)	84.36(5)	O(2)–Nb(2)–Cl(6)	84.34(6)
Cl(4)–Nb(1)–Cl(2)	95.46(2)	Cl(7)–Nb(2)–Cl(6)	95.09(2)
Cl(3)–Nb(1)–Cl(2)	96.09(2)	Cl(8)–Nb(2)–Cl(6)	96.14(2)
O(1)–Nb(1)–Cl(1)	83.51(6)	O(3)–Nb(2)–Cl(5)	83.85(7)
O(4)–Nb(1)–Cl(1)	83.43(5)	O(2)–Nb(2)–Cl(5)	84.16(6)
Cl(4)–Nb(1)–Cl(1)	95.60(2)	Cl(7)–Nb(2)–Cl(5)	95.59(3)
Cl(3)–Nb(1)–Cl(1)	95.74(2)	Cl(8)–Nb(2)–Cl(5)	95.06(3)
Cl(2)–Nb(1)–Cl(1)	162.84(3)	Cl(6)–Nb(2)–Cl(5)	163.62(3)
O(2)–C(1)–O(1)	125.7(2)	O(3)–C(3)–O(4)	125.9(2)
O(2)–C(1)–C(2)	117.49(19)	O(3)–C(3)–C(4)	116.10(19)
O(1)–C(1)–C(2)	116.77(19)	O(4)–C(3)–C(4)	117.96(19)



Scheme 2. Preparation of halo-acetato derivatives of Nb(V) and Ta(V).

The IR spectra display the symmetric and asymmetric vibrations of the [COO] group in the ranges 1386–1515 cm^{-1} and 1522–1635 cm^{-1}, respectively. In particular, the values available for **4g** are coherent with those reported for bridging trifluoroacetato complexes [11]. More in general, the fact that the difference $\nu_{as} - \nu_s$ results always smaller than 200 cm^{-1} indicates that the carboxylato units behave as bidentate ligands, rather than monodentate [8].

Major ^{13}C NMR feature is given by the resonance due to the carboxylic carbon, which falls in the range 166.2 (**4h**) –182.7 (**4j**) ppm. The ^{13}C signal related to the [CF_3] unit, in **4g–h**, appears as a quartet due to coupling with three adjacent fluorines (J = 286 Hz).

In addition, the ^{19}F NMR spectra (CD_2Cl_2 solutions) carried out on **4g–h** exhibit the singlet attributed to six equivalent fluorines, at *ca.* −74 ppm.

2.3. Reactivity of MF_5 (M = Nb, Ta) with haloacetic acids and haloacetic anhydrides

The pentafluorides MF_5 (M = Nb, Ta) react with RCOOH (R = Me, CH_2Cl), in 1:1 molar ratio, to give the ionic compounds $[MF_4(RCOOH)_2][MF_6]$ [M = Nb, R = Me, **5a**; M = Ta, R = Me, **5b**; M = Nb, R = CH_2Cl, **5c**; M = Ta, R = CH_2Cl, **5d**]:

$$2MF_5 + 2RCOOH \rightarrow \underset{\mathbf{5a-d}}{[MF_4(RCOOH)_2][MF_6]} \quad (4)$$

The products **5a–d** have been characterized by IR, ^1H, ^{13}C and ^{19}F NMR spectroscopies, and elemental analyses. The ^1H NMR spectra exhibit the resonance accounting for the R unit and a down-field resonance (11.61 ppm for **5c**) accounting for one oxygen-bound proton deshielded with respect to the uncoordinated acid [10]. In the ^{13}C NMR spectra, the carboxylic carbon is observed in the range 176.1(**5d**)–183.9(**5a**) ppm.[2] The ^{19}F NMR spectra are particularly diagnostic in determining the structure of compounds **5**, since they display a resonance occurring at typical negative δ values (*e.g.* −132.2 ppm for **5c**), accounting for the $[MF_6]^-$ anion, together with the broad resonance characteristic of the $[MF_4]$ moiety [7c,12].

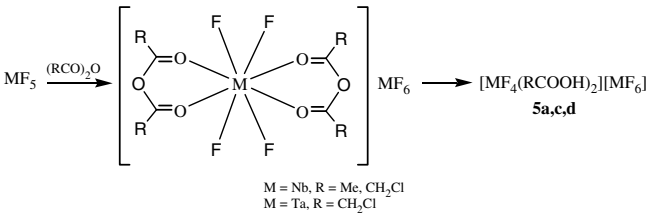
The IR spectra (solid state) are characterized by a strong absorption in the range 1616–1661 cm^{-1}, ascribable to the carboxylic C=O bond of the RCOOH ligands, rather than to carboxylato units. For instance, the C–O stretching vibration is observed at 1635 cm^{-1} in the IR spectrum of **5b**: this value is significantly closer to 1714 cm^{-1} (uncoordinated MeCOOH [9]), rather than to the wavenumbers (1545–1558 cm^{-1}) found for the bidentate carboxylato moiety within **2a–c**. These data are in agreement with those observed in other metal complexes containing carboxylic acids as ligands, such as $Ru_2(OOCPh)_6(PhCOOH)_2$ [13], $[TiCl_2(OOCR)(RCOOH)]_2O$, R = Et [14], Bu^t [15]. Unfortunately, due to the fact that we were not able to grow crystals suitable for X-ray investigation, we cannot describe in more detail the structural features of the cation of **5**.

The reaction of NbF_5 with $(MeCO)_2O$, in 1:1 molar ratio, resulted in the clean formation of complex **5a**. On the other hand, TaF_5 gave a complicated and not well reproducible mixture of products on reaction with $(MeCO)_2O$, thus this was not investigated further. As far as chloroacetic anhydride is concerned, compounds **5c–d**, in admixture with minor by-products, could be isolated from the reactions with MF_5:

$$MF_5 \xrightarrow[\substack{M=Nb,R=Me,CH_2Cl\\M=Ta,R=CH_2Cl}]{(RCO)_2O} \underset{\mathbf{5a,c,d}}{[MF_4(RCOOH)_2][MF_6]} \quad (5)$$

The chemistry of MF_5 with anhydrides deserves some further comments, because a C–O bond activation and a protonation of an oxygen atom should occur in order to obtain the products of reaction (5). Three hypothesis may be formulated regarding the origin of the proton: it could descend (i) from the anhydride itself, (ii) from the solvent (CH_2Cl_2), or (iii) from adventitious water.

In order to investigate the point, and paying particular attention to maintain strictly anhydrous conditions with anhydrides free from acid residues, we checked the reactions of NbF_5 with $(RCO)_2O$ (R = CH_3, CH_2Cl, one equivalent), in CD_2Cl_2, by NMR spectroscopy (see Section 4). The ^1H NMR spectra, taken 30 min after the mixing of the reactants, indicated clearly the formation of compounds **5a**, **c**. More specifically, the spectra exhibited the resonance of the O–*H* proton, which integrated for the correct ratio with respect to the resonance of the protons on the α-carbon atom, suggesting that the anhydride itself is the source of the proton.



Scheme 3. Mechanism proposed for the reactions of MF_5 with carboxylic anhydrides.

The reaction of NbF_5 with $(CH_2ClCO)_2O$, being well slower than that with acetic anhydride, allowed an intermediate product to be detected and characterized. As a matter of fact, 5 min after the mixing of the reactants, the ^1H NMR spectrum indicated the complete disappearance of the free anhydride, and displayed only one resonance at 4.54 ppm. A quick ^{13}C NMR acquisition allowed to identify two peaks, at δ 167.4 (*C*O) and 48.7 (*C*H_2) ppm, respectively. Contextually, the ^{19}F NMR spectrum revealed the presence of the $[NbF_6]^-$ anion (δ = 133.0 ppm [12]). Twenty minutes later, the resonances attributed to **5c** clearly came out, together with signals ascribable to minor products. These results point to the conclusion that the reactions of MF_5 (M = Nb, Ta) with anhydrides $(RCO)_2O$ (R = CH_3, CH_2Cl) probably proceed *via* the formation of ionic intermediate species such as that reported in Scheme 3, in which two anhydrides coordinate the metal centre in a symmetric fashion [3b]: C–H and C–O bonds activation, and hydrogen migration to the oxygen atom, give the final, stable, products **5**. Unfortunately, neither NMR nor GC–MS investigations allowed the characterization of the organic material derived from the fragmentation of the anhydride. It has to be remarked that activation of C–H or C–O bonds occurs in the reactions of Group 5 metal halides with excess ketones (*e.g.* acetone and acetophenone) [7a], or ethers (the C–O bond activation represents a key step in the polymerization of tetrahydrofuran initiated by **1**) [7b,7d].

In view of the fact that the reaction of MF_5 with carboxylic anhydrides without hydrogen atoms on the α-carbon atom may potentially lead to the isolation of the intermediate represented in Scheme 3, NbF_5 was treated with anhydrous $(CF_3CO)_2O$. Unfortunately, the reaction gave a mixture of inseparable and unidentifiable products. Notwithstanding, when the reaction was performed in a NMR tube (see Section 4), the ^{19}F NMR spectrum of the solution exhibited a peak awarded to the $[NbF_6]^-$ anion. Moreover, the ^1H NMR spectrum did not show any resonance, especially in the O–*H* region. Even though insufficient to establish the nature of the product, these observations are coherent with the structure placed into square brackets in Scheme 3.

3. Conclusions

In this paper, we have presented the results concerning our research on the chemistry of niobium(V) and tantalum(V) pentahalides, MX_5, with haloacetic acids and haloacetic anhydrides.

According to our previous findings, the outcomes of the reactions do not generally depend on the metal but are strongly influenced by the nature of the halide: MCl_5 and MBr_5 show a similar behaviour in the reactions with acetic acids or anhydrides, whereas

[2] The ^{13}C NMR spectrum of **5b** could not be recorded for the low solubility of this complex.

MF_5 show a fully different reactivity. To complete the picture, TaI_5 is inert towards both CH_3COOH and $(CH_3CO)_2O$.

The high stability of the $[MF_6]^-$ anion may be considered as the driving force of the reactions involving MF_5. As a consequence of such stability, HF is not released in the course of the reactions with acids, by contrast with what observed in the reactions of MX_5 (X = Cl, Br) with RCOOH. More in detail, the reactions of MX_5 (X = Cl, Br) with haloacetic acids, which resemble those reported previously regarding the reactivity of $NbCl_5$ with aryl-carboxylic acids, proceed with releasing of HX and afford neutral dimeric complexes containing bridging coordinated acetates. On the other hand, MF_5 react with haloacetic acids with coordination of two intact acid molecules to the metal centre and contextual fluoride migration to give the $[MF_6]^-$ anion.

The reactions of MX_5 with anhydrides result in anhydride fragmentation and afford the same inorganic products obtained by the reactions with the corresponding acids, although in minor yields. With MX_5 (X = Cl, Br), anhydride C–O bond activation occurs, and the reactions proceed with releasing of acetyl halides, being the Lewis acid–base adducts of these latter with MX_5 the prevalent by-products. Beside, when MF_5 are involved, activation of both C–O and C–H bonds takes place within the anhydride, and proton migration afford final stable ionic species. These latter reactions can be accompanied by formation of complicated mixtures of minor products, which have not been identified.

All these investigations were conducted at room temperature, at which no evidences for the formation of *O*-abstraction products were found.

4. Experimental

4.1. General procedures

All manipulations of air and/or moisture sensitive compounds were performed under an atmosphere of pre-purified argon using standard Schlenk techniques. The reaction vessels were oven dried at 150 °C prior to use, evacuated (10^{-2} mm Hg) and then filled with argon. All the reagents, including MX_5 (M = Nb, Ta, X = Cl; M = Nb, Ta, X = F), were commercial products (Aldrich) of the highest purity available. $TaBr_5$ and TaI_5 [16] were prepared according to published procedures. Solid anhydrides and solid $CH_2ClCOOH$ were dried over P_4O_{10} and stored under argon atmosphere as received. Liquid acids and liquid anhydrides were distilled before use under argon atmosphere from P_4O_{10}. MeCOCl and MeCOBr were distilled before use under argon atmosphere discarding a large fraction of liquid before the collection of the distillate. Liquid anhydrides were filtered through a short column of alumina immediately before use and their purity was verified by ^1H NMR. Solvents were distilled before use under argon atmosphere from appropriate drying agents: CH_2Cl_2, CD_2Cl_2, $CDCl_3$ from P_4O_{10}, pentane from $LiAlH_4$.

Infrared spectra were recorded at 298 K on a FT-IR Perkin–Elmer Spectrometer equipped with a UATR sampling accessory (solid samples). NMR measurements were performed at 298 K on Varian Gemini 200BB spectrometer. The chemical shifts for ^1H, ^{13}C, and ^{19}F NMR spectra were referenced to TMS and to $CFCl_3$, respectively.

Carbon and hydrogen analyses were performed at the Dipartimento di Chimica Farmaceutica of the University of Pisa on a Carlo Erba mod. 1106 instrument, paying particular attention to the more sensitive compounds which were weighed and directly introduced into the analyzer. The halide content was determined by the Volhardt method [17] after exhaustive hydrolysis of the sample. The chlorocarboxylic acids did not give a precipitate of AgCl upon treatment with $AgNO_3$ under the conditions used for the hydrolysis of the sample. Metals were analyzed as M_2O_5 obtained by hydrolysis of the sample followed by calcination in a platinum crucible. The halide and the metal analyses were repeated twice in order to get reproducible results.

4.2. Preparation of $[MX_4(\mu\text{-}OOCMe)]_2$ [M = Nb, X = Cl, **2a**; M = Ta, X = Cl, **2b**; X = Br, **2c**]

4.2.1. General procedure

Acetic acid (0.031 mL, 0.54 mmol) was added to a suspension of MX_5 (0.500 mmol) in CH_2Cl_2 (25 mL), in a Schlenk tube. The mixture was stirred for 1 h, and the final solution was layered with pentane (2 × 10 mL). A microcrystalline solid was formed after 24 h at room temperature. In the same conditions, no reaction between TaI_5 and MeCOOH was observed. Crystals suitable for X-ray analysis were collected from a solution of **2b** layered with pentane, at −20 °C.

2a: yellow; 78% yield. *Anal.* Calc. for $C_4H_6Cl_8Nb_2O_4$: C, 8.2; H, 1.0; Nb, 31.6; Cl, 48.3. Found: C, 8.4; H, 1.0; Nb, 31.0; Cl, 47.9%. ^1H NMR (CD_2Cl_2) δ = 2.63 (s, 6H, Me) ppm. ^{13}C NMR (CD_2Cl_2) δ = 185.4 (*CO*); 24.1 (Me) ppm. IR (solid state): ν = 2932w, 1545s [ν_{as}(COO)], 1489s [ν_s(COO)], 1387vs, 1340s, 1028w, m, 962w, 712vs cm^{-1}.

2b: colourless, 81% yield. *Anal.* Calc. for $C_4H_6Cl_8O_4Ta_2$: C, 6.3; H, 0.8; Ta, 47.4; Cl, 37.1. Found: C, 6.4; H, 0.7; Ta, 47.2; Cl, 36.7%. ^1H NMR (CD_2Cl_2) δ = 2.71 (s, 6H, Me) ppm. ^{13}C NMR (CD_2Cl_2) δ = 185.9 (*CO*); 23.5 (Me) ppm. IR (solid state): ν = 2932wm, 2856wm, 1558s [ν_{as}(COO)], 1461s [ν_s(COO)], 1376m, 1344m, 1030m, 652m cm^{-1}.

2c: orange, 75% yield. *Anal.* Calc. for $C_4H_6Br_8O_4Ta_2$: C, 4.3; H, 0.5; Ta, 32.3; Br, 57.1. Found: C, 4.5; H, 0.6; Ta, 31.6; Br, 56.1%. ^1H NMR (CD_2Cl_2) δ = 2.67 (s, 6H, Me) ppm. ^{13}C NMR (CD_2Cl_2) δ = 186.3 (*CO*); 24.3 (Me) ppm. IR (solid state): ν = 2927w, 1545m, sh [ν_{as}(COO)], 1489s [ν_s(COO)], 1444vs, 1387vs, 1348m, 1262m, 1078w, 1029m, 939m, 804s, 680vs cm^{-1}.

4.3. Reactions of MX_5, **1** (M = Nb, X = Cl; M = Ta, X = Cl, Br, I), with $(MeCO)_2O$

4.3.1. General procedure

Acetic anhydride (0.031 mL, 0.33 mmol) was added to a suspension of MX_5 (0.300 mmol) in CD_2Cl_2 (0.8 mL), inside a NMR tube, and the mixture was stirred for 30 minutes. Hence, a precipitate was present, and the ^1H NMR spectrum of the overlying solution appeared as follows: (a) $NbCl_5$: **2a**, CH_3COCl and **3a** (vide infra) were detected in 1:3:7 ratios. (b) $TaCl_5$: **2b**, CH_3COCl and **3b** in 1:3:3 ratios. (c) $TaBr_5$: **2c** and CH_3COBr in 1:3 ratio. (d) TaI_5: only resonances due to free anhydride were seen.

The reaction of acetic anhydride (0.50 mmol) with $NbCl_5$ (0.250 mmol), in CD_2Cl_2 (0.8 mL), gave a mixture consisting of **2a**, CH_3COCl and **3a** in 1:2:3 ratios.

4.4. Preparation of $MCl_5[OC(Cl)Me]$ [M = Nb, **3a**; M = Ta, **3b**]

4.4.1. General procedure

A suspension of MCl_5 (0.500 mmol) in CH_2Cl_2 (10 mL), in a Schlenk tube, was treated with MeCOCl (0.043 mL, 0.60 mmol). The mixture was stirred for 30 min, during which progressive dissolution of the solid occurred. The final solution was dried in vacuo, and the resulting residue was washed with pentane (2 × 10 mL), affording microcrystalline **3**. The addition of a fivefold excess of MeCOCl to $NbCl_5$ (0.300 mmol), in $CDCl_3$ suspension, did result in the prevalent formation of **3a**, according to ^1H NMR spectroscopy. The addition of MeCOBr (0.035 ml, 0.47 mmol) to $TaBr_5$ (0.180 g, 0.310 mmol) in $CDCl_3$ (0.8 mL), inside a NMR tube, resulted in partial dissolution of the solid, but only uncoordinated MeCOBr was detected in solution by ^1H NMR.

3a: orange, 85% yield. *Anal.* Calc. for $C_2H_3Cl_6NbO$: C, 6.9; H, 0.9; Nb, 26.6; Cl, 61.0. Found: C, 6.6; H, 0.9; Nb, 26.3; Cl, 61.2%. Yield: 0.148 g, 85%. ^{1}H NMR ($CDCl_3$) δ = 2.81 (s, 3H, Me) ppm. ^{13}C NMR ($CDCl_3$) δ = 177.5 (CO); 34.2 (Me) ppm. IR (solid state): ν = 2957w, 2922w, 1560m (CO), 1479m, 1446s, 1393s, 1345ms, 1266m, 1154m, 1095m, 1028m, 880ms, 804vs, 778vs cm^{-1}.

3b: yellow, 82% yield. *Anal.* Calc. for $C_2H_3Cl_6TaO$: C, 5.5; H, 0.7; Ta, 41.4; Cl, 48.7. Found: C, 5.4; H, 0.8; Ta, 40.9; Cl, 48.3%. ^{1}H NMR ($CDCl_3$) δ = 2.79 (s, 3H, Me) ppm. ^{13}C NMR ($CDCl_3$) δ = 175.6 (CO); 32.9 (Me) ppm. IR (solid state): ν = 2975w, 2922w, 1560s (CO), 1426m, 1391m, 1345m, 1265m, 1093m, 1031m, 940m, 807vs, 712s cm^{-1}.

4.5. Preparation of $[MCl_4(\mu\text{-}OOCCH_2Cl)]_2$ [M = Nb, **4a**; M = Ta, **4b**]

4.5.1. General procedure

Chloroacetic acid (47 mg, 0.50 mmol) was added to MCl_5 (0.450 mmol), in CH_2Cl_2 (15 mL) suspension. The mixture was stirred for 1 h and the final solution was layered with pentane (20 mL): precipitation of microcrystalline **4a**–**b** occurred after 12 h at room temperature. Alternatively, the reactions of MCl_5 (0.20 mmol) with a slight excess of $(CH_2ClCO)_2O$, in CD_2Cl_2 (0.8 mL) inside NMR tubes, afforded solutions containing $CH_2ClCOCl$ and **4a**–**b** in *ca.* 3:1 ratio.

4a: yellow, 70% yield. *Anal.* Calc. for $C_4H_4Cl_{10}Nb_2O_4$: C, 7.3; H, 0.6; Nb, 28.3; Cl, 43.2. Found: C, 7.1; H, 0.7; Nb, 27.9; Cl, 42.9%.[3] ^{1}H NMR (CD_2Cl_2) δ = 4.43 (s, 4H, CH_2) ppm. ^{13}C NMR (CD_2Cl_2) δ = 179.2 (CO); 45.9 (CH_2) ppm. IR (solid state): ν = 2932w, 2886w, 1558m, 1522s [ν_{as}(COO)], 1386vs [ν_s(COO)], 1257s, 1152ms, 965m, 808m, s cm^{-1}.

4b: light yellow, 71% yield. *Anal.* Calc. for $C_4H_4Cl_{10}O_4Ta_2$: C, 5.8; H, 0.5; Ta, 43.5; Cl, 34.1. Found: C, 5.6; H, 0.5; Ta, 43.1; Cl, 34.0%[3]. ^{1}H NMR (CD_2Cl_2) δ = 4.45 (s, 4H, CH_2) ppm. ^{13}C NMR (CD_2Cl_2) δ = 180.4 (CO); 45.8 (CH_2) ppm. IR (solid state): ν = 2999w, 2958w, 1558s, 1532vs [ν_{as}(COO)], 1386vs [ν_s(COO)], 1259s, 1174m, 970wm, 920m, 811m, s, 656m cm^{-1}.

4.6. Preparation of $[MCl_4(\mu\text{-}OOCCHCl_2)]_2$ [M = Nb, **4c**; M = Ta, **4d**]

4.6.1. General procedure

These compounds were prepared by a procedure analogous to that described for **4a**–**b**, by reacting MCl_5 (0.400 mmol) with $CHCl_2COOH$ (0.036 mL, 0.44 mmol), for 2 h. The reactions of MCl_5 (0.20 mmol) with a slight excess of $(CHCl_2CO)_2O$, in CD_2Cl_2 (0.8 mL) inside NMR tubes, afforded solutions containing $CHCl_2COCl$ and **4c**–**d**, in *ca.* 2:1 ratio.

4c: light brown, 75% yield. *Anal.* Calc. for $C_4H_2Cl_{12}Nb_2O_4$: C, 6.6; H, 0.3; Nb, 25.6; Cl, 39.1. Found: C, 6.4; H, 0.3; Nb, 25.1; Cl, 38.6%.[3] ^{1}H NMR (CD_2Cl_2) δ = 6.30 (s, 2H, CH) ppm. ^{13}C NMR (CD_2Cl_2) δ = 173.4 (CO); 63.9 (CH) ppm. IR (solid state): ν = 3003w, 2957w, 2924w, 1601vs [ν_{as}(COO)], 1408s [ν_s(COO)], 1266w, 1231vs, 1095m, 973w, 816vs, 783vs, 709vs cm^{-1}.

4d: light yellow, 71% yield. *Anal.* Calc. for $C_4H_2Cl_{12}O_4Ta_2$: C, 5.3; H, 0.2; Ta, 40.2; Cl, 31.5. Found: C, 5.2; H, 0.2; Ta, 39.3; Cl, 31.1%.[3] ^{1}H NMR (CD_2Cl_2) δ = 6.35 (s, 2H, CH) ppm. ^{13}C NMR (CD_2Cl_2) δ = 172.7 (CO); 64.5 (CH) ppm. IR (solid state): ν = 3006w, 2981w, 2969w, 1609vs [ν_{as}(COO)], 1450m, s [ν_s(COO)], 1422vs, 1264wm, 1236s, 1095w, 978w, 943w, 818s, 786m, 713s, 659ms cm^{-1}.

[3] Due to the fact that the carbon-bonded chloride does not precipitate with silver nitrate under conditions used for the analysis, the chloride content refers to the metal-bonded chloride ion.

4.7. Preparation of $[MCl_4(\mu\text{-}OOCCCl_3)]_2$ [M = Nb, **4e**; M = Ta, **4f**]

4.7.1. General procedure

These compounds were prepared by a procedure analogous to that described for **4a**–**b**, by reacting MCl_5 (0.420 mmol) with CCl_3COOH (0.048 mL, 0.48 mmol), for 3 h. Crystals suitable for X-ray analysis were collected by a CH_2Cl_2 solution of **4e**, layered with pentane, at −20 °C.

4e: yellow, 68% yield. *Anal.* Calc. for $C_4Cl_{14}Nb_2O_4$: C, 6.0; Nb, 23.4; Cl, 35.7. Found: C, 6.3; Nb, 23.2; Cl, 35.9%.[3] ^{13}C NMR (CD_2Cl_2) δ = 170.5 (CO); 90.0 (CCl_3) ppm. IR (solid state): ν = 1621vs [ν_{as}(COO)], 1505 m [ν_s(COO)], 1393s, 1362ms, 1262w, 978m, 855vs, 823vs, 726vs, 682vs cm^{-1}.

4f: colourless, 66% yield. *Anal.* Calc. for $C_4Cl_{14}O_4Ta_2$: C, 5.0; Ta, 37.3; Cl, 29.3. Found: C, 4.8; Ta, 36.9; Cl, 28.8%.[3] ^{13}C NMR (CD_2Cl_2) δ = 170.2 (CO); 90.1 (CCl_3) ppm. IR (solid state): ν = 2962w, 1627vs [ν_{as}(COO)], 1515m [ν_s(COO)], 1404s, 1365m, 1264w, 985m, 860s, 824s, 728s, 684vs cm^{-1}.

4.8. Preparation of $[MCl_4(\mu\text{-}OOCCF_3)]_2$ [M = Nb, **4g**; M = Ta, **4h**]

4.8.1. General procedure

These compounds were prepared by a procedure analogous to that described for **4a**–**b**, by reacting MCl_5 (0.500 mmol) with CF_3COOH (0.045 mL, 0.61 mmol). Alternatively, compounds **4g**–**h** were obtained in comparable yields by reacting MCl_5 (0.25 mmol) with one equivalent of $(CF_3CO)_2O$.

4g: yellow, 75% yield. *Anal.* Calc. for $C_4Cl_8F_6Nb_2O_4$: C, 6.9; Nb, 26.7; Cl, 40.8. Found: C, 6.7; Nb, 26.0; Cl, 39.2%. ^{13}C NMR (CD_2Cl_2) δ = 165.2 (m, CO); 114.3 (q, $^1J_{CF}$ = 286 Hz, CF_3) ppm. ^{19}F NMR (CD_2Cl_2) δ = −73.5 (s, 6F, CF_3) ppm. IR (solid state): ν = 2978m, 2932w, 1760m, 1635m, s [ν_{as}(COO)], 1464m [ν_s(COO)], 1383s, 1259w, m, 1208m, 1163m, s, 1099vs, 1011s, 918m, 832vs, 804vs cm^{-1}.

4h: colourless, 67% yield. *Anal.* Calc. for $C_4Cl_8F_6O_4Ta_2$: C, 5.5; Ta, 41.5; Cl, 32.5. Found: C, 5.2; Ta, 41.1; Cl, 32.0%. ^{13}C NMR (CD_2Cl_2) δ = 166.2 (m, CO); 114.9 (q, $^1J_{CF}$ = 286 Hz, CF_3) ppm. ^{19}F NMR (CD_2Cl_2) δ = −73.9 (s, 6F, CF_3) ppm.

4.9. Preparation of $[NbCl_4(\mu\text{-}OOCCHBr_2)]_2$, **4i**, and of $[NbCl_4(OOCCH_2I)]_2$, **4j**

4.9.1. General procedure

These compounds were prepared by a procedure analogous to that described for **4a**–**b**, by reacting $NbCl_5$ (0.600 mmol) with a slight excess of $CHBr_2COOH$ or CH_2ICOOH, respectively.

4i: yellow, 77%. *Anal.* Calc. for $C_4H_2Br_4Cl_8Nb_2O_4$: C, 5.3; H, 0.2; Nb, 20.6. Found: C, 5.1; H, 0.2; Nb, 19.8%. ^{1}H NMR (CD_2Cl_2) δ = 6.19 (s, 2H, CH) ppm. ^{13}C NMR (CD_2Cl_2) δ = 175.5 (CO); 34.7 (CH) ppm.

4j: yellow, 70% yield. *Anal.* Calc. for $C_4H_4I_2Cl_8Nb_2O_4$: C, 5.7; H, 0.5; Nb, 22.1. Found: C, 5.6; H, 0.6; Nb, 20.9%. ^{1}H NMR (CD_2Cl_2) δ = 4.19 (s, 4H, CH_2) ppm. ^{13}C NMR (CD_2Cl_2) δ = 182.7 (CO); −3.9 (CH_2) ppm.

4.10. Preparation of $[MF_4(RCOOH)_2][MF_6]$ [M = Nb, R = Me, **5a**; M = Ta, R = Me, **5b**; M = Nb, R = CH_2Cl, **5c**; M = Ta, R = CH_2Cl, **5d**]

4.10.1. General procedure

A suspension of MF_5 (0.400 mmol) in CH_2Cl_2 (15 mL) was treated with RCOOH (0.42 mmol; R = Me, CH_2Cl). The mixture was stirred for 30 min and the resulting solution was layered with pentane (20 mL). Compounds **5a**–**d** were obtained as microcrystalline solids after 12 h.

5a: orange, 85% yield. *Anal.* Calc. for $C_4H_8F_{10}Nb_2O_4$: C, 9.7; H, 1.6; Nb, 37.5. Found: C, 9.9; H, 1.5; Nb, 37.0%. ^{1}H NMR (CD_2Cl_2)

δ = 12.28 (s, 2H, O*H*), 2.35 (s, 6H, Me) ppm. ^{13}C NMR (CD_2Cl_2) δ = 183.9 (*C*O), 22.2 (Me) ppm. ^{19}F NMR (CD_2Cl_2) δ = 151.2 (Nb*F*$_4$), −132.3 (Nb*F*$_6$) ppm. IR (solid state): ν = 3186w, br (O–H), 2944m, 2795m, 2519w, m, 1616vs (C=O), 1555vs, 1407w, 1370w, 1247m, 1053w, 918m, 852ms cm^{-1}.

5b: pale yellow, 87% yield. *Anal.* Calc. for $C_4H_8F_{10}O_4Ta_2$: C, 7.1; H, 1.2; Ta, 53.9. Found: C, 7.0; H, 1.3; Ta, 53.5%. ^{1}H NMR (CD_2Cl_2) δ = 12.10 (s, 2H, O*H*), 2.21 (s, 6H, Me) ppm. ^{19}F NMR (CD_2Cl_2) δ = 81.2 (Ta*F*$_4$), −131.7 (Ta*F*$_6$) ppm. IR (solid state): ν = 3253br, m (O–H), 2942w, 2537w, m, 1635vs (C=O), 1397s, 1358m, 1230m, 1051m, 1012s, 883s, 829s cm^{-1}.

5c: orange, 83% yield. *Anal.* Calc. for $C_4H_6Cl_2F_{10}Nb_2O_4$: C, 8.5; H, 1.1; Nb, 32.9. Found: C, 8.3; H, 1.1; Nb, 32.0%. ^{1}H NMR (CD_2Cl_2) δ = 11.61 (s, 2H, O*H*); 4.38 (s, 4H, C*H*$_2$) ppm. ^{13}C NMR (CD_2Cl_2) δ = 176.8 (*C*O); 40.8 (*C*H$_2$) ppm. ^{19}F NMR (CD_2Cl_2) δ = 156.0 (Nb*F*$_4$); −132.3 (Nb*F*$_6$) ppm. IR (solid state): ν = 3228w, br (O–H), 2956w, 1661vs (C=O), 1551m, 1432m, 1395ms, 1275m, 1203br, m, 906vs, 797vs cm^{-1}.

5d: pale yellow, 81% yield. *Anal.* Calc. for $C_4H_6Cl_2F_{10}O_4Ta_2$: C, 6.5; H, 0.8, Ta, 48.8. Found: C, 6.4; H, 1.0; Ta, 48.6%. ^{1}H NMR (CD_2Cl_2) δ = 11.59 (s, 2H, O*H*); 4.34 (s, 4H, C*H*$_2$) ppm. ^{13}C NMR (CD_2Cl_2) δ = 176.1 (*C*O); 40.9 (*C*H$_2$) ppm. ^{19}F NMR (CD_2Cl_2) δ = 83.3 (Ta*F*$_4$); −132.4 (Ta*F*$_6$) ppm. IR (solid state): ν = 3225m, br (O–H), 3013w, 2958w, 1630vs (C=O), 1555m, 1450m, 1390m, s, 1270m, 1170m, 923s, 903s, 850m, s, 804s, 712m, s cm^{-1}.

4.11. Reactions of MF_5 (M = Nb, Ta) with $(MeCO)_2O$ and $(CH_2ClCO)_2O$

Compound NbF_5 (0.350 mmol), in CH_2Cl_2 suspension (15 mL), was treated with $(MeCO)_2O$ (0.036 mL, 0.38 mmol). The mixture was stirred for 1 h, then the solvent was removed under vacuum. Hence, the resulting residue was washed with pentane (2 × 10 mL), giving a dark yellow solid. An aliquot of this solid was analyzed by ^{1}H NMR spectroscopy (CD_2Cl_2 solution), which revealed the presence of a mixture of products, being **5a** the prevalent one. The reaction of TaF_5 with $(MeCO)_2O$, which was carried out three times in conditions analogous to that described for NbF_5, afforded complicated mixtures of products and did not appear reproducible.

The reactions of MF_5 (0.400 mmol; M = Nb, Ta) with $(CH_2ClCO)_2O$ (72 mg, 0.42 mmol) in CH_2Cl_2, yielded yellow solids upon removal of the solvent under vacuo. These solids were dissolved in CD_2Cl_2 and analyzed by ^{1}H NMR spectroscopy. The resonances related to **5c–d** were found, together with minor signals due to unidentified by-products. The formation of **5c–d** was confirmed by IR spectroscopy.

4.12. Reaction of NbF_5 with $(CH_2ClCO)_2O$ followed by NMR

Compound NbF_5 (120 mg, 0.639 mmol), CD_2Cl_2 (0.8 mL) and $(CH_2ClCO)_2O$ were introduced into a NMR tube in the order given, and the mixture was shaken for ca. one minute. ^{1}H, ^{13}C and ^{19}F NMR spectra were recorded after 5 min: ^{1}H NMR δ = 4.54 (s, C*H*$_2$) ppm; ^{13}C NMR δ = 167.4 (*C*O); 48.7 (*C*H$_2$) ppm; ^{19}F NMR δ = −133.0 (Nb*F*$_6$) ppm. After 30 min, the ^{1}H NMR spectrum of the mixture indicated complete disappearance of the resonance at 4.54 ppm and the formation of **5c** together with some by-products.

4.13. Reaction of NbF_5 with $(CF_3CO)_2O$

Complex NbF_5 (180 mg, 0.958 mmol), in suspension of CH_2Cl_2 (15 mL), was treated with $(CF_3CO)_2$ (0.12 mL, 0.90 mmol). The mixture was stirred for 2 h, then the solvent was removed in vacuo. The resulting residue was washed with pentane (2 × 15 mL), thus a pale yellow solid was obtained. ^{19}F NMR (CD_2Cl_2) δ = −133.1 (Nb*F*$_6$) ppm. ^{1}H NMR (CD_2Cl_2): no resonances in the O–*H* region.

Table 3
Crystal data and structure refinement for $[TaCl_4(\mu\text{-}OOCMe)]_2$, **2b**, and $[NbCl_4(\mu\text{-}OOCCCl_3)]_2$, **4e**

Complex	**2b**	**4e**
Formula	$C_4H_6Cl_8O_4Ta_2$	$C_4Cl_{14}Nb_2O_4$
F_w	763.59	794.16
T (K)	100(2)	100(2)
λ (Å)	0.71073	0.71073
Crystal system	triclinic	orthorhombic
Space group	$P\bar{1}$	$Pca2_1$
a (Å)	6.7746(9)	12.0031(7)
b (Å)	6.9224(9)	14.6579(8)
c (Å)	9.7855(13)	11.9975(7)
α (°)	99.843(2)	90
β (°)	104.818(2)	90
γ (°)	106.174(2)	90
Cell volume (Å^3)	411.33(9)	2110.8(2)
Z	1	4
D_c (g cm^{-3})	3.083	2.499
μ (mm^{-1})	14.588	2.867
F(000)	344	1504
Crystal size (mm)	0.20 × 0.18 × 0.12	0.19 × 0.17 × 0.15
θ limits (°)	2.23–26.99	1.39–27.99
Reflections collected	4501	17476
Independent reflections (R_{int})	1785 (0.0327)	4984 (0.0159)
Data/restraints/parameters	1785/0/83	4984/1/218
Goodness-of-fit on F^2	1.135	1.114
R_1 [$I > 2\sigma(I)$]	0.0216	0.0176
wR_2 (all data)	0.0561	0.0437
Largest difference peak and hole (e Å^{-3})	1.677/− 2.117	0.482/− 0.818

4.14. X-ray crystallographic study

Crystal data and collection details for $[TaCl_4(\mu\text{-}OOCMe)]_2$, **2b**, and $[NbCl_4(\mu\text{-}OOCCCl_3)]_2$, **4e**, are reported in Table 3. The diffraction experiments were carried out on a Bruker APEX II diffractometer equipped with a CCD detector using Mo Kα radiation. Data were corrected for Lorentz polarization and absorption effects (empirical absorption correction SADABS) [18]. Structures were solved by direct methods and refined by full-matrix least-squares based on all data using F^2 [19]. Hydrogen atoms bonded to C-atoms were fixed at calculated positions and refined by a riding model. All non-hydrogen atoms were refined with anisotropic displacement parameters. In the crystal structure of **2b**, the asymmetric unit contains only half of the molecule. The crystal of **4e** is racemically twinned with a refined Flack parameter of 0.23(3) [20], and it was, therefore, refined using the TWIN refinement routine of SHELXTL.

Acknowledgements

The authors wish to thank the Ministero dell'Istruzione, dell'Università e della Ricerca (MIUR, Roma) and the Consiglio Nazionale delle Ricerche (C.N.R.) for financial support.

Appendix A. Supplementary data

CCDC 674014 and 674013 contain the supplementary crystallographic data for **2b** and **4e**. These data can be obtained free of charge via http://www.ccdc.cam.ac.uk/conts/retrieving.html, or from the Cambridge Crystallographic Data Centre, 12 Union Road, Cambridge CB2 1EZ, UK; fax: (+44) 1223-336-033, or e-mail: deposit@ccdc.cam.ac.uk. Supplementary data associated with this article can be found, in the online version, at doi:10.1016/j.poly.2008.03.004.

References

[1] The fluorides of niobium(V) and tantalum(V) have tetranuclear structures in the solid state, while the corresponding heavier halides are dinuclear in the solid state and mononuclear in the vapour phase A.F. Wells, Structural

Inorganic Chemistry, 5th ed., Clarendon Press, Oxford, 1997. For sake of simplicity, in this paper the general formula MX5, when dealing with the niobium(V) and tantalum(V) halides, will be used.
[2] H. Funk, K. Niederländer, Chem. Ber. 62 (1929) 1688.
[3] (a) R. Kapoor, R. Sharma, P. Kapoor, Indian J. Chem. A 24 (1985) 761;
(b) B. Viard, M. Poulain, D. Grandjean, G. Amaudrut, J. Chem. Res. S (1983) 84;
(c) B. Viard, A. Laarif, F. Theobald, G. Amaudrut, J. Chem. Res. S (1983) 252;
(d) J.K. Puri, H. Anand, A. Miglani, Oriental J. Chem. 18 (2002) 445;
(e) J.K. Puri, H. Anand, A. Miglani, Chem. Abs. 140 (2002) 121475.
[4] D.A. Brown, M.G.H. Wallbridge, W.-S. Li, M. McPartlin, Polyhedron 13 (1994) 2265.
[5] D.A. Brown, M.G.H. Wallbridge, N.W. Alcock, J. Chem. Soc., Dalton Trans. (1993) 2037.
[6] D.A. Brown, W. Errington, M.G.H. Wallbridge, J. Chem. Soc., Dalton Trans. (1993) 1163.
[7] (a) F. Marchetti, G. Pampaloni, S. Zacchini, Dalton Trans. (2007) 4343;
(b) F. Marchetti, G. Pampaloni, S. Zacchini, Inorg. Chem. 47 (2008) 365;
(c) F. Marchetti, G. Pampaloni, S. Zacchini, Eur. J. Inorg. Chem. (2008) 453;
(d) F. Marchetti, G. Pampaloni, T. Repo, Eur. J. Inorg. Chem. (2008), doi:10.1002/ejic.200701348.
[8] G.B. Deacon, R.J. Phillips, Coord. Chem. Rev. 33 (1980) 227.
[9] C.J. Pouchert, The Aldrich Library of FT-IR Spectra, 1st ed., Aldrich Chemical Company Inc., Milwaukee, USA, 1985.
[10] C.J. Pouchert, J. Behnke, The Aldrich Library of ^{13}C and ^{1}H FT NMR Spectra, 1st ed., Aldrich Chemical Company Inc., Milwaukee, USA, 1993.
[11] C.D. Garner, B. Hughes, Adv. Inorg. Chem. Radiochem. 17 (1975) 1.
[12] (a) Yu.A. Buslaev, E.G. Ilyin, J. Fluorine Chem. 4 (1974) 271;
(b) N.A. Matwiyoff, L.B. Asprey, W.E. Wageman, Inorg. Chem. 9 (1970) 2014.
[13] M. Spohn, J. Strähle, W. Hiller, Z. Naturforsh. B: Chem. Sci. 41 (1986) 541.
[14] H. Barrow, D.A. Brown, N.W. Alcock, W. Errington, M.G.H. Wallbridge, J. Chem. Soc., Dalton Trans. (1994) 3533.
[15] H. Barrow, D.A. Brown, N.W. Alcock, H.J. Case, M.G.H. Wallbridge, J. Chem. Soc., Dalton Trans. (1994) 195.
[16] F. Calderazzo, P. Pallavicini, G. Pampaloni, P.F. Zanazzi, J. Chem. Soc., Dalton Trans. (1990) 2743.
[17] D.A. Skoog, D.M. West, Fundamentals of Analytical Chemistry, 2nd ed., Holt, Rinehart and Winston, Chatham, UK, 1974. p. 233.
[18] G.M. Sheldrick, SADABS, University of Göttingen, Göttingen, Germany, 1997.
[19] G.M. Sheldrick, SHELX97, University of Gottingen, Göttingen, Germany, 1997.
[20] H.D. Flack, Acta Crystallogr., Sect. A 39 (1983) 876.

ketyl before use. ε-CL was purchased from Acros, dried by stirring with CaH_2 for 48 h, and then distilled under reduced pressure. The complexes $Li_2L(THF)_{0.5}$ [3], LYbCl(THF)$_2$ (**1**) [4a] and anhydrous $LnCl_3$ [6] were prepared according to the literature procedures. All other reagents were purchased from Acros and used as received without further purification. IR spectra were recorded on a Magna-IR 550 spectrometer. ^{1}H NMR spectra were measured on a Unity Inova-400 spectrometer. Melting points were determined in sealed capillary tube, and uncorrected. Lanthanide analyses were carried out by complexometric titration. Carbon, hydrogen and nitrogen analyses were preformed by direct combustion with a Carlo-Erba EA 1110 instrument. Molecular weight and molecular weight distributions were determined against polystyrene standard by gel permeation chromatography (GPC) on a Waters 1515 apparatus with three HR columns (HR-1, HR-2 and HR-4), THF was used as an eluent at 30 °C.

2.2. Synthesis of metal complexes

2.2.1. LYCl(DME) (*2*)

Method A. A solution of $LLi_2(THF)_{0.5}$ (0.99 g, 2.1 mmol) in THF (15 mL) was added to a stirring suspension of YCl_3 (0.41 g, 2.1 mmol) in THF (30 mL). After stirring at r.t. for 48 h the solvent was removed in vacuo. The residue was extracted with toluene (30 mL) and the volume of the extract was reduced to 10 mL followed by addition of DME (1 mL). Cooling to 0 °C afforded **2** as colorless crystals. Yield: 0.80 g (60%), melt point: 120–123 °C. ^{1}H NMR (400 MHz, C_6D_6, 25 °C): δ 7.78–6.95 (m, 10H, Ph), 3.79 (m, 4H, OCH_2CH_2O), 3.34 (m, 6H, OCH_3), 3.12 (m, 4H, CH_2N), 1.23 (m, 2H, C*H*H), 1.01 (m, 2H, CH*H*), 0.31 (s, 18H, $SiMe_3$) ppm. IR (KBr pellet, cm^{-1}): 2956 (m), 1635 (s), 1568 (m), 1446 (m), 1383 (m), 1251 (w), 1206 (w), 1062 (w), 892 (w), 841 (w), 781 (w), 700 (m). *Anal.* Calc. for $C_{27}H_{44}Cl_1N_4O_2Si_2Y$ (M_W: 637.20): C, 50.89; H, 6.97; N, 8.79; Y, 13.95. Found: C, 51.05; H, 6.84; N, 8.96; Y, 13.78%.

Method B. A clear solution of **6** (1.21 g, 1 mmol) in THF (25 mL) was added to a stirring solution of YCl_3 (0.47 g, 1 mmol) in THF (20 ml). Complex **2** was isolated as colorless crystals by the same procedure as outlined for method A. Yield: 0.48 g (75%).

2.2.2. $Yb_2(\mu_2\text{-}L)_3 \cdot DME$ (*3*)

Method A. A solution of $LLi_2(THF)_{0.5}$ (0.47 g, 1 mmol) in THF (15 mL) was added to a stirring solution of **1** (1.55 g, 2 mmol) in THF (20 ml). The reaction mixture was stirred for 48 h at r.t. to become a clear solution. The volatiles were removed under reduced pressure and the residue was extracted with toluene (40 mL) and evaporated to dry. The solid was dissolved in DME (10 mL) and filtered. Cooling the solution to 0 °C afforded **3** as colorless crystals. Yield: 1.28 g (75%), melt point: 284–287 °C. IR (KBr pellet, cm^{-1}): 2959 (m), 1628 (m), 1570 (m), 1543 (m), 1385 (m), 1253 (w), 1060 (w), 891 (w), 844 (w), 783 (w), 756 (w), 702 (m). *Anal.* Calc. for $C_{73}H_{112}N_{12}O_2Si_6Yb_2$ (M_W: 1704.37): C, 51.44; H, 6.64; N, 9.86; Yb, 20.31. Found: C, 51.64; H, 6.21; N, 9.97; Yb, 20.03%.

Method B. A solution of $LLi_2(THF)_{0.5}$ (1.41 g, 3 mmol) in THF (30 mL) was added to a stirring suspension of $YbCl_3$ (0.56 g, 2 mmol) in THF (25 mL). Complex **3** was obtained as colorless crystals by the same procedure as outlined for method A. Yield: 1.02 g (60%).

Method C. A clear solution of **5** (2.59 g, 2 mmol) in THF (25 mL) was added to a stirring solution of **1** (2 mmol) in THF (20 ml). Complex **3** was isolated as colorless crystals by the same procedure as outlined for method A. Yield: 2.08 g (61%).

2.2.3. $Y_2(\mu_2\text{-}L)_3 \cdot DME$ (*4*)

Method A. A solution of $LLi_2(THF)_{0.5}$ (0.24 g, 0.5 mmol) in THF (20 mL) was added to a stirring solution of **2** (0.64 g, 1 mmol) in THF (20 ml). The reaction mixture was stirred for 48 h at r.t. to become a clear solution. The volatiles were removed under reduced pressure and the residue was extracted with toluene (40 mL) and evaporated to dry. The solid was dissolved in DME (5 mL) and filtered. Cooling the solution to 0 °C afforded **4** as colorless crystals. Yield: 0.42 g (55%), melt point: 170–173 °C. ^{1}H NMR (400 MHz, C_6D_6, 25 °C): δ 7.44–7.07 (m, 30H, Ph), 3.64 (m, 4H, OCH_2CH_2O), 3.44 (m, 6H, OCH_3), 3.23 (m, 12H, CH_2N), 1.64 (m, 3H, C*H*H), 1.45 (m, 3H, CH*H*), 0.26 (s, 54H, $SiMe_3$) ppm. IR (KBr pellet, cm^{-1}): 2955 (m), 1643 (m), 1605 (s), 1559 (s), 1381 (w), 1250 (w), 903 (w), 833 (w), 779 (w), 702 (m). *Anal.* Calc. for $C_{73}H_{112}N_{12}O_2Si_6Y_2$ (M_W: 1536.11): C, 57.07; H, 7.36; N, 10.94; Y, 11.58. Found: C, 56.93; H, 7.05; N, 11.21; Y, 11.24%.

Method B. A THF (40 mL) solution of $LLi_2(THF)_{0.5}$ (1.41 g, 3 mmol) was added to a stirring suspension of YCl_3 (1.41 g, 3 mmol) in THF (30 mL). Cooling to 0 °C afforded Complex **4** was isolated as colorless crystals by the same procedure as outlined for method A. Yield: 1.06 g (69%).

Method C. A clear solution of **6** (1.21 g, 1 mmol) in THF (25 mL) was added to a stirring solution of **2** (0.64 g, 1 mmol) in THF (20 ml). Complex **4** was isolated as colorless crystals by the same procedure as outlined for method A. Yield: 0.95 g (62%).

2.2.4. [Li(DME)$_3$][L$_2$Yb] (*5*)

Method A. A stirred suspension of $YbCl_3$ (0.42 g, 1.5 mmol) in THF (20 mL) was treated with $LLi_2(THF)_{0.5}$ (1.41 g, 3 mmol) in THF (15 mL). After the reaction mixture was stirred at r.t. for 48 h, the solvent was removed in vacuo. The residue was extracted with toluene (40 mL) and the volume of the extract was reduced to 10 mL followed by addition of DME (1 mL). Cooling to 0 °C afforded **5** as colorless crystals. Yield: 1.46 g (75%), melt point: 116–118 °C. IR (KBr pellet, cm^{-1}): 2963 (m), 1628 (m), 1543 (m), 1443 (m), 1381 (m), 1258 (w), 1204 (w), 1095 (w), 1026 (w), 895 (w), 841 (w), 787 (w), 702 (m). *Anal.* Calc. for $C_{58}H_{98}LiN_8O_6Si_4Yb$ (M_W: 1295.78): C, 53.76; H, 7.64; N, 8.65; Yb, 13.35. Found: C, 53.91; H, 7.35; N, 8.86; Yb, 13.54%.

Method B. A stirring solution of LYbCl(THF)$_2$ (0.78 g, 1 mmol) in THF (20 ml) was treated with $LLi_2(THF)_{0.5}$ (0.47 g, 1 mmol) in THF. Complex **5** was isolated as colorless crystals by the same procedure as outlined for method A (0.91 g, 70%).

2.2.5. [Li(DME)$_3$][L$_2$Y] (*6*)

Method A. A stirred suspension of YCl_3 (0.20 g, 1 mmol) in THF (20 mL) was treated with $LLi_2(THF)_{0.5}$ (0.94 g 2 mmol) in THF (20 mL). The reaction mixture was stirred at r.t. for 48 h, the solvent was removed in vacuo. The residue was extracted with toluene (50 mL) and the volume of the extract was reduced to 5 mL followed by addition of DME (1 mL). Cooling to 0 °C afforded **6** as colorless crystals. Yield: 0.91 g (75%), melt point: 109–112 °C. ^{1}H NMR (400 MHz, C_6D_6, 25 °C): δ 7.85–6.97 (m, 20H, Ph), 3.87 (m, 12H, OCH_2CH_2O), 3.58 (m, 18H, OCH_3), 3.20 (m, 8H, CH_2N), 1.46 (m, 2H, C*H*H), 1.12 (m, 2H, CH*H*), 0.31 (m, 36H, $SiMe_3$) ppm. IR (KBr pellet, cm^{-1}): 2948 (m), 1643 (m), 1605 (s) 1559 (m), 1489 (m), 1443 (m), 1373 (m), 1250 (w), 1196 (w), 980 (w), 903 (w), 833 (w), 779 (w), 702 (m). *Anal.* Calc. for $C_{58}H_{98}LiN_8O_6Si_4Y$ (M_W: 1211.65): C, 57.49; H, 8.17; N, 9.25; Y, 7.34. Found: C, 57.74; H, 8.05; N, 9.51; Y, 7.62%.

Method B. A stirring solution of **2** (0.64 g, 1 mmol) in THF (20 ml) was treated with $LLi_2(THF)_{0.5}$ (0.47 g, 1 mmol) in THF. Complex **6** was isolated as colorless crystals by the same procedure as outlined for method A (Yield: 0.95 g (78%)).

2.3. X-ray crystallographic study

Suitable crystals of complexes **2**–**6** for X-ray diffraction were sealed in a thin-walled glass capillary filled under argon for structural analysis. Diffraction data were collected on a Rigaku Mercury

CCD area detector. The structures were solved by direct methods and refined by full-matrix least-squares procedures based on $|F|^2$. All non-hydrogen atoms were refined with anisotropic displacement coefficients [7]. Hydrogen atoms were treated as idealized contributions. Crystal and refinement data are listed in Table 1.

2.4. Polymerization of ε-CL

To a stirred solution of ε-CL in toluene, a toluene solution of initiator was added with a syringe. The polymerization mixture was stirred for a definite time at the desired temperature and then quenched with an ethanol solution containing a small amount of hydrochloric acid. Polymer was precipitated from ethanol and washed with ethanol three times and dried under vacuum.

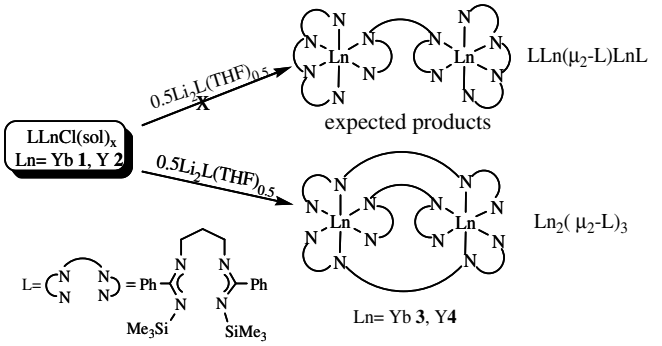
3. Results and discussion

3.1. Synthesis and molecular structure of LYClDME (2) and $Ln_2(\mu_2$-L)$_3 \cdot$ DME (Ln = Yb 3; Y 4)

Complex **1** [4a] was synthesized by the literature procedure as shown in Eq. (1). Treatment of **1** with 0.5 equiv. of $LLi_2(THF)_{0.5}$, followed by extraction with toluene, afforded colorless crystals upon crystallization from toluene. The full characterization by elemental analysis and X-ray crystal structural determination indicated that the product was the bimetallic complex $Yb_2(\mu_2\text{-L})_3 \cdot$ DME (**3**), not the expected complex LYb(μ_2-L)YbL as shown in Scheme 1

$$LnCl_3 + Li_2L(THF)_{0.5} \rightarrow LLnCL(sol)_xLn = Yb, sol = THF, x = 2, \mathbf{1}; Ln = Y, sol = DME, x = 1, \mathbf{2} \quad (1)$$

The isolation of **3**, instead of the complex LYb(μ_2-L)YbL, is somewhat surprised to us because the coordination mode of the L in **3** is quite different from that in LYb(μ_2-L)YbL. In **3** each of the three L acts as a bidented bridging ligand to link the two metals together, while each of the two L works as a chelating ligand and the third L as a bridging ligand to link the two YbL parts together in LYb(μ_2-L)YbL. Obviously, the formation of **3** should be included the change of coordination mode of L from a chelating fashion to a bridging one, i.e. the cleavage of two chelating Yb–amidinate bonds and then ligand redistribution during the reaction. In order to see whether this is the special case for Yb metal, the same reaction with Y was conducted. Complex **2** was then synthesized according to the procedure reported previously [4a] (Eq. (1)). The molecular structure of **2** was further determined by X-ray diffraction to be a monomeric structure with L as a chelating ligand (see the later part of this paragraph). Reaction of **2** with 0.5 equiv. of the dilithium salt went smoothly. After workup, colorless crystals were isolated in good yield. The crystals were fully characterized including elemental analysis, ^{1}H NMR and X-ray technique to be the analogous bimetallic complex $Y_2(\mu_2\text{-L})_3 \cdot$ DME (**4**) (Scheme 1). The results indicated that the occurrence of the ligand redistribution during the metathesis reaction here is independent on the metal used.



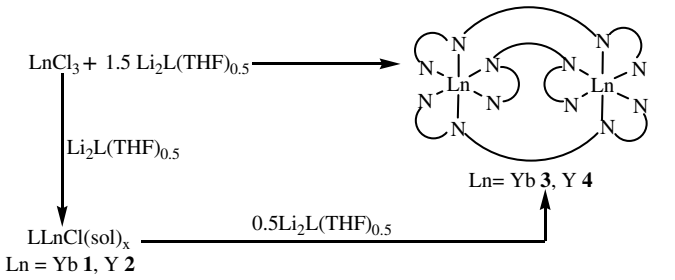
Scheme 1.

The pathway for the formations of **3** and **4** was proposed to be the same way that supposed for the preparation of the bimetallic lanthanocene hydride published [8]. The attack of lithium amidinate results in the cleavage of one of chelated Ln–bis(amidinate) bonds, followed by redistribution to another Ln metal. The same ligand redistribution, derived from the reaction of **1** with $NaN(TMS)_2$ was also described [4b]. These results indicate that the ligand redistribution of a linked bis(amidinate) ligand with a flexible bridge could be taken place under certain conditions and could become a strategy to various structure motifs by choice of right reagents and ligands.

Further study found that **3** and **4** can also be prepared directly by reaction of $LnCl_3$ with the dilithium salt in molar ratio of 1:1.5 (Scheme 2) in high yield. Its worth notice that **3**(**4**) was never isolated from the metathesis reaction of $LnCl_3$ with dilithium salt in 1:1 molar ratio, by prolonging reaction time and raising reaction

Table 1
Principal crystallographic data and parameters for complexes **2–6**

Compound	2	3	4	5	6
Chemical formula	$C_{27}H_{44}Cl_1N_4O_2Si_2Y$	$C_{73}H_{112}N_{12}O_2Si_6Yb_2$	$C_{73}H_{112}N_{12}O_2Si_6Y_2$	$C_{58}H_{98}LiN_8O_6Si_4Yb$	$C_{58}H_{98}LiN_8O_6Si_4Y$
Formula weight	637.20	1704.37	1536.11	1295.78	1211.65
T (K)	173(2)	193(2)	153(2)	193(2)	173(2)
Crystal system	monoclinic	triclinic	triclinic	trigonal	trigonal
Space group	$P2_1/c$	$P\bar{1}$	$P\bar{1}$	$P3_2$	$P3_2$
Unit cell dimensions					
a (Å)	17.7341(15)	12.2154(14)	12.1658(14)	15.679(2)	15.5959(8)
b (Å)	17.1032(13)	17.160(2)	17.189(2)	15.679(2)	15.5959(8)
c (Å)	21.9121(18)	21.107(3)	21.114(3)	24.222(3)	24.3310(13)
α (°)	90.00	107.239	107.233(3)	90.00	90.00
β (°)	96.275(2)	95.836(3)	95.831(3)	90.00	90.00
γ (°)	90.00	92.402(3)	92.204(3)	120.00	120.00
Volume (Å^3)	6606.3(9)	4191.6(9)	4184.4(9)	5156.9(12)	5125.2(5)
Z	8	2	2	3	3
D_{calc} (mg m^{-3})	1.281	1.350	1.219	1.252	1.178
θ Range for data collection (°)	3.03–25.35	3.05–25.35	3.05–25.35	3.00–27.48	3.02–25.31
Reflections collected	12101	15285	15236	15424	12262
Independent reflections	10020	13715	12613	13685	10862
Goodness-of-fit on F^2	1.173	1.098	1.081	1.079	1.105
R	0.0600	0.0266	0.0492	0.0523	0.0536
wR_2	0.1060	0.0579	0.0915	0.1340.	0.1375



Scheme 2.

temperature. Therefore, the formation of **3**(**4**) in this procedure may supposed through two steps: the metathesis reaction affords **1**(**2**) first and then **1**(**2**) reacts further with the dilithium salt to form **3**(**4**) via ligand redistribution reaction as shown in Scheme 2.

Complexes **2**, **3** and **4**, have been characterized by IR, single-crystal X-ray diffraction and also ^{1}H NMR spectroscopy for **2** and **4**. No ^{1}H NMR data were obtained for **3**, due to the paramagnetism of the ytterbium. In their IR spectra a strong absorption of C=N stretch at approximate 1640 cm^{-1} for both complexes was observed indicating the delocalized double bond of the N–C–N linkage [9].

The molecular structure of **2** is shown in Fig. 1. Selected bond distances and angles are listed in Table 2. Complex **2** has a monomeric structure, in which the yttrium atom is ligated by two linked bidentate amidinate moieties through nitrogen atoms, one chlorine atom, and two oxygen atoms of a coordinated DME molecule. The coordination geometry about the yttrium atom can be best described as a distorted trigonal bipyramid with each chelating bidentate amidinate ligand to occupy one coordination vertex, which is similar to that of **1** reported previously. The bond lengths of all Y–N are around 2.370(3) Å, which is comparable to that found in **1** if the deviation in ion radium between Y and Yb was considered.

The crystal structures of **3** and **4** are shown in Fig. 2. Selected bond distances and angles are listed in Table 3. Complexes **3** and **4** are isostructure having a free DME molecule in the unit cell. In the two complexes the central metals are connected together by three bridged bis(amidinate)s and each central metal coordinates to three amidinates in dihapto fashion through the nitrogen atoms with the Ln–N–C–N units only deviating slight from planarity (the largest one is 0.0003 Å from the plane Y1–N5–C24–N6). The whole molecule has a cage-like structure with the two planes formed by

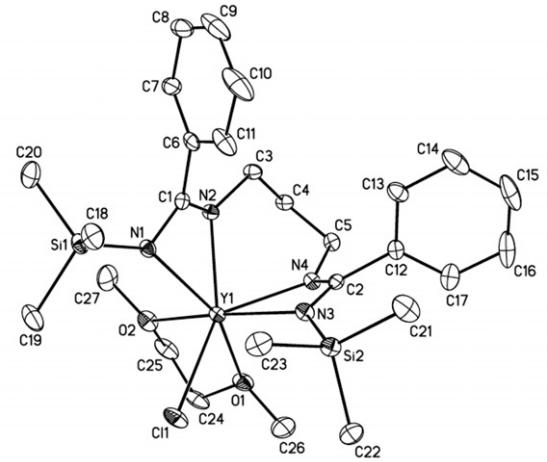


Fig. 1. Molecular structure of the complex **2**. Thermal ellipsoids are drawn at the 20% level. Hydrogen atoms are omitted for clarity.

Table 2
Selected bond distances (Å) and angles (°) for complex **2**

Y(1)–N(1)	2.360(3)	Y(1)–N(2)	2.365(3)
Y(1)–N(3)	2.379(3)	Y(1)–N(4)	2.375(3)
Y(1)–C(1)	2.695(4)	Y(1)–C(2)	2.765(4)
N(2)–Y(1)–N(1)	57.1(1)	N(4)–Y(1)–N(3)	56.8(1)

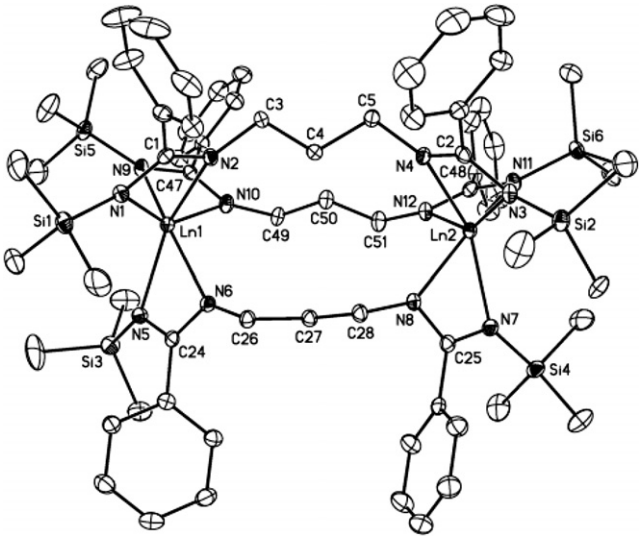


Fig. 2. Molecular structure of the complexes **3** (Ln = Yb) and **4** (Ln = Y). Thermal ellipsoids are drawn at the 30% level. Hydrogen atoms and a free DME molecule are omitted for clarity.

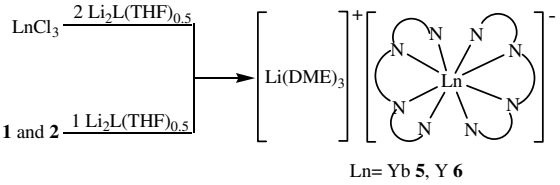
LnCCC occupying on top (Ln1–C1–C24–C47) and bottom plane (Ln2–C2–C25–C48). The coordinated geometries about each metal can be best described as a distorted octahedron in which four nitrogen atoms can be considered to occupy equatorial positions (N1, N2, N5 and N10; N3, N4, N7 and N12) with the angles sum about the lanthanide center of ΣN–Ln–N = 363.4° for Yb1 and 363.8° for Y1; 365.8° for Yb2 and 366.3° for Y2, while another two nitrogen atoms occupy axial positions and the N–Ln–N angle is distorted away from the idealized 180° (N6–Yb1–N9, 158.7° and N8–Yb2–N11, 159.2°; N6–Y1–N9, 157.6° and N8–Y2–N11, 158.6°). The angles of N–Ln–N in the Ln–N–C–N units are almost equal for the two complexes and the average value is 58.3° for **3** and 57.5° for **4**, which are comparable to the values found in homoleptic lanthanide tri(amidinates) [1a]. The bond lengths of Ln–N range from 2.352(2) to 2.392(2) Å for **3**, and 2.307(2) to 2.354(2) Å for **4**. The average Ln–N bond length of **3**, 2.361(2) Å, is comparable to 2.325(2) Å found in **4**, if the difference in ionic radii between the two metals is considered. The values are also comparable with 2.342(8) Å for $[CyNC(Me)Cy]_3Yb$ [1a] and 2.326(5) Å for $[CyNC(Ph)Cy]_3Yb$ [1a]. The bond lengths of Ln–C on N–C–N are around 2.765(3) Å for **3**, and 2.731(3) Å for **4** which are comparable to the values for lanthanide amidinate complexes published [1a]. All C–N bond distances within the chelating NCN units are nearly equal with the average value 1.332(4) Å for both complexes, which reflects the delocalization of the π bond in the N–C–N unit.

*3.2. Synthesis, molecular structure and reactivity of anionic complexes $[Li(DME)_3][L_2Ln]$ (Ln = Yb **5**;Y **6**)*

Treatment of $YbCl_3$ with $Li_2L(THF)_{0.5}$ in a molar ratio of 1:2, after workup afforded colorless crystals in good yield. The crystals were full characterized including X-ray analysis to be the target product $[Li(DME)_3][L_2Yb]$ (**5**) (Scheme 3). The same reaction with YCl_3 gave

Table 3
Selected bond distances (Å) and angles (°) for the complexes **3** and **4**

Compound	3	4		3	4
Ln(1)–N(1)	2.321(2)	2.352(2)	Ln(2)–N(3)	2.328(2)	2.365(2)
Ln(1)–N(2)	2.329(2)	2.364(2)	Ln(2)–N(4)	2.320(2)	2.355(2)
Ln(1)–N(5)	2.332(2)	2.365(2)	Ln(2)–N(7)	2.336(2)	2.373(2)
Ln(1)–N(6)	2.307(2)	2.350(2)	Ln(2)–N(8)	2.310(2)	2.351(2)
Ln(1)–N(9)	2.324(2)	2.360(2)	Ln(2)–N(11)	2.316(2)	2.351(2)
Ln(1)–N(10)	2.325(2)	2.358(2)	Ln(2)–N(12)	2.354(2)	2.392(2)
Ln(1)–C(1)	2.736(3)	2.769(3)	Ln(2)–C(2)	2.730(3)	2.768(3)
Ln(1)–C(24)	2.727(3)	2.765(3)	Ln(2)–C(25)	2.727(3)	2.762(3)
Ln(1)–C(47)	2.725(3)	2.760(3)	Ln(2)–C(48)	2.739(3)	2.768(3)
N(1)–Ln(1)–N(2)	58.25(8)	57.46(8)	N(4)–Ln(2)–N(3)	58.37(8)	57.56(8)
N(6)–Ln(1)–N(5)	58.13(8)	57.28(9)	N(8)–Ln(2)–N(7)	58.17(8)	57.34(8)
N(9)–Ln(1)–N(10)	58.52(8)	57.73(8)	N(11)–Ln(2)–N(12)	58.07(8)	57.29(8)



Scheme 3.

the analogous complex $[Li(DME)_3][L_2Y]$ (**6**) as colorless crystals in good yield (Scheme 3). ^1H NMR spectrum of **6** shows the signals of bis(amidinate) ligands [3], but no ^1H NMR data were obtained for**5** due to the paramagnetism of the ytterbium. In their IR spectra a strong absorption of C=N stretch at approximate 1640 cm^{-1} for both complexes was observed indicating the delocalized double bond of the N–C–N linkage [9].

Complexes **5** and **6** can also be prepared by reaction of **1** and **2**, respectively, with 1 equiv. of $Li_2L(THF)_{0.5}$ (Scheme 3).

The molecule structures of complexes **5** and **6** are shown in Fig. 3. Selected bond distances and angles are listed in Table 4. Complexes **5** and **6** have the same structure composed of a pairs of discrete cation and anion. The Ln atom in anion coordinates to two bis(amidinate)s to form a distorted tetrahedron, if each chelating amidinate ligand is considered to occupy a single coordination site. All four-membered rings Ln–N–C–N are essentially planar. The average bond angle of the N–Ln–N in the Ln–N–C–N unit, 54.8(2)°, for **5** is comparable to 54.4(1)° in **6**, but smaller than the corresponding values found in complexes **3** and **4**. The average bond length of the Ln–N (2.444(7) Å for **5** and 2.475(4) Å for **6)** and the bond lengths of the Ln– C on the N–C–N (around 2.869(7) Å for **5** and 2.890(5) Å for **6**) are longer than the corresponding values found in **1** and **2**. All these bond parameters reflect that four of amidinate groups make the coordinate sphere around the central metal more crowded. The coordinate geometry of the cation is normal.

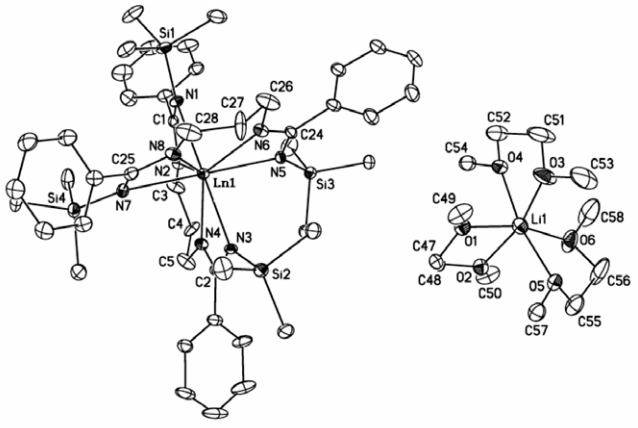


Fig. 3. Molecular structure of the complexes **5** (Ln = Yb) and **6** (Ln = Y). Thermal ellipsoids are drawn at the 30% level. Hydrogen atoms are omitted for clarity.

To see whether the complex LLn(μ_2-L)LnL (Ln = Yb, Y) could be prepared by the reaction of **5** and **6** with **1** and **2** respectively, the two reactions at room temperature were tried, respectively. Complexes **5** and **6** do react with **1** and **2** smoothly in THF, after workup, to afford colorless crystals in good yield for both metals, which were fully characterized to be complexes **3** and **4**, respectively, not the complexes LLn(μ_2-L)LnL as shown in Scheme 4. The results indicate again that complexes **3** and **4** are really much more stable than LLn(μ_2-L)LnL, which leads to the ligand redistribution reaction occurred easily during the present metathesis reaction.

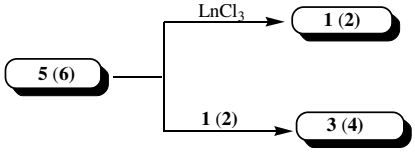
Complexes **5** and **6** can react with $LnCl_3$ to afford complexes **1** and **2**, respectively (Scheme 4).

3.3. Catalytic activity for ring-opening polymerization of ε-CL

The catalytic activity of **3**, **4**, **5** and **6** for ring-opening polymerization of ε-CL was examined under variety of conditions. The preliminary results are listed in Table 5. In comparison the reactivity of Li_2L was also tested, and no reactivity was found under the same conditions (Table 5, entry 8). It can be seen that all complexes are active initiators under mild conditions. All systems yield the polymers with a unimodal molecular weight distribution, indicating they function as single component catalysts. The anionic complexes of **5** and **6** are less active related to **3** and **4**. This may be contributed to the crowded coordination environment around the lanthanide metal by two bridged bis(amidinate) ligands. The center metal has profoundly effect on the activity and the active sequence of Yb < Y was observed for both the anionic complexes (**5** and **6)** and the bimetallic complexes (**3** and **4)**. This may result from the more crowded coordination environment around the smaller Yb metal than Y metal, which leads to the coordination of monomer to metal and then insertion of activated monomer more difficulty. Among the four complexes **4** is the most efficient catalyst. For example, quantitative yield was obtained within 30 min at room temperature with **4** at the molar ratio of monomer to catalyst of 2500:1, while the yields were only 87% and 57% for **3** and **6**, even the molar ratio of monomer to catalyst decreased to 2000:1 (Table 5, entries 1, 3 and 7). The polymerization system with **4** could still give 55% yield within 30 min, when the molar ratio of monomer to initiator increased to 4000:1 (Table 5, entry 2). All polymerization systems gave the polymers with rather broad molecular weight distributions. The polydispersity index M_w/M_n

Table 4
Selected bond distances (Å) and angles (°) for the complexes **5** and **6**

	5	6		5	6
Ln(1)–N(1)	2.492(10)	2.534(5)	Ln(1)–N(5)	2.525(6)	2.542(4)
Ln(1)–N(2)	2.372(5)	2.415(4)	Ln(1)–N(6)	2.377(7)	2.415(4)
Ln(1)–N(3)	2.519(11)	2.526(5)	Ln(1)–N(7)	2.521(6)	2.540(4)
Ln(1)–N(4)	2.373(5)	2.414(4)	Ln(1)–N(8)	2.374(7)	2.417(4)
Ln(1)–C(1)	2.851(6)	2.886(5)	Ln(1)–C(2)	2.861(6)	2.877(5)
Ln(1)–C(24)	2.886(7)	2.898(5)	Ln(1)–C(25)	2.878(7)	2.896(5)
N(2)–Ln(1)–N(1)	54.8(2)	54.3(1)	N(6)–Ln(1)–N(5)	54.6(2)	54.4(1)
N(4)–Ln(1)–N(3)	54.7(2)	54.4(1)	N(8)–Ln(1)–N(7)	55.0(2)	54.5(1)



Scheme 4.

Table 5
Polymerization of ε-CL initiated by complexes **3**, **4**, **5** and **6**[a]

Entry	Initiator	[M]/[I]	Time (min)	Yield[b] (%)	M_n($\times 10^4$)	PDI[c]
1	**3**	2000:1	30	87	13.1	1.87
2	**4**	2500:1	30	100	10.4	2.22
3	**4**	4000:1	30	55	6.9	2.80
4	**5**	500:1	30	84	0.66	2.25
5	**5**	700:1	30	65	0.96	2.66
6	**6**	1500	30	73	3.23	2.41
7	**6**	2000	30	57	4.11	2.50
8	**Li_2L**	700	30	0	–	–

[a] Conditions: room temperature, in toluene, solvent/monomer = 10 v/v.
[b] Yield = weight of polymer obtained/weight of monomer used.
[c] Measured by GPC calibrated with standard polystyrene samples.

ranged from 1.87 to 2.80. The values are comparable to those found for the systems with homoleptic lanthanide triamidinate complex as initiator [1a,1b,1c]. The reason for broad molecular weight distribution might be attributed to multi-active Ln–amidinate bonds existed in these catalysts [1a,1b,1c]. However, the activity of **4** is lower than that of the related complex with unbridged amidinate ligands [1a]. The reason for it may be attributed to the bimetallic structure skeleton of **4** which may not favor the coordination and insertion of monomer to active species.

4. Conclusion

In conclusion, four novel lanthanide complexes bearing bridged bis(amidinate) ligand L ($Me_3SiNC(Ph)N(CH_2)_3NC(Ph)NSiMe_3$) in different coordination modes were synthesized in high yields including $Ln_2(\mu_2\text{-}L)_3 \cdot DME$ and $Li(DME)_3LnL_2$ (Ln = Yb, Y). The change of the coordination mode of L from a chelating fashion to a bridging one was occurred during the metathesis reaction of $LLnCl(sol)_x$ with 0.5 equiv. of Li_2L. The results presented here demonstrated that the different coordination mode of L, which leads to the different structure motif, can be realized under different conditions. The further work on designing definite catalysts with the bridged bis(amidinate) ligands are currently proceeding in our laboratory.

Acknowledgement

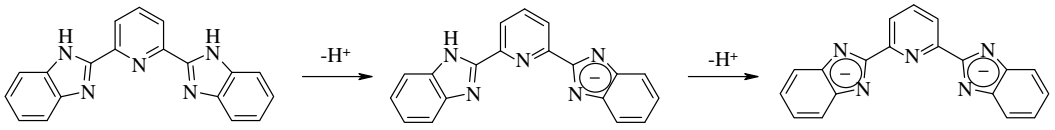
We acknowledge the National Natural Science Foundation for financial support.

Appendix A. Supplementary data

CCDC 612924, 612922, 612923, 612925 and 612926 contain the supplementary crystallographic data for LYCl(DME) (**2**), $Yb_2(\mu_2\text{-}L)_3 \cdot DME$ (**3**), $Y_2(\mu_2\text{-}L)_3 \cdot DME$ (**4**), $[L_2Yb][Li(DME)_3]$ (**5**), and $[L_2Y][Li(DME)_3]$ (**6**). These data can be obtained free of charge via http://www.ccdc.cam.ac.uk/conts/retrieving.html, or from the Cambridge Crystallographic Data Centre, 12 Union Road, Cambridge CB2 1EZ, UK; fax: (+44) 1223-336-033; or e-mail:deposit@ccdc.cam.ac.uk Supplementary data associated with this article can be found, in the online version, at doi:10.1016/j.poly.2008.03.006.

References

[1] (a) Y.J. Luo, Y.M. Yao, Q. Shen, J. Sun, L.H. Weng, J. Organomet. Chem. 662 (2002) 144;
(b) C. Li, Y.R. Wang, L.Y. Zhou, H.M. Sun, Q. Shen, J. Appl. Polym. Sci. 102 (2006) 22;
(c) C. Villiers, P. Thuery, M. Ephritikhine, Eur. J. Inorg. Chem. 23 (2004) 4624;
(d) R. Duchateau, C.T. van Wee, A. Meetsma, P.T. van Duijnen, J.H. Teuben, Organometallics 15 (1996) 2279;
(e) R. Duchateau, A. Meetsma, J.H. Teuben, Organometallics 15 (1996) 1656;
(f) R. Duchateau, C.T. van Wee, A. Meetsma, J.H. Teuben, J. Am. Chem. Soc. 115 (1993) 4931;
(g) C. Hagen, H. Reddmann, H.D. Amberger, F.T. Edelmann, U. Pegelow, G.V. Shalimoff, J. Organomet. Chem. 462 (1993) 69;
(h) R. Duchateau, C.T. van Wee, J.H. Teuben, Organometallics 15 (1996) 2291;
(i) M. Wedler, F. Knosel, U. Pieper, D. Stalke, F.T. Edelmann, H.D. Amberger, Chem. Ber. 125 (1992) 2171;
(j) A. Recknagel, F. Knosel, H. Gornitzka, M. Noltemeyer, F.T. Edelmann, U. Behrens, J. Organomet. Chem. 417 (1991) 363;
(k) M. Wedler, A. Recknagel, J.W. Gilje, M. Noltemeyer, F.T. Edelmann, J. Organomet. Chem. 426 (1992) 295;
(l) M. Wedler, M. Noltemeyer, U. Pieper, H.G. Schmidt, D. Stalke, F.T. Edelmann, Angew. Chem., Int. Ed. 29 (1990) 894.
[2] (a) J. Grundy, M.P. Coles, P.B. Hitchcock, J. Organomet. Chem. 662 (2002) 178;
(b) J.R. Hagadorn, M.J. McNevin, G. Wiedenfeld, R. Shoemaker, Organometallics 22 (2003) 4818;
(c) B. Clare, N. Sarker, R. Shoemaker, J.R. Hagadron, Inorg. Chem. 43 (2004) 1159;
(d) M.J. McNevin, J.R. Hagadorn, Inorg. Chem. 43 (2004) 8547;
(e) C. Roques, M.R. Mazières, J.P. Majoral, M. Sanchez, J. Jaud, Inorg. Chem. 28 (1989) 3931;
(f) J.R. Hagadorn, J. Arnold, Angew. Chem., Int. Ed. 37 (1998) 1729;
(g) J.F. Li, L.H. Weng, X.H. Wei, D.S. Liu, J. Chem. Soc., Dalton Trans. (2002) 1401;
(h) H. Kawaguchi, T. Matsuo, Chem. Commun. (2002) 958;
(i) C.T. Chen, L.H. Rees, A.R. Cowley, M.L.H. Green, J. Chem. Soc., Dalton Trans. (2001) 1761;
(j) S. Appel, F. Weller, K. Dehnicke, Z. Anorg. Allg. Chem. 583 (1990) 7;
(k) S.D. Bai, J.P. Guo, D.S. Liu, J. Chem. Soc., Dalton Trans. (2006) 2244;
(l) R.J. Baker, C. Jones, J. Organomet. Chem. 691 (2006) 65.
[3] S. Bambirra, A. Meetsma, B. Hessen, J.H. Teuben, Organometallics 20 (2001) 782.
[4] (a) J. Wang, Y. Yao, J. Cheng, X. Pang, Y. Zhang, Q. Shen, J. Mol. Struct. 743 (2005) 229;
(b) J. Wang, T. Cai, Y. Yao, Y. Zhang, Q. Shen, Dalton Trans. (2007) 5275.
[5] H. Sheng, L. Zhou, Y. Zhang, Y. Yao, Q. Shen, J. Polym. Sci. Part A: Polym. Chem. 45 (2007) 1210.
[6] M.D. Tayler, C.P. Carter, J. Inorg. Nucl. Chem. 24 (1962) 387.
[7] G.M. Sheldrick, SHELXTL 97. Program for the Refinement of Crystal Structures, University of Göttingen, Germany, 1997.
[8] (a) G. Desurmont, Y. Li, H. Yasuda, T. Maruo, N. Kanehisa, Y. Kai, Organometalics 19 (2000) 1811;
(b) D. Stern, M. Sabat, T.J. Marks, J. Am. Chem. Soc. 112 (1990) 9558.



LH_2 (*Diprotonated*) LH^- (*Mono-protonated*) L^{2-} (*Fully deprotonated*)

Scheme 1.

calomel reference electrode (SCE) were used in a three electrode configuration. The supporting electrolyte was $[NEt_4]ClO_4$ and the solute concentration was $\sim 10^{-3}$ M. The half-wave potential E^0_{298} was set equal to $0.5(E_{pa} + E_{pc})$, where E_{pa} and E_{pc} are anodic and cathodic cyclic voltammetric peak potentials, respectively. All experiments were carried out under a dinitrogen atmosphere and were uncorrected for junction potentials. The elemental analyses were carried out with Perkin–Elmer elemental analyser.

2.3. Crystallography

Single crystals were grown by slow diffusion followed by slow evaporation technique. The intensity data were collected using a Bruker SMART APEX-II CCD diffractometer, equipped with a fine focus 1.75 kW sealed tube Mo Kα radiation ($\lambda = 0.71073$ Å) at 273(3) K, with increasing ω (width of 0.3° per frame) at a scan speed of 3 s/frame. The SMART software was used for data acquisition. Data integration and reduction were undertaken with SAINT and XPREP [16] software. Multi-scan empirical absorption corrections were applied to the data using the program SADABS [17]. Structures were solved by direct methods using SHELXS-97 and refined with full-matrix least squares on F^2 using SHELXL-97 [18]. All non-hydrogen atoms were refined anisotropically. The hydrogen atoms were located from the difference Fourier maps and refined. Structural illustrations have been drawn with ORTEP-3 for Windows [19].

2.4. Synthesis of the ligand, LH_2

The tridentate ligand, LH_2 has been synthesized in a modified reported route [20]. A mixture pyridine 2,6-dicarboxylic acid (835 mg, 5 mmol) and ortho-phyenlenediamine (1080 mg, 10 mmol) in 10 ml orthophosphoric acid was refluxed for 8 h. Then cool down to room temperature and poured into 200 ml pre-cooled water with constant stirring which gives a light blue precipitate. On washing with 200 ml with 20% sodium carbonate solution, pinkish precipitate of the ligand LH_2 was obtained. It was then recrystallized from hot methanolic solution (Yield = 40%). *Anal.* Calc.: C, 73.30; H, 4.21; N, 22.49. Found: C, 73.21; H, 4.23; N, 22.51%.

2.5. Synthesis of the complexes [**1**] $(ClO_4)_2$ and **2**

$Ru^{III}(trpy)Cl_3$ (200 mg; 0.44 mmol) and ligand (142 mg; 0.46 mmol) was dissolved in 20 ml ethanol and NEt_3 (0.7 mmol) was added dropwise in the mixture. It was then heated to reflux with constant stirring for 4 h. Then the volume of mixture was reduced to 5 ml under reduced pressure and a precooled saturated aqueous $NaClO_4$ solution was added. The mixture was kept in refrigerator for overnight. The dark precipitate was then filtered off and washed with ice cold distilled water. The product was dried in vacuo over P_4O_{10}. It was then passed through the silica column with CH_2Cl_2/CH_3CN. The reddish brown color complex, [**1**]$(ClO_4)_2$ was separated first with 4:1 CH_2Cl_2:CH_3CN followed by complex **2**. Yield: complex [**1**]$(ClO_4)_2$, 30% and **2**, 40%. *Anal.* Calc. for [**1**]$(ClO_4)_2 \cdot 2H_2O$: C, 46.05; H, 3.84; N, 12.64. Found: C, 46.11; H, 3.86; N, 12.61%. *Anal.* Calc. for **2** $\cdot$ $2H_2O$: C, 59.38; H, 4.98; N, 16.29. Found: C, 59.35; H, 4.96; N, 16.25%.

2.6. Crystal data

2.6.1. Complex [**1**]$(ClO_4)_2 \cdot CH_3OH$

CCDC No. 658689, $C_{35}H_{28}Cl_2N_8O_9Ru$, $M = 876.62$, triclinic, $a = 8.9369(5)$, $b = 12.9441(6)$, $c = 16.6331(8)$ Å, $\alpha = 79.843(3)$, $\beta = 76.981(2)$, $\gamma = 81.413(3)$, $V = 1833.20(16)$ Å^3, space group $P\bar{1}$, $Z = 2$, $T = 298(2)$ K, μ (Mo Kα) = 0.637 mm^{-1}, $F(000) = 805$, GOF = 1.051; final R indices: $R_1 = 0.0495$ [$I > 2\sigma(I)$], $wR_2 = 0.2087$; R indices (all data): $R_1 = 0.0713$, $wR_2 = 0.02325$.

2.6.2. Complex **2** $\cdot$ $2H_2O$

CCDC No. 658688, $C_{34}H_{26}N_8O_2Ru$, $M = 679.67$, monoclinic, $a = 14.8580(4)$, $b = 13.2833(3)$, $c = 18.4269(5)$ Å, $\beta = 106.779(2)$, $V = 3481.96(15)$ Å^3, space group $P_2(1)/n$, $Z = 4$, $T = 298(2)$ K, μ (Mo Kα) = 0.493 mm^{-1}, $F(000) = 1500$, GOF = 1.009; final R indices: $R_1 = 0.0757$ [$I > 2\sigma(I)$], $wR_2 = 0.2084$; R indices (all data): $R_1 = 0.0931$, $wR_2 = 0.2274$.

3. Results and discussion

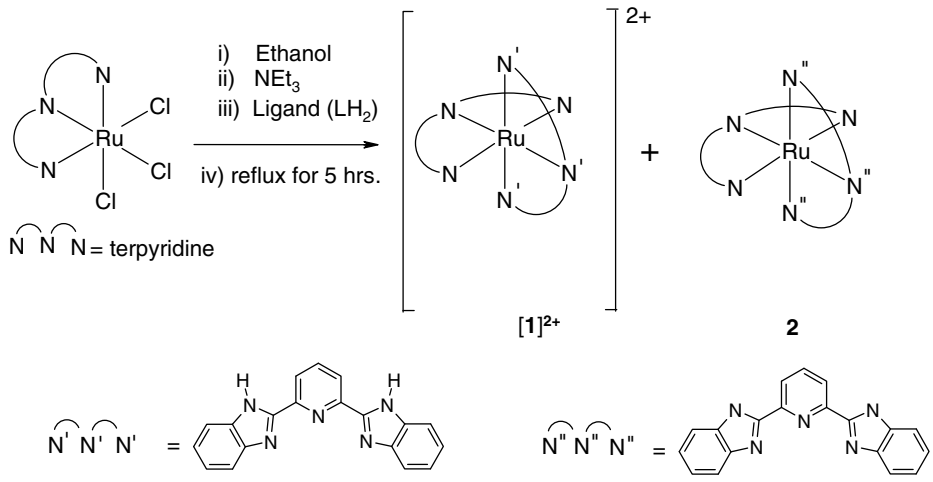
The ligand has been synthesized following a reported procedure [20]. The reaction of LH_2 with the ruthenium precursor complex $Ru(trpy)Cl_3$, in ethanol afforded a dark solution, from which a dark colored solid mass has been isolated on addition of excess saturated aqueous $NaClO_4$ solution (Scheme 2). Chromatographic purification of the crude product on a silica gel column using CH_2Cl_2:CH_3CN mixture (4:1) as eluent results in initially the reddish complex [**1**]$(ClO_4)_2$ (112 mg, yield, 30%) (this complex has been synthesized by other group in a different process [21]) followed by the pink colored neutral complex **2** (114 mg, yield, 40%).

The complexes exhibit satisfactory elemental analyses {see experimental section} and [**1**]$(ClO_4)_2$ shows 1:2 conductivity [$\Lambda_M(\Omega^{-1}\,cm^2\,mol^{-1})$, 248] in acetonitrile solution whereas **2** is neutral. The formulation of the complexes has been further supported by the FT-IR and ^1H NMR spectral features (see later). $[\mathbf{1}]^{2+}$, in presence of one equivalent of base affords $[\mathbf{1a}]^+$ which on successive addition of another equivalent of base gives **2**. The formations of [**1**]$(ClO_4)_2$ and **2** have been authenticated by their single crystal X-ray structures.

3.1. X-ray crystallographic studies

Single crystals of [**1**]$(ClO_4)_2$ were grown by slow diffusion of an acetonitrile solution of it in benzene followed by slow evaporation and for **2**, a dichloromethane solution of it was allowed to diffuse slowly in hexane followed by slow evaporation. The crystal structures of [**1**]$(ClO_4)_2$ and **2** are shown in Fig. 1.

The single crystal of [**1**]$(ClO_4)_2$ contains one methanol and **2** contains water as solvent of crystallization in the ratio of **2**: H_2O = 1:2. The RuN_6 chromophores in [**1**]$(ClO_4)_2$ and **2** are in distorted octahedral arrangement as can be seen from the angles subtended at the metal ions in Table 1. It is found that the ligands LH_2



Scheme 2.

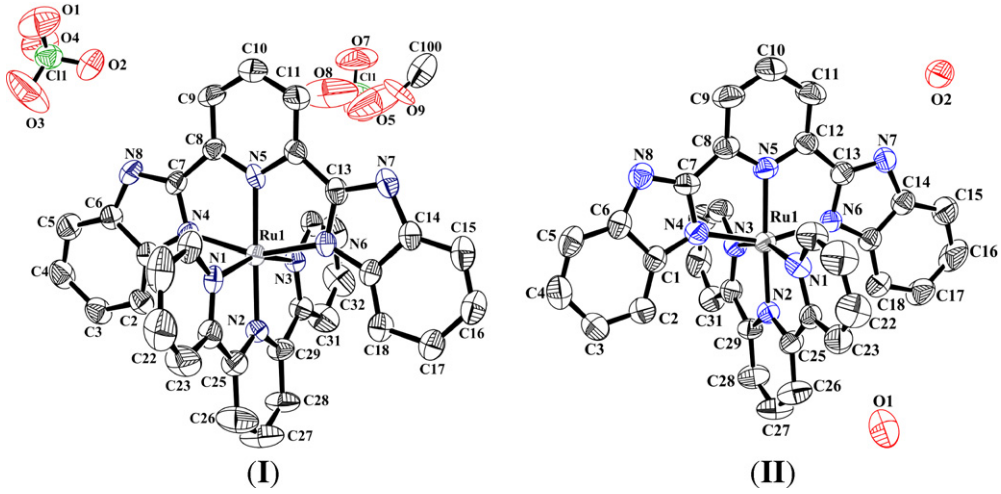


Fig. 1. ORTEP plot with atom numbering scheme of complexes (I) [**1**](**ClO**$_4$)$_2$ and (II) **2**. Hydrogen atoms are omitted for clarity.

Table 1
Selected bond distances (Å) and bond angles (°) of complexes [**1**](**ClO**$_4$)$_2$ and **2**

Complex [**1**](**ClO**$_4$)$_2$	Complex **2**
Ru1–N1 2.071(7)	Ru1–N1 2.051(8)
Ru1–N2 1.964(7)	Ru1–N2 1.951(7)
Ru1–N3 2.072(7)	Ru1–N3 2.050(8)
Ru1–N4 2.067(7)	Ru1–N4 2.064(8)
Ru1–N5 2.017(7)	Ru1–N5 2.029(8)
Ru1–N6 2.070(7)	Ru1–N6 2.075(7)
N2–Ru1–N5 177.8(3)	N2–Ru1–N5 176.1(3)
N2–Ru1–N4 103.9(3)	N2–Ru1–N1 79.9(3)
N5–Ru1–N4 78.1(3)	N5–Ru1–N1 96.7(3)
N2–Ru1–N6 100.1(3)	N2–Ru1–N3 79.6(3)
N5–Ru1–N6 77.9(3)	N5–Ru1–N3 103.8(3)
N4 Ru1–N6 156.0(3)	N1–Ru1–N3 159.5(3)
N2–Ru1–N1 79.5(3)	N2–Ru1–N6 99.9(3)
N5–Ru1–N1 99.5(3)	N5–Ru1–N6 78.2(3)
N4–Ru1–N1 90.8(3)	N1–Ru1–N6 91.4(3)
N6–Ru1–N1 93.1(2)	N3 Ru1–N6 92.4(3)
N2–Ru1–N3 79.1(3)	N2–Ru1–N4 103.3(3)
N5–Ru1–N3 101.8(3)	N5–Ru1–N4 78.6(3)
N4–Ru1–N3 94.3(3)	N1–Ru1–N4 91.8(3)
N6–Ru1–N3 90.6(3)	N3–Ru1–N4 92.5(3)
N1–Ru1–N3 158.6(3)	N6–Ru1–N4 156.8(3)

and L^{2-} in [**1**]$^{2+}$ and **2** are coordinated in the usual meridional fashion and terpyridine and LH_2 or L^{2-} in [**1**]$^{2+}$ or **2**, respectively, are in planes perpendicular to each other. The pyridine nitrogen of LH_2 or L^{2-} in [**1**]$^{2+}$ or **2** is in *trans* orientation with respect to the central pyridine nitrogen of terpyridine. Bond distances and angles associated with [**1**]$^{2+}$ and **2** match well with the reported analogous ruthenium-terpy [22–26] complexes. The geometrical constrains imposed on the meridional configurations of terpyridine and LH_2 in [**1**]$^{2+}$ and terpyridine and L^{2-} in **2** are reflected in the respective *trans* angles: N(1)–Ru(1)–N(3), 158.6(3)°/N(4)–Ru(1)–N(6), 156.0(3)° and N(1)–Ru(1)–N(3), 159.5(3)°/N(4)–Ru(1)–N(6), 156.8(3)°. Consequently, Ru(1)–N(2) (central pyridine nitrogen of terpyridine) distances in [**1**]$^{2+}$ and **2**, 1.964(7) and 1.951(7) Å, respectively, and the distance between ruthenium center and the central pyridine nitrogen (N_p) of the ancillary ligand (LH_2 and L^{2-}) in [**1**]$^{2+}$ and **2** are 2.017(7) and 2.029(8) Å, respectively, which are approximately 0.05 Å shorter than the corresponding terminal Ru–N bonds (Table 1). The average bite angles involving terpyridine/LH_2 in [**1**]$^{2+}$ and terpyridine/L^{2-} in **2** are 79.30°/78.00° and 79.75°/78.40°, respectively. It might be expected that an anionic ligand would be a better donor compared to the neutral and hence that will lead to shorter bonds. For complex [**1**](**ClO**$_4$)$_2$, the crystal

quality was not very good. We have tried several times to grow crystals from different solvent systems and at different conditions (e.g. at room temperature, at low temperature, etc.), also. However, we got the same results. The insignificant difference in the Ru–N bond distances in the two complexes might be because of this.

A poorly refined single crystal structure of complex $[\mathbf{1}](\mathbf{ClO_4})_2$ has been published previously along with spectroscopic and electrochemical measurements by Chattopadhyay et al. [21].

In the solid-state there is no π-stacking interactions due to the orthogonal orientation of the ligands in both the complexes. However, in complex $[\mathbf{1}](\mathbf{ClO_4})_2$, imidazole nitrogens are hydrogen bonded with perchlorate and methanol oxygen atoms. In addition to that they forms several weak C–HO and C–Hπ type hydrogen bond interactions. It is interesting to note that in solid-state it forms alternate hydrophobic and hydrophilic layers in the *bc* plane (Fig. 2a). On the other hand, complex **2** forms square boxes along *ab* plane in the solid-state with average dimension of the boxes is ~6 Å (Fig. 2b). Each box is filled with four water molecules of crystallization (Fig. 3).

One water molecule (O1) is double hydrogen bond donor while other one (O2) is as double hydrogen bond donor and single hydrogen bond acceptor. They form cyclic tetrameric water cluster with alternate arrangement of two symmetrically independent water molecules. This water cluster is highly stabilized by strong hydrogen bond between ligands.

3.2. UV–Vis spectroscopy

Complex $[\mathbf{1}]^{2+}$ exhibits metal-to-ligand charge transfer (MLCT) transition at 475 nm and intra-ligand $\pi \rightarrow \pi^*$ transitions appear at 347 and 314 nm at pH ~5 in acetonitrile/water (1:4 v/v) mixture. The MLCT band position is observed to change with the solution pH. It appears at 475 nm at a pH ⩽ 5; with increasing pH, 5–7, it is red shifted to 498 nm and finally, above pH 7, the band shifts further to 509 nm (Fig. 4). It is believed that in the acidic pH range of ⩽5, the di-protonated form of LH_2 exists in $[\mathbf{1}]^{2+}$ in solution, which with increasing pH gets transformed to $[\mathbf{1a}]^{+}$ containing the mono-protonated form of LH^- and the doubly-deprotonated form L^{2-} stabilizes in **2** in the alkaline pH range of 7–13 (Scheme 3, Fig. 4). The two pK_a values, 5.75 and 7.70 are determined from the spectral changes with the pH of the solution (Supporting Information). The similar spectral changes were reported for $[Ru(dtbimpy)(bimpyH_2)]^{2+}$ and $[Ru(dmbimpy)(bimpyH_2)]^{2+}$ in acetonitrile/buffer (1:1 v/v) with the pK_a values of 5.70, 7.33 and 6.35, 7.87, respectively [27]. Bond and Haga have reported similar pK_a values for $[Os(bpy)_2(BiBzImH_2)]^{2+}$ and $[Ru(bpy)_2(BiBzImH_2)]^{2+}$. The p$K_a$ values are also comparable to those of $[Ru(L18)(bimpyH_2)]^{2+}$ (L18 = 2,6-bis(1-octadecylbenzimidazol-2-yl)pyridine) in a micelle solution (10 mM Triton/0.1 M Na_2SO_4) (pK_a = 5.35 and 6.94) [28].

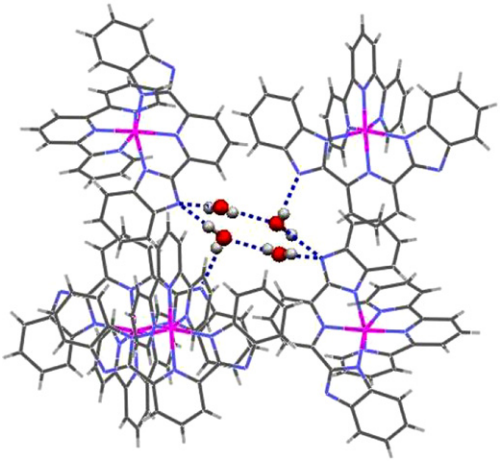


Fig. 3. Tetrameric water clusters inside hydrophilic pocket in complex **2**.

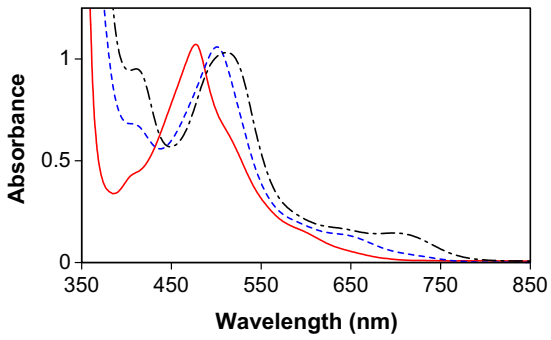


Fig. 4. UV–Vis spectra of $[\mathbf{1}]^{2+}$ (—), $[\mathbf{1a}]^{+}$ (- - -) and **2** (-·-·-) in acetonitrile:water (1:4 v/v) at pH: 1.25, 6.50 and 12, respectively.

3.3. IR spectroscopy

The FT-IR spectra of the complexes were recorded in KBr pellets (Figs. S1 and S2; Supporting Information). The strong, sharp per-

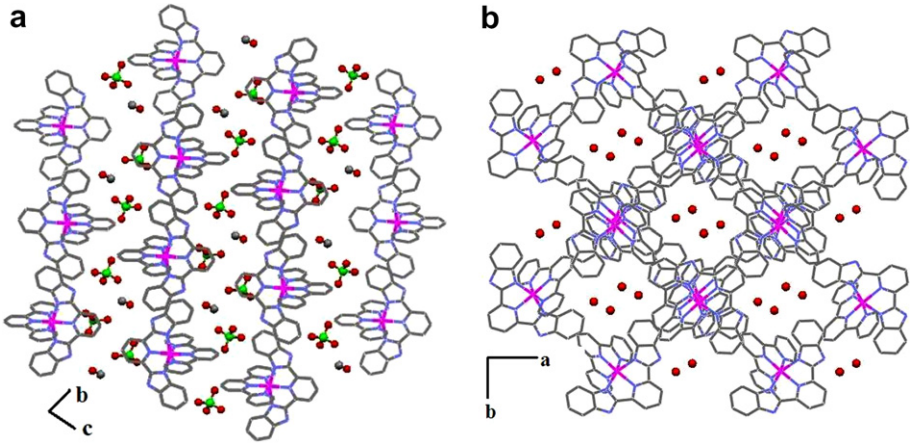
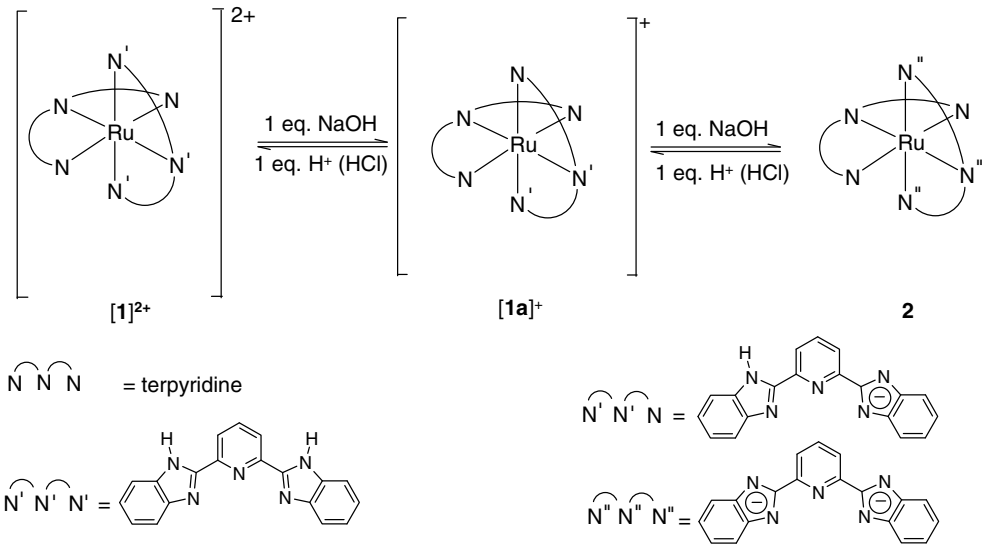


Fig. 2. Packing diagram of complexes (a) $[\mathbf{1}](\mathbf{ClO_4})_2$ viewed along *a*-axis and (b) **2** viewed along *c*-axis.



Scheme 3.

chlorate vibrations at ~1100 and ~625 cm^{-1} of complex $[\mathbf{1}]^{2+}$ were found to be absent in **2**; indicating the dianionic nature of the ligand LH_2 in complex **2**.

3.4. ^1H NMR spectroscopy

The ^1H NMR spectra of complexes $[\mathbf{1}]^{2+}$ and **2** in $(CD_3)_2SO$ (Supporting Information, Fig. S3) show the calculated number of 24 and 22 aromatic protons, respectively (overlapping between 5.5–9.2 ppm); eleven from the terpyridine group in each case; thirteen from the ancillary ligand LH_2 in case of complex $[\mathbf{1}]^{2+}$ and eleven from L^{2-} in **2**. The NH protons of LH_2 in $[\mathbf{1}]^{2+}$ are observed at 8.8 ppm, which have, as expected, disappeared on D_2O exchange [29]. The observed signals have been assigned to individual aromatic hydrogens (Supporting Information) with the aid of ^1H NMR correlation spectroscopic (COSY) experiments.

3.5. Electrochemical studies

Electrochemical studies have been performed in 1:4 acetonitrile–water solvent mixture since the complexes are not fully soluble in water. The Ru^{II}/Ru^{III} couple for **2** with fully deprotonated L^{2-} has been observed at 0.45 V versus SCE (I in Fig. 5) whereas the same for $[\mathbf{1}]^{2+}$ with doubly-protonated LH_2 appears at 0.99 V (II in Fig. 5). It is interesting to note that Ru^{II}/Ru^{III} couple for $[Ru(trpy)_2]^{2+}$ was reported to appear at 1.30 V [30]. Thus a decrease in potential of 0.30 V in case of $[\mathbf{1}]^{2+}$ and 0.85 V in case of **2** has been observed depending on the protonated (LH_2) or deprotonated (L^{2-}) form of the ancillary ligand. This can be attributed by the better σ-donor characteristic of the benzimidazol as compared to pyridine groups in trpy [31,32]. With the decrease in pH the redox wave (I in Fig. 5) of the fully deprotonated complex **2** is found to diminish with a gradual growth of a new redox wave at a higher anodic potential (II in Fig. 5, pH ~ 5) corresponding to $[\mathbf{1}]^{2+}$ with doubly-protonated LH_2 and no more significant change is observed with further decrease in pH. Thus Ru^{II}/Ru^{III} couple remains pH independent in the range of <5 and >8.5. The major Ru(II) species in these limits of pH are $[Ru(trpy)(LH_2)]^{2+}$ $[\mathbf{1}]^{2+}$ and $[Ru(trpy)(L^{2-})]$ **2**, respectively, and the electrode processes can be defined as

$$[Ru^{II}(trpy)(LH_2)]^{2+} \rightleftharpoons [Ru^{III}(trpy)(LH_2) + e^- \quad (pH < 5) \qquad (i)$$

$$[Ru^{II}(trpy)(L^{2-})] \rightleftharpoons [Ru^{III}(trpy)(L^{2-})]^{+} + e^- \quad (pH < 8.5) \qquad (ii)$$

Although pH dependent UV–Vis spectral changes clearly indicate the formation of singly-protonated intermediate $[\mathbf{1a}]^+$ (Fig. 4, Scheme 2), the voltammogram involving the singly-protonated species $[\mathbf{1a}]^+$ is not apparently (Fig. 5) involved. Bond and Haga have also reported same observation with $[Ru(bpy)(BiBzImH_2)]^{2+}$ [7]. Significantly, the shift in redox potential of the Ru^{II}/Ru^{III} couple with the change in pH is reversible in nature.

The plot of Ru^{II}/Ru^{III} potential as a function of pH is shown in Fig. 6. The redox process at 0.99 V going from region A to D involves only the protonated species, $[\mathbf{1}]^{2+}$ and the process at 0.45 V going from region C to F involves only the deprotonated species, **2** (Eqs. (i) and (ii)).

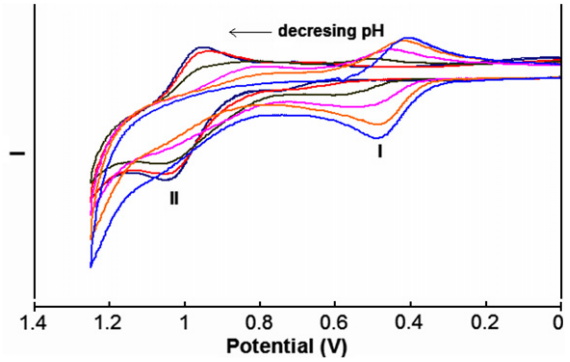


Fig. 5. pH (1.02–12.5) dependent cyclic voltammograms in acetonitrile:water (1:4 v/v).

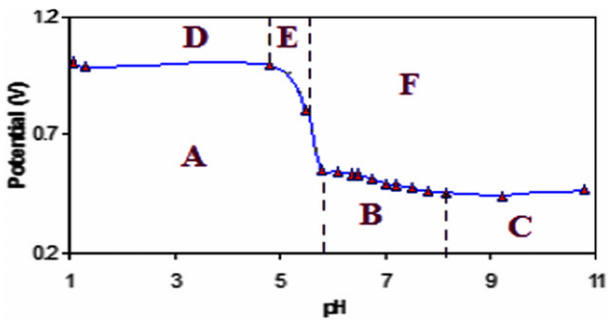


Fig. 6. The half-wave potential, $E_{1/2}$ vs. pH diagram for $[\mathbf{1}]^{2+}$ in acetonitrile:water (1:4 v/v).

The slope of the lines indicate the pH dependent processes in which proton transfer process is coupled with electron transfer (PCET). According to Nernst equation for a reversible electrode process, the slope of $\Delta E_{1/2}/\Delta pH = (m/n)59$ mV/pH-unit where m and n represent the number of protons and electrons involved in the process. From the plot (Fig. 6), it is evident that three distinct PCET processes are involved in the present case. The slope of 53 mV/pH in the region A–E implies one-electron/one-proton transfer process as follows (Eq. iii):

$$[Ru^{II}(trpy)(LH_2)]^{2+} \rightleftharpoons [Ru^{III}(trpy)(LH)]^{2+} + H^+ + e^- \quad \text{(iii)}$$

The change in slope to 114 mV/pH in the region A–F correlates with the expected two-proton/one-electron transfer process (Eq. iv):

$$[Ru^{II}(trpy)(LH_2)]^{2+} \rightleftharpoons [Ru^{III}(trpy)(L)]^{+} + 2H^+ + e^- \quad \text{(iv)}$$

Finally, the electrode reaction in the region B–F comes back to a one-proton/one-electron process with a slope 51 mV/pH (Eq. v):

$$[Ru^{II}(trpy)(LH)]^{+} \rightleftharpoons [Ru^{III}(trpy)(L)]^{+} + H^+ + e^- \quad \text{(v)}$$

Similar observations were reported by Ayers et al. [33] and Bond and Haga [7] with $[Ru(bpy\text{-}bzimH)_2]^{2+}$ and $[(bpy)_2Ru(bibzimH_2)]^{2+}$ (where bpy-bzimH = 6-(2-benzimidazole)-2,2′-bipyridyl; bpy = 2,2′-bipyridine and bibzimH = 2,2′-bibenzimidazole).

4. Conclusion

In conclusion, the present work demonstrates a unique example of a set of ruthenium monoterpyridine complexes, $[\mathbf{1}]^{2+}$ and **2**, with both the fully-protonated and deprotonated ancillary ligand. Both the complexes have been isolated as solid crystals. The complexes were characterized completely using various spectroscopic techniques and single crystal structures. The complex $[\mathbf{1}]^{2+}$, in solution, behaves as a dibasic acid. It, on successive addition of two equivalent of OH^-, results into complex **2**. The conversion of $[\mathbf{1}]^{2+}$ to **2** is found to be completely reversible in nature. The proton (or pH) dependency of the spectral and redox properties of the complexes have been studied in detail.

Acknowledgements

We would like to thank the Department of Chemistry, Indian Institute of Technology Guwahati, India for the support and DST India for FIST project. We would also like acknowledge that a poorly refined single crystal structure of complex $[\mathbf{1}](\mathbf{ClO_4})_2$ has been published previously along with spectroscopic and electrochemical measurements by Chattopadhyay et al. in Inorg. Chim. Acta 360 (2007) 2231.

Appendix A. Supplementary data

CCDC 658689 and 658688 contain the supplementary crystallographic data for $\mathbf{1(ClO_4)_2}$ and **2**, respectively. These data can be obtained free of charge via http://www.ccdc.cam.ac.uk/conts/retrieving.html, or from the Cambridge Crystallographic Data Centre, 12 Union Roda, Cambridge CB21EZ, UK; fax: (+44) 1223-336-033; or e-mail: deposit@ccdc.cam.ac.uk. The FT-IR, ^1H NMR spectra, absorbance versus pH plot are given as Supporting Information. Supplementary data associated with this article can be found, in the online version, at doi:10.1016/j.poly. 2008.03.008.

References

[1] T.A. Link, in: A. Muller, H. Ratajczak, W. Junge, E. Diemann (Eds.), Electron and Proton Transfer through the Mitochondrial Respiratory Chain, vol. 78, Elsevier Science Publishers, Amsterdam, 1992, p. 197.
[2] M. Nakamoto, K. Tanaka, T. Tanaka, Bull. Chem. Soc. Jpn. 61 (1988) 4099.
[3] A. Niemz, V.M. Rotello, Acc. Chem. Res. 32 (1999) 44.
[4] S.-W. Tam-Chang, J. Mason, I. Iverson, K.-O. Hwang, C. Leonard, Chem. Commun. (1999) 65.
[5] H.H. Thorp, Chemtracts: Inorg. Chem. 3 (1991) 171.
[6] S.A. Trammell, J.C. Wimbish, F. Odobel, L.A. Gallagher, P.M. Narula, T.J. Meyer, J. Am. Chem. Soc. 120 (1998) 13248.
[7] A.M. Bond, M. Haga, Inorg. Chem. 25 (1986) 4507.
[8] M. Haga, T. Ano, K. Kano, S. Yamabe, Inorg. Chem. 30 (1991) 3843.
[9] M. Haga, M.M. Ali, S. Koseki, K. Fujimoto, A. Yoshimura, K. Nozaki, T. Ohno, K. Nakajima, D. Stufkens, J. Inorg. Chem. 35 (1996) 3335.
[10] E.C. Constable, P.J. Steel, Coord. Chem. Rev. 93 (1989) 205.
[11] D.P. Rillema, R. Sahai, P. Matthews, A.K. Edwards, R.J. Shaver, L. Morgan, Inorg. Chem. 29 (1990) 167.
[12] M. Haga, A.M. Bond, Inorg. Chem. 30 (1991) 475.
[13] M. Haga, T. Matsumura-Inoue, S. Yamabe, Inorg. Chem. 26 (1987) 4145.
[14] K. Hutchison, J.C. Morris, T.A. Nile, J.L. Walsh, D.W. Thompson, J.D. Petersen, J.R. Schoonover, Inorg. Chem. 38 (1999) 2516.
[15] D.T. Sawyer, A. Sobkowiak, J.L. Roberts Jr., Electrochemistry for Chemists, 2nd ed., Wiley, New York, 1995.
[16] SMART, SAINT and XPREP, Siemens Analytical X-ray Instruments Inc., Madison, Wisconsin, USA, 1995.
[17] G.M. Sheldrick, SADABS: Software for Empirical Absorption Correction, University of Gottingen, Institut fur Anorganische Chemieder Universitat, Tammanstrasse 4, D-3400 Gottingen, Germany, 1999–2003.
[18] G.M. Sheldrick, SHELXS-97, University of Gottingen, Germany, 1997.
[19] L.J. Farrugia, J. Appl. Crystallogr. 30 (1997) 565.
[20] A.W. Addison, P.J. Burke, J. Heterocycl. Chem. 12 (1981) 4455.
[21] D. Mishra, A. Barbieri, C. Sabatini, M.G.B. Drew, H.M. Figgie, W.S. Sheldrick, S.K. Chattopadhyay, Inorg. Chim. Acta 360 (2007) 2231.
[22] B. Mondal, V.G. Puranik, G.K. Lahiri, Inorg. Chem. 41 (2002) 5831.
[23] B. Mondal, H. Paul, V.G. Puranik, G.K. Lahiri, J. Chem. Soc., Dalton Trans. (2001) 481.
[24] S. Sarkar, B. Sarkar, N. Chanda, S. Kar, S.M. Mobin, J. Fiedler, W. Kaim, G.K. Lahiri, Inorg. Chem. 44 (2005) 6092.
[25] N. Chanda, D. Paul, S. Kar, S.M. Mobin, A. Dutta, V.G. Puranik, K.K. Rao, G.K. Lahiri, Inorg. Chem. 44 (2005) 3499.
[26] C. Sans, M. Rodriguez, I. Romero, A. Llobet, Inorg. Chem. 42 (2003) 8385.
[27] M. Haga, H.-G. Hong, Y. Shiozaka, Y. Kawata, H. Monjushiro, T. Fukuo, R. Arakwa, Inorg. Chem. 39 (2000) 4566.
[28] A. Golzhauser, S. Panov, C. Woll, Surf. Sci. 314 (1994) 849.
[29] B. Sarkar, R.H. Laye, B. Mondal, S. Chakraborty, R. L Paul, J.C. Jeffery, V.G. Puranik, M.D. Ward, G.K. Lahiri, J. Chem. Soc., Dalton Trans. (2002) 2097.
[30] R.P. Thummel, S. Chirayil, Inorg. Chim. Acta 154 (1988) 77.
[31] M. Haga, T. Takasugi, A. Tomie, M. Ishizuya, T. Yamada, M.D. Hossain, M. Inoue, J. Chem. Soc., Dalton Trans. (2003) 2069.
[32] M. Maestri, N. Armaroli, V. Balzani, E.C. Constable, A.M.W.C. Thompson, Inorg. Chem. 34 (1995) 2759.
[33] T. Ayers, N. Caylor, G. Ayers, C. Godwin, D.J. Hathcock, V. Stuman, S.J. Slattery, Inorg. Chim. Acta 328 (2002) 33.

constant ionic strength (1 mol dm^{-3}), adjusted with lithium perchlorate. The disappearance of $[Co(III)W]^{5-}$ was followed at 390 nm using a Spectrochem MK II colorimeter as described [14]. At least three runs were studied for any given set of experimental conditions. The plots of $\log(A_t - A_\infty)$, where A_t and A_∞ are the absorbance at any time 't' and at infinite time (overnight), against time are linear for more than three half-lives of the reaction and some of the representative plots are shown in Fig. 1. These plots and the others were drawn using the EXCEL program, which also provided the least square values of the intercepts and slopes of the plots. The pseudo first-order rate constants, k_{obs}, were calculated from the slopes of these plots. The reproducibility of k_{obs} from the replicate runs was within ±3%. The mean of the pseudo first-order rate constant k_{obs} is reported in the tables.

2.4. Stoichiometry

A number of reaction mixtures having different concentration ratios of $[Co(III)W]^{5-}$ and $(NHNH_2)_2CO$ were prepared at different $[H^+]$ in a manner so that $[Co(III)W^{5-}]$ was always in excess over $[(NHNH_2)_2CO]$. These reaction mixtures were allowed to react at room temperature. The progress of the reaction was followed by measuring the absorbance from time to time, generally at 390 nm for the remaining $[Co(III)W]^{5-}$ but in few cases the absorbance was also measured at 625 nm, for the formation of $[Co(II)W]^{6-}$. The measurements were continued until a constant absorbance value was obtained. The computation of the results indicated that $\Delta[Co(III)W]^{5-}/\Delta[(NHNH_2)_2CO] = 3.96 \pm 0.08$. The results are reported in Table 1. Hence, the stoichiometry of the reaction is given by Eq. 1:

$$4[Co(III)W]^{5-} + (NHNH_2)_2CO \rightarrow 4[Co(II)W]^{6-} + HCHO + 4H^+ + 2N_2 \quad (1)$$

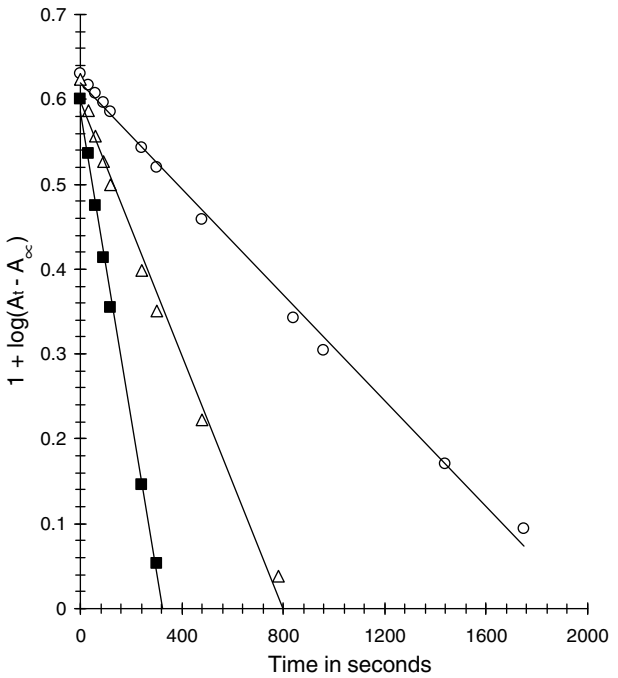


Fig. 1. The plots of $\log(A_t - A_\infty)$, where A_t and A_∞ are the absorbance at any time 't' and at infinite time, against time are linear for more than three half-lives of the reaction for the conditions: (■) $[H^+] = 0.35$, $[CO(NHNH_2)_2] = 0.03$ mol dm^{-3}, 40 °C; (△) $[H^+] = 0.35$, $[CO(NHNH_2)_2] = 0.005$ mol dm^{-3}, 40 °C and (○) $[H^+] = 0.1$, $[CO(NHNH_2)_2] = 0.01$ mol dm^{-3}, 30 °C. The ionic strength is held constant at 0.5 and $10^4[Co(III)W^{5-}] = 4$ mol dm^{-3}.

2.5. Spectral measurements

A HP 8452 UV–Vis spectrophotometer with a 2 nm band width and an integration time of 1 s was used to measure the spectra of the solutions at room temperature.[1] The spectra of the solutions were recorded at room temperature.

The method adopted for recording the spectra of the reaction mixtures is described below. The solutions of $NH_2NHCONHNH_2$ and $[Co(III)W]^{5-}$ ions of desired concentrations at appropriate $[H^+]$ were taken in test tubes. These test tubes were immersed in melting ice taken in a beaker and allowed to stand for sufficient time to attain thermal equilibrium. The melted water was drained out from time to time. The idea was to slow down the rate of the reaction to an extent that would permit the recording of meaningful spectra. These solutions were quickly mixed to give reaction mixtures which were immediately transferred to a silica cell which was placed in its compartment and the spectra were recorded immediately. These spectra are considered to be good enough for qualitative analysis only because the temperature and the time taken in mixing and recording the spectra are not precisely and uniformly maintained.

2.6. Characterisation of formaldehyde

According to the stoichiometric Eq. (1) formaldehyde is one of the products. The same product was characterised by a spot test with chromotropic acid, prepared in 12 N sulfuric acid, [15]. Its quantitative estimation was carried out by repeated extraction (×8) with 5 ml aliquots of ether. The ethereal solution was air evaporated. The liquid product was made up to 50 ml. Further dilution of 1 ml of this solution with 9 ml of chromotropic acid solution resulted in a purple solution which had λ_{max} at 507 nm with an optical density equal to 0.00677. The concentration of formaldehyde was calculated using $\varepsilon = 0.57$ cm^3 (μg)$^{-1}$ [16,17]. Computation of the results indicated that the amount of formaldehyde recovered from the reaction mixtures was 95 ± 4% of the theoretical value expected in terms of Eq. (1).

2.7. Characterisation of $[Co(II)W]^{6-}$

The other product in Eq. (1) is the $[Co(II)W]^{6-}$ ion. It was characterised by its spectra. In Fig. 2 spectra of authentic solutions of $10^5[Co(III)W^{5-}] = 9.85$ mol dm^{-3}, having λ_{max} at 390 nm, and $10^4[Co(II)W^{6-}] = 0.1$ mol dm^{-3}, which has λ_{max} at 625 nm, are given. The later spectra is superimposed by the spectrum of the spent reaction mixture ($10^5[Co(III)W^{5-}] = 1.0$, $[H^+] = 0.1$ and $10^3[H_2NNHCONHNH_2] = 5.0$ mol dm^{-3}). This indicates that the $[Co(II)W]^{6-}$ ion is the reduced product of $[Co(III)W]^{5-}$ ion and is produced quantitatively and that $[Co(III)W]^{5-}$ behaves as a one electron equivalent oxidant.

2.8. Characterisation of N_2

N_2 is another product in Eq. (1), and was qualitatively confirmed, with no attempt being made to quantify it. The qualitative method involved carrying out the reaction at room temperature in a conical flask fitted with standard joints with tubes for incoming and outgoing gases. The reaction was started and pure argon was passed through the reaction mixture. The outgoing gas was passed through a solution of $[Ru(NH_3)_5(H_2O)]^{2+}$, from which a red complex, $[(NH_3)_5Ru(N_2)Ru(NH_3)_5]^{4+}$, was isolated [18]. The Raman

[1] The instrument could not be used for the kinetics study since it had no facility for thermostating the solutions at the desired temperature.

Table 1
Study of the stoichiometry[a] of the reaction between $[Co(III)W]^{5-}$ and $(NHNH_2)_2CO$

S.no.	$[H^+]$	10^4 $[Co(III)W^{5-}]$ initial	10^4 $[(NHNH_2)_2CO]$ initial	10^4 $[Co(III)W^{5-}]$ final	$\frac{\Delta[Co(III)W]^{5-}}{\Delta[(NHNH_2)_2CO]}$
1	0.02	5.12	1.04	1.06	3.90
2	0.05	7.32	1.43	1.72	3.92
3	0.1	10.0	2.24	0.89	4.07
4	0.4	20.0	3.15	7.81	3.87
5	0.1	25.1	3.50	11.0	4.03
6	0.2	30.2	4.86	10.9	3.97

[a] Concentrations are in mol dm^{-3}; average $\Delta[Co(III)W]^{5-}/\Delta[(NHNH_2)_2CO] = 3.96 \pm 0.08$.

spectra of the complex showed a strong band of $\nu(N{\equiv}N)$ around 3100 cm^{-1} [18] which is due to the coordinated N_2.

2.9. Spectral changes effected by $[H_2NNHCONHNH_2]$ in the reaction mixture

The optical density measurements of a solution of the $[Co(III)W]^{5-}$ ion (**A**) and those of the reaction mixtures, soon after these were prepared, $10^4[Co(III)W]^{5-} = 1.0$, $[H^+] = 0.10$ and $10^4[H_2NHNCONHNH_2] = 1.25$ (**B**), 2.50 (**C**), 5.0 (**D**), 15.0 (**E**) and 25.0 mol dm^{-3} (**F**) are shown in Fig. 3. It is noted that the optical density of the reaction mixtures increased with the increase in $[H_2NHNCONHNH_2]$, indicating that a new species, probably a complex between the $[Co(III)W]^{5-}$ ion and $H_2NHNCONHNH_2$, is formed.

3. Spectral changes with $[H^+]$

In another series of experiments, several reaction mixtures having $10^5[Co(IIIW)^{5-}] = 9.4$ and $10^3[H_2NHNCONHNH_2] = 1.0$ mol dm^{-3} were prepared at different $[H^+]$ (between 0.001 and 0.07 mol dm^{-3}) in a manner analogous to that described above. The optical densities of these reaction mixtures are shown in Fig. 4 wherein it is noted that the optical density increases with increasing H^+ concentration, indicating that the species $^+H_3NHNCONHNH_2$ forms the complex, which is consistent with the protonation constant of $H_2NHNCONHNH_2$ because the $[Co(IIIW)]^{5-}$ ion is not affected by the presence of the H^+ ion [19]. It is seen later in the mechanism section that the complex so formed deprotonates in the subsequent step and that the decomposition of the deprotonated complex is rate controlling.

3.1. Results

The first-order dependence of the reaction on $[Co(III)W]^{5-}$ is confirmed by measuring the k_{obs} values over $1 \times 10^{-4} \leqslant [Co(III)W^{5-}] \leqslant 1 \times 10^{-3}$ mol dm^{-3} at $[H^+] = 0.35$, $[Co(NHNH_2)_2] = 0.025$ and $[\mu] = 0.50$ mol dm^{-3} at 40 °C. A mean value of 10^3 $k_{obs} = 3.45 \pm 0.04$ (s^{-1}) is obtained from several runs, indicating that the k_{obs} value is independent of the initial $[Co(III)W^{5-}]$.

The k_{obs} values were measured at different initial $[H_2NHNCONHNH_2]$ and at different temperatures, keeping the ionic strength and $[H^+]$ constant. The results, shown in Table 2, provided linear plots of k_{obs} against $[H_2NHNCONHNH_2]$, Fig. 5, that pass through the origin for all temperatures. This indicates that the reaction is first order with respect to $[H_2NHNCONHNH_2]$.

The dependence of k_{obs} was investigated over $0.02 \leqslant [H^+] \leqslant 0.40$ mol dm^{-3} at different temperatures. The results, shown in Table 3, indicate that k_{obs} decreases with an increase in $[H^+]$. The plots between k_{obs} and $[H^+]^{-1}$, Fig. 6, are linear and almost pass through the origin within the limits of the experiment.

The rate of catalysis by alkali metal ions (M^+) is considered characteristic of the redox reactions of 12-tungstocobaltate(III), both with inorganic and organic substrates [20]. Similar catalysis by M^+ has been reported in the oxidation of 12-tungstocobaltate(II) by the permanganate ion [10], oxidations of arsenous acid [21] and S(IV) [22] by 12-tungstocobaltate(III), from our laboratory too. Therefore, the effect of alkali metal ions ($M^+ = Li^+$, Na^+ and K^+) on k_{obs} was investigated at constant $[H^+]$ and $[CO(NHNH_2)_2]$ at 40 °C by adding the chloride salt of the respective ions. The higher concentrations of K^+ ions could not be used because of the insolubility of potassium perchlorate. The Cs^+ ion was also tried, but being

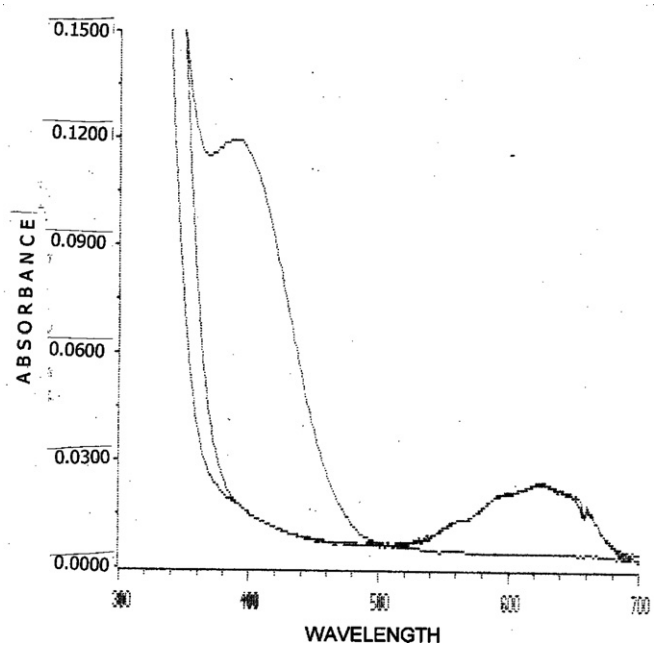


Fig. 2. Spectra of authentic solutions of $10^5[Co(III)W^{5-}] = 9.85$ mol dm^{-3} having λ_{max} at 390 nm and that of $10^4[Co(II)W^{6-}] = 0.1$ mol dm^{-3} and the spent reaction mixture ($10^5[Co(III)W^{5-}] = 1.0$, $[H^+] = 0.1$ and $10^3[H_2NHNCONHNH_2] = 5.0$ mol dm^{-3}). The spectra of $[Co(II)W]^{6-}$ and the spent reaction mixtures are seen to overlap indicating that $[Co(III)W^{5-}]$ is reduced to the $[Co(II)W]^{6-}$ ion.

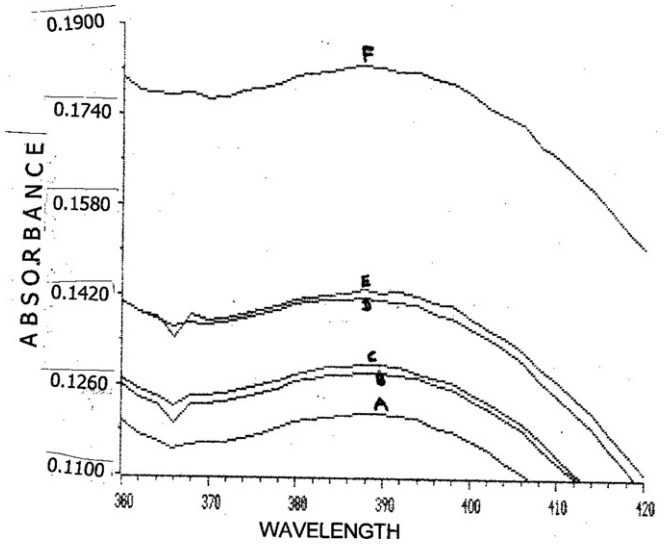


Fig. 3. The optical density changes in the spectra of the reaction mixtures with an increase in the concentration of $H_2NNHCONHNH_2$ at $[H^+] = 0.1$ and $10^4[Co(III)W^{5-}] = 1.0$ mol dm^{-3}. $10^4[H_2NNHCONHNH_2] = 0.0$ (A); =1.25 (B); =2.5 (C); =5.0 (D); =15.0 (E); =25.0 (F).

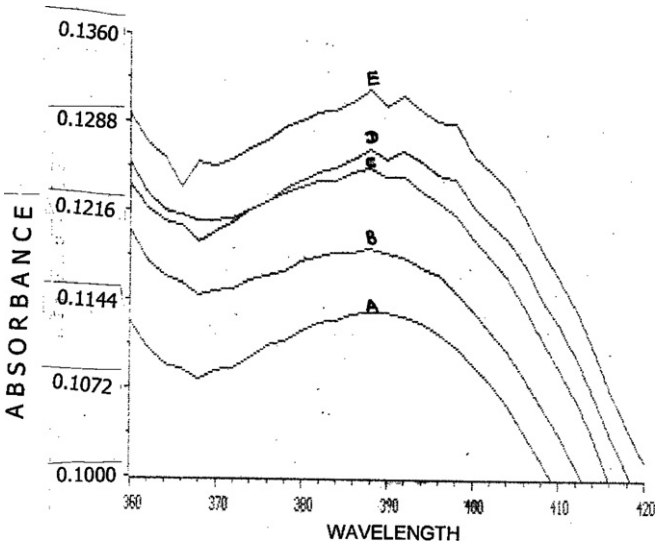


Fig. 4. The optical density changes in the spectra of the reaction mixtures with an increase in the H^+ ion concentration with initial $[H_2NNHCONHNH_2] = 0.001$ and $10^5[Co(III)W^{5-}] = 9.4$ mol dm^{-3}. $[H^+] = 0.0$ (A); =0.001 (B); =0.005 (C); =0.030 (D); =0.070 (E).

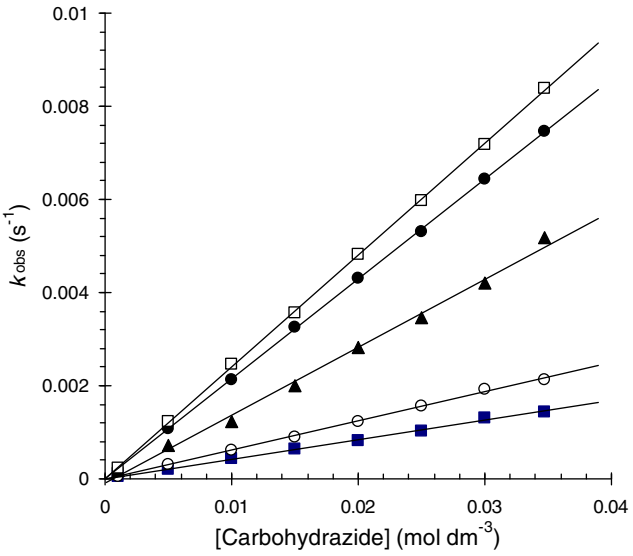


Fig. 5. The plots of k_{obs} against $[CO(NHNH_2)_2]$ pass through the origin or have negligible intercepts at the temperatures 30° (■), 35° (○), 40° (▲), 46° (●) and 49° (□).

more insoluble than $KClO_4$ the rate data could not be collected even for low concentrations. The results, Table 4, show that k_{obs} is retarded with an increase in $[M^+]$. The non-linear plot between k_{obs} and $[M^+]$ is shown in Fig. 7.

The Brønsted's treatment of the effect of the concentration of the alkali cation as ionic strength predicts that the reaction is occurring between oppositely charged ions. The data in Table 4 has been analysed in terms of Eq. (2), proposed by Davies [23].

$$\log k_{obs} = \log k_o + z_a z_b \left(\frac{\sqrt{\mu}}{1+\sqrt{\mu}} - B\mu \right) \quad (2)$$

where z_a and z_b are the charges on the reacting species and B is a constant. The plots, Fig. 8, in terms of Eq. (2) for $B = 0.1$ are linear with slope values −3.85, −3.97 and −2.84 corresponding to Li^+, Na^+ and K^+ ions, respectively, whereas for $B = 0.15$ the plot corresponding to K^+ is linear with slope = −3.82 (plot not shown). Thus the slope valve in each case is ≈ -4.0, indicating that the reaction is taking place between two oppositely charged ions carrying charges of 4 and 1.

3.2. Mechanism and discussion

The reaction is first order with respect to carbohydrazide, as is the oxidation of hydrazine by the 12-tungstocobaltate(III) ion [24]. A comparison of the rate constants of the two oxidations indicates that the oxidation of carbohydrazide is relatively faster than that of hydrazine. The two oxidations are also similar with respect to the dependence of the rate on H^+ concentration; the rate increased with the decrease in $[H^+]$. However, unlike the oxidation of hydrazine, the plots between k_{obs} against $[H^+]^{-1}$ pass through the origin. This indicates a different mechanism.

The first-order dependence in $[H_2NHNCONHNH_2]$ indicates that the complex formed from $[Co(III)W]^{5-}$ and $H_2NHNCONHNH_2$, suggested by the changes in the optical density of the reaction mixtures, is either weak in nature or the formation constant is small so that the complex is not formed in a sufficient quantity for its detection by the kinetics. Further, the participation of the protonated specie(s) in the formation of the complex is indicated by the increasing optical densities of the reaction mixtures with increasing $[H^+]$ at constant $[H_2NHNCONHNH_2]$ and $[Co(III)W]^{5-}$ ion. In an earlier study it was shown that the rapid scans of solutions of constant $[Co(III)W^{5-}]$ recorded in buffer solutions of different pH superimposed themselves, indicating that $[Co(III)W]^{5-}$ is not protonated [19]. The protonation of $H_2NHNCONHNH_2$ is well known, a value of $K_H = 1.38 \times 10^4$ is reported ($\mu = 0.1$ mol dm^{-3}) at 20 °C [25]. Therefore the equilibrium (3) is shifted far to the right[2] so that the analytical concentration of carbohydrazide mainly exists as $^+NH_3HNCONHNH_2$ in the acidic solution.

The alkali metal ions M^+ (Li^+, Na^+, K^+) either enhance or inhibit the rate of reactions [26–29]. The rate enhancement has been reported in several $[Co(III)W]^{5-}$ oxidations [30–32]. The effect of the alkali metal ions in the present reaction is interesting because k_{obs} decreased with the increasing concentration of the individual alkali cation and this is similar to the effect observed in the oxidation of $[Co(II)W]^{6-}$ by $S_2O_8^{2-}$ and IO_4^- ions [33]. However, the comparison of k_{obs} within the alkali metal ions indicated that k_{obs} increased in the order $K^+ > Na^+ > Li^+$.

The inhibition in k_{obs}, $Li^+ > Na^+ > K^+$, parallels with the ionic size of the strongly hydrated M^+_{aq} ions [34], which is in the order $Li^+ > Na^+ > K^+ > Rb^+ > Cs^+$ ion [35]. The M^+ ion, which plays the role of an effective bridge between the two reacting anions, is unlikely to have a similar role in the present case because the reactive species present in solution are $^+NH_3HNCONHNH_2$ and $[Co(III)W]^{5-}$ ions. The formation of an ion pair between M^+ and $[Co(III)W]^{5-}$ is

Table 2
The dependence of k_{obs} on $[CO(NHNH_2)_2]$ at different temperatures $10^4[Co(III)W^{5-}] = 4.0$, $[H^+] = 0.35$ and $[\mu] = 0.50$ mol dm^{-3}

k_{obs} (s^{-1})					
$[CO(NHNH_2)_2]$	30 °C	35 °C	40 °C	46 °C	49 °C
0.001	0.00005	0.00006	0.000189	0.000217	0.000237
0.005	0.000212	0.000318	0.000716	0.00108	0.00123
0.010	0.000565	0.000606	0.00114	0.00212	0.00245
0.015	0.000650	0.00091	0.00199	0.00325	0.00356
0.020	0.000820	0.00124	0.00281	0.00431	0.00481
0.025	0.00103	0.00156	0.00347	0.00531	0.00597
0.030	0.00131	0.00192	0.00421	0.00643	0.00719
0.0347	0.00144	0.00213	0.00517	0.00745	

[2] It can be shown that for the reported K_H value, $[H_2NHNCONHNH_2] = 0.01$, $[^+H_3NHNCONHNH_2]$ is 0.0092 and 0.0097 at $[H^+] = 0.01$ and 0.04 mol dm^{-3} at 20 °C.

Table 3
The dependence of k_{obs} on $[H^+]$ at different temperatures 10^4 $[Co(III)W]^{5-}$ = 4.0, $[CO(NHNH_2)_2]$ = 0.01 and [μ] = 0.50 mol dm^{-3}

$[H^+]$ (mol dm^{-3})	0.02	0.04	0.07	0.10	0.20	0.30	0.35	0.40
$10^3 k_{obs}$, 25 °C	5.06	2.65	1.42	1.04	0.517	0.342	0.302	0.268
$10^3 k_{obs}$, 30 °C	9.97	5.01	2.74	1.91	0.968	0.644	0.565	0.524
$10^3 k_{obs}$, 36 °C	15.4	7.63	4.48	2.92	1.43	0.978	0.864	0.754
$10^3 k_{obs}$, 40 °C	20.2	10.2	5.68	4.04	1.96	1.36	1.14	1.01
$10^3 k_{obs}$, 45 °C	29.6	14.6	8.72	6.09	2.94	2.02	1.81	1.44

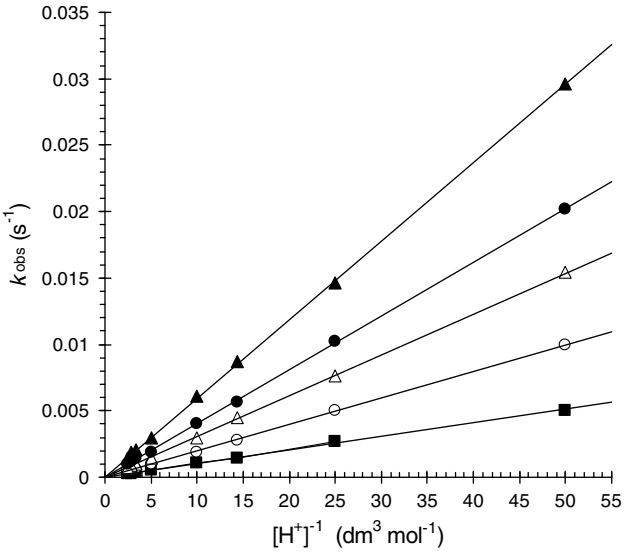


Fig. 6. The plots of k_{obs} against $[H^+]^{-1}$ pass through the origin or have negligible intercepts at the temperatures 25° (■), 30° (○), 36° (△), 40° (●) and 45° (▲).

supported by the increase in the optical density of the $[Co(III)W]^{5-}$ solution with increasing $[M^+]$, similar to that reported with $[Co(III)W]^{6-}$ [10].

In view of the above, the following sequence of reactions is considered to constitute the most likely mechanism of the reaction:

$$^{+}H_3NHNCONHNH_2 \overset{K_a}{\rightleftharpoons} H_2NHNCONHNH_2 + H^+ \quad (3)$$

$$[Co(III)W]^{5-} + M^+ \overset{K_m}{\rightleftharpoons} [Co(III)W \cdot M]^{4-} \quad (4)$$

$$[Co(III)W \cdot M]^{4-} + {}^{+}NH_3HNCONHNH_2 \overset{K}{\rightleftharpoons} [Co(III)W \cdot M \cdot NH_3HNCONHNH_2]^{3-} \quad (5)$$

$$[Co(III)W \cdot M \cdot NH_3HNCONHNH_2]^{3-} \overset{K_d}{\rightleftharpoons} [Co(III)W \cdot M \cdot NH_2HNCONHNH_2]^{4-} + H^+ \quad (6)$$

$$[Co(III)W \cdot M]^{4-} + H_2NHNCONHNH_2 \overset{K'}{\rightleftharpoons} [Co(III)W \cdot M \cdot NH_2HNCONHNH_2]^{4-} \quad (7)$$

$$[Co(III)W \cdot M \cdot NH_2HNCONHNH_2]^{4-} \overset{k}{\rightarrow} [Co(II)W \cdot M]^{5-} + H_2NHN\overset{+}{C}ONHNH_2 \quad (8)$$

$$3[Co(III)W \cdot M]^{4-} + H_2NHN\overset{+}{C}ONHNH_2 \overset{\text{fast}}{\rightarrow} 3[Co(II)W \cdot M]^{5-} + 2N_2 + 4H^+ + HCHO \quad (9)$$

Table 4
The dependence of k_{obs} on Li^+, Na^+ and K^+ ions at 40 °C 10^4 $[Co(III)W]^{5-}$ = 4.0, $[CO(NHNH_2)_2]$ = 0.020 and $[H^+]$ = 0.35 mol dm^{-3}

$[M^+]$ (mol dm^{-3})	0.03	0.04	0.05	0.06	0.08	0.10	0.14	0.18	0.26	0.42
10^3 k_{obs}, (Li^+)	3.01	2.95	2.87	2.82	2.71	2.62	2.48	2.38	2.20	2.00
10^3 k_{obs}, (Na^+)	3.03	2.97	2.91	2.86	2.76	2.67	2.54	2.40	2.21	1.99
10^3 k_{obs}, (K^+)	3.07	3.03	2.99	2.96	2.88	2.82	2.71			

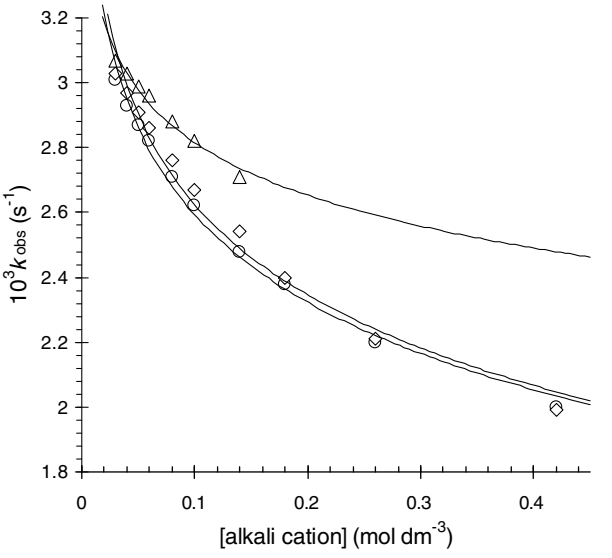


Fig. 7. The non-linear plot between k_{obs} and $[M^+]$ with M^+ = Li^+ (○), Na^+ (◇) and K^+ (△). $10^4[Co(III)W]^{5-}$ = 4.0, $[CO(NHNH_2)_2]$ = 0.020 and $[H^+]$ = 0.35 mol dm^{-3} and 40 °C.

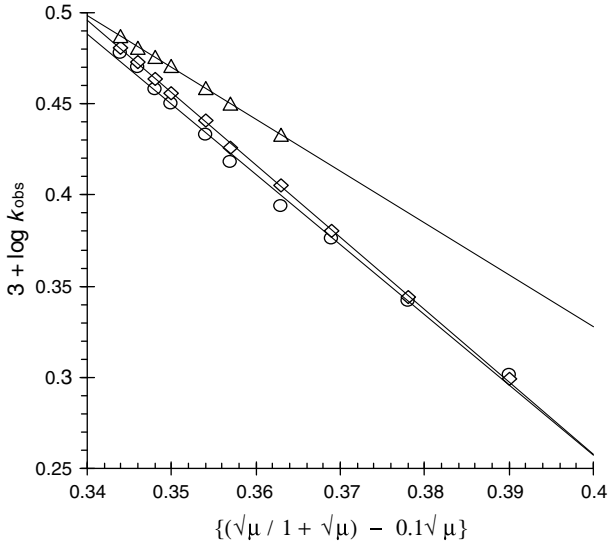


Fig. 8. The plots of log k_{obs} against $\{(\sqrt{\mu}/1+\sqrt{\mu}) - 0.1\sqrt{\mu}\}$ for Li^+ (○), slope = −3.85; Na^+ (◇), slope = −3.97 and K^+ (△), slope = −2.84. However, the slope of the plot between log k_{obs} against $\{(\sqrt{\mu}/1+\sqrt{\mu}) - 0.15\sqrt{\mu}\}$ is −3.82. $10^4[Co(III)W]^{5-}$ = 4.0, $[CO(NHNH_2)_2]$ = 0.020 and $[H^+]$ = 0.35 mol dm^{-3} and 40 °C.

Table 5
The dependence of k_o ($dm^3\ mol^{-1}\ s^{-1}$) at different temperatures

Temperature (°C)	30	35	40	46	49
k_o	0.015	0.022	0.051	0.075	0.084

The two alternate routes for the formation of the complex, $[Co(III)W \cdot M \cdot NH_2HNCONHNH_2]^{4-}$, equilibria (5) and (6), and equilibrium (7), are not kinetically distinguishable because it can be shown that $K_dK = K'K_a$.[3] The rate law deduced from reactions (3)–(9) is expressed by Eq. (10):

$$\frac{-d[Co(III)W]^{5-}}{dt} = kK'K_m[Co(III)W^{5-}][H_2NHNCONHNH_2][M^+] \quad (10)$$

The mass balance for $[Co(III)W]^{5-}$ from Eqs. (4) and (7) is given by Eq. (11), which is approximated to Eq. (12) because $1 \gg K'[H_2NHNCONHNH_2]$ due to the negligibly small concentration of $H_2NHNCONHNH_2$.

$$[Co(III)W^{5-}] = \frac{[Co(III)W^{5-}]_o}{1 + K_m[M^+](1 + K'[H_2NHNHCONHNH_2])} \quad (11)$$

$$[Co(III)W^{5-}] = \frac{[Co(III)W^{5-}]_o}{1 + K_m[M^+]} \quad (12)$$

In a similar manner Eq. (13) is obtained from the mass balance of carbohydrazide species from Eq. (3), remembering that $[H^+] \gg K_a$.

$$[NH_2HNCONHNH_2] = \frac{K_a[NH_2HNCONHNH_2]_o}{[H^+]} \quad (13)$$

The substitution of the respective values of $[Co(III)W^{5-}]$ and $[H_2NHNCONH_2]$ from Eqs. (12) and (13) into Eq. (10) gives the rate law in Eq. (14).

$$k_{obs} = \frac{-d[Co(III)W]^{5-}}{dt[Co(III)W^{5-}]_o} = \frac{kK'K_aK_m[NH_2HNCONHNH_2]_o[M^+]}{[H^+](1 + K_m[M^+])} \quad (14)$$

Eq. (14) is consistent with the plots of k_{obs} against $[H_2NHNCONHNH_2]_o$, Fig. 5, k_{obs} against $[H^+]^{-1}$, Fig. 6, and the non-linear plots of k_{obs} against $[M^+]$ shown in Fig. 7. Eq. (14), at constant concentrations of H^+ and M^+, is expressed by Eq. (15) where $k_o = kK'K_aK_m[M^+]/(1 + K_m)$. The values of k_o (=slope × $[H^+]$), calculated from the slopes of the plots in Fig. 5, are given in Table 5. Because k_o is a composite factor consisting of unknown equilibrium constants K_d and K, activation parameters were not calculated.

$$k_{obs} = \frac{k_o[NH_2HNCONHNH_2]_o}{[H^+]}m \quad (15)$$

It may be mentioned here that the reaction in buffered solutions pH ($\geqslant 2$) is good enough for study with the stopped-flow method. The attempts to control the rate at low concentrations and temperatures did not prove fruitful for the method employed. It was felt that the rate law of the reaction in buffer solutions might turn out to be similar to that obtained for the oxidation of hydrazine in the buffer solution [24].

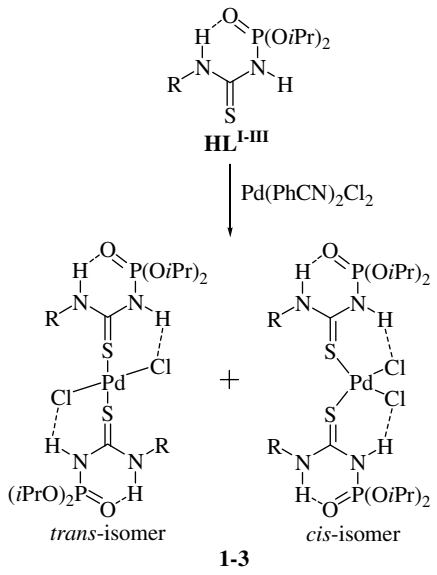
Acknowledgements

The financial grants from UGC (F.12-59/1997) and (F.12-147/2001) are acknowledged with thanks. Thanks are also due to the Department of Science and Technology (DST) for sanctioning the grant (2/17/83/STP-III) for the purchase of the stopped-flow instrument. Thanks are also due to Kriti Mehrotra, my grand daughter, at Cornell University, in helping with certain references.

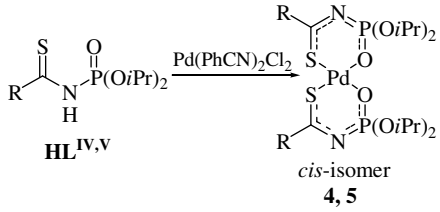
References

[1] M.J.M. Campbell, Coord. Chem. Rev. 15 (1975) 279. and references cited therein.
[2] F. Kurzer, M. Wilkinson, Chem. Rev. 70 (1970) 111. and references cited therein.
[3] G.R. Burns, Inorg. Chem. 7 (1968) 277.
[4] L.F. Audrieth, B.A. Ogg, The Chemistry of Hydrazine, Wiley, New York, 1951.
[5] B.T. Gowda, P. Vasi Reddy, P. Ramachandra, J. Indian Chem. Soc. 68 (1991) 220.
[6] B.T. Gowda, V. Pardhasaradhi, P. Ramachandra, Ind. J. Chem. 29 (1990) 1192.
[7] B.T. Gowda, P. Jagan Mohan Rao, Indian Acad. Sci., Chem. Sc. 103 (1991) 55.
[8] Ms. Rekha, A. Prakash, Raj N. Mehrotra, Can. J. Chem. 71 (1993) 2164.
[9] L.C.W. Baker, T.P. McCutcheon, J. Am. Chem. Soc. 78 (1956) 4503.
[10] Rupa Saha, Manu Mehrotra, A. Prakash, Raj N. Mehrotra, Indian J. Chem. A 40 (2001) 819.
[11] A.W. Chester, J. Org. Chem. 35 (1970) 1797.
[12] E. Baciocchi, M. Crecenzi, E. Feascella, M. Mattioli, J. Org. Chem. 57 (1992) 4684.
[13] A.L. Nolan, R.C. Burns, G.A. Lawrence, J. Chem. Soc., Dalton Trans. (1998) 3041.
[14] Vimal Soni, R.S. Sindal, Raj N. Mehrotra, Polyhedron 24 (2005) 1167.
[15] F. Feigl, Spot Tests in Organic Analysis, 7th ed., Elsevier, 1966.
[16] I.F. O'Dea, R.A. Gibson, Biochem. J. 55 (1953) 530.
[17] D.A. McFadyn, J. Biol. Chem. 158 (1945) 107.
[18] K.K. Sen Gupta, A. Sanyal, S.P. Ghosh, J. Chem. Soc., Dalton Trans. (1995) 1227.
[19] R.N. Mehrotra, S. Dholia (nee Gatiyala), K. Sharma, A. Prakash, Indian J. Chem. A 37 (1998) 973.
[20] S.K. Saha, M. Ali, P. Banerjee, Coord. Chem. Rev. 122 (1993) 41.
[21] S. Dholiya, A. Prakash, Raj N. Mehrotra, J. Chem. Soc., Dalton Trans. (1992) 819.
[22] Manu Mehrotra, Vimal Soni, Raj N. Mehrotra, Polyhedron 27 (2008) 609.
[23] C.W. Davies, Ion Association, Butterworths, London, 1962. p. 39.
[24] Rupa Saha, A. Prakash, Raj N. Mehrotra, Indian J. Chem. A 38 (1999) 680.
[25] A.E. Martell, R.S. Smith, Critical Stability Constants, vol. 3, Plenum, New York, 1989.
[26] P.G. Rasmussen, C.H. Brubaker, Inorg. Chem. 3 (1964) 977.
[27] R.J. Campion, C.F. Deck, P.J. King, A.C. Wahl, Inorg. Chem. 6 (1967) 672.
[28] G. Grtzner, K. Danksagmüler, V. Gutmann, J. Electroanal. Chem. 72 (1976) 177.
[29] M. Sphorer, G. Ron, A. Lowenstein, G. Navon, Inorg. Chem. 4 (1965) 4358.
[30] M. Ali, S.K. Saha, P. Banerji, J. Chem. Soc., Dalton Trans. (1990) 187.
[31] S. Dholiya, A. Prakash, Raj N. Mehrotra, J. Chem. Soc., Dalton Trans. (1992) 819.
[32] (a) S.K. Saha, M.C. Ghosh, P. Banerjee, J. Chem. Soc., Dalton Trans. (1986) 1301;
(b) M. Gupta, S.K. Saha, P. Banerjee, J. Chem. Soc., Perkin Trans. 2 (1988) 1781;
(c) S.K. Saha, P. Bhattacharya, M. Ali, P. Banerjee, Bull Chem. Soc. Jpn. 62 (1989) 3320;
(d) S.K. Saha, M.C. Ghosh, P. Banerjee, Inorg. Chim. Acta 126 (1987) 29;
(e) S.K. Saha, M.C. Ghosh, P. Banerjee, Int. J. Chem. Kinet. 20 (1988) 699.
[33] M. Ali, S.K. Saha, P. Banerjee, J. Chem. Soc., Dalton Trans. (1991) 2305.
[34] F.A. Cotton, G. Wilkinson, Advanced Inorganic Chemistry, 3rd ed., Wiley Eastern, New Delhi, 1986.
[35] K.H. Stern, E.S. Amis, Chem. Rev. 59 (1959) 1.

[3] $$[Co(III)W \cdot M \cdot NH_2HNCONHNH_2]^{4-} = \frac{K_dK[Co(III)W \cdot M^{4-}][^+H_3NHNCONHNH_2]}{[H^+]} = \frac{K'K_a[Co(III)W \cdot M^{4-}][^+H_3NHNCONHNH_2]}{[H^+]}$$



Scheme 1. Preparation of complexes **1–3** (R = *t*Bu, HL^{I} (**1**); Ph, HL^{II} (**2**); 4′-benzo-15-crown-5, HL^{III} (**3**)).



Scheme 2. Preparation of complexes **4** and **5** (R = Et_2N, HL^{IV} (**4**); morpholine-*N*-yl, HL^{V} (**5**)).

OCH), 9.61, 10.02 (2d, $^2J_{PNH}$ = 5.5 Hz, 1H, P(O)NH), 10.37, 10.49 (2s, 1 H, ArNH). $^{31}P\{^1H\}$ NMR ($CDCl_3$): δ −6.5, −6.8. IR: ν 1002 (POC), 1246 (P═O), 1534 (S═C–N), 3082, 3203 (NH) cm^{-1}. *Anal.* Calc. $C_{22}H_{50}Cl_2N_4O_6P_2PdS_2$ (770.06): C, 34.31; H, 6.54; N, 7.28. Found: C, 34.49; H, 6.62; N, 7.37%.

*2.2.2. $Pd(HL^{II}–S)_2Cl_2$ (**2**)*

Yield: 0.299 g (74%). M.p. 147–148 °C. ^1H NMR ($CDCl_3$): δ 1.41–1.48 (m, 12H, CH_3), 4.71–4.90 (m, 2H, OCH), 7.23–7.68 (m, 5H, C_6H_5), 9.80, 10.13 (2d, $^2J_{PNH}$ = 5.6 Hz, 1H, P(O)NH), 10.67, 10.79 (2s, 1H, PhNH). $^{31}P\{^1H\}$ NMR ($CDCl_3$): δ −5.6, −5.9. IR: ν 998 (POC), 1258 (P═O), 1521 (S═C–N), 3091, 3217 (NH) cm^{-1}. *Anal.* Calc. for $C_{26}H_{42}Cl_2N_4O_6P_2PdS_2$ (810.04): C, 38.55; H, 5.23; N, 6.92. Found: C, 38.32; H, 5.32; N, 6.78%.

*2.2.3. $Pd(HL^{III}–S)_2Cl_2$ (**3**)*

Yield: 0.483 g (81%). M.p. 139–141 °C. ^1H NMR ($CDCl_3$): δ 1.43–1.47 (m, 12H, CH_3), 3.65–4.21 (m, 16H, CH_2), 4.69–4.89 (m, 2H, OCH), 6.75–6.97 (m, 3H, C_6H_3), 9.88, 10.16 (2d, $^2J_{PNH}$ = 5.8 Hz, 1H, P(O)NH), 10.72, 10.83 (2s, 1H, ArNH). $^{31}P\{^1H\}$ NMR ($CDCl_3$): δ −6.0, −6.4. IR: ν 1008 (POC), 1140 (COC), 1241 (P═O), 1515, 1549 (S═C–N), 3094, 3211 (NH) cm^{-1}. *Anal.* Calc. for $C_{42}H_{72}Cl_2N_4O_{16}P_2PdS_2$ (1192.44): C, 42.30; H, 6.09; N, 4.70. Found: C, 42.72; H, 5.99; N, 4.59%.

*2.2.4. $Pd(L^{IV}–O,S)_2$ (**4**)*

Yield: 0.177 g (51%). M.p. 118–119 °C. ^1H NMR ($CDCl_3$): δ 1.03–1.26 (m, 12H, CH_3, Et_2N), 1.29–1.39 (m, 24H, CH_3, *i*PrO), 3.35–3.79 (m, 8H, CH_2, Et_2N), 4.57–4.74 (m, 4H, OCH). $^{31}P\{^1H\}$ NMR ($CDCl_3$): δ 9.4. IR: ν 1003 (POC), 1142 (P═O), 1529 (SCN) cm^{-1}. *Anal.* Calc. for $C_{22}H_{48}N_4O_6P_2PdS_2$ (696.15): C, 37.90; H, 6.94; N, 8.04. Found: C, 37.84; H, 6.99; N, 8.11%.

*2.2.5. $Pd(L^{V}–O,S)_2$ (**5**)*

Yield: 0.199 g (55%). M.p. 157–158 °C. ^1H NMR ($CDCl_3$): δ 1.33 (d, $^3J_{H,H}$ = 6.1 Hz, 12H, CH_3), 1.34 (d, $^3J_{H,H}$ = 6.1 Hz, 12H, CH_3), 3.62–3.97 (m, 16H, CH_2), 4.68 (d sept, $^3J_{P,H}$ = 7.6 Hz, $^3J_{H,H}$ = 6.1 Hz, 4H, OCH). $^{31}P\{^1H\}$ NMR ($CDCl_3$): δ 9.9. IR: ν 1005 (POC), 1144 (COC), 1154 (P═O), 1547 (SCN) cm^{-1}. *Anal.* Calc. for $C_{22}H_{44}N_4O_8P_2PdS_2$ (724.11): C, 36.44; H, 6.12; N, 7.73. Found: C, 36.49; H, 6.07; N, 7.68%.

2.3. Physical measurements

Infrared spectra (Nujol) were recorded with a Specord M-80 spectrometer in the range 400–3600 cm^{-1}. NMR spectra were obtained on a Varian Unity-300 NMR spectrometer at 25 °C. ^1H and $^{31}P\{^1H\}$ spectra were recorded at 299.948 and 75.429 MHz, respectively. Chemical shifts are reported with reference to $SiMe_4$ (^1H) and H_3PO_4 ($^{31}P\{^1H\}$). Elemental analyses were performed on a Perkin–Elmer 2400 CHN microanalyser.

2.4. Crystal structure determination and refinement

The X-ray data for **1** were collected at −173 °C using a KM4CCD diffractometer and graphite-monochromated Mo Kα radiation generated from Diffraction X-ray tube operated at 50 kV and 35 mA. The images were indexed, integrated and scaled using the KUMA data reduction package [10]. The structure was solved by direct method using SHELXS97 and refined by the full-matrix least-squares method on all F^2 data [11]. Non-hydrogen atoms were included in the refinement, with anisotropic displacement parameters. The hydrogen atoms were positioned geometrically and refined isotropically. The hydrogen atoms of NH groups were included from $\Delta\rho$ maps and fixed at a distance 0.92 and refined isotropically. Calculations were preformed using WINGX program [12].

*trans-[Pd(HL^{I}_2–S)$_2$Cl$_2$] (**1**).* $C_{22}H_{50}Cl_2N_4O_6P_2PdS_2$, M_r = 770.02 g mol^{-1}, yellow prisms, monoclinic, space group $P2_1/c$, a = 10.517(4), b = 17.316(5), c = 9.774(4) Å, β = 99.22(4)°, V = 1757.0(11) $Å^3$, Z = 2, D_c = 1.456 g cm^{-3}, μ(Mo Kα) = 0.929 mm^{-1}, reflections: 12196 collected, 4171 unique, R_{int} = 0.032, R_1(all) = 0.0285, wR_2(all) = 0.0605.

3. Results and discussion

3.1. Synthesis

N-Phosphorylated thioureas were prepared as previously described [9] and purified by recrystallization from dichloromethane–*n*-hexane mixtures.

Complexes **1–5** were prepared by the following procedure: $Pd(PhCN)_2Cl_2$ was dissolved in acetonitrile and added to a solution containing the corresponding ligand in the same solvent (Scheme 1). The compounds obtained are crystalline solids that are soluble in most polar solvents.

The molecular structures of complexes **1–5** were investigated by IR, ^1H, $^{31}P\{^1H\}$ NMR spectroscopy and elemental analysis. The crystal structure of **1** was established by single crystal X-ray diffraction analysis.

3.2. IR and NMR spectroscopy

The IR spectra of complexes **1–3** in Nujol are similar. The absorption bands of the P═O group of the neutral forms $HL^{I–III}$

are shifted by approximately 10–15 cm^{-1} to high frequencies relative to the band of the parent ligands. This confirms their nonparticipation in chelate complex formation. There are two signals for the NH proton in the IR spectra of complexes in the areas 3082–3094 and 3203–3217 cm^{-1} which are the characteristic range for amide protons participating in hydrogen bonds [4,7]. In the spectra of **1–3** there is an intense absorption band at 1515–1549 cm^{-1} corresponding to the S=C–N fragment. Besides very strong absorption bands for the POC group at 1008 cm^{-1}, there is a band of the COC group at 1140 cm^{-1} in the IR spectrum of **3**, containing crown-ether fragments. Presence of a wide absorption band of the POC fragment in the spectra of **1** and **2** in the area 998–1002 cm^{-1} also unequivocally confirms the substituted phosphoric fragment.

Application of the same procedure using the thioureas $\mathbf{HL}^{IV}$ and $\mathbf{HL}^{V}$ did not result in isolation of products with neutral forms of the corresponding ligand (Scheme 2). Complexes **4** and **5** obtained contain the central cation coordinated in a square-planar fashion by the C=S sulfur atoms and the P=O oxygen atoms of two anionic ligands. According to the IR, ^{1}H, $^{31}P\{^{1}H\}$ NMR spectroscopy, elemental analyses and melting point data complexes **4** and **5** are found to be the same as it was synthesized using the potassium salts of the thioureas $\mathbf{HL}^{IV}$ and $\mathbf{HL}^{V}$ in the aqueous ethanol medium [7].

The $^{31}P\{^{1}H\}$ NMR spectra of complexes **1–3** contain two singlet signals at −6.8 to −5.6 ppm, and a down-field shift, relative to that of the free ligands $\mathbf{HL}^{I–III}$, is observed. This confirms the preservation of neutral forms of ligands [4]. Two different signals correspond to the phosphorus atoms with *cis*- and *trans*-configuration of ligands in the structure of complexes in the solution.

The ^{1}H NMR spectra of **1–3** contain a double set of signals. This also confirms the presence of *cis*- and *trans*-complexes in the solution. The signals for the methyl protons are observed at 1.38–1.53 ppm. The signals at 4.58–4.90 ppm correspond to the OCH protons. The aromatic proton signals in complex **2** are at 7.23–7.68 ppm and shifted down-field relative to that in complex **3**. In the ^{1}H NMR spectrum of **3** signals for the CH_2 protons, corresponding to the crown-ether fragment, are in the area 3.65–4.21 ppm.

There is a double set of signals for the NH protons in the ^{1}H NMR spectra of complexes **1–3** in the areas 9.61–10.16 and 10.37–10.83 ppm. The high-field shifted signals for the P(O)NH group are shown as a doublet with a characteristic constant $^{2}J_{PNH}$ = 5.5–5.8 Hz. The low-field signals correspond to the RNH protons. Both set of signals are low-field shifted relative to that in parent ligands [9] because of the intramolecular hydrogen bonds formation of the RNH···O=P and PNH···Cl–Pd types.

The unrecrystallized, pure complexes **1–5** are presumed to be single isomers, in view of the sharp melting points, respectively. However, from the $^{31}P\{^{1}H\}$ NMR spectra of fresh $CDCl_3$ solutions of unrecrystallized complexes **1–3**, it appears that *trans*-isomers predominate. The $^{31}P\{^{1}H\}$ NMR spectra of **1–3** remain invariant for 72 h, suggesting that the isomer distribution rapidly reaches equilibrium on dissolution of the compound. By contrast to complexes **1–3**, the $^{31}P\{^{1}H\}$ NMR spectra of **4** and **5** contain the unique singlet signals in the region characteristic to the deprotonated *N*-phosphorylated thioureas and thioamides [4]. The signals observed correspond to the *cis*-isomer [7]. Moreover, the $^{31}P\{^{1}H\}$ NMR spectra of **4** and **5** remain invariant for 72 h, suggesting that the *trans*-isomer is not observed in the solution of $CDCl_3$.

3.3. Crystal structure of *1*

Crystals of **1** were obtained by slow evaporation of the solvent from dichloromethane–*n*-hexane solution of the complex.

The crystal structure of the *trans*-$[Pd(HL^{I}\text{-}S)_2Cl_2]$ complex **1** is shown in Fig. 1, while the geometrical data such as bond distances, angles, torsion angles and hydrogen bonds are given in Tables 1 and 2.

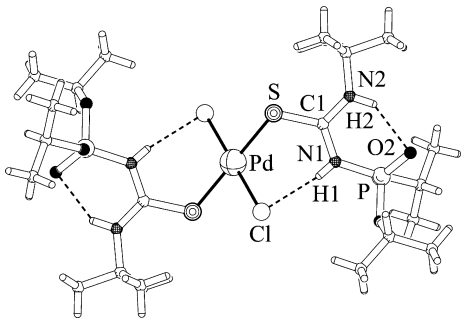


Fig. 1. Molecular structure of complex **1**.

Table 1
Selected bond lengths (Å), and bond angles (°) in complex **1**

Bond lengths			
Pd–Cl	2.3152(11)	P–N(1)	1.674(2)
Pd–S	2.3305(11)	N(1)–C(1)	1.370(3)
S–C(1)	1.708(2)	N(2)–C(1)	1.328(3)
P–O(2)	1.469(2)		
Bond angles			
Cl–Pd–S	85.31(4)	O(2)–P–N(1)	112.07(9)
Cl–Pd–Cl(A)	180.00	P–N(1)–C(1)	126.75(14)
Cl–Pd–S(A)	94.69(4)	S–C(1)–N(1)	120.82(15)
S–Pd–S(A)	180.00	S–C(1)–N(2)	121.71(15)
Pd–S–C(1)	113.86(8)	N(1)–C(1)–N(2)	117.5(2)
Torsion angles			
C(1)–S–Pd–Cl	128.09(9)	S–C(1)–N(1)–P	−170.94(11)
C(1)–S–Pd–Cl(A)	−51.91(9)	N(2)–C(1)–N(1)–P	10.5(3)
N(1)–C(1)–S–Pd	19.4(2)	C(1)–N(1)–P–O(2)	−38.1(2)
N(2)–C(1)–S–Pd	−162.02(14)		

Table 2
Parameters of hydrogen bonds for complex **1** [bond lengths (Å), and bond angles (°)]

N–H···A	*d*(N–H)	*d*(H···A)	D(N···A)	∠(NHA)
N(1)–H(1)···Cl	0.87(2)	2.26(2)	3.113(2)	167(2)
N(2)–H(2)···O(2)	0.90(2)	2.04(2)	2.832(3)	146(2)

Inspection of the structure shows the expected square-planar coordination with two ligands $\mathbf{HL}^{I}$ bonded through the sulfur atoms with Pd–S 2.316(1) Å. The bond lengths Pd–Cl are 2.442(1) Å, while the bond angles S(A)–Pd–Cl 95.54(3)° and S–Pd–Cl 85.46(3)° deviate significantly from 90°. The distortion being induced by the two hydrogen bonds between N1(H1)···Cl(A) and N1A(H1A)···Cl at 3.924 Å. Similar N(H)···Cl and N(H)···Br hydrogen bonds, and the resultant distortion of bond angles from 90°, have previously been observed for the *cis*-bis(*N*-benzoyl-*N*′-propylthioureato)dichloroplatinum(II) (**6**) and *trans*-bis(*N*-benzoyl-*N*′-propylthioureato)dibromopalladium(II) (**7**) complexes [3]. An additional hydrogen bond between the N2(H2) and the phosphoryl oxygen atom O2 of the coordinated ligand at 2.601(4) Å effectively locks the ring C1–N1–P–O2–H2–N2 into a planar structure. The structure, bond lengths and angles of the coordinated $\mathbf{HL}^{I}$ in *trans*-$[Pd(HL^{I}\text{-}S)_2Cl_2]$ complex **1** are similar to that of the unbound $RNHC(S)NHP(O)(OiPr)_2$ (R = alkyl, aryl) [4], as well as that of the coordinated ligand corresponding *cis*-platinum **6** and *trans*-palladium **7** complexes [3]. This mode of coordination of *N*-phosphorylated thiourea once again highlights the importance and relative stability of the intramolecular hydrogen bond between the thiourea NH group and the phosphoryl oxygen atom of this ligands in determining the preferred mode of S atom coordination.

4. Conclusions

The data presented allow to confirm that in the case of the investigated *N*-phosphorylthiourea ligands **HL**$^{I–III}$, containing secondary nitrogen at the *N*-thioacylamidophosphate moiety C(S)NHP(O)(O*i*Pr)$_2$ (Scheme 1), the pure *trans*-Pd(HL$^{I–III}$–*S*)$_2$Cl$_2$ complexes were obtained by reaction with palladium(II). These complexes undergoes partial isomerization in solution to yield *cis*/*trans* distribution. In contrast the palladium(II) complexes with thioureas **HL**^{IV,V}, containing tertiary nitrogen at the *N*-thioacylamidophosphate moiety, under the same synthesis conditions forms *cis*-Pd(L^{IV,V}–*O*,*S*)$_2$ chelate complexes with deprotonated forms of the ligands both in solution and solid state.

Thus, the formation of the intramolecular hydrogen bonds P═O···HNR is a necessary condition for the monodentate *S*-isomer stabilization in a square-planar complexes of Pd(II). When H-bonding in the coordinated ligands is not possible the deprotonation of them and a change of the coordination mode in the Pd(II) complexes occurs.

5. Supplementary data

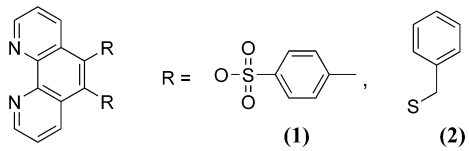
CCDC 669887 contains the supplementary crystallographic data for this paper. These data can be obtained free of charge via http://www.ccdc.cam.ac.uk/conts/retrieving.html, or from the Cambridge Crystallographic Data Centre, 12 Union Road, Cambridge CB2 1EZ, UK; fax: (+44) 1223-336-033; or e-mail:deposit@ccdc.cam.ac.uk.

Acknowledgements

This work was supported by the joint program of CRDF and the Russian Ministry of Education and Science (BRHE 2008 Y5-C-07-09); Russian Science Support Foundation.

References

[1] A.D. Garnovskii, D.A. Garnovskii, I.S. Vasilchenko, A.S. Burlov, A.P. Sadimenko, I.D. Sadekov, Russ. Chem. Rev. 66 (1997) 389.
[2] (a) G. Fitzl, L. Beyer, R. Sieler, R. Richter, J. Kaiser, E. Hoyer, Z. Anorg. Allg. Chem. 433 (1977) 237;
(b) L. Beyer, E. Hoyer, J. Liebscher, H. Hartmann, Z. Chem. 21 (1981) 81.
[3] (a) S. Bourne, K.R. Koch, J. Chem. Soc., Dalton Trans. (1993) 2071;
(b) K.R. Koch, Y. Wang, A. Goetzee, J. Chem. Soc., Dalton Trans. (1999) 1013.
[4] F.D. Sokolov, V.V. Brusko, N.G. Zabirov, R.A. Cherkasov, Curr. Org. Chem. 10 (2006) 27.
[5] D.A. Safin, F.E. Hahn, M.G. Babashkina, F.D.Sokolov, N.G. Zabirov, Materials of a scientific seminar of grant-aided students of the program "Michael Lomonosov", 2006/2007, p. 198.
[6] F.D. Sokolov, N.G. Zabirov, L.N. Yamalieva, V.G. Shtyrlin, R.R. Garipov, V.V. Brusko, A.Yu. Verat, S.V. Baranov, P. Mlynarz, T. Glowiak, H. Kozlowski, Inorg. Chim. Acta 359 (2006) 2087.
[7] F.D. Sokolov, S.V. Baranov, D.A. Safin, F.E. Hahn, M. Kubiak, T. Pape, M.G. Babashkina, N.G. Zabirov, J. Galezowska, H. Kozlowski, R.A. Cherkasov, New J. Chem. 31 (2007) 1661.
[8] D.A. Safin, Ł. Szyrwiel, S.V. Baranov, F.D. Sokolov, M.G. Babashkina, H. Kozlowski, Inorg. Chem. Commun. 11 (2008) 330.
[9] (a) F.D. Sokolov, D.A. Safin, N.G. Zabirov, P.V. Zotov, R.A. Cherkasov, Russ. J. Gen. Chem. 75 (2005) 1919;
(b) F.D. Sokolov, D.A. Safin, M.G. Babshkina, N.G. Zabirov, V.V. Brusko, N.A. Mironov, D.B. Krivolapov, I.A. Litvinov, R.A. Cherkasov, B.N. Solomonov, Polyhedron 26 (2007) 1550.
[10] Oxford Diffraction Poland Sp., CCD data collection and reduction GUI, Version 1.173.13 beta (release 14.11.2003) Copyright 1995–2003.
[11] G.M. Sheldrick, Acta Crystallogr., Sect. A 64 (2008) 112.
[12] L.J. Farrugia, WINGX, A Windows Program for Crystal Structure Analysis, University of Glasgow, Glasgow, 1998.



Scheme 1. 5,6-Substituted-1,10-phenanthrolines.

poured into ice (1 dm^3). A white solid formed immediately. The suspension was stirred to room temperature. After filtration the obtained solid was washed with MeOH and recrystallized from EtOH. The product is recovered as a crystalline white precipitate. Yield: 3.9 g, 7.5 mmol (80%); m.p. 227–230 °C. *Anal.* Calc. for $C_{26}H_{20}N_2O_6S_2$: C, 59.99; H, 3.87; N, 5.38; S, 12.32. Found: C, 58.65; H, 3.87; N, 5.36; S, 12.13%. ^{1}H NMR (300 MHz, $CDCl_3$): δ/ppm: 9.23 (dd, J = 1.5, 4, 2H, 2H), 8.44 (dd, J = 1.5, 8.1, 2H, H3), 7.66 (t, J = 4.2, 2H, H4), 7.62 (dd, J = 7.2, 4H, phenyl); 7.29 (dd, J = 9.3, 4H, phenyl), 2.48 (s, 6H, CH_3). ^{13}C NMR, (75.373 MHz, $CDCl_3$): δ 21.819, 123.430, 124.329, 128.744, 129.807, 132.035, 132.205, 135.819, 145.208, 146.143, 151.263.

2.2.2. 5,6-Dibenzylthiol-1,10-phenanthroline (*2*)

5,6-Dibromo-1,10-phenanthroline [5] (5.92 mmol; 2 g), $Pd_2(dba)_3$ (3 mol%; 0.184 g), bis-[2-(diphenylphosphino)phenyl]ether (PDEphos) (6 mol%; 0.191 g), *t*-BuOK (2.2 equiv., 13.01 mmol, 1.46 g), and 80 ml of dry and degassed toluene were mixed in a Schlenk tube under inert atmosphere. The solution was stirred for 1 h at room temperature. The benzylthiol (2.2 equiv., 13.01 mmol, 1.42 ml) was added by syringe. A condenser was adapted to the Schlenk tube and under argon atmosphere the reaction mixture was heated to 120 °C. After 48 h, the reaction mixture was allowed to reach room temperature, then filtered and concentrated under vacuum leading to an orange oil. This oil was chromatographed (Silica gel; AcOEt:MeOH:NH_3; (20:1:0.5)) and the product was recovered as a crystalline yellow precipitate. Yield: 1.78 g, 4.2 mmol (71%); m.p. 170–171 °C. *Anal.* Calc. for $C_{26}H_{20}N_2S_2$: C, 73.55; H, 4.75; N, 6.60; S, 15.10. Found: C, 73.53; H, 4.85; N, 5.76; S, 12.46%. ^{1}H NMR (300 MHz, $CDCl_3$): δ/ppm: 9.15 (dd, J = 1.8, 4.2, 2H, H2), 8.97 (dd, J = 1.8, 8.4, 2H, H4), 7.57 (dd, J = 4.2, 8.4, 2H, H3), 7.06 (m, 10H, phenyl), 4.06 (s, 4H, CH_2). ^{13}H NMR (75.373 MHz, $CDCl_3$): δ 42.172, 123.287, 130.293, 136.334, 137.116, 139.626, 146.202, 150.681.

2.2.3. [Fe(phdtos)$_3$](PF$_6$)$_2$ (*5*)

To a suspension of 5,6-bistosyl-1,10-phenanthroline (**1**) (3 equiv., 24.5 mg; 0.471 mmol) in 20 ml of a MeOH/H_2O (60/40) solution was added a MeOH/H_2O (50/50) solution of $FeCl_3 \cdot 6H_2O$ (1 equiv., 42.4 mg; 0.157 mmol). The reaction mixture was allowed to reflux with stir overnight, gradually turning to red. The hot mixture was filtered and a MeOH/H_2O (50/50) solution of $NaPF_6$ (3 equiv., 79.1 mg; 0.471 mmol) was added. The above reaction mixture was left in the refrigerated for several hours. A red precipitated was collected by vacuum filtration, washed with cold water and dried under vacuum. Yield: 101.8 mg, 0.0534 mmol (34%); m.p. 234–236 °C. *Anal.* Calc. for $C_{78}H_{60}F_{12}FeN_6O_{18}P_2S_6$: C, 49.11; H, 3.17; N, 4.41; S, 10.09. Found: C, 48.58; H, 3.26; N, 4.36; S, 9.22%.

2.2.4. [Fe(phdbt)$_3$](PF$_6$)$_2$ (*6*)

Following the previous procedure and using the 5,6-dibenzylthiol-1,10-phenanthroline (**2**) (3 equiv., 0.2 g; 0.471 mmol) instead of **1** a red precipitate was obtained. Yield: 104.7 mg, 0.0646 mmol (41%); m.p. 167–170 °C. *Anal.* Calc. for $C_{78}H_{60}F_{12}FeN_6P_2S_6$: C, 57.85; H, 3.73; N, 5.19; S, 11.88. Found: C, 57.76; H, 4.09; N, 5.18; S, 11.85%.

2.3. X-ray crystallographic study

Single crystals of **1** and **2** suitable for X-ray crystallographic analysis were obtained by slow evaporation in MeOH/CH_2Cl_2 solution and by slow diffusion of hexane into a CH_2Cl_2 saturated solution, respectively. Single crystals of the iron complexes (**5** and **6**) suitable for an X-ray structure determination were obtained by slow diffusion in an H shape cell. A saturated $NaPF_6$ solution in MeOH/H_2O (50:50) was placed in one compartment of a H cell and Fe(L)$_3$ (L = **5** and **6**) in a MeOH/H_2O (60:40) solution in the other compartment. Both solutions were layered with EtOH. Red crystals were obtained after a week.

The data collections of the single crystals suitable for single X-ray were obtained using graphite monochromated Mo Kα radiation

Table 1
Crystallographic data and refinement parameters for ligands the 5,6-bistosyl-1,10-phenanthroline (**1**) 5,6-dibenzylthiol-1,10-phenanthroline (**2**) and for the complexes [Fe^{II}(phendtos)$_3$] (PF$_6$)$_2$ (**5**) and [Fe^{II}(phendbt)$_3$] (PF$_6$)$_2$ (**6**)

Compound	**1**	**2**	**5**	**6**
Formula	$C_{26}H_{20}N_2O_6S_2$	$C_{26}H_{20}N_2S_2$	$C_{78}H_{60}F_{12}FeN_6O_{18}P_2S_6$	$C_{78}H_{60}F_{12}FeN_6P_2S_6$
Formula weight (g mol^{-1})	520.56	424.56	1907.47	1619.53
Crystal system, space group	orthorhombic, $P2_12_12_1$	monoclinic, $P2_1/c$	orthorhombic, $Pbcn$	monoclinic, $P21/n$
a (Å)	9.5073(15)	15.9858(7)	10.5444(7)	19.7632(7)
b (Å)	13.4731(19)	8.2106(3)	31.955(2)	32.8181(14)
c (Å)	18.112(2)	16.2844(8)	24.2972(16)	22.7482(9)
β (°)	90	107.749(2)	90	108.128(2)
V (Å^3); Z	2320.0(6); 4	2035.64(15); 4	8186.9(9); 4	14021.9(10); 4
ρ_{calc} (Mg/m^3); μ (mm^{-1})	1.490; 0.278	1.385; 0.278	1.548; 0.477	1.534; 0.523
F(000)	1080	888	3896	6640
Crystal size (mm)	0.4 × 0.3 × 0.08	0.35 × 0.30 × 0.10	0.28 × 0.20 × 0.16	0.20 × 0.08 × 0.04
θ Range (°)	1.88–25.99	2.63–25.35	2.56–25.35	1.65–25.46
Collected hkl	$-11 \leqslant h \leqslant 1$, $0 \leqslant k \leqslant 16$, $0 \leqslant l \leqslant 22$	$-18 \leqslant h \leqslant 18$, $-9 \leqslant k \leqslant 4$, $-15 \leqslant l \leqslant 18$	$-11 \leqslant h \leqslant 12$, $-38 \leqslant k \leqslant 38$, $-29 \leqslant l \leqslant 26$	$-23 \leqslant h \leqslant 23$, $-39 \leqslant k \leqslant 39$, $27 \leqslant l \leqslant 27$
Reflections collected	2888	6984	65 100	141 228
Independent reflections [R_{int}]	2850 [0.0136]	3443 [0.0292]	7482 [0.0831]	25 790 [0.2857]
Completeness to θ (%)	25.99, 99.7	25.35, 92.7	25.35, 99.7	25.46, 99.2
Maximum and minimum transmission	0.9992 and 0.9831	0.9727 and 0.9090	0.9276 and 0.8781	0.9794 and 0.9026
Data/restraints/parameters	2850/0/325	3443/0/271	7482/13/559	25 790/0/1891
Goodness-of-fit on F^2	1.037	1.027	1.100	0.855
Final R indices [$I > 2\sigma I$)]	R_1 = 0.0382, wR_2 = 0.0793	R_1 = 0.0423, wR_2 = 0.0992	R_1 = 0.0697, wR_2 = 0.1865	R_1 = 0.0838, wR_2 = 0.1514
R indices (all data)	R_1 = 0.0584, wR_2 =0.0851	R_1 = 0.0670, wR_2 = 0.1075	R_1 = 0.1160, wR_2 = 0.2070	R_1 = 0.2602, wR_2 = 0.1924
Largest difference in peak and hole (e Å^{-3})	0.192 and −0.226	0.510 and −0.336	0.702 and −0.799	0.844 and −0.781

(λ = 0.71073 Å). Crystallographic data of **1** were collected at 294 K on Enraf-Nonius CAD4 diffractometer in the $\omega - 2\theta$ scan mode. Empirical absorption correction (ψ-scans) and data reduction were performed with WINGX suite of programs [6].

Crystallographic data for compounds **2**, **5**, **6** were collected on a Bruker AXS APEX CCD area detector diffractometer equipped with an Oxford Cryosystems low-temperature device at 130 K (**2**) and 150 K (**5** and **6**) in the ω and ϕ scans mode. A semi empirical absorption correction was carried out using SADABS [7]. Data collection, cell refinement and data reduction were done with the SMART and SAINT programs [8].

The structures were solved by direct methods using SIR 97 [9] and refined by full matrix least-squares methods with the SHELXL 97 [10] program using the WINGX software package.

For **6** the crystals obtained were of poor diffraction quality, which results in a low percentage (35%) of observed data [$I > 2\sigma(I)$], even those, the number of reflections was enough for a satisfying structure refinement and unambiguously determination of the geometry of the complex, which is of interest for the present discussion.

In **5** one of the phenyl groups is disordered and in **6** one of the PF_6 anion is also disordered, we tried without success to applied disorder models but it was not possible to achieve a good structure solution refinement. Non-hydrogen atoms were refined with anisotropic thermal parameters, whereas H-atoms were placed in idealized positions and allowed to refine riding on the parent C atom. Molecular graphics were prepared using ORTEP3 [11] and MERCURY 1.4.2 [12]. A summary of the crystal data, structure solution and refinement are given in Table 1.

3. Results and discussion

3.1. Synthesis

Different synthetic strategies can be envisaged for the preparation of 5,6-dithiosubstituted-1,10-phenanthroline dithio-diazo ligands. As possible starting materials for these preparations both 5,6-dione-1,10-phenanthroline [4] and 5,6-dibromo-1,10-phenanthroline [5] (**4**) were considered as candidates.

However several of these approaches proved ineffective in our hands:

(1) Starting with the 5,6-dione-1,10-phenanthroline the thionation with P_4S_{10} or Lawesson's reagent [13,14] in the appropriated refluxing solvent proved to be ineffective, even after addition of a nickel chloride solution possibly leading directly to the bisdithiolene complex.

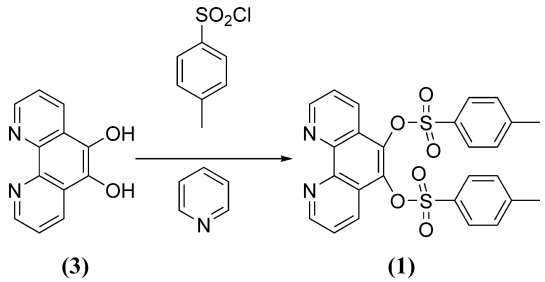
(2) As an alternative, also starting from the 5,6-dione-1,10-phenanthroline, it was envisaged the preparation of the 1,10-phenanthroline-5,6-bistosyl (**1**) via the corresponding dihydroxide [3] (**3**) compound treated with toluenesulfonyl chloride (Scheme 2). The preparation of (**1**) was achieved in good yield as demonstrated by single crystal X-ray structure analyses as well as by ^{1}H and ^{13}H NMR and elemental analyses.The tosyl groups on **1** could be good leaving groups for future nucleophilic aromatic substitution reactions. In spite of the successful preparation of **1** this compound proved to be ineffective for subsequent nucleophilic substitution reactions either with dithiooxamide for the obtention of the corresponding dithiol, or with potassium trithiocarbonate or sodium trithiocarbonate for the obtention of the corresponding 1,3-dithiole-2-thione. We also tried with **1**, without success, two further nucleophilic substitutions with either isopropyl mercaptan, or with benzyl mercaptan aiming at the obtention of the corresponding 5,6-dithiosubstituted 1,10 phenanthrolines.

(3) Starting from 5,6-dibromo-1,10-phenanthroline [5] (**4**) procedures based on the creation of the aryl-sulfur bond including nucleophilic aromatic substitutions, either with isopropyl mercaptan, or with benzyl mercaptan and also treatment of aryl lithium with sulfurated electrophiles, were first tried however all proved unsuccessful. The 5 and 6, 1,10-phenanthroline positions seem to be inactivated for the direct nucleophilic substitution as well as for the treatment of aryllithium with sulfurated electrophiles.

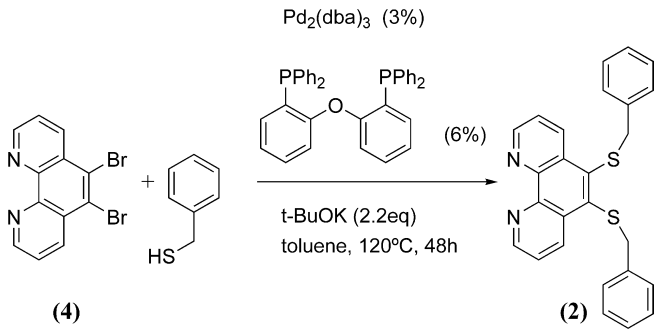
A successful synthesis to obtain the 5,6-dithiosubstituted phenanthroline was the synthesis of 5,6-dibenzylthiol-1,10-phenanthroline (**2**), achieved in good yield starting from **4** by a palladium cross-coupling catalyzed reaction with benzylthiol in the presence of a base and using as catalyst the $Pd_2(dba)_3$/DPEphos system (PDE = bis-[2-(diphenylphosphino)phenyl]ether) (Scheme 3). The compound **2** was unambiguously identified and characterized by single crystal X-ray diffraction, ^{1}H and ^{13}H NMR and elemental analysis.

This Pd-catalyzed cross coupling reaction is related to the one introduced by Migita in 1980 between aryl bromides and thiols [15] for which since then various efficient catalytic systems using bidentate phosphines have been described [16]. Our protocol for preparing **2** involves the deprotonation of the benzylthiol with *t*-BuOK, followed by heating, in refluxing toluene, the resulting potassium benzylthiolate with **4** in the presence of $Pd_2(dba)_3$/DPEphos. Compound **2** can be used as precursor to prepare the corresponding thio-azo ligand. Preliminary experiments aimed at deprotecting the thiolate function have shown that the Pyridine/Na treatment[17] is efficient to generate the 1,2-dithiolate function and the thereof transition metal complexes can be obtain. However, this requires an effective control of the coordination ability to different poles, as it will be published subsequently.

In this work, the diimine function coordination ability of these substituted phenanthroline ligands was explored by the synthesis of the iron(II) complexes **5** and **6** using standard conditions for the



Scheme 2. Synthesis of 5,6-bistosyl-1,10-phenanthroline (**1**).



Scheme 3. Synthesis of 5,6-dibenzylthiol-1,10-phenanthroline (**2**).

preparation of Fe(II) phenanthroline complexes. The elemental analyses of the two complexes are consistent with a 1:2 anion:cation stoichiometry, as confirmed by the X-ray crystal structure determination, indicating Fe(II) in spite of starting from $FeCl_3$.

3.2. Crystal structure

Compounds **1**, **2**, **5** and **6** have been characterized by single crystal X-ray diffraction technique. The ORTEP views of these compounds are shown in Figs. 1–4. Crystallographic data, selected bond angles and distances are given in Tables 1–3.

The compound **1** crystallizes in the orthorhombic system, $P2_12_12_1$ space group. Its asymmetric unit consists of one molecule shown in Fig. 1. The 1,10-phenanthroline core of the molecule and the two oxygen in the 5,6-substituted positions are almost planar (Rms deviation of fitted atoms = 0.0341 Å). The two tosyl groups are tilted 45.76(7)° and 26.30(8)° in opposite directions with respect to the 1,10-phenanthroline core plane, and the other bond distances and angles assume standard values (see Table 2).

The compound **2** crystallizes in the monoclinic system, $P2_1/c$ space group and the asymmetric unit contains one molecule (Fig. 2). Also in this compound the 1,10-phenanthroline core of the molecule and the two sulfur atoms in the 5,6 positions are almost planar (Rms deviation of fitted atoms = 0.1027 Å). The two benzyl groups are tilted 14.56(9)° and 17.98(10)° with respect to the 1,10-phenanthroline core plane. Bond lengths and angles assume standard values (see Table 2).

The compound **5** crystallizes in the orthorhombic system, *Pbcn* space group, with the iron atom lying on a twofold axis. The asymmetric unit has one half of the $[Fe^{II}(phdtos)_3]^{2+}$ cation and two PF_6^- anions (see ORTEP view Fig. 3). One of the 1,10-phenanthroline

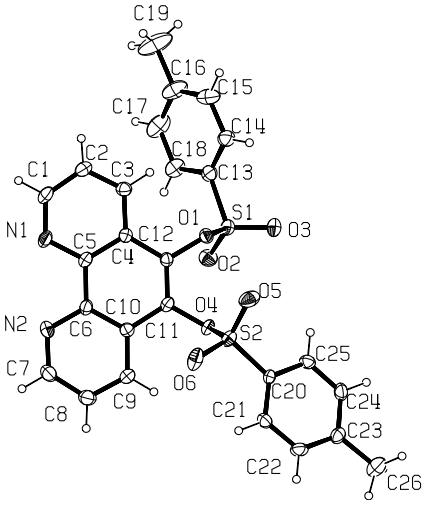


Fig. 1. ORTEP diagram of **1** drawn at a 40% probability level.

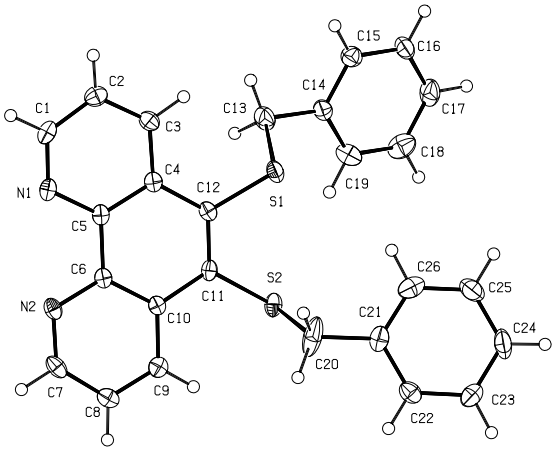


Fig. 2. ORTEP diagram of **2** drawn at a 40% probability level.

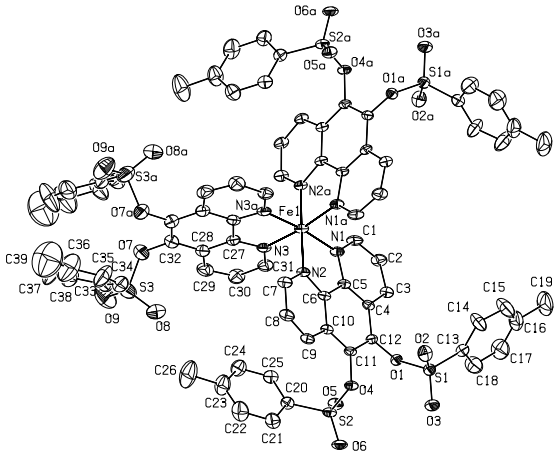


Fig. 3. ORTEP diagram of $[Fe(phdtos)_3]^{2+}$ cation in **5** drawn at a 30% probability level. *Symmetry code*: #*a*: $-x+2$, y, $-z+3/2$.

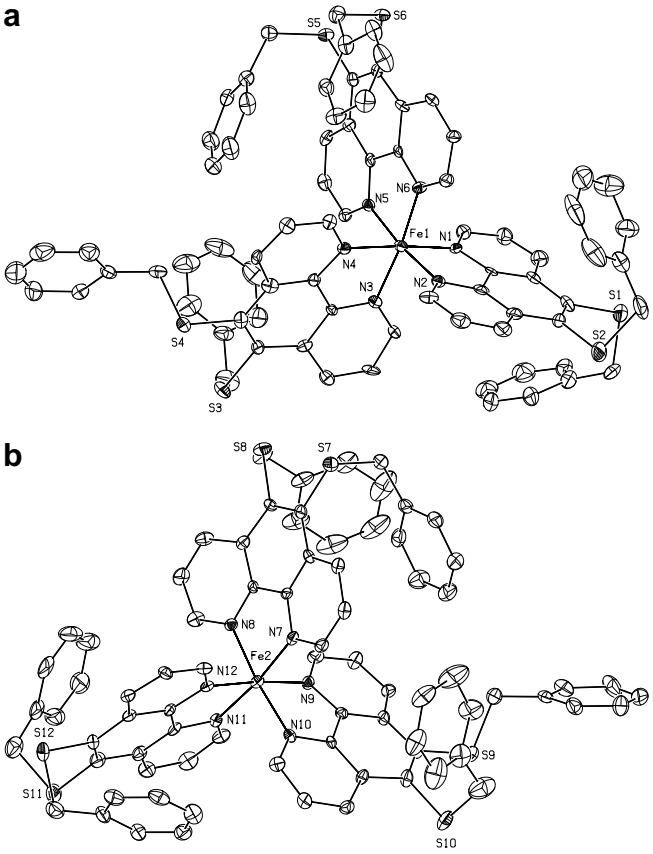


Fig. 4. ORTEP diagram of the two $[Fe(phdbt)_3]^{2+}$cations in the asymmetric unit of **6** drawn at a 40% probability level.

Table 2
Selected bond lengths (Å), angles (°) and torsion angles (°) for **1** and **2**

Bond lengths	Compound **1**	Compound **2**	Torsion angles	Compound **1**	Compound **2**
N(1)–C(1)	1.327(5)	1.323(3)	C10–C11–C12–C4	4.18(53)	−5.41(34)
N(1)–C(5)	1.367(4)	1.379(3)	O4–C11–C12–O1	1.27(50)	
N(2)–C(7)	1.321(5)	1.326(3)	S2–C11–C12–S1		−13.49(28)
N(2)–C(6)	1.353(5)	1.345(3)	C4–C12–O1–S1	−96.13(32)	
C(5)–C(6)	1.436(5)	1.451(3)	C10–C11–O4–S2	−91.96(32)	
C(12)–O(1)	1.398(4)		C13–S1–C12–C4		−70.05(21)
C(11)–O(4)	1.405(4)		C20–S2–C11–C10		−87.39(21)
S(1)–C(12)		1.763(2)			
S(2)–C(11)		1.800(2)			
Bond angles			Bond angles		
C1–N1–C5	116.47(29)	118.82(20)	C6–N2–C7	117.62(32)	115.83(20)
N1–C5–C6	117.98(29)	119.48(20)	N2–C6–C5	118.71(32)	116.49(20)

core units is almost planar (Rms deviation of fitted atoms = 0.0167 Å), the two other phenanthroline cores present a slight deviation from planarity (Rms deviation of fitted atoms = 0.0561 Å). As the uncoordinated ligand, the two tosyl groups are tilted, in opposite directions, with respect to the phenanthroline core plane 28.59(24)° in the ligand containing N3 and 28.16(16)° and 53.77(14)° on the two other ligands containing N1 and N2. The dihedral angles between the phenanthroline cores are 85.32(5)° and 88.07(5)°. The bond distances and angles of the coordinated ligands in complex **5** do not assume relevant deviation from the compound **1** values, except in the fact that the tosyl groups have different tilted directions and the associated torsion angles are necessarily different.

The compound **6** crystallizes in the monoclinic system, in the $P2_1/n$ space group. The asymmetric unit contains two independent cations $[Fe(phdbt)_3]^{2+}$ and four anions PF_6^- (see ORTEP view Fig. 4). In the Fe1 cation, one of the coordinated phenanthroline cores is almost planar (Rms deviation of fitted atoms 0.023 Å, for the ligand containing N1 and N2) and the two others present small deviation from planarity (Rms deviation of fitted atoms 0.104 and 0.061 Å, for the ligands containing N3–4 and N5–6, respectively). The Fe2 cation presents a similar planarity (Rms deviation of fitted atoms 0.121, 0.090 and 0.023 Å, for the ligands containing N7–8, N9–10, N11–12).

In each cation of **6** only one of the coordinating ligands has the 5,6-disubstituted groups tilted towards opposite sides of the core mean plane. In the Fe1 cation, two of the ligands have the benzyl groups tilted towards the same side of the core mean plane 61.3(2)°, 22.8(2)° and 30.7(2)°, 35.8(2)°. The other ligand has the two benzyl groups tilted towards opposite sides of the core mean plane, with angles of 36.8(2)° and 43.0(3)°. In Fe2 cation, the correspondent angles are 54.5(2)°, 35.8(2)° and 34.2(2)°, 63.3(2)° for the groups tilted towards the same side and 40.0(2)°, 31.6(2)° for the groups tilted towards opposite sides. Similarly to complex **5**, for **6** bond distances and angles of the ligands do not assume relevant deviations from the corresponding values in compound **2**. Also the benzyl groups have different tilted directions and the associated torsion angles are necessarily different.

A common characteristic of the crystal structures of **5** and **6** is the occurrence of parallel cation chains. However they have different packing patterns of anionic and cationic units (Figs. 5 and 6). Whereas in **6**, sheets of cationic layers alternate with anionic ones, in **5** there is not a so clear segregation of cations and anions. In all cases, due to the bulky substituted ligands the iron–iron distances are very large and the shortest Fe–Fe distance in both compounds is 10.5 Å.

The infinite chains of $[Fe(L)_3]^{2+}$ (L = **1** and **2**) complexes in **5** and **6** are shown in Figs. 7 and 8. These chains in **6** are composed of two crystallographic distinct complexes while those of **5** are made of only one complex. The shortest Fe–Fe distance within a chain is 12.2 Å for compound **5** and 10.5 Å for compound **6**.

Within the chains is possible to observe several short contacts but none of them correspond to π–π interactions. In compound **5**, hydrogen bonds between oxygen atoms of the tosyl groups and hydrogen atoms in the phenanthroline rings, O3···H30#*f* 2.327(4) Å, hydrogen bonds between oxygen atoms of the tosyl groups and hydrogen atoms of other tosyl group, O5···H25#*f* 2.601(3) Å, O8···H18#*f* 2.649(5) Å, and also a O···C short contact between a oxygen atom of a tosyl group and a phenanthroline carbon O3···C30#*f* 3.080(7)Å, #*f* = 2 − *x*, −*y*, 1 − *z* (see supplementary material SM1).

The short intrachain contacts in **6** are between sulfur and phenanthroline carbon atoms S3···C130#*b* 3.492(8) Å, #*b* = −1 + *x*, *y*, *z*; S5···C82#*a*, 3.487(22) Å, S5···C139#*a* 3.487(21) Å, S7···C1#*a* 3.483(18) Å, S8···C1#*a* 3.404(20) Å, S7···C58#*a* 3.434(16) Å, *a* = *x*, *y*, *z*. Between phenanthroline carbon atoms and benzyl carbon atoms C49···C132#*b* 3.393(11) Å. Hydrogen bonds between sulfur and phenanthroline rings S3···H130#*b* 2.7391(21) Å, S6···H139#*a* 2.836(19) Å, S8···H1#*a* 2.697(24) Å, S10··· H10#*c* 2.7785(22) Å, *c*# = 1 + *x*, *y*, *z*. Hydrogen mediated short contacts between benzyl groups C50···H151#*b* 2.897(13) Å and C51···H151#*b* 3.822(16) Å (see supplementary material SM2).

Although the mean Fe–N distances and the N–Fe–N angles are in the range usually found in other iron-phenanthroline derivatives [18] there are deviations from a regular octahedron more clearly denoted by other structural parameters. Shortest and longest Fe–N distances are 1.967(4) and 1.989(3) Å in compound **5** and 1.953(5) and 1.983(5) Å in compound **6**. This distortion is not merely an elongation and compression along an axis, as the angles between the phenanthroline moieties differ also from orthogonality, attaining values as low as 82.1(2)° both in **5** and **6**.

The comparison of the N–C bonds lengths in the free ligands and in these coordinating the Fe atom does not reveal any significant change within experimental uncertainty.

Magnetic susceptibility measurements[1] of the **5** and **6** compounds in the 4–300 K range indicate a diamagnetic behavior, indicative of the low spin *S* = 0 state as expected for Fe(II) complexes in an octahedral coordinating geometry.

These results show that the coordination distortion observed is not significant in order to allow an intermediate *S* = 1 spin state, as

[1] Magnetic susceptibility measurements were performed using a longitudinal Faraday system (Oxford Instruments) with a magnetic field of 5 T and gradient field of 1 T/m in a polycrystalline sample (~20 mg) placed inside a previous calibrated thin wall Teflon bucket. The force was measured with a microbalance (Sartorius S3D-V). Magnetization data were corrected for contributions due to the sample holder and core diamagnetism, estimated from tabulated Pascal constants as -11.8×10^{-4} and -9.5×10^{-4} emu/mol for **5** and **6**, respectively.

Table 3
Bond lengths d (Å) and angles ω (°) in the coordination polyhedron of the Fe atom

Bond	d (Å)	Bond	d (Å)	Bond	d (Å)
Compound ***5***					
Fe(1)–N(1)	1.970(4)	Fe(1)–N(3)	1.967(4)		
Fe(1)–N(2)	1.989(3)				
N(1)–C(1)	1.338(6);	N(1)–C(5)	1.357(5);		
N(2)–C(7)	1.346(6);	N(2)–C(6)	1.356(5);		
N(3)–C(31)	1.333(6)	N(3)–C(27)	1.342(6)		
Angle	ω (°)	Angle	ω (°)	Angle	ω (°)
N(3)#a–Fe(1)–N(3)	83.5(2)	N(1)#a–Fe(1)–N(1)	90.3(2)	N(3)#a–Fe(1)–N(2)	91.52(15)
N(3)#a–Fe(1)–N(1)#a	93.44(16)	N(3)#a–Fe(1)–N(2)#a	89.34(15)	N(3)–Fe(1)–N(2)	89.34(15)
N(3)–Fe(1)–N(1)#a	172.96(14)	N(3)–Fe(1)–N(2)#a	91.52(15)	N(1)#a–Fe(1)–N(2)	97.08(14)
N(3)#a–Fe(1)–N(1)	172.96(14)	N(1)#a–Fe(1)–N(2)#a	82.10(14)	N(1)–Fe(1)–N(2)	82.10(14)
N(3)–Fe(1)–N(1)	93.44(16)	N(1)–Fe(1)–N(2)#a	97.08(14)	N(2)#a–Fe(1)–N(2)	178.8(2)
C(1)–N(1)–C(5)	116.7(4);	C(7)–N(2)–C(6)	116.2(4);	C(31)–N(3)–C(27)	118.7(4)
#a −x + 2, y, −z + 3/2					
Bond	d (Å)	Bond	d (Å)	Bond	d (Å)
Compound ***6***					
Fe(1)–N(2)	1.953(5)	Fe(1)–N(4)	1.981(5)	Fe(2)–N(7)	1.970(5)
Fe(1)–N(1)	1.968(5)	Fe(1)–N(5)	1.981(5)	Fe(2)–N(10)	1.973(5)
Fe(1)–N(3)	1.971(5)	Fe(2)–N(11)	1.967(5)	Fe(2)–N(8)	1.980(5)
Fe(1)–N(6)	1.981(5)	Fe(2)–N(12)	1.968(5)	Fe(2)–N(9)	1.983(5)
N(1)–C(1)	1.319(8)	N(2)–C(10)	1.339(8)	N(3)–C(27)	1.334(8)
N(1)–C(5)	1.370(8)	N(2)–C(6)	1.371(8)	N(3)–C(31)	1.350(8)
N(4)–C(36)	1.338(8)	N(5)–C(53)	1.332(7)	N(6)–C(62)	1.312(8)
N(4)–C(32)	1.375(7)	N(5)–C(57)	1.376(7)	N(6)–C(58)	1.365(7)
N(7)–C(77)	1.339(8)	N(8)–C(86)	1.325(8)	N(9)–C(103)	1.354(8)
N(7)–C(81)	1.374(7)	N(8)–C(82)	1.348(7)	N(9)–C(107)	1.368(7)
N(10)–C(112)	1.314(8)	N(11)–C(130)	1.315(7)	N(12)–C(139)	1.339(7)
N(10)–C(108)	1.367(8)	N(11)–C(134)	1.378(8)	N(12)–C(135)	1.375(8)
Angle	ω (°)	Angle	ω (°)	Angle	ω (°)
N(2)–Fe(1)–N(1)	82.7(2)	N(2)–Fe(1)–N(5)	173.5(2)	N(7)–Fe(2)–N(10)	93.7(2)
N(2)–Fe(1)–N(3)	91.5(2)	N(1)–Fe(1)–N(5)	93.2(2)	N(11)–Fe(2)–N(8)	92.6(2)
N(1)–Fe(1)–N(3)	93.5(2)	N(3)–Fe(1)–N(5)	93.9(2)	N(12)–Fe(2)–N(8)	91.0(2)
N(2)–Fe(1)–N(6)	92.6(2)	N(6)–Fe(1)–N(5)	82.3(2)	N(7)–Fe(2)–N(8)	82.2(2)
N(1)–Fe(1)–N(6)	92.0(2)	N(4)–Fe(1)–N(5)	87.5(2)	N(10)–Fe(2)–N(8)	173.8(2)
N(3)–Fe(1)–N(6)	173.5(2)	N(11)–Fe(2)–N(12)	82.3(2)	N(11)–Fe(2)–N(9)	95.3(2)
N(2)–Fe(1)–N(4)	96.9(2)	N(11)–Fe(2)–N(7)	173.5(2)	N(12)–Fe(2)–N(9)	175.4(2)
N(1)–Fe(1)–N(4)	175.7(2)	N(12)–Fe(2)–N(7)	93.8(2)	N(7)–Fe(2)–N(9)	88.9(2)
N(3)–Fe(1)–N(4)	82.2(2)	N(11)–Fe(2)–N(10)	91.8(2)	N(10)–Fe(2)–N(9)	82.1(2)
N(6)–Fe(1)–N(4)	92.3(2)	N(12)–Fe(2)–N(10)	94.0(2)	N(8)–Fe(2)–N(9)	93.1(2)
C(1)–N(1)–C(5)	115.5(6)	C(27)–N(3)–C(31)	116.8(5)	C(53)–N(5)–C(57)	117.0(6)
C(10)–N(2)–C(6)	116.2(6)	C(36)–N(4)–C(32)	117.0(6)	C(62)–N(6)–C(58)	118.0(6)
C(77)–N(7)–C(81)	116.3(6)	C(86)–N(8)–C(82)	117.6(5)	C(103)–N(9)–C(107)	116.7(6)
C(112)–N(10)–C(108)	118.5(6)	C(130)–N(11)–C(134)	116.6(6)	C(139)–N(12)–C(135)	117.6(6)

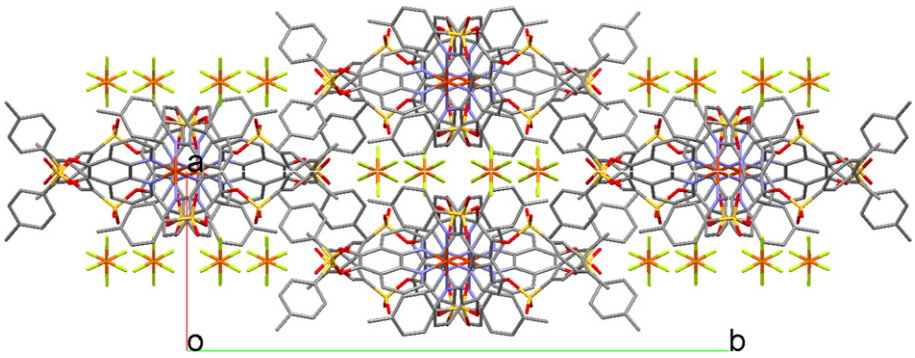


Fig. 5. Crystal structure of **5**, viewed along the *c*-axis.

it has been shown to occur in cases of more severely distorted hexacoordinated complexes. Several examples of iron (II) complexes with substituted phenanthrolines are known with this intermediate spin state [19], usually in square planar or heavily distorted hexacoordinated complexes. Examples of iron(II) complexes, where the metal atom is coordinated to six nitrogen atoms of bipyridine ligands, exhibiting magnetic moments varying with temperature and whose interpretation was based in a two-step transition involving also a $S = 1$ state, are also known [18c]. However the present complexes apparently are not so significantly, distorted from the ideal octahedral geometry to allow such intermediate spin state.

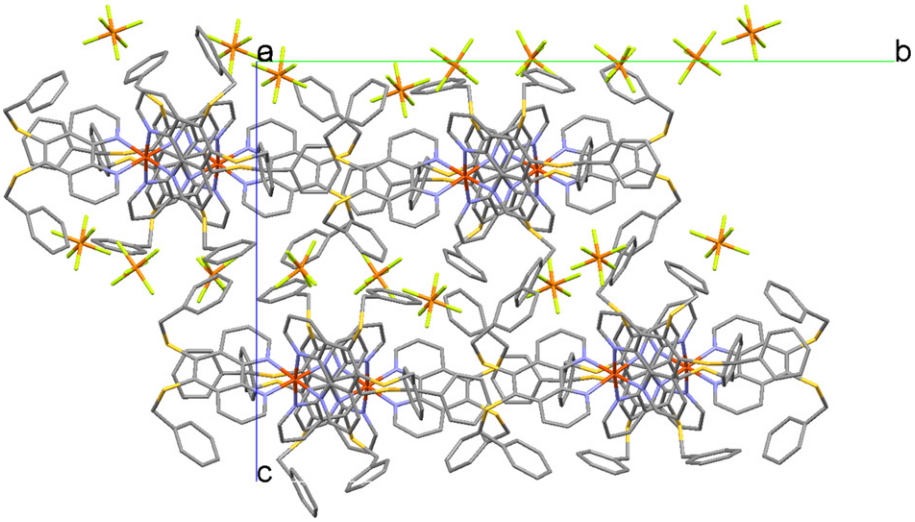


Fig. 6. Crystal structure of **6**, viewed along the *a*-axis.

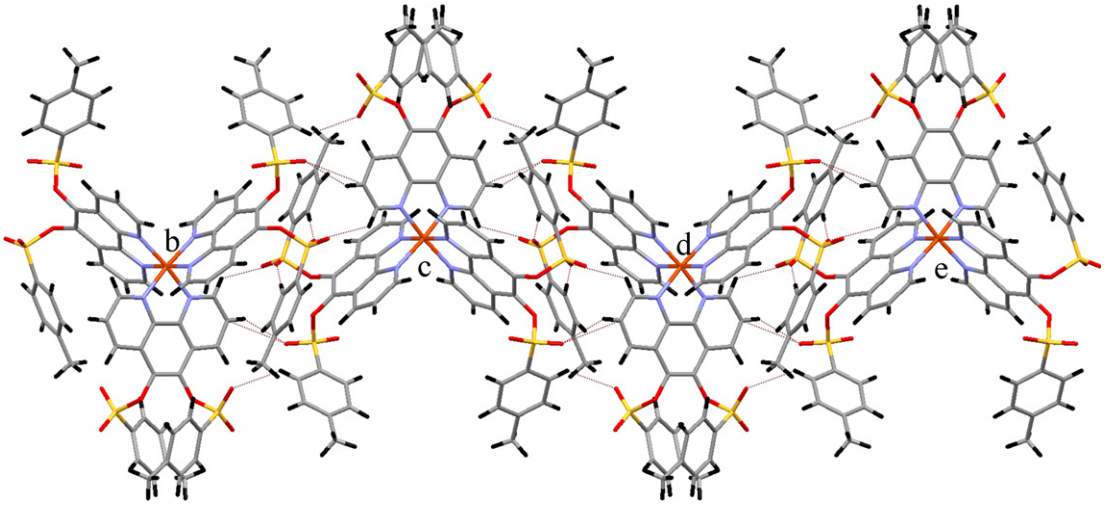


Fig. 7. Infinite chain of $[Fe(phdtos)_3]^{2+}$ complexes in compound **5**. View perpendicular to *a*-axis. [*Symmetry codes*: (b) $1-x, -y, 1-z$; (c) $-1+x, y, z$; (d) $1-x, -y, 2-z$; (e) $-1+x, y, 1+z$].

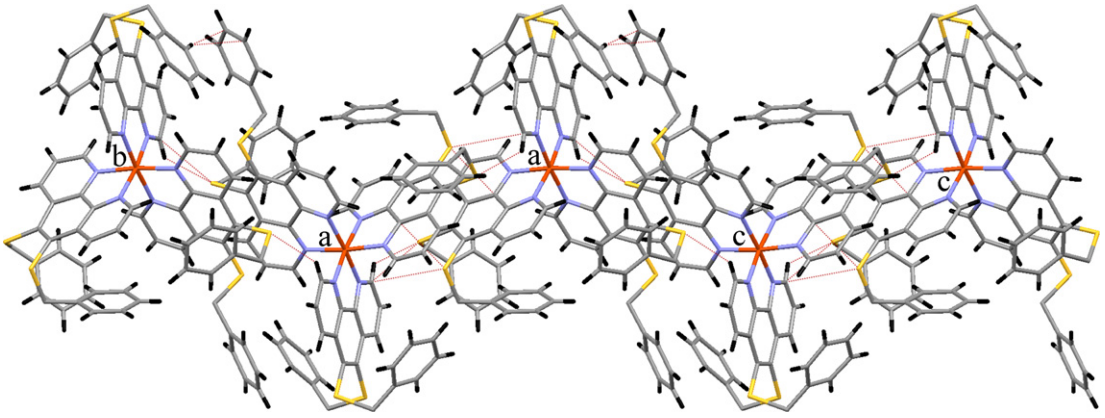


Fig. 8. Infinite chain of $[Fe(phdbt)_3]^{2+}$ complexes in compound **6**. View perpendicular to the *c*-axis. [*Symmetry codes*: (a) x, y, z; (b) $-1+x, y, z$; (c) $1+x, y, z$].

4. Conclusion

In summary, we achieved the synthesis of two new 5,6-substituted-1,10-phenanthrolines. Particularly, we have developed a convenient method for preparing sample quantities of the 5,6-dibenzylthiol-1,10-phenanthroline in two steps from commercially available phenanthroline. This is the first example of a cross-coupling reaction with a 5,6-dihalo-1,10-phenanthroline, achieving a new thio-azo ligand precursor, which can be explored in subsequent work for the preparation of thio-azo ligands. Preliminary

experiments have shown that is possible to generate the 1,2 dithiolate function and the thereof transition metal complexes can be obtained. However, this requires an effective control of the coordination ability to different poles. In this report, we have used the diimine function coordination ability of the 5,6-disubstituted-1,10-phenanthroline ligands, and these two new phenanthroline ligands allowed for the preparation of $[Fe(phdtos)_3](PF_6)_2$ and $[Fe(phdbt)_3](PF_6)_2$ complexes.

Acknowledgements

This work was partially supported by FCT through Contract (PTDC/QUI/64967/2006) and post-doctoral grant to S.R., and by GRICES-Ministère des Affaires Etrangères (France) Pessoa no. 07981RL bilateral agreement and it also benefited from the ESF COST action D35. We also thank Narcis Avarvari (Angers) for useful discussions concerning ligand synthesis.

Appendix A. Supplementary data

CCDC 601085, 601086, 656658 and 656659 contain the supplementary crystallographic data for **1**, **2**, **5** and **6**. These data can be obtained free of charge via http://www.ccdc.cam.ac.uk/conts/retrieving.html, or from the Cambridge Crystallographic Data Centre, 12 Union Road, Cambridge CB2 1EZ, UK; fax: (+44) 1223-336-033; or e-mail: deposit@ccdc.cam.ac.uk. Supplementary data associated with this article can be found, in the online version, at doi:10.1016/j.poly.2008.03.016.

References

[1] S. Rabaça, M.C. Duarte, I.C. Santos, M. Fourmigué, M. Almeida, Inorg. Chim. Acta 360 (2007) 3797.
[2] D.D. Perrin, W.L.F. Armarego, Purification of Laboratory Chemicals, Pergamon, Oxford, 1988.
[3] W. Paw, R. Eisenberg, Inorg. Chem. 36 (1997) 2287.
[4] F. Calderazzo, F. Marchetti, G. Pampaloni, V. Passarelli, J. Chem. Soc., Dalton Trans. (1999) 4389.
[5] M. Feng, K.S. Chan, Organometallics 21 (2002) 2743.
[6] L.J. Ferrugia, J. Appl. Crystallogr. 32 (1999) 837.
[7] G.M. Sheldrick, SADABS, Bruker AXS Inc., Madison, WI, USA, 2004.
[8] Bruker, SMART and SAINT, Bruker AXS Inc., Madison, WI, USA, 2004.
[9] A. Altomare, M.C. Burla, M. Camalli, G. Cascarano, G. Giacovazzo, A. Guagliardi, A.G.G. Moliterni, G. Polidori, R. Spagna, J. Appl. Cryst. 32 (1999) 115.
[10] G.M. Sheldrick, SHELXL 97, Program for Crystal Structure Refinement, University of Gottingen, Germany, 1997.
[11] L.J. Ferrugia, J. Appl. Cryst. 30 (1997) 565.
[12] MERCURY: visualization and analysis of crystal structures, C.F. Macrae, P.R. Edgington, P. McCabe, E. Pidcock, G.P. Shields, R. Taylor, M. Towler, J. van de Streek, J. Appl. Cryst. 39 (2006) 453.
[13] S. Scheibye, B.S. Pedersen, S.O. Lawesson, Bull. Soc. Chim. Belg. 87 (1978) 229.
[14] U.T. Mueller-Westerhoff, D.I. Yoon, K. Plourde, Mol. Cryst. Liq. Cryst. 183 (1990) 291.
[15] (a) T. Migita, T. Shimizu, Y. Asami, J. Shiobara, Y. Kato, M. Kosugi, Bull. Chem. Soc. Jpn. 53 (1980) 1385;
(b) M. Kosugi, T. Ogata, M. Terada, H. Sana, T. Migita, Bull. Chem. Soc. Jpn 58 (1985) 3657.
[16] (a) P.G. Ciattini, E.G. Morera, G. Ortar, Tetrahedron Lett. 36 (1995) 4133;
(b) S. Wendeborn, S. Berteina, W.K.D. Brill, A. McMesmaeker, Synlett (1998) 671;
(c) N. Zheng, J.C. McWilliams, J.D. Armstrong, R.P. Volante, J. Org. Chem. 63 (1998) 9606;
(d) J.C. McWilliams, F.J. Fleitz, N. Zheng, J.D. Armstrong, Org. Synth. 79 (2002) 43;
(e) U. Schopfer, A. Schlapbach, Tetrahedron 57 (2001) 3069;
(f) M. Murata, S.L. Suchwald, Tetrahedron 60 (2004) 7397.
[17] J. Larsen, K. Bechgaard, J. Org. Chem. 52 (1987) 3285.
[18] (a) A. Zalkin, D.H. Templeton, T. Ueki, Inorg. Chem. 12 (1973) 641;
(b) J. Baker, L.M. Engelhardt, B.N. Figgis, A.H. White, J. Chem. Soc., Dalton Trans. (1975) 530;
(c) D.C. Figgs, R.H. Herber, I. Felner, Inorg. Chem. 30 (1991) 2535.
[19] (a) E. König, Coord. Chem. Rev. 3 (1968) 471;
(b) H.A. Goodwin, Aust. J. Chem. 21 (1968) 83.